

PROCEEDINGS BOOK

SB³C

biomechanics.
bioengineering.
biotransport.

*2023 Summer Biomechanics, Bioengineering,
and Biotransport Conference*

June 4th – 8th, 2023

Vail, Colorado



*Building Interfaces Across Tissues,
Disciplines, and Communities*

Funding for this conference was made possible (in part) by the National Science Foundation and the National Institutes of Health. The views expressed in written conference materials or publications and by speakers and moderators do not necessarily reflect the official policies of the Department of Health and Human Services; nor does mention of trade names, commercial practices, or organizations imply endorsement by the U.S. Government. The 2023 Summer Biomechanics, Bioengineering, and Biotransport Conference (SB³C) organizers gratefully acknowledge the support of the National Science Foundation and the National Institutes of Health.



National Institute of Biomedical Imaging and Bioengineering
Creating Biomedical Technologies to Improve Health

Congratulations to the 2022 Cover Art Contest Winner:

Kacper Ostalowski, Joseph A. Insley, and Jifu Tan, Northern Illinois University.

Title: Direct Numerical Simulation of Blood Flow with Cells in Retina Vascular Network

Description: The photo depicts the transport of red blood cells through a patient-specific retina vascular network. The velocity magnitude is indicated by the background color in the tubes. The top inset illustrates the accumulation of cells in a T-branch vessel, while the bottom inset provides an enlarged view of cells in complicated vessels with branches and loops.

Permission to download, print, and photocopy a single, individual copy of any of the works contained in this file for personal use in research and/or educational pursuit is granted by the SB³C Foundation, Inc. For other uses, contact the Board of the SB³C Foundation, Inc., 20 South Duke Street, #1, Lancaster, PA 17602.

SB³C 2023 Meeting Pitch Competition

Sunday, June 4

4:00PM – 5:30PM MT

Translational Technologies Pitch Competition Finals

Zermatt

Session Chairs: **Ethan Kung**, *Clemson University of Utah*
Lyle Hood, *University of Texas at San Antonio*

- 4:00PM** **On-Demand, Volumetric Liquid Biopsy From Solid Tumors** SB³C2023-PC01
Y. Kimura¹, MC. Sheehan², NR. Raghuraman², D. Downing², G. Srimathveeravalli²
¹Osaka University Graduate School of Medicine, ²University of Massachusetts, Amherst
- 4:20PM** **Improving Clinical CT Image Data To Develop Better Fracture Risk Algorithms And Patient Outcomes** SB³C2023-PC02
Lance L. Frazer¹, Nathan Louis^{1,2}, Kal L. Clark³, Daniel P. Nicolella¹
¹Southwest Research Institute, ²University of Michigan, ³University of Texas Health Science Center at San Antonio
- 4:40PM** **SLIC-VAD: A Wirelessly Powered LVAD With Magnetic Levitation Bearings**
SB³C2023-PC03
Shweta Karnik¹, Huang Chen¹, Simon Kiang⁴, Arun Kumar Kota², Yaxin Wang³, Joseph Cavallaro⁴, Oscar H Frazier³, Lakshmi Prasad Dasi¹
¹Georgia Institute of Technology and Emory University, ²North Carolina State University, ³Texas Heart Institute, ⁴Rice University
- 5:00PM** **I-KinCor: Revolutionizing Pediatric Duct-Dependent Surgeries** SB³C2023-PC04
Luis René Mata Quiñonez¹, Shweta Karnik¹, Srujana S. Joshi¹, Leon Cheng¹, Holly Bauser-Heaton, MD^{1,2}, Lakshmi Prasad Dasi¹
¹Georgia Institute of Technology and Emory University, ²Children's Healthcare of Atlanta

Poster Session: Translational Technologies**Cascade ABC**

- P1 Solving the Problem of Bicycle Helmet Fit** SB³C2023-PC05
William J. Makowski, Thomas L. Martin, William A. Schaudt
Virginia Tech
- P2 Faciliflow: An Implantable Device to Prevent the Onset of Breast Cancer-Related Lymphedema** SB³C2023-PC06
A. Swarup¹, A. Vella¹, K. Rowley², J. Frattolin¹, J. Moore Jr.¹
¹Imperial College, ²Lympha Motus, Ltd.
- P3 Predicting Fracture Healing by Measuring Compliance Via Direct Electromagnetic Coupling** SB³C2023-PC07
Kevin M. Labus¹, Kirk C. McGilvray¹, Branislav Notaros¹, Milan Ilic², Julie Dunn³, Christian M. Puttlitz¹
¹Colorado State University, ²University of Belgrade, ³University of Colorado Health North
- P4 Tackling Antimalarial Drug Resistance in Africa Using Novel Drug Repurposing and Nanotechnology Strategies** SB³C2023-PC08
Samuel W. Uzundu, Petra O. Nnamani, Anthony A. Attama
University of Nigeria
- P5 Tapping into Ligament Tension with Our Ligament Tensiometer to Enhance Outcomes Following Orthopedic Procedures** SB³C2023-PC09
Lesley R. Arant, Kai M. Heineman, Josh D. Roth
University of Wisconsin-Madison
- P6 Orthopedic Cast Saw** SB³C2023-PC10
Ryan A. DeJesus, Nicholas J. Graham, Evan M. Lunney, Jaedan D. Morton
The Pennsylvania State University
- P7 Artificial Multi-Organ Replacement (AMOR) System** SB³C2023-PC11
Nanye Du, Suhail Ahmad, Shaohang Hao, Ziyuan Wang, Ye Jin, Alexander Novokhodko, Dayong Gao
University of Washington
- P8 A Novel Hardware and Software Device to Non-Invasively Predict Post Thrombotic Syndrome** SB³C2023-PC12
Cyrus J. Darvish, Pete H. Gueldner, Rabih A. Chaer, David A. Vorp, and Timothy K. Chung
University of Pittsburgh
- P9 Polymeric transcatheter aortic valve replacement (TAVR) for treating aortic stenosis** SB³C2023-PC13
B. Kovarovic¹, O.M. Rotman¹, M. Slepian², D. Bluestein¹
¹Stony Brook University, ²University of Arizona
- P10 Automatically perfusable human vessel chip platform for preclinical research in hazardous containment environments and space** SB³C2023-PC14
J. Eades¹, A. Kumar¹, A. Jain^{1,2}
¹Texas A&M University, ²Houston Methodist Hospital

SB³C 2023 Meeting Scientific Podium Sessions

Monday, June 5

9:45AM – 11:15AM MT

Machine Learning in Biofluids

Cascade ABC

Session Chairs: Amir Arzani, *University of Utah*
Fanwei Kong, *University of California, Berkeley*

- 9:45AM A Deep Learning Approach For Cardiac Model Construction For Congenital Heart Disease Patients** SB³C2023-402
Fenwei Kong, Alison L. Marsden
Stanford University
- 10:00AM Enhancing Corrupt Cardiovascular Flow Data With Machine Learning** SB³C2023-026
Hunor Csala, Amirhossein Arzani
University of Utah
- 10:15AM Automatic Model Construction For Patient-Specific Aortic Flow Simulations Using Geometric Deep Learning** SB³C2023-273
Pan Du, Delin An, Chaoli Wang, Jian-Xun Wang
University of Notre Dame
- 10:30AM Physics-informed Neural Networks with Fourier-based Activation Function To Model Complex Cardiovascular Flows** SB³C2023-015
Arman Aghaee, M. Owais Khan
Toronto Metropolitan University
- 10:45AM Data-Enhanced Personalized Models For Coronary Hemodynamics And Myocardial Perfusion** SB³C2023-014
Karthik Menon¹, Zachary Sexton¹, Owais Khan², Daniele Schiavazzi³, Koen Nieman¹, Alison Marden¹
¹Stanford University of Texas Dallas, ²Toronto Metropolitan University, ³University of Notre Dame
- 11:00AM Machine Learning-Based Reduced Order Modelling For The Simulation Of Braided Stent Deployment.** SB³C2023-303
Beatrice Bisighini^{1,2,3}, Miquel Aguirre^{1,4,5}, Baptiste Pierrat¹, David Perrin², Stéphane Avril¹
¹University of Lyon, ²Predisurge, ³University Tor Vergata, ⁴Universitat Politècnica de Catalunya, ⁵Gran Capità

Monday, June 5

9:45AM – 11:15AM MT

Soft Tissue Mechanics

Cascade D

Session Chairs: *Kyoko Yoshida, Univ of Minnesota*
Colleen Witzenburg, Univ of Wisconsin

- 9:45AM A Clot Composition Dependent Hyperelastic Model In The Simulation Of Direct Aspiration Thrombectomy** SB³C2023-362
K. Bein Snee¹, R. McCarthy², P.E. McHugh¹, B. Fereidoonenezhad³, J.P. McGarry¹
¹University of Galway, ²Cerenovus, ³TU Delft
- 10:00AM Using Bayes' Optimization For Inverse Finite Element Analysis Of The Tricuspid Valve In Hypoplastic Left Heart Syndrome** SB³C2023-338
Colton J. Ross¹, Jaden Norman¹, Arshid Mir¹, Harold M. Burkhart¹, Ming-Chen Hsu², Chung-Hao Lee¹
¹University of Oklahoma, ²Iowa State University
- 10:15AM Calcified Plaque Has A Local Effect On The Dissection Behavior Of Human Aortas** SB³C2023-563
Carly L. Donahue, Raturaj Badal, Victor H. Barocas
University of Minnesota
- 10:30AM Influence Of Material Parameter Variability On The Predicted Coronary Artery Biomechanical Environment Via Uncertainty Quantification** SB³C2023-413
David Jiang, Caleb C. Berggren, Y.F. Jack Wang, Jake A. Bergquist, Lindsay C. Rupp, Zexin Liu, Rob S. MacLeod, Akil Narayan, Lucas H. Timmins
University of Utah
- 10:45AM Spatial Configurations Of 3D Extracellular Matrix Density And Anisotropy Simultaneously Guide Angiogenesis** SB³C2023-084
Steven A. LaBelle¹, Steve A. Maas¹, Adam Rauff¹, Gerard A. Ateshian², Jeffery A. Weiss¹
¹University of Utah, ²Columbia University
- 11:00AM Spatiotemporal Evolution Of Collagen Micro-Mechanics Under Breast Cancer Cell Driven Remodeling** SB³C2023-125
Adil Khan, Jacopo Ferruzzi
University of Texas at Dallas

Monday, June 5

9:45AM – 11:15AM MT

Ocular and Lower Abdomen Biomechanics

Cascade E

Session Chairs: Jake Hermann, *University of Iowa*
Katrina Knight, *University of Pittsburgh*

- 9:45AM** **Lamina Cribrosa Beam Insertions. The Humble Heroes Of The Lamina-Sclera Interplay** SB³C2023-513
Fengting Ji, Hua Yi, Ian A. Sigal
University of Pittsburgh
- 10:00AM** **Mechanical Properties of Porcine Iris Stroma Using Micro-Indentation: The Effect Of Temperature And Hydration** SB³C2023-495
F. Sebastian¹, G. Bailey¹, V. Kondiboyina¹, S. Dorairaj², R. Amini¹
¹*Northeastern University*, ²*Mayo Clinic*
- 10:15AM** **Structural And Functional Heterogeneity Of The Uterosacral Ligaments In The Rat** SB³C2023-243
Joseph G. Thomas, Kandace Donaldson, Yizheng Zhu, Clara Gimenez, Raffaella De Vita
Virginia Tech
- 10:30AM** **Biaxial Mechanics Of The Murine Vagina During Postpartum Healing Before And After Elastic Fiber Disruption** SB³C2023-272
Shelby E. White¹, Lily M. Buchanan², Niyousha Karbasion³, Matthew R. Bersi³, Maria Florian-Rodriguez⁴, Kristin S. Miller^{2,4}
¹*Tulane University*, ²*University of Texas, Dallas*, ³*Washington University in St. Louis*, ⁴*University of Texas, Southwestern*
- 10:45AM** **Passive Mechanics Of Deep And Superficial Human Female Pelvic Floor Muscles** SB³C2023-455
Megan R. Routzong^{1,3}, Justin Dubik², Raffaella De Vita², Marianna Alperin³, Pamela A. Moalli¹, Steven D. Abramowitch¹
¹*University of Pittsburgh*, ²*Virginia Tech*, ³*University of California, San Diego*
- 11:00AM** **Bladder Wall Stress Is Lower In Female Compared To Male In A Murine Model Of Ex-Vivo Filling** SB³C2023-422
Eli Broemer, Pragya Saxena, Nathan R. Tykocki, Sara Roccabianca
Michigan State University

Monday, June 5

9:45AM – 11:15AM MT

Biotransport in Therapeutic Design and Analysis

Cascade F

Session Chairs: **Chris Rylander**, *University of Texas at Austin*
R. Lyle Hood, *University of Texas at San Antonio*

- 9:45AM A Biphasic Fluid-Structure Interaction Model Of Backflow During Infusion Into Agarose Gel** SB³C2023-090
Arthur D. Ayers, Joshua H. Smith
Lafayette College
- 10:00AM Thermodynamics Of Phase Transformation Of Water: Theory And Experiments** SB³C2023-301
Raphael J. Kepecs, Gerard A. Ateshian
Columbia University
- 10:15AM Model For Heat Conduction In Vaporizable Endoskeletal Droplet In Response To X-Ray Photon Absorption** SB³C2023-578
William N. Frantz, David H. Thomas, Mark A. Borden
University of Colorado
- 10:30AM Computational Modeling Of Machine Perfusion Of The Human Liver Vasculature** SB³C2023-585
Daniel Emerson, Yoed Rabin, Levent Burak Kara
Carnegie Mellon University
- 10:45AM Conformal Ablation Of Atherosclerotic Plaque Based On Multi- Electrodes And NSGA II** SB³C2023-590
Hongying Wang, Ruizhe Hou, Shiqing Zhao, Aili Zhang
Shanghai Jiao Tong University
- 11:00AM N-Acetyl Cysteine Rescues Chondrocytes From Oxidative Stress And Increases Their Metabolic Activity** SB³C2023-275
Austin C. Jenk^{1,2}, Elisabeth A. Lemmon^{1,2}, Sarah E. Gullbrand^{1,2}, Robert L. Mauck^{1,2}
1University of Pennsylvania, 2Veterans Affairs Medical Center

Monday, June 5

9:45AM – 11:15AM MT

Engineered *In Vitro* Models

Gore AB

Session Chairs: Nathaniel Dymnt, *University of Pennsylvania*

Kristan Worthington, *University of Iowa*

- 9:45AM Modeling Cardiac Fibrosis: Understanding the Effects of Exogenous Extracellular Matrix on 3D Cardiac Tissues** SB³C2023-229
Natalie Weiss-Pachter, Kristen Allen, Tracy Hookway
Binghamton University
- 10:00AM Engineered Composite Fibrous Hydrogels that Mimic Dynamic Developmental Signals during Fibrous Tissue Development** SB³C2023-376
Karen L. Xu¹, Jason A. Burdick^{1,2}, Robert L. Mauck¹
¹*University of Pennsylvania*, ²*University of Colorado*
- 10:15AM An explant-in-a-chip perfusion model for ex vivo preservation of tissue viability and function with applications for personalised medicine in cancer** SB³C2023-419
Evangelia E. Zeringa, Foivos Chatzidimitriou, Ester Reina-Torres, Larry O'Connell, Beatrice-Cristina Bezdadea, Alexandria Mitchell, Paula Cunnea, Christina Fotopoulou, Olivier Pardo, Joseph van Batenburg-Sherwood, Iain A. McNeish, Darryl R. Overby
Imperial College London
- 10:30AM Prolonged Subculture and Progerin Expression Sensitize VSMCs to Three Dimensional Fiber Structures** SB³C2023-374
Yu-Yu Hsueh, Pen-hsiu Grace Chao
National Taiwan University
- 10:45AM The Role Of Monocyte And Macrophages In The Development Of Aortic Valve Calcification In A 3D Tri-Culture In Vitro Model** SB³C2023-121
Fatemeh Saleemizadehparizi, Peter Huang, Mei-Hsiu Chen, Gretchen J. Mahler
Binghamton University
- 11:00AM Development of a Schlemm's canal "inner wall on a chip" for high content biomechanical screening** SB³C2023-417
Seyed Mohammad Siadat¹, Jacques A. Bertrand², Babak N. Safa¹, Darryl R. Overby², W. Daniel Stamer³, C. Ross Ethier¹
¹*Georgia Institute of Technology*, ²*Imperial College of London*, ³*Duke University*

Monday, June 5

9:45AM – 11:15AM MT

Cartilage: Composition and Lubrication

Gore CD

Session Chairs: Jennifer Puetzer, *Virginia Commonwealth University*

Phoebe Szarek, *University of Connecticut*

- 9:45AM Mechanical Weakening Precedes Cartilage Loss During Osteoarthritis Progression Across the Human Tapezium** SB³C2023-196
Brendan D. Stoeckl^{1,2}, Kendall M. Masada^{1,2}, Lorielle G. Laforest¹, Michael W. Hast¹, David R. Steinberg^{1,2}, Robert L. Mauck^{1,2}
¹University of Pennsylvania, ²Corporal Michael J. Crescenz VA Medical Center
- 10:00AM Quantitative Raman Measurement Of Cartilage Composition Via Tissue Phantom Calibration** SB³C2023-461
Erik Erslund¹, Dev Mehrotra¹, Mark W. Grinstaff¹, Brian D. Snyder², Mads S. Bergholt³, Michael B. Albro¹
¹Boston University, ²Beth Israel Deaconess Medical Center, ³King's College London
- 10:15AM Decorin Maintains Cartilage Surface Integrity And Chondrocyte Mechanotransduction During Aging** SB³C2023-159
M. Fan¹, B. Kwok¹, P. Singh¹, J. Xiang¹, L. Qin², D.E. Birk³, R.V. Iozzo⁴, R.L. Mauck², L. Han¹
¹Drexel University, ²University of Pennsylvania, ³University of South Florida, ⁴Thomas Jefferson University
- 10:30AM A chemo-mechano-biological model of cartilage in FEBio: Studies of pathological loading, homeostatic adaptation and bio-chemical treatments** SB³C2023-486
Muhammed M. Rahman¹, Paul N. Watton², Corey P. Neu³, David M. Pierce¹
¹University of Connecticut, ²University of Sheffield, ³University of Colorado
- 10:45AM Synovial Fluid Provides A Protective Effect In Articular Cartilage Fatigue Failure** SB³C2023-215
C.V. Sise, C.A. Petersen, J.X. Dewing, B.K. Zimmerman, J. Yun, R.J. Kepecs, C.T. Hung, G.A. Ateshian
Columbia University
- 11:00AM The Role of Hyaluronic Acid in the Synergistic Lubrication of Articular Cartilage** SB³C2023-082
Emily P. Lambeth, David L. Burris, Christopher Price
University of Delaware

Monday, June 5

9:45AM – 11:15AM MT

Translational Bioengineering

Powell

Session Chairs: Lin Li, *Eli Lilly*

Elizabeth Shih, *University of Minnesota*

- 9:45AM** **Shifting The Endovascular Paradigm: Patient-Specific Treatment Of Intracranial Aneurysms Using Shape Memory Polymers And Additive Manufacturing** SB³C2023-124
Sergio A. Pineda-Castillo¹, Tanner Cabaniss¹, Bradley N. Bohnstedt², Chung-Hao Lee¹
¹University of Oklahoma, ²Indiana University
- 10:00AM** **Impacts Of Type V Collagen Insufficiency On Cutaneous Wound Healing And Scar Formation** SB³C2023-153
Y. Liu¹, C. Wang¹, D.C. Stewart², E.M. O'Brien¹, B.K. Brisson², D.E. Birk³, K.L. Spiller¹, S.W. Volk², L. Han¹
¹Drexel University, ²University of Pennsylvania, ³University of South Florida
- 10:15AM** **Understanding Impacts Of Collagen Organization In An Infected Diabetic Wound Model Treated With A Novel Oxygenating And Antibacterial Hydrogel** SB³C2023-168
Hannah A. Durr¹, Samuel D. Salinas², Rouzbeh Amini², Nic D. Leipzig¹
¹University of Akron, ²Northeastern University
- 10:30AM** **Development And Utilization Of A Vascularized In Vitro Physiologically Representative Skin Tissue Platform For Burn Injury Investigation** SB³C2023-257
S. Brocklehurst, N. Ghousafim, K. Zuniga, D. Stolley, M.N. Rylander
University of Texas
- 10:45AM** **Proteomic Characterization And Metabolic Labeling Of A Fibrin-Based In Vitro Wound Healing Model** SB³C2023-418
Dalton Miles¹, Tyler Tuttle¹, Julian Jimenez², Yifan Guo², Adrian Buganza-Tepole², Sarah Calve^{1,2}
¹University of Colorado, ²Purdue University
- 11:00AM** **Experimental And Computational Analysis Of The Injection- Induced Mechanical Changes In The Skin Microenvironment During Subcutaneous Injection Of Biologics** SB³C2023-518
Yingnan Shen, Sameep R. Shah, Kejie Zhao, Bumsoo Han
Purdue University

Monday, June 5

9:45AM – 11:15AM MT

Cardiovascular Mechanobiology

Zermatt

Session Chairs: Bryan Good, *University of Tennessee*

Friederike Schäfer, *Norwegian University of Science and Technology*

- 9:45AM** **Effect of aging, sex, and gene (fibulin-5) on the arterial stiffness of mouse: 20 weeks adult mice with fibulin-5 knockout are older than 100 weeks wild-type mice** SB³C2023-341
H. Dong¹, J. Ferruzzi², M. Liu¹, L. Brewster³, R. Gleason¹
¹Georgia Institute of Technology, ²University of Texas, Dallas, ³Emory University
- 10:00AM** **Functional Differences in Human Aortic Valve Interstitial Cells from Patients with Varying Calcific Aortic Valve Disease** SB³C2023-458
R. Tuscher¹, A. Khang¹, T. West¹, G. Ferrari², M. Sacks¹
¹University of Texas, Austin, ²Columbia University
- 10:15AM** **Reduced Vascular Smooth Muscle Cell Mechanoadaptation in an in vitro Model of Cerebral Amyloid Angiopathy** SB³C2023-279
Samuel F. Boland, Patrick W. Alford
University of Minnesota
- 10:30AM** **Constitutive Modeling Of Mouse Arteries Suggests Changes In Directional Coupling And Extracellular Matrix Remodeling That Depends On Artery Type, Age, Sex And Elastin Amounts** SB³C2023-300
Keshav A. Kailash, Jie Z. Hawes, Austin J. Cocciolone, Robert P. Mecham, Jessica E. Wagenseil
Washington University in St. Louis
- 10:45AM** **Determining How VEGFR-2 Inhibition Affects Phosphorylation And Function In The Presence Of Mechanical Strain** SB³C2023-320
Bronte Miller, Michael Heim, Bryan Mortimer, M.K. Sewell-Loftin
University of Alabama at Birmingham
- 11:00AM** **A Testable Mechanism for Force Generation and Maintenance in the Tonic Smooth Muscle** SB³C2023-606
Suzzane E. Stasiak, Dhanajay T. Tambe, Harikrishnan Parameswaran
Northeastern University

Monday, June 5

11:30AM – 1:00PM MT

Thrombosis and Hemolysis

Cascade ABC

Session Chairs: Debanjan Mukherjee, *University of Colorado Boulder*
Bryan Good, *University of Tennessee*

- 11:30AM Numerical Predictions Of Flow-Induced Hemolysis: Can The Accuracy Of The Power Law Model Be Improved Using Calibrated Coefficients?** SB³C2023-371
Alberto Mantegazza¹, Nicolas Tobin², Keefe B. Manning², Brent A. Craven³
¹*Polytechnic University of Bari*, ²*Pennsylvania State University*, ³*US FDA*
- 11:45AM An In Vitro Assessment of Emboli Trajectories Within a Patient Specific Model: Investigation into the Influence of Thrombus Size, Mechanical Properties, and Cerebral Blood Pressure** SB³C2023-308
A. Glynn^{1,2}, A. Consoli³, B. Murphy^{1,4}, R. McCarthy², C. Lally^{1,4}
¹*Trinity College Dublin*, ²*Cerenovus*, ³*Hôpital Foch*, ⁴*RCSI & TCD*
- 12:00PM Hematocrit Is A Potent Driver Of Platelet Adhesion At Supraphysiological Shear Rates** SB³C2023-126
C. Watson¹, K. Manning^{1,2}
¹*Pennsylvania State University*, ²*Penn State Hershey Medical Center*
- 12:15PM Computational Simulation Of Patient-Specific Blood Coagulation In Stent Thrombosis** SB³C2023-404
Janneke M.H. Cruts¹, Mohammad Rezeimoghaddam², Frans N. van de Vosse², Frank J.H. Gijsen^{1,3}
¹*Erasmus Medical Center*, ²*Eindhoven University of Technology*, ³*Delft University of Technology*
- 12:30PM Image driven simulation of hemodynamics around a dynamic clot in vivo** SB³C2023-566
Chayut Teeraratkul¹, Timothy J. Stalker², Maurizio Tomaiuolo³, Debanjan Mukherjee¹
¹*University of Colorado*, ²*Thomas Jefferson University*, ³*Wills Eye Hospital*
- 12:45AM Multiscale, Cell-Resolved Simulations of Red Blood Cells in Macroscale Flows for Hemolysis Prediction** SB³C2023-105
Grant J. Rydquist, Mahdi Esmaily
Cornell University

Vascular Pathology and Fluid Flow

Cascade D

Session Chairs: Grant Rydquist, *Cornell University*

Alejandro Roldán-Alzate, *University of Wisconsin - Madison*

- 11:30AM Computational Fluid Dynamics Study To Investigate The Impact Of Sudden Physiological Actions On Cerebrospinal Fluid Pressure And Flow** SB³C2023-311
 Sarah Vandenbulcke¹, Paul Condron^{2,3}, Haribalan Kumar^{2,3,4}, Soroush Safaei³, Samantha Holdsworth^{2,3}, Joris Degroote¹, Patrick Segers¹
¹Ghent University, ²Tairāwhiti-Gisborne, ³University of Auckland, ⁴GE Healthcare
- 11:45AM Blood Flow Energy Profiles in Coronary Arteries Predict Myocardial Infarction** SB³C2023-309
 M. Lodi Rizzini¹, A. Candreva^{1,2}, V. Mazzi¹, C. Chiastra¹, B. De Bruyne³, C. Collet³, D. Gallo¹, U. Morbiducci¹
¹Politecnico di Torino, ²Zurich University Hospital, ³OLV-Clinic
- 12:00PM Evolution Of The Hemodynamic Properties And Arterial Wall Remodeling In Pulmonary Arterial Hypertension** SB³C2023-154
 H. Mu, D. Valdez-Jasso
University of California, San Diego
- 12:15PM Hemodynamics Of Coarctation Of The Aorta - Comparison Of A Distributed Lumped Parameter Model And 4D Flow MRI** SB³C2023-128
 Labib A. Shahid¹, Matthew A. Culver¹, James P. Rice¹, Haben Berhane², Cynthia K. Rigsby³, Joshua D. Robinson³, Lindsay M. Griffin³, Michael Markl², Colleen M. Witzenburg¹, Alejandro Roldán-Alzate¹
¹University of Wisconsin-Madison, ²Northwestern University, ³Lurie Children's Hospital of Chicago
- 12:30PM Mitigating Post-TAVR Thrombogenic Risk: Design And Optimization Of Novel Trileaflet and Bicuspid Aortic Valve Devices** SB³C2023-109
 Kyle J. Baylous¹, Brandon J. Kovarovic¹, Salwa B. Anam¹, Ryan T. Helbock¹, Marvin J. Slepian², Danny Bluestein¹
¹Stony Brook University, ²University of Arizona
- 12:45AM A Computational Assessment of Stroke Predictors After Transcatheter Aortic Valve Replacement** SB³C2023-491
 B. Vogl¹, Z. Wang², A. Chavez Ponce³, A. El Shaer³, M. Alkhouli³, H. Hatoum¹
¹Michigan Technological University, ²The Ohio State University, ³Mayo Clinic

Monday, June 5

11:30AM – 1:00PM MT

Ocular and Lung Biomechanics

Cascade E

Session Chairs: Yi Hua, *University of Mississippi*

Arina Korneva, *Virginia Tech*

- 11:30AM Eye-Specific Modeling Of Effects Of Intraocular Pressure On Optic Nerve Head Oxygenation** SB³C2023-297
Yuankai Lu, Yi Hua, Bingrui Wang, Fuqiang Zhong, Andrew Theophanous, Shaharoz Tahir, Po-Yi Lee, Ian A. Sigal
University of Pittsburgh
- 11:45AM Effects of Glaucoma and Optic Nerve Crush on the Biomechanical Behavior Of Mouse Astrocytic Lamina Cribrosa** SB³C2023-510
A Korneva, E. Kimball, T.V. Johnson, S. Quillen, M.E. Pease, T.D. Nguyen, H.A. Quigley
Johns Hopkins University
- 12:00PM Quantifying the Remodeling Strain in the Lamina Cribrosa Years After Pressure Lowering Surgery** SB³C2023-208
Cameron A. Czerpak, Harry A. Quigley, Thao D. Nguyen
Johns Hopkins University
- 12:15PM The Influence Of Recruitment Maneuvers On Localized Murine Lung Strains Assessed With Digital Image Correlation** SB³C2023-123
M. Shankel, T.M. Nelson, K.A.M. Quiros, T. Biddle, G.O. Ramirez, C.A. Mariano, J. Bebawy, D.D. Lo, M. Eskandari
University of California, Riverside
- 12:30PM Quantifying Temporal Dynamics Of Alveolar Recruitment During Mechanical Ventilation** SB³C2023-236
Daniel S. Meggo, Edward A. Sander, Jacob Herrmann
University of Iowa
- 12:45AM Probing Lung Function At High Spatiotemporal Resolution Via Crystal Ribcage** SB³C2023-434
Rohin Banerji, Gabrielle N. Grifno, Linzheng Shi, Dylan Smolen, Rob LeBourdais, Johnathan Muhvich, Cate Eberman, Bradley Hiller, Jisu Lee, Kathryn Regan, Siyi Zheng, Sue S. Zhang, John Jiang, Riley Pihl, Katrina Traber, Giovanni Ligresti, Joseph P. Mizgerd, Bela Suki, Hadi T. Nia
Boston University

Monday, June 5

11:30AM – 1:00PM MT

Sex, Age, and Disease in Brain and Head Injury

Cascade F

Session Chairs: Kaveh Laksari, *University of Arizona*

Ken Monson, *University of Utah*

- 11:30AM Sex Difference In Axon Dynamic Behavior Under Axial Loading And Unloading**
SB³C2023-324
C. Zhang, S. Ji
Worcester Polytechnic Institute
- 11:45AM Evolution Of Human Cortical Thickness And Morphology Throughout Growth And Development** SB³C2023-041
Nagehan Demirci, Maria A. Holland
University of Notre Dame
- 12:00PM Age- And Sex-Based Skull Thickness Distribution For Predicting Skull Fracture Patterns** SB³C2023-428
Yousef Alsanea, Timothy Dixon, Tagrid Ruiz-Maldonado, Brittany Coats
University of Utah
- 12:15PM Spatial Gradient in Brain Mechanical Properties Changes Through Development But Is Consistent During Adulthood** SB³C2023-239
Kyra E. Twohy¹, Grace McIlvain^{1,2}, Jeffrey M. Spielberg¹, Curtis L. Johnson¹
¹*University of Delaware*, ²*Georgia Institute of Technology*
- 12:30PM High Resolution MR Elastography of the Human Brain: Technical Development and Applications in Aging and Alzheimer's Disease** SB³C2023-132
E. Triolo¹, O. Khagai², A. Alipour², T. Hedden², P. Balchandani², M. Kurt^{1,2}
¹*University of Washington*, ²*Mount Sinai*
- 12:45AM The Relationship Between Imbalance Symptom And Cardiac Pulsation Induced Mechanical Strain In The Brainstem And Cerebellum For Chiari Malformation Type I** SB³C2023-471
Mohamad Motaz F. Al Samman¹, Alaaddin Ibrahimy², Blaise Simplicie Talla Nwotchouang³, John N. Oshinski⁴, Daniel L. Barrow⁴, Philip A. Allen³, Rouzbeh Amini¹, Rafeeqe A. Bhadelia⁵, Francis Loth¹
¹*Northeastern University*, ²*Yale University*, ³*University of Akron*, ⁴*Emory University*, ⁵*Harvard*

Monday, June 5

11:30AM – 1:00PM MT

Bioprinting and Emerging Technology in TCE

Gore AB

Session Chairs: Deva Chan, *Purdue University*
Edward Sander, *University of Iowa*

- 11:30AM Particulated ECM Biomaterial Inks Enable 3D Bioprinting of Osteochondral In Vitro Models With Multi-Scale Architecture** SB³C2023-535
Juliet O. Heye, Shannon A. Blanco, Jeanne E. Barthold, Emily Y. Miller, Corey P. Neu
University of Colorado
- 11:45AM Novel Metabolic Labeling Demonstrates A Critical Role Of Decorin In The Assembly And Turnover Of Cartilage Matrix** SB³C2023-399
T. Li¹, M. Fan¹, A. Porter², B. Kwok¹, C. Wang¹, D.E. Birk³, R.V. Iozzo⁴, X.L. Lu², R.L. Mauck⁵, L. Han¹
¹Drexel University, ²University of Delaware, ³University of South Florida, ⁴Thomas Jefferson University, ⁵University of Pennsylvania
- 12:00PM Modeling Human Sex-Specific Fibrotic Activation In 3D-Bioprinted Pulmonary Artery Adventitia** SB³C2023-039
Duncan J. Davis-Hall, Chelsea M. Magin
University of Colorado
- 12:15PM A Thermodynamic Framework For The Evolution Of Sarcomeres In Cardiomyocytes Subjected To Dynamic Loading** SB³C2023-522
Ryan J. Coleman¹, Vikram S. Deshpande², Patrick McGarry¹
¹University of Galway, ²University of Cambridge
- 12:30PM Effects of Conditional SV40-T Immortalization on Human Retinal Progenitor Cell Differentiation** SB³C2023-593
Qi Wang, Jessica A. Cooke, Budd A. Tucker, Kristan S. Worthington
University of Iowa
- 12:45AM Sub-Millimeter Stiffness Gradients Within 3d Printed Composite Scaffolds For Osteochondral Tissue Engineering** SB³C2023-517
Kevin N. Eckstein, A. Camila Uzcategui, John E. Hergert, Sarah A. Schoonraad, Stephanie J. Bryant, Robert R. McLeod, Virginia L. Ferguson
University of Colorado

Monday, June 5

11:30AM – 1:00PM MT

Cartilage: Imaging and Degeneration

Gore CD

Session Chairs: Jill Middendorf, *Johns Hopkins University*
David Pierce, *University of Connecticut*

- 11:30AM Enzymatic Digestion Does Not Compromise Sliding-Mediated Cartilage Lubrication** SB³C2023-182
Meghan E. Kupratis, Atia Rahman, David L. Burris, Elise A. Corbin, Christopher Price
University of Delaware
- 11:45AM Raman Probe Predicts Cartilage Functional Mechanical Properties Better Than ORSI Score And MRI T2* Mapping** SB³C2023-547
Masumeh Kazemi¹, Chenhao Yu¹, Farida Korna¹, Dev Mehrotra¹, Erik Ersland¹, Juncheng Zhang¹, Thomas P. Schaer², Julie B. Engiles², Mark W. Grinstaff¹, Brian D. Snyder³, Mads S. Bergholt⁴, Michael B. Albro¹
¹*Boston University*, ²*University of Pennsylvania*, ³*Beth Israel Deaconess Medical Center*, ⁴*King's College London*,
- 12:00PM Cartilage Strain And T1rho MRI Mapping In Response To Load In An Initial ACL-Reconstructed Patient Cohort** SB³C2023-169
Emily Y. Miller, Hongtian Zhu, Woowon Lee, Corey P. Neu
University of Colorado
- 12:15PM Cartilage Contact Pressures During Walking are Related to T2 Relaxation Times in Patients with Knee Osteoarthritis** SB³C2023-479
Benjamin D. Bernarding, Austin J. Garcia, Adam J. Bradshaw, Johnny Huard, Scott Tashman, Lauren E. Watkins, Colin R. Smilth
Steadman Philippon Research Institute
- 12:30PM In Vivo Assessment Of Passive And Active Articular Cartilage Strain Recovery** SB³C2023-283
Shu-Jin Kust, Dana Voinier, Kyle D. Meadows, Dawn M. Elliott, Daniel K. White, Axel C. Moore
University of Delaware
- 12:45AM Sensitivity Of Finite Element Models To Relationship Between T2 Relaxation And Modulus In Articular Cartilage** SB³C2023-483
Alexander A. Donabedian, Deva D. Chan
Purdue University

Monday, June 5

11:30AM – 1:00PM MT

Bioengineering Design I

Powell

Session Chairs: *Ria Mazumder, Widener University*
Sriram Balasubramanian, Drexel University

- 11:30AM Photo-Curing Extracellular Matrix Sealant For Stopping Vascular Hemorrhage**
SB³C2023-199
Luke E. Schepers¹, Brooke L. Martindale², Alycia G. Berman², Hannah L. Cebull¹, William Van Alstine³, Sydney E. Hollingshead², Tyler Novak², Craig J. Goergen¹
¹Purdue University, ²Cook Biotech Inc., ³Cook Research Inc.
- 11:45AM Evaluating The Effects Of Coordinate System Selection on Thumb Carpometacarpal Joint Angles** SB³C2023-387
Adam J. Chrzan¹, Nicole D. Arnold¹, Kevin Chan², Tamara Reid Bush¹
¹Michigan State University, ²Spectrum Health
- 12:00PM Development and Validation of a Smart Screwdriver (SSD) for Spine Surgery**
SB³C2023-436
Allison M. Tanner, Daniel Jacobson, Alexander W. Hooke, James S. Fitzsimmons, Chunfeng Zhao, Brett A. Freedman
Mayo Clinic
- 12:15PM Development of an Artificial Temporomandibular Joint Disc Replacement and Surgical Strategy** SB³C2023-584
Jason Kuiper, Ryan Dobbs, Jeremiah Easley, Christian Puttlitz, Kevin Labus
Colorado State University
- 12:30PM Regenerative Rehabilitation Of Muscle Defect Under Mechanical Stimulation: An Organ Culture Study** SB³C2023-381
D. Jacho, E. Yildirim-Ayan
University of Toledo
- 12:45AM Optimization Of A Bioprinted Pulsatile Fontan Conduit Using A Multiphysics Simulation Framework** SB³C2023-066
Zinan Hu¹, Jessica E. Herrmann¹, Mark A. Skylar-Scott¹, Tain-Yen Hsia², Alison L. Marsden¹
¹Stanford University, ²University of Central Florida

Monday, June 5

11:30AM – 1:00PM MT

Multiscale Models, Cardiovascular System

Zermatt

Session Chairs: Arianna Forneris, *University of Calgary*

Lei Fan, *Marquette University*

- 11:30AM Multiscale Model Predictions Of Heart Growth During Hypertensive Rat Pregnancies** SB³C2023-147
Molly S. Kaissar, Kyoko Yoshida
University of Minnesota
- 11:45AM A Computational Model of Coarctation of the Aorta in Rabbits** SB³C2023-235
Ashley A. Hiebing¹, Matthew A. Culver¹, John F. LaDisa Jr.², Colleen W. Witzenburg¹
¹*University of Wisconsin*, ²*Medical College of Wisconsin*
- 12:00PM Numerical and Computational Analysis of Artery Stresses Considering Active Contractility** SB³C2023-609
N. Goulbourne, Y. Li
University of Michigan
- 12:15PM Multiscale Modeling of Baroreflex Feedback Loop in Response to Acute Myocardial Infarction** SB³C2023-092
Hossein Sharifi, Kenneth S. Campbell, Jonathan F. Wenk
University of Kentucky
- 12:30PM Toward a biomechanical model of aortic development** SB³C2023-393
Bruno V. Rego, Sae-Il Murtada, Guangxin Li, George Tellides, Jay D. Humphrey
Yale University
- 12:45AM A 1D Model Characterizing The Role Of Spatiotemporal Contraction Distributions On Lymph Transport** SB³C2023-155
Farbod Sedaghati, J. Brandon Dixon, Rudolph L. Gleason
Georgia Institute of Technology

Tuesday, June 6

9:30AM – 11:00AM MT

**PhD-Level Student Paper Competition Session I:
Multiscale Biomechanics and Fluid Dynamics/Transport**

Cascade ABC

Session Chairs: Debanjan Mukherjee, *University of Colorado*
Lucas Timmins, *University of Utah*

- 9:30AM Characterizing Headform Friction Coefficient For Helmet Testing SB³C2023-142**
Nicole E-P. Stark, Steve Rowson
Virginia Tech
- 9:45AM Tuning Of The Mechanical Boundary Conditions Parameters For A Patient-Specific Thoracic Aorta Model SB³C2023-192**
Leonardo Geronzi¹, Antonio Martinez^{1,2}, Aline Bel-Brunon³, Michel Rochette², Marco Sensale², Pier Paolo Valentini¹, Marco E. Biancolini¹
¹University of Rome Tor Vergata, ²Ansys, ³INSA Lyon
- 10:00AM Toward Generalizable Brain Deformation Estimators For Head Impacts With Unsupervised Domain Adaptation And Deep Learning SB³C2023-030**
Xianghao Zhan, Jiawei Sun, Yuzhe Liu, Nicholas Cecchi, Enora Le Flao, Olivier Gevaert, Michael Zeineh, David Camarillo
Stanford University
- 10:15AM Learning Diffeomorphic Deformations for Whole Heart Mesh Generation SB³C2023-113**
Arjun Narayanan, Fanwei Kong, Shawn C. Shadden
University of California, Berkeley
- 10:30AM Correlations Between Mass Transport, Elastic Fiber Fragmentation, And Thoracic Aortic Aneurysm Severity SB³C2023-111**
Christie L. Crandall, Carmen M. Halabi, Jessica E. Wagenseil
Washington University in St. Louis
- 10:45AM Successful transplant of cryopreserved kidneys enabled by engineering-based protocol optimization SB³C2023-110**
Zonghu Han, Joseph S. Rao, Lakshya Gangwar, Bat-Erdene Namsrai, Jacqueline Pasek-Allen, Srivasupradha Ramesh, Michael L. Etheridge, Erik B. Finger, John C. Bischof
University of Minnesota

Tuesday, June 6

9:30AM – 11:00AM MDT

**PhD-Level Student Paper Competition Session II:
Cardiovascular Mechanics and Remodeling**

Cascade D

Session Chairs: Joao Soares, *Virginia Commonwealth University*
Joseph van Batenburg-Sherwood, *Imperial College London*

- 9:30AM Contribution Of Microtubule Network To The Passive Anisotropic Viscoelasticity Of Healthy Right Ventricle** SB³C2023-050
Kristen LeBar, Kellan Roth, Wenqiang Liu, Erith Evans, Jassia Pang, Adam Chicco, Zhijie Wang
Colorado State University
- 9:45AM Suppressing Leaflet Thickening and Stiffening May Restore Tricuspid Valve Function** SB³C2023-150
Mrudang Mathur¹, Marcin Malinowski^{2,3}, Tomasz A. Timek³, Manuel K. Rausch¹
¹*University of Texas, Austin*, ²*Medical University of Silesia*, ³*Spectrum Health*
- 10:00AM Sex Differences in Right Ventricular Chamber Elastance and Stiffness in an Animal Model of Pulmonary Arterial Hypertension** SB³C2023-177
Ethan D Kwan, Tsui Min Wang, Hao Mu, Becky A Hardie, Daniela Valdez-Jasso
University of California, San Diego
- 10:15AM Multiscale Model Translates Microscale Vascular Smooth Muscle Cell Mechanics to Tissue-Scale Aortic Contraction** SB³C2023-148
Shannon M. Flanary, Seokwon Jo, Emilyn U. Alejandro, Victor H. Barocas
University of Minnesota
- 10:30AM Heterogeneity Of Red Cell Mechanical Properties Drives Pathophysiology In Sickle Cell Disease** SB³C2023-064
Dillon C. Williams, David K. Wood
University of Minnesota
- 10:45AM Restored Normal Blood Flow Plus Atorvastatin Promotes Atherosclerosis Regression** SB³C2023-108
Morgan A. Schake, Ian McCue, Samuel Harvey, Evan Curtis, Forrest Kievit, Ryan M. Pedrigi
University of Nebraska-Lincoln

Tuesday, June 6

9:30AM – 11:00AM MT

Undergraduate Design Competition

Gore AB

Session Chairs: **Antonia Zaferiou**, *Stevens Institute of Technology*

- 9:30AM The History And Goals Of The Undergraduate Design Competition**
Anita Singh
Temple University
- 9:45AM Pulse Oximeter For Simulation Mannequin SB³C2023-624**
Marina Walsh, Benjamin Aon, Hatice S. Emanet, Cheyenne M. Miller, Chiamaka G. Oduah, Ria Mazumder
Widener University
- 10:00AM 3D Printed Mouth Guard For Temporomandibular Joint Dysfunction SB³C2023-635**
Christopher N. Barnes, Jorge M. Pumachagua, Elias P. Saliba
Embry-Riddle Aeronautical University
- 10:15AM Design Of A Prophylactic Knee Brace To Prevent ACL Injuries In Female Athletes SB³C2023-637**
J. DiVanna, E. LoVerde, M. Taibi
Manhattan College
- 10:30AM Elert: A Haptic Emergency Alert System For The Auditorily Impaired SB³C2023-643**
Emily Bartling, Ruth Hammon, Deven Cobb, Jerritt Gutierrez
Rose-Hulman Institute of Technology
- 10:45AM A Digital Incentive Spirometer for Aiding Lung Recovery Post-Surgery SB³C2023-647**
Isabella T. Mirro, Yi-An Hsieh, Jackson C. Dooley, Parth K. Mody, Josh Freedman
University of Pennsylvania

Tuesday, June 6

9:30AM – 11:00AM MT

**PhD-Level Student Paper Competition Session III:
Morphogenesis, Maternal/Abdominal Health**

Zermatt

Session Chairs: Sihong Wang, *The City College of New York*
Alix Deymier, *University of Connecticut*

- 9:30AM Vascular remodeling during late-gestation pregnancy: an in-vitro assessment of the murine thoracic aorta** SB³C2023-247
Ana I. Vargas, Samar Tarraf, Chiara Bellini, Rouzbeh Amini
Northeastern University
- 9:45AM Maternal Anatomy Drives Mechanical Loading in the Proximal Cervix During Pregnancy** SB³C2023-186
Erin Louwagie, Jada Hinds, Lindsey Carlson, Timothy Hall, Helen Feltovich, Kristin Myers
Columbia University
- 10:00AM Mechanical Changes of the Pregnant Murine Uterus** SB³C2023-207
Emily A. Hoffmann, Shanmugasundaram Nallasamy, Kyoko Yoshida
University of Minnesota
- 10:15AM Towards Enhanced Non-Invasive Assessment Of Bladder Urodynamics - Validation Of Dynamic 3D MRI In A Patient-Specific In Vitro Model Of The Bladder** SB³C2023-254
Jeams Rice, Jack Gwertzman, Alejandro Roldán-Alzate
University of Wisconsin - Madison
- 10:30AM Using Microinjected Fluid Droplets To Locally Perturb Epithelial Mechanics And Branching Morphogenesis In Cultured Embryonic Organs** SB³C2023-213
Shelby R. Mohr-Allen, Victor D. Varner
University of Texas
- 10:45AM Ectopic Changes in Tissue Stiffness Disrupt Epithelial Buckling and FGF-10-Induced Budding Morphogenesis in Cultured Embryonic Lungs** SB³C2023-234
Kara E. Peak, Victor D. Varner
University of Texas

Tuesday, June 6

11:15AM – 12:45AM MT

PhD-Level Student Paper Competition Session IV: Musculoskeletal and Mechanobiology/Tissue Engineering

Cascade ABC

Session Chairs: **Jacopo Ferruzzi**, *University of Texas at Dallas*
Stephanie Cone, *University of Delaware*

- 11:15AM Stiffness Of Direct-Write, Near-Field Electrospun Gelatin Fibers Generates Differences In Tenocyte Gene Expression** SB³C2023-240
Zachary G. Davis¹, Drew W. Koch¹, Grant M. Scull¹, Ashley C. Brown¹, Lauren V. Schnabel¹, Matthew B. Fisher^{1,2}
¹North Carolina State University, ²University of North Carolina at Chapel Hill
- 11:30AM Role Of Sex And Sex Hormones In Pulmonary Artery Adventitial Fibroblast Mechanosignaling** SB³C2023-120
Yufan Lin, Daniela Valdez-Jasso
University of California, San Diego
- 11:45AM Type V Collagen Plays An Essential Role In The Development Of Knee Articular Cartilage And Meniscus** SB³C2023-152
Bryan Kwok¹, Mingyue Fan¹, Prerana Singh¹, David Birk², Robert L. Mauck³, Nathaniel A. Dymant³, Eiki Koyama⁴, Lin Han¹
¹Drexel University, ²University of South Florida, ³University of Pennsylvania, ⁴Children's Hospital of Philadelphia
- 12:00PM Focal Adhesion Kinase Regulates Mechanosensitive Gene Transcription And Tendon Maturation** SB³C2023-230
Thomas P. Leahy, Srish S. Chenna, Louis J. Soslowsky, Nathaniel A. Dymant
University of Pennsylvania
- 12:15PM Mechanical Models Of Collagen Networks For Understanding Changes In The Failure Properties Of Aging Mouse Skin** SB³C2023-259
Nathan J. Witt¹, Alan E. Woessner², Jacob Herrmann¹, Kyle P. Quinn², Edward A. Sander¹
¹University of Iowa, ²University of Arkansas
- 12:30PM Moderated TGF-Beta Delivery Via Latent TGF-Beta Conjugated Scaffolds For Improving Engineered Articular Cartilage** SB³C2023-214
Tiabai Wang¹, Zhonghao Dai¹, Celina C. Maldonado¹, Prem Nelesh¹, Junhan Liao¹, Sung Yeon Kim¹, Andrew Martin¹, Joanne E. Murphy-Ullrich², Mark W. Grinstaff¹, Michael B. Albro¹,
¹Boston University, ²University of Alabama

Tuesday, June 6

11:15AM – 12:45PM MT

**PhD-Level Student Paper Competition Session V:
Musculoskeletal Biomechanics**

Cascade D

Session Chairs: Deva Chan, *Purdue University*
Spence Lake, *Washington University at St. Louis*

- 11:15AM A Novel Laser Ablation Model For Studying Local Microdamage Repair In Live Tendon Explants** SB³C2023-067
Anthony N. Aggouras, Matthew T. Lim, Jeroen Eyckmans, Brianne K. Connizzo
Boston University
- 11:30AM Collagen Crosslinking Dramatically Impairs the Frictional Performance of Articular Cartilage** SB³C2023-037
Meghan E. Kupratis, Uriel Gonzalez, Atia Rahman, David L. Burris, Elise A. Corbin, Christopher Price
University of Delaware
- 11:45AM Overexpression Of Enhanced Yellow Fluorescent Protein Fused With Channelrhodopsin Causes Contractile Dysfunction In Skeletal Muscle** SB³C2023-065
Syeda N. Lamia¹, Carol S. Davis¹, Peter C.D. Macpherson¹, T. Bradley Willingham², Yingfan Zhang², Chengyu Liu², Susan V. Brooks¹, Brian Glancy², Megan L. Killian¹
¹*University of Michigan*, ²*National Institutes of Health*
- 12:00PM Temporal and spatial dynamics of new bone formation in cyclic treatment regimens of parathyroid hormone-related peptide (PTHrP)** SB³C2023-114
Tala Azar, Kruti Desai, Justin Leggin, Yuanhang Li, Wenzheng Wang, Arie Jones, Wei-Ju Tseng, Nathaniel Dymment, X. Sherry Liu
University of Pennsylvania
- 12:15PM Shear Strain Stiffening In Ligaments Arises From Unaligned Fibers And Is Amplified By Axial Strain** SB³C2023-095
Jonathan L. Blank, Darryl G. Thelen, Joshua D. Roth
University of Wisconsin-Madison
- 12:30PM Development Of An In Vitro Model To Explore Collagen Fiber Regeneration With Aged Human Mensical Cells** SB³C2023-231
Austin G. Gouldin, Jennifer L. Puetzer
Virginia Commonwealth University

Tuesday, June 6

11:15AM – 12:45PM MT

**PhD-Level Student Paper Competition Session VI:
Emerging Tissue Mechanobiology & Biomechanics II**

Zermatt

Session Chairs: Erin Berlew, *University of Pennsylvania*
Jill Middendorf, *Johns Hopkins University*

- 11:15AM Damkohler Number Analysis For Predicting Biomolecule Gradients In Engineered Tissues** SB³C2023-187
Sedat Dogru, Matthew Simkulet, Halide Z. Haciguzeller, Michael B. Albro
Boston University
- 11:30AM Multiaxial Loading Attenuates Fibroblast Activation In An In Vitro Model Of Fibrosis** SB³C2023-181
Ghiska Ramahdita¹, Xiangjun Peng¹, Mohammad Jafari², David Schuftan¹, Guy M. Genin¹, Farid Alisafaei², Nathaniel Huebsch¹
¹*Washington University in St. Louis*, ²*New Jersey Institute of Technology*
- 11:45AM Deep Learning Enables Accurate Estimation Of Tissue Deformation In Vivo** SB³C2023-163
Reece D. Huff¹, Frederick C. Houghton¹, Conner C. Earl², Elnaz Ghajar-Rahimi², Ishan Dogra¹, Andrew J. Darling², Frederick W. Damen², Guoyang Zhou², Denny Yu², Craig J. Goergen², Carisa Harris-Adamson^{1,3}, Grace D. O'Connell^{1,3}
¹*University of California – Berkeley*, ²*Purdue University*, ³*University of California- San Francisco*
- 12:00PM Time And Strain Dependent Properties Of The Extracellular Collagen Matrix Regulate Cellular Mechanical Memory And Activation Level Of Fibroblast Cells** SB³C2023-209
Yuan Hong¹, Xiangjun Peng¹, Haomin Yu¹, Mohammad Jafari², Delaram Shakiba¹, Jacob Sandler¹, Kenneth M. Pryse¹, Justin M. Sacks¹, Elliot L. Elson¹, Guy M. Genin¹, Farid Alisafaei^{1,2}
¹*Washington University in St. Louis*, ²*New Jersey Institute of Technology*
- 12:15PM Nuclear Export Inhibition Jumbles Epithelial-Mesenchymal States and Gives Rise to Migratory Disorder in Healthy Epithelia** SB³C2023-134
Carly M. Krull, Haiyi Li, Amit Pathak
Washington University in St. Louis
- 12:30PM Collective Autologous Chemotaxis In Cancer Cells** SB³C2023-087
Louis González, Andrew J. Mugler
University of Pittsburgh

Wednesday, June 7

1:45PM – 3:15PM MT

Patient Specific Flow and Physiology

Cascade ABC

Session Chairs: Alejandro Roldán-Alzate, *University of Wisconsin -Madison*
Lucas Timmins, *University of Utah*

- 1:45PM Association of hemodynamic forces with patterns of coronary artery disease and atherosclerotic plaque phenotypes SB³C2023-370**
Diego Gallo¹, Alessandro Candreva¹, Maurizio Lodi Rizzini¹, Valentina Mazzi¹, Daniel Munhoz², Jean Paul Aben³, Bernard De Bruyne², Claudio Chiastra¹, Carlos Collet², Umberto Morbiducci¹
¹Politecnico di Torino, ²OLV-Clinic, ³Pie Medical Imaging BV
- 2:00PM Patient-Specific Flap Motion, False Lumen Flow, and Aortic Stiffness in Acute Uncomplicated Type B Aortic Dissections Using 4D Flow MRI and 2D PC MRI: A Preliminary Study SB³C2023-391**
H. Cebull¹, S. Hashemi², K. Porte¹, J. Oshinski^{1,3}, B.G. Leshnower¹, M. Piccinelli¹
¹Emory University, ²Children's Healthcare of Atlanta, ³Georgia Institute of Technology
- 2:15PM Predicting Hemodynamic Outcomes In Patients With Borderline Left Ventricles Under Uncertainty SB³C2023-156**
Yurui Chen¹, Isao A. Anzai¹, Justin S. Tran², David M. Kalfa¹, Vijay Vedula¹
¹Columbia University, ²California State University
- 2:30PM Non-Invasive Estimation of Pressure Drop Across Aortic Coarctation SB³C2023-149**
Priya J. Nair¹, Martin R. Pfaller¹, Seraina A. Dual², Doff B. McElhinney¹, Daniel B. Ennis¹, Alison L. Marsden¹
¹Stanford University, ²KTH Royal Institute of Technology
- 2:45PM Association Between Resistance To Cerebrospinal Fluid Flow And Cardiac-Induced Brain Tissue Motion For Chiari Malformation Type1 SB³C2023-475**
Saeed Mohsenian¹, Alaaddin Ibrahimy², John N. Oshinski³, Blaise Simplicie Talla Nwotchuang⁴, Rafeeqe A. Bhadelia⁵, Daniel L. Barrow³, Rouzbeh Amini¹, Francis Loth¹
¹Northeastern University, ²Yale University, ³Emory University, ⁴University of Akron, ⁵Harvard Medical School
- 3:00PM High-Fidelity Fluid-Structure-Interaction Modelling Explains Flow-induced Bruits and Murmurs in Cerebral Aneurysms SB³C2023-205**
David A. Bruneau¹, Kristian Valen-Sendstad², David A. Steinman¹
¹University of Toronto, ²Simula Research Laboratory

Fluid Velocity Mapping and Flow Characterization

Cascade D

Session Chairs: Jessica Oakes, *Northeastern University*

Ryan Pedrigi, *University of Nebraska*

- 1:45PM** **Towards High Spatiotemporal Resolution Blood Flow Velocity Field Mapping For Mice: A Validation Study** SB³C2023-583
Mingyi Tang^{1,2}, David A. Steinman¹, Craig A. Simmons^{1,2}
¹*University of Toronto*, ²*Ted Rogers Centre for Heart Research*
- 2:00PM** **The Generation of Synthetic Geometric Datasets for Flow Characterization in the Carotid Bifurcation** SB³C2023-440
Retta El Sayed^{1,2}, Paul Klein², John N. Oshinski¹, Tiziano Passerini²
¹*Georgia Institute of Technology*, ²*Siemens Healthineers*
- 2:15PM** **Surrogate Models For Pressure Gradients In Coronary Artery Stenoses** SB³C2023-527
Elizabeth R. Livingston, Siddhartha Srivastava, Krishna Garikipati, C. Alberto Figueroa
University of Michigan
- 2:30PM** **Impact of wall distensibility on emerging features of carotid bifurcation hemodynamics** SB³C2023-130
Sara Zamboni¹, Marachiara Arminio¹, David A. Steinman², Claudio Chiastra¹, Umberto Morbiducci¹, Diego Gallo¹
¹*Politecnico di Torino*, ²*University of Toronto*
- 2:45PM** **Quantification Of Embolus Transport To The Brain From Carotid Stenosis Sites** SB³C2023-497
Ricardo Roopnarinesingh¹, Neel Jani², Michelle Leppert¹, Debanjan Mukherjee¹
¹*University of Colorado*, ²*University of Wisconsin-Madison*
- 3:00PM** **Subject-Specific One-Dimensional Fluid Dynamics Model Of Chronic Thromboembolic Pulmonary Hypertension** SB³C2023-165
Amirreza Kachabi, Mitchel J. Colebank, Naomi C. Chesler
University of California, Irvine

Wednesday, June 7

1:45PM – 3:15PM MT

Reproductive Biomechanics and Pregnancy

Cascade E

Session Chairs: Megan Routzong, *University of California, San Diego*

Callan Luetkemeyer, *University of Illinois*

- 1:45PM** **Material Parametric Analysis Of Polypropylene During A Contact Sensitive Simulation Of A Ball Burst Test Of A Prolapse Mesh** SB³C2023-476
Madeline Hackett¹, Teseo Schneider², Zachary Ferguson³, Daniele Panozzo³, Denis Zorin³, Pamela Moalli¹, Steven Abramowitch¹
¹University of Pittsburgh, ²University of Victoria, ³New York University
- 2:00PM** **Modelling Of The Uterosacral Ligament Suggests Changes In Microarchitecture During Pregnancy** SB³C2023-179
Lea M. Savard¹, Catalina S. Bastías¹, Kathleen Connell¹, Sarah Calve¹, Callan M. Luetkemeyer², Virginia L. Ferguson¹
¹University of Colorado, ²University of Illinois
- 2:15PM** **Biaxial Contractility Of The Murine Cervix With Elastic Fiber Deficiency** SB³C2023-512
Mari J.E. Domingo¹, Avery G. Franques¹, Qinhan Zhou², Kristin S. Miller²
¹Tulane University, ²University of Texas
- 2:30PM** **Time-Dependent Material Properties Of Nonhuman Primate Uterine Layers Through Gestation** SB³C2023-529
Daniella M. Fodera¹, Echo Z. Xu¹, Shuyang Fang¹, Ivan Rosado-Mendez², Timothy Hall², Helen Feltovich^{2,3}, Michelle L. Oyen⁴, Kristin M. Myers¹
¹Columbia University, ²University of Wisconsin-Madison, ³Mount Sinai, ⁴Washington University in St. Louis
- 2:45PM** **A Longitudinal Study Of The Anatomical Changes Of The Pregnant Murine Vagina Using Magnetic Resonance Imaging** SB³C2023-217
Aileen C. Suarez¹, Clara J. Gimenez¹, Jennifer M. Munson¹, Kristin S. Miller², Kristin M. Myers³, Steven D. Abramowitch⁴, Raffaella De Vita¹
¹Virginia Tech, ²University of Texas, ³Columbia University, ⁴University of Pittsburgh
- 3:00PM** **Diffusion MRI Characterizes Microstructural Changes Of The Cervix During Pregnancy** SB³C2023-592
Noel Naughton¹, Amir Ostadi Moghaddam¹, Mariana Kersh¹, Sanmi Koyejo², Amy Wagoner Johnson¹, Bruce Damon^{1,3}
¹University of Illinois, ²Stanford University, ³Carle Health

Wednesday, June 7

1:45PM – 3:15PM MT

Biotransport in Drug Delivery

Cascade F

Session Chairs: Govind Srimathveeravalli, *UMass Amherst*
Nichole Rylander, *University of Texas at Austin*

- 1:45PM Lymph Node Conduit Modelling Offers Insight Into The Role Of Fluid Flow In Antigen Deposition** SB³C2023-457
Daniel J. Watson¹, Willy V. Bonneuil¹, James Marshall¹, Peter Xie¹, Thomas Adam¹, Jennifer Frattolin¹, Matthew J. Russell², Francesca Fasanella Masci³, Angela E. Goode¹, Shafa Balaram¹, Alexandra E. Porter¹, Anil A. Bharath¹, Bindi S. Brook², Robert J.B. Nibbs³, James E. Moore Jr¹
¹Imperial College London, ²Nottingham University, ³Glasgow University
- 2:00PM CD44 Mechanosignaling May Regulate Drug Resistance In Ovarian Cancer** SB³C2023-195
Maranda E. Kramer, Allison Criswell, Mary Kathryn Sewell-Loftin
University of Alabama at Birmingham
- 2:15PM Functionalized Particulate Carriers Targeting Abdominal Aortic Aneurysms Under Flow** SB³C2023-349
Moran Levi¹, Yevgeniy Kreinin¹, Ido Rachbuch¹, Perla Namour¹, Josué Sznitman¹, Meinrad Gawaz², Netanel Korin¹
¹Technion – IIT, ²Univesrity of Tuebingen
- 2:30PM Investigation Of Bioeffects From Microbubble And Focused Ultrasound Assisted Blood Brain Barrier Disruption** SB³C2023-423
Jane J. Song, Payton J. Martinez, Kang-ho Song, Jenna Steiner, Adam Green, Natalie Serkova, Mark A. Borden
University of Colorado
- 2:45PM Development Of A TGFβ2 Eluting Tissue Engineered Vascular Graft With Tunable Delayed Release** SB³C2023-369
Katarina M. Martinet, Tracey Moyston, Stephen C. Balmert, Steven R. Little, Jonathan P. Vande Geest
University of Pittsburgh
- 3:00PM A Lattice-Boltzmann Fluid-Structure Interaction Framework For The Inertial Transport Of Bioparticles In Microfluidic Devices** SB³C2023-469
Alberto Mantegazza, Dario De Marinis, Marco D. de Tullio
Polytechnic University of Bari

Wednesday, June 7

1:45PM – 3:15PM MT

Engineering Tissue Regeneration

Gore AB

Session Chairs: Jennifer Puetzer, *Virginia Commonwealth University*
Alejandro Almarza, *University of Pittsburgh*

- 1:45PM Optimization Of Lipid Nanoparticles For Localized mRNA Delivery In Fracture Repair** SB³C2023-498
Anna Laura Nelson^{1,2}, Chiara Mancino³, Josh Choe⁴, Gianluca Fontana⁴, Johnny Huard¹, William Murphy⁴, Francesca Taraballi³, Nicole Ehrhart², Chelsea Bahney^{1,2,5}
¹Steadman Philippon Research Institute, ²Colorado State University, ³Houston Methodist, ⁴University of Wisconsin-Madison, ⁵University of California, San Francisco
- 2:00PM Acellular ECM Powder Provides Lateral Integration And Structural And Cellular Signaling In A 12-Month Goat Implant** SB³C2023-539
Jeanne E. Barthold¹, Juliet Heye¹, Kaitlin McCreery¹, Katie Bizzaza², Jeremiah Easley², Ben Gadomski², Corey P. Neu¹
¹University of Colorado, ²Colorado State University
- 2:15PM Stem Cell-Derived Exosomes Promote Cell Homing and Angiogenic Differentiation For Dental Pulp Regeneration** SB³C2023-444
Venkateswaran Ganesh, Piedad C. Gomez-Contreras, Henry L. Keen, Kyungsup Shin, James A. Martin, Dongrim Seol
University of Iowa
- 2:30PM Superficial Meniscus Cells And Highly Proliferative And Migratory And Generate Functional Tissue Despite A Lower Cellular Mechanosensitivity** SB³C2023-112
Sereen SF. Assi¹, Elizabeth Bernstein¹, Edward D. Bonnevie^{1,2}, Emily E. Sharp¹, Ryan C. Locke^{1,2}, Robert L. Mauck^{1,2}
¹University of Pennsylvania, ²Crescenz VA Medical Center
- 2:45PM Viscoelasticity and Micro-phase Separation Mediate Meniscal Cell Migration through Hyaluronic Acid Hydrogels** SB³C2023-138
Karen L. Xu¹, Hooman Fallahi², Lin Han², Robert L. Mauck¹, Jason A. Burdick^{1,3}
¹University of Pennsylvania, ²Drexel University, ³Univesrity of Colorado
- 3:00PM Sustained-release losartan from peptide nanofibers promotes chondrogenesis** SB³C2023-485
Kohei Yamaura¹, Nicholas A. Sather², Anna Metlushko², Haruki Nishimura¹, Radoslav Z. Pavlović², Sealy Hambricht¹, Sudheer K. Ravuri¹, Marc J. Philippon^{1,3}, Samuel I. Stupp², Chelsea S. Bahney^{1,4}, Johnny Huard¹
¹Steadman Philippon Research Institute, ²Northwestern University, ³Steadman Clinic, ⁴University of California, San Francisco

Wednesday, June 7

1:45PM – 3:15PM MT

Predictive Models in Cardiovascular Biomechanics

Gore CD

Session Chairs: Lucas Timmins, *University of Utah*
Jonathan Wenk, *University of Kentucky*

- 1:45PM** **Towards Real-Time Predictive Models of Transcatheter Aortic Valve Replacement Procedures via Reduced Order Modeling** SB³C2023-328
I Shah^{1,3}, F. Ballarin², A. Veneziani³, L. Dasi¹
¹Georgia Institute of Technology, ²Università Cattolica del Sacro Cuore, ³Emory University
- 2:00PM** **Predicting Long-term Patient-Specific Outcome Of Cardiac Resynchronization Therapy Using A Fast Computational Model** SB³C2023-249
Clara E. Jones¹, Derek J. Bivona², Kenneth C. Bilchick², Pim J.A. Oomen¹
¹University of California, Irvine, ²University of Arizona
- 2:15PM** **Aortic Wall Stress Concentration As A Predictor Of Type A Aortic Dissection** SB³C2023-351
Christina Sun¹, Tongran Qin¹, Asanish Kalyanasundaram², Wei Sun¹, John Elefteriades², Liang Liang³
¹Lake Forest, ²Yale University, ³University of Miami
- 2:30PM** **A Modular Framework For Strong 3D/0D Coupling In Cardiac Mechanics Simulations** SB³C2023-032
Aaron L. Brown, Zinan Hu, Alison L. Marsden
Stanford University
- 2:45PM** **A Neural Network Finite Element Approach For High-Speed Cardiac Pressure-Volume Simulations** SB³C2023-459
Shruti Motiwale, Wenbo Zhang, Michael S. Sacks
University of Texas at Austin
- 3:00PM** **No Strings Attached: Predicting Tricuspid Valve Coaptation Without In Vivo Chordal Geometry** SB³C2023-473
Mrudang Mathur, Vijay Dubey, Manuel K. Rausch
University of Texas at Austin

Wednesday, June 7

1:45PM – 3:15PM MT

Bioengineering Design II

Powell

Session Chairs: Zhongping Huang, *West Chester University*
Anita Singh, *Temple University*

- 1:45PM** **Mixed Approaches to Noninvasive Ventilation Mask Design: Triphasic Mixture Theory Material Model Calibration and Global Finite Element Analysis** SB³C2023-290
Anne D. Zakrajsek¹, Marty O. Visscher¹, Vivek Narendran^{1,2}, Eric A. Nauman¹
¹University of Cincinnati, ²Cincinnati Children's Hospital
- 2:00PM** **Retropubic Trocar Temporal Characteristics Between Expert and Novice Surgeons** SB³C2023-438
Md A. Arif, Austin Bachar, Gregory W. King, Gary Sutkin, Antonis P. Stylianou
University of Missouri
- 2:15PM** **Continuous inter-limb gait coordination and stability in veterans and service members with transtibial limb loss: influences of prosthetic ankle-foot devices** SB³C2023-221
Alexis Sidiropoulos¹, Brad D. Hendershot², Jonathan Gladish², David Herlihy^{1,3}, Jason Maikos¹
¹New York Harbor Healthcare System, ²Extremity Trauma and Amputation Center of Excellence, ³Narrows Institute of Biomedical Research and Education
- 2:30PM** **Analysis of a New Socket Based Reference Frame for Ankle Rollover Shape for Transtibial Prostheses** SB³C2023-451
David Herlihy¹, John Chomack², Jason Maikos²
¹Narrows Institute of Biomedical Research and Education, ²New York Harbor Healthcare System
- 2:45PM** **Development Of A Novel Hand Worn Sensor For Objective Assessment Of Hand Dexterity In Neurodegenerative Conditions** SB³C2023-035
Conor D. Hayden¹, Deirdre Murray^{1,2}, Dara Meldrum¹, Dermot Geraghty¹, Orla Hardiman^{1,2}, Bruce P. Murphy¹
¹Trinity College Dublin, ²Beaumont Hospital
- 3:00PM** **The Impact Of Regulating The Plantarflexion And Dorsiflexion Resistance Of An Articulated Ankle Foot- Orthosis On Lower Limb Kinematics And Kinetics Of Stroke Survivors During Ambulation** SB³C2023-406
Oluwaseye P. Odanye¹, Emily E. Steffensen¹, Christopher J. Burcal¹, Aaron D. Likens¹, Elisa S. Arch², Brian A. Knarr¹
¹University of Nebraska, ²University of Delaware

Wednesday, June 7

1:45PM – 3:15PM MT

Cardiovascular Tissue Structure and Mechanics

Zermatt

Session Chairs: Jonathan Vande Geest, *University of Pittsburgh*

Lakshmi Dasi, *Georgia Institute of Technology*

- 1:45PM** **Right Ventricular Myocardium Remodeling in Pulmonary Arterial Hypertension is Sex Dependent** SB³C2023-265
Becky A. Hardie, Jessica Huberts, Daniela Valdez-Jasso
University of California, San Diego
- 2:00PM** **Cyclic Stretch Results in Directionally Dependent Recellularization Aligned with Cellular Stress Avoidance Reorientation** SB³C2023-267
Adam W.Y. Ley, Eric Slaughter, Victor H. Barocas, Robert T. Tranquillo
University of Minnesota
- 2:15PM** **Evaluation Of Hypertension And Intraluminal Vascular Injury On The Biomechanics Of The Murine Femoral Artery** SB³C2023-508
J. Caleb Snider¹, Zachary Tentor², Yujun Xu¹, Matthew R. Bersi¹
¹*Washington University in St. Louis*, ²*University of Virginia*
- 2:30PM** **Impact of local collagen architecture on rupture behavior of tissue-engineered atherosclerotic plaque caps** SB³C2023-012
Hanneke Crielaard¹, Tamar B. Wissing^{1,2}, Su Guvenir Torun¹, Pablo de Miguel^{1,3}, Gert-Jan Kremers¹, Frank J.H. Gijzen^{1,3}, Ali C. Akyildiz^{1,3}, Kim van der Heiden^{1,2}
¹*Erasmus Medical Center*, ²*Eindhoven University of Technology*, ³*Delft University of Technology*
- 2:45PM** **An Optimized Method For Constitutive Model Fitting Of Soft Tissues Bi-Directional Mechanical Stress-Stretch Data** SB³C2023-119
Sayed Ahmadrza Razian, Alexey Kamenskiy, Majid Jadidi
University of Nebraska at Omaha
- 3:00PM** **Mechanical Characterization of Porcine Tricuspid Valve Anterior Leaflets Over Time: Applications to Ex-vivo Studies** SB³C2023-582
Julia Clarin, Dominique Dang, Lucas Santos, Rouzbeh Amini
Northeastern University

Wednesday, June 7

3:30PM – 5:00PM MT

Heart Valve Fluid Mechanics

Cascade ABC

Session Chairs: Hoda Hatoum, *Michigan Tech*
Lucas Timmins, *University of Utah*

- 3:30PM Impact of Blood Pressure on Coronary and Sinus Flow Dynamics After Aortic Valve Replacement** SB³C2023-562
B. Vogl¹, S. Lilly², V. Thourani³, M. Alkhouli⁴, B. Lindman⁵, H. Hatoum¹
¹Michigan Technological University, ²The Ohio State University, ³Piedmont Heart Institute, ⁴Mayo Clinic, ⁵Vanderbilt University
- 3:45PM Biomechanical Analysis Of A Fetal Pulmonary Heart Valve Replacement**
SB³C2023-388
Sanchita S. Bhat, Katelynne Berland, Anna Farnan, Katherine Vietmeyer, Lakshmi Prasad Dasi
Georgia Institute of Technology
- 4:00PM On The Closure Kinematics Of Aortic Mechanical Heart Valves Versus Bioprosthetic Heart Valves** SB³C2023-044
Syed Samar Abbas, Iman Borazjani
Texas A&M University
- 4:15PM Bio-Inspired Polymeric TAVR To Improve Durability Outcomes** SB³C2023-204
Nipa Khair¹, Sanchita Bhat², Katie Vinterella², Satheesh Kumar Harikrishnan², Lakshmi Prasad Dasi², Susan James¹
¹Colorado State University, ²Georgia Institute of Technology
- 4:30PM Experimental Study of Flow-Mediated Fibrin Clot Accumulation in Prosthetic Heart Valves** SB³C2023-367
Yevgeniy Kreinin, Moran Levi, Yahel Talmon, Josué Sznitman, Netanel Korin
Technion - IIT
- 4:45PM Effect Of Sinotubular Junction Size In TAVR Leaflet Thrombosis And The Potential Of TAV-in-TAV Procedure: A Fluid Structure Interaction Based Thrombogenic Risk Assessment Analysis** SB³C2023-299
Symon Reza¹, David Oks², Brandon Kovarovic¹, Mariano Vázquez², Danny Bluestein¹
¹Stony Brook University, ²Computer Applications in Science and Engineering

Emerging Areas in Thrombosis and Vascular Modeling

Cascade D

Session Chairs: Diego Gallo, *Politecnico di Torino*

Hannah Cebull, *Emory University*

- 3:30PM Shear-Mediated Platelet Adhesion Dynamics And Multi-Platelet Aggregation: In Vitro Validated Multiscale Simulations Using Coarse-Grained Molecular Dynamics And Dissipative Particle Dynamics SB³C2023-288**
Peineng Wang, Yicong Zhu, Jawaad Sheriff, Peng Zhang, Yuefan Deng, Danny Bluestein
Stony Brook University
- 3:45PM Investigating Changes in Hematological and Hemorheological Parameters in a Mouse Stent Implantation Model SB³C2023-274**
D. Kokkinidou, E. Kaliviotis, C. Shamas, A. Anayiotos, K. Kaprnis
University of Technology
- 4:00PM Usability Of Low-cost 3D Visualization Sharing Interfaces For Cardiovascular Blood Flow Dynamics Data SB³C2023-509**
Zainab Husain¹, Noah Egnatis¹, Karol Calò², Diego Gallo², Umberto Morbiducci², Peter Coppin³, David A. Steinman¹
¹University of Toronto, ²Politecnico di Torino, ³Ontario College of Art and Design University
- 4:15PM Excessive Shear Rate, not Shear Stress, is Responsible for Cell Mechanolysis in Small Bore Needle Injections SB³C2023-368**
George Morgan, Lamis Elsayah, Alejandro Esclamado-Cadenas, Amelie Daudet, Jennifer Frattolin, Daniel Watson, Qian Xu, Nicola Negrini, Adam Celiz, James E. Moore Jr.
Imperial College London
- 4:30PM Real-Time Optimization of the Total Cavopulmonary Connection via Reduced Order Modeling SB³C2023-331**
I Shah^{1,2}, F. Ballarin³, T. Iliescu⁴, O. San⁵, L. Dasi¹, A. Wei⁶, A. Veneziani²
¹Georgia Institute of Technology, ²Emory University, ³Università Cattolica del Sacro Cuore, ⁴Virginia Tech, ⁵Oklahoma State University, ⁶University of Massachusetts
- 4:45PM Validation Of The Coupled Momentum Method Against A Compliant Aortic Phantom In A Hybrid Mock Circulatory Loop SB³C2023-358**
Francesco Bardi^{1,2,3}, Emanuele Gasparotti¹, Emanuele Vignali¹, Miquel Aguirre², Stéphane Avril², Simona Celi¹
¹BioCardioLab, ²INSERM, ³PrediSurge

Wednesday, June 7

3:30PM – 5:00PM MT

Multiscale Biomechanics

Cascade E

Session Chairs: Pim Oomen, *University of California – Irvine*
Chung-Hao Lee, *University of Oklahoma*

- 3:30PM Anisotropic Stiffness Measured Using A Toroidal Probe In Meso Level And Cell Level** SB³C2023-251
J. Li, T. Paradis, M. Vandadi, N. Rahbar, K.L. Billiar
Worcester Polytechnic Institute
- 3:45PM A Validated Data-Driven, Constitutive Model Of Type II Collagen Including Failure** SB³C2023-228
Phoebe Szarek, David M. Pierce
University of Connecticut
- 4:00PM Active Microtissue Arrays For Probing Tissue Response To Dynamic Conditioning** SB³C2023-366
William P. Cortes, Kalyn R. Younger, Thao D. Nguyen, Daniel H. Reich
Johns Hopkins University
- 4:15PM The Non-Affine Network Solver Plugin: A Generalized Fiber Network Material Model From Volume Averaging Theory** SB³C2023-287
Ryan R. Mahutga, Victor H. Barocas, Patrick W. Alford
University of Minnesota
- 4:30PM A Non-Contact Microfluidic Approach To Distinguish Large Extracellular Vesicles From Idh1-Mutated Glioblastoma Cells Based On Stiffness** SB³C2023-342
Mi Ho Jeong, Hyungsoon Im, Joanna B. Dahl
Massachusetts General Hospital
- 4:45PM Augmented Reality Visualization Of Biomechanical Wall Stresses On Abdominal Aortic Aneurysms Using Artificial Intelligence** SB³C2023-511
Timothy K. Chung, Nathan L. Liang, David A. Vorp
University of Pittsburgh

Wednesday, June 7

3:30PM – 5:00PM MT

Experimental Head and Injury Mechanics

Cascade F

Session Chairs: Brittany Coats, *University of Utah*
Mehmet Kurt, *University of Washington*

- 3:30PM Head Kinematics in Stock Car Racing: Quantifying Differences Between Tracks** SB³C2023-514
Sophia R. Zoch^{1,2}, Logan E. Miller^{1,2}, Cole M. Binder², Destiny R. Mason^{1,2}, John P. Patalak³, Matthew G. Harper³, Jillian E. Urban^{1,2}, Joel D. Stitzel^{1,2}
¹Virginia Tech-Wake Forest, ²Wake Forest School of Medicine, ³National Association for Stock Car Auto Racing
- 3:45PM Late Triggering of Tagged MRI for Measurement of In Vivo Brain Deformation during Head Rotation** SB³C2023-551
Yuan-Chiao Lu¹, Andy Knutsen¹, Ahmed Alshareef¹, Wen-Tung Wang², Joy Mojumder², Jerry L. Prince³, Philip Bayly⁴, John A. Butman², Dzung L. Pham^{2,5}
¹Henry M Jackson Foundation for the Advancement of Military Medicine, ²National Institutes of Health, ³Johns Hopkins University, ⁴Washington University at St. Louis, ⁵Uniformed Services University
- 4:00PM Non-Concussive Head Impact Kinematics And Brain Strain Distribution In Collegiate Football** SB³C2023-344
Enora Le Flao¹, Xianghao Zhan¹, Nicholas J. Cecchi¹, Yuzhe Liu¹, Ashlyn A. Callan¹, Landon P. Watson¹, Collin Pang¹, Gerald A. Grant^{1,2}, Michael M. Zeineh¹, David B. Camarillo¹
¹Stanford University, ²Duke University
- 4:15PM Behavioral Impairments In Repetitive Mild Traumatic Brain Injury** SB³C2023-262
S. Vafadar, H. Li, S. Assari, S.J. Ward, R.F. Tuma, K. Darvish
Temple University
- 4:30PM Influence of Fragment Impact Attributes in Cutaneous Injury** SB³C2023-086
O. Elsafty, R. Dauskardt
Stanford University
- 4:45PM A Methodology to Obtain Injury and Biomechanical Data from Live Swine Experimentation for Behind Armor Blunt Trauma** SB³C2023-302
Alok S. Shah¹, Narayan Yoganandan¹, Mary F. Otterson¹, Brian D. Stemper¹, Joost Op't Eynde², Cameron D. Bass², Justin McMahon³, Robert S. Salzar³, B. Joseph McEntire⁴
¹Medical College of Wisconsin, ²Duke University, ³University of Virginia, ⁴US Army Aeromedical Research Laboratory

Wednesday, June 7

3:30PM – 5:00PM MT

Biophysical Effects on Cells and Tissues

Gore AB

Session Chairs: Sarah Calve, *University of Colorado*
Victor Varner, *University of Texas at Dallas*

- 3:30PM** **Effect of the Physical Environment on Embryonic Kidney Progenitor and Explant Culture** SB³C2023-174
Aria (Zheyuan) Huang, Alex J. Hughes
University of Pennsylvania
- 3:45PM** **Elastic Fibers Confer Tensile Stiffness To The Dorsal Mesentery, Driving Buckling Morphogenesis Of The Small Intestine** SB³C2023-425
Elise A. Loffet, John F. Durel, Hyunjee Lim, Richard Kam, Nandan L. Nerurkar
Columbia University
- 4:00PM** **A Thermodynamic Framework For Sarcomere Formation In Cardiomyocytes Spread On Micro-Patterned Substrates** SB³C2023-253
Ryan J. Coleman¹, Vikram S. Deshpande², Patrick McGarry¹
¹*University of Galway*, ²*University of Cambridge*
- 4:15PM** **Cyclic Stretch Inhibits Cell Invasion And Migration In 3D Scaffolds** SB³C2023-017
Rozanne W. Mungai, Kevin Piskorowski, Grace Jolin, Ying Lei, Kristen L. Billiar
Worcester Polytechnic Institute
- 4:30PM** **Connecting Cyclic Stress To Nephron Induction In Kidney Organoids and 3D Co-Culture Models** SB³C2023-178
John M. Viola, Alex J. Hughes
University of Pennsylvania
- 4:45PM** **Delineating Effects of Substrate Stiffness, Chemistry, and Cyclical Strain on Lung Fibroblasts Gene Expression** SB³C2023-258
Qi Wang, Kristan S. Worthington, Edward A. Sander
University of Iowa

Wednesday, June 7

3:30PM – 5:00PM MT

Structure and Function in Biomechanics

Gore CD

Session Chairs: Stephanie Cone, *University of Delaware*
Kara Peak, *University of Texas - Dallas*

- 3:30PM Cell-Scale Measurements Of Tissue Viscoelasticity Using Thermoresponsive Mechanosensors In Engineered Tumor Models** SB³C2023-489
Benjamin E. Campbell, Stephanie Mok, Christina-Marie Boghdady, Nikita Kalashnikov, Luke McCaffrey, Christopher Moraes
McGill University
- 3:45PM Finite Elements Of Multiscale Mixtures (Fe2M): Theory, Numerical Implementation, And Analyses Of Size Effects** SB³C2023-389
Ashkan Almasi¹, Tim Ricken², David M. Pierce¹
¹University of Connecticut, ²University of Stuttgart
- 4:00PM Surgical Augmentation And Preservation Of Remnant ACL Tissue Best Restores Knee Function After Partial ACL Injury** SB³C2023-023
S. Cone^{1,2}, R. Salbego¹, J. Roth¹, P. Lang¹
¹University of Wisconsin, ²University of Delaware
- 4:15PM Characterizing The Biaxial Properties Of Skeletal Muscles Of The Mouse Hindlimb** SB³C2023-599
Katherine R. Knaus, Rebecca Hardie, Jessica Huberts, Daniela Valdez-Jasso
University of California, San Diego
- 4:30PM Cyclic Strain Induces Matrix Turnover To Better Maintain Tendon Composition In Explant Culture** SB³C2023-069
Anthony N. Aggouras, Brianne K. Connizzo
Boston University
- 4:45PM Microstructure-Based Estimation Of The Effective Stiffness Of Crosslinked, Embedded Fiber Networks** SB³C2023-330
Sotirios Kakaletsis¹, Emma Lejeun², Manuel Rausch¹
¹University of Texas at Austin, ²Boston University

Wednesday, June 7

3:30PM – 5:00PM MT

Growth and Remodeling I

Powell

Session Chairs: Colleen Witzenburg, *University of Wisconsin - Madison*
Jacopo Ferruzzi, *University of Texas - Dallas*

- 3:30PM Multiscale Model Predicts the Effect of Beta Blockers on Ventricular Remodeling in Dogs with Experimental Mitral Valve Regurgitation** SB³C2023-315
J. Bracamonte¹, L. Watkins², J. Saucerman², J. Holmes¹
¹University of Alabama at Birmingham, ²University of Virginia
- 3:45PM Computational Modeling Of Arterial Growth And Remodeling Including Mechanosensitive Notch Signaling** SB³C2023-420
Jordy van Asten¹, Marcos Latorre³, Cansu Karakaya¹, Frank Baaijens¹, Cecilia^{1,3}, Tommaso Ristori¹, Jay Humphrey⁴, Sandra Loerakker¹
¹Eindhoven University of Technology, ²Universitat Politècnica de València, ³Åbo Akademi, ⁴Yale University
- 4:00PM Growth And Remodeling Of The Pulmonary Arterial Tree For Evolution Of Pulmonary Arterial Hypertension** SB³C2023-546
Jason M. Szafron, Weiguang Yang, Jeffrey A. Feinstein, Marlene Rabinovitch, Alison L. Marsden
Stanford University
- 4:15PM Multiscale Computational Modeling Of TGF β 1/2 Knock-Out In Adult Mouse Aortas** SB³C2023-575
Ana C. Estrada, Linda Irons, Jay D. Humphrey
Yale University
- 4:30PM Semi-Automatic Quantification of Early Structural Remodeling Following Myocardial Infarction** SB³C2023-089
Catherine C. Eberman, Colleen M. Witzenburg
University of Wisconsin
- 4:45PM Mechanical Characterization of Sheep Lymphatic Growth and Remodeling** SB³C2023-106
Sophia M. Mavris, Zhanna V. Nepiyushchikh, J. Brandon Dixon, Rudolph L. Gleason
Georgia Institute of Technology

Wednesday, June 7

3:30PM – 5:00PM MT

Modeling in the Cardiovascular System

Zermatt

Session Chairs: Manuel Rausch, *University of Texas - Austin*
Beatrice Bisighini, *Mines Saint-Etienne*

- 3:30PM** **Classification-based super-resolution reconstruction in CMR to quantify four-dimensional myocardial strains in mice** SB³C2023-545
Tanmay Mukherjee¹, Sakthivel Sadayappan², Reza Avazmohammadi^{1,3}
¹Texas A&M, ²University of Cincinnati, ³Houston Methodist Academic Institute
- 3:45PM** **A Novel Image-based Computational Framework to Evaluate the Material Properties of Arterial Tissue from High-resolution Magnetic Resonance Image Data** SB³C2023-505
Y.F. Jack Wang, Samer S. Merchant, Edward W. Hsu, Lucas H. Timmins
University of Utah
- 4:00PM** **Novel Automated Aortic Root Echocardiography Feature Tracking Algorithm For Pediatric Aortopathy** SB³C2023-176
Elnaz Ghajar-Rahimi¹, Frederick W. Damen^{1,2}, Benjamin J. Landis², Craig J. Goergen^{1,2}
¹Prudue University, ²Indiana University
- 4:15PM** **3D Passive Strain Mapping of the Embryonic Zebrafish heart** SB³C2023-587
Alex L. Gendernalik^{1,2}, David Bark^{1,2}
¹Colorado State University, ²Washington University
- 4:30PM** **Computational modeling study of the effects of pulmonary hypertension on right heart perfusion** SB³C2023-024
Lei Fan¹, Jenny S. Choy², Ghassan S. Kassab², Lik Chuan Lee¹
¹Michigan State University, ²California Medical Innovations Institute
- 4:45PM** **Imaging And Mechanical Characterization Of Human Blood Clot Analogues With Different Compositions And Degrees Of Contraction** SB³C2023-395
Rachel Cahalane¹, Janneke M.H. Cruts¹, Ahlam Rachid², Kim van Gaalen¹, Heleen M.M. van Beusekom¹, Moniek de Maat¹, Marcel L. Kijkshoorn¹, Nikki Boodt¹, Aad van der Lugt¹, Frank Gijsen^{1,3}
¹Erasmus Medical Center, ²Eindhoven University of Technology, ³Delft University of Technology

Thursday, June 8

1:45PM – 3:15PM MT

Cardiovascular Devices and Design

Cascade ABC

Session Chairs: Zahra Keshavarz-Motamed, *McMaster University*

Ethan Kung, *Clemson University*

- 1:45PM Analyzing The Impact Of TAVR Device Orientation On Post-TAVR Paravalvular Leakage Severity And Thrombogenicity In Bicuspid Aortic Valve Patients**
SB³C2023-076
S. Anam¹, B. Kovarovic¹, A. Hamdan², R. Haj-Ali³, D. Bluestein¹
¹*Stony Brook University*, ²*Rabin Medical Center*, ³*Tel-Aviv University*
- 2:00PM In Silico Investigation on Stroke Risks from Left Ventricular Assist Device**
SB³C2023-538
Sreeparna Majee¹, Akshita Sahni¹, Erin E. McIntyre¹, Jay D. Pal², Debanjan Mukherjee¹
¹*University of Colorado*, ²*University of Washington*
- 2:15PM Hemodynamic Performance Of Dual Lumen VV ECMO Cannulas** SB³C2023-284
Louis P. Parker¹, Anders Svensson Marcial², Torkel B. Brismar², Lars Mikael Broman^{2,3}, Lisa Prohl Wittberg¹
¹*Royal Institute of Technology*, ²*Karolinska Institute*, ³*Karolinska University Hospital*
- 2:30PM A Preliminary In Silico Study On The Fluid Dynamic Changes With Central Venous Catheter Insertion** SB³C2023-414
B. Su, H. Palahnuk, T. Harbaugh, E. Rizk, S.W. Hazard, K.B. Manning
Penn State University
- 2:45PM Predicting Device Related Thrombosis After Left Atrial Appendage Occlusion Using Computational Fluid Dynamics** SB³C2023-151
B. Vogl¹, A. Chavez Ponce², A. El Shaer², A. Bavo³, M. De Buele³, M. Alkhouli², H. Hatoum¹
¹*Michigan Technological University*, ²*Mayo Clinic*, ³*FEops*
- 3:00PM Development Of A Novel Polymeric TAVR Valve: Design Optimization And Addressing TAVR Clinical Complications** SB³C2023-408
B. Kovarovic¹, R. Helbock¹, O.M. Rotman¹, K. Baylous¹, M. Slepian², D. Bluestein¹
¹*Stony Brook University*, ²*University of Arizona*

Savio Woo Session I: Joint, Ligament, and Muscle

Cascade D

Session Chairs: Daniel Cortes, *Pennsylvania State University*
Beth Winkelstein, *University of Pennsylvania*

- 1:45PM** **Strain Thresholds for Neuronal Activation During High-Rate Tensile Loading to Failure: Implications for Pain and Trauma** SB³C2023-078
Daniel Du, Sittinon Nuethong, Prabesh Ghimire, Beth A. Winkelstein
University of Pennsylvania
- 2:00PM** **Estimating Soleus Muscle Volume By Anthropometric And Ultrasound-Measurable Parameters** SB³C2023-372
Shabnam Rahimnezhad¹, Karin G. Silbernagel², Daniel H. Cortes¹
¹*Pennsylvania State University*, ²*University of Delaware*
- 2:15PM** **Quantifying The Effect Of Femoral Component Internal Rotation On Ligament Forces For Total Knee Arthroplasty With Varus Tibial Alignment** SB³C2023-448
Jonathan Glenday, Jonathan Vigdorchik, Peter Sculco, Cynthia Kahlenberg, David Mayman, Eytan Debbi, Joseph Lipman, Timothy Wright, Fernando Quevedo Gonzalez
Hospital for Special Surgery
- 2:30PM** **The Role of Posterior Cruciate Ligament on Femoral Rollback in Medial Congruent Total Knee Arthroplasty: A Computational Study** SB³C2023-525
Reza Pourmodheji, Jacob M. Hirth, Brian P. Chalmers, Cynthia A. Kahlenberg, William J. Long, Geoffrey H. Westrich, David J. Mayman, Peter K. Sculco, Timothy M. Wright, Carl W. Imhauser
Hospital for Special Surgery
- 2:45PM** **Blebbistatin As A Method To Improve Outcomes Following Joint Capsule Release Surgery In An In Vivo Rat Elbow Model** SB³C2023-083
Austin J. Scholp, Timothy P. Fowler, Emily Petersen, Douglas Fredericks, James A. Martin, Aliasger K. Salem, Edward A. Sander
University of Iowa
- 3:00PM** **Obesity Affects The Biomechanics Of The Posterior Kinetic Chain During Manual Lifting** SB³C2023-456
Sergio A. Lemus¹, Mallory Volz¹, Francisco Beron-Vera¹, Mitchell Hurtado¹, Eduard Tiozzo¹, Arlette Perry¹, Thomas M. Best^{1,2}, Francesco Travascio^{1,3}
¹*University of Miami*, ²*UHealth Sports Medicine*, ³*Mount Sinai*

Thursday, June 8

1:45PM – 3:15PM MT

Emerging Mechanobiology and Biomechanics I

Cascade E

Session Chairs: Soham Ghosh, *Colorado State University*

Ian Sigal, *University of Pittsburgh*

- 1:45PM** **Nuclear Deformation Of The Tricuspid Valve Interstitial Cells: The Effects Of Nuclear Orientation And Extracellular Matrix Structure** SB³C2023-222
Mina Pakzadmanesh, Samuel D. Salinas, Vineet S. Thomas, Rouzbeh Amini
Northeastern University
- 2:00PM** **Ultrasoft Edge-Labelled Hydrogel Sensors Reveal Internal Tissue Stress Patterns In Invasive Engineered Tumors** SB³C2023-223
C.M. Boghdady, W. Lee, V. Lelarge, R.L. Leask, L. McCaffrey, C. Moraes
McGill University
- 2:15PM** **Deep Learning Enhances Micro-Computed Tomography Image Resolution Of Murine Femurs** SB³C2023-604
Michael A. David¹, Tillman James², Douglas J. Adams¹
¹*University of Colorado*, ²*Washington University at St. Louis*
- 2:30PM** **The Role Of Skin Biomechanics In Tactile Perception Of Anti-Aging Formulations** SB³C2023-206
S. Hendrickx-Rodriguez, O. Elsafty, R. Dauskardt
Stanford University
- 2:45PM** **Constitutive Modeling Of The Airway Tree Informed By Experimental Biaxial Mechanical Behavior** SB³C2023-019
S. Sattari¹, CA. Mariano¹, T. Sigaeva², M. Eskandari¹
¹*University of California, Riverside*, ²*University of Waterloo*
- 3:00PM** **Integrated Right Ventricular-Pulmonary Artery Biomechanics In Pulmonary Hypertension** SB³C2023-197
Sunder Neelakantan¹, Peng Zhang^{2,3}, Gaurav Choudhary^{2,3}, Reza Avazmohammadi¹
¹*Texas A&M University*, ²*Providence VA Med Center*, ³*Brown University*

Thursday, June 8

1:45PM – 3:15PM MT

Biotransport in Directed Cell Migration

Cascade F

Session Chairs: Netanel Korin, *Technion*

Joanna Dahl, *University of Massachusetts*

- 1:45PM** **A Microfluidic Platform To Investigate Transport Phenomena In Chemokine Gradient Establishment** SB³C2023-380
J. Frattolin¹, D.J. Watson¹, W.V. Bonneuil¹, F. Fasanella Masci², M. Russell³, B.S. Brook³, R.J.B. Nibbs², J.E. Moore Jr¹
¹Imperial College London, ²University of Glasgow, ³University of Nottingham
- 2:00PM** **Quantitative Assessment Of The Role Of Chromatin Mechanics And Architecture In Monolayer Cell Migration** SB³C2023-397
Jack Forman, Brady Hine, Eric Havenhill, Samantha Kaonis, Soham Ghosh
Colorado State University
- 2:15PM** **The Mechanics And Morphodynamics Of 3D Migrating Cancer Cells** SB³C2023-432
Bo Sun
Oregon State University
- 2:30PM** **Interstitial Chemokine Gradients And Dendritic Cell Migration During Inflammation** SB³C2023-464
Matthew J. Russell¹, Francesca Fasanella Masci², Willy V. Bonneuil³, Daniel J. Watson⁴, Jennifer Frattolin⁴, James E. Moore Jr.⁴, Robert J.B. Nibbs², Bindi S. Brook¹
¹University of Nottingham, ²University of Glasgow, ³KTH Royal Institute of Technology, ⁴Imperial College London
- 2:45PM** **Mechanoregulation Of Cadherin Expression In A 3D Co-Culture** SB³C2023-431
Vaishali Bala, Faith Muriuki, M.K. Sewell-Loftin
University of Alabama at Birmingham
- 3:00PM** **Cellular Signal Processing Machinery During Directed Migration Of Cancer Cells** SB³C2023-359
Andrew Mugler, Bumsoo Han
¹University of Pittsburgh, ²Purdue University

Thursday, June 8

1:45PM – 3:15PM MT

Mechanobiology in Cancer, Inflammation, and Motility

Gore AB

Session Chairs: Jacopo Ferruzzi, *University of Texas at Dallas*
Alix Deymier, *University of Connecticut*

- 1:45PM** **Macrophage Signaling Alters Fibroblast Responses to Mechanical Loading**
SB³C2023-519
McKenzie E. Sup, Min Kyu M. Kim, Lee Song, Beth Ashinsky, Jieon J. Kim, Stavros Thomopoulos
Columbia University
- 2:00PM** **Stromal Cells Modulate Chemo-Mechanical Factors In The Tumor Microenvironment Required For Leader Cell Driven Collective Migration** SB³C2023-141
Jessanne Y. Lichtenberg¹, Trey P. Redman¹, Ella Ramamurthy^{1,2}, Christopher A. Lemmon¹, Priscilla Y. Hwang¹
¹*Virginia Commonwealth University*, ²*University of California, Berkeley*
- 2:15PM** **Mechanosensitivity of Naïve and Pro-inflammatory Macrophage Polarization upon Extravasation in 3D Musculoskeletal-like Tissue** SB³C2023-560
P. Babaniamansour, D. Jacho, A. Rabino, R. Garcia-Mata, E. Yildirim-Ayan
University of Toledo
- 2:30PM** **Mechanically Primed Cells Transfer Memory To Fibrous Matrices For Invasion Across Environments Of Distinct Stiffness and Dimensionality** SB³C2023-185
José Almeida, Jairaj Mathur, Ye Lim Lee, Bapi Sarker, Amit Pathak
Washington University in St. Louis
- 2:45PM** **Impact of Type V Collagen Deficiency on Fibroblast Mechanosensing Under Inflammatory Stimulation** SB³C2023-384
N. Patel¹, T. Li¹, J. Duggan¹, S.M. Kallish², K.L. Spiller¹, R.J. Petrie¹, L. Han¹
¹*Drexel University*, ²*University of Pennsylvania*
- 3:00PM** **Mechanical Stiffening of Extracellular Matrix by Neutrophil Extracellular Traps Promotes Breast Cancer Progression** SB³C2023-405
C.-M. Boghdady, N. Wong, A. Shen, E. Solymoss, M. de Meo, A. Chandrasekaran, R. Rayes, Y. Chen, A. Ghagre, A. Ehrlicher, L. McCaffrey, J. Spicer, P. Siegel, C. Moraes
McGill University

Thursday, June 8

1:45PM – 3:15PM MT

Fibrocartilage: Intervertebral Disc, Meniscus, TMJ

Gore CD

Session Chairs: Alejandro Almarza, *University of Pittsburgh*
Sonia Bansal, *University of Delaware*

- 1:45PM** **Non-enzymatic Glycation Strengthens Annulus Fibrosus Through Crosslinks Aligned With Primary Collagen Fibers** SB³C2023-031
Minhao Zhou, Erin Archibeck, Yarah Feteih, Yousuf Abubakr, Grace D. O'Connell
University of California
- 2:00PM** **Multiscale Biomechanics Across Scales: Micromechanics and Nonlinear Viscoelasticity of the Nucleus Pulposus in Inflammation** SB³C2023-573
Timothy D. Jacobson, Gerard A. Ateshian, Nadeen O. Chahine
Columbia University
- 2:15PM** **Influence of Multidirectional Loading On Meniscus Wear Behavior** SB³C2023-435
Kate J. Benfield, Katherine J. Fors, Trevor J. Lujan
Boise State University
- 2:30PM** **Identifiability of Poroelastic Model Parameters Using Uniaxial Tension Data: Role of 3D Strain and Unloading** SB³C2023-504
John M. Peloquin, Dawn M. Elliott
University of Delaware
- 2:45PM** **Comparison Of Mechanical Response of TMJ and Knee Cartilage Under Dynamic Loading** SB³C2023-143
Annie Porter¹, Michael Santare¹, Lin Han², John Peloquin¹, X. Lucas Lu¹
¹*University of Delaware*, ²*Drexel University*
- 3:00PM** **Tribological Assessment of PVA Hydrogels as Interpositional Implant Materials in the Temporomandibular Joint** SB³C2023-353
Kevin M. Labus, Jason P. Kuiper, Christian M. Puttlitz
Colorado State University

Thursday, June 8

1:45PM – 3:15PM MT

Educational Education: Challenges and Innovations

Powell

Session Chairs: Chiara Bellini, *Northeastern University*
Zhongping Huang, *West Chester University*

- 1:45PM** **Computation For Bioengineering And Mechanical Engineering Students: An Experiential Learning Opportunity In Norway** SB³C2023-318
Samuel D. Salinas¹, Ana I. Vargas¹, Turner Jennings¹, Sean Harington¹, Mohammad J. Sadeghinia², Mojgan Y. Jacobsen³, Trine Eide³, Cecilie Udberg-Helle³, Torill Andersen Eidsvaag⁴, Torjer A. Olsen⁵, Jonathan Crossen⁵, Victorien Prot², Bjørn H. Skallerud², Rouzbeh Amini¹
¹Northeastern University, ²Norwegian University of Science and Technology, ³Kinn Education and Resource Centre, ⁴Univesrity of Bergen, ⁵UiT The Arctic University of Norway
- 2:00PM** **Integration Of FEBio As An Instructional Tool For Undergraduate Biomechanics** SB³C2023-412
David Jiang, Jeffrey A. Weiss, Lucas H. Timmins
University of Utah
- 2:15PM** **ChatGPT And The Future Of Education In Biomedical And Mechanical Engineering** SB³C2023-588
Sara E. Wilson
University of Kansas
- 2:30PM** **Mega Data Analysis of Sex Distribution of Study Samples Reported in Summer Biomechanics, Bioengineering, & Biotransport Annual Meeting Abstracts** SB³C2023-093
F. Sebastian, A. Hurgoi, M. Schaenen, H. Shah, V. Rivera, K. Le, D. Ng, R. Amini
Northeastern University
- 2:45PM** **Bringing Discussions of Accessibility to Engineering Classrooms** SB³C2023-378
N. Rich¹, S. Johnson¹, C. Bellini²
¹Tatum Robotics, ²Northeastern University
- 3:00PM** **It Takes a Village: Catalyzing Clinically-driven Undergraduate Design Projects at the Nexus of Engineering, Medicine and Business** SB³C2023-337
Byron D. Erath, Laurel Kuxhaus
Clarkson University

Biomechanical Considerations in Cardio. Biomechanics

Zermatt

Session Chairs: Kyoko Yoshida, *University of Minnesota*
 Matthew R. Bersi, *Washington University in St. Louis*

- 1:45PM The Effects Of Strain History On Aortic Valve Interstitial Cell Activation In A 3D Hydrogel Environment** SB³C2023-071
 Toni M. West, Daniel P. Howsmon, Miles W. Massidda, Helen N. Vo, Athena A. Janobas, Aaron B. Baker, Michael S. Sacks
University of Texas at Austin
- 2:00PM Improving Anti-Thrombogenic Potential Of A Porohyperelastic Bilayered Vascular Graft Using Luminal Reversal Flow** SB³C2023-164
 Ali Behrangzade¹, Sang-Ho Ye^{1,2}, William R. Wagner^{1,2}, Jonathan P. Vande Geest^{1,2,3}
¹University of Pittsburgh, ²McGowan Institute for Regenerative Medicine, ³Vascular Medicine Institute
- 2:15PM Measurement of clot attachment forces to biomaterials and comparison to a hyperelastic simulation** SB³C2023-317
 Jose L. Monclova, Sara E. Almasy, Nicolas Tobin, Vikas Kannojiya, Francesco Costanzo, Scott Simon, Keefe B. Manning
Penn State
- 2:30PM Biomechanical Effects Of Annuloplasty Ring Sizing For Functional Mitral Regurgitation Repair** SB³C2023-140
 Gediminas Gaidulis, Muralidhar Padala
Emory University
- 2:45PM Investigating Elastin Fiber Kinematics In Porcine Epicardial Layer With Laser Scanning Confocal Microscopy** SB³C2023-345
 Sara R. McMahan¹, Alan Taylor¹, Duc Khang Chung¹, Jiazhu Xu¹, Matthias Peltz², Pietro Bajona^{1,2}, Yi Hong¹, Jun Liao¹
¹University of Texas, ²Drexel University
- 3:00PM Comparison of some novel 1D implementations of hyperelastic arterial models with 3D approaches for a cylindrical test case** SB³C2023-453
 Jacob Sturdy¹, Friederike Schäfer¹, Aleksander Sinek^{1,2}, Mateusz Mesek^{1,2}, Marek Rojczyk², Wojciech P. Adamczyk², Bartłomiej Melka², Ziemowit Ostrowski², Ryszard Białecki²
¹Norwegian University of Science and Technology, ²Silesian University of Technology

Thursday, June 8

3:30PM – 5:00PM MT

Emerging Areas in Biofluids

Cascade ABC

Session Chairs: Joseph van Batenburg-Sherwood, *Imperial College London*
Ellie Rahbar, *Wake Forest University*

- 3:30PM** **Effects of Wildland Fire Smoke Exposure on Airflow and Particle Deposition in the Mouse Respiratory Tract** SB³C2023-443
Matthew J. Eden, Jacqueline Matz, Chiara Bellini, Jessica M. Oakes
Northeastern University
- 3:45PM** **The Effects of Cerebrospinal Fluid and Hyperelastic Model on Aneurysm Wall Vibration Using High-fidelity Fluid-structure Interaction Simulations** SB³C2023-379
Kei Yamamoto¹, David Bruneau², David Steinman², Kristian Valen-Sendstad¹
¹*Simula Research Laboratory*, ²*University of Toronto*
- 4:00PM** **Dynamic Response Characterization Of Sheep Lymphatic Pumping During Growth And Remodeling** SB³C2023-541
Young Jae Ryu, Sophia Mavris, Zhanna Nepiyushchikh, Rudolph L. Gleason, J. Brandon Dixon
Georgia Institute of Technology
- 4:15PM** **Improved In Vivo Measurements Of Outflow Facility In Mice By Accounting For The Time-Varying Effects Of Anesthesia** SB³C2023-480
Michael Madekurozwa¹, Nicholas Tolman², Simon W. John², Darryl R. Overby², Joseph van Batenburg-Sherwood¹
¹*Imperial College London*, ²*Columbia University*
- 4:30PM** **Left Renal Vein Stenosis Alters Renal Venous Impedance During Murine Pregnancy** SB³C2023-200
Jennifer L. Anderson¹, Riley L. Holloway¹, Paula A. Torres Loza^{1,2}, David G. Reuter³, Craig J. Goergen¹
¹*Purdue University*, ²*National University of Colombia*, ³*Seattle Children's Hospital*
- 4:45PM** **Dynamics Of Shear Stress In Embryonic Chick Heart Anatomies Reconstructed From Light Sheet Fluorescence Microscopy** SB³C2023-219
K. Giesbrecht, S. Rossi, M. Bressan, B. Griffith
University of North Carolina at Chapel Hill

Thursday, June 8

3:30PM – 5:00PM MT

Savio Woo Session II: Ligament & Tendon Growth & Loading

Cascade D

Session Chairs: Jeffrey Weiss, *University of Utah*
Stephanie Cone, *University of Delaware*

- 3:30PM ACL Injury And Joint Instability Leads To Meniscal Hypertrophy In A Skeletally Immature Porcine Model** SB³C2023-536
Jacob D. Thompson, Margaret E. Easson, Danielle Howe, Lauren V. Schnabel, Jeffrey T. Spang, Brian G. Pietrosimone, Matthew B. Fisher
North Carolina State University
- 3:45PM Mechanical and Multiscale Structural Changes Due to Repetitive Fatigue Loading in an In Vivo Rat Overuse Model** SB³C2023-218
Pooja Chainani^{1,2}, Maria Buzo Mena¹, Diana Yeritsyan¹, Daniela Caro¹, Kaveh Momenzadeh¹, Joseph P. DeAngelis², Arun J. Ramappa², Ara Nazarian^{1,2}
¹*Harvard Medical School*, ²*Boston University*
- 4:00PM Changes in Viscoelastic Mechanical Properties and Gene Expression in Rat Achilles Tendon Due to Treadmill Running Depend on Exercise Intensity and Duration** SB³C2023-532
Margaret K. Tamburro, Kelsey A. Bonilla, Snehal S. Shetye, Thomas P. Leahy, Jeremy D. Eekhoff, Daniel C. Farber, Louis J. Soslowsky
University of Pennsylvania
- 4:15PM Reduced Postnatal Loading After Sciatic Nerve Resection Impairs Achilles Tendon Growth And Maturation** SB³C2023-454
Talayah A. Johnson¹, Natalie Fogarty¹, Alisia Lin¹, Tonia K. Tsinman¹, Xi Jiang¹, Eiki Koyama², Lin Han³, Josh R. Baxter¹, Robert L. Mauck¹, Nathaniel A. Dymment¹
¹*University of Pennsylvania*, ²*Children's Hospital of Pennsylvania*, ³*Drexel University*
- 4:30PM Tendon Overload Using A Rodent Model Of Synergist Ablation Leads To Mechanical Degeneration** SB³C2023-494
Lily M. Lin, Ellen T. Bloom, John M. Peloquin, Michael H. Santare, Justin Parreno, Karin G. Silbernagel, Dawn M. Elliott
University of Delaware
- 4:45PM Cellular Senescence Suppresses ECM Synthesis In Response To Mechanical Unloading in Tendon Explants** SB³C2023-047
Emma J. Stowe, Brianne K. Connizzo
Boston University

Thursday, June 8

3:30PM – 5:00PM MT

Emerging Mechanobiology and Biomechanics II

Cascade E

Session Chairs: Hannah Cebull, *Purdue University*
Chiara Bellini, *Northeastern University*

- 3:30PM Plasticity And Avalanche Failure In Computational Models Of Pulmonary Collagen-Elastin Fiber Networks** SB³C2023-598
Jacob Herrmann¹, Yuqing Deng², Béla Suki²
¹University of Iowa, ²Boston University
- 3:45PM Determining Strains From Intact Airway Inflation Tests As Compared To Isolated Uniaxial And Biaxial Tensile Tissue Testing** SB³C2023-166
Crystal A. Mariano¹, Stanislav Polzer², Mona Eskandari¹
¹University of California, Riverside, ²VSB-Technical University of Ostrava
- 4:00PM PolyFEM: Finite Element Solver For Complex Biomechanics Problems** SB³C2023-441
Pranav Jain¹, Liam Martin², Zachary Ferguson¹, Torkan Gholamalizadeh³, Faezeh Moshfeghifar⁴, Kenny Erleben⁴, Steven Abramowitch², Daniele Panozzo¹, Teseo Schneider⁵
¹New York University, ²University of Pittsburgh, ³3Shape ApS, ⁴University of Copenhagen, ⁵University of Victoria
- 4:15PM Spatial Mapping The Material And Structural Properties Of The Uterine Fibroid-Myometrium Boundary** SB³C2023-298
Daniella M. Fodera¹, Johanna L. Lund-Jackson¹, Shuyang Fang¹, Arnold Advincula¹, Michelle L. Oyen², Kristin M. Myers¹
¹Columbia University, ²Washington University in St. Louis
- 4:30PM Design And Evaluation Of A Floating Platform System For Mechanical Testing Of Mesoscale Gels And Tissues** SB³C2023-403
Tyler G. Tuttle, Sarah Calve
University of Colorado Boulder
- 4:45PM Modeling Ultrasound-Derived Acoustic Radiation Forces In Hydrogels Using 3D Force Microscopy** SB³C2023-096
Kevin P. Grassie, Fei Wang, Bryan D. Huey, Yusuf M. Khan
University of Connecticut

Thursday, June 8

3:30PM – 5:00PM MT

Innovative Brain Mechanics Characterization

Cascade F

Session Chairs: Maria Holland, *University of Notre Dame*
Reuben Kraft, *Pennsylvania State University*

- 3:30PM** **ElastUNet: Three-Dimensional Discovery of Elastic Material Parameters Using Deep Learning** SB³C2023-057
Ali Kamali, Kaveh Laksari
University of Arizona
- 3:45PM** **Inverse Finite Element Modeling Captures Wave Propagation in High-Rate Oscillatory Shear Tests on Porcine Brain Tissue** SB³C2023-172
Gregory M. Boiczyk, Noah R. Pearson, Kenneth L. Monson
University of Utah
- 4:00PM** **Identifying Commonalities of Harmonic Brain Deformation Induced by Magnetic Resonance Elastography in Vivo** SB³C2023-180
J.D. Escarcega¹, A.A. Alshareef², A.K. Knutsen², R.J. Okamoto¹, P.V. Bayly¹
¹Washington University, ²Henry M. Jackson Foundation for the Advancement of Military Medicine
- 4:15PM** **Investigating the Frequency-Dependent Skull-Brain Motion Transmissibility through MR Elastography** SB³C2023-600
F. Rezayaraghi¹, E. Triolo², C. Neher¹, M. Kurt^{1,2}
¹University of Washington, ²Mount Sinai
- 4:30PM** **Novel Magnetic Resonance Imaging Phantoms For Investigating Skull-Brain Mechanics** SB³C2023-576
Joy Mojumder¹, Suhas Vidhate², Yuan-Chiao Lu^{1,3}, Ahmed Alshareef^{3,4}, Curtis L. Johnson⁵, Dzung L. Pham^{1,6}, John A. Butman¹
¹National Institutes of Health, ²Intuitive Surgical, Inc., ³Henry M. Jackson Foundation, ⁴University of South Carolina, ⁵University of Delaware, ⁶Uniformed Services University
- 4:45PM** **Post-mortem Changes in Anisotropic Mechanical Properties of Brain Tissue Measured by MR Elastography** SB³C2023-033
Shuaihu Wang¹, Charlotte A. Guertler¹, Ruth J. Okamoto¹, Curtis L. Johnson², Matthew D.J. McGarry³, Philip V. Bayly¹
¹Washington University in St. Louis, ²Delaware University, ³Dartmouth College

Thursday, June 8

3:30PM – 5:00PM MT

Mechanobiology in Tissue and Cellular Engineering

Gore AB

Session Chairs: **Spencer Szczesny**, *Pennsylvania State University*
Virginia Ferguson, *University of Colorado*

- 3:30PM Prestress On Nascent Desmosomes Regulates Electrophysiology Of Stem Cell-Derived Heart Muscle** SB³C2023-346
Daniel W. Simmons, David R. Schuftan, Jingxuan Guo, Kasoorelope Oguntuyo, Ghiska Ramahdita, Mary Munsell, Brennan Kandalaft, Missy Pear, Nathaniel Huebsch
Washington University in St. Louis
- 3:45PM Epigenetic Treatments Restore Nuclear Architecture in Cardiomyocyte Cultures**
SB³C2023-556
Stephanie E. Schneider, Adrienne K. Scott, Corey P. Neu
University of Colorado
- 4:00PM Synaptopodin Enables Focal Adhesions To Resist Perpendicular Force** SB³C2023-224
Chengqing Qu¹, Shumeng Jiang¹, Farid Alisafaei², Jeffrey H Miner¹, Hani Y. Suleiman¹, Guy M. Genin¹
¹Washington University in St. Louis, ²New Jersey Institute of Technology
- 4:15PM Multiscale Mechanobiologically Optimized Scaffold Designs For Bone Tissue Engineering** SB³C2023-054
Timothy O. Josephson, Elise F. Morgan
Boston University
- 4:30PM In-Situ Viscoelasticity Measurement Of Cell Monolayer By Strain Sensing Of Elastohydrodynamic Force In Microfluidic Channel** SB³C2023-216
Tianzheng Guo, Xiaoyu Zou, Shalini Sundar, Xinqiao Jia, Charles Dhong
University of Delaware
- 4:45PM Development Of An Activating And Inactivating Optogenetic Toolbox For Perturbation Of Rhoa-Yap Mechanotransductive Feedback** SB³C2023-173
Erin E. Berlew, Annapurna Pranatharthi-Haran, Brian Y. Chow, Joel D. Boerckel
University of Pennsylvania

Thursday, June 8

3:30PM – 5:00PM MT

Spine and Shoulder Mechanics

Gore CD

Session Chairs: Arin Ellingson, *University of Minnesota*
Grace O'Connell, *University of California, Berkeley*

- 3:30PM Examination of the Coupled Motion of the Lumbar Functional Unit During Dynamic Motion** SB³C2023-558
Matthew R. MacEwen, Rebecca E. Abbot, Victor H. Barocas, Arin M. Ellingson
University of Minnesota-Twin Cities
- 3:45PM Risk Of Vertebral Endplate Failure During Vertebral Fracture** SB³C2023-060
Neilesh R. Frings, Elise F. Morgan
Boston University
- 4:00PM Cyclic Loading Comparison Between Standard Ultra-High Molecular Weight Polyethylene Blocks And Biofidelic Solid Rigid Polyurethane Blocks For ASTM Pedicle Screw Testing** SB³C2023-333
Jeremy G. Loss¹, Robb W. Colbrunn¹, Kevin J. Lawson²
¹*Cleveland Clinic*, ²*Ascension Medical Group*
- 4:15PM Bulk Properties of the Murine Spine are Maintained During 30-Days of Microgravity on the International Space Station** SB³C2023-088
Shiyin Lim¹, Joanna E. Veres¹, Eduardo A.C. Almeida², Grace D. O'Connell¹
¹*University of California – Berkeley*, ²*NASA Ames Research Center*
- 4:30PM Adaptive Changes In The Bat's Shoulder Anatomy Allow For Repetitive Overhead Motions** SB³C2023-528
Iden Kurtaliaj¹, Jennifer Kunes¹, K. Michael Rowley^{2,3}, Lynn Ann Forrester¹, Mikhail Golman¹, Guy M. Genin⁴, Sharon M. Swarz², Stavros Thomopoulos¹
¹*Columbia University*, ²*Brown University*, ³*California State University East Bay*, ⁴*Washington University at St. Louis*
- 4:45PM Evaluating The Effect Of Soft Tissue Forces On The Fixation Mechanics Of Reverse Shoulder Arthroplasty: A Finite Element Analysis Driven By Musculoskeletal Simulations** SB³C2023-400
Jonathan Glenday¹, Benjamin Johnston², Fernando Quevedo Gonzalez¹, Lawrence Gulotta¹, Andreas Kontaxis¹
¹*Hospital for Special Surgery*, ²*Cornell University*

Thursday, June 8

3:30PM – 5:00PM MT

Growth and Remodeling II

Powell

Session Chairs: Kyoko Yoshida, *University of Minnesota*
Adrian Buganza Tepole, *Purdue University*

- 3:30PM The mTOR Inhibitor Rapamycin Decreases Subchondral Thickness And Affects Variability In The Tibial Plateau Of Common Marmosets SB³C2023-336**
Michael D.K. Focht¹, Dennis M. Minton^{2,3}, Adam B. Salmon^{4,5}, Adam R. Konopka^{2,3}, Mariana E. Kersh¹
¹University of Illinois, ²University of Wisconsin-Madison, ³William S. Middleton Memorial Veterans Hospital, ⁴University of Texas, ⁵Audie L. Murphy Hospital
- 3:45PM Growth And Remodeling In Sparse And Semi-Sparse Tissues: Bridging The Gap Between The Constrained Mixture Model And Eshelby's Inclusion SB³C2023-446**
Ryan R. Mahutga, Elizabeth D. Shih, Patrick W. Alford
University of Minnesota
- 4:00PM Personalized Finite Element Model Of Pediatric Tissue Expansion SB³C2023-135**
Tianhong Han¹, Kaleem Ahmed², Arun Gosain², Taeksang Lee³, Adrian Buganza Tepole¹
¹Purdue University, ²Northwestern University, ³Myongji University
- 4:15PM Telocollagen Injectable Significantly Improves Supraspinatus Tendon Mechanical Strength After Full-Tendon Tear in Rats SB³C2023-553**
Alexandrea A. Silverman¹, Nicolo Rossi², Jeffrey A. Paten¹, Mark A. Randolph², Luke S. Oh^{2,3}, Jeffrey W. Ruberti¹
¹Northeastern University, ²Massachusetts General Hospital, ³Rothman Orthopaedics
- 4:30PM Computational Analysis of Heart Valve Growth and Remodeling in Pulmonary Autografts after the Ross Procedure SB³C2023-292**
Elmer Middendorp¹, Fabian Bräu^{2,3}, Frank P.T. Baaijens¹, Jay D. Humphrey⁴, Christian J. Cyron^{5,6}, Sandra Loerakker¹
¹Eindhoven University of Technology, ²Singapore National Eye Center, ³Singapore-MIT Alliance for Research and Technology, ⁴Yale University, ⁵Hamburg University of Technology, ⁶Helmholtz-Zentrum
- 4:45PM Identifying Contributors to Aneurysmal Progression in the Marfan Aorta Using a Constrained Mixture Model SB³C2023-295**
David S. Li¹, Cristina Cavinato², Marcos Latorre³, Jay D. Humphrey¹
¹Yale University, ²Univerity of Montpellier, ³Valencia Polytechnic University

Thursday, June 8

3:30PM – 5:00PM MT

Noninvasive Metrics for Cardio. Biomechanics

Zermatt

Session Chairs: Jun Liao, *University of Texas*

- 3:30PM Pre-Operative Functional Characterization Of Aortic Neck In Abdominal Aortic Aneurysms And Its Association With Type I Endoleak Following EVAR Procedure** SB³C2023-482
A Forneris^{1,2}, A. Satriano², R.A. Beddoes², R.D. Moore¹, E.S. Di Martino^{1,2}
¹University of Calgary, ²ViTAA Medical Solutions
- 3:45PM 4D Ultrasound-Based Strain Can Characterize Early Progression of Myocardial Infarction in Mice and Rats** SB³C2023-048
Conner C. Earl^{1,2}, Ana C.M. Omoto³, Karthik Annamalai¹, Alyssa Richards¹, Samuel X. Zhang¹, Adalyn M. Meeks¹, Alexandre A. de Silva³, Craig J. Goergen^{1,2}
¹Purdue University, ²Indiana University, ³University of Mississippi
- 4:00PM Comparison Between Material Properties Obtained from Ultrasound Image Based Inverse FE Method Against Ex-Vivo Inflation Test** SB³C2023-385
Hadi Wiputra¹, Sydney Q. Clark², Craig J. Goergen², Matthew R. Bersi³, Victor H. Barocas¹
¹University of Minnesota, ²Purdue University, ³Washington University in St. Louis
- 4:15PM Procedural Strategy Impact On Outcomes Of Transcatheter Aortic Valve Replacement For Bicuspid Aortic Valves** SB³C2023-131
Breandan Yeats¹, Sri Krishna Sivakumar¹, Milad Samaee¹, Pradeep Yadav², Venkateshwar Polsani², Vinod Thourani², Stephanie Sellers³, Janarthanan Sathananthan³, Lakshmi Dasi¹
¹Georgia Tech & Emory University, ²Piedmont Heart Institute, ³University of British Columbia
- 4:30PM A New Approach To Characterize Trabeculae Carneae Structures Using High-Resolution Human Heart Images** SB³C2023-567
Yasamin Seddighi¹, Keith Bartels², Hai-Chao Han¹
¹University of Texas at San Antonio, ²Southwest Research Institute
- 4:45PM Evaluating the use of Elastic Registration for Determining Atrioventricular Valve Annulus Mechanics** SB³C2023-390
Devin W. Laurence¹, Christian Herz¹, Silvani Amin¹, Ana Sulentic¹, Patricia Sabin¹, Andras Lasso², Matthew A. Jolley¹
¹Children's Hospital of Philadelphia, ²Queen's University

Poster Sessions

Posters will be presented in two sessions as listed below. Please see the “Instructions for Poster Presenters” on Page 8. The poster viewing area is located in the **Gore Pavilion** and will be open throughout the conference.

Poster Session I	Monday, June 5, 1:00PM – 2:30PM MT
Poster Session II	Tuesday, June 6, 12:45PM – 2:15PM MT

Poster Session I

Biotransport

- P1 Molecular dynamics studies of sugar solutions for controlling water rotational relaxation time** SB³C2023-098
Kang Hu, Ryo Shirakashi
University of Tokyo
- P2 Repeatability And Backlash Distances Of Microneedles Displaced Using A Novel Actuation Block** SB³C2023-241
Brianna E. Morales, Christopher G. Rylander
University of Texas at Austin
- P3 Non-Invasive Stroke Work As A Predictor Of Myocardial Contractility In Duchenne Muscular Dystrophy** SB³C2023-238
Israel O. Ajiboye¹, Navaneeth Chandran¹, Michael D. Taylor², Rupak K. Banerjee¹
¹University of Cincinnati, ²Cincinnati Children's Hospital Medical Center
- P4 MRI Guided Focused Ultrasound Drug Delivery to DIPG Tumors in a Mouse Model** SB³C2023-025
Payton J. Martinez, Genna Nault, Jenna Steiner, Natalie Serkova, Adam Green, Mark Borden
University of Colorado
- P5 A Cost Function Approach Applied to Muscle Cryopreservation** SB³C2023-013
Casey J. Kraft, Weston J. Upchurch, Michael L. Etheridge, Paul A. Iaizzo, John C. Bischof
University of Minnesota
- P6 Enabling Cryopreservation Through Vitrification And Rewarming At The Scale Of A Human Organ** SB³C2023-171
Lakshya Gangwar¹, Zonghu Han¹, Mikaela Hintz¹, Jacqueline L. Pasek-Allen¹, Robert C. Goldstein², Michael L. Etheridge¹, John C. Bischof¹
¹University of Minnesota, ²AMF Life Systems LLC
- P7 Frequency Optimization of a Novel Skin Blood Flow Transducer** SB³C2023-501
Georgia E. Robles, Christopher M. Francis, Saeed I. Latif, David A. Nelson
University of South Alabama

- P8 Characterization Of Cellular Response To Endovascular Ablative Therapies In 2D And 3D** SB³C2023-270
S. Brocklehurst, Amin Sabaghan, D. Stolley, N. Ghousifam, E. Cressman, D. Fuentes, M.N. Rylander
University of Texas at Austin

Design, Dynamics, & Rehabilitation

- P9 Joint Space Of The First Carpometacarpal Joint: Correlation Between Computed Tomographic And Simulated X-Ray Measurement** SB³C2023-063
David Jordan, C. Kent Kwok, Zong-Ming
University of Arizona
- P10 Changes In Thumb Force Due To Osteoarthritis** SB³C2023-427
Nicole D. Arnold¹, Adam J. Chrzan¹, Kevin Chan², Tamara Reid Bush¹
¹Michigan State University, ²Spectrum Health

Fluid Mechanics

- P11 Poroelastic Model Of Trabecular Structures In The Developing Heart** SB³C2023-305
Christine Miller Buffinton, James W. Bush
Bucknell University
- P12 A self-powered pump for patients with a single ventricle heart** SB³C2023-296
Mahdi Esmaily, Dongjie Jia
Cornell University
- P13 A Comparative Study on the Difference in Arteriovenous Fistula CFD Simulations Based on Geometry Length** SB³C2023-503
Kaitlin M. Southern, Fatemeh Bahmani, Veeranna Maddipati, Stephanie M. George
East Carolina University
- P14 Patient-Specific Pulmonary Hypertension Simulations in Sickle Cell Disease Patients, a Viscosity Model Study** SB³C2023-549
Fatimah Bahmani, Alex Vahdati, Veeranna Maddipati, Stephanie M. George
East Carolina University
- P15 Sensitivity of Platelet Activation in an ECMO Pump due to Different Modelling Approaches** SB³C2023-357
Francesco Fiusco¹, Lars Mikael Broman^{2,3}, Lisa Prahli Wittberg¹
¹KTH Royal Institute of Technology, ²Astrid Lindgren's Children's Hospital, ³Karolinska Institutet
- P16 Post-MitraClip Mitral Valve Gradient with MitraClip G4** SB³C2023-326
Shelley C. Gooden¹, Mani A. Vannan², Konstantinos D. Boudoulas³, Vinod H. Thourani², Pradeep K. Yadav², Lakshmi P. Dasi¹
¹Georgia Institute of Technology, ²Piedmont Heart Institute, ³Wexner Medical Center

- P17 Fluid-Structure Interaction Simulation In An Idealised Model Of The Dissected Aorta: Relation Between False Lumen Pressure And Outflow Via Side Branches** SB³C2023-383
Amith Balasubramanya¹, Lise Gheysen¹, Nele Famaey², Joris Degroote¹, Patrick Segers¹
¹Ghent University, ²KU Leuven
- P18 A Computational Model For The Roughness Of Coronary And Cerebral Artery Stenosis And Treatment For Diabetes Mellitus Disease** SB³C2023-433
S. Piskin
Istinye University
- P19 Effect of Aortic Curvature on Bioprosthetic Aortic Valve Performance** SB³C2023-490
B. Vogl¹, R. Gadhav¹, Z. Wang², A. Chavez Ponce³, A. El Shaer³, M. Alkhoul³, H. Hatoum¹
¹Michigan Technological University, ²The Ohio State, ³Mayo Clinic
- P20 Vorticity Transport In Aneurysms Of The Abdominal Aorta** SB³C2023-356
Valentina Mazzi¹, Karol Calò¹, Maurizio Lodi Rizzini¹, Ludovica Saccaro^{2,3}, Diego Gallo¹, Angelo Iollo^{2,3}, Umberto Morbiducci¹
¹Politecnico di Torino, ²Université de Bordeaux, ³Inria-Bordeaux Sud-Ouest
- P21 Investigating The Role Of Eccentric Inlet Conditions On Hemodynamic Results At Different Stages Of Aneurysm Growth** SB³C2023-601
Federica Galbiati^{1,2}, Emanuele Vignali³, Katia Capellini³, Claire Morin², Stéphane Avril², Emiliano Costa¹, Simona Celi³
¹RINA Consulting SpA, ²INSERM, ³BioCardioLab
- P22 A Fluid-Solid-Growth Framework For Simulating Patient-Specific Vascular Growth And Remodeling Using Constrained Mixture Theory** SB³C2023-268
Erica L. Schwarz¹, Martin R. Pfaller¹, Jason Szafron¹, Christopher Breuer², Jay D. Humphrey³, Alison L. Marsden¹
¹Stanford University, ²Nationwide Children's Hospital, ³Yale University
- P23 Towards Modeling Acute Ischemic Stroke: In Vitro Experiments and Simulations of Blood Flow and Mean Arterial Pressure in an Artificially Clotted Cerebrovascular Model** SB³C2023-447
Saurabh Bhardwaj¹, Brent A. Craven², Jacob E. Sever¹, Francesco Costanzo¹, Scott D. Simon¹, Keefe B. Manning¹
¹Pennsylvania State University, ²US FDA
- P24 The Influence Of Hemodiluted Blood Viscosity On Patient Hemodynamics During Cardiopulmonary Bypass** SB³C2023-162
Nafis M. Arefin, Allison R. Cripps, Bryan C. Good
University of Tennessee
- P25 Validating Multi-scale Coronary Simulation Pipeline Against Coronary Intravascular Velocity and Pressure Measurements** SB³C2023-016
Anahita A. Seresti¹, Alison L. Marsden², Andrew M. Kahn³, M. Owais Khan¹
¹Toronto Metropolitan University, ²Stanford University, ³University of California – San Diego

- P26 Multi-Omic Analysis Of Resected Thrombi Identifies Complex Traits Associated With Ischemic Stroke Etiology** SB³C2023-191
Briana A. Santo, Kerry E. Poppenberg, Andre Monteiro, Adnan H. Siddiqui
University of Buffalo
- P27 Laser Ablation: A New Leaflet Modification Strategy To Prevent Coronary Obstruction In Redo Tavr** SB³C2023-100
John T. Briansky, Masod Sadipour, Ali Azadani
University of Denver
- P28 Verification Errors In Eulerian Power-Law Hemolysis Model Predictions In Simple Flows** SB³C2023-280
Mohammad M. Faghih¹, Brent A. Craven¹, M. Keith Sharp²
¹US FDA, ²University of Louisville
- P29 Endothelial Nuclear Morphology is Incrementally Sensitive to Shear Stress Magnitude and Directionality** SB³C2023-515
Jaideep Sahni¹, Mehwish Arshad², Peter D. Weinberg², Ryan M. Pedrigi¹
¹University of Nebraska-Lincoln, ²Imperial College London
- P30 Computational Study of Role of Ultra Large Von Willebrand Factor in COVID-19 Related Thrombosis** SB³C2023-350
Nahid Rahmati, Nima Maftoon
University of Waterloo
- P31 Rotational Impact-Induced Brain Injury, a Biomimetic Study** SB³C2023-232
Q. Wang¹, J. Lang², R. Nathan³, Q. Wu¹
¹Villanova University, ²Southeast University, ³Pennsylvania State University

Solid Mechanics: Cardiovascular

- P32 High-Throughput Automated Mechanical Analysis of Human Induced Pluripotent Stem Cell Derived Cardiac Microtissue** SB³C2023-022
H. Kobeissi, E. Lejeune
Boston University
- P33 Changes In Right Ventricle Anisotropic Viscoelastic Behavior With Pulmonary Hypertension Development** SB³C2023-058
K. LeBar, K. Roth, W. Liu, B. Garcia, J. Pang, A. Chicco, Z. Wang
Colorado State University
- P34 A Three-node Rotation-free Kirchhoff-love Shell Formulation For Cardiovascular Applications** SB³C2023-570
L. Shi, Y. Chen, V. Vedula
Columbia University
- P35 Establishment Of A Validated Finite Element Framework To Predict The 3D, Patient-Specific Arterial Mechanical Environment** SB³C2023-597
Caleb C. Berggren, Y.F. Jack Wang, Lucas H. Timmins
University of Utah

- P36 Anisotropic Material Property and Local Strength Characterization of Human Carotid Plaques: A Bayesian Optimization Based Inverse Finite Element Modeling** SB³C2023-091
S. Guvenir Torun¹, B. Kaaij^{1,2}, P. de Miguel Munoz^{1,2}, H. Crielaard¹, H.J.M. Verhagen¹, G.J. Kremers¹, A.F.W. van der Steen¹, A.C. Akyildiz^{1,2}
¹Erasmus Medical Center, ²Delft University of Technology
- P37 Changes in Myocardial Deformation Induces Abnormalities in Valvular Dynamics Causing Mitral Valve Regurgitation** SB³C2023-294
Tawfik M. Hussein^{1,2}, Gediminas Gaidulis^{2,3}, Michael Silverman³, John N. Oshinski^{1,3}, Muralidhar Padala^{2,3}
¹Georgia Institute of Technology, ²Carlyle Fraser Heart Center, ³Emory University
- P38 Computational Assessment of Elastin in a Hybrid Modelling Approach of Arterial Biomechanics** SB³C2023-321
Yousof MA. Abdel-Raouf¹, Mathias Peirlinck², Nele Famaey³, Patrick Sips¹, Patrick Segers¹
¹Ghent University, ²Delft University of Technology, ³KU Leven
- P39 Pattern Of Aortic Valve Leaflet Calcification In As Patients: In-Vivo Geometric Description Of Calcific Progression** SB³C2023-006
Mohamed Abdelkhalek, Zahra Keshavarz-Motamed
McMaster University
- P40 An Inverse FE Method To Quantify The Relationship Between Mechanical Properties And Residual Stresses In The Myocardium** SB³C2023-478
Manoj Ghosh, Marissa Grobbel, Lik Chuan Lee, Sara Roccabianca
Michigan State University
- P41 Effects Of Chordae Rupture On Tricuspid Valve Septal Leaflet Strains: An Ex-Vivo Study On Porcine Hearts** SB³C2023-227
Julia Clarin¹, Keyvan Amini Khoiy², Samuel D. Salinas¹, Dipankar Biswas², Kourosh T. Asgarian³, Francis Loth¹, Rouzbeh Amini¹
¹Northeastern University, ²The University of Akron, ³Jersey Shore University
- P42 Right Ventricular Global Longitudinal Strain And Ventricular Dynamics In Patients With Pulmonary Hypertension** SB³C2023-521
Alexandra M. Janowski, Scott Visovatti, Raymond L. Benza, Rebecca R. Vanderpool
The Ohio State
- P43 Viscoelastic and Fracture Properties of Clot from Human and Bovine Blood** SB³C2023-104
Gabriella P. Sugerman, Sapun H. Parekh, Berkin Dortdivanlioglu, Manuel K. Rausch
University of Texas at Austin
- P44 Biomechanical Characterization Of Neonatal Aortic Coarctation Tissue Informs The Need To Design Bespoke Patient Therapies For Neonatal Coarctation Of The Aorta** SB³C2023-094
Niall Linnane^{1,2,3}, Robert Johnston¹, Damien P. Kenny^{2,3}, Caitriona Lally¹
¹Trinity College Dublin, ²Royal College of Surgeons, ³Children's Health Ireland

- P45 Ultrasound Imaging To Characterize Inflated Atherosclerotic Plaques** SB³C2023-327
 Yasmine Guendouz¹, Brooke Tronifoglio¹, Sherif Sultan^{2,3}, Niamh Hynes^{2,3}, Cleona Gray⁴,
 Caitriona Lally¹
*¹Trinity College Dublin, ²University Hospital Galway, ³Galway Clinic, ⁴Mater Misericordiae
 University Hospital*
- P46 Design, Computational And Experimental Evaluation, And 3D Printing Of Patient Specific
 Stents For Treatment Of Paediatric Aortic Coarctation** SB³C2023-286
 Robert D. Johnston¹, Niall Linnane^{1,2,3}, Samuel Geraghty¹, Conor O’Keeffe¹, Shirsha Bose¹,
 Damien Kenny³, Caitriona Lally¹
¹Trinity College Dublin, ²Royal College of Surgeons, ³Children’s Health Ireland at Crumlin
- P47 Using A Three-Dimensional Biventricular Mathematical Model To Help Understand Sex
 Differences In The Onset And Progression Of Pulmonary Arterial Hypertension**
 SB³C2023-211
 Kristen M. Garcia, Becky A. Hardie, Jennifer Stowe, Daniela Valdez-Jasso
University of California – San Diego
- P48 Multiscale Modeling of Myofiber Disarray In The Left Ventricle Using A Stress-Based
 Reorientation Law** SB³C2023-118
 Mohammad Mehri, Charles K. Mann, Hossein Sharifi, Kenneth S. Campbell, Jonathan F. Wenk
University of Kentucky
- P49 Method Of Applying Twist To Complex Femoropopliteal Artery Deformations In A Finite
 Element Study** SB³C2023-565
 Ali Ahmadi, Anastasia Desyatova
University of Nebraska-Omaha
- P50 Implementation Of Experimentally Acquired Tricuspid Valve Leaflet Pre-Strains To An In-
 Silico Finite Element Model** SB³C2023-137
 Colton J. Ross¹, Arshid Mir¹, Harold M. Burkhart¹, Ming-Chen Hsu², Devin W. Laurence³,
 Chung-Hao Lee¹
¹University of Oklahoma, ²Iowa State University, ³Children’s Hospital of Philadelphia
- P51 Patient-Specific Predictive Simulation of Transcatheter Edge-to-Edge Repair in Humans
 with Mitral Regurgitation** SB³C2023-452
 Natalie T. Simonian¹, Sneha Vakamudi², Mark J. Pirwitz², Alison M. Pouch³, Joseph H.
 Gormann, III³, Robert C. Gorman³, Michael S. Sacks¹
¹University of Texas at Austin, ²Ascension Texas Cardiovascular, ³University of Pennsylvania
- P52 Comparing The Elastic And Fracture Properties Between Fibrin And Whole Blood**
 SB³C2023-407
 Grace N. Bechtel¹, Gabrielle P. Sugerman¹, Sapun H. Parekh¹, Manuel K. Rausch^{1,2}
¹University of Texas at Austin, ²Oden Institute for Computational Engineering and Sciences

Solid Mechanics: Injury & Brain

- P53 Effect Of Muscle Activation on Head-Neck Response in Simulated Frontal Impact Compared To A Unique Military Data Set** SB³C2023-072
Jesse W. Gerringer^{1,2}, Karthik Somasundaram^{1,2}, Frank Pinter^{1,2}
¹Medical College of Wisconsin and Marquette University of Tennessee, ²VA Medical Center
- P54 Development of Three - Dimensional Finite Element Model of the Neonatal Brachial Plexus** SB³C2023-027
Sarah J. Wright, Michele J. Grimm
Michigan State University
- P55 Measurement Error Associated With Decoupling Of Instrumented Mouthguards** SB³C2023-245
Ryan A. Gellner, Mark T. Begonia, Matthew Wood, Lewis Rockwell, Taylor Geiman, Caitlyn Jung, Steve Rowson
Virginia Tech
- P56 Effect Of Excitation Direction And Frequency On Regional Dynamic Deformation Of The Human Brain** SB³C2023-561
Ruth J. Okamoto¹, Jordan D. Escarcega¹, Ahmed Alshareef², Curtis Johnson³, Philip V. Bayly¹
¹Washington University, ²Henry M. Jackson Foundation for the Advancement of Military Medicine, ³University of Delaware

Solid Mechanics: Musculoskeletal

- P57 Raman Spectroscopic Probe Predicts The Composition And Functional Mechanical Properties Of The Intervertebral Disc** SB³C2023-550
Chenhao Yu¹, Masumeh Kazemi¹, Farida Korna¹, Erik E. Ersland¹, Mark W. Grinstaff¹, Thomas P. Schaer², Mads S. Bergholt³, Edward J. Vresilovic⁴, Brian D. Snyder⁵, Michael B. Albro¹
¹Boston University, ²University of Pennsylvania, ³King's College London, ⁴University of Delaware, ⁵Beth Israel Deaconess Medical Center
- P58 The Effectiveness of Custom ACL Bracing in Adolescent Populations: A Finite Element Analysis** SB³C2023-009
Alexandria D. Mallinos¹, Brian L. Davis¹, Kerwyn C. Jones²
¹Cleveland State University, ²Akron Children's Hospital
- P59 Bendable Osteochondral Allografts for Improved Congruence: Comparison of Computational and Cadaveric Models** SB³C2023-194
Katherine A. Spack¹, Courtney A. Petersen¹, Peter T. Shyu¹, Edward Guo¹, James T. Cook², Melvin P. Rosenwasser¹, Clark T. Hung¹, Gerard A. Ateshian¹
¹Columbia University, ²University of Missouri
- P60 Mechanical Failure Properties Of Porcine Annulus Fibrosus: An I-PREDICT Study** SB³C2023-382
J. Seifert^{1,2}, A. Shah^{1,2}, L.L. Frazer⁴, N. Yoganandan^{1,2}, B.S. Shender³, J.B. Sheehy³, G. Paskoff³, T. Bentley⁵, D.P. Nicoletta⁴, B.D. Stemper^{1,2}

¹Medical College of Wisconsin, ²Zablocki VA Medical Center, ³Naval Air Warfare Center,
⁴Southwest Research Institute, ⁵Office of Naval Research

- P61 Calcium Signaling In In-Situ Chondrocytes Under Dynamic Compressive Loading**
SB³C2023-319
Vineel Kondiboyina, Timothy Boyer, Sandra J. Shefelbine
Northeastern University
- P62 Partial Meniscectomy Of The Meniscal Inner Part Increases The Meniscal Deformation And Extrusion** SB³C2023-343
Satoshi Yamakawa, Tomoki Ohori, Issei Ogasawara, Akira Tsujii, Shoji Konda, Seira Sato, Takashi Kanamoto, Ken Nakata
Osaka University
- P63 Effects Of External Bathing Solution Osmolarity On Tribological Rehydration And Cartilage Lubrication** SB³C2023-074
Shamimur R. Akanda, David L. Burris, Chris Price
University of Delaware
- P64 Slick Yet Stuck: Elucidating The Underlying Adhesive Mechanisms In Articular Cartilage**
SB³C2023-250
Jamie M. Benson, David L., Burris
University of Delaware
- P65 Partial Meniscus Transplant To Treat Horizontal Cleavage Tear Restores Contact Areas Similar to Partial Meniscectomy** SB³C2023-145
Farid Amirouche^{1,2}, Eric Chang¹, Asher Lichtig¹, Jason Koh²
¹University of Illinois, ²NorthShore University Health System

Solid Mechanics: Other

- P66 Multiscale Characterization of Human Tooth with Combination of SEM, AFM, and FEM**
SB³C2023-170
Y. Zhai¹, J. Wang¹, Z. Shi¹, T. Premaraj², S. Premaraj², T. Karpova¹, P. Dong¹, L. Gu¹
¹Florida Institute of Technology, ²Nova Southeastern University
- P67 Depth Map Image Based Inflation Test For Mechanical Characterization Of Soft Matter**
SB³C2023-468
Rahul L. Maurya¹, Yash K. Shrivastava², Samarth S. Raut¹
¹Indian Institute of Technology, ²Manipal University Jaipur
- P68 Micromechanical Model Of Mechanosensitive Collagen Tissues** SB³C2023-437
Kalyn G. Younger, William Cortes, Daniel H. Reich, Thao D. Nguyen
Johns Hopkins University
- P69 A Mesoscale Model Of Skin To Investigate The Role Of The Dermis-Epidermis Interface On The Tissue Biomechanics** SB³C2023-161
O. Moreno Flores¹, M. Rausch², A. Buganza Tepole¹
¹Purdue University, ²University of Texas at Austin

- P70 Deep Learning Framework For Stress Strain Analysis Over Point Cloud** SB³C2023-429
Jia Lu, Nishant Sundaravaradan
University of Iowa
- P71 An Inexpensive, Shared Biaxial Device To Study The Multiscale Mechanics Of Soft Materials** SB³C2023-332
Alberto Madariaga, Chien-Yu Lin, Mrudang Mathur, Manuel K. Rausch
University of Texas at Austin
- P72 Negative-Pressure Lung Mechanics Of Fibrotic And Emphysematous Mouse Lungs** SB³C2023-021
K.A.M. Quiros¹, T.M. Nelson¹, A. Ulu¹, E.C. Dominguez¹, T.M. Nordgren^{1,2}, M. Eskandari¹
¹University of California - Riverside, ²Colorado State University
- P73 The Material Properties of Healthy Versus Diseased Mouse Lung Parenchyma** SB³C2023-049
T.M. Nelson, K.A.M. Quiros, C.A. Mariano, S. Sattari, M. Eskandari
University of California – Riverside
- P74 Histopathology of Capsule and Cartilage Predict Elbow Biomechanics via Machine Learning** SB³C2023-605
Michael A. David¹, Spencer P. Lake²
¹University of Colorado, ²Washington University in St. Louis
- P75 Understanding mechanotransduction of the distal colon and rectum by multiscale and multimodal computational modeling** SB³C2023-516
Amirhossein Shokrani, Ashkan Almasi, Bin Feng, David M. Pierce
University of Connecticut
- P76 Effects Of GAGs On Microstructure Of Corneal Extracellular Matrix** SB³C2023-116
M.E. Emu, H. Hatami-Marbini
University of Illinois at Chicago
- P77 Effect Of GAGs On Tensile Properties Of Porcine Cornea** SB³C2023-363
H. Hatami-Marbini
University of Illinois at Chicago
- P78 Fibrous Finite Element Modeling Of Posterior Sclera** SB³C2023-278
Mohammad R. Islam, Fengting Ji, Manik Bansal, Yi Hua, Ian A. Sigal
University of Pittsburgh
- P79 Comparing Five Methods To Identify Fracture Toughness Of Soft Tissues** SB³C2023-540
Matthew J. Lohr, Manuel K. Rausch
University of Texas at Austin
- P80 Extracting Inhomogeneous Orientation Distribution Functions From 3d Image Data Of Fibrous Tissues For Finite Element Simulations** SB³C2023-242
Adam Rauff, Michael R. Herron, Steve A. Maas, Jeffrey A. Weiss
University of Utah

P81 Understanding Ciliary Waveforms Through Optimization SB³C2023-533

Louis G. Woodhams, Philip V. Bayly
Washington University in St. Louis

Tissue & Cellular Engineering

P82 Targeting the Chromatin Remodeling in Mesenchymal Stromal Cells Under Hyper Oxidative Stress for Maintaining Cell Phenotype and Viability SB³C2023-335

Lauren A. Monroe, Samantha Kaonis, Neda Kabi, Abigail Fennell, Jack Forman, Soham Ghosh
Colorado State University

P83 Mechanical Regulation of Lumen Growth SB³C2023-557

Wenhui Tang¹, Anqi Chen², Jessie Huang³, Darrell N. Kotton³, Shengqiang Cai⁴, Ming Guo¹
¹MIT, ²Harvard University, ³Boston University, ⁴University of California – San Diego

P84 Fabrication And Mechanical Characterization Of Direct Ink Write 3D Printed Methacrylated Hyaluronic Cerium Oxide Scaffolds SB³C2023-472

Aritra Chatterjee¹, Jordan Turner², Jonathan Banks², Joan Adebawale², Deva D. Chan¹, Juana Mendenhall²
¹Purdue University, ²Morehouse College

P85 Functionalized Nanowires Successfully Load And Sustain Release Of NGF SB³C2023-594

Molly E. Czachor¹, Joel A. Finbloom², Nafisa A. Elghazali², Darnell L. Cuylear², Kevin O. Rivera², Tejal A. Desai³, Chelsea S. Bahney^{1,2}
¹The Steadman Philippon Research Institute, ²University of California – Riverside, ³Brown University

P86 The Association Between Clot Presentation On Ct, Biological Composition, And Material Properties: Implications For Pre-Treatment Imaging Biomarkers SB³C2023-421

TaJania D. Jenkins^{1,2}, Briana A. Santo^{1,2}, Shiau-Sing K. Ciecierska¹, Tatsat R. Patel^{1,2}, Debanjan Mukherjee³, Adnan H. Siddiqui^{1,2}, Vincent M. Tutino^{1,2}
¹Canon Stroke and Vascular Research Center, ²University at Buffalo, ³University of Colorado

P87 A Vascularized Tissue Model To Investigate Human Synoviocyte - Endothelial Cell Crosstalk In Joint Health and Disease SB³C2023-410

Hannah M. Zlotnick¹, Abhishek P. Dhand^{1,2}, Matthew D. Davidson¹, Gabriel J. Rodriguez-Rivera¹, Christopher J. Calo¹, Hannah K. Weppner¹, Laurel E. Hind¹, Jason A. Burdick¹
¹University of Colorado, ²University of Pennsylvania

P88 Quantifying Alignment in Engineered Tissue Constructs Using Raman Spectroscopy and Computational Modeling SB³C2023-193

Maedeh Lotfi, Hui Zhou, Janny Piñeiro Llanes, Ghatu Subhash, Chelsey S. Simmons, Malisa Sarntinoranont
University of Florida

- P89 Amobarbital Prevents Intervertebral Disc Degeneration By Inhibiting Oxidative Stress** SB³C2023-146
Venkateswaran Ganesh¹, Deborah A. Vacek¹, Douglas C. Fredericks¹, Emily B. Petersen¹, Youssef W. Naguib^{1,2}, Anupam Tiwari¹, Yochana Kancharia³, Mitchell C. Coleman¹, James A. Martin¹, Aliasger K. Salem¹, Tae-Hong Lim¹, Dongrim Seol¹
¹University of Iowa, ²Deraya University, ³Des Moines University
- P90 Gelatin Hydrogel Poly-Caprolactone 3D Printed Composite Biomaterial Characterization For Meniscal Tissue Engineering** SB³C2023-531
Anthony J. El Kommos, Gabi Schwartz, Andy J. Morejon
University of Miami
- P91 Multi-physics Modeling of Neural Dendrite Growth With Electrical Polarization** SB³C2023-079
Shuolun Wang, Xincheng Wang, Maria A. Holland
University of Notre Dame
- P92 Highly Parallel Production of Designer Organoids by Mosaic Patterning of Progenitors** SB³C2023-202
Catherine M. Porter, Alex J. Hughes
University of Pennsylvania
- P93 Epithelial Monolayers Develop Density and Effective Temperature Differentials to Migrate across Confined Matrices** SB³C2023-225
W.J. Lin, A. Pathak
Washington University

Undergraduate Research and Design

- P94 3D Printed Patient-Specific Lower Extremity Model For Assessing Developmental Dysplasia Of The Hip** SB³C2023-638
E. Fontz¹, O. Burkowski¹, J. Palmer¹, E. Scott¹, C. Price^{2,3}, V. Huayamave¹
¹Embry-Riddle Aeronautical University, ²International Hip Dysplasia Institute, ³Orlando Health
- P95 Numerical Modeling For Infants With Ductal-Dependent Pulmonary Flow** SB³C2023-641
S. Mulla, M.H. Alzaeim, W.S. Basha, K.B. Kose
Istanbul Medipol University
- P96 Development of a Novel Animal Model for Osteochondritis Dissecans: A Radiofrequency Ablation Approach** SB³C2023-644
Kosisochukwu Ogbonna-ukuku, Boyuan Liu, Kristine Fischenich, Virginia L. Ferguson
University of Colorado
- P97 Significance of Vasa Vasorum Oxygen Supply in the Nourishment of the Aneurysmal Wall** SB³C2023-617
Manoela Neves, Alexis Throop, Rana Zakerzadeh
Duquesne University

- P98 Biomechanical Follow-Up And Evaluation Of Aneurysm Growth** SB³C2023-608
F.A.M. Garbou, O.O.M. Elnamla, W.A.K.A. Saber, K.B. Kose
Istanbul Medipol University
- P99 Heart Rate Impact On Plaque Deposition At The Carotid Artery Bifurcation** SB³C2023-571
Ramita Sajankila, Esha Navaneethakrishnan, Elvan Dogan, Amir K. Miri
New Jersey Institute of Technology

Bachelor's Level Research

- P100 The Effects Of Progeria On Central Vascular Tissue, Blood Flow, And Blood Pressure** SB³C2023-646
L. Roukoz¹, T. Hopper¹, S. Murtada², J. Humphrey², C.A. Figueroa¹
¹University of Michigan, ²Yale University
- P101 Computational Modeling Of Hemodynamics In Aortic Root Enlargement** SB³C2023-642
Surya Sanjay¹, Mia Bonini¹, Alexander Makkinejad¹, Maximilian Balmus², Marc Hirschvogel², Nicholas Burris¹, Bo Yang¹, David Nordsletten¹
¹University of Michigan, ²King's College London
- P102 High Aortic Diameter Variation Is Associated With Turbulent-Like Flow Conditions In Post-Norwood Patients** SB³C2023-611
Vivian Tan¹, Ankavipar Saprungruang², Brandon Peel², Christopher K. Macgowan², David J. Barron², Shi J. Yoo², M. Owais Khan¹
¹Toronto Metropolitan University, ²University of Toronto
- P103 Development and Assessment of a New Web Application to Measure the Orientation and Alignment of Fibrous Tissue** SB³C2023-652
Katherine J. Fors, Kyle Shannon, Kate J. Benfield, Trevor J. Lujan
Boise State University
- P104 Computational Modeling of Fluid Perfusion in a Biphasic Vocal Folds Tissue During Phonation: Potential Role of Permeability** SB³C2023-616
Isabella McCollum, Alexis Throop, Durwash Badr, Rana Zakerzadeh
Duquesne University
- P105 Failure in Articular Cartilage: Finite Element Predictions of Stress, Strain, and Pressure Under Micro-Indentation Inducted Fracture** SB³C2023-630
Brandon P. Chelstrom, Dipul Chawla, Corinne R. Henak
University of Wisconsin-Madison
- P106 Comparison Of Left Ventricular Function Estimated From Inverse Finite Element Modeling Using 3D Echocardiographic And Magnetic Resonance Images** SB³C2023-607
Chenghan Cai¹, Lei Fan¹, Jenny S. Choy², Ghassan S. Kassab², Lik Chuan Lee¹
¹Michigan State University, ²California Medical Innovations Institute
- P107 A New Method For Generating Virtual Bone Scans For The Purpose Of Investigating The Effects Of Cortical Microstructure** SB³C2023-614
Zachary B. Toth, Joshua Gargac
Ohio Northern University

- P108 Nintendo LABO For Serious Gaming** SB³C2023-621
Amanda M. Wells, Logan M. Suiter, Jacob G. Colwell, Joshua A. Gargac
Ohio Northern University
- P109 Fracture Risk Prediction Using Finite Element Modeling in a Canine Model of Osteosarcoma** SB³C2023-613
Chloe R. Brekhus¹, Kevin M. Labus¹, Bernard Seguin², Christian M. Puttlitz¹, Benjamin C. Gadowski¹
¹Colorado State University, ²VCA Central Victoria Veterinary Hospital
- P110 A Bioreactor towards Mechanically Stimulating Stem Cell Differentiation in Bioprinted Orthopedic Tissue Constructs** SB³C2023-658
Shreya Garg, Isadora S. Dos Passos, Hossein Vahid Alizadeh, Carolyn Kim, Jiannan Li, Yunzhi Peter Yang
Stanford University
- P111 Fisetin Treated Human Bone Marrow Aspirate Concentrate Rapidly Reduces Senescence Signatures** SB³C2023-466
Jacob B. Singer, Haruki Nishimura, Yoichi Murata, Sealy Hambright, Chelsea S. Bahney, Sudheer Ravuri, Johnny Huard, Marc J. Philippon
Steadman Philippon Research Institute
- P112 Evaluating The Understandability Of Real-Time Sonified Biofeedback Prototypes For Balance Training** SB³C2023-639
Vibha R. Iyer^{1,2}, Mitchel A. Tillman¹, Antonia M. Zaferiou¹
¹Stevens Institute of Technology, ²Georgia Institute of Technology
- P113 Analysis of Frictional Forces During Blood Clot Removal in Experimental Models of Acute Ischemic Stroke** SB³C2023-627
Omar N. Elkhayyat, Bryan C. Good
University of Tennessee
- P114 Micro-Computed Tomography For The Determination Of The Dentin-Enamel Junction Density Gradient Width** SB³C2023-650
Bradley S. Rosenberg, Michael Truhlar, Sobhan Katebifar, Alix C. Deymier
University of Connecticut Health
- P115 Directional Migration of Ovarian Cancer Cells in a 3D Microtissue Model** SB³C2023-625
Peyton E. Clark, Asha Kumari, Karthikeyan Mythreye, M.K. Sewell-Loftin
University of Alabama at Birmingham
- P116 Investigating sport-specific parameters of impacts in ice hockey** SB³C2023-618
D. Bondi, A. Clansey, K. Oxland, D. Luke, A. Rauscher, P. van Donkelaar, L. Wu
University of British Columbia
- P117 Normal Variation in Frequency- and Time-Domain Resting State EEG Metrics** SB³C2023-619
Eric Liu^{1,2}, Cidnee Luu¹, Lyndia Wu¹
¹University of British Columbia, ²University of Toronto

- P118 Optimization Of Mounting Methods For Tension-Compression Testing Of Murine Intervertebral Disc Joints SB³C2023-622**
J. Veres, S. Lim, G.D. O'Connell
University of California, Berkeley
- P119 Pregnancy And Age Differentially Affect Mechanically-Induced Collagen Damage in Murine Uterosacral Ligaments SB³C2023-628**
Catalina S. Bastías¹, Lea M. Savard¹, Kathleen Connell¹, Kathryn Jacobson¹, Sarah Calve¹, Virginia L. Ferguson¹, Callan M. Luetkemeyer^{1,2}
¹University of Colorado, Boulder, ²University of Illinois Urbana-Champaign
- P120 Simultaneous Measurements of Temperature and Blood Perfusion Rate During Surface Cooling to Evaluate Cooling Penetration in Human Shoulder Region SB³C2023-612**
Jacob Lombardo, Md Jawad Naseem, Liang Zhu
University of Maryland, Baltimore County
- P121 The Impact Of Lactation On Pregnancy-Induced Cardiac Hypertrophy During Postpartum In Mice SB³C2023-634**
Gracine H. Sime, Arden C. Shen, Molly S. Kaissar, Jennifer L. Anderson, Craig J. Goergen, Kyoko Yoshida
¹University of Minnesota, ²Purdue University
- P122 Application of 3D Printing in Shape Memory Polymer-Based Endovascular Embolization for Preventing Intracranial Aneurysm Rupture SB³C2023-631**
Tanner Cabaniss¹, Sergio A. Pineda-Castillo¹, Bradley N. Bohnstedt², Chung-Hao Lee¹
¹University of Oklahoma, ²Indiana University
- P123 Modulating The Axial Displacement Of Two Photon Polymerized Human Lamina Cribrosa Models SB³C2023-620**
Brock J. Pemberton, Remi J. Shittu, Jonathan P. Vande Geest
University of Pittsburgh
- P124 Eye-specific 3D Models Of Lamina Cribrosa Hemodynamics Show Shared Trends In Blood Flow, Oxygenation And Sensitivity To Vessel Diameter SB³C2023-629**
Andrew Theophanous¹, Shaharoz Tahir¹, Yuankai Lu¹, Yi Hua^{1,2}, Ian A. Sigal¹
¹University of Pittsburgh, ²University of Mississippi
- P125 Characterization Of A Polymeric Device For Localized And Controlled Drug Delivery To Cervical Cancer SB³C2023-657**
P. Phillips, M. Elbjorn, J. Provencio, D. Di Rocco, R.L. Hood
University of Texas at San Antonio
- P126 Investigating Anthropomorphic Hand Movement Patterns To Sign American Sign Language (ASL) Accurately And Repeatedly SB³C2023-655**
Lillie Bukzin¹, Sophi Schneider¹, Julia Zelevinsky¹, Ethan Danahy¹, Samantha Johnson²
¹Tufts University, ²Tatum Robotics
- P127 Quantitative Polarized Light Imaging of Porcine Pulmonary Valve Leaflets SB³C2023-626**
Shreya Sreedhar, Connor Link, Daniel P. Pearce, Colleen M. Witzenburg
University of Wisconsin-Madison

- P128 Handheld shear wave tensiometer measurements are sensitive to regional loading in phantom collateral ligaments** SB³C2023-653
Mary E. Laudon, Lesley R. Arant, Joshua D. Roth
University of Wisconsin-Madison
- P129 A Mechanical Model Of Glenohumeral Stability Across Species** SB³C2023-656
S. Li¹, I. Kurtaliaj², S. Swartz³, S. Thomopoulos², G.M. Genin¹
¹Washington University, ²Columbia University, ³Brown University
- P130 Automating Collagen Gel Image Segmentation Using Detectron2: An Application of Modern Computer Vision Techniques** SB³C2023-648
Michael I. Cafiero¹, Spencer P. Lake¹, Michael A. David²
¹Washington University, ²University of Colorado
- P131 Clinical Immersion of Undergraduate Biomedical Engineering Students: Best Practices for Short-Term Programs** SB³C2023-373
Emily L. Lothamer^{1,2}, Katherine R. Moravec^{1,2}, Amy Hoene¹, P. Mike Wagoner¹, Daniel J. Beckman¹, Craig J. Goergen^{1,2}
¹Indiana University, ²Purdue University

MS-Level Research

- P132 Tracking The Response Of A Sustained Dynamic Compression Device In An Ovine Tarsal Fusion Model** SB³C2023-465
Erin E. Estrada¹, Jeremiah T. Easley¹, David L. Safranski², Dave Latt³, Naohiro Shibuya⁴, Christian M. Puttlitz¹, Ben C. Gadowski¹
¹Colorado State University, ²Enovis Foot & Ankle, ³University of Arizona, ⁴Veterans Memorial Hospital
- P133 Fluid-Structure Interaction Simulation And Experimental Validation Of Bioprosthetic Heart Valves** SB³C2023-175
Masod Sadipour, Ali Azadani
University of Denver
- P134 A Novel Self-Sealing Dialysis Port** SB³C2023-493
Jacob M. Wright¹, Alan I. Benvenisty², Kenneth R. Nakazawa², Marina de Cos¹, Kirk N. Campbell¹, Eric G. Lima², Evren U. Azeloglu¹
¹Ichon School of Medicine, ²Cooper Union
- P135 An Anthropomorphic, Actuated Wrist for Achieving Biomimetic Motion of a Robotic Hand** SB³C2023-462
Jonathan M. Rooney¹, Samantha T. Johnson², Chiara Bellini¹
¹Northeastern University, ²Tatum Robotics
- P136 Multi-Modal Analysis Of Intracranial Aneurysms To Explore The Relationship Between Wall Enhancement, Phenotype, Internal Stress, And Intracardiac Hemodynamics** SB³C2023-460
Jay P. Shah, Sricharan S. Veeturi, Nandor Pinter, Ammad A. Baig, Munjal Shah, Tatsat R. Patel, Adnan H. Siddiqui, Vincent M. Tutino
University of Buffalo

- P137 A Multi Center Ilias Registry Based Diagnostic Cutoff For Pressure Drop Coefficient In Relation To The Current Pressure And Flow Endpoints In Patients With Coronary Artery Dysfunction** SB³C2023-304
Shreyash M Manegaonkar¹, Mohamed A Effat¹, Tim P van de Hoef², Rupak K Banerjee¹
¹University of Cincinnati, ²Amsterdam UMC
- P138 Reaction Kinetics In Electroosmotic Flow Driven Microfluidic Device For Detection Of Antigen** SB³C2023-603
Israel O. Ajiboye, Rupak K. Banerjee
University of Cincinnati
- P139 Quantification Of Tumor Biophysical Heterogeneity Through Mechanical And Ultrastructural Analysis** SB³C2023-537
Bradley J. Mahaffey, Zachary P. Fowler, Zoe Lung, Viven Dang, Neha Anil, Marco Munoz, Joseph Chen
University of Louisville
- P140 Studying The Mechanical Reference Domain Of The Heart For Cardiovascular Biomechanics** SB³C2023-502
John Sayut¹, Javiera Jilberto Vallejos¹, Sandra Hager¹, Mia Bonini¹, Marc Hirschvogel¹, David A. Nordsletten^{1,2}
¹University of Michigan, ²King's College London
- P141 Assessing Transmural Myocardial Perfusion In Healthy And Diseased Pigs Using Multi-Scale Computational Modeling** SB³C2023-507
Victoria E. Sturges¹, Alyssa Taylor-LaPole², Cooper M. Warne³, Hamidreza Gharahi¹, Elaleh Rahbar⁴, Jonathan D. Tune³, Daniel Beard¹, C. Alberto Figueroa¹
¹University of Michigan, ²NC State University, ³University of North Texas, ⁴Wake Forest
- P142 Bulk Material Density is Associated with Mechanical Response of Polydimethylsiloxane and Porcine Thoracic Aortic Tissue** SB³C2023-411
Pete H. Guelnder, Alexandria Trevino, Ronald Fortunato, Cyrus J. Darvish, Emma E. Ahlgren, Isabelle K.M. Chickanosky, Timothy K. Chung, Keshava Rajagopal, Kumbakonam R. Rajagopal, Spandan Maiti, Chandler C. Benjamin, David A. Vorp
University of Pittsburgh
- P143 Visualizing the Orifice of Visceral Arteries for In Situ Fenestration of AAA Endovascular Stent Grafts** SB³C2023-415
Cyrus J. Darvish, Nicholas P. Lagerman, Oldrich Virag, Mohammad H. Eslami, David A. Vorp, Timothy K. Chung
University of Pittsburgh
- P144 The Role Of Annuloplasty Ring Shape And Size On Tricuspid Valve Repair** SB³C2023-329
Collin E. Haese, Mrudang Mathur, Manuel K. Rausch
University of Texas at Austin
- P145 Coculture and Conditioned Media Enhance Mechanical Function of iPSC-Derived Cardiomyocytes on a 2D Micropatterned Substrate** SB³C2023-028
Mitchell Josvai, Alana Stempien, Jacob Notbohm, Jianhua Zhang, Timothy J. Kamp, Wendy C. Crone
University of Wisconsin-Madison

P146 Bladder Biomechanics - Filling And Voiding SB³C2023-543

Juan Pablo Gonzalez-Pereira, Cody J. Johnson, Wade A. Bushman, Shane A. Wells, Alejandro Roland-Alzate
University of Wisconsin-Madison

Poster Session II

Biotransport

P1 Focused-Ultrasound Mediated Gene Delivery To Brain Without Blood-Brain Barrier Opening SB³C2023-246

Hanwen Fan, Mohammadaref Ghaderi, Qi Cai, Shashank Sirsi, Zhenpeng Qin
University of Texas

P2 Effect of Acoustic Radiation Force and Microbubble Size Parameters on AvB₃ Integrins - Targeting In Microvessel Phantoms SB³C2023-544

Jair I. Castillo¹, J. Angel Navarro-Becerra¹, Federico Di Ruzza², Mark Borden¹
¹University of Colorado, ²University of Rome

P3 DMSO-free Cryopreservation Of Mammalian Cells Using Agarose Hydrogel Encapsulation SB³C2023-077

M Wang, A Mahajan, A Aksan
University of Minnesota

P4 Altered Oxygen Transport In Intracranial Aneurysms In Sickle Cell Disease SB³C2023-198

Marisa S. Bazzi, Hadi Wiputra, David K. Wood, Victor H. Barocas
University of Minnesota

P5 Toward Multiplexed Single-Cell Western Blotting Using DNA-Barcoded Readout SB³C2023-056

Mariia Alibekova Long, William KJ Benman, Lukasz J Bugaj, Alex J Hughes
University of Pennsylvania

P6 Technology For Rapid Rewarming Of Refrigerated Breast Milk SB³C2023-261

Melika Mehrabi Dehdezi, Marissa N. Rylander, Christopher G. Rylander
University of Texas at Austin

P7 Regulating Nanoscale Heat Transfer With Janus Nanoparticles SB³C2023-226

C. Xie, B. Wilson, Z. Qin
University of Texas at Dallas

P8 A Slim, Pulse-Driven Microfluidic Device for Insulin Delivery SB³C2023-255

Shuyu Zhang^{1,2}, Rafael V. Davalos^{1,2}, Anne E. Staples^{1,2}
¹Wake Forest, ²Virginia Tech

P9 Quantification Of Cationic Solute Diffusion And Fixed Charge Density In Human Synovium SB³C2023-101

Alexandra L. Davis, Ashish Vaidyanathan, Milad Rohanifar, Lori A. Setton
Washington University in St. Louis

Design, Dynamics & Rehabilitation

- P10 A Parabolic Modeling Of Carpal Arch Area Expansion** SB³C2023-062
David Jordan, Hui Zhang, Zong-Ming Li
University of Arizona
- P11 Understanding Fabric Friction to Reduce the Risk of Pressure Injuries in Wheelchair Users** SB³C2023-325
Archana Lamsal, Tamara R. Bush
Michigan State University
- P12 Kinematic Decomposition Of A Living Octopus: Application To Soft Robotic Assistive Devices** SB³C2023-365
Garrett S. Weidig, Brittany Bush, Fermin Jimenez, Galit Pelled, Tamara Reid Bush
Michigan State University
- P13 Fixation Analysis of Bone-Prosthesis Interface Micromotion of a Cementless Talar Component** SB³C2023-075
Irwan S.M. Moideen, Jun Wei Lee, Yu Shen Ong, Chin Tat Lim, Desmond Y.R. Chong
Singapore Institute of Technology, National University Hospital
- P14 Biomechanical Improvements In Gait With Carbon-Fiber Orthotic Insole For Post-Operative Tibiotalar Arthrodesis Patients** SB³C2023-424
Adam J. Bradshaw, Austin J. Garcia, Colin R. Smith, Thomas O. Clanton, Scott Tashman
Steadman Philippon Research Institute
- P15 Reduced Sensor Set For Assessment Of Hand Posture** SB³C2023-559
Ranjith Madhana-Gopal, Sara E. Wilson
University of Kansas
- P16 Individuals With Rotator Cuff Tears Requiring Surgery After Exercise Therapy Have Less Inferiorly Directed Muscle Forces Post-Exercise Therapy** SB³C2023-167
Luke T. Matter, Arash B. Mahboobin, Adam J. Popchak, William J. Anderst, Volker Musahl, James J. Irrgang, Richard E. Debski
University of Pittsburgh
- P17 Developing and Testing a Novel Device for Detecting Peripheral Artery Disease Using Radio Frequency Energy** SB³C2023-615
J Nelson, C Cobb, J Keller, D Nelson, M Francis
University of South Alabama
- P18 Performance comparison of portable suction devices** SB³C2023-264
Saketh R. Peri, Forhad Akhter, Robert A. De Lorenzo, R. Lyle Hood
University of Texas
- P19 Testing the Validity of Various Viscosity Values for a Versatile Oxygenating Perfusion System** SB³C2023-623
A Fasci, S Salazar, J Oseghale, M Garcia, A Khalil, B Wearden, L Muenchow, J Gonzalez, C Villareal, D Portillo
University of Texas at San Antonio

- P20 Multifiber Computational Modeling of Hollow-Fiber Hemodialyzers** SB³C2023-256
Ruhit Sinha, Anne E. Staples
Virginia Tech
- P21 An Intravascular Catheter With Switchable Flexural Rigidity** SB³C2023-269
D.G. Rucker, J.W. Osbun, M.A. Zayed, G.M. Genin
Washington University
- P22 Tissue Diffusion and Two Component Computational Model to Predict Leaching from Medical Devices** SB³C2023-068
Martin L. Tanka¹, David M. Saylor², Robert M. Elder²
¹*Western Carolina University*, ²*US FDA*

Education

- P23 Building Entrepreneurial Mindset: Motivating Curiosity, Connections, and Creating Value in an Assistive-Device Design Project** SB³C2023-316
Joshua A. Gargac
Ohio Northern University
- P24 Scaffolded And Iterative Course Design In a Biomechanics Laboratory Course** SB³C2023-352
S Bansal, J Benson, S Sullivan, E Corbin
University of Delaware
- P25 Effect Of Standards-Based Grading On The Course Grade Distribution In A Biomechanics Course** SB³C2023-488
Kenneth J Fischer, Christopher J Fischer
University of Kansas

Fluid Mechanics

- P26 Investigating the impact of aortic root geometry on TAVI implantation using 3D reconstructions and FSI** SB³C2023-053
K Bates, K Lachapelle, G Martucci, RL Leask
McGill University
- P27 Advance In Hybrid Cardiovascular Modeling: Coupling Volumetrically Dynamic In-Vitro Experiments To Numerical Physiology Simulation** SB³C2023-103
Abraham E. Umo, Ethan O. Kung
Clemson University
- P28 Toward Real-Time Simulation of Cardiovascular Flows by Introducing a Stabilized Time-Spectral Finite Element Method** SB³C2023-085
Dongjie Jia, Mahdi Esmaily
Cornell University

- P29 Computational Modeling Of Coronary Venous Retroperfusion Treatments For Ischemia** SB³C2023-052
Haifeng Wang, Lei Fan, Jenny S. Choy, Ghassan S. Kassab, Lik Chuan Lee
¹Michigan State University, ²California Medical Innovation Institute
- P30 Impact of the Coronary Stent Footprint on Wall Shear Stress in Patient-Specific Arteries - Analysis from the Shear-Stent Trial** SB³C2023-322
I Shah^{1,2}, D Molony³, K. Crawford^{2,3}, A. Lefieux², A. Veneziani², H. Samady^{2,3}
¹Georgia Institute of Technology, ²Emory University, ³Northeast Georgia Medical Center
- P31 A 3D Particle Tracking Study on the Blood Residence Time in a Cerebral Aneurysm under Different Inflow Conditions** SB³C2023-552
Huang Chen, Roya Kamali, Thangam Natarajan, Satheesh Kumar Harikrishnan, Lakshmi Dasi
Georgia Institute of Technology
- P32 Biomechanical Follow-Up and Evaluation of Aneurysm Growth** SB³C2023-323
F.A.M Garbou, O.O.M. Elnamla, W.A.K.A. Saber, K.B. Kose
Istanbul Medipol University
- P33 The Impact Of Transcatheter Aortic Valve Replacement Deployment Parameters On Coronary Artery Hemodynamics** SB³C2023-007
Seyedvahid Khodaei, Zahra Keshavarz-Motamed
McMaster University
- P34 Developing a Perfusion Optimization Framework For Synthetic Vasculature In Biofabrication Applications** SB³C2023-564
Zachary A. Sexton, Karthik Menon, Lazaros Papamanolis, Alison Marsden
Stanford University
- P35 Quantitative comparison of flow parameters in rigid vs compliant aneurysm models using 4D particle image velocimetry (PIV)** SB³C2023-157
Nikhil S. Shirdade, Sandy Karam, Baha T. ElKhader, Ephraim W. Church, Guha Manogharan, Melissa C. Brindise
Penn State
- P36 Tomographic X-ray Particle Tracking Velocimetry And Possible Applications In Biological Fluid Dynamics** SB³C2023-496
Jason T. Parker, Simo A. Mäkiharju
University of California - Berkeley
- P37 Vascular Cross-Section Morphometrics Can Predict First Pass Outcome Of Mechanical Thrombectomy For Ischemic Stroke** SB³C2023-188
Briana A. Santo, S.M.M. Janbeh Sarayi, Muhammad Waqas, Andre Monteiro, Adnan H. Siddiqui, Vincent M. Tutinio
University at Buffalo
- P38 Bovine Pericardium Density Measurement And Its Implications On Leaflet Stress Distribution In Bioprosthetic Heart Valves** SB³C2023-107
Masod Sadipour, Ali Azadani
University of Denver

- P39 A Novel Electrochemical Catheter For Cardiac Output Monitoring** SB³C2023-055
Marco A. Nino, Abdulsattar H. Ghanim, Syed Mubeen, Suresh M.L. Raghavan
University of Iowa
- P40 Computational Fluid Dynamics Simulations Of Aortic Dissection Using Immersed Boundary Method** SB³C2023-117
Gokul G. Anugrah, Sam Tyagi, Mary B. Sheppard, Christoph Brehm, Jonathan F. Wenk
University of Kentucky
- P41 Peristalsis Alone Is Inconsistent With Measured Flow In The Paravascular Space** SB³C2023-281
M. Keith Sharp
University of Louisville
- P42 An Euler-Lagrange Approach For Modeling Particle-Laden Flows In Biological Applications** SB³C2023-401
Abhilash Reddy Malipeddi, Jesse Capecehatro, C. Alberto Figueroa
University of Michigan
- P43 Pulse Wave Velocity Increases With Extending The Length Of Vascular Stent-Grafts** SB³C2023-189
Ramin Shahbad, Anastasia Desyatova
University of Nebraska Omaha
- P44 Design and characterization of a silicone venous valve model** SB³C2023-306
Matthew S. Ballard, Dallin Brimhall, Sarah Dayley, Andrew Rasmussen
Utah Valley University

Solid Mechanics: Cardiovascular

- P45 Comparing Approaches to Estimate Failure Strength of Sutured Patches Used in Pediatric Cardiac Surgery** SB³C2023-580
Shannen B. Kizilski^{1,2}, Dominic P. Recco^{1,2}, Lauren E. Marshall¹, Nicholas E. Kneier¹, Patrick D. Earley¹, Peter E. Hammer^{1,2}, David M. Hoganson^{1,2}
¹Boston Children's Hospital, ²Harvard College
- P46 Simulation of a Repair on a Dynamic Patient-Specific Left Atrioventricular Valve Model** SB³C2023-520
Stephen Ching¹, Christopher Zelonis¹, Christian Herz¹, Patricia Sabin¹, Muhammad Nuri¹, Yan Wang¹, Andras Lasso², John Moore³, Terry Peters⁴, Matthew A. Jolley¹
¹Children's Hospital of Philadelphia, ²Queen's University, ³Archetype Medical Inc., ⁴Western University
- P47 4D Ultrasound-Based Regional Mechanical Characterization Of Abdominal Aortic Aneurysms Using Virtual Fields Method** SB³C2023-360
Mirunalini Thirugnanansambandam^{1,2}, Esther J Maas^{1,2}, Arjet HM Nievergeld^{1,2}, Marc RHM van Sambeek^{1,2}, Stephane Avril³, Richard Lopata¹
¹Eindhoven University of Technology, ²Catharina Hospital Eindhoven, ³Ecole des MINES Saint-Etienne

- P48 Influence of Wall Shear and Mechanical Stress on Atherosclerotic Artery Disease in Human Coronaries** SB³C2023-293
Aikaterini Tziotziou¹, Eline Hartman¹, Suze-Anne Korteland¹, Antonius F.W. van der Steen¹, Joost Daemen², Jolanda Wentzel¹, Ali C. Akyildiz^{1,3}
¹Erasmus Medical Center, ²Delft University of Technology
- P49 Development of a System for Measuring Aortic Valve Deformation Using Digital Image Correlation** SB³C2023-442
Alexander W Hooke, Christopher Noble, David Morse, Melissa Young, Amir Lerman
Mayo Clinic
- P50 Personalized Intervention Cardiology For Transcatheter Aortic Valve Replacement With A Doppler-Exclusive Diagnostic Framework** SB³C2023-008
Nikrouz Bahadormanesh, Zahra Keshavarz-Motamed
McMaster University
- P51 Mechanical Properties Of Cardiac Tissue Surrogates And How They Compare To Human Cadaveric Cardiac Tissue** SB³C2023-122
Emily A. Bermel, Kevin O'Brien
Therapy Delivery Systems
- P52 Anatomical Location-Specific Quantification of Tissue Composition of Perivascular Adipose Tissue** SB³C2023-334
D. McClintock, E. Flood, S.W. Watts, W. Jackson, S. Roccabianca
Michigan State University
- P53 Altering Metabolic Cost Function Of Pulmonary Arteries To Understand Hemodynamic Response To Pah** SB³C2023-542
Haritha N. Mullagura, C. Alberto Figueroa, Seungik Baek
University of Michigan
- P54 Do Age And Sex Matter In A 1D Simulation Study Targeting Arterial Stiffness?** SB³C2023-276
Friederike Schäfer, Jacob Sturdy, Leif Rune Hellevik
Norwegian University of Technology
- P55 A Machine Learning Approach To Estimate Size And Location Of Myocardial Infarction** SB³C2023-252
RR Mehdi, EA Mendiola, R Avazmohammadi
Texas A&M University
- P56 Effective Strain Sharply Captures the Rupture Point of Aneurysm Tissues** SB³C2023-038
Ali Kamali, Kaveh Laksari
University of Arizona
- P57 Elucidating The Longitudinal Impact Of Solid Mechanics On Atherosclerotic Plaque In Patient-Specific Coronary Arteries** SB³C2023-426
Jeremy L Warren, Clark A Meyer, Heather N Hayenga
University of Texas at Dallas

- P58 Optimization and Implementation of a Carotid Quantitative Susceptibility Mapping Sequence for Atherosclerotic Plaque Vulnerability Assessment** SB³C2023-313
Brooke Tornifoglio¹, Sarah McElroy², Alan J Stone³, Karin Shmueli⁴, Catriona Lally¹
¹Trinity College London, ²Siemens Healthcare, ³St. Vincent's University Hospital, ⁴University College London
- P59 Development of Melt Electrowriting Based Polymer Heart Valve Leaflets Informed Through Finite Element Modelling** SB³C2023-285
Celia Hughes^{1,2}, Robert D Johnston¹, Alix Whelan¹, David O'Reilly², Evelyn Campbell², Caitriona Lally¹
¹Trinity College London, ²Boston Scientific Corporation
- P60 Changes In Elastin Structure And Extensibility Induced By Hypercalcemia And Hyperglycemia** SB³C2023-439
C. Yang¹, A.S. Weiss², A Tarakanova¹
¹University of Connecticut, ²The University of Sydney
- P61 Development Of A Representative Artery Model For Stent Fatigue Testing** SB³C2023-220
Jude M Hussain, Ankush Aggarwal, Andrew McBride, Robbie Brodie, Craig MacLean
University of Glasgow
- P62 Integration Of Deep Neural Networks And Finite Element Method For Biomechanical Analysis Of The Aorta** SB³C2023-499
Liang Liang¹, Minliang Liu², Wei Sun³
¹University of Miami, ²Georgia Institute of Technology, ³Sutra Medical Inc
- P63 Effect Of Aortic Root Motion On Aortic Wall Stresses In Thoracic Aortic Aneurysms** SB³C2023-201
T Kim, N Tjahjadi, X He, H Patel, N Burris, CA Figueroa
University of Michigan
- P64 Regional Heterogeneity In The Biomechanics Of Human Aorta** SB³C2023-307
M Kazim, S Razian, D Varandani, M Jadidi
University of Nebraska-Omaha
- P65 Investigation Into Clot And Stent Retriever Parameters Affecting Removal Forces In An Experimental Model Of Acute Ischemic Stroke** SB³C2023-158
Demitria A Pouls¹, Jordis E Blackburn¹, Michael T Froehler², Bryan C Good¹
¹University of Tennessee, ²Vanderbilt University Medical Center
- P66 Viscoelastic And Shear Mechanical Properties Of Human Hypertrophied Septum** SB³C2023-347
Katherine M Copeland¹, Uday Chintapula¹, Alan M Taylor¹, Duc Khang Chung¹, Yi Hong¹, Kytai T Nguyen¹, Zhi-Ping Liu¹, Matthias Peltz¹, Pietro Bajona^{1,2}, Jun Liao¹
¹University of Texas, ²Drexel University
- P67 Phase-field Modeling of Deep Vein Thrombus Embolization** SB³C2023-011
Osman Gültekin, Matthew J Lohr, Sapun H Parekh, Manuel K Rausch
University of Texas at Austin

- P68 A Neural Network-Finite Element Approach For Multibody Contact in Soft Biological Materials** SB³C2023-487
Christian L Goodbrake, Michael S Sacks
University of Texas at Austin
- P69 On The Association Of Rupture Potential Index With Abdominal Aortic Aneurysm Geometric Measures In Patients Under Surveillance** SB³C2023-394
Juan C Restrepo-Perez¹, Pratik Mitra¹, Satish C Muluk², Mark K Eskandari³, Ender A Fino¹
¹University of Texas at San Antonio, ²Allegheny Health Network, ³Northwestern University
- P70 A Computational Framework For Surgical Planning Of Pulmonary Artery Stenosis Repair In Tetralogy Of Fallot Patients** SB³C2023-474
Alessia De Nardo, Leslie Louvelle, David A. Romero, Matthew Doyle, Thomas L Forbes, Cristina H Amon
University of Toronto
- P71 A Constitutive Model That Incorporates A Microstructural Mechanism Of Homogenizing Transmural Stress Distributions In Arteries** SB³C2023-450
Taisiya Sigaeva¹, Yanhang Zhang²
¹University of Waterloo, ²Boston University
- P72 A Complete Physics-Based Model For The Full Flow Mediated Dilation (FMD) Response** SB³C2023-291
B Sidnawi¹, B Zhou¹, S Santhanam¹, Z Chen², C Sehgal², P Kaufmann³, Q Wu¹
¹Villanova University, ²University of Pennsylvania, ³University of Nevada
- P73 A Tale Of Two Mice - Hypertension, Inflammation, And Insights From Immuno-Mechanical Modeling** SB³C2023-289
Jay D Humphrey¹, Marcos Latorre², Bart Spronck³
¹Yale University, ²Universitat Politecnica de Valencia, ³Maastricht University

Solid Mechanics: Growth and Remodeling

- P74 In Vivo Multiscale Measurements Of Solid Stresses In Primary And Metastatic Tumors** SB³C2023-555
Sue Zhang¹, Rachel Passaro¹, Kathryn Regan¹, Muhamed Hadzipasic^{1,2}, Gabrielle Grifno¹, Siyi Zheng¹, Logan O'Connor¹, Vinson Chu¹, Sung Yeon Kim¹, Jiarui Yang¹, Rohin Banerji¹, Kavon Karrobi¹, Darren Roblyer¹, Mark Grinstaff^{1,2}, Hadi T. Nia¹
¹Boston University, ²Massachusetts General Hospital
- P75 Pin Loosening In External Fixation: A Finite Element Analysis To Develop An Ovine Bone Transport Model** SB³C2023-579
Michael J Poland, Yunzhi Peter Yang, Jeremiah T Easley, Jeffrey Young, Holly L Stewart, Chloe Brekhus, Christian M Puttlitz, Benjamin C Gadowski
¹Colorado State University, ²Stanford University
- P76 Validation Of A Strain-Based Lower-Limb Fracture Healing Algorithm** SB³C2023-036
George Morgan¹, Lucas Low¹, Arul Ramasamy^{1,2}, Spyros Masouros¹
¹Imperial College London, ²Royal Centre for Defence Medicine

- P77 Modeling the fracture mechanical properties of load-bearing soft biological tissues**
SB³C2023-409
Christopher Miller¹, T Christian Gasser^{1,2}
¹KTH Royal Institute of Technology, ²University of Southern Denmark
- P78 FSGe: A Computational Model for Equilibrated Cardiovascular Fluid-Solid-Growth Interaction** SB³C2023-586
Martin R Pfaller¹, Marcos Latorre², Erica L Schwarz¹, Fannie M Gerosa¹, Jason M Szafron¹, Jay D Humphrey³, Alison L Marsden¹
¹Stanford University, ²Universitat Politècnica, ³Yale University
- P79 Predictive Growth Analysis of Abdominal Aortic Aneurysms Under Surveillance Using Geometric Measures** SB³C2023-602
Pratik Mitra¹, Juan C Restrepo-Perez¹, Satish C Muluk², Mark K Eskandari³, Ender A Finol¹
¹University of Texas at San Antonio, ²Allegheny Health Network, ³Northwestern University
- P80 Vascular Smooth Muscle Cells Retain Their Material Properties in Mechanically Variant Microenvironments** SB³C2023-043
Elizabeth D Shih, Ryan R Mahutga, Katriel S Ng, Patrick W Alford
University of Minnesota
- P81 Determining The Geometrical Properties of Urinary Bladder Wall During Passive Filling**
SB³C2023-314
F Azari
University of Pittsburgh
- P82 Tropocollagen Denaturation Is Not Responsible For Sub-Yield Softening** SB³C2023-160
Noah R Pearson, Gregory M Boiczyk, William J Anderl, S Michael Yu, Kenneth L Monson
University of Utah
- P83 Contact Mechanics Based Formulation To Examine The Role Of Cellular Adhesion In Epithelial Mechanics** SB³C2023-595
M Talukder, S Kale
Virginia Tech
- P84 A Predictive Model For The Coverage Of Wounds By Skin Grafts** SB³C2023-572
Haomin Yu¹, Mohammad Jafari², Yuan Hong¹, Jacob Sandler¹, Guy M Genin¹, Farid Alisafaei^{1,2}
¹Washington University, ²New Jersey Institute of Technology

Solid Mechanics: Injury & Brain

- P85 Mathematical Dynamic Modeling (MADYMO) of the Maternal Pelvis and Neonate for Simulating Shoulder Dystocia and Delivery Maneuvers** SB³C2023-248
J Iaconainni¹, B Gonik², M Grimm³, S Balasubramanian¹, Anita Singh⁴
¹Drexel University, ²Wayne State University, ³University at Albany, ⁴Temple University
- P86 Validation of Steering Wheel Forces And Upper Extremity Loading During Rear-End Collisions Using MADYMO** SB³C2023-133
Dominic R Demma, Stephanie M Rossman, Nicole A Johns, Steven A Rundell
Explico Inc.

- P87 Rate Effects and Material Characterization of Skin During Puncture** SB³C2023-190
Joseph S LeSueur, Frank A Pintar
Medical College of Wisconsin
- P88 Impact Forces of Division 1 Collegiate Offensive and Defensive American Football Players Using Practice Sled** SB³C2023-445
Sloan Kanat, Ryan Harth, William Burghardt, Tamara Reid Bush
Michigan State University
- P89 Evaluating Material Models For Low-Frequency Magnetic Resonance Elastography Of Agarose Gels Via Finite Element Simulations** SB³C2023-396
Julian A Rey¹, Kulam N Magdoom^{1,2}, Thomas T Jones¹, Marcial Garmendia-Cedillos¹, Randall Pursley¹, Michal E Komlos^{1,2}, Thomas Pohida¹, Peter J Basser¹
¹National Institutes of Health, ²Henry M Jackson Foundation
- P90 Modal Analysis Of Natural Vibration Frequencies Of The Brain And Head** SB³C2023-051
Turner Jennings, Rouzbeh Amini, Sinan Müftü
Northeastern University
- P91 Using An Investigative Microscale Model To Study Mechanical White Matter Properties In Demyelinating Diseases** SB³C2023-046
Xuesong Zhang, Johannes Weickenmeier
Stevens Institute of Technology
- P92 Analyzing Real World Head Impacts Using The Brain Simulation Research Platform** SB³C2023-569
Ritika R Menghani, Reuben H Kraft
Pennsylvania State University
- P93 A Large Deformation Multiphase Continuum Mechanics Model For Shock Loading Of Soft Porous Materials** SB³C2023-018
Zachariah T Irwin^{1,2}, John D Clayton², Richard A Regueiro^{1,2}
¹University of Colorado, ²Army Research Laboratory
- P94 A Constitutive-Finite Element Model of Cyclic Head Rotations in the Neonatal Piglet** SB³C2023-260
Ruhit Sinha¹, Qianhong Wu², Ji Lang³, Anne E Staples¹
¹Virginia Tech, ²Villanova, ³Southeast University
- P95 Characterizing Natural Frequencies of the Hybrid III and NOCSAE Headforms** SB³C2023-526
Kristin J Dingelstedt, Steven Rowson
Virginia Tech
- P96 Comparison Of Dominant Modes Of Human Brain Deformation From Simulation And Experiment** SB³C2023-183
Amir HG Arani¹, Jordan D Escarcega¹, Antoine Jerusalem², Ruth J Okamoto¹, Philip V Bayly¹
¹Washington University, ²University of Oxford

Solid Mechanics: Joint & Spine

- P97 Superposition Testing On A Functional Spinal Unit Within A Multi-Level Spine Construct** SB³C2023-340
Callan M Gillespie, Robb w Colbrunn
Lerner Research Institute
- P98 Virtual Tensile Test Experiments To Reconcile The Meso- And Micro-Scale Mechanical Properties Of The Lung Parenchyma** SB³C2023-524
E Dimbath¹, L de Castro Brás², S George², A Vadati²
¹Duke University, ²East Carolina University
- P99 Computational and Experimental Based Guidance for Personalized Implant Selection and Alignment in Reverse Total Shoulder Arthroplasty** SB³C2023-470
Colin R Smith, Rony-Orijit Dey Hazra, Alex Brady, Matthew T Provencher, Peter J Millett, Scott Tashman
Steadman Philippon Research Institute
- P100 Effect of Labrum Size on Cartilage Mechanics in a Patient with Cam-Type Femoroacetabular Impingement Syndrome** SB³C2023-097
Luke T Hudson^{1,2}, Travis G Maak¹, Andrew E Anderson^{1,2}, Gerard A Ateshian³, Jeffrey A Weiss¹
¹University of Utah, ²Scientific Computing and Imaging Institute, ³Columbia University

Solid Mechanics: Musculoskeletal

- P101 Glutaraldehyde Crosslinking Of Collagen Is A Time Dependent Reaction On The Order Of 24 Hours** SB³C2023-589
Kimberly R Kroupa, CV Sise, Jason Fan Sinisa Vukelic, Gerard A Ateshian
Columbia University
- P102 Force Direction Is Different From Fiber Direction At The Anterior Cruciate Ligament Attachments In Porcine Knees** SB³C2023-596
D Ishii, S Koseki, S Sato, H Fujie
Tokyo Metropolitan University
- P103 Transverse Carpal Ligament Elongation After Injection Of Collagenase In Situ** SB³C2023-061
Jocelyn Hawk, David Margolis, Zong-Ming Li
University of Arizona
- P104 Evaluation of The Relative Stiffness Of Surgically Treated Ruptured and Contralateral Achilles Tendon During Healing** SB³C2023-386
Sarah Thompson Murray¹, Shabnam Rahimnezhad¹, Dov Bader², Cristy French², Karin G Silbernagel³, Daniel H Cortes¹
¹Pennsylvania State University, ²Hershey Medical Center, ³University of Delaware

- P105 Multiscale Simulations Show Role Of Diffuse Damage In Anomalous Fiber Realignment**
SB³C2023-484
Jacob S Merson, Catalin R Picu, Mark S Shephard
Rensselaer Polytechnic Institute
- P106 Muscle Err-Gamma Overexpression Mitigates The Muscle Atrophy After ACL Rupture**
SB³C2023-477
Aiping Lu¹, Katie Sikes², Ping Guo¹, Matthieu Huard¹, Kelly Santangelo², Scott Tashman¹,
Vihang A Narkar³, Johnny Huard¹
¹Steadman Philippon Research Institute, ²Colorado State University, ³University of Texas
- P107 Variable Gradients In Mineral Content And Crystallinity May Be Responsible For Mechanical Resilience Of The Dentin-Enamel Junction** SB³C2023-099
Michael Truhlar¹, Sobhan Katebifer¹, Roland Kröger³, Alix Deymier¹
¹University of Connecticut, ²University of York
- P108 Applied Stress Promotes Mineralization of Substituted Bioapatites: A Thermochemical Equilibrium Study** SB³C2023-102
Pierre A Deymier¹, Marat Latypov¹, Krishna Muralidharan¹, Alix C Deymier²
¹University of Arizona, ²University of Connecticut
- P109 Extracellular Matrix Composition And Viscoelasticity Are Longitudinally Heterogeneous In Tendon** SB³C2023-449
Hannah M Larson, Olivia J Ward, Sarah Calve
University of Colorado
- P110 In Vivo Human MRI with Loading to Evaluate Disc Mechanical Function in Young and Older Subjects** SB³C2023-184
H.R. Newman, K.D. Meadows, T.B. Elia, E.H. Williams, E.J. Vresilovic, D.M. Elliott
University of Delaware
- P111 Stress Quantification On Intact And Torn Rotator Cuff Tendons** SB³C2023-210
Nicole Tueni¹, Farid Amirouche^{1,2}
¹University of Illinois, ²Northshore University
- P112 A Single-Sensor Approach for Tracking Phase Velocity as a Proxy for In Vivo Tendon Loading** SB³C2023-080
D Schmitz¹, D Thelen¹, S Cone²
¹University of Wisconsin-Madison, ²University of Delaware
- P113 Determination Of Biomechanical Effects Of Histotripsy On Osteosarcoma In A Canine Comparative Oncology Model** SB³C2023-212
Preeya F Achari¹, Jackson Comer¹, Elliana Vickers¹, Lauren Ruger¹, Joanne Tuohy², Eli Vlaisavljevich¹, Caitlyn J Collins¹
¹Virginia Tech, ²Virginia-Maryland College of Veterinary Medicine

Solid Mechanics: Skin, Ocular, Reproductive, & Other Emerging Topics

- P114 In Vivo Testing Of Hysteresis Of The Uterine Suspensory Tissue In Chinese Women With Pelvic Organ Prolapse** SB³C2023-136
Hui Wang¹, Zhuowei Xue², Chenxin Zhang¹, Fei Feng², Chengsheng Huang², Da He², Xinyi Wang², Qingkai Wu², Jiajia Luo¹
¹Peking University, ²Shanghai Jiao Tong University
- P115 End-to-end 3D Geometric Model Reconstruction Of Pelvic Organs Based On 3D Magnetic Resonance Imaging And Deep Learning** SB³C2023-375
Hui Wang, Xiaowei Li, Chenxin Zhang, Xiuli Sun, Jianliu Wang, Jiajia Luo
Peking University
- P116 A Multi-Curve Inverse Finite Element Approach Towards Simulating Vertical Tooth Extraction Mechanics** SB³C2023-040
Timothy J Gadzella¹, Lindsey Westover¹, Owen Addison^{1,2}, Dan L Romanyk¹
¹University of Alberta, ²King's College London
- P117 Development Of A Finite Element Birthing Model To Assess Pelvic Floor Biomechanics** SB³C2023-530
M Mounzer¹, A Singh², S Balasubramanian¹
¹Drexel University of Pennsylvania, ²Temple University
- P118 A Review of the State of Soft Tissue Material Property Data for Human Body Modeling** SB³C2023-416
Justin Scott, Nicole Arnold, Tamara Reid Bush
Michigan State University
- P119 Nonlinear and Anisotropic Mechanical Response of Fish Skin** SB³C2023-581
Sean T Harrington, Frederick Sebastian, Rouzbeh Amini
Northeastern University
- P120 Mechanical Characterization Of Human Penile Tissues To Inform The Development Of Pre-clinical Testbeds** SB³C2023-312
Shirsha Bose^{1,2}, Majid A Khorshidi^{1,2}, Robert D Johnston^{1,2}, Brian Watschke³, Evania Mareena³, Daragh Nolan³, Sean Cooney³, Caitríona Lally^{1,2}
¹Trinity College Dublin, ²Royal College of Surgeons, ³Boston Scientific Corp,
- P121 Simulation Of Uterus Active Contraction And Fetus Delivery In LS-DYNA** SB³C2023-034
R Tao, M Grimm
¹Michigan State University, ²University at Albany
- P122 Visceral Pleura Mechanics: A Comparison Between Porcine And Rat Lung Tissue** SB³C2023-203
Gustavo O Ramirez, Crystal A Mariano, Talyah M Nelson, Samaneh Sattari, David Carter, Erica C Heinrich, Mona Eskandari
University of California - Riverside
- P123 Effect Of GAGs On Shear Properties Of Cornea** SB³C2023-364
H Hatami-Marbini, ME Emu
University of Illinois

- P124 Effect Of GAGs On Tensile Properties Of Posterior Cornea** SB³C2023-392
ME Emu, H Hatami-Maribini
University of Illinois
- P125 Characterization of Lung Lobar Sliding Kinematics Using Finite Element Modelling and Helmholtz-Hodge Decomposition** SB³C2023-042
Adam E Galloy, Joseph M Reinhardt, Suresh ML Raghavan
University of Iowa
- P126 Quantifying Lower Birth Canal Viscoelastic Properties During The First Stage Of Labor** SB³C2023-073
Mariana Masteling, John O DeLancey, James A Ashton-Miller
University of Michigan
- P127 Are Mice A Good Model System to Study Sex And Age-Dependent Skin Properties?** SB³C2023-020
Chien-Yu Lin¹, Gabriella P Sugerman¹, William D Meador¹, Sotirios Kakaletsis¹, Adrian B Tepole², Manuel K Rausch¹
¹University of Texas at Austin, ²Purdue University
- P128 Finite Element Modeling Of C-Section Scars And Scar Defects** SB³C2023-430
Adrienne K Scott¹, Erin M Louwagie², Kristin M Myers², Michelle L Oyen¹
¹Washington University in St. Louis, ²Columbia University

Tissue & Cellular Engineering

- P129 A Novel Strain Energy-Based Method to Dynamically Stimulate Three-Dimensional Cellular Constructs** SB³C2023-500
Amevi M Semodji, Faith R Wilder, Anamaria G Zavala, Sean M Howard, Gunes Uzer, Trevor J Lujan
Boise State University
- P130 Substrate Mechanical Stiffness Regulates Epigenetic Modifications and Chromatin Remodeling in Mesenchymal Stromal Cells During Monolayer Culture Over Passaging** SB³C2023-081
Samantha Kaonis, Lauren Monroe, Emily Kaplan, Jack Forman, Soham Ghosh
Colorado State University
- P131 Transmembrane Hydrostatic Pressure Differentials As A Biophysical Basis For Air-Liquid Interface Differentiation** SB³C2023-523
Chen Li, Tanvi A Javkar, Syeda SZ Zaidi, John W Hanrahan, Alex Gregorieff, Christopher Moraes
McGill University
- P132 Design of a collagen hydrogel with embedded smooth muscle cells for the 3D study of cell-matrix interactions** SB³C2023-129
Chloe Techens¹, Amira Ben Hassine¹, Edwin-Joffrey Courtial², David Eglin¹, Stéphane Avril¹
¹Université Jean Monnet Saint-Etienne, ²ICBMS

- P133 A Pneumatically Controlled Device For Uniaxial And Biaxial Cell Stretching** SB³C2023-310
Jue Wang, Aritra Chatterjee, Clarisse M Zigan, Alex Chortos, Deva D Chan
Purdue University
- P134 Local ECM Stiffness Modulates Epithelial Cell Response To Micropatterns** SB³C2023-127
Tasnim Shireen, Rajath D Prabhu, Deekshitha Jetta, Susan Z Hua
University at Buffalo
- P135 Investigating The Effect Of Tensile Strain On The Mechanical Memory Of Endothelial Cells** SB³C2023-633
Michael Heim, Bronte Miller, Mary-Kathryn Sewell-Loftin
University of Alabama at Birmingham
- P136 Human iPSC Hydrogel Encapsulation For Efficient Production Of Embryoid Bodies** SB³C2023-266
Matthew T Conway, Edward A Sander, Kristan S Worthington
University of Iowa
- P137 Mesenchymal Transitions in Glioblastoma Enhance Confined Migration Through Nuclear Softening** SB³C2023-233
Landon Teer, Dominic Armagno, Bradley Mahaffey, Neha Anil, Marco Muñoz, Sihan Sun, Joseph Chen
University of Louisville
- P138 Tailoring the release profile of a small molecule agonist to stimulate hedgehog signaling during tendon-to-bone integration** SB³C2023-467
J Marcelin, R Madi, T Kamalidinov, X Jiang, S Assi, DH Kim, S Keith Lang, RL Mauck, A Kuntz, N Dymant
University of Pennsylvania
- P139 A Mathematical Model Of Kidney Podocyte Responses To Fluid Shear And Actomyosin Contractility Predicts Changes To Kidney Filtration In A Mouse Model Of Kidney Injury** SB³C2023-244
S Jiang¹, YY Huang¹, P Puapatanakul¹, JH Miner¹, F Alisafaei², HY Suleiman¹, GM Genin¹
¹Washington University, ²New Jersey Institute of Technology
- P140 Endothelin-1 Expression Is Dependent On The Stability Of Endothelial Glycocalyx Heparan Sulfate** SB³C2023-070
Santiago Rivero, Solomon A Mensah
Worcester Polytechnic Institute
- P141 Biomechanics of Cancer Cell Invasion Across the Vascular Endothelium** SB³C2023-045
Chaohui Jiang, Guangsong Xie, Baohua Ji
Zhejiang University

Undergraduate Research and Design

- P142 Assistive Paddle Mounting System For Para-Kayaking Sports** SB³C2023-636
Betsabe Hernandez, Dinh L. Le, Weston J. Randall, Erin C. Ray
Embry-Riddle Aeronautical University

P143 3D Reconstruction of Syndactylized Hand in Autodesk ReCap Photo with Arduino

SB³C2023-632

Caleb E Scheideger, Anna S Dillenbeck, Hui Shen, Xiangyi Cheng
Ohio Northern University

P144 Ultraportable Extracorporeal Membrane Oxygenation Machine SB³C2023-645

D Kurtz, L Windover, C Davies
Queen's University

P145 CogniGuard SB³C2023-654

J Funk, J Aikens, C Davies
Queen's University

P146 Tracking of Pedicle Screws Using Extenders and Lenticular Arrays SB³C2023-649

Alicia C Repka¹, Jacob Sandler¹, Halle Lowe¹, Peter Brunner¹, Robert B Pless², Camilo A Molino¹, Eric C Leuthardt¹, Carl D Hacker¹, Daniel W Moran¹, Guy M Genin¹
¹Washington University in St. Louis, ²George Washington University

MS Research

P147 Development And Characterization Of A Low Intensity Vibrational System For Microgravity Studies SB³C2023-577

Omor M Khan¹, Chess Necessary², Maximilien DeLeon³, Mary Farach-Carson³, Elizabeth Blaber⁴, Danielle Wu³, Aykut Satici¹, Gunes Uzer¹

¹Boise State University, ²Space Tango, ³University of Texas, ⁴Rensselaer Polytechnic Institute

P148 Local Nonlinear Elastic Response of Extracellular Matrices SB³C2023-377

Haiqian Yang, Ming Guo
Massachusetts Institute of Technology

P149 Impact Of Vimentin Intermediate Filament On 3D Multicellular Development and Morphogenesis SB³C2023-339

Camille D Rodriguez, Ming Guo
Massachusetts Institute of Technology

P150 Aging Influences Static and Dynamic Properties of Primary Mouse Pulmonary Fibroblasts through Cellular Senescence SB³C2023-398

Lani Lee¹, Krishna Penumatsa², Ming Guo¹
¹Massachusetts Institute of Technology, ²Tufts Medical Center

P151 Wavy Microchannels Suppress Persistent Cell Migration SB³C2023-492

Ze-Hao Lin, Pen-Hsiu Grace Chao
National Taiwan University

P152 Promotion Of Chronic Wound Healing By Aligned Fiber Scaffolds: Modeling And Model Verification SB³C2023-534

Yin-Yuan Huang^{1,2}, Xiangjun Peng¹, Chengli Li², Kunkoo Kim², Peilun Hu², Chun-Yi Yang², Pengchao Ma², Yuxuan Huang¹, Shumeng Jiang¹, Chengqing Qu¹, Farid Alisafaei^{1,3}, Xiumei Wang², Guy M Genin¹

¹Washington University, ²Tsinghua University, ³New Jersey Institute of Technology

- P153 Computational Mechanobiology Model Evaluating Healing Of Postoperative Cavities Following Breast-Conserving Surgery** SB³C2023-277
Zachary J Harbin¹, Emma L Vanderlaan^{1,2}, Sherry L Voytik-Harbin¹, Adrian Buganza Tepole¹
¹Purdue University, ²Indiana University
- P154 Effects of dynamic compressive loading on mechanical and biochemical properties of chondrocyte-embedded hydrogels** SB³C2023-348
Clarisse Zigan, Honganh Nguyen, Aritra Chatterjee, Alex Chortos, Deva D Chan
Purdue University
- P155 Correlating Ball Delivery Parameters With Head Impact Kinematics For A Common Soccer Heading Protocol In Brain Injury Research** SB³C2023-354
Keili R Shepherd, David Luke, Rebecca Kenny, Lyndia C Wu
University of British Columbia
- P156 Clustered Low Severity Impacts May Lead To Concussions** SB³C2023-355
David S Luke, Marko M Elez, Daniel R Bondi, Adam C Clansey, Alexander Rauscher, Paul van Donkelaar, Lyndia C Wu
University of British Columbia
- P157 Micromechanical Response Of Fibrous Networks Subjected To Far Field And Local Contractile Forces** SB³C2023-463
Ashutosh Mishra, Hamed Hatami-Marbini
University of Illinois - Chicago
- P158 Rheological characterization of collagen-hyaluronic acid co-gels for 3D cell culture** SB³C2023-481
Jared A Tucker, Benjamin L Clarke, Victor K Lai
University of Minnesota-Duluth
- P159 Click Chemistry-Based Injectable Hydrogel for Repair of the Annulus Fibrosus Following Intervertebral Disc Herniation** SB³C2023-139
Emily E Sharp¹, Karen L Xu¹, Ryan C Locke^{1,2}, Zhiliang Cheng¹, Jason A Burdick³, Sarah E Gullbrand^{1,2}, Robert L Mauck^{1,2}
¹University of Pennsylvania, ²Crescenz VA Medical Center, ³University of Colorado
- P160 Strength, Stiffness, And Toughness Of Tendons, And Their Variation With Tendon Function** SB³C2023-282
Yuxuan Huang¹, Ulrike GK Wegst², Victor Birman³, Stavros Thomopoulos⁴, Guy M Genin¹
¹Washington University, ²Northeastern University, ³Missouri University, ⁴Columbia University

CONFERENCE ABSTRACTS

ESTIMATION OF AORTIC SYSTOLIC BLOOD PRESSURE FROM BRACHIAL BLOOD PRESSURE WAVEFORM USING DEEP LEARNING

Vasiliki Bikia (1,2), Marija Lazaroska (1), Sokratis Anagnostopoulos (1), Georgios Rovas (1), Hao-min Cheng (3,4), Chen-Huan Chen (4,5), Nikolaos Stergiopoulos (1)

- (1) Laboratory of Hemodynamics and Cardiovascular Technology, Institute of Bioengineering, Swiss Federal Institute of Technology, Lausanne, Vaud, Switzerland.
- (2) Division of Vascular Surgery, School of Medicine, Stanford University, California, USA.
- (3) Ph.D. Program of Interdisciplinary Medicine (PIM), National Yang Ming Chiao Tung University College of Medicine, Taipei, Taiwan.
- (4) Division of Faculty Development, Taipei Veterans General Hospital, Taipei, Taiwan.
- (5) College of Medicine, National Yang Ming Chiao Tung University, Taipei, Taiwan.

INTRODUCTION

Analysis of the arterial pressure waveforms can offer a deep insight into the hemodynamic status of a patient and might be a promising prognostic factor of cardiovascular disease. The central aortic blood pressure, measured in the ascending aorta, has been shown to be a more accurate predictor of clinical outcomes in comparison to blood pressure measurements acquired in the periphery, such as the brachial artery [1].

METHODS

In this study, we developed and validated a deep learning method for estimating aortic systolic blood pressure (aSBP) from the brachial blood pressure waveform (brBP_{wave}) using convolutional neural networks (CNNs). We used *in vivo* invasive data collected from 38 subjects [2] and *in silico* data (3'748 virtual individuals) [3] generated from a previously validated mathematical model of the cardiovascular system [4]. Simultaneous high-fidelity, invasive central aortic and brachial pressure waveforms were recorded for 20–30 consecutive beats to cover at least two respiratory cycles. A 2F custom-made dual pressure sensor catheter (Model SSD-1059, Millar Instruments Inc. Houston, TX, USA) was advanced within a standard 6F Judkins coronary artery catheter. The first pressure sensor was placed at the ascending aorta and the second pressure sensor was positioned in the brachial artery at the level of the mid humerus. We performed two training experiments for the CNN models: 1) a CNN was trained and tested using the *in vivo* dataset (CNN_{in vivo}), and 2) a second CNN was trained using *in silico* data and tested using the *in vivo* data (CNN_{TL}). The idea behind the second experiment (transfer learning) was to assess whether the *in silico* data can simulate accurately the content of human data in the prediction of aSBP from the brBP_{wave}.

RESULTS

The CNN trained and tested using the *in vivo* data yielded the highest accuracy with an RMSE loss of 6.46 mmHg (bias = -0.4 mmHg,

limits of agreement (LoA) = [-13, 12] mmHg, $r=0.95$). The performance of the CNN trained with the *in silico* was similarly highly satisfactory, achieving an RMSE loss of 8.61 mmHg (bias = 0.2 mmHg, LoA = [-20, 21] mmHg, $r=0.87$). A slight systematic bias was reported in the Bland-Altman analysis of CNN_{TL} (aSBP was underestimated at higher BP level and overestimated at lower BP level). The comparison between the model predictions and the reference data is presented in Figure 1.

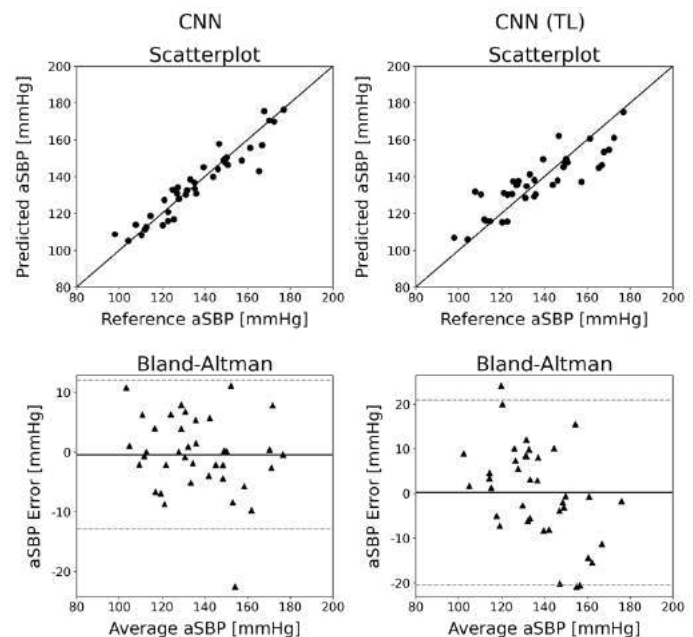


Figure 1: Scatter plots and Bland-Altman plots: Predicted versus reference data for CNN_{in vivo} (left panel) and CNN_{TL} (right panel).

DISCUSSION

The results showed that the methods used to obtain the predictions of aSBP are accurate and may facilitate the acquisition of aSPB in the clinical setting. Importantly, *in silico* data may offer a valuable alternative for training purposes when high-volume *in vivo* data are difficult to find. Future work will focus on improving the CNN architecture to correct for potential bias resulted from transfer learning. Pending validation using non-invasively measured brachial pressure waveforms, the proposed methodology provides plausible aSBP estimation from the morphology of the raw brBP_{wave}.

ACKNOWLEDGEMENTS

None to declare.

REFERENCES

- [1] R. R. Townsend *et al.*, “American Society of Hypertension position paper: central blood pressure waveforms in health and disease,” *J Am Soc Hypertens*, vol. 10, no. 1, pp. 22–33, Jan. 2016, doi: 10.1016/j.jash.2015.10.012.
- [2] Y.-T. Shih, H.-M. Cheng, S.-H. Sung, W.-C. Hu, and C.-H. Chen, “Application of the N-point moving average method for brachial pressure waveform-derived estimation of central aortic systolic pressure,” *Hypertension*, vol. 63, no. 4, pp. 865–870, Apr. 2014, doi: 10.1161/HYPERTENSIONAHA.113.02229.
- [3] V. Bikia *et al.*, “Estimation of Left Ventricular End-Systolic Elastance From Brachial Pressure Waveform via Deep Learning,” *Front. Bioeng. Biotechnol.*, vol. 9, p. 754003, Oct. 2021, doi: 10.3389/fbioe.2021.754003.
- [4] P. Reymond, F. Merenda, F. Perren, D. Rüfenacht, and N. Stergiopulos, “Validation of a one-dimensional model of the systemic arterial tree,” *Am. J. Physiol. Heart Circ. Physiol.*, vol. 297, no. 1, pp. H208–222, Jul. 2009, doi: 10.1152/ajpheart.00037.2009.

PATTERN OF AORTIC VALVE LEAFLET CALCIFICATION IN AS PATIENTS: IN-VIVO GEOMETRIC DESCRIPTION OF CALCIFIC PROGRESSION

Mohamed Abdelkhalik (2), Zahra Keshavarz-Motamed (1,4,5)

(1) Department of Mechanical Engineering,
McMaster University, Hamilton, Ontario,
Canada

(2) School of Biomedical Engineering,
McMaster University, Hamilton, Ontario,
Canada

(3) School of Computational Science and
Engineering, McMaster University, Hamilton,
Ontario, Canada

INTRODUCTION

Procedural planning for transcatheter aortic valve replacement (TAVR) is routinely performed using contrast computed tomography (CT) in patients with severe aortic stenosis (AS) (1). Despite its potential, little investigation has been done into the possibility of aortic valve (AV) calcification (AVC) scoring in contrast-enhanced CT (2). This is valuable because contrast-enhanced CT has better dynamic contrast and spatial resolution than non-contrast CT, allowing for better descriptors of calcific lesions in the aortic valve (3, 4). Previous calcification scoring techniques (3,4) based on luminal attenuation or fixed HU thresholds have been widely used only to predict post-TAVR complications.

We developed a new method that automatically finds a threshold to minimize the false positive rate (FPR), defined as the ratio of falsely labeled calcific pixels to the total number of calcific pixels (Fig.1A). We also introduce a scheme for describing the geometric and relative concentration of calcification via intensity as well as radial and longitudinal maps (Fig.1B). The method was evaluated on a retrospective cohort of 178 patients diagnosed with AS from a single center (Hamilton General Hospital, ON, Canada) between 2020 and 2022. Non-consecutive data collection only included patients that have undergone 2D doppler echocardiography and both gated contrast and non-contrast CT to allow for a wide variety in gender (46%/54% female/male) and AS severity (28%/72% non-severe/severe). Severity was categorized by recommended thresholds for aortic valve area, peak aortic jet velocity and mean valve pressure gradient (1, 2). The data was collected after

approval from the Hamilton integrated research ethics board (HiREB) and waiver of informed consent.

Scores produced using the proposed method were compared to the standard scores produced from non-contrast images using commercially available software (Calcium scoring application, Syngovia; Siemens Healthineers). Correlations and comparisons between continuous variables were evaluated using Spearman's rank test and Bland-Altman analysis of difference. Interobserver variability was assessed on a random sub-group of 49 patients using intraclass correlation coefficient (ICC; two-way random agreement) showing excellent reproducibility (ICC:0.95; 95%CI 0.94-0.96; raters=2).

METHODS

Calcium Detection (Global Calcium Volume Score). We developed a method that does not explicitly rely on luminal attenuation. Initial leaflet calcification regions are determined instead based on the intensity characteristics of a bounding aortic root segmentation. Using those initial conditions, an iterative region growing method adjusts the Hounsfield band for calcific detection gradually, until satisfying a minimum false positive (0.01/1%) ration between calcific and non-calcific segments in the local region of interest.

Calcium Regional Map (Local Regional Calcium Deposition). We developed an anatomical 18 region mapping scheme based on standardized measurements of height to sino-tubular-junction, annular area derived radius and angles of the inter-leaflet triangle which we used to parametrize distance thresholds (18 regions from coaptation zone to attachment) in order to quantify regional calcific volume across the cohort.

RESULTS

Calcium Detection (Global Calcium Volume Score). We compared techniques based on average luminal attenuation (LA) plus constant multiplier to standard deviation (SD) in the ascending aorta. We showed that calcification volume using the FPR method showed the best correlation against non-contrast volume and Agatston scores ($r = 0.919$; $p < .001$) ($r = 0.913$; $p < .001$) in contrast-enhanced images (Fig. 1). Visual differences between detected calcific volumes using the proposed method (FPR) and other LA methods are shown in (Fig. 1). Moreover, comparative analysis showed the FPR method had the highest correlation to ground truth non-contrast volume and Agatston scores as shown in the correlation matrix heatmap (Fig. 1).

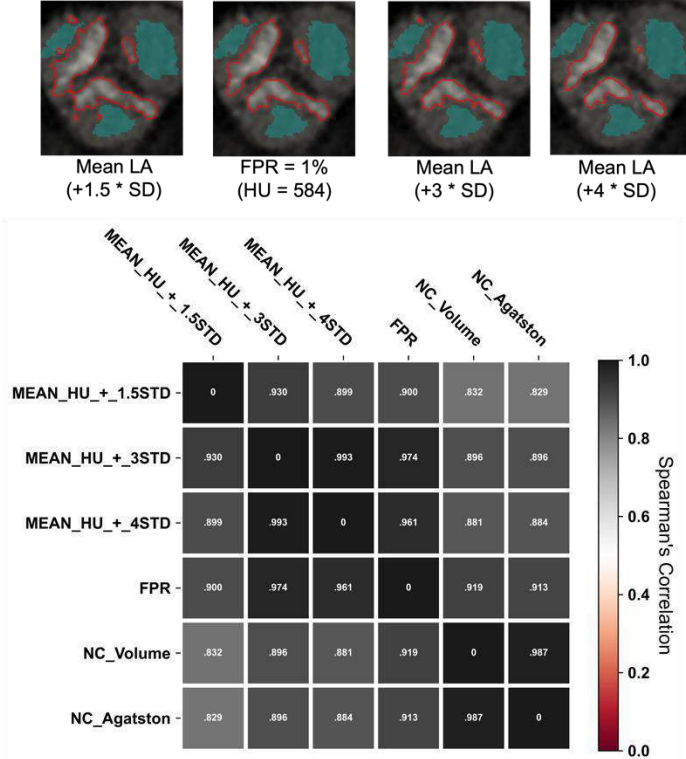


Figure 1. Top panel : The detected calcification is identified with a red outline around the region of interest in each subplot with high thresholds (+3*SD, +4*SD) missing small calcific nodules and low thresholds (+1.5*SD) merging large calcific regions between the leaflets. **Bottom panel:** Spearman’s correlation heatmap between all contrast calcific volume scores and non-contrast volume and Agatston scores.

Aortic root and coronary arteries fluid dynamics (local hemodynamics).
Calcium Regional Map (Local Regional Calcium Deposition). The high contrast and spatial resolution in contrast images combined with a precise calcific detection method provides a unique opportunity to examine the regional presentation of calcific deposition in AS. In that respect, we generated topographic distance maps for both radial and longitudinal distance relative to each patient’s aortic valve

dimensions (annular radius and STJ height) as presented in Fig. 2. These maps were then used to map calcific volume concentrations onto shape invariant 2D polar map with 18 regions organized by cusp (3 sectors), distance to center (3 levels) each radial distance level was further decomposed by angle (Distal to center – 3 angles, Mid – 2 angles and Proximal – 1 angle).

In terms of the regional presentation of calcification for each cusp, we observed four primary patterns of calcific distribution as follows:

1. Severe: Maximal calcific deposition in near the belly region of all leaflets followed by root attachment edges with significantly lower calcification near the coaptation zones. In males the amount of calcification is significantly higher across most regions. While in females a lower calcific progression rate, presents calcific arcs primarily near free edges of the leaflets, that have not yet developed in rings at the fixed edge (Fig. 2).
2. Non-severe: Maximal calcific deposition near sites of root attachment and belly, prominent near the non and left coronary cusps. At this stage calcification primarily presents as disconnected deposits. With males presenting with significantly higher calcific deposition near leaflet attachment edges between the non and right coronary leaflets than females (Fig. 2).

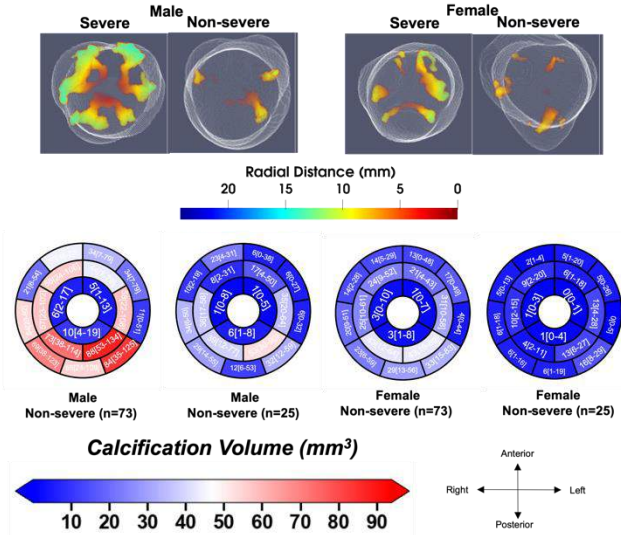


Figure 2. Top panel: Distance map of detected calcification, color mapped by a normalized radial distance range of [0-25.4 mm]. **Bottom panel:** Bullseye aortic valve plot with 18 region map localizing the radial and angular location for each cusp. Median volume values for each categorical group (sex and severity) were used to color the volume with median [IQR] values were annotated inside the borders of each region.

DISCUSSION

Calcific AS is the most common valvular disease, with high mortality rate once symptoms are presented. AVR intervention is currently the only treatment option in which aortic valve calcification in and around the valve is an important factor for procedural risk assessment and predicting complications in TAVR. The presented computational assessment tool can be

used to characterize the complex patterns of calcification at different stages of the disease. We found that calcific progression appears to follow distinctive patterns for each leaflet (5–8), with differences emerging in the stage of calcific progression between the leaflets. This difference in rate of progression is also significantly affected by sex which cannot be explained by the difference in valve sizes (3, 9, 10). In addition, we provide a new method for calcific detection that could potentially overcome the inherent variability of contrast material effect on HU attenuation (1–4), which could enable additional quantitative criteria for calcific assessment in routinely used contrast CT for TAVR planning(1). All in all, detailed quantitative description of the complex patterns of leaflet calcification, combined with accurate anatomical assessment of aortic valve morphology, could be critical for simultaneously monitoring the progression of AS, and determining the best treatment options, especially for asymptomatic patients who might eventually need an aortic valve replacement.

ACKNOWLEDGEMENTS

This study was supported by NSERC Discovery Grant (RGPIN-2017-05349).

REFERENCES

1. P. Blanke, *et al.*, Computed tomography imaging in the context of transcatheter aortic valve implantation (TAVI) / transcatheter aortic valve replacement (TAVR): An expert consensus document of the Society of Cardiovascular Computed Tomography. *Journal of Cardiovascular Computed Tomography* **13**, 1–20 (2019).
2. T. Pawade, T. Sheth, E. Guzzetti, M. R. Dweck, M. A. Clavel, *Why and How to Measure Aortic Valve Calcification in Patients With Aortic Stenosis* (Elsevier Inc., 2019).
3. T. R. Cartlidge, *et al.*, Contrast-enhanced computed tomography assessment of aortic stenosis. *Heart* **0**, heartjnl-2020-318556 (2021).
4. W.-K. Kim, *et al.*, Accuracy of device landing zone calcium volume measurement with contrast-enhanced multidetector computed tomography. *International Journal of Cardiology* **263**, 171–176 (2018).
5. M. J. Thubrikar, J. Aouad, S. P. Nolan, Patterns of calcific deposits in operatively excised stenotic or purely regurgitant aortic valves and their relation to mechanical stress. *The American Journal of Cardiology* **58**, 304–308 (1986).
6. M. Bäck, T. C. Gasser, J.-B. Michel, G. Caligiuri, Biomechanical factors in the biology of aortic wall and aortic valve diseases. *Cardiovascular Research* **99**, 232–241 (2013).
7. R. Halevi, *et al.*, Progressive aortic valve calcification: Three-dimensional visualization and biomechanical analysis. *Journal of Biomechanics* **48**, 489–497 (2015).
8. A. Arzani, M. R. K. Mofrad, A strain-based finite element model for calcification progression in aortic valves. *Journal of Biomechanics* **65**, 216–220 (2017).
9. V. A. Myasoedova, *et al.*, *Sex-specific differences in age-related aortic valve calcium load: A systematic review and meta-analysis* (Elsevier Ireland Ltd, 2020).
10. J. J. Thaden, *et al.*, Sex-related differences in calcific aortic stenosis: correlating clinical and echocardiographic characteristics and computed tomography aortic valve calcium score to excised aortic valve weight. *European Heart Journal* **37**, 693–699 (2016).

THE IMPACT OF TRANSCATHETER AORTIC VALVE REPLACEMENT DEPLOYMENT PARAMETERS ON CORONARY ARTERY HEMODYNAMICS

Seyedvahid Khodaei (1), Zahra Keshavarz- Motamed (1,2,3)

(1) Department of Mechanical Engineering,
McMaster University, Hamilton, Ontario,
Canada

(2) School of Biomedical Engineering,
McMaster University, Hamilton, Ontario,
Canada

(3) School of Computational Science and
Engineering, McMaster University, Hamilton,
Ontario, Canada

INTRODUCTION

Transcatheter aortic valve replacement (TAVR) is becoming popular for patients who are of a high, intermediate, or low risk, indicating that it may become the superior treatment modality for aortic stenosis (AS) for the whole risk spectrum and younger populations (1,2). While coronary artery disease (CAD) is present in up to two third of the TAVR population (3), CAD severity assessment is challenging and the decision for coronary lesion revascularization is currently mainly based on invasive procedures (4). However, invasive coronary access is limited in significant proportion of patients who undergo TAVR, due to anatomical restrictions such as overlap between transcatheter heart valve and the coronary ostia (5). Consequently, this presents a dilemma among patients with post-TAVR complications, regarding the relative contribution of CAD versus the valve insufficiencies on long term symptoms and prognosis, and more studies are needed to understand how TAVR affect coronary hemodynamics (3).

Computational simulations are a powerful tool for accurate and early diagnosis of long-term hemodynamic complications that are difficult or impossible to infer in clinical practice. Some technical challenges and concerns of the effect of TAVR on both short term and long-term coronary hemodynamics can be predicted through numerical simulation (3). However, such simulations should be personalized for each patient and be able to capture the effect of global and local hemodynamics on a case-by-case basis to provide a clinically meaningful tool based on patient anatomy and valve implantation parameters (6,7).

In this study, we propose a novel strategy to quantitatively investigate the impact of TAVR on coronary artery hemodynamics. We developed a personalized lumped parameter model and computational fluid dynamics framework based on patient-specific hemodynamic and anatomical parameters to examine the effect of factors such as valve to coronary distance, aortic root diameter, coronary ostium height and commissural misalignment on coronary artery hemodynamics. We showed that coronary flow improvement depends on post-TAVR aortic root remodeling and ventricular-vascular coupling hemodynamics. We quantified the effect of TAVR on coronary flow and cardiac function and investigated the correlation of hemodynamic parameters with the metrics currently used in clinical practice.

METHODS

Global hemodynamics. We have previously developed a non-invasive diagnostic computational-mechanics framework for complex valvular, vascular, and ventricular disease (C3V-LPM), described in detail elsewhere (6). In this study, the C3V-LPM was developed to a greater extent to compute global hemodynamics in patients with mixed valvular, vascular, mini-vascular and ventricle diseases. The model uses a limited number of input parameters all of which can be reliably obtained using Doppler echocardiography and a sphygmomanometer.

Local hemodynamics. A computational fluid dynamics and lumped parameter modeling framework was developed to compute 3D blood flow dynamics in all main coronary artery branches, aortic root, ascending aorta, sinus, and neo-sinus

regions for both pre- and post-TAVR (Figure 2). This framework is based on lumped parameter modelling and 3D FSI modelling as implemented in open-source foam-extend library and validated against in-vivo DE data (7).

RESULTS

LV workload and coronary artery flow (global hemodynamics). The LV workload is an effective metric of the LV load and clinical state and represents the energy that the ventricle delivers to the blood during ejection plus the energy necessary to overcome the viscoelastic properties of the myocardium itself. Pre-TAVR, untreated AS increased the load on the LV due to the augmented flow resistance which caused a LV pressure overload. Although the flow resistance and consequently the LV pressure decreased greatly post TAVR, the LV workload did not improve (Figure 1a). Interestingly we observed a reduction in coronary flow after TAVR (figure 1b), while improvement of coronary flow is expected after AS removal. This could probably explain why TAVR might not be associated with reduced workload if the coronary flow is not improved.

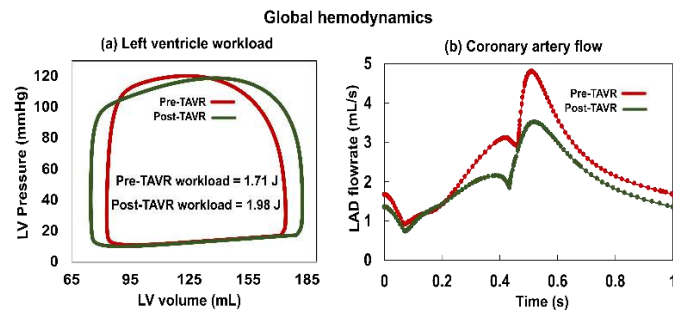


Figure 1. Global hemodynamics in a sample patient between baseline and 90 days post-TAVR: (a) Left ventricular workload: LV workload did not improve after TAVR. (b) Coronary artery flow: TAVR was associated with a reduced coronary flow during both systole and diastole phases

Aortic root and coronary arteries fluid dynamics (local hemodynamics). It has been shown that after TAVR the coronary flow influences the flow patterns of aortic root and neo-sinus and favors the transfer of blood flow towards ostium during diastole (8). However, our results showed that due to the extra anatomical nature of transcatheter valve stent, the aortic root vortices might not favor the transfer of blood flow towards ostium in the aortic root and neo-sinus region (figure 2a). TAVR can also lead to a pro-inflammatory state of endothelial cells due to the reduced wall shear stress microenvironment after intervention which is linked to plaque progression. Our findings demonstrate that TAVR might exacerbate the washout mechanism for the sinus and neo-sinus regions and lead to a significantly lower shear stress at the coronary walls due to the decreased blood supply during diastole after TAVR. This makes the coronary arteries susceptible to atherosclerosis, due to the low wall shear stress-induced inflammatory activation of

endothelium mainly at the inner bend of curved arteries, ostia of branches and lateral walls of bifurcations.

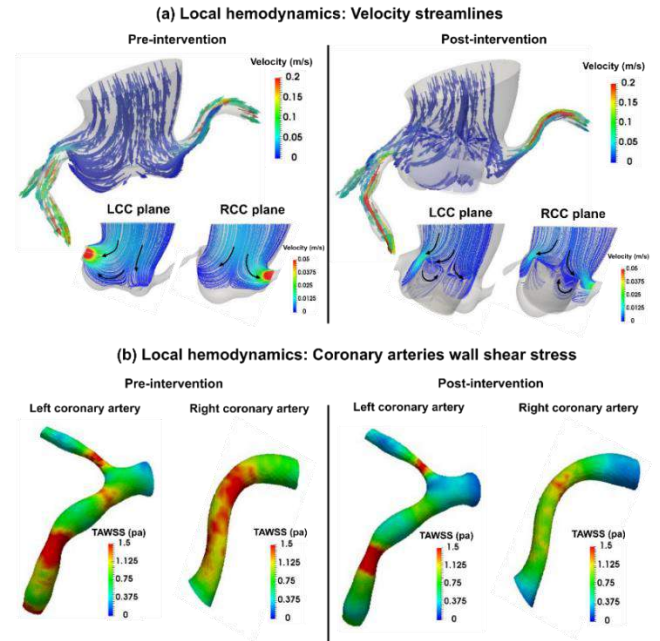


Figure 2. Flow modeling in an aortic root and coronary arteries in a sample patient. (a) Velocity vector at peak diastole. (b) Left and right coronary time averaged wall shear stress during diastole.

DISCUSSION

TAVR prosthetic and its influence on natural flow pathways in the sinus of Valsalva attributes to disturbance of the blood entering the coronary circulation which might limit the benefit of TAVR: may increase the LV load, may potentially worsen coronary perfusion, and worsens heart failure. Atherosclerosis promotion through loss of physiological flow-oriented alignment of endothelial cells and its exacerbation will likely play an important hindering role in success of TAVR. The findings of this study suggest that beyond routine clinical indices for hemodynamic evaluation of the valvular disease (e.g, Doppler pressure gradients), valvular, vascular, and ventricular hemodynamics and their interactions should be clinically quantified and considered to better conduct the aortic valve management and treatment planning.

ACKNOWLEDGEMENTS

This study was supported by NSERC Discovery Grant (RGPIN-2017-05349).

REFERENCES

- [1] Leon, MB et al., *NEJM*: 374, 1609-1620 ,2016.
- [2] Popma, JJ et al., *NEJM*: 380, 1706-1715 ,2019.
- [3] Patel, KP et al., *JACC interventions*: 14, 2083-2096 ,2021.
- [4] Vendrik, J et al., *JAHA*: 9, e015133,2020.
- [5] Ochiai, T et al., *JACC interventions*: 13, 693-705 ,2016.
- [6] Keshavarz-Motamed, Z et al., *Sci. Rep*: 10, 1-19 ,2020.
- [7] Khodaei, S et al., *Sci. Rep*: 11, 1-28 ,2021.
- [8] Madukauwa-David, ID et al., *Ann Biomed Eng* 48, 169-180, 2020.

PERSONALIZED INTERVENTION CARDIOLOGY FOR TRANSCATHETER AORTIC VALVE REPLACEMENT WITH A DOPPLER-EXCLUSIVE DIAGNOSTIC FRAMEWORK

Nikrouz Bahadormanesh (1), Zahra Keshavarz-Motamed (1,2,3)

(1) Department of Mechanical Engineering,
McMaster University, Hamilton, Ontario,
Canada

(2) School of Biomedical Engineering,
McMaster University, Hamilton, Ontario,
Canada

(3) School of Biomedical Engineering,
McMaster University, Hamilton, Ontario,
Canada

INTRODUCTION

Transcatheter aortic valve replacement (TAVR) is an emerging treatment alternative to surgical aortic valve replacement that covers a range of patients suffering from moderate to severe aortic stenosis (AS). AS is one of the most common and serious cardiovascular problems and if left untreated, often leads to death. Surgical valve replacement remains the standard treatment method for AS, however, many patients suffering from this pathology are at a high risk for surgery and may suffer death or other complications [1].

TAVR is a growing alternative for intervention of AS patients across a broad risk spectrum and has lower death rates in severe cases compared to a surgical approach. Although TAVR has critical benefits for surgical high-risk patients, there are several drawbacks that patients may experience [2]. *Given the associated risks with TAVR, it is crucial to determine: how the implant will affect the cardiac function? when is the proper timing for intervention? Will TAVR improve or worsen the outcome of the patient [3].*

The condition of the heart valves heavily relies on the geometry and material properties of the leaflets as well as the interaction between the flow and the valve [3,4,5,6]. Valvular disease, including AS, often results in, or is a result of abnormal stress and strain distributions on aortic valve leaflets for both pre- and post-interventional cases.

In this study, we developed a highly innovative non-invasive Doppler-exclusive computational-mechanics framework that can function as a diagnostic tool to assess aortic

valve dynamics in pre and post-TAVR states at no risk to the patients. The developed diagnostic tool is able to dynamically couple the local valve dynamics with the global circulatory system [4] which provides a platform for testing intervention scenarios (e.g. TAVR) and evaluating their effects.

METHODS

We developed a Doppler-based computational mechanics diagnostic framework to non-invasively investigate the dynamic behavior of the aortic valve (e.g., transient 3-D distribution of stress and displacement field, 3-D deformed shape of leaflets, geometric orifice area, angular positions of leaflets, stiffness, etc.). This framework is based on a Doppler-based patient-specific lumped parameter algorithm (LPM) [4] along with a 3-D Doppler-based nonlinear (using anisotropic hyper elastic) finite element solver CalculiX with some supplements. The developed LPM algorithm [4] consists of a parameter estimation algorithm and a lumped-parameter model that includes several sub-models allowing analysis of any combination of complex valvular, vascular and ventricular diseases. A Doppler-based parametric method was developed to construct the 3-D geometry of the asymmetric aortic valve leaflets. Calculations of this Doppler-based computational mechanics diagnostic framework were validated against clinical Doppler echocardiography data in patients with AS.

RESULTS

In patients with aortic stenosis, the healthy instantaneous LV pressure and/or volume are altered which ultimately overloads the heart. We investigated metrics of cardiac function (global hemodynamics) computed by our Doppler-based lumped parameter algorithm to determine the effects of TAVR on patient condition. The impacts of the TAVR on the aortic valve pressure gradient were not always be associated with reduction in LV function parameters, e.g., LV workload, normalized LV workload to stroke volume and maximum LV pressure. LV hemodynamics metrics worsened in some patients, and they were not significantly improved in the others (Figure 1, panel c)

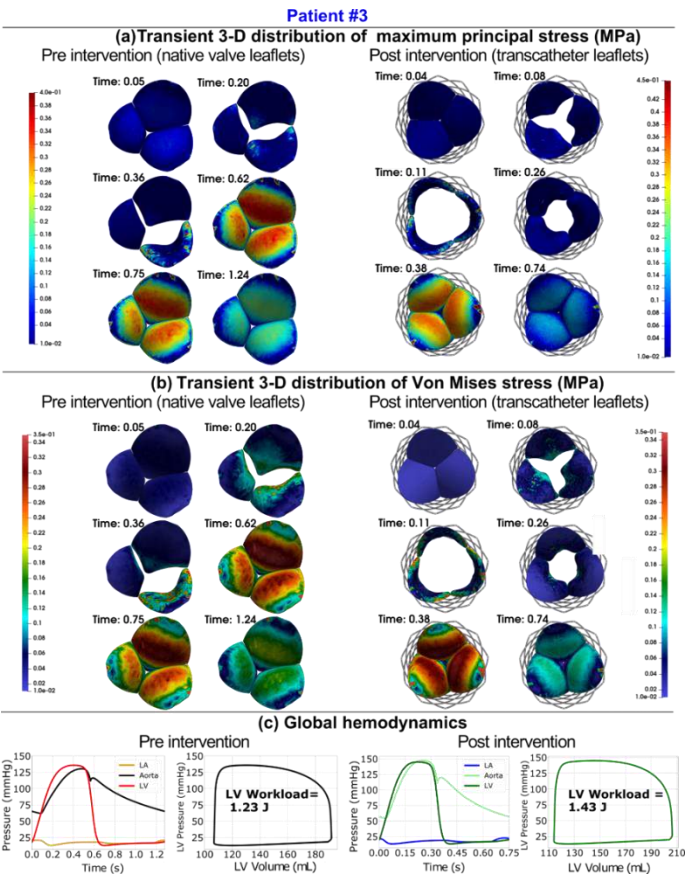


Figure 1. Changes in valve dynamics and global hemodynamics in patient #3 between baseline and 90-day post-TAVR.

Biomechanical factors resulting from hemodynamic loads are a common dominator of a variety of vascular diseases. Various mechanical metrics including 3-D Mises stress (the derivative format of principle stress), 3-D major principal stress (the maximum value of the three principal stresses), as well as displacement magnitude resulted from our Doppler-based computational framework reveled that TAVR worsened valve dynamics in some patients. Indeed, mechanical forces are the driving force behind the degeneration and failure of prosthetic heart valves and must be measured regularly to prevent the deterioration of the replacement valve.

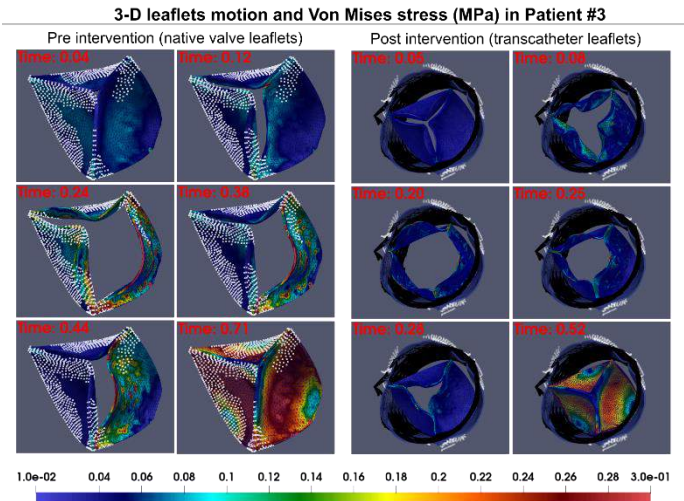


Figure 2. 3D motion and 3D distribution contours of Mises stress in patient #3 at six time points throughout the cardiac cycle in both pre- and post-intervention states

DISCUSSION

TAVR does not always improve cardiac function metrics. LV hemodynamics metrics worsened in some patients, and they were not significantly improved in the others. TAVR does not always improve valve dynamics metrics. Valve dynamics post-intervention should be quantified and monitored to ensure the improvement of patient conditions and prevent any further complications. Improper evaluation of biomechanical valve features pre-intervention as well as post-intervention may result in harmful effects post-TAVR in patients including paravalvular leaks, valve degeneration, failure of TAVR and heart failure.

ACKNOWLEDGEMENTS

This work was supported by NSERC Discovery Grant (RGPIN-2017-05349).

REFERENCES

[1] Pibarot, P et al., *JACC Cardiovasc Imaging*, 8:340–360, 2015.
[2] Ben-Assa, E et al, *Sci Transl Med*, 1(509): eaaw0181, 2019.
[3] Keshavarz-Motamed Z, et al, *J Am Heart Assoc*, 9:e015063, 2020.
[4] Keshavarz-Motamed Z, *Sci Rep*, 10:1–19, 2020.
[5] Khodaei S, et al, *Sci Rep*, 11:10888, 2021.
[6] Khodaei S, *Int J Mech Sci*, 202–203:106506, 2021.

THE EFFECTIVENESS OF CUSTOM ACL BRACING IN ADOLESCENT POPULATIONS: A FINITE ELEMENT ANALYSIS

Alexandria D. Mallinos (1), Brian L. Davis (2), Kerwyn C. Jones (3)

- (1) Department of Chemical & Biomedical Engineering, Cleveland State University, Cleveland, OH, USA
(2) Department of Mechanical Engineering, Cleveland State University, Cleveland, OH, USA
(3) Department of Orthopedic Surgery, Akron Children's Hospital, Akron, OH, USA

INTRODUCTION

Functional Anterior Cruciate Ligament (ACL) orthoses are prescribed to patients with the goal of preventing anterior tibial translation and valgus moments at the joint [1]. However, despite the prevalence of ACL tears, there has been much debate within the medical community on the effectiveness of functional bracing after reconstructive surgery [2-4]. Part of the controversy surrounding this discussion is due to the insufficient amount of data supporting the theory that ACL functional orthoses “control joint translation and prevent re-injury” [2].

The limited and inconsistent data available on knee orthosis (KO) biomechanics make it difficult to assess the effectiveness of functional ACL bracing. Fortunately, advancements in finite element technology have opened the possibility for accurate and quantitative assessments of subject-specific knee orthoses.

The purpose of this study was to determine how effective custom functional ACL bracing is in preventing anterior tibial translation. The contact pressures of custom ACL orthoses exerted along the tibia obtained by Ghadikolaei et al. [5] were replicated in the patient-specific finite element models. Our previously developed baseline knee models that have been validated in accurately predicting anterior tibial displacement [6] were utilized to determine how effective this orthosis design is in preventing joint translation when subject to Lachman and pivot shift tests.

METHODS

A total of 22 CT images of juvenile knees were utilized (ages: 9-18, m: n=16, f: n=6). 3D Slicer was used to convert the CT images into a three-dimensional representation of the bony

anatomy. FEBio was used to construct each tibiofemoral joint and perform the finite element analyses.

Two sensor pads (C1 = 5.08 kPa; C2 = 6.75 kPa) of 400mm² area were placed along the tibial crest following the sensor placement established by Ghadikolaei et al. [5] (Figure 1).

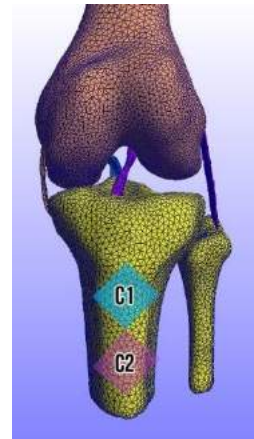


Figure 1: Finite element model of adolescent knee. C1 and C2 depict pressure sensor placement.

To replicate the Lachman test, anteriorly directed forces of 67 N, 89 N, and 133 N were applied to the tibia [7]. To simulate the pivot shift test, an anteriorly directed force of 133 N was applied to the tibia in addition to a combined rotatory load of 4 Nm internal tibial torque and 10 Nm valgus [8].

A 95% confidence interval was used to determine statistical significance between the bracing and non-bracing groups for each loading condition.

RESULTS

As expected, the custom ACL orthosis simulation resulted in less anterior tibial translation than the non-bracing models for both loading conditions (Table 1).

Table 1: Descriptive statistics of FEBio anterior tibial translation of Lachman and pivot shift test simulations with and without bracing.

FEBio - Lachman Test (mm)				
<i>Mallinos et al. - Without Bracing</i>		<i>Ghadikolaee et al. - Custom KO</i>		
	Mean	SD	Mean	SD
67 N	5.53	0.33	4.82	0.39
89 N	6.53	0.28	5.60	0.30
133 N	7.54	0.34	6.58	0.42
FEBio - Pivot Shift Test (mm)				
<i>Mallinos et al. - Without Bracing</i>		<i>Ghadikolaee et al. - Custom KO</i>		
	Mean	SD	Mean	SD
	4.38	0.78	3.64	0.18

The 95% confidence intervals demonstrate that the custom ACL knee orthosis provides a significant ($p<0.05$) resistance to anterior tibial translation compared to the non-bracing models (Figures 2 and 3).

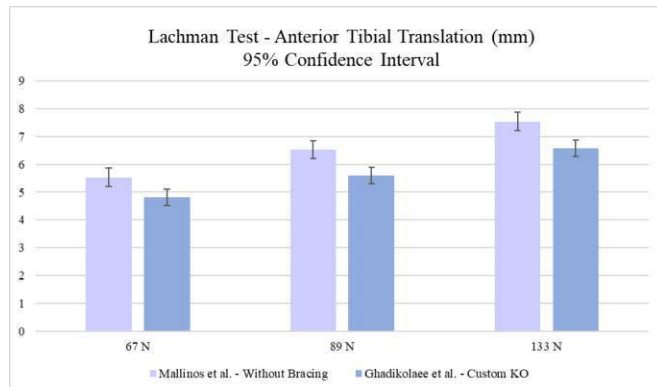


Figure 2: 95% confidence interval for the Lachman test anterior tibial translation between bracing and non-bracing simulations.

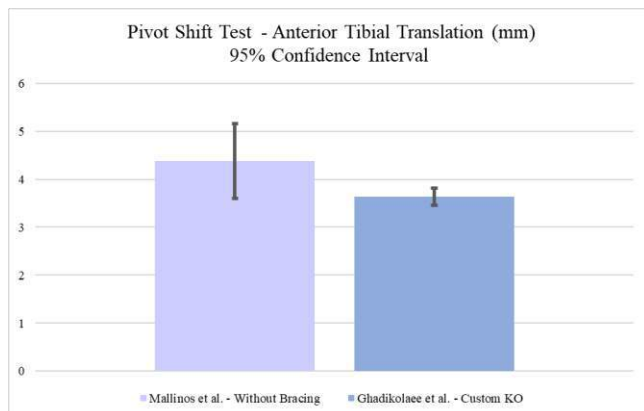


Figure 3: 95% confidence interval for the pivot shift test anterior tibial translation between bracing and non-bracing simulations.

DISCUSSION

The finite element simulations showed that custom knee orthosis designs statistically minimize anterior tibial translation when subject to loading conditions that can harm the healing graft. The custom knee orthosis design resulted in approximately 1 mm less anterior tibial translation than the non-bracing options.

This highlights the importance of accurately fitting a knee orthosis to a patient. If the fit of the orthosis is not sufficient, it is likely that the device will not be effective in preventing anterior tibial translation. This is especially significant if there is a gap of 1 mm between the orthosis and the tibia as this might result in minimal resistance to anterior tibial movement.

As demonstrated in the simulations, gapping between the orthosis and the patient can place the healing ACL graft at risk for reinjury by allowing less resistance to ligament translation. Incorrect orthosis fitting that allows gapping between the device and the tibia is ultimately ineffective in preventing excess stress and strain to the healing graft. This highlights the significance of having orthotic designs that are contoured to fit the patient's unique anatomy and size because the posterior directed forces along the tibial pad provide significant resistance to unwanted anterior tibial translation.

Understanding the biomechanical impact ACL knee orthoses have in protecting the healing ACL can provide clinicians with the opportunity to prescribe the best orthosis that will significantly minimize the risk of reinjury and provided further justification for insurance purposes.

Future studies will utilize this methodology to assess the biomechanical effectiveness of the different knee orthosis designs (four-point force system vs total contact; custom vs custom-fit/off-the-shelf) to determine which offers the greatest protection to an ACL-deficient knee.

In conclusion, utilizing finite element technology makes it possible to assess knee orthosis biomechanics in manner that cannot be assessed in a clinical setting. Custom functional ACL knee orthosis provide a significant resistance to anterior tibial displacement – ultimately protecting the healing graft from significant stress and strain.

ACKNOWLEDGEMENTS

This research has been made possible by the Cleveland State University's Cellular and Molecular Medicine Fellowship.

REFERENCES

- [1] Pereira, S et al., *J Ind Text*, 36:279-300, 2007.
- [2] Wojtys, E et al., *Am J Knee Surg*, 14:157-162, 2001.
- [3] Birmingham, T et al., *Am J Sports Med*, 36:648-655, 2008.
- [4] Soma, C et al., *Orthop*, 27:307-310, 2004.
- [5] Ghadikolaee, M et al., *J Pros Orth*, 32:142-148, 2020.
- [6] Mallinos, A et al., *J Biomech*, 136:1-7, 2022.
- [7] Highgenboten, C et al., *Am J Sports Med*, 20:450-454, 2012.
- [8] Wan, C et al., *Med Biol Eng Comput*, 55:2097-2106, 2017

PHASE-FIELD MODELING OF DEEP VEIN THROMBUS EMBOLIZATION

Osman Gültekin (1), Matthew J. Lohr (2), Sapun H. Parekh (2), Manuel K. Rausch (1,2,3)

- (1) Department of Aerospace Engineering and Engineering Mechanics, University of Texas at Austin, Austin, Texas, USA
(2) Department of Biomedical Engineering, University of Texas at Austin, Austin, Texas, USA
(3) Oden Institute for Computational Engineering and Sciences, University of Texas at Austin, Austin, Texas, USA

INTRODUCTION

Blood clot is a natural bio-adhesive that prevents bleeding after vascular injury. It comprises three constituents: fibrin, platelets, and red blood cells. In its role as a wound sealant, blood clot is critical to our health. On the other hand, if pathologically formed within the intact vessels (i.e., giving rise to a thrombus), it can also be deadly. That is, when blood clots break (or fracture), they may shed small emboli that can travel downstream and occlude vital arteries or veins, leading to deadly sequelae such as ischemic strokes, heart attacks, and pulmonary emboli. Together, thromboembolic diseases cause one in four deaths worldwide [1].

Given this high mortality, it is imperative to understand when, why, and in whom blood clot breaks off, i.e., embolizes. This breaking-off may be interpreted as a fracture process. It is, therefore, vital to learning to describe and predict blood clot fracture. We are not the first to identify the importance of studying blood clot fracture. In fact, several experimental and numerical studies have reported on the fracture toughness of blood clot, which is a critical measure of its resistance (or lack thereof) to fracture, see for example [2-6]. Among other questions, previous studies investigated how blood clot's aforementioned constituents contribute to its fracture toughness [4,5]. Despite this important prior work, the in vivo mechanisms of blood clot fracture remain incompletely understood. In other words, we still do not know when, why, or in whom blood clot breaks off.

Among the many questions that remain unanswered about in vivo blood clot embolization is that of the driving force. That is, blood clot is exposed to wall shear stress due to blood flow in cases where clot is non-occlusive, as well as tensile and shear from wall-stretch and blood pressure. To date, it is not clear which of those mechanical loading conditions are most critical in causing blood clot fracture. Please note, this question is difficult to answer experimentally. For example, in experiments it is difficult to deconvolute different loading scenarios and identify their relative contributions to blood clot fracture. In contrast,

computational tools allow us to investigate the driving factors behind thrombus embolization by applying shear stress, wall stretch, and blood pressure in isolation and in combination. Therefore, the goal of this study is to use a computational model of an idealized blood clot geometry to investigate the driving forces behind clot embolization. To this end, we will first inform a phase-field finite element model of an idealized occlusive clot embedded within a vessel wall and then investigate its response to different loading scenarios. Specifically, we chose a deep vein thrombus as a model problem.

METHODS

This section is devoted to the phase-field modeling of blood clot fracture. To this end, let \mathcal{B} and \mathcal{S} denote the reference and deformed configurations for the body of interest. The coupled problem of fracture is described by the deformation map $\boldsymbol{\varphi}_t$ and the assisting field variable, which we call the crack phase-field d . While the deformation map transforms a point $\mathbf{X} \in \mathcal{B}$ onto its spatial counterpart $\mathbf{x} \in \mathcal{S}$, the phase-field continuously interpolates between the intact, i.e., $d = 0$, and the ruptured state of the solid, i.e., $d = 1$. Upon establishing the standard kinematical descriptions for hyperelasticity and the crack phase-field approach, see [7-8], we choose the one-term Ogden model to describe the isotropic mechanical response of the clot. Having only two parameters – one accounting for the shear modulus and the other one giving the degree of nonlinearity – the one-term Ogden model is well-suited for the numerical representation of blood clot [9].

The present study features a variational principle based on the power balance of the rate of the internal and external energy functionals and the dissipation functional. The corresponding minimization of the field variables yield the governing equations, i.e., strong forms, of the mechanical problem, namely the balance of the linear momentum,

$$\text{div}(\boldsymbol{\sigma}) + \boldsymbol{\gamma} = \mathbf{0} \quad (1)$$

and the evolution equation of the crack phase-field

$$\eta l \dot{d} = l(1 - d)\mathcal{H} - (d - l^2 \Delta d) \quad (2)$$

In Equation (1), σ and γ represent the Cauchy stress tensor and the body force vector per unit volume. In Equation (2) we introduce the artificial viscosity η stabilizing the algorithm, the length-scale l , and the crack driving source term

$$\mathcal{H} = \max_{s \in [0,1]} \left(\frac{\Psi_0}{G_c} - 1 \right), \quad (3)$$

which is irreversible and filters out positive values. Therein Ψ_0 denotes the effective free energy function of the Ogden model, whereas G_c represents the fracture toughness. \mathcal{H} can be interpreted as an isotropic failure criterion as cracking does not initiate until $\Psi_0 \rightarrow G_c$. Finally, Equations (1) and (2) are discretized in time and space via Galerkin-type weak formulations and solved for the respective primary field variables, i.e., displacement and phase-field. We implemented this framework in the nonlinear finite element solver FEAP.

RESULTS

We first used our phase-field modeling approach to inversely identify the fracture toughness G_c from Mode-I fracture experiments on in vitro blood clot, see Figure 1. Please note, details on the coagulation conditions and experimental aspects of the Mode-I fracture experiments can be found in [10]. Also, note that the hyperelastic Ogden material parameters for this numerical experiment were informed from pure shear experiments on blood clot that was coagulated from the same blood as those samples used for the Mode-I experiments ($\mu = 10.4 \times 10^{-4}$ [MPa] and $\alpha = 7.2$). After inversely identifying an optimal G_c (9.6×10^{-4} [N/mm]) the numerical, predicted Mode-I experiment and the experimental data show great agreement, see Figure 1A. Additionally, snapshots throughout simulation time show the fracture process which agrees qualitatively with our experimental observations, see Figure 1B.

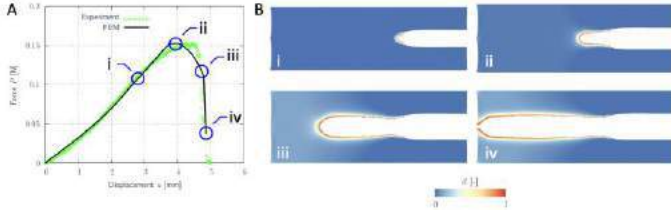


Figure 1: A phase-field model of Mode-I fracture agrees well with experimental data. A) Mode-I fracture test with force-displacement results obtained from phase-field simulations (black solid line) and experiment (green circles). B) Snapshots i-iv) show the predicted evolution of the crack phase-field in the solid, which agree well with our experimental observations. Elements are blanked if $d \geq 0.95$.

Next, we used our calibrated phase-field approach to investigate likely drivers for venous blood clot embolization. As a first example, we modeled an occlusive blood clot. To this end, we modeled an octant of the entire solid domain with the fully occlusive clot sitting on the inner surface of the venous wall. We tested two different scenarios: Scenario I) wall-stretch as a driver of clot fracture (wall stretch of $\lambda = 2$) and Scenario II) blood pressure as a driver of clot fracture (10 mmHg). For both scenarios the hyperelastic material parameters of the blood clot were the same as above, similarly the fracture toughness was based on the identification in Figure 1. The venous wall was modeled as a neo-Hookean material [11]. In Scenario I, we subjected the venous wall to cyclic extension in the longitudinal z -direction. Figure 2 depicts the results of this first simulation. Snapshots A (inner surface view) and B (outer surface view) at the end of the simulation show the severely

damaged zones (iso-surfaces) where $d \geq 0.8$. From the complete evolution of the fracture field along the venous wall, it is clear that the clot separated from the venous wall at their interface. Clinically, this would lead to embolization and traveling of the embolus downstream. Additionally, the crack also branched into the center of the clot, likely leading to multiple emboli.

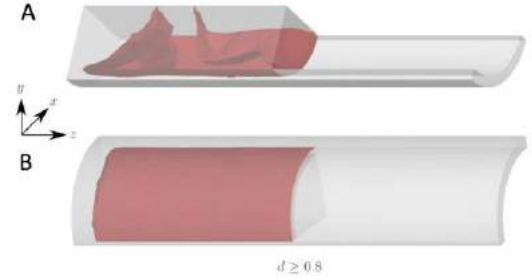


Figure 2: Blood clot delaminates from the venous wall due to wall stretch. Snapshots A and B illustrate the inner and outer surface view of the crack growth within the thrombus. Areas (iso-surfaces) subjected to severe damage, i.e., $d \geq 0.8$ are shown.

On the other hand, Scenario II, where we applied only blood pressure without wall stretch, did not lead to any fracture development and thus embolization (results not shown). Interestingly, even when applying super-physiological pressures of 50 and 100 mmHg no significant crack propagation was observed.

DISCUSSION

In our current work, we accomplished two goals. First, we used an inverse finite element approach to inform a phase-field model of blood clot fracture. Second, we used our calibrated phase-field model to investigate the likely driving force of blood clot embolization. To this end, we studied venous blood clot as a model problem. Interestingly, we found that blood pressure alone, even when as high as 100 mmHg, does not lead to clot fracture and embolization. On the other hand, we found that wall stretch can lead to mismatched stress between the venous wall and the clot and the subsequent development of a delamination-type fracture process. Our goal is to extend our model through sensitivity analyses and by also including non-occlusive clots. Overall, we expect that our work will shed light on venous thromboembolism in particular and other thromboembolic diseases in general.

ACKNOWLEDGEMENTS

We acknowledge support from ONR with grant N00014-22-1-2073 and NSF with grants 2046148, 2105175, and 2127925.

REFERENCES

- [1] Wendelboe et al., *Circ. Res.*, 118:1340-1347, 2016.
- [2] Tutwiler, V et al., *Sci Adv*, 6:eabc0496, 2020.
- [3] Tutwiler, V et al., *Acta Biomater*, 131:355-369, 2021.
- [4] Liu, S et al., *Extreme Mech Lett*, 48:101444, 2021.
- [5] Fereidoonhezad, B et al., *Acta Biomater*, 127:213-228, 2021.
- [6] Ghezelbash, F et al., *J Mech Behav Biomed Mater*, 128:105101, 2022
- [7] Gültekin, O et al., *Comput Methods Appl Mech Engrg*, 312:542-566, 2016
- [8] Gültekin, O et al., *Comput Methods Appl Mech Engrg*, 331:23-52, 2018
- [9] Lohr, MJ et al., *Phil Trans R Soc A*, 380: 20210365, 2022
- [10] Sugerman, GP et al., *Current Protocols*, 1, e197, 2021
- [11] Rausch, MK and Humphrey JD, *J Elast*, 129, 125-144, 2017

IMPACT OF LOCAL COLLAGEN ARCHITECTURE ON RUPTURE BEHAVIOR OF TISSUE-ENGINEERED ATHEROSCLEROTIC PLAQUE CAPS

Hanneke Crielaard (1), Tamar B. Wissing (1,2), Su Guvenir Torun (1), Pablo de Miguel (1,3), Gert-Jan Kremers (4), Frank J.H. Gijzen (1,3), Ali C. Akyildiz (1,3), Kim van der Heiden (1,2)

(1) Department of Biomedical Engineering, Erasmus Medical Center, Rotterdam, the Netherlands

(2) Department of Biomedical Engineering, Eindhoven University of Technology, Eindhoven, the Netherlands

(3) Department of Biomechanical Engineering, Delft University of Technology, Delft, the Netherlands

(4) Erasmus Optical Imaging Center, Erasmus Medical Center, Rotterdam, the Netherlands

INTRODUCTION

Stroke is commonly initiated by rupture of the atherosclerotic plaque fibrous cap in a carotid artery. However, cap rupture mechanisms are not well understood yet. Understanding the impact of the structural components of the cap on its local mechanics may provide critical insights into plaque rupture. Various limitations within studying plaques *in vivo* and *ex vivo* highlight the need for additional methods to investigate rupture mechanics. Therefore, we created collagenous tissue-engineered plaque cap analogs [1]. In the current study, we obtain local collagen structural parameters, local mechanical properties, and rupture characteristics of these analogs to analyze the relationship between the local collagen architecture and local rupture mechanics of cap analogs.

METHODS

Development of fibrous cap analogs

Nine cap analogs were created by seeding human vena saphena cells (HVSCs) in 1 x 1.5 cm-sized fibrin gels (Fig 1A). After seeding, the samples were cultured statically (no loading) for 7 days, whereafter a 2 mm \varnothing soft inclusion (SI) was created by punching a hole in the center of each analog and filling this hole with fibrin (Fig 1B). This fibrin inclusion mimics the soft lipid core of atherosclerotic plaques. The analogs were statically cultured for 7 more days, after which they were

exposed to 7 days of dynamic loading (Fig 1C) using the Flexcell FX-4000T (Flexcell Int, 196 McKeesport, PA).

Collagen imaging

On day 21, samples were imaged with multiphoton microscopy (MPM) with second harmonic generation (SHG) to visualize the collagen architecture. First, an overview scan splitting the sample into tiles (728x728 μm) was made (Fig 2A). From the tile scan, two horizontal lines of adjacent tiles were selected for further analysis. One line of the selected tiles overlaid the shoulder region of the sample while the other overlaid the mid-cap, including the soft inclusion (Fig 2B). For each selected tile, z-stack imaging in the depth direction was performed (pixel size of $\sim 1.4 \mu\text{m} \times 1.4 \mu\text{m}$, 3- μm steps).

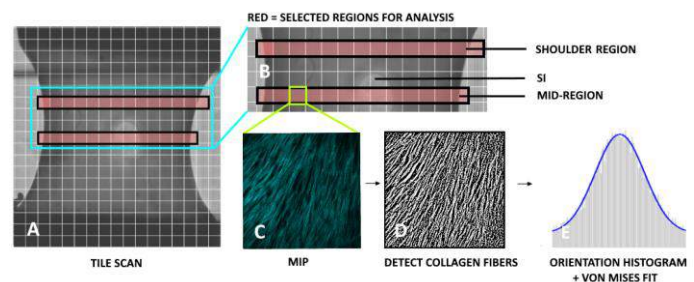


Figure 2: Collagen imaging and fiber orientation analysis pipeline.

Maximum intensity projection (MIP) image of each tile (Fig 2C) was analyzed with a MATLAB-based fiber orientation analysis tool (FOAtool [2]) to calculate the orientation of individual collagen fibers (Fig 2D). A von Mises distribution was fit to the histogram of all detected collagen fiber orientations (Fig 2E). From this distribution, the predominant fiber orientation (θ in degrees) and kappa value (κ), an

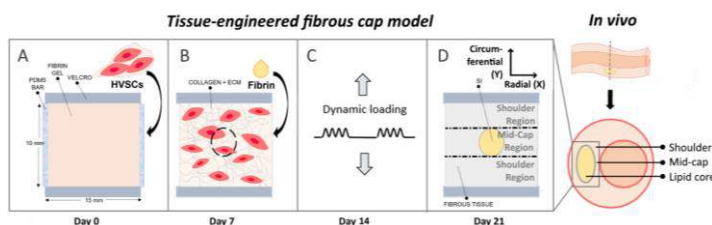


Figure 1: Protocol for developing fibrous cap analogs.

indicator of the degree of fiber anisotropy, were determined for each tile.

Uniaxial tensile tests and DIC

After imaging, the samples were mechanically tested. A speckle pattern for digital image correlation (DIC) was applied to the top surface of each sample using an airbrush and a tissue dye. After pre-stretch (15 mN) and preconditioning (10 cycles of 10% strain), the samples were uniaxially strained until complete failure at a speed of 100%/min in the y-direction, which biologically corresponds to circumferential strain (Fig 1D). Tissue deformation, rupture initiation location, and rupture propagation path were recorded with a high-speed camera (PL-D725, Pixelink). To obtain local strains (Green-Lagrange), DIC analysis was performed in MATLAB using the open-source software Ncorr [3].

RESULTS

Local collagen architecture

The predominant direction, θ (90° if y-direction), and the dispersion, κ (range=0-0.33), of the fibers for the tiles scanned are shown in Fig 3 for a representative sample. For all 9 cap analogs, the fibers were mainly oriented in the y-direction, and more so if they are located close to the sample's edges (16° vs central region: 37°). Moreover, the fibers at the sample edges showed slightly less dispersion than the ones in the central region (κ , 0.27 vs. 0.24).

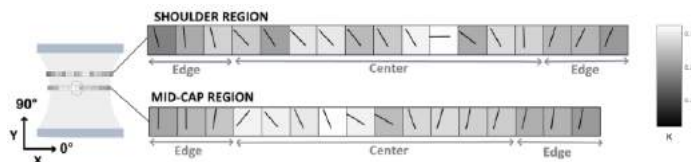


Figure 3: Predominant fiber orientation (black line) and dispersion, κ , (background color) in mid-cap and shoulder regions of a plaque cap analog. A larger κ indicates greater fiber dispersion.

Rupture initiation

In three samples, the rupture initiated at a clamping site whereas in the other six samples, rupture initiated in the SI or at the SI-fibrous tissue interface. The DIC-derived local tensile strain (E_{yy}) analysis at the timepoint of rupture initiation (Fig 4A) showed statistically significantly higher strain levels at the rupture initiation locations (Fig 4B). This finding also indicates that the average tissue strain commonly used for plaque tissue rupture characterization underestimates the real, local rupture strain.

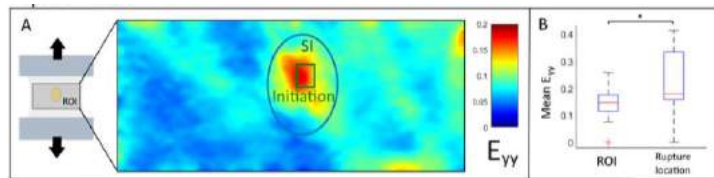


Figure 4: A) DIC-derived local tensile strains (E_{yy}). The blue oval shape indicates the soft inclusion and the green rectangle marks the location of rupture initiation. B) DIC-derived average tensile strains in the ROI are significantly lower than those in the rupture initiation region.

Rupture propagation

Qualitative analysis of rupture propagation paths showed inter-sample variation. In some samples, multiple ruptures were found, which were connected by the rupture propagation (Fig. 5A). Moreover, the shape of the rupture propagation path differed between samples. The local predominant fiber angles and the rupture propagation path in a cap

analog are shown in Fig 5A. The figure demonstrates that at most locations within the analog, the rupture propagated parallel to the local

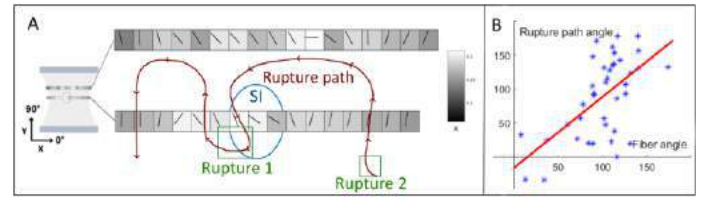


Figure 5: A) Rupture path (red line) in a representative cap analog. B) Fiber orientation vs rupture path direction, linear regression curve in red

predominant fiber angle. Similar results were found in the other samples. Fig. 5B shows the rupture path versus the local predominant fiber orientation. The linear regression curve in figure 5B ($R=0.60$, $\beta_1=1.04$, $p < 0.001$) shows that the rupture path angle approximates the fiber angle, again supporting the hypothesis that rupture in the analogs propagated parallel to the local fiber angle.

DISCUSSION

We successfully visualized the collagen orientation and obtained local mechanical (strain) fingerprints in tissue-engineered cap analogs to study atherosclerotic plaque rupture. The results demonstrated that the created cap analogs correctly replicate the predominant circumferential collagen orientation in real plaque caps [4]. Yet, there is local variation in the fiber architecture in the analogs. In the central region, larger deviations of the predominant fiber orientation from the circumferential direction and a more dispersed fiber architecture were observed compared to the edges. Local strain measurements showed that rupture in the analogs initiated at the elevated tensile strain regions. The strains found in the analog are similar to the local rupture strain found in a previous DIC-analysis of ex vivo human plaque tissue [5]. Despite the inter-sample variation in the rupture propagation path, it was found that the ruptures usually propagated parallel to the local predominant fiber angle.

As a next step, we will investigate the rupture surfaces with scanning electron microscopy (SEM) to test our new hypothesis proposing that rupture propagation in the cap analogs is mostly parallel to the local predominant fiber direction. We will also use these SEM images to determine if fibers at the rupture location are still intact. This information will help us to gain better understanding of the underlying failure mechanisms of plaque tissue.

ACKNOWLEDGEMENTS

This research, HC, TBW and KvdH are funded by an NWO-Vidi grant 18360.

REFERENCES

- [1] Wissing TB et al. *Sci. Rep.*, 12: 5434, 2022
- [2] <https://gitlab.tue.nl/stem/FibLab/blob/master/Fibertracking/manual.pdf>. (2016)
- [3] Blaber J et al. *Exp. Mech.*, 55: 1105-1122, 2015
- [4] Akyildiz AC et al. *J Struct Biol.* 200(1): 28-35, 2017
- [5] Guvenir, S. et al. *Proceedings book of SB³C 2022*, 209, 2022

A COST FUNCTION APPROACH APPLIED TO MUSCLE CRYOPRESERVATION

Casey J. Kraft (1), Weston J. Upchurch (2), Michael L. Etheridge (3), Paul A. Iazzo (1)(2), John C. Bischof (1)(3)

- (1) Department of Biomedical Engineering, University of Minnesota, Minneapolis, MN, USA
(2) Department of Surgery, University of Minnesota, Minneapolis, MN, USA
(3) Department of Mechanical Engineering, University of Minnesota, Minneapolis, MN, USA

INTRODUCTION

Tissue samples are valuable *in vitro* models for basic and preclinical research. A key research objective is to develop a cryopreservation protocol that preserves tissue viability for extended periods of time. Such a protocol may be especially beneficial in cases where the experiment or the sample is extremely valuable, such as muscle biopsies from a patient with muscular dystrophy.

To cryopreserve tissue without ice formation, a technique known as vitrification, high concentrations of cryoprotective agents (CPAs) must be used. These high concentrations of CPAs may reach a toxicity threshold, depending on factors such as tissue type and the protocol by which the CPAs are delivered.

The focus of this work is on the protocol of CPA delivery. The CPA toxicity for a given CPA cocktail and sample type is generally considered to be a function of concentration, exposure time, and temperature. The research objective, therefore, is determining the optimal “CPA exposure profile”—CPA concentration as a function of time and temperature. This profile needs to achieve the goal of sufficient CPA transport while at the same time minimizing toxicity: an optimization problem. Here, we present our solution to this optimization problem for muscle tissue, which has not been successfully cryopreserved.

METHODS

Computational

Toxicity cost function

As formulated by Davidson et al., the CPA toxicity cost function is as follows:

$$J = \int_0^{t_f} k_{\infty} \exp(-E_a/RT) C^{\alpha} dt \quad (1)$$

Where toxicity J is exponentially related to temperature T (K) and intracellular CPA concentration $C(t)$ for a given exposure time t_f . The temperature relation follows an Arrhenius-type model, with gas constant R (kJ/mol/K) and parameters k_{∞} (1/min) and E_a (kJ/mol),

which give the toxicity rate at infinite temperature and the activation energy, respectively.¹ The concentration relation is determined by the parameter α (typically $\alpha > 1$).

The goal is to minimize J while satisfying constraints of sufficient CPA loading (Eq. 2) and minimal osmotic damage (Eq. 3).

$$C \geq C_{desired} \quad (2)$$

$$V \geq V_{low} \quad (3)$$

Here, $C_{desired}$ gives the desired intracellular [CPA] at the center of the tissue and V_{low} gives the minimal fraction of initial cell volume.²

To achieve this optimization, various CPA exposure profiles— $c=f(t,T)$ —were generated in Mathematica. The profiles which failed either constraint (Eqs2-3) were removed from consideration. For each remaining profile, the CPA toxicity (Eq1) was calculated at various penetration depths within the 1.4 mm-thick tissue. The code then outputs the profile with the lowest total toxicity along the thickness of the tissue as the optimum.

Diffusion simulation

The system was modeled as two-sided one-dimensional diffusion through a rectangular slab of 1.4 mm in thickness. To calculate extracellular CPA concentration as a function of penetration depth, the finite medium solution (Eq4) was used:

$$\theta = \int_0^1 1 - 2 \sum_{i=1}^{\infty} \frac{(-1)^{i-1}}{(i+.5)\pi} \cos((i+.5)\pi\eta) \exp(-(i+.5)^2\pi^2 \frac{tD}{L^2}) d\eta \quad (4)$$

Here, the key parameter is effective diffusivity, D , which was modeled as a function of temperature via parameters given by Jomha et al.³

Shrink-swell simulation

To calculate the intracellular CPA concentration, C (Eqs1-2), and the cell volume, V (Eq3), the 2 parameter formalism for water and CPA transport was used:

$$\frac{dV_w}{dt} = -L_p A R T (c + c_n - C - C_n) \quad (5)$$

$$\frac{dN}{dt} = P_s A (c - C) \quad (6)$$

In which the two parameters are L_p , which gives the hydraulic conductivity, and P_s , which gives the CPA permeability. These two parameters were modeled as a function of temperature in accordance with parameters given by Fry et al.⁴

Experimental

To date, values for the above toxicity parameters (k_{ω} , E_a , and α in Eq1) have only been determined for glycerol exposure in endothelial cells¹. Here, we determine these parameter values for a vitrification-relevant CPA cocktail (VS55 in Celsior) in muscle tissue.

Tissue preparation and muscle bath protocol

Porcine diaphragm muscle was cut into strips of approximately 40 mm in length and 2.5 mm in diameter.

To assess CPA toxicity, the twitch force before and after CPA treatment was recorded. The muscle bath apparatus functions to electrically stimulate the muscle every 10 s, while also providing oxygenation and temperature control. In the initial stage, the temperature was 37°C and the solution was Krebs-Henseleit Buffer. In the treatment stages, the temperature was adjusted (if necessary) and a step-loading procedure (20 min, 2 M CPA steps) was used to reach the treatment CPA concentration whilst avoiding osmotic damage. In the 150 min assessment stage, the temperature was set back to 37°C and the solution was changed back to Krebs. The median initial force divided by the median assessment force was defined as the force recovery.

Extracting toxicity parameters from experimental data

This force recovery (% of initial) was used to calculate the toxicity parameters (k_{ω} , E_a , and α in Eq1). Multiple CPA concentrations and temperatures were tested (Fig. 1). For each concentration and temperature, multiple exposure times were tested (data not shown). The decline in force recovery as a function of exposure time, t , was fit to the equation $100e^{-kt}$, and the value of k was calculated and plotted in Figure 1. This k is defined as the toxicity constant, and is related to CPA toxicity, J , by the following equation:²

$$J = \int_0^t k dt \quad (7)$$

RESULTS

As expected, we found that CPA toxicity (Eq. 7) was higher at higher concentrations and higher temperatures (Fig. 1).

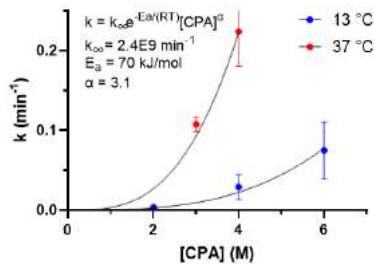


Figure 1: Toxicity of porcine diaphragm muscle exposed to different temperatures and concentrations of VS55 over time. Curves were generated using nonlinear regression ($R^2 = 0.89$)

One key finding was the relatively high parameter values for k_{ω} and α (Fig. 1, top left), which indicate that our system is quite sensitive to CPA toxicity, especially at high temperatures (k_{ω}) and high concentrations (α). For comparison, Davidson et al. report $k_{\omega} = 1E7 \text{ min}^{-1}$ and $E_a = 56 \text{ kJ/mol}$ ¹, and Benson et al.² report $\alpha = 1.6$. This discrepancy may simply be a result of procedural differences in CPA type and toxicity metric, though the idea that muscle tissue is more sensitive to CPA would explain the lack of successful muscle cryopreservation protocols.

These parameter values were used as inputs in the mathematical simulation, which outputs the profile (Fig. 2A) that has the least toxicity

(Eq. 1) of all the profiles which passed both the osmotic and loading constraints (Equations 2-3 with $V_{low} = 0.5$ and $C_{desired} = 3.5 \text{ M}$). As expected, the optimal profile is at the edge of these constraints (Fig. 1B).

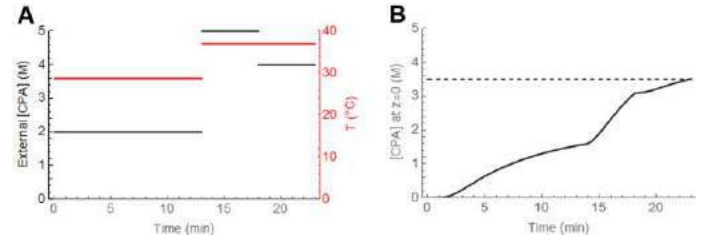


Figure 2: Simulation results for CPA loading in 1.4 mm-thick tissue. A: Toxicity-optimal CPA step-loading profile. B: Intracellular CPA concentration at the midline, with the dashed line giving the desired CPA concentration.

One key finding is the non-monotonic increase in CPA concentration (Fig. 1A, black). This is consistent with the simulation results of Benson et al., in which they argue that a higher penultimate step results in a more uniform concentration throughout the length of the tissue, and therefore less toxicity⁵.

Another key finding is the high temperature (Fig. 1A, red). This is inconsistent with conventional wisdom, which advises to use a low temperature to minimize toxicity. The explanation for our conflicting result is that, for this simulated system, the benefit of using a high temperature (faster mass transport and therefore shorter exposure time and therefore reduced toxicity) outweighs the downside of using a high temperature (increased metabolism and therefore increased toxicity). This finding has implications for CPA protocol development generally: a low temperature may not always be best.

There is some precedent for this result. In the simulation from Davidson et al., they identify an E_a threshold for the first CPA loading step in their system. At $E_a < 89 \text{ kJ/mol}$, they found that it was better to load CPA in a manner that was fast and hot instead of slow and cold.¹

DISCUSSION

In 2018, Benson et al. proposed a cost function approach for developing a toxicity-optimal CPA exposure profile in tissue systems. In their work, they determined the optimal time for each CPA loading step.⁵ In our simulation, we also determined the optimal temperature for each CPA loading step, in addition to the optimal time. By exploiting the fact that mass transport parameters are higher at higher temperatures, it may be possible to develop a successful cryopreservation protocol for sensitive systems such as muscle tissue.

In the development of CPA loading protocols, many researchers start with a historical protocol from the literature. The approach described here offers a better experimental starting point. Experimental development may still be necessary, but in this case the experimenter will be iterating from the theoretical optimum, likely saving time and resources. The vision is for every cryobiologist to employ a computational approach such as this for developing CPA loading and unloading profiles.

ACKNOWLEDGEMENTS

This work was supported by research funding from the NSF (EEC 1941543) and traineeship funding from the NIH (T32HL139431).

REFERENCES

- [1] Davidson, A et al., *PLOS ONE*, 10:1-22, 2015.
- [2] Benson, J et al., *Cryobiology*, 64:144-151, 2012.
- [3] Jomha, N et al., *Cryobiology*, 58:110-114, 2009.
- [4] Fry, A et al., *Cellular and Molecular Bioeng.*, 5:287-298, 2012.
- [5] Benson, J et al., *Cryobiology*, 80:144-155, 2018.

DATA-ENHANCED PERSONALIZED MODELS FOR CORONARY HEMODYNAMICS AND MYOCARDIAL PERFUSION

Karthik Menon^{*1}, Zachary Sexton², Owais Khan³, Daniele Schiavazzi⁴, Koen Nieman⁵ and Alison Marsden^{1,2}

(1) Department of Pediatrics (Cardiology), Institute for Computational and Mathematical Engineering, and Stanford Cardiovascular Institute, Stanford University, Stanford, CA, USA

(2) Department of Bioengineering, Stanford University, Stanford, CA, USA

(3) Department of Electrical, Computer, and Biomedical Engineering, Toronto Metropolitan University, Toronto, Ontario, Canada

(4) Department of Applied and Computational Mathematics and Statistics, University of Notre Dame, Notre Dame, IN, USA

(5) Department of Medicine (Cardiovascular Medicine), Stanford University, Stanford, CA, USA

INTRODUCTION

Coronary artery disease (CAD) is the leading cause of death globally. Current treatment to restore flow in occluded coronary arteries is often guided by anatomy-based risk assessment, which has poor outcomes compared to treatment based on hemodynamic metrics [1]. To address this, personalized computational fluid dynamics (CFD) simulations are an emerging way to improve CAD treatment outcomes via non-invasive hemodynamic risk assessment and virtual treatment planning.

The accuracy of patient-specific CFD, which uses anatomical models constructed from non-invasive clinical imaging, depends on the quality of imaging on which it is based. A major source of error in current CFD models is the exclusion of arteries in the anatomical model that are under-resolved by clinical imaging. This causes erroneous flow distributions amongst coronary arteries in the model. Moreover, the flow distribution amongst arteries in CFD models is also affected by the boundary conditions specified at the outlet of each artery. The widely-used Murray's law [2], which empirically splits flow amongst arteries based on diameter, does not account for occluded and collateral arteries, metabolic regulation or anatomical uncertainty.

To address these issues, this work demonstrates a framework for more accurate and personalized coronary hemodynamics models that are enhanced by clinical and morphometric data. To create more anatomically realistic models, we combine conventional image-based models with synthetic vascular trees to represent arteries that are under-resolved in clinical imaging. Furthermore, these models are informed by novel non-invasive CT myocardial perfusion imaging (MPI_{CT}) [3] and clinical measurements of cardiac function, to estimate more accurate and personalized model parameters and boundary conditions. We also couple the coronary hemodynamics to patient-specific simulations of myocardial blood flow, which

allows quantitative estimates of hemodynamic CAD severity as well as myocardial ischemic risk.

METHODS

We use patient-specific coronary anatomical models based on CT angiography (CTA). The models are created using the segmentation and model building tools available in the open-source *SimVascular* software. We augment these image-based models with synthetic vascular trees generated using Constrained Constructive Optimization (CCO) [4] to represent vessels that are under-resolved in CTA. CCO can generate multiple non-intersecting trees in concave ventricle-like volumes that are constrained by hemodynamics and vascular scaling laws while minimizing vascular volume.

The hemodynamics is simulated using multi-scale 3D and reduced order models. The 3D flow in large arteries is simulated using the finite element solver, *svSolver*, included with *SimVascular*. The flow in synthetic and distal vasculature is simulated using 0D lumped-parameter models of flow (electric circuit analogy).

We enforce patient-specific flow distributions in the coronary tree based on clinical dynamic CT myocardial perfusion imaging (MPI_{CT}) [3]. MPI_{CT} is a non-invasive contrast-based imaging modality that quantifies the spatial distribution of blood flow/volume perfusing the left ventricle myocardial tissue. From clinically-acquired MPI_{CT}, we extract patient-specific left ventricle (LV) volumes and myocardial blood flow (MBF) distributions. Using co-registered 3D models of each patient's coronary vascular tree obtained from CTA and the MBF distribution in the LV obtained from MPI_{CT}, we estimate the LV perfusion regions and MBF volumes corresponding to each coronary artery. These are incorporated into the out-flow boundary conditions for the simulated hemodynamics. We compare

this novel method to specify flow splits with the conventionally used modified Murray's law [2] with an exponent of 2.6.

We use closed-loop lumped parameter network (LPN) boundary conditions at inlets and outlets of the aorta and coronary arteries in the 3D simulations [5] to capture the coupling with downstream systemic circulation. This includes blocks to model the resistance and capacitance of distal vasculature, each heart chamber, and the intramyocardial pressure in coronary arteries that causes out-of-phase flow with respect to the cardiac cycle. This model also incorporates the distribution of flow amongst coronary arteries, described above. Parameters are tuned using an automated surrogate-based optimization framework so that the resulting simulations reproduce clinically measured flow splits, heart rate, aortic pressure, cardiac output and ejection fraction for each patient within a specified error tolerance.

Finally, the coronary hemodynamics models are coupled to finite element simulations of myocardial blood flow based on Darcy flow through porous materials. A single compartment Darcy model is used to simulate myocardial blood flow, which is coupled to the coronary hemodynamics via pressure sources in the myocardium that are driven by coronary flow [6].

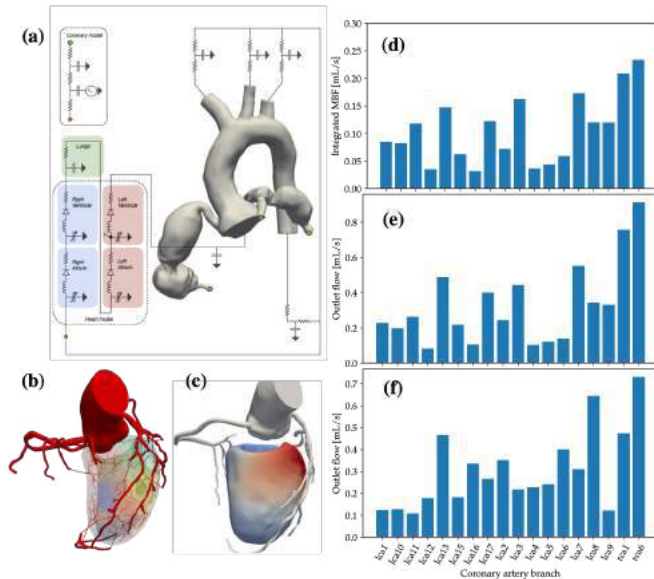


Figure 1: (a) Schematic of the simulation setup. (b) Sample case with synthetic vascular trees. (c) Myocardial perfusion simulation showing capillary pressure. (d) Flow in each coronary artery evaluated from MPI_{CT}. (e) Simulated flow in each coronary artery when using perfusion-informed boundary conditions. (f) Simulated flow in each coronary artery when using Murray's law boundary conditions.

RESULTS

Figure 1(a) shows a schematic of the image-based coronary hemodynamics model used in this study (shown without synthetic vascular trees for clarity) which is coupled with reduced-order models for systemic circulation and the four heart chambers. Figure 1(b) shows a sample case of an image-based anatomical model augmented with synthetic vascular trees that are constrained to grow in the patient-specific LV volume. This example shows 15 vascular trees perfusing the LV volume with 30 outlets in each tree. A sample myocardial perfusion simulation result is shown in figure 1(c), where the colors on the myocardium represent capillary pressure.

Preliminary results indicate that our automated framework to personalize and tune coronary hemodynamics models accurately recapitulates patient-specific clinical measurements. Figure 1(d) shows the clinically measured flow in each branch of the coronary tree, estimated from vessel-specific MPI_{CT} perfusion territories. This is compared with the simulated

flow using boundary conditions based on the novel imaging-informed technique and conventional Murray's law. The flow splits tuned based on perfusion imaging, shown in figure 1(e), qualitatively reproduce the measured distribution of flow (from MPI_{CT}) amongst the coronary arteries. However, the flow distribution obtained from using Murray's law, shown in figure 1(f), does not show good agreement with the clinically measured flow splits in figure 1(d). We note that the absolute volume of flow differs between the clinical measurement and both simulation cases because MPI_{CT} is known to underestimate flow volumes. We therefore focus on relative flow distributions in this study. Although not shown here, the automated parameter estimation framework used to tune the coronary hemodynamics simulations also produces good agreement between simulations and clinically measured metrics of cardiac function such as cardiac output, stroke volume and ejection fraction.

DISCUSSION

This work presents a novel framework for simulations of patient-specific coronary hemodynamics and myocardial perfusion that are enhanced by non-invasive myocardial perfusion imaging and morphometric synthetic vascular trees. We seek to address two significant sources of error in current coronary hemodynamics CFD models; (1) the exclusion of anatomical features of the coronary tree that cannot be resolved from clinical imaging; and (2) the use of empirical flow splits amongst arteries that are not patient-specific. Preliminary results indicate good success with the automated framework for tuning simulation parameters to reproduce patient-specific clinical measurements of coronary flow distributions as well as cardiac function.

Previous studies have highlighted the inaccuracies introduced in coronary hemodynamics simulations due to inaccurate branching in the model anatomy [7] as well as uncertainty in outflow boundary conditions [8]. We expect that the inclusion of synthetic vascular trees in place of under-resolved arteries will aid in producing more physiological flow distributions and, in the future, will also allow more rigorous studies of the effect of branching. Moreover, the incorporation of non-invasive perfusion imaging into the tuning of coronary flow boundary conditions is a novel method to obtain personalized flow distributions in the coronary tree, which in turn leads to more accurate estimates of clinically relevant hemodynamic metrics such as fractional flow reserve.

ACKNOWLEDGEMENTS

This work is supported by NIH grant 5R01HL141712-03. High performance computing resources were provided by XSEDE and the Stanford Research Computing Center.

REFERENCES

- [1] Tonino PA et al. *New England Journal of Medicine* 360.3 (2009). DOI: 10.1056/nejmoa0807611.
- [2] Zhou Y et al. *Physics in Medicine and Biology* 44.12 (1999). DOI: 10.1088/0031-9155/44/12/306.
- [3] Giordano M et al. *Medical Physics* 44.4 (2017). DOI: 10.1002/mp.12126.
- [4] Schreiner W et al. *IEEE Transactions on Biomedical Engineering* 40.5 (1993). DOI: 10.1109/10.243413.
- [5] Tran JS et al. *Computers and Fluids* 142 (2017). DOI: 10.1016/j.compfluid.2016.05.015.
- [6] Papamanolis L et al. *Annals of Biomedical Engineering* 49.5 (2021). DOI: 10.1007/s10439-020-02681-z.
- [7] Wellnhofer E et al. *Atherosclerosis* 213.2 (2010). DOI: 10.1016/j.atherosclerosis.2010.09.007.
- [8] Sankaran S et al. *Journal of Biomechanics* 49.12 (2016). DOI: 10.1016/j.jbiomech.2016.01.002.

PHYSICS-INFORMED NEURAL NETWORKS WITH FOURIER-BASED ACTIVATION FUNCTION TO MODEL COMPLEX CARDIOVASCULAR FLOWS.

Arman Aghaee(1), M. Owais Khan (1)

(1) Electrical, Computer and Biomedical Engineering, Toronto Metropolitan University, Toronto, ON, Canada

INTRODUCTION

Physics-Informed Neural Networks (PINNs) has emerged as a powerful approach to encode governing partial differential equations (PDEs) and training data to solve complex engineering problems. In cardiovascular applications, PINNs can be designed to encode Navier-Stokes equations and clinically-acquired hemodynamic data (e.g., from 4D Flow MRI) into the loss function to improve predictions. However, minimizing the loss function during the training process is challenging.

One key strategy to improve the training operation is to use more robust activation functions that maintain nonlinearity, differentiability, with minimal vanishing gradients. However, majority of the popular activation functions, such as Swish or Tanh, lack some of these properties, which can consequently make the training process tedious. Additionally, these functions cannot capture high-frequency signals, for example, those observed in quasi-turbulent cardiovascular flows, such as in aorta, aneurysms, and ventricles.

We propose to use a recently-introduced Fourier-based activation function that utilizes a periodic *sine* function [1]. The derivative of a *sine* function is a cosine, a phase-shifted *sine*, and thus, inherit the properties of the original function. *Sine* activation functions have shown to outperform others in computer vision problems, but their applicability in cardiovascular fluid applications is not known [1].

METHODS

PINNs Model: The solution $u(\mathbf{x}, t)$ was approximated with a deep learning network $f(\mathbf{x}, t; \theta)$, where θ represents the trainable parameters of the neural network. The loss function is defined as:

$$\mathcal{L}_{\text{total}}(\theta) = \mathcal{L}_{PDE} + \lambda_{BC}\mathcal{L}_{BC} + \lambda_{data}\mathcal{L}_{data} \quad (1)$$

where \mathcal{L}_{PDE} , \mathcal{L}_{BC} and \mathcal{L}_{data} correspond to the loss term for the Navier-Stokes equation, boundary conditions, and known sensor data, respectively. The parameters λ_{BC} and λ_{data} aim to balance the interplay of the different terms in the loss function. The training parameter θ is

optimized by minimizing the total training loss, $\mathcal{L}_{\text{total}}(\theta)$ via a standard gradient descent optimization (i.e., ADAM).

The weighting coefficients in the loss function, λ_{BC} and λ_{data} , are problem-specific and tedious to choose for complex flow cases. Hence, we applied the strategy of dynamic weights that adaptively update the coefficients by utilizing the back-propagated gradient statistics during training. The iterative formulation for the adaptive weight can be expressed as [2]:

$$\theta^{k+1} = \theta^k - \eta \nabla_{\theta} \mathcal{L}_{PDE} - \eta \lambda_{BC} \nabla_{\theta} \mathcal{L}_{BC} - \eta \lambda_{data} \nabla_{\theta} \mathcal{L}_{data} \quad (2)$$

where k is the iteration step, and η is the learning rate. The coefficients λ_{BC} and λ_{data} can be estimated using the following relation [2]:

$$\lambda_{BC} = \frac{\max_{\theta} (|\nabla_{\theta} \mathcal{L}_{PDE}(\theta_n)|)}{(|\nabla_{\theta} \mathcal{L}_{BC}(\theta_n)|)}, \lambda_{data} = \frac{\max_{\theta} (|\nabla_{\theta} \mathcal{L}_{PDE}(\theta_n)|)}{(|\nabla_{\theta} \mathcal{L}_{data}(\theta_n)|)} \quad (3)$$

Activation Functions: We compared two standard activation functions, SWISH and Tanh against a Fourier-based, periodic *sine* function (i.e., SIREN[1]). Compared to other activation functions, *sine* function has shown better convergence and differentiability for high-frequency signals. The formulation of the three activations functions is

$$\text{SWISH: } f(x) = x \cdot \text{sigmoid}(x) \quad (4)$$

$$\text{Tanh: } f(x) = \frac{e^x - e^{-x}}{e^x + e^{-x}} \quad (5)$$

$$\text{Sinus: } f(x) = \sin(\omega_0 x) \quad (6)$$

Sine requires special initialization for the first layer and normalization of the input components from -1 to 1. We applied the strategy proposed by Pan et al. in our work [3].

Test Case A – 1D Advection Diffusion Equation: We tested the three activation functions on a 1D steady advection-diffusion equation:

$$\alpha \frac{\partial u}{\partial x} = v \frac{\partial^2 u}{\partial x^2} \quad (7)$$

where $\alpha = 1$ and $v = 0.001$ were chosen for advection and diffusion coefficients, respectively. The neural network consisted of 2-10 layers with 100 neurons per layer. Three sensor points were chosen along x .

Test Case B – 2D Eccentric Stenosis: A 2D eccentric stenosis geometry was created based on Varghese et al [4]. An asymmetry of 5% was introduced at the stenosis throat that served as a geometric perturbation to the flow field.

CFD simulations were performed using a higher-order finite-element solver, *Oasis* [5], that is designed to minimize numerical dissipation and dispersion errors. The geometry was meshed into 60k second-order tetrahedra, which corresponds to 480k linear tetrahedra. CFD simulations were run for 25000 timesteps for $t^* = tu_i/D = 125$.

The PINNs architecture consisted of 4 layers with 128 neurons/layer. The boundary conditions and velocity field at the mesh nodes were treated as unknown quantities. Sensitivity to sensor data (obtained from CFD) were tested by increasing sensor points from 25 to 400. The sensor points were equally distributed along the domain.

RESULTS

1D Advection Diffusion Equation: Figure 1 shows that even with 2 layers, *sine*-based PINNs is able to reconstruct the analytical solution with an order of magnitude lower errors compared to other activation functions. In addition, *sine* activation function shows a monotonic decrease in error while other activation functions require 10 layers to produce any notable reduction in error.

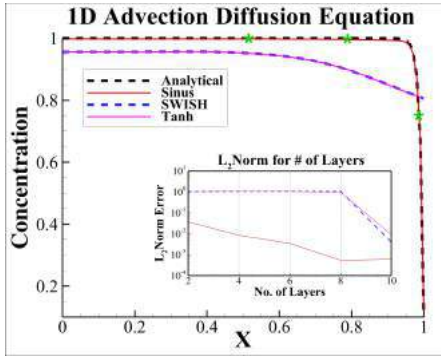


Figure 2: PINNs solution with different activation functions using 2 neural network layers. The inset shows error with increasing neural network layers. The green asterisk marks the location of sensor (known) data.

2D Eccentric Stenosis at Re=5000: While PINNs model with *sine* and *swish* activation functions converged, the *tanh* solution diverged due to its gradient diminishing properties.

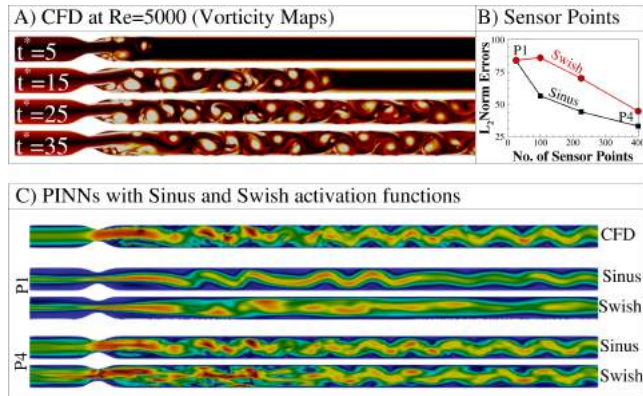


Figure 1: A) Temporal evolution of vortical structures over non-dimensional time, t^* . B) Decrease in error with increasing sensor data, and C) PINNs-predicted velocity for *sine* and *Swish* activation functions at $t^* = 35$.

The results for *sine* and *swish* functions are summarized in Figure 2:

- **CFD Flow Field:** Figure 2A shows that at $Re=5000$, the velocity field is unsteady and dynamic. The geometric asymmetry leads to formation of periodic vortical structures that shed at a constant frequency. Initial transients wash out by $t^* = tu_i/D = 35$.
- **Sensitivity to # of Sensor Points:** Figure 2B shows a monotonic decrease in L_2 errors as the number of sensor data increases from 25 to 400. There is a rapid decrease in error norm from 25 to 100 points for *sine* function compared to *swish* function.
- **PINNs-predicted Velocity Field:** Figure 2C shows the velocity field estimated by PINNs for 25 and 400 sensor points, marked with P1 and P4 respectively. We note that even with 25 sensor points, the *sine*-predicted velocity field shows the oscillatory behavior that is not captured by *Swish* activation function. At 400 sensor points *swish* and *sine* show similar L_2 norms; however, the qualitative velocity maps demonstrate that *sine*-based predictions closely match the CFD ground-truth data.

DISCUSSION

We have demonstrated that *sine* activation function provides a notable improvement in velocity field predictions compared to conventional activation functions. Although *sine* function requires specialized treatment (i.e., initialization and normalization), they provide a notable improvement in velocity predictions.

Another observation is that *sine* activation function was able to reconstruct the gross velocity field even with 25 sensor points. The reduced requirements on sensor data are beneficial since clinically-acquired hemodynamic data is often scarce and sparse, for example, in 4D Flow MRI or dynamic perfusion CT imaging.

Lastly, we note that due to the vanishing gradient problems pervasive in some of the activation functions (e.g., Tanh), these functions are unsuitable for more dynamic and complex flow problems.

Relationship to Previous Literature: We note that our study is the first to use a *sine*-based activation function for cardiovascular flow application. Previous study by Arzani et al. [6] have demonstrated that PINNs could predict wall shear stresses using sparse measurements away from the wall. Those authors used a *Swish* activation function and demonstrated excellent agreement with CFD data; however, the flow field used in their study was steady, uniform and thus, had low spatial gradients. As seen in our study, if the flow complexity and spatial gradients are increased, training with conventional activation function can produce inaccurate results, especially when sensor data is sparse.

We have demonstrated that *sine*-based activation function can better capture complex flow fields compared to conventional activation functions. Further work is needed to demonstrate the applicability of the proposed approach for patient-specific three-dimensional models.

ACKNOWLEDGEMENT

This work is support by NSERC Discovery Grant awarded to M.O.K.

REFERENCES

- [1] Sitzmann, V et al., Advances in Neural Information Processing Systems, 33: 7462 – 7473, 2020.
- [2] Jin, X. et al., Journal of Computation Physics, 109951, 2021.
- [3] Pan, Shaowu et al., arXiv preprint, 2204.03216, 2022.
- [4] Varghese, S. et al., Journal of Fluid Mechanics, 582: 253-80, 2007.
- [5] Mortensen, M. et al., Computer Physics Communication, 188: 177-188, 2015.
- [6] Arzani, A. et al., Physics of Fluids, 33(7): 071905, 2021.

VALIDATING MULTI-SCALE CORONARY SIMULATION PIPELINE AGAINST CORONARY INTRAVASCULAR VELOCITY AND PRESSURE MEASUREMENTS

Anahita A. Seresti (1), Alison L. Marsden (2), Andrew M. Kahn (3), M. Owais Khan (1)

(1) Electrical, Computer and Biomedical Engineering, Toronto Metropolitan University, Toronto, ON, Canada

(2) Department of Pediatrics, Stanford University, Stanford, CA, USA

(3) Division of Cardiovascular Medicine, University of California San Diego, La Jolla, CA, USA

INTRODUCTION

Ischemic heart disease is caused by restricted coronary blood flow. Thus, the availability of coronary blood flow would be helpful to guide clinical interventions or evaluate biomechanical stresses (e.g., wall shear stresses) as a proxy of plaque remodeling. However, coronary flow is challenging to measure non-invasively and routinely in clinic.

One non-invasive approach to obtain coronary pressure and velocity is to use CTA-based computational fluid dynamics (CFD) simulations, commercially popularized by HeartFlow's FFR-CT technology. A key disadvantage of CTA-based CFD simulation is related to the assumptions of inflow and outflow boundary conditions.

Boundary conditions are typically estimated using empirically-derived flow-diameter relations; however, there is no clear evidence whether these assumptions produce patient-specific results when used for CTA-based CFD simulations.

The goal of this study was to utilize a fully non-invasive approach to coronary CFD and evaluate the impact of inflow and outflow boundary conditions against intravascular velocities and pressures.

METHODS

Patient Data: Imaging and hemodynamic data were acquired for N=13 patients at the University of California San Diego, including coronary CTA, echocardiography, intravascular Doppler velocity, and pressure. Intravascular measurements were made using ComboWire XT Pressure and Flow Wire (Volcano, San Diego California) at rest and stress for multiple cardiac cycles (see Figure 1A). Only rest values were used in our analyses. For each patient, intravascular recordings were obtained for 120 ± 55 cardiac cycles. These flow waveforms were assessed for quality (e.g., peak in diastolic phase, gradual decline, noise) using an automated in-house tool. Only waveforms that had an acceptance rate of $>70\%$ were included in the study.

Computational Fluid Dynamics Simulations: All 13 coronary CTA images were segmented and meshed in the SimVascular software

package (simvascular.github.io). Fluid-structure interaction (FSI) simulations were coupled to a lumped parameter network (LPN) to model heart and closed-loop circulation (Figure 1B). An automated approach was used to tune the input variables of LPN to match clinical targets, such as heart rate, blood pressures, ejection fraction, cardiac output [1]. Briefly, $\sim 4.6\%$ of the cardiac output fed the coronary arteries, with a 70-30% flow split between left and right coronary tree. Within each coronary tree, the flow was split based on modified Murray's Law using the following relationship [2]:

$$\frac{Q_i}{\sum Q_i} = \frac{D_i^{2.6}}{\sum D_i^{2.6}} \quad (1)$$

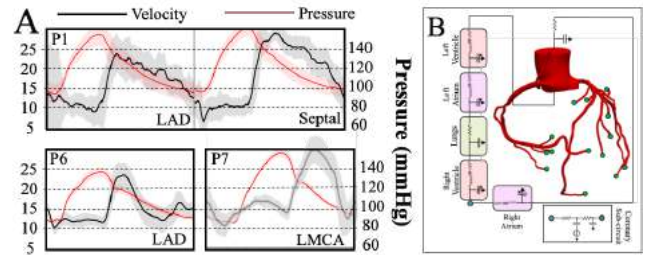


Figure 1: A) Doppler velocity (black) and pressure (red) tracings in three representative patients. B) Multi-scale CFD pipeline, combining FSI with closed-loop LPN.

Coronary Flow Rate Estimation: Cardiac cycle-averaged intravascular Doppler flow rate was estimated assuming a parabolic velocity profile, according to the following formula:

$$Q_{Doppler} = Area \cdot \frac{AVP}{2} \quad (2)$$

where Area is obtained from coronary CTA at the location where intravascular data was recorded. AVP is the averaged peak velocity and was taken by averaging multiple cardiac waveforms. The intravascular

probe location was recorded by the interventional radiologist during the procedure and marked onto the 3D reconstructed coronary model by an experienced cardiologist (A.M.K).

CFD Post-processing: Cross-sectional slices were made at locations where intravascular data was measured. CFD flow rates were estimated using equation (2) and pressures were averaged across the cross-section.

Statistical Analysis: A Shapiro-Wilks test was performed to check for normality. Since all anatomic and hemodynamic variables were found to be non-normally distributed, a two-sided paired Wilcoxon signed rank-sum test was used to compare CFD vs. intravascular data.

RESULTS

A total of 19 vessel were analyzed from 13 patients, including left anterior descending artery (N=11), right coronary artery (N=5), left main coronary artery (N=2) and septal artery (N=1). Table 1 compares cohort-averaged intravascular vs. CFD hemodynamics.

Table 1: Hemodynamic measurements in N=19 vessels.

	Intravascular	CFD	p-value
Pressure (mmHg)	89 ± 18	63 ± 11	<0.01
Velocity (cm/s)	8.76 ± 2.80	11.7 ± 5.9	0.16
Q, Flow rate (mL/min)	38.5 ± 26.2	55 ± 48	0.16

Pressure Analysis: Figure 2 (top panel) shows that there was a statistically significant correlation between CFD derived pressures and intravascular pressures ($p < 0.01$). Bland-Altman plot showed a positive bias of 26.5 [49 – 3.4] mmHg, indicating that CFD simulations tended to underestimate the intravascular pressures. This underestimation can be attributed to differences between cuff pressures, used to compute resistances in CFD simulations, and intravascular pressures.

Velocity and Flow Rate Analysis: Figure 2 (bottom panel) shows that there was no statistically significant correlation between CFD-derived velocity vs. intravascular Doppler velocity. The same was true for flow rates. Bland-Altman plot showed a negative bias of -3 [-16.3 – 10.4] cm/s for velocity (Figure 2, bottom panel), and a negative bias of -16.5 [-86 – 53] mL/min for flow rate, with a wide 95% limits of agreement.

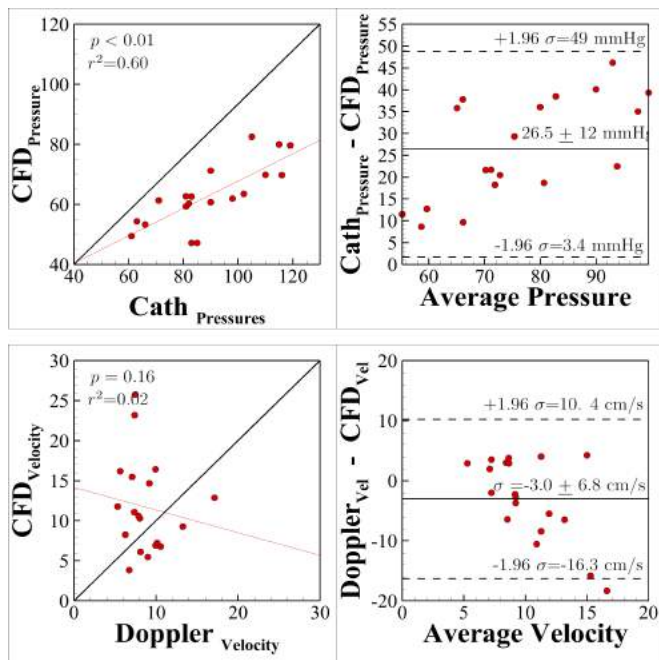


Figure 2: Correlation and Bland-Altman plots comparing CFD vs. intravascular pressure and velocity data.

DISCUSSION

CTA-based CFD simulations of coronary arteries are used widely in research and, more recently, in commercial applications; however, based on our findings, there is no clear evidence of how accurately these simulations predict in-vivo hemodynamics, particularly absolute pressures and velocities. Although we found that CFD-predicted pressures correlated well with intravascular pressures, there was a lack of correlation with intravascular Doppler velocity. These findings have important implication for coronary CFD-based technologies.

Implications for Coronary CFD-based applications: There is a strong clinical and research interest in estimating absolute coronary flow, for example to predict coronary wall shear stresses as a proxy of plaque vulnerability [3]. Additionally, recent efforts have focused on using CFD to assess coronary physiology in heart bypass surgeries for pre-planning [4], or to computationally predict myocardial blood flow perfusion [5]; all of which depends on accurate estimation of coronary hemodynamics. Our findings demonstrate that even when using highly detailed patient-tailored CFD simulations, there are still significant errors in coronary velocities and flow rate, which would naturally lead to errors in other velocity-derived quantities, such as wall shear stresses.

Interestingly, our findings demonstrate that CFD-derived pressures correlated well with those measured invasively. This good correlation can be attributed to the use of patients' cuff pressures to estimate coronary vascular resistances in our CFD strategy. Additionally, there is recent interest in simulating myocardial blood flow perfusion by coupling coronary and myocardial perfusion physiology [5]. These dynamics are dependent on accurate prediction of coronary pressures, and thus, would benefit from our coronary CFD strategy.

Relationship to Previous Literature: Previous studies have compared Doppler- vs. scaling-law approach for coronary inflow estimation [6,7], but most of these studies are limited to coronary models that have been reconstructed from 2D angiography, and consequently, permit only 2-5 outlets. In contrast, since we used CTA, we were able to reconstruct ~20 branches per model, and without the need for invasive imaging.

A recent study by Lodi Rizzini et al. investigated the impact of different inflow estimation methods (e.g., thermodilution, Doppler, and scaling law) on coronary hemodynamics [7]. Those authors reported a cohort-averaged $Q_{Doppler}$ of 44 mL/min, which is in close agreement with $Q_{Doppler}$ of 38.5 mL/min reported in our study. Similar to our findings, those authors found significant differences between their baseline approach (i.e., thermodilution) and scaling-law based flow rates.

In conclusion, our findings indicate that while CFD-derived predictions correlate well with intravascular pressures, there is no statistical correlation with intravascular velocity or flow rates. These findings highlight the need to improve inflow boundary condition estimation if absolute coronary flow rate or velocities are needed.

ACKNOWLEDGEMENT

This work is support by NSERC Discovery Grant awarded to M.O.K.

REFERENCES

- [1] Tran, JS. et al., *Computers and Fluids*, 142:128-138, 2017.
- [2] Changizi, M. et al., *Can. J. Physiol. Pharmacol.*, 78:603-611, 2000.
- [3] Candreva, A. et al., *Atherosclerosis*, 342: 28-35, 2022.
- [4] Rezaeimoghaddam, M. et al. *Cardiovasc. Eng. Technol.*, 11: 663-678, 2020.
- [5] Papamanolis, L. et al., *Annals of Biomedical Engineering*, 49 (5): 1432 – 1447, 2021.
- [6] Van de Giessen, AG. et al., *Journal of Biomechanics*, 44(6):1089-1095.
- [7] Lodi Rizzini, M. et al., *Computer Methods and Programs in Biomedicine*, 106882, 2022.

CYCLIC STRETCH INHIBITS CELL INVASION AND MIGRATION IN 3D SCAFFOLDS

Rozanne W. Mungai (1), Kevin Piskorowski (1), Grace Jolin (1), Ying Lei (1) and Kristen L. Billiar (1)

(1) Department of Biomedical Engineering, Worcester Polytechnic Institute, Worcester, MA, USA

INTRODUCTION

Cell invasion and migration are driving factors for various biological events such as development, wound healing, tumor invasion and host cell infiltration of implanted scaffolds. These events involve cells invading and/or migrating in response to chemical or mechanical cues [1]. Extracellular features such as matrix porosity, substrate topography, matrix stiffness and density are among a few static mechanical cues that influence cell invasion and migration [2, 3]. Dynamic mechanical stimuli such as fluid shear and stretch may also play a role [4]. Many organs experience dynamic loading (e.g., cardiovascular tissues, skin, tendons) which induces changes in cell alignment and forces [5]. It is possible that dynamic stretch also alters cell invasion and migration.

Studies utilizing 2D substrates have demonstrated reduction of cell migration in response to cyclic stretch [6-8]. Most cell types reorient away from stretch in these 2D systems. In contrast, in 3D biopolymer gels, cells and extracellular matrix (ECM) fibers generally align in the direction of uniaxial stretch [9, 10]. This cell and fiber alignment could promote contact guidance and subsequent increased directional migration, yet migration and invasion have not been studied in these 3D biopolymer systems.

We hypothesize that uniaxial cyclic strain inhibits cell invasion and migration in 3D scaffolds. Herein we describe a system for testing this hypothesis consisting of applying 10% cyclic strain at 1Hz to a collagen hydrogel containing cell spheroids and quantification of the extent and directionality of cell invasion using a custom MATLAB program and present representative data.

METHODS

Cell-spheroids were generated from male porcine aortic valvular interstitial cells (VIC) and male human neonatal dermal fibroblasts (HDF) using non-adherent microwells (Microtissues®) and combined

with collagen solution (2.0mg/mL rat tail type I). The hydrogel-spheroid mixture was plated into 8mm x 8mm square wells in a stretchable silicone well plate (CellScale) and mounted on a uniaxial stretching device (MechanoCulture FX™, CellScale). Fresh medium was added over the samples, and they were cultured at 37°C in a humidified 10% CO₂-containing incubator for two days at either a static or stretched condition (10% uniaxial stretch at 1Hz frequency).

Fluorescent z-stack images were captured using a Keyence BZ-X800 fluorescence microscope to assess the extent of cell invasion by visualizing cell nuclei. The cells were stained with Hoechst 33342 before spheroid formation and imaged at Day 0 prior to stretching. They were fixed in 4% paraformaldehyde at Day 2, permeabilized using 0.25% Triton-X 100 and further stained with Hoechst and Alexa Fluor® 488 phalloidin for nuclei and F-actin visualization. The images in each z-stack were processed to create maximum z-projection images (Figure 1A). 3D reconstruction images were processed from Z-stack images captured using a Leica SP5 point scanning confocal microscope.

Image quantification was carried out using a custom MATLAB program using the image processing package. The images were thresholded and the boundaries of the Day 0 images were traced to determine the boundary of cell invasion. The spheroid centroids were identified as well as the locations of the pixels of the Day 2 images that lay outside of the boundary of invasion. The distances (d) (Equation 1) of each of these pixels from the boundary and the centroid was calculated as well as their angles of invasion (θ) (Equation 2, Figure 1B-D).

$$d = \sqrt{(x_2 - x_1)^2 + (y_2 - y_1)^2} \quad (1)$$

$$\theta = \tan^{-1} \frac{y_2 - y_1}{x_2 - x_1} \quad (2)$$

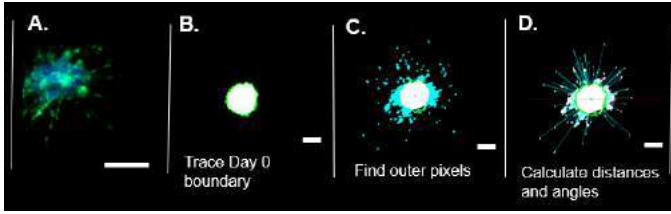


Figure 1: Z-stack image processing and quantification. Day 2 images were processed to create maximum z-projection images from each z-stack (A). The distances and angles of the migrated pixels were calculated with reference to the spheroid boundary and center (B-D). Scale: 200µm.

These data were used to calculate the invasion area (sum of number of pixels), persistence speed (boundary distances (d_b) divided by the culture time (t)) and area moment of inertia (where $dA = 1 \mu m^2$) in the stretch (x) and cross(x)-stretch (y) directions as weighted measures of invasion (Equation 3)

$$I_{stretch} = \sum_{i=0}^n y^2 dA ; I_{x-stretch} = \sum_{i=0}^n x^2 dA \quad (3)$$

RESULTS

At Day 2, we observed reduced invasion in VICs as shown by a decreased number of migrated nuclei while HDF invasion appeared similar for both static and dynamic conditions (Figure 2).

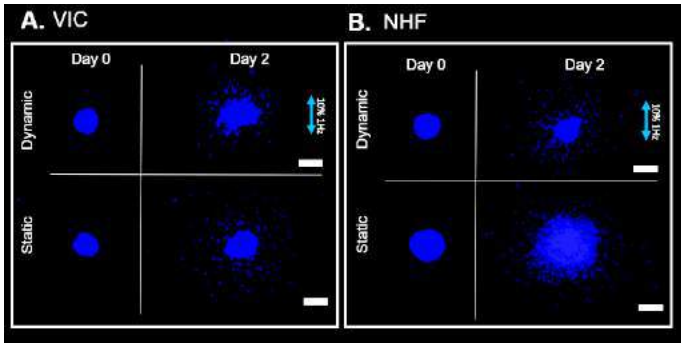


Figure 2: Dynamic stretch reduces cell invasion area. Representative images of invasion Day 0 vs Day 2, VICs (A) and HDFs (B). Scale: 200µm.

Similarly, the invasion persistence speed for VICs was significantly slower ($p < 0.05$) in the dynamic spheroids compared to the static spheroids as assessed by a paired t-test ($p = 0.0076$) (Figure 3A). This trend further indicates that dynamic stretch reduces cell invasion in VICs. In addition, differences in the directional area moment of inertia ($I_{stretch}$ and $I_{x-stretch}$) (Figure 3B) were not significant different ($p = 0.707$) under dynamic stretch for VICs revealing that invasion was not dependent on the direction of stretch.

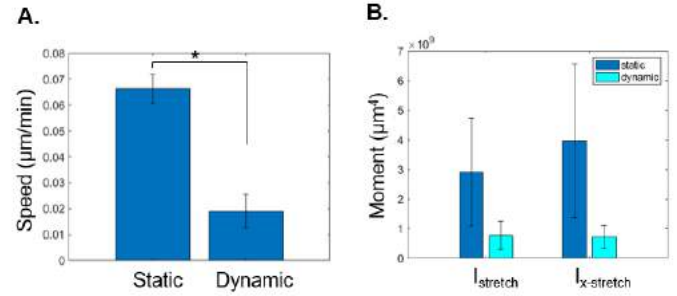


Figure 3: Representative persistence speed and directional area moment of inertia at Day 2 for representative VIC spheroids of one experiment. Quantified mean persistence speed, * $p = 0.0076$ from paired t-test (A). Directional area moment of inertia ($I_{stretch}$, $I_{x-stretch}$) (B). Error bars are standard error of the mean.

DISCUSSION

In this work, we developed a spheroid-based *in vitro* model utilizing collagen hydrogels to study the effects of cyclic stretch on cell invasion. We designed a custom MATLAB program to analyze captured images to robustly discern directional and speed trends. We observe that VIC invasion into a collagen hydrogel is strongly affected by stretch, whereas HDF invasion is less sensitive. These results indicate that in the 3D microenvironment, the effects of cyclic stretch on cell invasion and migration may be cell-type dependent. It is unclear why there is not a directional dependence of stretch on the VICs.

This study can be expanded by exploring the roles that different ECM proteins and growth factors play in the cell response to cyclic stretch. Although collagen is the major protein constituent of the ECM, other proteins such as fibronectin, glycosaminoglycans and elastin are also known to influence cell invasion and migration [11]. In addition, the mechanism by which cyclic stretch inhibits cell invasion in VICs but not HDFs could be further explored. This work has the potential to inform how tissues exposed to cyclic stretch can be more or less susceptible to cell invasion with possible applications in wound healing, cancer metastasis and the repopulation of scaffolds such as tissue engineered heart valves.

ACKNOWLEDGEMENTS

This work was supported by the NSF (CMMI 1761432) and the AHA (20AIREA35120448).

REFERENCES

- [1] SenGupta, S., *et al.*, *Nat Rev Mol Cell Biol* 2021. **22**(8): p. 529-547.
- [2] Throm Quinlan, A.M., *et al.*, *PloS one* 2011. **6**(8): p. e23272.
- [3] Zonderland, J. and Moroni, L., *Biomaterials* 2021. **268**: p. 120572.
- [4] Stroka, K.M. and Konstantopoulos, K., *Am J Physiol Cell Physiol* 2014. **306**(2): p. C98-c109.
- [5] Cirka, H., *et al.*, *Biophys J* 2016. **110**(8): p. 1845-1857.
- [6] Desai, L.P., *et al.*, *Am J Physiol Lung Cell Mol Physiol* 2008. **295**(5): p. L958-65.
- [7] Zhang, B., *et al.*, *Stem Cell Research* 2015. **14**(2): p. 155-164.
- [8] Song, J., *et al.*, *Biosci Rep* 2020. **40**(6).
- [9] Marquez, J.P., *et al.*, *Philos Trans A Math Phys Eng Sci* 2010. **368**(1912): p. 635-54.
- [10] Obbink-Huizer, C., *et al.*, *Biomech Model Mechanobiol* 2014. **13**(5): p. 1053-63.
- [11] Eble, J.A. and Niland, S., *Clinical & Experimental Metastasis* 2019. **36**(3): p. 171-198.

A LARGE DEFORMATION MULTIPHASE CONTINUUM MECHANICS MODEL FOR SHOCK LOADING OF SOFT POROUS MATERIALS

Zachariah T. Irwin (1,2), John D. Clayton (2), Richard A. Regueiro (2,3)

(1) Department of Mechanical Engineering, University of Colorado Boulder, Boulder, CO, USA

(2) Soldier Protection Sciences Branch, Army Research Laboratory, Aberdeen, Maryland, USA

(3) Department of Civil, Architectural and Environmental Engineering, University of Colorado Boulder, Boulder, CO, USA

INTRODUCTION

Shock wave-induced deformations (e.g., from local detonations) of smaller lung tissue (lung parenchyma) are responsible for larger-scale injuries, such as hemorrhage, long term diseases, such as pneumonia, and in many cases, immediate death [1, 2]. The progression of “damage”, the biological processes that govern pathology and eventual tissue healing, and mitigation of damage through personal protective equipment (PPE) to reduce the likelihood of Behind-Armor Blunt Trauma (BABT) is an active area of research. The goal of the research is to advance our understanding of the physiology through numerical modeling given that experimental data is limited for high-strain rate loadings on lung tissue, human or otherwise.

A large deformation, coupled finite-element (FE) model is developed to simulate the multiphase response of soft porous materials subjected to high-strain rate loading. For the soft porous material of particular interest here, the lung parenchyma, conventional computational fluid dynamics (CFD) fluid-structure interaction (FSI) models are prohibitively expensive for the length scales of interest. Our approach is based on the theory of porous media (TPM) at large deformations [3–5]. Prior computational modeling of lung parenchyma treats the soft porous network (solid skeleton) of lung tissue and enclosed pore fluid (e.g., air) as a single constituent [6, 7]; TPM treats them as separate constituents to describe more physically realistic FSI. Herein, our aim is to address differences in the kinematics, with future work focusing on the assessment of differences in the quantification of damage of the soft porous material.

METHODS

We assume that the lung parenchyma continuum body constitutes a control space \mathcal{B} (current configuration of the solid skeleton) and that only liquids or gases in the pores can leave this pore space. Rather than modeling the exact microstructure of the lung parenchyma, we assume that the pores are modeled in a statistical sense such that their specific locations are arbitrary. This concept of volume fraction is illustrated in Figure 1(a).

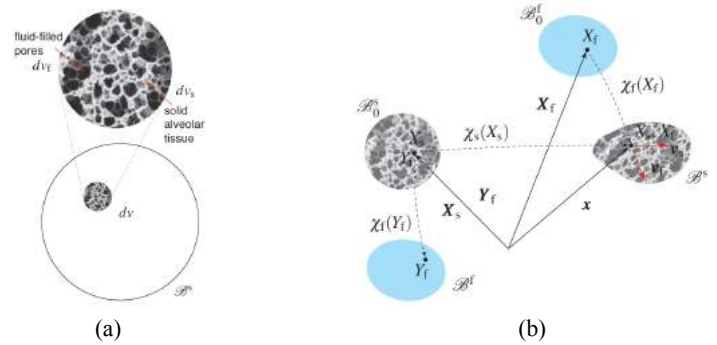


Figure 1: (a) Concept of volume fraction for biphasic (solid(s)-fluid(f)) mixture theory, showing solid skeleton composed of alveolar tissue. Note that in the theory of porous media, it is assumed that the control space is that of the solid phase $\mathcal{B} := \mathcal{B}^s$, also known as “solid skeleton.” (b) Kinematics of a biphasic (solid-fluid) mixture theory.

Detailed derivations for constituent and mixture balance of: mass, linear momentum, energy and entropy are provided in [5]. To describe the kinematics, we solve the following equations for balance of mass of the mixture, balance of momenta (mixture and fluid) in the reference configuration \mathcal{B}_0 of the solid skeleton (assuming immiscible constituents, negligible mass supplies and a nearly-inviscid pore fluid):

$$\frac{J_s n^f}{K_f} D_t^s p_f + D_t^s J_s + \frac{J_s}{K_f} \text{GRAD}_s p_f \cdot \mathbf{F}_s^{-1} \cdot (n^f \tilde{\mathbf{v}}_f) + J_s \text{GRAD}_s (n^f \tilde{\mathbf{v}}_f) : \mathbf{F}_s^{-T} = 0 \quad (1)$$

$$\text{DIV}_s \mathbf{P}_s + \rho_{0(s)} \mathbf{g} = \rho_{0(s)}^s \mathbf{a}_s + \rho_{0(s)}^f \mathbf{a}_f \quad (2a)$$

$$\mathbf{P}_s = \mathbf{P}_E - J_s p_f \mathbf{F}_s^{-T} \quad (2b)$$

$$\rho_{0(s)}^f \mathbf{a}_f + J_s n^f \text{GRAD}_s p_f \cdot \mathbf{F}_s^{-1} + \frac{J_s (n^f)^2}{\hat{k}} (\mathbf{v}_f - \mathbf{v}_s) - \rho_{0(s)}^f \mathbf{g} = \mathbf{0} \quad (3)$$

All constitutive assumptions follow from thermodynamic conjugacy laid out in [5]. For the solid skeleton stress response, we assume a neo-Hookean hyperelastic material, and for the pore fluid pressure response, an exponential relationship between pore fluid real mass density and pore fluid pressure (see [8]). Mixed constituent temperatures are also assumed (sans thermo-mechanical coupling), and Darcy's law with inertia terms is used to describe the seepage velocity $n^f \tilde{\mathbf{v}}_f$. Thereafter, simplifications to the one-dimensional uniaxial strain regime are made for the numerical implementation. To stabilize numerical noise arising from shock-like pressure loadings, the canonical shock viscosity Q is added to the solid skeleton stress response [9], and pressure stabilization is added to the balance of mass of the mixture [10]. The balance equations are discretized in space via FE method and discretized in time via implicit or explicit numerical time integration methods; a fifth-order accurate adaptive time-stepping Runge-Kutta scheme [11] provides greatest computational cost-to-accuracy ratio for shock-like loading and is thus preferred.

RESULTS

We impose a Friedlander wave overpressure boundary condition to the top of the lung parenchyma column mesh, represented here as a traction on the biphasic mixture (refer to Figure 2). Peak overpressure was chosen to be 25 kPa, which is above the injury threshold for exposed rabbit lung [12]. The base and sides of the column are held fixed; an impermeable, no-slip boundary condition for the motion of the pore air is imposed at the top of the column to be able to provide a comparison to [7] wherein the pore air is assumed to be trapped in the pores. However, in contrast to that model, pore air in the multiphase model is allowed to move freely within the lung parenchyma column.

DISCUSSION

The stress response of the single-phase and multiphase models is shown in Figure 3. We observe good agreement between both models for the total (tissue + air) axial stress, but the advantage to our multiphase model is that we can directly compute the axial stress of the solid skeleton, i.e., the lung parenchyma, which goes into tension sooner than the aggregate response of the single-phase model. Fung has suggested that excessive tensile forces in the walls of the lung aveoli can lead to rupturing of the alveoli and local injury [13]. These findings have implications for predicting injury sooner by accounting for relative motion of the air to the lung parenchyma in the multiphase model. Further work is needed to quantify damage and local injury in the multiphase solid skeleton constitutive model to say for certain.

ACKNOWLEDGEMENTS

The authors acknowledge support of the US Army Combat Capabilities Development (DEVCOM) Army Research Laboratory (ARL). This work utilized resources from the University of Colorado Boulder Research Computing Group, which is supported by the National Science Foundation (awards ACI-1532235 and ACI-1532236), the University of Colorado Boulder, and Colorado State University. Helpful discussions with Alan Freed of Texas A&M University on soft tissue biomechanics are acknowledged. ZTI gratefully acknowledges funding from the Department of Defense Science, Mathematics and Research for Transformation (SMART) scholarship-to-service program and computing hours provided by Bobby Doney at ARL.

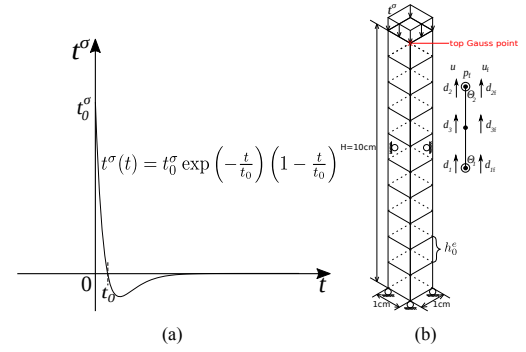


Figure 2: (a) Friedlander impulse traction application, and (b) schematic of multiphase column mesh for examples of lung parenchyma deformations. Note that element size h_0^e is not to scale in (b).

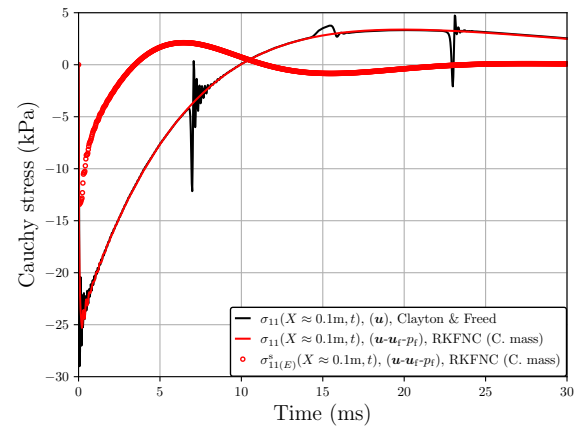


Figure 3: Overpressure loading from the Friedlander impulse at 25 kPa showing a comparison of the total axial Cauchy stress between the single-phase and multiphase model, as well as the solid skeleton effective axial Cauchy stress for the multiphase model.

REFERENCES

- [1] Cohn S et al. *World J. Surg.* 34.8 (2010).
- [2] Maynard R et al. *In Trauma* (1989).
- [3] Truesdell C et al. *Handbuch der Physik* (1960).
- [4] Bowen R. *Continuum Physics*. Elsevier, 1976.
- [5] Boer R de. Springer, 2005.
- [6] Clayton JD et al. *Mechanics of Soft Materials* 2.3 (2020).
- [7] Clayton J et al. Tech. rep. 9138. Aberdeen, MD, USA: Aberdeen Proving Ground (MD): CCDC Army Research Laboratory, 2021.
- [8] Regueiro R et al. *Comput. Methods Appl. Mech. Eng.* 199.29-32 (2010).
- [9] Neumann J von et al. *J. Appl. Phys.* 21.3 (1950).
- [10] Truty A et al. *Comput. Methods Appl. Mech. Eng.* 195.13-16 (2006).
- [11] Cash JR et al. *ACM Trans. Math. Softw.* 16.3 (1990).
- [12] Yen R et al. *J. Biomech.* 21.9 (1988).
- [13] Fung Y. Springer, 1990.

CONSTITUTIVE MODELING OF THE AIRWAY TREE INFORMED BY EXPERIMENTAL BIAXIAL MECHANICAL BEHAVIOR

S. Sattari (1), CA. Mariano (1), T. Sigaeva (2), M. Eskandari (1,3,4)

- (1) Department of Mechanical Engineering, University of California, Riverside, CA, USA
(2) Department of Systems Design Engineering, University of Waterloo, Ontario, CANADA
(3) Department of Bioengineering, University of California, Riverside, CA, USA
(4) BREATHE Center, School of Medicine, University of California, Riverside, CA, USA

INTRODUCTION

Understanding the mathematical relationship between applied forces and tissue deformations through constitutive modeling can improve our understanding of lung function and remodeling due to pathological conditions [1]. This is particularly key for airway mechanics, the site of occlusion in lungs diseases such as asthma and chronic obstructive pulmonary disease. Despite its importance, few studies have constructed constitutive models for the airways which have tend to opt for oversimplifying assumptions (e.g., linear, isotropic) due to the scarcity of experimental data [2]. These previous models were also limited to extrapolating trachea properties for use in whole bronchial tree modeling analyses due to challenges associated with characterizing the distal airway network [3]. Contrary to these modeling limitations, recent experimental studies of the airway tree concluded these oversimplifications to be invalid given the tissue demonstrates non-linear, anisotropic, and heterogenous behavior [4,5].

To address this knowledge gap, we analyze the performance of a purely phenomenological model (Fung) and two structurally motivated constitutive models (Four Fiber Family and Holzapfel) in simultaneously fitting experimental data from multiple biaxial loading conditions collected from the proximal and distal airways. These constitutive models capture the nonlinear, anisotropic, and heterogenous behavior of the airways and ultimately improve our understanding of lung structure by establishing a much needed foundation for generating predictive computational models for future pulmonary disease characterization as well as airway stent design.

METHODS

Four fresh porcine lungs were acquired from a local abattoir and the whole airway tree was extracted and divided into three distinct regions, including the trachea, large and small bronchi, based on their inner diameters of 18.6 ± 2.6 , 8.4 ± 1.5 , and 4.9 ± 1 mm, respectively [4]. Square soft tissue specimens (5-5.2 mm) were prepared by peeling

away the cartilage layer while noting the circumferential and axial directions of the airway. Graphite powder was used to enable tracking of the tissue surface deformation via digital image correlation (DIC) [6]. Six samples were collected from each airway region, and specimens with poor speckling or tearing were excluded, resulting in a total of 60 samples. Specimens were loaded in a commercial planar biaxial machine (CellScale Biomaterials Testing) while hydrated with 1X phosphate-buffered saline bath at 37°C. Samples were preconditioned five times. A strain rate of 1%/s was used with a maximum strain value of 60% to implement various displacement ratio protocols of 1:1 (circumferential:axial), 1:0.75, 1:0.5, 0.5:1, and 0.75:1. The first Piola-Kirchhoff engineering stress was calculated, and DIC informed the actual tissue strain using commercial software (CellScale Biomaterials Testing).

The experimental data for all five protocols were simultaneously fit to three constitutive models [1]. Four-parameter phenomenological Fung strain energy density function was used in the form of

$$\psi = \frac{C}{2} e^Q; \text{ with } Q = b_1 E_\theta^2 + b_2 E_z^2 + 2b_3 E_\theta E_z \quad (1)$$

where C , b_1 , b_2 , and b_3 are material constants obtained from experimental data and E_θ and E_z are the circumferential and axial components of the Green strain tensor, respectively [7].

Additionally, the four fiber family (4FF) model with perfectly aligned fiber families in the circumferential and axial directions along with two symmetric diagonal directions [8] was used in the form of:

$$\psi = \psi_{iso} + \psi_{aniso} = \frac{C}{2} (I_C - 3) + \sum_{i=1}^4 \frac{C_{1i}}{2C_{2i}} (e^{C_{2i}(I_{4i}-1)^2} - 1) \quad (2)$$

where C , C_{1i} , and C_{2i} are material parameters (i denotes a fiber family), I_C is the first invariant of the right Cauchy-Green tensor and $I_{4i} = \mathbf{C} : \mathbf{M}_i \otimes \mathbf{M}_i$ is the square of the stretch of i^{th} fiber family. The direction of each fiber family is denoted as $\mathbf{M}_1 = (0,1,0)^T$, $\mathbf{M}_2 = (1,0,0)^T$, $\mathbf{M}_{3,4} = (\pm \cos \varphi, \sin \varphi, 1)^T$, where φ is the angle between each diagonal fiber family and the circumferential direction [1,8,9].

The third utilized model was proposed by Holzapfel et al. (2015)

[10] to account for in-plane and out-of-plane fiber dispersions in two diagonal fiber families with the form of

$$\psi = \frac{c}{2}(I_C - 3) + \sum_{i=4,6} \frac{C_i}{2C_2} (e^{C_1(I_i-1)^2} - 1); \quad (3)$$

$$I_i^* = AI_C + BI_i + (1 - 3A - B)I_n; \quad (4)$$

$$A = 2\kappa_{op}\kappa_{ip}; \quad B = 2\kappa_{op}(1 - 2\kappa_{ip}); \quad (5)$$

$$I_i = C: \mathbf{M}_i \otimes \mathbf{M}_i; \quad I_n = C: \mathbf{M}_n \otimes \mathbf{M}_n; \quad \mathbf{M}_{4,6} = (\cos \varphi, \pm \sin \varphi, 1)^T \quad (6)$$

Here $\mathbf{M}_{4,6}$ are mean fiber family directions composing angle φ with the circumferential direction, and \mathbf{M}_n is an out-of-plane vector. Parameters of κ_{ip} and κ_{op} are related to in-plane/out-of-plane fiber dispersions [10].

Hyperfit was used to facilitate fitting the data by regression, maximizing the coefficient determination of R^2 [1]. One way ANOVA and Bonferroni correction were performed to further evaluate all model performances and assess the success of each model in capturing airway heterogeneity with significances set at * $p < 0.05$, ** $p < 0.01$, *** $p < 0.001$, and **** $p < 0.0001$ [GraphPad Prism].

RESULTS

A representative specimen's experimental response fit to each model is shown in Figure 1. 4FF outperformed capturing the non-linear shape of stress-strain curve, while Fung and Holzapfel models' curve convexity underestimates/overestimates the experimental behavior.

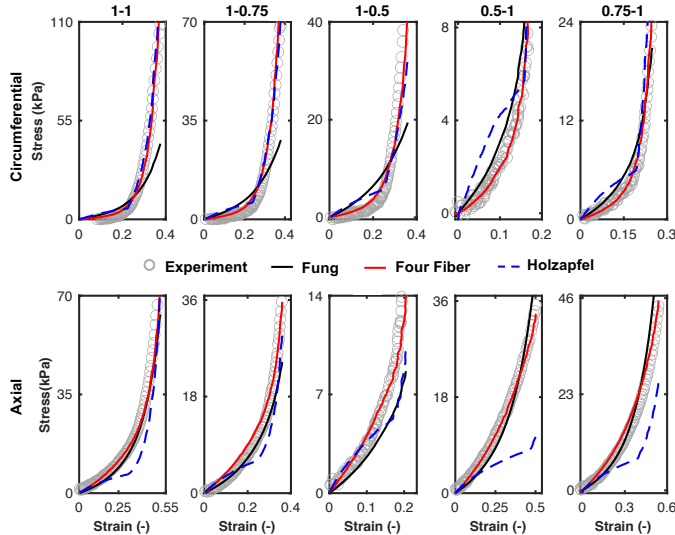


Figure 1: Representative specimen's experimental data fitted to three models. Scales vary for visualization.

The performance of these three models in simultaneously fitting all five experimental biaxial loading profiles were evaluated for each specimen as shown in Figure 2; box plots inform fit performances for all airway regions. Among the three models tested in this study, 4FF fit the region-specific data significantly better with the highest overall average R^2 and the least variability of $R^2 = 0.94 \pm 0.05$, while Fung and Holzapfel models were $R^2 = 0.89 \pm 0.07$ and 0.80 ± 0.15 , respectively.

The material parameters and R^2 values of 4FF were further analyzed to explore any notable differences between airway regions and are reported in Table 1. Parameters of C_{11} , C_{234} , and φ were found to be significantly different between the trachea and other regions.

DISCUSSION

This study is the first attempt to explore the capability of various constitutive models in describing simultaneous biaxial experimental protocols for the proximal and distal airway tree. The 4FF model, with perfectly aligned fiber families, exhibited superior performance in

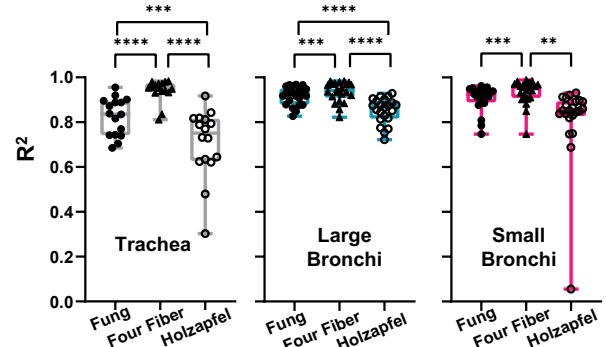


Figure 2: Box plots demonstrating Four Fiber, Fung, and Holzapfel model performances to biaxial tensile tests.

Table 1: Averages \pm standard deviations of the Four Fiber model parameters fitted to experimental data from each airway region.

Four Fiber	Trachea	Large Bronchi	Small Bronchi
C (kPa)	2.05 ± 2.41	1.15 ± 3.46	0.29 ± 0.75
C_{11} (kPa)	14.3 ± 8.13	5.56 ± 8.05 (**)	5.71 ± 5.59 (**)
C_{21}	0.06 ± 0.08	5.43 ± 24.06	0.24 ± 0.77
C_{12} (kPa)	1.53 ± 1.89	2.4 ± 1.74	1.25 ± 1.18
C_{22}	2.38 ± 1.59	1.35 ± 2.69	1.28 ± 1.65
C_{134} (kPa)	3.82 ± 3.55	6.06 ± 4.81	5.66 ± 3.57
C_{234}	2.26 ± 1.8	0.26 ± 0.34 (**)	0.97 ± 2.77
φ ($^\circ$)	40.1 ± 12.95	56.9 ± 0.04 (**)	53.6 ± 14.06 (*)
R^2	0.94 ± 0.05	0.93 ± 0.04	0.93 ± 0.05

capturing the experimental biaxial mechanical behavior of all five loading protocols compared to the Fung and Holzapfel models. These results are in agreement with cardiovascular studies reporting better performance of 4FF in modeling of human abdominal aorta, porcine thoracic aorta, as well as rabbit and mouse arteries [1,8,9].

The 4FF also well represents heterogeneity within the airway tree, with significant differences in diagonal fiber families' directions between proximal and distal airways: fiber families are found to be aligned closer to the circumferential direction in tracheal specimens (40°), while they are closer to the axial direction in distal airways (57° and 54°). These results align with regional heterogeneities observed from our previous histological analyses, in which the fiber architecture of proximal and distal airways differ [3].

Despite simultaneously utilizing multiple experimental data sets to constrain the solution, constitutive models are often affected by non-unique fits [11] and pose a limit to this study. Similarly, noted regional differences in C_{11} and C_{234} parameters are not necessarily independent due to the exponential functional form in the strain energy density (Eq. 2). Nonetheless, the model parameters provided in this study yield essential information central to the development of predictive pulmonary tools and help to inform the design of airways' replacements.

REFERENCES

- [1] Schroeder, F et al. *JMBBM*, 78:369-80, 2018; [2] Zhao, J et al. *Phys Fluids*, 33:101906, 2021; [3] Eskandari, M et al. *Acta Biomater*, 97:513-23, 2019; [4] Sattari, S et al. *Acta Biomater*, in press, 2022; [5] Eskandari, M et al. *J App Physiol*, 125:878-88, 2018; [6] Javani, S et al. *Ann Biomed Eng*, 44:3266-83, 2016; [7] Fung, YC et al. *Am J Physiol*, 237:630-31, 1979; [8] Ferruzzi, J et al. *J R Soc Interface*, 8:435-50, 2011; [9] Baek, S et al. *Comput Methods Appl Mech Engrg*, 196:3070-8, 2007; [10] Holzapfel, GA et al. *J R Soc Interface*, 12: 20150188, 2015; [11] Billiar, KL and Sacks MS. *J Biomech Eng*, 122, 2000.

ARE MICE A GOOD MODEL SYSTEM TO STUDY SEX AND AGE-DEPENDENT SKIN PROPERTIES?

Chien-Yu Lin (1), Gabriella P. Sugerman (1), William D. Meador (1), Sotirios Kakaletsis (2),
Adrian B. Tepole (3), Manuel K. Rausch (1,2,4)

(1) Department of Biomedical Engineering, University of Texas at Austin, Austin, TX, USA

(2) Department of Aerospace Engineering and Engineering Mechanics, University of Texas at Austin, Austin, TX, USA

(3) Department of Mechanical Engineering, Purdue University, West Lafayette, IN, USA

(4) Oden Institute for Computational Engineering and Sciences, University of Texas at Austin, Austin, TX, USA

INTRODUCTION

Mice are a widely used model system in engineering and life sciences as mice are inexpensive, easy to handle, and genetically highly malleable. Interestingly, much remains to be understood about the suitability of mouse skin as a model system for human skin. This is especially true for skin mechanics. For example, we have recently published a study showing only minor differences between the mechanics of young and mature mouse skin. Thus, whether mechanical changes due to skin aging are well-represented in mouse skin is unclear. Similarly, there is a sparsity of data on sex differences in mouse skin mechanics as compared to those in human skin mechanics. Therefore, the goal of our work is to answer some of these questions. Specifically, we set out to systematically study the histo-mechanical properties of young and old mouse skin of both sexes and to compare our observed differences to what is known about human skin.

METHODS

Towards this objective, we used 12-week (young) and 80-week (old) C57BL/6 mice, both male and female. After sacrificing the mice, we applied a 6 mm x 6 mm square ink stamp to dorsal and ventral skin regions of the mice and excised the tissue as 10 mm x 10 mm square samples. Subsequently, we photographed the excised tissue while floating on 1x PBS to compare the stamp size before and after the excision. Thereby, we determined the prestrain between the *in vivo* (pre-excision) and floating (post-excision, stress-free) configurations (Figure 1). Prior to mounting the samples for biaxial testing, we measured their average thicknesses with a digital thickness gauge and speckled the epidermal side with graphite powder for digital image correlation (DIC). We then mounted, preconditioned, and tested each sample in equibiaxial tension. In the following analysis, we isolated and analyzed the final downstroke of the equibiaxial tests. Next, we transformed the force-displacement data into Cauchy stress-stretch data via the samples' cross-sectional areas and the acquired true strains via DIC. To

quantitatively compare biaxial data from different groups, we next computed three metrics for each sample: toe stiffness (i.e., stiffness at small strains), calf stiffness (i.e., stiffness at large strains), and transition stretch (i.e., the stretch at which data showed clear strain-stiffening), in the lateral and cranial-caudal directions.

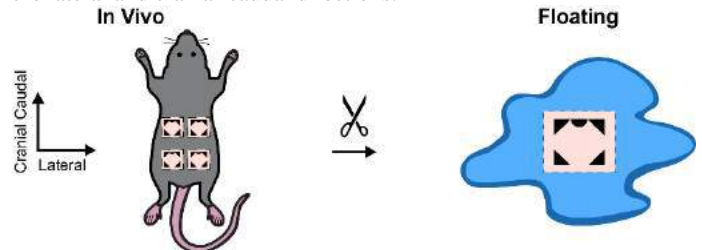


Figure 1: We stamped skin regions *in vivo* before excision and photographed them while floating on 1x PBS.

We also determined the thicknesses of different skin layers of each group from Masson's Trichrome histological images. Moreover, we performed hydroxyproline and BCA assays to acquire the normalized collagen content of the skin samples from each group. Lastly, to analyze the *in vitro* collagen fiber orientation, we used second harmonic generation (SHG) with a two-photon microscope. We used the orientation distribution analysis with a Gaussian gradient method in ImageJ-FIJI OrientationJ, and subsequently fit a symmetric von Mises distributions to the raw data to estimate the distribution's location parameter $\tilde{\mu}$ and concentration parameter $\tilde{\kappa}$ as a function of imaging depth. Please note, we only showed representative results for each experiment given the constraints of the abstract format.

RESULTS

In Figure 2, we showed that skin samples shrank upon excision as quantified by Green-Lagrange strain. This strain differed significantly between the lateral and cranial-caudal directions ($p < 0.001$) in all

groups. Additionally, we observed differences due to sex in some groups, but not due to age.

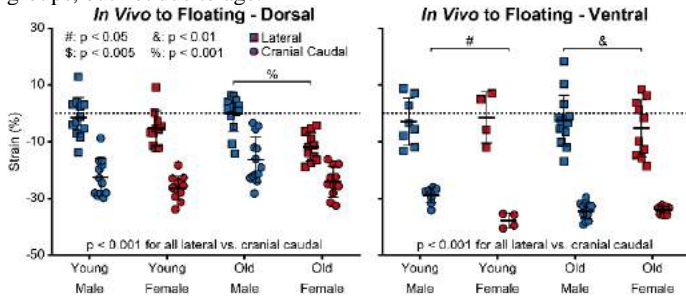


Figure 2: Green-Lagrange strain between *in vivo* configurations and floating configurations.

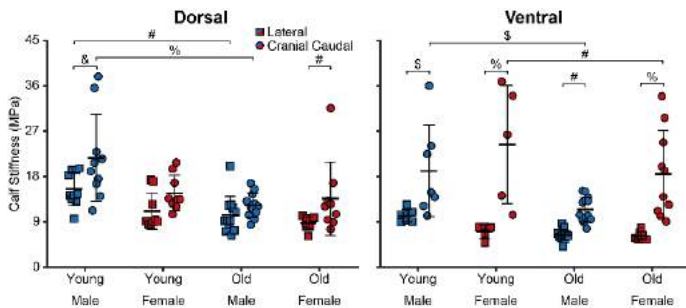


Figure 3: Biaxial mechanics showed that mouse skin is more compliant in lateral direction on the ventral side.

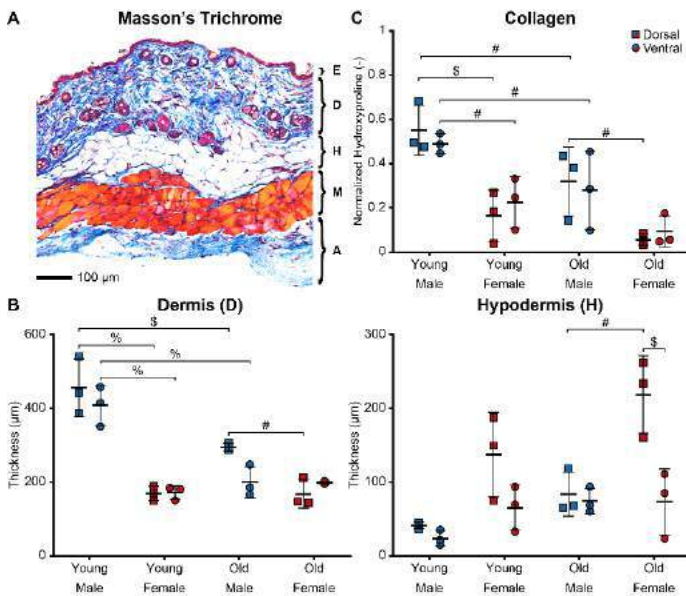


Figure 4: (A) Representative image of mouse skin layers stained with Masson's Trichrome. (B) Thickness measurements of dermis and hypodermis layers of mouse skin from each group. (C) Normalized collagen content of mouse skin from each group.

We observed a classic J-shaped stress-stretch curve for all samples in the biaxial data. In Figure 3, we reported skin stiffness as the tangent moduli (i.e., the slopes of the equibiaxial data) in the “calf region” at 0.15 MPa. We found some differences with age, but none with sex. The calf stiffness significantly varied between the lateral and cranial-caudal directions ($p < 0.05$) in all groups on the ventral side.

Figure 4A depicted a histological image of mouse skin: epidermis (E), dermis (D), hypodermis (H), muscle (M) and adventitia (A). We found significant differences with both sex and age in dermal thickness (Figure 3B) and also found that the differences among the groups were consistent with the normalized collagen content shown in Figure 4C. That is, the collagen content of mouse skin decreased with age in both male and female mice. Moreover, hypodermis layers of old and female skin appeared to be thicker (Figure 4B). However, these differences were only significant in two comparisons.

Figure 5A illustrated the representative von Mises probability density function of collagen fiber orientation from three young male mouse skin samples by depth, with the averaged orientation distribution projected underneath. Qualitatively, these data suggested that collagen fibers are widely dispersed with a mean orientation in the lateral direction (Figure 5B). Statistically comparing the distribution's location parameter $\tilde{\mu}$ and concentration parameter $\tilde{\kappa}$ of the collagen orientation distributions for sample sex, age, location, and depth only revealed differences due to depth ($p < 0.01$).

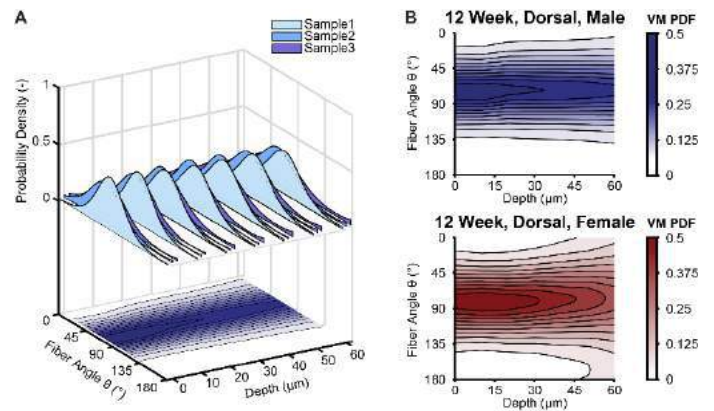


Figure 5: (A) Representative plot of von Mises collagen orientation histograms by depth and the projected orientation distribution. (B) Collagen orientation distributions of dorsal skin samples from young male and female mice ($n = 3$).

DISCUSSION

We investigated sex and age-dependent histo-mechanical properties of mouse skin using young/old, male/female, dorsal/ventral mouse skin samples (a total of 152 individual skin samples). Of note in our findings was that the calf stiffness dropped significantly during normal aging in male mice, yet there were almost no significant differences between young and old female mice. This contrasts with findings in human skin, where the mechanical properties of male and female skin have both been found to decline with age [1]. In contrast, we found that mouse skin thinned with age, independent of sex, which is congruent with findings in humans [2]. Specifically, mouse skin thinned with age, and collagen concentration – the principal component of the dermis – also decreased with age (mostly in old mice). In summary, we found good agreement between aging skin from male and female mice with aging skin in humans.

ACKNOWLEDGEMENTS

We acknowledge the National Science Foundation for their support of this project via Grant #1916663.

REFERENCES

- [1] Luebbeberding, S et al., *Skin Res Technol*, 20(2):127-135, 2014.
- [2] Quan, T et al., *Gerontology*, 61(5):427-434, 2015.

NEGATIVE-PRESSURE LUNG MECHANICS OF FIBROTIC AND EMPHYSEMATOUS MOUSE LUNGS

K.A.M. Quiros (1), T.M. Nelson (1), A. Ulu (2), E.C. Dominguez (2,3),
T.M. Nordgren (5,2,3,4), M. Eskandari (1, 4, 6)

1. Department of Mechanical Engineering, University of California, Riverside CA, USA
2. Division of Biomedical Sciences, University of California, Riverside School of Medicine, Riverside, CA, USA
3. Environmental Toxicology Graduate Program, University of California Riverside, Riverside, CA, USA
4. BREATHE Center, School of Medicine University of California, Riverside, CA, USA
5. Department of Environmental and Radiological Health Sciences, Colorado State University, Fort Collins, CO, USA
6. Department of Bioengineering, University of California, Riverside, CA, USA

INTRODUCTION

Chronic pulmonary diseases are devastating, lifelong conditions, affecting an estimated 545 million people worldwide, with annual per-patient costs of over \$200,000¹⁻³. Despite the egregious effects of conditions such as pulmonary fibrosis and chronic obstructive pulmonary disease (COPD), diagnostics and treatment tools are lacking^{1,2,4}. In recent years, research into early detection of chronic conditions has received more attention⁵, as current diagnostic strategies consisting of expensive imaging and invasive biopsies limit clinicians' disease detection capabilities to only advanced stages². Improved inexpensive and noninvasive screening processes are necessary to facilitate the potential for early medical intervention.

Lung mechanics, determined from pressure-volume (PV) curves, are altered in diseased states, and may serve as an effective diagnostic tool^{6,7}. However, explorations of changes to the PV curve in diseased states as conducted in the laboratory on animal models are principally limited to artificial positive pressure ventilation as opposed to negative pressure ventilation, which more closely mimics physiological breathing⁸. To fully evaluate the diagnostic potential of PV curves, it is crucial to determine whether pulmonary mechanics are also measurably altered in curves collected under physiologically representative negative pressure breathing. As such, here we investigate the comparability and potential dissimilarity of PV curves collected from healthy, emphysemic, and fibrotic lungs under negative-pressure ventilation compared to previously published positive-pressure ventilation studies.

METHODS

Twenty mouse lungs (29.4 ± 2.9 g, 8-12 weeks old) were collected from male C57BL/6J mice purchased through Jackson Laboratory (Bar Harbor, ME, USA) and separated into four treatment groups following published protocols^{9,10}. The treatment groups are as follows: (1) Mice (n=5) were subjected to a single intranasal instillation of elastase and housed for 4 weeks to simulate emphysema. (2) Mice (n=5) were given

a single instillation of phosphate buffered saline (PBS) and aged for 4 weeks to provide an aged-matched control for group 1. (3) To induce fibrosis, mice (n=5) were subjected to chronic dust exposure via intranasal agricultural dust thrice weekly for 21 weeks. (4) Mice (n=5) intranasally received PBS thrice weekly to serve as the aged-matched control group to the fibrosis treatment group 3¹⁰. Lungs were dissected as previously outlined¹¹ and negative pressure cyclic inflation was imposed, utilizing our validated electromechanical testing apparatus⁸. A 5 cmH₂O preload was applied followed by four inflation-deflation cycles. The first three cycles served to precondition the lungs and the fourth cycle was analyzed. Two breathing frequencies (10 and 20 breaths per minute, BPM) and two inflation volumes (0.7 and 0.9 ml) were tested¹². The emphysema and fibrotic groups were most sensitive to 10 BPM and 20 BPM, respectively; as such, these results are reported.

Four pulmonary measures (e.g., compliance, peak pressure, inflation compliance C_{inf} , and deflation compliance C_{def}) were analyzed for each treatment group (control and exposed represented by grey and orange, respectively in Figure 1). C_{def} and C_{inf} were calculated as the PV curve tangent via linear regression ($R^2 > 0.99$) using MATLAB, according to previously described methods^{8,12} (Figures 1A, 1F). Mean \pm standard deviation (SD) of calculated measures for emphysema and fibrosis groups are represented by Figures 1B-F and 1G-J respectively. Statistical analysis of mean \pm SD of all samples was investigated by Wilcoxon signed-rank test (GraphPad Prism 9).

RESULTS

Representative specimens PV curves, generated from the pressure and volume data collected during cyclic inflation testing, demonstrate disparate healthy (grey) and diseased (orange) PV curve shapes and contrasting slopes (Figures 1A, F).

For three of the four mechanical measures considered (static compliance, peak pressure, and inflation compliance), alterations between control and exposed groups were significant. Specifically, in

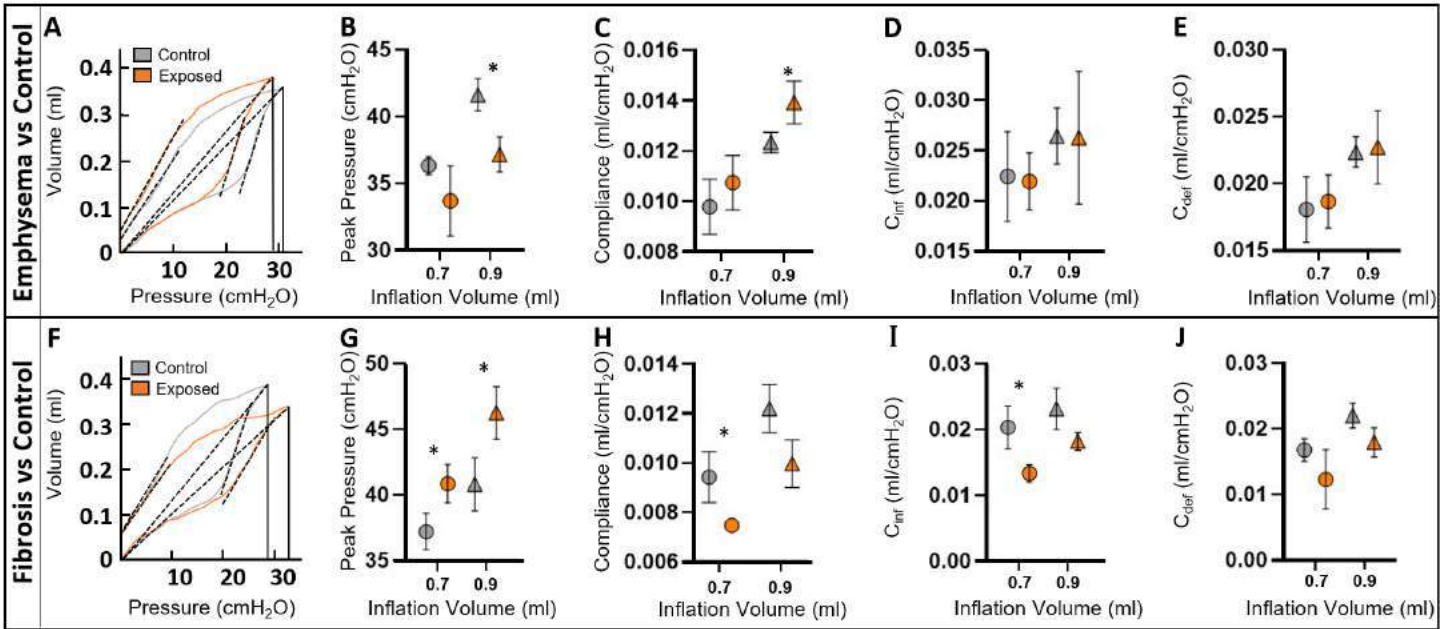


Figure 1: (A & F) PV curves and analyzed features demonstrating healthy controls (grey) compared to exposed diseased (orange) subjects. Resulting lung mechanics reported as mean \pm SD comparing control (grey) and exposed (orange) groups: (B & G) peak pressure, (C & H) static compliance, (D & I) inflation compliance, (E & J) deflation compliance. (Top) Results from emphysema treatment group at 10 BPM for inflation volumes 0.7 (circle) and 0.9 ml (triangle). (Bottom) Results from fibrosis treatment group at 20 BPM for inflation volumes 0.7 (circle) and 0.9 ml (triangle).

the emphysema treatment group, significancies occurred solely at 0.9 ml for static compliance and peak pressure (Figure 1B and 1C). In the fibrosis treatment group, static compliance, peak pressure, and inflation compliance were significantly altered at 0.7 ml (Figure 1G-1I). Peak pressure was also significantly varied between the control and exposed group at the larger volume of 0.9 ml.

DISCUSSION

We find that under negative pressure loading, static compliance and peak pressure are significantly altered in both emphysema and fibrosis with reverse trends between the two exposure groups (i.e., in comparison to healthy counterparts, peak pressure increases in fibrotic lungs but decreases in emphysemic lungs and the compliance increases in emphysema but decreases in fibrosis). Characteristic bulk lung inflation and deflation compliances measured from the PV curves are not significantly altered in emphysematous lungs, indicating comparable behavior despite alveolar damage. Conversely, the inflation compliance of fibrotic lungs is shown to significantly decrease compared to healthy counterparts; similarly, the deflation compliance exhibits a decreasing trend.

The static compliance trends seen in this negative-pressure study agree with reports from clinical studies^{6,13}. Altered compliance in fibrotic states is thought to result from the modified structure of the extracellular matrix, where increased levels of collagen result in stiffening of the entire structure, thereby limiting distensibility^{10,14,15}. Similarly, in emphysema, marked alveolar damage lowers the concentration of elastin, modifying lung compliance and shifting the PV curve upward and leftward^{16,17}. These respective trends are in agreement with both disease groups presented here.

Another potential biomarker of disease is deflation compliance⁷. In contradiction with our findings, prior investigation of positive-pressure PV curves from emphysema and fibrosis treatment groups indicates C_{def} is altered in both disease treatment groups⁷; C_{def} significancies are not observed in this study. The lack of C_{def} dependencies under negative

pressure ventilation is unexpected, suggesting differences between the two ventilation modes. This prompts further study to investigate differences between lung mechanics under the two modes specific to behaviors manifesting in diseased states^{8,17}.

While C_{def} significancies are not present in this negative-pressure ventilation study, the use of tangential slopes as diseased markers is still promising. We find that when ventilating with negative pressure, C_{inf} is lower in fibrosis compared to control groups. Due to the connection between C_{inf} and alveolar recruitment, this suggests recruitment may differ in fibrotic lungs^{12,18}. The contrasting lack of C_{inf} dependencies in emphysematous tissue is unexpected given the known manifestation of alveolar damage. In conclusion, we find in this study that biomarkers traditionally present under positive pressure loading are not consistently translatable to negative pressure physiological loading.

REFERENCES

- [1] Vaidya, S. *et al. Lung* **195**, 1–8 (2017).
- [2] King *et al. Lancet* **378**, 1949–1961 (2011).
- [3] Labaki, W. W. *et al. The Lancet Respiratory Medicine* **8**, 531–533 (2020).
- [4] Konstantinos K., *et al. Respir. Med.* **119**, e2–e9 (2016).
- [5] Christe, A. *et al. Invest. Radiol.* **54**, 627–632 (2019).
- [6] West, J. R. & Alexander, J. K. *Am. J. Med.* **27**, 529–544 (1959).
- [7] Limjunyawong, N. *et al. J. Vis. Exp.* 52376 (2015).
- [8] Sattari, S. *et al. Am. J. Respir. Crit. Care Med.* (2022)
- [9] Nordgren, T. M. *et al. Transl. Res.* **166**, 57–69 (2015).
- [10] Dominguez, E. C. *et al. Cancers* **14**, (2022).
- [11] Nelson, T.M. *et al. Submitted*
- [12] Quiros, K. A. M. *et al. Sci. Rep.* **12**, 7094 (2022).
- [13] Sansores, R. H. *et al. Lung* **174**, 315–323 (1996).
- [14] Suki, B. & Bates, J. H. T. *Respir. Physiol. Neurobiol.* **163**, 33–43 (2008).
- [15] Nelson, T.M. *et al. SB3C* (2022)
- [16] Vindin, H. J. *et al. Curr. Opin. Biotechnol.* **74**, 15–20 (2022).
- [17] Quiros, K.A.M. *Submitted*
- [18] Namati, E. *et al. Am. J. Respir. Cell Mol. Biol.* **38**, 572–578 (2008).

HIGH-THROUGHPUT AUTOMATED MECHANICAL ANALYSIS OF HUMAN INDUCED PLURIPOTENT STEM CELL DERIVED CARDIAC MICROTISSUE

H. Kobeissi (1), E. Lejeune (1)

(1) Department of Mechanical Engineering, Boston University, Boston, MA, USA

INTRODUCTION

Despite recent advances in cardiovascular disease prevention and diagnosis [1,2], heart disease remains the most common cause of death among adults globally [3]. To be able to alleviate this immense health burden, the disease mechanisms must be understood. Furthermore, human cardiac tissue has poor regenerative ability, and any damage to the heart muscle is irreversible [4]. More than a decade since their development in Yamanaka's lab [5], human induced pluripotent stem cells (hiPSCs) differentiated into cardiomyocytes (CMs) offer promising in-vitro platforms for different applications including disease modeling, drug discovery, and regenerative tissue engineering [6,7,8]. Yet, with the attractive opportunities that hiPSCs offer for advancing cardiac research comes a key limitation: they are physiologically immature. They resemble fetal CMs that are not only morphologically distinct from adult CMs, but also function differently [8].

One method to promote physical maturity of hiPSC-CMs involves employing different culture platform designs that allow for mechanical, electrical, or magnetic actuation. Each of these two-dimensional or three-dimensional constructs has its own advantages and challenges [9,10,11,12] (Fig. 1). With the variability of implemented setups and preparation methods arises a need to develop protocols to collect and compare testing data on these different constructs and assess cardiac microtissue characteristics and functional maturity. Available image-based data extraction and analysis software at the microtissue scale measure contractile kinetics such as contraction/relaxation velocities and contraction frequency in 2D cultures where the contractile direction is preferably organized in the uniaxial direction [13]. Despite this prior work, the research community is still lacking software tools to reliably assess the mechanical function of these tissue constructs. Here, we present our ongoing work in: (1) developing methods and metrics for analyzing the mechanical function of beating hiPSC derived microtissue

constructs, and (2) deploying these methods as automated analysis tools released under open-source software licenses.

METHODS

In this Section, we present our open-source computational framework, "Microbundle Compute", that tracks the contractile action of beating microtissue across bright-field frames and computes full-field displacement and subdomain-averaged strain results. In brief, our software builds on OpenCV's implementation of the Lucas-Kanade sparse optical flow algorithm [14]. In our implementation, the tracking points are Shi-Tomasi corner points (points at which a slight shift in location leads to "large" changes in intensity along both main horizontal and vertical axes) [15] computed on the first frame of the movie (Fig. 1). Notably, our approach relies solely on the natural contrast of bright-field microtissue images and the resulting intensity gradients which makes it straightforward to implement in the experimental setting. From tracking these points across consecutive frames, we are able to compute full-field displacement, strain, and strain derived metrics to quantitatively capture mechanical function.

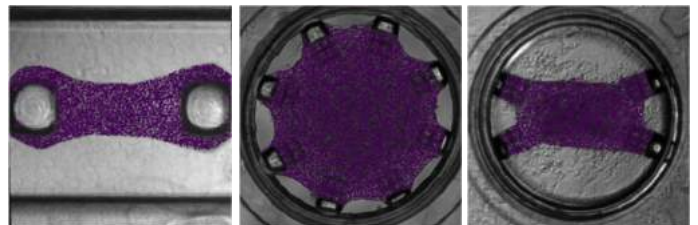


Figure 1: Examples of different cardiac microtissue culture platform designs with detected track points in a segmented mask region of the microtissue domain.

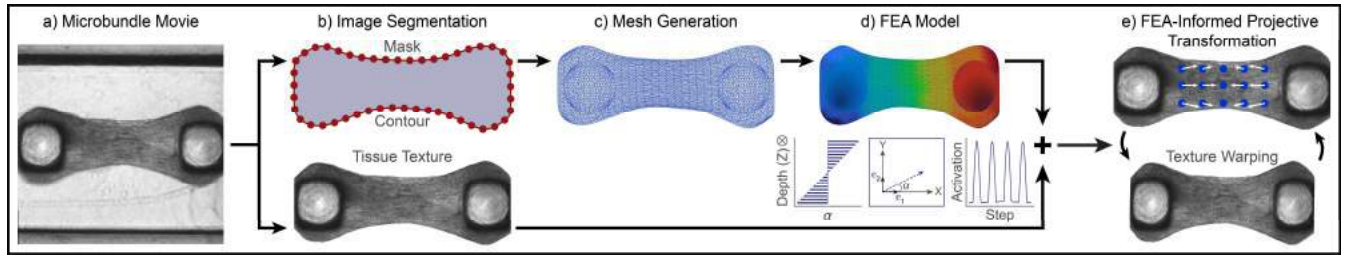


Figure 2: Pipeline for generating synthetic data. The main steps include segmenting a real movie frame to extract both the tissue contour coordinates and the tissue texture. FEA simulation results are used to warp the tissue texture following a realistic deformation pattern.

To validate our approach and ensure that experimental images have sufficient spatial and temporal resolution for the chosen algorithms, we implemented a pipeline for generating synthetic data with a known ground truth. Specifically, we extracted the microtissue component of a microbundle movie frame and generated, from its contour coordinates, a microtissue mesh. We ran Finite Element simulations and extracted displacement results. Finally, we estimated projective transformations based on the deformed microtissue model and warped the image texture accordingly (see Fig. 2). Notably, this pipeline combined with our diverse set of sample experimental datasets, led to many improvements in our software such as image drift correction and smoothing. In addition, this synthetic data pipeline made it possible to design metrics (e.g., synchrony metrics derived from Green-Lagrange subdomain strain timeseries) that would be robust to confounding factors such as image corruption with realistic experimental noise.

RESULTS

In this Section, we briefly present example results from applying our computational framework to the multiple cardiac microtissue platform designs shown in Figure 1. In Figure 3, we show results for full-field absolute displacement (top left), full-field displacement in x-direction (top right), and average subdomain strain in x-direction (E_{xx}) (bottom left) and its time series plot (bottom right) at the automatically identified peak of the first beat of the movie. These plots show the heterogeneous behavior of the cardiac tissue and highlight regions where the microtissue experiences tensile versus compressive strains.

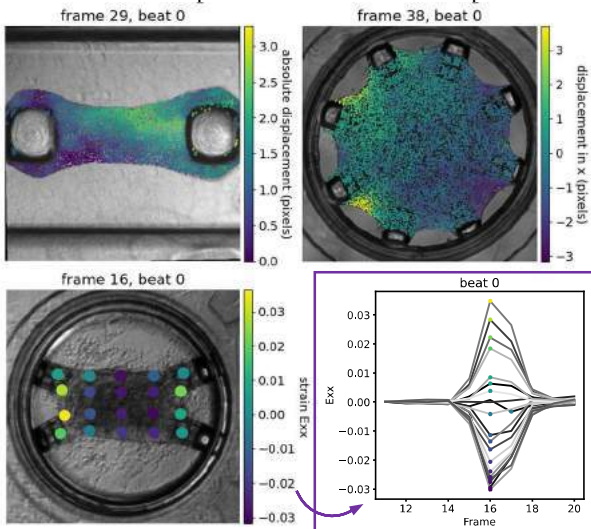


Figure 3: Example results of “Microbundle Compute” software.

Notably, all software functionality is implemented in a test-driven development framework with 100% code coverage and automatic testing on ubuntu, windows, and macOS platforms implemented through GitHub Actions. To date, the lite version of our software (with

the more robustly tested functions) is available under an open-source MIT License on GitHub (<https://github.com/elejeune11/MicroBundleCompute-Lite>). In addition, the code to implement our synthetic data pipeline and the entire synthetic dataset are available on GitHub (<https://github.com/HibaKob/SyntheticMicroBundle>) under MIT license.

DISCUSSION

Here, we briefly presented a summary of the main capabilities of our software in analyzing movies of beating cardiac microtissue. The results clearly show the feasibility and significance for developing computational tools to automatically extract meaningful mechanical metrics from this type of imaging data. Without such tools, the anticipated heterogeneous contractile behavior of the microtissue would be very challenging to quantify. Furthermore, being able to implement the same pipeline and extract quantitatively related results on different testing platforms allows us to meaningfully assess microtissue behavior across multiple in-vitro culture conditions. Ongoing work includes: (1) adding functionality to automatically assess additional experimental platforms, (2) integrating with calcium imaging, (3) integrating with microstructural imaging, (4) using machine learning based data analysis techniques to identify patterns in these datasets, and (5) using these results to directly inform computational models. By making our software open-source and disseminating it from this early stage, we aim to collect feedback from potential users to further improve the software interface, computed output, and result visualization to maximally benefit the research community.

ACKNOWLEDGEMENTS

This work was supported by the CELL-MET Engineering Research Center NSF ECC-1647837, the Boston University Hariri Junior Faculty Fellowship and Graduate Student Fellowship, the David R. Dalton Career Development Professorship, and an American Heart Association Career Development Award #856354.

REFERENCES

- [1] Vardas, P E et al., *European Heart Journal* 43(4):271-279 (2022)
- [2] Brush Jr., John E., et al., *BMJ*, 376 (2022):e064389
- [3] World Health Organization, Cardiovascular Diseases. Accessed 12/13/2020.
- [4] Bursill, C A et al., *Heart, Lung and Circulation*, 31(10), 2022.
- [5] Takahashi, Kazutoshi, *Cell*, 131(5):861-872, 2007.
- [6] Brandão, K O et al., *Dis Model Mech*, 10(9):1039-1059, 2017.
- [7] Nacho, S et al., *Eur Cardiol*, 15:e02, 2020.
- [8] Hnatiuk, A P et al., *Cell Chemical Biology*, 28(3):271-282, 2021.
- [9] Batalov, I et al., *Sci Rep*, 11:11502, 2021.
- [10] DePalma, S et al., *Biomater. Sci.*, 9:93-107, 2021.
- [11] Jayne, R K et al., *Lab Chip*, 21:1724-1737, 2021.
- [12] Javor, J et al., *JMEMS*, 30(1):96-104, 2021.
- [13] Ufford, K et al., *Stem Cell Reports*, 16(3):470-477, 2021.
- [14] OpenCV Optical Flow. Accessed 12/13/2020.
- [15] Shi, J et al., *CVPR*, 593-600, 1994.

SURGICAL AUGEMENTATION AND PRESERVATION OF REMNANT ACL TISSUE BEST RESTORES KNEE FUNCTION AFTER PARTIAL ACL INJURY

S Cone (1,2,3), R Salbego (2), J Roth (1,4), P Lang (4)

- (1) Department of Mechanical Engineering, University of Wisconsin, Madison, Wisconsin, USA
(2) Department of Biomedical Engineering, University of Wisconsin, Madison, Wisconsin, USA
(3) Department of Biomedical Engineering, University of Delaware, Newark, Delaware, USA
(4) Department of Orthopedics and Rehabilitation, University of Wisconsin, Madison, Wisconsin, USA

INTRODUCTION

Partial anterior cruciate ligament (pACL) injuries pose a treatment dilemma in skeletally immature athletes. Particularly in cases where the pACL injury is local to the posterolateral bundle (PLB), pACL injuries are associated with recurrent instability and high risk of reinjury with return to sports [1]. Standard surgical treatments for these pACL injuries require removal of any remaining intact ACL tissue for adequate visualization in the ACL reconstruction (ACLR) procedure. However, physeal sparing ACLR using an iliotibial band (ITB) graft instead supplements any remaining ACL tissue with two stages of the reconstruction procedure: a lateral extra-articular tenodesis (LET) and the ITB ACLR fixation [2]. LET procedures independently have gained popularity as a secondary procedure during standard ACLR surgeries in patients with hyperlaxity or a high risk of reinjury. The purpose of this study was to evaluate the biomechanical responses at both the joint and tissue level of the knee to pACL injuries in the PLB, and to assess LET and ITB ACLR procedures both with and without maintenance of the remnant ACL tissue. We hypothesized that tissue-retaining surgical procedures will result in the closest kinematics to the native knee, and that graft tissue and remnant ACL tissue will share loads in cases where both are present, limiting the risk of secondary failure for either.

METHODS

Five cadaveric human knees (2F/3M) were collected and prepared for robotic testing [3]. Mechanical testing was performed on a 6 degree-of-freedom (6DOF) universal force-sensing robotic testing system (Figure 1) [3] to assess knee joint kinetics and kinematics under three common clinical testing modalities: the Lachman, Slocum, and Pivot-Shift exams. The Lachman exam consisted of kinematically fixing the knee in 30° of flexion, applying a ramped anterior tibial load from 0N-100N-0N, maintaining a compression load of 50N, and minimizing loads in all other directions. The Slocum exam involved kinematically fixing the knee in 80° of flexion, applying a ramped anterior tibial load

from 0N-100N-0N, maintaining kinetic internal and valgus moments of 3N*m, and maintaining 50N of compression. The Pivot-Shift exam was designed to maintain 5N*m of internal and valgus moments and 50N of compression loads, and vary the flexion angle of the knee from 10°-50°-10° during the test.

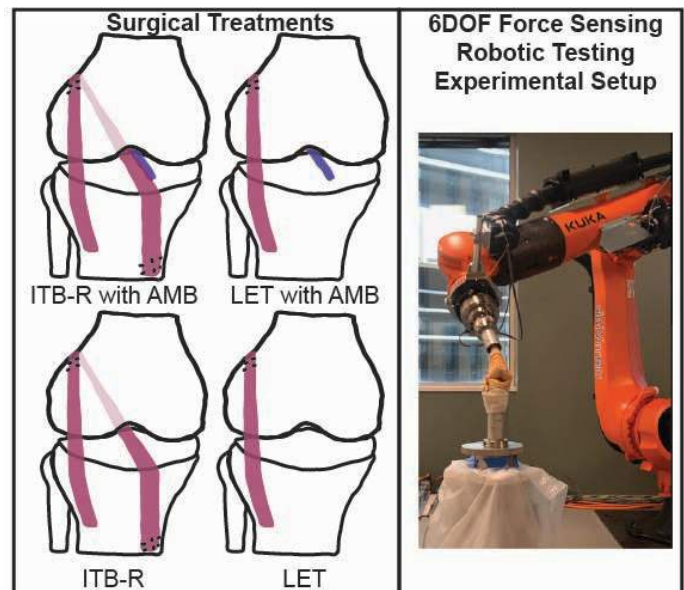


Figure 1: Surgical treatments consisted of lateral extra-articular tenodesis (LET) and all-outside iliotibial band (ITB-R) anterior cruciate ligament reconstructions (ACLR) with or without the anteromedial bundle (AMB) or the ACL intact. Testing was performed on a multiaxial robotic system.

Each test was performed with hybrid kinetic and kinematic controls in the following states: intact ACL, partial injury (PL bundle injury), AM bundle + LET, AM bundle + ITB ACLR, LET, and ITB ACLR (Figure 1). Kinematics were repeated after serial dissections of the tissues of interest: the AM bundle, PL bundle, LET graft, and the ITB ACLR graft. Knee joint kinematics were collected directly from the robotic software (simVITRO, Cleveland Clinic), and calculations were performed using the principle of superposition to assess the 6DOF and resultant loads carried in each tissue [4]. Statistical comparisons consisted of ANOVA testing with kinematic path and knee state as main effects, while individual knees were treated as repeated measures.

RESULTS

Partial and complete ACL injuries both resulted in kinematic destabilization of the knee joints, with respective increases in anterior translation of 0.1 mm and 4.6 mm for the Lachman exam, 0.1 mm and 3.4 mm for the Slocum exam, and 0.03 mm and 0.03 mm for the Pivot-Shift exam. These effects were compounded by destabilization in the other DOFs, with the average resultant translations for each exam shown in Figure 2. Knee joint kinematics were best restored to the intact state in cases where the ITB ACLR was performed with the anteromedial (AM) bundle of the ACL remaining intact. However, in the Pivot-Shift exam, this approach resulted in a slight over-constraint of the knee in the immediate outcome. Across tests, maintenance of the AM bundle resulted in significantly lower laxity measurements compared to LET or ITB ACLR procedures without the AM bundle.

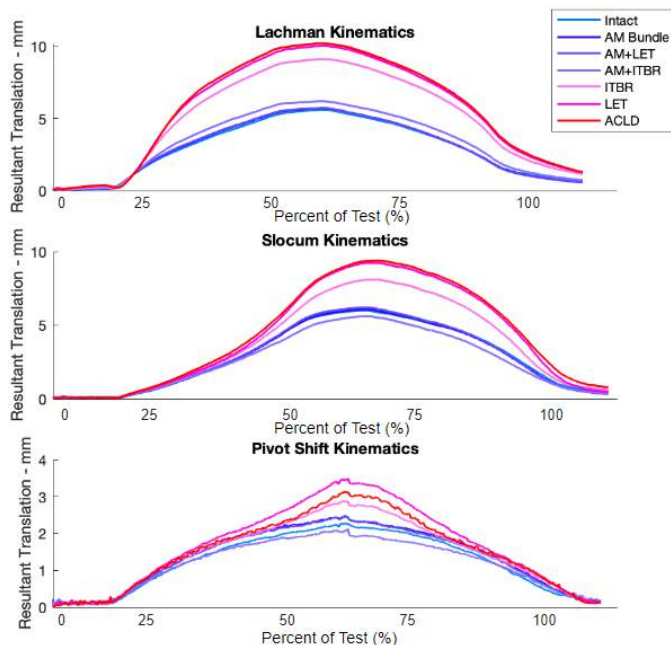


Figure 2: Resultant translations of the tibia during Lachman, Slocum, and Pivot-Shift testing across all joint states of interest.

With applied anterior loads of 100N (Lachman and Slocum) and valgus and internal moments of 3N*m (Slocum) or 5N*m (Pivot-Shift), resultant forces in the knee reached peaks at or slightly above 100N during robotic testing. In the intact knee, these loads were carried primarily by the ACL, with forces split between AM and PL bundles. Specific splits varied between testing modalities, with the AM bundle carrying 70% of the peak ACL load in the Lachman exam, 38% in the Slocum exam, and 74% in the Pivot-Shift exam (Table 1).

Table 1: Peak resultant loads carried in anteromedial (AM) and posterolateral (PL) bundles of the anterior cruciate ligament (ACL) and graft tissues in each surgical case.

Peak Resultant Loads in Tissues Across Clinical Exams			
Test Kinematics	Lachman	Slocum	Pivot-Shift
Intact Case			
ACL	106.5 N	71.3 N	67.7 N
AM Bundle	74.6 N	27.0 N	49.8 N
PL Bundle	24.9 N	32.2 N	81.8 N
Augmented LET Surgical Treatment			
AM Bundle	110.6 N	38.4 N	52.9 N
LET Graft	13.7 N	18.1 N	20.7 N
Augmented ITB ACLR Surgical Treatment			
AM Bundle	87.7 N	28.9 N	44.6 N
ITB Graft	22.8 N	24.4 N	29.5 N
LET Surgical Treatment			
LET Graft	21.9 N	21.6 N	25.8 N
ITB ACLR Surgical Treatment			
ITB Graft	64.8 N	32.5 N	44.8 N

Surgical treatments resulted in significant changes to the loading in the knee joint tissues, with both the grafts and the remnant AM bundle carrying substantial loads (Table 1). When the AM bundle remained in the knee, it carried at least 28.9N of resultant load at peak translation, relieving the forces experienced in the surgical graft tissue. In all cases, removal of the AM bundle resulted in significant increases in the load carried by the graft tissue for both LET and ITB ACLR procedures, with remaining loads accounted for by secondary restraining tissues.

DISCUSSION

The AM bundle-retaining ITB ACLR procedure resulted in the greatest stability, best replicating intact knee kinematics after a partial ACL injury, especially in Lachman and Slocum tests. Interestingly, the AM bundle retaining ITB ACLR procedure overconstrained the knee in the Pivot-Shift test. All surgical interventions restored some stability to the joint compared to partial and complete ACL injury cases, and both techniques were improved when maintaining the AM bundle. The AM bundle relieved loads in both the LET and ITB ACLR graft tissues, suggesting that in cases where the remnant ACL is left intact, load-sharing across tissues should decrease the likelihood of future graft rupture. This study was limited to analysis of partial injury to the PL bundle, with the entire AM bundle remaining intact. In the clinic, partial ACL injuries may affect any percentage of each bundle, potentially limiting the translation of this study to clinical cases with varied injury characteristics. Additionally, this study was limited to assessing the acute functional impacts of these treatments, while clinical outcomes may be affected by graft lengthening or other known long-term effects. Overall, this study suggests that in partial ACL injury cases, LET and ITB ACLR treatments preserving the remnant ACL tissue may be ideal solutions for restoring knee function, especially in young populations where all-outside treatments are desirable.

ACKNOWLEDGEMENTS

This work was supported by the UW Department of Orthopedics and Rehabilitation and NIH NIAMS (F32 AR076267).

REFERENCES

- [1] Kocher, MS et al., *Am J Sports Med*, 30(5): 697-703, 2002. [2] Trentacosta, N et al., *J Ped Ortho*, 40(1): 8-16, 2020. [3] Cone, SG et al., *Clin Orthop Rel Res*, 477(9): 2161-2174, 2019. [4] Xerogeanes, JW et al., *Ann Biomed Eng*, 26(3): 345-352, 1998.

COMPUTATIONAL MODELING STUDY OF THE EFFECTS OF PULMONARY HYPERTENSION ON RIGHT HEART PERFUSION

Lei Fan (1), Jenny S. Choy (2), Ghassan S. Kassab (2), Lik Chuan Lee (1)

(1) Department of Mechanical Engineering, Michigan State University, East Lansing, MI, USA
(2) California Medical Innovations Institute, San Diego, CA, USA

INTRODUCTION

Right heart failure is the leading cause of death in patients with pulmonary hypertension (PH), which is associated with an elevated mean pulmonary artery pressure (mPAP) greater than 25 mmHg. The underlying mechanisms of how PH affects right heart perfusion (that may in turn cause right heart failure) are not well-understood. While several computational models have been developed to investigate PH, they do not consider right heart perfusion. To address this limitation, a novel computational model coupling a biventricular finite element (FE) model with the main coronary branches and their corresponding microvascular networks, including those in the right ventricle (RV) is developed. The model is applied to quantify the effects of acute and chronic PH on biventricular mechanics and perfusion on both the left ventricle (LV) and RV.

METHODS

The computational framework that couples a biventricular FE model with blood flow in the microvascular networks associated with right coronary artery (RCA), left anterior descending (LAD) and left circumflex (LCx) arteries is developed. Besides the coronary circulation, the framework also considers the systemic and pulmonary circulations in a closed-loop system (**Fig. 1**). The framework consists of four cardiovascular components associated with the ventricle, atrium, arteries and veins, each in the systemic and pulmonary circulations. Conservation of total mass of blood in the circulatory model requires the change of inflow and out flow rates of each compartment be related to the rate of change of the volume. The functional relationship between the LV and RV pressures and volumes is obtained by minimizing a Lagrangian function consisting of myocardial tissue strain energy function and terms associated with the enforcement of constraints on 1) myocardial tissue incompressibility, 2) zero-mean rigid body translation and rotation, and 3) cavity volume [1]. Mechanical behavior of the biventricular unit is modeled using an active stress formulation, in

which the passive and active mechanical behaviors are described, respectively, by a Fung-type strain energy function and a modified time-varying elastance model [2-3]. The left atrium and right atrium are described by time-varying elastance models. There are a total of 12 microvascular 400-vessel networks [4] located at the endocardium, mid-wall and epicardium regions associated with the perfusion territories of RCA, LAD, LCx and posterior descending artery (PDA).

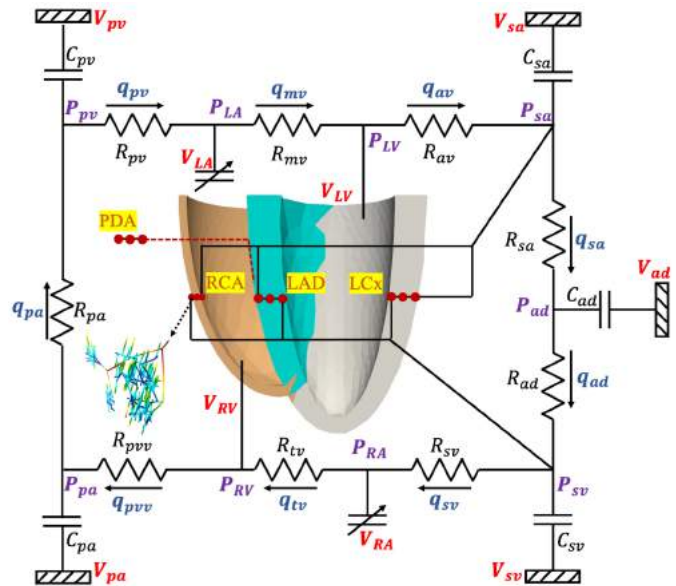


Fig. 1: Schematic of the closed-loop lumped parameter framework that couples the FE biventricular model with coronary networks at endocardium, mid-wall and epicardium regions of the RCA, LAD and LCx.

Intramyocardial pressure (IMP), which varies across regions in the biventricular unit, is imposed on each vessel. Invoking mass conservation across different vessels in each network results in a system of ODEs in terms of the unknown pressures in each vessel. The ODEs are solved using the backward differentiation formula in the freely available library CVODE.

The model was first calibrated to predict cavity pressure and volume waveforms of the LV and RV, as well as the PAP waveform associated with a health human (baseline). The calibrated model was then applied to simulate **1)** different degree of acute PH (without remodeling) by increasing the PA resistance, R_{pa} , and reducing the preload, V_{sv0} to keep the ratio of end-diastolic volume (EDV) of RV/LV below 1.5; **2)** chronic PH (with remodeling) by increasing the RV free wall (FW) thickness from 3 mm to 9 mm. For each simulation, we also considered the case when the PDA was supplied by RCA or LCx in right- and left-dominant heart, respectively.

RESULTS

Peak RV pressure and mPAP are increased from 23 to 60 mmHg and from 14 to 49 mmHg, respectively, from baseline (base) to acute PH at different degree (PH+ and PH++) (Fig. 2a). LVEDV is reduced by 5 ml but RVEDV is increased from 96 to 111 ml (Fig. 2b). Intramyocardial pressures at different transmural locations are increased in the RVFW and septum but is unchanged in the LVFW in acute PH compared to baseline (Fig. 2c). As a result, transmural distribution of total coronary flow is reduced in the RCA and the RV in acute PH. This reduction is more significant in right-dominant heart than left-dominant heart (Fig. 2d). Transmural distribution of total coronary flow is relatively unchanged in the LCx of the right-dominant heart as both perfusion pressure and IMP in the LVFW do not change with in acute PH. Flow in the LCx of left-dominant heart, however, is reduced because the increased IMP at the septum impedes more flow in the PDA (Fig. 2e). Flow rate waveform of the RCA is also different in the left- and right-dominant heart (Fig. 2f). In the right-dominant heart, flow rate in the RCA is reduced during systole due to effects of higher IMP at septum on PDA whereas in the left-dominant heart, RCA flow rate waveform follows the perfusion pressure waveform. In chronic PH where RV wall thickness is increased, the model predicts that blood flow is reduced more in the RCA, LAD and LCx microvascular networks at the endocardium than acute PH (Fig. 2g-i). This reduction is more than that found at the epicardium.

DISCUSSION

We developed a novel computational modeling framework coupling a biventricular FE model with coronary perfusion at different transmural locations in the RVFW, septum and LVFW. We apply the model to investigate the effects of PH on heart perfusion. The key findings are **1)** IMPs at different transmural locations of the RVFW and epicardium of the septum are increased in PH, which reduce coronary flow in the RVFW and septum, as well as in the LCx network in the chronic PH; **2)** the coronary flow in RVFW is reduced more at the endocardium than epicardium in PH, suggesting that endocardium is more vulnerable to ischemia with PH; **3)** the coronary flow in LCx is reduced more in the left-dominant heart than the right-dominant heart in PH, suggesting left-dominant LCx is more vulnerable to ischemia with PH. These findings suggest that right heart perfusion is affected by PH and may contribute to the development of right heart failure in PH.

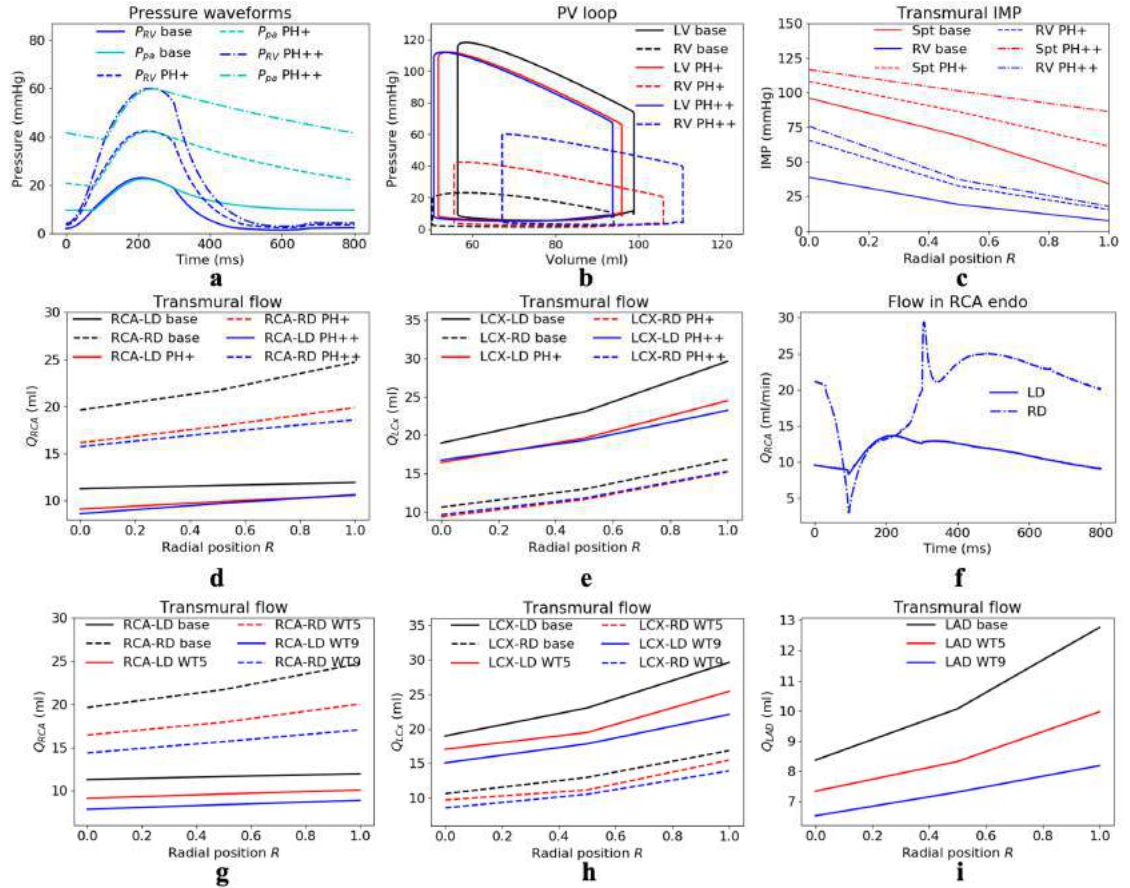


Fig. 2: Comparison of **a.** RV and PA pressures; **b.** LV and RV PV loops; transmural distribution of **c.** IMP in the LVFW, septum and RVFW; **d.** RCA total flow; **e.** LCx total flow, in baseline and acute PH. **f.** representative RCA flow rate waveforms at endocardium in the left- and right-dominant heart. Comparison of total flow in **g.** RCA; **h.** LCx; **i.** LAD, in baseline and chronic PH.

ACKNOWLEDGEMENTS

This work was supported by the National Institute of Health (R01 HL160997) and American Heart Association Postdoctoral Fellowship (AHA835298).

REFERENCES

- [1] Guccione, J. M. et al., J. Biomech., 28, 1167–1177, 1995.
- [2] Fan, L. et al., Front. Physiol., 2105, 2021.
- [3] Fan, L. et al., Comput. Biol. Med., 141, 105050, 2022.
- [4] Fan, L. et al., Am. J. Physiol. - Hear. Circ. Physiol., 2021.

MRI GUIDED FOCUSED ULTRASOUND DRUG DELIVERY TO DIPG TUMORS IN A MOUSE MODEL

Payton J. Martinez (1,2), Genna Nault (3), Jenna Steiner (3),
Natalie Serkova (3), Adam Green (4), Mark Borden (1,2)

(1) Biomedical Engineering, University of Colorado Boulder, Boulder, Colorado, USA
(2) Mechanical Engineering, University of Colorado Boulder, Boulder, Colorado, USA
(3) Animal Imaging, University of Colorado Anschutz Medical Campus, Aurora, Colorado, USA
(4) Pediatric Oncology, University of Colorado Anschutz Medical Campus, Aurora, Colorado, USA

INTRODUCTION

Diffuse midline glioma, specifically pontine and H3 K27M-altered, is the most common and unfortunately the deadliest brainstem tumor in children [1]. Current clinical treatment methods only involve palliative radiotherapy. These do not significantly improve survival beyond its poor mean survival of 9 months [2]. These tumors remain difficult to treat with chemotherapy as they maintain an intact blood brain barrier (BBB). Although, a technique using focused ultrasound (FUS) and microbubbles (MBs) has been shown to disrupt the blood brain barrier (BBBD) allowing larger chemotherapeutics to enter the parenchyma [3]. Panobinostat is one of the chemotherapeutics that has difficulty crossing the BBB however it has promising effects in vitro [4]. Therefore, in this study we hypothesized that using FUS, we could disrupt the BBB allowing a higher concentration of Panobinostat to enter the tumor region and provide a therapeutic effect.

METHODS

Mice were injected with BT-245 (DIPG tumor cell line) orthotopically into the pons, 1 mm laterally to the right hemisphere. Initial set of mice (n=12) had two weeks of growth. Magnetic Resonance (MR) images were then taken and used to guide FUS targeting to the center of the tumor location. In house microbubbles were size isolated to $3 \mu\text{m} \pm 0.5 \mu\text{m}$ and half of the mice (n=6) were injected via tail vein at 25 $\mu\text{l/kg}$ right before (10-20 seconds) sonication. Sonication parameters were as follows: center frequency: 1.515 MHz, peak negative pressure: 0.77 MPa, pulse length: 1 ms, pulse repetition frequency: 1 Hz. Sonication lasted for 3 minutes and passive cavitation data was collected and analyzed as previously described [5]. Directly after FUS Panobinostat (LBH-589) was given (10 mg/kg) intraperitoneally (IP) and MR images were taken to determine extent of BBBD. After 1.5 hours, mouse serum and brains were extracted and split at the midbrain and cerebellum. All three samples were sent in for liquid chromatography and mass spectrometry to determine concentration of

Panobinostat at each location.

The second set of mice (n=20) were treated weekly for three weeks. Half of which were treated with both FUS and Panobinostat with the same parameters to the first set, the other half was only given Panobinostat. After 3 weeks no treatment was done on either set. MR images were taken and body weight was examined weekly prior to treatment and after treatment period ended to evaluate extent of BBBD and tumor progression.

RESULTS

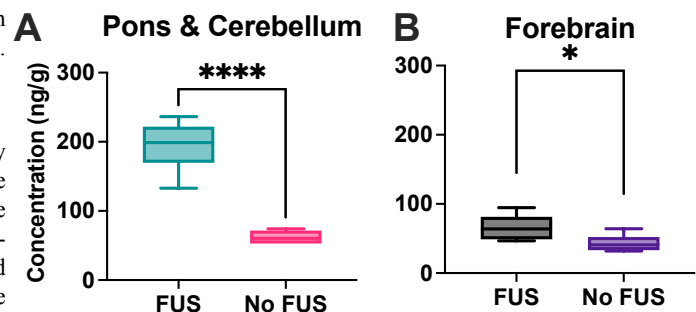


Figure 1: Concentration of Panobinostat found in the pons and cerebellum (A) and forebrain (B) 1.5 hours after FUS-mediated BBBD occurred (if applicable) and Panobinostat was injected IP. Analysis was done using mass spectrometry. Wiskers illustrate 10-90 percentile. Significance testing was done using student's t test (n=6). *, ** indicates $P < 0.05$ and $P < 0.0001$ respectively.**

We have demonstrated that FUS-mediated BBBD can successfully deliver Panobinostat (LBH-589) to the pons and cerebellum region with DMG tumors over 3-fold (Fig.1a) while only slightly increasing the concentration of the forebrain 51 percent (Fig. 1b).

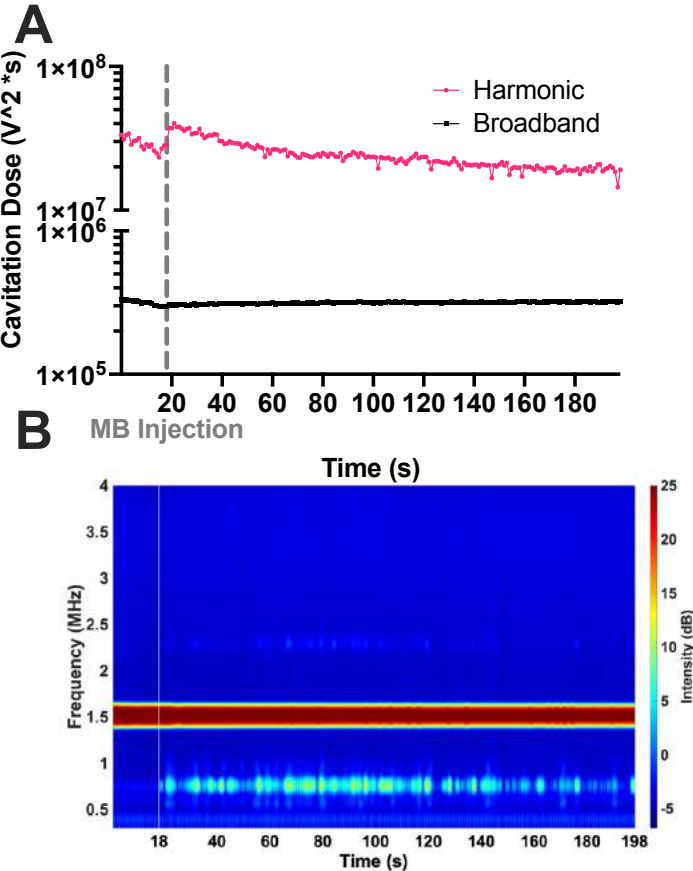


Figure 2: Passive cavitation detection during 3 minute treatments. A) Illustrates the harmonic and broadband cavitation dose (HCD and BCD respectively) found during each 10 ms pulse. Gray dotted line at 18 seconds represents the point where all microbubbles were injected. **B)** Spectrogram of total treatment. Non-sonication time between pulses were removed. White line at 18 seconds represent the time at which microbubbles were injected.

Passive cavitation detection (PCD) during treatments showed ideal harmonic cavitation throughout the 3 minutes while not having any significant broadband cavitation (Fig. 2a). Harmonic cavitation doses showed a spike right after injection of microbubbles and decay that matches the pharmacokinetics found for similar doses and compositions of microbubbles. PCD illustrates the presence of microbubbles in focal region with the introduction of sub- and ultra-harmonic responses only when microbubbles were injected (Fig. 2b).

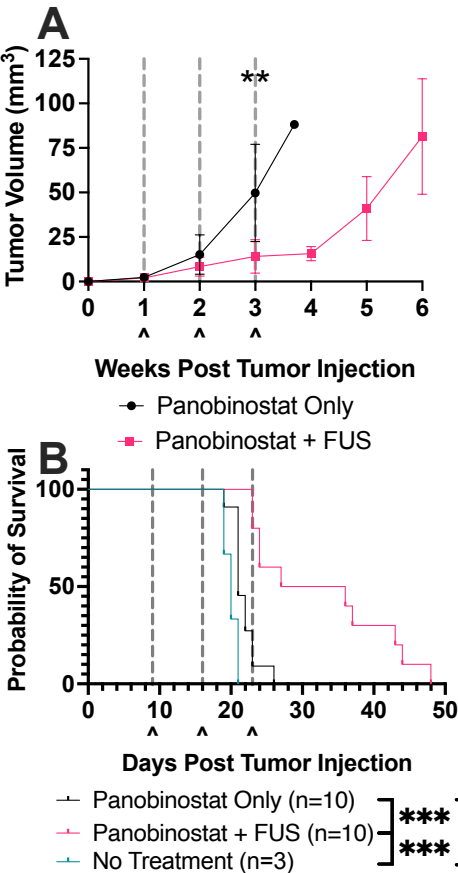


Figure 3: Longitudinal analysis of tumor volume using MR images obtained weekly (A) and survival (B). Dotted gray lines on both plots represent the treatment days. Significance testing was done using student's t test for A, and Mantel-Cox test (n=10) for B, where *, **, *** indicates P <0.05, 0.01, and 0.001 respectively.

The combination of both Panobinostat and FUS showed major decreases in tumor growth by 71 percent by the end of the treatment weeks when compared to Panobinostat without FUS (Fig. 3a). A significant survival benefit was also demonstrated when treated with both Panobinostat and FUS improving the mean survival from 21 to 31.5 days (Fig. 3b).

DISCUSSION

Our study demonstrates that FUS-mediated BBBD can increase the delivery of Panobinostat (LBH-589) to an orthotopic DMG tumor (BT-245). The increased concentration exclusively at the tumor site was shown to significantly decrease tumor growth (71 percent) and significantly increase survival (50 percent). Therefore, we see a strong indication that this methodology can be used to improve the treatment of DMGs in patients.

ACKNOWLEDGEMENTS

This material is based upon work supported by The Cancer League of Colorado, and in part by the National Science Foundation Graduate Research Fellowship under Grant No. (2040434).

REFERENCES

- [1] Zanten SEV van et al. *Expert Review of Anticancer Therapy* 15.2 (2015). DOI: 10.1586/14737140.2015.974563.
- [2] Packer RJ et al. *Cancer* 74.6 (1994).
- [3] Woodworth GF et al. *Frontiers in Oncology* 4 (2014).
- [4] Grasso CS et al. *Nature medicine* 21.6 (2015).
- [5] Martinez P et al. *Pharmaceutics* 14.9 (2022). DOI: 10.3390/pharmaceutics14091925.

ENHANCING CORRUPT CARDIOVASCULAR FLOW DATA WITH MACHINE LEARNING

Hunor Csala (1,2), Amirhossein Arzani (1,2)

(1) Department of Mechanical Engineering, University of Utah, Salt Lake City, UT, USA
(2) Scientific Computing and Imaging Institute, University of Utah, Salt Lake City, UT, USA

INTRODUCTION

Obtaining clean, high resolution velocity measurements of blood flow inside small arteries such as cerebral vasculature is challenging, as the existing experimental techniques have several limitations. Time-resolved three-dimensional phase contrast magnetic resonance imaging (4D flow MRI) is a popular approach in research settings, however it is constrained by low spatio-temporal resolution, noise, and other artifacts [1]. Particle image velocimetry (PIV) often considered the gold-standard in experimental fluid dynamics also suffers from some limitations. Therefore, handling corrupt blood flow data is key challenge towards developing more accurate and robust cardiovascular flow models. There are well developed algorithms in the machine learning community that can tackle similar issues, such as data imputation, denoising or outlier detection. Existing methods have been less frequently used and leveraged for complex real-world fluid flow problems [2], such as cardiovascular flows [3]. Specifically, we do not understand which one of these approaches commonly used in the machine learning community perform better for hemodynamics data. This study investigates and compares several techniques for filling in missing values and denoising unsteady blood flow data in an image-based 3D intracranial aneurysm model.

METHODS

Voxel-based data mimicking some of 4D flow MRI data features was created from computational fluid dynamics (CFD) simulation results. Pulsatile blood flow inside an internal carotid artery (ICA) aneurysm was simulated using SimVascular, a finite element numerical solver. The Reynolds number was 555, based on the maximum systolic inlet velocity and inlet diameter. A population averaged inlet waveform was used, 1000 snapshots were saved through one cardiac cycle. The unstructured mesh consisted of 6.6M elements, which was resampled to a voxelized grid with a uniform spatial resolution of 0.5 mm, resulting in 27000 voxels. Two types of data corruption were investigated here, missing data and Gaussian noise. These were artificially added to the voxelized data. Voxels were randomly removed in space and time for the missing data case and Gaussian noise was added for the noisy case. The process of creating corrupt synthetic voxel-

based data is illustrated in Figure 1. For the missing data case, the fraction of missing data was varied between 10% and 90%. For the denoising case, the fraction of noisy data was varied between 10% and 70%. The standard deviation of the added noise was 10% of the maximum velocity value.

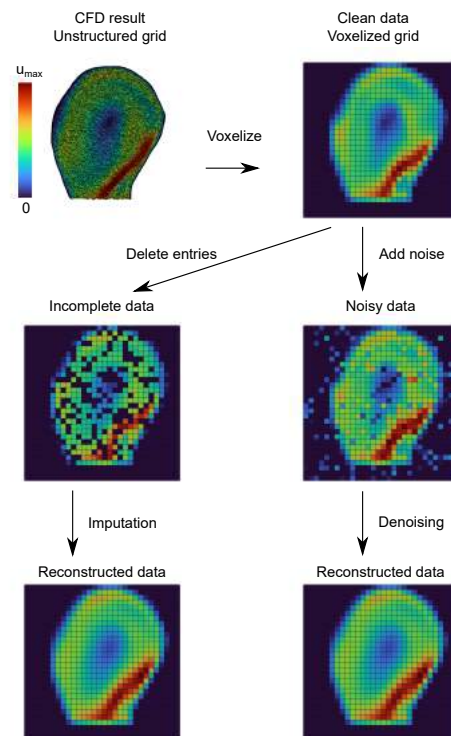


Figure 1: Process of creating corrupt voxel-based data from CFD results.

Imputation is the process of filling in missing data based on some statis-
SB³C2023-026

tics of the observable dataset. Four methods were used for data imputation: probabilistic principal component analysis (PPCA), iterative singular value decomposition (itSVD), softImpute, and an autoencoder. PPCA is a probabilistic version of PCA using the expectation-maximization (EM) algorithm. itSVD and softImpute are two techniques based on iterative low-rank SVD decompositions and soft-thresholding. The autoencoder approach is a fully-connected deep neural network that has a bottle-neck layer in the middle, whose dimensionality is much smaller than the input and output, therefore the network learns a low-dimensional embedding of the data.

Three algorithms were used for denoising: robust principal component analysis (RPCA), Noise2Noise autoencoder (N2N), and a conventional denoising autoencoder (DAE). RPCA tries to separate the data into a low-rank matrix containing the noise-free data and a sparse noise matrix. N2N is a neural network based denoising algorithm that does not require clean training data. That is, the input and the target data are both noisy data representing two samples from the same noise distribution. The DAE approach does denoising in a supervised fashion. It was trained with 7 simulations with different mean inlet velocities (Reynolds number ranging between 380 and 650, based on the systolic maximum inlet velocity) on the same geometry, then tested on unseen velocity data ($Re_{max} = 555$). The noise and missing data characteristics (fraction of data missing or noisy and noise standard deviation) were the same during training and testing. It is important to note that the matrix completion (itSVD, softImpute) and PCA-based methods (PPCA, RPCA) do not require training data.

RESULTS

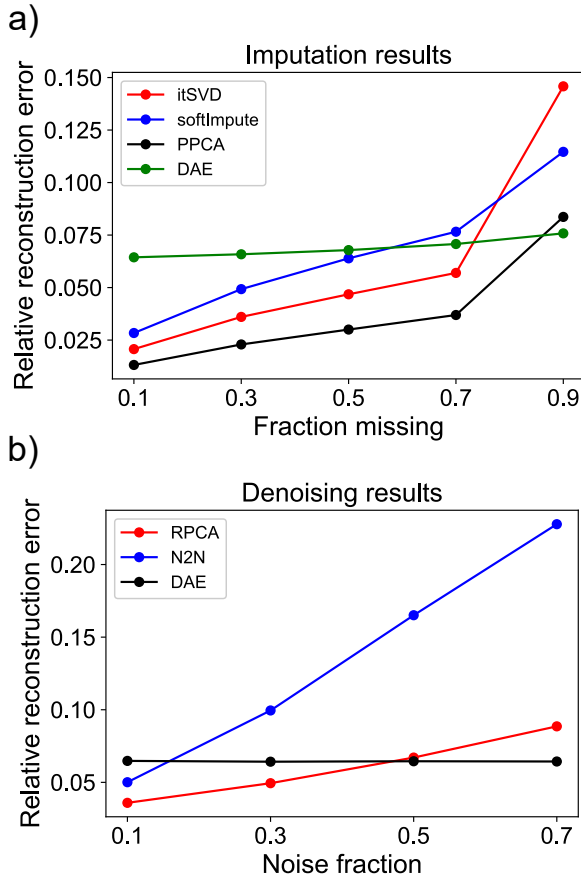


Figure 2: a) Imputation relative reconstruction error with different percentage of data missing. b) Denoising relative reconstruction error with different percentage of data being noisy.

Imputation and denoising results are shown in Figure 2, top and bottom panel, respectively. The relative reconstruction error ϵ is defined as

$$\epsilon = \frac{\|\mathbf{X} - \mathbf{X}_{rec}\|}{\|\mathbf{X}\|}, \quad (1)$$

where \mathbf{X} is the clean ground-truth data, \mathbf{X}_{rec} is the filled in or denoised data, and the Frobenius norm is used. In case of imputation, the two matrix completion methods (itSVD and softImpute) have similar results. PPCA has the lowest error in almost all cases. As the percentage of missing data grows the error increases, and a sharp rise can be seen at 90% missing data for these three methods. The autoencoder is much less sensitive to the amount of data missing, probably due to the nature of supervised learning, and its error is only slightly increasing as the fraction of missing data increases. Overall, all methods perform well and can fill in the missing entries in the aneurysm velocity data, as the relative reconstruction error is below 10% for most cases, and even for the highest missing fraction of 0.9 the error is less than 15% for all four techniques. This suggests that blood flow inside an aneurysm can be described well by an intrinsic low-dimensional model that can be inferred from a few data points.

For denoising, N2N has clearly inferior performance to the other methods. RPCA achieves good performance in the low-noise setting, while the DAE outperforms RPCA in the high-noise scenario. Again, the autoencoder errors does not seem to be depending too much on the fraction of noisy data. RPCA and DAE achieve an error smaller than 10% for all noise fractions, while for N2N the error exceeds 20% at 70% of noisy data.

DISCUSSION

We investigated several machine learning algorithms for handling corrupt blood flow data inside an ICA aneurysm. Matrix completion, PCA-based, and neural network-based techniques proved to be able to enhance blood flow data corrupted with randomly missing voxel entries and added Gaussian noise. Matrix factorization methods seem to be more useful in the low-corruption case, while for highly corrupted datasets neural networks perform better. Overall, these machine learning algorithms have the potential to significantly improve hemodynamic data quality and enable the creation of robust cardiovascular models.

Our findings suggest that neural networks are more valuable when dealing with highly corrupted datasets with available data for training. On the other hand, matrix completion and PCA-based methods can achieve excellent results with mildly corrupted data, without the need for clean training data. However, there is a serious limitation to the matrix completion and PCA methods. These methods assume that the missing data is random in space and time, and the noise is Gaussian noise. Without these assumptions, these methods could fail. On the other hand, if there is enough training data available, the autoencoder based methods can achieve good results, no matter the pattern of missing data or the characteristic of the noise. Obviously it is desired that the training and testing data have the same type of corruption. Creating models that can handle multiple noise or missing data characteristics is a future challenge that needs to be investigated.

Our future work includes extending this setup to real experimental data. Additionally, we are working on other types of data corruptions such as aliasing in 4D flow MRI, which could be treated using outlier detection algorithms.

ACKNOWLEDGEMENTS

This work was supported by NSF grant No. 2246916.

REFERENCES

- [1] Fathi MF et al. *Computer Methods and Programs in Biomedicine* 197 (2020). ISSN: 0169-2607. DOI: <https://doi.org/10.1016/j.cmpb.2020.105729>.
- [2] Scherl I et al. *Phys. Rev. Fluids* 5 (5 2020). DOI: 10.1103/PhysRevFluids.5.054401.
- [3] Arzani A et al. *Journal of the Royal Society Interface* 18.175 (2021).

DEVELOPMENT OF THREE – DIMENSIONAL FINITE ELEMENT MODEL OF THE NEONATAL BRACHIAL PLEXUS

Sarah J. Wright (1,2), Michele J. Grimm (1,2)

- (1) Department of Biomedical Engineering, Michigan State University, East Lansing, MI, USA
(2) Department of Mechanical Engineering, Michigan State University, East Lansing, MI, USA

INTRODUCTION

The brachial plexus is a complex system of nerves that connect to the cervical (C5-C8) and thoracic spinal cord (T1). This system of nerves is responsible for motor and sensory functions of the upper extremities. During the birthing process, vaginal or cesarian, these nerves are susceptible to an injury known as Neonatal Brachial Plexus Palsy (NBPP). NBPP occurs approximately 1-4/1,000 total births [1]. It has been documented clinically and through research that, for cephalic presentations with the fetal arm adducted against or across the body, the injury is initiated at C5 and progresses down to sequentially include the lower nerve roots.

Conducting research into the mechanism of NBPP is a challenge due to the vulnerable populations that it involves. Computational modeling is an ethically sound and scientifically valid method to explore this injury, as it allows parameters to be precisely controlled and varied within a known range of values – including nerve diameter and nerve root angle.

Key to obtaining precise estimates of localized stress and strain in the brachial plexus is having accurate anatomy, which has been a challenge to obtain. Medical images of the infant brachial plexus may be used; however, they have limitations due to obscured visuals that result from other anatomical structures (e.g., clavicle). Exploratory surgery is unlikely to occur as it is not ethically sound to experiment on this age of subjects.

The main objective of this study was to develop a 3D model of the brachial plexus and then conduct a simulation study to determine how injury to the upper nerve roots, through complete rupture or avulsion, affects the stress along the remainder of the brachial plexus.

METHODS

A computational neonatal brachial plexus model was created and analyzed using Solidworks software. The initial dimensions to create this model – diameters and lengths of the nerve roots and trunks – were

collected by the University of Michigan Neurosurgery Department during primary reconstructive surgery of infants [2]. The dimensions for the divisions, cords, and branches were determined based on their calculated ratios to the root and trunk dimensions, as estimated from images of adult brachial plexus using ImageJ. Figure 1 demonstrates the entire model that was created, including the anterior and posterior portions of the divisions.

Due to the lack of research done on human neonatal nerves, the material properties are unavailable. For this reason, properties determined from neonatal piglet brachial plexus nerves in an *in vivo* tensile stress analysis were used [2].

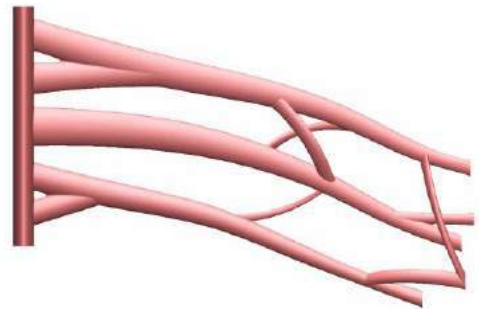


Figure 1: Three – Dimensional Brachial Plexus Model

The material properties, boundary conditions and external loads were added to the model within Solidworks. The entire spinal cord was subjected to an encasté boundary condition, in which all active structural degrees of freedom are constrained. No boundary conditions were used to constrain the anterior and posterior surfaces of the nerves. A tensile force was applied at the distal end of each nerve branch, as would occur with the depression of the shoulder while the head and neck remained aligned with the axis of the spine. The force was applied as a

surface stress perpendicular to the face of the nerve, and the tensile stress was calculated based on the maximum load (1.08N) [2] normalized by the estimated cross-sectional area of each nerve branch. The stress in each nerve root was determined for the complete, intact brachial plexus. The simulation was repeated with a complete discontinuity between C5 and the spinal cord, representing an avulsion or rupture, and then a discontinuity at C5 and C6 (Figure 2).

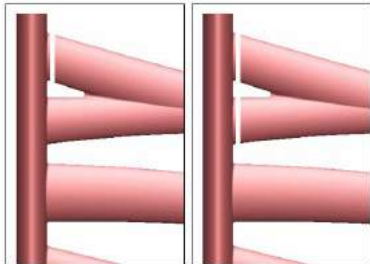


Figure 2: (A) C5 avulsion and (B) C5 and C6 avulsion

RESULTS

When a complete avulsion or rupture occurs only at C5, a significant increase in stress ($> 16x$) occurs to the C6 nerve root, as seen in Figure 5. The stress in C7 also increased, but to a lesser extent ($3x$). When an avulsion occurs to the entire upper plexus (C5 and C6), the predicted increase in the stress at C7 nerve root was about 8 times higher than in the intact brachial plexus (Figure 5). Figure 3 illustrates the stress on a non-injured brachial plexus. Within this model, the stress is distributed along the entire brachial plexus beginning from the nerve roots and continuing down to the five branches. A higher stress occurred at the anterior and posterior portions of the divisions than at the nerve roots.

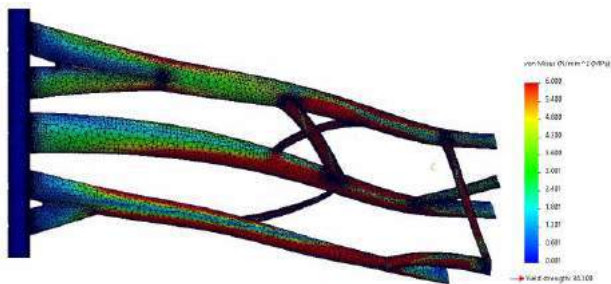


Figure 3: Control - Von Mises Stress (MPa)

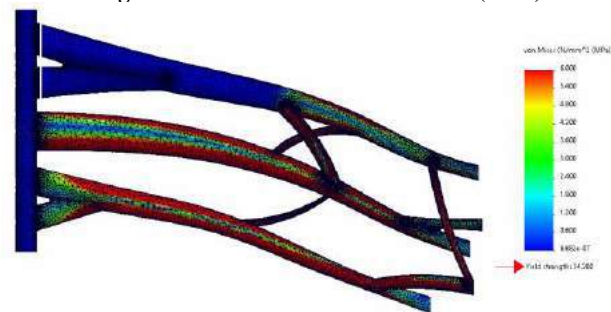


Figure 4: C5 and C6 Avulsion - Von Mises Stress (MPa)
** Displacement is not shown

Figure 4 illustrates the impact of a C5 and C6 discontinuity, in which the nerve roots separate from the spinal cord. When this injury occurs, it is shown that less stress occurs in the upper plexus. The roots and trunks of the upper plexus are essentially unstressed. This

displaces the stress within the nerve root to the nerve root levels below the avulsion. In this case, a large increase of stress occurs within the C7 nerve root.

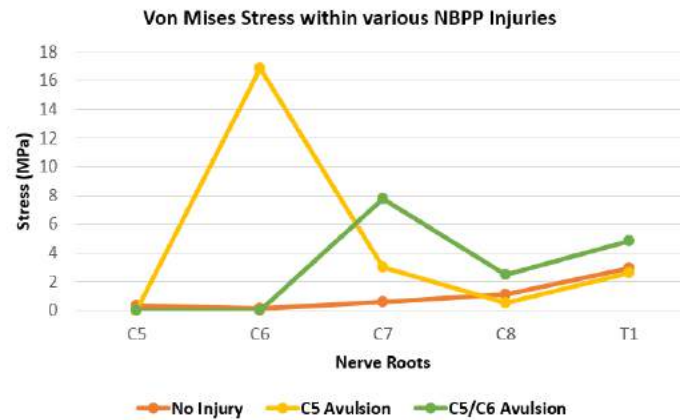


Figure 5: Von Mises (MPa) stress comparison for different injuries

DISCUSSION

In some children, there may be more than one level of nerve root in the brachial plexus that is injured. An anatomically accurate model of the complex, 3D plexus allows for more detailed assessment of the stresses and injury progression to be evaluated. It also allows for the effect of full or partial disruption of the nerve roots to be investigated.

Clinical patterns of brachial plexus injury and some experimental work demonstrate that C5 and C6 experience higher stress under initial loading of the brachial plexus than do the lower roots and that these levels are damaged first [3]. This simulation confirms this outcome. While this may be an obvious result to biomechanical engineers, it is not obvious to neurosurgeons or obstetricians.

While two three-dimensional models of the adult brachial plexus have been published [4, 5], they are anatomically accurate only through the level of trunks. This is the first 3D model of the complete brachial plexus, for either neonates or adults, that extends through the distal branches. This complete computational model will allow in-depth analysis of NBPP injuries by providing a better understanding of the stress distribution within the nerves that occurs during the birthing process.

ACKNOWLEDGEMENTS

We dedicate our research to the late Dr. Lynda Yang. We thank our colleagues from University of Michigan who provided insight and expertise that assisted the research and data collected. The lead author was supported through NSF Award CBET 2028474.

REFERENCES

- [1] Gherman, *Obstet Gynec*, 123(4):902, 2014. doi: 10.1097/01.AOG.0000445582.43112.9a.
- [2] Singh, *J Brachial Plex Peripher Nerve Inj*, 13(1):e8, 2018, doi: 10.1055/s-0038-1669405.
- [3] Metaizeau, *Chir Pediatr*, 20(3):159, 1979.
- [4] Perruisseau-Carrier, A *Annales De Chirurgie Plastique Esthétique*, vol. 62, no. 6, 2017, pp. 664-668., doi: 10.1016/j.anplas.2017.03.002
- [5] Mihara, *Experimental and Therapeutic Medicine*, 2017, doi: 10.3892/etm.2017.5607.

COCULTURE AND CONDITIONED MEDIA ENHANCE MECHANICAL FUNCTION OF iPSC-DERIVED CARDIOMYOCYTES ON A 2D MICROPATTERNED SUBSTRATE

Mitchell Josvai (1,2), Alana Stempien (1,2), Jacob Notbohm (1,3,4), Jianhua Zhang (5), Timothy J. Kamp (5,6), Wendy C. Crone (1,2,3,4)

- (1) Department of Biomedical Engineering, University of Wisconsin-Madison, Madison, WI, USA
- (2) Wisconsin Institute for Discovery, University of Wisconsin-Madison, Madison, WI, USA
- (3) Department of Engineering Physics, University of Wisconsin-Madison, Madison, WI, USA
- (4) Department of Mechanical Engineering, University of Wisconsin-Madison, Madison, WI, USA
- (5) Department of Medicine, Division of Cardiovascular Medicine, University of Wisconsin-Madison, Madison, WI, USA
- (6) Department of Cell and Regenerative Biology, University of Wisconsin-Madison, Madison, WI, USA

INTRODUCTION

Cardiomyocytes (CMs) are the primary contractile cells of the native heart, responsible for executing coordinated contractions sufficient to maintain cardiac function. While not mechanically active, cardiac fibroblasts (CFs) are prevalent in cardiac tissue, necessary for maintenance and remodeling the extracellular matrix (ECM), direct cell-to-cell communication, and paracrine signaling factor secretion [1], [2]. CFs play a role in cardiac development, homeostasis, and repair in response to myocardial injury or disease [3], [4], though their effects on CM mechanical function and maturation remain unclear.

Despite recent advances, potential applications and cell therapies involving iPSC-CMs are hindered by relative immaturity of these myocytes in comparison to primary adult CMs [5]. iPSC-CMs display electrophysiological, morphological, and mechanical characteristics of embryonic CMs [6]-[8]. Methods to influence iPSC-CMs towards a more mature phenotype *in vitro* have been developed, such as chronic mechanical and electrical stimulation [9],[10], metabolic cues [11], and coculture with alternative cell types [12], [13]. CM-CF coculture increases the amplitude of force generation by CMs [14], as well as the spontaneous rate of contraction [15]. We have previously shown that CFs improve calcium kinetics and increase contractile strain when in coculture with CMs [16]. Such findings demonstrate the importance of developing models of myocyte-fibroblast-ECM interactions to understand the bidirectional communication between cell types, and their role in mechanical function.

This work explores the differential effects of CM-CF coculture and CF conditioned media on iPSC-CM mechanical function on an engineered 2D platform. We seek to determine to what extent coculture and conditioned media enhance mechanical function of CMs and to elucidate if the observed improvements are the result of ECM remodeling and direct cell contact through the concurrent presence of CFs, the result of CF-mediated paracrine signaling not requiring direct cell contact, or a more complex interplay of the two.

METHODS

Human induced pluripotent stem cell-derived cardiomyocytes (iPSC-CMs) were differentiated using a modified version of the small molecule GiWi method and purified using lactate medium [17], [18]. iPSC-CFs were differentiated as described previously [19]. Microcontact printing and soft lithography was used to generate compliant substrates with patterned ECM proteins in defined geometries as previously described [20]. Decellularized ECM substrates were produced by Matrigel patterning as described and seeding iPSC-CFs at a density of 253 CFs/mm². CFs were cultured and allowed to remodel the deposited ECM for 14 days before decellularizing [21].

CM only and CF conditioned samples were seeded with purified iPSC-CMs at a density of 2,528 CMs/mm². CM-CF coculture samples were seeded at an equivalent CM density, as well as a density of iPSC-CFs of 253 CFs/mm². CM only and CM-CF coculture samples were maintained with EB2 medium: DMEM/F12, 2% FBS, 1% NEAA, 0.5% GlutaMax, and 0.07% 2-Mercaptoethanol. For CF conditioned samples, EB2 media was conditioned by a CF monoculture before being transferred to the samples unaltered or at a 1:1 dilution with fresh EB2.

Mechanical analysis was performed using digital image correlation (DIC) to quantify maximum contractile strain and spontaneous contraction rate [22], [23]. Statistical analysis of two groups was performed using an unpaired two sample t-test. Analysis of more than two conditions used a one-way ANOVA test followed by multiple comparison test to perform pairwise comparisons using Tukey's honestly significant difference criterion.

RESULTS

iPSC-CMs were seeded either alone or in coculture with iPSC-CFs on platforms of micropatterned ECM or ECM remodeled by CFs and decellularized. CMs cultured alone remained within the boundaries of the defined ECM pattern through 18 days and demonstrated a similar arrangement to CMs conditioned by CF media. CM-CF coculture

demonstrated progressive remodeling of the patterned ECM and migration to previously unoccupied regions of the substrate, resulting in an appearance similar to a confluent monolayer under brightfield microscopy although stained images reveal that the underlying CMs retain their organization [16].

Videos of coordinated cell contractions were captured using brightfield microscopy, and the contractile strains were calculated using digital image correlation (DIC). At each time point, there was a significant difference in the maximum strain generated in the CM-CF coculture condition and the CM Only condition (Fig. 1). However, a significant difference between the CF conditioned media condition and CM only condition was only present at the Day 12 and Day 18 timepoints, and the magnitude of the difference was less pronounced.

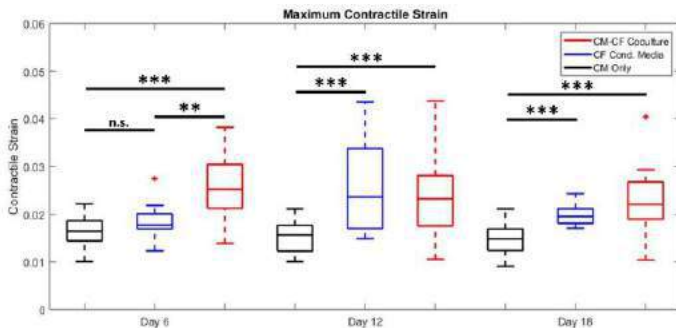


Figure 1: Matrigel strain analysis; The maximum contractile strain is significantly higher in the CM-CF coculture condition than the CM Only condition at Days 6, 12, and 18. Strain is significantly higher in the CF conditioned media condition than the CM Only condition at only Days 12, and 18. ** $p < 0.01$, *** $p < 0.001$.

To understand other features of contractile behavior, the spontaneous contraction rate was evaluated. Only videos collected at Day 6 were included as not all samples at later timepoints captured greater than one contraction. CM-CF coculture resulted in increased rates of contraction on both ECM conditions (Fig. 2A), while CF conditioned media had no effect on rate on either ECM condition. A similar trend was observed at later experimental timepoints for samples capturing multiple contractions. The contraction rate was significantly decreased on decellularized ECM in comparison to Matrigel (Fig. 2B). No correlation was observed between the amplitude of contractile strain and the spontaneous rate of contraction (data not shown).

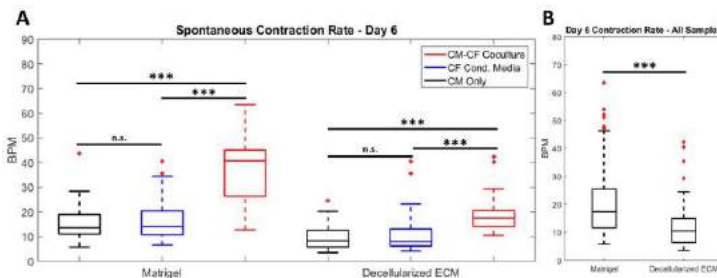


Figure 2: (A) Spontaneous contraction rate is significantly higher in the CM-CF coculture condition compared to the CM only and CF conditioned media condition on both Matrigel and decellularized ECM. (B) Spontaneous contraction rate is increased on Matrigel in comparison to decellularized ECM. (***) $p < 0.001$

DISCUSSION

While CMs are the contractile cells of the heart, CFs contribute to the structural, biochemical, mechanical, and electrical properties of the myocardium. In this work, we sought to characterize the effects of CF coculture and CF conditioned media on the mechanical function of CMs. We demonstrated that CM-CF coculture increases the maximum contractile strain achieved by CMs, matching the literature and our previous findings. We also found that media that has been conditioned by CFs, with no direct coculture, results in an increase in maximum strain, albeit at a lower magnitude. Interestingly, direct CM-CF coculture resulted in an increase in the spontaneous rate of contraction for both ECM conditions, while CF conditioned media had no effect on the rate of contraction for either ECM condition.

Taken together, these results suggest that CFs may influence CM activity and functional maturity through a mechanism that requires both paracrine signaling and direct cell-to-cell interactions. These findings may have implications in enhancing iPSC-CM maturity *in vitro*, an increasingly important goal in cardiac tissue engineering, as well as in potential future cell-free therapies *in vivo*. Future work will explore the mechanisms of the differential enhancement through characterization of the CF conditioned media and the CM-CF coculture microenvironment.

ACKNOWLEDGEMENTS

This research was funded by the University of Wisconsin-Madison, through the Karen Thompson Medhi Professorship, Graduate School, and Office of the Vice Chancellor for Research and Graduate Education (WCC). Support also provided by the National Institutes of Health (NIH), under Ruth L. Kirschstein National Research Service Award T32 HL 007936 (AS). TJK and JZ were supported for this work by NIH U01HL134764 and National Science Foundation (NSF) 1648035. This material is based upon work supported by (while serving at) the NSF (WCC). The content is solely the responsibility of the authors and does not necessarily represent the official views of the NIH nor the NSF.

REFERENCES

- [1] Camelliti, P. et al., *Cardiovascular Res*, 65(1):40-51, 2005.
- [2] MacKenna, D. et al., *Cardiovascular Res*, 46(2):257-263, 2000.
- [3] Sounders, C.A. et al., *Circ Res*, 105(12):1164-1176, 2009.
- [4] Hall, C. et al., *J Am Heart Assoc*, 10(5):e19338, 2021.
- [5] Chen, H.S. et al., *Circ Am Heart Assoc*, 120(24):2496-2508, 2009.
- [6] Zhang, J. et al., *Circ Res*, 104(4):e30-e41, 2009.
- [7] Denning, C. et al., *Biochim Biophys*, 1863(7):1728-1748, 2016.
- [8] Bedada, F.B. et al., *Stem Cell Rep*, 3(4):594-605, 2014.
- [9] Tulloch, N.L. et al., *Circ Res*, 109(1):47-59, 2011.
- [10] Ma, R. et al., *Antioxid Redox Signal*, 28(5):371-384, 2018.
- [11] Horikoshi, Y. et al., *Cells*, 8(9):1095, 2019.
- [12] Dunn, K.K. et al., *Biotechnol J*, 14(8):e1800725, 2019.
- [13] Beauchamp, P. et al., *Front Mol Biosci*, 7:14, 2020.
- [14] Zhang, D. et al., *Biomaterials*, 34(23):5813-5820, 2013.
- [15] Giacomelli, E. et al., *Cell Stem Cell*, 26(6):862-879, 2020.
- [16] Napiwocki, B.N. et al., *Physiological Rep*, 9(19):e15045, 2020.
- [17] Lian, X. et al., *Proc Natl Acad Sci*, 109(27):E1848-E1857, 2012.
- [18] Tohyama, S. et al., *Cell Stem Cell*, 12(1):127-137, 2013.
- [19] Zhang, J. et al., *Nature Communications*, 10(1):1-15, 2019.
- [20] Napiwocki, B.N. et al., *Biotech Bioeng*, 118(1):442-452, 2021.
- [21] Xing, Q. et al., *Adv Funct Mater*, 24(20):3027-3035, 2014.
- [22] Bar-Kochba, E. et al., *Exp. Mech*, 55(1):261-274, 2015.
- [23] Stempien, A. et al., *Front Bioeng Biotechnol*, 10:873531, 2022.

TOWARD GENERALIZABLE BRAIN DEFORMATION ESTIMATORS FOR HEAD IMPACTS WITH UNSUPERVISED DOMAIN ADAPTATION AND DEEP LEARNING

X. Zhan (1), J. Sun (1), Y. Liu (1), N. Cecchi (1), E. Le Flao (1), O. Gevaert (2), M. Zeineh (3), D. Camarillo (1)

- (1) Department of Bioengineering, Stanford University, Stanford, CA, USA
(2) Department of Biomedical Data Science, Stanford University, Stanford, CA, USA
(3) Department of Radiology, Stanford University, Stanford, CA, USA

INTRODUCTION

Traumatic brain injury (TBI) has become a global health threat. In 2016, over 27 million cases of TBI were reported globally [1]. The fast diagnosis and early warning approaches of TBI are significant to helping prevent repetitive sport-related TBI [2]. Physiologically, the brain is damaged because of the brain deformation resulted from the inertial movement of the brain after the head sustains an impact or suffers rapid acceleration and deceleration. Therefore, metrics of brain deformation are effective predictors of TBI. Brain strain, particularly the maximum principal strain (MPS) and MPS rate (MPSR), has been shown to correlate with TBI pathologies [3-5]. To calculate MPS and MPSR, the state-of-the-art approach, finite element modeling (FEM), can take hours to model one impact. Recently developed machine learning head models (MLHMs) trained on large quantities of simulated impacts or lab-reconstructed impacts, in contrast, can substantially reduce the computational cost [6-8].

Despite their superiority in the computational time, MLHMs are often biased towards data similar to the distribution of their training data, which can vary with the type of the impact (i.e., football impacts, car crash impacts) [9]. The dependence on training data distribution raises the issue of generalizability across datasets. For example, in our previous study, a promising prediction accuracy was found using a simulation dataset of 2,130 impacts, and the accuracy decreased when the model was applied to the combined datasets of simulation impacts and the on-field impacts (college football (CF, size of 302) or mixed martial arts (MMA, size of 457)) [9]. The reason for the decreasing accuracy was the remarkably different data distribution in different contact sports [10]. To address this problem, transfer learning has been applied and successfully reduced the MPS and MPSR estimation errors. However, transfer learning requires labeled data (FEM-computed reference MPS and MPSR for the kinematics are required to fine-tune the deep learning models) of a particular type of head impacts, which are typically not available to the user [11]. In this study, to improve the

brain strain estimation across types of head impacts without labeled data, we perform unsupervised domain adaptation by establishing mapping between domains represented by different datasets, including the simulation dataset and two different on-field datasets, or from these domains to a unified regularized domain, followed by brain deformation modeling with an MLHM. We compare the approach of deep-learning unsupervised domain adaptation based on the cycle-generative adversarial network (cycle-GAN) architecture with a non-deep-learning approach, domain regularized component analysis (DRCA), and attempted the approach of combining both DRCA and cycle-GAN.

METHODS

We collected a total of 13,539 samples of head impact data from diverse but representative impact types, including: 1) 12,780 laboratory head impacts simulated from a validated FEM of the Hybrid III anthropomorphic test device headform (labeled as HM for head model); 2) 302 college football head impacts recorded by the Stanford instrumented mouthguard (labeled as CF); 3) 457 MMA head impacts recorded by the Stanford instrumented mouthguard (labeled as MMA)[10]. From each sample, we extracted 510 temporal and spectral features according to four physical quantities describing the head translation and rotation: linear acceleration at the brain's center of gravity, angular velocity, angular acceleration and angular jerk. Four channels are associated with each quantity: the three anatomical axes (x: posterior-to-anterior, y: left-to-right, z: superior-to-inferior) and the magnitude. Feature extraction details are shown in [11]. The reference MPS and MPSR are computed with a validated finite element head model: the KTH finite element model (Stockholm, Sweden) [12], which modeled the human brain with 4,124 brain elements. We firstly developed the baseline deep neural networks to estimate MPS and MPSR based on dataset HM, as in our previous studies [10,11].

Then, to compensate for the data distribution drift (also known as domain drift in machine learning), we applied two types of unsupervised domain adaptation approach: the DRCA and cycle-GAN. The convex-

optimization-based DRCA looks for a projection hyper-plane (i.e., the domain-invariant feature subspace) on which the difference between the projected source domain (the dataset HM) and target domain (the dataset CF/MMA) is minimized while the within-domain variance is maximized [13]. The linear projection matrix was found by the optimization of constrained Rayleigh Quotient [13]. Upon projecting the data onto the hyper-plane, deep-learning MLHMs are developed on the features along the projection hyper-plane.

Alternatively, we used the deep-learning approach for domain adaptation: mapping on-field data to the domain of the HM dataset before prediction of brain deformation via cycle-GAN [14]. To further address the potential domain drift from the real data and the cycle-GAN-generated data, we performed the Kernel Means Matching (KMM, also referred as shift-GAN) or the DRCA on the top of the cycle-GAN, which are compared against the cycle-GAN alone, the DRCA method, and the baseline without any domain adaptation. The model development and evaluation processes are visualized in Fig. 1.

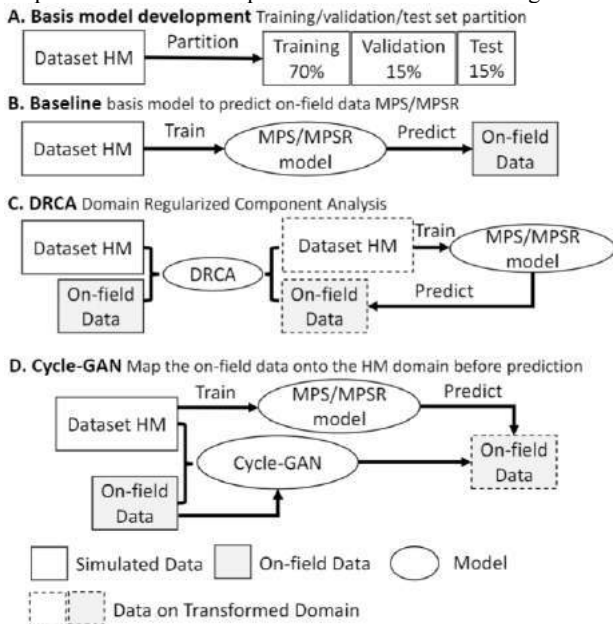


Figure 1: The pipeline of the model development and evaluation. The pipeline consists of a deformation prediction model and domain adaptation models with DRCA or cycle-GAN. On-field data: CF or MMA.

RESULTS

To evaluate the model performance, the brain-element-wise prediction error in MPS and MPSR were calculated and shown in Fig. 2. The DRCA method outperformed all the competing methods with the smallest prediction errors in both the MPS prediction and MPSR prediction, on both dataset CF and dataset MMA. The DRCA method significantly reduced the MPS/MPSR prediction error when compared with the baseline approach without any domain adaptation ($p < 0.001$, Wilcoxon signed-rank test). Furthermore, the DRCA method enables significantly more accurate predictions when compared with three cycle-GAN-based methods ($p < 0.001$, Wilcoxon signed-rank test). To quantify the overall accuracy of the prediction and compare with the previous study which reported model accuracy on simulated head impacts [11], we computed the mean absolute error (MAE) of MPS over all brain elements and then calculated the mean over all test impacts. For the MPS prediction, the DRCA method reduces the mean MAE from 0.036 to 0.017 (MPS, dataset CF), from 0.103 to 0.020 (MPS,

dataset MMA). The MAE was in the same order as that reported in our previous studies when the model (trained on the dataset HM) predicts the test impact from dataset HM (MAE: 0.015), on which the models were trained with the same kinematics features [11].

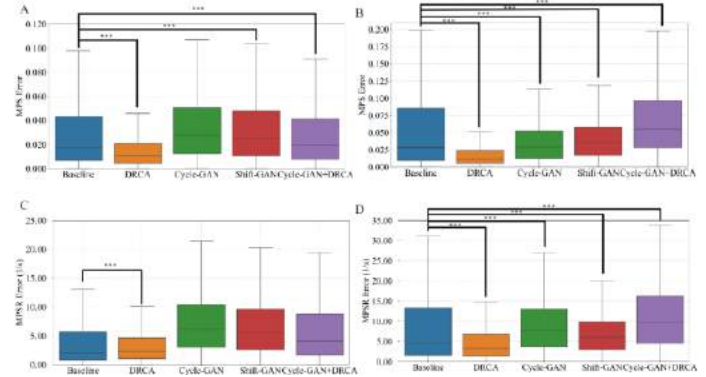


Figure 2: Absolute values of the MPS/MPSR prediction error over all the brain elements and test impacts. The prediction error of MPS on dataset CF (A) and MMA (B). The prediction error of MPSR on dataset CF (C) and (D). (*: $p < 0.001$)**

DISCUSSION

The lack of generalizability in MLHMs hinders their application in TBI detection due to the data distribution drifts in different impact datasets. In this work, we are the first to propose a generalizable brain deformation estimator that integrates domain adaptation with a deep-learning brain deformation prediction network. To perform domain adaptation, we apply either a cycle-GAN-based architecture or a non-deep-learning method, DRCA, and find that although both methods reduce the prediction error, DRCA achieves a substantially higher accuracy as quantified by the mean absolute error of the brain deformation field estimation. Our results indicate that domain adaptation can improve the accuracy of brain deformation estimation for different types of on-field head impact data to be in the same order of accuracy on the simulated head impacts, and therefore, this study address the generalizability problem of MLHMs without labeled data. As a derivative of MLHM, this study significantly enables fast and accurate brain deformation estimation for TBI detection in potential clinical applications and for better protection of soldiers, contact-sports players and motorists who are frequently at risk of sustaining TBIs.

ACKNOWLEDGEMENTS

This research was supported by the Pac-12 Conference's Student-Athlete Health and Well-Being Initiative, the National Institutes of Health (R24NS098518), Taube Stanford Children's Concussion Initiative and Stanford Interdisciplinary Graduate Fellowship.

REFERENCES

- [1] James, S. *et al. Lancet Neur.* 18(1):56-87 (2016).
- [2] Guiza, F. *et al. Neurosurgery.* 45(3):e316-e320 (2017).
- [3] Wu, T. *et al. J. Neurotrauma.* 38(13): 1879-1888 (2021).
- [4] Hajiaghamemar, M. *et al. J. Neurotrauma.* 38(1):144-157 (2021).
- [5] Ji, S. *et al. Ann. Biomed. Eng.* 1-20 (2022).
- [6] Ghazi, K. *et al. J. Neurotrauma.* 38(8):1023-1035 (2021).
- [7] Wu, S. *et al. Sci. Rep.* 9(1):1-11 (2019).
- [8] Wu, S. *et al. Comput. Methods in Appl. Mech. Eng.* 394 (2022).
- [9] Zhan, X. *et al. J. R. Soc. Interface.* 18(179):20210260 (2021).
- [10] Zhan, X. *et al. IEEE Trans. Biomed. Eng.* 68(11):3424-3434 (2021).
- [11] Zhan, X. *et al. arxiv:* 2108.13577 (2021).
- [12] Kleiven, S. *et al. SAE Tech. Pap.* (2007).
- [13] Wang, H. *et al. IEEE Trans. Instrum. & Meas.* 71: 11 (2022).
- [14] Sanabria, A. *et al. IEEE Access.* 9:19421-19438 (2021).

NON-ENZYMATIC GLYCATION STRENGTHENS ANNULUS FIBROSUS THROUGH CROSSLINKS ALIGNED WITH PRIMARY COLLAGEN FIBERS

Minhao Zhou* (1), Erin Archibeck* (1), Yarah Feteih (1), Yousuf Abubakr (1),
Grace D. O'Connell (1, 2)

*: These authors contributed equally to this work

(1) Department of Mechanical Engineering, University of California, Berkeley
Berkeley, CA, United States

(2) Department of Orthopaedic Surgery, University of California, San Francisco
San Francisco, CA, United States

INTRODUCTION: The annulus fibrosus (AF) in the intervertebral disc is a fiber-reinforced tissue consisting of collagen fibers embedded in a proteoglycan-rich extracellular matrix, resulting in great load-bearing and energy absorption capacities. However, due to the disc's avascularity, the AF is susceptible to catabolic remodeling with disease and degeneration, causing debilitating back pain and disability.¹⁻² Diabetes mellitus, a prevalent metabolic disorder that has been shown to cause or aggravate irreversible disc tissue damage, is a significant risk factor low back pain.³⁻⁶ A well-documented diabetes-induced AF structural change is the accumulation of advanced glycation end-products (AGEs), which can form irreversible covalent crosslinks with AF collagens due to their slow biological turnover and long half-life.⁷⁻⁸ Understanding AF structure-function relationships with diabetes-induced non-enzymatic glycation (i.e., AGEs) can provide insight into tissue failure mechanisms, which is pivotal for developing injury prevention measures and effective therapeutic interventions.

Previous studies reported an increased AF stiffness and toughness with non-enzymatic glycation.⁹⁻¹⁰ Our recent work examined AF uniaxial tensile mechanics at physiologically relevant AGEs levels and observed significantly increased tensile modulus and failure stress in circumferential-axial (circ-ax) samples (Fig. 1A).¹¹ Thus, how diabetes increases or accelerates AF tissue mechanical failure remains unclear.

Crosslinking schematics with AGEs are still unclear due to experimental limitations.¹² Finite element models (FEMs) are a valuable tool for predicting stress-strain distributions in complex tissue structures. We recently developed and validated a robust multiscale structure-based FEM framework for the disc. Tissue-level FEMs were able to accurately predict multiscale AF mechanics under different loading configurations (e.g., uniaxial and biaxial tension, simple shear) and specimen geometries.¹³⁻¹⁴ Thus, the objectives of this study were to: (1) examine the effect of AGEs on AF uniaxial tensile mechanics in loading directions with less fiber engagement, and (2) to expand our FEM framework to describe AF mechanics with non-enzymatic glycation.

METHODS: *Experimental:* Bovine caudal discs were dissected from mature coccygeal spines. Circumferential-radial (circ-rad) and radial samples were prepared using a freezing stage microtome to obtain 2 mm-thick rectangular specimens. The lengths of circ-rad and radial specimens were ~10 and ~5 mm; specimen widths were ~5 mm for both orientations. For repeatable midlength failure, a 1-mm full-width notch was created using a custom-made cutting jig in the thickness direction for circ-rad specimens.¹⁵ Radial specimens exhibited limited grip failure during preliminary testing and were thus unnotched (Fig. 1A).

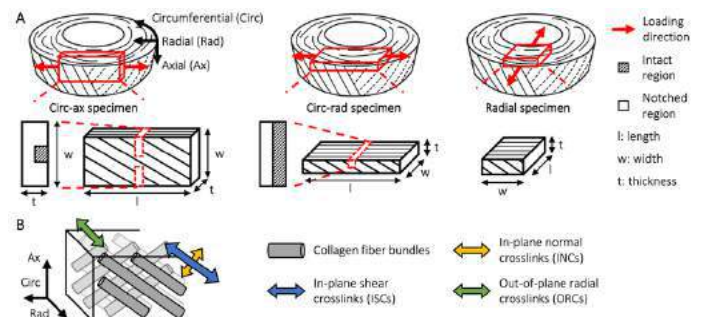


Fig. 1: (A) Specimen orientation, loading direction, and notch geometry. **(B)** Model schematics demonstrating possible crosslinking mechanisms.

AF specimens were prepared at three physiologically relevant glycation levels (18 hr soak). Control samples were soaked at 25 °C in a SPEG5 solution to minimize excessive swelling (CTRL, $n_{\text{circ-rad}} = 15$, $n_{\text{radial}} = 7$).¹⁶ Glycated samples were soaked in 0.3 M methylglyoxal pH-balanced to 7.4 at 25 °C (GLY25, $n_{\text{circ-rad}} = 15$) or 50 °C (GLY50, $n_{\text{circ-rad}} = 15$, $n_{\text{radial}} = 7$). Samples were gripped with custom-made clamps and tested in SPEG5 to maintain hydration. Quasi-static monotonic uniaxial tension was applied at 0.1 mm/min until failure. Linear-region modulus, failure stress, and failure strain were evaluated for specimens that failed at midlength post-testing. AGE content was also measured.

Computational: The multiscale structure-based FEM framework previously developed and validated for the AF was adapted to describe crosslinks within the extrafibrillar matrix with model geometries determined using experimental samples.¹¹ Non-enzymatic crosslinks, whose orientations are still unknown, were described in three possible directions, including crosslinks parallel to collagen fibers (in-plane shear crosslinks, ISCs), crosslinks perpendicular to collagen fibers (in-plane normal crosslinks, INCs), and out-of-plane radial crosslinks (ORCs, Fig. 1B). All crosslink components were modeled as directional homogeneous interfibrillar reinforcements with identical mechanical properties. A higher AGE content was assumed to generate denser AGEs compounds per unit volume, leading to a larger overall crosslink stiffness. Crosslink modulus was calibrated by comparing model-predicted bulk AF tensile modulus to experimental data; other model parameters were directly linked to reported AF physical or biochemical properties.¹³ Simulated boundary and loading conditions replicated those of experiments. Multivariate linear regression was conducted based on a parametric group of FEMs with varying crosslink modulus to estimate the relative contribution of crosslink modulus to the increase in bulk AF tensile modulus with non-enzymatic glycation.

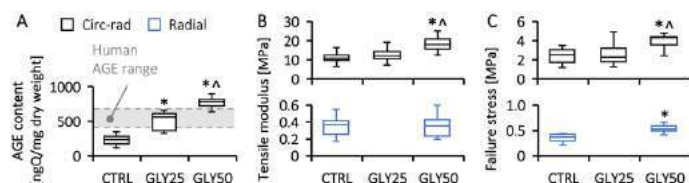


Fig. 3: (A) AGE content, (B) modulus, and (C) failure stress at each glycation level. *: $p < 0.05$ vs CTRL; ^: $p < 0.05$ vs GLY25.

RESULTS: Experimental: 51/59 specimens experienced midlength failure and exhibited a nonlinear stress-strain response. AGEs content normalized by dry weight increased by 95% in GLY25 and 206% in GLY50 samples ($p < 0.001$ vs CTRL; Fig. 3A). For circ-rad specimens, non-enzymatic glycation increased linear-region modulus and failure stress by 62% (18.13 vs 11.22 MPa; $p < 0.001$) and 60% (4.09 vs 2.55 MPa; $p < 0.01$) in GLY50 samples. For radial specimens, AGEs did not increase tissue modulus but increased failure stress by 42% (0.54 vs 0.38 MPa; $p = 0.04$; Fig. 3B-C). Failure strain was not affected by the non-enzymatic glycation treatment in both directions.

Computational: Preliminary FEMs predicted that ORCs could result in a 10 to 100× increase in AF radial tensile modulus. However, experimental work showed that AF radial modulus did not increase with glycation (Fig. 3B). Thus, ORCs were excluded from the model.

Model predictions agreed well with experiments when the crosslink modulus was 12.5% and 25% of collagen fibers in GLY25 and GLY50 specimens, respectively (7.5 and 15 vs 60 MPa). For circ-ax specimens, model-predicted linear-region modulus were 25.2, 38.4, and 48.7 MPa for CTRL, GLY25, and GLY50 samples, respectively ($< 0.35\times$ standard deviation (std) from experimental means; Fig. 4A).¹¹ Model-predicted linear-region modulus were 8.7, 13.0, and 17.3 MPa for CTRL, GLY25, and GLY50 circ-rad samples, respectively. Model predictions were within $0.8\times$ std from experimental means except for Werbner et al. (8.7 vs 11.3 ± 1.8 MPa; Fig. 4A).¹⁷ Model-predicted tensile modulus was 0.38 MPa for both CTRL and GLY50 radial specimens ($< 0.23\times$ std from the experimental means; Fig. 4A).

Models with only ISCs or INCs greatly underestimated AF linear-region modulus for circ-ax and circ-rad GLY50 specimens (Fig. 4B). Thus, ISCs and INCs were both required to accurately describe the effect of non-enzymatic glycation. Multivariate linear regression suggested that the increase in AF circumferential tensile modulus with glycation was more sensitive to ISC modulus than INC modulus.

Particularly, ISC and INC modulus contributed $\sim 90\%$ and $\sim 10\%$ to the increase in tensile modulus for both circ-ax and circ-rad specimens.

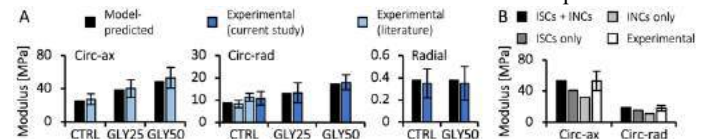


Fig. 4: Model-predicted (A) tensile modulus in three specimen orientations and (B) GLY50 sample tensile modulus with different crosslinking schematics vs experimental data (mean \pm std).^{11, 15, 17}

DISCUSSION: Non-enzymatic glycation modifies AF collagen structure via crosslinking. The current study found that glycation increased AF tensile modulus and failure stress without affecting failure strain. These findings agreed with previous studies for circ-ax samples,⁹⁻¹¹ indicating that AGEs accumulation is unlikely to cause premature tissue failure by adversely affecting AF quasi-static monotonic uniaxial tensile mechanical properties. However, tendon studies have reported a significantly reduced tissue viscoelasticity (i.e., energy dissipation capabilities) with AGEs,¹⁸⁻¹⁹ suggesting that non-enzymatic glycation with diabetes could cause premature disc failure by compromising tissue performance under dynamic, especially fatigue loading.

Observations from the current study indicated that non-enzymatic crosslinks had a larger effect along the primary collagen fiber direction. Particularly, glycation did not stiffen the AF in the radial direction. Model predictions also showed that including out-of-plane radial crosslinks led to unrealistically high radial tensile modulus, suggesting that interlamellar crosslinks, most likely through elastic fibers,²⁰ were not probable. Furthermore, glycation had a greater effect in directions with more fiber engagement. With GLY50 treatment, AF tensile modulus increased by $\sim 100\%$ in circ-ax specimens but by only $\sim 60\%$ in circ-rad samples ($p < 0.001$ for both orientations).¹¹ Multivariate linear regression suggested that the increase in bulk AF tensile modulus was more sensitive to the mechanics of in-plane shear crosslinks aligned with collagen fibers. These findings agreed with previous tendon studies, where AGEs treatment increased tendon uniaxial tensile modulus along the fiber direction by $\sim 100\text{--}400\%$.^{12, 21} Our findings also agreed with a previous quantitative imaging study, which showed that collagens were more responsive to AGEs formation than interlamellar elastic fibers, which are mainly oriented in the radial direction.^{20, 22}

FEMs in the current study accurately and robustly predicted AF uniaxial tensile mechanics with AGEs. Since collagen mechanics were not altered in the glycated FEMs, model predictions indicated that glycation could strengthen bulk AF without stiffening individual collagen fibers or fibrils, which remains a debate in the field.¹²

Determining the effect of non-enzymatic glycation on AF mechanics plays a pivotal role in understanding diabetes as a risk factor for tissue injury, which is essential for developing preventive measures and therapeutic interventions for low back pain. Adding to previous literature, the current study showed that AGEs did not compromise AF monotonic quasi-static uniaxial tensile mechanical properties. The proposed FEM framework also provided a powerful tool for examining multiscale AF mechanics with disease and degeneration. Future work aims to examine the effect of glycation on AF damage accumulation.

ACKNOWLEDGEMENTS: The work was supported by the National Science Foundation (BMMB 1760467).

REFERENCES: [1] Adams+, *Spine*, 2006; [2] Vergroesen+, *Osteoarthritis Cartilage*, 2015; [3] Hoy+, *Arthritis Rheumatol*, 2012; [4] Zhou+, *Lancet*, 2016; [5] Jhawar+, *Spine J*, 2006; [6] Liu+, *J. Orthop Surg Res*, 2018; [7] Vlassara+, *J Intern Med*, 2002; [8] Verzijl+, *JBC*, 2000; [9] Wagner+, *J Biomech*, 2006; [10] Chuang+, *Clin Biomech*, 2007; [11] Werbner+, *JMBBM*, 2022a; [12] Svensson+, *Acta Biomater*, 2018; [13] Zhou+, *BMMB*, 2020; [14] Zhou+, *JMBBM*, 2021; [15] Werbner+, *J Biomech Eng*, 2017; [16] Werbner+, *JMBBM*, 2022b; [17] Werbner+, *J Biomech*, 2019; [18] Li+, *Matrix Biol*, 2013; [19] Gautieri+, *Matrix Biol*, 2017; [20] Tavakoli+, *Acta Biomater*, 2017; [21] Reddy+, *Arch Biochem*, 2017; [22] Tseng+, *Biomed Opt Express*, 2010

A MODULAR FRAMEWORK FOR STRONG 3D/0D COUPLING IN CARDIAC MECHANICS SIMULATIONS

Aaron L. Brown (1), Zinan Hu (1), Alison L. Marsden (1,2)

(1) Department of Mechanical Engineering, Stanford University, Stanford, CA, USA
(2) Departments of Pediatrics and Bioengineering, Stanford University, Stanford, CA, USA

INTRODUCTION

In numerical simulations of cardiac mechanics, the circulatory system, which is typically represented with a 0D lumped-parameter model, is important for capturing the physiological behavior of the heart. Due to the strong *physical* coupling between the heart and the circulation, accurate and efficient *numerical* coupling methods remain an active area of research [1,2,3]. In this work, we present a modular, strong coupling framework for coupling a 3D mechanical (fluid or structural) simulation of the heart to a 0D fluid model of the circulation. “Modular” denotes that we take advantage of separate, preexisting 3D and 0D solver codes, which operate independently except for communication of select information during the iterative solution. We demonstrate that fluid models (e.g., blood flow in the aorta) and structural models (e.g., contracting left ventricular myocardium) can be coupled to a 0D circulation model in a uniform manner. The present coupling is a generalization of the 3D fluid – 0D fluid coupling of [4] to a 3D structure – 0D fluid coupling. Interestingly, that coupling, as well as the present work, was found to be an application of the Approximate Newton Method (ANM) [5]. This connection provides a rigorous mathematical basis and proven convergence results for our coupling algorithm, both of which were lacking in [4].

METHODS

The 3D fluid or structure equations are discretized in space with the finite element method and discretized in time with the generalized-alpha method. This results in a system of nonlinear equations to be solved at the unknown time step $n + 1$

$$\mathbf{R}^{3D}(\Phi_{n+1}) = \mathbf{0}, \quad (1)$$

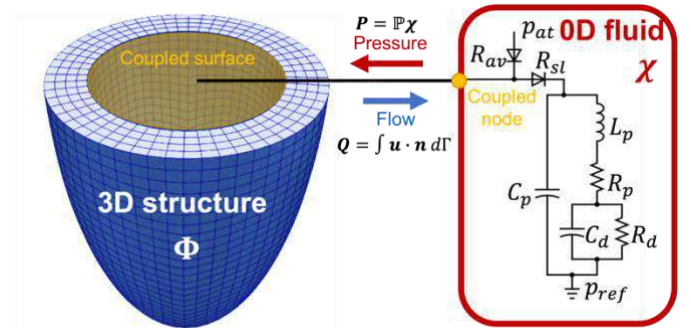


Figure 1: Schematic showing an idealized left ventricle (3D structure) coupled to an open-loop lumped-parameter model of circulation (0D fluid). The 3D state vector is Φ while the 0D state vector is χ . The 0D imposes a pressure (Neumann) boundary condition on the 3D coupled surface, while the 3D imposes a flow (Dirichlet) boundary condition on the 0D coupled node.

where \mathbf{R}^{3D} is called the 3D residual and is a function of the 3D state vector Φ at the unknown time step $n + 1$. Φ in general, contains the nodal degrees of freedom of the finite element model.

Blood flow in the circulatory system (not including the heart) is modeled using a lumped-parameter network (LPN), following common practice in the field. This amounts to a 0D model of blood flow, described only by pressure and flowrate. This model yields a system of nonlinear ODEs, which upon application of a suitable time-stepping scheme yields a system of nonlinear equations,

$$\mathbf{R}^{0D}(\chi_{n+1}) = \mathbf{0}, \quad (2)$$

where \mathbf{R}^{0D} is the 0D residual and is a function of the 0D state vector χ at the unknown time step $n + 1$. χ in general, contains the pressure and flowrate at and into each node, respectively.

The 3D and 0D models are coupled in that they impose boundary conditions on each other, as follows. The pressure imposed on a coupled surface of the 3D model is taken as the pressure at the corresponding coupled node of the 0D model (see Figure 1). Analogously, the flow rate imposed on a coupled node of the 0D model is taken as the flow rate through the corresponding coupled surface of the 3D model. Mathematically, this means that the 3D residual \mathbf{R}^{3D} is also a function of the 0D variables χ through the coupling pressure \mathbf{P} . Likewise, the 0D residual \mathbf{R}^{0D} is also a function of the 3D variables Φ through the coupling flow rate \mathbf{Q} . Thus, in the time-discrete setting, the coupling problem reduces to a coupled system of nonlinear algebraic equations

$$\begin{cases} \mathbf{R}^{0D}(\chi_{n+1}, \mathbf{Q}_{n+1}(\Phi_{n+1})) = \mathbf{0} \\ \mathbf{R}^{3D}(\Phi_{n+1}, \mathbf{P}_{n+1}(\chi_{n+1})) = \mathbf{0} \end{cases} \quad (3)$$

Solving these two nonlinear equations simultaneously via Newton's method yields the monolithic system

$$\begin{bmatrix} \frac{\partial \mathbf{R}^{0D}}{\partial \chi} & \frac{\partial \mathbf{R}^{0D}}{\partial \Phi} \\ \frac{\partial \mathbf{R}^{3D}}{\partial \chi} & \frac{\partial \mathbf{R}^{3D}}{\partial \Phi} \end{bmatrix}_{n+1} \begin{bmatrix} \Delta \chi \\ \Delta \Phi \end{bmatrix} = - \begin{bmatrix} \mathbf{R}^{0D} \\ \mathbf{R}^{3D} \end{bmatrix}_{n+1}^{(k)} \quad (4)$$

Performing Schur Complement Reduction yields an equivalent system

$$\begin{bmatrix} \frac{\partial \mathbf{R}^{0D}}{\partial \chi} & \frac{\partial \mathbf{R}^{0D}}{\partial \Phi} \\ \mathbf{0} & \frac{\partial \mathbf{R}^{3D}}{\partial \Phi} - \frac{\partial \mathbf{R}^{3D}}{\partial \chi} \left(\frac{\partial \mathbf{R}^{0D}}{\partial \chi} \right)^{-1} \frac{\partial \mathbf{R}^{0D}}{\partial \Phi} \end{bmatrix}_{n+1} \begin{bmatrix} \Delta \chi \\ \Delta \Phi \end{bmatrix} = - \begin{bmatrix} \mathbf{R}^{0D} \\ \mathbf{R}^{3D} - \frac{\partial \mathbf{R}^{3D}}{\partial \chi} \left(\frac{\partial \mathbf{R}^{0D}}{\partial \chi} \right)^{-1} \mathbf{R}^{0D} \end{bmatrix}_{n+1}^{(k)} \quad (5)$$

We point out that the effect of the 0D model is to modify the 3D equation with particular tangent and residual contributions. In this work, borrowing ideas from [5, 6], Eq. 5 is solved in an approximate and modular manner using separate 0D and 3D solvers, with proper communication of pressure \mathbf{P} and flow rate \mathbf{Q} between the two. This involves approximating the 0D contributions in a finite difference manner. Communication between 0D and 3D solvers is required each Newton iteration, as shown in Figure 2.

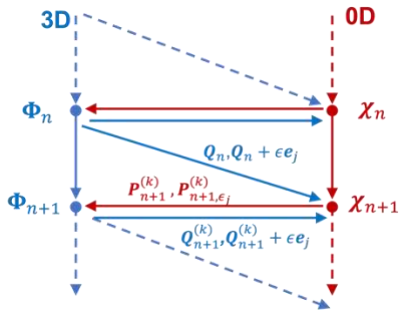


Figure 2: Communication scheme between 3D and 0D solvers [4]. Pressure and flow rate are communicated every Newton iteration.

RESULTS

Figure 3 shows a pressure-volume (PV) loop obtained by coupling an idealized left ventricle (LV) structural model to a 0D circulation model (Figure 1). We model the contracting myocardium using an active stress approach with a prescribed temporal profile. As seen in the figure, we obtain a realistic pressure-volume loop. In particular, the four cardiac phases – isovolumic contraction, ejection, isovolumic relaxation, filling – are easily identified.

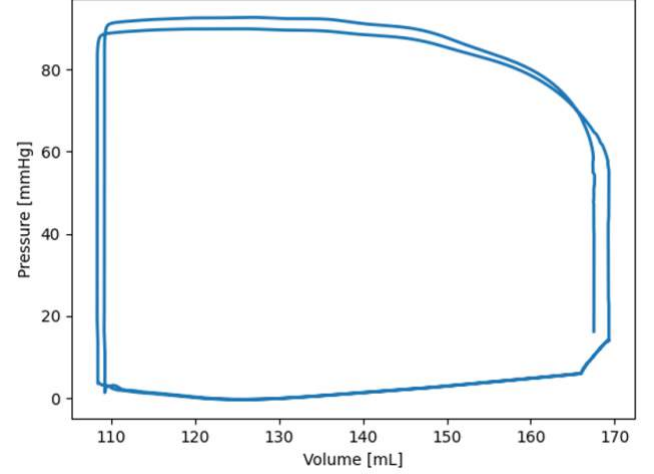


Figure 3: PV loop obtained by coupling a structure simulation of an idealized left ventricle with active stress to a 0D circulation model (as shown in Figure 1).

DISCUSSION

Compared to an uncoupled 3D simulation, our coupling additionally requires evaluating the 0D solver each Newton iteration. In our application, the 0D solver is far cheaper to evaluate than the 3D solver, so this presents a minimal extra cost. In addition, the present coupling method retains the quadratic convergence of Newton's method, as proven by [5]. We do not require the additional volume constraint (for structure solver) nor the ad hoc stabilization found in the partitioned coupling strategies of [1,2,3]. Finally, we reiterate that the coupling uniformly treats a 3D fluid – 0D fluid coupled system and a 3D structure – 0D fluid coupled system. To our knowledge, none have previously pointed out the equivalence between fluid and structure in the context of this cardiovascular coupling problem.

ACKNOWLEDGEMENTS

The authors would like to thank National Institutes of Health (R01HL129727) and the National Science Foundation (1663671) for grant funding for this project, and the members of the Cardiovascular Biomechanics Computation Lab at Stanford for many helpful discussions.

REFERENCES

- [1] Augustin, C.M. et al., *Comp. Meth. App. Mech. And Eng.* 386, 114092 (2021)
- [2] Regazzoni F., et al., *J. Comp. Phys.* 457, 111083 (2022)
- [3] Regazzoni F., et al., MOX report 17 (2022)
- [4] Moghadam M.E., et al., *J. Comp. Phys.* 244, 63-79 (2013)
- [5] Chan T.F., *SIAM Journal on Numerical Analysis*, 22(5), 904-913 (1985)
- [6] Matthies H.G., *Computers & structures* 81(8-11), 805-812 (2003)

POST-MORTEM CHANGES IN ANISOTROPIC MECHANICAL PROPERTIES OF BRAIN TISSUE MEASURED BY MR ELASTOGRAPHY

Shuaihu Wang (1), Charlotte A. Guertler (1), Ruth J. Okamoto (1), Curtis L. Johnson (2),
Matthew D. J. McGarry (3), Philip V. Bayly (1,4)

- (1) Mechanical Engineering & Material Science, Washington University in St. Louis, St. Louis, MO, USA
(2) Biomedical Engineering, Delaware University, Newark, DE, USA
(3) Thayer School of Engineering, Dartmouth College, Hanover, NH, USA
(4) Biomedical Engineering, Washington University in St. Louis, St. Louis, MO, USA

INTRODUCTION

Computational models of brain biomechanics are emerging as important tools to simulate traumatic brain injury (TBI) and improve methods for injury prevention, diagnosis, and treatment. These models require accurate material properties of brain tissue [1], but the mechanical behavior of the intact, living brain remains incompletely characterized, due to its complexity and inaccessibility. Most mechanical testing of brain tissue has been performed using animal tissue post-mortem (either *in vitro* or *in situ*) [2, 3], which may not necessarily reflect *in vivo* mechanical behavior [4]. Thus, understanding how brain mechanical properties change after death is important in order to correctly interpret post-mortem measurements.

Magnetic resonance elastography (MRE) provides estimates of mechanical properties non-invasively in soft tissue by imaging harmonic wave motion and inverting the full-field displacement data [5]. White matter (WM) brain tissue is structurally anisotropic, consisting of aligned neural fibers, and exhibits strongly anisotropic diffusion, so is expected to be mechanically anisotropic as well. MRE inversion has typically assumed material isotropy [5] to estimate only shear modulus and damping, but recently we have developed anisotropic (transverse isotropic) inversion [6] to also estimate shear and tensile anisotropy. The objective of this research is thus to measure anisotropic mechanical properties in the porcine brain before and after death and use MRE to characterize changes that occur post-mortem.

METHODS

Three female Yucatan minipigs (age 7-8 months, weight 21-32 kg) were scanned using a Siemens Prisma® 3T scanner. Each animal was scanned *in vivo* and immediately after death. The anesthetized minipig was positioned supine on the scanner table with head placed in the bottom half of the Siemens Head/Neck 20 coil. Shear waves in the brain were induced at a frequency of 100 Hz using a pneumatic driver (Resoundant™) and custom jaw actuator in three different

configurations, exciting both, left or right sides of the jaw. MRE imaging was performed with a 2D multishot spiral sequence with OSCILLATE acceleration [7]. Phase contrast images proportional to displacement (1.497 microns/rad) were acquired with 8 samples per period of harmonic motion; TR/TE = 4800/60 ms; FOV = 180×180×72 mm³ with 1.5 mm isotropic spatial resolution. The displacement field data were fitted to a model of rigid-body displacement to estimate rigid-body motion. Wave motion was isolated by subtracting the rigid-body motion from the total displacement field. T1- and T2-weighted anatomical MR images were also acquired at 0.8 mm isotropic resolution. Diffusion tensor imaging (DTI) was performed to estimate WM fiber direction and diffusion fractional anisotropy (FA). DTI parameters included: single-shot echo-planar imaging acquisition; 30 diffusion-weighted directions with two averages; and FOV = 192×192×72 mm³ with 1.5 mm isotropic resolution. After *in vivo* scanning was completed, the minipig was euthanized by intravenous (IV) injection of sodium pentobarbital; extension lines were used to allow IV injection while the animal is in the scanner without inducing motion between *in vivo* and *in situ* scanning. *In situ* scanning was initiated 5 minutes after heartbeat cessation was determined by pulse oximeter. Identical imaging procedures were used *in situ*. The interval between *in vivo* and *in situ* MRE scanning was ~35 min, corresponding to the time needed for euthanasia and anatomical imaging.

A transversely isotropic (TI) material model was recently incorporated into a non-linear inversion (NLI) framework [6]. TI-NLI inversion was performed using MRE displacement data from all three actuator configurations and DTI-derived fiber directions to estimate anisotropic mechanical properties of the minipig brain. The medulla, pons, and olfactory bulbs were removed from the mask prior to the estimation of material parameters since the size of these regions are relatively small compared to both the wavelengths of shear waves and the subzone size. Four parameters (baseline shear stiffness, μ_1 , damping ratio, ξ , shear anisotropy $\phi = \mu_{\parallel}/\mu_1 - 1$, and tensile

anisotropy, $\zeta = E_{\parallel}/E_{\perp} - 1$) as well as diffusion anisotropy (FA), were analyzed using a repeated-measures two-way ANOVA.

RESULTS

Figure 1 shows examples of anatomical structure, fiber direction, and wave displacement fields. The three configurations of the MRE jaw actuator imparted different types of wave motion to the brain, providing four combinations of input data for the TI-NLI algorithm. The dorsal-ventral ('V') component of wave motion is the dominant component, and the maximum displacement amplitude is about $2 \mu\text{m}$. Figure 2 displays representative TI-NLI-estimated material properties for both *in vivo* and *in situ*. The difference of baseline shear stiffness refers to ratio difference, $(\mu_{iv} - \mu_{is})/\mu_{iv}$, and difference for other three parameter, for example, $\xi_{iv} - \xi_{is}$. For baseline shear stiffness, μ_{\perp} , estimated values are generally higher after death, which is consistent with longer wavelength after death in Figure 1C, but for the damping ratio, ξ , shear anisotropy, ϕ , tensile anisotropy, ζ , estimated values appear generally lower after death.

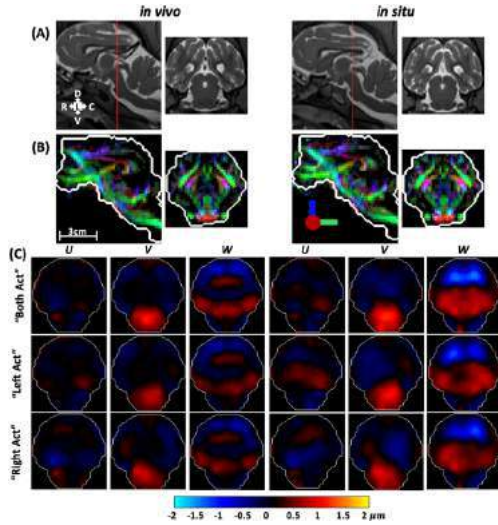


Figure 1: Example images. (A) T2-weighted image slices in sagittal and axial planes. (B) Directionally encoded DTI color map where colors (red = RL, green = RC, blue = DV) indicate direction of maximum diffusivity and brightness indicates diffusion anisotropy (FA). (C) MRE data: U, V and W wave displacement components corresponding to RL, DV, RC motion, respectively. DV: dorsal-ventral; RC: rostral-caudal; RL: right-left.

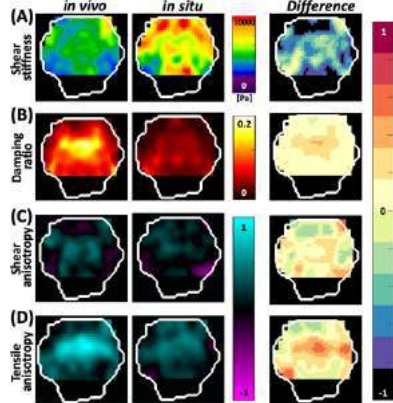


Figure 2: Mechanical properties before and after death estimated by TI-NLI and their difference for an axial slice of minipig brain in animal MP2. (A) Baseline shear stiffness (μ_{\perp}). (B) Damping ratio (ξ). (C) Shear anisotropy (ϕ). (D) Tensile anisotropy (ζ).

The means and standard deviations of the parameters in WM and GM sub-volumes for both before and after death are plotted in Figure 3. For all these four parameters, the differences between *in vivo* and *in situ* were statistically significant. The shear stiffness and diffusion anisotropy increase obviously right after death, but other parameters decrease after death. The difference between WM and GM decrease after death.

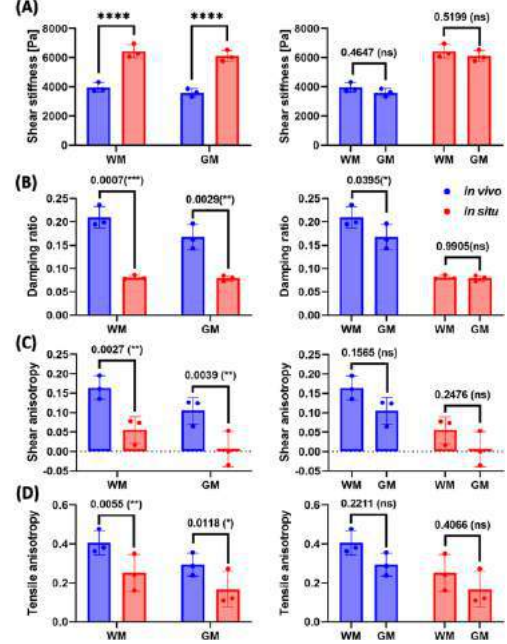


Figure 3: Mean NLI-estimated mechanical properties of WM and GM for all 3 minipigs. Each marker represents the mean value for an individual minipig at a specific age. Bars denote standard deviations. (A) Baseline shear stiffness (μ_{\perp}). (B) Damping ratio (ξ). (C) Shear anisotropy (ϕ). (D) Tensile anisotropy (ζ).

DISCUSSION

MRE measurements reveal significant mechanical anisotropy in brain tissue, both *in vivo* and post-mortem. Mechanical anisotropy arises from tissue microstructure, which is also reflected in diffusion anisotropy measured by DTI. All parameters of the anisotropic material model of brain tissue change post-mortem, some by a large fraction of their mean value *in vivo*. Baseline shear stiffness increases, damping decreases, and anisotropy (particularly tensile anisotropy) decreases post-mortem. These changes all represent important differences between the behavior of the intact, living brain and brain tissue *ex vivo*. Computer models of brain mechanics that are parameterized or evaluated using experimental data from *ex vivo* brain tissue should account for the differences in brain properties post-mortem.

ACKNOWLEDGEMENTS

This work was supported by NIH Grant R01EB027577 and ONR Grant N00014-22-1-2198.

REFERENCES

- [1] Sierra, H et al., *J Invest Dermatol*, 135:612-615, 2015.
- [2] Shen, F et al., *J Biomech Eng*, 128:797-801, 2006.
- [3] Chatelin, S et al., *Biorheology*, 47:255-76, 2010.
- [4] Gefen, A et al., *J Biomech*, 37:1339-52, 2003.
- [5] Manduca, A et al., *Med Image Anal*, 5:237-54, 2001.
- [6] McIlvain, G et al., *Magn Reson Med*, 88: 1659-1672, 2022.
- [7] McGarry, M et al., *Med Image Anal*, 78:102432, 2022.

SIMULATION OF UTERUS ACTIVE CONTRACTION AND FETUS DELIVERY IN LS-DYNA

R. Tao (1), M. Grimm (2)

(1) Department of Mechanical Engineering, Michigan State University, East Lansing, MI, US
(2) College of Engineering and Applied Sciences, University at Albany, Albany, NY, US

INTRODUCTION

Childbirth, also known as delivery or labor, is the final phase of pregnancy when one or more fetuses pass through the birth canal from the uterus and is a biomechanical process [1]. However, approximately twenty percent of labors are difficult or dysfunctional, which leads to a high risk of injuries to both the infant and the mother resulting from the stress, strain and stretch of the biological tissues or anatomical structures of the fetus and the mother during the delivery process [2].

Normal biomechanical function and regulation of the uterus is vital for childbirth. Poor quality uterine contractions contribute to many labor problems, including labor dystocia (a delay in labor progression), which has proven to be a significant reason for the rising Caesarean section rate [1]. In addition, the interaction of the uterus, the fetus, the maternal pelvis, and the vagina results in both the normal cardinal movements of labor and abnormalities of descent. Therefore, it is important to understand the mechanical process of labor and delivery so that mechanisms of injury can be more realistically investigated.

In this study, we developed an FEM model in LS-DYNA to simulate uterine active contraction, which was driven by the contractile fibers inside the uterine wall, and the fetus delivery through the birth canal.

METHODS

The geometry of the uterus was designed in NX software with a length of 35 cm, a maximum width of 15.6 cm, a thickness of 1 cm, and diameter of 10 cm at the cervix, as shown in Figure 1a. The fetus model included head, neck and body (Figure 1a). Meshing was done in Hypermesh software using hexahedral elements (Figure 1b), which was then exported to LS-DYNA. Each element was bonded with truss beam elements. These beams were assigned to seven regions in LS-DYNA (Figure 1c). These beams were used to provide the contraction force based on the Hill material model [3] (MAT_156 in LS-DYNA). The activation curves for the seven beam regions were assumed as shown in

Figure 1d, based on uterine physiologic behavior [4]. The solid portion of the uterus, representing the non-contractile portions of the tissue, was modeled as a hyperelastic material with a Neo Hookean model ($c1 = 0.07$ MPa) [5].

The bony pelvis and fetus were modeled as rigid bodies. The pelvic muscle floor, rectum, and vagina were modeled as hyperelastic materials with a Mooney Rivlin model ($c1 = 0.026$ MPa, and $c2 = 0.014$ MPa) [6]. For the boundary conditions, the cervix and the bony pelvis were fixed in x, y, and z translation directions in space. The nodes connecting the pelvic soft tissues and the bony pelvis as well as the nodes on the top edge of the vagina were also fixed in all translation directions. No external loads were applied.

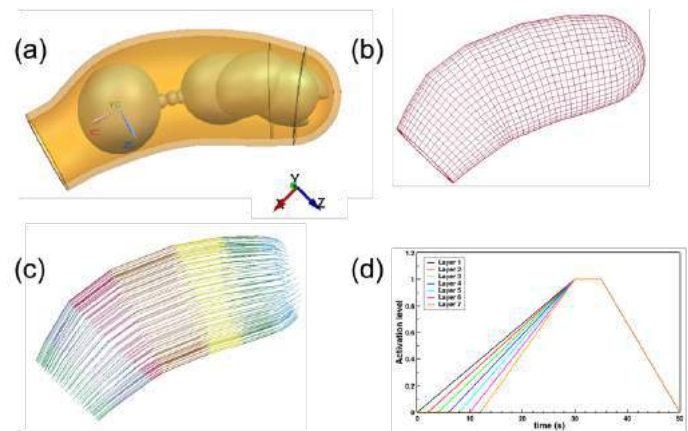


Figure 1: Modeling details: (a) uterus and fetus geometry; (b) meshwork; (c) seven regions of contractile beams; and (d) activation level curves.

RESULTS

The simulation results showing contraction of the uterus are shown in Figure 2. At $t = 0$ s, there was no deformation (Figure 2a). After that, the uterus started to contract from the fundus region and the contraction wave started to propagate to the lower part. By $t = 5$ s, the first three regions had started to contract, and the largest effective strain was 32.0% at the top of the fundus area (Figure 2b). By $t = 10$ s, the contraction wave had propagated to the first five regions. The largest strain was 51.4% (Figure 2c). By $t = 15$ s, all of the regions had started to contract, and the largest strain was 68.4% (Figure 2d). The entire uterus continued to contract until 22 s, when the largest strain was 94.5%.

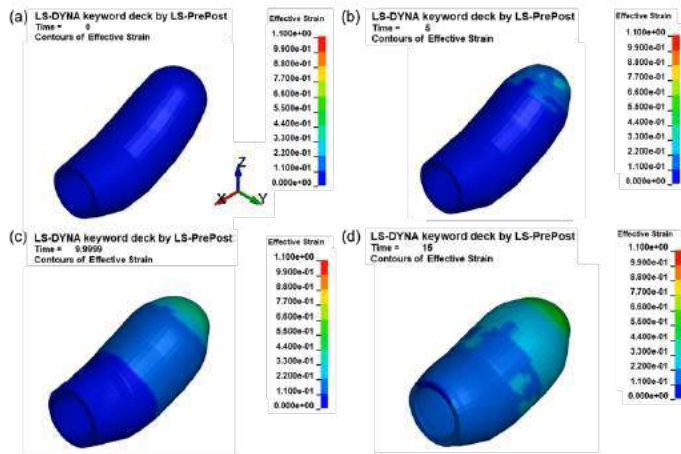


Figure 2: Representation of the deformation for the uterus at times of (a) 0 s, (b) 5 s, (c) 10 s, and (d) 15 s.

The simulation results for the pelvic soft tissue structures are shown in Figure 3. The pelvic muscle floor had no deformation until the fetus contacted with the structure (Fig 3a). At time = 10 s, the largest strain of the pelvic muscle floor was 23.6% (Fig 3b). As the fetus continued to move forward, the strain of the pelvic muscle floor and vagina became much larger. At time = 15 s, the largest strain was 77.9% (Fig 3c). At time = 20 s, the fetal head filled the vagina, and the largest strain was 213.8%, occurring in the contact surface (Fig 3d) between the fetus head and the vagina. At time = 22 s, the fetal head was out of the vagina. The strain started to drop, with a maximum value of 52.6%.

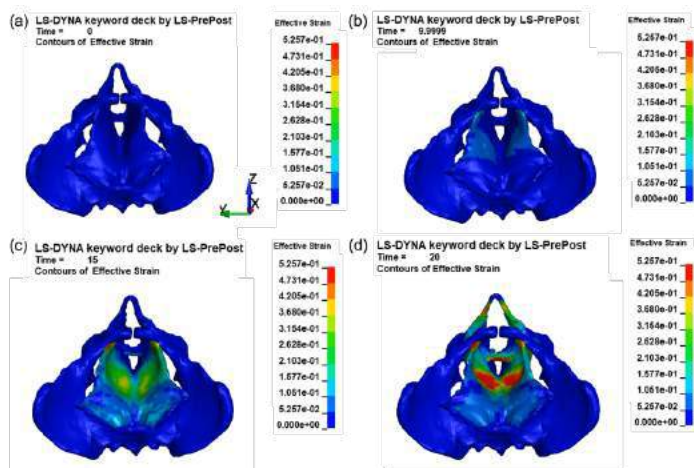


Figure 3: Representation of the deformation for the uterus at times of (a) 0 s, (b) 5 s, (c) 10 s, and (d) 15 s.

The simulation result of the fetal displacement with time is shown in Figure 4. The fetus started to move at time = 2 s, when the uterus' fundal region contracted and contacted with the fetus. The contraction of the uterus pushed the fetus to move forward through the pelvic structures and the vagina. Since this fetus was modeled as a rigid body, no deformation occurred to the fetus during the delivery process. The fetus rotated clockwise as it moved through the birth canal. The velocity of the movement was almost a constant from the beginning of the fetus' motion to time = 21 s. After that, there was a sudden acceleration of the fetus' movement, and the fetal head was delivered at 22 s. The overall displacement of the fetus during the delivery process was about 320 mm.

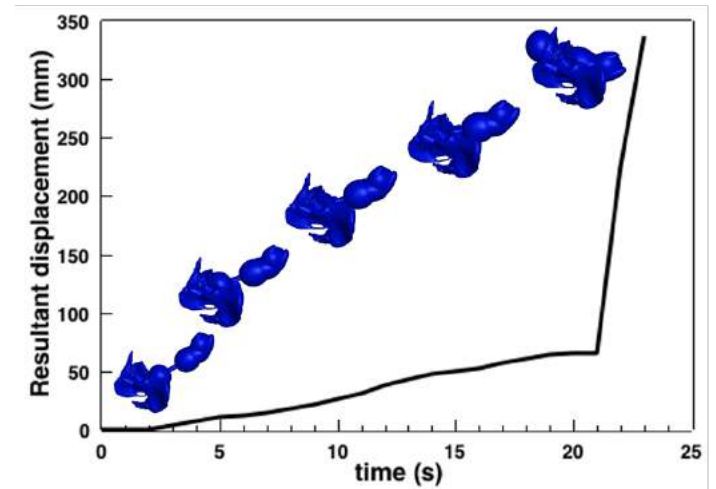


Figure 4: Representation of the deformation for the uterus at times of (a) 0 s, (b) 5 s, (c) 10 s, and (d) 15 s.

DISCUSSION

In this study, we developed a FEM model to simulate the uterine active contraction and fetus delivery. The fetus in our current model was modeled as a rigid body. However, in order to investigate the mechanisms of injuries to the fetus during the labor, especially brachial plexus injury, the fetus has to be modeled as a deformable structure, and the nerves inside the neck of the fetus will also need to be modeled. This work is currently being conducted within our group.

We recognize that we are currently modeling a single contraction to deliver the fetus. We are currently working to simulate the second stage of labor more accurately, so that multiple contractions bring the fetus through the pelvis and birth canal.

In addition, this uterus model is not linked to the cellular level models to study how cell-level electrical, chemical, and mechanical behaviors influence tissue and organ-level behaviors. However, such cellular-level models could be incorporated into the Hill muscle model to develop a new multi-scale constitutive model in the future.

ACKNOWLEDGEMENTS

This project was supported by NSF Award CBET-2028474.

REFERENCES

- [1] Alrubaii, B, *Med J of Babylon*, 2(1), 2005.
- [2] Myers, K., *Systems Biol Med*, 9(5):e1388, 2017.
- [3] Hill, V., *Proc Royal Soc London. Series B-Biol Sci*, 126(843):136,1938.
- [4] Caldeyro-Barcia, R., *Triangle*, 2:41–52, 1955.
- [5] Buttin, R, *Comp Meth Prog Biomed*, 111(2):389, 2013.
- [6] Silva, M.E.T., *Comp Meth Biomech BME*, 20(8): 842, 2017.

DEVELOPMENT OF A NOVEL HAND WORN SENSOR FOR OBJECTIVE ASSESSMENT OF HAND DEXTERITY IN NEURODEGENERATIVE CONDITIONS

Conor D. Hayden (1,2,4), Deirdre Murray (4,5), Dara Meldrum (4), Dermot Geraghty (2), Orla Hardiman (4,5), Bruce P. Murphy (1,2,3)

(1) Trinity Centre for Biomedical Engineering, Trinity College Dublin, Ireland

(2) Department of Mechanical, Manufacturing and Biomedical Engineering, Trinity College Dublin, Ireland

(3) Advanced Materials and Bioengineering Research Centre (AMBER), Trinity College Dublin, Ireland

(4) Academic Unit of Neurology, Trinity Biomedical Sciences Institute, Trinity College Dublin, Ireland.

(5) Neurocent Directorate, Beaumont Hospital, Beaumont, Ireland

INTRODUCTION

Upper limb and hand dexterity impairment is common in neurological conditions such as Parkinson's Disease, Stroke or Amyotrophic Lateral Sclerosis. The most widely used measurement methods for these conditions are multi-item ordinal performance rating scales that are either condition specific or generic in application [1]. These scales have inherent subjective biases and lack sensitivity to small but meaningful changes. To address this, performance-based tests such as the nine-hole peg test (NHPT) or grip strength dynamometry have been utilized but these tests are limited by floor and ceiling effects, reliability or accessibility in the clinical setting. This may contribute to failed clinical trials, as the lack of sensitive objective endpoints hamper the ability to assess the impact of novel treatments.

We hypothesized that the development of a new measurement tool for hand dexterity could provide an enhanced outcome measure that would be able to detect small but meaningful changes in patient function.

METHODS

The new tool was designed to satisfy predefined user needs and design requirements. It digitises the Finger Tapping Test (FTT), a widely used clinical test in neurological practice [2]. This involves tapping the index finger against the thumb rapidly, while the clinician visually evaluates the size, speed and accuracy of the movement. This approach is subjective, insensitive and yields a bivariate result of normal or abnormal. The novel device (Figure 1) is comprised of two sections, a mechanical system attached to a participant's thumb and index finger and an electronic system which captures and transmits the data to an app on an Android phone for instant evaluation. The two primary outputs of the device are distance travelled and the associated time in milliseconds. Testing was carried out to validate the mechanical reliability and accuracy of the device.

This study evaluated the device in a healthy population and in people with a neurodegenerative condition that affects hand function (pwNDC). It was approved by the School of Medicine Research Ethics Committee, Trinity College Dublin for healthy people (REC 20190209) and the Beaumont Hospital Medical Ethics Research committee (REC 18/25) for pwNDC. Potential participants were invited to participate, provided with an information leaflet and written consent obtained.

Participants were tested using the novel dexterity device and using three traditional tests; grip strength dynamometry, pinch gauge and the NHPT. A hand function questionnaire, the Disability of Arm, Shoulder and Hand (DASH) was completed by pwNDC. Participants who were unable to complete the NHPT were given a score of 200 seconds. The testing method for the dexterity device was as follows: participants rested their hand in a custom hand support to standardise orientation and were instructed to place the tip of their index finger on the distal crease of their thumb and to extend their finger as high and as fast as they could, returning to the starting point of the distal crease between each tap, for eleven taps, with ten taps used in the analysis. Participants completed three FTTs for both hands with a 'best test' chosen. The maximal passive height of the index finger was also recorded once for each hand, where the tester passively extended the participant's index finger to the maximum potential height. **180** healthy participants (90 Males, mean age \pm SD = 49.7 \pm 17.3). **58** pwNDC (36 Males, mean age \pm SD = 62.6 \pm 11.3) participated.

RESULTS

The accuracy of the dexterity device (four prototypes were manufactured) was confirmed by plotting the known displacements against the calculated displacements; this test was conducted using a static testing machine (Zwick Instron, UK) (Fig. 2A). The R^2 values were high (R^2 greater than 0.99 for every device). The maximum forces recorded were 0.51N, 0.39N, 0.51N and 0.44N for Devices 1-4 respectively (Fig.2B).

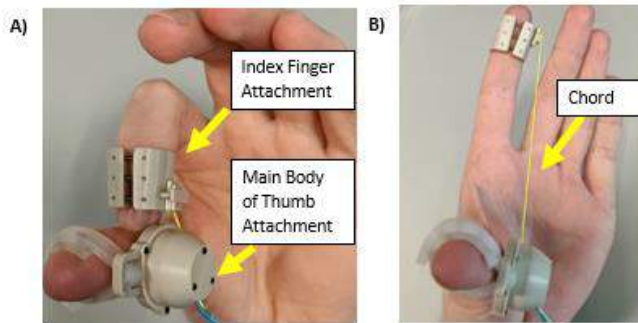


Figure 1: Photographs of the system in place on a person's hand.

Despite significant hand impairment only four pwNDC (6.9%) were unable to complete the FTT using the device using their dominant hand with two (3.4%) unable using the non-dominant hand. In comparison, ten (17.2%), were unable to complete both the NHPT or grip strength test using their dominant hand and 13 (22.4%) were unable to complete the NHPT and ten (17.2%) the grip strength using their non-dominant hand (Figure 3).

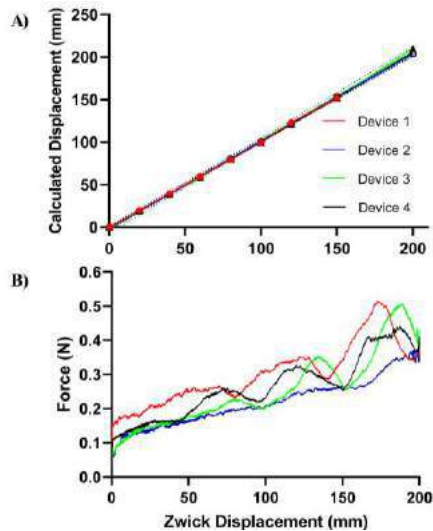


Figure 2: (A) calculated displacement for four devices when the associated calibration factors were used, plotted against known measurement points. (B) average force for the four devices over five tests using the force recorded at a displacement of 200 mm.

15 features were extracted from a participant's raw data graph (time, accuracy, speed etc.). All features (along with age and gender) were used as inputs to a logistic regression which was carried out on a combined healthy and patient dataset. The linear predictor of the logistic regression output was used to determine the objective 0-1 (0 = maximum impairment) score for a participant's hand function.

The objective score accounts for the effects of age and gender on the features. Figure 4A shows the objective score plotted against age for healthy controls with lower scores seen in older participants. The score was plotted against the traditional measures (Figure 4B and 4C). The score was negatively correlated with the NHPT ($r = -0.69$ D/ -0.73 ND) and positively with the grip strength test ($r = 0.50$ D/ 0.50 ND). A negative correlation was observed between the score and the DASH questionnaire ($r = -0.55$ D/ -0.44 ND).

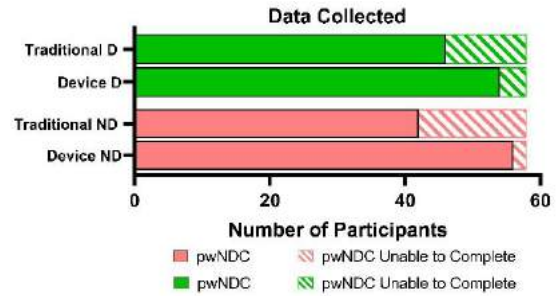


Figure 3: Data collected from participants with a neurodegenerative condition affecting hand function (pwNDC) dominant and non-dominant hands using the traditional measures and the novel dexterity device.

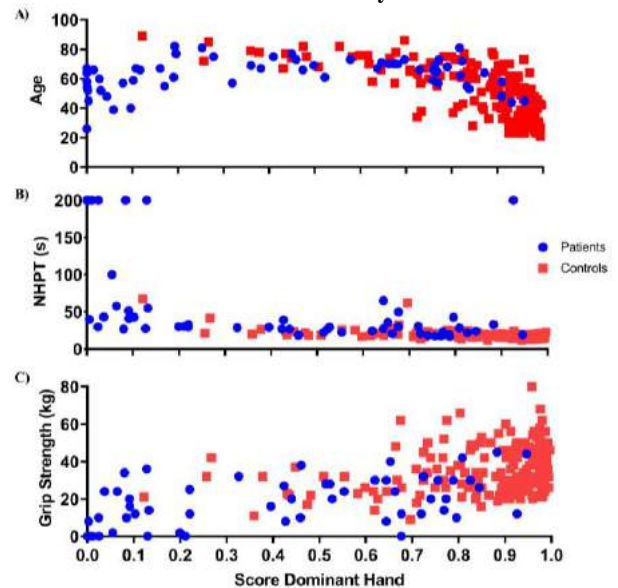


Figure 4: Objective score for participant's dominant hands plotted against ages (A) and corresponding traditional measures; NHPT (B) and Grip Strength Test (C).

DISCUSSION

Our novel hand dexterity measurement device is more sensitive than standard measurement techniques, with a low floor effect despite patients demonstrating significant hand impairment. It accurately records the finger tapping movement with a high degree of sensitivity and has potential as a small and simple to use device for remote monitoring. Our new calculated score is an objective measure of hand dexterity that is sensitive and correlates with the traditional measures. It has the potential to record changes in hand function and enables longitudinal data collection - vital for clinical trials. No previous technology-based solutions for hand dexterity assessment have been adopted in clinical practice, due to limitations in usability, cost and clinical meaningfulness, this new system overcomes these limitations.

ACKNOWLEDGEMENTS

Thanks to participants, Health Research Board (HRB/MRCG 2018-03) Ireland and Research Motor Neurone Ireland.

REFERENCES

- [1] J. M. Cedarbaum *et al.*, *Journal of the Neurological Sciences*, 169:13-21,1999.
- [2] A. Shirani *et al.*, *BMC Neurology*,17:55,2017.

VALIDATION OF A STRAIN-BASED LOWER-LIMB FRACTURE HEALING ALGORITHM

George Morgan (1), Lucas Low (1), Arul Ramasamy (1,2), Spyros Masouros (1)

(1) Department of Bioengineering, Imperial College London, London, UK
(2) Academic Department of Trauma and Orthopaedics, Royal Centre for Defence Medicine, ICT Centre, Birmingham, UK

INTRODUCTION

Despite continued progress in fracture treatment, non-unions, which can lead to additional surgeries and significant morbidity, are still prevalent and the best-practices to avoid them remain under debate. Specifically, questions regarding the optimal surgical fixation method for distal femoral fractures have been investigated through conventional clinical trials and bench-top tests. However, most remain unanswered due to the constraints of *in vivo* and *in vitro* trials, such as limited patient and surgeon recruitment capacity [1] and limitations of *in vitro* callus development. *In silico* trials have successfully addressed questions left unanswered by clinical trials and *in vitro* testing [2].

Fracture healing algorithms, such as the Ulm Fracture Healing Model [3], simulate the progression of fracture healing and can be used to compare fixation methods and configurations. The algorithms model callus chondrogenesis and ossification based on the mechanical strain environment at each location in the callus. A finite-element (FE) model of fracture and fixator calculates the strains due to expected external loading. The healing algorithm calculates updated material properties for each callus finite element, representing the progression of healing; the simulation is repeated in an iterative process. Despite the progress of fracture healing algorithms, they are not fully validated. Specifically, they have not been validated across different fracture geometries, healing metrics, and applied strains [4].

This study presents a qualitatively validated fracture healing model of an ovine metatarsal fracture stabilized with a custom external fixator. We compared it against corresponding experimental data from literature [5] across 3 different initial interfragmentary gap sizes and 2 different initial interfragmentary strains. These experimental data were chosen for comparison against the simulations due to the controlled mechanical properties of the external fixator used and the variety of fracture geometries and loads analyzed. Bending stiffness is used as the primary comparison metric since interfragmentary movement has been shown to be a poor indicator of successful union [5].

METHODS

An FE model was developed in MSC.Marc (v2021, MSC Software) of a simple transverse mid-diaphyseal metatarsal ovine osteotomy secured with an external fixator with a pre-defined callus domain. A 40 mm long section of the fracture region was modelled with the metatarsus represented as a hollow cylinder, with outer diameter and thickness of 16 mm and 2 mm, respectively. The external fixator was represented as an axial spring according to the specified design criteria of the original experiment [5]. The bone fragments were meshed using quadratic tetrahedral elements with an average element size of 1 mm. The callus domain was meshed using quadratic tetrahedral elements with an element size of 0.7 mm at the fracture gap and an average element size of 1.2 mm. A diagram of the FE model is shown in Figure 1. An axial compressive load of 500 N was applied.

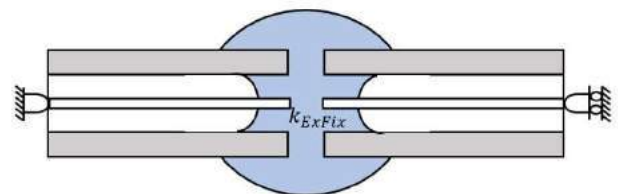


Figure 1: Diagram showing the longitudinal section of the 3D FE model of the healing simulation, with bone fragments shown in grey and the callus domain shown in blue, with the external fixator represented as an axial spring.

The fracture healing algorithm was developed based on a modified version of the Ulm Fracture Healing Algorithm [3] which assumes unconstrained callus perfusion [4]. 6 different initial conditions were simulated, representing the experimental conditions of Claes et. al. [5] (Table 1). Gap sizes of 1, 2, and 6 mm, and allowable interfragmentary

strains of 7 and 31%, were used (Table 1). The simulations were run for 56 iterations, representing 56 days.

Table 1: Model set up: fracture gap width and interfragmentary strain allowed in each of the developed models, recreating the experimental conditions of Claes et. al. [5].

Group	Gap Size (mm)	Strain (%)
A	1	7
B	1	31
C	2	7
D	2	31
E	6	7
F	6	31

A mesh convergence study and a callus domain-size independence study were performed on the Group C (Table 1) simulation. The converged callus domain size was 26 mm long and 32 mm in diameter.

Bending stiffness of the simulated fracture region at the final iteration was assessed using virtual mechanical testing [4]. The bone fragments were extended in length for an overall limb length of 200 mm, matching the experimental conditions [5]. An *in silico* four-point bending rig was developed and the bending stiffness of the metatarsus was assessed.

RESULTS

Simulations which yielded successful union displayed an initial bony outgrowth from the periosteum followed by initial bony bridging at the external callus, followed by cartilage ossification in the interfragmentary region, thus demonstrating the qualitative physiological secondary fracture healing stages [6].

The simulated bending stiffness of the ovine metatarsus at 8 weeks for groups A-F were 19.8, 19.7, 19.8, 1.8, 18.5, and 0.3 N mm⁻¹, respectively, and are shown against the experimental results of Claes et. al. [5] in Figure 2.

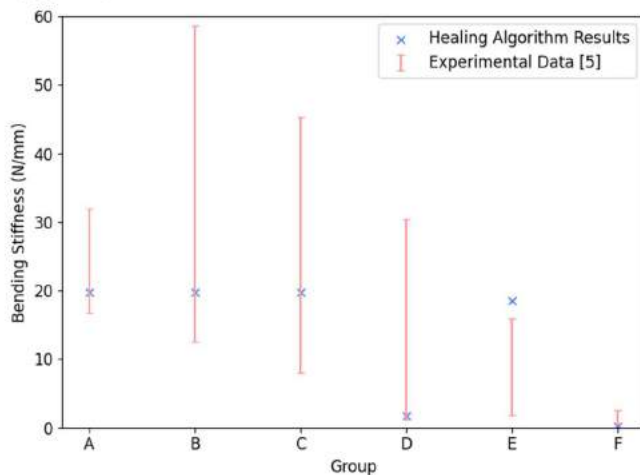


Figure 2: Bending stiffness of the simulated callus region of each case at 8 weeks post-fixation as measured by a four-point bending simulation compared against bending stiffnesses of corresponding cases reported in experimental results by Claes et. al. [5].

The simulated daily progression of interfragmentary movement (IFM) for Group C is shown in Figure 3 against the weekly measured IFM of Group C in the experimental results reported by Claes et. al. [5].

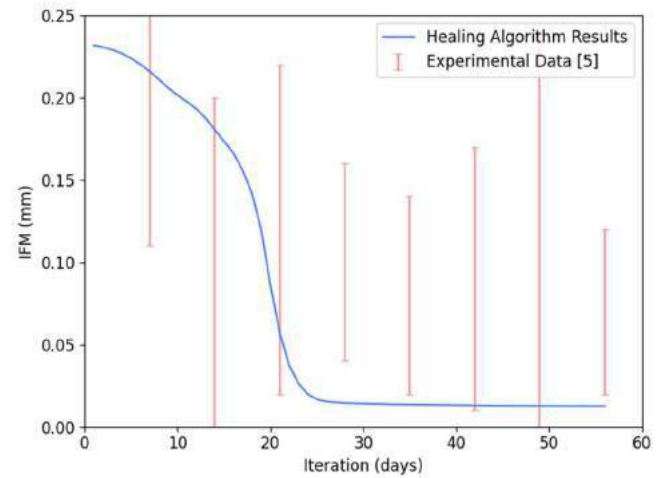


Figure 3: Simulated interfragmentary movement (IFM) compared against the experimental results by Claes et. al. for Group C [5].

DISCUSSION

Simulations of successful fracture healing groups (A, B, C, E) displayed physiologically accurate qualitative ossification patterns as demonstrated by callus healing radiography studies [6]. This contrasts the healing patterns displayed by previous fracture healing algorithms which frequently suffered from spontaneous ossification at the extremities of the callus domain due to strain artefacts [3].

The simulated callus bending stiffness at 8 weeks post-fixation (Figure 2) agrees with the data of Claes et. al. [5] for Groups A, B, C, and F. However, the detrimental effect of high strain is over-stated (Group D) and the detrimental effect of a large initial gap size is understated (Group E). The dependence of the algorithm to these input parameters could be addressed with a broad sensitivity study to quantify their effect on the algorithm outcomes.

The simulated IFM values at week 8 fall outside of the published experimental values, however, IFM has been shown to be a poor indicator of fracture healing [5]. Instead, the time period during which the largest reductions in IFM occur, likely related to initial bony bridging of the callus, are considered a better indicator. Specifically in Group C, this occurs during weeks 2-3 (Figure 3).

This study demonstrates the qualitative physiological validation of a fracture healing algorithm and an initial quantitative validation for four of the six simulated fracture fixation conditions. The discrepancies between the presented model and experimental data will be addressed with a further sensitivity study of the model. The model will then be applied to an *in silico* clinical trial to investigate the optimal fracture fixation treatment for distal femoral fractures for a variety of loading conditions and fracture types.

ACKNOWLEDGEMENTS

This research was supported by an EPSRC Doctoral Training Partnership.

REFERENCES

- [1] Griffin, X et al., *BMJ Open*, 2019; 9:e026810.
- [2] Sarrami-Foroushani, A et al., *Nat Commun*, 2021; 12:3861.
- [3] Simon, U et al., *Comp Meth Biomech Biomed Eng*, 2011; 14:79-93.
- [4] Ren T & Dailey H, *Biomech Model Mechan*, 2020; 19:2307-2322.
- [5] Claes, L et al., *J Orthop Res*, 1997; 15:577-584.
- [6] Vetter, A et al., *J Orthop Res*, 2010; 28:1440-1447.

COLLAGEN CROSSLINKING DRAMATICALLY IMPAIRS THE FRICTIONAL PERFORMANCE OF ARTICULAR CARTILAGE

Meghan E. Kupratis (1), Uriel Gonzalez (1), Atia Rahman (2), David L. Burris (2),
Elise A. Corbin (1), Christopher Price (1)

(1) Biomedical Engineering, University of Delaware, Newark, DE, USA
(2) Mechanical Engineering, University of Delaware, Newark, DE, USA

INTRODUCTION

In osteoarthritis (OA), loss of tissue stiffness is thought to expose cartilage to elevated compressive and shear strains, leading to chondrocyte dysfunction and degeneration [1-3]. As a result, reversing cartilage softening has been suggested as a means to slow or halt OA progression. For example, collagen crosslinking (CXL) can reinforce native and tissue engineered cartilage [4-7], and thus has seen interest as a method for stabilizing cartilage and preventing degeneration.

Classical stationary contact area (SCA) tribology studies support cartilage softening as a driver of elevated cartilage friction. In depressurized and slowly slid (~1mm/s) SCA contacts, equilibrium friction coefficients of 'OA' cartilage ($\mu_{eq}=0.2-0.3$) are ~2X higher than healthy tissue [2-4]. Paradoxically, though, similarly elevated SCA frictions have been reported following CXL [6]. However, the clinical relevance of such SCA-based findings are unclear given that articular cartilage operates at higher average sliding speeds (30-80mm/s) and sustains markedly lower frictions ($\mu_{eq}<0.005$) *in vivo* [8].

Alternatively, our team has pioneered the use of the convergent SCA (cSCA) to investigate cartilage function under biofidelic sliding conditions. In the cSCA, modest sliding speeds (>30mm/s) i) facilitate interstitial fluid recovery and ii) sustain near-physiological friction coefficients ($\mu_{eq}\leq 0.01$) via tribological rehydration [8-10]. Critically, cSCA tribomechanical outcomes are largely insensitive to tissue mechanical properties in both healthy [8-9] and OA-like cartilage [10]. Thus, while CXL can increase cartilage tensile and compressive moduli [6-7], whether the restoration of tissue stiffness alters articular cartilage lubrication under biofidelic articulation conditions (such as those replicated in the cSCA) remains unknown. Here, our objective was to determine if reinforcement of cartilage via CXL alters its lubricity under sliding conditions that better represent those of the intact joint.

METHODS

Osteochondral explants ($\varnothing 19$ mm) were extracted from mature bovine femoral condyles. Specimens underwent sequential

microindentation and cSCA-based tribomechanical testing in their naïve state and after treatment with crosslinking agents (**Fig. 1**).

A $\varnothing 4$ mm glass probe was used to indent each specimen in creep-relaxation (at 50 μ m/s to a 150mN load), and the time-dependent normal force and indentation depth were fit to Hertz biphasic theory (HBT) to determine tensile modulus (E_{y+}), compressive modulus (E_{y-}), and permeability (k_0) [10]. Tribological testing consisted of ramp loading to 7N ("force-matched") or 4N ("stress-matched"), followed by 30min static compression and 15min reciprocal sliding. Explants were crosslinked with 0.6% glutaraldehyde (GTA) for 1h or 10mM genipin (GP) for 24h (n=5/treatment). Differences in mechanical properties and tribomechanics following CXL were assessed via paired *t*-tests and two-way ANOVA with Tukey's post-hoc test, respectively.

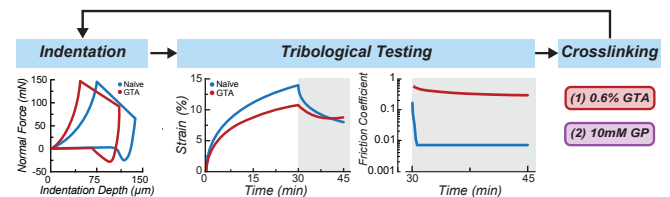


Fig. 1: Experimental overview. Pairwise assessment of indentation-based mechanical properties and cSCA tribology of naïve cartilage and following reinforcement with collagen crosslinking agents (naïve and 1hr of 0.6% GTA shown).

RESULTS

Collagen crosslinking significantly increased both cartilage tensile and compressive moduli. Tensile moduli increased from 2.65 ± 0.80 to 6.31 ± 0.22 and from 3.72 ± 1.18 to 5.10 ± 1.37 MPa following GTA and GP treatment, respectively ($p<0.001$, **Fig. 2A**). Similarly, compressive moduli increased from 0.51 ± 0.08 to 1.35 ± 0.17 MPa in the GTA group

and from 0.54 ± 0.09 to 0.80 ± 0.09 MPa in the GP group ($p < 0.001$, Fig. 2B). Consistent with prior findings [6-7], these crosslinkers had no significant effect on permeability ($p > 0.2$). Dilatation under 7N loading (“force-matched” tests) was reduced by CXL, resulting in 66% higher contact stresses compared to the naïve state (Fig. 2C). Thus, “stress-matched” tests, wherein CXL cartilage was loaded to 4N, were performed, resulting in contact stresses of 0.26 ± 0.03 MPa (Fig. 2C).

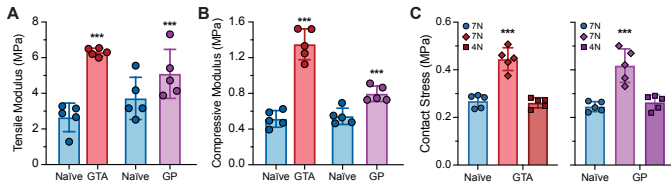


Fig. 2: Cartilage tensile (A) and compressive moduli (B) increased significantly following CXL. (C) cSCA contact stresses for naïve, and “force”- and “stress”-matched CXL tribomechanical tests. Data shown as mean \pm SD ($p < 0.001$ vs. naïve).**

CXL significantly decreased elastic strain during ramp loading relative to naïve tissue ($p < 0.001$). In force-matched tests, exudative strain decreased following GTA ($p = 0.02$), but not GP treatment ($p = 0.28$, Fig. 3A). However, both treatments decreased exudative strain in stress-matched tests ($p < 0.001$, Fig. 3A). Tribological rehydration drove average strain recovery of $4.7 \pm 1.7\%$ in naïve cartilage (Fig. 3B). Following GTA treatment, strain recovery decreased to $1.2 \pm 1.0\%$ and $2.8 \pm 0.6\%$ in force- and stress-matched tests, respectively ($p < 0.05$, Fig. 3B). GP had no significant effect on strain recovery ($p > 0.35$, Fig. 3B).

In naïve cartilage, transient friction coefficients of 0.08-0.22 were observed at start-of-sliding, which then rapidly dropped to near-physiological values (median $\mu = 0.005$, Fig. 3C). In contrast, start-of-sliding friction coefficients increased after CXL (to 0.19-0.58) and remained elevated through the end-of-sliding. For GTA-treated explants median end-of-sliding friction coefficients were 0.31 and 0.23 for force- and stress-matched tests, respectively (Fig. 3C). For GP-treated explants end-of-sliding friction coefficients were significantly elevated for force-, but not stress-matched tests (Fig. 3C).

DISCUSSION

Here, we introduce the first biofidelic assessment of articular cartilage lubrication following tissue CXL with agents proposed for ‘preserving’ native cartilage or ‘strengthening’ graft materials [4-7]. Following GTA treatment, elastic and exudative strain were significantly reduced, indicating enhanced tissue resistance to compressive loads. However, GTA compromised tribological rehydration-mediated strain recovery under equivalent applied forces. At 7N, only 11% of the exudative strain was recovered in GTA-treated explants vs. 35% in their naïve condition, indicating significant reduction in the rehydration capacity of crosslinked cartilage at equivalent loads. CXL also decreased cartilage contact area expansion under load. Consequently, contact stresses at 7N nearly doubled after crosslinking (from 0.25 to 0.46 MPa). The concomitant reduction in strain recovery observed here under equivalent forces is consistent with recent findings that modestly elevated contact stresses suppress tribological rehydration [11].

To disentangle the effects of elevated contact stress on tribological rehydration from those of CXL alone, cSCA tests were repeated at 4N (0.26 ± 0.03 MPa). As expected, exudative strains were lower in these “stress-matched” tests. However, ~40% of exudative strains were recovered by tribological rehydration, suggesting that elevated contact stresses indeed impaired fluid recovery in the “force-matched” tests.

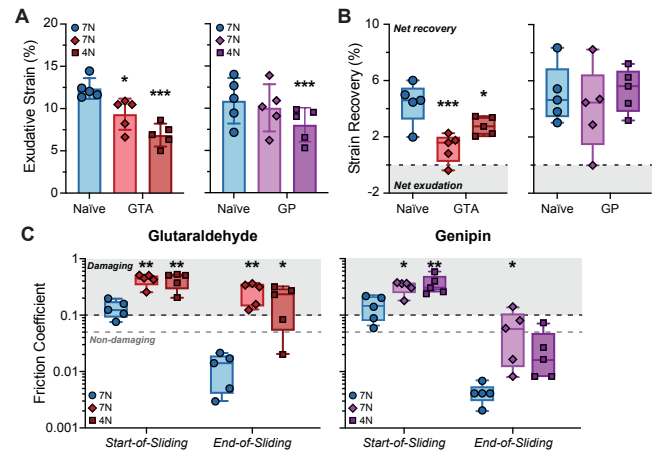


Fig. 3: (A) Exudative strain and (B) strain recovery of naïve and CXL cartilage. (C) Friction coefficients were elevated following CXL. Data shown as (A) mean \pm SD and (B-C) median \pm IQR (* $p < 0.05$, ** $p < 0.01$, * $p < 0.001$ vs. naïve).**

Most importantly, our friction outcomes revealed incontrovertible detrimental impacts of CXL on cartilage lubrication, despite the persistence of strain recovery (*i.e.*, tribological rehydration). In PBS-bathed cSCA contacts, naïve cartilage sustained near-physiological equilibrium friction coefficients (average $\mu_{eq} = 0.005$), whereas average μ_{eq} of 0.26 and 0.06 were observed among force-matched tests of GTA- and GP-crosslinked samples, respectively. Furthermore, reducing the applied contact stress failed to restore friction coefficients of CXL cartilage to those in the naïve state. Exposure to such elevated friction coefficients is likely detrimental to chondrocytes, as multiple studies report marked cell death after just 30-60min of sliding at $\mu \geq 0.10$ [1,12].

In summary, this study demonstrates that increased cartilage stiffness does not automatically equate to improved, or even adequate, tribomechanical function under biofidelic sliding conditions (*i.e.*, high sliding speeds, incomplete interstitial fluid depressurization). Marked reduction in the frictional performance of crosslinked cartilage despite their “improved” stiffness and load-bearing capacity indicates that CXL is ill-suited for cartilage preservation and/or joint resurfacing. Even if CXL were to improve the tribomechanical properties of ‘compromised’ cartilage, its effect on healthy tissue within the joint would likely preclude CXL-based OA mitigation approaches. Ongoing work will investigate if the presence of natural cartilage lubricants (*i.e.*, synovial fluid) can mitigate the deleterious effects of CXL on cartilage lubrication, or if alternative tissue reinforcement strategies (GAG-replacement) might be more suitable for rescuing articular cartilage’s tribomechanical function.

REFERENCES

- [1] Bonnevill, *J Biomech*, 74: 72-78, 2018.
- [2] Gleghorn, *Arthritis Rheum*, 60(2): 440-449, 2009.
- [3] Basalo, *J Biomech*, 38: 1343-1349, 2005.
- [4] Santos, *OA&C Open*, 4: 100233, 2022.
- [5] Bonitsky, *J Orthop Res*, 35: 558-565, 2017.
- [6] Oungoulouian, *J Biomech*, 47(3): 694-701, 2014.
- [7] Lima, *J Biomed Mat Res A*, 91(3):692-700, 2009.
- [8] Graham, *Conn Tiss Res*, 61(3-4): 375-388, 2020.
- [9] Kupratis, *Acta Biomater*, 138: 375-389, 2022.
- [10] Kupratis, *BMES*, 2022.
- [11] Akanda, *ORS*, 2022.
- [12] Farnham, *CMBE*, 14(4): 349-356, 2021.

EFFECTIVE STRAIN SHARPLY CAPTURES THE RUPTURE POINT OF ANEURYSM TISSUES

Jia Lu (1), Xuehuan He (1,2)

(1) Department of Mechanical Engineering, The University of Iowa, Iowa City, IA, USA
(2) Department of Radiology, University of Michigan, Ann Arbor, MI, USA

INTRODUCTION

Strain- or stress-based rupture criteria have been gradually introduced into aneurysm risk assessment. However, values of ultimate strain or stress in the literature exhibit significant intra- and inter-subject heterogeneities. This brings in a certain level of uncertainties in patient-specific application if one is to rely on literature values, and eventually hinders the application of mechanics-based risk analysis. We submit that the total strain is not a suitable failure metric because it does not reflect the true strain level in the collagen network. In recent works [1,2], we introduced an effective strain to measure the net strain in the collagen after excluding the part of strain spent to straighten the fibers. In light of this new metric, we examined the effective strain of 156 sets of uniaxial tension data and 13 sets of bulge inflation test data of ascending thoracic aortic aneurysm (ATAA) tissues [3,4]. The waviness properties, which were required for evaluating the effective strain, were obtained from constitutive regression. The study found that all samples ruptured sharply around 10% of effective strain.

METHODS

Effective Strain. The effective strain was introduced in [1]. It is a tissue-scale strain measure derived in a multi-scale context. At the fiber-scale, the true stretch of a fiber is defined as the ratio of the deformed length over the undeformed arclength. If the deformation is insufficient to straighten the fiber, the true stretch is set to be unit. The effect stretch is the ensemble average of the fiber true stretch over the probability distribution of fiber waviness. In the seminal work, Rezakhanlou et al [5] showed that the waviness of arterial collagen was best described by beta distribution. Using the beta distribution, the effective stretch was derived as

$$\bar{\lambda} = F(\lambda^{-1}; \alpha, \beta) + \frac{\lambda\alpha}{\alpha+\beta} F(\lambda^{-1}; \alpha+1, \beta, upper) \quad (1)$$

Here, λ is the kinematic stretch, (α, β) are the shape parameters of the beta distribution, $F(x; \alpha, \beta)$ is the incomplete beta function, and $F(x; \alpha, \beta, upper) := 1 - F(x; \alpha, \beta)$ is its tail. The effective stretch $\bar{\lambda}$

is a monotonically increasing function of λ and is bounded above by $\lambda \cdot E(p)$ where $E(p)$ is the mean waviness. Note that $\bar{\lambda}$ is a directional stretch measure; the directional dependence enters through λ . The corresponding effective strain is

$$\bar{E} = 0.5(\bar{\lambda}^2 - 1) \quad (2)$$

Determination of waviness parameters. The effective stretch depends on the beta distribution parameters (α, β) . These parameters were identified from constitutive regression; the stress-strain response data were fitted to constitutive models that employed the effective strain as a deformation measure. For uniaxial extension, the strain energy function assumed the form

$$W = \mu_1(\lambda^2 + 2\lambda^{-1} - 3) + \mu_2\bar{E}^2 \quad (3)$$

The first term represents the strain energy of the ground substances. It is reduced from a neo-Hookean function after imposing the incompressibility condition and the assumption of isotropic transverse contraction. The second term is the contribution from the collagen network, formulated as a quadratic function of the effective strain. The model contains four constitutive parameters: $(\mu_1, \mu_2, \alpha, \beta)$.

For bi-axial response, the following constitutive model was used:

$$W = \mu_1(I_1 - \log I_2 - 2) + \mu_{21}\bar{E}_1^2 + \mu_{22}\bar{E}_2^2 \quad (4)$$

Again, the first term represents the ground substance contribution, now a function of the principal invariants (I_1, I_2) of the in-plane deformation tensor. The strain energy of the collagen network is described by quadratic functions of effective strain in two sampling directions. The angles of these two directions were also determined by regression. This model contains seven parameters: $(\mu_1, \mu_{21}, \mu_{22}, \alpha, \beta, \theta_1, \theta_2)$.

Experimental data. The uniaxial extension data were collected in Professor Ferdinando Auricchio's laboratory. Approximately 180 sets of data were obtained from ATAA tissues samples from 52 patients who underwent surgery, and 156 sets were used in this study. Some scattered data points were removed. This was accomplished by fitting the raw data to a NURBS curve, and then

computing the stress and stretch at uniformly spaced knots. Third order NURBS with 7 knot intervals was found to accurately replicate the curves.

The biaxial response data were extracted from bulge-inflation tests conducted in Professor Stephane Avril's laboratory. Briefly, ATAA tissue samples of ~3cm radius where subjected to incremental transverse pressure till rupture. At each pressure pause, the surface geometry was recorded by Digital Image Correlation. A NURBS mesh that corresponded through all deformed configurations was extracted, and the strain fields were computed from the deforming mesh. Stress field in each configuration was computed individually using an inverse analysis method [6]. In this manner, stress-strain curves were obtained at multiple material points, approximately 2300 in each specimen.

RESULTS

Constitutive regression. The optimal parameters were obtained by minimizing the squared difference of the experimental and modeled stresses. The 1D quadratic model (3) fitted the uniaxial data very well. The R^2 values were above 0.95 for 148 specimens (94.8% of the total). The 2D model (4) also described the planar response well. Sample-wise median R^2 were over 0.95 for all 13 samples. Forward finite element analyses were conducted to simulate the inflation motion. The displacement, strain and stress fields in all deformed states were replicated to high fidelity.

Rupture Strain. Figure 1 presents histograms of the effective strain at rupture, denoted by $\bar{\epsilon}_f$, from the uniaxial tests. Evidently, the ultimate effective stretches are closely packed, with nearly 70% of them cluster around 0.1. In contrast, the values of total stretch are wide-spread. The statistics are summarized in Table 1.

Table 1. Statistics of ultimate strains.
 $\bar{\epsilon}_f$: effective strain; ϵ_f : total strain

Variable	Mean \pm SD	Median ([interquartile])
$\bar{\epsilon}_f$	0.113 ± 0.049	0.109 ([0.079, 0.146])
ϵ_f	0.365 ± 0.207	0.326([0.240, 0.432])

For the planar response we define the effective strain norm as

$$\bar{\epsilon} = \sqrt{\bar{E}_{major}^2 + \bar{E}_{minor}^2} \quad (5)$$

where $(\bar{E}_{major}, \bar{E}_{minor})$ are the effective strains in the two principal strain directions. The norm of the total strain, ϵ , is defined in the same way. Note that $\bar{\epsilon}$ applies to the uniaxial extension as well because $\bar{E}_{minor} = 0$ in this case. Distributions of $\bar{\epsilon}$ and ϵ at rupture are presented in Figure 2. Again, the effective failure strains are closely clustered around 0.1 while the other spread over a wider range.

DISCUSSION

The present study underscores the importance of considering collagen waviness in assessing the ultimate strain that the tissue can sustain. The result implies that failure is dictated by the level of true strain in the collagen network, not the total strain that measures the bulk deformation of the continuum. This is reasonable, because near failure the mechanical load is sustained primarily by the collage fibers and hence, the mechanical condition of the collagen network is likely the leading factor that determines rupture. The finding suggests that the effective failure strain could be much more homogeneous than the total strain. The heterogeneity seen in the total strain could be attributed to the difference in collagen waviness (more generally, the collagen microstructure). It should be cautioned, however, that the waviness

properties were obtained from constitutive regression, not direct measurement. Lack of direct experimental measurement, or validation, of the waviness properties is a major limitation of the present work. Nonetheless, the study points to a new direction for establishing failure metrics which are hopefully more applicable, and more reliable in patient-specific studies.

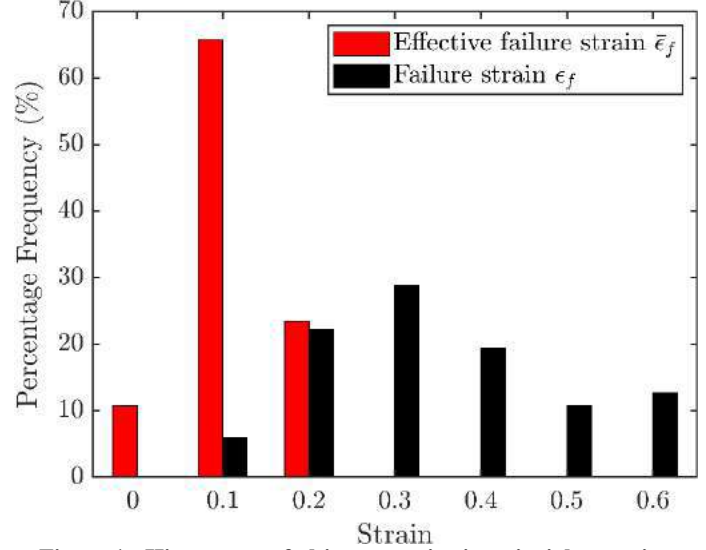


Figure 1: Histograms of ultimate strains in uniaxial extension

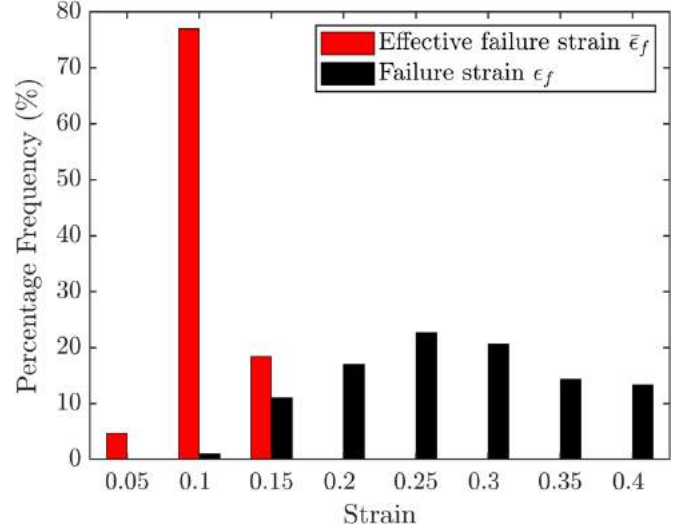


Figure 2: Histograms of the ultimate strains in bi-axial extension

ACKNOWLEDGEMENTS

The authors thank Professors Auricchio and Avril for providing the experimental data, and acknowledge funding from ANSYS Inc.

REFERENCES

- [1] Lu, J and He, X *Biomech Model Mechanobiol*, 20:1833-185, .2012
- [2] He, X and Lu, J *J. Mech. Phys. Solids* 163:104837,2022.
- [3] He, X and Lu, J *Acta Biomaterialia*, 136:303-313, 2021
- [4] He, X and Lu, J *Acta Biomaterialia*, 149:51-59, 2022
- [5] Rezakhaniha, R et al., *Biomech Model Mechanobiol* 11:461-473, 2012
- [6] Lu, J et al, *Biomech Model Mechanobiol*, 7:477-486, 2008

MODELING HUMAN SEX-SPECIFIC FIBROTIC ACTIVATION IN 3D-BIOPRINTED PULMONARY ARTERY ADVENTITIA

Duncan J. Davis-Hall (1), Chelsea M. Magin (1,2,3)

- (1) Department of Bioengineering, University of Colorado Denver □Anschutz Medical Campus, Aurora, CO, USA
(2) Department of Pediatrics, University of Colorado Anschutz Medical Campus, Aurora, CO, USA
(3) Division of Pulmonary Science and Critical Care Medicine, University of Colorado Anschutz Medical Campus, Aurora, CO, USA

INTRODUCTION

Interactions between cells and the extracellular matrix (ECM) are critical drivers of fibrotic diseases like pulmonary arterial hypertension (PAH), a progressive and incurable pathology characterized by aberrant cell proliferation and ECM remodeling. This pathology narrows blood vessels, increases blood pressure in the arteries of the lungs, and ultimately leading to right heart failure. Female patients are diagnosed with idiopathic PAH (IPAH) as much as four times more frequently than male patients, but there is no clear reason for this discrepancy [1].

Synthetic tissue culture platforms made from 3D hydrogel biomaterials are a powerful tool for studying cell-ECM interactions. Poly(ethylene glycol)-alpha methacrylate (PEG- α MA) is the backbone of a dynamic hydrogel system that undergoes an initial base-catalyzed Michael addition and can be stiffened *in situ* by photoinitiated homopolymerization. These two polymerization reactions allow the formation of an initially soft hydrogel with an elastic modulus (E) of 1-5 kPa that can be stiffened up to an E > 10 kPa. These E values recapitulate healthy and fibrotic pulmonary arterial adventitia mechanical properties [2], which allows PEG- α MA to be used as a culture platform to study human pulmonary artery adventitia fibroblast (HPAAF) behavior in a reproducible synthetic microenvironment.

Here, we use 3D bioprinting techniques to create vascular constructs with PEG- α MA hydrogels and male or female HPAAFs. These constructs are used to probe sex-specific fibrotic activation associated with PAH pathology, including cell proliferation, production of the myofibroblast marker alpha-smooth muscle actin (α SMA).

METHODS

PEG- α MA Synthesis and Hydrogel Characterization: PEG- α MA was synthesized as previously described and functionality was verified by ¹H NMR [3]. Hydrogels were fabricated by combining 17.2 wt% PEG- α MA off-stoichiometry ([thiol]:[ene] = 0.375) with dithiothreitol and MMP2-degradable peptide crosslinkers (70:30

peptide ratio). Hydrogels contained 2 mM of the adhesive peptide CGRGDS and 2.5 wt% poly(ethylene oxide) to facilitate cell attachment and suspension. Hydrogel discs were allowed to swell overnight with 2.2 mM lithium phenyl-2,4,6-trimethylbenzoylphosphine (LAP) photoinitiator. Then, storage modulus was measured on a Discovery HR-2 rheometer [4].

Cell Culture: HPAAFs from male and female IPAH patients and control donors were cultured according to supplier instructions (Pulmonary Hypertension Breakthrough Initiative). Following bioprinting, constructs were cultured with complete media supplemented with 1% sex-matched human serum (Innovative Research, Inc.). Sera from three donors between the ages of 20 and 50 years old were pooled for each sex.

3D Bioprinting: Constructs were 3D bioprinted using the Freeform Reversible Embedding of Suspended Hydrogels method [5]. Hydrogel components were dissolved in pH 9 growth media. LifeSupport gelatin microparticles were dissolved in pH 7 growth media. HPAAFs were suspended in hydrogel precursor solution, then printed in 48-well plates containing LifeSupport and allowed to polymerize for one hour. Then, the plates were placed in a tissue culture incubator for two hours. Melted support slurry was aspirated off and replaced with growth media containing 1% sex-matched human serum. On day 6, 2.2 mM LAP was added. On day 7, half of the constructs were stiffened by exposure to 10 mW/cm² 365-nm light for 5 minutes.

Immunofluorescent Staining: Control male samples were 3D bioprinted and immunostained as part of previous work [4]. Constructs were incubated with EdU overnight on day 8, then fixed, quenched, and flash-frozen on day 9. Constructs were cryosectioned and then stained with α SMA antibody, EdU staining solution, and Hoechst dye. Slices were imaged at 10x on an Olympus BX63 microscope.

Statistical Methods: Sample means were compared using ordinary two-way ANOVA with α = 0.05 and Tukey tests for multiple

comparisons. Data are presented as mean \pm standard error of the mean (SEM) for three technical replicates of each condition.

RESULTS

EdU positivity was used to assess fibroblast proliferation, and this metric was greater in stiffened bioprinted constructs compared to soft (**Fig 1A**). Control male cells in soft and stiffened bioprinted constructs were $39 \pm 6\%$ and $66 \pm 6\%$ proliferative, respectively ($p < 0.05$). Control female cells in soft and stiffened constructs were $48 \pm 4\%$ and $64 \pm 4\%$ proliferative, respectively. IPAHA male cells were $47 \pm 4\%$ proliferative in soft constructs and $66 \pm 6\%$ proliferative in stiffened constructs. IPAHA female cells in soft constructs were $63 \pm 3\%$ proliferative and $83 \pm 4\%$ proliferative in stiffened constructs ($p < 0.05$). All fibroblast conditions saw statistically significant increased activation in stiffened constructs compared to soft constructs ($p < 0.05$; **Fig 1B**). Control male cells in soft and stiffened constructs were $65 \pm 4\%$ and $88 \pm 2\%$ α SMA-positive, respectively. Control female cells were $64 \pm 5\%$ activated in soft constructs and $83 \pm 3\%$ activated in stiffened constructs. IPAHA male cells were $66 \pm 3\%$ activated in soft constructs and $81 \pm 3\%$ activated in stiffened constructs. Finally, IPAHA female cells in soft and stiffened constructs were $71 \pm 4\%$ and $90 \pm 2\%$ activated, respectively. These differences can be seen in representative images (**Fig 1C**).

DISCUSSION

Matrix stiffness is a well-established modulator of myofibroblast activation, with stiffer substrates producing more activated fibroblasts [6]. The significant increases in α SMA positivity seen in stiffened constructs lines up with the body of research done on 2D hydrogels and builds upon 3D culture studies by using an MMP2-degradable crosslinker that allows activation in 3D as well [7]. The greater percentage of activation observed in IPAHA female HPAAFs compared to other conditions was expected due to prevalence of PAH in female patients and prior research that saw increased α SMA positivity in fibroblasts treated with female serum compared to male serum [8]. Estrogen has been shown to increase cell proliferation in clinical studies, which supports our findings of increased EdU positivity in IPAHA female cells [9]. The increased proliferation we observed in male control HPAAFs is indicative of those cells' susceptibility to stiffening and may be related to the worse outcomes generally seen in male PAH patients [1]. Results shown here are preliminary, and further studies are underway to measure fibrotic gene expression through qRT-PCR, as well as characterize the effect of estrogens on activation. This platform can be used to study sex-specific fibrotic behavior in the context of pulmonary vascular disease with a reproducible 3D microenvironment.

ACKNOWLEDGEMENTS

This work was supported by the Ludeman Family Center for Women's Health Research (DDH and CMM), the Rose Community Foundation (DDH and CMM), and the NIH NHLBI under Awards F31 HL151122 (DDH) and R01 HL153096 (CMM).

REFERENCES

- [1] Mair, K.M. et al., *Br J Pharmacol*, 171(3):567-579, 2014.
- [2] Liu, F et al., *JCI Insight*, 1(8):e86987, 2016.
- [3] Petrou, C.L. et al., *J Mater Chem B*, 8(31):6814-6826, 2020.
- [4] Davis-Hall, D et al., *Biofabrication*, 15(1):015017, 2022.
- [5] Hinton, T.J. et al., *Sci Adv*, 1(9):e1500758, 2015.
- [6] Kloxin, A.M. et al., *Biomaterials*, 31(1):1-8, 2010.
- [7] Mabry, K.M. et al., *Biomaterials*, 49:47-56, 2015.
- [8] Aguado, B.A. et al., *Sci Transl Med*, 11(509):eaav3233, 2019.
- [9] Benisty, J.I. et al., *Chest*, 126(4):1255-1261, 2004.

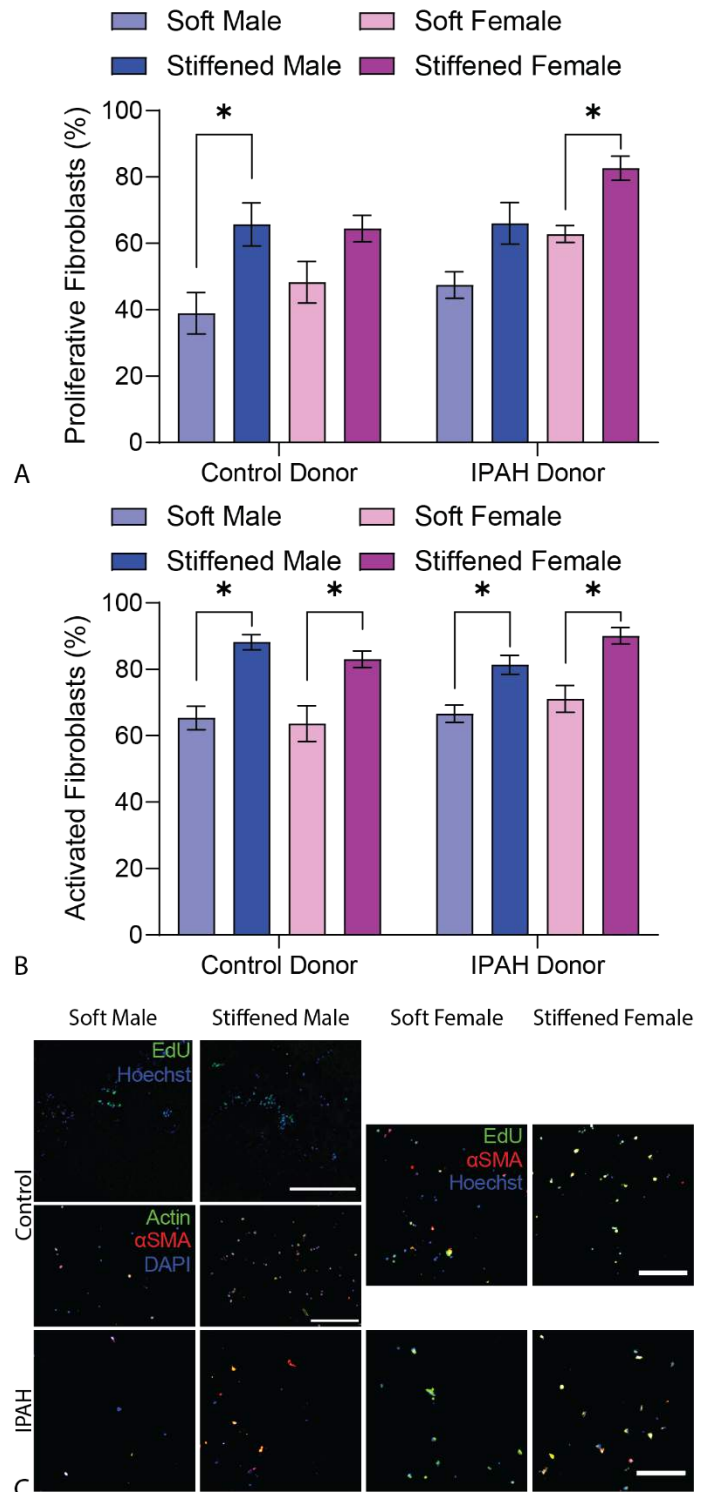


Figure 1: HPAAf behavior in 3D-bioprinted constructs. A) Proliferation measured by EdU immunostaining. B) Activation measured by α SMA immunostaining. Columns represent mean \pm SEM, $n = 3$, * $p < 0.05$. C) Representative images of immunostaining. Control male samples: proliferation with EdU (green) and Hoechst (blue), activation with actin (green), α SMA (red), and DAPI (blue). Scale bars = 300 μ m. All other samples: EdU (green), α SMA (red), and Hoechst (blue). Scale bars = 200 μ m.

A MULTI-CURVE INVERSE FINITE ELEMENT APPROACH TOWARDS SIMULATING VERTICAL TOOTH EXTRACTION MECHANICS

Timothy J. Gadzella (1), Lindsey Westover (1), Owen Addison (2,3), Dan L. Romanyk (1,2)

- (1) Department of Mechanical Engineering, University of Alberta, Edmonton, Alberta, Canada
(2) School of Dentistry, University of Alberta, Edmonton, Alberta, Canada
(3) Faculty of Dentistry, Oral and Craniofacial Sciences, King's College London, Kent, UK

INTRODUCTION

Reducing the damage caused to the remaining bone during a tooth extraction is an important consideration to improve patient recovery times and can influence the success of subsequent implantation at the extraction site [1,2]. Atraumatic extraction applies different forms of extraction load compared to conventional forceps extraction to minimize this damage and improve outcomes. One example, the Benex extraction system [3], uses a cable and threaded insert to apply a purely vertical extraction force to the tooth as demonstrated in Figure 1.

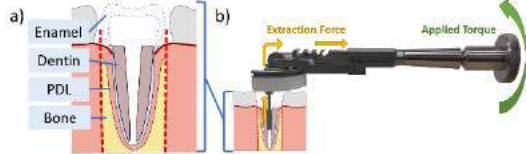


Figure 1: a) Cross-section of a tooth prepared for Benex extraction; b) vertical extraction force via Benex device.

Finite element (FE) models of the dental complex are important tools for the development of dental appliances and procedures, but to date there are few models suitable for studying tooth extraction. These models either offer a limited representation of the tooth geometry [4] or are computationally-expensive subject specific models with custom material models for the periodontal ligament (PDL; the soft tissue which attaches the tooth to the surrounding bone) [5]. The focus of this study is the development of an axisymmetric FE model of the dental complex with PDL properties determined via an inverse FE problem.

METHODS

Experimental Data Collection and Preparation: Force-time data was collected from partial swine incisors in an ex-vivo experiment. Incisors were extracted in three displacement-controlled schemes: 0.2mm/min, 2mm/min, and intermittent periods of 2mm/min displacement followed by 10s of relaxation. Experimental data from after 50N to the peak extraction force were parsed from full data sets.

50N was the minimum force found across all tests to align the custom-built testing apparatus, beyond which the measured crosshead displacement acts on the dental complex solely and not alignment of components. The time at which each curve passed the 50N threshold was averaged to obtain the mean transition time to which all force-time curves were shifted.

Model Boundary Conditions and Mesh: The model is composed of simplified planar bodies representing bone, PDL, dentin, and a threaded insert from a Benex extraction kit. These bodies were meshed as a revolution of planar geometry in SALOME. Symmetry boundary conditions were used to enforce axisymmetric behaviour as demonstrated in Figure 2.

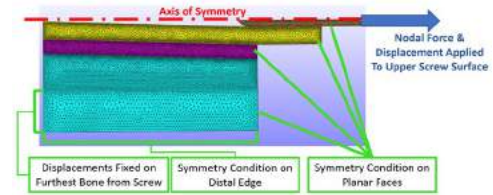


Figure 2: Mesh bodies and boundary conditions; Benex insert (screw), dentin (yellow), PDL (purple) and bone (blue).

Nodal fixation was applied to the bone far from the screw. Isotropic Hookean material properties were assigned to the steel, dentin, and bone with a principal-strain based damage model for the dentin and bone using FEBio[6]. The Arruda-Boyce model [7] was selected as the hyperelastic base for the PDL:

$$W = \mu \sum_{i=1}^N \frac{C_i}{N^{i-1}} (I_1^i - 3^i) + \frac{1}{2} k (\ln(J))^2 \dots (1)$$

where μ is the initial material modulus, N the number of modelled chains, k the bulk modulus, and C_i pre-determined constants. Viscoelasticity was modelled with a single-branch quasi-linear model:

$$S_v(t) = \int_{-\infty}^t G(t-s) \left(\frac{dS_e}{ds} \right) ds \dots (2a)$$

$$G(t) = 1 + g_1 \exp\left(-\frac{t}{t_1}\right) \dots (2b)$$

where g_1 is the relaxation constant and t_1 the relaxation time, Damage was applied with a quintic polynomial and a maximum principal stress criterion:

$$\sigma = (1 - D) * dev(\sigma_v) + pI \dots (3a)$$

$$D(\epsilon) = x^3(10 - 15x + 6x^2) \dots (3b)$$

$$x = \frac{\epsilon - \epsilon_{min}}{\epsilon_{max} - \epsilon_{min}} \text{ when } \epsilon \in (\epsilon_{min}, \epsilon_{max}) \dots (3c)$$

where ϵ_{min} and ϵ_{max} are the damage-limiting strains.

Formulation of the Inverse FE Problem: Simulation loading was initiated with a linear force-controlled ramp to the 50N transition force determined by the experimental data. After the 50N transition, displacement-controlled loading was applied to match the experimental crosshead loading scheme. Only data beyond the 50N transition is used to determine the PDL properties using an optimization error function as given in Equation 4.

$$Err = \sum_{i=1}^n [(SSE_i/10^5) \Delta t_{rupture,i}^2 \Delta F_{rupture,i}^2] \dots (4)$$

where n is the number of experimental curves in the data set and Δ terms are the differences in rupture time and force between each experimental curve and the FE model response. The error function was minimized in MATLAB using the `fminsearchbnd()` function [8] with the GIBBON toolbox [9]. Seven PDL parameters were passed into the search algorithm: g_1 , t_1 , μ , N , k , ϵ_{min} , and ϵ_{max} . Limits were only applied for numerical stability. Each optimization was performed using a random initial guess, bounded only for physically permissible values (e.g. relaxation times and coefficients forced greater than zero).

RESULTS

The force-time response of each inverse result is compared to the adjusted experimental data in Figure 3. Curve shapes and peak forces and times appear to match the experimental data. The determined material parameters are presented in Table 1.

Table 1: PDL material parameters from multi-curve fits

	0.2mm/min	2mm/min	Intermittent
g_1 [n.u.]	0.997	0.929	0.695
t_1 [s]	10.3	10.29	19.6
μ [MPa]	0.464	0.545	0.506
N [n.u.]	9.94	10.9	11.7
k [MPa]	9.97	9.62	7.55
ϵ_{min} [m/m]	4.95	5.00	5.00
ϵ_{max} [m/m]	13.2	12.6	18.8

DISCUSSION

The PDL hyperelasticity and damage parameters found in this study are similar among load cases despite being fit independently. This trend indicates systematic (rather than random) relationships between the dental complex response captured in the experimental data and the FE model. This finding indicates that the model is suitable for testing extraction loading schemes similar in rate to the cases tested here.

The viscoelastic parameters obtained from the continuous displacement cases require further investigation, as they exceed 0.90, indicating an even greater load-rate dependency than the intermittent-fit model ($g = 0.695$) which clearly demonstrated relaxation behaviour. However, the initial guess for g in these fits was 1 and the magnitudes have changed very little. It may be that the effect of PDL viscoelasticity in these cases is being masked by the sensitivity to other parameters and an agreeing inverse FE result can still be obtained if viscoelasticity is not included. Future work will investigate the sensitivity of the inverse FE outcomes to the initial guess for viscoelasticity and its inclusion in the material model.

The intermittent FE model demonstrates relaxation behaviour that approximates the initial relaxation periods present in the data

immediately after the 50N transition. At later times, the reductions in force in the FE model response are not as great as those seen in the experimental data. The optimization may not be as sensitive to the difference in relaxation shape because two of the experimental curves end earlier than the FE curve where the agreement is better. Additionally, the viscoelasticity model assumes a quasi-linear response which may not capture nonlinear viscoelastic effects. Further work will investigate these possibilities and their influence on the predictive capability of the FE model.

The findings of this study indicate that the axisymmetric FE model is appropriate for modelling the case of vertical tooth extraction, although further validation of the results are required. Future work will focus on validating the material parameters and testing the model response against load schemes other than those used in the inverse FE problem to demonstrate its suitability as a predictive tool for improving tooth extraction procedures.

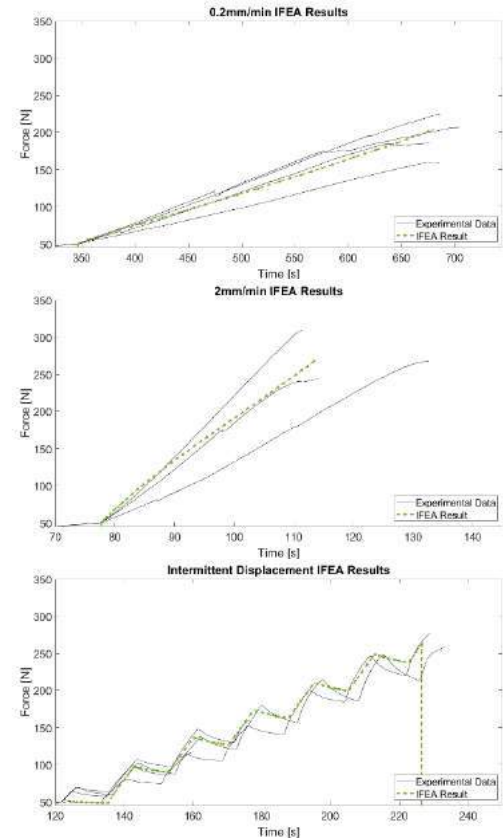


Figure 3: Experimental force-time curves and inverse FE results

ACKNOWLEDGEMENTS

The authors gratefully acknowledge the support of the Natural Sciences and Engineering Research Council of Canada (NSERC) Canada Graduate Scholarship and Discovery Grant Programs.

REFERENCES

- [1] Bergmann, G et al., *J Biomech*, 34:859-871, 2001.
- [2] Dym, H and Weiss, A., *Dent Clin North Am*, 56:245-66, 2012.
- [3] Muska, E et al., *Oral Surg Med Pathol Radiol*, 116:e303-10, 2013
- [4] Natali, A et al., *Comput Methods Biomech Biomed Eng*, 6:5-6, 2003
- [5] Genna F and Paganelli C, *J Mech Mat Struct*, 9:497-514, 2014.
- [6] Maas SA et al., *J Biomech Eng*, 134:011005, 2012.
- [7] Arruda, EM and Boyce, MC. *J Mech Phys Solid*, 41:389-412, 1993
- [8] D'Errico J, MATLAB Central File Exchange, 2021.
- [9] Moerman KM, *J Open Source Softw*, 3:506, 2018

EVOLUTION OF HUMAN CORTICAL THICKNESS AND MORPHOLOGY THROUGHOUT GROWTH AND DEVELOPMENT

Nagehan Demirci (2), Maria A. Holland (1,2)

- (1) Aerospace and Mechanical Engineering, University of Notre Dame, Notre Dame, Indiana, USA
(2) Bioengineering Graduate Program, University of Notre Dame, Notre Dame, Indiana, USA

INTRODUCTION

The brain is one of the most intricate structures of the mammalian body. Its outermost layer, i.e., the cerebral cortex, is folded with outer gyral ridges and inner sulcal valleys. The degree of foldedness (i.e., gyrification) varies across species, such that smaller species tend to have less folded cortices, and gyrification increases gradually with an increase in size [1]. A similar picture is observed throughout the growth and development of individual species. For example, fetal cortices are relatively smooth for humans until the later stages of gestation, in which cortical folds begin to emerge and the cortex is highly folded at full-term birth (Figure 1).



Figure 1: Human brain development from gestation week 25 to 43

The folding patterns are unique to each individual, similar to fingerprints, but one common feature is that gyri are thicker than sulci [2,3]. In our previous work, we developed an open-source computational pipeline that explores patterns of cortical thickness, incorporating outer and inner folds at each depth [4]. Utilizing public imaging resources, we investigated the consistent patterns of cortical thickness for multiple primate species [1,3]. Our previous results indicate that cortical thickness patterns are consistent for primate cortices with varying shapes, sizes, and degrees of foldedness – outer folds are consistently thicker than inner folds. However, not much is known about how these patterns emerge throughout development.

MRI of the human fetal brain has been a clinical tool for many years. Advances in MRI acquisition techniques enable high-resolution, complete 3D imaging of the brain *in utero*. This allows emerging cortical folding patterns to be characterized accurately. Successful quantification of the folding patterns of the cortex *in utero* is indispensable for understanding changes in folding, which are linked to

atypical brain development, as well as early and objective diagnosis of neurological deficits and disorders via reliable and accurate biomarkers.

In this study, we are interested in understanding the evolution of cortical thickness and folding patterns throughout human brain growth and development. By this, we aim to link structural changes spatially and temporally to ontogenetic (e.g., proliferation and myelination) and biomechanical determinants (e.g., differential growth).

METHODS

Here, we investigated the ontogeny of the human cortex from gestation week (GW) 25 to 43 using publicly available fetal and neonatal structural magnetic resonance images (MRIs).

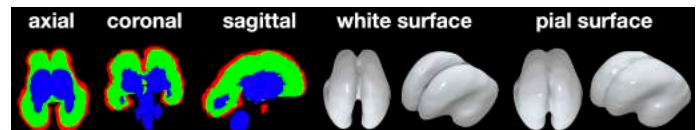


Figure 2: Fetal human brain at GW25. Left: MRIs (axial, coronal, and sagittal views) depicting manual, three-tissue class segmentation labels (red: gray matter, green: white matter, blue: subcortical structures). Middle: Reconstructed white surface. Right: Reconstructed pial surface.

To achieve this, we obtained N=7 (N=3 at GW23, N=1 at GW25, and N=3 at GW27) T2-weighted fetal brain MRIs from the FeTA (Fetal Tissue Annotation and Segmentation Challenge) public data set [5]. The images were manually segmented into seven tissue classes (external cerebrospinal fluid, gray matter, white matter, ventricles, cerebellum, brainstem, and deep gray matter). We carefully reviewed the manual annotations at each slice from each direction (axial, sagittal, coronal) and refined them further using openly available medical image visualization and editing tools MRICroGL and ITK-SNAP. Next, we

converted the gray and white matter segmentations into 3D surfaces using AFNI and Freesurfer to create triangulated surfaces with spherical topology (Figure 2).

Additionally, we accessed N=76 (N=2 at GW29 and 31, N=11 at GW33, N=21 at GW35, N=5 at GW37, N=8 at GW39, N=6 at GW41, and N=2 at GW43) neonatal human brain MRIs from the ‘Developing Human Connectome Project Neonatal Data Release’ [6]. The data set includes labels of 3 tissue classes, subcortical structures, and reconstructed pial and white surfaces.

To analyze the local and global variations of cortical thickness and morphology during the growth and development of the human brain, we used our open-source computational pipeline [4] and calculated cortical thickness, cortical thickness ratio, curvature, shape index, sulcal depth, surface area, volume, and gyrification index (GI) at each growth stage. This extensive data allows us to track the evolution of each measure and the correlations between the measures.

RESULTS

First, we observed the evolution of each morphometry measure individually. For example, we observed the gradual emergence of sulci by plotting the distribution of shape index, which reveals the maturation of cortical folds. At GW27, we observe few concave and saddle-shaped points; however, at GW37, the frequency of concave shapes increases with the formation of distinct sulci and gyri (Figure 3A).

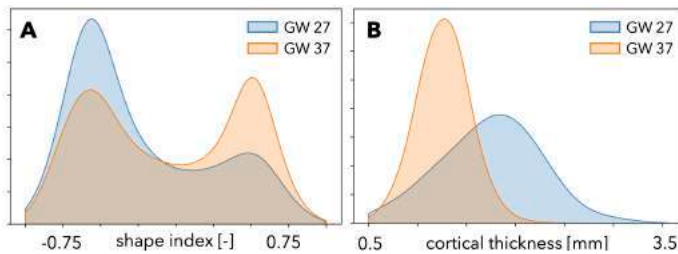


Figure 3: Evolution of shape index (A) and cortical thickness (B) before (GW 27) and after (GW 37) cortical folding

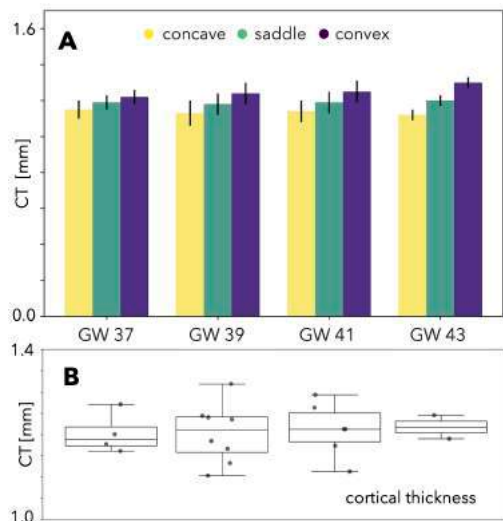


Figure 4: Cortical thickness (CT) is strongly correlated with shape (A), thickness is stable between GW 37 and 43 (B)

Second, we investigated the evolution of cortical thickness. Surprisingly, we found a thicker cortical plate at early stages of

gestation, when the cortex is still smooth. Then, the cortex thins significantly with the maturation of folds (Figure 3B).

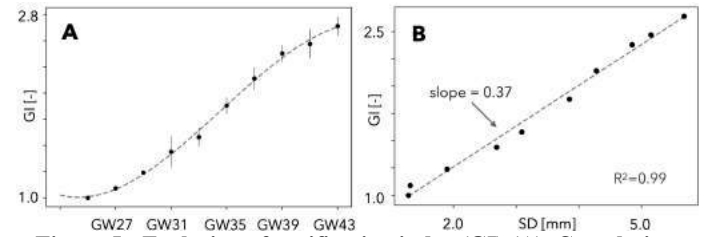


Figure 5: Evolution of gyrification index (GI) (A). Correlation between GI and sulcal depth (SD) (B)

Third, we investigated the correlation between cortical thickness and shape. Our preliminary data for the neonatal brains reveals a similar patterning between shape and cortical thickness: the convex shape is consistently thicker than the concave shape, which is thinner than saddle shape between GW37 to 43 (Figure 4A). We also found that sulci thin and gyri thicken. As a result, the gap between gyri and sulci widens, but the average cortical thickness remains stable (Figure 4B).

Finally, we tracked the evolution of GI (measure of foldedness). We observed that GI increases immediately with the emergence of folds but then reaches a plateau towards the end of maturation of folds (Figure 5A). We also found a strong correlation between GI and average sulcal depth (Figure 5B).

DISCUSSION

Human brain growth and development are distinct before and after birth. Gyrification mainly occurs during prenatal growth, evolutionarily and genetically dissociated from postnatal growth. Primary folds, which are more consistent across species, form first, right before the emergence of secondary folds, around the second trimester of pregnancy. On the other hand, the tertiary folds continue to form after birth throughout the first years of life.

We captured the dynamic growth of cortex and gyral-sulcal patterns from GW23 to 43 using the shape index, which yields better results than sulcal depth. In this study, following our prior approach, we investigated the correlation between cortical thickness and shape and detected that at GW37, the correlation between cortical thickness and shape becomes significant and consistent. GW37 coincides with the emergence of tertiary folding patterns. This finding will help us also determine the emergence of abnormal cortical folding patterns, which might be associated with neurological diseases and disorders. In addition, we showed that cortical folding strongly affects global cortical thickness. The bending and folding of the cortex at GW25 lead to the gradual thinning of the cortical plate. As a result, the variation of the morphological measures with gestational age would give us more insight into understanding typical and atypical cortical growth rates and patterns.

ACKNOWLEDGEMENTS

This work was supported by NSF Grant No. CMMI-2144412.

REFERENCES

- [1] Demirci, N. et al., (*under revision*).
- [2] Consolini, J. et al., *Brain Multiphysics*, 3, 2022.
- [3] Demirci, N. et al., *Human Brain Mapping*, 43 (6), 2022.
- [4] <https://github.com/mholla/curveball>.
- [5] Payette, K. et al., *Scientific Data* 8 (1): 167, 2021.
- [6] Edwards, A. D. et al., *Frontiers in Neuroscience* 16 (5), 2022.

CHARACTERIZATION OF LUNG LOBAR SLIDING KINEMATICS USING FINITE ELEMENT MODELLING AND HELMHOLTZ-HODGE DECOMPOSITION

Adam E. Galloy (1), Joseph M. Reinhardt (1), Suresh M. L. Raghavan (1)

(1) Roy J. Carver Department of Biomedical Engineering, University of Iowa, Iowa City, Iowa, United States of America

INTRODUCTION

Delineating the differences in motion between healthy and diseased lungs during breathing can improve clinical diagnoses. Treatment strategies such as radiation therapy and mechanical ventilation can potentially reduce the amount of harm delivered to healthy tissue by being delivered in conjunction with the lung's natural motion. One often-overlooked aspect of lung motion is the sliding between the different lobes of the lung along the lobar fissures. Little research exists identifying the anatomical features and mechanical forces that drive lobar sliding. This knowledge gap limits our understanding of the role of lobar sliding in lung mechanics and consequently our ability to distinguish normal from diseased lung motion.

One way to improve our understanding of lobar sliding is to decompose this complex motion into simpler components. For example, Hubmayr et al. described lobar sliding in dog lungs by quantifying differences in rotations between lung lobes [1]. However, the lung lobes undergo significant nonuniform parenchymal deformation which cannot be described by a single set of rotations [2]. Helmholtz-Hodge decomposition (HHD) is promising for the characterization of sliding kinematics because it can decompose a highly nonuniform vector field into three comprehensive components associated with stretching, rotation, and translation. The goal of this study was to use finite element models (FEM) to simulate lobar sliding in the left lung and demonstrate the use of HHD to characterize sliding kinematics with physically meaningful components that still capture the full nonuniformity and complexity of sliding motion.

METHODS

Six healthy subjects (ages 22-37) underwent CT scans following a procedure approved by our institutional review board. Scans were obtained with the subjects in the supine position during breath holds at total lung capacity (TLC) and functional residual capacity (FRC). The

two left lung lobes (upper and lower) and thoracic cavity were segmented from the images. From the segmentations at TLC, solid meshes representing the lung lobes were generated along with a surface mesh of the thoracic cavity.

Exhalation was simulated by prescribing displacements to the thoracic cavity surface to drive deformation of the lobar tissue with contact constraints. Thoracic cavity displacements were derived by registering the thoracic cavity mask at FRC to the mask at TLC. Contact was assumed to be frictionless between each of the lung lobes and between the lobes and thoracic cavity. Thoracic cavity displacements were applied incrementally (minimum of 20 increments) to allow the trajectories of points throughout the deformation to be tracked. Simulations were quasi-static and assumed no viscoelasticity in the lung tissue. This contact mechanics model of lobar sliding has been described in detail in Galloy et al. [3].

After the simulations, at each node of the lower lobe along the lobar fissure, a sliding displacement vector at time increment n was computed as follows:

$$\Delta \mathbf{s}_n = \boldsymbol{\pi}^U(\mathbf{u}_{n+1}^L - \mathbf{u}_n^L - \mathbf{u}_{n+1}^U + \mathbf{u}_n^U) \quad (1)$$

Where a superscript U and L signify the upper and lower lobe respectively and $\boldsymbol{\pi}^U$ is the projection operator onto the tangent plane of the upper lobe.

For each of the six subjects, HHD was performed on the sliding displacement vector field at the 10th time increment. HHD identifies three orthogonal components for a vector field on a surface homeomorphic to an open disc: the exact component, the coexact component, and the harmonic component [4]. The exact component is rotation-free and describes sliding motion arising from one lobe stretching differently than the other. The coexact component is divergence-free and describes the sliding motion arising from one lobe rotating about the other. The harmonic component is both rotation and

divergence-free and describes translational sliding motion. An example HHD of a sliding displacement field is shown in figure 1. The square magnitude of each HHD component was normalized to the square magnitude of the whole vector field to determine the relative contribution of each component.

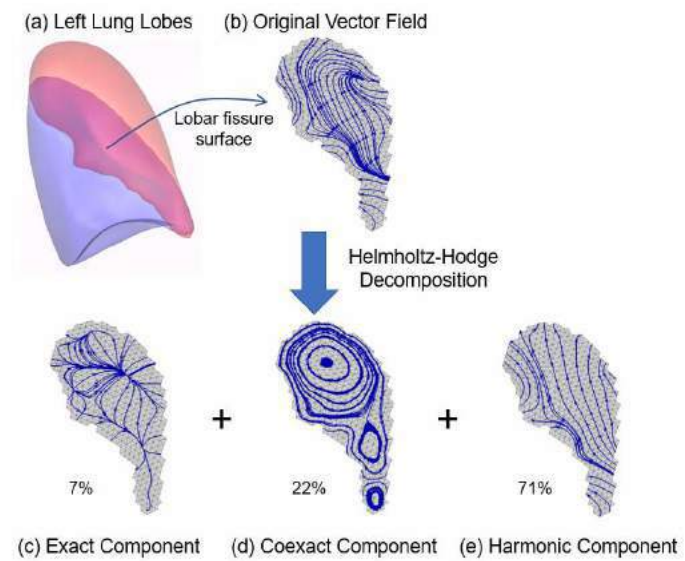


Figure 1: 3D model of the left lung showing the lobar fissure (a) with the streamlines of the sliding displacement vector field (b). The vector field was decomposed into three HHD components: a stretch induced exact component (c), a rotational coexact component (d), and a translational harmonic component (e).

RESULTS

The relative contributions of the three HHD components to the overall sliding displacement vector field are displayed for each subject in figure 2. On average, 88% of the sliding displacement vector field was captured by the harmonic component, 7.5% by the coexact component, and 4.2% by the exact component. The dominating harmonic component suggests that lobar sliding primarily conforms to the curvature of the fissure in a motion similar to translation that has little relative stretching or rotation between lobes.

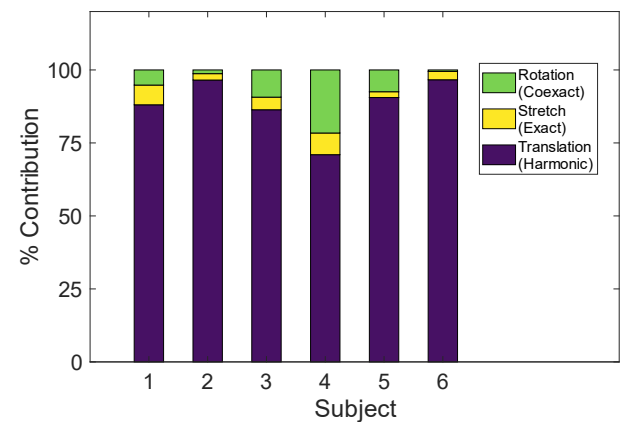


Figure 2: Relative contributions of HHD components in the study subjects shows that lobar sliding is predominantly translational (harmonic) with lesser contributions from rotational (coexact) and stretch induced (exact) motions.

The exact and coexact components had varied contributions to the overall sliding motion ranging from 2.0% to 7.4% and 0.5% to 21.6% respectively. Figure 3 compares the sliding displacement field streamlines of subject 4 who had the largest exact and coexact contributions to subject 6 whose motion was almost entirely harmonic. Subject 4 exhibits an inward spiral towards the top right (corresponding anatomically to an apical lateral location) indicating both rotation and compression of the lower lobe relative to the upper lobe at that location. On the other hand, subject 6’s streamlines form a nearly parallel field.

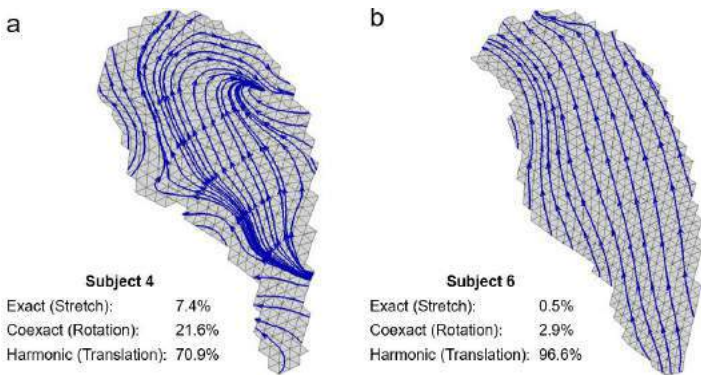


Figure 3: Subject 4’s streamlines (a) exhibit an inward spiral that is reflected by larger exact and coexact components. In contrast, subject 6 (b) exhibits nearly parallel streamlines and has small exact and coexact components.

DISCUSSION

In this study we sought to better understand lobar sliding by decomposing the sliding motion into physically meaningful components. Interestingly, we found that a large portion of the sliding motion could be described by translational motion. On the other hand, rotational motion between lobes played a smaller, sometimes negligible, role. This finding is consistent with the fact that the primary force driving lobar sliding during exhalation is the upward motion of the diaphragm which slides the lower lobe upward against the upper lobe (figure 3b). Rotation still plays a significant role in some subjects (figure 3a) but will not be an adequate descriptor of sliding motion on its own as in Hubmayr et al. [1] even when the non-uniformity of the rotation is accounted for.

A limitation to this study is that the FEM neglects three aspects of lung motion: deflection from the lung’s self-weight, the viscoelasticity of the lung tissue, and nonlinear thoracic cavity shape changes (we linearly interpolated between the TLC and FRC thoracic cavity shape for each displacement increment). Additionally, boundary effects on the HHD can potentially cause parts of the exact and coexact components to “bleed in” to the harmonic component and inflate its value. However, these limitations are unlikely to affect our finding that translation predominates lobar sliding in the left lung. Future work will examine the impact of these limitations.

ACKNOWLEDGEMENTS

This work was supported in part by training grant T32 HL144461 and research grant R01 HL142625 from the National Institutes of Health.

REFERENCES

[1] Hubmayr, R. et al., *J Appl Physiol.*, 63:2467-2475, 1987.
[2] Amelon, R. et al., *J Biomech.*, 44:2489-2495, 2011
[3] Galloy, A. et al., *Appl. Eng. Sci.*, 10:10098, 2022.
[4] Poelke, K. and Polthier, K., *Comput.-Aided Des.*, 78:126-136, 2016.

VASCULAR SMOOTH MUSCLE CELLS RETAIN THEIR MATERIAL PROPERTIES IN MECHANICALLY VARIANT MICROENVIRONMENTS

Elizabeth D. Shih (1), Ryan R. Mahutga (1), Katriel S. Ng (1), Patrick W. Alford (1)

(1) Department of Biomedical Engineering
 University of Minnesota
 Minneapolis, MN, USA

INTRODUCTION

Arterial mechanical properties are often changed in diseased tissues, such as in aneurysms and atherosclerosis.¹ Many cell functions are influenced by changing extracellular properties, guiding tissue rehabilitation or disease progression.² Vascular smooth muscle cells (VSMCs) are the mechanically dominant cells in arteries and actively respond to mechanical signals via contraction, dilation, or phenotypic switching.³ To date, it is not known whether VSMCs' nonlinear mechanical properties themselves depend on extracellular mechanics.

Here, we used cellular micro-biaxial stretching (CμBS) to examine how VSMC mechanics are influenced by extracellular mechanics.⁴ To do so, we first determined how traction force microscopy (TFM) analysis assumptions are influenced by substrate mechanics.⁵ Next, we measured mechanical properties of individual VSMCs micropatterned on substrates of varying mechanical properties. We found that VSMC mechanical properties are relatively unchanged over a physiological range of extracellular moduli. This finding has important implications for understanding the cellular mechanics of arterial disease, how they are influenced by tissue-scale properties, and how they subsequently respond to and remodel their local environments.

METHODS

Substrate Fabrication and Cell Culture. Polyacrylamide (PA) gels doped with fluorescent microspheres were synthesized onto elastomer membranes using previously described methods.⁴ PA gel modulus was varied from 14.0 kPa to 240 kPa by increasing ratios of 2% bis-acrylamide to 40% acrylamide. A layer of patterned 32 x 128 μm² fibronectin islands was stamped onto the top of the PA gel to facilitate cell adhesion onto the substrates. Human umbilical artery VSMCs (Lonza) in between passages 5-7 were micropatterned onto the gels. The VSMCs were cultured overnight in supplemented Medium 199 (Gibco), incubated at 37 °C and 5% CO₂. 24 hours before stretching, a contractile state was induced in the cells by exchanging the media with supplemented serum-free media.

Biaxial Stretching. The elastomer constructs were mounted in a custom designed CμBS apparatus on an inverted microscope (**Fig. 1A**). The CμBS device equibiaxially stretched the constructs in increments of 5% up to 20%, with brightfield and fluorescent images taken at each stretch increment of the cells and the underlying beads in the gel. The cells were then lysed and the bead layer was imaged again at the same location at each stretch increment. The fluorescent images of the gel layers with the adhered cells were paired with respective images of the gels without the cells to perform traction calculations (**Fig. 1B**).

Traction Calculation. Displacement of the beads due to cellular contraction was tracked and measured using a particle image velocimetry (PIV) ImageJ plugin between the paired images with and without the adhered VSMCs.⁶ Taking the displacement data and the known material properties of the substrate, an unconstrained Fourier

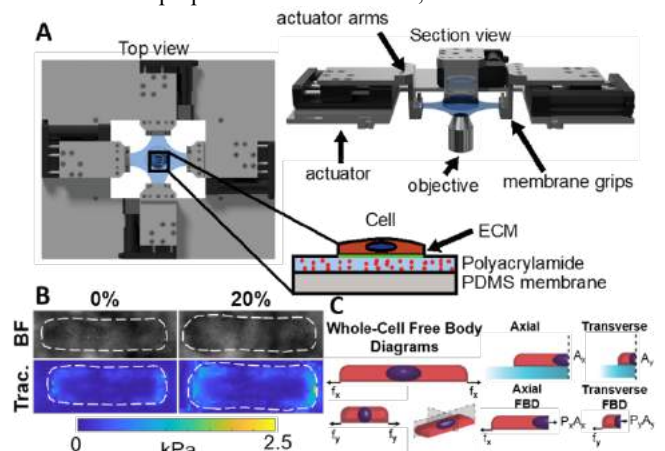


Figure 1. A. CμBS apparatus.⁴ B. Brightfield images of undeformed and stretched cell with corresponding traction maps. C. Calculation of axial and transverse PK1 stresses in a single cell.⁷

transform traction cytometry (FTTC) ImageJ plugin calculated traction stress vectors throughout the area occupied by the cell.⁶ During FTTC, a regularization factor λ is used to improve resolution and account for noise in the displacement data such that⁵

$$\iint [\tilde{G}_{ii}G_{ij}T_j - G_{ji}u_j]dr''dr' + \lambda^2 \int H_{ij}T_j dr' = 0 \quad (1)$$

λ drives the solution towards a default solution described by $\int H_{ij}T_j dr'$. G_{ij} is the Green function that maps the displacement vector u_j to the traction vector T_j . r is the absolute value of the displacement of surface point r to r' . For 0th order regularization, H_{ij} is the identity tensor.

Surface tractions were used with confocal imaging of the actin cytoskeleton to calculate the midplane first Piola-Kirchoff (PK1) stress P_i of the cell as previously described (Fig. 1C).⁴ For biaxial stretching, P_i was calculated for each stretch increment from 0% to 20% to obtain stress-stretch data. The stress-stretch curves were fit to a Holzapfel-Gasser-Ogden (HGO) strain energy density function given by

$$W = \frac{\mu_m}{2} (F_{mi}F_{mi} - 3) + \frac{C_f}{4} (K_{ij}(A_{ki}^{-1}(F_{mk}F_{mi})A_{lj}^{-1})) - 1)^2 \quad (2)$$

where F_{ij} is the deformation gradient and K_{ij} describes the actin fiber distribution.⁸ In its principal axes, A_{ij} may be described as $\lambda_a \delta_{ij}$. Eq. 2 was fit to obtain values for parameters μ_m , C_f , and λ_a , reflective of the shear modulus, actin stiffness, and activation stretch, respectively.

Finite Element Model. A finite element (FE) model was developed to simulate deformation of the gel by VSMCs during biaxial stretching in COMSOL Multiphysics. The model was comprised of the elastomer substrate, PA gel, and a micropatterned VSMC. Quarter symmetry conditions were imposed to simplify the model (Fig. 2A). The elastomer membrane and the gel were both modeled as nearly incompressible Neo-Hookean materials, and the cell was modeled as an HGO material. FTTC regularization levels were optimized using error minimization between the experimental displacement and the displacement calculated by the simulated forward problem.

RESULTS

Determining an optimal level of regularization. Prior studies in unstretched cells showed that regularization factor value (λ in Eq. 1) affects the calculated traction magnitude in TFM experiments.⁹ To determine the effect of regularization on our experiment, we first performed $C\mu$ BS studies using varying regularization, then the fitted HGO parameters from the experimental data were assigned to a finite element model of the VSMC and an that replicated the experimental protocol. The resulting simulated displacement of the gel by VSMC contraction was compared to the PIV data, and a regularization factor was calculated that minimized error between the simulation and the experiment (Fig. 2B). In cellular biaxial stretching assays, we found that as substrate Young's modulus increases, VSMCs deform the substrate less. Thus, as substrate modulus increases, the simulations using the parameters with lower regularization levels, or less filtering, are in better agreement with the experimental data (Fig. 2C).

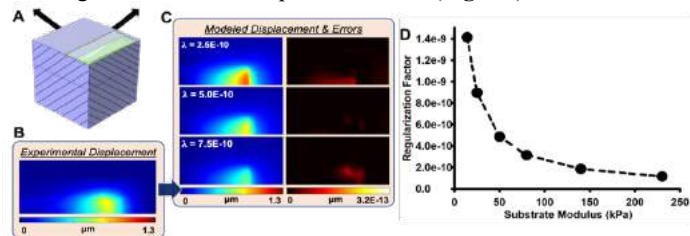


Figure 2. Identification of an optimal regularization factor for each substrate group. A. FE model geometry and boundary conditions. B. Average experimental displacement for one group. C. Model results at different regularization factors compared against experimental data. D. Optimal regularizations plotted.

Effect of extracellular stiffness on VSMC properties. We calculated traction forces with the optimized regularization factors. PK1 stresses were calculated and average stress-strain curves were generated for VSMCs on substrates of different moduli. From the stress-strain data, we calculated basal tones as the initial axial stress (Fig. 3A), apparent axial moduli, or the fitted linear slope of the axial stress-strain curve (Fig. 3B), actin activation stretches (λ_a) (Fig. 3C), and actin stiffnesses (C_f) (Fig. 3D). On the lowest modulus substrates, VSMCs had higher basal tones, apparent moduli, and actin stiffnesses than on all other substrates. However, the VSMCs seeded on all other substrates showed little difference in the four investigated properties.

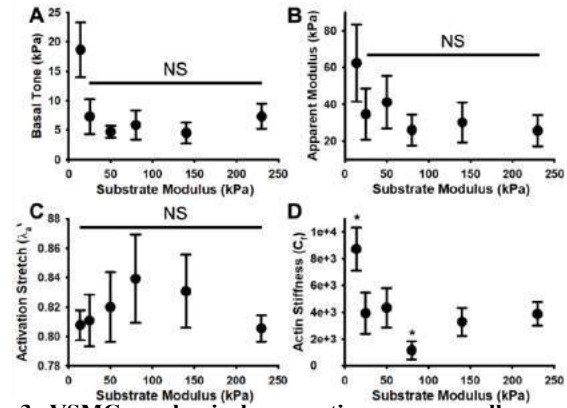


Figure 3. VSMC mechanical properties are generally consistent across substrate groups. A. Basal tones. B. Apparent moduli. C. HGO-fitted actin stiffnesses. D. HGO-fitted actin activation stretches. * denotes that that condition is statistically different ($p < 0.05$) from all other conditions and NS stands for Not Significant.

DISCUSSION

Using $C\mu$ BS with a varied regularization approach, we find that VSMC mechanical properties for cells seeded on substrates of moduli from 25 kPa up to 240 kPa are generally consistent. Prior studies have shown arterial moduli at small inflations lie in the range of 72-134 kPa.¹⁰ Taken with our data, this suggests that VSMC properties change very little in healthy arteries. Diseased tissues like cerebral aneurysms can be much softer than healthy tissue.¹¹ Here we find that in very soft environments, VSMC mechanics are altered, suggesting that in these very soft tissues, changes in extracellular mechanics might influence VSMC mechanics and potentially influence disease progression.

This work has important implications for understanding how VSMCs respond to a range of microenvironmental conditions like those observed in aneurysms. VSMC response might be a key determinant in whether an artery is able to successfully adapt to hazardous conditions or maladapt into dysfunction, such as the formation of an aneurysm susceptible to rupture or a plaque that inhibits tissue elasticity. Our results allow us to model VSMC mechanical responses as generally consistent in response to changing microenvironments, simplifying the mathematical complexity while retaining physiological accuracy.

ACKNOWLEDGEMENTS

NSF (CMMI 1553255). Doctoral Dissertation Fellowship (U of M).

REFERENCES

- [1] Lacolley, P et al., *Arterioscler Thromb Vasc Bio*, 40(5). 2020.
- [2] Wang, T et al., *ChemBioChem*, 21(9). 2020.
- [3] Liu, S et al., *J Vasc Res*, 59(2). 2022.
- [4] Win, Z et al., *J Biomech Eng*, 139(7). 2017.
- [5] Butler, JP et al., *Am J Phys*, 232. 2002.
- [6] Tseng, Q et al., *PNAS*, 109. 2011.
- [7] Win, Z et al., *Biophys J*, 115(10). 2018.
- [8] Gasser, TC et al., *J R Soc Interface*, 3(6). 2006.
- [9] Stricker, J et al., *J Phys Condens Matter*, 22(19). 2010.
- [10] Bernal, M et al., *J Acoust Soc AM*, 129(3). 2011.
- [11] Shih, ED et al., *J Vasc Res*. 59(1) 2021.

ON THE CLOSURE KINEMATICS OF AORTIC MECHANICAL HEART VALVES VERSUS BIOPROSTHETIC HEART VALVES

Syed Samar Abbas (1), Iman Borazjani (1)

(1) J. Mike Walker '66 Department of Mechanical Engineering, Texas A&M University, College
Station, Texas, USA

INTRODUCTION

Only in the United States each year, over 100,000 patients undergo the replacement of malfunctioning aortic heart valves with prosthetic/Artificial Heart Valves (AHVs) [1]. AHVs could be mainly classified into two types: (i) Bioprosthetic Heart Valves (BHV), composed of material from live tissues [2] or (ii) Mechanical Heart Valves (MHVs), generally made up of Pyrolytic Carbon [3]. The BHVs offer an excellent hemodynamic performance, however, their constituent tissues degenerate over time, gradually resulting in their invincible deterioration. The MHVs are although durable, they have been reported to cause platelet activation that leads to thrombotic events [4]. The closure kinematics of typical MHVs bear critical importance, as they have been strongly related to their non-physiological hemodynamics, for instance, a higher regurgitation volume in comparison to the natural valves/BHVs [5] and promotion of platelet activation [6]. New designs of MHVs are therefore required to emulate the closing behavior and hemodynamics of natural valves/BHVs, such that a less thrombogenic and simultaneously durable AHV could be attained. This research, for the first time, numerically investigates the closure kinematics and hemodynamics of a newly designed Trileaflet MHV (TMHV) and compare them with a conventional Bileaflet MHV (BMHV) and a BHV under similar conditions.

METHODS

For the TMHV and the BMHV, the designs of the TRIFLO Valve (Novostia SA, Switzerland) and the On-X Valve (CryoLife Inc., USA), respectively, were selected. The BHV leaflets are modelled as non-linear, membrane-like, thin shell structures composed of anisotropic material undergoing deformations to replicate the experimentally observed stress-strain behavior of a heart valve tissue [7].

Numerical Fluid-Structure Interaction (FSI) simulations were carried out by employing the Curvilinear Immersed Boundary

(CURVIB) method as a flow solver, strongly coupled with a robust FSI algorithm for calculating the leaflet kinematics of the three AHVs [8].

Owing to the elastic deformation of the BHV leaflets, it is not possible to graphically plot the FSI angles they cover in response to the cardiac flow against time and compare them with the two MHVs. Thus, to enable the graphical visualization and facilitate a comparison of the AHVs' leaflet kinematics, the projected area of each AHV on a plane perpendicular to the streamwise direction (the z-plane) was calculated by using Equation 1 and plotted against time.

$$PA_V = \frac{IOA_V - \sum_{i=1}^n PAL_i}{IOA_{BHV}} \quad (1)$$

where, PA_V is the projected area of the AHV on the z-plane, IOA_V is its inner orifice area, PAL_i is the projected area of the '*i*th' leaflet, *n* is the number of leaflets in the AHV, being 3 for the TMHV and the BHV, whereas 2 for the BMHV, while IOA_{BHV} is the inner orifice area of the BHV, being the largest and therefore used for normalization.

RESULTS

Figure 1 illustrates the projected area on the z-plane for the three AHVs under consideration, showing that the BHV has the largest projected area during the peak systolic phase of the cardiac cycle in comparison to the TMHV and the BMHV. The BMHV has a slightly larger projected area during the peak systole in comparison to the TMHV, owing to the BMHV's non-circular housing geometry. During the forward deceleration phase of the cardiac cycle, the projected area starts to decrease for the TMHV and the BHV, indicating the commencement of the closure kinematics of their leaflets, while remains constant at the maximum for the BMHV, indicating fully opened leaflets. The projected area of the TMHV and the BHV reduces to its near minimum by the early regurgitation phase of the cardiac cycle. In contrast, the BMHV has a relatively higher projected area during early regurgitation, which reduces to its minimum by the mid-diastolic phase of the cardiac cycle. These results imply that the leaflets

of the TMHV and BHV begin to close while there still exists forward flow during the systolic deceleration phase of the cardiac cycle and complete the major fraction of their closing excursion by early regurgitation in comparison to the BMHV, for which the two leaflets start undergoing closure due to the onset of regurgitation.

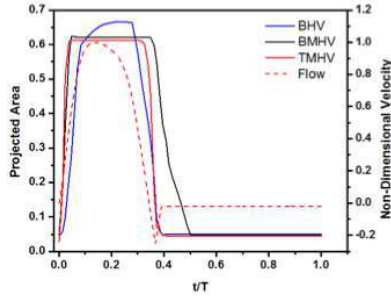


Figure 1: Projected Area for the three AHVs

To understand the closing behavior of the three AHVs, the Transvalvular Pressure Gradient (TPG), calculated as shown by Equation 2, has been plotted against time in Figure 2.

$$\frac{\Delta P}{\rho U^2} = TPG = P_u - P_d \quad (2)$$

where, ΔP is the net pressure, P_u is the pressure on the upstream ventricular side of the AHV, while P_d is that on the downstream aortic side. A continuous decrease in the TPG could be observed during the systolic deceleration phase for all AHVs, with high oscillations occurring at the instant of the valve closure.

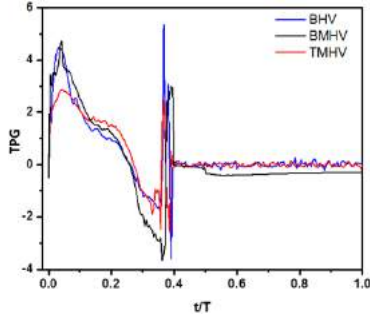


Figure 2: TPG for the three AHVs

Augmented with a decreasing TPG for the TMHV, it is observed that the sinus-sides of its leaflets develop a higher pressure in comparison to their central flow-sides during the systolic deceleration, as shown for various instants by Figure 3. Consequently, a pressure force is created which is directed towards the closure of each leaflet.

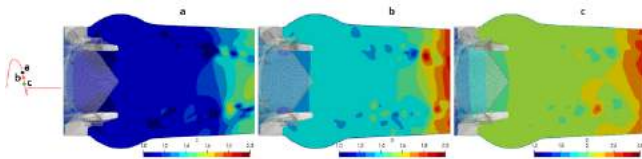


Figure 3: Pressure variation in TMHV during deceleration

In contrast, since the leaflets of the BMHV are oriented within the central flow region, the pressure on the sinus-sides of its leaflets remains nearly the same as that on their central flow-sides as shown in Figure 4 for various instants of the systolic deceleration phase. The BMHV leaflets therefore wait for the regurgitation to begin closing.

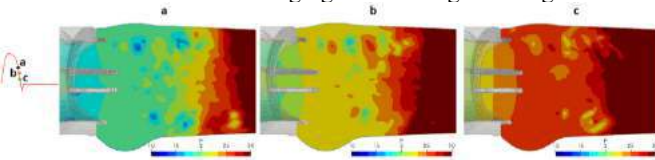


Figure 4: Pressure variation in BMHV during deceleration

The elastic deformation of the BHV leaflets as they move towards their fully closed positions causes high spatial variations in the pressure on the sinus- and central flow-sides of its leaflets. For this reason, the net fluid pressure (*Pressure Difference*) on the BHV leaflets was calculated as shown in Equation 3 and has been illustrated for one of the three BHV leaflets during the systolic deceleration, granted the three leaflets respond similarly to the pressure variations across them.

$$Pressure\ Difference = P_s - P_c \quad (3)$$

Where, P_s is the pressure on the sinus-side of the BHV leaflets, while P_c is that on their central flow-side.

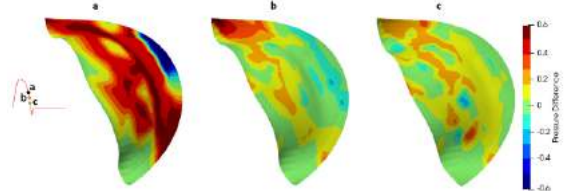


Figure 5: Pressure variation on a BHV leaflet during deceleration

From Figure 5a, it could be observed that the *Pressure Difference* is positive for the belly region and the other major portion of the leaflet's surface excluding the fixed edge for early systolic deceleration, indicating a higher P_s in comparison to P_c , thereby creating a pressure force directed towards the closing position. As the cardiac cycle advances in time, the *Pressure Difference* decreases, however, remains positive and the leaflet continues its closing excursion.

DISCUSSION

This numerical study compares the closing kinematics, and the associated hemodynamics of two designs of MHVs, the TMHV and the BMHV, against a BHV under similar conditions for the first time. The leaflets of the TMHV and the BHV start to close during the systolic deceleration phase, and complete most of their closing excursion by the early regurgitation, with similar and smooth closing pattern towards the center as earlier observed in experiments [9]. Congruous to the native aortic valves which have been reported to begin their closure during the systolic deceleration [5], the leaflets of the TMHV and BHV also start to close as the flow decelerates in response to a higher pressure developed on the sinus-sides of their leaflets compared to their central flow-sides. The BMHV leaflets, however, begin their closing excursion by the onset of regurgitation as previously observed by several studies [5, 6], with high oscillations occurring in TPG at the valve closure, as earlier experimentally observed [10]. The early closure of the TMHV and the BHV is a physiologically desired feature, whereas the delayed closure of BMHV might generate a high regurgitant volume and consequently cause an additional workload on the heart [5].

ACKNOWLEDGEMENTS

The authors acknowledge the financial support from Novostia SA, Switzerland and computational resources from the High-Performance Research Computing (HPRC) group at Texas A&M University.

REFERENCES

1. Tsao, C.W., et al., Circulation, 2022. **145**(8): p. e153-e639.
2. Mohammadi, H, et al. Med. Eng. and Phy, 2011. **33**(2): p. 131-147.
3. Hatoum, H., et al., J Mech Behav Biomed Mater, 2020.
4. Bozzi, S., et al., Int J of Art Organs, 2021. **44**(12): p. 1013-1020.
5. Borazjani, I., et al., Ann Biomed Eng, 2010. **38**(2): p. 326-344.
6. Abbas, S.S., et al., Artificial Organs, 2020. **44**(2): p. E20-E39.
7. Borazjani, I., Comput Methods Appl Mech Eng, 2013.
8. Borazjani, I., L. Ge, et al., J Comput Phys, 2008.
9. Vennemann, B., et al., ASAIO journal, 2018. **64**(5): p. 651-661.
10. Dasi, L., et al., Physics of Fluids, 2007. **19**(6): p. 067105.

BIOMECHANICS OF CANCER CELL INVASION ACROSS THE VASCULAR ENDOTHELIUM

Chaohui Jiang (1), Guangsong Xie (1), Baohua Ji (1) *

(1) Institute of Biomechanics and Applications, Department of Engineering Mechanics, Zhejiang University, Hangzhou 310027, China

* Corresponding author

INTRODUCTION

Tumor metastasis is one of the leading causes of death in cancer patients. Intravasation and extravasation are critical processes in tumor metastasis. The process of cancer cells crossing the endothelium of a blood vessel or lymphatic vessel into the circulatory system is called intravasation, and the process of cancer cells penetrating the vessel and entering the tissue parenchyma from the blood vessel is called extravasation[1]. Most studies on intravasation and extravasation had been focused on the influence of biochemical factors, such as transforming growth factor- β (TGF β) or vascular endothelial growth factor (VEGF), which increase the number of cancer cells entering into blood vessels, increasing metastasis[2, 3]. However, the underlying mechanisms of how cancer cells invade across the vascular endothelium and the biomechanical interactions between cancer cells, vascular endothelium, and extracellular matrix are poorly understood.

In this study, we focus on the biomechanics of cancer cells invading across the vascular endothelium to reveal biomechanical properties and biomechanical interactions of cancer cells, vascular endothelial cells, and extracellular matrix (ECM).

METHODS

Human umbilical vein endothelial cells (HUVEC) were seeded on a confocal dish to form a cell monolayer. Colorectal cancer cells LoVo cells were seeded on the HUVECs monolayer for invasion, forming a model for the process of tumor cell invasion of the vascular endothelium (Figure 1). After being seeded with LoVo cells, the dish with experimental samples was placed in a live cell workstation for time-series photography. In order to make living cells fluorescent, we use lentiviral transfection and actin tracking staining. To explore the role of actin polymerization and cell contraction, we used several kinds of inhibitors to inhibit actin polymerization and cell contraction. To visualize the expression of focal adhesions, we used immunofluorescence. In the measurement of cell traction, we used the

micropattern printing technique, and we measured the cell traction force by analyzing the displacement of the substrate fluorescent microbeads. The image data were processed and analyzed in ZEN BLUE 3.1, Imaris9.0.1, and ImageJ. GraphPad Prism 8 software was used for statistical analysis and graphing. The cell layer is modeled as a two-dimensional, continuous elastomer with pre-strain for considering the active contraction of cytoskeleton. The stresses in the cell layer under various conditions are obtained by solving the equation of elasticity using the numerical method in COMSOL.

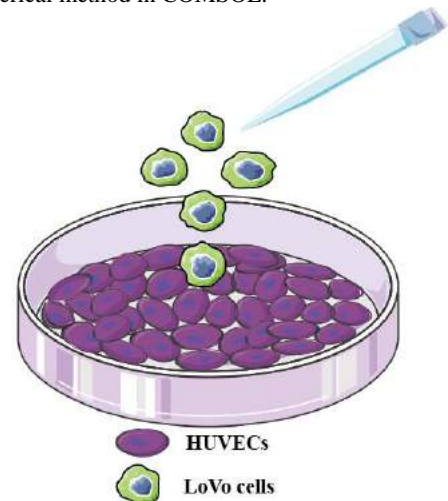


Figure 1: LoVo cells were seeded on the HUVECs monolayer.

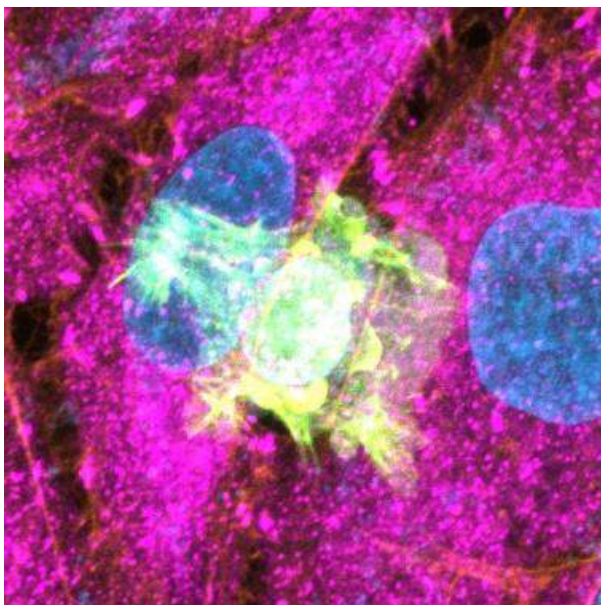
RESULTS

Our results suggest that cancer cells invade across the vascular endothelial cell layer through protruding pseudopodia, establishing adhesions and cancer cell extrusion (Figure 2). These three processes

are continuous, interrelated, and intertwined. Among these three processes, the polymerization of cancer cell actin and cell contraction plays crucial roles. With cancer cells invading and the adhesion becoming stronger, the traction force was developed.

We observed two important approaches in which the vascular endothelial cell layer acts as a barrier to the invasion of cancer cells. The first one is the density of vascular endothelial cells. A higher cell density leads to a stronger barrier and, thus, a lower invasion rate of cancer cells (Figure 3). The second one is the formation of actin rings among vascular endothelial cells, in which case the actin ring could block the nucleus of the cancer cell and prevent its passage. We further found that the stiffness of the cancer cell nucleus is critical in determining whether the actin ring between vascular endothelial cells could block the invasion of cancer cell.

The mechanical properties of the extracellular matrix also play a vital role. We found that substrate stiffness can affect cancer cells' invasion and crossover efficiency.



F-actin/F-actin/Paxillin/Hoechst

Figure 2: The invasion of cancer cell into the vascular endothelial monolayer.

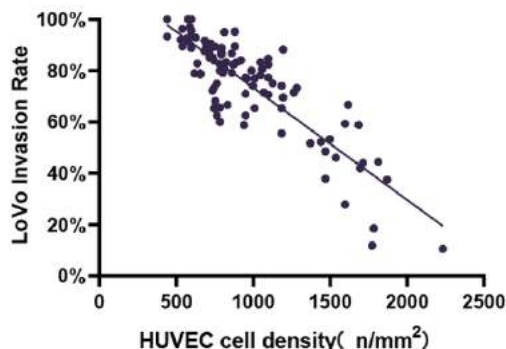


Figure 3: The invasion rates of LoVo cells under different levels of HUVECs density.

DISCUSSION

Our research revealed the process of tumor cell invasion across the vascular endothelium. We found that substrate stiffness affects the

barrier capacity of the cell layer. And the actin ring structure formed a physical blockade to the invasion of the cancer cell. The ring-shaped actin structure of actin has been described in cell division, wound healing, epithelial cell extrusion, and *Drosophila* dorsal closure[4]. But the role of actin-ring in the cancer invasion has not been reported before. In addition, we found that the softening of the nuclei significantly reduced the chances of cancer cell nuclei being blocked by actin rings among vascular endothelial cells. Our results revealed the relationship between the stiffness of the nucleus and invasion ability. This finding differs from the previous researches on the endothelial barrier, which were mostly focused on the intercellular connection.

This study gives useful insights into the mechanics of cancer cell invasion and may provide clues for searching for potential targets and developing novel cancer therapies.

ACKNOWLEDGEMENTS

This work was supported by fund from National Natural Science Foundation of China (Grants No. 11932017)

REFERENCES

- [1] S. Valastyan, Robert A. Weinberg, Tumor Metastasis: Molecular Insights and Evolving Paradigms, *Cell* 147(2) (2011) 275-292.
- [2] S. Giampieri, C. Manning, S. Hooper, L. Jones, C.S. Hill, E. Sahai, Localized and reversible TGF β signalling switches breast cancer cells from cohesive to single cell motility, *Nature Cell Biology* 11(11) (2009) 1287-1296.
- [3] C. Anderberg, S.I. Cunha, Z. Zhai, E. Cortez, E. Pardali, J.R. Johnson, M. Franco, M. Pérez-Ribes, R. Cordiner, J. Fuxe, B.R. Johansson, M.-J. Goumans, O. Casanovas, P. ten Dijke, H.M. Arthur, K. Pietras, Deficiency for endoglin in tumor vasculature weakens the endothelial barrier to metastatic dissemination, *Journal of Experimental Medicine* 210(3) (2013) 563-579.
- [4] C. Schwyer, M. Sikora, J. Slovakova, R. Kardos, C.P. Heisenberg, Actin Rings of Power, *Dev Cell* 37(6) (2016) 493-506.

USING AN INVESTIGATIVE MICROSCALE MODEL TO STUDY MECHANICAL WHITE MATTER PROPERTIES IN DEMYELINATING DISEASES

Xuesong Zhang (1), Johannes Weickenmeier (1)

(1) Department of Mechanical Engineering,
Stevens Institute of Technology
Hoboken, NJ, United States

INTRODUCTION

Myelin plays a significant role during early brain development and strongly influences the mechanical environment of brain white matter [1]. Weickenmeier et al. studied white and gray matter of fresh bovine brain and found a proportional relation between myelin density and tissue stiffness [2]. Some other methods have been used to reveal the relationship between myelin and stiffness. Among these methods, indentation is considered as a promising approach to study mechanical white matter properties. However, the exact correlation between indentation tested stiffness and microstructure of white matter remains unclear.

Here, we present a computational approach that uses an investigative microscale model (IMM) to rationalize the microstructural origin of mechanical white matter properties. Our study will allow us to systematically explore mechanical white matter tissue behavior in diseases such as multiple sclerosis and aging.

METHODS

Model Creation. We reconstruct a representative white matter model from a transmission electron microscopy (TEM) image of an axon bundle and obtain myelin sheath properties from literature (inner diameter (0.75-2.5μm), g-ratio (0.5-0.74), and sheath length (5-35μm)) [3,4]. Specifically, as shown in Figure 1, the TEM image (1A) was binarized (1B), and subsequently imported into Simpleware to create the IMM (1C-G). First, each axon was segmented individually (1C). Next, up to four concentric layers were created around each axon to represent myelin sheaths (1D). The remaining space was filled to represent extracellular matrix (ECM). This approach allows us to model demyelination by changing material properties for each distinct ring around axons. The final 3D model included additional details such as variable sheath length and inter-sheath distance (1E). The axon, myelin, and ECM were meshed with linear tetrahedral elements (1F-G).

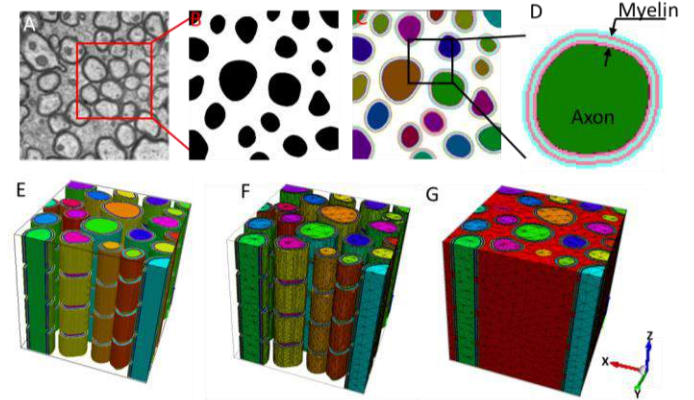


Figure 1: The creation of IMM, (A) TEM microstructure image of white matter, (B) the created axon (black) and ECM (white) image, (C) the created masks for axons and myelin sheaths, (D) the illustration of a single axon with four layers of myelin sheath, (E) 3D view of the IMM model with axons and myelin sheaths, (F) the axons and myelin sheaths with meshed elements, (G) the meshed model with axons, myelin sheaths, and ECM.

Material Properties and Boundary Conditions. Our model differentiates between axon, myelin, and ECM. All are posed to be well characterized by the Neo-Hookean model given by

$$U = C_{10}(\bar{I}_1 - 3) + \frac{1}{D_1}(J - 1)^2, \quad (1)$$

where U is the strain energy function, C_{10} is a material constant and equals half of the shear modulus, \bar{I}_1 is the first invariant of the isochoric part of the right Cauchy–Green deformation tensor, D_1 is the material's incompressibility parameter and is related to bulk modulus κ_0 by $\kappa_0 = 2/D_1$, and J is the determinant of the deformation gradient tensor.

We assume that the Young's modulus of myelin is twice as high as of axons and ten times higher than of ECM. Based on previous work, we assume E_{axon} to be 1.02 kPa and the Poisson's ratio to be 0.495 due to the nearly incompressible behavior of white matter [5]. Here, we study the anisotropic behavior of our IMM by simulating uniaxial tension, compression, and shear with respect to directions that align with axons (AA) and are transverse to axons (TT). We explore the mechanical response of these models for up to 30% strain, respectively.

Homogenized Stiffness Acquisition and Myelin Area Fraction Calculation. To determine the IMM's homogenized stiffness value, a simple cubic model with homogeneous material was created and meshed with linear hexahedral elements. The simple cubic model was subjected to the same boundary conditions as the IMM. An inverse method was used to determine the material property C_{10} of the simple cube by minimizing the root-mean-square error of the resulting stress and strain data between simple cubic model and IMM. The optimized C_{10} was obtained and converted to Young's modulus.

To calculate the myelin area fraction, we sliced each IMM model along the TT direction into 279 slices. In each slice, the area fraction of myelin was calculated by dividing the number of myelinated pixels by the total number of pixels.

RESULTS

The Heterogeneous and Anisotropic Response of IMM. The simulation results are summarized in Figure 2. We show von Mises stress and consistently observe that stress is highest in the myelin sheaths (2A). Loading in axon direction (AA) results in a higher stress-strain response than TT simulations under all three conditions (2B). The resulting homogenized stiffness values of AA simulations are higher than the TT simulations (2C). Specifically, the mean and standard deviation of stiffness is 0.86 ± 0.04 kPa for AA simulations and 0.76 ± 0.01 kPa for TT simulations.

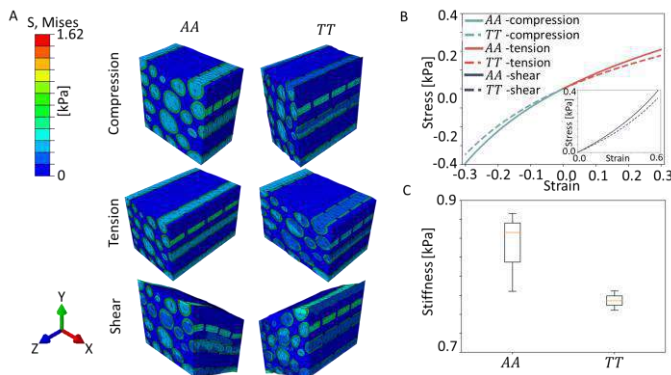


Figure 2: The simulation result of 4-layer IMM on different directions under compression, tension, and shear, (A) deformed configuration and contour plots of stress distributions, (B) the resulted stress-strain curves, (C) the boxplot of the resulted homogenized stiffness values on AA and TT direction.

The Myelin Area Fraction Changes in the IMM. Figure 3A shows the myelin content, calculated as the myelin area fraction, for each model. Myelin area fraction is proportional to the number of layers and decreases from 0.58 ± 0.14 in the 4-layer model to 0.51 ± 0.14 in the 3-layer model, 0.46 ± 0.14 in the 2-layer model, 0.40 ± 0.14 in the 1-layer model, and 0.34 ± 0.14 in the 0-layer model. This trend agrees well with decreasing myelin scores in the demyelinating cuprizone mouse model most frequently used to study white matter disease. Specifically, Gudi et al. presented myelin scores that decreased from 3 ± 0.05 at baseline to

2.30 ± 0.1 at week 3, 2.0 ± 0.1 at week 4, 1.0 ± 0.37 at week 4.5, and 0.49 ± 0.5 at week 5 [6].

Stiffness Changes with the Changing Number of Myelin Layer.

Figure 3B shows how the homogenized stiffness value increases with the number of myelin layers. For example, for TT-compression, the homogenized stiffness decreased from 780.78 Pa in the model with 4 layers to 627.19 Pa with 3 layers, 537.59 Pa with 2 layers, 447.99 Pa with 1 layer, and 391.1 Pa for the model without any myelin. Similar trends can also be found in TT-tension, TT-shear, AA-compression, AA-tension, and AA-shear.

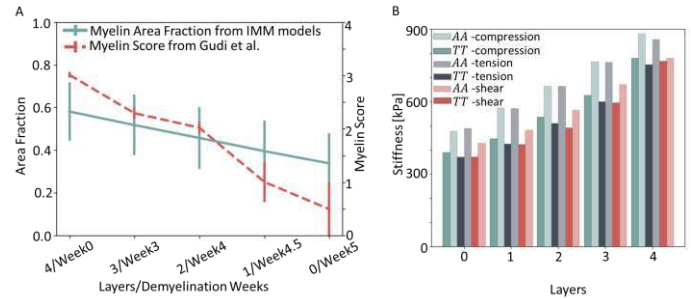


Figure 3: The area fraction of the IMM models with different myelin layers and the resulted homogenized stiffness of total 30 simulations, (A) the myelin area fraction (solid blue)) changes with the number of myelin layers in our models, and the myelin score (dash red) changes with cuprizone-induced demyelination weeks on literature [6], (B) the homogenized stiffness results of the IMM models with different myelin layers (0-4) under compression, tension, and shear on both AA and TT.

DISCUSSION

We created an investigative microstructural finite element model of white matter to systematically study the mechanical response as a result of varying anatomy. Our results suggest a highly heterogeneous and anisotropic white matter behavior. Our model reproduces previously reported softening behavior during progressive demyelination [7].

This model has great significance in the fundamental understanding of mechanical white matter behavior in some white matter diseases, such as multiple sclerosis. Going forward, this model will be used to investigate the mechanical response of white matter in acute and chronic demyelination and remyelination, which will help to predict the macroscale tissue response in white matter disease.

ACKNOWLEDGEMENTS

None

REFERENCES

- [1] Beirowski, B et al., *J. Cell Biol.*, 215, 2016.
- [2] Weickenmeier, J et al., *Acta Biomater.*, 42 2016.
- [3] Lee, H et al., *Brain Struct Funct*, 224.4, 2019.
- [4] Bechler, M et al., *Curr. Biol.*, 25.18, 2015.
- [5] Spedden, E et al. *Biophys. J.*, 103.5 2012.
- [6] Gudi, V et al., *Brain Res.*, 1283, 2009.
- [7] Schregel, K et al. *PNAS*, 17, 2012.

CELLULAR SENESENCE SUPPRESSES ECM SYNTHESIS IN RESPONSE TO MECHANICAL UNLOADING IN TENDON EXPLANTS

Emma J. Stowe (1), Brianne K. Connizzo (1)

(1) Department of Biomedical Engineering, Boston University, Boston, MA, USA

INTRODUCTION

Musculoskeletal injuries, including tendinopathies, present a large clinical burden for aging and elderly populations. Aged tendons are at increased risk for tendon injuries, exhibit poor healing outcomes, and show a loss in regenerative capacity [1]. While the biological drivers of this age-related degeneration are poorly understood, it is well accepted that deregulation of balanced matrix turnover plays a role in tendon injury. Remodeling of tendon extracellular matrix (ECM), through matrix synthesis, organization, and breakdown, is essential in the ability of the resident cells to respond and adapt to altered mechanical environments.

The accumulation of senescent cells is documented to play a role in the phenotype of aging tissues, including tendon [2]. Senescent cells are anti-apoptotic and secrete a highly pro-inflammatory senescence-associated secretory phenotype (SASP) that has potential to promote ECM breakdown. However, the role of senescent cells in the dysregulation of tendon ECM homeostasis is unknown. Our group has recently developed *in vitro* models of cellular senescence in live tendon explants using the chemotherapy drug, doxorubicin, and irradiation [3]. Using these models, we aim to investigate how ECM remodeling and homeostasis are altered with natural aging and cellular senescence.

The objective of this study is to compare the remodeling response of native young, native aged, and senescent tendons to an altered mechanical stimulus. We hypothesize that both aged and senescent tendons will exhibit altered ECM remodeling following a mechanical unloading injury, with a shift to processes that promote ECM degradation over synthesis.

METHODS

Flexor digitorum longus (FDL) tendon explants were harvested from young (4m) and aged (24m) male C57BL/6J mice [4]. Tendon explants were cultured under stress-deprived conditions (mechanical unloading) in standard culture medium for up to 14 days. Cellular

senescence was induced *in vitro* in young explants following tissue harvest with irradiation (RAD) and doxorubicin (DOX) [3]. Live/dead confocal imaging was performed to quantify cell viability and total cell density. A resazurin reduction assay was used to evaluate metabolism. To measure matrix composition, tendons were digested, and biochemical assays were performed for DNA content (PicoGreen), GAG content (DMMB), and total collagen content (OHP) [4]. Matrix biosynthesis was assessed using 24-hr incorporation of radiolabels ³H-proline and ³⁵S-sulfate to measure synthesis of total protein and sulfated GAGs, respectively [4]. Assays were normalized to tendon dry weight to account for tendon size. Changes in gene expression were evaluated using qPCR for genes encoding matrix proteins and matrix metalloproteinases (MMPs) [4]. qPCR data is presented as a change in relative expression, normalized to both a housekeeping gene, β -Actin, and day 0 expression. Generic MMP activity was assessed using fluorometric detection kit (AnaSpec). Statistical evaluation was performed using two-way ANOVAs with appropriate post-hoc t-tests, significance at $p < 0.05$ (solid lines) and trends at $p < 0.1$ (dashed lines). All data is presented as mean \pm 95% confidence interval.

RESULTS

All groups were viable for the duration of the experiment, with RAD tendons exhibiting a higher percentage of live cells than young tendons at both time points (Fig. 1a). Cell density was the same in all groups at day 7 but was reduced in senescent groups by day 14 (Fig. 1b). Similarly, while no differences in DNA content were seen at day 7, significant reductions of DNA content in aged, RAD, and DOX tendons were found at day 14 (Fig. 1c). Explant metabolism was significantly reduced in the aged, RAD, and DOX groups when compared to the young tendons at days 7 and 14 (Fig. 1d). After 7 days, no significant differences were seen in hydration, collagen content, or GAG content between groups. However, by day 14 water content and GAG content were significantly reduced in aged and senescent groups (Fig. 2).

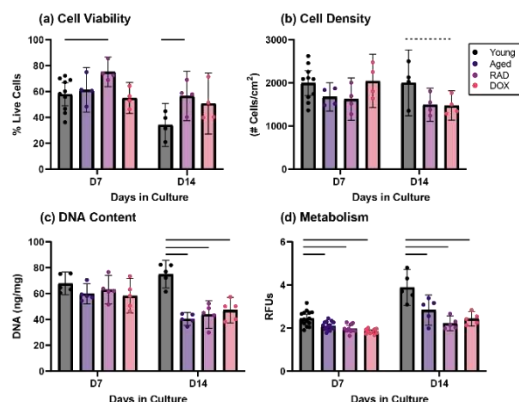


Figure 1: Explant Health. (a) Viability, (b) cell density, (c) DNA content, and (d) metabolism.

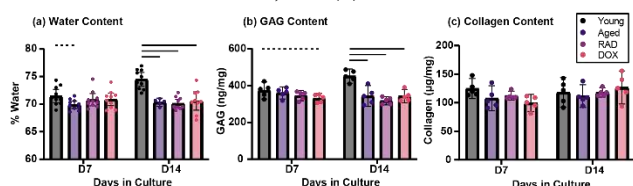


Figure 2: Matrix Composition. (a) Water content, (b) GAG content, and (c) collagen content.

Total protein and sGAG synthesis were diminished in aged and senescent cultures at both time points (Fig. 3a,b). Gene expression data at day 14, showed significant reduction in expression of matrix proteins collagen 1 (Col1α1), fibromodulin (FMOD), and decorin (DCN) in DOX and RAD tendons (Fig 3c,d,e). MMP activity increased in young FDLs over time in culture, peaking at 10 days of stress deprivation. Although non-significant, MMP activity was slightly elevated in senescent cultures compared to young at days 4 and 14 (Fig. 4a). Day 14 MMP gene expression showed downregulation of MMP-1, upregulation of MMP-3, and no changes in MMP-13 in senescent groups compared to young (Fig. 4b,c,d).

DISCUSSION

Excitingly, supporting our original hypothesis, we found that senescent tendons exhibit altered responses to changes in mechanical unloading compared to young tendons. Decreases in protein and sGAG synthesis, as well as downregulation in gene expression of key ECM components, signifies a compromised ability of cells to synthesize ECM. Despite a reduction in total number of cells, which is typically seen in natural aging, the remaining cells also appeared to be functionally different than young cells, exhibiting both reduced metabolism and capacity to synthesize matrix. In addition, while young tissues undergo swelling and GAG accumulation between 7-14 days of stress deprivation, senescent tendons lack a similar adaptation.

Interestingly, changes in ECM remodeling found here were similar between the naturally aged and senescent-induced tendons, suggesting that senescence likely contributes to divergent remodeling outcomes in aged tissues. In some cases, the response appears graded, with more severe changes in the senescent groups than in aged tissues. Since aged tissues are documented to contain a low number of senescent cells (5-10%) [5], this is expected. Future work aims to quantify numbers of senescent cells in aged and senescent-induced tendons to determine thresholds at which bulk tissue response are altered.

Contrary to expectations, MMP expression and activity, signifying matrix breakdown, were not strikingly elevated with senescence. However, stress deprivation injury itself initiates a high degradative response in young FDLs, shown by increasing MMP activity following

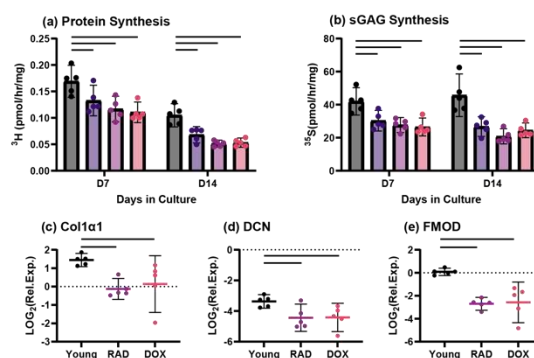


Figure 3: Matrix Production. (a) Protein and (b) sGAG synthesis. Day 14 gene expression of (c) Col1α1, (d) DCN, and (e) FMOD.

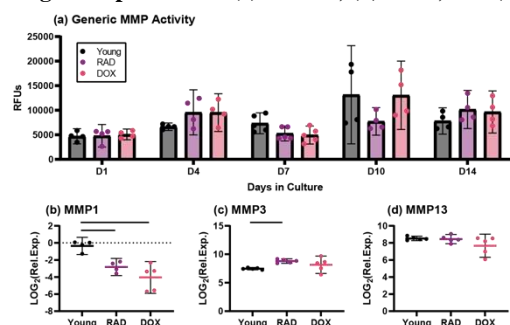


Figure 4: Matrix Degradation. (a) Generic MMP activity and day 14 expression of (b) MMP-1, (c) MMP-3, and (d) MMP-13.

injury. Thus, the senescent response is on-par with that of a mechanical injury and appears to be elevated for a sustained period. Gene expression data shows divergent trends with different MMPs. It's likely that senescence affects functionally different MMPs in distinct ways, potentially muddling the generic activity results. Elevated expression of MMP-3, responsible for breakdown of proteoglycans, could explain the lack of GAG accumulation later in culture in senescent groups.

Overall, this study is the first to investigate the response of senescent cells to altered mechanical stimuli within the native matrix environment. Compared to young tendons under identical mechanical stimuli, senescent tendons exhibit reduced matrix synthesis with similar or increased MMP activity, thus shifting the remodeling balance towards degradation over production. This lack of adaptation in aged and senescent tendons shows a reduced capacity to respond to altered mechanical environments and likely contributes to increased tendon injury and poor healing outcomes. This suggests senescence-targeting therapies may be a promising strategy for preventing age-related tendon degeneration. Ongoing work aims to investigate the ability of senescent explants to respond and adapt to physiological and injurious levels of mechanical loading, as well as explore the potential of senescence therapies to recover homeostatic ECM remodeling.

ACKNOWLEDGEMENTS

This study was supported by NIH/NIA R00-AG063896, NSF GFRP, the Boston University Micro and Nano Imaging Facility, and the National Institute of Health (S10OD024993).

REFERENCES

- [1] Thomopoulos, S et al., *J Orthop Res.*, 33(6):832-839, 2015.
- [2] Hernandez-Segura, A et al., *Trends in cell bio*, 28(6):436-453, 2018.
- [3] Stowe, E et al., *Trans. Orthop. Res. Soc.*, 2022.
- [4] Connizzo, B et al., *Connect Tissue Res.*, 61(1):48-62, 2019.
- [5] Liu, J et al., *Proc. Natl. Acad. Sci.*, 116(7): 2603-2611, 2019.

4D ULTRASOUND-BASED STRAIN CAN CHARACTERIZE EARLY PROGRESSION OF MYOCARDIAL INFARCTION IN MICE AND RATS

Conner C. Earl (1,2), Ana C. M. Omoto (3), Karthik Annamalai (1), Alyssa Richards (1), Samuel X. Zhang (1), Adalyn M. Meeks (1), Alexandre A. da Silva (3), Craig J. Goergen (1,2)

(1) Weldon School of Biomedical Engineering, Purdue University, West Lafayette, IN, USA

(2) Indiana University School of Medicine, Indianapolis, IN, USA

(3) Department of Physiology and Biophysics, University of Mississippi Medical Center, Jackson, MS, USA

INTRODUCTION

Coronary heart disease is the number one cause of mortality worldwide, contributing to nearly 15% of all deaths [1]. Early characterization of myocardial ischemia (MI) is essential for improving surgical and medical outcomes. While two-dimensional ultrasound is often used to evaluate left ventricular function and monitor disease progression, it is insufficient to completely characterize the complex myocardial biomechanics involved in pathologic remodeling leading to heart failure, a common outcome of coronary ischemic injury. Many interventions for preventing heart failure development following ischemic injury are time dependent and rely on implementation within at least 7 days of the index MI for therapeutic benefit [2], however traditional image-base wall-thinning or histological metrics in rodents can only estimate infarct size 7-14 days following ischemic injury [3].

Here we present a method for quantifying myocardial mechanics in an ischemia reperfusion (I/R) and permanent ligation (PL) model of myocardial infarction for both mice and rats using four-dimensional ultrasound imaging (4DUS). We also describe the use of a custom MATLAB graphical user interface to leverage the value of 4D imaging (3D plus time) while streamlining analysis and processing.

While many studies examine the longer-term effects of myocardial infarction, the objective of this study is to examine the early/acute phase of cardiac remodeling following myocardial infarction during the first 7 days following the procedure. We hypothesize that 4DUS strain-based infarct size estimations within one day following myocardial infarction will be similar to estimations after one week for both rats and mice. Identifying the extent of myocardial injury at early time points could be a powerful asset for guiding surgical and medical intervention.

To our knowledge, this is the first study to describe the use of 4DUS-based mechanical characterization for I/R and PL in both mice and rats. Characterizing the progression of myocardial infarct injury during this early stage of remodeling has far-reaching implications for studying and understanding the complex mechanical response of the heart to ischemic injury.

METHODS

Mouse surgeries: We performed coronary artery ligation surgeries on 10 male, wild-type, C57BL/6J mice (age 13-15 weeks). For surgery, each mouse was anesthetized with 1–3% isoflurane and endotracheally intubated using a small-animal ventilator (SomnoSuite, Kent Scientific, Torrington, CT). A small incision was made in the third intercostal space of the left thorax and the ribs were retracted to expose the left ventricle. The pericardium was removed to visualize the left coronary artery (LCA). In the I/R group (n=5), we used PE-10 tubing in combination with a suture to temporarily ligate the LCA for 30 min before restoring blood flow to the ischemic myocardium (reperfusion) as described previously [4,5]. In the PL group (n=5), the LCA was permanently ligated to induce an infarct [4,5].

Rat surgeries: For rat surgeries, male Sprague-Dawley rats (n=10, age 12-14 weeks) were anesthetized with 1–3% isoflurane, followed by endotracheal intubation and mechanical ventilation (Harvard Apparatus, USA). The chest was opened at the fourth left intercostal space, the pericardium was removed, and the LCA was identified. In the I/R group (n=5), the LCA was temporarily ligated using 4-0 prolene suture (Ethicon, USA) for 60 minutes followed by reperfusion. For the PL group (n=5), the LCA was permanently ligated. Following each procedure, the chest retractor was removed, the ribs were drawn together, thoracic pressure was reestablished, and the skin was closed.

Imaging: 4D ultrasound images were obtained prior to surgery, 24 hours post-surgery, and 7 days post-surgery using the Vevo3100 or Vevo2100 ultrasound system (FUJIFILM, VisualSonics). We analyzed the 4DUS data using a custom-built graphical user interface in MATLAB (MathWorks, Natick, MA) to manually segment the left ventricle by tracking 48 points on the endo- and epicardial surfaces over a representative cardiac cycle. The 4D mesh generated through these tracked points was sampled uniformly at 60 interpolated time points across one cardiac cycle, with 60 rotations around the longitudinal axis, and 60 slices from base to apex for a total of 3,600 nodes at each timepoint [6]. We then estimated surface area strain (E_a) calculated as:

$$E_a(z, \theta, t) = \left[\frac{A(z, \theta, t) - A_D(z, \theta)}{A_D(z, \theta)} \right] \times 100\% \quad (1)$$

Where A represents the surface area on the endocardial surface between two sequential slice locations along the longitudinal axis z and rotational location θ over time t . We estimated infarct size by identifying nodes with low E_a magnitude ($>-20\%$) as previously described [2].

RESULTS

We found that regions with surface area strain values greater than -20% at day 1 were similar to those found at day 7 for the rat PL and I/R groups (Figure 1) and for the mouse PL groups. Mild infarct for some mice in the I/R groups was not detected at day 1 (Figure 2).

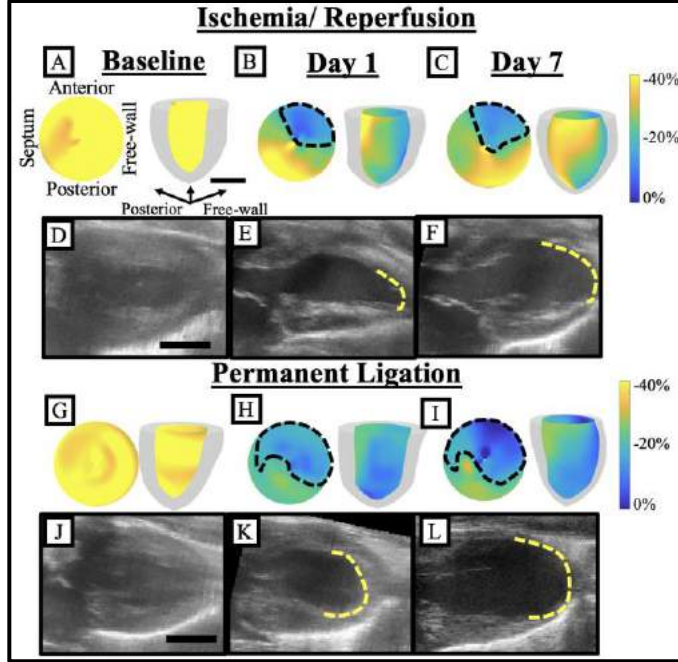


Figure 1: 4D ultrasound strain-based infarct size estimation. Example rat left ventricular surface area strain colorized polar plot (left) and 3D model (right) at baseline (A,G), day 1 (B,H), and day 7 (C,I) following ischemia reperfusion (I/R; A,B,C) or permanent ligation (PL; G,H,I). Dotted black lines represent estimated infarct. Representative 2D long axis slices identified from the rat 4D image volume at peak systole at baseline (D,J), day 1 (E,K), and day 7 (F,L) following I/R (D,E,F) or PL (J,K,L). (Yellow lines represent areas of akinesis; black scalebar=5mm).

We also found that strain estimated infarct was significantly different ($p<0.0001$) between I/R and PL groups at day 1 and day 7 for both mice and rats (Figure 2). For rats we found that left ventricular ejection fraction (LVEF) dropped from $57.4 \pm 5.9\%$, $53.7 \pm 4.8\%$ (mean \pm SD); I/R and PL respectively) at baseline to $38.2 \pm 3.6\%$, $29.7 \pm 3.7\%$ at day 1 and $36.2 \pm 3.1\%$, $27.1 \pm 3.7\%$ at day 7 post-infarction. For mice we found a similar drop from baseline $73.6 \pm 6.1\%$, $66.7 \pm 11.4\%$ (I/R and PL respectively) to $54.1 \pm 6.1\%$, $42.2 \pm 10.4\%$ at day 1 and $59.3 \pm 5.8\%$, $37.3 \pm 8.4\%$ at day 7 post-infarction.

DISCUSSION

In this study, we used a mechanics-based approach to identify infarct size in both mice and rats with varying levels of ischemic injury. Our results showed that infarct size measured using E_a estimated from 4DUS at 24 hours following the ischemic event is predictive of infarct size at day 7 for both mice and rats. This is highly impactful to the field

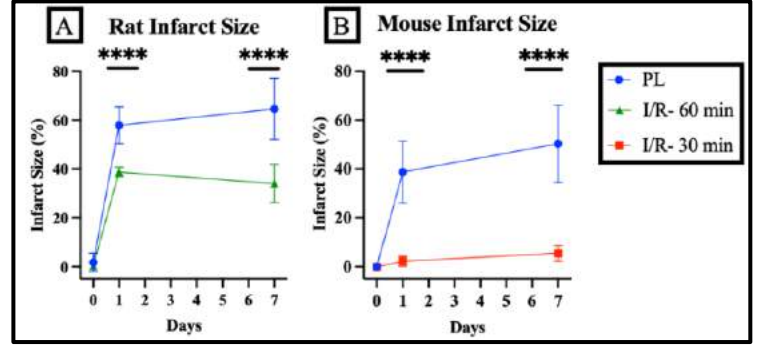


Figure 2: Rat and mouse infarct size over time. (A) Rat and (B) mouse infarct size over time for permanent ligation (PL; n=5) and ischemia reperfusion (I/R; n=5). ****PL vs I/R, $p<0.0001$, error bars: mean \pm SD.

because traditional wall-thinning or histological metrics in rodents can only assess this infarct size after 7-14 days [2]. This method is also non-invasive and can be used to track infarct progression longitudinally-limiting the need to use large numbers of animals to achieve statistical significance. Additionally, unlike traditional 2D assessment, 4D analysis can account for infarct asymmetry and heterogeneity.

Another advantage of this study is the scope of our methodology. We showed how our strain estimation method can be applied to both I/R and PL models in mice and rats. This is powerful as I/R models more closely recapitulate percutaneous coronary intervention [7], while PL models produce more severe infarcts and may represent better the response of untreated myocardial infarction more common in low-resource settings without ready access to percutaneous interventions.

It should be noted that our strain estimation technique relies on gross akinesis of myocardium to estimate infarct size. This technique has the potential to overestimate large infarcts by including the “at-risk” border zone. This may be partially reflected in the slight (but not significant) decrease we see in the moderate infarction size produced by the I/R model in rats from day 1 to day 7. We also may underestimate mild infarcts that do not induce damage throughout the entire thickness of the myocardium, which may partially explain the small infarcts we calculated in the I/R mouse group.

In summary, we demonstrated that 4DUS is an effective and useful tool for examining myocardial mechanics following experimentally induced ischemia in both mice and rats and can be used for early assessment of infarct size. Similar clinical techniques could be implemented in future preclinical research to comprehensively characterize the myocardial response to help guide interventions and decrease the burden of heart failure after MI.

ACKNOWLEDGEMENTS

Research reported in this publication was supported by the National Heart, Lung, And Blood Institute of the National Institutes of Health under Award Number F30HL162452, NIGMS P20GM104357, NIGMS U54GM115428, and AHA – POST835218. The content is solely the responsibility of the authors and does not necessarily represent the official views of the National Institutes of Health

REFERENCES

- [1] Jayaraj, J.C., et al., Myocardial Infarction, 2018: p. 9-19.
- [2] Dann, M.M., et al., AJP-Heart and Circ. Physiology, 2022.
- [3] Bahit, M.C., et al., JACC: Heart failure, 2018 6(3): p. 179-186.
- [4] Hashmi, S. et al., Int. J. clin. and exp. pathology, 2015. 8(8): p. 8786.
- [5] Soepriatna, A.H., et al., J. Royal Soc. Int., 2019 16(160): p. 20190570.
- [6] Damen, F.W., et al., Tomography, 2017. 3(4): p. 180-187.
- [7] De Villiers, C., et al., Mechanisms, 2020. 13(11): p. dmm046565.

THE MATERIAL PROPERTIES OF HEALTHY VERSUS DISEASED MOUSE LUNG PARENCHYMA

T.M. Nelson (1), K.A.M. Quiros (1), C.A. Mariano (1), S. Sattari (1), M. Eskandari (1,2,3)

- (1) Department of Mechanical Engineering, University of California, Riverside CA, USA
(2) BREATHE Center, School of Medicine University of California, Riverside CA, USA
(3) Department of Bioengineering, University of California, Riverside CA, USA

INTRODUCTION

Pulmonary diseases are progressive, often incurable, and shorten life-expectancies [1]. Despite the critical role of the lungs in oxygen delivery throughout the body, rudimentary lung mechanical function is not well understood, neither in healthy nor diseased states; moreover, mechanical characterization of lung tissue is fundamental for developing predictive models and advancing disease treatment and mitigation but remains scarce [2]. Parenchymal tissue is understudied, despite being the site of injury and disease manifestation [1, 3]. Existing parenchymal studies often use precision cut lung slices (PCLS), which can alter properties due to agarose injection [4, 5]. In addition, such small-scale studies only examine uniaxial rather than more physiologically representative multi-directional loading [6]. These limitations often present challenges for evaluating physiologically relevant lung tissue behavior [7, 8, 9].

In this timely COVID-19-era pulmonary mechanics study, we characterize and compare unaltered healthy mouse lung mechanics to diseased counterparts using biaxial tensile testing for the first time. We analyze the tissue stress-strain response and viscoelastic behaviors to formulate a better local-scale understanding of the changes in diseased lungs that are witnessed at the global, pressure-volume level of the whole lung [10, 11]. Ultimately, this study quantifies lung biaxial material properties, which have been thus far absent in the field, and provides measures for future use in computational models and for comparisons to other pulmonary diseases.

METHODS

Ten male C57BL/6J mice were obtained from Jackson Laboratory (Bar Harbor, ME, USA) at 8-12 weeks old as part of a larger ventilation study [11, 12]. Half the specimens were intranasally exposed to agricultural dust, while the other half were exposed to 1X phosphate-buffered saline (PBS) three times weekly for 21 weeks, modeling fibrosis or healthy states, respectively [13]. In accordance with

Institutional Animal Care and Use Committee protocols, left lungs were extracted noting the cranial-caudal (CC) and medial-lateral (ML) directions. Uniform lung parenchymal sample dimensions were obtained using a custom-designed cutter (Figure 1A). The 1.9 \pm 0.5 mm thickness samples were loaded onto four planar rakes [8], producing a 3x3 mm testing area, and submerged in 1X PBS at 37°C. The experimental setup is shown in Figure 1A. Equibiaxial tests were executed with a BioTester 5000 and 1.5N load cells (CellScale Waterloo, ON, Canada). Tissue was stretched to 40% at 2.5%/s, selecting testing parameters mirroring whole-organ strain inflation tests [3, 10]. A 0.5mN tare was applied similar to previous studies [4]; the tissue was then preconditioned with three loading-unloading cycles followed by an analyzed fourth stress-strain load and a 300s hold for viscoelastic considerations [9].

First Piola-Kirchoff stress-strain loading curves were averaged across samples (Figures 1B and C) [2, 9], and the tangent at strain values of 15, 25, and 35% were found using the least-squares method with $R^2 > 0.9$, (MATLAB, MathWorks Inc.) [14]. Maximum stress values at 40% strain were also measured. Stress versus time plots were used to characterize percent relaxation, determined as the difference between maximum stress at the beginning of the hold and asymptotic stress, normalized by maximum stress (Figures 1D and E) [9, 15]. Statistical differences between healthy versus diseased tissue comparisons and directional differences were assessed for calculated slopes, maximum stress values, and percent relaxation values, using the Mann-Whitney and Wilcoxon nonparametric tests [GraphPad Prism, San Diego, CA, USA]. Statistical significance was designated with $p < 0.05$.

RESULTS

Parenchymal tissue stress-strain curve slopes trended greater for diseased compared to healthy tissue for the average slope measured at 35% strain (Figure 1B and C). This slope was notably steeper for diseased tissue, particularly for the CC direction, with values of 25.7

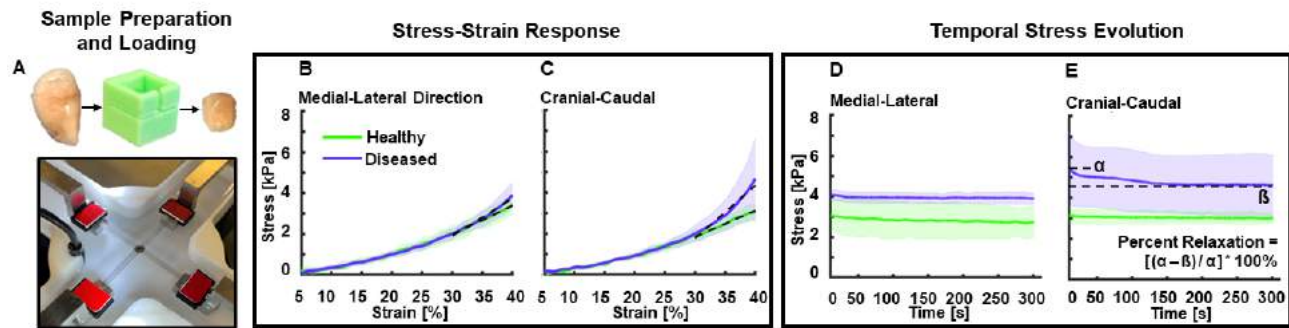


Figure 1. Murine lung parenchyma was diced into slices using a custom-designed cutter and biaxially loaded (A). Average \pm standard deviation (SD) of healthy and diseased tissue stress-strain curves, shown in the medial-lateral (B) and cranial-caudal (C) loading directions, respectively (with shown slopes fitted at 35% strain). Averaged \pm SD stress-time viscoelastic relaxation plots are similarly illustrated in the medial-lateral (D) and cranial-caudal (E) orientations (with percent relaxation calculation shown).

and 12.8 kPa/% for healthy and diseased samples, respectively. Slopes measured at 15 and 25% did not reveal measurable differences between healthy and diseased states. Comparisons of ML and CC slopes did not show significant differences; however, directional slope differences were most discernable for diseased tissue at 35% which, on average, was less steep for the ML compared to CC direction (18.4 and 25.7 kPa/%, respectively).

Maximum stress values measured from stress-strain curves did not significantly differ between healthy and diseased states (Figures 1B and C). However, diseased tissue tended to yield greater stress values at maximum loading, with 3.9 kPa in disease compared to 3.4 kPa in healthy tissue for the ML direction, and 4.7 (diseased) compared to 3.0 kPa (healthy) for the CL direction. Differences between the two directions' maximum stress values were not significant.

Stress-time plots demonstrated healthy versus diseased tissue percent relaxation trended greater for healthy (12.8%) compared to diseased (5.8%) tissue in the ML direction (Figure 1D), but greater for diseased (16.0%) compared to healthy (5.0%) tissue in the CC direction (Figure 1E). ML and CL directional comparisons were not significant.

DISCUSSION

In this study, we characterize murine lung parenchymal biaxial material properties between healthy and diseased states for the first time, broadening our understanding of how tissue mechanics are altered due to chronic lung disease. The steepened stress-strain slopes and greater maximum stress values observed in diseased tissue (Figures 1B and C) are indicative of the increased parenchymal stiffness that is a hallmark of fibrosis and ultimately restricts breathing [1, 11, 16, 17]; it is widely understood that collagen deposition in the extracellular matrix (ECM) governs this pathological remodeling. Additionally, local stiffening may result in augmented forces within the ECM which exacerbate disease progression [1, 16], further underscoring the need for characterizing diseased tissue mechanics.

Given the absence of previous murine studies and biaxial tests, we compare the stress values obtained here to those of rat parenchymal uniaxial studies [4]; we find that biaxially loaded healthy mouse tissue exhibits a near order of magnitude higher stress values when compared to the same deformation values of uniaxial loading. This agrees with the nature of uniaxial versus biaxial loading, where the Poisson's ratio raises the effective stiffness of the tissue, as also observed in studies of soft airway tissue [18].

In contrast to uniaxial methods, biaxial testing allows for simultaneous comparisons between orthogonal loading orientations. Tissue anisotropic behavior is important for understanding disease effects, as the spatial orientation of collagen is a key factor in fibrotic

tissue mechanics [1]. We observe that the CC direction consistently reveals the most evident fibrosis-induced mechanical alterations: this direction shows the greatest degree of stiffening (stress-strain slopes at 35%, Figure 1C), and the greatest amount of relaxation (Figure 1E), indicating changes in viscoelasticity. Such alterations suggest the organization of deposited collagen fibers in fibrosis may influence the CC direction more drastically, and warrants further analyses regarding the role of pulmonary collagen fiber properties and architecture [1].

We note that use of planar loading may overlook physiologically relevant tissue responses (e.g., shear stresses), and future aims include testing parenchymal cubes in three dimensions to address this limitation [7]. In addition, individual pulmonary constituents would ideally be fully isolated to elucidate their distinct roles; this challenge posed by mouse lung size, will be further explored in future work. Nevertheless, the fundamental healthy versus diseased murine lung mechanics established in this study are essential, as mice are regarded for their pragmatism and potential to advance human pulmonary research, due to shared physiology, ease in procurement, and manipulability for therapy models [15]. To the best of our knowledge, we provide the first mechanical characterization of tissue-level mouse parenchymal biaxial material properties in a diseased state, enabling future material modeling and laying the foundation for comparisons to other manifestations of pulmonary disease.

ACKNOWLEDGEMENTS

This material is based on work supported by the National Science Foundation Graduate Research Fellowship Program, awarded to Talyah Nelson (Grant No. DGE-1840991).

REFERENCES

- [1] Suki, B & Bates, JHT, *Respir Physiol Neurobiol* 163, 33–43, 2008.
- [2] Vande Geest, JP, et al., *J Biomech* 39, 1324–1334, 2006.
- [3] Andrikakou, P, et al., *Sci Rep* 6, 2016.
- [4] Birzle, AM, et al., *Biomech Mod Mechanobiol* 18, 1383–1400, 2019.
- [5] Rausch, SMK, et al., *J Mech Behav Biomed Mater* 4, 583–592, 2011.
- [6] Faffe, DS, et al., *J Appl Physiol* 90, 1400–1406, 2001.
- [7] Budday, S, et al., *Acta Biomater* 48, 319–340, 2017.
- [8] Sacks, MS, *J Elast* 61, 199, 2000.
- [9] Sattari, S & Eskandari, M, *JMBBM* 110, 103824, 2020.
- [10] Nelson, TM, et al., *Physiol Rep* 10, e15466, 2022.
- [11] Nelson, TM, et al., *Sci Rep*, 2022 (submitted).
- [12] Quiros, KAM, et al., *Ann Biomed Eng*, 2022 (submitted).
- [13] Nordgren, TM, et al., *Trans Res J Lab Clin Med* 166, 57–69, 2015.
- [14] Eskandari, M, et al., *J Appl Physiol* 125, 878–888, 2018.
- [15] Quiros, KAM, et al., *Sci Rep* 12, 7094, 2022.
- [16] Haak, AJ, et al., *Matrix Biol* 73, 64–76, 2018.
- [17] Nelson, TM, et al., SB3C, 2022.
- [18] Sattari, S, et al., *Acta Biomater*, 2022.

CONTRIBUTION OF MICROTUBULE NETWORK TO THE PASSIVE ANISOTROPIC VISCOELASTICITY OF HEALTHY RIGHT VENTRICLE

K. LeBar (1), K. Roth (1), W. Liu (2,3) E. Evans (1,2), J. Pang (4), A. Chicco (5), Z. Wang (1,2)

- (1) Department of Mechanical Engineering, Colorado State University, Fort Collins, CO, USA
(2) School of Biomedical Engineering, Colorado State University, Fort Collins, CO, USA
(3) Stanford Cardiovascular Institute, Stanford University, Stanford, CA, USA
(4) Laboratory Animal Resources, Colorado State University, Fort Collins, CO, USA
(5) Department of Biomedical Sciences, Colorado State University, Fort Collins, CO, USA

INTRODUCTION

The myocardium is viscoelastic, which means that there exist both viscous and elastic resistive forces over the cardiac cycle. Prior studies on cardiac muscles have demonstrated significant viscoelastic behavior of the myofibers and its impact on the contractile function [1-3]. However, the tissue-level investigation of the anisotropic viscoelasticity of ventricular free wall is much less compared to that of the elastic behavior of the tissue.

The right ventricle free wall (RVFW) is a complex tissue composed of myofibers, collagen, vasculature, and other extracellular matrix (ECM) components, all of which exhibit viscoelastic behavior and contribute to the anisotropic mechanical behavior of the tissue. It is thought that myofibers are the main determinant of mechanical properties of the RV at low strains and the myofiber elasticity is associated with the RV diastolic function [4]. Microtubules (MT) are key intracellular elements contributing to the myofiber viscoelasticity. The enhancement or reduction of the MT network has been shown to increase or decrease cardiomyocyte viscoelasticity, respectively [1,2,5]. However, these findings are based on 1D cell mechanics. The realignment and reassembly of MT network can lead to significant changes in anisotropy and viscoelastic properties of the entire tissue, but the exact impact remains unknown. Thus, the **aim of this study** is to investigate the effect of the MT network on the healthy RVFW anisotropic viscoelasticity. We **hypothesize** that MT hyper- and de-polymerization differentially alter RVFW viscoelastic properties and lead to the opposite changes in the ratio of viscosity to elasticity.

METHODS

All procedures and methods were approved by the Colorado State University IACUC. Healthy adult male Sprague-Dawley rats (n=6) were euthanized, and the heart was excised and placed in phosphate buffer solution (PBS) on ice. The RVFW was then dissected in cardioplegic solution (CPS) and placed in 30mM 2,3-butanedione

monoxime (BDM) solution at body temperature (37C) for 30 minutes to remove the contractility of the myocardium. The outflow tract direction was defined as the longitudinal (L) direction. RV tissue then underwent equibiaxial stress relaxation to obtain the passive, biaxial viscoelastic behavior. Preconditioning was performed before data collection. Then, the RV was stretched to a maximum strain of 6% and at a ramp speed of 0.95 mm/s using an in-house biaxial tester. After the intact tissue was tested at baseline condition (base), the RV was treated with colchicine (COL) (0.3mM) for 30 minutes to de-polymerize the MT, and the same mechanical testing was performed. The RV was then rinsed with PBS and let rest in CPS solution to remove the effect of colchicine, treated with 50% of deuterium oxide (D₂O) for up to one hour to hyper-polymerize the MT, and the same mechanical tests were repeated. Relaxation modulus [6], stored energy (elasticity), dissipated energy (viscosity) (**Fig. 1**), and the ratio of dissipated to stored energy (V/E ratio) were examined. Paired student t-test was performed and p<0.05 was considered significant.

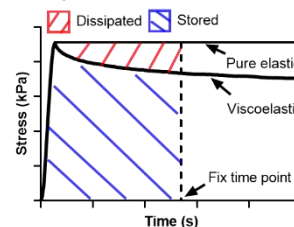


Figure 1: Calculation of the stored (W_s ; blue shaded area) and dissipated (W_d ; red shaded area) energy at any fixed time point.

RESULTS

MT de-polymerization reduces RV circumferential elasticity but does not affect viscosity. Colchicine treatment led to a significant reduction in relaxation modulus from the baseline in the circumferential (C) direction only (**Fig. 2**), indicating a reduction in RV elasticity.

Moreover, there was a trend of decrease in stored energy ($p=0.09$) (Fig. 3A) after MT de-polymerization in the C direction. However, we observed no change in dissipated energy (Fig. 3B) in either direction, indicating that the viscosity was not changed. Lastly, a trend of decreased V/E ratio was observed in the L direction only (Fig. 3C).

MT hyper-polymerization enhances RV longitudinal elasticity and viscosity in both directions. D₂O treatment led to a significant increase in relaxation modulus in the L direction only (Fig. 2), suggesting an enhanced RV elasticity. We also observed increases in both stored and dissipated energies, although the increase in stored energy was only observed in the L direction (Fig. 3A&B). As a result, the V/E ratio remained unchanged in the L direction but was greater in the C direction with the enhanced MT network (Fig. 3C).

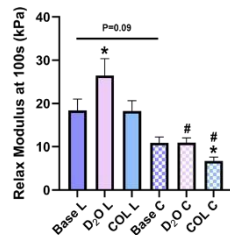


Figure 2: Relaxation modulus measured at equilibrium (100s) of relaxation in different conditions. * $p<0.05$ vs. baseline in the same direction. # $p<0.05$ vs. longitudinal direction in the same condition.

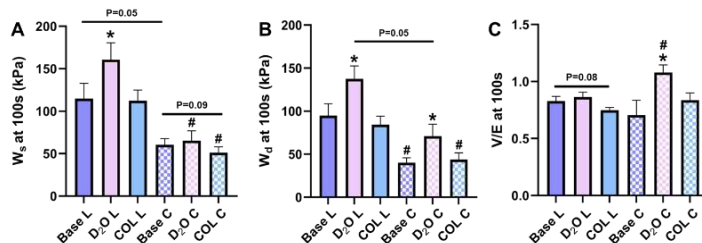


Figure 3: Stored energy (W_s) (A), dissipated energy (W_d) (B), and the V/E ratio (W_d/W_s) (C) measured at equilibrium (100s) of relaxation in different conditions. * $p<0.05$ vs. baseline in the same direction. # $p<0.05$ vs L in the same condition.

Enhanced RV anisotropy with MT hyper- and de-polymerization.

At the baseline state, we observed no significant anisotropy in RV relaxation modulus. However, after MT hyper- or de-polymerization, the relaxation modulus in the C direction was significantly lower than that of the L direction (Fig. 2), leading to marked tissue anisotropy. A similar behavior was seen in the stored energy (Fig. 3A). But the anisotropic behavior in RV dissipated energy (viscosity) was differently altered by the two treatments. At the baseline state, the RV exhibited marked anisotropy in dissipated energy and MT de-polymerization did not affect such behavior. However, MT hyper-polymerization caused a weakening of the anisotropy in dissipated energy (Fig. 3B).

DISCUSSION

To the best of our knowledge, this is the first investigation of the effect of MT network on healthy RVFW anisotropic viscoelasticity. A key condition of our test is applying a strain level of 6% to the RV tissue. In myocardial mechanics, the main microstructural components at play are myofibers and collagen. At lower strain levels (5%-7%), myofibers are the main determinant of the tissue mechanical properties. As the strain increases to late diastole (9%-20%), collagen is recruited and begins to dominate the RV mechanical behavior [4]. Therefore, by examining the tissue viscoelasticity at a lower strain level, we can better delineate the contribution of MT to RVFW viscoelasticity.

We firstly observed that **MT de- or hyper-polymerization did not necessarily result in equivalent changes in elasticity and viscosity in each direction.** For instance, after COL treatment, the circumferential elasticity (relaxation modulus, W_s) was reduced but the viscosity (W_d) was not changed in either direction. Similarly, MT hyper-polymerization increased viscosity (W_d) but did not alter the elasticity (W_s) in the C direction. In prior length-tension studies using cyclic test and/or stress relaxation, both cardiomyocyte elasticity and viscosity were reduced by COL [1,2,5]. Our results suggest that **the cell-level findings cannot be directly translated into tissue-level mechanical behavior, and an impaired MT network may result in the recruitment of other intracellular or ECM proteins to compensate and strengthen the tissue's overall mechanical behavior.** These data also imply that the RV elastic and viscous properties are decoupled within the myofiber domain range. More work should be performed to confirm this finding and investigate the potentially different sources to confer MT elasticity and viscosity.

Interestingly, both de- and hyper-polymerization of MT led to enhanced RV anisotropy with a larger elasticity in the L than C direction. **The anisotropic changes in RVFW viscoelasticity indicate that the MT network not only affects the viscoelastic parameter values (stronger or weaker viscoelasticity), but also impacts the structural organization and, consequently, tissue anisotropy.**

Second, we observed that **MT de- and hyper-polymerization led to opposite changes in RVFW viscoelasticity.** 1) As shown in Fig. 2 and Fig. 3A, MT de-polymerization reduced RV relaxation modulus (in C direction) and hyper-polymerization increased RV relaxation modulus (in the L direction), suggesting that an enhanced MT network is associated with stiffer myocardium. 2) The de-polymerization of MT did not affect tissue viscosity in either direction, whereas the MT hyper-polymerization leads to greater viscosity in both directions (Fig. 3B). 3) MT de-polymerization tended to decrease the V/E ratio in the L direction, whereas MT hyper-polymerization significantly increased V/E ratio in the C direction (Fig. 3C). The last two findings suggest that different sources may be responsible for the tissue viscosity and the V/E ratio with high and low content of MT, and these changes may be associated with the reorganization of MT network and recruitment of other load bearing components (e.g., titin).

Finally, our data may provide some insights on the role of MT in myocardial remodeling in heart diseases. Increases in elasticity and viscosity result in more resistance of the tissue during the passive stretch or active shortening. Therefore, an enhanced myocardial viscoelasticity is overall considered harmful to cardiomyocytes as the 'resistance' to muscle shortening is elevated. However, there may be another side of the story as some *in vitro* studies have shown a beneficial role of matrix viscosity in cell behavior (e.g., migration and proliferation) [7,8]. The viscous property to 'damp' mechanical energy may prevent wall stress elevation and cell damage in diseased conditions, and thus the MT proliferation in hypertrophied myocardium may be an adaptive response of the tissue. Future study should further investigate the roles of substrate's viscosity and the V/E ratio in cardiomyocyte function.

REFERENCES

- [1] Caporizzo M.A. et al., *Biophys. J.*, 1796-1807, 2018.
- [2] Caporizzo M.A. et al., *Circulation*, 902-915, 2020.
- [3] Tsutsui, H. et al., *Circulation*, 533-555, 1994.
- [4] Jang, S. et al., *J. Am. Heart Assoc.*, 2017.
- [5] Harris, T et al., *Heat and Circ. Phys.*, 2173-2182, 2002.
- [6] Liu, W. et al., *J. Biomech. Eng.*, 2021.
- [7] Curtis, M.W et al., *J. Cardio. Nursing*, 87-92, 2009.
- [8] Ryan, A.J. et al., *Biomat.*, 296-307, 2015.

MODAL ANALYSIS OF NATURAL VIBRATION FREQUENCIES OF THE BRAIN AND HEAD

Turner Jennings (1), Rouzbeh Amini (1,2), Sinan Müftü (1)

(1) Department of Mechanical and Industrial Engineering, Northeastern University, Boston, MA, USA

(2) Department of Bioengineering, Northeastern University, Boston, MA, USA

INTRODUCTION

Physical structures in the absence of outside forces tend to passively vibrate at specific natural frequencies. If an outside vibration is applied with a frequency equal to one of the natural frequencies of that structure, it induces potentially harmful resonance, leading to a larger vibration amplitude than the input force. Quantifying the natural frequencies of a structure, whether it is manmade or not, is critical in identifying potentially harmful vibration sources. Individuals experience exposure to vibrations in both low intensity long duration, such as riding in a car or operating machinery, and high intensity short duration, such as sports collisions or car accidents. As such, categorizing the natural frequencies of critical parts of the body, such as the brain, can help identify dangerous sources of vibration and improve protective technologies through attunement of dangerous frequencies.

The natural frequencies of the brain have been studied both experimentally [1,2] and numerically [3,4] in the past. Experimental measurement of natural frequencies is limited due to ethical limitations with testing with live subjects. Tests with cadavers have shown that vibrations are difficult to detect due to the soft layers of skin and muscle that inhibit amplitude measurement. The accuracy of previous finite element (FE) studies to calculate the natural frequencies have been limited by the simplicity of the models used, which frequently omit organs or sections of the head to reduce computational cost. The purpose of this study was to validate the use of a more complete and detailed FE model to calculate the natural frequencies of the head and the brain.

METHODS

We calculated the natural frequencies of the head and brain using the Total Human Model for Safety (THUMS) [5]. The THUMS model is a full-body FE model developed using the LS-DYNA (Ansys, Inc., Canonsburg, PA) FE solver for crash test safety applications. For this investigation only the head model, segmented at the base of the skull, was used. The addition of the neck was found to have no effect on the

natural frequencies (data not provided). The model features a highly detailed head (Fig. 1), including a brain fully modeled with separate white and gray matter, meninges, and cerebrospinal fluid (CSF). The geometry of the model is based on a 50th percentile male. It includes components of the head frequently omitted in previous studies, such as the eyes, facial musculature, and skin.

The head model is comprised of 257 parts made of 256,935 elements, with the brain model making up 195,783 of those elements. Different parts of the head are all modeled using linear material modeling approaches; linear piecewise plasticity (MAT_024) for the skull, viscoelasticity (MAT_006 and MAT_061) for the brain and meninges, and simple elasticity (MAT_001) for the skin, muscles, and other tissues. The linearized material models reduce computation time and enable modal analysis of the natural frequencies of the model.

Modal analysis was performed using LS-DYNA implicit analysis. The first 10 natural frequencies were calculated for six different subsections of the head: the brain matter alone, brain with falx and tentorium, brain with falx, tentorium, CSF, and meningeal layers, skull alone, skull with all contents, and the full head model. Vibration modes associated with rigid body motion of the full head, as well as nonphysical vibration modes calculated in the CSF, were rejected.

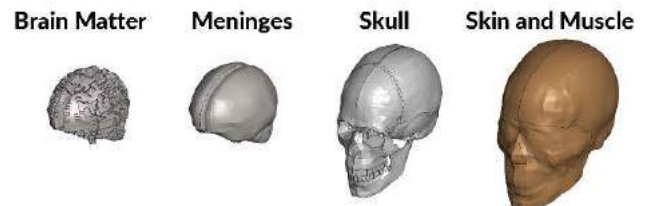


Figure 1: Layers of the THUMS head model

RESULTS

The range of the first ten natural frequencies for each sub-section of the head tested are summarized in Table 1. The vibration modes associated with the natural frequencies of the full head model are shown in Fig. 2. The type of deformation observed for each of the vibration modes shown in Fig. 2, and their associated natural frequencies are listed in Table 2.

As expected, the stiffer parts of the head, such as the skull and meningeal layers, had much higher natural frequencies than the softer brain matter. The natural frequencies of the skull alone were two to three orders of magnitude larger than the other sections tested. The brain alone had the lowest natural frequency, but the addition of the CSF and meningeal layers as supporting structures around the brain increased the natural frequency response. The natural frequencies of the full head model fell between those of the skull and the brain. The frequency range was closer to the response of the brain, consistent with the corresponding vibration modes showing deformation primarily in the cerebral brain matter.

Table 1: Range of the first 10 natural frequencies for different sub-sections of the head model

Section	1 st Natural Frequency [Hz]	10 th Natural Frequency [Hz]
Brain matter	1.1	6.1
Brain matter, falx, tentorium	1.1	5.0
Brain, falx, tentorium, CSF, meningeal layers	12.6	16.0
Skull	1026.2	2301.3
Skull with cranial cavity contents	11.2	16.2
Full head	11.1	16.2

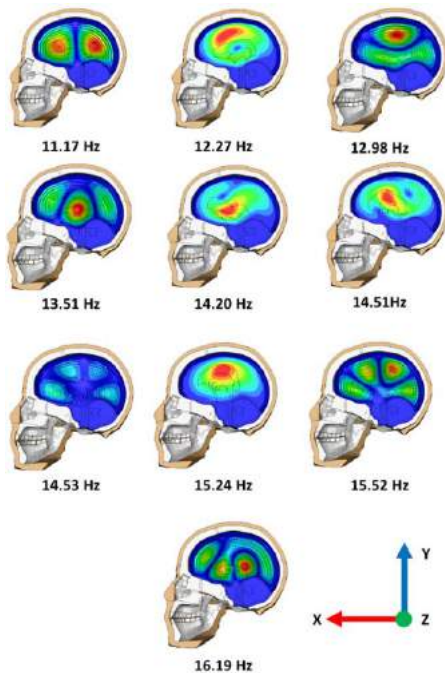


Figure 2: Vibration modes for the first ten natural frequencies of the full head model. The color plot represents the relative magnitude of displacement, with blue indicating zero displacement and red indicating maximum relative displacement.

Table 2: Description of vibration modes for the full head model

Frequency [Hz]	Vibration mode
11.17	Flexural rotation around y-direction
12.27	Flexural rotation around z-direction
12.98	Flexural rotation around x-direction
13.51	Flexion normal to x-y plane
14.20	Flexural rotation in the z-direction
14.51	Flexural rotation in the z-direction
14.53	Flexion normal to x-y plane
15.24	Flexural translation in the y-direction
15.52	Flexion normal to x-y plane
16.19	Flexion normal to x-y plane

DISCUSSION

The results of the head section analysis are consistent with expectations and prior research. The natural frequencies calculated for the skull align closely with previous experimental results measured on dry skulls [6,7]. The vibration modes observed in the full head model are similar to those observed in Tse et al [4]; however, the natural frequencies calculated in this study are an order of magnitude smaller. This discrepancy may be due to differences in the modelling techniques used. Another reason could be that the dynamic behavior of the model in Tse et al.'s work was not validated against previous experimental results.

The natural frequencies of any object are dependent on the geometry and material properties. The frequency ranges calculated in this study are estimates based on 50th percentile adult male dimensions, and average material properties. Future simulations using geometry representative of different head sizes, as well as varying the material properties according to uncertainty observed in the literature, could clarify the sensitivity of the natural frequencies to natural variations in size, shape, and material stiffness of the head. The natural frequency ranges calculated coincide with the frequency range of other physiological functions, such as heart rate (1-3 Hz) and brain waves (0.1-40 Hz). It is unknown whether the brain's mechanical preference toward these frequencies is related in any way.

The objective of this study was to validate the modal analysis results of this model against existing literature on the topic. The natural frequency response of the model is close to previous experimental and numerical results, which lays the foundation for using this model to test the effects of variation in tissue properties or subject-to-subject geometric variation on natural frequencies, as well as further investigation into cellular-level response to these vibration frequencies.

ACKNOWLEDGEMENTS

Funding for this project was provided by the United States Army Research Lab Soldier Protection Program Cooperative Agreement #W911NF2120208.

REFERENCES

- [1] Franke, E, *J. Acoust. Soc. Am.*, 28:1277-1284, 1956.
- [2] Stalnaker, R et al., *J. Biomech.*, 4:127-139, 1971
- [3] Meyer, F, *Int. J. Crashworthiness*, 9:535-545, 2004
- [4] Tse, K et al., *CM Biomech. Biomed. Eng.*, 18:961-973, 2015
- [5] Iwamoto, M et al., *Traffic Inj. Prev.*, 16:S36-S48, 2015
- [6] Khalil, T B et al., *J. Sound Vib.*, 63:351-376, 1979
- [7] Horáček, J et al, *Nat. Conf. Eng. Mech.*, paper no. 318, 2003

COMPUTATIONAL MODELING OF CORONARY VENOUS RETROPERFUSION TREATMENTS FOR ISCHEMIA

Haifeng Wang (1), Lei Fan (1), Jenny S. Choy (2), Ghassan S. Kassab (2), Lik Chuan Lee (1)

(1) Department of Mechanical Engineering, Michigan State University, East Lansing, Michigan, USA
(2) California Medical Innovation Institute, San Diego, California, USA

INTRODUCTION

Coronary venous retroperfusion, such as coronary sinus occlusion (CSO) and selective auto-retroperfusion (SARP) [1], is proposed as a treatment for coronary artery diseases. Unlike existing treatments of coronary artery diseases such as coronary artery bypass grafting, coronary venous retroperfusion seeks to deliver blood through the coronary venous system (i.e., “back door”) to the ischemic region either by occluding the coronary sinus in CSO or shunting arterial blood to the coronary veins in SARP. Their mechanisms and effects on the coronary microvasculature are, however, not well understood largely because it is especially extremely difficult, if not impossible, to measure all the relevant hemodynamic quantities in the microcirculation *in vivo*. To address this limitation, we developed a novel computational framework that couples the coronary arterial-capillary-venous microcirculation with cardiac mechanics in a closed-loop to investigate coronary venous retroperfusion treatments.

METHODS

The computational framework consists of the coronary arterial, venous and capillary networks (with cross-connections) as well as the Thebesian vessels that are not considered in most existing computational models (Figure 1). The entire network consists of 1996 vessels and each vessel is represented by a 0D nonlinear lumped model consisting of the 2 vascular resistances and compliance (as indicated in the square inset in Figure 1). Geometry (radius and length) and mechanical properties of the vessels are prescribed based on measurements. To account for the branching ratios measured in experiments [2], the equivalent resistance, R_{eq} , and capacitance, C_{eq} , for the vessel of order n are determined by

$$R_{eq}^n = \frac{128\mu L}{\pi D^4} \frac{N_{num}^n}{N_{exp}^n}, \quad C_{eq}^n = \frac{\partial V}{\partial P} \frac{N_{exp}^n}{N_{num}^n} \quad (1)$$

where N_{num}^n and N_{exp}^n are the total number of vessels of order n in the present numerical model and experimentally measured in pigs,

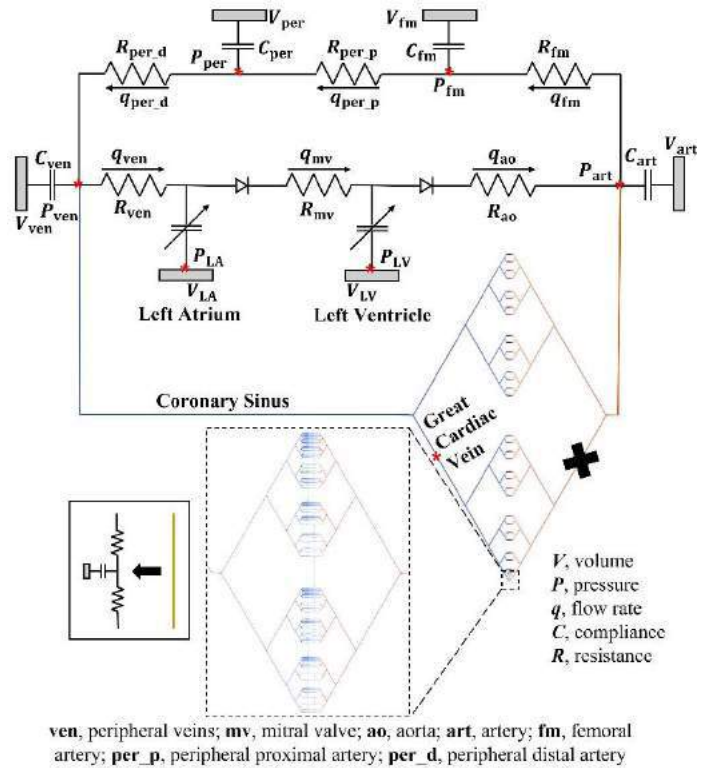


Figure 1: Schematic of the computational framework modeling coronary venous retroperfusion treatments. Dashed lines represent the microvascular network containing coronary arteries, capillaries and veins. The black cross indicates the occluded arterial vessel.

respectively. In Eq. (1), L , D , V and P are the length, diameter, volume, and transmural pressure of an individual vessel, respectively; μ denotes the blood viscosity. The function of left ventricle (LV) and left atrium (LA) are each described using a time-varying elastance model [3]. Ischemia due to the occlusion of a coronary artery (as indicated by the black cross symbol in **Figure 1**) is simulated by setting the artery resistance to infinitely large. CSO and SARP are simulated, respectively, by occluding the coronary sinus and connecting the great cardiac vein (GCV) to the femoral artery via a catheter, respectively (**Figure 1**).

RESULTS

The predicted blood pressure and flow rate distribution across different vessel order of the entire coronary network (without ischemia) are consistent with that in the arteries in previous measurements (**Figure 2**). The model predicts both SARP and CSO lead to higher intravascular pressure (**Figure 3A**), larger vessel diameter (**Figure 3B**) and slower flow (**Figure 3C**) in capillaries compared the ischemic case. The capillary transit time (CTT), which is calculated by dividing capillary blood volume by flow rate, is increased as a result (**Figure 3D**). Between the two coronary venous retroperfusion treatments, SARP produces a lower intravascular pressure (55 mmHg vs. 80 mmHg) and smaller capillary diameter (7.25 μm vs. 7.38 μm) but higher capillary transit time than CSO (25 s vs. 20 s).

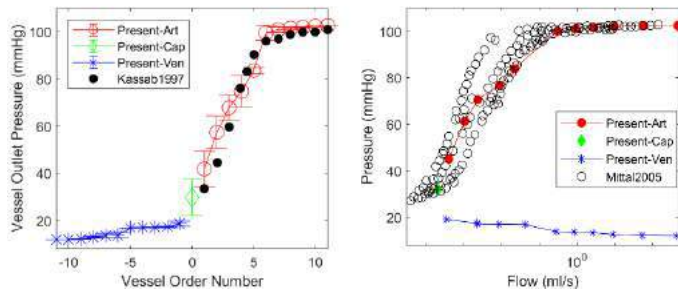


Figure 2: Model predictions of the pressure-vessel order relationship (left) and pressure-flow relationship (right) without ischemia. Reference data is taken from [2] and [4], respectively. Pressure and diameter are averaged over one cardiac cycle for arterial (Art), capillary (Cap) and venous (Ven) vessels.

DISCUSSION

Capillary transit time is closely associated with tissue oxygenation. High capillary transit time, in principle, allows more oxygen and nutrients to be transported to the tissue in the ischemic region, which in turn, improves coronary microvascular function and reduces infarct size. Our results show that both CSO and SARP increase the capillary transit time substantially, which can help in increasing tissue oxygenation. The increase in capillary transit time is larger in SARP, which shunt blood from the femoral artery to the coronary veins. An interesting finding here is that while CSO produces higher GCV pressure, it does not translate to a higher capillary transit time compared to SARP. This framework can be further extended to account for myocardial contractility and oxygen transport, and eventually for optimizing coronary venous retroperfusion treatments.

ACKNOWLEDGEMENTS

NIH R01 HL160997

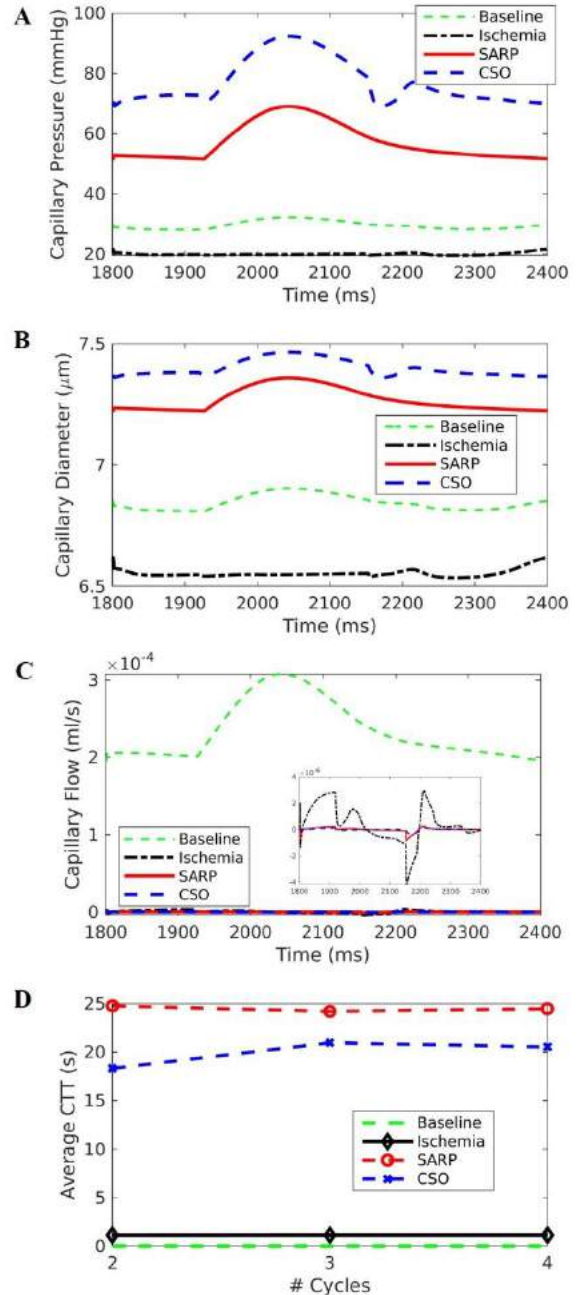


Figure 3: Effects of CSO and SARP on (A) capillary pressure, (B) diameter, (C) flow rate, and (D) capillary transit time (CTT). Pressure, diameter and flow rate are averaged over all capillaries for each time step. CTT is averaged per cardiac cycle per capillary.

REFERENCES

- [1] Choy JS et al., *Acute Card Care*, 13(2):99-108, 2011.
- [2] Kassab GS et al., *Ann Biomed Eng*, 25(1):204-17, 1997.
- [3] Fan L et al., *Am J Physiol Heart Circ Physiol*, 320(3):H1037-H1054, 2021.
- [4] Mittal N et al., *Am J Physiol Heart Circ Physiol*, 289(1):H439-46, 2005

INVESTIGATING THE IMPACT OF AORTIC ROOT GEOMETRY ON TAVI IMPLANTATION USING 3D RECONSTRUCTIONS AND FSI

K. Bates (1), K. Lachapelle (2), G. Martucci (3), R.L. Leask (1)

- (1) Chemical Engineering, McGill University, Montreal, QC, Canada
(2) Division of Cardiac Surgery, McGill University, Montreal, QC, Canada
(3) Division of Cardiology, McGill University, Montreal, QC, Canada

INTRODUCTION

Transcatheter aortic valve implantation (TAVI) has emerged as an alternative method to treat heart valve disease, especially in those patients with a high surgical risk. Severe aortic stenosis in tricuspid aortic valves (TAV) is now routinely treated with this minimally invasive procedure. As TAVI devices have become safer and longer lasting [1], the procedure is becoming an option for populations at a lower surgical risk and with different valve phenotypes. Recently TAVI has been approved for aortic stenosis for moderate surgical risk populations by the FDA [2].

Lower surgical risk patient populations, however, tend have different valvular and surrounding structural anatomies. In particular, bileaflet aortic valves (BAV) have unique anatomical characteristics that have led to BAV patients being excluded from official clinical trials for TAVI devices [3]. As a result, a BAV is typically a counterindication for TAVI. However, BAV patients have with varying degrees of frequency been chosen as candidates for TAVI, but this is not yet the standard of care. With the approval of TAVI devices for lower risk populations, there is a need to investigate new ways of assessing patients for TAVI and the impact on BAV patients.

This study seeks to investigate the hemodynamic effects of a variety of geometrical parameters on native and TAVI device function. Parametrized 3D models are used as the basis for fluid-structure interaction (FSI) numerical modeling of flow across the aortic valve. This paper presents preliminary work to create a TAVI simulator for evaluating the impact of root geometry, hemodynamics and future implantation training. Mechanical properties of the aorta are investigated using a large-scale tensile testing study and a patient-specific parametrized 3D model of the aorta and aortic valve is developed. Initial FSI studies are also presented.

METHODS

The aortic valve and surrounding anatomy are complex structures that are often simplified to save computational power. FSI models often reduce the geometry to a symmetrical aortic valve and a straight channel [4]. Other models reconstruct fully patient-specific aortic roots with idealized leaflets to maximize fidelity [5], [6]. In this study, to better understand which parts of the anatomy affect the flow dynamics through the aortic valve, a highly parametrizable model of the aortic root, valve and ascending aorta was build using SolidWorks (Dassault Systèmes, SolidWorksCorp., Waltham MA). The parameters used allow for a patient-specific idealized model to be generated and are shown in Table 1. A retrospective study of patients having undergone TAVI were reconstructed to begin validation of the FSI simulations.

Table 1: List of geometrical parameters in 3D model

Parameter	Description
LVOT_D	Left ventricular outflow tract diameter
STJ_D	Sinotubular junction diameter
Sinus_D	Sinus diameter (one for each region)
STJ_H	Height from base of LVOT to sternotubular junction
Sinus_H	Height from base of LVOT to the maximal sinus diameter
α	LVOT-aorta angle
Commisure H	Height of each commissure (one per commissure)
Coaptation_H	Height of the central coaptation
Geometric_H	Geometric height, or total length, of the aortic valve profile
Fusion type	If case is a BAV or not
Ellipticity	Ellipticity index of the LVOT Diameter

Material properties of the aortic tissue were determined from samples obtained from aortic aneurysm resection surgeries. Biaxial tensile testing was done using a TA Electroforce (TA Instrument, New Castle, DE) planar biaxial tensile tester. Testing samples are prepared by punching four 15x15mm samples from the collected tissue. Samples are then placed in a heated saline bath using suture holders to connect the samples to the load cells. The test consists of 8 pre-conditioning cycles of loading to 60% strain at 0.4 mm/s, followed by identical loading at 0.1 mm/s. Modulus of elasticity was calculated as the slope of the stress-strain relationship at 50% strain.

Numerical simulations are performed in COMSOL Multiphysics 6.1® (COMSOL AB, Stockholm, Sweden, 2022) using a fully-coupled arbitrary Lagrangian-Eulerian method (ALE) for the FSI components. Mechanical properties of the aortic valve were taken from the literature, and blood was assumed to be a Newtonian fluid with a viscosity of 3.5 cP and density of 1060 kg/m³. Pressure boundary conditions were applied at the ventricular inlet and aortic outlet. Transvalvular gradient, effective orifice area (EOA) and maximum jet velocity were used as validation measures to compare numerical modeling results with patient data.

RESULTS

Accurate mechanical properties are key to having a robust numerical model. The aortic tissue tensile testing study allows for a large cohort of patients to be used to get an average value of aortic stiffness of patients with diseased aortas, who also often present with valvular disease. The modulus of elasticity at 50% strain was on average 0.18 MPa ± 0.07 MPa.

The parametric 3D models were built using CAD software, with an example shown in Figure 1. The parameters encompass a wide variety of parameters and capture the asymmetry of the aortic root and valve. Based on clinician evaluation, these models visually resemble the native aortic root and valve.

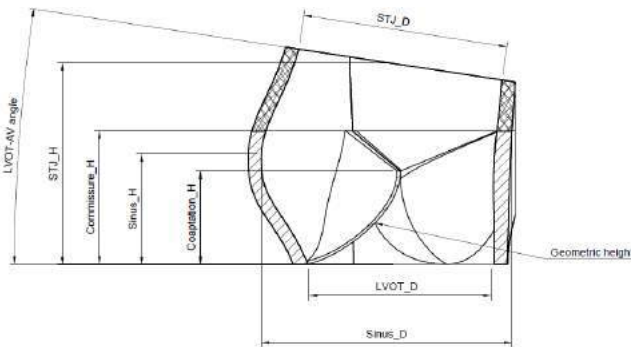


Figure 1: Cross-section view of the parametric 3D model

Simulations were run using these patient-specific models to start preliminary quantitative validation. The results show that the valve leaflets deform similarly to the native leaflets. The transvalvular pressure gradients, EOA and velocity profiles were comparable to the preprocedural evaluations. Figure 2 shows a visualization of the FSI results for a patient with an LVOT-aorta angle (α) of 10° at a mean

gradient of 3 mmHg (mid opening). Note the asymmetrical opening due to the higher value of α .

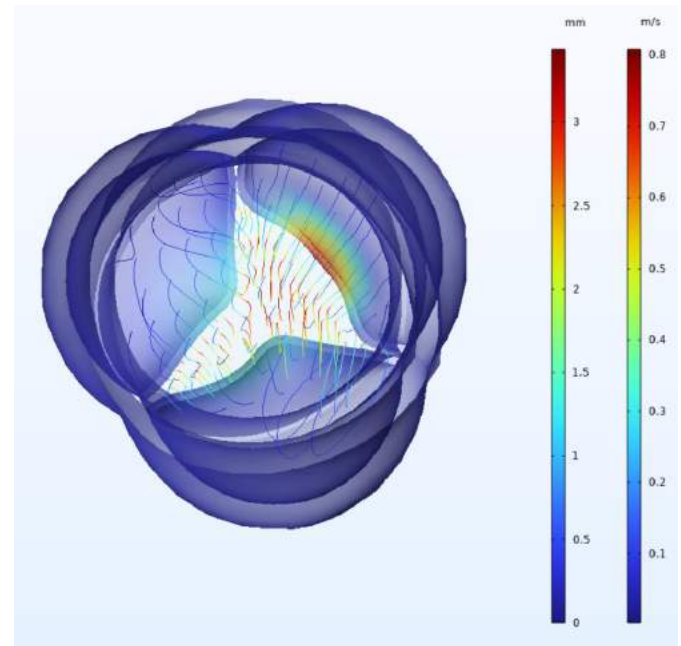


Figure 2: Top view of a FSI simulation with $\alpha = 10^\circ$

DISCUSSION

This preliminary work shows that an idealized 3D geometry that utilizes a multitude of input parameters can be used as the basis for patient-specific simulations without the need for a complete 3D reconstruction. Future studies plan for the investigation of these geometrical parameters. Geometry is one of the main aspects where BAV patients are different from TAV patients. They more often have an asymmetrical LVOT, increased LVOT-aorta angle, and larger ascending aortic diameters. Virtual deployment of a TAVI device in the 3D models coupled with a parametric analysis will allow for the determination of which of these parameters are responsible for the greatest disruption to flow, and how these could impact TAVI success.

Future work will also involve the investigation of implantation issues, different flow profiles, as well as coronary flow and how these affect TAV and BAV patients differently. Physical models can be 3D-printed to create catheterized models for procedural training.

ACKNOWLEDGEMENTS

This work was supported by the McGill University Health Centre Foundation, NSERC Discovery (RGPIN 2018-0616) and an FRQNT doctoral research award.

REFERENCES

- [1] Mack, M. J. et al., *N. Engl. J. Med.* 380, 1695–1705 (2019).
- [2] FDA. *FDA News Release* 2–4 <https://www.fda.gov/news-events/press-announcements/fda-expands-indication-several-transcatheter-heart-valves-patients-low-risk-death-or-major> (2019).
- [3] Halim, S. A. et al., *Circulation* 1071–1079 (2020) doi:10.1161/CIRCULATIONAHA.119.040333/FORMAT/EPUB.
- [4] Tango, A. M., Salmons-Smith, J., Ducci, A. & Burriesci, G., *Cardiovasc. Eng. Technol.* 9, 739–751 (2018).
- [5] Luraghi, G. et al., *Cardiovasc. Eng. Technol.* 10, 437–455 (2019).
- [6] Mohammadi, H., Cartier, R. & Mongrain, R., *Biomech. Model. Mechanobiol.* 17, 263–283 (2018).

MULTISCALE MECHANOBIOLOGICALLY OPTIMIZED SCAFFOLD DESIGNS FOR BONE TISSUE ENGINEERING

Timothy O. Josephson (1,3), Elise F. Morgan (1,2,3)

- (1) Department of Biomedical Engineering, Boston University, Boston, MA, USA
(2) Department of Mechanical Engineering, Boston University, Boston, MA, USA
(3) Center for Multiscale and Translational Mechanobiology, Boston University, Boston, MA, USA

INTRODUCTION

Scaffolds for bone tissue engineering aim to treat large bone defects, such as those that occur from severe skeletal trauma. Yet, how to design a scaffold for optimal bone formation remains an open question. A variety of physical stimuli, including substrate curvature and strain, can promote osteogenic differentiation of skeletal progenitor cells. The design of scaffold architectures can thus be used to regulate the mechanical stimuli to which cells are exposed, and for the purpose of testing mechanobiological hypotheses and promoting bone repair.

Mechanically informed scaffold designs can be lumped broadly into two categories: macro-mechanical and micro-mechanical. Macro-mechanically informed designs use the concept of “mechanical homeostasis,” matching the apparent modulus of the scaffold to that of the bone the scaffold is intended to replace [1,2,3]. On the other hand, micro-mechanically informed designs rely on the concept of the cellular microenvironment [4,5] to generate designs that possess large shares of osteogenically favorable microenvironments [6,7]. However, these designs are typically only based on a single stimulus and/or are limited in the variety of designs that they consider.

Various studies have examined the role of curvature and strain in the cellular microenvironment. For this work, curvature will be represented using curvedness (C) and the shape index (SI) [8]. Swanson et al. [9], found that smaller values ($C \in [4.7, 8] \text{ mm}^{-1}$) of curvedness promoted osteogenesis while larger values ($C \in [16, 33.3] \text{ mm}^{-1}$) maintained stemness. Werner et al. [10] found that convex curvatures ($SI > 0$) led to increased osteogenic gene expression in osteoprogenitor cells. Some studies have noted that saddles ($SI = 0$) may be preferable for osteogenesis [11,12]. Triply periodic minimal surfaces (TPMSs) have thus grown in popularity as a basis for scaffold designs, because TPMSs are saddles at all points.

In addition to substrate curvature, the scaffold architecture also determines the local strains that develop throughout the scaffold when subjected to loading. Results of numerous studies support the

mechanobiological hypothesis of Prendergast and colleagues [13,14,15] which proposes that octahedral shear strain (ϵ) and fluid velocity are the predominant stimuli regulating differentiation of osteoprogenitor cells. Under that paradigm in the absence of fluid flow, strains from 0.04% to 1% and from 1% to 3.75% promote formation of mature and immature bone, respectively [15].

This study develops a “mixed-topology TPMS” optimization scheme to generate both macro- and micro-mechanically informed scaffold designs and proposes several ways to evaluate the osteogenic fitness of a scaffold architecture.

METHODS

Scaffold surfaces were defined implicitly as a weighted sum of equations defining three different TPMSs (Fig. 1): primitive ($p(x, y, z)$), gyroid ($g(x, y, z)$), and diamond ($d(x, y, z)$). The mixed topology surface is a function of three parameters, α , β , and γ :

$$s(\alpha, \beta, \gamma) = \alpha p(x, y, z) + \beta g(x, y, z) + \gamma d(x, y, z) \quad (1)$$

and corresponds to where $s(\alpha, \beta, \gamma) = \pm \frac{1}{2}$. This scheme gives α , β , and γ control over both the architecture and wall thickness of the scaffold.

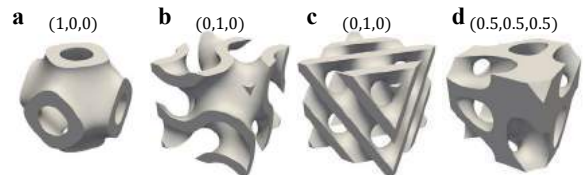


Figure 1: Scaffold unit cells for (a) primitive, (b) gyroid, (c) diamond, and (d) the starting design for the optimizations. The parameters (α, β, γ) that define each architecture are given above.

Meshes of the implicit surfaces were constructed through a process involving the marching cubes algorithm [16], a dynamic mesh optimization procedure for implicit surfaces [17], a constructive solid geometry technique [18], and finally the fTetWild [19] tetrahedral mesh

generator to produce 1mm cubic unit cells. Scaffolds were simulated in Ansys (Ansys Inc., PA, USA) with a linear-elastic material model ($E=13$ GPa, $\nu=0.3$), the bottom surface fixed, and the top surface compressed with a strain of $2500 \mu\epsilon$. Equations for C and SI of the scaffolds were derived analytically [8,20] and then evaluated at each node in the surface.

For each stimulus (SI, C, and ϵ), values were first calculated at all surface nodes and then averaged over each triangular surface facet in the mesh. Linear piecewise scoring functions were used to assign a score in the range [0,1] to each triangle. For the curvedness score f_c , a maximum score was assigned to 6 mm^{-1} , decreasing outward to 0 at $C=3$ and 9 mm^{-1} . For the SI score f_{si} , the score was maximal for the interval $SI=[0.25,0.5]$ and decreased outwards to 0 at $SI=-0.25$ and 0.5 at $SI=1$, thus targeting a saddle-like-convex surface. For the shear strain score f_ϵ , the maximal score was at 0.52% and decreased outwards to 0 at 0.04% and 3.75% , targeting the midpoint of the “mature bone” range of shear strains (according to [15]). Scores for multiple stimuli were multiplied together to obtain a curvature score (eq. 2) and a total score considering curvature and strain (eq. 3):

$$f_{\text{curv}} = f_c f_{si}, \quad (2)$$

$$f_{\text{total}} = f_c f_{si} f_\epsilon. \quad (3)$$

Each of the scoring functions was used to generate a single scalar score quantifying the overall fitness F of a given scaffold design:

$$F_{\text{stimuli}} = \sum_t^n \text{Triangles} A_t f_{\text{stimuli},t}, \quad (4)$$

where A_t is the area of a triangular facet and $f_{\text{stimuli},t}$ is the facet's score for a particular stimulus or combination of stimuli.

Five optimal scaffolds were determined, each corresponding to a different objective (Fig. 2), using the gradient-free COBYLA optimizer [21], as implemented in the SciPy library [22], with α , β , and γ each constrained between 0 and 1. The starting point for each case was $\alpha, \beta, \gamma = 0.5$ (Fig. 1.d). In two of the five optimization runs (cases 4 and 5), the apparent modulus was constrained to be within the interval $[0.475, 0.525]$ GPa, an example target modulus representative of trabecular bone in the human proximal tibia and greater trochanter [23]. This constraint required the optimizer to explore micro-mechanically informed designs while simultaneously achieving a macro-mechanically informed structure.

RESULTS

For each of the first three cases, the optimized design had a fitness score greater than those of the original TPMSs, the starting design, and the results of all other cases, though the optimal design for F_ϵ converged to a diamond-like scaffold (Fig. 2). Adding the modulus constraint slightly reduced fitness in regards to the curvature score (case 4), and more than halved the fitness in regards to the total curvature & strain score (case 5). All cases converged to designs that were heavily weighted towards the diamond TPMS (large γ) and only lightly weighted towards the gyroid TPMS (small β), while the weight for the primitive TPMS (α) varied among cases.

DISCUSSION

These results demonstrate the potential of mixed-topology TPMS designs to achieve optimal architectures for various macro- and micro-mechanical objectives. The mixed-topology TPMS strategy provides a larger design space than has been considered in studies using only traditional TPMS designs, and the design space could be further expanded to four or more TPMS base structures, simply by adding more parameters. The flexibility of the scoring functions could allow for additional stimuli, such as fluid shear stress or hydrostatic pressure, to be considered within the same framework—a notable advantage over other approaches that only consider a single stimulus.

These results also emphasize that considering different stimuli leads to different “optimal” designs and thus highlight the need for

experiments that explore what combinations of stimuli (e.g. curvedness, shape index, and strain) are most favorable for osteogenesis. At present, knowledge of which stimuli, at what magnitudes, and in what combinations is insufficient to establish that the designs obtained here are truly optimal. Our approach can be used to generate designs for these future experiments, to compare scoring functions and accelerate development of scaffolds that provide requisite stimuli for bone repair.

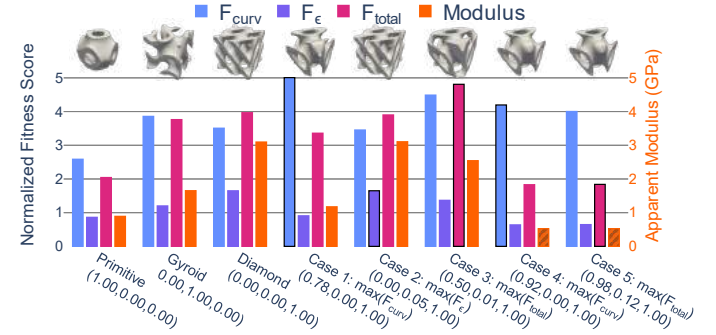


Figure 2: Normalized scaffold fitness scores and apparent moduli for the 3 TPMS designs and the final design of each optimization. Scores are presented as the score for that design normalized by the score F of the starting point design ($\alpha, \beta, \gamma = 0.5$). For each case, the score that was optimized is outlined in black, constraints are indicated by striped bars. The final parameters (α, β, γ) are listed for each case.

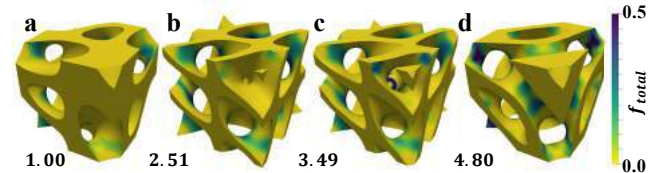


Figure 3: Iteration progress for the case 5 optimization, showing the f_{total} score on each surface facet. The normalized scaffold fitness scores are reported below each design. (a) Initial design (iteration 1), (b) iteration 15, (c) iteration 25, (d) final design (iteration 49).

ACKNOWLEDGEMENTS

NIH AG073671.

REFERENCES

- [1] Wu S et al., *Mat. Sci.&Eng R: Reports*. 80(1):1–36, 2014.
- [2] Ghose S et al., *Appl. Mat. Today*. 15:377–88, 2019.
- [3] Vijayavenkataraman S et al., *ACS Appl. Bio Mat.* 1(2):259–69, 2018.
- [4] Moraes C et al., *Int. Bio*. 3(10):959–71, 2011.
- [5] Werner M et al., *Materials*. 13(4):1–18, 2020.
- [6] Perier-Metz C et al., *Front. in Bioeng&Biotech.* 10, 2022.
- [7] Pires THV et al., *Materials*. 15(20), 2022.
- [8] Koenderink JJ et al., *Img&Vis Comp.* 10(8):557–64, 1992.
- [9] Swanson WB et al., *Int. J of Mol Sci.* 23(9):4499, 2022.
- [10] Werner M et al., *Advanced Sci.* 4(2):1600347, 2017.
- [11] Callens SJP et al., *Biomat.* 232:119739, 2020.
- [12] Jinnai H et al., *Bone*. 30(1):191–4, 2002.
- [13] Prendergast PJ et al., *J Biomech.* 30(6):539–48, 1997.
- [14] Huiskes R et al., *J. of Mat Sci.* 8(12):785–8, 1997.
- [15] Lacroix D et al., *Med. and Bio Eng and Comp*, Vol. 40. p. 14–21, 2002.
- [16] Chernyaev E, *Inst. for High Eng Phys, Moscow, Russia*, :1–8, 1995.
- [17] Ohtake Y et al., *Vis Computer*. 19(2-3):115–26, 2003.
- [18] Laidlaw DH et al., 13th *Conf. on Comp. Graphics & Interactive Techniques, SIGGRAPH* 1986. :161–70, 1986.
- [19] Hu Y et al., *ACM Trans. on Graphics*. 39(4):18, 2020.
- [20] Goldman R, *CAD Design*. 22(7):632–58, 2005.
- [21] Powell MJD, *Adv. in Opt.&Num. Analysis*. (1):51–67, 1994.
- [22] Virtanen P et al., *Nature Methods*. 17(3):261–72, 2020.
- [23] Morgan EF et al., *Ann Rev of Biomed Eng*. 20:119–43, 2018.

A NOVEL ELECTROCHEMICAL CATHETER FOR CARDIAC OUTPUT MONITORING

Marco A. Nino (1), Abdulsattar H. Ghanim (2), Syed Mubeen (2), Suresh M.L. Raghavan (1)

(1) Roy J. Carver Department of Biomedical Engineering, University of Iowa, Iowa City, IA, USA
(2) Department of Chemical and Biochemical Engineering, University of Iowa, Iowa City, IA, USA

INTRODUCTION

Cardiac output (CO) monitoring is important in critically ill patients and for those undergoing cardiac procedures to check for adequate tissue oxygenation and effectiveness of cardiac repair. The current standard for CO monitoring is the use of the specialized pulmonary artery catheter (PAC) that works on the thermodilution principle. In thermodilution, a clinician will make controlled injections of cooler-than-blood saline into the flowing blood to induce a small drop in temperature of the blood. The transient change in local blood temperature – generally less than 0.5°C – is monitored and used to estimate blood flow rate (greater the blood flow, quicker recovery to normal temperature). Thermodilution-based CO measurement can be highly operator dependent and affected by uncontrolled confounding factors. As a result, measurements are known to have poor repeatability resulting in about 20% window of error. Overall, thermodilution is notoriously error-prone and may lead to wrong interpretations. Nishikawa et al. states that, “Knowledge of the errors inherent in thermodilution measurement is essential for the anaesthetists and other clinicians engaged in the management of critically ill patients. The erroneous estimation of CO may lead to inappropriate management and adverse outcomes”^[1].

Principle of electrodilution

We proposed the novel electrodilution method, which is operationally similar to thermodilution, but uses a distinctly different physiochemical principle allowing us to circumvent many of its known challenges^[2]. The electrodilution method for measuring flow rate leverages transient electrochemical behavior of a redox-active tracer molecule that is injected or released directly into the blood stream. The principle is that when a voltage applied to electrodes in contact with specific tracers released in blood, a measurable current is observed due to charge redistribution or electron transfer processes. Similar to thermodilution, the current response will also dissipate as a function of

CO and thus help recover it through calibration. This method avoids the use of temperature and its associated sources of error and hence holds the potential to be more reliable. Our initial findings showed that electrodilution metrics are correlated to flow rate. However, that proof-of-concept study did have some limitations – electrochemical cell design and flow conditions tested were not representative of physiological conditions. The study used steady flow conditions, but CO is pulsatile. In addition, the study used a flow-through electrochemical cell instead of a catheter and as a result it limited the flow rates tested to those that constitute neonate/pediatric regimes.

In this study, the electrochemical cell was miniaturized and an electrodilution catheter prototype was developed. A flow loop apparatus was designed to test the novel catheter using a broad range of flow rates under pulsatile flow conditions for bovine blood with hypertonic saline injections.

METHODS

Saline electrodilution experiments

To test electrodilution under conditions that more closely mimic a clinical setting, *in vitro* high-fidelity flow injection analysis experiments were conducted under physiologically representative pulsatile flow conditions. Anticoagulated bovine blood solution was prepared to have a 9:1 ratio of bovine blood to 3.2 wt% sodium citrate. Bovine blood samples were acquired from a local abattoir as needed. Hypertonic saline solution (7 wt%) was prepared as the analyte solution. Hypertonic saline was selected as it allows for greater current response in blood compared to isotonic saline. A 2.5 Fr quad-lumen PAC intended for thermodilution (131F7, Edwards Lifesciences Corp., Irvine, CA United States) was adapted to fabricate an electrodilution catheter, equipped with an electrochemical cell as a sensor, for physiological fluid flow characterization. This was achieved by threading copper wire with electrode material in two of the individually insulated catheter lumens and the catheter tip was

sealed using silicone. Only 1.5 mm of the electrode material wire was exposed at the catheter tip and the electrode spacing was 2 mm. The PAC is equipped to have analyte released from the catheter itself – operationally similar to thermodilution. The analyte release port is located 15 cm proximal to the sensing cell at the catheter tip.

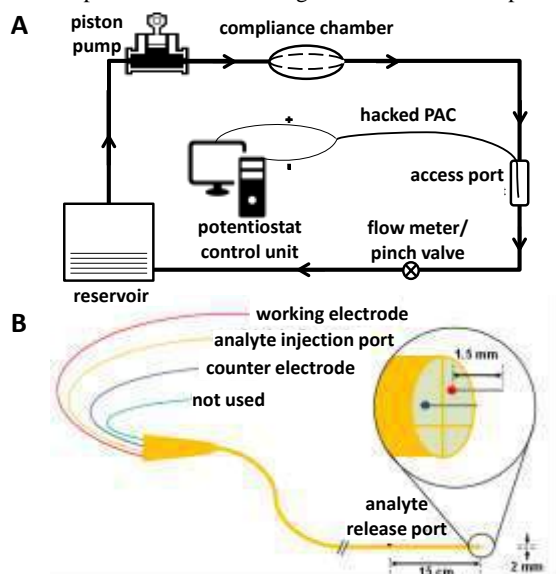


Figure 1: (A) Schematic of the flow loop apparatus. (B) Schematic of the fabricated electrodilution catheter prototype.

Experiments were conducted at various flow rates to characterize how the electrodilution curves are influenced by the flow rate of the medium. A programmable piston pump (SuperPump pulsatile pump, ViVitro Labs Inc., Victoria, BC Canada) was used to drive flow using a physiologically representative velocity waveform of large-artery blood flow. A tunable compliance chamber and pinch valve were used to target physiologically representative pressure waveforms (see Figure 1A). The electrodilution catheter was introduced into the flow loop via a catheter access port and the catheter was advanced so that 30 cm of the catheter was exposed to the flowing media. The catheter described above was connected to a potentiostat control unit (VSP-300, BioLogic Science Instruments, Seyssinet-Pariset, France). Using large-amplitude sinusoidal voltammetry (LASV), a potential waveform with AC parameters of $4 V_{pk}$ and 10 Hz was applied to the working electrode and the resulting current signal was continuously recorded at a sampling rate of 1 kHz. The pump was set to a predetermined flow rate, and the medium was allowed to flow until the measured current of the cell reached equilibrium. Next, multiple manual injections of 5 mL analyte was delivered over 1 sec into the flowing medium proximal to the sensing electrodes. The resulting current response and recovery were recorded. The process was repeated for various flow rates ranging from 0.5 to 4 L/min which constitute the ranges of blood flow for pediatric and adult patients. Experiments were repeated to test for reliability and reproducibility.

RESULTS

The current response to the analyte bolus follows a typical dilution curve – a steep rise and gradual fall back to the baseline. To characterize the temporal current response, data was post-processed using a semi-automated algorithm to identify the metrics that best correlate to flow rate of the media. The electrodilution curve is represented as the positive envelope of the current response (see Figure 2A). To quantitatively assess the relationship between flow rate

and the electrodilution curve in the time domain, an electrodilution metric was calculated for each curve: $\Delta Total Charge$ is defined as the charge observed during the duration of the rise from the baseline and fall back to baseline of current (area under the dilution curve). A description of how the metric is calculated can be found in our previous study^[2]. A schematic illustration of the prototype electrodilution catheter developed is shown in Figure 1B.

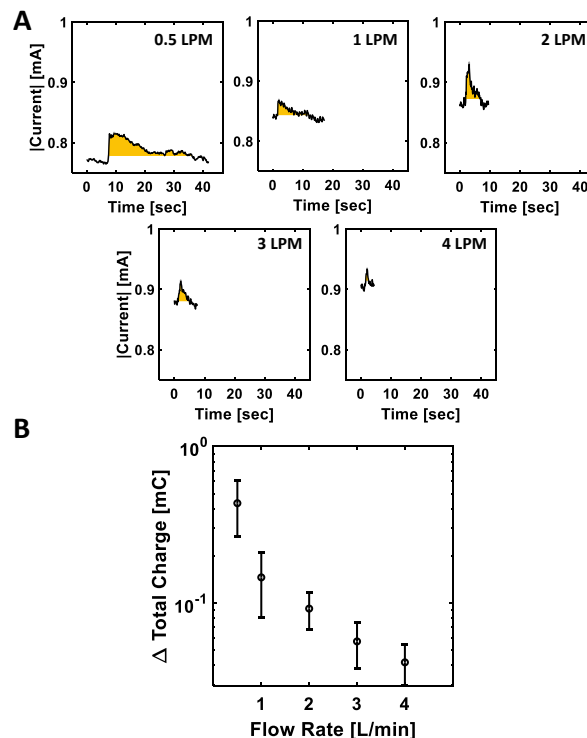


Figure 2: (A) Representative electrodilution curves for each flow rate tested. Shaded regions indicate $\Delta Total Charge$. (B) $\Delta Total Charge$ metric (mean and standard deviation for $n=5$) for five different pulsatile flow rates.

DISCUSSION

A novel electrodilution catheter was developed and tested for its ability to characterize flow rate under high-fidelity physiological conditions (see Figure 1B). The catheter has similar form factor to a clinically used PAC and is operationally identical to thermodilution. Figure 2B shows a summary of the key electrodilution metric for the novel catheter in blood under pulsatile flow conditions. Our results are consistent with our previous findings; there is a negative correlation with flow rate for $\Delta Total Charge$ ^[2].

We found that the electrodilution method using a novel electrochemical catheter is a feasible approach to characterizing blood flow rate in the body. This electrochemical approach to fluid flow measurement circumvents the major challenge that exists with thermodilution – measuring minute changes in temperature – providing the opportunity for more reliable flow rate measurement.

ACKNOWLEDGEMENTS

This work was supported in part by National Institutes of Health under Grant Nos. R03EB027299 (to Mubeen and Raghavan).

REFERENCES

- [1] Nishikawa, T et al., *Can J Anaesth*, 40:142-153, 1993.
- [2] Sarathy, S et al., *Frontiers on Chem*, 9, 2021.

TOWARD MULTIPLEXED SINGLE-CELL WESTERN BLOTTING USING DNA-BARCODED READOUT

Mariia Alibekova Long (1), William KJ Benman (1), Lukasz J Bugaj (1,3), Alex J Hughes (1,2,3,4)

(1) Department of Bioengineering, University of Pennsylvania, Philadelphia, Pennsylvania, USA

(2) Center for Soft and Living Matter, University of Pennsylvania, Philadelphia, Pennsylvania, USA

(3) Institute for Regenerative Medicine, University of Pennsylvania, Philadelphia, Pennsylvania, USA

(4) Department of Cell and Developmental Biology, University of Pennsylvania, Philadelphia, Pennsylvania, USA

INTRODUCTION

Cell functional states can change rapidly, especially during development and differentiation¹. Changes in cell function can affect nearby cells, leading to the development of heterogeneous tissues that are different from the starting cell population. While cell states collectively set tissue homeostasis, disease processes like cancer are characterized by increases in state variability (heterogeneity) and changes in normal tissue composition². Proteins and their post translational modifications (PTMs) are thought to more proximally set cell state relative to its genome or transcriptome. However, elucidating single cell proteomes poses a major technical challenge as mammalian cells are estimated to contain $> 10^4$ types 400 different types of PTMs of each moment in time^{3,4}, and unlike transcripts proteins cannot be amplified to aid their detection. Antibody-based protein detection is highly sensitive relative to mass spectrometry but suffers from limited specificity and multiplexing limits imposed by spectral overlap of fluorescent labels. Therefore, single-cell proteomics has significantly lagged scRNA-seq, particularly in scalability to whole-proteome quantitation.

We are tackling this significant technological gap using a novel tool called single-cell proteome sequencing, or *scProteome-seq*. We analyze proteins from single cells using electrophoretic separations similar to existing scWestern technology⁵ and then perform DNA-based protein information encoding. The physical separation of analytes mitigates non-specific binding of analytes, while the use of DNA-labeled antibodies enables sensitivity by amplification and circumvents optical multiplexing limits. We developed readout of protein information comprising two barcodes 1) *Antibody ID* delivered via DNA-tagged antibodies to identify protein targets, 2) *Size ID* oligonucleotide delivered via a DNA microarray that encodes spatial coordinates. The size ID allows us to determine both the cell of origin of a particular analyte and to confirm antibody binding specificity by inferring the

molecular weight of the analyte from its migration distance. Our scProteome-seq workflow is performed as follows (see Fig.1). First, we settle single cell in microwells patterned in a polyacrylamide gel sheet, lyse them and separate proteins by single-cell SDS-PAGE, followed by protein immobilization on a nitrocellulose blotting membrane. Next, we add Antibody ID and Size ID and enzymatically couple, extend, and extract the full barcode. Lastly, we analyze barcodes by next-generation sequencing (NGS) for high throughput analysis. We can then compare cell-cell protein abundance and construct a profile of cell heterogeneity (see Fig 1). In this abstract, we present several performance aspects of technology development including protein immobilization efficiency, feasibility of protein DNA barcoding and compatibility of DNA barcoding with NGS. Our long-term research objective is to obtain high resolution snapshots of single-cell proteomes using our tool for applications in cell development, differentiation, and disease.

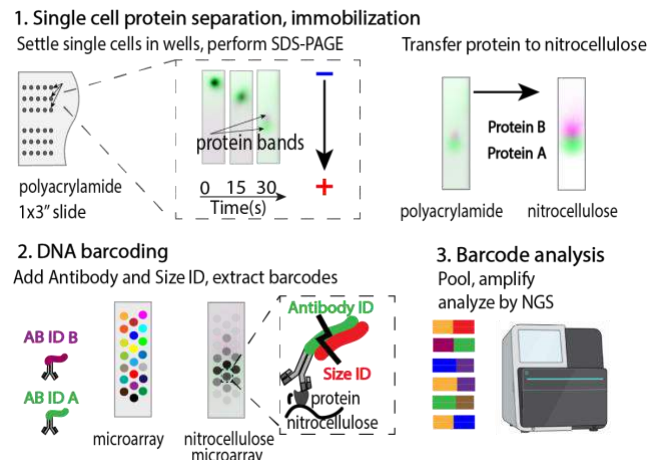


Figure 1: Schematic of the scProteome-seq workflow.

METHODS

1. Efficiency of protein transfer from polyacrylamide gel to nitrocellulose. We blotted 5 μ M GFP, Ovalbumin-Alexa 555, IgG-Alexa-555 on polyacrylamide gel and transferred to nitrocellulose while varying transfer time. We computed % efficiency as difference in AUC of fluorescence distribution peaks of protein post- and pre-separation divided by initial protein spot AUC, adjusted for background.

2. Single cell protein transfer resolution loss. We performed single-cell SDS-PAGE on GFP+ HEK-293 cells, transferred proteins to nitrocellulose and compared full width at half maximum (FWHM) of fluorescence distribution peaks adjusted for background to find increase in spot size during diffusive transfer.

3. Feasibility of DNA barcoding. We blotted serial dilutions (5 μ M to 5 nM) of purified GFP on nitrocellulose. We then performed scProteome-seq workflow as follows: blocked the membrane, fixed protein with paraformaldehyde and performed probing with anti-GFP-DNA conjugate. Next, we added size IDs via a DNA microarray spotted with 80,000 unique IDs. We used restriction enzymes to cut DNA and allow Antibody ID to hybridize to Size ID, Klenow polymerase to extend DNA. We then extracted and analyzed barcodes via qPCR.

4. Compatibility of the tool with NGS. We performed single-cell SDS-PAGE on GFP+ and tdTomato-FLAG+ HEK-293 cells. We then performed scProteome-seq workflow as described above. We used NGS to analyze extracted barcode library by mapping location of each Size ID as DNA “coordinate” and adding counts of extracted barcodes to each location to reconstruct protein information in DNA form.

RESULTS

1. Use of nitrocellulose as protein immobilization media in ScProteome-seq enables high protein transfer efficiency. Previous scWestern versions have relied on in-gel capture of proteins after separation, which severely limits antibody probing efficiency. We instead tested the feasibility of diffusive blotting to a nitrocellulose sheet as the protein immobilization strategy in scProteome-seq and studied transfer efficiency over a wide range of protein target molecular weights. We determined that purified protein transfer efficiency from polyacrylamide gel to nitrocellulose for low MW proteins like GFP (27kDa) exceeds 95% and exceeds 80% for high MW proteins like IgG (150 kDa) in just 2 minutes (see Figure 2A). Transfer efficiency decreases with increasing molecular weight and increases for all proteins with increase in transfer time.

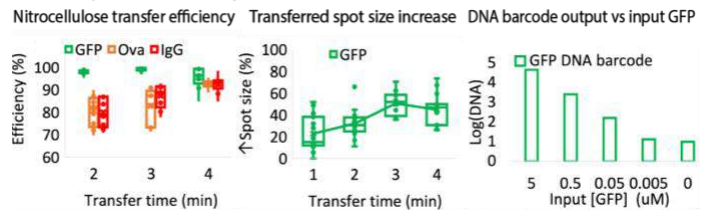
2. Immobilization of single-cell protein on nitrocellulose membrane via diffusive transfer preserves single-cell separation resolution. One potential tradeoff for protein blotting is that target bands could spread significantly during transfer from polyacrylamide to nitrocellulose, especially for small band sizes (~100 μ m). We therefore studied resolution loss during this transfer. When comparing FWHM of protein spot on polyacrylamide pre-transfer and on nitrocellulose post-transfer, we found that band widths increase modestly over blotting times, up to 50% at 3 minutes, and does not increase after 3 minutes, thus adequately preserving single-cell separations on nitrocellulose (see Figure 2A).

3. ScProteome-seq DNA barcode output is linearly correlated with protein input concentration. We aimed to determine whether amount of detected DNA barcodes encoding protein information correlates with protein input as well as quantify limit of detection. To achieve this, we performed scProteome-seq workflow on serial dilutions of purified eGFP and used qPCR as readout of resultant DNA barcode abundance. We detected concentrations of eGFP as low as 5nM (see Figure 2A). In future work, we will study lower protein concentrations down to 5 fM.

4. scProteome-seq is compatible with next-generation sequencing. We next sought preliminary data that would establish the feasibility of

highly multiplexed analyte detection in scProteome-seq using next-generation sequencing. We added Illumina adapters to our barcodes extracted from a spatially restricted zone of nitrocellulose bearing single-cell separations of GFP+ and tdTomato-FLAG+ cells. We were able to reconstruct a spatially restricted distribution of barcodes corresponding to the correct region of interest on the nitrocellulose patch probed by scProteome-seq (see Figure 2B). While the separation map reconstructed from NGS was not yet at single-cell resolution, we anticipate that with a higher density of Size ID probes we will be able to read out single-cell levels of protein information.

A. Feasibility of scProteome-seq workflow



B. Confirmation of scProteome-seq compatibility with NGS

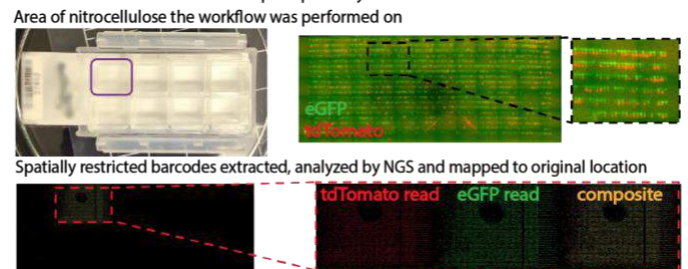


Figure 2: (A) Evaluation of scProteome-seq assay performance (B) scProteome-seq reconstruction of protein information via NGS

DISCUSSION

In this work, we evaluated feasibility of scProteome-seq as novel single-cell protein analysis tool and assessed several aspects of its performance. We effectively immobilized spatially separated single cell proteins on nitrocellulose while preserving single cell resolution. We also confirmed ability to encode protein information via DNA barcoding and made progress toward assay integration with NGS with the goal to increase throughput. In future work we will address the following gaps necessary for successful implementation of the scProteome-seq including 1) determine assay sensitivity and LOD, 2) assess multiplexing capacity and 3) optimize resolution for high-throughput single-cell protein detection. A full implementation of scProteome-seq would represent a major advance in single-cell proteomics including 1) increased multiplexing capacity due to DNA barcoding allowing us to encode many protein targets, 2) high throughput as we can simultaneously analyze ~1600 cells in a 75x25mm polyacrylamide gel, 3) high sensitivity as DNA-based readouts allow amplification of low abundance proteins.

ACKNOWLEDGEMENTS

Funding: University of Pennsylvania NEMO grant, ASN Pre-doctoral fellowship

REFERENCES

- [1] Ko, M. S et.al, *N. EMBO J.* 9, 2835–2842 (1990).
- [2] Jamal-Hanjani, M. et al, *Clin. Cancer Res.* 21, 1258–1266 (2015).
- [3] Fisher, R. et al, *Br. J. Cancer* 108, 479–485 (2013).
- [4] Milo, R., *Bioessays*, 35, 1050–1055 (2013).
- [5] Hughes, A.J. et al, *Nat.Methods.* 11(7), 749-55 (2014)

ELASTUNET: THREE-DIMENSIONAL DISCOVERY OF ELASTIC MATERIAL PARAMETERS USING DEEP LEARNING

Ali Kamali (1), Kaveh Laksari (1,2)

(1) Department of Biomedical Engineering, University of Arizona, Tucson, Arizona, United States
(2) Department of Aerospace and Mechanical Engineering, University of Arizona, Tucson, Arizona, United States

INTRODUCTION

The ability to measure the spatially varying mechanical properties of solid materials is useful in biomedical engineering, materials science, and imaging. Soft biological tissues often have complex mechanical properties due to variation in structural components or fiber alignments.

Elasticity imaging is a technique to reconstruct distribution of mechanical properties using available deformation and force measurements. Quasi-static elasticity imaging, in particular, has been the subject of many experimental, theoretical, and numerical studies in 1D and 2D geometries over the past three decades, and various methods have been introduced to solve the inverse problem. These approaches include direct¹, virtual field methods², or domain decomposition³. While all these methods reveal distributions of elastic modulus (E) with varying levels of accuracy, they share two main drawbacks. First, they have been mostly validated using non-complex geometries, e.g., a stiff spherical inclusion inside a soft background. Second, they assume uniform Poisson's ratio (ν) distributions across the domain, an assumption which might not be valid for all biological tissues and might negatively affect the validity of the elastic modulus estimation⁴.

In recent years researchers have leveraged the power of neural networks as universal function approximators to solve elasticity imaging inverse problems^{5,6}. These studies are limited to 1D and 2D geometries and have their own shortcomings, as we reviewed in our previous work⁴. In this study, we introduce ElastUNet, an inversion algorithm based on convolutional neural networks, which discovers the distributions of E and ν using 3D strain distributions and normal stress boundary conditions on the sides of the domain.

METHODS

We generated a synthetic dataset by simulating the 3D deformation of brain tissue under compressive loading. We collected a T1 scan of the brain from a 28-year-old male using a 3.0 Tesla MRI scanner (Skyra, Siemens Healthcare, Germany) and a 32-channel head coil to perform

the simulation (human subject imaging approved by University of Arizona Institutional Review Board, February 2020). We used BrainSuite⁷ to segment the T1-weighted image volume and exported masks for different regions of the brain (Figure 1A). We simplified the segmentation by grouping deep brain structures under white matter. Therefore, the resulting geometry had three distinct regions: gray matter, white matter, and the ventricles. After manually refining some sharp edges of the geometry, we converted the masks to STL files using Slicer⁸, and re-meshed the STL's in InStep 3.0 (Solveering LLC, NM, USA) to reduce the number of triangles down to 10-15% to simplify the finite-element (FE) modeling.

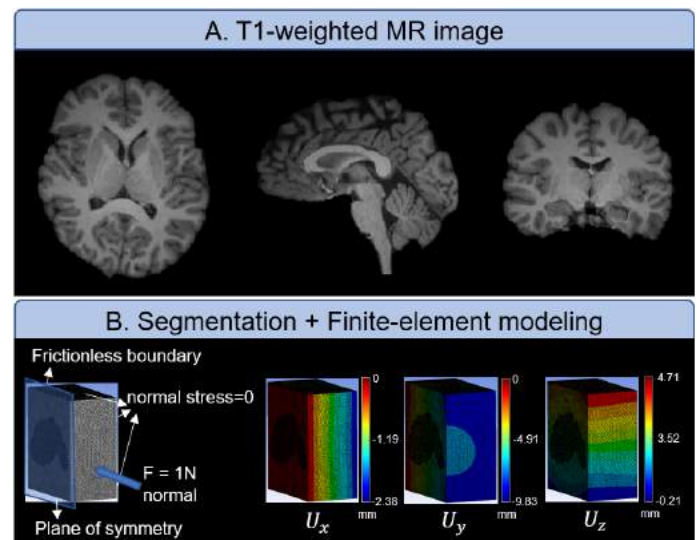


Figure 1: Creating the validation 3D deformation data.

Next, we performed the FE simulation steps on the geometry. We imported the remeshed STLs to SpaceClaim, part of the Ansys Workbench suite (Ansys, Inc, PA, USA), and created solid models out of the surface geometries, created a 200mm×200mm×200mm background region around the brain, and made a model of the right hemisphere only, with a symmetry boundary condition at the midsagittal plane. We performed this step to simplify the FE forward simulation. In Ansys Mechanical, we assigned E values of 1, 1.5, and 2kPa, and ν values of 0.45, 0.4, and 0.35 to the background, gray matter, and white matter regions, respectively. The ventricle's properties were assigned similar to the background. The geometry was discretized using tetrahedral mesh and uniaxial compressive loading was applied in the y direction by a uniform force of 1N (leading to maximum axial strain of about -0.07) on one side and frictionless boundary condition on the other. The other sides (other than the symmetry plane) were free boundaries. After running the simulation, we interpolated the unstructured data into a structured grid of 160×160×160 using the natural neighbor interpolation method due to the nature of convolution kernels requiring structured arrays as inputs. It should be noted that we exported the entire field by mirroring the results with respect to the plane of symmetry.

For solving the inverse problem, we developed ElastUNet, an encoder-decoder structure based on the original UNet architecture⁹ (Figure 2). In brief, compared to the original work, we used 3D convolutions instead of 2D, removed bias parameters and used batch normalization in the double-convolution sections, and transposed convolutions in the upward path of the network. The network takes in a 6-channel input, each channel containing the volumetric distribution of a strain tensor term (three normal and three shear terms) and estimates two volumetric distributions: first and second dimensionless Lamé parameters (λ and M). The algorithm then uses the isotropic linear elasticity constitutive equations to compute stress terms across the domain using the estimated Lamé parameters and given strains. It then computes the mean squared error loss values for balance of linear momentum in three directions (by using finite central difference approximation to compute the partial derivatives), and normal stress on the boundaries. We used the Adam optimizer with a learning rate of 0.001 to minimize the loss value and trained the model for 50,000 epochs on Nvidia v100 GPUs (taking ~6 hours to finish). The ElastUNet was not given prior knowledge about symmetry conditions of the domain.

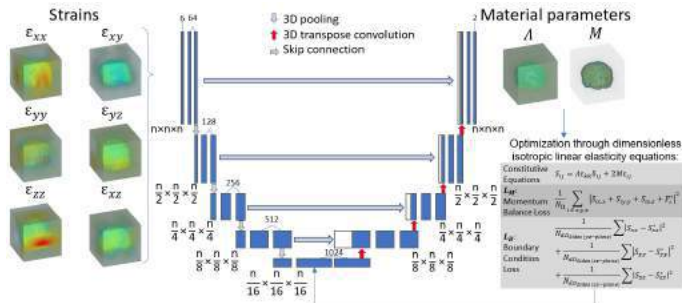


Figure 2: ElastUNet overview.

RESULTS

Distributions of E and ν estimated through ElastUNet generally followed the ground truth values (Figure 3). The model accurately estimated the sharp transitions between the different regions of the 3D geometry, as can be seen in the complex folds of white matter and gray matter captured in the estimated fields. Absolute relative error values for elastic modulus estimation were the highest inside the brain reaching about 10% while Poisson's ratio errors remained below 5% in most

parts, including inside the brain. Mean absolute relative errors were 2.51% and 0.65% for E and ν , respectively.

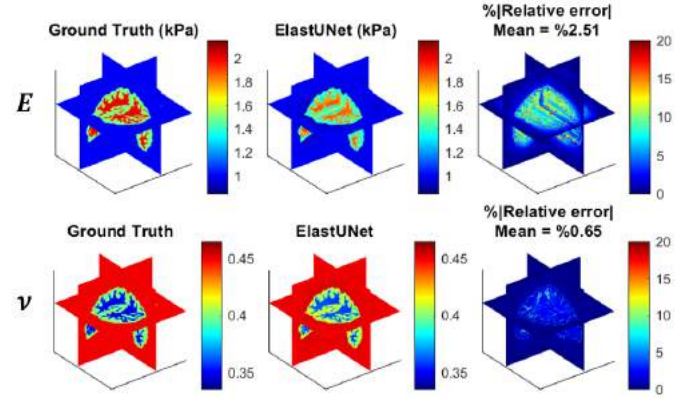


Figure 3: Comparing estimated distributions vs. ground truth.

DISCUSSION

We proposed a deep learning model to estimate the spatial distribution of linear elastic material properties in 3D given the strain fields and normal stress boundary data. In this approach, the network learns the material parameters by taking in normal and shear strain distributions, enforces constitutive equations, balance of linear momentum, and normal stress boundary conditions at the 6 sides of the model. The finite difference approximation to compute the partial derivatives is much faster than graph-based differentiation, which takes the derivative of the network with respect to inputs in the form of spatial coordinates, and is compatible with the convolutional neural network architecture. More generally, the current method improves existing models in two main aspects: It reconstructs both unknown material parameters in isotropic linear elasticity and is validated using a complex heterogeneous geometry.

Two main areas can be improved in future work. Although this model requires further development to show robustness in noisy datasets such as clinical and experimental applications, our study shows significant promise for solving the inverse mathematical problem. Secondly, we trained the on the entire volume and needed GPU memories exceeding 16 gigabytes to meet the demand from this large simulated dataset. Strategies to train the network in minibatches of data can be developed to tackle this problem in the future.

Our approach can be adopted in scenarios where 3D deformation fields can be obtained, especially MR or ultrasound, to aid diagnostics, in vitro or ex vivo tissue characterization, and defect analysis.

ACKNOWLEDGEMENTS

This work was supported by the National Institutes of Health (NIH) National Institute of Biomedical Imaging and Bioengineering (NIBIB) Trailblazer award number R21EB032187.

REFERENCES

1. Barbone PE, Oberai AA. Phys Med Biol. 2007;52(6):1577-1593.
2. Nguyen TT, et al. Strain. 2017;53(5):e12229.
3. Moussawi A, et al. Int J Num Meth Eng. 2015;102(7):1431-1448.
4. Kamali A, et al. Acta Biomater. 2022;155:400-409.
5. Zhang E, et al. arXiv Prepr arXiv200904525. 2020.
6. Chen CT, Gu GX. Proc Natl Acad Sci U S A. 2021;118(31).
7. Shattuck DW, Leahy RM. Med Image Anal. 2002;6(2):129-142.
8. Fedorov A, et al. Magn Reson Imaging. 2012;30(9):1323-1341.
9. Ronneberger O, et al. Springer; 2015:234-241.

CHANGES IN RIGHT VENTRICLE ANISOTROPIC VISCOELASTIC BEHAVIOR WITH PULMONARY HYPERTENSION DEVELOPMENT

K. LeBar (1), K. Roth (1), W. Liu (2,3), B. Garcia (1), J. Pang (4), A. Chicco (5), Z. Wang (1,2)

- (1) Department of Mechanical Engineering, Colorado State University, Fort Collins, CO, USA
(2) School of Biomedical Engineering, Colorado State University, Fort Collins, CO, USA
(3) Stanford Cardiovascular Institute, Stanford University, Stanford, CA, USA
(4) Laboratory Animal Resources, Colorado State University, Fort Collins, CO, USA
(5) Department of Biomedical Sciences, Colorado State University, Fort Collins, CO, USA

INTRODUCTION

Right ventricle failure (RVF) is the leading cause of death in patients of pulmonary hypertension (PH), heart failure with preserved ejection fraction and congenital heart disease. Moreover, the passive elasticity of the RV has been found to be associated to the organ function [1,2]. However, the myocardium is viscoelastic, meaning that there exist two types of resistive forces during the diastolic stretch: viscous and elastic. Historically, there has been a lack of experimental evidence of hysteresis from the myocardial tissue. Strong hysteresis was reported recently in adult human left and right ventricles (LV, RV) [3], neonatal porcine LV and RV [4], and adult ovine LV and RV [5]. But these studies did not examine the changes in ventricular tissue viscoelasticity during disease progression. In contrast, prior cellular research has shown increased cardiac muscle viscoelasticity with PH development [6-8]. However, these measurements were performed with 1D length-tension tests only. The changes in RV free wall (RVFW) anisotropic viscoelasticity with PH progression remain largely unknown. Therefore, **the aim of this study** is to investigate the changes in RVFW anisotropic viscoelasticity during PH development. We **hypothesize** that PH enhances RV viscoelasticity (elasticity and viscosity), and the RV exhibits different frequency-dependent elastic and viscous behaviors.

METHODS

All procedures and methods were approved by Colorado State University IACUC. 6-week-old male Sprague Dawley rats (n=8) were injected with monocrotaline (MCT) (60 mg/kg) and housed in normal conditions for three weeks to induce PH. Healthy age-matched rats (n=7) served as control (CTL). Echocardiography and pressure-volume (PV) measurements were then performed to confirm the establishment of RV failure. Animals were euthanized via urethane (1.2 g/kg) or CO₂. The tissue was harvested and placed in phosphate buffer solution (PBS) on ice. The entire RVFW was dissected in cardioplegic solution (CPS) and then placed in 30 mM 2,3-butanedione monoxime (BDM) solution

for 30 minutes to remove the muscle contraction. The outflow tract direction was defined as the longitudinal (L) direction. The tissue then underwent equibiaxial, sinusoidal cyclic tensile tests. All samples were preconditioned at 1Hz and 20% of strain before data collection. Next, the RV was stretched to a maximum strain of 20% and was loaded at 5 varied strain rates corresponding to: 0.1Hz (quasi-static), 1Hz and 2Hz (sub-physiological), 5Hz (resting heart rate), and 8Hz (heart rate under acute stress). A rest period was applied between tests to fully remove previous tests' effect on the tissue viscoelasticity. Stored energy (W_s ; elasticity), dissipated energy (W_d ; viscosity), the ratio of dissipated to stored energy (V/E ratio), and damping ($W_d/(W_d+W_s)$) were examined as previously described [5]. Student t-test was performed and $p < 0.05$ was considered significant.

RESULTS

RV failure establishment in MCT rats

In vivo RV function measurements showed the establishment of PH development and RV impairment in the MCT rats. There were marked RV dilation and reduced fractional shortening and cardiac output in the MCT rats ($p < 0.05$, data not shown), confirming the development of RV failure.

PH increased RV viscoelasticity in the longitudinal direction only

Compared to the CTL rats, the MCT rats had significant increases in RV dissipated energy (W_d) at 0.1Hz, 1Hz, and 5Hz (**Fig. 1A**). Similarly, the stored energy (W_s) was also significantly increased in MCT rats at 0.1Hz and 1Hz, with strong trends of increase in RV W_s at 5Hz and 8Hz (**Fig. 1B**). However, all these changes were observed in the L direction only, and there were no marked changes in the circumferential (C) direction. There were no changes in the V/E ratio or damping between healthy and diseased RVs at all frequencies.

PH led to significant anisotropy in RV elasticity and viscosity only

The healthy RV did not exhibit significant anisotropy in any viscoelastic parameter (**Fig. 2**). However, in diseased RVs, the W_d and

W_s in the C direction were significantly lower compared to those in the L direction at all frequencies, indicating strong anisotropy (Fig. 3A&B). We did not, however, observe any significant anisotropy in the V/E ratio or damping in the diseased RVs (Fig. 3C&D).

RV viscosity and elasticity had distinct frequency-dependent behaviors

In the healthy RVs, the W_d at 5Hz and 8Hz was significantly elevated compared to 1Hz in the L direction only (Fig. 2A). In the diseased RVs, we observed similar frequency-dependent behaviors. The W_d at 5Hz and 8Hz was significantly elevated compared to 0.1Hz and 1Hz and the increase was more pronounced in the C direction. However, there were moderate frequency-dependent changes in W_s in both groups (Fig. 2B, 3B). We further examined the relative change of RV viscosity to elasticity. In healthy RVs, there was no frequency-dependent change in the V/E ratio or damping up to 5 Hz. But in diseased RVs, the V/E ratio and damping were significantly elevated at 5Hz in the L direction (Fig. 3C&D). These results showed that the RV (both healthy and diseased) had different frequency-dependent viscous and elastic behaviors, and the diseased RV had pronounced frequency-dependent behavior in the V/E ratio and damping.

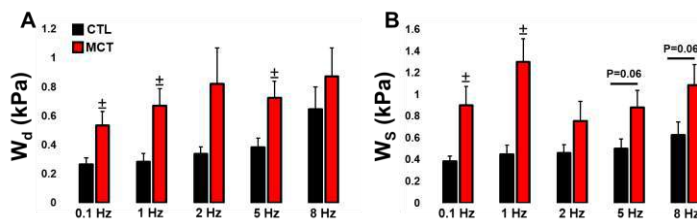


Figure 1. (A) The dissipated (W_d) and (B) stored energy (W_s) in CTL and MCT RVs in the L direction. $\pm p < 0.05$ compared to CTL.

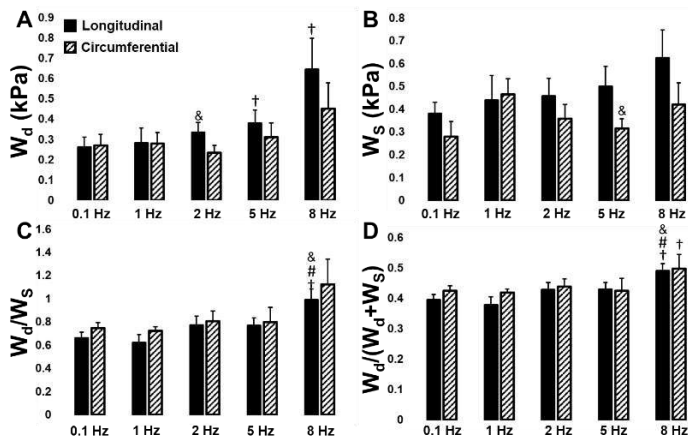


Figure 2. (A) The dissipated (W_d), (B) stored energy (W_s), (C) the ratio of dissipated to stored energy (W_d/W_s), and (D) damping ($W_d/(W_d+W_s)$) in CTL RVs. $\& p < 0.05$ compared to 0.1Hz; $\dagger p < 0.05$ compared to 1Hz; $\# p < 0.05$ compared to 5Hz.

DISCUSSION

In this study, we originally measured the RVFW anisotropic viscoelasticity by hysteresis analysis obtained across multiple testing frequencies, including the physiologically relevant frequencies of the rat (5Hz). We observed significant increases in RV viscoelasticity and altered frequency-dependent damping behavior with PH development.

Firstly, we observed an enhanced RV viscoelasticity (i.e., both viscosity and elasticity) in the L direction with PH progression. However, this increase was absent in the C direction. This led to an anisotropic viscoelastic behavior with pressure overload. It's known

that the PH RVs have marked cardiomyocyte hypertrophy and collagen accumulation, and both microstructural components are key to the tissue mechanical behavior. The increased RVFW viscoelasticity (mainly in the L direction) in MCT rats could be a result of reorganization of these microstructures such that the myo- and collagen fibers are more aligned along the L direction. This is consistent with prior findings of RV hyperelastic mechanics [1, 2, 10].

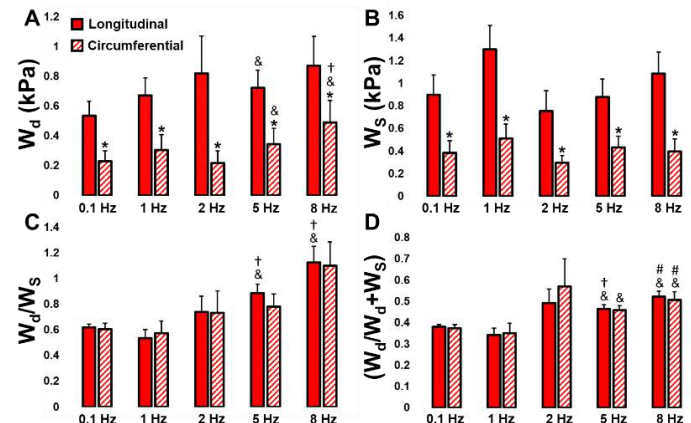


Figure 3. (A) The dissipated (W_d), (B) stored energy (W_s), (C) the ratio of dissipated to stored energy (W_d/W_s), and damping ($W_d/(W_d+W_s)$) in MCT RVs. $* p < 0.05$ compared to L direction in the same testing frequency; $\& p < 0.05$ compared to 0.1Hz; $\dagger p < 0.05$ compared to 1Hz; $\# p < 0.05$ compared to 5Hz.

Second, we observed that in both healthy and diseased RVs, the RV viscosity (W_d) at the physiological frequency was significantly higher than that at quasi-static testing frequency. But the RV elasticity (W_s) did not show such frequency-dependent behavior in either group. These data show that the RV display inequivalent elastic and viscous behavior at higher strain rates, and the potentially different “sources” of these mechanical properties should be investigated further. To better compare viscous and elastic changes, we used the parameters (W_d , W_s) with identical units. But we acknowledge that the use of W_s (instead of elastic modulus) to measure RV elasticity is non-traditional, and other elastic parameters should be investigated in the next step.

Finally, we found some frequency-dependent changes in the RV V/E ratio and damping, but the changes were more pronounced in the MCT rats. The V/E ratio and damping were elevated at 5Hz (resting heart rate of rats) and 8Hz compared to the sub-physiological frequencies. This indicates an enhanced ability of the tissue to damp mechanical energy at physiological strain rates during the pathological remodeling. Nevertheless, the MCT rats did not have an altered RV V/E ratio or damping compared to the CTL rats, indicating that the viscous and elastic changes in the pressure overloaded RV are equivalent. Future research should confirm this finding with other viscoelastic parameters and/or tests.

REFERENCES

- [1] Liu, W et al., *J. Integr. Cardio.*, 1-6, 2020.
- [2] Jang, S et al., *J. Am. Heart Assoc.*, 2017.
- [3] Sommer, G et al., *Acta Biomater.*, 172-192, 2015.
- [4] Ahmad, F et al., *J. Mech. Behav. Biomed. Mat.*, 18-28, 2018.
- [5] Liu, W et al., *J. Biomech. Eng.*, 2021.
- [6] Cooper, G et al., *Heart and Circ. Phys.*, 1003-1014, 2006.
- [7] Harris, T et al., *Heart and Circ. Phys.*, 2173-2182, 2002.
- [8] Stroud, J.D et al., *Heart and Circ. Phys.*, 2324-2335, 2002.
- [9] Hill, M.R et al., *Ann. Biomed. Eng.*, 2451-2465, 2014.

RISK OF VERTEBRAL ENDPLATE FAILURE DURING VERTEBRAL FRACTURE

Neilesh R. Frings (1,3), Elise F. Morgan (1,2,3)

- (1) Biomedical Engineering Department, Boston University, Boston, MA, USA
(2) Mechanical Engineering Department, Boston University, Boston, MA, USA
(3) Center for Multiscale and Translational Mechanobiology, Boston University, Boston, MA, USA

INTRODUCTION

Vertebral fracture (VF) is the most common type of osteoporotic fracture¹ and is associated with back pain, loss of mobility, and excess mortality [1,2]. The *vertebral endplate region*, located at the superior and inferior end of each vertebra, is made up of the cartilage endplate, vertebral endplate (VEP), and underlying subchondral trabecular bone (STB). This region plays a critical role in how loads are distributed to the rest of the vertebral body [3] and is also frequently involved in VF. Depression of the VEP is a clinical diagnostic of fracture occurrence [4], but this deflection does not always involve fracture of the VEP [5,6]. This distinction is key: VF that do involve fracture of the VEP are associated with a higher risk of future disc degeneration and worsening of the fracture over time [6-8]. Despite the importance of VEP involvement in VF, the conditions responsible for these different modes of failure are unclear. Identification of these conditions can aid in evaluation of injury risk and need for preventative treatment [9]. Although compression testing of the vertebra is often used to create VF in the laboratory setting, finite element modeling provides an alternative that allows for precise identification of volumes of interest and evaluation of tissue yield at much higher spatial resolution. This study aimed to use high-resolution micro-finite element (μ FE) models to evaluate relative risk of failure in the VEP, STB, and other portions of the vertebral body at the point of onset of VF, and whether the relative risk of VEP failure is associated with VEP and STB microstructure.

METHODS

μ FE models (0.074mm cubic elements) were constructed from micro-computed tomography (μ CT) images of L1 vertebrae (n=18) that were previously scanned (μ CT 80; Scanco Medical; 70kV, 114 μ A) and mechanically tested [5]. Each vertebra was compressed axially in steps of 1 mm and imaged at each step after a resting period. Further, in that study, digital volume correlation (DVC) was used to compute internal displacements throughout the vertebra from the μ CT images.

In the present study, the μ FE models focused on the superior endplate region, as it is more likely than the inferior endplate region to fail during VF [10,11]. Therefore, models included the superior portion of the vertebra down to a depth 1.5 mm above the inferior boundary of the available DVC-computed displacements, or to a maximum depth of 29.6 mm; models typically included 80-85% of the total vertebral height. Models contained between 11-22 million nodes and 6-12 million elements. Bone tissue was modeled as an isotropic, linear elastic solid with Young's Modulus of 13 GPa and Poisson's ratio of 0.3 [12,13]. Superior and inferior boundary node sets for each sample were defined in Matlab and prescribed experimentally matched displacements by interpolating the DVC-measured values corresponding to the yield point identified on the load-displacement plot for the vertebra. μ FE simulations were run in parallel in Abaqus (Dassault). Simulations completed after 1-10 hours of runtime, using 10-90 hours of CPU time.

Using the μ FE-computed element strains, tissue yield was determined based on principal strain thresholds of 0.41% in tension and 0.83% in compression, as previously reported for trabecular bone tissue [14]. The amount of tissue yield was then computed for volumes of interest (VOIs) corresponding to the VEP, STB, and the rest of the vertebra. The VOIs were identified first in 2D on coronal slices of the μ CT image volumes and then mapped to the 3D model (Figure 1). The VEP VOI was identified from each superior surface bone pixel to the first empty pixel directly beneath it, after using an image dilation-erosion process to fill in endplate pores. The STB VOI extended 4mm below the inferior surface of the endplate. The remaining portion of the vertebra was defined as the mid-vertebral body (MVB). For each VOI, the *yield fraction* was computed as the ratio of the number of yielded elements in the VOI to the total number of elements in the VOI (eq. 1). This fraction was then divided by the *total yield fraction*, defined as the ratio of the number of yielded elements in the entire model to the total number of elements in the model (eq. 2), to obtain the *normalized yield fraction* for that VOI (eq. 3). The resulting value quantifies the yield in

each VOI normalized to that of the full model; a value above one indicates that the VOI contained a proportionally greater amount of yield than the vertebra as a whole.

$$VOI \text{ yield fraction} = \frac{\# \text{ yielded elements in } VOI}{\# \text{ elements in } VOI} \quad (1)$$

$$Total \text{ yield fraction} = \frac{\# \text{ yielded elements in model}}{\# \text{ elements in model}} \quad (2)$$

$$Normalized \text{ yield fraction} = \frac{VOI \text{ yield fraction}}{Total \text{ yield fraction}} \quad (3)$$

Pearson correlation was used to evaluate associations between the yield fractions and several measures of microstructure: VEP thickness, VEP BV/TV, and STB BV/TV. Repeated measures ANOVA tested for differences among VOIs in 90th percentile strains, yield fraction, normalized yield fraction, and tensile/compressive yield ratio.

RESULTS

High strains in the vertebrae were frequently observed in the superior endplate and cortical shell (Figure 2). In the VEP, tensile strains were typically of greater magnitude than compressive strains, whereas in the other two VOIs, the tensile and compressive strain magnitudes were comparable to each other. Given the lower yield point in tension, however, tension was the dominant mode of yield. In each VOI, the number of elements yielded in tension exceeded that in compression by at least three-fold in all vertebrae. Tensile/compressive yield ratio was highest in the VEP ($p=0.048$). Ninetieth percentile tensile strains were higher in the VEP than in the other VOIs ($p=0.003$), but 90th percentile compressive strains did not differ among VOIs ($p=0.600$).

VOI yield fraction varied among vertebrae (Figure 3A), and was not different across VOIs ($p=0.104$). Although the VEP constituted only 12-24% of the total number of elements in the models, the VEP's normalized yield fraction was greater than one for 15 out of the 18 vertebrae (Figure 3B), indicating a higher risk of yield in the VEP compared to the other two VOIs. The normalized yield fraction in the STB hovered around one, while that for the MVB was below one for most vertebrae, indicating that the portions of the vertebra outside the endplate region were at relatively low risk of yield. Normalized yield fraction was greater in the VEP than in the MVB ($p=0.001$).

VEP and STB yield fraction both correlated negatively with STB BV/TV ($p=0.018$, $p=0.023$). No other correlations were found.

DISCUSSION

Simulations of vertebral compression using high-resolution micro-finite element models indicated that at the onset of vertebral fracture—defined by the yield point on the force-displacement curve generated during compression testing—tissue-level yield typically occurs in the VEP, and to a lesser extent, the rest of the vertebral body. The normalized yield fraction was highest in the VEP, indicating a greater relative risk of failure in the endplate region compared to the rest of the vertebra. These results are consistent with prior observations that VF frequently involve the superior endplate region [10,11] and suggest that this region, and the VEP in particular, is where VF initiates.

Tension was the dominant mode of yield in all regions of the vertebra. This suggests that, during macroscopic compressive deformation of the vertebra, large deformations of the trabeculae and endplate are occurring that produce tensile tissue-level failure. Tensile strains were higher in the VEP than in other VOIs, in line with prior μ FE observations of higher tensile strains in the vertebral endplate relative to the underlying trabeculae [15]. However, the same prior study found the highest compressive strains during vertebral compression to occur in the trabecular centrum; in this study, compressive strains did not significantly differ across VOIs. This difference may be due to the difference in boundary conditions, as the prior study used uniaxial compression rather than physiologically matched displacements.

The associations between STB BV/TV and the yield fractions in the VEP and STB indicate that a vertebra with a more porous STB is at greater risk of failure in the endplate region during the onset of VF. Other factors may also influence which regions fail during VF; future studies are needed to determine whether the relative risk of VEP failure is affected by age, sex, and disc degeneration, which are known to influence VF risk and the microstructure of the endplate region [16,17].

ACKNOWLEDGEMENTS

NIH AR054620

REFERENCES

- [1] Cooper, C., et al., *Am J Epi*, 137(9):1001-1005, 1993.
- [2] Cooper, C., *Osteo Int*, 21(2):425-429, 2010.
- [3] Ferguson, S.J., et al., *The Aging Spine*, 15-21, 2005.
- [4] Oei, L., et al., *JBMR*, 33(4):560-568, 2018.
- [5] Hussein, A.I., et al., *J Biomech Eng*, 140(2), 2018.
- [6] Holmes, A.D., et al., *Spine*, 18(1):128-135, 1993.
- [7] Holm, S., et al., *Clin Spine Surg*, 17(1):64-71, 2004.
- [8] Dudli, S., et al., *Spine J*, 14(7):1256-1264, 2014.
- [9] Khosla, S., et al., *JBMR*, 32(3):424-430, 2017.
- [10] Jackman, T.M., et al., *J Ortho Res*, 32(7):880-886, 2014.
- [11] Jackman, T.M., et al., *JBMR*, 31(4):777-788, 2016.
- [12] Wu, D., et al., *Acta Biomater*, 78:1-12, 2018.
- [13] Liu, X.S., et al., *J Biomech*, 42(3):249-256, 2009.
- [14] Bayraktar, H.H., et al., *J Biomech*, 37(1):27-35, 2004.
- [15] Fields, A.J., et al., *J Biomech*, 43(16):3126-3131, 2010.
- [16] Edidin, A.A., et al., *Osteo Int*, 24(2):451-458, 2013.
- [17] Wasnich, R.D., *Bone*, 18(3):S179-S183, 1996.

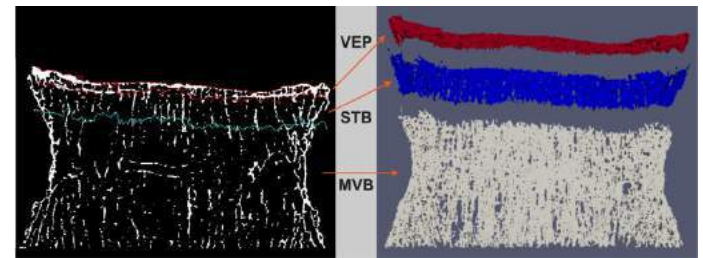


Figure 1: VOI identification.

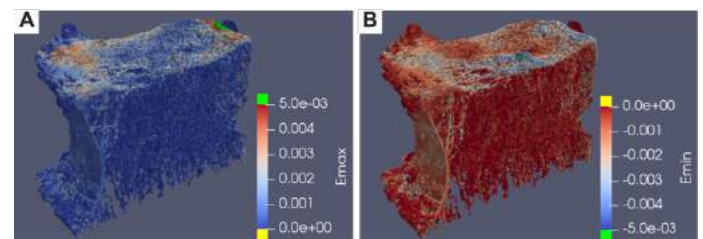


Figure 2: Principal strains rendered on a sagittal half-section of one vertebra: (A) Maximum and (B) Minimum principal strains. Elements experiencing strains outside the range [0,0.5%] or [-0.5%,0] are colored in green and yellow, for ease of visualization.

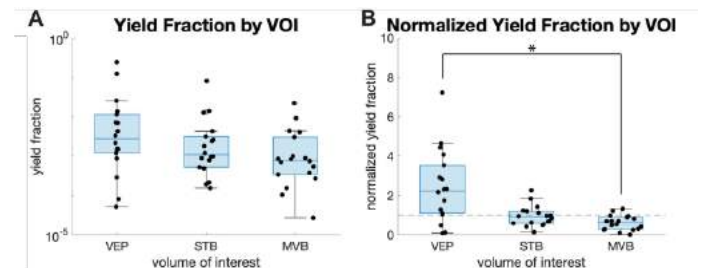


Figure 3: (A) Yield fraction and (B) Normalized yield fraction by VOI.

TRANSVERSE CARPAL LIGAMENT ELONGATION AFTER INJECTION OF COLLAGENASE IN SITU

Jocelyn Hawk, David Margolis, Zong-Ming Li

Hand Research Laboratory, Department of Orthopaedic Surgery, University of Arizona College of Medicine, Tucson, Arizona, US

INTRODUCTION

The transverse carpal ligament (TCL) forms the volar boundary of the carpal tunnel, making it relevant compression neuropathy of the median nerve at the wrist. Although the etiology of carpal tunnel syndrome is unclear, it has been associated with higher carpal tunnel pressure, sometimes reaching above 200mmHg [1]. The current standard treatment for carpal tunnel syndrome is to surgically transect the TCL in order to increase carpal tunnel space and decompress the median nerve. However, this can disrupt the important biomechanical functions of the TCL and result in side effects such as pillar pain or hand weakness [2]. A potential alternative to surgery could be to increase TCL elasticity, allowing it to elongate in response to elevated carpal tunnel pressure. Collagenase Clostridium Histolyticum (CCH) is an enzyme that breaks down collagen fibers and can be injected into the TCL to increase its elasticity. The purpose of this study was to investigate the effects of CCH injections on the elongation of TCL tissue when carpal tunnel pressure is applied.

METHODS

Six fresh-frozen cadaveric hands were used in this study. The carpal tunnel contents were emptied, and a medical balloon connected to a pressure regulator was inserted into the tunnel. 18 retroreflective markers ($\Phi = 1\text{mm}$) were attached to the volar surface of the transverse carpal ligament in a 6x3 grid, such that the 3 rows were placed along the distal border, the proximal border, and centered between the proximal and distal border. The six markers in each row were evenly spaced between the radial and ulnar borders of the TCL. Nine evenly spaced injection sites were marked along the TCL midline (Figure 1) using tissue marking dye. Collagenase solution with a concentration of 50U/ μL was prepared by dissolving CCH in phosphate buffered saline. Each injection site was injected with 5 μL of the solution so that it received 250U of CCH, and the specimen was placed in an incubator set to 37°C.

The specimen was removed from the incubator 24 hours after injection and placed on a table with the wrist in a neutral position. Four Vicor cameras were set up to capture the marker positions (Figure 1). The medical balloon in the carpal tunnel was connected to a pressure regulator using plastic tubing. Using the pressure regulator, the carpal tunnel was inflated to 10, 30, 60, 90, 120, 150, 180, and 210 mmHg. At each pressure level, 3 seconds of video were recorded by the Vicor cameras.



Figure 1: Four Vicor cameras recording marker positions at each pressure level.

The 3D coordinates of each marker at each pressure level were obtained. The injection group for each row consisted of the centermost pairs of markers that contained a CCH injection between them. The control group consisted of all other pairs of markers. Distances between adjacent markers in the same row were calculated using MATLAB. Percent elongation was calculated for each pair of adjacent markers in the same row using the following equation:

$$\% \delta = \frac{d_i - d_{10}}{d_{10}} \quad (1)$$

Where d_{10} is the distance between the markers at the baseline carpal tunnel pressure of 10 mmHg and d_i is the distance between the markers at the i^{th} pressure.

Mean percent elongations of the injection group and control group were calculated for the proximal, middle, and distal rows. Pearson's correlation coefficient and linear regression analysis was used to determine the relationship between pressure and percent elongation for the injection group. Two-way RM ANOVA was performed to determine the effect of pressure and CCH injection on percent elongation. Pairwise comparisons were determined using Tukey's test.

RESULTS

Percent elongations of each group are shown in Figure 3. The proximal, middle, and distal TCL in the injection group had significantly greater elongation than the control group at pressure levels 60 mmHg and above ($p < 0.001$), 60 mmHg and above ($p < 0.001$), and 120 mmHg ($p < 0.002$) and above, respectively. For the injection group, the percent elongations at 210 mmHg for the proximal, middle, and distal rows were $6.3 \pm 0.7\%$, $5.8 \pm 1.0\%$, and $4.9 \pm 2.8\%$, respectively. For the control group, the percent elongations at 210 mmHg for the proximal, middle, and distal rows were $0.4 \pm 0.3\%$, $0.4 \pm 0.3\%$, and $0.5 \pm 0.3\%$, respectively. In some specimens, visible tearing of the TCL occurred at high pressure levels (≥ 180 mmHg) where CCH was injected.

In the injection group, Pearson's correlation coefficient showed a strong positive correlation between pressure and percent elongation for the proximal ($r = 0.79$) and moderate positive correlations for the middle ($r = 0.64$), and distal ($r = 0.53$) rows. The fitted regression models of the proximal, middle, and distal rows for the injection group were $y = 2.6 \times 10^{-4}x + 0.01$, $y = 2.2 \times 10^{-4}x + 0.02$, and $y = 1.68 \times 10^{-4}x + 6.5 \times 10^{-3}$, respectively. In the control group, weak positive correlations were found for the proximal row ($r = 0.13$), the middle row ($r = 0.23$), and the distal row ($r = 0.07$).

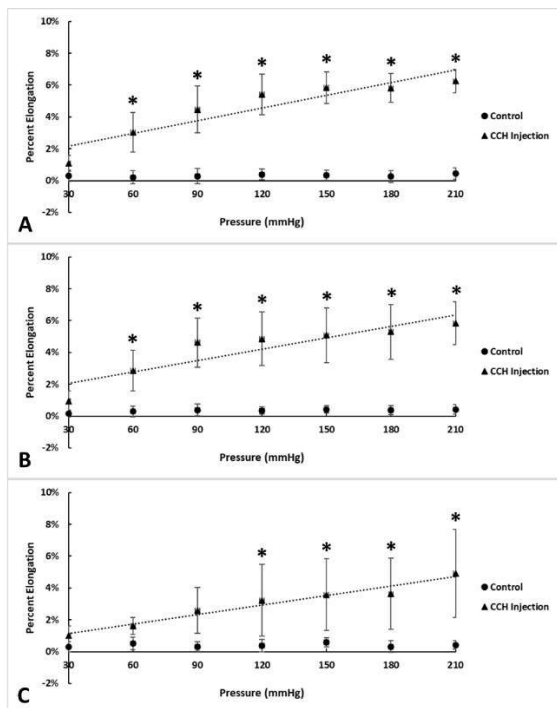


Figure 2: Percent elongation at each pressure level for the proximal (A), middle (B), and distal (C) regions of the TCL.

DISCUSSION

This study investigated the relationship between carpal tunnel pressure and percent elongation of TCL tissue injected with CCH. We found that the intact locations experienced no elongation, while the injection locations experienced significant percent elongation at elevated pressure levels and had a strong positive correlation between pressure and percent elongation.

The proximal, middle, and distal regions of the control group had percent elongations of 0.5%, 0.4%, and 0.5%, respectively, when 210 mmHg of carpal tunnel pressure was applied. These results agree with previous literature that the TCL is relatively unable to be stretched [3]. The proximal, middle, and distal regions of the injection group experienced 6.3%, 5.8%, and 4.9% elongation when 210 mmHg of carpal tunnel pressure was applied. While healthy people can have a carpal tunnel pressure around 2.5 mmHg, those with carpal tunnel syndrome tend to have tunnel pressures above 30 mmHg [1]. When CCH breaks down the collagen fibers in the TCL, the TCL becomes more elastic, allowing it to elongate and yield to carpal tunnel pressure. This elongation also creates more carpal tunnel space, alleviating pressure off the median nerve.

In the injection locations, the distal region of the TCL had lower percent elongations than the proximal and middle regions and required higher carpal tunnel pressure to reach significantly greater percent elongation than the intact locations. Because median nerve compression usually occurs at the distal end of the carpal tunnel [4], elongating the distal region of the TCL would be most important for nerve decompression. Previous studies have found that the TCL tends to be thickest distally in the center [5], which could explain the distal region experiencing less elongation than the middle and proximal regions. To account for this, a higher dose of CCH could be used in the distal region to achieve the same elongation as the proximal and middle regions.

In the injection group, tearing of the TCL occasionally occurred in the middle region when pressures of 180 mmHg or greater were applied. This tearing of the TCL could allow CCH to leak into the carpal tunnel and cause undesired effects to the tunnel contents. Also, tearing could disrupt the biomechanical functions of the TCL, such as providing an anchor for the thenar muscles. A possible solution to this is to decrease the amount of CCH injected to the middle region.

Our results suggest that CCH injection is effective in elongating the surrounding TCL tissue under elevated carpal tunnel pressure. One line of injections was delivered along the TCL midline to achieve these results, but multiple lines of injections could be delivered for greater elongation of the entire TCL. Also, the distal region of the TCL is less affected by CCH injection and may require a higher dose of CCH, while the middle region may require a lower dose to prevent tearing of the tissue. These findings support that CCH injection has potential as a treatment for carpal tunnel syndrome and should be further explored. While we investigated the local effects of CCH injection on TCL tissue, future studies can investigate the effects of CCH injection on total TCL length and carpal arch morphology.

ACKNOWLEDGEMENTS

NIH R21AR075402A1

REFERENCES

- [1] Gelberman et al., *J Bone Joint Surg Am.*, 3:380-3, 1981
- [2] Karl et al., *Orthop Clin North Am.* 2:425-33, 2016
- [3] Li et al., *J Biomech Eng.*, 8:081011, 2009
- [4] Luchetti et al., *J Hand Surg Br.* 5:598-602, 1998
- [5] Goitz et al., *J Wrist Surg.* 4:233-4, 2014

A PARABOLIC MODELING OF CARPAL ARCH AREA EXPANSION

David Jordan, Hui Zhang, Zong-Ming Li

Hand Research Laboratory, Department of Orthopaedic Surgery, University of Arizona College of Medicine, Tucson, Arizona

INTRODUCTION

Treatment of carpal tunnel syndrome has been shown to be achievable through non-surgical augmentation of the carpal arch, leading to increases in tunnel space and decreases in median nerve compression [1]. The carpal arch is formed by the transverse carpal ligament, which has attachments at the hook of hamate and ridge of trapezium at the distal carpal tunnel. Methods of carpal arch space augmentation can take advantage of this anatomical configuration, either through compressing the distance between the ligament attachment points [1, 2], or through direct ligament lengthening [3]. The primary outcome of this method is to increase the carpal arch area. These methods have been evaluated individually, however, their collective influences on the carpal arch morphology and the identification of how this influence is affected by the initial arch morphological condition is unknown.

The efficacy of therapeutic treatments is determined by a multitude of factors, including the treatment method and the conditions of the patient. Therefore, it is important to identify which patients will benefit most from a particular treatment and the extent to which the patient-specific treatment needs to be implemented to achieve the desired degree of therapeutic outcome. With respect to carpal arch space augmentation, the primary augmentation outcome is the increase in the carpal arch area, which has been shown to decompress the median nerve in vivo [2, 3]. A primary variable in determining the magnitude of the carpal arch area is the arch height, which is variable between patients.

The carpal arch area depends on the arch height and width and has been geometrically modeled in previous studies [3], demonstrating the usefulness of the modeling approach. The benefits of modeling methods lies in the ability to simulate a wide range of effects, driven by a wide variety of tunnel morphology, which is necessary given the variability in tunnel characteristics between patients.

The purpose of this work is to examine (1) the change of carpal arch area in response to the shortening of the carpal arch width, (2) the

change of carpal arch area in response to the elongation of the TCL, and (3) the change of carpal arch area in response to the combined shortening and elongation of the carpal arch width and TCL, respectively. These effects will be evaluated with varying initial arch heights in order to determine the effect of initial patient morphology on carpal arch space augmentation effectiveness.

METHODS

The carpal arch was modeled as the following horizontal parabola function,

$$y(x) = H - 4H \left(\frac{x}{W}\right)^2 \quad (1)$$

where H was the length of the semi-minor axis and W was the length of the major axis. H and W represent the width and height of the carpal arch, respectively.

There were three simulation cases: (1) shortening the carpal arch width while keeping the carpal arch length (the curve length of the parabola) constant, (2) elongating the carpal arch length while keeping the carpal arch width constant, and (3) shortening the carpal arch width and increasing carpal arch length simultaneously. Each simulation was performed for an initial carpal arch height H_0 , of 0 and 2 mm.

The initial carpal arch width was specified as 20 mm for all simulations. For simulation (1), the carpal arch width was decreased by a maximum of 2 mm in steps of 0.2 mm. For simulation (2), the TCL length was increased by a maximum of 2 mm in 0.2 mm increments from the initial length value. For simulation (3), the arch width and length were simultaneously shortened and elongated in similar fashion. The carpal arch area A, was calculated using Equation 2. The arch length L, was calculated using the integral of Equation 3 and is given by Equation 4.

$$A = \int_{-W/2}^{W/2} y dx = \frac{2}{3} HW \quad (2)$$

$$L = \int_{-W/2}^{W/2} \sqrt{1 + \left(\frac{dy}{dx}\right)^2} dx \quad (3)$$

$$L = \frac{1}{2} \sqrt{W^2 + 16H^2} + \frac{W^2}{8H} \ln \left(\frac{4H + \sqrt{W^2 + 16H^2}}{W} \right) \quad (4)$$

RESULTS

The carpal arch formation was different between each simulation for the different combinations of morphological augmentation and within each simulation for the different values of H_0 . The arch formations for $H_0 = 0$ mm resulting from the conditions of each simulation are given by Figure 1 (a-c).

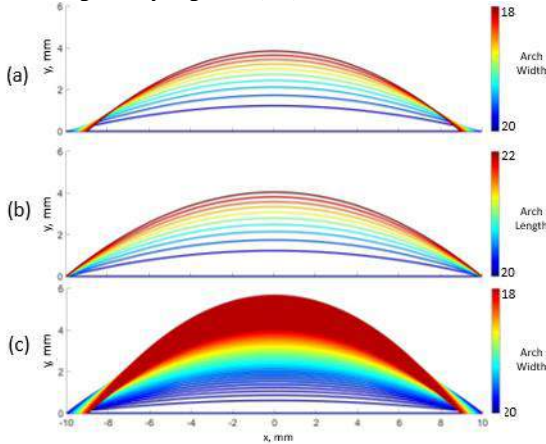


Figure 1: Carpal arch formation for an initial arch height of $H_0 = 0$ mm for (a) decreasing arch width with constant arch length, (b) increasing arch length with constant arch width and (c) simultaneously decreasing arch width and increasing arch length

For the initial arch heights of $H_0 = 0$ and $H_0 = 2$ mm, the maximum increase in arch area was 46.2 and 25.8 mm² for the decreasing of the arch width with constant arch length (Figure 2); and 53.8 and 34.4 mm² for elongating the arch length with constant arch width (Figure 3).

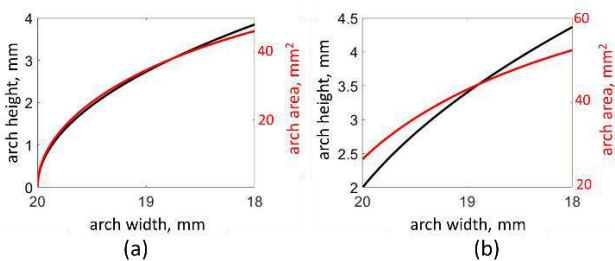


Figure 2: Carpal arch height (black) and area (red) as a function of arch width for initial arch heights of (a) $H_0 = 0$ mm and (b) $H_0 = 2$ mm

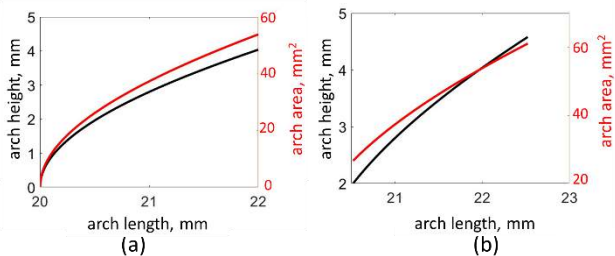


Figure 3: Carpal arch height (black) and area (red) as a function of arch length for initial arch heights of (a) $H_0 = 0$ mm and (b) $H_0 = 2$ mm

The simultaneous altering of the carpal arch width and arch length allowed the carpal arch height and area to increase in a bivariate formulation for the initial arch heights of $H_0 = 0$ mm (Figure 4) and $H_0 = 2$ mm, respectively. For the maximum 2 mm narrowing and lengthening of the arch width and arch length, the maximum change in carpal arch height was 5.7 and 4.1 mm, respectively. The maximum change in carpal arch area was 68.0 and 46.3 mm², respectively.

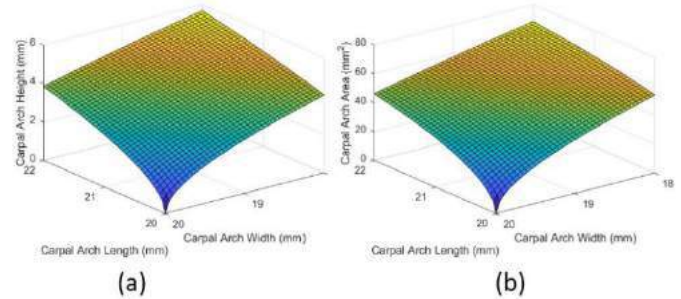


Figure 4. (a) Carpal arch height and (b) carpal arch area as a function of arch width and arch length ($H_0 = 0$ mm)

DISCUSSION

This study simulated the morphological changes of the carpal tunnel with the narrowing of the carpal arch width, the lengthening of the arch length and the simultaneous narrowing and lengthening of the arch width and length, respectively, for different initial arch heights. Large initial arch heights yielded less carpal arch morphological changes than small initial arch heights for equivalent degrees of arch width narrowing and arch length increase. These results show that patient specific morphology is critically relevant for carpal arch space augmentation.

Specifically, the initial arch height varied the gain of both the arch height and area for both the two arch space augmentation approaches. For the 2 mm narrowing of the arch width with constant arch length, the increase in arch height and area was decreased from a gain of 3.8 mm and 46.2 mm²; to a gain of 1.6 mm and 14.3 mm², for initial arch heights of 0 and 2 mm, respectively. Similar results were obtained for the 2 mm elongation of the arch length with constant arch width. The increase in arch area and arch height was decreased from a gain of 4 mm and 53.8 mm²; to a gain of 1.9 mm and 25.3 mm². These results show that a patient with a larger value of initial arch height may be less responsive to carpal arch space augmentation, with respect to increasing the arch area.

The simultaneous shortening of the arch width and lengthening of the arch length provided the greatest increases in arch area and arch height. More research is required for the development of a practical means of in vivo application of the arch length increasing, alongside the established method of radial-ulnar compression for decreasing the arch width [1, 2].

Limitations with the simulation include the parabolic assumption and the omission of the bony portion of the carpal arch. In conclusion, this work provides a foundation for determining the amount of carpal arch space augmentation necessary to achieve a specific degree of arch area increase, necessary for median nerve decompression, for carpal tunnel syndrome patients with different morphological characteristics.

REFERENCES

- [1] Li, ZM et al., *Clin Biomech*, 28(4): 402-407, 2013.
- [2] Marquardt, T et al., *Clin Biomech*, 30(3): 248-253, 2015.
- [3] Li, ZM et al., *J Biomech Eng*, 131(8): 081011, 2009.

JOINT SPACE OF THE FIRST CARPOMETACARPAL JOINT: CORRELATION BETWEEN COMPUTED TOMOGRAPHIC AND SIMULATED X-RAY MEASUREMENT

David Jordan (1), C. Kent Kwoh (2), Zong-Ming Li (1, 2)

(1) Hand Research Laboratory, Department of Orthopaedic Surgery, University of Arizona, Tucson, Arizona, US

(2) University of Arizona Arthritis Center, Tucson, Arizona, US

INTRODUCTION

The thumb carpometacarpal (CMC) joint has a highly complex morphology. This complexity presents difficulties with quantitatively evaluating the joint via two-dimensional x-ray radiography, which is commonly used to visualize and diagnose various joint pathologies, such as osteoarthritis [1]. This is particularly true when considering measurements of joint space, which is a crucial parameter for the scoring of osteoarthritic severity [2]. Conversely, computed tomography (CT) is an imaging modality that can readily evaluate the complex three-dimensional joint structure and make accurate measurements of joint space. Given that the two-dimensional x-ray visualization is derived from the three-dimensional joint structure, there may exist a relationship between the two visualizations that can be used to predict the true CMC joint space based on x-ray measurement alone.

X-ray visualization of the CMC joint has been extensively studied in regard to optimizing the resulting projection by finding complimenting combinations of hand, wrist and thumb postures. A clear view of the trapezium-metacarpal articulation has been achieved using a combination of wrist flexion, wrist supination, ulnar deviation and thumb pronation [3]. It is in such a view that the trapezium-metacarpal articulation can be clearly observed, absent of any overlapping projections from the adjacent bones. Such a view can potentially provide a foundation for a relation to the three-dimensional equivalent.

Evaluation of the CMC joint using CT imaging has been regularly achieved, producing accurate and varied quantifications of joint space. These can include distance maps, showing the distribution of the joint spacing within a given tolerance or singular values typically given as the minimum distance between the articular joint surfaces [4]. These CT measurements are considered the gold standard and can serve as guidelines for related expectations in the two-dimensional space.

Given the frequency of x-ray radiography in the evaluation of various hand pathologies, it is necessary to improve the quantifiable accuracy of the imaging modality with respect to joint space

measurement. The improvement of this accuracy could be achieved by the development of a relationship between the gold standard CT measurement and what is objectively visible within a clearly defined x-ray projection of the CMC joint, effectively combining the accessibility of x-ray imaging with the accuracy of analysis by CT.

METHODS

Seven full-arm cadaveric specimens (female, 68.2 ± 3 years) were prepared for testing. Each specimen was secured onto a custom platform that secured the upper forearm and wrist. The four fingers were wrapped around a cylindrical extension and the thumb was angled in 45 degrees of extension. The prepared specimen was placed into a CT machine. A custom device which allowed for the application of thumb traction within the CT machine was used to apply a 1 N load along the long axis of the thumb via a finger trap and a set of pulleys. A single CT scan was taken of each specimen in this configuration.

The metacarpal and trapezium of the first CMC joint were segmented and meshed. The articular surfaces of the two bones were manually identified (Figure 1a) and a fifth order polynomial was fit to each for the metacarpal PM (Figure 1b), and the trapezium PT. The saddle-point of the metacarpal polynomial surface has been used previously in CMC-related studies and was similarly determined in this work by calculating the gradient field of the polynomial surface, finding the critical points and using the second derivative test [5] (Figure 1b).

Two spheres of radii 1 and 2 mm, respectively, were centered at the saddle point of the articular surface of the first metacarpal (Figure 1b). The intersection of these spheres with the polynomial surface was defined as the three-dimensional contours κ_1 and κ_2 (Figure 1b), respectively.

The joint space was defined as the minimum distance between the metacarpal and trapezium polynomial surfaces calculated over a 100 x 100 grid, which was confined to lie within the boundaries of κ_1 and κ_2 . For each point on the constrained grid (x, y), the joint space D (Figure

2), was calculated as the solution to the unconstrained minimization of Equation (1). This equation describes the distance from a given point on the metacarpal polynomial surface (x_M, y_M, z_M) to an arbitrary point on the trapezium polynomial surface ($x_T, y_T, PT(x_T, y_T)$). The average and standard deviation of the joint space was calculated in both regions over the constrained grid.

$$D = \sqrt{(x_M - x_T)^2 + (y_M - y_T)^2 + (z_M - PT(x_T, y_T))^2} \quad (1)$$

A spherical projection region (Figure 3a) was then defined centered at the centroid of the CMC joint articulation and with a radius $R = 40$ mm (arbitrary for visualization purposes). At a discrete number of points ($n = 441$), along the spherical surface, a plane of projection was defined with unit normal vector \hat{R} . Every point of the metacarpal and trapezium articular surfaces was projected on the n planes (Figure 3a). The 2D projections were made into polygon shapes and the optimum projection, defined as the projection with the minimal amount of overlap between the polygons, was determined (Figure 3b). This optimum projection is meant to mimic an x-ray projection of the CMC joint with clear view of the trapezoid-metacarpal articulation [3].

In the optimum 2D projection, the 2D joint space was calculated as the distance between the corresponding projected points defining the 3D joint space within the two domains (κ_1 and κ_2) (Figure 3b). The average and standard deviation of the 2D joint space was calculated for both regions. The average 2D and 3D measures of joint space were plotted against one another and a Pearson correlation test was performed ($\alpha = 0.05$).

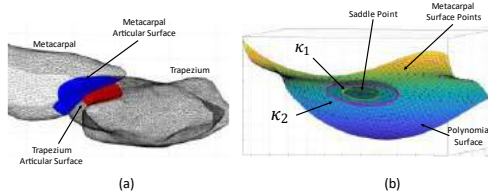


Figure 1: (a) First CMC joint with manually identified articular surfaces (b) Intersection of spherical regions with the metacarpal polynomial surface defining the three-dimensional contours κ_1 and κ_2 .

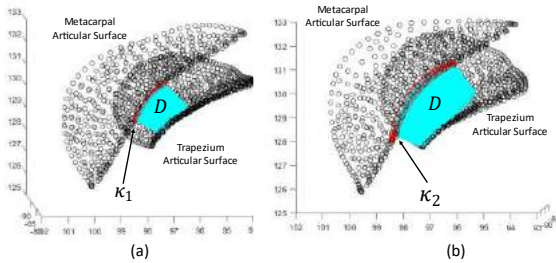


Figure 2: Representative example of the CMC joint space calculated within the boundaries of regions (a) κ_1 and (b) κ_2 .

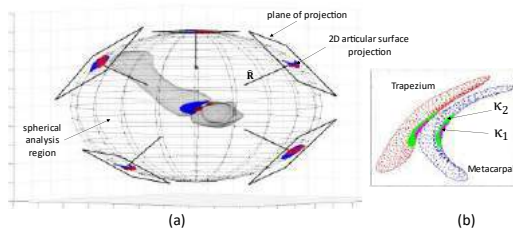


Figure 3: (a) First CMC joint with spherical projection region, representative 3D planes of projection and 2D projections of articular surfaces. (b) Optimal 2D projection with joint space analysis regions κ_1 and κ_2 .

RESULTS

Figure (4) gives the results for the correlation between the average 2D and 3D measures of CMC joint space. The slope of the regression line for the regions κ_1 and κ_2 were 0.7807 and 0.7837, respectively. The Pearson correlation coefficients, $r = 0.965$ for κ_1 and $r = 0.963$ for κ_2 , were both statistically significant ($p < 0.001$).

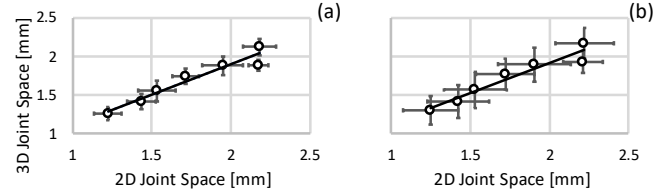


Figure 4: 2D vs 3D joint space for regions (a) κ_1 and (b) κ_2

DISCUSSION

This work aimed to develop a relationship between thumb carpometacarpal joint space as measured in 3D, using conventional computed tomography, and 2D, using simulated x-ray radiography. The joint space was calculated within constrained regions in order to eliminate outliers which may exist closer to the boundaries of the respective bones. The joint space measures in 3D and 2D were taken between corresponding points whose designations were maintained through the 3D-to-2D projection, providing a one-to-one comparison.

The correlation between the 2D and 3D joint space was strong positive and significant. This may be a result of the measurements being taken around constrained regions centered at the saddle point, which defines the point on the articular surface where the derivatives in orthogonal directions are all zero. This would mean that the rate of change of the surface features in neighboring regions around this point would be minute, resulting in small deviations of space between these points and the trapezium.

Limitations with the work include the specimen sample size and simulated radiography, which needs to be validated using conventional radiography. In conclusion, the developed relationship between 3D and 2D joint space can potentially allow for the identification of the CMC joint space through x-ray analysis alone. This can result in an x-ray defined measure of joint space for measurement regions κ_1 and κ_2 , whose locations can be standardized between patients for similar x-ray views.

ACKNOWLEDGEMENTS

NIH/NIAMS 3R01AR078187

REFERENCES

- [1] Melville, D et al., *Skeletal Radiol*, 44:165-177, 2015.
- [2] Altman, R et al., *J Osteoarthr. Cartil*, 15: A1-A56, 2007.
- [3] Shin, Y et al., *J Orthop Surg*, 26(1): 1-5, 2018.
- [4] Halilaj, E et al., *J Biomech*, 48(13): 3634-40, 2015.
- [5] Halilaj, E et al., *J Biomech*, 46(5): 1031-4, 2013.

HETEROGENEITY OF RED CELL MECHANICAL PROPERTIES DRIVES PATHOPHYSIOLOGY IN SICKLE CELL DISEASE

Dillon C. Williams (1), David K. Wood (2)

(1) Biomedical Engineering, University of Minnesota, Minneapolis, MN, United States

(2) Biomedical Engineering, University of Minnesota, Minneapolis, MN, United States

INTRODUCTION

Sickle cell disease (SCD) is an inherited blood disorder that arises from a single nucleotide mutation in the β -globin gene [1]. This mutation leads to an abnormal hemoglobin, known as sickle hemoglobin or HbS. HbS monomers can bind to other hemoglobin proteins that are in the deoxygenated T-conformation. When sufficient HbS proteins bind together they form polymer domains that decrease the red blood cell's (RBC) oxygen carrying capacity and can develop into long inflexible strands that deform and stiffen the cell giving it the characteristic sickle morphology [1].

Sickled red blood cells are the main driver of the adverse effects of SCD [2]. The decreased oxygen carrying capabilities and mechanical changes in SCD blood lead to disrupted flow, vascular occlusions, and increased inflammation and cell adhesion. This can lead to thrombosis, stroke, ischemia, hemolytic anemia, and organ failure. In the United States, patients with SCD have an average life expectancy of 54 years compared to the national average of 76 years [3].

The molecular mechanisms of SCD have been well studied, and the mechanical differences between healthy red blood cells and SCD red blood cells have been measured at normoxic conditions [1]. However, there have been limited studies investigating the mechanics of deoxygenated, sickled red blood cells [4]. Since the stiffness of these sickled cells is a major driver of the pathophysiology it is imperative to understand their mechanics. Further, research has shown that for a given oxygen tension the fraction of cells with sickled morphology can vary greatly between patients [5]. In order to design targeted, patient specific treatment it is crucial to be able to measure both the mechanical changes of SCD red blood cells as they deoxygenate, and how this response varies between patients. To accomplish this, we have developed a high throughput microfluidic device that simultaneously measures single red blood cell deformability and oxygen saturation for up to 10,000 RBCs per patient at a range of physiological oxygen tensions (0mmHg-90mmHg).

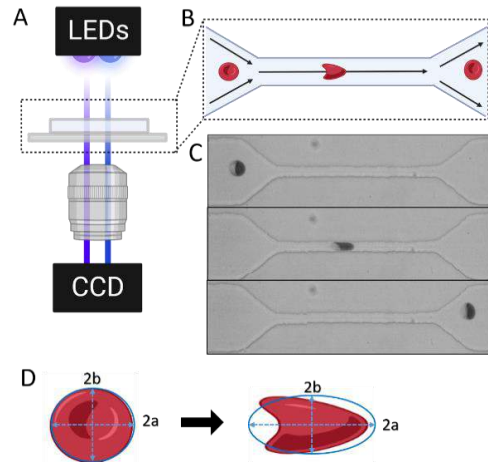


Figure 1: Experimental setup for the RBC Mechanics assay. (A) The microfluidic and optical set up showing the alternating Soret Band LEDs, objective, and high speed camera. (B) ROI section of the microfluidic device showing cell deformation. (C) High Speed images of red blood cell deformation. (D) Taylor deformation parameters to calculate change in RBC shape

METHODS

A novel microfluidic technique, optical analysis instruments and software were developed to quantify saturation and deformability of individual red blood cells under controlled oxygen tension (fig. 1). A dilute solution of washed red blood cells in 25% human albumin serum was perfused through the microfluidic device at a controlled pressure of 800 mbar. The oxygen tension in the microfluidic device was regulated by PDMS channels supplied with a controlled mixture of air and nitrogen. Individual RBC oxygen saturation was calculated using

alternating LEDs in the Soret band and measuring the ratio of absorption (fig. 1A), similar to the method in the 2019 Di Caprio et. al paper [5]. After sufficient time to reach steady state oxygen saturation, red blood cells were subject to controlled stress by passing through a 6x8μm capillary channel (fig. 1B). A high speed camera imaged the RBCs at 1000 fps (fig. 1C) as they underwent this mechanical testing. Cells were imaged passing through the constriction at a rate of 30 cells per second, and the experiment was performed at eight different oxygen tensions ranging from 0 mmHg to 160 mmHg recording ~1000 cells at each oxygen tension.

A custom Python software package was developed to label each cell passing through the constriction and identify key parameters such as shape, velocity, saturation, and cross sectional area. From this data, cell deformation was calculated by taking the difference in Taylor deformation (eq. 1) of the cell inside and outside the constriction (fig. 1D).

$$\Delta Ta = \left(\frac{a-b}{a+b}\right)_1 - \left(\frac{a-b}{a+b}\right)_0 \quad (1)$$

Previous work has suggested that second order, non-dimensional shape parameters such as Taylor deformation and eccentricity are less sensitive to imaging noise making these parameters a robust choice for measuring changes in cell shape in this experiment [6].

RESULTS

Each patient sample displayed unique, heterogeneous behavior. A contour plot of saturation and deformability of every cell at the eight different oxygen tensions for one patient sample highlights the abnormal mechanical behavior of SCD blood cells (fig. 2). At normoxic conditions (90 – 160 mmHg) RBC saturations are high and the ΔTa of cells is normally distributed. As oxygen tension decreases two distinct populations appear, one with relatively lower saturation and decreased change in Taylor deformation; this stiffer population is the sickled cells.

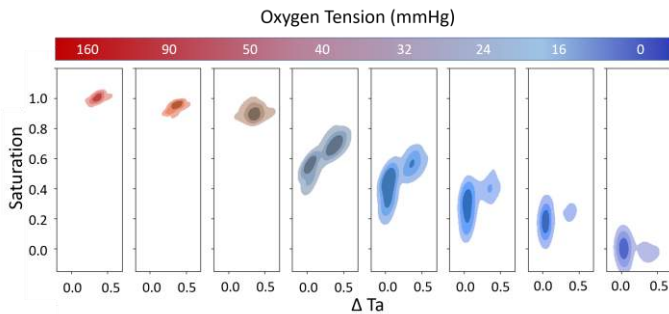


Figure 2: Density plots of one patient sample showing ΔTa and saturation for cells imaged at eight different oxygen tensions. As oxygen tension decreases two population emerge separated by both saturation and deformability

We used unsupervised k-means clustering to separate the stiff and deformable cells at each oxygen tension. Within each patient sample, changing oxygen tensions did not change the mean ΔTa for the two distinct populations, however it did change the fraction of cells in each population. This can be seen in Figure 2. For each patient sample we calculated an overall deformable ΔTa and stiff ΔTa by averaging each ΔTa across oxygen tensions. In a cohort of nine SCD patients (SS), three healthy patients (AA), and two Sickle Cell Trait patients (AS) the average stiff cell ΔTa was significantly decreased compared to the average deformable cell change in Taylor deformation with a p-value < 0.0001 in a Welch's t-test (fig. 3).

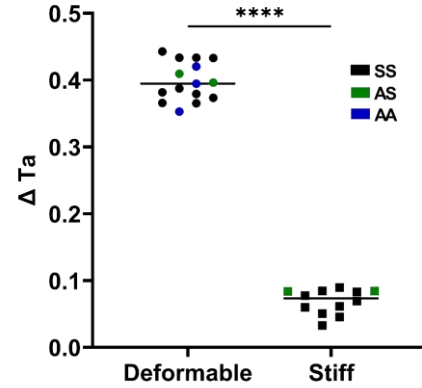


Figure 3: Average ΔTa for deformable and stiff cell populations for 9 SS patient samples, 2 AS patient samples, and 3 AA patient samples. The stiff cell populations show a statistically significant decrease in ΔTa with a p-value < 0.0001

DISCUSSION

The data in this study agrees with and extends the current understanding of SCD pathophysiology. As oxygen tension decreases, hemoglobin in SCD red blood cells will polymerize, and as a result oxygen carrying capacity will decrease and cell stiffness will increase [4]. Before now, the actual change in mechanical properties of stiffening RBCs had not been measured with high throughput at this level of precision. Current studies suggest polymerized hemoglobin fraction within the RBC will continuously increase with decreasing oxygen tension [2], and indeed in this study we see that as oxygen decreases, the fraction of stiff cells increases. However, after the initial sickling the stiffness of these cells does not seem to change. This suggests that despite constantly increasing hemoglobin aggregation, RBCs will reach a threshold in which they 'jump' from the deformable, high saturation population to the stiff, low saturation population and additional hemoglobin polymerization will not significantly increase stiffness. If this is the case, treatments strategies should focus on shifting this threshold to lower oxygen tensions. Once RBCs pass this point they significantly increase in stiffness and become hazardous, and further deoxygenation leads to little or no change. With this in mind, potential next steps for this project would be to test current FDA approved therapeutics to see how they affect this threshold point.

ACKNOWLEDGEMENTS

Portions of this work were conducted in the Minnesota Nano Center, which was supported by the National Science Foundation through the National Nano Coordinated Infrastructure Network (NNCI) under Award No. ECCS-1542202. This work was supported by the NHLBI under Grant Nos. HL130818 and HL132906.

REFERENCES

- [1] Barabino, Gilda A., Manu O. Platt, and Dhananjay K. Kaul *Annual review of biomedical engineering* 12 (2010): 345-367.
- [2] Henry, Eric R., et al. *Proceedings of the National Academy of Sciences* 117.26 (2020): 15018-15027.
- [3] Lubeck, Deborah, et al *JAMA network open* 2.11 (2019): e1915374-e1915374.
- [4] Li, Xuejin, et al *Journal of biomechanics* 50 (2017): 34-41.
- [5] Di Caprio, Giuseppe, et al. *Proceedings of the National Academy of Sciences* 116.50 (2019): 25236-25242.
- [6] Saadat, Amir, et al *Lab on a Chip* 20.16 (2020): 2927-2936.

OVEREXPRESSION OF ENHANCED YELLOW FLUORESCENT PROTEIN FUSED WITH CHANNELRHODOPSIN CAUSES CONTRACTILE DYSFUNCTION IN SKELETAL MUSCLE

Syeda N. Lamia (1, 2), Carol S. Davis (1), Peter C.D. Macpherson (1), T. Bradley Willingham (3), Yingfan Zhang (3), Chengyu Liu (3), Susan V. Brooks (1), Brian Glancy (3), Megan L. Killian (1)

- (1) Department of Orthopaedic Surgery, University of Michigan, Ann Arbor, MI, USA
(2) Department of Mechanical Engineering, University of Michigan, Ann Arbor, MI, USA
(3) Intramural Research Program, National Institutes of Health, Bethesda, MD, USA

INTRODUCTION

Skeletal muscle activation with optical stimuli (i.e., optogenetics) is a novel alternative to established electrical stimulation approaches [1]. Direct optogenetic stimulation (OS) of excitable muscle cells can induce contraction noninvasively via transdermal light exposure [2-4]. Recently, we have used established transgenic mice (Ai32) to control expression of light-sensitive channelrhodopsin-2 (ChR2) fused with enhanced yellow fluorescent protein (EYFP) in skeletal muscle [4, 5]. When exposed to blue light (455 nm), the transmembrane ChR2 opens to allow non-selective cation flow for muscle cell depolarization and contraction [6]. EYFP is useful for detecting Cre recombination in our tissues, however we observed its unusual clustering in cryosections of skeletal muscle [4]. This high EYFP and/or ChR2 expression may lead to contractile and electrophysiological dysfunction [7, 8]. To address this concern, we have generated a new transgenic mouse to express ChR2 in skeletal muscle without the EYFP fusion gene. We hypothesized that muscles with ChR2 but without EYFP would mimic physiological contractility (i.e., electrical stimulation) similar to wildtype mice and more accurately replicate physiological properties when excited using optogenetic stimulation compared to muscles which express both ChR2 and EYFP. To test this hypothesis, we compared muscle contractility in three mouse strains (wildtype, muscle expressing ChR2 with EYFP, and muscle expressing ChR2 without EYFP) using electrical stimulation *in situ* and *in vitro* and OS *in vitro*. We also evaluated skeletal muscle structure using light and electron microscopy.

METHODS

The Institutional Animal Care and Use Committee at the University of Michigan approved all animal procedures. Mouse models: Mice expressed ChR2 with EYFP (ChR2-EYFP, i.e., Ai32) [5] or ChR2 without EYFP (ChR2-only) in skeletal muscle using doxycycline inducible Acta1-Cre (for contractility and imaging) or muscle creatine kinase (CK)-Cre (for imaging). ChR2-only mice (developed by BG laboratory) were generated by removing both the woodchuck hepatitis

virus post-transcriptional regulatory element (WPRE) and EYFP fusion gene and adding a non-fluorescent V5 tag. Wildtype Cre-negative littermates (WT) were used as controls. Microscopy: EDL muscle was flash frozen and cryosectioned (for confocal) or fixed and embedded (glutaraldehyde, Spurr's resin) then ultramicrotomed (for ultrastructure) of WT, ChR2-EYFP, and ChR2-only mice (n=1/group). Tissues were imaged with confocal and transmission electron microscope (TEM), respectively. In situ contractility: We compared isometric contractile properties of gastrocnemius muscles *in situ* with nerve stimulation [9]. In brief, mice were anesthetized using tribromoethanol and gastrocnemius muscles were carefully separated from surrounding musculature without damaging the blood vessels and nerves. Suture was tied around the Achilles tendon and then the tendon was dissected from the calcaneus. The knee and the foot were secured to posts to limit knee motion. The Achilles tendon was then tied to a dual mode lever system (6650LR, Cambridge Technology). The sciatic nerve was exposed and stimulated using bipolar platinum wire electrode. Voltage and muscle resting length were adjusted until maximum twitch force was achieved. Isometric contractile forces were then measured for three groups: WT, ChR2-EYFP, and ChR2-only mice (n=3, 3, and 5 respectively, all male) in response to increasing frequencies from 40 to 220 Hz. Maximum isometric tetanic force was normalized by the physiological cross-sectional area (PCSA) of individual gastrocnemius muscles. In vitro contractility with electrical stimulation: We measured isometric contractile properties of isolated extensor digitorum longus (EDL) muscles with electrical stimulation *in vitro* [10]. EDL muscles were dissected and placed in buffered Ringer's solution bath. Distal and proximal tendons were tied with suture to a fixed post and force transducer (BG-50, Kulite Semiconductor), respectively. Two platinum plate electrodes were placed on either side of the muscle parallel to its long axis. An electrical field was applied between the electrodes, and the muscle was tested using the same stimulation protocol as *in situ* test for the three groups: WT (n=2, male only), ChR2-EYFP (n=2, male

only), and Chr2-only (n=2, 1 male, 1 female). Maximum isometric tetanic force was normalized to PCSA of individual EDLs. **In vitro contractility with OS:** In the same setup as *in vitro* tests, EDL muscles were optically stimulated using a blue (455 nm) light emitting diode (LED; Thorlabs; ~140mW/cm²). We measured peak twitch force with incremental pulse duration ranging from 1 to 100 ms. The ability of muscle to undergo tetanus was also tested by varying LED pulse duration/frequency over 300 ms duration. **Statistics:** Data from experiments with n≥3 per group were compared using one- or two-way ANOVA in experiments with Tukey's multiple comparison tests on GraphPad. Akaike information criterion (AIC) was used to identify the best fit model to describe the relationship between OS twitch force and light pulse durations.

RESULTS

In addition to confirming EYFP overexpression in Chr2-EYFP muscle (Fig1A&B), we also found whorls/vacuoles along Chr2-EYFP sarcolemma (Fig1C), which were absent in WT or Chr2-only muscle (data not shown). Body weights were similar in WT, Chr2-EYFP, and Chr2-only mice (data not shown), however gastrocnemius muscle mass from Chr2-EYFP mice was significantly lower compared to WT and Chr2-only mice (p<0.01, Fig2A). Isometric tetanic force of Chr2-EYFP mice was significantly reduced compared to WT and Chr2-only mice at all test frequencies (p<0.05, Fig2B). We observed a significant reduction in max. specific tetanic force with nerve stimulation for gastrocnemius muscles of Chr2-EYFP mice compared with WT *in situ* (p=0.007, Fig2C). Reduced force was also observed in EDL muscles *in vitro* (Fig3A,B). However, both time to peak twitch tension and half relaxation time in EDL muscles were similar among groups (Fig3C,D). Based on AIC, force vs pulse duration response was modeled using one phase decay (R²>0.7). EDL twitch forces from Chr2-only mice were higher at shorter pulses than Chr2-EYFP EDLs (Fig3E,F) and plateaued at shorter pulse durations (Fig3E). Similarly, Chr2-only EDLs generated higher forces with partially fused tetanus at 50Hz (10ms pulse, Fig3G), which was not achieved in Chr2-EYFP muscles.

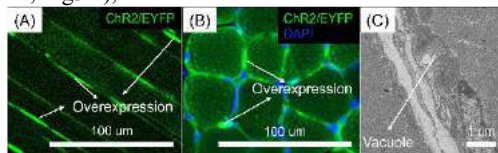


Fig 1. EYFP overexpression and vacuole formation in Chr2-EYFP EDL muscles. (A) Fluorescence microscopy of CKCre;Ai32 (longitudinal) and (B) Acta1Cre;Ai32 (transverse), as well as (C) TEM of CKCre;Ai32, showed (A,B) increased aggregates of EYFP overexpression and (C) vacuole formation.

DISCUSSION

In this study, we determined the contractile properties and ultrastructure of skeletal muscle expressing Chr2 with (Ai32) and without EYFP reporter. This study is of high importance for the field of musculoskeletal bioengineering as it elucidates a detrimental role of fluorescent Cre reporters in muscle physiology. Cre reporter strains are widely used for cell lineage tracing, validating recombination, tracking cellular processes, and monitoring expression in living tissues and cultured cells. However, we observed significant deficits in contractile properties of skeletal muscle that expresses Chr2 with EYFP (i.e., Ai32) using both electrical and optogenetic stimulation. When EYFP was removed (Chr2-only), we found a repeatable and significant improvement in muscle contractility and physiological response to stimulation. This work has significant impact to the field, as it has potential to improve Chr2 delivery and efficacy in skeletal muscle, strengthening the translational potential for use of optogenetics for controlling muscle function. The attenuated muscle force with Chr2/EYFP expression that we observed can be explained by at least

two mechanisms: (1) decreased calcium handling in muscle cells limited by Chr2/EYFP fusion protein, and (2) structural damage caused by excessive accumulation of EYFP in vacuoles. In our mouse models, Chr2-EYFP colocalizes at the sarcolemma, T-tubules and dihydropyridine (DHP) calcium channel ([2] and Fig1A,B). Although no major disruption was observed in these networks in microscopy, it is possible that Chr2/EYFP colocalization may hinder the functionality of voltage gated DHP channels, which could negatively impact the Ca²⁺ transient, thereby reducing contractile force. However, we did not see any change in the twitch times (Fig3C,D), suggesting that calcium handling during excitation-contraction coupling was not affected by Chr2/EYFP. Thus, we have ruled out the effects of structural changes as a driver of contractility dysfunction in EYFP-expressing muscle cells. In our new Chr2-only mouse model, it is likely that Chr2 expression is lower, as WPRE was removed in addition to EYFP. Elevated Chr2 can increase membrane capacitance [11] which could decrease conduction velocity of action potentials and inadvertently limit force generation capacity. However, if EYFP or Chr2 alone are responsible for functional deficit needs further study. In the future, we will measure Chr2 levels in our models.

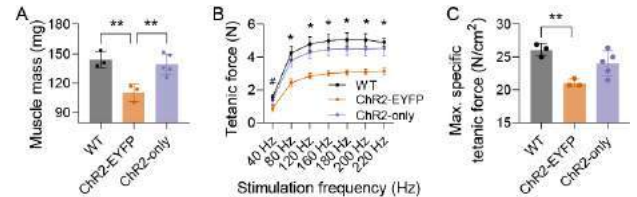


Fig 2. *In situ* contractile forces were significantly decreased in gastrocnemius muscles expressing Chr2-EYFP but not in Chr2-only muscles. (A) Muscle mass, (B) force–frequency relationship, and (C) specific tetanic force were reduced in Chr2-EYFP compared to WT and Chr2-only muscles. **, p<0.01; *, #, p<0.05.

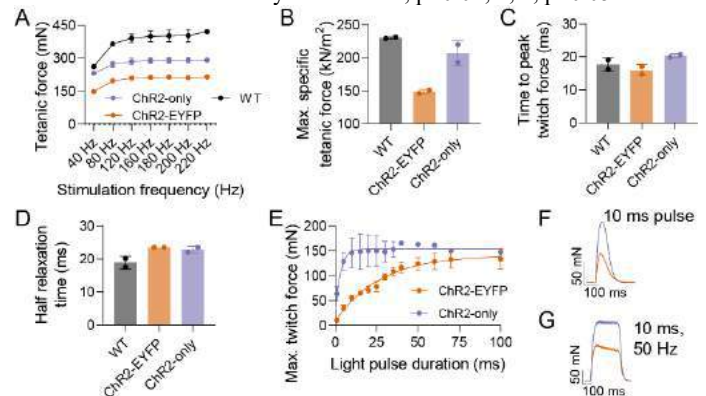


Fig 3. Chr2-only EDL muscles generated higher force in both electrical and OS compared to Chr2-EYFP EDLs *in vitro*. Using electrical stimulation, (A) force–frequency relationship and (B) max. specific tetanic force was reduced for Chr2-EYFP EDLs compared to WT EDLs. However, (C) time to peak twitch force and (D) half relaxation time were not different. Using OS, Chr2-EYFP had reduced (E) twitch force compared to Chr2-only. Representative (F) OS twitch force at 10 ms pulse and (G) 10 ms at 50 Hz.

ACKNOWLEDGEMENTS: R01 AR079367, NSF CAREER 1944448, P30AR069620, UM BRCF, Robert Balaban, NHLBI EM.

REFERENCES: [1] Gundelach, *Euro J Phys*, 2020. [2] Magown, *Nat Comm*, 2015. [3] Bruegmann, *Nat Comm*, 2015. [4] Ganji, *Conn Tiss Res*, 2021. [5] Madisen, *Nat Neuro*, 2012. [6] Nagel, *Curr Biol*, 2003 [7] Meng, *Cell Mol Prop Neurons*, 2019. [8] Lipták, *Phys Res*, 2019. [9] Larkin *Am. J. Phys*, (2011). [10] Brooks & Faulkner *J Phys*, 1988. [11] Zimmermann, *Biochem Biophys Res Comm*, 2008.

OPTIMIZATION OF A BIOPRINTED PULSATILE FONTAN CONDUIT USING A MULTIPHYSICS SIMULATION FRAMEWORK

Zinan Hu (1), Jessica E. Herrmann (2), Mark A. Skylar-Scott (3),
Tain-Yen Hsia (4), Alison L. Marsden (3,5)

- (1) Department of Mechanical Engineering, Stanford University, Stanford, CA, USA
(2) School of Medicine, Stanford University, Stanford, CA, USA
(3) Department of Bioengineering, Stanford University, Stanford, CA, USA
(4) College of Medicine, University of Central Florida, Orlando, FL, USA
(5) Department of Pediatrics, Stanford University, Stanford, CA, US

INTRODUCTION

Over the past decades, the rapid development of tissue engineering has increasingly held promise for creating tissues for a variety of applications, including in vivo regeneration, and organ repair and replacement. Three-dimensional bioprinting now has potential to spatially controlled deposition of biomaterials and cells in 3D with remarkable accuracy. Our team is investigating creation of a bioprinted pulsatile conduit as a possible substitute for the standard Gore-Tex conduit used in the Fontan surgery. Fontan surgery, which places the pulmonary and systemic circulations in series, is the final stage of three palliative surgical procedures for single ventricle congenital heart disease patients. Lacking a ventricular power source to pump flow to the lungs, patients with Fontan physiology experience a condition known as the Fontan paradox, in which central venous pressure is abnormally elevated, while pulmonary artery pressure and pulsatility are decreased [1]. Overtime, this unusual physiology leads to multiple morbidities and mortality, including early demise, liver fibrosis, arrhythmias, and reduced exercise tolerance [2]. The bioprinted pulsatile conduit, which connects the inferior vena cava (IVC) to the pulmonary arteries, has the potential to improve the adverse Fontan hemodynamics by providing the missing power source.

Currently, bioprinting of large-scale contractile materials is an expensive and complex procedure. Computational modeling provides a means to accelerate design by allowing for efficient performance evaluation and exploration of the design space. Here, we construct a multi-physics computational framework combining electrophysiology, cardiac mechanics with active contraction, fluids mechanics, and valves. In this study, we first demonstrate the performance of the prototype of pulsatile conduit, then discuss its feasibility to resolve the Fontan paradox, and finally optimize the design by evaluating the different contraction mechanisms.

METHODS

The proposed pulsatile Fontan will be 3D bioprinted using a combination of two printing techniques: freeform reversible embedding of suspended hydrogels [3] and sacrificial writing of functional tissues [4]. The myocardial walls will be manufactured using a cardiac organoid-laden bioink, while the valves will be printed with a collagen ink. The vasculature will be created by bioprinting a sacrificial gelatin ink into the myocardial walls and later evacuating the ink to yield perfusable channels. We place the valves at both ends to prevent backflow in the conduit. Based on the standard conduit used in the Fontan surgery, our initial design is a straight cylinder with a height of 7.5 cm, an inner radius of 10 cm, and a thickness of 4.4 cm. The thickness is optimized based on hoop stress calculations. Given the current bioprinted myocyte's capabilities, the conduit is expected to have a 3 mN/mm² passive stiffness and generate a 5 mN/mm² active stress. A human value of 60 mN/mm² was also simulated for comparison.

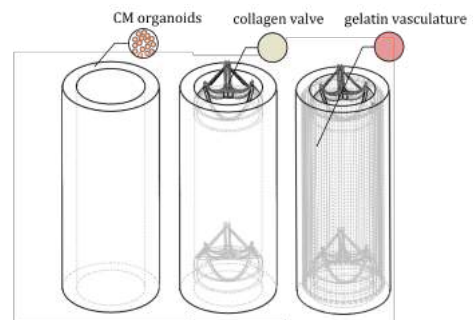


Figure 1: Demonstration of the bioprinted Fontan Conduit

Simulations of the 3D finite element conduit model are performed in a multi-physics computational framework, which includes physics

modules for electrophysiology, active stress generation, fluid-solid interaction, and valves in a single solver. All the simulations are performed in the svFSI finite element solver provided by the open-source software SimVascular [5]. A representative Purkinje network is generated on the exterior surface and coupled to the myocardium wall at the node endpoint. Electric signal propagation is simulated using a diffusion equation, with the tenTusscher-Panfilov model chosen to model the electrophysiology [6]. Holzapfel's orthotropic material model is used for the solid mechanics simulations to represent the anisotropic nonlinear material behavior [7]. The action potential in the myocardium triggers its contraction along the defined directions; a rule-based method is used to prescribe fiber directions. The FSI simulation enables us to assess the performance of the conduit via local hemodynamics. We also obtain global physiologic parameters by coupling inlet and outlet boundaries to a lumped parameter model of the single ventricle circulation following prior work [8,9]. LPN values were tuned to match typical clinical values. Primary quantities of interest for evaluating pump performance include reduction in central venous pressure and pulsatility in the pulmonary arteries. We explore the impact of several design parameters on conduit performance, including pure circumferential contraction vs. twist motion by varying the fiber orientations, and simultaneous contraction vs. peristaltic pumping by defining the timing of fiber activation.

RESULTS

With a value of 5 mN/mm² active stress, representative of current bioprinted myocyte values, the simulated bioprinted conduit generates a 4.4-mmHg interior pressure rise and an 5.7% change in volume amplitude. This pumping source is unable to either lower the liver pressure, or alter the pulmonary mean pressure and pressure waveform, which indicates the conduit fails to transfer the generated pulsatility forward. These negligible changes in hemodynamics may at first lead to concerns about the feasibility of the bioprinted pulsatile conduits. However, with the higher human myocyte contractility value (60 mN/mm²), the model predicts a 21 mmHg pressure amplitude and a 48% volume amplitude. The liver pressure falls by 5mmHg to 11.7 mmHg, while the mean pulmonary pressure increases 2.5 mmHg (figure 2). Other hemodynamics are also affected by the implementation of conduit with strong contractility. The pressure in the superior vena cava (SVC) rises from 15.8 to 18.4 mmHg.

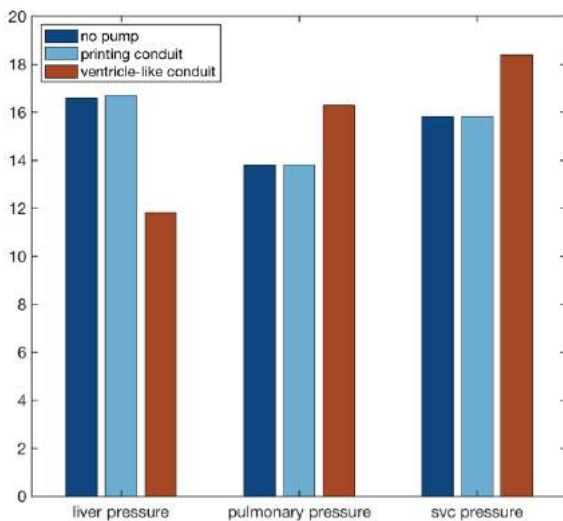


Figure 2: Comparisons of hemodynamics without pump, with bioprinted myocyte and with human myocyte.

By exploring different contraction patterns, we aim to maximize the myocyte's effectiveness. We assign the fibers helically around the conduit, varying the angle between the fibers and the horizontal plane. The circularly oriented fiber produces a pure circumferential contraction with a maximum volume pulse of 9.4% and a 5.8 mmHg pressure increment. Other longitudinal orientations create a twisting motion of conduit, and the change in volume lowers gradually to 2.6% with increasing helical angle. Moreover, we implement the peristaltic pumping by manipulating the activation time of the myocardium fibers. When we partition the conduit into two halves with one part before the other, the volume amplitude drops to 2.3% since only one portion is transporting blood. With the conduit divided into three parts, the volume amplitude decreases further to 2% as expected. Due to the small active stress, the effects of fiber angles or activation time on Fontan hemodynamics are insignificant. Further exploration of the parameter space is underway to optimize overall conduit performance.

DISCUSSION

We introduce a multi-physics computational framework to investigate how pulsatile conduit designs parameter choices can impact the hemodynamics and physiology of Fontan patients. The 5-mmHg reduction in central venous pressure demonstrates that adding a pumping source could improve adverse hemodynamics significantly and possibly reverse the Fontan paradox in the presence of strong contractility. However, the conduit implementation did not result in the expected increase in pulsatility in the pulmonary arteries. One reason is that the pulsatile flow from the conduit is dampened by the flow from the SVC at the Fontan junction. Future studies should examine more complicated geometries to maximize pump efficiency. The considerable increase in SVC pressure raises concerns about possible unfavorable clinical outcomes. Further conduit improvements or design changes could be considered to prevent high SVC pressure. By altering the contractility, fiber angles, and contraction mechanism, we have illustrated that contractility plays an essential role in the conduit's performance. To maximize the utility of contraction, the circumferential simultaneous contraction is preferred to generate as much volume amplitude as possible and further reduce the central venous pressure. However, this contrasts with the finding that the twist motion helps to produce a larger ejection fraction from the conduit. Such differences may arise from our boundary condition implementation. The clamped boundary conditions in the simulation fix the total length of the conduit and may negate the effects of the twist motion. Future work should explore alternative boundary condition implementations.

ACKNOWLEDGEMENTS

The authors would like to thank the Additional Ventures Foundation Cures Collaborative Grant for grant funding.

REFERENCES

- [1] de Leval, MR. *Pediatric cardiology* 19.4 (1998): 316-320.
- [2] Gewillig, M, et al., *Heart* 102.14 (2016): 1081-1086.
- [3] Lee, A. R. H. A., et al., *Science* 365.6452 (2019): 482-487.
- [4] Skylar-Scott, M A., et al. *Science advances* 5.9 (2019): eaaw2459
- [5] Updegrove, A, et al. *Annals of biomedical engineering* 45.3 (2017): 525-541.
- [6] ten Tusscher, K H W J, et al., *American journal of physiology. Heart and circulatory physiology*, vol. 286,4 (2004).
- [7] Holzapfel, G. A., et al., *Philosophical Transactions of the Royal Society A*, 367(1902), 3445-3475.
- [8] Kung, E, et al. *Journal of biomechanical engineering* 136.8 (2014).
- [9] Schwarz, E L., et al. *NPJ Regenerative Medicine* 6.1 (2021): 1-17.

A NOVEL LASER ABLATION MODEL FOR STUDYING LOCAL MICRODAMAGE REPAIR IN LIVE TENDON EXPLANTS

Anthony N. Aggouras (1), Matthew T. Lim (1),
Jeroen Eyckmans (1), Brianne K. Connizzo (1)

(1) Department of Biomedical Engineering, Boston University, Boston, MA, USA

INTRODUCTION

Tendinopathy is a common pathology that affects 10% of adults under the age of 45 and results in pain, degradation of tendon structure, and diminished tissue function [1]. One factor thought to contribute to the pathogenesis of tendinopathy is overuse, or the accumulation of microdamage in the extracellular matrix [2]. While the accumulation of microdamage in response to overuse is well known, it is still unclear if resident tenocytes have an innate capacity to respond to and heal tendon matrix microdamage. Previous work has looked at the innate response of tenocytes to widespread load-induced microdamage and found that they were unable to heal [3]. However, few studies have explored localized microdamage. Current methods induce microdamage by the means of high strain, load, or loading cycles. This widespread microdamage may be far over the threshold of damage tenocytes can heal without support from extrinsic factors. In other tissue types, such as in cardiac tissue constructs, the healing response of resident cells to localized microdamage has been identified by using a laser ablation model [4]. Therefore, the purpose of this study was to establish a novel laser ablation model to induce localized microdamage to live tendon explants and characterize the response to localized microdamage. We hypothesized that resident tenocytes would have the ability to initiate healing by remaining closely around the site of injury and removing denatured collagen from the site of injury.

METHODS

Flexor digitorum longus (FDL) tendon explants were harvested from mature 4-month-old C57BL/6J mice (BU IACUC Approved), as described [5]. FDL explants were then loaded into custom grips with a gauge length of 10 mm. Samples were transferred to culture wells in a custom-built imaging bioreactor and standard culture media was added to each well (Figure 1A,B). Tendons were hand tensioned using a custom tensioning bar until taut. The bioreactor was then transported to stage of a Zeiss Axiovert S100 microscope equipped with a 10x

objective and a 1,064-nm pulsed Nd:YAG nanosecond laser (Minilite, Continuum). The midportion of the tendon was ablated using a single laser pulse of 10 mJ (Figure 1C), and a bright field image was captured before and after to ensure an injury was produced (Figure 1D). Explants were then cultured in place for up to 10 days. Collagen damage and cell location were determined by Cy3 Collagen Hybridizing Peptide (CHP) and NucBlue nuclear fluorescent stains, respectively, at day 0, 3, 7, and 10. Tendons were transferred to 1.8 μ M Cy3 CHP in PBS solution and incubated at 4C for 16 hrs. After incubation, tendons were stained with NucBlue (Fischer Scientific) for 5 minutes. Confocal image z-stacks of the ablation damage and hole were then captured on an Olympus FV3000 with a 20x objective. Volume of the damage was estimated by using the equation for an elliptical frustum [6], with the measured length and width of the damaged region stained with CHP and distance between z stacks. Cells in the damaged area were determined by tracing

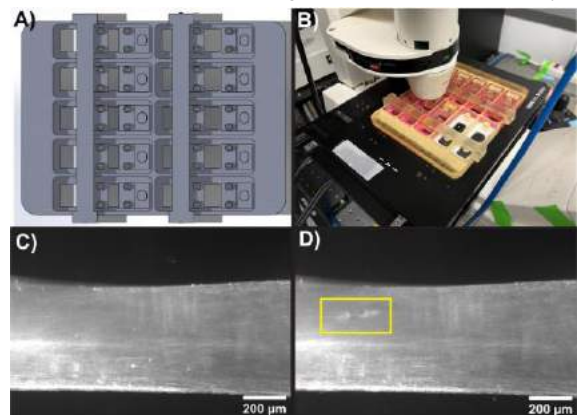


Figure 1: (A) 3D model of the bioreactor and (B) an image of the bioreactor in use. (C) Before and (D) after images of an ablated tendon. Yellow box highlights area of damage after ablation.

the area of CHP stain and counting the number of cells in the NucBlue channel. Peak and average collagen damage intensity were determined from a max intensity projection of the CHP channel using a rectangular ROI with dimensions equivalent to the max width and length of all damaged regions. Statistical evaluation was performed using one-way ANOVAs with post-hoc Bonferroni corrected t-tests. Significance was noted at $*p<0.05$.

RESULTS

We created a repeatable injury model that produced a $\sim 50 \times 100 \mu\text{m}$ elliptical hole in the tissue (estimated from day 0 images, not shown). Representative images show a progressive reduction in CHP stain around the hole during the culture period (Figure 2). By day 10, there is no visible CHP staining around the hole in most samples (Figure 2D). We found a significant reduction in the average intensity of collagen damage from days 0 and 3 to days 7 and 10 (Figure 3A). This was accompanied by a reduction in peak CHP signal (Figure 3B). There is also a significant reduction in the volume of damage marked by CHP staining from day 0 to day 7 and 10 (Figure 3C). There were no differences in cell number within the damage area until day 7, but the number of cells decreased from day 7 to day 10 (Figure 3D).

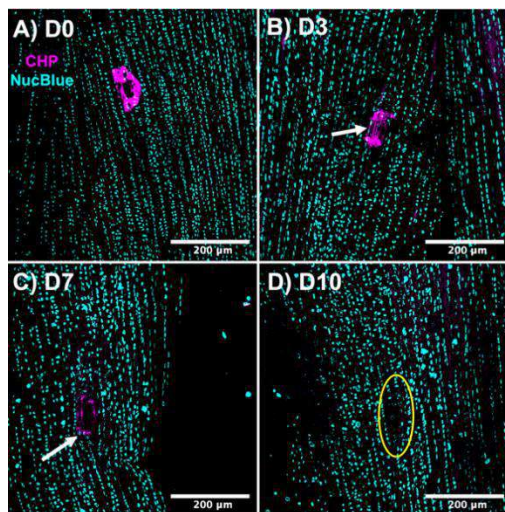


Figure 2: Representative max intensity projection images of collagen damage (magenta) and cell nuclei (blue) at days (A) 0, (B) 3, (C) 7, and (D) 10. White arrow highlights area CHP stain around cells. Yellow ellipse highlights area of ablation damage.

DISCUSSION

Our data demonstrate that resident tenocytes can initiate healing of localized microdamage by removing denatured collagen, and specifically that resident tenocytes are not reliant on extrinsic factors to initiate healing. The reduction in damage volume also demonstrates that this is not a superficial process occurring at the surface of the tendon, where tendon stem cells are expected to reside. The removal of stain is likely to be an active process by resident cell types, such as fibroblast-like tenocytes or a recently identified macrophage-like cell population, known as tenophages [7]. Both cell types can produce the collagen type 1 degrading matrix metalloproteinase MMP-9 [8], which has been shown to selectively remove denatured collagen in mechanically overloaded tendons [9]. Future studies will explore the local expression of matrix degrading enzymes around the injury site to identify mechanisms and cellular drivers of denatured collagen removal.

In agreement with our hypothesis, we did find cells co-localized with CHP stain in the damaged regions of ablated explants, particularly

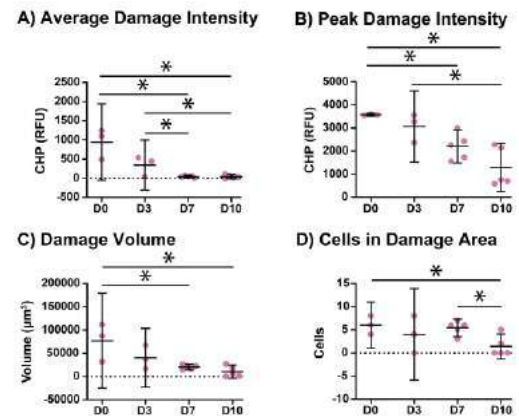


Figure 3: (A) Average intensity, (B) peak intensity, (C) volume, and (D) cell count of damaged area. Data is mean \pm 95% confidence interval.

at early time points. While cells in the damaged region were easily identifiable at earlier time points, identifying the borders of the damaged area at day 10 was more difficult as there was a lack of CHP staining. In addition, the cells at day 0 appeared to be small and fragmented, potentially indicating that they were dead. It's not clear whether damaged cells remained at the injury site throughout culture or at what point they were cleared, and we are now performing viability assessment to confirm cell health in these areas. Given the necessity of cell-mediated signaling to remove damaged ECM, we believe this process does directly involve tenocytes as observed in Fig. 2B and 2C. Areas with reduced stain clearly have visible tendon cells in the damaged area, suggesting that these cells are actively removing denatured collagen from those regions. Future studies will aim to identify the cells in the damaged region and characterize their behavior following the initial injury.

In summary, we present here a novel model for studying innate tissue healing processes following a microscale injury without interference from extrinsic factors. Future studies will take advantage of this model to explore thresholds of microdamage repair by modulating hole size and volume. We also aim to identify what provisional matrix is produced at the injury site, and the cell types responsible for this healing response. Regardless, this novel model system enables the direct visualization and study of local tissue repair, which will be a powerful asset for understanding mechanisms of microdamage accumulation and/or healing, as well as identifying local tendon-specific factors that can be leveraged for therapeutics.

ACKNOWLEDGEMENTS

This study was supported by NIH R00-AG063896 and R21-EB028491. Research reported in this publication was supported by the Boston University Micro and Nano Imaging Facility and the National Institutes of Health (S10OD024993).

REFERENCES

- [1] Voleti, P et al, Annu. Rev. Biomed. Eng., 14:47–71, 2012.
- [2] Millar, N et al, Nat. Rev. Dis. Primers, 7(1):1, 2021.
- [3] Stauber, T et al, Matrix Biol., 85-86:68-79, 2019.
- [4] Das, SL et al, Am J Physiol Heart Circ Physiol., 323(4):H738-H748, 2022.
- [5] Connizzo, BK et al, Connect Tissue Res., 61(1):48-62., 2019
- [6] Mayrovitz HN, Lymphology, 36(3):140-3., 2003.
- [7] Lehner, C et al, Dis Model Mech., 12(12):dmm04138., 2019.
- [8] Watanabe, R et al, Circ Res., 123(6):700-715., 2018.
- [9] Baldwin, SJ et al, J Mech Behav Biomed Mater., 95:67-75., 2019.

Tissue Diffusion and Two Component Computational Model to Predict Leaching from Medical Devices

Martin L. Tanaka (1), David M. Saylor (2), Robert M. Elder (2)

(1) College of Engineering and Technology, Western Carolina University, Cullowhee, NC, USA
(2) US Food and Drug Administration, Silver Spring, MD, USA

INTRODUCTION

Implanted polymeric medical devices can pose a risk to human health when they contain potentially hazardous materials that leach into the body. Historically, extraction experiments and animal studies have been used to estimate the amount of material released. However, these approaches are changing. Fueled by increases in computational capabilities, computer models can now be used to predict the amount of material released over time. These simulations can complement traditional extraction studies and yield several benefits for regulatory science. First, the models can be used to simulate a more realistic environment than the harsh conditions used in extraction studies. Second, because the models contain system specific input parameters, they can be easily adapted to other polymer types or leachable chemicals making it easy to analyze a multitude of different systems. Third, once the models are developed and validated, simulations can often be run in seconds saving the weeks or months needed for extraction studies. This can help medical device companies to accelerate new product development getting new devices to market faster. Finally, reducing the effort needed to meet regulatory requirements will reduce overall product development costs.

The FDA has already developed regulatory science tools for rapid risk assessments of color additives in medical devices. These tools use physics-based models to predict the amount of material that may be released from an implanted polymeric medical device. In this research, models will be extended beyond a one component system (implant only) to a two-component system that also includes the surrounding tissue.

METHODS

A two-component mathematical model was developed to characterize the migration of leachable chemicals from an implanted polymeric device into the surrounding tissue (Figure 1). The model assumes that the leachable chemical is homogeneously distributed throughout the implant and that the implant will remain structurally

consistent throughout the duration of the simulation (i.e., no degradation or swelling). Human tissue surrounding the implant was also modeled. Tissue was assumed to be quasi-static with consistent material parameters over the duration of the simulation. The mathematical model estimates the amount of material released over a time period of one day (24 hours). When this quantity is less than the allowable daily dose for the leachable chemical, the risk associated with potential exposure to the chemical is considered acceptable.

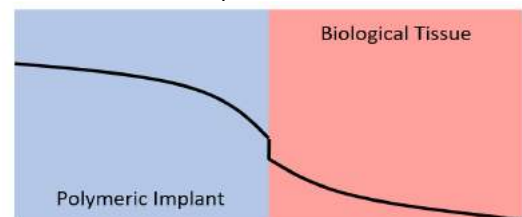


Figure 1: Two-component model shows diffusion through the implant (blue), across the partition, and into the surrounding tissue (red).

Fick's law was used to predict diffusion through the implant and the tissue.

$$\frac{\partial C(x,t)}{\partial t} = D_p \nabla^2 C(x,t) \quad (1)$$

where, the concentration of the leachable substance, C , is a function of the position within the polymer, x , and time, t . D_p is the effective (macroscopic) diffusion coefficient of the leachable in the polymer. D_p is scalar and independent of C , x , and t .

The polymer-tissue partition coefficient, K , was used to predict migration across the polymer-tissue interface. Due to differences in hydrophilicity/lipophilicity, the migrating chemical can have a different affinity for the polymer than the tissue which can lead to a step change in concentration at the interface. Our model utilizes equations originally developed by Gandek to characterize migration of potentially hazardous

materials into food from its surrounding packaging [1]. The amount of material release, M_τ is, given by,

$$M_\tau(\tau) = \left[\frac{2\beta}{1+\beta} \right] \sqrt{\frac{\tau}{\pi}} \left\{ 1 - \frac{2\beta}{1+\beta} \sum_{n=1}^{\infty} \left[\frac{1-\beta}{1+\beta} \right]^{n-1} \left[e^{\left(\frac{-n^2}{\tau} \right)} - \frac{n\sqrt{\pi}}{\sqrt{\tau}} \operatorname{erfc} \left[\frac{n}{\sqrt{\tau}} \right] \right] \right\} \quad (2)$$

$$\tau = \frac{D_p \tau}{L^2} \quad (3) \quad \beta = K \sqrt{\frac{D_t}{D_p}} \quad (4)$$

where, τ is a dimensionless time parameter, β is a dimensionless parameter that consists of the partition coefficient, K , and the tissue and polymer diffusion coefficients D_t and D_p . Values for D_p for various chemical-polymer combinations were obtained from FDA databases and polymer tissue partition coefficients were previously developed by the co-authors [2]. Tissue diffusion coefficients were determined through literature review. Searches on Scopus, SciFinder, and Google Scholar were utilized. Forward and backward snowballing was also used to expand the search. Models were verified by comparing results to those developed by Crank [3].

$$M(\tau) = \begin{cases} 2M_0 \sqrt{\tau/\pi} & \tau \leq 0.2 \\ M_0 (1 - 8 \exp[-\tau\pi^2/4]/\pi^2) & \tau > 0.2 \end{cases} \quad (5)$$

Equations 2 and 5 are identical models with different boundary conditions that converge to the same solution at low values of K and high D_t . While it is not feasible to analyze all possible combinations of polymer types, leachable chemicals, and tissue types, several cases were considered that represent a broad range of input parameter combinations. Furthermore, results over the expected range of parameter values were calculated.

RESULTS

Tissue diffusion values were found for 307 different combinations of chemicals and tissues (Figure 2). These were grouped into barrier tissues (red) and non-barrier tissues (blue). Because an implanted device is often located against cut tissue the higher diffusion rates associated with non-barrier tissues were used for the model.

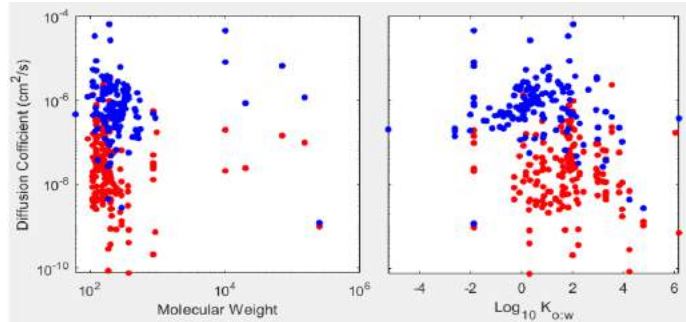


Figure 2: Tissue diffusion data as a function of molecular weight and octanol-water partition coefficient (hydrophobicity)

Table 1 shows the mean value by group and the two inner quartiles (25% and 75%). The 5% and 95% values were estimated from these inner quartiles, but values are only estimates because there is no confirmation that the distribution is normal.

Table 1: Diffusion for barrier and non-barrier tissues ($\times 10^{-6} \text{ cm}^2/\text{s}$)

Tissue Type	5%	25%	mean	75%	95%
Barrier	0.0010	0.0057	0.0201	0.0612	0.3387
Non-Barrier	0.1145	0.3510	0.6500	1.6657	5.1055

Using the values for K , D_t and D_p , the results of equation 2 were calculated. Large variability in D_p led to large variability in τ causing it to range in value from 10^{-13} to 10^1 . Similarly, β spans a large range from

10^{-3} to 10^9 . This yields material release quantities that span over 20 orders of magnitude.

One of the main objectives of the two component model was to determine conditions where use of the more complex model (Eq. 2) yields more clinically relevant results than the simpler one component model (Eq. 5). Several cases were considered. The case that yielded the greatest difference (1), several intermediate combinations (2 – 6), and the case that yielded the smallest difference (7). Results showed that for case 1, the one-component model could overestimate material release by as much as 445 times (Figure 4). Several intermediate cases are also shown in the figure. For case 7 (not shown), there was no difference in results between the one and two component models.

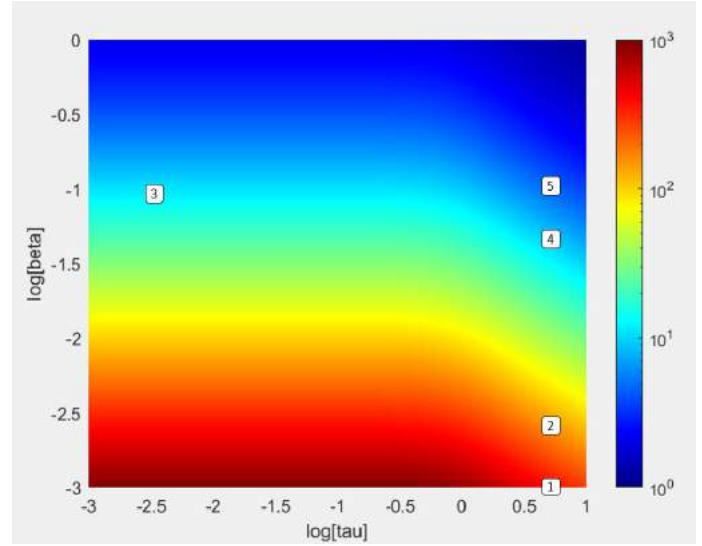


Figure 4: Ratio of one-component to two-component models. Results for case 1-5, respectively; 445, 188, 13.4, 12.6, 5.8

DISCUSSION

When analyzed over a large range of values, the more complex two-component model predicted lower quantities of leached material than the more conservative one component model. Differences in predictions could imply that the more clinically relevant two component model should be adopted. However, when clinically relevant values for K , D_t and D_p are used, it was apparent that the conditions where the two-component model is needed is limited. Conditions where this occurs include migration through high diffusion rate polymers such as silicones, hydrophobic leachables that have reduced transport across the implant-tissue barrier, and tissues with lower chemical diffusion rates. Overall, these findings have enhanced our understanding of chemical migration across multicomponent systems.

ACKNOWLEDGEMENTS

This research was supported by a grant from the National Science Foundation – Award #2149517.

REFERENCES

- [1] Gandek, T. P., 1986, "Migration of phenolic antioxidants from polyolefins to aqueous media with application to indirect food additive migration," Ph.D. Thesis, Massachusetts Institute of Technology.
- [2] Tanaka ML, Elder RM, and Saylor DM, 2022, "Polymer Tissue Partition Coefficient in Implant Leaching and Biotransport," ASME International Mechanical Engineering Congress and Exposition (IMECE), Columbus, Ohio.
- [3] Crank, J., 1975, The mathematics of diffusion. (2nd ed.), Clarendon Press, Oxford.

CYCLIC STRAIN INDUCES MATRIX TURNOVER TO BETTER MAINTAIN TENDON COMPOSITION IN EXPLANT CULTURE

Anthony N. Aggouras (1), Brianne K. Connizzo (1)

(1) Department of Biomedical Engineering, Boston University, Boston, MA, USA

INTRODUCTION

Resident tendon cells, called tenocytes, remodel the extracellular matrix (ECM) to repair normal microdamage and maintain mechanical function, balancing matrix production in response to increased exercise and matrix removal when unnecessary [1]. This balance is disrupted in tendinopathy, a common pathology affecting 10% of adults under the age of 45, leading to pain, degeneration of tendon structure, and diminished tissue function [2]. One factor thought to contribute to the pathogenesis of tendinopathy is excessive mechanical loading or exercise [2], termed overuse. While we understand that matrix turnover has a role in tendon degeneration, the innate cellular mechanisms that control the balance between matrix synthesis and degeneration are still unknown.

Explant culture allows for the maintenance of cell-cell and cell-matrix interactions and the assessment of the innate cellular responses without influence from the systemic environment. However, a major challenge to the field of tendon explant culture is establishing a consensus on the loading conditions that best maintain the tendon in culture [3]. While the field has learned much about adaptive changes to mechanical loading, previous work has mainly focused on changes to gene expression and tissue composition rather than alterations in cell behavior [4]. Studies that have focused on protein synthesis explored the short-term effects only [5]. Therefore, the purpose of this study is to investigate long-term effects of cyclic loading on matrix turnover at the protein level. We hypothesized that 3% cyclic strain would be sufficient to maintain baseline values of composition with balanced matrix turnover.

METHODS

Flexor digitorum longus (FDL) tendon explants were harvested from mature C57BL/6J (B6) mice at 4 months of age (BU IACUC Approved), as described [6]. Explants were then loaded into custom grips with a gauge length of 10 mm. Samples were transferred to culture

wells in our incubator-housed tensile loading bioreactor (Figure 1), and subjected to stress deprivation (SD), 3% static strain (SS), or 3% cyclic strain (CS) for 7 days in standard culture medium [6]. For SD, gripped tendons were placed into culture wells of the bioreactor and were left slack between the grips. Both static and cyclic loaded tendons were preloaded to a 0% strain of 20 g to ensure consistent loading between all explants. SS tendons were loaded on day 0 and held at 3% strain for the duration of the culture. CS tendons were loaded using a sinusoidal waveform from 0% to 3% strain at 1 Hz for 1 hour followed by a 5 hour hold at 0% strain. This protocol was repeated 4 times a day for the duration of the culture (Fig. 1). Explant metabolism, biosynthesis, and matrix composition were assessed on the last day of culture. Explant metabolism was measured using a resazurin reduction assay. Sulfate and proline incorporation, indicating sulfated glycosaminoglycan (sGAG) and total protein synthesis, respectively, were measured via the addition of 20 $\mu\text{Ci}/\text{ml}$ ³⁵S- sulfate and 10 $\mu\text{Ci}/\text{ml}$ ³H-proline to the media for the final 24 hours of culture. Activity of matrix metalloproteinases (MMPs) was determined in day 7 culture media. Finally, tendons were digested to facilitate the measurement of GAG

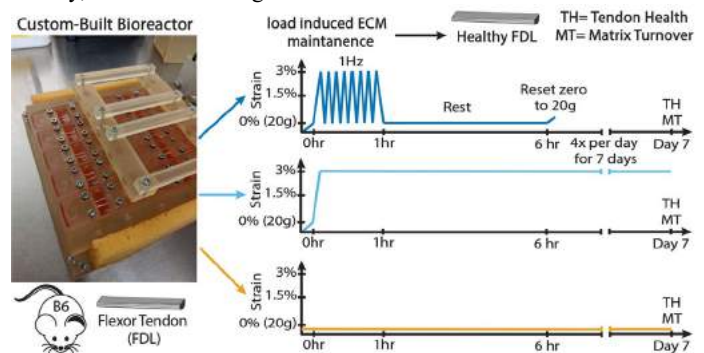


Figure 1: Study Design.

content (DMMB assay), DNA content (PicoGreen assay), and total collagen (OHP assay). All biochemical assays were normalized to tendon dry weight. Statistical evaluation was performed using one-way ANOVAs with post-hoc Bonferroni corrected t-tests. Significance was noted at $p < 0.05$. Significance from day 0 marked with an asterisk (*) and significance between the groups with a bar (-). All data is presented as mean \pm 95% confidence interval.

RESULTS

Water content of the SD group was significantly greater than that of the loaded groups and baseline value (Figure 2A), while cellularity reduced (Figure 2B). SS cellularity was also reduced from baseline values. The SD (not significant) and SS group had decreased GAG content compared to baseline values and was reduced compared to CS (Figure 2C). In collagen content, the SD group was significantly increased compared to baseline and loaded groups (Figure 2D). Metabolic activity was increased from day 0 in all groups with the CS group displaying the greatest increase (Figure 3A). There was no difference in MMP activity between groups (Figure 3B), although it appeared to increase with SD compared to SS and CS. In both protein synthesis and sGAG synthesis, the CS group has greater incorporation than the SS and the SD groups (Figure 3C,D).

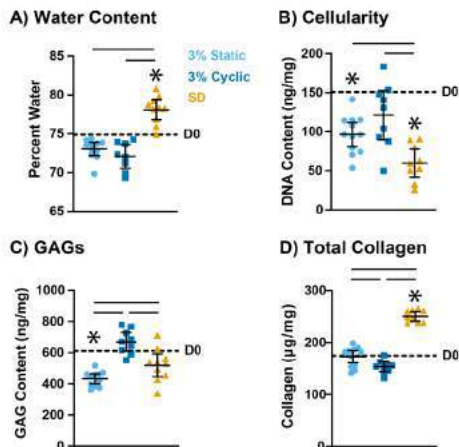


Figure 2: (A) Water content, (B) cellularity, (C) glycosaminoglycan, and (D) total collagen at day 7. Dashed line represents day 0 baseline measures.

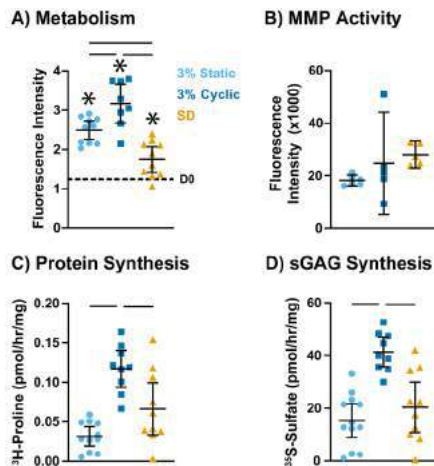


Figure 3: (A) Metabolism, (B) MMP activity, (C) protein synthesis, and (D) sGAG synthesis at day 7. Dashed line represents day 0 baseline measures.

DISCUSSION

Under SS and SD, the explants lose cellularity, indicating that static strain may not be sufficient for retaining cells within the tendon structure. This reduction in cellularity may be due to cells migrating out of the matrix or cell necrosis. While we did not measure either of these parameters, we know tenocytes rely on mechanotransduction for maintenance of cell viability and homeostasis [7] and without sufficient stimulus the cells may start to seek more favorable environments or die. We also found that SD has the greatest impact on the composition of the tendon with significant deviations from the other groups and baseline, suggesting potential pathological changes to the tissue. This is expected as SD is a common model for tendinopathy [8].

Cyclic loading appeared to maintain tendon composition throughout culture better than the other conditions, which could be a result of the higher metabolic activity and the greater synthesis in the CS group. The high synthesis rate and high metabolic activity may be sufficient to replace matrix loss while adjusting to culture conditions. Furthermore, the high MMP activity in the SD group may have led to increased breakdown of matrix. This is consistent with previous studies indicating that tendons may substantially increase matrix turnover to maintain function or to initiate repair [9]. It's also possible that higher matrix turnover is necessary to incorporate newly synthesized matrix effectively into the existing structure, but this remains unknown.

A noteworthy finding is the increase of collagen in the SD group, most likely due to an imbalance in collagen synthesis. While the higher protein synthesis appears to be balanced by an increase in MMP activity, these measures are non-specific. Although a good estimation of collagen synthesis given the primary function of tendon fibroblasts in synthesizing collagen, proline is used in the production of many other proteins as well. Furthermore, the MMP activity assay used measures many MMPs. More specific assays are necessary to truly identify type 1 collagen and collagenase levels, and this remains an avenue of inquiry in the lab.

Regardless, this study demonstrated that 3% cyclic strain is sufficient for maintaining tendon composition. It also indicates that an increased metabolic function and an increase in matrix synthesis may be helpful in tissue maintenance. Future studies will aim to explore more strain levels with the goals of identifying the optimum loading protocol for maintaining physiologic conditions and developing clinically relevant injury models. We also aim to look at the impact on the cells through gene expression, as well as matrix organization function to ensure a comprehensive analysis of tendon health. Regardless, this study identifies a baseline loading condition against which the effects of loading on matrix turnover can be explored, providing a strong model for exploring mechanosensitive cellular mechanisms that induce matrix adaptation or pathological degeneration.

ACKNOWLEDGEMENTS

This study was supported by NIH/NIA R00-AG063896.

REFERENCES

- [1] Andarawis-Puri, N et al, J Orthop Res., 33(6):780-4., 2015.
- [2] Voleti, P et al, Annu. Rev. Biomed. Eng., 14:47-71, 2012.
- [3] Wunderli, SL et al, Connect Tissue Res., 61(3-4):262-277, 2020.
- [4] Wang, T et al, Biotechnol Bioeng., 110(5):1495-507, 2013.
- [5] Screen, HR et al, Biochem Biophys Res Commun., 336(2):424-9, 2005.
- [6] Connizzo, BK et al, Connect Tissue Res., 61(1):48-62., 2019.
- [7] Killian, ML et al, J Shoulder Elbow Surg., 21(2):228-37., 2012.
- [8] Arnoczky, SP et al, Clin Orthop Relat Res., 466(7):1583-91., 2008.
- [9] Riley GP, et al, Matrix Biol., 21(2):185-95., 2002.

ENDOTHELIN-1 EXPRESSION IS DEPENDENT ON THE STABILITY OF ENDOTHELIAL GLYCOCALYX HEPARAN SULFATE

Santiago Rivero (1), Solomon A. Mensah, PhD (1,2)

- (1) Department of Biomedical Engineering, Worcester Polytechnic Institute, Worcester,
Massachusetts, United States
(2) Department of Mechanical and Materials Engineering, Worcester Polytechnic Institute,
Worcester, Massachusetts, United States

INTRODUCTION

Endothelin-1 (ET-1) is a vasoconstrictor produced by the vascular endothelium [1]. After ET-1 is produced, it is secreted into the extracellular space where it binds to endothelial B receptor on the endothelial cells or endothelial A receptor on the smooth muscle cells [2]. Increased ET-1 has been observed in the endothelial and smooth muscle cells of patients with moderate to severe hypertension [3]. It has also been correlated with different stages of atherosclerosis [4]. Several studies suggest that the expression of ET-1 depends on the magnitude and time of the shear stress produced by the blood flow and that disruption of cytoskeletal structures could mediate its production [5,6,7]

Endothelial B receptor (ETB) is a plasma membrane bound receptor present in the endothelial cell surface [8]. Studies have revealed that G-protein-coupled receptors like ETB, are flow-sensitive and lectin based [9].

The vascular endothelial glycocalyx (GCX) coats the luminal surface of endothelial cells [10]. This component senses the flow of blood and then translates it into biochemical activities [11,12]. The GCX consists of several transmembrane solid core proteins like syndecans and glypicans [13,14]. Linked to the core protein is one or more glycosaminoglycan (GAG) chains, which are made up of lectins and N-acetylglucosamine [13,15]. There are five types of GAGs: heparan sulfate, chondroitin sulfate, dermatan sulfate, keratan sulfate, and hyaluronan (or hyaluronic acid) [13]. However, the most abundant is heparan sulfate (50 – 90%) [13]. Studies have shown that the GCX is connected to the cytoskeleton and the core proteins act as a torque on the cytoskeleton structures which then leads to rearrangement and several biochemical activities [16]. There has also been noted that a degraded GCX promotes endothelial cell disfunction which leads to several diseases like atherosclerosis [10].

Both the GCX and ETB are located in the surface of the endothelial cells and are flow sensitive, therefore we suspect that there is a relationship between these components. Figure 1 describes the main

hypothesis of this study. We hypothesize that the ETB is connected to the GCX, which is also connected to the cytoskeleton. The shear stress induced upregulation of the GCX could lead to an increase in ETB which will trigger the release of ET1.

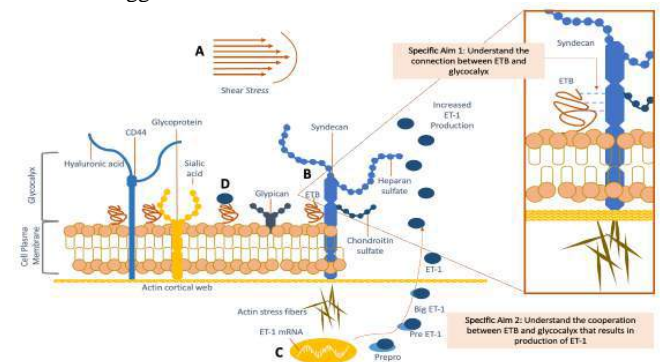


Fig 1. Schematic of the proposed hypothesis: **A.** Introduction of shear stress results in the structural changes of GCX and ETB. **B.** Shear stress triggers an interplay between the GCX and ETB that results in cytoskeletal changes which causes conformational changes leading to the synthesis of ET-1 mRNA. **C.** EC nucleus synthesizes ET-1 mRNA and produces Prepro ET-1, which undergoes post transcriptional modifications leading to the release of ET-1 which **D.** then binds to ETB on the surface of EC.

Figure 1: Schematic of proposed hypothesis

The goal of this study is to understand the involvement of the GCX in the expression of ETB receptors and ET-1 expression. Once this pathway is understood, new therapies can be developed to mitigate the detrimental effect of ET-1.

METHODS

Human Lung Microvascular Endothelial cells (HLMVEC) were maintained in Microvascular Endothelial Cell Growth Medium (Sigma-Aldrich) at 37 °C. These cells were passaged using 0.05% trypsin-EDTA at 70–80% confluence. The cells will then be cultured on a 24mm X 60mm X 1mm glass slide (Fisher Scientific) at an initial

concentration of 100,000 cell/ml. Once the glass slide is confluent, it was placed in a parallel plat flow chamber. This chamber consists of a base plate with an inlet and outlet port, and a gasket that controls the flow chamber thickness. The setup was connected to a peristaltic pump (Cole Palmer) via silicon tubing (Cole Palmer) to create a continuous flow loop. Media flowed through the tubing and flow chamber, exposing the HLMVEC to 10dynes/cm² of shear stress for 12 hours. This shear stress is within the range reported for microvascular endothelial cells [17,18].

To mimic disease progression the GCX were degraded with two different enzymes. Neuraminidase targets the lectin components of GCX and Heparinase III targets the heparan sulfate of the GCX. An initial dose of 15mU/mL represented disease onset and 3645mU/mL represented extreme disease progression [15].

Immunostaining was used to determine the expression of GCX lectin and HS. GCX lectin was labeled using biotinylated maakia amurensis lectin II (MAL II) (Thermo Fisher Scientific) as primary antibody and Alexa-fluor 488 conjugated anti biotin (Thermo Fisher Scientific) as secondary antibody. HS was labeled using 10E4-epitope heparan sulfate antibody (Amsbio) for primary detection and Alexa Fluor 488 conjugated goat anti-mouse IgG/IgM (H+L; Life Technologies) for secondary detection. ETB was labeled using anti-endothelin B receptor/ET-B antibody (ab117529 from abcam) for primary detection and horseradish peroxidase (HRP)-conjugated secondary antibodies (Pepro Tech Inc) for secondary detection. ET-1 was labeled with endothelin 1 monoclonal antibody (MA3-005), secondary detection was achieved using goat anti-mouse IgG1 cross-adsorbed Alexa fluor 488. Image J was used to quantify the results. Western blotting will also be conducted to confirm the results of immunostaining.

RESULTS

Preliminary testing was performed with two different timepoints, 4 hours and 6 hours. Results are shown in figure 2. First, the HLMVEC were stained with Wheat Germ Agglutinin, which targets all the components of the GCX (Fig 2A, 2B, 2C). The green represents the GCX and the blue the nucleus. The coverage and thickness of GCX was quantified and revealed a statistically significance difference between the control and the flow conditions (Fig 2G, 2H). There was not statistically significance difference between the 4 to 6 hours in coverage and thickness. HS was also labeled and shown in green in fig 2D, 2E and 2F. The coverage of HS has a statistically significance difference between the control and the 6-hour flow cells (Fig 2I). The thickness of the HS increased with time and the quantification showed that in fact there was a statistically significance difference between the three conditions (Fig 2J).

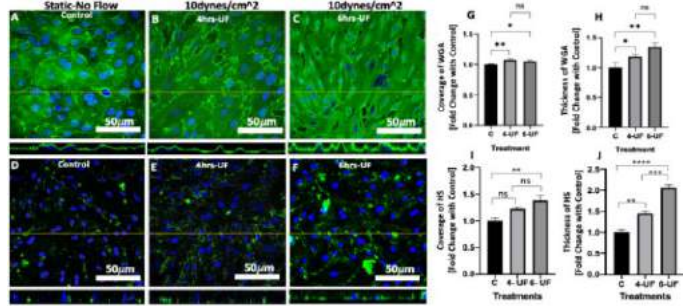


Figure 2: The effect of shear stress and time on the expression of glycocalyx and its sub-component HS on HLMVEC

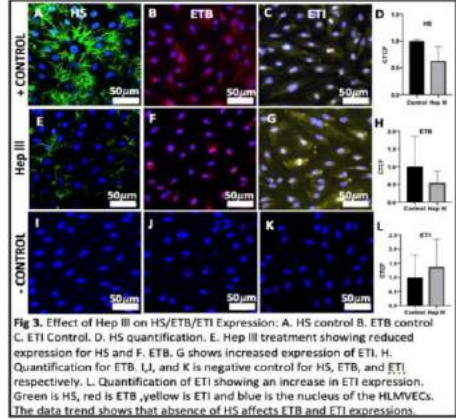


Fig 3. Effect of Hep III on HS/ETB/ET-1 Expression: A. HS control B. ETB control C. ET-1 Control. D. HS quantification. E. Hep III treatment showing reduced expression for HS and F. ETB. G shows increased expression of ET-1. H. Quantification for ETB. I, J, and K are negative control for HS, ETB, and ET-1 respectively. L. Quantification of ET-1 showing an increase in ET-1 expression. Green is HS, red is ETB, yellow is ET-1 and blue is the nucleus of the HLMVECs. The data trend shows that absence of HS affects ETB and ET-1 expressions.

DISCUSSION

The preliminary results from, immunostaining reveals a potential co-participation of GCX HS and ETB in the expression of ET-1. However, there is a possibility that HS is not the only glycosaminoglycans interacting with ETB. If that is the case, targeting other GCX GAGs and lectins independently will provide insight into the role of GCX in the regulation of ETB and ET-1.

Future work will be focused on understanding the cellular mechanisms and pathways by which cooperation between GCX and ETB could trigger the release of ET-1 in the endothelial cells.

ACKNOWLEDGEMENTS

This research was supported with startup funds from Worcester Polytechnic Institute awarded to Dr. Mensah. I want to thank Victoria Bicchieri from the BME imaging core facility for support with confocal images.

REFERENCES

- [1] Sutton. G. et al, *American Journal of Hypertension*, 32:813-815, 2019.
- [2] Inoue, A. et al, *Proc Natl Acad Sci U S A*, 86:2863-2867, 1989.
- [3] Dhaun, N. et al, *Hypertension*, 52:452-459, 2008.
- [4] Lerman, A. et al, *N Engl J Med*, 325:997-1001, 1991.
- [5] Morawietz, H. et al, *J Physiol*, 525:761-770, 2000.
- [6] Kuchan, M.J. et al, *Am J Physiol*, 264:H150-H156, 1993.
- [7] Morita, T. et al, *J Clin Invest*, 92:1706-1712, 1993.
- [8] Pollock, D.M. et al, *Hypertension*, 48:211-212, 2006.
- [9] Perez-Aguilar, S. et al, *Am J Physiol Heart Circ Physiol*, 306:H699-H708, 2014.
- [10] Ebong, E.E. et al., *Integr Biol (Camb)*, 6:338-347, 2014.
- [11] Tarbell, J.M. et al., *Sci Signal*, 1:8, 2008.
- [12] Fu, B.M et al, *Wiley Interdiscip Rev Syst Biol Med*, 5:381-390, 2013.
- [13] Reitsma, S. et al, *Pflugers Archiv : European journal of physiology*, 454:345-359, 2007.
- [14] Bartosch, A.M.W. et al, *Sci Rep*, 11:11386, 2021.
- [15] Mensah. S.A. et al, *AIChE J*, 65, 2019.
- [16] Thi, M.M et al, *Proc Natl Acad Sci U S A*, 101:16483-16488, 2004.
- [17] Wu, D. et al, *Front Bioeng Biotechnol*, 7:172, 2019.
- [18] Paszkowiak, J.J. et al, *Vasc Endovascular Surg*, 37:47-57, 2003.

THE EFFECTS OF STRAIN HISTORY ON AORTIC VALVE INTERSTITIAL CELL ACTIVATION IN A 3D HYDROGEL ENVIRONMENT

Toni M. West (1), Daniel P. Howsmon (1), Miles W. Massidda (2), Helen N. Vo (1), Athena A. Janobas (1), Aaron B. Baker (2), Michael S. Sacks (1)

(1) James T. Willerson Center for Cardiovascular Modelling and Simulation
Oden Institute for Computational Engineering and Sciences
and the Department of Biomedical Engineering,
University of Texas at Austin, Austin, TX, USA

(2) Department of Biomedical Engineering, University of Texas at Austin, Austin, TX USA

INTRODUCTION

Aortic valves (AVs) undergo a unique stretch history which includes high stretch rate and magnitude [1,2]. While major differences in deformation patterns have been observed between normal and congenitally defective bicuspid aortic valves (BAVs) [1-3], the relation to underlying mechanisms of rapid disease onset in BAV patients remains unclear. Such altered deformation patterns in BAVs may be related to early onset of disease. Therefore, hydrogels impregnated with aortic valve interstitial cells (AVICs) were mechanically conditioned to determine how AVIC activation is affected by specific properties of strain waveforms (peak strain, strain rate, and average strain history). Since bicuspid AVICs have higher cytoskeletal polymerization, we hypothesized that altering strain waveforms would alter alpha smooth muscle actin (α SMA) and vimentin (VMN) polymer formation, modify the activity of the transcription factor SMAD 2/3, and affect the nuclear shape.

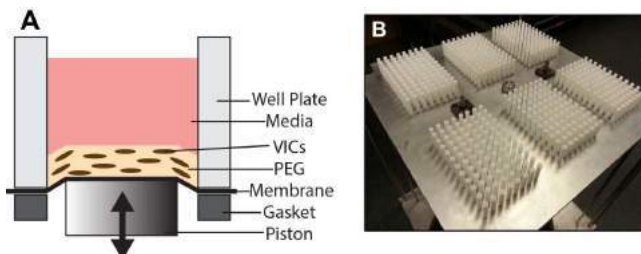


Figure 1: 3D Poly(ethylene) Glycol (PEG)-Imbedded Aortic Valve Interstitial Cell (AVIC) Cultures in the High-Throughput Biaxial Oscillatory Strain System.

METHODS

To evaluate how stretch histories affect AV interstitial cell (AVIC) activation, the high-throughput biaxial oscillatory strain system on which we have previously reported [4] was further developed to impart varied cyclical biaxial stretch histories into 3D poly(ethylene) glycol hydrogels impregnated with AVICs for 48 hours (**Figure 1**). Specifically, a physiologically-mimicking stretch history was compared to two subsequent stretch histories that separately varied peak stretch and stretch rate (**Figure 2**). Post-conditioned AVICs were imaged for nuclear shape, α SMA and VMN polymerization, SMAD 2/3 nuclear activity, and nuclear shape.

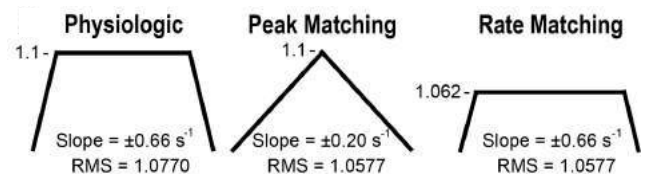


Figure 2: 1-Hz Waveforms Applied to 3D PEG Gel AVIC Cultures for 48 h. The physiologic waveform moved to the peak stretch of 1.1 as quickly as the motor could do so; the peak matching wave moved to 1.1 within 0.5 s; and the rate matching waveform maintained the same slope as the physiologic wave and the same root mean squared (RMS) value of the peak matching wave, making the peak stretch 1.062.

RESULTS

Results indicated that bulk gel deformations were accurately transduced to the embedded AVICs. Lower peak stretches lead to increased α SMA polymerization. In contrast, VMN polymerization was a function of stretch rate, with SMAD 2/3 nuclear localization and nuclear shape also trending towards stretch rate dependency (**Figure 3**).

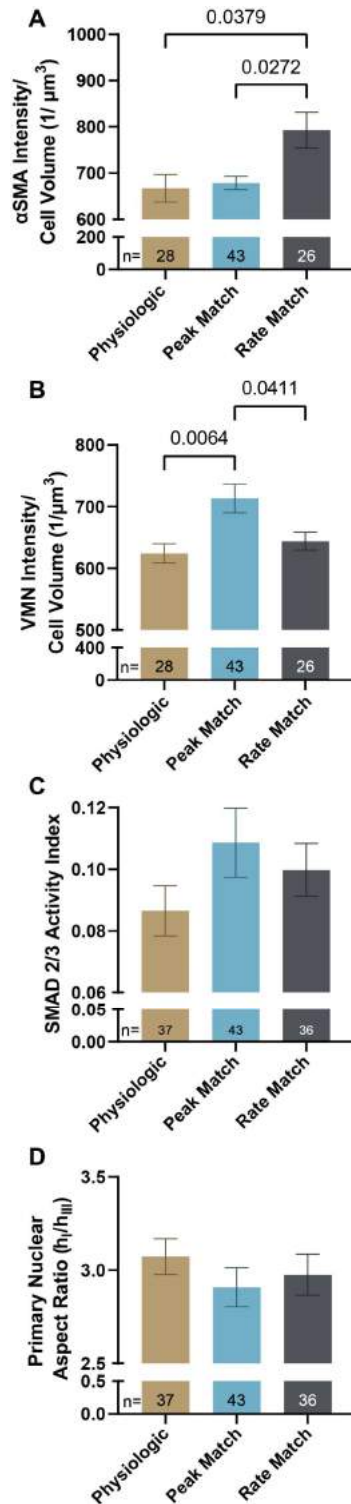


Figure 3: Waveform vs. AVIC Activation. (A) α SMA and (B) VMN intensity per cell volume in gels conditioned for 48 hours with designated waveforms. (C) SMAD 2/3 nuclear intensity divided by cell intensity from cells conditioned with indicated waveforms. (D) Primary nuclear aspect ratio measured as the longest hemi-axis divided by the shortest hemi-axis of the nuclear best fit ellipsoid from cells conditioned with indicated waveforms.

Lower than physiological levels of stretch rate led to higher SMAD 2/3 activity, higher VMN polymerization around the nucleus, and lower nuclear elongation. α SMA polymerization did not correlate with VMN polymerization, SMAD 2/3 activity, nor nuclear shape (Figure 4).

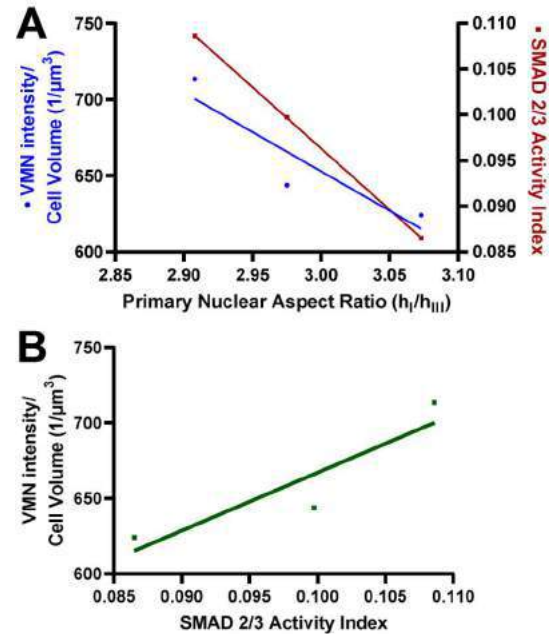


Figure 4: Strong correlations between VMN polymerization, SMAD 2/3 activity, and nuclear shape. (A) Average nuclear eccentricity correlated to average VMN intensity per cell volume ($y = -516.2x + 2201$, $R^2 = 0.8336$) and average SMAD 2/3 activity ($y = -0.1340x + 0.4982$, $R^2 = 1.000$) from AVICs conditioned for 48 hours of stretch waveforms. (B) Average SMAD 2/3 nuclear localization correlated to average VMN intensity per cell volume from AVICs conditioned for 48 hours of stretch waveforms ($y = 3843x + 282.7$, $R^2 = 0.8294$).

DISCUSSION

These results suggest that a negative feedback loop may form between SMAD 2/3, VMN, and nuclear shape to maintain AVIC homeostatic nuclear deformations, which is dependent on cyclic stretch rate. These novel results suggest that AVIC mechanobiological responses are sensitive to stretch history and provide insights into the mechanisms of AV disease.

ACKNOWLEDGEMENTS

MSS (5R01HL129077-03, 1R01HL142504-01, 2R01HL073021-10A1, 1R01HL157829-01A1, R01EB032533) and ABB (1R21EB024147-01A1; 1R01HL141761-01) have funding from NIH that supported this work. TMW is an American Heart Association post-doctoral fellow (826414) and DPH is an F32 NIH post-doctoral fellow (F32HL149210). ABB has US Patent US20200268801A1 for the HT-BOSS system described.

REFERENCES

- [1] Yap, C et al., *Am J Physiol Heart Circ Physiol*, 298:H395-405, 2009.
- [2] Rego, B et al., *Ann Biomed Eng*, 50:1-15, 2022.
- [3] Cao, K & Sucusky, P et al., *Int J Numerical Meth in Biomed Eng*, 2017.
- [4] Lee, J et al., *Nature Biomed Eng*, 5:89-102, 2021.

EFFECT OF MUSCLE ACTIVATION ON HEAD-NECK RESPONSE IN SIMULATED FRONTAL IMPACT COMPARED TO A UNIQUE MILITARY DATA SET

Jesse W. Gerringer (1,2), Karthik Somasundaram (1,2), Frank Pintar (1,2)

(1) Joint Department of Biomedical Engineering, Medical College of Wisconsin and Marquette
University, Milwaukee, WI, USA

(2) Neuroscience Research Facility, VA Medical Center, Milwaukee, WI, USA

INTRODUCTION

While survivable severe cervical spine (c-spine) injuries are rare in vehicle crashes, the rehabilitation is often difficult and long-term consequences debilitating [1]. Despite advances in the biomechanical understanding of c-spine injuries, not much is understood about ligamentous damage in severe injury cases, specifically in frontal impacts. Post-mortem studies on the c-spine ligamentous response to frontal impact have been performed in the past, but without active musculature the measured strains may be artificially high [2]. Human Research Volunteer (HRV) studies have been utilized to create and validate a human head-neck model that has been optimized multiple times for improved efficacy [3,4]. Additional HRV frontal impact studies available from the Air Force were performed at higher accelerations and shorter duration but have yet to be summarized for model development. Therefore, it is crucial to verify the available Head-Neck model to accurately represent this dataset by optimizing model parameters to the specific kinematics of the experiment. Once verified, the ligamentous response to frontal impact can be further studied at higher impacts in live humans.

METHODS

All HRV kinematic data was downloaded from the Collaborative Biomechanics Data Network (CBDN), courtesy of the Wright-Patterson Air Force Base, OH. HRVs were positioned on a seat fixture mounted to a horizontal accelerator sled and restrained with double-shoulder strap harness and lap belt. The peak frontal acceleration pulse ranged from 10 G-30 G in the -X direction. For present analysis, HRV runs with a rise-time of 13-20 ms were selected for consistency. All subjects were within 10% of 50th percentile male stature. A total of n=16 and n=9 subjects were selected from the 10 G and 30 G test series, respectively.

Linear accelerations were measured from accelerometers located on the upper thoracic spine and the subject's mouth (bite-block). An additional rotational accelerometer measured rotational head

acceleration from the subject's mouth as well. The first 0.1 seconds of measured kinematics was used for present study.

To simulate the c-spine response, the Global Human Body Model Consortium (GHBMC M50 v6.0) isolated Head-Neck model [4] was driven at T1 with the experiment measured upper thoracic X acceleration. According to frontal impact literature, the extensor and flexor muscles activate in response to impact approximately 74 ms after the start of acceleration [4]. Given the rise-times are no more than 20 ms for sled accelerations from the selected corridors, the impact event is already close to complete by 74 ms. Therefore, the first simulated condition studied was a passive muscle condition, meaning no muscle activity implemented. Given the subjects of this study underwent multiple sled tests, it is assumed that they would likely brace for the impact event. Under this assumption, the second condition had a muscle activation curve [4,5] started at 0 ms, the start of the sled acceleration. The activation curve starts at a magnitude of 0 and increases in activation peaking at 0.87 over 100 ms, progressively contracting the 1D muscle elements. Additionally, using GHBMC documentation and literature suggestions [5], flexors muscles were activated to 100% and extensors to 70% of maximum activation. All simulations were performed using LS-DYNA MPP version R8.0.0 and 64 cores on a high performance cluster..

A CORrelation and Analysis (CORA) method was used to score the biofidelity of the head-neck model. CORA was performed for two of the kinematic outputs measured from the simulation: Head X acceleration and Head Rotational Y acceleration, collected from the same area of the bite-block in the experiment. Biofidelity was deemed fair if CORA rating was between 0.440 and 0.650, and good if between 0.650 and 0.860 [6].

RESULTS

Figure 1 presents the output kinematics of the GHBMC Head-Neck model for both passive and active muscle conditions. Experiment kinematics include one standard deviation. The passive muscle

condition for both Head X acceleration and Head Rotational Y acceleration in 10 G and 30 G fall outside the standard deviation of the experiment, resulting in worse biofidelity. Table 1 describes the biofidelity of each metric using the CORA rating, color coded to indicate quality. In both 10 G and 30 G, Head X acceleration improves from fair to good when muscles are activated beginning at 0 ms under the proposed assumptions. Additionally, Head Rotational Y acceleration biofidelity increases by 0.09 or more in both 10 G and 30 G, to at least fair.

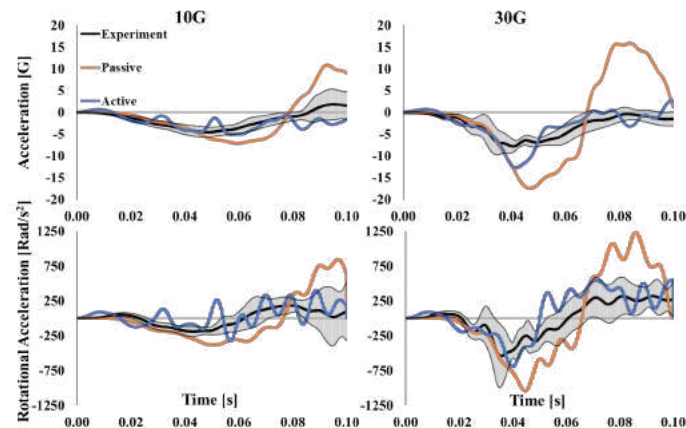


Figure 1: Head X-acceleration (top) and Rotational Y Acceleration (bottom) for 10G (left) and 30G (right) sled corridors.

Table 1: CORA rating for 10G and 30G, passive and active conditions. Orange is marginal, yellow fair, and green good.

Condition	Head X Accel	Rot. Y Accel
10G Passive	0.532	0.365
10G Active	0.758	0.640
30G Passive	0.503	0.545
30G Active	0.738	0.631

DISCUSSION

When comparing the passive simulations to the active simulations, it is clear that the muscle activation scheme implemented improved the model response outcomes compared to the human response corridor. The biofidelity increased significantly, with both Head X acceleration and Rotational Y acceleration being at least fair, and the Head X specifically being considered good. This would indicate the GHBM Head-Neck model is capable of validating multiple HRV datasets, with varying experimental characteristics. Further investigation is needed to improve oscillations in the 10 G corridor, as well as the peak response in the 30 G corridor. It is possible the muscle activation differs between the two, but as the muscle responses were not measured in the experiment, iterative optimization may be necessary.

The main difference in the methodology of the present study is the timing of the muscle activation in response to acceleration. As the literature suggests, the typical timing of the muscle response is 74ms after the start of acceleration [4]. However, 74 ms into acceleration for this dataset would be well past the peak response of the head, therefore

it was assumed this condition would be an overall passive response. As the experimental kinematics would suggest, however, there is a clear dampening effect on the linear and rotational accelerations of the head. This would indicate muscle activity starting much earlier. Many of the subjects in this study were well aware of the experimental set-up and had undergone multiple sled tests prior to the data shown. Qualitative analysis of video recordings of each subject presumably showed tension in the neck, further supported by the modeling outcome. Thus, adjusting the muscle activation to start at 0 ms is one assumption to account for muscle response in lieu of measured muscle activity from these experiments.

With this current set of data validated against the GHBM Head-Neck model, further analysis can determine the response of the ligaments in the c-spine during frontal impact at non-injurious Gs. Preliminary analysis suggests the passive simulation ligament strains were only moderately lower than isolated post-mortem studies [2], meaning the ligaments were on the borderline of failure. With the active muscle simulation, ligament strain was decreased by as much as 50% from passive muscle. The ligament strains in the active muscle simulations seems more reasonable than those recorded in post-mortem studies, or passive simulations due to the nature of using HRVs and having no reported injuries post-experiment. Further optimization of the active muscle simulations for this unique dataset will produce more accurate ligament strains along the c-spine and help to identify areas of injury in the c-spine during higher g-loading in real world frontal impacts.

ACKNOWLEDGEMENTS

The authors would like to acknowledge the Collaborative Biomechanics Data Network (CBDN), Wright-Patterson AFB OH for use of their kinematic datasets (<https://biodyn.istdayton.com/CBDN>). The simulation was completed in part with computational resources and technical support provided by the Research Computing Center at the Medical College of Wisconsin.

REFERENCES

- [1] Freeman, MD et al., *Accid. Anal. Prev.*, 142:105571, 2020.
- [2] Panjabi MM et al., *SPINE*, 29:2395-2403, 2004.
- [3] Gayzik, FS et al., *Ann. of Biomed. Eng.*, 39:2568-2583, 2011.
- [4] Panzer, MB et al., *MedEngPhys*, 37:1147-1159, 2011.
- [5] Correia, MA et al., *J Biomech*, 104:109754, 2020.
- [6] Somasundaram, K et al., *Mech.Behav.Bio.Mat.*, 100:103398, 2019.

Quantifying Lower Birth Canal Viscoelastic Properties During The First Stage Of Labor

Mariana Masteling (1), John O. DeLancey (2), James A. Ashton-Miller (1)

(1) Department of Biomedical Engineering, University of Michigan, Ann Arbor, MI, USA
(2) Department of Obstetrics and Gynecology, University of Michigan, Ann Arbor, MI, USA

INTRODUCTION

Up to 19% of nulliparous women sustain pelvic muscle injuries while giving vaginal birth. Since these injuries, which are not repairable, can have life-long sequelae, including pelvic organ prolapse and incontinence, we need better ways of preventing them. From a biomechanical perspective, it seems reasonable that if women have unusually stretch-resistant lower birth canals they should expect longer labors and perhaps a higher risk for muscle and tissue injury, a hypothesis yet untested.

In the present work, a novel vaginal dilator, (PREP, Maternal Medical, LLC, Mountain View, CA) used during the first stage of labor to ease the birth of the baby during the second stage of labor has allowed us to quantify inter-individual differences in lower birth canal hoop tension during dilation, as well as lower birth canal viscoelastic properties using a Fractional viscoelastic Zener Model.

METHODS

The PREP dilator was introduced into the first 4 cm of the vaginal canal in nulliparous women in their first stage of labor during the ongoing EASE clinical trial (NCT 03973281). A semi-automatic, dilation-controlled actuation system was programmed to mechanically expanded the device to ~80 mm diameter in a step-wise manner over ~60 minutes (Figure 1). The dilation force, time and diameter were recorded. The measured dilation force was then used to calculate the hoop tension, T , in the lower birth canal tissues.

We quantified the variation in T across 56 subjects at three points during PREP insertion: 1) at initial 20 s expansion to 55 mm of diameter (T_e); 2) after a 5 min “hold” at 55 mm of diameter (T_r); 3) at maximum diameter (T_m). Canal hoop stiffness during the 20s ramp (S_i) was calculated as the difference in hoop tension divided by the increase in dilation diameter (Figure 1).

The canal tissue 20 s ramp-and-5-minute-hold response was initially characterized using a Fung quasilinear viscoelastic model,

similar to that using a constant-force vaginal dilator during the first stage of labor [1] but we found it had no predictive power outside the fitting interval. Considering the strong linear relationship after the 5-minute hold (Figure 1), we also tried classical viscoelastic models but they also had poor predictive power. However, when using a fractional approach, the simplest model with predictive power was found to be the fractional viscoelastic Zener Model (FZM) (a SpringPot (constants C_α and α) in series with a spring in one arm (k_β), lying in parallel with a spring (k_γ) in the other arm). For each subject, RHEOS.jl – an open-source Julia-based rheology package [2]- was used to obtain the four FZM constants. First, dilation diameter and lower birth canal hoop tension data from the ‘hold’ relaxation were used to obtain the constants. Then using the four constants, the equivalent lower birth canal hoop tension, T , was predicted using the experimentally recorded dilation diameter and temporal data for the remainder of the insertion (Figure 1, peach colored background). Relative error of the prediction was calculated as the squared error relative to the maximum hoop tension, T , for each subject.

Data management and statistical analyses were performed using Julia and Python.

RESULTS

We found a remarkable variation (Figure 2) in the measured T across all subjects. Specifically, when reaching 55 mm dilation T varied 5.5-fold and was 22% greater in older women (age ≥ 30 years) ($p = 0.05$) and correlated strongly with both relaxation (T_r) during the 5-minute hold and with the maximum tension (T_m) ($r = 0.80$, $r = 0.59$ with $p < 0.001$). Hence the 20 s-ramp-and 5-minute-hold behavior of T was therefore a reasonable predictor of the resistance the lower canal would later develop during the full 60 minutes of dilation. The stiffness of the initial 20 s ramp (S_i) varied 6.8-fold and was 31% higher in older women.

When the four FZM constants were calculated from the 20 s ramp-and-5-minute-hold data the relative fit error was $8.1 \pm 3.6\%$. The relative prediction error of T after 60 minutes of dilation of $10.0 \pm 5.4\%$. FZM constants varied 742, 64 and 23-fold for C_α , k_β and k_γ ; α varied between its acceptable range of 0 and 1. k_β was 33% higher in the older versus the younger group ($p = 0.03$).

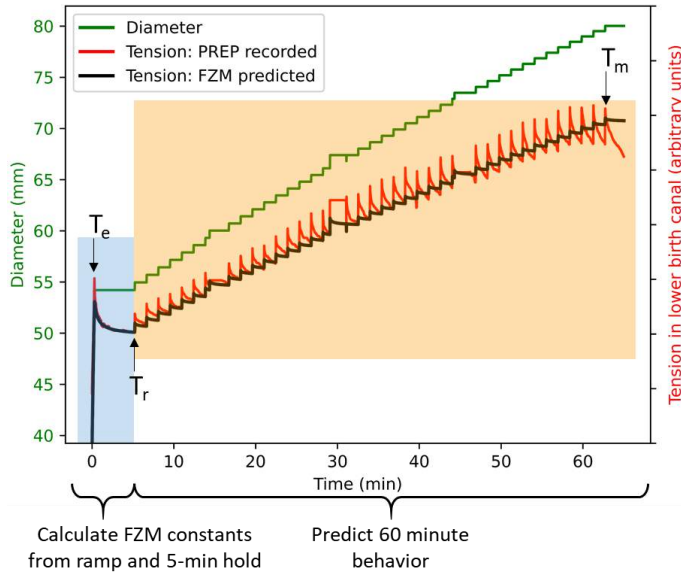


Figure 1: An example of *in vivo* PREP data from a single participant. Lower birth canal dilation is shown (in mm) on the left ordinate axis with the 20 s ramp-and-5 minute-hold dilation and subsequent cyclic 1 mm step dilation-and-hold cycles up to 80 mm dilation plotted in green, at top). The measured lower birth canal hoop tension, T , is shown on the right ordinate axis (arbitrary units and plotted in red) shows the effect of the initial ramp in tension (T_e) followed by tissue relaxation over the first 5 minutes (T_r) followed by the increases to T_m , the maximum. The predicted FZM tension in the lower birth canal over the 60-minute dilation protocol, based only on the initial 20 s ramp-and-5-minute-hold data, is plotted in black with a reasonable fit between the measured (red) and FZM predicted (black) curves.

DISCUSSION

This is the first quantification of normal human lower birth canal viscoelastic properties during the first stage of labor using a constant displacement dilator. These results reflect the response of the term-pregnant, nulliparous, lower birth canal to its first-ever dilation to 80 mm diameter in preparation for the second stage of labor when the fetus is pushed through the birth canal. T is a measure of the resistance of the canal to dilation: the stiffer and more viscous the canal wall is, the greater the tensional resistance to the passage of the fetal head during the second stage of labor. T was governed principally by the elastic nature of the lower birth canal, as seen from the linear course of the force-dilation curve (Figure 1) during a slow dilation regime. But clearly, the viscous behavior of the lower birth canal also played an important role in its response to step increases in canal dilation, as can be seen by its relaxation following the initial 20 s ramp-and-5-minute-hold dilation, as well as its relaxation following each 0.9 mm step every ~90 s (Figure 1).

[4]

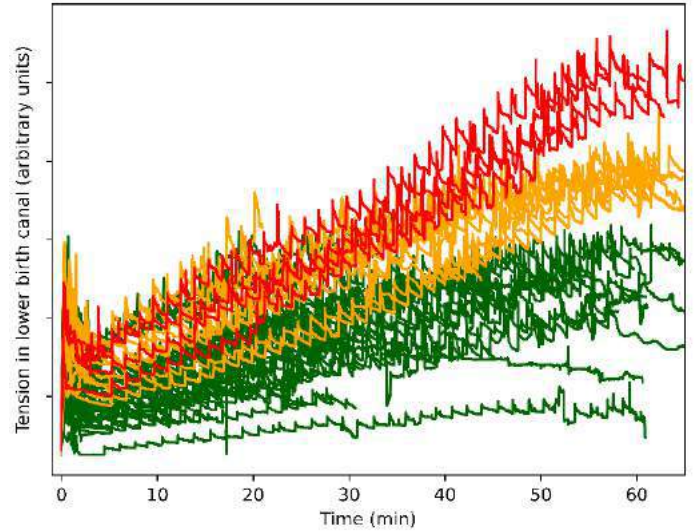


Figure 2: Range of measured PREP lower birth canal hoop tensions over time across all 56 subjects in their first stage of labor. Red curves are $>99.7^{\text{th}}$ centile ($n = 4$) in maximum tension, orange between the 95^{th} and 99.7^{th} centiles ($n = 13$) and green those $<95^{\text{th}}$ centile ($n = 39$). Those $>99.7^{\text{th}}$ centile might be expected to endure longer second stages, and have elevated risk for injury, clinical outcomes will be available for analysis once the EASE trial ends in Fall 2023.

The large range in T_e , T_r , T_m and the FZM constants quantifies clinical experience that a large range of viscoelastic properties can lead to successful vaginal delivery (Figure 2). Those above the 95^{th} in T_m , however might logically be expected to have difficult vaginal deliveries. The insight that T_e and S_i , as well as, k_β , are higher in older women has direct bearing on the known risk of levator ani injury and longer second stage of labor in older women [3], [4].

A strength is that all the participants were nullipara, because they are the highest higher risk for long second stages and levator avulsions (compared with multiparous women). A caveat is that each PREP insertion time-displacement-tension dataset is unique for that subject at the specific time of insertion, somewhat limiting generalizability.

When the labor outcomes become available upon completion of the EASE trial in late 2023, we will be able to test the hypothesis that the PREP can be used to identify women abnormally stiff birth canals with a brief ramp dilation during the first stage of labor, so preparations can be made to ease her second stage delivery. When combined with existing obstetric variables, the PREP dilator could prove helpful in mitigating the risks of difficult vaginal deliveries.

ACKNOWLEDGEMENTS

MM, JAAM and JOLD received salary support via a subcontract to the University of Michigan from the National Institute of Child Health and Disease grant R44 HD 096987 awarded to Materna Medical, LLC and separately from NIDDK 1 RC2 DK122379. MM received funding from the Portuguese Foundation of Science and Technology under grant number SFRH/BD/138822/2018.

REFERENCES

- [1] Tracy, P et al., *J Mech Behav Biomed Mater*, 79:213-218, 2018
- [2] Kaplan, J et al., *J Open Source Softw*, 4:1700, 2019
- [3] Doxford-Hook, E et al., *Midwifery*, 115:103494, 2022
- [4] Papadiaz, K et al., *Ann N Y Acad Sci*, 1092:414-417, 2006

EFFECTS OF EXTERNAL BATHING SOLUTION OSMOLARITY ON TRIBOLOGICAL REHYDRATION AND CARTILAGE LUBRICATION

Shamimur R. Akanda (1), David L. Burris (1), Chris Price (2)

(1) Mechanical Engineering, University of Delaware, Newark, DE, USA
(2) Biomedical Engineering, University of Delaware, Newark, DE, USA

INTRODUCTION

Articular cartilage, the unique biological bearing material of our diarthrodial joints sustains millions of articulation cycles while maintaining vanishingly low friction coefficients.^[1] This phenomenal lubricity has been ascribed to interstitial lubrication,^[1] a mechanism dependent on cartilage's triphasic nature. Triphasic tissue theory, developed by Mow et al., describes cartilage as a mixture of a solid phase (i) and a fluid phase containing water (ii) and monovalent ions (iii; *e.g.*, Na⁺ and Cl⁻)^[2] in which an ionic imbalance between cartilage's interstitial fluid and bathing solution generates a Donnan osmotic swelling pressure. Subsequently, tissue swelling is dictated by bath osmolality;^[2-5] hypotonic solutions result in stiffer cartilage.^[6-8]

While cartilage swelling supports interstitial lubrication and the maintenance of high fluid load support (FLS) levels and low tissue strains and frictions,^[1] habitual quasi-static loading drives fluid out of cartilage leading to high tissue strains and frictions. Such changes are detrimental to joint function unless they can be reversed/recovered (which was only thought to occur because of free swelling during cartilage unloading). However, using our convergent stationary contact area (cSCA) testing configuration, we recently discovered a sliding dependent fluid recovery mechanism that can combat fluid exudation absent unloading, via 'tribological rehydration'.^[9-10]

Tribological rehydration fosters active fluid recovery and the long-term maintenance of biofidelic strains, frictions, and fluid load support in a sliding speed dependent manner. However, whether bathing solution osmolality (and physiochemistry) influences tribological rehydration and lubrication remains unknown. Such a question has both basic science and clinical significance. Understanding the effects of osmolality on tribological rehydration may elucidate the underlying mechanisms by which cartilage fluid recovery during articulation sustains the tissues remarkable tribomechanical function and longevity. Furthermore, the synovial fluid of osteoarthritic joints exhibits altered osmolality (as well as composition),^[11] yet knowledge of the impacts of

such changes on cartilage tribomechanics is incomplete. Thus, the objective of this study was to investigate the influence of bathing solution osmolality on tribological rehydration and cartilage lubrication under the biofidelic sliding conditions of the cSCA configuration.

METHODS

First (study 1), the effect of bath osmolality on tribological rehydration and friction was examined when high-speed sliding was initiated from a condition of low FLS (*i.e.*, quasi-equilibrium compression). Φ 19mm osteochondral cSCA explants (N = 8) were removed from the femoral condyles of mature bovine stifles, then stored in 280mOsm PBS with protease inhibitors (1X PBS) for no more than 24 hours.¹² Explants were then compressed (in 1X PBS) against the glass counterface of a linear reciprocating tribometer^[12] to a specified compression value, the PBS was removed, and bathing solutions of various osmolality/composition were added. Explants were then slid for 8 min at 80mm/s while compression, normal and friction forces, and friction coefficients (μ) were recorded. Six bathing solutions were utilized: 1) 1X PBS (280mOsm), 2) sucrose in DI water (280mOsm), 3) sucrose in 0.5X PBS (280mOsm), 4) DI water (0mOsm) 5) 1X PBS plus sucrose (1350mOsm) and 6) 5X PBS (1350mOsm). Between testing conditions explants were allowed to free-swelling in 1X PBS (2-hours) before tribological characterization was repeated.

In study 2, the influence of bath osmolality on explant tribomechanics when slid from high FLS (*i.e.*, compression and sliding initiated simultaneously) was investigated. Explants (N = 10) bathed in either 1) 1X PBS (280mOsm), 2) 5X PBS (1350mOsm), or 3) DI water (0mOsm) were compressed to 7N (over ~2-seconds) while reciprocal sliding, at 80mm/s, was initiated simultaneously and maintained for 10-minutes. As in study 1, explants were allowed to free-swelling in 1X PBS (for 2-hours) before their characterization was repeated in subsequent bathing solutions.

RESULTS

Despite bathing solution osmolarity having a significant influence on the equilibrium compression behaviors of cartilage explants, which is explained by triphasic tissue theory, osmolarity had no meaningful effect on cSCA cartilage lubricity, regardless of the level of fluid load support at the start-of-sliding.

In study 1, when high-speed sliding was initiated from near-zero FLS (**Fig 1A**), explants exhibited robust tribological rehydration in all but the 1X PBS + sucrose (1350mOsm) bath. However, the degree of compression recovery observed during sliding varied with bath osmolarity (**Fig 1B**). Low osmolarity baths exhibited the largest recoveries and high osmolarity baths the smallest, a response aligned perfectly with cartilage's triphasic nature ($p < 0.05$ for all pairs). However, rates of compression recovery initiated by sliding (i.e., tribological rehydration rates) were indistinguishable across bathing solutions (**Fig 1C**) ($p > 0.05$ all pairs). Lastly, frictions at both start- and end-of-sliding appeared insensitive to bath osmolarity ($p > 0.05$).

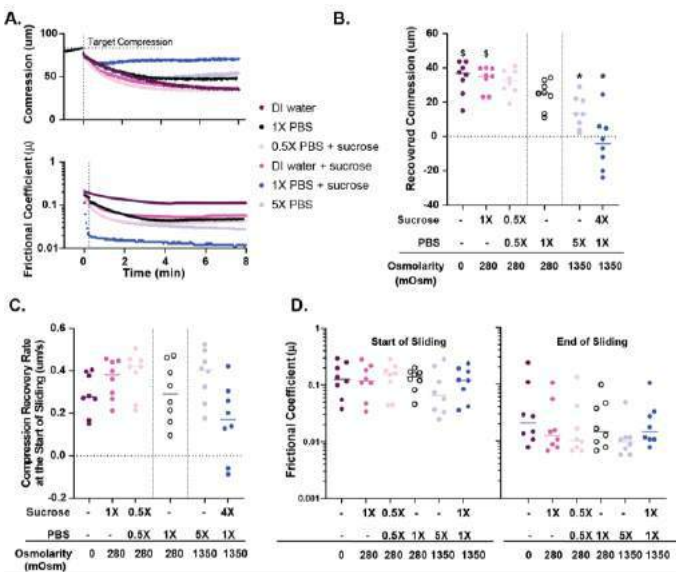


Figure 1: A) Representative compression and frictional behaviors of a cSCA bovine explant - study 1 (low FLS). B) Recovered compression, C) initial compression recovery rates and D) start- and end-of-sliding friction outcomes under different bathing solutions. Data analyzed via repeated measures one-way ANOVA; * and \$ denote significant differences from 1X PBS for hypertonic and hypotonic solutions respectively ($p < 0.05$).

Tribological outcomes in study 2, where sliding was initiated from near maximal FLS (**Fig 2A**) qualitatively reflected those of study 1. Again, equilibrium compression magnitudes varied with bathing solution (**Fig 2B**)—as predicted by triphasic theory; end-of-sliding compressions were less for DI water and greater for 5X PBS than for a given load and testing time (7N & 10 min) in 1X PBS ($p < 0.01$ for all pairs). Again, initial compression rates, which are dictated by the competition between rehydration and exudation rates during sliding did not differ among baths (**Fig 2C**) ($p > 0.05$). Frictional behaviors were again insensitive to bath osmolarity in the cSCA (**Fig 2D**) ($p > 0.05$).

These findings revealed a generalized lack of influence of bathing solution osmolarity on tribological rehydration and lubricity in the cSCA regardless of FLS levels.

DISCUSSION

The present study demonstrated the robustness of tribological rehydration in rescuing compression and lubricity under all bathing

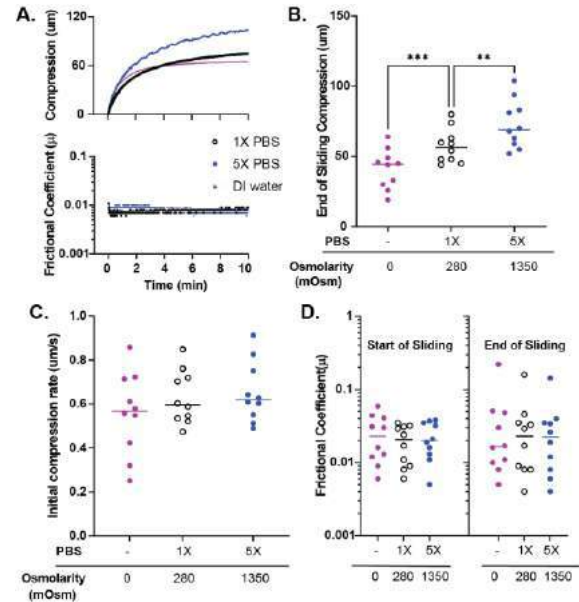


Figure 2: A) Representative cSCA explant compression and frictional behaviors - study 2 (high FLS). B) End-of-sliding compression, C) initial compression rates, and D) start- and end-of-sliding outcomes for different bathing solutions. Data analyzed via repeated measures one-way ANOVA ($p < 0.01$, *** $p < 0.001$).**

solutions except 1X PBS + sucrose (1350 mOsm). The defeat of tribological rehydration in the 1350 mOsm PBS + sucrose solution appears likely mediated by both the increased osmolarity and hygroscopic nature of the solution, which acted to “pull” water out of the tissue at a rate greater than sliding could replenish it, resulting in significantly increased equilibrium compressions. Nevertheless, both studies validated the triphasic-driven equilibrium swelling behavior of cartilage even in the face of tribological rehydration—hypotonic solutions “stiffened” explants and limited load-induced compression while hypertonic solutions resulted in tissue “softening” and greater overall compression.

Of more interest was the observation that both initial recovery (study 1) and compression rates (study 2) upon sliding were unaffected by bath solution osmolarity. Findings that support our postulate of tribological rehydration being dictated by sliding speed driven hydrodynamics, as opposed to Donnan swelling behaviors. The fact that high-speed cartilage lubrication in the cSCA was not meaningfully altered by extremes in bath osmolarity suggests that the hydrodynamic pressures generated by rapid sliding can be quite large. In fact, these rates appear large enough to “pump up” the interfacial surface fast enough to both compete against load-induced fluid exudation and mask the influence of large changes in bath osmolarity. Besides contributing to a better understanding of cartilage lubrication mechanisms, these results hold immense clinical significance for the cartilage lubrication field as they support a paradigm shift discounting the common wisdom that compromised osteoarthritic synovial fluid, with altered osmolarity, is an inherently inferior lubricant; it instead might be fully capable of supporting vanishingly low frictions in the cSCA.

REFERENCES [1] Ateshian, *J Biomech*, 2009 [2] Lai, *J Biomech*, 1991 [3] Maroudas, *Adult Articular Cartilage*, 1979 [4] Donnan, *Chem Rev*, 1924. [5] Gu, *J Biomech*, 1998. [6] Eisenberg, *J Orthop Res*, 1985 [7] Lu, *Ann Biomed Eng*, 2004 [8] Zimmerman, *J Biomech* 2021 [9] Burris, *OA&C*, 2017 [10] Burris, *Tribol Let*, 2019 [11] Shanfield, *Clin Orthop Relat Res*, 1988 [12] Farnham, *JMBB*, 2020.

FIXATION ANALYSIS OF BONE-PROSTHESIS INTERFACE MICROMOTION OF A CEMENTLESS TALAR COMPONENT

Irwan S.M. Moideen (1), Jun Wei Lee (1), Yu Shen Ong (1), Chin Tat Lim (2), Desmond Y.R. Chong (1)

(1) Engineering Cluster, Singapore Institute of Technology, Singapore
(2) Department of Orthopedic Surgery, National University Hospital, Singapore

INTRODUCTION

The golden standard treatment for an ankle arthritis is arthrodesis especially for the end-stage ankle arthritis [1]. Ankle arthrodesis is a salvage procedure that involves direct fusion of vital bones such as tibia, fibula and talus using standard orthopedic screws such as Herbert and cortical bone screws that can be made of stainless steel, cobalt chrome or titanium [2]. Baumhauer et al. reported that ankle arthrodesis was effective in pain alleviation, possibility of normal increased activities and lower infection rate postoperatively with minimal procedural cost [3].

Nevertheless, arthrodesis procedure is still far from an ideal treatment for the ankle arthritis patients. Short term complications upon post-arthrodesis procedure were bone non-union, malunion and contralateral joint arthritis as noted in previous studies [4]. Clinically reported non-union rates could be as high as 41% of the total patients whom undergo the arthrodesis procedure [4]. Patients were also subjected to difficulties relating to walking on an uneven surface, staircase ascent and descent, picking up objects on the floor and wearing shoes or boots. Long term follow up studies indicated that post-arthrodesis patients may be at risk of joint deterioration on the ipsilateral hind and midfoot [4] in which could cause severe handicap to the gait cycle leading to ambulation [5].

Alternative treatment to ankle arthrodesis would be the total ankle replacement (TAR). The main advantage of the TAR is the ability to preserve the joint motion and function of the ankle in comparison to the ankle arthrodesis procedure [6]. The resulted loading conditions of the patient on the ankle joint will be similar to the physiological walking gait cycle postoperatively thus lowering the risk of a long-term adjacent ankle arthritis [6]. Therefore, it is of interest of this study to understand further on the total ankle replacement in attempting to replace the arthrodesis as the golden standard.

METHODS

One of the commercial talar components of the cementless STAR Ankle (Stryker Corporation, Kalamazoo, Michigan) was used for this study. The STAR Ankle was selected as it has been the most widely used total ankle prosthesis in the market [7] and was generally having good short to intermediate term clinical outcomes [8]. This study employed both the simulation and experimental approaches. The three-dimensional model of the talar prosthesis was obtained through the scanning technique using Artec Spider (Artec 3D, Luxembourg). The polka dot design features were then modified from the scanned model through SolidWorks (Dassault Systemes, France) software. Material properties were assigned to the model using Abaqus CAE-SIMULA (Dassault Systemes, France) software for finite element analysis (FEA).

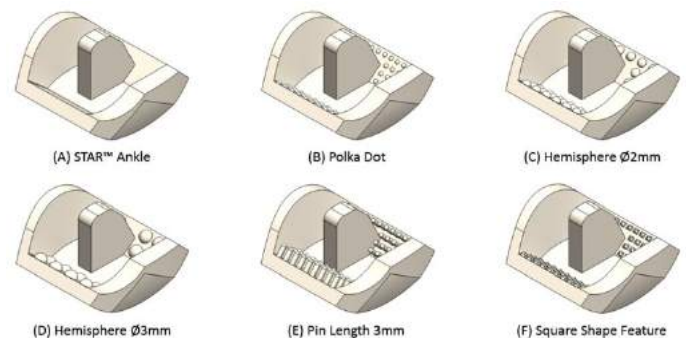


Figure 1: The STAR Ankle (A) and the polka-dot designs (B to F).

The three-dimensional model of the talus bone was obtained through computed tomography (CT) scanning of a right cadaveric foot and ankle joint of a female donor (48 years old, 182 cm tall, and weighed

60 kg with no osteoporosis complications). The CT radiographic images were then constructed into three-dimensional model using the software Materialise Mimics (Materialise, Leuven, Belgium). The heterogeneous material properties of the talus bone were assigned using the element-by-element method, with properties of each element mapped through linear relationship between the CT Hounsfield and apparent density [9].

The experimental study was conducted to validate the finite element analysis results, and mechanical responses of bone strain and bone-prosthesis interface relative micromotion (BPIRM) were measured. The simulation and experimental results were compared and correlated to validate the FE model that has been created.

RESULTS

The contour plots of the BPIRM for the STAR Ankle talar component and other polka-dot design features were obtained. The predicted results included three specified critical loading conditions of heel strike, midstance and toe-off of a gait cycle. The interface micromotion values extracted and mapped from Abaqus corresponded to three different contact output variables of COPEN, CSLIP1 and CSLIP2. In addition, the predicted minimum principal bone stresses (MPBS) extracted from FE analysis were compared as well.

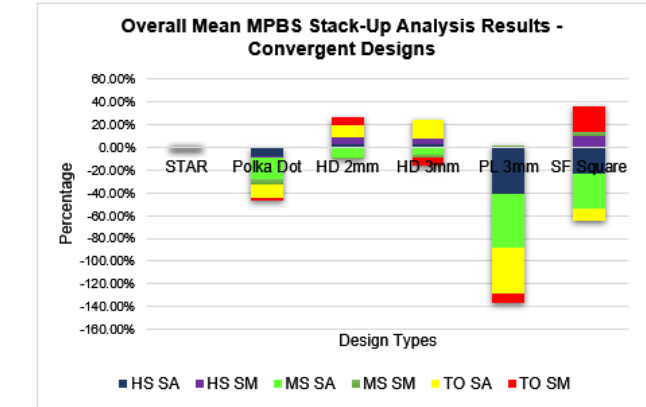


Figure 2: The mean MPBS stack-up predicted results in comparison to the STAR Ankle.

The experimental validation study results were obtained through the STAR Ankle and the polka-dot designs. Results were compared through two different parameters of bone strain and BPIRM.

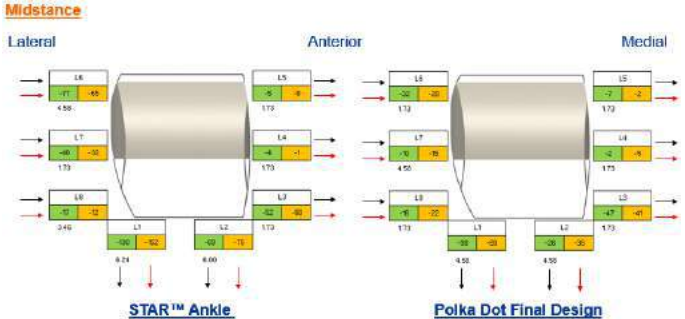


Figure 3: BPIRM measurement results.

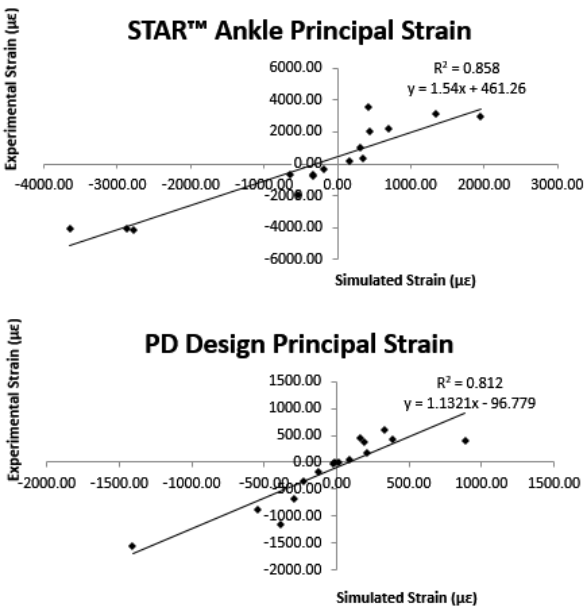


Figure 4: Linear regression between experimental and finite element analysis bone strain values.

DISCUSSION

The FE predicted bone strain and BPIRM results have shown a good correlation with the strain and interface micromotion values measured, indicating the validity of the FE models generated and can be used for reliable future studies. Another prevalent finding of the study was to understand the specific primary stability issues of the TAR leading towards aseptic loosening. The clinical outcome studies [10] and FE results from this study also assimilated well with the predicted BPIRM and MPBS, showing the accuracy of the predicted simulation and experimental validation results from this study. In conclusion, this study has shown that the proposed new polka dot design is potentially able to mitigate aseptic loosening issue of TAR.

ACKNOWLEDGEMENTS

Not applicable.

REFERENCES

1. Van, A., S.V. Heuvel, and G. Dereymaeker, *Acta Orthopaedica Belgica*, 2010. **76**: p. 150-161.
2. Pellegrini, M.J., et al., *JBJS*, 2015. **97**(24): p. 2004-2013.
3. Baumhauer, J.F., *Clinical Orthopaedics and Related Research*, 2013. **471**(8): p. 2439-2442.
4. Doets, H.C., R. Brand, and R.G. Nelissen, *JBJS*, 2006. **88**(6): p. 1272-1284.
5. Giannini, S., A. Leardini, and J. O'Connor, *Foot and ankle surgery*, 2000. **6**(2): p. 77-88.
6. Hong, C.C. and K.J. Tan, *Clinical Research on Foot & Ankle*, 2014. **2014**.
7. Zhao, H., et al., *International orthopaedics*, 2011. **35**(12): p. 1751-1758.
8. Brunner, S., et al., *The Journal of bone and joint surgery. American volume*, 2013. **95**(8): p. 711.
9. Rho, J.Y., M.C. Hobatho, and R.B. Ashman, *Medical Engineering and Physics*, 1995. **17**(5): p. 347-355.
10. DeOrto, J.K. and S.G. Parekh, 2014: Lippincott Williams & Wilkins.

ANALYZING THE IMPACT OF TAVR DEVICE ORIENTATION ON POST-TAVR PARAVALVULAR LEAKAGE SEVERITY AND THROMBOGENICITY IN BICUSPID AORTIC VALVE PATIENTS

S. Anam (1), B. Kovarovic (1), A. Hamdan (2), R. Haj-Ali (3), D. Bluestein (1)

- (1) Department of Biomedical Engineering Stony Brook University, Stony Brook, New York, U.S.A
(2) Department of Cardiology, Rabin Medical Center, Petah Tikva, Israel
(3) School of Mechanical Engineering, Tel-Aviv University, Tel-Aviv, Israel

INTRODUCTION

Bicuspid aortic valve (BAV) is the most common congenital heart defect with an incidence of 0.4 – 2.25% in general population [1]. Unlike normal tri-leaflet aortic valves, BAV is marked by the fusion of two aortic leaflets with a thick, fibrous raphe present at the location of fusion in most cases. In addition to the abnormal valve fusion, BAV is also associated with other structural anomalies including aortic root dilatation and severe cusp asymmetry [2]. The structural malformation and altered hemodynamics result in an early onset of calcific aortic valve disease in most BAV patients, eventually leading to aortic stenosis (AS) and regurgitation, which often require these patients to undergo aortic valve replacement procedure. A minimally invasive and alternative to surgical aortic valve replacement, transcatheter aortic valve replacement (TAVR) has emerged as a lifesaving treatment option for severe AS. As current TAVR devices are intended to treat trileaflet aortic valves in AS patients, its initial use to treat BAV patients with AS was marked as an “off-label” use. Recently the FDA officially approved their use for treating BAV patients. Despite showing promising performances, TAVR is reported to be associated with various clinical complications including paravalvular leakage (PVL) and thrombogenicity. Currently, PVL remains one of the most persistent and significant post-TAVR clinical complications. PVL severity depends on the positioning and orientation of the device and device-tissue interaction, which are often hampered in BAV patients due to their morphological heterogeneity and severe leaflet calcification, exacerbating PVL complications in them. Post-TAVR PVL may eventually lead to life threatening complications including heart failure, hemolytic anemia and increased left ventricular load. In patients with PVL, high pressure gradient across narrow leaks during diastole creates a prothrombotic environment by increasing the shear stress on the platelets, which increases the risk of flow induced-thrombogenicity and may eventually lead to stroke in TAVR patients. Recently, few clinical studies focused on analyzing the impact of device orientation on post-

TAVR coronary occlusion [3]. However, none of these studies address its impact on PVL, which we hypothesize to be associated with the device orientation. Moreover, these studies excluded BAV patients due to their morphological variations and anatomical complexities. In order to maximize the benefit of TAVR in each patient, it is important to understand the complex device-tissue interaction, the risk of post-TAVR PVL and thrombogenicity, and how this risk varies with different devices and their orientation- in a patient-specific manner, which is challenging to do in clinical settings. Our goal is to address these concerns and optimize the post-TAVR outcomes using predictive computational modeling. In our current study, we analyzed the impact the TAVR device orientation on the post-TAVR PVL and associated flow-induced thrombogenicity using patient-specific BAV models. We also quantified the differences in severity and compared the outcomes between different devices, which has a tremendous clinical significance.

METHODS

Anonymized Pre-TAVR Cardiac CT scans of 3 type 1 BAV patients who had different degrees of post-TAVR PVL, were obtained from Rabin Medical Center (Israel) with the approval of the Stony Brook University IRB protocol. All of them received older generation 29 mm self-expandable (SE) TAVR devices (Medtronic plc, Minneapolis, MN, USA) (Patient 1 and 2 – CoreValve and patient 3 Evolut R). Patient-specific surface meshes were reconstructed and optimized for finite element (FE) analysis using ANSYS SpaceClaim and Fluent (Ansys, Inc. Canonsburg, PA). A 4-step FE simulation (crimping, insertion, deployment, and relaxation) was performed in order to deploy the original devices in virtual patient model, using Abaqus Explicit 2019 (Dassault Systèmes Simulia Corp., Johnston, RI). Computational fluid dynamics (CFD) analysis was then performed to assess PVL degree, location, and quantify stress accumulation (SA) on platelets, using a method that depicts the device “thrombogenic footprint” based on the accumulated shear stresses on the platelets [4]. In order to analyze the impact of device orientation, the skirt and leaflets were rotated by 24 ° increments

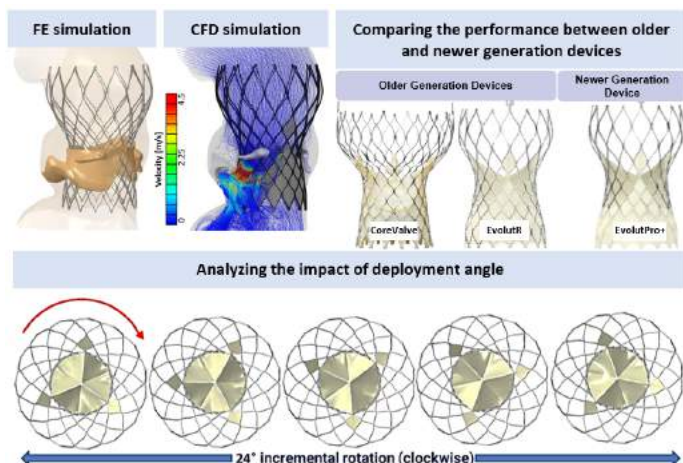


Figure 1: (Top row) – FE simulation of TAVR procedure, CFD simulation of PVL analysis in BAV patients and, comparing the performance between older and newer generation devices (Bottom row) –as a function of the device radial orientation

from the initial configuration (R0), resulting in four additional configurations (R1, R2, R3 and R4). R0 marks the initial orientation with which clinical validations were performed in our previous study [5]. PVL and thrombogenicity analysis were performed for each orientation case. All the in-silico steps were repeated in each patient model using newer generation device (Evolut Pro+).

RESULTS

In patient 1 CoreValve cases, the PVL volume difference between the worst and the best configuration was 22 mL/beat (Figure 2, table 1),

Table 1: Variation in PVL volume with device orientations

		Regurgitant volumes [mL/beat]					Average regurgitant volume
		R0	R1	R2	R3	R4	
Patient 1	CoreValve	17.87	6.86	9.11	26.31	28.89	17.81 mL/beat
	Evolut Pro+	11.17	2.88	4.42	19.56	21.16	11.84 mL/beat
Patient 2	CoreValve	28.49	28.16	28.14	26.43	17.84	25.81 mL/beat
	Evolut Pro+	1.83	1.82	1.62	0.93	0.50	1.34 mL/beat
Patient 3	Evolut R	1.1	0.71	0.67	0.65	0.63	0.75 mL/beat
	Evolut Pro+	0	0	0	0	0	0 mL/beat

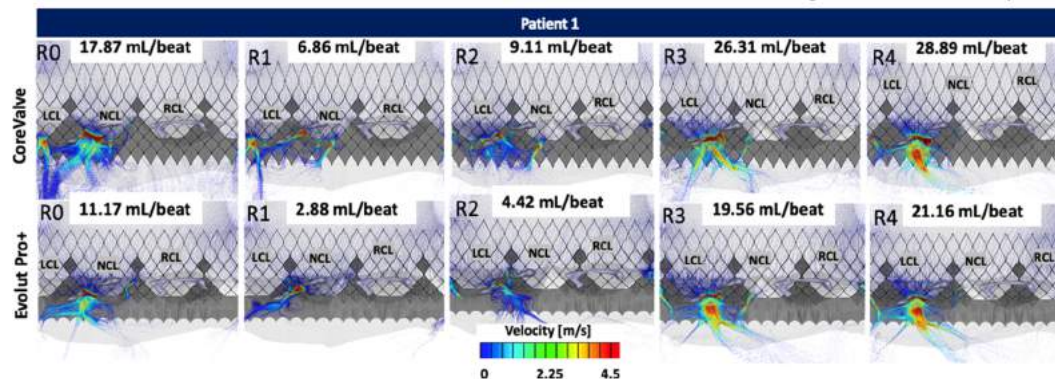


Figure 2: (Polar representation of CFD simulations) Velocity streamlines from peak diastole, highlighting the variation in PVL locations and severity with different generations and orientations of SE devices (NCL – non-coronary leaflet, LCL – left coronary leaflet, RCL – right coronary leaflet

which went down to 18.3 mL/beat for Evolut Pro+ cases. In patient 2 CoreValve cases, the PVL volume difference between worst and best configuration was 10.7 mL/beat, which went down to 1.3 mL/beat for Evolut Pro+ cases. The average regurgitation volume decreased significantly with Evolut Pro+ device, in both patient 1 and 2 (Table 1). In patient 3 Evolut R cases, the PVL volume differed by ~0.5 mL/beat between the worst and the best configuration (table 1). There was virtually no leak channel associated with any Evolut Pro+ orientation in this patient. All the patients have demonstrated an overall decrease in thrombogenic risk with the implantation of newer generation device (Figure 3).

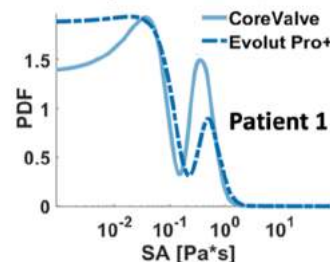


Figure 3: Probability density functions of accumulated stress values on platelets, comparing the PVL flow-induced device thrombogenicity in one patient

DISCUSSION

This study highlights the importance of understanding the complex device-tissue interaction in BAV patients and how they get impacted by different procedural factors, affecting the post-TAVR outcomes. In all the patient cases, deployment of newer generation device demonstrated significant improvement in PVL complications regardless of the device orientation. This trend supports the effectiveness of design improvement in newer generation Evolut Pro+, which is marked by an outer pericardial skirt. While major leak channel locations were consistent in all patients, PVL volume varied with different device and orientation. In patient 1, simply changing the orientation decreased the PVL complications significantly, regardless of the device generation. Whereas in patient 2, implantation of newer device rather than modified orientation, improved the PVL. These observations indicate a complex relationship between the device and the native aortic root features, which determines the origin, flow path and severity of the PVL. Clinicians may find it challenging to predict the variations in possible outcomes, which emphasizes the significance of using personalized computational modeling approach during pre-TAVR planning, especially in complex BAV anatomies. Future study will focus on including additional patients with balloon-expandable devices, analyzing the impact of additional deployment parameters on PVL and other complications and finding optimum set of parameters based on the patient anatomies. An engineering design challenge that should be addressed in future study is - developing a delivery profile that allows complete re-orientability of the TAVR device, which will fulfill the translational potential of this study.

ACKNOWLEDGEMENTS

Funding-NIH-NIBIB U01EB026414 (DB). Industry Partners- ANSYS, Simulia Living Heart Project.

REFERENCES

- [1] Das, R, and Puri, R. *Frontiers in cardio medicine*, 2018, 5:91-91.
- [2] Wang, X., et al. *JACC. Cardiovascular interventions*, 2022, 15(2), 123–134.
- [3] Tang GHL. Et al. *JACC Cardiovasc Interv.* 2020 11;13(9):1030-1042.
- [4] Xenos M, et al. (2010). *J Biomech.* 43(12):2400-9.
- [5] Anam S., et al. *J Cardiovasc Transl Res.* 2022; 15(4):834-844.

DMSO-FREE CRYOPRESERVATION OF MAMMALIAN CELLS USING AGAROSE HYDROGEL ENCAPSULATION

M Wang (1), A Mahajan (1), A Aksan (1)

(1) Department of Mechanical Engineering, University of Minnesota, Minneapolis, Minnesota
55455, United States

INTRODUCTION

With the rapid development of immunotherapy and regenerative medicine, there has been an urgent need to improve both the efficiency and safety of cell/tissue cryopreservation methods. During freeze/thaw, mechanical, thermal, and osmotic stresses associated with ice formation may cause damage and compromise cell function and viability. To minimize cryoinjury, cryoprotectant agents (CPAs) such as dimethyl sulfoxide (DMSO) are widely used. As a membrane-permeable CPA, DMSO can diffuse into cells and thus inhibit both intra- and extracellular ice formation during cryopreservation. However, DMSO is toxic. Also, mild to severe side effects have been reported for patients who were injected with therapeutic products cryopreserved with DMSO.

In recent years, hydrogel encapsulation has been proposed as a strategy for the cryopreservation of mammalian cells.^[1,2] Encapsulation of cells in hydrogels before freeze/thaw has shown the advantage of maintaining high post-thaw cell survival while decreasing the need for using higher concentrations of membrane-permeable CPAs.^[2,3] Two hypotheses for the protection offered by hydrogel encapsulation have been proposed through observations made in transmitted light cryomicroscopy experiments: (1) hydrogel enables vitrification of cells through inhibition of extracellular/intracellular ice crystallization during cooling, and (2) hydrogel inhibits devitrification and ice recrystallization during warming. However, these hypotheses have not been validated using thorough thermodynamic and kinetic analyses.

In this work, our objective is to develop a cryopreservation method for mammalian cells using agarose hydrogel encapsulation, eliminating the need for toxic membrane-permeable CPAs such as DMSO. As the sole CPA, trehalose was incorporated into the agarose solution before gelling to enhance the cryoprotective effect of the hydrogel matrix. We used MDA-MB-231 cells as a model. Also, we characterized the thermodynamics and kinetics changes of the hydrogel matrix with trehalose during freeze/thaw using Fourier Transform Infrared Spectroscopy (FTIR) and Differential Scanning Calorimetry (DSC) to establish the physicochemical mechanisms of cryoprotection offered by hydrogel encapsulation.

METHODS

(1) Hydrogel encapsulation

To encapsulate in an agarose-trehalose hydrogel, MDA-MB-231 cells were first suspended and incubated in a cell culture medium containing 10%, and then in 20% trehalose for 15 minutes. Stepwise exposure was conducted to minimize hyperosmotic stress on the cells. To encapsulate the cells in an agarose hydrogel, the cell pellet was resuspended in 1xPBS agarose solution containing trehalose at 37°C to achieve a cell concentration of 10⁷ cells/ml. The solution was gently and

thoroughly mixed in a microtube and then stored at 4°C to induce gelation.

(2) Freeze/thaw protocol and post-thaw viability measurements

The hydrogel with encapsulated cells was cooled down from 10°C to -150°C at a rate of 2°C/min. Once the temperature reached -150°C, the sample was rapidly rewarmed to room temperature at a warming rate of 100°C/min. Post-thaw viability of the encapsulated cells was measured using acridine orange (AO)/propidium iodide (PI) fluorescent dyes. The live (green) and dead (red) cells in the sample were counted in five representative areas for each sample, and the final percent viability was calculated with respect to the freshly harvested MDA-MB-231 cells.

(3) Differential Scanning Calorimetry (DSC) analysis

To prepare DSC samples, 2-10 mg solution or hydrogel was weighed in a Tzero hermetic pan and sealed with a lid. Each sample was initially cooled from room temperature to -150°C at 2°C/min, then heated back to 10°C at 2°C/min.

(4) Fourier Transform Infrared Spectroscopy (FTIR) analysis

0.1-1 µL of experimental and control samples were first cooled from 10°C to -150°C at a rate of 2°C/min, then warmed back to 10°C at 2°C/min, following the identical freeze/thaw protocol used in the DSC analysis. Infrared (IR) spectra were collected every 2°C, and 64 IR scans at a resolution of 4 cm⁻¹ were averaged in 9000 to 900 cm⁻¹ wavenumber range to obtain each spectrum. Changes in the ν-(OD) band (2500 cm⁻¹), δ-(OH) band (1650 cm⁻¹), and the glycosidic band (995 cm⁻¹) were examined as the sample was cooled and warmed.

RESULTS

(1) Post-thaw viability of cells encapsulated in agarose hydrogel with trehalose

Table 1. Viability of MDA-MB-231 cells cooled at 2°C/min to -150°C, and warmed at 100°C/min to 10°C

Sample	Normalized Viability (%)
1xPBS	0.4 ± 0.3 %
10% DMSO	70.9 ± 3.6 %
20% trehalose	28.7 ± 7.2 %
0.75% agarose	15.8 ± 3.6 %
0.75% agarose + 20% trehalose	78.7 ± 3.4 %

The viability of MDA-MB-231 cells frozen/thawed in different samples is shown in Table 1. Poor survival was observed when the cells were frozen and thawed in the presence of trehalose or encapsulated in agarose hydrogel alone. However, when MDA cells were encapsulated and frozen/thawed in 0.75% agarose hydrogel with 20% trehalose, the

post-thaw cell viability increased significantly (to $78.7 \pm 3.4\%$), which is comparable to the positive control group, where cells were frozen in a PBS solution that contained 10% DMSO ($70.9 \pm 3.6\%$).

(2) Identifications of the thermodynamic and kinetic transitions in agarose hydrogels during freeze/thaw

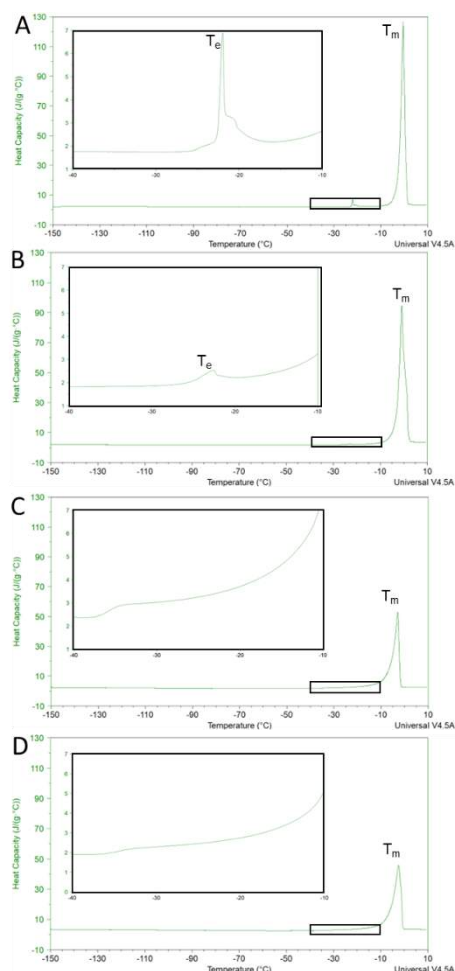


Figure 1. DSC warming scans of (A) 1xPBS solution, (B) 2.5% agarose in 1xPBS, and (C) 20% trehalose in 1xPBS and (D) 2.5% agarose + 20% trehalose in 1xPBS. (T_e : eutectic melting temperature, T_m : ice melting temperature)

The large endothermic peak around 0°C shown in each DSC scan corresponds to the melting of ice (T_m), and the area under the endotherm peak (heat of fusion, ΔH) is proportional to the total amount of ice crystals formed during cooling. The decrease of ΔH (from Figure 1A to Figure 1D) indicates that less amount of ice crystallized during cooling in the combination system of agarose and trehalose. On the other hand, the small endothermic peaks around -22°C seen in the 1xPBS (Figure 1A) and 2.5% agarose (Figure 1B) samples correspond to the eutectic melting of $\text{NaCl}\cdot 2\text{H}_2\text{O}$ -ice in the PBS solution.^[4] The significant decrease in eutectic melting peak in Figure 1B indicates that agarose hydrogel inhibited the eutectic crystallization/melting of PBS during the freeze/thaw process. Furthermore, no eutectic melting peak was observed in the sample with trehalose (Figure 1C and Figure 1D), suggesting that trehalose eliminated the eutectic crystallization/melting

of PBS and therefore minimize related kinetic/mechanical damage on cells during cryopreservation.

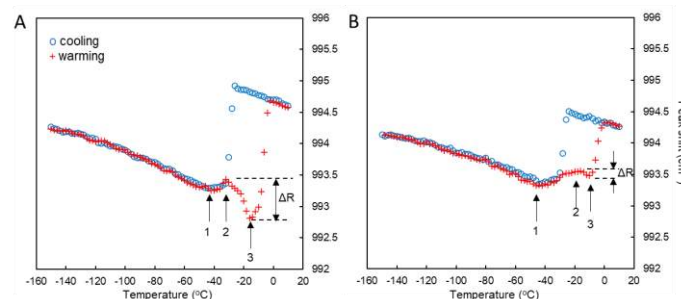


Figure 2. Peak shift of the glycosidic band ($\sim 995\text{ cm}^{-1}$) during cooling (blue) and warming (red) processes of 20% trehalose (A) and 4% agarose + 20% trehalose (B).

To investigate the water-trehalose and trehalose-trehalose HB interactions during the freeze/thaw event, temperature-induced shift of the trehalose glycosidic linkage peak was analyzed. During the warming process, three transitions were observed in the plots. The first transition located around -45°C corresponds to the glass melting temperature of the freeze concentrate liquid (FCL) in the sample.^[5] Similarly, a significant increase of peak shift was observed after the third transition, corresponding to the melting of the bulk ice. Transition 2 is a non-equilibrium process, and it only occurs in the temperature range between T_g and T_m , which corresponds to ice recrystallization. Therefore, the significant decrease of ΔR (the magnitude of ice crystallization) from 20% trehalose (Figure 2A) to 4% agarose + 20% trehalose (Figure 2B) indicates that the ice recrystallization was greatly inhibited by agarose in the combination system during warming.

DISCUSSION

Here, we report a hydrogel encapsulation method using agarose and trehalose for cryopreservation of MDA-MB-231 cells. The results demonstrate that the encapsulated cells were well protected from kinetic mechanical damage during the freeze/thaw process, as reflected by very high viability post-thaw even in the absence of DMSO. Through the identifications of the thermodynamic and kinetic transitions in agarose hydrogels during freeze/thaw, the mechanisms of cryoprotection offered by agarose encapsulation in the presence of trehalose can be attributed to: 1) agarose hydrogel encapsulation decreases the amount of ice formed in the combination system. 2) Ice recrystallization during warming is inhibited when water molecules are confined in the agarose hydrogel. 3) the eutectic crystallization/melting of PBS can be eliminated in the presence of trehalose.

ACKNOWLEDGEMENTS

The research was supported by an NIH grant (CA261734).

REFERENCES

- [1] Gurruchaga, H. et al. *J. Controlled Release*, 281, 119-138, 2018
- [2] Huang, H. et al. *Adv Functional Materials*, 25, 6839-6850, 2015
- [3] Li, Y. et al. *ACS Biomaterials Sci & Eng*, 5, 5273-5283, 2019
- [4] Thorat, A. A. et al. *Pharm Res*, 36, 98, 2019
- [5] Goff, H et al. *Thermochimica acta*, 399, 43-55, 2003

STRAIN THRESHOLDS FOR NEURONAL ACTIVATION DURING HIGH RATE TENSILE LOADING TO FAILURE: IMPLICATIONS FOR PAIN AND TRAUMA

Daniel Du (1), Sittinon Nuethong (1), Prabesh Ghimire (1), Beth A. Winkelstein (1,2)

(1) Department of Bioengineering, University of Pennsylvania, Philadelphia, PA, USA

(2) Department of Neurosurgery, University of Pennsylvania, Philadelphia, PA, USA

INTRODUCTION

The facet capsule is a common source of pain in the neck and low back [1,2]. The capsular ligament is primarily composed of collagen fibers arranged in an extracellular matrix (ECM) network with afferent neurons embedded in that ECM [3,4]. Injury and/or damage to the capsular ligament can induce laxity and collagen disorganization in the ligament [5,6] and can induce pain and injury responses in afferent nerve fibers via mechanotransduction [1,7,8]. ECM biomechanics are not only associated with neuronal physiological responses, but such neuronal regulatory pathways are activated when strains exceed thresholds [9,10]. Both neuronal upregulation of phosphorylated ERK (pERK) and NMDA receptors, like the NR2B subunit, which are related to neuroplasticity and dysfunction, are sensitive to local strains [9,10]. In fact, pERK is not only correlated with tissue-level strains but the strain threshold (11.7%) for its increase corresponds to that strain at which collagen fiber reorganization occurs (11.3%) [9]. While that study found no difference in pERK expression following distractions sufficient to produce pain applied at 0.5mm/s or 3.5mm/s [9], those loading rates only vary by 7-fold. Yet, the biomechanical response of ligaments varies with loading rate [11-14], neuronal injury is rate-dependent [15-18], and higher rate loading affects matrix kinematics and kinetics [19]. If and how, a higher rate of loading alters the threshold for neuronal pERK activation has not been examined.

Our neuron collagen gel construct (NCC) in vitro platform enables the integrated investigation of macroscale and local mechanics, along with neuronal responses, and has been used to define relationships between local mechanics, collagen fiber responses and neuronal mechanisms relevant to nociception [9,10,20-22]. While most work with the NCC system to date has been limited to a slow strain rate (i.e. 1%/s) [9,10,20-22], ligament trauma occurs at much faster rates [13]. Tensile loading at 127%/s not only increases the failure force and stiffness, but also doubles the extent of collagen realignment over those responses observed for 1%/s [9,19,20]. Since neuronal responses may

similarly be differentially modulated by loading rate, this study extends that high rate tensile study of NCCs to characterize the neuronal pERK response to tensile failure loading at 10.5mm/s. Regional strains are also integrated with neuronal pERK expression to define a strain threshold for neuronal activation [9,10] after a high rate NCC failure [19].

METHODS

NCCs (n=6) were prepared using 2.0mg/mL of rat tail collagen I solution cast in 12-well plates [9,19-22]. Collagen gels self-assembled at 37°C in 5% CO₂ for at least 45mins and were seeded with DRG neurons (3x10⁵cells/mL) dissociated from embryonic day 18 rats [9,10,19]. Collagen was added after 3 days in vitro to encapsulate the neurons. Four days later, NCCs were transferred to sterile PBS and cut into a strip (21mm x 8mm). A grid was drawn on each NCC surface to facilitate elemental strain analyses (Figure 1). NCCs were affixed to a planar testing machine (TestResources) that was integrated with a high-speed camera (Phantom-v9.1; Vision Research), and gels were submerged in a 37°C PBS bath [9,19-22]. NCCs were stretched to failure with each arm distracted at 10.5mm/s. Force and displacement data were recorded at 500Hz; high speed imaging (500fps) was acquired and synchronized with the force and displacement data [19].

Force and displacement data were filtered using a 25-point moving average filter [9,20-22]. Failure was defined as the peak of the force-displacement curve for each loading arm. Each of the failure force and displacement was averaged across both arms for each NCC. Each NCC was marked with fiducial markers to define elemental nodes (Figure 1) and the nodal displacements were measured using ProAnalyst software (Xcitem). Those nodal displacements were input into LS-DYNA (LSTC) to compute the mean maximum principal strain (MPS) for each element and averaged across all elements for each NCC (Figure 1) [9,20-22].

NCCs were incubated for 24hrs after loading in warm culture medium supplemented with 1% Pen-Strep [10] and then fixed in 4% paraformaldehyde for immunolabeling of pERK and β III-tubulin. Matching unloaded gel samples (n=6) were similarly fixed and labeled

to serve as controls for analyses. Fixed NCCs were blocked using 10% normal goat serum with 0.3% Triton X-100 in PBS for 2hrs and treated with rabbit anti-pERK antibody (1:200; Cell Signaling) and mouse anti- β III-tubulin antibody (1:200; Biolegend) overnight at 4°C to label pERK and neurons, respectively [9]. After PBS washes, NCCs were incubated for 2hrs in goat anti-rabbit AlexaFluor647 (1:500; Invitrogen) for pERK and goat anti-mouse AlexaFluor568 (1:500; Invitrogen) for β III-tubulin. Images (3-6) were taken within each element of each NCC as defined by the markers (Figure 1) using a Leica TCS SP8 confocal microscope at 63X. Quantitative densitometry was used to determine the percent of pixels positive for pERK that were colocalized with β III-tubulin and averaged across images in each element [10]. The response of loaded NCC elements was assigned a value of 1 if expression levels were greater than the mean level plus one standard deviation in the matching unloaded control gel; an element was assigned 0 if expression in a loaded NCC element was less than or equal to that value [9,10].

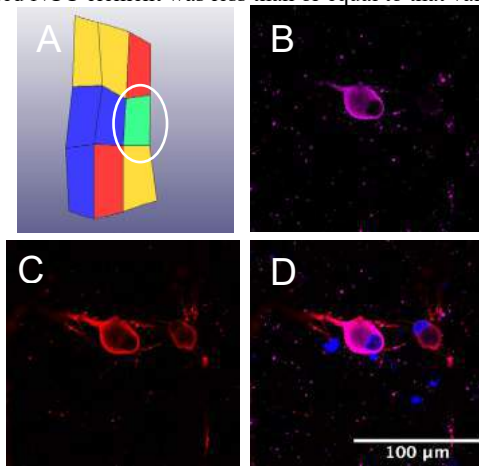


Figure 1. MPS map and immunofluorescent images of NCC (#14) showing (A) elemental strain map at failure and confocal images from Element 6 (circled in A) for (B) pERK and (C) β III-tubulin. Their colocalization is in (D) with scale that applies to all panels.

RESULTS

The measured displacement rate across all NCCs is 7.9 ± 0.3 mm/s, corresponding to a strain rate of $122 \pm 16.5\%$ /s. At that rate of applied stretch, NCCs failed at 23.1 ± 16.4 mN and a corresponding displacement of 4.4 ± 0.5 mm. The mean elemental MPS at failure is 0.33 ± 0.07 . The pERK expression at 24hrs increases by approximately 2.5-fold to 1.02 ± 1.22 over expression in unloaded controls (0.40 ± 0.47). Corresponding colocalized neuronal pERK is generally unchanged after loading (0.95 ± 1.6 fold greater than unloaded controls). Logistic regression of the binarized neuronal pERK is significant ($p=0.005$) against elemental MPS and predicts a 50th-percentile threshold of 55.7% (95% confidence interval: 55.6-56.6%) and 95th-percentile threshold of 78.7% (95% confidence interval: 76.7-78.9%) (Figure 2).

DISCUSSION

This is the first study to define the relative levels of pERK expression after a tensile failure at a rate ($122\%/s$) consistent with that of ligament trauma. Indeed, the force at failure is comparable to that previously reported for similar loading conditions (26.5mN) and twice that using the same NCC system used here (12.6mN) at a measured strain rate much lower ($1\%/s$) than the rate used here [19,22]. The displacement at failure is similar regardless of the strain rate (4.68 ± 1.6 mm for $1\%/s$; 4.35 ± 1.1 mm for $122\%/s$) [19,22]. Interestingly, the mean MPS (0.33 ± 0.07) is higher than the average MPS (0.12 ± 0.07) found using a $1\%/s$ distraction rate [22].

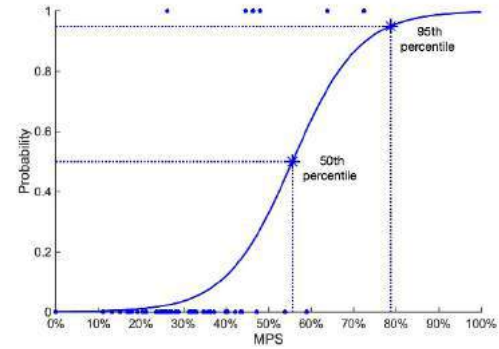


Figure 2. Logistic regression of binarized pERK colocalized with β III-tubulin against elemental MPS. The predicted 50th-percentile and 95th-percentile thresholds for increases are 55.7% and 78.7%.

Consistent with increased failure forces and strains at this higher strain rate, the strain thresholds for pERK activation are also about 5-times higher than for the lower rate, with prior work identifying thresholds of 11.7% for 0.5 mm/s and 10.2% for 3.5 mm/s [9]. Those thresholds aligned with the transition point for collagen activation at 11.3% [9], suggesting that altered collagen fiber kinematics are associated with mechanotransduction signaling in neurons. Of note, that prior study did not stretch NCCs to failure, but to a degree known to generate pain with corresponding mean elemental MPS of 0.15-0.17 [9], which would skew the threshold lower. While analyses of the relationships between MPS and CV have not been performed at the faster loading rate in this study, CV values increase 10-fold after failure [19]. Additional studies defining relationships between strain, collagen alignment, and neuronal morphology and health are important in understanding trauma-related insults.

Since neuronal responses are known to be rate-dependent [15-18], it is not surprising that there is a lack of pERK upregulation despite a prior report of significant increases [9]. Notably, that response was detected immediately after loading, but was also found to correlate with MPS. Additional work is needed to better understand the relationship between rate of loading, its severity and the time after exposure, as well as additional physiological responses suggestive of injury, dysfunction and excitability, particularly for painful injury.

ACKNOWLEDGEMENTS

Funding for this study was provided by the NCCIH (AT010326).

REFERENCES

- [1] Lee K & Winkelstein B, *J Pain*, 10:436-45, 2009; [2] Kallakuri S et.al, *Eur Spine J*, 17(4):556-63, 2008; [3] Yamashita T et al, *Spine J*, 21(5):538-43, 1996; [4] Yahia L & Garzon S, *Ann Anat*, 175(2):185-88, 1993; [5] Quinn K et al, *J Biomech*, 43(10):1870-75, 2010; [6] Quinn K et al, *Stapp Car Crash J*, 51:169-87, 200; [7] Chen C et al, *J Bone Joint Surg Am*, 88(8):1807-1816, 2006; [8] Dong L & Winkelstein B, *J Neurotrauma*, 27(1):163-174, 2010; [9] Zhang S et al, *J Biomech Eng*, 138:021013, 2016; [10] Singh S & Winkelstein B, *Biomech Model Mechanobiol*, 21:885-98, 2022; [11] Bass C et al, *Spine J*, 32(1): E7-13, 2007; [12] Noyes F et al, *J Bone Joint Surg*, 56(2):236-53, 1974; [13] Stephen F et al, *J Mech Behav Biomed Mater*, 10: 216-26, 2012; [14] Yoganandan N et al, *Spine J*, 14(10):1102-10, 1989; [15] Geddes D et al, *J Neurotrauma*, 20(10):1039-49, 2003; [16] Cullen D & LaPlaca M, *J Neurotrauma*, 23(9):1304-19, 2006; [17] Tang-Schomer M et al, *FASEB J*, 24(5):1401-10, 2010; [18] Kochba E et al, *Sci Rep*, 6:1-11, 2016; [19] Nuethong S, et al, *SB3C*, 2022; [20] Zhang S & Winkelstein B, *SB3C*, 2016; [21] Zhang S et al, *J Orthop Res*, 36(2):770-7, 2018; [22] Ita M & Winkelstein B, *J Biomech Eng*, 138(2):021013, 2019.

MULTI-PHYSICS MODELING OF NEURAL DENDRITE GROWTH WITH ELECTRICAL POLARIZATION

Shuolun Wang ⁽¹⁾, Xincheng Wang ⁽¹⁾, Maria A. Holland ^(1,2)

⁽¹⁾ Department of Aerospace and Mechanical Engineering, University of Notre Dame, Notre Dame, IN, USA

⁽²⁾ Bioengineering Graduate Program, University of Notre Dame, Notre Dame, IN, USA

INTRODUCTION

The nervous system comprises many neurons with different morphologies [1]. A typically-developed neuron roughly consists of a soma/cell body, dendrites, a single axon, and synapses [2]. Neural dendrites are tree-like protrusions from the soma and receive incoming electrical signals from other neurons' synapses. The axon also protrudes from the soma. At the other end of the axon are synapses, where the fired electrical signal goes across and passes down to the subsequent neurons.

Neural dendrites, in particular among other neural components, are highly distinctive for their intricate morphologies, which perform vital functionalities and bring a sense of beauty. Its signature branching feature allows multiple connections between neurons, thus facilitating high connectivity in our brain [3]. The question of how neural dendrites morphology is formed needs to be better understood. This work aims to elucidate this myth via mathematical modeling and numerical simulation.

A critical feature of neural dendrite morphology is "tiling" – nonredundant innervation of a receptive area by the same type of neurons – which serves a universal organizing principle across the species. Experiments have shown that similar visual neurons in rabbits form their territory and barely overlap [4]. It makes functional sense because this arrangement allows the incoming light to fall onto visual neurons with as many types as possible. As for now, the molecular basis of "tiling" is still under debate, and no popular paradigm has been formed.

Many extrinsic factors could also influence dendrite growth. Endogenous electric field, in particular, changes in space and time throughout embryonic development, and such endogenous electrical cues influence neuronal migration [5]. Early work showed that neurites in embryonic chick grow faster towards the cathode than the anode in an applied electric field [6].

In this work, we propose a multi-physics model that captures the neural dendrite growth polarized by external electrical stimuli via an advective diffusion-reaction system and implement it by writing a user element subroutine (UEL) for the finite element program Abaqus/Standard [7]. Furthermore, we set up a convolutional neural network to identify physical parameters inversely from real neuron images.

METHODS

Evolution of neural dendrite: To capture the essence of the dendrite growth, we borrowed the idea of the Gray-Scott model and incorporated an advection term for electrical polarization [8, 9],

$$\begin{cases} \dot{u} = D_u \nabla^2 u - uv^2 + F(1 - u), \\ \dot{v} + \sigma \mathbf{E} \cdot \nabla v = D_v \nabla^2 v + uv^2 - (F + k)v, \end{cases} \quad (1)$$

where u and v are two diffusive morphogens that interact with each other through diffusion and reaction, D_u and D_v are diffusivities, F and k are "feed" rate of u and "kill" rate of v , respectively. Additionally, the parameter σ in Eqn. (1) controls the strength of the polarization induced by electric field \mathbf{E} .

Next, we use a phase variable c to track regions occupied by the neural dendrite, the evolution of which is given by

$$\dot{c} = \gamma c(a(v) - c)(c - 1), \quad (2)$$

where γ is a rate constant, $a(v)$ serves as a saddle point, at which the dynamic response of phase variable c flips.

Gauss's law: As a simplification, we treat the brain tissue as the dielectric material; thus, the governing equation of the applied electric field is given by

$$\nabla \cdot \mathbf{E} = 0, \quad (3)$$

where the electric field is given by the negative of the gradient of the electric potential $\mathbf{E} = -\nabla \Phi$.

Finite-element implementation: Our coupled system was numerically implemented in Abaqus/Standard [7] by writing user-defined element (UEL) subroutines, following our previous work [10].

Inverse pattern recognition via convolutional neural network To inversely obtain parameters of F and k from real neural dendrite images, we utilized a convolutional neural network (CNN) as a surrogate model and trained with our finite-element simulations.

RESULTS

We explored the impact of various material parameters, including diffusivity ratio D_u/D_v and rate constant pair (F, k) , on neural dendrite growth *without* any applied electric fields. We first varied the diffusivity ratio D_u/D_v while fixing the rate constant pair and then vice-versa. It shows that vibrant patterns emerge when $D_u/D_v \approx 3$, and the number of branching increases with an increasing diffusivity ratio. Next, holding at a constant $D_u/D_v = 3$, the simulated phase field variable c confirmed that intricate patterns emerge along the bifurcation curve $F = 4(F + k)^2$ (Figure 1, left). Various representative patterns in $F - k$ space have been identified and dubbed with fancy names [11].

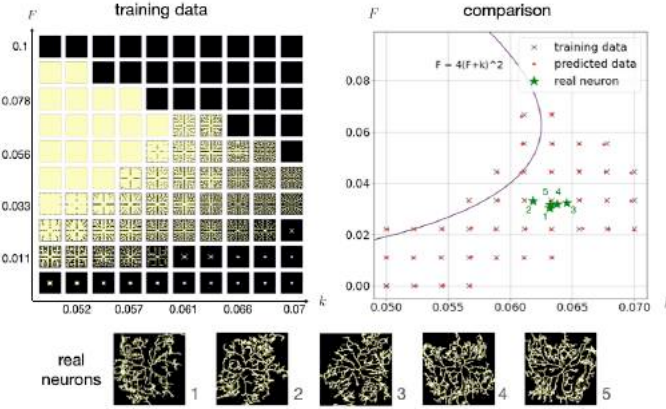


Figure 1: Results of inverse neural dendrite pattern detection via CNN.

To relate our model to real-world problems, we first trained a CNN with our simulated phase variable c covering a labeled parameter space of $k \in [0.05, 0.07]$ and $F \in [0, 0.1]$ (Figure 1, left). The fully-trained CNN can replicate the original model and give reasonable predictions of five real IV neural dendrites in drosophila larva (Figure 1, right and bottom). As we expected, our model resembles branching in real neurons.

Our model can also reproduce features of space-filling and self-avoidance. We simulated neural dendrite growth on ideal geometries with multiple soma seeds. Two neurons in the oval domain formed a “flat” boundary in between, while the pentagon domain with five neurons formed a pentagonal “pizza” (Figure 2).

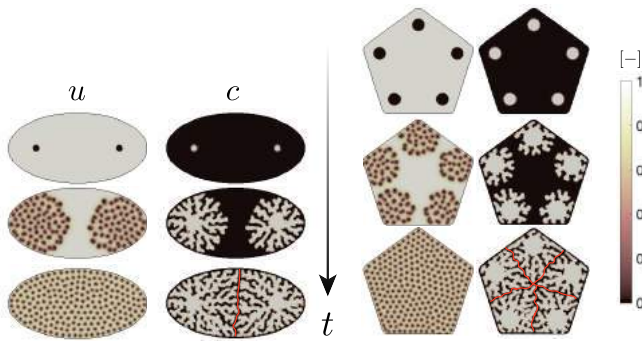


Figure 2: The interactions between morphogen u and v accomplish features of space-filling and self-avoidance.

It has been reported that polarizations of neural dendrites could be guided by stimuli, such as chemo-attractant gradients, electric fields, and mechanical deformations [12–14]. Here we focus on simulating electric field-induced polarizations. We considered two different electrode setups in which the anode and cathode have potentials of $\Phi = \pm 75$ mV, respectively (Figure 3). As expected, our electrode setups yield highly inhomoge-

neous electric potential distributions. The neural dendrites’ growth aligns with the electric field \mathbf{E} (red unit vectors) pointing toward the cathode.

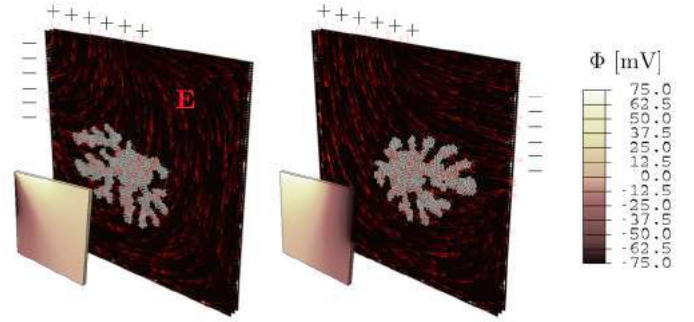


Figure 3: 3-D Simulation of neural dendrites growth with electrical polarization.

DISCUSSION

In this work, we have developed a multi-physics model for neural dendrite growth with electrical polarization. The model is a coupled PDE system that combines an advective Gray-Scott model with Gauss’s law. We have implemented it numerically in Abaqus/Standard [7]. The results show that our model accounts for critical features of branching, space-filling, self-avoidance, and polarization under the applied electric field. Additionally, we have set up a CNN pipeline for real neural dendrites pattern detection.

Looking toward the future, much has to be done to advance our understanding of the process and refine our mathematical formulations. Well-designed experiments are needed to confirm the underlying mechanism, such as the specific genes and pathways involved in the process. Additionally, we will incorporate other external stimuli, such as gradients of chemo-attractants and mechanical environments, into our multi-physics modeling endeavors.

ACKNOWLEDGEMENTS

This work is supported by National Science Foundation (CMMI 2144412).

REFERENCES

- [1] Ascoli GA et al. *Journal of Neuroscience* 27.35 (2007).
- [2] Lefebvre JL et al. *Annual review of cell and developmental biology* 31 (2015).
- [3] Denk W et al. *Nature Reviews Neuroscience* 13.5 (2012).
- [4] MacNeil MA et al. *Neuron* 20.5 (1998).
- [5] Yao L et al. *Tissue Engineering Part B: Reviews* 17.3 (2011).
- [6] Jaffe LF et al. *Journal of Experimental Zoology* 209.1 (1979).
- [7] Abaqus/Standard. Providence, RI: Dassault Systemes Simulia, 2022.
- [8] Gray P et al. *Chemical Engineering Science* 38.1 (1983).
- [9] Gray P et al. *Chemical Engineering Science* 39.6 (1984).
- [10] Wang S et al. *PLOS Computational Biology* 18.6 (2022).
- [11] Pearson JE. *Science* 261.5118 (1993).
- [12] Polleux F et al. *Nature* 404.6778 (2000).
- [13] McCaig C et al. *Developmental dynamics: an official publication of the American Association of Anatomists* 217.3 (2000).
- [14] Ladoux B et al. *Trends in cell biology* 26.6 (2016).

A SINGLE-SENSOR APPROACH FOR TRACKING PHASE VELOCITY AS A PROXY FOR IN VIVO TENDON LOADING

D. Schmitz (1), D. Thelen (1), S. Cone (2)

(1) Department of Mechanical Engineering, University of Wisconsin–Madison, Madison, WI, USA
(2) Department of Biomedical Engineering, University of Delaware, Newark, DE, USA

INTRODUCTION

Shear wave tensiometry uses external excitation and skin-mounted accelerometers to noninvasively measure tension in soft tissues [1]. This exciting new technology holds promise in many clinical applications, ranging from intraoperative monitoring of ligament forces to evaluating functional tendon recovery through rehabilitation [2]. There are two notable challenges limiting the use of tensiometry. The first challenge is dispersion, or the frequency dependent nature of wave propagation in layered media, which is prevalent in soft tissues [3]. Our current approach tracks the waves emergent from an impulsive excitation. However, as inherent tissue stiffness modulates with loading, the system resonance changes as well. Consequently, dynamic loading conditions during movement cause changes in the dominant wave frequencies and could introduce variability into the measured wave speeds. A second challenge is that the overall footprint of the device (~30 mm) is not suitable on ligaments and tendons with short free lengths. The footprint size is predicated by the need for two accelerometers, which are used to monitor wave travel time between two fixed locations. This study investigated the use of a shaped excitation waveform to measure phase velocity at a prescribed dominant frequency using a single sensor.

METHODS

Shear waves were excited in the Achilles tendon using a miniature surface transducer (Fig. 1a). The input excitation ψ was an amplitude modulated harmonic wavelet:

$$\psi = \begin{cases} A \cdot \sin(\omega_A t) \cdot \sin(\omega_H t + \varphi) & \text{for } 0 \leq t \leq t_0 \\ 0 & \text{otherwise} \end{cases} \quad (1)$$

where A is the excitation amplitude and ω_H is the dominant wavelet frequency. Amplitude modulation frequency ($\omega_A = \omega_H/7$) and wavelet duration ($t_0 = 3.5 \cdot (2\pi/\omega_H)$) produced a seven-lobe wavelet (Fig. 1b).

Surface mounted accelerometers (PCB Piezotronics, Depew, NY) were used to measure the wave propagation along the tendon (Fig. 1a). The envelope of the measured acceleration was computed via Hilbert

transform [4]. The envelope and intact signal were then used to compute the group and phase arrival times of the shear wave, respectively, by correlating the ideal input as defined in Eq. 1 with the measured signal [5]. Kalman filters were implemented for group and phase arrival times, with *a priori* estimates based on the changes in arrival time between consecutive excitations [6]. Phase velocity for the shear wave was computed from the known distance from the transducer (20 mm) to the accelerometer and the arrival times. A frequency-based excitation latency was determined via a system response characterization (Fig. 1c).

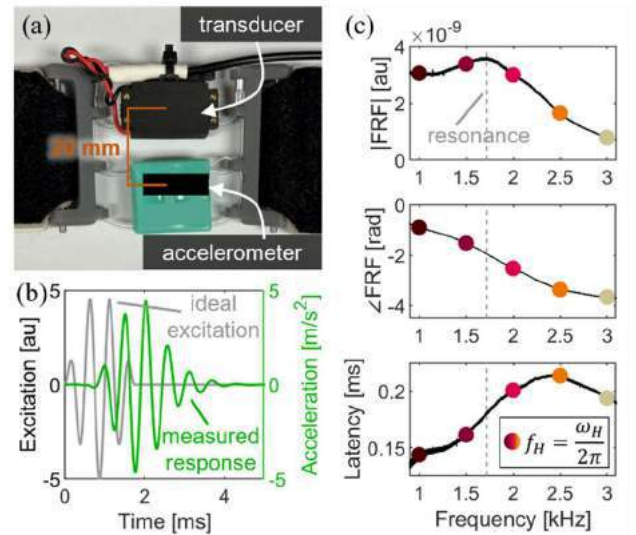


Figure 1: (a) Shear wave tensiometry was performed using only the first sensor in a standard two-sensor device. (b) Example of the input modulated harmonic wavelet and measured response. (c) Measured frequency response of the transducer.

Two healthy young adults (1F/1M) were recruited to participate in the study (2018-0487-CP019). The tensiometer was placed over the right Achilles tendon. The test conditions included 3 walking speeds (1.33, 1.67, 2 m/s) and 3 running speeds (2, 2.33, 2.67 m/s) with the wavelet frequency f_H set to 2 kHz. Additionally, f_H was varied from 1-3 kHz in 500 Hz increments at the 1.33 m/s walking speed. Wave speed profiles were ensemble averaged across multiple (15-26) strides per trial. Statistical significance was tested using ANOVAs ($p < 0.05$). Significant results are in **bold**.

RESULTS

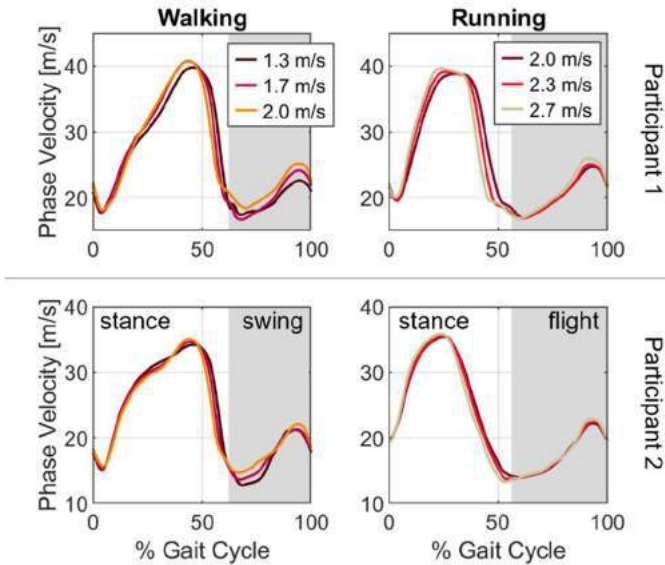


Figure 2: Phase velocity across speeds for each participant.

Phase velocity modulated with load in walking and running (Fig. 2). Peak phase velocity during stance showed a minor increase with walking speed (**2.5-2.6%**) and running speed (**0.4-1.7%**). Only participant 2 showed a significant increase in peak velocity from walking to running.

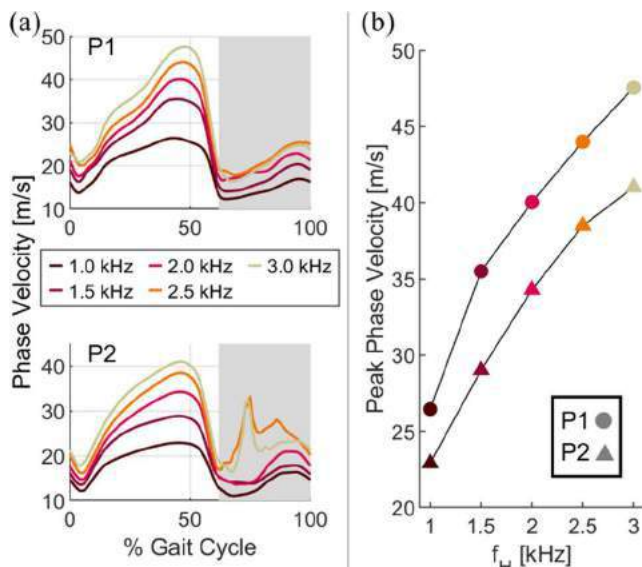


Figure 3: (a) Phase velocity for walking at 1.33 m/s. (b) Peak phase velocity vs. the dominant wavelet frequency f_H .

The computed phase velocities were frequency dependent, consistent with the dispersive nature of biological tissues [7]. Most notably, an increase in the excitation frequency resulted in an increase in the magnitude of the peak phase velocity, which varied by 25 m/s across the excitation frequencies considered (Fig. 3).

DISCUSSION

This study introduces a promising single-sensor approach for tracking tendon phase velocity during dynamic movement. Wave speed profiles were consistent with stance phase ankle torque measured via inverse dynamics and wave speeds measured with a two-sensor approach [1,8]. Peak wave speeds tended to increase with speed for a fixed locomotion pattern, though changes were relatively small and did not change substantially between walking and running [9]. From a tensioned beam model [1], tendon force scales with wave speed squared such that the relative changes in force may be greater than the change in wave speed. It is also worth noting that tensiometry is designed to monitor loading in specific tendons, whereas net ankle torque superimposes contributions from all agonistic and antagonistic muscles active about a joint. Hence, wave speed can modulate with locomotion speeds differently than torque.

The tendons exhibited dispersive behavior as expected for soft tissues. Peak wave speeds increased with wavelet excitation frequency for both participants. Analytical models of wave propagation suggest that wave speed can increase with frequency due to wave-guided behavior [3] or the viscoelastic nature of the tissue [7]. Data collected above f_H of 2.0 kHz yielded the most consistent results. This is likely due to the physical constraints of the device implementation, as well as the transducer resonances. Further investigation is needed to determine if there is a single optimum frequency in this range, or whether the best choice for ω_H is device and individual specific.

A primary outcome of this study is the single-sensor tensiometer that may greatly expand the range of ligaments and tendons that can be monitored. The footprint of the device on the tendon is reduced by ~30%, allowing the tensiometer to be used on children and shorter structures such as quadriceps and hamstring tendons. Additionally, since the wave speeds can be computed using only one sensor close to the excitation source, the overall signal to noise ratio should be higher. Finally, the hardware resources required to acquire the necessary data to perform tensiometry are essentially halved. This further expands on the potential of this implementation to simultaneously quantify the loading patterns on multiple tendons using fewer resources.

To conclude, we have demonstrated a single-sensor approach to shear wave tensiometry which can noninvasively track tendon wave speeds under dynamic loading conditions. We believe this advance could significantly expand the use of tensiometry for biomechanical studies, and in orthopedic and rehabilitation applications.

ACKNOWLEDGEMENTS

We would like to acknowledge Karen Walker and Elizabeth Schmida for their contributions. This work was funded by the NSF DARE (2019621) and the NIH (F32-AR076267).

REFERENCES

- [1] Martin, J et al., *Nat Commun*, 9(1):1592, 2018.
- [2] Blank, J et al., *Ann Biomed Eng*, 50:751–768, 2022.
- [3] Brum, J et al., *Phys. Med. Biol.*, 59:505, 2014.
- [4] Ulrich, T, Technical Report, 2006.
- [5] Crespo, B et al., *Appl Sci*, 8:1253, 2018.
- [6] Schmitz, D et al., *Sensors*, 22(6):2283, 2022.
- [7] Cortes, D et al., *Ultrasound Med Bio*, 41(6):1518-1529, 2015.
- [8] Keuler, E et al., *Sci Rep*, 9(1):1-9, 2019.
- [9] Ebrahimi, A et al., *Exp Gerontol*, 137:110966, 2020.

SUBSTRATE MECHANICAL STIFFNESS REGULATES EPIGENETIC MODIFICATIONS AND CHROMATIN REMODELING IN MESENCHYMAL STROMAL CELLS DURING MONOLAYER CULTURE OVER PASSAGING

Samantha Kaonis (1,3), Lauren Monroe (1,3), Emily Kaplan (1,3),
Jack Forman (1,3), Soham Ghosh (1,2,3)

(1) School of Biomedical Engineering, Colorado State University, Fort Collins, CO, USA
(2) Department of Mechanical Engineering, Colorado State University, Fort Collins, CO, USA
(3) Translational Medicine Institute, Colorado State University, Fort Collins, CO, USA

INTRODUCTION

Mesenchymal stromal or stem cells (MSC) are one of the most promising candidates for a myriad of cell therapy applications because of their multipotency, trophic properties and immunomodulatory properties. Despite showing promises in numerous preclinical and clinical studies, MSC based therapy is not yet a reality for regenerative medicine due to their suboptimal outcome at the clinical endpoint. Suboptimal function of MSC is often attributed to the monolayer expansion process on cell culture plate, which is a necessary condition to reach the therapeutically relevant number, and also to their response to a fibrotic environment post transplantation. In both scenarios of plastic culture and fibrotic conditions, the substrate mechanical stiffness experienced by the MSC is completely different from the natural mechanical niche of the MSC. Accordingly, the role of mechanical environment has been shown to be a critical determinant of MSC gene expression, function, and heterogeneity as shown by the work from our group and other groups [1, 2]. Despite several mechanisms that have been proposed to explain how the MSC gene expression is affected by the substrate mechanical stiffness, new mechanisms that involve the epigenetic modifiers are emerging [3].

In this present study we investigated how the chromatin architecture, specific histone modifiers and chromatin remodelers in bone marrow-derived MSC are affected by the substrate mechanical stiffness over multiple passages. Subsequently, we show preliminary evidence that targeting the epigenetic mechanism of histone modification and chromatin remodeling in MSC can enhance their functionality, as shown by the enhanced gene expression of the Vascular Endothelial Growth Factor (VEGF).

METHODS

Design of experiment: Soft substrates mimicking the bone marrow is known to maintain the MSC phenotype over multiple passages. P3 MSC (Lonza) were seeded on mechanically soft (sylgard 527 PDMS) or stiff (plastic) substrate until P5 in order to understand how chromatin

architecture changes over passing in a stiffness-dependent manner (Figure 1A). Cells were cultured in a petri dish (with or w/o PDMS) for passing and on ibidi 8-well plate (with or w/o PDMS) for imaging.

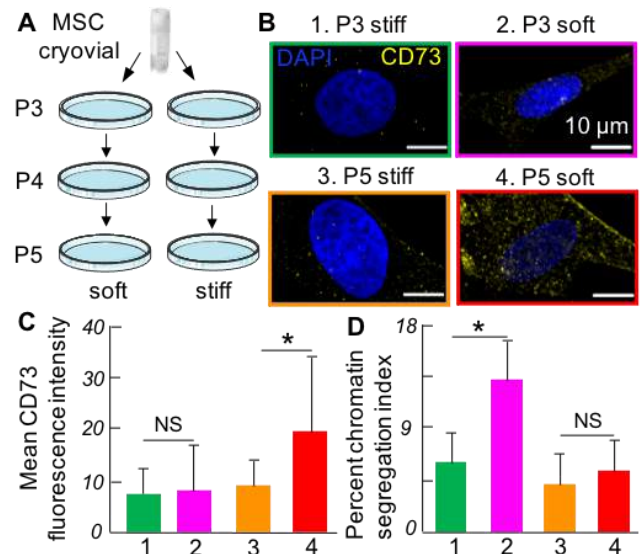


Figure 1: (A) Passaging of MSC on a soft and a stiff substrate. (B) Images of chromatin and MSC-specific marker CD73. (C) CD73 expression increases but (D) chromatin is less segregated in MSC on the soft substrate at the later passage. (* $p < 0.001$, $n > 20$ cells).

Immunofluorescence: Cells were fixed, permeabilized and blocked prior to antibody (Invitrogen) staining. Dilution of primary antibodies were as follows: CD73 - 1:100, ARID1A - 1:400, H3K9me3 - 1:400, H3K9Ac - 1:400. All secondary antibodies were used at 1:200 dilution. Cells were imaged across their midsection using a confocal microscope

(Zeiss LSM 980) using a 63X oil objective and the Airyscan mode. **Gene expression analysis:** All gene expression data was normalized to the reference genes *GAPDH*. Pre-designed and validated primers was purchased from IDT. **Statistical analysis:** Statistical analysis was performed using Student's t-test (RStudio). Results are expressed as mean \pm standard deviation. Sample and replicate numbers and p-values are provided in the figure legends.

RESULTS

The expression of MSC specific marker CD73 increases with priming on soft substrate (Figure 1B,C) but decreases with priming on a stiff substrate. Interestingly, although an open chromatin architecture, characterized by a higher chromatin segregation index (CSI), which is a hallmark of MSC, by passage 5, the CSI value was the same in cells on both substrate stiffness (Figure 1D). Therefore, in contrast to previous report [2], openness of the chromatin architecture is not the absolute phenotype of MSC stemness.

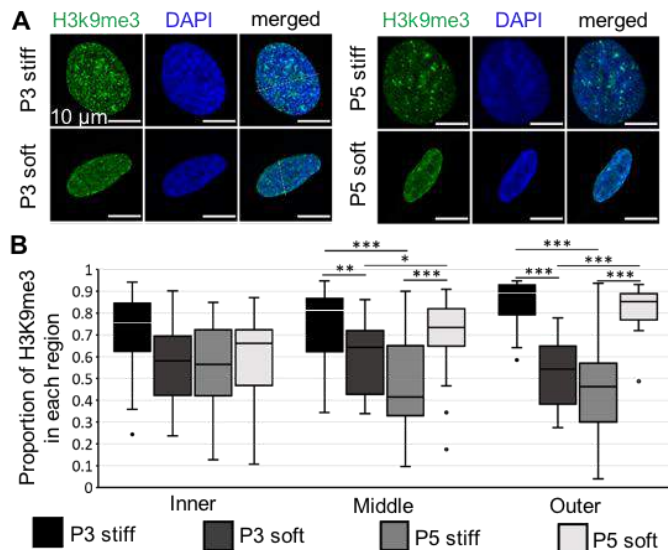


Figure 2: The repressive epigenetic marker H3K9me3 showed more peripheral enrichment on soft substrate in later passages compared to early passage. On stiff substrate, they are homogeneously located in the nucleus, with larger puncta size in later passages. *p<0.05, **p<0.01, *p<0.001. n>20 nuclei for each group.**

Loss of stemness and hence, transcription of genes is associated with global repression. Therefore, we investigated the expression and localization of the repressive epigenetic marker H3K9me3 in the nucleus. Interestingly, when we looked into the distribution of H3K9me3, we found that it was more localized in the nuclear periphery in soft substrate at passage 5, compared to passage 3 (Figure 2). For stiff substrates, H3K9me3 tends to be more localized as puncta in the entire nucleus and those puncta grew bigger over passing on the stiff substrate. Overall, a key finding was that MSC culture on soft substrate promotes the localization of H3K9me3 to the periphery, opening more regions inside the nucleus for gene transcription. Moreover, the intensity of the H3K9me3 remained the same on the soft substrate while they increased on stiff substrate by serial passaging. Overall, this data shows that H3K9me3 is a key driver of mechanics-mediated chromatin architecture and repressive status during serial passaging of MSC.

Histone acetylation and methylations are signatures of chromatin architecture status in MSC. However, it is not clear what really causes the chromatin architecture change. Of note, H3K9me3 showed more peripheral enrichment on the soft substrate, especially during serial passaging. This suggests that the chromatin is dynamic on soft substrate.

To investigate the possible cause of such dynamic chromatin architecture, we visualized ARID1A, the core subunit of the Chromatin Remodeling Complex (CRC) SWI/SNF. SWI/SNF is highly conserved in mammalian cells and has never been investigated before in the context of mechanobiology of MSC. We found that on soft substrate the intensity of ARID1A is high, but also, large clusters form, which further increases in the later passage (Figure 3B,C). On stiff substrate, the intensity is not only low, but also, they make smaller puncta which further decreases in size in later passages. We further found that the gene expression of several SWI/SNF CRC complex subunits also increased on soft substrate (Figure 3A). When the MSC on stiff substrate is treated with cytoskeletal mechanics disrupting drugs, their expression increases again, indicating a clear role of mechanics in the gene expression. Overall, this data suggests that SWI/SNF CRC-mediated chromatin remodeling is critical to maintain the stemness and to maintain the dynamic chromatin architecture for MSC on the soft substrate. Very interestingly, when MSC were treated with GSK126, an inhibitor of ARID1A, the dynamics of chromatin remodeling was stopped. As a result, even on a stiff plastic substrate the MSC secreted VEGF expression remains high (Figure 3D).

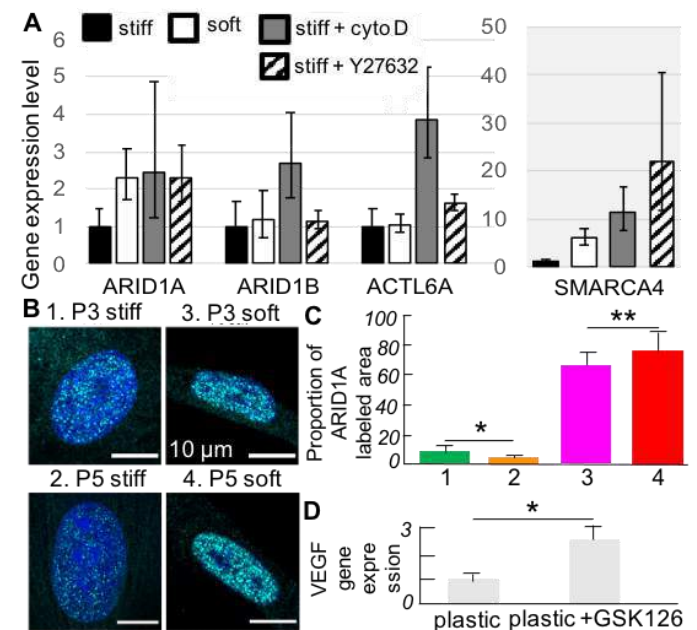


Figure 3: (A) The gene expression of SWI/SNF CRC associated proteins is high on soft substrate. On a stiff substrate, the gene expression increases with the application of 0.05 µM cyto D and 10 µM Y27632. (B, C) ARID1A distribution in nucleus is stiffness and passaging dependent. *p<0.01, **p<0.05. n>20 nuclei for each group. (D) Application of ARID1A inhibitor GSK126 (10 µM) increases the VEGF expression in MSC even on a plastic surface.

DISCUSSION

We report the discovery of mechanics-driven H3K9me3 and SWI/SNF CRC regulation in MSC. We show that inhibition of the chromatin remodeling can enhance the quality of MSC. In the future we will investigate if the inhibition of SWI/SNF CRC and H3K9me3 can improve the MSC stemness, thus increasing the MSC functionality.

REFERENCES

- [1] Kureel, S et al., *Biology Open*, 8:312-319, 2019.
- [2] Kaonis, S et al., bioRxiv, 2022
- [3] Heo, SJ et al., *Nature BME*, 8, 2022.

THE ROLE OF HYALURONIC ACID IN THE SYNERGISTIC LUBRICATION OF ARTICULAR CARTILAGE

Emily P. Lambeth (1), David L. Burris (2), Christopher Price (1)

(1) Biomedical Engineering, University of Delaware, Newark, DE, USA
(2) Mechanical Engineering, University of Delaware, Newark, DE, USA

INTRODUCTION

Articular cartilage is a phenomenal lubricating material, facilitating remarkably low friction coefficients *in vivo* ($\mu \leq 0.005$).¹ Only recently have innovative *ex vivo* studies been able to recapitulate cartilage's unmatched *in vivo* lubricity on the benchtop, a feat enabled via our re-deployment of the convergent stationary contact area (cSCA) testing configuration.^{2,3} In the cSCA, and in the presence of PBS, sliding promotes the speed-dependent, hydrodynamically mediated recovery and maintenance of high fluid load support (FLS), interstitial lubrication (ISL), and low friction values ($\mu \sim 0.03$), via a mechanism termed 'tribological rehydration'.² Intriguingly, when synovial fluid (SF) was introduced into high-speed cSCA studies, truly *in vivo*-like equilibrium frictions ($\mu < 0.004$) were recorded on the benchtop for the first time.³ We have termed this frictional benefit, arising from the presence of SF and hydrodynamically driven recovery of ISL by tribological rehydration, 'synergistic lubrication'.

The unanticipated discovery of SF-mediated 'synergistic lubrication' in rapidly articulated cSCA contacts raises two critical questions: 1) What is the mechanism underlying lubrication synergy in cartilage? And 2) what aspects of SF mediate this synergy? SF is composed of numerous macromolecules postulated to influence cartilage lubrication in a variety of ways, from mediating viscous to boundary lubrication.^{3,4} One of these is hyaluronic acid (HA). HA is a non-sulfated high-molecular weight glycosaminoglycan (typically $> 7\text{MDa}$) found in SF at concentrations ranging from 1-3mg/mL.⁵

While HA contributes to increasing the viscosity of SF⁵⁻⁷ and has been traditionally thought to provide boundary lubricating activates to articular cartilage^{5,8,9}, the role that HA plays in promoting/regulating synergistic lubrication is unknown. Here, we explored friction mitigating interactions among hydrodynamics and ISL recovery (both titrated through sliding speed-dependent behaviors in cSCA explants) and HA presence (titrated by varying HA concentration and molecular weight [MW]) on the benchtop.

METHODS

$\Phi 19\text{mm}$ osteochondral explants were extracted from the femoral condyles of skeletally mature bovine stifles.^{2,3} Explants were rinsed and stored in 1X PBS to which sucrose was added to approximate the osmolality of synovial fluid (400mOsm¹⁰; hereon referred to as PBS).

Two studies were performed to examine the effects of HA concentration and MW on cSCA explant lubrication using a custom reciprocating tribometer.² All explants were preconditioned (**Fig 1A**) by being statically compressed against a glass counterface for 30 min at 9N, followed by a load reduction to 5N for 15 min, before being slid at 10, 80, and 10mm/s for 15 min each (under 5N).

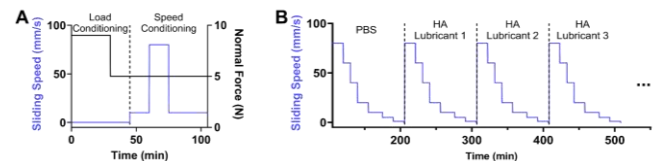


Figure 1: Schematic showing: (A) cSCA explant preconditioning and (B) the “speed sweep” conditions of HA concentration/molecular weight tests. All sliding tests were conducted under a constant 5N compressive load ($\sim 0.2\text{MPa}$).

In study 1, after preconditioning, sliding “speed sweep” tests were conducted (at 5N) to investigate the effect of HA concentration on speed-dependent friction coefficients in the cSCA (**Fig 1B**). 1-1.8MDa. HA dissolved in PBS was sequentially tested at 0, 0.1, 1.5, and 5.0mg/mL. For all tests, sliding conditions (*e.g.*, sliding speed or bathing solution) were only changed when deformation and friction equilibria (*i.e.*, rates of change $< 1\mu\text{m/min}$ & $< 0.01\mu\text{m/min}$ or $< 0.001\mu\text{m/min}$ [for $\mu > 0.1$ & < 0.1 , respectively] were achieved at the prior condition).

In study 2, “speed sweep” tests, as described in study 1, were performed to explore the effect of HA MW on cSCA lubrication (**Fig**

1B). Tested HA MW included 20-40kDa, 301-450kDa, and 1.01-1.8MDa HA (each at 1.5mg/mL).

Equilibrium compression and kinetic friction coefficients for each sliding speed and HA combination were recorded in LABVIEW and analyzed in MATLAB.

RESULTS

In a manner unique to the cSCA configuration, the lowest observed equilibrium friction (μ_{eq}) values always occurred at sliding speeds $>40\text{mm/s}$, while maximum μ_{eq} values occurred at speeds $<5\text{mm/s}$ regardless of HA concentration (Fig 2A). Both maximal and minimal μ_{eq} (at slow and high-sliding speeds, respectively) decreased with increasing HA concentration (Fig 2B,C). The lubrication benefit associated with tribological rehydration at high sliding speeds in the cSCA ranged from 8.8-fold in PBS to 25-fold in 5mg/mL HA; with increasing HA concentration associated with increased lubrication synergy. Finally, increasing HA concentration monotonically reduced the sliding speeds at which equivalent levels of lubrication—defined as μ_{eq} corresponding to that of PBS at 80mm/s—was achieved (Fig 2D; e.g., for 5mg/mL HA equivalent lubricity was achieved at 20mm/s).

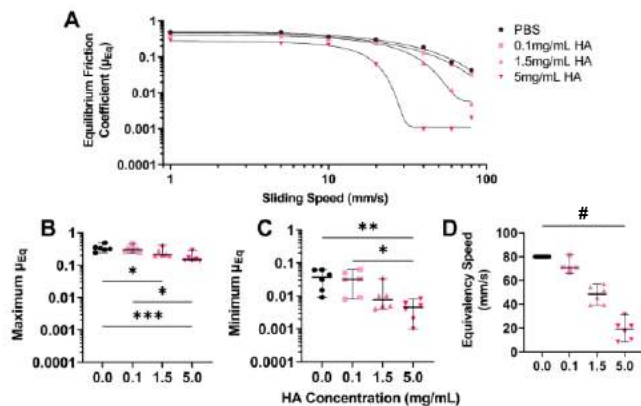


Fig 2: (A) Representative equilibrium friction (μ_{eq}) vs. sliding speed curves for a sample in PBS (black) vs. three HA concentrations (pink). (B) Maximum, (C) minimum μ_{eq} values, and (D) equivalency speeds at each HA concentration. (* $p<0.05$, ** <0.01 , * <0.001 , one-way ANOVA; # all comparisons $p<0.05$).**

Study 2, investigating the impact of HA MW—at 1.5mg/mL—on cSCA lubrication, produced results consistent with the speed-dependent synergistic lubrication effects seen above (Fig 3A). Tests using HA of increasing MW—from ~30kDa to ~1.4MDa—suggested a trend of molecular weight-dependent reductions in μ_{eq} at high sliding speeds (Fig 3B,C) and reduction in sliding speeds at which equivalent levels of lubricity were encountered (Fig 3D). Studies on further samples will be required to power this data similarly to synergy experiments in study 1.

DISCUSSION

The cSCA configuration, because it can precisely titrate interfacial hydrodynamics and FLS through speed-dependent control of tribological rehydration represents a novel tool for studying the role of HA (and other SF components) in mitigating articular cartilage friction.

In the absence of hydrodynamics and tribological rehydration (e.g., at slow sliding speeds), HA appears to function as a modest, classically understood boundary lubricant - one that is marginally impacted by concentration and MW. However, as hydrodynamic forces are generated by increasing cSCA sliding speeds the effect of HA on friction evolves dramatically. As sliding-induced tribological rehydration drives the recovery of interstitial pressure (i.e., FLS), HA

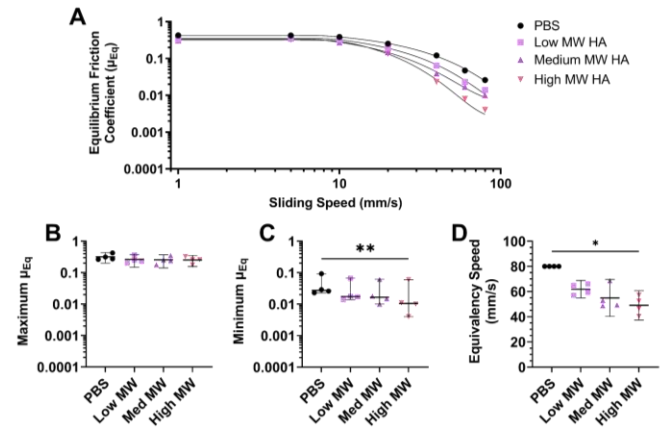


Fig 3: (A) Representative equilibrium friction (μ_{eq}) vs. sliding speed curves for a sample in PBS (black) vs. three HA molecular weights (purple). (B) Maximum, (C) minimum μ_{eq} values, and (D) equivalency speeds at each HA molecular weight. (* $p<0.05$, ** $p<0.01$, paired t-test or ANOVA)

transitions from a modest boundary lubricant to one having tremendous synergism with ISL.

High concentration and high MW HA provided the largest synergistic benefits (e.g., friction reductions) upon ISL recovery, generating μ_{eq} values at the limit of our detection ($\mu \sim 0.002$) at high sliding speeds. Furthermore, these benefits increased in proportion to HA concentration; findings that were confirmed through refined “concentration sweep” tests on 1.01-1.8MDa HA at 0, 0.1, 0.5, 1, 1.5, 2, 3, 4, and 5mg/mL under 50mm/s sliding (data not shown)—50mm/s was chosen because it was the sliding speed (in study 1) associated with the largest variance in μ_{eq} across HA concentrations due to its fostering of sub-maximal levels of tribological rehydration and FLS.

Because lubricant viscosity increases with HA concentration and MW⁵⁻⁷, careful consideration of the sliding-speed and HA-dependent behaviors of the cSCA contact suggest—indirectly—the renewed possibility of interfacial fluid film-mediated lubrication of cartilage. However, such fluid films only appear to be generated upon the ‘full’ recovery of interstitial pressure and ISL by TR. Considering mass/fluid-balance under such conditions, the ‘porous’ cartilage interface could be made ‘effectively’ impermeable to fluid influx by the presence of large interstitial pressures and maximal FLS; presenting a possible solution to the nagging paradox of how a ‘porous’ cartilage surface could support fluid film-based lubrication.^{4,11,12} Studies characterizing the effect of bath viscosity, in the presence and absence of HA, are continuing to explore the role of viscosity in articular cartilage lubrication (and in fluid film generation).

Overall, the present study highlights a crucial synergy between interstitial hydration and HA-presence in regulating cartilage lubrication under biofidelic conditions of high FLS and high sliding speeds. These insights continue to advance our objective of identifying a unifying framework to explain cartilage’s unmatched lubricity *in vivo* and to better understand how healthy and diseased cartilage works.

REFERENCES

- [1] Linn, *J Biomech*, 1968.; [2] Moore & Burris, *OA&C*, 2017; [3] Farnham et al, *Trib Let*, 2021; [4] Bonnevie & Bonassar, *J Biomech Eng*, 2020; [5] Fam et al, *Biorheol*, 2007; [6] Krause et al, *Biomacromol*, 2001; [7] Miyazaki et al, *J Appl Polym Sci*, 1998; [8] Ogsten & Stanier, *J Physiol*, 1953; [9] Bonnevie et al, *PLoS One*, 2015; [10] Baumgarten et al, *J Bo Join Surg*, 1985; [11] McCutchen, *Wear*, 1961; [12] Dowson, *Proc Instn Mech Engrs*, 1967.

BLEBBISTATIN AS A METHOD TO IMPROVE OUTCOMES FOLLOWING JOINT CAPSULE RELEASE SURGERY IN AN *IN VIVO* RAT ELBOW MODEL

Austin J. Scholp (1), Timothy P. Fowler (2), Emily Petersen (2), Douglas Fredericks (2), James A. Martin (2), Aliasger K. Salem (3), Edward A. Sander (1,2)

- (1) Roy J. Carver Department of Biomedical Engineering, University of Iowa, Iowa City, IA, USA
(2) Department of Orthopedics and Rehabilitation, University of Iowa, Iowa City, IA, USA
(3) Department of Pharmaceutical Science, University of Iowa, Iowa City, IA, USA

INTRODUCTION

Elbow trauma can lead to joint contracture and a reduced range of motion (ROM) that can limit one's ability to perform activities of daily living¹. Contracture is characterized by thickening and stiffening of the joint capsule. Nonsurgical interventions such as physical therapy or splinting may be able to improve ROM. When these approaches are not always successful, capsule release surgery is a treatment option. While surgery can improve ROM, ROM typically does not return to pre-injury ranges. Thus, alternative or adjuvant therapies are needed².

Activated myofibroblasts are a common feature found in fibrotic tissue³. Myofibroblasts, which can be distinguished by their expression of alpha smooth muscle actin (α -SMA), can generate large traction forces and deposit collagen and other extracellular matrix (ECM) proteins at the site of injury⁴. Biomechanical and biochemical interactions between myofibroblasts and their environment produce a feedback loop that can result in either normal or pathological healing³. We hypothesize that this feedback loop can be manipulated so that myofibroblast activity is reduced, normal healing is achieved, and ROM is improved or restored.

One strategy for controlling this feedback loop we are exploring is to temporarily block non-muscle myosin II (NMMII)-actin engagement in myofibroblasts with the drug blebbistatin. We have previously demonstrated that blebbistatin and blebbistatin-loaded PLGA microparticles significantly reduced fibroblast force development and collagen production *in vitro*^{5,6}. Use of this drug in conjunction with capsule release surgery might offer a way to improve and maintain outcomes. Thus, we tested the effects of capsule release surgery with and without blebbistatin in an established Long-Evans rat model of elbow contracture developed by Lake et al.⁷

METHODS

Injury Model: This protocol was approved by the University of Iowa IACUC (Protocol 2072222-004). Joint contracture was induced in 9 groups of 4 rats (n=36) using the procedure described by Lake et al.⁷ Briefly, the left elbow of each rat underwent an anterior capsulotomy,

transection of the lateral collateral ligament, and joint subluxation. The injured arm was then immobilized for 6 weeks.

Blebbistatin: Blebbistatin was administered two different ways. First, racemic blebbistatin was delivered using poly(lactic-co-glycolic acid) (PLGA) microparticles. These were produced using an oil-in-water single-emulsion technique described in our previous work². Microparticles were delivered in a hydrogel solution made up of 22.3% F-127 PluronicTM, 1% GelOne®, and 1x phosphate buffered saline with proportions of 76.4%, 20%, and 3.6%, respectively. The hydrogel and microparticles were delivered to the elbow after capsule release surgery. Second, daily systemic injections of blebbistatin were also tested following capsule release surgery. Blebbistatin was diluted to 1 mg/mL in a vehicle of 0.9% saline with 6.7% dimethyl sulfoxide (DMSO) and 25% hydroxypropyl β -cyclodextrin (w/v). Blebbistatin was delivered at a dosage of 5 mg/kg. For the first 4 days post-release, rats received injections intraperitoneally to ensure that peak drug concentrations were reached quickly during the early phases of healing. Subcutaneous injections were performed thereafter to reduce handling of the forelimbs during injection, which could aggravate the healing elbow and to lessen the potential for internal injury or injection into organs.

Mechanical Testing: At the end of the study, all arms were mechanically tested. The uninjured contralateral arms of each rat were used as a control group. Mechanical testing for this study was similar to the protocol outlined by Lake et al.⁷ Briefly, the upper limb was disarticulated at the glenohumeral joint, and the paw was removed at the wrist. The humeral head and wrist were mounted into polycarbonate tubing. A custom-built flexion-extension device interfaced with an ElectroForce® Planar Biaxial Test Bench Instrument (shown in figure 1). It was operated in load control and cycled between 10 N-mm in flexion and extension.

Statistical Analysis: One-way ANOVA with post-hoc Tukey's tests were used to assess significant differences ($p < 0.05$) between groups. Statistical analysis was performed in Prism GraphPad 9.4.1.

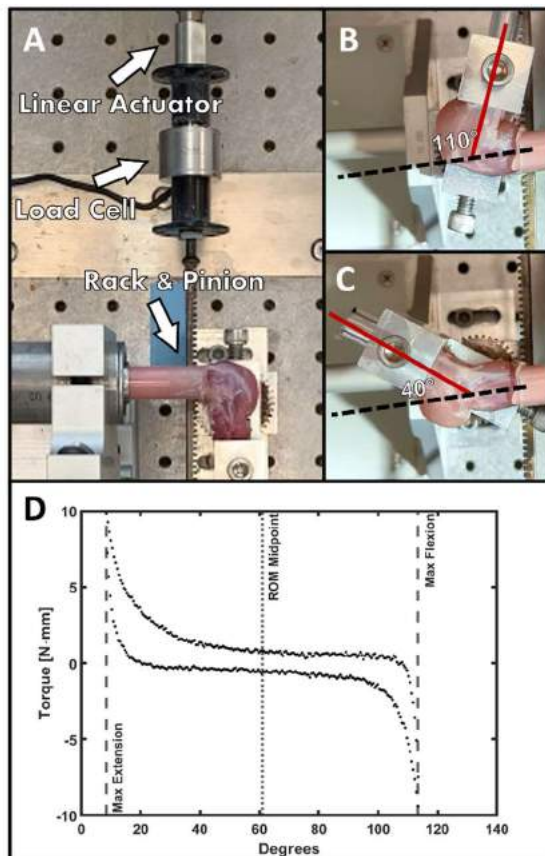


Figure 1: (A) Image of the mechanical testing setup. (B & C) Examples of how flexion and extension angles are measured. (D) Plot of typical torque-angle curve for an uninjured arm.

Study Timeline: After contracture was established (6 weeks post-injury) the first group of 4 rats was euthanized. The remaining 8 groups had restraints removed and were allowed to freely use their injured arms (remobilization) for 3 weeks. At this point (9 weeks post-injury), the second group of rats was euthanized. The last 7 groups received the following treatments:

- 3 additional weeks of free use of injured arm (euthanized 12 weeks post-injury)
- Capsule release surgery with a 1-week recovery period (euthanized 10 weeks post-injury)
- Capsule release plus blebbistatin hydrogel and a 1-week recovery period (euthanized 10 weeks post-injury)
- Capsule release with a 3-week recovery period (euthanized 12 weeks post-injury)
- Capsule release plus hydrogel and a 3-week recovery period (euthanized 12 weeks post-injury)
- Release followed by 3 weeks of daily vehicle injections (euthanized 12 weeks post-injury)
- Release followed by 3 weeks of daily blebbistatin injections (euthanized 12 weeks post-injury)

RESULTS

Remobilization: Free use of the injured arm did not improve max extension angles significantly after either 3 or 6 weeks (9 or 12 weeks post-injury). Remobilization was also not significantly different from capsule release 3 weeks after surgery. Note that a lower max extension angle equates to a better outcome.

Capsule Release: By itself, capsule release significantly ($p < 0.05$) improved the angle of maximum extension 1 week after surgery (10 weeks post-injury) compared to the injury-only group and was not significantly different from the uninjured group. Three weeks after surgery (12 weeks post-injury), the max extension angle was also significantly better than injury but was also significantly ($p < 0.05$) worse than the uninjured arms.

Microparticles: One week post-release, the max extension angle for arms that received blebbistatin microparticles was significantly greater than that of the uninjured arms ($p < 0.05$) while the arms that did not receive blebbistatin were not significantly different from the uninjured. Three weeks post-release, both the release-only and the blebbistatin groups had significantly worse max extension.

Injections: Maximum extension angles between the groups that received daily blebbistatin and daily vehicle injections were not significantly different. Both groups were significantly different from the uninjured control ($p < 0.05$). Comparisons between groups can be found in figure 2.

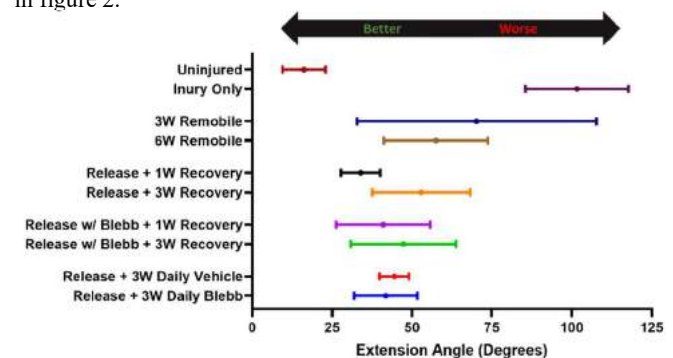


Figure 2: Comparison of maximum extension angles (mean \pm standard deviation) between all groups. Dashed lines mark the mean angles for the uninjured and injury-only arms; dotted lines mark the standard deviations. Note that a lower max extension equates to a better outcome.

DISCUSSION

Overall, capsule release surgery improved maximum extension. However, the improvement seen at 1 week was reduced at 3-weeks post-surgery, indicating that the contracture may return following surgery. This is often observed clinically in patients undergoing capsular release surgery. Blebbistatin did not provide a significant improvement in maximum extension compared to capsule release surgery alone, but it may have reduced the loss of ROM observed three weeks after release surgery. Future work will investigate the long-term effects of capsule release and other treatments on this contracture model.

ACKNOWLEDGEMENTS

Support for this work was provided by the National Institutes of Health (NIH 1R21AR075137-01A1). We would also like to thank the Lake lab at Washington University for their assistance

REFERENCES

- [1] Morrey et al., *J Bone Joint Surg Am*, 63:872-877, 1981
- [2] Lindenhovius et al., *J Hand Surg Am*, 34:858-865, 2009
- [3] Hinz, *J Biomech*, 43:146-155, 2010
- [4] Hildebrand, et al. *Clin Orthop Relat Res*, 419:189, 2004
- [5] Scholp, et al., *Front Bioeng Biotechnol*, p1180, 2022
- [6] Atluri, et al., *ACS Biomater Sci Eng*, 2:1097-1107, 2016
- [7] Lake, et al., *J Orthop Res*, 34:354-364, 2016

SPATIAL CONFIGURATIONS OF 3D EXTRACELLULAR MATRIX DENSITY AND ANISOTROPY SIMULTANEOUSLY GUIDE ANGIOGENESIS

Steven A. LaBelle (1,2), Steve A. Maas (1,2), Adam Rauff (1,2), Gerard A. Ateshian (3), Jeffrey A. Weiss (1,2)

- (1) Department of Biomedical Engineering, University of Utah, Salt Lake City, UT, USA
(2) Scientific Computing and Imaging Institute, University of Utah, Salt Lake City, UT, USA
(3) Department of Mechanical Engineering, Columbia University, New York, NY, USA

INTRODUCTION

Extracellular matrix (ECM) collagen fibril anisotropy and density have mechanoregulatory roles during cellular growth and guidance. The configuration of matrix fibril alignment and density are thought to affect the development of new vasculatures during pathologic and homeostatic angiogenesis [1]. For instance, healing and disease progression may be influenced by gradients and discontinuities in ECM density and anisotropy such as those in entheses (bone-tendon/ligament/fascia attachment sites) and in peri-tumoral regions.

We recently demonstrated that microvascular growth rate and orientation simultaneously depend on the ECM density and anisotropy [1]. While ECM density generally reduced neovessel growth, microvessel growth rate returned to baseline levels when the degree of anisotropy (DA) was high. These results suggested that the spatial configuration of ECM density and anisotropy influence neovascularization at tissue boundaries and structural gradients.

Computational simulation is emerging as a tool to investigate the role of matrix structural configurations on cell guidance. Prior computational models of angiogenesis and cell guidance have only been sensitive to ECM density and the dominant ECM collagen direction regardless of the DA [2]. Thus, the objective of this study was to incorporate our prior experimental finding that angiogenic neovessels are simultaneously sensitive to ECM density and ECM anisotropy (orientation and DA). We found that high DAs embolden neovessels to migrate long distances and persist through high ECM collagen density.

METHODS

Simulations of microvascular guidance: Biomechanical simulations of angiogenesis were performed using Finite Elements for Biomechanics (FEBio) [3]. The mechanical model was coupled with AngioFE, a growth model that simulates angiogenic neovessel growth from parent microvessels suspended in hydrogels [2]. The ECM was

represented as a biphasic viscoelastic material with a solid mixture comprising a neo-Hookean ground matrix and a continuous collagen fibril distribution governed by an exponential-power law response. During model initialization, AngioFE suspended parent microvessel fragments within the ECM and prescribed the local ECM density and collagen fibril orientation distribution function (ODF). Microvessel tips sprouted into neovessels that grew and contracted the ECM during simulation. We modified AngioFE such that the growth rate simultaneously depended on the ECM density and the DA. Growth parameters were calibrated from prior experiments [1].

Initial collagen ODFs, \mathbf{P}^0 , were assumed to be ellipsoidal, symmetric, positive-definite (SPD) tensors. \mathbf{P}^0 were constructed via: the spectral-decomposition:

$$\mathbf{P}^0 = \sum_{i=1}^3 \beta_i^0 \mathbf{n}_i^0 \otimes \mathbf{n}_i^0, \quad (1)$$

where β_i^0 were the initial semiprincipal axis lengths of the ellipsoid and \mathbf{n}_i^0 were the initial directions of the semiprincipal axes. As the ECM deformed due to cellular tractions some ODFs became distorted and were no longer elliptical (SPD). For the mechanical model, the directional response of deformed collagen fibrils at each finite element integration point was calculated via Gauss-Kronrod-trapezoidal integration [4]. For the growth model the deformed ODF was approximated as an SPD via ODF pseudo-deformation [5]. This was necessary to allow spatial interpolation of ODFs because neovessel growth was sensitive to the local collagen ODF [6].

Simulations of anisotropy gradients: Microvessel growth was simulated across an isotropic matrix or an anisotropy gradient to determine how structural configurations affect neovascular recruitment. A rectilinear geometry was separated into 3 regions (near, middle, far) with microvessels originating in the near region. Anisotropy increased (positive) or decreased (negative) between the near and far regions.

Simulations of tumor associated collagen signatures: Tumor-associated collagen signatures (TACS) are configurations of matrix density and structure found near some tumors [7]. To explore how different TACS affect tumor angiogenesis, microvessels were suspended in a tissue separated from a nearby tumor by an interface. The interface structural properties were modified to include high-density collagen (TACS-1), circumferential alignment (TACS-2), radial alignment (TACS-3), or a combination (TACS-1+2, TACS-1+3).

RESULTS

Anisotropy gradients recruit neovessels: In the baseline case (isotropic ECM), microvessels modestly vascularized the middle but not the far region (Fig. A). In the cases with anisotropy gradients, neovessels grew into the middle and far regions. Microvessels grown in a negative anisotropy gradient more thoroughly vascularized the middle region of the simulation domain than those originating near a positive gradient but there was no difference in vascularization of the far region.

Anisotropy enhances neovessel recruitment at TACS: In the baseline case (no TACS), microvessels grew from the periphery into the tumor (Fig. B). A high-density interface (TACS-1) greatly reduced tumor vascularization. Circumferential fibril alignment (TACS-2) led to microvascular growth along the interface but baseline levels of tumor vascularization. Radial fibril alignment (TACS-3) facilitated the highest level of tumor vascularization. The combined presence of elevated density and circumferential fibril alignment (TACS-1+2) resulted in the least tumor vascularization. Alternatively, the combined presence of elevated density and radial fibril alignment (TACS-1+3) resulted in a similar level of vascularization as the baseline case.

DISCUSSION

This research improved predictive tools to understand the impact of ECM structural configuration during cell guidance. Previously, the DA was not used as a model input in studies of cell migration, despite evidence that the DA affects cell behaviors and guidance [1].

Anisotropy gradients potentially recruited neovessels across long distances regardless of gradient orientation. However, the middle region of the positive gradient was less vascularized in comparison to the negative gradient; thus, positive gradients are more efficient at vascularizing across long distances since. As neovessels grew up the positive gradient, the potency of matrix growth and guidance cues increased. In contrast, the potency of guidance cues decreased as neovessels grew along the negative anisotropy gradient.

To explore the roles of matrix density and anisotropy in tumor angiogenesis, we simulated angiogenesis between a host and a tumor. Radial fibril alignment (TACS-3, TACS-1+3) dramatically increased tumor vascularization. This is consistent with clinical observations that TACS-3 appears in aggressive cancers with poor prognoses [7]. Interestingly, circumferential fibril alignment (TACS-2, TACS-1+2) had a negligible effect on tumor vascularization since the DA increased the persistence of deflected neovessels. Such neovessels would likely be susceptible to tumor cytokines which were absent in our simulations.

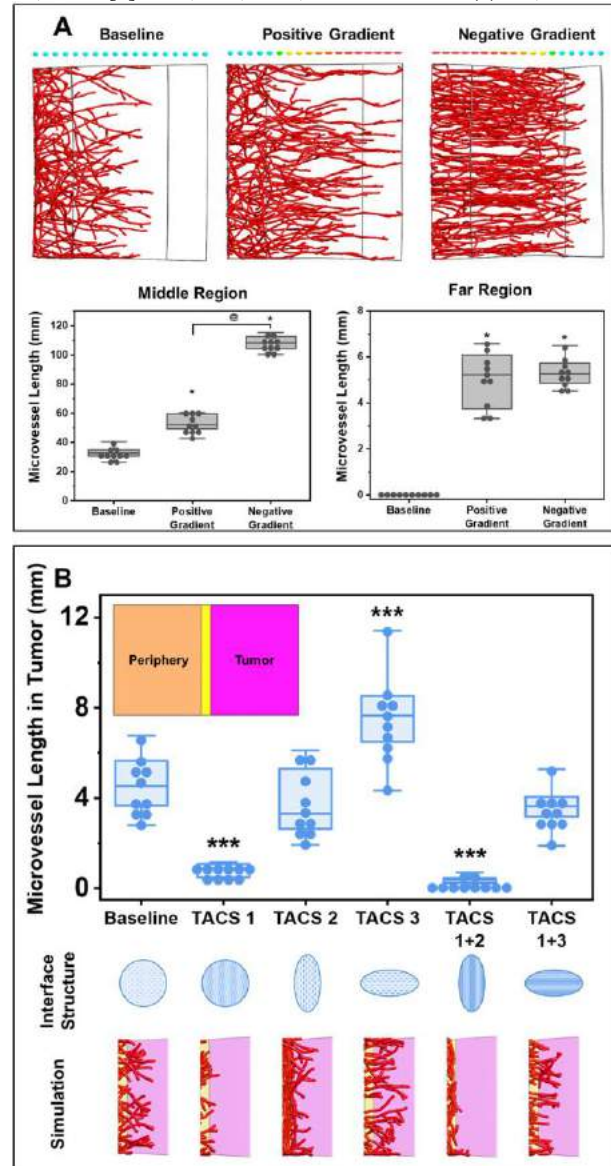
Our simulations were performed in the absence of biochemical signaling which allowed us to explore the isolated role of matrix structural patterning during neovessel guidance. AngioFE will be expanded in the future to include biochemical signaling to understand the coordination of biophysical and biochemical stimuli.

ACKNOWLEDGEMENTS

Funding from NIH R01HL131856, NIH R01GM083925, and NIH R01AR069297 are gratefully acknowledged.

REFERENCES

- [1] LaBelle, SA., et al., *AJP Heart Circ. Phys.* 322(5): H806-18, 2022.
- [2] Edgar, LT., et al., *Ann. Biomed. Eng.* 43(7): 1531-1542, 2015.
- [3] Maas, SA., et al., *J. Biomech. Eng.* 134(1):011005, 2012.
- [4] Hou, C. & Ateshian, GA., *Comput. Methods Biomech. Biomed. Engin.* 19(8): 883-93, 2016.
- [5] Barocas, VH. & Tranquillo, RT., *J Biomech Eng.* 119(2): 137-45, 1997.
- [6] Fletcher, PT. & Joshi, S., *Signal Process.* 87(2): 250-62, 2007.
- [7] Brett, EA., et al., *Cancer Metab.* 8(1): 14, 2020.



Figures. **A) Anisotropy gradients influence long-range neovessel recruitment.** Growth was either simulated in an isotropic ECM (baseline) or an ECM characterized by a positive or negative anisotropy gradient. Top: Simulation results. Ellipsoidal glyphs indicate the DA (blue: low; red: high). Bottom: Relative vascularization of each region (*: $p < 0.05$ w.r.t baseline; @: $p < 0.05$ pairwise comparison, 1 way ANOVA with Holm-Sidak post hoc). **B) Anisotropy increases tumor vascularization while ECM density decreases it.** Top: Tumor vascularization of each TACS. Model geometry presented as an inset (top left). Middle: Corresponding glyphs indicating interface structure (anisotropy, density). Bottom: Corresponding simulation visualizations (***: $p < 0.001$. 1 Way ANOVA with Sidakholm post hoc test).

TOWARD REAL-TIME SIMULATION OF CARDIOVASCULAR FLOWS BY INTRODUCING A STABILIZED TIME-SPECTRAL FINITE ELEMENT METHOD

Dongjie Jia (1), Mahdi Esmaily (1)

(1) Sibley School of Mechanical and Aerospace Engineering, Cornell University, Ithaca, New York, USA

INTRODUCTION

The finite element methods for the solution of the Navier-Stokes equation have found common use for simulating cardiovascular flows [1]. These simulations typically use periodic boundary conditions for physiological relevance. In another word, it is common to impose a periodic pressure or flow-rate profile at the boundaries given that the heart beats in cycles. This results in a solution that is unsteady and often periodic. To capture this behavior, a conventional finite element method uses time-stepping to resolve the unsteady behavior of the flow. That is done so by starting from a zero-velocity field and simulating multiple cardiac cycles to wash the initial condition and obtain cycle-to-cycle convergence. As a result, the overall cost of these simulations is significant, potentially taking days for a typical cardiovascular simulation to complete. For example, the cardiac flow in a Norwood procedure requires simulating 10 cardiac cycles to ensure numerical convergence (Figure 1) [2]. In the end, results are only taken from one cardiac cycle after the simulation is converged. More than 90% of the computational cost is spent on numerical convergence due to the unsteady and periodic nature of cardiovascular simulations.

What we propose is an alternative way of simulating these flows that can significantly reduce this cost. The key idea here is to perform simulations in the frequency rather than the time domain, thereby obviating the need to simulate many cycles for convergence. Also, since the periodic flows can be represented with a few frequency modes (spectral modes) in the frequency domain, we no longer need to rely on thousands of time steps to resolve the unsteady nature of these flows. It is by exploring these two major cost savings strategies that a time-spectral formulation can reduce the overall cost of a cardiovascular simulation from hours or days to seconds or minutes.

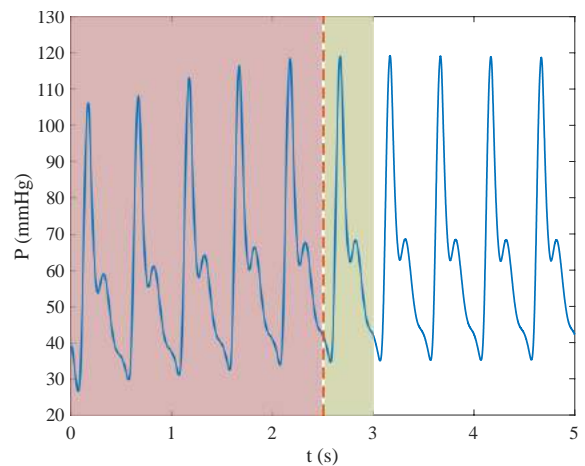


Figure 1: Pressure history for a cardiovascular simulation starting from a zero-velocity field. The converging phase is colored in red, and the converged solution is colored in green.

In our previous study, we introduced a stabilized finite element formulation for solving the linear Stokes equation in the frequency domain [3] that improved upon a non-stabilized earlier formulation of the same problem [4]. By decomposing the Stokes equation into different modes and separating the real and imaginary parts. This formulation eliminates the need for time-stepping, thus eliminating the computational cost of reaching a cycle-to-cycle converged solution. In addition, due to the periodic nature of the cardiovascular simulation, the flow information can be fully represented with a handful of modes. Furthermore, since the spectral modes are independent, they can be calculated in parallel, which further shortens the simulation wall-clock time. Using a patient-specific geometry, we achieved a 1% error with less than 1% of the simulation time compared to the conventional finite

element method. However, due to the Stokes limit, this method is only realistic for the blood flow in the smallest blood vessels in the human circulatory, where Reynolds number approaches zero. Extending this method to finite-Reynolds numbers for most cardiovascular simulations requires solving the Navier-Stokes equation in the frequency domain.

In this talk, we will introduce the spectral-Navier-Stokes finite element formulation that solves the Navier-Stokes equation in the frequency domain. First, we will present the formulation and numerical methods we used to build this formulation. We will use two cases, one single vessel flow, and one Norwood flow, to compare our method to the conventional method in terms of both accuracy and computational speed. Lastly, we will discuss the real-life clinical indications of our method and potential shortcomings.

METHODS

The Spectral-Navier-Stokes equation is formulated as the following. For each spectral mode m ,

$$\begin{aligned} i\rho\omega_m \mathbf{u}_m + \mathbf{u}_a \nabla \mathbf{u}_b &= -\nabla p_m + \mu \nabla^2 \mathbf{u}_m \quad \text{in } \Omega, \\ \nabla \cdot \mathbf{u}_m &\quad \text{in } \Omega, \\ \mathbf{u}_m &= \mathbf{g}_m \quad \text{on } \Gamma_g, \\ (-p_m \mathbf{I} + \mu \nabla \mathbf{u}_m) \cdot \mathbf{n} &= \mathbf{h}_m \quad \text{on } \Gamma_h, \end{aligned} \quad (1)$$

where a and b are all modes that satisfies $a + b = m$, $i = \sqrt{-1}$, ω_m is the oscillation frequency, \mathbf{u}_m is the velocity, p_m is the pressure, \mathbf{g}_m is the imposed modal velocity on the Dirichlet boundary Γ_g , and \mathbf{h}_m is the imposed modal traction on the Neumann boundary Γ_h .

We will derive an appropriate stabilized finite element method that will be similar to the Streamline upwind/Petrov-Galerkin method [5]. Mode-coupling techniques for the non-linear term in the Navier-Stokes equation between different spectral modes will also be developed and presented.

RESULTS

This is an ongoing study. The first planned simulation result is a flow in a straight pipe, which is the simplest flow in a blood vessel. We will use this case to demonstrate the stability, accuracy, and speed of our numerical method by comparing the solution to that of the conventional method and the analytical solution.

Afterward, we plan to simulate a realistic cardiac flow, namely the Norwood procedure with a Blalock-Taussig shunt (Figure 2), using both the proposed spectral method and the conventional finite element method. With this complex simulation, we can demonstrate the significant simulation speed advantage of our method. We will also show that the difference in simulation results is within acceptable margins.

Expected results should show a significant reduction in computational cost and overall simulation time. The differences in results between the conventional method and the introduced method should be within 1%.

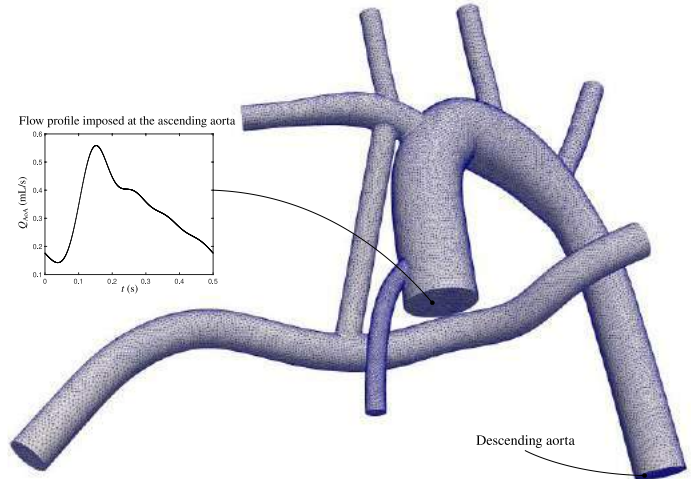


Figure 2: Simulation setup for the Norwood procedure with Blalock-Taussig shunt. A flow rate profile is imposed at the ascending aorta

DISCUSSION

Earlier studies have shown that the proposed method at the Stokes limit significantly shortens the simulation time and reduces computational costs [3,4]. It is the goal of this study to show the same cost-saving advantage for the finite Reynolds number periodic flow simulations, such as simulating cardiovascular flow. This improvement will enable various clinical and surgical applications, such as same-day diagnostic, surgical planning, and virtual surgery. Currently, CFD is mostly used as a diagnostic tool in the clinical environment, where the simulation will be built from a patient-specific MRI scan but must be run on a dedicated computer cluster for several days. With the proposed method, the CFD simulations could potentially be run on an on-site computer within the same day, or even within an hour, which provides critical hemodynamical information to clinicians in a timelier manner. This improvement in computational efficiency can also help advise surgical planning, where multiple geometries and flow configurations need to be simulated, which was not possible due to prohibiting large computational costs using the current CFD methods.

A limitation of the proposed method is that it relies on the assumption that the simulation can be resolved with a small number of frequency modes, which is the case for most cardiovascular simulations. However, there could be instances that a significant number of modes need to be used, most likely when an assist device is present in the circulatory system. In this case, the cost advantage might not be as significant.

REFERENCES

- [1] Updegrave, A. et al., *Annals of biomedical engineering*, 45(3), 525-541, 2017.
- [2] Jia, D. et al., *Journal of Biomechanical Engineering*, 143(7), 2021.
- [3] Esmaily, M. et al., *Journal of Computational Physics*, 473, 111736, 2023.
- [4] Meng, C. et al., *Journal of Computational Physics*, 445, 110601, 2021.
- [5] Brooks, A. N. et al., *Computer methods in applied mechanics and engineering*, 32(1-3), 199-259, 1982

INFLUENCE OF FRAGMENT IMPACT ATTRIBUTES ON CUTANEOUS INJURY

O. Elsafty (1), R. Dauskardt (1,2)

(1) Department of Mechanical Engineering, Stanford University, Stanford, CA, USA
(2) Department of Materials Science and Engineering, Stanford University, Stanford, CA, USA

INTRODUCTION

Fragment impact injuries are one of the most common cutaneous injuries observed, often caused by flying glass shards in vehicle accidents, impacting debris in construction blasts, and from improvised explosive devices [1]. These injuries can lead to infection, function loss, and extensive scarring, particularly in the facial and extremity regions, severely deteriorating the affected individual's wellbeing. However, despite their significance, there is a poor understanding of the damage processes involved and the influence of projectile attributes on injury severity.

Previously, we characterized the damage mechanisms involved in cutaneous fragment impact injuries through experimental techniques and by developing a high-fidelity finite element (FE) model to predict cutaneous injuries [2]. We found that the two prevalent damage mechanisms were epidermal tearing, where the epidermis layer is peeled from the dermis layer, and dermal crushing, where permanent compression and damage to the dermis layer is observed, see Figures 1a and 1b, respectively. However, the contribution of each damage mechanism can vary significantly depending on fragment attributes, such as projectile shape and orientation at impact, necessitating a deeper understanding of the factors affecting these injuries. Here, we utilize our model to ascertain the effect of projectile shape on cutaneous injury severity and illustrate that fragment shape asymmetry can alter the injury type and damage process.

METHODS

A 3D multi-layered finite element damage model of skin was developed using ABAQUS EXPLICIT (2019) to analyze partial-thickness cutaneous injuries caused by projectile impact, see Figure 1c. To capture all the damage mechanisms involved in the injury process, it was essential to incorporate the three layers of the skin individually, including the stratum corneum, the living epidermis, and the dermis, as well as the hypodermis, which is the subcutaneous fatty tissue.

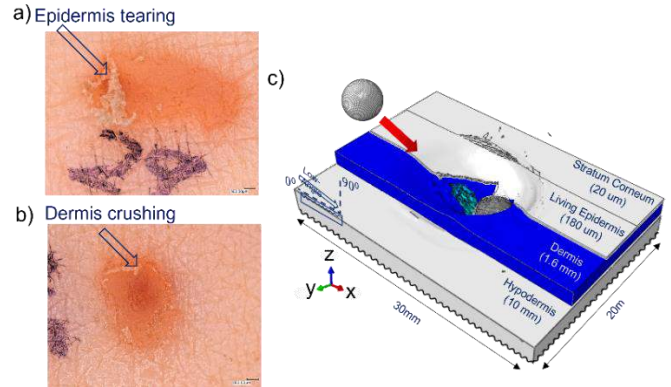


Figure 1: a) Epidermal tearing. b) Dermis crushing. c) Multi-layered 3D FE model for cutaneous fragment impact injuries.

The Ogden hyperelastic constitutive model was used for skin layer, apart from the dermis which was supplied the Gasser-Ogden-Holzapfel (GOH) constitutive model to capture its anisotropic behavior. The Ogden strain energy density, W , can be written in the form

$$W_{Ogden} = \sum_{i=1}^N \frac{2\mu_i}{\alpha_i^2} (\bar{\lambda}_1^{\alpha_i} + \bar{\lambda}_2^{\alpha_i} + \bar{\lambda}_3^{\alpha_i} - 3) \quad (1)$$

where λ_1 , λ_2 , and λ_3 are the principal stretches, $N=1$, and coefficients μ_i and α_i are temperature-dependent material parameters. The GOH strain energy density, W , can be written in the form

$$W_{GOH} = C(\bar{I}_1 - 3) + \frac{k_1}{2k_2} \sum_{i=4,6} [\exp\{k_2[\kappa \bar{I}_i + (1 - 3\kappa)\bar{I}_i - 1]^2\} - 1] \quad (2)$$

where C , k_1 , and k_2 are temperature-dependent material parameters. I_1 is the first deviatoric strain invariant, relating to the pressure, and I_4 and I_6 are the invariants relating to the stretches in the fiber directions for two families of collagen fibers. Finally, κ , describes the level of dispersion in the fiber direction.

Viscoelastic Prony series parameters were applied to the dermis and hypodermis, and inverse analysis was used to determine the failure parameters of each layer, using a critical stress damage criterion.

Displacement boundary conditions were implemented along the base of the hypodermis in the z-plane, and perpendicularly along the side surfaces in the x-direction and y-direction. 8-node linear hex elements with reduced integration (C3D8R) were used to mesh the model. A dynamic explicit analysis was performed for a 1.5ms duration.

The model was validated experimentally using a kinetic impact system designed to accelerate projectiles to impact full-thickness samples of near-live cadaverous abdominal human skin. The impact process and resulting wound morphology were analyzed using high-speed imaging techniques. Further details on the experiments and the parameters of the model can be found in our previous publication [2].

RESULTS

Spheres and cylinders were used in our analysis as they are the two most common fragment shapes found in explosive devices [3]. Due to the symmetric attributes of the cylinder, three impact orientations were tested, see Figure 2a, at impact angles varying from 15° to 90° and at 5.6 J/cm^2 . The resulting wound depths were measured both computationally and experimentally, averaged among the differing orientations, and a plot of the results, see Figure 2b, revealed a bifurcation in the cylinder curve with increasing impact angle. R^2 values of 0.71 and 0.91 were obtained for the sphere and cylinder projectiles, respectively. Wound depths for each individual orientation were also plotted for 90° impacts at energy densities ranging from $5.6\text{--}16.8 \text{ J/cm}^2$, see Figure 2c. The results indicate that the edge orientation (red) caused the largest wound depths and was the first orientation to cause injury perforation (wound depth $\geq 1.8\text{mm}$) where the projectile penetrates through all skin layers. However, both spheres and cylinders exhibited a positive relation between wound depth and energy density.

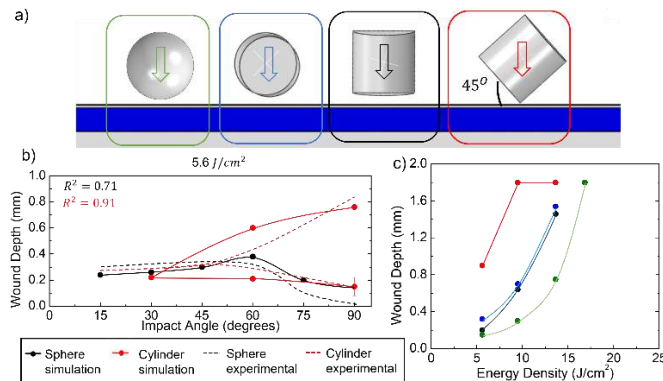


Figure 2: a) Projectile orientations at impact. b) Wound depth vs impact angle for spheres and cylinders at 5.6 J/cm^2 . c) Wound depth vs energy density for spheres and cylinders at 90° impact.

In addition to spheres and cylinders, common fragment shapes include cubes, tetrahedrons, and stellate octahedrons [3]. Simulations of projectile impact at 30° and 90° impact angles and at 5.6 J/cm^2 were performed for three times for each projectile, at different impact orientations, apart from the sphere due to its perfect symmetry, see Figure 3a. The results show significant differences in wound shape for the same impact input parameters. Stellate octahedrons showed a large chaotic wound pattern along with multiple wound depth segments. Tetrahedrons also had three wound depth segments, though its wound shape was not as complex as the stellate. The results also show an increasing trend in wound depth with shape complexity, and, apart from the sphere, a larger wound depth for 90° impacts compared to 30° , see

Figure 3b. However, large variations in wound depth (standard deviation of $\pm 0.58\text{mm}$) were observed for cubic projectiles at 90°

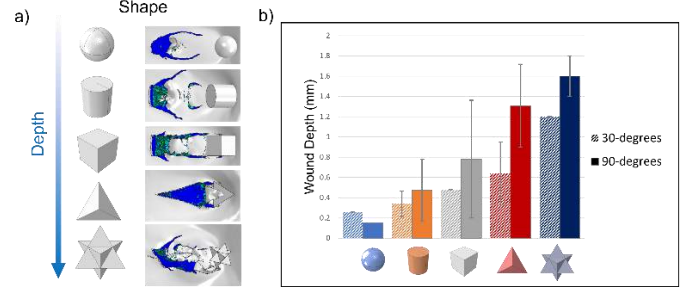


Figure 3: a) Fragment shapes and resulting injury at 30° impact. b) Wound depth vs fragment shape for 30° and 90° impact.

DISCUSSION

Results indicate that cylinders whose first point of impact with the skin was an edge showed a larger wound depth than other orientations. The edge effect was more significant at high-angled impacts due to larger perpendicular forces relative to low-angled impacts at the same energy density, causing a larger variation in wound depth for the former, leading to the bifurcation of the wound depth curve for cylindrical projectiles. Wound depths caused by spherical projectiles were shallower than cylindrical projectiles due to a lack of edges.

Comparing the five shapes, projectiles with sharper edges caused larger wound depths for both low-angled and high-angled impacts, and the sequence of increasing wound depth with projectile shape can be seen in Figure 3a. However, the orientation at impact was a key factor in determining the severity of the edge effect, causing a large variation in wound depth for the cubic projectile at 90° impacts. Depending on impact orientation, cubic projectiles could have lower or higher wound depths at low-angled impacts than at high-angled impacts. Moreover, due to larger forces perpendicular to the skin, wound depths were, on average, larger at 90° impacts than at 30° impacts, with spheres being the exception due to their reliance on friction to remove the epidermal layer at 30° impacts; thus, increasing the wound depth. However, the effect of friction is reduced at high-angled impacts, and so, spheres caused larger wound depths for low-angled impacts at small energy densities, since they were unable to peel off the epidermal layer.

It should be noted that due to the heterogenous nature of biological material, continuum-based models cannot perfectly replicate the microscopic mechanical behavior of human skin. Furthermore, the model can overestimate wound depth as element deletion removes mass and energy from the system, causing the removal of dead tissue that would have otherwise carried compressive load. However, reasonable results were still obtained when compared to experimental data.

These results indicate the importance of accounting for projectile shape and impact orientation when analyzing cutaneous fragment impact injuries. We expect our data to be used to guide the design optimization process for personal protective equipment that aim to reduce these types of injuries.

ACKNOWLEDGEMENTS

This work was supported by the Irregular Warfare Technical Science Directorate, an affiliate of the U.S. Department of Defense, under Contract N4175620C3013.

REFERENCES

- [1] Mathews, Z. et al., *J. Emerg. Med.*, 49:573–587, 2015
- [2] Berkey, C. et al., *Comms Eng*, 1:33, 2022
- [3] J. Breeze et al., *Br. J. Oral Maxillofac. Surg.*, 51:263–266, 2013

COLLECTIVE AUTOLOGOUS CHEMOTAXIS IN CANCER CELLS

Louis González (1), Andrew J. Mugler (1)

(1) Department of Physics and Astronomy, University of Pittsburgh, Pittsburgh, Pennsylvania, USA

INTRODUCTION

In complex dynamic microenvironments, cells are subjected to multiple stimuli that yield contradictory outcomes. How cells integrate these multiple signals into a collective action is an open question. A tumor and its surroundings is one of the many complex environments in which this question is relevant and fundamental. One of the hallmarks of cancer progression is an increase in interstitial fluid pressure which facilitates signal transport to provoke cellular migratory response. A ubiquitous mode of migration is a process called ‘autologous chemotaxis’ where cells use self-secreted signaling molecules that are biased by flow and then bind to receptors [1]. A simplified schematic is shown below, where tumor cells secrete a diffusible autocrine (CCL21) that is biased in the direction of lymphatic drainage that binds to the receptor CCR7 which causes the cells to travel to the lymphatic vessel during cancer metastasis (Figure 1, from [2]).

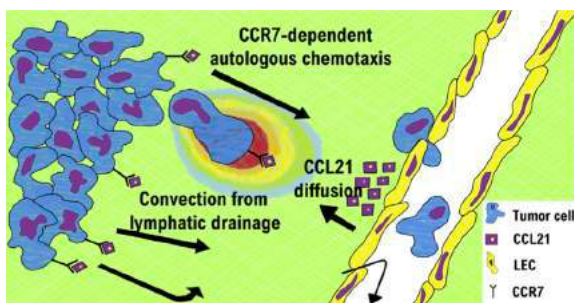


Figure 1: A depiction of tumor cells performing autologous chemotaxis in an attempt to migrate to the endothelium to begin intravasation, a necessary step in cancer metastasis. Both the tumor cell and the endothelium secrete the signaling molecule. This contributes to an autocrine concentration background.

In contrast, cells also use the pressure exerted on their surface membranes generated by fluid flow to stimulate mechanotransduction pathways for a variety of functions, including cell migration. The former induces downstream migration in cells due to the flow biasing molecules along the flow direction and the latter induces an upstream response as the cell travels

along higher pressure gradients.

Experiments have shown that at low density, tumor cells travel downstream using autologous chemotaxis. However, at high density, the cells travel upstream, suggesting that autologous chemotaxis fails, and that the pressure-sensing mechanism takes over [3]. We found that this is due to a saturation in secreted molecule concentration, distorting a cell’s ability to determine a directional bias in the signal and consequently act upon it [4]. Previous work in our group found that cells can sense chemical concentrations better when acting together as a collective unit by integrating each cell’s molecule count and then averaging amongst all cells in the collective [5]. Given that tumors are multicellular environments and cancer cells often travel as clusters, here we ask whether cancer cells can overcome the density-dependent failure of autologous chemotaxis by acting as a collective instead of as individuals.

METHODS

To this end, we assumed a simplified model of a human breast cancer cell as a spherical cell in the presence of other identical cells within a spherical cluster. To model chemo-sensing, we solved the N -body advection-diffusion equation, with N being the number of cells within the cluster. Each cell thus produces a local concentration gradient that is biased in the flow direction, with cells downstream being in the path of upstream secreted molecules. The molecules bind asymmetrically along the surface of the cell, creating a surface concentration anisotropy. Whereas individual cells would integrate the anisotropy to determine flow direction, a cluster would instead integrate whole cells and average each cell’s singular measurement with its position in the cluster. This approach will directly compare the effectiveness of single-cell integration versus multi-cell integration. Since solving the N -body advection-diffusion equation only yields a stationary solution to an evolving concentration field, we introduced a dynamical simulation to simulate autologous chemotaxis. We then turn to Monte Carlo simulation to create a biased random walk where the cells choose subsequent steps that are weighted by the static solution at each time step.

RESULTS

We found that collective chemo-sensing outperforms individual chemo-sensing, similarly to the findings of cells responding to externally sourced gradients in other works [5] as the anisotropy is found to be

$$A_C = \left(\frac{4}{3}\pi\epsilon\right) (V^{1/3}a^3)\rho^{4/3}. \quad (1)$$

Whereas the anisotropy for individual-based chemo-sensing goes as $A_I \sim \rho^{-1}$. This is shown in Figure 2 where collective sensing avoid the density-dependent falloff in concentration sensing as individual sensing as the local cellular environment becomes more crowded.

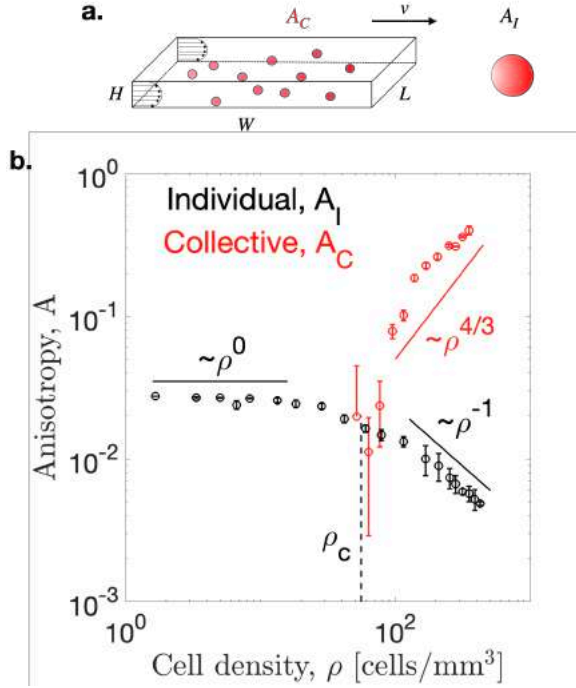


Figure 2: (a) A schematic that shows the difference in how a cell cluster computes collective anisotropy by summing the molecule counts over all cells and weighting it with the position of the box with respect to the cluster center, $\cos \theta_0$ (left diagram) and how an individual cell computes individual anisotropy sums the molecule count across its surface weighted by $\cos \theta$ of the cell (right diagram). **(b)** Anisotropy as a function of cell density for both individual and collective autologous chemo-sensing regimes.

The individual anisotropy A_I represents the failure of autologous chemotaxis at high cell density, a result found in our previous work [4]. As cell density increases, the cells fail to determine flow direction and consequently act (migrate) on it. This is due to a homogenization of the autocrine concentration field. On the contrary, cells performing collectively instead improve as more cells contribute and sense autocrine. This allows clusters to avoid density-dependent failure.

The N -body simulation represents a stationary solution so we must therefore turn to dynamical simulation. Using Monte Carlo simulation, we found that a cell collective will also outperform single cells here as cells are able to resolve more concentration by using the entire cells as “probes” instead of receptors on a single cell’s surface in the individual autologous chemotaxis case. Example trajectories of the collective and individual regimes are shown in Figure 3 below.

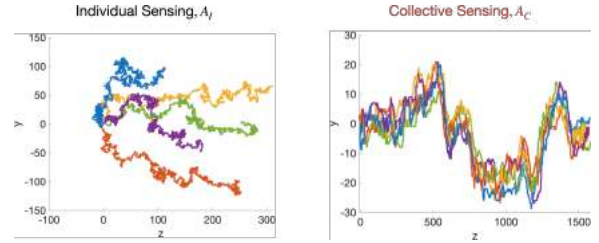


Figure 3: Example trajectories of both the collective and individual regimes using a lattice-based Monte Carlo simulation. In the collective regime, the cells are attracted to one another, forming a cluster and constraining their intercellular distance. This increases their speed and their chemotactic index, the distance moved in the direction of the gradient. The opposite is true in the individual regime, however, as the cells do not maintain a cluster formation and instead travel as individual agents. This causes a slowdown despite moving in the flow direction as well. Fluid flow is in the positive z direction.

Thus, we found that not only do cell clusters resolve concentration anisotropy better than single cells, but that this leads to increased speed. This shows that it is advantageous for cancer cells to travel together, something that has been observed experimentally [6]. This increased speed is the result of resolving the flow direction more efficiently and with higher fidelity than the individual regime.

DISCUSSION

Understanding how cancer cells can overcome apparent failure of their sensory mechanism by operating as a collective unit can provide new insights on drug treatment and therapies. Interrupting or completely disrupting this collective could be a target for a treatment regimen for patients. Our results importantly do not cover why pressure-sensing is subdominant to chemo-sensing at low cell density. We hypothesize that this is due to cells being able to more precisely determine flow direction through chemo-sensing than with pressure-sensing. Whether or not that is the case remains an open question.

ACKNOWLEDGEMENTS

We would like to thank Bumsoo Han, Hye-ran Moon, and Soutick Saha for useful discussion. This work was supported by National Science Foundation Grants No. MCB-1936761 and No. PHY1945018.

REFERENCES

- [1] Shields JD et al. *Cancer Cell* 11.6 (2007). DOI: 10.1016/j.ccr.2007.04.020.
- [2] Waldeland JO et al. *Chemical Engineering Science* 191 (2018). ISSN: 0009-2509. DOI: <https://doi.org/10.1016/j.ces.2018.06.076>.
- [3] Polacheck WJ et al. *Proceedings of the National Academy of Sciences* 108.27 (2011). DOI: 10.1073/pnas.1103581108.
- [4] Vennetilli M. *Physical Review E* 106.2 (2022). DOI: 10.1103/PhysRevE.106.024413.
- [5] Varennes J. *Physical Review Letters* 119.18 (2017). DOI: 10.1103/PhysRevLett.119.188101.
- [6] Cheung KJ et al. *Proceedings of the National Academy of Sciences* 113.7 (2016). DOI: 10.1073/pnas.1508541113.

BULK PROPERTIES OF THE MURINE SPINE ARE MAINTAINED DURING 30-DAYS OF MICROGRAVITY ON THE INTERNATIONAL SPACE STATION

Shiyin Lim (1), Joanna E. Veres (2), Eduardo A.C. Almeida (3), Grace D. O'Connell (1,4)

- (1) Department of Mechanical Engineering, University of California, Berkeley, Berkeley, CA, USA
(2) Department of Bioengineering, University of California, Berkeley, Berkeley, CA, USA
(3) NASA Ames Research Center, Moffett Field, CA, USA
(4) Department of Orthopaedic Surgery, UCSF, San Francisco, CA, USA

INTRODUCTION

As NASA prepares to send astronauts on longer duration spaceflight missions, understanding the detrimental effects of microgravity on human health is important. It has been well established that spaceflight negatively affects bone, with bone loss up to 1-2% for every month in space [1, 2]. Furthermore, astronauts are 4.3X more likely to experience lumbar disc herniation after returning to Earth [3]. While measures have been established to counteract bone loss, there are outstanding questions regarding the impact of spaceflight on spine mechanobiology.

Previous reports from short duration missions (≤ 15 days) showed changes in rodent disc biochemical content and mechanical properties after spaceflight [4-7]. However, the impact of longer duration microgravity on disc biomechanics is not well understood and may provide insight into elevated risk of herniation after spaceflight. Thus, the primary aim of this study was to examine murine disc biochemical content and lumbar vertebral body microstructure after 30-days on the International Space Station (ISS).

METHODS

Rodent Research-10. Lumbar spines from the Rodent Research-10 (RR-10) mission were collected as part of a collaboration with the RR-10 Investigator Team. Mice (B6129SF2/J) were 16 weeks at launch (day 0) and included four groups: a baseline control (BL, euthanized on day 0, $n=10$), a ground control (GC, Rodent Research housing on Earth, $n=10$), a vivarium control (VIV, normal mouse housing on Earth, $n=12$), and a spaceflight experimental group (SF, $n=10$). After 30 days, mice were euthanized in orbit and carcasses were flash frozen and returned to Earth for dissection. Lumbar spines were collected and stored at -80°C until processing for biochemistry and μCT imaging.

Biochemical Analysis. The L1-L2 discs were removed and refrozen at -80°C . Frozen discs ($n=8-10/\text{group}$) were lyophilized overnight before digestion in papain. Digests were evaluated for DNA content with the PicoGreen Assay, sulfated glycosaminoglycan (GAG) content with the Dimethylmethylene blue (DMMB) assay, and collagen

content with an oxidized hydroxyproline content (OHP) assay. GAG content and OHP content were normalized to DNA content, as the weights of the small discs could not be reliably measured.

μCT . The L3-L5 lumbar columns were wrapped in saline-polyethylene glycol-soaked gauze to maintain hydration and scanned at $4.0\ \mu\text{m}$ voxel size (60 kV, 166 μA , 0.25 mm aluminum filter) using a Skyscan 1272 (Bruker). The L4 vertebra was reconstructed and segmented in nRecon to isolate the middle 50% of the vertebral body. Trabecular bone was manually segmented from cortical bone, and automated analyses for bone volume fraction (BV/TV), trabecular thickness (Tb.Th), trabecular separation (Tb.Sp), and trabecular number (Tb.N) were conducted by CT Analyser.

Statistics. To provide robust statistical analysis against normality assumptions, a one-way ANOVA and permutation test combined approach was used. Briefly, the F-statistic generated by the one-way ANOVA was compared to a distribution of F-statistics generated from 10^3 permutations of the experimental data. Post-hoc pairwise comparisons were conducted similarly, using a combined t-test and permutation approach. A Bonferroni post-hoc adjustment was used to account for multiple comparisons. Significance was determined at $p \leq 0.05$ and data is presented as mean \pm standard deviation.

RESULTS

Biochemical Analysis. Spaceflight did not affect intervertebral disc DNA, GAG, or OHP contents (**Figure 1**). Discs from the spaceflight group had an average of 1771.8 ± 294.2 ng of DNA per disc, which did not differ from discs in the baseline control, ground control, or vivarium control groups ($p > 0.6$). Similarly, loading did not affect GAG or OHP contents, with spaceflight discs containing an average of $21.94\ \mu\text{g}$ GAG/ μg DNA and $15.59\ \mu\text{g}$ OHP/ μg DNA ($p > 0.4$).

μCT Analysis. Similarly, spaceflight did not affect lumbar vertebral body bone microstructure (**Figure 2**), with one-way ANOVA indicating no statistically significant effects of loading on BV/TV

($p=0.17$), Tb.Th ($p=0.056$), Tb.Sp. ($p=0.44$), and Tb.N ($p = 0.37$; Figure 3).

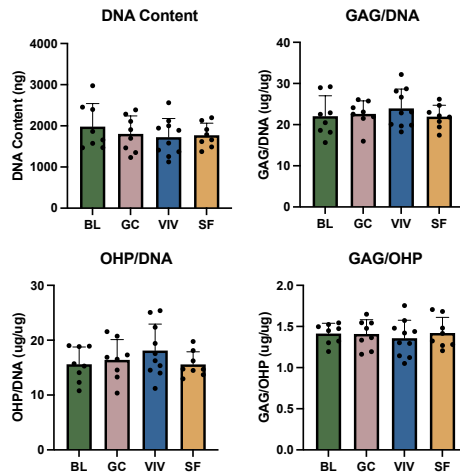


Figure 1. Disc biochemical content is not significantly affected by spaceflight ($p > 0.4$). BL=baseline control, GC=ground control, VIV=vivarium control, SF=spaceflight.

DISCUSSION

Results presented here differ from previously reported data. In one of the first studies on spaceflight and the intervertebral disc, Pedrini-Mille et al. reported decreases in the proteoglycan/OHP ratio in the annulus fibrosus of lumbar discs from rats flown on COSMOS 2044 (14-day flight) [4]. This was supported by a later publication from STS-48, which reported decreases in proteoglycan/OHP ratio in lumbar and thoracic discs of neonatal rats after 5 days of spaceflight [5]. While data presented here investigates GAG content, sulfated GAGs compose the major proteoglycans of the disc, and GAG content is directly proportional to proteoglycan content. Furthermore, numerous studies utilizing simulated weightlessness demonstrated decreases in disc GAG content after unloading [8, 9]. Thus, the consistency in disc biochemical content between spaceflight and control groups in this study was unexpected.

Similarly, the lack of changes in trabecular bone of the vertebral body were also surprising. While data presented here show no significant spaceflight effect on BV/TV, Gerbaix et al. report a 36% decrease in L3 BV/TV after 30-days of spaceflight on Bion-M1 [10]. Berg-Johansen et al. report similar results from the same flight in the caudal vertebrae [11]. On the contrary, a recent study from Rodent-Research 4 demonstrated less bone loss, with changes in L4 BV/TV marked as significant by two-way ANOVA, but not after pairwise post-hoc comparisons [12]. Notably, preliminary results from other weight bearing sites such as the femoral head (unpublished), show significant losses in BV/TV, suggesting that bone loss may be dependent on anatomical location and loading modality rather than spaceflight itself.

There are several factors that may contribute to differences between previous reports and observations presented here, including flight duration and animal housing. While Bion-M1 was the same duration as RR-10, Bion-M1 housing utilized smooth walled cylinders that limited ambulation [13], whereas the Rodent Research hardware has wire mesh. After 14 days in the wire mesh habitat, mice have been observed to develop a unique compensatory mechanism of “race tracking”, which involves highly repetitive, fast running in circles around the habitat. Another behavior is backflipping, whereby mice somersault repeatedly [15]. Though not quantified, these behaviors were observed in the mice used for this study. Lastly, the Animal Enclosure Module (AEM), used in the space shuttle era, also utilized

wire mesh, but experiments did not last longer than 15 days [14]. Given that axial spinal loading of quadrupeds is primarily due to muscle contraction, the lack of differences seen here may be explained by the compensatory mechanisms developed by mice in longer duration spaceflight (> two weeks).

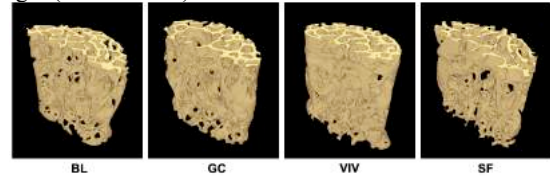


Figure 2. Representative reconstructions of lumbar vertebral body.

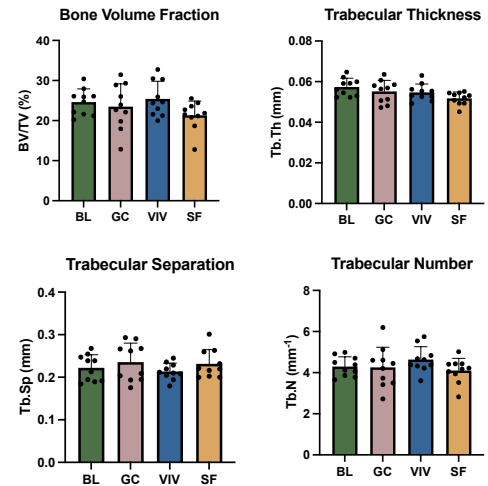


Figure 3. Vertebral body microstructure ($p > 0.05$).

However, as with all spaceflight studies, there are challenges that limit these findings, including a small sample size limiting statistical power. Furthermore, it is possible that other properties, such as mechanical behavior, bone remodeling rates, and other skeletal sites in the same mice experience more drastic differences with longer spaceflight.

Rodent spaceflight studies are extremely helpful in understanding the effects of microgravity on the human body, but the difference in loading modalities between quadrupeds and bipeds is critical for lumbar spine loading. Data presented here suggests that adaptation to the Rodent Research hardware after 30-days of spaceflight may reload the quadruped spine, compensating for microgravity. Further research into this topic may help clarify appropriate rodent models for understanding the impact of long duration spaceflight on spine health in humans.

ACKNOWLEDGEMENTS

This study was supported in part by the NSF (1751212, G. O’Connell) and by NASA (NNH14ZTT001N 14-14SF Step2-0063, E. Almeida).

REFERENCES

- [1] Le Blanc et al., *J. Musculoskelet. Neuronal Interact.*, 1(2):157-160, 2000.
- [2] Gabel et al., *Sci. Rep.*, 12(1):1-13, 2022.
- [3] Johnston et al., *Aviat. Sp. Environ. Med.*, 81(6):566-574, 2010.
- [4] Pedrini-Mille et al., *J. Appl. Physiol.*, 73(1):26S-32S, 1992.
- [5] Sinha et al., *Spine J.*, 2(4):239-243, 2002.
- [6] Bailey et al., *J. Biomech.*, 47(12):2983-2988, 2014.
- [7] Bailey et al., *Gravitational Sp. Biol.*, 26(2):38-47, 2012.
- [8] Hutton et al., *Spine*, 27(12):1286-1290, 2002.
- [9] Yasuoka et al., *Spine*, 32(25):734-740, 2007.
- [10] Gerbaix et al., *Sci. Rep.*, 7(1):2659, 2017.
- [11] Berg-Johansen et al., *J. Orthop. Res.*, 24(1):48-57, 2016.
- [12] Dadwal et al., *Sci. Rep.*, 9(1):1-11, 2019.
- [13] Andreev-Andrievskiy et al., *PLoS One*, 9(8), 2014.
- [14] Choi et al., *Sci. Rep.*, 10(1):1-17, 2020.
- [15] Ronca et al., *Sci. Rep.*, 9(1):1-14, 2019.

SEMI-AUTOMATIC QUANTIFICATION OF EARLY STRUCTURAL REMODELING FOLLOWING MYOCARDIAL INFARCTION

Catherine C. Eberman (1), Colleen M. Witzenburg (1, 2)

(1) Department of Mechanical Engineering, University of Wisconsin Madison, Madison, WI, USA
(2) Department of Biomedical Engineering, University of Wisconsin Madison, Madison, WI, USA

INTRODUCTION

Following myocardial infarction (MI) there are significant changes in the cellular and extracellular content and structure of ventricular tissue. This highly dynamic response is commonly separated into three healing phases: necrotic, fibrotic, and long-term remodeling [1]. The latter two phases have been extensively studied for their role in heart failure [2]. There has been less focus on the short-term changes that occur during necrosis, despite associated rupture events being a leading cause of sudden death [3] and its importance as the foundation for long-term adverse remodeling and ventricular dysfunction [1]. In more recent years, quantitative or computational histology has become more widely used, particularly in cancer diagnosis [4]. However, algorithmic image processing methods can also be utilized to identify pathologies and assess regional heterogeneities [5]. Here we applied algorithmic image processing methods to quantify structural changes in the left ventricle during the necrotic phase of post-MI healing. We hypothesize that image processing methodology can be used to quantify tissue remodeling post-MI semi-automatically, including immune cell infiltration, changes in collagen content, and border topology.

METHODS

Animal Experiments. For this study, 3 male Sprague-Dawley rats (440-490g) were subject to infarction by permanent ligation of the coronary artery. Animal experiments were reviewed and approved by the University of Wisconsin Institutional Animal Care and Use Committee. Hearts were harvested on day 1, 3, and 5 post infarction. The heart was arrested by retrograde aortic perfusion with phosphate-buffered saline and frozen at -80 degrees. Upon thawing, the left ventricle was dissected from the heart and fixed in 10% formalin for 24hrs prior to histological staining.

Histology. The ventricles were cut to produce longitudinal slices in the plane of the heart wall. Samples were stained with H&E, Masson's Trichrome, and Picrosirius Red (PSR) with two replicates for a total of

6 slices per heart. Histology sections were imaged using brightfield and polarized light microscopy (Nikon Eclipse, OpenPolScope).

Image Processing and Data Analysis. Images were processed using custom MATLAB code to determine immune cell infiltration, collagen content, as well as infarct and border topology. The images were analyzed to determine immune cell content in the infarcted region by spatial variation in color of H&E stained slides (Fig. 1 top row). Immune cell density was calculated as the ratio of segmented immune cell pixels to total image area. Regional collagen content was determined from pixel density of PSR slides (Fig. 2 top row). A polarizing filter isolated collagen from the muscle fibers. Images were segmented into 100x100 pixel blocks and the ratio of light to dark pixels within each region was determined via a binarization threshold to assess collagen density. Infarct collagen density was determined from blocks localized within infarct region. Infarct regions were segmented by applying a K-means clustering algorithm to the Trichrome stained slides (Fig. 3 top row). The pixels were clustered into six color bins to group regions of similar coloration, which allowed for separation of the infarct core, border, and periphery.

RESULTS

Cell Infiltration. Fig. 1 (bottom row) shows the immune cell infiltration into the infarct region. The immune cell density, quantified by percent cell area, was largest at day 3 post MI, with percent areas of 5.34, 12.32, and 9.18% at days 1, 3, and 5 respectively.

Collagen Density. Fig. 2 (bottom row) shows the change in collagen content within the infarct region over the 5-day period. Initially there is a decrease in the collagen level at day 1 compared to the remote regions. At day 3 the collagen level in the infarct region appears to have returned to the level of the healthy surrounding tissue, and by day 5 the infarct region has increased collagen content in comparison to the surrounding tissue. The infarct regions have a collagen pixel density of 0.0033, 0.0064, and 0.0156, respectively.

Area and Border Topology. Fig. 3 shows the segmented infarct regions. This segmentation shows the change in the infarct core, as well as the development of the border over time. On day 1 no clear core or border are present, on day 3 a core and border region are present, and on day 5 the infarct core shows a sharper delineation compared to day 3. Finally, Fig. 4 shows the transition from infarct core to periphery, at higher resolution on day 5. Here, the transition from the highly collagenous infarct core, through the variable border, to healthy myocytes with clear sarcomere units and Z-discs can be seen.

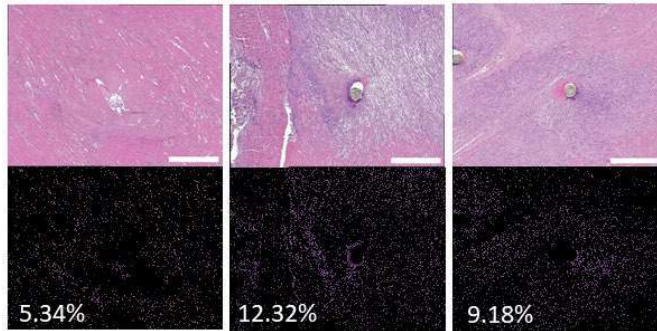


Figure 1: Immune cell infiltration surrounding suture point from H&E stained images; bright field images (top), immune cell density (bottom); left to right: day 1, day 3, day 5, scale = 500µm

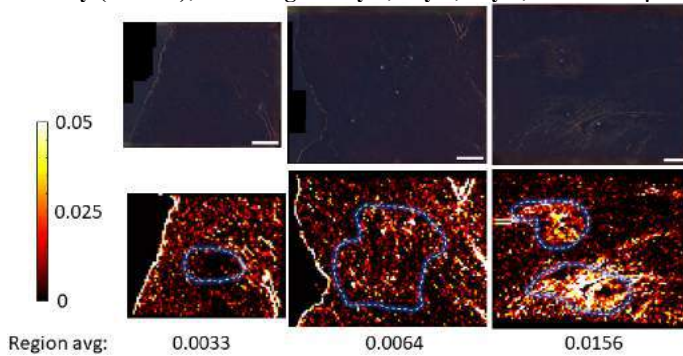


Figure 2: Collagen content in infarct region in PSR stained images; polarized light images (top), regional collagen density (bottom); left to right: day 1, day 3, day 5, scale = 1000µm

DISCUSSION

Semi-automated image processing can be used to assess changes in the tissue structure and content post-MI. Previous work has shown immune cell upregulation during the early stages of healing [2]. Here, we were able to verify this response using image processing by segmenting out the immune cells. Additionally, collagen content in the tissue is known to drop during the early stages of healing prior to the new collagen matrix being laid down. Again, we were able to verify this finding by isolating the collagen using a polarizing filter and determining local collagen density. Finally, we were able to segment and separate the infarct region from the surrounding border region. This allows for quantification of the change in regional topology of the infarct and the border over time. Quantification of the structural changes during this early healing phase could provide important insights into later structural changes during remodeling and the occurrence of rupture events.

ACKNOWLEDGEMENTS

This work was funded by an NSF grant to CMW (2030173). The Cardiovascular Physiology Core Facility performed animal surgeries and the Experimental Animal Pathology Laboratory did histologic staining. CMW is a Carbone Cancer Center member.

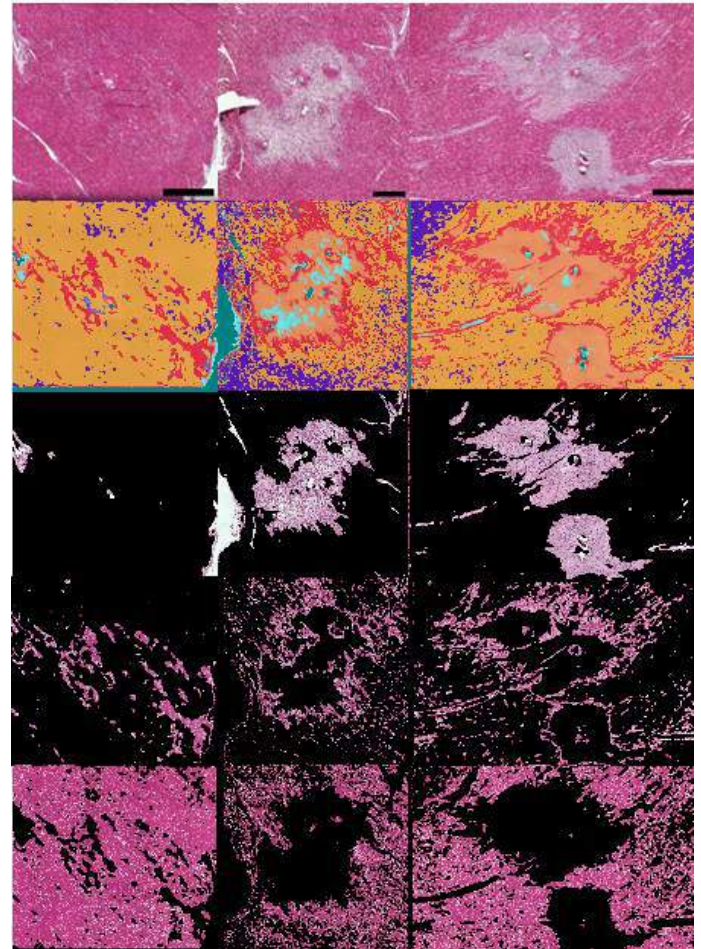


Figure 3: Infarct region segmentation on Masson's Trichrome stained slides, top to bottom: raw images, K-means clustering result, infarct core, border, periphery; left to right: day 1, day 3, day 5, scale = 1000µm

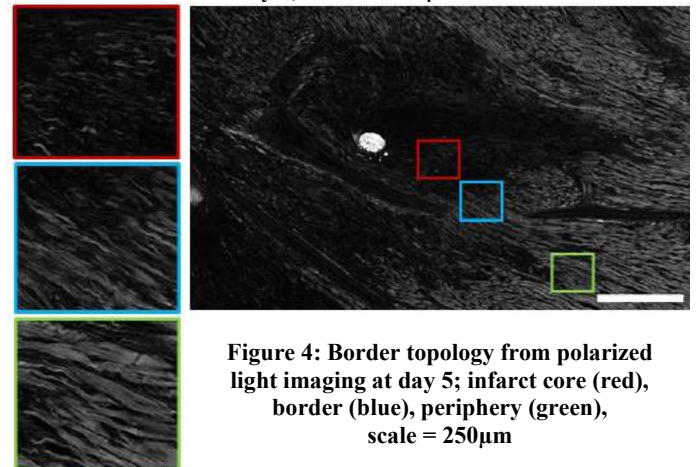


Figure 4: Border topology from polarized light imaging at day 5; infarct core (red), border (blue), periphery (green), scale = 250µm

REFERENCES

- [1] Holmes, J et al., *Annu. Rev. Biomed. Engineering*, 7:223-53, 2005.
- [2] Talman, V et al., *Cell Tissue Res.*, 365:56-581, 2016.
- [3] Birnbaum, Y et al., *Coronary Artery Disease*, 14:463-470, 2003.
- [4] Niazi M et al., *Lancet Oncol*, 20:253-262, 2019.
- [5] Reyes-Fernandez, P et al., *Skeletal Muscle*, 9:1-15, 2019.

A BIPHASIC FLUID-STRUCTURE INTERACTION MODEL OF BACKFLOW DURING INFUSION INTO AGAROSE GEL

Arthur D. Ayers and Joshua H. Smith

Mechanical Engineering, Lafayette College, Easton, PA, USA

INTRODUCTION

Convection-enhanced delivery is a medical procedure in which therapeutic agents are infused directly into the brain to treat diseased tissue. However, its efficacy is limited by a phenomenon called backflow, in which the infused fluid flows preferentially along the side of the catheter toward the surface of the brain, resulting in a poor distribution of the therapeutic agents. Experimental studies have explored novel step-design catheters with a geometry that involves a sudden increase in the radius of the catheter a short distance from its tip. These designs are successful at preventing backflow during infusions into agarose gel, even at infusion rates that were significantly higher than the standard for convection enhanced delivery [1].

Analytical [2] and numerical [3] methods have been employed to explore the physics of backflow but have done so only for catheters with straight geometries. Furthermore, the existing finite element model of backflow [3] is predicated on an assumption of Poiseuille flow in the annular gap that forms around the catheter and, therefore, cannot be extended to stepped catheters. As a first step towards developing a model of backflow in a stepped catheter, in this study, we present a model of backflow for a straight catheter in FEBio using biphasic fluid-structure interaction that avoids the assumption of Poiseuille flow.

METHODS

Our finite element model was created in FEBio [4]. Consistent with experimental infusions into agarose gel [2], we modeled backflow for infusions from catheters of radii 0.33 mm, 0.5 mm, and 0.98 mm. The geometry consists of an upper

cylindrical portion, 40 mm in height, with a hemispherical bottom, both of which have outer radius of 20 mm. This geometry was modeled using an axisymmetric wedge domain and, following a mesh convergence study, the mesh for the

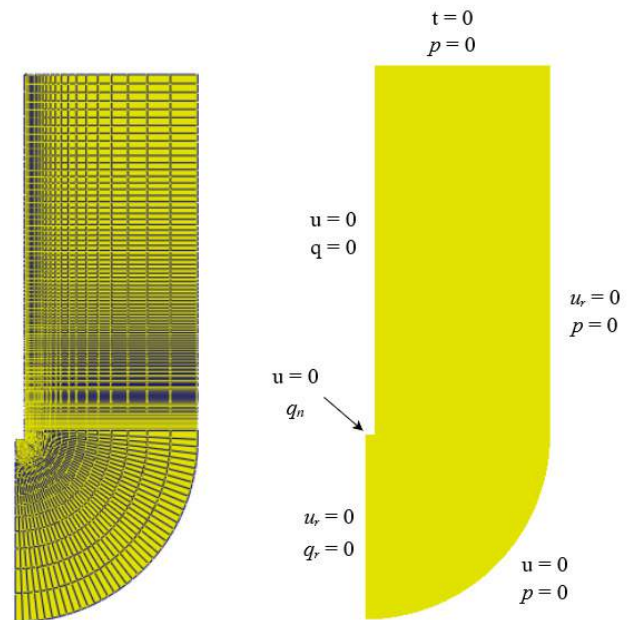


Figure 1: Mesh (left) and boundary conditions (right) represented as surface traction t , fluid pressure p , displacement u , radial displacement u_r , fluid velocity q , radial fluid velocity q_r , and prescribed normal fluid velocity q_n .

0.98 mm catheter consisted of 11,736 linear hexahedral elements and 72 linear pentahedral elements (Figure 1).

Similar to the previous finite element model of backflow [3], a thin layer of elements was placed along the tip and side of the catheter to represent the fluid-filled gap that develops between the catheter and the tissue during backflow. The primary difference between our model and the previous one is in the formulation of this layer of elements. Whereas the previous model used biphasic elements with a hydraulic conductivity formulated to replicate Poiseuille flow, our model utilized FEBio’s fluid-FSI element type [5].

Fluid-FSI elements have a stiffness property that allows them to conform with their solid and biphasic interfaces. The fluid-FSI elements directly under the tip of the catheter were assigned a negligibly small stiffness value to allow those elements to freely deform, while the elements along the side of the catheter were assigned a stiffness value determined through a fit of backflow length and fluid pressure results from our 0.98 mm catheter model against those from experimental infusions into agarose gel [2]. Consistent with the previous model of backflow [3], the backflow length was defined to be the distance from the tip of the catheter to the nearest point along the side of the catheter where the radial tissue displacement is 5% of its maximum. The boundary conditions applied for this simulation are shown in Figure 1.

A neo-Hookean material model was used for the behavior of the biphasic domain, with property values taken from the previous study [3]. The infusion flow rate ranged from 1–8 $\mu\text{L}/\text{min}$, consistent with experimental gel infusions [2] and the previous model of backflow [3].

RESULTS

For the three catheter sizes and infusion rates ranging from 1–8 $\mu\text{L}/\text{min}$, our biphasic-FSI model yielded results for the fluid pressure and backflow length that showed good agreement with the agarose gel infusion results of Raghavan et al. [2] (comparisons not shown).

For the 0.98 mm catheter, our biphasic-FSI model produced a spherical fluid pressure distribution for an infusion flow rate of 1 $\mu\text{L}/\text{min}$ and ellipsoidal fluid pressure distribution for a flow rate of 8 $\mu\text{L}/\text{min}$ that is representative of backflow (Figure 2). The biphasic-FSI model produced flow distributions comparable to the previous model, with some differences at the larger flow rate (Table 1).

DISCUSSION

A biphasic fluid-structure interaction finite element model for backflow was developed that reproduces experimental results of backflow length and fluid pressure to a good degree of accuracy. Additionally, it produces flow distributions and fluid pressure profiles that align with our physical understanding of backflow.

Unlike other backflow models, our model does not require the assumption of Poiseuille flow in the annular gap that forms around the catheter. It, therefore, has the potential to be extended to stepped catheter geometries, for which it would be difficult to

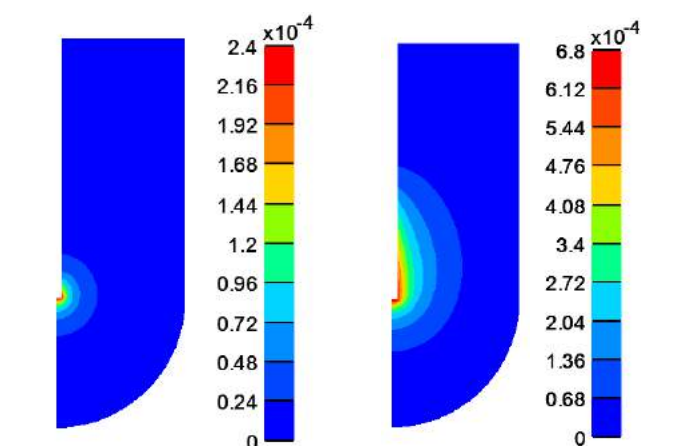


Figure 2: Fluid pressure distribution (MPa) at steady state during an infusion of 1 $\mu\text{L}/\text{min}$ (left) and 8 $\mu\text{L}/\text{min}$ (right) through a 0.98 mm radius catheter.

Table 1: Comparison of distribution of infused fluid flow with the finite element model of Garcia et al. [3].

	Percentage of Flow into Region	
	Hemispherical	Cylindrical
1 $\mu\text{L}/\text{min}$		
Biphasic-FSI model	22.6%	77.1%
Garcia et al. [3] model	22.4%	77.6%
8 $\mu\text{L}/\text{min}$		
Biphasic-FSI model	7.4%	92.5%
Garcia et al. [3] model	9.8%	90.2%

apply that assumption. The results from this model have some differences with the ones produced by the model by Garcia et al. [3], which may be attributed to their assumption of Poiseuille flow.

In the future, this model may be used as a basis for models of backflow for infusions with stepped catheters. One challenge in extending it to a stepped catheter geometry may be determining an appropriate value for the stiffness of the fluid-FSI elements along the step.

ACKNOWLEDGEMENTS

J. H. Smith thanks the EXCEL Scholar program at Lafayette College for funding support for A. D. Ayers during Summer 2022.

REFERENCES

1. Krauze, M., et al., *Journal of Neurosurgery*, 103:923–929, 2005.
2. Raghavan, R., et al., *Physics in Medicine and Biology*, 55:281–304, 2010
3. Garcia, J.J., et al., *Journal of Computational and Nonlinear Dynamics*, 8:011017, 2013.
4. Maas, S.A., et al., *Journal of Biomechanical Engineering*, 134:011005, 2012
5. Shim, J.J., et al., *Journal of Biomechanical Engineering*, 141:051010, 2019

ANISOTROPIC MATERIAL PROPERTY AND LOCAL STRENGTH CHARACTERIZATION OF HUMAN CAROTID PLAQUES: A BAYESIAN OPTIMIZATION BASED INVERSE FINITE ELEMENT MODELING

S. Guvenir Torun (1), B. Kaaij (1,2), P. de Miguel Munoz (1,2), H. Crielard (1), H.J.M. Verhagen(3), G.J. Kremers (4), A.F.W. van der Steen (1), A.C. Akyildiz (1,2)

- (1) Department of Biomedical Engineering, Erasmus Medical Center, Rotterdam, Netherlands
- (2) Department of Biomechanical Engineering, Delft University of Technology, Delft, Netherlands
- (3) Department of Vascular Surgery, Erasmus Medical Center, Rotterdam, Netherlands
- (4) Erasmus Optical Imaging Center, Erasmus Medical Center, Rotterdam, Netherlands

INTRODUCTION

Atherosclerotic plaque rupture in arteries is a major cause of fatal or disabling cardiovascular events. Plaque rupture is a mechanical event, hence analyses of local mechanical stress in plaques can be of great help for clinical event risk prediction [1]. Plaque stress analyses require accurate information of plaque tissue material properties. However, the current knowledge is limited to average tissue properties based on tissue homogeneity and isotropy assumptions [2], although the fibrous plaque tissue has highly collagenous and heterogenous structure.

In this work, we aim to provide the currently missing critical knowledge on local anisotropic hyper-elastic material properties and strength of fibrous plaque tissue. Our pipeline comprises uniaxial tensile testing of human carotid plaques, digital image correlation (DIC) derived local deformation measurements, second harmonic generation (SHG) microscopy imaging for local collagen information, and a Bayesian optimization based inverse finite element modeling (iFEM) for sample-specific local material property prediction.

METHODS

Sample Collection and Structural Calcium and Collagen Imaging

Nine atherosclerotic human carotid artery (CEA) samples were collected at Erasmus Medical Center in Rotterdam, the Netherlands. Firstly, the samples were scanned with a micro-CT scanner (Quantum GX 2, Perkin Elmer) to identify non-calcified regions for rectangular fibrous plaque tissue strip preparation (n=9). Afterwards, strips were scanned by using a multiphoton microscope (Leica SP5) SHG imaging. Preliminary to the imaging, a tile scan was performed on each sample. In every other tile element (with size of 738 x 738 μm , 512x512 pixels), in-plane Z stack images were obtained at every 3 μm depth up to ~150 μm depth from the luminal side [3]. Maximum intensity projection (MIP) images were obtained per each tile, and were analyzed by using a combination of the Fiblab Software [4] and a custom-built Matlab script to obtain the collagen pre-dominant angle (pDA) and dispersion

(κ) information, as defined by Holzaphel et al. [5], by fitting a von Misses distribution to the obtained collagen orientation histogram data.

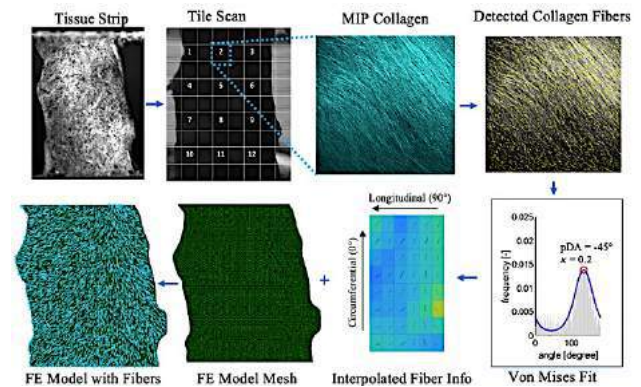


Figure 1: Second harmonic generation (SHG) imaging, collagen fiber predominant angle (pDA) and dispersion (κ) assessment, and element-specific fiber embedded finite element (FE) model.

Mechanical Testing and Digital Image Correlation (DIC)

Following the structural imaging, a speckle pattern was applied to the luminal side of the strips. Then, the strips were placed into the uniaxial tensile testing setup (filled with 37°C PBS), such that the tensile stretching was applied in the circumferential direction of the strips. A pre-load of 0.05N was applied, and in the pre-stretched configuration, samples were scanned by using a 3-D ultrasound (Vevo 3100, Fujifilm) with 21 MHz central frequency 2-D linear transducer (MX250) for thickness measurements. Then, they were preconditioned up to %10 strain for 10 cycles with a speed of 0.05mm/s and a final stretching was applied until complete tissue failure. The tissue stretching was recorded by a 5.3 MP CMOS camera (PL D 725,

Pixelink), and the videos were analyzed by NCorr 2-D DIC Software [6] to obtain local displacements until rupture.

Finite Element Modeling

For each tested strip ($n=9$), the pre-stretched reference image from the tensile testing was used to create finite element (FE) model geometry in ABAQUS (Dassault Systèmes). The tile specific collagen fiber pDA and κ information from the SHG was incorporated in the FE model, element-specific, based on the interpolation of measured parameters (Fig.1). The fibrous plaque was modelled as anisotropic, hyper-elastic, incompressible, Holzapfel-Gasser-Ogden solid [5]. The mesh was composed of plane stress, triangular CPS3 elements. For the thickness, global measured ultrasound-based thickness of ~ 0.7 mm was used. The experimental uniaxial stretching until rupture initiation was simulated by applying experimentally measured tensile loading in four force steps and local plaque displacements were computed for each step.

Inverse Finite Element Modeling (iFEM)

The iFEM framework [7,8] is used to iteratively run FE models with newly generated material model parameters C_1 , k_1 and k_2 until the normalized mean square error (NMSE) between the computed and experimentally measured displacements is minimized (Fig.2). The iFEM framework uses Deep Partitioning Tree based Bayesian Optimization (DPTBO) [9] that chooses a new sample set minimizing the NMSE by training a stochastic Gaussian Process at every iteration.

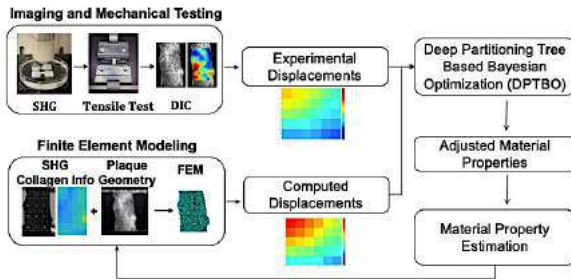


Figure 2: The Bayesian optimization based iFEM pipeline.

RESULTS

For all nine human CEA fibrous plaque tissue strips, structural imaging, collagen fiber measurements, mechanical testing and DIC were successfully conducted. For one sample, the iFEM approach was performed. At the end of the analysis, an NMSE of 4% was reached. The obtained C_1 , k_1 and k_2 values were 0.4 MPa, 0.4 MPa and 400, respectively. The representation of the iFEM predicted material constant-based computational and the DIC based experimental displacement results are shown in Fig.3. Their trends were similar with elevating levels of displacements from lower right to the top left region.

Based on the predicted material properties, tensile strain distribution on the test strip at the final loading step (1.2N) was computed for qualitative comparison with the experimentally measured strain distribution (Fig.4A and B). Both strain maps were observed to have similar patterns (high strains on the left corner and low strains on right top region of the strip), with a range up to 35%. However, local differences were observed in various regions.

The FE model predicted maximum principal stress patterns were observed to have also local variation (range up to 2 MPa) (Fig.4C). This behavior was similar to the observations in the measured and FE computed strain patterns. Interestingly, the rupture was observed to initiate at a local high strain (obtained by both measured and FE-based analysis) and stress (obtained by FE-based analysis) region for the representative case demonstrated in Figure 4.

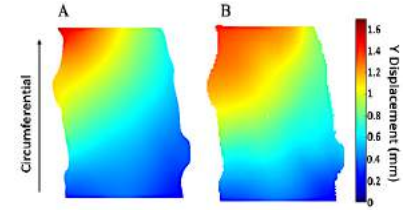


Figure 3: iFEM predicted computational (A) and experimental (B) displacement results

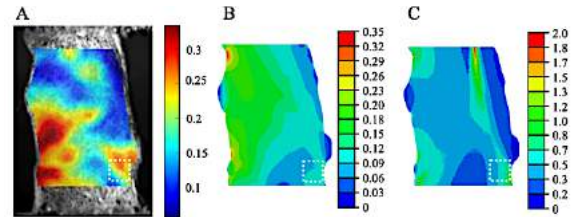


Figure 4: Correlation of the rupture location and local DIC based strain (A), FE model predicted strain (B) and stress (C) patterns. Rupture initiation region was located within the white square.

DISCUSSION

In this study, we have developed an experimental-computational framework to characterize the anisotropic material properties of atherosclerotic human fibrous plaques. The analysis of the representative human carotid plaque case achieved a successful NMSE result. The FE strain simulation based on the iFEM predicted material properties was observed to have similar patterns to the DIC-based experimentally measured strains. Local differences between two modalities could be due to local thickness variations not captured in the FEM. Furthermore, incorporating the collagen fiber data in the FEM in higher resolution may also improve the final outcome. The FE stress simulation was observed to have local variations through the sample, similar to strain distribution. These local variations are not surprising for the heterogeneous structure of the fibrous plaque tissue. The rupture initiation spot on the sample demonstrated both high stress and strain, which may be an important indicator for further investigation. However, not all high stress and strain regions showed tissue failure. Hence, this could emphasize other structural metrics, i.e., collagen content or cross-linking, as possible candidates, in combination with structural stress and strain, leading to the complex pathways of plaque rupture. As the next step, the remaining eight strips will be characterized with the iFEM approach, and their local stress patterns will be obtained.

To the best of our knowledge, this is the first study on the characterization of local anisotropic material properties of fibrous plaque tissue. The findings of this research hold great potential for identification of local stress fingerprints that are highly crucial for fibrous plaque rupture risk assessment tool development.

ACKNOWLEDGEMENTS

This project is funded by the European Commission's Horizon 2020 under the Marie Skłodowska-Curie grant agreement # 749283.

REFERENCES

- [1] Cheng, G C et al., *Circulation*, 87.4:1179-1187, 1993.
- [2] Akyildiz, A C et al., *J Biomech*, 47.4:773-783, 2014.
- [3] Crielaard, H et al., *JOVE*, 189, 2022.
- [4] van Haaften, E et al., *Tissue Eng Part C: Methods*, 24:418-429, 2018.
- [5] Holzapfel, G et al., *J Elasticity*, 61.1:1-48, 2000.
- [6] Blaber, J et al., *Exp Mech*, 55.6:1105-1122, 2015.
- [7] Guvenir Torun, S et al., *JMBM*, 126:104996, 2022.
- [8] Guvenir Torun, S et al., *Frontiers in Physiology*, 1480, 2021.
- [9] Torun, H M et al., *IEEE Trans. Microw. Theory Tech*, 67:2128-2142, 2019.

MULTISCALE MODELING OF BAROREFLEX FEEDBACK LOOP IN RESPONSE TO ACUTE MYOCARDIAL INFARCTION

Hossein Sharifi (1), Kenneth S. Campbell (2), Jonathan F. Wenk (1,3)

(1) Department of Mechanical Engineering, University of Kentucky, Lexington, KY, USA
(2) Department of Physiology & Division of Cardiovascular Medicine, University of Kentucky, Lexington, KY, USA
(3) Department of Surgery, University of Kentucky, Lexington, KY, USA

INTRODUCTION

Although the 30-day survival rate of patients who suffer from a heart attack (myocardial infarction, MI) is 87% [1], it can result in reduced cardiac function with increased incidence of cardiomyopathy and heart failure, which is the most common cause of death post-MI.

Infarcted hearts undergo various types of remodeling, including changes in structure and mechanics of the scar region, and changes in contractility and architecture of myofibers in the remote region. Such a change in contractile behavior of remote regions is mainly driven by acute response of the baroreflex loop to compensate for the loss of contractile properties of infarcted myocardium.

In this study we utilized a high-fidelity FE model of the left ventricle that is coupled with a baroreflex feedback loop that maintains arterial pressure at a setpoint level by modulating heart rate, intracellular Ca^{2+} handling, molecular-level function of both the thick and the thin myofilaments, and vascular tone. The baroreflex loop predicted higher heart rate with increased contractile function of remote regions and higher vascular tone in response to acute MI.

METHODS

The model described in Figure 1 is called MyoFE, which was built using the FEniCS open-source finite element software. This framework is an enhanced version of a simplified model of cardiovascular function named PyMyoVent [2] in which the 1-D model of LV mechanics was replaced with a high-fidelity 3-D finite element model of the LV. In the current framework, a pacing stimulus activates a 2-compartmental model of electrophysiology that drives the Ca^{2+} transient at each gaussian point across the mesh. The Ca^{2+} transient then triggers the contractile behavior of myocardium, which is being driven by a myosin-level model of contraction named MyoSim [3]. Finally, the LV chamber pumps blood through a lumped parameter model of systemic circulation.

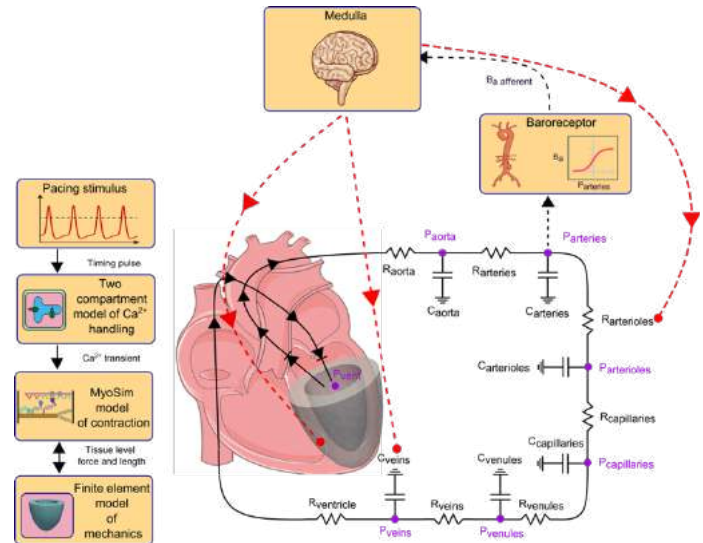


Figure 1: Overview of MyoFE framework.

The baroreflex control was implemented using an algorithm mimicking the underlying biology. In this module, arterial pressure (P_{arteries}) transduces into a normalized afferent signal B_a via a sigmoidal relationship (1), where S is the slope of function around its midpoint, and P_{set} is the setpoint for arterial pressure.

$$B_a(t) = \frac{1}{1 + e^{-S(P_{\text{arteries}}(t) - P_{\text{set}})}} \quad (1)$$

B_a drives the balance signal (B_b) that is a normalized representation of the difference between sympathetic and parasympathetic efferent

activity. The rate of change of B_b is defined in (2) where k_{drive} is a rate constant.

$$\frac{dB_b(t)}{dt} = \begin{cases} -k_{drive} (B_a(t) - 0.5) B_b(t) & B_a \geq 0.5 \\ -k_{drive} (B_a(t) - 0.5) (1 - B_b(t)) & B_a < 0.5 \end{cases} \quad (2)$$

The control signals $B_{c,i}$ capture how each of the eight reflex-sensitive parameters in the cardiovascular model respond to the balance signal. Similar to equation (2), their rates of change were defined as

$$\frac{dB_{c,i}(t)}{dt} = \begin{cases} k_{control,i} (B_b(t) - 0.5) (1 - B_{c,i}(t)) & B_b \geq 0.5 \\ k_{control,i} (B_b(t) - 0.5) B_{c,i}(t) & B_b < 0.5 \end{cases} \quad (3)$$

where i ranges from 1 to $5n+3$, with n equal to the total number of integration points across the geometry and $k_{control,i}$ is the rate constant for system i . The final step in the algorithm used mapping functions M_i to link the normalized control signals $B_{c,i}$ to actual parameter values

$$M_i(B_{c,i}(t)) = \begin{cases} M_{base,i} + \frac{1}{2} (B_{c,i}(t) - 0.5) (M_{symp,i} - M_{base,i}) & B_{c,i} \geq 0.5 \\ M_{base,i} + \frac{1}{2} (B_{c,i}(t) - 0.5) (M_{param,i} - M_{base,i}) & B_{c,i} < 0.5 \end{cases} \quad (4)$$

where $M_{base,i}$ is the default value for parameter i , and $M_{symp,i}$ and $M_{param,i}$ are its limits during maximum sympathetic and maximum parasympathetic drive respectively.

RESULTS

Figure 3 summarizes how the baroreflex feedback loop responds to modeling acute MI. The simulation started with default parameters for ~5 cardiac cycles with heart rate of 65 bpm. Then the baroreflex module was activated (at first vertical dashed line) to start regulating the system to maintain arterial pressure at a setpoint level of 90 mmHg, representing a healthy subject. Once the simulation was at steady state, the infarct region was modeled by reducing the density of cross-bridge myosin heads to 0 for prescribed region of interest shown in Figure 2.

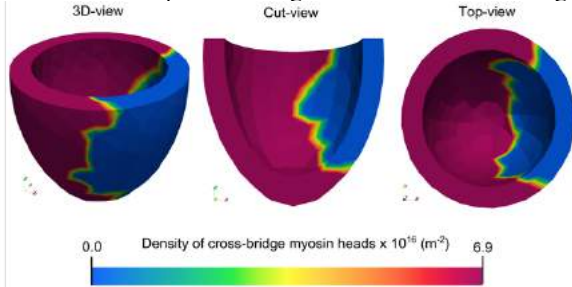


Figure 2: Simulated acute myocardial infarction by decreasing the density of cross-bridge myosin heads to 0 in infarcted regions.

In response to such a loss in contractile behavior within the LV (starting at 2nd vertical dashed line), arterial pressure started to fall below the setpoint level of 90 mmHg (i.e. between 2nd and 3rd vertical dashed lines). However, the baroreflex restored arterial pressure by increasing heart rate, vascular tone ($R_{arterioles}$, C_{veins}), contractility of remote regions (by increasing k_1 , k_3 and decreasing k_{on}), and Ca^{2+} transient of remote regions (via k_{act} and k_{SERCA}).

DISCUSSION

The current study demonstrated a multiscale computational model of cardiovascular function, which is coupled with a baroreflex feedback loop, and is able to maintain arterial pressure in response to a disease mimicking perturbation, such as acute MI. In addition to an increase of

heart rate and vascular tone, the baroreflex increased the contractility of remote regions to compensate for the loss of contractile properties in the infarcted region (Figure 4).

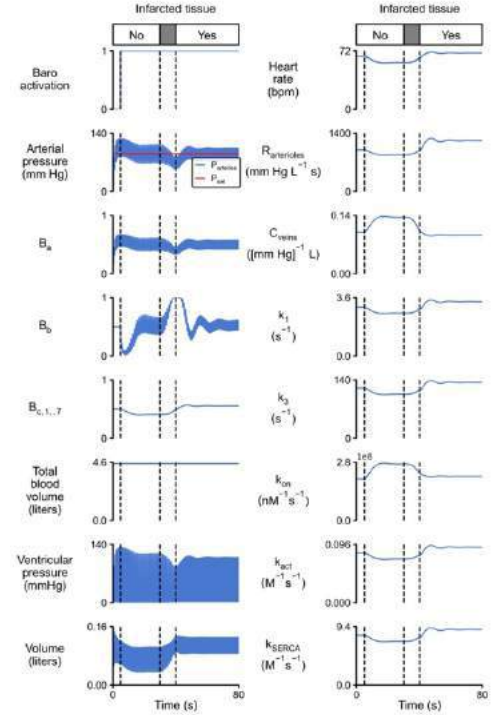


Figure 3: Baroreflex stabilizes the arterial pressure after perturbing the simulation of a healthy subject by mimicking acute MI.

In another simulation, the model was run in the absence of the baroreflex feedback loop, which predicted a non-physiological drop in arterial pressure range due to the loss of contractile function.

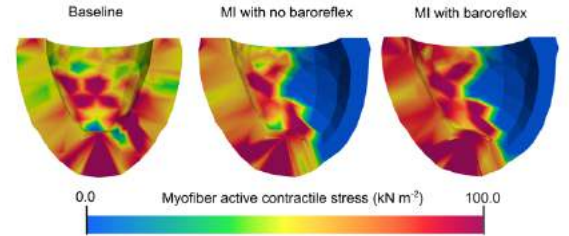


Figure 4: Effect of baroreflex in compensating for MI by increasing the contractile behavior of remote regions.

ACKNOWLEDGEMENTS

Supported by NIH U01 HL133359 to JFW and KSC.

REFERENCES

- Virani, S.S., et al., *Heart Disease and Stroke Statistics-2021 Update: A Report From the American Heart Association*. Circulation, 2021. **143**(8): p. e254-e743.
- Sharifi, H., et al., *A multiscale model of the cardiovascular system that regulates arterial pressure via closed loop baroreflex control of chronotropism, cell-level contractility, and vascular tone*. Biomech Model Mechanobiol, 2022. **21**(6): p. 1903-1917.
- Campbell, K.S., *Dynamic coupling of regulated binding sites and cycling myosin heads in striated muscle*. J Gen Physiol, 2014. **143**(3): p. 387-99.

MEGA DATA ANALYSIS OF SEX DISTRIBUTION OF STUDY SAMPLES REPORTED IN SUMMER BIOMECHANICS, BIOENGINEERING, & BIOTRANSPORT ANNUAL MEETING ABSTRACTS

F. Sebastian, A. Hurgoi, M. Schaenen, H. Shah, V. Rivera, K. Le, D. Ng, R. Amini

Department of Bioengineering, Department of Mechanical and Industrial Engineering, Northeastern
University, Boston, MA, USA

INTRODUCTION

For decades, the outcomes of biomedical research have been limited due to the exclusive use of male subjects. The inclusion of women as research subjects—both in hypothesis-driven investigations and in tool-development efforts—is vital to extend our understanding of medicine and to improve human health. It also ensures that generalized inferences about health and diseases can be made accurately. Evidence has shown that certain areas of biomedical engineering suffer from extensive disparity between its effects on women and men, including but not limited to cardiovascular disease, biomechanical response to concussion, and motor vehicle crash injury outcomes [1-3].

In recent years, rules and regulations have been implemented to encourage higher recruitment of women and minorities in research studies. In the US, title 42 U.S.C. § 289(a)(2) of federal statutes requires the National Institutes of Health (NIH) to ensure that women are included as subjects in clinical research. Additionally, in 1993 the NIH Revitalization Act was executed to further bridge the gap in sex inclusivity in research studies.

These measures have proven effective with data showing that approximately 50% of participants in NIH-funded research studies were women [4]. However, data for studies that were not funded by NIH are not readily available. Some research has been done to assess the inclusivity of sexes in studies that also encompass animals and cells. One of which was done by Bach et al. in 2015 [5] to evaluate the macroscopic trends regarding sex sampling in abstracts presented at the annual meetings of the American Society of Biomechanics (ASB). With similar motivations, the purpose of this study was to examine the sex inclusions in the abstracts of the Summer Biomechanics, Bioengineering, & Biotransport (SB³C) conference from 2015, the inception year of the conference, to 2022 (sans 2018). With increasing awareness of the scientific community, we hypothesized that the number of research projects with both sexes included would have increased over the past seven years.

METHODS

To assess trends of sex inclusion in biomedical studies, we analyzed abstracts from seven years of SB³C proceedings. The abstracts from 2018 were omitted since the conference was jointly run with the World Congress of Biomechanics. Identification of sex in human or animal experimental studies was straightforward. To identify sex in computational and mathematical studies, we examined if the animal or human data/geometry used as input parameters were reported.

For each abstract, the title, applicable population, and summary of the study were recorded. Given the large number of abstracts ($n = \sim 600/\text{year}$), each year was assigned to an examiner. For each abstract, we first examined if any information about sex was provided. If the answer was yes, we then identified if, only female, only male, or both sexes were included. If both sexes were included, we examined if a balanced number of both sexes were used. It was determined that a study was “balanced” if each sex accounted for $50 \pm 10\%$ of the total study population. If only one sex was included, we examined if the study had a sex-specific and biologically relevant purpose (e.g., biomechanics of pregnancy or prostate cancer) and thus the reason for using only one sex was considered “justified”. Once every abstract from each conference proceeding was analyzed, the examiners were randomly assigned a different year from their initial assignment, the process was repeated, and any discrepancies were rectified. A final review of all reported data in the studies that included sex was conducted by a single examiner to ensure the assessments were accurate.

Statistical analyses were performed in R (R Core Team). Unpaired Student’s t-test was used to determine differences between two groups when the distribution was determined to be normal using the Shapiro-Wilk test. If the distribution was not normal, a Mann-Whitney U test was performed. The differences were considered significant if $p < 0.05$. Additionally, a regression and/or correlation model was used to determine trends over the years where applicable.

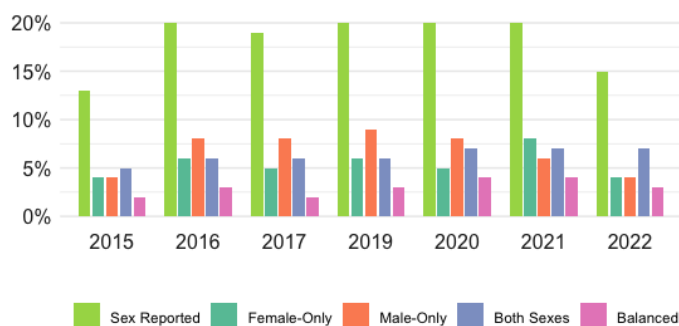


Figure 1: Distribution of sex inclusion in SB³C abstracts per year

RESULTS

The overall number of abstracts that included sex in their study stayed at approximately 20% for every year ($R = 0.2$, $R^2 = 0.04$, $p = 0.7$; Fig. 1). The numbers for 2015 and 2022 were slightly lower than the rest. To better visualize the data from the abstracts that reported sex, a normalized distribution of female-only, male-only, or both sexes is provided in Fig. 2. It was determined that the number of female- and male-only abstracts submitted each year were not significantly different ($p = 0.2$) using an unpaired t-test.

Using a regression model, we found that the total number of abstracts that included both sexes increased over the years ($R = 0.91$, $R^2 = 0.82$, $p = 0.005$). However, of these abstracts, those with balanced sex groups did not increase significantly ($R = 0.70$, $R^2 = 0.49$, $p = 0.08$) as seen in Fig. 3. In fact, the number of balanced abstracts were significantly lower than the total number of abstracts that included both sexes according to an unpaired t-test ($p < 0.001$).

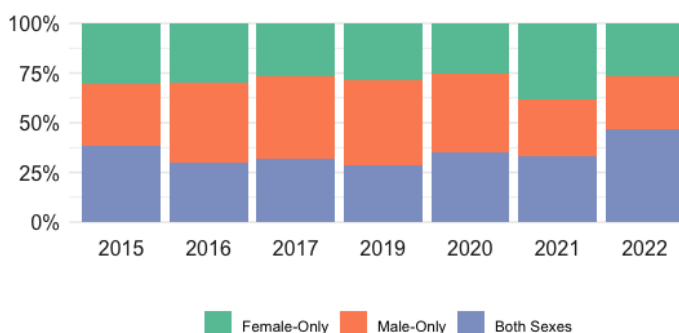


Figure 2: Normalized distribution of sex groups per year

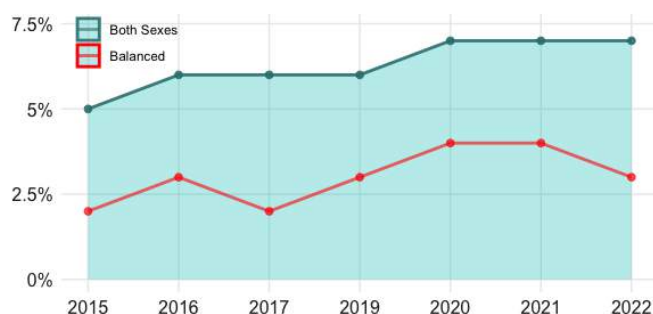


Figure 3: Trend of abstracts that include both sexes and balanced inclusion of female and male sexes over the years.

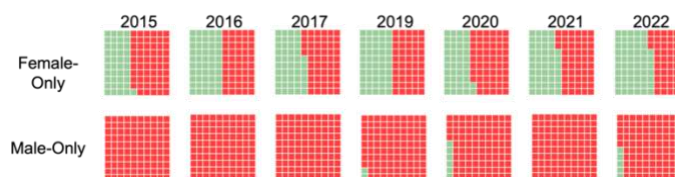


Figure 4: Comparison of single-sex abstracts (green = justified; red = unjustified). The reasons for the exclusion of the other sex were based on the research purposes in the “justified” category.

Finally, the female- and male-only data were categorized for justification in each year. The percentage of justified versus unjustified abstracts were plotted using a waffle chart (Fig. 4). A Mann-Whitney U test determined that across all years, female-only group had significantly higher “justified” abstracts ($p = 0.002$).

DISCUSSION

The objective of this study was to obtain an overarching perspective of sex sampling in abstracts submitted to SB³C over the years. We hypothesized that the number of papers that included both sexes, and those with balanced sex groups would increase over the years. The results indicate that there was a significant increase in the inclusion of both sexes; however, the number of balanced abstracts is significantly lower than expected. Ideally, all studies that include *both sexes* should have a 100% rate of balanced groups, but current results leave more to be desired.

Additionally, it was hypothesized that *female-only* studies would be performed due to more justifiable research-specific reasons as compared to *male-only* studies. Such a hypothesis was chosen based on the historical male-only bias toward non-sex-specific research. The stark difference between the justification of male- and female-only studies is apparent from this analysis. Even though the number of female-only studies being justified is higher than the male-only studies, the need for more balanced studies in biomechanics is apparent.

One of the limitations of our analysis is the assumption that the SB³C abstracts encompass all the information of the full study. The papers that result from the abstracts might include a larger and more comprehensive subject population that has not been described in the abstracts due to space constraints. Additionally, there were many studies that included both sexes, but the abstracts did not include the number of male and female subjects, skewing the “balanced” assessment.

In summary, while the overall trend of using both sexes in biomedical research is optimistic, our analysis has shown that the disparity is still prominent. We encourage scientists to be mindful of sex (i.e., the biological differences between females and males) and gender (i.e., the socially constructed identity of the individuals) inclusion to ensure the full benefit of biomedical research.

ACKNOWLEDGEMENTS

We thank SB³C Foundation for making all proceedings readily available online free of charge. Funding for this study was provided in part by the National Science Foundation (CAREER 2049088).

REFERENCES

- [1] Solomito, M. J. et al. *Brain Injury* 33:105–110, 2019
- [2] Ryan, A. et al. *J Transportation Safety & Security* 14:818, 2022
- [3] Woodward, M. *Int. J. Env. Res & Pub Health* 16(7):1165, 2019
- [4] Committee on Ethics *Am Coll of OB & GYN*, 126: e100, 2015
- [5] Bach, S. et al., *PLoS One* 0(3): e0118797, 2015

BIOMECHANICAL CHARACTERISATION OF NEONATAL AORTIC COARCTATION TISSUE INFORMS THE NEED TO DESIGN BESPOKE PATIENT THERAPIES FOR NEONATAL COARCTATION OF THE AORTA.

Niall. Linnane (1,2,3), Robert. Johnston (1,4), Damien P. Kenny (2,3), Caítriona. Lally (1,4)

- (1) Trinity Centre for Biomedical Engineering & School of Engineering, Trinity College Dublin, Ireland.
- (2) Royal College of Surgeons, St Stephen's Green, Dublin 2, Ireland.
- (3) Children's Health Ireland at Crumlin, Dublin 12, Ireland.
- (4) Advanced Materials and Bioengineering Research Centre (AMBER), Royal College of Surgeons in Ireland and Trinity College Dublin, Dublin, Ireland.

INTRODUCTION

Coarctation of the aorta has an incidence of 0.3 to 0.6 in 1000 live births, accounting for 5% to 12% of all congenital heart disease [1,2]. Coarctation is associated with structural pathologies of the aortic wall and is considered as a continuum of a disease process which affects the entire aorta [3].

Balloon angioplasty of native coarctation *in vitro* was reported in 1982 by Lock *et al.* [4]. Intimal tears were observed in all patients but no cases of aortic wall rupture. Examination under light microscopy demonstrated intimal hyperplasia, medial thickening and confirmed the presence of tissue tears [4].

A prospective randomised trial by Shaddy *et al.* demonstrated the safety and efficacy of balloon angioplasty in native coarctation when compared with surgery [5]. In the angioplasty group, however, there was a higher rate of aneurysm formation and long-term data showed that aneurysms can occur as late as 5 years post procedure [6]. These early reports [4-6] demonstrate the importance of advancing the knowledge of the wall structure of coarcted aortic tissue and how, at a microscopic level, the vessel responds to intravascular interventions such as balloon angioplasty and stenting.

The ductus arteriosus is a foetal blood vessel which connects the pulmonary arteries to the aorta allowing blood to bypass the lungs. Ho *et al.* demonstrated that ductal tissue is a common cause of coarctation and that ductal tissue is histologically different to the surrounding aorta [7].

The current treatment for neonatal coarctation is surgery, however, the treatment has evolved for older children and adults to include percutaneous stent implantation [8]. Newer stent designs, such as the Minima stent (Renata medical, CA, USA) [9], have opened the door for percutaneous treatment in neonates but further understanding of the underlying vessel properties is needed.

The aim of this study is to examine the differences between neonatal vessels at coarctation sites, in terms of mechanical properties and histology. Understanding these differences is key to designing bespoke patient therapies and to understanding the potential impact of neonatal stenting.

METHODS

Five specimens of neonatal aortic coarctation tissue were harvested during surgery from Children's Health Ireland at Crumlin following ethical approval by the hospital research ethics board. The vessels were cut into 3mm ring samples and uniaxial tensile testing was performed after 5 cycles of pre-conditioning to predetermined stretch levels before being fixed for histological analysis, see Figure 1.

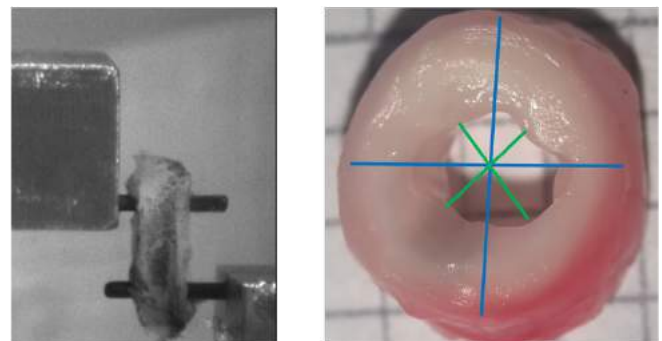


Figure 1: Neonatal aorta sample set-up for ring testing and demonstration of calculating stretch level, (outer diameter - inner diameter)/inner diameter.

RESULTS

Five sections were harvested of which three (samples 3 – 5) were further subdivided into two test specimens. Samples were labelled “A, B and C” with “B” being at the ductal-insertion point and “A” and “C” being proximal and distal, respectively.

Figure 2 shows the Force versus Diameter Change behaviour of the samples and highlights the inter- and intra-specimen variability. Specimens have quite variable mechanical properties depending on their relative location with respect to the ductus arteriosus insertion point (i.e. proximal or distal).

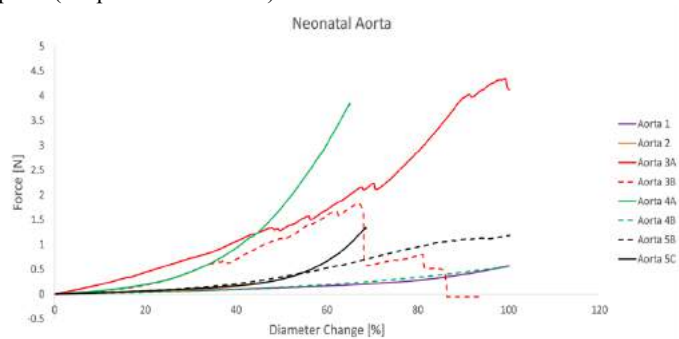


Figure 2: Force-Diameter Change (%) curves from uniaxial testing of neonatal coarcted tissue

Preliminary histological assessment of the ductus arteriosus tissue demonstrates the different histological structure of the ductal tissue when compared to the aortic wall tissue (Figure 3 & 4). The ductal tissue has very little elastin or collagen thus inferring that its load bearing capability is likely quite limited when undergoing stretch.

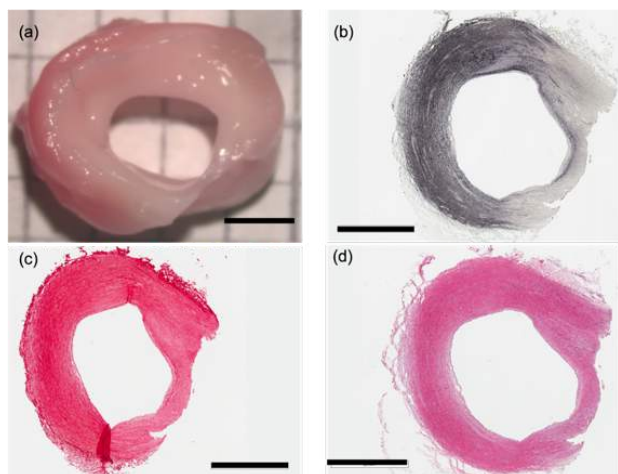


Figure 3: Neonatal aorta representative sample (Aorta 1) (a) Gross sample, (b) Verhoeff's stain (elastin), (c) Picrosirius red (collagen), (d) H&E stain (cell content). [Scale bars 2mm]

DISCUSSION

Neonatal coarcted aortic tissue has variable mechanical properties and the amount of ductal tissue which invades into the healthy aortic tissue likely plays a significant role in this variability. The composition of the coarcted tissue needs to be accounted for in any bespoke device-based patient treatment.

Previous work has demonstrated that bespoke titanium stents can be designed *in silico*, 3D printed and post-processed to match the patient specific geometry from a paediatric patient with coarctation of the aorta [10]. Our data will provide new insights into patient vessel properties and help inform such computational models to enable the optimum stent to be designed to achieve lumen gain while minimizing tissue damage.

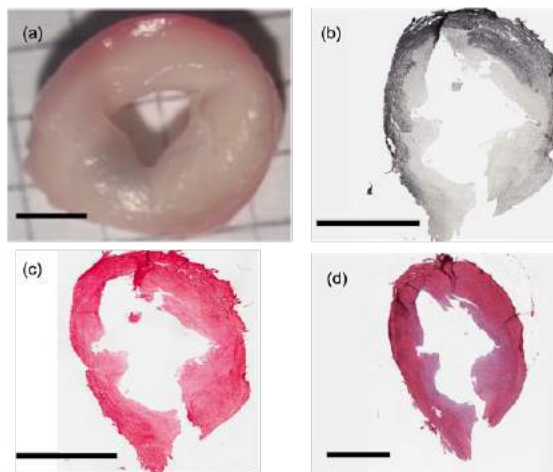


Figure 4: Neonatal aorta representative sample (a) Gross sample, (b) Verhoeff's stain (elastin), (c) Picrosirius red (collagen), (d) H&E stain (cell content). [Scale bars 2mm]

CONCLUSION

Individualised treatment plans will be the way of the future for many conditions. This study confirms the need to further understand the complex interplay between mechanical properties and tissue composition when designing less invasive treatment options in neonatal coarctation of the aorta.

ACKNOWLEDGEMENTS

The authors acknowledge the RCSI StAR MD program and Beacon Hospital, Dublin, Ireland who have provided funding for this project.

REFERENCES

1. Mai CT et al. Birth Defects Res. 2019 Nov 1;111(18):1420-1435.
2. Rosenthal E. Heart. 2005 Nov;91(11):1495-502.
3. Niwa K et al. Circulation. 2001; 103 (3):393-400.
4. Lock JE et al. Radiology. 1982 Jun;143(3):689-91.
5. Shaddy RE et al. Circulation 1993 Mar;87(3):793-9.
6. Cowley CG et al. Circulation. 2005 Jun 28;111(25):3453-6.
7. Ho SY et al. Coarctation, tubular hypoplasia, and the ductus arteriosus. Histological study of 35 specimens. Br Heart J. 1979 Mar;41(3):268-74.
8. Kenny D, Hijazi ZM. Coarctation of the aorta: from fetal life to adulthood. Cardiol J. 2011;18(5):487-95.
9. Zahn EM et al. Catheter Cardiovasc Interv. 2021 Jul 1;98(1):117-127.
10. McGee OM et al. J Mech Behav Biomed Mater. 2022 Oct;134:105388.

SHEAR STRAIN STIFFENING IN LIGAMENTS ARISES FROM UNALIGNED FIBERS AND IS AMPLIFIED BY AXIAL STRAIN

Jonathon L. Blank (1), Darryl G. Thelen (1,2), Joshua D. Roth (1,3)

- (1) Department of Mechanical Engineering, University of Wisconsin-Madison, Madison, WI, USA
(2) Department of Biomedical Engineering, University of Wisconsin-Madison, Madison, WI, USA
(3) Department of Orthopedics and Rehabilitation, University of Wisconsin-Madison, Madison, WI, USA

INTRODUCTION

Ligaments are hierarchical soft tissues that guide joint mechanics and prevent aberrant motion. In these roles, they often undergo a combination of tensile and shear loading. Resistance to shear is the primary mechanism by which ligament loading is dispersed across the tissue and is traditionally thought to arise from the non-collagenous matrix and interfibrillar bonds.¹ However, we recently showed using a computational model that the tissue's resistance to shear increases substantially with axial tissue strain when collagen fibers are not aligned in the loading direction.² These model predictions have yet to be empirically validated. It was previously shown that the shear modulus of ligament is shear strain-stiffening¹, but those tests were conducted in an axially unloaded state, which does not represent the combined loading that ligaments undergo *in vivo*.

The objective of this study was to characterize changes in the effective shear modulus of computational, electrospun nanofiber, and *ex vivo* models of human ligaments with axial loading. **Our primary hypothesis** is that effective shear modulus increases with axial load. **Our secondary hypothesis** is that the relationship between shear modulus and axial load is dependent on the shear region's fiber alignment.

METHODS

Finite element model: We created a finite element (FE) model of a ligament loaded both axially and in shear (Fig. 1 bottom). We modeled the tissue as transversely isotropic³ with distributed fibers⁴ according to a fiber alignment factor, k_f . Fibers were embedded in a Neo-Hookean matrix material. We simulated loaded shear with variable fiber alignment (i.e., from isotropic fibers, $k_f = 0$, to relatively aligned fibers, $k_f = 50$) on a high-throughput computing grid using FEBio v3.1.0.⁵

Electrospun nanofiber phantom: We dissolved PCL in hexafluoroisopropanol at 0.15 g/mL. The polymer was driven through a 22-gauge needle at 3 mL/hr with a 15kV potential through a distance of 15 cm. A rotating drum was placed in the polymer jet path. We controlled rotation speed to generate an isotropic nanofiber phantom.

Ex vivo ligaments: We procured 9 ligament specimens from the medial collateral ligaments (MCL) of three human donors (1M, 65.3 ± 7.0 years). We sectioned specimens to a uniform thickness of < 2 mm, ensuring that collagen fibers without overlying tissue constituents were visible on either side of the sample. We determined the tissue thickness using a portable ultrasound system (26 μ m resolution) prior to mechanical testing (1.27 ± 0.47 mm (mean \pm s.d.)).

Mechanical testing: We mounted specimens between sandpaper grips in a 1X PBS bath (ligament) or in air (phantom) on a custom axial-shear dynamic testing fixture (Fig. 1 top). The fixture consists of four motor-driven linear actuators (< 20 μ m backlash, 2 proximal, 2 distal) that load the specimen both in axial tension and shear. We preloaded each specimen to 0.05-0.1 N with approximately equal tension on either side. After preloading, we loaded the specimen in shear with a sawtooth displacement profile from 0-40% shear strain at a rate of 10%/s for 10

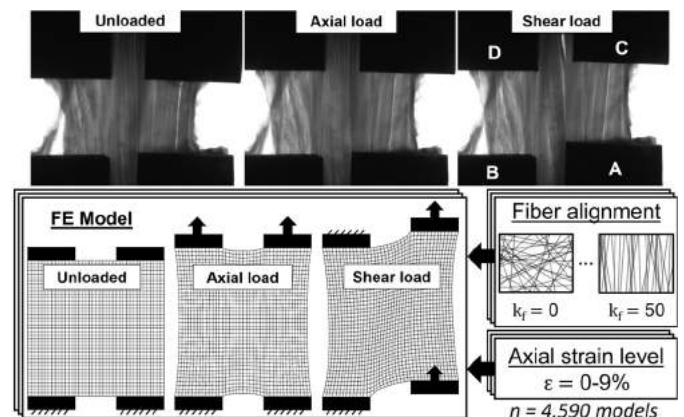


Figure 1: (top) Loaded shear force was computed as the force balance on the right side of the specimen ($F_C - F_A$). **(bottom)** Our FE model simulated loaded shear across fiber alignments and axial strain levels.

cycles. We then loaded specimens to axial strains of 3, 6, and 9% at a rate of 1%/s, and at each axial strain we applied the same sawtooth shear displacement profile. We recorded all measurements during the last cycle to minimize viscoelastic effects. The testing order of axial strains after 0% axial strain was randomized for all specimens.

Fiber alignment determination: We determined fiber alignment in our ligament samples using quantified polarized light imaging.⁶ A high-intensity backlight projected circularly polarized light through the specimen, and we captured images at 10 Hz using a machine vision camera (FLIR Blackfly S USB3). We computed the degree of linear polarization (DoLP), which represents fiber alignment, from interpolated polarized greyscale intensities.⁷ Our electrospun phantom was sputter-coated with gold and imaged using a scanning electron microscope (Zeiss Gemini 450) to verify isotropic fiber alignment.

Statistical analysis: We assessed the shear modulus (τ) at each axial strain level (ϵ). We determined the linear region of the shear stress response using an exponential-linear optimization function.⁸ In ligaments, we evaluated differences in shear modulus across axial strains using one-way analyses of variance (ANOVAs) with $\alpha = 0.05$. We additionally used a repeated measures ANOVA with an interaction effect between axial strain and fiber alignment (DoLP).

RESULTS

FE Model: The model predicted that shear modulus increased by up to 2.8 MPa at 9% strain when fiber alignment was varied. Increasing levels of axial preload increased shear modulus by up to 1.03 MPa in tissues with isotropic fibers (Fig. 2a,b) but were also present when fibers were relatively aligned (up to a 115 kPa increase) (Fig. 2a,c).

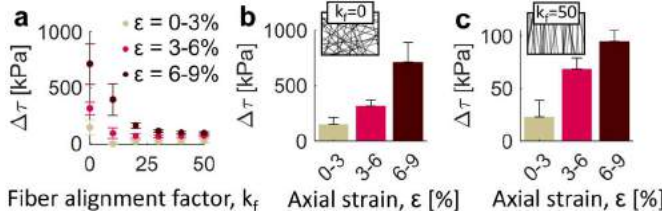


Figure 2: (a) The FE model revealed that changes in shear modulus ($\Delta\tau$) from the unloaded state were higher for (b) models with unaligned fibers ($k_f=0$) than those for (c) models with relatively more aligned fibers ($k_f=50$). Error bars represent standard deviation.

Electrospun Phantom: The shear stress-shear strain behavior of the electrospun nanofiber phantom (Fig. 3b) was qualitatively similar to that of the FE model with randomly aligned fibers ($k_f = 0$) (Fig. 3a). Both the model and phantom exhibited shear strain stiffening behavior when the tissue was not axially preloaded.

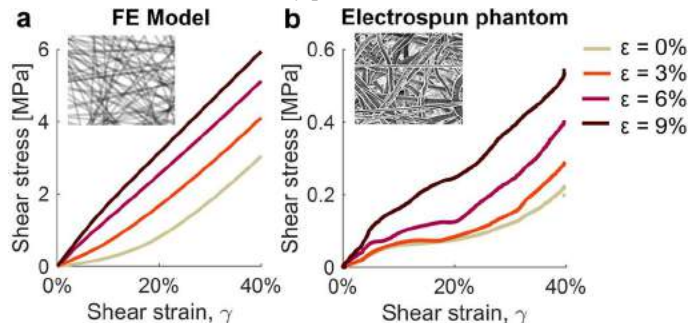


Figure 3: (a) The shear response of our FE model with unaligned fibers ($k_f=0$) qualitatively agreed with (b) the shear response of an isotropic electrospun phantom.

Ligaments: Ligament specimens exhibited shear strain-stiffening behavior on average for all levels of axial preload (Fig. 4a). The shear modulus of the linear region at 9% axial strain was greater than that at

0% ($p < 0.001$) and that at 3% axial strain ($p < 0.05$) (Fig. 4b). Axial strain was the primary contributor to an increase in shear modulus ($p < 0.01$). We did not detect a relationship between fiber alignment and shear modulus ($p=0.34$) or a significant interaction between fiber alignment and axial strain ($p=0.32$).

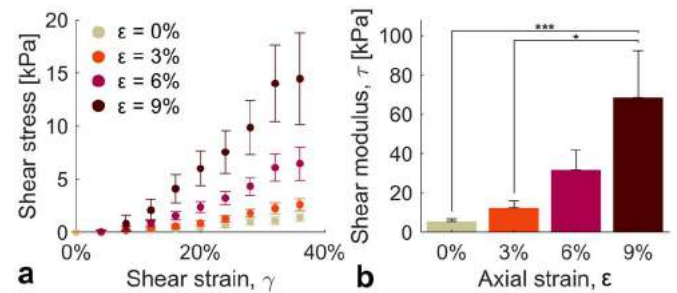


Figure 4: (a) The shear stress-shear strain relationship was nonlinear in the ligament specimens tested. (b) Shear moduli in ligaments generally increased with increasing axial load at both low and high-shear strains. Error bars represent standard error (* $p < 0.05$, *** $p < 0.001$).

DISCUSSION

The objective of this study was to characterize ligament shear modulus under combined axial and shear loading. Consistent with our primary hypothesis and prior FE model predictions,² the linear shear modulus increased up to 12-fold on average when ligaments were axially loaded prior to undergoing shear deformation (Fig. 4b). We also observed a nonlinear relationship between the ligament shear stress and shear strain, which agrees with prior studies.¹ However, we observed much smaller max shear stresses in ligaments than the same prior study (1.6-5.5 kPa vs 15-25 kPa) in the axially unloaded state. This may be caused by loss of ligament matrix material and supporting structures other than the fibers from cryosectioning or by changes to the shear loading setup (i.e., gripping anterior/posterior¹ vs proximal/distal).

Our secondary hypothesis that increases in shear modulus correspond to fiber realignment due to axial loading was not supported. However, our FE model suggests that the initial fiber alignment in the shear region of the tissue is an important factor that can affect shear modulus (Fig. 2a). Because this strain-stiffening relationship exists in electrospun nanofiber phantoms (Fig. 3b), we are currently expanding our study of the relationship between fiber alignment and shear modulus by systematically varying fiber alignment in the phantoms.⁹

The findings from this study have several applications. First, we developed and implemented a novel technique to measure shear modulus in axially loaded tissues, which can be used to study the mechanics of ligaments and other fibrous soft tissues. Second, we showed that axial loading modulates ligament shear modulus, a relationship that has functional relevance but is not captured in current constitutive models of ligament³ that are used most commonly. Third, because noninvasive sensing and imaging using shear waves, such as in tensiometry or elastography, is dependent on the tissue's axially preloaded shear modulus,² the analysis presented in this study may be useful for resolving how shear wave speeds can change with axial load and shear modulus.

ACKNOWLEDGEMENTS

NSF GRFP DGE-1747503. We thank Drs. Wan-Ju Li and Terry Lee for their support in fabricating nanofiber scaffolds.

REFERENCES

- [1] Weiss, *J. Biomech.*, 2002.
- [2] Blank, *JMBBM*, 2021.
- [3] Weiss, *Comput. Meth. Appl. Mech. Eng.*, 1996.
- [4] Gouget, *Biomech. Model. Mechanobiol.*, 2012.
- [5] Maas, *J. Biomech. Eng.*, 2012.
- [6] York, *J. Biomed. Optics*, 2014.
- [7] Zhang, *Optics Express*, 2016.
- [8] Tanaka, *J. Biomech. Eng.*, 2011.
- [9] Li, *J. Biomech.*, 2007.

MODELING ULTRASOUND-DERIVED ACOUSTIC RADIATION FORCES IN HYDROGELS USING 3D FORCE MICROSCOPY

Kevin P. Grassie (1), Fei Wang (2), Bryan D. Huey (2), Yusuf M. Khan (1,2,3)

(1) Biomedical Engineering, University of Connecticut, Storrs, CT, USA

(2) Materials Science & Engineering, University of Connecticut, Storrs, CT, USA

(3) Orthopaedic Surgery, CT Convergence Institute, UConn Health, Farmington, CT, USA

INTRODUCTION

Biophysical stimuli have gained attention in the growing field of bone regenerative engineering for their potential to augment cell behavior and enhance bone repair. In an effort to treat large-scale bone defects not amenable to traditional grafting techniques, our group has combined hydrogel-based cell therapy with low-intensity pulsed ultrasound (LIPUS). Hydrogels serve as implantable, biomimetic, 3D environments in which encapsulated cells can be delivered to and retained within bone defects. LIPUS stimulation, an FDA approved treatment for fracture healing, is used in our approach to deliver low-level acoustic radiation force (ARF) to cells [1]. Physical forces are well-known as important regulators of cell behavior and bone homeostasis. Therefore, LIPUS-derived ARF applies supplementary mechanical forces to hydrogel-encapsulated cells. Previous work has demonstrated that LIPUS can upregulate osteogenic markers *in vitro* and stimulate bone formation *in vivo* in cells encapsulated in collagen hydrogels [2,3]. However, the local mechanical environment that LIPUS imparts on hydrogel-encapsulated cells is not well understood. Here, we have developed a 3D force microscopy (3D-FM) technique based on traditional traction-force microscopy (TFM) to predict the mechanical forces imparted to cells and their surroundings during LIPUS stimulation. Briefly, this technique involved tracking fluorescent microspheres embedded in cell-laden hydrogels and measuring their ultrasound-induced displacements. These displacements were then used to computationally reconstruct and predict the associated 3D forces applied locally to cells and their hydrogel environment. The objectives of the work herein were to: 1) develop the theoretical framework and MATLAB algorithm for the 3D-FM technique, 2) validate its performance using simulated displacement data from simple, user-defined force distributions, and 3) use 3D-FM to estimate the forces near isolated cells in a collagen hydrogel subject to ARF. Modeling the ARF-induced cell-scale forces across different ultrasound and hydrogel parameters will permit a better understanding of how these inputs

correspond to cell behavior, and ultimately optimize the regenerative capacity for bone defect repair.

METHODS

Theoretical Framework and Implementation of 3D-FM: The 3D-FM algorithm developed in MATLAB was an extension of traditional TFM techniques. While almost all applications of TFM focus on cell-generated forces and most analyze 2D culture conditions, our novel algorithm was designed to compute forces near cells fully encapsulated in 3D hydrogels resulting from externally-applied mechanical stimulation, outlined visually in Figure 1. First, fluorescent beads embedded in the hydrogels were tracked and their ultrasound-induced displacements were measured, representing local values of gel deformation. Interpolation of these bead displacements then produced a 3D displacement vector field $\vec{u}(\vec{r})$ for the region of gel imaged.

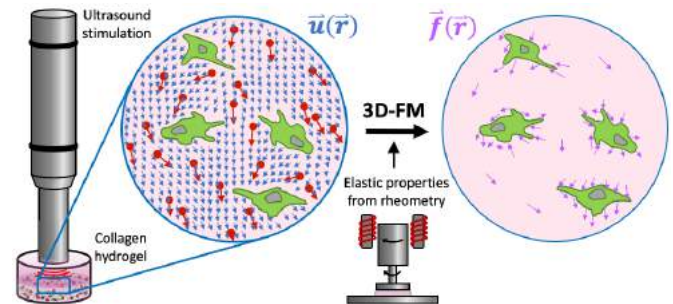


Figure 1. Diagram illustrating the concept and experimental setup of the 3D-FM technique for predicting the local forces in cell-laden hydrogels due to ultrasound stimulation.

The 3D force-density vector field $\vec{f}(\vec{r})$ was reconstructed from the displacement field via a regularized Fourier transform method for solving the otherwise ill-posed inverse problem of linear elasticity. This

method approximated the hydrogel as a linear-elastic, isotropic, homogeneous medium satisfying the conditions of mechanical equilibrium with ultrasound-induced deformations that were small compared to the bulk hydrogel dimensions. These assumptions for the medium admit a closed-form matrix Green's function $\mathbf{K}(\vec{r})$ in terms of its elastic properties (E_Y, ν) that characterizes the displacements produced from a concentrated force in the 3D medium. $\mathbf{K}(\vec{r})$ was then used as a mathematical "building block" for a general solution relating $\vec{f}(\vec{r})$ and $\vec{u}(\vec{r})$ (Eqs. 1 and 2).

$$\vec{u}(\vec{r}) = \int \mathbf{K}(\vec{r} - \vec{r}') \vec{f}(\vec{r}') d^3 r' \quad (1)$$

$$K_{ij}(\vec{r}) = \frac{1 + \nu}{8\pi E_Y (1 - \nu)} \left[\frac{3 - 4\nu}{r} \delta_{ij} + \frac{x_i x_j}{r^3} \right], \quad i, j = 1, 2, 3 \quad (2)$$

Inverting this general solution to obtain $\vec{f}(\vec{r})$ from $\vec{u}(\vec{r})$ involved transforming Eq. 1 into discrete Fourier space (denoted by tilde marks below) and employing zeroth-order L^2 Tikhonov-regularization (Eq. 3) to stabilize the reconstruction of $\vec{f}(\vec{r})$ [4].

$$\vec{\tilde{f}} = (\mathbf{K}^\dagger \mathbf{K} + \lambda^2 \mathbf{1})^{-1} \mathbf{K}^\dagger \vec{\tilde{u}} \quad (3)$$

Here, \dagger denotes the conjugate transpose of a matrix. The choice of the real-valued regularization parameter λ was based on the tradeoff between suppressing the undesirable amplification of high-frequency noise in $\vec{u}(\vec{r})$ and excessively dampening the entire reconstructed force-density field. Finally, the results of Eq. 3 were transformed back into physical space to yield the estimated local force-density field $\vec{f}(\vec{r})$ corresponding to the measured ultrasound-induced displacements within the cell-laden hydrogel.

Validation of 3D-FM Algorithm: To test the accuracy of the 3D-FM algorithm, simulated displacement data were generated without added noise from known, randomized point-force distributions. First, the ability for the algorithm to reconstruct accurate force magnitudes was assessed for 50 randomly-generated forces of various magnitude ranges. Second, the ability for the algorithm to accurately reconstruct force distributions of increasing complexity was tested, using 10, 100 and 1000 randomly-generated forces.

Cell-Hydrogel Construct Synthesis: Bone marrow stromal cells (BMSCs) were harvested from the long bones of reporter mice and cultured for 7 days before osteogenic induction to enhance expression of a green fluorophore. BMSCs ($10^6/\text{mL}$) were then co-encapsulated with red fluorescent beads ($1 \mu\text{m}$ diameter, $10^8/\text{mL}$) in 3 mg/mL (0.3%) collagen hydrogels formed on plasma-treated microwell dishes with glass coverslip bottoms and immersed in 3 mL α -MEM.

Estimation of Local 3D Forces near Encapsulated Cells: Continuous-wave ultrasound with $1000 \text{ mW}/\text{cm}^2$ intensity was applied to the BMSC/bead-laden hydrogels. Z-stacks containing an isolated cell were acquired with a Leica DMi8 epifluorescence microscope before ultrasound, 30 seconds after the onset of stimulation, and 30 second after the cessation of a 2 minute bout of stimulation. Tracking and displacement measurements were performed with Velocity software. Elastic parameters for the 3D-FM algorithm were derived from previous rheometry experiments on 0.3% collagen hydrogels. A user-defined Boolean mask enclosing the green fluorescence from a cell was used to isolate and quantify the estimated ultrasound-derived forces in the region occupied by the cell.

RESULTS

Figure 2 shows that the 3D-FM algorithm was able to reconstruct force-distributions with different magnitude ranges and complexity to with normalized errors less than 15%. Other data (not shown) showed that reconstructed force-density magnitudes increased with increasing magnitudes of simulated displacement, thereby demonstrating the validity of the algorithm. Figure 3 displays top-down views of the Z-

stack and tracked bead displacements for a representative region of collagen hydrogel containing an isolated cell and deformed by incident $1000 \text{ mW}/\text{cm}^2$ ultrasound. The 3D-FM results in Figure 4 reveal a cluster of ultrasound-induced forces localized around the cell.

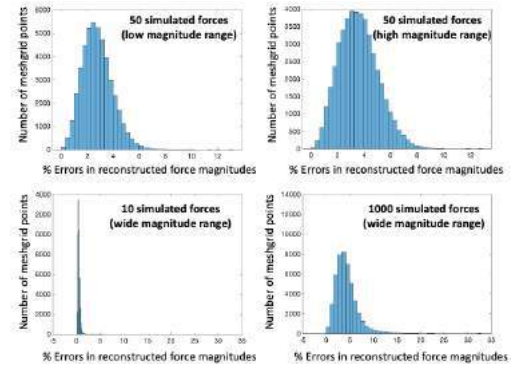


Figure 2. Histograms of percent normalized errors in the forces reconstructed from various simulated displacement datasets.

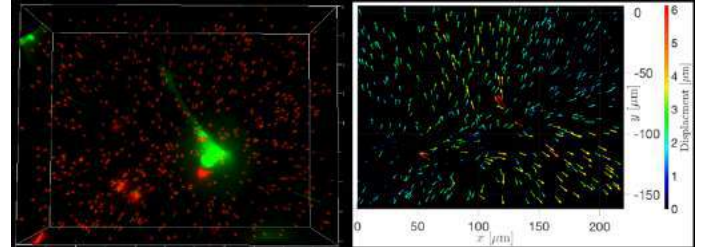


Figure 3. Top views of a cell and beads in a 3D hydrogel (left) and associated ARF-induced displacements of the beads (right).

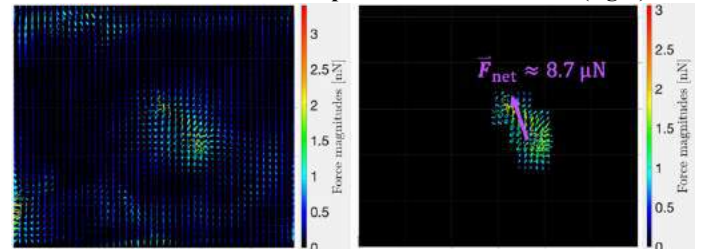


Figure 4. Local ARF-induced force field (left) and estimated net force (right) around the cell, predicted by the 3D-FM algorithm.

DISCUSSION

Here we present a novel application and modification of TFM to quantify the local mechanical forces on cells encapsulated in hydrogels stimulated by LIPUS-derived ARF. The 3D-FM model suggested that mechanical forces are transmitted directly to cells and their immediate surroundings as a result of ARF propagating through the hydrogel. Quantifying these forces in various ultrasound and hydrogel conditions will contribute to a clearer picture of the mechanisms of LIPUS stimulation in order to improve bone regeneration.

ACKNOWLEDGEMENTS

Research reported in this abstract was supported by the National Institutes of Arthritis and Musculoskeletal and Skin Diseases of the National Institutes of Health under award number R01AR073206.

REFERENCES

- [1] McCarthy C. Micromachines, 12: 1488, 2021. [2] Veronick JA. Exp Biol Med, 241: 1149-1156, 2016. [3] Veronick JA. Tiss Eng Part A, 24: 254-263, 2018. [4] Mulligan JA. Adv Exp Med Biol, 1092: 319-349, 2018.

EFFECT OF LABRUM SIZE ON CARTILAGE MECHANICS IN A PATIENT WITH CAM-TYPE FEMOROACETABULAR IMPINGEMENT SYNDROME

Luke T. Hudson^{1,2}, Travis G. Maak³, Andrew E. Anderson^{1,2,3},
Gerard A. Ateshian⁴, Jeffrey A. Weiss^{1,2,3}

- (1) Department of Biomedical Engineering, University of Utah, Salt Lake City, UT, USA
(2) Scientific Computing and Imaging Institute, Salt Lake City, UT, USA
(3) Department of Orthopaedics, University of Utah, Salt Lake City, UT, USA
(4) Department of Mechanical Engineering, Columbia University, New York City NY, USA

INTRODUCTION

The acetabular labrum plays a crucial role in the hip, serving as a mechanical boundary to enhance joint stability and sharing load with the acetabular cartilage. Labral injuries can impair these functions, leading to instability and potentially accelerated degeneration of the acetabular cartilage. In individuals with cam-type femoroacetabular impingement syndrome (FAIS), secondary labral tears are common. Tears are often repaired during arthroscopic surgery for FAIS¹. Suture anchor repair is currently considered the gold standard for labral repair, though labral reconstruction procedures are also utilized to modify the labrum's natural morphology. There is ongoing debate among surgeons as to whether reconstruction or augmentation of hypotrophic (undersized) labra is necessary, as there is a lack of biomechanical or clinical data demonstrating reduced efficacy of such labra². The aim of this study was to assess the influence of labral size on the mechanical environment of the cam-type FAIS hip during gait. We tested the null hypothesis that there were not differences in contact mechanics between different sized labra, and thus the likelihood of cartilage damage would remain unchanged.

METHODS

For our finite element models, we adapted closed bounded surfaces of the bones, cartilage, and labrum segmented from CT arthrogram image data of a single patient with cam-type femoroacetabular impingement syndrome (FAIS)³. Three clinical morphologies were considered in our modeling cases: (1) an anatomically normal labrum, corresponding to the segmented geometry, (2) a hypotrophic labrum with an average

thickness less than 3mm, and (3) a hypertrophic labrum with an average thickness greater than 4 mm^{2,4}. The labrum and cartilage surfaces were discretized using quadratic tetrahedral elements in ANSA (BETA CAE Systems SA), and elements were manually offset, modulating the height and thickness, to reflect the hypertrophic and hypotrophic morphologies (Fig. 1).

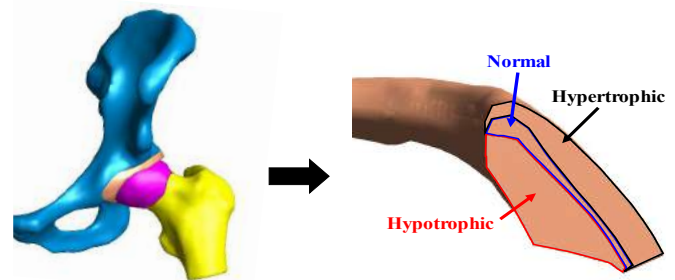


Fig. 1: (Left) Surfaces from a volunteer with cam-type FAIS were used for FE model creation. (Right) The anatomically normal labrum was modified to reflect the hypotrophic and hypertrophic cases.

The acetabular and femoral cartilage layers were modeled as anisotropic hyperelastic materials with a continuous ellipsoidal fiber distribution of tension-only collagen fibers that varied in primary orientation through the thickness of the cartilage (tangent to the articular surface in the superficial zone, isotropic distribution in the middle zone, and perpendicular to the articular surface in the deep zone)⁵. The labrum was represented as a transversely isotropic material with circumferentially oriented collagen fibers⁵. Patient-specific kinematics from skin-marker motion tracking during gait and joint reaction forces collected by

Bergmann et al. were incorporated into the finite element models⁶. All models were analyzed in FEBio (www.febio.org). The labral load support was examined for the three modeling cases, defined as the total load across the labrum divided by the total load across the cartilage-labrum interface. Additionally, the magnitude of displacement for the labrum was evaluated for each morphology at heel-strike. Contact pressure, 1st principal (tensile) strain on the articular surface, and maximum shear stress at the osteochondral interface were also evaluated throughout the gait cycle to compare the distribution of load.

RESULTS

A larger labrum resulted in greater load supported by the labral surface (Normal – 2.1%; Hypertrophic – 3.0%; Hypotrophic – 1.8%) throughout the gait cycle. Greater load across larger labra also lead to greater displacement during heel-strike for the hypertrophic (2.63 mm) and normal (2.29 mm) cases compared to the hypotrophic cases (2.26 mm) (Fig. 2). However, this did not result in measurable changes in contact pressure anterosuperiorly at heel-strike (Fig. 3).

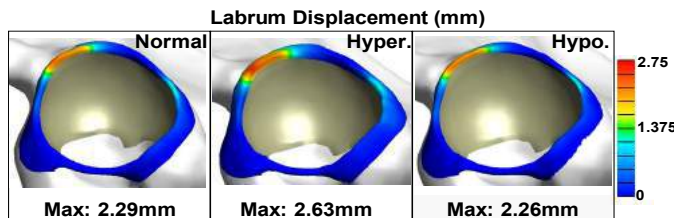


Fig. 2: Labrum displacement at heel-strike for each morphology. Larger labra lead to greater displacement across the three modeling cases.

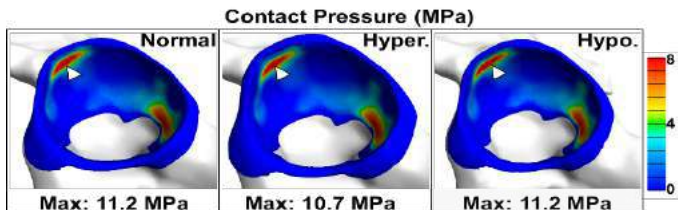


Fig. 3: Contact pressure at heel strike for the three labrum geometries. Note the lack of difference in max contact pressure located anterosuperiorly.

There were small differences in the 1st principal strain, with the hypotrophic labrum model presenting the largest tensile strain within the same region for the cartilage (25.6%), followed by the hypertrophic (24.3%) and normal (20.2%) cases (Fig. 4). Similarly, the peak shear stress at the osteochondral interface was slightly elevated for the hypotrophic labrum (13.1 MPa) followed by the hypertrophic (12.8 MPa) and normal (12.2 MPa) labra (Fig. 5).

DISCUSSION

The difference in labral load support between the hypertrophic and hypotrophic morphologies indicates that labral size modifies the load transferred to the labrum during walking. These findings are consistent with the larger magnitude of displacement in both the hypertrophic and normal cases compared to that of the hypotrophic case. These results are also consistent with a study

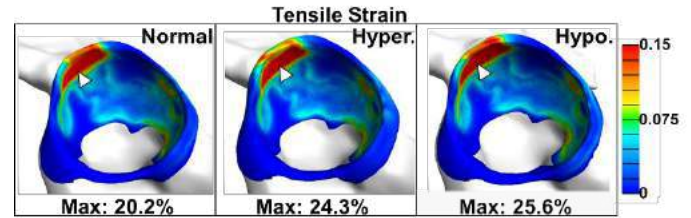


Fig. 4: 1st principal strain at heel-strike for the three labrum geometries. Max strain was located anterosuperiorly with similar values for each case.

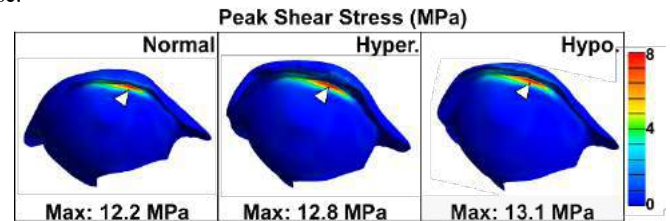


Fig. 5: Peak shear stress at heel-strike for the three labrum geometries. The highest shear stress occurred at the osteochondral surface for each case.

of acetabular dysplasia, where dysplastic hips with larger labra had higher values for labral load support⁷.

Despite the differences in load transmission between different sizes of labra, the contact pressure and tensile strain across the articular cartilage were minimally affected and were within similar ranges previously reported for normal and cam-type hips, respectively^{3,8}. Similarly, the variation in max shear stress was minimal between the three cases and was above the reported magnitude of shear stress within normal hips⁹. These findings indicate that the mechanical loading on the acetabular cartilage in cam-type hips is left unchanged regardless of labral size, suggesting similar levels of susceptibility to cartilage damage.

Our results could have implications for clinical decision making during primary arthroscopic surgery for cam-type FAIS, particularly regarding management of the labrum. Notably, model predictions for this patient suggest that labral reconstruction would not have a major effect on cartilage stress. It is possible that labral repair with native labral fibers may be enough to restore functionality to the hip regardless of labral morphology. Still, additional patients and asymptomatic controls need to be modeled to better understand the role of the size of the labrum. Future research could also evaluate the effect of labrum size by using more advanced approaches to scaling the dimensions of this tissue, and incorporating the use of statistical shape model to better represent anatomical variation in the size and shape of the labrum that occurs across this population.

ACKNOWLEDGEMENTS: NIH #R01AR077636

REFERENCES

- [1] Buzin, S.D. et al., *Orthop Res Rev*, 14:121-132, 2022.
- [2] Ejnisman, L et al., *Clin Sports Med*, 30:317-329, 2011.
- [3] Todd, J.N. et al., *Clin Orthop Relat Res*, 480:602-615, 2022.
- [4] Nwachukwu, B.U. et al., *HIP Int.*, 29:198-203, 2019.
- [5] Todd, J.N. et al., *J Biomech*, 69:113-120, 2018.
- [6] Bergmann, G et al., *J Biomech*, 34:859-871, 2001.
- [7] Henak, C.R. et al., *J Biomech*, 44:2210-2206, 2011.
- [8] Henak, C.R. et al., *J Biomech Eng*, 136:021021, 2014.
- [9] Ng, K.C. et al., *HSS J*, 8:206-212, 2012.

MOLECULAR DYNAMICS STUDIES OF SUGAR SOLUTIONS FOR CONTROLLING WATER ROTATIONAL RELAXATION TIME

Kang Hu (1,2), Ryo Shirakashi (1)

(1) Institute of Industrial Science, The University of Tokyo, Meguro, Tokyo, Japan
(2) Department of Mechanical Engineering, The University of Tokyo, Bunkyo, Tokyo, Japan

INTRODUCTION

Along with the advancements in therapeutic proteins, stabilization methods are in urgent demand to maintain their quality, given the necessity of protein stability for successful therapy. Protein drugs are usually in a liquid formulation and the dynamics of surrounding water (hydration layers, abbreviated as HLs hereafter) are known to have a significant influence on protein conformation. During the stabilization processes, protective agents are usually added to help the preserved biological materials overcome the induced physiochemical stresses, such as ice crystallization, low temperature, dehydration, etc. Therefore, the investigations of the effect of additives on water dynamics may advance our knowledge of controlling water dynamics, thus the design of protein stabilizers. Molecular dynamics (MD) simulations have been a powerful tool to probe the structure, dynamics, and interactions of biological molecules, providing adequate spatial and temporal resolution at a reasonable computational cost¹.

Among the protective agents, sugars have been widely employed to protect protein drugs and food during the freezing and drying processes. The sugar-water interactions are deemed to be responsible for its unique protection mechanism². It has also reached a consensus that water dynamics close to sugars are retarded relative to bulk water, by a variety of experiments³ and MD simulations⁴. However, the basic principles for retarding water rotational dynamics thus for the design of protective agents is rarely discussed, although all these above works explored how different additives influence water dynamics through water-structure-making or water-structure-breaking effect⁵. Therefore, a systematic investigation to extract the essential parameters for developing protective agents is of great significance.

In order to facilitate the design of the protein stabilizer, the present work aims to have a better understanding of how the protective additives slow down the water dynamics from a molecular level. Rotational relaxation times of individual water molecules in bio-protective sugar solutions (glucose, trehalose) are calculated by MD simulation. Water

relaxation time is found to increase exponentially with its residence time. Furthermore, the normal distribution of water residence time suggests how the solute size (specific surface area) governs water residence time. The basic laws acquired here for controlling water dynamics will have a meaningful impact on the development of protein stabilizers.

METHODS

MD simulation was adopted in the present work. Initial structures of glucose and trehalose were downloaded from the GlycoSciences Database. The corresponding topology files for MD simulation in GRMACS were prepared by the CHARMM Graphical User Interface (CHARMM-GUI). Sugars were described by the CHARMM36m force field, and the simple point charge (SPC/E) model was used for water. For these carbohydrate-water systems, tens of solute molecules were solvated in a cubic box of length around 3 nm with 6~10 hundreds of water molecules, corresponding to a mass percent ranging from 10 to 40 wt%. The subsequent simulation protocols such as the energy minimization, NVT equilibration, NPT equilibration, and the final production run were similar with those used for the simulation of aqueous lysozyme solution⁶.

The rotational relaxation time of water molecule was derived from its dipole moment time autocorrelation function (ACF), which is defined as

$$\psi(t) = \frac{\langle \mu(0) \cdot \mu(t) \rangle}{\langle \mu(0) \cdot \mu(0) \rangle}, \quad (1)$$

where dipole vector $\mu(t)$ is the summation of single water OH-bond vector e at time t . The dipole moment ACF obtained was then approximated with a multi-decaying exponential by the least squares method to extract the rotational relaxation time constants⁶.

By terahertz absorption measurements, Heyden et.al found that the THz absorption of the hydration water was increased in a range of 3.7

$\pm 0.9 \text{ \AA}$ and defined the HL thickness of 3-4 \AA , for monosaccharide solutions⁷. EDLS experiments by Lupi et al. suggested the evident retardation of water within 3.1 \AA from any solute atom relative to the bulk water, for monosaccharide and disaccharide solutions⁸. Based on these experimental determinations, the sugar HL in this work was also adopted as a 3 \AA water layer from the sugar surface. Consequently, the residence time which is the time water spends within the HL was obtained for each water molecule in all the studied sugar solutions.

RESULTS

The relationship between water rotational relaxation time and residence time is explored and shown in **Figure 1** where the abscissa, residence time t_R , is normalized by the sampling time (5 ns). For all the solutions studied here, water relaxation time shows a decent exponential correlation with its residence time, as suggested by the linear fit (the solid black line in **Figure 1**) between the relaxation time in a logarithmic scale and the residence time. The intercept ($t_R = 0$) of around 0.68 corresponds to the relaxation time of HMW, which is ~ 5.0 ps. The slope is around 0.40 for monosaccharide (glucose), while it is about 0.56 for disaccharide (trehalose) solutions. Obviously, the increasing rate of the water relaxation time with the residence time is faster in disaccharide solutions than that in monosaccharide solutions. Particularly, this observation implies that slowing down water rotation dynamics might be achieved by promoting the increment rate and elongating the water residence time.

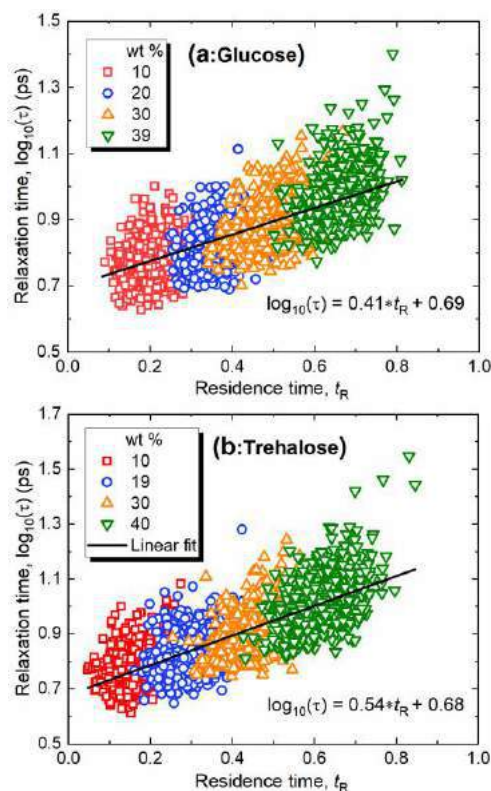


Figure 1: Correlation between rotational relaxation time and residence time for water in sugar solutions. Each symbol represents one single water molecule. (a) glucose, (b) trehalose.

Achieving a broader distribution of water relaxation time necessitates a longer residence time spectrum. In light of this, PDF of the water residence time in various concentrations of trehalose solutions

together with the approximated Gaussian curve is obtained and shown in **Figure 2**. For each condition, water residence time PDF is perfectly fitted to a normal distribution. This observation suggests that residence time distribution of water in sugars solutions is uniform and that water molecule has an equivalent probability of entering the sugar HLs. This result was also observed in glucose solutions.

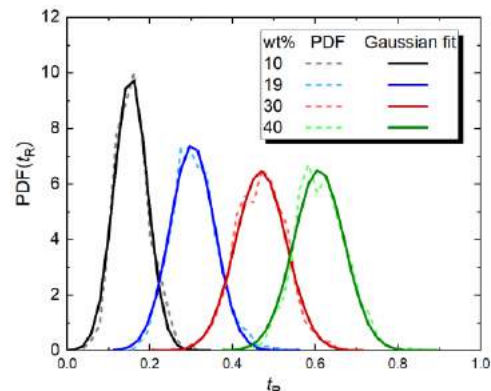


Figure 2. PDF of normalized water residence time in various concentrations of trehalose solutions.

DISCUSSION

According to the geometric definition of HL in this work, a water molecule is hydration water when its distance from the solute surface is less than 3 \AA . Water residence time is obtained by counting the time it stays within the HLs. Now that the normal distribution of water residence time in sugar solutions (**Figure 2**) has suggested the random walk of water within sugar solutions, the ratio of sugar HLs volume to the total solvent-accessible space should be equivalent to the normalized water residence time on the assumption that water density is uniform within the sugar solutions. Ignoring the HL overlapping, the volume of sugar HLs is the geometric summation of a single HL space. Therefore, the ratio of sugar HLs volume (V_{HLs}) to the total solvent-accessible space (V_{access}) is

$$\frac{V_{HLs}}{V_{access}} = \frac{SSA \cdot \Delta L}{1/(\rho_{solute} V_{solute}) - 1}, \quad (2)$$

where SSA is the specific surface area of the solute, ρ_{solute} is the solute number density, and V_{solute} is the molecular volume of solute. Eq. (2) indicates that a larger solute SSA is necessary for a longer residence time. Therefore, in the design of a protective agent, the molecular size is one of the keys to controlling water rotational dynamics. A smaller protective agent with larger specific surface area is more effective.

ACKNOWLEDGEMENTS

This work was supported by the Grant-in-Aid for Scientific Research from Japan Society of Promotion of Science (JSPS) (KAKENHI), Grant Numbers 21K18684 (Grant-in-Aid for Challenging Research/Pioneering).

REFERENCES

- [1] Weng, L et al., *Annu. Rev. Biomed. Eng.*, 21:1-31, 2019.
- [2] Cordone, L et al., *Curr. Org. Chem.*, 19:1684-1706, 2015.
- [3] Shiraga, K et al., *J. Chem. Phys.*, 142:234504, 2015.
- [4] Magno, A et al., *J. Phys. Chem. L*, 2:977-982, 2011.
- [5] Hishida, M et al., *J. Phys. Chem. B*, 126:2466-2475, 2022.
- [6] Hu, K et al., *J. Phys. Chem. B*, 126:4520-4530, 2022.
- [7] Evans, M et al., *Phys. Rev. A*, 36:226-231, 1987.
- [8] Lupi, L et al., *J. Phys. Chem. B*, 116:14760-14767, 2012.

VARIABLE GRADIENTS IN MINERAL CONTENT AND CRYSTALLINITY MAY BE RESPONSIBLE FOR MECHANICAL RESILIENCE OF THE DENTIN-ENAMEL JUNCTION

Michael Truhlar (1), Sobhan Katebifer (2), Roland Kröger(3), Alix Deymier (2)

- (1) School of Dental Medicine, UConn Health, Farmington, CT, USA
 (2) Biomedical Engineering, UConn Health, Farmington, CT, USA
 (3) Department of Physics, University of York, York, U.K.

INTRODUCTION

The introduction should establish the importance of the subject, briefly explain what is known, state what is unknown or problematic, and then provide a clear statement of the objectives and/or research questions associated with the study.

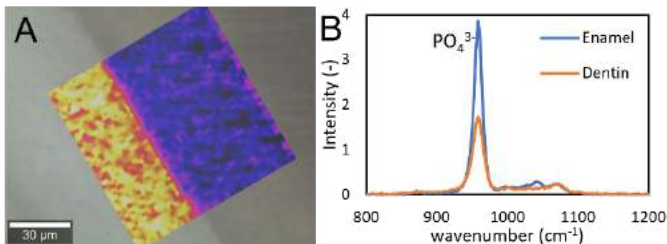


Figure 1: (A) Image showing an overlay of the 960 cm⁻¹ phosphate peak intensity over an optical image of the murine DEJ. (B) representative spectra showing the 960 cm⁻¹ in enamel and dentin.

METHODS

Data acquisition:

All animal protocols were completed in accordance with the UConn Health Institutional Animal Care and Use Committee. The lower left incisors of 5-6 month old CD-1 mice (n=5) were extracted, mounted onto glass slides and polished with a diamond embedded polishing wheel. A Witec Alpha 300 Raman Spectrometer was used to obtain spectra over a 25x25 μm² area encompassing the DEJ near the incisal edge of the tooth (Fig 1). Spectra were collected every 0.5 μm with a 785 nm laser, 50X objective, and a 20 sec integration time.

Data analysis:

All spectra were corrected for cosmic rays and background subtraction using Witec Program 5.1 software. The 960 Δcm⁻¹ v₁ phosphate peak, Fig 1B, was then fit using the MATLAB Voigt-fit function to calculate

the peak maximum intensity (Max Int) and full width half max (FWHM). Matrices of Max Int and FWHM were then aligned such that line profiles were taken perpendicular to the DEJ. Max Int and FWHM values were then averaged across the line profiles in order to obtain average values for each as a function of position across the DEJ (Fig 2). These plots exhibited 3 distinct gradients: a 1st shallow gradient in Max Int, a 2nd sharp gradient in Max Int, and a single gradient in FWHM. The 2nd Max Int gradient and the FWHM gradient were fit with a logistic function using MATLAB. The derivative of this function was then used to determine the center of the gradient (location of the derivative peak) and the gradient width (FWHM of the derivative peak). The first Max Int gradient was not accurately fit by a logistic function. Its width and center were thus determined manually by an experienced user.

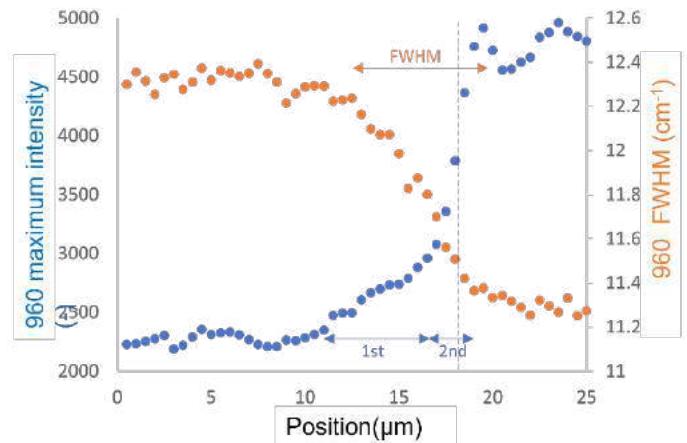


Figure 2: Representative plots of the gradients in 960 cm⁻¹ peak intensity (blue) and peak FWHM (orange) with the identified gradients. Dotted lines indicated the optical DEJ.

Modeling:

The logistic function fits were used to predict the change in moduli of the tissue as a function of position considering both the mineral content and crystallinity. Changes in mineral crystallinity were assumed to follow the logistic fit of the FWHM experimental data. The relationship between modulus and crystallinity was determined to be positive and linear based on previous work using Raman spectroscopy and X-ray diffraction to link modulus, compositional changes, and crystallinity [1, 2]. From this we predicted the change in modulus based on crystallinity as a function of position across the DEJ. The mineral content as a function of position was assumed to follow the logistic fit of the 2nd Max Int experimental data. The modulus was then calculated as a function of position assuming an isostrain system where the mineral content varies according to the MaxInt and the mineral modulus varies as a function of FWHM (Fig 3). Using a span of 10 μm , the total tissue modulus was estimated by averaging the varying moduli across the tissue.

RESULTS

Gradient widths: The Max Int, which is an indicator of mineral content across the DEJ, exhibited two graded regions in all samples. Both gradients indicated that the amount of mineral increased as one traveled from the dentin towards the enamel. The first gradient was a shallow gradient which had an average gradient width of $7.7 \pm 2.5 \mu\text{m}$. The second gradient was a much sharper gradient and had a calculated average width of $2.9 \pm 0.8 \mu\text{m}$.

The FWHM of the 960 cm^{-1} peak, which is inversely correlated to the mineral crystallinity [3], was also graded across the DEJ showing a decrease as one travels from dentin to enamel. The width of this gradient was $6.7 \pm 0.7 \mu\text{m}$.

Gradient locations: The inflection point positions for the three measured gradients were staggered. The sharp increase seen in the 2nd Max Int gradient aligns well with the optically determined DEJ and remained on the enamel side of the gradient compared to the other two gradient centers. The center of the FWHM gradient was located $1.3 \pm 0.8 \mu\text{m}$ away while the 1st Max Int gradient was located $5.6 \pm 2.3 \mu\text{m}$ away from the center of the 2nd Max Int gradient.

Modelling: The overall calculated modulus of the tissue surrounding the DEJ was significantly reduced when the gradient in crystallinity was considered in addition to the gradient in mineral content. It decreased by 13% from an estimated 80 GPa to 69.6 GPa. The gradient in modulus as a function of position when only the change in mineral content, as determined from Max Int, is considered is shown in blue in Fig 3. When the gradient in crystallinity is considered, the mechanical gradient is broadened as shown in orange.

DISCUSSION

The murine DEJs investigated here exhibited 3 distinct gradients: 2 separate gradients in Max Int and one in FWHM. The presence of two Max Int gradients suggests that there are likely two features present at this interface regulating mineral content. The 1st gradient has a width of approximately $8 \mu\text{m}$ located within what is visually considered the dentin. Although this width is slightly smaller than those previously reported [4], this 1st gradient is likely representative of changes in mineral content in the mantle dentin near the DEJ. The 2nd much steeper gradient is likely the “true” interface between the dentin and enamel tissues. This gradient exhibits a width of $\sim 3 \mu\text{m}$. This is in agreement with previous studies using nano-scratch and X-ray techniques [5-7] but smaller than that previously reported with Raman spectroscopy [8, 9].

Interestingly, the slope of the FWHM of the 960 cm^{-1} peak did not correlate with the intensity slope across the junction. It was found to be broader and its inflection point did not coincide with that of the intensity slopes with a total width of transition for the FWHM from dentin to

enamel being $\sim 7 \mu\text{m}$. This difference of the inflection point positions suggests that the crystallinity of the mineral around the DEJ is not associated with a specific tissue, like the mantle dentin, but instead spans the regions of varying composition. Mineral crystallinity, or atomic order, is often correlated with changes in mineral composition or maturity. Reduced crystallinity has been associated with reduced crystal size and stiffness as well as increased solubility [1, 2]. These studies have shown that reduced crystallinity caused by changes in composition lead to significant decreases in the mineral stiffness. Biologically, this gradient in mineral crystallinity may play a role in reducing stress concentrations at the DEJ by broadening the gradient in mechanical properties.

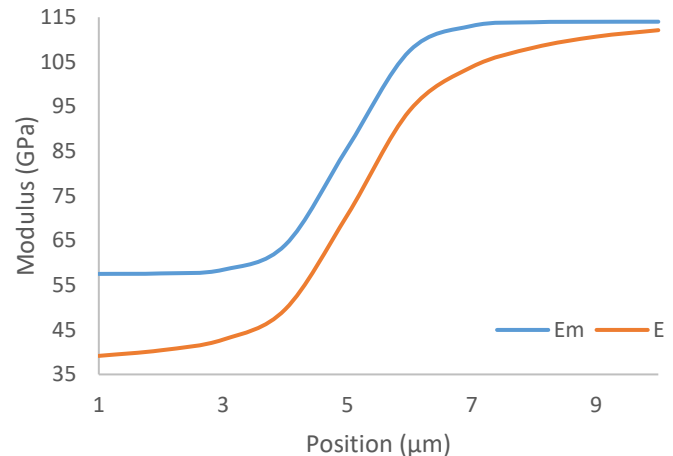


Figure 3: Plot of the estimated modulus as a function of position across the DEJ considering changes in mineral content (Em) as well as changes in mineral crystallinity (E).

To examine this, we developed a basic model examining the effect of gradients in both mineral content and crystallinity, based on the measured gradients of Max Int and FWHM respectively. We find that the added gradient in crystallinity broadens the overall mechanical gradient helping to reduce the formation of possible stress concentrators. In addition, it reduces the overall tissue modulus around the DEJ. This local reduction in modulus has been previously proposed as a possible mechanism for crack absorption at the DEJ [10].

ACKNOWLEDGEMENTS

We acknowledge NIH R03 GRANT13319573 and NSF CAREER grant 2044870 as well as the UConn Dental School Summer Research Program.

REFERENCES

1. Wingender, B., et al. *Acta Biomaterialia*, 2021. **122**: p. 377-386.
2. Deymier, A.C., et al. *Biomaterials*, 2017. **127**: p. 75-88.
3. Amel, S., et al. *Journal of Biomedical Optics*, 2017. **22**: p. 086003.
4. Goldberg, M., et al. *Front Biosci (Elite Ed)*, 2011. **3**: p. 711-35.
5. Fong, H., et al. *Microscopy and Microanalysis*, 1999. **5**: p. 1010-1011.
6. Wang, R., et al. *Microscopy Research and Technique*, 2021. **84**: p. 881-890.
7. Marshall, S.J., et al. *Journal of the European Ceramic Society*, 2003. **23**: p. 2897-2904.
8. Gallagher, R.R., et al. *J Dent Biomech*, 2010. **2010**: p.
9. Schulze, K.A., et al. *Journal of Biomedical Materials Research Part A*, 2004. **69A**: p. 286-293.
10. Almer, J.D., et al. *Journal of Biomechanics*, 2010. **43**: p. 2294-2300.

LASER ABLATION: A NEW LEAFLET MODIFICATION STRATEGY TO PREVENT CORONARY OBSTRUCTION IN REDO TAVR

John T. Brlansky (1), Masod Sadipour (1), Ali Azadani (1)

(1) Department of Mechanical and Materials Engineering, University of Denver, Denver, Colorado, United States

INTRODUCTION

Transcatheter aortic valve replacement (TAVR)-in-TAVR is a promising treatment option for transcatheter aortic valve degeneration. This involves implanting a secondary valve internal to the degraded valve, and pinning the degraded leaflets to the first TAVR stent (Fig. 1).

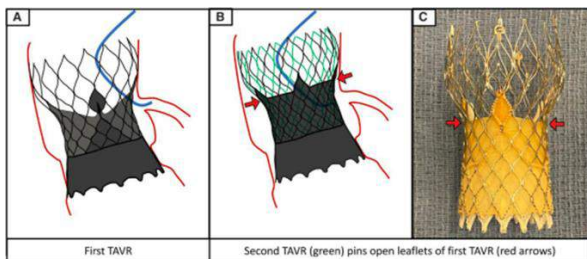


Figure 1: Coronary Obstruction in Repeat TAVR [1].

The prevalence of TAVR-in-TAVR is expected to grow significantly in the immediate future. The risk of coronary obstruction after redo-TAVR is affected by several factors, including the first TAV design, implantation depth, commissural alignment, degree of frame expansion, and choice of the second TAV type for redo-TAVR. CT simulations have predicted that the supra-annular leaflet position and tall frame of Evolut devices may cause coronary obstruction in 23% and hinder future coronary access in 78% of redo-TAVR patients. [2].

Leaflet modification techniques may be required in case of high coronary obstruction risk. BASILICA has been utilized to prevent coronary artery obstruction by creating a bisecting incision on the leaflet (Figure 2). However, this procedure may not be effective in the presence of commissural misalignment (Figure 3) and a high depth of implantation of the second valve. Furthermore, BASILICA may not be feasible or suboptimal in patients having challenging anatomy (minimal valve-to-coronary distance) and diffusely calcified and rigid leaflets.

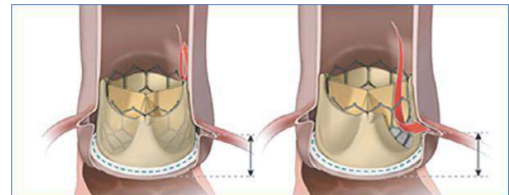


Figure 2: BASILICA leaflet modification procedure [3].

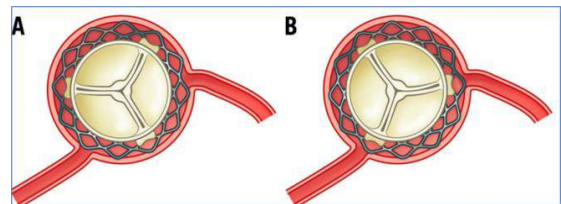


Figure 3: TAVR implantation with aligned commissures (A) and misaligned commissures (B) [4].

We sought to develop a new leaflet modification strategy using laser ablation (Figure 4) of the initial TAVR leaflets to prevent coronary obstruction and reduce leaflet blood residence time repeat TAVR.

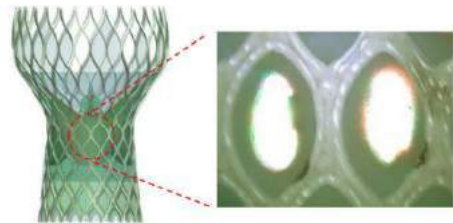


Figure 4: Laser ablation leaflet modification.

METHODS

Initial pericardium lasing feasibility testing was conducted using a Philips laser system and fiber optic laser ablation catheter, with full ablation of the tissue observed (Figure 5).

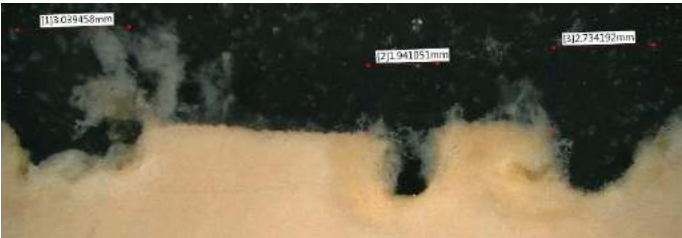


Figure 5: Pericardium laser ablation feasibility testing.

To quantify the impact of increased coronary flow due to laser ablation modification of the initial TAVR leaflets, a two-way fluid-structure interaction (FSI) model was generated, which evaluated flow over two heartbeat cycles at a rate of 60 beats per minute. The geometry for the model was constructed in SolidWorks using patient CT data and Medtronic CoreValve geometries. Simulated laser ablation modifications were then made by inserting 10F size holes in the initial TAVR leaflets oriented at the left coronary, right coronary, or the non-coronary. For analysis, a control model (Figure 6A) and the following laser ablation models were considered:

- 1. Single ablations at the left and right coronary (Figure 6B).
- 2. Single ablations at the left and right coronary, one on the non-coronary (Figure 6C).
- 3. Double ablation at the left coronary, single at the right coronary (Figure 6D).
- 4. Double ablation at the left and right coronary (Figure 6E)

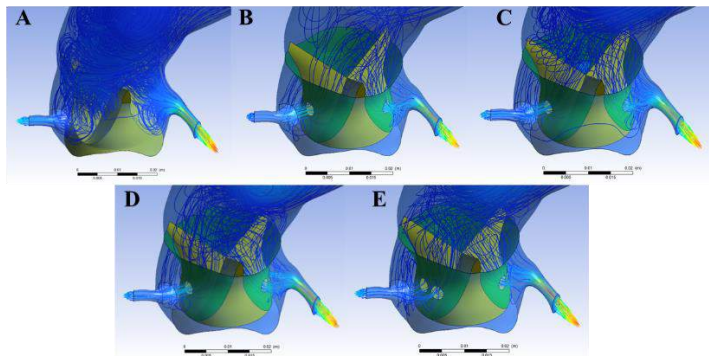


Figure 6: Model geometries. Aorta pictured in translucent blue, initial TAVR in yellow, and secondary TAVR in green.

A mesh was generated for each model using Pointwise, and simulations were run using ANSYS Fluent. The working fluid, blood, was modeled as Newtonian, and flow was modeled as laminar. The density and the viscosity of blood was 1,060.0 kg/m³ and 0.0035 kg . s/m², respectively. Moreover, mesh densities were optimized by conducting mesh dependency studies for all models. FSI modeling was conducted using ANSYS Fluent within the Workbench. Simulations were run over three cycles at 60 beats per minute.

RESULTS

Laser ablation modification of TAVR-in-TAVR improved coronary flow in all cases resulting in left coronary artery flow increases

of 87% to 96% from total occlusion and right coronary artery flow increases of 40% to 74% from total occlusion (Figure 7).

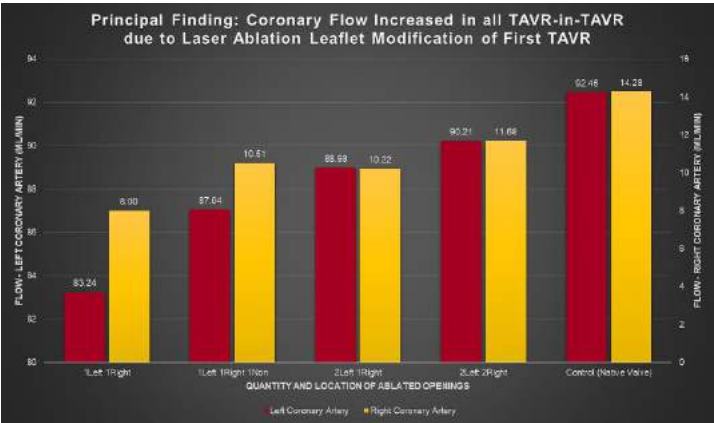


Figure 7: Impact on coronary flow due to laser ablation modification of initial TAVR leaflets.

This improved coronary flow resulted in a proportional reduction in blood residence time due to the increased flow velocities in the coronary arteries, which increased with the number of ablated openings, as shown in Table 1.

Table 1: Coronary flow velocities.

Maximum Flow Velocity (m/s)		
Ablated Openings	LCA	RCA
1 Left 1 Right	0.3191	0.0492
1 Left 1 Right 1 Non	0.3338	0.0645
2 Left 1 Right	0.3394	0.0630
2 Left 2 Right	0.3436	0.0724
Control (Native Valve)	0.3516	0.0885

DISCUSSION

Laser ablation is a viable treatment strategy, especially for patients who are ineligible for BASILICA. The new leaflet modification strategy resulted in increased coronary flow and velocity in the sinus and neo-sinus, which may allow safer redo-TAVR in selected patients at high risk of coronary obstruction and coronary access impairment. Moreover, this may also reduce the risk of leaflet thrombosis due to the decrease in leaflet blood residence time.

ACKNOWLEDGEMENTS

This work was supported by the University of Denver [Grant number: 84993-142235].

REFERENCES

[1] Forrestal BJ et al., *Cardiovascular Interventions*, 13:375-3830, 2020.
[2] Ochiai T et al., *Cardiovascular Interventions*, 13:2617-2627, 2020.
[3] Khan JM et al., *Cardiovascular Interventions*, 14:941-948, 2021.
[4] Søndergaard L et al., *EuroIntervention*, 14:147-149, 2018.

QUANTIFICATION OF CATIONIC SOLUTE DIFFUSION AND FIXED CHARGE DENSITY IN HUMAN SYNOVIUM

Alexandra L. Davis (1), Ashish Vaidyanathan (1), Milad Rohanifar (1), Lori A. Setton (1,2)

- (1) Department of Biomedical Engineering, Washington University in St. Louis, St. Louis, MO, United States
(2) Department of Orthopedic Surgery, Washington University in St. Louis School of Medicine, St. Louis, MO, United States

INTRODUCTION

The synovium is a thin, multilayer tissue that lines the diarthrodial joint. Its blood and lymphatic vessels rapidly clear both small and large molecules, respectively, from the joint space, hindering the efficacy of intra-articular (IA) drug delivery to treat degenerative joint diseases such as osteoarthritis (OA) [1,2]. In vivo models may underestimate drug clearance times due to parameters that vary across species such as synovial thickness and synovial fluid volume. However, experimental-computational approaches can be used to quantify intrinsic solute diffusivities that enable comparisons across species, solutes, and pathologies. We previously developed a multiphasic finite element model (FEM) to study diffusion through synovium and found that solute effective diffusivity (D_{eff}) decreased with increasing molecular weight (MW) [3,4].

Factors other than MW such as charge could affect solute diffusivity through synovium. Like cartilage, synovium contains collagen and anionic glycosaminoglycans (GAGs) that may contribute to solute-matrix interactions during drug transport. Therefore, the aim of this study was to quantify the D_{eff} of a cationic solute through human synovium using our FEM optimization and compare it to that of an uncharged solute of similar MW. In doing so, the fixed charge density (FCD) of synovium was also reported for the first time.

METHODS

Tissue preparation: Human synovium was harvested from anonymized donor knee tissues procured through an agreement with the Mid-America Transplant Foundation (St. Louis, MO). Synovium was isolated from the posterior aspects of the knee joint into $\sim 10 \times 10$ mm pieces that were cryoprotected by immersing in 15% sucrose in PBS for 24 hours followed by 30% sucrose for 24 hours at 4 °C. The samples were devitalized by flash freezing in an isopentane (Sigma-Aldrich) bath cooled by liquid nitrogen and stored at -80 °C for at least 48 hours before trimming, where a sledge microtome (Leica SM2400, Allendale,

NJ) was used to trim the tissues to less than 1-mm thickness. Trimmed samples were soaked in PBS overnight at 4 °C to remove any remaining sucrose, after which their thicknesses were measured with a scanning profilometer (Keyence LJ-V700, Itasca, IL).

FCD quantification: A 1,9-dimethylmethylene blue (DMMB) assay was performed to quantify the sulfated glycosaminoglycan (sGAG) concentration and subsequently the FCD of synovium. Synovium samples (~ 50 mg each) were lyophilized and digested overnight at 60 °C in papain digest buffer (125 $\mu\text{g/mL}$ in PBS; 1 mL/100-mg dry mass). Digested human synovium was diluted 1:2 to ensure that its sGAG concentration fell within the linear range of a chondroitin sulfate (CS) standard curve (0–80 $\mu\text{g/mL}$). DMMB (Sigma-Aldrich) dye was prepared as previously described; however, its pH was shifted to 1.5 to minimize DNA interference [5]. 200 μL DMMB dye were added to three 20- μL replicates of each sample, whose sGAG concentrations were quantified based on the absorbance difference between 525 nm and 595 nm to compensate for reduced sensitivity to CS at lower pH. The amount of sGAG per dry weight of synovium {mg/g} and FCD {mM} were calculated assuming two moles of charge per sGAG and using the MW of CS (502.5 g/mol).

Diffusion experiment: Unsteady diffusion of a 4-kDa cationic dextran, fluorescein isothiocyanate-diethylaminoethyl-dextran (FITC-DEAE) (TdB Labs, Uppsala, Sweden) through devitalized human synovial explants ($n=4$) was studied as previously described. Briefly, each explant was secured between two platens that separated “donor” and “sink” baths of a custom-built diffusion chamber. One mL of FITC-DEAE at a known concentration ($C_0=0.25$ mg/mL) was pipetted in the donor bath, while a syringe pump (New Era Pump Systems NE-300, Farmingdale, NY) replenished PBS in the 1-mL sink bath at a rate of 2 mL/hour to maintain dilute downstream conditions. The diffusion chambers remained under ambient pressure at 37 °C on a 3D rotating shaker (Benchmark Scientific Biomixer™, Sayreville, NJ) to establish one-dimensional, unsteady diffusion. The concentration of FITC-DEAE

in the donor bath was determined by measuring the fluorescence intensities of eight 5- μ L aliquots collected over a three-day period using a multimode plate reader (Perkin-Elmer, Waltham, MA). The zeta potential of FITC-DEAE was measured separately using a Zetasizer ZEN3600 (Malvern Instruments, Malvern, UK).

Model predictions of unsteady diffusion: An FEM model of cationic solute diffusion through synovium was created in FEBio [6]. The synovial matrix was modeled as an uncharged, porous, and fluid-saturated mixture based on the negligible FCD calculated from the DMMB assay results. The solid phase was assumed to be neo-Hookean and assigned previously measured material properties [7]. Specimen-specific meshes of thickness L contained eight-node hexahedral elements that were refined at the interface between the synovium and the donor bath. Notably, the model was adapted to simulate charged solute transport using two steps to satisfy electroneutrality and ensure convergence:

- 1) A 100s-phase during which FITC-DEAE and an anionic counter-ion were introduced into the donor bath at $t=0$; their concentrations were linearly ramped up and down, respectively, to C_0 and 0 mM at $t=100$ s.
- 2) Modeling of unsteady diffusion of FITC-DEAE through human synovium after $t=100$ s.

Freely mobile Na^+ and Cl^- ions were also included at a physiologically relevant concentration (150 mM) to ground the electrical potential and match experimental conditions. Together these four ions dictated the effective fluid pressure

$$\tilde{p} = p + RTC\varphi \quad (1)$$

in the synovium, donor bath, and sink bath (Figure 1), where R is the ideal gas constant (8.314 J/mol K), T is the absolute temperature (310 K), and C is the total concentration of solute and ion. The hydrostatic fluid pressure (p) and osmotic coefficient (φ) were taken to be zero and unity, respectively [3,4].

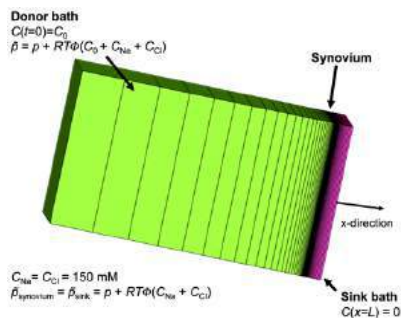


Figure 1: Finite element mesh and boundary conditions to model charged solute diffusion through human synovium of thickness L [3,4]. The solute and its counter-ion, whose initial concentrations in the model sum to C_0 , as well as Na^+ and Cl^- contribute to an effective fluid pressure in the donor bath, sink bath, and synovium.

Statistical analyses were performed in GraphPad Prism 9.0 (La Jolla, CA). The Mann-Whitney U Test was performed to determine if the D_{eff} of FITC-DEAE through human synovium was significantly different ($p<0.05$) from that of 3 kDa Texas Red dextran measured in our previous study. Data are presented as mean \pm standard deviation.

RESULTS

According to the DMMB assay, human synovium contains low amounts of sGAG (0.112 ± 0.0213 mg/g synovium) and therefore a

negligible FCD (-0.013 ± 0.0025 mM) orders of magnitude lower than that measured in other soft tissues (Table 1). Thus, the synovial matrix was assigned a FCD of zero in FEBio to model charged solute diffusion. The zeta potential of FITC-DEAE was 1.69 ± 0.342 mV.

Table 1: Fixed charge density (FCD) of synovium measured here compared to that of articular cartilage and nucleus pulposus.

Tissue	Species	FCD (mM)	Reference
Synovium	Human	-0.013	–
Articular cartilage	Bovine	-150	[8]
Nucleus pulposus	Bovine	-138	[9]

The D_{eff} of 4-kDa FITC-DEAE ($2.21\text{E-}4 \pm 2.66\text{E-}5$ mm²/s) through human synovium was significantly greater ($p=0.0286$) than that of 3-kDa Texas Red ($9.73\text{E-}5 \pm 2.66\text{E-}5$ mm²/s from prior study). Table 2 summarizes the data on FITC-DEAE and Texas Red diffusivity through human synovium.

Table 2: Effective diffusivity (D_{eff}) of cationic FITC-DEAE and neutral Texas Red through human synovial explants of thickness L .

Solute	MW (g/mol)	Charge	n	L (μ m)	D_{eff} (mm ² /s)
FITC-DEAE	4 kDa	Cationic	4	921 ± 64.1	$2.21\text{E-}4 \pm 2.66\text{E-}5$
Texas Red	3 kDa	Neutral	4	813 ± 148	$9.73\text{E-}5 \pm 2.35\text{E-}5$

DISCUSSION

Here, a cationic solute of low MW diffused faster than a neutral solute of similar MW through human synovium in vitro. This suggests that factors other than MW regulate solute transport through synovium such as tissue porosity and charge in addition to solute size, shape, and charge. In vivo studies should also consider cell-mediated uptake, IA pressure, and the density of draining lymphatic vessels. Here, human synovium had a low sGAG concentration that agrees with previous studies [10,11] and a FCD orders of magnitude lower than that of other soft tissues [8,9]; therefore, the FCD of synovium was not expected to accelerate diffusion of a cationic solute. However, sGAG content may decline with age and should be measured in synovium from younger donors to further elucidate the role that FCD plays in solute transport. Although DMMB assays cannot measure hyaluronic acid (HA), an unsulfated GAG largely produced by synovial fibroblasts, it likely does not contribute to significant negative charge in the matrix [10]. HA may instead elicit a boundary-layer effect at the synovial intima and impede transport through an alternative mechanism. Altogether these results invite further studies on charged solute-matrix interactions in synovium that inform drug design for IA drug delivery.

ACKNOWLEDGEMENTS

This work was funded by NIH AR070975 and AR077678. We thank Mid-America Transplant for providing human donor knee tissues.

REFERENCES

- [1] Evans CH et al., *Nat Rev Rheumatol*, 10:11–22, 2014.
- [2] Levick JR et al., *Ann Rheum Dis*, 54:417–423, 1995.
- [3] Guang Y et al., *J Biomech Eng*, 142:0410101–0410108, 2020.
- [4] Guang Y et al., *Ann Biomed Eng*, 49:1245–1256, 2021.
- [5] Zheng C & Levenston ME. *Eur Cell Mater*, 29:224–236, 2015.
- [6] Maas SA et al., *J Biomech Eng*, 134:011005, 2012.
- [7] Rohanifar M et al., *Biophys J*, 121:575–581, 2022.
- [8] Lesperance LM et al., *J Orthop Res*, 10:1–13, 1992.
- [9] Wang C et al., *Magn Reson Med*, 64:1721–1727, 2010.
- [10] Price FM et al., *J Physiol*, 495:803–820, 1996.
- [11] Hanai H et al., *Front Cell Dev Biol*, 8:581972, 2020.

APPLIED STRESS PROMOTES MINERALIZATION OF SUBSTITUTED BIOAPATITES: A THERMOCHEMICAL EQUILIBRIUM STUDY

Pierre A. Deymier (1), Marat Latypov (1,2), Krishna Muralidharan (1), Alix C. Deymier (3)

(1) Department of Materials Science and Engineering, University of Arizona, AZ, USA
(2) Graduate Interdisciplinary Program in Applied Mathematics, University of Arizona, AZ, USA
(3) Department of Biomedical Engineering, UConn Health, Farmington, Connecticut, USA

INTRODUCTION

Bone's ability to increase its mineral content and mass in response to mechanical loads, also known as Wolff's law [1], has been well established with Galileo describing this effect in 1638[2]. This ability of bone to adapt to the mechanical environment has primarily been attributed to cellular mechanotransduction. Specifically, it has been shown that osteocytes respond to changes in fluid flow through the bone porosity by increasing pro-osteoblastic signaling [3]. These signals recruit and activate osteoblasts resulting in the deposition of greater quantities of more highly mineralized bone tissue. This process has been shown to be in part responsible for the increase in bone density in high-intensity athletes and conversely the bone loss seen in astronauts [4, 5].

However, mineralization of bone has also been shown to be physiochemically controlled in the absence of cellular activity. Many studies have shown that the chemistry of the protein matrix enhances the nucleation and growth of bone mineral by reducing the energy barriers to mineralization [6, 7]. Further, recent investigations of the effects of fluid shear stress and cyclic loading on collagen matrix mineralization, have shown that increased loading promoted induced matrix mineralization due to improved fluid transport [8, 9]. These results suggest that, beyond cellular activity chemistry and mechanical loading may play a central role in the physiochemical mineralization of bone tissue.

Biological apatite is not hydroxyapatite but a highly substituted apatite that undergoes both anionic and cationic substitutions. In terms of anions carbonate (CO_3^{2-}) substitutes for phosphate (PO_4^{3-}) in bone mineral. This charge imbalance is then rectified by a sodium (Na^+) substitution for calcium (Ca^{2+}). These substitutions give the apatites unique properties, but they also allow the material to act thermodynamically as a substitutional solid. Larché and Cahn showed that thermodynamically the composition of substitutional solids is significantly affected by applied stress [10]. This huge advancement in thermodynamics was recently experimentally confirmed [11]. Here we

use the Larché and Cahn theory to predict not only the change in mineral composition but the effect of mechanical loading on bioapatite mineral growth.

METHODS

Assumptions: Based on the known chemistry of bioapatite we established a closed system with a number of assumptions. The system is composed of an apatite crystal containing CO_3^{2-} , PO_4^{3-} , Ca^{2+} , and Na^+ in equilibrium with water containing the same ions. We assume the exchange only occurs between the $\text{Na}^+/\text{Ca}^{2+}$ and $\text{CO}_3^{2-}/\text{PO}_4^{3-}$ and that the system has charge conservation. Finally, the total volume of the system cannot change although the relative volumes of solid and liquid can change. In addition, using literature values, we assume that the lattice deformation caused by the exchange of Na^+ for Ca^{2+} is negligible compared to that of CO_3^{2-} for PO_4^{3-} .

The system is designed as shown in figure 1, where the mineral centered on the origin and has an initial thickness of $2l$. The mineral is surrounded by liquid water on both sides with the total length of the system adding up to $2L$. The reference state is a state of hydrostatic

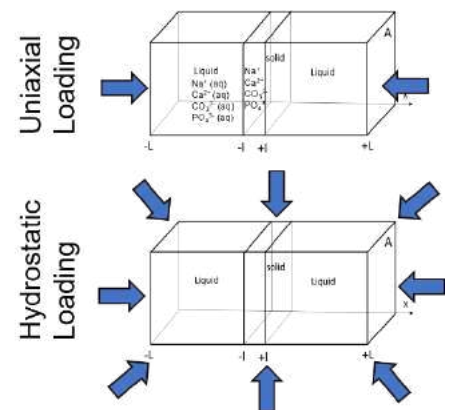


Figure 1: Schematic of the setup showing the ionic distribution, geometry, and loading states being studied.

pressure while the stressed state undergoes uniaxial stress (σ) along the x-axis. A change in the mineral size is denoted by Δl .

Variables: We define the following compositional variables for the cationic and anionic species in aqueous solution, $C_{Na}^L, C_{Ca}^L, C_C^L, C_P^L$. The upper script refers to a liquid solution. We use short-hand notation for the lower indices, Na, Ca, C and P for Na^+, Ca^{2+}, CO_3^{2-} and PO_4^{3-} , respectively. The ionic compositions in the solid apatite are defined as $C_{Na}^S, C_{Ca}^S, C_C^S, C_P^S$ where the upper script S stands for solid. We use a bar ($\bar{C}_{Ca}^L, \bar{C}_{Na}^L, \bar{C}_C^L, \bar{C}_P^L, \dots$) as an accent above thermodynamic quantities to denote that they are under hydrostatic pressure. Δ'_{Ca} and Δ'_C are the change in cation and anion compositions due to stress relative to the compositions under hydrostatic conditions.

Calculations: Using the work of Larché and Cahn and Johnson et al. [10, 12] we can establish the cationic condition for equilibrium as:

$$\Delta'_{Ca} \sim -\frac{\Delta l}{L-l} \left[\frac{\bar{C}_{Ca}^S}{\bar{C}_{Ca}^L} - \frac{\bar{C}_{Na}^S}{\bar{C}_{Na}^L} \right] / \left(\frac{1}{\bar{C}_{Ca}^S} + \frac{1}{\bar{C}_{Na}^S} + F \left[\frac{1}{\bar{C}_{Ca}^L} + \frac{1}{\bar{C}_{Na}^L} \right] \right) \quad (1)$$

where F is the ratio of solid and liquid volumes under uniaxial stress.

Similarly, the anionic condition for equilibrium is:

$$\Delta'_C \sim -Z - \frac{\Delta l}{L-l} \left[\frac{\bar{C}_C^S}{\bar{C}_C^L} - \frac{\bar{C}_P^S}{\bar{C}_P^L} \right] / \left(\frac{1}{\bar{C}_C^S} + \frac{1}{\bar{C}_P^S} + F \left[\frac{1}{\bar{C}_C^L} + \frac{1}{\bar{C}_P^L} \right] \right) \quad (2)$$

where Z is a function of mineral mechanical properties and composition. Finally, we can approximate the condition for dissolution/recrystallization by:

$$\mathcal{E} - \bar{C}_{Ca}^S - Z \bar{C}_C^S = \left[\frac{1}{\bar{C}_{Na}^S} \left(1 + F \frac{\bar{C}_{Na}^S}{\bar{C}_{Na}^L} \right) \right] \Delta'_{Ca} + \left[Z + \frac{1}{\bar{C}_P^S} \left(1 + F \frac{\bar{C}_P^S}{\bar{C}_P^L} \right) \right] \Delta'_C + \frac{\Delta l}{L-l} \left[\left(1 - \frac{\bar{C}_{Na}^S}{\bar{C}_{Na}^L} \right) + \left(1 - \frac{\bar{C}_P^S}{\bar{C}_P^L} \right) \right] \quad (3)$$

where $\mathcal{E} = \frac{\sigma^2}{2Y}$, σ is the applied stress and Y is the mineral Young's modulus. By inserting Eqs 1 and 2 into Eq 3 we can solve for $\frac{\Delta l}{L-l}$,

which represents the change in crystal size, as a function of the magnitude of the uniaxial stress σ .

To obtain information about the relative concentrations of Na^+, Ca^{2+}, CO_3^{2-} and PO_4^{3-} in the liquid and solid at equilibrium, we turn to Moynahan et al. [13] where concentrations were measured for biomimetic apatites in equilibrium with water. This gives us the values of $\bar{C}_{Ca}^L, \bar{C}_{Na}^L, \bar{C}_C^L, \bar{C}_P^L, \bar{C}_{Ca}^S, \bar{C}_{Na}^S, \bar{C}_C^S$, and \bar{C}_P^S . Relationships between the mineral modulus and the composition have also been identified by Wingender et al. [14] that allow us to approximate $Z \sim 5 \times 10^{-5} \mathcal{E}$.

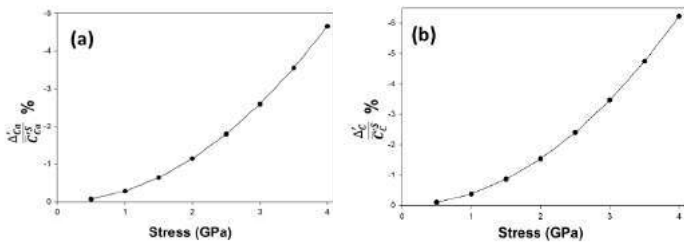


Figure 2: Plot of the change in Ca^{2+} (a) and CO_3^{2-} (b) in the solid with applied stress. (Note the negative y-axis)

RESULTS

Compositional changes with applied stress

Using equations 1 and 2 and the known compositions for biomimetic apatites under hydrostatic stress, we were able to predict how an applied uniaxial stress would affect the substitutional exchange of Na^+/Ca^{2+} and CO_3^{2-}/PO_4^{3-} . We find that increasing applied stresses lead to preferential substitution of Na^+ for Ca^{2+} and of PO_4^{3-} for CO_3^{2-} in biological apatite.

Crystal growth with applied stress

Using Equations 1, 2, and 3 we find that the normalized crystal thickness, $\frac{\Delta l}{L-l}$, increases with increasing applied stress. This suggests

that the substitutional nature of biological apatites allows them to crystallize upon loading instead of dissolve.

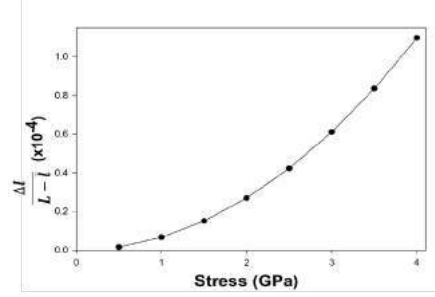


Figure 3: Plot of the relative thickness of the solid apatite in equilibrium with an aqueous solution as a function of applied uniaxial stress

DISCUSSION

The recommendations that individuals engage in weight bearing exercise to promote bone growth and mineralization have mainly centered on the idea of cellular mechanotransduction. Only recently has physiochemical stimulation of mineralization been suggested as possible benefit of exercise [8, 9]. However, the results presented here show another layer of benefit, indicating that applied stress during weight bearing activities promotes mineralization via crystal growth irrespective of cellular and matrix contributions.

In addition, the bone mineral composition is shown to shift towards reduced calcium and carbonate content with applied stress. This would suggest a decrease in Ca^{2+}/PO_4^{3-} and CO_3^{2-}/PO_4^{3-} ratios with applied stress. Reduction in these markers has historically been associated with bone immaturity or increased cellular remodeling [15, 16]. However, the measurements presented here report these compositional changes in response to applied load irrespective of cellular or maturation behaviors. Therefore, it is important to understand the thermodynamics of bone mineral in stressed environments like bone when considering the meaning or cause of compositional changes.

In conclusion, we have shown thermodynamically that applied stress promotes compositional changes and crystal growth in biological apatites in equilibrium with aqueous liquids. This reinforces the importance of understanding both cellular and physiochemical process when studying biological materials.

ACKNOWLEDGEMENTS

ACD was supported by NSF CAREER grant 2044870. P.A.D would like to acknowledge many discussions with F.C. Larché on the topic of thermochemical equilibrium of stressed solids prior to his passing.

REFERENCES

1. Wolff, J. 1892, Berlin: Hirschwald.
2. Galilei, G. 1990: Gli Elsevirii.
3. Choi, J.U.A., et al. Front Cell Dev Biol. 2021, **9**: p. 770143
4. Iandolo, D., et al. Curr Osteoporos Rep. 2021, **19**: p. 626-636
5. Scott, A., et al. Sports medicine. 2008, **38**: p. 139-60
6. Jee, S.S., et al. Acta Biomater. 2010, **6**: p. 3676-3686
7. Wang, Y., et al. Nat Mater. 2012, **11**: p. 724-33
8. Kim, D., et al. Biomaterials Science. 2021, **9**: p. 5907-5916
9. Du, T., et al. Journal of Materials Chemistry B. 2020, **8**: p. 2562-2572
10. Larché, F.C., et al. J Res Natl Bur Stand. 1984, **89**: p. 467-500
11. Shi, S., et al. PNAS. 2018, **115**: p. 10914-10919
12. Johnson, W.C., et al. J. Am. Ceram. Soc. 1993, **76**: p. 1713-1719
13. Moynahan, M.M., et al. PLOS ONE. 2021, **16**: p. e0250822
14. Wingender, B., et al. Acta Biomater. 2021, **122**: p. 377-386
15. Boskey, A.L., et al. Ann N Y Acad Sci. 2017, **1410**: p. 93-106
16. Eanes, E.D., et al. Calcified Tissue Research. 1977, **23**: p. 259-269

ADVANCE IN HYBRID CARDIOVASCULAR MODELING: COUPLING VOLUMETRICALLY DYNAMIC IN-VITRO EXPERIMENTS TO NUMERICAL PHYSIOLOGY SIMULATION

Abraham, E. Umo (1), Ethan, O. Kung (1,2)

(1) Bioengineering, Clemson University, Clemson, SC, USA
 (2) Mechanical engineering, Clemson University, Clemson, SC, USA

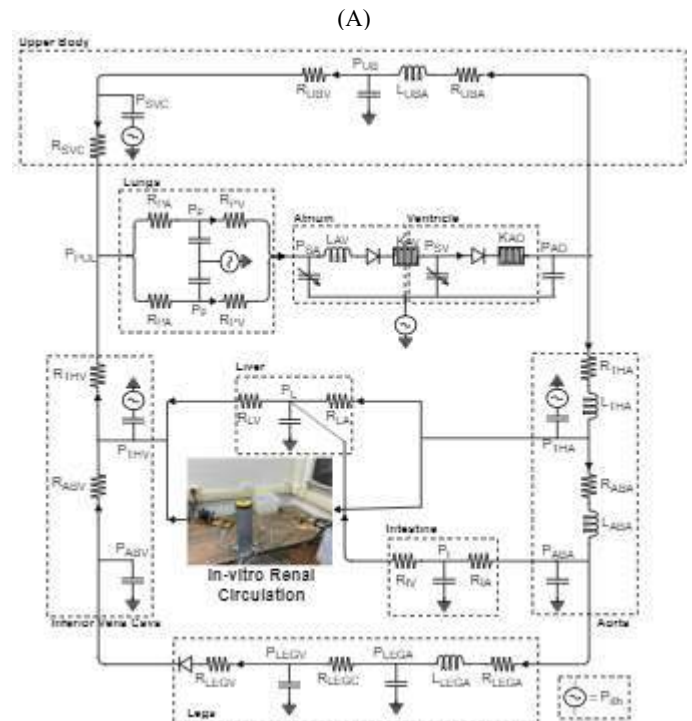
INTRODUCTION

The Physiology Simulation Coupled Experiment (PSCOPE) is a cardiovascular modeling approach that couples an in-vitro experiment to a numerical physiology simulation in a hybrid framework. This framework enables investigation of the closed-loop physiological response of the cardiovascular system in the context of dynamic conditions modeled in a physical fluid experiment. The experiment is coupled to the simulation via a protocol that directs the exchange of pressure and flow rate information to identify the hybrid model's solution. Previous PSCOPE coupling methods^{1,2} successfully coupled rigid and multi-branch experiments to a lumped parameter physiology simulation (LPN) but are incompatible with volumetrically dynamic experiments where fluid volume is not constant. In this study, we present an iterative protocol for coupling several types of physical experiments, including rigid, multi-branch, and volumetrically dynamic in-vitro experiments to an LPN.³

METHODS

The protocol begins with an initial guess of the model's solution and utilizes a weighted averaging algorithm to iteratively generate boundary conditions (pressure or flow rate) prescribed to each in-vitro and numerical domain. The prescribed boundary conditions ensure that both domains share identical pressure waveforms and minimize the differences between their corresponding flow rate waveforms (residual). The exact model solution corresponds to a residual of zero; we can specify the target accuracy of our coupling solution via setting an NRMSE threshold. We first confirm the accuracy of the PSCOPE solutions by using mathematical surrogates for in-vitro experiments. The mathematical surrogates were directly integrated into LPNs to derive the reference solutions, which serve as the gold standard to validate the solutions obtained from using our proposed method to couple the same mathematical surrogates to the LPNs. We also demonstrate the real-world applicability of the protocol by coupling an

in-vitro renal circulation model to a fontan LPN (Fig.1a). A <5% NRMSE threshold was set as the target residual between the LPN and in-vitro renal flow waveforms.



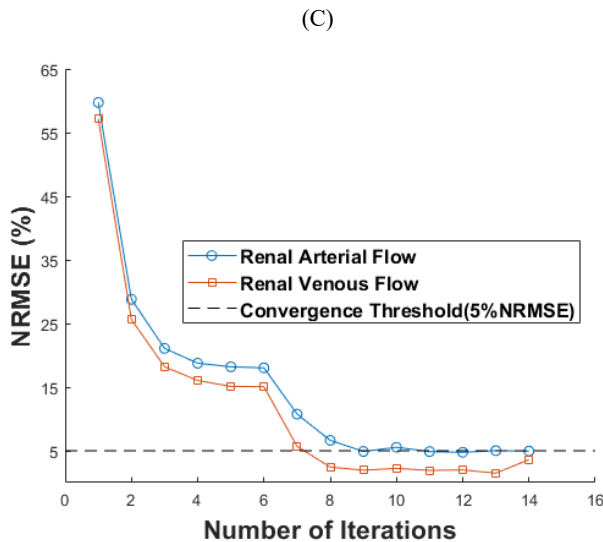
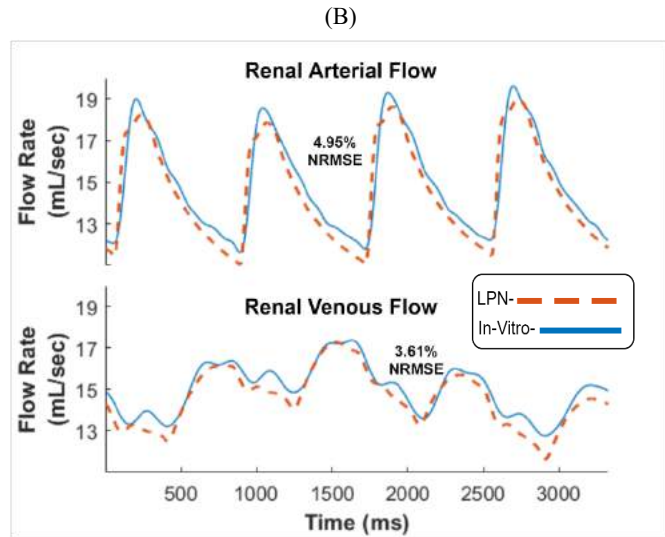


Fig. 1 (A) Illustration of a hybrid model setup coupling an in-vitro Renal circulation model to an LPN—(B) Renal Flow waveforms from the LPN and in-vitro model were successfully converged below the 5% NRMSE threshold; (C) Convergence trend of flow waveforms.

RESULTS

The NRMSE values (0.001% - 1.36%) between the reference and PSCOPE solutions obtained from integrating and coupling mathematical surrogates to LPNs, respectively, demonstrate a high degree of accuracy achieved by the coupling method. The in-vitro renal circulation model was successfully coupled to the LPN with the algorithm converging their corresponding renal flow waveforms below the 5% NRMSE threshold (Fig. 1b) after 9 iterations. Subsequent iterations were continued to confirm stabilization of the model solution convergence (Fig. 1c).

DISCUSSION

This work introduces a protocol capable of coupling volumetrically dynamic in-vitro experiments to a lumped parameter physiology simulation, overcoming the limitations of previous PSCOPE coupling methods. Its real-world applicability includes experimental investigation of medical devices and anatomies that exhibit volume changes within the context of a closed-loop hybrid model.

ACKNOWLEDGEMENTS

This work was supported in part by Clemson University, an award from the American Heart association and The Children's Heart Foundation under Grant 16SDG29850012 and in part by an award from the National Science Foundation under Grant 1749017.

REFERENCES

- [1] Kung, Ethan & Farahmand, Masoud & Gupta, Akash. (2019). A Hybrid Experimental-Computational Modeling Framework For Cardiovascular Device Testing. *Journal of Biomechanical Engineering*. 10.1115/1.4042665.
- [2] Mirzaei, E, Farahmand, M, Kung, E. An algorithm for coupling multibranch in vitro experiment to numerical physiology simulation for a hybrid cardiovascular model. *Int J Numer Meth Biomed Engng*. 2020; 36:e3289. <https://doi.org/10.1002/cnm.3289>
- [3] Umo A, Kung EO. A Protocol for Coupling Volumetrically Dynamic In vitro Experiments to Numerical Physiology Simulation for A Hybrid Cardiovascular Model. *IEEE Trans Biomed Eng*. 2022 Oct 21;PP. doi: 10.1109/TBME.2022.3216542. Epub ahead of print. PMID: 36269903.

VISCOELASTIC AND FRACTURE PROPERTIES OF CLOT FROM HUMAN AND BOVINE BLOOD

Gabriella P. Sugerman (1), Sapun H. Parekh (1), Berkin Dortdivanlioglu (2), Manuel K. Rausch (1,3,4)

- (1) Department of Biomedical Engineering, University of Texas at Austin, Austin, TX, USA
(2) Department of Civil, Architectural, and Environmental Engineering, University of Texas at Austin, Austin, TX, USA
(3) Department of Aerospace Engineering and Engineering Mechanics, University of Texas at Austin, Austin, TX, USA
(4) Oden Institute for Computational Engineering and Sciences, University of Texas at Austin, Austin, TX, USA

INTRODUCTION

Blood clots play critical roles in both health and disease. On the one hand, blood clotting prevents hemorrhage after vascular injury and is thus vital to our survival. On the other hand, blood clotting and blood clot embolization (i.e., fracture) lead to deadly diseases such as heart attacks, strokes, and pulmonary embolisms. In both diametrical roles, the mechanical behavior of blood clots is clearly important. Despite its importance in health and disease, significant gaps in our knowledge about blood clot mechanics persist. We have developed experimental techniques to robustly characterize the fracture mechanics of blood clots coagulated in vitro with the aim of probing this clinical question. Bovine, porcine, and ovine blood have all been used to understand clot mechanics [1-3], but the correlation between the behavior of these clots and clots made from human blood is unclear and variability in experimental modalities limits direct comparisons across studies. Towards understanding this relationship, in this study we describe the viscoelastic and fracture properties of clots made from human and bovine blood measured using identical protocols.

METHODS

Blood collection: Bovine blood drawn in CPDA-1 anticoagulant was purchased from a commercial vendor (Lampire Biological Laboratories, PA, USA). Human blood was drawn into ACD anticoagulant. Time between draw and testing was 48 hours for both samples.

Sample preparation: Samples were prepared according to previously published protocols [4]. Briefly, samples were mixed with calcium chloride to a final concentration of 20 mM and cast into rectangular molds lined with Velcro (see Figure 1A). After 60 minutes, the samples were assigned to one of four experimental groups: (i) mode-I, (ii) pure shear, (iii) cyclic loading, or (iv) stress relaxation (see Figure 1B). Mode-I samples received a notch of 1/3 the width of the sample.

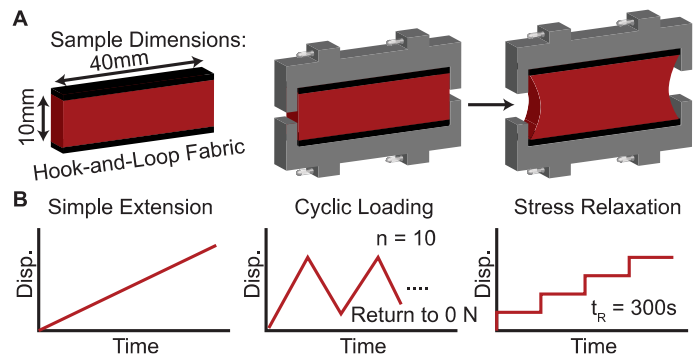


Figure 1: (A) Sample dimensions are 40 mm x 10 mm x 3 mm and molds are lined with Velcro so they can be tested without gluing or clamping. (B) We used a tensile tester to displace the samples using three protocols: simple extension, cyclic loading, and stress relaxation. Figure adapted from [5].

Note that both mode-I and pure shear samples underwent simple extension.

Mechanical testing: Mode-I and pure shear samples were extended to failure. Cyclic loading samples were extended to 40% clamp-to-clamp strain and returned to 0 N force for ten cycles. Finally, stress relaxation samples were consecutively displaced to 10%, 20%, 30%, and 40% clamp-to-clamp strain with 300 s holds after each loading step. All tests were conducted at a displacement rate of 0.2 mm/s (equivalent strain rate 2%/s). High-resolution images were captured of the mode-I samples at a rate of 5 Hz.

Statistics: For direct comparisons between two groups, we used two-tailed Student's t-tests implemented in R. We fit a linear mixed model to our stress relaxation time constants using the “afex” library in R and used the “emmeans” library to run pairwise comparisons. Differences with p-value ≤ 0.05 were considered significant. All data are reported as mean \pm standard deviation.

RESULTS

Figure 2 shows that human blood clots are softer, weaker, and more susceptible to fracture than bovine blood clots. In Figure 2A, Cauchy stress-stretch curves for pure shear (left) and mode-I (right) samples show that bovine clots (gray) yield higher stress for a given stretch value. Figure 2B compares scalar metrics derived from these curves. Bovine clots have higher fracture toughness, calculated as

$$\Gamma_c = W(\lambda_c)H, \quad (1)$$

where H is the reference sample height and $W(\lambda_c)$ is the strain energy density of the pure shear sample at the fracture stretch λ_c . They also have higher strength (peak stress in pure shear geometry), tangent modulus, and work to rupture.

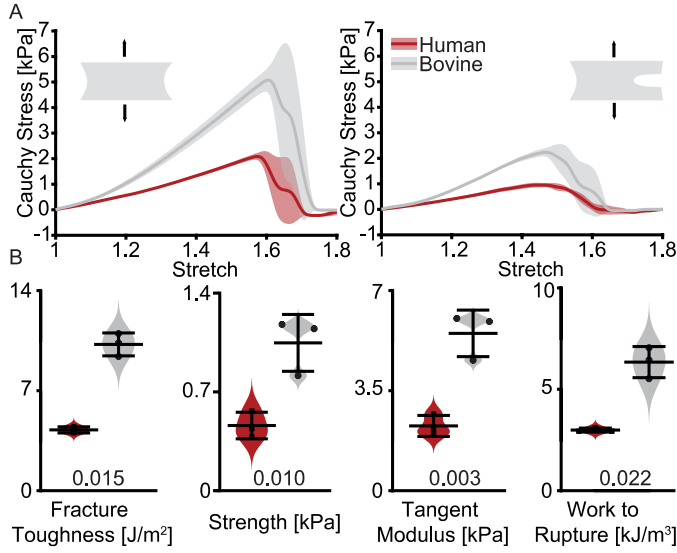


Figure 2: (A) Stress-stretch curves of pure shear and mode-I experiments (B) Bovine clots show higher fracture toughness, strength, stiffness, and work to rupture than human clots. P-values are from two-tailed Student's t-tests.

Cyclic loading experiments showed that both human and bovine blood clots equilibrate after ten cycles but differ in magnitude of work lost in hysteresis, peak force, and set (data not shown). Work lost to hysteresis and peak force are higher in bovine samples while the amount of set is greater in human samples. Set is measured as the effective strain that samples return to when unloaded to zero force. The presence of set implies that the samples lengthened during loading. Each of these metrics change substantially from the first cycle to the second with the difference between cycles decreasing steadily and trending toward an equilibrium response by the tenth cycle.

Figure 3 shows the strain-dependent stress relaxation response of clots made from human and bovine blood. Each clot relaxes at every strain step. To compare the stress-relaxation response, we fit each step with a two-term exponential decay function

$$\hat{\sigma} = 1 - \sum_i^n c_i \left(1 - \exp\left(-\frac{t}{\tau_i}\right)\right), \quad (2)$$

where $\hat{\sigma}$ is the normalized stress at each strain step, t is time, c_i are scaling parameters, and τ_i are the time constants. We have previously reported that this two-term exponential decay function captures the response well and that additional terms are not beneficial [5]. The first time constant, τ_1 , does not differ significantly between bovine and human samples. The second time constant, τ_2 , differs significantly at each strain level ($p = 0.011$) though the values are within the same order

of magnitude. This similarity may suggest that time-dependent dissipative mechanisms are conserved between species.

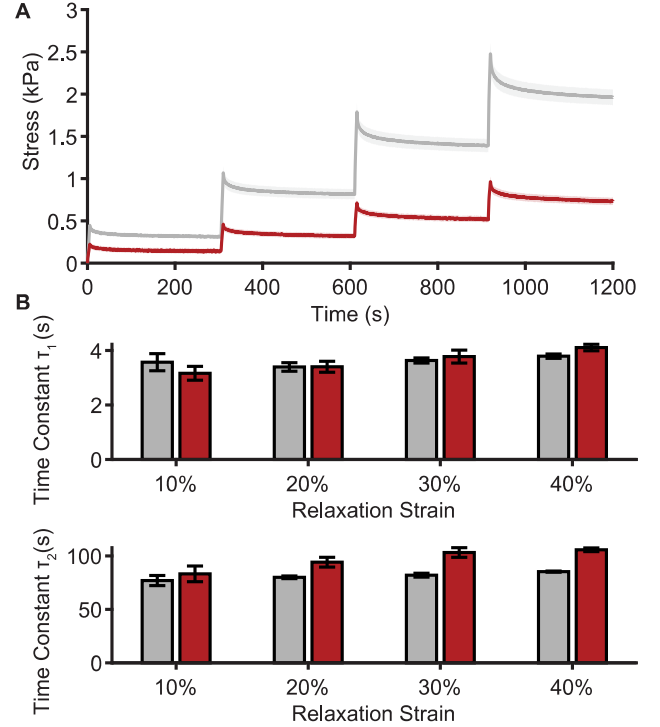


Figure 3: (A) Stress relaxation curves for bovine (gray) and human (red) samples (B) Time constants of a two-term exponential decay function fit to each strain step vary across species within the same order of magnitude.

DISCUSSION

While animal blood is more easily accessible than human blood, our findings suggest that the mechanical behavior of clots made from bovine blood are not interchangeable with the behavior of those made from human blood. The data presented here are based on one subject, and data from five additional subjects will be included in the final presentation to better assess this relationship. Many of the same phenomena are present in both clots, including preconditioning effects, hysteresis, set, and stress relaxation, however the magnitude of these effects differs. There are many possible mechanisms for this discrepancy, and further study will help us distinguish between inter-species variability and subject-to-subject variability.

ACKNOWLEDGEMENTS

We acknowledge support from ONR with grant N00014-22-1-2073 and NSF with grants 2046148, 2105175, and 2127925.

REFERENCES

- [1] Ghezelbash, F et al., *JMBBM*, 128:105101, 2022.
- [2] van Kempen, T et al., *BMMB*, 15:279-291, 2016.
- [3] Johnson, S et al., *Ann Biomed Eng*, 49:420-431, 2021.
- [4] Sugerman, G et al., *Curr Protoc*, 1:e197, 2021.
- [5] Sugerman, G et al., *Soft Matter*, 16:9908-9916, 2020.

MULTISCALE, CELL-RESOLVED SIMULATIONS OF RED BLOOD CELLS IN MACROSCALE FLOWS FOR HEMOLYSIS PREDICTION

Grant J. Rydquist (1), Mahdi Esmaily (1)

(1) Sibley School of Mechanical and Aerospace Engineering, Cornell University, Ithaca, NY

INTRODUCTION

The rupture of red blood cells (RBCs), known as hemolysis, is a common problem in many blood flow scenarios. In particular, hemolysis commonly occurs when the flow of blood has been artificially altered, such as in blood pumps or surgical treatments, since this can expose the RBCs to unphysiologically large shear stresses. There are several medical problems associated with hemolysis, so it is important to be able to predict its incidence. However, most algorithms for detecting hemolysis use empirical relationships [1] that may not be general in all situations (e.g., any turbulence may make the results unreliable). One approach that has yet to be fully explored is to simulate the RBCs in these types of macroscale flows directly to obtain a cell-resolved picture of the RBCs' response to it. If the effects of the flow on the cell are properly represented, the resulting framework will be fully general and agnostic to the actual character of the flow. Additionally, the results provide a more mechanistic, realistic picture of the cells' response to the flow than the empirical relationships typically used to evaluate the amount of hemolysis in a flow. The purpose of the current work is to construct a computational framework to resolve the behavior of individual RBCs in macroscale flows.

The main difficulties in the construction of this framework lie in the accurate reproduction of the flow's effect on the RBCs. For example, the number of cells in the flows this framework is intended for is larger than is computationally feasible. Thus, only a sample of the total number of cells are used, and the behavior of the cells is resolved in a statistical sense. However, cell-cell interactions are an essential component of the way RBCs behave, and these interactions have long decay distances relative to the size of the RBCs, so a collection of cells need to be simulated with periodic boundary conditions to mimic these long-range interactions.

METHODS

Since there is a difference in scales of multiple orders of magnitude between the characteristic lengths of the RBCs and the macroscale flow, some assumptions must be made to couple the simulations of the two. First, since the effects of the cells on the fluid are typically modeled, for example by using a shear-thinning viscosity, only the effects of the fluid on the cells are resolved. Thus, the periodic box containing the collection of cells is advected through the flow as a one-way coupled tracer. At each time step, the fluid velocity in the vicinity of the cells is used in conjunction with their current deformation to evaluate their relative velocities. Since the curvature and higher order terms of the velocity become negligible at the scale of the cells, only the velocity gradient is used.

Since the RBCs are small, the Stokes equations can be used to solve for their relative velocity. A suitable method of solving for this velocity is the boundary integral method. This method utilizes the Stokes equations recast into integral form. Taking account of the above assumptions, this equation is

$$\begin{aligned} u_j(\mathbf{x}_0) - \frac{1-\lambda}{4\pi(1+\lambda)} \sum_p \sum_{k=1}^N D_{ij}^k [u_i^p](\mathbf{x}_0 - \mathbf{x}_p) \\ = \frac{2}{1+\lambda} u_j^\infty(\mathbf{x}_0) \\ - \frac{1}{4\pi\mu(1+\lambda)} \sum_p \sum_{k=1}^N S_{ij}^k [\Delta f_i^p](\mathbf{x}_0 - \mathbf{x}_p). \quad (1) \end{aligned}$$

The above equation is evaluated at the point \mathbf{x}_0 , which must be on the surface of a cell. μ is the viscosity of the ambient fluid, λ is the ratio of the viscosity of the fluid inside the cell to the viscosity of the ambient fluid, \mathbf{u}^∞ is the ambient fluid velocity in the absence of the cells (i.e., the velocity gradient obtained from the macroscale simulations), and $\Delta \mathbf{f}$ is the jump in the hydrodynamic traction over the cell membrane. This last term is obtained using the Skalak constitutive model [2] to represent the

cells' resistance to shear and area dilatation and the Helfrich constitutive model [3] to represent the cell's resistance to bending. k describes the sum over the total number of cells N in the box, and p describes the sum over the infinite periodic lattice, where \mathbf{x}_p describes the distance from the primary periodic box to the p^{th} box. D_{ij} and S_{ij} are the boundary integral operators taken over the surface of the cells γ , described by

$$D_{ij}[\phi](\mathbf{x}_0) = \int_{\gamma} T_{ijk}(\mathbf{x}, \mathbf{x}_0) n_k(\mathbf{x}) \phi(\mathbf{x}) dS_{\mathbf{x}}, \quad (2)$$

$$S_{ij}[\phi](\mathbf{x}_0) = \int_{\gamma} G_{ij}(\mathbf{x}, \mathbf{x}_0) \phi(\mathbf{x}) dS_{\mathbf{x}}. \quad (3)$$

T_{ijk} and G_{ij} are fundamental solutions of Stokes flow, known as the *stresslet* and *Stokeslet*, respectively. Due to the singular nature of these operators, these integrals require special care to evaluate accurately. Additionally, to truncate the sum over the periodic lattice, fast Ewald sums [4] are used to split the *stresslet* and *Stokeslet* into two components, one that decays rapidly in Fourier space and one that decays rapidly in real space. This leaves the velocity of the cells as the only unknown, so once all other items are calculated, the equation is discretized and inverted to solve for the velocity.

RESULTS

One major test of the validity of the framework is whether it can reproduce the macroscale behavior of blood. For example, blood is shear-thinning, and the solver should show a decreasing effective viscosity of the blood as the shear rate increases. This behavior is illustrated in Figure 1, where the effective viscosity (relative to the viscosity of the plasma) of the entire periodic box in shear flow at 45% hematocrit is compared against experimental measurements.

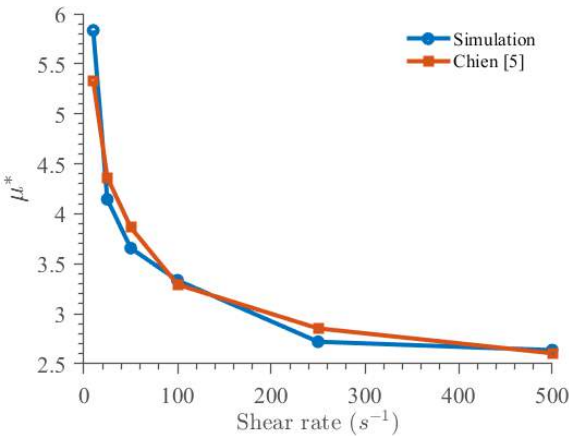


Figure 1: Relative effective viscosity calculated over a periodic box (blue circle) and experimental measurements of relative effective viscosity gathered from Chien [5] (red square) plotted against shear rate.

A primary goal of the solver is to accurately evaluate stresses and strains on a statistically significant sample of cells to gain a statistical picture of how they respond to a given flow. A representative example of this process is displayed in Figure 2, where the deformation of RBCs is tracked through a Blalock-Taussig shunt [6]. The parameter λ_1/λ_2 is a representation of the shear strain on the surface of the cells, where λ_1 is the larger principal strain on the surface of the cell and λ_2 is the smaller principal strain.

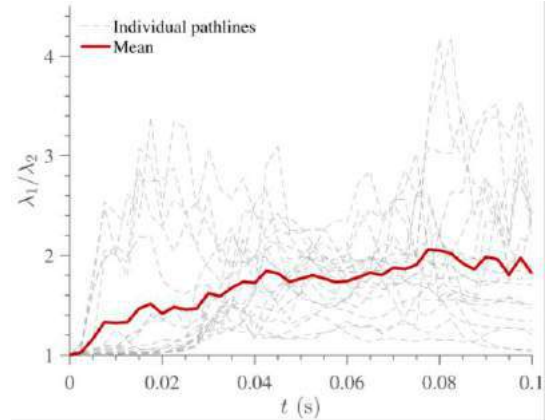


Figure 2: Maximum value of shear parameter λ_1/λ_2 on the surface of 20 cells (dashed grey) and their average (solid red) as they travel through a Blalock-Taussig shunt [6].

DISCUSSION

The current framework provides a novel method of understanding the way RBCs behave in macroscale flows. However, it is important that it faithfully reproduces what the cells actually experience. Figure 1 demonstrates an important characteristic of the solver in this regard: the microscale behavior of the cells is consistent with some of the macroscale properties of blood. One difficulty with this solver is that properties of the blood can vary, especially between patients. That considered, however, the agreement between the experimental and computational cases is good.

Figure 2 demonstrates an expected use of the solver: obtaining a statistical picture of the cells' response to a flow. However, the solver also provides additional information other than only average maximum strain on the cell, including the peak strain experienced overall, expected time over which the cell will experience this strain, and potential information on fatigue. Such information could be useful in obtaining a mechanistic understanding in how hemolysis occurs in flows on this scale.

The immediate extension of this work involves modifying it to include a measurement of hemolysis. Hemolysis occurs in multiple stages, with initial stages being the formation of pores that cause hemoglobin to leak from the cells, and later stages being the full-scale rupture of the cells [7]. Incorporating these effects in a way that accurately captures the release of hemoglobin is essential for using the solver to predict hemolysis. Additionally, there are several ways that the solver can be reduced in cost before it is used in time-sensitive procedures. However, even without these extensions, the current work provides a high level of detail about the behavior of RBCs not typically available for macroscale flows.

ACKNOWLEDGEMENTS

Research reported in this work was supported by National Heart, Lung, and Blood Institute of the National Institutes of Health under award number R01HL089456-10.

REFERENCES

- [1] Faghih, M et al., *Biomech Model Mechanobiol*, 18:845-881, 2019
- [2] Skalak, R et al., *Biophys J*, 13:245-264, 1973.
- [3] Helfrich, W, *Z Naturforsch C*, 28:693-703, 1973.
- [4] Deserno, M et al., *J Chem Phys*, 109:7678-7693, 1998.
- [5] Chien, S, *Science*, 168:977-979, 1970.
- [6] Rydquist, G et al., *J Comp Phys*, 461:111204, 2022.
- [7] Evans, E et al., *Biophys J*, 85:2342-2350, 2003.

MECHANICAL CHARACTERIZATION OF SHEEP LYMPHATIC GROWTH AND REMODELING

Sophia M. Mavris (1), Zhanna V. Nepiyushchikh (2), J. Brandon Dixon (1,2), Rudolph L. Gleason (1,2)

(1) Wallace H. Coulter Department of Biomedical Engineering, Georgia Institute of Technology and Emory University, Atlanta, GA, USA

(2) George W. Woodruff School of Mechanical Engineering, Georgia Institute of Technology, Atlanta, GA, USA

INTRODUCTION

Approximately 1 in 1000 Americans are affected by secondary lymphedema (SL), a vascular disease characterized by excess fluid buildup in the extremities from severe damage to the lymphatic system [1,2]. This form of lymphatic dysfunction can disrupt proper function and maintenance of the cardiovascular system and of nearly every organ in the body [3,4]. The lymphatic system is responsible for maintaining fluid and protein homeostasis and transporting lipids, immune cells, and antigens [5,6]. The leading cause of SL is a secondary complication to the surgical removal of lymph nodes for breast and gynecological cancer treatment [7]. If left untreated, patients with SL have an increased risk of developing lymphangiosarcoma, infection, and cardiovascular disease [1,2].

Standard SL treatments are limited to pressure garments and lymphatic drainage massages [8]. While these methods help to temporarily reduce pressure within the affected limb, there is a lack of evidence that these methods aid in the repair of the lymphatic vasculature itself in the presence of disease [9]. Little data is available regarding growth and remodeling (G&R) of the lymphatic vasculature in health and disease; however, previous literature suggests the mechanical properties and behavior of the lymphatic vasculature are vital for lymph flow [10,11]. With the absence of impactful therapies and no available cure, there exists a pressing need to better characterize the G&R response of the lymphatic vasculature following disruption or damage to the lymphatic system.

In this study we introduce a large-scale lymphatic model to characterize post-injury changes in the geometry and mechanical behavior of lymphatics. This large animal model considers the impact of gravitational force on the lymphatic network within the hindlimbs of female sheep - an element that is absent in previous rodent models yet substantial in clinical cases [12]. We aim to progress towards better preventions and treatments for patients with lymphatic injury by

investigating how the lymphatic vasculature adapts to alterations in its mechanical environment.

METHODS

The caudal popliteal lymphatic vessel in one hindlimb of the sheep (n=12) was occluded with an ~1cm in length excision, while the other hindlimb received a sham surgery. The experiment was terminated at 2, 4, and 8 weeks (n=4 at each time point). Post-euthanasia, the cranial popliteal lymphatic vessels from each hindlimb were isolated and sutured onto two opposing glass cannulas within a 37°C calcium-free PSS bath connected to a custom cylindrical biaxial mechanical testing device. The computer-controlled device comprised of a trinocular stereoscope at 0.7x magnification with an attached camera to visualize the cannulated vessel, an edge detection subroutine in LabView for measuring diameter, inlet and outlet pressure sensors, a 50 g load cell force transducer, manual axial length actuators, and a syringe pump. This system controls transmural pressure and axial stretch, while measuring outer diameter and axial force. To evaluate passive mechanics, vessels underwent one cycle of preconditioning of a pressure range of 3-40 cm H₂O at stretches below in vivo, at in vivo, and above in vivo, respectively, followed by three loading cycles with the same pressure range and stretches. The in vivo stretch for each vessel was determined by finding the intersection point of axial stretch versus axial force curves for fixed pressures. Pressure-diameter and pressure-compliance curves were plotted at the in vivo axial stretch. Compliance was calculated as

$$C = \frac{\Delta D / \bar{D}}{\Delta P} \quad (1)$$

where D is vessel outer diameter and P is transmural pressure.

RESULTS

At each termination time point, the cranial popliteal vessels from the injured hindlimbs exhibited an increased outer diameter compared to the sham hindlimbs when exposed to pressures of 3-40 cm H₂O (Fig 1). No significant difference in compliance (Fig 2), in vivo axial stretch (Fig 3), or axial length (Fig 4) were observed between the injured and sham vessels at any of the time points. The ratio of in vivo stretches from the injured to sham vessels from the same animal showed a high degree of variability (Fig 4).

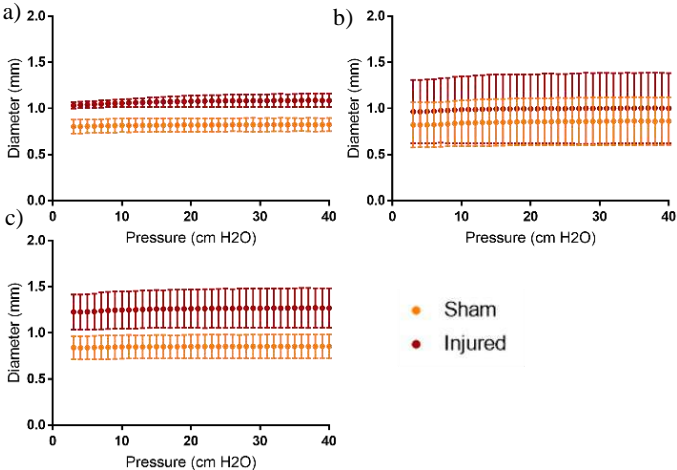


Figure 1: Pressure-diameter curves for sham and injured lymphatic vessels at 2 week (a), 4 week (b), and 8 week (c) time points.

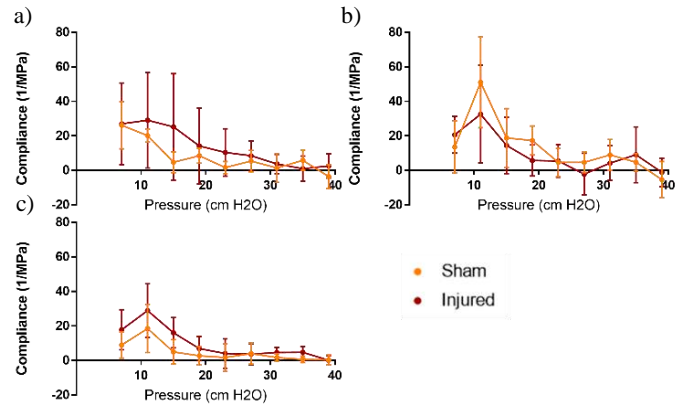


Figure 2: Pressure-compliance curves for sham and injured lymphatic vessels at 2 week (a), 4 week (b), and 8 week (c) time points.

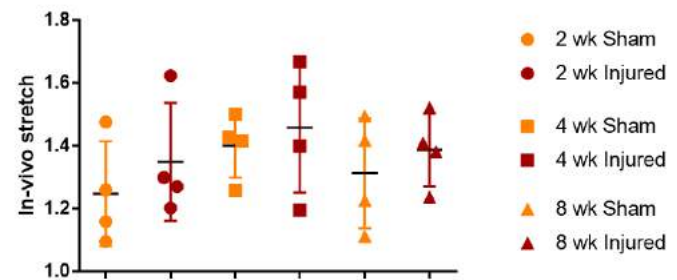


Figure 3: Comparison of in vivo stretches between sham and injured vessels at each time end point (2, 4 and 8 weeks).

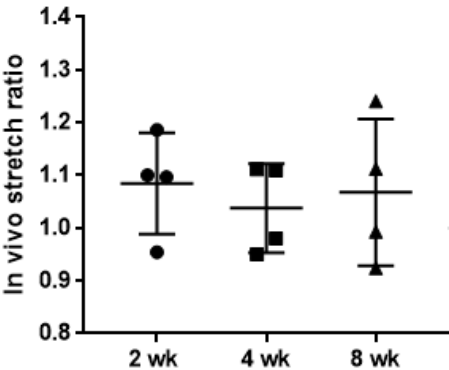


Figure 4: Comparison of the in vivo stretch ratio between the injured and sham vessel for each sample at all time points.

DISCUSSION

This study highlights that remodeled lymphatic vessels adapt by growing with a significant increase in circumferential size (outer diameter) while showing no observable changes in mechanical properties (compliance), in vivo stretch, and axial length. Another observation was that there was a high degree of variability in vessel diameters and in vivo stretch ratios between the samples. This showcases that the lymphatic vasculature anatomy within a standardized experimental group (adult female sheep) can differ greatly, indicating that there may not be a “one-size-fits-all” treatment for lymphatic injury. Some limitations of this experiment include having a small sample size within each termination group and the presence of systematic inflammation within the sheep due to the sham and injury vessels being isolated from the animal. There was also observed local inflammation at the site of both the sham and injured surgical wounds at the time of tissue collection. Our findings help to create a better understanding of lymphatic biomechanics and its relation to disease progression by translating these findings to improve and uncover better treatments and preventions for SL.

ACKNOWLEDGEMENTS

We respectfully acknowledge this research was funded by a grant from the National Institutes of Health (R01-HL152152).

REFERENCES

[1] Sleight, B et al., *StatPearls*, 2022.
[2] Grada, A et al., *JAAD*, 77:1009-1020, 2017.
[3] Breslin, J et al., *Compr Physiol*, 9:207-299, 2018.
[4] Oliver, G et al., *Cell*, 182:270-296, 2020.
[5] Yousef, M et al., *JPPS*, 24:533-547, 2021.
[6] Margaritis, K et al., *J R Soc Interface*, 9:601-612, 2012.
[7] Rockson, S et al., *Nat Rev Dis Primer*, 5:22, 2019.
[8] Bernas, M et al., *Clin Exp Metastasis*, 35:547-551, 2018.
[9] Kareh, A et al., *Mo Med*, 117:143-148, 2020.
[10] Scallan, J et al., *J Physiol*, 594:5749-5768, 2016.
[11] Munn, L et al., *Semin Cell Dev Biol*, 38:67-74, 2015.
[12] Nelson, T et al., *Nat Biomed Eng*, 4:649-661, 2020.

BOVINE PERICARDIUM DENSITY MEASUREMENT AND ITS IMPLICATIONS ON LEAFLET STRESS DISTRIBUTION IN BIOPROSTHETIC HEART VALVES

Masod Sadipour (1) and Ali Azadani (1)

(1) Department of Mechanical and Materials Engineering, University of Denver, Denver, Colorado, United States

INTRODUCTION

Bovine pericardium (BP) is one of the common materials in manufacturing BHVs. It has been shown that valve performance is highly dependent on leaflet material properties. Finite element analysis (FEA) has been widely used to study prosthetic and natural heart valves, reducing the costly and lengthy process required for in vivo and in vitro analysis. To obtain reliable solutions in computational modeling, it is essential to consider accurate properties of bioprosthetic heart valves (BHVs), such as density and mechanical properties. Previous computational studies assume BP density to be close to the density of water or blood. However, BP leaflets undergo multiple treatments, such as fixation and anti-calcification. The goal of the present work is to measure the density of bovine pericardial patches and analyze the impact of density on BHV leaflet stress and strain distribution. To the best of our knowledge, this is the first study to measure the density of commercially available bovine heart valves and compare leaflet deformation and stress with different densities.

METHODS

First, we measured the density of eight square BP samples laser cut from Edwards BP patches. The weight of specimens was measured using an A&D Analytical Balance, and volume was measured by high-resolution imaging. An FE analysis was then conducted on the effect of density deviation on the deformation and stress distribution of PERIMOUNT Magna aortic heart valve (Edwards Life Sciences, CA), a well-known and commercially available surgical valve. For this purpose, we conducted a dynamic analysis on the 25 mm PERIMOUNT Magna Bioprosthesis with different densities based on our findings in the first part of the study. Abaqus/Explicit was used to carry out the FE analysis. A thickness of 0.56 mm was taken into account in the simulations. A non-linear anisotropic Fung-type elastic constitutive model was employed for the leaflets:

$$w = \frac{c}{2}(e^Q - 1), \quad Q = E : (\mathbf{h}E) \quad (1)$$

where E is the Green–Lagrange strain tensor and \mathbf{h} is a non-dimensional symmetric tensor entailing 21 independent coefficients of the Fung model. Material orientation was given to the leaflet's elements utilizing a homemade MATLAB code [1]. A pressure waveform obtained from a previous study using in vitro analysis was used as the simulation physiological loading condition²⁴. Finally, A material optimization was carried out for the leaflets based on the deformation experimental results obtained by Mostafa et al. [1].

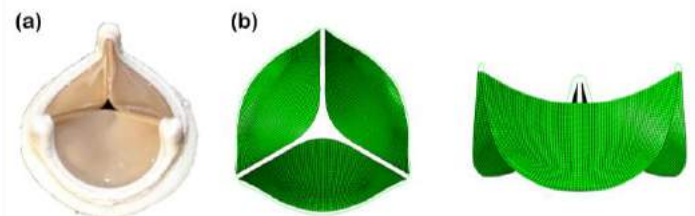


Figure 1: (a) 25-mm PERIMOUNT Magna surgical bioprosthetic aortic valve (b) The FE model showing the leaflets' geometric configurations attached to the frame.

RESULTS

The average density value of the BP samples was 1,410 kg/m³, and the standard deviation (SD) was 0.07 kg/m³. In previous simulations and analyses [1-3], the density of bovine and porcine pericardium was considered 1,000 kg/m³ and 1,100 kg/m³. We compared the stress on the leaflets with different densities (1,000 and 1,410 kg/m³) in both the acceleration and deceleration phases of the cardiac cycle (Figure 2). As

presented in the figure, the leaflet stress distribution was dependent on the density of the leaflets. In the acceleration, high-stress regions were detected in the fixed edges between the middle of the fixed edge and commissure, and the maximum principal stress reached to 1.89 MPa for a density value of 1,410 kg/m³, and 2.47 MPa for a density of 1,000 kg/m³ (30.7% difference). The maximum principal stress of the higher density showed lower stress during the acceleration. However, high-stress regions were observed mainly near the commissures during deceleration, and the maximum stress reached 0.713 MPa. A decrease in density from 1,410 kg/m³ to 1,000 kg/m³ resulted in decreased magnitudes of the maximum in-plane principal stress in the deceleration.

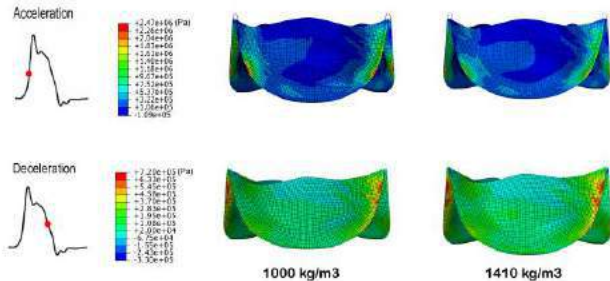


Figure 2: Max in plane principal stress of 25 mm premium Magna surgical valve in the acceleration and deceleration with 1,000 kg/m³ and 1,410 kg/m³ density

In addition, the maximum in-plane principal stress histogram of the leaflets in the acceleration is presented in Figure 3. The histogram indicates that 2% of the leaflet elements with density of a 1,000 kg/m³ had a maximum in-plane principal stress of more than 1.2 MPa while in the density=1,410 Kg/m³ case we just have 0.5% of elements within 1.2-1.87 MPa and no elements more than 1.87 MPa.

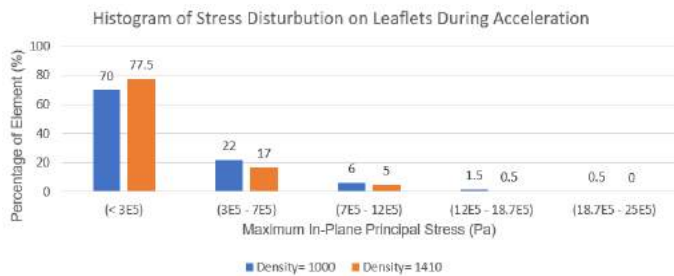


Figure 3: The maximum in-plane principal stress histogram of PERIMOUNT Magna leaflets in the Acceleration with 1,000 kg/m³ and 1,410 kg/m³ density

DISCUSSION

This study improves our understanding of the structural performance of surgical heart valves. To obtain the mechanical behaviors of bioprosthetic aortic valve leaflets, accurate properties of tissues are essential, helping us design and manufacture novel prosthetic valves. Stress distribution and deformation of the BHV leaflets depend on the magnitude of density; by considering 1,410 kg/m³ as the reference value for density, the difference of taking the value of 1,000 kg/m³ into account as the density value would be remarkable. Through dynamic simulations of a 25-mm PERIMOUNT Magna aortic valve, it was shown that the maximum principal stress was significantly higher in the acceleration phase of the cardiac cycle than the deceleration phase in all

cases. Relevant differences in stress distribution have a strict correlation with different kinematics of the leaflets. In computational models, it is essential to consider an accurate value for the density of BHV leaflets. Simulating the interaction between fluid and structure could offer a simulation with a higher level of precision which we will consider in future studies. Also, adding more samples could increase the accuracy of the current study.

ACKNOWLEDGEMENTS

This work was supported by the University of Denver [Grant number: 84993-142235].

REFERENCES

- [1] Abbasi M, Barakat MS, Dvir D, Azadani AN. A non-invasive material characterization framework for bioprosthetic heart valves, *Ann Biomed Eng*.47(1):97–112, 2019.
- [2] Borazjani I, Fluid-structure interaction, immersed boundary-finite element method simulations of bio-prosthetic heart valves, *Comput Methods Appl Mech Eng*, 257:103–16, 2013.
- [3] Jermihov PN, Jia L, Sacks MS, Gorman RC, Gorman JH, Chandran KB, Effect of geometry on the leaflet stresses in simulated models of congenital bicuspid aortic valves, *Cardiovasc Eng Technol*. 2(1):48–56, 2011.

RESTORED NORMAL BLOOD FLOW PLUS ATORVASTATIN PROMOTES ATHEROSCLEROSIS REGRESSION

Morgan A. Schake (1), Ian McCue (1), Samuel Harvey (1), Evan Curtis (2), Forrest Kievit (2),
Ryan M. Pedrigi (1)

- (1) Department of Mechanical and Materials Engineering, University of Nebraska-Lincoln, Lincoln, NE, USA
(2) Department of Biological Systems Engineering, University of Nebraska-Lincoln, Lincoln, NE, USA

INTRODUCTION

Blood flow within an artery is a key determinant of its susceptibility to the development of atherosclerotic plaques [1, 2]. Unidirectional blood flow at a normal velocity (i.e., normal flow) in straight arterial segments protects against plaque development. Multidirectional blood flow at a low velocity (i.e., disturbed flow) in curved or bifurcated arterial segments promotes plaque development [3]. These relationships are well established, yet our understanding remains incomplete. It is unknown how normal blood flow affects plaque fate, and whether flow can be restored within an atherosclerotic artery. To address this knowledge gap, a blood flow-modifying cuff was initially placed around the left carotid arteries of ApoE^{-/-} mice to induce plaque development and then it was removed to allow restoration of normal blood flow. Restored normal blood flow was confirmed using magnetic resonance imaging (MRI) for lumen area and Doppler ultrasound for blood velocity. Serially-collected histology sections demonstrated that plaques in decuffed mice exhibited compositional changes indicative of a more stable phenotype compared to those in untreated mice. Because the primary therapeutic strategy for atherosclerosis is systemic lipid lowering via statins, we also evaluated the effects of atorvastatin. Plaques in mice treated with atorvastatin also exhibited plaque stabilization comparable to those treated with restored normal blood flow via decuffing and the combination promoted both plaque stabilization and regression.

METHODS

Mouse Model. A total of 56 mice were acquired from Jackson Labs at 11 weeks of age and immediately placed on an atherogenic diet for the duration of the experiments. Two weeks later, mice were instrumented with a blood flow modifying cuff around the left carotid artery and the contralateral carotid artery served as a control. The cuff induces an unstable plaque in the upstream artery segment and stable plaque in the downstream segment. Mice were randomly assigned to

one of four experimental groups: (1) untreated with the cuff maintained for nine weeks (9U), (2) treated with decuffing (to restore normal blood flow) after five weeks of cuff placement and maintained without the cuff for an additional four weeks (9D), (3) treated with atorvastatin daily after five weeks of cuff placement and maintained with the cuff for an additional four weeks (9A), and (4) treated with the combination of atorvastatin plus decuffing (9AD). All mice were humanely sacrificed nine weeks after initial cuff placement.

Histology. Carotid arteries were serially cryosectioned at 8 μ m thickness. Three stains were evaluated: oil red O for lipids, picrosirius red for collagen, and CD68 for macrophages. The stained sections were imaged with a Zeiss Axio Observer 5 microscope at 10x magnification for basic stains and a Zeiss LSM 800 confocal microscope for the immunostain. Sections were segmented with a custom MATLAB program that quantified percentage of stain area to intima area.

Medical Imaging. Magnetic resonance imaging (MRI) and Doppler ultrasound were used to quantify lumen patency at the point of maximum artery stenosis and peak blood velocity, respectively, at -1, 1, 4, 7, and 9 weeks after initial cuff placement. Both quantities are normalized to week -1.

Statistics. All quantities are reported as mean \pm standard deviation. Normality was determined by a Shapiro-Wilks test and either a *t*-test or Mann Whitney U test with equal or unequal variances (F-test) were performed. Multiple comparisons were accounted for using a Bonferroni-Holm correction and an adjusted *p*-value of less than 0.05 was considered statistically significant.

RESULTS

MRI and Doppler ultrasound demonstrated that placement of the blood flow-modifying cuff caused a significant reduction in lumen patency and blood velocity, while latter cuff removal in the 9D mice restored these quantities to near baseline values (Figure 1B & C). One week after cuff placement, MRI revealed a dramatic reduction in

lumen area ($13.7 \pm 5.2\%$ versus $99.6 \pm 17.4\%$, $p < 0.0001$), which was similar at 4 weeks. However, two weeks after decuffing, the maximum stenosis had improved ($74.8 \pm 21.2\%$ versus $103.9 \pm 19.5\%$, $p = 0.005$) and, after 4 weeks, there was no significant difference between the left and right carotid arteries ($84.3 \pm 18.1\%$ versus $97.3 \pm 14.6\%$, $p = 0.07$) (Figure 1B). Similarly for peak systolic blood velocity, the left carotid artery exhibited a dramatic reduction compared to the control at week 1 ($55.9 \pm 8.8\%$ versus $107.9 \pm 16.8\%$, $p = 0.0002$) and 4 ($56.5 \pm 10.6\%$ versus $113.8 \pm 18.5\%$, $p = 0.0002$). Two weeks after decuffing, the peak blood velocity had increased in the instrumented arteries and was no longer statistically different from the control arteries (Figure 1C).

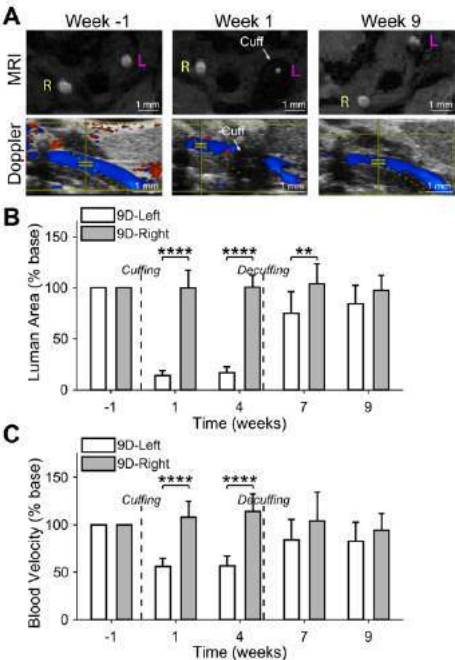


Figure 1: MRI and Doppler ultrasound of decuffed carotid arteries compared to right contralateral control arteries. (A) MRI and ultrasound images before (week -1), during (week 1), and after (week 9) cuffing. (B) Quantification of lumen area from MRI. (C) Quantification of peak blood velocity from ultrasound.

Histological analysis revealed that restored normal blood flow alone promoted plaque stabilization and the combination with atorvastatin caused plaque regression. In the upstream (unstable) plaque region, decuffed mice exhibited significant changes in plaque composition compared to the untreated group (9D vs 9U), wherein lipid content was lower ($4.3 \pm 3.6\%$ versus $17.2 \pm 9.4\%$, $p = 0.003$), macrophage content was lower ($1.1 \pm 0.8\%$ versus $4.0 \pm 1.8\%$, $p = 0.0009$), and collagen content was higher ($9.3 \pm 3.1\%$ versus $4.9 \pm 2.0\%$, $p = 0.0009$) (Figure 2A). Similar results were seen with atorvastatin (9A). The combination of the two therapies (9AD) exhibited similar plaque lipid and macrophage contents, but a higher collagen content versus each therapy individually ($15.5 \pm 4.4\%$ versus $8.2 \pm 5.4\%$, $p = 0.01$ and $9.3 \pm 3.1\%$, $p = 0.013$ for the 9A and 9D groups respectively). Furthermore, the 9AD group was the only group that exhibited a significant decrease in plaque burden from the 9U group ($22.7 \pm 18.0\%$ versus $43.7 \pm 12.7\%$, $p = 0.013$).

In the downstream (stable) plaque region, there was no significant differences in lipid and macrophage content between the groups. However, collagen concentrations were significantly higher in all treatment groups compared to the untreated 9U group with 9AD having the highest collagen concentration compared to 9U and 9D ($9.6 \pm 5.4\%$, $p < 0.0001$ and $17.1 \pm 5.0\%$, $p = 0.04$, respectively).

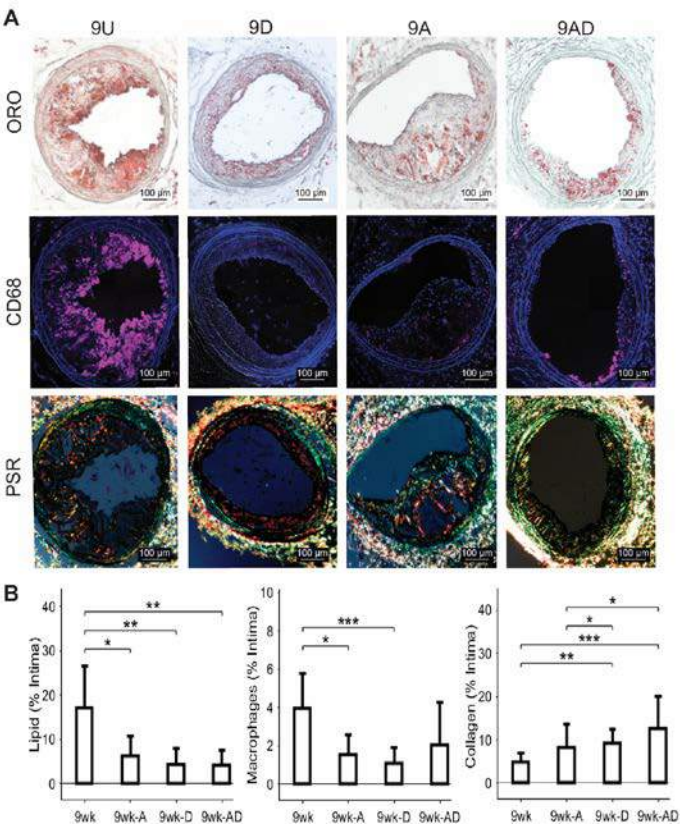


Figure 2: Histological results from the unstable plaque region upstream of the cuff. (A) Mouse carotid artery sections for lipids (ORO), macrophages (CD68), and collagen (PSR) in each mouse group. (B) Histology quantification of each group across each stain.

DISCUSSION

Atorvastatin is a first-line therapeutic for atherosclerosis that primarily causes plaque stabilization. Studies in patients have shown that it promotes increased fibrous cap thickness, decreased lipids, and decreased macrophages [4]. Remarkably, our study herein demonstrated a similar degree of plaque stabilization with restored normal blood flow. We also found that the combination of restored normal blood flow and atorvastatin had additive beneficial effects, including a significant reduction in plaque burden, lipid, and macrophage content, and increased collagen content compared to the untreated mice. This suggests that atorvastatin and mechanical stimuli operate along different cell signaling pathways and could be administered in parallel within patients for additive therapeutic effects.

ACKNOWLEDGEMENTS

We gratefully acknowledge support for this work from the AHA (grant number 19CDA34660218) and NIH (grant R21EB028960).

REFERENCES

- [1] Pedrigi, RM et al., *Circulation*, 132:1003-1012, 2015.
- [2] Davies, PF et al, *Cardiovascular Res*, 99:315-327, 2013.
- [3] Chatzizisis, YS et al, *J Am Coll Cardiol*, 49:2379-2393, 2007.
- [4] Komukai K, *J Am Coll Cardiol*, 64:2207-2217, 2014.

MITIGATING POST-TAVR THROMBOGENIC RISK: DESIGN AND OPTIMIZATION OF NOVEL TRILEAFLET AND BICUSPID AORTIC VALVE DEVICES

Kyle J. Baylous (1), Brandon J. Kovarovic (1), Salwa B. Anam (1), Ryan T. Helbock (1), Marvin J. Slepian (2), Danny Bluestein (1)

(1) Department of Biomedical Engineering, Stony Brook University, Stony Brook, NY, USA
 (2) Department of Medicine and Biomedical Engineering, Sarver Heart Center, University of Arizona, Tucson, AZ, USA

INTRODUCTION

Transcatheter aortic valve replacement (TAVR) is a minimally invasive treatment used to treat severe aortic stenosis. The efficacy of TAVR has been shown over the past 20 years and the number of TAVR procedures is constantly increasing, surpassing surgical aortic valve replacement (SAVR). TAVR is expanding to younger, lower-risk patients, and is even being used for bicuspid aortic valve (BAV) patients in addition to the common trileaflet aortic valve (TAV) patients for

which TAVR was originally used [1,2]. However, TAVR is associated with several clinical complications, including long-term, life-threatening thrombotic events that may be a consequence of prolonged exposure of platelets to elevated cyclic stresses. Flow-induced thrombogenicity increases the risk of platelet activation, and microthromboemboli formation can lead to prosthetic leaflet thrombosis. The rapid expansion of TAVR into younger and lower-risk patients highlights the importance of developing alternatives to current

tissue-based TAVR devices that may suffer from structural deterioration and thrombus formation – as the device must remain functional and safe for the long-term. New polymer technologies facilitate the creation of more durable TAVR valves and mitigate such adverse complications [3,4].

Optimization of polymeric TAVR leaflets can reduce the risk of flow-induced thrombogenicity and mitigate the need for post-TAVR anticoagulation therapies, which are widely debated. Optimizing the valve design to improve its hemodynamics and minimize the associated potential thrombotic events is the preferred approach. Furthermore, given that current devices deployed in BAV patients are designed for treating common trileaflet aortic valve patients, having a dedicated TAVR stent and leaflet design for BAV patients can lead to better device performance. The goal of this study is to use advanced computational modeling approaches, including fluid-structure interaction (FSI) simulations, to assess the thrombogenic potential and hemodynamic performance of current commercial TAVR valves. We demonstrate how these devices compare to our dedicated polymeric TAVR leaflet designs for both trileaflet and bicuspid AV patients, which are optimized in multiple steps involving various design features. Specifically, in this work we highlight a thrombogenic risk

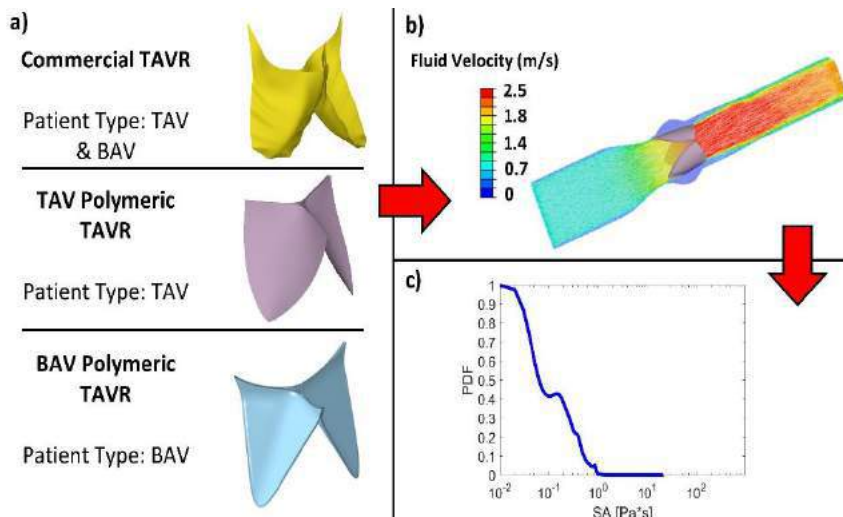


Figure 1: Thrombogenic optimization workflow in which the various valve types in (a) are used to simulate TAVR and run hemodynamic analyses via FSI (b). The thrombogenic risk of each valve can be examined via PDFs (c).

assessment workflow that utilizes a fully integrated TAVR FSI approach, leading to reduced thrombogenicity.

METHODS

Commercial TAVR models were generated for older, self-expandable CoreValve (23 and 26 mm) and newer generation Evolut (23 and 26 mm) devices, in addition to the balloon-expandable SAPIEN (23 mm). The valve models were generated along with their stents as described in our previous work [5]. With the constructed leaflets and stents, a TAVR deployment was simulated in ABAQUS Explicit v2019 (Dassault Systemes, Vélizy-Villacoublay, France) and the resulting post-deployment geometry - with a native trileaflet valve - was taken into ANSYS LS-DYNA to perform FSI analysis for two beat cycles (Fig. 1).

To validate the constructed TAVR valves, FSI flow data for the commercial devices were compared to particle image velocimetry (PIV) data in the literature [6]. Following the validation, each FSI simulation was post-processed using ANSYS EnSight in which ~150,000 platelets were seeded in the systolic flow via the implementation of Lagrangian particles. Stress accumulation (SA) was calculated and tracked for all the particles seeded in the fluid domain, with the continuous seeding of particles at the inlet to accurately model new platelets introduced into the flow [7]. With this data, the probability density function (PDF) of the accumulated stresses of the large population of flowing platelets was computed for each valve type, which represents the “thrombogenic footprint” for each respective device [7]. To analyze the thrombogenic potential of different leaflet designs, the PDFs of the various commercial devices were compared amongst each other and to multiple parametric trileaflet valve geometries that have varying belly and attachment profiles. Additionally, the thrombogenic potential of our BAV-dedicated TAVR design, PolyV-B, was assessed and compared to commercial devices currently used for BAV patients by utilizing this workflow with an idealized native geometry consisting of a bicuspid aortic valve (Fig. 2).

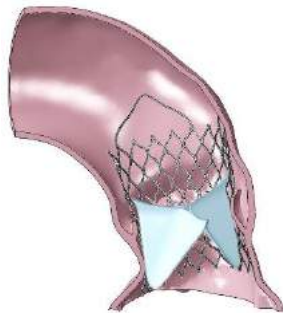


Figure 2: Deployment of the PolyV-B polymeric valve in a patient-specific anatomy.

RESULTS

The FSI results for the commercial valves showed peak systolic jet velocities in the range of 2.5 to 3.0 m/s (Fig. 3), comparable to the PIV velocity data found in the literature [6]. Data was also compared for the

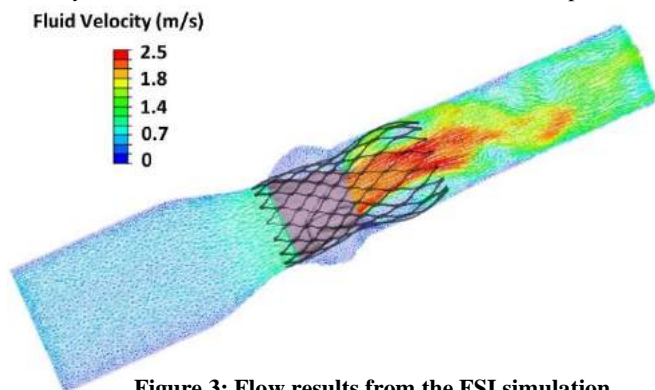


Figure 3: Flow results from the FSI simulation for the Evolut 29 mm commercial valve.

CoreValve and SAPIEN, and after validation, the thrombogenic risk simulations were performed for the commercial valves, followed by the polymeric TAV valves and PolyV-B. Upon comparison of the PDFs for the polymeric TAV valves, different degrees of stress accumulation were highlighted. In particular, the B1A1 valve showed more stress accumulation on a much larger number of platelets than the B1A2 or B1A3 valves. Valves designed with attachment regions with large tapering angles (least-gradual curvature), and comparatively large surface areas tended to show higher thrombogenic risk due to excessive leaflet fluttering, irregular GOA shapes, and other characteristics that would likely activate platelets over time (Fig 4.). Various commercial valves also showed comparatively high thrombogenic risk, thereby highlighting that the commercial leaflets are not optimized for mitigating flow-induced thrombogenicity.

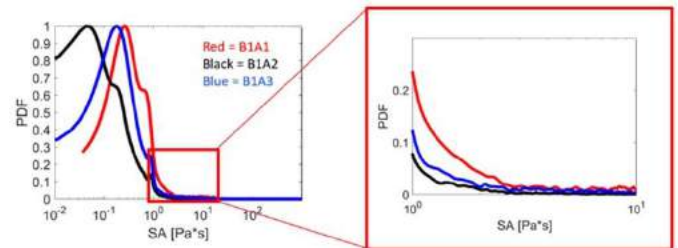


Figure 4: PDFs for three of the polymeric TAV leaflet geometries showing variation in thrombogenic risk due to changes in leaflet design.

DISCUSSION

This study demonstrates the ability to analyze post-TAVR thrombogenic risk by studying hemodynamics of prosthetic devices via a fully integrated TAVR FSI approach. The devices studied here include both self-expandable and balloon-expandable commercial valves currently on the market, old and new generation devices, novel polymeric TAV devices, and our BAV-specific device, PolyV-B. More specifically, we can analyze the impact of TAVR leaflet designs on hemodynamics and thrombogenicity to develop novel devices that are safe and durable with reduced thrombogenicity for younger patient cohorts. Limitations of this study include the use in few cases of idealized anatomies for TAVR deployments. Nevertheless, this study points to key parameters of TAVR leaflet design most critical for the mitigation of thrombogenic risk and other essential hemodynamic criteria. Optimized TAVR devices of the future may finally reduce the need for post-TAVR antithrombotic therapies. In the future, we wish to use patient-specific anatomies, especially for the PolyV-B device. Additionally, we plan to perform our own in-vitro hemodynamics testing (ViVitro) with TAVR devices that we are developing.

ACKNOWLEDGEMENTS

Funding provided by NIH-NIBIB Phase II-U01EB012487 (DB); NIH-NIBIB 1U01EB026414-01 (DB). Industry Partners: ANSYS, Dassault Systemes.

REFERENCES

- [1] Travaglini, S et al., *J Biomech*, 142(1) (2020).
- [2] Li, K et al., *Int J Num Meth Biomed Eng*, 33(3): e02814 (2017)
- [3] Abbasi, M et al., *J Mech Behav Biomed Mat*, 102: 103491 (2020)
- [4] Kovarovic, B et al., *J Biomech Eng*, 144(6) (2022)
- [5] Helbock, R et al., *Annals of Biomed Eng*, (2022): 1-13
- [6] Hatoum, H et al., *JTCVS Open*, 9 (2022): 43-56
- [7] Xenos, M et al., *J Biomech*, 43(12): 2400-2409 (2010)

SUCCESSFUL TRANSPLANT OF CRYOPRESERVED KIDNEYS ENABLED BY ENGINEERING-BASED PROTOCOL OPTIMIZATION

Zonghu Han (1), Joseph S. Rao (2,3), Lakshya Gangwar (1), Bat-Erdene Namsrai (2), Jacqueline Pasek-Allen (4), Srivasupradha Ramesh (1), Michael L. Etheridge (1), Erik B. Finger (2), John C. Bischof (1,5)

- (1) Department of Mechanical Engineering, University of Minnesota, Minneapolis, MN, USA
- (2) Department of Surgery, University of Minnesota, Minneapolis, MN, USA
- (3) Schulze Diabetes Institute, University of Minnesota, Minneapolis, MN, USA
- (4) Department of Biomedical Engineering, University of Minnesota, Minneapolis, MN, USA
- (5) Institute for Engineering in Medicine, University of Minnesota, Minneapolis, MN, USA

INTRODUCTION

A method to cryopreserve or “bank” kidneys prior to transplant would effectively remove the influence of time from the organ transplantation process. It would transform transplantation from an emergency procedure that must be accomplished within hours of organ acquisition to a planned procedure that can equitably reach patients regardless of geographical and time constraints. A promising approach to organ banking is vitrification – that is, cooling organs perfusion-loaded with cryoprotective agents (CPAs) so quickly that they cannot undergo the phase transition from liquid water to ice and instead enter a stable glass-like state wherein viable storage is theoretically indefinite. While vitrification of rabbit kidneys was first successfully demonstrated decades ago[1], the ability to reproducibly rewarm whole organs while preserving viability and function has proven elusive. Addressing this long-standing issue requires mitigating the effects of two interrelated sources of damage to the organ: CPA toxicity (including osmotic stress) during perfusion loading/unloading and ice crystallization or cracking due to slow or non-uniform rewarming. Here we apply engineering-based optimization of CPA loading and vitrification to allow fast and uniform rewarming (i.e., RF nanowarming) and demonstrate the first repeatable organ cryopreservation and rewarming with success in an in vivo transplant model.

While CPAs help mitigate damage due to ice formation, the required concentrations can become toxic. The toxicity to the organ is determined by the CPA components, exposure time, temperature, and osmotic stress during loading. Carefully balancing these factors allows vitrifiable concentrations to be achieved within the organ while minimizing toxicity. Successful rewarming then becomes critical; if rewarming is too slow, ice crystals form (i.e., devitrification), and if rewarming is not uniform, thermal stress causes cracking. Increasing the CPA concentration reduces the rewarming rates required but can increase toxicity, so overall protocol optimization is a delicate balance between

these factors. Traditional rewarming approaches (i.e., convection, microwave, or dielectric) fail to meet both requirements[2]. While whole kidney vitrification has been achieved with a high concentration CPA (9.3 M M22), rewarming has been largely unsuccessful. Only a single kidney has been successfully transplanted with any function [3], and that kidney was cryopreserved for only 8 min and only restored partial function. Further, even that partial success has never been repeated.

In this work, we show the ability to load, vitrify, and store (up to 100 days) kidneys at lower concentrations of CPA than M22 and the ability to use RF nanowarming to achieve a robust fast and uniform rewarming protocol with transplantation success. Physical success with RF nanowarming has been reported in earlier work from our group. Briefly, the technique employs alternating magnetic fields to remotely couple to and heat iron oxide nanoparticles (IONPs) that are perfused in CPA throughout the organ vasculature. Once the organ is vitrified, the IONPs provide the ability to rewarm in a fast and uniform manner in an RF field, which allows rewarming to occur independent of organ size [4, 5]. We systematically modeled the CPA transport and toxicity to achieve lower CPA concentration (8.4M) while still allowing vitrification. To demonstrate organ function and viability, we nanowarmed and transplanted the rat kidneys and showed restoration of renal function that solely sustained the lives of nephrectomized transplant recipients for 30 days post-transplant.

METHODS

We first established a target CPA concentration of ~7.8M based on our ability to nanowarm at rates of ~60 °C/min (needs to exceed CWR of 7.8 M CPA which is ~51 °C/min)[6]. We then applied combined CPA transport and toxicity models to predict the tissue CPA concentration and toxicity “cost function” to achieve vitrification and minimize toxicity for loading with 8.4M VMP, a vitrifiable CPA with acceptable toxicity in kidneys[7]. Here 8.4 M CPA concentration is used to drive rapid CPA loading in the tissue to 7.8 M without seeking full equilibration. To study this process, we used a two-compartment Krogh cylinder

model as a representative unit to study the CPA transport and osmotic stress between the vascular and cellular compartments of the organ, where the transport kinetics between the compartments are described by Kedem-Katchalsky (KK) equations[8]. The 3 parameters (L_p , P_s , and σ) related to compartmental exchange in the Krogh model were measured by fitting the observed pressures and flow during organ perfusion (as described below and previously by Pegg et al.). Then, the model was used to predict the CPA concentration inside the organ. We also applied a toxicity cost function model ($J = \int_0^t \beta C^\alpha dt$) to study the cumulative toxicity during CPA exposure[9]. The parameters in the toxicity cost function were determined by fitting viability data of kidney slices after exposing them to a range of CPA concentrations and times. All the models are coded in MATLAB R2020b (MathWorks). The combined models were then used to identify a CPA loading protocol that achieved vitrifiable organ-CPA concentrations (i.e. 7.8 M) while minimizing osmotic stress and CPA toxicity to the organs. The organ CPA concentration after loading and vitrification was then assessed by micro-CT [10]. The organs were vitrified following previously demonstrated cooling protocols at 20 °C/min with annealing [5].

Once established, the loading protocol was used to perfuse load CPA and IONP into rat kidneys, followed by vitrification and storage. The viability/function of the organ was then tested after nanowarming, CPA removal, and transplantation. First, the rat kidney was harvested from the donor and flushed with cold University of Wisconsin (UW) preservation solution and connected to a pressure- and flow-controlled multi-thermic (20 °C to -4 °C) perfusion system. CPA was loaded following the optimized VMP protocol. IONPs were perfused along with the final step of CPA loading assuming the IONP as an inert additive (<1 wt.%). Following CPA and IONP loading, the organ was placed in a controlled rate freezer and vitrified. The vitrified organ was then transferred to a -150 °C freezer for storage. At pre-determined times (n = 5 kidneys, 1-100 days), organs were removed from cryogenic storage, rapidly placed in an RF coil, and rewarmed at > 60°C/min. The CPA and IONPs were then unloaded in a gradual fashion.

Organ function and viability were tested in a rat transplant model. The recipient had both native kidneys removed, followed by transplant of the nanowarmed and CPA-unloaded donor kidney. Thus, renal function and survival of the animal depended solely on the transplanted organ. The animals survived for the full 30-day study period, over which the organs were assessed by blood serum and urine analysis (e.g., creatinine level and venous blood gas). The animal's body weight was also measured. Nanowarmed kidneys were compared directly to fresh control kidney transplants (n = 5).

RESULTS

In the Krogh model, the water permeability (L_p), CPA permeability (P_s), and reflection coefficient (σ) were measured as $1.5 \times 10^{-14} \text{ m}^3/(\text{N} \cdot \text{s})$, $7.0 \times 10^{-13} \text{ mol}/(\text{N} \cdot \text{s})$, and 0.10 (mean values), respectively. The toxicity cost function parameters were estimated as $\alpha = 3.12$ and $\beta = 9.39 \times 10^{-6}$ for VMP (n=3 for each parameter determination).

Guided by the CPA transport model, we optimized existing perfusion loading protocols by modifying the perfusion pressure, CPA exposure time, and temperature. Using the toxicity cost function model, we optimized the loading to achieve a vitrifiable concentration of 7.8 M (this value was predicted by the model and determined by DSC) as shown in Figure 1.

After vitrification, the rat kidneys were stored for 1-100 days followed by nanowarming and transplant. Intraoperatively, all nanowarmed kidneys reperfused rapidly and homogeneously upon restoration of blood flow (Fig. 1f) and grossly appeared similar to fresh control organ transplants. Postoperatively, all fresh control and nanowarmed kidney transplants continued to produce urine, and all animals survived for the full 30-day study period. During the first two postoperative

weeks, nanowarmed kidney recipients experienced more metabolic dysfunction (e.g., higher creatinine level) than control transplants, but all the nanowarmed kidney values reached the control kidney levels by day 14 and renal function was completely normal at sacrifice on day 30.

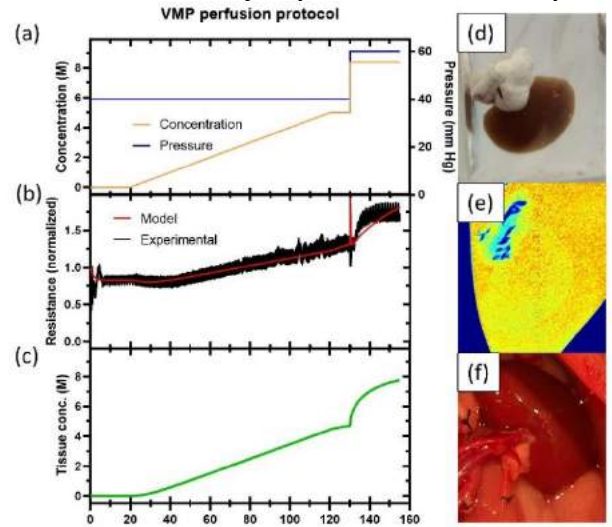


Figure 1: (a) VMP perfusion loading protocol. (b) The model-predicted and experimental perfusion resistances (representative case). (c) The model-predicted CPA concentration inside kidney tissue for the case shown in Fig. 1b. (d, e) Photo and micro-CT image of vitrified kidney after perfusion loading. (f) Intra-operative photo of nanowarmed transplanted kidney showing reperfusion.

DISCUSSION

This work presents several new findings: 1) Krogh cylinder permeability parameters (L_p , P_s , and σ) for rat kidney and VMP loading, 2) toxicity cost function parameters (α and β) for kidney and VMP exposure, 3) combination of Krogh and toxicity cost function modeling to achieve a vitrifiable kidney with improved viability, and 4) demonstration that these viable vitrified kidneys can be nanowarmed, transplanted, and used to preserve the life of a recipient after cryobanking for up to 100 days. While we demonstrate success in the rat kidney, our approach is scalable to human-sized organs, and we are conducting further studies to demonstrate this. Further, this systematic approach to protocol optimization can be broadly applied to other organs.

This result is an important step on the path to clinical organ banking. Cryobanking would improve donor/recipient matching, allow for better patient preparation and scheduled procedures, facilitate tolerance induction protocols in recipients, and increase organ utilization – all while supporting graft and patient survival.

ACKNOWLEDGEMENTS

This work was supported by NIH grants DK117425 and HL135046, and NSF grant EEC-1941543.

REFERENCES

- [1] Fahy GM, et al. *Cryobiology*. 1984;21(4):407-26.
- [2] Manuchehrabadi N, et al. *Science translational medicine*. 2017;9(379):eaah4586.
- [3] Fahy GM, et al. *Organogenesis*. 2009;5(3):167-75.
- [4] Gao Z, et al. *Advanced Science*. 2020;7(4):1901624.
- [5] Sharma A, et al. *Advanced Science*. 2021;8(19):2101691.
- [6] Han Z, et al. *CryoLetters*. 2020;41(4):185-93.
- [7] Fahy GM, et al. *Cryobiology*. 2004;48(1):22-35.
- [8] Pegg D, et al. *Cryobiology*. 1986;23(2):150-60.
- [9] Benson JD, et al. *Cryobiology*. 2012;64(3):144-51.
- [10] Han Z, et al. *Advanced healthcare materials*. 2020;9(19):2000796.

CORRELATIONS BETWEEN MASS TRANSPORT, ELASTIC FIBER FRAGMENTATION, AND THORACIC AORTIC ANEURYSM SEVERITY

Christie L. Crandall (1), Carmen M. Halabi (2), Jessica E. Wagenseil (1)

(1) Department of Mechanical Engineering and Materials Science, Washington University in St. Louis, St. Louis, MO

(2) Department of Pediatrics, Washington University School of Medicine, St. Louis, MO

INTRODUCTION

Thoracic aortic aneurysm (TAA) is characterized by a >50% dilation in the aortic diameter and can lead to aortic dissection, which is often fatal. Some TAAs are linked to genetic mutations that affect elastic fiber formation and cross linking, and elastic fiber fragmentation is a common pathology in TAA [1]. However, the mechanisms relating elastic fiber fragmentation to TAA formation and growth are not well understood. In this study, we investigate the connection between elastic fiber fragmentation and TAA severity by quantifying transmural mass transport as a possible mechanism contributing to TAA progression.

Previously we reported that enzymatic degradation and genetic mutations in fibulin-5 or lysyl oxidase facilitate arterial mass transport [2,3]. These studies showed that elastic fiber fragmentation can impact transmural convection and diffusion, yet, did not specifically model TAA. This study uses a TAA mouse model with a missense mutation in fibulin-4 (E57K), a protein necessary for elastic fiber formation [4]. *Fbln4*^{E57K/E57K} mice develop TAA with 50% penetrance, and when bred with lysyl oxidase (a crosslinking enzyme) haploinsufficient mice, *Fbln4*^{E57K/E57K};*Lox*^{+/-} mice have 100% TAA penetrance.

We present data from transmural mass transport experiments measuring hydraulic conductance and solute permeability of the mouse ascending thoracic aorta (ATA). We then compare mass transport properties with ATA geometries and quantification of elastic fiber fragmentation. We hypothesized that elastic fiber fragmentation would cause an increase in mass transport properties that would correlate with increased TAA severity, as measured by ATA diameter.

METHODS

Mouse Model. Mice with a missense mutation in fibulin-4 (E57K) were used and compared to wild-type (WT) littermates. *Fbln4*^{E57K/E57K} *Lox*^{+/-} mice were categorized into MU-A (aneurysm, >50% dilation) and MU-NA (non-aneurysm, <50% dilation) groups by comparing the ATA diameter to the average WT diameter. *Fbln4*^{E57K/E57K};*Lox*^{+/-} mice are

referred to MU-XA (extreme aneurysm) and always had >50% diameter dilation. Mice were sacrificed at 3-4 months of age and the ATA was isolated by dissection. All procedures were approved by the IACUC.

Mass Transport. ATAs were mounted into a Myograph (DMT). The outlet was closed off, and a hydrostatic fluid column was attached to the inlet to maintain an internal pressure of 100 mmHg. An air bubble was introduced into the lead tubing and the bubble displacement was tracked over time. This measurement was performed with phosphate buffered saline (PBS) in the fluid column, and then PBS containing 5 mg/mL of 4 kDa FITC Dextran. When Dextran was present, the concentration of the external bath was recorded over time. These values were used to calculate hydraulic conductance, with (L_{ps}) and without (L_p) solute present, and solute permeability (ω) [2, 3].

Elastic Fiber Fragmentation. After experimentation, a subset of ATAs were fixed while pressurized for 12-20 hours in 4% paraformaldehyde. Samples were flash frozen and 5 μ m thick cross sections were cut using a cryostat microtome and cover slipped. Samples were imaged using a Leica Sp-8 DIVE multiphoton microscope with a 40x objective. Collagen and elastin were excited at 880 nm and imaged using second-harmonic generation (emission: 420-460 nm) and autofluorescence (emission: 495-540 nm), respectively. After imaging, the elastin channel was isolated and analyzed in ImageJ (NIH). A 144 x 192 μ m section was thresholded to create a binary image of the laminae and the built-in skeletonize function and analysis was used to measure end points, junctions and slabs, which are defined by pixels with <2, >2, and 2 neighboring pixels, respectively.

Statistics. Statistical analysis was done using GraphPad Prism. Data are presented as means and standard deviations. Experimental groups were compared using one-way ANOVA and Sidak's multiple comparisons. Correlation matrices were made using the Pearson r correlation test. Pearson r values >0.6 can be considered moderate correlation, and >0.8 strong correlation. P-values <0.05 were considered significant.

RESULTS

Hydraulic conductance was calculated from the velocity of an air bubble in the fluid system and assumed 1-D advection-diffusion flow. Hydraulic conductance's are 60% and 68% lower in aneurysm groups (MU-A and MU-XA) compared to WT (Fig. 1A-B). Solute permeability of these groups, however, is no different compared to WT, but MU-NA solute permeability is 397, 52, and 81% higher than WT, MU-A, and MU-XA (Fig. 1C). These results demonstrate distinct mass transport differences between TAA and non-TAA groups.

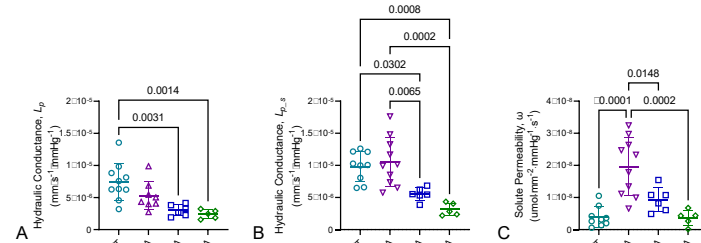


Figure 1: Calculated values of hydraulic conductance with solute absent (A), and solute present (B), and solute permeability (C) from 1-D advection diffusion analyses. N = 5 – 10/group.

Cross-section images of the elastic laminae (Fig. 2A) were analyzed to quantify elastic fiber fragmentation. Thickness measurements show a 54% thicker wall in MU-XA groups only compared to WT. Using a skeletonized thresholded image, limited differences are found in the measurements of junctions and average slab size, but end point voxels are 81, 76, and 70% higher in MU-NA, MU-A, and MU-XA groups compared to WT, respectively.

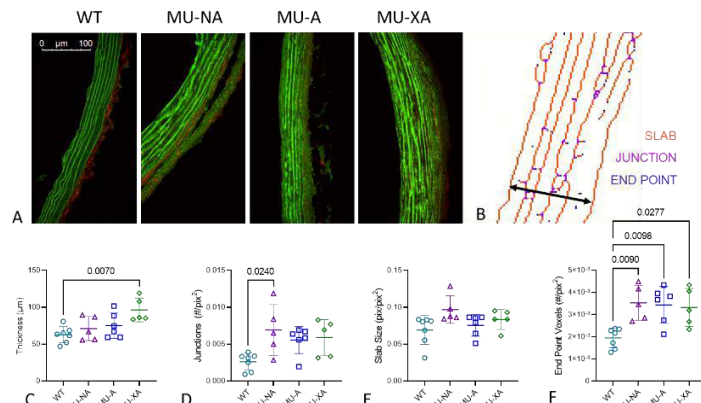


Figure 2. Representative cross section images (A) where elastin is shown in green and collagen in red. Skeleton analysis was used in ImageJ (B). Measurements of thickness (C), and skeleton values for junctions, branches, and end points (C-E) from the cross section images. N = 5-6/group.

Data from MU groups only were compared using correlation matrices which show the Pearson r values (Fig. 3). Hydraulic conductance values (L_p , L_{ps}) are significantly, negatively correlated with diameter ($p = 0.021$, 0.003), demonstrating mass transport properties that correlate with aneurysm severity. Solute permeability (ω) is not well correlated with any of the other metrics (Fig. 3A-B). The number of elastic fiber endpoints and average slab size are positively correlated with L_p and L_{ps} , ($p = 0.0010$, 0.015). Slab size is negatively correlated with diameter ($p = 0.012$) and thickness ($p = 0.009$), which demonstrates elastic fiber remodeling that correlates with TAA severity.

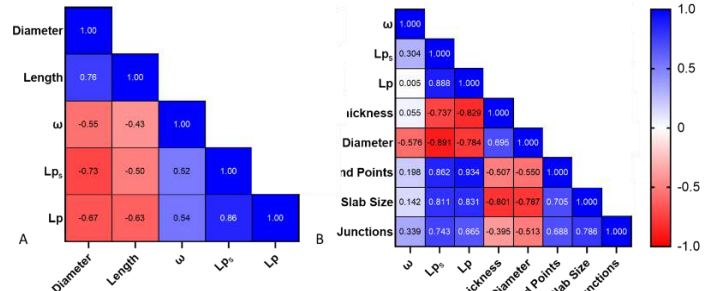


Figure 3. Correlation matrices for all measured MU data from mass transport experiments (A, N = 19-21) and elastic fiber fragmentation images (B, N = 8-9).

DISCUSSION

We investigated the effect of TAA caused by elastic fiber fragmentation on transmural mass transport in the ATA. Because *Fbln4*^{E57K/E57K} mice have only 50% TAA penetrance, we were able to compare pathological, but non-aneurysmal (MU-NA) to aneurysmal (MU-A and MU-XA with *Lox*^{+/+}) conditions. We found a decrease in hydraulic conductance specific to aneurysm groups (Fig. 1) and an increase in solute permeability specific to pathological, non-aneurysm groups. Previously, we studied mass transport in a different genetic mouse model which causes TAA in humans, but does not independently cause TAA in mice [2]. These ATAs had similar properties to our MU-NA, suggesting that an initial increase in solute permeability due to elastic fiber fragmentation may allow confounding conditions, such as increased cytokine trafficking, to contribute to TAA formation and growth. Increased growth factors and matrix metalloproteinases are found in human TAA [1]. As TAA progresses with extensive matrix remodeling, solute permeability returns to normal, but hydraulic conductance decreases which could cause hypoxia in medial layer cells and contribute to ongoing pathology.

Our elastic fiber quantification shows fragmentation in all MU groups and does not explain the linkage between TAA and elastic fiber defects. Using just the MU data, we further investigated these relationships through correlation analyses. The results show that hydraulic conductance is correlated with diameter dilation and also with elastic fiber endpoints and slab size. Formed elastic fibers may increase initially in compensation for the genetic mutation, and fragment further during TAA progression due to the genetic mutation. Areas between elastic fibers may be filled with proteoglycans which could affect mass transport and weaken the ATA wall due to their highly charged nature.

Overall, our results suggest that convective flow (hydraulic conductance) is decreased in fully-developed TAA and diffusion of small molecules (solute permeability) is increased at early TAA stages. These data could inform drug treatments for TAA or computational models of the TAA process. Limitations include only consideration of 1-D flow and the use of a mouse model, which differs in structure from human ATA. However, our work provides an initial understanding of how elastic fiber fragmentation may contribute to TAA pathology through alterations in mass transport.

ACKNOWLEDGEMENTS

Funding partially provided by AHA 19TPA-34910047 and NIH HL 164800.

REFERENCES

- [1] Pomerance, et al., *Histopathology*, 1:257-2776, 1977.
- [2] Cocciolone, et al., *J Biomech Eng*, 141:021013, 2018.
- [3] Crandall, et al., *J Biomech*, 145:111360, 2022.
- [4] Igocheva, et al., *J Bio Chem*, 290(35):21445-21459, 2015.

SUPERFICIAL MENISCUS CELLS ARE HIGHLY PROLIFERATIVE AND MIGRATORY AND GENERATE FUNCTIONAL TISSUE DESPITE A LOWER CELLULAR MECHANOSENSITIVITY

Sreen SF. Assi (1,2), Elizabeth Bernstein (2), Edward D. Bonnevie (1,2,3), Emily E. Sharp (1,2), Ryan C. Locke (1,2,3), Robert L. Mauck (1,2,3)

(1) Department of Bioengineering, University of Pennsylvania, Philadelphia, PA, U.S.A
(2) Department of Orthopedic Surgery, University of Pennsylvania, Philadelphia, PA, U.S.A
(3) Translational Musculoskeletal Research Center, Crescenz VA Medical Center, Philadelphia, PA, U.S.A

INTRODUCTION

The knee meniscus supports dynamic joint motion and load transmission through its specialized extracellular matrix (ECM). The meniscus contains an outer vascularized zone, an inner avascular zone, and two horns that anchor the meniscus to the tibia. Covering the entire tissue is a thin, specialized superficial layer. Cells within this superficial layer express progenitor cell markers and play a critical role in meniscus injury response [1]. Specifically, in both small and large animal models, these cells migrate to injury sites, proliferate rapidly, and deposit a disorganized repair tissue [2]. Thus, while these cells appear to direct some level of endogenous repair, the disorganized ECM they form lacks in mechanical integrity relative to native tissue [3], and so may not provide for a durable repair.

To determine whether differences in response to the injury microenvironment and matrix formation arise from cell origin or is a consequence of the wound repair environment, this study investigated the response of superficial cells to changes in the mechanical environment as well as their migration and proliferation potential, relative to cells from the central region of the meniscus body. We additionally probed the functional matrix production capacity of these cells, relative to body cells, via culture in nanofibrous scaffolds and evaluation of their mechanical properties and ECM deposition. Understanding of the differences in functional ECM-deposition potential between the superficial and body cells may guide tissue engineering approaches to enhance the quality of meniscus repair.

METHODS

***In vitro* culture:** Juvenile bovine medial menisci were dissected, and biopsy punches (12 mm diameter) used to isolate samples (**Figure 1**). A custom device was used to separate the superficial (~100 μ m depth) from the deeper (body) zones (1 mm depth). Tissue segments were minced and cultured at 37°C in basal media (BM – DMEM with 10% fetal bovine serum and 1% penicillin / streptomycin / fungizone).

2D Wound Healing Assay:

Cells were plated in six-well tissue culture plates and cultured until confluence. Next, a 200 μ l pipette tip was used to scratch the cell monolayer. Brightfield images were taken every 2 – 4 hours and wound closure was computed using ImageJ. **Proliferation and Mechanosensation Assays:** 5, 10, and 55 kPa polyacrylamide gels were prepared as in [4]. Cells

were seeded on substrates for 24 hours and then incubated in Hoechst 33342 (nuclear stain), phalloidin (f-actin stain), and goat anti-YAP/TAZ (1:1000 in 1% BSA) or Click-iT EdU reagent (Proliferation) followed by confocal imaging. **Traction force microscopy (TFM):** 10 kPa gels polyacrylamide gels were prepared on glass coverslips and seeded with cells from the superficial or body zones. Phase and fluorescent microscopy was used to measure substrate displacement, followed by image analysis using a TFM plugin for ImageJ and a MATLAB code to generate traction force maps [5]. **Nanofibrous Scaffold Fabrication and Analysis:** Aligned poly(ϵ -caprolactone) (PCL) and polyethylene oxide (PEO) sheets were co-electrospun (40% PEO) and seeded with superficial or body cells as in [6]. Constructs were cultured for 12 weeks in basal media supplemented with Transforming Growth Factor Beta-3 (10ng/mL), changed three times weekly. On weeks 3, 6, and 12, constructs were mechanically tested in uniaxial tension, and the tensile modulus and yield strain calculated. Additional scaffolds were fixed, cyrosectioned (10 μ m), and stained Picrosirius red or Alcian Blue. Additional scaffolds were digested and assessed for collagen and proteoglycan content [6]. Statistics: Fig 2: t-test, Fig 3, 4, 5B: ANOVA.

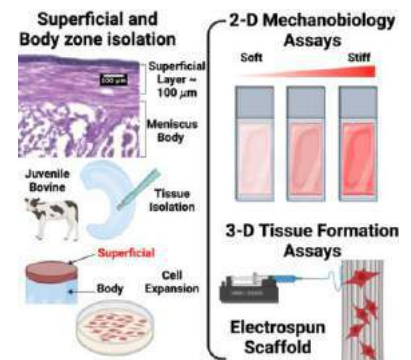


Figure 1: Experimental Layout

RESULTS

Scratch assay results showed that superficial cells migrated faster than body cells (**Figure 2A**). 36 hours after the scratch wound, superficial cells completely closed the gap, whereas the wound remained ~50% open for body cells. TFM analysis showed that superficial cells had a smaller cell area than body cells, and that the total force exerted by superficial cells was lower than that of body cells (**Figure 2B**).

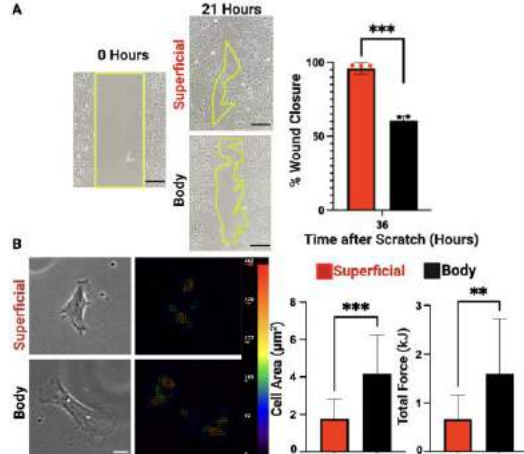


Figure 2: 2D Migration Assay and Traction Force Microscopy. A) Superficial cells closed the wound faster than cells from the body of the meniscus. Sample number: 5 per group, B) Superficial cells had a smaller area and generated less force than body cells.

*** $p < 0.001$, ** $p < 0.01$. Scale bars: A) 150 μm , B) 10 μm .

When placed on substrates of differing stiffness, superficial layer cells showed differences in mechano-response (**Figure 3A**). Specifically, superficial cells had a decreased level of nuclear YAP/TAZ across all substrate stiffnesses, in comparison to body cells. This indicated that superficial were not as responsive to substrate stiffness as body cells. Superficial cells also showed a higher proliferation rate across all substrate stiffnesses (**Figure 3B**). Notably, superficial cells were highly proliferative, even on softer substrates (5 and 10 kPa).

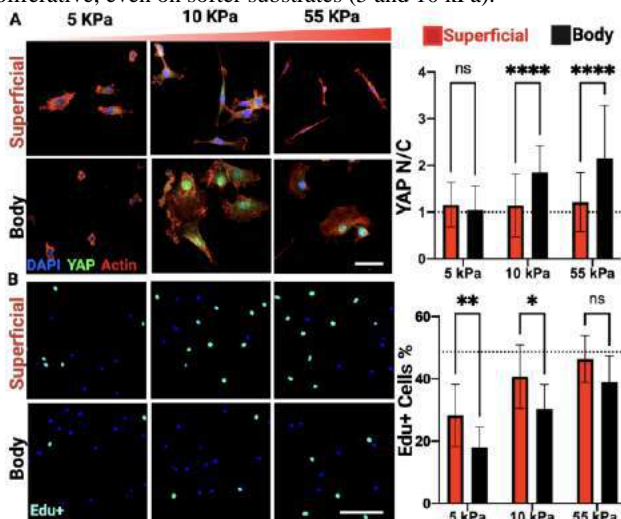


Figure 3: Response to Substrate Stiffness. A) Superficial cells showed no change in nuclear YAP with an increase in stiffness, unlike cells of the meniscus body. B) Superficial cells proliferated more at a lower stiffness (5 kPa) compared to body cells. Dashed line: % Edu+ cells on glass, N/C: Nuclear/Cytoplasmic ratio, sample number: 5 per group, **** $p < 0.0001$, ** $p < 0.01$, * $p < 0.1$.

Scale bars: A) 150 μm B) 150 μm .

When seeded in nanofibrous scaffolds and subjected to long-term culture, analysis showed that superficial cells produced a similar amount of collagen as body cells (**Figure 4A**). Proteoglycan (GAG) assessment showed that constructs seeded with body cells produced more proteoglycans by week 12 in culture than those seeded with superficial cells (**Figure 4B**). Superficial- and body-cell seeded constructs increased in tensile moduli and yield strains as a function of time in culture and were not different from one another (**Figure 4C**).

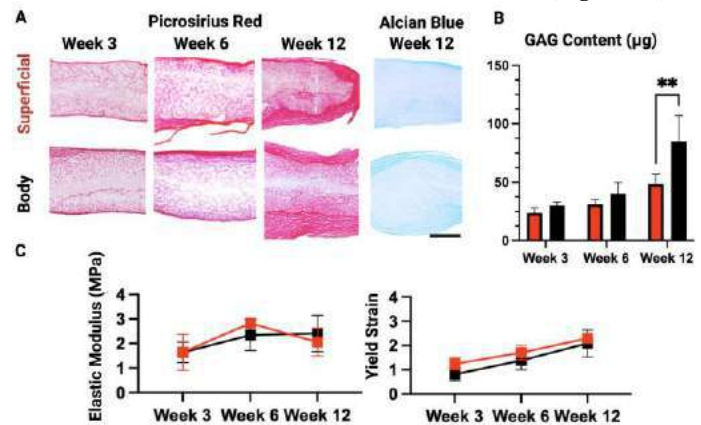


Figure 4: Histology and Mechanical Properties of Cell-Seeded Scaffolds. A) Histological images and B) GAG content of constructs at 3, 6, and 12 weeks. C) Elastic modulus and yield strain of constructs (n=4). ** $p < 0.01$. Scale bar: A) 500 μm .

DISCUSSION

This study highlights that superficial cells are less mechanosensitive and exert less force/cell on their surrounding ECM. This, coupled with their higher proliferative potential (compared to body cells) may explain their superior performance in the 2D wound closure assay. In the context of wound repair, the finding that superficial cells proliferate more, even in softer environments, may explain why these cells colonize meniscus injury sites faster than cells from the body. Interestingly, when these superficial cells were placed in a 3D context, they produced functional tissue, with mechanical properties that were similar to scaffolds seeded with body cells. These findings indicate that, despite their decreased response to change in substrate stiffness and lower traction forces, superficial cells are able to produce functional tissue. In the setting of tissue repair, this may suggest that superficial zone cells can be functional contributors to new tissue formation. However, supplemental scaffolds and factors at the site of tissue repair that can direct the organization of ECM produced by these superficial cells may improve repair outcomes. Taken together, these results establish the regenerative potential of superficial meniscus cells and direct future tissue engineering and drug delivery approaches to harness their full potential for functional meniscus repair.

ACKNOWLEDGEMENTS

This work was supported by the NIH/NIAMS (R01 AR075418, R01 AR056624, P30 AR069619).

REFERENCES

- [1] Wei Y. et al., *eLife*, 10:62917, 2021.
- [2] Doral M. et al., *EFORT*, 5:260-268, 2018.
- [3] Arnoczky S. et al., *Arthroscopy*, 33:278-283, 2017.
- [4] Assi S. et al., *ORS*, 2022.
- [5] Bonnevie E. et al., *SciRep*, 11:5950, 2021.
- [6] Baker B. et al., *Biomaterials*, 29(15), 2348-2358, 2017.

LEARNING DFFEOMORPHIC DEFORMATIONS FOR WHOLE HEART MESH GENERATION

Arjun Narayanan¹, Fanwei Kong², Shawn C. Shadden¹

¹Department of Mechanical Engineering, University of California Berkeley, Berkeley, California, USA.

²Department of Pediatrics, Stanford University, Stanford, California, USA.

INTRODUCTION

Image-based computer modeling is playing an increasing role in understanding the mechanisms of cardiac disease and personalized care.¹ Broadly, this paradigm uses medical imaging (CT or MR) to construct an anatomically accurate computer model of the heart in order to mathematically model physiological processes and probe functional information. Reconstructing an accurate, personalized computer model of the heart is challenging because of imaging artifacts, limited resolution and difficulty differentiating between cardiac and surrounding tissues.

Segmentation is the process of identifying structures of interest in an image. Machine learning has been utilized to automate segmentation of cardiac structures from CT or MR images.² However, segmentation often generates artifacts that are unfit for simulation-based modeling. Recently, we have developed alternative template based deep-learning methods that are able to generate simulation-ready computer models of cardiac structures automatically from cardiac images.³ However, these are mostly surface models of the blood pool boundaries since only these boundaries can be discerned from clinical imaging. Developing models wherein *tissue thickness* is assigned to all cardiac structures has remained challenging since most tissues are too thin to be accurately discerned.

We present here a deep learning method to produce whole-heart meshes with tissue thickness from clinical image data. We employ a template-based method to ensure accurate, simulation compatible models. Briefly, we use deep learning to deform a template mesh using a combination of linear-transformations and diffeomorphic flow deformations.⁴ We present a novel physics-informed loss term that penalizes vanishing volumes thereby preventing self-penetrations in thin walled structures. The model can be trained on data containing no thickness information and subsequently evaluated on a template with thickness. We demonstrate that this approach is able to successfully deform this new template in a realistic manner without interpenetration. The predictions of our model can be readily used to generate full 3D tetrahedral meshes.

METHODS

Dataset information. We used the multi-modality whole heart segmentation challenge (MMWHS)² dataset. We split the

dataset into 16 CT and 16 MR samples for training and used the remaining 4 CT and 4 MR samples for validation. We augmented the training dataset by introducing small perturbations including random scaling, translation, rotation, shear and local b-spline deformations to produce a final dataset size of 1920 samples.

Neural network architecture. We observed a large difference in scale and position across the data-set. This can be attributed to the different field-of-view in the image samples along with inter-patient variations. Hence, our framework consists of two modules (1) a 3D convolutional neural network (CNN) that performs a linear transformation on the template, and (2) a 3D Unet that learns to deform the template by integrating mesh vertices along a diffeomorphic flow vector field. The linear transformation is effective at scaling and positioning the template, and the flow deformation captures the finer details. For memory reasons the modules are trained separately. We use a weighted sum of the 2-way chamfer distance and geometrical regularizations such as normal consistency, mesh edge loss, and laplace loss as objective. We introduce a novel physics-informed loss term that penalizes vanishing volumes. A reference volume V_0 at time t_0 evolves to a volume V_1 at time t_1 in a flow vector field f as,

$$\frac{V_0}{V_1} = \exp \left(- \int_{t_0}^{t_1} \text{div}(f) dt \right) \quad (1)$$

If a finite initial volume V_0 collapses to an infinitesimal volume V_1 after deformation, equation 1 evaluates to a very large value. We incorporate this term into the objective function to discourage collapsing volumes. The divergence of the flow field is computed using a central finite difference scheme. Fig. 1 shows a schematic of our network architecture.

RESULTS

Dice scores. We use 4 CT and 4 MR samples from the MMWHS training data for validation. The predicted final meshes are converted to segmentations. We compute the dice score between predicted and ground truth segmentations which is presented in Table 1. The predictions of our model for a typical validation sample are shown in Fig. 2.

Self-intersections. We measured self-intersections using PyMesh. The predicted final meshes contained *zero* self-intersections within cardiac structures. For the predictions to

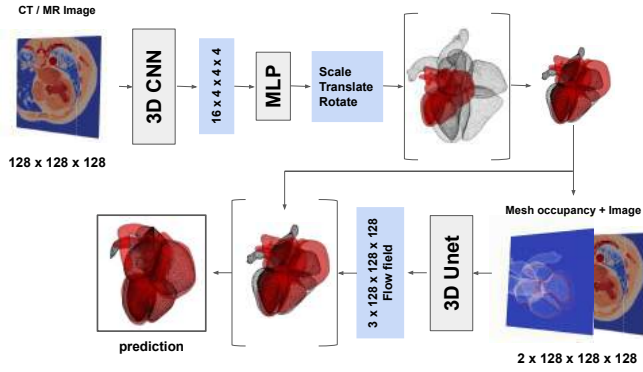


Figure 1: 128^3 input image processed by 3D CNN to produce 4×16^3 encoding. Linear network predicts 3 scale, 3 translate, and 3 rotate parameters from encoding to transform the template mesh. Transformed vertices embedded in an occupancy map and passed with image as input to 3D Unet which generates 3D flow vector field. Vertices are integrated along flow field to produce final prediction.

Table 1: Median and minimum dice scores on validation data for the converged model.

Cardiac structure	CT		MR	
	Median	Min	Median	Min
Myo	0.83	0.78	0.80	0.72
LA	0.91	0.87	0.83	0.75
LV	0.91	0.82	0.94	0.88
RA	0.89	0.86	0.84	0.76
RV	0.90	0.85	0.89	0.85
Ao	0.94	0.86	0.83	0.70
PA	0.73	0.63	0.70	0.10

be intersection-free it is important that the initial template is also intersection-free.

Patient-specific myocardium. An advantage of our framework is that once the network is trained, different templates can be used without re-training. For example, Fig. 3(a) shows a myocardium template that was produced by fusing the myocardium mesh with parts of the left atria and aorta and adding thickness to these openings. It is important that these regions have thickness because (a) they are used for solid modeling in FSI simulations (b) we apply boundary conditions on these surfaces. Note that this template contains about 47k triangular faces which is significantly more than the template used for training. Fig. 3(b) shows a patient-specific prediction for a model trained without the loss term eq. 1. This model collapses the thickness of the mitral and aortic tissue into an unphysical thin surface. It is not possible to generate a 3D volumetric mesh from such a surface mesh. The worst case predicted mesh contained 234 self-intersecting faces. Fig. 3(c) shows a patient-specific prediction for a model trained with the loss term eq. 1. This model preserves the thickness of the mitral and aortic openings. The worst case predicted mesh contained 8 self-intersecting faces which is a 97% improvement. The remaining self-intersections can be readily eliminated by running a constrained smoothing algorithm. Subsequently, we were able to generate full 3D tetrahedral meshes from these surface

meshes.

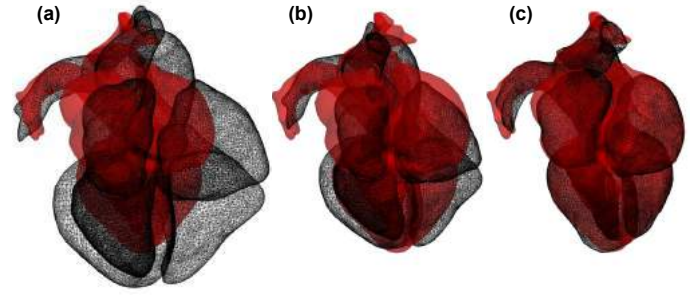


Figure 2: Predictions of the model for a typical validation sample. Red surface is the ground truth and black wireframe is the template. (a) Undeformed initial template (b) after linear transformation (c) after flow deformation. The final average dice score was 0.86 for this sample.

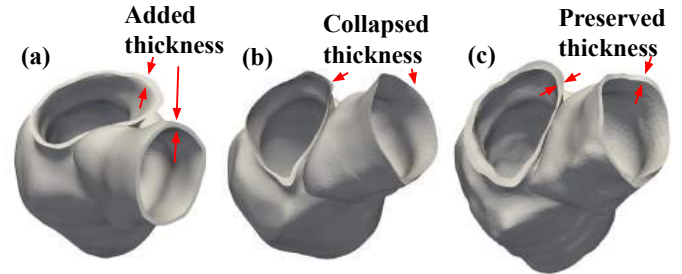


Figure 3: (a) Initial myocardium template with added thickness for mitral and aortic openings (b) prediction of model trained without divergence loss collapses thin walls resulting in self-intersections (c) prediction of model with divergence loss preserves thickness.

DISCUSSION

We have developed an automated deep learning method for generating patient-specific meshes of the human heart directly from biomedical images. These meshes are anatomically accurate and physically realistic. We presented a novel physics-informed loss term that penalizes collapsing volumes. This enables us to represent cardiac structures with tissue thickness even when this information is missing in the image data. Our predictions are almost entirely free of self-intersections, and the few that remain can be fixed by simple smoothing procedures. Our model predictions can be used to generate full 3D tetrahedral meshes with tissue thickness. We hope to soon present results of our model trained on a larger training dataset, provide detailed comparisons of our results against prior state of the art, and utilization of this method to applications of cardiac physiology simulation.

ACKNOWLEDGMENTS

This work was supported by NSF Award 1663671.

REFERENCES

- [1] Prakosa et al. In: *Nature Biomed Eng.* 2.10 (2018), pp. 732–740.
- [2] Zhuang et al. In: *Med Image Analysis* 58 (2019), p. 101537.
- [3] Kong et al. In: *Med Image Analysis* 74 (2021), p. 102222.
- [4] Lebrat et al. In: *NeurIPS* 34 (2021), pp. 29491–29505.

TEMPORAL AND SPATIAL DYNAMICS OF NEW BONE FORMATION IN CYCLIC TREATMENT REGIMENS OF PARATHYROID HORMONE-RELATED PEPTIDE (PTHrP)

Tala Azar (1), Kruti Desai (1), Justin Leggin (1), Yuanhang Li (1), Wenzheng Wang (1), Arie Jones, (1), Wei-Ju Tseng (1), Nathaniel Dyment (1), X. Sherry Liu (1)

(1) McKay Orthopaedic Research Laboratory
University of Pennsylvania
Philadelphia, PA, United States

INTRODUCTION

Anabolic agents, such as PTH and PTHrP, rapidly promote new bone formation and improve bone mass but are initially administered for only up to 24 months of combined use in a patient's lifetime. Interestingly, our recent *in vivo* micro computed tomography (μ CT) and histomorphometry studies in ovariectomized (OVX) rats demonstrated an extended anabolic period (EAP) during the first week of PTH/PTHrP discontinuation, where alkaline phosphatase activity by osteoblasts was found on over 60% of newly formed bone surfaces, resulting in continuous mineral deposition and an increased bone volume fraction (BV/TV) [1,2]. These data support the use of a cyclic treatment regimen to improve the efficacy of existing anabolic treatments. However, by testing a cyclic PTH-vehicle (VEH) treatment regimen (3-week PTH, 3-week VEH, repeat for 3 cycles) in OVX rats, we found that the EAP was not enough to fully prevent PTH discontinuation-induced bone loss by the end of an off-PTH cycle [1]. Indeed, a histomorphometry study indicated that after 1 week of discontinuation from PTH/PTHrP, BV/TV began to decrease and TRAP activity by osteoclasts over newly formed bone surfaces increased from 8% in week 1 to 71% in week 3 [2]. This supports the addition of an antiresorptive during the off-PTH/PTHrP cycle to inhibit bone resorption during the off-treatment period. Furthermore, we hypothesized that a cyclic treatment regimen is able to activate new bone formation sites on quiescent surfaces with each new anabolic cycle. To test these hypotheses, we investigated the dynamics of new bone formation and changes in trabecular bone microstructure in cyclic treatment regimens of alternating PTHrP and either VEH or alendronate (ALN, an antiresorptive agent), and a standard PTHrP treatment regimen followed by ALN. We hypothesized that the cyclic PTHrP-ALN treatment regimen would yield the greatest new bone formation and bone microstructure.

METHODS

Animal protocol and treatment: All animal experiments were IACUC approved. Female Sprague-Dawley (SD) rats received bilateral ovariectomy (OVX) surgery at 4 months of age to simulate post-menopause estrogen deficiency and developed osteopenia for 4 weeks. For histomorphometry (n=6/group), rats underwent either two cycles of 3 wk PTHrP followed by 3 wk VEH (CPV), 3 wk PTHrP followed by 3 wk ALN (CPA), or 6 wk PTHrP followed by 6 wk ALN (Standard PTHrP-ALN, SPA). For μ CT (n=8-9/group), three cycles of treatments were performed for a total of 18 wks and the SPA group received 9 wk PTHrP followed by 9 wk ALN. PTHrP (PTHrP 1-34, 20 μ g/kg/day for histomorphometry, 40 μ g/kg/day for μ CT) and saline (VEH) were administered 5x/wk, and ALN (28 μ g/kg/day) was administered 2x/wk. Histomorphometry: Fluorochrome labels of calcein green (G), alizarin complexone (red/R), and tetracycline (yellow/Y) were injected in the sequence of G-G-R-R-Y at wks 0, 3, 6, 9, and 12 (Fig.1A). Two 8 μ m-thick, undecalcified cryosections were obtained from the left proximal tibia and imaged with darkfield and a fluorescent microscope to capture trabecular structure and multi-color fluorochrome labels. A 1.5 mm-thick region of the metaphysis from each section was analyzed by OsteoMeasure to assess mineralizing surface (MS/BS), mineral apposition rate (MAR), and bone formation rate divided by bone surface (BFR/BS) for each double label. Total new bone formation from all double label periods was also quantified. μ CT: For longitudinal analysis, a 4-mm region of the proximal tibia was scanned at 10.5 μ m voxel size using *in vivo* μ CT (Scanco vivaCT40) at wks 0, 3, 6, 9, 12, 15, and 18. Bone volume fraction (BV/TV) and trabecular thickness (Tb.Th) were obtained. Statistics: A one-way ANOVA or Student's t-tests were used to compare histomorphometry groups. A two-way, repeated measures ANOVA was used to compare μ CT treatment groups over time.

RESULTS

Histomorphometry (Fig. 1B-P): Throughout two cycles of treatment, various double labels were observed: mineralization during PTHrP treatment of cycle 1 (C1-ON, G to G) and cycle 2 (C2-ON, R to R) of PTHrP, as well as the off anabolic periods of C1 (C1-OFF, 2nd G to 1st R) and C2 (C2-OFF, 2nd R to Y). Most C2-ON sites mineralized on existing C1-ON sites, as C2-ON sites that did not form on or adjacent to existing C1-ON sites only accounted for 2% of C2-ON sites. MS/BS and BFR/BS for C1-ON were 64% and 77% greater in CPA vs. CPV, indicating that ALN minimized resorption of C1-ON sites during the PTHrP-OFF cycle. C2-ON MS/BS, MAR, and BFR/BS were 32%, 51%, and 95% higher in CPV vs. CPA, respectively. During C1-OFF, MAR and BFR/BS trended towards a 110% and 187% greater difference in CPV vs. CPA, respectively. There was minimal but non-zero C2-OFF bone formation activity for CPV, but none during C2-OFF was detected in CPA. These data suggest that ALN blunted bone formation during C2-ON and the off anabolic periods. For histomorphometry groups, BV/TV was not different between CPA and SPA or CPV and SPA but was 47% greater in CPA vs. CPV. SPA gained 36% more total new bone than CPV and there was no difference between that of CPA and SPA. Therefore, CPA and SPA resulted in the greatest bone gain.

In vivo μ CT (Fig. 2A-B): By wk 18 in CPA and SPA, BV/TV was 119% and 109% greater and 92% and 107% greater for Tb.Th compared to baseline, respectively. For CPV, although Tb.Th still increased by 76%, BV/TV decreased by 20% at wk 18 compared to baseline. Adding ALN during the off anabolic periods in CPA vs. CPV minimized discontinuation-induced bone loss and resulted in a 21-138% greater BV/TV and a 9-16% greater Tb.Th during wks 6, 9, 12, 15, and 18.

DISCUSSION

This study elucidated how new bone is formed and maintained during cyclic treatment regimens of PTHrP with and without an antiresorptive. We originally hypothesized that an additional cycle of PTHrP would activate new bone formation sites on quiescent bone surfaces. Surprisingly, most of the new bone formation during C2-ON occurred on existing mineralizing sites activated during C1-ON, regardless of treatment during the off-PTHrP period.

Without the addition of ALN, there is a greater withdrawal effect in both histomorphometry and μ CT groups, supporting our hypothesis that adding ALN between cyclic anabolic treatments helps minimize the withdrawal effect and maintains newly formed bone. However, the finding that ALN may blunt new bone formation during the EAP and into the next PTHrP cycle contradicts our original hypothesis. Since resorption of newly formed bone occurs in CPV following C1-ON and C2-ON [1, 2], we expected more bone formation observed in the anabolic periods of CPA vs. CPV groups. However, greater new bone formation parameters in CPV vs. CPA during C2-ON suggest that ALN may have blunted the effect of PTHrP in the second anabolic period. There may also be a blunting effect in the CPA group for μ CT, however, we only observe a net increase at the end of the 3 wk anabolic periods.

Considering complete treatment cycles, SPA and CPA resulted in a similar BV/TV, suggesting that a CPA regimen can yield similar results as a SPA regimen with the added benefit of extending the duration of active bone formation under anabolic treatments. We conclude that the timeline of different cyclic treatment regimens of an anabolic agent and an antiresorptive need to be further explored to account for the blunting effect of ALN while still minimizing bone loss upon discontinuation of an anabolic agent.

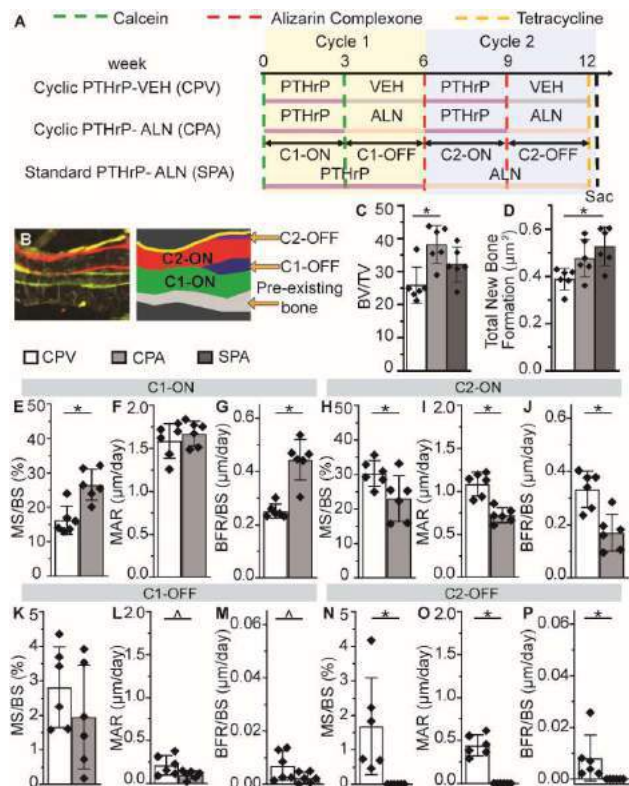


Figure 1: (A) Histomorphometry study design. (B) Schematic of the four double-label areas on top of pre-existing bone. (C) Bone volume fraction (BV/TV) and (D) total new bone formed. MS/BS, MAR, and BFR/BS for C1-ON (E-G), C2-ON (H-J), C1-OFF (K-M), and C2-OFF (N-P). *: $p < 0.05$ and ^: $p < 0.1$.

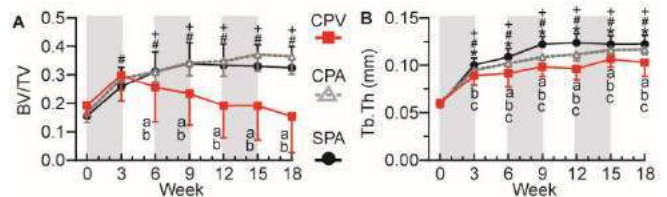


Figure 2: Changes in tibial trabecular microstructure measurements for (A) bone volume fraction (BV/TV) and (B) trabecular thickness (Tb.Th) in all groups during three cycles of treatment. Gray shadows indicate PTHrP treatment in the cyclic groups. “a” indicates a significant difference between CPV and CPA groups. “b” indicates a significant difference between CPV and SPA groups. “c” indicates a significant difference between CPA and SPA groups. *, #, and + indicate a significant difference from wk 0 in CPV, CPA, and SPA groups, respectively.

ACKNOWLEDGEMENTS

NIH/NIAMS R01-AR077598, Penn Center for Musculoskeletal Disorders (P30-AR069619), and 5-T32-AR007132.

REFERENCES

- [1] Tseng, W et al., *J Bone Miner Res*, 37(4):616-28, 2022.
- [2] Wang, W et al., *J Bone Miner Res*, 37(11):2215-25, 2022.

EFFECTS OF GAGS ON MICROSTRUCTURE OF CORNEAL EXTRACELLULAR MATRIX

M.E. Emu (1), H. Hatami-Marbini (1,2,3)

- (1) Mechanical and Industrial Engineering, University of Illinois at Chicago, Chicago, IL USA
(2) Biomedical Engineering, University of Illinois at Chicago, Chicago, IL USA
(3) Civil, Materials & Environmental Engineering, University of Illinois at Chicago, Chicago, IL USA
Email: hatami@uic.edu

INTRODUCTION

The cornea is a transparent tissue with precise curvature that contributes significantly to the total refractive power of the eye while protecting the delicate internal components of the eye. The cornea consists of several different layers, among them corneal stroma accounts for 90% of total corneal thickness. The stroma consists of several hundreds of collagen lamellar layers containing regularly organized collagen fibrils [1,2]. The precise spacing of collagen fibrils in the corneal stroma is believed to be maintained by proteoglycans (PGs) that exist in between and around the collagen fibers [3]. PGs are composed of a core protein to which glycosaminoglycan (GAG) side chains are attached. Our recent studies have shown that PGs and their GAG side chains are one of the microstructural elements of the cornea that play a role in providing strength to the cornea. The present study investigates their effects on corneal microstructure and arrangement of collagen fibers in corneal stroma.

The imaging techniques such as transmission electron microscopy (TEM) and X-ray scattering technique have been used to study the collagen fibril diameter and interfibrillar spacing of the corneal stroma. For example, Hayes et al. quantified collagen fibril diameter and interfibrillar spacing of porcine cornea using the X-ray scattering technique [4]. The second-harmonic-generated (SHG) images have also been used to show the nearly orthogonal corneal collagen organization [5]. The electron microscopy of bovine corneal tissue revealed the arrangement of PGs around the collagen fibrils, suggesting that they are important for highly regular corneal collagen fibril spatial order, Fig. 1 [6]. Here, we removed enzymatically keratan sulfate (KS) GAGs from the cornea and used TEM to characterize their effects on collagen fibril diameter and interfibrillar spacing of porcine cornea.

METHODS

The excess muscles were removed from porcine eye globes by a sharp scissor. Then, a scalpel and scissors were used to prepare corneal

samples with a 2 mm scleral ring from eyeballs. Corneal strips of about 5 mm width were cut in the nasal-temporal direction using a custom-made double bladed device. The strips were divided into control and enzyme treated groups. In order to remove KS GAGs from corneal strips in the enzyme treated group, they were first dried completely in a desiccator. The dried corneal strips were then kept in a container filled with 0.1M sodium acetate buffer and 0.1 U/ml keratanase II enzyme at pH of 6.0 for 18 hours at 37°C. The success of this method of removing KS GAGs from the corneal strips was previously shown by performing biochemical and histological studies using Blyscan assays and Alcian blue staining [7].

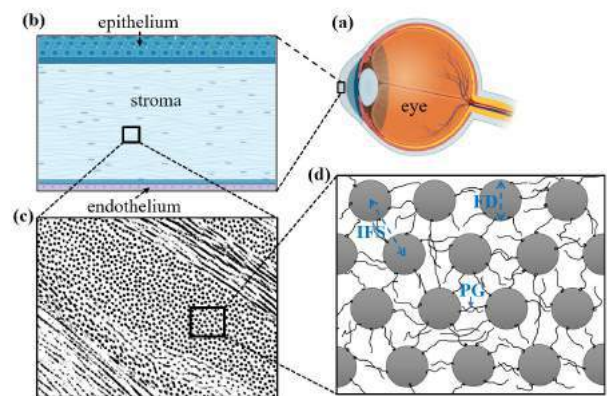


Figure 1: Schematic of the (a) eyeball, (b) corneal stroma, and (c, d) ultrastructural features of the corneal stroma. IFS and FD indicate interfibrillar spacing and collagen fibril diameter, respectively.

For TEM studies, small blocks excised from each corneal strip were fixed in 2.5% phosphate-buffered (0.1M) glutaraldehyde. The specimens were washed in 0.1M Sorensen's sodium phosphate buffer (SPB, pH 7.2) and were then fixed in buffered 1% osmium tetroxide to

sharpen the contrast of the ultrastructure. After further processing, the 70 to 80 nm thick sections were cut using an ultra-microtome (Leica Ultracut UCT model). The ultra-thin sections were collected onto 200-mesh copper grids and contrasted with 6% uranyl acetate and Reynolds lead citrate stains. The grids were dried, inserted into the specimen holder, and were examined using a JEOL JEM-1400 Flash transmission electron microscope (operating at 80 kV). Several images were captured around the viewing area. The image analysis was performed using the open-source software Image J. Two-way ANOVA and t-test were performed to find any significant difference between the results. A p-value less than 0.05 was considered statistically significant.

RESULTS

The ultrastructural features were shown for typical control and enzyme-treated specimens in Fig. 2. The hexagonal arrangement of the collagen fibrils (CF) was visible in the images. The dark clouds situated in the interfibrillar spacing between collagen fibrils were considered as PGs. The PG clouds appeared significantly reduced in the enzyme-treated specimens (Fig. 2c-d), which was because KS GAGs were removed from these specimens. The collagen fibrils appeared to be hexagonally arranged in the control samples (Fig. 2a) whereas hexagonal patterns seemed to collapse in images obtained for enzyme-treated specimens (Fig. 2c-d).

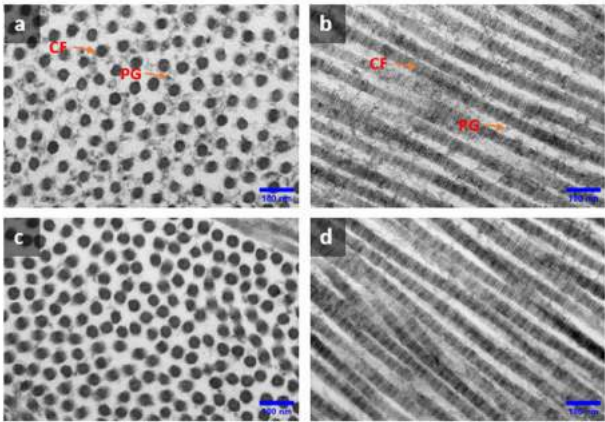


Figure 2: Electron micrographs of control (a and b) and enzyme-treated (c and d) corneal samples. Collagen fibrils (CF) and proteoglycan (PGs) are shown by arrows. (a) and (c) represent transverse direction fibrils whereas (b) and (d) represent longitudinal direction fibrils. The enzyme-treated specimens showed significant PG reduction.

Using TEM images (Fig. 2), the collagen fibril diameter and interfibrillar spacing for both control and enzyme-treated specimens were quantified, Table 1. No significant difference was observed in the fibril diameter (FD) of the control and enzyme treated samples but the interfibrillar spacing (IFS) increased significantly in the enzyme-treated specimens ($P < 0.05$).

Table 1: The collagen fibril diameter and interfibrillar spacing of each specimen group.

group	Fibril Diameter (nm)	Interfibrillar Spacing (nm)
Control	34.77 ± 1.66	54.28 ± 0.23
Enzyme-treated	35.85 ± 1.26	57.71 ± 1.94

DISCUSSION

The main goal of this study was to reveal the porcine corneal ultrastructure and the quantitative analysis of the effect of KS GAG removal using transmission electron microscopy. The TEM images

showed that the mean collagen fibril diameters were 34.77±1.66 nm and 35.85±1.26 nm in control and enzyme-treated specimens, respectively. The previous X-ray scattering measurements gave the collagen fibril diameter of 35.7±0.6 nm for control porcine cornea, which agrees very well with the present measurements using TEM [4]. The slight differences could be because of different measuring techniques and intrinsic difference in the specimens. The quantified values presented in Table 1 imply that the keratanase enzymatic digestion did not affect collagen fibril diameter, i.e. we did not observe a significant difference in fibril diameter (FD) of two specimen groups.

Similar to the collagen fibril diameter, the interfibrillar spacing (IFS) of control specimens of the present work was in agreement with previous studies. The IFS in enzyme-treated specimens significantly increased compared to that of the control specimens. Furthermore, the collagen fibrillar arrangement showed slight distortion in enzyme-treated specimens compared to control samples, Fig. 2. The enzyme treatment significantly reduced GAG content in enzyme treated group, Fig. 2c-d. GAGs work as structural elements and binders connecting neighboring collagen fibrils [1-2, 7]. Since GAG density was reduced in the enzyme-treated specimen, the collagen fibrils move away from each other causing the IFS to increase.

The present study had a number of limitations. First, we used a limited number of samples for each group. However, we took extra precautions during dissection, fixation, and all other steps to ensure the accuracy of the results, which was confirmed by comparing our data with previous studies. Another limitation of our work was that Cuprolineic Blue stain was not used to enhance the contrast of PGs. Using Cuprolineic Blue during the fixation process could allow better visualization of PGs between collagen fibrils. However, the absence of dark cloud in enzyme treated samples, seen here, was because of removing GAGs from samples. The present work provided valuable and novel data for the influence of KS GAGs on corneal microstructure and can be used to interpret and explain the changes in mechanical response of GAG depleted samples. Furthermore, the crosslink group may be included in future studies to identify any role of PGs visually and quantitatively in crosslink treatment.

ACKNOWLEDGEMENTS

The authors acknowledges the support in part from NIH-EY030264.

REFERENCES

1. Maurice D.M. The structure and transparency of the cornea. J. Physiol. 1957;136: 263–286.
2. Cheng, X., Hatami-Marbini, H., Pinsky, P.M. Modeling Collagen-Proteoglycan Structural Interactions in the Human Cornea. In: Holzapfel, G., Kuhl, E. (eds) Computer Models in Biomechanics. Springer, Dordrecht. 2013, 11-24.
3. Meek, K.M., Corneal collagen-its role in maintaining corneal shape and transparency. Biophys Rev, 2009. 1(2): 83-93.
4. Hayes, S., et al., The effect of riboflavin/UVA collagen cross-linking therapy on the structure and hydrodynamic behaviour of the ungulate and rabbit corneal stroma. PLoS One, 2013. 8(1): p. e52860.
5. Winkler, M, et al., A Comparative Study of Vertebrate Corneal Structure: The Evolution of a Refractive Lens. Invest. Ophthalmol. Vis. Sci. 2015; 56(4):2764-2772
6. Lewis, PN, Pinali C, Young RD, Meek KM, Quantock AJ, Knupp C. Structural interactions between collagen and proteoglycans are elucidated by three-dimensional electron tomography of bovine cornea. Structure. 2010, 18(2):239-45.
7. Hatami-Marbini, H. On mechanical roles of Glycosaminoglycans in tensile properties of the porcine corneal stroma, Invest. Ophthalmol. Vis. Sci., accepted

COMPUTATIONAL FLUID DYNAMICS SIMULATIONS OF AORTIC DISSECTION USING IMMERSED BOUNDARY METHOD

**Gokul G. Anugrah (1), Sam Tyagi (2), Mary B. Sheppard (2,3),
Christoph Brehm (4), Jonathan F. Wenk (1,2)**

- (1) Department of Mechanical Engineering, University of Kentucky, Lexington, KY, USA
(2) Department of Surgery, University of Kentucky, Lexington, KY, USA
(3) Department of Family Medicine, University of Kentucky, Lexington, KY, USA
(4) Department of Aerospace Engineering, University of Maryland, College Park, MD, USA

INTRODUCTION

The mortality and morbidity rate of patients with Aortic Dissection (AD) in the United States has been on a steep rise since 2012 [1]. This could be attributed to the lack of proper diagnostic criteria and our inadequate knowledge about the progression of the disease. It has been shown recently that AD could be predicted from the vortex flow pattern in the ascending aorta and the consequent changes in Time Averaged Wall Shear Stress (TAWSS) and Oscillatory Shear Index (OSI) [2]. The current standard of care among clinicians for deciding on a surgical intervention is based on the size of the aorta. If the diameter of the artery is larger than a threshold value (usually 5-5.5 cm), the condition is severe [3]. This is based on a crude approximation using Laplace's law, where the hoop stress (or the circumferential stress on the artery wall) is given as

$$P_{\theta\theta} = \frac{PD}{2t} \quad (1)$$

Where P is the pressure inside the artery, D is the diameter and t is the thickness of the wall. It is clear from the equation above that for a given blood pressure and thickness of the artery wall, the wall stress increases with an increase in diameter. However, more than sixty percent of AD occurs at a diameter less than 5 cm [4][5], which means this practice cannot be followed for a successful diagnosis of the disease.

Use of Computational Fluid Dynamics (CFD) for the simulation of flow inside human arteries is gaining popularity due to its capability of predicting the flow physics accurately inside the aorta without the involvement of any invasive methods. The current study focuses on the CFD simulation of patient-specific geometries of AD using the Immersed Boundary Method (IBM) [6]. We will demonstrate that this method could predict the velocity variation in the artery with good accuracy based on comparison to ultrasound data of the patients.

METHODS

Figure 1 shows the workflow that is adopted for the simulations. The CT scan data is pre-processed to attain the mesh using the open-source software, 3D slicer. The mesh is further cleaned using a commercial tool, STAR-CCM+. The CFD simulations are performed using an in-house code that solves the incompressible Navier-Stokes equations in three dimensions. The solver solves the mass conservation and momentum conservation equation using a fractional-step method on collocated grids [7]. The boundary conditions for the Navier-Stokes equations are obtained from the Duplex ultrasound data. The velocity data were fitted with polynomials, which are used as the inlet boundary condition and at the five outlets; pressure boundary conditions were prescribed based on a 3 element Windkessel model. In this model, the pressure (P) and flow rate (Q) are related by the equation

$$P = (R_1 + R_2)Q - R_2C \frac{dP}{dt} + R_1R_2C \frac{dQ}{dt} \quad (2)$$

In the equation, R_1 , R_2 and C are different parameters that are tuned to achieve the desired flow rate at the outlet. The ultrasound data is also used to compare the results from CFD.

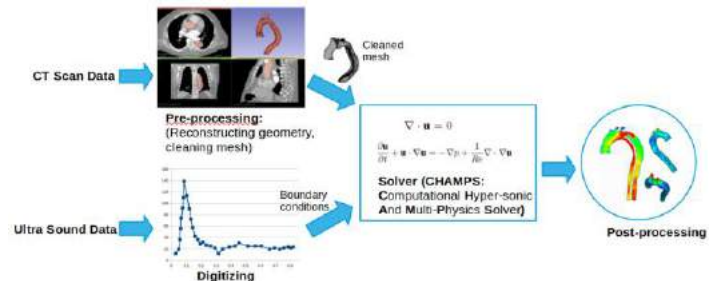


Figure 1: Process flow chart

The study protocol complies with the Declaration of Helsinki and was approved by the University of Kentucky Institutional Review Board and Ethics Committees.

RESULTS

Simulations were performed on the aorta of a patient with Stanford- type B dissection. A small entry tear is located at the arch of the aorta, approximately 2 cm away from the root of the left subclavian artery. The ultrasound scans show that there is a retrograde flow in the false lumen. The flow is directed towards the heart in the false lumen and away from the heart in the true lumen. For simulating this flow, the Windkessel model at the false lumen outlet is tuned in such a way that the flow is reversed. Figure 2 shows the variation of the velocity in z-direction (longitudinal from bottom to top) over the course of a complete cardiac cycle. The velocity peaks at systole (approximately 0.1 s) and the magnitudes of velocity are high everywhere in the artery. The direction of velocity is reversed in the false lumen during this phase. In addition to the major tear, there were some minor tears further downstream of the artery (near the pelvic region). These minor tears could be partially responsible for the retrograde flow.

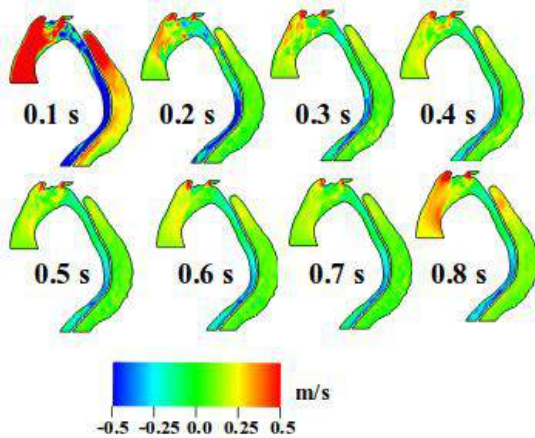


Figure 2: Cross-section view of aorta with z-component of velocity at different time points.

Figure 3 shows the comparison of velocity magnitude variation in the root of Common Carotid Artery (CCA) and Left Subclavian Artery (LSA) obtained from the ultrasound data with the CFD results. There is good agreement in the variation of velocity during the cardiac cycle. It should be noted that there are potential uncertainties in the ultrasound measurements, regarding the location and timing of the measurements. These could be a reason why there are minor variations in the comparison (especially in the diastolic phase).

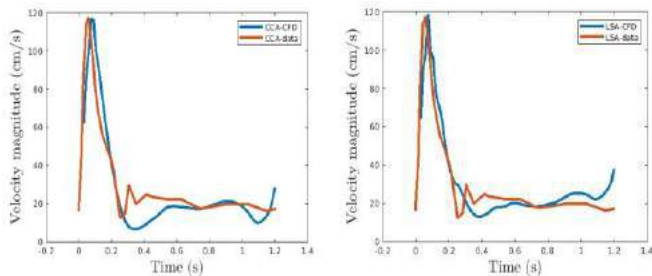


Figure 3: Velocity comparison at different branches of the aorta. Measurements were taken at the centerline of the artery.

TASS and OSI are metrics used for the prediction of occurrence and progression of several cardiovascular diseases, including AD. A high TAWSS at the wall near the dissection (Figure 4) could suggest that there is a good chance of progression of the disease as the tear could enlarge over the course of time due to high stress. The OSI values are observed to be relatively low in the true lumen as compared to the false lumen and this suggests that there is a large variation in the velocity field of the false lumen. This could also suggest that the flow is more turbulent in the false lumen. It has been reported that high OSI is associated with the production of reactive oxygen species in endothelial cells, which leads to injury of these cells. Although it is not certain what value of OSI would lead to a tear, it could be assumed that there is a higher probability of tear development in the places where there is abnormally large OSI.

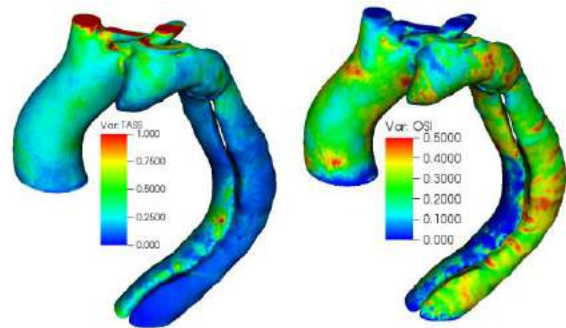


Figure 4: TAWSS and OSI

DISCUSSION

A significant advancement in performing CFD simulations using IBM for patient-specific models of AD is presented in the current study. Even though IBM was developed for studying blood flow simulations in the heart and arteries, earlier studies were limited to over simplified geometric models and boundary conditions. For example, the inlet boundary velocities were assumed to be that of a healthy artery and outlet pressures were assumed to be constant. These assumptions affect the accuracy of predicted velocity variation and shear stress development in the artery. In the current work, it is also shown that pressure values close to physiological (for example, 80 to 120 mm Hg) could also be achieved in the simulations. A well-defined and reliable protocol is established through this study that could be used for clinical decision making. The major limitation in the current study is the use of rigid wall for the simulations. Even though the rigid wall assumption could be made for the arterial wall and obtain reliable wall shear stresses for a healthy artery, studying the role of flap (that separates true and false lumen) is a big challenge. For this, Fluid Structure Interaction (FSI) would be performed in the future.

ACKNOWLEDGEMENTS

The authors would like to thank the Gill Heart and Vascular Institute for providing the patient-specific data and the Center for Computational Sciences at the University of Kentucky for the computing time for performing the simulations pertinent to this study.

REFERENCES

- [1] Nazir, S et al., *J of the American Heart Association*, 11(7), 2022
- [2] Hohri, Y et al., *European J of Cardio-thoracic Surgery*, 60(2):384-391, 2021
- [3] Karachaliou, GA et al., *Physics of fluids*, 33(11):1-8, 2021
- [4] Pape, LA et al., *Circulation*, 116(10):1120-1127, 2007
- [5] Parish, L. M. et al., *European J of Cardio-thoracic Surgery*. 35 2009
- [6] Peskin, C et al., *J of Computational Physics*, 25(3):220-252, 1977
- [7] Kim, J. et al., *J of Computational Physics*, 59(2):308-323, 1985

MULTISCALE MODELING OF MYOFIBER DISARRAY IN THE LEFT VENTRICLE USING A STRESS-BASED REORIENTATION LAW

**Mohammad Mehri (1), Charles K. Mann (1), Hossein Sharifi (1),
Kenneth S. Campbell (2), Jonathan F. Wenk (1,3)**

(1) Department of Mechanical Engineering
University of Kentucky
Lexington, KY, USA

(2) Department of Physiology & Division of
Cardiovascular Medicine
University of Kentucky
Lexington, KY, USA

(3) Department of Surgery
University of Kentucky
Lexington, KY, USA

INTRODUCTION

The effect of myofiber architecture on cardiac muscle mechanics has a direct impact on global pumping performance. In a healthy heart, muscle myofibers are transmurally arranged in parallel with helical angles ranging from $\sim +60$ degrees at the endocardium to ~ -60 degrees at the epicardium. However, abnormal helical angles of myofibers can lead to a deterioration in cardiac performance. [1]

Myofiber disarray is one type of adverse remodeling, which is characterized by disorganized cardiomyocyte spatial distributions. Cellular level heterogeneity in cardiac muscle (material properties and contractile behavior) can lead to myofiber disarray. “Replacement fibrosis” is an example of a heterogeneous change (stiffening) in muscle material properties, which is a collagen-based healing mechanism observed, but not limited to hypertrophic cardiomyopathy (HCM) [2].

In this study, we have developed a myofiber remodeling approach (Figure 1) for addressing disarray induced in the LV with HCM, due to replacement fibrosis. The models are developed in our modular cardiac modeling framework (MyoFe), which was built using the FEniCS open-source finite element software, enabling us to model cardiac diseases such as HCM that affect the heart at different scales.

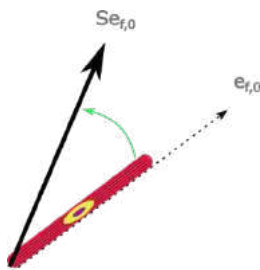


Figure 1: Schematic of fiber reorientation using the stress-based reorientation law. Fiber is initially oriented in the $e_{f,0}$ direction and would reorient gradually toward the traction vector $S e_{f,0}$.

METHODS

Many cardiac models have been developed using rule-based assignment of myofiber distributions based on experimental measurement. Considering the importance of cardiac myofiber organization on global pumping performance, and disorganization of cardiac myofibers due to some cardiac disease conditions, myofiber orientations in cardiac models may need to change due to the effects of remodeling.

In the current study, we present a novel fiber remodeling algorithm that is inspired by previous fiber adaptation algorithms by Kroon et al [3] and Washio et al [4]. Our work establishes a stress-based reorientation law in which fibers tend to reorient towards local traction vectors, which optimizes force generation during contraction (maximizing pumping capacity) and elevates the load bearing capacity of the fibers (by redirecting them in a direction with pure normal stress).

In Figure 1, $e_{f,0}$ represents the initial unit vector along a muscle fiber, and its multiplication to the referential stress tensor (S) (known as second Piola-Kirchhoff stress), generates the traction vector on the fiber ($S e_{f,0}$). Our stress-based reorientation law incrementally reorients each fiber to be aligned with the traction vector ($S e_{f,0}$) as below:

$$\frac{d e_{f,0}}{dt} = \frac{1}{\kappa} \left(\frac{S e_{f,0}}{\|S e_{f,0}\|} - e_{f,0} \right)$$

where κ is a time constant which allows us to employ the idea of separation of time scales, i.e., where the change in fiber orientation over a long time-scale (say days to weeks) can be achieved in several heart beats. Gradual reorientation would minimize the difference between $S e_{f,0}$ and $e_{f,0}$ until each fiber is aligned with the direction of its experienced traction. The stress tensor S is the summation of both active and passive stress, which reflects required remodeling for optimized systolic and diastolic performance.

We have developed a multiscale framework called MyoFe, where an implicit finite element scheme is implemented with MyoSim [5] as the contraction law and a Windkessel model of circulation. The main goal is evaluation of fiber disarray and cardiac performance induced by heterogeneous (het) fibrosis of different severity (Figure 2 (a)). Therefore, we prepared 4 different LV models based on an idealized ellipsoidal geometry that matches the dimensions of a rat LV with different percentages (0, 10, 20, 30) of stiff regions (representing necrotic cells replaced by diffuse fibrosis). Regions in the LV with fibrotic characteristics are distributed randomly throughout the LV and are set to be 15 times stiffer, as well as being isotropic. Additionally, the cross-bridge density in these regions is zero, representing dead myocytes that cannot contract. To reach steady state, models were run for 2 cardiac cycles of normal performance and then 5 additional cycles for fiber reorientation purposes.

RESULTS

The epicardial fibers are shown in Figure 2 (b), with their final angle from the last time step of the model overlaid on the fibers with their initial angles. It is observed that fibrotic regions in the LV induce considerable myofiber reorientation.

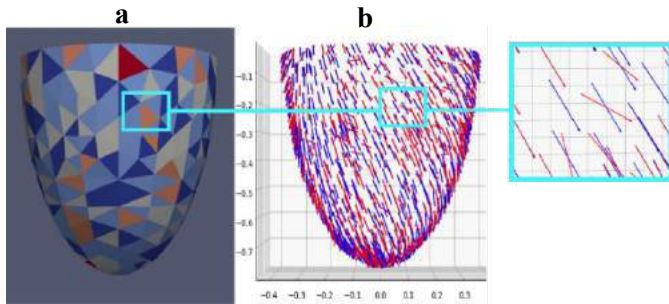


Figure 2: (a) Distribution of stiff regions within the LV mesh (Dark blue: Cells with 4 normal gaussian points, Dark red: Cells with 4 stiff gaussian points) (b) Epicardial fiber representation before (blue) and after (red) fiber reorientation in model with 30% heterogeneous stiffness.

Figure 3 shows the disarray of myofibers in 5 different transmural layers of the LV wall. The mean and standard deviation of fiber angle values were calculated within each transmural layer. As a result of the normal variation in transmural distribution of fiber angles, a baseline standard deviation is expected in each layer. Standard deviation bars vary

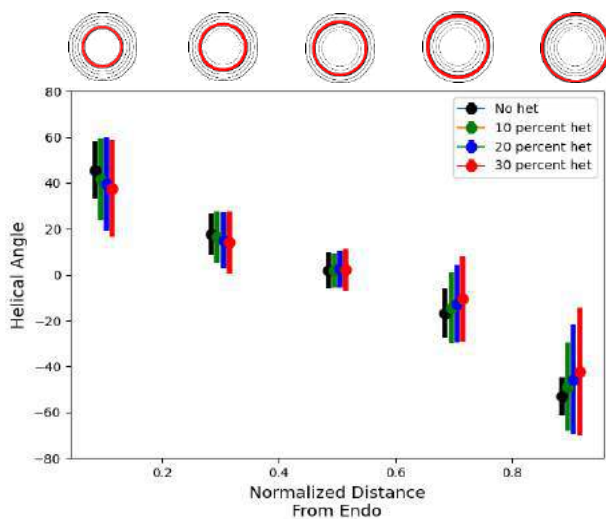


Figure 3: Disarray of myofibers in 5 transmural locations in LV wall (LV top view of each region is shown on the top). Standard deviation bars and mean of fiber angles are plotted to show the disarray and dominant fiber angle in each layer.

proportionally to the percentage of heterogeneity, and when the location is closer to endo or epi, the standard deviation increases substantially. Myofibers become more circumferential (seen in the mean value of fiber angles) and disorganized as stiffness heterogeneity increases. Both of these phenomena become more pronounced at the endo and epi.

Heterogeneity of cardiac muscle stiffness also affects the final PV loop in a proportional manner. The ejection fraction (EF) and stroke volume (SV) are reduced from 71% and 0.17 ml at baseline to 58% and 0.1 ml in the model with 30% heterogeneity. An increase in heterogeneity is associated with a substantial reduction in end diastolic (ED) volume. Increasing material stiffness due to diffuse fibrosis, which replaces dead myocytes, is responsible for such ED volume reduction. The induced myofiber disarray could also contribute to the reduction of ED volume. A disorganized distribution of myofibers is expected to reduce passive relaxation of heart muscle during filling.

It is also evident that muscle heterogeneity affects the pressure in the same way as LV volume. The primary cause of such pressure reduction is the absence of cross bridges in the fibrotic regions, which thus reduces the active stress in the LV thereby lowering systolic pressure. It has also been shown that induced myofiber disarray can reduce cardiac pumping performance [4], which is another contributing factor for pressure reduction. As a result of fiber disarray, not all cardiac muscle cells are oriented in their most efficient angle for muscle contraction and LV torsional motion. Thus, LVs with greater myofiber disarray will generate lower systolic pressures.

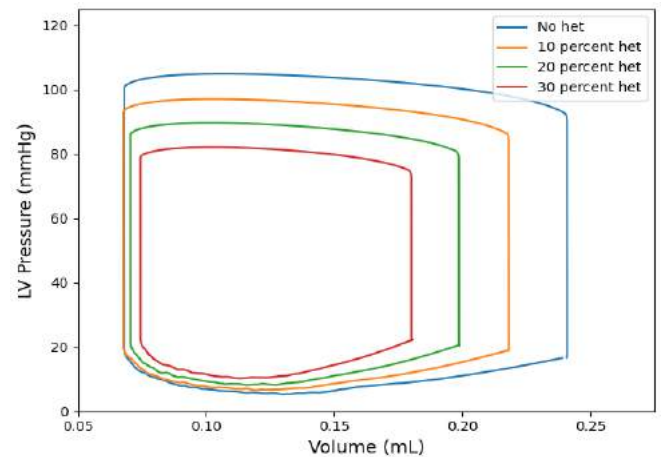


Figure 4 Pressure-volume loops for LV models with no heterogeneity (blue), 10% (orange), 20% (green) and 30% (red) heterogeneous stiffness.

DISCUSSION

This study developed a multiscale modular framework to simulate cardiac behavior with a stress-based myofiber reorientation law. The prominent mechanical effects of replacement fibrosis (increased stiffness and lack of contraction in the necrotic cells) were applied to the model at the cell level. Considerable disarray is observed relative to the percentage of fibrosis in the LV. Fibrosis and its consequent disarray highly affects the global pumping performance of the heart.

ACKNOWLEDGEMENT

This study was supported by National Institutes of Health grant U01HL133359 (JFW and KSC).

REFERENCES

- [1] Zhang, X.Y., et al., J Biomech Eng, 2015. 137(4).
- [2] Liu, J., et al., Radiology, 2022. 302(2): p. 298-306
- [3] Kroon, W., et al., Med Image Anal, 2009. 13(2): p. 346-53.
- [4] Washio, T., et al., Int J Numer Method Biomed Eng, 2016. 32(7)
- [5] Campbell, K.S., J Gen Physiol, 2014. 143(3): p. 387-99

AN OPTIMIZED METHOD FOR CONSTITUTIVE MODEL FITTING OF SOFT TISSUES BI-DIRECTIONAL MECHANICAL STRESS-STRETCH DATA

Sayed Ahmadrza Razian (1), Alexey Kamenskiy (1), Majid Jadidi (1)

(1) Department of Biomechanics, University of Nebraska at Omaha, Omaha, NE, USA

INTRODUCTION

The mechanical properties of arteries are often assessed with biaxial testing. Mathematical relations, often known as constitutive models, are then used to describe the experimental stretch-stress response to determine relations describing the intrinsic mechanical characteristics of the material. If these models describe the complex experimental data well, they can be utilized in computational models investigating repair devices and treatment methods[1].

Several constitutive models are proposed to describe the mechanical behavior of soft tissues and capture their response. A constitutive model inputs the experimental stretch tensor and calculates the theoretical stress tensor. Each model has one or several parameters, referred to as material parameters, that need to be determined from the experimental data[2]. Values of these material parameters cannot be predicted analytically, and numerical methods are utilized to iteratively try different sets of parameters and find the optimal convergent solution that minimizes the error function.

The Levenberg-Marquardt and Trust-Region-Reflective algorithms are two of the most commonly used numerical methods for nonlinear least square optimization in tissue biomechanics[3]. They are used to find the material parameters which yield the best fit, i.e., the lowest error. However, these techniques may not always produce the best fit for the experimental data.

In this work, we utilize a different optimized fitting routine based on Differential Evolution (DE) [4] algorithm, and Minkowski and Chebyshev Distance relations as the objective function (OF) to improve the constitutive model fit quality.

METHODS

Human arterial specimens from 60 donors of a wide range of ages (average 42±19 years, range 14-92 years, 45% male) were obtained within 24 hours of death after obtaining consent from next of kin. Samples were selected from a wide range of ages and both sexes to

include different mechanical properties in the analysis. Tissues were tested fresh within 4 hours of procurement. We performed planar biaxial tests (Figure 1) on 13×13 mm stress-free specimens using a CellScale BioTester at 37°C PBS. The experimental stresses, $T_{\theta\theta}^{exp}$ (circumferential) and T_{zz}^{exp} (longitudinal), and stretches, λ_{θ} (circumferential) and λ_z (longitudinal), were determined from the experimental tests and used in constitutive modeling.

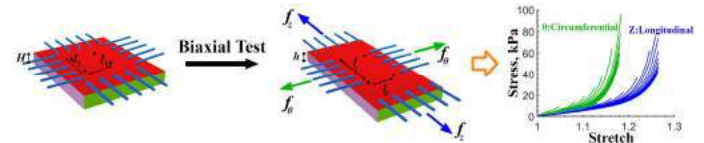


Figure 1. Schematic of the planar biaxial test. The right panel displays the experimental stress-stretch response. f_{θ} and f_z represent the applied forces in the circumferential (θ) and longitudinal (z) directions of the arterial wall specimen, respectively.

In this work, we used the Four-Fiber Family constitutive model [5] to assess the optimization routine based on the DE algorithm. DE is a population-based evolutionary method that iteratively improves the fit to minimize the objective loss function and find the global minimum. There are different loss functions to measure the difference between the experimental and theoretical stresses calculated through constitutive modeling and determine the parameters that produce the best fit. Among them, Mean Absolute Error (MAE), and Root Mean Square Error (RMSE) methods are common. Herein, we implemented an error function based on the Minkowski Distance function as follows:

$$MD = \left[\left(\sum_i^n |T_{\theta\theta}^{exp,i} - T_{\theta\theta}^{fit,i}|^p \right) + \left(\sum_i^n |T_{zz}^{exp,i} - T_{zz}^{fit,i}|^p \right) \right]^{\frac{1}{p}}, \quad (1)$$

where n is the total number of experimental data points.

If $p = 2$, we obtain Root Square Error (RSE), or Euclidean Distance, and if $p = 1$, we obtain the Absolute Error (AE), or Manhattan Distance. In addition to the Minkowski Distance relation, we used an extended version of the Chebyshev Distance with a power of $p > 0$ for the error function:

$$CD_{ext} = \left[\left(\sum_i \max \left\{ |T_{\theta\theta}^{exp,i} - T_{\theta\theta}^{fit,i}|^p, |T_{zz}^{exp,i} - T_{zz}^{fit,i}|^p \right\} \right) \right]^{\frac{1}{p}} \quad (2)$$

RESULTS

We first found the best fit for each sample using the Levenberg-Marquardt and Trust-Region-Reflective algorithms by RMSE objective relation implemented through the MATLAB lsqnonlin function. These results are represented in Figure 2.A,3.A,4.A,5.A, and 6.A for five representative samples.

The Four-Fiber Family model was then fitted on the same datasets using DE and the described Minkowski and Chebyshev distance functions. The DE algorithm has several parameters, such as the number of individuals in each population (NP), the maximum number of generations (G_{max}), scaling factor (F), and crossover rate (CR). Therefore, for each sample, we performed a hyperparameter tuning to find the optimized DE settings as well as the best objective function. These results are represented in Figure 2.B,3.B,4.B,5.B, and 6.B.

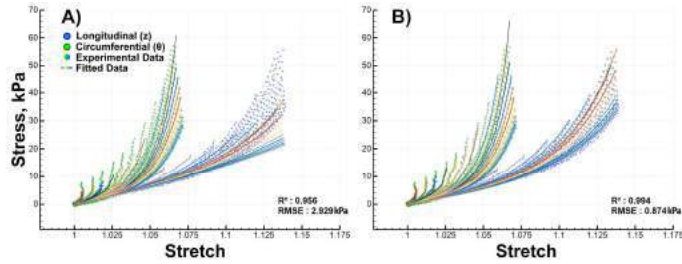


Figure 2.A) The MATLAB lsqnonlin function fit, and **B)** the DE algorithm fit obtained by hyperparameter tuning ($NP = 32$, $G_{max} = 200$, $F = 0.35$, $CR = 0.5$, $OF = MD$, and $P = 1$) for a 63-year-old female subject.

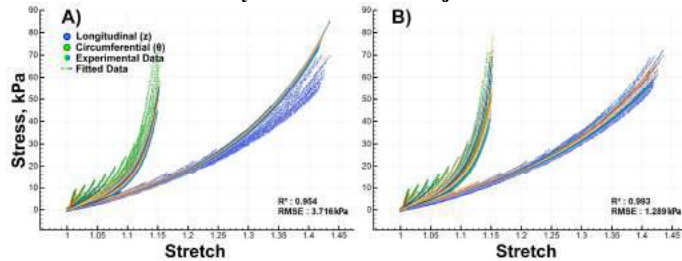


Figure 3.A) The MATLAB lsqnonlin function fit, and **B)** the DE algorithm fit obtained by hyperparameter tuning ($NP = 32$, $G_{max} = 200$, $F = 0.35$, $CR = 0.5$, $OF = CD_{ext}$, and $P = 2.5$) for a 33-year-old subject.

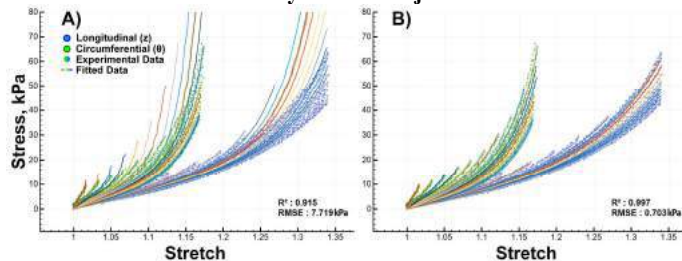


Figure 4.A) The MATLAB lsqnonlin function fit, and **B)** the DE algorithm fit obtained by hyperparameter tuning ($NP = 32$,

$G_{max} = 200$, $F = 0.35$, $CR = 0.5$, $OF = CD_{ext}$, and $P = 1.5$) for a 35-year-old subject.

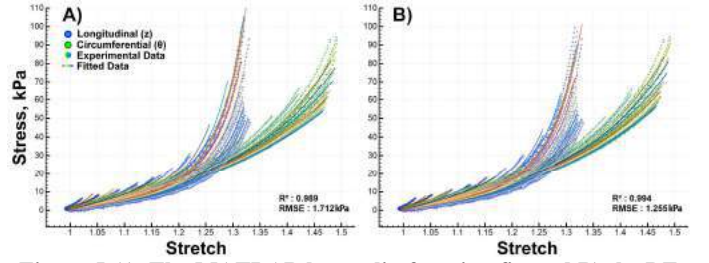


Figure 5.A) The MATLAB lsqnonlin function fit, and **B)** the DE algorithm fit obtained by hyperparameter tuning ($NP = 32$, $G_{max} = 200$, $F = 0.35$, $CR = 0.5$, $OF = MD$, and $P = 1.5$) for a 25-year-old male subject.

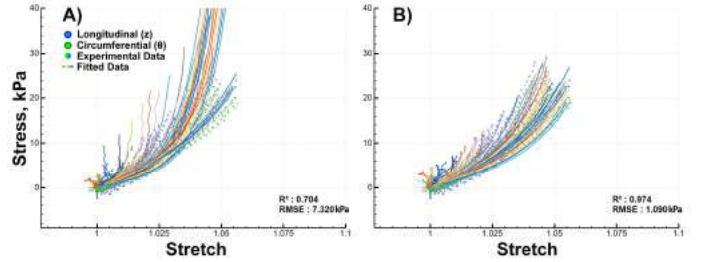


Figure 6.A) The MATLAB lsqnonlin function fit, and **B)** the DE algorithm fit obtained by hyperparameter tuning ($NP = 32$, $G_{max} = 200$, $F = 0.35$, $CR = 0.5$, $OF = MD$, and $P = 1.5$) for a 92-year-old male subject.

DISCUSSION

In this work, we introduced a metaheuristic population-based algorithm and implemented the Minkowski and Chebyshev Distance functions to improve the quality of the constitutive model fit to bi-directional experimental stress-stretch data. Constitutive modeling of soft tissues involves multiple aspects, from experimental data collection to developing or selecting a physics-based mathematical relation and estimating the material parameters. If a model does not represent the experimental data very well, it is common to choose a more complex constitutive model with more material parameters. However, in this work, we highlighted that instead of using a more complex relation, by using algorithms, such as the implemented DE and Minkowski Distance function, we could obtain a superior fit with fewer material parameters. In addition, by using the DE algorithm with hyperparameter tuning, we were able to decrease the error between experimental and theoretical, i.e., fitted, data.

ACKNOWLEDGEMENTS

We wish to acknowledge LiveOn Nebraska for their help and support in collecting the blood vessels and thank donors and their families for making this study possible. This work was supported in part by NHLBI HL125736.

REFERENCES

- [1] Holzapfel, GA et al., *Proc. R. Soc.*, 466, 1551–1597, 2010.
- [2] Jadidi, M et al., *Acta Biomaterialia*, 121, 431–443, 2021.
- [3] Levenberg, K, *Appl. Math.*, 2, 164–168, 1944.
- [4] Storn, R et al., *J. of Global Optimization volume*, 11, 341–359, 1997.
- [5] Kamenskiy, A et al., *Biomech. Model. Mechanobiol.*, 16, 681–692, 2017.

ROLE OF SEX AND SEX HORMONES IN PULMONARY ARTERY ADVENTITIAL FIBROBLAST MECHANOSIGNALING

Yufan Lin (1), Daniela Valdez-Jasso (1)

(1) Department of Bioengineering, University of California, San Diego, La Jolla, California, United States

INTRODUCTION

Pulmonary arterial hypertension (PAH) is a progressive disease driven by the abnormal activities of mechanosensitive cells in pulmonary arteries (PAs) [1]. PAH is more prevalent in women than men, but pre-menopause females have better outcomes than man and post-menopausal women [2]. To investigate the cellular-level mechanism behind this estrogen paradox, we are currently studying how the mechanosignaling activities of pulmonary artery adventitial fibroblasts (PAAFs), the cell type that is attributed for vasculature stiffening in PAH, and how they are regulated by the intrinsic sex of the animal and the presence of sex hormones. Our approach include combining *in-vitro* experiments with *in silico* experiments to test our understanding and validate the PAAF signaling network model. Based on studies relating 17 β -estradiol (E2) to collagen type I and III expression, we hypothesize that E2 regulates the pro-fibrotic PAAF mechanosignaling via components including BMPR2 and apelin, which are found to be downstream of E2 and its receptor in right ventricle [3].

METHODS

PAAFs isolated from healthy male, female, and ovariectomized (OVX) female rats are cultured in polyacrylamide gels. These scaffolds are made to represent healthy (0.5 kPa), mild (3 kPa) and severe (10 kPa) disease stages as previously done [4]. Strain due to the increase in pulmonary blood pressure ranges was mimicked by stretching the substrates 10% biaxially for 24 hours [4]. Cells are then harvested and lysed for RNA isolation, which is followed by cDNA synthesis and quantitative PCR (qPCR) to measure the expression levels of profibrotic genes and myofibroblast-activation marker shown previously to be upregulated in PAs from animals treated with sugen-hypoxia (SuHx), a well-established animal model of PAH. After being normalized against housekeeping gene *18S*, qPCR results are analyzed with 3-way ANOVA followed by Dunnett's *post-hoc* multiple comparisons test.

A logic-based differential equation model is constructed to represent the target signaling network, where:

$$\frac{dy_i}{dt} = \frac{1}{\tau_i} (\sum_j \omega_j f_j y_j^{max} - y_i) \quad (1)$$

where y_i is the activation level of species i , τ_i and y_i^{max} are the time constant and maximal fractional activation, while f_j and ω_j are the associated Hill activation/inhibition functions and corresponding reaction weights, respectively [5]. Based on the PAAF signaling model [6], we isolated and modified a portion of the network to study the role of E2 in regulating fibrotic genes. The logical relationships between components are generated based on literature data [3,7-9].

RESULTS

The study is currently in progress. Preliminary data (**Figure 1**) show that stretch and stiffness generally up-regulate the mRNA level of fibrotic genes. Female PAAFs exhibits a higher stiffness response threshold and lower stretch sensitivity compared to both male and OVX cells, while OVX cells show higher general response levels than males.

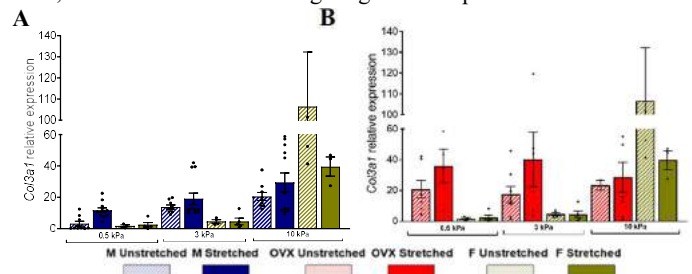
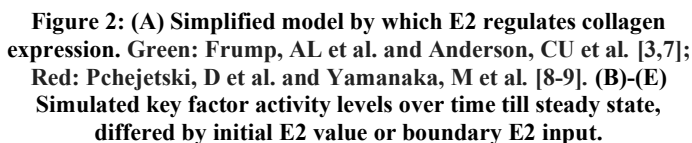


Figure 1: Effect of stiffness and stretch on *Col3a1* expression in PAAFs derived from male rats and female rats (A), and intact vs. OVX female rats (B). Note that the groups have different response thresholds, degrees, and patterns, both when male is compared to OVX (A) and when OVX is compared to female (B).

This study suggests that the presence of estrogen would down-regulate fibrotic gene expressions during PAAF mechanosignaling activities, while the intrinsic sex of the cells plays an also significant but unclear role in the process. The suggested signaling model helps decipher and explain how estrogen plays a role in the mechanosignaling network by connecting it to BMPR2 and apelin, providing a potential direction for further investigation and understanding of sex dependent PAAF mechanosignaling and PAH development in general.

This work was funded by American Heart Association Grant 16SDG29670010 (to D. Valdez-Jasso); National Heart, Lung, and Blood Institute Grants 1R25HL145817-01 and 1R01HL155945-01 (to D. Valdez-Jasso) and 1R32HL160507-01A1 (to Y. Lin); and National Science Foundation CAREER Award 2046259 (to D. Valdez-Jasso).

- [1] Maron, BA et al., *Global Cadiol Sci*, vol.2020,1 e202003 (2020).
- [2] Umar, S et al., *Am J Respir Crit Care Med*, 186(2):125-131, 2012.
- [3] Frump, AL et al., *J Clin Invest*, 131(6):e129433, 2021.
- [4] Wang, A et al., *Cells*, 10(5):1000, 2021.
- [5] Kraeutler, MJ et al., *BMC Syst Biol*, 4:157, 2010.
- [6] Wang, A et al., *Phil Trans R Soc A*, 378:20190338, 2020.
- [7] Anderson, CU et al., *Pulm Circ*, 1(3):334-346, 2011.
- [8] Pchejetski, D et al., *Eur Heart J*, 33(18):2360-9, 2012.
- [9] Yamanaka, M et al., *J Biol Chem*, 279(52):53994-4001, 2004.



In addition to the general up-regulation of profibrotic gene expressions under both stiffness and stretch, the qPCR data suggest a difference in the response thresholds, degrees, and patterns between

THE ROLE OF MONOCYTES AND MACROPHAGES IN THE DEVELOPMENT OF AORTIC VALVE CALCIFICATION IN A 3D TRI-CULTURE IN VITRO MODEL

Fatemeh Salemizadehparizi (1), Peter Huang (2), Mei-Hsiu Chen (3), Gretchen J. Mahler (1)

- (1) Department of Biomedical Engineering, Binghamton University, Binghamton, NY, USA
(2) Department of Mechanical Engineering, Binghamton University, Binghamton, NY, USA
(3) Department of Mathematics and Statistics, Binghamton University, Binghamton, NY, USA

INTRODUCTION

Globally, calcific aortic valve disease (CAVD) is becoming more common and causes significant mortality and morbidity [1]. When calcific nodules form on aortic valve leaflets, the valve becomes stenotic. This makes it hard for the heart valve to open and close properly, prevents the heart from pumping blood to other parts of the body easily, and can lead to a stroke or other diseases. There is no proven effective pharmacological treatment for CAVD and the underlying mechanisms in CAVD development are not fully understood. A 3D, *in vitro* model of CAVD can provide a method for an improved understanding of the biological mechanisms in CAVD development [2].

The initiation and progression of aortic valve calcific nodules can be caused by inflammatory processes that are induced by numerous stimuli such as aging, hypertension, and metabolic disease, resulting in increased oxidative stress. H_2O_2 is a critical molecule in oxidative stress and is produced during normal metabolism in mammalian cells. H_2O_2 diffuses across cells and tissues as a messenger molecule, causing rapid biological effects such as cell shape changes, proliferation, and migration [3]. However, greater levels of exposure cause immune cell recruitment, inflammatory response, growth inhibition, and cell apoptosis through a variety of pathways (Figure 1) [3]. This inflammatory environment induces macrophages, valvular endothelial cells (VECs), and valvular interstitial cells (VICs) to produce extracellular vesicles, and triggers apoptosis in macrophages and VICs, which results in the production of apoptotic bodies. Both processes result in

dystrophic calcification, which causes macrocalcifications [4]. The goal of this work is to study the role of monocytes and macrophages in the development of aortic valve calcification as a result of elevated reactive oxygen species (ROS) (in this study by adding H_2O_2) in a 3D *in vitro* model of the aortic valve.

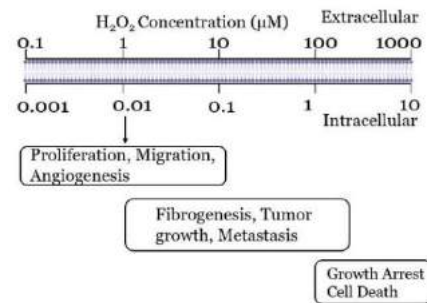


Figure 1: Hydrogen peroxide concentrations in oxidative stress and biological responses of the cell. Reproduced from [3].

METHODS

Porcine aortic VICs (PAVICs) were seeded within a 3D collagen type I hydrogel at 1×10^6 cells/mL and porcine aortic VEC (PAVECs) were seeded on top of the matrix at 95,000 cells/cm² in a 24-well plate. 100 mM H_2O_2 was added to the DMEM + 10% fetal bovine serum (FBS), which was changed every other day for up to 7 days. On the 8th day, THP-1 (a human monocyte cell line) was seeded onto 3D gels at 1×10^5 cells/mL in fresh medium with 200 ng/mL phorbol 12-myristate-13-

acetate (PMA) for 12 hours to induce differentiation to M₀ macrophages. M₀ macrophages were then differentiated toward M₁ with 12 hours incubation with 200 ng/mL of lipopolysaccharide (LPS). Then the both tri-culture matrix were fed with 400 µL of fresh medium, and then fed every other day by adding 100 µL to the old medium until the 14th day. Alizarin Red Staining (ARS) was used to show and quantify calcified nodule formation. The microstructure of calcified nodules was assessed by scanning electron microscopy with energy dispersive X-ray (SEM/EDX) spectroscopy. EDX was used to quantify calcium-phosphate atomic ratios (Ca/P). Crystal violet and live/dead assays were used to quantify THP-1 monocyte activation. Results were analyzed using Kruskal-Wallis tests and the Wilcoxon rank-sum test at each time point with adjustment for multiple comparisons with P-value < 0.05.

RESULTS

H₂O₂ induced calcification in PAVIC-only, PAVEC-only, and co-culture (Figure 2). While the ARS results show that calcific nodules were present in the co-culture and PAVIC-samples but not in the PAVEC-only samples, the SEM images showed calcified nodules in all three conditions. The PAVEC-only calcified nodules have a higher Ca/P ratio than other samples. The ARS and SEM images showed H₂O₂ induces calcification in tri-culture samples and causes monocytes to differentiate toward M₀ macrophages. According to EDX results, tri-culture samples with monocytes and macrophages have a lower Ca/P ratio compared to both mono-cultures (PAVIC-only and PAVEC-only culture) and co-culture samples. However, the number of calcific nodules of tri-culture samples (according to quantified ARS results) is significantly increased compared to mono-culture and co-culture samples.

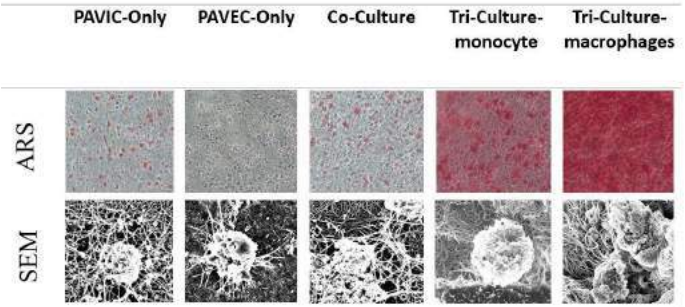


Figure 2: Alizarin Red Staining (ARS) qualitative images, Scanning Electron Microscopy (SEM) shows the existence of calcified nodules in samples treated with H₂O₂ (100 µM).

DISCUSSION

The amount of mineralization is shown by Ca/P ratios which indicates the pathobiological calcium phosphates range in different diseases such as cardiovascular diseases and cancer [5]. Pathobiological calcium phosphates can develop which is resulting in the creation of hydroxyapatite (Ca/P = 1.67). The primary calcium phosphate phases leading to the formation of

hydroxyapatite are monocalcium phosphates (Ca/P = 0.5), dicalcium phosphates (Ca/P = 1), and octacalcium phosphates (Ca/P = 1.33) [6, 7]. The Ca/P ratios of calcified nodules in PAVIC-only, PAVEC-only, and co-cultures treated with H₂O₂ (100 µM) samples were determined to be 1, 1.53, 1.32, which shows that the calcific nodules of these three conditions were made of different forms of calcium phosphates found in the body. Ca/P = 1.53 of PAVEC-only culture is close to the Ca/P ratio of hydroxyapatite (Ca/P = 1.67). SEM/EDX results indicated Ca/P ratio in tri-culture samples with monocytes (Ca/P = 0.83) is higher than in tri-culture samples with macrophages (Ca/P = 0.52).

Based on the SEM images with calcified nodules in all conditions, H₂O₂ likely induces PAVECs to differentiate into endothelial-derived PAVICs which further differentiate into osteoblastic PAVICs and result in valve calcification. ARS images showed the presence of the calcified nodules in tri-culture samples pre-treated with H₂O₂ (100 µM). Compared to tri-culture samples with monocytes, the concentration of ARS stain increased in the presence of activated macrophages (M1), which shows an increase in the number of calcified nodules.

According to SEM/EDX results, the model forms calcified nodules of different calcium phosphate maturity phases as found in *ex vivo* calcified human aortic valves. This 3D aortic valve model can be useful for understanding the role of immune cells including both macrophages and monocytes in disease progression in response to increased oxidative stress. These tri-culture models could be used to test new pharmacological treatments for CAVD in the presence of immune cells.

ACKNOWLEDGEMENTS

Funding for this work was provided by NSF (CMMI 1919438).

REFERENCES

1. Yi, B., et al., Aging (Albany NY), 2021. 13(9): p. 12710.
2. Goody, P.R., et al., Arteriosclerosis, thrombosis, and vascular biology, 2020. 40(4): p. 885-900.
3. Sies, H., Redox biology, 2017. 11: p. 613-619.
4. Broeders, W., et al., Basic Research in Cardiology, 2022. 117(1): p. 1-22.
5. Bazin, D., et al., Chemical Reviews, 2012. 112(10): p. 5092-5120.
6. Mikroulis, D., et al., Journal of Materials Science: Materials in Medicine, 2002. 13(9): p. 885-889.
7. Griffanti, G., et al., Biomaterials science, 2019. 7(3): p. 1064-1077.

MECHANICAL PROPERTIES OF CARDIAC TISSUE SURROGATES AND HOW THEY COMPARE TO HUMAN CADAVERIC CARDIAC TISSUE

Emily A. Bermel, PhD¹, Kevin O'Brien¹

[¹Medtronic, Cardiac Rhythm Management, Therapy Delivery Systems, Mounds View, MN, USA

INTRODUCTION

During development of implantable devices and their delivery systems, mechanical testing is required to ensure the devices will function properly during its implanted life. Many different medical devices interact with many different types of tissue, for this study we focused on cardiac tissues and their surrogates. Many different cardiac therapy devices interact with cardiac tissue, creating a need for tissue surrogates suitable for accelerated bench testing. Current surrogates in use are Ballistic gel¹, SynDaver synthetic tissues², LifeLike Bio Tissues³ and 3D printed materials⁴. Mechanical characterization of these surrogates is required to determine their suitability for replicating cardiac tissue behavior.

There are several modes of mechanical loading that surrogates can be compared. In this study we looked at three types: Uniaxial tension, uniaxial compression, and friction.

METHODS

Sample Preparation

Ballistic gel was cast in molds to create samples. SynDaver sheets and LifeLike Bio sheets were cut using a sample punch. Tissue was resected from cadavers, dissected into flat sheets, and the samples were punched out. Tissue samples were stored in a fridge, wrapped in saline soaked gauze and synthetic tissue surrogates were stored as directed by the manufacturer when not in use.

Testing Types

To fully characterize each material three different types of testing were done: Uniaxial Tension, Uniaxial Compression, and Friction.

Uniaxial tension tests were done on dog bone samples, shown in Figure 1. Each test included pre-strain to account for relaxation, 10 preconditioning cycles to 10% strain, then five cycles of 25%, 50%, and 100% strain, then a pull to failure. Uniaxial compression was done on one inch diameter samples, Figure 1. Each test included a pre-load of

1% and then five cycles of 50% strain was applied. All testing was done at a rate of 1.2mm/sec in saline at 37°C.

Friction testing was done to characterize the interaction of the surrogates with a needle. A 0.020-inch stainless steel wire was sharpened at the distal end. The tissue and surrogate samples were clamped in a fixture that allowed the wire to fully penetrate the sample, while trying to minimize tenting of the tissue. The test pushed the needle through a sample's thickness to a maximum displacement of 25 mm, then pulled back at a rate of 25mm/min so that there was a constant surface area interacting with the needle during pull-out.

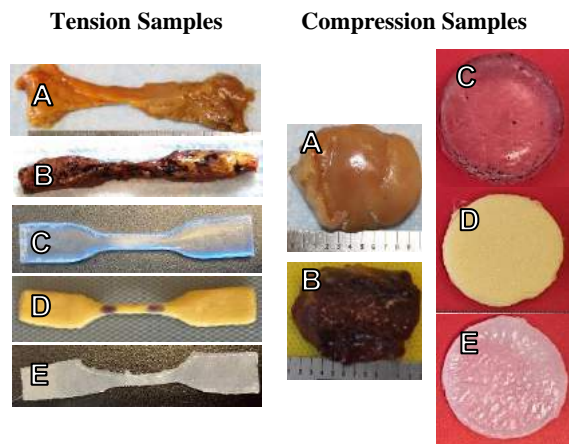


Figure 1: Tension and Compression Samples. A) Cadaveric Cardiac Fat, B) Cadaveric Cardiac Muscle, C) Ballistic Gel, D) SynDaver Bulk Fat, and E) SynDaver Cardiac Muscle

Data Analysis

Force and displacement data was collected for all tests at a sampling rate of 100Hz. To compare surrogates to cadaveric tissue we looked at the average tension and compression moduli for the linear loading region of the data. For friction data analysis, the maximum pull-out force was used to as the representative frictional force and had comparable results to using the average pull-out force (Figure 2).

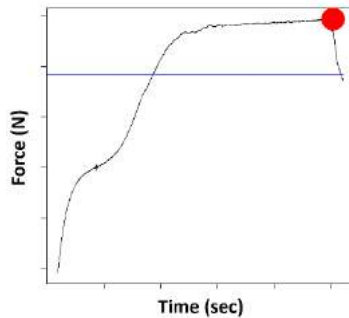


Figure 2: Maximum Frictional Force. Red dot indicates the max force during retraction of wire and the blue line represents average pull-out force.

RESULTS

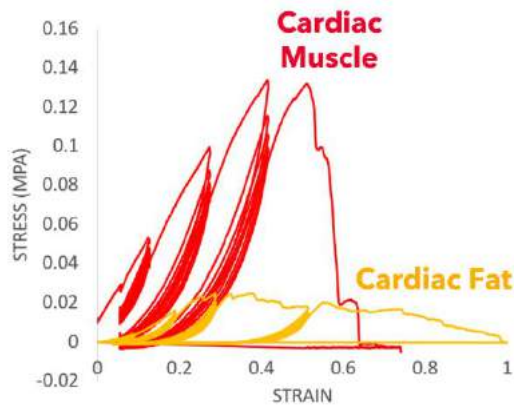


Figure 3: Cadaveric Tissue Tension.

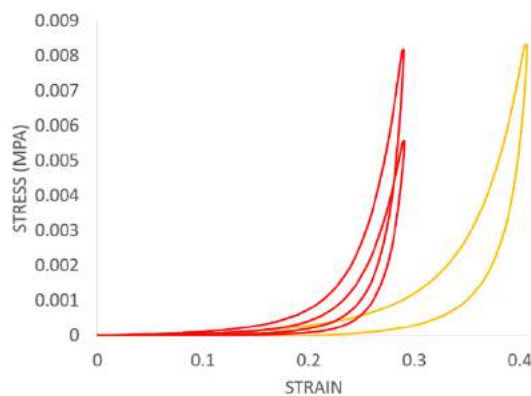


Figure 4: Cadaveric Tissue Compression.

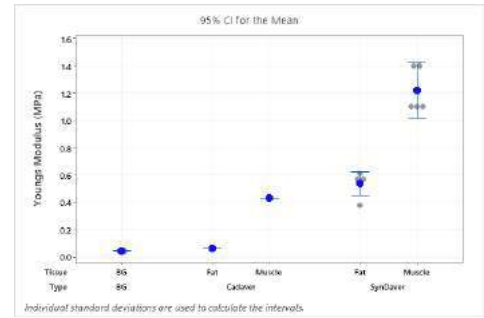


Figure 5 : Tension Moduli

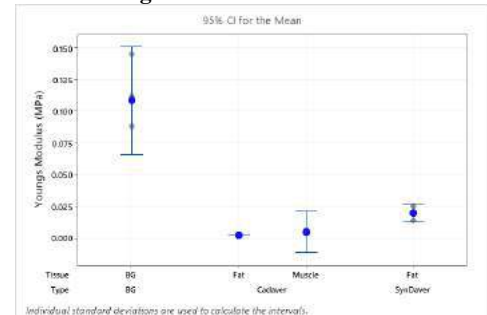


Figure 6 : Compression Moduli

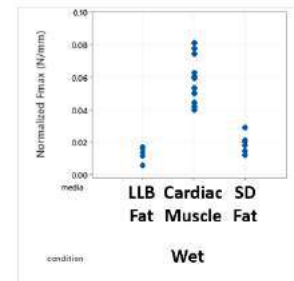


Figure 7: Max Friction Force Normalized by Sample Thickness. LifeLife Bio (LLB) Fat, Porcine Cardiac Muscle, and SynDaver (SD) Fat.

DISCUSSION

SynDaver materials are stiffer than cadaveric tissue in tension, but the SynDaver fat seems to mimic the compression modulus of the cardiac muscle and fat the best. In addition to a tissue's response to tension and compression, friction between cardiac tissues and medical device engineering materials is critical for chronic fixation of a device inside the body. Real tissue has higher frictional forces than any surrogate tested to-date, further testing of surrogate materials is needed. We have developed a reproducible test that is representative of use conditions and may be used to evaluate surface coatings, tip sharpness, and device-tissue interactions relevant for medical implants.

ACKNOWLEDGEMENTS

The authors would like to acknowledge Medtronic Physiologic Research Laboratory, SynDaver, and LifeLike BioTissue.

REFERENCES

- [1] Clear Ballistics LLC., <https://www.clearballistics.com/resourcescenter/>, 2023.
- [2] SynDaver, <https://syndaver.com/what-we-do/>, 2023.
- [3] LifeLike BioTissue, <https://lifelikebiotissue.com/about-us>, 2023.
- [4] Stratasy, <https://www.stratasy.com/en/industries-and-applications/3d-printing-industries/medical/>, 2023.

THE INFLUENCE OF RECRUITMENT MANEUVERS ON LOCALIZED MURINE LUNG STRAINS ASSESSED WITH DIGITAL IMAGE CORRELATION

M. Shankel (1), T.M. Nelson (1), K.A.M. Quiros (1), T. Biddle (2,3), G.O. Ramirez (1),
C.A. Mariano (1), J. Bebawy (1), D.D. Lo (2,3), M. Eskandari (1,2,4)

- (1) Department of Mechanical Engineering, University of California, Riverside CA, USA
(2) BREATHE Center, School of Medicine University of California, Riverside CA, USA
(3) Division of Biomedical Sciences, School of Medicine, University of California, Riverside CA, USA
(4) Department of Bioengineering, University of California, Riverside CA, USA

INTRODUCTION

Mechanical ventilation is often used to support gas exchange and lung function during surgery, since pulmonary muscles relax under anesthesia. However, the lungs may undergo regional atelectasis (partial lung collapse) if improperly ventilated, which can be harmful and lengthen recovery [1]. To mitigate this, maneuvers are performed during ventilation to improve alveolar recruitment, protecting against atelectasis [2-3]. Common recruitment maneuvers include escalation of pressure with incremental cycling to sufficiently recruit alveoli, or a sustained inflation maneuver, where inhalation is followed by a pause and volumetric hold of air.

Previous studies discourage sustained inflation methods, as they may heterogeneously over distend open alveoli adjacent to closed alveoli groups, resulting in lung damage [4-5]. In contrast, recent research suggests that escalation maneuvers more homogeneously recruit non-aerated alveolar groups, which gradually open as the air is incrementally cycled, and may be a more ideal method [2, 5-6]. Previous studies have employed global mechanical characterization, such as pressure-volume curves, or non-continuous time methods, such as internal imaging with magnetic resonance imaging (MRI) [2,6] to examine the effect of differing recruitment maneuvers. However, such methods neglect local lung mechanics, including the development of lung strains during ventilation [2], which can reveal critical information about regions susceptible to damage [7]. Measuring tissue-level stretch during these maneuvers may provide insights regarding each maneuvers' comparable efficacy [8].

This novel study characterizes regional tissue-level lung mechanics recruitment maneuvers using digital image correlation (DIC). Strains on the surface of the ex-vivo lung are compared between the sustained inflation and the escalation maneuvers when specimens are inflated to matched lung volumes, complementing established global insights with new local assessments of pulmonary mechanics. The results of the study can contribute to identifying optimal maneuvers

and provide clinically applicable insights regarding pulmonary overdistension during ventilation.

METHODS

Six male C57BL/6J mice were obtained from Jackson Laboratories (Bar Harbor, ME, USA), aged 12-15 weeks, and were anesthetized and sacrificed according to IACUC protocol. Lungs were removed and cannulated to enable mechanical ventilation and were speckled for digital image correlation measurements. Specimens were placed in a custom-designed, electromechanical pressure-volume tank for ventilation testing [9], where three lungs were subjected to an escalation maneuver (EM) and three to the sustained inflation maneuver (SIM).

For both recruitment maneuvers, lungs were preloaded to 6 cmH₂O [10], then preconditioned to a volume of 0.3 mL for 3 cycles, at a rate of 20 breaths per minute (Figure 1). For the EM, the lungs were subsequently cycled with incrementally increasing volumes to 0.9 mL. For the SIM, the preloading and preconditioning process was repeated 5 times to match the number of cycles of EM; then, a volumetric hold to 0.9 mL was performed. DIC data [Trilion Quality Systems, King of Prussia, PA, USA] was recorded for analogously matched inflation legs of the SIM and EM, as highlighted in Figure 1 [8].

The major strain was tracked over time for randomly selected locations points between a representative EM and SIM mouse for qualitative comparisons (Figure 2A and B); the reduced Jacobian was calculated to ensure equivalent DIC surface areas and displaced volumes between specimens [11]. Histograms (average \pm standard deviation) were generated from the DIC tissue surface strains at peak inflation (0.9 mL) for both maneuvers and all mice (Figure 2C and D). The coefficient of variability (CV) was also calculated to compare the strain distribution and tissue deformation heterogeneity [12]. Metrics were compared between the two maneuvers using a one-way ANOVA with a significance level of $p < 0.05$ [GraphPad Prism, San Diego, CA, USA].

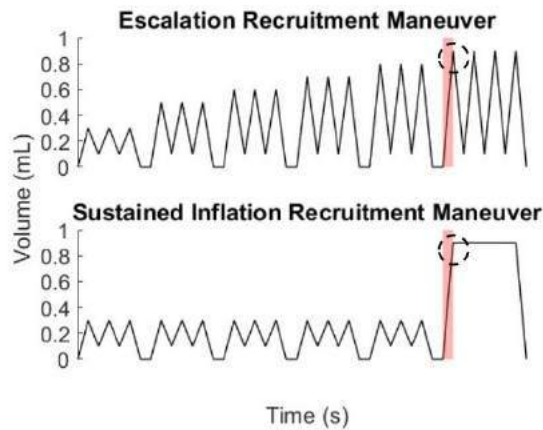


Figure 1: Illustrated escalation and sustained inflation recruitment maneuvers. The red highlighted inflation limb is analyzed by DIC to assess the temporal strain evolution (Figure 2A-B), and the strain distributions at the peak volume stage (dotted circle) are evaluated (Figure 2C-D).

RESULTS

For both maneuvers, lung tissue surface strains were found to increase over time with greater air delivery as expected (Figure 2A and B). Qualitatively, the EM demonstrated a more steady and progressive increase in strains, whereas the SIM demonstrated decreased strain slopes followed by a sharp increase, resulting in more populated high peak strains at the maximum volume.

Statistically significant differences were not found between the peak strain values, mean, standard deviation, and CV between EM and SIM (Figure 2C and D). However, EM strains were more uniformly distributed about the mean value of 22% with a CV of 63%, compared to SIM, which demonstrated reduced mean strain of 19% with greater strain heterogeneity with a CV of 82%.

DISCUSSION

In this study, the SIM group was associated with a greater fraction of low strains across the analyzed left lung and superior and inferior right lobes, which is considered to be associated with more unopened alveolar groups compared to EM [1-2,13]. The higher CV value within the SIM group exhibits greater surface strain spread and implies greater alveolar recruitment heterogeneity. Analogously, the comparatively reduced CV value for EM implies more uniform recruitment of alveolar units and therefore, greater lung homogeneity.

Previously, based on MRI imaging and global pressure-volume hysteresis curves, Cereda et al. [2] found that the EM in rat lungs led to the opening of smaller alveolar groups versus over aeration of opened alveoli, associated with a homogeneous versus heterogenous response respectively. However, such methods are limited in that they cannot characterize the progressive behaviors nor the regionality of tissue strains that result from alveolar recruitment, which may yield an understanding regarding the development of lung damage [7-8]. Nonetheless, our local findings substantiate the conclusions of these discrete and global mechanics studies, observing that EM results in more homogenous lung tissue expansion, while also tending to do so continuously throughout inflation.

Although EM and SIM are both utilized clinically, these studies and recent clinical research [1] has led to a consensus highlighting the benefits of EM and the risk of injury with SIM. The mechanical substantiation for these results is still currently debated, and our local to lung injury [5,6]; in this study, the inflation limb of EM results in

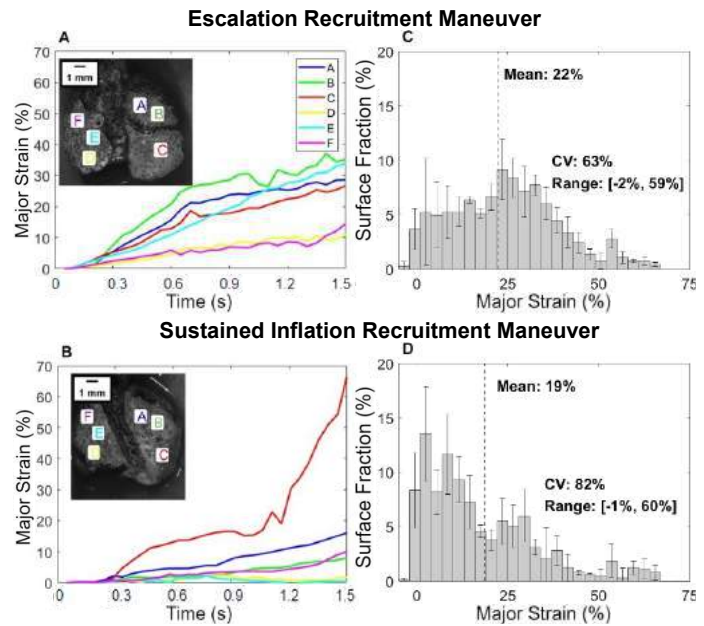


Figure 2: Representative major strain temporal evolution for the escalation recruitment maneuver (A) and sustained inflation maneuver (B) are shown. Histograms quantify the fraction of the surface exhibiting various strain levels and corresponding distributions for the escalation maneuver (C) and sustained inflation (D).

steadier and more homogenous strain response when compared to the heterogenous and abrupt tissue expansion found in SIM. This may lend insights into the cause of lung damage during ventilation and help to improve identifying optimal methods of lung recruitment.

While our findings did not exhibit statistical significance, more conclusive results may be revealed with greater mice sample sizes, as currently planned for future work. Additionally, this study was conducted ex-vivo, without the presence of the chest cavity encapsulating the lungs, which may change deformation measures during tissue expansion; however, relative measures, such as tissue strains and regional patterns, would likely persist [8]. Despite these limitations, this study is the first of its kind to characterize the development of strain during different recruitment maneuvers, with future work aimed at connecting global to local mechanical characteristics to lend additional clinically applicable insights.

REFERENCES

- [1] Tusman, G et al., *Anaesthesia and Critical Care* 21 (5): 244-49, 2010.
- [2] Cereda et al. *Anesthesiology* 119 (6): 1402-9, 2013.
- [3] Lachmann, B., *Intensive Care Medicine* 18 (6) 319-21, 1992.
- [4] Silva, Pedro L et al., *Critical Care Medicine* 39 (5): 1074-81, 2011.
- [5] Marini, J., *Intensive Care Medicine* 37 (10): 1572-74, 2011.
- [6] Pellicano, A et al., *Intensive Care Medicine* 35 (11): 1990-98, 2009.
- [7] Roan, E., et al., *American Journal of Physiology-Lung Cellular and Molecular Physiology* 301 (5) 625-35, 2011.
- [8] Nelson, TM et al., *Physiological Reports* 10 (19): e15466, 2022.
- [9] Sattari, S et al., *Frontiers in Bioengineering and Biotechnology* 578762, 2020
- [10] Cannizzaro, V et al., *Respiratory Physiology & Neurobiology* 169 (3): 243-51, 2009.
- [11] Amelon, R et al., *Journal of Biomechanics* 44 (13): 2489-95, 2011.
- [12] Ito, S et al., *Journal of Applied Physiology* 97 (1): 204-12, 2004.
- [13] Castellón, E et al., *Histology and Histopathology* 0213-3911, 2002.

SHIFTING THE ENDOVASCULAR PARADIGM: PATIENT-SPECIFIC TREATMENT OF INTRACRANIAL ANEURYSMS USING SHAPE MEMORY POLYMERS AND ADDITIVE MANUFACTURING

Sergio A. Pineda-Castillo (1,2), Tanner Cabaniss (2), Bradley N. Bohnstedt (3),
Chung-Hao Lee (2)

- (1) Stephenson School of Biomedical Engineering, The University of Oklahoma, Norman, Oklahoma, USA
(2) Biomechanics and Biomaterials Design Laboratory (BBDL), School of Aerospace and Mechanical Engineering, The University of Oklahoma, Norman, Oklahoma, USA
(3) Department of Neurological Surgery, Indiana University School of Medicine, Indianapolis, IN, USA

INTRODUCTION

Intracranial aneurysms (ICA) affect approximately 3-5 % of the overall population. 3-50 in every 100,000 ICAs will rupture if left untreated, making prophylactic treatment a pressing urgency. Current methods for ICA treatment involve surgical clipping or endovascular embolization: the latter being preferred for its low invasiveness and lower in-hospital mortality. Nonetheless, endovascular therapies face challenges related to incomplete ICA occlusion, which can lead to aneurysm recurrence and rupture [1,2]. Therefore, research efforts can be made towards advancing technologies for ICA endovascular embolization that aim to promote complete occlusion and improve the long-term effectiveness.

Traditionally, endovascular embolization using Guglielmi detachable coils (GDCs), or other biomaterials for the occlusion of ICAs, have non-patient-specific approach (i.e., the material does not match the aneurysm geometry). In this study, we aim to develop a *paradigm-shifting* technology for ICA endovascular treatment: shape memory polymers (SMP) that can be tailored to *aneurysm-specific* geometries. Specifically, our polymeric formulation and manufacturing show great promise for ICA embolization, as demonstrated by the occlusion of *in vitro* aneurysm models. In addition, our material is fabricated using a facile method that allows fast production of foams. Overall, our SMP device exhibits potential to improve complete occlusion rates of ICAs.

METHODS

SMP Synthesis and Material Fabrication: Polyurethane was synthesized using hexamethylene isocyanate (HDI), triethanolamine (TEA) and N,N,N',N'-tetrakis (hydroxypropyl) ethylenediamine (HPED), as described previously [3], in a nitrogen-rich environment. SMP solution was poured on a polyvinyl alcohol (PVA) 3D-printed template with a grid infill structure. SMP was cured in a vacuum oven and, once solid, PVA was washed out using a sonicator. SMP foams (Fig. 1) were then dried in a vacuum oven and stored in a desiccator.

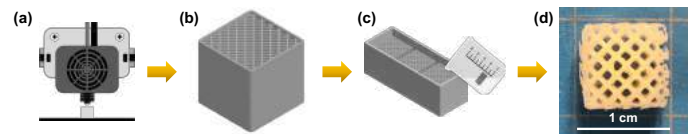


Figure 1. Schematic of 3D SMP foam fabrication pipeline: (a) 3D printing of (b) PVA template with a grid infill design. (c) Pouring of SMP solution and (d) the final SMP foam after washout.

Calorimetry and Shape Recovery Analysis: Differential scanning calorimetry (DSC) was used to quantify the glass transition temperature (T_g) of the synthesized SMP foams ($n = 3$). Further, shape recovery of the SMP specimens ($n = 3$, $1 \times 1 \times 1$ cm) was characterized by bringing the material above T_g and measuring the shape recovery using:

$$SR\% = \frac{h(t) - h_c}{h_0 - h_c} \quad (1)$$

where $SR\%$ is the shape recovery percentage, $h(t)$ is the height of the foam at a given time, h_c is the height of the compressed foam, and h_0 is the original (prior-to-compression) height of the foam. The shape recovery experiments were performed at both the room temperature and the freezing condition to characterize the shape storage. A heat ramp from room temperature to $T_g + 10^\circ\text{C}$ was also applied to characterize the triggering of shape recovery as a response to heat stimuli.

Thermo-mechanical Testing: An Instron 5969 machine was used to characterize the compressive properties of the SMP foams: Foams ($n = 6$) of $1 \times 1 \times 1$ cm were uniaxially compressed up to 80% strain, with mechanical parameters derived from the stress-stretch curves.

Polypyrrole Coating & Thermal Analysis: To induce conductivity of the polyurethane matrices, polypyrrole (PPy) was polymerized on the surface of the foam [4]. Cubic foams were first submerged in FeCl_3 for 10 min and subsequently suspended over 1 mL of pyrrole in an air-tight container for 2 h at -20°C . PPy-coated foams were then dried overnight in a fume hood and stored in a desiccator.

Fabrication of Patient-Specific Foams and Aneurysm Models:

Aneurysm geometries were obtained via segmentation of computerized tomography angiography (CTA) images of human subjects (IRB #7932) using AMIRA software. Geometries were used to print PVA templates for foam synthesis and for phantom fabrication. Phantoms were fabricated by pouring polydimethylsiloxane (PDMS) on solid PVA 3D-printed templates. PDMS was cured at 70 °C for 1 h and PVA was thoroughly rinsed in a sonicator until completely dissolved.

RESULTS

Material Synthesis and Microstructure: SMP foams replicated the computer-designed infill structure of PVA templates (Fig. 1). Wall thickness of the infill design was significantly higher in SMP foams than in PVA templates ($p < 0.01$, not shown here), demonstrating that the SMP solution cured around the PVA filament, thus creating a sheath-like structure. Overall, the SMP foam mimicked the PVA template geometry and infill producing a porous compressible 3D SMP foam.

Calorimetry & Shape Recovery Analysis: DSC demonstrated that the 3D-printed foams exhibited significantly lower T_g than solid SMP specimens (not shown). By fine-tuning the molar compositions, we found that a TEA-to-HDI ratio of 0.22 yielded a $T_g \approx 41^\circ\text{C}$ that is the desired working temperature for the endovascular embolization procedure. At this molar ratio, we found that the material maintained its deformed configuration when stored at freezing temperatures ($<0^\circ\text{C}$, Fig. 2a), but an average of 40 % shape recovery was observed when foams were stored at room temperature after 10 min. In addition, we observed that a heat ramp from room temperature to $T_g + 0^\circ\text{C}$ increased the rate of shape recovery (Fig. 2b). These experiments demonstrate the thermal dynamic behavior of our SMP with customized T_g .

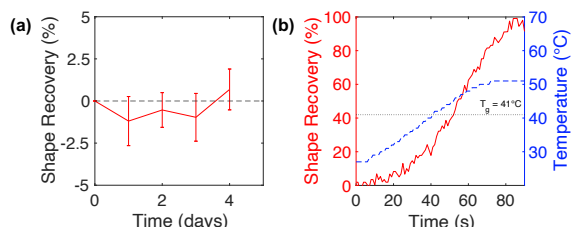


Figure 2. (a) Shape recovery storage at -20°C . (b) Shape recovery measurements as a response to a heat ramp.

Mechanical Properties: SMP foams exhibited a nonlinear anisotropic mechanical behavior. The x - and y -axes did not exhibit significant differences in the characterized mechanical parameters, while the z -axis exhibited significantly *greater peak stresses* and *elastic moduli* than the other two axes. Overall, the foam exhibited a unique behavior that promoted guided compression along the x - and y -axes.

Occlusion of Patient-Specific Phantoms: SMP foams with patient-specific geometries (Fig. 3a) were successfully used for the occlusion of aneurysm models. The foam was transported in its deformed configuration into the aneurysm and shape recovery was triggered by applying external heat. The SMP foam successfully recover and completely occlude the aneurysm space (Fig. 3b).

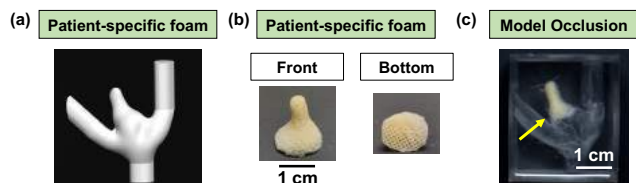


Figure 3. (a) 3D aneurysm model obtained from patient CTA imaging. (b) SMP foams with patient-specific geometry and a grid infill pattern design. (c) Proof-of-concept aneurysm occlusion using a patient-specific aneurysm model and our 3D-printed SMP foam (arrow).

Joule-Heating Properties of the PPy-Coated Foams: The PPy-coated foams had a black appearance, demonstrating pyrrole polymerization [4]. Resistivity measurements ($n = 3$) of the PPy-coated foams yielded an average of $6.16 \pm 1.94 \text{ k}\Omega$. In addition, the uncompressed foams were able to conduct heat during electrical stimulation (30V DC) using a parallel copper plate setup, reaching temperatures $>T_g$ in less than 10 s, as demonstrated in an infrared (IR) thermal analysis (Fig. 4).

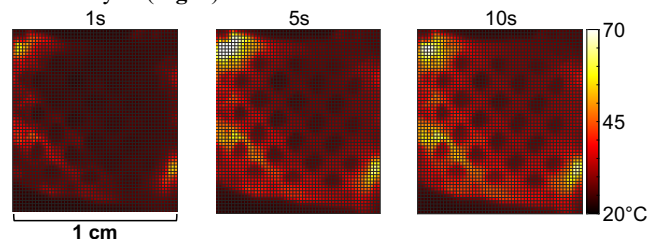


Figure 4. IR camera snapshots of a PPy-coated SMP foam with a grid infill pattern being subjected to DC voltage at different timepoints.

DISCUSSION

In this present work, we have developed a facile method for the fabrication of porous SMP foams with customized T_g and patient-specific geometries. For the first time, we have developed a biomaterial that can be fabricated with aneurysm-specific geometries, custom infill microstructure, and anisotropic mechanical properties. A material with these properties and unique features had been elusive in our previous efforts [5], where SMP shape recovery could be triggered using Joule-heating but had less desirable mechanical behaviors and structural integrity, preventing its fabrication with guided compression patterns nor with patient-specific geometries. Overall, these features are the cornerstone to develop a coil-free endovascular device that can achieve higher complete occlusion than the currently available technologies.

To achieve this longer-term goal, the ongoing research will optimize the polypyrrole coating methods to obtain low resistivity, while maintaining T_g of the pure SMP matrix without deteriorating its mechanical behavior. With this future optimization process, testing of phantom occlusion using PPy-coated foams will be performed in dry and wet conditions. In addition, we will characterize the biocompatibility of the material via cell culture with endothelial cells. Future directions of the project will also include the preclinical effectiveness assessment of the device using our established New Zealand rabbit animal model [6].

Overall, this research presents a novel technology for the treatment of ICAs using an SMP-based endovascular approach. Our 3D SMP foam material exhibits features with great potential for improved aneurysm occlusion using endovascular embolization.

ACKNOWLEDGEMENTS

We would like to acknowledge the University of Oklahoma Graduate College Alumni Fellowship and Dissertation Excellence Award for sponsoring Mr. Pineda-Castillo's research. This project is funded through the NIH R01HL159475-01A1 grant.

REFERENCES

- [1] Pineda-Castillo, S.A. *et al.*, *Polymers*, 14(13):2526, 2022.
- [2] Toth, G. *et al.*, *Vasc Med*, 23(3):276-288, 2018.
- [3] Kunkel, R. *et al.*, *J Mech Behav Biomed Mater*, 88:422-430, 2018.
- [4] Zhang, F. *et al.*, *ACS Mater & Interf*, 10:35526-35532, 2018.
- [5] Pineda-Castillo, S.A. *et al.*, *Adv Eng Mater*, 2100322, 2021.
- [6] Pineda-Castillo, S.A. *et al.*, *bioRxiv*, 2021.

SPATIOTEMPORAL EVOLUTION OF COLLAGEN MICRO-MECHANICS UNDER BREAST CANCER CELL DRIVEN REMODELING

Adil Khan (1), Jacopo Ferruzzi (1)

(1) Department of Bioengineering, The University of Texas at Dallas, Richardson, TX, USA

INTRODUCTION

Mechanical interactions between cells and the surrounding extracellular matrix (ECM) play a key role in regulating physiological processes as well as numerous diseases [1]. Cell-ECM interactions are particularly relevant in breast cancer, where rogue signaling from transformed epithelial cells leads to increased deposition, alignment, and stiffening of peritumoral collagen. While mechanical remodeling of the collagenous ECM continues to be implicated with cancer cell invasion and overall patient survival [2], the underlying relationship between cancer cell driven remodeling and collagen micro-mechanics remains poorly understood. This is primarily due to inherent complexities in measuring 3D micro-mechanical properties of the collagen networks, which are known to be highly heterogeneous, nonlinear, and anisotropic. To describe such complexity, an integrated method for defining the local structure-function relationship in collagen networks is of the essence, though not currently available.

To address this unmet need, we have developed a novel approach for characterizing the micro-mechanics of fibrous ECM scaffolds. Our method employs iron oxide beads embedded into collagen networks as localized micro-scale actuators. Through the application of coordinated magnetic fields, the beads experience a homogenous torque and generate heterogeneous deformations, which depend on the local material properties of the network. By combining magnetic twisting, confocal microscopy, and finite element analysis, we have thus established a platform capable of interrogating local cell-ECM mechanical interactions. Here, we demonstrate this capability by mapping the spatial and temporal evolution of mechanical heterogeneities in a collagen matrix as it is remodeled by breast cancer cells of different invasive potentials.

METHODS

Ferromagnetic beads made of pure iron oxide with an average diameter of 4.8 μm were distributed evenly in a collagen solution, which

was polymerized using established protocols [3]. To enable the beads to bind with collagen fibrils, their surface was functionalized with NHS groups [4]. In brief, the beads were incubated in a solution of nitrodopamine (ND) – polyethylene glycol (PEG) – succinimidyl carbonate (NHS) in 0.1 M triethylammonium acetate (TEA) for 2 hours, following which they were washed 4 times by centrifugation and resuspension in TEA. Finally, the beads were resuspended in 20 μL of TEA and mixed with the unpolymerized collagen solution at a density of 10^5 particles/ml. Micro-mechanical experiments were conducted on acellular collagen gels of varying density (1 to 4 mg/ml) and on collagen networks of fixed collagen density (2 mg/ml) populated with either a homogenous distribution of single cancer cells ($\sim 250 \times 10^3$ cells/ml) or with embedded tumor spheroids ($\sim 10^3$ cells/spheroid).

The micro-structural organization of the collagen network around selected beads was assessed using a Nikon AX confocal microscope equipped with a 20 \times objective lens and operating in reflection mode with an excitation wavelength of 488nm. The Nikon NIS-Elements software was used to control independently two orthogonal sets of coils mounted on a custom microscope insert. A strong magnetizing pulse B^M in one direction, followed by a weaker twisting field B^T in the perpendicular direction were used to impose a magnetic torque (T) on all the beads within a sample (Figure 1a). Confocal image stacks acquired before and after the magnetic stimulation were compared using an augmented Lagrangian digital image correlation algorithm to measure the displacements generated in the collagen network [5]. The magnitude of the 3D displacement field around each bead was compared with that produced by a finite element model (Figure 1b), and the difference was minimized to estimate the unknown material properties of the local collagen network. For the sake of simplicity, collagen was modeled as a neo-Hookean material $W = \mu/2 (I_c - 3)$ and the associated Young's modulus $E = 2\mu(1 + \nu)$ was used to report local material properties, where the Poisson's ratio ν was determined in preliminary experiments by means of uniaxial unconfined compression.

RESULTS

To validate our novel approach, we imposed finite element-based synthetic deformations onto experimentally measured confocal stacks taken from acellular collagen gels. Our method was able to recover the imposed Young's moduli with a mean error of 6.8%. Direct measurements via magnetic twisting in acellular collagen gels indicate that material stiffness gradually increases with increasing collagen density: $E = 11 \pm 5$ Pa for 1 mg/ml, $E = 14 \pm 7$ Pa for 2 mg/ml, $E = 20 \pm 4$ Pa for 3 mg/ml, and $E = 25 \pm 11$ Pa for 4 mg/ml.

Next, we used the non-tumorigenic MCF-10A and post-metastatic MDA-MB-231 breast cancer cell lines to investigate the mechanical signatures of cancer cell mediated matrix remodeling. First, we performed a collagen gel contraction assay by dispersing single cells in 2 mg/ml collagen gels. Once polymerized, the cylindrical collagen matrices were physically detached from their Petri dish, leaving them floating and free to contract over the course of four days. The more contractile MDA-MB-231 cells compacted the collagen matrices by up to 60% of their original area. While acellular gels remained mechanically stable over time, cell-mediated compaction was accompanied by a near 3.7-fold increase in material stiffness (Figure 1c). Subsequently, we embedded multicellular tumor spheroids in 2 mg/ml collagen gels and monitored their growth and invasion over time. By day 4, the more epithelial MCF-10 spheroids invaded collectively with modest remodeling of the surrounding collagen. During the same time frame, the more mesenchymal MDA-MB-231 spheroids aligned collagen fibers radially and invaded as single cells in a highly dynamic manner. This heterogeneous reorganization of the peritumoral collagen network (Figure 1d, left) resulted in spatially varying material properties, with a marked stiffening in areas of elevated compaction and alignment of collagen fibers (Figure 1d, right). Magnetic twisting is therefore capable of monitoring the spatiotemporal evolution in material properties driven by highly contractile and invasive breast cancer cells.

DISCUSSION

During invasion and metastasis, breast cancer cells interact with the surrounding ECM to enable mutual regulation of cell signaling and ECM mechanics, ultimately resulting in cellular migration into adjacent tissues. While various endogenous and exogenous fluorescent reporters are already available to track intracellular signaling in a spatially and temporally resolved manner, methods to measure extracellular micro-mechanics in a 3D setting are still limited. Currently available methods, such as atomic force microscopy (AFM) and optical tweezers (OT) are limited, respectively, by the fact that AFM is a 2D technique and that OT involve complex and low-throughput 3D measurements. More importantly, other approaches are limited by the often implicit assumption of linear and isotropic elasticity [4,6]. Similarly, this work is currently limited by the adoption of a neo-Hookean material model, but our approach lends itself to the exploration of more realistic constitutive models as it inherently incorporates both structural and mechanical information by combining confocal reflection imaging and magnetic twisting.

Future work will focus on evaluating structure-based constitutive models of collagen network mechanics and on investigating the mechanisms of cancer cell driven remodeling by selectively inhibiting key processes mediating cell-ECM interactions such as contractility, proteolysis, and cross-linking. Furthermore, the capacity of measuring evolving material properties in 3D can potentially improve the accuracy of traction force estimation in 3D [7]. We conclude that our method represents a new semi-automated approach to map 3D spatiotemporal heterogeneities in nonlinear collagen micro-mechanics. This capability will enable mechanistic studies on cell-ECM interactions in the context of breast cancer and other fibrotic conditions.

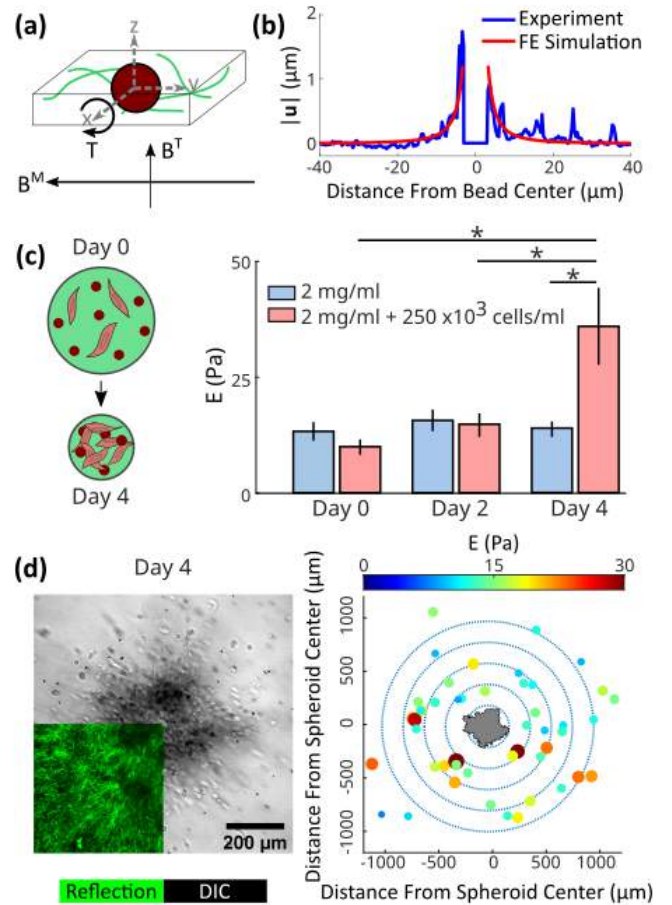


Figure 1: (a) Schematic representation of a ferromagnetic bead (red) embedded into a collagen network (green) and torqued about a specific axis (herein indicated as x) using coordinated magnetic fields B^M and B^T . (b) Iterative simulations are conducted to match the experimental and computational displacements and estimate the local material properties of the collagen network. (c) Compaction of collagen gels seeded with MDA-MB-231 cancer cells (250×10^3 cells/mL) occurs gradually over time and is accompanied by a corresponding increase in Young's modulus. (d) Confocal imaging (left) and spatial mapping of Young's moduli (right) around an invading MDA-MB-231 tumor spheroid reveal a correspondence between structural and mechanical remodeling of collagen after 4 days of culture. Data presented as mean \pm standard deviation. Statistical significance was determined using a one-way ANOVA with a Tukey post-hoc test. (* $p < 0.05$).

ACKNOWLEDGEMENTS

We acknowledge Professor Jeffrey J. Fredberg and Dr. Emil Millet (Harvard T.H. Chan School of Public Health) for their support with ferromagnetic beads, and Professor Jin Yang (University of Texas at Austin) for expert assistance with digital image correlation algorithms.

REFERENCES

- [1] Yamada K. et al., *Trends Cell Biol*, 32: 883-895, 2022
- [2] Ray A. and Provenzano P., *Curr Opin Cell Biol*, 72: 63-71, 2021
- [3] Ferruzzi J. et al., *Sci Rep*, 9: 1-16, 2019.
- [4] Asgeirsson D.O. et al., *Lab Chip*, 21: 3850-3862, 2021.
- [5] Yang J. and Bhattacharya K., *Exp Mech*, 4: 719-735, 2021
- [6] Krajina B. et al., *Sci Adv*, 7: 1969-1983, 2021
- [7] Mark C. et al., *Elife*, 9: 51912-51933, 2020

HEMATOCRIT IS A POTENT DRIVER OF PLATELET ADHESION AT SUPRAPHYSIOLOGICAL SHEAR RATES

C. Watson (1), K. Manning (1,2)

- (1) Department of Biomedical Engineering, The Pennsylvania State University, University Park, PA, USA
(2) Department of Surgery, Penn State Hershey Medical Center, Hershey, PA, USA

INTRODUCTION

Supraphysiological shear rates ($>1\text{--}2,000\text{ s}^{-1}$) have been well established as a driving factor in the incidence of pathological and device-mediated thrombosis [1]. Excessive shear rates cause not only increased platelet activation but amplified unfurling of the von Willebrand factor (vWF), leading to increased tethering of platelets and thrombus formation [2]. vWF is an ultralarge, mechanosensitive glycoprotein circulating within plasma, acting to permit platelet arrest within arterial shear stress ranges at sites of injury. Supraphysiological shear forces drive the upregulation of vWF-mediated platelet capture. This clinically relevant phenomenon is tied to the shear-sensitive structure of vWF multimers, leading to pathological thrombosis by increased platelet activation and vWF unfurling [3].

Due to the severity of adhesion associated complications, it is crucial that the mechanisms behind vWF-mediated platelet deposition are further mapped to improve predictive modeling and inform the development of novel anticoagulant and antiplatelet agents. The unfurling behavior of vWF is tied to local fluid dynamics, chiefly the wall shear rate or shear rate gradient, of a potentially adhesive surface [4]. Flow perturbation during or following a period of exorbitant shear rates ($\geq 5,000\text{ s}^{-1}$) can cause sudden wall contact following a period of acceleration or deceleration. Similarly, margination by red blood cells displaces vWF and platelets into the near wall region of high shear and has been demonstrated to play a role in vWF adhesion efficacy [5]. Hematocrit (HCT) is therefore hypothesized to play a crucial role in thrombus deposition at supraphysiological shear rates. The primary objective of this study was to observe the effect of variable hematocrit and shear rate on platelet deposition in a sudden expansion model.

METHODS

Using established methods of soft lithography [6], polydimethylsiloxane (PDMS) microchannels were fabricated to act as a testing platform for shear-altered deposition. A sudden expansion

geometry was fabricated to induce rapid deceleration, with an expansion ratio of 2:1 at a backwards facing step (BFS). Microchannels had a cross-section of $200 \times 50\text{ }\mu\text{m}$ in the upstream region and a cross-section of $400 \times 50\text{ }\mu\text{m}$ in the downstream region. PDMS chips were cleaned in 70% ethanol and sealed to glass microslides using a plasma cleaner (Harrick Plasma, Ithaca NY). Shear rates were calculated in ANSYS FLUENT (ANSYS, Canonsburg PA) and verified by acquiring velocity data with a micro-PIV system (TSI Inc., Shoreview MN). Prior to experiments, channels were coated with human type I collagen at 50 or $100\text{ }\mu\text{g/mL}$ as noted to create a reactive surface. Human blood was acquired via a Penn State IRB approved protocol and anticoagulated with sodium citrate at a final concentration of 0.32%. Blood was centrifuged at 300g for 30 min to obtain separated platelet rich plasma (PRP), which was used to quantify platelet concentration. Blood was then reconstituted to the desired HCT (0%, 20%, 40%) with PRP and buffered with saline, maintaining native platelet concentration ($264 \pm 55.3 \times 10^6/\text{mL}$). Platelets were stained with DiOC₆ and incubated for 30 min at 37°C. Blood was not recalcified to avoid triggering of the coagulation cascade. Blood was then perfused for 3 min through microchannels with a Harvard syringe pump (Kd Scientific, MA) at 5, and 25 $\mu\text{L/min}$ to achieve wall shear rates of 1,000 and $5,000\text{ s}^{-1}$, correlating to arteriolar and pathological shear rates, respectively ($n = 6\text{--}7$). Following these experiments, a second study was conducted using the A2A9 antibody (Biolegend, San Diego CA) to inhibit $\alpha_{\text{IIb}}\beta_{\text{III}}$ function ($n = 7$). Blood reconstituted to 40% HCT was incubated with 5 $\mu\text{g/mL}$ A2A9 for 30 min prior to perfusion through straight channels at 500 and $5,000\text{ s}^{-1}$. Real-time immunofluorescence images were acquired at 1 frame per second with an Olympus IX71 inverted microscope and DP74 4MP CMOS camera (Olympus, Tokyo Japan). Pixel resolution was $0.586\text{ }\mu\text{m/pixel}$ edge. Images were converted to binary and processed in ImageJ (NIH, Bethesda MD) and MATLAB (Mathworks, Natick MA).

RESULTS

Hematocrit was observed to have a notable effect on platelet deposition that was compounded by flow deceleration. Thrombus surface coverage (% total area) within the 50 $\mu\text{g/mL}$ collagen coated BFS channel was affected by hematocrit at all shear rates (**Figure 1**), and the increase in deposition was pronounced in the step region. A two-way ANOVA assessment followed by Tukey's multiple comparisons test was performed. Hematocrit was a very significant factor ($p < 0.01$) in thrombus deposition, while shear rate was positively correlated with surface area coverage of only 40% HCT.

Hematocrit had an additional notable effect on thrombus morphology, as measured by mean area of thrombus deposits (μm^2). Increasing hematocrit resulted in larger and more prevalent thrombus surface deposits. Hematocrit was a significant factor in determining mean thrombus area ($p < 0.05$). Shear rate was not a determining factor in mean thrombus area.

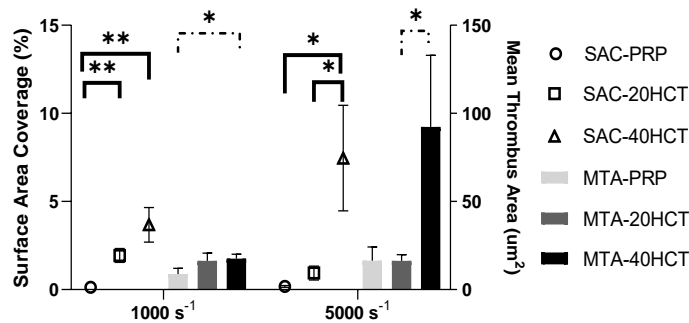


Figure 1: Surface area coverage (SAC) and mean thrombus area (MTA) related to increasing hematocrit and shear rate. Statistical significance of SAC is denoted by solid lines while significance of MTA is denoted by dashed lines. Data are presented as mean \pm SEM.

Additional experiments at 40% HCT were conducted to investigate the change in thrombus morphology observed. The function of the $\alpha_{\text{IIb}}\beta_{\text{III}}$ integrin was inhibited prior to perfusion over 100 $\mu\text{g/mL}$ collagen coated straight channels with a 200 x 50 μm cross section. A two-way ANOVA assessment followed by Tukey's test was performed. Shear rate and receptor inhibition were both significant factors in determining SAC ($p < 0.05$, $p < 0.01$) and MTA ($p < 0.01$, $p < 0.001$). Pairwise comparisons demonstrated that receptor inhibition significantly reduced both SAC ($p < 0.001$) and MTA ($p < 0.001$) at 5,000 s^{-1} . This effect was insignificant at 500 s^{-1} (**Figure 2**).

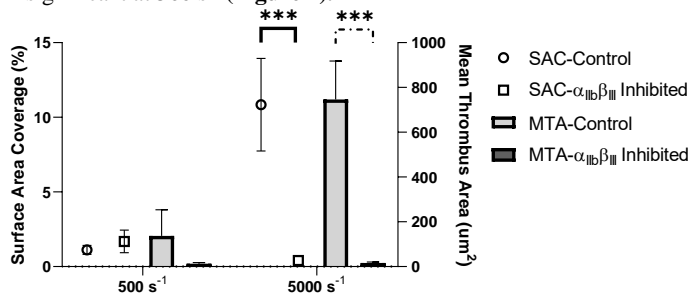


Figure 2: Surface area coverage (SAC) and mean thrombus area (MTA) related to receptor inhibition and shear rate. Data are presented as mean \pm SEM.

DISCUSSION

The presence of red blood cells is a critical contributor to vWF-mediated thrombus formation, despite remaining primarily biochemically passive. Platelet deposition at shear rates relevant to

arteriolar and pathological flow was quantified. Hematocrit was observed to mediate platelet adhesion at all shear rates investigated, and larger thrombi tended to form at higher shear rates at physiological hematocrit. Thrombus deposition for PRP was minimal at all shear rates, suggesting reduced platelet delivery to the collagen surface. While platelet deposition at 20% HCT was comparable to 40% HCT at 1,000 s^{-1} , attachment decreased as shear rate increased, indicating a lack of clot stabilization. Thrombus formation at 40% HCT was dramatically amplified at supraphysiological shear rates (**Figure 3**).

The observed changes in thrombus morphology suggest a switch from platelet-collagen binding to platelet-platelet binding, possibly linked to a change in platelet integrin activity. This potential mechanism was investigated by selective inhibition of the $\alpha_{\text{IIb}}\beta_{\text{III}}$ receptor in a subsequent experiment. This treatment resulted in a significant loss in surface area coverage and reduced platelet-platelet interactions, albeit only at the higher shear rate of 5,000 s^{-1} . This supports a shift in receptor binding activity at supraphysiological shear rates towards $\alpha_{\text{IIb}}\beta_{\text{III}}$ -dominated platelet adhesion.

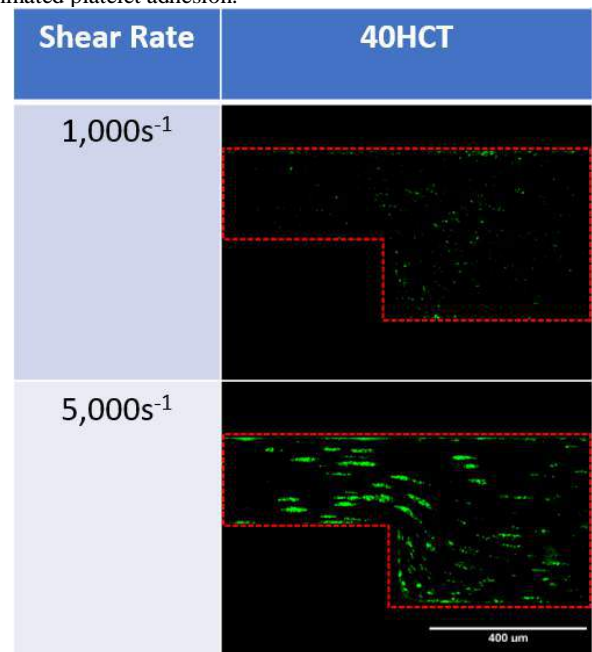


Figure 3: Representative images of thrombus deposition for 40% HCT blood perfused over 50 $\mu\text{g/mL}$ collagen at variable shear.

The increased thrombus deposition associated with supraphysiological shear rates was shown to be dependent on physiological hematocrit levels. Changes in thrombus morphology and an observed affinity for platelet-platelet interactions were linked to activity of the $\alpha_{\text{IIb}}\beta_{\text{III}}$ integrin. Further investigation of this phenomenon is required to determine clinical impact and how modulation of platelet binding receptors might influence adhesive behavior.

ACKNOWLEDGEMENTS

This work is generously supported by NIH HL136369.

REFERENCES

- [1] Manning, K. B., et al., *Curr Opin Biomed*, 2021.
- [2] Sadler JE., Annual Review of Biochemistry, 1998, 67.1: 395-424.
- [3] Kreuziger, LB., ASAIO, 2018, 64.6: 754.
- [4] Westein, E., Proc Natl Acad., 2013, 110.4: 1357-1362.
- [5] Rack, K., Scientific reports, 2017, 7.1: 1-12.
- [6] Jamiolkowski, MA., Biomaterials, 2016, 96: 72-83.

LOCAL ECM STIFFNESS MODULATES EPITHELIAL CELL RESPONSE TO MICROPATTERNS

Tasnim Shireen (1), Rajath D. Prabhu (1), Deekshitha Jetta (1), Susan Z. Hua (1,2)

(1) Department of Mechanical and Aerospace Engineering, University at Buffalo, Buffalo, NY, USA

(2) Department of Physiology and Biophysics, University at Buffalo, Buffalo, NY, USA

INTRODUCTION

Cells respond to substrate mechanical confinements with changes in morphology, proliferation, and motility. It is widely observed that cells grown on narrow stripes stretch themselves along the orientation of the stripes [1-3]. Such cells develop thick stress fibers along the stripes suggesting a reinforcement of the cytoskeleton in response to the geometrical constraints [4]. Nucleus of the cell is connected to the surrounding cytoskeleton via linker of nucleoskeleton and cytoskeleton complex. The alteration of mechanical environments around the nucleus can also trigger the change in nucleus shape. In human endothelial cells, the mechanical confinement caused nuclear deformation is attributed to the enhanced apical stress fibers that press the nucleus envelope [5-7]. However, in epithelial cells, shear stress disassembles stress fibers, the nucleus shrinks through Piezo1 mediated Ca^{2+} signaling [8]. Thus, the cells utilize complex force transduction mechanisms in response to external mechanical signals.

In this study, we have created fibronectin stripe patterns on substrates of varying stiffness and investigated the roles of substrate stiffness on cell response to mechanical confinements in MDCK cells. To assess the involvement of Piezo1, we knockdown Piezo1 with miRNA. Our results show that cells grown on soft patterns are significantly longer than cells on stiffer patterns. The cell elongation coincides with nuclear deformation. Knockdown of mechanosensitive Piezo1 protein significantly reduced the elongation on stiffer substrates but has minimal effect in cells on soft substrates. This result shows that increasing tension in stress fibers is not required for MDCK cell expansion on soft substrate, thus, different mechanisms are involved.

METHODS

PDMS substrates of various stiffness were made using Sylgard 184 and Sylgard 527. Four stiffness were tested, hard substrate (184 sylgard 10:1, stiffness ~ 1 MPa), semi-soft substrate (184 Sylgard 40:1, stiffness ~ 25 KPa) and soft substrate (527 Sylgard 1:0.8 ~1 KPa), and glass

substrate (stiffness >1 GPa). To create micropatterns on the soft substrate, a reverse microcontact printing technique was used. Briefly, the substrate was plasma treated, followed by coating with monolayer of Fibronectin. The PDMS stamp (10 μm feature, 6 μm groove) was plasma treated for 30 s and then placed in contact with the substrate for 1 hr. The substrate was then treated with Pluronic F-127 for 1 hr to block non-selective cell attachment.

Prior to experiments, MDCK cells were seeded onto the patterned substrates and placed in incubator for 150 min. Following live-cell imaging, the cells were fixed and stained with Phalloidin Alexa Fluor 568 and Hoechst 33342 dye. Images were captured with a Zeiss inverted microscope with a CCD camera.

Statistical analysis used two-sample t-test. Values of $p < 0.005$ were considered statistically significant.

RESULTS

Substrate stiffness regulates cell elongation on micropatterns

To test the effect of substrate stiffness on MDCK cell response to narrow fibronectin stripes, we patterned micro-stripes (6 μm wide and 10 μm spacing) on substrates with various stiffness, namely, glass, hard, semi-soft, and soft. Cells have shown elongation on fibronectin stripes on all substrates. Interestingly, the cell elongation on soft substrate is significantly longer than stiffer substrates (Fig. 1a). The typical cells linear expansion on soft substrate are ~2 times longer than cells on glass. Cells showed similar expansions on semi-soft and soft substrates. The aspect ratio of cells on different substrates were analyzed using previously developed method [3]. Statistical analysis shows that the difference between soft and stiffer substrates is significant (Fig. 1b). Immunostaining F-actin with phalloidin showed that cells exhibit stronger actin stress fibers on the hard substrates compared with soft substrates. This suggests that stress fiber generated tension is not responsible for MDCK cell expansion on the soft substrates.

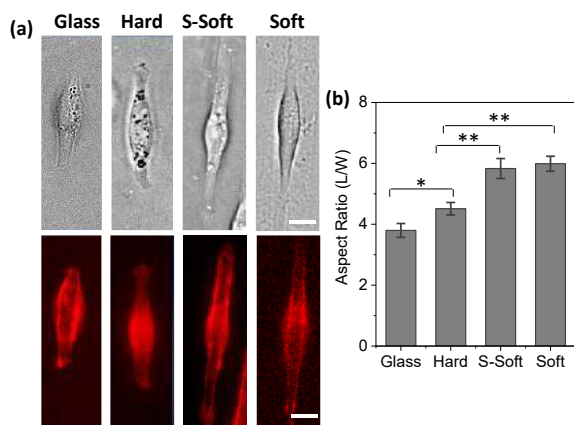


Figure 1: MDCK cell elongation on micropatterns with various stiffness. (a) Cells on soft stripes show maximal elongation but weaker stress fibers. (b) Aspect ratio of cell body on each substrate ($n = 50$ for all substrates, $*p < 0.05$, $**p < 0.005$). Scale bars represent $20 \mu\text{m}$.

Nuclear deformation coincides with cell elongation

To assess whether the ECM mechanical signals can be transmitted to the nucleus, we stained nucleus with Hoechst dye following the cell stretching and analyzed the shape of nuclei on different substrate. We found that nuclear deformation coincides with cell elongation in MDCK cells (Fig. 2). This effect is also modulated by substrate stiffness. On softer substrate, cells consistently show larger elongation and larger nucleus deformation. However, on soft substrate the thick stress fibers were not observed, therefore, mechanical stress arising from tension in stress fibers are not responsible for the nuclear deformation. We have previously reported that nuclear deformation in MDCK cell under shear stress is mediated by intracellular Ca^{2+} that increases through activation of Piezo1 channels [8].

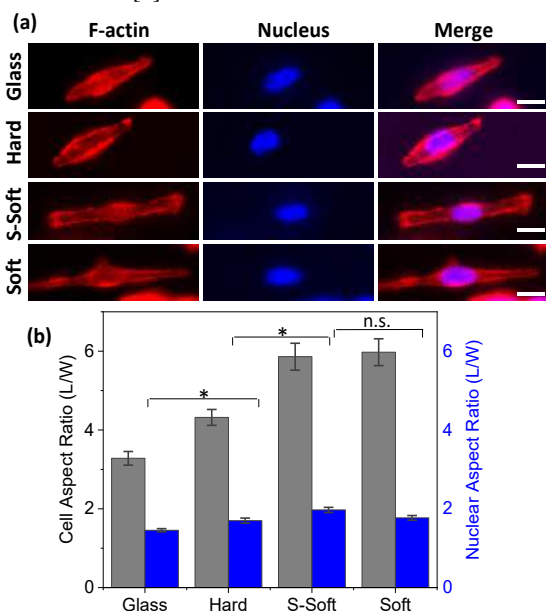


Figure 2. Nuclear deformation coincides with cell elongation. Images of actin (red) and nuclei (blue) in cells grown on micro-stripes on different substrates, showing soft substrate caused larger cell and nuclear deformation. Scale bar = $20 \mu\text{m}$. (b) Statistical analysis of cell elongation and corresponding nuclear deformation ($n = 40$ for hard and semi-soft substrates; $n = 30$ for glass and soft substrates. $*p < 0.005$).

Role of Piezo1 in cell response to substrate confinements

MDCK cells endogenously express mechanosensitive Piezo1 channels. To investigate the role of Piezo1 in cell elongation, we targeted Piezo1 miRNA to knockdown Piezo1 (PIKD). Cells were transfected with Piezo1 miRNA and co-expressed with EGFP to verify transfection (Fig. 3a). Knockdown of Piezo1 significantly reduced the elongation on patterns on glass substrate (Fig. 3b). The mean elongation of PIKD cells was ~ 2.5 , that was 40% lower than nearby control cells. The statistical analysis shows consistent results (Fig. 3c). This result shows that Piezo1 mediated Ca^{2+} uptake participated in the cell elongation on hard substrate, which is consistent with our previous findings [3]. Our recent results show that inhibiting Piezo1 only reduced the stress fibers, however, it did not alter the cell shape (data not shown). It suggests that different stiffness may activate different mechanisms for MDCK cell elongation.

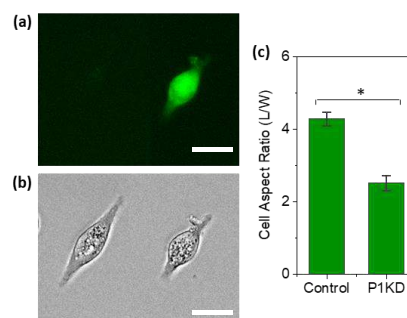


Figure 3: Elongation of Piezo1 knockdown cells. (a) MDCK cells expressing miRNA that target *Piezo1* (green). (b) Elongation of control cell (left) and PIKD cell (right), showing that Piezo1 knockdown significantly reduced elongation. Scale bar = $20 \mu\text{m}$. (c) Mean cell elongation in PIKD and control, showing Piezo1 knockdown reduced elongation by 40% (Control: $n = 29$; PIKD: $n = 14$, $*p < 0.005$).

DISCUSSION

MDCK cells elongate on micropatterned stripes, the cell response depends on the substrate stiffness. Cells showed maximal elongation on the soft substrate compared to stiffer ones. Nuclear deformation coincides with the cell elongation. It has been reported that mechanical confinements change tension in actin stress fibers, causing changes in cell shape and nuclear deformation [5, 7]. Our results show that the cytoskeleton tension may not be responsible for deformation, depending on the substrate stiffness. On stiffer substrates, Piezo1 mediated Ca^{2+} uptake may cause increase in myosin contractility and cytoskeletal tension resulting in cell expansion. On soft substrates, stress fibers were reduced significantly, cytoskeleton may only serve as guidelines for cell adhesion. Epithelial cells utilize different force transmission mechanisms in response to varying local stiffness.

ACKNOWLEDGEMENTS

This work was supported by National Science Foundation (CMMI-2015964).

REFERENCES

- [1] Suffoletto K, et al. J Biomech. 2014;48:627-35.
- [2] Thery M, et al. Nat Cell Biol. 2005;7(10):947-53.
- [3] Jetta D, et al. Sci Rep. 2021;11(1):5088.
- [4] Thery M, et al. Cell Motil Cytoskeleton. 2006;63(6):341-55.
- [5] Versaevel M, et al. Sci Rep. 2014;4:7362.
- [6] Swift J, et al. Science. 2013;341(6149):1240104.
- [7] Bray MA, et al. Biomaterials. 2010;31(19):5143-50.
- [8] Jetta D, et al. J Cell Sci. 2019;132(11).

HEMODYNAMICS OF COARCTATION OF THE AORTA - COMPARISON OF A DISTRIBUTED LUMPED PARAMETER MODEL AND 4D FLOW MRI

Labib A. Shahid (1), Matthew A. Culver (2), James P. Rice (1), Haben Berhane (3,4), Cynthia K. Rigsby (5), Joshua D. Robinson (5), Lindsay M. Griffin (5), Michael Markl (3,4), Colleen M. Witzenburg (1,2), Alejandro Roldán-Alzate (1,2,6)

- (1) Mechanical Engineering, University of Wisconsin-Madison, Madison, WI, USA
- (2) Biomedical Engineering, University of Wisconsin-Madison, Madison, WI, USA
- (3) Radiology, Northwestern University, Chicago, IL, USA
- (4) Biomedical Engineering, Northwestern University, Evanston, IL, USA
- (5) Medical Imaging, Lurie Children's Hospital of Chicago, Chicago, IL, USA
- (6) Radiology, University of Wisconsin-Madison, Madison, WI, USA

INTRODUCTION

Coarctation of the aorta (COA) is one of the most common congenital heart defects. It is characterized by a narrowing in the aortic arch or proximal descending aorta. Treatment procedures for COA include surgery, intravascular stent placement, and balloon angioplasty. However, the selection criteria for the optimal treatment strategy are not well defined, and interventionalists often rely on their preference rather than patient-specific conditions [1]. 1 in 3 COA patients have post-interventional secondary complications [2], likely due to suboptimal treatment.

4D Flow MRI is a diagnostic imaging technique capable of measuring time-resolved 3D blood velocities within a volumetric acquisition region. Numerous studies have used 4D Flow MRI to evaluate patient-specific blood flow information in COA [3-4]. 4D Flow MRI has high potential to be used as a tool for treatment planning, however, imaging on its own provides no predictive capabilities. Image-based computational fluid dynamics (CFD) can be used to complement medical imaging, such as virtually testing and simulating interventions [5]. A major challenge hindering image-based CFD from achieving widespread clinical adoption is its high computational cost. This calls for reduced order modeling strategies.

A distributed lumped parameter (DLP) model of blood flow was recently published by Mirramezani and Shadden [6]. The results of the DLP model were consistent with CFD. However, to our knowledge, the DLP model has not been compared against in-vivo 4D Flow MRI. The aim of this study was to compare hemodynamic flow rates from the DLP model against in-vivo 4D Flow MRI in COA patients.

METHODS

In-vivo 4D Flow MRI was performed in two male pediatric patients before and after COA repair following an IRB-approved HIPAA-compliant protocol. Patient 1 was 10 and 12 years old during the two scans, and Patient 2 was 4 and 12 years old during the two scans.

The thoracic aorta was segmented, and centerlines were generated using semi-automatic software Mimics (Materialise NV, Leuven, Belgium). Flow rates at the ascending aorta (AAo), brachiocephalic (BCA), left common carotid (LCCA), left subclavian arteries (LSA), and descending aorta (DAo) were obtained using EnSight (Ansys, Inc., Canonsburg, PA, USA).

Most image-based CFD models use medical imaging to define the geometry and numerically solve the 3D incompressible Navier-Stokes equations. The DLP model formulates the mass and momentum conservation as ordinary differential equations (ODEs) in terms of cross-sectionally averaged pressure $P(x, t)$ and volumetric flow rate $Q(x, t)$, where x denotes the axial coordinate along a given vessel and t is time. Conservation of momentum yields

$$\left(\frac{\rho}{\pi} \int_0^L \frac{1}{R(x)^2} dx \right) \frac{\partial Q}{\partial t} + \mathcal{R}Q + \Delta P = 0 \quad (1)$$

where ρ is fluid density, $R(x)$ is vessel radius, L is the length of the vascular segment, and \mathcal{R} is a resistance. Mirramezani and Shadden [6] explains how to implement \mathcal{R} as a function of viscous dissipation, curvature, expansions, bifurcations, and unsteadiness.

The flow rate in the AAo was imposed as the inlet boundary condition and 3-element Windkessel model was set as the outlet boundary conditions. The DLP model was implemented on MATLAB where the resistance \mathcal{R} was calculated for each patient case (pre- and post-repair). The system of ODEs (Equation 1) was solved using the Levenberg-Marquardt algorithm. The DLP model calculated the flow rates at the four outlets (BCA, LCCA, LSA, DAo) and these were compared against the in-vivo 4D Flow MRI data.

RESULTS

A total of four 4D Flow MRI scans were performed. Figure 1 shows the velocity contour during peak systole of the in-vivo data at peak systole.

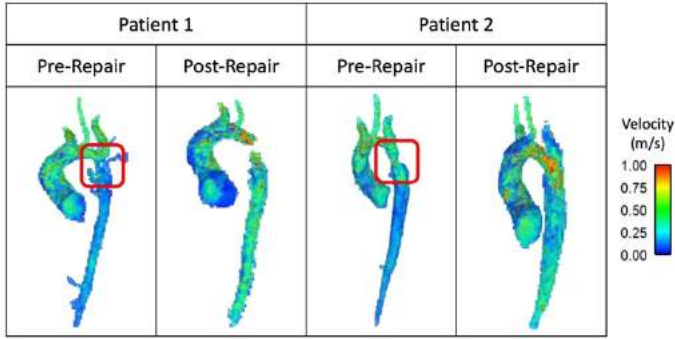


Figure 1: Peak systolic velocity contours from in-vivo 4D Flow MRI. Coarctations in red boxes.

The luminal narrowing (in red boxes) in the descending aorta caused by COA can clearly be seen in both patients' aorta pre-repair. Patient 1 underwent stenting, and the stent was not visible in the 4D flow MR images due to signal loss as a result of susceptibility effects caused by the stent material. Patient 2 underwent surgical repair.

For each patient case, the DLP model was successfully executed. Figure 2 shows the blood flow rates from the DLP model and 4D Flow MRI in the DAo of Patients 1.

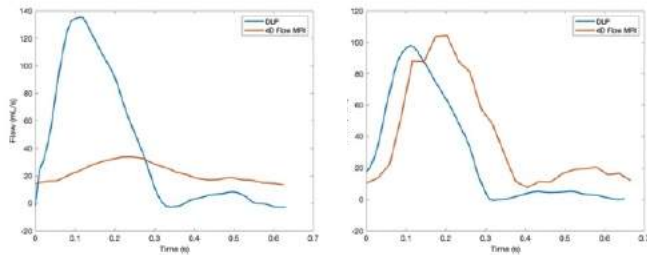


Figure 2: Flow rates in the DAo from DLP model and 4D Flow MRI for Patient 1 pre-repair (left) and post-repair (right).

Table 1: Flow rates (mL/s) at outlets over one cardiac cycle

Patient 1					
Pre-repair	4D Flow MRI	DLP Model	Post-repair	4D Flow MRI	DLP Model
BCA	31.2	5.5	BCA	5.1	12.5
LCCA	3.2	12.4	LCCA	3.3	5.7
LSA	13.2	28.5	LSA	N/A	18.7
DAo	22.3	40.5	DAo	40.6	28.3
Patient 2					
Pre-repair	4D Flow MRI	DLP Model	Post-repair	4D Flow MRI	DLP Model
BCA	16.7	14.1	BCA	14.5	13.8
LCCA	3.9	6.4	LCCA	2.7	4.7
LSA	6.1	20.6	LSA	8.3	27.0
DAo	23.5	32.2	DAo	51.6	51.7

By visual inspection, flow curves from the DLP model matched closer to the in-vivo 4D Flow MRI data post-repair compared to pre-repair. The flow rates in the BCA, LCCA, LSA, and DAo were calculated for all four patient cases over one cardiac cycle. These values are given in Table 1.

The average flow rate in the ascending aorta over one cardiac cycle was approximately 70 mL/s. Previous 4D Flow MRI studies have shown a 10% flow rate discrepancy using mass conservation analysis [7]. Therefore, we categorized < 7 mL/s difference between in-vivo and DLP model flow rate to be good agreement (green), between 7 and 10 mL/s to be moderate agreement (yellow), and > 10 mL/s to be poor agreement (red). All DLP models ran in less than 5 minutes, which is significantly faster than standard image-based CFD simulations.

DISCUSSION

Overall, we conclude that the flow rates calculated using the DLP model agreed moderately with in-vivo 4D Flow MRI in COA patients. We made several assumptions in our DLP model implementation. Due to the lack of pressure data from catheterization, we assumed normal aortic pressures (120/80 mmHg) at each outlet. This could be the reason the DLP model performs poorer in patients pre-repair because COA stenosis exhibits higher blood pressure. Temporal resolution of 4D Flow MRI was not sufficient to reliably measure patient-specific pulse wave velocities. Therefore, we assumed pulse wave velocity to be 7 m/s [8] when calculating the Windkessel parameters. To our knowledge, this is the first attempt at comparing the novel DLP model against in-vivo 4D Flow MRI. Additional patient-specific measurements are warranted to better understand model versus 4D Flow MRI differences and improve agreement between methods.

The DLP model of blood flow is an attractive method for modeling hemodynamics. Particularly when flow rates and pressure drops need to be calculated quickly, this DLP model has potential to outperform CFD. In the future, methods for imposing patient-specific boundary conditions should be investigated, and validation studies with in-vivo datasets need to be performed. Despite significant reduction in simulation times, we still envision 3D CFD as the standard tool in studying wall shear stress or turbulence.

ACKNOWLEDGEMENTS

Funding was provided by the American Heart Association (Grant No. 19TPA34850066).

GE Healthcare, which provides research support to the University of Wisconsin.

Ryan Pewowaruk, for assistance in implementing the DLP model.

REFERENCES

- [1] Torok RD, et al. Coarctation of the aorta: Management from infancy to adulthood. *World J Cardiol* 2015; 7(11): 765-775
- [2] Canniffe C, et al. Hypertension after repair of aortic coarctation—a systematic review. *Int J Cardiol*. 2013 Sep 10;167(6):2456-61.
- [3] Desai L, et al. Four-Dimensional flow Magnetic Resonance Imaging for Assessment of Pediatric Coarctation of the Aorta. *J Magn Reson Imaging*. 2022 Jan;55(1):200-208.
- [4] Hope MD, et al. Clinical evaluation of aortic coarctation with 4D flow MR imaging. *J Magn Reson Imaging*. 2010 Mar;31(3):711-8.
- [5] LaDisa JF Jr, et al. Three-dimensional computational fluid dynamics modeling of alterations in coronary wall shear stress produced by stent implantation. *Ann Biomed Eng*. 2003 Sep;31(8):972-80.
- [6] Mirramezani, M., Shadden, S.C. A Distributed Lumped Parameter Model of Blood Flow. *Ann Biomed Eng* 48, 2870–2886 (2020).
- [7] Roldán-Alzate A, et al. In vivo validation of 4D flow MRI for assessing the hemodynamics of portal hypertension. *J Magn Reson Imaging*. 2013 May;37(5):1100-8.
- [8] Koivisto T, et al. Pulse wave velocity reference values in healthy adults aged 26-75 years. *Clin Physiol Funct Imaging*. 2007 May;27(3):191-6.

DESIGN OF A COLLAGEN HYDROGEL WITH EMBEDDED SMOOTH MUSCLE CELLS FOR THE 3D STUDY OF CELL-MATRIX INTERACTIONS

Chloe Techens (1), Amira Ben Hassine (1), Edwin-Joffrey Courtial (2), David Eglin (1),
Stéphane Avril (1)

(1) Mines Saint-Etienne, Université Jean Monnet Saint-Etienne, INSERM, U 1059 SAINBIOSE, F-42023 Saint-Etienne, France

(2) 3d.FAB, Université Lyon1, CNRS, INSA, CPE-Lyon, ICBMS, UMR 5246, Lyon, France

INTRODUCTION

Aortic aneurysm is a life-threatening pathology requiring immediate intervention. In absence of upstream symptoms, a better analysis of the causes and mechanisms leading to this abnormal dilatation of the aorta wall would support prevention and reduce preemptive surgery. In particular, Smooth Muscle Cells (SMCs) play an active role in maintaining mechanobiological homeostasis in the healthy aorta wall and the dysfunction of their contractile phenotype was established in case of aortic aneurysm [1]. Because SMCs change their mechanical behavior depending on the extracellular environment, a neat understanding of the biological, chemical and mechanical interactions occurring between the cells and their environment is clearly needed.

Traction Force Microscopy (TFM) is an *in vitro* method apprehending cell mechanoregulation, measuring traction forces between the cell and the extracellular matrix [2]. Initially performed on single cells grown on a hydrogel surface, research is now heading toward 3D models with embedded cells [3], [4] to better describe the *in situ* cell-matrix interface. However, the matrix itself can induce phenotypic transitions for SMCs.

There is still a pressing need for adapting hydrogel to host SMCs, maintain their contractile phenotype and measure their traction forces using TFM. Thus, the objectives of this study were 1/ to assess how SMCs behave when they are embedded in collagen hydrogels with variable microstructure, chemical composition and mechanical properties, 2/ to design a hydrogel where embedded SMCs keep a contractile phenotype for future TFM applications.

METHODS

Twelve chemically different hydrogels were prepared from a 10 mg/ml bovine Type I collagen solution (TeloCol-10, Advanced Biomatrix) varying the collagen solution dilution (from 2.5 to 10 mg/ml) and the pH (from 7.4 to 8 to allow cell viability). Solutions were prepared on ice to prevent early gelation, mixing 8 parts of collagen

dilution, 1 part of PBS 10X (Fisher, US), pH-corresponding NaOH volume and completed to 10 parts with basal medium (SmBM, Lonza).

Primary aortic SMCs (AoSMC, Lonza) were cultivated in growth medium (SmGM-2, Lonza) at 37°C with 5% CO₂. Cells at passage P10 were then detached (0.025% Trypsin, Sigma) and gently mixed with the hydrogel solutions at three cellular densities (from 50 000 to 150 000 cells/ml) thus reaching 16 different seeded hydrogels. The confection of the seeded hydrogels matched a Design Of Experiment (DoE) using a modified L16 orthogonal array [5]. Each seeded hydrogel was reproduced three times.

Hydrogels were formed at 37°C for 1h before immersion in basal medium. Embedded cells differentiated for 5 days. Then, cell nuclei and actin fibers were stained by fluorochromes, and imaged with confocal microscope (Axio Observer Z1 station, Zeiss). In each hydrogel, three volumes of interest (0.90 mm x 0.67 mm) were defined at three different locations near the center of the well, along the whole gel thickness (~1mm) (Figure 1). There, the number of observed nuclei was reported. Based on the observations, cells were sorted into five phenotypes based on their length and form: uniaxial cell length <100µm and >100µm, multiaxial cell length <100µm and >100µm, and round.

The 12 hydrogel compositions used before were also mechanically tested. The acellular hydrogel viscoelastic behaviors were characterized with a stress-controlled rheometer (Discovery HR 2, TA Instruments) with 15mm plate-plate geometry at 37°C in oscillatory uniaxial compression and shear at frequencies in the range 0.1-10.0 Hz.

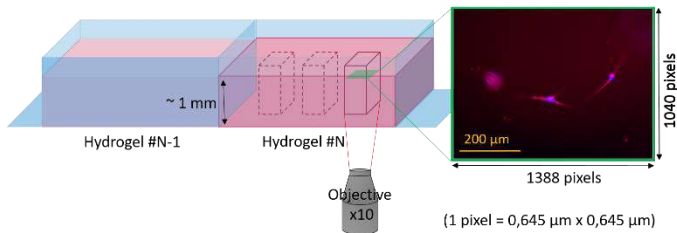


Figure 1: Acquisition of the cell images in the collagen hydrogel (pink) by fluoroscopy. Three acquisitions per gel were made using blue (465 nm) and red (673 nm) channels.

RESULTS

Cells showed great diversity of behaviors among the 16 tested combinations. The overall number of cells in a hydrogel significantly depended on the collagen concentration ($p < 0.001$, Kruskal-Wallis test). Stable at low concentrations, the mean cell number reduced by a factor 2 from 5 mg/ml to 10 mg/ml.

The number of round cells was only significantly impacted by the collagen concentration of the hydrogels ($p = 0.004$, ANOVA 1-way), with a sudden increase for 10 mg/ml.

In vivo, the SMC contractile phenotype manifests with an elongated (length $> 100 \mu\text{m}$) uniaxial cell. The fraction of such elongated cells increased when the initial cell density increased ($p = 0.008$, ANOVA 2-ways) and when the collagen concentration decreased ($p = 0.001$, ANOVA 2-ways). Their average length ranged between 132 and 244 μm , depending on the seeded hydrogel. Only the initial cell density seemed to significantly affect this length ($p = 0.011$, ANOVA 1-way).

Using the DoE approach, we found that a collagen hydrogel concentrated at 2.5 mg/ml with a pH=8, and seeded with 100 000 cells/ml offers the maximum fractions of contractile SMCs and seems well suited for TFM investigations.

Oscillatory shear tests revealed a predominant elastic behavior for all hydrogels. The shear storage and loss moduli of each hydrogel had parallel variations across the frequency range (Figure 2). The storage modulus approximated Coulomb's modulus at low frequency and ranged between 0.05 and 3 kPa. It increased with the collagen concentration ($p = 0.037$, Kruskal-Wallis test). Conversely, oscillatory compression exhibited storage and loss moduli intersecting at various frequencies depending on the hydrogel. Variations of behavior in between hydrogels were observed, with a general increase of storage modulus at the lowest frequencies. At low frequencies, the storage modulus ranged between 0.03 and 7 kPa.

DISCUSSION

Our study showed that SMCs embedded in a collagen hydrogel may have different behaviors and phenotypes depending on the collagen hydrogel composition. Collagen concentrations above 5 mg/ml tend to induce significant rates of cell death. Dense hydrogel meshes could limit the diffusion of nutrients and cell respiration from the surface to the center of the gels. Thus, only the cells at the surface of the gels could grow and differ as observed in some 10mg/ml collagen hydrogels. Conversely, low-concentration collagen hydrogels tend to induce SMC contractile phenotype more homogeneously distributed. Sufficient initial cellular densities also seem to be crucial to induce a high fraction of SMC contractile phenotype, as they enable sufficient interactions and communication between cells. For TFM applications, an optimal initial cellular density would provide the largest fractions of contractile SMCs while avoiding cell-cell contact.

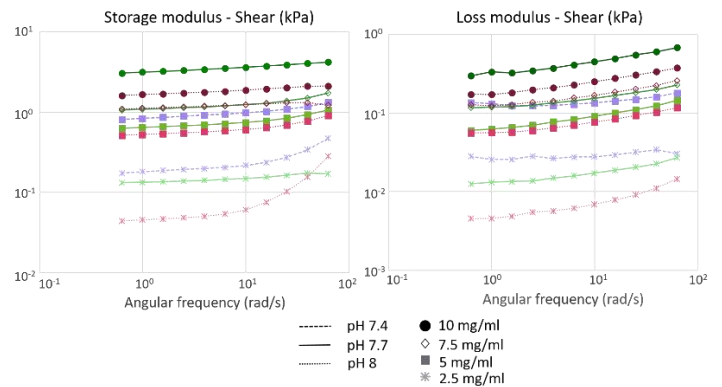


Figure 2: Variations of storage and loss moduli in parallel plates shear oscillations. The pH (line types) and concentration of collagen (symbols and brightness) varied among the hydrogels.

The acellular hydrogels demonstrated a viscoelastic behavior in shear and in compression. The hydrogel mechanical properties play a crucial role in the SMCs mechanobiology. First, SMCs adapt their basal tone to the changes of extracellular matrix stiffness [1], [6]. The cell contractibility also changes depending on the strain perceived by the cell membrane [6]. Thus, the design of an *in vitro* model for SMCs behavior study requires the management of the hydrogel properties. The difference of viscoelastic response observed between compression and shear suggested that hydrogels had a less isotropic fibrillary organization or a difference in cross-link point density along the axial axis. This supported the necessity to study embedded SMCs traction forces with 3D TFM in order to assess potential force heterogeneity.

Our study has a number of limitations such as the high passage number of the SMCs and the uncertainties of volumes during hydrogel preparation because of collagen high viscosity. Each was either controlled either taken into consideration in the DoE. Moreover, SMC phenotype was simply characterized based on the shape and length of the cells, but we will consider other markers (alpha-actin and myosin) in the future.

In conclusion, a hydrogel was designed to serve as a 3D *in vitro* model for the study of SMCs mechanobiology and their interactions with a collagen matrix. Future work will include the quantification of SMCs basal tone with 3D TFM and the analysis of their mechanobiological response to matrix loading.

ACKNOWLEDGEMENTS

This research was partially supported by the European Union's Horizon 2020 research and innovation programme SimInSitu (Grant Agreement 101017523). We thank Claudie Petit from Sainbiose F-42023 Saint-Etienne, France), for training us to AoSMC culture.

REFERENCES

- [1] Petit, C *et al.*, *Biomech Model Mechanobiol*, 20(2):717-731, 2021.
- [2] Lekka, M *et al.*, *Micron*, 150:103-138, 2021.
- [3] Hazlett L. *et al.*, *Sci Rep*, 10:16599, 2020.
- [4] Franck, C *et al.*, *PLOS ONE*, 6(3):e17833, 2011.
- [5] Roy, R., *A primer on the Taguchi method*, Soc. Manuf. Eng., 2010.
- [6] Lacolley, P *et al.*, *Card. Research*, 114(4):513-528, 2018.

IMPACT OF WALL DISTENSIBILITY ON EMERGING FEATURES OF CAROTID BIFURCATION HEMODYNAMICS

**Sara Zambon (1), Mariachiara Arminio (1), David A. Steinman (2),
Claudio Chiastra (1), Umberto Morbiducci (1), Diego Gallo (1)**

(1) Polito^{BIO}Med Lab, Department of Mechanical and Aerospace Engineering,
Politecnico di Torino, Turin, Italy

(2) Biomedical Simulation Lab, Department of Mechanical & Industrial Engineering,
University of Toronto, Toronto, ON, Canada

INTRODUCTION

Recent evidence suggests that near-wall as well as intravascular hemodynamics are of pivotal importance in the onset and progression of atherosclerosis at the carotid bifurcation [1,2]. In detail, helical flow has been associated with *in vivo* markers of early atherosclerosis [1], and a 5-year longitudinal study has shown that intra-cycle variability of the wall shear stress (WSS) topological skeleton (i.e., contraction/expansion action on the endothelium) is associated with intima-media thickening after carotid endarterectomy [2]. However, all those studies relied on computational fluid dynamics (CFD) modeling under the rigid wall assumption. Here, the effect of wall distensibility on these emerging features of the carotid bifurcation hemodynamics is explored by implementing fully coupled two-way fluid-structure interaction (FSI) simulations accounting for prestress of the arterial wall, anisotropic material properties, and external tissue support. Furthermore, the relationship between hemodynamic and structural quantities is explored.

METHODS

The diastolic volumetric fluid domains of five ostensibly healthy carotid bifurcations were reconstructed from contrast-enhanced magnetic resonance (MR) angiography, including at least 15 radii of the proximal common carotid artery (CCA) [1]. The carotid structural domains were generated with constant subject-specific thickness derived from edge-enhanced black blood MR images. Subject-specific volumetric flow rates were extracted from phase-contrast MR measurements [1] and prescribed as boundary condition at the CCA inflow section. A 3D-0D coupling scheme was applied at the external and internal carotid artery (ECA and ICA) outflow sections with three-element Windkessel models tuned to match subject-specific measured flow splits and age-adjusted pressure curves [3]. On each geometry, FSI and CFD simulations were carried out using Simvascular [4]. For the

FSI simulations, the arbitrary Lagrangian-Eulerian formulation was used [4]. The anisotropic nonlinear Holzapfel-Gasser-Ogden model was implemented to simulate the wall mechanical properties accounting for the presence of two families of collagen fibers aligned along two directions $\hat{\mathbf{a}}$ and $\hat{\mathbf{b}}$, according to the following strain energy function:

$$\bar{\Psi} = \frac{\mu}{2}(\bar{I}_1 - 3) + \frac{k_1}{2k_2} \sum_{j=4,6} [e^{k_2[\kappa \bar{I}_1 + (1-3\kappa)\bar{I}_j - 1]} - 1] \quad (1)$$

where μ is the isotropic matrix shear modulus, $\bar{I}_1 = \text{trace}(\bar{\mathbf{C}})$, $\bar{I}_4 = \hat{\mathbf{a}} \cdot \bar{\mathbf{C}} \cdot \hat{\mathbf{a}}$ and $\bar{I}_6 = \hat{\mathbf{b}} \cdot \bar{\mathbf{C}} \cdot \hat{\mathbf{b}}$, with $\bar{\mathbf{C}}$ being the isochoric right Cauchy-Green tensor, $\hat{\mathbf{a}}$ and $\hat{\mathbf{b}}$ are the fiber orientation unit vectors obtained from the directions $\hat{\mathbf{e}}_1$ and $\hat{\mathbf{e}}_2$ of the principal stresses σ_1 and σ_2 , k_1 and k_2 are stress-like and dimensionless nonlinearity parameters respectively, and κ accounts for the dispersion of each fiber family around its principal direction. The material parameter values proposed in [5] by fitting experimental data were adopted. The fiber orientations were determined from the initial loading state [5]. To do so, the so-called prestress tensor was iteratively obtained by balancing diastolic intraluminal blood pressure from CFD simulations until zero displacement is obtained [4], as illustrated in Fig. 1. Viscoelastic support of the tissue surrounding the carotid outer wall was accounted for by imposing a Robin-type boundary condition [4]. For the purpose of comparison, rigid wall CFD simulations were carried out with the same fluid mesh and simulation settings as in FSI simulations. Maximum edge sizes of the tetrahedral radius-based meshes were 0.17 mm (fluid domain) and 0.39 mm (solid domain).

In addition to the canonical time-average WSS (TAWSS) and oscillatory shear index (OSI), the variability of the WSS contraction/expansion action along the cardiac cycle was quantified by the topological shear variation index (TSVI) [2], defined as:

$$\text{TSVI} = \left\{ \frac{1}{T} \int_0^T [\text{DIV}_w - \overline{\text{DIV}_w}]^2 dt \right\}^{\frac{1}{2}} \quad (2)$$

where DIV_w represents the divergence of the normalized WSS vector field [2] and T is the duration of the cardiac cycle. Data from all cases were pooled to identify the 20th percentile value of TAWSS and 80th percentile values of OSI and TSVI. These threshold values were used to obtain the burden of disturbed WSS by quantifying the relative surface area (SA) exposed to TAWSS below (OSI, TSVI above) the corresponding threshold value. Analogously, wall regions exposed to elevated structural stress and strain were obtained by calculating the 80th percentile of the cycle-average maximum principal stress (σ_1) and strain (ϵ_1) at the fluid-solid interface. The Similarity Index (SI, here defined as two times the SAs intersection over the SAs union) was adopted to quantify the co-localization of hemodynamic and structural quantities [1]. The intravascular flow was characterized in terms of cycle-average local normalized helicity (LNH) and helicity intensity h_2 , given by the cycle- and volume-average of the norm of the internal product of velocity and vorticity [1]. The bifurcation region was delimited by sections CCA3, ICA5 and ECA2 (Fig. 1).

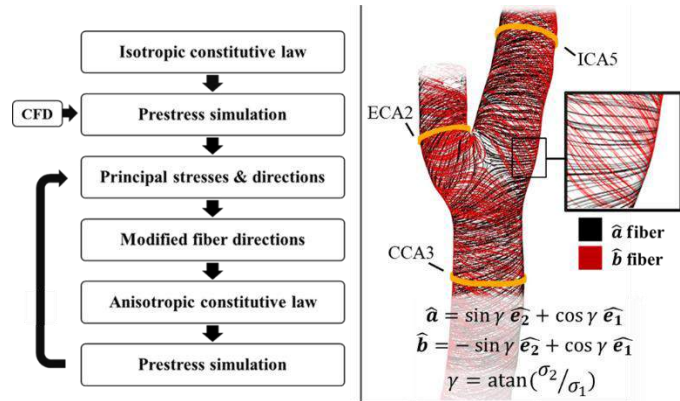


Figure 1: Prestress iterations (left panel) to determine fiber directions (right panel) and the initial loading state.

RESULTS

FSI simulations provided average values of luminal area variation at the CCA3 of $14.5\% \pm 3\%$, consistent with in vivo measurements [6]. TAWSS, OSI, and TSVI distributions were comparable in distensible vs. rigid wall simulations, both qualitatively (Fig. 2; TAWSS and OSI not shown) and quantitatively (surface-averaged TSVI values $305.1 \pm 141.0 \text{ m}^{-1}$ vs. $313.1 \pm 172.4 \text{ m}^{-1}$, respectively). Counter-rotating helical flow patterns characterized the flow field of all models, as highlighted by LNH isosurfaces of opposite signs (Fig. 2). Rigid wall models were characterized by higher h_2 values (Fig. 2).

Maximum values of both σ_1 and ϵ_1 were localized at the apex of the bifurcation (Fig. 3). SI values for the couplets of hemodynamic and structural quantities are reported in Table 1. The highest co-localization was found between σ_1 and OSI or TSVI ($\text{SI}=0.55$, Table 1). Low SI values were found between low TAWSS and high σ_1 or ϵ_1 regions. SI values between high σ_1 and ϵ_1 regions were 0.88 ± 0.07 .

DISCUSSION

The near-wall and intravascular hemodynamic quantities investigated here were only moderately affected by wall distensibility. Thus, the rigid wall assumption seems to be acceptable when linking the considered emerging hemodynamic features and atherosclerosis initiation at the carotid bifurcation. Considering the increased complexity, cost, and inherent introduction of additional uncertainties to model wall distensibility, our findings suggest that rigid wall CFD

modeling might be considered reasonable in view of a future clinical translation. With that said, the implemented FSI approach allows exploring the synergistic action between hemodynamic stresses on the endothelium and wall structural stress [7], potentially uncovering distinct or synergistic effects of these biomechanical stimuli on atherosclerosis initiation.

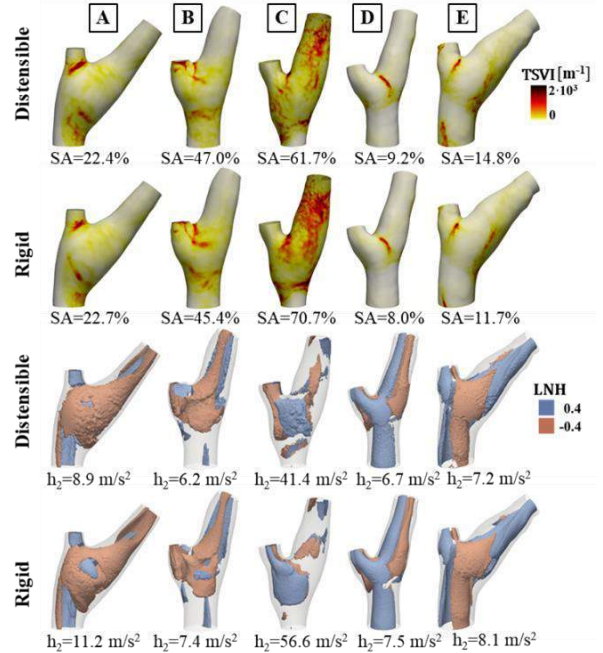


Figure 2: TSVI and LNH distributions.

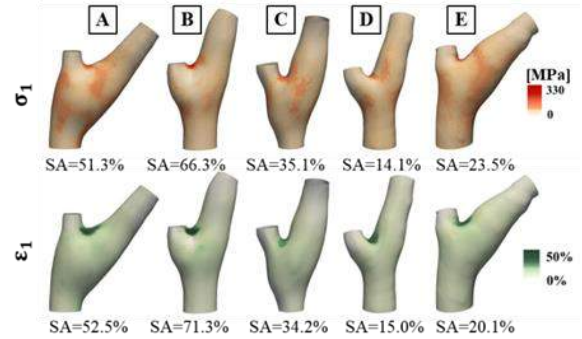


Figure 3: σ_1 and ϵ_1 distribution at the fluid-solid interface.

Table 1: SIs between hemodynamic and structural quantities

SI (MEAN \pm STD)	TAWSS	OSI	TSVI
σ_1	0.12 ± 0.11	0.55 ± 0.18	0.55 ± 0.12
ϵ_1	0.10 ± 0.08	0.53 ± 0.18	0.55 ± 0.12

REFERENCES

- [1] Gallo, D et al., *J R Soc Interface*, 15(147):20180352, 2018.
- [2] Morbiducci, U et al., *Ann Biomed Eng*, 48(12):2936–2949, 2020.
- [3] Hirata, K et al., *Stroke*, 37(10):2552–2556, 2006.
- [4] Bäumlér, K et al., *Biomech Model Mechanobiol*, 19(5):1607–28, 2020.
- [5] Hariton, I et al., *J Theor Biol*, 248(3):460–470, 2007.
- [6] Segers, P et al., *J Hypertens*, 42(5):638–638, 2004.
- [7] Qiu, Y and Tarbell, JM, *J Vasc Res*, 37(3):147–57, 2000.

PROCEDURAL STRATEGY IMPACT ON OUTCOMES OF TRANSCATHETER AORTIC VALVE REPLACEMENT FOR BICUSPID AORTIC VALVES

Breandan Yeats (1), Sri Krishna Sivakumar (1), Milad Samaee (1), Pradeep Yadav (2), Venkateshwar Polsani (2), Vinod Thourani (3), Stephanie Sellers (4), Janarthanan Sathananthan (4), and Lakshmi Dasi (1)

- (1) Biomedical Engineering, Georgia Institute of Technology and Emory University, Atlanta, GA, United States
(2) Cardiology, Marcus Valve Center, Piedmont Heart Institute, Atlanta, GA, United States
(3) Cardiovascular Surgery, Marcus Valve Center, Piedmont Heart Institute, Atlanta, GA, United States
(4) Cardiovascular Translational Lab, Centre for Heart Lung Innovation & Centre for Cardiovascular Innovation, University of British Columbia, Vancouver, Canada

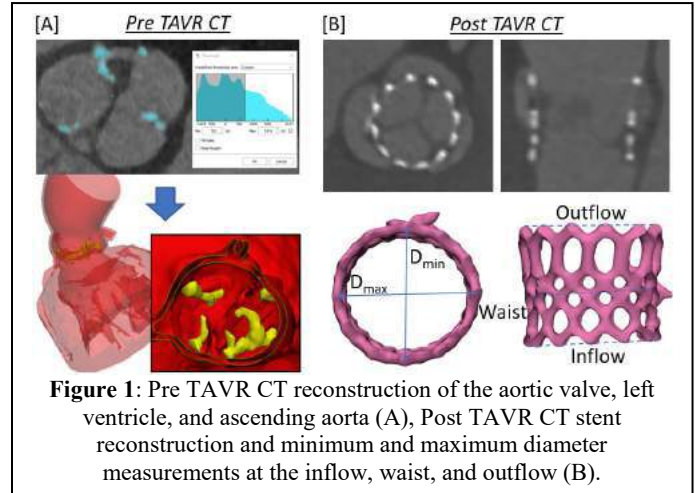
INTRODUCTION

Bicuspid aortic valve (BAV) disease is the most common form of congenital valve defect present in 2-4% of the general population [1]. Calcific aortic valve disease (CAVD) is the progressive formation of calcium nodules within the tissue causing stiffening of the valve and aortic stenosis [2]. Currently, the only treatment for aortic stenosis is valve replacement where ~50% of patients with CAVD also have BAV disease [2]. Historically, BAV patients with aortic stenosis have been treated with surgical aortic valve replacement. However, in recent years clinicians have been transitioning to transcatheter aortic valve replacement (TAVR) in BAV patients due to fast patient recovery times and TAVR for low surgical risk tricuspid aortic valve patients showing similar results to surgery [3].

Stent under expansion and non circularity occur to varying degrees following deployment and have been correlated to poor hemodynamic outcomes [4-6]. Under expansion and non circularity are more of a concern in BAV patients due to their higher calcium volume on average and elliptical openings. Currently, it is unclear if fracturing the calcium nodules allows for increased stent expansion by lowering the resistance of the native valve. Additionally, it is unknown if intentionally over expanding the balloon beyond the nominal amount would expand the device closer to intended nominal values. The goal of this study is to determine if calcium fracture or balloon over expansion results in increased stent expansion and stent circularity.

METHODS

BAV patients treated with the Edwards SAPIEN 3 balloon-expandable device with both pre and post TAVR CT scans were analyzed (n=8). From the pre TAVR CT, the aortic valve (with leaflets and calcium), left ventricle, and ascending aorta were reconstructed in Materialise Mimics 23.0 (Leuven, Belgium) (**Figure 1A**). From the post TAVR CT, the TAV stent and calcium were reconstructed and the minimum and maximum diameter at the inflow, waist, and outflow was measured (**Figure 1B**).



The amount of stent expansion was assessed by calculating the expansion ratio which was defined by the ratio of the measured diameter derived area to the nominal area at the inflow, waist, and outflow (**Eq. 1**). The amount of stent non-circularity was assessed by calculating the aspect ratio defined by the ratio of the minimum to maximum diameter (**Eq. 2**). Any noticeable regions of calcium fracture were identified via qualitative comparison to the pre TAVR calcium reconstruction.

$$\text{Expansion Ratio} = \frac{\left(\frac{\text{Min Diameter} + \text{Max Diameter}}{4}\right)^2}{\left(\frac{\text{Nominal Diameter}}{2}\right)^2} \quad (1)$$

$$\text{Aspect Ratio} = \frac{\text{Minimum Diameter}}{\text{Maximum Diameter}} \quad (2)$$

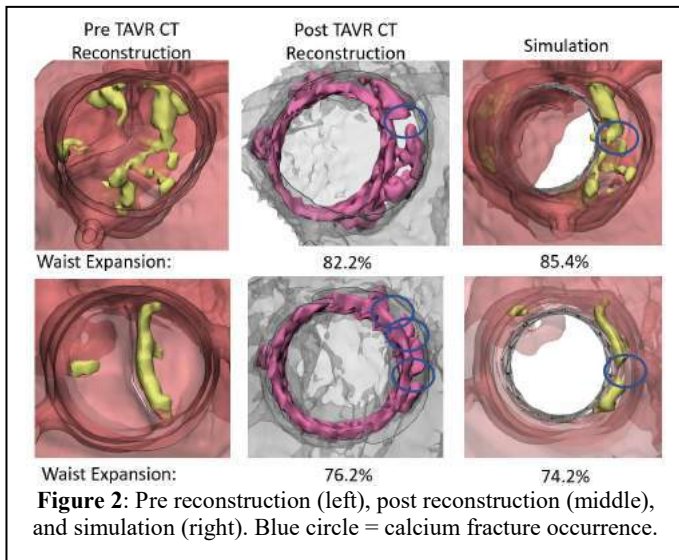
Using a finite element model, a balloon-expandable TAV stent was deployed in the pre TAVR reconstruction for each case (Abaqus, Waltham, MA, USA).

CAD models of the 23, 26, and 29 mm sizes were created from micro CT scans of the SAPIEN 3 Ultra device (Solidworks, Waltham, MA, USA) and meshed ensuring four elements through the thickness with hexahedral elements (Hypermesh, Powell, OH, USA). Balloons were created for each size from measurements taken from the device delivery system and meshed with rectangular membrane elements. Native tissues were meshed with tetrahedral volume elements with 0.7 mm element length. Material properties included the stent being elastic with a plastic yield stress, the balloon being elastic, native soft tissue with hyperelastic Ogden 3rd order, and calcium nodules elastic, all parameters used in previous studies [7-10]. To simulate calcium fracture, a stress fracture threshold was created at 1 MPa where if an element reached the threshold it was no longer mechanically included in the simulation [10, 11]. The stent was rigidly crimped and the balloon was folded using radial and circumferential forces to ensure uniform expansion. The balloon was then filled using a volumetric flow rate to a set end volume, tuned by deploying the device with no native anatomy to the manufacturer specified diameter, then the balloon was deflated.

The stent minimum and maximum diameter at the inflow, waist, and outflow were measured and the incidence and location of calcium fracture was recorded. The expansion ratio and aspect ratio were calculated and compared to the post CT measurements. Two additional simulation scenarios were then performed (1) removal of the calcium fracture threshold and (2) expansion using a balloon 1mm larger in diameter. Both scenarios were compared to the baseline simulation in terms of expansion ratio and aspect ratio in each case.

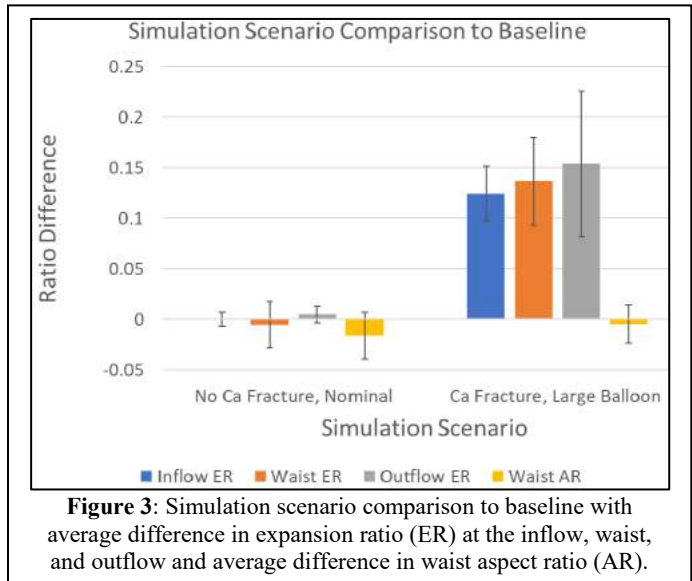
RESULTS

Patient characteristics included 62.5% female, 50% Sievers Type I and 50% Type 0, 3 patients each had the 23 and 26 mm devices and 2 patients had the 29 mm, and a range of calcium volume from 135 to 1718 mm³. Post CT device expansion ratio was < 100% at all levels in all cases with $90.1 \pm 5.3\%$, $79.9 \pm 4.7\%$, and $94.4 \pm 3.2\%$ averages and standard deviations for the inflow, waist, and outflow respectively. Noticeable calcium fracture was observed in 2/8 cases which were similar in location compared to the simulation (Figure 2).



The average and standard deviation in expansion ratio differences between the post TAVR CT and simulation were $6.72 \pm 3.9\%$, $2.50 \pm 4.5\%$, and $3.73 \pm 2.9\%$ for the inflow, waist, and outflow with a $2.95 \pm$

4.9% difference in waist aspect ratio. All data points had < 15% error indicating reasonable agreement between post CT and simulation. Simulation baseline expansion ratios and aspect ratio are compared to the no calcium fracture scenario and the over expansion scenario (Figure 3). Minimal differences were observed in the absence of calcium fracture with the exception of cases with extreme calcification (all average differences < $\pm 2\%$). Over expansion resulted in consistent increase in expansion with an average waist expansion increase of 13.7% but did not impact waist aspect ratio (-0.5% difference).



DISCUSSION

This study demonstrated a detailed analysis of a group of post TAVR CTs in BAV patients (n=8), validation of a TAV deployment computational model, and investigation of the impact of calcium fracture and balloon over expansion on the overall expansion of the device. Waist expansion was < 90% in 100% of cases and circularity was < 90% in 37.5% of cases. Currently, it is impossible for clinicians to predict the final stent expansion and circularity due to anatomical and procedural biomechanical complexities. Computational modeling has the potential to aid in pre procedural planning demonstrated by its high accuracy (all data points < 15% error). The impact of calcium fracture on the stent expansion was low even in the presence of very large calcium nodules (maximum -4.8% waist expansion difference). Balloon over expansion was found to have a significant increase in the overall device expansion bringing the waist much closer to nominal size, 96.1% compared to the post CT 79.9% waist expansion average. However, did not impact the stent circularity. In conclusion, calcium fracture has a low impact on the stent expansion and circularity in most cases and slight balloon over expansion can avoid significant waist under expansion, common in TAVR for BAV patients.

REFERENCES

- [1] Siu, S.C., J Amer Col Cardiol, 2010. 55(25): p. 2789-2800.
- [2] Yutzy, K.E., Arterioscler Thromb Vasc Biol, 2014. 34(11): p. 2387-2393.
- [3] Leon, M.B., J Amer Col Cardiol, 2021. 77(9): p. 1149-1161.
- [4] Fukui, M., Circ, 2022. 146(6): p. 480-493.
- [5] Gunning, P.S., Ann of Biomed Eng, 2014. 42(6): p. 1195-1206.
- [6] Khodae, F., Int Cardio Thorac Surg, 2020. 30(1): p. 39-46.
- [7] Tzamtzis, S., Med Eng Phys, 2013. 35(1): p. 125-130.
- [8] Martin, C., J Biomed Mater Res Part A, 2012. 100(6): p. 1591-1599.
- [9] Reza, S., Artificial Organs, 2022. 46(11): p. 1305-1317.
- [10] Holzapfel, G.A., J Biomech Eng, 2004. 126(5): p. 657-665.
- [11] Morany, A., 2022: p. 1-14.

HIGH RESOLUTION MR ELASTOGRAPHY OF THE HUMAN BRAIN: TECHNICAL DEVELOPMENT AND APPLICATIONS IN AGING AND ALZHEIMER'S DISEASE

E. Triolo (1), O. Khagai (2), A. Alipour (2), T. Hedden (2,3), P. Balchandani (2), M. Kurt (1,2)

- (1) Department of Mechanical Engineering, University of Washington, Seattle, WA, USA
(2) The Biomedical Engineering and Imaging Institute, Icahn School of Medicine at Mount Sinai, New York City, NY, USA
(3) Department of Neurology, Icahn School of Medicine at Mount Sinai, New York City, NY, USA

INTRODUCTION

Magnetic resonance elastography (MRE) is a technique for determining the mechanical response of tissues using applied harmonic deformation and motion-sensitive MRI¹. Performing MRE on human brain can provide information on different structures within brain tissue based on their mechanical properties, which can then be used to diagnose pathologies such as Alzheimer's disease (AD) and dementias, or indicate disease progression²⁻⁶. Studies using MRE to investigate the mechanical properties of the human brain are most commonly performed at conventional field strength (3 Tesla (T) or 1.5T), although there have been a few attempts at the ultra-high field strength, 7T, in an attempt to achieve higher resolution scans. Aiming for higher resolution scans of the human brain at 7T, MRE presents unique challenges of decreased octahedral shear strain-based signal-to-noise ratio (OSS-SNR)⁷ and lower shear wave motion sensitivity. Additionally, it has been shown that quantitative values of MRE, i.e., the magnitude of the complex shear modulus estimate ($|G^*|$), are sensitive to changes in OSS-SNR⁸, so 7T MRE can present a challenge of not only quality, but accuracy.

Performing MRE at 7T, and more specifically at high resolution, proves to be an attractive option for investigations into small brain structures, such as in the progression of Alzheimer's disease. Early diagnosis of Alzheimer's disease is still challenging, because of the subtlety of the microstructural changes it initially causes in the brain and the difficulty of identifying them with traditional neuroimaging techniques such as MRI, PET, or CT scans. Recent evidence has revealed that the neurodegeneration characterizing AD is accompanied by effective tissue softening, which can be quantified *in vivo* using MRE²⁻⁶. However, MRE at conventional field strengths has a resolution limitation in studying finer microstructure details, such as hippocampal subfields, that are important in the investigation of AD tissue microstructure. *Overall, this work seeks to investigate advanced reconstruction and noise reduction techniques to improve accuracy of*

ultra-high field (7T) MRE in determining the mechanical properties of small brain tissue structures, with applications in aging and early detection of dementias.

METHODS

Full brain coverage MRE using our custom 2D multi-slice SE-EPI 7T MRE pulse sequence^{9,10} was performed on twenty healthy human subjects (young adults, Avg. Age 26.9±3.4 years) at 1.1mm³ isotropic resolution at 50Hz vibration frequency, using a 32-channel head coil (Nova Medical) on a 7T Siemens Magnetom MRI Scanner. Using the same methods, MRE was also performed on a custom silicone MRE phantom (CIRS 049)⁹ with 20mm diameter spherical inclusions. The custom MRE sequence was synchronized with our custom pneumatic acoustic actuator^{9,11} by TTL triggering at the beginning of every TR (TR/slice=140ms, TE=65ms, GRAPPA=3, Partial Fourier=7/8). We also performed 7T MRE on our phantom at an isotropic resolution of 2.5mm³ for comparison (GRAPPA=2).

For the scanner-reconstructed image series, we employed the MP-PCA denoising¹² and our Algebraic Inversion of the Helmholtz Equation (AIDE) to calculate $|G^*|$ ¹⁰. To improve the default scanner reconstruction method, we used Gadgetron¹³, an open-source MRI image reconstruction software, on the raw data files to generate magnitude and phase images before performing the same pre-processing and inversion method. We also calculated OSS-SNR⁷ after

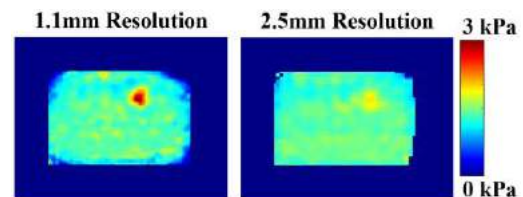


Figure 1: Custom Phantom with Spherical Inclusions Scanned at 7T Using Low and High Resolutions

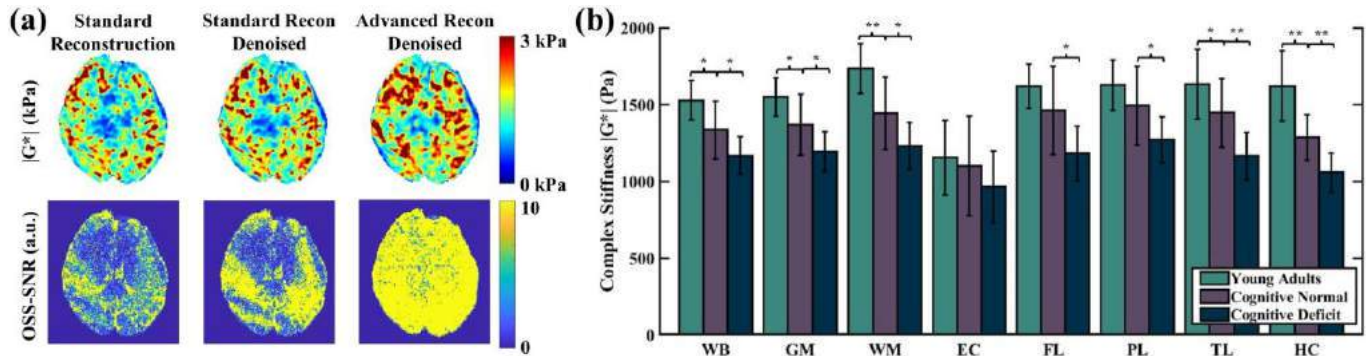


Figure 2: (a) High resolution Elastograms and OSS-SNRs with Advanced Reconstruction methods in One Young, Healthy Subject. (b) Average $|G^*|$ for Young Adults, CN, and CD individuals in all Segmented Brain Regions (* $p < 0.05$, ** $0 < 0.01$)

each post-processing method after performing SEGUE¹⁴ unwrapping on the displacement fields. Segmentation of whole brain (WB), all gray matter (GM), all white matter (WM), the Entorhinal Cortex (EC), Frontal Lobe (FL), Parietal Lobe (PL), Temporal Lobe (TL), and Hippocampus (HC) were performed on the MP2RAGE T1scans (0.7mm³) using Freesurfer¹⁵ and were co-registered using SPM¹⁶. Differences between WB post-processing groups were analyzed using a one-way, repeated measures ANOVA with multiple comparisons.

Using the previously described 1.1mm³ 7T acquisition, denoising¹¹, advanced reconstruction, and segmentation, full brain coverage 7T MRE was performed on six human subjects that presented with cognitive deficits (CD, Avg. age 75.8 ± 6.5 years) and nine age-matched ($p > 0.10$) subjects with normal cognition (CN, Avg. age 69.0 ± 8.0 years). In our CD group, two subjects have previously been diagnosed with AD, two have been diagnosed with mild cognitive impairment, and two had no specific diagnosis. Average $|G^*|$ of each brain region listed were compared between CD and CN, and CN and young adult groups using one-tailed, unequal variance, t-tests.

RESULTS

Using our phantom as validation of accuracy and as a rationale for using ultra-high resolution MRE to investigate small brain regions, the calculated shear stiffness values are within the manufacturer's specified range (1.67 ± 0.33 kPa) at both 2.5mm³ (1.43 ± 0.01 kPa) and 1.1mm³ resolutions (1.42 ± 0.01 kPa). However, at 2.5mm resolution, the inclusion (specification 2.67 ± 0.33 kPa) is not in the correct range at a mean of only 1.77kPa, but is in the correct range at 1.1mm resolution at a mean of 2.39kPa (Figure 1).

Investigating the advanced post-processing techniques on the 20 young healthy human subjects, we observed a whole-brain average 127% significant increase in OSS-SNR using just denoising and a 375% significant increase using both advanced reconstruction and denoising. Using advanced reconstruction, we observed the removal of artifacts introduced by scanner reconstruction error (Figure 2a). Investigating differences between CN and CD groups in regional averages of $|G^*|$, we observe a significant decrease in $|G^*|$ in each brain region apart from the EC (12.6% decrease in WB*, 13.0% in GM*, 14.8% in WM*, 19.1% in FL*, 15.0% in PL*, 19.6%** in TL, and 17.9% in HC**); * $p < 0.05$; ** $p < 0.01$; Figure 2b). Additionally, we observe a significant decrease in $|G^*|$ between young adult and CN groups in WB (12.5%*), GM (11.6%*), WM (16.8%*), TL (11.4%**), and HC (20.6%**), simply due to the effect of aging (* $p < 0.05$; ** $p < 0.01$; Figure 2b).

DISCUSSION

Overall, in this work we successfully developed and implemented high resolution MRE at ultra-high field (7T) to determine the mechanical properties of small brain tissue structures, showing

regional differences in brain stiffness in subjects with cognitive deficits. Our initial phantom validation experiments clearly indicate the motivation for use of high resolution MRE in investigating small structures with accuracy, achieved using 7T. Additionally, we can achieve sufficiently high OSS-SNR for accurate quantification at this high resolution by using both denoising and post-hoc advanced reconstruction, as denoising removes thermal and gaussian noise while advanced reconstruction removes errors caused by the scanner reconstruction. Noise reduction in the case of scanning subjects with cognitive deficits is of particular importance, as it also allows us to keep the scan time relatively short.

Using these advanced techniques and high resolution allows us to observe differences in smaller brain structures than previous studies, and with a higher level of accuracy. Previous investigations at courser resolutions (3mm³ or 2.5mm³)^{2,3,5,6} typically only investigate larger regional or WB differences between groups, or report particularly low values of smaller regions such as HC⁶ compared to what is reported in this study. A more recent study using a slightly higher resolution (1.6mm³) reported changes in individual lobes of HC in subjects with AD⁴, which can likely be further observed with our ultra-high resolution. This more accurate information on smaller structures will allow us to better investigate neurodegeneration effects or other relevant brain disorders, e.g. traumatic brain injury, *in vivo*.

Our study has several limitations that need to be addressed as analysis continues. First, a more robust inversion algorithm, such as nonlinear inversion¹⁷ would benefit the high-resolution scan, resulting in even more detail. Additionally, individual corrections for changes in brain volume, age, and sex would allow for more accurate comparison between groups. Finally, this study has a relatively small sample size of individuals with CD, although recruitment is still ongoing.

ACKNOWLEDGEMENTS

We acknowledge funding support from NSF CMMI 1953323, NIH R21AG071179, NIH P30AG066514, and the Sanford Grossman Interdisciplinary Center in Neural Circuitry and Immune Function.

REFERENCES

- [1] Muthupillai, *et al.*, *Magn Reson Med*, 1996
- [2] Murphy, *et al.*, *NeuroImage Clin*, 2016
- [3] Murphy, *et al.*, *J. Magn. Res. Img.*, 2011
- [4] Hiscox, *et al.*, *Brain Commun*, 2019
- [5] ElSheikh, *et al.*, *AJR Am J Roentgenol*, 2017
- [6] Gerischer, *et al.*, *Clin. Neurophys.*, 2016
- [7] McGarry, *et al.*, *Phys Med Biol*, 2011
- [8] Murphy, *et al.*, *PLoS One*, 2013
- [9] Triolo, *et al.*, *Proc. SB3C 2021*
- [10] Triolo, *et al.*, *Proc. ISMRM 2021*
- [11] Triolo, *et al.*, *Curr Protoc*, 2022
- [12] Veraart, *et al.*, *NeuroImage*, 2016
- [13] Hansen & Sørensen, *Magn Reson Med*, 2013
- [14] Karsa & Shmueli, *IEEE Trans Med Imag*, 2019
- [15] Reuter, *et al.*, *NeuroImage*, 2019
- [16] SPM12
- [17] McGarry, *et al.*, *Med Phys*, 2012

VALIDATION OF STEERING WHEEL FORCES AND UPPER EXTREMITY LOADING DURING REAR-END COLLISIONS USING MADYMO

Dominic R. Demma (1), Stephanie M. Rossman (1), Nicole A. Johns (1), Steven A. Rundell (1)

(1) Explico Inc., Novi, MI, USA

INTRODUCTION

Rear-end collisions (RECs) are the largest portion of reported crash incidents in the United States. RECs with a change in velocity (delta-V) below 15 kph generally report minor, or no injuries at all [1]. Nevertheless, complaints of more serious injuries resulting from generally lower severity RECs continue to persist and require further investigation.

One injury type that remains scarcely discussed in the context of RECs is shoulder injuries. Lucas, et al (2009) began a discussion analyzing the potential for acromioclavicular (AC) and coracoclavicular (CC) ligament injuries in low-speed RECs [2]. This study used kinematic data collected via video during physical rear-end crash tests to mathematically calculate the resulting loads at the AC and CC ligaments and compared them to reported failure forces. Lucas, et al. concluded that the kinematics associated with a REC are not likely to result in injury to these ligamentous structures. However, this study did not directly measure upper extremity loads. Furbish, et al (2011) [3] conducted full-scale, rear-end crash tests, and directly measured the steering column loads resulting from the volunteers' grip on the steering wheel.

The objective of the current study was to develop and validate a computational occupant dynamics model that measures upper extremity loading during RECs by accurately predicting loading in the steering wheel column. We hypothesized that the computational model could accurately predict steering wheel column loads and therefore quantify the reaction loads acting at the occupant's upper extremity. Furthermore, the upper extremity loading experienced during low-speed RECs was hypothesized to be consistent with loads experienced during ADLs and generally non-injurious activities.

METHODS

Simulation Setup. Furbish et al. included 7 male subjects (average height 1.70 m and weight 91.6 kg) who were submitted to RECs with

delta-V's ranging from 8.5 to 11.6 kph (average 9.1 kph). Each subject experienced multiple, full-scale, rear-end crash tests as the driver of a 1996 Ford Taurus. For the purposes of this study, only subjects that maintained both hands on the steering wheel were evaluated. The steering column load time-histories reported for these subjects were digitized using Web Plot Digitizer (v4.2). These time-histories were averaged, and corridors (± 1 SD) were created.

A validated, scalable 50th Percentile Male Hybrid III (HIII) ellipsoid model from MADYMO (Siemens v.2020.1) [4] was scaled to the average subject anthropometry and placed into a virtual vehicle sled with geometry representative of a 1996 Ford Taurus. A publicly available REC sled test of an exemplar vehicle was used as a reference for positioning the virtual occupant.

The steering wheel-column was tilted to a position of 18 degrees above the horizontal, as reported in Furbish et al, and was positioned within the virtual subject's reach consistent with a normal driving position. A loadcell was positioned at the kinematic joint connecting the steering wheel to the steering column and the steering column was attached directly to the vehicle sled joint. The loadcell was oriented in accordance with Federal Motor Vehicle Safety Standard 203 and the steering wheel was given a mass of 4.3 kg. A finite element 3-point belt was added to the simulation in accordance with the documented subjects' restraint use (Figure 1).

Control Test Validation. Furbish et al. (2011) documented a control test in which one subject was seated in the target vehicle without his hands on the steering wheel. This test measured the inertial loading response at the steering wheel. A corresponding simulation was run using the MADYMO model without the HIII's hands tied to the steering wheel. A haversine, forward acceleration was applied to the virtual sled at a delta-V of 10.5 kph and a duration of 80 ms, followed by a triangular deceleration. These vehicle dynamics were designed to match the documented dynamics from prior physical testing [5] and included the immediate deceleration of the vehicle from braking.

Physical Test Validation. The acceleration profile for the control test was modified to represent an average delta-V of 9.1 kph. The hands of the HIII were secured to the steering wheel at clock positions 10-and-2 using restraint points. A triangular force-displacement function was applied to the restraint points that exerted a maximum force of 550 N at a displacement of 7.5 cm. This represents the average male grip strength reported in Young et al. (2009) [6].

Upper Extremity Loading. A series of simulations were conducted using the validated model to quantify the compressive loads experienced by the HIII's upper extremities. Loadcells were added to the HIII wrists to measure hand loads, and the simulations were rerun without subsequent vehicle deceleration. All steering column loads were filtered at CFC 60 and wrist loads were filtered at CFC 1000.



Figure 1: MADYMO build position matched to IHS SER01040 and steering wheel loadcell orientation.

RESULTS

Control Test Validation. The results of the physical control test [3] were compared with the inertial loading seen in the modeled MADYMO steering-wheel column (Figure 2). Qualitatively, the virtual steering-wheel column loadcell mirrors the tension-compression response reported in the control test. Quantitatively, the peak inertial tension recorded in the MADYMO is within 6% of the reported physical test. The results of the control test validation verified that the inertial response of the virtual steering-wheel column loadcell was consistent between the physical and virtual environments.

Physical Test Validation. The corridors along with the average time versus tension-compression response of the steering-wheel column was plotted with the MADYMO model's predictive response in Figure 3. The simulated sinusoidal tension-compression shape of the steering-wheel column loading follows the trends from the physical testing. The maximum compression and tension were within 5.2% and 6.1% of the peak corridors from the physical testing, respectively. The results of the physical test validation verified that the MADYMO model was a robust method for predicting steering-wheel-occupant loading interactions.

Upper Extremity Loading. The compression phase of the HIII hand loads during these tests was plotted alongside compressive hand loads in published activities of daily living (ADLs) and was found to be comparable with generally non-injurious loads (Figure 4). This was consistent with the result of the physical testing that did not result in traumatic injuries to the upper extremities of the subjected occupants.

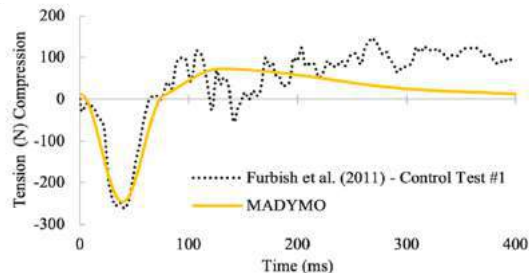


Figure 2: Inertial steering column loads from the control test compared to the simulation.

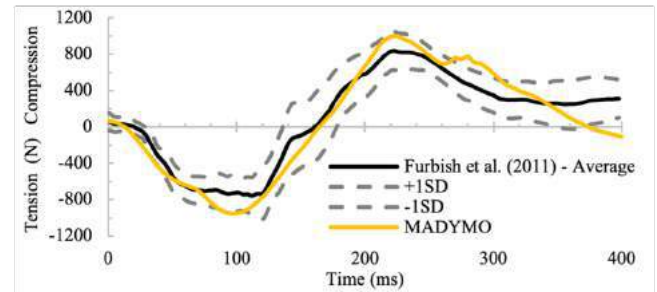


Figure 3: Steering-wheel column time vs. tension-compression responses from the physical test compared to the simulation.

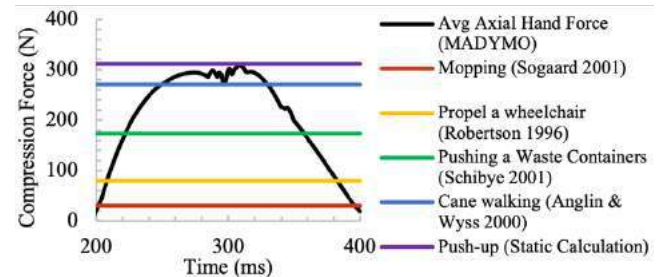


Figure 4: Comparing predicted hand loads to ADLs.

DISCUSSION

Results of the current study confirmed our hypothesis that a computational model could accurately predict steering-wheel column loads and be used to quantify the reaction loads acting on an occupant's upper extremity during a REC. The reaction forces experienced by the upper extremities during ADLs and generally non-injurious activity can provide context to the injury potential during a REC event. Specifically, the reaction forces occurring at the volunteer's upper extremities were relatively minimal, which was consistent with a) the lack of reported injuries during the physical testing, and b) the general lack of scientific studies and field data that links the potential for upper extremity injury to RECs.

Future development of this model should consider simulation of the deformation of the seat and belts per the data in Furbish et al. (2011). In the present study, average anthropometry and average time-history response from the physical testing was used. Future work might consider modeling each subject-specific anthropometry and delta-V reported in the study. A future study might also consider a peak strength switch for occupants who lose grip with the steering wheel during a REC. These scenarios may be used to analyze inertial shoulder loads for drivers who do not maintain their grip on the steering wheel.

In conclusion, this experiment was a modeling effort that presents a method to better understand upper extremity loading during low-speed REC utilizing MADYMO. This study also supports the hypothesis that RECs are not a physiologically relevant mechanism to shoulder injuries.

REFERENCES

- [1] Goertz A. et al., *SAE International*, 2010-01-0139, 2010.
- [2] Lucas S, et al., *SAE International*, 2009-01-1203, 2009.
- [3] Furbish C et al., *SAE International*, 2011-01-0275, 2011.
- [4] Siemens, *MADYMO Reference Manual* (v.2020.1), 2020.
- [5] Ivory MA, et al. *SAE International*, 2010-01-0067, 2010.
- [6] Young JG, et al. *Hum Factors*, 51(5), 705-717, 2009.

NUCLEAR EXPORT INHIBITION JUMBLES EPITHELIAL-MESENCHYMAL STATES AND GIVES RISE TO MIGRATORY DISORDER IN HEALTHY EPITHELIA

Carly M. Krull (1), Haiyi Li (2), Amit Pathak (1,3)

(1) Department of Biomedical Engineering, Washington University, St. Louis, MO, USA
(2) Department of Computer Science & Engineering, Washington University, St. Louis, MO, USA
(3) Department of Mechanical Engineering & Materials Science, Washington University, St. Louis, MO, USA

INTRODUCTION

Epithelial-mesenchymal (E-M) gradients support collective cell migration to facilitate normal physiological activities, like embryogenesis and tissue repair, as well as malignant processes, like cancer invasion. At the leading edge of a migrating group, cells exhibiting partial E-M transition (EMT) extend protrusions and apply traction to drive migration. Meanwhile, from behind, more epithelial-like cells supply lower tractions, retaining higher cell-cell adhesions to preserve the collective [1]. This E-M gradient transpires from tactful regulation of transcription factors (TFs) and migration-related proteins [2]. While it is known that these proteins individually promote or inhibit EMT, it is unknown whether opposing factors compete, cooperate, or cancel during the construction of cell phenotypes. To explore this question, we consider that transcription changes from EMT-TFs and related proteins hinge on their nuclear localization. Therefore, we perform nuclear export inhibition (NEI), using leptomycin B (LMB) to co-localize EMT-related proteins in the nucleus. We then survey interactions between opposing EMT factors by assessing changes in E-M cellular traits and collective migration characteristics (*preprint*: [3]).

METHODS

Polyacrylamide gels were synthesized using 4%:0.2% acrylamide:bis-acrylamide to yield 0.5 kPa stiffness, and were coated with type I collagen. MCF10A monolayers were seeded on each gel and treated with 100 nM LMB or 100% ethanol (vehicle) for 24 h. Time-lapse imaging was performed, acquiring phase contrast images every 10 min for 24 h with 10x objective. Particle image velocimetry was used to extract spatiotemporal velocity profiles from time-lapse images of migrating monolayers ($n > 6$). Fixed samples were immunostained for I κ B α , p120, vimentin, and YAP, and phalloidin was used to visualize F-actin. Images were captured using confocal at 40x objective. YAP nucleocytoplasmic ratio was quantified by dividing integrated density of nuclei by that of cytoplasm ($n = 8$). Actin coherency was measured

in OrientationJ ($n > 1000$). Expression of EMT marker genes PTEN and SNAIL1 was measured via reverse transcription quantitative polymerase chain reaction, using established protocols ($n = 12$).

RESULTS

Nuclear localization of I κ B α is an established measure for NF κ B inhibition [4], and junctional expression of p120 reflects the degree of cell-cell adhesion reinforcement [5] (Fig. 1A-i). We found that NEI contributed to higher I κ B α nucleocytoplasmic (N:C) ratios and increased p120 junctional intensity in both leader and follower cells (Fig. 1A-ii). To determine whether other traditionally epithelial markers were affected, we measured expression of the epithelial marker gene PTEN, and found it was upregulated following NEI (Fig. 1A-iii). These findings indicate that NEI reinforces epithelial characteristics. We then assessed mechanoactivation and mesenchymal features. NEI increased vimentin expression, YAP N:C ratio, and actin coherency, while giving rise to leader cells with highly polarized, protrusive morphology (Fig. 1B-i). NEI also elevated expression of the mesenchymal marker gene SNAIL1 (Fig. 1B-ii). Overall, these results indicate that NEI simultaneously enhances epithelial and mesenchymal cellular traits.

Because epithelial cells balance intercellular adhesion and mechanoactivation gradients to facilitate collective movement, we hypothesized that the observed disturbances could interfere with typical patterns of migration. Indeed, results reveal time-dependent changes in migration velocity and order. Previous studies have exclusively shown that NEI inhibits migration; yet, strikingly, on 0.5 kPa, NEI elevated collective migration velocity (Fig. 2A, B). Meanwhile, progressive disorder contributed to the decline of net velocity toward control levels (Fig. 2B, C). These findings depict changes to the conventional patterns of collective migration, where NEI initially promotes migration, while disorder predominates at later timepoints.

Force propagation through adherens junctions is fundamental to collective migration [6]. The protein α -catenin mechanically couples

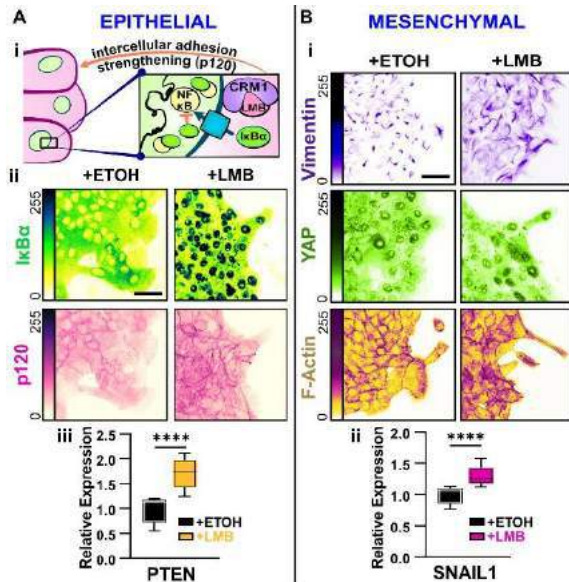


Figure 1: NEI enhances epithelial and mesenchymal traits.
A) Epithelial traits in MCF10A cells: **i)** Schematic depicting known mechanism for intercellular adhesion strengthening via CRM1 inhibition. **ii)** Images for IκBα and p120 epithelial markers. **iii)** PTEN gene expression. **B)** Mesenchymal traits: **i)** Images for vimentin, YAP, and F-actin. **ii)** SNAIL1 gene expression. Graphs show mean ± SEM with significance levels for unpaired t-test (n = 12). Scale bars: 50 μm.

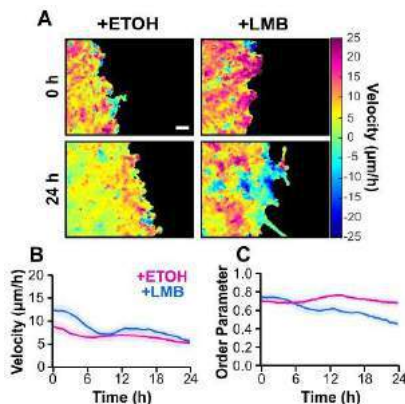


Figure 2: Time-dependent changes in collective velocity and disordered migration arise during NEI.

A) Velocity heat maps at 0 and 24 h. Graphs for **B)** collective velocity and **C)** order parameter over 24 h timelapse. Scale bar: 100 μm. Graphs show mean as solid line and ± SEM as shaded region (n > 6).

cells, recruiting F-actin to E-cadherin-based cell junctions. To characterize the role of intercellular force propagation in the observed NEI outcomes, we used α-catenin depleted MCF10A cells (α-cat KD). α-cat KD cells treated with LMB exhibited higher YAP N:C ratios and higher actin coherency compared to wild type (WT) cells (Fig. 3A,B). However, this elevation of mesenchymal characteristics did not extend to functional cellular changes. Remarkably, during NEI, α-cat KD cells lost front-back polarity, formed discrete colonies, and dissolved leader-follower relationships (Fig. 3C). At the same time, while NEI elevated net migration velocity initially above that for control α-cat KD cells, net velocities were lower than WT cells across timepoints, and migration arrested by 24 h. Ultimately, these findings suggest that α-catenin functionally couples concurrent epithelial and mesenchymal traits.

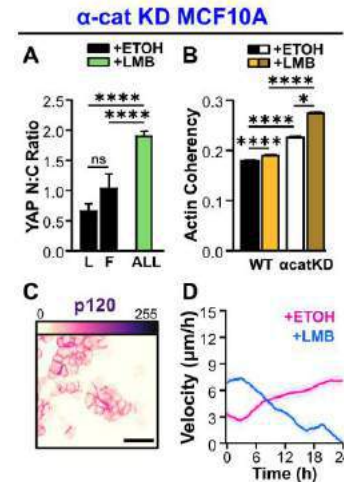


Figure 3: Removing α-catenin from NEI enhances mesenchymal traits without translating functionally to cell shape or migration.

Changes in **A)** YAP nucleocytoplasmic (N:C) ratio (n = 8) and **B)** actin coherency (n > 1000) following NEI for wild type (WT) and α-catenin knockdown (α-cat KD) cells. **C)** Sample morphology following NEI shown via p120. **D)** Velocity over 24 h for NEI and vehicle (n > 6). Graphs show mean as bar or solid line ± SEM, with significance levels for one- or two-way ANOVA.

DISCUSSION

Classically, epithelial (E) and mesenchymal (M) phenotypes exist along a single continuum, where cells traverse from E to M via the loss of epithelial characteristics precisely in step with the gain of mesenchymal ones. Here, we show that NEI promotes biological (gene, protein expression) and functional (morphological, migratory) changes that expand the traditional epithelial-mesenchymal continuum. We propose these changes constitute a concurrent E-M state in which highly epithelial and highly mesenchymal characteristics coexist. From this atypical phenotype, what results is progressively disordered cell migration during NEI. This outcome emphasizes that epithelial and mesenchymal characteristics can exist in high degrees concurrently but not necessarily cooperatively. Meanwhile, results from MCF10A α-catenin knockdown cells indicate that the simultaneous phenotype hinges on cooperation between intercellular adhesion and intracellular force, with adherens junctions emerging as the operative link.

Ultimately, the concurrent states we observe expand the classical interpretation of phenotypes, and indicate that epithelial and mesenchymal traits may exist on separate continua. These findings highlight an increasingly diverse range of epithelial-mesenchymal phenotypes and thus further encourage a more comprehensive assessment of E-M cellular features as a basis for phenotypic categorization. Overall, this expanded understanding of E-M states could help further characterize how cells manipulate phenotypes to promote cancer, wound healing, and embryonic development.

ACKNOWLEDGEMENTS

Supported by NIH/NIGMS MIRA (R35GM128764).

REFERENCES

- [1] Trepac, X & Sahai, E, *Nat Phys*, 14(7):671-682, 2018.
- [2] Yang, J et al., *Nat Rev Mol*, 21(6):341-352, 2020.
- [3] Krull, C et al, *BioRxiv*, 2022. [\[Link to preprint\]](#)
- [4] Arenzana-Seisdedos, F et al, *J Cell Sci*, 110(3):369-378, 1997.
- [5] Kourtidis, A et al, *Prog Mol Biol Transl Sci*, 116:409-432, 2013.
- [6] Ladoux, B, & Mège, RM, *Nat Rev Mol*, 18(12):743-757, 2017.

PERSONALIZED FINITE ELEMENT MODEL OF PEDIATRIC TISSUE EXPANSION

Tianhong Han (1), Kaleem Ahmed (2), Arun Gosain (2), Taeksang Lee (3), Adrian Buganza Tepole (1)

(1) Mechanical Engineering, Purdue University, West Lafayette, Indiana, United States
(2) Feinberg Medical School, Northwestern University, Chicago, Illinois, United States
(3) Mechanical Engineering, Myongji University, Yongin, Korea

INTRODUCTION

Tissue expansion (TE) is a commonly used procedure to repair large skin defects including breast reconstruction after mastectomy and large congenital defects. Because skin grows in response to stretch, tissue expander, a balloon-like device, can be inserted subcutaneously and gradually inflated with saline to promote skin growth. After inflation, the excess skin can then be harvested for reconstructive purposes. However, due to the lack of ability of predicting the amount and shape of the newly grown skin, the postoperative complication rate can be as high as 20 percent [1]. We have done extensive work calibrating a mathematical model of skin growth in response to stretch based on a porcine animal model [2]. Here we leverage that model and adapt it to the clinical setting to predict deformation and growth of skin in a patient-specific model.

METHODS

Patient Protocol

One pediatric case of TE was studied shown in Figure 1. Three dimensional photos were taken before the insertion of the expander, before initial inflation of the expander, and after the expansion process right before the excess skin was going to be harvested. A tissue expander with base 50×80 mm² was inserted and inflated in increments over a 2 month period. The details of inflation protocol are included in Table 1.

Table 1: Inflation Protocol of Patient

Date [MM/DD]	Volume [ml]	Time [Days]
01/24	15	0
02/03	30	10
02/10	45	17
02/17	60	24
02/24	70	31
03/03	80	38
03/10	90	45
03/17	100	52
03/24	110	59
03/31	120	66

Finite Element Model of Tissue Expansion

The finite element model of tissue expansion is an extension on our previous work [2]. The initial state of the skin is discretized with C3D8 elements in Abaqus from the 3D scan after the insertion of the expander. The expander is modeled with shell elements CPS4 and fluid cavity elements. We also assumed no friction between the expander and the skin. Skin area deformation is split into growth and elastic parts, see Figure 2,

$$\theta = \theta^g \theta^e \quad (1)$$

with the area growth rate being proportional to the elastic deformation

$$\dot{\theta}^g = k(\theta^e - \theta^{crit}) \quad (2)$$

Copyright 2023 SB³C Foundation, Inc.

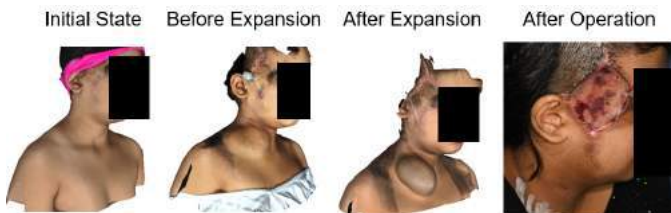


Figure 1: Photos of the patient with tissue expander at different states

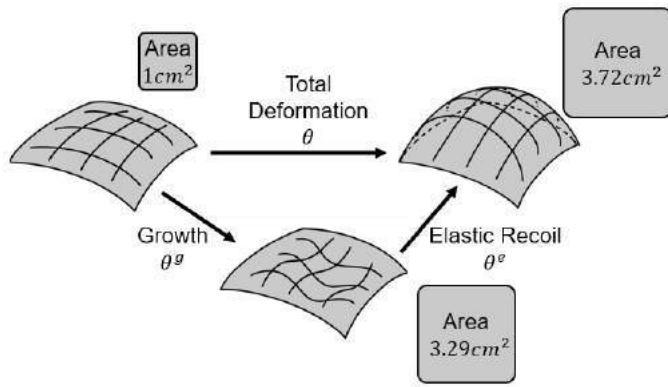


Figure 2: Skin deformation schematic at the apex of the expander

where k is the growth parameter calibrated in our previous work [2].

Uncertainty Analysis

Our previous work has quantified the uncertainty in the biological parameter k . Furthermore, there are other uncertain quantities associated with the process, including mechanical properties for human skin [3]. Additional uncertainties are on boundary conditions. To account for the uncertainty analysis, we ran a series of simulations with different growth rate k , material properties, and boundary conditions. Among material properties, we varied shear modulus μ . For the boundary conditions, we varied the expander's distance to skin h to account for the inaccuracy in volume and the fixed skin distance from expander tol to account for the uncertainty in the procedure. The parameter sets were generated with Latin hypercube sampling. The ranges of different variables are detailed in Table 2.

Table 2: Ranges for Material Properties and Boundary Conditions

Parameter	Range
μ [MPa]	[0.1, 1.0]
k [hr ⁻¹]	[0.02, 0.1]
tol [mm]	[15, 30]
h [mm]	[1, 3.5]

RESULTS

With the expander inflated to the volume following the protocol, we are able to show the development of total deformation over time. To show the skin's recoil, we added a deflation process to the expander in the simulation as shown in Figure 3. The full simulation spanned the 80 days of the protocol.

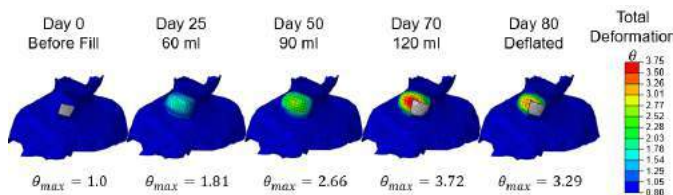


Figure 3: Total deformation of skin over time.

Based on the post operation picture in Figure 1, we estimated the harvested skin area to be [23.8, 26.8]cm². Based on our simulations, the final skin growth area has a range of [13.0, 30.9]cm² with a median of 20.2 cm² (Fig. 4).

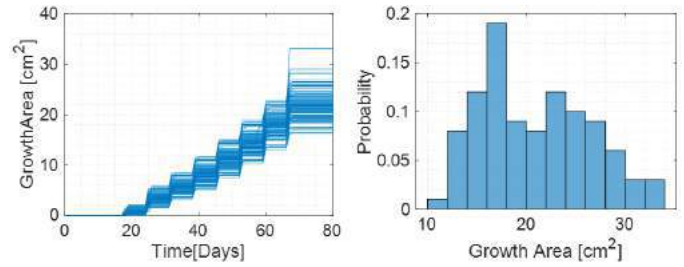


Figure 4: Skin growth area results from simulations.

To further confirm the accuracy of our model, we compared the final coordinate location of the nodes on the skin to the 3D scan of the patient after expansion. For each simulation, the shortest distance from the nodes to the 3D scan were calculated and recorded as shown in Figure 5. To compute the shortest distance, the simulation and scan were first aligned using software CloudCompare. For most cases, the average distance from the node at the end of the simulation to the scan is 3.5mm.

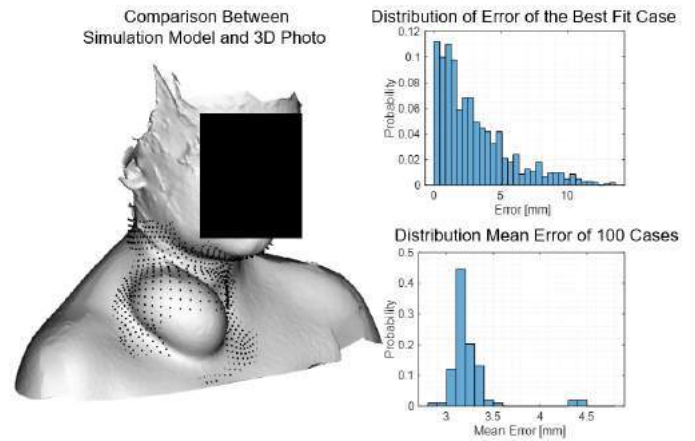


Figure 5: Error calculation comparing predicted geometry from finite element model to 3D scan at the end of procedure.

DISCUSSION

Currently, the designing of TE protocols solely relies of the surgeon's individual training and experience. This lack of standardization can limit the potential use of the technique and also lead to sub-optimal final results. Based on our understanding of skin mechanobiology from porcine models, we simulated skin growth in response to a clinical protocol. Our results show that computational modeling can not only be utilized in predicting the outcome of TE, but also take the uncertainty in the procedure into account. While we cannot fully validate the model, the geometry at the end of the process has very small error distributions. With ongoing

ACKNOWLEDGEMENTS

This work was supported by NIAMS R01AR074525.

REFERENCES

- [1] Bergmann G et al. *J Biomech* 34.7 (2001). DOI: 10.1016/s0021-9290(01)00040-9.
- [2] Han T et al. *Acta Biomaterialia* 137 (2022).
- [3] Luebberding S et al. *Skin Research and Technology* 20.2 (2014).

IN VIVO TESTING OF HYSTERESIS OF THE UTERINE SUSPENSORY TISSUE IN CHINESE WOMEN WITH PELVIC ORGAN PROLAPSE

Hui Wang (1), Zhuowei Xue (2), Chenxin Zhang (1), Fei Feng (3), Chengsheng Huang (2), Da He (3), Xinyi Wang (3), Qingkai Wu (2), Jiajia Luo (1)

- (1) Biomedical Engineering Department, Peking University, Beijing, China
(2) Department of Obstetrics and Gynecology, Shanghai Jiao Tong University Affiliated Sixth People's Hospital, Shanghai, China
(3) University of Michigan-Shanghai Jiao Tong University Joint Institute, Shanghai Jiao Tong University, Shanghai, China

INTRODUCTION

Pelvic organ prolapse (POP) refers to downward displacement and deformation of the female pelvic organs [1]. In the United States, more than 200,000 surgeries are performed each year [2], with a 25% recurrence rate 10 years after surgery [3]. In China, the prevalence of symptomatic pelvic organ prolapse was 9.6% [4].

Pelvic organ prolapse usually occurs about 20-30 years after vaginal delivery, which is most likely closely related to prolonged and repeated loading and unloading of the uterine suspensory tissue (UST) over many years. The UST, consisting of the cardinal ligament (CL) and the uterosacral ligament (USL), is thought to play an important role in resisting pelvic organ prolapse [5]. However, the underlying mechanisms of tissue damage of the UST and prolapse caused by long-term repetitive loading remains unclear. Therefore, the aim of this study was to develop an MRI-based preoperative measurement technique to quantify the *in vivo* hysteresis of the UST in women with pelvic organ prolapse and to help understand the temporal mechanisms of the occurrence of pelvic organ prolapse.

METHODS

Six Chinese women with POP scheduled for surgery were selected from an ongoing POP research at the Shanghai Jiao Tong University Affiliated Sixth People's Hospital (Shanghai, China) with the approval of the Institutional Review Board.

Prior to surgery, the mechanical behavior of the CL and USL was tested using a newly designed computer-controlled linear servo system (Figure 1), similar to our previous work [6]. First, the patient's information and the max force used were entered through the computer. To obtain the initial position, a force of 1 N was preloaded to remove the slack of the UST. Then the linear actuator pulls the uterine cervix until the force reaches its maximum. Finally, the linear actuator was reversed to gradually release the UST. Force and displacement were recorded in real time during the test. A total of three trials were

performed for each patient, with a two minutes interval for tissue recovery.

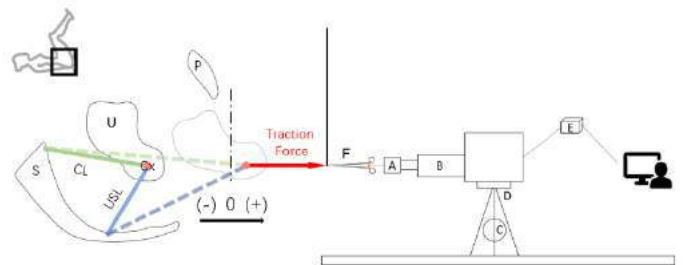


Figure 1: Schematic of the test setup. Zero indicates the location of the hymen, with $-/+$ meaning above or below the hymen. Cx, cervix; P, pubic bone; S, sacrum; U, uterus; A, B, and D denote the force sensor, linear actuator, and shell; C, the tripod; E, the motor controller; and F, the cervical forceps. The vertical dashed-dotted line represents the initial location of the hymenal ring. The green and blue dashed lines indicate CL and USL under load, respectively. Modified from [6].

Similar to our previous study [7], we used MRI scans of the CL and USL to create a specific 3D model for each individual, measuring the length, angle, and cross-sectional area of the CL and USL for each individual. A four-wire model was used to calculate the forces on the ligaments.

A typical loading and unloading of the UST is shown in Figure 2. The UST stiffness is defined by $\frac{f_2 - f_1}{d_2 - d_1}$, where f_2 and f_1 denote the maximum force and minimum force, and d_2 and d_1 denote the maximum displacement and minimum displacement. The hysteresis is defined by $\theta_1 - \theta_2$, where θ_1 is the area under the loading curve and θ_2

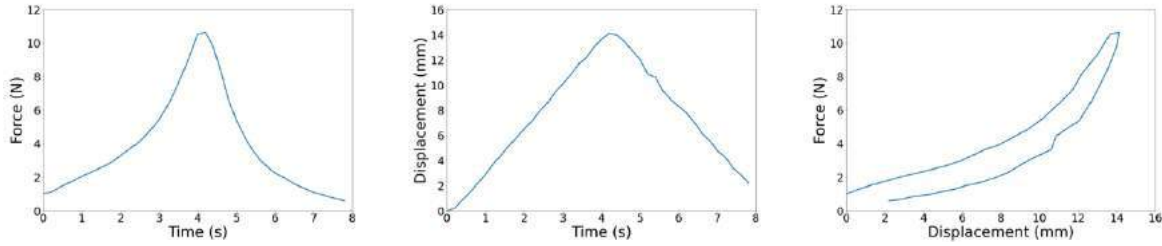


Figure 2: A typical loading and unloading test result (trial 1) for the UST (Patient #003).

is the area under the unloading curve of each trial. Python (v 3.7.2) and the corresponding NumPy (v 1.20.2) library were used to process the data and calculate the hysteresis and stiffness per person per trial.

For simplicity, CL and USL were assumed as incompressible isotropic hyperelastic materials, and the strain energy density was assumed to be a function of the first and second invariants of the strain tensor. A three-parameter hyperelastic Moony-Rivlin material model was thus selected to fit the CL and USL loading behavior, and the model was defined as follows:

$$W(0) = C_{10}(I_1 - 3) + C_{01}(I_2 - 3) + C_{11}(I_1 - 3)(I_2 - 3) \quad (1)$$

Where C_{01} , C_{10} , and C_{11} are material constants; I_1 and I_2 are the first and second invariants of rights Cauchy deformation tensor. A customized MATLAB (v.2019a) program was used to solve the strain and stress and fit the strain-stress curve.

Descriptive statistical analysis and two-sided T-test were used to compare the differences between the three trials.

RESULTS

The six Chinese women with POP had an age of 68 ± 12 years old (*mean* \pm *SD*), and parity of 1.8 ± 0.8 . They all had anterior vaginal prolapse. The stiffness and hysteresis of the UST for those Chinese women are shown in Figure 3.

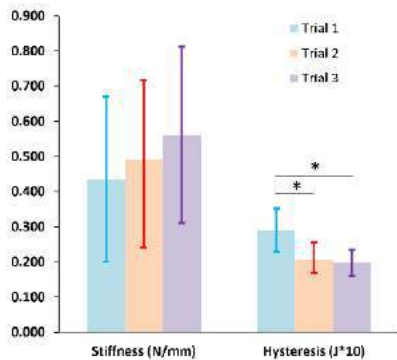


Figure 3: Uterine suspensory tissue stiffness and hysteresis in Chinese women with prolapse from trial 1 to trial 3 (*, $p < 0.05$). For demonstration purposes, we change the unit of hysteresis from J to $10J$.

For the UST, the stiffness was 0.434 ± 0.235 N/mm for trial 1, 0.492 ± 0.227 N/mm for trial 2, and 0.560 ± 0.250 N/mm for trial 3. The hysteresis was 0.029 ± 0.006 J for trial 1, 0.021 ± 0.005 J for trial 2, and 0.019 ± 0.004 J for trial 3. As can be seen from the results, the UST continues to harden with repeated loading. The hysteresis of the UST was significantly reduced from trial 1 to trial 2, not significantly from trial 2 to trial 3.

The stress-strain behavior in each trial and the fitted curves of CL and USL are shown in Figure 4. The three-parameter hyperelastic

Moony-Rivlin material constants were fitted according to Eq. (1). For CL, C_{10} was -0.04 ± 0.05 MPa, C_{01} was 0.04 ± 0.06 MPa, and C_{11} was 0.04 ± 0.05 MPa. For USL, C_{10} was -0.02 ± 0.02 MPa, C_{01} was -0.02 ± 0.02 MPa, and C_{11} was -0.02 ± 0.02 MPa.

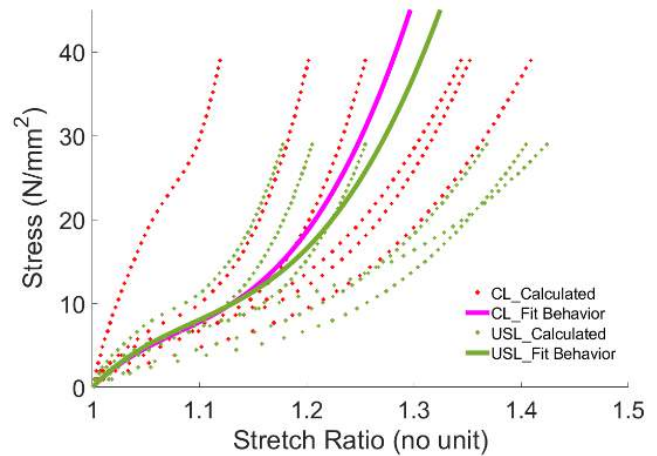


Figure 4: Stress-strain behaviors of the CL and USL. The calculated stress-strain data for each subject are shown as dotted lines, and the fitted stress-strain curves are shown as solid lines. The R^2 value for the CL is 0.6311 and for the USL is 0.6674.

DISCUSSION

This study is the first to examine *in vivo* hysteresis of the uterine suspensory tissue in Chinese women with pelvic organ prolapse. This helps us to understand the changes in uterine suspensory tissue and the temporal mechanism of pelvic organ prolapse under long-term repeated loading. This will allow us to better understand why vaginal delivery leads to pelvic organ prolapse after 20 to 30 years. So far, we have only provided partial results. In future work, a larger sample size might help us to find statistical differences between different categories of patients.

ACKNOWLEDGEMENTS

NSFC 31870942, Peking University Clinical Medicine Plus X-Young Scholars Project PKU2020LCXQ017 and PKU2021LCXQ028, PKU-Baidu Fund 2020BD039.

REFERENCES

- [1] Haylen et al., *Int Urogynecol J*, 27(4), 655-684, 2016.
- [2] Boyles et al., *Am J Obstet Gynecol*, 188(1):108-115, 2003.
- [3] Fialkow et al., *Int Urogynecol J*, 19(3), 437-440, 2008.
- [4] Pang et al., *Bjog-Int J Obstet Gy*, 128(8):1313-1323, 2021.
- [5] Summers et al., *Am J Obstet Gynecol*, 194(1):1438-1443, 2006.
- [6] Luo et al., *J Biomech Eng*, 136(2):021016, 2014.
- [7] Luo et al., *Int Urogynecol J*, 25(2):197-203, 2014.

IMPLEMENTATION OF EXPERIMENTALLY ACQUIRED TRICUSPID VALVE LEAFLET PRE-STRAINS TO AN *IN-SILICO* FINITE ELEMENT MODEL

Colton J. Ross (1), Arshid Mir (2), Harold M. Burkhart (3)
Ming-Chen Hsu (4), Devin W. Laurence (5), Chung-Hao Lee (1)

(1) School of Aerospace and Mechanical Engineering, University of Oklahoma, Norman, OK, USA

(2) Department of Pediatrics, University of Oklahoma Health Sciences Center, Oklahoma City, OK, USA

(3) Department of Surgery, University of Oklahoma Health Sciences Center, Oklahoma City, OK, USA

(4) Department of Mechanical Engineering, Iowa State University, Ames, IA, USA

(5) Department of Anesthesiology and Critical Care Medicine, Children's Hospital of Philadelphia, Philadelphia, PA, USA

INTRODUCTION

The bodily soft tissues are naturally under tension, or, in other words, pre-strained. These pre-strains were first discovered by Chuong and Fung (1986) in their pivotal experiments measuring the opening angles of the blood vessels [1]. Following this seminal work, other researchers sought to quantify the pre-strains of other soft tissues, such as the heart valve leaflets. Of specific interest, Amini *et al.* (2012) measured the areal contraction of the ovine mitral valve anterior leaflet between the *in vivo* and *ex vivo* configurations and found 18% and 30% contractions in the circumferential and radial directions, respectively [2]. Inspired by this work, our laboratory recently characterized the pre-strains of the tricuspid valve (TV) leaflets using a novel 3D photogrammetry and reproducing kernel method [3]. Briefly, in that work, porcine hearts were acquired, fiducial markers were placed on the TV leaflets, and photographs were captured throughout the tissue dissection and biaxial testing process, including a standard equibiaxial loading preconditioning protocol. Overall, we found that the quantification of the tissue material behaviors was greatly influenced by the selected reference configuration, which will have a profound impact for the *in-silico* modeling of the *in vivo* TV behaviors. As a logical next step in our investigations, we proceed to implementing these pre-strains into finite element models to elucidate the implications of these findings for applications such as patient-specific modeling.

In this work, we will perform an *in-silico* investigation of the effects of pre-strains on modeling of the tricuspid valve closing. Utilizing the data from our previous work [3], we will conduct simulations for $n = 8$ porcine tricuspid valves to make comparisons between the valve closing predictions with and without consideration of the experimentally acquired, subject-specific pre-strains. Furthermore, we will investigate how the chosen reference configuration from the *ex vivo* material characterizations influences the simulated TV closing behaviors and biomechanics (e.g., tissue stresses).

METHODS

Building upon our existing parametric TV finite element analysis framework [4], we construct subject-specific valvular geometries based upon the leaflet and commissure heights measured from our experimental photographs (Fig. 1(a)). Due to the nature of our experiments, we are unable to acquire subject-specific annulus and free edge contours, and thus we use a simplified, flat, elliptical annulus geometry for our preliminary investigations. Afterwards, we generate the leaflet free edge curve using the measured valvular heights and a periodic smoothing cubic spline. Then, the leaflet surface is constructed between the two curves and discretized using 4-node shell elements (S4) in ABAQUS (Dassault Systèmes, Simulia Corp., Johnson, RI). The shell thicknesses are prescribed based upon our experimental measurements of the porcine leaflets. Meanwhile, the leaflet material parameters are determined by fitting an isotropic Lee-Sacks model to the biaxial tensile testing data:

$$\psi = \frac{c_0}{2}(I_1 - 3) + \frac{c_1}{2}(e^{c_2(I_1 - 3)^2} - 1) - \frac{p}{2}(J - 1). \quad (1)$$

Here, c_0 , c_1 and c_2 are the material parameters, I_1 is the first invariant of the right Cauchy-Green tensor ($\mathbf{C} = \mathbf{F}^T \mathbf{F}$, where \mathbf{F} is the deformation gradient), and p is a penalty parameter to enforce the incompressibility condition (i.e., $J = \det(\mathbf{F}) = 1$). For our preliminary investigations, the material parameters are prescribed uniformly across all three leaflets with the following values: $c_0 = 10$ kPa, $c_1 = 0.209$ kPa, and $c_2 = 9.046$.

Due to limitations with our photogrammetry-based analysis, we generate the chordae tendineae using the simplified representation from our previous work [5]. For the material behaviors, the chordae are modeled as linearly elastic solids, with a Young's modulus of 10 MPa. Finally, the model boundary conditions include a transvalvular pressure of 25 mm Hg applied to the ventricular surface of the leaflets, and pinning of the annulus and papillary muscles.

The pre-strains are embedded to the model using a three-step procedure [6] (Fig. 1(b)): (i) the original TV geometry is shrunk based upon the leaflet-specific pre-strains measured in our experiments; (ii) the shrunk TV geometry is imported to ABAQUS, and the nodes are displaced to restore the original TV shape, embedding the pre-strains; and (iii) the forward simulation of the valve closing is performed. To prescribe the pre-strains, all transformations are performed within the cylindrical coordinate system. For the radial pre-strains, the annulus-to-free edge distance of each node is adjusted using the Z-coordinates. Meanwhile, the circumferential pre-strains are prescribed by manipulation of the radius coordinate value (i.e., displacement of the nodes towards the valve origin), effectively contracting the annulus segment lengths. For numerical continuity, the pre-strains in the commissural regions are constructed as a gradient between the leaflet-specific pre-strains.

Following the completion of the valve simulations, post-processing metrics include quantities such as the projected regurgitant orifice area (ROA), the Green-Lagrange leaflet strains, and the Cauchy stresses. All values are reported as the mean \pm standard deviation.

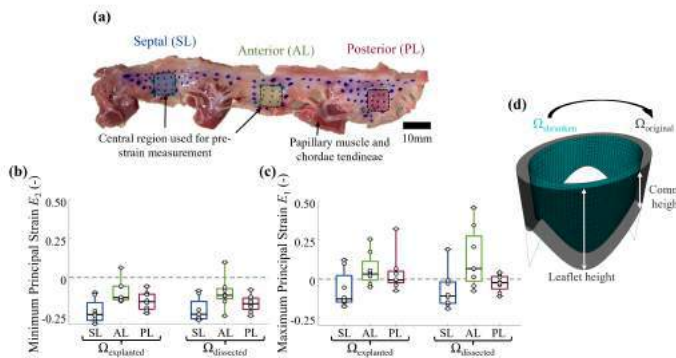


Figure 1: (a) Explanted TV for pre-strain and dimensional measurements; (b) measured pre-strains in the E_2 and (c) E_1 principal directions at the explanted and sectioned tissue configurations (Ω) from [3]; (d) surfaces constructed for embedding a homogenous 20% pre-strain by displacing the mesh from the shrunk to the original configuration

RESULTS

For our preliminary analysis, we performed a systematic investigation of the effects of pre-strains on the simulated TV closing by applying incremental, homogenous pre-strains (i.e., the same for all three leaflets) of 0% – 30% with a 10% increment. In this early study, we used the valvular measurements from Figure 1: septal leaflet (SL), 19.9 mm; anterior leaflet (AL), 15.8 mm; posterior leaflet (PL), 19.4 mm. Meanwhile, the commissure heights were measured as: posterior-septal, 9.6 mm; antero-posterior, 8.4 mm; antero-septal, 11.9 mm.

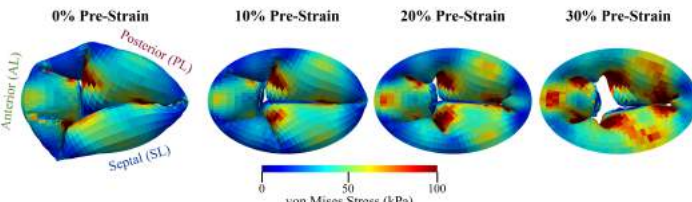


Figure 2: Superior view of the simulated TV closing and von Mises Cauchy strains for the representative specimen without and with embedded pre-strains.

In our preliminary results, we found that an increase in the pre-strains resulted in severely diminished valve coaptation (Fig. 2). Specifically, for

the models with 10% and 30% pre-strain, we calculated a projected ROA of 22 mm² and 514 mm², respectively. Analyzing the leaflet stresses, we noted profound increases with larger applied pre-strains, and comparing the 0% and 30% pre-strain levels we found von Mises stress increases of 116%, 89%, and 89% for the SL, AL, and PL, respectively. Similar trends were observed for the leaflet strains. For example, comparing the strains in the circumferential direction between the 0% and 30% pre-strain levels: SL, 35% increase; AL, 25% increase; PL, 20% increase. We also found 35% larger reaction forces at the papillary muscle tips between the 0% and 30% pre-strain levels.

DISCUSSION

Our preliminary investigation provided a clear demonstration that the inclusion of pre-strains in the simulated tricuspid valve results in the development of a regurgitant orifice. At the same time, the stresses, strains, and papillary muscle reaction forces became larger with increasing amounts of pre-strain. It is likely that the presence of TV regurgitation is caused by using the same leaflet material parameters across all of our simulations, and that the valve closing may be better simulated by performing data fitting to our biaxial tensile data using a different stress-free reference configuration (e.g., the explanted valve vs. the post-preconditioned tissue). Comparing our findings to the mitral valve-focused inverse finite element analysis study by Rausch and Kuhl (2013), they found that consideration of the pre-strains yielded variations in the estimated membrane stiffnesses by up to four magnitudes [6], providing support to our theory.

Motivated by these observations, as we continue this study, we will systematically test the influence of the leaflet- and subject-specific material parameters and pre-strains on the simulated valve closing. Through this experimentally supported *in-silico* work, we will provide *novel findings* for the effects of pre-strains on the TV closing, which will have major implications on the refinement of the protocols used in benchtop material characterizations. For example, the equibiaxial tensile preconditioning protocol typically used in previous studies may not effectively restore the *in vivo* tissue operating condition, and thus the material parameters obtained from subsequent tensile testing may not be an accurate representation [3].

Overall, our results demonstrate the necessity for considering pre-strains both during the experimental characterizations of tissue and while performing *in-silico* simulations of valve function. Specifically, a careful selection of the reference configuration is required to ensure proper material parameter estimation and accurate simulation results. In the long-term, advancements in pre-strain-focused research will lead to more improved finite element models and enable the next steps in simulation-informed, personalized medicine.

ACKNOWLEDGEMENTS

We gratefully acknowledge the supports from the Presbyterian Health Foundation, American Heart Association Scientist Development Grant Award (16SDG27760143), and the National Science Foundation Graduate Research Fellowship (GRF 2020307284).

REFERENCES

- [1] Chuong CJ *et al.* *Frontiers in Biomechanics*. Springer, 1986. DOI: 10.1007/978-1-4612-4866-8_9.
- [2] Amini R *et al.* *Ann Biomed Eng* 40.7 (2012). DOI: 10.1007/s10439-012-0524-5.
- [3] Laurence DW *et al.* *Acta Biomater* 152 (2022). DOI: 10.1016/j.actbio.2022.08.046.
- [4] Laurence DW *et al.* *Int J Numer Method Biomed Eng* 36.7 (2020). DOI: 10.1002/cnm.3346.
- [5] Johnson EL *et al.* *Comput Methods Appl Mech Eng* 384 (2021). DOI: 10.1016/j.cma.2021.113960.
- [6] Rausch MK *et al.* *J Mech Phys Solids* 61.9 (2013). DOI: 10.1016/j.jmps.2013.04.005.

VISCOELASTICITY AND MICRO-PHASE SEPARATION MEDIATE MENISCAL CELL MIGRATION THROUGH HYALURONIC ACID HYDROGELS

Karen L. Xu (1), Hooman Fallahi (2), Lin Han (2), Robert L. Mauck (1), Jason A. Burdick (1,3)

(1) Department of Bioengineering, University of Pennsylvania, Philadelphia, PA, USA

(2) School of Biomedical Engineering, Science and Health Systems, Drexel University, Philadelphia, PA, USA

(3) BioFrontiers Institute and Department of Chemical and Biological Engineering, University of Colorado, Boulder, USA

INTRODUCTION

The meniscus is a load-bearing structure that supports knee stability and motion and has a limited capacity for repair after damage [1]. Untreated torn menisci often result in the rapid progression of osteoarthritis in patients due to changes in joint loading, underscoring the critical need to develop therapeutics that promote meniscus repair. Injectable, acellular, and degradable biomaterials have been explored for tissue repair due to their ability to support and promote endogenous cell migration, proliferation, and extracellular matrix deposition. In our approach, we seek to introduce biophysical cues that are present in native tissues to enhance cellular infiltration into engineered hydrogels. First, we introduce tissue viscoelasticity, a property that has been shown to support cell migration within biomaterials [2]. Second, we investigate the micro-phase separation that occurs during hydrogel formation to introduce micro-scale heterogeneity and micro-interfaces at the cellular level. This study explores how these biophysical cues promote important cellular behaviors (e.g., migration) needed for meniscal repair.

METHODS

Material Fabrication: Interpenetrating network (IPN) hydrogels were fabricated through the mixing of guest-host (GH) physical networks (adamantane-modified hyaluronic acid (AD-HA) and cyclodextrin-modified HA (CD-HA)) with covalent gelatin networks (transglutaminase crosslinked) (Fig 1A). All studies performed were conducted with 5 wt% gelatin, 1 U/mL transglutaminase and 0, 1 or 3 wt% GH. **IPN Hydrogel Characterization:** Bulk mechanical properties were assessed with oscillatory time sweeps. Structural features of an 800 x 800 μm region were evaluated through confocal fluorescent microscopy. Microscopic mechanical characterization across a 105 x 105 μm grid was performed via atomic force microscopy (AFM). Heterogeneity was assessed by determining the spatial coefficients of variation across both fluorescent intensity and AFM measurements. **In vitro Cell Interactions:** Meniscal fibrochondrocyte (MFC) spheroids

were formed through 48-hour culture and then embedded within IPNs. Cell outgrowth was assessed by staining actin cytoskeletons and averaging radii of outgrowth from the spheroid edge. The 3% GH experimental group was treated with a broad spectrum MMP inhibitor (Marimastat), a DMSO vehicle control, soluble RGD, and a PBS vehicle control for 3 days and their influence on cell outgrowth was measured. **Cell Infiltration into Hydrogels:** 5 mm juvenile bovine meniscus explants were placed atop hydrogels and cells were allowed to infiltrate for 6 days. **Quantification:** Mechanical testing (n=3-5), spheroid outgrowth (n=3-8) and explant studies (n=5) were pooled per experimental group and timepoint and compared with 1- or 2-way ANOVA with Bonferroni posthoc or Student's T-Test.

RESULTS

We developed a viscoelastic (Fig 1B, C) IPN hydrogel due to the combined guest-host (GH) physical crosslinking [3] of HA and covalent (i.e., transglutaminase) crosslinking of gelatin (Fig 1). Injectability was possible at early times after mixing, prior to complete crosslinking. Increasing the physical network concentration (0 to 3 wt%) correlated with increased $\tan(\delta)$ (Fig 1C), a measure of viscoelasticity. Heterogeneity of the IPN networks was observed through labeling of the distinct microphases of gelatin and quantification of the domain variations (Fig 2A,B). Further, micro-scale heterogeneity was observed mechanically, as measured and quantified with AFM mapping of hydrogel films (Fig 2C,D). Single network gelatin hydrogels without the GH component exhibited less variation than the IPN hydrogels.

The combined attributes of these biophysical properties in the 1% and 3% IPN hydrogels promoted rapid migration of meniscal fibrochondrocytes (Fig 3) compared to pure gelatin 0% group. Cell outgrowth decreased when cell mediated degradation (Fig 3D) or cell adhesion to the hydrogel (Fig 3E) was inhibited. Finally, increased migration of cells into hydrogels from juvenile meniscus explants into the IPN hydrogels was greater (Fig 4A, B). Qualitatively, cells tracked along the borders of the gelatin-rich regions in these studies.

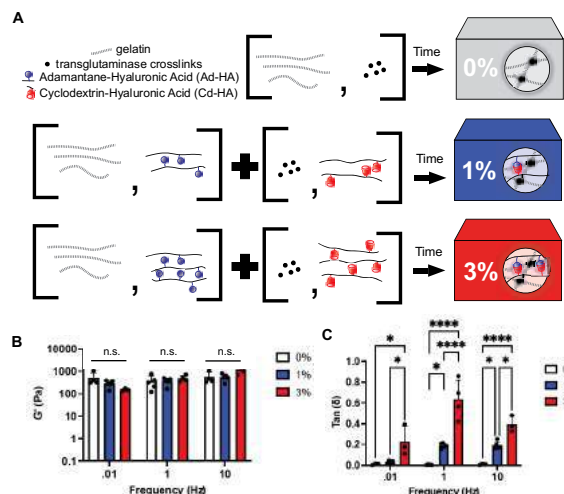


Figure 1: Schematic of control (0%) and IPN (1%, 3%) hydrogel fabrication (A) and resulting storage modulus (B) and tan (δ) (C) at various frequencies. * $p \leq 0.05$, ** $p \leq 0.0001$**

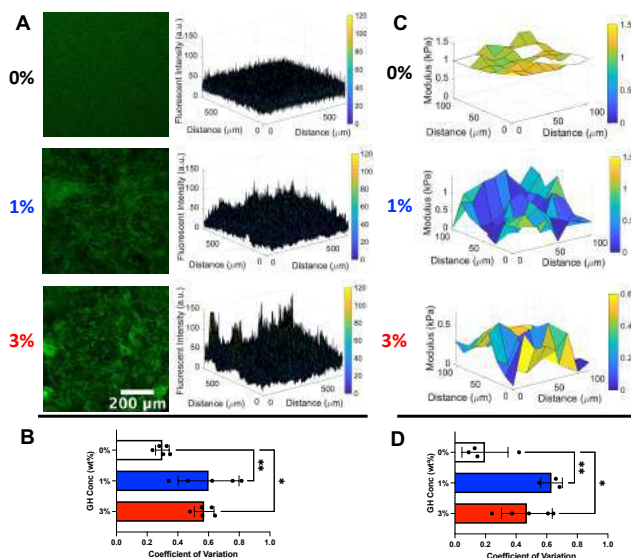


Figure 2: Representative fluorescent images (A; green: gelatin) and corresponding intensity profiles and coefficients of variation (CV) (B) and representative AFM maps (C) and CV (D) for control (0%) and IPN (1%, 3%) hydrogels. * $p \leq 0.05$, ** $p \leq 0.01$

DISCUSSION

This work addresses how key biophysical cues presented through the micro-phase separation of IPN hydrogels influences cell migration, looking towards improved platforms for mechanobiology and translational materials for tissue repair. The IPN hydrogel design allowed for both control over both the hydrogel viscoelasticity and micro-scale properties (e.g., gelatin content, mechanics) (Fig 1,2). This increased viscoelasticity and micro-scale heterogeneity altered cellular migration into hydrogels, including from embedded MFC spheroids or from adjacent meniscal tissues (Fig 3,4). Interestingly, the rapid migration was not observed for gelatin hydrogels alone and depended at least partially both on the cells' ability to remodel its extracellular environment (Fig 3D) and on adhesion to its extracellular environment via integrin-based interactions (Fig 3E). Given that gelatin is rich in these adhesive moieties and that hyaluronic acid is not, this behavior is dependent on both the structure and the composition of the hydrogels.

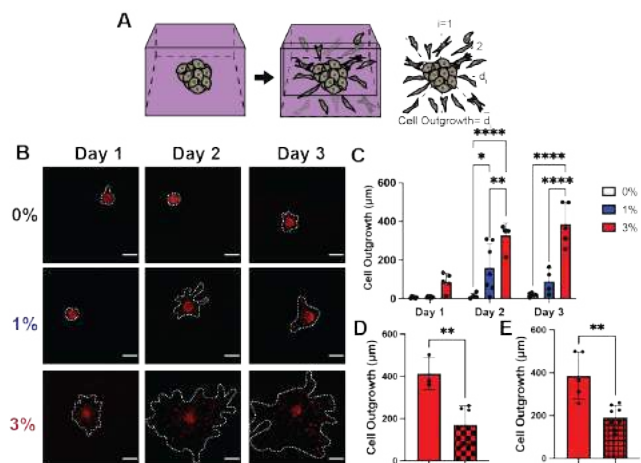


Figure 3: Schematic of cell outgrowth studies (A). Actin (red, dashed line of outgrowth) visualization (B; Scale bar=200 μm) and quantification (C). Outgrowth was assessed in the presence of matrix metalloproteinase inhibitor (MMPi, D) and soluble RGD (sRGD, E). * $p \leq 0.05$, ** $p \leq 0.01$, ** $p \leq 0.0001$**

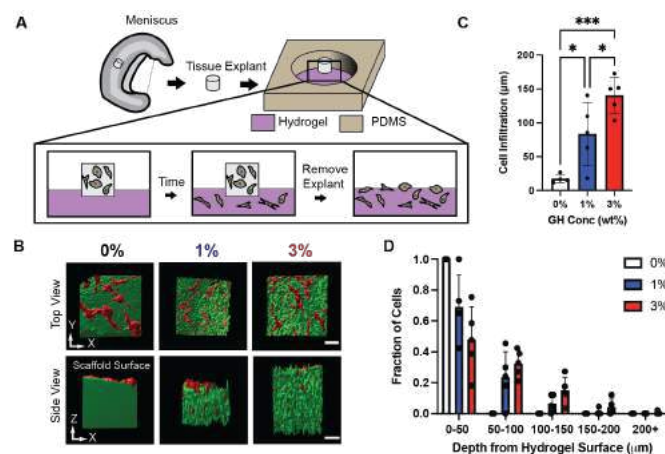


Figure 4: Schematic of experimental set up for outgrowth studies from explants (A; green: gelatin, red: actin). Rendering of outgrown cells within hydrogels (B; Scale bar=50 μm), quantification of maximum cell infiltration into hydrogels (C) and infiltration throughout hydrogel depth (D). * $p \leq 0.05$, ** $p \leq 0.001$**

Qualitatively, we have observed that migrating cells remain along the interfaces of regions of gelatin but did not necessarily infiltrate into these regions (Fig 4C,D). However, further analysis is needed.

Future work will further explore physiologic activities in migrating cells, namely exploring their proliferation, nascent matrix deposition and differentiation states. Gaining a greater understanding of the basis behind cell migration and other critical steps involved in tissue repair will enable a more targeted design of therapeutics to promote healing of connective tissues, such as the meniscus.

ACKNOWLEDGEMENTS

This work was supported by the Center for Engineering Mechanobiology (CMMI: 1548571) and the National Institutes of Health (F30 AG074508, R01 AR056624).

REFERENCES

- [1] Mauck et al. *Ann Biomed. Eng.* 43(3) 529-54, 2015
- [2] Alberto Elosegui-Artola, *Nat. Mater.* 22, 117-127, 2023
- [3] Rodell et al. *Biomacromolecules.* 14, 11, 4125-4134, 2013

CLICK CHEMISTRY-BASED INJECTABLE HYDROGEL FOR REPAIR OF THE ANNULUS FIBROSUS FOLLOWING INTERVERTEBRAL DISC HERNIATION

Emily E. Sharp (1,2), Karen L. Xu (1,2), Ryan C. Locke (1,2,3), Zhiliang Cheng (1), Jason A. Burdick (4), Sarah E. Gullbrand (2,3), Robert L. Mauck (1,2,3)

- (1) Department of Bioengineering, University of Pennsylvania, Philadelphia, PA, USA
(2) Department of Orthopedic Surgery, University of Pennsylvania, Philadelphia, PA, USA
(3) Translational Musculoskeletal Research Center, Crescenz VA Medical Center, Philadelphia, PA, USA
(4) BioFrontiers Institute and Department of Chemical and Biological Engineering, University of Colorado, Boulder, CO, USA

INTRODUCTION

The intervertebral discs (IVDs) are the soft tissues bridging adjacent spinal vertebrae, providing flexibility, load transfer, and shock absorption during multi-axial movement. IVDs are comprised of the highly organized annulus fibrosus (AF) that surrounds the gel-like nucleus pulposus (NP), which are separated from adjacent vertebrae by thin cartilaginous end-plates (CEPs). Trauma, overuse, or degeneration can result in AF tears or ruptures that disrupt the crucial role that the IVD plays in daily activities and can lead to NP herniation. The standard of care after herniation is microdiscectomy, where the herniated NP tissue is surgically excised. While effective in relieving symptoms that arise from herniation (i.e., pain, motor and sensory deficits), the mechanical integrity of the AF remains compromised, and a large defect persists through which remaining NP tissue can reherniate.¹

Successful annular repair following herniation offers immense potential in transforming clinical practice and creating superior surgical alternatives and outcomes for patients. To that end, next-generation multifunctional biomaterials enable complete customization to achieve ideal design criteria. In addition to common design criteria like biocompatibility and biodegradability, an ideal annular repair material would be injectable and have the capacity for controlled delivery of a therapeutic. Injectability enables the repair material to interdigitate with the AF to precisely fill the complex defect created by AF tears or ruptures. Controlled delivery of a therapeutic would not only minimize patient discomfort (by controlling inflammation, for example), but could also create a more favorable environment for tissue regeneration and annular repair. However, many proposed strategies for annular repair, such as hyaluronic acid and fibrin-based materials, lack this significant controlled delivery component.^{2,3}

Here, we developed an injectable hydrogel capable of spatiotemporal controlled delivery via click chemistry. Click chemistry describes a class of chemical reactions where two small molecules rapidly and strongly bind to one another. Specifically, we

utilize strain-promoted azide-alkyne cycloaddition (SPAAC) click reactions. Norbornene-modified hyaluronic acid (NorHA) hydrogels were azide-modified to click-functionalize the hydrogels, which was first confirmed using alkyne-modified fluorophores. Towards enabling controlled delivery, we demonstrate that alkyne-modified micelles can selectively attach to these azide-modified NorHA hydrogels. We confirmed that this azide-modification is cytocompatible with AF cells *in vitro*. While additional characterization and customization of these hydrogels is necessary for optimal use as an annular repair material, **this novel multifunctional biomaterial has the potential to revolutionize how we approach dense connective tissue repair and regeneration.**

METHODS

Hydrogel Synthesis and Click-Functionalization: NorHA synthesis was accomplished using well-established protocols.⁴ UV photocrosslinking of NorHA hydrogels was achieved using a di-thiol photocrosslinker that reacts with a portion of the pendant norbornene groups via a thiol-ene Michael addition. To click-functionalize these hydrogels, a thiol-PEG-azide (TPA) (MW: 1 kDa) was added to the hydrogel solution in a 50:50 ratio with the photocrosslinker (i.e., 50% of available norbornene groups were azide-modified and the remaining 50% were used to crosslink the hydrogel). Click Validation: Confirmation of click-functionalization was achieved by incubating non-modified (NorHA) and azide-modified (NorHA-TPA) hydrogels in an alkyne-modified fluorophore solution (30 μ M Alexa Fluorophore (AF)-488-Dibenzocyclooctyne (DBCO)) for 1 hour and assessing attachment via confocal microscopy. These same hydrogels were imaged after 1 week and 1 month of incubation in a PBS bath. The concentration of fluorophore was also varied to demonstrate concentration-dependent attachment via the click reaction. Quantification of the fluorophore attachment was carried out in ImageJ. Micelle Attachment: DBCO-modified micelles labelled with Rhodamine were fabricated as previously described.⁵ As a proof of

concept, these micelles were loaded with a secretory phospholipase A2 inhibitor (sPLA2i). sPLA2 mediates inflammation and tissue damage and is upregulated in injured AF scenarios.⁶ Non-modified (NorHA) and azide-modified (NorHA-TPA) hydrogels were incubated in a 30 μ M solution of these micelles overnight and then were vigorously shaken (500 RPM) for 24 hours prior to imaging via confocal microscopy. **Cytotoxicity Evaluation:** To ensure azide-modification did not impact hydrogel biocompatibility, we performed a non-contact cytotoxicity assay using bovine AF cells (P3-P4). AF cells were seeded in 96-well plates at a seeding density of 6,000 cells/cm². Cells were incubated at 37 °C in basal media for 24 hours before exposure. Cells either received no exposure or were indirectly exposed to NorHA-TPA hydrogels using 0.8 μ m transwell inserts (n=12/treatment group). AlamarBlue was used to assess cell viability and proliferation by measuring absorbance (at 590 nm) at days 1, 3, and 7 of exposure. Measurements were subtracted from media only (i.e., no cells) controls and plotted using GraphPad (Statistics: unpaired t-tests).

RESULTS

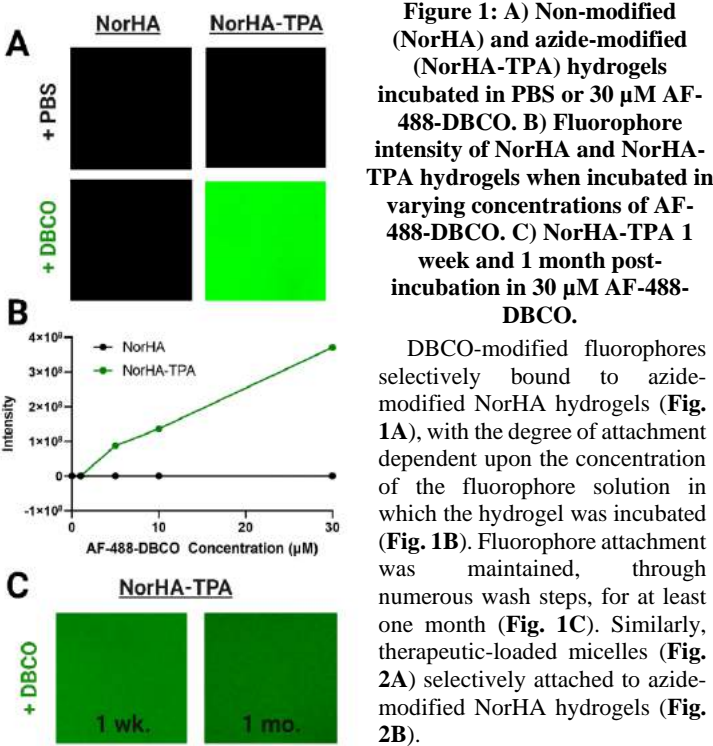


Figure 1: A) Non-modified (NorHA) and azide-modified (NorHA-TPA) hydrogels incubated in PBS or 30 μ M AF-488-DBCO. B) Fluorophore intensity of NorHA and NorHA-TPA hydrogels when incubated in varying concentrations of AF-488-DBCO. C) NorHA-TPA 1 week and 1 month post-incubation in 30 μ M AF-488-DBCO.

DBCO-modified fluorophores selectively bound to azide-modified NorHA hydrogels (Fig. 1A), with the degree of attachment dependent upon the concentration of the fluorophore solution in which the hydrogel was incubated (Fig. 1B). Fluorophore attachment was maintained, through numerous wash steps, for at least one month (Fig. 1C). Similarly, therapeutic-loaded micelles (Fig. 2A) selectively attached to azide-modified NorHA hydrogels (Fig. 2B).

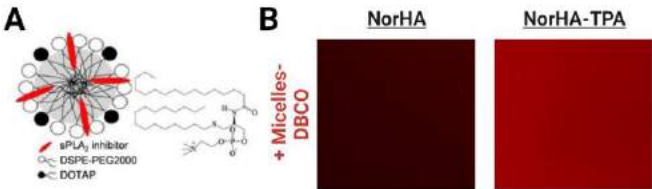


Figure 2: A) Schematic of sPLA2i-loaded micelles, which were DBCO-modified for this study. B) NorHA and NorHA-TPA hydrogels incubated in 30 μ M micelles-DBCO labelled with Rhodamine.

The biocompatibility of NorHA hydrogels has been rigorously investigated and confirmed.^{4,7} As expected, NorHA-TPA hydrogels were not cytotoxic when cultured in the presence of AF cells (Fig. 3). Apart from day 1, there were no significant differences in viability for cells exposed to hydrogels and controls. Further, cell number increased over time in both groups.

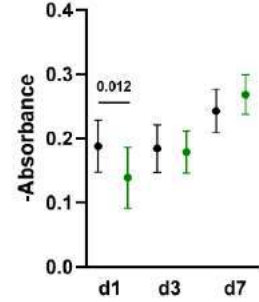


Figure 3: Cell viability and proliferation for controls (no hydrogel, AF cells only, black dots) and with NorHA-TPA exposure (green dots). An increase in (negative) absorbance corresponds to an increase in cells number.

DISCUSSION

NorHA hydrogels are promising candidates for biomedical applications due to their injectability and inherent biocompatibility and biodegradability. However, these hydrogels lack a mechanism for controlled therapeutic delivery, which is desirable in nearly all biomedical applications. For instance, an ideal AF repair material would possess all these characteristics to precisely repair the wound defect while utilizing controlled delivery to minimize inflammation and promote tissue regeneration.

Here, we showed that the incorporation of thiol-PEG-azide (TPA) successfully click-functionalizes NorHA hydrogels. This was demonstrated through the selective attachment of DBCO-modified fluorophores to NorHA-TPA (Fig. 1A), which was stable for at least one month. This suggests that therapeutic-loaded nanoparticles could be attached to NorHA-TPA and subsequently localized to the site of injury for delivery. We demonstrated this with loaded DBCO-modified micelles (Fig. 2B). Notably, both the therapeutic and the specific type of nanoparticles (e.g., micelles, liposomes, polymeric, etc.) could be altered based on the specific delivery requirement for the hydrogel system. Additionally, the number of particles attached can be tailored by varying solution concentration (Fig. 1B) or by altering the ratio of photocrosslinker relative to the amount of TPA. Regardless, the attachment of DBCO-modified particles is highly stable for considerable durations (Fig. 1C). Importantly, TPA incorporation did not impact AF cell viability or proliferation (Fig. 3).

Future work will explore the fabrication and click-functionalization of injectable fibrous NorHA hydrogels, which may better mimic the microstructure of the AF.⁷ We will optimize injection parameters to best fill complex AF ruptures and examine total disc mechanics using *ex vivo* and *in vivo* AF injury models. We will also investigate the impact of sPLA2 inhibition in injured AF scenarios. Ultimately, this multifunctional material may improve outcomes in a variety of dense connective tissue repair scenarios.

ACKNOWLEDGEMENTS

This work was supported by the National Institutes of Health and the Department of Veterans Affairs.

REFERENCES

[1] Hudson, K et al., *Curr Opin Biotech*, 24:872-9, 2013. [2] Sloan, S et al., *Sci Trans Med*, 12:eaay2380, 2020. [3] Peredo, A et al., *JOR Spine*, 4:e1133, 2021. [4] Gramlich, W et al., *Biomater*, 34: 9803-11, 2013. [5] Wei, Y et al., *Sci Adv*, 7, 2021. [6] Franson, R et al., *Spine*, 17: S129-32, 1992. [7] Davidson, M et al., *Sci Adv*, eabi8157, 2021.

BIOMECHANICAL EFFECTS OF ANNULOPLASTY RING SIZING FOR FUNCTIONAL MITRAL REGURGITATION REPAIR

Gediminas Gaidulis (1,2), Muralidhar Padala (1,2)

- (1) Structural Heart Research and Innovation Laboratory, Carlyle Fraser Heart Center at Emory University Hospital Midtown, Atlanta, GA, USA
(2) Division of Cardiothoracic Surgery, Emory University School of Medicine, Atlanta, GA, USA

INTRODUCTION

Functional mitral regurgitation (FMR) is the leakage of blood through the mitral valve (MV), that occurs in nearly 60% of the patients with heart failure after surviving a myocardial infarction [1]. The geometry of the MV is distorted by the left ventricular dilatation and the restricted motion of the infarcted ventricular wall, causing the mitral annulus to dilate, and preventing proper valve closure during systole. The geometric distortions of the MV that lead to such a condition, however, differ between individual patients [2], thus making the effective surgical or transcatheter repair of FMR challenging.

Of the many FMR repair techniques available today, undersizing mitral annuloplasty (UMA) is a surgical technique that has gained the most clinical adoption [3]. In this technique, the dilated mitral annulus is reduced by placing sutures into the native annulus and tying them onto a prosthetic ring of a smaller size. Such surgery is hypothesized to draw the native leaflets closer to each other and enable easier and better systolic valve closure and correction of FMR. Though effective in some patients, clear guidance is lacking on which MV geometries may benefit from this repair, and which may not. The lack of standardization with this technique is reflected in the 29% persistent FMR rates at 30 days after annuloplasty procedure, and 58.8% reported recurrence rate of moderate or greater degree of FMR within 24 months after UMA [4]. Furthermore, the annuloplasty rings are available in several sizes, and optimal sizing of the ring to the patient remains a challenge [5]. Though the smallest size ring could be chosen in all patients, the risk of increasing the transmitral diastolic pressure gradient and creating MV stenosis after the repair is high [6]. Therefore, a better understanding of the individualized, patient-specific impact of UMA on MV mechanics could have a significant impact on FMR repair.

In this study, we present a patient-specific, clinically relevant, computational modeling framework to investigate the impact of different annuloplasty ring sizes on the outcomes of UMA for FMR repair.

METHODS

Three patient-specific computational disease models of the MV were created from the 3D epicardial echocardiography data obtained in three pigs with FMR. For each case, the geometry of the MV annulus, leaflets, and papillary muscle (PM) tips was reconstructed from echo images. The model was completed by adding a branched network of chordae, connecting the MV leaflets to the PMs. FMR state of the MV was created by displacing the PMs apically, thus stretching the chordae and imposing a pre-strain on both chordae and MV leaflets. To simulate the MV closure before the repair, physiological transvalvular pressure gradient was applied to the leaflets, and patient-specific annular contraction and movement of the PMs were prescribed as kinematic boundary conditions.

The outcomes of UMA were examined by simulating the effects of differently sized annuloplasty rings on each MV computational model. Seven annuloplasty ring models of different sizes (40, 38, 36, 34, 32, 30, 28 mm) were created based on the shape and measurements of Carpentier-Edwards Physio I ring. For each investigated case, all seven rings were used to downsize the mitral annulus in diastole, mimicking implantation of the ring on the arrested heart during surgery. After each ring was positioned, the mitral annulus was deformed to the ring configuration by prescribing appropriate displacements to the annular nodes (Fig 1A). Lastly, dynamic simulations of the valve closure were run for each model with different size rings. Physiological transvalvular pressure gradient was applied to the leaflets, and movement of the PMs was prescribed as a boundary condition. For the mitral annulus, fixed boundary condition was applied to avoid deformation of the annulus or the ring during the MV closure (Fig 1B).

After each simulation, i.e., pre-repair (or FMR) and UMA (7 ring sizes), the following parameters were evaluated for each investigated case: mitral annular area, regurgitant gap area, leaflet coaptation length, tenting height, stress distribution on the leaflets, and tension forces in the chordae.

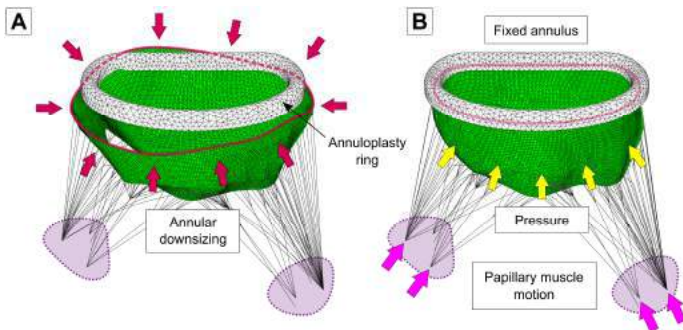


Figure 1: Deformation of mitral annulus to annuloplasty ring dimensions (A) and simulation of MV closure (B).

RESULTS

The average simulation results for the three valves are presented in **Table 1** and **Table 2**. In all pre-repair models, regurgitant gaps at A1-P1 and A3-P3 segments of the valve were present, and poor leaflet coaptation as well as increased tenting height were observed. In addition, high leaflet stresses and chordal tension forces were present. After UMA, regurgitant gaps were completely eliminated only with annuloplasty rings smaller than 34 mm. Leaflet coaptation length increased with all ring sizes, still, a value considered clinically adequate for long term repair durability (> 5 mm) was acquired only with rings smaller than 36 mm. Similarly, tenting height was reduced with all ring sizes, however, clinically acceptable value (< 5 mm) was not achieved with any ring size. Annuloplasty rings larger than 36 mm were not able to reduce leaflet stresses. Tension forces in the strut chordae were reduced only with the rings smaller than 38 mm, while forces in the marginal chordae decreased with all annuloplasty ring sizes.

Table 1: Geometric parameters of the valve.

	Annular area (mm ²)	Regurgitant gap area (mm ²)	Coaptation length (mm)	Tenting height (mm)
FMR	1120.0±65.9	13.5±6.0	2.3±0.5	10.9±0.4
UMA 40	1049.8	16.0±3.8	2.7±1.1	8.2±1.5
UMA 38	944.0	6.3±3.2	3.9±0.7	7.4±1.0
UMA 36	846.7	1.9±2.2	4.8±0.6	6.7±0.9
UMA 34	758.4	0.9±1.5	5.5±0.5	6.4±0.8
UMA 32	649.7	0	6.5±0.3	6.0±0.5
UMA 30	578.8	0	7.1±0.3	5.6±0.7
UMA 28	510.8	0	7.8±0.6	5.1±0.9

Table 2: Leaflet stresses and chordal tension forces.

	Max leaflet stress (MPa)	Max strut force (N)	Max marginal force (N)
FMR	0.76±0.27	2.305±0.79	0.399±0.24
UMA 40	1.241±1.24	3.338±3.47	0.354±0.20
UMA 38	0.952±0.86	2.582±2.41	0.31±0.20
UMA 36	0.751±0.63	2.099±1.65	0.272±0.18
UMA 34	0.629±0.49	1.667±1.34	0.284±0.15
UMA 32	0.502±0.22	1.194±0.74	0.241±0.12
UMA 30	0.50±0.25	1.044±0.63	0.211±0.10
UMA 28	0.468±0.17	0.86±0.43	0.18±0.07

DISCUSSION

In this study, we presented the application of computational modeling approach to simulate and evaluate the outcomes of UMA and

the impact of different annuloplasty ring sizes on FMR repair. The results showed that large rings (≥ 34 mm) were not effective in repairing FMR. The use of smaller annuloplasty rings (< 34 mm) eliminated regurgitant gaps in all investigated cases and demonstrated better outcomes while reducing leaflet stresses and chordal tension forces.

The best results defined in terms of valve coaptation were achieved after annuloplasty with the smallest 28 mm ring (**Fig 2**). Such ring increased leaflet coaptation length, restoring an adequate (> 5 mm) coaptation level. Still, even with the smallest ring, post-repair valve biomechanics remained unphysiological. Firstly, while such ring greatly reduced leaflet tenting, an adequate (< 5 mm) tenting height was not achieved. Also, after UMA with 28 mm ring, peak leaflet stresses were still high, exceeding threshold value of 0.5 MPa for healthy valve in two investigated cases. Finally, while the smallest annuloplasty ring reduced tension in the chordae and rebalanced force distribution across the whole chordal network, peak marginal and strut chordal forces in all three cases were higher than those we measured earlier in the ex vivo model of FMR [7]. Therefore, even with 28 mm ring, the excessive valve tethering was not eliminated.

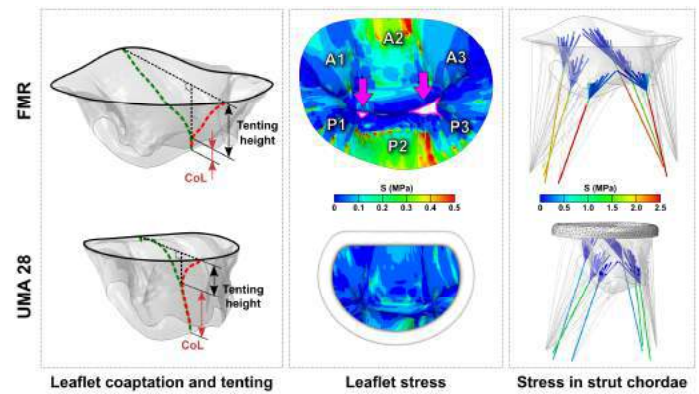


Figure 2: Simulation results: pre-repair vs UMA with 28 mm ring.

In addition, though the data from our simulations indicates that the smallest ring can eliminate FMR and aid in better systolic valve closure, the risk of creating MV stenosis after such excessive annular downsizing should be considered. On average, the 28 mm ring reduced annular area by $54.3 \pm 2.7\%$. From the Gorlin formula [8], 50% reduction of the annular area increases transmitral gradient by four times, worsening intracardiac hemodynamics, patient's functional capacity, and affecting repair durability. For this reason, UMA with the smallest ring might appear as a durable repair at first, but it may lead to greatly increased transmitral gradients later after the surgery, and that could limit the benefit of this repair technique.

We conclude that conservative annular downsizing with large annuloplasty rings (≥ 34 mm) is not suitable for FMR repair. The use of smaller rings (< 34 mm) provides better systolic valve closure but at the same time increases the risk of elevated transmitral gradients, and that could limit the repair benefits.

REFERENCES

- [1] Milwidsky, A et al., *Circ Heart Fail*, 15(9):e009689, 2022.
- [2] Reid, A et al., *J Cardiovasc Comput Tomogr*, 16(5):431-441, 2022.
- [3] Quinn, R et al., *JTCVS Tech*, 13:53-57, 2022.
- [4] Goldstein, D et al., *N Engl J Med*, 374(4):344-353, 2016.
- [5] Hiraoka, A et al., *Int J Cardiol Heart Vasc*, 28:100517, 2020.
- [6] Li, B et al., *Cardiol J*, 26(4):350-359, 2019.
- [7] Zhan-Moodie, S et al., *JTCVS Open*, 7:91-104, 2021.
- [8] Gorlin, R et al., *Am Heart J*, 41(1):1-29, 1951.

STROMAL CELLS MODULATE CHEMO-MECHANICAL FACTORS IN THE TUMOR MICROENVIRONMENT REQUIRED FOR LEADER CELL DRIVEN COLLECTIVE MIGRATION

Jessanne Y. Lichtenberg (1), Trey P. Redman (1), Ella Ramamurthy (1,2),
Christopher A. Lemmon (1), Priscilla Y. Hwang (1)

(1) Department of Biomedical Engineering, Virginia Commonwealth University, Richmond,
Virginia, USA

(2) Department of Bioengineering, University of California, Berkeley, Berkeley, California, USA

INTRODUCTION

The tumor microenvironment (TME) consists of extracellular matrix (ECM) proteins, secreted factors, and various populations of cells, all of which can change ECM properties that trigger tumor cell migration or metastasis. Metastasis of breast cancer can occur via collective cell migration (CCM), the coordinated movement of a cluster of interconnected cells. CCM is guided by a subset of cells at the front known as leader cells. Previous *in vitro* studies in our lab demonstrate that in order for CCM to occur, there is associated fiber alignment and stiffening of the collagen matrix, which correlates with *in vivo* observations [1]. Further, selective knockout of collagen receptor discoidin domain receptor 2 (DDR2) in stromal cells (i.e. cancer associated fibroblasts (CAFs)), resulted in loss of fiber alignment and matrix stiffening in the TME with associated decrease in metastatic lung lesions *in vivo*. [2]. Further, without DDR2, CAFs lost their ability to lay down organized, aligned fibers *in vitro* [2]. However, how these changes in the TME effect leader cell activation that is required for directional collective migration is not well understood.

The objective of this study is to investigate how changes in the TME due to stromal cell remodeling activate leader cells. Specifically, our goal is to investigate how changes in mechanical matrix properties effect leader cell mechanosensing. We hypothesize changes in collagen architecture and mechanical properties altered by stromal cells via DDR2 are used by leader cells to sense directional migration. Further, we hypothesize leader cells sense TME cues required for migration via cell protrusions and traction forces transmitted by focal adhesions. In this study, we used decellularized primary tumor tissue as a

biologically relevant microenvironment to investigate the response of breast tumor leader cells to ECM where CAFs are depleted of DDR2. Our work begins to reveal how leader cell mechanics and ECM cues work together to impact directional migration that contributes to cancer progression.

METHODS

We isolated primary tumors from established collective migration breast cancer mouse model, MMTV-PyMT (WT MMTV-PyMT) or where we depleted DDR2 in CAFs (FSP1cre;Ddr2^{-/-}), and generated decellularized matrix (dECM [3]). Using the dECM, we generated 3D dECM hydrogels and cultured WT MMTV-PyMT tumor organoids. After culture for 3 days, we quantified fiber orientation and changes in tumor organoid morphology. To study how tumor organoids interact with the matrix, we cultured primary MMTV-PyMT tumor organoids for 1 day on 2D plates coated with dECM, and stained for leader cell marker (cytokeratin-14 (K14)), focal adhesions (vinculin), and nuclei (DAPI). Finally, we measured forces exerted by tumor organoids onto their surrounding matrix using a HexForce method [4] in order to compare differences in force generation by leader (K14+) and follower (K14-) cells.

RESULTS & DISCUSSION

Findings reveal the action of DDR2 in CAFs contributes to matrix remodeling factors that are used by tumor organoids to reorganize their surrounding, as aligned collagen fibers were observed in FSP1cre;Ddr2^{-/-} dECM but not in WT dECM after culturing tumor organoids (Fig 1A-B). Additionally, organoids cultured in FSP1cre;Ddr2^{-/-} dECM were unable to spread out or

form protrusions, resulting in decreased invasion phenotype compared to organoids cultured in WT dECM, as indicated by the greater roundness, smaller spread area, and reduced aspect ratio (Fig. 1A-B).

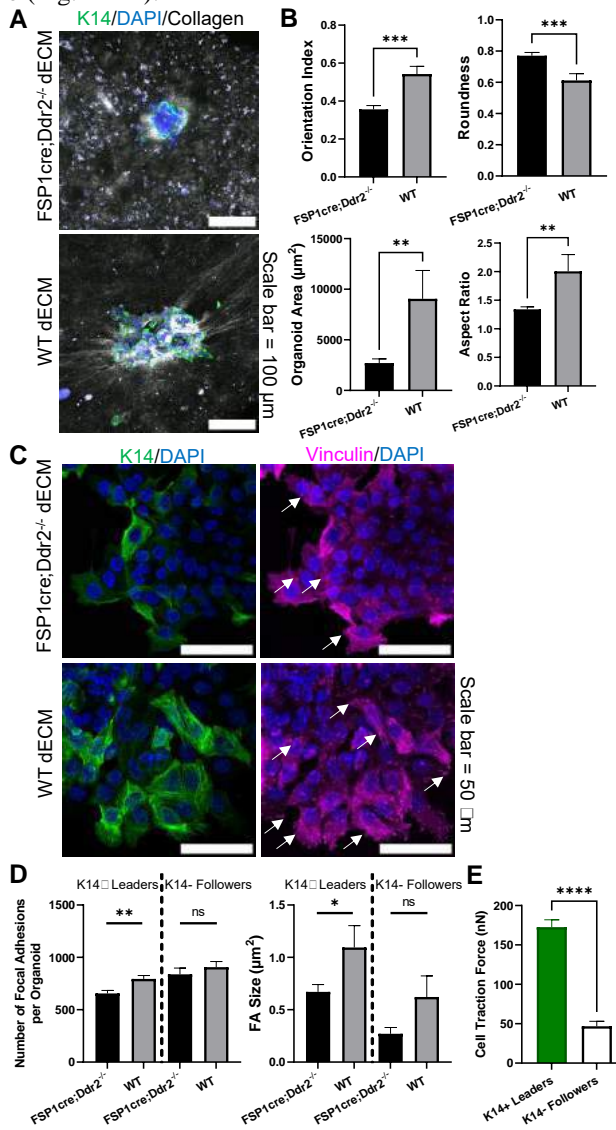


Figure 1: (A) Representative immunofluorescence images of tumor organoids in 3D FSP1cre;Ddr2^{-/-} dECM and WT dECM hydrogels. (collagen = gray, K14= green, DAPI=blue; scale bar = 100 μm) (B) Quantification of matrix fiber orientation and tumor organoid morphology: roundness (1 = perfectly round), spread area, and aspect ratio (greater value = more elongated). n= 36-39 organoids from three independent mice. (C) Representative immunofluorescence images of tumor organoids on 2D FSP1cre;Ddr2^{-/-} dECM and WT dECM. (K14=green, DAPI=blue, vinculin=pink. white arrows highlight vinculin focal adhesions; scale bar = 50 μm) (D) Quantification of focal adhesion count and size for K14+ leader and follower cells. n= 56-61 organoids from three independent mice. (E) Quantification of K14+ leader and follower cell traction forces. n=42 organoids from three independent mice. All data shown as mean ± SEM. *p<0.05, **p<0.01, *p<0.001, ****p<0.0001, ns=p>0.05, unpaired student's T-test.**

To understand what factors are responsible for leader cell sensing of the TME, we stained tumor organoids for mechanosensitive focal adhesion marker, vinculin, which has been shown to be crucial for directed cell migration [5]. On 2D dECM, K14+ leader cells formed fewer and smaller focal adhesions on FSP1cre;Ddr2^{-/-} dECM compared to follower cells (K14-) (Fig. 1C-D). The differences in number and size of focal adhesions suggest the K14+ leader cells are forming more mechanically active interactions with their surrounding matrix compared to follower cells and perhaps increased traction forces. Further, since focal adhesions are known to regulate force transmission between the cell cytoskeleton and ECM as a route of mechanosensing, we measured the traction forces exerted by leader cells on their surrounding environment: we observed leader cells (K14+) exert higher pulling forces on the ECM compared to follower cells (K14-) (Fig. 1E). Increased traction forces and focal adhesion number and area could be physical mechanisms utilized by leader cells to signal for collective migration. Further, these differences point to a distinct mechanical phenotype of K14+ leader cells when they are activated to collectively migrate where they generate increased traction forces mediated by focal adhesions.

Altogether, our findings suggest mechanical matrix cues modulated by stromal helper cells can activate leader cells to mechanically engage with their surroundings through the recruitment of vinculin at the focal adhesions as the cytoskeleton contracts and generates traction forces. This suggests a possible mechanism for how leader cells sense physical matrix cues in the TME and direct collective migration.

CONCLUSIONS

Together, this work demonstrates breast tumor leader cells are mechanically responsive to tumor microenvironment mechanical cues. Further, our findings reveal the importance of stromal helper cells in regulating leader cell mechanical behavior that contributes to metastasis. In future studies we will investigate specific ECM receptors activated in focal adhesions, such as integrins, and the downstream mechanosignaling pathways in leader cells that are responsible for driving collective cell migration. Ultimately, the outcomes of our work will inform the development of future therapies to target key cell types responsible for promoting metastasis.

ACKNOWLEDGEMENTS

Thanks to NSF CAREER (Hwang), REU (Redman) and VCU Mechanobiology REU (1852116, Ramamurthy) Grants for support. Thanks to the Nanomaterials Characterization Core Facility and the Puetzer and Heise labs for equipment use.

REFERENCES

- [1] Hwang, PY et al., *Cancer Research*, 79:1899-1912, 2019.
- [2] Bayer, SVH et al., *eLife*, 8:e45508, 2019.
- [3] Link, PA et al., *J Vis Exp*, 119:55094, 2017.
- [4] Griffin, BP et al., *MethodsX*, 6:1343-1352, 2019.
- [5] Rothenberg, KE et al., *Biophys*, 114:1680-16944, 2018.

CHARACTERIZING HEADFORM FRICTION COEFFICIENT FOR HELMET TESTING

Nicole E-P. Stark (1), Steve Rowson (1)

(1) Biomedical Engineering and Mechanics, Virginia Tech, Blacksburg, VA, USA

INTRODUCTION

Evaluating the impact response of helmets is essential in reducing the number of head injuries across varying sports. Helmets are evaluated using dummy headforms to simulate the impact response of the head. However, there are various standards and independent test methods that use different headforms, each with unique properties. The outer material composition of the headform differs significantly, resulting in different frictional interfaces between the headform and helmet lining. The head and helmet frictional interface affects the head's impact response during a helmeted impact. Reducing the friction between the headform and helmet correlates with lower head rotational velocity and corresponding injury risk during oblique impacts [1, 2]. Therefore, the headforms' frictional properties must accurately represent that of the human head.

Multiple studies have evaluated the frictional characteristics of Hybrid III and magnesium/EN960 headforms. The Hybrid III headform, developed for automotive crash testing but now also used in helmet testing, has a vinyl plastisol skin with a high friction coefficient [3]. The coefficient of friction (COF) reported for Hybrid III is 0.75-1.07 [4-6]. Due to Hybrid III's high friction coefficient, some test methods cover the headform with a stocking to reduce friction [5, 7, 8]. The magnesium headforms, which are commonly used in standards for helmet testing, have no outer layer and have been reported to have a lower friction coefficient, 0.16-0.23 [1, 2, 5]. Other helmet test methods use a National Operating Committee on Standards for Athletic Equipment (NOCSAE) headform. The NOCSAE headform was developed exclusively for helmet testing, and its outer layer is composed of polyurethane skin [9, 10]. Though widely used for helmet testing [10], there are no reported friction coefficients for the NOCSAE headform.

Although there are defined friction coefficients for magnesium and Hybrid III headform, various testing methods and materials were used, making it hard to compare across headforms. Trotta et al. did evaluate the COF of a magnesium and Hybrid III headform against a helmet lining material, but the comparison to human heads was based on cadaveric samples [5]. Furthermore, no previous study has quantified the COF of the NOCSAE headform, and previous studies have yet to evaluate new headforms to older headforms that have been used for impact testing. Polyurethane and vinyl plastisol oxidize and degrade over time, and many headforms undergo repetitive impacts resulting in wear markings or scratches [11, 12].

This study's objectives were to (1) quantify the NOCSAE headform friction coefficient, (2) measure COF across three new and used headforms using the same methods, and (3) compare each headforms' biofidelity. Each headforms' biofidelity will be determined through the comparison against previously determined human head COF under similar testing conditions. Comparing COF between headforms and defining their biofidelity will lead to modifications of headforms and the development of more realistic helmet testing standards.

METHODS

Using a specially designed tribometer, the NOCSAE, Hybrid III, and EN960 headforms static friction coefficients were measured against multiple materials, including EPP high-density foam, a helmet liner, Teflon, aluminum, and polyester fabric. Each headform was weighted to apply an 80 N normal force to the tested material. The headforms tested included new and used NOCSAE, Hybrid III, and EN960 headforms to evaluate the effects of degradation and oxidation. The Hybrid III and NOCSAE were also tested with a skull cap applied.

The normal force was measured using a compression load cell, and tangential force was measured using an inline load cell during the five trials at 400 Hz. The raw force data for each trial were processed in MATLAB (Mathworks; Natick, Massachusetts, USA). The force and tension data were filtered using a 4-pole phaseless lowpass Butterworth filter with a 17 Hz cut-off frequency. Bias in the signals was removed, and the data were smoothed using a 50 ms moving average window. For each trial, the COF was calculated, and the static friction coefficient was extracted. The static COF was defined as the maximum friction right before movement occurred. The static COF of all the headforms was measured across five trials, averaged, and compared. An ANOVA and post-hoc Tukey test was used to evaluate the differences between headforms, materials, and new versus old. Each headforms static COF was also compared to the previously determined 95% confidence interval (CI) of human head static COF at 80 N.

RESULTS

The COF against each material varied and increased in order: Teflon, aluminum, polyester, helmet liner, then foam (Figure 2). The material also significantly affected COF ($P < 0.001$). Comparing headforms, the NOCSAE and Hybrid III ($P = 0.60$) are not significantly different from one another, but the NOCSAE and Hybrid III are significantly different from the EN960 ($P < 0.001$).

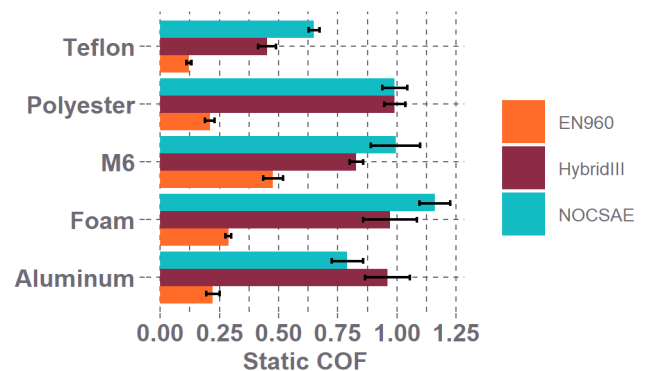


Figure 2: Static friction coefficients of the EN960, Hybrid III, and NOCSAE headforms against multiple materials.

The new headforms' static friction coefficients against foam and a helmet lining material varied compared to the used headforms ($P < 0.001$).

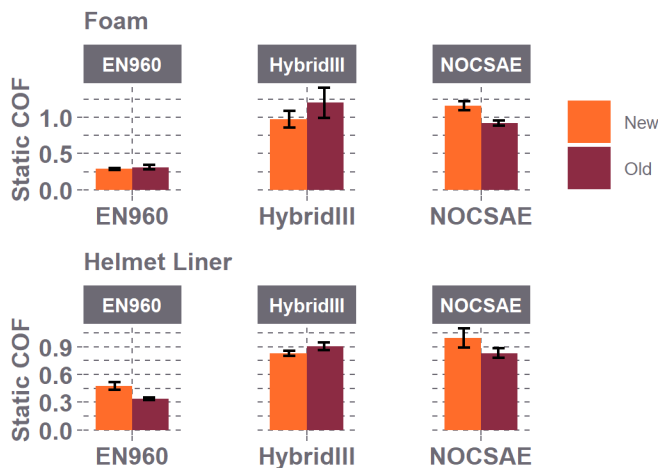


Figure 3: Friction coefficients against foam and a helmet lining material vary between new and old/used headforms.

The previously defined 95% CI of the human head static COF at 80 N against helmet foam was 0.30-0.34. The EN960 COF 0.29-0.31, NOCSAE with a skull cap COF 0.27-0.31, and the Hybrid III with a skull cap COF 0.27-0.30, all fall within the 95% CI for the human head at 80 N (Figure 4).

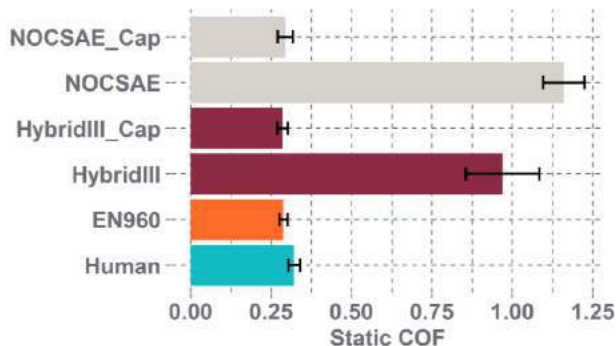


Figure 4: Comparing previously determined human head friction coefficients to different headforms against high-density foam.

DISCUSSION

At 80 N, the static friction coefficient of the EN960 headform is 0.30 ± 0.01 , the Hybrid III is 1.08 ± 0.07 , and the NOCSAE is 1.44 ± 0.06 against a high-density foam (Figure 2).

Previous studies reported a friction coefficient of 0.75 and 1.07 for the Hybrid III headform against a polyester material [4-6]. This study found a friction coefficient of 1.15 ± 0.05 for the Hybrid III against a polyester material. When a stocking cap or skull cap was applied to the Hybrid III, Bootlang et al. reported a COF of 0.26 comparable to the COF we found of 0.28 ± 0.02 . These differences could be due to differences in the polyester materials tested. The magnesium EN960 bare headform has reported COF of 0.16 ± 0.03 and 0.20 ± 0.02 against polyester [2,5], while we found a similar COF of 0.20 ± 0.02 for the EN960 against polyester. Another study found a COF of 0.23 for the EN960 against padding inside an HJC helmet [1]. Although we did not

test against similar padding, when compared against high-density foam, another compressive material, we found a higher COF for the EN960 0.30 ± 0.01 .

Previous studies have not compared the biofidelity of the NOCSAE, EN960, and Hybrid III headform to human head friction coefficients using similar testing methods. In an earlier study involving 74 participants, we defined the 95% CI for the static friction coefficient of the human head at 80 N against helmet foam to be 0.30-0.34. The NOCSAE and Hybrid III had over three times the COF of the human head against foam. However, when covered with a skull cap the static COF reduced and were within the 95% CI of the human head's COF (Figure 4). The EN960 static friction coefficient of 0.30 ± 0.01 was within the human head's 95% CI static COF (Figure 4). Therefore, the EN960 or similar magnesium headforms are the most biofidelic and should be used when considering friction properties to accurately represent the impact response of the human head and if a Hybrid III or NOCSAE headform are used a skull cap should also be used.

Furthermore, our results showed that the degradation and oxidation of the Hybrid III vinyl plastisol and NOCSAE polyurethane affect their static COF (Figure 3). The NOCSAE headform had the most extensive alteration in COF, most likely due to oxidation [11]. There was also an increase in COF for the new Hybrid III compared to the used Hybrid III against foam, polyester, Teflon, and aluminum, but not for the helmet liner. Due to the friction changes for each headforms with use and time, we suggest that each individual headform is tested before use.

One limitation of this study was quantifying the COF at an 80 N normal force. 80 N is well below the normal forces experienced by headforms during impact testing, and friction coefficients will follow a power law as friction is a function of normal force [13]. However, testing at 80 N allowed a direct comparison to the human head COF. Another limitation of this study was that there was no quantification of the degradation or oxidation of the used headforms tested. Quantifying the degradation or oxidation should be a consideration for future work. Future work should also investigate how frictional properties of these headforms affect linear and rotational impact kinematics.

Standardization of headform frictional properties is necessary to ensure accurate representation of the human head during helmet testing. This study was the first to quantify NOCSAE COF, measure COF across three headforms using the same methods with a defined normal force, and directly compare their biofidelity. These results will also lead to modifications of headforms, develop more realistic helmet testing standards, and aid the optimization of helmet designs.

ACKNOWLEDGEMENTS

KASK S.p.a. ad Unico socio provided funding support for the completion of this project.

REFERENCES

- [1] Ebrahimi, I et al., *Traffic Inj. Prev.*, 16:404-408, 2015.
- [2] Juste-Lorente, O et al., *Applied Sci.*, 11:11318, 2021.
- [3] Hubbard, R et al., *18th Stapp Car Crash Conf.* 741193, 1974.
- [4] Bonin, S et al., *Ann Biomed Eng.* 50:860-870, 2022.
- [5] Trotta, A et al., *J. Biomech.* 75:28-34, 2018.
- [6] Yu, X et al., *Front Bioeng Biotechnol.* 10:860435, 2022.
- [7] DiGiacomo, G et al., *Ann Biomed Eng.* 49:2805-2813, 2021.
- [8] Takhounts, E et al., *Stapp Car Crash Conference*, 2013.
- [9] Gwin, J et al., *J Biomech Eng.* 132:011006, 2010.
- [10] V. R. Hodgson, V. *Med and Sci in Sports*, 7:225-232, 1975.
- [11] Christenson, E et al., *Int. J. Corros.* 42:312-323, 2013.
- [12] Perito, E et al., *Journal of Elastomers & Plastics*, 54, 2022.
- [13] Katano, Y et al., *Sci Rep.* 4:6324, 2014.
- [14] Bottlang M. et al., *Ann Biomed Eng* 48: 68-78, 2020.

COMPARISON OF MECHANICAL RESPONSE OF TMJ AND KNEE CARTILAGE UNDER DYNAMIC LOADING

Annie Porter (1), Michael Santare (1), Lin Han (2), John Peloquin (3), X. Lucas Lu (1)

(1) Department of Mechanical Engineering, University of Delaware, Newark, Delaware, USA
(2) School of Biomedical Engineering, Drexel University, Philadelphia, Pennsylvania, USA
(3) Department of Biomedical Engineering, University of Delaware, Newark, Delaware, USA

INTRODUCTION

Disorders of the temporomandibular joint (TMJ), the only moving joint in the human head, affect over 10 million Americans. TMJ condylar cartilage however remains an understudied tissue [1]. It has a unique, hybrid bi-layered structure (Fig 1), distinctive from articular cartilage in other diarthrodial joints [2]. The top layer is fibrocartilage dominated by type I collagen fiber bundles. The bottom layer is primarily hyaline cartilage, composed of type II collagen fibrils and proteoglycans. The two layers are integrated by type I collagen bundles which extend from the top layer and root into the subchondral bone [3].

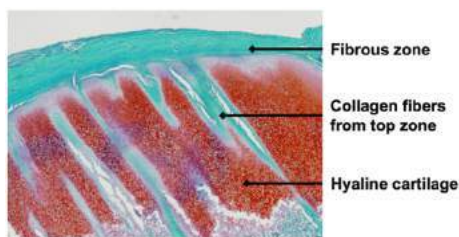


Figure 1. Porcine TMJ condylar cartilage (Safranin O).

A primary mechanical function of TMJ condylar cartilage is shock absorption through energy dissipative deformation to reduce concussion on the brain [4]. Previously, we found that in static loading the hyaline layer has a much lower modulus than knee cartilage, but the hybrid mandibular cartilage, reinforced by the fibrous layer, has a similar equilibrium stiffness [2]. In this study we hypothesized that the unique bilayer structure endows the TMJ condylar cartilage with a low dynamic stiffness, especially under small stress and high frequency loads, to minimize the impact on the brain from TMJ daily functions, *i.e.*, eating and talking.

METHODS

Cylindrical cartilage samples (diameter = 2.5 mm) were harvested from either TMJ condyles or the knee femoral condyle heads of the

same porcine (6-9 months old). Subchondral bone was removed (TMJ $h = 1.12 \pm 0.17$ mm; Knee $h = 1.03 \pm 0.20$ mm) and samples were stored at -80°C before testing ($n = 8$ for each group).

Dynamic Loading. Dynamic compression was applied on the samples with an ElectroForce 3230 test frame (TA Instruments) with previously described profiles [5]. In brief, a constant load of 0.2 N (~ 40.7 kPa) was applied to the cylindrical sample with an unconfined compression setup and held for 1 hr to reach equilibrium deformation. The final reduction in thickness under 0.2 N was $40.7 \pm 18.8\%$ for TMJ cartilage and $14.8 \pm 2.6\%$ for knee cartilage. Compressive Young's modulus was calculated based on the equilibrium strain.

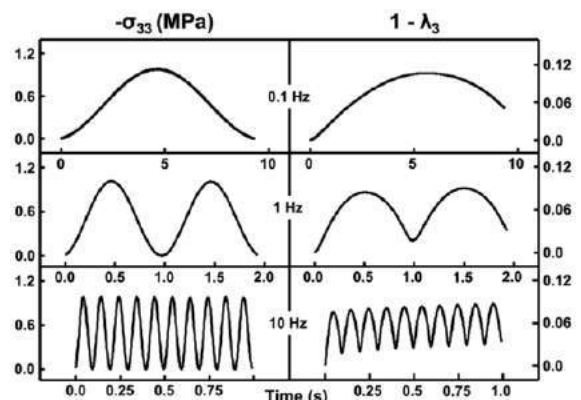


Figure 2. Stress and strain vs. time response of a typical TMJ cartilage sample under dynamic compression at select frequencies.

Cyclic compressive loading was then applied in a sinusoidal waveform with an amplitude of 6 N (~ 1.0 MPa), consisting of 20 cycles at 20 Hz, 15 cycles at 15 Hz, 10 cycles at 10 Hz, 5 cycles at 5 Hz, 3 cycles at 3 Hz, 2 cycles at 1 Hz, and 1 cycle at 0.1 Hz (Fig. 2). Samples rested for 5-10 minutes between each loading frequency [5].

Theoretical Analysis. During the testing, cartilage was assumed to be incompressible and was evaluated with Cauchy normal stress component ($\sigma_{33} = hF/h_0A_0$) versus stretch ratio ($\lambda_3 = h/h_0$). To calculate dynamic modulus ($\partial\sigma_{33}/\partial\lambda_3$) as a function of strain, the slope of an exponential function $y = A(e^{Bx} - 1)$ was fit to the stress (σ_{33}) versus strain (λ_3) curve at each frequency [5]. The strain energy integral of the loading (W_l) and unloading (W_u) σ_{33}/λ_3 curves was used to calculate the phase angle δ according to $\tan\delta = 4(W_l + W_u)/\pi(W_l - W_u)$.

RESULTS

The equilibrium modulus of TMJ condylar cartilage under unconfined compression was significantly lower than that of knee cartilage (116±45 kPa vs. 276±44 kPa, $p < 0.001$). Representative stress-strain plots of dynamic loading are presented in Fig. 3a. For TMJ tissue, the dynamic modulus increased with the loading frequency, but this correlation diminished at higher stress levels. The dynamic modulus increased significantly with loading stress, e.g., > 100% increase from 0.2 to 0.8 MPa at all frequencies. At low stresses, the dynamic modulus of knee cartilage was higher than that of TMJ (e.g., 14.9±2.6 vs 10.6±4.0 MPa at 10 Hz), but the opposite was true at higher stresses (16.8±3.0 vs 22.0±7.8 MPa at 10 Hz) (Fig. 3b). The minimum dynamic modulus of TMJ was always lower than cartilage at all frequencies, while the maximum modulus was higher than cartilage (Table 1). Phase angle derived from energy dissipation analysis was similar for both knee and TMJ cartilage, and both decreased significantly with increased loading frequency (Fig. 3c).

DISCUSSION

The loading profile in this study reflects the low loading levels during daily functions of TMJ. The typical frequency of a pig chewing is 2-3 Hz, whereas a human chews at 1 Hz and achieves up to 5-6 Hz while speaking [4,6,7]. At low stresses, the dynamic modulus of TMJ cartilage was lower than that of the knee. This trend implies that during daily activities, such as talking, TMJ cartilage provides better shock absorption than knee cartilage, potentially reducing impact on the brain.

Table 1. Minimum and maximum modulus using the fit $\sigma_{33} = A(\exp[B(1-\lambda_3)] - 1)$, evaluated at the minimum and maximum λ_3 for each frequency (*: $p < 0.05$ vs Knee at each frequency).

Frequency	Minimum Modulus (MPa)		Maximum Modulus (MPa)	
	Knee	TMJ	Knee	TMJ
0.1 Hz	7.1±1.8	5.2±1.9*	12.0±2.5	15.1±6.6
1 Hz	8.7±2.2	7.3±2.8	15.9±2.9	20.1±7.7
3 Hz	10.4±2.2	8.2±3.3	16.4±3.0	20.8±7.5
5 Hz	11.9±2.2	9.3±3.3*	16.7±3.1	21.2±7.7
10 Hz	14.9±2.6	10.6±4.0*	16.8±3.0	22.0±7.8
15 Hz	16.3±2.6	11.5±4.5*	17.4±3.0	21.7±7.9
20 Hz	17.2±2.7	11.5±4.6*	18.1±2.9	22.9±7.8

We previously found that in static loading the hybrid mandibular cartilage has a similar equilibrium stiffness with knee cartilage under indentation tests [2]. In this study, cartilage was cut into cylinders with subchondral bone removed. The cutting significantly compromised the mechanical functions of the type I collagen bundles in TMJ cartilage, which resulted in the low equilibrium stiffness. The top fibrocartilage is essential for the mechanical function of TMJ condylar cartilage.

It is critical to note that the dynamic moduli here were obtained when the knee and TMJ tissues were under the same initial load (0.2 N), but different initial strains (15% vs 41%). Thus, the dynamic moduli of TMJ could be even lower than the knee with similar initial strain. We will quantify this trend by testing the TMJ tissue under 15% strain.

ACKNOWLEDGEMENTS

NSF Graduate Research Fellowship.

REFERENCES

- [1] *Int J Oral Maxillofac Implants*. 2013; 28(6): 393-414. [2] *J Dent Res*. 2015 Jan; 94(1): 85-92. [3] *Ann Biomed Eng*. 2015 Nov; 43(11): 2652-2662. [4] *J Dent Res*. 2006 Jun; 85(6): 571-575. [5] *Osteoarthritis Cartil*. 2004 Jan; 12(1): 65-7. [6] *J Dent Res*. 2000 Oct; 79(10): 1740-1746. [7] *Arch Oral Biol*. 1989; 34(9): 685-693.

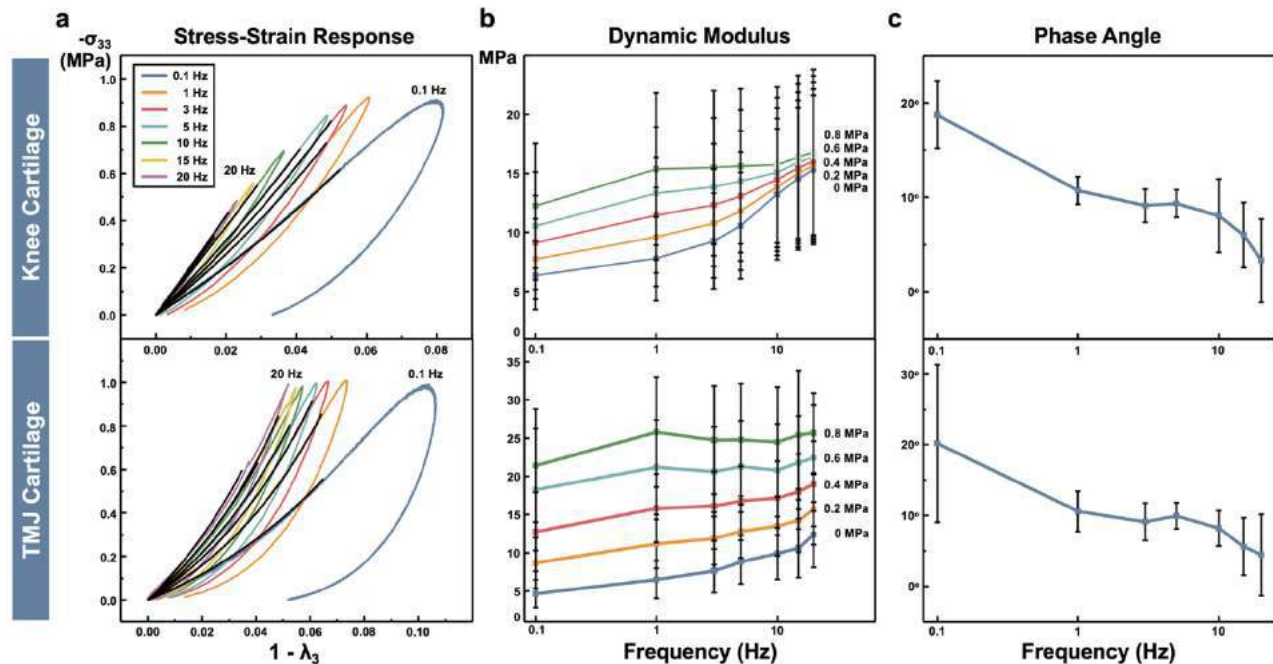


Figure 3. (a) Stress-strain response of typical knee and TMJ specimens with corresponding exponential curve fits (black). (b) Incremental dynamic modulus ($\partial\sigma_{33}/\partial\lambda_3$) at selected Cauchy stress levels as a function of frequency. Open squares indicate data was extrapolated using the curve fits. (c) Phase angle as a function of frequency.

PARTIAL MENISCUS TRANSPLANT TO TREAT HORIZONTAL CLEAVAGE TEAR RESTORES CONTACT AREAS SIMILAR TO PARTIAL MENISCECTOMY

Farid Amirouche (1, 2), Eric Chang (1), Asher Lichtig (1), Jason Koh (2)

(1) Department of Orthopaedics, University of Illinois, Chicago, IL, USA
(2) Department of Orthopaedics, NorthShore University Health System, Skokie, IL, USA

INTRODUCTION

While partial meniscectomy is an established treatment for horizontal cleavage tear to allow for rapid return to sport at competitive levels, partial meniscus transplant is a newly emerging operative technique that has been studied as a non-inferior alternative for restoration of native knee biomechanics. Data from previous studies that delved into *in vitro* porcine knees demonstrated that partial meniscus transplant restored knee biomechanics to that of partial meniscectomy and that of intact knees.¹ In spite of the advancements made to better understand biomechanical outcomes of partial meniscus transplant, there is currently a paucity of data comparing the effects on contact area of partial meniscectomy and partial meniscus transplant in the human knee. We hypothesized that partial meniscus transplant, as treatment for horizontal cleavage tears, can produce contact areas that are not significantly different from those achieved by partial meniscectomy.

METHODS

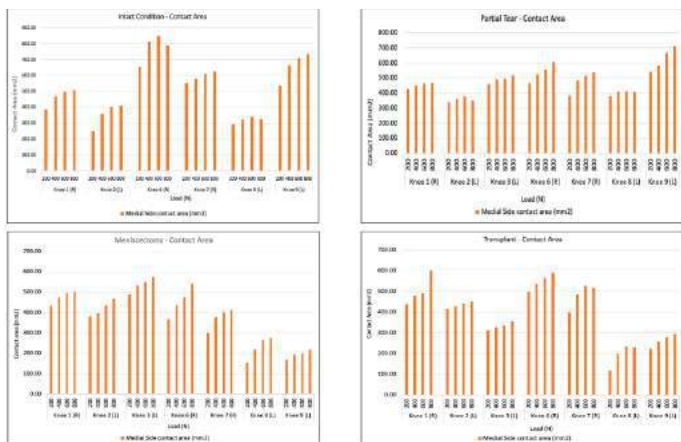
7 fresh-frozen human cadaveric knees were removed of muscular structures and extensor mechanisms while leaving ligaments intact. Femoral condyle osteotomy was performed to access the tibiofemoral joint, and submeniscal arthrotomy was performed to place pressure-mapping sensors (Tekscan). Knees were tested each at full extension and at 30 degrees flexion under the 4 experimental conditions of (1) intact medial meniscus, (2) posteromedial horizontal cleavage tear of medial meniscus, (3) partial meniscectomy, and (4) partial medial meniscus transplantation. Triplicate results of tibiofemoral contact pressure and contact area in the medial and lateral compartments were obtained at 200 N, 400 N, 600 N, and 800 N of axial load for each experimental condition using a uniaxial load frame (MTS 30/G machine).

RESULTS

The average contact areas at full extension and across the 3 non-intact, experimental meniscus conditions of the medial compartment in the knee was observed to be 477.93 mm², 383.29 mm², and 394.08 mm² for partial tear, partial meniscectomy, and partial meniscus transplant conditions respectively. There was a statistically significant difference between the tear and meniscectomy conditions ($p = 0.005256$) as well as between the tear and transplant conditions ($p = 0.00842$), while there was no statistically significant difference between meniscectomy and transplant conditions ($p = 0.58282$). The average contact areas at 30 degrees flexion of the knee in the medial compartment was observed to be 487.15 mm², 343.00 mm², and 413.69 mm² for the same conditions respectively. There was statistical significance found when comparing contact areas of tear to meniscectomy conditions ($p < 0.00001$) and tear to transplant conditions ($p = 0.000267$). Contact area comparisons between meniscectomy and transplant conditions yielded statistically significant differences ($p = 0.000979$).



Figure 1: MTS 30/G Machine with Tekscan sensors in knee.



Graph 1: Contact area comparisons of all knees at full extension.

DISCUSSION

Partial transplantation of the meniscal tissue showed no statistically significant change in contact area when compared to that of partial meniscectomy when the knee is positioned at full extension. Data obtained from the knee in a position of 30 degrees of flexion yielded considerably different results. It was found that comparisons of tear to treatment conditions, intact to treatment conditions, and treatment to treatment all yielded significantly different results. Solely comparing the average contact areas across all knees and all tested axial loads would reveal that the partial transplant condition was able to restore and increase contact area in a way that the meniscectomy condition was unable to. In this way, the data offers some support to the notion that partial transplantation is non-inferior to partial meniscectomy in terms of the contact area achievable in the repair of horizontal cleavage tears. These findings may provide evidence of partial meniscal transplantation as a viable treatment option for meniscal tears. While the results obtained from the knees at 30 degrees of flexion were inconclusive compared to the results obtained from the knees at 0 degrees of flexion, this study offers support for further investigation into the biomechanical differences between meniscectomy and partial meniscus transplant treatments. Due to the novelty of the partial transplant method, continued improvements to the surgical procedure, graft shaping and matching, and suturing method could play important roles in altering the outcome of this operative technique.

REFERENCES

- [1] Nyland J, Campbell K, Kalloub A, Strauss EJ, Kuban K, Caborn DNM. Medial meniscus grafting restores normal tibiofemoral contact pressures. Arch Orthop Trauma Surg. 2018;138(3):361-367. doi:10.1007/s00402-017-2849-x

AMOBARBITAL PREVENTS INTERVERTEBRAL DISC DEGENERATION BY INHIBITING OXIDATIVE STRESS

Venkateswaran Ganesh (1,2), Deborah A. Vacek (1), Douglas C. Fredericks (1), Emily B. Petersen (1),
Youssef W. Naguib (3,4), Anupam Tiwari (1), Yochana Kancherla (5), Mitchell C. Coleman (1,6), James A.
Martin (1,2,3), Aliasger K. Salem (3), Tae-Hong Lim (2), and Dongrim Seol (1,7)*

- (1) Department of Orthopedics and Rehabilitation, University of Iowa, Iowa City, IA 52242, USA
- (2) Department of Roy J. Carver Biomedical Engineering, University of Iowa, Iowa City, IA 52242, USA
- (3) Department of Pharmaceutical Sciences and Experimental Therapeutics, University of Iowa, Iowa City, IA 52242, USA
- (4) Department of Pharmaceutics, Faculty of Pharmacy and Pharmaceutical Manufacturing, Deraya University, New Minia City, Minia 61768, Egypt
- (5) School of Osteopathic Medicine, Des Moines University, Des Moines, IA 50312, USA
- (6) Department of Radiation Oncology, University of Iowa, Iowa City, IA 52242, USA
- (7) Department of Orthodontics, University of Iowa, Iowa City, IA 52242, USA

* Correspondence: dongrim-seol@uiowa.edu

INTRODUCTION

Intervertebral disc (IVD) degeneration (IDD) is clinically considered as a significant source of back pain. While one of the most common causes is aging, traumatic injuries to the spinal joints including disc herniation, accounts for up to 2% IDD in people aged 30-50 years, and lead to IDD in adolescent and young adult discs. Current surgical and conservative treatment options for IDD cannot restore normal tissue integrity or function; thus, IDD remains a critical public health problem. We hypothesize that oxidative stress contributes to the progression of post-traumatic IDD and therapies targeting oxidative stress may prevent disease progression based on mounting evidence [1-3]. The objective of this study was to investigate the preventive effects of amobarbital (Amo) on the progression of disc degeneration.

METHODS

***In-vitro* study:** Rabbit nucleus pulposus (NP) cells were pre-treated with Amo for 2 hours (h) prior to exposure of 50 μ M *tert*-butyl hydroperoxide (tBHP) for 1 h. *N*-acetylcysteine (NAC) was used as a positive control. Toxicity of tBHP, Amo, and NAC were analyzed by CellTiter 96[®]Aqueous One Solution (Promega). Apoptotic and necrotic cells were quantified *via* Annexin V/propidium iodine (PI) staining. Further the levels of reactive oxygen species (ROS) generation and corresponding mitochondrial membrane potential were quantified with MitoSOX and JC-1 staining, respectively.

***Ex-vivo* study:** Amo (2.5 mM; Amytal[®] sodium; Bausch Health) was encapsulated in a lyophilized hydrogel (HG; PF-72[®]; TGel Bio) composed of F127 and hyaluronic acid. *In-vitro* release profile of Amo was performed by high-performance liquid chromatography incorporated with ultra-violet spectroscopy (HPLC-UV) (Agilent Technologies) at 220 nm. Thirty-six rabbit thoracic and lumbar motion segments (T11/L2) from New Zealand White (NZW) rabbit cadavers (10 months old) were subject to an IVD puncture using a 20-gauge needle and treated with HG with or without Amo. Following 2- or 7-day organ culture, the samples were harvested for histological examination with Weigert's iron hematoxylin/Fast Green/Safranin-O staining. A modified histological classification was adapted based on

two well-established grading systems [4,5]. Three blinded evaluators independently and blindly scored twice according to 4 categories: morphology of the annulus fibrosus (AF), border between the AF and NP, cellularity of the NP, and matrix of the NP. For oxidative stress response to NP cells, voltage-dependent anion channel 1 (VDAC1) and nuclear factor (erythroid-derived 2)-like 2 (Nrf2) immunohistochemical stains were performed. To quantify the amount of IHC positive expression, we followed a semi-quantification procedure using ImageJ Fiji software (Version 1.53c; NIH) [6].

***In-vivo* study:** A total of 24 (11 male and 13 female) young adult NZW rabbits (7-8 months old) were randomly assigned for intact control, injury + HG only, and injury + Amo/HG (n = 6/group/time-point). Under sterile surgical conditions, two of three randomly assigned lumbar IVDs (L2/3, L3/4, or L4/5 levels) were punctured percutaneously with an 18-gauge needle using fluoroscopic guidance. With the needle confirmed in the NP, a 5 cc syringe was attached to the needle, the plunger drawn back to the 5 cc line, and aspiration held for 5 seconds. After the puncture, the syringe was removed and an intradiscal injection of 100 μ l HG with or without Amo was performed using a 27-gauge needle inserted through the 18-gauge needle, then both needles removed. At 2 and 8 weeks, disc height index (DHI) was calculated by two independent observers using ImageJ (Fig. 3B) [7]. Additional glycosaminoglycan (GAG), glutathione, and histology are under analysis.

RESULTS

***In-vitro* study:** Concentrations of up to 10 mM NAC and 2.5 mM Amo were found to be non-toxic, and these doses were used for further studies (Fig. 1A). Amo and Amo/NAC pre-treatment significantly prevented the rate of apoptotic and necrotic cell death (Fig. 1B). The levels of mitochondrial ROS production and membrane potential were similar with control (Fig. 1C and D). Thus, Amo has potential for protection against tBHP-induced oxidative damage to mitochondrial function in NP cells.

***Ex-vivo* study:** Amo was more slowly released in higher concentration of F-127 and HA, however, there was no significant differences among

the groups. In contrast, Amo only (no HG) was completely dissolved within 24 h (Fig. 2A). Histological analysis revealed a superior preventative effect of Amo in the degenerative grading system and representative images (Fig. 2B and C). Scoring of the Amo-treated group were statistically significant at day 2 ($p = 0.002$) and day 7 ($p = 0.007$) compared to that of HG only group (Fig. 2B). VDAC1 quantification at day 7 was significantly higher in HG only group compared uninjured control ($p = 0.005$), but there was no difference between intact and Amo/HG (Fig. 2D). This result implies that Amo inhibits VDAC1 opening, eventually reducing the apoptosis of NP cells from oxidative stress-mediated discal injuries. Nrf2 found in the cytosol of protected cells from oxidative stress was significantly over-expressed in Amo/HG at 7 days ($p > 0.001$ vs. HG) (Fig. 2E).

In-vivo study: In representative images of rabbit IVDs, the treatment of Amo/HG induced less severe damages in the NP compared to HG only group represented by apparent water loss and color change (Fig. 3A). Quantified DHI values denoted protective role of Amo in disc height at week 2 ($p = 0.003$ vs. HG) and week 8 ($p = 0.002$ vs. HG) (Fig. 3C).

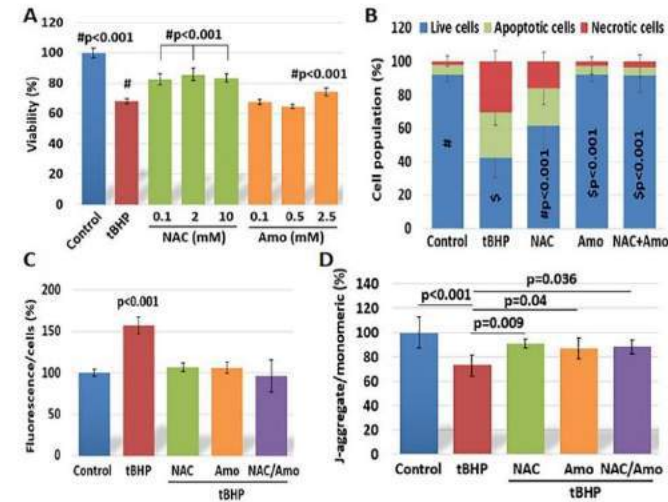


Figure 1: In vitro effect of Amo on targeting oxidative stress. (A) Viability assay ($n = 4$). (B) Annexin V/PI staining ($n = 4$). (C) Quantified MitoSOX Red fluorescence ($n=4$). (D) JC-1 staining ($n=6$). Reproduced with permission [8]. Copyright 2021, The Spine Journal.

DISCUSSION

Taken together, in-vitro, ex-vivo, and in-vivo studies highlight the role of Amo in preventing mitochondrial damage. Next, we plan to analyze GAG and glutathione concentrations, alongside histological indications of disease and damage *in-vivo*. In conclusion, Amo treatment targeting oxidative stress has great potential for preventing degenerative disc degeneration.

ACKNOWLEDGEMENTS

This work was supported by the Assistant Secretary of Defense for Health Affairs endorsed by the Department of Defense, through the Peer Reviewed Medical Research Program under award no. W81XWH2010152.

DISCLOSURE

The authors declare that there is a potential intellectual property regarding data presented here.

REFERENCES

- [1] Dimozi *et al.*, *Eur Cell Mater*, 30:89-102, 2015.
- [2] Feng *et al.*, *Oxid Med Cell Longev*, 2017:1-12, 2017.
- [3] Suzuki *et al.*, *Arthritis Res Ther*, 17:316, 2015.
- [4] Lu *et al.*, *Spine*, 22(16):1828-34, 1997.
- [5] Masuda *et al.*, *Spine*, 30(1):5-14, 2005.
- [6] Crowe *et al.*, *Bio Protoc*, 9(24), 2019.
- [7] Rutges *et al.*, *Osteoarthritis Cartilage*, 21(12):2039-47, 2013.
- [8] Seol *et al.*, *Spine J*, 21(6): 1021-1030, 2021.

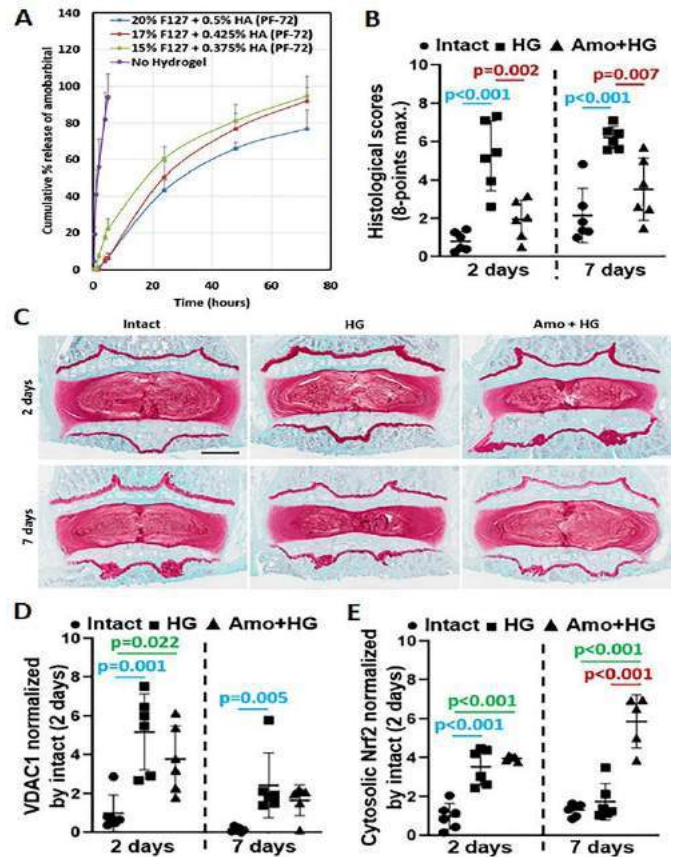


Figure 2: Ex vivo effect of Amo on targeting oxidative stress. (A) *In vitro* Amo release profile over 72 h ($n=3$). (B) Histological grading of IVD at day 2 and 7 ($n=6$). (C) Representative histological images of IVD. (D) Quantified VDAC1 expression ($n = 6$). (E) Quantified cytosolic Nrf2 expression ($n = 5-6$).

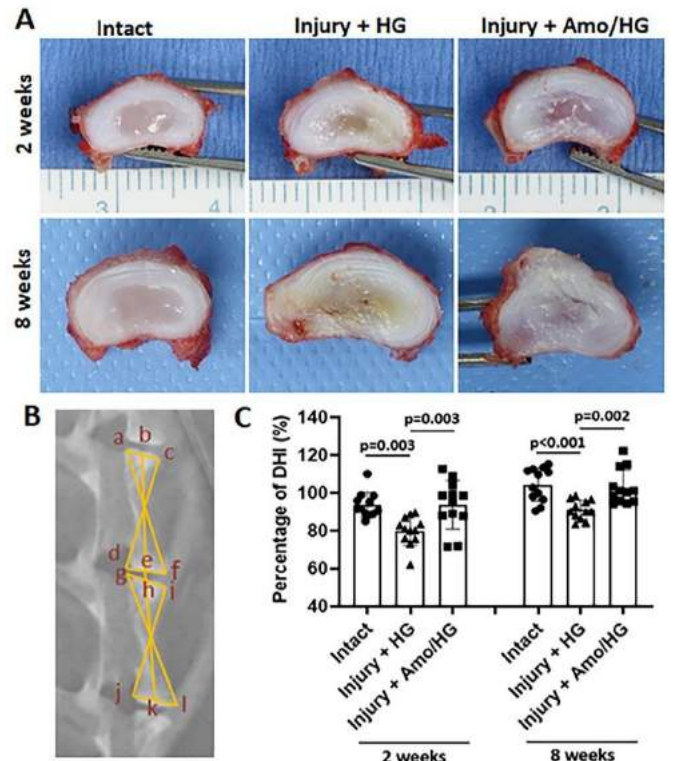


Figure 3: In vivo effect of Amo on targeting oxidative stress in a rabbit disc herniation model. (A) Representative images of IVDs. (B) DHI = $e-h / (b-e + h-k)$. (C) Quantified DHI ($n=12$).

MULTISCALE MODEL PREDICTIONS OF HEART GROWTH DURING HYPERTENSIVE RAT PREGNANCIES

Molly S. Kaissar (1), Kyoko Yoshida (1)

(1) Department of Biomedical Engineering, University of Minnesota, Minneapolis, MN, USA

INTRODUCTION

Throughout pregnancy, the patient's body adapts to accommodate the growing fetus. For example, the cardiovascular system meets rising demands by expanding total blood volume, reducing systemic vascular resistance, and increasing cardiac output.¹ Hemodynamic adaptations work alongside changing hormone concentrations to induce significant cardiac growth, culminating in a ~30% increase in both left ventricular (LV) mass and cavity volume by term pregnancy.² This heart growth often helps the pregnant patient maintain normal cardiac function to meet the increased workload.

In some cases, the heart can have a maladaptive response to the stresses of pregnancy and trigger cardiovascular conditions, which constitute the leading causes of pregnancy-related mortality in the United States. One of the biggest culprits is hypertension, which accounts for 10% of deaths during pregnancy and up to a year after delivery.³ Hypertension impacts 1 in 10 pregnancies worldwide, but only half of these cases can be attributed to pre-existing conditions.³ Gestational hypertension and preeclampsia are both hypertensive disorders of pregnancy identified by new elevated blood pressure after 20 weeks' gestation – when significant cardiac growth has already occurred.³ However, providers are left to treat unavoidable diagnoses without a clear etiology. To anticipate these conditions earlier, we must first uncover the mechanisms behind pregnancy-induced heart growth.

Towards this goal, we developed a multiscale model of heart growth, where we incorporated a set of hormonal and hemodynamic mechanisms that we hypothesize describe heart growth in normal and perturbed pregnancies. We previously demonstrated that this model could predict LV growth during a normal rat pregnancy.⁴ Here, we assessed whether our model could predict perturbed pregnancies by applying it to three different animal models of hypertensive pregnancies.⁵⁻⁷ We simulated case-dependent changes in hormones and hemodynamics and compared our predictions to the experimental results. We demonstrate that our multiscale model can capture heart

growth in some cases of perturbed pregnancies and illustrate the importance of considering both hormonal and hemodynamic cues in models of cardiac hypertrophy.

METHODS

Multiscale Model of Heart Growth We previously published a multiscale model of heart growth during normal pregnancy in rats.⁴ Briefly, an intracellular signaling network model (Fig 1A) that predicts cell-level growth in response to key pregnancy and cardiovascular hormones (Progesterone, *P4*; Estrogen, *E2*; Angiotensin II, *Ang II*) plus a generic stretch term (*myoStretch*) is coupled to a systemic mechanical compartmental model (Fig 1B) that predicts organ-level deformation in response to changes in heart growth and hemodynamics. Organ-level growth is simulated using the kinematic growth framework within the compartmental model, in which the total observable deformation of the heart is a product of the growth deformation tensor and the elastic deformation tensor ($F_{tot} = F_e F_g$). The growth deformation tensor is determined by the network model's predicted changes in the cell area. In return, the maximum elastic fiber stretch, calculated by the compartmental model, is fed into the network model as *myoStretch*, closing the loop between the two models.

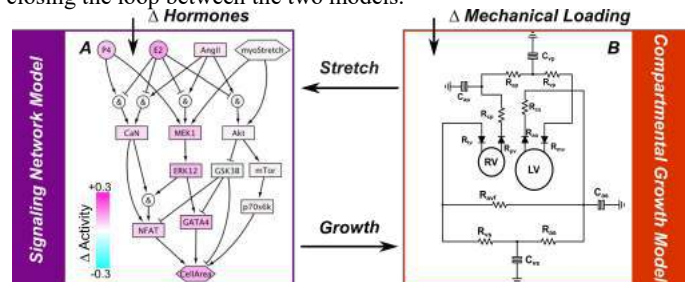


Figure 1: Multiscale model of heart growth during pregnancy. A schematic of (A) the cell-level intracellular signaling network model coupled to (B) the organ-level systemic compartmental growth model.

Simulating Hypertensive Pregnancies We simulated a range of hormonally and hemodynamically induced rat models of hypertensive pregnancy to test the breadth of our model. First, we simulated hormonally-induced hypertension, where osmotic mini-pumps containing a low pressor dose of *Ang II* (+**Ang II**) were implanted between days 8.5 and 9.5 of pregnancy.⁵ Second, we simulated hemodynamically-induced hypertension with a reduced uterine perfusion pressure (+**RUPP**) model, where the uterine arteries and the abdominal aorta below the renal arteries were banded on day 14 of pregnancy.⁶ Finally, we simulated a hormonally and hemodynamically induced hypertension, where transverse aortic constriction (+**TAC**) – known to elevate circulating *Ang II* levels – was induced between days 5.5 and 8.5 of pregnancy.⁷ All experimental studies saw elevated blood pressure and additional heart growth when compared to their gestation-day-matched normal pregnant counterparts.

Table 1: Changes in simulations of hypertensive rat pregnancies

Induced by...	+Ang II Hormones	+RUPP Hemodynamics	+TAC Hormones + Hemodynamics
Resistance (R_{as})	↑	↑	↑
Compliance (C_{as})	–	↓	↓
<i>Ang II</i>	↑	–	↑
<i>E2</i>	–	↓	–

For each case, normal pregnancy was simulated until the average time of pump implantation or banding. Then, we implemented the changes summarized in Table 1 to reflect each of the hypertensive models. To simulate hypertension, the systemic arterial resistance, R_{as} , was increased to fit the reported mean arterial pressure. The reported reductions in vascular compliance in the +**TAC** and +**RUPP** models were considered by decreasing the systemic arterial capacitance, C_{as} .^{7,8} Time-appropriate changes in hormones, such as increases in *Ang II* in the +**Ang II** and +**TAC** models and observed decreases in *E2* in the +**RUPP** models, were also implemented.^{7,9} Lastly, each simulation was re-run twice, once with only hemodynamic changes (R_{as} , C_{as}) and once with only hormonal changes (*Ang II*, *E2*), to investigate their influences on predicted heart growth.

RESULTS

During the 21-day pregnancy in rats, our model predicted additional heart growth in 2 out of 3 cases, which were quantitatively consistent with the reported data (Fig 2A). For +**RUPP**, our model predicted negligible increases in LV mass, which disagreed with the reported experimental growth.⁶

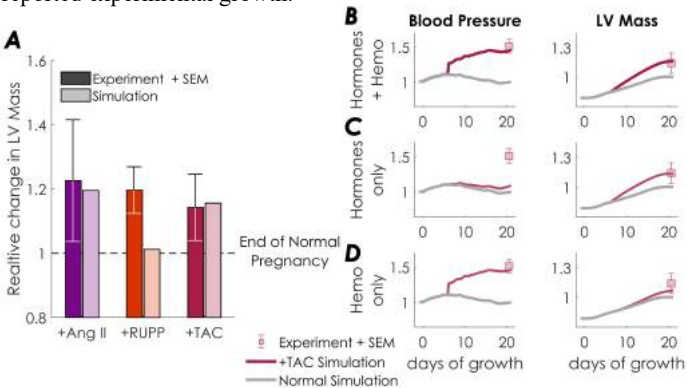


Figure 2: (A) Heart growth in rat models of hypertensive pregnancy. (B-D) Simulated changes in blood pressure and heart growth for the +TAC model. Y-axis values are reported as relative to the end of a normal pregnancy.

Next, we investigated the contributions of hormones and hemodynamics on the predicted growth in the +**Ang II** and +**TAC** simulations. Our model predicted the experimental increase in LV mass in the +**Ang II** and +**TAC** cases when both hormones and hemodynamics were included, suggesting that both cues are necessary to capture heart growth in our model (Fig 2A,B).^{5,7} When only hormonal changes were included, we could predict changes in LV mass on par with the experimental results for +**Ang II** and +**TAC**, but we could not induce the elevated blood pressure that defines these hypertensive rat models (Fig 2C). When only hemodynamic changes were included, we could not capture the mass changes in the experimental models (Fig 2D).

DISCUSSION

This work assessed if the mechanisms proposed in our multiscale model could predict heart growth in perturbed pregnancies. Our model correctly captured the additional heart growth in 2 of 3 animal models of hypertensive pregnancies (+**Ang II** and +**TAC**), demonstrating its ability to predict heart growth in these perturbed pregnancies.^{5,7} Further, our analysis indicates the need to incorporate both biological and mechanical cues to predict heart growth and hemodynamics. These results align with previous simulations of +**TAC** in non-pregnant mice, where a similar multiscale modeling approach required both hemodynamic and hormonal cues to predict appropriate growth.¹⁰

An important finding here is the inability of our model to capture the increase in heart growth associated with +**RUPP**, suggesting the need to include additional mechanisms into the model.⁶ Unlike +**Ang II** and +**TAC**, +**RUPP** does not elevate plasma levels of *Ang II*, which contributed to heart growth in these simulations.¹¹ Instead, +**RUPP** triggers other potent vasoconstrictors, including Endothelin-1 (*ET-1*).¹¹ *ET-1* is a good candidate to incorporate into our intracellular signaling network since it impacts cardiomyocyte growth and it is also elevated in preeclampsia in humans.^{11,12}

In conclusion, we demonstrate that our multiscale framework can capture heart growth in two animal models of hypertensive pregnancies. Based on our initial findings, we are improving our model to include *ET-1* to see if we can capture heart growth due to +**RUPP**. In future studies, we will explore our model’s capacity to capture other hemodynamic and growth parameters, such as changes in stroke volume and wall thickness, and its ability to accommodate biological perturbations, including heart growth in pregnant transgenic mouse models. Ultimately, we aim to apply this multiscale model as a clinical tool for screening and treating perturbed heart growth in pregnant patients to facilitate early diagnosis of cardiovascular disease and inform personalized patient care.

ACKNOWLEDGEMENTS

This work was supported by the National Institutes of Health through the Cardiovascular Engineering Training Program at the University of Minnesota (T32-HL139431).

REFERENCES

[1]Hunter S et al. *Br Heart J* 68.6 (1992). [2]Savu O et al. *Circ Cardiovasc Imaging* 5.3 (2012). [3]Sutton ALM et al. *Obstet Gynecol Clin North Am* 45.2 (2018). [4]Yoshida K et al. *Biomech Model Mechanobiol* 21.3 (2022). [5]Aljabri MB et al. *Acta Physiol Scand* 201.4 (2011). [6]Richards C et al. *Biol Sex Differ* 12.1 (2021). [7]Songstad NT et al. *PLoS ONE* 9.2 (2014). [8]Mazzuca MQ et al. *Biochem Pharmacol* 208 (2023). [9]Neves LA et al. *Am J Physiol Regul Integr* 294.1 (2008). [10]Estrada AC et al. *Biomech Model Mechanobiol* 20.1 (2022). [11]Li J et al. *Am J Physiol Heart Circ* 303.1 (2012). [12]Frank DU et al. *J Mol Cell Cardiol* 121 (2018).

MULTISCALE MODEL TRANSLATES MICROSCALE VASCULAR SMOOTH MUSCLE CELL MECHANICS TO TISSUE-SCALE AORTIC CONTRACTION

Shannon M. Flanary (1), Seokwon Jo (2), Emilyn U. Alejandro (2), Victor H. Barocas (3)

(1) Department of Chemical Engineering & Materials Science, University of Minnesota, Minneapolis, MN, USA

(2) Department of Integrative Biology & Physiology, University of Minnesota, Minneapolis, MN, USA

(3) Department of Biomedical Engineering, University of Minnesota, Minneapolis, MN, USA

INTRODUCTION

Despite \$2 billion of public funding being dedicated to cardiovascular disease (CVD) research each year, CVD remains the leading cause of death in the US.¹ Vascular smooth muscle cells (VSMC) and extracellular matrix (ECM), which compose the medial layer of blood vessels, often play a role in CVD. Biochemical and mechanical stimuli influence VSMCs to contract and secrete ECM modifying proteins, ultimately impacting vessel geometry and mechanics.² The responsiveness of VSMCs, however, can drive maladaptation when signaling is perturbed due to disease, such as in pre-diabetic chronic hyperglycemia.³ VSMC behavior has been greatly investigated *in vitro*,^{2,4,5} but cell-scale results do not always translate to the tissue scale, hindering the development of VSMC-active therapeutics.

Multiscale computational and experimental techniques, applied together, can translate information across length scales and help tease out the role of perturbed VSMC behavior in CVD pathogenesis. Previously, multiscale models of perturbed biochemical signaling have been employed to predict tissue-scale behaviors, but they lack modalities to compare mechanical results at varying length scales.^{6,7} The objective of this study was to create a multiscale vasculature model connecting cell-scale biochemical signaling and cytoskeletal structure to arterial mechanics. We hypothesized that the multiscale model would capture VSMC contractile behavior observed in both *in vitro* cell-scale and *ex vivo* tissue-scale experiments, which was supported by the correct model prediction of hyperglycemic aortic hypercontractility.

METHODS

Overall Strategy. Our strategy consisted of construction of a multiscale computational model based on biochemical signaling and cellular mechanics, coupled with experimental characterization at the tissue-scale via an isometric ring contraction assay.⁸

Multiscale Model Formulation. The model consists of (1) biochemical signaling, (2) single-actin-filament mechanics in response

to the signal, (3) actin stress fiber / ECM fiber network mechanics, and (4) tissue-scale FE model. Each component is described in turn below.

Biochemical Signaling Model (Fig. 1). The signaling network model was based on a previous VSMC model validated against existing traction force microscopy data⁹, modified to include known glucose relationships. Elevated glucose levels increase VSMC contractility through RhoA pathway activation and Ca²⁺ sensitization.⁴ Following established methods⁶, the model reactions were defined by ordinary differential equations and connected by Boolean logic.

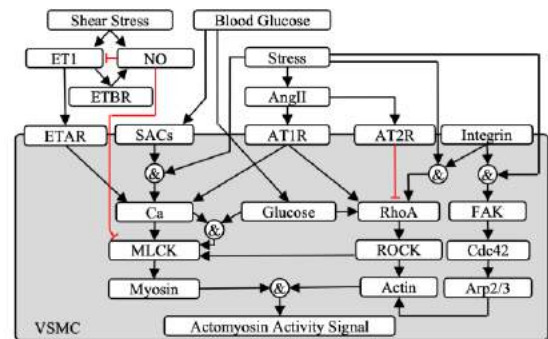


Figure 1: Biochemical signaling network.

Actomyosin Contraction. The resulting biochemical signal was transferred to stress fibers as an input signal for a contraction model.¹⁰ The actin stress was constructed from a Hill-type active component and a linear passive component. Similar, but purely passive models, were used for collagen and elastin fibers.

Cell-Scale Modeling. A 2D, cell-only model (Fig. 2A) was used to simulate traction force microscopy and cellular microbiaxial stretching (CμBS).¹¹ The network was anchored to a substrate by focal adhesions in each corner of the rectangular VSMC. Simulation results were compared to previously published experimental data.¹¹

Tissue-Scale Modeling. For tissue-scale predictions, the full multiscale model was implemented by imposing test deformations on the micro-network and fitting the output to a continuous macroscale model with a neo-Hookean matrix and three fiber families. Microscale contraction translated into a prestrain in the macroscale model, in which the finite-element model was applied to a tissue ring wrapped around two pins, which were modeled as rigid and in sliding contact with the tissue (Fig. 2B).

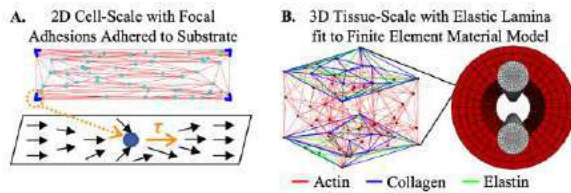


Figure 2: Fiber networks for A) cell and B) tissue modeling.

Ring Contraction Assay. Aortic ring contraction studies were performed with tissue explants from male wildtype (WT) and OGT^{KO} mice, the latter a well-established model of progressive, chronic hyperglycemia.¹² Tissue was dissected into ~2mm long sections and then loaded onto 0.2 mm diameter pins in a DMT Tissue Myograph with a 37°C PBS bath supplemented with 5.6 mM glucose. Contraction was induced with 100 mM KCl at each strain (10%, 20%, 25%, and 30%).

RESULTS

Multiscale Model Predicts Cell-Scale Strain Dependence. To investigate the strain-dependence of individual VSMCs, we compared the multiscale model to published *CμBS* data.¹¹ In the cell-scale predictions, the multiscale model predicts that the substrate deformation is localized near the focal adhesions in each corner (Fig. 3A). The displacements increase in prominence when the VSMC is transversely strained (Fig. 3B). The increasing strain results in increased passive actin fiber stress (Fig. 3C), as well as a small increase in active stress (Fig. 3D). With no fitting parameters, the model predicts experimental VSMC transverse traction stress-strain behavior (Fig. 3E).¹¹

Tissue-Scale Passive and Contractile Stresses are Captured by the Multiscale Model. When the multiscale model is expanded to the tissue scale, the stress near the pins and along the luminal side increases with increasing pin distance (Fig. 4A). The force on the loading pins prior to KCl addition, defined as the passive reaction force, increases with increasing pin strain both experimentally and in the model prediction without the need for additional fitting (Fig. 4B).

To demonstrate the power of the multiscale model, the value of the “Blood Glucose” signaling node (Fig. 1) was increased from 0.5 (normal) to 0.95 to mimic hyperglycemia, and the results were

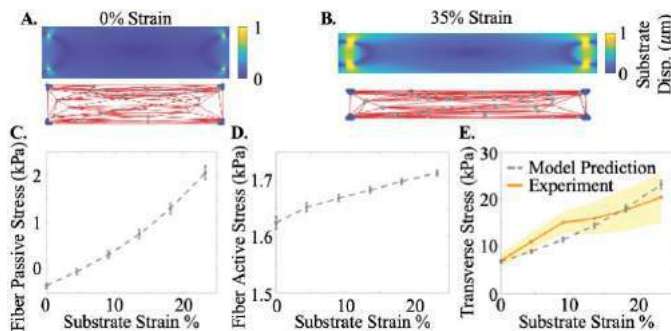


Figure 3: Representative substrate displacement and fiber network for VSMC at A) 0% and B) 35% strain. Predicted C) passive and D) active fiber stress. E) Total predicted and experimental VSMC traction stress. Error is STD for n=10.

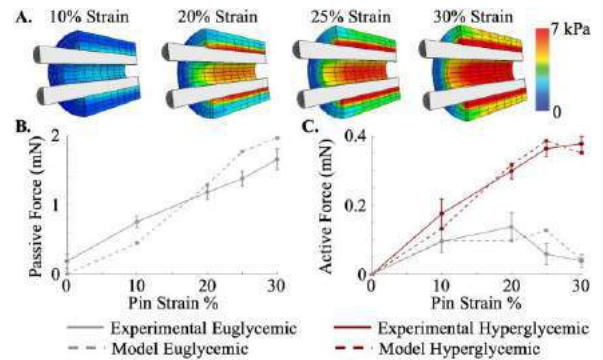


Figure 4: A) Predicted total stress distributions. B) Model-predicted and experimental aortic passive (prior to induced contraction) force. C) Model and experimental active (difference between during and prior to contraction) force for euglycemic and hyperglycemic aortas. Error is STD for n = 8.

compared to experimental data collected from hyperglycemic aortic explants. The euglycemic (normal) active reaction force, defined as the difference between total measured force and passive force, is well-predicted by the model (Fig. 4C). Additionally, the imposed *in silico* increase in glucose biochemical signaling was enough to capture the experimentally observed increase in hyperglycemic aortic contractility.

DISCUSSION

These results demonstrate the capability of our multiscale model to describe VSMC contractility observed in both *in vitro* cell-scale and *ex vivo* tissue-scale experiments. To our knowledge, this model is the first of its kind that predicts VSMC mechanical contractility across such a wide range of length scales. Previous models have been developed that predict the long-term growth and remodeling due to disease^{6,7}, however they did not consider short-term contractility changes due to chronic signaling perturbations.

The significance of our model is demonstrated in its recapitulation of the hypercontractile aortic phenotype observed in chronic hyperglycemia. VSMC hypercontractility due to hyperglycemia is subtle at the single-cell scale, and therefore it is easily lost in experimental techniques with large variability, leading to conflicting reports.^{4,5} However, at the tissue scale, endothelium-independent hypercontractility is consistently observed.¹³ The multiscale model reveals a possible source of this discrepancy in that the while the impetus is localized in cell-scale biochemical signaling, the phenotype must be amplified to be resolved experimentally at the tissue-scale.

In its current form, the model does not account for long-term ECM remodeling. For example, chronic hyperglycemia leads to ECM crosslinking.³ Currently, the model only considers contractility changes, leading to an inability to predict passive mechanical changes. Despite this limitation, the multiscale model still has potential to elucidate mechanisms behind contractile vessel hyperreactivity.

ACKNOWLEDGEMENTS

Support was provided by NIH (U01-HL139471, R01-HL164800). We thank Ryan Mahutga for his expertise in multiscale mechanics.

REFERENCES

- [1] Stockmann, C et al, *Int J Cardiol*, 172, 2014.
- [2] Frisantiene, A et al, *Cell Signal*, 52, 2018.
- [3] Raaz, U et al, *Circ Res*, 117, 2015.
- [4] Hien, T et al, *J Biol Chem*, 291, 2016.
- [5] McCallinhart, P et al., *Am J Physiol Hear Circ Physiol*, 318, 2020.
- [6] Irons, L et al, *Ann Biomed Eng*, 49, 2021.
- [7] Yoshida, K et al, *BMMB*, 21, 2022.
- [8] Caulk, A et al., *JBME*, 141, 2019.
- [9] Flanary, S et al., *Under review*.
- [10] Deshpande, V et al., *PNAS*, 103, 2006.
- [11] Win, Z et al., *JBME*, 139, 2017.
- [12] Alejandro, E et al., *Cell Rep*, 13, 2015.
- [13] Guo, Z et al. *Cardiovasc Res*, 67, 2005.

NON-INVASIVE ESTIMATION OF PRESSURE DROP ACROSS AORTIC COARCTATION

Priya J. Nair (1), Martin R. Pfaller (2), Seraina A. Dual (3), Doff B. McElhinney (4), Daniel B. Ennis (5), Alison L. Marsden (1,2)

- (1) Bioengineering, Stanford University, Stanford, CA, USA
(2) Pediatric Cardiology, Stanford University, Stanford, CA, USA
(3) Biomedical Engineering and Health Systems, KTH Royal Institute of Technology, Stockholm, Sweden
(4) Cardiothoracic Surgery, Stanford University, Stanford, CA, USA
(5) Radiology, Stanford University, Stanford, CA, USA

INTRODUCTION

Coarctation of the aorta (CoA) is a congenital heart defect characterized by a constriction of the aorta, and with an estimated incidence of 3 per 10,000 births.¹ The narrowing of the aorta causes a drop in blood pressure (BP) across the CoA which can be alleviated using surgical and catheter-based treatments. The current guideline for treatment is a BP gradient ≥ 20 mmHg at rest.

Computational fluid dynamics (CFD) simulations are used to characterize local hemodynamics in patients with CoA. Previous studies have demonstrated the capability of three-dimensional (3D) simulations in modeling CoA and predicting the trans-coarctation pressure gradient.^{2,3} However, these studies either had small sample sizes or assumed the aortic walls to be rigid. Additionally, 3D simulations are computationally expensive and time-intensive, which currently may limit the translation to routine clinical applications. Reduced-order models, specifically zero-dimensional (0D) models, that are less computationally expensive, can be applied to perform patient-specific simulations. 0D circuit analogy models have no spatial dependency; they only depend on time but can be evaluated at different locations along the cardiovascular system by creating models comprising multiple circuit elements. However, the simplified nature of 0D models and lack of features such as wave propagation can affect the accuracy of 0D hemodynamic estimates.

The objective of this study was to non-invasively predict the pressure drop across the CoA using patient-specific simulations. Both 0D and 3D simulations were performed for a cohort of patients using the open-source software SimVascular.⁴ The peak systolic pressure drops measured across the CoA using both 0D and 3D models (ΔP_{0D} and ΔP_{3D} respectively) were compared and validated using invasive cardiac catheterization measurements (ΔP_{Cath}).

METHODS

Acquisition of Patient Data: CT/4D-Flow MRI datasets (obtained as part of the standard clinical care for CoA patients and approved by the IRB) were acquired from the Lucile Packard Children's Hospital for 17 patients with CoA (12 CT, 5 MRI, age = 28 ± 10.99 years, 13 male/4 female) prior to their undergoing an invasive catheterization and stent placement. Invasive BP measurements were obtained via cardiac catheterization in the ascending and descending aorta. Cuff BP measured on the day of the catheterization was also acquired.

Anatomic Model Generation: Anatomic images were imported into SimVascular and manually segmented to generate 3D geometries of the aorta and branches arising from the aortic arch: brachiocephalic trunk, left carotid artery, and left subclavian artery (Figure 1). Centerlines were automatically extracted from the 3D geometry to create the 0D model which consists of individual lumped parameter elements (resistors, capacitors and inductors) that connect to form a lumped parameter network. The 3D volume was meshed using tetrahedral elements and contained 1.5-2 million elements. A boundary layer mesh consisting of three layers was incorporated to resolve velocity gradients at the wall. The mesh was refined at the CoA and the post-stenotic dilation region to capture the jet formed by the stenosis.

Boundary Conditions: Boundary conditions were tuned using flow measurements and cuff BP measurements. For patients who had MRI, eddy-current corrected images from the 4D-Flow MRI dataset were analyzed to measure 2D time-resolved flow at the inlets and outlets using Arterys (Arterys, San Francisco, USA). For patients who had a CT, a generalized waveform was created by averaging MRI-derived waveforms of 7 additional CoA patients from the Vascular Model Repository (vascularmodel.org). The waveform was then scaled to match the patient's cardiac output and heart rate measured during catheterization. The patient-specific temporally varying parabolic flow profile was prescribed to the inlet of the 0D and 3D models. A three-element Windkessel model (proximal resistance R_p , capacitance C , distal resistance R_d) was imposed at each of the outlets. Total resistance

($R_p + R_d$) for each of the branches was determined based on flow splits to each of the branches for patients who had MRI, and by vessel cross-sectional area for patients who had CT. 0D simulations were performed first and used to fine-tune the prescribed boundary conditions. The value of C , along with R_p/R_d ratio, were adjusted to fine-tune the boundary conditions until the calculated pressures matched the patient's systolic and diastolic cuff BP within 5 mmHg.

0D and 3D simulations: For the 0D simulation, the values of the lumped parameter elements were determined from the geometric and material properties of the blood and blood vessel: fluid density 1.06 g/cm^3 , viscosity 4cP , Young's modulus $3 \times 10^6 \text{ dyne/cm}^2$, and vessel thickness defined as 20% of the vessel radius. Simulations were run for ten cardiac cycles to reach a periodic state of the solution. A stenosis loss model was included to incorporate an additional non-linear resistance that would account for flow separation effects at the stenosis.⁵ Results from the last time step of the 0D simulation were projected onto the model's 3D mesh and used as the initial condition for the 3D simulation.⁶ 3D simulations were performed using a coupled-momentum method with the same boundary conditions as the 0D simulation. Deformable walls with Young's modulus $3 \times 10^6 \text{ dyne/cm}^2$, Poisson ratio 0.5, and shear correction factor 0.8333 were used. Simulations were run for ten cardiac cycles to reach a periodic state of the solution. Pressure along the centerline before and after the CoA were measured at peak systole in the 0D and 3D models. ΔP was calculated as the difference between the mean of the pressure measured in a region defined as the last 20% of the length of the ascending aorta, and the centerline pressure measured at a point in the descending aorta two vertebral spaces above the diaphragm to match typical catheter location. ΔP_{0D} and ΔP_{3D} were compared to ΔP_{Cath} .

Statistical Analysis: Paired Student's t-test was used to compare ΔP_{0D} and ΔP_{3D} to ΔP_{Cath} . A p-value of 0.05 was considered significant. The agreement of ΔP_{0D} and ΔP_{3D} with ΔP_{Cath} was characterized with Bland-Altman plots.

RESULTS

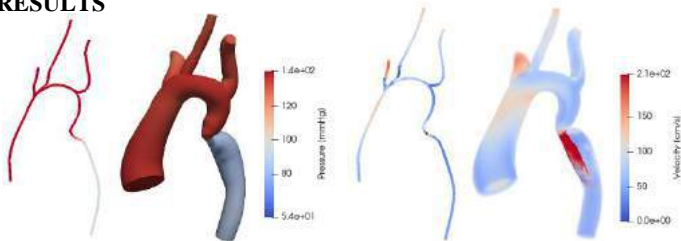


Figure 1. Pressure (left) and velocity (right) features captured in 0D and 3D patient-specific simulations.

CoA anatomy and hemodynamics were observed and captured in the simulations (Figure 1).

ΔP_{0D} and ΔP_{3D} resulted in an underestimation of ΔP_{Cath} on average but was more severe in the case of ΔP_{0D} as shown in Figure 2 (0D: $11.5 \pm 13.2 \text{ mmHg}$; 3D: $18 \pm 11.2 \text{ mmHg}$; Catheter: $18.8 \pm 10.4 \text{ mmHg}$).

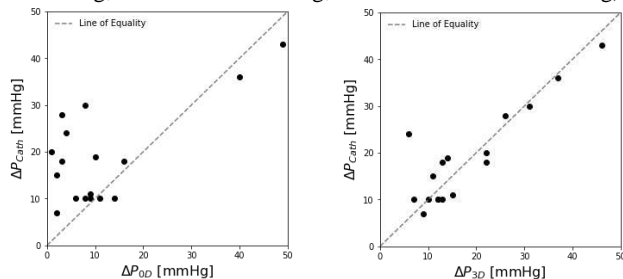


Figure 2. ΔP_{Cath} plotted against ΔP_{0D} (left) and ΔP_{3D} (right).

Using a BP gradient $\geq 20 \text{ mmHg}$ at rest as a treatment guideline, ΔP_{0D} and ΔP_{3D} would result in the right treatment recommendation in 76.5% and 94% of cases, respectively.

The root-mean-square error between simulation pressure drop estimates and catheter-derived measurements was smaller for 3D simulations, than for 0D simulations (0D: 12.05 mmHg ; 3D: 5.26 mmHg).

Paired Student's t-test between ΔP_{0D} and ΔP_{Cath} had a p-value < 0.001 indicating that the ΔP_{0D} was not always a good estimate of clinical catheter-derived pressures. The t-test between ΔP_{3D} and ΔP_{Cath} had p-value = 0.565, indicating that the null hypothesis was not rejected and that ΔP_{3D} can provide good non-invasive estimates of catheter pressures.

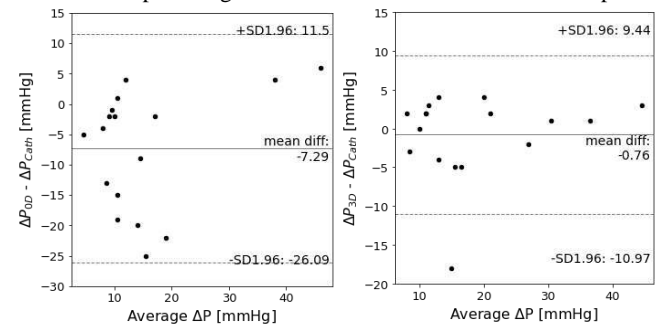


Figure 3. Bland-Altman plot of catheter-derived pressure drop and estimates from 0D (left) and 3D (right) simulations, difference plotted against the mean. Upper and lower dotted lines correspond to mean difference $\pm 1.96 \text{ SD}$.

DISCUSSION

This study demonstrates the capability of using CFD to non-invasively estimate pressure drops in patients with CoA. 0D models (constructed automatically from 3D models) were used to efficiently tune boundary conditions, to initialize 3D simulations, and to compute flow and pressure in patient-specific models of CoA. Methods were also introduced to generate patient-specific inflow waveforms for patients with CTs where such information is typically lacking. Pressure drops predicted from 0D and 3D simulations validated using invasive catheter measurements showed that the 3D model estimated pressure gradient within 5 mmHg in most cases. The 0D model was also a good estimator of catheter-derived pressure gradients in cases where the CoA was in a non-junction region. The significantly lower computational time of the 0D models makes them more feasible to use in a clinical setting in scenarios where the CoA is not located at a vessel junction. With improvements to 0D models, like more comprehensive stenosis loss models, they have the potential to become more accurate. Therefore, while 0D simulations cannot currently replace 3D simulations, they can be used to speed up the model personalization process. Future studies should explore the prediction of the CoA pressure gradient in exercise conditions, as well as before and after stent intervention.

ACKNOWLEDGEMENTS

This work is funded by a National Science Foundation Graduate Research Fellowship to PJN and by the Stanford Maternal and Child Health Research Institute (award K99HL161313) to MRP.

REFERENCES

- [1] Dijkema, EJ et al., *Heart*, 103(15):1148-1155, 2017.
- [2] LaDisa, JF et al., *J Biomech Eng*, 133(9), 2011.
- [3] Saitta, S et al., *J. Biomech*, 94:13–21, 2019.
- [4] Updegrave, A et al., *Ann Biomed Eng*, 45, 525-541, 2017.
- [5] Mirramezani, M et al., *Ann Biomed Eng* 48, 2870–2886, 2020.
- [6] Pfaller, MR et al., *Ann Biomed Eng*, 49:3574–3592, 2021.

SUPPRESSING LEAFLET THICKENING AND STIFFENING MAY RESTORE TRICUSPID VALVE FUNCTION

Mrudang Mathur (1), Marcin Malinowski (2,3), Tomasz A. Timek (3), Manuel K. Rausch (4,5,6)

- (1) Department of Mechanical Engineering, UT-Austin, Austin, TX, USA
(2) Department of Cardiac Surgery, Medical University of Silesia School of Medicine, Katowice, Poland
(3) Division of Cardiothoracic Surgery, Spectrum Health, Grand Rapids, MI, USA
(4) Department of Aerospace Engineering and Engineering Mechanics, UT-Austin, Austin, TX, USA
(5) Department of Biomedical Engineering, UT-Austin, Austin, TX, USA
(6) Oden Institute for Computational Engineering and Sciences, UT-Austin, Austin, TX, USA

INTRODUCTION

Tricuspid valve leaflets have long been considered inert tissues, or “passive flaps” [1]. However, recent studies indicate that they are highly complex, biochemically active, hierarchical structures populated by valve interstitial and endothelial cells, or VICs and VECs, respectively [2]. VICs and VECs maintain a homeostatic environment in the extracellular matrix (ECM) of leaflet tissue through regular collagen degradation and deposition. However, when “activated”, hypersecretory VICs drive an excess deposition of collagen in the ECM. This, in turn, may increase the thickness as well as stiffness of valve leaflets and alter the nonlinearity of their constitutive response. Interestingly, we recently observed such changes in sheep with functional tricuspid regurgitation (FTR) [3]. We posit that this increase in leaflet thickness as well as stiffness and change in material nonlinearity fundamentally alters the leaflets’ ability to bend and stretch, thereby affecting valve function. Furthermore, we hypothesize that the suppression of these changes in tricuspid valve leaflets will, in fact, promote leaflet coaptation and restore valve function. Thus, the objective of our current study is to test this hypothesis.

METHODS

To test our hypothesis, we use a reverse-engineered, openly available finite element model of the healthy human tricuspid valve, “Texas TriValve 1.0”, see **Figure 1**. Detailed descriptions of the creation and validation of this model are provided in our previous work [4]. To study the effects of excess collagen deposition by activated VICs on valve function, we alter three properties of our model. As seen in our animal studies, we increase leaflet thickness and stiffness. Additionally, we decrease the stretch at which the material enters the strain-stiffening regime, which we refer to as “transition- λ ”. Together, we call these changes maladaptive leaflet remodeling. Upon altering each of the above, we compare valve function between all cases by quantifying three metrics at end-systole: (i) average stresses in leaflet

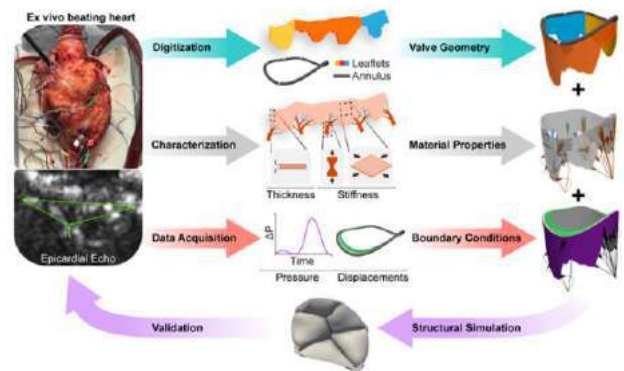


Figure 1: Texas TriValve 1.0 reverse-engineering pipeline

centers, (ii) anterior leaflet opening angle, and (iii) leaflet coaptation area.

RESULTS

Effect of Isolated Changes: To study the sensitivity of valve function to maladaptive leaflet remodeling, we first increased leaflet thickness and leaflet stiffness, and decreased transition- λ in isolation. To this end, we increased thickness by 20-100%, increased stiffness by 20-100%, and decreased transition- λ by 1-5%.

We first examined the effect of isolated maladaptive changes on leaflet stresses. Specifically, we found that a 20-100% increase in leaflet thickness reduced average stresses by 14-69% in the anterior, 7-59% in the posterior, and 7-49% in the septal leaflet. In contrast, we found that a 20-100% increase in leaflet stiffness increased average stresses by 3-15% in the anterior and septal leaflets, and 6-35% in the posterior leaflet. Finally, we found that a 1-5% decrease in transition- λ increased average stresses by 10-22% in the anterior, 10-46% in the posterior, and 6-12% in the septal leaflet.

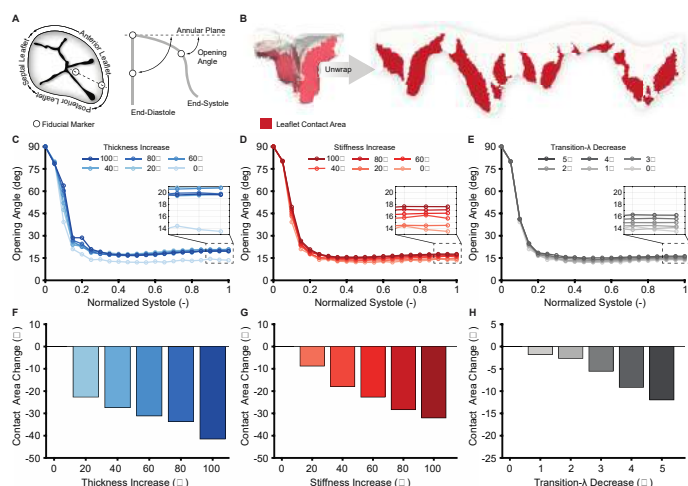


Figure 2: (A) Anterior leaflet opening angles and (B) end-systolic leaflet coaptation areas for valves with increased thickness, increased stiffness, and decreased transition- λ

Next, we examined the effect of isolated maladaptive changes on anterior leaflet opening angle, see **Figure 2A**. Here, we found that a 20-100% increase in thickness increased opening angle by 45-54% at end-systole (**Figure 2C**). Next, we found that a 20-100% increase in stiffness increased opening angle by 7-30% at end-systole (**Figure 2D**). Similarly, we found that a 1-5% decrease in transition- λ increased opening angle by 4-20% at end-systole (**Figure 2E**).

Additionally, we examined the effect of isolated maladaptive changes on leaflet coaptation area at end-systole, see **Figure 2B**. Here, we found that a 20-100% increase in thickness led to a 22-41% decrease in coaptation area (**Figure 2F**). Next, we found that a 20-100% increase in stiffness led to a 9-32% decrease in coaptation area (**Figure 2G**). In contrast, we found that a 1-5% decrease in transition- λ led to only a 2-12% decrease in coaptation area (**Figure 2H**).

Effect of Combined Changes: In addition to studying the effect of an isolated increase in leaflet thickness and leaflet stiffness, and decrease in transition- λ , we also studied their combined effect, see **Figure 3**. To this end, we combined a 40% increase in thickness with a 30% increase in stiffness and a 3% decrease in transition- λ , as observed in our previous animal studies. Furthermore, to contrast the combined effect of maladaptive changes with their isolated effects, we introduced four cases. A control case (I), cases examining isolated changes only (IIa/b/c), cases combining two changes together (IIIa/b/c), and a final case with all changes combined (IV), see **Figure 3**.

In case IV we found that simultaneously increasing leaflet thickness and stiffness and decreasing transition- λ by previously measured magnitudes led to a decrease in average stresses of 26% in the anterior, 17% in the posterior, and 20% in the septal leaflet (**Figure 3A**). This change was primarily driven by changes in thickness (case IIa) and less so by changes in stiffness or transition- λ (cases IIb and IIc, respectively). Next, in case IV we found that remodeling-induced leaflet changes increase anterior leaflet opening angle by 10% at end-systole (**Figure 3C**). This change was driven by the simultaneous increase in stiffness and decrease in transition- λ (case IIIb). To that end, an increase in stiffness and decrease in transition- λ by previously measured magnitudes led to a 26% increase in opening angle. Finally, in case IV we found that remodeling-induced leaflet changes decrease leaflet coaptation area by 29% (**Figure 3D**). This change was primarily driven by an increase in thickness (case IIa) and less so by an increase in stiffness or decrease in transition- λ (cases IIb and IIc, respectively).

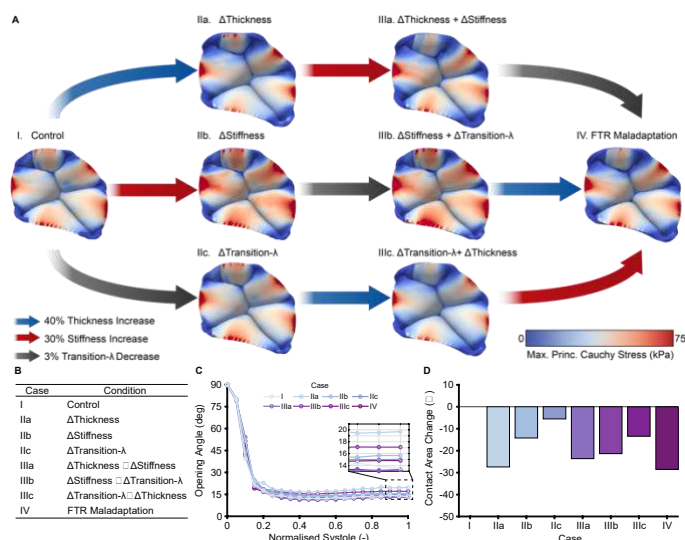


Figure 3: (A) Maximum principal Cauchy stress at end-systole varies among (B) the simulated cases. Similarly, (C) anterior leaflet opening angle and (D) coaptation area varies among cases.

DISCUSSION

Through structural finite element simulations, we show that isolated and combined changes to leaflet thickness, stiffness, and transition- λ disrupt tricuspid valve function. Specifically, in isolation, we found that thicker or stiffer leaflets increasingly resist both bending and buckling. Furthermore, thicker leaflets better support membrane forces and experience lower stresses. In contrast, stiffer leaflets experience greater stresses due to increased membrane forces. Notably, we also found that stresses decrease when maladaptive effects are combined. Here, the leaflets' buckling resistance likely dominates their material stiffness. That is, reduced buckling yields a larger area to support pressure loads, limiting leaflet inflation and reducing stresses.

The clinical significance of our findings is two-fold. Firstly, they may inspire new pharmacological targets for treating FTR. Specifically, pharmaceuticals may be used to suppress the thickening and stiffening of leaflets while preserving beneficial area growth. For example, Losartan was used to suppress leaflet thickening and stiffening in regurgitant mitral valves [5]. Secondly, our results may help understand the sub-optimal outcomes of surgical tricuspid repair. For example, mitral annuloplasty causes leaflet thickening and stiffening, leading to post-repair dysfunction [6]. Suppressing similar changes due to tricuspid annuloplasty may, thus, improve valve function and repair outcomes.

Here, we provide the first computational evidence that suppressing isolated and combined increases in leaflet thickness and stiffness may promote leaflet coaptation and restore tricuspid valve function. Future experimental studies will be needed to support our findings.

ACKNOWLEDGEMENTS

AHA 18CDA34120028 (to MKR) & 902502 (to MM), as well as NIH R21HL161832 (to MKR) & R01HL165251 (to MKR)

REFERENCES

- [1] Marron, K et al, *Circulation*, 94:368-375, 1996.
- [2] Meador, WD et al., *Acta Biomater*, 102:100-113, 2020.
- [3] Meador, WD et al., *eLife*, 9:1-22, 2020.
- [4] Mathur, M et al., *Eng Comput*, 38:3835-3848, 2022.
- [5] Bartko, PE et al., *J Am Coll Cardiol*, 70(10):1232-1244, 2017.
- [6] Sielicka, A et al., *J Am Heart Assoc.*, 7(21):1-18, 2018.

PREDICTING DEVICE RELATED THROMBOSIS AFTER LEFT ATRIAL APPENDAGE OCCLUSION USING COMPUTATIONAL FLUID DYNAMICS

B. Vogl (1), A. Chavez Ponce (2), A. El Shaer (2), A. Bavo (3), M. De Beule (3), M. Alkhouli (2), H. Hatoum (1)

- (1) Department of Biomedical Engineering, Michigan Technological University, Houghton, MI, USA
(2) Department of Cardiovascular Medicine, Mayo Clinic, Rochester, Minnesota, USA
(3) FEops, Gent, Belgium

INTRODUCTION

Atrial fibrillation (AF) is the most common arrhythmia that can cause cardioembolic events. Stroke prevention is the main concern in the management of AF. Blood stasis in the atrium is associated with thrombus development and often occurs in the left atrial appendage (LAA). While anticoagulants are effective in mitigating strokes, bleeding risk, noncompliance, and other side effects make them unused in more than 50% of eligible patients. Instead, another method for reducing LAA related cardioembolic stroke, is left atrial appendage occlusion (LAAO) using an occlusion device such as the WATCHMAN™ (Boston Scientific Corporation, St. Paul, Minnesota). Although this device has shown improved long-term outcomes, studies have also shown that about 4% of patient's develop device related thrombosis (DRT)¹. The factors leading to DRT are still unclear despite several clinical studies investigating potential predictors.

The aim of this study is to evaluate the hemodynamic profiles of the left atrium (LA) in patients who have received a WATCHMAN™ device, and to identify potential predictors for DRT. We hypothesize that DRT is more likely to occur in patients with blood stasis and complex flow patterns at and around the WATCHMAN™ device. We propose a combined finite element analysis (FEA) and computational fluid dynamics (CFD) approach to investigate this hypothesis.

METHODS

Contrast-enhanced computed tomography (CT) and echocardiographic (ECHO) images of patients pre- and post-device implantation with DRT and without (control group) were obtained from Mayo Clinic under an IRB approved protocol. The datasets included full cardiac cycles and ECHO data of the mitral valve (MV) and pulmonary veins (PVs). The CT images were imported into Mimics Research 23.0 (Materialise, Belgium) and segmented to generate patient specific 3D digital models. Finite element analysis performed by FEops (Gent, Belgium) was used to deploy the WATCHMAN™ in the patient digital

models. The digitally implanted devices were deformed and positioned in the LAA to replicate the clinical deployment for each patient. The digital models were imported into Ansys Workbench 2020 R1 (Canonsburg, PA), where extensions equivalent to 10 times the diameter the MV and each PV were applied in order to overcome entrance effects and to have an appropriate velocity profile. The LA models were then meshed with a polyhedral mesh after mesh independent results were performed and an element size of 0.8mm was selected.

Computational fluid dynamic simulations were performed on the patient-specific models (pre- and post- device implantation) using Ansys Fluent (Canonsburg, PA). The simulations were transient, used a laminar flow model (Reynolds number < 2000), with blood properties being a density of 1060kg/m³ and a viscosity of 0.0035Pa.s. The boundary conditions (BC) for the PVs were set to pressure inlets with 0Pa total pressure. No slip BCs were imposed on the LA surface and WATCHMAN™ device. A velocity inlet BC was used for the MV, with the velocity magnitude following the patient specific MV profile from ECHO. In addition, the velocity direction was normal to the MV (0, 0, -1). The time averaged wall shear stress (TAWSS; **EQ1**), oscillatory shear index (OSI; **EQ2**), and endothelial cell activation potential (ECAP; **EQ3**) were calculated for the top surface of each WATCHMAN™ device.

$$TAWSS = \frac{1}{T} \int_0^T |\overline{WSS}| dt \quad (\text{EQ1})$$

$$OSI = 0.5 \left(1 - \frac{\left| \int_0^T \overline{WSS} dt \right|}{\int_0^T \overline{WSS} dt} \right) \quad (\text{EQ2})$$

$$ECAP = \frac{OSI}{TAWSS} \quad (\text{EQ3})$$

The patient-specific heart rates (taken from the ECHO reports) were used as the period for TAWSS and OSI calculations. An example schematic of the workflow used to generate the digital models and run CFD simulations in this study is shown in **Figure 1**.

RESULTS

TAWSS on the top surface the WATCHMAN™ device for each patient is shown in **Figure 2**. Elevated TAWSS values were observed in the control patients compared to the respective DRT patients.

ECAP quantifies the response of endothelial cells which can be used to determine regions where thrombus formation is more likely to occur. ECAP on the top surface of the WATCHMAN™ device is shown in **Figure 3**. More elevated ECAP was found with DRT patients compared with the control patients in the top region of the device.

DISCUSSION

Herein, various hemodynamic parameters were investigated using CFD in order to better predict the development of DRT in patients who have received a WATCHMAN device. This was accomplished using a combined FEA (for device deployment) and CFD approach. The DRT patients had higher ECAP and lower TAWSS on the surface of the device compared to the respective control patients.

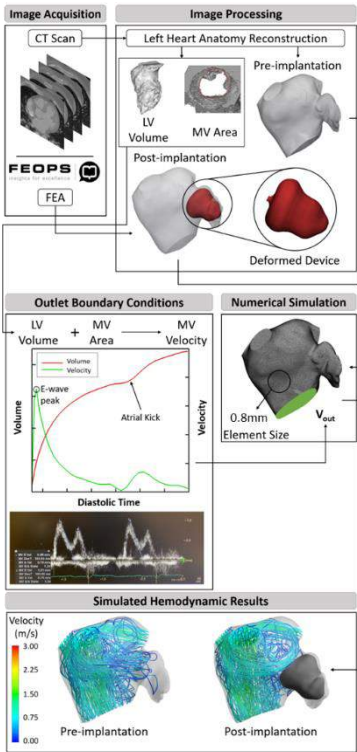


Figure 1. Combined FEA and CFD workflow.

It has been reported that non-physiological levels of WSS are associated with an increased risk of thrombus formation². In this study, we observed lower TAWSS on the top surface of the WATCHMAN™ device in DRT patients compared with the respective control patients.

Understanding ECAP is of particular importance due to the endothelialization — the formation of endothelial cells — that occurs after the deployment of the WATCHMAN™ device. Flow abnormalities/disturbances and stasis have been reported for patients with AF³. These disturbances can result in endothelial cell dysfunction which is associated with adverse cardiovascular outcomes like thrombogenesis⁴. Achille et al.⁵ proposes ECAP as a measurement for thrombogenic susceptibility for endothelial cells by taking the ratio of TAWSS and OSI. A high ECAP value indicates a high OSI and a low TAWSS, both of which have been shown to be related to increased likelihood of thrombus formation. Endothelial cells naturally provide an antithrombotic surface⁶, but when activated, this property is negated which can result in thrombus formation⁷. This activation can occur due to blood stagnation. Regions of high oscillatory flow can induce an inflammatory response⁸. This response may also promote thrombus formation.

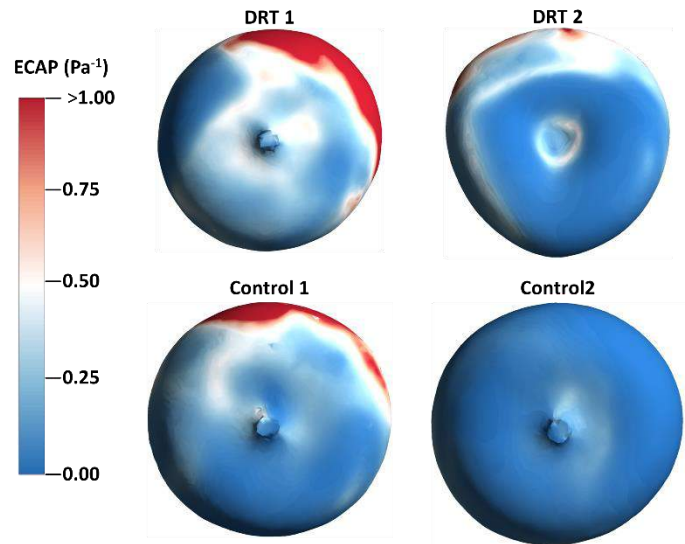


Figure 1. ECAP on the top surface of the WATCHMAN™ device.

In this study, we have demonstrated the feasibility of a combined FEA and CFD approach for the assessment of DRT in the LAA after LAAO. Thus far, we have observed a higher ECAP and lower TAWSS values in the DRT patients. The addition of more patients is needed to better understand and predict DRT after LAAO.

ACKNOWLEDGEMENTS

We would like to acknowledge the DeVlieg Foundation, the Blue Cross Blue Shield of Michigan Foundation, and the Health Research Institute at Michigan Technological University.

REFERENCES

[1] Lempereur M, *Cath. and Cardiovasc. Interv.* 2017;90(5):E111-E121
[2] Nesbitt WS, *Nature Medicine.* 2009;15(6):665-673
[3] Lip G, *Lancet*, 1995; 346(8986):1313-1314
[4] Khan A, *Annals of Medicine*, 2020; 52(1-2):1-11
[5] Achille P, *Proc. Math. Phys. Eng.*, 2014; 470(2172):20140163
[6] Wood J, *ATVB*, 2014; 34(1):169-176
[7] Mackman N, *J. Clin. Investig.* 2012; 122(7): 2331-2336
[8] Hathcock J, *ATVB*, 2006; 26(8):1729-1737

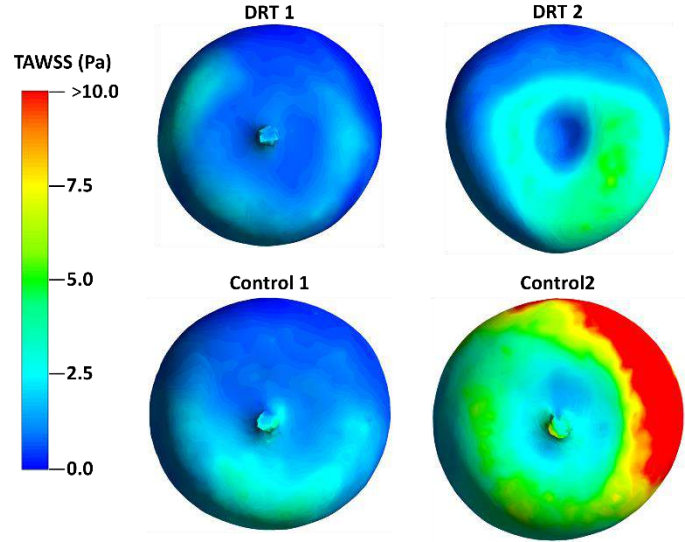


Figure 2. TAWSS on the top surface of the WATCHMAN™ device.

TYPE V COLLAGEN PLAYS AN ESSENTIAL ROLE IN THE DEVELOPMENT OF KNEE ARTICULAR CARTILAGE AND MENISCUS

B. Kwok (1), M. Fan (1), P. Singh (1), D. Birk (2)
R. L. Mauck (3), N. A. Dyment (3), E. Koyama (4), L. Han (1)

(1) School of Biomedical Engineering,
Science and Health Systems
Drexel University
Philadelphia, PA, United States

(3) McKay Orthopaedic Research Laboratory
University of Pennsylvania
Philadelphia, PA, United States

(2) Department of Molecular Pharmacology
and Physiology
University of South Florida
Tampa, FL, United States

(4) Department of Surgery
The Children's Hospital of Philadelphia
Philadelphia, PA, United States

INTRODUCTION

The extracellular matrix (ECM) of articular cartilage is characterized by a porous network of type II collagen fibrils that entrap aggrecan aggregates [1]. The meniscus, the loading counterpart of cartilage, is a fibrocartilage mainly consisting of collagen I fibers, with minor collagen II content [2]. Collagens V and XI are regulatory collagens that serve as the nucleation cores for initiating fibrillogenesis of collagens I and II, respectively [3,4]. To date, little is known about how these two regulatory collagens work in concert to regulate initial development and growth of the knee joint that encompasses both hyaline and fibrocartilage. Such knowledge could provide a crucial benchmark for designing novel regenerative strategies to repair and restore the function of degenerative joints [5]. This study aims to elucidate the role of collagen V by assessing the development phenotype of cartilage and meniscus resulting from targeted knockout of *Col5a1* gene in the knee joint.

METHODS

Immunofluorescence (IF) was applied to C57BL/6J murine knees to assess the protein distributions of collagens V (ab7046, Abcam) and XI (Ms #309–322, Zymed) for wild-type (WT) mice at embryonic (E17.5), newborn (P0) and adult (P90) ages, following established protocols [6]. To confirm that the gene expressions complement the protein expressions, *RNA-scope* was applied to assess the spatial gene expressions of collagens V (521291, ACD bio) and XI (439241, ACD bio) for WT mice at P0, following established protocols [7]. *Conditional Col5a1 knockout mice* (*Col5a1^{fl/fl}/Gdf5Cre*, or *Col5a1^{cko}*) were established by crossing *Col5a1^{fl/fl}* mice [8] with joint-specific *Gdf5Cre* mice [9]. Knee joints were harvested from newborn (P0), as well as 3 and 8 months of age (P90 and P240) *Col5a1^{cko}* and control *Col5a1^{fl/fl}* mice. We applied *histology* and μ CT imaging to assess cartilage and meniscus morphology, cell morphology, sGAG staining, and

subchondral bone structure, as well as *AFM-nanoindentation* to quantify the indentation modulus, E_{ind} , of the loading regions of articular cartilage and meniscus via a microspherical tip ($R \approx 5 \mu\text{m}$, $k \approx 8.9 \text{ N/m}$) [10]. Mann-Whitney U tests were applied to detect differences in E_{ind} between genotypes at $\alpha = 0.05$.

RESULTS

In WT mice, at both E17.5 and P0, as expected, we detected strong staining for collagen XI in epiphyseal cartilage (Fig. 1a, EC) and collagen V in meniscus (Fig. 1a, M). Surprisingly, articular cartilage showed higher staining for collagen V than for collagen XI (Fig. 1a). This finding was also validated by gene expression at P0 using *RNA-scope* (Fig. 1b), with *Col5a1* enrichment in the articular vs. epiphyseal cartilage and vice versa for *Col11a1*. In adult joints, staining of both collagens V and XI were low, with collagen V mainly localized to the pericellular domain of superficial layer cells (Fig. 1a).

Corroborating the presence of collagen V in developing articular cartilage and meniscus, we found profound developmental defects in newborn (P0), young adult (P90) and middle-aged (P240) *Col5a1^{cko}* mice. In *Col5a1^{cko}* mice, we confirmed the deletion of collagen V by the absence of IF staining at P0 (Fig. 2a). Also, even at the newborn age, loss of collagen V already resulted in disrupted joint formation, as marked by the formation of smaller menisci and wider cartilage plateaus (Fig. 2a). At young adult (P90) age, loss of collagen V resulted in much smaller menisci (Fig. 2b). For articular cartilage, although we did not detect changes in tissue thickness or sGAG staining, chondrocytes appeared to undergo aberrant clustering in *Col5a1^{cko}* group (Fig. 2b). Notably, both articular cartilage and meniscus of *Col5a1^{cko}* mice had significantly reduced modulus relative to the control (Fig. 3a), indicating impaired matrix integrity and mechanical functions with the loss of collagen V (Fig. 2b). Furthermore, μ CT analysis showed aberrant calcification in joints, with a loss of expected ossification at the

horns of lateral meniscus in P90 *Col5a1^{cko}* joints, and excessive osteophyte formation in P240 joints, which is a sign of severe osteoarthritis (OA) [11] (Fig. 3b).

DISCUSSION

This study highlights a crucial role for collagen V in the development and maintenance of articular cartilage. For years, the consensus has been that the fibrillar collagen network of hyaline cartilage consists of collagen types II, IX and XI [12], with collagen XI being highly expressed at embryonic and neo-natal stages [13]. While the high expression of collagen XI is confirmed in developing epiphyseal cartilage, we show here, for the first time, that developing articular cartilage is rich in collagen V, but not in collagen XI (Fig. 1) [13,14]. The importance of collagen V in cartilage integrity is further highlighted by the altered cartilage shape in newborn *Col5a1^{cko}* mice (Fig. 2a), and aberrant cell clustering and reduced tissue modulus in adult mice (Fig. 2b). Recent studies have suggested that collagen V may regulate stem cell quiescence in muscle through the Notch-Col V-CALCR axis [15]; it is thus possible that collagen V may play a similar role in regulating progenitor cell fate in developing articular cartilage. Collagen V is present at low concentrations in young adult cartilage, and according to our recent study, induced knockout of *Col5a1* during post-natal growth led to no clear phenotype in articular cartilage [6]. Therefore, the role of collagen V in regulating articular cartilage integrity is most likely limited to early embryonic and neo-natal stages, and the observed phenotype in *Col5a1^{cko}* mice is due to cell and/or tissue defects resulting from the lack of collagen V in early development.

The reduced size, modulus and absence of horn ossification in *Col5a1^{cko}* menisci (Figs. 2, 3) also suggest a crucial role of collagen V in the developing meniscus. The reduction of meniscus size cannot be explained by the canonical role of collagen V in regulating collagen I fibril assembly [16]. In early development, articular cartilage and meniscus are both initiated from *Gdf5*-expressing progenitors in the interzone [17]. Given the high expression of collagen V in this region, it is possible that collagen V regulates the activities of progenitors that give rise to multiple joint tissues, including the meniscus. In fact, the osteophytes in P240 *Col5a1^{cko}* knees (Fig. 3) support the importance of collagen V in the initial growth and development of the knee structures, which are critical to overall joint health in adulthood. Meanwhile, lack of collagen XI in this region suggests that collagen V may be more crucial than collagen XI in the initial development of articular cartilage, while collagen XI could be essential for the development of epiphyseal cartilage and secondary ossification. Building on these results, our ongoing studies aim to elucidate the mechanisms by which collagen V regulates cartilage and meniscus integrity, and delineate the roles of collagen V versus XI in initial joint development.

ACKNOWLEDGEMENTS

This work was supported by NSF CMMI-2047073, NIH R01 AR075418 and UPenn PCMD NIH P30 AR069619.

REFERENCES

- [1] Han, L et al., *Annu. Rev. Mater. Sci.* 41:133-168, 2011.
- [2] Vanderploeg, EJ et al., *J. Anat.* 221:174-186, 2012.
- [3] Wenstrup, RJ et al., *J. Biol. Chem.* 279:53331-53337, 2004.
- [4] Wu, JJ et al., *J. Biol. Chem.* 270:18865-18870, 1995.
- [5] Wang, C et al. In *Musculoskel. Tissue Eng.* pp 133-166, 2022.
- [6] Chandrasekaran, P et al., *Matrix Biol.* 102:1-19, 2021.
- [7] Koyama, E et al., *J. Bone Miner. Res.* 36:1387-1402, 2021.

- [8] Sun, M et al., *J. Cell. Sci.* 124:4096-4105, 2011.
- [9] Rountree, RB et al., *PLoS Biol.* 2:e355, 2004.
- [10] Wang, C et al., *Matrix Biol.* 85-86:47-67, 2020.
- [11] Felson, DT et al., *Rheumatology (Oxford)* 44:100-104, 2005.
- [12] Eyre, D, *Arthritis Res. Ther.* 4:30, 2001.
- [13] Mendler, M et al., *J. Cell Biol.* 108:191-197, 1989.
- [14] Petit, B et al., *Histochemistry* 100:231-239, 1993.
- [15] Baghdadi, MB et al., *Nature* 557:714-718, 2018.
- [16] Birk, DE, *Micron* 32:223-237, 2001.
- [17] Schwartz, Y et al., *Cell Rep.* 15:2577-2587, 2016.

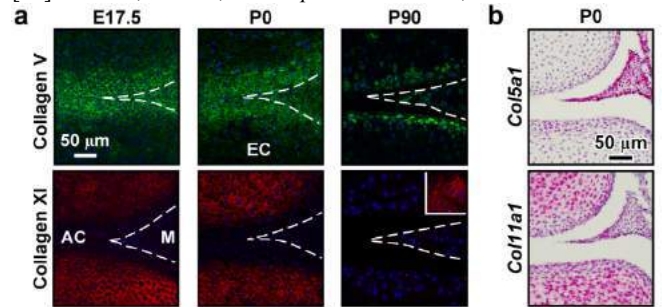


Fig. 1 a) Immunofluorescence (IF) images of collagens V and XI in WT mice at E17.5, P0 and P90 (Inset: positive control for high collagen XI content in growth plate cartilage). b) RNA-scope in situ hybridization depicting *Col5a1* and *Col11a1* expressions at P0. (AC: articular cartilage, EC: epiphyseal cartilage, M: meniscus).

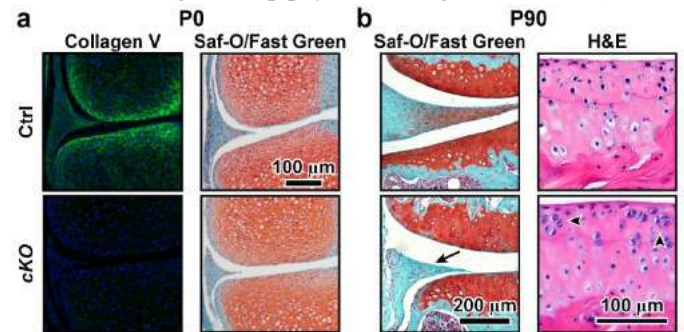


Fig. 2 a) Representative collagen V IF and Saf-O/Fast green histology images show the absence of collagen V and reduced meniscus size in *Col5a1^{cko}* (*cKO*) mice relative to control at P0. b) Representative Saf-O/Fast green and H&E histology images show reduced size and proteoglycan content in meniscus (black arrow) and aberrant chondrocyte clustering (black arrowheads) in *cKO* mice at P90.

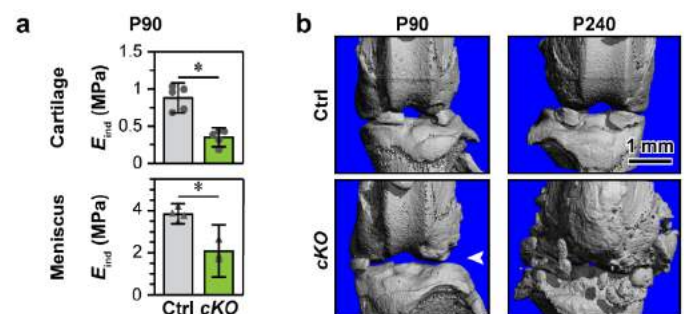


Fig. 3 a) Nanoindentation modulus of cartilage and meniscus at P90 (mean \pm 95% CI, $n \geq 3$, *: $p < 0.05$ via Mann-Whitney test). b) Reconstructed 3D μ CT of knee joints from *cKO* and control mice at P90 and P240 (white arrowhead: absence of meniscus horn ossification at P90, repeated for $n \geq 3$ mice).

IMPACTS OF TYPE V COLLAGEN INSUFFICIENCY ON CUTANEOUS WOUND HEALING AND SCAR FORMATION

Y. Liu (1), C. Wang (1), D. C. Stewart (2), E. M. O'Brien (1), B. K. Brisson (2),
D. E. Birk (3), K. L. Spiller (1), S. W. Volk (2), L. Han (1)

(1) School of Biomedical Engineering, Science and Health Systems, Drexel University,
Philadelphia, Pennsylvania, United States

(2) School of Veterinary Medicine, University of Pennsylvania, Philadelphia, Pennsylvania, United States

(3) Department of Molecular Pharmacology & Physiology,
University of South Florida, Tampa, Florida, United States

INTRODUCTION

Pathological wounds are a prevalent healthcare problem, affecting more than 40 million Americans [1]. Imbalanced healing often results in fibrotic scar formation, marked by excessive deposition and aberrant assembly of type I collagen fibers. Type V collagen, a minor fibril collagen, initiates the initial fibrillogenesis of collagen I [2], and thus, could be an important player in wound healing [3]. For patients with classic Ehlers-Danlos syndrome (cEDS), a genetic disorder caused by mutation of human *COL5A1* gene, one major symptom is the formation of atrophic scars [4]. Understanding the role of collagen V in wound healing will provide new insights for improved cEDS patient care and new targets for regeneration therapies. This study aims to determine the impact of collagen V insufficiency on the wound healing and scar formation in vivo using collagen V heterozygous mice, *Col5a1*^{+/-}, an established animal model of cEDS [5].

METHODS

Two 6-mm diameter circular full-thickness dermal punch wounds were created on the lower dorsal skin of *Col5a1*^{+/-} and wild-type mice at 7 weeks of age [6]. Both wound tissue and surrounding intact skin tissue were harvested on post-wound day (PWD) 14 and 21 [7]. We applied Picrosirius Red staining to assess scar size and collagen I fiber structure, and immunofluorescence (IF) imaging to assess the distributions of collagen V (1:200, Ab7046) and α -smooth muscle actin (α -SMA, 1:1000, Ab5694), a biomarker of myofibroblast activation [8]. Freshly dissected skin tissue was cryotomed into 20- μ m

thick cross-sections in OCT for scanning electron microscope (SEM) imaging and atomic force microscope (AFM) analyses. For SEM, cryo-sections were treated with trypsin and hyaluronidase and imaged at 10k \times magnification. AFM nanoindentation was applied to quantify the micromodulus, *E*_{ind}, using a microspherical tip (*R* \approx 5 μ m, *k* \approx 0.03 N/m) and a BrukerNano AFM in 1 \times PBS, following established procedures [9]. We separated the moduli of intact epidermis, dermis, wound edge (WE), as well as granulation tissue (GT) at PWD14, and scar tissue at PWD21 (Fig. 3a). Two-way ANOVA followed by Tukey-Kramer post-hoc test was applied to detect differences with region and genotype at the significance level of $\alpha = 0.05$.

RESULTS

The reduction of collagen V in *Col5a1*^{+/-} murine skin was validated by the decreased staining of collagen V (shown for granulation tissue, Fig. 1a). With the reduction of collagen V, we observed an appreciable increase in the size of scar tissue (Fig. 1b, dashed line), which was in alignment with aggravated activation of myofibroblast, as illustrated by α -SMA staining (Fig. 1c). Also, at the nanoscale, for both genotypes, the scar tissue showed more aligned, densely packed collagen fibers relative to the intact dermis, illustrating aberrant assembly of collagen fibrils (Fig. 2, arrowheads). Comparing to the WT control, both the intact dermis and scar tissue of the *Col5a1*^{+/-} skin exhibited thicker collagen fibrils, indicating aggravated scar formation with the loss of collagen V. Furthermore, *Col5a1*^{+/-} group also showed lower micromodulus relative to WT control throughout intact, granulation (PWD14) and scar tissues

(PWD21) (Fig. 3), supporting impaired biomechanical functions with the loss of collagen V.

DISCUSSION

This study highlighted the crucial role of collagen V in regulating the healing process and scar formation in dermal wounds. Here, we validated that collagen V insufficiency leads to widened scar and abnormal collagen density indicated by picrosirius red (Fig. 1b). Furthermore, SEM imaging confirms the difference between collagen fibril thickness of WT and *Col5a1*^{+/-} groups (Fig. 2). These thickened collagen fibrils within the *Col5a1*^{+/-} group might be an indication of excessive fibrosis which is a classic symptom of cEDS [4]. In addition, IF staining of α -SMA suggests that PWD21 *Col5a1*^{+/-} scar tissue retains aggravated activation of myofibroblast when compare with WT group (Fig. 1c). This indicates collagen V could play important role in mediating fibroblast migration and activation during cutaneous wound healing.

It has been well established that symptoms of cEDS include hyperflexible skin, easy bruising, retardation in wound healing, and widened scar [10]. However, the degree of pathological changes in tissue biomechanics of reconstructed tissue is affected by the insufficiency of collagen V is not well understood. Here, we show for the first time, that across all regions of skin, whether intact or regenerated tissue, collagen V insufficiency leads to significantly softer tissue stiffness when compared with tissue with normal collagen V quantity (Fig. 3b). Building on these results, our ongoing studies aim to investigate the fiber alignment and density of granulation and scar as well as healthy tissue, as well as the cell proliferation and general MMP activity during the remodeling of wound tissue.

ACKNOWLEDGEMENTS

This work is supported by NSF CAREER CMMI-1751898.

REFERENCES

- [1] Birk, DE et al., *J. Cell Sci.* 95: 649-657, 1990.
- [2] Wenstrup, RJ et al., *J. Biol. Chem.* 279:53331-53337, 2004.
- [3] DeNigris, J et al., *Connect Tissue Res.* 57:1-9, 2016.
- [4] Mak, KM et al., *Anat Rec.* 299:613-29, 2016.
- [5] Wenstrup, RJ et al., *J. Biol. Chem.* 281: 12888-12895, 2006.

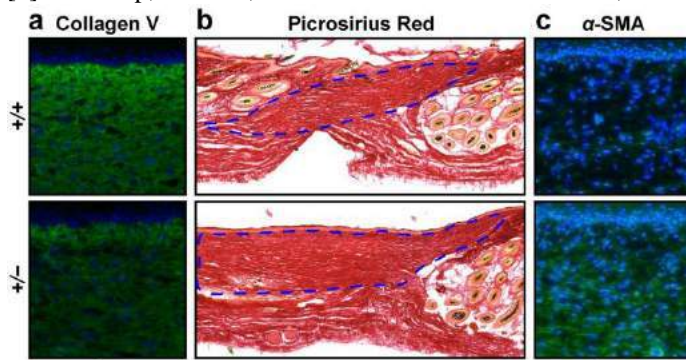


Fig. 1 a) Representative Collagen V IF, b) Picrosirius Red histology and c) α -smooth muscle actin (α -SMA) IF images of dermal scar tissue for WT (+/+) and *Col5a1*^{+/-} (+/-) mice at post-wound day (PWD) 21. Scale bar: 100 μ m.

- [6] Müller-Röver, S et al., *J. Invest Dermatol.* 117:3-15, 2001.
- [7] Volk, SW et al., *Cells Tissues Organs.* 194:25-37, 2011.
- [8] Nagamoto, T et al., *IOVS.* 41:1122-9, 2000.
- [9] Han, B et al., *ACS Biomater. Sci. Eng.* 9:2033-2049, 2017.
- [10] Malfait, F et al., *Genet Med.* 12:597-605, 2010.

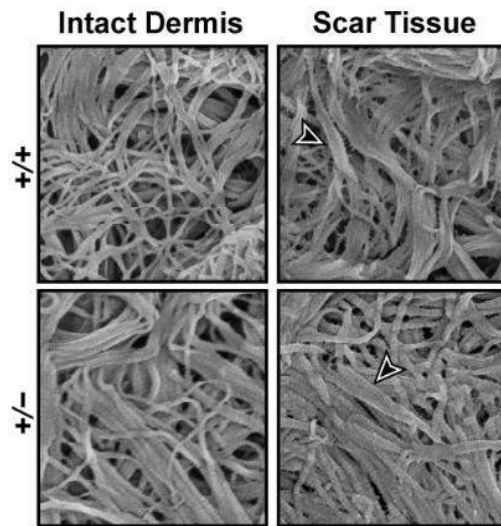


Fig. 2 Representative SEM images of intact dermis and scar tissue for WT (+/+) and *Col5a1*^{+/-} (+/-) mice at post-wound day (PWD) 21. Scale bar: 500 nm.

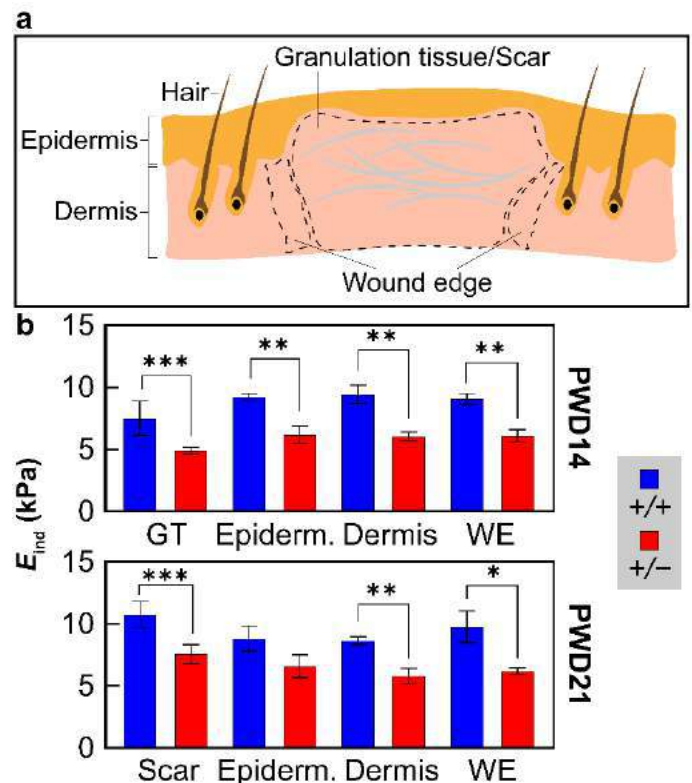


Fig. 3 a) Regions of interest for AFM-nanoindentation, b) Comparison of E_{ind} between of WT (+/+) and *Col5a1*^{+/-} (+/-) mice at post-wounding day (PWD) 14 and 21 (mean \pm SD, $n = 3$, GT: granulation tissue, WE: wound edge, *: $p < 0.05$, **: $p < 0.01$, ***: $p < 0.001$).

EVOLUTION OF THE HEMODYNAMIC PROPERTIES AND ARTERIAL WALL REMODELING IN PULMONARY ARTERIAL HYPERTENSION

H. Mu (1), D. Valdez-Jasso (1)

(1) Department of Bioengineering
University of California San Diego
La Jolla, CA, United States

INTRODUCTION

Pulmonary arterial hypertension (PAH) is characterized by sustained elevation of mean pulmonary arterial pressure and vascular remodeling. Recent studies have shown that changes in vascular compliance, characteristic specific attributed to the large pulmonary arteries, plays an important role in PAH. [1,2,3] Our studies on pressure and flow data analyzed using a three element Windkessel model have shown that female and male rats have different patterns of hemodynamic changes, with a significant decrease in vascular compliance for both sexes, but total resistance decreases to be specific to male rats [4]. This difference in the hemodynamic implies different types of vascular remodeling between female and male rats. To better understand wave propagation along the large vessels and impact of vascular remodeling, we investigated these hemodynamic measurements using a one-dimensional fluid model.

METHODS

Male Sprague-Dawley rats (Charles River Lab) were injected with sugen 5416 (SuHx) and kept in 10% O₂ hypoxia chamber for three weeks to induce PAH. Taking the injection day as week 0, SuHx rats of week 6 was selected for analysis. Control rats received no injection and were kept in normoxia. Rats underwent a thoracotomy to expose the heart and great vessel and simultaneously measure pulmonary arterial pressure and flow with a dual-pressure catheter and a flow probe (Transonic Science), respectively (Figure 1). The data were collected in LabChart Software (ADInstruments Inc.) and processed in a custom-built Matlab code. After obtaining the hemodynamic measurements, the lungs were harvested, and the left and right pulmonary arteries *ex-vivo* radius and length were measured using ImageJ. Biaxial tests were carried out using the BioDynamic chamber (ElectroForce Systems Group) as previously described [5]. Briefly, segments of the pulmonary arteries are cannulated, perfused, and in inflated using pulsatile flow, temperature-controlled PBS. Measured pressure, arterial diameter, and

axial tension were used to compute circumferential strain and stress, and modeled using the quasi-linear viscoelastic model to obtain the elastic modulus E .

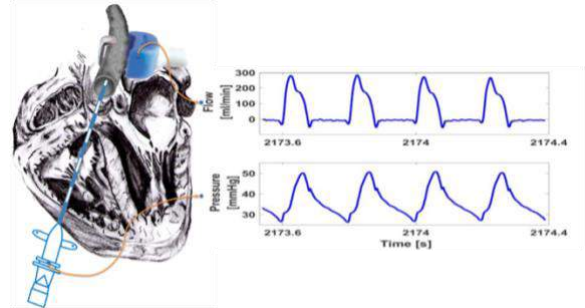


Figure 1. *In-vivo* pressure and flow data measured at the inlet of main pulmonary artery.

Our model spans the main, left, and right pulmonary arteries (M, L, and RPA) with assumptions of incompressible, Newtonian blood and axisymmetric, inviscid, laminar flow. Blood flow is formulated with the conservation of mass (Equation 1) and momentum (Equation 2), and a linear thin-wall state equation (Equation 3). [6]

$$\frac{\partial A(x,t)}{\partial t} + \frac{\partial Q(x,t)}{\partial x} = 0 \quad (1)$$

$$\frac{\partial Q(x,t)}{\partial t} + \frac{\partial}{\partial x} \left(\frac{Q^2(x,t)}{A(x,t)} \right) + \frac{A(x,t)}{\rho} \frac{\partial P(x,t)}{\partial x} = - \frac{2\pi\nu r(x,t)Q(x,t)}{\delta A(x,t)} \quad (2)$$

$$P = P_0 - \frac{4Eh}{3r_0} \left(1 - \sqrt{\frac{A_0}{A}} \right) \quad (3)$$

Here A is the vessel's cross-sectional area, Q is the volumetric flow, P blood pressure, r is the artery radius, t is time, x is the longitudinal distance with inlet as $x = 0$, ρ is blood density, ν is kinematic viscosity, δ is the boundary layer thickness, P_0 is the end-diastolic pressure, E is the circumferential elastic modulus obtained from the mechanical tests,

h is the artery wall thickness, r_0 and $A_0 = \pi r_0^2$ are the end-diastolic radius and cross-sectional area.

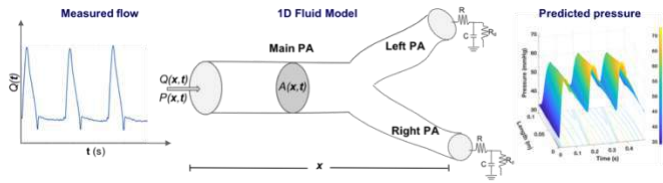


Figure 2. One-dimensional model of the large, proximal pulmonary arteries is initiated with *in-vivo* flow to predict pressure waveforms.

The model is initialized using *in-vivo* flow measured at the inlet of the pulmonary vasculature. At the bifurcation, flow and pressure conservations are enforced. For the outlet boundary conditions of LPA and RPA, three-element Windkessel models are applied to quantify the effect of downstream vessels (Figure 2), in which the Windkessel parameters are previously calculated from the pressure-flow data measured at the inlet. [7]

Windkessel parameters and MPA elastic modulus are then optimized to best fit the measured hemodynamics. The minimization algorithm uses the sum of squares error between the simulated and measured pressure at MPA inlet as the objective function, where extra weight is added to the end-diastole pressure. After obtaining the baseline simulation for the control and PAH rats, the simulation parameters of the control rat are substituted with SuHx value to explore the effect of different PA remodelings on hemodynamics.

RESULTS

The simulated pressure resembles the *in-vivo* pressure measurement (Figure 3A). The baseline simulation parameters differ greatly between the control and SuHx groups (Figure 3B), with the elastic modulus of the MPA increased the most by about 17 folds. When the elastic moduli (stiffness) of the large pulmonary arteries in the control are substituted with the SuHx values, the simulated pressure greatly increases systolic pressure and the rate of change of pressure, while the diastolic pressure remains the same. In contrast, replacing the Windkessel parameters of the control simulation increases the diastolic pressure slightly with the unchanged systolic pressure. (Figure 3C)

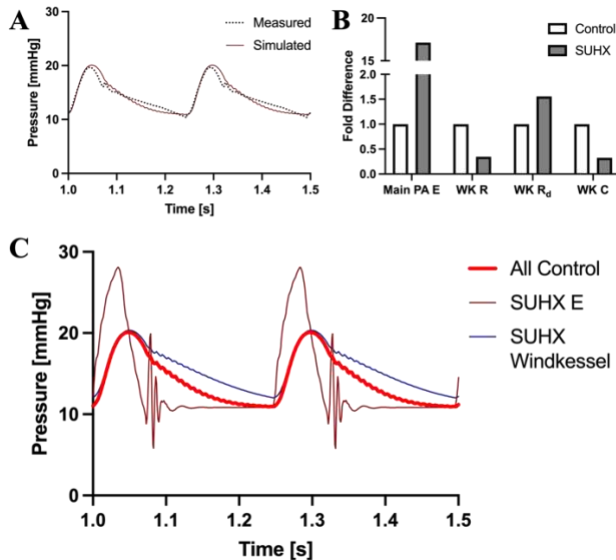


Figure 3: Simulated pressure waveforms at the inlet of MPA and the baseline simulation parameters in control and SuHx rats. (A)

Comparison of measured and simulated pressure. (B) Comparison of optimized baseline simulation parameters, where E is the circumferential elastic modulus, WK R and R_d are Windkessel proximal and distal resistances, and WK C is the Windkessel Compliance. (C) Comparison of control simulation, control rat with SuHx large artery stiffness (SuHx E), and control rat with SuHx downstream vessels (SuHx Windkessel).

DISCUSSION

Our one-dimensional model can predict the pulmonary arterial pressure waveforms. By substituting the simulation parameters based on the control simulation, the effect of different remodeling on the hemodynamics can be distinguished. The stiffening of the proximal pulmonary arteries produces a much greater change in the simulated pressure waveform than remodeling of the distal vasculature. When there is only the stiffening of the proximal pulmonary arteries, there is a much greater pulse pressure in the simulated pressure waveform which increases the afterload experienced by the right ventricle. In addition, the shortened and heightened pressure peak could direct more pulsatile flow to the distal pulmonary vasculature and cause damage. [3,8] The great hemodynamic change suggests the importance of proximal pulmonary stiffening in PAH. When there is only the remodeling of the distal pulmonary vasculature, the elevated diastolic pressure may indicate blood retention in the pulmonary arteries and slightly elevated right ventricle afterload.

When comparing the hemodynamics from control, normotensive animals to those of the SuHx rats, we find the MPA stiffness E and Windkessel resistance R_d to increase, while the compliance decrease. This finding generally aligns with other modeling studies [1,6].

The limitation of this study includes the single SuHx group simulated. In the future, more SuHx groups will be added to show a time-course of pulmonary artery remodeling and how the hemodynamics is affected at different stages.

In conclusion, our modeling approach identifies the hemodynamics changes due to different aspect of vascular remodeling. With more SuHx groups to analyze in the future, we can see how the pulmonary arteries adapt to the raising pressure in different stage of PAH, and thus better understand the physiopathology of PAH.

ACKNOWLEDGEMENTS

This work was funded by AHA grant 16SDG29670010, NIH grants 1R01 HL155945-01, 1R25HL145817-01 and NSF CAREER Award 2046259. The authors would also like to acknowledge discussions with Yasser Aboelkassam and Dr. Joakim Sundnes.

REFERENCES

- [1] Zambrano BA, et al. *J Biomech*, 2018.
- [2] Lai, YC et al. *Circ Res*, 1:115, 2014.
- [3] Thenappan, T et al. *Ann Am Thorac Soc*, 13 :2, 2016.
- [4] Giri, S. *UC San Diego*, 2022.
- [5] Pursell, ER et al. *J Biomech Eng*, 11:138, 2016.
- [6] Olufsen, MS. *IMFUF*, 345:98, 1998.
- [7] Gerringer, JW et al. *Physiol Rep*, 3:6, 2018.
- [8] Li, Min et al. *Ann Biomed Eng*, 37:6, 2009.

A 1D MODEL CHARACTERIZING THE ROLE OF SPATIOTEMPORAL CONTRACTION DISTRIBUTIONS ON LYMPH TRANSPORT

Farbod Sedaghati (1), J. Brandon Dixon, PhD (1,2), and Rudolph L. Gleason, Jr., PhD (1,2)

- (1) The George W. Woodruff School of Mechanical Engineering, Georgia Institute of Technology, Atlanta, GA, USA.
(2) The Wallace H. Coulter Department of Biomedical Engineering, Georgia Institute of Technology, Atlanta, GA, USA.

INTRODUCTION

The lymphatic system transports the interstitial lymph fluid from tissues back to the venous system (usually) against an adverse pressure gradient. To achieve this goal, secondary lymphatics contract autonomously to drive the lymph through one-way valves. This autonomous contractile behavior is governed by numerous factors and computational models have proven useful in characterizing the contractile behavior and lymph transport. It is becoming increasingly clear that the timing of contractions may be governed by pacemaking cells within the lymphatics but much is unknown regarding the orchestration of contractions across multiple lymphangions. Lumped-parameter models are the most commonly used approach to study the lymphatic mechanics and simulate lymph transport. The drawbacks of such models are that the pacemakers cannot specifically be located, the contraction propagation speed is not applied, and the pressure/flow waves along the lymphangions are missing. Therefore, this study aims to construct a 1-D mathematical model that is based on fluid-solid governing equations and utilizes a general activation function which is created based on pacemaking parameters and drives the lymph transport in the healthy and Connexin-45 knock-out (KO) mice.

METHODS

We modeled a lymphatic vessel consisting of three lymphangions and four secondary valves (Figure 1). The inlet and outlet pressures were set at 3.5 and 4 cmH₂O, respectively, for all illustrative simulations. Each lymphangion was modeled as a tapered, elastic tube in a one-dimensional pulsatile fluid flow framework. To determine the diameter for a given pressure and muscle activation, we employed a weighted-average of pre- and peak-twitch diameters where the weight function was a general activation function (Eq. 1). We used a sigmoidal valve behavior introduced by Bertram *et al.* [1]. A 2-D bivariate Gaussian function was used to quantify the temporal and spatial propagation of contractions (Eq. 2) (Figure 2). The normal case was

based on the wild-type (Cx45^{flx/flx}) (WT) mouse data and the abnormal case was from Smmhc-CreER^{T2}; Cx45^{flx/flx} [TMX] (2-4 weeks) (KO) mouse line (Table 1) [2]. The effect of the direction of contraction wave propagation is an ongoing challenge. To investigate the extent that direction of propagation would affect lymphatic pumping in the KO mouse, three scenarios were considered: 1) all signals were antegrade, 2) every other signal was retrograde, and 3) all signals were retrograde.

Equations

$$d(z, t) = (d_{peak} - d_{pre})t_{act} + d_{pre} \quad (1)$$

$$f(x, t) = \frac{1}{2\pi\sigma_x\sigma_t\sqrt{1-\rho^2}} e^{\left[\frac{1}{2(1-\rho^2)} \left(\frac{(x-\mu_x)^2}{\sigma_x^2} - \frac{2\rho(x-\mu_x)(t-\mu_t)}{\sigma_x\sigma_t} + \frac{(t-\mu_t)^2}{\sigma_t^2} \right) \right]} \quad (2)$$

RESULTS

The time-space mapping of contractions illustrates that the peak contraction arrives at different times within the lymphangion chain, depending on both the propagation speed and how close the vessel region is from the pacemakers (Figure 1). Ejection fraction (EF), which is the ratio of the volume of fluid dispenses at peak systole relative to the diastolic volume, was 0.78 for the WT model but only 0.20 to 0.33 in the KO models. In the WT model, all lymphangions experienced a pressure rise equivalent to the total pressure gradient of the chain and the mean pressure in all lymphangions was near the average of P_{in} and P_{out} (Table 2). However, in the KO models, only pressure in L3 oscillated between P_{in} and P_{out}, while the L1 and L2 pressures stayed near P_{in}, suggesting that the work done on the fluid was performed primarily by a single lymphangion. The flow patterns showed a sudden impulse in flow at the mid-point of each lymphangion that was concurrent to systole in the WT model followed by a dip due to relaxation and lumen expansion resulting in flow retracement and provided a net pumped lymph flow of 5.44 μL/hr (Figure 3). Similar behavior was not observed in the KO models. Although a relatively high

flow passed the last lymphangion during systole, simultaneously the first two lymphangions had opposing (zero or negative) flows. Similarly, in diastole the flow in L3 was reversed but L1 and L2 had forward flows. The net cycle-averaged lymph flow was 2.9, 2.8 and 1.17 $\mu\text{L/hr}$ in Cases 1, 2, and 3 of the KO models. It is notable that in all KO models, the peak systolic and diastolic velocities did not exceed 0.5 and -0.8 mm/s, while in the WT model they reached up to 2.4 and -3.8 mm/s.

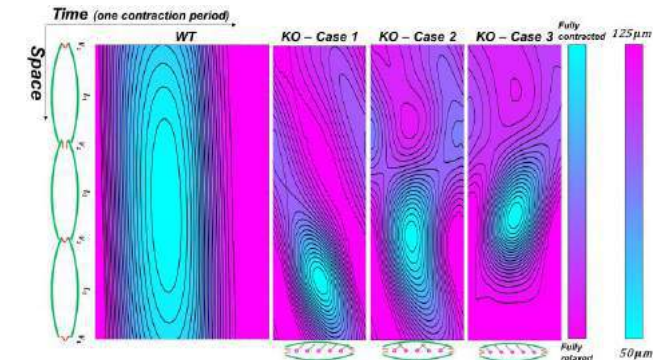


Figure 1: Time-space mapping of contractions of the lymphatic vessel during a contraction cycle.

Figure 2: The constitutive data. a) Data of the mesenteric lymphatic vessel from male Sprague-Dawley rats [3]. b) Secondary valve resistance [4].

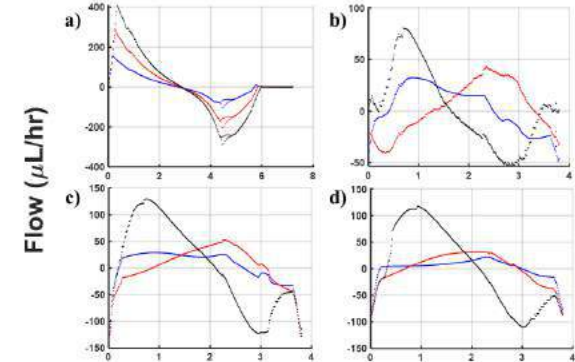


Figure 3: Lymph axial flow profiles during a contraction cycle. Results belong to the middle node of the first (Blue), second (Red), and third (Black) lymphangion.

Table 1: Contractility metrics used to prescribe the activation function.

Mouse line	Conduction Speed (cm/s)	Number of Initiation Sites (1/cm)	Contraction Frequency (1/min)	Contraction Period (sec)
WT	0.98	10	8.3	7.23

KO	0.07	31	15.8	3.80
----	------	----	------	------

Table 2: Mean pressure in each lymphangion during a contraction cycle.

Mean pressure (cmH ₂ O)			
(Average of P_{in} and P_{out} is 3.75 cmH ₂ O)			
Model	L1	L2	L3
WT	3.73	3.73	3.74
KO – Case 1	3.50	3.50	3.71
KO – Case 2	3.52	3.52	3.72
KO – Case 3	3.52	3.55	3.73

DISCUSSION

EF and fractional pump function for the WT and KO models resemble well published experimental results. Zawieja et al. showed that the mean WSS is 0.4 to 0.6 dyn/cm² with the peak of 3 to 10 dyn/cm², which are close to our model calculations [5]. If the KO model is comparable to the wounded case presented in a study, contractile frequency of the remodeled vessel is 2-3 times more than the control case, which is consistent with our results [6]. The current model could be a useful tool in studying the lymph transport in conjunction with an imaging technique. One limitation was that due to uncertainties the chemical couplings in the contractions were not included in the model. To advance the model, one may add pressure/WSS and contraction couplings that provide feedback to regulate contractions.

A 1-D mathematical model along with contractility metrics obtained from the experimental data of the WT and KO mouse lines were used to study the mechanical behavior and pumping function of a lymphatic vessel under the health and Cx45 knocked out conditions. The model proves that only by analyzing some aspects of the mechanical behavior of a lymphatic vessel, we cannot get a clear picture of the pump efficiency. For example, the model showed that a high contraction velocity and valve functioning, do not guarantee efficient lymph transport. Lastly, disparities between KO models suggest that the directionality of pacemaking signals matters and the antegrade contraction propagation seems to be more efficient in lymph transport which complies with the accepted paradigm.

ACKNOWLEDGEMENTS

We gratefully acknowledge the support from the National Institutes of Health (award number 1R01HL152152).

REFERENCES

[1] Bertram, C. D., Macaskill, C. & Moore, J. E., Jr, *J Biomech Eng* 133, 011008, 2011

[2] Castorena-Gonzalez, J. A. et al. *Circ Res* 123, 964-985, 2018.

[3] Davis, M. J., Rahbar, E., Gashev, A. A., Zawieja, D. C. & Moore, J. E., Jr., *Am J Physiol Heart Circ Physiol* 301, H48-60, 2011

[4] Bertram, C. D., Macaskill, C., Davis, M. J. & Moore, J. E., Jr. *Am J Physiol Heart Circ Physiol* 310, H847-860, 2016.

[5] Zawieja, D. C. Contractile Physiology of Lymphatics. *Lymphat Res Biol.* 7(2), 87–96, 2009.

[6] Nelson, T. S. et al. *Nat Biomed Eng* 4, 649-661, 2020.

PREDICTING HEMODYNAMIC OUTCOMES IN PATIENTS WITH BORDERLINE LEFT VENTRICLES UNDER UNCERTAINTY

Yurui Chen (1), Isao A. Anzai (2), Justin S. Tran (3), David M. Kalfa (2), Vijay Vedula (1)

(1) Mechanical Engineering, Columbia University, New York, NY
(2) Department of Surgery, Columbia University Irving Medical Center, New York, NY
(3) Mechanical Engineering, California State University Fullerton, Fullerton, CA

INTRODUCTION

Borderline left ventricle (BLV) patients are neonates born with an undeveloped left ventricle, often resulting from aortic valve stenosis, hypoplastic aortic arch, and hypoplastic left heart complex.¹ They often undergo critical decisions as neonates between a biventricular repair (BiVR) or a single ventricle palliation procedure (SVPP). Current surgical decision-making is primarily based on morphological measurements,² and incongruent pursuit of any approach will increase the risk of multiple interventions and mortality. Providing the surgeons with the ability to predict hemodynamics post-intervention and inform decision-making will transform the treatment planning for these high-risk patient groups.

Novel tools have been developed recently for predicting hemodynamics in response to surgical intervention in complex congenital heart disease applications.³ A majority of these models rely on lumped parameter networks (LPN), resembling electrical circuits to simulate blood flow, due to their computational efficiency and robustness in representing organ-level hemodynamic interactions in complex pathologies. However, closed-loop LPN models involve tens of parameters that need to be tuned to personalize the model and are driven by clinically acquired data, including catheter-based and/or echocardiographic measurements, often associated with uncertainties.

We developed a computational framework to model the hemodynamics in BLV patients undergoing virtual BiVR and SVPP.⁴ A Bayesian-based semi-automatic tuning framework is applied to personalize the preoperative LPN model for a BLV patient and propagate the uncertainties in the clinical data through the model. In this approach, we treat the unknown LPN parameters are treated as random variables and apply a Metropolis-Hastings (MH) type Markov chain Monte Carlo (MCMC) algorithm: DREAM,⁵ to sample from their joint posterior distribution. We then perform a Monte Carlo simulation on all the parameter samples to obtain a set of preoperative LPN solutions and quantify the variability in the hemodynamic outputs. The framework

then allows simulating virtual surgeries (BiVR and Norwood – 1st stage SVPP) using the post-operative LPN models and quantifying the confidence intervals on the predicted hemodynamics.

METHODS

Data Collection: We selected four patients for this IRB-approved study who clinically underwent either BiVR or SVPP (P1, P2 for SVPP, and P3, P4 for BiVR). Patients were described as having ‘moderately hypoplastic left ventricle’ on their ultrasound reports, and their mitral (-3.11 ± 1.53) and aortic valve z-scores (-2.61 ± 1.46) are below average. In this study, we do not include any cath data and base our model entirely on echocardiographic measurements. Clinical targets include pressures and flow rates derived from Doppler measurements. Atrium and ventricular chamber pressures were derived based on Doppler-based transvalvular pressure gradients, and cuff-based aortic pressure.⁶ Patient-specific vascular resistances (PVR, SVR) were extracted as the ratios of the pressure gradients across the pulmonary and systemic arteries and the corresponding atria to the respective flow rates.

Uncertainty Quantification (UQ) and Parameter Estimation: We adopted a framework (Figure 1) that allows for both UQ and automatic parameter estimation.^{7,8} We define a set of parameters: $\mathbf{y} = \{y_1, y_2, \dots, y_n\}$ statistically characterized by their joint probability $\rho(\mathbf{y})$, where y^k is defined as a generic sample based on $\rho(\mathbf{y})$. We also define a set of model outputs $\mathbf{o} = \{o_1, o_2, \dots, o_m\}$ corresponding to m clinical targets outputs $\mathbf{d} = \{d_1, d_2, \dots, d_m\}$. Considering the LPN model as a map $\mathbf{G}: \mathbb{R}^n \rightarrow \mathbb{R}^m$, which satisfies $o^k = G(y^k)$, the error between model outputs and clinical targets is defined as, $\epsilon = \mathbf{d} - \mathbf{G}(\mathbf{y})$. Given the model observations \mathbf{y} , the Bayesian formulation describes the relation between posterior density $P(\mathbf{y}|\mathbf{d})$ and the prior density $P(\mathbf{y})$ as,

$$P(\mathbf{y}|\mathbf{d}) = \frac{P(\mathbf{d}|\mathbf{y})P(\mathbf{y})}{P(\mathbf{d})} \quad (1)$$

Here, we set uniform $P(\mathbf{y})$ as priors in reasonable ranges based on previous manual tuning experience. Due to the lack of knowledge about

how clinical measurements are correlated, we adopt a weighted Gaussian distribution as the likelihood function $P(\mathbf{d}|\mathbf{y})$ given by,⁷

$$\frac{1}{\sqrt{(2\pi)^m \prod_{i=1}^m \omega_i \sigma_i^2}} \exp\left(-\frac{1}{2} \sum_{i=1}^m \frac{[d_i - G_i(\mathbf{y})]^2}{\omega_i \sigma_i^2}\right) \quad (2)$$

where d_i denotes the i^{th} clinical targets with a weighting factor ω_i and variance σ_i^2 , $G_i(\mathbf{y})$ is the i^{th} model output. Since it is difficult to calculate the marginal density of $P(\mathbf{d})$, we applied the DREAM algorithm as an alternative route to sample only from the density $P(\mathbf{d}|\mathbf{y})P(\mathbf{y})$.⁹ We set 20 chains in parallel and ran DREAM algorithm for 1000 steps, resulting in 20000 samples from the joint posterior distribution of the parameters. Upon convergence, the results depict a set of parameters characterized by the maximum posterior probability. We then applied a Monte Carlo step for each parameter set by calculating the model outputs of the last 1000 sampled candidates generated to yield the mean and standard deviations for the hemodynamic quantities of interest. Finally, we performed LPN simulations of both virtual surgeries (BiVR, SVPP) for these parameter samples to predict post-operative hemodynamics with confidence intervals.⁴ Our framework allows for automatic parameter estimation by using the parameter set corresponding to the maximum posterior following MCMC as an initial guess for the subsequent Nelder-Mead optimization. However, we focus on UQ analysis in the current work.

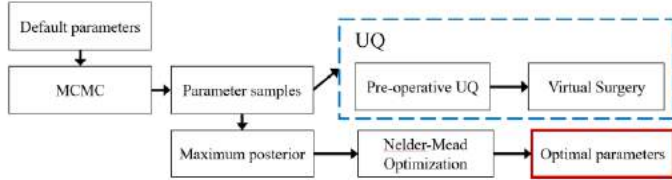


Figure 1: Workflow for uncertainty quantification and automated parameter estimation.

RESULTS

We present the computed statistics for the post-operative hemodynamic indicators in BLV patients (Figure 2). Both the virtual surgeries significantly lower pulmonary artery pressures (Figure 2a, $p < 0.01$), except for performing BiVR in patient A (38.66 ± 0.98 vs. 38.42 ± 2.94 mmHg, $p = 0.02$). BiVR resulted in a significantly higher PAP_{mean} ($p < 0.01$) than Norwood for patients P1 and P2, but PAP_{mean} for patients P3 and P4 remained in the normal PAP range. Mean aortic pressure (AOP_{mean}) generally increased after surgery in all the patients (Figure 2b) except for performing BiVR on patient P1 (AOP_{mean} decreased from 49.76 ± 1.53 to 40.66 ± 1.73 mmHg, $p < 0.01$). Our LPN-based UQ model predicts a balanced pulmonary to systemic flow ratio after BiVR compared Norwood (Figure 2c; P1: 1.04 ± 0.03 vs. 0.66 ± 0.03 ; P2: 1.00 ± 0.04 vs. 1.27 ± 0.04 ; P3: 0.93 ± 0.01 vs. 1.42 ± 0.07 ; P4: 0.96 ± 0.01 vs. 1.67 ± 0.08 ; $p < 0.01$). Significant differences were also demonstrated in oxygen deliveries (O_2D) between BiVR and Norwood procedures for patients P3 and P4 (Figure 2d; P3: 864.53 ± 51.78 vs. 542.98 ± 64.52 ; P4: 796.48 ± 45.74 vs. 429.23 ± 76.48 ; $p < 0.01$).

DISCUSSION

We developed a robust and efficient computational framework to personalize and predict post-operative hemodynamics in BLV patients by considering the uncertainty in clinical data acquisition. Our model only relies on non-invasively acquired echocardiographic data and does not employ cath, although regarded as the 'gold standard' because these patients often do not undergo cath. We have analyzed the model outputs by comparing the hemodynamic characteristics of four patients who underwent either BiVR or Norwood.

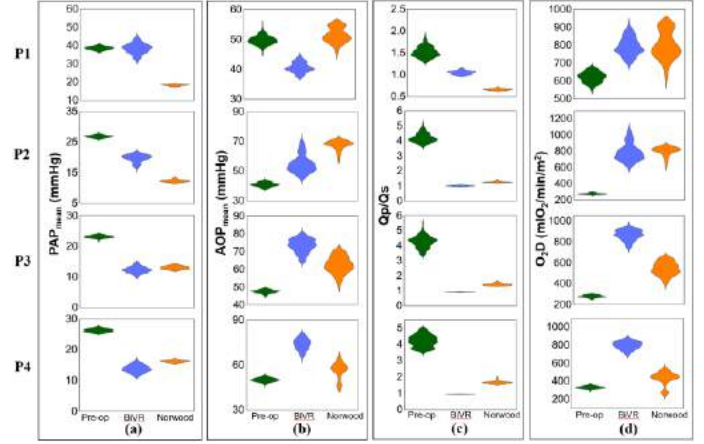


Figure 2: UQ analysis of predicted post-operative hemodynamic indicators in BLV patients. (a) Mean pulmonary artery pressure (PAP_{mean}) (b) Mean aortic pressure (AOP_{mean}) (c) Qp/Qs ratio (d) Oxygen delivery (O_2D) to the systemic circulation. Rows represent data for different patients (P1-P4).

Our results indicate that performing either virtual surgery in most cases will significantly affect the pulmonary and systemic pressures, flow rates, and oxygen deliveries. The utility of the model is demonstrated by comparing the predicted hemodynamics between the two surgical procedures. Our model predicts higher pulmonary pressures in patients P1 and P2 in response to BiVR but showed no significant differences in patients P3 and P4.

Further, our model predicts a more balanced Qp/Qs after BiVR with negligible variances but shows substantial variability after performing Norwood among the study group. These model findings suggest that SVPP is the better choice for patients P1 and P2. At the same time, the model suggests that BiVR is the optimal choice for patients P3 and P4, restoring two-ventricular circulation with an improved O_2D .

Limitations The current study has limitations we plan to overcome in the future. While the present study only considers uncertainty from model inputs, operator variability is not accounted for. We must also demonstrate the model's utility over a larger and a prospective patient group. We also aim to explore other surgical options for BLV patients, such as the staged LV recruitment following LV rehabilitation.¹¹

ACKNOWLEDGEMENTS

Y.C. would like to acknowledge a fellowship received through SEAS of Columbia University.

REFERENCES

- [1] Corno, A.F., et al., Euro. J. Card Surg., 27(1), 67-73, 2005.
- [2] Rhodes, et al., Circulation, 84(6), 1991.
- [3] Yang, W., et al., J Biomech, 199, 33-36, 2010.
- [4] Chen, Y., in preparation for JTCVS.
- [5] Vrugt, J.A., et al., Hyd. Earth Syst. Sci. 15(3701-3713), 2011.
- [6] Harris, P., et al., BJA Edu., 16(2): 46-52, 2016.
- [7] Tran, J. S., et al., Comp. and Fluids, 142, 128-138, 2017.
- [8] Schiavazzi, D.E., et al., Int. J. Num. Meth. In BioMed. Eng., e02737, 2016.
- [9] Hastings, W.K., et al., 57(1) 97-109, 1970.
- [10] Dennis, J.E., et al., New Com. Envir.: Microcomp. In Large-scale Comp, 116-122, 1987
- [11] Emani, S.M., et al., Ope. Tech. in Th. And Card. Surg., 21(2), 112-123, 2016

QUANTITATIVE COMPARISON OF FLOW PARAMETERS IN RIGID VS COMPLIANT ANEURYSM MODELS USING 4D PARTICLE IMAGE VELOCIMETRY (PIV)

Nikhil S. Shirdade (1), Sandy Karam (1), Baha T. ElKhader (1), Ephraim W. Church (2), Guha Manogharan (1), Melissa C. Brindise (1)

- (1) Department of Mechanical Engineering, The Pennsylvania State University, State College, PA, USA
(2) Department of Neurosurgery, Penn State Health, Hershey, PA, USA

INTRODUCTION

It is estimated that 1 in 12 persons harbors an unruptured intracranial aneurysm (IA) [1]. Clinical evaluation of IAs requires clinicians to decide whether the aneurysm is likely to grow, rupture, and requires treatment or if it should be simply monitored. However, assessing an IA's risk of rupture remains challenging as the physiology of the aneurysm is complex and it exists in a dynamic environment. Both morphological and hemodynamic factors have been correlated to the growth and rupture of an aneurysm [2]. However, prior studies have reported conflicting results regarding the role of specific hemodynamic and morphological risk mechanisms [3].

The motivation for this study lies in addressing a major contributing factor to these conflicting results due to the varying and non-physiological assumptions which are made among hemodynamic studies in this domain. In particular, we focus on the assumption that *in-vitro* IA models are most often manufactured to be rigid and have no compliance contrary to expected *in vivo* conditions [4]. In part because of the use of this assumption, there is a lacking consensus as to whether or not the aneurysms deform *in vivo*, and if so, if the deformation is a significant parameter affecting its growth and rupture [8, 9]. Experimental particle image velocimetry (PIV) studies usually use a block model or models made of plastics/ glass [5, 6, 7]

In this work, we will compare hemodynamics in an IA using a rigid block model as well as a compliant, thickness-controlled model. We will conduct this study using 4D PIV and an in-house developed additive-manufacturing based method for making compliant IA models. Further, we will evaluate the conditions under which deformation is observed with the compliant aneurysm model.

METHODS

R MCA aneurysm: The aneurysm model in this study is based on a patient specific unruptured 7 mm right middle cerebral artery (R MCA) aneurysm treated at Penn State's Hershey Medical Center.

PDMS Block model: The block model manufactured in this investigation is a 1:1. Computed tomography (CT) images of the IA were obtained as a digital imaging and communications in medicine (DICOM) file as shown in Figure 1(a). Using this, a 3D reconstruction in Slicer 3D software is performed. Figure 1(b) shows the segmented SolidWorks part file. The segmented stereolithography (STL) geometry was 3D printed in polyvinyl alcohol (PVA). The 3D printed part was placed in an acrylic box and polydimethylsiloxane (PDMS) silicone was poured around the printed part. The PVA model was subsequently dissolved out with warm water. Figure 1(c) shows the final PDMS block model based on the R MCA aneurysm.

Compliant model: The compliant model was manufactured using a concentric mold in which the PDMS is encased. The PDMS model was then cured for 5-6 hours in an oven set to a temperature of 70°C. The compliant model is shown undergoing pressure testing in Figure 2.

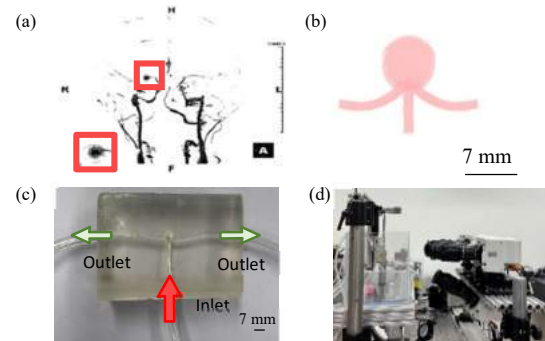


Figure 1: (a) Patient specific R middle cerebral artery (MCA) aneurysm, Digital Imaging and Communications in Medicine (DICOM) file (b) Derived SolidWorks file (c) Block model (d) PIV setup

Experimental methods: The aneurysm models were subjected to physiologically-relevant flow. The inflow waveform was inferred from prior studies that reported flow rate waveforms in the MCA artery. A blood analog working fluid seeded with fluorescent particle tracers was used. We conducted time-resolved volumetric PIV experiments using four cameras for both models. Figure 1(d) shows the experimental setup used. Shake-the-box processing was used to evaluate velocity fields from the particle images [10]. Subsequently, relevant flow parameters such as wall shear stress (WSS), oscillatory shear index (OSI), relative residence time (RRT) and turbulent intensity were evaluated.

Deformation pressure test: To evaluate the expected amount of deformation using the compliant model, a preliminary test was conducted where the model was subjected to a total pressure difference of 100mmHg for 10 seconds and the deformation in the aneurysmal sac was measured.

RESULTS

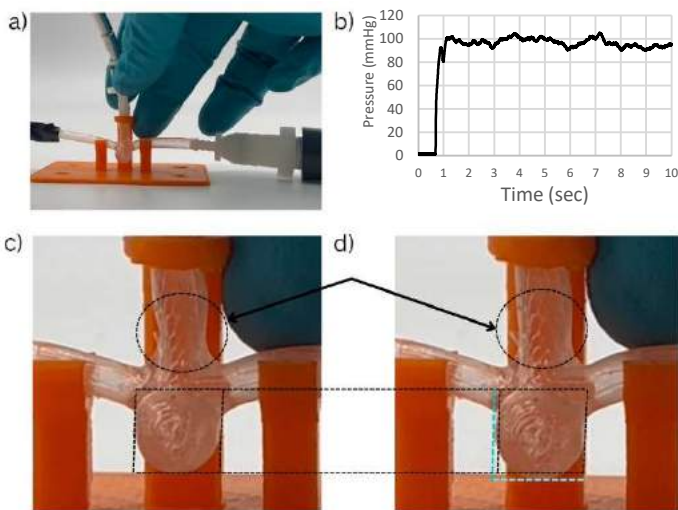


Figure 2: (a) the setup of the model by closing the left side with tape, connecting the right side by a pressure transducer, and the inlet connected to the air compressor. (b) Graph illustrating the pressure measurements over 10 s taken using a pressure transducer. (c) Snapshot taken at $t = 0$ s. (d) Snapshot taken at $t = 1$ s showing a bulge visible as seen in the circles and by comparing the blue lines to the initial black square lines.

Figure 2 shows the results of the pressure test conducted using the compliant IA model. Comparing the observed deformation in Figures 2(b) and 2(c), it was observed that the aneurysm expanded by approximately 10% relative to its original size. It was qualitatively found that deformation was occurred uniformly in all directions. These results are preliminary; further experiments are needed to test across reduced pressure difference ranges as well as to account for natural cranial pressure. Moreover, the PIV results will further expand the extent to which this deformation affects the IA hemodynamics.

DISCUSSION

The preliminary results of this work highlight the importance of studying compliant geometries experimentally. Further studies can help to build a consensus on the role of deformation and wall compliance on IA hemodynamics *in vivo*. Compliant model deformation studies, such as ours herein, can be used in conjunction with fluid structure interaction (FSI) studies where deformation evaluation in cases of IAs with

irregular wall thickness is more easily controlled. However, the experimental study conducted in this work can be critical to validation of FSI models [11].

A limitation of this work so far is that only one compliant model and thus only a single value of compliance with a single value for material strength was assessed. Moving forward, other models with different material properties are needed to conclusively report differences in hemodynamic parameters in compliant models.

ACKNOWLEDGEMENTS

Authors acknowledge funding support from American Heart Association CDA grant #940354. Authors further acknowledge Drew Mosser for all the logistics regarding the manufacturing of PDMS block model.

REFERENCES

- [1] Leemans, Eva L., et al. "Intracranial aneurysm growth: consistency of morphological changes." *Neurosurgical Focus* 47.1 (2019): E5.
- [2] Sforza, D. M., Lehner, R., Putman, C., & Cebal, J. R. (2010). Hemodynamic analysis of intracranial aneurysms with moving parent arteries: basilar tip aneurysms. *International Journal for Numerical Methods in Biomedical Engineering*, 26(10), 1219-1227
- [3] H. Meng, V. M. Tutino, J. Xiang, and A. Siddiqui, "High WSS or Low WSS? Complex interactions of hemodynamics with intracranial aneurysm initiation, growth, and rupture: Toward a unifying hypothesis," *Am. J. Neuroradiol.*, vol. 35, no. 7, pp. 1254–1262, 2014
- [4] Ruedinger, K. L., Medero, R., & Roldán-Alzate, A. (2019). Fabrication of low-cost patient-specific vascular models for particle image velocimetry. *Cardiovascular engineering and technology*, 10(3), 500-507.
- [5] Moore, J. A., et al. "A numerical study of blood flow patterns in anatomically realistic and simplified end-to-side anastomoses." (1999): 265-272.
- [6] Tupin, S., Saqr, K. M., & Ohta, M. (2020). Effects of wall compliance on multiharmonic pulsatile flow in idealized cerebral aneurysm models: comparative PIV experiments. *Experiments in Fluids*, 61(7), 1-11.
- [7] Arcaute, K., & Wicker, R. B. (2008). Patient-specific compliant vessel manufacturing using dip-spin coating of rapid prototyped molds.
- [8] Scotti, C. M., Shkolnik, A. D., Muluk, S. C., & Finol, E. A. (2005). Fluid-structure interaction in abdominal aortic aneurysms: effects of asymmetry and wall thickness. *Biomedical engineering online*, 4(1), 1-22.
- [9] Leng, X., Wang, Y., Xu, J., Jiang, Y., Zhang, X., & Xiang, J. (2018). Numerical simulation of patient-specific endovascular stenting and coiling for intracranial aneurysm surgical planning. *Journal of translational medicine*, 16(1), 1-10.
- [10] Brindise, M. C., Rothenberger, S., Dickerhoff, B., Schnell, S., Markl, M., Saloner, D., ... & Vlachos, P. P. (2019). Multi-modality cerebral aneurysm haemodynamic analysis: in vivo 4D flow MRI, in vitro volumetric particle velocimetry and in silico computational fluid dynamics. *Journal of the Royal Society Interface*, 16(158), 20190465.
- [11] Valencia, A., & Solis, F. (2006). Blood flow dynamics and arterial wall interaction in a saccular aneurysm model of the basilar artery. *Computers & structures*, 84(21), 1326-1337.

INVESTIGATION INTO CLOT AND STENT RETRIEVER PARAMETERS AFFECTING REMOVAL FORCES IN AN EXPERIMENTAL MODEL OF ACUTE ISCHEMIC STROKE

Demitria A. Poulos (1), Jordis E. Blackburn (1), Michael T. Froehler (2), Bryan C. Good (1)

(1) Mechanical, Aerospace, and Biomedical Engineering
University of Tennessee
Knoxville, TN, USA

(2) Department of Neurology
Vanderbilt University Medical Center
Nashville, TN, USA

INTRODUCTION

Acute ischemic stroke (AIS) due to large vessel occlusions (LVOs) accounts for 90% of 6-month post-stroke mortality [1]. The standard treatment for an LVO AIS is mechanical thrombectomy (MT) that, when compared to standard therapeutic treatment, results in improved patient outcomes [2]. Current MT procedures require the use of stent retrievers (SRs) or aspiration techniques to restore blood flow. Despite the clinical success of MT, adverse outcomes including hemorrhage and thrombus embolization to distal vessels can occur [3]. To improve the degree of revascularization for SR MT, the interaction between SRs and thrombi, as well as the overall thrombus removal forces need to be better understood. Previous experimental research of SR MT has investigated the effects of vascular geometry on thrombi removal forces and found that they increase with tortuosity of the anatomical occlusion location [4]. These results are the motivation for investigating additional parameters of SR MT including the effects of clot hematocrit, length, and diameter on SR removal forces and for comparisons between different commercially available SRs on their removal forces. These findings will lead to better clinical training and inspire new SRs to further improve AIS patient outcomes.

METHODS

To accurately represent AIS in a benchtop model, a circulatory flow loop was developed with a peristaltic pump, flow meter, fluid reservoir, and a constricting cerebral artery model (PVC tubing) (**Fig. 1**). To ensure embolus analog (EAs) lodging within the artery model, the vascular geometry,

highlighted in **Fig. 1**, was tapered from 5.5 to 3.3 mm in diameter. To represent a MT procedure, a SR within a microcatheter was passed through a hemostatic valve into the flow loop. The SR was then connected to a force gauge attached to a stepper motor which ensured the SR was pulled at a constant speed and the maximum removal force was recorded. For these experiments, two different Medtronic microcatheters, Phenom21 and Phenom27, and three different Medtronic SRs of varying diameters and lengths were used (**Fig. 2A-C**): Solitaire Platinum (4x20 mm) and two sizes of Solitaire2 (4x15 and 6x30 mm).

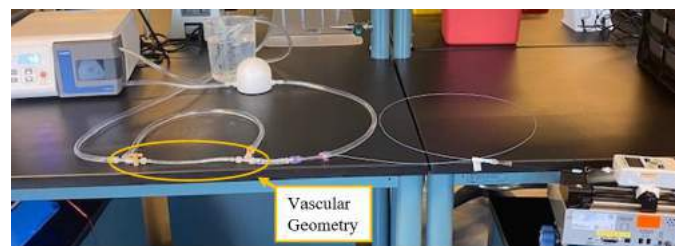


Fig 1: Benchtop circulatory flow loop with the cerebral artery model highlighted.

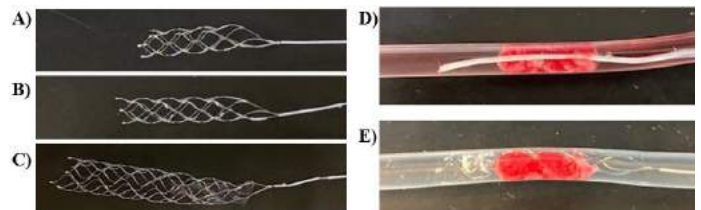


Fig 2: Images of A) Solitaire2 4x15 mm, B) Solitaire Platinum 4x20 mm, and C) Solitaire2 6x30 mm SRs used. D) Example of microcatheter passed across the EA with E) SR deployment.

To fabricate EAs for these experiments, bovine blood was collected in CPDA-1 anticoagulated bags, centrifuged to separate red blood cells and platelet rich plasma, and reconstituted to achieve a specific hematocrit (0, 25, or 50%) before CaCl_2 was introduced to promote coagulation. The reconstituted blood was injected into 6 mm diameter tubing and placed in a Chandler Loop system where the EAs were formed under dynamic flow conditions for 2 hours. The EAs were removed from the Chandler loop, cut to length, and inserted into the flow loop upstream of the arterial model. The EAs flowed downstream and were allowed to lodge within the vascular geometry for 5 minutes. The microcatheter with the SR was then passed across the EA as shown in **Fig. 2D**. The microcatheter was pulled back to deploy the SR over the entire EA (**Fig. 2E**) and the SR was attached to the force gauge which pulled the SR while recording the removal forces. This protocol was also repeated for each SR without the presence of a lodged EA to collect baseline (control) removal forces. In these control tests, the removal forces represent the frictional interaction forces between the SR and the vascular model (PVC tubing).

RESULTS

The maximum removal forces for each of the experimental test parameters are summarized in **Table 1**.

Table 1: Sample size and removal forces for each test parameter

Test Parameter	Sample Size	Average Removal Force (N)
Solitaire Platinum		
4 × 20 mm		
Controls (w/out EA)	20	0.24 ± 0.012
50% Hematocrit	20	0.59 ± 0.162
Solitaire2		
4 × 15 mm		
Controls (w/out EA)	20	0.29 ± 0.011
50% Hematocrit	20	0.55 ± 0.076
25% Hematocrit	20	0.54 ± 0.071
0% Hematocrit	20	0.57 ± 0.075
6 × 30 mm		
Controls (w/out EA)	20	0.39 ± 0.025
50% Hematocrit	20	0.69 ± 0.093

As seen in **Fig. 3**, the removal forces varied only slightly between the different hematocrit EAs. However, there was a slight, but not significant, increase in the removal forces for the 0% hematocrit EAs, which was expected based on lower clinical removal success for fibrin-rich clots [5].

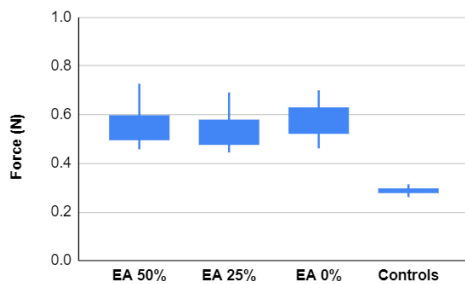


Fig 3: Maximum removal forces with the Solitaire2 4×15 mm SR.

Fig. 4 compares the removal forces for 50% hematocrit EAs of varying geometry using the 6 mm diameter SR. The results

are presented for EAs with diameters 4.5-6.5 mm and lengths 14.3-18.7 mm. The relationship between EA diameter and removal force indicates a slight positive correlation, while EA length does not appear to correlate with overall removal force. Similar trends in EA diameter and length were observed for all hematocrit and SR dimension test parameters.

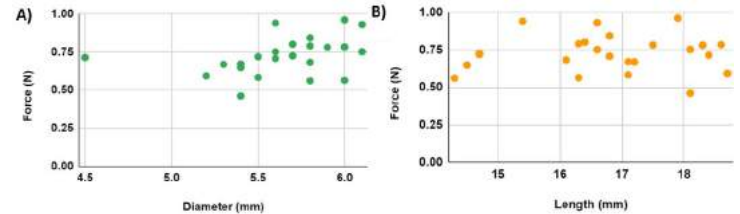


Fig 4: Maximum removal forces with the Solitaire2 6×30 mm SR for EAs of varying A) diameter and B) length.

DISCUSSION

The results of the experiments indicate that EA hematocrit does not have a significant influence on their SR removal force. These data also supports previous work [4] which showed that vascular tortuosity significantly influenced EA removal force, while other factors were minor. A comparison of the control test data across the various model geometries is displayed in **Fig. 5A**. From the average forces listed in **Fig. 5B**, it is observed that increasing complexity will increase the force by at least 0.1 N.

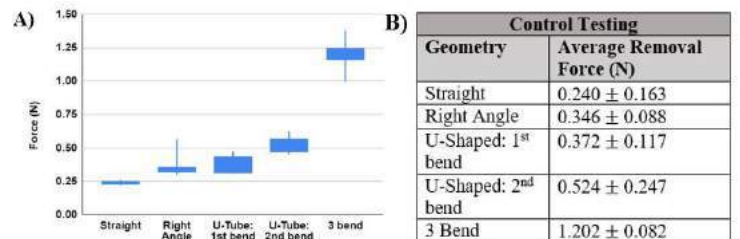


Fig 5: Control test removal forces from flow loop experiments with varying model geometries.

The 0% hematocrit EAs with the 4×15 mm Solitaire2 had the highest removal force. This was expected since fibrin rich clots are associated with lower recanalization rates [5]. For 50% hematocrit EAs, the average removal force with the 4×20 Solitaire Platinum SR was 0.59 N, 4×15 Solitaire2 SR was 0.55 N, and 6×30 Solitaire2 SR was 0.69 N. Based on these results, we have shown that removal forces increase as the diameter of the SR increases. From this, we hypothesize that the diameter of the SR has a greater influence on the removal force than its length. However, further testing with SRs of the same length and varying diameters is necessary to prove this. Further investigation is also needed to observe the range of removal forces collected with the various SRs with varying EA hematocrits, although similar trends are expected.

REFERENCES

- [1] Hui, W et al., *AHA Journals*, 51:2026-2035, 2020.
- [2] Pérez, MA et al., *JNIS*, 2011.
- [3] Luraghi, G et al., *Interface Focus*, 11, 2021.
- [4] Poulos, D et al., *SB3 Conference* 2022.
- [5] Gunning, G et al., *Journal of NeuroInterventional Surgery*, 2018

DECORIN MAINTAINS CARTILAGE SURFACE INTEGRITY AND CHONDROCYTE MECHANOTRANSDUCTION DURING AGING

M. Fan (1), B. Kwok (1), P. Singh (1), J. Xiang (1), L. Qin (2),
D. E. Birk (3), R. V. Iozzo (4), R. L. Mauck (2), L. Han (1)

- (1) School of Biomedical Engineering, Science and Health Systems, Drexel University, Philadelphia, PA, United States
- (2) McKay Orthopaedic Research Laboratory, University of Pennsylvania, Philadelphia, PA, United States
- (3) Department of Molecular Pharmacology and Physiology, University of South Florida, Tampa, FL, United States
- (4) Department of Pathology, Anatomy and cell Biology, Thomas Jefferson University, Philadelphia, PA, United States

INTRODUCTION

Aging is the leading risk factor for osteoarthritis (OA), which afflicts more than 10% of adults over 60 years of age [1]. Many efforts have been dedicated to elucidating the cellular hallmarks of aging [2]. In contrast, despite the importance of extracellular matrix (ECM) in cartilage biomechanical function and chondrocyte mechanosensing, there is limited knowledge regarding how aging impacts ECM integrity. Our recent studies found that decorin, a small proteoglycan, plays indispensable roles in regulating the integrity of aggrecan network in cartilage ECM [3] and mediating chondrocyte mechanotransduction [4] during post-natal growth. In post-traumatic OA, up-regulation of decorin delays loss of fragmented aggrecan and thus attenuates surface fibrillation [5]. Decorin is actively expressed in both young and old human cartilage [6], indicating a potentially important role of decorin in regulating cartilage aging. This study tests whether decorin plays a crucial role in cartilage ECM maintenance during aging.

METHODS

Animal model. Cartilage-specific knockout of *Dcn* was induced by i.p. injection of tamoxifen to conditional decorin knockout mice (*Dcn^{fllox/fllox}/AcanCre^{ER}*, or *Dcn^{CKO}*) at 3 months of age (3M), and the phenotype was evaluated at 9 and 18 months (9M, 18M), and compare to age-matched controls. Additional global decorin-null (*Dcn^{-/-}*) and wild-type (WT) mice were evaluated at 3M and 18M. **Histology and immunofluorescence** (IF) imaging were applied to sagittal sections to assess joint morphology, sulfated glycosaminoglycan (sGAG) staining and presence of collagen I, indicating surface fibrillation [7]. **SEM** was applied to measure collagen fibril nanostructure [5]. **AFM-nanoindentation** was applied to the condyle cartilage surface to quantify tissue modulus [3]. **IF-guided AFM-nanomechanical mapping** was applied to delineate the local modulus, E_{ind} , between the territorial and interterritorial (T/IT)-ECM and PCM using unfixed cryo-sections of tibial cartilage, guided by the PCM biomarker, collagen VI, following

our established procedure [4]. For *in situ intracellular* $[Ca^{2+}]_i$ signaling, tibial cartilage explants were labeled with intracellular calcium indicator Calbryte-520, and time-series of confocal images were taken in isotonic, hypotonic and hypertonic DMEM [4]. The responsive rate, % R_{cell} , was calculated as the fraction of responsive cells over a 15 min period. A non-parametric Mann-Whitney U test was applied to compare E_{ind} , and the proportion z -test was applied to compare % R_{cell} , between genotypes at each age and/or osmotic condition at $\alpha = 0.05$, followed by Holm-Bonferroni correction to account for family-wise errors.

RESULTS

In 9M *Dcn^{CKO}* mice, loss of decorin led to an overall reduction of sGAG staining in cartilage, as well as the appearance of a surface layer devoid of sGAGs (Fig. 1a). IF imaging further confirmed that this sGAG-depleted layer was rich in collagen I, evidencing surface fibrillation. Furthermore, the surface collagen fibrils formed highly aligned bundles along the mediolateral split-line direction (Fig. 1a). A more severe phenotype was observed in 18M *Dcn^{CKO}* mice, including nearly full depletion of sGAG staining, disrupted cartilage surface integrity, as signified by the increased collagen I at uncalcified cartilage layer and a phenotype shifting of the surface layer cell to more elongated morphology (Fig. 1b). Applying AFM-nanoindentation, we did not detect significant changes of E_{ind} in 9M *Dcn^{CKO}* cartilage relative to the control. However, we found a substantially increased modulus in both *Dcn^{CKO}* and *Dcn^{-/-}* groups at 18M, which was in stark contrast to our previously observed modulus reduction in 3-month-old *Dcn^{-/-}* mice (Fig. 2a). This increase in modulus was also associated with a change in the nature of the indentation response. Specifically, we observed a linear F - D curve in 18M decorin groups (Fig. 2b), instead of the non-linear F - $D^{3/2}$ Hertzian indentation response typically observed for cartilage [3].

Interestingly, contrary to the increased E_{ind} in *Dcn^{CKO}* femoral condyle cartilage at 18M, we detected significantly reduced E_{ind} in tibial cartilages for both T/IT-ECM and PCM relative control (Fig. 3a,b). The

disrupted local mechanical environment of PCM did lead to altered chondrocyte mechanotransduction. For both 9M and 18M groups, loss of decorin led to a reduction in chondrocyte $[Ca^{2+}]_i$ responses in situ, as marked by significantly lower $\%R_{cell}$, under both physiological (isotonic) and osmotically instigated (hypotonic and hypertonic) conditions (Fig. 3c,d).

DISCUSSION

This study highlights a crucial role of decorin in maintaining the integrity of the cartilage surface during aging. The surface of healthy cartilage is characterized by a transversely isotropic mesh of thin collagen II fibrils [8], which plays an important biomechanical role in resisting shear forces and mediating boundary lubrication [9]. The absence of sGAGs and presence of highly aligned collagen I fibers (Fig. 1) clearly evidence cartilage surface fibrillation. Also, the non-Hertzian, linear $F-D$ response in the 18M *Dcn* group (Fig. 2) is a typical indentation response of fibrous tissues with inherent tensile pre-stress, such as the meniscus [10]. This surface fibrillation may be attributed to several mechanisms. First, decorin increases the retention of aggrecan in cartilage during post-natal growth [3], and the loss of sGAG staining observed here suggests that decorin continues playing this role during aging. Second, decorin also directly provides collagen interfibrillar spacing through its GAG chain [11]. Thus, the loss of decorin and aggrecan together may result in reduced biophysical resistance against collagen fibril fusion and alignment under shear forces during aging, thus accelerating surface fibrillation.

In addition, our results illustrate a crucial role of decorin in maintaining the PCM integrity and chondrocyte in situ mechanosensing during aging (Fig. 3). This role is likely manifested through its regulation of aggrecan network integrity [3], and support decorin as an

indispensable constituent of cartilage throughout lifespan. Our ongoing studies aim to pinpoint the mechanobiological roles of decorin in regulating chondrocyte fate and signaling, which will provide justification for using decorin as a molecular therapy to modulate cartilage aging.

ACKNOWLEDGEMENTS

This work was supported by NIH R01 AR074490, NSF CMMI-1751898 and UPenn PCMD NIH P30 AR069619.

REFERENCES

- [1] Zhang, Y et al., *Clin. Geriatr Med.*, 26(3):355-69, 2010.
- [2] Loeser, F et al., *Nat. Rev. Rheumatol.*, 12(7):412-20, 2016.
- [3] Han, L et al., *ACS Nano*, 13(10):11320-11333, 2019.
- [4] Chery DR et al., *Matrix Biol.*, 96, 1-17, 2021.
- [5] Li, Q et al., *Arthritis Rheumatol.*, 72(8):1266-1277, 2020.
- [6] McAlinden, A et al., *Osteoarthritis Cartilage*, 9(1):33-41, 2001.
- [7] Tschakowsky, M et al., *Acta Biomater.*, 2022.
- [8] Vanden Berg-Foels, WS et al., *J Microsc.*, 246(2):168-76, 2012.
- [9] McNary, SM et al., *Tissue Eng. Part B Rev.*, 18(2):88-100, 2012.
- [10] Li, Q et al., *J Biomech.*, 48(8):1364-70, 2015.
- [11] Danielson, KG et al., *J Cell Biol.*, 136(3):729-43, 1997.

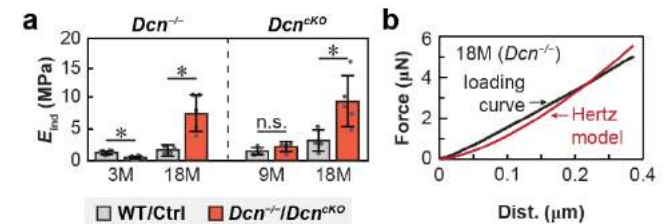


Fig. 2: a) AFM-nanoindentation modulus, E_{ind} , of medial condyle cartilage between WT vs *Dcn*^{-/-} at 3M and 18M, and control vs *Dcn*^{cKO} at 9M and 18M (mean \pm 95% CI, $n \geq 4$, *: $p < 0.05$; n.s.: not significant). b) Representative $F-D$ curve of 18M *Dcn*^{-/-} cartilage shows non-Hertzian indentation response.

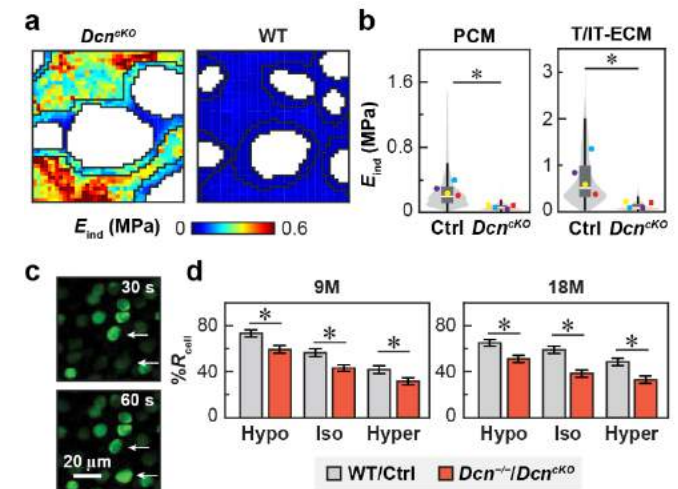


Fig. 3: a) Representative E_{ind} maps of *Dcn*^{cKO} and Control tibial cartilage at 18M. b) Violin plots show reduced E_{ind} of tibia cartilage PCM and T/IT-ECM in *Dcn*^{cKO} at 18M ($n = 4$, *: $p < 0.05$). Each circle shows the average E_{ind} from one animal. Circles with the same color indicate values from the same animal. c) Confocal images of chondrocyte in situ $[Ca^{2+}]_i$ signaling. d) Comparison of $[Ca^{2+}]_i$ cell responsive rate, $\%R_{cell}$, between Control vs *Dcn*^{cKO} at 9M, and WT vs *Dcn*^{-/-} at 18M (≥ 300 responding cells pooled from $n \geq 4$ animals for each group, mean \pm 95% CI, *: $p < 0.05$).

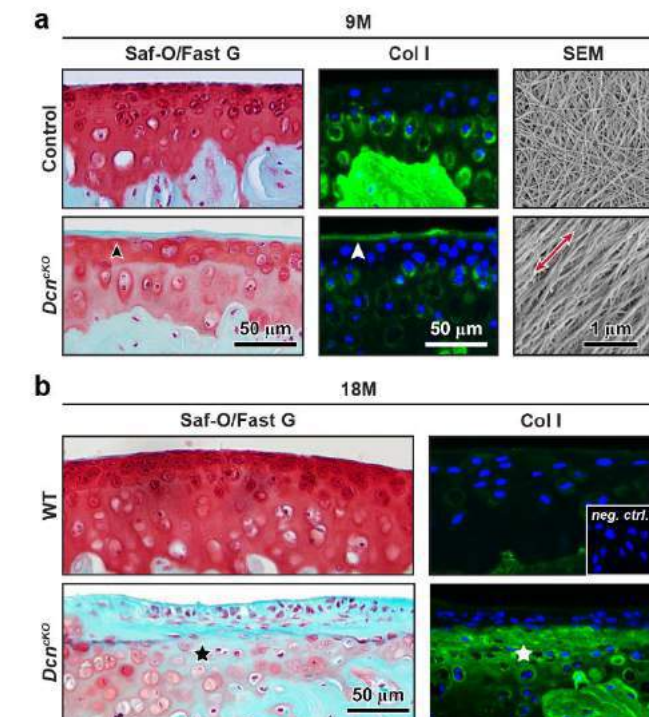


Fig. 1: Safranin-O/Fast Green histology, IF of collagen I and cartilage surface SEM images of Control vs *Dcn*^{cKO} at a) 9M and b) 18M. a) Black and white arrows indicate the layer devoid of sGAGs and rich in collagen I. Red arrow: mediolateral direction. b) Stars indicate the same location in the section between histology and IF images ($n \geq 4$ animals for each age and genotype).

TROPOCOLLAGEN DENATURATION IS NOT RESPONSIBLE FOR SUB-YIELD SOFTENING

Noah R. Pearson (1), Gregory M. Boiczuk (2), William J. Anderl (1), S. Michael Yu (2,3), Kenneth L. Monson (1,2)

(1) Mechanical Engineering, University of Utah, Salt Lake City, UT, USA
(2) Biomedical Engineering, University of Utah, Salt Lake City, UT, USA
(3) Molecular Pharmaceuticals, University of Utah, Salt Lake City, UT, USA

INTRODUCTION

Computational models suggest that the cerebrovasculature plays a significant role in the brain's structural response in traumatic brain injury [1]. However, recent studies have shown that cerebral arteries soften following supraphysiologic deformations [2]. Previous studies, such as that by Converse et al., have identified tropocollagen denaturation as a critical failure location in the collagen hierarchy of cerebral arteries, but have not evaluated its association with tissue softening after mechanical injury [3]. To understand the connection between softening of tissue and changes in the extracellular matrix (ECM), this study explores the relationship between tropocollagen denaturation and softening of the tissue following mechanical overstretch at various rates. By examining this link, this study aims to inform potential therapeutics to counteract the effects of TBI.

METHODS

We isolated middle cerebral arteries from Göttingen minipigs that had been euthanized under the supervision of the University of Utah Institutional Animal Care and Use Committee. We mounted the arteries onto cannulas attached to a custom high-rate tester using suture and cyanoacrylate. We then preconditioned the tissue according to a previously published protocol [4].

After preconditioning, we subjected the arteries to axial harmonic oscillations at five frequencies ranging from 0.32 to 32 Hz between stretch magnitudes of 1.0 to 1.1 times the in vivo length to define the baseline dynamic moduli of the tissue at various rates at near-physiologic stretch. We then axially overstretched the arteries to stretch magnitudes ranging from 1.1 to 1.4 times the in vivo length at one of four targeted strain rates ranging from 0.05 to 50 s⁻¹. We then repeated the harmonic oscillations to calculate overstretch-induced softening of the tissue.

After mechanical testing, we stained the samples with CHP using a previously published protocol. This involved staining the arteries overnight in 20 μM F-CHP (3-Helix, Salt Lake City, UT), rinsing them three times in phosphate buffered saline, cutting them open, and mounting them luminal side down on a glass slide for imaging. A confocal microscope (FV1000, Olympus Corporation, Tokyo, Japan)

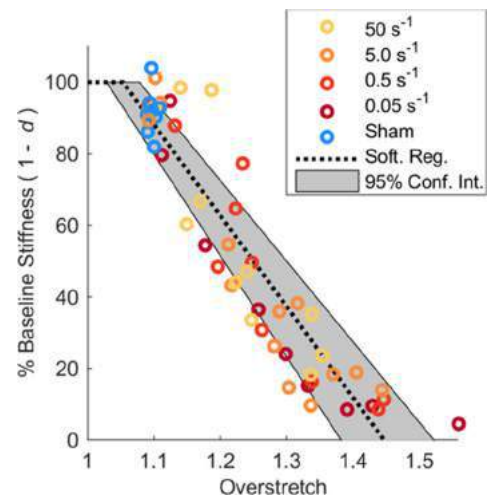


Figure 1: Softening (% of baseline stiffness) as a function of overstretch for all samples; regression line shown. Note that softening happens following low degrees of overstretch and is independent of overstretch rate.

was used to image the fluorescence of stained samples. We also performed the same staining and imaging protocol on undamaged, animal-matched controls for comparison. All pixels having an intensity greater than two standard deviations above the mean control intensity

were taken as representing collagen denaturation. We then tallied the number of pixels in test samples that exceeded this threshold and normalized them by the total number of pixels, providing a tropocollagen damage metric of percent bright pixels.

Dynamic moduli were calculated by dividing the peak-to-peak change in the first Piola-Kirchoff stress by the peak-to-peak strain. Softening (% baseline stiffness) was defined by the average post-overstretch dynamic modulus divided by the average baseline dynamic modulus for each sample. A linear regression was fit to the softening data as a function of magnitude of overstretch. A softening threshold was identified as the intersection of the softening regression with 100 % of the baseline stiffness. Overstretch curves were evaluated for yielding by monitoring for a sustained decrease in stiffness.

RESULTS

Softening progressed linearly with magnitude of overstretch but was notably independent of overstretch rate (Figure 1). The slope of the softening regression was 2.73 ± 0.31 (mean \pm 95% conf) with the threshold of softening calculated to be 1.05 ± 0.025 . The substantial softening of the dynamic moduli (>80% reduction) was observed in the absence of tropocollagen denaturation; denaturation was not readily identified at overstretches up to 1.4 (at any strain rate), although several samples (possible outliers) showed high amounts of CHP expression (Figure 2). Inspection of the overstretch curves for these odd CHP samples did not show any unusual activity (not shown). The overstretch curves did not show evidence of yielding, indicating that all observed softening was due to sub-yield deformations.

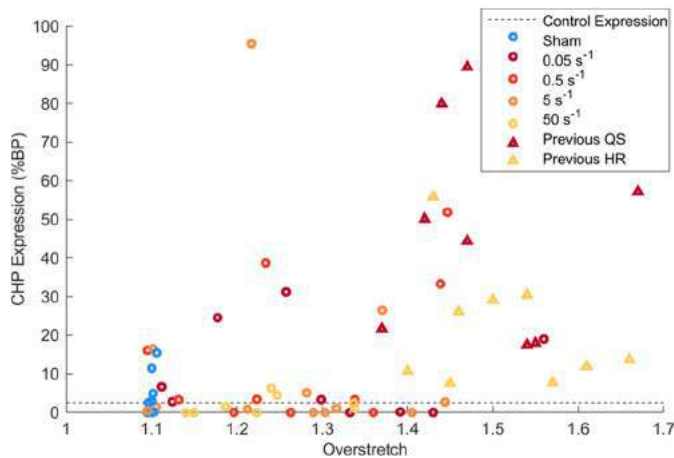


Figure 2: CHP expression showing the amount of denatured tropocollagen in each sample. Note that seven samples from the present study show elevated levels of CHP at a relatively low (<1.3) magnitude of overstretch. Additional data from arteries pulled to failure either quasi-statically (QS) or at high-rate (HR) in a previous study are added for comparison.

DISCUSSION

The purpose of this study was to examine the connection between sub-yield softening and tropocollagen denaturation. Results demonstrate that tissue softening is dependent upon extent of overstretch but not overstretch rate. Further, this softening occurs in the absence of tropocollagen denaturation at sub-yield overstretch levels.

Error! Reference source not found. illustrates the current understanding of the relationship between the degree of overstretch, the softening of the tissue, and ECM damage. This illustration is consistent

with previous research linking tropocollagen denaturation to the yielding of the native stress-stretch curve [3, 5].

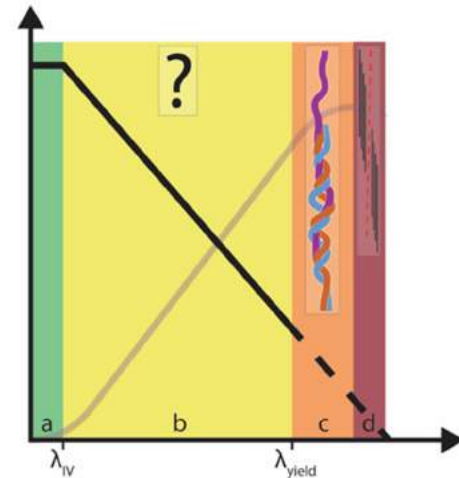


Figure 3: A schematic showing the relationship of softening with ECM alterations, including the following regimes: (a) undamaged (no softening); (b) large range of deformations with clear mechanical softening, yet no evidence of ECM alterations; (c) post-yield regime characterized by tropocollagen denaturation; (d) gross fibril failure leading to final tissue failure. Note that the softening regression becomes dashed as we exit the presently explored softening region. A stress-stretch curve (pink) is provided for the convenience of the reader to relate landmarks in the mechanical curve with softening and ECM alterations.

These findings suggest that even mild TBI causes significant changes in cerebral vessel properties. Given their role in the structural response of the brain, these changes could potentially lead to increased susceptibility to subsequent injury. Unrecoverable vessel changes and associated dysfunction could also lead to disease development. These risks highlight the need to determine what molecules or structures in the collagen hierarchy are being changed to cause the significant softening observed following sub-yield overstretch. This information may be key to the development of post-TBI therapies, even where injury is considered to be mild.

ACKNOWLEDGEMENTS

Funding for this project was provided by the National Science Foundation (Award No. 2027367) with contributions from the Henry Jackson Foundation (Contract No. W81XWH-17-2-0008). We'd like to thank Kolbi Dietmeier and J. Kevin Lee for their assistance in imaging. We acknowledge Cell Imaging Core at the University of Utah for use of equipment (Olympus FV1000).

REFERENCES

- [1] Subramaniam, D. R. *et al.*, BioMed. Eng. Online, 20(1) 2021.
- [2] Bell, E. D. *et al.*, Front Bioeng Biotechnol, 3(2):2, 2015.
- [3] Converse, M. I. *et al.*, Acta Biomater, 67:307-318, 2018.
- [4] Pearson, N. *et al.*, J Biomech Eng, 144(8), 2022.
- [5] Lin, A. H. *et al.*, Acta Biomater, 118:153-160, 2020.

A MESOSCALE MODEL OF SKIN TO INVESTIGATE THE ROLE OF THE DERMIS-EPIDERMIS INTERFACE ON THE TISSUE BIOMECHANICS

O. Moreno Flores (1), M. Rausch (2) A. Buganza Tepole (1,3)

(1) School of Mechanical Engineering, Purdue University, West Lafayette, Indiana, USA
(2) School of Biomedical Engineering, The University of Texas at Austin, Austin, Texas, USA
(3) Weldon School of Biomedical Engineering, Purdue University, West Lafayette, Indiana, USA

INTRODUCTION

Understanding and correctly simulating the mechanics of skin is crucial for many medical applications, e.g. planning reconstructive surgery or monitoring wound healing. The field of skin biomechanics has often modeled this tissue as a homogeneous material because its response at finite deformations is governed by its collagen content. However, skin consists of two main layers with different constituents and microstructure: epidermis and dermis. Additionally, there are skin appendages such as hair follicles. Recently, multi-layer models of skin have been developed to study wrinkling and transport [1]. However, these models have considered skin as a stack of the multiple layers but have ignored the interface geometry between layers and the presence of skin appendages. Here we fill this gap using a computational model of a representative volume element (RVE) of the skin mesoscale.

METHODS

The interface geometry between epidermis and dermis is a sinusoidal-like surface (Figure 1a). A RVE $0.4002 \times 0.4002 \times 1 \text{ mm}^3$ shown in Figure 1b consist was created, consisting of two layers. The epidermis is the top layer and has thickness 0.1 mm. The dermis below has thickness 0.9 mm. The two layers are separated by a parametric surface described by equations

$$\begin{aligned} x(t) &= t & (1) \\ y(t) &= A \sin(Bt) & (2) \\ z(t) &= A \sin(Bt_1) + A \sin(Bt_2) & (3) \end{aligned}$$

with $A=0.015 \text{ mm}$ and $B=78.5 \text{ mm}$ as seen in Figure 1b. The sine wave parameters were determined by measuring thickness variations in histological images of skin e.g. Figure 1a. Another RVE was created with a hair follicle according to an anatomical study in [2]. A control model with flat layers was also created.

The epidermis and epithelium surrounding the hair follicle were modelled using the Ogden model parameters based on [3]. The dermis was modelled using the Gasser–Ogden–Holzapfel (GOH) model with parameters from [4]. The hair follicle was modeled as neo-Hookean with parameters C_{10} of 789.57 MPa and D_1 of 0.0003 MPa^{-1} (notation corresponds to Abaqus) The geometry was discretized mostly with linear hexahedra with a hybrid formulation for incompressible behavior, C3D8RH in Abaqus. Due to the complexity of the geometry, a small number of elements are linear wedge or tetrahedral elements C3D6H. A mesh convergence study was performed to select the appropriate element number. The final mesh of the RVE in Figure 1b consisted of 195704 elements. The hair follicle mesh had 202074 elements. The control geometry needed 68850 elements.

We were interested in the response of skin under multiple modes of deformation, e.g. biaxial deformations and shear. For this study we focus on the equi-biaxial response. Periodic boundary conditions were enforced in the simulations with linear constraints between pairs of nodes in Abaqus. The top surface was assumed stress-free.

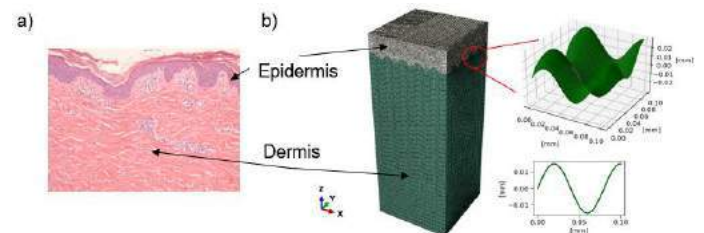


Figure 1: a) Porcine histology image used to create RVE. b) Finite element model of RVE with sinusoidal interface.

RESULTS

We first investigated the homogenized behavior of the composite by simulating the RVE under biaxial loading, averaging the stress over the RVE, and comparing against the analytical solution of homogeneous tissue made from either Ogden or GOH materials. We also compared against the homogenized response of the control RVE with flat interface. The interface geometry did not have an influence on the homogenized response, confirming that multi-layer models with a flat interface are accurate to capture the macroscale response (data not shown). Furthermore, the response matched closely the rule of mixtures. However, the sinusoidal interface resulted in a heterogeneous stress distribution with higher stresses at the valleys and lower stresses at the peaks on the dermis side (Figure 2a-b). We tested how changes in period and amplitude of the interface affected the stress distribution. Figure 2a shows that increasing the amplitude further increased the maximum stress at the high saddles and decreased the stresses at the low saddles. Changing the period in the RVE implies simply a different control volume and scaling. Thus, we didn't expect the change in period would affect the magnitudes of the stresses. Indeed, changing the period just scaled the pattern of stress but values remained the same at the locations of interest (Figure 2b).

One question we were interested in was whether or not the sinusoidal interface would have an effect on the stress jump across the dermis-epidermis junction. For the model with amplitude of 0.015 mm the average stress jump was lower compared to a flat surface (Figure 2d), with the difference increasing at larger stretches. This last result suggests that even though the homogenized response is the same regardless of the interface geometry, the stress variation and in particular the stress jump is affected by the non-flat interface. The sinusoidal interface could offer a protective mechanism against delamination. Indeed, fracture mechanics studies on curved interfaces suggests an increase in fracture toughness with wavy interfaces compared to flat ones [5].

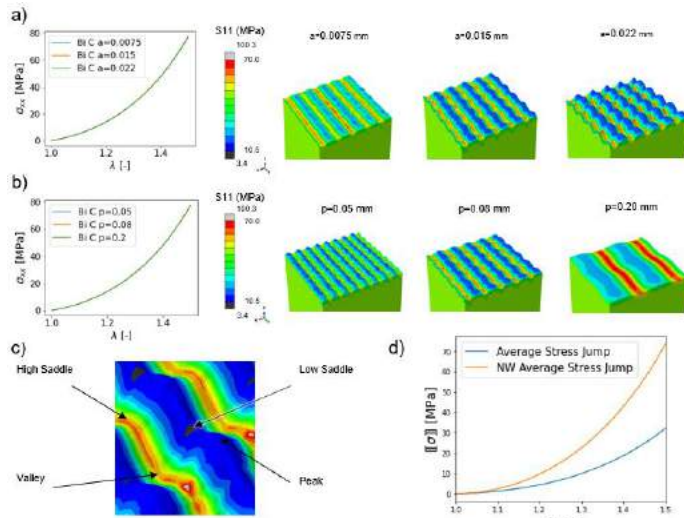


Figure 2: a) Stress vs stretch plots for amplitude variation along with their contour plots. Homogenized response remains unchanged but maximum stresses increases and minimum stresses decrease with increased amplitude. b) Stress vs stretch plots for period variation along with their contour plots. Neither the homogenized response nor the stress change at locations of interest change identified in c). d) Stress jump vs stretch plots comparing the sinusoidal interface and flat interface models.

We then looked into the RVE with the hair follicle. Hair follicles are known to be crucial in mechanosensation as part of our sense of touch [6]. The RVEs with the hair follicle exhibited strain concentrations in the epithelial tissue surrounding the hair follicle (Figure 3), where mechanoreceptors are expected [6].

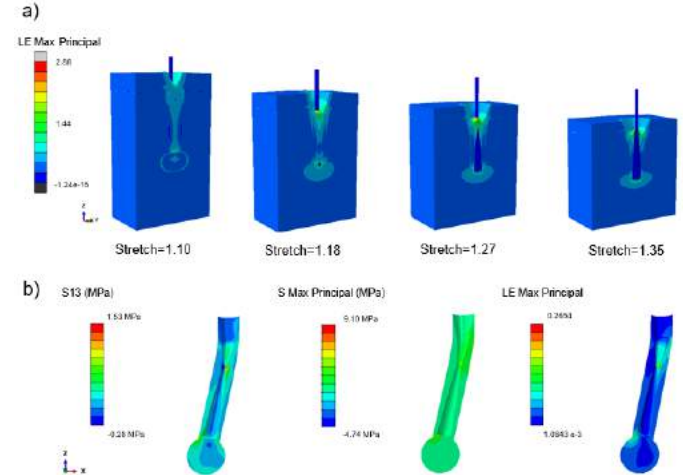


Figure 3: a) Contour plots of the strain as it progresses in a biaxial deformation. b) contour plots of the epithelium after experiencing shear.

DISCUSSION

Our analysis shows that the homogenized stress does not depend on interface geometry. Thus, flat interface models or even rule of mixtures can be used to predict the overall stress-stretch response of skin in biomechanics simulations (provided there is no damage or fracture). The interface geometry leads to heterogeneous stress at the mesoscale, in particular the dermis stresses are highest at the valleys and smallest at the peaks of the sinusoidal interface. It remains to determine if this heterogeneous stress distribution correlates with biological function. For example, do higher stresses and strains in some region of the epidermis correlate with different stem cell population density or presence of mechanoreceptors? This is an area of future research that we intend to pursue. From a purely mechanical standpoint, a sinusoidal interface does have the advantage of reducing the stress jump across the interface of the two materials and this has similarly been studied in the context of fracture of composites [5]. Future work will focus on modeling fracture at the interface for skin RVEs. Beyond the interface versus flat geometry, one of the salient features of skin is that it hosts several appendages. We show that hair follicles also cause heterogeneous mechanical response, with strain concentrations at specific locations in the epithelium surrounding the hair follicle. These result open research avenues for how the mechanics of the mesoscale can affect skin physiology, e.g. haptics and sense of touch.

ACKNOWLEDGEMENTS

Supported by NIAMS R01AR074525, NSF CMMI 1916668

REFERENCES

- [1] Zhao et al., *J Mech Behav Biomed Mat*, 105:103694, 2020.
- [2] Vogt et al., *Exp Dermatol*, 16:946, 2007.
- [3] Groves et al., *PhD thesis*, Cardiff University, 2012.
- [4] Ni-Annaidh et al., *Ann Biomed Eng*, 40:1666, 2012.
- [5] Zavattieri, PD et al., *I J Fracture*, 145:167-80, 2007.
- [6] Lumpkin, EA et al., *Nature*, 445:858-65, 2007.

THE INFLUENCE OF HEMODILUTED BLOOD VISCOSITY ON PATIENT HEMODYNAMICS DURING CARDIOPULMONARY BYPASS

Nafis M. Arefin (1), Allison R. Cripps (1), Bryan C. Good (1)

(1) Department of Mechanical, Aerospace, and Biomedical Engineering, University of Tennessee
Knoxville, TN, USA

INTRODUCTION

Perioperative complications with cardiopulmonary bypass (CPB) are still common and are associated with concerning rates of mortality and morbidity. Emboli formed during CPB can cause severe complications including thromboembolic stroke [1]. Therefore, it is critical to understand their delivery to the cerebral arteries to help minimize various neurological complexities. Previous experimental transport studies in the aorta have found that emboli trajectory paths are proportional to the flow rate split within the aortic branches during normal flow conditions [2]. However, no studies have investigated emboli distribution in hemodiluted blood during CPB. Hemodilution is an imperative procedure during CPB to reduce blood viscosity and improve microcirculatory flow and oxygen delivery. To address these shortcomings and inadequacies, an experimental mock circulatory flow loop (MCFL) was built and used to observe emboli distribution through the aorta under varying hemodiluted blood viscosities for the first time. This experimental dataset was then used to validate computational simulations of emboli transport in a patient aorta model, hence producing original and state-of-the-art results that can be used to help reduce stroke risk during CPB.

METHODS

A silicon model of an aorta consisting of the ascending aorta (AA), brachiocephalic artery (BCA), left common carotid artery (LCCA), left subclavian artery (LSCA), and descending aorta (DA) has been developed. A patient-specific CAD model of an aortic arch anatomy, 26-year-old male with no cardiovascular complications was obtained from the Vascular Model Repository [3] (Fig. 1) and 3D printed. The material used for 3D printing the CAD model was polyvinyl alcohol (PVA), which is a biodegradable polymer highly sensitive to moisture. A rectangular box was also 3D printed with polylactic acid (PLA). The PVA-printed aorta was kept inside the PLA-printed box and the box was filled with *SYLGARD 184*, a two-component silicone-based elastomeric kit. After curing in the box for 3 days, the model was submerged in hot

water for another 2 days to allow for the PVA aorta to dissolve out, leaving a cavity representative of the fluid domain within the aorta. Tube connectors were fixed to each of the model's inlets and outlets to allow for incorporation into an MCFL. The MCFL included a Sorin Stockert Roller Pump (10-10-00 CAPS Module 10H), a fluid reservoir, tubing clamps to control the flow rate, and a flow meter (Transonic) (Fig. 1).

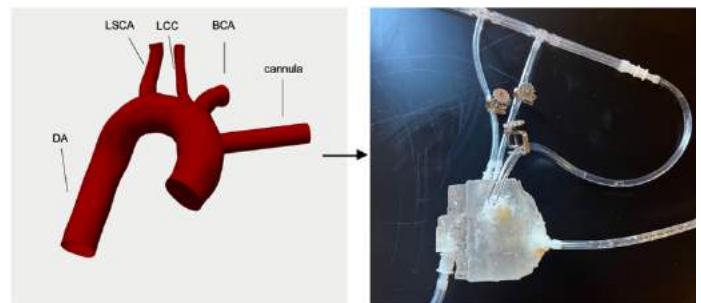


Figure 1: CAD model of the patient aorta and the constructed MCFL with silicon aorta geometry

To cover the range of hemodiluted blood viscosities observed clinically during CPB, four blood analog solutions were created by mixing water and glycerin at specified ratios; 1) 80:20 for $\mu \approx 2$ cP, 2) 74:26 for $\mu \approx 3$ cP, 3) 70:30 for $\mu \approx 3$ cP, and 4) 67:33 for $\mu \approx 3.5$ cP. To represent emboli formed in the CPB system, nylon beads of two different diameters (3/32" and 1/16") were used. For each trial, run with a 3-LPM pump flow rate, a single bead was injected into the flow loop and its path and exit through one of the aortic branches was noted.

OpenFOAM, a C++ open-source computational software, was used for the computational studies. For meshing, high-grade unstructured meshes were developed using the *snappyHexMesh* utility. All four

outlets were prescribed resistance boundary conditions for pressure to achieve physiological flow splitting according to the following equation: $p=RQ+p_0$, where p is the pressure, Q is the flow rate, R is a resistance constant, and p_0 is the baseline mean arterial pressure. Several computational simulations were carried out to determine the correct resistance constants (R) at each outlet such that the total flow splitting into the vessels was 15.67%, 7.83%, 7.83%, and 68.67% in the BCA, LCCA, LSCA, and DA, respectively (based on patient data collected by Benim *et al.* [4]). For the hemodiluted blood viscosity of 3 cP, the resistance constants were found to be 2e3, 0.1e0, 4.3e3, and 4e0 Pa*s/m3 for the BCA, LCCA, LSCA, and DA, respectively.

Computational particle transport studies were also performed using OpenFOAM. Lagrangian particle transport capabilities to observe emboli distribution through the aortic arch branches (Fig. 3), mimicking the experimental study presented above. The simulations utilized OpenFOAM's validated solver 'particleFoam' for modelling the transport of a kinematic particle cloud.

RESULTS

Fig. 2 shows the experimental embolus trajectory results for both small and large beads and at each fluid viscosity investigated. It was found that for all the experimental blood viscosities, more small beads entered the BCA than large beads. Also, higher percentage of large beads were found to enter the DA compared to the small beads.

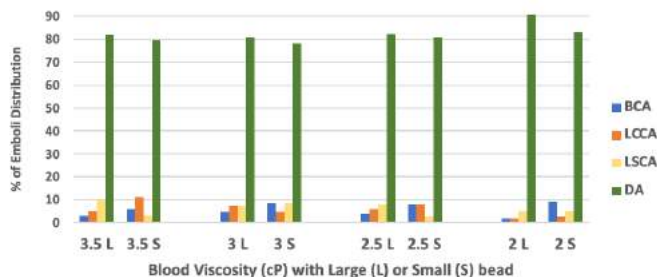


Figure 2: Distribution of two different-sized Nylon beads with fluid viscosities varying from 1.5 to 3.5 cP in the MCFL.

As shown in Fig. 3, a 6 mm diameter cannula was connected to the ascending aorta with a constant flow rate of 3 L/min to mimic anastomosis from the CPB circuit. Emboli transport is shown over time as the injected particles flow in through the CPB pump cannula and are distributed to one of the aortic outlets.

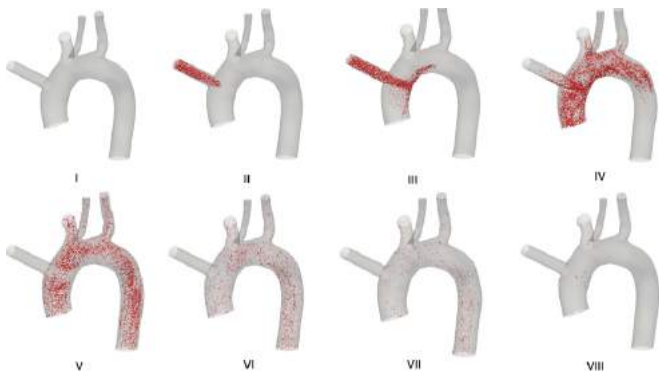


Figure 3: Visualization of emboli trajectories over time during computational emboli transport simulations in the aortic arch.

The particles were tracked until they exited through one of the aortic outlets. In phase II, the injection of the emboli into the aorta model is observed. The particles begin exiting through the outlets of the

model in phase IV until nearly all have been transported out of the fluid domain by phase VIII.

Figs. 4 and 5 compare emboli distribution in the 3-cP fluid during CPB in the experimental and computational studies, respectively.

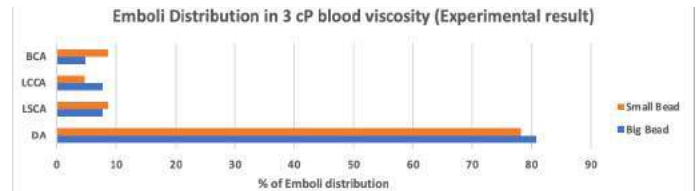


Figure 4: Experimental emboli distribution with 3-cP fluid.

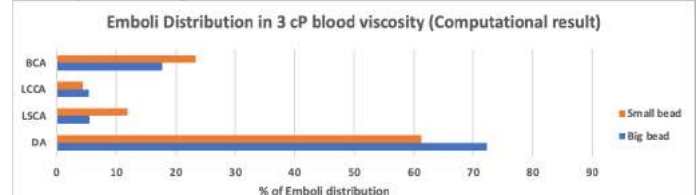


Figure 5: Computational emboli distribution with 3-cP fluid.

DISCUSSION

The computational simulations predict similar emboli distribution trends to those observed experimentally, with the small and large emboli entering specific aorta branches during CPB (Fig. 5). Similar to what was observed in the experimental study, the CFD simulation for 3-cP blood viscosity showed that the percentage of small emboli entering the BCA is greater than that of the large emboli. Likewise, the percentage of large emboli entering the DA was more than that of the small emboli. Also, for both embolic sizes, their tendency to enter the LCCA was found to be minimal. Figures 4 and 5 show that in both the experimental and computational studies, emboli distribution for small and large emboli was similar for each of the aortic branches.

The results of these experimental and computational studies indicate that larger emboli generated in CPB roller pumps are most likely to exit through the DA travelling to the abdomen and lower body. Likewise, smaller emboli have a higher tendency of exiting through the BCA which carries blood to the right arm and right side of the brain. Emboli exiting through the BCA thus increases the potential stroke risk in patients and can cause severe impairments due to a lack of oxygen supply to the brain. The experimental studies (Fig. 2) also observed that with decreasing hemodiluted blood viscosity, the beads have lower tendency of exiting through the LCCA and LSCA and higher tendency of exiting through the DA. Further studies will be carried out to understand how emboli travel to the brain during CPB and what techniques and pump operating conditions can be used to minimize this.

Further studies will be carried out to understand how emboli travel to the brain during CPB and what techniques and pump operating conditions can be used to minimize this. Also, future studies will also incorporate more realistic emboli sizes and compositions. Hence, through computational studies, the behavior of varying emboli sizes in the cerebral vasculature will be understood as to their risk of causing a stroke. Real embolus analogs (EAs) will also be injected into the MCFL to observe their distribution and to determine if the elastic properties of the EAs will play a role in their transport. Upon completion, this study will contribute to reducing stroke risk and CPB complications, hence increasing the overall safety of cardiovascular surgery.

REFERENCES

- [1] Raffa, G et al., *Journal of Cardiothoracic Surgery*, 2019.
- [2] Malone, F et al., *Journal of Biomechanical Engineering*, 2019.
- [3] Wilson, N et al., *Journal of Medical Devices*, 2013
- [4] Benim, A et al., *Applied Mathematical Modeling*, 2011.

DEEP LEARNING ENABLES ACCURATE ESTIMATION OF TISSUE DEFORMATION *IN VIVO*

Reece D. Huff¹, Frederick C. Houghton¹, Conner C. Earl², Elnaz Ghajar-Rahimi²,
Ishan Dogra¹, Andrew J. Darling², Frederick W. Damen², Guoyang Zhou²,
Denny Yu³, Craig J. Goergen², Carisa Harris-Adamson^{4,5}, Grace D. O'Connell^{1,6}

¹Department of Mechanical Engineering, University of California, Berkeley, Berkeley, CA, USA.

²Weldon School of Biomedical Engineering, Purdue University, West Lafayette, IN, USA.

³School of Industrial Engineering, Purdue University, West Lafayette, IN, USA.

⁴School of Public Health, University of California, Berkeley, Berkeley, CA, USA.

⁵Department of Occupational and Environmental Medicine, University of California, San Francisco, CA, USA.

⁶Department of Orthopaedic Surgery, University of California, San Francisco, San Francisco, CA, USA.

INTRODUCTION

Measuring tissue deformations using medical images allows researchers to noninvasively track tissue mechanics with degeneration or rehabilitation. Researchers have used *image texture correlation* algorithms to compare pixel intensities between successive images and calculate the displacement field between pixels, which is then numerically differentiated to obtain a strain field. These techniques have been applied in various contexts, including quantifying forces in myocardial cells,¹ detecting breast cancer,² and studying impact of disease on tissue mechanics *in vitro*.³ However, these algorithms often struggle with *in vivo* images, partly due to low signal-to-noise ratio and out-of-plane motion.⁴ Therefore, the objective of this study was to develop a new technique using deep learning (called **StrainNet**) to accurately predict tissue deformation and ignore image artifacts (*e.g.*, noise). We hypothesized that **StrainNet** would outperform traditional image texture correlation algorithms on synthetic images with known deformations and a real dataset of a wrist flexor tendon undergoing contraction *in vivo*. Our results showed that **StrainNet** reduced error by up to 84% when compared to traditional image texture correlation algorithms in the synthetic datasets. Moreover, the measurements made by **StrainNet** in the *in vivo* experiments were strongly correlated with the measured grip force distributed to the wrist flexor tendons.

METHODS

Experimental Procedure. To investigate *in vivo* tendon mechanics, a participant was asked to perform maximum voluntary contraction (MVC) of their forearm using an IRB-approved protocol (IRB-2020-497). A dynamometer was used to track and measure applied forces during contraction, and the MVC was calculated as the average of three trials. Next, the participant was instructed to contract their forearm to 10%, 30%, or 50%

of their MVC in three seconds, hold the contraction for five seconds, and relax their forearm in three seconds. High-frequency ultrasound images (Vevo3100, FUJIFILM VisualSonics Inc., Toronto, Ontario, Canada) of the participant's *flexor digitorum superficialis* tendon were collected throughout the contraction and release. This protocol was repeated five times for each effort level, resulting in a total of 15 trials.

Synthetic Test Cases. To test the accuracy of our strain analysis method on a dataset with known deformations, five synthetic test cases were created by artificially imposing a non-linear strain field onto collected ultrasound images. These test cases simulated the process of contraction and relaxation in our experimental procedure described above. Additionally, the prescribed non-linear strain field was designed to reflect reported observations for *in vivo* tendon mechanics. Specifically, the strain in the superficial layer was set to 75% of the deep layer,⁵ and the tendon was modeled as an incompressible material.^{6,7} The five test cases differed in their maximum longitudinal strain, ϵ_{long}^{max} , which was set to 4%, 7%, 10%, 13%, and 16% to cover the range of strains observed *in vivo*.^{5,7-9} Noise was added to all synthetic test cases to simulate the level of noise present in the experimental dataset. By using synthetic test cases with known deformations, we were able to compare the performance and accuracy of our deep learning based approach with existing texture correlation algorithms.

StrainNet. **StrainNet** is a deep learning model designed to predict 2D Lagrangian strain from a sequence of ultrasound images of the wrist flexor tendon. It consists of a two-stage architecture, with the first stage classifying the type of bulk deformation present in the image pair (tensile, compressive, or rigid-body) and the second stage predicting the strains throughout the image. To train the model, a set of synthetic images with random deformations was utilized. The deformations in these images were generated using a generalized mathematical model of tendon mechanics, SB³C2023-163
Copyright 2023 SB³C Foundation, Inc.

with the governing parameters being randomly varied to produce a diverse range of strain distributions (e.g., 2% - 20% bulk strain in the longitudinal direction). The training set included 1,000 images in tension, 1,000 images in compression, and 1,000 images undergoing rigid deformation. The model was trained using the Adam optimizer for 100 epochs, allowing it to learn the patterns and features associated with different types of deformation and accurately predict strain in unseen images.

Data Analysis and Statistics. StrainNet, digital image correlation (DIC),¹⁰ and direct deformation estimation (DDE)¹¹ were applied to synthetic test cases and experimental images. For the synthetic test cases, the strain error was calculated as the ℓ_2 -norm between the ground truth strain tensor and the algorithm-predicted strain tensor. A pairwise permutation test was conducted on the median strain error for each of the five test cases, with significance set at $p \leq 0.05$. For experimental images, the true strain was unknown, so the analysis was limited to a qualitative assessment. However, linear regression was conducted between the maximum longitudinal strain predicted by the three algorithms during contraction and the percentage of MVC. A strong correlation was defined as an $|r| > 0.7$.

RESULTS

Of the 15 trials conducted, two trials were discarded due to corruption of data file containing the forces measured by the dynamometer.

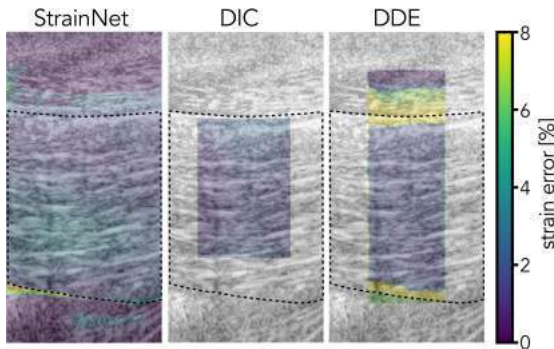


Figure 1: Spatial distribution of errors incurred by StrainNet, DIC, and DDE during maximum contraction in the synthetic test case with maximum longitudinal strain of 10%. Black dashed line represents the boundary between the flexor tendon and the surrounding soft tissue.

In the synthetic test cases, errors were largest at the boundary between the tendon and surrounding tissue. StrainNet achieved pixel-wise strain estimation while DIC and DDE were limited to the central area of interest (Fig. 1). The median strain error from StrainNet was 48-84% lower than the strain error from both DIC and DDE (Fig. 2; $p < 0.001$ in all strain cases).

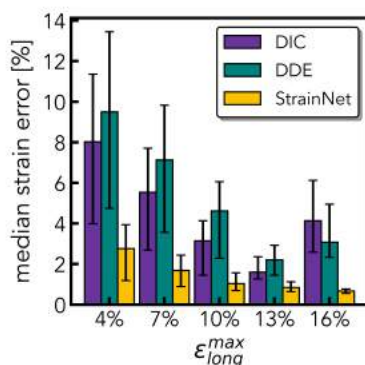


Figure 2: Median strain error across all five synthetic test cases. Median strain error was statistically significantly lower than DIC and DDE across all test cases ($p < 0.001$).

For the real experimental images, both DIC and DDE underperformed and many pixels were lost during image analysis. StrainNet, on the other hand, was able to learn around much of the noise and accurately predict the longitudinal strain in the tendon, which increased as effort level increased. There was a strong linear relationship between the predicted longitudinal

strain and percent MVC (Fig. 3; $r = 0.784$, $p = 0.002$), which is comparable to the expected linear relationship between strain and stress for tendon mechanics.

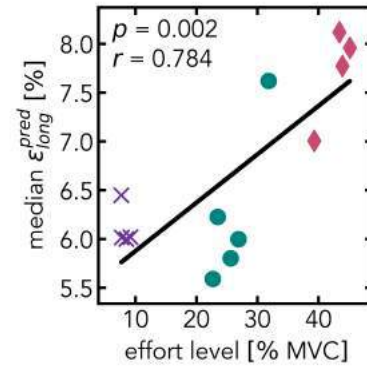


Figure 3: Median longitudinal strain predicted by StrainNet during tendon contraction across all of the trials ($n = 13$). \times 's, \bullet 's, and \blacklozenge 's correspond to 10% , 30%, and 50% MVC.

DISCUSSION

StrainNet was able to accurately measure and quantify the different strain levels using ultrasound images of the flexor tendon. For synthetic datasets, StrainNet detected subtle differences in deformations with a high degree of accuracy ($< 3\%$ error), outperforming existing approaches (e.g., DIC and DDE), which had median strain errors as high as 10%. Additionally, when applied to *in vivo* images, StrainNet predicted a strong linear correlation between the measured strain and effort level (percentage of the MVC), further validating the performance of the model. These findings suggest that deep learning models have the potential to significantly advance the accuracy of *in vivo* biomechanics studies.

There are several limitations to our model that will be addressed in future work. First, the model was evaluated on a single tissue type and location, so it is not clear whether it can be applied to a wider range of tissue types. Additionally, the current architecture is specialized to handle only three types of deformation, and it would be useful to explore expanding its capabilities to a wider range of deformations (e.g., shear). Lastly, improvements to the architecture or training the model on a larger dataset may also allow us to remove the need for the first stage of the model, which currently classifies the type of deformation present in the image pair.

The potential applications of StrainNet are numerous and exciting. Our results indicate that StrainNet greatly outperforms traditional image texture correlation algorithms in controlled settings, such as the synthetic test cases (Fig. 2). In more challenging environments where image texture correlation is prone to error due to image artifacts, such as *in vivo* measurements of tendon mechanics in real time, StrainNet has demonstrated the ability to provide reasonable and expected levels of tissue deformation (Fig. 3). Taken together, these findings suggest that StrainNet could be applied to a wide range of biomedical contexts, including *in vivo* studies of muscle function, blood flow, and tissue viability. Overall, the design and capabilities of StrainNet are ripe for continued research and development, with the potential for significant advancements in these areas.

The code, trained models, and tutorial for using StrainNet will be available at strainnet.net.

ACKNOWLEDGEMENTS

This study was supported by the NIH (NIH R21 AR075127-02), the NSF (NSF GRFP), and the Training Grant, T42OH008429, funded by the National Institute for Occupational Safety and Health (NIOSH) / Centers for Disease Control and Prevention (CDC).

REFERENCES

- [1] Ribeiro+. *PNAS* (2015).
- [2] Han+. *J Mech Behav Biomed Mater* (2012).
- [3] O'Connell+. *JOR* (2011).
- [4] Sutton+. *Opt Lasers Eng* (2008).
- [5] Lee+. *Scand J Med Sci Sports* (2017).
- [6] Suydam+. *J Biomech* (2014).
- [7] Vergari+. *J Biomech* (2011).
- [8] O'Brien+. *J Biomech* (2010).
- [9] Sheehan+. *Clin Orthop Relat Res* (2000).
- [10] Sutton+. *Correlated Strain* (2014).
- [11] Boyle+. *J R Soc Interface* (2014).

IMPROVING ANTI-THROMBOGENIC POTENTIAL OF A POROHYPERELASTIC BILAYERED VASCULAR GRAFT USING LUMINAL REVERSAL FLOW

Ali Behrangzade (1), Sang-Ho Ye (2,4), William R. Wagner (1,2,4),
Jonathan P. Vande Geest (1,3,4,5)

(1) Department of Bioengineering, University of Pittsburgh, Pittsburgh, PA, USA

(2) Department of Surgery, University of Pittsburgh, Pittsburgh, PA, USA

(3) Department of Mechanical Engineering, University of Pittsburgh, Pittsburgh, PA, USA

(4) McGowan institute for Regenerative Medicine

(5) Vascular Medicine Institute

INTRODUCTION

Cardiovascular diseases (CVD) resulted in around 1 million deaths in 2017 in the U.S. [1]. Atherosclerosis is a form of CVD and a major cause of CVD-related mortality rate. In atherosclerotic arteries, fatty plaques are formed in the arterial wall and block the blood flow, depriving downstream tissue from nutrients and oxygen. This disease can affect both coronary and peripheral arteries. One of the treatments for these patients is bypass surgery using vascular grafts. One of the failure mechanisms of vascular grafts is thrombosis. Platelets are critical in formation of thrombosis. Particularly, non-homeostatic shear stress and the exposure to foreign material can trigger platelet activation. Variety of chemical methods have been studied to prevent thrombosis following vascular graft implantation. These efforts include but are not limited to conjugation of Heparin, Poly-ethylene Glycol, and vascular endothelial growth factor to the luminal surface of the vascular grafts. In contrast, there has been very limited number of studies focusing on mechanical approaches to interrupt coagulation cascade and thrombus formation process. In this regard, surface topology has been studied that has shown lower surface roughness decreases platelet adhesion. In another study, platelet adhesion was lowered using surface wrinkling during diastole. Herein, we have developed a layered and porous vascular graft to reduce thrombogenicity. During systole, fluid can penetrate through the porous structure of a vascular graft. We have optimized the porohyperelastic (PHE) response of the graft such that the fluid velocity through the vascular graft wall is reversed during diastole – Luminal Reversal Flow (LRF) – and the fluid is moved back into the luminal space. We hypothesized that the momentum carrying LRF can repel the platelets and drive self-cleaning.

METHODS

We have previously shown that the PHE response of a bilayered vascular graft can be optimized to promote luminal reversal fluid velocity [2]. Our results showed that a highly permeable inner

layer and a highly impermeable outer layer in a deformable vascular graft are required to boost the LRF. In another effort, we have shown that electrospun Polycaprolactone (PCL) fibers will fuse into each other under thermal treatment (thermobonding) and create a highly impermeable scaffold [3]. Leveraging the results of these two studies, we fabricated LRF- generating bilayered vascular grafts (1.1mm ID - rat aortic size) to assess the hemocompatibility. The Inner layer of the vascular graft is composed of electrospun Tecoflex and the outer layer is made of electrospun PCL. Following electrospinning, the bilayered grafts underwent thermal treatment in a convection oven at 60°C for 3 minutes. This post-processing creates a bilayered graft with an impermeable PCL outer layer that is relatively stiff. The outer layer thickness was minimized in the anti-thrombogenic grafts with high LRF to reduce its effect on deformability. Control grafts were fabricated using the same procedure but with a thicker outer layer to significantly reduce LRF. Both groups had the same blood contact area and material. We have also computationally predicted the LRF in each experimental group. **Figure 1** illustrates the geometry used in the axisymmetric PHE finite element model of a bilayered vascular graft. To predict the LRF,

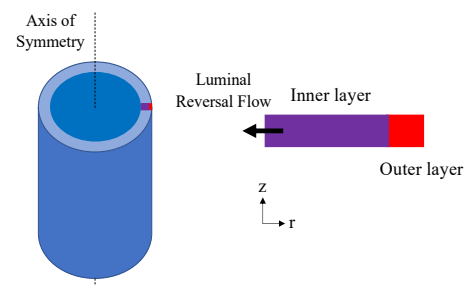


Figure 1. Geometry used in the axisymmetric PHE finite element model of a bilayered vascular graft (computational predictions of LRF)

we mechanically characterized electrospun Tecoflex and thermobonded PCL constructs using a microbiaxial tensile testing device. We also measured the thickness of the layers and surface porosity of the scaffolds using SEM images. A void-dependent permeability finite element porohyperelastic model (ABAQUS) was used to inversely find the material properties and then computationally predict the LRF values. **Figure 2** represents cross-sectional SEM images of the LRF-generating grafts (Higher LRF) and controls (Lower LRF). These grafts were sutured and glued at both ends and connected to a mock flow loop (Figure 3). Fresh citrated ovine whole blood was circulated in the loop using roller pumps. The test was performed at 37°C for 1.5 hours. The flow rate was set to 10 mL/min. The grafts were then washed with PBS and stored in Triton-X and glutaraldehyde solutions for Lactate dehydrogenase (LDH) assay and SEM imaging, respectively. LDH assay was performed to measure the absorbance of the solutions containing blood contact samples. A standard curve was generated

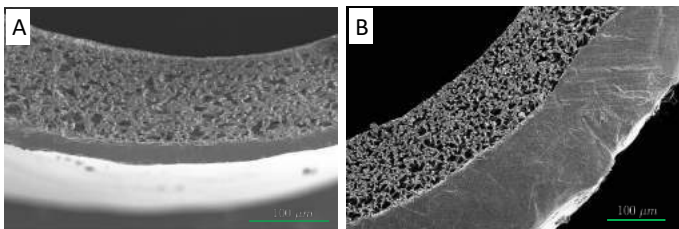


Figure 2. Representative SEM images of the grafts with higher LRF (A) and lower LRF (B - controls).

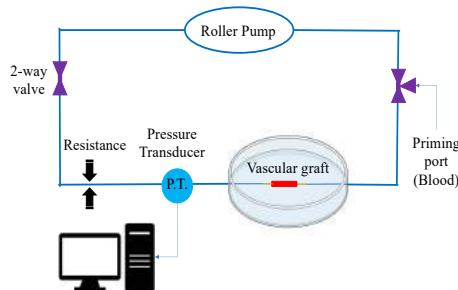


Figure 3. Mock flow loop for assessment of hemocompatibility

using fresh blood to correlate the absorbance values with the number of platelets. SEM imaging was done to visualize the platelets and validate the LDH results. A student t test was used to infer the statistical difference between groups ($p < 0.05$).

RESULTS

Figure 4 represents the number of platelets per luminal surface area of each experimental group. The vascular grafts with higher LRF had an average of 66% lower number of platelets. **Figure 5** shows the SEM images from the luminal surface of vascular grafts with higher LRF and the controls. The high LRF group had a lower number of platelets on the luminal surface of the grafts compared to the low LRF group which confirms the results of the LDH assay. Computationally predicted values of LRF for high LRF grafts were approximately -11.2 mm/s. The LRF value of the control group was about -4.2 mm/s. Higher LRF was associated with lower platelet adhesion.

DISCUSSION

Our results indicated an improved hemocompatibility in the vascular grafts with higher luminal reversal flow compared to the grafts

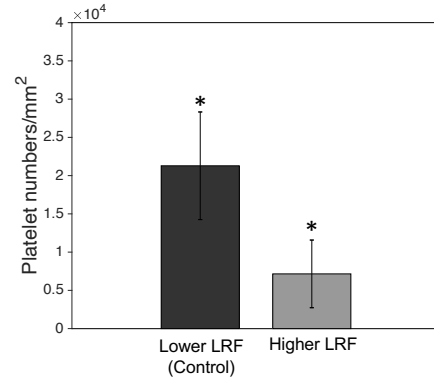


Figure 4. Number of platelets per luminal surface area of vascular grafts with higher (n=5) and lower LRF (n=4).

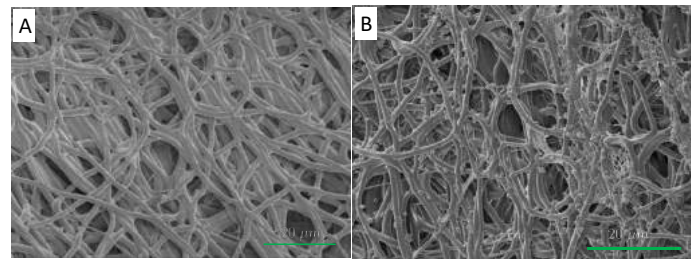


Figure 5. Platelet adhesion to the luminal surface of the vascular grafts. Control group (B) has significantly higher number of platelets on the surface.

that generated lower reversal flow. The presence of LRF has been computationally confirmed in another study on intraluminal thrombosis in abdominal aortic aneurysms [4]. Soldani et. al. have also demonstrated that the formation of thrombosis (in-vivo) is reduced in bilayered grafts with a highly porous inner layer and a low porosity outer layer compared to the grafts with a reversed porosity of the layers [5]. However, they attributed these findings to less available surface area in the inner layers of their grafts. This study had several limitations. The compliance of the high-LRF grafts was relatively low compared to rat aortic tissue. Therefore, a new method is required to achieve an impermeable outer layer. The pressure range of the roller pumps was 20-220 mmHg. The material model used for the computational predictions did not take material anisotropy into account. Thrombosis is considered a major clinical problem with no permanent solution. We have used local mechanics manipulation to improve hemocompatibility [6] and shown a significant reduction in platelet adhesion.

ACKNOWLEDGEMENTS

This research was funded by the NIH R01HL157017 and the American Heart Association pre-doctoral fellowship (20PRE35211036 to A. Behrangzade). The computational resources of this research were supported by University of Pittsburgh Center for Research Computing (CRC). We also appreciate all the assistance from Bruce. R Simon, Hannah R. Keeney, and Katarina M. Martinet.

REFERENCES

- [1] American Heart Association, *Circulation*, 2021.
- [2] Behrangzade, A. et al., *J Biomech Eng.*, 145(2): 021002, 2023.
- [3] Behrangzade, A. et al., *J Biomed Mat. Res. Part B*, 2022.
- [4] Ayyalasomayajula, et. al., *J Biomech Eng*, 123(10): 104502, 2010.
- [5] Soldani et. al., *Biomaterials.*, 31(9): 14, 2009.
- [6] PCT Application No. PCT/US2021/037582. 2021.

SUBJECT-SPECIFIC ONE-DIMENSIONAL FLUID DYNAMICS MODEL OF CHRONIC THROMBOEMBOLIC PULMONARY HYPERTENSION

Amirreza. Kachabi (1), Mitchel J. Colebank (1), Naomi C. Chesler (1)

(1) University of California Irvine – Edwards Lifesciences Foundation Cardiovascular Innovation
and Research Center, and Department of Biomedical Engineering, University of California, Irvine
Irvine, CA, USA

INTRODUCTION

Pulmonary emboli, blood clots that lodge in the small vessels of the lung, increase blood pressure in the lung circulation and can overload the heart. Chronic thromboembolic pulmonary hypertension (CTEPH) is a debilitating disease that is curable with early diagnosis and surgery, but, if left untreated, can lead to right ventricular failure and death [1].

CTEPH is diagnosed by a mean pulmonary artery pressure (mPAP) ≥ 20 mmHg at rest, pulmonary capillary wedge pressure (PCWP) ≤ 15 mmHg, and imaging data confirming clot burden [2]. Measurement of these pressures requires an invasive right heart catheterization (RHC). To study disease progression, large animal models of CTEPH have been developed, e.g., injecting microspheres into the pulmonary arteries (PAs) serially until a chronic disease develops. These data can be integrated with computational models to simulate subject-specific pulmonary hemodynamics and identify novel indicators of progression.

Here, we use an image-based nonlinear one-dimensional (1D) computational fluid dynamics (CFD) model to predict hemodynamics throughout the pulmonary arterial network in canines before and after CTEPH induction. We calibrate our model to available hemodynamic and imaging data and then use the model to quantify the impact of CTEPH on hemodynamic metrics not feasible to measure. Our image experimental-computational framework gives insight into the proximal and distal effects of CTEPH and provides a future tool for understanding changes in hemodynamic forces in the progression of the disease as seen clinically.

METHODS

All experimental data were obtained retrospectively; a detailed protocol and complete reporting of measurements can be found in [3]. Briefly, CTEPH was induced by injecting multiple microspheres into the PAs using an indwelling catheter in five, adult male canines (12 ± 1 kg body weight). Measured hemodynamic data included systolic and diastolic

proximal PA pressures and PCWP from RHC. Imaging data included time series velocity and area at the main, left, and right pulmonary artery (MPA, LPA, and RPA, respectively, i.e., the extralobar PAs) from chest magnetic resonance imaging (MRI). All data were collected at baseline and after CTEPH development. Dynamic flow was calculated as a product of velocity and cross-sectional area for each extralobar PA. From MRI, extralobar and intralobar PA geometries for fluid dynamic simulations were segmented using 3D slicer. We used the vascular Modeling Toolkit [4] to convert the segmentations to 1D centerline networks, and then post-processed the networks using custom MATLAB (Natick, MA) software to create the 1D CFD domain.

Assumptions include that: blood vessels are impermeable and cylindrical, that flow is axially driven, and that the blood is an incompressible, Newtonian fluid with a dynamic viscosity $\mu=0.049$ Pa·s and density $\rho=1055$ (kg/m³). The governing mass conservation and momentum equations are given by:

$$\frac{\partial q}{\partial x} + \frac{\partial A}{\partial t} = 0 \quad (1)$$

$$\frac{\partial q}{\partial t} + \frac{(\gamma + 2)}{(\gamma + 1)} \frac{\partial}{\partial x} \left(\frac{q^2}{A} \right) + \frac{A}{\rho} \frac{\partial p}{\partial x} = - \frac{2\pi\mu(\gamma + 2)}{\rho} \frac{q}{A} \quad (2)$$

where x and t represent the axial and temporal coordinates, and q , p and A are the volumetric flow (mL/s), pressure (mmHg), and cross-sectional area (cm²). We assumed the blood velocity follows a power-law profile,

$$u(x, t) = U(t) \frac{\gamma + 2}{\gamma} \left(1 - \frac{r^\gamma}{R(t)^\gamma} \right) \quad (3)$$

with $\gamma = 9$, where $R(t)$ (cm) is the time-dependent inner radius and $U(t)$ (cm/s) is the mean axial velocity. To close the system of equations, we assume that the vessels are linearly elastic, thin walled, incompressible, and isotropic. This gives the constitutive law

$$p = \frac{4 Eh}{3 r_0} \left(\sqrt{\frac{A}{A_0}} - 1 \right) + p_0 \quad (4)$$

where E is the circumferential Young's modulus (mmHg), h (cm) is the wall thickness of the artery, and $A_0 = \pi r_0^2$ (cm²) is the diastolic arterial area at the diastolic pressure p_0 (mmHg). Vessel mechanical properties are governed by $4Eh/3r_0$, which is determined analytically using systolic and diastolic pressure and area data.

Boundary conditions are specified at the inlet of the network and at each terminal vessel outlet. Dynamic flow from MRI is used at the network inlet, while 3 element Windkessel models including a proximal (R_1) and distal (R_2) resistance and one capacitance (C) are used at the network outlets. Nominal Windkessel resistance is calculated based on a Poiseuille argument, i.e. $R_T = 8\mu L/\pi r^4$ for each vessel. We assume that proximal and distal resistances are equal. Nominal capacitance is determined by fitting an exponential decay from systolic to diastolic MPA pressure over the time-course of diastole. We calibrate the Windkessel parameters of the 1D model using a combination of systolic and diastolic pressure-area data, as well as time-series LPA and RPA flow. All Windkessel parameters are scaled using the reduced parameter set $\phi_{wk} = \{r_1, r_2, c\}$ using weighted nonlinear least squares [5]. We investigate how CTEPH affects pressure, flow, and time averaged wall shear stress (TAWSS)

$$TAWSS = \frac{1}{T} \int_0^T |\tau| dt \quad \text{where} \quad \tau = \mu \left(\frac{\partial u}{\partial r} \right)_{r=R} \quad (5)$$

throughout the network. Here, τ (dyne/cm²) is the arterial wall shear stress and T (s) is the cardiac cycle length.

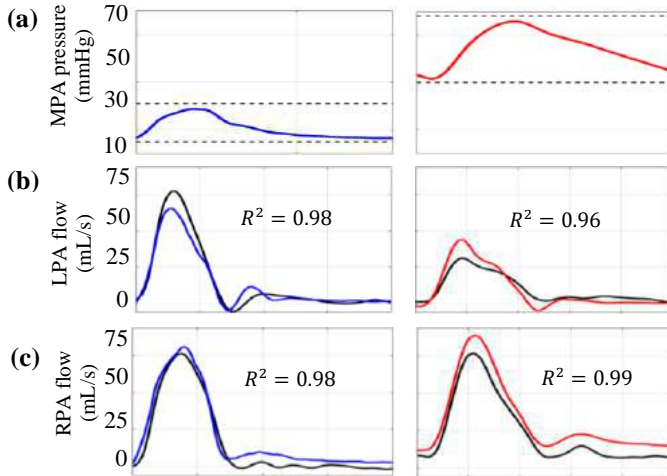


Figure 1: (a) MPA pressure, (b) LPA flow, and (c) RPA flow for a representative subject at baseline (blue; left) and with CTEPH (red; right).

RESULTS

Figure 1(a) shows model pressure predictions (solid lines) and measured systolic and diastolic pressure (dashed lines) for a representative animal in which mPAP increased from 20 to 51 mmHg from baseline (blue; left) to CTEPH (red; right) [3]. For the same animal, Figures 1(b) and 1(c) show LPA flow and RPA flow, respectively, from measurements (black) and model predictions (blue, left at baseline and red, right with CTEPH). The averaged R^2 between the measured and simulated flow improved after optimization: the averaged R^2 increased from 0.94 (± 0.04 SD) (without optimizing) to 0.96 (± 0.03) (after optimizing) in the LPA and 0.97 (± 0.025) to 0.986 (± 0.009) in the RPA at baseline. The average R^2 improved from 0.76 (± 0.2) to 0.88 (± 0.09) in the LPA and 0.94 (± 0.06) to 0.97 (± 0.027) in the RPA with CTEPH. All animals

had a reduced cardiac output and network flow after CTEPH induction. However, significant asymmetries and heterogeneity were evident. The animal shown in Figure 1 had a decrease in mean flow from 0.73 to 0.5 (mL/s) ($\approx 30\%$) in the distal pulmonary arteries of the left lung with CTEPH and an increase ($\approx 70\%$) in the distal arteries of the right lung. Figure 2 shows a 3D map of average TAWSS distribution in baseline (left) and CTEPH (right) in this animal. Despite high flows to the right lung, TAWSS decreased due to arterial dilation. Considering only the extralobar arteries (MPA, LPA, and RPA), on average CTEPH significantly decreased TAWSS in the LPA ($\approx 42\%$; $p=0.049$) and tended to decrease TAWSS in the MPA ($\approx 43\%$; $p=0.152$) and RPA ($\approx 60\%$; $p=0.144$), as shown in Figure 3.

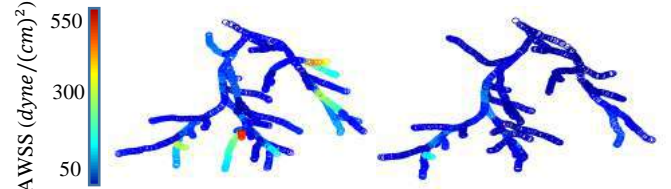


Figure 2: 3D map of TAWSS distribution in the network for baseline(right) and CTEPH (left)

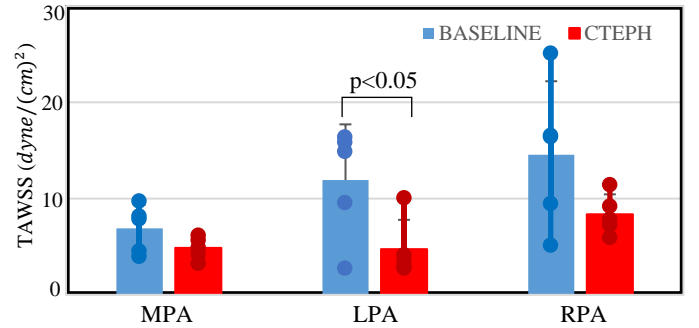


Figure 3: MPA, LPA, and RPA TAWSS under baseline (blue) and CTEPH (red) conditions; n=5.

DISCUSSION

We used a 1D CFD model to simulate arterial hemodynamic features (i.e., wall shear stress) that are infeasible to measure based on experimentally obtained pressure and imaging data. One novelty of this study is that we efficiently calibrated our model with systolic and diastolic pressures and areas, as well as dynamic flow data from each subject in both baseline and CTEPH conditions to increase accuracy. Qualitatively, the model matches measured pressures (Figure 1) and quantitatively, the model matches measured flows (high R^2 values). Our finding of asymmetry is supported by the experimental observation that more microspheres were delivered to the left lung [3]. We also investigated changes in TAWSS with CTEPH, and our results agree with previous clinical studies predicting reduced TAWSS with CTEPH [6]. Thus, our synergistic experimental-computational framework shows promise as a future, patient-specific simulator of proximal and distal hemodynamics under CTEPH conditions.

ACKNOWLEDGEMENTS

Funding support from Inari Medical, Inc.

REFERENCES

- [1] Miller, D, et al. *J Pulmonol Respir Res* 6: 012-015, 2022.
- [2] Lang, IM, et al. *CIRCULATION* 5:130(6):508-18, 2014.
- [3] Mulchrone, A, et al. *Front Cardiovasc Med* 9:5:189, 2019.
- [4] Antiga, L, et al. *Med Biol Eng Comput* 46:1097-1112, 2008.
- [5] Qureshi, M.U et al. *Biomech Model Mechanobiol* 18, 219–243, 2019.
- [6] Spazzapan, M, et al. *Front Physiol* 13:9:223, 2018.

DETERMINING STRAINS FROM INTACT AIRWAY INFLATION TESTS AS COMPARED TO ISOLATED UNIAXIAL AND BIAxIAL TENSILE TISSUE TESTING

Crystal A. Mariano (1), Stanislav Polzer (2), Mona Eskandari (1,3,4)

- (1) Department of Mechanical Engineering, University of California Riverside, Riverside, CA, USA
- (2) Department of Applied Mechanics, VSB-Technical University of Ostrava, Ostrava, Czech Republic
- (3) BREATHE Center, School of Medicine, University of California Riverside, Riverside, CA, USA
- (4) Department of Bioengineering, University of California Riverside, Riverside, CA, USA

INTRODUCTION

Lung diseases are continually rising as one of the leading causes of death in the United States with no indication of major improvement [1]. While common respiratory illnesses manifest from airway obstruction [2], characterization of airway mechanics is still lacking. Airway morphology has been explored using optical coherence tomography (OCT) [3], but such methods are limited to stepwise regional analysis rather than a real-time assessment of whole airway evolution when inflated. Previous studies have employed mechanical testing on the trachea [4,5], and the bronchial airways [6,7], but tissue samples were isolated from the branch structure when subjected to uniaxial or biaxial loading. Physiological expansion of the airways however, includes multi-axial deformations, which has remained elusive to date.

This novel study aims to broaden our understanding of airway mechanical properties by utilizing digital image correlation (DIC) coupled with continuous global pressure-volume inflation to assess the stress and strains of whole and intact main airway branches for the first time. By analyzing the heterogeneous and anisotropic surface strains of the bronchial tree in real-time, we offer new insights regarding the compound structural effects of the soft tissue and cartilaginous constituents of the airway and compare our findings to past results from isolated tissue strips. These observations improve our understanding of the physiological strains present in the airway tree and enable future predictive computational modeling of the lung.

METHODS

Four porcine lungs were extracted from 6-8 month old, 200–250lb pigs obtained from an abattoir (IACUC exempt). Preliminary investigations observed no difference between right and left branching airway mechanics; as such, the primary left airways were used. Airways were cut 1cm above the anatomical accessory lobe and 14cm beyond the main left and right airway junction to ensure uniformly comparable samples between pigs. Regions were distinguished by their location and

inner diameters as follows: the trachea (>17mm) was above the main airway junction, the large bronchi (>9mm) was 7cm below the junction, and the small bronchi (>3mm) was 7cm beyond the large bronchi.

A latex condom was traversed within the airway; having a notable inner diameter greater than the airway allowed for unconstrained inflation which circumvented the need to suture shut each adjacent branch, thus providing a leak-free testing set up. The whole airway sample was speckled for DIC analysis using an airbrush and connected to our custom pressure-volume system [8,9]. Each airway was preloaded to 0.7 cmH₂O, which ensured the condom was inflated to fill the airway's resting state. Preliminary tests deemed the airways exhibited a reproducible response when cycled, and thus, there was no need for preconditioning [10]. The specimens were inflated once to 200ml at a rate of 15 breaths per minute, corresponding to physiological lung pressures of 30 cmH₂O [11], and DIC was simultaneously recorded [Trilion Quality Systems, King of Prussia, PA].

Virtual tissue sections (6x6mm) measured the strain of the compliant airway soft tissue between the cartilage fragments for each of the trachea, large bronchi, and small bronchi regions to compare with analogous regions from previous airway mechanical test samples [6, 7]. For the full inflation cycle, axial and circumferential strains of each region were averaged (Figure 1). Airway pressure, radii, and thickness were used to calculate stresses according to thin-walled cylindrical pressure vessel theory. Airway inflation stress-strain profiles for each region and orientation were compared to previous studies (Figure 2).

RESULTS

A contour map for both axial and circumferential strain of a representative porcine airway (Figure 1A), and the associated average strain temporally evolving during the inflation cycle is shown (Figure 1B). Highest tissue strains were observed at the junctures between cartilage rings of the trachea with values of nearly 30% strain in the circumferential direction and 8% in the axial direction.

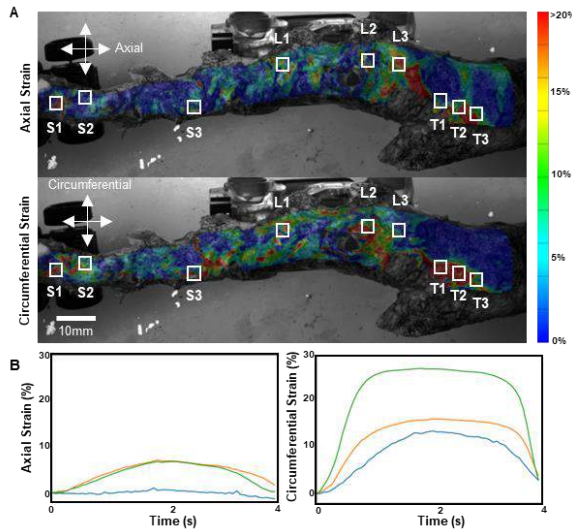


Figure 1: (A) Directional strain contour maps of a representative porcine airway sample inflated to 200ml corresponding to physiological pressures of 30cmH₂O [11]. (B) Strain values from three virtual soft tissue samples were averaged for each lung region and direction during the inflation cycle.

Axial strains were notably decreased compared to circumferential strains for all three lung regions, with nearly a two-fold difference within the trachea and small bronchi regions. The bronchial airway regions observed lower strains than the trachea in the circumferential direction. However, the large bronchi exhibited similar axial strains to the tracheal region, sharing a maximum strain value of 8%. Circumferentially, the trachea and large bronchi also shared an asymptotic stop-length response once the maximum strain was reached.

Stress-strain curves of the three lung regions and two orientations were compared to previous uniaxial and biaxial mechanical airway tissue studies as shown in Figure 2. This study found greater peak stress values at the maximum strain values seen during inflation. The tracheal samples showed consistently higher stresses compared to bronchial regions, similar to the biaxial and uniaxial data, except for the case of the uniaxial circumferential response, where the tracheal stresses were found to be lower than their bronchial counterparts. As with other testing methods, circumferential stress values at the maximum strain for this study were lower than their corresponding axial stresses, except for the uniaxial tests of the small bronchi region, which were found to be lower axially than circumferentially. Inflation test curves diverged from the planar isolated tissue strip studies at ~10% strain in the circumferential direction and at <5% strain for the axial orientation.

DISCUSSION

Our novel DIC divulged airway mechanics report notably higher circumferential and axial stresses in the trachea compared to the bronchial airways, in agreement with prior biaxial studies and axial trends from the uniaxial study [6,7]. Airway open angle experiments have concluded residual stresses in the trachea [12] and a lack thereof in the bronchial airways [13], posing a potential explanation for the noted heterogeneity between proximal and distal airways. Additionally, the cartilage structure varies within the airway tree, potentially dictating the high strain regional behaviors which further differentiate the trachea and bronchial regions: in the trachea, c-shaped cartilage rings are joined by smooth muscle [14], whereas the cartilage in the distal bronchi is segmented with multiple strips [15]. As such, the soft tissue response is evident in the strain contour maps (Figure 1A), where a single area of

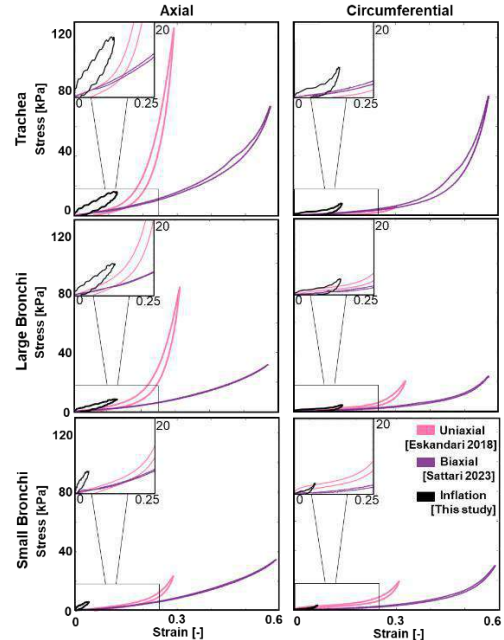


Figure 2: Regional stress-strain curves of airway tissue samples subjected to uniaxial, biaxial, and inflation mechanical testing in the circumferential and axial direction.

high strain is noted to develop axially and circumferentially within the trachea [16]; alternatively, high strain locations are observed to be scattered across the large and small bronchi, corresponding to the soft tissue sections of the discontinuous cartilage.

It is important to note that previous uniaxial and biaxial tests focused solely on airway soft tissue [6,7], excluding the role of the cartilage altogether due to the independence and asynchrony between the cartilage plates and airway tissue [3]; however, inflating the compound, whole airway with the unaltered presence of the cartilage layer in this study yielded a notably stiffer mechanical response compared to studies of isolated tissue strips. The role of the cartilage appears to not be negligible, stiffening the overall response while acting as a stop-length for the soft tissue; as such, comprehensively characterizing the intact airway structure is more physiologically representative and can better inform computational lung models.

ACKNOWLEDGEMENTS

National Science Foundation Graduate Research Fellowship under Grant No. DGE – 1840991, awarded to Crystal A. Mariano.

REFERENCES

- [1] Mokdad, A. H. et al., *Jama*, 319(14):1444-1472, 2018. [2] Macklem, P. T., *Physiol Rev*, 51(2):368-436, 1971. [3] Noble, P. B. et al., *J Appl Physiol*, 108:401-411, 2010. [4] Trabelsi, O. et al., *Med Eng Phys*, 32:76-82, 2010. [5] Safshekan, F. et al., *Materials*, 9(6):456, 2016. [6] Eskandari, M et al., *J Appl Physiol*, 125:878-888, 2018. [7] Sattari, S. et al., *Acta Biomater*, 155:410-422, 2023. [8] Mariano, C. A. et al., *Front Physiol*, 11:600492, 2020. [9] Sattari, S. et al., *Front Bioeng Biotechnol*, 8:578762, 2020. [10] Mariano, C. A. et al., *Respir Res*, 23(92), 2022. [11] Berend, N. et al., *J Appl Physiol*, 49(4):558-565, 1980. [12] Han H. C. et al., *J Biomech*, 24(5):307-309, 1991. [13] McKay, K. O. et al., *J Appl Physiol*, 92:1261-1266, 2002. [14] Hyde, D. M. et al., *J Allergy Clin Immunol*, 124(6):S72-S77, 2009. [15] Su, Z. Q. et al., *Chest*, 156(5):915-925, 2019. [16] Bagnoli, P. et al., *J Biomech*, 46(3):462-469, 2013

INDIVIDUALS WITH ROTATOR CUFF TEARS REQUIRING SURGERY AFTER EXERCISE THERAPY HAVE LESS INFERIORLY DIRECTED MUSCLE FORCES POST-EXERCISE THERAPY

Luke T. Mattar (1), Arash B. Mahboobin (1), Adam J. Popchak (3), William J. Anderst (1,2),
Volker Musahl (1,2), James J. Irrgang (2,3), Richard E. Debski (1,2)

(1) Department of Bioengineering, University of Pittsburgh, Pittsburgh, PA, USA
(2) Department of Orthopaedic Surgery, University of Pittsburgh, Pittsburgh, PA, USA
(3) Department of Physical Therapy, University of Pittsburgh, Pittsburgh, PA, USA

INTRODUCTION

Exercise therapy for individuals with rotator cuff tears fails in approximately 25.0% of individuals [1]. One reason for failure of exercise therapy may be the inability to strengthen and balance the muscle forces crossing the glenohumeral joint that act to center the humeral head on the glenoid. The coronal and transverse plane force couples are responsible for centering the humeral head on the glenoid in the superior-inferior and anterior-poster directions, respectively [2,3]. If the magnitude of the joint reaction force is decreased and the muscle forces are imbalanced, the humeral head may not be centered on the glenoid. The objective of the study was to determine the magnitude and direction of the joint reaction force in individuals with symptomatic isolated supraspinatus tears after a 12-week personalized exercise therapy program. Individuals that opted for surgery (exercise therapy failed) because exercise therapy did not resolve their symptoms were compared to individuals successfully treated with exercise therapy (exercise therapy successful).

METHODS

Twelve individuals (6 exercise therapy failed, 6 exercise therapy successful, 57.9 \pm 10.9 years) provided IRB-approved consent before participation. Primary inclusion criteria included: 1) symptomatic tear isolated to the supraspinatus tendon, 2) partial-($>50\%$) or full-thickness tear, 3) and age >40.0 years. Eleven individuals had a full- and one had a partial-thickness tear. Individuals underwent a 12-week personalized exercise therapy program. Time to surgery for individuals in the exercise therapy failed group was 1.6 \pm 0.9 years and all individuals completed the 12-weeks of exercise therapy. Isometric muscle strength was measured by a licensed physical therapist in four joint positions (each position biased a rotator cuff muscle). Tear size and location was measured by a musculoskeletal radiologist via ultrasound and glenohumeral kinematics were quantified during scapular plane abduction using a biplane radiography system and validated model-

based tracking technique (accuracy $\pm 0.5^\circ$) [4]. All variables were collected pre- and post-exercise therapy. Glenohumeral joint models were created in OpenSim [5] using individual-specific bone geometries segmented from computed tomography images (slice thickness 0.625mm) for the humerus and scapula.

The maximum isometric force a muscle could produce pre-exercise therapy was based on muscle volume from computed tomography images and scaled post-exercise therapy by percent changes in isometric strength [6]. Maximum isometric force for each muscle was determined pre-exercise therapy using muscle volume since utilization of individual specific muscle parameters has been shown to influence joint reaction forces [6]. The supraspinatus, infraspinatus and subscapularis were represented by 3 muscle-tendon units each and the teres minor and middle deltoid with one unit each. Maximum isometric force for each supraspinatus unit was scaled by the amount of tendon torn based on tear size, location and thickness measured.

The experimentally measured kinematics acted as the input to drive the model. The resulting motion was utilized to determine the muscle forces (static optimization, minimizing muscle activation) at each step of the simulation and muscle-tendon units were assumed to be ideal force generators. Joint reaction force analysis was used to determine the magnitude and direction of the glenohumeral joint reaction force during scapular plane abduction from the initiation of abduction to maximum humerothoracic abduction. The magnitude of the joint reaction force was normalized to bodyweight (BW). Elevation and deviation angles were calculated as previously described to report the direction of the joint reaction force (Figure 1) [7]. The movement was normalized from initiation of abduction to maximum abduction (0-100%). Statistical parametric mapping was used to compare elevation and deviation angles and the magnitude of the joint reaction force between the exercise therapy failed and successful groups post-exercise therapy [8]. Significance was $p < 0.05$.

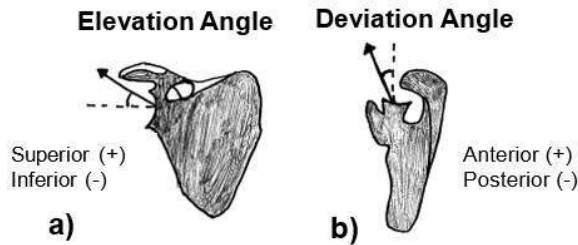


Figure 1: Depictions of the direction of the joint reaction force: a) elevation angle in scapular plane and b) deviation angle in transverse plane.

RESULTS

For the direction of the joint reaction force, the elevation angle for the exercise therapy successful group was greater between 58-71% of the movement ($108.5\text{--}124.8^\circ$ humerotheracic abduction, $p=0.045$) compared to the exercise therapy failed group post-exercise therapy (Figure 2). No difference in deviation angle was observed between groups post-exercise therapy ($p>0.05$). For both groups, the direction of the joint reaction force pointed superiorly and posteriorly. No difference in the magnitude of the joint reaction force was observed between groups ($p>0.05$, Figure 3). For the successful and failed exercise therapy groups, the peak magnitude of the joint reaction force was $0.67 \pm 0.14 \times \text{BW}$ and $0.61 \pm 0.16 \times \text{BW}$, respectively. The magnitude of the joint reaction force either increased with abduction to a maximum and then decreased or continued to increase (Figure 3).

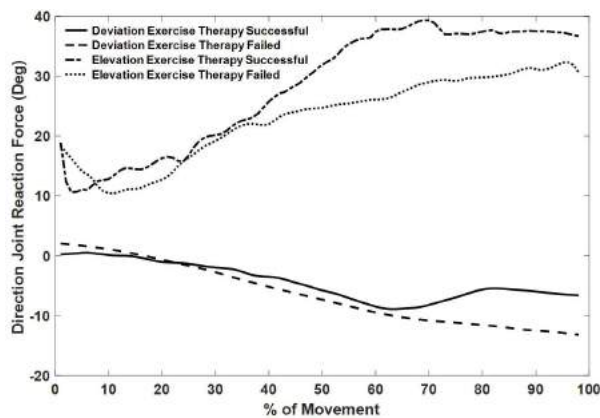


Figure 2: Average directions of joint reaction force post-exercise therapy.

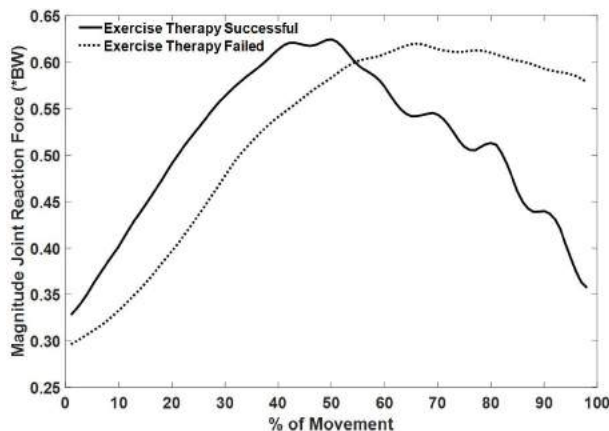


Figure 3: Average magnitudes of joint reaction force post-exercise therapy.

DISCUSSION

The main findings of the current study were post-exercise therapy: 1) the exercise therapy failed group had less superiorly oriented magnitudes of the joint reaction force compared to the exercise therapy successful group and 2) no differences were observed in deviation angle and magnitude of the joint reaction force between the groups. The implications of the first finding are that the exercise therapy successful group has more inferiorly directed muscle forces, resulting in a more superiorly oriented joint reaction force. Biomechanically, this implies that the intact rotator cuff of the successful exercise therapy group produced more inferiorly directed forces that could prevent superior migration of the humeral head. Interestingly, the difference occurred within the range of motion in which individuals with rotator cuff tears typically experience a painful arc thought to be due to impingement. This novel finding may be used to identify individuals that will successfully respond to exercise therapy and provide motivation to modify current treatment algorithms. For example, improvements in the direction of the joint reaction force may be achieved by improving strength of the subscapularis, infraspinatus and teres minor. For individuals with lower elevation angles, additional exercise therapy sessions may be warranted to avoid surgery.

An experimental study using cadavers found contradicting results for the elevation angle but similar results for the deviation angle [9]. The joint reaction force for simulated incomplete and complete supraspinatus tears initially pointed inferiorly and became less inferiorly oriented with abduction. The discrepancy is likely influenced by the scapula being rigidly fixed preventing upward rotation that supports the humeral head. No differences were found in the magnitude of the joint reaction force, which is reasonable given both groups have similar pathology.

One limitation of the current study is that no electromyography data were collected to compare to the simulated muscle activation data. However, the muscle activation results were compared to the available literature and followed similar trends [10,11]. Thus, the current study produced novel models for individuals with rotator cuff tears that included individual specific muscle forces, tear characteristics and accurate in-vivo kinematics. The models were able to distinguish differences in joint function between individuals that required surgery after exercise therapy and those that were successfully treated with exercise therapy alone. Future directions will include determining if individuals with decreased elevation angles require additional exercise therapy sessions to improve joint function.

ACKNOWLEDGEMENTS

The authors would like to thank the National Institutes of Health (grant #5R01AR069503) for providing financial support to this project.

REFERENCES

- [1] Kuhn, JE et al., *JSES*, 22:1371-1379, 2013.
- [2] Inman, VT et al., *CORR*, 330:3-12, 1944.
- [3] Burkhart, SS et al., *Orthop Clin North Am.*, 28:125-132, 1997.
- [4] Bey, MJ et al., *J Biomech Eng.*, 128:604-609, 2006.
- [5] Delp, SL et al., *IEEE Trans Biomed Eng.*, 54:1940-1950, 2007.
- [6] Vidt, ME et al., *Clin Biomech*, 60:20-29, 2018.
- [7] Fujie, H et al., *J Biomech Eng.*, 117:1-7, 1995.
- [8] Pataky, TC, *J Biomech.*, 43:1976-1982, 2010.
- [9] Parsons, IM et al., *JOR*, 20:439-446, 2002.
- [10] Hawkes, DH et al., *PloS One*, 14:e0211800, 2019.
- [11] Alenabi, T et al., *Clin Biomech*, 32:194-200, 2016.

UNDERSTANDING IMPACTS OF COLLAGEN ORGANIZATION IN AN INFECTED DIABETIC WOUND MODEL TREATED WITH A NOVEL OXYGENATING AND ANTIBACTERIAL HYDROGEL

Hannah A. Durr (1), Samuel D. Salinas (2) Rouzbeh Amini (2,3) Nic D. Leipzig (1,4)

(1) Department of Integrated Biosciences, University of Akron, Akron, OH, USA

(2) Department of Bioengineering, Northeastern University, Boston, MA, USA

(3) Department of Mechanical and Industrial Engineering, Northeastern University, Boston, MA, USA

(4) Department of Chemical, Biomolecular, and Corrosion Engineering, University of Akron, Akron, OH, USA

INTRODUCTION

Diabetic wounds are often chronic and show slow healing responses. Infection is common to these wounds and can lead to sepsis or amputation if not addressed. Combating bacteria requires effective antibacterial agents, in this case polyhexamethethylene biguanide (PHMB), which has been shown clinically to effectively clear wound infections. However, direct transdermal use of antiseptics requires high doses resulting in necrotic tissue effects or biocide resistance development; both of which impair endogenous healing. In addition, oxygen has been shown to improve collagen regeneration in diabetic wounds via our novel fluorinated methacrylamide chitosan (MACF) hydrogel dressings. The overall goal of this work is to examine the ability of MACF hydrogels to supply both oxygen and an antiseptic to combat infection in infected diabetic wounds while improving collagen network regeneration and regularity after infection is resolved.

METHODS

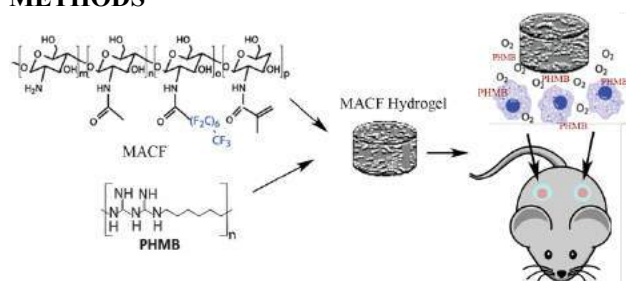


Figure 1: MACF hydrogels to supply oxygen and PHMB to treatment of infected diabetic wounds.

Materials synthesis: Chitosan and methacrylic acid were reacted together, then reacted with pentadecafluorooctanoyl chloride to result in MACF. After dialysis purification and freeze-drying, MACF was mixed with ultrapure water, loaded with PHMB, and photo-crosslinked to create hydrogel dressings that were saturated with ultrapure oxygen before application.

Wound Infection and treatment: Transgenic diabetic (db/db) mice (BKS.Cg-Dock7^m/+Lepr,^{db}/J) were confirmed to be diabetic via blood glucose readings of over 110 mg/dL. Under anesthesia, sterile silicon splints were sutured to prevent healing via contraction. Two 6 mm diameter full-thickness wounds were created in the center of each splint. Wounds were infected by applying 200 μ L of *P. aeruginosa* liquid culture to wounds. After 24 h, wounds were treated with oxygenated MACF hydrogels and/or PHMB, alongside a commercial PHMB dressing from Kendal, and controls. All wounds and treatments were covered with Tegaderm films. Dressings were changed approximately every other day. Samples were collected at the endpoint (D21) for histology, immunohistochemistry (IHC), and collagen organization/mechanical assessments[1].

Collagen analyses: Biaxial mechanical testing was performed on harvested tissues to determine tissue strength. Briefly, excised tissues were tested after 10 cycles of preconditioning using a five-protocol testing approach including stress ratios of 1:2, 3:4, 1:1 (equibiaxial), 4:3, and 2:1, similar to previous reports [2]. To explore the connection between strength of fiber networks and collagen organization, we used second harmonics generation (SHG) confocal microscopy to image type I fibrillary collagen and analyzed angle patterns of resulting images.

RESULTS

The equibiaxial stress versus strain curves (Fig. 2) showed that treatment with MACF mimicked the isotropic responses of the native tissues, whereas the commercial Kendal dressing revealed an anisotropic pattern similar to the no treatment infected control.

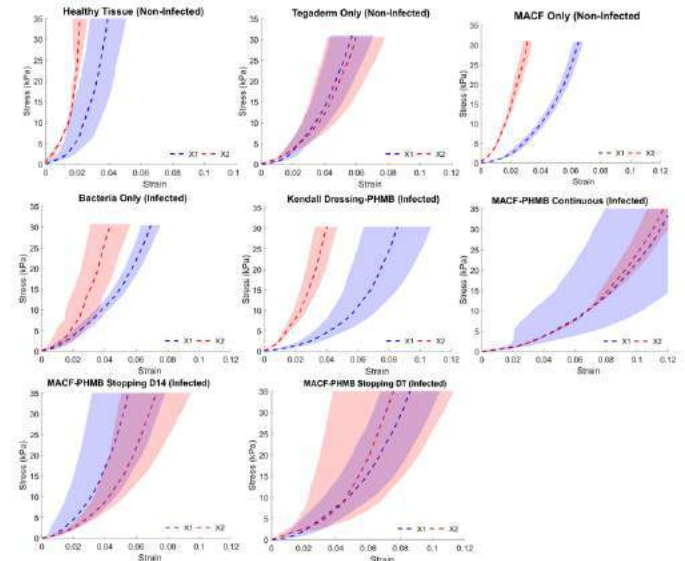


Figure 2: Average equi-biaxial stress-strain response curves for control groups and treatments (both n=3) from D21 post wounding with commercial dressing and MACF with PHMB application stopped at various time points (D7, D14) before completion of the study. Shaded regions represent standard error of the mean, X1 shows radial stretching and X2 shows circumferential stretching (1:1).

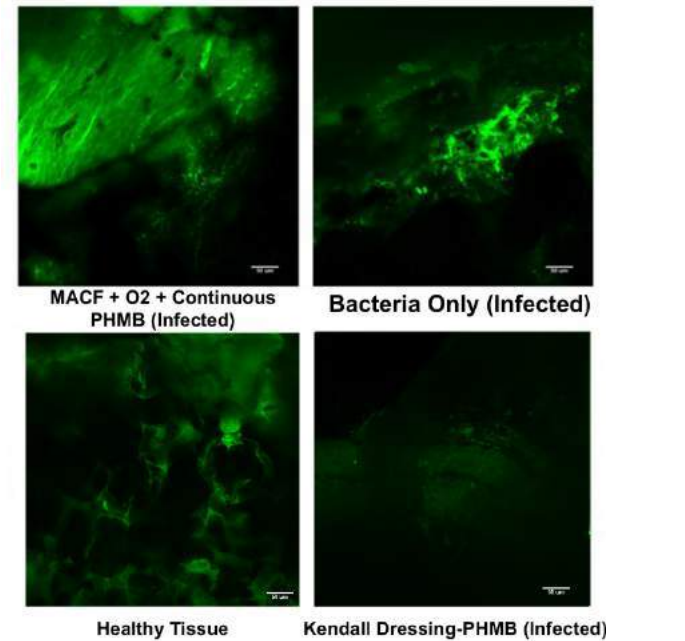


Figure 3: SHG images of wound margins showing organization of collagen networks from D21.

SHG was used to image granulation tissue (Fig 3), and organization of collagen networks present in biaxial testing was corroborated by mapping of angle of collagen fibers. As shown in Figure 4, collagen fiber angles showed more regularly organized collagen networks, reflective of healthy tissue, when treated with MACF. Treatment with commercial dressing and no treatment infected control showed increased grouping of angles in one principal direction instead of multiple directions, indicating improved network regularity.

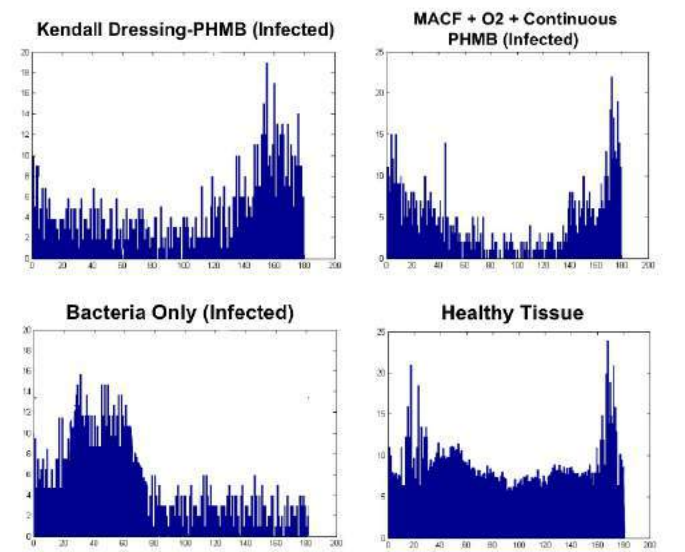


Figure 4: Histograms of collagen fiber angles in D21 wound samples showing fiber angle distributions calculated from SHG images using DiameterJ plugin (ImageJ).

DISCUSSION

These data confirm the successful development of a non-healing chronic wound model infected with biofilm-forming bacteria (*P. aeruginosa*). Further, these data show that our treatment can both resolve infection and improve collagen synthesis and organization toward successful healing outcomes. Through these experiments we have narrowed the effective window (14 days) of localized topical PHMB treatment to effectively treat infection while minimizing necrotic effects of localized high dosages, as was seen in the commercial Kendal dressings. Our introduction of oxygen into the system via MACF hydrogels improved wound healing post infection and showed improved collagen network development with improved isotropic collagen patterning. This pattern is indicative of multi-directional strength, while treatment with bacteria only and commercial dressing showed stronger tissues in a singular direction. Tissues progressing toward isotropic collagen organization is representative of overall strength of healing tissues.

ACKNOWLEDGEMENTS

Funding for this project was provided by the National Institutes of Health, R21 Grant #R21AR074743.

REFERENCES

1. Patil, PS et al., *Acta Biomaterialia*, 36:164-174, 2016.
2. Salinas, SD, Clark, MM, and Amini, R, *J Biomech*, 98:109462, 2020.

CARTILAGE STRAIN AND T1RHO MRI MAPPING IN RESPONSE TO LOAD IN AN INITIAL ACL-RECONSTRUCTED PATIENT COHORT

Emily Y. Miller (1), Hongtian Zhu (2), Woowon Lee (2) Corey P. Neu (1,2)

(1) Biomedical Engineering Program, University of Colorado Boulder, Boulder, CO, USA
(2) Paul M. Rady Department of Mechanical Engineering, University of Colorado Boulder, Boulder, CO USA

INTRODUCTION

Knee osteoarthritis (OA) is a degenerative joint disease that is a leading cause of joint pain, disability, and health care costs worldwide. OA affects the whole joint and is characterized by a gradual loss of articular cartilage often due to repeated microtraumas from injury, overuse, or ageing. A subset of OA, post-traumatic OA, often arises due to ligament injuries and occurs in a younger subgroup of patients than traditional ageing-related OA. Diagnosing early-stage post-traumatic OA can be difficult due to a lack of validated outcome measures for individuals with early knee OA [1]. The most common diagnosis metric, morphological changes to the cartilage, is limited to patients with moderate to severe OA, after irreversible changes to the joint have occurred. As post-traumatic OA may progress from an initial injury in the superficial zone of cartilage to more widespread biochemical and mechanical changes throughout the zonal tissue cartilage, quantifying changes to cartilage mechanical and biochemical properties non-invasively *in vivo* is of substantial interest.

MRI is unique among imaging tools as it can characterize tissues with high contrast and spatial detail, and has a deep penetration depth [2]. Recent work supports that T1rho MRI mapping, which is the time constant of spin lattice (T1) in the rotating frame, can discriminate between subjects with mild OA and controls.[1] In T1rho mapping the relaxation constants have been shown to be affected by both water and proteoglycan content in articular cartilage [1]. In other works, displacement encoded stimulated echo MRI (DENSE) has been used to calculate pixel level full field displacement maps of cartilage under repetitive motion [3]. In this study, we first utilized T1rho mapping before and after cyclic load along with DENSE MRI in a control cohort, in order to capture *in vivo* biochemical and biomechanical changes of the human knee cartilage exerted by the mechanical load. We then applied this technique to a cohort of patients who recently experienced an ACL reconstructive surgery (ACLR). This is our first application of the technique in a clinical population.

METHODS

Subjects: Research participants who underwent an ACL reconstructive surgery between 4 and 7 months (average 5.97 months) prior to the MRI date were recruited under IRB-approved protocols (n = 12, 6 females and 6 males). Participants received either a bone-patellar tendon-bone or quadriceps tendon autograft from one of our collaborating surgeons. Average subject age was 27.3 ± 4.8 and subjects had a mean BMI of 25.5 ± 3.5 . An age, sex, and BMI-matched group of control subjects with no history of knee pain or surgery were also recruited (n = 12, 6 females and 6 males). Average subject age in the control cohort was 27.1 ± 3.5 years old and subjects had a mean BMI of 24.6 ± 3.1 . A paired t-test was performed to determine that there were no significant differences in age or BMI between the ACLR and control groups.

MRI Scanning and Loading Protocol: Both ACLR and control groups underwent the same scanning and loading protocol (**Fig 1A**). Each participant's knee was imaged using a 3.0 T magnetic resonance (MR) scanner (Siemens Prisma^{fit}) with a knee coil (15-channel transmitter/receiver, Siemens). ACLR groups underwent imaging of their surgically reconstructed knee whereas all control participants were imaged on the leg of their choice. Prior to the application of load, T1rho-weighted MR images were acquired using the following parameters: Echo/repetition time (TE/TR)= 3/6 ms; spin-lock frequency = 500 Hz; spin-lock durations = 50,100,150,200 ms; field of view = 100×100 mm². Following imaging, medial compartment of participant knees underwent varus loading using a cyclic loading regime (0.5× body weight; pneumatic, 1s load, 1s unload) to mimic a walking cadence (**Fig 1B**). To apply the load, an MRI-compatible apparatus for varus-valgus loading was manufactured and validated, leading to compression of the medial condyle [4]. Moment conservation was used to estimate the load applied at the medial condyle. Importantly, eight (8) minutes of cyclic loading was applied prior to imaging to achieve a quasi-steady-state

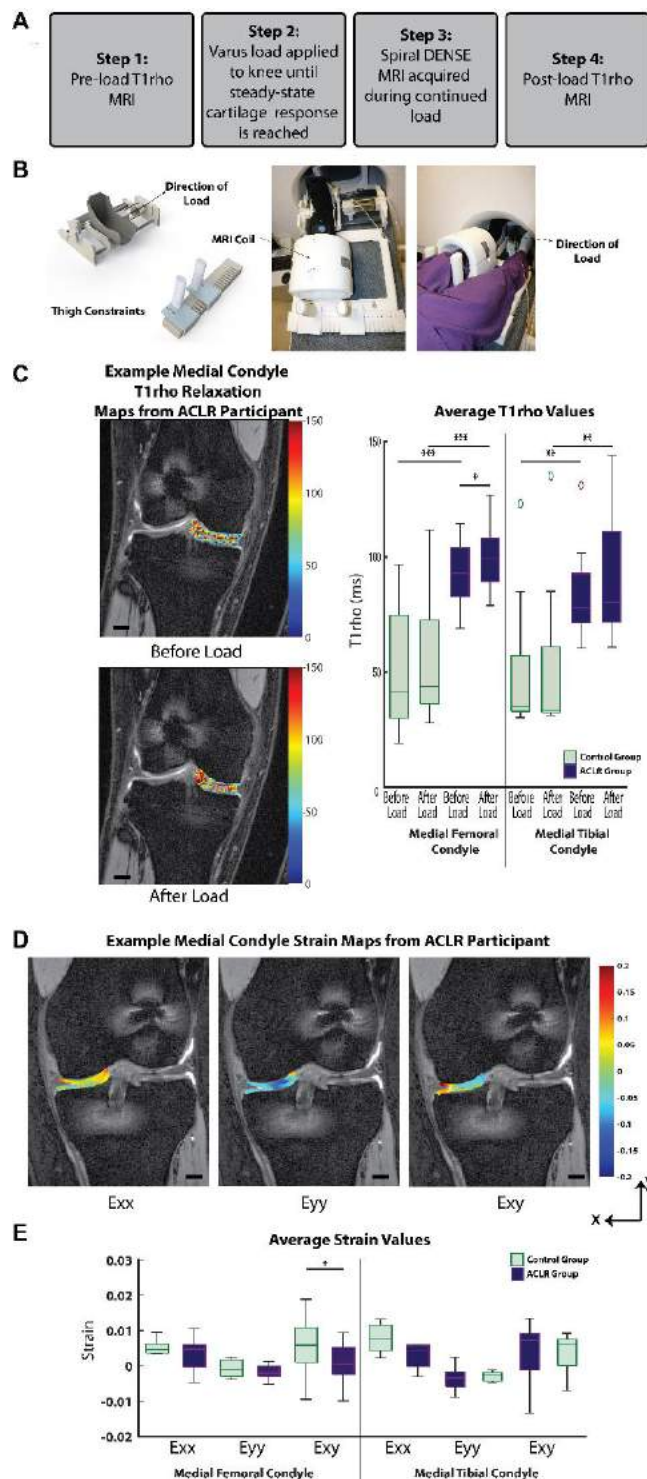


Figure 1: Multiple imaging techniques were used to assess cartilage response to load in control and ACLR cohorts. (A) MRI scanning session workflow. (B) Varus-valgus MRI compatible loading device. (C) T1rho relaxation maps and average values in control and ACLR groups. Scale bars indicate 10mm. *** indicates $p < 0.001$, ** indicates $p < 0.01$, * indicates $p < 0.05$ (D) Example strain maps from DENSE MRI. Scale bars indicate 10mm. (E) Average strain values. * indicates $p < 0.05$.

response and to minimize the viscoelastic response in the articular cartilage. Spiral DENSE MRI was collected following preconditioning. 27 time-sequenced coronal plane DENSE MR images were collected using 8 averages, 10 spiral interleaves, at a temporal resolution of 40 ms, TE was 2.5 ms and TR was 20 ms. FOV, slice thickness, and displacement encoding gradient were $160 \times 160 \text{ mm}^2$, 1.7 mm and 0.64 cycles/mm, respectively [5]. Total imaging time was 13.6 minutes. Following DENSE MRI, load was ceased, and T1rho-weighted MR images were acquired again using the same parameters as previously described (Fig 1C).

Data Analysis: The medial cartilage tibial and femoral regions of interest (ROIs) were manually segmented for all T1rho and DENSE images. DENSE MRI phase data was unwrapped using a custom Goldstein branch-cut phase unwrapping algorithm. Displacements for each pixel within the cartilage ROIs were determined from unwrapped phase data and smoothed using a locally weighted Gaussian filter with a kernel size of 3 [5]. A nearest neighbor transform was used to minimize bias at the ROI edges during smoothing. In-plane Green-Lagrange strains were calculated from the smoothed displacements [5] (Fig 1D). T1rho MR intensity images were fitted to a monoexponential relaxation model to obtain the T1rho relaxation map. An analysis of variance was used to determine the significance between control and ACLR groups for all strains and T1rho values (Fig 1C, Fig 1E).

RESULTS

There were significant differences in average T1rho values between control and ACLR groups. The medial femoral condyle and tibial condyle regions displayed significant differences between groups at before and after load timepoints (femoral condyle, $p < 0.001$, tibial condyle, $p < 0.01$). In response to load, only the ACLR group displayed a significant difference in T1rho values ($p < 0.05$). Shear strain (E_{xy}) in the medial femoral condyle was the only strain that displayed a significant difference between the ACL and control groups ($p < 0.05$) [6]. Multiple regression analysis was used to test if both group and change in T1rho value due to load can predict shear strain. The results of the regression indicate that there is a significant interaction between change in T1rho due to load and shear strain ($p < 0.05$).

DISCUSSION

This work provides a small cohort proof of concept of an MRI framework to non-invasively determine cartilage mechanical and biochemical information in a clinical setting. Although the cohort size is limited, the results support the use of both DENSE MRI and T1rho changes in response to load as a potential diagnostic tool to evaluate early cartilage degeneration in a clinical population. Ultimately, we hope to apply this framework in a larger population to further the development of diagnostic biomarkers for OA.

ACKNOWLEDGEMENTS

This work was supported by NIH grant 2 R01 AR063712. We also acknowledge Dr. Rachel Frank, Dr. Jonathan Bravman, and Dr. Eric McCarty.

REFERENCES

- [1] MacKary J.W., et al., *Osteoarthritis Cartilage*, 26:1140–52. 2018
- [2] Weaver J.S., et al., *Polish J Radiol*, 87:e93–112, 2022.
- [3] Chan, D.D., et al., *Sci Rep.*, 6:19220, 2016.
- [4] Zhu H., et al., SB3C 2022 Proceedings, 6/21/2022
- [5] Lee W., et al. *Magn Reson Med*. 2023; 89: 694- 709.
- [6] Griebel A.J., et al., *Magn Reson Med*. 2013; 71: 807-814.

MULTISCALE MECHANICAL CHARACTERIZATION OF HUMAN TOOTH WITH COMBINATION OF SEM, AFM, AND FEM

Y. Zhai (1), J. Wang (1), Z. Shi (1), T. Premaraj (2), S. Premaraj (2), T. Karpova (1), P. Dong (1), L. Gu (1)

(1) Biomedical Engineering, Florida Institute of Technology, Melbourne, Florida, USA
(2) Department of Orthodontics, Nova Southeastern University, Davie, Florida, USA

INTRODUCTION

As dental hard tissue, including enamel and dentin, is the major structure withstanding biomechanical loading, knowledge of tooth mechanical properties has been determined in bulk and nano scales. Previous studies have elucidated Young's modulus of enamel and dentin with a compression test and nanoindentation test¹⁻⁴. However, the previous research only determined tooth mechanical properties without consideration of tooth microstructure. In this research, the microstructure of enamel and dentin was characterized with scanning electron microscopy (SEM) and atomic force microscopy (AFM), and Young's modulus of enamel and dentin was determined through AFM. The enamel rod, dental tubules, and odontoblast processes were observed. Furthermore, the mechanical properties of dentin at the macro scale were determined by finite element method (FEM) simulation with a representative volume element (RVE) model. The influence of the dentin tubules on the mechanical properties of dentin was investigated.

METHODS

Extracted teeth was used. Before tooth sample preparation, the samples were stored in self-sealing sterilization pouches at room temperature. To prepare the tooth section, each tooth was embedded in resin for fixing. The fixed sample was machine-cut by a saw to get the occlusal section at the bottom of the tooth crown.

For SEM characterization of tooth occlusal cross-section, an unpolished tooth section was gold sputter coated. The section was imaged with JEOL JSM-6380 LV Scanning Electron Microscopy with an acceleration voltage of 15 kV to examine the microstructures of enamel and dentin at the occlusal section. Enamel micro-feature were observed under 600× magnification to see the enamel rods exposed through mechanical fracture after machine cutting. Dentin is the structure beneath enamel with tubules and odontoblast processes. To characterize dentin microstructure, the SEM image was obtained under

1200× magnification to observe the open dental tubules and odontoblast process.

For the AFM test, the sample surface was first exposed in 1× phosphate buffered solution (PBS) for 30 minutes to avoid the effects of surface charge. The AFM test was conducted with JPK force Robot 300. A probe, RTESPA-150 (Bruker, Billerica, MA), was utilized for morphology characterization, with a scanning area of $20 \times 20 \mu\text{m}^2$, and grids of 50×50 . A probe, RTESPA-525, was adopted for mechanical characterization with a scanning area of $5 \times 5 \mu\text{m}^2$, a grid of 8×8 . Six locations were selected in both enamel and dentin for mechanical characterization. The force-indent curves were fitted with Hertz Model to get Young's modulus at each point.

The FEM simulation of the compression test was implemented to quantify the mechanical properties of dentin in the presence of dentin tubules. A 2-dimensional (2-D) RVE model with a size of $38.4 \mu\text{m} \times 28.0 \mu\text{m}$ was reconstructed based on an SEM image (Figure. 1). Plane stress was set as 2-D behavior with $3.84 \mu\text{m}$ thickness to have the free movement horizontally. The material properties, Young's modulus of dentin, were determined by AFM test results. The boundary conditions were set as 2 nm downward displacement on the upper boundary and frictionless support on the lower boundary. The Young's modulus of dentin, E_{RVE} , was calculated from the simulation.

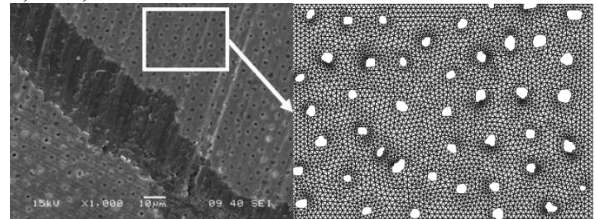


Figure 1: The selection of the region for FE simulation and meshes of selected dentin region in 2-D with tubules.

RESULTS

The morphology of enamel and dentin characterized with SEM and AFM are shown in Fig. 2. Different magnifications were adopted for each image to get a better visualization. The enamel rods and dentin tubules are observed (marked by white arrows in each figure). The dentin tubules observed with AFM showed a consistence with the SEM image. The enamel rod had a diameter of $\sim 5\mu\text{m}$, the tubules had a diameter of $\sim 2\mu\text{m}$. The odontoblast process in dental tubules was also observed. The alignment of enamel rods and dental tubules may indicate anisotropic mechanical properties of the teeth material.

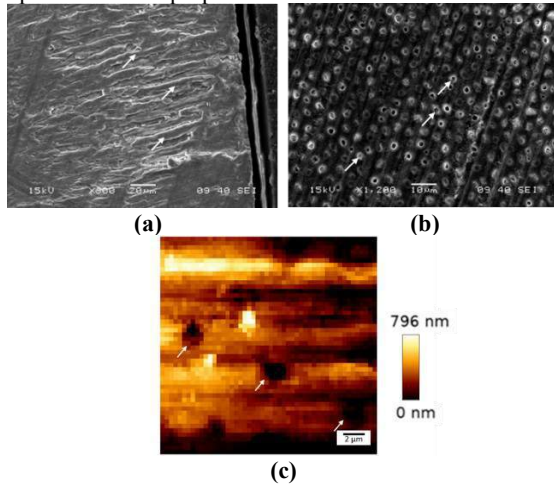


Figure 2: Morphology of (a) enamel and (b) dentin characterized with SEM scanning, and (c) AFM scanning of dentin at a relative local region (enamel rods and dental tubules are marked with white arrows in each image).

The Young's modulus of enamel and dentin were quantified at six locations, as depicted in Fig. 3(a)&(b). The Young's modulus of enamel ranged from 19.8 to 77.8 GPa, with an average value 49.6 ± 20.4 GPa. The Young's modulus of dentin ranged from 16.0 to 47.4 GPa, with an average value of 35.4 ± 11.6 GPa. The representative Young's modulus mapping images indicated that both enamel and dentin show a highly heterogeneous behavior (Fig 3(c)&(d)).

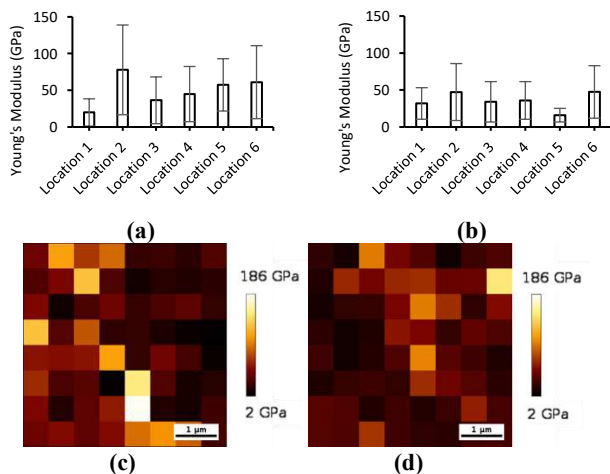


Figure 3: Young's modulus quantified at six locations in (a) enamel and (b) dentin, and a representative Young's modulus mapping image of (c) enamel, (d) dentin.

The mechanical property of the dentin at the macro scale was determined by a compression simulation with an RVE model. Following simulation, the Young's modulus was determined by curve

fitting of the extracted stress-strain curve. The Young's modulus calculated by RVE model, $E_{RVE} = 29.2$ GPa, which is 17.5% less than the value quantified with AFM (35.4 GPa) due to the presence of dentin tubules, which undertook less load (Figure 4).

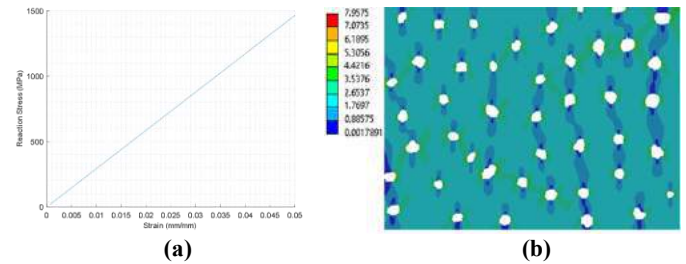


Figure 4: FEA simulated result of (a) reaction stress vs. strain curve of dentin for Young's modulus calculation, (b) the representative 2D dentin von Mises stress.

DISCUSSION

The mechanical property of enamel and dentin were determined through AFM nanoindentation, and the microstructure of dental hard tissue (enamel and dentin) is characterized by AFM scanning and SEM imaging. The Young's modulus of enamel and dentin is anisotropic with 49.6 ± 20.4 GPa and 35.4 ± 11.6 GPa, which are corresponding to previous compression and nanoindentation test results ranging from 1.3 GPa to 98.3 GPa for enamel and 1.6 GPa to 100 GPa for dentin⁴. The tested Young's modulus of enamel in general is higher than the value of dentin⁴. Since the difference in enamel and dentin microstructures leads to various mechanical properties, the compositions of dental hard tissue play an intrinsic role in the wear-resistant outer layer (enamel)⁵ and dental structure support (dentin)⁶.

Enamel rods and dental tubule structures with the odontoblast processes can be observed with SEM. Enamel rods are perpendicular to the dentinal-enamel junction (DEJ) with a diameter of approximately 5 μm. Rod sheath between enamel rods containing more protein than the mineralized enamel⁷⁻⁸. While dentin is main supporting structure of the tooth⁶ composed of tubules, peritubular dentin, and intertubular dentin⁹. Correspondingly, the superficial morphology of dentin cross-section is detected through AFM topography. The size of open tubules and the distance between tubules show consistency between AFM and SEM images.

The Young's modulus quantified with the RVE model is 17.24% less than that quantified by AFM due to the presence of dentin tubules. Combining the SEM, AFM, and FEM, we build a frame for multiscale mechanical characterization of the hard dental tissues considering the microstructures, which can be further applied to the study of enamel and the whole tooth.

ACKNOWLEDGEMENTS

Thanks to Florida Institute of Technology core facilities for SEM and machine cutting.

REFERENCES

- [1] Craig, R. G et al., *J Dent Res*, 40:936-945, 1961.
- [2] Fong, H et al., *Mater Sci Eng C*, 7:119-128, 1999.
- [3] He, L. H et al., *Biomaterials*, 27:4388-4398, 2006.
- [4] Chun, K et al., *J Dent Biomech*, 5:5/0/1758736014520809, 2014.
- [5] Lacruz, R. S et al., *Physiol Rev*, 97:939-993, 2017.
- [6] Tjäderhane, L et al., *Endod Top*, 20:3-29, 2009.
- [7] Zhang, Y et al., *Int J Oral Sci*, 6:61-69, 2014.
- [8] Poole, D. F. G et al., *Arch Oral Biol*, 5:14-IN5, 1961.
- [9] Weiner, S et al., *J Struct Biol*, 126:27-41, 1999.

ENABLING CRYOPRESERVATION THROUGH VITRIFICATION AND REWARMING AT THE SCALE OF A HUMAN ORGAN

Lakshya Gangwar (1), Zonghu Han (1), Mikaela Hintz (1), Jacqueline L. Pasek-Allen (2), Robert C. Goldstein (3), Michael L. Etheridge (1), John C. Bischof (1,2)

- (1) Department of Mechanical Engineering, University of Minnesota, Minneapolis, MN, USA
(2) Department of Biomedical Engineering, University of Minnesota, Minneapolis, MN, USA
(3) AMF Life Systems LLC, Auburn Hills, MI, USA

INTRODUCTION

Cryopreservation of human organs has immense potential to save lives by increasing the shelf life and usage of donor organs, which may then help achieve long term banking and reduce or eliminate the organ transplant wait list [1]. Vitrification is a viable and promising approach to achieve cryopreservation of organs for theoretically indefinite time. To achieve this, an organ perfused with cryoprotective agent (CPA) is cooled rapidly to below its glass transition temperature to form an amorphous glassy state free of damaging ice crystallization [2, 3]. Cooling is typically achieved using forced convection of cold nitrogen vapor in a commercial freezer such as a Planar Control Rate Freezer [4]. Cooling is intrinsically size/volume dependent since it occurs through convective flux at the sample boundaries. While this approach works well for small systems, it can be a challenge for larger systems, both in i) achieving rapid enough cooling throughout the volume to avoid ice formation and ii) sufficiently uniform cooling to avoid significant thermal stresses that can lead to cracking [5,6]. Critical cooling (CCR) & warming (CWR) rates are thresholds to detect presence of ice formation (if cooling rate < CCR or warming rate < CWR- Table 1). To our knowledge successful vitrification has not yet been achieved for human organ scale systems (roughly ranging from 500 mL to 2.5L). Once vitrified, samples can be stored below the glass transition temperature (roughly < -120°C) and can be rewarmed at any time when needed. Rewarming of smaller vitrified samples (typically < 3 mL) in a water bath has been successful, however, alternative approaches intending to produce volumetric heating in larger samples, such as nanowarming or dielectric heating are being investigated [7,8]. Water bath rewarming is again a convective approach, where rewarming rates in the middle of the organ will naturally drop as organ size increases. To address this, a recent technique termed nanowarming was developed by our group. In this approach, magnetic iron oxide nanoparticles suspended in CPA are perfused throughout the vasculature of an organ to couple directly with

a radiofrequency field, thereby achieving more uniform rewarming independent of the size of the organ [7]. So far, successful vitrification and rewarming has been demonstrated in models such as rabbit kidneys and rat hearts, kidneys and livers, where the total preserved volumes were around 10-30mL [9-12]. To extend these results to the scale of human organs this study shows that vitrification and rewarming of up to 2.5L volumes of CPAs without crystallization or cracking is possible. This includes testing with three common CPAs including VS55, M22, and 40%EG+0.6M-sucrose (EG-Suc), all of which have been studied for use in cryopreservation of mammalian organ systems. Further, we present here the first demonstration of uniform nanowarming at the liter scale, performed with a state of art 120kW RF coil capable of 0-34 KA/m field strength at 360 kHz (2.5L uniform field volume).

Table 1: Critical rates of the studied three CPAs

CPA	CCR(°C/min)	CWR(°C/min)	Ref.
VS55	~2.5	~50	[10]
40%v/vEG+0.6MSucrose	<~1	45	[12]
M22	0.1	0.4	[3]

METHODS

A controlled rate freezer (CRF) is used to convectively cool the CPA samples in a polyethylene bag. Standard thermometry is employed to record temperature for estimating cooling/rewarming rates (3 fiber optic temperature probes at center, left & right edge of the CPA inside cryobag). Visual photos are used for confirmation of vitrification success (ice results in white clouding) and verified by μ CT imaging. Expected ice crystallization at the observed cooling rates is also compared to results measured on the same CPAs measured using differential scanning calorimetry (DSC). For nanowarming, magnetic field is mapped in 120kW RF coil using a 2D high frequency probe.

RESULTS

Using a CRF, a cooling protocol is designed by introducing fast cooling ($-40^{\circ}\text{C}/\text{min}$ in the chamber was chosen to avoid ice crystallization by achieving cooling rate above CCR) from a starting temperature (0°C) until reaching an annealing temperature (-122°C , just above the glass transition) at which point the sample is held for complete thermal equilibration. This helps to alleviate thermal stress prior to entering the brittle glassy phase. The protocol ends with a very slow cooling step ($< -1^{\circ}\text{C}/\text{min}$) in the glassy state until reaching the storage temperature of -150°C . This step is needed to avoid introducing additional thermal stresses. VS55 formed ice during cooling (i.e. failed to vitrify) at all volumes whereas EG-Suc and M22 vitrified without crystallization or cracking at volumes of 0.5L, 1L. M22 seems to be best cocktail for vitrification as we were able to vitrify up to 2.5L due to its exceptionally low CCR (Table1). Average center cooling results vs. volume are also listed below Figure 1.

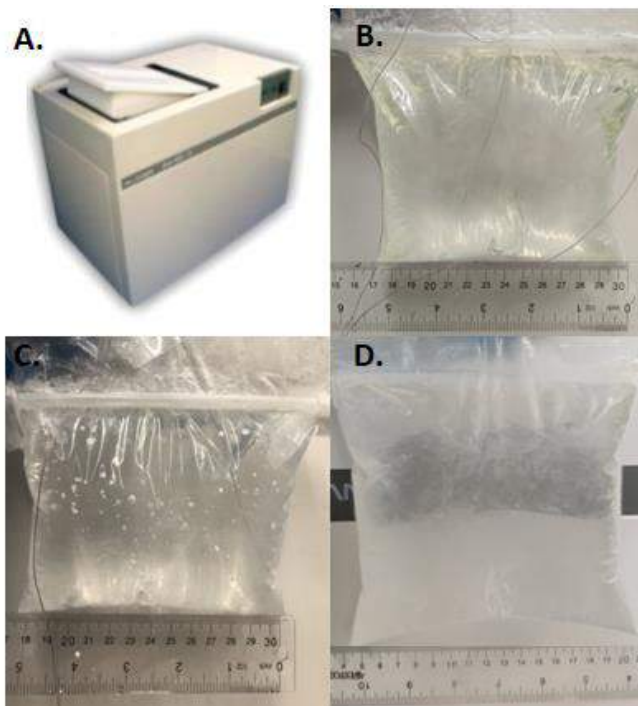


Figure 1: Examples of 0.5 L cryobags of CPA cooled in a CRF. Photos of A. CRF; B. M22 (vitrified); C. VS55 (crystallized); D. EG-Sucrose (vitrified). (Note: 0.5 L cryobag can hold a human kidney) (Center cooling rates: 0.5L $\sim 1.4^{\circ}\text{C}/\text{min}$; 1L $\sim 1^{\circ}\text{C}/\text{min}$)

To achieve sufficiently uniform & rapid rewarming of these larger systems through nanowarming we used a new state of the art 120kW RF coil with a sample capacity of up to 2.5L (Figure 2A). A magnetic field strength of up to 34 kA/m (at 360 kHz) is generated at the full 100% operational power of RF coil. Figure 2C shows the variation of generated magnetic field with the % power output of the 120kW RF coil. The magnetic field variation in axial and radial direction inside the coil is uniform (within $\pm 5\%$) as in Figure 2B. Finally, to demonstrate uniform rewarming of these vitrified large volumes, a solution of 1L M22 with 7 mgFe/mL iron oxide nanoparticles (Ferrotec EMG-308) was vitrified with the protocol above, stored at -150°C , and then nanowarmed in the RF coil. Heating rates of $\sim 100^{\circ}\text{C}/\text{min}$ were measured with negligible temperature variation measured at three different points ($\sim 3\text{cm}$ spacing) within the volume (Figure 2D) exceeding highest CWR of all CPAs (VS55 $\sim 50^{\circ}\text{C}/\text{min}$).

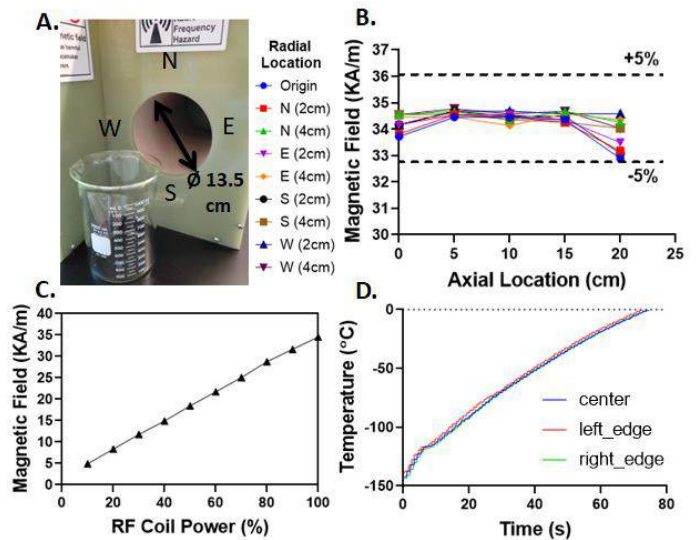


Figure 2: Nanowarming system characterization: A. 120kW RF coil (AMF Life Systems); B. Magnetic Field variation within coil (N, S, E, W vs. axial depth); C. Magnetic field vs. % Power in coil; D. Temperature curve for 1L nanowarming of EMG-308+M22.

DISCUSSION

Cooling rates at center decrease with increasing volume of CPAs ($\sim 1.4^{\circ}\text{C}/\text{min}$ at 0.5L to $\sim 1^{\circ}\text{C}/\text{min}$ at 1L). Thus to maintain cooling rate greater than CCR we would need to either utilize CPAs with extremely low CCR such as M22 ($\sim 0.4^{\circ}\text{C}/\text{min}$) or new technologies are needed to enhance cooling in larger volumes. Long annealing time is required (~ 2 hrs at 0.5L to ~ 4 hrs at 1L) to achieve isothermal equilibration prior to final cooling and storage. Furthermore, a very slow cooling rate ($< 1^{\circ}\text{C}/\text{min}$) is then needed when cooling below the glass transition temperature ($\sim -123^{\circ}\text{C}$). Both of these approaches are designed to minimize thermal gradients which can induce fractures. Once the system is vitrified, we show that nanowarming in a 120KW RF coil (0-35KA/m at 360 KHz) can uniformly rewarm CPA volumes up to 1L and our characterization suggests further scaling to 2.5L will be possible. This study demonstrates physical success in vitrification and rewarming of human organ scale systems (0.5-2.5L), suggesting that vitrification and nanowarming of human organs will be possible, an provided needed "organ banking" technology for the future.

ACKNOWLEDGEMENTS

This work was supported by the NIH Grant (5R01DK117425-03, 5R01HL135046-04) and NSF Grant EEC 1941543.

REFERENCES

- [1] Lewis, JK et al., Cryobiology 72(2):169-82, 2016.
- [2] Fahy, GM et al., Cryobiology 21(4):407-26, 1984.
- [3] Fahy, GM. et al., Cryobiology 48(2):157-78, 2004.
- [4] <https://planer.com/products/cryo-freezers/medium-crf/kryo560.html>
- [5] Gangwar, L. et al., CryoLetters 43.6:303-315, 2022.
- [6] Fahy, GM et al., Cryobiology 27(5):492-510, 1990.
- [7] Etheridge ML et al., Technology Vol.02, No.03, 229-242, 2014.
- [8] Burdette EC et al., Cryobiology 17: 393-402, 1980.
- [9] Fahy GM et al., Organogenesis 5: 167-175, 2009.
- [10] Sharma, A. et al., Advanced Science 8: 2101691, 2021.
- [11] Gao Z et al., Advanced Materials Technologies 7: 2100873, 2022.
- [12] Sharma, A. et al., Annals of biomedical engineering:1-12, 2022.

INVERSE FINITE ELEMENT MODELING CAPTURES WAVE PROPAGATION IN HIGH-RATE OSCILLATORY SHEAR TESTS ON PORCINE BRAIN TISSUE

Gregory M. Boiczuk (1), Noah R. Pearson (2), Kenneth L. Monson (1,2)

(1) Department of Biomedical Engineering, University of Utah, Salt Lake City, UT, USA
(2) Department of Mechanical Engineering, University of Utah, Salt Lake City, UT, USA

INTRODUCTION

Traumatic brain injury (TBI) is a major cause of injury and death in the United States [1]. Due to difficulties in studying the mechanics of TBI in vivo, finite element (FE) simulations have become an important tool in studying TBI. These simulations require accurate material parameters of brain tissue to achieve relevant results. Due to the viscoelastic nature of brain tissue [2], experimentally derived constitutive models should be validated over a large range of strain rates relevant to TBI, ranging from on the order of tens per second to several hundred per second [3]. To date, high-rate characterized models of brain tissue in shear in literature either achieve low strain amplitudes and high strain rates [4] or higher amplitudes but lower peak strain rates below 100 s⁻¹ [5].

We previously performed oscillatory shear frequency sweeps, between strain rates of 0.025 and 250 s⁻¹, on cerebral tissue from freshly euthanized Göttingen minipigs. The objective of the present study was to fit a hyper-viscoelastic constitutive model to the experimental data using both an inverse FE model and MATLAB and to compare the results.

METHODS

Previously, cerebral tissue from freshly euthanized Göttingen minipigs was cut into 8 x 8 x 5 mm samples and subjected to a simple-shear frequency sweep having an amplitude of 20% shear strain, with strain rates ranging from 0.025 s⁻¹ to 250 s⁻¹ for 5 cycles each.

First Piola-Kirchhoff (1st PK) stress and shear strain were calculated from the recorded load and displacement data, respectively, and used to generate average strain vs time and stress vs time curves. We then fit these curves with a hyper-viscoelastic constitutive model with the stress defined by

$$\mathbf{S}(t) = \int_0^t G(t-s) \frac{\partial \mathbf{S}^e}{\partial s} ds \quad (1)$$

where the elastic stress \mathbf{S}^e is given by a one-term Ogden model defined by the strain energy function

$$W^{matrix} = \frac{\mu}{\alpha} (\lambda_1^\alpha + \lambda_2^\alpha + \lambda_3^\alpha - 3) \quad (2)$$

where μ is the shear stiffness, α is a non-linearity parameter and λ_i is a principal stretch. The reduced relaxation function $G(t)$ is defined by a six-term Prony series

$$G(t) = \sum_{i=1}^6 g_i \exp\left(-\frac{t}{\tau_i}\right) \quad (3)$$

where τ_i are fixed time constants, each spaced one decade from another and ranging from $\tau_1 = 1$ s to $\tau_6 = 1 * 10^{-5}$ s, and g_i are viscoelastic coefficients. The parameters μ , α , and g_i were fit to the average stress and strain curves in MATLAB using the *fmincon* function.

In addition to the MATLAB fits, we also constructed an inverse FE model of the experiments in FEBio [6]. Briefly, we modeled an 8 x 4 x 5 mm half-symmetry cube of brain tissue. The top face was attached via rigid contact to a fixed 8 x 4 x 1 mm rigid body representing the load cell-attached plate in our tester, while a displacement corresponding to the average experimental displacement waveform was applied to the bottom face in the X direction.

To correspond with the constitutive model fit in MATLAB, we used an uncoupled viscoelastic material for the brain tissue cube with an uncoupled Ogden model selected for the elastic material. All analysis was performed with the implicit dynamics solver. A convergence was performed study using the material parameters from the MATLAB fit. We selected a mesh of 400 20-node hex elements for the brain tissue and 16 20-node hex elements the rigid plate. We then used the FEBio optimization module to define the 8 material parameters by minimizing the error between the X reaction force at the rigid contact and the

average experimentally recorded force. Finally, we performed a forward simulation using the optimized parameters, converting the X reaction force at the fixed plate back to 1st PK stress, for comparison with the experimental and MATLAB fit curves.

RESULTS

The MATLAB and inverse FE fits for the first two loading cycles of selected strain rates are shown in **Figure 1**. At the lowest rate (0.025 s^{-1}), both the MATLAB and inverse FE fits underpredict peak stresses. At intermediate rates from 0.25 s^{-1} to 12.5 s^{-1} (not shown), the inverse FE model tends to overpredict stresses while the MATLAB model tends to underpredict them. At 50 s^{-1} and 100 s^{-1} , both models underpredict maximum stresses and overpredict minimum stresses, though the inverse model provides a better prediction. At the highest rate (250 s^{-1}), both models show a marked phase shift, with the MATLAB model leading the experimental data while the inverse model slightly lags it. Additionally, both models substantially underpredict minimum stresses.

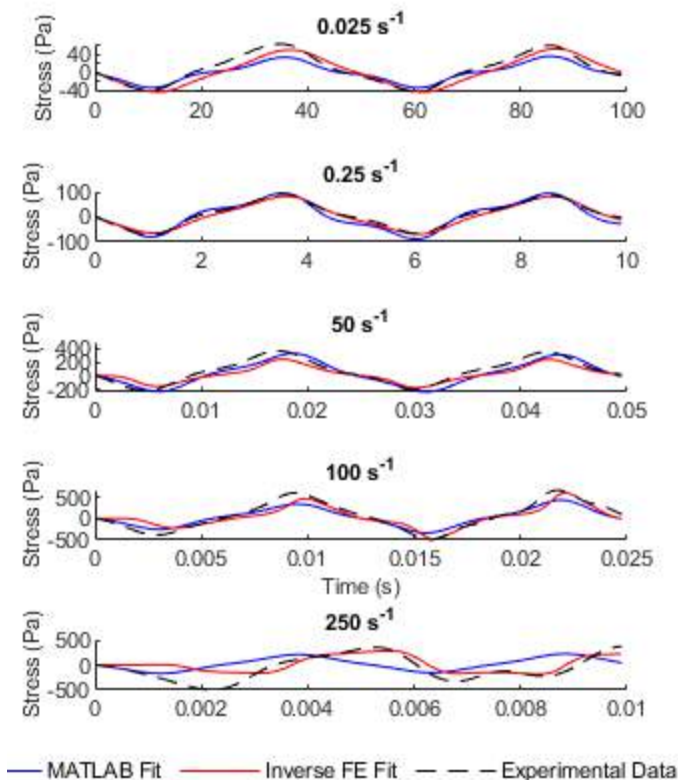


Figure 1 | Comparison of MATLAB and FE fits and experimental data for the first two loading cycles of selected rates.

R^2 values for overall fit quality show that the FE fit performs better than the MATLAB fit (0.75 vs 0.58), though both perform relatively poorly. Examining R^2 values for each oscillation, the FE model performs best for rates below 50 s^{-1} (0.81-0.94 vs 0.60-0.85) and above 100 s^{-1} (0.48-0.66 vs -0.42-0.51), while the MATLAB fit performs best at 50 and 100 s^{-1} .

DISCUSSION

The purpose of this work was to fit a hyper-viscoelastic constitutive model to previously acquired oscillatory shear data from brain using both conventional fitting in MATLAB as well as inverse FE methods.

Generally, the inverse FE model performed better than the MATLAB model. Overall, both models perform worse at rates above 100 s^{-1} , with the worst performance at 250 s^{-1} . While this was somewhat expected, due to increased noise and variation present in the experimental data at these rates, it is clear that additional revisions of the model may be needed to capture this, especially at 250 s^{-1} .

At rates of 100 s^{-1} and above, noticeable wave propagation is present in the FE model, suggesting that inertial effects are playing an important role at these rates. This is consistent with the experimental data, which show a noticeable leftward shift of the strain-time waveform relative to the stress waveform present at higher rates. For a viscoelastic material, stress should always lead or be in phase with strain, but strain should never lead stress. This suggests that there is some degree of shear wave propagation through the tissue from the moving platen, where displacement was measured, to the fixed platen, where load was measured. This is further evidenced by thicker samples tending to exhibit more phase shift at these rates compared to thinner samples. Because our MATLAB methodology assumes a homogeneous deformation and does not account for inertial effects, it cannot account for wave propagation, helping explain why it is typically outperformed by the inverse FE approach. Further constitutive model refinement will thus use inverse FE.

Attempts to weight the g_i terms corresponding to the smallest τ_i values in the inverse FE model in order to better fit high-rate oscillations led to better fitting of the first cycle of all oscillations above 100 s^{-1} but caused the stresses of subsequent cycles to be substantially overpredicted, up to several times peak stress values for the 5th cycle. This may suggest that either the model is in need of increasing damping or possibly that the tissue does not exhibit frequency independent damping as assumed by the Fung quasi-linear viscoelastic formulation used here [7]. However, we are unable to verify this from experimental data as the phase shift present at high rates precludes accurate calculation of the loss modulus at high rates. Fitting may still be improved by implementing a material model with frequency dependent damping [8]. Future work will aim to improve predictive accuracy of the inverse FE models by both investigating different materials as well as implementing anisotropy to model additional experiments.

ACKNOWLEDGEMENTS

Funding for this project was provided by the Henry M. Jackson Foundation for the Advancement of Military Medicine, Inc. and the National Science Foundation. The authors would like to thank Dr. Jeffery Weiss, Dr. Steve Maas, Dr. Aravind Sundaramurthy, and Dr. Jose E. Rubio for their assistance with the FE models in this work.

REFERENCES

- Centers for Disease Control and Prevention, 2014
- Budday, S., et al., *Arch Comput Methods Eng*, 27:1187-1230, 2019.
- Wu, T., et al., *J Neurotrauma*, 38:1879-1888, 2021.
- Nicolle, S., et al., *Biorheology*, 42:209-223, 2005.
- Hrapko, M., et al., *Biorheology*, 45:663-76, 2008.
- Maas, S.A., et al., *J Biomech Eng*, 134:011005, 2012.
- Fung, Y.C., Springer. 277-292, 1993.
- Yang, L., et al., *Wave Motion*, 50:334-346, 2013.

DEVELOPMENT OF AN ACTIVATING AND INACTIVATING OPTOGENETIC TOOLBOX FOR PERTURBATION OF RHOA-YAP MECHANOTRANSDUCTIVE FEEDBACK

Erin E. Berlew (1,3), Annapurna Pranatharthi-Haran (2), Brian Y. Chow (1), Joel D. Boerckel (1,3)

- (1) Department of Bioengineering, University of Pennsylvania, Philadelphia, PA 19104, USA
- (2) Department of Cancer Biology, University of Pennsylvania, Philadelphia, PA 19104, USA
- (3) Department of Orthopaedic Surgery, University of Pennsylvania, Philadelphia, PA 19104, USA

INTRODUCTION

The Rho family of small GTPases coordinate actin cytoskeletal rearrangements underlying crucial cell processes including migration and mechanotransduction [1]. Rho GTPase signaling is tightly controlled in space and time: GTPases are activated by guanine nucleotide exchange factors (GEFs) and inactivated by GTPase accelerating proteins (GAPs) at the plasma membrane. RhoA activation and interaction with downstream effector proteins leads to actin polymerization, which drives transcriptional mechanotransduction in part through Yes-associated protein (YAP) [2,3]. Previously, we found that YAP is not only activated by RhoA-signaling, but also regulates RhoA by a negative feedback loop through expression of RhoA-inactivating GAPs, including ARHGAP7. This negative feedback loop is necessary for persistent cell motility. However, in order to define the role of this loop in cell motility, which is dynamic and spatially regulated in the cell, we need to understand its temporal and spatial control during cell migration. Solving this problem requires a new set of tools.

Here we describe the engineering of a novel set of single-component (i.e., one-protein) optogenetic tools to control activation and termination of RhoA signaling using the BcLOV4 membrane recruitment platform [6]. These tools allow us to control the subcellular localization of the RhoA GTPase and its associated GEF and GAP domains and systematically perturb signaling interactions involved in cell motility and mechanotransduction with precise spatial and temporal control.

METHODS

We generated both RhoA-activating and RhoA-inactivating tools. For activation, we generated tools for RhoA itself as well as the RhoA-activating GEF11. For inactivation, we generated tools for RhoA-inactivating GAPs (GAP1, GAP7/DLC1).

Fusions of BcLOV4, effector protein (wildtype RhoA GTPase, the Dbl homology domain of ARHGAP11, and the GAP domain of

ARHGAP1 or ARHGAP7), and mCherry visualization tag were Gibson cloned into the pcDNA3.1 backbone. To measure RhoA activation-induced cell contraction, mCherry fluorescence was imaged before and after a 5-second pulse of whole-field blue light activation (N = 82-93 cells per condition). Change in cell area was calculated using a custom Python script. Cytoskeletal changes were assessed by fixing tool-expressing cells in the dark-adapted state and after two hours of pulsed blue light stimulation and staining with Alexa Fluor 488-tagged phalloidin (N = 40 cells per condition).

For mechanotransduction assays, HEK293T cells were co-transfected with mCherry-tagged tools and EGFP-tagged YAP in a 4:1 ratio. EGFP-YAP was imaged every 15 seconds using a 250 msec excitation pulse that also stimulated BcLOV4, and mCherry fluorescence was imaged every minute. Nuclear and cytosolic fluorescence normalized to the area of each region was calculated every minute by manual segmentation in ImageJ, with N = 20 cells per condition.

YAP-TEAD-dependent transcriptional activity was quantified using a dual luciferase reporter system (Promega, E1910). HEK293T cells were serum starved and co-transfected with plasmids encoding 8XGT1C-luciferase, a YAP-sensitive promoter driving firefly luciferase expression; *Renilla* luciferase; and mCherry-tagged tool in a 1:1:3 ratio. Half the cells were incubated under pulsing blue light with a 1.6% stimulation duty cycle for 12 hours. Cells were lysed and luminescence was measured in white 96-well plates with a 10 second integration time. The firefly luminescence value for each sample was normalized to its *Renilla* luciferase readout. N = 8 lysate samples per condition.

RESULTS

Activation tools: Blue light stimulation of cells expressing opto-RhoA (RhoA-BcLOV4-mCherry) and opto-RhoGEF (BcLOV4-ARHGAP11-mCherry) drove robust cell contraction and actin polymerization measured by phalloidin staining, compared to control

BcLOV4-mCherry (Figure 1). To assess whether synthetic RhoA activation using optogenetic tools was sufficient to drive transcriptional mechanotransduction, we next co-expressed tagged YAP with either opto-RhoA-mCherry or BcLOV4-mCherry and observed that blue light stimulation of the opto-RhoA condition again caused cell contraction and a rapid increase in nuclear localization of YAP. A synthetic YAP-sensitive promoter driving luciferase expression showed a significant increase in YAP-mediated transcription in photoactivated opto-RhoA-expressing cells compared to dark-state cells or control BcLOV4 (Figure 2).

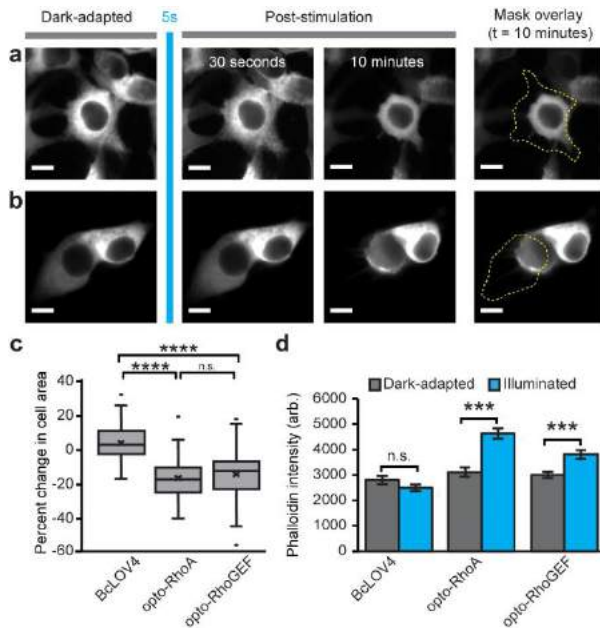


Figure 1: Characterization of optogenetic RhoA activation in HEK293T cells. Opto-RhoA (a) and opto-RhoGEF (b) drive potent cell contraction after one 5-s pulse of whole-field blue light illumination, leading to a significant change in cell area (c) and a significant increase in actin polymerization measured by phalloidin intensity (d). (*) $p < 0.001$, (****) $p < 0.0001$, n.s. not significant by Mann-Whitney U test.**

Inactivation tools: Cells expressing opto-ARHGAP1 (ARHGAP1-BcLOV4-mCherry) exhibited less actin polymerization in the photoactivated state compared with dark-adapted cells (Figure 3), measured by phalloidin staining. Untransfected cells observed in this assay exhibit higher actin signal than the GAP tool-expressing cells in the photoactivated state, suggesting that opto-GAP-mediated RhoA inactivation lowers cytoskeletal tension.

DISCUSSION

We created single-component optogenetic tools to both activate (opto-RhoA, opto-RhoGEF) and inactivate (opto-ARHGAP1, opto-ARHGAP7) RhoA signaling in mammalian cells. The use of a single protein for optogenetic signaling perturbation in this toolbox reduces the genetic payload of plasmid delivery to targeted cells and eliminates the need for stoichiometric tuning of multiple optogenetic components. The toolbox also occupies only one visualization channel for tool excitation, freeing up optical bandwidth in experimental setups.

We plan to use these tools to investigate how RhoA signaling protein identity and subcellular localization drive mechanotransductive feedback and cell migration with greater spatiotemporal precision than is afforded by traditional inhibitors or cell-wide genetic manipulations.

Opto-RhoA activation generated sufficient cytoskeletal tension to drive YAP nuclear localization and transcriptional co-activation, presenting an opportunity change the mechanical and transcriptional state of the cell using light. Finally, opto-ARHGAP1 is one of two reported Rho-family optogenetic termination tools [8], expanding the capabilities of optogenetics to control cell physiology.

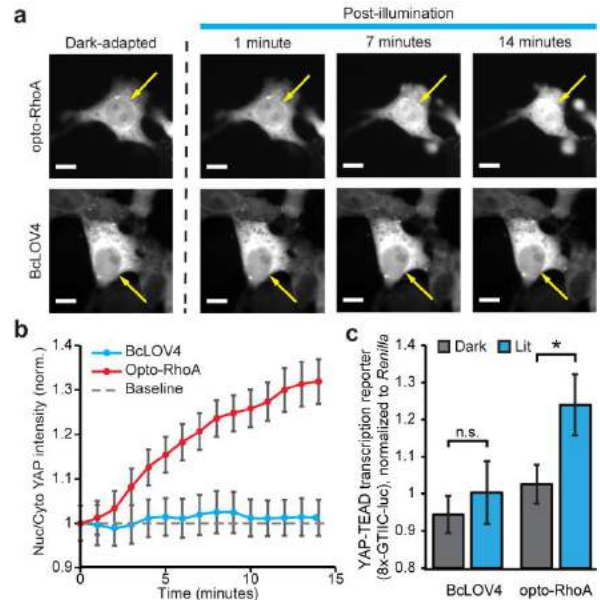


Figure 2: Opto-RhoA drives YAP-EGFP nuclear localization in HEK293T cells (a-b) and an increase in YAP-TEAD-mediated transcription (c). (*) $p < 0.05$ by Mann-Whitney U test.

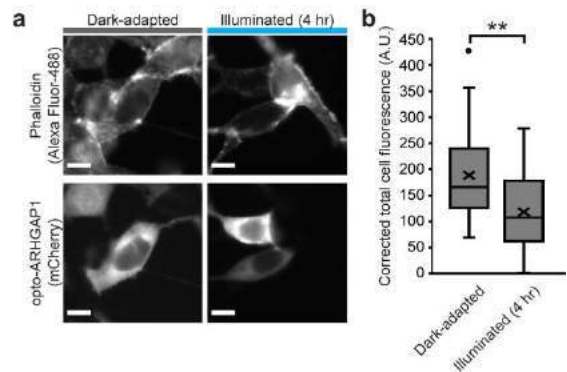


Figure 3: Opto-ARHGAP1-expressing cells HEK293T cells show lower actin density in their photo-activated state.

ACKNOWLEDGEMENTS

This work was funded by the NSF (MCB 1652003) and the NIH (T32 NS091006).

REFERENCES

- [1] Denk-Lobnig, M et al., *Small GTPases*, 10:122-129, 2019.
- [2] Dupont, S et al., *Nature*, 474:179-183, 2011.
- [3] Mason, D et al., *J Cell Biol*, 218:1369-1389, 2019.
- [4] Bugaj, L et al., *Nat Methods*, 10:249-252, 2013.
- [5] Glantz, S et al., *PNAS USA*, 115:E7720-E7727, 2018.
- [6] Berlew, E et al., *Adv Biol*, e2100810, 2021.
- [7] Herrera-Perez, R et al., *Biophys J*, 120:4214-4229, 2021.

EFFECT OF THE PHYSICAL ENVIRONMENT ON EMBRYONIC KIDNEY PROGENITOR AND EXPLANT CULTURE

Aria (Zheyuan) Huang (1), Alex J. Hughes (1,2)

(1) Bioengineering, University of Pennsylvania, Philadelphia, PA, USA
(2) Cell & Developmental Biology, University of Pennsylvania, Philadelphia, PA, USA

INTRODUCTION

Kidney development is a dynamic and highly coordinated dance between branching of the future urinary collecting tubules and induction of nephrons. While genetic and biochemical factors involved in this process have been the primary focus in the past, the role of mechanics is an emergent interest in the field. Studies from other branched organ systems suggest that mechanical factors are crucial in guiding branching morphogenesis [1, 2, 3]. However, the role that mechanics play during kidney development has yet to be elucidated. Our lab recently reported that the mechanical stress generated by jamming of nephron-forming progenitor niches at the tips of tubules may serve as a pace-making cue that instructs nephron commitment. We also showed that pharmacologically inhibiting tension in an iPSC-derived model alters nephron commitment outcomes [4].

To further understand the signaling-level regulation of mechanotransduction during kidney development, we are now perturbing the physical environment at the cellular and whole-organ scales. In this abstract, we present preliminary data on the effect of matrix stiffness on YAP nuclear localization in nephron progenitor cells (NPCs) and on 3D branching in kidney explants. We show that NPCs plated on substrates of different stiffness have varying levels of YAP nuclear localization. Jumping to the whole-organ level, we first develop a 3D explant culture system that enables ex vivo development in a controlled mechanical environment. Current thought in the field is that 3D explant culture is impossible due to nutrient or oxygen transport limitations, necessitating flattened culture at air-liquid interfaces [5]. However, our preliminary work demonstrates that embedding kidney explants in a high-concentration collagen gel supports ex vivo, 3D branching morphogenesis and nephron development for the first time. Future experiments will focus on altering the 3D gel's stiffness to study the impact of the mechanical 3D environment on kidney branching morphogenesis and nephrogenesis..

METHODS

Kidney microdissection and progenitor dissociation: Kidneys were microdissected from CD1 mouse embryos at different embryonic age. For progenitor dissociation, E17 kidneys were further dissected to remove the capsule and ureter. Mouse nephrogenic zone cells were dissociated from E17 kidneys following published protocol [6].

PA gel fabrication and fibronectin coating: Polyacrylamide (PA) gels were fabricated and coated with fibronectin as described by Prah et al. [7]. Soft gel contained 3% Acrylamide (Am) and 0.1% Bisacrylamide (Bis) and stiff gel contained 7.5% Am and 0.25% Bis. After fabrication, the gels were incubated in 10 µg/ml bovine serum fibronectin at 4°C overnight and sterilized under UV light before use.

Cell culture on PA gels: Culture media was made by adding maintenance factors except ROCK-inhibitor Y-27632 to advanced RPMI media [6]. Fibronectin solution was aspirated before adding progenitor cells of various densities. Rock inhibitor was added to half of the chambers and removed 24 hours after cells were plated.

Kidney explant culture at air-liquid interface: Protocol modified from Sebinger et al. [5]. 10% Polydimethylsiloxane (PDMS) was casted to a dish and baked at 60°C overnight. The cured PDMS was first cut into rectangles and a 12 mm circular hole was punched in the center. The PDMS was then plasma-bonded to a 35mm glass-bottom dish. Dissected E12 kidneys were placed in the circular cutout and cultured in 85µL DMEM with 10% FBS. The space between the PDMS and the dish was filled with DI water. The inner surface was coated with 10% Matrigel before culture.

3D kidney explant culture: 3D explant culture utilized the same PDMS dish. In addition to placing the kidney in the dish, a drop of Matrigel or neutralized 3mg/ml rat tail collagen I was added to cover the explant. The embedded kidney was left at room temperature for a few minutes for the gel to solidify and the media was added.

Immunofluorescence: Immunofluorescence staining was performed as described before [4]. Primary antibodies used were YAP,

SIX2, JAG1, and E-cadherin. Secondary antibodies used were donkey anti-rabbit Alexa 647, anti-mouse Alexa 488, anti-mouse Alexa 555 and anti-goat Alexa 555. PA samples were also stained with DAPI. Explants were further cleared with scale A and scale B for two days each.

Imaging and data analysis: PA gels were imaged at 20-40x magnifications on a spinning-disk confocal microscope. Z-stacks of the explants were taken at 4-10x magnification. Fluorescence signals were thresholded using FIJI to assign identity to each cell. YAP nuclear translocation is defined as the ratio of nuclear signal to the cytoplasmic signal. The ratio was calculated using CellProfiler and compared within each cell identity group. Prism was used to perform unpaired t-test to determine statistical significance.

RESULTS

We previously showed that jamming of NPC niches is instructive for cell commitment. We also reported that ROCK-pathway inhibitor (RI), which decreases cell collective tension, promotes stem cell plating efficiency and nephrogenesis in vitro [4]. Moreover, crosstalk between the mechanosensitive YAP pathway and ROCK pathway can regulate stem cell fate in many contexts [8, 9]. Therefore, we decided to characterize NPC's sensitivity to the mechanical environment with and without RI. We fabricated fibronectin-coated PA gels and seeded NPCs obtained from either dissociating mouse embryonic kidneys or differentiating human iPSCs (h-iPSCs) [6, 7, 10]. NPCs were cultured on PA gels of different stiffness at varying density (Figure 1a) with and without RI. The elastic modulus (E) for the soft gel was ~8.7kPa and the stiff gel was ~36.3 kPa. NPCs were stained for undifferentiated NPC marker SIX2, committed NPC marker JAG1, and YAP two days after. h-iPSC-derived NPCs plated at higher density expressed more mature markers, agreeing with published result [10] (Figure 1a). We hypothesized that cells expressing different NPC markers have different YAP nuclear translocation levels which is indicated by the YAP nuclear-to-cytoplasmic (N/C) ratio [8] (figure 1b). We built an analysis pipeline to segment NPCs based on their identity and calculate the YAP N/C ratio in individual cells. We compared the YAP N/C ratios of JAG1-expressing cells and found significant higher N/C ratio in cells on soft gel with RI than in cells on stiff gel with and without RI (figure 1c). Currently, we are determining the mechanosensitivity of other NPC subtypes and the link between NPC commitment and the mechanosensitive YAP activation.

We also sought to study the effect of the physical properties of the matrix on the whole-organ level. Studies of mechanical regulators in cultured kidney explants are limited by the need for an air-liquid interface which disrupts the 3D morphology of the tissue. We aimed to develop a culture system that preserves the 3D architecture of the explants and supports ex vivo branching morphogenesis. The current standard culture method places the explant in a silicon ring exposed at an air-liquid interface [5]. We incorporated a 3mg/ml collagen I gel with reported $E \sim 2.48$ kPa to fully encapsulate the explant (figure 1d) [11]. We also added a 3D Matrigel droplet with reported $E \sim 331$ Pa to the culture device as a separate control [12]. All the groups were cultured under the same conditions and fixed after two days. Kidneys were stained with SIX2 and E-cadherin to visualize the mesenchyme and the ureteric tree (figure 1e). The explant cultured in the 3D Matrigel failed to develop (data not shown). However, the kidney cultured in collagen gained a spherical morphology as compared to the flattened tissue at air-liquid interface while maintaining comparable branch numbers. These data indicate that explant viability may depend not on nutrient or oxygen availability, but rather on an appropriate stiffness and/or adhesive microenvironment. Ongoing experiments are investigating optimal biomaterial and mechanical properties both to achieve a step-change in long-term 3D explant culture capabilities, translate our findings to

regenerative medicine applications, and to understand the fundamental mechanobiology of kidney morphogenesis.

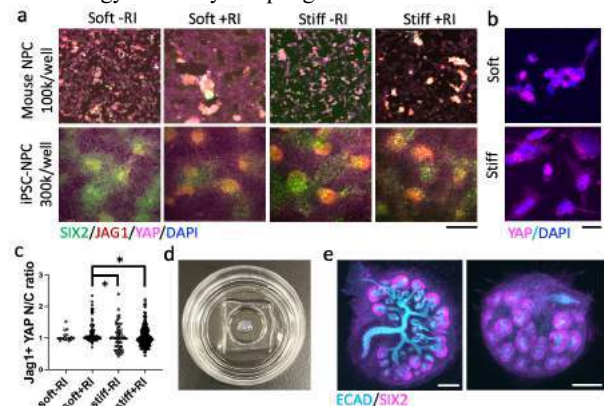


Figure 1. Effect of matrix stiffness on NPCs and 3D explant culture. a. Immunofluorescence micrographs of mouse and h-iPSC-derived NPCs on soft/stiff PA gels with/without RI. b. YAP and nuclear DAPI signals on soft vs stiff substrates. c. Quantification of YAP nuclear translocation of JAG1-expressing cells. Asterisk indicates significant difference. d. 3D culture device with a collagen I gel. e. Z-projection of kidney grown in Matrigel-coated air-liquid interface dish (left) and 3D collagen droplet (right). Scale bar: a&e:200um, b:20um.

DISCUSSION

In the present study, we have presented preliminary data effects of the physical environment on kidney development at both the cellular and whole-organ scales. On the cellular scale, this work contributes preliminary characterization of nephron progenitor mechanosensitivity. We are also testing different tension inhibitors in ongoing work to illuminate the cell-scale details of niche geometry, mechanics, and pace-making of nephron progenitor differentiation. On the organ scale, we introduce a culture technique that supports 3D, ex vivo branching morphogenesis of kidney explants for the first time. We are currently determining the role of gel stiffness, adhesion, and viscoelasticity on branching timing and geometry in this system. A 3D culture method that resembles the in vivo environment offers tremendous opportunities for future studies of kidney branching morphogenesis. This work will create a new cell-to-organ-level mechanics perspective that impacts kidney regenerative medicine efforts seeking to address the high burden of congenital and adult kidney disease.

ACKNOWLEDGEMENTS

We thank members of the Hughes laboratory for helpful discussions and assistance with experimental protocols, especially Louis and John for the gel fabrication and animal work.

REFERENCES

- [1] Varner, V et al., *PNAS*, 112 (30):9230-9235, 2015.
- [2] Wang, S et al., *Cell*, 184:3702–3716, 2021.
- [3] Buchmann, B et al., *Nat Comm*, 12:2759, 2021.
- [4] Viola, J et al., *BioRxiv*, 2022.
- [5] Sebinger, D et al., *PLoS*, 5(5): e10550, 2010.
- [6] Brown, A et al., *Dev Cell*, 34:229–241, 2015.
- [7] Pahl, L et al., *BioRxiv*, 2022.
- [8] Cai, X et al., *Front Cell Dev Biol*, 9, 2021.
- [9] Scott, K et al., *PNAS*, 118 (20) e2021571118, 2021
- [10] Morizane, R et al., *Nat Biot*, 33(11):1193-200, 2015.
- [11] Tirella, A et al., *Mat Letters*, 74: 58–61. 2012.
- [12] Abbas, Y et al., *Human Repr*, 34(10):1999–2008, 2019.

FLUID-STRUCTURE INTERACTION SIMULATION AND EXPERIMENTAL VALIDATION OF BIOPROSTHETIC HEART VALVES

Masod Sadipour (1) and Ali Azadani (1)

(1) Department of Mechanical and Materials Engineering, University of Denver, Denver, Colorado, United States

INTRODUCTION

Bioprosthetic heart valves (BHVs) are designed to closely resemble the flow patterns of a normal human aortic valve, reducing the need for long-term chronic anticoagulation treatment. However, BHVs are usually prone to failure after 10-15 years of being implanted, often due to calcification and degeneration, which can lead to additional surgical procedures to replace the bioprosthetic valve. Design and development of bioprosthetic heart valves (BHVs) require extensive and expensive pre-clinical and clinical testing. The process limits opportunities to thoroughly refine BHVs' design and explore novel ideas. In the past decade, the role of computational modeling has been becoming increasingly important in the design of BHVs. Computational modeling provides a framework for a quantitative description of BHVs' function to address concerns such as long-term valve durability, hemodynamic performance, and thrombogenicity. Several studies have primarily concentrated on modeling the valve using finite element techniques and did not consider the valve interaction with blood flow [1-3]. Fluid-solid interaction (FSI) simulations can examine the interaction between the flow of blood and the mechanics of the valve. In the present study, we have developed a 3D FSI computational model representing a surgical bioprosthesis (25-mm PERIMOUNT Magna Ease) inside a pulse duplicator system (BDC Labs). The simulation results were validated against experimental data obtained by particle image velocimetry (PIV) measurements.

METHODS

A 25-mm PERIMOUNT Magna Ease valve was examined in a BDC pulse duplicator to acquire both valves dynamic and hemodynamic data. We used experimental measurements of pressure gradient and flow rate data as boundary conditions in the FSI simulation [5]. A conventional two-dimensional TSI PIV system was also employed to measure planar velocity downstream of the bioprosthetic valves [5]. PIV data were used to validate the FSI simulation. A NextEngine 3D Laser Scanner was used to obtain the geometry of the surgical valve leaflets [6]. The final geometry model of the leaflet and one-third of the pulse duplicator was created in Solidworks (Figures 1a and 1b). We used Ansys Workbench for the FSI modeling.

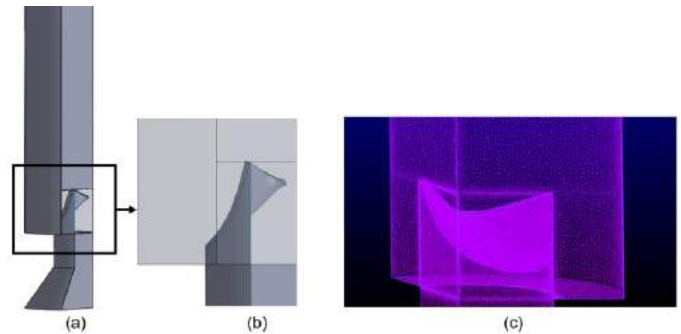


Figure 1: (a) Computational model; (b) magnification of leaflet area; (c) Fluid computational mesh near the valve region.

For solving the structural part of the simulation ANSYS Transient structural and for fluid dynamics, ANSYS FLUENT was used. HyperMesh FE preprocessor was employed to discretize the leaflet geometry using a mapped mesh with 18,610 hexahedral elements. The mesh was then imported to Ansys Transient structural. Leaflets were assumed to be hyperelastic isotropic materials. Yeoh 3rd order strain energy function was used to model the mechanical properties of the leaflets. The strain energy potential equation is:

$$W = \sum_{i=1}^3 C_i (I_1 - 3)^i \quad (1)$$

where C_i are the material mechanical constants and I_1 represents the first deviatoric invariant of the deviatoric right green deformation tensor. The mechanical constants were found by fitting Yeoh 3rd order equation to the experimental strain-stress results of the biaxial test by Mostafa et. al [7]. The fluid domain was discretized via approximately 1.2 million tetrahedral elements using Pointwise- Mesh Generation Software for CFD (Figure 1-c). Mesh independency for both the structure and the fluid mesh was done through four different element numbers. The blood passing through was specified as a homogeneous, Newtonian incompressible fluid with a density of $\rho = 1,060 \text{ kg/mm}^3$ and a viscosity of $\eta = 0.0035 \text{ Pa.s}$. Because the fluid and structure behavior are mutually dependent and data was exchanged in both directions between the solid and fluid domains, we employed a two-way coupled FSI solver. Figure 2 illustrates the flow chart of the system coupling. The process of iterating between FEM and CFD solvers continues until a converged solution was achieved in each FSI iteration.

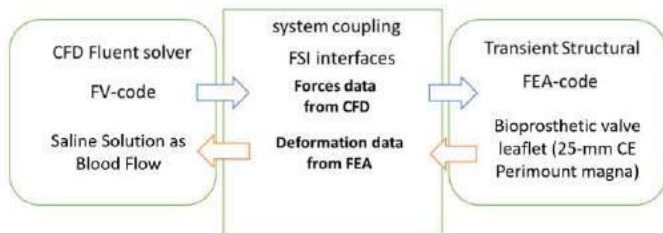


Figure 2: Flow chart of each FSI iterations (data exchanging)

RESULTS

Instantaneous velocity contour from 2-way FSI simulation of the 25-mm Carpentier-Edwards PERIMOUNT Magna bioprosthesis is compared with PIV results at peak systole (presented in Figure 3). At the peak flow, the maximum jet velocity in FSI and PIV are 2.07m/s and 2.1 m/s at the center of the jet respectively, with a diameter of about 14.6 in FSI and 15.2 mm in PIV. Also, jet length is the same in both FSI and PIV. As can be seen, the velocity dropped significantly from the central jet to the surrounding area in both FSI and PIV results. The plane at which the flow parameters are shown in Figure 3 (left) is the mid-plane cutting through the bioprosthetic valve. Good agreement between the experiment and the simulation results was observed.

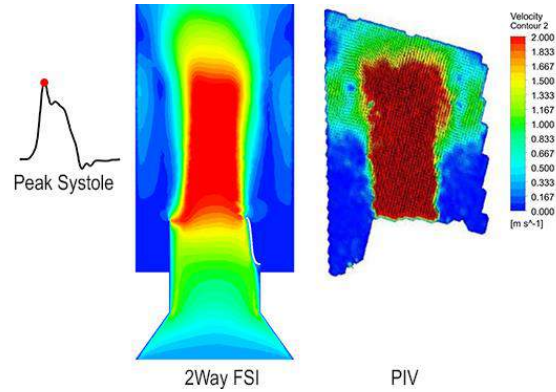


Figure 3: Two-way FSI simulation results (left) and PIV measurement (right) of 25-mm surgical Carpentier-Edwards PERIMOUNT Magna at peak of systole.

DISCUSSION

This study has developed an FSI simulation of a BHV in a pulse-duplicator platform. The study improves our understanding of structural and hemodynamic performance of BHVs. The simulation results were validated against experimental data obtained by flow velocity measurements using PIV. We found a good agreement between them. Our validated platform is applicable for different bioprosthetic and transcatheter heart valves. FSI methodology offers a reliable tool to assess the structural and hemodynamic performance of BHVs. This project is a step toward the experimental validation of this FSI modeling platform for evaluating tissue heart valves. The methodology can be used effectively for the quantitative description of the structural and hemodynamic performance of BHVs and mitigate the need to perform time-consuming bench-top and pre-clinical animal testing.

ACKNOWLEDGEMENTS

This work was supported by the University of Denver [Grant number: 84993-142235].

REFERENCES

- [1] Haj-Ali R. et al., Structural simulations of prosthetic tri-leaflet aortic heart valves, *J. Biomech*, 41:1510–1519, 2008.
- [2] Huang X. et al., A two-dimensional finite element analysis of a bioprosthetic heart valve, *J. Biomech*, 23:753–762, 1990.
- [3] Kim H. et al., Dynamic simulation of bioprosthetic heart valves using a stress resultant shell model, *Ann. Biomed. Engrg*, 36:262–275, 2008.
- [4] Borazjani I, Fluid-structure interaction, immersed boundary-finite element method simulations of bio-prosthetic heart valves, *Comput Methods Appl Mech Eng*, 257:103–16, 2013.
- [5] Barakat, M. et al., Fluid dynamic characterization of transcatheter aortic valves using particle image velocimetry, *Artificial Organs*, 42(11): 357-368.
- [6] Abbasi M et al., A non-invasive material characterization framework for bioprosthetic heart valves, *Ann Biomed Eng*, 47(1):97–112, 2019.
- [7] Abbasi, M. et al., Leaflet stress and strain distributions following incomplete transcatheter aortic valve expansion, *Journal of biomechanics*, 48(13): 3663-3671, 2015.

NOVEL AUTOMATED AORTIC ROOT ECHOCARDIOGRAPHY FEATURE TRACKING ALGORITHM FOR PEDIATRIC AORTOPATHY

Elnaz Ghajar-Rahimi (1), Frederick W. Damen (1,2), Benjamin J. Landis (3,4), Craig J. Goergen (1,2)

(1) Weldon School of Biomedical Engineering, Purdue University, West Lafayette, IN, USA

(2) Indiana University School of Medicine, Indianapolis, IN, USA

(3) Herman B Wells Center for Pediatric Research, Indiana University School of Medicine, Indianapolis, IN, USA

(4) Division of Pediatric Cardiology, Department of Pediatrics, Indiana University School of Medicine, Indianapolis, IN, USA

INTRODUCTION

Transthoracic echocardiography is important for the diagnosis and monitoring of aortopathy involving the proximal aorta (e.g., bicuspid aortic valve, Marfan syndrome) [1]. Maximal aortic diameters measured from the parasternal long axis (PSLAX) window often guide treatment strategies. However, these measurements remain an incomplete marker of disease status and even the slightest inter-observer variability may lead to vastly different management plans [2]. Gross displacement and aortic root expansion across the cardiac cycle may further complicate precise measurement. Here we present a feature tracking algorithm that accounts for these factors to extract aortic root information accurately and efficiently from routine echocardiography data.

METHODS

This algorithm simultaneously estimated aortic root expansion and gross displacement from PSLAX echocardiography images, and automatically extracted diameter measurements across the length of the aortic root. The Indiana University School of Medicine IRB approved the collection and de-identification of all echocardiography images.

Algorithm Development: A feature tracking algorithm was developed in MATLAB, which specifically quantifies five parameters at every time point across the cine loop: x-displacement, y-displacement, rotation angle, aortic root expansion, and slope (**Figure 1**). Simultaneous tracking of these parameters reduced the impact of translation and rotation of the aorta to align measurements perpendicularly to the axis of the vessel. To mitigate effects of image artifacts during tracking, the algorithm iteratively built a reference template-image based on previously tracked frames. Image artifacts were identified through regional variability of image intensity across time, from which a new iteration of temporal template weights was estimated.

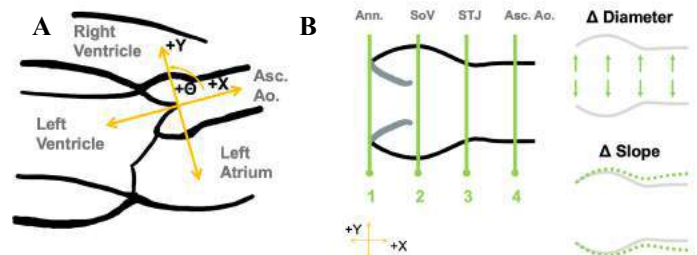


Figure 1: Algorithm Parameters A) x- and y-displacement and rotational component ($\Delta\theta$) are used to track gross movement B) Change in diameter and slope are used to estimate aortic root size and function. (Asc. Ao.= ascending aorta, Ann.= annulus, SoV= sinus of Valsalva, STJ= sinotubular junction).

Algorithm Verification: To ensure that derived maximum diameter measurements were comparable to standard clinical techniques, we compared our algorithm against manual aortic root diameter measurements obtained in the clinic. Clinical transthoracic echocardiography images were obtained in the PSLAX view from a group of healthy control patients (11.5-21.5 years old; $n=7$) and patients with known aortopathy (0.2-18.6 years old; $n=3$). Diameter measurements were obtained at the aortic annulus, sinus of Valsalva, sinotubular junction, and ascending aorta segments in up to three cardiac cycles using 1) the feature tracking algorithm and 2) manually by a board-certified pediatric cardiologist. The maximal systolic diameter measurements at each aortic segment were then compared between estimation methods using linear regression and goodness-of-fit statistics.

Healthy vs. Diseased: After preliminary assessment of our algorithm against clinical methods, the patient data set was expanded.

The algorithm was used to compare healthy and aortopathy patients. Automated tracking was performed on clinical PSLAX echocardiograms of 43 control patients ($n=21$ female, 0.2-16.5 years old; $n=22$ male, 2.6-18.6 years old) and 45 patients with known aortopathy ($n=21$ female, 2.2-17.7 years old; $n=24$ male, 5.0-14.3 years old). Aortic root diameter measurements were estimated with the algorithm for each patient. Linear regression analysis of tracking results focused on maximum systolic diameters extracted from curves at the sinus of Valsalva compared against patient age and body surface area (BSA).

RESULTS

Image Stabilization: The algorithm successfully tracked the anterior and posterior surfaces of the proximal aorta in the PSLAX window. Stabilization of the aorta with respect to gross translation facilitated measurement of aortic diameters in consistent anatomic planes throughout the cardiac cycle at the sinus of Valsalva (**Figure 2**) and other specified segments. Stabilization of the PSLAX B-Mode allowed for retroactive generation of M-Mode images in which the aortic valve movement and anatomy were more clearly seen in stabilized M-Modes (**Figure 2A**) compared to non-stabilized M-Modes (**Figure 2C**).

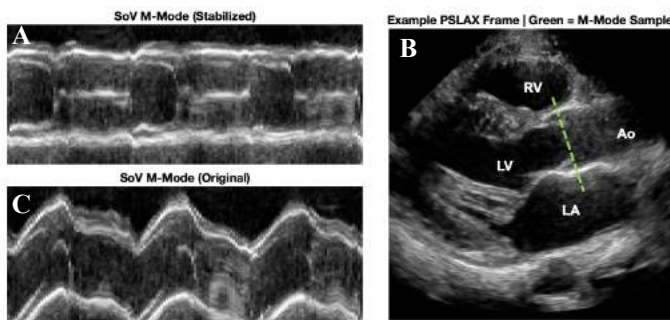


Figure 2: A) Stabilized M-mode at the sinus of Valsalva (SoV) retroactively generated from B) B-Mode image, across the green marker. C) Original, non-stabilized M-Mode.

Diameter Extraction & Algorithm Performance: After stabilizing the inputted PSLAX echocardiograph images, the algorithm successfully estimated the diameters across the aortic root from the annulus to the start of the ascending aorta across all periods of time (**Figure 3**). When compared to standard of care techniques, the algorithm derived and manually derived diameter measurements were highly correlated ($r^2 > 0.96$) for each analyzed segment in both healthy and aortopathy groups.

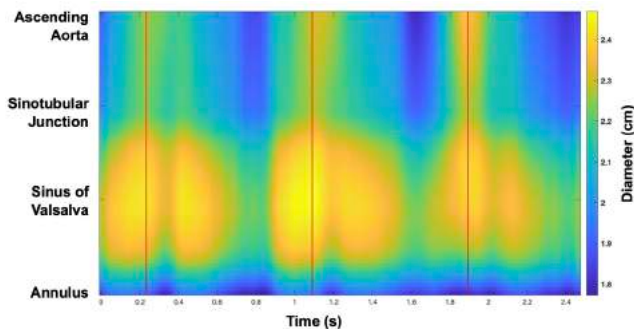


Figure 3: Diameter time courses from tracking results across aortic root throughout cardiac cycle.

Application in Aortopathy Cohorts: The maximum diameters at the sinus of Valsalva were larger in the aortopathy patient cohort compared to the controls across both BSA and age. In both the control and aortopathy cohorts, a stronger linear relationship was observed between maximum diameter and BSA than between maximum diameter and age: control males ($r^2=0.82$ vs. 0.75), control females ($r^2=0.54$ vs. 0.49), aortopathy males ($r^2=0.57$ vs. 0.40), and aortopathy females ($r^2=0.64$ vs. 0.60; **Figure 4**). Aortic diameters extracted by the algorithm do not appear to vary significantly between sexes.

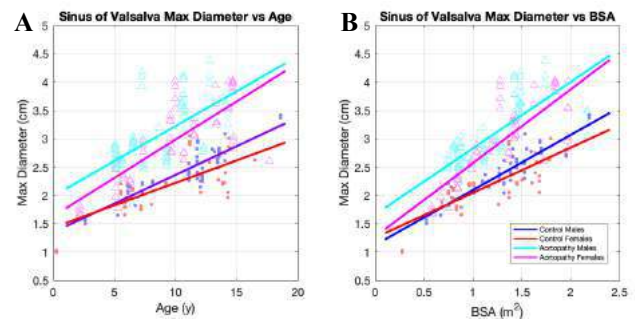


Figure 4: Maximum diameter at sinus of Valsalva versus A) age and B) body surface area (BSA) in controls and aortopathy patients. As expected, the aortic diameter extracted by the algorithm are higher in the aortopathy cohort versus controls across a range of ages and body sizes.

DISCUSSION

Our novel tracking algorithm successfully stabilized images and precisely measured aortic diameters when compared to manual measurements. Ultimately, our algorithm may reduce inter-observer variability and significantly increase throughput compared to current standard manual measurement techniques. Initial results suggest that differences in aortic root diameters are detectable between healthy and aortopathy cohorts, and that BSA and maximum diameter have a strong linear relationship. This further supports the use of our algorithm, as it reflects current clinical guidelines in which Z-scores for aortic root dimensions are assessed with respect to BSA [3]. A notable limitation, however, is that the data utilized in this study was collected from patients at a single timepoint. Applying the algorithm to a longitudinal study to assess disease progression overtime may allow us to better test the robustness and predictive capabilities of our algorithm. This study provides a foundation for expanding the algorithm to include machine learning techniques and biomechanical analyses, such as Green-Lagrange strain [4], vessel diastology, and aortic root pulsatility. We anticipate that further development and application of this algorithm to incorporate other rigorous biomechanics estimates will help elucidate vessel wall dynamics throughout the cardiac cycle and eventually improve the quality of care for patients with aortopathy.

ACKNOWLEDGEMENTS

This work was partially supported by the NIH (HL141667). Elnaz Ghajar-Rahimi was supported by the Purdue Doctoral Fellowship.

REFERENCES

- [1] Wheeler A.P., et al., *Pediatr Cardiol.*, 42(1):148-157, 2021
- [2] Rutten D.W.E., et al., *Cardiol Young.*, 31:1962-1968, 2021
- [3] Lopez, L., et al., *Circ Cardiovasc Imaging*, 10(11): e006979, 2017
- [4] Damen, F.W., et al., *Appl. Sci.*, 11: 1690, 2021

SEX DIFFERENCES IN RIGHT VENTRICULAR CHAMBER ELASTANCE AND STIFFNESS IN AN ANIMAL MODEL OF PULMONARY ARTERIAL HYPERTENSION

ED Kwan (1), TM Wang (1), H Mu (1), BA Hardie (1), D Valdez-Jasso (1)

(1) Department of Bioengineering, University of California San Diego, La Jolla, California, USA

INTRODUCTION

The health and function of the right ventricle (RV) is the most important predictor of outcomes in patients with pulmonary arterial hypertension (PAH). Both clinical and preclinical studies have demonstrated the association of sex with RV hemodynamic function¹. Women present less severe RV remodeling and improved function compared to men, for unknown reasons. Importantly, women also show different responses pre- and post-menopause, with more severe RV remodeling and worse health outcomes post-menopause¹. Despite this, most animal studies have focused on males so sex-dependent RV remodeling data is particularly sparse. Previous studies have correlated endogenous estrogen to improved RV function as well as demonstrated positive effects of exogenous estrogen², however the regulation and role of estrogens in progressive human PAH remains unclear.

In a recent 10-week study of male PAH-treated rats, we found that RV hypertrophy and diastolic stiffening explained almost all measured changes to RV chamber end-systolic and end-diastolic pressure-volume relationships³. While RV hypertrophy and diastolic stiffening are well established prognostic indicators in PAH patients⁴, their relative contributions to RV function in both male and female PAH remains unclear. It is possible that sex-differences in RV myocardial structural and material remodeling may also underlie the progression of PAH disease often attributed to estrogens. Therefore, we designed a study to investigate the pathology of RV remodeling by combining hemodynamic and morphologic measurements with a biomechanics model previously described. We investigated RV remodeling in PAH-induced male and female rats, as well as ovariectomized female rats to model the effects of estrogen depletion post-menopause.

METHODS

Seven-week old male and eight-week old female and ovariectomized female rats were treated with a subcutaneous injection of 20mg/kg sugen, a vascular endothelial growth factor receptor

inhibitor, then placed in a hypoxia chamber (10% oxygen) for 3 weeks to induce PAH. The animals were then returned to normoxia for 5 weeks. Age-matched normotensive animals kept in normoxia were the control groups. During terminal surgeries, a 1.9F admittance catheter (Transonic Scisense, Ontario, Canada) was inserted apically into the RV chamber and used to take invasive pressure-volume (PV) measurements during steady state and during occlusion of the inferior vena cava. Right ventricular pressure, myocardial wall mechanics, and morphology were analyzed using a Laplace-type reduced-order model³. Briefly, the RV geometry was modeled as a fraction of a sphere comprised of RV chamber, RV free-wall, and septum wall volumes. The geometric model-derived RV radius to wall thickness remained greater than 5:1 in all three SuHx-treated groups, so the thin-walled assumption was used to relate RV blood pressure to myocardial circumferential wall stress using Laplace's Law³. Here, passive stress (T_p) was modeled as an exponential function with two material stiffness parameters optimized to match the model to end-diastolic (ED) PV measurements. Passive stress plus an additional active fiber stress (T_a), modeled as saturation equation, was computed and matched to end-systolic (ES) PV measurements by optimizing a third material parameter of calcium-dependent myofilament activation. Fitted rat-specific model parameters were then used to predict and analyze resting and active sarcomere length-stress relations.

Measurements of right-ventricular myocyte mechanics were taken to validate model predictions of myofiber contractility upregulation. Right ventricular myocytes were isolated using enzymatic digestion (.001M collagenase II, .0015M protease) *via* Langendorff's perfusion⁵, then incubated in [1.8mM]_{Ca2+} Tyrode's solution (.0018M CaCl₂, .134M NaCl, .00268M KCl, .00556M glucose, .0119M NaHCO₃) with 2uM Fura 2-AM. RV myocytes were field stimulated at 1Hz and fluorescence at 340nm and 380nm excitation wavelength. Sarcomere length was recorded with a laser scanning fluorescent photometer (IonOptix, MA, USA). Myocyte shortening was measured as the

difference between baseline sarcomere length at rest and peak sarcomere length during contraction.⁶

Descriptive statistics were performed in JMP Pro Statistical software (version 16, SAS Institute Inc., NC, USA)). For normally distributed data, two-factor ANOVA were used to test for differences based on the two factors treatment and sex, followed by the Dunnett's *post-hoc* test for treatment and the Tukey test for sex. Otherwise, non-parametric Wilcoxon-Kruskal-Wallis statistic was used followed by the Dunnett's *post-hoc* test for treatment and the Dunn test for sex. Statistical significance was determined at a level of $\alpha < 0.05$.

RESULTS

Male, female, and ovariectomized female rats treated with SuHx reached hypertension (mean pulmonary arterial pressure >20 mmHg), with group mean pulmonary arterial pressure of 39.1mmHg in males, 42.7mmHg in females, and 42.8mmHg in OVX female rats. End-systolic RV chamber pressures were almost identical across sex groups at baseline (22.4-23.1mmHg), but with the largest increases in male SuHx (62.7mmHg male compared to 60.4mmHg female and 58.7mmHg OVX female). While RV mass was greater in males than females at baseline and in SuHx, the Fulton index (not shown) indicated similar relative RV mass hypertrophy in all three SuHx groups when normalized by the LV+septum masses. End-diastolic pressure increased in SuHx groups, with the largest increases in the male rats (6x increase vs 2x increase in females compared to controls). End-systolic pressures increased in all three SuHx groups, with similar increases across sex.

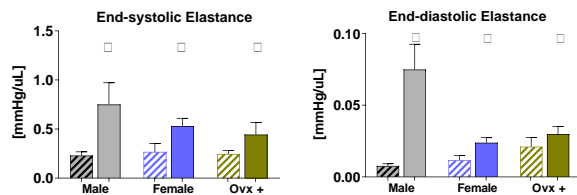


Figure 1: RV ES and ED chamber elastance increased in all SuHx groups (solid bars) compared to respective controls (dashed bars). Increases to ES and ED chamber elastance were the largest in the male SuHx group.

From rat-specific models fitted to PV data, sarcomere length-stress relations were predicted (Figure 2). Male, female, and OVX passive and active sarcomere length-tension relations were similar at baseline, so only a single control group curve is shown (dashed). Active length-tension relations showed small increases (n.s., $p>0.05$) in all three SuHx groups compared to controls.

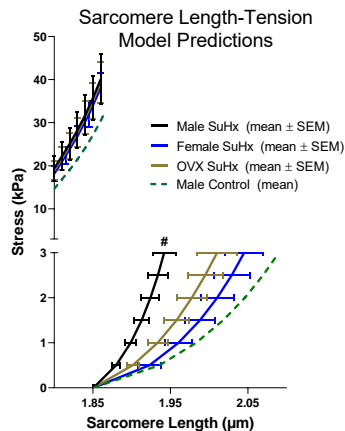


Figure 2. Model predictions showed significant increases ($p<0.05$) in passive stiffness (bottom) in male SuHx (black)

compared to control (green dashed) that was not seen in female (blue) and OVX (gold) groups ($p>0.05$).

RV myocytes isolated from SuHx-treated rats showed small increases (between 0.1-2.8% shortening, n.s.) with the largest changes in the male and OVX groups.

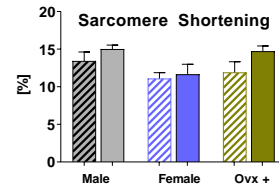


Figure 3. RV myocytes showed no significant increases in contractile shortening from baseline (dashed) to SuHx (solid).

DISCUSSION

Elevated pulmonary pressures resulted in RV remodeling as shown by hemodynamic and morphologic measurements and showed sex-dependent changes to end-systolic and end-diastolic chamber mechanics. End-systolic chamber elastance increased in all SuHx-treated groups. Model predictions of sarcomere length-tension relations showed only small changes in the active length-tension relation, indicating the significant RV wall hypertrophy and geometric remodeling identified by the model largely explained the increases to end-systolic chamber elastance. Significant contributions of RV hypertrophy to remodeling of ES chamber mechanics were found independent of sex or ovariectomy. Small increases in model-predicted myofiber contractility were validated by myocyte contraction experiments which showed small increases in sarcomere shortening in myocytes isolated from SuHx-treated rats. Both compensatory RV hypertrophy and contractility upregulation have been reported in clinical⁴ and preclinical studies⁷ of PAH.

Model predictions of sarcomere length-tension relations found significant passive myocardial stiffening in male SuHx rats, that was not present in female or ovariectomized female rats, which reflects the large increases to diastolic elastance seen at the organ level. Correspondingly, diastolic stiffness, found to be most severe in male rats, has been correlated to RV dysfunction in PAH patents. While diastolic stiffness in this study was not associated with significant extracellular matrix collagen accumulation, it could be explained by fibrillar collagen structural changes. Diastolic stiffness has been well established as a prognostic indicator⁴, yet this study identifies sex-differences in the severity of chamber stiffening and myocardial passive stiffening. Further studies investigating sex-differences in addition to the role of estrogen in the remodeling of the RV myocardium would address the gaps between results reported in isolated myocytes⁶ (increased calcium transient amplitudes and improved cell contractility) and the progressive loss of RV function⁴ reported *in vivo*.

ACKNOWLEDGEMENTS

This work was funded by AHA-16SDG29670010; NHLBI 1R25HL145817-01, NHLBI 1R01HL155945-01; NIH-NHLBI-1T32HL105373; NSF 2045269

REFERENCES

- [1] Lahm, T et al., *Am J Physiol – Lung Cell Mol*, 307(1):L7-26, 2014.
- [2] Frump, AL et al., *J Clin Invest*, 131(6):e129433, 2021.
- [3] Kwan, ED et al., *Am J Physiol – Heart Circ*, 321(4):H702-715, 2021.
- [4] Rain, S et al., *Circulation*, 128(18):2016-2025, 2013.
- [5] Li, D et al., *J Vis Exp*, 98:51357, 2014.
- [6] Sabourin, J et al., *J Mol Cell Card*, 118:204-224, 2018.
- [7] De Man, FS et al., *Circ Heart Fail*, 5(1):97-105, 2012

CONNECTING CYCLIC STRESS TO NEPHRON INDUCTION IN KIDNEY ORGANOID AND 3D CO-CULTURE MODELS

John M. Viola (1), Alex J. Hughes (1,2)

(1) Bioengineering
University of Pennsylvania
Philadelphia, PA, USA

(2) Cell & Developmental Biology
University of Pennsylvania
Philadelphia, PA, USA

INTRODUCTION

Nephrogenesis is the process by which collections of mesenchymal progenitor cells within a stem cell niche transition to form the epithelial filtration units of the kidney. The nephron progenitor stem cell niche must balance differentiation and self-renewal of nephron progenitor cells as new nephrons form continuously throughout development¹. Understanding how this balance is maintained for continuous nephron formation is crucial for creating nephron-dense and structurally organized kidney organoids or replacement tissues. *In vivo*, the nephron progenitor niche exists in a dynamic environment at the actively branching tips of a rapidly growing epithelial tubule network and is surrounded by stromal cells. Therefore, biochemical and physical properties within the niche that oscillate due to the migration and branching of the adjacent epithelial tissue are promising targets to regulate this balance in nephron progenitor differentiation outcomes.

We have shown through modeling and physical measurements that newly branching tips must overcome mechanical resistance from neighboring niches, which generates increased mechanical stress within the niche that then dissipates over time before the next branch event². In a reductionist human iPSC-derived nephron progenitor spheroid model that also contains stromal cells, we saw increased early nephron differentiation in the presence of the cell tension inhibitors². To further examine the role of a changing mechanical environment on nephron formation outcomes in the niche, we separately purified nephron progenitor and cells surrounding the niche specifically including stroma from the mouse embryonic kidney and found that the inclusion of stroma in a co-culture model changes the nephron progenitor differentiation response to mechanical perturbations. Crosstalk between these two cell types impacting nephron formation has been identified in other work³, however the nature of this crosstalk in the context of cyclic mechanical stress remains unexplored. Understanding the mechanisms

by which nephrogenic niche cell types interact with each other and the mechanical environment to influence nephrogenesis could allow for new engineering control strategies for nephron formation *in vitro*. This advance would contribute to development of kidney replacement tissue for the estimated 15% of adults that experience kidney disease⁴.

METHODS

Kidney immunofluorescence imaging. Immunofluorescence staining and imaging was performed as previously published^{5,6}.

Force inference. Bayesian force inference was applied according to a recently published procedure that infers maps of tissue tension and pressure based on observed variations in edge lengths and angles at cell vertices. Ureteric tip Voronoi diagrams were processed in the *Tissue Analyzer* plugin in FIJI⁷, and anisotropic stress was computed using Batchelor's formula using previously published MATLAB code^{8,9}.

Laser ablation. E17 mouse embryonic kidney explants were incubated in Alexa Fluor 488-PNA to label the ureteric bud and CellTracker red in culture media and placed in PDMS wells plasma bonded to a quartz coverslip. Individual cap mesenchyme niches at the kidney surface were ablated using an ultraviolet laser through a 10X objective. Cut opening time-lapses were imaged from the microscope monitor using an iPhone 8 video camera.

Nephron progenitor and stroma co-culture differentiation assay. Mouse embryonic kidneys were partially dissociated to isolate nephron progenitor and niche surrounding cells including stroma from the organ surface per published protocols¹⁰. Nephron progenitor cells were sorted using magnetic activated cell sorting by previously published protocols to generate nephron progenitor spheroids¹⁰. 50,000 nephron progenitor or stromal cells were plated in low attachment round bottom plates and centrifuged to generate spheroids. Cells were plated directly into treatment media that was removed after overnight

incubation and replaced with control media for overnight incubation. Spheroids were then fixed and stained by immunofluorescence.

Quantification of spheroid cell differentiation. Maximum intensity projections of spheroids were generated and further processed in FIJI. LHX1 and SIX2 signals were segmented using 200 pix rolling ball background subtraction and thresholded to remove background signal. The total numbers of positive pixels were divided by total number of pixels within the spheroid to normalize by spheroid area.

RESULTS

In kidney development the urinary collecting duct tree is formed through iterative branching of the epithelial precursor tissue, the ureteric bud. The nephrogenic stem cell niches exist at the tips of this branching tissue and periodically form nephrons that will later merge with the nearest collecting duct. As branching continues and more niches are generated, they become crowded at the surface of the developing organ (fig. 1A). Each niche is separated from others by a thin layer of stromal cells. Recent work has shown that niche positions at the surface are partially predicted by a physical model that includes mutual repulsion and crowding¹¹. We used a force inference model^{8,9} to infer interfacial tensions at niche boundaries as well as internal niche stresses (fig. 1B). We found that higher niche anisotropic stress is positively correlated with shape index of individual niches (fig. 1C). Shape index is highest just as the ureteric bud tip is bifurcating, and then steadily decreases until the next bifurcation event. We confirmed this result experimentally through measuring rebound velocity of laser ablated niche boundaries in mouse embryonic kidney explants (fig. 1D). These data suggest a model in which the niche is cycling between low and high internal stress states during branching cycles of the ureteric bud.

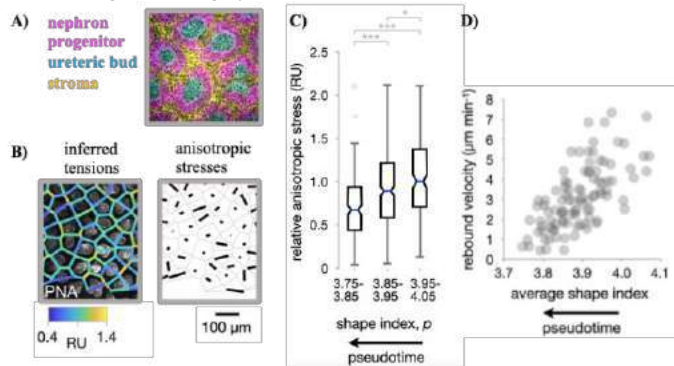


Figure 1. Nephron progenitor niche mechanical environment is correlated with shape index **a.** Immunofluorescence image of whole mount E17 mouse embryonic kidney **b.** PNA stained ureteric bud tips overlaid with Voronoi diagram showing inferred tensions and anisotropic stresses by force inference modeling **c.** Plot of relative anisotropic stress in niches grouped by shape index. **d.** scatter plot of rebound velocity after laser ablation of the interface between two neighboring nephron progenitor niches.

Cell membrane tension is influenced by cell crowding, can be predicted by cell shape, and affects signaling outcomes within the cell^{9,12}. We hypothesize that, at the larger scale of the developing kidney, stromal cell boundaries between stem cell niches may play an analogous role to the cell membrane. As the stromal cell boundaries are sculpted through niche shape index changes, they experience different tensional loads depending on niche life cycle. It has also been shown that stroma - nephron progenitor contact signaling affects differentiation³. Therefore, we asked if changes in mechanical state are instructive to nephron progenitor cell differentiation outcomes either directly or mediated by nearby stromal cells. To test this, we partially

dissociated and sorted mouse embryonic kidney tissue per published protocols¹⁰ to isolate either nephron progenitor cells along with surrounding niche cells including stroma or nephron progenitor cells only. We then cultured these cells as spheroids in the presence of pulse treatment of cell tension inhibitors as well as a low level of a Wnt signaling agonist to mimic the mechanical and biochemical environment of the niche *in vivo* (fig. 2A-D). We found that in spheroids consisting of nephron progenitor cells only, differentiation decreased compared to controls. However, in spheroids consisting of nephron progenitor cells and stromal cells, differentiation increased compared to controls. These results suggest that stromal cells could mediate niche mechanosensitivity. Future work will determine the mechanosensitivity of stromal - nephron progenitor signaling for nephron induction.

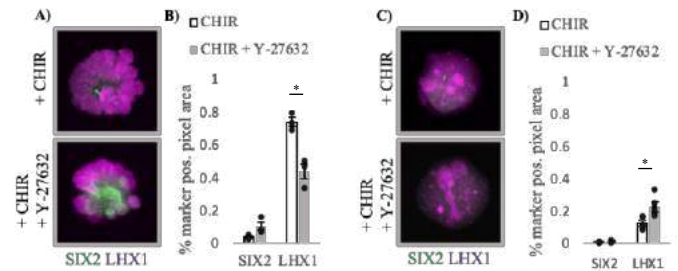


Figure 2. Nephron progenitors have different differentiation responses to mechanical transients in the presence of kidney stromal cells **a.** Immunofluorescence of nephron progenitor spheroids after pulse treatment of Wnt agonist (CHIR) +/- cell tension inhibitor (Y-27632). Stained for differentiation marker LHX1 and progenitor marker SIX2. **b.** Quantification of **a.** **c.** Immunofluorescence of nephron progenitor + stroma spheroids after pulse treatment of Wnt agonist (CHIR) +/- cell tension inhibitor (Y-27632). Stained for differentiation marker LHX1 and progenitor marker SIX2. **d.** Quantification of **c.**

DISCUSSION

Here, through modeling and physical measurements, we show that the nephron progenitor niche is subject to cyclical mechanical stress. We then show that mechanical perturbations are sufficient to alter nephron progenitor differentiation outcomes *in vitro*. However, co-culture with native kidney stroma that borders the niche *in vivo* alters the nephron progenitor differentiation response to mechanical perturbations. In future work, we aim to uncover how the niche as a whole interprets mechanical signals to influence nephron formation.

ACKNOWLEDGEMENTS

We thank members of the Hughes laboratory for helpful discussions and assistance with experimental protocols. This work was supported by NIH grants T32HD083185 and R35GM133380.

REFERENCES

- Kopan, et al., *Curr. Top. Dev. Biol.* **107**, 293–331 (2014).
- Viola, J. M. et al., *bioRxiv* 2022.06.03.494718 (2022).
- Wilson, S. B. et al., *Development* **148**, (2021).
- CDC. 322964-A (2021).
- O'Brien, L. L. et al., *Elife* **7**, (2018).
- Combes, A. N. et al., *Nat. Protoc.* **9**, 2859–79 (2014).
- Aigouy, B. et al., *Methods Mol. Biol.* **1478**, 227–239 (2016).
- Ishihara, S. et al., *J. Theor. Biol.* **313**, 201–211 (2012).
- Kong, W. et al., *Sci. Rep.* **9**, 14647 (2019).
- Brown, A. C. et al., *Proc. Natl. Acad. Sci.* **110**, 4640–4645 (2013).
- Prahl, L. S., et al., *bioRxiv* 2021.11.29.470441 (2021).
- Sitarska E. et al., *Curr Opin Cell Biol.* **66**, 11-18 (2020).

MODELLING OF THE UTEROSACRAL LIGAMENT SUGGESTS CHANGES IN MICROARCHITECTURE DURING PREGNANCY

Lea M. Savard (1), Catalina S. Bastías (2), Kathleen Connell (3)
Sarah Calve (1, 2, 4), Callan M. Luetkemeyer (5), Virginia L. Ferguson (1, 2, 4)

- (1) Department of Mechanical Engineering, University of Colorado at Boulder, Boulder, CO, USA
- (2) Biomedical Engineering Program, University of Colorado at Boulder, Boulder, CO, USA
- (3) Department of Obstetrics and Gynecology, University of Colorado Anschutz, Aurora, CO, USA
- (4) BioFrontiers Institute, University of Colorado at Boulder, Boulder, CO, USA
- (5) Department of Mechanical Science and Engineering, University of Illinois at Urbana-Champaign, Urbana, IL, USA

INTRODUCTION

In the United States, nearly one half of all females between the ages of 50 to 79 years old have uterine prolapse, which is characterized by the descent of the uterus from its normal anatomical position, or other forms of pelvic organ prolapse (POP) [1]. The strongest factors known to be associated with POP include parity (i.e., the number of times a woman has given birth), and vaginal childbirth, but the mechanisms in which these lead to prolapse remains unknown [2,3]. The uterosacral ligament (USL), which connects from the cervix to the sacrum, is the primary suspensory support structure for the uterus, which provides apical support and suspends the uterus [3]. Damage to and failure of the USL due to biomechanical injury may result in the protrusion of the uterus and/or vagina, or POP; hence, we focus our research on understanding how the mechanics of the USL change during pregnancy and parturition, and how that may lead to POP.

Ligaments, like the USL, serve primarily mechanical functions; therefore, it is critical to have a mechanistic understanding of the USL to elucidate mechanisms of ligament deformation and damage. USL mechanical behavior is governed by the extracellular matrix (ECM), which primarily derives tensile support from collagenous fibers [2,3]. A constitutive model describes the material mechanical behavior in a mathematical framework. In particular, structural constitutive models incorporate information on tissue composition and microarchitecture to study the structural and functional relationship in response to changes in mechanical loading. The Holzapfel-Gasser-Ogden (HGO) is a hyperelastic anisotropic model that includes terms that represent the tissue histoarchitecture, including collagen fiber stiffness and alignment, to describe the tissue mechanics [4]. The free energy of the HGO model is a combination of energy from the non-collagenous surrounding matrix, the collagenous substance, or the fibers, and a volumetric correction due to assumptions of incompressibility.

Although this model is commonly used to describe biological tissues with one main axial loading direction, to the authors knowledge

it has not yet been used to describe the USL mechanical behavior. In this study, we used the HGO model to capture the tensile loading behavior of the murine USL before, during, and after pregnancy to understand how changes in the USL microarchitecture influence the mechanical behavior of intact ligaments under tension.

METHODS

Female C57BL/6J mice were obtained and euthanized as nulliparous (NP, $n = 4$), late pregnancy gestation day 18.5 (E18.5, $n = 2$), and 1 day postpartum (PP1, $n = 2$), according to the University of Colorado Boulder's Animal Care and Use Committee. USLs were isolated and a suture was tied at the cervical end. The USL was then cut proximal to the suture. The other USL was removed and saved for later biochemical analysis. The pelvic tissue, with the one USL still attached to the sacrum, was dissected from the mouse, yielding a cervix-USL-pelvis complex. Each sample was placed at 4°C in Ghost Dye Red 780 (Tonbo Biosciences) and stained for 2 hours followed by Sytox Deep Red Fluorescent Stain (Thermo Fischer Scientific) for 10 minutes.

Each USL sample was placed under a confocal microscope (Leica STELLARIS) in a custom loading chamber with PBS bath and connected to a 100 mN FemtoTools microforce load sensor. The sample was placed in a reference configuration based on a 500 μ N preload, and then subjected to four displacement-controlled stress relaxation tests, returning to the reference configuration after each test. Applied displacements were 1000 μ m, 1500 μ m, 2000 μ m, and 2500 μ m at a loading rate of 50 μ m/s, and the sample was held at each displacement state for 5 minutes. In each reference and relaxed configuration, the sample surface was imaged at 10 \times magnification. The confocal images of the stained USL were used to map deformation with the Matlab function 'imregdemon'. Global displacement was calculated from the maximum and minimum image-tracked displacement values.

The strain energy density function of the HGO model with an additional fiber dispersion parameter (Gasser et al., 2006) is given as:

$$\Psi_{HGO} = c \left(J^{-\frac{2}{3}} I_1 - 3 \right) + \frac{k_1}{2k_2} \{ \exp[k_2(\kappa I_1 + (1 - 3\kappa)I_4 - 1)^2] - 1 \} + \frac{B}{2} (J - 1)^2 \quad (1)$$

where c is the isotropic shear modulus, k_1 is a measure of the fiber phase stiffness, k_2 describes fiber nonlinearity, κ measures the degree of collagen fiber alignment ($\kappa=0$ is perfectly aligned, $\kappa=1/3$ is perfectly isotropic), and B is the bulk modulus. We followed methods outlined in [5] to characterize the USL samples with the HGO model. Briefly, with the image-based deformation fields, we utilized the virtual fields method to construct a cost function from the equilibrium equation, and we iterated through model parameters to minimize the difference between internal and external virtual work.

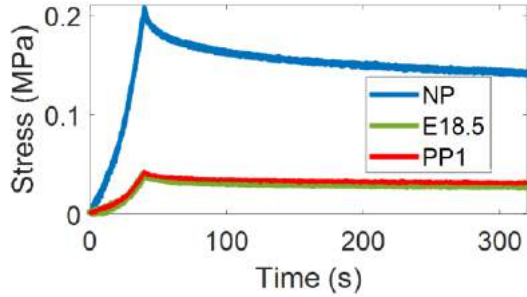


Fig 1. Average stress relaxation curves for the nulliparous, late gestation, and postpartum USL.

RESULTS

The USL stress relaxation response differed across the NP, E18.5, and PP1 groups as evaluated by the magnitude of stress relaxation, tangential loading stiffness, and average peak stress (Fig 1). Image-based deformation tracking showed that USL deformation is inhomogeneous (Fig. 2). Strains and global displacements increased with increased applied displacement. Deformation maps demonstrate heterogeneous tensile and compressive strains in the transverse loading direction, as well as large shear strains.

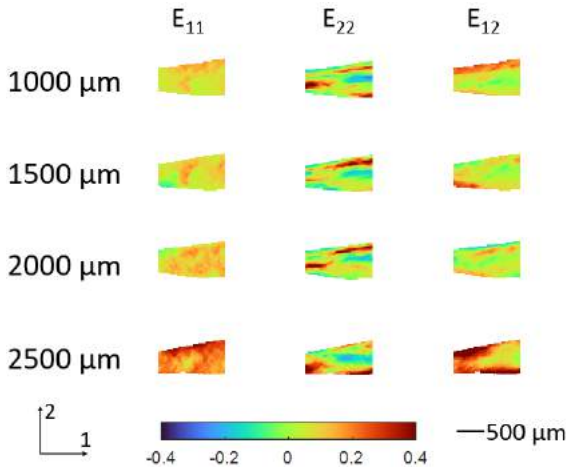


Figure 2: Representative deformation maps at increasing levels of applied displacement for a nulliparous murine USL exhibit heterogeneous axial (11), transverse (22), and shear (12) Lagrangian strain fields.

Initial model parameter values show slight differences in USL material parameters before, during, and after pregnancy (Table 1). The nulliparous USL had a larger fiber stiffness, k_1 , as compared to the late pregnancy and postpartum USLs. The measure of fiber alignment, κ ,

was smallest for the postpartum and nulliparous USL, both reaching values on the order of magnitude of $1e-14$, and was largest for the late pregnant USLs. The fiber nonlinearity, k_2 , and bulk modulus, B , parameters often converged on their default values and are not currently identifiable.

Table 1: Model parameters for nulliparous (NP, n=4), late pregnancy (E18.5, n=2), and 1 day postpartum (PP1, n=2), given as mean \pm standard deviation.

	c (MPa)	k_1 (GPa)	$k_2 \times 10^{-2}$	$\kappa \times 10^{-14}$	B (kPa)
NP	18 \pm 33	57 \pm 73	5.8 \pm 11	2.9 \pm 0.77	1.1 \pm 0.17
E18.5	1.7 \pm 1.6	5.9 \pm 0.22	12 \pm 16	3.5e07 \pm 5.0e07	950 \pm 380
PP1	51 \pm 70	5.3 \pm 3.0	0.1 \pm 0	2.4 \pm 0.24	1.0 \pm 0

DISCUSSION

The nulliparous USL exhibited a different mechanical response under stress relaxation than the late pregnant and postpartum USL. This finding is consistent with studies that have observed changes in the ECM and mechanical behavior of the cervix and vagina in pregnancy and postpartum [6]. It is well-documented how the microarchitecture and mechanics of the cervix and vagina evolves with pregnancy, but a similar analysis has yet to be done for the USL. Elucidating how the microarchitecture of the USL evolves due to pregnancy and leads to an altered mechanical response will allow us to better understand how parturition can lead to POP.

Two important parameters of the HGO model are the fiber stiffness and fiber alignment. Of the three groups evaluated, fiber stiffness was greatest in the NP USL, like the NP cervix [4]. The USL directly integrates with the cervix, and therefore may behave similarly to the cervix during pregnancy to allow for childbirth. Thus, we hypothesize that fiber stiffness decreases due to a decrease in fiber density during pregnancy which facilitates stretching of the USL during parturition. Similarly, the increase in κ in the E18.5 samples suggests that fiber alignment in the USL may decrease during pregnancy, further decreasing axial stiffness in preparation for childbirth.

This work provides preliminary results for describing the mechanical behavior of the USL using the HGO model. These methods adopted for the USL will allow us to further characterize its stress-strain relationship. Current limitations of this study are being addressed by ongoing work and include a limited sample size, inconsistent global displacements, and lack of direct measurement of USL microstructure to validate our results. Future studies seek to attain $n = 8$ samples/group and evaluating USLs at 4 weeks postpartum and USLs from older nulliparous and retired breeders to characterize the effects of pregnancy, parturition, and age on the murine USL. In combination with proteomics and histology, this work will lend insight into the role of pregnancy in USL injury and POP.

ACKNOWLEDGEMENTS

This work was supported by the NSF Graduate Research Fellowship (LS), the Schmidt Science Fellowship (CL) and other funding provided by the University of Colorado Innovative Grant Program and the Anschutz Boulder AB Nexus Seed Grant Program.

REFERENCES

- [1] "Uterine Prolapse". John Hopkins Medicine. 2022
- [2] Kerkhof, MH *et al.*, *Int Urogynecol J Pelvic Floor Dysfunct.* 2009
- [3] Donaldson, K *et al.*, *Annals of Biomed. Eng.*, 2021
- [4] Gasser, TC *et al.*, *J. R. Soc. Interface*, 2006
- [5] Luetkemeyer, CM *et al.*, *J. Mech. Phys. Solids*, 2021
- [6] Yoshida, K *et al.*, *Acta Biomaterialia*, 2016

IDENTIFYING COMMONALITIES OF HARMONIC BRAIN DEFORMATION INDUCED BY MAGNETIC RESONANCE ELASTOGRAPHY IN VIVO

J.D. Escarcega (1), A.A. Alshareef (2), A.K. Knutsen (2) R.J. Okamoto (1), P.V. Bayly (1)

(1) Mechanical Engineering and Materials Science, Washington University, St. Louis, MO, USA
(2) Henry M. Jackson Foundation for the Advancement of Military Medicine, Bethesda, MD, USA

INTRODUCTION

Traumatic brain injury (TBI) is widespread and associated with the possibility of debilitating emotional and cognitive deficits. TBIs are caused by rapid brain deformations that arise from skull acceleration. The mechanics of TBI are incompletely understood; improved insight and ability to simulate injury could help reduce, diagnose, and treat TBI.

To bridge the gap in knowledge surrounding the mechanics of TBI, both physical experiments and computational measures can be used to better understand the relationship between skull motion and brain deformation. One technique to study low-amplitude, dynamic, brain deformation in human subjects in vivo is magnetic resonance elastography (MRE). In MRE, harmonic acceleration of the skull induces shear waves in the brain, which are then imaged and analyzed.

In previous work [1, 2] we showed that shear waves induced in the brain via MRE propagate differently depending on the frequency and direction of actuation. Different regions of the brain (i.e. cerebrum and cerebellum) show different levels of deformation. Intriguingly, qualitatively similar patterns appeared in different subjects; we speculate that these common patterns of deformation may illuminate common injury mechanisms. The objective of this study is to quantitatively compare strain fields from different subjects at each frequency and brain region to characterize the similarity of brain deformation patterns between several human subjects.

METHODS

MRE was used to image dynamic brain deformation in 4 different human subjects (2M, 2F, 27-28 yrs.) undergoing harmonic skull motion at 10, 20, 30, and 50 Hz. Skull motion was driven by an inflatable silicone actuator pre-loaded against the side of a subject's head. Harmonic pressure waves were delivered to the actuator by a pneumatic driver (Resoundant, Rochester, MN) for 20-50 Hz or customized PL-300 sub-woofer, (BIC America, Anaheim CA) for 10 Hz. A custom MRE sequence [3] was used to obtain all components of 3D harmonic

displacement in 3×3×3 mm voxels at eight time points. Displacement fields were Fourier-transformed in time and numerically differentiated in space to estimate complex-valued, 3D strain tensors at each voxel. Strain amplitude was quantified by octahedral shear strain (OSS, Eq. 1).

$$\epsilon_{OSS} = \frac{2}{3} \sqrt{(E_1 - E_2)^2 + (E_2 - E_3)^2 + (E_3 - E_1)^2} \quad (1)$$

To compare harmonic strain fields from MRE in different subjects, we performed a series of spatial transformations to register the brains to a common space. Anatomical T1-weighted images were used to rigidly register each subject's brain to a standard structural template (MNI152 T1-weighted 0.8 mm brain atlas) using Advanced Normalization Tools (ANTs) [4]. T1- and T2-weighted images were rigidly registered to the MNI-152 space [5] using ANTs, and resampled to 0.8 mm isotropic resolution. Strain tensor components were re-computed in the rigidly-registered space based on the rotation matrix associated with the rigid registration.

The nonlinear transform from each subject's T1 volume to the MNI152 template was calculated using the cross-correlation standard symmetric normalization (SyN) model in ANTs. Then the SyN transformation was applied to each 2D strain tensor (ϵ_{xx} , ϵ_{yy} , ϵ_{xy}) and OSS strain field calculated from MRE data.

Each subject's MNI registered T1-weighted images were segmented using the SLANT algorithm [6] to extract the whole brain falx and tentorium. Custom segmentation tools (MaCRUISE [6, 7] and SLANT) were used to segment each brain into three binary masks: the cerebrum (~85% vol.), the brainstem (~1.5% vol.), and the cerebellum (11% vol.). These subject-specific brain region masks were then transformed to the MNI atlas using the same transformation matrices.

Comparisons between strain fields were visualized using volume-normalized, strain cross-correlation fields $\hat{\epsilon}_V$ (Eq. 2a-b) and quantified by the scalar tensor product (STP) correlation values C_V (Eq. 3). $\hat{\epsilon}_V$ is a

qualitative representation showing similarity between regions of the brain. The STP correlation C_V is a quantitative metric which defines similarity over an image volume by a value between 0 and 1 ($C_V = 1$ for two identical strain fields).

$$\varepsilon_n^{(p)} = \sqrt{\sum (\varepsilon_V^{(p)} \cdot \bar{\varepsilon}_V^{(p)})} \quad (2a) \quad \hat{\varepsilon}_V = \left(\frac{\varepsilon_V^{(p)}}{\varepsilon_n^{(p)}} \cdot \frac{\bar{\varepsilon}_V^{(q)}}{\varepsilon_n^{(q)}} \right) \quad (2b)$$

$$C_V = |\sum \hat{\varepsilon}_V| \quad (3)$$

Strain fields in four subjects were compared for each pair of subjects (a total of 6 comparisons) for four frequencies and three brain regions for a total of 72 comparisons. A two-way analysis of variance with repeated measures (ANOVA; Prism 9, GraphPad, San Diego, CA) was used to compare the effects of the interaction between excitation frequency and brain region, the effects of excitation frequency alone, and the effects of brain region alone on the mean STP correlations (Fig. 2). Mean OSS for each subject was computed for each combination of frequency and brain region to describe the magnitude of shear deformation (Fig. 3).

RESULTS

Volume-normalized 3D strain cross-correlation fields (Fig. 1) were plotted to identify regions of the brain that shared consistent, large deformations. We found high cross-correlations across the entire cerebrum at lower frequencies (10-20 Hz). At higher frequencies (30-50 Hz) cross-correlation values increased around the posterior of the cerebrum and the cerebellum.

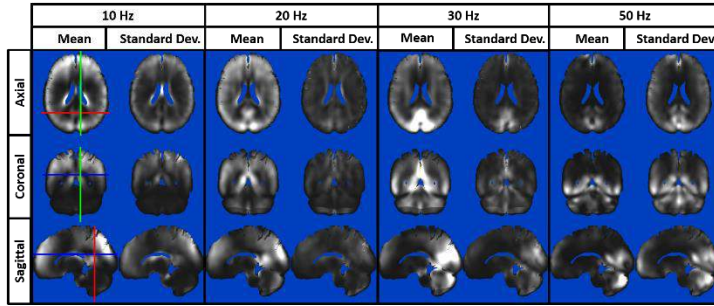


Figure 1: Cross-correlation strain field $\hat{\varepsilon}_V$ visualization. Each column represents the arithmetic mean and standard deviation across 6 strain field comparisons at a single frequency. Rows indicate each 3D anatomical plane with red, blue, and green lines to indicate slice locations. Lighter regions indicate high similarity and dark regions indicate low similarity.

The highest OSS (largest deformations) occurred at 10 Hz in all subjects and brain regions, and decreased with frequency (Fig. 2). The cerebrum and brainstem exhibited higher OSS than the cerebellum at 10 Hz, but at other frequencies deformations were similar in all regions.

Volumetric STP correlations C_V (Fig. 2) were higher in the cerebrum than both other regions at 10 Hz (Fig. 2). At higher frequencies the average correlation values in the cerebellum did not differ significantly from those in the cerebrum. The correlation values in the brainstem remained significantly lower than those in the cerebrum at all frequencies. The individual effects of frequency ($P = 0.0007$) and brain region ($P < 0.0001$) were both statistically significant, as was the interaction between frequency and brain region ($P = 0.0021$).

DISCUSSION

Strain cross-correlations between harmonic brain motion at 10, 20, 30, and 50 Hz in different subjects reveal common patterns of deformation in the cerebellum, brainstem, and cerebrum. The magnitudes of correlation differ by frequency and brain region.

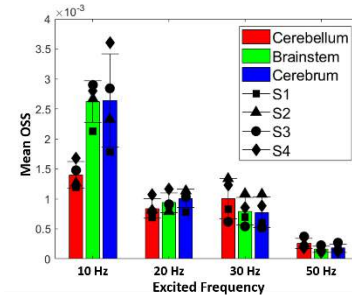


Figure 2: Mean OSS averaged across subjects and brain region. Larger values of mean OSS indicate higher amounts of shear deformation during MRE. Each symbol present on the bar plot represents the mean OSS for that subject in that brain region.

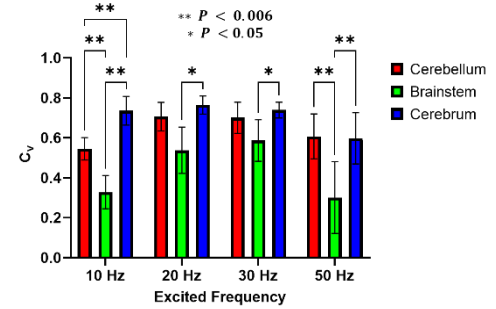


Figure 3: Volumetric STP comparisons C_V averaged across frequency and brain region. Each star indicates a comparison was found to be significantly different.

To perform these comparisons between strain fields in four different human subjects it was necessary to register and transform strain fields to the MNI-152 atlas.

We acknowledge some limitations. Data from only four subjects of similar age were used. The brains of older subjects (50+) may exhibit more differences as the brains tend to shrink and the ventricle size increase with age. These changes may exacerbate the challenges of registering images to a common template. In future studies we plan to incorporate more human subjects over a larger range of ages and both sexes. We also plan to introduce other frequencies and directions of skull motion. Nevertheless this study shows clear patterns of cross-correlation between strain fields in different subjects, which may correspond to regions likely to experience higher strains (and injury) at higher skull accelerations.

ACKNOWLEDGEMENTS

Research was supported by NIH grant U01 NS112120, NIH Fellowship F31 NS122281-01A1

REFERENCES

- [1] Escarcega, JD et al., *J Biomech Eng*, in review.
- [2] Okamoto, RJ et al., *J Biomech Eng*, in review.
- [3] Bayly, PV et al., *Ann Biomed Eng*, 49(10): 2677-2692, 2021.
- [4] Avants, BB et al., *Neuroimg*, 54(3): 2033-2044, 2011.
- [5] Fonov, VS et al., *Neuroimg*, 47:S102, 2009.
- [6] Huo, Y et al., *Neuroimg*, 194: 105-119, 2019
- [7] Huo, Y et al., *Neuroimg*, 138:197-210, 2016

MULTIAXIAL LOADING ATTENUATES FIBROBLAST ACTIVATION IN AN IN VITRO MODEL OF FIBROSIS

Ghiska Ramahdita^{1,2}, Xiangjun Peng², Mohammad Jafari³, David Schuftan⁴, Guy M. Genin^{1,2},
Farid Alisafaei^{3*}, Nathaniel Huebsch^{2,4*}

- (1) Department of Mechanical Engineering and Materials Science, Washington University, St. Louis, MO, USA
(2) NSF Science and Technology Center for Engineering Mechanobiology, Washington University, St. Louis, MO, USA
(3) Department of Mechanical and Industrial Engineering, New Jersey Institute of Technology, Newark, NJ, USA
(4) Department of Biomedical Engineering, Washington University, St. Louis, MO, USA

INTRODUCTION

Fibrosis contributes to one third of natural deaths worldwide and currently has no cure [1]. A critical step in the pathway to fibrosis in all organs is the fibroblast-to-myofibroblast transition (FMT), a largely irreversible event in which mechanical stimuli trigger tissue resident fibroblasts to express a subset of smooth muscle genes that enhance stress fiber formation and contractility [2]. Understanding the mechanisms behind FMT will be impactful for efforts to slow fibrosis or potentially restore organ function.

The mechanical environment of cells, including stress and substrate or ECM stiffness, can induce FMT in both 2D and 3D culture settings [3,4], but the role of stress directionality and isotropy is not clear [5]. Our specific objective was therefore to study how directionality of loading regulates FMT phenotype.

To achieve this, we tested the hypothesis that tension isotropy attenuates fibroblast contractility and FMT. To test the hypothesis, we developed a mathematical model of the effects of tension anisotropy on FMT, and tested predictions of the model against 3D platforms with geometries predicted to induce either isotropic or anisotropic contraction in collagen-encapsulated high-density fibroblasts. Results suggest that tension isotropy attenuates FMT, even in the presence of TGF- β , a well known agonists of FMT.

METHODS

Tissue constructs comprised of NIH-3T3 fibroblasts and rat-tail collagen type I were formed around micro-posts in microwells. Cells were provided anisotropic stress states using 4-post devices, and isotropic stress states using 8-post devices (Fig. 1).

Modeling: Our multiscale continuum computational model was used to design and interpret experiments on how cells respond to the polarity of extracellular mechanical signals. In this model [5], tissues are treated as a continuum of representative volume elements composed of an active contractile cell in collagen matrix. Equations

were solved using the Abaqus (Dassault Systemes) finite element software with finite strain hyperelasticity for the posts and a user-written constitutive law for the cells. Because simulations showed the evolution of tissue shape in 4-post and 8-post tissue designs to produce regions of strong anisotropic and isotropic stress fields, respectively (Fig. 1), we tested our hypothesis on tissues in these configurations.

Device Design & Fabrication: Devices had wells (3.26 mm diameter, 1.25 mm depth) with posts (200 μ m diameter, with wider caps. Master molds were 3D printed, then replicated using the HASTE technique [6] to produce PDMS devices with pillars of known stiffness. These enabled testing of the hypothesis by providing microtissues with controlled stress fields.

3D Microtissues: 8 μ L of mixture (2x10⁷ cells/ml, 1.5 mg/ml collagen, 0.5 mM Hepes, 12.5 mM NaOH, 1X DMEM) was seeded in each well. Devices were centrifuged at 4°C, 300 g for 3 min. Collagen gels set for 20 minutes at 37°C before adding media. In some specimens, TGF- β (10 ng/ml) was added.

Imaging: To test whether TGF- β induces higher compaction in the devices, we compared the morphology of the control versus treatment. Bright field images were taken 3 hours and 4 days post-seeding (Fig. 1), and side-view fluorescence images at 4 days post-seeding (Fig. 2) using a Nikon eclipse TsR microscope.

Immunofluorescence Microscopy: The microtissues were fixed and immuno-stained for α -SMA, actin (phalloidin), and DNA (Hoechst), then imaged (Olympus IX83 confocal microscope). Maximum intensity projection images from the z-stacks were analyzed using a custom-built MATLAB code to calculate mean fluorescence intensity at specific regions and test model predictions and the hypothesis.

Statistical Analysis: Two-way ANOVA with Holm-Sidak mean comparison test was used. P value < 0.05 was considered statistically significant difference. * = p < 0.05; ** = p < 0.005; *** = p < 0.0005; **** = p < 0.0001.

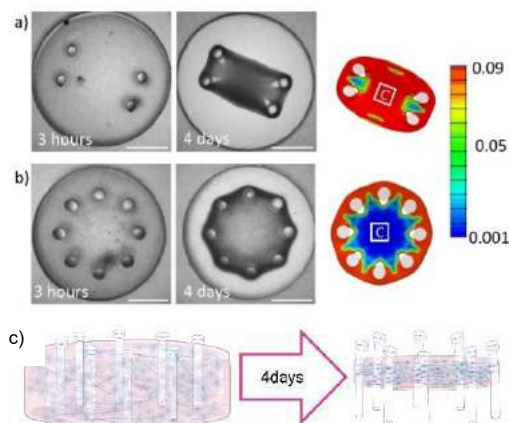


Figure 1: Tissue-generated compaction and collagen remodeling in (a) 4-posts devices and (b,c) 8-posts devices with predicted high tensional anisotropy (red) and low tensional anisotropy at the central region [C], respectively. Scale bar = 1 mm

RESULTS

Three significant results emerged. First, TGF- β condition promotes higher volumetric compaction (Figure 2). After 4 days of compaction, in 4-posts tissues, the 2D-projected areas of control and TGF- β treated tissues were 27.6% versus 21.5% of initially seeded area ($p < 10^{-4}$). On the 8-posts tissues, the 2D-projected area was 47.34 and 44.64 (p-value: 0.0198) of control and TGF- β , respectively.

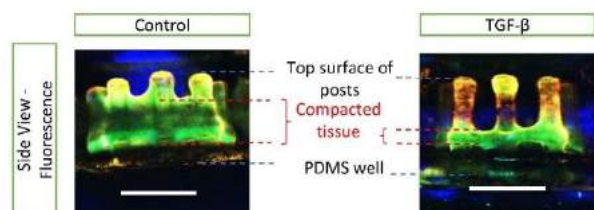


Figure 2: Addition of TGF- β enhanced the 3D tissue-generated compaction. Scale bar = 1 mm

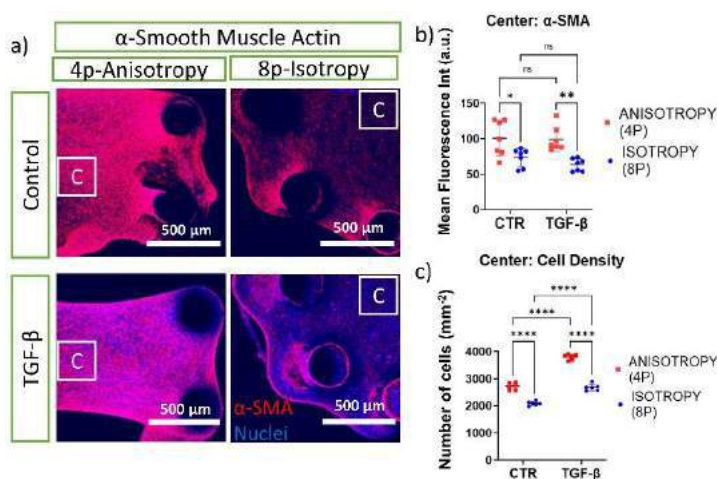


Figure 3: TGF- β conditioning does not enhance myofibroblast marker expression as strongly as tensional anisotropy in the 3D tissues. (a) α -SMA and nuclei protein expression (fluorescence); Quantitative data on (b) α -SMA intensity and (c) cell density of central regions of each tissue. Scale bar = 500 μ m

Second, across different designs (Figure 3a), we observed significantly higher α -SMA within the central region of geometrically anisotropic 4-posts tissues as compared to within geometrically isotropic 8-posts tissues. Treatment with TGF- β increased the impact of anisotropy on α -SMA expression (Fig. 3b). Observations of stress fiber density via F-actin staining were similar to observations from α -SMA visualization. These data are consistent with our hypothesis and as predicted by computational model.

Surprisingly, we observed that the effect size of anisotropy was more pronounced than the effect size of TGF- β at inducing α -SMA (Figure 3b) and stress fibers (data not shown). Nevertheless, TGF- β exposure increased cell density within micro-tissues, as gauged by overall nuclear intensity (Hoechst staining) and direct quantification of nuclear density in tissues with either geometry (Fig. 3c). TGF- β treatment also led to higher individual cellular polarization, as gauged by nuclear shape and alignment, regardless of tissue geometry. These results suggest a model in which tissue and cellular mechanical anisotropy, which may themselves be influenced by chemical cues like TGF- β , play a central role in promoting FMT.

DISCUSSION

Several new, interesting results emerged. Key facets of FMT, including expression of smooth-muscle associated contractile proteins, are more strongly regulated by tensional anisotropy than the addition of exogenous TGF- β . This discrepancy was not strongly linked to changes in individual cell geometry, as TGF- β still induced higher cellular alignment and nuclear elongation regardless of predicted overall tissue-level tension anisotropy. This trend is contradicted with another study in 3D system, in which TGF- β induced higher myofibroblast marker expression but not necessarily proliferation [1,4]. Insensitivity to exogenous of TGF- β in driving FMT in this study is potentially linked with some factors, including cell-contraction driven changes in mechanical liberation of latent TGF- β stored in extracellular matrix [7], and/or mechanically-driven changes in endogenous TGF- β secreted by the fibroblasts themselves [8]. Indeed, others have observed that localized changes in matrix stiffness induce TGF- β receptor dependent changes in α -SMA expression that were insensitive to the addition of exogenous TGF- β [3].

These results are significant. Results revealed that stress directionality is a central determinant to FMT, which further can induce fibrotic response, suggesting that while chemical cues are necessary for these processes, they may require a mechanically permissive environment for their action.

These results are potentially impactful, highlighting the importance of microenvironment, especially loading directionality of organs in attenuating FMT leading to fibrosis.

ACKNOWLEDGEMENTS

This work was supported by the National Institutes of Health, (RO1HL159094) and the Center for Engineering Mechanobiology (CEMB), an NSF Science and Technology Center (CMMI: 15-48571).

REFERENCES

- [1] Asmani, M. et al., *Nat. Commun*, 2018.
- [2] Guo, X., et al. *Sci. Rep.*, 2022.
- [3] Farrell, E., et al., *Acta Biomater*, 2022.
- [4] Gladilin, E. et al., *Sci. Rep.*, 2019
- [5] Alisafaei, F., et al. *BioRxiv*, 2022.
- [6] Simmons, D., et al. *BioRxiv*, 2022.
- [7] Shi, M., et al., *Nature*, 2011.
- [8] Frangogiannis, N.G., *J Exp Med*, 2020.

ENZYMATIC DEGRADATION DOES NOT COMPROMISE SLIDING-MEDIATED CARTILAGE LUBRICATION

Meghan E. Kupratis (1), Atia Rahman (2), David L. Burris (2),
Elise A. Corbin (1), Christopher Price (1)

(1) Biomedical Engineering, University of Delaware, Newark, DE, USA
(2) Mechanical Engineering, University of Delaware, Newark, DE, USA

INTRODUCTION

Articular cartilage serves as the near-frictionless bearing material of synovial joints. In osteoarthritis (OA), degeneration reduces cartilage's compressive modulus and increases its permeability. According to classical tribological theory, these changes should drastically impair lubrication by increasing load-induced interstitial fluid exudation and diminishing fluid load support (FLS) [1-2]. Although reduced stiffness is associated with high strains and frictions in fully depressurized cartilage interrogated under boundary lubrication conditions (sliding speeds $\leq 1\text{mm/s}$), new evidence suggests such relationships may not hold under more biofidelic sliding conditions. Recently, we demonstrated that the introduction of hydrodynamic pressurization, which occurs with high-speed ($>40\text{mm/s}$) sliding in convergent stationary contact area (cSCA) explants having curved cartilage surfaces, replenishes interstitial fluid lost to compressive loading via tribological rehydration. In healthy cartilage, tribological rehydration recovers and sustains high FLS and near-physiological friction coefficients ($\mu \leq 0.01$) in PBS-lubricated contacts with little sensitivity to variation in cartilage stiffness or permeability [3-4]. Here, we investigated whether OA-associated changes to cartilage mechanical properties, modeled via enzymatic digestion, impair cartilage lubrication under biofidelic articulation conditions.

METHODS

Osteochondral explants ($\varnothing 19\text{mm}$; $n=51$) were extracted from mature bovine femoral condyles. Specimens were indented with a $\varnothing 4\text{mm}$ spherical probe at $50\mu\text{m/s}$ to a target force of 150mN , then allowed to equilibrate under creep relaxation (Fig. 1A). The time-dependent normal force and indentation depth were fit to Hertz biphasic theory (HBT) to determine the compressive modulus (E_y), tensile modulus (E_{y+}), and permeability (k_0) [3]. Tribological characterization comprised ramp loading to a target of 7N , followed by 30min static compression and 15min reciprocal sliding against a glass counterface

(Fig. 1B). Two sliding speeds were investigated (10 vs. 80mm/s), corresponding to speeds that facilitate high and low tribological rehydration and FLS recovery, respectively. Explants were lubricated with 1X PBS or bovine synovial fluid (SF), which synergizes with tribological rehydration to enhance lubricity in the cSCA ($\mu \sim 0.003$) [4]. Following characterization in the naive state, explants were digested with 0.1U/mL chondroitinase-ABC (chABC) or 1U/mg wet weight bacterial collagenase-IV. Indentation and tribological testing were repeated after 40min , 4h , and 12h of digestion. SF-lubricated explants were characterized after 2h of digestion. Differences between groups were assessed via two-way ANOVA (significance at $p < 0.05$).

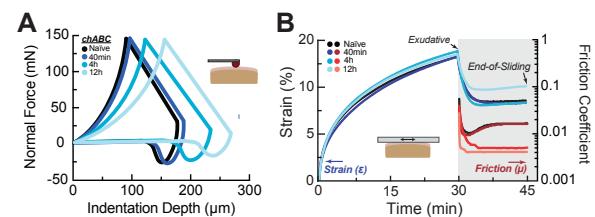


Fig. 1. Representative indentation tests (A) and high-speed cSCA tribological characterization (B) for naive and chABC-digested cartilage in PBS (note: initial ramp loading not shown).

RESULTS

Brief exposure ($\leq 4\text{h}$) to chABC or collagenase produced mechanical properties consistent with human OA samples (ICRS 1-2) as reported previously by our group [5]. After 4h , E_y decreased from 0.57 ± 0.20 to $0.41 \pm 0.18\text{MPa}$ and 0.68 ± 0.19 to $0.37 \pm 0.15\text{MPa}$ for chABC- and collagenase-treated samples, respectively ($p < 0.0005$, Fig. 2A). k_0 increased from 0.0038 ± 0.0012 to $0.0056 \pm 0.0020\text{mm}^4/\text{Ns}$ and 0.0029 ± 0.0007 to $0.0053 \pm 0.0012\text{mm}^4/\text{Ns}$ in chABC- and collagenase-treated explants, respectively ($p < 0.005$, Fig. 2B). After 12h , tissue compromise exceeded that observed in ICRS 1-2 human samples [5].

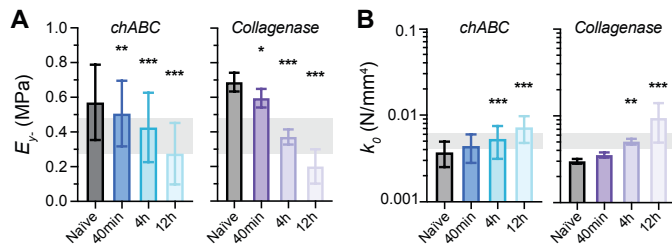


Fig. 2. Compressive moduli decreased (A) and permeability increased (B) following digestion. Data as mean \pm SD (* p <0.05, ** p <0.005, *** p <0.0005 vs. naïve). Grey shaded regions indicate the properties of human OA cartilage from Graham *et al.* [5].

Elastic strain during the initial ramp loading phase of cSCA testing increased significantly following ≥ 4 h of digestion ($p \leq 0.001$ vs. naïve, **Fig. 3A**). Nonetheless, exudative strain during 30min of subsequent static compression did not vary between naïve and digested cartilage ($p > 0.15$, **Fig. 3B**). This can be attributed to decreased contact stresses experienced following ≥ 4 h digestion (**Fig. 3C**). Furthermore, we found no evidence of altered tribological rehydration in digested cartilage. When slid at 80mm/s, strain recoveries of $6.83 \pm 1.46\%$ were seen in naïve cartilage and $6.60 \pm 1.47\%$ after 12h digestion, respectively ($p = 0.50$, **Fig. 3D**). Similarly, all explants exhibited negative strain recovery (*i.e.*, net fluid exudation) of -1.0 to -2.5% when slid at 10mm/s ($p > 0.2$ vs. naïve, **Fig. 3D**).

Remarkably, digestion had little to no influence on cartilage lubricity in the cSCA. Under conditions of low FLS (10mm/s), end-of-sliding friction coefficients were elevated (~ 0.3) but not different among naïve and digested tissue ($p > 0.2$). Importantly, under conditions of high FLS, driven by high-speed cSCA sliding (80mm/s), consistently low end-of-sliding friction coefficients of $\mu < 0.1$ were observed in both naïve and digested cartilage ($p > 0.15$, **Fig. 4A**).

Next, we examined if digestion alters lubrication synergy fostered by tribological rehydration and synovial fluid presence [4]. At 80mm/s, strain recoveries of $7.08 \pm 1.68\%$ and $7.84 \pm 2.05\%$ were observed in the naïve state and following 2h digestion, respectively ($p > 0.12$). Furthermore, indistinguishable, and physiologically consistent friction coefficients (0.003-0.006) were observed for both naïve and digested explants at the end-of-sliding in SF ($p = 0.25$, **Fig. 4B**).

DISCUSSION

Our results demonstrate that OA-like articular cartilage retains the strain recovery and lubricity of healthy cartilage under biofidelic articulation conditions (*i.e.*, high-speed sliding at high FLS). In human OA samples (ICRS 1-2), E_y decreased by 0.056MPa (12%) and k_0 increased by $0.0005 \text{ mm}^4/\text{Ns}$ (20%) for each increase in ICRS score [6]. Here, just brief chABC or collagenase exposure replicated similar OA-like mechanical properties: 40min and 4h of digestion reduced E_y by 13% and 36%, respectively. The cartilage tribology field has typically relied on exposure of cartilage to degradative enzymes or inflammatory cytokines for much longer durations to model tissue degeneration (7-48h) [1-2, 6]. Predictably, this results in more extreme degeneration ($>80\%$ decrease in modulus and $>200\%$ increase in permeability), exceeding the ranges reported for ICRS 1-2 cartilage in our work [5] and by Kleemann ($<70\%$ reduction in modulus for severe OA; ICRS 3) [7]. Thus, we demonstrate that relatively minor, but clinically aligned OA-like changes in cartilage mechanical properties can be achieved with <4 h enzymatic digestion.

As expected, digested cartilage experienced elevated axial elastic strains during load application compared to naïve cartilage. Digestion also increased contact dilatation, as quantified by *in situ* optical measurements of cSCA contact area. For example, cSCA contact areas

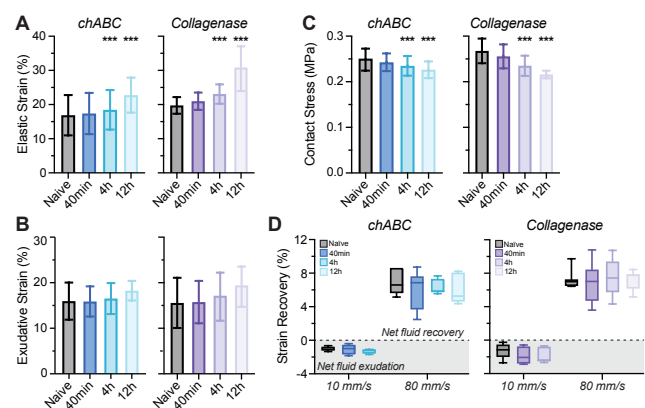


Fig. 3. (A) Elastic strain during ramp loading to 7N increased following enzymatic digestion. (B) Exudative strain during static compression did not differ among groups. (C) Contact stress at 7N decreased with ≥ 4 h digestion (D) Strain recovery at low- and high-FLS was not significantly affected by digestion. Data as mean \pm SD (A-C) and median \pm IQR (D), *** p <0.001.

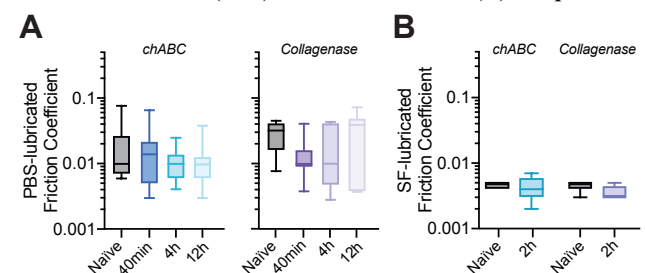


Fig. 4. Friction coefficients under high-speed sliding. (A) End-of-sliding (*i.e.*, equilibrium) friction coefficients in PBS were insensitive to digestion ($p > 0.12$) (B) In SF, end-of-sliding friction coefficients approached *in vivo*-like values in both naïve and digested cartilage ($p = 0.25$). Data as median \pm IQR.

increased from $28.4 \pm 2.5 \text{ mm}^2$ in naïve cartilage to $31.1 \pm 2.3 \text{ mm}^2$ after 12h chABC digestion, resulting in $\sim 9\%$ lower contact stress under 7N normal force. As a result, exudative strain during 30min of creep relaxation did not differ between naïve and digested cartilage, despite substantial softening (up to 85% reduction in E_y after 12h digestion). Furthermore, even extensively digested cartilage supported robust tribological rehydration when slid at 80mm/s, as evidenced by strain recovery magnitudes and PBS-lubricated friction coefficients indistinguishable from naïve cartilage. This was further confirmed in our SF-lubricated tests, which revealed that digested cartilage sustains near-physiological friction coefficients (0.003-0.006) during high-speed cSCA sliding. Together, these results suggest OA cartilage is more mechanically resilient than previously credited. Furthermore, increased elastic (or “habitual”) strain in digested tissue absent meaningful differences in “activity-mediated” (or “diurnal”) strain and friction coefficients during sliding suggest that the biomechanical consequences of OA could be mitigated through behavioral modifications that reduce total cartilage strain and promote fluid recovery (*i.e.*, weight loss and physical activity) [8].

REFERENCES [1] Bonnevill, *J Biomech*, 36: 1456-1464, 2018. [2] Basalo, *J Biomech*, 38: 1343-1349, 2005. [3] Kupratis, *Acta Biomater*, 138: 375-389, 2022. [4] Farnham, *CMBE*, 14: 349-356, 2021. [5] Graham, *J Orthop Res*, 36: 3256-3267, 2018. [6] Han, *Sci Rep*, 11: 9527, 2021. [7] Kleemann, *OA&C*, 13:958-963, 2005. [8] Graham, *Conn Tiss Res*, 61: 375-388, 2020.

COMPARISON OF DOMINANT MODES OF HUMAN BRAIN DEFORMATION FROM SIMULATION AND EXPERIMENT

Amir H.G. Arani (1), Jordan D. Escarcega (1), Antoine Jerusalem (2), Ruth J. Okamoto (1), Philip V. Bayly (1)

(1) Mechanical Engineering and Materials Science, Washington University in St. Louis, MO, USA
(2) Engineering Science, University of Oxford, Oxford, UK

INTRODUCTION

Traumatic brain injury (TBI) affects an estimated 70 million people worldwide each year [1, 2]. Computer models of brain biomechanics are emerging as important tools to understand and develop approaches to prevent or treat TBI [3,4], however such models should be parameterized and evaluated by comparison to experiments. Magnetic resonance elastography (MRE) and tagged magnetic resonance imaging (MRI) experiments provide mechanisms to image the response of the brain to harmonic motion and mild impact to the skull, respectively. Both MRE and tagged MRI can identify dominant modes of oscillation in brain deformation [5], which can provide important insight into the mechanics of TBI.

In this study, we compare dominant modes of brain deformation predicted by a computer model to those identified by MRE and tagged MRI experiments. The results not only assess the ability of the computer model to predict actual strain fields in the intact living brain, but also illustrate common features of strain fields obtained in different subjects by the two experimental methods.

METHODS

The model used in this study is an existing model developed in ABAQUS (SIMULIA) and was used initially for the time-domain simulation of brain response to an impact (see ref. [3] for more model information). The computer model in this study uses a set of boundary conditions and excitation amplitude similar to those of the experimental setup. Two different sets of viscoelastic material properties were used to predict the first (dominant) oscillatory mode of the brain.

The head model has 792,773 hybrid tetrahedral/quadratic elements, including the brain, skull, and scalp. Material properties of all element sets can be found in ref. [3] and the brain material properties were converted to frequency-domain parameters for this study. Two constitutive models for brain tissue were considered: (1) the hyperviscoelastic (HVE) material properties in the original model [3];

(2) a linear viscoelastic (LVE) model reported in ref. [4]. In the HVE model, the deviatoric stress includes a convolution integral with respect to time, as described in ref. [6]. For the viscoelastic properties in both LVE and HVE cases, the relaxation modulus is time-dependent, defined by the Prony series with $N = 2$:

$$\bar{\mu}(t) = \bar{\mu}_{\infty} + \sum_{i=1}^N \bar{\mu}_i \exp\left(-\frac{t}{\tau_i}\right) \quad (1)$$

Here $\bar{\mu}$ is the effective relaxation modulus at time t , and $\bar{\mu}_{\infty}$ is the long-term relaxation modulus. Viscoelastic parameters are summarized in Table 1 where λ_1 and λ_2 are dimensionless forms of $\bar{\mu}_1$ and $\bar{\mu}_2$ in equation (1) with respect to the instantaneous relaxation modulus $\bar{\mu}_0$.

In MRE, dynamic deformation of brain tissue is induced by harmonic vibration of the skull; here lateral excitation at the frontal temporal bone induces left-right skull translation and rotation about the superior-inferior axis (SI-axis). Tissue displacement is measured by a phase-contrast MRI sequence and differentiated to estimate strain [7]. In tagged MRI, brain deformation is induced by a mild angular acceleration of the head, and displacement is measured by tracking “tag” lines (imposed variations of tissue magnetization) [1,4,5]. Dominant modes from tagged MRI [5] and strain fields from MRE are represented as fields of complex-valued coefficients of complex exponential (sinusoidal) functions of time. Each coefficient represents the amplitude and phase of the oscillatory strain field.

Dominant modes of deformation predicted by the computer model were compared to the modes extracted from experimental data. Strain fields from MRE during lateral harmonic excitation of the skull and from tagged MRI during rotation about the SI-axis were obtained from publicly-available datasets [8]. Frequency-domain and modal analyses were performed for the model, and modes that are excited by rotation of the brain around the SI-axis were identified.

Because brain size and anatomical features vary among human subjects, a framework is needed to register the anatomical images and strain fields of simulation and experiment to the same standard space of

MNI-152 atlas, as used in many studies (see ref. [4]), for comparison. Using the *antsRegistration* module of ANTS software [9], we applied three types of transformations (rigid, affine, and SyN transformations) to the model's image (Figure 1) in order to rotate, align, scale, shear, and nonlinearly warp the model to the MNI-152 atlas image.

The correlation value (CV) between two normalized complex strain fields $\bar{\epsilon}_1$ and $\bar{\epsilon}_2$ can be described as a complex dot product with a value close to 1 showing a high similarity:

$$0 < CV = |\bar{\epsilon}_1 \cdot \bar{\epsilon}_2| < 1 \quad (2)$$

Table 1: Viscoelastic parameters used in the computer simulation

Parameter case		λ_1	λ_2	$\tau_1(s)$	$\tau_2(s)$
1. HVE	White	0.650	0.204	3.460	735
	Gray	0.540	0.250	2.170	235
2. LVE model in [4]		0.710	0.055	0.001	0.028

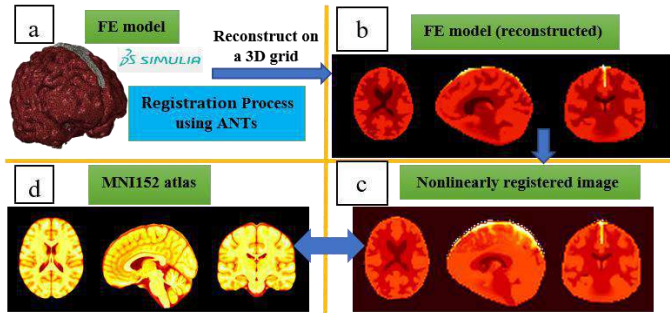


Figure 1. Registration process: (a) The Finite Element model in ABAQUS. (b) The model's reconstructed image in MATLAB R2022a. (c) The model's image fully registered to MNI-152 atlas (nonlinear registration), and (d) The fixed image in the standard space. The image array is $241 \times 286 \times 241$ with 0.8 mm voxels for panels c,d and $80 \times 80 \times 60$ with 3 mm voxels for panel b. The left to right views in each panel b-d show the axial slice (SI), the sagittal slice (RL), and the coronal slice (AP), respectively.

RESULTS

Qualitative and quantitative comparisons for two different types of simulations and two different experiments are shown in Figure 2 and Table 2. Figure 2(a,b) shows the strain fields of dominant mode of model from (i) modal analysis and (ii) harmonic response (simulated MRE), respectively. Figure 2(c,d) shows dominant modes from tagged MRI and MRE experiments for two different human subjects. Table 2 shows the average values for correlations of strain fields corresponding to two simulation cases and two imaging experiment types (each involving three different human subjects). Positive correlations are seen between experiment and simulation (case 1 slightly higher than case 2).

DISCUSSION

Dominant modes of oscillation in the brain predicted by computer simulation were quantitatively compared to modes in different human subjects when the skull is excited around the SI axis harmonically (as in MRE) or by impact (as in tagged MRI). To enable this comparison, simulated and measured fields were registered to the MNI-152 atlas. The range of values for the correlation between simulated and experimental strain fields was 0.40 to 0.56. The experimental strain fields found in MRE at low frequencies are correlated to modes excited by mild impact (from tagged MRI). The modes predicted by computer models are similar to modes identified from both MRE and tagged MRI [5], and share characteristic features of brain response to mild impact. There are inherent limitations with registering strain fields from

different subjects (as the strain fields are modified, in the process) but registration is required for quantitative comparisons. The framework developed here allows evaluation of models by comparison of predicted modes to modes observed in MRE and tagged MRI experiments. Dominant modes of brain deformation excited in a particular direction provide key information about the brain's response to mild impact.

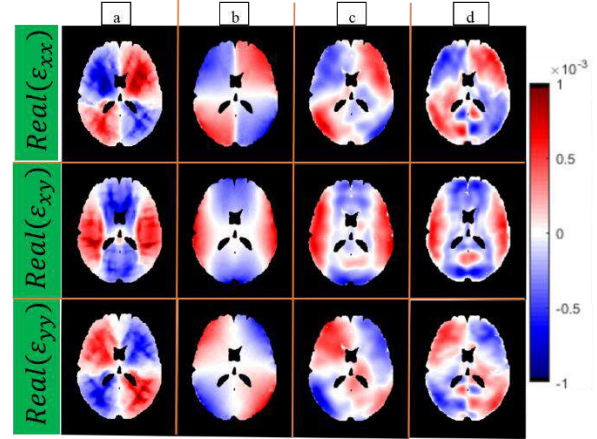


Figure 2. Visual comparison of strain fields from simulation case 2 (see Table 1) and experiment: (a) Dominant mode of simulation from modal analysis with a frequency of 6.28 Hz. (b) MRE simulation at 10 Hz. (c) Dominant mode of tagged MRI experiment with a frequency of 5.52 Hz from a 24-year-old female subject. (d) MRE experiment at 10 Hz from a 27-year-old female subject. The slice number is 119 out of 1 to 241 in the SI direction for all panels.

Table 2: Correlation values over the volume of the brain in two simulation cases (Table 1) reporting average values (standard deviation) of each experiment type involving three subjects

Case 1	Sim Mode	Sim MRE	Exp TMRI	Exp MRE
Sim Mode	1	0.86(0.00)	0.50(0.04)	0.46(0.10)
Sim MRE		1	0.56(0.06)	0.52(0.08)
Exp TMRI			1	0.52(0.08)
Exp MRE				1
Case 2	Sim Mode	Sim MRE	Exp TMRI	Exp MRE
Sim Mode	1	0.78(0.00)	0.45(0.03)	0.40(0.10)
Sim MRE		1	0.56(0.06)	0.52(0.08)
Exp TMRI			1	0.52(0.08)
Exp MRE				1

ACKNOWLEDGEMENTS

This study was funded by NIH grant U01 NS112120.

REFERENCES

- [1] Knutsen, A.K. et al., *Comp Biomech for Medicine*, 113-122. Springer, Cham, 2021.
- [2] Haarbauer-Krupa, J. et al., *J Neurotrauma*, 38:3235-3247, 2021.
- [3] Garcia-Gonzalez, D. et al., *J Mech Behav Biomed Matls*, 69:342-54, 2017.
- [4] Alshareef, A. et al., *Brain Multiphysics*, 2:100038, 2021.
- [5] Escarcega, J.D. et al., *J Biomechanics*, 119:110259, 2021.
- [6] J. C. Simo, *Comp Meth Appl Mech Engrg*, 60:153-173, 1987.
- [7] Okamoto, R.J. et al., *J Exp Neurosci*, 13:1179069519840444, 2019.
- [8] (Brain biomechanics imaging resources) <https://www.nitrc.org/projects/bbir/>
- [9] Avants, B.B. et al., *Neuroimage*, 54:2033-2044, 2011.

IN VIVO HUMAN MRI WITH LOADING TO EVALUATE DISC MECHANICAL FUNCTION IN YOUNG AND OLDER SUBJECTS

H.R. Newman, K.D. Meadows, T.B. Elia, E.H. Williams, E.J. Vresilovic, D.M. Elliott

Biomedical Engineering, University of Delaware, Newark, DE, USA

INTRODUCTION

The intervertebral disc maintains and distributes large multiaxial loads as a part of regular activity. We and others recently measured disc mechanics in young subjects using MRI^{1,2}. However, the disc undergoes large degenerative changes with age that are difficult to distinguish from pathology. Therefore, the purpose of this study was to non-invasively measure disc mechanical function in Young and Older pain-free subjects using our recently developed methods¹. To this end, magnetic resonance imaging (MRI) was used at four loading conditions to evaluate the differences in healthy disc function and spine behavior.

METHODS

Sixteen healthy women were divided evenly between Young (23-27 years old) and Older (63-77 years old) groups. Subjects were all asymptomatic, having no significant or chronic back pain, never had back surgery, scored less than 5 on the Oswestry Index low back pain disability questionnaire, and a back VAS pain score of less than 10/100.

Subjects underwent MRI in four loading states (Fig 1)¹. Loading states were achieved by postural changes and diurnal loading. Subjects were imaged first thing in the morning, following an hour of laying down to unload their spine. The supine scan was conducted first, followed by the extension and flexion positions (Fig 1). The postural positions were within the subjects' normal range of motion. The subject then conducted their daily routine and returned in the evening for a repeat supine scan.



Figure 1: Schematic of postural loading for supine, extension, and flexion positions for MRI scanning.

At each position, established MRI protocols (Table 1) were used to evaluate MRI variables and determine changes between loading states. The Supine AM, Extension, and Flexion scans were all within an hour of each other and therefore no measurable change in T2 relaxation time occurred between them, so the T2 scan was only done for Supine scans. Additionally, the gross health of the disc did not change within an hour, so the Pfirrmann TSE scan was only taken for the Supine scans.

All morning scans (Supine AM, Extension, Flexion) are taken within an hour of each other, which is insufficient time for significant fluid changes in the discs, therefore the T2-weighted scans are completed for the Supine AM and Supine PM states; while only the T1-weighted FLASH was conducted for the extension and flexion positions to assess disc geometry changes.

Table 1: MRI sequence protocol and scan details.

Sequence	Scan Time	Resolution (mm)	Slices	Imaging Parameters (ms)	Outcomes
T1-w FLASH	10.3 mins	0.5 x 0.5 x 3	20	TE=3.65, TR=9.6	Disc Geometry
T2 Map CPMG	15.9 mins	0.5 x 0.5 x 5	1	TE=13.6, ... 81.6, TR=3000	T2 Relax Time
T2-w TSE	6 mins	0.5 x 0.5 x 5	17	TE=124, TR=4540	Pfirrmann Grade

The 3D T1-weighted (T1-w) FLASH sequence provided detailed anatomic images of the disc which were used to evaluate disc geometry (Fig 2). From the mid-sagittal slice, spine cobb angle was determined as the total angle of the lumbar spine in the AM supine scan (Fig 2A). Disc height was calculated as the disc area divided by the anterior-posterior width (Fig 2A). The disc volume was evaluated by manual segmentation of the disc in all slices of the image sequence which were extruded based on the 3mm slice thickness to create a 3D volume of the disc (Fig 2B).

A T2 map sequence was used to quantify T2 relaxation time which is highly correlated with water content^{3,4} and we and others have shown that T2 time correlates with disc degeneration^{3,5-7}. To calculate T2 time, the image intensity decay in the nucleus pulposus was fit to a

noise-corrected exponential (Fig 2C)³. Lastly, a T2-weighted TSE sequence was used to determine the discs' degeneration grade by using the Pfirrmann scale (Fig 2)⁸. The grade is a disc health ranking from one to five where one is healthiest; the homogeneity of disc intensity and disc height largely determine the disc's score.

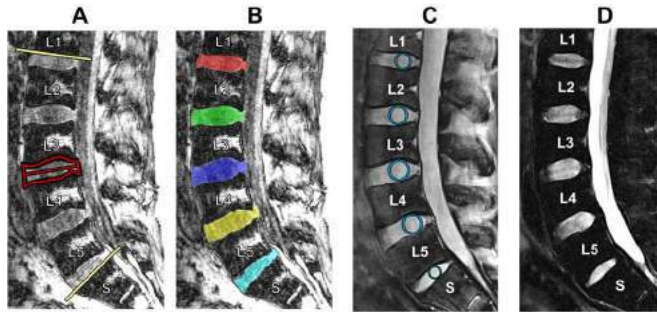


Figure 2: FLASH sequence with (A) yellow lines indicating Cobb angle, red lines showing disc area and width measures and (B) colored segmentations. (C) T2 map with regions of interest shown. (D) TSE sequence used for Pfirrmann grading discs.

For all evaluations, the Supine AM scan served as the baseline such that changes with diurnal loading and extension/flexion are the difference between Supine AM and Supine PM, extension, and flexion, respectively. A mixed model with fixed effect of age group and random effect of subject and disc level was used to evaluate differences between age groups ($p < 0.05$). A mixed model with fixed effect of Group and Loading and random effect of Subject and Disc Level was used to evaluate changes between loading conditions ($p < 0.05$).

RESULTS

Subject Data: There was no significant difference between the groups' BMI or physical activity on the day of scanning (steps taken between AM and PM scanning). The Young group had significantly lower Pfirrmann grades than the Older group (Fig 3A).

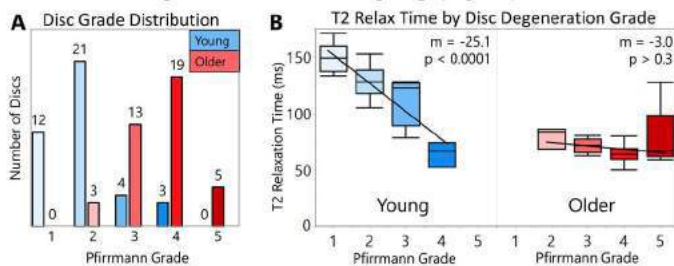


Figure 3: (A) Distribution of Pfirrmann grade by age group, where the Older group had significantly higher disc grades. (B) Correlation between grade and T2 relaxation time by age group, where the Young group had a significant correlation, and the Older group did not.

Supine AM Baseline: For comparing between age groups, the baseline disc T2 time (Fig 3B) and disc height were significantly reduced in the Older group but there was no significant difference in disc volume or baseline Cobb angle between age groups. The Young group had a significant correlation between T2 time and Pfirrmann grade, but the Older group did not.

Postural Loading: Both groups had significant differences in Cobb angle with the imposed postural changes to extension and flexion (Fig 4A). The Young group achieved 28% greater flexion than the Older group (Fig 4A), but there were no significant differences in achieved

extension. The change in disc height, change in volume, and change in T2 time were not significantly different between age groups in extension or flexion.

Diurnal Loading: With diurnal loading, there was no significant difference in Cobb angle as the result of diurnal loading both within and between age groups (Fig 4A). There was a significant decrease in disc height (Fig 4B), disc volume, and T2 relaxation time in both groups. The change in disc height (Fig 4B), change in volume, and change in T2 time were not significantly different between age groups.

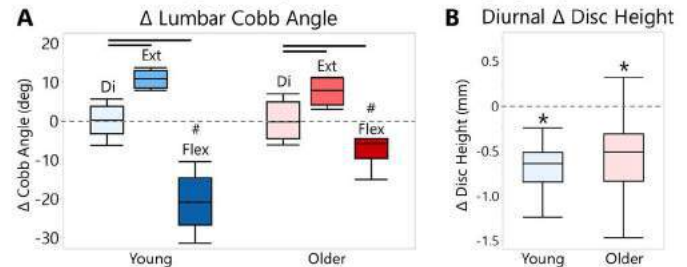


Figure 4: (A) Spine Cobb Angle was not impacted by diurnal loading (Di) but was significantly different in the extension (Ext) and flexion (Flex) positions. Flexion Cobb angle was significantly different between age groups (#), the Young group achieved greater flexion. (B) There was a significant decrease in disc height diurnally (*) for both age groups; they were not significantly different from each other.

DISCUSSION

We found that the disc exhibited age-dependent traits measurable with multi-positional MRI acquisition. The age groups had expected differences in Pfirrmann grade, where Young discs tended to have lower degeneration scores. The Young discs also had a strong correlation between the Pfirrmann grade and baseline T2, this is expected as a primary criterion of the Pfirrmann grading is nucleus visual intensity which coincides with higher T2 times. Interestingly, the Older discs had no correlation, despite a distribution of Pfirrmann grades. This suggests a potential limitation in using the Pfirrmann grading scheme, whereby intensity of a single image slice could be insufficient for assessing disc fluid content and subsequently disc health. The reduced T2 times in the Older cohort were expected, as aging discs tend to lose proteoglycans and subsequently water; there is also potential for changes in matrix composition reducing matrix integrity.

Importantly, while the groups had different baseline disc heights and T2 times, the Older group experienced diurnal changes similar to those of the Young group indicating that the geometric changes and water loss experienced throughout the day is maintained with varying age. Furthermore, Cobb angle changes confirmed postural positions were successfully achieved and did not change diurnally, as expected. The Older group achieved 28% less flexion than the Young group, this could be due to reduced flexibility in the spinal muscles. We found that disc health (degeneration) and flexion capacity were significantly impacted by age and provide valuable insights for changes to expect with age in the healthy disc.

REFERENCES

- [1] Meadows, KD et. al., JOR Spine, e1243:1-12, 2023. [2] Martin, JT et. al., Eur Spine J, 31(3):746-754, 2022. [3] Meadows, KD et. al., JOR Spine, 3(3):1-12, 2020. [4] Antoniou, J et. al., Magn Reson Med, 40(6):900-907, 1998. [5] Marinelli, NL et. al., Am J Neurorad, 31(7):1278-1282, 2010. [6] Ellingson, AM et. al., J Ortho Res, 32(8):1083-1089, 2014. [7] Yoon, M et. al., Magn Reson Imag, 34(7):932-939, 2016. [8] Pfirrmann, C et. al., Spine, 26(17):1873-1878, 2001.

MECHANICALLY PRIMED CELLS TRANSFER MEMORY TO FIBROUS MATRICES FOR INVASION ACROSS ENVIRONMENTS OF DISTINCT STIFFNESS AND DIMENSIONALITY

José Almeida (1), Jairaj Mathur (2), Ye Lim Lee (1), Bapi Sarker (2), and Amit Pathak (1,2)

- 1) Department of Biomedical Engineering, Washington University, St. Louis, United States
- 2) Department of Mechanical Engineering & Materials Science, Washington University, St. Louis, United States

INTRODUCTION

In fundamental biological processes of development, disease, and regeneration, cells move to and from mechanically distinct environments. For example, neural crest cells move throughout the embryo to lay the foundation for structurally complex organs [1], and cancer cells escape stiff tumors and invade through softer healthy tissue to initiate metastasis [2,3]. In any given environment, cells sense and respond to stiffness of their extracellular matrix (ECM) through actin-myosin force generation and focal adhesion signaling [4,5]. However, it remains unknown how grouped cells negotiate such mechanically dissimilar interfaces in fibrous three-dimensional (3D) environments. Further complicating this cross-environment mechanical heterogeneity, cells not only sense their current environment but also remember their past environments by retaining activated expression of mechanosensitive genes. In the context of collective cell migration, as epithelial cells move from stiff to soft 2D surfaces, adequate stiff-priming enhances their migration on future soft surfaces due to a YAP-based mechanical memory [6]. However, it is not yet clear whether such memory of cellular mechanical priming can be imparted to 3D collagen microenvironments, and whether this remodeled collagen can alter future cell invasion strategies into new, mechanically distinct environments. Here, we investigate these questions through an *in vitro* system to capture this cross-environment behavior by spatiotemporal invasion measurements and collagen remodeling done by primed cells implanted in collagen.

METHODS

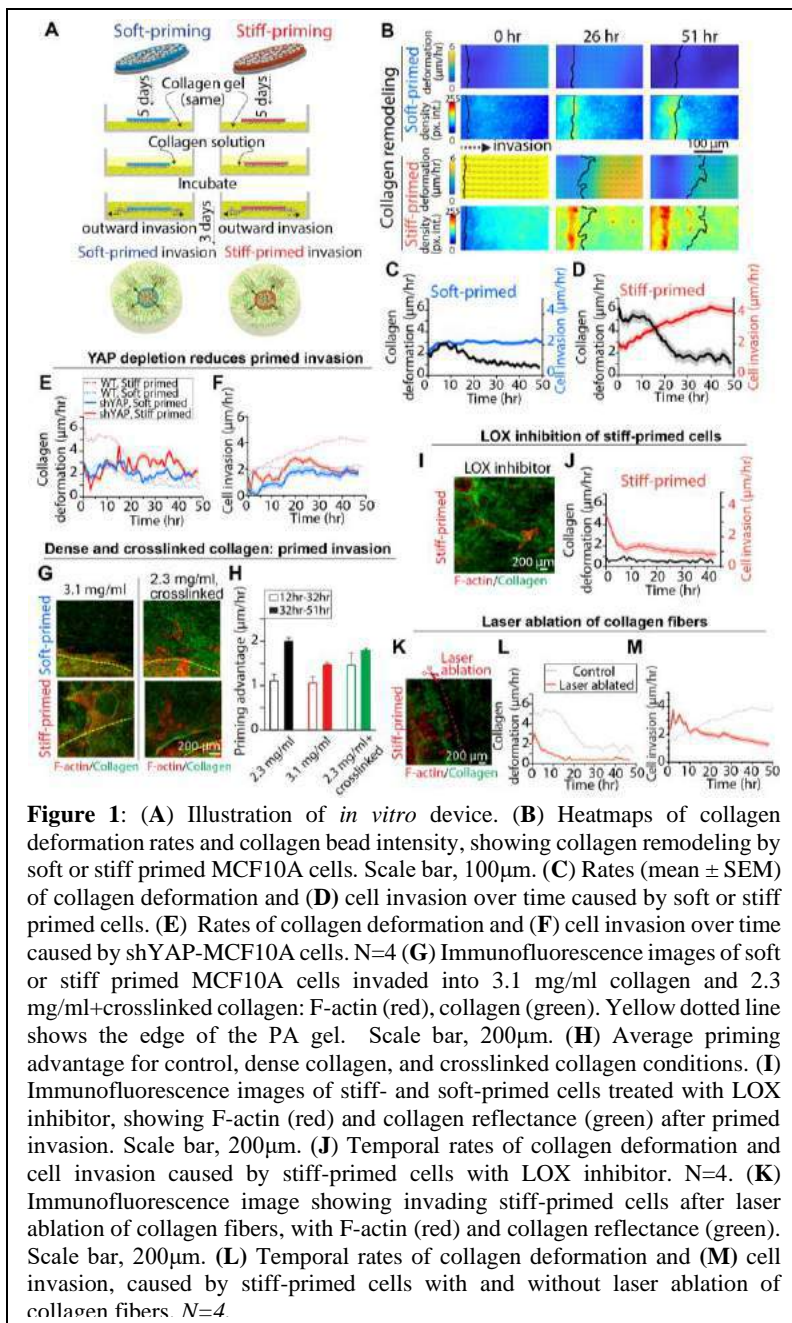
To combine two mechanically distinct environments for cellular mechanical priming and future invasion within one assay, we developed a dual-matrix scaffold with synthetic hydrogels and 3D collagen type I (Figure 1A). We first cultured MCF10A human breast epithelial cells on soft (0.08kPa) or stiff (16kPa) hydrogel substrates. Next, we implanted these hydrogel discs with adhered cells within 3D collagen (2.3 mg/ml) to allow spontaneous invasion of soft- or stiff-primed cells

into a new and mechanically different environment without intermediate detachment. We analyzed the cellular invasion by tracking the invasion front using an ROI (387 μm x 213 μm). Collagen deformation was tracked using embedded fluorescent beads and quantified using particle image velocimetry (PIVLab) and fixed images were visualized using a reflectance microscopy through confocal microscopy. To test the memory-independent invasion in case of an unstable priming, we depleted YAP in MCF10A cells.

RESULTS

Given the known importance cell-matrix engagement in cell migration, the differential collagen remodeling caused by soft versus stiff primed cells could also result in different outcomes for 3D cell invasion. In our measurements, stiff priming led to almost double the invaded distance and higher number of invaded cells, compared to soft priming (Figure 1, B-C). Notably, these differences in the number of invaded cells grew larger as the invasive front moved farther away from the priming environment (Figure 1B). When tracked over time and distance from the PA gel, stiff-primed cells pull and accumulate collagen behind the invasive front (Figure 1B-D). These high-density collagen 'anchors', shown as red band in the collagen intensity plots (Figure 1B), remain stable over the duration of observed invasion. After the initial ~12 hours period of rapid matrix remodeling, collagen deformation rate reduced, which could indicate establishment of pretension within the collagen matrix (Figure 1B).

As a result of memory-dependent collagen remodeling, invasion speed of stiff-primed cells almost doubled compared to their soft-primed counterparts. By plotting spatial maps of collagen bead density over time (Figure 1B, bottom row), we show that regions of high-density collagen accumulation are larger and more pronounced in case of stiff primed cells; and once formed, these regions do not dissolve over time. Here, collagen deformation rate around soft-primed cells remained too low (Figure 1C) to cause collagen accumulation or tension generation (Figure 1B, top row).



To test the memory-independent invasion in case of unstable priming, we used MCF10A-shYAP that were depleted YAP, a known regulator of cellular mechanical memory [6,7] and repeated the experiments of primed cell invasion. As cells invade their surrounding matrix, the resulting collagen deformation was priming-independent, somewhat temporally uncoordinated, and lower compared to the control case (Figure 4E). In addition, this lower collagen deformation by shYAP cells coincided with their slower invasion speeds (Figure 4F), regardless of soft or stiff priming.

To understand how differentially primed cells behave in dense or stiffened collagen matrices, we repeated experiments in two collagen compositions: higher collagen density of 3.1 mg/ml, and second with crosslinking to increase stiffness but maintain density by mixing 2.3 mg/ml collagen with the photo-crosslinker Riboflavin followed by UV

exposure. We found that in these challenging matrices of higher density and crosslinking, the priming advantage, a term we defined as the difference in the invasion speeds of soft and stiff primed cells, was preserved and persisted over time (Figure 1G-H). Overall, our experiments show that prior mechanical priming continues to be advantageous in denser and stiffened collagen matrices (Figure 1H).

To experimentally test the role of stable collagen remodeling in primed invasion, we used β -aminopropionitrile (BAPN) to inhibit lysyl oxidase (LOX) that crosslinks collagen. After soft or stiff priming of cells, BAPN was added, and cells were allowed to invade into collagen (Figure 1I). When tracked over time (~2 days), both collagen deformation and invasion rates of stiff-primed cells remained low (Figure 1J).

We next asked whether cellular forces are necessary only near the invasive front, or whether they need to be propagated over long distances into the matrix to enable collagen remodeling (Figure 1K). To implement an analogous spatial disruption of force-based collagen remodeling in experiments, after the stiff-primed cells invaded into the collagen and at the onset of invasion, we performed laser-based ablation of collagen fibers ahead of the invasive front. Collagen deformation was substantially reduced within a few hours after laser ablation of fibers and remained in a low net deformation state over time (Figure 1L). This depleted effect of ablated matrix indicates the importance of long-distance force propagation within collagen for its bulk remodeling. Similarly, although the invasion rate of stiff-primed cells started at a high level, it subsided within 6-8 hours and remained low over two days of tracking (Figure 1M).

DISCUSSION

Here, we developed a novel hydrogel-collagen device to combine mechanical priming and cross-environment invasion. Using this system, we show that cells previously primed by stiff environments continue to invade through softer 3D collagen matrices – a multifaceted process mediated by collagen fiber remodeling. We show that priming-based cellular forces and matrix remodeling are such intimately coupled processes that any disruptions in collagen crosslinking or force propagation disrupt the connection between past cellular priming and future invasion. These basic mechanisms of priming-dependent matrix remodeling and invasion hold true for multiple cell types and collagen compositions. Overall, our results show that past ‘stiff-priming’ provides cells a previously unappreciated advantage in navigating new challenging environments. This memory-dependent cell-matrix coupling could apply to wide-ranging biological processes wherever cells remodel their environments over time and distance, e.g., fibrosis, cancer, and aging.

ACKNOWLEDGEMENTS

The authors acknowledge all members of the A.P. laboratory for discussions and feedback on this work. We acknowledge financial support from following sources: NIH grant R35GM128764 (to A.P.) and NSF CEMB grant CMMI:154857 (to A.P.).

REFERENCES

- [1] Shellard, A et al., *Science* 362, 339 – 343.
 - [2] Paszek, M.J et al., *Cancer Cell* 8, 241 – 254.
 - [3] Acerbi, I et al., *Integr Biol (Camb)* 7, 1120 – 1134.
 - [4] Pelham, R.J et al., *Proceedings of the National Academy of Sciences, USA* 94, 13661 – 13665.
 - [5] Li, C.X et al., *Nat Mater* 16, 379-389.
 - [6] Nasrollahi, S et al., *Biomaterials* 146, 146 – 155.
 - [7] Yang, C et al., *Nat Mater* 13, 645 – 652
- (Preprint for this work: Almeida et al., 2022, [bioRxiv](https://doi.org/10.1101/2022.08.18.501111))

MATERNAL ANATOMY DRIVES MECHANICAL LOADING IN THE PROXIMAL CERVIX DURING PREGNANCY

Erin Louwagie (1), Jada Hinds (1), Lindsey Carlson (2,3), Timothy Hall (2), Helen Feltovich (2,3),
Kristin Myers (1)

(1) Mechanical Engineering, Columbia University, New York, NY, USA
(2) Maternal Fetal Medicine, Intermountain Healthcare, Provo, UT, USA
(3) Medical Physics, University of Wisconsin-Madison, Madison, WI, USA

INTRODUCTION

Preterm birth (PTB) rates in the United States have remained largely unchanged since the first year when definitive national data were available, with the 2007 PTB rate being 10.44% and the 2021 PTB rate being 10.48% [1]. PTB is delivery before 37 weeks gestation, and babies born prematurely are at an increased risk of death and disability [2]. The current gold standard for PTB prediction is the sonographic measurement of cervical length, with a typical cutoff of 25mm or less placing a pregnant patient at increased risk of PTB [3]. However, this method of PTB prediction is only 30-60% sensitive, depending on other patient risk factors [3]. The structural integrity of maternal reproductive tissues is essential to a successful pregnancy. Thus, a better knowledge of maternal reproductive tissue loading on an individual basis will improve PTB prediction and provide a rationale for PTB prevention.

Because pregnancy is a protected environment, we use computational modeling to study pregnancy biomechanics. We have developed a method to create parametric patient-specific solid models of the maternal uterus and cervix from 2D ultrasound images [4,5]. These solid models have been utilized in finite element analysis to calculate cervical loading in the early second trimester in patients considered at low- and high-risk for PTB. In addition, we have explored the repeatability of these ultrasonic measurements by calculating the inter-class correlation coefficient (ICC) for each dimension, which were rated as ‘excellent’, ‘good’, ‘fair’, and ‘poor’ using the Cicchetti guideline [5]. This research aims to study the sensitivity of proximal cervical loading to variations in maternal anatomy measured via ultrasound. These measurements will lay the foundation for PTB prediction related to the mechanical overloading of the cervix.

METHODS

Previously collected sonographic measurements from the early second trimester (14-16 weeks gestation) were used in this study from a cohort of 29 patients who delivered at-term [5]. A “normal” early

second-trimester maternal anatomy was determined by finding the median value for each of the 15 ultrasonic measurements collected and a parametric 3D model built of the “normal” uterus and cervix in Solidworks (Dassault Systemes, Vélizy-Villacoublay, France). Four additional 3D solid models were built for each parametric ultrasonic measurement by varying the median value by $\pm 10\%$ and $\pm 20\%$, covering most maternal dimension values observed, and holding all other parametric values at the median. One measurement, the lower uterine segment thickness (UT4), was varied to $\pm 50\%$ and $+100\%$ to cover the range of values found in the patient cohort. In addition to the cervix and uterus, a fetal membrane and supporting abdomen was included in each geometry. The left half of each geometry was used for computational efficiency and discretized into elements using Hypermesh (Altair Engineering Inc., Troy, MI). FEBio Studio (v1.3.0) was used for finite element analysis (FEA), and the meshed geometry was imported into it [6].

Within FEBio, the material properties, boundary conditions, and contacts were defined. The same material properties were assigned to each geometry. Material properties used were based on existing mechanical tests. The cervix and uterus were modeled as passive fiber composite materials and the fetal membrane as a transversely isotropic fiber-based material with a compressible neo-Hookean ground substance [7-9]. Cervical fiber stiffness was assumed to be normal for the gestational age based on existing cervical aspiration data [10]. The boundary conditions applied were as follows: fetal membranes tied to the intrauterine wall and sliding on the cervix, the uterus sliding on the abdomen, the proximal cervix tied to the abdomen and the distal cervix sliding on the abdomen, and the model fixed in the normal direction at the superior, inferior, posterior, and sagittal plane surfaces. A gestationally appropriate intrauterine pressure was applied to the inner membrane surface [11]. Heat maps of stretch in the proximal cervix were compared between models with varying measurement values and cylindrical stretches at points in the anterior, left, and posterior cervical

midstroma plotted against percentage change in measurement value. Changes of 1% or more stretch at these points were deemed notable. This limit was used to ensure notability in results is due to changes in the maternal anatomy and not variances that may arise from the computation.

RESULTS

The measurements with reported excellent ICCs that affected proximal cervix loading are inferior-superior intrauterine diameter (UD1), left-right intrauterine diameter (UD4), and lower uterine segment thickness (UT4), with table 1 summarizing which parameters had notable effects in proximal cervical loading. An example of how the proximal cervix heat maps change is shown for the lower uterine segment thickness (Fig. 1).

Table 1: Percent change in stretch from lowest to highest dimension value dimensions with noticeable changes. Stretches at (Pos)itions in the (Ant)erior, Left, and (Post)erior cervical midstroma are reported in the (R)adial, (C)ircumferential, and (L)ongitudinal (Dir)ections. Percent change in stretch $\geq 1\%$ are bolded.

ICC Rating		Excellent			Good		Fair
Dimension		UD1	UD4	UT4	UD3b	AUCA	CD1
Pos.	Dir.						
Ant.	R	-0.2%	0.6%	0.5%	1.5%	-0.6%	-0.3%
	C	-0.5%	1.8%	1.4%	0.8%	0.3%	-0.3%
	L	0.2%	-1.3%	-1.0%	0.7%	1.0%	-0.6%
Left	R	-0.6%	2.5%	1.0%	0.5%	0.0%	0.4%
	C	0.2%	0.2%	0.2%	1.3%	0.7%	-0.7%
	L	0.7%	-2.2%	-0.7%	0.3%	-1.4%	-1.1%
Post.	R	1.0%	0.6%	0.1%	0.8%	0.8%	0.2%
	C	-0.3%	1.9%	0.4%	0.7%	-0.4%	0.0%
	L	0.0%	-1.5%	0.2%	0.5%	-0.5%	-1.8%

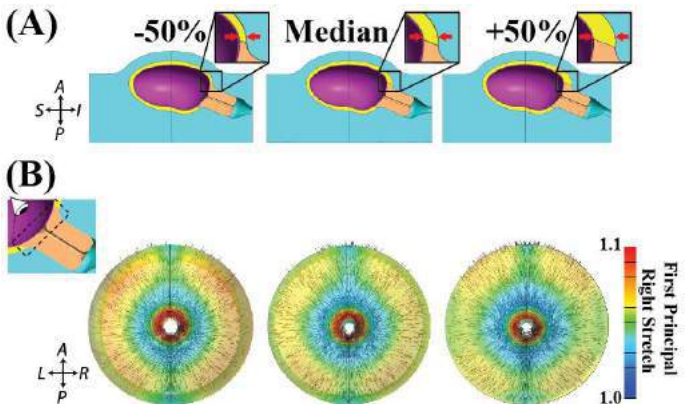


Figure 1: (A) Varying one measurement, the lower uterine segment thickness (UT4), while holding all other dimensions at the median value changes stretch in the proximal cervix. (B) First principal stretch decreases in the proximal cervix as UT4 increases. Anatomical directions are provided.

Ultrasonic measurements with reported good ICCs that affect loading in the proximal cervix are the anterior uterocervical angle (AUCA, angle between cervical canal and lower uterine segment) and the posterior intrauterine diameter in the inferior uterus (UD3b, controls curvature of posterior uterine wall in the inferior uterus). Only one measurement with a reported good ICC had a notable effect on proximal

cervical loading, the outer cervical diameter (CD1). No measurements with reported poor ICC values had notable effects on proximal cervix loading. Cervical length, which has a reported good ICC, did not have notable effects on proximal cervical loading.

DISCUSSION

Dimension measurements that had the largest effects on cervical loading were those that dictate the overall width of the uterus (UD4), the shape of the posterior intrauterine wall near the cervix (UD3b), and the thickness of the lower uterine segment (UT4). The overall length of the uterus (UD1) along with the width (CD1) and angle (AUCA) of the cervix were also important to cervical loading. Given the criteria of 1% change in stretch or greater, only 6 of the 15 investigated parametric ultrasonic measurements have a notable effect on loading results in the proximal cervix when varied, and none of them have reported poor ICCs. Our ongoing clinical studies have shown that patients with large radial stretches tend to deliver extremely preterm, so dimensions that change radial stretch (UD1, UD4, UT4, and UD3b) are likely highly important to capture. Several clinical studies have investigated using the anterior uterocervical angle to predict preterm birth [12,13]. It is known that the stiffness of the cervix also affects cervical loading, so in the future we will repeat this study with varying cervical fiber stiffness [4]. Additionally, an investigation of how these parameters affect stretch in other cervical locations and the uterus and fetal membranes is warranted. More methods of analysis will also be undertaken in the future, such as stretch comparisons across the entire proximal cervix rather than at select points.

Limitations to this work are non-trivial. The measurements used in this study are from pregnant anatomy, so the configurations used are inherently not in a stress-free state. Additionally, the dataset from which the dimension measurements were taken was only patients who ended up delivering at term, so measurements reflective of maternal anatomy who deliver preterm may not be covered by the range of values investigated in this work. Also, the analysis was only done in the contact condition where the fetal membrane was tied to the intrauterine wall and allowed to slide on the cervix, which may have artificially increased the degree to which the outer cervical diameter (CD1) affected proximal cervix loading.

ACKNOWLEDGEMENTS

This work is supported by the Eunice Kennedy Shriver National Institute of Child Health & Human Development of the National Institutes of Health under award number 1R01HD091153-01. The content is solely the responsibility of the authors and does not necessarily represent the official views of the National Institutes of Health. It was also supported by the Columbia University and Amazon Summer Undergraduate Research Experience (SURE) Program.

REFERENCES

[1] Hamilton, B et al., Vital Statistics Rapid Release; no 20, 2022.
[2] Center for Disease Control, "Preterm Birth", 2022.
[3] *Int J Gynecol Obstet*, 144(3):340-346, 2019.
[4] Westervelt, A et al., *J Biomed Eng*, 139:051004, 2017.
[5] Louwagie, E et al., *PLOS ONE*, 16(1):e0242118, 2021.
[6] Maas, S et al., *J Biomech Eng*, 134(1):011005, 2012.
[7] Myers, K et al., *J Biomech*, 48:1533-1540, 2015.
[8] Conrad, J et al., *Am J Ob Gynecol*, 96:1055-1059, 1966.
[9] Bürzle, W and Mazza, E., *J Biomech*, 46:1777-1783, 2013.
[10] Badir, S et al., *Prenat Diagn*, 33:737-741, 2013.
[11] Fisk, N et al., *BJOG*, 99(1):18-22, 1992.
[12] Dziadosz, M et al., *Am J Obstet Gynecol*, 215(3):376.e1-7, 2016.
[13] Uquillas, K et al., *J Matern-Fetal Neo M*, 30(1):50-53, 2017.

DAMKOHLE NUMBER ANALYSIS FOR PREDICTING BIOMOLECULE GRADIENTS IN ENGINEERED TISSUES

Sedat Dogru (1), Matthew Simkulet (2), Halide Z. Haciguzeller (2), Michael B. Albro (1,2)

- (1) Department of Mechanical Engineering, Boston University, Boston, MA USA
(2) Department of Biomedical Engineering, Boston University, Boston, MA USA

INTRODUCTION

Tissue engineering (TE) is an emerging treatment strategy for an assortment of trauma/degenerative pathologies (e.g., cardiac/skeletal muscle, musculoskeletal connective tissue), consisting of the fabrication and clinical implantation of cellularized replacement tissues [1]. Cell-seeded tissue constructs are initially cultivated *in vitro* with an array of anabolic biomolecules, consisting of nutrients, vitamins, hormones, and growth factors (GFs), to accelerate tissue growth. In contrast to native developmental processes—whereby biomolecule transport is aided through delivery via dense vascular networks—in TE applications, biomolecules are supplemented in culture medium and expected to transport sizable diffusion distances through thick avascular constructs to reach their cell targets [2,3]. Consequentially, growth-stimulating biomolecules can encounter significant transport limitations in constructs, giving rise to sustained, steady-state spatial concentration gradients, which in turn, can lead to detrimental non-uniformity in the viability and composition of developing tissues [2,3]. As such, the development of novel TE platforms to improve the delivery of transport-limited biomolecules may considerably improve clinical treatment outcomes.

The identification of transport-limited biomolecules constitutes a significant challenge. On a theoretical basis, steady-state concentration gradients of biomolecules arise when the rate of cell-mediated chemical degradation/consumption of a biomolecule (via membrane transporters or receptor-mediated endocytosis) exceeds its rate of diffusive transport through the construct [3,4]. Accordingly, more pronounced gradients are observed for a higher biomolecule consumption rate and/or lower biomolecule diffusivity. Generally, for small nutrients (e.g., glucose, oxygen) gradients can arise as a result of their characteristic high rates of cellular consumption, but are also mitigated due to their high diffusivity. In contrast, large protein biomolecules (e.g., GFs) are

expected to exhibit lower consumption rates but also possess far reduced diffusivities. As such, it remains challenging to predict how these parametric variations for different types of biomolecules manifest into differential concentration gradients in engineered tissues.

Non-dimensional parametric ratios have traditionally been used in the field of thermofluids to provide insights into mass/energy distributions in response to complex transport phenomena. The non-dimensional Damkohler number, derived from the 1D reaction-diffusion equation, has classically been used to relate chemical reaction rates to mass transfer rates, providing an analytical estimate of the steady-state spatial distribution of reactants in a chemical system [5]. In this work, we explore the utility of adopting the Damkohler number to serve as a novel analytical tool for evaluating the steady-state gradients that arise for specific biomolecules in engineered tissues. Here, we utilize a cartilage TE model system, consisting of chondrocyte-seeded agarose constructs to examine: 1) the ability of the Damkohler number to quantitatively predict the 1D steady-state distribution of biomolecules in TE cartilage, and 2) the variation of Damkohler number and accompanied steady state concentration gradients in TE cartilage for a range of different classes of growth-stimulating biomolecules: nutrients (glucose), vitamins (ascorbic acid 2-phosphate (AAP)), protein hormones (insulin), and GFs (TGF- β 3, IGF-1, BMP-2).

METHODS

Reaction-diffusion equation analytical solution:

The steady-state 1D reaction-diffusion equation reduces to:

$$D \frac{d^2 C}{dx^2} - R_i C = 0 \quad (1)$$

where D : diffusivity, C : biomolecule concentration, R_i : consumption rate constant. The non-dimensional form of Eq. (1) reduces to:

$$\frac{d^2 \bar{C}}{d\bar{x}^2} - \pi \bar{C} = 0 \quad (2)$$

where $\bar{C} = \frac{C}{C_s}$; C_s : construct surface conc.; $\bar{x} = \frac{x}{L}$; L : tissue thickness;

Damkohler number (π) = $\frac{R_i L^2}{D}$. Solving for the boundary conditions (BC) to Eq. (2), where

BC1: $\bar{C} = 1$ when evaluated at $\bar{x} = 0$ and

BC2: $\frac{d\bar{C}}{d\bar{x}} = 0$ when evaluated at $\bar{x} = 1$, results:

$$C = C_s \frac{1}{1 + e^{2\sqrt{\pi}}} \left(e^{2\sqrt{\pi} - \sqrt{\pi} \frac{x}{L}} + e^{\sqrt{\pi} \frac{x}{L}} \right) \quad (3)$$

Damkohler number for growth stimulating biomolecules:

The Damkohler number (π) for each biomolecule in chondrocyte-seeded cartilage constructs was computed based on measures of diffusivity, chondrocyte-mediated consumption rate constant (R_i), and tissue thickness (prescribed at a conventional 3mm). Diffusivity values of biomolecules in 2% agarose scaffolds were adopted from the literature (glucose and AAP [4] and others [6]). R_i values were experimentally measured for cartilage constructs fabricated via immature bovine chondrocytes (30×10^6 cells/mL) seeded in 2% agarose. Here, small-size constructs ($\varnothing \times 1$ mm) were exposed to chondrogenic medium, consisting of glucose [4.5mg/mL], AAP [0.45mg/mL], and insulin [6 μ g/mL], and supplemented with either IGF-1 (10ng/mL), TGF- β 3 (10ng/mL), or BMP-2 (10ng/mL). The transient concentration decrease of each biomolecule in medium was monitored over 48h and curve-fit for R_i using a reaction-diffusion model and finite element model solver, as previously described [3].

Analytical model validation: Large-size constructs ($\varnothing \times 3$ mm) were exposed to CM supplemented with TGF- β 3 (10 ng/mL) for 5 days to reach steady-state conditions, as determined by FE analysis (not shown). Constructs were sub-punched, axially sectioned. Biomolecules in each section were buffer extracted and subjected to glucose assay or TGF- β 3 ELISA, yielding depth-dependent concentration profiles. Analytical model computed spatial gradients of glucose and TGF- β 3 were determined (Eq. (3)) using the diffusivity (D) and consumption rate constant (R_i) values given in Fig 2B.

RESULTS

Biomolecule gradient with respect to Damkohler number: The normalized biomolecule concentration \bar{C} versus normalized tissue depth \bar{x} in a TE construct was plotted for a wide range of Damkohler numbers ($\pi = 0.01$ -1000; Fig 1). Steady state gradient severity increases with π . For $\pi \leq 0.2$ gradients were largely absent. For $\pi > 10$, severe gradients were observed where the concentration at the construct bottom decays to a near zero value.

Damkohler number for growth stimulating biomolecules: Measured R_i for biomolecules varied by four orders of magnitude, ranging from $2.8 \times 10^{-7} \text{ s}^{-1}$ for insulin to $1.8 \times 10^{-3} \text{ s}^{-1}$ for BMP-2 (Fig 2A). Calculated Damkohler numbers also varied by four orders of magnitude, ranging from $\pi = 0.02$ to $\pi = 725$ (Fig 2B). Predicted steady-state gradients reflected these Damkohler numbers—modest gradients were observed for insulin and glucose, intermediate gradients for AAP and IGF-1, and severe gradients for TGF- β 3 and BMP-2 (Fig 2C).

Analytical model validation: Analytical model predictions of steady-state gradients of glucose and TGF- β 3 exhibited strong agreement with the experiment measures ($R^2=0.67$, $R^2=0.89$ respectively, Fig. 3).

DISCUSSION

This work advances the use of the nondimensional Damkohler number as a novel tool for estimating biomolecule concentration gradients in engineered tissues. Here we demonstrate that Damkohler number analysis can accurately predict the steady-state distribution of biomolecules in TE cartilage, allowing for a parametric analysis of concentration gradients of different classes of growth-stimulating biomolecules. An intriguing outcome of this analysis is the substantially elevated Damkohler number observed for TGF- β 3 ($\pi=53$) and BMP-2

($\pi=723$) GFs relative to glucose ($\pi=0.42$). Physically, this disparity arises from the combination of the significantly higher consumption rates and lower diffusivity of GFs relative to glucose—ultimately, these GFs are consumed by cells at a faster rate and replenished from the medium bath more slowly. This observation suggests that GF transport limitations may constitute the dominant contributor to heterogeneities of developing engineered tissues. This represents an unanticipated outcome given the primary focus of small nutrients in prior transport analysis investigations [4,7].

Damkohler number analysis can serve as an easy-to-implement analytical framework for identifying the dominant transport-limited biomolecules in a wide range of TE applications. This analysis requires measures of two easy-to-measure biomolecule parameters: D and R_i . D can be readily determined via transport characterizations of size-matched fluorescent tracers or estimated from prior literature characterizations in TE scaffolds. R_i can be determined by monitoring biomolecule depletion in culture media for small-sized, gradient mitigated constructs, as performed in this study. It is worth noting that curve-fitting of R_i was performed using an FE model to account for residual biomolecule gradients of GFs in small-sized tissues. However, future R_i measures can be performed on tissues with further reduced gradients (i.e., thinner tissues or cell monolayers), thus enabling curve-fitting with analytical models, thus avoiding need for FE models entirely. In the future, we envision that Damkohler analysis will guide the development of novel TE cultivation systems to optimize growth-stimulating biomolecule delivery, leading to control of engineered tissue composition and mechanics in order to improve their performance after clinical implantation.

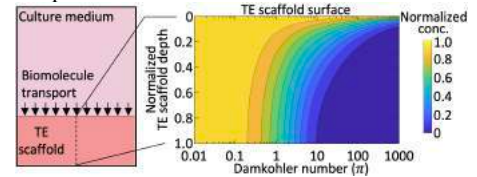


Fig 1: Variation of steady-state biomolecule concentration gradient with respect to Damkohler number in TE construct.

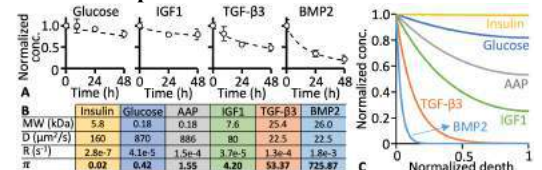


Fig 2: (A) Monitored transient concentration decrease of glucose, IGF-1, TGF- β 3 and BMP-2 and FE curve fit (dashed line) for R_i determination. (B) Molecular weight, diffusivity, consumption rate constant and Damkohler number (π) of biomolecules. (C) Spatial gradient of different biomolecules in TE cartilage constructs.

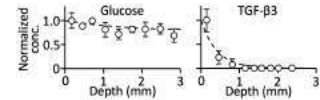


Fig 3: Experimentally measured (circles) and analytically predicted (dashed line) steady-state spatial gradient of glucose and TGF- β 3 in cartilage construct after 5 days.

ACKNOWLEDGEMENTS: Supported by NSF (CMMI 1906469) and NIH (R01AR078299).

REFERENCES: [1] Huang BJ+ 2016 Biomaterials; 98:1-22. [2] Bian L.+ 2009 Osteoarthr. Cartil. 17:677-685; [3] Albro MB+ 2016 Biomaterials 77:173-85; [4] Nims RJ+ 2014 J. Biomech. 47:2165-2172; [5] Damkohler G. 1947 angew. phys. chem. 46: 1112; [6] Albro MB+ 2009 CBME 2.3:295-305. [7] Carroll, S. F.+ 2021 Front. Bioeng. Biotechnol. 328

VASCULAR CROSS-SECTION MORPHOMETRICS CAN PREDICT FIRST PASS OUTCOME OF MECHANICAL THROMBECTOMY FOR ISCHEMIC STROKE

Briana A. Santo (1,2), S.M.M. Janbeh Sarayi (1,3), Muhammad Waqas (1,4), Andre Monteiro (2,3), Adnan H. Siddiqui (2,3), Vincent M. Tutino (1,2,3)

- (1) Canon Stroke and Vascular Research Center, University at Buffalo, Buffalo, NY, United States
- (2) Department of Pathology and Anatomical Sciences, Jacobs School of Medicine and Biomedical Sciences, University at Buffalo, Buffalo, NY, United States
- (3) Department of Mechanical and Aerospace Engineering, School of Engineering and Applied Sciences, University at Buffalo, Buffalo, NY, United States
- (4) Department of Neurosurgery, Jacobs School of Medicine and Biomedical Sciences, University at Buffalo, Buffalo, NY, United States

INTRODUCTION

Large vessel occlusions (LVO) are associated with increased mortality and morbidity among stroke patients, bearing a high incidence rate of ~30% [1]. Mechanical thrombectomy has become a standard of care for LVOs [1]. In this method, a device (stent retrievers, aspiration catheters, or their combination) is navigated through a network of arteries to access the occlusion site in the neurovasculature and physically remove a blood clot. The primary goal of mechanical thrombectomy is to establish near-perfect reperfusion (indicated by an extended Thrombolysis in Cerebral Infarction, eTICI, score of $\geq 2c$) in one treatment pass, referred to as first pass effect (FPE) [1]. However, studies have demonstrated that mechanical thrombectomy only achieves FPE in ~29-40% of cases. When FPE cannot be not achieved, the treatment requires additional passes, and poses greater mortality and morbidity risks [1]. To improve thrombectomy outcomes, the underlying causes of first pass failure must be studied.

Several publications have demonstrated that the vascular morphology plays a critical role in procedural outcomes. Tortuosity and angulation have been the most studied characteristics to date, as reports have shown that it is difficult to maneuver stent delivery devices or to place aspiration catheters adjacent to (or in contact with) clots in tortuous vessels. Mokin et.al. measured the 3D tortuosity and angulation of vessels from the aortic arch to the terminal internal carotid artery (ICA), found that greater angulation was associated with longer procedure times due to difficulty in navigation. More recently, several studies have examined ICA tortuosity and its impact on thrombectomy outcome. While some studies identified an association between ICA tortuosity and reduced likelihood of FPE, none tested whether predictive models could be developed to predict FPE based on tortuosity alone. The existing literature tends to be either overly simplistic (only evaluating 2D morphology), limited in scope (only evaluating macro-scale characteristics like tortuosity), or limited in location (not investigating the vessels distal to the ICA). Moreover, most of the prior

work hasn't tested if morphological parameters could predict first pass outcome or if one treatment approach exhibited a greater success rate in tortuous vessels over another.

To our knowledge, no study has investigated quantitative measures other than tortuosity and angulation when analyzing 3D geometry of thrombectomy vascular pathways. In several medical specialties (e.g., congenital disorders), geometric morphometric analysis and feature engineering have demonstrated success in pinpointing subtle and highly informative anatomical differences that aid in disease assessment. Therefore, in this study, we aimed to investigate whether GMM could be used to more precisely identify regions associated with first pass failure, and if so, design new features that quantified informative vessel characteristics at cross-sections corresponding to these regions. Specifically, we also sought to test the predictive power of engineered cross-sectional features, relative to traditional measures (like tortuosity and angulation), through development and evaluation of machine learning (ML) models for classification of FPE and first pass failure.

METHODS

This study was approved by the institutional review board at the University at Buffalo (study 00005640). All methods were performed in accordance with the approved protocol. Pre-MT computed tomography (CT) angiography (CTA) and noncontrast CT (nCCT) images were retrospectively collected from patients undergoing MT by either stent retriever, aspiration, or a combined therapy between November 2018 and November 2019 at the Gates Vascular Institute in Buffalo, New York. Pre-MT and post-MT digital subtraction angiography were also collected. Patients considered for this study met the following inclusion criteria: (1) they had undergone MT for AIS because of an occlusive clot in the intracranial vasculature, (2) they had pretreatment (pre-MT) CT available with sufficient image quality and an identifiable clot, and (3) they had complete treatment outcome data. In total, 56 cases were considered; however, 6 were removed from

analysis, as portions of the ICA region could not be properly segmented.

We analyzed CTA and non-contrast CT (nCCT) from 50 anterior circulation stroke thrombectomy patients. A summary of our image processing and feature engineering pipeline is provided in **Figure 1**. As previously described, vessels and clots were segmented together and the vessel region about the occlusion was reconstructed [3]. Geometries were trimmed to the device path, from the base of the ICA through to the proximal portion of the M2 segment, and centerlines were extracted. All analysis was completed in *3d Slicer*. After segmentation, traditional metrics (vessel tortuosity, and angulation) were calculated from vessel centerlines that were transformed into the same coordinate system and same ROI through mirror reflection of vessels for cases featuring right-sided occlusions to align with left-sided cases. Univariate statistical analysis and geometric morphometrics (GMM) were used to explore differences in geometry between cases that did and did not achieve FPE, which traditional metrics could not discern. To describe these differences complex cross-section features were engineered and quantified using a semi-automatic pipeline. These features were preliminarily ranked using univariate statistics and correction for multiple testing based on their ability to differentiate between cases that did and did not achieve FPE.

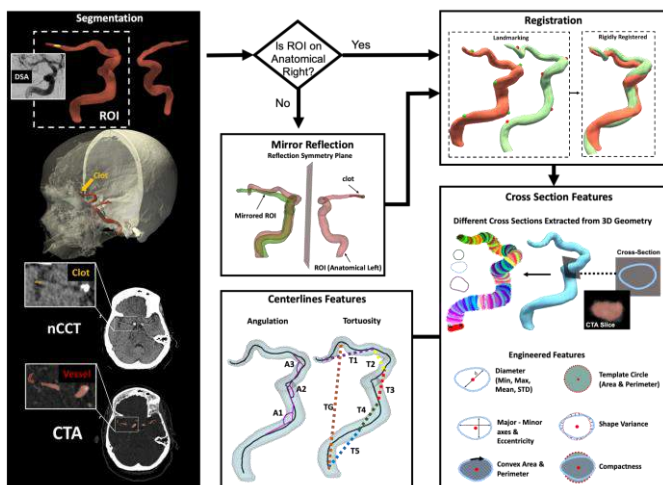


Figure 1: Image processing and feature engineering pipeline for quantification of vascular cross-sections from pre-treatment CT.
Figure adapted from Sarayi and Santo et al. SVIN, 2022.

ML was used to train predictive models of FPE based on significant cross-section features. Feature selection was completed using recursive feature elimination (RFE), while hyperparameter tuning and model evaluation were completed using stratified, 5-fold cross-validation over 50 randomizations. Evaluated classifiers included support vector machine (SVM), logistic regression (LR), extreme gradient boosting (XGB), and artificial neural network (ANN). Classification performance was summarized as accuracy, area under the receiver operating characteristic curve (AUC), and F1-Score.

RESULTS

Our data set was balanced across demographic, treatment, and stroke presentation. Overall, 48% of patients were women (n=24) and the mean age of the population was 71.1 years (SD=13.1 years). Average National Institutes of Health stroke scale at presentation was 16.1 (SD=7.6), and the thrombectomy techniques used included stent retriever (n=9, 18%), aspiration (n=9, 18%), and Solubra (n=32, 64%). A total of 54% (n=27) of occlusions occurred on the left and were

primarily located at M1 (n=27, 54%), the ICA/M1 junction (n=5, 10%), and M2 (n=18, 36%). The frequency of FPE was 42% (n=21).

With respect to standard tortuosity and angulation measures, only one local tortuosity metric was significantly different ($q=0.019$) between FPE and first pass failure cases. The most significant Principal Component score ($q=0.012$) from GMM highlighted M1 and upper Cavernous ICA variation as morphological indicators of first pass outcome. 15 cross-section features, corresponding to ICA and MCA regions, and selected through RFE, were significantly different between cases that did and did not achieve FPE. Each of these cross-section features was mapped back to patient vessels for clinician interpretation (**Figure 2**) and were described as caliber changes at critical locations in the device path as well as the clot region itself, aligning with the theory that clot properties also affect device success. Classifiers exhibited strong prediction of FPE, with the best model (SVM) achieving an $AUC=0.98\pm0.05$. All classifiers trained using cross-section features far outperformed complementary trained using traditional tortuosity and angulation features alone.

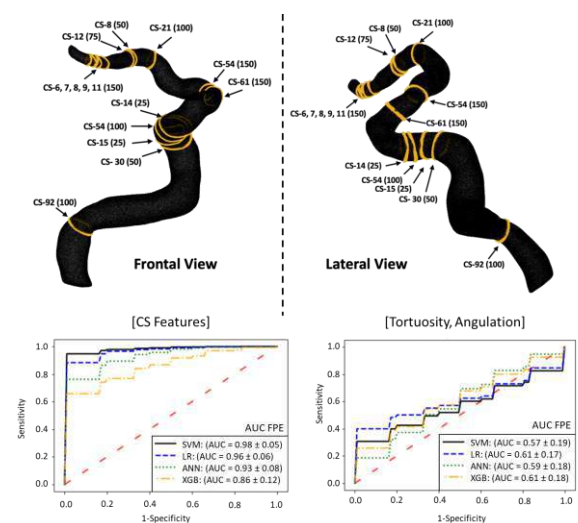


Figure 2: Models trained with cross-section features demonstrated superior performance to those trained using standard measures.
Figure adapted from Sarayi and Santo et al. SVIN, 2022.

DISCUSSION

In conclusion, computational analyses enabled us to develop and test a novel set of cross-section features that can predict FPE with high accuracy and highlighted important local changes in the thrombectomy device path. Our results not only showed that vessel cross-section features are better morphological indicators than the current standard, but also suggested that for patient-specific cross-sectional geometries, particular thrombectomy techniques are associated with greater likelihood of FPE. Anatomically-informed feature sets, such as the developed cross-sections, are clinically interpretable and may be applied in patient-specific, data-driven intervention techniques.

ACKNOWLEDGEMENTS

Research was supported, in part, by the National Center for Advancing Translational Sciences of the NIH under award number UL1TR001412 to the University at Buffalo.

REFERENCES

- [1] Papanagiotou et al., *Circ Cardiovasc Interv*, 2018.
- [2] Ciurică et al., *Hypertension*, 2019.
- [3] Santo et al., *Circulation Proceedings*, 2022.

PULSE WAVE VELOCITY INCREASES WITH EXTENDING THE LENGTH OF VASCULAR STENT-GRAFTS

Ramin Shahbad (1), Anastasia Desyatova (1)

(1) Department of Biomechanics, University of Nebraska Omaha, Omaha, Nebraska, USA

INTRODUCTION

A vital characteristic of the aorta is elasticity. This feature of elastic arteries plays a pivotal role in maintaining blood pressure and blood flow at a stable rate [1]. Several studies on aortic hemodynamic properties have reported an increase in arterial stiffness (i.e., a decrease in elasticity) in patients with the aortic disease who have experienced endovascular aortic repair [2]. Multiple evidence accumulated from recent studies reveals a consistent association between stent-graft deployment and aortic stiffening in the long term [3]. Aortic stiffening is now accepted as one of the most critical self-reliant predictors of cardiovascular morbidities and mortalities. Therefore, understanding the effects of stent grafting on aortic compliance and cardiac hemodynamics may play a key role in either improving the design of current stent grafts or developing a new generation of stent-graft to protect the heart and aorta from these complications.

Stent-graft factors thought to be influencing aortic stiffness have been explored in several studies. However, there is a current paucity of studies focusing specifically on the contribution of stent-graft length in aortic stiffening. The present study aimed to address this discrepancy and investigate the effect of stent-graft length on vascular conduit stiffening by measuring the pulse wave velocity (PWV) in a mock flow loop.

METHODS

Mock flow loop setup. In this study, a custom-made mock flow loop has been built in conjunction with a pulsatile pump system to replicate human blood circulation. As shown in Figure 1, this mock loop consists of two main components: a pulsatile pump with a heart function emulator (HFE) and an afterload system based on a three-element Windkessel model. The pulsatile pump and heart function emulator serve as the left ventricle and supply pulsatile flow to the loop. The afterload system is a lumped model of the arterial system and imitates

the load on the heart. It includes a compliance chamber, a resistant valve, and a resistor that mimics the total arterial compliance, peripheral resistance, and characteristic impedance, respectively.

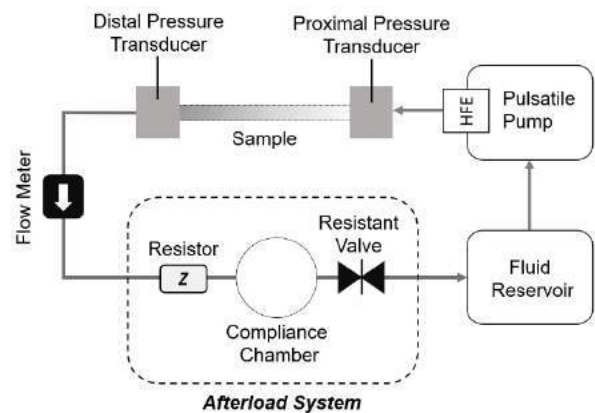


Figure 1: A schematic illustration of the developed mock loop.

Models. The human aorta was approximated as a silicone tube with tuned mechanical and geometrical properties to achieve the pulsatility of young human aortas. Four identical 320mm silicone aortas were used in this study (shore 20A). These mock vessels were connected to tee-shape connectors and placed between the pump and the afterload system. The flow and cardiac cycle rates were set at 2.5 L/min and 60 bpm, respectively, to imitate the physiological condition of the abdominal aorta. To perform all experiments at the same hemodynamics conditions, proximal pressure at baseline conditions was targeted at ~120/100/80 mmHg, representing the systolic, mean, and diastolic

pressures, respectively. Pressure data were recorded at proximal and distal locations (Figure 1) using two digital pressure transducers for about 30 continuous stable pulse waves. Upon the completion of data recording for baseline condition, a 40mm long stent graft with a diameter of 20mm was deployed in the silicone aorta. These stent grafts were made by sewing a P5010 Palmaz biliary stent and a Maquet Hemashield Platinum vascular graft. The proximal and distal pressures were recorded for 30 cycles in this condition. The stent graft was then extended with a second and a third 40mm stent grafts to 80mm and 120mm lengths. Pressure data were recorded for each of these conditions as well. When the stent grafts were deployed in each step, the pressure transducers and fluid level in the compliance chamber were calibrated and adjusted as necessary to ensure that the flow and pressure conditions of the system were the same in every situation.

Pulse wave velocity measurements. Pulse wave velocity (PWV) is an arterial hemodynamics parameter that refers to blood flow velocity through the circulatory system and provides information regarding the artery's mechanical characteristics. Since PWV is positively associated with arterial stiffness, it is commonly measured and used as an indirect quantification of arterial stiffness and risk assessments [4]. Before PWV measurement, a low pass fifth-order Butterworth filter with a cutoff frequency of 5 Hz was used to smooth out the high-frequency noises associated with pressure transducers. PWV was calculated for all four samples based on pressure pulse waves and using the intersecting tangent algorithm, which is the most reliable technique among others. In this technique, the line with the steepest slope at the systolic upstroke part of the wave was intersected with the line passing through the foot of the wave, and the intersection point was chosen as the reference point. PWV was computed as the wave traveling distance (distance between pressure transducers) divided by wave travel time (time delay between the reference points) (Figure 2).

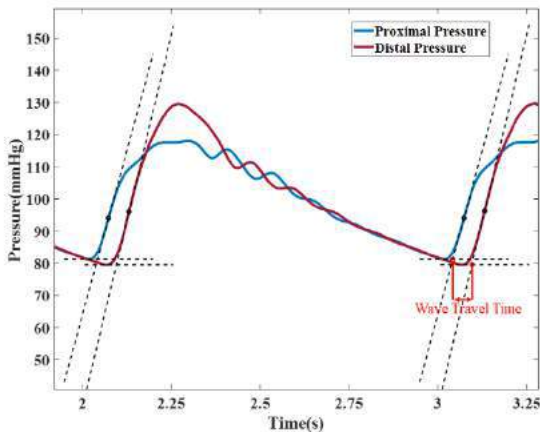


Figure 2: A pressure wave sample at two proximal (blue) and distal (red) sites and the principle of calculating wave travel time via intersecting tangent algorithm.

RESULTS

The PWV was calculated for all four conditions of each mock aorta using the intersection tangent algorithm. The PWV was obtained at $6.81 (\pm 0.41)$ m/s for aortas without stent grafts (baseline), $7.52 (\pm 0.42)$ m/s for aortas with 40mm long stent-grafts, $8.365 (\pm 0.37)$ m/s for aortas with 80mm long stent grafts and $9.98 (\pm 0.87)$ m/s for aortas with 120mm long stent grafts (Figure 3). A single-way ANOVA was conducted to compare the effect of stent graft length on PWV. Comparisons were made among baseline, 40mm, 80mm, and 120mm

stent graft conditions. There was a significant difference in PWV among the different lengths of stent grafts at the $p < 0.05$ level for the four groups $F = 23.60$ and $p = 2.54E-05$. Tukey's HSD post hoc test results revealed that in four conditions, including baseline-80mm stent graft, baseline-120mm stent graft, 40mm-120mm stent graft, and 80mm-120mm stent graft, the latter had significantly higher PWV compared to the former. There was no significant difference in PWV between the baseline-40mm stent graft and 40mm-80mm stent graft conditions.

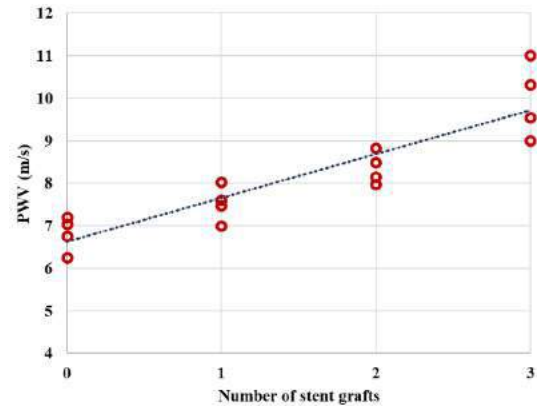


Figure 3: PWV values for different number of stent grafts.

DISCUSSION

Though several studies have revealed the responsibility of stent-graft factors in aortic stiffening, the effect of length is still unclear. The main result of the present study is that in the same pressure condition, PWV increased significantly by increasing the length of stent grafts. This result is in line with the previous experimental studies, which found higher PWV associated with deploying stent grafts [5]. This finding may be explained by the fact that PWV is a measurement method directly related to the modulus of elasticity of the aortic wall and aortic distensibility. The deformation range of the aorta in the circumferential direction decreases in the region where the stent graft is implanted. Increasing the length of the stent graft will reduce the distensibility of the aorta for a more extended length. The lower pulsatility of the aorta is associated with increased stiffness and impedance resulting in rapid propagation of forward waves, reflected waves, and higher PWV.

The main limitation of this study is that, instead of the actual human or porcine aorta, the project used mock vessel samples made from silicone rubber. The silicone rubber's mechanical behavior and compliance have been tested and shown to be in the range of human aorta tissue properties within the range of 60-69 years old. However, due to the high non-linearity in young aorta characteristics, it cannot cover young aorta tissue properties with lower stiffness than aged ones.

ACKNOWLEDGEMENTS

This work was supported by the NHLBI HL147128.

REFERENCES

- [1] Belz, G.G., *Cardiovascular Drugs and Therapy*, 1995. 9(1): p. 73-83.
- [2] Lantelme, P., et al., *J hypertension*, 2009. 27(6): p. 1268-1276.
- [3] Kadoglou, N.P., et al., *J Endovascular Therapy*, 2014. 21(6): p. 850-858.
- [4] Hermeling, E., et al., *Ultrasound in medicine & biology*, 2007. 33(5): p. 774-781.
- [5] De Beaufort, H.W., et al., *PLoS One*, 2017. 12(10): p. e0186080.

RATE EFFECTS AND MATERIAL CHARACTERIZATION OF SKIN DURING PUNCTURE

Joseph S. LeSueur (1), Frank A. Pintar (1,2)

(1) Joint Department of Biomedical Engineering, Marquette University & Medical College of Wisconsin, Milwaukee, WI, USA

(2) Department of Neurosurgery, Medical College of Wisconsin, Milwaukee, WI, USA

INTRODUCTION

As the primary mechanical barrier between the internal and external environment, skin functions to prevent puncture and penetration [1]. In military and law-enforcement environments, protective armor may reduce the likelihood of penetrating debris from blast events [2]. However, to develop effective protection, the failure thresholds of skin during penetration must be known.

The mechanical properties of skin have been thoroughly studied in indentation, suction, and tensile testing [3], but limited attention has been given to high-rate, traumatic failure of skin during puncture [4], stabbings [5], and ballistic impact [6]. Dynamic loading rates have shown to increase the stiffness response of skin in tension due to viscoelastic properties [3]. In previous puncture studies, skin simulants were used as surrogates to reduce variability but lacked representative boundary conditions of anisotropic, viscoelastic skin with natural pre-tension [4,5]. To accurately simulate the mechanical behavior of skin, hyperelastic constitutive models [1,3] and 3D digital image correlation (DIC) have been utilized for development and validation of computational models [7].

The purpose of this study was to experimentally characterize rate effects in puncture of skin and provide 3D-DIC surface strain maps for implementation and validation of computational models.

METHODS

Frozen porcine tissue was thawed at 4°C for two days. Skin samples were cut into discs of diameter 97.6 ± 6.8 mm with a smooth layer of adipose tissue ($n = 72$). A circle of diameter 25.0 ± 0.47 mm was stamped onto the center of the skin during its relaxed state. To achieve a state of natural tension determined from previous experiments, the skin was biaxially stretched with pulleys on a custom apparatus, and the circle was measured again to determine major (30.9 ± 15.3 %) and minor strain (13.4 ± 10.6 %). After testing, cutis thickness (epidermis and dermis: 2.13 ± 0.52 mm) and total sample

thickness (epidermis, dermis, and adipose: 4.55 ± 1.79 mm) were measured with digital calipers adjacent to the puncture site.

An electrohydraulic piston actuator with an attached load cell, LVDT (MTS) and a uniaxial accelerometer (DTS) provided deformation of the skin and recorded force, displacement, and acceleration at 20 kHz; acceleration was filtered with an SAE class 180 low-pass Butterworth filter. A custom tapered impactor with a 5 mm stainless steel spherical end was fixed to the load cell. With constant biaxial pre-tension, the skin was preconditioned to a displacement of 15 mm for eight trials then clamped with a custom ring clamp. Sub-failure trials were conducted to a displacement of 15 mm at 50 and 500 mm/s, allowing the sample to recover between runs. Finally, a failure trial was performed at a rate of 5, 50, 500, or 5000 mm/s.

3D digital image correlation (DIC) was performed using two high-speed cameras (NX-Air series, IDT) at sampling rates up to 4230 Hz for 13 failure runs to measure local surface strains during puncture. A black speckle pattern was randomly applied using a custom 3D-printed stamp with micro-projections to the adipose surface of the specimen. Maximum, minimum, and mean principal strains were calculated with a median spatial filter of 5 pixels (GOM Correlate Pro, Trilion).

To calculate the resistive force of skin, inertial effects were accounted for by subtracting the inertial force, derived from acceleration and load cell mass, from the total force measured by the load cell. Engineering stress and strain of the clamped skin sample were calculated from piston force and displacement measurements.

Two trials were excluded due to mechanical damage during sub-failure runs since 1) the second sub-failure run resulted in a reduction of maximum force greater than 5% of the failure force, and 2) strain energy of the second sub-failure run decreased by more than 10% from the first sub-failure run. Strain energy was calculated by computing the area under the force-displacement curve from 0 to 13 mm displacement.

Paired t-tests were performed to determine significance of loading rate for strain energy between the failure and two sub-failure runs on the

same skin sample. A generalized linear mixed model with repeated measures for pig specimen was developed to determine significant variables and predict strain energy at failure (SPSS, IBM). Utilizing a hyperelastic constitutive model, first-order Ogden coefficients were determined by curve fitting experimental stress-strain data and averaged for all trials by strain rate using Hyperfit software (Equation 1).

$$\Psi = \sum_{p=1}^N \frac{\mu_p}{\alpha_p} (\lambda_1^{\alpha_p} + \lambda_2^{\alpha_p} + \lambda_3^{\alpha_p} - 3) \quad (1)$$

where Ψ is strain energy density, λ is strain, and μ and α are constants.

RESULTS

The 500 mm/s sub-failure run resulted in significantly greater ($p < 0.001$) average strain energy (0.272 ± 0.029 J) compared to the 50 mm/s sub-failure run (0.191 ± 0.012 J). Higher loading rates between sub-failure and failure runs resulted in significantly greater strain energy at 13 mm displacement ($p < 0.001$), except for 50 mm/s sub-failure and 5 mm/s failure ($p = 0.084$). For sub-failure and failure runs at the same loading rate, two-tailed paired t-tests resulted in non-significant differences in strain energy for 50 mm/s ($p = 0.047$) and 500 mm/s ($p = 0.096$) with an alpha of 0.01. For loading at the same rate, failure trials always had greater average strain energy than sub-failure trials.

For prediction of strain energy at failure, the generalized linear mixed model resulted in significant effects ($p < 0.01$) for major tension, minor tension, cutis thickness, total sample thickness, sample mass, and failure rate. The model predicted failure strain energy values of 1.73, 1.80, 2.32, and 1.88 J for 5, 50, 500, and 5000 mm/s loading rates, respectively, with fixed average values of 32.0 %, 14.1 %, 2.1 mm, 4.6 mm, and 48.2 g for major tension, minor tension, cutis thickness, total sample thickness, and sample mass, respectively.

Average force-displacement curves were generated to show effect of loading rate (Figure 1).

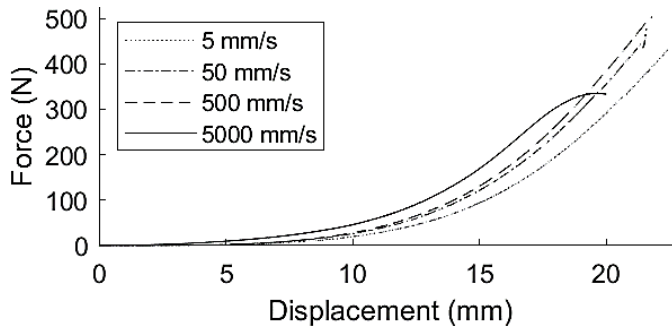


Figure 1: Force-displacement during skin puncture at varying loading rates to failure

A one-term Ogden constitutive model was used to quantify the material behavior of skin subjected to puncture with all R^2 values greater than 0.97. Ogden coefficients were averaged for loading rates of 5, 50, 500, and 5000 mm/s, which represented strain rates of 0.15, 1.5, 15, and 150 s^{-1} , respectively (Table 1).

Table 1: One-term Ogden coefficients for varying strain rate

Strain Rate	μ_1	α_1	R^2
0.15 s^{-1}	0.0095 ± 0.0049	13.04 ± 2.9	0.990 ± 0.004
1.5 s^{-1}	0.0113 ± 0.0045	12.88 ± 3.37	0.990 ± 0.006
15 s^{-1}	0.0128 ± 0.0029	13.03 ± 3.37	0.990 ± 0.004
150 s^{-1}	0.0225 ± 0.0086	10.19 ± 1.31	0.978 ± 0.008

Since 3D-DIC displacement was measured on the bottom of the specimen, maximum surface displacement (13.78 ± 2.29 mm) was compared to piston displacement minus total sample thickness (13.58 ± 2.76 mm). A paired t-test determined the displacement measurements were not significantly different ($p = 0.71$) and resulted in a root-mean-square error (RMSE) of 1.80 mm. The maximum principal strain map with directional vectors was computed for each trial (Figure 2). For the 13 failure trials, the average maximum principal strain (33.71 ± 8.30), average mean principal strain (14.60 ± 4.69), and average minimum principal strain (-12.93 ± 5.99) were computed. The average engineering strain (23.29 ± 4.55) served as an approximation for the global strain of the skin, whereas maximum principal strains were localized to the area in contact with the impactor.

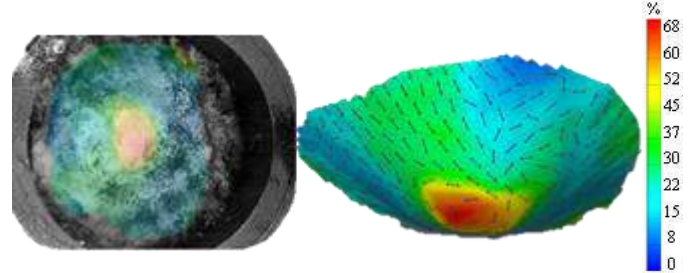


Figure 2: Representative 3D-DIC maximum principal strain map on the adipose surface of the specimen near puncture

DISCUSSION

Rate-dependency was shown in strain energy between sub-failure and failure puncture runs. Similarly, Ottenio et al observed an increase in strain energy and ultimate strength with increased strain rates up to 167 s^{-1} in tensile testing of cadaveric human skin [8]. Trotta et al reported increased elastic modulus, slightly increased ultimate strength, and decreased stretch at failure for dynamic tensile tests of porcine scalp up to strain rates of 100 s^{-1} [9]. Analogous to previous material characterizations of skin [10,11], an Ogden one-term constitutive model was sufficient with all R^2 values greater than 0.97.

Due to mass compensation from inertial effects, the 5000 mm/s force-displacement curves exhibited a more rounded failure region compared to a linear stiffness region in slower rates, which may have resulted in decreased ultimate strength. 3D-DIC and piston displacement measurements were not identical since the skin experienced some compression during puncture.

Rate-dependency was observed in strain energy during dynamic puncture of skin. Ogden material model coefficients and a 3D-DIC principal strain map were presented for development and validation of a computational model of skin during penetration.

ACKNOWLEDGEMENTS

This research was supported by resources at the Zablocki VA Medical Center, Milwaukee, Wisconsin. This research was funded by DEVCOM ARL Cooperative Agreement W911NF-21-2-0004.

REFERENCES

- [1] Yazdi SJM & Baqersad J, *J Biomech.* 2022;130.
- [2] Rozen N & Dudkiewicz I, *Springer*; 2011. p. 21–33.
- [3] Joodaki H & Panzer MB, *Proc Inst Mech Eng H.* 2018. p. 323–43.
- [4] Parmar K et al., *Int J Legal Med.* 2012;126:43–53.
- [5] Gilchrist MD et al., *Forensic Sci Int.* 2008;177:52–65.
- [6] Breeze J & Clasper JC, *J R Army Med Corps.* 2013. p. 265–70.
- [7] Moerman KM et al., *J Biomech.* 2009;42:1150–3.
- [8] Ottenio M et al., *J Mech Behav Biomed Mater.* 2015;41:241–50.
- [9] Trotta A & Ni Annaidh, *J Mech Behav Biomed Mater.* 2019;100.
- [10] Comley K & Fleck N, *Int J Impact Eng.* 2012;46:1–10.
- [11] Lim J et al., *Int J Impact Eng.* 2011;38:130–5.

MULTI-OMIC ANALYSIS OF RESECTED THROMBI IDENTIFIES COMPLEX TRAITS ASSOCIATED WITH ISCHEMIC STROKE ETIOLOGY

Briana A. Santo (1,2), Kerry E. Poppenberg (1,3), Andre Monteiro (2,3), Adnan H. Siddiqui (2,3), Vincent M. Tutino (1,2,3)

- (1) Canon Stroke and Vascular Research Center, University at Buffalo, Buffalo, NY, United States
- (2) Department of Pathology and Anatomical Sciences, Jacobs School of Medicine and Biomedical Sciences, University at Buffalo, Buffalo, NY, United States
- (3) Department of Neurosurgery, Jacobs School of Medicine and Biomedical Sciences, University at Buffalo, Buffalo, NY, United States

INTRODUCTION

The determination of stroke etiology, which is mainly defined by the Trial of Org 10172 in Acute Stroke Treatment (TOAST) score, is critical for preventing secondary strokes, which have a recurrence rate of 11% and 26% at 1 and 5 years, respectively. Typically, secondary stroke prevention relies on mitigating the underlying cause of clot generation. For example, strokes of cardioembolic (CE) origin are treated with anticoagulation, while large artery atherosclerotic (LAA) strokes undergo revascularization surgery, and lacunar strokes can be treated with lifestyle changes and antiplatelet therapy. Unfortunately, 30-40% of all cases remain cryptogenic [1]. The increased use of mechanical thrombectomy has enabled wide-spread investigation of resected clots, and opened the door to the promise of new methods for diagnosing stroke etiology through biological analysis of the retrieved tissue. To date, many histological studies have found that clot percent composition of fibrin/platelet (FP), red blood cell (RBC), and white blood cell (WBC) components are associated with etiology [2], and thus may be biomarkers of stroke subtype. However, this body of work has been plagued with conflicting findings [3], and reports of no histologic association with etiology.

We believe that additional information is likely needed for stroke diagnosis from analysis of retrieved clots. This led us to hypothesize that the complex molecular biology and cellular architecture of the clot, rather than mere percent composition, may provide important biologic insights into stroke etiology. To this end we have begun to explore both the molecular biology and histological structure and makeup of ischemic stroke blood clots. Recently we have performed next generation RNA sequencing and gene expression analysis on clot RNA to identify expression differences between each TOAST classes and determine expression patterns that are characteristic of each etiology. Concurrently, we have developed state-of-the-art computational histopathology pipelines to quantify spatial distribution of clot components and their relation to one another. In particular, a validated

nucleotyping pipeline was implemented to characterize white blood cell (WBC) populations in each clot.

With the goal of developing etiology-specific biomarkers, we are now investigating whether paired clot transcriptomics and H&E histologic image features can be used to identify robust WBC image-omic correlates using canonical correlate analysis (CCA).

METHODS

This study was approved by the Human Research Institutional Review Board at the University at Buffalo (STUDY00002092). All methods were carried out in accordance with the approved protocol and written informed consent was obtained for all subjects. Clot samples were collected from patients receiving MT between November 2018 and December 2022 at the Gates Vascular Institute in Buffalo, NY. Clot fragments retrieved from intracranial locations were studied if they were of sufficient size and quality for histopathology (if multiple fragments were collected, the largest one was studied). Cases were excluded if they received intraarterial tissue plasminogen activator. Stroke etiology was defined using the trial of TOAST score. A combination of clinical features and results of ancillary diagnostic studies were used to classify each clot into 5 subtypes: large artery atherosclerosis (LAA), small-vessel occlusion, cardioembolic (CE), stroke of other determined etiology (OTH), and undetermined etiology or cryptogenic (CR).

We analyzed paired H&E histology and transcriptome data from 31 clots (LAA=5; CE=18; OTH=3; CR=5). A published computational pipeline for WBC segmentation and characterization was used to quantify 46 image features (e.g., textures representative of heterochromatin-euchromatin ratio) from >100,000 WBC instances. Features were used to classify WBCs into 1 of 10 validated classes and calculate clot class frequency distributions. To test associations among image features and expression data we used SparseCCA (significance defined by Pearson's $R \geq 0.4$ and $p < 0.01$). First, we tested the strength of correlation between canonical covariates (transformed WBC image and

expression features), and found that canonical covariates (e.g., histology canonical variate [CV] 1 and transcriptome CV1) were strongly and significantly correlated ($R>0.9$, $p<0.001$). Gene ontology (GO) enrichment analysis was used to identify biological process (BP) ontologies associated with positively correlated genes for each etiology.

RESULTS

In pairwise correlation analysis between CVs and original dataset features (e.g., to identify original WBC image features captured in histology CV1) we found 3 canonical covariates that were highly enriched in LAA (CV6), CE (CV14), and OTH (CV17). In LAA, WBC Class 1 was representative of cells that were primarily leukocytes. Gene ontology enrichment analysis of positively correlated genes supported this interpretation, as it indicated significantly ($q<0.05$) greater T-cell regulatory mechanisms and cytokine production. In CE, we observed granulocyte enrichment in both the histology (WBC class 9, neutrophils and other eosin-rich granular structures) and positively correlated genes. Lastly, in OTH, we found histologic enrichment of WBC Class 3 (WBCs embedded in RBC clot regions) was highly positively correlated with genes involved in heme biosynthesis. Enriched WBC classes were also found to be significantly different among TOAST groups based on a final ANOVA analysis, supporting the potential application of the WBC image and expression feature pairs as etiology biomarkers: WBC Class 1 ($p=0.035$), WBC Class 9 ($p=0.001$), and WBC Class 3 ($p=0.047$). The image-omic correlates enriched in each etiology aligned well with the results of our prior study, with T-cells enriched in LAA, Granulocytes enriched in CE, and RBC constituents enriched in OTH.

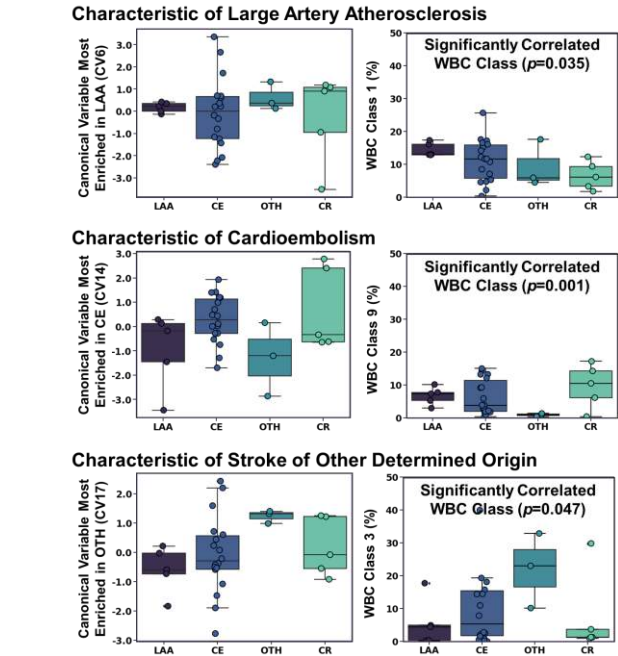


Figure 1: Enriched WBC image and expression features among TOAST classes. Top Row). Canonical covariate (CV) 6 was significantly enriched in LAA, with WBC Class 1 in histology. The frequency distribution of WBC Class 1 was significantly different among TOAST classes ($p=0.035$). Middle Row). CV14 was enriched in CE and found to represent neutrophils on histology (WBC Class 9, $p=0.001$ among TOAST groups). Bottom Row). In OTH, CV17 was significantly enriched and represented WBCs embedded in RBC-rich regions of thrombi, Class 3. Figure adapted from Tutino et al., WNS, 2022.

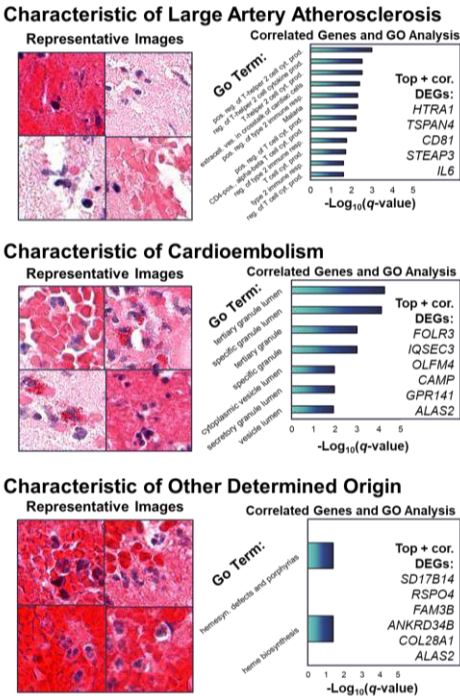


Figure 2: Enriched WBC image and expression features among TOAST classes. Top Row). For CV6, there was high correlation of histology with T-Cell GO biological processes. Middle Row). For CV14, polymorphonuclear cells corresponding to neutrophils are readily apparent among eosin-rich granular structures. These WBCs were positively correlated genes related to granule enzymes. Bottom Row). For CV17 WBC Class 3 was highly correlated with heme biosynthesis. Figure adapted from Tutino et al., WNS, 2022.

DISCUSSION

CVs were strongly and significantly correlated ($R>0.9$, $p<0.001$). Pairwise correlation of CVs and original feature sets showed the most enriched CVs in LAA (CV6, top row of Figures), CE (CV14, middle row of Figures), and OTH (CV17, bottom row of Figures). These represented distinct WBC subtypes on histology and unique GO signatures. LAA clots had enrichment of leukocytes (and greater T-cell regulation and cytokine production), while CE clots had granulocyte enrichment, and OTH clots had many WBCs embedded in RBC-rich regions with greater heme biosynthesis. Through joint analysis of clot histology and gene expression data, we engineered and validated unique structure-expression covariates that are highly correlated, biologically interpretable traits with practical application. While seldom studied, computational investigations of histomics and transcriptomics in stroke are rapidly developing. We hope our findings motivate continued research to develop biological markers of stroke etiology. Together, computational biomarkers and routine clinical data (workups and imaging) will facilitate robust identification of stroke etiology, reducing cryptogenic diagnoses and aiding secondary stroke prevention efforts.

ACKNOWLEDGEMENTS

Research was supported, in part, by the National Center for Advancing Translational Sciences of the NIH under award number UL1TR001412 to the University at Buffalo.

REFERENCES

[1] Bang et al., *Ann Neurol*, 2003
[2] Brinjikiet al., *J Neurointerv Surg*, 2017

TUNING OF THE MECHANICAL BOUNDARY CONDITIONS PARAMETERS FOR A PATIENT-SPECIFIC THORACIC AORTA MODEL

**Leonardo Geronzi (1,2), Antonio Martinez (1,2), Aline Bel-Brunon (3), Michel Rochette (2),
Marco Sensale (2), Pier Paolo Valentini (1), Marco E. Biancolini (1)**

(1) Department of Enterprise Engineering “Mario Lucertini”, University of Rome Tor Vergata, Via
del Politecnico, 1, 00133 Rome, Italy

(2) Ansys France, 69100, Villeurbanne, France

(3) INSA Lyon, LaMCoS, CNRS UMR5259, Lyon, France

INTRODUCTION

Cardiovascular patient-specific modelling aims to recreate vascular anatomies with the goal of improving diagnosis and optimizing clinical treatments [1]. In the study of pathologies such as thoracic aortic aneurysm, a patient-specific model should integrate the tissue material properties [2] and the zero-pressure state of the vessel [3] and should consider the interaction of the aorta with the surrounding structures, especially the spine and soft tissue [4]. The importance of including the aortic root motion and its role in increasing the wall stress has already been described in [5]. A first approach to calibrate the mechanical boundary conditions (BCs) presented in [4] exploiting multi-phase CT and a 3-parameter Windkessel model was presented in [6].

In this work, we describe a procedure to tune 4 parameters governing the mechanical BCs of a thoracic aorta (TA) model considering the displacement due to heartbeat at the level of the aortic annulus. The mechanical BCs we introduced consist in a set of visco-elastic components (Robin BCs) representing the support provided by the soft tissue and able to reproduce the interaction of the aorta with the spine. The model, which also involves the whole area of the Valsalva sinuses and includes the modeling of the aortic valve, accounts for the zero-pressure state. Exploiting information on the position of the aorta from a set of 2D cine-MRI sequences, we tune the parameters governing the BCs to obtain an improved correspondence between the displacement of the simulated model and that derived from the images.

METHODS

The procedure, here applied for a single TA geometry, consists of two steps: in the first one, we manually segmented a MRI-Angiography dataset to obtain the anatomies (Fig. 1a) and 11 cine-MRI sequences to extract the aortic boundaries during 25 different cardiac phases. We performed then a rigid-wall computational fluid-dynamic (CFD) analysis coupled with a 0D closed loop, whose lumped parameters were calibrated following what reported in [7, 8], to extract the pressure field

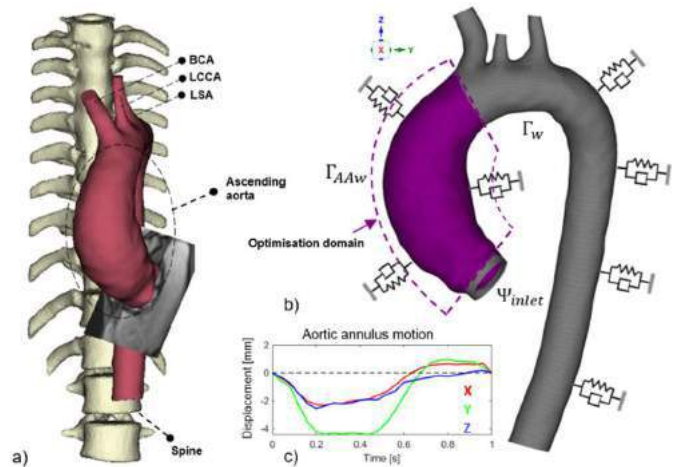


Figure 1: a) The segmented aorta and spine. b) The structural model. c) The displacements imposed at the inlet boundary.

at the aortic wall $P_w(t)$. Besides, we created the structural model (Fig. 1b) and from cine-MRI tracked the motion of the annulus deriving its displacement in space: $Dx(t)$, $Dy(t)$ and $Dz(t)$ (Fig. 1c). Concerning the mechanical BCs, we connected each i -node of the wall Γ_w to three dampers and springs, each for a j -direction of the space. The stiffness of each spring was defined as:

$$K_{ji} = K_{ST} + W_{di} W_j K_{SPINE} \quad (1)$$

where K_{ST} was the first sought parameter representing the stiffness of the soft tissue, W_j the weight to be optimised for each j -direction of the space, $K_{SPINE} = 10^6$ Pa/m the stiffness linking the aorta to the spine [9] and W_{di} the scaling factor to represent the distance to the vertebrae:

$$W_{di} = 1 - \alpha \frac{d_i}{d_{\max}} \quad (2)$$

with $\alpha = 0.95$, \mathbf{d} the vector containing the minimum Euclidean distance of each node to the spine and $d_{\max} = \max(\mathbf{d}) = 142$ mm.

In the second step, with the aim of minimising a cost function described below, we performed an iterative procedure, computing each time a new zero-pressure model and running a structural simulation with $P_w(t)$ applied at Γ_w and $D_x(t)$, $D_y(t)$ and $D_z(t)$ at the inlet boundary Ψ_{inlet} . Starting with $\mathbf{p}^0 = [W_x^0, W_y^0, W_z^0, K_{ST}] = [1, 1, 1, 10^5 \text{ Pa/m}]$ and using Levenberg-Marquardt, we minimised the following loss function:

$$f(\mathbf{p}) = \sqrt{\sum_{\varphi} \sum_{l=1}^m \sum_{k=1}^{n_l} |d_{l,k}^{\varphi}(\mathbf{p})|^2} \quad (3)$$

where $\varphi = 25$ was the number of cine-MRI frames from which we retrieved the motion of the ascending aorta wall Γ_{AAW} , $m=11$ the number of splines from the full 2D dataset, n_l the number of points for the l -spline and $d_{l,k}^{\varphi}(\mathbf{p})$ the nearest neighbour distance of each k -point belonging to the l -spline and all the points of the spline derived from the intersection between the cine-MRI plane and the deformed aortic model. Four additional initial guesses were selected to verify each time the minimum reached.

RESULTS

The calculation took 32 hours in total. The loss function $f(\mathbf{p})$ was reduced from 0.343 m to 0.227 m (34%) after 19 iterations. The value of the parameters at the end of the calibration was $\bar{\mathbf{p}} = [0.6, 0.02, 0.04, 1.5 \times 10^4 \text{ Pa/m}]$. The values of the cost function, the maximum and mean neighbour distance, normalised with the corresponding value at the first iteration, are shown in Fig. 2. In addition, the same figure shows the baseline model related to the first iteration and the final calibrated model with the splines used to compute the distance at the systolic peak. The relative displacement of the computational grid in systole compared to the configuration in late diastole is shown in Fig. 3 for the model simulated with the initial parameters from \mathbf{p}^0 and the calibrated model.

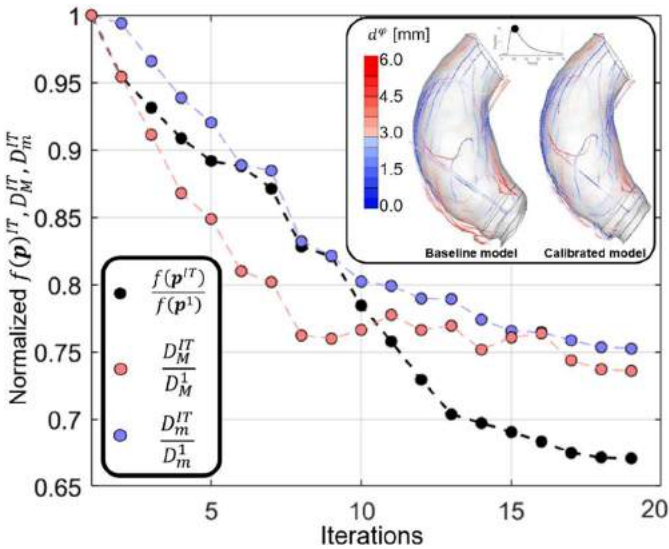


Figure 2: Normalized loss function $f(\mathbf{p}^{IT})$, maximum (D_M^{IT}) and mean (D_m^{IT}) neighbour distance for each of the iterations of the Levenberg-Marquardt optimisation. The top right-hand box shows the splines with which the calibration is performed.

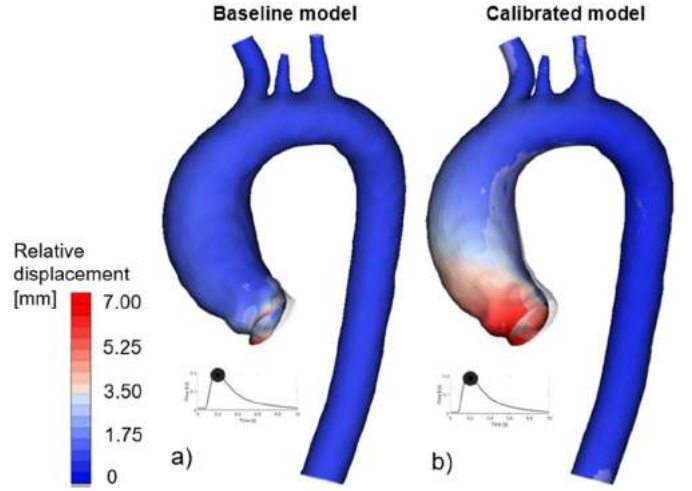


Figure 3: Relative systolic-diastolic displacement contours for a) the model with non-calibrated parameters and b) the tuned model.

DISCUSSION

In this work, we proposed a method to tune 4 parameters governing the mechanical boundary conditions of a thoracic aorta model. As shown in Fig. 2, the loss function (3) could not be reduced to 0 because the full set of mechanical BCs was controlled by only 4 variables. Fig. 3 shows how the baseline model was strongly constrained and the motion applied at the level of the annulus was propagated exclusively to the nearest elements up to the central part of the Valsalva sinuses. For the calibrated case, on the other hand, it was the entire ascending aorta that absorbed the impulse caused by the heart muscle. Although cine-MRI was here used, this workflow can be repeated with every image set that considers dynamic acquisitions during the cardiac cycle, such as multiphase-CT or even 4D-Flow MRI. To ensure the robustness of this procedure, it should certainly be extended to more patients. Combining mechanical BCs parameters with shape parameters derived from statistical shape modelling (SSM) and building reduced-order models (ROMs) could be one of the keys to exploit patient-specific models in clinical practice.

ACKNOWLEDGEMENTS

The research has received funding from the European Union's Horizon 2020 research and innovation programme under the Marie Skłodowska-Curie grant agreement No 859836, MeDiTATe: "The Medical Digital Twin for Aneurysm Prevention and Treatment".

REFERENCES

- [1] Neal, M. L. et al., *Brief Bioinform*, 11(1), 111-126, 2010.
- [2] Silver, F. et al., *Crit Rev Biomed Eng*, 17(4), 323-358, 1989.
- [3] Liu S. et al, *J Biomech Eng*, 110(1), 82-84, 1988.
- [4] Taylor C.A. and Figueroa C., *Annu Rev Biomed Eng*, 11, 109-134, 2009.
- [5] Beller, C.J. et al., *Circulation*, 109(6), 763-769, 2004
- [6] Moireau P. et al., *Biomech. Model Mechanobiol*, 12(3), 475-496, 2013.
- [7] Tomasi, J. et al., *Med Hypotheses*, 135, 109477, 2020.
- [8] Korakianitis T. and Shi Y., *Med Eng Phys*, 28(7), 613-628, 2006.
- [9] Gindre et al., *IEEE. Trans Biomed Eng*, 64(5), 1057-1066.

QUANTIFYING ALIGNMENT IN ENGINEERED TISSUE CONSTRUCTS USING RAMAN SPECTROSCOPY AND COMPUTATIONAL MODELING

Maedeh Lotfi (1), Hui Zhou (1), Janny Piñeiro Llanes (2), Ghatu Subhash (1), Chelsey S. Simmons (1,2), Malisa Sarntinoranont (1,2)

- (1) Department of Mechanical and Aerospace Engineering, Herbert Wertheim College of Engineering, University of Florida, Gainesville, Florida, United States
(2) J. Crayton Pruitt Family Department of Biomedical Engineering, Herbert Wertheim College of Engineering, University of Florida, Gainesville, Florida, United States

INTRODUCTION

Tissue engineering is recognized as a translational approach to replacing damaged tissue or whole organs. However, it faces challenges preventing the successful repair or replacement of biomechanically functioning tissues. Low mechanical integrity is a crucial problem faced during the clinical translation of these constructs¹. Understanding the relationship between changes in microscopic structure and macroscopic mechanical response provides insight into biological function, which can help in the design of new biomaterials and enable monitoring of changes during biomaterial fabrication and deformation^{2,3}. Within these constructs, collagen fiber and cell compaction often produce local mechanical stress, which influences the structure and mechanical behavior of the engineered tissues⁴. Since the orientation of cells and collagen fibers is essential for proper tissue functioning, several studies have focused on estimating the alignment of cells and collagen fibers. However, some of these techniques are limited in their widespread application since they are incompatible with hydrated tissue or are destructive.

To overcome the limitations of previous techniques, our research group is using a polarized Raman spectroscopy (PRS) method, which provides advantages such as label-free preparation, high molecular specificity, non-contact, non-invasive, real-time imaging of cell-laden scaffolds under normal physiological conditions, and good compatibility with hydrated tissue^{5,6}. Raman spectroscopy is a spectroscopic technique that is typically used to determine the vibration modes of molecules⁷. Since Raman spectra can be collected for a small volume of samples (less than 1 μm in diameter), are insensitive to aqueous absorption bands, and can be used on live cells, it is suitable for testing cells and proteins. In addition to identifying chemical composition, polarization effects on Raman spectra can provide information on the orientation of molecules in anisotropic materials and single crystals. In this study, we are using noninvasive polarized Raman spectroscopy combined with computational modeling to quantify the

alignment in engineered tissue constructs. Such tools can be used to non-destructively evaluate whether engineered tissue constructs approach the same structure as native tissues.

METHODS

Engineered tissue constructs: 1-mm thick polymer molds were fabricated using polydimethylsiloxane (PDMS). Selective functionalization of the surface of two anchorage wings increased the adhesion strength between the hydrogel and the PDMS mold. A microtissue precursor solution was prepared by mixing high-concentration rat tail collagen type-I (Corning) with 0.2% acetic acid (Glacial, Fisher Scientific), Matrigel (Corning), 10x DMEM (Sigma), HEPES (Gibco) solution, and phosphate buffered saline (PBS). The precursor solution contained a 4 mg/ml final concentration of Collagen I and 10% v/v of Matrigel. The precursor solution for the two parts (wings and central part) was separated. C2C12 myoblasts were gently admixed to the precursor solution for the central part until it reached a density of 5.0×10^5 cells/ml. Then, to ensure an equivalent Collagen I concentration of 4 mg/ml in the central part and wings, the volume of the wing's precursor solution was adjusted using PBS according to the volume of myoblasts added (Figure 1).

Polarized Raman spectroscopy: Two regions, 10 μm each, were scanned at a step size of 1 μm (11 points) at each location of interest (middle center, middle edge, and corner edge). For each point, a 10 s acquisition time and 12 accumulations were chosen. Measurements were performed for the sample submerged in PBS at room temperature, neglecting thermal effects. The PRS measurements were conducted with a linear polarizer. To capture the anisotropy, the tissue sample was rotated from 0° to 180° in 30° increments to measure the different polarization angles between the laser polarization direction and the sample alignment axis. After measuring the spectra of the tissue sample, the PBS background was subtracted in software. A Savitzky-Golay finite impulse response (FIR) smoothing filter to smooth the spectra.

Next, Standard Normal Variate (SNV) was performed to normalize the spectra. Principal component analysis (PCA) was used to provide Primary Principal Component (PC1) for the tissue sample using the loading coefficient for every normalized intensity at a given wavenumber⁶. The PCA converted the spectra of different polarized angles into a single score (PC1) as a function of polarized angles. By fitting a sine function to this output and comparing the Amplitude Alignment Metric (sine amplitude), the protein fiber alignment variation in one tissue sample in different regions was determined.

Computational modeling: A solid structure similar to the experimental mold was first modeled in Abaqus, including the wings (collagen gel without cells) and the center part (collagen gel including cells). A compressible, Neo-Hookean model was applied as the constitutive model. Also, uniform shrinkage was only applied to the center part to capture the deformation of the tissue structure due to cell contraction. A geometrical treatment was used to visualize the state of local deformation in the neighborhood of a point by mapping to the material points a quadratic surface ellipsoid (initially a circle). The decomposition of the calculated deformation gradient to stretch tensor (chosen as the square root of right Cauchy-Green stretch tensor) and rotation tensor was used to find the deformed ellipse at each point. The ratio of the maximum and minimum axes of the deformed ellipse (alignment factor) was used to show the ratio of fiber alignment in different locations.

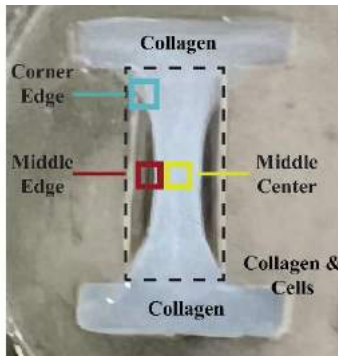


Figure 1. Engineered tissue construct constructed of collagen. Cells (C2C12) are only within the central part. Three select locations (middle center, middle edge, and corner edge) were measured.

RESULTS

Tissue constructs deformed due to cell contraction (as shown in Figure 1), resulting in changes in fiber alignment as confirmed by microscopy. The PRS method was used to find the variation of alignment in different locations after 12 days. Figure 2 shows the alignment metric that was calculated by fitting the sine function $y = y_0 + A \sin\left(\frac{\pi(x-45^\circ)}{90^\circ}\right)$ at adjusted PC1 Score at each point at each select location. The corner edge was found to have a higher level of alignment. Computational models also predict higher alignment in corner regions as predicted by alignment factor. Dominant directions of fiber alignment predicted by the model also matched with image analysis of stained fibers.

DISCUSSION

We have implemented an experimental, analytical, and computational procedure to quantify the variation of alignment in engineered tissue constructs. By utilizing PCA of PRS spectra, we were able to identify peaks in the spectra that corresponded to the alignment of biological proteins. Comparing the amplitude of sine fit for select

locations shows that we have maximum alignment at the corner edge of our samples. In addition, the alignment factor of the computational model was useful for further predicting the spatial variation of alignment within the construct.

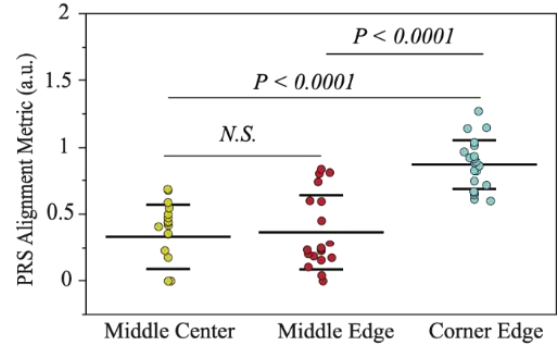


Figure 2. Alignment within test samples as determined by PRS. The Amplitude Alignment Metric was calculated by amplitude analysis of the PC1 Score at select locations.

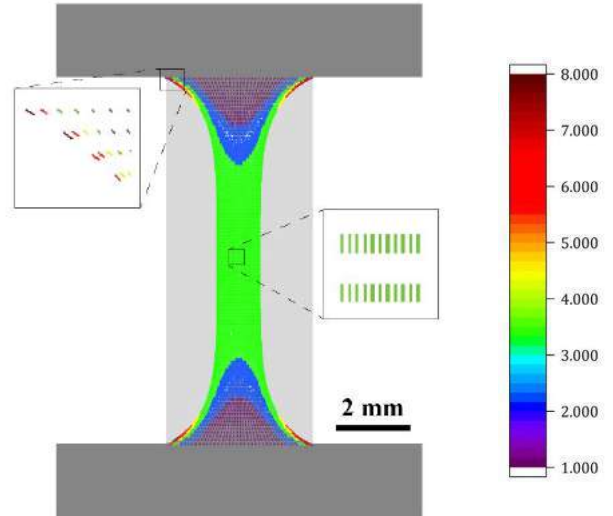


Figure 3. Alignment factor and directions calculated from the FEA model.

ACKNOWLEDGEMENTS

This work was supported by NSF CMMI 1762791.

REFERENCES

- (1) Isenberg, B. C., et al. *Circ Res* 98, 25–35 (2006).
- (2) Rehfeldt, F., et al. *Adv. Drug Delivery Rev.* 59, 1329–1339 (2007).
- (3) Samir, M. & Joerg, L. *Nat Mater* 8, 15–237 (2009).
- (4) Sander, E. A., et al. *Ann Biomedical Engineering* 39, 714–729 (2011).
- (5) Zhou, H., et al. *Biomacromolecules* 21, 3485–3497 (2020).
- (6) Zhou, H., et al. *Acta Biomaterialia* 136, 363–374 (2021).
- (7) Gardiner, D. J., et al. *Springer Berlin Heidelberg* (1989).

BENDABLE OSTEOCHONDRAL ALLOGRAFTS FOR IMPROVED CONGRUENCE: COMPARISON OF COMPUTATIONAL AND CADAVERIC MODELS

Katherine A. Spack (1), Courtney A. Petersen (2), Peter T. Shyu (1), Edward Guo (1),
James T. Cook (3), Melvin P. Rosenwasser (4), Clark T. Hung (1), Gerard A. Ateshian (1,2)

- (1) Department of Biomedical Engineering, Columbia University, New York, NY, United States
- (2) Department of Mechanical Engineering, Columbia University, New York, NY, United States
- (3) Department of Orthopaedic Surgery, University of Missouri, Columbia, MO, United States
- (4) Department of Orthopedic Surgery, Columbia University, New York, NY, United States

INTRODUCTION

Post-traumatic osteoarthritis (PTOA), a subclassification of osteoarthritis (OA), results after a major impact or injury to the joint, such as dislocations or ligament tears. Significant clinical interventions for PTOA remain elusive. Patients with a prior history of joint injury present with OA on average more than ten years younger than OA patients without a history of joint injury¹. Because total joint replacements have limited *in-vivo* lifespans, these younger patients make poor candidates for this current gold-standard treatment. Osteochondral allografts (OCAs) provide a biologic alternative for the treatment of large cartilage defects, and may provide better long-term results for younger OA patients. While plug and shell style OCAs have so far shown promising clinical results, particularly in the knee^{2,3,4}, the challenges of size and curvature-matching between donor articular cartilage and recipient native joint anatomy currently limit their use.

Previously, our lab proposed creating bendable osteochondral allografts (BOCAs) to increase joint congruence between donor and recipient by machining grooves through the depth of the bone to the tidemark, leaving a flexible layer of articular cartilage.⁵ These BOCAs may be especially advantageous in joints such as the patellofemoral joint. Chondral lesions in the patellofemoral joint are present in >33% of patients undergoing knee arthroscopy, and these defects are considered more difficult to manage in clinical settings due to patellar malalignment in the femoral groove, lateral tilt, and attachment to the patellar tendon. Studies investigating the feasibility of using BOCAs to restore joint congruence in the patellofemoral joint (PFJ) have included computational⁵ and cadaveric analysis. Our prior finite element analyses found that patellofemoral contact in the knee with either non-grooved patellar OCAs or patellar BOCAs was maintained at a level comparable to that assessed in the native joint⁵. The encouraging outcomes of the finite element study motivated further cadaveric investigation of BOCAs in order to validate the

computational results in a more physiologically representative environment and over a greater range of flexion.

In the present study, we aimed to validate these prior computational results against our recent cadaveric experiments. In both computational and cadaveric studies, we found that BOCAs in the patellofemoral joint produce contact values equivalent to those observed in the native joint.

METHODS

Computational Analysis: Simplified finite element models of three native PFJs and 12 allograft PFJ models were employed in the finite element analyses⁶. Knee models included femur, tibia, patella, articular cartilage, patella tendon, and quadriceps muscles⁶. Active contractile forces of 178 N, 89 N, and 267 N were prescribed to represent the vastus lateralis, vastus medialis obliquus, and combined rectus femoris and vastus medialis longus, respectively⁷. To ensure numerical convergence despite the exclusion of some stabilizing capsular tissues in the PFJ, knees were articulated from 40 to 70 degrees of flexion⁸. PFJ contact area was compared between knees with either the native patella, non-bendable OCA, BOCA bent at 60 degrees flexion and fixed in that configuration through the flexion cycle, OCA shifted distally by 6 mm (SOCA), and 6 mm shifted BOCA (SBOCAs)⁶.

Cadaveric Analysis: Five fresh-frozen human cadaver knee joints obtained from the Anatomy Gift Registry were dissected to expose and separate the major muscle groups and mounted on a custom-built kinematic loading rig designed to support the knee at 15-degree increments of flexion from 15 to 90 degrees. Pressure-sensitive paper (fujifilm.com) was positioned in the PFJ space, tensile loading forces of 189 N, 44.5 N, and 133.5 N were placed on the vastus lateralis, vastus medialis obliquus, and combined rectus femoris, vastus intermedius and vastus medialis longus, respectively⁷. Additionally, to represent the contribution of the hamstring muscles, 55.5 N, 55.5 N, and 22.5 N were applied to the biceps femoris, semimembranosus, and combined

sartorius, gracilis, and semitendinosus. A further 44.5 N was loaded via the iliotibial band. These loads were applied to their respective tendons for 60 seconds at each flexion angle. Five additional cadaveric patellae were used to create non-bending OCAs by first milling a uniform planar surface on the anterior side of each patella resulting in an allograft bone depth of 12 mm. Non-bending OCAs replaced the native patellae and contact area measurements were taken using the same loading regimen. A 6 mm distal shift of the OCA (SOCA) was implemented to match the computational study, and the knee was loaded again. Finally, this loading regimen was repeated using BOCA or shifted BOCA (SBOCA), which were created from the OCA patellae by machining a set of two proximal-distal 2 mm-wide grooves through the depth of the subchondral bone. Pressure-sensitive film was used to measure contact area at each loading angle⁹. Contact measurement comparisons were calculated using the *stats* package for R Statistical Software (v4.2.2, R Core Team 2022) and the *Estimated Marginal Means* package (Length, 2022). Plots were generated using the *ggplot2* package (Wickham, 2016).

RESULTS

Statistical analyses of both the computational and cadaveric studies yielded very similar trends in the data. In both studies, the *in-silico* and *ex-vivo* results indicated that none of the treatment groups (OCA, BOCA, S-OCA, S-BOCA), showed a statistically significant difference between the respective group's average contact throughout all angles of flexion compared to the native PFJ contact area ($p > 0.05$, Figure 1). Although treatment groups did not show an overall statistically significant difference in contact area relative to the native group, there were observable differences in measured contact areas between the different treatment groups at smaller angles of flexion (Figure 2), with the most significant differences seen between the OCA and SBOCA groups. The differences observed from the cadaveric study were more modest than the results seen in the *in-silico* models of the treatment groups, as computational models of patellofemoral contact generally resulted in greater measured contact areas and smaller in-group standard deviation of contact measurements.

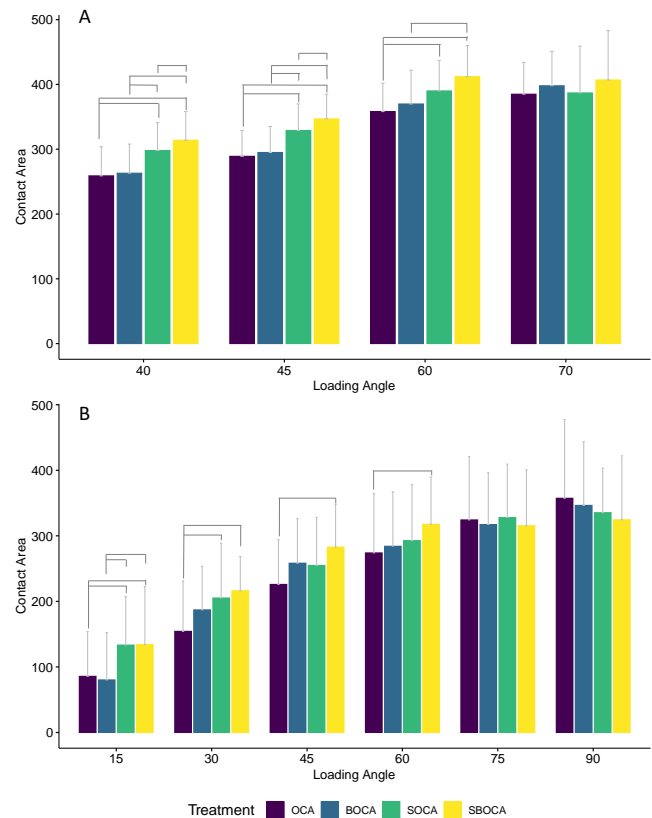


Figure 1: Measured contact areas by flexion angle for (A) computational models and (B) cadaveric models. Bars show groups for which there is a significant difference ($p < 0.05$)

computational model represented twice the load applied to the cadaveric knee models, which may account for the greater measured joint contact area *in silico*.

While the results of the cadaveric analysis of surface contact area and the computational results show similar trends, it is notable that the results from the cadaveric joints show a much higher average standard deviation in the contact area. The joint measurements from cadaveric knees likely had greater variability due to the fact that more human knee joints from a wider range of donor heights and weights were used, as donor cadaveric total knees and patellae were not initially screened for size. In summary, the cadaveric results substantially support the predictions of the computational models of bendable osteochondral allografts, showing that BOCA can match the joint contact area of native patellae.

ACKNOWLEDGEMENTS

This study was supported with funds from the United States Department of Defense (W81XWH-18-1-0361/PR171360). We thank Thomas Gardner (Columbia University) for his assistance in the cadaveric study.

REFERENCES

- [1] Gelber A. et al., *Annals of Internal Medicine* 2000 [2] Cook, J. et al *Orthop J Sports Med* 2021 [3] Chahla, J. et al *Clinical Sports Medicine* 2019 [4] Familiari, F. et al., *Am J Sports Med* 2018 [5] Rosenwasser, M. et al., US Patent, 2019 [6] Petersen, C. et al., *J Biomech.* 2022 [7] Kwak, D. et al., *J orthopedic* [8] Jones, B. et al. *J Knee Surg.* 2016 [9] Schindelin, J. et al. *Nat Methods.* 2012

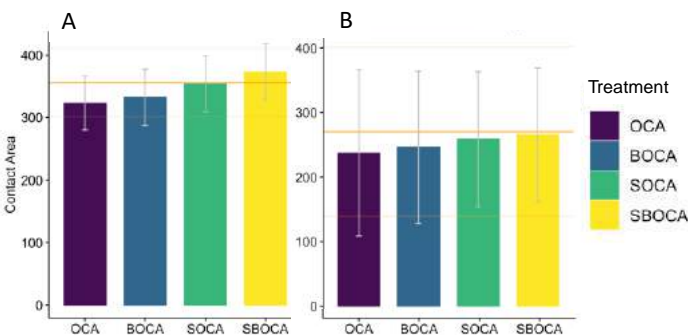


Figure 2: Overall averages of contact values across all angles of flexion for computational knee models (left) and cadaveric knee models (right). Orange bars represent average \pm the standard deviation of native knee average contact.

DISCUSSION

Significant differences in applied loads and range of loading exist between the computational and cadaveric models due to the limitations of each model. The computational model could not load across the full 15-to-90-degree range of flexion due to the inability of the model to converge at low angles of flexion without additional soft tissue support. Moreover, the simulated load of the quadriceps muscle group in the

CD44 MECHANOSIGNALING MAY REGULATE DRUG RESISTANCE IN OVARIAN CANCER

Maranda E. Kramer (1), Allison Criswell (2), Mary Kathryn Sewell-Loftin (1,3)

- (1) Biomedical Engineering, University of Alabama at Birmingham, Birmingham, Alabama, USA
(2) Biomedical Sciences, University of Alabama at Birmingham, Birmingham, Alabama, USA
(3) O'Neal Comprehensive Cancer Center, Heersink School of Medicine, University of Alabama at Birmingham, Birmingham, Alabama, USA

INTRODUCTION

Ovarian cancer is the 5th most common and the deadliest gynecologic cancer. Despite its five-year survival rate being less than 50%, little is understood about the role of biomechanics in the tumor microenvironment (TME) on the progression of ovarian cancer [1]. The CD44 receptor is found on the surface of ovarian cancer cells and is associated with increased invasive properties and maintenance of stemness in ovarian cancer cells. CD44 regulates these processes through signaling pathways associated with cancer proliferation, migration, and drug resistance including the Ras-MAPK pathway [2]. Hyaluronic acid (HA), a ligand of CD44, is prevalent in the ovarian TME and required for metastatic invasion [3]. Furthermore, previous studies have shown that an increase in HA in the ovarian TME is associated with a worse prognosis [4]. In the clinic, ovarian cancer is commonly initially treated with chemotherapy drugs including paclitaxel; recurrent disease can occur when a patient develops a decrease in sensitivity to the drug, and this may be regulated by mechanotransductive factors in the MAPK pathway. We hypothesize that mechanosignaling in the HA-CD44 axis enhances ovarian cancer growth and metastasis and increases chemoresistance. The objective of this study was to evaluate the combinatorial effects of HA-CD44 signaling and mechanical strain on ovarian cancer cell response to paclitaxel in 2D and 3D environments.

METHODS

Studies utilized the non-serous, highly invasive OVCAR8 cell line for all experiments. Using shRNA, we previously generated genetically-modified OVCAR8 cells including a knockdown of CD44 (shCD44) and a scramble control (shSCR). The shCD44 knockdown cells exhibit a stable decrease of ~60% as measured by Western blot. In 2D studies, HA was introduced to the cells by coating the tissue culture plates with 1 μ M HA in HBSS overnight, before seeding the cells (PLT HA). No treatment (NT) controls were incubated with HBSS only. OVCAR8

wildtype (WT), shSCR, and shCD44 cells were seeded at 2x10⁵ cells per well in a 6 well plate on to the PLT HA plates or NT (no HA) controls. The cells were allowed to adhere to the plates for 24 hours before treatment with 5 μ M paclitaxel or vehicle (Veh) control. After 24 hours, the treatment was removed, and samples were incubated with Sytox (ThermoFisher, S11381) and DAPI stains. After 30 minutes, the cells were washed and imaged. Images were processed in FIJI to determine the relative number of dead cells normalized to total cell count.

To further explore the effects of mechanical tension on the cells, a Flexcell (FX-6000T) system was used for monolayer, uniaxial strain studies. Samples were exposed to 9% strain at 0.3Hz for 24h. Control samples utilized the same Flexcell plates but were not exposed to cyclic strain. OVCAR8 WT, shSCR, and shCD44 cells were seeded at 2x10⁵ cells per 6 well plate on Flexcell plates and were allowed to adhere overnight prior to strain exposure. To facilitate Sytox image analysis, the cells were trypsinized after strain treatment and re-plated at 1x10⁶ cells per well in a 24 well plate. The cells were allowed to adhere for 6h before treatment with 5 μ M paclitaxel or vehicle control. After 24h, the treatment was removed and Sytox analysis was completed as described previously.

For 3D studies, a microfluidic device consisting of 3 diamond-shaped tissue chambers connected in series was utilized [5]. The devices were loaded with fibrin only (F only) or fibrin embedded with HA (F+GEL HA, 9:1 ratio). OVCAR8 WT cells were loaded at 1x10⁶ cells/mL and cultured for 7 days, with fresh media added every day. Devices were then treated with 5 μ M paclitaxel or vehicle control. After 24 hours, the treatment was removed and Sytox and DAPI stains were added and allowed to diffuse overnight before imaging analysis. As cell growth in the microfluidic devices was denser than that observed in 2D studies, we analyzed total positive-area for Sytox and normalized to total DAPI area to quantify chemoresponse of the cells.

RESULTS

As expected, paclitaxel treatment increases cell death for all tested cell types with and without HA compared to Veh treated samples. However, WT cell death is decreased for PLT HA samples treated with the drug compared to the no HA (NT) group. (Figure 1). The shCD44 cells demonstrate no significant difference in cell death in NT groups but do have increased cell death in response to both PLT HA and paclitaxel (Figure 1).

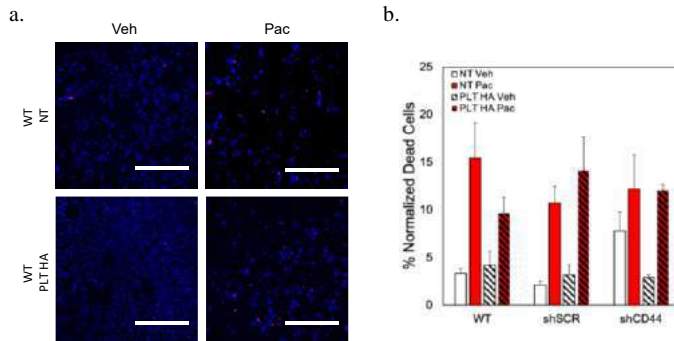


Figure 1: a. Representative images of OVCAR8 WT cells grown in the presence of no HA (NT) or PLT HA and treated with vehicle (Veh) or 5µM paclitaxel. Sytox (dead cells) are shown in red; blue is DAPI. Scale bar = 500 µm. b. Quantification of cell death for OVCAR8 cells normalized to total cell count for each sample. Data shown are averages + SEM.

Pre-treating cells with tensile strain before treatment with paclitaxel abrogated cell death in WT and shSCR samples but not shCD44 samples (Figure 2). To expand our studies to a 3D TME model, we cultured OVCAR8 WT cells in a microfluidic device to investigate how HA in the matrix altered response to paclitaxel. In Fibrin only samples, paclitaxel treatment caused a significant increase in cell death; however this was not observed in F+GEL HA samples (Figure 3).

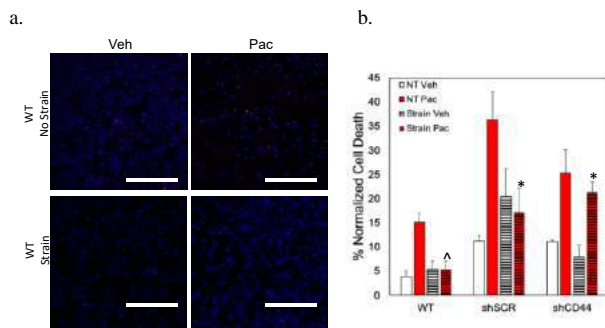


Figure 2: a. Representative images of OVCAR8 WT cells pretreated with strain via the Flexcell for 24h before treatment with vehicle or 5µM paclitaxel. Sytox (dead cells) are shown in red; blue is DAPI. Scale bar = 500 µm. b. Quantification of cell death for OVCAR8 cells normalized to total cell count for each sample. Data shown are averages + SEM; NT = no strained controls. N=3; ^ p > 0.05 versus WT NT Pac. * p < 0.05 versus shSCR NT Pac.

DISCUSSION

The results show that OVCAR8 cells expressing CD44 (WT and shSCR) can exhibit chemoresistance when cultured in the presence of HA before drug treatment paclitaxel in both 2D and 3D environments. Alternatively, OVCAR8 cells with CD44 knockdown (shCD44) do not exhibit the same chemoresistance shown in WT or shSCR cells. Interestingly, the absence of HA in these experiments may indicate that CD44 can be mechanically-activated without HA ligand-induced signaling. This suggests that there is a mechanotransduction phenomenon occurring through CD44 that could be affecting the drug resistance and potentially altering ovarian cancer disease progression.

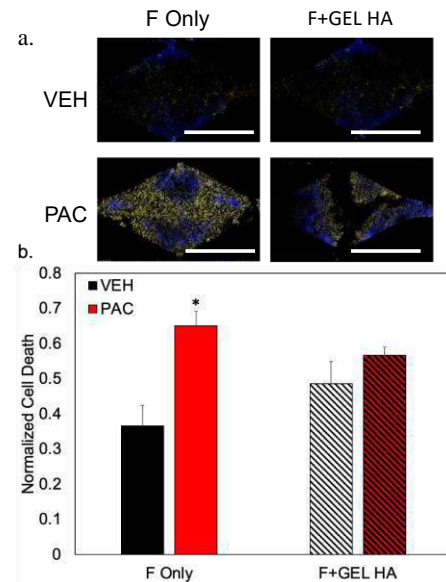


Figure 3: a. Representative images of OVCAR8 WT cells grown in F or F+GEL HA in microtissue TME models and treated with vehicle or 5µM paclitaxel. Sytox is shown in yellow; DAPI shown in blue. Scale bar = 500 µm. b. Quantified showing area of dead cells normalized to total cell area. N = 3; * p > 0.05 versus F VEH.

Future directions for this project incorporating HA into Flexcell studies to investigate crosstalk between HA-CD44 signaling and mechanical stimulation on OVCAR8 chemoresistance behaviors. We also plan to perform proliferation and migration studies in microfluidic models to determine the role of mechanosignaling via HA/CD44 in on these behaviors. These proof-of-concept studies help explain the role HA and strain plays in mechanically stimulating CD44. Ultimately, this project will help elucidate proliferation, metastasis, and drug resistance observed in ovarian cancer and open the doors for researching new diagnostics and therapeutics.

ACKNOWLEDGEMENTS

The Authors would like to acknowledge funding for the project. T32EB023872-04 (M.E.K.), R00-CA2302022 (M.K.S.L.), IMPACT Award, O'Neal Comprehensive Cancer Center (M.K.S.L.), Fine Family Grant (M.K.S.L.).

REFERENCES

- [1] Momenimovahed, Z et al., *Int J Women's Health*, 11:287-299, 2019
- [2] Price, Z et al., *Cancers*, 10(12):482, 2018
- [3] Thapa, R et al., *Stem Cells Int*, 2016
- [4] Ween, M et al., *Int J Mol Sci*, 12(2):1009-1029, 2011
- [5] Moya et al. *Tissue Eng. Part C*, 12(9): 730-737, 2013.

MECHANICAL WEAKENING PRECEDES CARTILAGE LOSS DURING OSTEOARTHRITIS PROGRESSION ACROSS THE HUMAN TRAPEZIUM

Brendan D. Stoeckl (1,2,3), Kendall M. Masada (1,3), Lorie G. Laforest (1), Michael W. Hast (1), David R. Steinberg (1,3), Robert L. Mauck (1,2,3)

- (1) Department of Orthopaedic Surgery, University of Pennsylvania, Philadelphia, PA, USA
(2) Department of Bioengineering, University of Pennsylvania, Philadelphia, PA, USA
(3) Translational Musculoskeletal Research Center, Corporal Michael J. Crescenz VA Medical Center, Philadelphia, PA, USA

INTRODUCTION

Trapeziometacarpal (TMC) osteoarthritis (OA) is one of the most common conditions affecting middle and older aged adults¹. Given that the opposable thumb is central to activities of daily living, loss of function has a significant impact on quality of life. Patients with TMC OA are initially managed with activity modification, non-steroidal anti-inflammatory drugs, splinting, and occasionally corticosteroid injections². These conservative treatments often fail in the long term, and many patients will eventually require surgical intervention. Despite the prevalence of this disease, and the paucity of effective treatments, diagnosis largely relies on patient reported outcomes.² However, analysis of radiographs, the gold standard for OA diagnosis, shows little correlation to pain or functional deficits.^{3,4} In this study we sought to close gaps in knowledge related to the initiation and progression of TMC OA by evaluating the morphology and gross appearance, wear patterns, mechanical properties, subchondral bone morphology, and histological characteristics of the tissue across a spectrum of disease severity.

METHODS

Thirty-two human hands were acquired from fresh frozen cadaveric donors with approval from the University of Pennsylvania committee for cadaveric testing. Fluoroscopic images were recorded for each specimen in five anatomic views (posterior-anterior, lateral, oblique, stressed oblique, and Robert view). A board-certified hand surgeon used these images to assign a semiquantitative modified Eaton OA grade³ to each sample, in a blinded manner. Next, the trapezia were isolated and stained with India Ink to assess areas of cartilage wear⁵. Indentation creep testing was then performed on the cartilage at nine anatomic locations from dorsal to volar and from radial to ulnar, and the creep displacement curve was fit to a Hertzian biphasic model in order to compute the compressive and tensile moduli and tissue permeability.⁶ Locations where the cartilage was completely worn away were

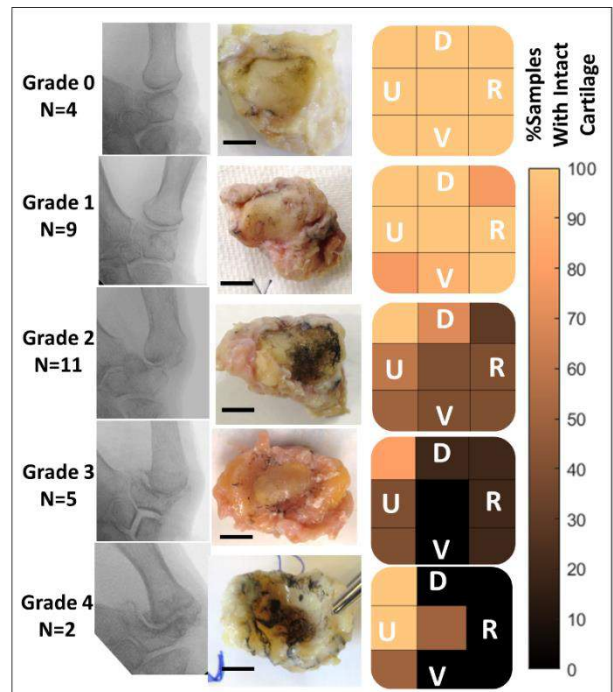


Figure 1: From left to right: Number of samples at each modified Eaton grade, with a representative Robert view radiograph for each. Representative gross images of the trapeziometacarpal surface of the trapezium with India ink staining. Scale=5mm. Regional maps showing the percent of samples with intact cartilage at each of nine anatomic regions for each grade. Photos and maps are each oriented so that Dorsal is up, Volar down, Ulnar to the left, and Radial to the right.

excluded. Each specimen was then fixed in formalin, and scanned via microCT at 70kVp, 85μA, with a voxel size of 10.3 μm. This was repeated after a 24 hour immersion in Lugols solution (10% KI, 5% I₂ in water) to increase the radiopacity of the cartilage. These contrast-enhanced images were used to compute the cartilage thickness across each sample. Specimens were then decalcified, paraffin processed, embedded, sectioned, and stained with Safranin O/Fast Green. All quantitative data were compared with one-way ANOVA followed by Tukey's post hoc tests, with significance set at p<0.05.

RESULTS

Radiographic assessment yielded a range of modified Eaton grades assigned to specimens, with grade 0 showing no evidence of OA to grade 4 representing a severely degenerated joint. (Fig. 1). One of the 32 specimens was excluded from this study due to past trapeziectomy. Macroscopically, samples with a higher Eaton grade showed a greater degree of gross degeneration, with increased cartilage eburnation, especially on the radial and volar aspects of the joint (Fig 1). Higher Eaton grades also showed greater evidence of bone abnormalities, including subchondral sclerosis and osteophyte formation, as well as a narrowing of the trapezium (Fig 2A-B). Histologically, specimens with higher Eaton scores showed evidence of major cartilage degeneration, with grade four specimens showing little if any Safranin-O positive staining for proteoglycans (Fig. 2C). Cartilage was thickest at grades 0 and 1, with thinning starting on the radial and volar edges by grade 2 (Fig 3A). Cartilage compressive modulus was significantly lower beginning at grade 1 in comparison to grade 0, with tensile moduli showing similar trends (Fig 3C-D), while cartilage permeability increased from grade 0 through grade 4 (Fig 3E). However, loss in mechanical properties did not seem to follow the same pattern of regionality as the cartilage erosion.

DISCUSSION

This study assessed the tissue and micro-scale properties of human trapezia throughout the stages of radiographically-diagnosed osteoarthritis, in order to better understand the progression of the disease. Our findings indicate that the onset of thumb OA is characterized by increased wear at the volar edge of the joint, progressing toward the dorsal side; this is well supported in the biomechanics literature^{7,8} as well as imaging studies of healthy specimens.⁹ Interestingly, loss of mechanical integrity of the cartilage preceded volumetric tissue loss, but did not follow the same pattern of regionality. Future work using this data set will include quantification of subchondral bone abnormalities, semi-quantitative scoring of osteochondral histology, and the assessment of synovium and synovial fluid harvested from these joints. As with any study involving donated human tissue, one limitation of this study is the low sample number. Another limitation is our inability to correlate any of our tissue and micro-scale outcomes to clinical measures of pain and functional deficit. Despite this, this data provides a rich data set for the evaluation of TMC OA and effectiveness of regenerative therapeutics.

ACKNOWLEDGEMENTS

This work was supported by the NIH and the Department of Veteran's Affairs.

REFERENCES

[1] Becker+, *CORR*, 2013. [2] Weiss+ *JAAOS* 2018. [3] Ladd+, *ASSH* 2015. [4] Weinstock-Zlotnick+, *HSSJ* 2019. [5] Bansal+ *OJSM* 2021. [6] Moore+, *J. Tribol.* 2016. [7] D'Agnostino+, *Clinical Biomechanics* 2017. [8] Ateshian+, *JOR* 1995. [9] Dourthe+, *Clinical Biomechanics* 2019.

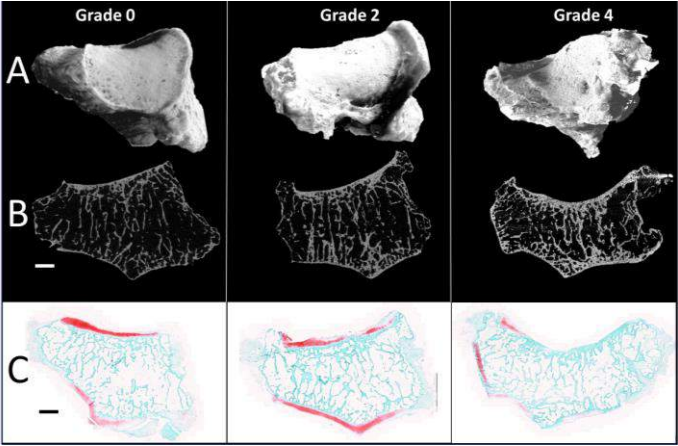


Figure 2: (A) Representative 3D reconstructions and (B), central 2D slices from microCT scans of grade 0, 2 and 4 trapezia. Scale = 2mm. (C) Representative Safranin O /Fast green stained trapezia for grade 0, 2, and 4. Scale = 2mm.

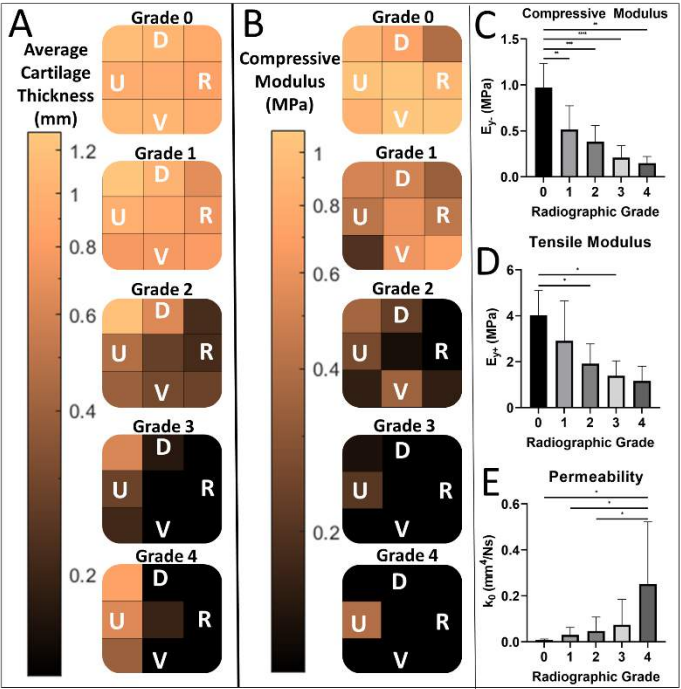


Figure 3: (A) Average cartilage thickness at nine anatomic locations for each modified Eaton grade. Values of zero were included in the average when no soft tissue was present. (B) Average cartilage compressive modulus at nine anatomic locations for each modified Eaton grade. Zeros were used in the average when no soft tissue was present. (C-E) Compressive modulus, tensile modulus and permeability of the remaining cartilage averaged across all testable locations for each modified Eaton grade.

INTEGRATED RIGHT VENTRICULAR-PULMONARY ARTERY BIOMECHANICS IN PULMONARY HYPERTENSION

Sunder Neelakantan (1), Peng Zhang (2,3), Gaurav Choudhary (2,3), Reza Avazmohammadi (1,4)

(1) Department of Biomedical Engineering, Texas A&M University, College Station, TX, USA

(2) Vascular Research Lab, Providence VA Med Ctr, Providence, RI, USA

(3) The Warren Alpert Medical School, Brown University, Providence, RI, USA

(4) J. Mike Walker '66 Department of Mechanical Engineering, Texas A&M University, College Station, TX, USA

INTRODUCTION

Pulmonary hypertension (PH) is defined as an elevation in mean pulmonary arterial pressure (mPAP) and is believed to affect 1% of the world population [1]. PH increases the afterload in the right ventricle (RV) leading to dysfunction and remodeling of the RV. PH also leads to the remodeling of the pulmonary artery (PA) and pulmonary vasculature following the increased resistance in the downstream capillary bed. The correlation between the severity of RV and PA remodeling is unknown. The increased stiffness and resistance in the pulmonary vasculature require a larger pressure head at the main pulmonary artery to maintain the flow rate in the capillaries. The RV contracts harder to achieve this increased pressure head leading to RV stiffening and remodeling. Our objectives in this study were to i) investigate the correlation between RV and proximal PA stiffening in rodents under mild and severe PH conditions, and ii) deconvolute the effects of increased stiffness and resistance in the pulmonary vasculature on the stress experienced by the RV free wall (RVFW).

METHODS

Two severities of PH were induced in rats for this study. The mild model of PH was developed by placing Sprague Dawley (SD) rats (n=6) in a hypoxia (Hx) chamber (10% O₂) for 3 weeks. The wild-type (WT) control rats for the Hx group (n=6) were placed in normoxia. The severe model of PH was developed by injecting a single dose of SU5416 (20 mg/kg sc) into Fischer (CDF) (n=6) and placing the animal in a hypoxia chamber for 3 weeks, followed by 1 week of normoxia (SuHx). The WT control rats for the SuHx group (n=6) were placed in normoxia and were injected with vehicle instead of SU5416. Both male and female rats were used in this study (male=12, female=12). Hemodynamic parameters were measured through echocardiography and catheterization. RVFW and right proximal PA tissues were harvested and subjected to biaxial and uniaxial loading, respectively.

To analyze the PA remodeling, the lungs of two rats (1 control and 1 SuHx) were isolated and fixed using the method described in Knutsen et al [2]. The lungs were imaged using micro-CT to obtain the morphology of the pulmonary vasculature (Fig. 2A). The images were segmented and processed to obtain the dimensions of individual vessels (slicer VMTK). This information was used to reconstruct the major vessels in the pulmonary vasculature (Fig. 2B) and the connectivity information was used for in-silico experiments. For the in-silico model, a 1-D fluid-structure interaction (FSI) model, originally developed by Colebank et al. [3], was extended to include nonlinear vessel elasticity and was integrated with our existing biventricular model [4]. The pressure at the inlet of the pulmonary vasculature was translated into the stress on the RVFW via our integrated RV-PA model. The stiffness and resistance of the PA vasculature were altered (3x stiffness and 10x resistance) to determine the contributions of narrowing and stiffening of the pulmonary vasculature on RVFW stress. In addition, the terminal resistance was also increased to determine the contribution of the increased capillary bed resistance to elevating RV afterload and increasing RVFW stress.

RESULTS

RVFW stiffness increased in both mild and severe PH, but the increase observed in the case of SuHx was significant (Fig. 1A). There was a strong correlation between the change in RVFW stiffness and change in hemodynamic parameters such as RV systolic pressure (RVSP) (Fig. 1B) and mPAP (results not shown here). In addition, there was a hyperbolic relation observed between RVFW stiffness and the ratio RVSP/TAPSE (Tricuspid annular plane systolic excursion) as a measure of RV-PA coupling (result not shown). These results indicate a strong relationship between RVFW remodeling and RV-PA uncoupling, which is the hallmark of RV maladaptation and triggers RV failure. The uniaxial testing of the PA specimen revealed that the PA stiffness increased significantly in the circumferential direction for the

SuHx rats, but remained unchanged in the Hx rats (control vs Hx: 237.6 kPa vs 216.9±12.72 kPa at 40% strain: control vs SuHx: 441.19.9±189.2 kPa vs 1139.3±309.3 kPa at 40% strain).

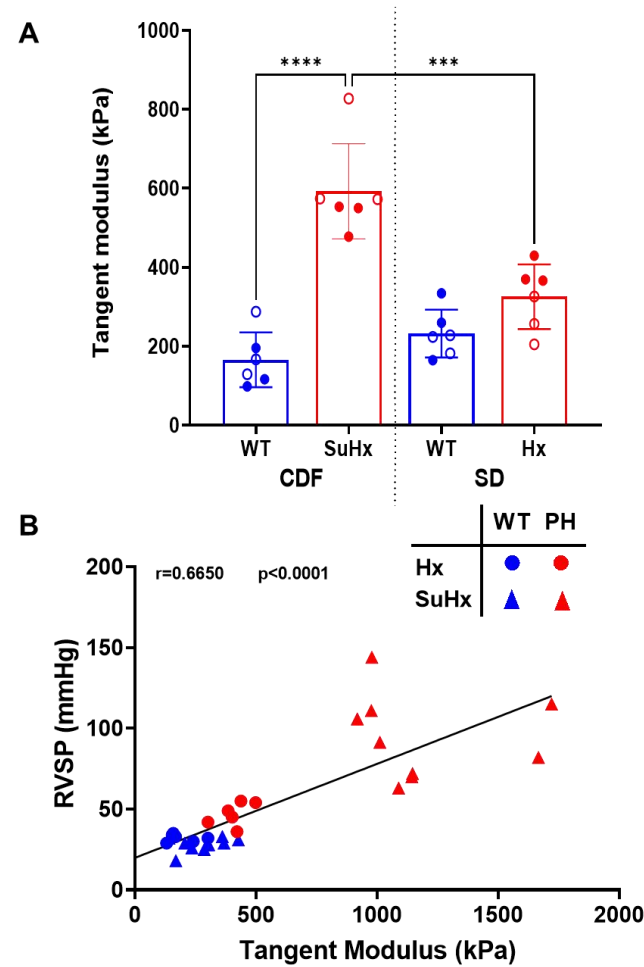


Figure 1: A) Ensemble tangent modulus of RVFW (Male - solid symbol, Female – hollow). B) Correlation of ensemble tangent modulus with RVSP.

The imaging of the pulmonary vasculature with the addition of the contrast agent allowed for the segmentation of extremely fine details such as the distal vasculature (Fig. 2A). Analysis and reconstruction of the vasculature provided morphological information of 342 vessels, which was reduced to 241 vessels after discarding extremely small features. Preliminary flow simulations were mapped onto the segmented vasculature geometry (Fig. 2B). In-silico experiments reveal that pulmonary vessel stiffness significantly affects the predicted stress in the RVFW (Fig. 2C). Simulations indicate that RVFW stress is doubled for SuHx rats based on the measured increase in pulmonary artery stiffness (PA stiffness tripled in SuHx) (Fig. 2C). Based on the measured change in pulmonary resistance (through the measurement of pulmonary vascular resistance using catheterization) and the change in pulmonary artery stiffness (through ex-vivo testing), we were able to replicate the increase in mPAP (Fig. 2D)

DISCUSSION

PH resulted in RV hypertrophy measured by increases in RV weight and RV thickness. The stiffness of the PA in the circumferential direction

increased significantly in the case of the severe PH model, but not in the mild form of PH. The RV stiffness significantly in SuHx rats, but not in Hx rats, and the result was expected according to the PH severity.

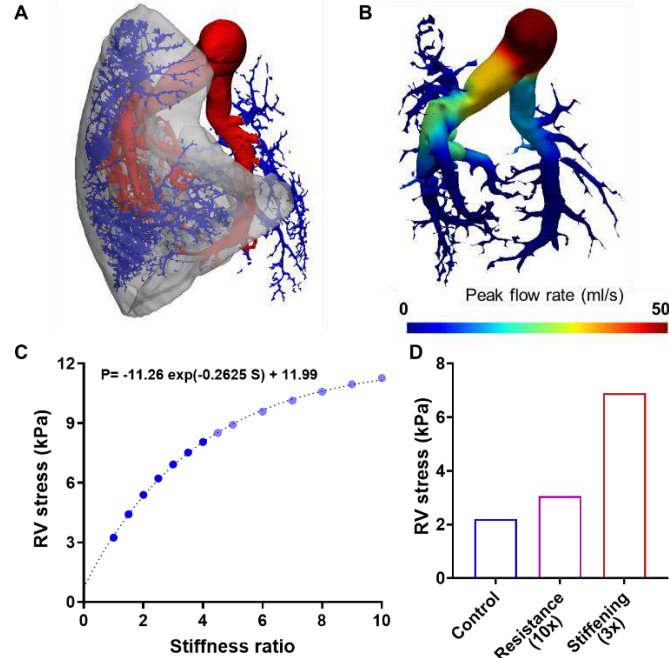


Figure 2: A) Segmented lung and pulmonary vasculature (Red – proximal, blue – distal). B) Flow rate mapped to pulmonary tree (preliminary result from rigid wall simulation). C) The effect of vessel stiffness on RV wall stress. D) Preliminary results on effects of increased resistance and stiffness on RV stress (n=1).

Preliminary results from in-silico experiments indicate the stiffening of the PA, increasing vascular resistance, and narrowing of vessels contribute to increased RV stress during PH. The results from the in-silico experiments combined with mechanical testing of the PA indicate that the SuHx rats will experience a significant increase in RV stress and RVSP, and the Hx rats will experience a mild increase (Fig. 1A). These results agree with the measured hemodynamic parameters (Fig. 1B). The combined effect of these remodeling events triples the RV stress (Fig 2D), with vessel stiffening being an important contributor. The method used in this study offers provides insights into the biomechanical coupling between the PA and RV and determines the larger contributor to RV remodeling on the PA side. Results from the study indicate that both the RVFW and pulmonary vasculature undergo significant remodeling due to PH. Distinguishing the contributions of various remodeling events of the vasculature on the function of the right heart can provide us with additional risk-stratification tools and aid in identifying optimal therapeutic targets.

ACKNOWLEDGEMENTS

This work was supported by the National Institutes of Health (K99HL138288 to R.A.).

REFERENCES

- [1] Hoeper, M. M. et al. Deutsches Arzteblatt international 114, 73-84 2017.
- [2] Knutsen, R. H., et al. J. Vis. Exp. (160), e61242, 2020.
- [3] Colebank, M. J. et al. J. The Royal Soc. Interface 16, 20190284 2019
- [4] Avazmohammadi, et al. Ann Biomed Eng 47, 138–153 2019

ALTERED OXYGEN TRANSPORT IN INTRACRANIAL ANEURYSMS IN SICKLE CELL DISEASE

Marisa S. Bazzi (1), Hadi Wiputra (2), David K. Wood (2), Victor H. Barocas (2)

- (1) Department of Chemical Engineering and Materials Science, University of Minnesota,
Minneapolis, MN, USA
(2) Department of Biomedical Engineering University of Minnesota, Minneapolis, MN, USA

INTRODUCTION

Neurological complications are more common in patients with sickle cell disease (SCD), with subarachnoid hemorrhage (SAH) of an intracranial aneurysm (ICA) among the most common¹. Given the life-threatening risk of SAH, understanding the relationship between development and rupture of ICA with SCD is highly important.

In SCD, under moderate to low oxygen conditions, the sickle hemoglobin undergoes a polymerization process that leads to stiffer and sickle-shaped cells². The apparent viscosity of the blood increases³, most obviously affecting blood flow resistance but also potentially affecting oxygen advection, which could further reduce oxygen levels and drive a cascade contributing to ICA formation and weakening.

Our aim in this study was to investigate how the geometry and blood rheology affect oxygen transport and consequently oxygen availability in the blood of an idealized ICA, testing the hypothesis that feedback between oxygen level, blood viscosity, and oxygen transport can aggravate the reduction in available oxygen in SCD.

METHODS

Primitive geometries were used, in which an arched 4-mm diameter cylindrical tube represented the vessel, and an attached 9-mm diameter spherical bulge represented the aneurysm. Two parameters were studied: (1) the ratio between the aneurysm throat length and the aneurysm diameter (L/D^a), and (2) the vessel curvature (κ).

The Carreau-Yasuda model was used to describe the shear thinning of the blood, with parameters dependent on the level of sickle hemoglobin (HbS) in the blood stream, based on our previous study⁴. The computed flow fields were validated against published in vitro data on flow in an idealized aneurysm model⁵.

Oxygen transport in the blood was described by

$$\frac{\partial O^T}{\partial t} = D^P K \nabla^2 O^T - v \cdot \nabla O^T \quad (1)$$

where O^T is total (hemoglobin-bound and free) oxygen in the blood. $K = O^P/O^T$ is the equilibrium constant for association and disassociation

of oxygen, where O^P is the free (plasma) oxygen concentration⁶. D^P is the diffusion coefficient for oxygen in plasma, and v is blood velocity.

Oxygen level in the vessel wall (O^W) was modeled using Fickian diffusion without convection for transport and Michaelis-Menten kinetics for consumption⁶:

$$\frac{\partial O^W}{\partial t} = D^W \nabla^2 O^W - \frac{A O^W}{B + O^W} \quad (2)$$

where D^W is the diffusion coefficient of oxygen in the wall, and A and B are kinetic constants⁶. A pulsatile velocity waveform and constant oxygen concentration were imposed at the model inlet. Outlet boundary conditions were fixed pressure and no axial oxygen gradient.

A full factorial study was done on three factors: HbS level (0, 10, 30, 50, 70, and 90%); aneurysm throat / aneurysm diameter ratio (0.07, 0.1, 0.3, 0.6, 0.8, 1.0); vessel curvature (-0.44, -0.14, -0.06, 0, 0.06, 0.14, 0.44 cm^{-1}) for a total of 36 geometries and over 140 cases. Simulations were performed at the Minnesota Supercomputing Institute.

RESULTS

Thirty-six geometries were studied, for both sickle (~90% HbS) and non-sickle (0% HbS) blood. Figure 1 shows one example geometry and the corresponding oxygen distribution during mid-systole for the non-sickle (Fig. 1A) and sickle (Fig. 1B) cases.

The average Peclet number in the aneurysm ranged from 30-4000, meaning that even for more the extreme cases, oxygen transport was dominated by advection. Figure 1C and 1F compare the normalized blood oxygen level for the non-sickle and sickle cases, respectively. Values range from 0 (no oxygen present) to 1 (oxygen level is the same as in the vessel). For throat sizes >0.7 times aneurysm size, oxygen distribution is not affected by the increased viscosity of the SCD system. However, for smaller throat sizes, there is reduced blood flow into the aneurysm, as shown by a smaller throat Reynolds number for the SCD. (Fig. 1G vs. 1D). Oxygen transport through the aneurysm wall was also lower in the sickle case (Fig. 1H vs. Fig. 1E), even for large throat sizes.

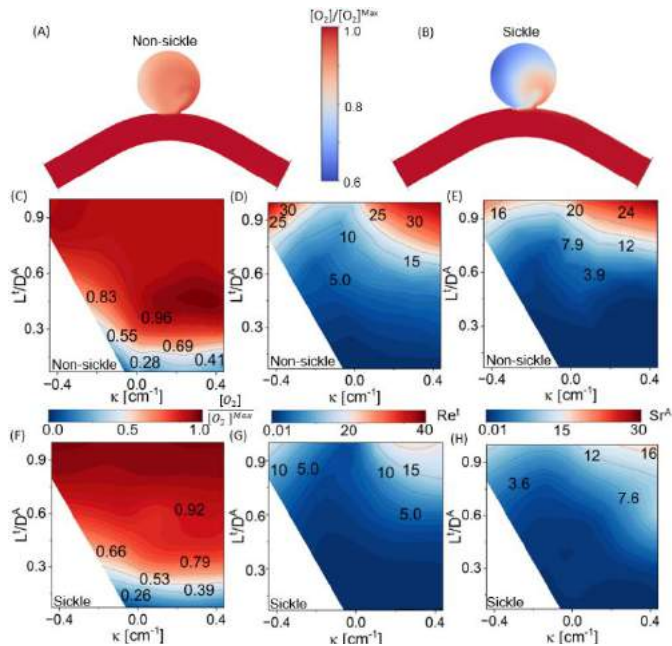


Figure 2: Normalized oxygen distribution for (A) non-sickle and (B) sickle in a plane cut for $\kappa=0.14 \text{ cm}^{-1}$ and $L/D^a=0.3$ calculated at peak of the cardiac cycle. Color maps show time average values for different curvatures (κ) and aneurysm throat diameter to vessel diameter ratio (L/D^a), for (C, F) normalized oxygen (D, G) throat Reynolds number and (E, H) Sheerwood number.

Figure 2 shows the results of the parametric study, with each column of the figure corresponding to a different aneurysm throat size (increasing left to right) and each row showing a different measured quantity. The first row (A-C) shows the normalized oxygen level in the aneurysm as a function of vessel curvature and HbS level. Increased HbS (more severe disease) decreases the oxygen level, especially for smaller throat sizes. The next three rows show the oxygen distribution (D-F), the blood viscosity (G-I), and the blood velocity (J-L) in a midplane slice through the geometry. For the small throat (A, D, G, J) in particular, oxygen is depleted in the aneurysm, leading to increased viscosity, but some effect was seen even at moderate throat sizes (B, E, H, K). The blood recirculated in the aneurysm for all cases (J-L).

The effect of curvature on oxygen transport is less consistent (Fig 2A-C). For small and large throats (Fig 2A, C), the higher curvature leads to lower oxygenation, but for intermediate throats (Fig. 2B), there was little effect or slightly increased oxygenation with curvature.

DISCUSSION

The most significant finding of this work is that oxygen availability is a potential issue in intracranial aneurysms, especially in large aneurysms with small throats. This effect was seen in all simulations, even those using healthy blood parameters, and the problem as more pronounced for SCD blood parameters. The higher viscosity of the sickle blood increases the effect of the narrow throat, and the poor oxygen transport can lead to even greater increase in blood viscosity. This sequence could create a positive feedback loop, wherein smaller throats produce less flow inside the aneurysm, leading to lower shear rates and lower levels of oxygen; the lower oxygen level could then lead to more sickling and greater viscosity, aggravating the problem.

The *geometrical* analysis showed that throat size seems to be a more important determinant of oxygen distribution than vessel

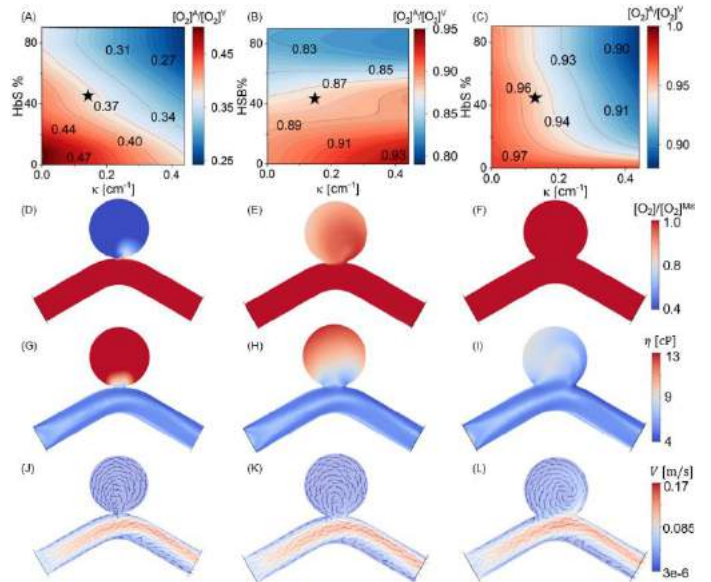


Figure 1: Normalized oxygen distribution maps for (A) $L/D^a=0.1$, (B) $L/D^a=0.3$, (C) $L/D^a=0.6$ at different level of sickle hemoglobin (HbS%) and different vessel curvatures (κ). Values are time averaged. Plan cuts show (D-F) oxygen distribution, (G-I) apparent viscosity distribution, and (J-L) velocity magnitude and direction.

curvature. For the sickle cell case, a larger throat is required to maintain full oxygenation of the aneurysm wall. Smaller throat Reynolds numbers and mass transfer coefficients measured for the SCD case suggested that less oxygen is available for the tissue in SCD patients who have aneurysms with smaller throats.

Synergizing with the geometrical effects, the *rheological* effects, in which a higher percentage of sickle cells leads to a higher apparent viscosity inside the aneurysm, also impact the oxygen distribution. The effects of the HbS% in the deoxygenation of the aneurysm site is higher for smaller throats and more curved geometries.

Finally, it is important to recognize certain considerations that were not addressed in the current study. Perhaps most importantly, this study did not address the mechanisms by which an aneurysm might form or by which a small aneurysm might grow into a larger and more fragile one. The process of intracranial aneurysm formation and growth is incredibly complex⁷ and this work focused only on fluid mechanics and oxygen transport. While oxygen's central role in SCD makes it important to study in the context of elevated ICA rates for SCD patients, the larger process of ICA formation requires more detailed and thorough study.

ACKNOWLEDGEMENTS

This work was supported by NIH (U01HL139471) and an AHA predoctoral fellowship to MSB. Computational support from the Minnesota Supercomputing Institute (MSI) is gratefully acknowledged.

REFERENCES

- (1) Anson, J. A.; *et. al. Journal of Neurosurgery* 75 (4), 552.
- (2) Piel, F. B. *et. al. New England Journal of Medicine* 2017, 376 (16)
- (3) Usami, S. *et. al. Microvascular Research* 1975.
- (4) Bazzi, M. S. *et. al. Biophysical Journal* 119 (11), 2307–2315.
- (5) Chassagne, F. *et. al. Journal of Fluid Mechanics* 2021, 915, 1–19..
- (6) Popel, A. S. *Crit. Rev. Biomed. Eng* 1989, 17 (3), 257–321.
- (7) Zimmermann, J. *et. al. Scientific Reports* 2021, 11 (1).

PHOTO-CURING EXTRACELLULAR MATRIX SEALANT FOR STOPPING VASCULAR HEMORRHAGE

Luke E. Schepers (1), Brooke L. Martindale (2), Alycia G. Berman (2), Hannah L. Cebull (1), William Van Alstine (3), Sydney E. Hollingshead (2), Tyler Novak (2), Craig J. Goergen (1)

- (1) Weldon School of Biomedical Engineering, Purdue University, West Lafayette, IN, United States
(2) Cook Biotech Inc., West Lafayette, IN, United States
(3) Cook Research Inc., West Lafayette, IN, United States

INTRODUCTION

Hemorrhage from traumatic injury is the leading cause of death in the United States in patients under 46 years of age [1]. Timely cessation of hemorrhage prevents hemorrhagic shock that results from severe blood loss and lack of tissue oxygenation [2]. Applying pressure to a vessel is the first line of defense in stopping hemorrhage and buys time to locate the source of the bleed, transport the patient, and prepare them for long-term treatment. However, prolonged pressure from a tourniquet or localized pressure such as a finger or clamp on the lacerated vessel occludes blood flow to surrounding tissue as well. Thus, the goal for long-term care is to repair the laceration and revascularize the vessel as soon as possible to restore oxygen-rich blood to the surrounding tissue.

One method of long-term vessel repair is the use of surgical sutures or staples, but these are associated with increased risk of infection or non-favorable wound healing outcomes [3]. Another strategy is the use of bioadhesives that come in the form of sealants, tissue adhesives, or hemostatic agents. Bioadhesives and sealants have shown advantages in ease of application and stable wound healing compared to sutures and staples [4,5]. With a wide array of bioadhesives and sealants available, it is important to consider the mechanical properties, application method, storage conditions, and biocompatibility of the sealant before choosing the one that achieves the greatest clinical efficacy. Multiple biomedical sealants and hemostatic agents have shown clinical efficacy in stopping bleeds and initiating the wound healing process, and each has its own set of advantages and limitations in terms of mechanical properties, storage conditions, and application method [5].

In this project, we investigate the use of a photo-curable, porcine-gelatin based sealant [6] in a murine venous hemorrhage model. The photo-curing extracellular matrix sealant (pcECM, Cook Biotech Inc., West Lafayette, IN) has the potential to address limitations in mechanical properties and storage conditions of currently available sealants, potentially expanding use for situations in ambulances, battlefields, and other remote settings. In this study, we tested pcECM

for its mechanical properties and use in venous hemorrhage cessation against a popular commercially available sealant (Tisseel, Baxter Healthcare, Deerfield, IL) to evaluate viability in stopping hemorrhage, promoting wound healing and revascularization of the lacerated vessel, and its effects on vessel hemodynamics and morphology.

METHODS

Sample Preparation: pcECM (low, medium, and high modified gelatin %) formulations consist of a 1mL syringe filled with 0.9mL precursor solution and 0.1mL of activator solution. Two 1mL syringes were attached with a luer lock connector and mixed back and forth 100 times. The mixture was dispensed via cannula and crosslinked with a visible light source for 1-4 minutes. Tisseel consisted of 2mL syringes in a double barrel configuration filled with human thrombin solution and human sealer protein solution. We thawed the syringes at 37°C, attached the provided mixing tip, and dispensed Tisseel via cannula allowing 2-5 minutes for crosslinking to take place.

Mechanical Properties: Low, medium, and high modified gelatin pcECM formulations and Tisseel samples (n=6-9/group) were tested for swelling, burst strength, and tensile strength. In addition, the density and viscosity of the three pcECM precursor formulations were measured.

Murine Venous Hemorrhage Model: Purdue University Institutional Animal Care and Use Committee approved all procedures under protocol #2002002016. After anesthetizing mice with 1.5-2.5% isoflurane, we made an incision in the abdomen, isolated the infrarenal portion of the vena cava (VC), and passed 2 nylon sutures around the VC. The VC was lacerated with a 27G needle, pressure was applied to the vessel with sutures immediately proximal and distal to the laceration, and the vessel was treated with either low modified gelatin percentage pcECM (n=9) or Tisseel (n=4).

Ultrasound Image Acquisition: A small animal, high frequency ultrasound system (Vevo3100, FUJIFILM VisualSonics, Toronto, CAN) was used to acquire B-mode, ECG-gated kHz video, 3-dimensional

ultrasound, and color and pulsed-wave Doppler images of the VC at baseline and days 1, 7, 14, 21, and 28 after surgery.

RESULTS

We found that varying the percentage of modified gelatin in the three pcECM formulations had significant effects on each formulation's mechanical properties, and Tisseel also had significantly different mechanical properties compared to the three pcECM formulations.

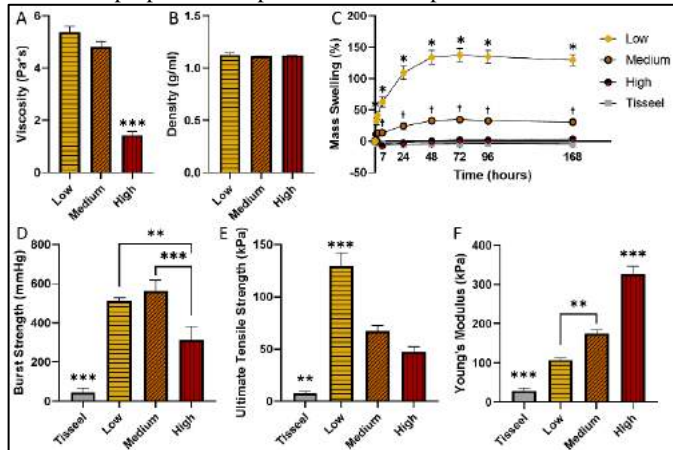


Figure 1: Mechanical properties of pcECM can be modified by adjusting the percentage of modified gelatin to fit different applications. A-D) The low and medium modified gelatin percentage pcECM formulations had significantly greater viscosity, swelling, and burst strength compared to the highly modified pcECM and Tisseel. E-F) The low modified gelatin pcECM had significantly greater tensile strength and a lower Young's modulus compared to the other pcECM formulations.

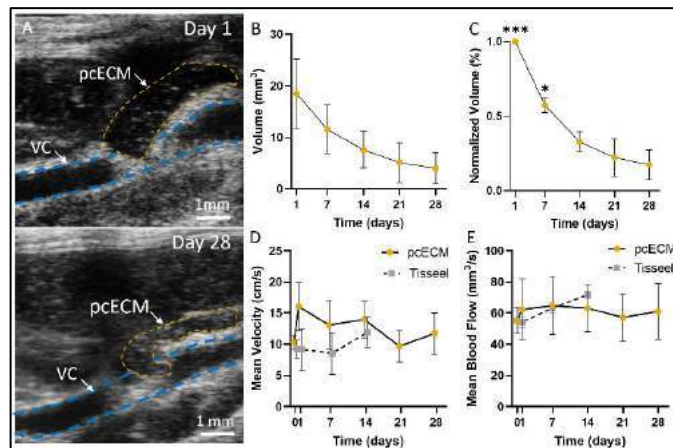


Figure 2: 3DUS volume measurements showed that pcECM degrades significantly but was robust and adhered/sealed the VC up to 28 days after surgery. A) B-mode ultrasound images show pcECM covering the laceration site on the vena cava and degradation over 28 days. B-C) Total pcECM volume degraded significantly over 28 days. D-E) The presence of pcECM or Tisseel did not significantly affect mean velocity or volumetric blood flow compared to baseline measurements.

We also found that pcECM significantly degrades over time and only small volumes of pcECM remained at the 28 day explant (Fig. 2). While pcECM compressed the VC after implant, only mild increases in

velocity (+5.7 mm/s) and volumetric flow (+7.8 mm³/s) were observed with pulsed-wave Doppler and luminal area measurements.

DISCUSSION

In this study we found pcECM to be a mechanically robust, biocompatible sealant capable of stopping venous hemorrhage without significantly altering vessel hemodynamics and morphology after application. All three pcECM formulations and Tisseel were tested to determine their respective mechanical properties, but only the low percentage modified gelatin pcECM and Tisseel were tested *in vivo*. The low modified gelatin formulation was selected due to its significantly higher viscosity that provided ease of application to the ~1.0mm diameter murine VC, as well as its high burst strength and tensile strength (Fig. 1) that make it suitable for vascular applications. However, the low formulation experienced the greatest amount of swelling which may cause it to compress veins and surrounding tissue structures depending on the volume implanted. Nevertheless, pcECM is crosslinked by a visible light source allowing the user to clear unwanted pcECM, reposition it on the tissue, or apply more before crosslinking.

Tisseel also successfully stopped venous hemorrhage in this study with little effect on mean velocity and morphology of the vessel. It is important to note that bleeding was well controlled while applying either pcECM or Tisseel to the vessel. One limitation of Tisseel is that it cannot be applied to severe or brisk bleeds as the sealant is quickly washed away before crosslinking. We observed that both sealants can be crosslinked in an aqueous environment with little or no active flow. While pcECM and Tisseel performed similarly in this venous hemorrhage application, pcECM's significantly greater burst strength, tensile strength, Young's modulus, and its crosslinking method/time make it a suitable candidate for arterial hemorrhage applications in the future. While bleeding can be controlled with pressure to a lacerated vessel in real-world cases, future experiments will also test pcECM application and crosslinking in both venous and arterial hemorrhage cases where active flow is present.

3DUS volume approximations showed pcECM degrades significantly to 17.4±8.1% of its initial implant volume 28 days after application. We were unable to visualize Tisseel with ultrasound and could not perform volume degradation analysis, but there were no traces of Tisseel present at the 14 day explant. Both sealants were significantly degraded and cleared by the body over time, and histology results showed minimal inflammatory response to pcECM or Tisseel suggesting both have a high degree of biocompatibility. pcECM can also be stored and quickly prepared at room temperature whereas Tisseel is stored at -20°C and must be thawed. Low modified gelatin pcECM's high burst strength, tensile strength, and room temperature storage and preparation conditions provide the possibility for future use in remote location emergencies and arterial bleeds, and the ability to adjust pcECM's mechanical properties by changing the percentage of modified gelatin open an array of surgical applications where a fast-curing, durable, naturally degraded sealant is needed.

ACKNOWLEDGEMENTS

Research reported in this publication was supported by the NIH/NIDDK T32 Training Fellowship, NSF Graduate Research Fellowship, Cook Biotech Inc., and Cook Research Inc., West Lafayette, IN.

REFERENCES

- [1] Chambers, J et al., *Mil. Med.*, 184:67-71, 2019. [2] Donley, E, and Loyd, J., *StatPearls*, 2022. [3] Scognamiglio, F. et al., *Biomed. Mat. Res. B Appl. Biom.*, 104:626-639, 2016. [4] Doria C. And Vaccino S., *Exp. Opin. Biol. Ther.*, 9:243-247, 2009. [5] Zhu W et al., *Acta Biometer.*, 74:1-16, 2018. [6] Elvin C., et al., *Biomaterials*, 30:2059-2065, 2009.

LEFT RENAL VEIN STENOSIS ALTERS RENAL VENOUS IMPEDANCE DURING MURINE PREGNANCY

Jennifer L. Anderson (1), Riley L. Holloway (1), Paula A. Torres Loza (1,2), David G. Reuter (3),
Craig J. Goergen (1)

(1) Weldon School of Biomedical Engineering, Purdue University, West Lafayette, IN, United States of America

(2) School of Medical Education, National University of Colombia, Bogotá, Colombia

(3) Division of Cardiology, Seattle Children's Hospital, Seattle, WA, United States of America

INTRODUCTION

Significant cardiovascular changes occur with the metabolic demands of growing a child. Cardiac output and glomerular filtration increase, the cardiac muscle is physically remodeled, and an entirely new organ is made to regulate this demand: the placenta [1]–[4]. This complex and delicate process is upset in hypertensive disorders of pregnancy, but the etiology of these is still poorly understood. Study of preeclampsia – hypertension in pregnancy with end-organ dysfunction – focuses on placental biomarkers and associated changes in hemodynamics which explain some cases, but not the majority [5].

Conversely, the role of renal venous compression, known to occur in early- and late-term preeclampsia, is underexplored [6]. The short gestation (19-21 days) and similar placental structure of mice is ideal for evaluation of this. Herein we explore the impact of compromised renal perfusion in pregnancy through a murine model of left renal vein (LRV) stenosis with the hypothesis that renal injury occurs (such as that seen in preeclampsia) when adequate collateralization does not exist.

METHODS

This study was approved by Purdue University's Institute for Animal Care and Use Committee. Thirty-four nulliparous female mice were paired with male mice (C57Bl/6J) and imaged with high-frequency ultrasound (Vevo3100 Imaging system, FUJIFILM VisualSonics, Inc., Toronto, ON, Canada) every 3-4 days to date the gestation [7]. On gestational day 6.5 (e6.5) a proximal (PS, n=14), distal (n=15), or sham stenosis (n=5, Figure 1) was induced by placing a 30g needle parallel to the LRV, tying a suture around both, and removing the needle. Ten distal animals also underwent mini-osmotic pump implantation (Alzet, Durect) filled with angiotensin II (n=5, 1000ng/kg/min) or saline (n=5).

All distal, all sham, and a subset (n=5) of PS animals underwent blood pressure (CODA, Kent Scientific) and ultrasound imaging at pairing, e12.5, e15.5, and e18.5 using a 40MHz central frequency

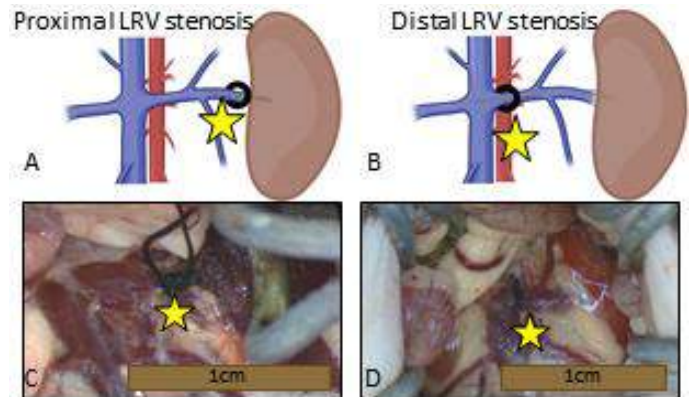


Figure 1: Proximal stenosis (A, C) provides no alternate route for blood to return to the heart. Conversely, a distal stenosis (B, D) assumes detours. A and B created with biorender.com.

transducer (Figure 2A). Renal volumes and velocities were noted. Impedance index was calculated using peak systolic velocity (PSV) and end diastolic velocity (EDV, Eq. 1). At e18.5 animals were euthanized. Maternal kidneys were weighed and fixed in 4% paraformaldehyde for histology. Renal weights were normalized to the contralateral control.

Renal impedance index

$$\text{Impedance Index} = (PSV - EDV)/PSV \quad (1)$$

Glomerular changes throughout gestation

To better assess renal injury progression, we euthanized six PS animals earlier in gestation at e12.5 and e15.5 (n=3 each). Kidneys were weighed, fixed in 2% glutaraldehyde and compared with PS animals euthanized at e18.5 (n=8, 3 of whom did not undergo ultrasound).

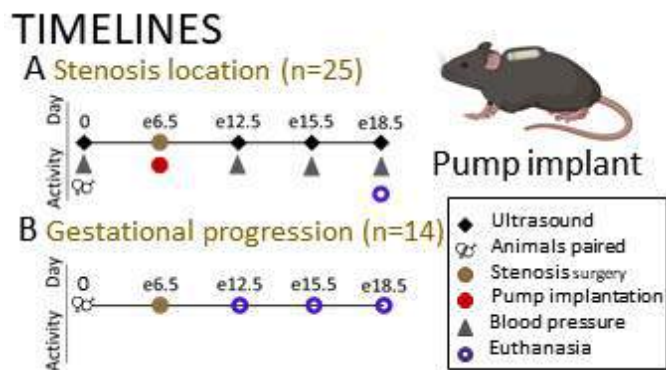


Figure 2: General timelines. (A) focuses on changes with differing stenosis location. (B) focuses on longitudinal changes with the PS group only. Pump implant created with biorender.com.

RESULTS

Renal weight difference (right – left) was significantly higher in the PS group compared to all other groups. (Figure 3B, 34.3 ± 21.8 mg vs. 6.1 ± 17.6 mg in the distal stenosis (DS) group, $p=0.026$). Histological and gross pathological analysis demonstrated evidence of acute infarct (Figure 3C). There was no significant difference in renal weight difference between other stenosis location groups. In the PS group left renal weight increased initially (at e12.5), then decreased until euthanasia at e18.5, with a significant difference between e12.5 and e18.5 (-30.4 ± 34.6 and 31.4 ± 24.0 respectively, $p=0.01$). Left renal venous impedance index (VII) was significantly higher in the PS group at e18.5 compared with other groups (0.76 ± 0.16 , PS, $p=0.03$) (Figure 4). There was no significant difference in left renal VII between other groups.

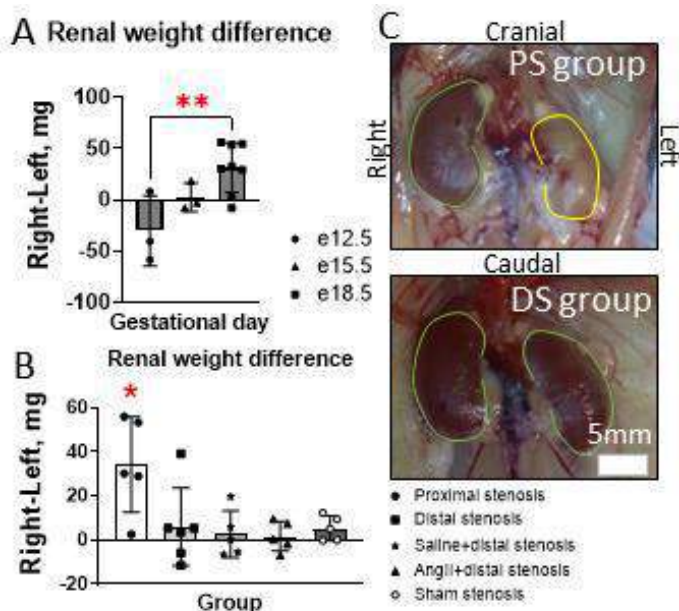


Figure 3: Difference in PS right and left renal weight as gestation progresses was significantly higher at e18.5 than e12.5 (A) and in the PS group (B). Gross pathology demonstrated necrosis (yellow outline) in the PS group compared with distal groups (C). PS, proximal stenosis; DS, distal stenosis.

Left renal venous impedance

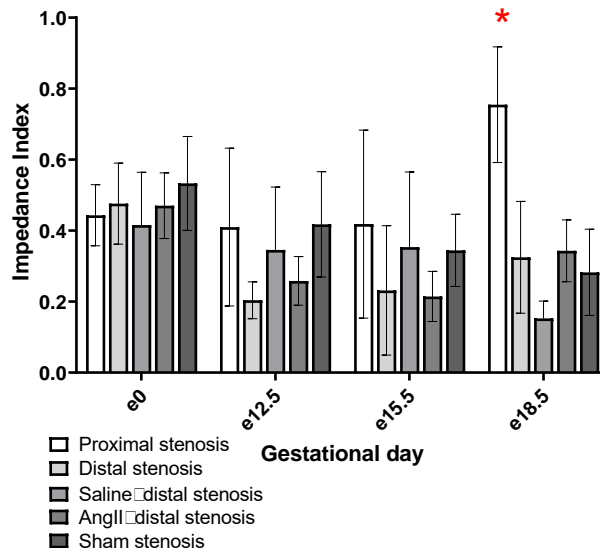


Figure 4: Venous impedance index what significantly higher in the proximal group at e18.5, suggesting increased intrarenal pressure.

DISCUSSION

Proximal renal vein stenosis results in decreased renal weight, increased venous resistance, and acute infarct as pregnancy progresses. While not statistically significant at e15.5, changes to the difference in PS right and left renal weight throughout gestation (Figure 3A) otherwise agree with our hypothesis – an initial decrease due to left renal congestion, followed by an increase as ischemia and atrophy of the left kidney begins to occur. This surgically induced murine stenosis is likely more severe than that experienced during human pregnancy, with positional changes causing a more intermittent stenosis and anatomic variation resulting in differing degrees of collateral vascularization. In the context of preeclampsia and no collaterals to re-route blood to the heart these results demonstrate a potential link to the renal injury in these patients. Future work is needed to explore the impact on glomeruli. Scanning electron microscopy and histological analysis will provide additional insight on glomeruli integrity.

Combined, these highlight the importance of collateral vessels in the mitigation of renal injury from renal venous compression by the gravid uterus. Therapies which reduce compression (positional changes, etc.) in patients without adequate collaterals may prevent renal injury.

ACKNOWLEDGEMENTS

We acknowledge funding from the Gates Foundation, Indiana CTSI and Purdue University Women's Global Health Institute. JLA was supported by the National Science Foundation under the Graduate Research Fellowship Program (GRFP; DGE-1842166).

REFERENCES

- [1] Lees, C and Gyzaers, W, Eds., *Maternal hemodynamics*. 2018.
- [2] Thornburg, K et al., *Knobil and Neill's Physiology of Reproduction*, 1927-1955, 2015.
- [3] Hall, J.E. et al., *Circ Res*, 116(6):991-1006, 2015.
- [4] Sanghavi, M and Rutherford, J.D., *Circulation*, 130(12):1003-1008, 2014.
- [5] Lisonkova, S and Joseph, K.S., *Am J of Ob and Gyn*, 209(6):544.e1-544.e.12, 2013.
- [6] Tokunaga, N et al., *J of Maternal-Fetal Medicine*. 9(6):356-359, 2000.
- [7] Greco, A et al., *PLOS ONE*, 8(10):e77205

EFFECT OF AORTIC ROOT MOTION ON AORTIC WALL STRESSES IN THORACIC AORTIC ANEURYSMS

T. Kim (1), N. Tjahjadi (2), X. He (3), H. Patel (2), N. Burris (3), and C.A. Figueroa (1,4)

(1) Department of Biomedical Engineering, University of Michigan, Ann Arbor, MI, USA

(2) Department of Cardiac Surgery, University of Michigan, Ann Arbor, MI, USA

(3) Department of Radiology, University of Michigan, Ann Arbor, MI, USA

(4) Department of Surgery, University of Michigan, Ann Arbor, MI, USA

INTRODUCTION

Thoracic aortic aneurysms (TAA) carry the risk of potentially lethal complications such as type A aortic dissection (TAAD). Current known risk factors of TAAD are aortic dilation and hypertension [1]. Most TAAD occur a few centimeters above the sinotubular junction (STJ) and along the greater curvature of the ascending aorta [2]. In TAAD, the intimal tear is normally oriented in the circumferential direction. However, risk factors such as aortic dilation and hypertension fail to explain the strong predilection for circumferential intimal tearing.

In each cardiac cycle, the aortic annulus is displaced downward during cardiac contraction. We hypothesize that such aortic root motion may impart significant stress on the ascending aorta in the axial direction that are ultimately responsible for the direction of intimal tearing. Several studies have investigated the effect of aortic root motion on the wall stress of the ascending aorta using finite element analysis (FEA) [3,4]. These studies showed increased aortic wall stress when aortic root motion was considered in the model. However, these studies used idealized and non-aneurysmal aortic geometries or prescribed simplified, unidirectional (e.g., axial) aortic root motion. Furthermore, validation of simulation results against motion data over the cardiac cycle was also lacking.

In this study, our goal is to investigate the effect of aortic root motion on axial and circumferential stresses in patient-specific models of TAAD using 3D dynamic data on vessel motion and a novel nonlinear rotation-free shell FEA model [5].

METHODS

A patient-specific aortic model was constructed from a 69-year-old male with a history of TAA (maximum diameter: 48mm), hypertension, and mild aortic regurgitation. The blood pressure was 131/85 mmHg. Dynamic computed tomography (CTA) images were available to define systolic and diastolic aortic configurations. The configurations were segmented using a custom U-Net neural network. Subsequently, a

patient-specific aortic model for the FEA was constructed by trimming the aortic inflow and outflow branches to define flat faces (Figure 1.A). 3D root motion was then extracted using a technique recently developed by our group, termed vascular deformation mapping (VDM), which can define 3D aortic displacement (both axial and in-plane) from dynamic CTA imaging [6] (Figure 1.B).

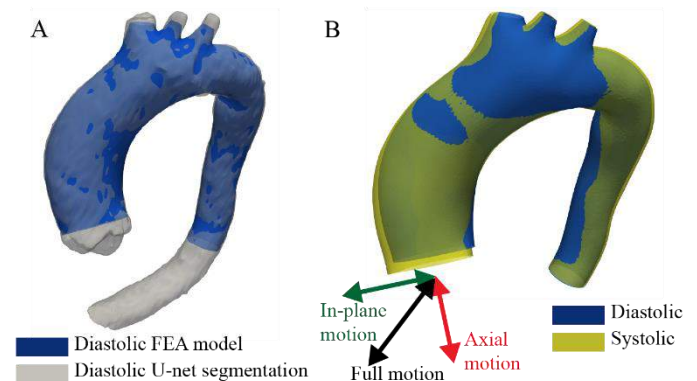


Figure 1: A: Diastolic U-net segmentation (gray) overlaid with FEA aortic model (blue). B: diastolic (blue) and systolic (yellow) patient-specific aortic models.

An incompressible Neo-Hookean constitutive model was used to characterize the aortic wall. The unloaded configuration of the aortic model was estimated using a pre-stressing technique [5]. Literature values of ascending and descending aortic material stiffness [7] were first prescribed in the analysis. Then, comparisons of systolic configurations between FEA and segmentation data were used to iteratively adjust ascending and descending aorta material stiffnesses until the difference between computed and segmentation cross-sectional areas was smaller than 5% (Figure 2).

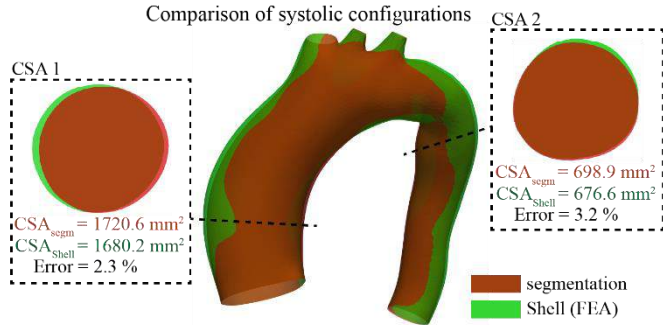


Figure 2: Comparison of systolic configurations between segmentation and shell FEA. CSA: Cross-Sectional Area.

To understand the impact of pressure and root motion in aortic wall axial stress, a combination of the following loading scenarios was considered: no root motion, in-plane motion, axial motion, and full root motion, both under diastolic and systolic pressures. For all loading scenarios, a full 3D displacement was prescribed for the three arch branch vessel outlets, whereas a free radial, fixed axial displacement was assigned to descending aorta outlet [5]. A mesh independence study was performed. The results reported here were obtained with a 17,681 triangular element mesh.

RESULTS

Aortic root displacement magnitude was 4.3, 5.6, and 7.0 mm in the in-plane, axial, and full components (Figure 1.B), respectively. Figure 3 shows the axial stress for the different pressure and aortic root motion scenarios described above. We report representative values of axial stress in the ascending aorta 2 cm above the STJ along the greater curvature of the aorta, noted by the red star. This is the location where TAAD is more likely to occur. For the case of diastolic pressure and no aortic root motion, the axial stress was 88.5 KPa (Figure 3a). Loading the aortic to the systolic pressure without considering root motion increased the axial stress to 140.3 KPa, a 58% increase (Figure 3b). Considering both systolic pressure and full 3D root motion resulted in an axial stress of 176.7 KPa, a further 26% increase (Figure 3h). As expected, Figure 3d and f show that the axial motion has a much greater impact on axial stress than in-plane.

DISCUSSION

We used a nonlinear rotation-free shell FEA and 3D aortic root displacement data extracted via VDM to study the impact of aortic root motion and blood pressure on axial stress in a patient-specific TAA model. Our results suggest that the contribution of aortic root motion to axial stress in the ascending aorta may be just as important as the blood pressure. Therefore, aortic root motion is critically important when performing aortic stress analysis in the ascending TAA, especially in studies examining risk of TAAD. Further studies will apply these techniques to a large cohort of TAAD subjects.

REFERENCES

- [1] Isselbacher EM, *Circulation*, 111(6):816-828, 2005
- [2] Hirst AE, *Medicine*, 37(3):217, 1958
- [3] Beller, CJ et al., *Circulation*, 109(6):763-769, 2004
- [4] Martin, C et al., *American J of Physiology-Heart and Circulatory Physiology*, 308(10):H1306-1316, 2015
- [5] Nama, N et al., *Scientific reports*, 10(1):1-17, 2020.
- [6] Bian, Z et al., *Medical Physics*, 49(4):2514-2530, 2022.
- [7] Roccabianca, S et al., *J mechanical behavior of biomedical materials*, 29:618-634, 2014

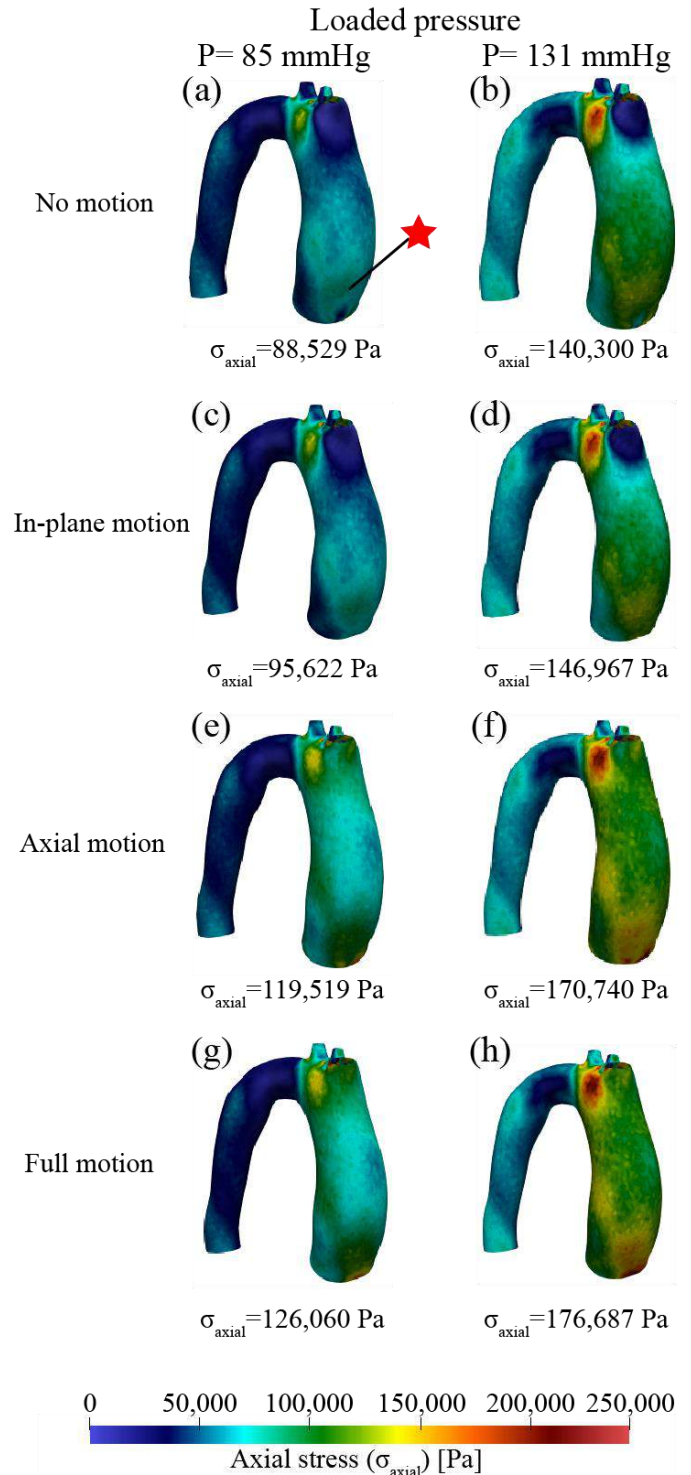


Figure 3: Axial stress under 8 different loading conditions. Representative values are given in the greater curvature of the ascending aorta, 2 cm above the STJ (red star).

HIGHLY PARALLEL PRODUCTION OF DESIGNER ORGANOIDS BY MOSAIC PATTERNING OF PROGENITORS

Catherine M. Porter (1), Alex J. Hughes (1,2,3,4)

- (1) Bioengineering, University of Pennsylvania, Philadelphia, PA, USA
- (2) Institute for Regenerative Medicine, University of Pennsylvania, Philadelphia, PA, USA
- (3) Cell & Developmental Biology, University of Pennsylvania, Philadelphia, PA, USA
- (4) Center for Soft and Living Matter, University of Pennsylvania, Philadelphia, PA, USA

INTRODUCTION

Organoids derived from human induced pluripotent stem cells (iPSCs) are a promising approach for congenital and adult disease modeling, regenerative medicine, and gaining fundamental understanding of organogenesis [1]. However, organoids are limited in their production scale, reproducibility, and physiologic function and structure [2], posing a considerable barrier to their application. Thus, an important open question is the extent to which engineering control over culture conditions guides organoids toward specific outcomes in composition and organization.

Here, we build upon a DNA ‘velcro’ approach to achieve precise control over initial iPSC-derived progenitor cell numbers and ratios in arrays of microwells, independently of well geometry. We focus on kidney organoids as a model system. We show significant control over organoid size and morphological trajectory after 15-day differentiation of nephron progenitor (NP)-derived organoids. We then create mosaic organoids by establishing precise ratios of NPs and ureteric bud (UB) tip cells, which give rise to the ureteric epithelium (UE, the urinary collection network) *in vivo*. Preliminarily, we find that transition of 2D mosaic cell patterns to 3D suspension culture facilitates cell sorting and discrete compartment formation early in organoid development, which resembles physiologic organization. Furthermore, UB tip cells and NPs synergistically upregulate the stromal cell population. Our approach achieves significant advances in organoid homogeneity relevant to disease modeling and drug screens as well as improved control over tissue interface formation crucial to engineered morphogenesis efforts.

METHODS

Derivation of kidney precursors. Prior to organoid culture, NPs and UB tip cells were derived from iPSCs using established protocols [3]. Briefly, intermediate mesoderm was induced from iPSCs by CHIR99021—a Wnt agonist—and transitioned to NPs under exposure to FGF9. For UB tip cells, NPs were fully differentiated into distalized

nephron organoids and transdifferentiated into UB tip cells by TTNPB (a retinoic acid analog), GDNF, CHIR99021, FGF2, and rock inhibitor.

Fabrication of integrated DNA-cell-patterning technology with microwell arrays. Photoactivatable polyacrylamide (PAA) gels on glass slides were patterned with single-stranded DNA (ssDNA) using UV light exposure through a photomask [4]. To create microwell walls, silicone (PDMS) through-hole sheets were replica micro-molded on 3D-printed pillar arrays and passivated with a polyacrylamide (PA) brush layer [5]. Silicone through-hole sheets were then aligned and adhered to ssDNA-patterned PAA gels. Finally, chamber walls were clamped onto PAA base gels, making 8 separate culture compartments.

Progenitor cell patterning in microwells. NPs and UB tip cells were each functionalized with unique lipid-conjugated ssDNA, which was complementary to an oligo sequence patterned on PAA substrates. During gentle mixing, the lipid moieties passively inserted into cell membranes, decorating cells with ssDNA that was accessible for base-pairing with PAA-bound ssDNA. Cells were then serially patterned by settling them in microwells and washing away excess, unadhered cells.

Kidney organoid culture. Once patterned cells had spread and formed cell junctions with adjacent neighbors, DNase was added to cleave ssDNA tethers, initiating lifting and aggregation. Organoids underwent differentiation in suspension culture for 15 days, receiving minimal medium supplements during the first 2 days. Kidney organoids were then fixed and immunostained for well-established markers of nephron, ureteric epithelium, and stromal tissues.

Image acquisition and analysis. Images of fluorescently labeled patterns of ssDNA and cells, as well as immunostained organoids, were acquired using a Nikon spinning disk confocal microscope. A subset of evenly spaced planes from each organoid z-stack was manually segmented in Fiji to measure the area of proximal tubules, distal tubules, and podocytes. The proportion of each tissue was calculated as the area of the tissue divided by the total area of all segmented tissues of interest (sum of proximal tubule, distal tubule, and podocyte areas).

RESULTS

We began by adapting cell patterning technology to a microwell format suited to long-term organoid culture (**Figure 1**). We targeted three design criteria: 1) using cell patterning to achieve precise cell number and compositional control, 2) inducing the transition of 2D patterns to self-organized 3D spheroids open to continued differentiation, and 3) sequestering individual organoids in passivated microwells throughout long-term culture. For cell patterning, we used our modified photolithographic technique [4], in which base-pairing between cell- and PAA-bound ssDNAs creates temporary cell-substrate adhesions. Nonspecific cell adhesion was reduced by grafting a PA brush layer on the PDMS microwell walls [5]. Furthermore, the addition of DNase, which enzymatically cleaved paired ssDNAs, aided in the transition of patterned cells to a single spheroid per microwell.

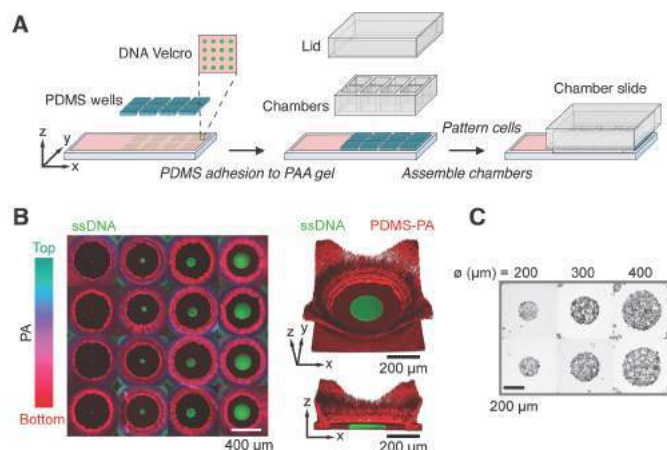


Figure 1: Integration of DNA-cell-patterning with microwells.

(A) Schematic of culture device fabrication. (B) Fluorescently probed ssDNA patterns on PAA base gels and aligned within PA-grafted PDMS microwell walls in array (left) and single-well (right) formats. (C) An example of patterned iPSC-derived NPs on ssDNA spots with variable diameters (\emptyset) in microwells.

Next, we applied our culture system to study the effect of initial NP number on organoid morphogenesis (**Figure 2A**). We discovered that throughout culture, organoid sizes directly depended on NP number, as set by the ssDNA spot sizes used to pattern them. Moreover, larger nephron organoids displayed a shift in final composition, with a significant increase in proximal tubule proportion from $40\% \pm 8.6\%$ to $61\% \pm 7.3\%$ from pattern size diameters 200 to 500 μm (\pm S.D., $n = 10$ organoids per diameter, Tukey's multiple comparisons test, $*p < 0.0332$, $**p < 0.0021$, $***p < 0.0002$, $****p < 0.0001$). These data suggest that the initial NP quantity modulates cell differentiation.

During kidney organogenesis, reciprocal interactions between NPs and UB tip cells influence nephron endowment, a major predictor of kidney disease [6]. We therefore examined how modulating NP to UB tip cell ratios affects organoid morphogenesis *in vitro* (**Figure 2B**). 24 hours post orthogonal cell patterning of UB tip cells and NPs on ssDNA patterns within microwells, we observed lifting, integration, and condensation of both populations to form early mosaic organoids. Interestingly, cells sorted to a single NP and a single UB tip cell compartment. Furthermore, regardless of starting ratio, an outer shell of NPs consistently covered UB tip cell cores, much like the wrapping of the NP cap mesenchyme around UB tips *in vivo* (**Figure 2B, 2C**). Preliminary assessment of immunostained late-stage mosaic organoids suggests an upregulation in stromal cell differentiation, as compared to NP- or UB tip cell-only organoids.

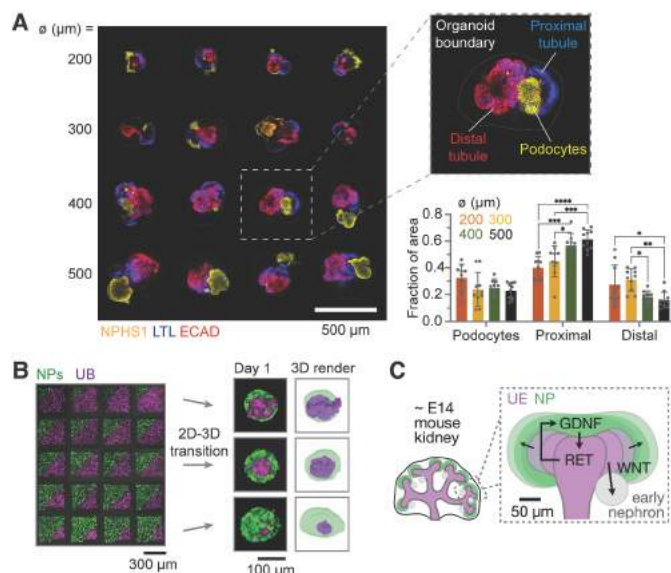


Figure 2: Modulated organoid morphogenesis by controlled variation in initial cell numbers and ratios. (A) Immunostained nephron organoids, derived from NPs patterned on various ssDNA spot sizes, and quantification of segmented tissues (bottom right). (B) Transition of UB tip cells and NPs from 2D patterns to 3D spheroids. (C) Organization and crucial interactions between NPs and UE *in vivo*.

DISCUSSION

Here, we contribute an integrated cell patterning and long-term culture platform that decouples organoid size from well geometry, enables 3D suspension culture, and maintains discrete organoid cultures. Using this technology, we first discovered a positive correlation between initial NP number, organoid size, and resulting proximal tubule proportion. In a second application, we observed the formation of NP caps around UB tip cell cores in early mosaic organoids, mimicking the organization of these cellular compartments *in vivo*. This cell sorting was likely primarily driven by differential cadherin-based cell-cell adhesion [7]. Preliminary analysis of final mosaic organoids suggests that NPs and UB tip cells synergistically upregulate stromal differentiation, an area of ongoing work.

Future studies are needed to gain mechanistic insight into our resulting organoid phenotypes. Furthermore, it may be necessary to identify, source, and incorporate additional cell types into organoids and/or engineer further control over culture conditions to achieve the structure and function needed for applications in regenerative medicine.

ACKNOWLEDGEMENTS

We thank members of the Hughes Lab for insightful discussion and assistance in protocol development and M. Little and S. Howden for sharing expertise in kidney organoid culture. This work was supported by an NSF Graduate Research Fellowship to CMP, an NIH NIGMS MIRA R35GM133380 to AJH, an NIH NIDDK R01DK132296 to AJH, and an NSF CAREER award 2047271 to AJH.

REFERENCES

- [1] Clevers, H., *Cell*, 165:1586-1597, 2016.
- [2] Zeng, Z et al., *Nat Commun*, 12:3641, 2021.
- [3] Howden, SE et al., *Cell Stem Cell*, 28:671-684, 2021.
- [4] Viola, JM, Porter, CM et al., *Adv Mater*, 36:2002195, 2020.
- [5] Beh, CW et al., *Lab Chip*, 12:4120-4127, 2012.
- [6] Cebrian, C et al., *Cell Rep*, 7:127-37, 2014.
- [7] Lefevre, JG et al., *Development*, 144:1087-1096, 2017.

VISCERAL PLEURA MECHANICS: A COMPARISON BETWEEN PORCINE AND RAT LUNG TISSUE

Gustavo O. Ramirez (1), Crystal A. Mariano (1), Talyah M. Nelson (1), Samaneh Sattari (1), David Carter (2), Erica C. Heinrich (3), Mona Eskandari (1,4,5)

- (1) Department of Mechanical Engineering, University of California, Riverside, CA, USA
(2) Department of Molecular, Cell, and Systems Biology, University of California, Riverside CA, USA
(3) Division of Biomedical Sciences, School of Medicine, University of California, Riverside
(4) Department of Bioengineering, University of California, Riverside CA, USA
(5) BREATHE Center, School of Medicine University of California, Riverside CA, USA

INTRODUCTION

The visceral pleura is a thin layer of stiff tissue on the surface of the lung, encapsulating the spongy parenchyma. Among its many roles, the visceral pleura helps seal the lung tissue which conducts air exchange. Visceral pleura injuries cause air leaks and are amongst the most common complications in thoracic surgery [1]. Patients undergoing a lobectomy have an 8% to 26% chance of experiencing a prolonged air leak (PAL), defined as air seepage into the pleural cavity persisting for more than 5 days after the procedure [2,3]; Patients experiencing PAL after a lung resection experience higher morbidity rates and lengthier hospital stays [4]. Today there are many lung sealants both on the market and in development to help reduce PAL in thoracic surgery, however, the ability of the sealants to reduce PAL are often inconclusive [5]. Sealants must adhere to and synchronously stretch with the visceral pleura at the site of injury, and therefore characterizing the mechanical properties of this biological tissue is central to understanding how to improve sealants and patient outcomes [6].

Currently, only a few studies characterize the mechanics of the visceral pleura and such studies are limited to uniaxial tests [7]. In-vivo rat and porcine lung studies focus on the rupture performance of lung sealants, not the mechanical behavior of the visceral pleura [8,9]. To date, there has been no mechanical characterization of rat visceral pleura while porcine pleura has been tested only uniaxially. Given the multi-axial loading experienced by the visceral pleura with each dynamic breath, unidirectional testing is an inadequate representation of tissue physiology. This study addresses this knowledge void in the literature by investigating the material properties of both rat and porcine visceral pleura using equibiaxial tensile tests, and considering regional and anisotropic dependencies.

METHODS

Fresh porcine (N=3) and rat (N=3) lungs were obtained from local vendors (Sierra for Medical Science, IACUC exempt). Visceral pleura

specimens were collected from both ventral and dorsal sides of the lung for both porcine and rat lungs (Figure 1). The sheets of visceral pleura tissue were carefully separated from underlying parenchyma while tracking of sample orientation to be aligned with the cranial-caudal (CC) and medial-lateral direction (ML). A total of six rat visceral pleura specimens (4x4mm test area) were collected (Figure 1A). Porcine lobes (Figure 1B) were substantially larger than the rat, allowing for additional consideration of upper (cranial) versus lower (caudal) lobe pleural mechanics. A total of 16 porcine samples (1x1cm test area) were collected.

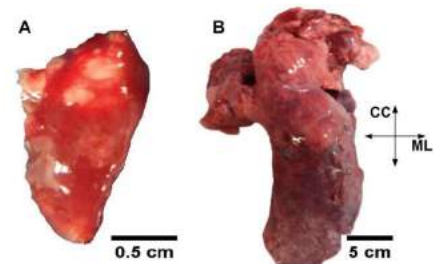


Figure 1: (A) Rat lung and (B) pig lung single lobes where the reflective outermost layer is the intact visceral pleura. Cranial-caudal (CC) and medial-lateral (ML) orientations are shown.

Tissue thickness was measured using a digital thickness gauge for porcine specimens (Mitutoyo, Kawasaki, Japan) and a confocal microscope for rat specimens (Zeiss, Oberkochen, Germany) [10]. Each specimen was loaded onto rakes and immersed in a 1X phosphate buffered saline solution bath maintained at 37°C [11]. Samples underwent equibiaxial tension tests using a commercial planar biaxial machine (1.5N load cell, BioTester, CellScale Biomaterials Testing, Waterloo, ON, Canada). Extensive preliminary tests informed the testing parameters utilized to avoid tissue damage: 60% strain was applied simultaneously in both the CC and ML directions at a strain rate

of 0.2%/s. Two preconditioning cycles were followed by a third cycle used for data analysis [11]. All tissues were refrigerated at 4°C upon receipt and experiments were conducted within 72 hours postmortem [12].

The First Piola-Kirchhoff engineering stress was calculated and the resulting bilinear stress-strain loading curves (Figure 2) were analyzed by fitting lines through both the initial and final slopes of the curve ($R^2 > 0.95$) to determine the tissue initial and final moduli [11,13]. The maximum stress at 60% strain was noted and the strain energy was calculated as the area under the loading portion of the stress-strain curve. Each metric was explored for the CC and ML orientations, and the ventral and dorsal sides of the lung. Additionally, thickness variations in the porcine visceral pleura suggested upper ($79 \pm 12 \mu\text{m}$) versus lower ($104 \pm 25 \mu\text{m}$) regions should also be examined; the rat visceral pleura thickness was consistent ($11 \pm 1 \mu\text{m}$). No region dependent mechanics were found, and thus ventral-dorsal and upper-lower sample groups were pooled together. Data comparisons were performed using a student's t-test. Statistical significance was defined at $*p < 0.05$, where **, ***, and **** are $p < 0.01$, $p < 0.001$ and $p < 0.0001$ respectively.

RESULTS

The stress-strain response shown in Figure 2 illustrates rat and porcine CC and ML directional responses. Overall, rat visceral pleura experienced higher stresses throughout the strain range compared to porcine tissue.

Maximum stress, strain energy, initial, and ultimate moduli were compared between species. Porcine visceral pleura had an initial modulus of $1.21 \pm 0.11 \text{ kPa}$ and $0.97 \pm 0.09 \text{ kPa}$ in the CC and ML directions respectively, while rat was nearly double that of the porcine moduli (CC: $2.82 \pm 0.41 \text{ kPa}$; ML: $2.80 \pm 0.35 \text{ kPa}$). The ultimate modulus between species differed only in the CC direction (pig: $14.3 \pm 1.26 \text{ kPa}$; rat: $8.64 \pm 0.87 \text{ kPa}$). Despite the greater ultimate modulus for porcine tissue, the maximum stress was greater in rat specimens along both CC and ML directions compared to porcine counterparts. The strain energy was also significantly greater along both CC and ML orientations for the rat compared to porcine visceral pleura.

Intraspecies comparisons were also made. Regional dependencies were not found when comparing ventral and dorsal samples within each species. Despite the sizeable variation in upper versus lower lobe thicknesses of porcine samples, no regionally dependent differences were observed in the mechanical responses of porcine tissue. Anisotropic CC and ML analysis of rat visceral pleura did not exhibit any significant differences. However, porcine specimens demonstrated statistically significant greater CC values for the ultimate modulus, maximum stress, and strain energy compared to ML (Figure 3).

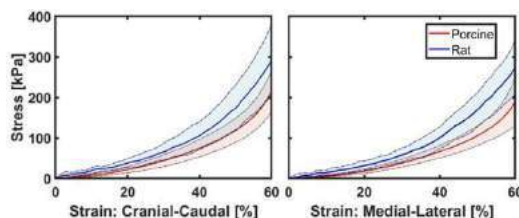


Figure 2: Average \pm standard deviation stress-strain behavior for rat and porcine visceral pleura tissue in both the cranial-caudal and medial-lateral orientations.

DISCUSSION

This study compares porcine and rat visceral pleura mechanical properties via equibiaxial planar testing for the first time. Intraspecies'

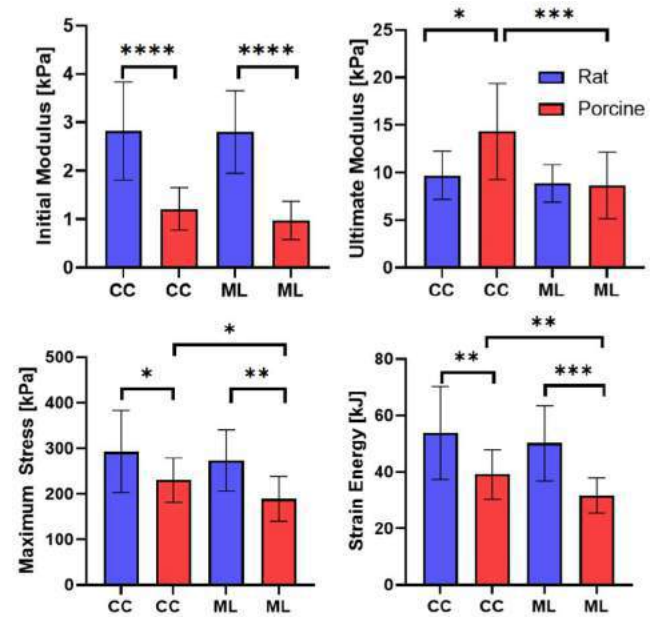


Figure 3: (A) Initial and (B) ultimate moduli, in addition to the (C) maximum stress and (D) strain energy values in both the cranial-caudal (CC) and medial-lateral (ML) directions.

mechanical properties demonstrate that porcine and rat visceral pleura are homogenous with no regional variation across the lung. Rat visceral pleura was observed to behave isotropically, however, porcine specimens were anisotropic. Previous literature notes potential anisotropy for canine visceral pleura but concluded isotropic behavior due to experimental errors while determining the tissue reference state [14]. This current study is the first to report biaxial species variability and directional dependency of the visceral pleura. The anisotropic response documented in this biaxially analyzed study will be further substantiated histologically in the future, to investigate the role of the underlying fiber orientation on the directional dependency observed in porcine but not rat visceral pleura.

Rat and porcine visceral pleura material properties are notably disparate and indicate variability from species to species. As such, the effects of differing visceral pleura mechanics among animal models should be considered when constructing and testing pleural sealants. The mechanical properties of modern tissue sealants are often tunable, and thus, comprehensively characterizing the mechanics of the visceral pleura can aid the optimization and effectiveness of pleural sealants [6]. Our future studies will also investigate human cadaveric visceral pleura lung tissue to assess the applicability of animal models for clinical translation.

REFERENCES

- [1] Mueller MR, et al., *J Thorac Dis*, 6:271-284, 2014. [2] Yoo A, et al., *Clinicoecon Outcomes Res*, 9:373-383, 2017 [3] Adeyinka A, et al., *StatPearls Publishing*, 2022 [4] Varela G, et al., *Eur J Cardiothorac Surg*, 27:329-333, 2005 [5] McGuire AL, et al. *J Thorac Dis*, Suppl 32:S3728-S3739, 2018 [6] Annabi N, et al. *Eur J Pharm Biopharm*, 95:27-39, 2015 [7] Lu X., *Front Bioeng Biotechnol.*, 10:796076, 2022 [8] Servais AB, et al. *Tissue Eng Part A*, 24:695-702, 2018 [9] Kawai N., *Ann Thorac Surg.*, 102:282-6, 2016. [10] Petroll, M.W. *Curr Opin Ophthalmol* 9:59-65, 1998 [11] Sattari, S, et al., *J Mech Behav Biomed Mater* 110:103824, 2020. [12] Eskandari, M. et al. *J Appl Physiol*, 125:878-888, 2018. [13] Quiros, K.A.M., et al., *Sci Rep* 12:7094, 2022. [14] Humphrey, J.D., *Ann Biomed Eng*, 14:451-466, 1986.

BIO-INSPIRED POLYMERIC TAVR TO IMPROVE DURABILITY OUTCOMES

Nipa Khair (1), Sanchita Bhat (2), Katie Vinterella (2) Satheesh Kumar Harikrishnan (2), Lakshmi Prasad Dasi (2), Susan James (1,3,4)

1. School of Advanced Materials Discovery, Colorado State University, Fort Collins, Colorado
2. Department of Biomedical Engineering, Georgia Institute of Technology, Atlanta, Georgia,
3. School of Biomedical Engineering, Colorado State University, Fort Collins, Colorado
4. Department of Mechanical Engineering, Colorado State University, Fort Collins, Colorado

INTRODUCTION

Rheumatic and calcified aortic heart valve disease is prevalent globally among all aged people, and the number is rapidly increasing. Minimally invasive xenograft-based transcatheter aortic heart valve replacement (TAVR) shows limited durability (<10 years)¹. Hyaluronic acid (HA) enhanced polyethylene polymeric TAVR shows excellent *in vitro* and *in vivo* anti-calcific, anti-thrombotic, and hydrodynamic performance. HA, a glycosaminoglycan, is one of the major constitutive elements of the native heart valve leaflet¹. The long dynamic chains of HA over low-density linear polyethylene (LLDPE) thin-film surface interpenetrated at the molecular level provides a robust and durable hydrophilic biomaterial. LLDPE thin film has high tear strength and excellent flexibility, making it a suitable candidate for heart valve leaflets. However, during durability testing, impact wear causes early valve failure in a consistent fashion related to TAVR assembly (figure 1. b). TAVR leaflets were assembled into a cylinder from a flat film by welding two ends together where they meet over the commissure post and the TAVRs were tested in an accelerated wear tester (AWT). The welded areas never failed and always tore at the cusp opposite the weld commissure post (figure 1. a). The weld at the commissure post is mechanically stronger than the rest of the leaflet, protecting this region. Therefore, this research investigates failure mechanisms and provides methods to increase durability by strategic strengthening of the leaflets in the region of the commissure posts.

METHODS

Fiber-reinforced valve fabrication: We fabricated polymeric heart valves by reinforcing the commissure posts with polyester fiber. One polyester fiber (0.2 mm diameter) was hand-laid upon a thin sheet of LLDPE (80 μ m) along the commissure posts **parallel** to the valve height (figure 1. c). Another thin sheet was laid on top and melt-pressed to create a composite structure. The melt press applied 500 lbs. pressure at 125 °C for 1 minute. The flat laminate was further melt-pressed (i.e.,

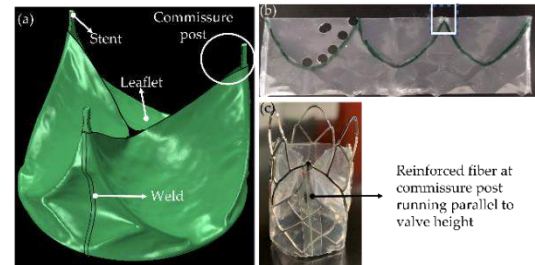


Figure 1 (a) Simulated polymeric TAVR assembled over cobalt chromium stent and (b) Tested in AWT. The white rectangle shows torn commissure and dark curve shows stent line and the round holes are where test samples were punched out of leaflets. (c) Fiber reinforcement at the commissure post.

welded) at the two ends to create cylindrical leaflets that were fitted over the stent to complete the valve².

Hydrodynamic Testing: This valve was tested for hydrodynamic performance in an *in-vitro* left heart simulator (LHS) under adult physiologic pressure (120/80 mmHg), heart rate (70 bpm), and cardiac output (5 L/min) using a 60/40 water/glycerin mixture to simulate blood properties. Eighty consecutive cardiac cycles of flow waveforms data were recorded at a sampling rate of 100 Hz³. The fiber-reinforced valves (n=2) were compared to an unreinforced (control) valve⁴. After averaging all cardiac cycles, we calculated the effective orifice area (EOA) and mean transvalvular pressure gradient (PG) and compared them with a control valve without any fiber reinforcement. In this study, particle image velocimetry (PIV) was also performed to measure flow velocity magnitude. Time-resolved recordings were acquired at a temporal resolution of 1000 Hz³. Later the valves (n=3) were tested for durability in an AWT according to ISO 5840¹.

Finite Element Analysis: SolidWorks was used to create a CAD model assembly of cylindrical leaflet and stent to simulate the TAVR in

ABAQUS. The internal diameter and height of the stent (cobalt chromium) were 26 mm and 18.5mm, respectively. The fiber-reinforced valve CAD file was created by thickening a 3mm width of the commissure post with a peak thickness of 0.28mm, which was tapered down to 0.08 mm of the rest of the valve thickness. The thickest region housed the fiber (0.2 mm diameter) **parallel** to the valve height (figure 1 c). In another iteration, a fiber (0.1 mm diameter and 6 mm long) was wrapped over the leaflet **perpendicular** to valve height in the CAD model and simulated in ABAQUS. The stent and the leaflet were discretized in Hypermesh 2021, and mesh convergence was achieved on the leaflet. Cobalt-Chromium alloy and fiber were modeled using the linear elastic material model: elastic modulus 210 GPa and 4 GPa, respectively, and Poisson's ratio of .33. LLDPE leaflet was modeled with 2nd order Ogden hyperelastic material properties. The model simulated the mid-diastolic or leaflet closure part of a cardiac cycle and applied a 100 mm Hg pressure load on the outer surface of the leaflet. Appropriate boundary conditions were applied to the leaflet bottom edge and the entire stent to restrict their movement completely.

RESULTS

The fiber-reinforced valves were tested in LHS and compared with the unreinforced valve. The fiber-reinforced valves had a pressure gradient of 13.2 ± 2 mmHg and EOA of 1.5 ± 0.5 cm². Reinforced valve peak velocity was 2.2 m/s (figure 3) compared to 2.2 m/s for the control group³. In AWT the reinforced valve survived for 73 million cycles compared to 4 million cycles for the control group.

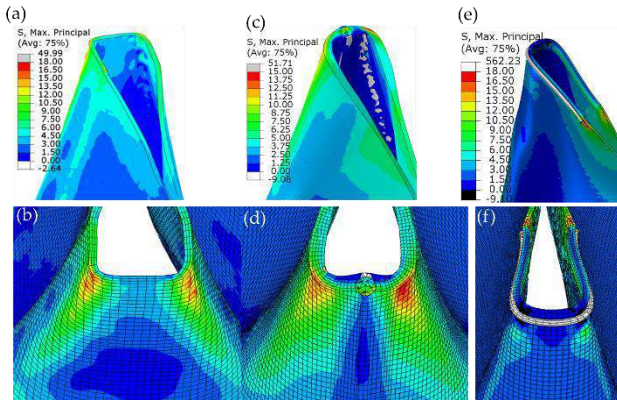


Figure 2. FEA results of (a-b) control valve and (c-f) fiber-reinforced valve. Fiber running parallel to valve height shows (c) compression on the inner surface and (d) lower max principal stress on the outer surface compared to (a-b) unreinforced control group. Fiber running perpendicular to valve height shows (f) a drastic reduction of stress at the commissure post yet (e) height stress concentration at the fiber endpoint.

Max. principal stress reduced from an average of 18 MPa to 15 MPa (n=3) for parallel fiber reinforced group and had compression on the high bending region instead of tension compared to the control group. On the other hand, the valve of fiber running perpendicular to valve height tensile stress at the commissure post was replaced with compressive stress, but fiber tip had high-stress (22 MPa) concentration.

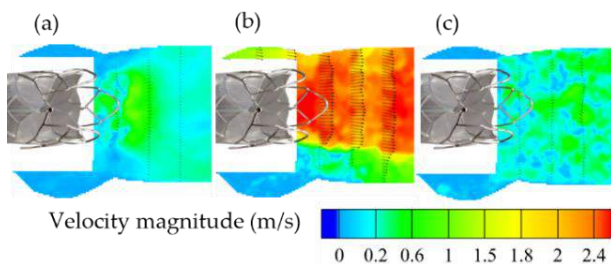


Figure 3 Velocity magnitude of fiber (parallel to valve height) reinforced valve: mid to late acceleration (a), peak (b), and mid to late deceleration (c)

DISCUSSION

The fiber-reinforced valve hydrodynamics were comparable to the previously published control group (pressure gradient 9.5 mm Hg and EOA 1.91 cm²) because the strong reinforcement was tucked behind the stent⁴. The results showed a slightly higher standard deviation, indicating inconsistent valve assembly during testing. Interestingly the fluid velocity did not significantly change, indicating the overall good performance of the valve. This parallel-to-valve-height-fiber reinforced valve showed drastic improvements in durability as the highly stressed commissure posts were strengthened and protected, confirming the initial hypothesis. However, FEA simulation results did not show significant peak stress reduction due to the parallel fiber reinforcement, although thickened commissure post-bending area had compressive stress compared to tensile stress in the control group. Which indicates that the strong composite at the post was more of a surface protection from abrasion between the leaflet and stent than stress reduction in the leaflet itself.

Tensors of the deformed valve showed high stresses perpendicular to valve height instead of parallel to valve height (figure 1 c). Therefore, a fiber with an aspect ratio 60 was placed perpendicular to valve height to transfer the maximum load from the matrix to the fiber. The FEA showed promising results where leaflet stresses near the commissure post were drastically reduced to negative tensile stress (compressive stress). The fiber was 16 times stiffer than the matrix, so showed 562 MPa stress while transferring load from matrix LLDPE. However, the perpendicular fiber placement could cause a new failure mode due to the high leaflet stresses at the fiber ends.

Critical fiber length determines the minimum length required to transfer the maximum load from matrix to fiber. The perpendicular-to-valve height fiber modeled above was longer than the estimated critical fiber length. For a thermoplastic composite like LLDPE, yield shear stress is generally below 10 MPa, and polyester fiber strength is ~400 MPa depending on braiding and diameter⁵. Therefore, the critical aspect ratio is below 50. Thus, for a 0.1 mm diameter, the critical fiber length is below 5 mm. Therefore, the perpendicular-to-valve height fiber modeled above was able to carry commissure post load and thus protect the leaflet in the region of commissure from failure. It should also provide protection from abrasive failure, as the parallel fiber did. However, the perpendicular fiber does create new areas of stress concentration in the leaflets at the ends of the fiber.

The CAD models can be readily devised into a composite valve where the fiber is embedded into the LLDPE matrix between two layers of LLDPE instead of laying over only one layer. Future simulations will compute embedded fiber in two layers of LLDPE to create a geometry contour at the fiber tip to reduce stress concentration. In addition, strategic bio-inspired fiber orientation, like collagen fiber orientation in native valves, will also be studied in computational modeling. Finally, these strategically reinforced valves will be devised using melt press technology and tested for hydrodynamic testing.

This research has shown drastic improvement in polymeric valve durability outcomes by strategic fiber placement. The fibers tucked at the back of the stent retained valve hydrodynamic performance. Therefore, this research can be considered a gateway towards improving durability outcomes using bio-inspired fiber placement strategies.

ACKNOWLEDGEMENTS

THIS WORK WAS SUPPORTED BY AMERICAN HEART ASSOCIATION GRANT #837028/Nipa Khair/2022.

REFERENCES

1. Bui, HT. et al., *Adv Healthc Mater.* 2021;10:e2100115.
2. Bui, HT. et al., 2022, US20220133474A1.
3. Heitkemper, M. et al., *Journal of the Mechanical Behavior of Biomedical Materials.* 2019;98:163-171.
4. Bui, HT. et al., *TCT-326 J Am Coll Cardiol.* 2021;78:B133-B133.
5. Sanadi, AR. et al., *MRS Online Proceedings Library.* 1992;266:81-92.

HIGH-FIDELITY FLUID-STRUCTURE-INTERACTION MODELLING EXPLAINS FLOW-INDUCED BRUITS AND MURMURS IN CEREBRAL ANEURYSMS

David A. Bruneau (1), Kristian Valen-Sendstad (2), David A. Steinman (1)

- (1) Department of Mechanical and Industrial Engineering, University of Toronto, Toronto, Ontario, Canada
(2) Department of Computational Physiology, Simula Research Laboratory, Oslo, Norway

INTRODUCTION

Cerebral aneurysms are prevalent (3-5% of adults), and with high mortality and morbidity if the aneurysm ruptures. For unruptured aneurysms discovered incidentally, there is a need for more reliable indicators of rupture risk than the basic systemic and morphological characteristics currently used [1]. Some aneurysms are known to produce sound in the range of 100-800Hz [2], and the wall vibration producing this sound could be a mechanobiological stimulus for deleterious wall remodelling or rupture.

The source and mechanism of aneurysm sounds has been debated for decades. It has been suggested that sounds could be caused by the aneurysm wall simply transmitting the frequency content of fluid vortex-shedding or “turbulence” [3], or that resonance of the aneurysm structure is creating the sound [4]. If we assume resonance is taking place, the dominant modes of vibration are not clear from the literature. “Breathing” mode vibration (aka “flexible Helmholtz resonator”), consisting of expansion and contraction of the aneurysm sac [4], has been considered as the only mode of vibration by most mathematical modelling studies (e.g., [5]), but recent studies have identified axisymmetric or “rocking” modes of vibration [6,8].

We have been the first to perform proof-of-concept FSI studies of aneurysm wall vibration, but only under steady [7] or ramped [6] flow conditions. In this study we performed the first pulsatile FSI simulations of vibrating intracranial aneurysms, the most detailed analysis of cerebral aneurysm vibration to date, to elucidate the mechanism of aneurysm wall vibrations.

METHODS

Three cerebral aneurysms (Cases 3, 9 and 16) previously shown by CFD to exhibit unstable flow at physiological flow rates [9] plus one stable-flow control (Case 8) were subjected to pulsatile inflow and pressure profiles (Figure 1) based on a 10% damped older-adult waveform [10]. Three cycles were run, with results shown from the

last cycle. Cycle-averaged, cross-sectional mean velocity was assumed to be 0.37 m/s [9], with a fully-developed Womersley velocity profile applied at the inlet.

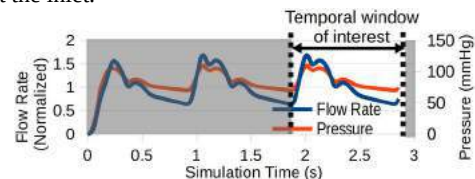


Figure 1 – Inlet flow (normalized to cycle-average flow rate) and pressure applied to the inner wall as a function of time, for all cases, starting from initial conditions.

Simulations were performed using a monolithic FSI solver (“turtleFSI”) [11], with solver settings as detailed in [6]. FSI meshes were generated using the Vascular Modelling Toolkit, with ~100k tetrahedral fluid elements and ~40k solid elements in each case. The solid was constructed as two additional layers of elements, with a total uniform wall thickness of 0.25 mm and an elastic modulus of 1 MPa. To prevent over-estimation of the pressurized aneurysm geometry, an approximate zero-pressure geometry was calculated and prescribed to these meshes, as detailed in [6]. Dynamic viscosity and density of the blood were 0.0035 Pa-s and 1000 kg/m³ respectively. A zero-pressure boundary condition was applied to the fluid at the outlets, with the physiological perfusion pressure prescribed as a distributed force normal to the FSI interface. The deformable region of the aneurysm geometry was a spherical region that fully enclosed the aneurysm sac, with the proximal and distal arteries fixed in space and rigid.

For comparison with sonic and Doppler ultrasound recordings in previous studies, sac-averaged spectrograms of the fluid velocity and wall displacement were generated to demonstrate the onset and nature of flow instability and vibration, following methods detailed in [6]. Wall displacements were band-pass filtered to obtain the mode shapes.

RESULTS

The three cases known to exhibit flow instability from previous CFD-only studies exhibited flow instability under pulsatile FSI conditions, as exhibited by the high-power (green to bright yellow) regions of the spectrograms (Figure 2), while the control Case 8 did not. Cases 3, 9 and 16 all exhibited high-frequency wall vibrations that persisted into diastole, after the flow had re-laminarized, as exhibited by the return to a flat, dark indigo in the fluid spectrograms. Visualizations of the sac motion showed that these persistent frequencies corresponded to “rocking” modes of the whole aneurysm sac (e.g., Figure 3), and a modal analysis showed that these were the natural vibration modes of the structure. These frequencies were related to the size of the aneurysm, with the largest aneurysm exhibiting the lowest frequencies (120–190 Hz in Case 16) and the smallest aneurysm exhibiting the highest frequencies (360 Hz in Case 9). Case 3 exhibited the largest amplitudes of vibration, indicated by the bright yellow band at ~220 Hz in the wall spectrogram. This prominent band is visible in the fluid spectrogram as well, suggesting feedback from the structure back to the fluid.

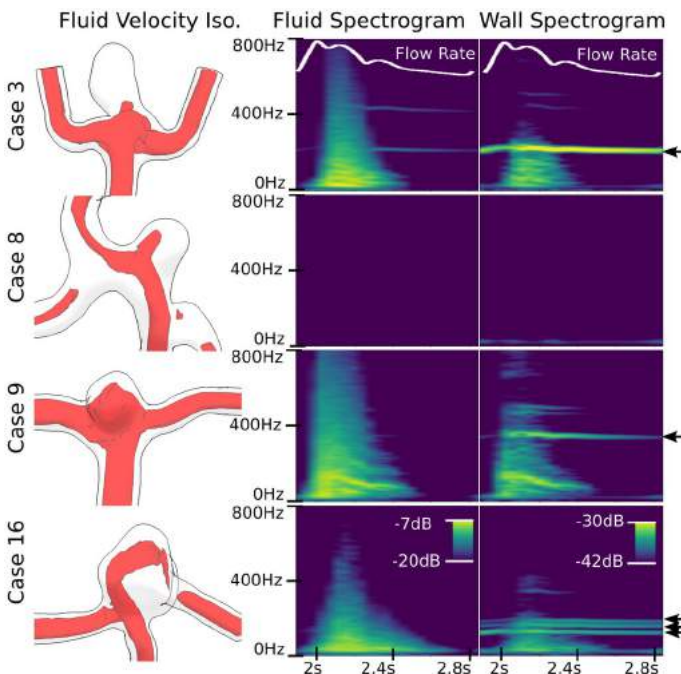


Figure 2 – (left) Peak systolic velocity isosurfaces at 0.5 m/s. (middle and right) Fluid and Wall spectrograms. The persistent bands in the wall spectrograms (indicated by arrows on the right) represent “rocking” modes of the aneurysm sac.

DISCUSSION

This study has some limitations, namely the linear elastic wall model with uniform walls, and the simplistic support method with no external damping, which may lead to some vibrations persisting longer than in a real aneurysm. However, the spectrograms do bear a striking resemblance to the Doppler ultrasound recordings of blood flow sounds from cerebral aneurysms with vasospasm reported by Aaslid and Nornes [12] (Figure 3). Those recordings consisted of a broadband systolic “bruit” with a narrowband “murmur” (or “spike”, as described by Sekhar and Wasserman [4]) superimposed; this murmur persisted until mid-diastole, after the bruit had subsided. In our results, the persistent band in the wall spectrogram (like the “murmur” in [12]) was due to vibration in a “rocking” mode of the aneurysm structure, where the sac “rocked” back and forth, while the underlying broadband wall response (like the “bruit” in [12]) mirrored the turbulent-like

fluid response. In other words, there is a resonant phenomenon taking place, with additional transitional or turbulent flow superimposed, exactly like the “turbulent” fluid bruit with superimposed resonant spikes suggested by Sekhar and Wasserman to describe their aneurysm recordings [4]. However, the “breathing mode” vibration described there [4] (and in most previous studies [5]) was not the primary source of narrow-band vibration in our study; “rocking” modes were the main cause. Similar to previous studies (for example, [5]), our results suggest that aneurysms do not self-excite in response to *stable* pulsatile flow, as shown by the control Case 8.

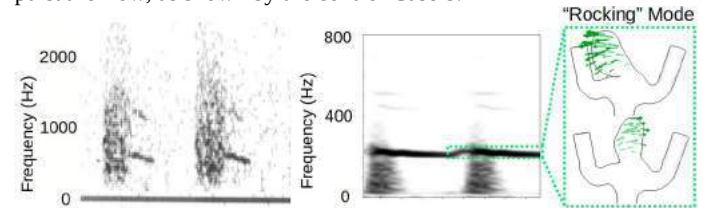


Figure 3 – (left) Two cycles of a Doppler ultrasound recording of cerebral vasospasm and aneurysm (from [12], with permission); (middle) wall spectrogram from Case 3 for the second and third cardiac cycle, shown in grayscale to highlight the similar broadband “turbulent” bruit and descending narrowband murmurs, the latter corresponding to “rocking” modes (right). The deformation of this mode shape was scaled by 1000x.

To explain the differences among the cases, it is thought that Case 3 vibrates most due to its oblong shape and therefore its lower resistance to bending about the neck, while Case 16 vibrates the least of the unstable-flow aneurysms, as it is the largest aneurysm and requires exposure to more prolonged flow instability to vibrate more, due to its larger mass and inertia.

Our simulations are the first to demonstrate the wall response of a cerebral aneurysm due to flow instability under pulsatile conditions. In multiple studies, it has been shown that vibration can disrupt the normal behaviour of mural cells, either by inhibition of the active force in smooth muscle cells and subsequently damaging to the passive structures [13] or damaging endothelial cells [14]. Future work aims to quantify the strains and stresses on the wall, to estimate the mechanobiological stimulus and relate this to the mechanobiological changes in the wall, and to assess the impact of more realistic wall and surrounding properties.

ACKNOWLEDGEMENTS

This work was supported by grants from the Natural Sciences and Engineering Research Council of Canada (DAS) and the Research Council of Norway (KVS) through the SIMMIS project (262827). DAB was supported by an NSERC Canada Graduate Scholarship.

REFERENCES

- [1] Turjman, A. et al., *Circulation* 129(3): 373–82, 2014
- [2] Kurokawa, Y. et al., *Stroke* 25(2): 397–402, 1994
- [3] Ferguson, G. *J Neurosurg* 33(5): 485–497, 1970
- [4] Sekhar, L., and Wasserman, B., *J Neurosurg* 60(3): 553–559, 1984
- [5] Shah, A. and Humphrey, J., *J Biomech* 32(6): 593–599, 1999
- [6] Bruneau, D. et al., *Biomech Model Mechanobiol* (in press), 2023
- [7] Souche, A. et al., *J Biomech* 145(Dec): 111369, 2022
- [8] Lamarquette, A., *PhD thesis, University of Cambridge*, 2021
- [9] Khan, M. O. et al., *Am J Neuroradiol* 36(7): 1310–16, 2015
- [10] Hoi, Y. et al. *Physiol Meas* 31(3): 291–302, 2010.
- [11] Bergersen, A.W. et al. *J Open Source Softw* 5(50): 2089, 2020
- [12] Aaslid, R., and Nornes, H., *J Neurosurg* 60(1): 32–36, 1984
- [13] Ljung, B., and Sivertsson, R., *Blood Vessels* 12: 38–52, 1975
- [14] Cho, J.G. et al., *Sleep* 34(6): 751–757, 2011

THE ROLE OF SKIN BIOMECHANICS IN TACTILE PERCEPTION OF ANTI-AGING FORMULATIONS

S. Hendrickx-Rodriguez (1), O. Elsafty (1), R. Dauskardt (2)

(1) Department of Mechanical Engineering, Stanford University, Stanford, CA, USA
(2) Department of Materials Science, Stanford University, Stanford, CA, USA

INTRODUCTION

Human skin regulates tactile perception of the world around us through interplay of the tissue's material properties and a system of mechano-sensitive cells. These mechanoreceptors transduce deformations in the skin to electro-chemical signals in the central nervous system [1]. Changes in the skin's microstructure, which could stem from UV exposure or moisturizer application, induce alterations in the skin's biomechanical state that trigger these mechanoreceptors. However, the relationship between skin biomechanics and how we perceive sensations remains unclear.

Anti-aging cosmetic formulations are associated with feelings of tightness and discomfort due to a contracting polymer film formed on the skin surface. A substantial amount of effort has been made in the development of formulations that assuage this discomfort while retaining skincare and aesthetic benefits. However, primary focus has been on optimizing chemical composition [2] and there remains no clear mechanism explaining why certain formulations outperform others.

In this work, we bolster a fundamental link between mechanical stresses in the top layer of skin, the stratum corneum (SC), and feelings of skin tightness. Furthermore, we show how careful combination of polymer films and moisturizers in anti-aging formulations can optimize both skin comfort and appearance.

METHODS

A three-pronged approach was used to connect the skin's biomechanical state to tactile perception, combining *in vitro*, *in vivo*, and *in silico* methods. First, SC from human cadaver skin was used to characterize the tissue's material properties in response to dehydration before and after application of cosmetic treatments. In particular, the substrate

curvature technique (Fig. 1) was used to measure stresses, σ_{SC} , in the thin SC ($h_{SC} \approx 20 \mu\text{m}$):

$$\sigma_{SC} = \frac{E_{sub}}{1 - \nu_{sub}} \frac{h_{sub}^2}{6h_{SC}} \kappa \quad (1)$$

E_{sub} and ν_{sub} are the elastic modulus and Poisson ratio of the substrate, h_{sub} is the thickness of the substrate ($\sim 174 \mu\text{m}$), and κ is the curvature of the substrate. Importantly, no information is needed about the elastic properties of the SC.

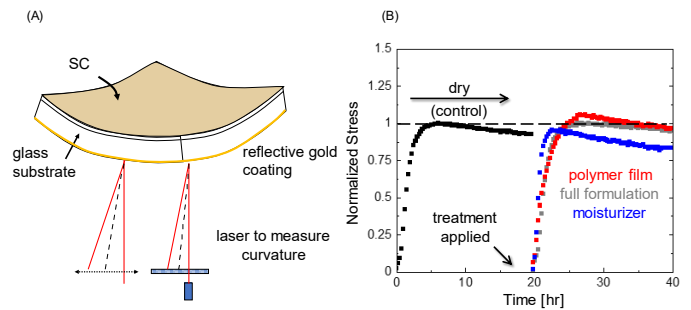


Figure 1: (A) Substrate curvature technique to measure SC stresses. The substrate's curvature increases as stress develops during dehydration. (B) Following application of either a contracting polymer film (red) or moisturizer (blue), peak stress increases or decreases. However, combining both components in the full formulation (grey) results in no peak stress change.

Stresses measured in the laboratory were used as inputs to a finite element (FE) model of a histologically accurate skin section. We used the FE model to calculate strains at mechanoreceptor locations. These strains correlate with the firing rate (number of neurological impulses sent per second) of these cells.

Complementary to the laboratory experiments and computational simulations, a consumer survey was conducted where volunteers assess the effectiveness and comfort of the full formulation.

RESULTS

The relationship between measured SC stresses and consumer perception for the full anti-aging formulation is compared with previous results for cleansers and moisturizers [3] in Fig. 2. Given the measured peak stress, we predict consumers would report tighter feeling skin for the polymer film by itself (red dashed arrow). However, these feelings could be assuaged by adding a soothing moisturizer (blue dashed arrow) in the full formulation (grey dashed arrow). In fact, 70% of consumers report the formulation combining polymer film and moisturizer feels comfortable on skin directly after application. This further establishes the connection between biomechanical state of the SC and feelings of tightness. Specifically, as SC stress increases due to application of a polymer film, increased deformation at mechanoreceptor sites leads to a higher firing rate which corresponds to augmented sensations of discomfort. However, inclusion of a moisturizer that reduces SC stress results in less deformation leading to lower firing rates and dampened feelings of tightness. Importantly, this reduction in skin discomfort had no adverse consequences on the effectiveness of the treatment.

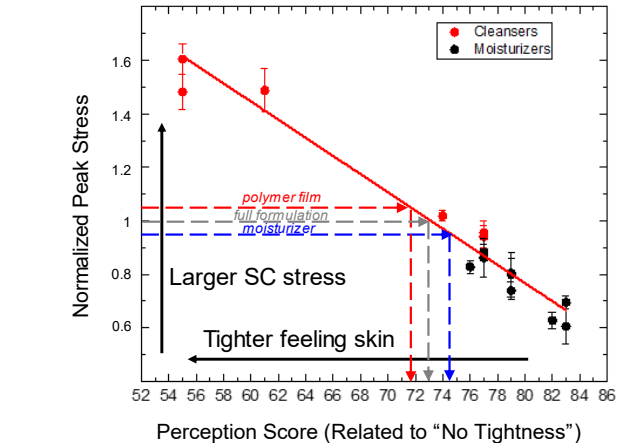


Figure 2: Relationship between consumer perception scores and measured SC stresses. Cleansers (red) and the polymer film increase SC peak stress and lead to tighter feeling skin. Moisturizers (black) decrease SC stress and soothe skin discomfort. The full anti-aging formulation (grey) combines a specific moisturizer (blue) with the stress-increasing polymer film.

The FE model provides the capability to explore the effect of topology on perception of skin tightness. Particularly, by inputting cheek and forehead histological sections, we see that different geometries propagate strains through the full-thickness skin in different ways (Fig. 3). Differing amounts of deformation at mechanoreceptors will lead to differing sensations.

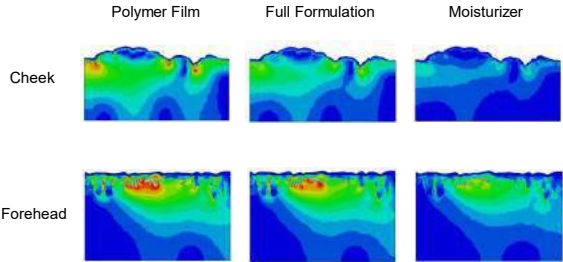


Figure 3: FE simulations of cheek and forehead histological sections after application of a polymer film, moisturizer, or full formulation that combines both. Topology as well as mechanoreceptor density and location affect the sensorial perception of our skin in response to topical treatments.

DISCUSSION

In this study, we establish a fundamental link between the SC’s biomechanical state and tactile perception, and use this to quantitatively understand the mechanism underlying sensorial perception of our skin in response to topical treatments. We demonstrate a new approach to understand and predict modifications of skin SC biomechanics by polymer films and moisturizers, and resulting consumer perception of comfort. The resulting model links SC modifications to the stimulation of mechanoreceptors well below the skin surface.

The synergistic integration of *in vivo*, *in vitro*, and *in silico* methods provides a novel framework for rapid testing of new formulations. Laboratory measurements allow for quick assessment of the SC’s biomechanical properties over time. Computational simulations can be used to explore skin regions and topographies that would be difficult in the lab. Finally, consumer surveys provide the necessary information to place computed firing rates in the appropriate neurological context.

Future studies will focus on further expanding the capabilities of the FE model to account for 1) 3D topological affects, 2) mechanoreceptor density in various body sites, and 3) precise mechanoreceptor location in full-thickness skin (e.g., higher concentrations near hair-shafts). Furthermore, the psychophysical framework developed can be extended to a full range of stimulations provided by haptic devices including wearable actuators and sensors. It also provides a novel way to study the body’s sensing system which could serve as inspiration for the design of soft robotics and stimuli responsive materials.

ACKNOWLEDGEMENTS

S.H.R. is supported by the National Defense and Engineering Graduate (NDSEG) Fellowship.

REFERENCES

[1] Johnson, K.O., *Curr. Opin. Neurobiol.*, 11(4):455-461, 2001.
[2] Hendrickx-Rodriguez, S. *Int. J. Cosmet. Sci.*, 44(5):486-499, 2022.
[3] Dauskardt, R., *32nd IFSCC Congress*, Lecture #31, 2022.

MECHANICAL CHANGES OF THE PREGNANT MURINE UTERUS

Emily A. Hoffmann (1), Shanmugasundaram Nallasamy (2), Kyoko Yoshida (1)

(1) Department of Biomedical Engineering, University of Minnesota, Minneapolis, MN, U.S.A.
(2) Department of Obstetrics, Gynecology and Reproductive Sciences, University of Vermont, Burlington, VT, U.S.A.

INTRODUCTION

Proper growth, remodeling, and mechanical function of the uterus are critical for a safe, term pregnancy. Abnormalities can lead to conditions like preterm birth, which can occur when the uterus contracts prematurely [1]. Preterm birth is the leading cause of infant and early childhood mortality and affects over 10% of pregnancies in the U.S. [1,2]. Mechanical and hormonal factors influence uterine contractility, but their mechanisms of action and how they influence the timing of labor is unknown. Our long-term goal is to understand the mechanisms of uterine growth, remodeling, and mechanical function during pregnancy to guide better diagnostics and treatments of preterm birth. Here, we characterize the mechanical environment that may affect uterine contractility: changes in *in situ* stretch, stiffness, and uterine material properties during pregnancy. These mechanical factors are important to understand because they result from, and drive, the growth (changes in size), remodeling (changes in material properties), and mechanical function of the uterus during gestation.

Therefore, the objectives of this study are to 1) experimentally measure biaxial *in situ* stretch and stiffness during gestation, and 2) fit a constitutive material model to our data to determine material properties and for future computational model development. In this work, we conduct biaxial stress-relaxation tests using the *in situ* stretch as a reference state to determine the most relevant mechanical properties for each gestation day. We use a mouse model for the advantages of a short gestation period, access to healthy tissue, and pregnancy-induced changes comparable to those in humans [3].

METHODS

Mouse uterine tissue was acquired at gestation days 12, 15, and 18 of a 19-day pregnancy (n=5-6 per group for *in situ* measurements; n=1 animal per group for biaxial testing). We isolated the reproductive tract, then marked a 5mm length in the longitudinal and circumferential directions on the regions around the pups (FIG. 1A). We removed the

pups to calculate the *in situ* stretch as the ratio of the lengths in the stretched and unstretched states (FIG. 1B). This measurement indicates the stretch that the uterus experiences during pregnancy and was used to calculate the stretch range for tensile testing.

Next, we cut a cruciform sample from the isolated uterus and conducted equibiaxial stress-relaxation tests (FIG. 1C). Each sample was stretched to 40%, 70%, 100%, 140%, and 180% of its *in situ* stretch and held for 30 minutes to allow stress relaxation. We calculated the maximum slope of the equilibrium stretch-force curve to assess stiffness. While previous studies have reported only longitudinal material properties of the uterus [4], our biaxial testing more closely replicates the pregnant loading condition.

To determine tissue material properties, we generated sample-specific finite element (FE) models and simulated biaxial stretching using FEBio (v. 3.6.0). We modeled two layers of tissue, one with longitudinal fibers and one with circumferential fibers, to reflect the fiber distribution of the mouse uterus [5]. We then fit a transversely isotropic Mooney-Rivlin (TIMR) material model to our equilibrium stretch versus force data by sweeping a range of values for the parameters $c1=[0.0005-0.1]$, $c3=[0.003-0.1]$, and $c4=[1.4-25]$, while fixing the parameters $c2=0$, $c5=0$, $k=100$, and $\lambda_{max}=10$ to avoid overfitting. We determined the best-fit parameter set that minimized the sum of squared error between experimental and model forces.

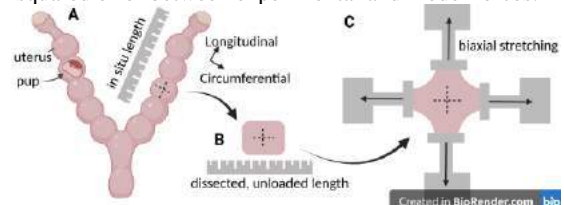


Figure 1: The *in situ* lengths were measured in the longitudinal and circumferential directions by comparing A) stretched versus B) unstretched lengths. C) Biaxial stretching setup.

RESULTS

In situ stretches in both the longitudinal and circumferential directions remained constant between gestation day 12 (long.: 1.06, circ.: 1.23) and day 15 (long.: 1.09, circ.: 1.19), then increased significantly by day 18 in the longitudinal direction (long.: 1.19, circ.: 1.22) (FIG. 2A, one-way ANOVA $p < 0.05$). There were no significant changes with gestation in the circumferential direction and no significant differences between the longitudinal and circumferential directions at each timepoint. These results suggest that the amount of stretch the pregnant uterus experiences is similar during mid-gestation (between days 12 and 15) and increases near term. They also indicate that that tissue experiences isotropic stretch.

In the biaxial tensile tests, maximum stiffness was higher in the circumferential direction compared to longitudinal (FIG. 2B). As pregnancy progressed, the maximum stiffness values increased. Longitudinal maximum stiffness values were 0.30, 0.62, and 0.93 [N/-] and circumferential maximum stiffnesses were 0.58, 0.84, and 1.48 [N/-] at days 12, 15, and 18, respectively. While the maximum stiffness increased, the toe region of the stretch-force curve elongated as gestation progressed (longitudinal: FIG. 2C, circumferential: FIG. 2D).

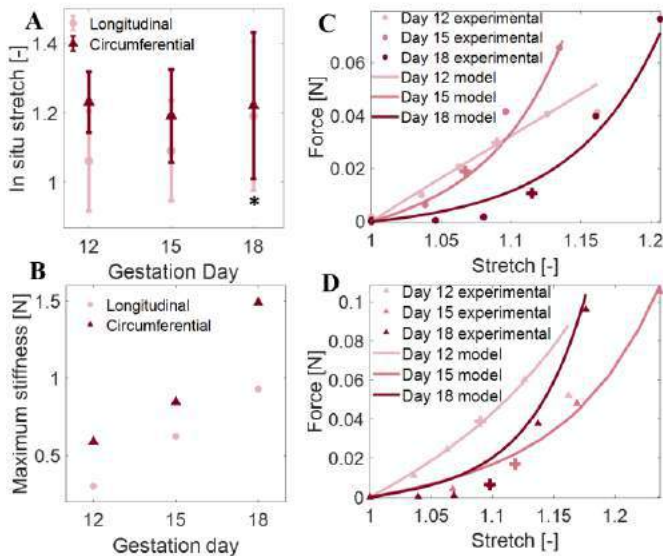


Figure 2: A) *In situ* stretch (*significant in the longitudinal direction compared to day 12 ($p < 0.05$)). B) Maximum stiffness increased with pregnancy. C) Biaxial stretch-force (dots) and model fits (lines) for the longitudinal direction and D) circumferential direction (+ indicates *in situ* stretch).

Our FE model was able to capture the material behavior on days 12, 15, and 18 of pregnancy, indicating that a TIMR material model can describe the material behavior of the pregnant mouse uterus (lines in FIG. 2C, 2D and Table 1). Over the course of gestation, the parameters $c1$ and $c3$ generally decreased, reflecting the elongated toe region, while $c4$ increased to reflect the increase in maximum stiffness (FIG. 2B).

Table 1: Best-fit TIMR material parameters.

	Longitudinal			Circumferential		
	Day12	Day15	Day18	Day12	Day15	Day18
$c1$ [Pa]	0.03	0.005	0.0005	0.02	0.006	0.003
$c3$ [Pa]	0.04	0.01	0.003	0.05	0.008	0.003
$c4$ [-]	5	21	18	11	16	24
r^2 value	0.93	0.87	0.96	0.99	0.99	0.95

DISCUSSION

The objective of this study was to characterize changes in the mechanical environment of the murine uterus during pregnancy. We report changes in biaxial *in situ* stretch and stiffness at three gestational timepoints. We conduct mechanical testing around the sample-specific *in situ* stretch measurements to determine relevant material property changes during pregnancy. Finally, we fit a TIMR material model to our experimental data and report material parameter changes of the mouse uterus throughout gestation.

Our results show that *in situ* stretch remains constant until day 15 of a 19-day gestation, suggesting that the uterus grows at a similar pace to the growing pups during this period. By day 18, *in situ* stretch increases, indicating that pup growth begins to outpace uterine growth at term. Our measurements of *in situ* stretch (FIG. 2A) agree with previous results from rabbit uteri that show a similar increase in *in vivo* length towards the end of gestation [6].

Our biaxial data show that the toe region of the stretch-force curve elongated and the maximum stiffness increased as pregnancy progressed. The toe region elongation agrees with changes seen in the pregnant murine cervix [7] and in previous uniaxial tests on uterine tissue [4,8], although the increase in maximum stiffness was not observed in these prior studies. However, our results generally agree with a recent study that demonstrated an increase in collagen fiber organization with progressing gestation in the mouse uterus [5], as increased fiber organization would suggest an increase in stiffness. Disagreements in our maximum stiffness measurements with previous mechanical data could be due to differences in the loading conditions (uniaxial vs. biaxial) or in how the reference state was defined. We are testing additional samples to further investigate these results.

Finally, we were able to capture our experimental stretch-force curves with our FE simulations using a TIMR material model, indicating that TIMR is an appropriate constitutive model to describe the mechanics of pregnant uterine tissue. We were able to describe the elongation of the toe region in our data with the decrease in the $c1$ and $c3$, while the increase in $c4$ (the exponential parameter) reflects the increase in maximum stiffness.

In conclusion, we develop and report a novel method to assess uterine material property changes during pregnancy in mice. Specifically, we connect *in situ* stretch measurements to *ex vivo*, biaxial stress-relaxation tests to determine the most relevant material property changes of the uterus during pregnancy. The main limitation of our current work is the low animal number ($n=1$) for mechanical testing and we are conducting additional tests to determine statistical significance. These data will inform our FE model of the uterus, through which we will examine how mechanical signaling controls uterine growth and remodeling during pregnancy. In the future, we aim to use this knowledge to improve prediction and prevention of preterm birth.

ACKNOWLEDGEMENTS

The work was supported in part by the University of Minnesota's College of Science and Engineering Fellowship.

REFERENCES

- [1] Romero, R. et al., Science, 345, no.6198:760–765, 2014.
- [2] WHO, [Online] Organisation mondiale de la Santé, 2017.
- [3] Mahendroo, M. Reprod. Camb. Engl., 143, no.4:429–438, 2012.
- [4] Wu, X. et al., J. Cell. Mol. Med., 12, no. 4: 1360–1373, 2008.
- [5] Ouellette, A. et al., Biol. Reprod., p. ioac102, 2022.
- [6] Schofield, B. and Wood, C., J. Physiol., 175, no. 1:125–133, 1964.
- [7] Yoshida, K. et al., Acta Biomater., 36:195–209, 2016.
- [8] Conrad, J. et al., Am.J. Obstet. Gynecol., 96,no.8:1055–1059, 1966.
- [9] Shynlova, O. et al., REPRODUCTION, 139, no.1:247–253, 2010.

QUANTIFYING THE REMODELING STRAIN IN THE LAMINA CRIBROSA YEARS AFTER PRESSURE LOWERING SURGERY

Cameron A. Czerpak (1) Harry A. Quigley (2), Thao D. Nguyen (1)

(1) Mechanical Engineering, Johns Hopkins University, Baltimore, MD, United States

(2) Ophthalmology, Johns Hopkins University, Baltimore, MD, United States

INTRODUCTION

The lamina cribrosa (LC) is a collagenous tissue at the end of the optic nerve head (ONH). The cribriform plates of the LC resemble a network of beams and pores when viewed *en face*. Retinal ganglion cells (RGC) exit the eye through the LC, and the LC supports the RGCs from intraocular pressure (IOP) [1,2]. Glaucoma is a blinding disease associated with a chronic elevation in IOP, and the human LC is the primary site of RGC axon injury in glaucoma [3]. The LC also remodels with glaucoma. The LC thins and becomes more curved with axon damage [4]. The pores become smaller and the collagen and elastin composition changes [5,6]. Therefore, mechanical deformations in the LC caused by changes in IOP or remodeling may be a biomarker for developing glaucoma or glaucoma progression.

Optical coherence tomography (OCT) has recently been used to measure the motion of structural features of the ONH *in vivo* in response to changes in IOP and remodeling [7,8]. We and others have measured the change in the anterior LC depth and strain to changes in IOP using digital volume correlation (DVC) [9,10]. Our study of 29 suturelysis procedures measured the acute strain response in the LC from IOP lowering by suturelysis. Radial OCT scans were acquired of the ONH before and 20 minutes after suturelysis and DVC was applied to the before and after-lysis scans to calculate the strain field [10]. We found tensile anterior-posterior strain of $0.95 \pm 1.2\%$ and LC border movement of $1.3 \pm 6.3 \mu\text{m}$ posterior (out of the eye).

In contrast, previous studies have used only the displacement of the anterior LC border to characterize the long-term remodeling response to a change in IOP. Kadziauskienė et al. showed the largest movement of the LC border occurred 3-10 days after pressure lowering and was $37 \mu\text{m}$ anterior [11]. The LC border continued to move anterior at a slower rate up to 6 months following pressure lowering ($65 \mu\text{m}$ anterior). Krzyżanowska-Berkowska et al. found that the LC border had the largest anterior motion at 1 month following pressure lowering ($60 \mu\text{m}$ anterior), then remained at a constant depth at follow-up measurements

up to a year [12]. These results suggest there is a passive viscoelastic response shortly after IOP lowering, followed by a period of active remodeling. However, the motion of the anterior LC border may not predict the strains the LC experiences from remodeling [10]. This study aims to quantify the active biomechanics in the LC by measuring the long-term deformation response in the LC years after IOP lowering by suturelysis.

METHODS

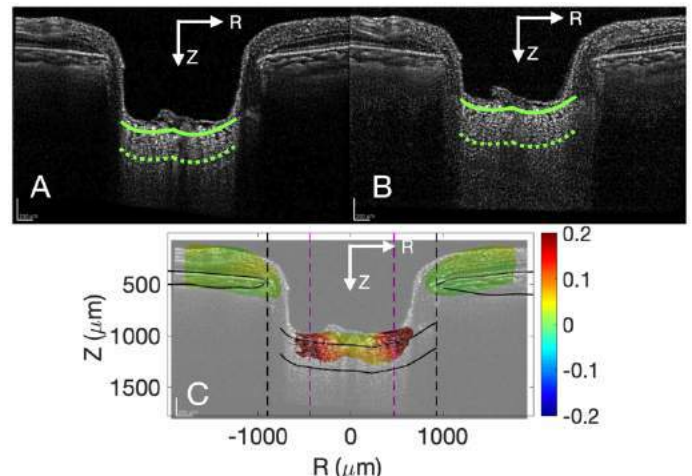


Figure 1: A) OCT image of the optic nerve head after suturelysis, B) 1 year later, and C) the anterior-posterior strain map.

Twelve patients who previously had trabeculectomy and suturelysis surgery were reimaged 1–4 years following the suturelysis surgery. The average patient age was 65.8 ± 6.7 years and glaucoma damage, as measured by mean deviation (MD), ranged from -1.3 to $-$

27.4 dB at the time of suturelysis. IOP was measured by an iCare tonometer and applanation. IOP before the trabeculectomy surgery was calculated from the average of up to 3 applanation IOP measurements. The iCare tonometer was used to measure IOP immediately before and 20 minutes after suturelysis, and at the follow-up appointment 1-4 years after suturelysis. We also recorded the average and maximum of applanation IOP measurements taken between the suturelysis surgery and the follow-up appointment.

Heidelberg Spectralis (Heidelberg, Germany, Heidelberg Engineering) was applied to capture 24 radial scans of the ONH. Three sets of OCT images were captured 20 minutes after suturelysis, and at the follow-up appointment 1-4 years after suturelysis. Images were preprocessed to increase contrast and reduce noise by contrast-limited adaptive histogram equalization (CLAHE) and Gamma correction (Fig. 1). The Bruch's membrane opening and the anterior border of the LC were marked, and a curve was drawn 250 μm posterior to delineate the anterior portion of the LC.

DVC was applied between follow-up scans and after-lysis scans to estimate follow-up LC strains and anterior LC displacement, which include the effects of creep, IOP change over time, and tissue remodeling in response to IOP-lowering. We calculated E_{zz} , $E_{\theta\theta}$, E_{rr} , $E_{r\theta}$, $E_{\theta z}$, E_{rz} over R, θ , and Z, and calculated the maximum principal strain (E_{max}) and maximum shear strain (Γ_{max}) in the RZ plane. Baseline DVC error was calculated by measuring the strain response from subsequent image sets 20 minutes after-lysis to measure the repeatability of the strain measurements. We calculated correlation error by numerically applying a deformation to an after-lysis image and measuring the difference between the numerically applied strain and the strain measured from DVC. We used t-tests to determine the significance of the mean LC strains and to compare strain to the baseline error and correlation error. Relationships between the follow-up strain, IOP, LC border movement, and glaucoma damage (MD, and nerve fiber layer (RNFL)) were analyzed using linear regression.

RESULTS

Remodeling produced a mean tensile anterior-posterior strain (E_{zz}) $11.5 \pm 20.0\%$ in the LC ($p=0.073$) and the LC border displaced by an average of $62.7 \pm 59.8 \mu\text{m}$ anteriorly ($p=0.004$). The mean E_{zz} was borderline larger than the baseline error ($p=0.078$) and the correlation error ($p=0.085$). The follow-up strains in the radial direction ($E_{rr} = 0.36 \pm 1.14\%$) and circumferential direction ($E_{\theta\theta} = -0.61 \pm 2.35\%$) were over an order of magnitude smaller than E_{zz} and not significant. Follow-up shear strains ($E_{r\theta} = 0.48 \pm 1.28\%$), ($E_{\theta z} = -0.28 \pm 1.41\%$), ($E_{rz} = -0.58 \pm 1.41\%$) were also small and not larger than 0 or error. Maximum principal strain ($E_{max} = 15.3 \pm 18.9\%$) and maximum shear strain ($\Gamma_{max} = 9.40 \pm 9.07\%$) were both larger than 0 ($p=0.017$, 0.004 respectively).

Multiple measures of IOP were associated with $E_{\theta\theta}$ and anterior LC displacement. More tensile $E_{\theta\theta}$ was associated with higher pre-trabeculectomy IOP ($p=0.045$) and greater IOP decrease from before trabeculectomy to after suturelysis ($p=0.057$) (Fig. 2). Lower IOP measured immediately before the suturelysis was associated with greater anterior movement of the LC at follow-up ($p=0.025$).

A larger anterior movement of the LC border at follow-up was associated with tensile E_{zz} ($p=0.007$), E_{max} ($p=0.005$), and Γ_{max} ($p=0.004$). More negative MD ($p=0.052$), indicating worse damage to the visual field, and a greater decrease in MD ($p=0.015$), indicating greater worsening of the visual field, measured at the follow-up appointment were associated with greater tensile $E_{\theta\theta}$ strain. Thinner RNFL thickness, indicating worse damage, at suturelysis was associated with larger follow-up E_{zz} ($p=0.035$) and E_{max} ($p=0.045$) (Fig. 2). Eyes

with a greater after-lysis shear compliance (after-lysis $E_{\theta\theta}$ /IOP decrease from lysis) had a greater follow-up E_{zz} ($p=0.004$).

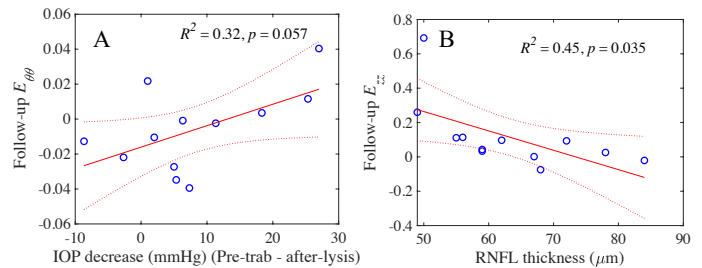


Figure 2: A) Greater tensile follow-up $E_{\theta\theta}$ was associated with greater IOP decrease from before trabeculectomy to after-lysis. B) Greater tensile follow-up E_{zz} was associated with thinner RNFL thickness.

DISCUSSION

The study suggests that the LC deformation can be reliably and accurately measured years after IOP lowering by suturelysis. The acute after-lysis deformation from IOP lowering was up to 10 times smaller than those measured years later. The anterior border movement was 47 times larger at follow-up. Remodeling increased LC thickness, reduced LC circumference and produced an anterior border movement.

LC remodeling has a complicated relationship with IOP change. We did not find that a greater IOP decrease from before trabeculectomy to after suturelysis produced greater anterior motion of the LC border nor larger tensile E_{zz} . A limitation of the method is the small sample size, and a larger sample size may be needed to determine the relationship between IOP change and ONH remodeling.

Eyes with greater glaucoma damage at suturelysis, as measured by MD and RNFL, and greater worsening of glaucoma damage, measured by MD change from suturelysis to follow-up, experienced more remodeling. Furthermore, a more compliant LC measured at suturelysis was associated with greater glaucoma damage and greater remodeling at follow-up. The structural compliance of the LC at suturelysis and LC strains at long-term follow-up may represent new potential biomarkers for early diagnosis of glaucoma and glaucoma progression.

ACKNOWLEDGEMENTS

Supported by NIH NEI EY 02120, Brightfocus G2021012S, and Research to Prevent Blindness

REFERENCES

- [1] Burgoyne, CF et al., *Prog Retin Eye Res.* 24(1),2005
- [2] Sigal, IA et al., *Exp Eye Res.* 88:799-907,2009
- [3] Quigley, HA et al., *Ophthalmology.* 86(10),1979
- [4] Quigley, HA et al., *J Glaucoma.* 8(6),1999
- [5] Summers Rada, JA et al., *Exp Eye Res.* 82(2),2006
- [6] Wang B, et al., *Invest Ophthalmol Vis Sci.* 54(13),2013
- [7] Quigley, H et al., *Invest. Ophthalmol Vis. Sci.* 58, 2566, 2017.
- [8] Rhodes, LA et al., *Invest Ophthalmol Vis Sci.* 55:8123-8133, 2014.
- [9] Girard, MJA et al., *Ophthalmology.* 123(6),2016
- [10] Czerpak, CA et al., *Ophthalmol Glaucoma.* 2022.
- [11] Kadziauskienė, A et al., *Ophthalmology.* 125(11),2018
- [12] Krzyżanowska-Berkowska, P et al., 256(4),2018

TIME AND STRAIN DEPENDENT PROPERTIES OF THE EXTRACELLULAR COLLAGEN MATRIX REGULATE CELLULAR MECHANICAL MEMORY AND ACTIVATION LEVEL OF FIBROBLAST CELLS

Yuan Hong (1,2), Xiangjun Peng (1), Haomin Yu (1,2), Mohammad Jafari (3), Delaram Shakiba (1), Jacob Sandler (1,2), Kenneth M. Pryse (1,2), Justin M. Sacks(4), Elliot L. Elson (1), Guy M. Genin (1,2), Farid Alisafaei (1,3)

- (1) NSF Science and Technology Center for Engineering Mechanobiology, Washington University, St. Louis, Missouri, United States
- (2) Department of Mechanical Engineering and Materials Science, Washington University, St. Louis, Missouri, United States
- (3) Department of Mechanical Engineering, New Jersey Institute of Technology, Newark, New Jersey, United States
- (4) Division of Plastic and Reconstructive Surgery, Washington University School of Medicine, St. Louis, Missouri, United States

INTRODUCTION

Each year only in America 8.2 million suffer a chronic wound arising from burns, diabetic ulcers, skin cancer surgery, or infection¹. Surgical repair of chronic wounds often requires split-thickness skin grafts in which epidermis and a thin part of the dermis from one site are harvested, cut into a meshwork, and stretched to cover a larger wound area (Fig.1A). In the process of skin grafting and as a result of skin graft stretching, cells within the skin graft experience static tensile strains. The main drawback of split-thickness skin grafting is excessive contracture of the skin graft in the wound site which is caused by the activation and transition of low-contractile fibroblasts to hyper-contractile myofibroblast cells². While a low amount of cellular contractile forces is required for wound healing, excessive contractile forces generated by hyperactivated cells can cause tightening of the skin graft, pain, scarring, and even graft failure³. On top of that, factors such as aging, obesity, and peripheral vascular disease postpone the wound healing process⁴, causing cells to remain under tension for a longer period in stretched skin grafts until new skin is produced and tension decreased.

We hypothesized that the magnitude and duration of the tensile strain that cells experience within a meshed graft regulate the activation of fibroblasts and can induce long-term mechanical memory in cells. To test the hypothesis, we first measured the strain fields that cells experience within a meshed graft and we found that the strain magnitude can significantly change by altering grafting parameters such as meshing ratio. We then evaluated the responses of human dermal fibroblasts to these strain levels within tissue constructs, and we found that cell activation and memory induction change with strain magnitude in a biphasic manner. Finally, using an integrated computational and experimental approach, we showed that the biphasic response is regulated by the time and strain-dependent behavior of the extracellular matrix (ECM).

METHODS

The human dermal fibroblasts (HDFs) at P4-8 were trypsinized, resuspended in fresh DMEM and then added to mouse rat tail-derived

type I collagen in acetic acid and 2X DMEM. After neutralizing the pH with sodium hydroxide, 1 mL of the mixture containing 1.5×10^6 cells/mL HDFs and 1.2 mg/mL collagen was poured into each cylindrical casting well and was incubated at 37 °C with 5% CO₂ for 2 d for the polymerization and compaction of the tissue. These casting wells for tissue construction were made with Teflon and have a mandrel with a diameter of 9.65 mm at the center to construct a tissue ring for the tensile test (Fig. 2A).

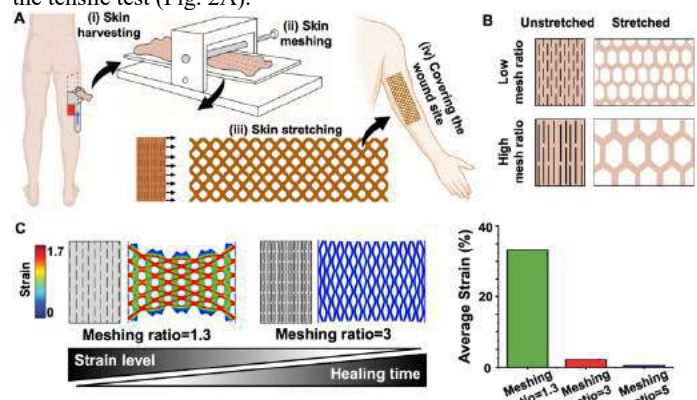


Figure 1: Skin graft meshing ratio can be tuned to tailor strain levels by an order of magnitude during graft stretching.

The custom-made tensile tester with sensitive isometric force transducers and stepper motors was plugged into an Arduino for applying displacement precisely (Fig. 2B). The tissue rings removed from the casting wells were hung onto the attachment bars, bathed with 25 mM HEPES buffered DMEM with 10% FBS and 1% PS at 37 °C. Then the attachment bars were separated at a 13.3 mm distance under the control of the Arduino. The initial force was measured by removing the lower attachment bars away from the samples to define the zero-force points. The samples were moved to a pre-strain setup in normal DMEM at 37 °C with 5% CO₂ for desired strain levels with 3D printed spacers with different lengths for 1h or 24h. Then the spacers were

removed to relax the tissues for another day. Then, the samples were treated with 2 μ M cytochalasin-D (cyto-D) for 1h. The cyto-D treated samples were tested with the 5% strain for 10 mins (Fig. 3A) for ECM mechanical property.

RESULTS

To test the hypothesis that the strain field within a graft varies with the meshing ratio, we evaluated how the strain field that cells experience in a skin graft is affected by altering grafting parameters such as meshing ratio (Fig. 1B). Using Holzapfel-Gasser-Ogden model, we found that the strain distribution in stretched skin grafts depends strongly on the meshing ratio (Fig. 1C). Skin meshed with higher meshing ratios has higher numbers and longer cuts, and can be stretched easily without undergoing high tensile strains. These lower macroscopic strains mean that cells within skin grafts with higher meshing ratios experience lower strain levels. Note that meshing ratios of 1 to 5 are frequently used in skin graft surgeries and our results show that the choice of meshing ratio can induce more than an order of magnitude change in the average strain level that cells experience in the skin graft with average strains of over 30% possible (Fig. 1C).

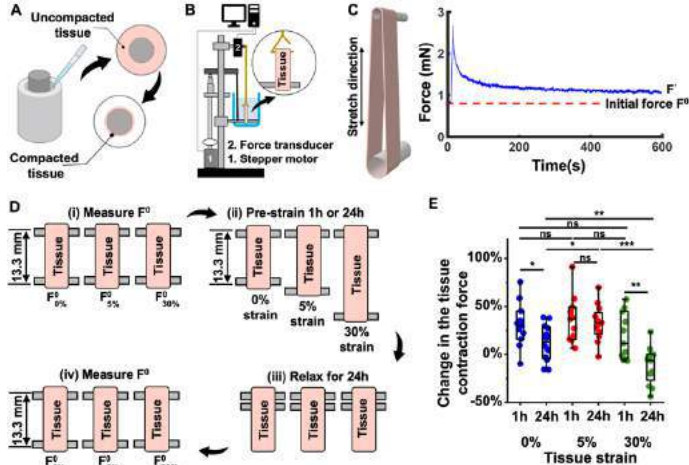


Figure 2: The strain field generated in stretched skin grafts determines the activation level of fibroblast cells.

We next studied whether the 30% change in the strain level of cells can affect their behavior by inducing a long-term increase or decrease in cell contractility level. Our results showed that the contractility level of cells and the traction force they generate depend in a biphasic manner on the magnitude of strain that they experience in their skin grafts (Fig. 2E); tissue stretching even with a small strain of 5% for 24h drove cells permanently into a higher contractile state, while very large strains significantly reduced tissue contractile force. This indicates that the level of strain that cells experience in skin grafts can cause permanent activation/deactivation of cells and therefore affect the outcome of skin graft surgeries as hypercontractility of cells can cause excessive tissue contraction, while low contractility of cells can delay and even curtail the wound healing process. Interestingly, the biphasic strain magnitude-dependent behavior was only observed in tissues loaded for 24 h, while the tissues loaded for 1h showed no significant change in contraction force. This indicates that the cell memory induction and thus permanent activation/deactivation of cells in tissues are not only a function of the strain level but also highly depend on the loading duration. As external forces are transmitted to cells through the extracellular collagen matrix^{5,6}, we next studied the role of ECM mechanical properties in cell memory induction.

To decouple the effects of cells and matrix on the total tissue contractile force F^0 , we treated the tissues with cyto-D to disrupt the actomyosin contractility of the cells. Then we tested the cyto-D treated tissues with the relaxation test to determine whether the ECM stiffness in any of the tissues has been affected by the magnitude and duration of external stretching (Fig. 3A). We found that the ECMs of the tissues loaded for 1h showed the same stiffness, independent of the strain magnitude in the tissue. They also exhibited higher stiffness than the ECMs of the tissues loaded for 24h. Interestingly, the softening in the 24h group increased with the strain magnitude in the tissue where the tissue loaded with 30% strain showed significantly lower stiffness (Fig. 3E). Note that cells in this group showed the lowest level of actomyosin contractility and activation level (Fig. 2E). This indicates that long-term loading on tissues can cause opposite permanent effects on cell behavior: long-term tissue stretching with small strain magnitudes can promote actomyosin contractility of cells and permanently transmit them to a hypercontractile phenotype, while long-term tissue stretching with large strain magnitudes can damage and soften the ECM and subsequently deactivate cells (Fig. 3F).

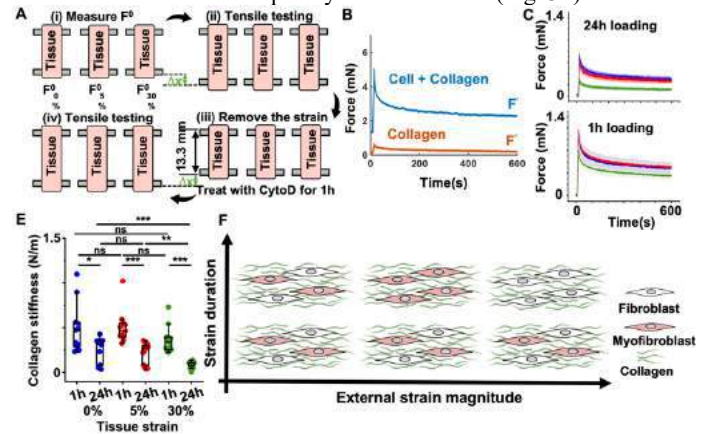


Figure 3: The long-term effect of pre-straining on tissue contractility is due to cell activation and not due to the ECM.

DISCUSSION

Cells in skin grafts undergo stresses whose magnitude depends on surgical parameters including meshing ratio, meshing orientation, skin physical properties, and wound site geometry. While current grafting protocols do not account for these mechanobiological factors, our results showed that these stresses and their durations can activate mechanosensing pathways and drive fibroblast cells to a higher or lower contractile phenotype. Using an integrated experimental and theoretical approach, we showed that by tailoring of meshing configuration, we can harness the molecular machinery of mechanotransduction to enable skin graft contracture that prevents excessive contracture while keeping the baseline contractility required for wound closure.

ACKNOWLEDGEMENTS

This work was funded by National Science Foundation Center for Engineering Mechanobiology.

REFERENCES

- 1 Sen, C. K. *Advances in Wound Care* 10, 281–292 (2021)
- 2 Elson, E. L. *et al. Prog Biophys Mol Biol* 144, 30–40 (2019)
- 3 Davidson, M. D. *et al. Adv Healthc Mater* 9, (2020)
- 4 Khalil, H. *et al. Wound Repair and Regeneration* 23, 550–556 (2015)
- 5 Alisafaei, F. *et al. Proc Natl Acad Sci U S A* 116, 13200–13209 (2019)
- 6 Discher, D. E. *et al. Science* (1979) 310, 1139–1143 (2005)

STRESS QUANTIFICATION ON INTACT AND TORN ROTATOR CUFF TENDONS

Nicole Tueni (1), Farid Amirouche (1,2)

- (1) University of Illinois at Chicago Department of Orthopaedic Surgery, Chicago, Illinois, USA
(2) Northshore University Department of Orthopaedic Surgery, Evanston, Illinois, USA

INTRODUCTION

The rotator cuff is a set of muscles attached to the humeral head via tendons. They surround the shoulder joint and securely retain the upper arm bone's head within the scapula's shallow socket, hence ensuring the glenohumeral joint stability. The tendon-to-bone attachment connects two very different materials: a compliant tendon and a stiff bone. It is thus prone to high-stress concentrations and an increased risk of failure. This study aims at developing a full numerical model of the glenohumeral joint, comprising cartilage, muscles, tendons, and ligaments, in order to shed light on the mechanisms of rotator cuff tears.

METHODS

From CT scans, the scapula, humerus, and clavicle bones were generated using *Materialise MIMICS* for bone segmentation. The surfaces of the four muscles were then designed using the bone surfaces and then extruded to obtain the muscle volumes in *Ansys SpaceClaim*. Each volume was then sectioned into two parts, separating the tendon from the muscle. Moreover, the muscles were sectioned into several parts representing the local orientations of the fibers (See Figure 1, Left).

Three cases were investigated: (a) an intact shoulder, (b) a shoulder with an induced partial tear of half of the subscapularis tendon width, and (c) a shoulder with an induced subscapularis tendon total transverse tear and a partial attachment to the humerus (See Figure 1, Right).

The complete assembly was then imported into *Abaqus CAE*, where the local fiber orientations were defined using the *Orientation* function.

Elastic material parameters with a Young modulus and a Poisson's ratio were assigned to the bones [1], while hyperelastic material properties were assigned to the muscles, tendons, cartilage, and ligaments. For the ligaments and cartilages, isotropic Arruda-Boyce and Neo-Hookean models were adopted respectively [2,3], and transversely isotropic Holzapfel-Ogden model parameters were assigned for the muscles and tendons [4,5].

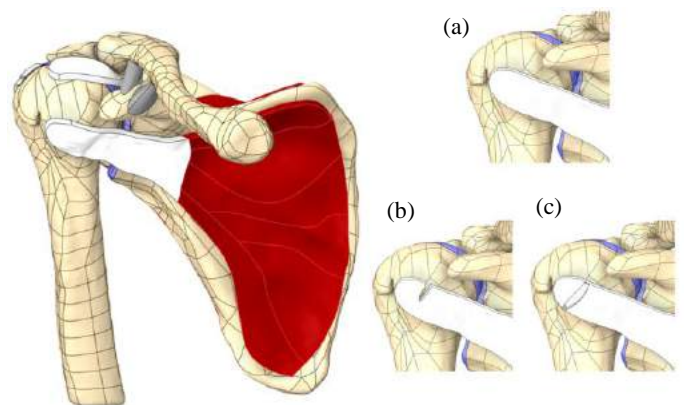


Figure 1: Left: Complete 3D model. Yellow: bones, Red: muscles, White: tendons, Gray: ligaments, Blue: cartilage. Right: (a) Intact tendon (b) Tendon with partial transverse tear (c) Tendon with total transverse tear with partial attachment to the humerus

A tie connection was considered between the four muscles and the scapula and humerus bones, as well as between the ligaments linking the clavicle to the scapula. The glenohumeral joint was modeled using a frictionless contact, consisting of a normal and a tangential component. Furthermore, in order to mimic an abduction motion of the shoulder, the scapula was fixed, and a displacement was imposed on the humerus.

RESULTS

Figure 2 shows the stress distribution map for the three cases. The intact shoulder shows a stress concentration with a peak at mid-width of the tendon-bone attachment (Figure 2, a). We induced the partial tear on this region and observed a local increase of the stress by approximately 160% (Figure 2, b), with a peak stress on the inner edge of the tear. Interestingly, the total transverse tear (Figure 2, c), showed a 120% decrease of peak stress compared to the partial tear, implying a more homogeneous distribution of the stress in the case of a total transverse tear.

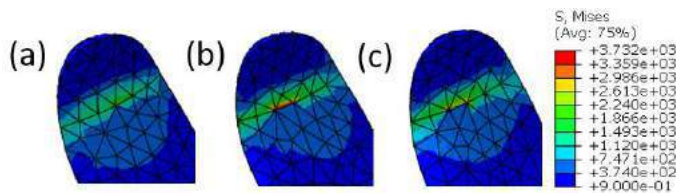


Figure 2: Stress distribution maps on the tendon-to-bone attachment for the three studied cases.

DISCUSSION

The developed model predicts the injury location in the tendon and quantifies the medically observed stress evolution in case of a tear. To improve this model, muscles should be segmented using high-definition MRI. Furthermore, the results should be validated using experimental data. In future work, different repair techniques, commonly used by orthopaedic surgeons, will be simulated and compared. Moreover, the impact of tendon tears on the glenohumeral joint stability could be analyzed.

ACKNOWLEDGEMENTS

The authors would like to thank the University of Illinois at Chicago and the Northshore University Health Systems for their support.

REFERENCES

- [1] Seki, N et al., *J Orthop Sci*, 13:348-353, 2008.
- [2] Velasquez Garcia, A et al., *J Orthop Surg*, 17:73, 2022.
- [3] Junior, A et al., *Med Eng Phys*, 110:103898, 2022.
- [4] Kuravi, R et al., *JMBBM*, 117: 104375, 2021.
- [5] Diniz, P et al., *J Orthop Res*, 2022.

USING A THREE-DIMENSIONAL BIVENTRICULAR MATHEMATICAL MODEL TO HELP UNDERSTAND SEX DIFFERENCES IN THE ONSET AND PROGRESSION OF PULMONARY ARTERIAL HYPERTENSION

Kristen M. Garcia (1), Becky A. Hardie (1), Jennifer Stowe (1), Daniela Valdez-Jasso (1)

(1) Department of Bioengineering, University of California San Diego, La Jolla, CA, US

INTRODUCTION

Pulmonary arterial hypertension (PAH) is a vasculopathy of the arteries of the lungs associated with vasoconstriction, stiffening, and *in-situ* thrombosis, raising the mean arterial pressure.¹ This pressure overload induces right ventricle (RV) remodeling. The RV initially maintains cardiac output by increasing muscle contractility recruitment and wall hypertrophy, however, when left untreated, RV remodeling can become maladaptive and lead to right heart failure and premature death.² Thus, RV function is an important predictor of disease severity.

PAH is four times more prevalent in women than men. Premenopausal women have a better outcome and higher survival rates than postmenopausal women and men.³ Thus, the RV remodeling process is sex dependent, where sex hormones play an important, yet unknown role. Here we study these sex-dependent differences in the sugen-hypoxia (SuHx) rat model of PAH. To study the role of sex hormones, a group of ovariectomized female rats was included.

Here we present a mathematical and experimental framework for building a three-dimensional biventricular model of the heart. By combining hemodynamic data, geometry of the heart, myocardial wall properties and fiber architecture information together, we hope to understand what factors contribute to the changes in RV mechanics that give rise to RV hypertrophy and functional changes that are sex-dependent, along with the role of sex hormones in the progression of PAH.

METHODS

All protocols were in accordance with the Institutional Animal Care and Use Committee (IACUC) at the University of California San Diego. PAH was induced in rats by a single injection of a vascular endothelial growth factor receptor inhibitor (SU5416, S8442 MilliporeSigma, CAS Number 204005-46-9, PubChemSubstance ID 24278606 Sigma-Aldrich, MO) followed by three weeks in hypoxia (10% oxygen levels). Male, female intact (OVX-), and ovariectomized

female (OVX+) Sprague-Dawley rats of four- and eight-weeks post PAH induction are studied. PAH is confirmed by invasive measurements of blood pressure at the inlet of the pulmonary artery with a mean pulmonary arterial pressure above 20 mmHg. A control group was matched to each week and referred to as week 0.

Hemodynamics and Tissue Mechanics: *In vivo* blood pressure-volume relationships are recorded during open chest surgery. The heart is harvested and a square sample from the RV free-wall aligned along the apex to the outflow-tract (AOT) is biaxed as previously described by Vélez-Rendón et. al.⁴

Cardiac magnetic resonance imaging (Cardiac MRI): Cardiac MRI was performed at three time points – weeks 0, 4 and 8 in one male, one OVX+, and one OVX- animal at the Molecular Imaging Center at Sanford Consortium (University of California San Diego) using a 11.7-T magnetic strength preclinical scanner (Bruker Biospec, Billerica, MA). Rats were anesthetized with 1-2% isoflurane in 100% oxygen while maintaining body temperature at 37 degrees Celsius. Short axis slices ranging from the apex to the base of the heart were taken every 1.5 mm. Respiration and electrocardiogram were continuously monitored which allowed for us to determine the end-systolic and end-diastolic frames. Image spatial resolution is 200 x 200 microns, with a 250 x 250 pixels image matrix, from a 50 x 50 mm field of view, acquired over a period of 318 ms per frame.

Diffusion-tensor magnetic resonance imaging (DT-MRI): Two male, one OVX- and one OVX+ rats were imaged using DT-MRI to obtain unloaded geometry of the hearts and fiber orientation. To mimic the unloaded state, the heart was fixed by an initial flush of phosphate buffer saline through the cannulated aorta, followed by a flush of 4% paraformaldehyde. The four unloaded control hearts were then sent to the Small Animal Imaging Core Facility (University of Utah) where the imaging and post-process analysis was performed. DT-MRI scans were performed at 100 μ m resolution (TR 500 ms, and TE 26.9 ms) over a period of 16 hours in a 7T horizontal bore Bruker Biospec Avance II

(Bruker Biospin, Ettlingen, Germany). Samples were placed in a custom-built 20 mm surface coil and immersed in fomblin to suppress background signal for imaging.

Image segmentation: Segmentation of the cardiac MRI and DT-MRI were performed manually to create meshes of the left ventricle, right ventricle, and epicardium using *itk-SNAP* (version 3.8.0). After outlining the two ventricles and the epicardium, the files were inputted into a graphic-based software, *Autodesk Meshmixer* (version 3.5.474), in which the segmented ventricles were smoothed out (Figure 1). Lastly, using an open-source 3D finite element generator, *Gmsh* (version 4.10.5), a 3D mesh of each ventricle and the epicardium was built. End-systolic and end-diastolic volumes were calculated using the cardiac magnetic resonance disc summation method, which includes finding the area of the ventricle at each of the slices in the heart and then adding them up and multiplying by the slice thickness.⁵ Using ImageJ (version 1.53) wall thickness measurements of each ventricle and septum were made. Based on the end-systolic and end-diastolic volumes, we computed stroke volume and ejection fraction.

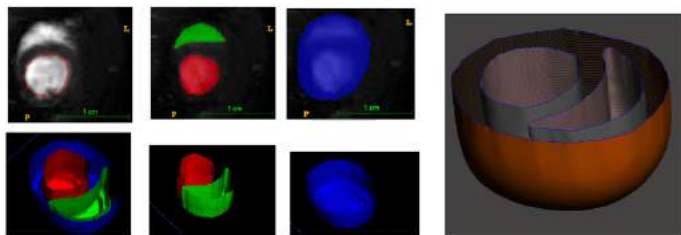


Figure 1: Manual Segmentation of a Cardiac MR Image and an example of Autodesk Meshmixer used to smooth the free wall.

After creating the mesh of the full heart, *3D slicer* (version 5.0.3) was used to determine the location from which the RV sample was taken for mechanical testing.

From the DT-MRI data, we obtain a fiber orientation file (150 x 200 x 150 x 3 array) containing the pixel position of the x- and y-axis, the slice number (z-axis) and the matrix of the fiber vectors at each location (Figure 2A). The primary eigenvector for each location and the fractional anisotropy for each voxel was provided, ranging between 0.3 to 0.6 for fibrous tissues. Once the location of the RV square sample is identified in the 3D mesh (Figure 2B-C), we can assign the fiber orientation to that region.

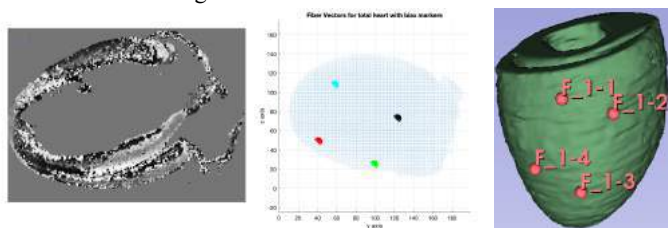


Figure 2: Longitudinal DT-MRI slice (left, A). Vector field of fibers measured with DT-MRI of the heart (y-axis goes from apex to base and z-axis goes from posterior to anterior) (middle, B). The markers on the RV free wall represent the region where the biax sample was taken (right, C).

RESULTS

The goal is to map the fiber directions onto the geometry of the heart for male, OVX-, and OVX+ control and PAH animals, and to determine how fiber direction influences the movement of the heart. The results from this step are still in progress, however Figure 3 shows preliminary results. Here, an element model (Figure 3A) and mesh

(Figure 3B) were created to represent the portion of the tissue that is biaxed. Using *Continuity* (version 6.4), the finite element (FE) mesh will be reduced to fewer elements and the fiber angles will be interpolated using a nearest neighbor interpolation method onto the nodes of each element. Once the fiber angles are mapped onto the nodes of the mesh, *Continuity* will be used again to test the biomechanical properties of this slab, and to compare the stress-strain relationships of this biax mesh with the *ex vivo* results from harvested RV tissue from control animals.

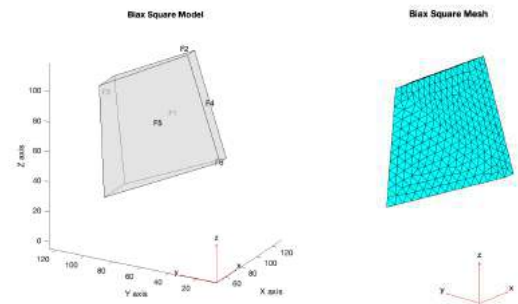


Figure 3: Model of the biax square (left, A) and the FE Mesh that was created in MATLAB (right, B). The model will be used in Continuity to create a mesh with fewer elements that the fiber vectors will be interpolated onto.

DISCUSSION

The major goal of our work is to use different data modalities to get a more comprehensive understanding of the remodeling process of the RV during PAH. Cardiac MRI and DTI-MRI data allow us to build a realistic biventricular model of the heart with actual geometry and fiber directions. The addition of fiber directions onto the geometry of the heart allows us to determine direction of motion.

Data obtained from these computer simulations will help us discriminate the different changes undergone by the ventricle from health to disease. *In vivo* hemodynamic measurements will be used as input into the model to investigate how changes in pressure impacts RV hypertrophy and changes in mechanical properties of the RV myocardial wall during the progression of PAH. This computational framework will help guide our next set of experiments and help us understand organ level sex differences in RV remodeling.

ACKNOWLEDGEMENTS

We would like to thank Edward Hsu at the University of Utah Small Imaging Core for the Diffusion Tensor Imaging and the University of California San Diego Graduate Interfaces Program for the funding under the T32 EB 009380 training grant.

REFERENCES

1. Lai, Y.-C. et al. *Circ. Res.* **115**, 115–130 (2014).
2. Franco, V. *Pulm. Hypertens.* **8**, 403–412 (2012).
3. Shapiro, S. et al. *CHEST* **141**, 363–373 (2012).
4. Vélez-Rendón, D. et al. *J. Biomech. Eng.* **141**, 091011 (2019).
5. Huttin, O. et al. *Medicine (Baltimore)* **94**, e1856 (2015).

DETERMINATION OF BIOMECHANICAL EFFECTS OF HISTOTRIPSY ON OSTEOSARCOMA IN A CANINE COMPARATIVE ONCOLOGY MODEL

Preeya F. Achari (1), Jackson Comer (1), Elliana Vickers (2), Lauren Ruger (1), Joanne Tuohy(3),
Eli Vlasisavljevich (1), Caitlyn J. Collins (1)

- (1) Department of Biomedical Engineering and Mechanics, Virginia Tech, Blacksburg, VA, USA
(2) Translational Biology, Medicine, and Health, Virginia Tech, Roanoke, VA, USA
(3) Virginia-Maryland College of Veterinary Medicine, Blacksburg, VA, USA

INTRODUCTION

Osteosarcoma (OS) is a rare, aggressive bone cancer that accounts for <1% of all cancers in humans. The survival rate for OS has not improved in decades due to the refractoriness of metastatic disease to therapy.¹ Non-surgical options for treating the primary tumor remain extremely limited. Recently, comparative tumor models such as canine OS have been explored for the development of effective clinical treatments. OS accounts for over 85% of bone tumors in canines, with 95% of patients presenting with spontaneous micrometastases and high levels of pain at time of diagnosis.² Current treatment options for canine OS are limited, the most common involving tumor resection via limb-salvage or limb-amputation surgery and adjuvant chemotherapy.¹⁻² Some dogs may not qualify for limb amputation, and serious complications after limb-salvage surgery such as implant failure and infection occur in 20-50% of patients. Histotripsy is a noninvasive, non-thermal ablation technique that uses ultrasound to mechanically destroy tissue.³ Previous *ex vivo* studies have demonstrated that histotripsy effectively ablates primary OS tumor tissue without causing cell death or damage to normal tissue.⁴⁻⁵ However, the relationship between histotripsy dose and bone mechanical properties has yet to be established. The objective of the current study was to explore the effects of histotripsy on OS tumor and adjacent grossly normal bone tissue by analyzing the biomechanical integrity of treated and untreated bone. We hypothesized that histotripsy does not significantly alter the biomechanical properties of treated bone and can be used as an alternative to surgery for treatment of canine OS.

METHODS

Two amputated limbs from canine patients with OS tumors undergoing standard-of-care limb amputation were acquired under an approved institutional IACUC protocol (22-091). *Ex vivo* histotripsy ablation was then applied to the OS tumor and a matching volume of grossly normal bone with a custom setup utilizing 1-2 cycle histotripsy pulses at a pulse repetition frequency of 500 Hz (**Figure 1**).



**Figure 1: Osteosarcoma tumor in the canine distal radius (left).
Ex-vivo histotripsy treatment of the tumor (right).**

Bone tissue from the ablated tumor (AT), the ablated grossly normal bone (AN), and a segment of unablated grossly normal bone (UN) were then extracted for biomechanical testing. Cubic (7.5mm x 7.5mm x 7.5 mm; n=3 per group) and rectangular beam specimens (15mm x 2mm x 1mm; n=3 per group) were tested under compressive loading and 3-point bending until failure to assess trabecular and cortical bone biomechanics, respectively. Mechanical testing was performed at a quasi-static loading rate of 1% s⁻¹. Cubic specimens were subjected to compressive loading in the three principal directions (D1, D2, and D3) until just below the yield point to assess potential differences in anisotropy, with D1 being the primary axis of loading. Compression tests were repeated (n=3) in all directions to ensure an accurate measure of the elastic properties of each tissue was achieved. A final compression test to failure in D1 was performed to determine the maximum compressive stress of the tissues. Bending mechanical testing

was performed to failure for all specimens. Compressive and bending moduli, calculated from the slope of the linear region of the stress-strain curves, and maximum stresses were determined to assess the impact of histotripsy on tissue stiffness and strength, respectively. A two-way repeated measures ANOVA was used to assess the impact of loading direction and tissue on the compressive moduli of the trabecular bone specimens. One-way ANOVAs were used to assess elastic and post-yield behavior of the cortical bone specimens and post-yield behavior of the trabecular bone specimens. If significant differences were detected, Tukey's Honest Significant Difference (HSD) tests were performed to compare data between groups if they followed a normal distribution. If data were skewed, non-parametric Mann-Whitney U tests were implemented. The alpha value was set 0.05 and p-values were adjusted for multiple comparisons.

RESULTS

Regarding anisotropy, stiffness was often higher in D1; however, no significant differences were found between the three loading directions for UN, AN or AT samples from either donor. As such, data was grouped by tissue for the remainder of the statistical analyses. No significant differences were detected in the compressive or bending mechanical properties of the trabecular or cortical bone of the AN and UN specimens (**Figures 2 & 3, Table 1**). No statistical comparison could be made between the compressive properties of the AT trabecular bone and those of the UN and AN tissue, as only one cube could be extracted from the ablated tumor tissue of either donor. Regarding the cortical bone, the bending modulus of the AT tissue was not significantly different from the UN and AN tissue. In contrast, max bending strength was significantly lower in the AT (192 ± 66.6 MPa) compared to UN (304 ± 42.5 MPa, $p=0.010$) and AN (327 ± 64.6 MPa, $p=0.002$) cortical bone.

Table 1: Biomechanical properties of UN, AN, and AT bone tissue, measured via compression and 3-point bending testing. Data reported as mean ± standard deviation or median (IQR).

	Property	Condition		
		UN	AN	AT
Compression	Maximum stress (MPa)	8.56 ± 3.51	11.2 ± 6.39	1.31
	Elastic modulus (MPa)	116 (70.6)	200 (58.7)	60.6 (60.3)
Bending	Maximum stress (MPa)	304 ± 42.5	327 ± 64.6	192 ± 66.6
	Elastic modulus (GPa)	32.5 ± 4.94	30.4 ± 10.7	23.3 ± 10.9

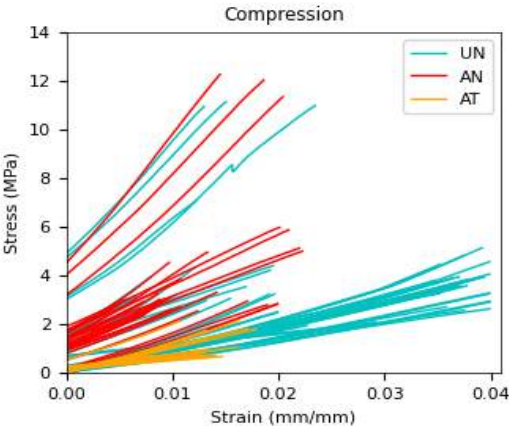


Figure 2: Stress vs strain compression test results for UN, AN, and AT trabecular bone.

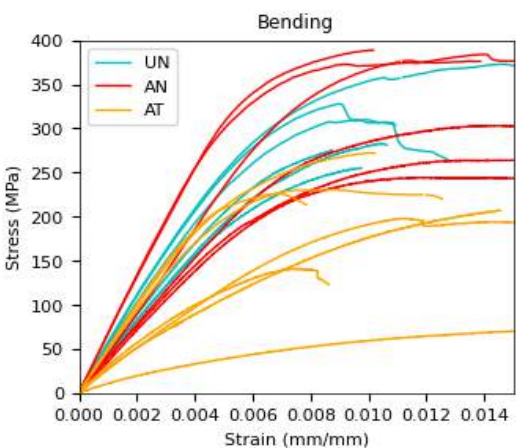


Figure 3: Stress vs strain 3-point bending test results for UN, AN, and AT cortical bone.

DISCUSSION

The similarities between the biomechanical properties of UN and AN tissue shown in **Figures 2 and 3** support our hypothesis that histotripsy tumor ablation does not detrimentally affect the biomechanical properties of treated OS bone. Despite the limited dataset, our results also indicate that the compressive and flexural properties of cortical and trabecular tumor tissue are compromised even before histotripsy treatment is applied; however, further analysis must be done to verify these results. Although our current sample size and number of trabecular AT tissue samples were limited in the current work, the study is ongoing. To fully power our statistical analysis, additional limbs and sample preparation are in process to gain a clearer understanding of the biomechanical effects of histotripsy treatment on OS bone tissue. The clinical nature of this pilot study prevented complete control over key variables such as tissue donor characteristics (age, weight, breed, etc.), the anatomical location from which sample tissue was extracted (i.e., radius, ulna, tibia, femur), and sample size. As such, the detected differences between groups may have been influenced by the anatomical location of each of the samples as well as donor demographics. To address these limitations, future controlled studies on the biomechanical effects of histotripsy dose on healthy and OS tissue should be performed to establish treatment guidelines. Ultimately, the results of the current work will aid in the development and advancement of effective, non-invasive treatments for clinical OS patients.

ACKNOWLEDGEMENTS

The authors gratefully acknowledge the support of the Veterinary Memorial Foundation.

REFERENCES

[1] Szewczyk, M et al., *Vet Res Commun.*, 39(1):61-67, 2015.
[2] Khokhlova, VA et al., *Int J Hyperthermia*, 31(2):145-62, 2015.
[3] Xu, Z, et. Al., *Int J Hyperthermia*, 38(1):561-575, 2021.
[4] Arnold L, et al. *Ultrasound Med Biol*, 47(12):3435-3446, 2021.
[5] Mason, N.J., *Adv Exp Med Biol*, 1258:199-221, 2020.

USING MICROINJECTED FLUID DROPLETS TO LOCALLY PERTURB EPITHELIAL MECHANICS AND BRANCHING MORPHOGENESIS IN CULTURED EMBRYONIC ORGANS

Shelby R. Mohr-Allen (1), Victor D. Varner (1,2)

(1) Department of Bioengineering, The University of Texas at Dallas, Richardson, TX, USA

(2) Department of Surgery, UT Southwestern Medical Center, Dallas, TX, USA

INTRODUCTION

Numerous organs in the bodies of animals consist of branched networks of epithelial tubes, which arise during development via a process known as branching morphogenesis. In many of these organs, changes in tissue mechanics have been shown to affect the formation of new branches, but this work has often relied on experimental techniques, such as microfluidic control of luminal fluid pressure or pharmacological modulation of epithelial fluid secretion, which macroscopically alter the mechanical environment in the entire branched network [1, 2]. As a consequence, it is not well understood how local changes in mechanics impact the formation of new branches or the patterns of proliferation associated with incipient buds. Recent experiments, however, have shown that small, functionalized fluid droplets can be microinjected within the mesenchyme of mechanically accessible embryonic tissues (like the developing limb bud or the presomitic mesoderm) and can be used to quantify the mechanical forces exerted by either individual cells or cell-clusters [3]. Here, we modified this technique to locally perturb the mechanical environment within cultured epithelial organs. Small fluid droplets were microinjected into the luminal space of embryonic lungs to locally alter epithelial tension in the developing airway. These microinjected explants were then cultured *ex vivo* to dynamically assess how local changes in mechanics influence branching morphogenesis and proliferation during embryonic lung development.

METHODS

A pulled glass micropipette was filled with a bioinert fluorocarbon oil (Fluorinert Electronic Liquid FC-70; 3M, St. Paul, MN) and then manually inserted into the luminal space of the developing airway in either embryonic day (E) 5 chicken lung explants or E12.5 mouse lung explants. Using a pneumatic pump, a small volume of oil was injected into the luminal space to create a local dilation within the primary bronchus. The microinjected explants were then cultured for 24-48 hr

on Nucleopore filter membranes at the air/fluid interface in DMEM/F12 medium supplemented with 5% fetal bovine serum (FBS) and antibiotics. Bright-field and epifluorescence images were captured at either discrete time-points (e.g., at 0 and 24 hr) or at 30 min intervals during time-lapse culture. In some experiments, Confetti^{+/+} female mice were crossed with ShhCreEGFP^{+/+} male mice to generate transgenic embryos that randomly express one of four fluorescent reporters within cells along the airway epithelium. At the end of each experiment, explants were fixed in 4% paraformaldehyde and stained for E-cadherin immunofluorescence, EdU incorporation, and DAPI. (The explants were pulsed with EdU for 20 min prior to fixation.) The fixed explants were then optically cleared, mounted in custom imaging chambers, and imaged as whole mounts using a laser scanning confocal microscope. Quantitative image analysis of bright-field and epifluorescence images was performed in ImageJ.

RESULTS

To locally perturb the mechanical environment within the embryonic airway, we injected a small volume of bioinert oil into the lumen of the primary bronchus in E5 chicken lung explants. The

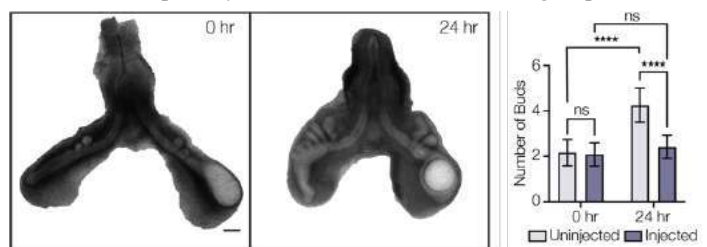


Figure 1: Microinjected oil droplets locally dilate the embryonic airway and disrupt branching morphogenesis.
Scale bar, 200 μ m.

microinjected droplet rounded up over 24 hr of ex vivo culture and created a local distension of the airway (Fig. 1). This local dilation inhibited the formation of new epithelial buds, as compared to uninjected controls (Fig. 1). Smaller volumes of microinjected oil, however, did not dilate the airway, were morpho-logically similar to controls, and did not disrupt branching morphogenesis (Fig. 2), suggesting that a local distension of the airway – and thereby an increase in epithelial tension – is needed to suppress bud formation.

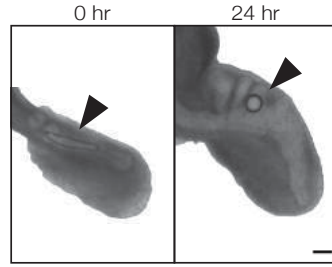


Figure 2: Smaller volumes of microinjected oil do not affect normal branching morphogenesis. Scale bar, 150 μ m.

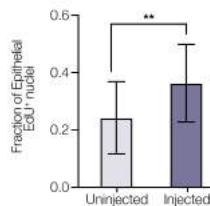
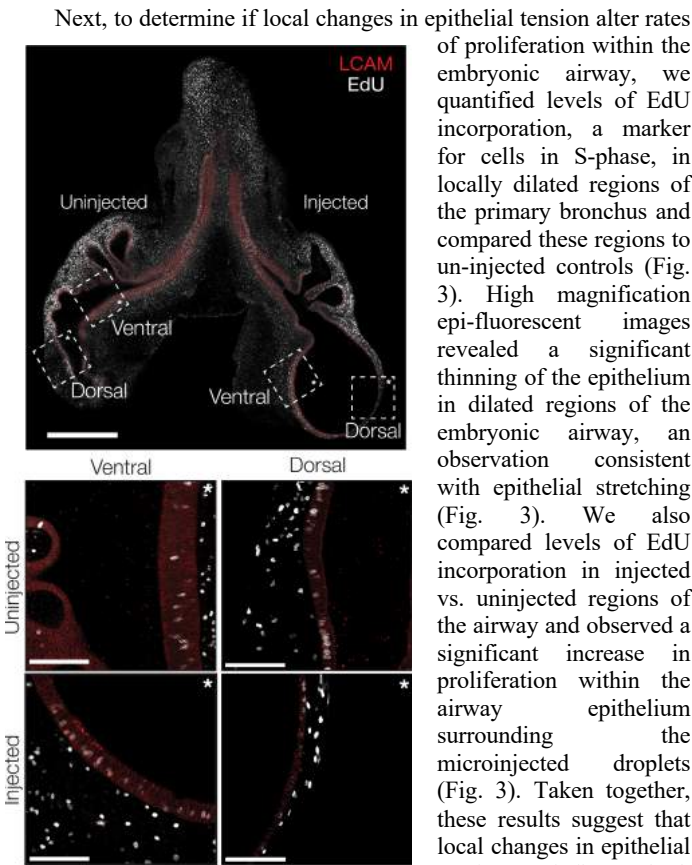


Figure 3: Epithelial proliferation is elevated within injected regions of cultured embryonic lungs. Scale bar, 200 μ m (inset scale bars, 50 μ m).

Next, to determine if local changes in epithelial tension alter rates of proliferation within the embryonic airway, we quantified levels of EdU incorporation, a marker for cells in S-phase, in locally dilated regions of the primary bronchus and compared these regions to un-injected controls (Fig. 3). High magnification epi-fluorescent images revealed a significant thinning of the epithelium in dilated regions of the embryonic airway, an observation consistent with epithelial stretching (Fig. 3). We also compared levels of EdU incorporation in injected vs. uninjected regions of the airway and observed a significant increase in proliferation within the airway epithelium surrounding the microinjected droplets (Fig. 3). Taken together, these results suggest that local changes in epithelial tension can influence both branching morphogenesis and proliferation in cultured embryonic lungs.

Next, to observe cellular dynamics within locally dilated regions of the airway epithelium, and to determine if similar results were observed in the developing mammalian lung, we repeated these experiments using

transgenic mouse embryos, which express dynamic fluorescent reporters within the airway epithelium. Time-lapse epi-fluorescent images revealed a similar local dilation of the embryonic airway (Fig. 4). In this case, however, branching morphogenesis was not completely suppressed. Instead, cells within the airway epithelium moved distally around the microinjected fluid droplet and accumulated within the distal tip of the dilated embryonic airway before forming new epithelial buds (Fig. 4). The branching pattern and dynamics within these dilated regions, however, were significantly different than uninjected regions of the cultured lungs. Taken together, these results indicate local changes in mechanics alter epithelial morphogenesis in cultured avian and mammalian lungs.

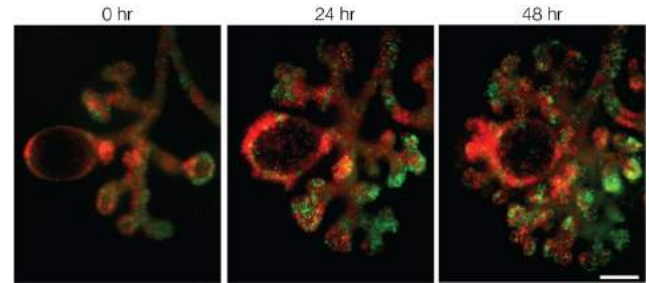


Figure 4: Injection of oil droplets within the epithelium of transgenic mice allows for dynamic evaluation of branching. Scale bar, 200 μ m.

DISCUSSION

Although biophysical cues have been shown to regulate embryonic development [4], few experimental tools exist to locally alter epithelial mechanics in cultured embryonic organs [5]. Here, we have shown how microinjected fluid droplets can be used to create a local dilation within the luminal space of the embryonic airways to focally modulate epithelial tension in developing lung explants. The microinjected droplets disrupted normal branching morphogenesis and altered patterns of proliferation along the embryonic airway epithelium. Our technique can be readily adapted to other developing epithelial organs, such as the embryonic kidney [6], intestine [7], or salivary gland [8], in which mechanical forces are thought to influence epithelial morphogenesis. In addition, going forward, our microinjection experiments can be combined with time-lapse imaging and quantitative cell tracking to determine how changes in the mechanical environment influence the epithelial deformations that sculpt incipient branches. The bioinert oil can also be substituted for ferrofluid droplets, which would enable them to be used as mechanical actuators to apply time-varying forces during ex vivo culture, as has been reported during the axial elongation of developing zebrafish embryos [9].

ACKNOWLEDGMENTS

This work was supported, in part, by the NIH grant R01HL145147 to VDV.

REFERENCES

- [1] Nelson, C., et al., *Development* 144, 4328-4335, 2017.
- [2] Peak, K., et al., *Biology Open* 11, 2022.
- [3] Campàs, O., et al., *Nat Methods* 11, 183-189, 2014.
- [4] Nelson, C. & Gleghorn, J., *Annu Rev Biomed Eng* 129-154, 2012.
- [5] Gómez-González, M., et al., *Nat Rev Phys* 2, 300-317, 2020.
- [6] Costantini, F. & Kopan, R., *Dev Cell* 18, 698-712, 2010.
- [7] Savin, T., et al., *Nature* 476, 57-62, 2011.
- [8] Wang, S., et al., *Cell* 184, 3702-3716, 2021.
- [9] Serwane, F., et al., *Nat Methods* 14, 181-186, 2017.

MODERATED TGF- β DELIVERY VIA LATENT TGF- β CONJUGATED SCAFFOLDS FOR IMPROVING ENGINEERED ARTICULAR CARTILAGE

Tianbai Wang (1), Zhonghao Dai (2), Celina C. Maldonado (2), Prem Nelesh (2), Junhan Liao (3), Sung Yeon Kim (2,3), Andrew Martin (2), Joanne E. Murphy-Ullrich (4), Mark W. Grinstaff (1,2), Michael B. Albro (1,2,3)

- (1) Materials Science and Engineering, Boston University, Boston, MA USA
(2) Biomedical Engineering, Boston University, Boston, MA USA
(3) Mechanical Engineering, Boston University, Boston, MA USA
(4) Department of Pathology, University of Alabama at Birmingham, Birmingham, AL USA

INTRODUCTION

Cartilage tissue engineering (TE) is a promising osteoarthritis (OA) treatment strategy where neocartilage is generated with chondrogenic cell-seeded scaffolds. Transforming growth factor beta (TGF- β) is widely utilized due to its ability to enhance the biosynthesis of cartilaginous extracellular matrix (ECM). Conventionally, tissue constructs are exposed to highly supraphysiologic doses of TGF- β (10-100 ng/mL) supplemented in culture medium, representing activity levels that are 10-1,000-fold higher than those present during native development. While accelerating ECM biosynthesis, conventional TGF- β doses are associated with promoting features detrimental to hyaline cartilage function, including the induction of cellular hyperplasia ^[1], hypertrophy ^[1], and fibrocartilage ^[2]. Further, media-supplemented TGF- β exhibits severe penetration limitations into engineered cartilage, inducing undesirable ECM heterogeneities ^[1]. Together these detrimental outcomes can compromise the clinical survival of tissues post-implantation.

In contrast to conventional TE delivery methods, the natural process of TGF- β delivery in native cartilage occurs differently, whereby chondrocytes are surrounded by TGF- β in an inactive complex, termed latent TGF- β (LTGF- β). LTGF- β is highly concentrated throughout the cartilage ECM (100-300 ng/mL ^[3]) but is activated by chondrocytes at a low, tightly controlled rate (0.1-0.7 ng/mL ^[4]), giving rise to an advantageous, need-based and spatially uniform activity throughout the cartilage tissue. This regulatory mechanism functions to maintain requisite ECM biosynthesis, while avoiding pathological tissue formation from TGF- β excesses.

Inspired by native TGF- β regulatory mechanisms, we explore the novel hypothesis that the delivery of moderated, physiologic TGF- β doses can improve neocartilage formation, marked by achieving native-matched functional mechanical properties, while reducing detrimental features of development: hyperplasia-induced cell clusters, cell hypertrophy, and fibrocartilage-associated type-I collagen. This

hypothesis is examined in two studies. In study 1, we directly examine the effect of physiologic-range TGF- β doses on neocartilage development by exposing small-size constructs to varying doses of media-supplemented TGF- β . These small-size constructs exhibit mitigated TGF- β gradients, allowing for a better assessment of the intrinsic effect of TGF- β doses on tissue development. In study 2, we directly examine the ability of a bio-inspired LTGF- β conjugated scaffold to improve the mechanical properties, composition, cell morphology, and cell phenotype in conventional sized constructs. Here, LTGF- β is conjugated to a methacrylate agarose (MeAgr) hydrogel scaffold, providing a stable LTGF- β reservoir for seeded chondrocytes, allowing for controlled cell-mediated activation to promote sustained, and spatially uniform levels of physiologic TGF- β activity.

METHODS

Tissue Constructs: For both studies, constructs were fabricated with immature bovine primary chondrocytes (30×10^6 cells/mL) and 2% w/v agarose and cultivated in chondrogenic medium. **Study 1: Intrinsic effect of physiologic TGF- β doses.** Small-size constructs ($\varnothing 2 \times 2$ mm) were exposed to a range of physiologic (0.1, 0.3, 1 ng/mL) and conventional supraphysiologic (3, 10 ng/mL) active TGF- β 3 doses supplemented in media for the initial two weeks of culture, or maintained TGF- β free continuously. Compressive Young's modulus (E_y) was analyzed at day 56 ($n=5$) ^[2]. Cell morphology was analyzed at day 30 ($n=3$) via confocal microscopy (Live/Dead) and the fraction of cells in a clustered versus isolated morphology was measured (cluster area fraction [CAF]) ^[5]. Deposition of type-I and type-II collagen were assessed at day 56 via immunostaining ($n=2$). **Study 2: Delivery via LTGF- β conjugated scaffolds.** LTGF- β 1 (R&D) was covalently conjugated to methacrylate agarose ^[6] (MeAgr) by incubating at 37°C overnight with high (3000 ng/mL), medium (1500 ng/mL), and low (600 ng/mL) doses prior to cell encapsulation. Constructs were fabricated at $\varnothing 5 \times 2$ mm. LTGF- β construct development was compared to unconjugated control constructs exposed to media supplemented

(MS) active TGF- β 3 for the initial 2 weeks of culture at a physiologic dose (0.3 ng/mL; MS-0.3), supraphysiologic dose (10 ng/mL; MS-10), or no added TGF- β (TGF- β free). LTGF- β conjugation yields were measured via ELISA. Constructs were analyzed for E γ (n=5) at day 28 and 56. GAG distribution were assessed at day 56 via Safranin O/Fast Green staining (n=1). Spatial strain distributions were analyzed at day 56 via digital image correlation [7] (n=5) with 10% platen-to-platen axial compression, strain profiles were discretized into 6 evenly spaced domains through the tissue depth and used to characterize the degree of heterogeneity in tissue stiffness, determined by a strain ratio (SR)—the ratio of mean strain in each domain to mean strain in the top first domain. CAF was assessed at day 42 (n=3). Type X collagen expression levels were analyzed at day 56 via qPCR (n=3).

RESULTS

Study 1: Intrinsic effect of TGF- β Doses. Small-size constructs (\varnothing 2 \times 2 mm) exhibited increases in both E γ and hyperplasia cell clusters with TGF- β dose. At low TGF- β doses (\leq 0.1 ng/mL), clusters were mitigated, but construct E γ remained low (Fig. 1A). At supraphysiologic doses ($>$ 1 ng/mL), constructs yielded native-matched mechanical properties (E γ ~590 kPa) but exhibited type-I collagen deposition (Fig. 1C) and a pronounced degree of cell clustering—at 10 ng/mL 58% of cells presented as clusters (Fig. 1A-B). However, for physiologic TGF- β doses (0.1-1 ng/mL), constructs exhibited native-matched mechanical properties while maintaining low clustered cellularity and low type-I collagen (Fig. 1), thus representing an optimal dosing regimen for neocartilage development.

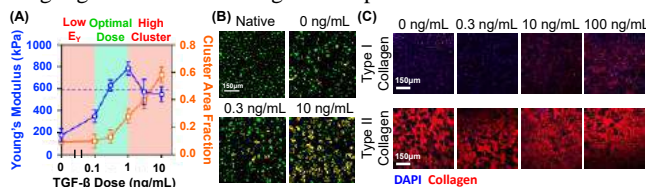


Fig 1: (A) E γ and CAF vs. TGF- β dose. Dashed line represents native cartilage E γ level. (B) Cell morphology images depicting clustered (yellow) and isolated (green) cell regions. (C) immunostaining of type-I and type-II collagen in constructs.

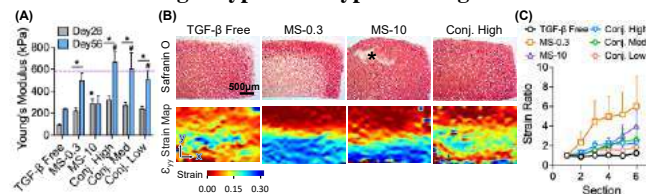


Fig 2: (A) E γ , (B) Safranin O staining (* indicates tissue crack region) and strain color maps, and (C) SR of large-size constructs subjected to active TGF- β media-supplementation and LTGF- β conjugation. Dashed line represents native cartilage E γ level. * #p<0.05: significantly above the TGF- β free and MS-10 levels, respectively

Study 2: LTGF- β conjugated scaffolds. LTGF- β conjugation levels increased with incubation dose, reaching native cartilage levels (290 \pm 19 ng/mL) with the high dose. At day 56, all LTGF- β groups exhibited significant enhancement in E γ relative to TGF- β free (p<0.005) and MS-10 (p<0.05) groups, approaching native cartilage E γ (Fig. 2A). GAG gradients were observed in MS-0.3, but not in LTGF- β constructs (Fig. 2B; only high LTGF- β construct depicted). Severe cracks were present near the surface of the MS-10 constructs. At day 56, MS-0.3 and MS-10 groups exhibited large stiffness heterogeneities with SR values of 6.03 \pm 2.99 and 4.00 \pm 1.62, respectively (Fig. 2B-C). In contrast, strain heterogeneities were reduced for LTGF- β groups to an average value of

2.23 \pm 0.68. Minimal cell clusters were present for TGF- β free and MS-0.3 groups (CAF<0.21; Fig. 3A-B), but increased significantly for MS-10 (CAF=0.56 \pm 0.08). For all LTGF- β groups, CAF was significantly reduced below MS-10 levels (p<0.05) (Fig. 3A-B). The expression level of a chondrocyte hypertrophy biomarker, type X collagen was also reduced for LTGF- β groups relative to MS-10 (p<0.05; Fig. 3C).

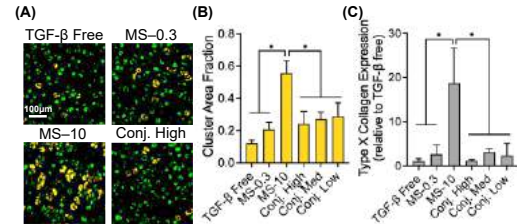


Fig 3: (A) Cell morphology images depicting clustered (yellow) and isolated (green) cell regions, (B) CAF, and (C) type X collagen expression in constructs from TGF- β media supplementation and LTGF- β conjugation groups. *p<0.05.

DISCUSSION

These results offer a new perspective in cartilage tissue engineering, demonstrating that the administration of moderated, physiologic doses of TGF- β can improve the quality of regenerating neocartilage. In our first study, through our small construct model, we observe that, in the absence of concentration gradients, physiologic doses can yield neocartilage with native-matched functional properties while mitigating the emergence of hyperplasia-induced cell clusters and fibrocartilage-associated type-I collagen. However, due to transport limitations, the delivery of physiologic TGF- β doses to larger, clinical-sized constructs remains a significant challenge. In our second study, we address this hurdle by establishing the benefit of achieving uniform delivery of moderated, physiologic TGF- β doses in large-size constructs via LTGF- β conjugated scaffolds. Results first highlight the limitations of conventional media supplemented delivery approaches. The administration of a supraphysiologic 10 ng/mL TGF- β dose leads to tissue quality deficits in the form of cell clusters and ECM heterogeneities. The administration of a physiologic 0.3 ng/mL TGF- β dose reduces cell clustering but leads to more pronounced heterogeneities, due to TGF- β transport limitations [5]. It is reasonable to surmise that these deficits may compromise the clinical longevity of constructs—heterogeneities can lead to failure of soft tissue regions when subjected to physiologic loading and cell clusters, a hallmark of OA, can lead to propagation of excessive cellular strains under loading due to a lack of sufficient ECM buttressing. The use of LTGF- β conjugation doses that match those present in native cartilage allows for an examination of the regenerative potential of this bio-inspired delivery platform. LTGF- β -conjugated scaffolds appear to create an optimal dynamic where cell-mediated activation of LTGF- β leads to the generation of moderated and uniform TGF- β activity, akin to that present during native development. Here, we observe that this moderated activity promotes requisite ECM biosynthetic enhancements while mitigating cell hyperplasia and cell hypertrophy, leading to engineered cartilage with native-matched mechanical properties, reduced heterogeneities, and improved cell morphology.

ACKNOWLEDGEMENTS

This work was supported by NIAMS AR078299, NIH S10OD024993, and the Boston University Dean's catalyst award.

REFERENCES

- [1] Albro+ 2016 Biomaterials 77:173-85.
- [2] Cigan+ 2014 J Biomech 47:3847-54.
- [3] Morales+ 1991 Arch. Biochem. Biophys 288:397-405.
- [4] Kim+ 2020 SB3C (No. 409).
- [5] Wang+ 2021 ORS (No. 0713).
- [6] Paepe+ 2002 Polym. Int 51:867-70.
- [7] Wang+ 2002 J. Biomech. Eng 124:557-67

SYNOVIAL FLUID PROVIDES A PROTECTIVE EFFECT IN ARTICULAR CARTILAGE FATIGUE FAILURE

C.V. Sise (1), C.A. Petersen (2), J.X. Dewing (1), B.K. Zimmerman (2), J. Yun (1), R.J. Kepecs (2),
C.T. Hung (1), G.A. Ateshian (1,2)

(1) Department of Biomedical Engineering, Columbia University, New York, New York, USA
(2) Department of Mechanical Engineering, Columbia University, New York, New York, USA

INTRODUCTION

Osteoarthritis (OA) is a disease of the joint characterized by the degeneration of articular cartilage. Previously, we have shown the primary wear mechanism in immature bovine articular cartilage is caused by fatigue failure [1]. While cartilage wear is often assumed to occur in conjunction with frictional sliding, recent results suggest that fatigue failure in articular cartilage is specifically due to cyclical compression and not reciprocal frictional sliding [2,3]. Pure reciprocal frictional sliding did not produce damage in human articular cartilage when articulated against stainless steel [2]. However, when slid against glass in a migrating contact configuration (MCA), immature bovine tissue that was cyclical compressive loading during sliding cycles consistently delaminated between the superficial and middle zones of the cartilage tissue. In contrast, tissue that was subjected to a static compressive load during frictional sliding in a stationary contact configuration (SCA) did not result in visual or sub-surface damage [3].

In the aforementioned studies, articular cartilage was submerged in phosphate buffered saline (PBS) for the duration of the experiment. While PBS allows proper hydration of the tissue and can maintain the native osmotic environment, a more physiologic testing bath should be considered. Synovial fluid (SF), the fluid found within each joint space, is known to lower the friction coefficient relative to PBS in cartilage sliding [1,4]. However, the friction coefficient appears not to be a direct indicator of wear. Caligaris et al. found no statistical differences in the friction coefficient between human cartilage with more or less arthritis [4]. Similarly, Durney et al. reported no difference in average friction coefficient between damaged and undamaged immature bovine samples after MCA sliding tests [1]. In our most recent study, we showed that damage occurred in immature bovine cartilage samples in the low-friction MCA test configuration, but not in the high-friction SCA configuration [3]. Though SF reduces the friction coefficient in cartilage sliding, the above outcomes suggest that friction alone is not driving cartilage damage.

The purpose of this study was to investigate how SF affects wear propagation in immature bovine articular cartilage in both the MCA and SCA configurations, and whether it provides a protective effect against damage. We also investigated potential mechanisms for SF to impart protection against damage progression, such as the role of viscosity, molecular diffusion, or friction.

METHODS

Frictional Tests: Full thickness cartilage tibial plateaus were harvested from immature bovine knee joints (2-3 months old), and microtomed to an average thickness of 1.41 ± 0.05 mm. Paired strips were cut from each tibial plateau for the MCA in SF (MCA-SF) test group (10 mm \times 30 mm, $n = 5$) and SCA in SF (SCA-SF) test group (10 mm \times 10 mm, $n = 5$). Samples were mounted onto petri dishes, submerged in mature bovine SF, and placed on a custom frictional testing device equipped with a multiaxial load cell and motorized stage which recorded position and load data during testing. The MCA-SF testing configuration consisted of a hemispherical glass lens ($\varnothing 25$ mm) under a compressive load of 4.45 N, and the SCA-SF configuration consisted of a flat glass lens ($\varnothing 25$ mm) with a compressive load of 44.5 N. Compressive loads were selected to produce equal average contact stress for both configurations. Sliding was prescribed at 1 mm/s across a distance of $U_x = \pm 4$ mm for 24 h (5,400 cycles).

Quantitatively, pressure sensitive Fuji film was used to measure the contact area between each platen-sample pair. Laser scans were taken of the sample surfaces to produce a dense point cloud (50,000 points/cm²). Root-mean-square surface deviation (R_q) of the samples from a plane were quantified to detect the presence and degree of cartilage surface damage. Qualitatively, photographs were taken of the sample before and after testing, and histology was performed on the sample after complete relaxation.

Mechanical Tests: A second set of experiments was conducted to investigate how SF affects fluid exudation from articular cartilage boundaries. Cylindrical plugs (1.4 mm \times $\varnothing 3$ mm, $n = 8$) were harvested

from the femoral condyle of immature bovine knee joints. Biphasic material properties were assessed by fitting transient unconfined compression data assessed using a custom mechanical testing device with a creep tare load (0.1 N, 600 s) and a stress-relaxation test to 10% strain (0.5 $\mu\text{m/s}$ ramp, 1800 s). Samples were mechanically tested in PBS, allowed to recover, and then tested again in SF.

RESULTS

The friction coefficient for the MCA-SF group (0.014 ± 0.0032) was significantly lower than that previously reported in the MCA-PBS group (0.025 ± 0.009 , $p < 0.05$, Fig. 1) [3]. The average friction coefficient for the MCA-SF group was significantly lower than the friction coefficient in the SCA-SF group (0.056 ± 0.027 , $p < 0.01$). Surface deviation measurements showed no statistical difference between the MCA-SF and SCA-SF groups either before ($R_{q\text{-MCA}} = 0.034 \pm 0.006$ mm, $R_{q\text{-SCA}} = 0.046 \pm 0.031$ mm) or after ($R_{q\text{-MCA}} = 0.051 \pm 0.025$ mm, $R_{q\text{-SCA}} = 0.041 \pm 0.013$ mm) testing ($p > 0.3$). Average contact stresses, σ , were similar among SF groups ($\sigma_{\text{MCA-SF}} = 0.74 \pm 0.13$ MPa, $\sigma_{\text{SCA-SF}} = 0.63 \pm 0.14$ MPa, $p > 0.2$). Contact stresses in SF tests were not statistically different from those previously reported in PBS tests ($p > 0.5$) [3].

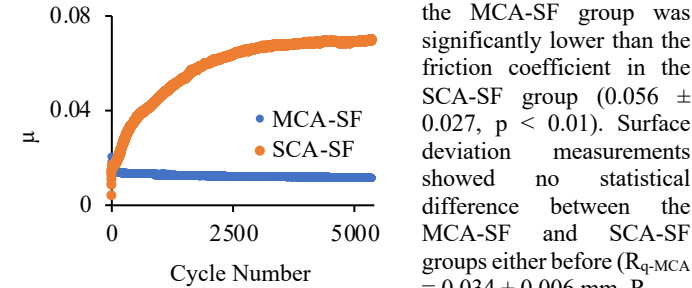


Fig. 1: Friction coefficient for one representative sample set.

One of the five samples in the MCA-SF group exhibited surface damage after testing, in the form of delamination resulting in tearing of the superficial zone (Fig. 2a,d). An additional sample exhibited

initiation of superficial zone delamination in the form of a blister (Fig. 2b,e), while the remaining three exhibited no evidence of delamination (Fig. 2c,f). The SCA-SF group showed no evidence of delamination.

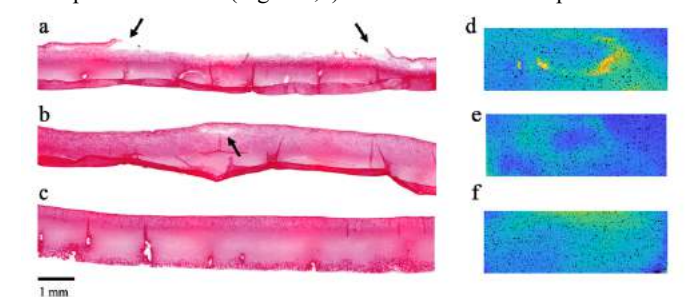


Fig. 2: Cartilage histological cross-sections (left) and surface scans (right) for samples with a torn superficial zone (top), initial delamination (middle), and no damage (bottom).

The stress-relaxation tests showed similar equilibrium moduli and relaxation times between samples tested in SF and PBS (Fig. 3).

The stress-relaxation tests showed similar equilibrium moduli and relaxation times between samples tested in SF and PBS (Fig. 3).

DISCUSSION

Our results indicate SF delays fatigue failure due to compressive loading in the MCA testing configuration. Only one out of the five samples tested in the MCA-SF test group exhibited superficial zone tearing and one showed initial sub-surface damage, while the remaining three samples exhibited no indication of damage. Additionally, the lack of change in surface deviation of MCA-SF samples before and after testing suggests minimal fatigue failure, even when delamination occurred. In contrast, previously reported results in an identical testing configuration in PBS found that all five samples tested in that study exhibited gross visual damage in the form of superficial zone tearing, producing a significant increase in R_q after testing [3]. The results

presented here show that SF reduces, or even prevents, damage when compared to PBS, indicating that SF provided a protective effect against fatigue failure during frictional sliding.

One hypothesis to explain why samples tested in SF resulted in less damage than those tested in PBS could be that the more-viscous SF prevented the interstitial fluid from escaping from the cartilage tissue as quickly. However, examining the creep in the cartilage tissue during the first 30 minutes of sliding showed nearly identical creep deformation in both SF and PBS tests (results not shown). This result was further supported by the unconfined compression mechanical tests performed on the articular cartilage cylindrical plugs which showed identical stress-relaxation responses when tested in either SF or PBS (Fig. 3).

Taken together, these results suggest that SF viscosity does not impede the exudation of interstitial fluid from cartilage, thus it plays no role in reducing tissue damage by extending the duration of elevated fluid load support.

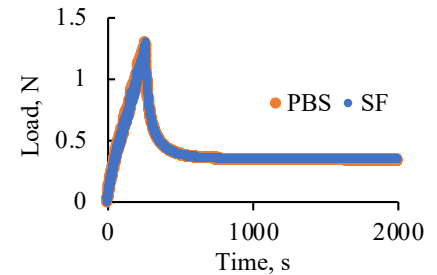


Fig. 3: Representative stress-relaxation curves for a sample tested in PBS and SF.

Another explanation could be the diffusion into the articular cartilage of SF molecules such as hyaluronic acid (HA) or lubricin which may protect the tissue against fatigue damage. Lubricin is known to play an important role in cartilage integrity and HA has been suggested to potentially protect cartilage against wear [5]. We estimated that these SF constituents can diffuse from the cartilage surface to the site of initial delamination in as little as ~12 hours, based on their molecular weights [6]. Further investigations are necessary to determine if these molecules indeed provide protection against fatigue damage.

While the primary lubrication of articular cartilage surfaces has often been attributed to boundary or fluid film lubrication due to SF and its constituents [5], several studies have shown that a more significant mode of lubrication in articular cartilage is the interstitial fluid load support [3,7,8]. The results reported here support this finding: while SF reduces the friction coefficient relative to PBS, maintaining the fluid load support has a more significant effect on the friction coefficient (Fig. 1). However, perhaps the reduced friction coefficient observed in SF tests compared to PBS tests results in an overall reduction of damage by reducing the likelihood that subsurface fatigue damage (Fig. 2b) can propagate to the articular surface (Fig. 2a). The friction coefficient is not the primary predictor of damage, as shown previously [1,3,4] as well as in the present study, with damage occurring in a low-friction MCA environment but not in a high-friction SCA environment. However, once fatigue failure has been initiated, the friction coefficient may play a role in the extent of damage observed. Damage progression due to friction may be conducted using computational models in future investigations, to help resolve differences between PBS and SF.

ACKNOWLEDGEMENTS

Prof. X. Edward Guo (Columbia University) for use of microscope. National Institutes of Health (R01 AR073289, R01 GM083925).

REFERENCES

- [1] Durney, KM+, *J Biomech*, 107. 2020.
- [2] Sise, CV+, *SB3C 2022*, 2022.
- [3] Petersen, CA+, *ORS Annual Conference 2023*, In Press.
- [4] Caligaris, M+, *Osteoarthr Cartil*, 17(10). 2009.
- [5] Lin, W+, *Adv Mater*, 33(18). 2021.
- [6] Albro, MB+, *CMBE*, (2)3. 2009.
- [7] Ateshian, G.A., *J Biomech*, 42(9). 2009.
- [8] Caligaris, M+, *Osteoarthr Cartil*, 16(10). 2008.

IN-SITU VISCOELASTICITY MEASUREMENT OF CELL MONOLAYER BY STRAIN SENSING OF ELASTOHYDRODYNAMIC FORCE IN MICROFLUIDIC CHANNEL

Tianzheng Guo (1), Xiaoyu Zou (1), Shalini Sundar (2), Xinqiao Jia (1,2), Charles Dhong (1,2)

(1) Materials Science and Engineering, University of Delaware, Newark, Delaware, United States

(2) Biomedical Engineering, University of Delaware, Newark, Delaware, United States

INTRODUCTION

Maturing developments in understanding the mechanical properties of cells has led to developing cell stiffness as novel biomarkers for understanding pathogenesis and pathophysiology¹ because the mechanical stiffness of cells is well known to correlate with cellular function and state in basic biology and disease modeling. Cell monolayers play a critical role in most of the physiological functions where cells interact collectively with neighboring cells and surrounding extracellular matrix (ECM) through biochemical exchange and mechanotransduction^{2,3}. Measurement of mechanical properties of cell monolayers is beneficial to the development of disease-specific biomarkers. Current techniques are often difficult to scale and operationally complex, due to their reliance on optical or microscope-based characterization methods. In addition, they are usually limited by low repeatability, low throughput, fragility, and few of them achieve *in-situ* measurement of mechanical properties.

To access the mechanical stiffness of cell monolayers, we presented a microfluidic-based platform which relies on the principle of elastohydrodynamics as measured through piezoresistive metal-nanoisland-on-graphene strain sensors. Therefore, throughput is improved by relying on relatively simple voltage measurements, which can be performed in parallel. The platform is capable of non-invasive stiffness measurements within conventional cell culturing conditions, without the need for optical design considerations. Our toolkit provides a new facile route for investigating dynamic cellular mechanics at the multicellular level.

METHODS

Standard soft lithographic techniques were used to fabricate microfluidic devices. A rectangular piece of metallic nanoisland-bearing graphene strain sensor (12 mm × 4 mm, GrollTex Inc.) was embedded which spans the short axis of the channel.

The platform is based on the fluid-induced deformation of soft elastic walls, or elastohydrodynamics. Under a constant flow rate, the

relationship between the flow rate and the pressure and the channel deformation are given by⁴:

$$Q = \frac{h_0^4 E}{48 c_2 \mu (L-z)} \left[\left(1 + c_2 \frac{p(z)W}{E h_0} \right)^4 - 1 \right] \quad (1)$$

$$\frac{\Delta h}{h_0} = 2^4 \sqrt{\frac{3 Q \mu (L-z)}{E h_0^4} + 1} - 2 \quad (2)$$

where Q is the flow rate, h_0 is the initial channel height, E is the elastic modulus of the channel walls, L is the length of the channel, z is the axial position along the channel, μ is the fluid viscosity, W is the width of the channel, $p(z)$ is the pressure distribution along the channel.

If a constant stress is applied to a Kelvin-Voigt material and then released at time t_1 , the relaxation obeys the following equation:

$$\varepsilon(t > t_1) = \varepsilon(t_1) e^{-\frac{t-t_1}{\tau}} \quad (3)$$

where E is the modulus of elasticity, η is the viscosity.

A brief stress is applied by flowing fluid droplet in the channel and the wall deformation relaxes over finite time due to its viscoelastic properties⁵. As the sensor resistance signal is proportional to wall deformation, the voltage change can be described in terms of the viscoelastic relaxation as:

$$V(t) = V_0 - V(t_1) e^{-\lambda t} \quad (4)$$

where $\lambda = \frac{1}{\tau} = \frac{E}{\eta}$ is the relaxation time constant. To fit the viscoelastic relaxation curve, the equation is linearized as:

$$\ln \left(1 - \frac{V(t)}{V_0} \right) = -\lambda t + \ln \left(\frac{V(t_1)}{V_0} \right) \quad (5)$$

where the negative slope of the function is the relaxation time constant. A MATLAB (The MathWorks, Inc.) program is used to do the linear fitting.

RESULTS

The relationship between channel deformation and water flow rates and voltage signal is linear (**Fig. 1b**).

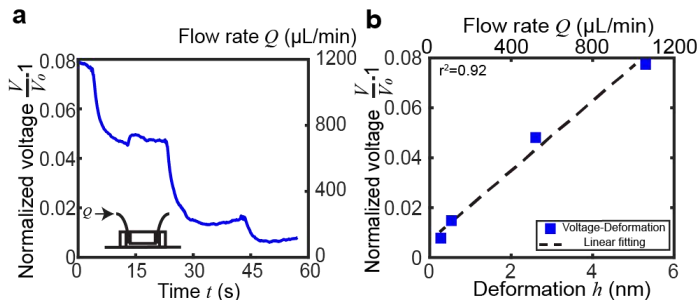


Figure 1: Calibration of microfluidic devices through elastohydrodynamics

We demonstrated measurements of dynamic *in-situ* stiffness changes of the Madin-Darby canine kidney (MDCK) cell monolayer. We observed a continuous decrease in relaxation time constant over treatment time. The treatment sequence was shown in Fig. 2a.

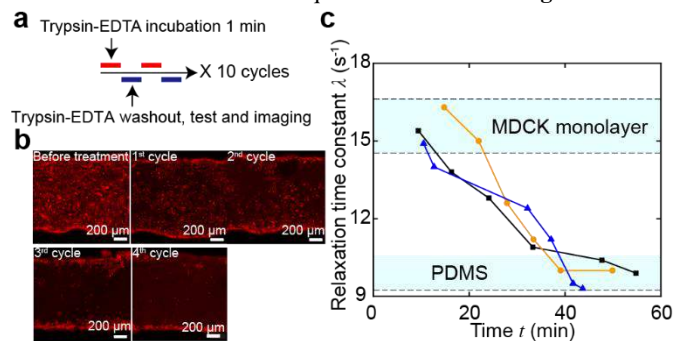


Figure 2: In-situ measurement of trypsinization process of MDCK cells.

Hepatocyte growth factor (HGF) treated MDCK cells showed lower relaxation time constant than the untreated group (Fig. 3b).

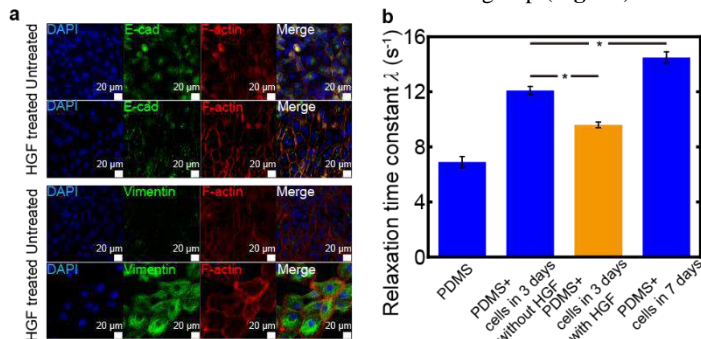


Figure 3: Epithelial-to-mesenchymal transition (EMT) induced by HGF.

DISCUSSION

A normalized electrical voltage signal from the strain sensor with different flow rates is shown in Fig. 1a. Pressure drop changes linearly with the imposed flow rate at low pressures in a rigid channel⁴. In Fig. 1b, the relationship between channel deformation and voltage signal is linear. This demonstrates that strain sensor is sensing deformation due to elastohydrodynamics and the voltage readings are proportional to channel deformation.

We obtained a λ of $14.5 \pm 0.4 s^{-1}$ ($n=10$) for channels with a MDCK cell monolayer. This relaxation time constant is greater compared to that of the bare PDMS channel wall ($6.9 \pm 0.4 s^{-1}$, $n=10$), indicating increased stiffness upon introduction of the MDCK cell monolayer. The composite structure of PDMS with MDCK cell

monolayer is stiffer than the PDMS structure alone. The mechanical contributions of MDCK cell monolayer are provided by a combination of the MDCK cells, intercellular adhesion junctions, and extracellular matrix proteins⁶.

During trypsinization process, the loss of cells and the extracellular matrix proteins led to an expected decrease in stiffness (Fig. 2c). However, the simultaneous stiffness measurements, when compared to cell count (Fig. 2b), were better able to capture the degradation of the cellular layer. At earlier time points, cell loss preceded the loss in stiffness, while at later time points, residual basement membrane proteins had a small, but detectable contribution to the channel stiffness, even after the cells were virtually absent. Compared with the slope of overall relaxation time constant decrease, the speed of cell count loss was quicker. However, compared to the earlier decrease of relaxation time constant—which was mostly due to cell count loss—the later decrease of relaxation time constant was more gradual. This suggested that MDCK cell bodies contributed more to the monolayer stiffness relative to the ECM and basement membrane proteins. Previous studies by Sorba et al.⁷ in MDCK cell monolayers through tensile testing found that cell covered region had higher relaxation time constant ($10.09 \pm 1.42 s^{-1}$) than the bare PDMS region ($3.18 \pm 1.47 s^{-1}$). They also found that EDTA treated MDCK cell had lower Young's modulus ($6.86 \pm 3.27 kPa$) than untreated group ($23.3 \pm 6.3 kPa$) due to softening effect.

For the *in vitro* EMT experiment, immunostaining images confirmed morphological changes resulting from HGF treatment (Fig. 3a). Down regulation of E-cadherin and up regulation of vimentin were observed. With HGF treatment, MDCK cells adopted a spindle-shaped morphology and vimentin expression was significantly higher. In untreated MDCK cells, polarized cells interact with the basement membrane and are held together through the adherent junction. During EMT, the monolayer stiffness decreases due to weakened cell-cell adhesions and rearrangements in the cytoskeleton. In addition, extracellular matrix undergoes significant mechanical change. There is diminished E-cadherin staining, which is present both in the cytoplasm as punctuated dots and at the periphery of the cells, indicating the disintegration of cell-cell adhesions. Previous study showed that the presence of vimentin networks reduced the effective cytoskeletal mesh size and viscoelastic relaxation time constant of the cytoskeleton, resulting in a softer cell layer⁸.

In conclusion, our toolkit provides a new facile route for investigating dynamic cellular mechanics at the multicellular level by the demonstration of the platform utility through minute-resolution of cellular monolayer dissociation via trypsinization and through multi-day *in vitro* EMT experiment. In the future, we envision this microfluidic platform to be scalable to multi-channel for more complex cellular processes and to be applied for different cell types in the field of drug discovery and disease modeling.

ACKNOWLEDGEMENTS

The research was supported by National Institute of Health (NIH) under award number: NIGMS 1P20GM139760-01 and NIDCD 2R01DC014461-06.

REFERENCES

- [1] Suresh, S. *Acta biomaterialia*, 34: 413-438, 2007
- [2] Barnes, J. M. et al., *Journal of cell science*, 1301: 71-82, 2017
- [3] Guillot, C. et al., *Science*, 3406137: 1185-1189, 2013
- [4] Gervais, T. et al., *Lab on a Chip*, 64: 500-507, 2006
- [5] Guyard, G. et al., *Physical Review Letters*, 12920, 204501, 2022
- [6] Jamora, C. et al., *Nature cell biology*, 44: E101-E108, 2002
- [7] Sorba, F. et al., *Lab on a Chip*, 1912: 2138-2146, 2019
- [8] Patteson, A. E. et al., *Physical biology*, 181: 011001, 2020

A LONGITUDINAL STUDY OF THE ANATOMICAL CHANGES OF THE PREGNANT MURINE VAGINA USING MAGNETIC RESONANCE IMAGING

Aileen C. Suarez (1), Clara J. Gimenez (1), Jennifer M. Munson (1), Kristin S. Miller (2,3), Kristin M. Myers (4), Steven D. Abramowitch (5), Raffaella De Vita (1)

(1) Department of Biomedical Engineering and Mechanics, Virginia Tech, Blacksburg, VA, USA

(2) Department of Bioengineering and Mechanical Engineering, University of Texas Dallas, Richardson, TX, USA

(3) Department of Obstetrics and Gynecology, University of Texas Southwestern Medical Center, Dallas, TX, USA

(4) Department of Mechanical Engineering, Columbia University, New York City, NY, USA

(5) Department of Bioengineering, University of Pittsburgh, Pittsburgh, PA, USA

INTRODUCTION

The United States has the highest maternal morbidity rate among high-income countries with 23.8 deaths per 100,000 live births in 2020 [1]. Patients who survive pregnancy have an increased risk of pelvic floor disorders like urinary and fecal incontinence, overactive bladder, and pelvic organ prolapse [2]. Studying the female reproductive organs and their remodeling during pregnancy and post-partum could help in the prevention and treatment of maternal trauma but it remains challenging due to the lack of appropriate animal models. Thus, there still are unknowns about the mechanical alterations that are associated with pregnancy and how the pelvic tissues recover after parturition.

Previous research to establish murine animal models have used terminal studies to measure anatomical and mechanical changes of the vagina throughout pregnancy or magnetic resonance imaging (MRI) for studying embryonic development [3,4,5]. There is currently no research that aims to quantify how murine vaginas change prepartum to postpartum within the pelvic floor, surrounded by other organs and tissues. Therefore, we conducted a pilot study using MRI to non-invasively quantify the changes in the murine vagina throughout pregnancy. This longitudinal study is the first to observe the anatomical changes of the entire murine reproductive tract from a non-pregnant state up to three weeks postpartum. The scans from this study provide *in vivo* images that will serve to create robust finite element models to recapitulate the effect of pregnancy on the pelvic system.

METHODS

Three sexually mature (12-16 weeks old) CD-1 mice were used for this study. These animals were imaged in a small animal bore 9.4 Tesla

BioSpec 94/20 MRI scanner (Bruker, Billerica, MA) at five different time points: virgin (V), mid-pregnancy (gestation day 9-10, MP), late pregnancy (gestation day 16-17, LP), 24-72 hours postpartum (PP), and 3 weeks PP. At each timepoint, the mouse was sedated via inhalation (Harvard Apparatus, Holliston, MA) of a dose of 1-3% isoflurane in oxygen at a flow rate of 0.6 liters per minute to immobilize the mouse during imaging. Once immobilized, the animal was transferred onto the bed of the MRI scanner equipped with a radio frequency volume coil with a 40:70 mm inner to outer diameter. A pressure sensor was placed underneath the mouse's upper chest to monitor respiration. Feedback from this probe was collected by a respiration monitoring and gating system (SAII, Stony Brook, NY) and used to trigger the MRI scanner to avoid imaging when the abdomen was in motion during respiration.

The 2D imaging sequences protocol consisted of a T1 weighted FLASH (fast low angle shot) axial, T2 weighted turboRARE (rapid acquisition with relaxation enhancement) axial, and a T1 weighted FLASH sagittal scan with a spatial resolution of 10 pixels per mm³, slice thickness of 0.8 mm, and fat suppression. The number of slices and the dimension of the slices were varied across time points to accommodate the size of each mouse ([minimum – maximum] # of axial slices: 32-56, axial slice dimensions: 280 x 280 mm²-320 x 320 mm², # of sagittal slices: 32-40, sagittal slice dimensions: 360 x 360 mm²-480 x 480 mm²). Depending on the timepoint, scans were averaged between 8 to 16 times to adjust for time and animal welfare constraints.

The acquired MRI scans were exported to a DICOM format and processed in 3D Slicer [6]. The axial and sagittal scans at each timepoint were registered using the pubic symphysis as reference to visualize the volume of the vagina in both T1 and T2 sequences (Figure 1A-1F). The

T1 scan established the external contours of the vagina, while the T2 scans provided more information on the internal structures of the tissue (e.g., vaginal rugae seen in Figure 1A, 1D). Label maps and closed surface models (without smoothing) were created by segmenting the registered T1 and T2 axial scans (Figure 1G-1I) to quantify the volume of the vagina (including the enclosed volume). Circularity (which ranges roughly from 0 to 1; where 1 marks a perfect circle) of cross sections of the vagina was calculated using parameters given by the SegmentGeometry plugin [7]. Positions of each segment cross section were defined by percentages relative to their distance with respect to the introitus and total vaginal length, with 0% representing the vaginal opening (introitus) and 100% the cervix. The longitudinal length of the vagina was measured in the sagittal scan using ImageJ (NIH).

RESULTS

Computed from segmentations of the vaginas, the virgin mice had vaginal volumes of 72.2, 56.1, and 46.6 mm³ (Figure 2A). After normalizing the volume during and after pregnancy to the virgin volume, each mouse had a fold change of 0.48, 0.73, and 1.26 by MP, 0.70, 1.26, and 2.36 by LP, 0.48, 0.96, 1.94 by PP and 0.64, 1.06, 1.28 by 3WPP. The maximum vaginal length measured at each time point was also averaged across mice and normalized to the virgin timepoint. The average fold change in vaginal length and its standard deviation were 1.18 ± 0.07 at MP, 1.35 ± 0.06 at LP, 1.35 ± 0.08 at PP, and 1.03 ± 0.10 at 3WPP. Preliminary results show the circularity of the vaginal cross sections near the introitus are increased throughout pregnancy and postpartum while near the cervix, they decreased. This can be observed in Figure 2B for one mouse where at each timepoint the maximum circularity value of the vagina with its respective position (%) was: 0.56 (at 36%) at V, 0.91 (at 30%) at MP, 0.77 (at 31%) at LP, 0.87 (at 42%) at PP, and 0.85 (at 23%) at 3WPP. The minimum circularity value and position were: 0.41 (at 55%) at V, 0.31 (at 80%) at MP, 0.36 (at 75%) at LP, 0.34 (at 100%) at PP, and 0.31 (at 77%) at 3WPP.

DISCUSSION

In this pilot study, we designed and optimized an MRI protocol to capture for the entire volume of the murine pelvic floor throughout pregnancy and the postpartum recovery period. To our knowledge, this is the first MRI study that focuses on visualizing and measuring the changes to the vagina up to 3 weeks post-delivery. The properties of the MRI scan (i.e., sequences, averages, volume coil size) had to balance animal wellbeing, signal to noise ratio (scan quality), and cost.

The vaginal volume decreased by mid-pregnancy, peaked in late pregnancy, and then decreased to a similar virgin value. The vaginal length follows this trend where length peaks at late pregnancy before decreasing by 3 weeks postpartum, suggesting that the vagina may lengthen in preparation for delivery or due to the strains imposed by the growing uterine horn. Prior results using *ex vivo* rat tissues support the trends seen here [3]. The circularity of the segmented cross sections suggests that the vagina is not uniform across its length *in vivo* and that the shape varies throughout pregnancy. By 3 weeks postpartum, the range of vaginal circularity differs from its virgin state indicating irreversible changes to the vagina due to pregnancy.

A limitation of the study is the low sample size due to high cost of the MRI scans. Additionally, data collection on set gestational and delivery days was difficult to manage, so data were grouped together within a two-day range, possibly contributing to variations between mice. The estrous cycle was not accounted for at the virgin time point and can also contribute to the variation seen since murine vaginal openings appear swollen during proestrus and estrus [3]. For quantification, image resolution and software tools impeded segmentation of the enclosed volume across the length of the vagina at

certain timepoints. Overall, this MRI study acquired the first longitudinal *in vivo* images of the murine pelvic floor throughout pregnancy and postpartum recovery. With these geometric models of the vagina detailing its longitudinal changes, we can improve previously simplified finite element models that describe the biomechanical changes of the vagina during and after pregnancy to improve the women's health field.

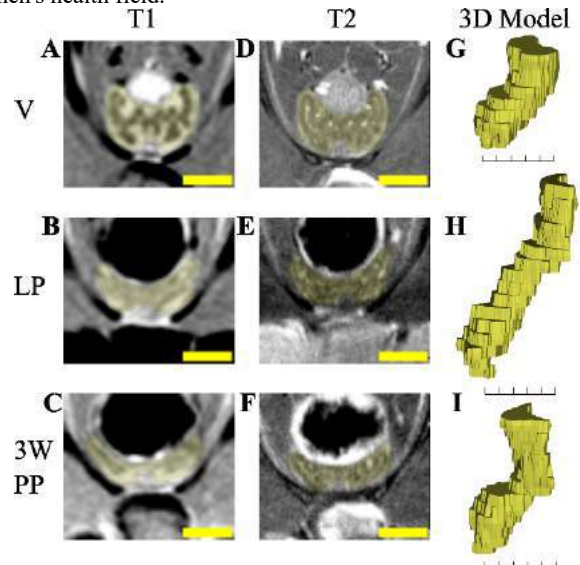


Figure 1: T1 (A-C) and T2 axial scans (D-F) (scale bar 2 mm) depicting vaginas (yellow overlay) at virgin (V), late pregnancy (LP) and 3-week postpartum (3W PP) timepoints for one mouse with its 3D model representation (G-I) (scale bar 5 mm).

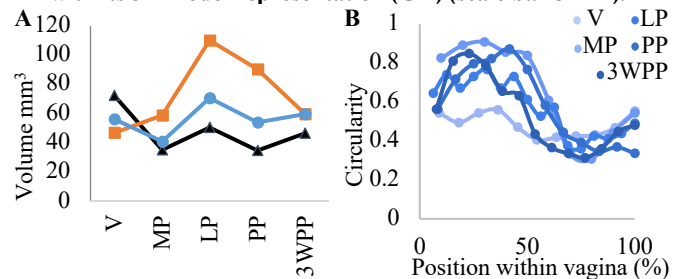


Figure 2: (A) Volume (mm³) of each individual mouse vaginal segmentations over time. (B) Circularity of vaginal cross sections for one mouse over time. Horizontal axis describes position along the vaginal length, from 0% (introitus) to 100% (cervix). Data depicted in Figure 2B is collected from the mouse whose volume is reported using blue circle in Figure 2A and seen in Figure 1.

ACKNOWLEDGEMENTS

Dr. Maosen Wang at the Fralin Biomedical Research Institute at Virginia Tech for operating the MRI. This work was supported by the National Science Foundation under award #2053851.

REFERENCES

- [1] Hoyert, DL. Maternal mortality rates in the US, 2020. *NCHS Health E-Stats*. 2022.
- [2] Hallock, J., *Obstet. Gynecol. Clin. North Am.*, 43(1): 1–13, 2016.
- [3] Feola, A. et al., *Ann. Biomed. Eng.*, 39:549–558, 2011.
- [4] Pang, S.C. et al., *Academic Press*, eds. The Guide to Investigation of Mouse Pregnancy: 3–19, 2014.
- [5] Krishnamurthy, U. et al., *Gynecol. Obstet. Invest.*, 78(1): 33–40, 2014.
- [6] Fedorov, A. et al., *Magn. Reson. Imaging*, 30(9):1323–41, 2012.
- [7] Huie, JM., et al. *Integr. Org. Biol.*, 4(1): obac009, 2022.

MECHANICAL AND MULTISCALE STRUCTURAL CHANGES DUE TO REPETITIVE FATIGUE LOADING IN AN *IN VIVO* RAT OVERUSE MODEL

Pooja Chainani (1,3), Maria Buzo Mena (1), Diana Yeritsyan (1), Daniela Caro (1), Kaveh Momenzadeh (1), Joseph P. DeAngelis (2), Arun J. Ramappa (2), Ara Nazarian (1,2,3)

- (1) Musculoskeletal Translational Innovation Initiative, Beth Israel Deaconess Medical Center and Harvard Medical School, Boston, MA, USA
(2) Carl J. Shapiro Department of Orthopedic Surgery, Beth Israel Deaconess Medical Center and Harvard Medical School, Boston, MA, USA
(3) Department of Mechanical Engineering, Boston University, Boston, MA, USA

INTRODUCTION

Tendon injuries, such as ruptures and tendinopathies, account for nearly 46% of the 33 million reported musculoskeletal injuries per year, affecting occupational- and sports-related events (1). As load bearing structures that are primarily composed of type I collagen and connect muscle to bone, tendons play a key role in daily activities and exercise (2). Although some levels of physical activity can lead to increased tendon mechanical function, without sufficient rest periods, an imbalance in matrix proteins, such as collagen, and net degradation of the tendon's extracellular matrix, can leave the tendon susceptible to injury (2, 3). The clinical presentation of tendinopathies is limited to later stages of injuries and occur after pain and loss of function. Tendinopathy is considered to be caused by a result of accumulated fatigue damage from overuse repetitive cyclic loads, although the threshold between normal and overuse is not clearly defined (4, 5). This demonstrates the need to investigate the initiation and progression of early tendon damage. The hierarchical nature of tendons contributes to their strength, therefore, investigations of tendon damage on multiple scales is important to understand how damage propagates spatially as well as temporally. The objective of this study is to assess rat Achilles tendon's mechanical, structural, and biological temporal and spatial changes and responses to noninvasive *in vivo* repetitive cyclic fatigue loading.

METHODS

Forty-two 13-week-old Sprague Dawley female rats were anesthetized using isoflurane per IACUC approved protocols. The rats' left hindlimb was fixed in full-leg extension using a splint to isolate the Achilles tendon. The foot was attached to an ankle joint actuator that allowed for passive ankle dorsiflexion up to 40° relative to neutral and the rats were secured in a prone position in a full-body platform. The ankle was cyclically dorsiflexed to an angle that loaded the tendon to the exponential region at ~1 Hz to mimic normal gait for 500 cycles.

Mechanical measurements before and after each cyclic loading bout were performed to assess the effect of loading on tendon mechanical properties. The rats were divided into three groups, where each group was subjected to either 1, 2, or 3 bouts of 500 cycles of loading with two days of cage activity between each loading bout. Following two days after each group's final bout of loading, the rats were euthanized via CO₂ inhalation.

The loaded Achilles tendon tissue was harvested for RT-qPCR analysis of gene expression (n = 5 per group), histological assessment (n = 3 per group), and transmission electron microscopy analysis of transverse and longitudinal sections (n = 6 per group). Samples of 5µm thickness from each group were sectioned and stained with hematoxylin & eosin (H&E) to assess changes in cells shape, size, and quantity. For collagen fibril assessment, sections of 50-70 nm thickness from the midsection of the tendon were cut perpendicular to the longitudinal axis of the tendon. Ten representative images from each sample were preprocessed and quantified for collagen morphological parameters (collagen fibril radius, collagen area fraction, and specific fibril contact area) using Fiji. The hysteresis curves of the baseline measurement prior to the loading protocol and the post-measurement immediately after the last loading bout for each group were analyzed to obtain the percentage change in peak stress, hysteresis, and loading and unloading modulus of the stress-strain curves. Statistical analysis was done using GraphPad (version 9.3.0 for Windows; GraphPad Software, San Diego, CA). The Kolmogorov-Smirnov test was used to determine whether the data was normally distributed. For normally distributed data, an ordinary one-way ANOVA test was used to test significance between the three load groups on the mechanical and morphological properties, otherwise, the Kruskal-Wallis test was performed. Statistical significance was considered for p-values < 0.05.

RESULTS

Histological evaluation of loaded tendons stained with H&E revealed increased rounded cells, hypercellularity, and fiber disorganization with increased loading, specifically for 3 bouts of loading (Figure 1A). Qualitative assessment of collagen fibrils showed larger amounts of fibrils with smaller radii compared to larger radii in the 1 load group in comparison to the 2 and 3 load groups (Figure 1B).

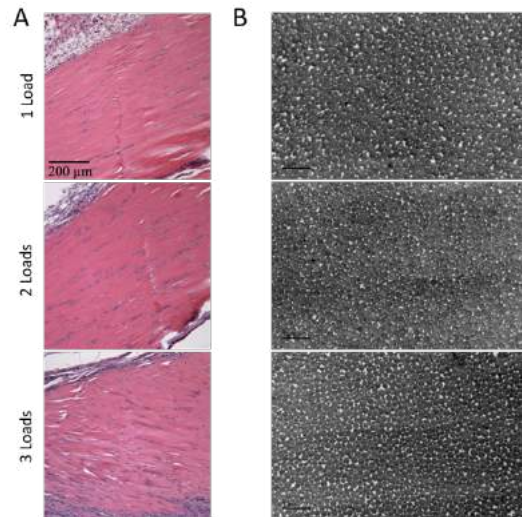


Figure 1: Structural assessment of collagen fibers and fibrils. (A) Representative images of tendons stained with hematoxylin and eosin (H&E) staining, (B) Representative transmission electron images for the three load groups used to calculate the mean fibril radius, collagen fibril area fraction, and specific fibril surface area.

Quantitative evaluation of transmission electron images revealed significant difference between each bout of loading for mean fibril radius, with larger mean radii after 2 bouts of loading, while the collagen area fraction was considered similar for each load group. Specific fibril surface area was significantly lower for the 3 loads group compared to the 1 and 2 loads groups (Figure 2). When comparing the histograms of collagen fibril distributions between each group, there are higher number of smaller fibrils after 1 bout of loading, similar fractions of smaller and larger fibrils after 2 bouts of loading, and a closer to normal distribution after 3 bouts of loading (Figure 3).

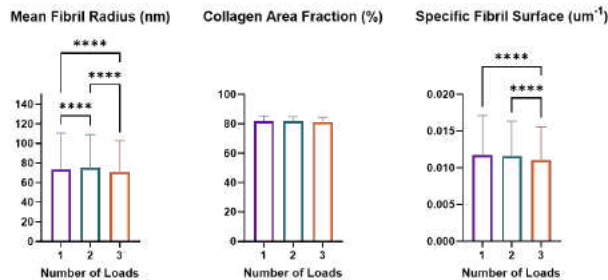


Figure 2: Calculated morphological parameters of collagen fibrils

Overall, there was a decrease in mechanical properties with increased number of loading, with a significant difference between 1 bout of loading when compared to the 2 and 3 bouts for peak stress, hysteresis, and loading modulus. Additionally, there was a significant difference between 2 and 3 loads for hysteresis ($p < 0.05$) (Figure 4).

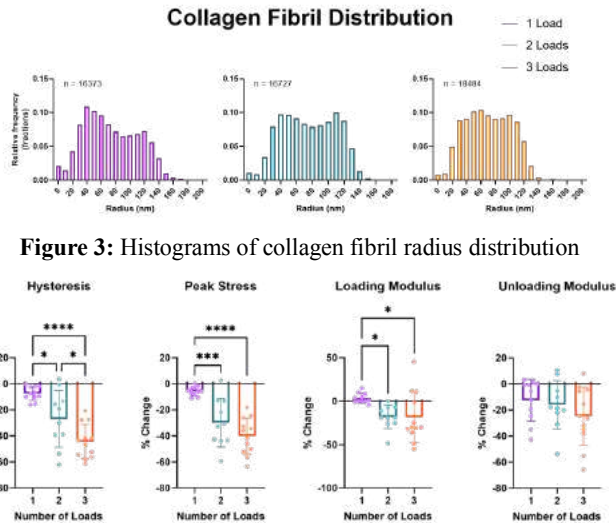


Figure 3: Histograms of collagen fibril radius distribution

Figure 4: Mechanical changes between the post-measurement of the final load and the baseline measurement before loading

DISCUSSION

These structural and mechanical results provide insight to evaluate structure-function relations of damaged tendon from repetitive fatigue loading. The decreased mechanical properties suggest loss in collagen in contributing to the overall stress of the tendon response to load. The increased cellularity and rounded cells in stained histological samples demonstrates matrix damage with increased bouts of loading. The difference in mean fibril radius shows that there are significant changes occurring in loss and formation of collagen fibrils between loads. This could be attributed either to the healing of the fibrils, the disruption of fibers and fibrils due to overuse loading, or a combination of both. Although each group has similar area fractions, the distribution of fibril radii demonstrates a shift in the formation and growth of collagen fibrils throughout the course of loading. The changes in specific fibril surface between 1 and 3 loads and 2 and 3 loads relates to fibril-fibril interactions, showing decreased interactions with more loads applied. Although macroscopically, mechanical properties reveal that the tendons become progressively more damaged with more loads, microstructurally, the change in distribution of collagen fibril radius over the course of more loads suggests growth of smaller fibrils to larger fibrils. Microscale mechanical testing can be done in future studies to understand the collagen fibril mechanical changes. Gene expression of collagen types I and III, MMPs and TIMPs, as well as inflammatory cytokines will be done to further understand and link biological changes with the quantified microstructural and mechanical changes.

We have been able to assess mechanical and multi-scale structural changes to rat Achilles tendon subjected to repetitive fatigue loading in a noninvasive, *in vivo* setting. Taken together with further analysis of remaining data of gene expression of collagen, matrix, and inflammatory markers, these results will help us understand the initiation and propagation of tendon injury and the relations between the mechanical, structural and biological healing responses to for better clinical understanding of the initiation of tendinopathy.

REFERENCES

[1] Li, ZJ et al, *Frontiers in Medicine*, 1192, 2021.
[2] Svensson, RB et al, *J Appl Physiol*, 121(6):1237-1246, 2016.
[3] Magnusson, SP et al, *Nat Rev Rheumatol*, 6(5):262-8, 2010.
[4] Andarawis-Puri, N, Flatow, EL, *Musculoskeletal Neuronal Interact*, 11(2):106-14, 2011.
[5] Neviasser, A, et al, *J Shoulder Elbow Surg*, 21(2):158-63, 2012.

DYNAMICS OF SHEAR STRESS IN EMBRYONIC CHICK HEART ANATOMIES RECONSTRUCTED FROM LIGHT SHEET FLUORESCENCE MICROSCOPY IMAGING

K. Giesbrecht (1), S. Rossi (1), M. Bressan (2), B. Griffith (1)

(1) Department of Mathematics, University of North Carolina at Chapel Hill, Chapel Hill, NC, USA
(2) Department of Cell Biology and Physiology, University of North Carolina at Chapel Hill, Chapel Hill, NC, USA;

INTRODUCTION

Congenital heart defects are the most common birth defect and are present in approximately 1% of newborns¹. Yet, only 20-30% of congenital heart defects can be traced to genetic or environmental causes²⁻⁴. Altered hemodynamic environments account for many congenital heart defects⁵⁻¹⁰. As the first functioning organ in vertebrates, the heart relies on many hemodynamic queues, such as intracardiac blood velocity, blood pressure, and shear stress, while developing. Particularly, shear stress has been shown to regulate many aspects of cardiogenesis by modulating gene expression, such as aortic and pulmonary trunk diameters¹¹. When these hemodynamic factors are altered, abnormalities may arise.

Most congenital heart defects occur in the outflow tract, a region that eventually gives rise to the pulmonary trunk and aorta¹². Outflow tract congenital heart defects are severe and have a high mortality rate¹³. However, it's unclear what role shear stress plays in outflow tract development partially due to the difficulty of obtaining shear stress measurements in the outflow tract and surrounding vasculature experimentally. Measuring shear stress in animal models is challenging due to the delicate nature and continuous pumping of the embryonic heart. Computational fluid dynamics modeling is an attractive method to simulate blood flow and the resulting shear stress throughout the heart and surrounding vasculature, capturing precise spatial and temporal patterns of shear stress.

This is the first computational fluid dynamics modeling study, to our knowledge, that uses light sheet fluorescence microscopy to image the embryonic chick heart and supporting vasculature throughout several stages of development. Light sheet fluorescence microscopy offers higher resolution than other imaging techniques for capturing embryonic heart anatomies, such as optical coherence tomography (OCT) imaging¹⁴. Shear stress is mapped throughout the outflow tract, aortic arches, and dorsal aorta of the captured anatomies. We also compare the geometric properties of aortic arches imaged by light sheet

fluorescence microscopy throughout the stages of development to areas of elevated shear stress. Together this information is critical to establishing baseline measurements of anatomical features and hemodynamic factors necessary for understanding if altered intracardiac shear stress contributes to the outflow tract and supporting vasculature abnormalities.

METHODS

Chick embryos staged at Hamburger-Hamilton (HH)16, HH18, HH19, and HH21 were imaged using light-sheet fluorescence microscopy. The imaging data were segmented and meshed. Using the finite element method, we model blood flow through the meshed anatomies described by the momentum equation (1) and the continuity equation (2):

$$\rho \frac{Du}{Dt} + \nabla p - \mu \nabla^2 u - f = 0 \quad (1)$$

$$\nabla \cdot u = 0 \quad (2)$$

The continuity equation (2) describes blood as an incompressible fluid. The blood pressure and velocity fields are p and u , respectively. Fluid density is $\rho = 1060 \text{ kg}\cdot\text{mm}^{-3}$. We model blood to have a constant viscosity of $\mu = 3.7 \cdot 10^{-3} \text{ Pa}\cdot\text{s}$ since many studies consider embryonic chick blood as a Newtonian fluid¹⁵. We impose pulsatile pressure-driven flow in the inflow modeled from previously measured pressure profiles¹⁶ and no-slip boundary conditions on intracardiac and vessel walls ($u=0$). Aortic arch diameters, curvatures, and lengths were measured for all embryos.

RESULTS

Blood velocity streamlines are plotted throughout the four examined stages (Fig. 1) during peak flow, decreasing flow, and minimum flow throughout the cardiac cycle. The streamlines reveal expected laminar flow throughout the embryonic heart, aortic arches, and dorsal aorta.

Velocity increased in narrow anatomical regions such as the aortic arches and narrow regions preceding the outflow tract.

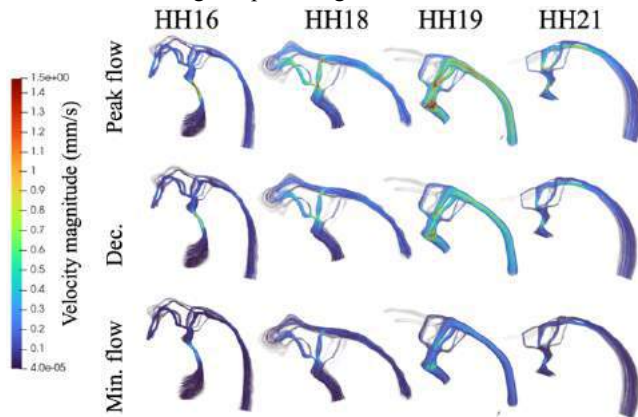


Figure 1: Blood flow is laminar at each stage. Peak velocity occurs in aortic arches and in narrowed intracardiac luminal regions.

Shear stress is shown during peak flow, decreasing flow, and minimum flow throughout the cardiac cycle (Fig. 2). Peak shear stress is observed in many of the same regions and stages of the cardiac cycle where peak velocity is observed.

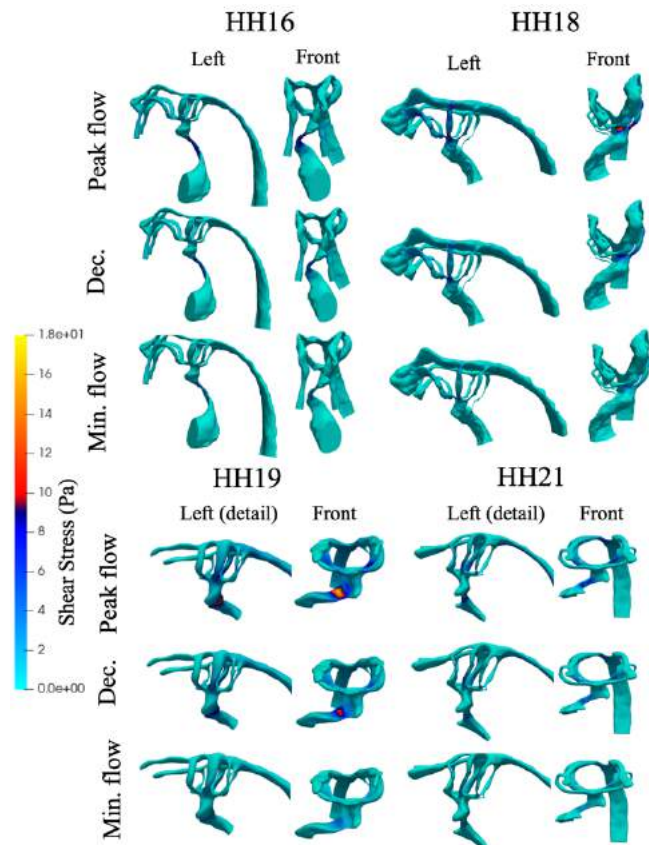


Figure 2: Shear stress is elevated in similar regions and time points where peak velocity occurs.

At the intermediate stages, HH18 and HH19, peak shear stress and velocities in the aortic arches occur in the second pair of aortic arches, which is the shortest pair of the three at these stages (Fig. 3).

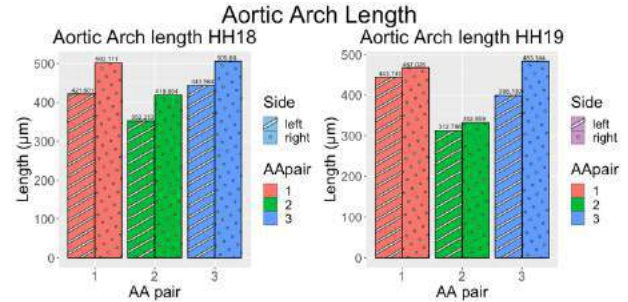


Figure 3: The second pair of aortic arches is the shortest pair and experiences high shear stress.

DISCUSSION

This is the first computational study examining shear stress spanning stages HH16 through HH21 to include the heart, aortic arches, and dorsal aorta using light sheet fluorescence microscopy to reconstruct the embryonic anatomies. Light sheet fluorescence microscopy is also an excellent imaging technique to observe gene expression¹⁴. Future studies could use light sheet fluorescence microscopy to both reconstruct anatomies and indicate regions of activated shear-sensing genes to complement computational fluid dynamics modeling.

Additionally, shear stress is elevated in both the aortic arches and heart, which is typically lost on most models with smaller fluid domains, which omit either the aortic arches and dorsal aorta or ventricle. The observed velocity profiles produced expected laminar flow and are consistent with the observed shear stress throughout the stages.

We measured several geometric features of the aortic arches including the average diameter, curvature, and lengths of each aortic arch across the stages. Aortic arches undergo extensive remodeling during these stages, with some arches persisting between stages, while others disappear and new ones develop¹⁵. Yet, across all stages, the second pair of aortic arches was the shortest among the pairs. In the intermediate stages, the aortic arches that experienced the highest shear stress were the second pair arches. However, these arches were not necessarily the narrowest. Increasing the number of embryos used in the analysis is necessary to further explore this relationship between aortic arch length and hemodynamics.

ACKNOWLEDGEMENTS

This research is supported through the NIH IVB training program at UNC-Chapel Hill (# T32HL069768-19) and the American Heart Association Predoctoral Fellowship (# 899419).

REFERENCES

- [1] Hoffman, J Kaplan, S, *J Am Coll Cardiol*, 39:1890-1900, 2002.
- [2] Grech, V Gatt, M, *Int J Cardiol*, 68:151-156, 1999.
- [3] Meberg, A et al., *Acta Paediatr*, 96:1142-1145, 2007.
- [4] Kučienė, R Dulskienė, V, *Medicina (Mex)*, 44:827, 2008.
- [5] Dyer, L Rugonyi, S, *J Cardiovasc Dev Dis*, 8:90, 2021.
- [6] Alser, M et al., *J Cardiovasc Dev Dis*, 8:32, 2021.
- [7] Midgett, M et al., *Am J Phys-Heart Circ Phys*, 312:H632-42, 2017.
- [8] Midgett, M et al., *Front Physiol*, 8:56, 2017.
- [9] Hogers, B et al., *Cardiovasc Res*, 41:87-99, 1999.
- [10] Menon, V et al., *J Cardiovasc Dev Dis*, 2:108-124, 2015.
- [11] Baeyens, N et al., *eLife* 4:e04645, 2015.
- [12] Courchaine, K et al., *J Cardiovasc Dev Dis*, 6:11, 2019.
- [13] Rothenberg, F et al., *Birth Def Res C Emb Today*, 69:38-45, 2003.
- [14] Karim, M et al., *Multimod Biom Imag XVII*, 11952:1195202, 2022.
- [15] Kowalski, W et al., *PLoS One*, 8: e60271, 2013.
- [16] Shi, L et al., *Am J Phys-Heart Circ Phys*, 305: H386-96, 2013.

DEVELOPMENT OF A REPRESENTATIVE ARTERY MODEL FOR STENT FATIGUE TESTING

Jude M. Hussain (1), Ankush Aggarwal (1), Andrew McBride (1), Robbie Brodie (2), Craig MacLean (2)

(1) School of Engineering, University of Glasgow, United Kingdom, (2) Terumo Aortic, Inchinnan, United Kingdom

INTRODUCTION

Stents are devices employed in the treatment of arterial injuries including abdominal aortic aneurysms. They apply a continuous chronic outward force (COF) that resists artery-imposed hoop stresses to maintain lumen patency. Their failure conditions are difficult to predict computationally as they depend on the compliance properties of the representative (often hyperelastic) vessel. To capture arterial compliance faithfully is to select a suitable model and identify its parameter values that would yield the desired compliance. However, aleatory and epistemic uncertainties associated with parameter identification and model selection, respectively, hinder models in reproducing compliance values. Aleatory uncertainty arises from the variability in data procurement methods and subject-to-subject differences. Epistemic uncertainty is associated with the choice of a particular model [1]. To account for such uncertainties, a systematic approach to selecting hyperelastic models that outlines objective criteria for a parsimonious model in capturing arterial compliance is necessary. To this end, a Bayesian approach to hyperelastic model selection and parameter identification wall modeling is detailed and proposed. This framework employs pre- and postoperative compliance data of abdominal aortic aneurysms (AAA) patients treated with the self-expanding Nitinol stent-graft, the *Anaconda*TM, to inform the choice of a representative hyperelastic model for future 3-D computational fatigue testing.

METHODS

1. Patient sample and collected data

15 patients with abdominal aortic aneurysms underwent elective EVAR (endovascular aneurysm repair) with the *Anaconda*TM stent-graft. Anonymized collected data \mathbf{d}_{pat} of the 15 abdominal aortae are categorized into preoperative \mathbf{v}_{pre} and postoperative \mathbf{v}_{post} measures. The vector of preoperative data, $\mathbf{v}_{\text{pre}} = [r_{\text{dias,pre}} \quad p_{\text{sys}} \quad p_{\text{dias}}]$, contains the preoperative diastolic radius $r_{\text{dias,pre}}$, systolic pressure p_{sys} , and diastolic pressure p_{dias} . The vector of postoperative measures, $\mathbf{v}_{\text{post}} = [d \quad \varepsilon]$, contains the postoperative arterial compliance d_{post} and expansion ε

$$d_{\text{post}} = \frac{r_{\text{sys,post}} - r_{\text{dias,post}}}{r_{\text{dias,post}}} \frac{1}{p_{\text{sys}} - p_{\text{dias}}} \quad \varepsilon = \frac{r_{\text{dias,post}} - r_{\text{dias,pre}}}{r_{\text{dias,pre}}} \quad (1)$$

A statistical model of \mathbf{v}_{pre} and \mathbf{v}_{post} , formulated as a multivariate normal distribution, was used to construct the conditional distribution $p(\mathbf{v}_{\text{post}} | \mathbf{v}_{\text{pre}}) \sim \mathcal{N}(\mu_c, \Sigma_c)$, defined by the conditional mean μ_c and covariance Σ_c .

2. Vascular mechanics: Kinematics

The abdominal aorta is modeled as a hyperelastic tube subject to axisymmetric deformation. The tube begins at a reference configuration Ω_0 , and is subjected to arterial pressure and a chronic outward force in the deformed configuration Ω_L . The coordinates of the map $\Omega_0 \mapsto \Omega_L$ are

$$\begin{aligned} \Omega_0 : R_i \leq R \leq R_o, \quad 0 \leq \Theta \leq 2\pi, \quad 0 \leq Z \leq L, \\ \Omega_L : r_i \leq r \leq r_o, \quad 0 \leq \theta \leq 2\pi, \quad 0 \leq z \leq l, \end{aligned} \quad (2)$$

where R_i is the inner radius in the reference configuration, r_o is the outer radius in the deformed configuration, and L and l are the tube lengths in Ω_0 and Ω_L , respectively. Assuming axisymmetric deformation along the length of the tube and the incompressibility of the tube wall, the aortic radius after loading is obtained as

$$\Omega_0 \mapsto \Omega_L : r(R) = \sqrt{\frac{R^2 - R_i^2}{\lambda_z} + r_i^2}. \quad (3)$$

In cylindrical coordinates, the components of $\mathbf{F} = \text{diag}[\lambda_r, \lambda_\theta, \lambda_z] = \text{diag}\left[\frac{R}{r\lambda_z}, \frac{r}{R}, \lambda_z\right]$ map a point in Ω_0 to Ω_L , where λ_r , λ_θ , and λ_z are the principal stretches. The hyperelastic response of the aortic wall is quantified by a strain energy density function Ψ , which is related to the Cauchy stress via $\boldsymbol{\sigma} = 2\mathbf{F} \frac{\partial \Psi}{\partial \mathbf{C}} \mathbf{F}^T - p\mathbf{I}$, where $\mathbf{C} = \mathbf{F}^T \mathbf{F}$ is the right Cauchy-Green tensor. The principal stresses

$$\sigma_{rr} = -p + \lambda_r \frac{\partial \Psi}{\partial \lambda_r}, \quad \sigma_{\theta\theta} = -p + \lambda_\theta \frac{\partial \Psi}{\partial \lambda_\theta}, \quad \sigma_{zz} = -p + \lambda_z \frac{\partial \Psi}{\partial \lambda_z} \quad (4)$$

follow from the assumptions of axisymmetric loading and arterial tube incompressibility. The equilibrium condition $\text{div } \boldsymbol{\sigma} = \mathbf{0}$ holds in the absence of body forces, where $\text{div}(\bullet)$ is the spatial divergence operator. Assuming constant λ_z and thus the dependence of the inflation problem solely on r , the equilibrium equations reduce to

$$\frac{d\sigma_{rr}}{dr} + \frac{1}{r}(\sigma_{rr} - \sigma_{\theta\theta}) = 0. \quad \text{SB}^3\text{C2023-229}$$

Integrating Eq. (5) and imposing boundary conditions $\sigma_{rr}(r_i) = -p_i$ and $\sigma_{rr}(r_o) = 0$, the equation for the pressure at r_i is deduced as

$$p_i = \int_{r_i}^{r_o} \left(\lambda_\theta \frac{\partial \Psi}{\partial \lambda_\theta} - \lambda_r \frac{\partial \Psi}{\partial \lambda_r} \right) \frac{dr}{r}. \quad (6)$$

The *Anaconda*TM is modeled as a locally linear spring. The force F exerted by the spring is

$$F = k(r_{\text{dias,post}} - r_{\text{dias,pre}}) + f_0, \quad (7)$$

where k is the stent stiffness from radial force testing, and f_0 is the COF exerted by the stent graft. To calculate the expansion ε , Eq. (6) is solved by calculating the radius $r_{\text{dias,post}}$ due to the chronic outward pressure resulting from f_0 . After setting $R_i = r_{\text{dias,post}}$, $r_{\text{sys,post}}$ due to $p_i = p_{\text{sys}} - p_{\text{dias}}$ is calculated, and d_{post} is acquired.

3. Bayesian model selection framework

The proposed Bayesian approach to hyperelastic model selection and corresponding parameter identification is now detailed. Bayes' theorem is used to update prior distributions $p(\theta_k | m_k)$ of parameters θ_k given patient data \mathbf{d} and the choice of the k^{th} model m_k to give the posterior distribution of parameters $p(\theta_k | \mathbf{d}, m_k)$,

$$p(\theta_k | \mathbf{d}, m_k) = \frac{p(\mathbf{d} | \theta_k, m_k) p(\theta_k | m_k)}{p(\mathbf{d} | m_k)}. \quad (8)$$

$p(\theta_k | m_k)$ is uniformly distributed in the absence of knowledge regarding values of θ_k . $p(\mathbf{d} | \theta_k, m_k)$ is the likelihood of observing patient data $\mathbf{d} = \mathbf{d}_{\text{pat}}$ given model m_k and corresponding θ_k . The candidate models m_k include the 4-term Yeoh and Neo-Hookean isotropic models for rubber elasticity, and the GOH, Holzapfel, and HGO anisotropic models for arterial walls [2]. The evidence $p(\mathbf{d} | m_k) = \int p(\mathbf{d} | \theta_k, m_k) p(\theta_k | m_k)$ may be interpreted as the probability mass contained under the posterior distribution over the parameter space for a given model. The Monte Carlo integral $p(\mathbf{d} | m_k) \approx \frac{1}{S} \sum_{s=1}^S p(\mathbf{d} | \theta_k^s, m_k)$ is used to approximate the evidence for $n_s = 2^{17}$ samples of S . The likelihood, $p(\mathbf{d} | \theta_k, m_k)$, for a sample parameter vector θ_k^s assumes the Gaussian form

$$p(\mathbf{d} | \theta_k^s, m_k) = \frac{1}{\sqrt{2\pi} \det \Sigma_c} \exp \left(-\frac{1}{2} (\mathbf{v}_{\text{post}}^s - \mu_c)^T \Sigma_c^{-1} (\mathbf{v}_{\text{post}}^s - \mu_c) \right). \quad (9)$$

To calculate $p(\mathbf{d} | \theta_k^s, m_k)$, $\mathbf{v}_{\text{post}}^s$ is evaluated using the kinematics described in Section 2 for a given m_k and θ_k^s , and is substituted into Eq. (9).

Preoperative compliance was not measured for the patient cohort, and is incorporated as an output of the framework. Compliance data from literature, \mathbf{d}_{lit} , for subjects within the same age group [3], is compiled to form the independent distribution $p(d_{\text{pre}}) \sim \mathcal{N}(\mu_{d_{\text{pre}}}, \sigma_{d_{\text{pre}}}^2)$. Given the independence of datasets \mathbf{d}_{pat} and \mathbf{d}_{lit} , the likelihood of reproducing d_{post} and ε from \mathbf{d}_{pat} and d_{pre} from \mathbf{d}_{lit} is the product of their individual likelihoods

$$p(\mathbf{d} | \theta_k, m_k) = p(\mathbf{d}_{\text{pat}} | \theta_k, m_k) \times p(\mathbf{d}_{\text{lit}} | \theta_k, m_k). \quad (10)$$

The expected values of d_{post} and ε from $\mathbf{d} = \mathbf{d}_{\text{pat}}$ and d_{pre} from $\mathbf{d} = \mathbf{d}_{\text{lit}}$ for given m_k are

$$\mathbb{E}(\mathbf{v}_{\text{post}}) = \int \mathbf{v}_{\text{post}}(\theta) p(\theta | \mathbf{d}) d\theta = \frac{1}{n_s} \sum_{i=1}^{n_s} \mathbf{v}_{\text{post}}(\theta_i) p(\theta_i | \mathbf{d}), \quad (11)$$

with expected variance $\text{Var}(\mathbf{v}_{\text{post}}) = \mathbb{E}((\mathbf{v}_{\text{post}} - \mathbb{E}(\mathbf{v}_{\text{post}}))^2)$.

RESULTS

Figure 1 presents the predicted expected value of d_{pre} , d_{post} , and ε from various models to that of \mathbf{d}_{pat} and \mathbf{d}_{lit} . For all models, the compliance of the artery decreases after stenting. Table 1 presents the normalized model evidence values as well as parameter values that maximize the likelihood of the respective models in representing the data, also known as maximum likelihood estimates (MLEs). The models with the highest evidence values are the Neo-Hookean, GOH, and Holzapfel models.

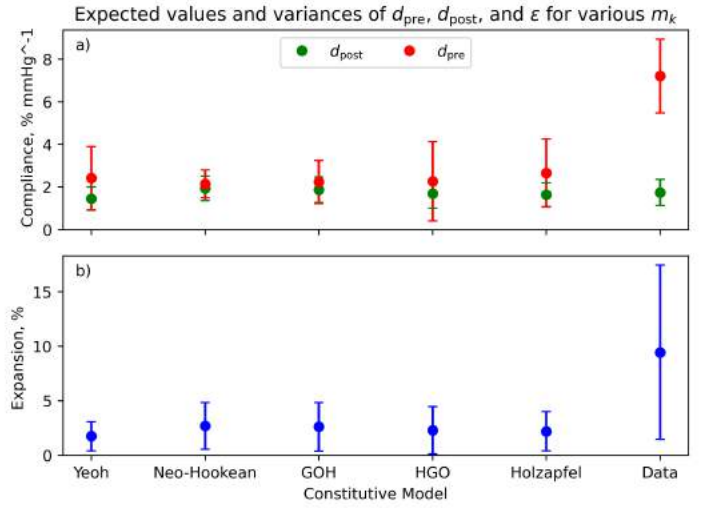


Figure 1: Expected values of (a) pre- and postoperative compliance d_{pre} and d_{post} , and (b) expansion ε compared to \mathbf{d}_{pat} and \mathbf{d}_{lit} ("Data").

Table 1: Normalized evidence and maximum likelihood estimates of θ_k for models three models with greatest evidence values.

	Neo-Hookean	GOH	Holzapfel
Evidence	1.00	0.61	0.35
θ_1 (kPa)	$\mu = 30.3$	$k_1 = 14.1$	$k_1 = 47.4$
θ_2	—	$k_2 = 29.0$	$k_2 = 13.5$
θ_3	—	$\kappa = 0.11$	$\kappa = 0.98$
θ_4 (kPa)	—	$\mu = 98.4$	$\mu = 98.1$

DISCUSSION

The decrease in arterial compliance for all m_k in Figure 1 is consistent with reported data, and is a function of the compliance mismatch between the artery and the stent [4]. Moreover, the primacy of the Neo-Hookean model indicates that evidence-based model selection intrinsically favors parsimonious models, as more complex models yielded no improvement in predictive capacity. This is corroborated by the work of [1], who show an inverse relationship between model evidence and increasing order of the Ogden in the reproduction of bovine liver compression data. In addition, the Neo-Hookean provides the poorest match for \mathbf{d}_{lit} , as its formulation is unable to capture the characteristic stiffening of compliant arteries at large strains. Nevertheless, informed prior distributions may ameliorate current predictions of d_{post} and ε . [1] also recommend the inclusion of parameter identifiability and goodness of fit via the log-likelihood (LLH) function landscape and maximum LLH values, respectively, as model selection criteria. Such improvements would render the current framework an assistive tool in the construction of representative arterial models.

ACKNOWLEDGEMENTS

J. M. Hussain discloses partial funding from the British Engineering and Physical Sciences Research Council (EPSRC).

REFERENCES

- [1] Madireddy S et al. *Computer Methods in Applied Mechanics and Engineering* 291 (2015). ISSN: 0045-7825. DOI: 10.1016/j.cma.2015.03.012.
- [2] Aggarwal A et al. *Journal of the Mechanical Behavior of Biomedical Materials* 138 (2023). ISSN: 1751-6161. DOI: 10.1016/j.jmbbm.2023.105657.
- [3] Langewouters G et al. *Journal of Biomechanics* 17.6 (1984). ISSN: 0021-9290. DOI: 10.1016/0021-9290(84)90034-4.
- [4] Long A et al. *Annals of Vascular Surgery* 23.1 (2009). ISSN: 1615-5947. DOI: 10.1016/j.avsg.2008.08.006. SB³C2023-220

CONTINUOUS INTER-LIMB GAIT COORDINATION AND STABILITY IN VETERANS AND SERVICE MEMBERS WITH TRANSTIBIAL LIMB LOSS: INFLUENCES OF PROSTHETIC ANKLE-FOOT DEVICES

Alexis Sidiropoulos, PhD¹, Brad D. Hendershot, PhD², Jonathan Gladish, MS², David Herlihy, BS^{1,3}, Jason Maikos, PhD¹

¹Department of Veteran Affairs New York Harbor Healthcare System, New York, NY, USA

²Extremity Trauma and Amputation Center of Excellence, Falls Church, VA, USA

³Narrows Institute of Biomedical Research and Education, Inc., Brooklyn, NY, USA

INTRODUCTION

The number of Veterans and Service members (SMs) with transtibial limb loss (TLL) is growing due to the aging population with dysvascular disease and diabetes, as well as from U.S. military involvements abroad [1,2]. With high associated healthcare costs [3], it is expected that conclusive research is available to clinicians for proper prosthetic prescription. However, most research is noncommittal and lacks guidance for clinical practice [4]. Metabolic and biomechanical parameters, the primary outcomes traditionally used to determine effectiveness of prosthetic devices, indicate mixed results, limiting evidentiary support for optimal prescription guidelines [5]. Conversely, continuous measures of coordination and stability, evaluated using Relative Phase (RP) analysis, provide superior sensitivity over traditional spatiotemporal measures and detect changes at a greater resolution [6]. The first aim of this study was to quantify levels of continuous inter-limb gait coordination and stability among Veterans and SMs with TLL. It was hypothesized that individuals with vs. without TLL will walk with lower levels of inter-limb coordination and stability. The second aim was to determine the extent to which gait coordination and stability of Veterans and SMs with TLL are influenced by different Energy Storing and Returning (ESR) ankle-foot devices (i.e., ESR, articulating ESR (ART), and powered ESR (PWR)). It was hypothesized that the PWR device will indicate greater levels of coordination and stability compared to the other devices.

METHODS

Thirty individuals with unilateral TLL were fit and evaluated with 3 different prosthetic ankle-foot devices: ESR, ART, and PWR. Participants separately utilized each prosthetic foot for 1 week at home. After each 1-week trial, participants with TLL underwent biomechanical gait analysis. Ten

individuals without TLL performed a single gait analysis session. All participants walked at 1.3 m/s across a 10-meter instrumented walkway until at least 15 steps per foot were recorded. RP analysis calculated continuous measures of coordination, Mean Absolute Relative Phase (MARP), and stability, Deviation Phase (DP), between limbs.

MARP is calculated using the following equation:

$$\text{MARP} = \Sigma(|\Phi_{\text{Rel.}}|/N) \quad (1)$$

where Φ_{relative} is the relative phasing relationship between the two segments and N is the number of points in the RP mean ensemble curve.

A low MARP value (closer to 0°) indicates a more in-phase relationship, while a high MARP value (closer to 180°) indicates a more anti-phase relationship.

DP is calculated using the following equation:

$$\text{DP} = (\Sigma|\text{SD}_i|)/N \quad (2)$$

where N is the number of points in the RP mean ensemble curve and SD is the SD of the mean ensemble curve at the i th point.

A low DP value (closer to 0°) indicates a more stable organization of the neuromuscular system and a high DP value (closer to 180°) indicates less stability.

Two sample T-tests determined differences between the Control participants and each device (PWR, ESR, ART) for MARP and DP separately. Linear mixed effect models compared MARP and DP between devices, while accounting for repeated observations. Pairwise comparisons were conducted using estimated marginal means. Significance was set at $p < 0.05$.

RESULTS

Aim 1: Veterans and SMs with vs. without TLL experience deficits in coordination and stability (Table 1).

Table 1. Differences in coordination (MARF) and stability (DP) in Veterans and SMs with TLL compared to intact individuals.

	MARP	t-value	p-value
Arm to Arm			
Control	157.6	-3.1	0.004
ART	162.6		
Prosthetic-side Arm to Intact-Side Ankle			
Control	17.3	-2.1	0.03
ART	22.8		
	DP	t-value	p-value
Leg to Leg			
Control	2.9	-2.2	0.03
PWR	3.6		
Control	2.9	-2.3	0.03
ART	3.5		
Prosthetic-Side Wrist to Intact-Side Ankle			
Control	5.5	-2.0	0.04
PWR	7.8		
Control	5.5	-2.1	0.04
ART	7.4		

Aim 2: The PWR device indicates a less coordinated gait pattern than the ART device between the prosthetic-side arm and leg, and lesser coordination than both the ESR and ART devices between the prosthetic-side arm and intact-side leg (Figure 1). However, the PWR device indicates a more stable gait pattern than the ESR device between the intact-side arm and leg and is more stable than the ART and ESR devices between the intact-side arm and prosthetic-side leg (Figure 2).

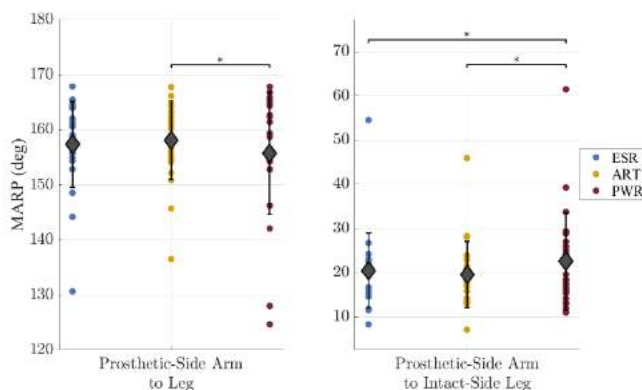


Figure 1. Inter-limb coordination as Mean Absolute Relative Phase (MARF) between groups and devices (only significant differences illustrated).

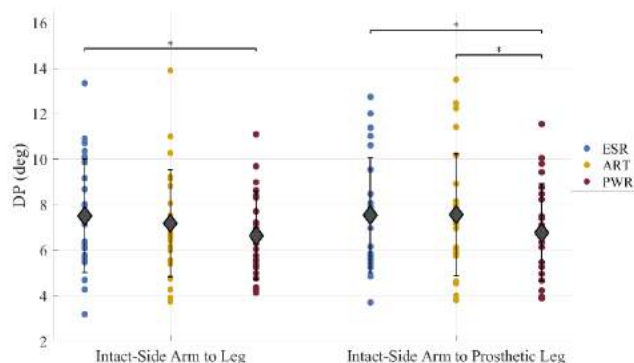


Figure 2. Inter-limb stability as Deviation Phase (DP) between groups and devices (only significant differences illustrated).

DISCUSSION

Preliminary analysis of this dataset indicates that RP analysis is sensitive enough to identify differences between individuals with vs. without TLL and between the PWR, ART, and ESR devices. As expected, individuals with vs. without TLL experience deficits in both coordination and stability.

Interestingly, the PWR device was associated with both greater levels of stability and lower levels of coordination compared to the ESR and ART devices. This discrepancy may be due to the novelty of the device for some individuals with TLL (notwithstanding the 1-week acclimation). It is possible that the active push-off provided by the PWR device disrupts the coordinative pattern the individual is accustomed to with a non-powered device, while the new pattern associated with the device allows for greater consistency of the motor pattern compared to the other devices. However, it should be noted that this device is also associated with large outliers in the coordination measure. It is possible that removal of such outliers may eliminate the significant coordination deficits observed between the PWR device and both the Control group and the other devices. If so, a clear advantage of the PWR device would become evident, as it provides the greatest stability advantage to individuals with TLL. Though, device acclimation is an important consideration for future work.

Given the identified deficits in gait coordination and stability among Veteran and SMs with TLL, particularly across different types of prosthetic ankle-foot devices, such findings can help support development of rehabilitation programs focused on improving these parameters. Importantly, findings can directly influence prescription guidelines to optimize healthcare for all Veterans and SMs with TLL, helping them to live high quality, active lives.

ACKNOWLEDGMENTS

We thank Dr. Timothy Moore for his statistical support, the VISN 2 BRAVO lab and Walter Reed National Military Medical Center for data collection contributions, and the Narrows Institute for their support. The views expressed herein are those of the authors, and do not necessarily reflect the official policies of the U.S. Departments of the Army, Navy, or Air Force, nor the U.S. Government. The identification of specific products or instrumentation is considered an integral part of the scientific endeavor and does not constitute endorsement or implied endorsement on the part of the authors nor by the U.S. Government. This investigation is funded by the DoD Orthotics and Prosthetics Outcomes Research Program (OPORP) (W81XWH2-1-0409) and expands upon an ongoing study (DoD OPORP, W81XWH-17-2-0014).

REFERENCES

1. Ziegler-Graham, K., et al., *Arch Phys Med Rehab*, 89: 422-429, 2008.
2. Krueger, C., et al., *J Trauma Acute Care Surg*, 73: 438-444, 2012.
3. Blough, D., et al., *J Rehab Res Dev*, 47: 387-402, 2010.
4. Highsmith, M., et al., *J Rehab Res Dev*, 53: 157-184, 2016.
5. Healy, A., et al., *PLoS ONE*, 13(3): 1-42, 2018.
6. Haddad, J., et al., *J App Biomech*, 26(1): 109-113, 2010.
7. Donker, S., et al., *Acta Psych*, 110: 265-288, 2002.

NUCLEAR DEFORMATION OF THE TRICUSPID VALVE INTERSTITIAL CELLS: THE EFFECTS OF NUCLEAR ORIENTATION AND EXTRACELLULAR MATRIX STRUCTURE

Mina Pakzadmanesh (1), Samuel D. Salinas (2), Vineet S. Thomas (2), Rouzbeh Amini (1,2)

(1) Department of Bioengineering, Northeastern University, Boston, MA, USA

(2) Department of Mechanical and Industrial Engineering, Northeastern University, Boston, MA, USA

INTRODUCTION

The micro-scale mechanical environment of the heart valves is comprised of individual components that make up the extracellular matrix (ECM) and the residing valve interstitial cells (VICs) [1]. The VICs have an important role in maintaining the mechanical integrity of the valve [2]. In the tricuspid valve (TV), proper leaflet coaptation is required for normal valvular function. Any change in the mechanical integrity of the ECM constituents, such as collagen and/or elastin, may cause improper valve coaptation and lead to a variety of cardiac diseases [3]. For example, Marfan Syndrome (MFS) is a connective tissue disorder, in which fragmented elastin fibers are present in the ECM. Valvular diseases are more frequent in MFS patients and other connective tissue disorders.

Among different functions, the VICs contribute to ECM protein synthesis and maintain a structurally competent leaflet. As such, it is important to identify changes in the biomechanical micro-environment of the TV interstitial cells in response to the ECM structural changes. For example, previous experiments have shown that alignment of cells with the ECM affects ECM protein production [4]. While existing computational models can capture the overall responses of the TV, they fail to accurately predict cellular deformation in response to the changes of the ECM. Our multi-scale framework has the potential to bridge this gap and help us identify the interplay between macro-scale and micro-scale alterations in the TV complex.

The objective of this study was to identify how deformation of VICs changes when they are aligned in different angles relative to ECM fibers. For this purpose, a computational framework was used to analyze the cellular deformation and orientation of cells within the ECM. This computational model was also validated using experimental measurements using microscopy.

METHODS

An analysis using a multi-scale finite element model was conducted to predict alteration in the micro-structure of the ECM under equibiaxial tension (Fig. 2). This method was applied to data sourced from two groups that had been the subject of previous experimental studies: (1)

native leaflets (control) and (2) leaflets treated with elastase to remove native elastin [5]. The dimensions of the models were $7 \times 7 \times 0.406$ mm and $7 \times 7 \times 0.313$ mm for the native and elastin-digested group, respectively. Both groups were discretized into 2352 macro-scale elements and approximately 450 micro-scale elements per each ECM representative volume element with a total of $\sim 10^8$ degrees of freedom, as described previously [6].

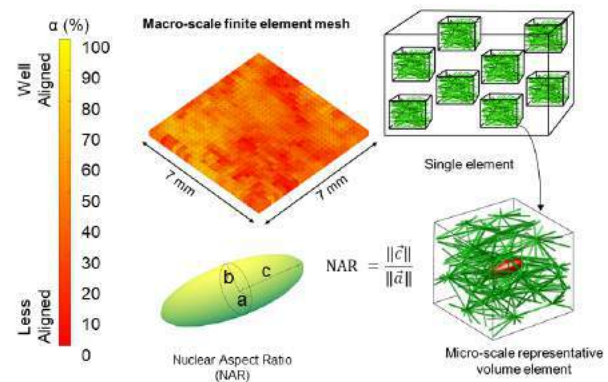


Figure 1: Schematic of the model. An ellipsoid located in the micro-scale representative volume element was used to quantify nuclear aspect ratio (NAR) at different macro-scale loading levels.

The nuclear deformation was chosen as a measure of cellular deformation under mechanical loading. To model VIC nuclei, an ellipsoid was chosen in each representative volume element at the undeformed configuration. The nuclear deformation was quantified via alteration of the aspect ratio of the ellipsoid, referred to as the nuclear aspect ratio (NAR) [7]. The initial undeformed NAR in the control group and the elastin-digested group were 2.57 and 2.72, respectively, based on preliminary experimental findings. Initially, the nuclei were aligned with the mean fiber direction of each network in both groups.

The points of intersection of the ellipsoid and surrounding fibers represent the ECM integrins. These intersections were tracked throughout a series of simulated loading levels, and the associated NAR was measured at each point. The average NAR under different levels of stress were computed for approximately 50 elements in each group. The results of the elastin-digested and control groups were compared to experimental results obtained from microscopy.

To investigate the impact of nuclear alignment, the NAR was calculated under load-controlled conditions for a representative fiber network in three different orientations relative to the mean fiber direction. In particular, the following case studies were performed: (1) the largest axis of the nucleus was aligned with the main fiber direction, (2) the largest axis of the nucleus had a 45° angle with the main fiber direction, and (3) the largest axis of the nucleus had a 90° angle with the main fiber direction.

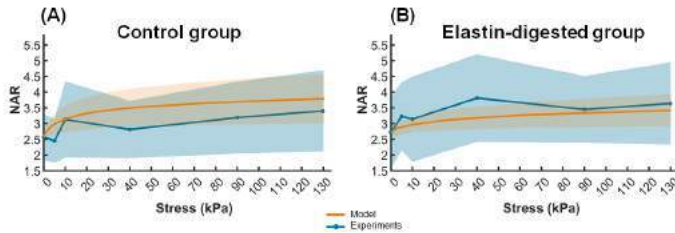


Figure 2: Nuclear aspect ratio (NAR) alteration under different levels of macro-scale stress.

RESULTS

Figure 2 shows the alteration of NAR under different stress levels in the control and elastin-digested group. In Fig. 1A, the NAR of the control group model went up from 2.57 to 3.75 under the stresses from 0 to 130 kPa. In the elastin-digested group (Fig. 1B), the NAR increased from 2.72 to 3.28 under the stresses from 0 to 130 kPa. In both groups, the changes were consistent with values measured experimentally via microscopy.

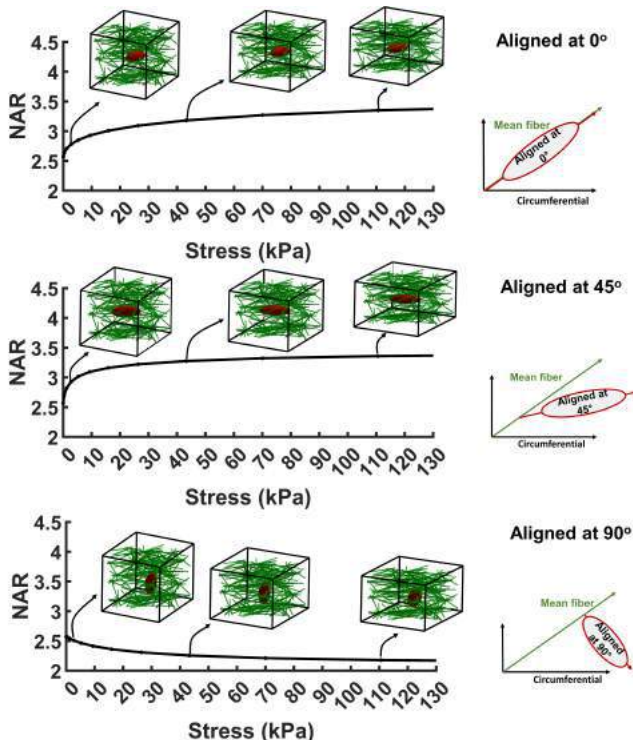


Figure 3: Changes in the nuclear aspect ratio (NAR) with stress in different orientation case studies.

Figure 3 illustrates changes in NAR that occur at various loading levels when the nucleus is oriented at three different angles relative to the mean fiber direction. The NAR increased with loading when the nucleus was aligned with the ECM fiber direction. In contrast, when the nucleus was oriented perpendicular to the main fiber direction at the undeformed configuration, the NAR decreased with increasing stress.

DISCUSSION

Both control and elastase-digested groups exhibited a rapid initial increase in NAR, followed by a plateau. This increase was due to a reduction in the undulation of ECM fibers, which plateaued once the collagen was fully recruited. As such, we hypothesized that the NAR in the elastin-digested group would plateau earlier than the control group. The simulation that we conducted had results that were similar to those found in earlier experimental studies.

Given the assumptions made in the simulation, this model can be utilized to predict the cellular deformation of the TV anterior leaflet when nuclei are oriented at various angles relative to the ECM fibers. We investigated alignment of cells with mean fibers direction in both control and elastin-digested groups and compared the results with the average orientations of VICs to a concurrent experimental study conducted in our lab. Our simulation results showed more similarity in cell orientation in the control group, while the elastin-digested group showed a slightly wider span in mean orientation.

Figure 3 displays how the initial configuration of nuclei may affect how the NAR changes under different levels of equibiaxial load. When the cell is aligned with 45° to the mean fiber direction, NAR plateaued later than when cell was aligned parallel to the mean fiber direction. Also, when the nuclei are perpendicular to the ECM fibers, NAR decreased with increasing load levels.

In the simulation, we assumed that the nuclei deform affinely with the positional changes of the integrins of the ECM in each representative volume element. Our model can be improved upon by addition of the non-affine deformation of the intra-cellular structure such as actin microfilaments, microtubules, and/or intermediate filaments.

In summary, comparing the average nuclei deformation of designated elements in two groups, we observed that elastin degradation and mechanical loading affected the shape of the nuclei. Although in MFS elastin is not compromised in the same manner as in this research, some differences in collagen structure were observed that may lead to the change of NAR with different loads. As changes in NAR can lead to deviations in gene expression and protein synthesis, it may consequently affect the mechanobiology and function of the TV. Future work will focus on computing more numbers of networks among the TV leaflet with different orientations to the ECM and comparing with the results obtained from our concurrent experimental study to statistically analyze how the orientation of cells and alignment with the ECM impact nuclear deformation.

ACKNOWLEDGEMENTS

Computational facilities from Research Computing at Northeastern University and the funding provided for this work by the National Science Foundation (NSF CAREER award 2049088) are acknowledged.

REFERENCES

- [1] Fung Y. J. *Biomech* 103 (1981).
- [2] *Biochem. Cell Biol.* 35.2 (2003). ISSN: 1357-2725.
- [3] Chen JH et al. *Circ. Res* 108.12 (2011).
- [4] Lee CH et al. *Biomaterials* 26.11 (2005). ISSN: 0142-9612.
- [5] Salinas SD et al. *PLoS One* 17.5 (2022).
- [6] Thomas VS et al. *ACTA BIOMATER* 94 (2019). ISSN: 1742-7061.
- [7] Huang HYS et al. *Biomech Eng J* 129 (2007).

ULTRASOFT EDGE-LABELLED HYDROGEL SENSORS REVEAL INTERNAL TISSUE STRESS PATTERNS IN INVASIVE ENGINEERED TUMORS

C.-M. Boghdady (1,2), W. Lee (1), V. Lelarge (2), R.L. Leask (1,3), L. McCaffrey (2,4,5), C. Moraes (1,2,6)

- (1) Department of Chemical Engineering, McGill University, Montreal, Quebec, Canada
(2) Rosalind Morris Goodman Cancer Institute, McGill University, Montreal, Quebec, Canada
(3) McGill University Health Centre, Montreal, Quebec, Canada
(4) Division of Experimental Medicine, McGill University, Montreal, Quebec, Canada
(5) Gerald Bronfman Department of Oncology, McGill University, Montreal, Quebec, Canada
(6) Department of Biological and Biomedical Engineering, McGill University, Montreal, Quebec, Canada

INTRODUCTION

Within the human body, tissues are in a continuous state of remodelling. From development to disease, cell-generated forces play a key role in this remodelling, contributing to tissue shape, structure, and function. While bulk measurements are useful, they provide little insight into how local stresses arise and evolve within tissues over time, as they provide either an end-point snapshot of stress state or a global measurement of tissue-generated stress [1]–[3]. Cell-sized microspheres have recently emerged as a powerful technique to probe tissue mechanobiology at the cellular scale, as they can be sufficiently soft as to deform within remodelling tissues, and optically imaged to measure internal stresses. Oil microdroplets can be used to measure anisotropic forces [4], [5] while hydrogel-based approaches can measure isotropic stresses like tension and compression [6], [7].

However, measuring stresses with dispersible hydrogel sensors requires ultrasoft, low-polymer content gel formulations to create measurable stress sensor deformations at the ~10s of Pa stress loading conditions expected within tumors. Such low-polymer content materials are challenging to label with sufficiently fluorescent materials to support repeated measurements without photobleaching, particularly in optically dense tissues over 100 μm thick, as required in cancer tumor models [7]. Here, we leverage thermodynamic partitioning of hydrogel components to create “edge-labelled” ultrasoft hydrogel microdroplets, in a single polymerization step. Bright and stable fluorescent nanoparticles preferentially polymerize at the hydrogel droplet interface, and can be used to repeatedly track sensor surfaces over long-term experiments, even when embedded deep in light-scattering tissues. We use these edge-labelled microspherical stress gauges (eMSGs), in inducible breast cancer tumor models of invasion, and demonstrate distinctive internal stress patterns that arise from cell-matrix interactions at different stages of breast cancer progression.

METHODS

High-throughput fabrication of eMSGs was performed via water-in-oil emulsion with incorporation of fluorescein (green; polymer backbone) and interface-partitioning fluorescent microspheres (red) that preferentially polymerize at the sensor edges. eMSGs were functionalized for cell adhesion, mechanically characterized via osmotic compression [7], and imaged using fluorescence microscopy to monitor shape dimensions (Fig. 1).

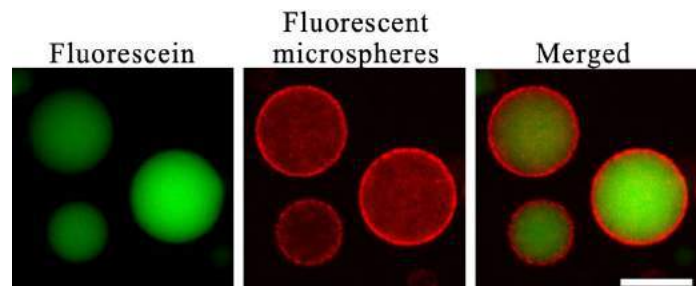


Figure 1: Fluorescent microspheres enhance microspherical stress gauge visibility (scale bar = 100 μm)

We then embedded eMSGs to monitor internal tissue stress evolution within multiple engineered tumor models that recreate stages of breast cancer progression (Fig. 2). eMSGs were incorporated into collagen-embedded spheroids formed from either non-invasive T-47D, inherently invasive MDA-MB-231, or MCF7 with an inducible Src oncogene or green fluorescent protein (EGFP) expression as a control. eMSGs were imaged prior to spheroid formation (day 0) for stress-free dimensions, and finite element modelling was used to calculate radial and circumferential stresses based on deformed bead dimensions.

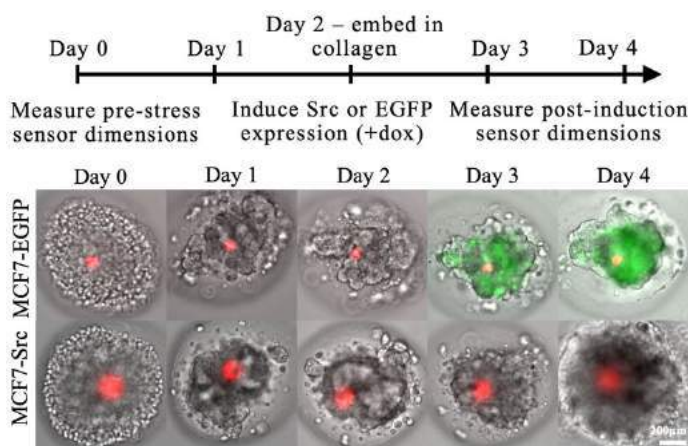


Figure 2: Inducible breast cancer model with embedded eMSGs

RESULTS

We found homogeneously low stresses within invasive MDA cell lines, compared to non-invasive T-47Ds which showed relatively high and heterogenous internal stress patterns (Fig. 3). We also demonstrate that although tissues are measurably compacted once encapsulated within a matrix, internal tumor stresses only increase in the short term, as non-invasive tumors rapidly make small internal reorganizations that reduce the mechanical stress to baseline levels (data not shown).

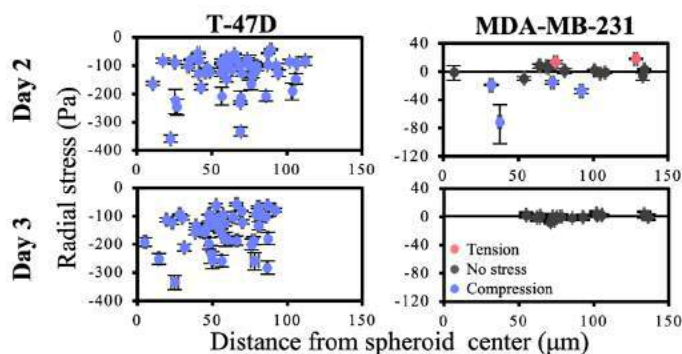


Figure 3: Non-invasive T-47D spheroids remain compressive while invasive MDA-MB-231 spheroids lose internal stress with invasion

Similarly, models induced to overexpress Src, which triggers growth and migration programs, exhibited a significant reduction in stress, while control EGFP-expressing spheroids changed internal stress levels minimally in both radial and circumferential directions. (Fig. 4).

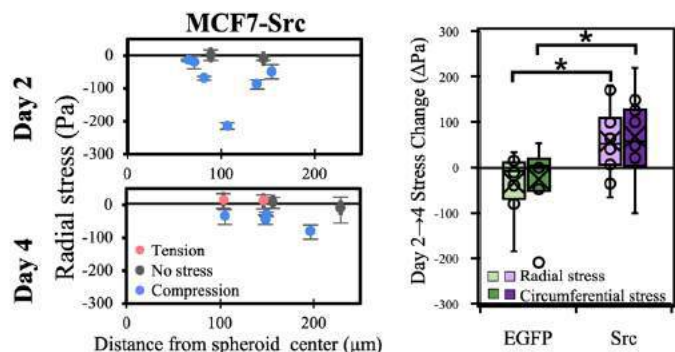


Figure 4: Breast cancer spheroids exhibit loss of internal stress with invasion triggered by Src overexpression

DISCUSSION

The eMSGs developed in this study enable enhanced visualization and long-term monitoring of cell-generated stresses within multicellular aggregates, through their engineered compliance and surface-localized fluorescent labelling. Their resistance to photobleaching even after repeated measurements at high-power excitations uniquely allowed us to characterize the heterogenous time-evolution of internal tumor stress states within breast cancer models, while simultaneously activating and monitoring gene-inducible tissue invasion.

In all cases, significant internal tumor stress heterogeneity was observed in these model systems; an emerging picture that is also supported by a recent study in our lab demonstrating that invasive tumors have highly heterogenous internal stiffnesses [10], which must correlate with local stress-generating cell behaviours. Internal stresses were also generally greater in non-invasive models, while invasive models including MDA-MB-231 and induced MCF7-Src cells consistently form relatively loose aggregates [8], [9] with low internal stresses. Speculatively, this transition to a low-stress architecture is consistent with the transition of tumor cells towards low-levels of cell-to-cell adhesion during invasion. Interestingly however, although the internal stresses are highly heterogenous, our ability to track individual sensors during a non-invasive to invasive transition in the same inducible cell system allows us to conclude that internal stresses within the tumor are collectively reduced once invasion is triggered. This finding is particularly important in potentially explaining widely varying clinical observations of tumor stress under metastatic and non-metastatic conditions; and also suggests a potential biophysical marker to determine whether a metastatic event has occurred.

More broadly, this work demonstrates that mapping internal mechanical stress in tumors may have utility in understanding the fundamental tumor microenvironment and in understanding the highly dynamic and local mechanical processes of disease and development.

ACKNOWLEDGEMENTS

This work was supported by funding from the Canadian Cancer Society (Grant Nos. 704422 and 706002) and the Canadian Institutes for Health Research (Grant No. 01871-000) to C.M. and L.M., the Natural Sciences and Research Council of Canada (NSERC) Discovery grants (RGPIN-2022-05165) and the Canada Research Chairs in Advanced Cellular Microenvironments to C.M.

REFERENCES

- [1] H. T. Nia *et al.*, *Nat Biomed Eng*, vol. 1, p. 0004, 2016.
- [2] T. Stylianopoulos *et al.*, *Cancer Res*, vol. 73, no. 13, pp. 3833–3841, Jul. 2013.
- [3] T. Boudou *et al.*, *Tissue Eng Part A*, vol. 18, no. 9–10, pp. 910–919, May 2012.
- [4] O. Iampàs *et al.*, *Nat. Methods*, vol. 11, no. 2, pp. 183–189, Feb. 2014.
- [5] A. Mongera *et al.*, *Nature*, vol. 561, no. 7723, Art. no. 7723, Sep. 2018.
- [6] E. Mohagheghian *et al.*, *Nature Communications*, vol. 9, no. 1, Art. no. 1, May 2018.
- [7] W. Lee *et al.*, *Nat Commun*, vol. 10, no. 1, pp. 1–14, Jan. 2019.
- [8] A. Ivasku and M. Kubbies, *International Journal of Oncology*, vol. 31, no. 6, pp. 1403–1413, Dec. 2007.
- [9] L. Zhao *et al.*, *Biofabrication*, vol. 11, no. 4, p. 045013, Aug. 2019.
- [10] S. Mok *et al.*, *Nature Communications*, vol. 11, no. 1, Art. no. 1, Sep. 2020.

SYNAPTOPODIN ENABLES FOCAL ADHESIONS TO RESIST PERPENDICULAR FORCE

Chengqing Qu (1), Shumeng Jiang (1), Farid Alisafaei (3), Jeffrey H Miner (2),
 Hani Y Suleiman (2) and Guy M. Genin (1)

- (1) NSF Science and Technology Center for Engineering Mechanobiology, Washington University in St. Louis, MO, USA
 (2) Division of Nephrology, Department of Medicine, Washington University School of Medicine, St. Louis, MO, USA
 (3) NSF Science and Technology Center for Engineering Mechanobiology, New Jersey Institute of Technology, NJ, USA

INTRODUCTION

Focal adhesions resist shear forces in nearly all cell types. Kidney podocytes are unusual in that they must resist stresses perpendicular to their basement membrane arising from fluid shear stress as pressurized fluid from capillaries passes through glomerular slit diaphragms [1]. Kidney podocyte cells are lost daily and never regenerated. As the spare supply from birth is lost, a process that is accelerated dramatically in kidney injury and disease, kidney failure and chronic kidney disease arise [2-5]. Our objective was thus to identify the protein structures responsible for enabling kidney podocyte focal adhesions to resist forces perpendicular to their basement membrane.

A search of the literature turned up several candidate proteins near the basement membrane. Of these, the protein synaptopodin arose as a likely target. Synaptopodin, a unique actin-associated protein that is highly expressed in podocytes. Synaptopodin is implicated as a protective factor for kidney function following in acute kidney injury [1]. Compared with wild type mouse models, synaptopodin knockout mice have significantly decreased numbers of podocytes and significantly impaired kidney function; however, the mechanism of this disease exacerbation is not known [2].

We therefore hypothesized that that synaptopodin serves as a linker to enable focal adhesions to resist perpendicular forces.

METHODS

Normal force loading system: We developed an *in vitro* system to study the effect of perpendicular forces on cells cultured on hydrogels of defined stiffness, coated with defined extracellular matrix (ECM) proteins. Cells were cultured on substrates that were linked to a centrifuge, in swinging buckets that enabled the cells to face outwards (force perpendicular to and away from the substrate) while still staying submerged in culture medium. Accelerations of 400 m/s² (500 RPM) were applied for 1-2 minutes, producing forces at the upper extreme of what a cell might experience in an injury setting [7]. By varying

stiffness, surface proteins, culture conditions, and the mechanical loading/centrifugal forces applied, this setup allowed us to simulate perpendicular forces that podocytes experience in their native glomerular microenvironment.

Mouse models: We used primary podocytes taken from control (WT) mice as well as mice lacking synaptopodin (Synpo KO). We compared these cells to osteosarcoma cells (U2OS) as well as NIH 3T3 cells (no synaptopodin) cultured in both undifferentiated and differentiated conditions. Animal studies were approved by Wash. Univ. IACUC.

Histology: We tested our hypothesis by assessing the cellular responses to centrifugal forces using morphological analysis as well immunostaining for integrins, synaptopodin, α -actinin-4, myosin II and actin. We predicted that cells with synaptopodin would exhibit improved stability against perpendicular force.

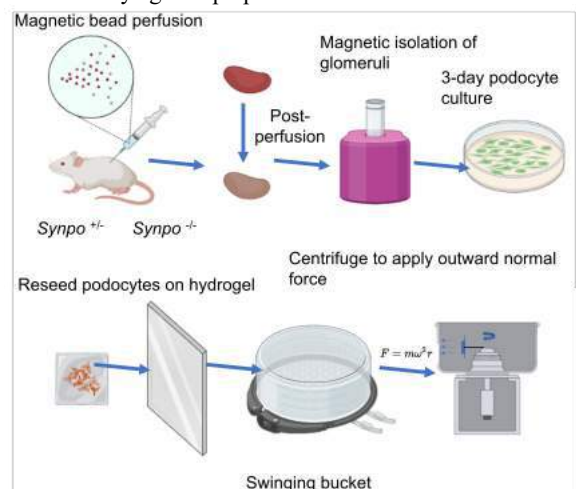


Figure 1: Centrifugal loading apparatus.

Quantitative microscopy: We also used a quantitative scoring system for showing the degree of phenotypic change in response to perpendicular force. Confocal immunofluorescence staining and confocal microscopy at 60X showed that cell morphology changed in response to perpendicular force. Cells that had clean and continuous integrin at the periphery, were scored as 1, and cells that had integrin spreading over the whole cell were scored as 0.

RESULTS

Consistent with expectations for standard models of focal adhesions [8], NIH 3T3 cells, which do not express synaptopodin, elongated into spindle shapes or detached in response to perpendicular forces (Fig. 2). However, wild type (WT) primary podocytes spread and formed a continuous skirt of integrins at their periphery, staying largely stable. Synaptopodin (Synpo) KO primary podocytes did not show this continuous integrin $\beta 1$ pattern at the cell periphery but rather showed a diffuse pattern and were more likely to detach.

For the wild-type primary podocytes, when bearing normal forces, the $\beta 1$ -integrin relocated to the periphery of the cells and accumulated to form a continuous adhesive structure, rather than the discrete focal adhesions observed at baseline.

For the *Synpo*^{-/-} primary podocytes, integrin accumulation at the periphery of the podocytes was diminished when bearing normal force. This phenotype suggests a role for synaptopodin in mechanotransduction and integrin regulation.

For the osteosarcoma cells (U2OS), the integrin was stronger in the wild-type than in the *Synpo*^{-/-} U2OS. The myosin structure was clearer in the wild-type; however, it became cloudy in the *Synpo*^{-/-} U2OS. These phenotypes suggested that synaptopodin in U2OS had similar function as it had in primary podocytes. In addition, the absence of synaptopodin also caused the deconstruction of myosin protein.

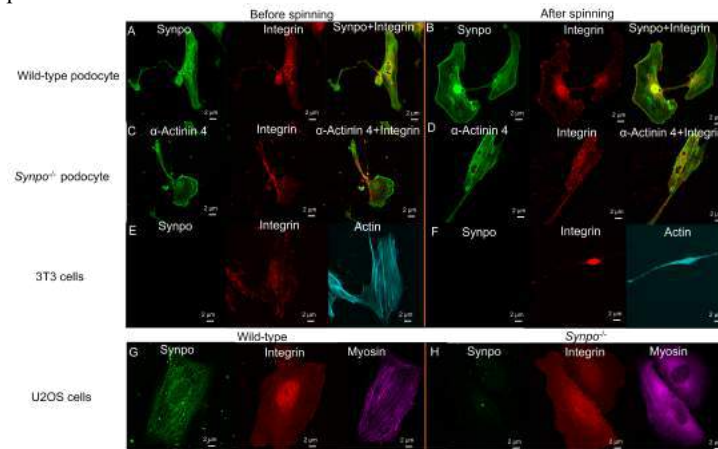


Figure 2: Immunostaining of wild-type primary podocytes. Synpo (green), integrin (red) and synaptopodin + integrin (merged). Immunostaining of *Synpo*^{-/-} primary podocytes. α -Actinin-4 (green), integrin (red) and α -Actinin-4 + integrin (merged). Immunostaining of 3T3 cells. Integrin (red) and actin (blue). Immunostaining of osteosarcoma cells and *Synpo*^{-/-} osteosarcoma cells. Synpo (green), integrin (red) and myosin (purple). (A) No normal (perpendicular) force. (B) 500 RPM for 1min. (C) *Synpo*^{-/-} primary podocyte, no normal force. (D) *Synpo*^{-/-} primary podocyte, 500 RPM for 1min. (E) 3T3, no normal force. (F) 3T3, 500 RPM 1min.

For the wild-type primary podocyte, when we increased the time of bearing perpendicular force, the shape score significantly increased, which indicated a more resistant phenotype. For the *Synpo*^{-/-} primary podocyte, the score did not change when the time of force applied increased and is similar to the control in wild-type primary podocytes, indicating that after synaptopodin was knocked out, the primary podocytes did not have phenotype.

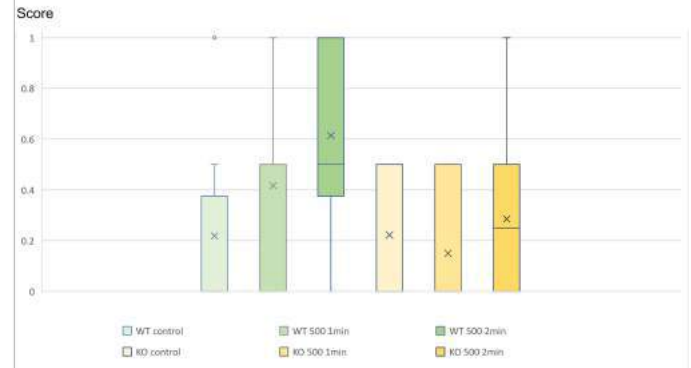


Figure 3: Shape index of cells following perpendicular force.

DISCUSSION

Results suggest that synaptopodin may have a mechano-resistance role in podocytes, enabling podocytes to respond adaptively to normal forces. The mechanism underlying this was relocation of focal adhesions to resist acute normal forces. This buffering process could be a characteristic of healthy podocytes *in vivo* for maintaining adhesion to the GBM after injury.

Results suggest a mechanistic, mechanobiological explanation for why synaptopodin is protective and predictive of improved prognosis following kidney injury. These results motivate further study exploring synaptopodin targeted therapies could be protective after kidney injury.

ACKNOWLEDGEMENTS

This work was funded by NIH grants (R01DK058366, R01DK078314, R01DK128660, R01DK131177), and the National Science Foundation Center for Engineering Mechanobiology (CMMI 1548571).

This work was also supported by the Washington University Institute of Clinical and Translational Sciences which is, in part, supported by the NIH/National Center for Advancing Translational Sciences (NCATS), CTSA grant #UL1TR002345

REFERENCE

- [1] Kannan N, Tang VW. *J Cell Biol.* 2015
- [2] Ning L, Suleiman HY, Miner JH. *J Am Soc Nephrol.* 2020 Dec
- [3] Levey et al, *The Lancet*, 379(9811); 165-80, 2012.
- [4] Ebefors et al, *Frontiers in Physiology*, 12; 689083-689083, 2021.
- [5] Jefferson J A et al, *Kidney International*, 74(1); 22-36, 2008.
- [6] Hu G et al, *Biomedicine & Aging Pathology*, 3(1); 36-42, 2013.
- [7] Elseguí-Artola A et al, *Nature Cell Biology*, 18(5); 540-8, 2016.
- [8] Suleiman H Y et al, *JCI insight*, 2; 2017.

Epithelial Monolayers Develop Density and Effective Temperature Differentials to Migrate across Confined Matrices

W.J. Lin (1), A. Pathak (1)

(1) Mechanical Engineering, Washington University, St. Louis, MO, USA

INTRODUCTION

Collective migration of epithelial cells across physically heterogeneous environments regulates vital physiological and pathological processes, such as embryogenesis, wound healing, tissue regeneration, and cancer metastasis. In response to matrix stiffness and topography, epithelial cell monolayers undergo jamming-unjamming transitions. Although previous studies have shown different migration phenotypes separately in confined and unconfined environments, physical transitions required for collective cell populations to negotiate confined regions remain unclear. To address this question, we fabricated polydimethylsiloxane (PDMS) substrates with contiguous microchannels and studied collective migration of MCF10A (10A) human mammary epithelial cell line epithelial cells.

We found that cells develop a density differential in wide regions, relative to narrow channels, which could generate enough pressure for their eventual migration into confinement. To understand whether cell-cell cohesivity alters this requirement of a density differential, we used cells with constitutively-active RhoA (+RhoA) for higher cohesivity and overexpressed ErbB2 (+ErbB2) for cancer-like reduced cohesion. We found that more cohesive cells (+RhoA) developed a higher density differential relative to less cohesive cells for migration across confinement. While confined channels allowed for faster migration in WT cells, this confinement sensitivity was diminished for both alternations in cell cohesivity. With migration into confinement, cells deformed their shape and increased their effective temperature, calculated by treating cells as a granular thermodynamic system. Further, more cohesive cells (+RhoA) and those in confined regions were effectively 'warmer'.

Overall, our results show that collective cell populations build a pressure differential between narrow and wide matrices to enter confined environments and these differentials vary for cell types of varying cohesivity. These findings show that collective cell migration across confinements can be interpreted in terms of basic physical

principles of pressure and temperature of granular matter, which could inform our understanding of more complex living systems.

METHODS

We cultured MCF10A (10A) monolayers on PDMS substrates and allowed cells to migrate through rectangular PDMS microchannels of varied widths. Microchannels were fabricated following standard soft lithography with 10:1 mixing ratio. Wide and narrow channels of widths 200 μ m and 50 μ m (with 70 μ m height), respectively, were used.

We tracked cell dynamics within the monolayers for 2-3 days as 10A cell monolayers expanded and entered microchannels (Fig. 1A.) Migration of 10A cells was compared with their 10A+ErbB2 and 10A+RhoA variants. We used the ImageJ plugin TrackMate for cell velocity and density analyses. After imaging, the monolayers were fixed and stained with F-actin (phalloidin) and p120 (antibody for δ -catenin to label cell-cell junctions) for cell segmentation. The statistics of cell morphologies including distribution of cell areas (A), shape indices ($SI = P/\sqrt{A}$, P : cell perimeter), and aspect ratios (AR) were calculated from cell outlines generated by the Python program SeedWaterSegmenter with custom MATLAB scripts. Metformin (MFM; 2 mM) was used for enhancing cell-cell junctions and reversing EMT in 10A+ErbB2 cells.

RESULTS

We found that epithelial monolayers developed density differentials when cells went across confined matrices across various cell lines (Fig. 1A.) The 10A (Fig. 1B i) and 10A+RhoA (Fig. 1B ii) monolayers built up more cell densities outside the narrow channels while 10A+ErbB2 (Fig. 1B iii) monolayers maintained smaller density difference outside narrow channels. Comparing root-mean-square velocities (v_{rms}) of cell clusters outside and inside the microchannels [1], we found that there was a v_{rms} difference between 10A cells in wide and narrow channels (Fig. 1C i,v.) For 10A+RhoA cell clusters (Fig. 1C ii, vi), the

difference in v_{rms} between outside and inside the wide channels was larger compared to narrow channels. In comparison, 10A+ErbB2 cells showed some v_{rms} outside-inside difference in wide channels (Fig. 1C iii) but not in narrow (Fig. 1C vii.)

To understand whether cell spreading responds to confinement and cell cohesivity, we calculated cell areas. We found that cell spreading was the highest in 10A+ErbB2 cells in narrow channels (Fig. 1D.) By analyzing and visualizing cell aspect ratio and shape index, we found that 10A and 10A+RhoA cells were slightly jammed (Fig. 1D i, ii, dark blue) when cell monolayers were crowded against channel walls, with some unjamming in open areas (Figure 1D, light purple). The less cohesive 10A+ErbB2 cells showed unjamming when

going through narrow channels (Figure 1D iii, light pink and light purple) [2]. Treatment with Metformin (reinforces epithelial phenotype) shifted the phenotype of 10A+ErbB2 monolayers from unjamming to slightly higher jamming (Fig. 1D, darker blue and fragmented).

By utilizing our measurements of cell shapes, we calculated effective temperatures of cell colonies from distribution of aspect ratio of cells within a region: $PDF(x; k) = k^k x^{k-1} e^{-kx} / \Gamma(k)$ and $T_{eff} = s.d.(AR) / \sqrt{k}$ [3]. We found that correlation between effective temperature (T_{eff}) and local cell density was higher in narrow channels (Fig. 1E ii) compared to wide channels (Fig. 1E i.)

DISCUSSION

Through biophysical analyses of collective cell migration on substrates with contiguous microchannels of narrow and wide regions, we discovered that cell colonies develop density and migration differentials to enter confined environments. Since microchannels either warm or cool cell monolayers according to cellular cohesivity and matrix confinement, this could be interpreted as a thermal circuit that could induce tissue liquefaction or solidification [4],[5]. The narrow microchannels significantly lower effective temperature (T_{eff}) of 10A+RhoA monolayers, shifting them from a liquid-like state to a jammed state. This is consistent with their innate properties because RhoA GTPases are known to increase cell contractility and enable mechanosensing.

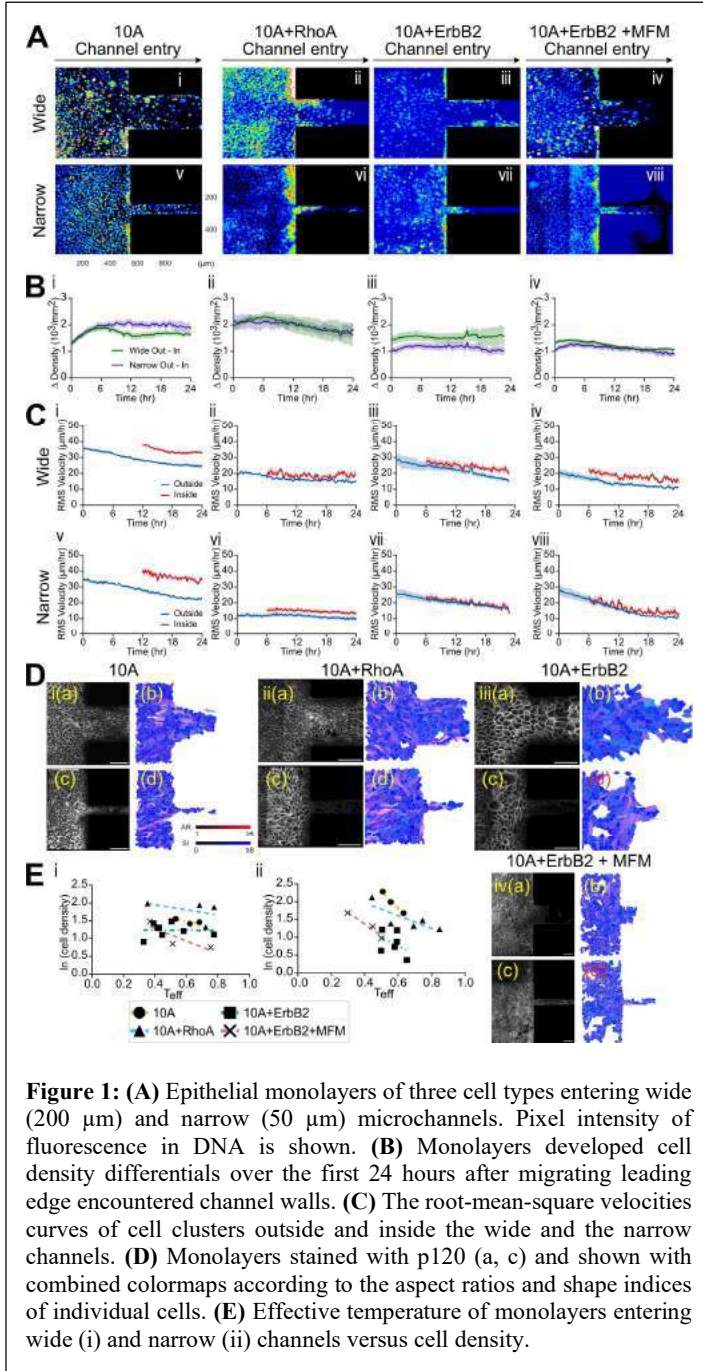
As proposed by Recho *et al.* [6], bulk stresses within an expanding monolayer are spatially constant and equal to a homeostatic stress: $\sigma_h = -E \log \frac{\rho_d}{\rho_e}$, where E, ρ_e are constants. We suppose cell surface density is a measure of effective pressure experienced by monolayers near channel walls and inside channels. Effective temperature (T_{eff}) reflects elongated and protrusive cell shape, which could indicate migration potential. When the more cohesive 10A+RhoA cells enter narrow microchannels, their effective temperature varies in concert with local cell density, which is not the case in other cell types or wider channels. By contrast, when the less cohesive 10A+ErbB2 cells enter confinement, their migration, temperature and density are weakly correlated. These difference across cellular properties indicate that cells with innately healthy and diseased phenotypes negotiate confinement environment differently, dictated by their ability to adapt cell shape, manage rise in cell density, and migratory potential.

ACKNOWLEDGEMENTS

This work was supported by NIH (R35GM128764) grant to AP.

REFERENCES

- [1] S. Garcia, et al., *Proc. Natl. Acad. Sci. U. S. A.*, vol. 112, no. 50, pp. 15314–15319, 2015.
- [2] J. A. Mitchel *et al.*, *Nat. Commun.*, vol. 11, no. 1, pp. 1–14, 2020.
- [3] J. A. Park *et al.*, *Nat. Mater.*, vol. 14, no. 10, pp. 1040–1048, 2015.
- [4] D. Bi, *et al.*, *Phys. Rev. X*, vol. 6, no. 2, pp. 1–13, 2016.
- [5] X. Yang, *et al.*, *Proc. Natl. Acad. Sci. U. S. A.*, vol. 114, no. 48, pp. 12663–12668, Nov. 2017.
- [6] P. Recho, *et al.*, *Soft Matter*, vol. 12, no. 8, pp. 2381–2391, 2016.



REGULATING NANOSCALE HEAT TRNSFER WITH JANUS NANOPARTICLES

C. Xie (1), B. Wilson (1), Z. Qin (1, 2, 3, 4)

- (1) Department of Mechanical Engineering, University of Texas at Dallas, Richardson, Texas, USA
- (2) Department of Bioengineering, University of Texas at Dallas, Richardson, Texas, USA
- (3) Department of Surgery, University of Texas at Southwestern Medical Center, Dallas, Texas, USA
- (4) Center for Advanced Pain Studies, University of Texas at Dallas, Richardson, Texas, USA

INTRODUCTION

Materials advances can lead to breakthroughs in novel applications. Recently, Janus nanoparticles (JNPs) with heterogeneous compositions and multiple interfacial physical properties can lead to directional heating and bring new possibilities for novel nanotechnology and biomedical applications^[1-2]. The critical issue for JNP heating is thermal transport and temperature management. Wilson et al. have systematically investigated interfacial thermal resistance (ITR), and they found that the interfacial curvature and the wettability play important roles in the thermal transport across the interface^[3]. Rajabpour et al. analyzed the directional heating with JNPs with heterogeneous coating and ITRs and demonstrated a temperature difference (~10K) with octanethiolate/mercaptohexanol-coated JNPs^[4]. While these seminal works have advanced our understanding of directional heating with JNP, a comprehensive analysis of directional heating with JNP under steady-state and transient conditions is missing.

In this work, we developed a numerical framework to analyze the thermal transport induced by JNP heating with heterogeneous interfacial thermal resistance. By introducing a dimensionless parameter (ζ) to characterize the temperature contrast, we systematically investigated the key factors that affect the temperature contrast under both steady-state and transient heating scenarios. We found strong size dependence and polar angle dependence of the temperature contrast. Furthermore, we discovered a significant enhancement of the temperature contrast during the pulsed JNP heating. We expect that this work can bring new insights into the thermal responses of JNP heating and can guide future applications.

METHODS

We first constructed and validated the numerical model. Here we consider a plasmonic JNP with a gold core and asymmetric coating on its surface and thus heterogeneous ITR (Fig. 1) along the interface, and the governing equation for temperature is given by:

$$\begin{cases} \frac{\partial^2 T_{JNP}}{\partial r^2} + \frac{2}{r} \frac{\partial T_{JNP}}{\partial r} + \frac{g}{k_{JNP}} = \frac{1}{D_{JNP}} \frac{\partial T_{JNP}}{\partial t}, & r \leq r_{1D} \\ \frac{\partial^2 T_{JNP}}{\partial r^2} + \frac{2}{r} \frac{\partial T_{JNP}}{\partial r} + \frac{\cot(\theta)}{r^2} \frac{\partial T_{JNP}}{\partial \theta} + \frac{1}{r} \frac{\partial^2 T_{JNP}}{\partial \theta^2} + \frac{g}{k_{JNP}} = \frac{1}{D_{JNP}} \frac{\partial T_{JNP}}{\partial t}, & r_{1D} < r \leq r_{JNP} \\ \frac{\partial^2 T_w}{\partial r^2} + \frac{2}{r} \frac{\partial T_w}{\partial r} + \frac{\cot(\theta)}{r^2} \frac{\partial T_w}{\partial \theta} + \frac{1}{r} \frac{\partial^2 T_w}{\partial \theta^2} = \frac{1}{D_w} \frac{\partial T_w}{\partial t}, & r > r_{JNP} \end{cases} \quad (1)$$

And it's subjected to the boundary and initial conditions:

$$\begin{aligned} \frac{T_{JNP} - T_w}{R} &= -k_{JNP} \frac{\partial T_{JNP}}{\partial r} = -k_w \frac{\partial T_w}{\partial r}, \quad r = r_{JNP} \\ T_w &= 0, \quad r = r_{boundary}; \quad T_{JNP} = 0, \quad T_w = 0, t = 0 \end{aligned} \quad (2)$$

$$R = \begin{cases} R_1, & 0 \leq \theta \leq \theta_0 \\ R_2, & \theta_0 < \theta \leq \pi \end{cases}$$

Here we discretized the Equation (1&2) with a Crank-Nicolson scheme and all solutions were calculated in Matlab 2019b software. To quantify the temperature contrast, we developed a dimensionless parameter ζ which is defined as the ratio between the temperature rise in water at north pole (ΔT_1) and south pole (ΔT_2) (Fig. 1).

RESULTS

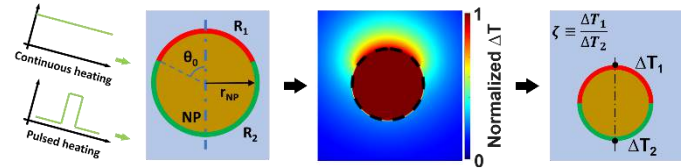


Figure 1. Schematic illustration of the modeling of JNP heating and temperature contrast.

Several factors can affect the thermal transport and temperature profile with JNP heating. We first focus on the directional heating under steady-state scenarios and start with the symmetric JNP with a $\theta_0 = \pi/2$ (Fig. 1). Nonuniform ITR can stem from the heterogeneous coating and can lead to heterogeneous thermal transport. Fig. 2A shows that for a JNP with $R_1 = 1 \times 10^{-9} \text{ m}^2\text{KW}^{-1}$ and $R_2 = 100 \times 10^{-9} \text{ m}^2\text{KW}^{-1}$, the temperature increase (ΔT) near the north pole is significantly higher than ΔT near the south pole due to the ITR contrast. This heterogeneous thermal transport

and temperature contrast is known as directional heating. For more generalized cases with various combinations of R_1 and R_2 , we plotted the 2D map of $\zeta_{s.s.}$ as functions of R_1 and R_2 (Fig. 2B). On this map, we can readily read the relative temperature contrast with arbitrary combinations of R_1 and R_2 . For instance, $R_1 = 1 \times 10^{-9} \text{ m}^2\text{KW}^{-1}$ and $R_2 = 100 \times 10^{-9} \text{ m}^2\text{KW}^{-1}$ gives $\zeta_{s.s.} = 2.5$, indicates significant directional heating with the temperature rise near the north pole is 2.5 times higher than that near the south pole.

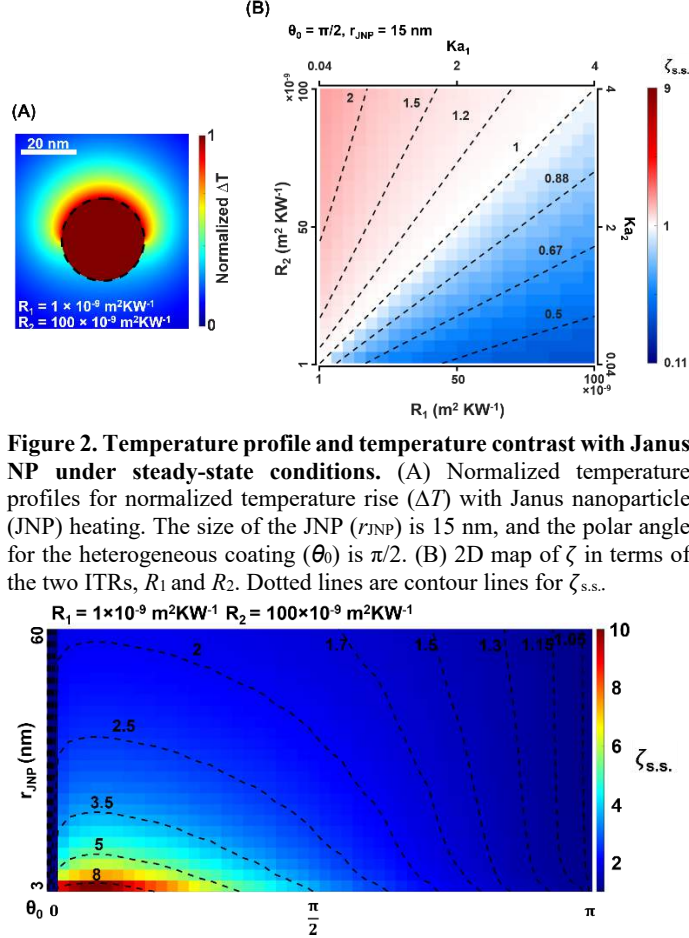


Figure 2. Temperature profile and temperature contrast with Janus NP under steady-state conditions. (A) Normalized temperature profiles for normalized temperature rise (ΔT) with Janus nanoparticle (JNP) heating. The size of the JNP (r_{JNP}) is 15 nm, and the polar angle for the heterogeneous coating (θ_0) is $\pi/2$. (B) 2D map of ζ in terms of the two ITRs, R_1 and R_2 . Dotted lines are contour lines for $\zeta_{s.s.}$.

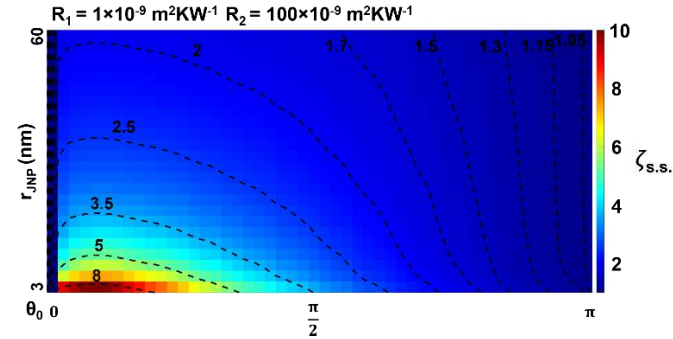


Figure 3. $\zeta_{s.s.}$ map in terms of r_{JNP} and θ_0 under steady-state.

Next, we studied the effect of the polar angle (θ_0) and the size of the JNP (r_{JNP}) on temperature contrast under steady-state heating. Here we demonstrate this combined effect by plotting the map of $\zeta_{s.s.}$ in terms of r_{JNP} and θ_0 with a given ITR contrast under steady-state (Fig. 3). Fig. 3 demonstrates a strong size dependence of temperature contrast with JNP heating, increasing r_{JNP} will end up with less temperature contrast. This size dependence agrees with Kaptiza number analysis, where for larger NP, the ITR has an insignificant effect on heat conduction across the interface^[5]. Additionally, we found that θ_0 has a significant impact on the temperature profile and on $\zeta_{s.s.}$ when $\theta_0 = 0$ & π , the JNP is homogeneously coated, leading to $\zeta_{s.s.} = 1$. As we slightly increase θ_0 above 0, $\zeta_{s.s.}$ rises drastically and reaches its peak value at $\theta_0 \sim \pi/12$. Within the range of our parameter scanning, a greatest temperature contrast ($\zeta_{s.s.} = 10$) under-steady state is observed for a 3 nm JNP with $\theta_0 \sim \pi/12$ ($R_2/R_1 = 100$).

Finally, we analyzed the evolution of temperature contrast with JNP heating during the transient process. Here we imposed 100 ns pulsed constant heating on a 30 nm JNP with $R_1 = 1 \times 10^{-9} \text{ m}^2\text{KW}^{-1}$, R_2

$= 100 \times 10^{-9} \text{ m}^2\text{KW}^{-1}$, and $\theta_0 = \pi/2$. Fig. 4A illustrates the temperature profiles during the transient heating process. We can observe a greater temperature contrast as no obvious heating is observed near the southern hemisphere at $t = 1 \text{ ns}$ & 10 ns , leading to a much-enhanced ζ for pulsed heating (Fig. 4B). As heating continues, thermal energy continuously diffuses, ending up with ζ asymptotically reducing to steady state level (Fig. 4B, $\zeta_{s.s.} = 2.5$). Moreover, we expand our investigation into more generalized cases and discuss the combined effects of geometric parameters (r_{JNP} and θ_0) on temperature contrast during the transient heating process. Fig. 4C&D show a strong geometry dependence of the temperature contrast during the transient heating process. Smaller JNP and moderate polar angle can lead to greater enhancement of temperature contrast for pulsed JNP heating.

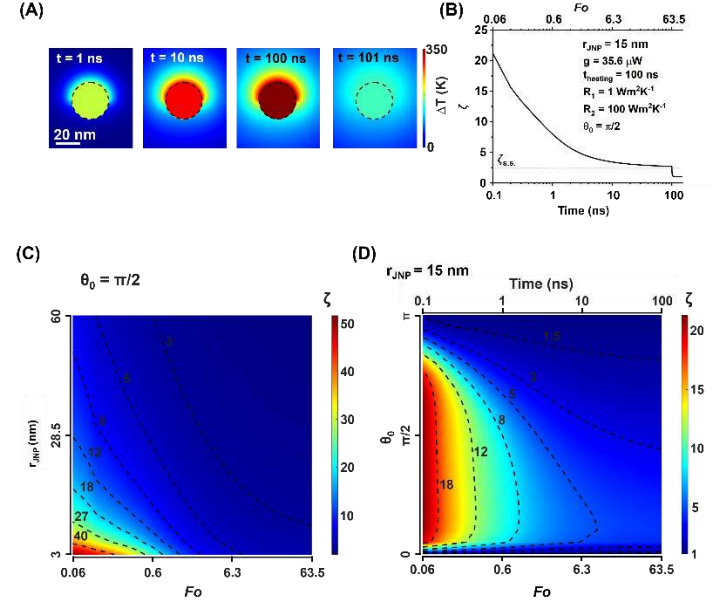


Figure 4. The temperature evolution during the transient heating. (A) ΔT profiles during the transient heating process with JNP. (B) The evolution of ζ during the transient heating process. (C) ζ map in terms of r_{JNP} and Fo . (D) ζ map in terms of θ_0 and t .

DISCUSSION

In this work, we found that shorter heating time can lead to drastic enhancement of ζ . Therefore, it is reasonable to speculate further enhancement of temperature contrast with picosecond heating. However, our numerical model is limited in estimating the thermal transport during the picosecond range as it is too short for electron-phonon energy transfer^[6]. In our future work, a two-temperature model can be a starting point to reveal the JNP heating during the picosecond pulsed energy excitation.

ACKNOWLEDGEMENTS

We acknowledge the support from National Science Foundation (1631910), National Institute of Health (R35GM133653).

REFERENCES

- [1] Xuan M, et al., *J. Am. Chem. Soc.*, 138: 6492-6497, 2016.
- [2] Wei H, ET AL., *PNAS*, 117: 15473-15481, 2020.
- [3] Wilson B A, et al., *J. Phys. Chem.*, 157: 054703, 2022.
- [4] Olarte-Plata J D, et al., *ACS nano*, 16: 694-709, 2021.
- [5] Baffou G, et al., *Laser Photonics Rev.*, 7: 171-187, 2013.
- [6] Nguyen S C, et al., *ACS Nano*, 10: 2144-2151, 2016.

EFFECTS OF CHORDAE RUPTURE ON TRICUSPID VALVE SEPTAL LEAFLET STRAINS: AN EX-VIVO STUDY ON PORCINE HEARTS

**Julia Clarin (1), Keyvan Amini Khoiy (2), Samuel D. Salinas (1), Dipankar Biswas (3),
Kourosh T. Asgarian (4), Francis Loth (1,5), Rouzbeh Amini (1,5)**

(1) Department of Bioengineering, Northeastern University, Boston, MA, USA

(2) Department of Biomedical Engineering, The University of Akron, Akron, OH, USA

(3) Department of Mechanical Engineering, The University of Akron, Akron, OH, USA

(4) Jersey Shore University Medical Center, Neptune, NJ, USA

(5) Department of Mechanical and Industrial Engineering, Northeastern University, Boston, MA, USA

INTRODUCTION

The tricuspid valve (TV) maintains unidirectional blood flow in the pulmonary side of the heart through precise and complex interactions of the TV leaflets and sub-valvular components. Proper function of these sub-valvular components is critical to overall TV function. Alterations to sub-valvular anatomy or function can result in tricuspid regurgitation (TR) and reduced RV function. Specifically, the TV chordae tendineae prevent prolapse of the leaflet cusps or edges into the right atrium when the ventricle is pressurized during systole [1]. Alterations or lesions on the chordae may lead to primary TR. Complete chordae tendineae rupture (CTR) may cause TV leaflet flail into the right atrium, increasing the severity of regurgitation.

Though a majority of TV regurgitation is associated with left-sided heart disease, an estimated 8-10% of TR occurs in the presence of primary TV pathology (primary TR) [2]. Primary TR resulting from chordae abnormalities may occur due to both congenital and acquired causes. Congenital causes include Ebstein's anomaly and Marfan syndrome, while acquired causes include endocarditis, rheumatic disease, blunt force trauma (e.g., vehicular accidents), and most commonly, iatrogenic injury (e.g., endomyocardial biopsy, interference from pacing or defibrillator leads) [3, 4]. However, the mechanics of TR development following CTR are not well understood, especially for acquired causes of TR.

To address this knowledge gap, we experimentally modeled CTR in whole porcine hearts using our ex-vivo beating heart simulator to assess the mechanical impact of CTR on TV leaflet deformation [5]. TV septal leaflet strains were quantified to gain insight into acute TR development following CTR. We hypothesized that CTR further disturbs normal deformation of the TV leaflets, leading to insufficient leaflet coaptation and acute TR.

METHODS

Fresh porcine hearts were obtained from a local slaughterhouse (3D meats, Dalton, OH) for investigation using a previously developed ex-vivo beating heart system [5]. The positive displacement pump's standard

70 bpm waveform was used to circulate phosphate buffered saline (PBS) through intact porcine hearts at physiological pressures and flow rates, in accordance with the International Standard Organization (ISO 5840) guidelines for heart valve testing. The circulating fluid generates a transvalvular pressure gradient that causes the TV leaflets to open and close, mimicking native leaflet deformation.

Eight porcine hearts ($n = 8$) were evaluated in the native state (chordae intact) and then after simulating CTR. Chordae rupture was modeled by severing one of the septal chordae adjacent to the posteroseptal commissure, closest to sonocrystal 1 (Fig. 1). Sonomicrometry techniques were used to obtain displacements of the TV septal leaflet, consistent with our previous publications [5, 6]. Eight sonocrystals (Sonometrics Co., London, ON, Canada) were sutured onto septal leaflet in a predefined arrangement, with sonocrystals 6 – 8 placed along the TV annulus (Fig. 1).

Right atrial pressure (RAP), right ventricular pressure (RVP), pulmonary artery pressure (PAP) and mean flow rate were recorded throughout the cardiac cycle for all experiments. Leaflet coaptation was visually assessed using an endoscopic camera prior to data collection. The pressure signals and sonocrystal displacements were recorded for 20 seconds for both the intact and post-chordae rupture (PCR) conditions.

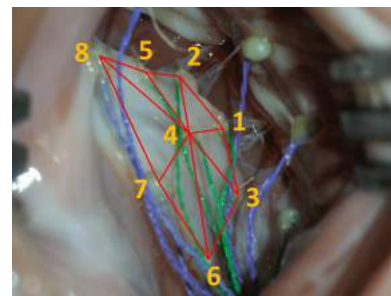


Figure 1: Arrangement of eight sonocrystals on the surface of the septal leaflet, with surface triangulation outlined in red. SB³C2023-227

Positional data were extracted from sonocrystal signals to determine the deformation of the septal leaflet surface with respect to the reference configuration at minimum RAP. A custom Matlab code was used to calculate strains over the septal leaflet surface throughout the cardiac cycle for intact and post-rupture conditions. Details on the triangulation and strain calculation can be found in our previous publication [5].

RESULTS

Following CTR, the maximum RVP dropped from 31 to 25 mmHg, and the flow rate decreased by 26%, indicating that regurgitation occurred immediately after CTR. The observed delay in opening and closing of the pulmonary valve (PV) further indicated regurgitation following chordae rupture (PCR) (Fig. 2). Comparison of the pressures with principal strain values calculated throughout the cardiac cycle revealed that the maximum strains occurred at peak RVP (approximately 0.4 s). After this peak, strains rapidly dropped towards the end of the systole and remained closed to zero during diastole.

Chordae rupture notably altered the strain distribution across the septal leaflet surface (Fig. 3a). A significant increase in peak principle strain was observed after rupture at the distal edge of the septal leaflet, near sonocrystal 1 (Fig. 3b). However, no significant difference was observed in maximum principal strains (mean \pm standard error) averaged across the septal leaflet between intact (14.6 \pm 3.0%) and PCR (18.2 \pm 3.4%) conditions.

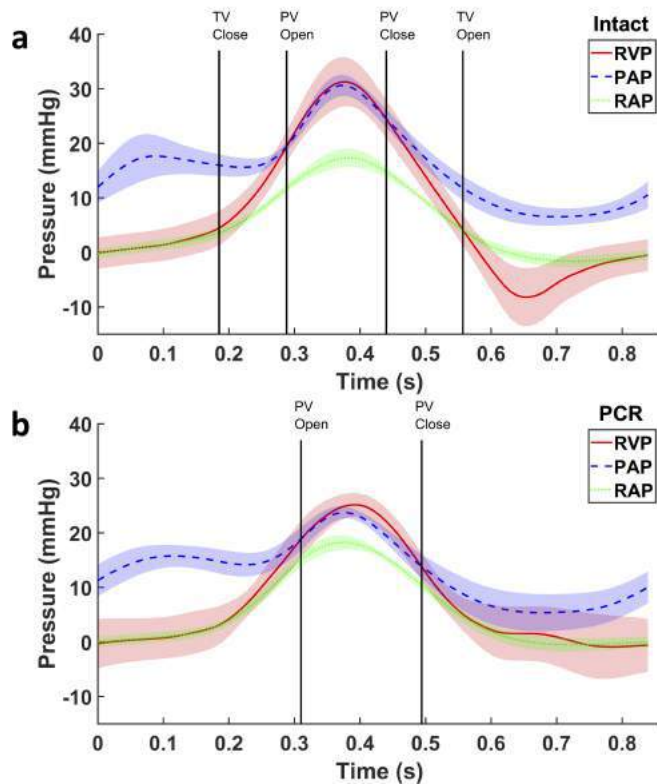


Figure 2: Mean right atrial pressure (RAP), right ventricular pressure (RVP), and pulmonary artery pressure (PAP) during the cardiac cycle for (a) intact and (b) post chordae rupture (PCR) conditions ($n=8$, paired samples), where shaded regions represent standard error. Vertical lines indicate opening and closing of the tricuspid valve (TV) and pulmonary valve (PV).

DISCUSSION

Chordae rupture was observed to prevent proper TV leaflet coaptation which caused acute primary TR, confirmed by the changes in hemodynamic pressures, flow rates and time of PV opening and closure (Fig. 2). Septal leaflet regional strains were immediately altered in PCR conditions, with a significant increase in peak principal strain occurring along the leaflet free edge, nearest the ruptured chordae (Fig. 3). Such results support our hypothesis that CTR disturbs native TV leaflet deformation and coaptation, leading to acute TR.

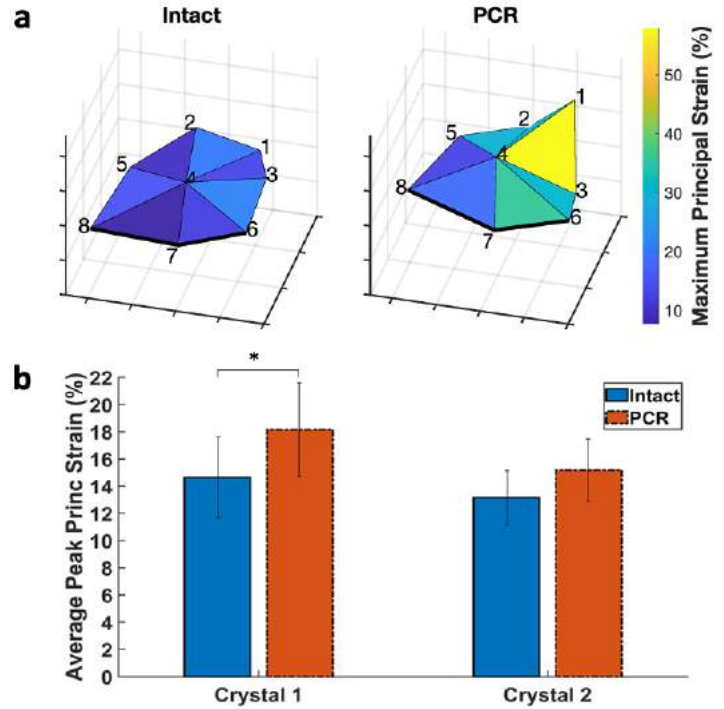


Figure 3: (a) Maximum principal strain on the TV septal leaflet calculated at maximum RVP (approximately 0.4 s) for intact and ruptured (PCR) conditions, shown for a representative sample. (b) Average peak principal strains between intact and PCR conditions for Crystals 1 and 2. Error bars show standard error and an asterisk (*) indicates significance ($p < 0.05$).

The observed changes in septal leaflet strain distribution post-CTR shows that the TV's biomechanical environment is immediately altered by chordae rupture. While we can only directly quantify acute mechanical changes with our experimental system, the presence of altered mechanical strains is indicative of potential long-term effects. Specifically, alterations in mechanical strains may elicit tissue remodeling responses that affect TV function, potentially exacerbating existing TR or accelerating its development. However, further investigation is required to determine the exact tissue remodeling mechanisms.

It is important to note that while our ex-vivo porcine model provides detailed mechanical data that cannot be readily obtained in a clinical setting, conclusions from ex-vivo animal studies do not directly translate to humans. These limitations, however, do not invalidate the overall findings of this study.

In summary, our work provides insight into the mechanics of tricuspid regurgitation development following chordae tendineae rupture. The significant alterations in leaflet strain resulting from chordae rupture highlight a need to further investigate potential maladaptive remodeling responses that may be detrimental to long-term cardiac function. Such investigations are critical to improve treatment strategies and timing of intervention for primary TR, which is currently associated with a high risk of surgical mortality for valve repair and a poor prognosis if left untreated [2, 4].

ACKNOWLEDGEMENTS

Funding for this project was provided in part by the National Science Foundation (CAREER 2049088).

REFERENCES

- [1] Carpentier A et al. Elsevier Health Sciences, 2011.
- [2] Adler DS. *Ann Cardiothorac Surg* 6.3 (2017).
- [3] Lin SJ et al. *KJMS* 22.12 (2006).
- [4] Höke U et al. *Heart* 100.12 (2014).
- [5] Khoiy, K. et al. *J Biomech Eng* 138.11 (2016).
- [6] Khoiy K et al. *PLOS ONE* 13.11 (2018).

A VALIDATED, DATA-DRIVEN CONSTITUTIVE MODEL OF TYPE II COLLAGEN INCLUDING FAILURE

Phoebe Szarek (1), David M. Pierce (1,2)

(1) Biomedical Engineering, University of Connecticut, Storrs, CT, USA
(2) Mechanical Engineering, University of Connecticut, Storrs, CT, USA

INTRODUCTION

Collagen plays a crucial mechanical role in most biological tissues and some biomaterials. Inhomogeneity and anisotropy of the individual constituents, e.g., collagen, within tissues affect mechanics at all scales. Type I collagen ($\varnothing \sim 350 \text{ nm} - 1 \mu\text{m}$) is both the most prevalent type in the mammalian world and the most studied [1]. Type II collagen ($\varnothing \sim 20 - 200 \text{ nm}$) is next in prevalence and is the primary source of tensile stiffness in some load-bearing soft tissues yet is relatively understudied.

Continuum-level constitutive models of soft tissues often use an exponential function to model the tensile response of type II collagen but these models rely primarily on untested assumptions or phenomenological fits to macroscale experimental data. In this study we aim to: 1) directly measure the stress-stretch response of networked type II collagen, 2) establish a data-driven constitutive model for individual collagen fibers in tension, 3) similarly establish a failure model for individual collagen fibers in tension, and 4) validate the final constitutive model against data from independent mechanical tests.

METHODS

Tensile Testing. We employed our previously established methods to measure the stress-stretch responses of isolated networks of type II collagen to failure [2]. We sourced bovine cartilage from the patellofemoral groove and produced dumbbell-shaped specimens (thickness of 140-160 μm) oriented along the primary fiber orientation (Fig. 1a). We performed quasi-static uniaxial tension tests to failure and converted force-displacement data to Cauchy stress σ and stretch λ .

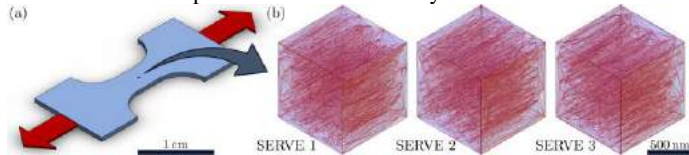


Figure 1. (a) Mechanical test. (b) SERVEs with statistically equivalent orientation, dispersion, and volume fraction of fibers [7].

Constitutive Modeling and Inverse Finite Element Analysis. We created three $1 \mu\text{m}^3$ cubic statistically equivalent representative volume elements (SERVEs) of the superficial zone of healthy, human articular cartilage (Fig. 1b) using previously quantified data on the morphology of collagen networks in the superficial zone, specifically matching the orientation, dispersion, and volume fraction of fibers [3]. We modeled each collagen fiber as a 1-D spring element with one of ten constitutive models (Table 1, subscript c denotes critical). We filled the remaining volume with four-node linear tetrahedra using a biphasic neo-Hookean.

Table 1. Candidate models for individual collagen fibers.

Stress (σ) – Stretch (λ) $\lambda > 1$	<i>polyI1</i>	$\sigma = 4\lambda^2 c_1 (\lambda^2 - 1)$
	<i>polyI2</i>	$\sigma = 2\lambda^2 [2c_1 (\lambda^2 - 1) + 3c_2 (\lambda^2 - 1)^2]$
	<i>polyI3</i>	$\sigma = 6\lambda^2 c_2 (\lambda^2 - 1)^2$
	<i>polyS1</i>	$\sigma = 2\lambda c_1 (\lambda - 1)$
	<i>polyS2</i>	$\sigma = \lambda [2c_1 (\lambda - 1) + 3c_2 (\lambda - 1)^2]$
	<i>polyS3</i>	$\sigma = 3\lambda c_2 (\lambda - 1)^2$
	<i>expI1</i>	$\sigma = 2\lambda^2 c_1 (\lambda^2 - 1) [\exp(c_3 (\lambda^2 - 1)^2)]$
	<i>expS1</i>	$\sigma = 2\lambda c_1 (\lambda - 1) [\exp(c_3 (\lambda - 1)^2)]$
	<i>powI1</i>	$\sigma = 2\lambda^2 c_1 c_3 (\lambda^2 - 1)^{c_3 - 1}$
	<i>powS1</i>	$\sigma = \lambda c_1 c_3 (\lambda - 1)^{c_3 - 1}$
Failure $\lambda > \lambda_c$	<i>Failure stretch</i>	$\sigma = 0$
	<i>Failure stress</i>	$\sigma = 0, \text{ for } \sigma > \sigma_c$
	<i>Fiber damage</i> [4]	$\sigma = [1 - (\lambda - \lambda_f)/(\lambda_c - \lambda_f)]\sigma$
	<i>Fiber softening</i> [5]	$\sigma = \exp[-(\psi_{fib}(\lambda^2) - \psi_{fib}(\lambda_c^2))/m]\sigma$

We applied boundary conditions to the SERVEs to match the tensile experiments on isolated collagen networks. Leveraging the SERVEs we used an inverse finite element scheme (with the Constrained Levenberg-Marquardt method) to fit the candidate stress-stretch models (Table 1) to the experimental data prior to bulk softening. We repeated this process with the complete experimental data, i.e., to failure, to fit the failure models (Table 1). We determined the best fit model using $n=6$ experiments and then fit this model to all $n=27$ experiments. We completed all modeling using FEBio (R3.7.0, University of Utah) [6].

Independent Validation. We created finite element (FE) models, i.e., SERVEs, of pristine, healthy human cartilage from the superficial zone and simulated both uniaxial tensile testing [7] and large-strain shear testing [8] to exercise our best-fit fiber model including failure. We modeled intact proteoglycan as a biphasic neo-Hookean (shear stiffness 0.23 MPa and permeability $1 \times 10^{-14} \text{ } \mu\text{m}^4/\text{Ns}$ [9]). We compared our model predictions in uniaxial tension and shear to experimental measurements from these two independent studies.

Statistical Analyses. We used two-way ANOVAs to assess the variance due to both network models (SERVEs) and experiments, with $p=0.05$ for significance. We established the best models (stress-stretch and failure) by ranking R^2 regression values for each fit, and by considering the number of model parameters (i.e., penalizing additional parameters). We used the root-mean-squared-error to assess model performance in validation.

RESULTS

Tensile Testing. We performed 27 uniaxial tension tests of networks of collagen to failure. The median failure stretch was 1.51 and the median failure stress was 7.71 MPa.

Constitutive Model. We fit ten individual fiber models with three SERVEs to $n=6$ experimental bulk responses (Fig. 2a) and found the best-fit parameters for each model (Table 2). Fitting the model to all experiments, we propose the first data-driven constitutive model for individual type II collagen fibers as

$$\sigma = \lambda c_1 c_3 (\lambda - 1)^{c_3 - 1}, \quad (1)$$

with $c_1 = 0.48$, $c_3 = 4.09$ for $\lambda \geq 1$. We also established that the differences in SERVEs had no effect on the resulting fitted parameters.

Table 2. Best-fit model parameters for individual collagen fibers.

Fiber Model	c_1 [MPa]	c_2 [MPa]	c_3 [-]	R^2	Rank
<i>polyI1</i>	0.011	-	-	0.902	8
<i>polyI2</i>	0*	0.024	-	0.970	4
<i>polyI3</i>	-	0.015	-	0.983	1
<i>polyS1</i>	0.076	-	-	0.836	10
<i>polyS2</i>	0*	0.258	-	0.963	7
<i>polyS3</i>	-	0.255	-	0.961	5
<i>expI1</i>	0.010	-	1.21	0.974	5
<i>expS1</i>	0.048	-	6.59	0.934	8
<i>powI1</i>	0.017	-	3.50	0.992	3
<i>powS1</i>	0.857	-	4.09	0.994	1

* optimization process found the best fit at the lower limit, interpreted as 0

Failure Model. We fit four fiber failure models with one SERVE to $n=6$ experimental bulk responses (Fig. 2b). We established the best failure/damage model as

$$\sigma = \begin{cases} \sigma, & \lambda < \lambda_c \\ \exp\left[-\frac{\psi_{fib}(\lambda^2) - \psi_{fib}(\lambda_c^2)}{m}\right] \sigma, & \lambda \geq \lambda_c \end{cases}, \quad (2)$$

with $\lambda_c = 1.39$ and $m = 0.178$, and $\psi_{fib}(\lambda^2) = c_1(\lambda - 1)^{c_3}$.

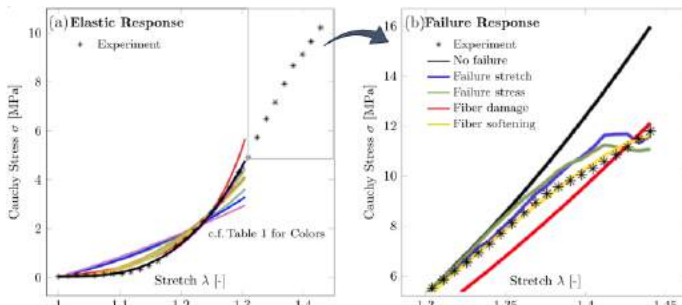


Figure 2. Representative best fits of (a) elastic and (b) failure models to experimental data from a network of type II collagen.

Model Validation. We successfully predicted data from two independent modes of mechanical testing on healthy human cartilage (Fig. 3). Predicted tensile and shear stresses generally lie within one standard deviation of the experiments with a root mean squared error of 0.251 MPa and 40.0 kPa, respectively.

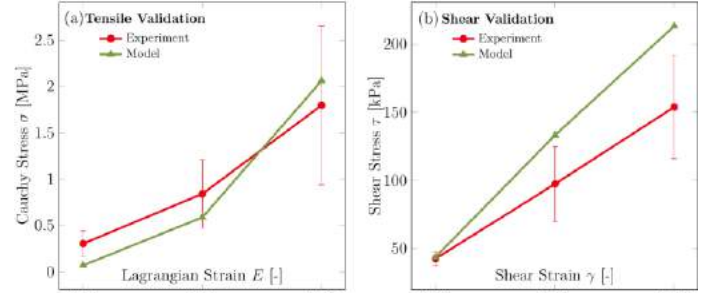


Figure 3. Validation of fitted constitutive model against independent tests on human cartilage: (a) tension [7], (b) shear [8].

DISCUSSION

We established a new validated, data-driven model for networked, type II collagen fibers within cartilage, and potentially within other soft tissues containing type II collagen. Our power-law model for single fibers presents comparable toe and linear regions to those seen in tension testing of soft tissues containing highly aligned networks of collagen. Many of the candidate stress-stretch response models performed equally well at small strains (e.g., *expI1*, *expS1*), but at large strains these models were not able to fit the experimental data. While we tested and modeled tension to rupture, physiological stretches are generally much less extreme, possibly explaining the usability of such models. Introducing fiber failure into our constitutive model, while increasing complexity and computational cost, improved the fit of our model to the gradual bulk softening present in the experimental data.

The data used for validation derived from independent experiments on human cartilage, while our tensile experiments used bovine cartilage. Thus, some discrepancy likely derives from differences in species and location. Our model produced a more non-linear response than the tensile experiments [7]. Our model also predicted higher stresses in the superficial zone under large-strain shear, potentially due to overestimation of the recruitment within the superficial zone [8].

Limitations and Outlook. We assumed that collagen was undamaged in the experimental preparation and was only type II, when collagen within cartilage is heterotypic with small quantities of types IX and XI. We assumed that there was no cross-linking between fibers in our SERVEs and that fibers had no stiffness in bending. We established constitutive models for the stress-stretch and failure responses of individual type II collagen fibers. This novel and fundamental understanding may inform the experimental study and computational modeling of tissues containing type II collagen.

ACKNOWLEDGEMENTS

NSF CAREER 1653358, NSF 1662429, GE Fellowship.

REFERENCES

- [1] Sherman, VR et al., *J. Mech. Behav. Biomed. Mater.* 52:22-50, 2015.
- [2] Szarek, P & Pierce, DM, *J. Mech. Behav. Biomed. Mater.* 136: 105466, 2022.
- [3] Szarek, P et al., *Osteoarthritis Cartilage Open*, 2:e100086, 2020.
- [4] Lemaitre, J, *J. Engr. Mater. Technol.*, 1:83-89, 1985.
- [5] Holzapfel, GA & Ogden RW, *Proc. R. Soc. Lond. A*, 476:17249-17254, 2020.
- [6] Maas, SA et al., *J Biomech. Eng.*, 134:110005, 2012.
- [7] Elliot, DM et al., *J. Biomech. Eng.*, 124:223-228, 2002.
- [8] Maier, F et al., *Osteoarthritis Cartilage*, 27:810-822, 2019.
- [9] Pierce, DM et al., *Biomech. Model Mechanobiol.*, 15:229-244, 2016.

MODELING CARDIAC FIBROSIS: UNDERSTANDING THE EFFECTS OF EXOGENOUS EXTRACELLULAR MATRIX ON 3D CARDIAC TISSUES

Natalie Weiss-Pachter (1), Kristen Allen (1), Tracy Hookway, PhD (1)

(1) Department of Biomedical Engineering, Binghamton University, Binghamton, NY, USA

INTRODUCTION

Cardiac injury results in the death of many cardiomyocytes (CMs), which have a very limited regenerative capacity. Following injury, cardiac fibroblasts (CFs) infiltrate the heart and attempt to repair the wound by depositing large amounts of extracellular matrix (ECM), mostly collagen I. However, this excess ECM forms scar tissue with a greater stiffness than native tissue, impairing the heart's ability to contract. This stiffening is termed cardiac fibrosis and has very few treatment options, motivating the development of accurate tissue engineered heart models for screening new therapeutics.

Current fibrosis models lack multiple human cardiac cell types, a defined ECM environment, or a 3D environment to enable better cell-cell communication^{1,2}. Because cardiac fibrosis is so dependent on both ECM composition and contractile function, we have designed a model incorporating both CMs, the contractile cells of the heart, and CFs, which produce and resorb ECM, along with exogenous ECM to provide a more defined ECM environment. Most current models induce fibrosis with a compound such as transforming growth factor- β , but few have modeled fibrosis by modulating the cellular environment as opposed to cellular signaling. By changing the amount of ECM in the system, we hypothesize that we will be able to model environments corresponding to varying degrees of fibrosis.

Our goal is to create a physiologically relevant cardiac tissue model which can be used to understand the heart's response to various fibrotic factors and to develop new therapeutics for cardiac fibrosis.

METHODS

2 different types of 3D cardiac tissues were generated- spherical aggregates and tissue rings³. Human induced pluripotent stem cells (iPSCs) were encoded with a GCaMP calcium reporter to enable calcium flux analysis in differentiated CMs (Gladstone Institutes). CMs were differentiated from iPSCs via modulation of the Wnt pathway using GSK3 inhibitor CHIR99021 followed by Wnt pathway inhibitor

IWP2⁴. For each tissue, CMs and primary human adult ventricular CFs (Cell Applications) (3 : 1) were combined with collagen I, laminin 221, a collagen-laminin mix, or Matrigel/Geltrex at concentrations of 0.1-0.5 mg/mL. The ratio of collagen I to laminin (1 : 0.86) in rings containing both ECM types together was based on physiologically relevant *in vivo* ratios of collagen and laminin reported in literature⁵. Aggregates were formed in round bottom, ultra-low attachment 96 well plates. Tissue rings were formed in custom agarose molds.

Bright field microscopy was used to assess tissue phenotype and formation. High frame rate calcium flux videos were assessed with MuscleMotion in ImageJ to measure contractile parameters⁶.

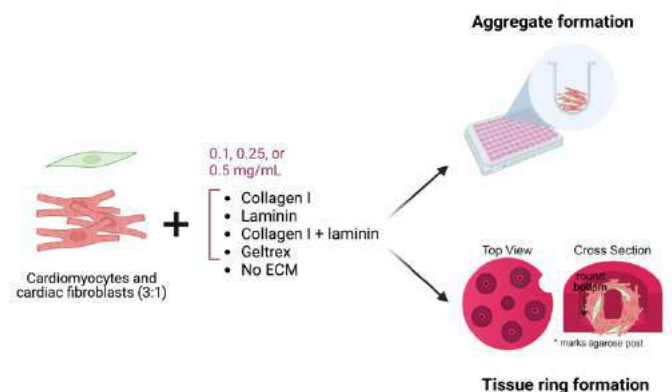


Figure 1: 3D cardiac tissue formation. Schematic of experimental design showing production of spherical aggregates and tissue rings.

RESULTS

Both spherical aggregates and tissue rings were able to form in the absence of exogenous extracellular matrix (Fig. 2). However, the

addition of collagen I, either independently or together with laminin, resulted in less robust formation of both tissue types. Aggregates with no ECM compacted efficiently and formed with an average diameter of 400 μm , but those containing collagen had inferior compaction and less defined edges (Fig. 2a). Aggregates with no ECM had 100% tissue formation as opposed to 7% formation in aggregates with collagen I alone and 0% formation when collagen I and laminin were combined (Fig. 3). Tissue rings with no ECM formed uniformly with an average thickness of 500 μm , but rings containing collagen had inconsistent thickness and highly irregular formation (Fig. 2b).

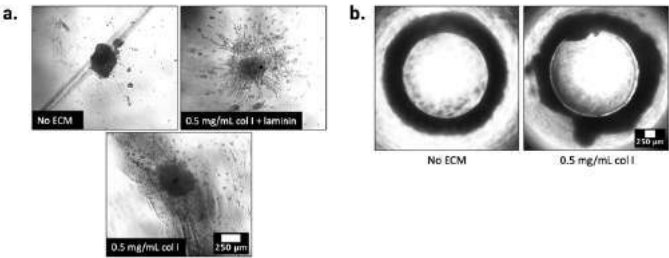


Figure 2: Morphology of aggregates and tissue rings. (a) Representative images of aggregates containing no exogenous ECM, collagen I + laminin, and collagen I alone. (b) Representative images of rings containing no ECM and collagen I. Scale bars = 250 μm .

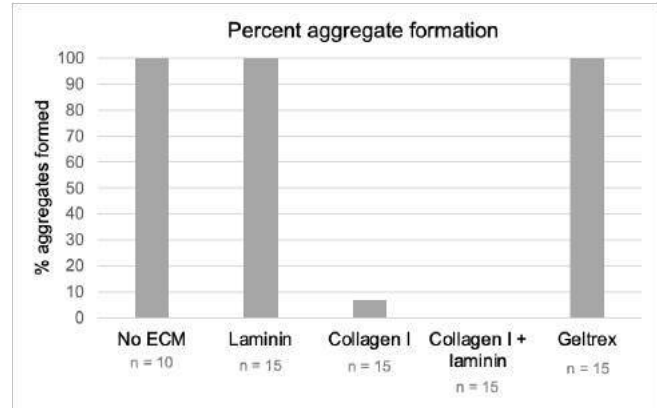


Figure 3: Percent aggregate formation. Quantitative aggregate formation data under various ECM conditions. Figure 2 shows examples of formed (top left) and unformed (top right and bottom) aggregates.

Tissue rings showed robust beating, as shown by calcium flux (Fig. 4a-b). Calcium flux analysis also showed decreased contraction duration in rings containing both collagen I and laminin, comparable to that of rings containing no ECM and significantly lower than all other ECM groups (Fig. 4c). No significant differences in contractile parameters were found between different ECM concentrations.

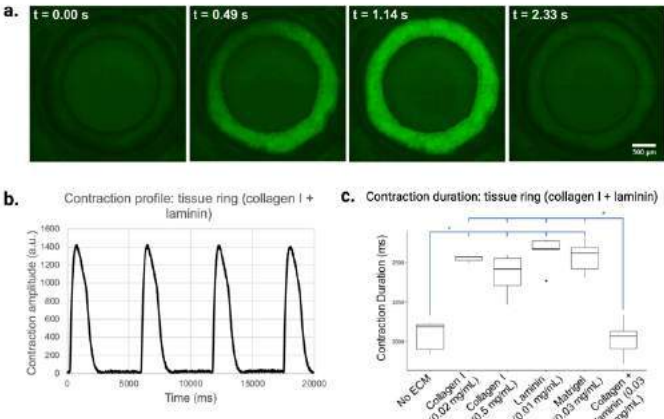


Figure 4: Calcium flux analysis of tissue ring. (a) Calcium flux time lapse of beating ring containing collagen I and laminin. Scale bar = 500 μm . (b) Contraction profile of beating ring. Obtained by analyzing calcium flux video in MuscleMotion for ImageJ. (c) Statistical analysis of contraction duration between different ECM groups. *p < 0.05.

DISCUSSION

We have shown that the addition of collagen I negatively impacts tissue formation across multiple 3D cardiac tissue platforms (Fig. 2). This indicates that exogenous ECM can modulate the environment of these tissues. Notably, rings containing collagen still showed robust beating, and the presence of collagen I and laminin together resulted in decreased contraction duration, which is a characteristic of more mature contractile function (Fig. 4). This decreased contraction duration was similar to that of rings containing no ECM, whereas all other ECM groups had a higher contraction duration. Though more studies are required, this may suggest that the presence of multiple ECM types combined in physiologically relevant ratios encourages more robust beating.

Interestingly, no major differences in either formation or contractile efficiency were seen between different concentrations of ECM. This may suggest that not all the exogenous ECM was incorporated into the tissues during formation, or that CMs were not in contact with ECM for long enough to induce functional change in tissue stiffness and/or beating.

Additionally, the robust formation of both aggregates and rings in the absence of exogenous ECM may suggest that the CFs provide a level of endogenous ECM sufficient to support the formation of these tissues. As such, the “no-ECM” conditions may instead be more reflective of a healthy heart’s ECM environment, and the addition of collagen to the system may reflect a more fibrotic-like environment that inhibits tissue formation and remodeling. Future studies will measure endogenous ECM to determine the CFs’ role in shaping our model’s ECM environment.

One limitation of our study is that CFs are cultured on tissue culture plastic prior to their use in 3D tissues. The stiffness of these plates may induce a fibroblast to myofibroblast transition, causing CFs to deposit more ECM than if they were cultured on a softer substrate⁷. Our model also lacks immune cells such as resident macrophages, which have been shown to inhibit fibrosis and mitigate adverse tissue remodeling⁸.

In addition to measuring endogenous ECM, future studies will measure tissue stiffness using atomic force microscopy to determine whether increased ECM in the system affects the stiffness of the overall tissue. These measurements will help determine the level of fibrosis represented by this model, and further optimization will enable screening of compounds for new potential therapeutics.

ACKNOWLEDGEMENTS

NWP is supported by the American Heart Association predoctoral fellowship. Thank you to the Hookway lab. Figures created with BioRender.

REFERENCES

[1] Mainardi, A. et al., *Lab. Chip*, 21, 4177–4195 (2021). [2] van Spreeuwel, A. C. C. et al., *J Cardiovasc. Transl. Res.*, 10, 116–127 (2017). [3] Gwyther, T. A., Hu, J. Z., Billiar, K. L. & Rolle, M. W. *J. Vis. Exp. JoVE*, e3366 (2011). [4] Lian, X. et al., *Nat. Protoc.*, 8, 162–176 (2013). [5] Hanson, K. P. et al., *Tissue Eng. Part A*, 19, 1132–1143 (2013). [6] Sala, L. et al., *Circ. Res.* 122, e5–e16 (2018). [7] Andrysiak, K., Stepniowski, J. & Dulak, J., *Pflugers Arch.* (2021). [8] Wang, J. et al., *Curr. Probl. Cardiol.*, 101570 (2022).

FOCAL ADHESION KINASE REGULATES MECHANOSENSITIVE GENE TRANSCRIPTION AND TENDON MATURATION

Thomas P. Leahy (1,2), Srish S. Chenna (1,2), Louis J. Soslowsky (1,2), Nathaniel A. Dymant (1,2)

(1) McKay Orthopaedic Research Laboratory, University of Pennsylvania, Philadelphia, PA, USA
(2) Department of Bioengineering, University of Pennsylvania, Philadelphia, PA, USA

INTRODUCTION

Throughout development and postnatal growth, resident tendon cells respond to mechanical cues from the nascent tendon extracellular matrix (ECM) to regulate tissue properties. Focal adhesion kinase (FAK, gene: *Ptk2*) is an intracellular protein kinase that regulates the actin cytoskeleton and cell-ECM adhesions. In *in vitro* tendon cell culture, FAK inhibition alters cell morphology and attenuates the cell's tenogenic gene expression response to growth factor stimulation and mechanical stretching.¹⁻⁴ In addition, FAK inhibitor treatment of explanted tendons attenuates ECM to nuclei strain transmission, indicating that FAK plays an active role in regulating cell-ECM attachment within the native tendon ECM.⁵ Finally, tendon-targeted FAK conditional knockout mice demonstrate altered development of tendon structure compared to wildtype (WT) mice at 30 days of age (P30), specifically exhibiting reduced cross-sectional area (CSA) yet mostly normal mechanical properties.⁴ Despite these known roles for FAK in tendon, the degree to which FAK regulates mechanotransduction within the native tendon ECM as well as the regulatory role of FAK-dependent mechanotransduction in maintaining tendon homeostasis throughout postnatal growth remain unknown. Therefore, the objectives of this study were to define the role of FAK in (1) regulating mechanotransductive gene expression in response to de-tensioned free-floating explant conditions and (2) regulating tendon homeostasis during postnatal growth. We hypothesized that (1) FAK inhibition will attenuate the tendon gene expression response to free-floating explant conditions and that (2) tendon-targeted FAK conditional knockout will negatively impact tendon maturation and maintenance of homeostasis during postnatal growth, specifically by eliciting a reduction in tendon CSA and mechanical properties.

METHODS

Free-Floating Tendon Explant: Flexor digitorum longus (FDL) tendons from male and female P30 WT mice were freshly dissected and randomized to receive FAK-inhibitor (FAK-I; 10 μ M PF-573228;

Tocris; Minneapolis, MN) or control (DMSO) media (DMEM supplemented with 5% FBS and 25 mM HEPES). Tendons were maintained in explant culture conditions at 37°C for 1.5, 4, or 12 hours to assess the initial mechano-response to acute de-tensioning (n=5/treatment group/timepoint). **Gene Expression:** Following explant treatment, RNA was immediately isolated from all tendons to quantify mechanotransductive gene expression using Taqman assays (*Acta2*, *Cyr61*, *Mmp3*, *Mmp13*, *Ptk2*; Housekeeper control: *Abl1*).

In Vivo Mouse Model: We utilized tendon-targeted FAK knockout (Scx-Cre;FAK^{F/F}; FAK-KO) mice,⁶ in which we validated reduced *Ptk2* expression.⁴ Achilles tendons (ATs), FDL tendons, and patellar tendons (PTs) from P60 FAK-KO and WT littermate controls were used for viscoelastic mechanical testing (males only) and histology (males and females). **Viscoelastic Mechanics:** Tendon CSAs were measured (n=11-13/genotype), and tendons were subjected to a viscoelastic mechanical testing protocol (preconditioning, viscoelastic stress relaxation and dynamic frequency sweep, and a quasi-static ramp to failure). **Histology:** Whole ankle and knee joints were fixed, decalcified, paraffin embedded, and sectioned in the sagittal plane (n=3-5/genotype). Additional knee joints were sectioned in the transverse plane to visualize the PT cross-section (n=4-7/genotype). Overall tissue morphology was visualized via toluidine blue staining.

RESULTS

Free-Floating Tendon Explant: In DMSO-treated tendons, we observed substantial increases in *Mmp3* (~90-fold) and *Mmp13* (~15-fold) gene expression with time under de-tensioned free-loading conditions, while expression of genes involved in cell contractility (*Acta2*, the Yap/Taz target gene *Cyr61*, and *Ptk2*) were not dramatically affected at these timepoints (Fig. 1A-C). Strikingly, FAK-I treatment resulted in differences in mechanotransductive gene expression at all timepoints evaluated. Specifically, compared to DMSO treated tendons, FAK-I treated tendons demonstrated reduced *Mmp3* expression at all timepoints and reduced *Mmp13* expression at the 12 hour-timepoint

(Fig. 1A-C). In addition, FAK-I treatment modulated the expression levels of *Acta2* and *Cyr61* throughout the experiment (Fig. 1A-C).

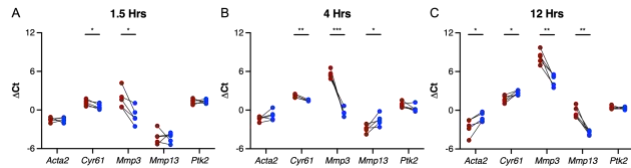


Figure 1: Mechanotransductive gene expression response to de-tensioning was significantly affected by FAK-I treatment. Gene expression levels (represented as ΔC_t) for **DMSO** and **FAK-I** treated tendons following A) 1.5, B) 4, and C) 12 hours of free-floating explant conditions. Data represented as mean \pm standard deviation with plotted individual datapoints. Connected datapoints indicate contralateral FDLs. Bars indicate significant differences (t-test: * $p<0.05$; ** $p<0.01$; *** $p<0.001$).

In Vivo Mouse Model: For tendon viscoelastic mechanical properties, we observed reduced CSA in all FAK-KO tendons, with the greatest effects in the ATs and PTs (Fig. 2A). Structurally, FAK-KO resulted in reduced stiffness in the ATs (Fig. 2B) and reduced maximum load in the FDLs (Fig. 2C) compared to WT tendons. Interestingly, material properties including modulus and maximum stress were increased in FAK-KO ATs and PTs (Fig. 2D-E). Finally, dynamic moduli were increased in the FAK-KO ATs and PTs at all frequencies evaluated (Fig. 2F).

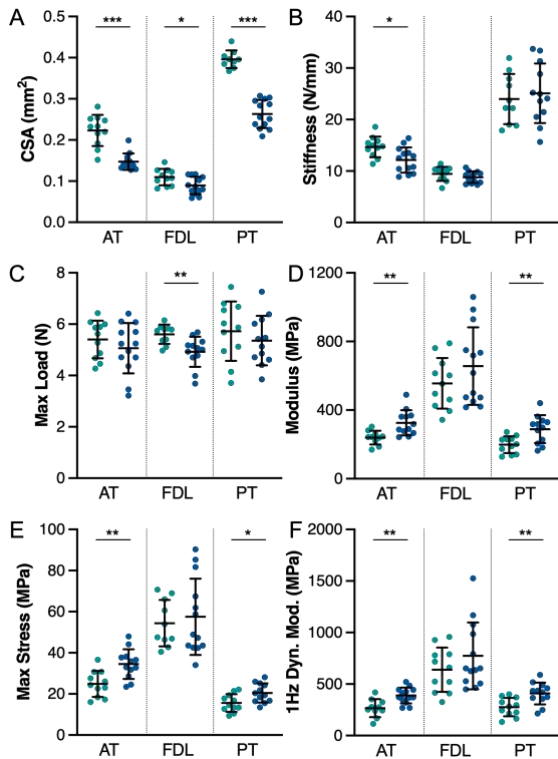


Figure 2. FAK-KO tendons demonstrated reduced size yet increased material properties at P60. A) CSA, B) stiffness, C) max load, D) modulus, E) max stress, and F) 1 Hz (shown as representative of all frequencies) dynamic modulus values for **WT** and **FAK-KO** tendons. Data represented as mean \pm standard deviation with plotted individual datapoints. Bars indicate significant differences (t-test: * $p<0.05$; ** $p<0.01$; *** $p<0.001$).

In sagittal sections, FAK-KO tendons were generally thinner than WT controls as expected (Fig. 3A; PT sections shown as an example). Transverse knee sections further illustrated the reduced CSA of FAK-KO PTs compared to WT PTs (Fig. 3B).

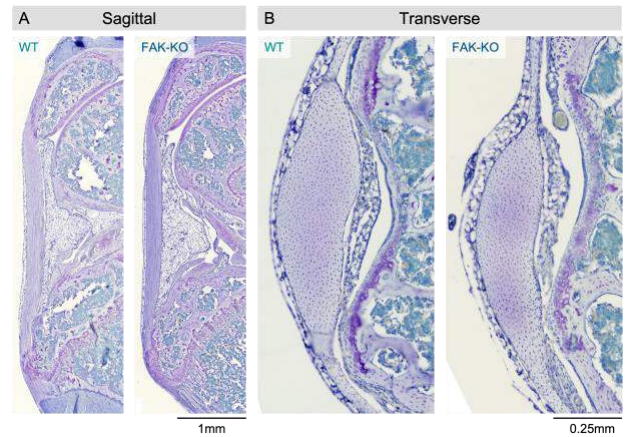


Figure 3. Paraffin histology confirmed the reduced size of FAK-KO tendons at P60. A) Sagittal and B) transverse sections of patellar tendons from **WT** and **FAK-KO** mice.

DISCUSSION

This study investigated the regulatory roles of FAK on cell mechanotransduction within the native tendon ECM and on maintaining tendon homeostasis during postnatal growth. Consistent with our first hypothesis, FAK inhibition affected mechanotransductive gene expression levels in response to de-tensioned, free-floating explant conditions. Previous experiments demonstrated that tendons respond to de-tensioning by increasing expression of matrix remodeling genes such as *Mmp3* and *Mmp13* and decreasing expression of mechanotransductive genes such as *Acta2* and *Cyr61*.⁷⁻¹⁰ In the present study, we observed similar severe increases in *Mmp3* and *Mmp13* with increased duration of explant treatment. Interestingly, FAK-I treatment suppressed this catabolic response to de-tensioning. In addition, we observed that FAK-I alters *Acta2* and *Cyr61* expression throughout our experimental timepoints. Taken together, these results indicate that FAK regulates the sensation of and response to changes in mechanical tension in the tendon *in situ* ECM.

Consistent with our second hypothesis, we observed substantially reduced CSA with FAK-KO in all tendons evaluated. Interestingly, despite their reduced size, FAK-KO tendons generally demonstrated increased material properties compared to WT tendons. Collectively, these results indicate that FAK regulates tendon size throughout postnatal development and that FAK-KO ultimately yields a tendon with increased material properties. Ongoing work will define the mechanism by which FAK regulates tendon size during development and postnatal growth. Specifically, we will investigate the regulatory role of FAK on tendon cell proliferation and ECM deposition. In addition, future work will investigate how mechanical loading regulates FAK-dependent mechanotransduction and tendon response *in vivo*.

ACKNOWLEDGEMENTS

We acknowledge support from NIH/NIAMS (T32AR007132 and P30AR069619).

REFERENCES

1. Liu *et al.*, Stem Cells Int, 2018; 2. Xu *et al.*, J Cell Physiol, 2012; 3. Li *et al.*, J Orthop Res, 2019; 4. Leahy *et al.*, ORS, 2023; 5. Leahy *et al.*, ORS, 2022; 6. Beggs *et al.*, Neuron, 2003; 7. Jones *et al.*, bioRxiv, 2022; 8. Gardner *et al.*, Dosabil Rehabil, 2008; 9. Arnoczky *et al.*, J Orthop Res, 2004; 10. Lavagnino *et al.*, J Biomech, 2005.

DEVELOPMENT OF AN *IN VITRO* MODEL TO EXPLORE COLLAGEN FIBER REGENERATION WITH AGED HUMAN MENSICAL CELLS

Austin G. Gouldin (1), Jennifer L. Puetzer (1,2)

(1) Biomedical Engineering
Virginia Commonwealth University
Richmond, VA, USA

(2) Orthopaedic Surgery
Virginia Commonwealth University
Richmond, VA, USA

INTRODUCTION

Menisci are semi-lunar wedge shaped discs that aid in load transfer in the knee.¹ Menisci are able to distribute these loads due to a complex collagen organization dominated by circumferentially aligned fibers.^{1,2} With age, menisci have increased injuries with reduced healing (Fig 1A),^{2,3} resulting in progressive osteoarthritis (OA) and total knee replacements.¹ Generally, injuries are thought to increase with age in musculoskeletal tissues due to cells remodeling collagen less as they become less active or senescent.¹ However, previous work has shown that adult tenocytes isolated from their aged ECM regain the ability to form aligned collagen fibrils *in vitro*,⁴ suggesting reduced healing with age may be due to changes in the ECM rather than aged cells. We and others have reported that meniscus ECM changes with age.¹⁻³ In particular, we have found significant increases in glycosaminoglycans (GAGs) and advanced glycation end product (AGEs) with age (Fig 1B), both of which can alter ECM mechanics, contributing to increased inflammation and injury.³ There is a need to better understand the aging process in order to regenerate collagen fibers after injury and reduce degeneration. Our long-term goal is to develop a model system to dissect the aging process so to better develop therapeutic interventions.

Previously, we developed a novel cell-seeded culture device that guides neonatal bovine cells in high density collagen gels to produce native-sized hierarchically organized collagen fibers over 6 weeks.⁵ Specifically, mechanical restrains (clamps) at the edge of constructs

restricts contraction and guides neonatal cells to produce aligned collagen fibrils by 2 weeks, which develop into native-sized fibers and fascicles by 4 and 6 weeks (Fig 1C).⁵ The objective of this work is to evaluate whether human cells isolated from aged OA menisci maintain an ability to form organized collagen fibers in our culture system, similar to neonatal cells. We hypothesize aged meniscal cells will produce fibers similar to neonatal cells by 6 weeks in culture.

METHODS

Meniscal cells were isolated from 5 deidentified human OA menisci ranging from 57 to 87 years old (IRB exempt, HM20019726). Each human donor was seeded individually into high density collagen gels as previously described,⁵ with cells being cast into 1.5 mm thick sheet gels and gelled at 37°C for 1 hour to obtain 20 mg/ml collagen gels at 5x10⁶ cells/ml.⁵ Rectangles (8x30mm) were cut from gels and cultured for up to 6 weeks either unclamped as a negative control or clamped in our culture device to guide cellular development of hierarchical collagen fibers (Fig 1C).⁵ The aged human constructs were compared to constructs seeded with cells isolated from bovine neonatal menisci (1-3 days old, 3 donors pooled). Timepoints were taken at 0, 2, 4, and 6 weeks to assess differences in organization, composition and mechanics with time in culture. Once removed from culture, constructs were photographed and weighed to assess differences in contraction. Collagen organization was assessed using confocal reflectance microscopy. DNA, GAG, and collagen were determined via PicoGreen, DMMB, and hydroxyproline (Hyp) assays.⁵ Tensile properties were determined by ramping to failure at 0.5% strain/sec.⁶ Significance was calculated using 2-way ANOVAs with Tukey post-hoc ($p < 0.05$).

RESULTS

Collectively, neonatal constructs seeded with cells from 1-3 day old bovine mirrored results previously obtained with more mature cells isolated from 2-6 week old bovine menisci.⁵ Specifically, unclamped neonatal constructs had significant contraction with time in culture and no change in collagen organization, while clamped neonatal constructs developed aligned collagen fibrils by 2 weeks, fibers by 4 weeks, and larger fascicle bundles by 6 weeks (Fig 2). Aged human constructs also contracted with time in culture, however less than neonatal cells (Fig 2A), suggesting aged cells are less contractile than neonatal cells. Specifically, unclamped neonatal constructs were ~6% their original weight by 6 weeks, while unclamped aged constructs were ~24% their

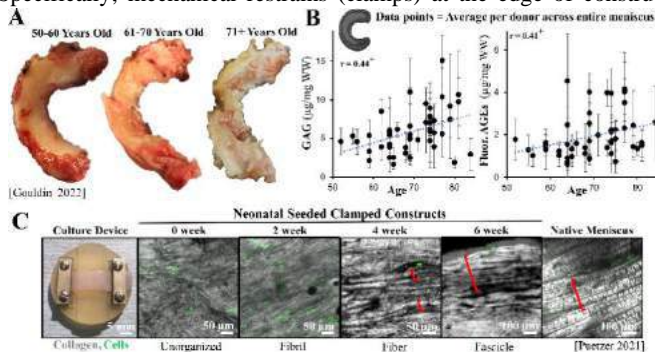


Fig 1: A) Human menisci showing increased degeneration with age.³ B) GAG & AGE accumulation normalized to wet weight in OA human menisci with age. +Significant correlation with age.³ C) Culture device that guides cells to form aligned hierarchical collagen fibers by 6 weeks.⁵ Brackets denote fibers & fascicles.

original weight by 6 weeks (not shown). Despite reduced contraction, confocal reflectance revealed clamped aged constructs were able to develop aligned collagen fibrils by 2 weeks, which matured into fibers by 4 and 6 weeks (Fig 2B). Clamped aged constructs produced similar fiber organization as neonatal constructs; however lacked larger collagen bundles observed in neonatal constructs at 6 weeks (Fig 2B).

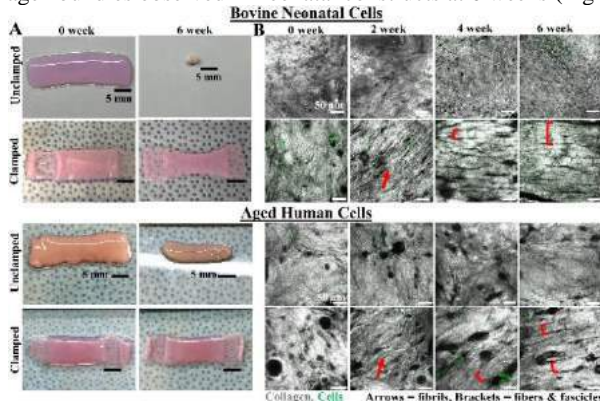


Fig 2: A) Gross morphology & B) confocal of collagen organization in constructs seeded with neonatal bovine or aged human cells

Compositionally, clamped neonatal constructs had a significant increase in DNA and GAG with time in culture, and no change in collagen (hypro) content (Fig 3), while unclamped neonatal constructs largely maintained consistent composition throughout culture. Clamped and unclamped aged constructs had no significant differences in composition, but aged cells isolated from OA menisci were able to maintain DNA, GAG, and collagen content throughout culture, suggesting a possible shift in OA cells becoming less inflammatory (Fig 3). Interestingly, while aged constructs did not reach GAG levels of 6 week clamped neonatal constructs, several individual younger donors did accumulate higher concentrations closer to neonatal levels, demonstrating donor variability. Also, aged constructs matched clamped neonatal GAG levels at 4 weeks, suggesting more time in culture might be needed to further increase GAG accumulation (Fig 3).

Mirroring collagen organization, clamped neonatal constructs had significant increases in toe modulus (not shown), elastic tensile modulus, and ultimate tensile strength (UTS) with time in culture (Fig 4). Aged human constructs had no significant differences between unclamped and clamped constructs mechanically (Fig 4), however clamped aged constructs had an increasing trend in tensile modulus and UTS with time in culture, mirroring increased collagen organization. Further, while clamped aged constructs did not match the mechanical properties of clamped neonatal constructs, they did have similar tensile

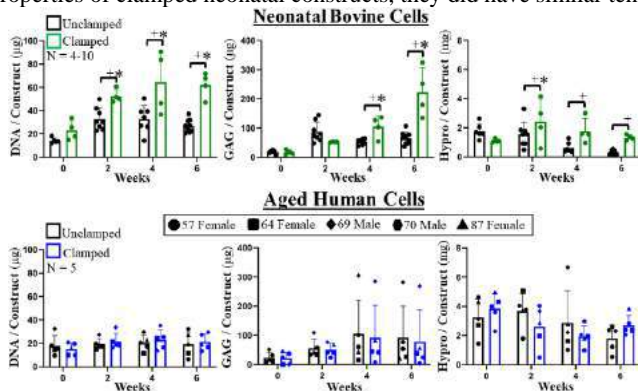


Fig 3: DNA, GAG, & collagen (represented by hypro) per construct for neonatal and aged constructs. Significance to *day 0 or + bracketed group.

moduli and UTS as previously reported clamped constructs seeded with cells isolated from immature bovine menisci (2-6 wks old, Fig 4 line).⁵

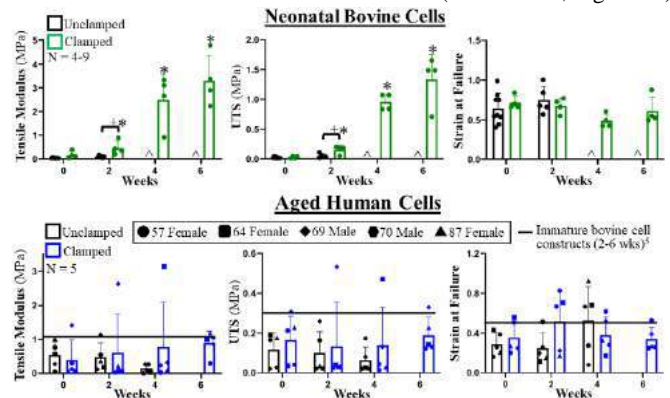


Fig 4: Tensile elastic modulus, UTS, and strain at failure for neonatal and aged constructs. Significance to *day 0 or + bracketed group. ^ denotes too small to test.

DISCUSSION

This data illustrates that human OA meniscal cells, isolated from their aged matrix, are capable of remodeling their surrounding matrix when presented with correct mechanical cues. Specifically, aged human cells cultured with boundary conditions in high density collagen gels were capable of producing aligned collagen fibrils by 2 weeks which matured into larger fibers by 6 weeks. Despite aged cells having reduced contraction compared to neonatal bovine cells, they appeared to produce aligned collagen fibrils and fibers in the same time-frame as neonatal cells (Fig 2B). However, aged constructs did lack larger collagen bundles at 6 weeks, possibly due to reduced cellular contraction.

While collectively composition and mechanics did not significantly change in clamped aged constructs, individual donors did match GAG concentrations and mechanics of neonatal constructs. Specifically, the younger human donors (age 57-69) tended to have greater contraction, increased fiber formation (data not shown), increased GAG production (Fig 3), and greater tissue mechanics (Fig 4) than the older human donors (age 79 & 87). This data suggests that within the older donors there is a shift in cellular contractility or activity with age, with the younger cells being able to organize the matrix a bit quicker. Older donors may need extended culture or the addition of chemical or mechanical stimulation to produce similar changes.⁴ However, despite these differences between the aged constructs, they did still produce mechanical properties similar to clamped constructs seeded with immature meniscal cells (2-6 wks old),⁵ suggesting differences between juvenile and aged cells may not be so extreme.

Overall, we have developed a model system to better understand how collagen regeneration is impacted with age and disease. These findings suggest that reduced healing with age may be less cell driven and more environmentally driven, which could point to future therapies targeting the matrix rather than cells to treat age-related degeneration. Ongoing work is evaluating gene expression with time in culture to elucidate whether aged cells become less inflammatory once removed from their aged matrix, as well as inducing AGEs into the system to evaluate their impact on cell function and fiber regeneration.

ACKNOWLEDGEMENTS

We acknowledge Drs. N. Patel and G. Golladay for providing tissue.

REFERENCES

- [1] Tsujii, A et al., *Knee*, 24:1262-70, 2017.
- [2] Pauli, C et al., *OARSI*, 19:1132-41, 2011.
- [3] Gouldin, A et al., *OARSI*, In Press, 2022.
- [4] Bayer, M et al., *Biomater*, 31:4889-97, 2010.
- [5] Puetzer, J et al., *Biomater*, 26:120527, 2021.
- [6] Ansorge, H et al., *Biomed Eng*, 29:1904-13, 2011.

ROTATIONAL IMPACT-INDUCED BRAIN INJURY, A BIOMIMETIC STUDY

Q. Wang (1), J. Lang (2), R. Nathan (3), Q. Wu (1)

- (1) Department of Mechanical Engineering, Villanova University, Villanova, PA, USA
(2) School of Mechanical Engineering, Southeast University, Nanjing, China
(3) Pennsylvania State University Berks, Reading, PA, USA

INTRODUCTION

Each year, millions of people worldwide suffer from traumatic brain injury (TBI) [1-3], a serious health issue that can result from falls, collisions, and other accidents [4, 5]. While the causes of TBI can vary, impacts on the head are a common mechanism of injury and can be divided into two categories: translational and rotational [6-8]. In this study, we focus on rotational impacts and use a novel experimental setup to investigate their effects on the brain.

The cerebrospinal fluid (CSF) around the brain may result in the difference between translational and rotational impacts. The CSF is a thin layer (1 to 5 mm) of water-like fluid that fills the gap between the arachnoid and pia mater, which is an important constituent of the head [9-11]. The CSF acts as a dampening buffer when the brain suffers translational impacts [12]. On the other hand, when the head experiences rotational impacts, the CSF acts as a slippery layer, which increases the relative motion between the brain and the skull.

While TBI has attracted wide attention, the brain response under rotational impacts is still unclear. Studies to investigate TBI can be categorized into two sections: experiment and numerical modeling. From the experiment side, animal tests were performed, including sheep [13], monkeys [14], rabbits [15], etc. These animal investigations all obtained satisfactory conclusions from the post-impact observations. Also, cadavers were mounted with sensors to investigate the movement of the head during the rotational impacts [16-18]. However, animal and cadaver tests can only obtain limited results due to the opaque skull. The motion of the brain can not be captured during the impact process. From the numerical modeling side, the finite element (FE) modeling has received more attention [19, 20]. However, validating the numerical model is difficult because the dataset from the experiments is limited. For example, the stress and strain data during the brain impact process are not available for numerical modeling comparison [21, 22]. Furthermore, the TBI process involves large brain deformation, highly

transient CSF flow, and intense fluid-solid interaction, which is still tricky for numerical simulation.

In this study, we develop a novel methodology to treat these challenges. An artificial transparent surrogate with biomimetic brain matter and CSF was built to reveal the response of brain matter under rotational impact. This included displacement between the skull and the brain, the stress, and the strain distributions.

METHODS

Figure 1 (A-C) shows that rotational impacts can be categorized into three directions: horizontal, sagittal, and coronal impacts. A novel experimental setup was developed to produce these three directional brain impacts. Figure 1 (D-F) shows that the experimental setup consists of an artificial head surrogate, a spring-controlled spinner, an impacting apparatus, and an accelerometer. The head surrogate was originally built based on previous work [23]. It consists of a transparent skull filled with distilled water and an artificial soft brain. On one side of the head surrogate, there is a spring-based spinner. This spinner provides a constant initial force to rotate the head surrogate. The whole setup can be adjusted to simulate the three directional impacts by changing the impacting apparatus. The accelerometer is mounted on the frame to measure the acceleration of the head surrogate.

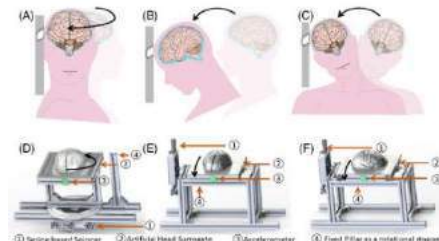


Figure 1: The schematic of rotational impact from three directions: (A) horizontal, (B) sagittal, (C) coronal.

RESULTS

Figure 2 shows the brain response under a horizontal impact. Each subplot represents a time frame since the impact. The red line, which is the centerline of the brain, indicates the rotation and the deformation of the brain matter. As the spinner drove the head surrogate to rotate in an anti-clockwise direction, the first three subplots suggest that the brain kept moving after the skull was stopped. Then, the brain began to rotate back and slowly stopped. This relative motion between the brain matter and the skull is caused by the inertia of the brain and the slippery effect of the CSF. This motion was restricted by the geometry of both the brain and skull, which would cause scratches on the surface and further deformation of the brain. This response may lead to diffusive brain injury near the surface and blood vessel damage inside the brain.

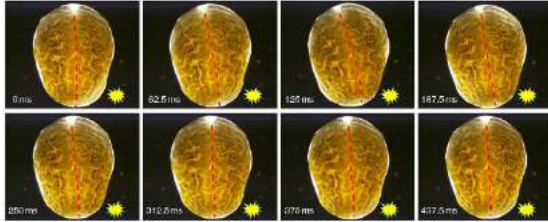


Figure 2: Photography of the brain response after the head surrogate was horizontally stopped by the pillar.

Figure 3 shows the transient strain distribution under horizontal impact. The first row of the pictures shows the minimum principal strain (ϵ_{min}) map at different time frames. The dark blue color represents that this region has been severely compressed. From the time 0 ms to 200 ms, the ϵ_{min} at the coup region (the impact side, right bottom in the figures) and the left side show significant dark blue regions. This indicates that these two regions suffer stronger compression during the horizontal impact. The compression of the coup region is due to the brain inertia and the skull restriction. The compression of the left side is due to the bounce-back effect of the brain, where the brain bounces back from the right-bottom side and compresses to the left side. On the other hand, the second row of figure 3 shows the maximum principal strain (ϵ_{max}), indicating the material extension degree at different time frames. These figures state that the countercoup region (the far end from the impact point) has been stretched more seriously. The reason is that the negative pressure causes the extension at the far end, which impedes the brain from moving.

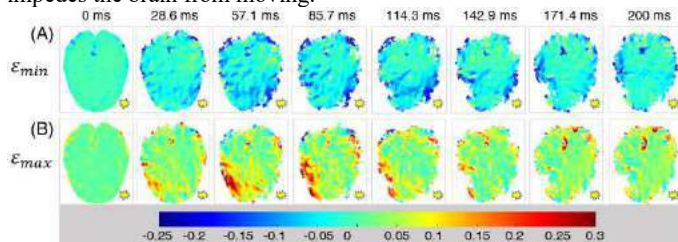


Figure 3: The first row shows the minimum principal strain distribution, and the second row shows the maximum principal strain distribution. The yellow icon on the left bottom represents the impact position.

DISCUSSION

In this study, we employed a novel experimental setup to elucidate the biomechanics of rotational impacts on the brain. Our findings reveal that under rotational impacts, the brain undergoes significant motion and deformation within the skull, which is modulated by the brain's material properties, the skull's geometry, and the slippery effect of cerebrospinal fluid (CSF). The CSF's slippery effect facilitates brain

rotation within the skull, leading to friction between the brain and the skull, which affects most areas of the brain surface, as observed in diffuse brain damage. The brain's motion also generates positive and negative pressure responses in the CSF, compressing and stretching the brain tissue and introducing positive and negative principal strains. Principal strains are a reliable indicator of tissue and vessel damage during a concussion. The skull's geometry also affects the brain's response to rotational impacts, with the least restriction in the horizontal direction and the highest restriction in the sagittal direction. Our experimental findings strongly suggest that rotational impacts can cause significant brain damage and could inform the development of advanced concussion diagnostic tools and protective devices.

ACKNOWLEDGEMENTS

This work is supported by National Science Foundation CBET Fluid Dynamics Program under Award #2003077 and the funding from Pennsylvania state.

REFERENCES

- [1] De Ramirez, S. S. *et al.*, *Annual review of public health*: 175-191, 2012.
- [2] Kamal, V. K. *et al.*, *Journal of neurosciences in rural practice*, 04: 515-525, 2016.
- [3] Peterson, A. B. *et al.*, *Surveillance report*, 2019.
- [4] Bruns Jr, J. *et al.*, *Epilepsia*: 2-10, 2003.
- [5] Kasmaei, V. M. *et al.*, *Emergency*, 4: 141, 2015.
- [6] Anderson, R. W. *et al.*, *Journal of neurotrauma*, 10: 961-974, 2003.
- [7] Gennarelli, T. *et al.*, "Acceleration induced head injury in the monkey. I. The model, its mechanical and physiological correlates," in *Experimental and Clinical Neuropathology*: Springer, 1981, pp. 23-25.
- [8] Lissner, H. *et al.*, *Surgery, gynecology*: 329-338, 1960.
- [9] Atsumi, N. *et al.*, *International journal of vehicle safety*, 1: 1-23, 2016.
- [10] Duckworth, H. *et al.*, *International Journal for Numerical Methods in Biomedical Engineering*, 4: e3440, 2021.
- [11] Pudenz, R. H. *et al.*, *Journal of neurosurgery*, 6: 487-505, 1946.
- [12] Morley, W. A. *et al.*, *Surgical neurology international*, 2014.
- [13] Grimmelt, A.-C. *et al.*, *Central European Neurosurgery-Zentralblatt für Neurochirurgie*, 03: 120-126, 2011.
- [14] Gennarelli, T. A. *et al.*, *Annals of Neurology: Official Journal of the American Neurological Association*, 6: 564-574, 1982.
- [15] Härtl, R. *et al.*, "Blood-brain barrier breakdown occurs early after traumatic brain injury and is not related to white blood cell adherence," in *Brain Edema X*: Springer, 1997, pp. 240-242.
- [16] Alshareef, A. *et al.*, *Journal of neurotrauma*, 5: 780-789, 2018.
- [17] Hardy, W. N. *et al.*, *Stapp car crash journal*: 17, 2007.
- [18] Knutsen, A. K. *et al.*, "3D brain deformation in cadaveric specimens compared to healthy volunteers under non-injurious loading conditions," in *Computational Biomechanics for Medicine*: Springer, 2021, pp. 113-122.
- [19] Kimpara, H. *et al.*, *Annals of biomedical engineering*, 1: 114-126, 2012.
- [20] Laksari, K. *et al.*, *Journal of neurotrauma*, 7: 982-993, 2020.
- [21] Toma, M. *et al.*, *International journal of crashworthiness*, 2: 175-182, 2020.
- [22] Zhou, Z. *et al.*, *Biomechanics modeling in mechanobiology*, 1: 155-173, 2019.
- [23] Lang, J. *et al.*, *Physics of Fluids*, 3: 031908, 2021.

MESENCHYMAL TRANSITIONS IN GLIOBLASTOMA ENHANCE CONFINED MIGRATION THROUGH NUCLEAR SOFTENING

Landon Teer (1), Dominic Armagno (1), Bradley Mahaffey (1), Neha Anil (1), Marco Muñoz (1),
Sihan Sun (3), Joseph Chen (1,2)

(1) Department of Bioengineering, University of Louisville, Louisville, KY, USA
(2) Department of Pharmacology and Toxicology, University of Louisville, Louisville, KY, USA
(3) Department of Biology

INTRODUCTION

Glioblastoma (GBM) is an incurable and highly aggressive brain cancer with a median survival rate of only 15-months. [1] GBM progression is coupled with a molecular event known as proneural-to-mesenchymal transition (PMT) that consists of a phenotypic shift that heightens cell invasion and spread. Interestingly, this increase in cell invasion occurs despite the dense parenchyma, which contain tight pores that act as physical barriers to cell migration. Recent studies have suggested that highly invasive cells display enhanced cell deformability to bypass these barriers [3]; however, the underlying mechanisms permitting these cellular changes remain unclear. Here, we examine these mechanisms through a biophysical lens by investigating the relationship between mesenchymal transitions in GBM and mechanical changes that facilitate efficient confined migration.

We hypothesize that TGF- β 1 promotes increased confined migration by inducing PMT-dependent mechanical softening, which enables efficient navigation of the tight, natural barriers in the brain microenvironment. Further, we hypothesize that PMT specifically softens the nucleus as it represents a critical limiting factor for confined migration. In this study, we induced mesenchymal transitions via TGF- β 1 and assessed changes in structural protein expression and organization, cellular mechanical rigidity, functional confined migration, and the impact of nuclear mechanics on confined migration. Our data suggests an important role for nuclear mechanics in facilitating confined migration and spread of GBM. These data reveal the biophysical alterations that arise from mesenchymal transitions and provide insight into the mechanical features that underlie GBM aggressiveness.

METHODS

GBM cells were cultured in 1X DMEM (Corning: 10-017-CV) supplemented with 10% FBS, 1% NEAA, and 1% PenStrep at 5 % CO₂ and 37°C and treated with 10 ng/mL TGF- β 1 for 72 h to induce

mesenchymal transitions. Western blots were used to verify mesenchymal pathway activation (pSMAD2, pSTAT3, ZEB1), and evaluate nuclear and cytoskeletal protein expressions (pLamin, Lamin A/C, F-Actin/G-Actin). Confocal imaging was used to qualify organizational patterns of lamin A/C and actin before and after TGF- β 1 treatment. To assess nuclear and cytoskeletal mechanics, AFM was employed following induction of mesenchymal transitions. Confined migration was examined using PDMS microchannel platforms consisting of 1D channels at varied levels of confinement (5 μ m, 10 μ m, 20 μ m, and 50 μ m) and were imaged via time lapse microscopy on a Nikon Eclipse TE2000-U. To assess the role of nuclear mechanics in confined migration, cells were treated with 10 uM of CDK1 inhibitor (RO-3306) to increase nuclear stiffness and then plated on microchannel platforms.

RESULTS

TGF- β 1 was sufficient for inducing mesenchymal transitions in the GBM cell lines. First, TGF- β 1 activation was verified via Smad2 phosphorylation (Figure 1A). Next, we evaluated the mesenchymal marker Stat3 and the mesenchymal transcription factor ZEB1. As expected, TGF- β 1 led to significant increases in both Stat3 phosphorylation and ZEB1 expression (Figure 1B, C), indicating a mesenchymal phenotype. We wondered how structural proteins in the nucleus and the cytoskeleton might be affected by mesenchymal transitions, so we evaluated Lamin A/C expression and the ratio of F-actin to G-actin. Both Lamin A/C and F-actin/G-actin decreased with TGF- β 1 treatment at varied levels of significance (2A,B). Interestingly, we also observed significantly more irregularly shaped and porous nuclei in the TGF- β 1 treated cells (2C,D) as well as decreased F-actin across the cell (2B), indicating dysregulation among the different structural proteins.

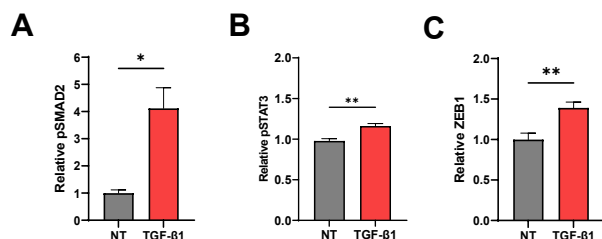


Figure 1: TGF-β1 activates canonical signaling (A) and STAT3 signaling (B), leading to increased ZEB1, a mesenchymal transcription factor (C).

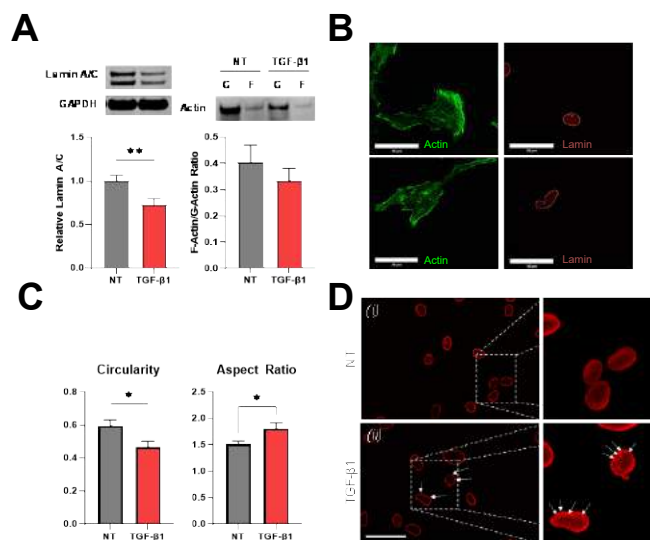


Figure 2: Both lamin A/C and F-actin/G-actin saw reductions in expression levels (A), but lamin A/C saw more pronounced dysregulation with TGF-β1 causing increased shape irregularity (B,C) as well as the formation of pores in the nuclear envelope (D).

Next, we employed AFM to determine how the protein level changes of the nucleus and cytoskeleton might affect cell rigidity. We discovered that TGF-β1 treatment led to reduced cell stiffness in both the nucleus and the cytoskeleton (3A,B). Interestingly, the nuclear stiffness was softest in both treatment groups (3A). Histograms show a narrower distribution of stiffness values were obtained following TGF-β1 treatment. Next, we evaluated the functional changes in the cells using 2D motility assays and microchannel platforms. Notably, 2D cell speed and persistence did not change significantly with TGF-β1 addition; however, microchannel platforms revealed that while NT cells struggled to migrate under tight confinement ($< 5\mu\text{m}$), TGF-β1 cells migrated more rapidly through the same channels. Ongoing work suggests that stiffening the nucleus of TGF-β1 treated cells may be sufficient to limit confined migration.

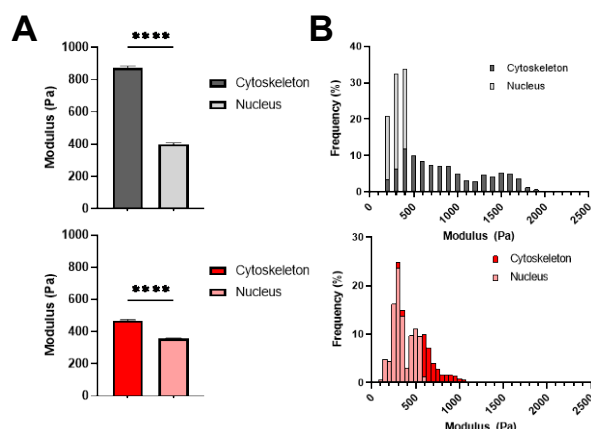


Figure 3: AFM analysis reveals that TGF-β1 treatment significantly reduces nuclear and cytoskeletal stiffnesses (A). Histograms illustrate a shift in moduli values with $> 90\%$ of the scan area exhibiting a stiffness of $< 1\text{ kPa}$ after being exposed to TGF-β1 (B).

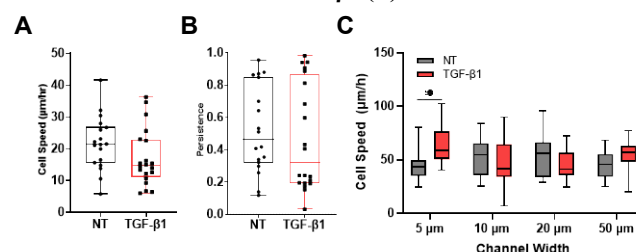


Figure 4: Traditional 2D motility assays show minimal differences between the NT and TGF-β1 treated cells (A,B). When exposed to confinement via microchannel platforms, TGF-β1 treated cells exhibit a significant increase in speed as compared to the NT cells (C).

DISCUSSION

In this study, we demonstrate that TGF-β1 induced mesenchymal transitions are accompanied by reductions in Lamin A/C expression and F-actin G-actin ratios. Further, we show that these reductions change the organization and porosity of the nuclear lamins. Moreover, we demonstrate via AFM mapping that TGF-β1 treatment reduces cell rigidity in both the nucleus and cytoskeleton. With the increase in nuclear compliance, TGF-β1 cells navigated the constricted environment more quickly, suggesting that nuclear mechanics and organization may provide a basis for efficient confined migration.

This study uncovers a novel relationship between mesenchymal transitions and mechanical rigidity. Further, it adds to the growing appreciation for the impact of cell mechanics on cancer aggression and disease progression. Further investigations of this relationship may aid in the development of novel diagnostic tools and help identify new targets for pharmacological intervention.

ACKNOWLEDGEMENTS

The authors gratefully acknowledge the Huson Imaging & Characterization Laboratory at the University of Louisville.

REFERENCES

- [1] Omuro, A. And DeAngelis, L.M., JAMA, 310(17): 1842-50, 2013
- [2] Fedele, M., et al. International Journal of Molecular Sciences, 20(11): 2746, 2019
- [3] Krakhmal, N.V., et al. Acta Naturae, 7(2): 17-28, 2015

ECTOPIC CHANGES IN TISSUE STIFFNESS DISRUPT EPITHELIAL BUCKLING AND FGF-10-INDUCED BUDDING MORPHOGENESIS IN CULTURED EMBRYONIC LUNGS

Kara E. Peak (1), Victor D. Varner (1,2)

(1) Department of Bioengineering, The University of Texas at Dallas, Richardson, TX, USA
(2) Department of Surgery, UT Southwestern Medical Center, Dallas, TX, USA

INTRODUCTION

Ramified networks form the basic architecture for many organs in the body, including the lung, kidney, and salivary gland. In the embryonic lung, these structures arise via a process known as branching morphogenesis, wherein the airway epithelium undergoes a series of branching events to build the bronchial tree [1]. Focal regions of FGF-10 expression within the pulmonary mesenchyme are thought to provide a biochemical template for the overall branching pattern, with individual sources of FGF-10 stimulating the formation of new epithelial branches. But it is still unclear how FGF-10 signaling drives the macroscopic changes in tissue form that sculpt incipient buds. In previous work, we have shown that a focal source of FGF-10 can promote epithelial buckling morphogenesis and stimulate the formation of multiple supernumerary buds [2]. Here, to investigate how FGF-10-induced buckling is impacted by changes in the mechanical properties of the tissue, we developed a new technique to locally and ectopically stiffen the pulmonary mesenchyme in explanted embryonic lungs. We then combined ex vivo explant culture experiments with microindentation testing, quantitative fluorescence microscopy, and computational modeling to determine how changes in tissue stiffness impact the formation of epithelial buds in response to a focal source of FGF-10 in the developing lung.

METHODS

Experimental methods: Fertilized White Leghorn chicken eggs were incubated at 37°C until embryonic day (E) 5, and lung explants were dissected in phosphate-buffered saline (PBS) using fine forceps and a stereomicroscope. In the presence of green (555 nm) light, treatment with Rose Bengal has been shown to photocrosslink the extracellular matrix (ECM) and to alter the measured mechanical properties of soft tissues, such as the cornea [3]. To photocrosslink cultured embryonic

lungs, agarose beads, soaked in either 100 µg/ml FGF-10 or 100 µg/ml Rose Bengal (RB) + 100 µg/ml FGF-10, were implanted into the pulmonary mesenchyme of explanted embryonic lungs. The explants were then cultured on Nucleopore membranes at the air-liquid interface in DMEM/F12 medium (without HEPES) supplemented with 5% fetal bovine serum (FBS) and antibiotics. To photoactivate RB, some explants were exposed to green (555 nm) light after 3 hr of culture to deliver an irradiance of 25 mW/cm² and a fluence of either 0.5 or 1 J/cm² (control explants were not exposed to any light). Bright-field images were captured at 0 and 24 hr to quantify changes in epithelial morphology. We also used the MicroSquisher mechanical testing system (CellScale), equipped with a custom 70 µm-diameter cylindrical microindenter, to measure the mechanical properties of the cultured explants. The Click-iT EdU Imaging Kit was used to quantify rates of cell proliferation and cleaved caspase-3 (CC3) staining was used to visualize apoptotic cells. Whole-mount explants were co-stained for E-cadherin immunofluorescence and imaged using a laser scanning confocal microscope.

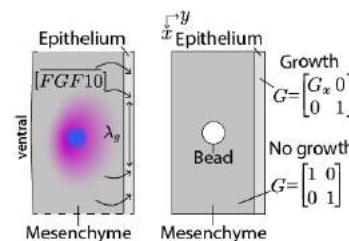


Figure 1: Schematic of computational model for FGF-10-induced epithelial buckling.

Computational methods: We created a computational model of FGF-10-induced budding morphogenesis using COMSOL Multiphysics. As a first approximation, we modeled the airway epithelium as a growing hyperelastic layer supported by an underlying foundation, which represented the pulmonary mesenchyme (Fig. 1). Both tissue layers were prescribed a Blatz-Ko

strain-energy density function, and growth was included by decomposing the overall deformation gradient tensor (\mathbf{F}) into a component due to growth (\mathbf{G}) and a component due to elastic deformation (\mathbf{F}^*) via $\mathbf{F} = \mathbf{F}^* \cdot \mathbf{G}$. The growth rate within the epithelium was assumed to depend on the local concentration of FGF-10 ([FGF10]), which diffused outward from a focal source embedded in the pulmonary mesenchyme (Fig. 1). FGF-10 diffusion was assumed to follow Fick's second law, and, as a first approximation, [FGF10] was assumed to be at steady-state at each time-point. The growth rate within the epithelium \dot{G}_x was therefore defined by the growth law $\dot{G}_x/G_x = \alpha[\text{FGF10}]$, where α is a growth constant and [FGF10] represents the local concentration of FGF-10. The computed Cauchy stresses depended only on \mathbf{F}^* [4].

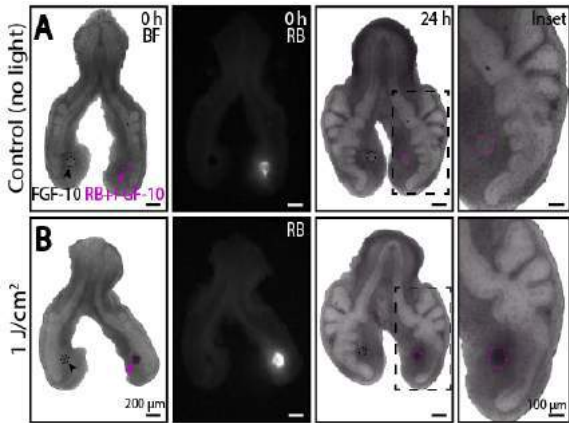


Figure 2: (A-B) Photocrosslinking with RB disrupts FGF-10-induced budding morphogenesis in cultured embryonic lungs.

RESULTS

We have shown previously that ectopic focal sources of FGF-10 can elicit the formation of multiple supernumerary buds within cultured embryonic lungs via a growth-induced buckling mechanism [2]. To determine how changes in the mechanical properties affect FGF-10-induced buckling morphogenesis, we developed a new technique to alter the stiffness of the pulmonary mesenchyme in cultured embryonic lung explants. Agarose beads containing either FGF-10 alone or FGF-10 + RB, a potent photocrosslinker of the ECM [3], were embedded within the pulmonary mesenchyme of explanted embryonic lungs and exposed to green light to initiate photocrosslinking. Treatment with activated RB was sufficient to suppress the formation of FGF-10-

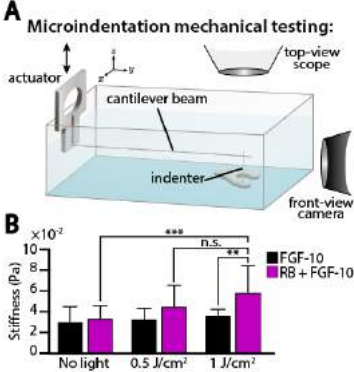


Figure 3: (A-B) Microindentation tests indicate an increase in stiffness within RB-treated embryonic lungs.

induced epithelial buds, as compared to either contralateral controls or explants exposed to no light (Fig. 2). Microindentation experiments revealed that photocrosslinking with RB significantly increased the stiffness of the pulmonary mesenchyme (Fig. 3), without influencing levels of either proliferation or apoptosis within the tissue (data not shown).

We then created a computational model of the airway epithelium to investigate the mechanics of

FGF-10-induced buckling morphogenesis (Fig. 1). Growth within the epithelium was assumed to depend on the local concentration of FGF-10, which diffused from an individual focal source embedded within the pulmonary mesenchyme, in a manner consistent with previous experiments [2]. In our simulations, FGF-10-induced growth caused the epithelium to buckle and form multiple buds, similar to those observed in control explants (Fig. 4). Interestingly, if the stiffness of the pulmonary mesenchyme was increased in the model, FGF-10-induced buckling was substantially suppressed (Fig. 4), similar to that observed in our photocrosslinking experiments (Fig. 2). Taken together, these results suggest that ectopic sources of FGF-10 can promote the buckling morphogenesis within the embryonic airway epithelium and that FGF-10-induced bud formation depends crucially upon the mechanical properties of the tissue.

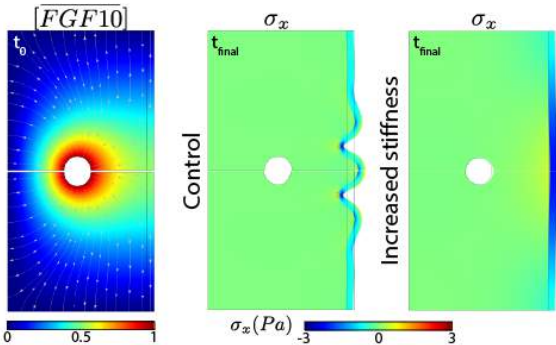


Figure 4: Computational model of buckling morphogenesis predicts that increased mesenchymal stiffness will suppress the formation of FGF-10 induced epithelial buds.

DISCUSSION

Although biophysical cues have long been known to influence tissue morphogenesis [5], there is a dearth of experimental techniques to alter the mechanical properties within intact embryonic organs [6]. Here, we used RB to photocrosslink the pulmonary mesenchyme in cultured embryonic lungs and investigated how changes in tissue stiffness influence FGF-10-induced budding morphogenesis. This assay can be readily adapted to the study of other morphogenetic processes, such as heart tube formation [7] and gut looping [8], as well as a variety of different model organisms, including frog, mouse, and zebrafish embryos. Within the context of embryonic lung development, our data indicate that the overall branching pattern, though certainly regulated by FGF-10 signaling, is also substantially influenced by the mechanical properties of the tissue. Future work will be necessary to disentangle more completely how various biochemical and biophysical cues are integrated together to properly sculpt the bronchial tree in the developing lung.

ACKNOWLEDGEMENTS

This work was supported, in part, by NIH grant R01HL145147 to VDV.

REFERENCES

- [1] Metzger RJ, Krasnow MA, *Nature*, 453:745-751, 2008.
- [2] Peak KE, et al., *Biol Open*, 11(9):bio059436, 2022.
- [3] Cherfan D, et al., *Invest Ophth Vis Sci*, 54:3426-3433, 2013.
- [4] Taber LA, *Continuum Modeling in Mechanobiology*, 2020.
- [5] Miller CJ, Davidson L, *Nat Rev Genet*, 14(10):733-744, 2013.
- [6] Gómez-González M, et al., *Nat Rev Phys*, 2:300-317, 2020.
- [7] Jackson TR, et al., *Curr Biol*, 27(9):1326-1335, 2017.
- [8] Nerurkar NL, et al., *Proc Natl Acad Sci U S A*, 114(9):2277-2282, 2017.

A COMPUTATIONAL MODEL OF COARCTATION OF THE AORTA IN RABBITS

Ashley A. Hiebing (1), Matthew A. Culver (1), John F. LaDisa, Jr. (2), Colleen M. Witzenburg (1)

(1) Department of Biomedical Engineering, University of Wisconsin, Madison, WI, USA
(2) Department of Medicine, Division of Cardiovascular Medicine, Medical College of Wisconsin, Milwaukee, WI, USA

INTRODUCTION

Coarctation of the aorta (CoA) is a common congenital cardiovascular lesion that typically presents as a localized narrowing of the descending aorta just distal to the left carotid and subclavian arteries. While improvements in surgical and catheter-based techniques have increased short-term survival, long-term complications such as re-coarctation, aortic aneurysm, and hypertension frequently occur after CoA correction, leading to a reduced average lifespan [1].

Though ventricular and vascular remodeling has been implicated in many of these morbidities [2,3], it is not possible to measure these alterations *in vivo*. Computational models can be used to investigate potential mechanisms driving ventricular and arterial remodeling and to generate predictive estimations of remodeling [4].

The purpose of this study was to simulate CoA by modifying an existing computational model of the heart and circulation. To match non-invasive hemodynamic measurements from an experimental study on rabbits with CoA [2] it was necessary to simulate both ventricular and vascular remodeling.

METHODS

A previously published lumped parameter computational model [4] capable of predicting left ventricular growth in adult canines under hemodynamic overload was modified for rabbits with CoA. Briefly, the ventricles were simulated using time-varying elastances, aortic and pulmonary artery behavior was simulated by three-element Windkessels, distal vessels were represented by capacitors in line with resistors, and valves were represented by pressure-sensitive diodes. To model CoA, the systemic arterial pool was divided into ascending aorta, descending aorta, and upper body arteries compartments (Figure 1). To simulate the inertial effect of blood flow through the aortic valve, an inductor was also added.

These additional components, along with stressed blood volume, systemic characteristic resistance, and end-systolic elastance were fitted

to match sham data (see Table 1). Ventricular parameters governing the end-systolic and end-diastolic pressure-volume relationships were fitted to measured sham hemodynamics. Heart rate was input directly from measured data. All other parameters were allometrically scaled from the original values for canines [4].

Aortic coarctation was simulated in three steps, wherein model parameters were fitted to experimental data [2]. First, CoA is characterized by a stenosis in the descending aorta, therefore its associated resistance (R_{da}) was increased and its compliance (C_{da}) decreased. Second, following prolonged CoA, ventricular hypertrophy has been observed, therefore ventricular elastance and passive stiffness were increased to reflect increased left ventricular wall thickness. Third, following prolonged CoA, remodeling of the proximal aorta involving increased thickness, elastin fragmentation, and reduced smooth muscle function has been observed [4], therefore the characteristic aortic resistance (R_{cs}) and the ascending aortic resistance (R_{aa}) were increased along with a decrease in ascending aortic capacitance (C_{aa}).

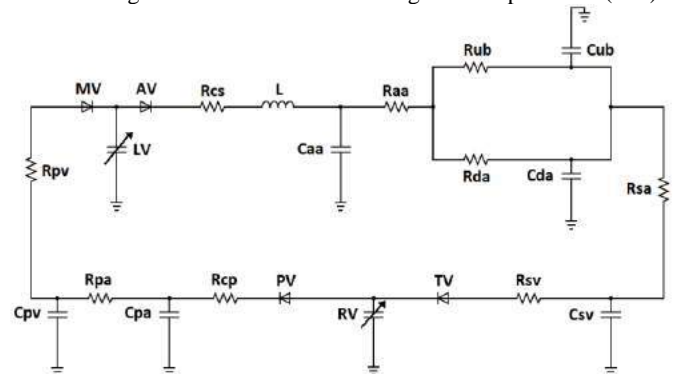


Figure 1: Schematic of the circuit model used to simulate the pressure-volume behavior of the cardiovascular system

RESULTS

To match the observed peak and mean blood pressure gradients in the CoA rabbits manyfold increases in the descending aortic parameters were required: Rda was increased 4.5x and Cda was decreased 19x. Subsequently, consistent with the significant increase in left ventricular mass observed in the CoA rabbits, to match left ventricular stroke volume (SV) and ejection fraction (EF), ventricular elastance and passive stiffness were increased 1.8x. Finally, to match reported ascending aortic pressures and flow, Raa was increased 8x, Rcs was increased 3.3x, and Caa was decreased 2.1x.

Model results agreed well with experimental data, as shown in Figures 2-3 and Table 1. Outputs for mean and peak blood pressure gradients (BPG) between the ascending and descending aorta, left ventricular SV and EF, as well as maximum flow, systemic blood pressure (SBP) and diastolic blood pressure (DBP) in the ascending aorta, and the flow split between the upper and lower body (not shown) all fell within half a standard deviation of measured data.

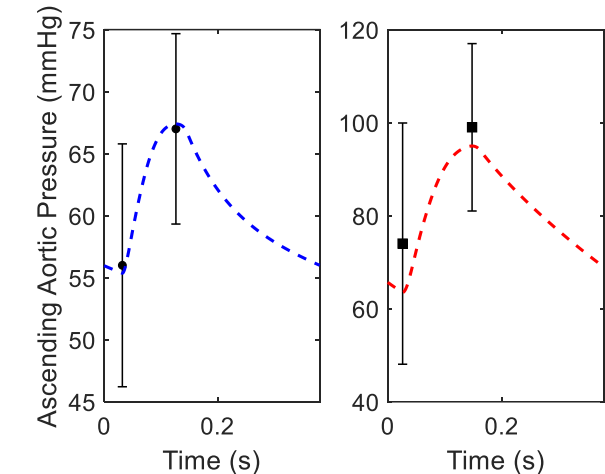


Figure 2: Pressure predicted in the ascending aorta throughout the cardiac cycle for sham (left) and coarctation (right) compared to measured data in rabbits [2]

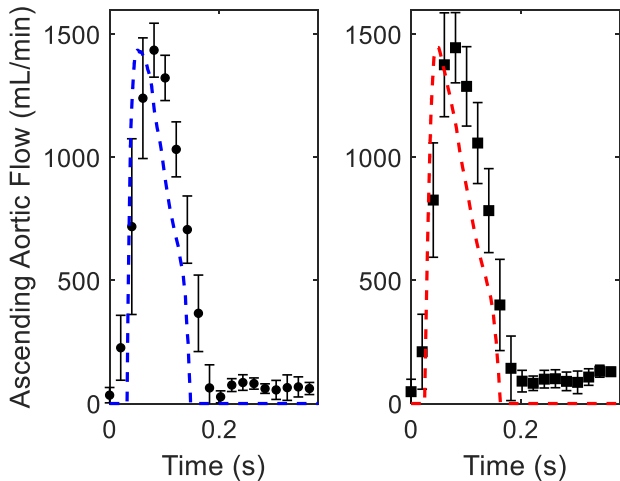


Figure 3: Flow predicted in the ascending aorta throughout the cardiac cycle for sham (left) and coarctation (right) compared to measured data in rabbits [2]

Table 1: Experimental data and model outputs. Z-scores indicate the number of standard deviations model outputs are from experimental means

Index	Sham	Model	Z-score	Coarc	Model	Z-score
BPG, mean (mmHg)	3.27 ± 4.32	3.66	0.09	20.1 ± 4.75	21	0.2
BPG, peak (mmHg)	10.8 ± 7.34	10.1	0.09	31.0 ± 8.64	32.1	0.12
SV (mL)	1.87 ± 0.53	1.85	0.04	1.99 ± 0.56	1.99	0
EF %	60.6 ± 4.82	60.7	0.02	66.4 ± 6.24	66.5	0
Maximum AA flow (mL/min)	1435 ± 110	1435	0	1445 ± 143	1446	0.01
AA SBP (mmHg)	67 ± 7.67	67	0	99 ± 17.99	95	0.22
AA DBP (mmHg)	56 ± 9.79	55	0.1	74 ± 25.93	64	0.39

DISCUSSION

Our model successfully matched reported hemodynamics in sham and CoA rabbits. To capture the ventricular behavior accurately it was necessary to simulate not just the coarctation (change in descending aortic parameters) but also ventricular hypertrophy, by increasing the ventricular parameters associated with increased thickness. Similarly, simulating coarctation and ventricular hypertrophy was insufficient to match the ascending aortic pressure and flow shown in Figures 2 and 3. A decrease in the compliance and an increase in the resistances proximal to the descending aorta was required, suggesting the rabbits with CoA underwent vascular remodeling.

Previous studies of CoA have shown an increase in the stiffness of the proximal aorta before and after corrective surgery [5,6]. Thus, the degree of vascular and ventricular remodeling—and its potential for reversal post-correction—is likely linked to the duration and severity of CoA. Future simulations will model rabbits with CoA of varying severity and corrections at various timepoints. From this, we can investigate the trade-off in severity and duration of CoA to evaluate their individual roles on the timecourse and reversibility of ventricular and vascular remodeling.

ACKNOWLEDGEMENTS

We thank Callyn Kozitza for her help implementing the inductor in the model and Luis Mañán Mejías for his help fitting the sham parameters. This work was supported by the American Heart Association (20CDA35210754) and the NSF (GRFP).

REFERENCES

[1] Choudhary, P et al., *Heart*, 101:1190-1195, 2015.
[2] Wendell, D et al., *J Surg Res*, 218:194-201, 2017.
[3] Menon, A et al., *Am J Physiol Heart Circ Physiol*, 303:H1304-H1318, 2012
[4] Witzenburg, C and Holmes, J, *J Cardiovasc Trans Res*, 11(3):109-122, 2018.
[5] Vogt, M et al., *Circ*, 111(24):3269-3273, 2005.
[6] Xu, J et al., *Am Heart J*, 134:93-98, 1997

QUANTIFYING TEMPORAL DYNAMICS OF ALVEOLAR RECRUITMENT DURING MECHANICAL VENTILATION

Daniel S. Meggo (1), Edward A. Sander (1), Jacob Herrmann (1)

(1) Roy J. Carver Department of Biomedical Engineering, University of Iowa, Iowa City, Iowa, USA

INTRODUCTION

Ventilator-induced lung injury (VILI) poses a serious risk for patients suffering from acute respiratory distress syndrome (ARDS). Protective lung ventilation strategies aim to mitigate VILI, including atelectrauma associated with repetitive alveolar recruitment and derecruitment. However, heterogeneity of alveolar dynamics in ARDS obstructs reliable bedside assessment of VILI risk and treatment efficacy. Limitations of current lung-protective strategies call for a reevaluation of our understanding of alveolar recruitment dynamics during mechanical ventilation.

In a 2011 study, Arnal et al. [1] discovered that most alveolar recruitment occurred within the first 10 seconds of a sustained inflation recruitment maneuver in ARDS patients, and that hemodynamic impairment increased significantly after 10 seconds. In another study, researchers investigating the role of time and pressure on alveolar recruitment found that 80% of alveolar recruitment was achieved in as little as 2 seconds after the application of positive pressure [2]. Although

these studies provide insights into the time dependency of alveolar recruitment, they quantified recruitment from a macroscopic perspective rather than at the level of individual alveoli. Additionally, the quasi-static conditions used in these studies may not accurately recapitulate what occurs when alveoli experience the dynamic and cyclic conditions associated with physiological or mechanical breathing. To overcome both of these challenges, we are investigating the use of a dynamic microscopic imaging modality to quantify the temporal dynamics of individual alveolar recruitment during pressure-controlled mechanical ventilation. Such data will be vital for prescribing novel ventilation strategies that can account for the heterogeneity of alveolar dynamics so that VILI can be reduced.

METHODS

Subsegmental samples of porcine lung tissue were carefully dissected to preserve airtight structure. A micro-ventilator, consisting of a microcontroller-timed solenoid valve and two adjustable pressure

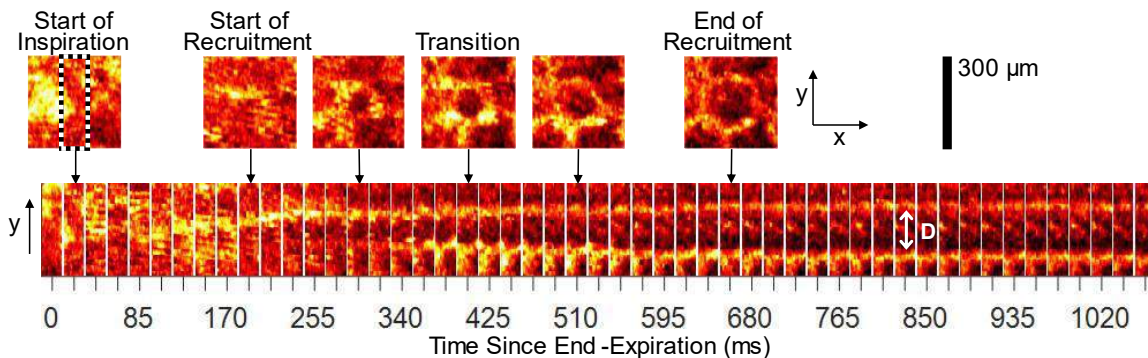


Figure 1: Top: A region of interest in the x-y plane showing a cross-section of a cyclically recruiting alveolus at selected time points during inspiration. Bottom: A time series showing a cropped region, highlighting changes in alveolar diameter (D) at each consecutive time point.

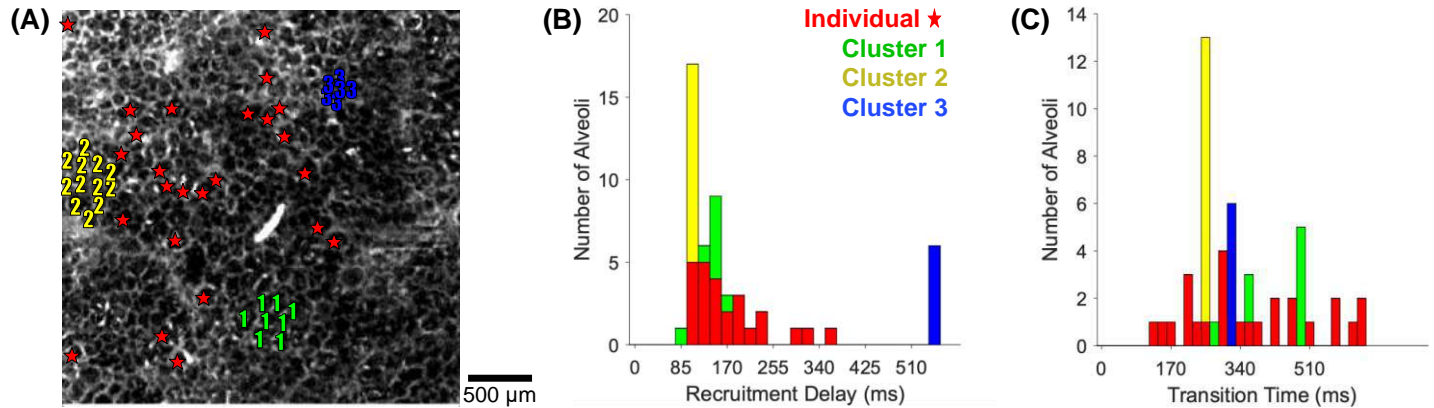


Figure 2: (A) Image at end-inspiration with 51 recruiting alveoli labeled as individuals (red ★), or in clusters 1 (green), 2 (yellow), and 3 (blue). (B) Delay times between end-expiration and start of recruitment. (C) Transition times between start of recruitment and end of recruitment.

relief valves, was connected to the airway opening of the samples to simulate pressure-controlled mechanical ventilation with an inspiratory pressure of 25 cmH₂O and expiratory pressures between 0 to 15 cmH₂O. The respiratory rate was 14 min⁻¹ with 1:1.3 inspiratory:expiratory ratio.

During uninterrupted mechanical ventilation, a series of images was acquired continuously with a Nikon A1+ laser scanning confocal microscope using 561 nm excitation and 595/50 nm emission over a 3.18-mm field of view. Assuming periodic motion of the sample during ventilation, retrospectively gated image reconstruction was performed according to the respiratory rate [3]. The respiratory cycle was partitioned into N phase bins, and each acquired pixel was associated with one of the N phases based on acquisition timing. Pixels belonging to the same phase of ventilation were assembled into a frame. After reconstruction, a sequence of N phase-binned frames was generated with each frame capturing the alveolar structure at one phase of the periodic ventilation cycle.

Alveoli exhibiting cyclic recruitment were identified in the subset of frames corresponding to inspiration (Figure 1). The spatial trajectory of each recruiting alveolus was annotated across frames. For each alveolus, frames associated with the start of recruitment (SOR) and the end of recruitment (EOR) were used to calculate the time delay from end-expiration to SOR and the transition time from SOR to EOR.

RESULTS

Alveolar recruitment was only apparent during ventilation with zero end-expiratory pressure. The 4.27-s ventilation cycle was reconstructed with 201 phase-binned frames, yielding a temporal resolution of 21 ms. Cyclic recruitment was observed in 51 alveoli, including 3 clusters defined as multiple adjacent recruiting alveoli (Figure 2A). Clusters 1, 2, and 3 comprised 8, 12, and 6 alveoli, respectively. After end-expiration, the delay before SOR was 197 ± 143 ms (mean \pm SD) (Figure 2B). After SOR, transition times to EOR were 345 ± 129 ms (Figure 2C). Relative to end-expiration, the shortest total time for an alveolus to reach EOR was 319 ms, while the longest observed time was 871 ms. Total inspiratory time was 1874 ms. A correlation between the delay to SOR and transition time to EOR was nearly nonexistent ($R^2 = 0.0001$). For clusters 2 and 3, alveoli within each cluster exhibited identical SOR and EOR timing. By contrast, heterogeneity of recruitment timing was observed in cluster 1.

DISCUSSION

In this study, the temporal dynamics of intratidal recruitment of individual alveolar structures during *ex vivo* mechanical ventilation were investigated. The absence of cyclic recruitment and derecruitment

events observed with positive end-expiratory pressure (PEEP) supports the efficacy of PEEP in clinical settings. Without PEEP, all cyclically recruiting alveoli were fully inflated within 900 ms of inspiration. This differs from the studies of Albert et al. [2] and Arnal et al. [1] who found that the majority of alveoli become recruited up to 2 s and 10 s after applying positive pressure, respectively. These differences could be attributed to the *ex vivo* preparation; however, it is also likely that intratidal alveolar recruitment behavior is different during the dynamic conditions of ventilation as opposed to the quasi-static conditions used in other studies. Individual alveolar transition times in Figure 2C are consistent with 250-ms recruitment events observed in just two alveoli during quasi-static inflation of healthy mouse lungs [4], but generally, injured lungs exhibit a wide distribution of critical opening pressures and transition times extending over seconds to minutes [5].

Observations of cyclic recruitment in alveoli indicate that cyclic derecruitment must also occur in those same alveoli. However, derecruitment events were not reliably detected. One possible explanation is that the 21-ms temporal resolution was insufficient, which would imply that derecruitment occurs much more rapidly than recruitment, and with almost no delay following end-inspiration. This explanation contradicts data reported in experimental lung injury [5]. Alternatively, the inability to identify cyclic derecruitment could imply that derecruitment occurs aperiodically, such that it cannot be reliably reconstructed using assumptions of motion periodicity, despite consistent periodic recruitment in the same alveoli. If true, the latter explanation supports the notion that reducing the time allowed for exhalation may benefit alveoli that can collapse with irregular or unpredictable timing. These results may support the development of lung-protective strategies that target dynamic recruitment based on inspiratory and expiratory timing.

ACKNOWLEDGEMENTS

Support provided by the Carver Charitable Trust. Lung samples provided by AF da Cruz, EA Akor, and DW Kaczka.

REFERENCES

- [1] J-M Arnal et al., *Intensive Care Med* 37(10):1588-1594, 2011.
- [2] SP Albert et al, *J Appl Physiol* 106(3):757-765, 2009.
- [3] J Herrmann, EA Hoffman, DW Kaczka, *IEEE Trans Med Imaging*, 36(8):1722-1732, 2017.
- [4] E Namati et al., *Am J Respir Cell Mol Biol* 38(5):572-578, 2008.
- [5] CB Massa, GB Allen, JHT Bates. *J Appl Physiol* 105(6):1813-1821, 2008.

NON-INVASIVE STROKE WORK AS A PREDICTOR OF MYOCARDIAL CONTRACTILITY IN DUCHENNE MUSCULAR DYSTROPHY

Israel O. Ajiboye (1), Navaneeth Chandran (1), Michael D. Taylor (2), Rupak K. Banerjee (3)

(1) Department of Mechanical and Materials Engineering, College of Engineering and Applied Science, University of Cincinnati, Cincinnati, OH, USA

(2) The Heart institute, Cincinnati Children's Hospital Medical Center, Cincinnati, OH, USA

(3) Department of Biomedical Engineering, College of Engineering and Applied Science, University of Cincinnati, Cincinnati, OH, USA

INTRODUCTION

Duchenne muscular dystrophy (DMD) is the most common inherited muscle disease, affecting ~1 in 10,000 male children [1-3]. Loss of functional dystrophin protein results in progressive skeletal muscle weakness loss of ambulation, and eventually DMD-associated cardiomyopathy (DMDAC) [3,4]. With the advent of effective respiratory support, left ventricular (LV) dysfunction is the most common cause of morbidity and mortality in DMD [2,3].

Although cardiomyopathy is inexorably progressive, markers of myocardial dysfunction are necessary for starting therapies and monitoring therapeutic efficacy. LV stroke work (SW) is an established parameter proven as a marker of myocardial health in other diseases. It may be helpful in the risk stratification of DMD patients with DMD. As the line integral of intracardiac pressure and volume, simultaneous pressure, and volume measurements are required. Intracardiac pressure measurement is invasive and requires cardiac catheterization [5]. Noninvasive techniques have been established to measure stroke work indirectly. They can detect subclinical signs of LV dysfunction. Cardiac magnetic resonance (CMR) is a routine modality for cardiac evaluation in DMD [3,5]. Ejection fraction (EF) is the most commonly measured parameter. However, a decline in EF is a late finding in the temporal dynamics of heart failure [7]. Consequently, earlier measures of cardiac function are needed. Seeman et al. [7] developed a noninvasive method to compute left ventricular PV loops using CMR data, ventricular elastance curves, and non-invasive blood pressure. They showed agreement with *in vivo* PV loop measurements.

This study aims to measure non-invasive LV stroke work in DMD patients and investigate the correlation of LV SW.

METHODS

We performed a retrospective case-control study of Duchenne muscular dystrophy (DMD) patients who underwent serial CMR from 2014 to 2022. Patients were divided into two groups: those who

maintained an LV ejection fraction $\geq 55\%$ on serial CMR studies were grouped into controls (-DMDAC) and those who had a decrease of LVEF $< 55\%$. We compared the LV SW with EF for all subjects. Also, the SW of the +DMDAC group was compared with the control groups.

Study Population. Human data from 7 controls (-DMDAC) and seven patients with +DMDAC were included. Brachial systolic and diastolic blood pressures from cuff sphygmomanometer and CMR short axis steady-state free-precession images covering the LV were acquired and analyzed (Figure 1). Our Institutional Review Board approved the study, and informed consent was not required.

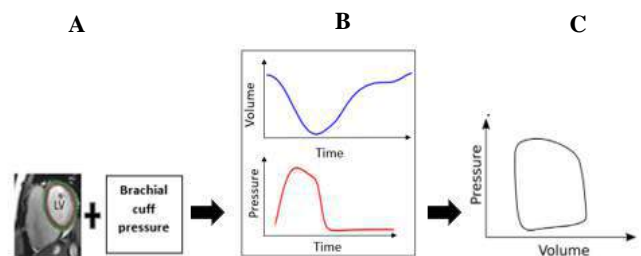


Figure 1. Schematic of pressure-volume loop acquisition. A) Biventricular segmentations are performed in Segment. Brachial pressure is used as input; B) Using Elastance model, pressure and volume curves are obtained in segment; and C) Pressure-volume loops are generated.

CMR protocol. CMR studies were performed on a 1.5 Tesla magnetic resonance scanner (Ingenia; Philips Healthcare; Best, The Netherlands). Study parameters: temporal resolution of 30 to 40 ms, slice thickness 8 mm, and pixels 1.5x1.5 mm. The cine images were obtained during end-expiratory breath-holds. Images were acquired in the vertical and horizontal ventricular long-axis planes and a stack of slices in a ventricular short-axis plane from the atrioventricular junction

through the cardiac apex. The imaging plane was aligned perpendicular to the aorta.

Data Analysis. Images were analyzed using Segment v3.2 R9074. LV was automatically delineated over the entire cardiac circle (usually 30-time frames), and manual corrections were performed when necessary. Our study used LV stroke work to predict cardiac dysfunction. Student t-tests were used to compare two groups of parametric variables. Paired t-tests were used to compare the LV stroke work measures with $p < 0.05$ considered statistically significant. Variation between distributed variables was estimated using the Pearson correlation coefficient.

RESULTS

Figure 2 shows the relationship of LV SW with LV EF for all subjects. A moderate negative correlation existed between LV SW and LV EF for all subjects ($r = -0.46$, $p < 0.0001$).

Figure 3 shows the correlation between the change in LV SW variation and with change in EF. Interestingly, a reasonable positive correlation was observed between LV SW and LV EF for all subjects ($r = 0.53$, $p = 0.34$).

Figure 4 shows the LV SW for the +DMDAC and control groups. The left ventricular SW of the +DMDAC group (0.77 ± 0.23 J) was higher by 50.98% ($p = 0.00093$) than that of the control group (0.51 ± 0.14 J).

DISCUSSION

This study found that SW mildly correlated with EF, which suggests that SW contains other information that the EF in the subjects may not capture. This may provide additional information on global cardiac function compared to EF in the DMDAC population. However, a better correlation was observed between the change in SW and the change in EF. A positive correlation shows that the change in SW agrees well with the change in EF. Although some patients did not follow the same trend, future extensive studies are required to validate the observation.

This study also shows that the SW of +DMDAC patients (0.77 ± 0.23 J) was higher (50.98%, $p = 0.00093$) than that of the controls (0.51 ± 0.14 J). In addition, the +DMDAC group had significantly lower EF (39.90 \pm 8.15%, $p < 0.0001$) than the control group (60.25 \pm 3.73%).

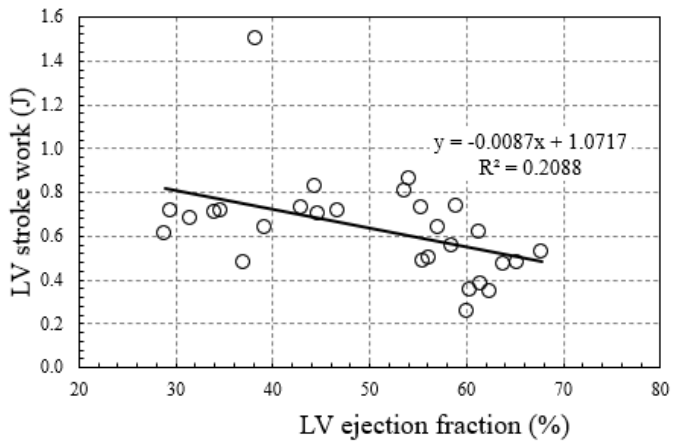


Figure 2. a Correlation of LV SW with left ventricular ejection fraction. LV SW had a moderate negative correlation with LV EF in the DMD group.

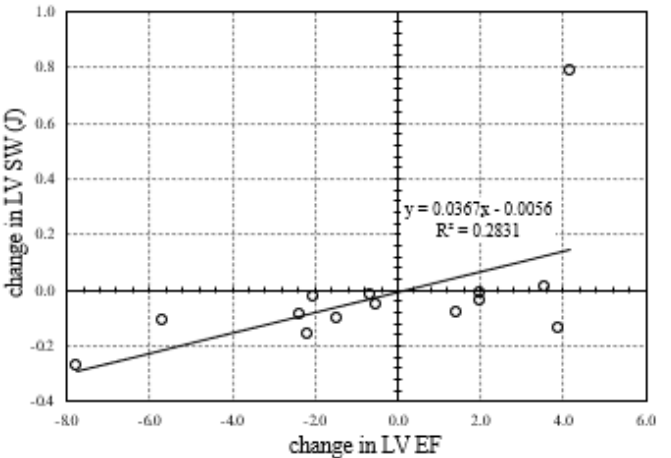


Figure 3. a Correlation of change in ejection fraction with change in left ventricular stroke work. Change in EF showed a moderately positive correlation with change in LV SW in the DMD group.

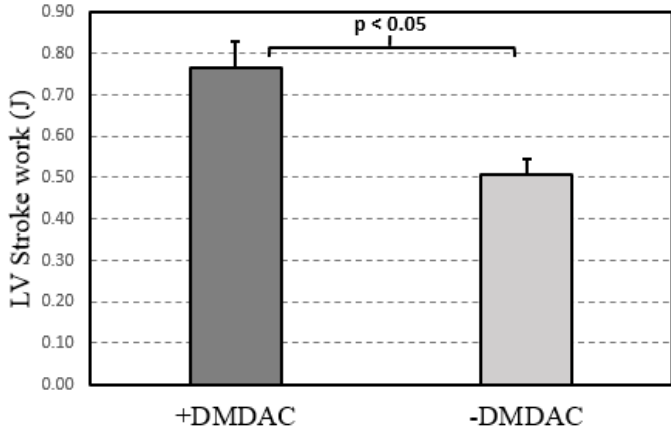


Figure 4. Comparison of left ventricular stroke work (LV SW) between the +DMDAC and control groups. The +DMDAC group had a higher LV than the control (-DMDAC) group.

ACKNOWLEDGEMENTS

This work was funded by the Cincinnati Children’s Hospital Medical Center (CCHMC) (grant no. 16814).

REFERENCES

[1] Norwood, F. L et al., *Brain*, 132(11), 3175-3186.
[2] Yamamoto, T et al., *Circulation: Genomic and Precision Medicine*, 11(1), e001782.
[3] Siddiqui, S et al., *Circulation: Cardiovascular Imaging*, 13(11), e011526.
[4] Kaspar, R. W et al., *Circulation: Cardiovascular Genetics*, 2(6), 544-551.
[5] Lee, N et al., *Heart and vessels*, 28(1), 76-85.
[6] McNally, E. M et al., *Circulation*, 131, 1590-1598.
[7] Seemann, F et al., *Circulation: Cardiovascular Imaging*, 12(1), e008493.

SPATIAL GRADIENT IN BRAIN MECHANICAL PROPERTIES CHANGES THROUGH DEVELOPMENT BUT IS CONSISTENT DURING ADULTHOOD

Kyra E. Twohy (1), Grace McIlvain (2,3), Jeffrey M. Spielberg (4), Curtis L. Johnson (1,2,4)

- (1) Department of Mechanical Engineering, University of Delaware, Newark, DE, USA
(2) Department of Biomedical Engineering, University of Delaware, Newark, DE, USA
(3) Biomedical Engineering Department, Emory University & Georgia Institute of Technology, Atlanta, GA, USA
(4) Department of Psychological and Brain Sciences, University of Delaware, Newark, DE, USA

INTRODUCTION

Human brain development begins with dynamic morphological changes, such as cortical folding, starting *in utero* and extending through childhood [1]. Additional changes continue to occur through to adulthood in a period of maturation. The role of internal forces and stresses in driving early brain development is commonly studied; however, the role that forces play in driving structural remodeling during maturation is unknown [1]. Measurement of internal forces *in vivo* is limited due to the invasive nature of these techniques. A non-invasive alternative is magnetic resonance elastography (MRE), which allows for *in vivo* quantification of tissue mechanical properties and has previously been shown to be sensitive to microstructural changes in brain tissue [2], but application of MRE to brain maturation has been limited. Current work has shown large scale changes in mechanical properties in regional brain structures, as well as marked differences in mechanical properties of interior and exterior brain structures [3]. We hypothesize that spatial variation of these tissue properties could create imbalances in internal force distribution creating stress concentrations, which in turn may influence maturational remodeling, such as localized synaptic pruning and myelination, through mechanotransduction processes. This study aims to quantify shear stiffness gradients in the brain and how this measure varies during maturation through extended aging. This expands on previous work that developed this measure only in the frontal lobe during a limited time period.

METHODS

MRE data from a total of 358 participants with ages ranging from 5-82 years (145M/213F, Age: 32.7 +/- 22.4 years) were included in this study. MRE scans were pooled from multiple sites to create this database, all scans were performed on a Siemens 3T Scanner including Prisma, Trio, and Verio models. The MRE portion of the protocol used a custom high-resolution 3D multiband, multishot spiral sequence [4,5]. Vibrations were applied at 50 Hz to the back of the head to induce shear

displacements. A T₁-weighted MPRAGE (resolution: 0.9 x 0.9 x 0.9 mm³) was also completed for anatomical segmentation. Displacement data was converted to shear stiffness using a nonlinear inversion algorithm (NLI) [6]. Complex shear modulus (G) is calculated using the storage (G') and loss (G'') moduli. From complex shear modulus, shear stiffness (μ) can be calculated using Equation 1.

$$\mu = 2 |G|^2 / (G' + |G|) \quad (1)$$

For each subject, shear stiffness maps were converted into standard space for comparison across the age range and between multiple studies, shown in Figure 1. The boundaries of each lobe were defined using the WFU-Pick Atlas and the average lobe stiffness was calculated. To determine gradients in stiffness from the interior to the exterior of the lobe, sequential 3D volume erosions were completed. The average stiffness of voxels removed with each erosion was calculated, with the gradient quantifying the change in this measure over the distance. Since average brain stiffness also changes with age, and thus could influence the magnitude of the stiffness gradient, we normalized the gradient measure by dividing by the average lobe stiffness.

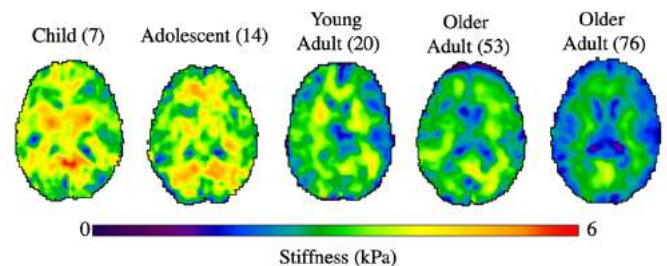


Figure 1: Representative stiffness maps of a single slice for participants across the age range with specific ages given in parentheses. The gradient can be seen as stiffer interior tissue, shown in red, transitions to softer exterior tissue, shown in blue.

Change in the normalized gradient measures during maturation was examined using partial correlations controlling for sex in MATLAB, with separate analyses for each of the four lobes. To test the hypothesis that changes in gradient occur during maturation, but plateau in adulthood, we fit a piecewise function with two slopes using a nonlinear least squares model and calculated the inflection point, using Equation 2, where IP is the inflection point where the slope with age, A , switches from being defined by m_1 to $m_1 + m_2$.

$$F(A) = b + m_1 A + m_2 (A - IP) \quad (2)$$

RESULTS

Normalized gradients changed significantly across all lobes from childhood to young adulthood (< 32 years) as shown in Figure 2. The gradient measure was negative for all participants across the cerebrum indicating greater tissue stiffness in the interior of the brain compared to the exterior.

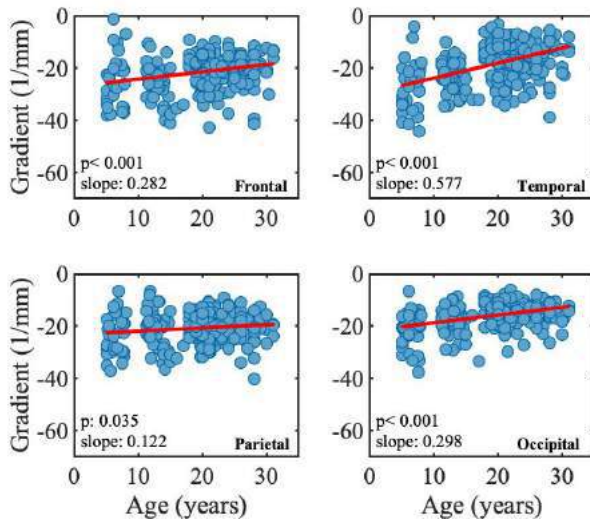


Figure 2: Average normalized gradient change, shown in red, for each cerebral lobe calculated cross sectionally from childhood to young adulthood.

Partial correlations seen in Figure 2 show consistent increase in average stiffness gradient with age, indicating less of a difference between interior and exterior mechanical properties. The greatest changes were observed in the temporal lobe, while the smallest were in the parietal lobe.

Table 1 shows the change in normalized gradient with age both before and after the inflection point. When two slopes are used to model normalized gradient change with age, the increase in gradient is seen again from childhood to the beginning of young adulthood. The inflection points shown in Figure 3 range from 18 to 22 years and mark

the start of only slight decreases in the gradient measure during adulthood, indicating that spatial gradients in mechanical stiffness, appear to reach an equilibrium in young adulthood.

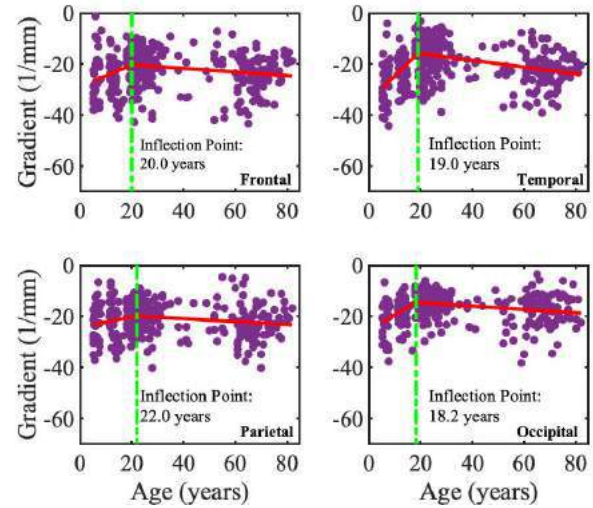


Figure 3: Average normalized gradient for each cerebral lobe fit to a piecewise function with two slopes, shown in red, that change at the marked inflection point shown in green.

DISCUSSION

This study examined the spatial variation of shear stiffness across the brain during development by calculating gradients in stiffness in each lobe of the brain. Significant age-related increases in gradient (i.e. decreasing magnitude becoming less negative) are found from childhood to young adulthood. The change in gradient shows that interior and exterior stiffness of the brain become more similar with age during maturation. Significant changes in this measure were found despite normalization by average lobe stiffness for each individual, thus the gradient measure is not biased by overall average stiffness changes but by spatial distribution of mechanical properties.

To confirm if the gradient measure captures age-related changes due to maturation, we continued to track this measure cross-sectionally through adulthood. In each of the four lobes, the increase in the gradient measure stopped between 18 and 22 years old – the beginning of young adulthood. The gradient measure then plateaus through adulthood, indicating a stabilization in the spatial distribution of properties (despite continued average softening into old age), potentially indicating a mechanical equilibrium achieved. This may mean that reduction of internal stresses reaches a desired threshold and is sustained throughout adulthood even as the tissue begins to atrophy. Future work will include longitudinally assessing these gradients to understand if individual maturation confirms age-related changes and if the magnitude of the gradient present impacts structural development across the brain.

ACKNOWLEDGEMENTS

This work was supported in part by NIH grants R01-EB027577, R01-MH123470, R01-AG058853, and U01-NS112120.

REFERENCES

- [1] Bayly, PV et al., J. Mech. Behav. Biomed. Mater., 29:568-581, 2014.
- [2] Hiscox, LV et al., Neuroimage, 232:117889, 2021.
- [3] McIlvain G et al., Neuroimage, 263:119590, 2022.
- [4] Hiscox, LV et al., Hum. Brain Mapp., 41:5282-5300, 2020.
- [5] McIlvain, G et al., Magn. Reson. Med., 88:1659-1672, 2022.
- [6] McGarry, MDJ et al., Med. Phys., 39:6388-6396, 2012.

STIFFNESS OF DIRECT-WRITE, NEAR-FIELD ELECTROSPUN GELATIN FIBERS GENERATES DIFFERENCES IN TENOCYTE GENE EXPRESSION

Zachary G. Davis (1,3), Drew W. Koch (2,3), Grant M. Scull (1,3), Ashley C. Brown (1,3),
Lauren V. Schnabel (2,3), Matthew B. Fisher (1,3,4)

- (1) Joint Department of Biomedical Engineering, North Carolina State University, Raleigh and the University of North Carolina at Chapel Hill, Chapel Hill, NC, USA
(2) College of Veterinary Medicine, North Carolina State University, Raleigh, NC, USA
(3) Comparative Medicine Institute, North Carolina State University, Raleigh, NC, USA
(4) Department of Orthopaedics, University of North Carolina at Chapel Hill, Chapel Hill, NC, USA

INTRODUCTION

Tendon injuries are a leading cause of morbidity with ~50% of musculoskeletal injuries involving tendons.¹ Tendinopathy is characterized by changes in tendon matrix composition and structure as well as changes to tenocyte protein and gene expression.^{2,3} The mechanisms of tendinopathy formation at the single cell-matrix level remain unclear.² *In vitro* models are promising for studying tendon pathology as they provide a controlled environment for single cell investigation.⁴ Direct-write, near field electrospinning (DWNFE) can be used to fabricate scaffolds with precise placement of physiologically relevant fibers.⁵ These scaffolds provide an effective framework for constructing *in vitro* models with control over the structure, composition, orientation, stiffness, and mechanical stimulation; which are all needed to understand how cells respond to specific changes to their environment.⁴ Prior work with DWNFE has produced gelatin fibers that mimic native tendon collagen fiber diameters.⁵ Beyond mimicking orientation, structure, and size, gelatin fiber stiffness can be controlled through crosslinking. This is important as the stiffness of a substrate has been shown to alter cell gene expression.⁶ The objective of this research was to analyze how varying stiffness of direct-written gelatin fibers can influence tenocyte phenotype and gene expression.

METHODS

Type A, 300 bloom gelatin was mixed at 625mg/mL in 70% acetic acid and direct-written in aligned fibrous patterns following an established protocol⁵ (Fig. 1A). Scaffolds were crosslinked with 1-ethyl-3-(3-dimethylamino propyl) carbodiimide hydrochloride (EDC) and N-hydroxy-succinimide (NHS) in 90% EtOH at a 10:1 ratio for 1, 6, or 24 hours (Low, Mid, and High stiffness, respectively). The stiffness of fibers (n=16 per crosslinking group) was determined via contact force mapping mode of atomic force microscopy (AFM) with a silicon nitride pyramidal tip (0.32N/m spring constant). Fiber diameter was measured from brightfield images (0, 1, 2, and 3 weeks

of culture in 1X PBS). Tenocytes isolated from an equine superficial digital flexor tendon were seeded onto scaffolds (one week after scaffold fabrication) or neutrally-charged slides at 75,000 cells/sample and cultured for 2 weeks. Cell viability was determined via a commercial cell viability kit (Invitrogen). Nuclear aspect ratio, cytoskeletal and nuclear peak orientation, and orientation index (OI) were determined via phalloidin and DAPI staining. Image processing was accomplished with ImageJ (NIH). Multiplex gene expression of matrix mechanotransduction-associated, and remodeling proteins (COL1A2, COL2A1, COL3A1, DCN, MMP1, MMP3, and PIEZO1; ACTB, GAPDH, and HPRT1 served as housekeeping genes) was determined via Nanostring (nCounter MAX system) from RNA isolated at 1 and 2 weeks. Samples were run in triplicate for analysis. Outliers were removed (ROUT 5%), and one-way ANOVA with Tukey's test ($\alpha=0.05$) was used for statistical analysis. One sample t-tests were used for statistical analysis of peak direction from the hypothetical value of 90°. Two-tailed t-tests was used for analyzing statistical significance in gene expression.

RESULTS

Fiber stiffness decreased from 0 to 1 week, then remained consistent to 3 weeks for all groups (Fig. 1B). Stiffness increased with increasing crosslinking time (High and Mid groups were 10- and 6-fold higher than Low group at 1 week) while maintaining similar fiber diameters (Fig. 1B and C). Cellular viability remained >94% for all groups at 1 and 2 weeks. Cytoskeletal and nuclear peak orientation was not different from the direction of the fibers (90°) for all groups except glass at 1 week (mean: 51°). Nuclear OI was 45-60% lower for all scaffolds vs. glass both 1 and 2 weeks (Fig. 2B). Cytoskeletal OI was 63-78% lower for all scaffolds vs. glass at 1 and 2 weeks (Fig. 2B). Nuclear aspect ratio was 71%, 59%, and 53% higher for the Low, Mid, and High groups respectively compared to neutral glass slides (1.7±0.1) at 1 week. At 2 weeks, the nuclear aspect ratio for the Low and Mid groups were 70% and 74% higher than neutral glass slides,

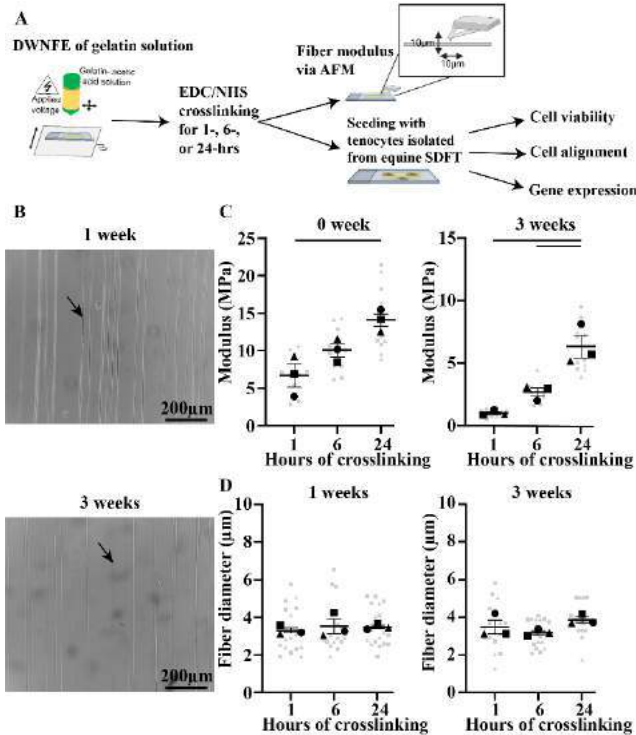


Figure 1: A) Schematic of the study design. B) Representative images of 1- and 3-weeks fibers. Black arrow indicates one fiber. C) Stiffness of EDC/NHS crosslinked gelatin fibers increased with time. Modulus of fibers crosslinked for 1-, 6-, or 24-hrs. Top 0 week to bottom 3 weeks. D) Fiber diameter did not change with time. Top 1 week to bottom 3 weeks. Bars represent statistical significance between connected groups.

while the High group was not significantly different from neutral glass slides. Multiplex gene expression showed no differences between stiffness groups at 1 week except for MMP1 which was upregulated for the High vs. Low groups. However, at 2 weeks upregulation of COL1A2, COL3A1, DCN, MMP3, and PIEZO1 was found for the High vs. Low groups (Table 1). Fewer changes were found between High and Mid as well as Mid and Low groups. Comparing changes in gene expression from 1 to 2 weeks, these same five genes (COL1A2, COL3A1, DCN, MMP3, and PIEZO1) along with MMP1 were upregulated with time for all groups. MMP1 and MMP3 showed the greatest fold change for all groups with time. The Low group showed upregulation of COL2A1 with time, while the Mid and High groups did not.

DISCUSSION

Gelatin scaffolds with similar fiber orientation and size, but varied stiffness caused similar cellular orientation but different levels of expression of genes related to matrix proteins, remodeling, and mechanotransduction. This follows previous work that has shown tenocytes aligning along the direction of fibers.⁷ Increased expression of COL1A2, COL3A1, DCN, and PIEZO1 in the High stiffness group compared to the Low stiffness group shows tenocytes are sensitive to changes in stiffness between 1 and 10 MPa. The changes over this range may be relevant for mimicking the decreased stiffness of a tendon with the onset of tendinopathy.⁸ PIEZO1 especially has been shown to be a positive marker for tendon development specifically for mechanotransduction.⁹ The increased MMP1 and MMP3 expression in all scaffold groups may represent the desire of the cells to remodel the collagenous fibers. Changes in COL2A1 and COL3A1 are relevant to

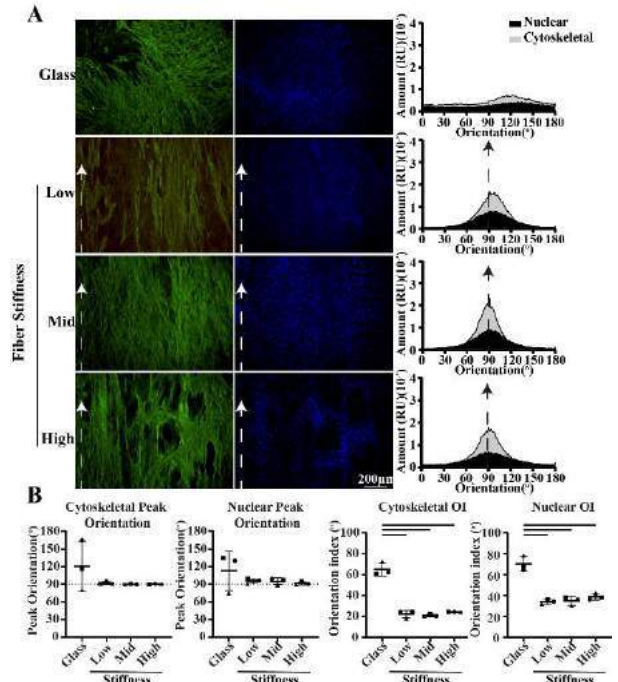


Figure 2: Tenocytes seeded on scaffolds or neutral glass slides at 2 weeks. A) Fluorescent images stained with phalloidin (green) left column and DAPI (blue) middle column. Histograms of the orientation distribution (grey=cytoskeletal; black=nuclear) right column. Arrow indicates direction of fiber orientation. RU= arbitrary relative units. B) Cytoskeletal and nuclear peak orientation and index are improved with fibers. Bar indicates statistical significance between groups.

Table 1: Gene expression fold changes (p-values) between varying scaffold stiffness groups and within scaffold stiffness over culture time. Shaded cells are statistically significant.

	2 weeks			Low	Mid	High
	High vs. Low	High vs. Mid	Mid vs. Low	2 weeks vs 1 week	2 weeks vs 1 week	2 weeks vs 1 week
COL1A2	1.28 (p=0.03)	1.19 (p=0.08)	1.08 (p=0.27)	3.1 (p<0.001)	3.27 (p<0.001)	4.03 (p=0.001)
COL2A1	1.04 (p=0.92)	-1.29 (p=0.13)	-1.24 (p=0.60)	3.35 (p=0.006)	2.66 (p=0.07)	2.92 (p=0.27)
COL3A1	1.44 (p=0.01)	1.16 (p=0.06)	1.24 (p=0.02)	2.21 (p<0.001)	2.35 (p<0.001)	2.79 (p=0.004)
DCN	1.43 (p=0.02)	1.36 (p=0.02)	1.05 (p=0.60)	4.78 (p<0.001)	4.6 (p<0.001)	5.18 (p<0.001)
MMP1	1.43 (p=0.08)	1.28 (p=0.17)	1.11 (p=0.32)	59.28 (p<0.001)	52.09 (p<0.002)	39.12 (p<0.001)
MMP3	1.77 (p<0.001)	1.73 (p=0.10)	1.02 (p=0.92)	15.4 (p<0.001)	15.4 (p<0.001)	17.07 (p<0.001)
PIEZO1	1.2 (p=0.04)	1.19 (p=0.08)	1.01 (p=0.88)	1.49 (p=0.06)	1.48 (p=0.01)	1.59 (p=0.003)

changes seen with tendinopathy with transition to a fibrotic or cartilage-like behavior. Further analysis is needed to understand how differences in gene expression translate to changes in protein expression. Additionally, it is unclear how changes to the fiber composition or external mechanical stimulation, often altered in tendinopathy, may alter these responses. In conclusion, DWNFE gelatin fibers represent an effective platform for studying the response of tenocytes to fibrous matrix properties, such as stiffness.

ACKNOWLEDGEMENTS

We thank the Comparative Medicine Institute at NC State University for funding and support. Funding by NSF (DGE-1746939).

REFERENCES

- [1] Wu, Y et al., *J Tissue Eng Regen Med*, 12:1798-1821, 2018.
- [2] Meeremans, M et al., *Front Cell Dev Biol*, 9:1051, 2021.
- [3] Jacobsen, E et al., *PLOS ONE*, 10:e0122220, 2015.
- [4] Calejo, I et al., *Adv Healthc Mater*, 11:2102863, 2022.
- [5] Davis, Z et al., *Biomed Mater*, 16:045017, 2021.
- [6] Acevedo-Acevedo, S et al., *J Negat Results Biomed*, 14:22, 2015.
- [7] Schoenenberger, A et al., *Acta Biomater*, 71:306-317, 2018.
- [8] Arya, S et al., *J Appl Physiol*, 108:670-675, 2010.
- [9] Passini, F et al., *Nat Biomed Eng*, 5:1457-1471, 2021.

REPEATABILITY AND BACKLASH MEASUREMENTS OF MICRONEEDLES DISPLACED USING A NOVEL ACTUATION BLOCK

Brianna E. Morales (1) and Christopher G. Rylander (2)

(1) Department of Biomedical Engineering, The University of Texas at Austin, Austin, Texas, USA
(2) Walker Department of Mechanical Engineering, The University of Texas at Austin, Austin, Texas, USA

INTRODUCTION

The Central Brain Tumor Registry of the United States estimated that there would be over 13,000 new diagnoses of glioblastomas (GBM) in 2022 [1]. Given that the current standards of treatment (surgery, radiation, and chemotherapy) have not effectively cured this grade IV glioma, the number of new diagnoses will continue to increase. There is a pressing need to develop an improved method of treatment delivery for GBMs.

An experimental method of improved treatment is convection-enhanced delivery (CED) of drugs using a minimally-invasive catheter. CED has shown promise and there are currently several clinical studies that are recruiting patients [2]. Our lab has designed an arborizing catheter known as the Convection Enhanced Thermochemotherapy Catheter System (CETCS), as shown in Figure 1 [3].

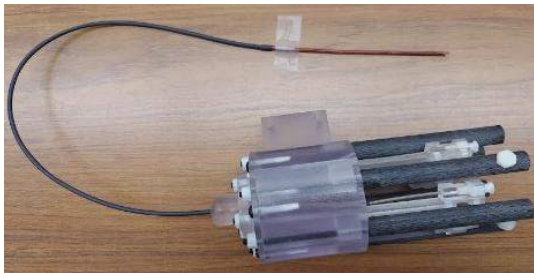


Figure 1: CETCS; main cannula (top) and actuation block (bottom).

The CETCS consists of a main cannula connected to the actuation block, and six microneedles capable of extending past the main cannula. Once the main cannula is deployed and secured using a conventional neuronavigational positioning system, the novel CETCS actuation block provides the ability to deploy the CETCS microneedles

individually, up to 4.5 cm from the main cannula tip into the target regions surrounding the tumor. Microneedle movement is driven by the actuation block using a lead screw that allows for unidirectional positioning. A retaining clip is used to ensure the microneedles are secured to the lead screw mechanism. Based on the fixed pitch of the lead screw, for each complete revolution, the microneedle is displaced 0.72 mm. The current mode of operation is manual, but later iterations of CETCS will have remote controlled capability. Control will be provided to the neurosurgeon user through the implementation of a software interface which will drive individual stepper motors and rotating rods which will deploy or retract the microneedles from the main cannula. Figure 2 shows a representation of the microneedles in a deployed state from the end of the main cannula.



Figure 2: Main cannula with deployed microneedles.

The end goal for the CETCS device is to be used clinically for the treatment of GBM. To reach this goal, we have been advised to apply for and receive 510(k) FDA clearance. For this process it is imperative to demonstrate the device is as safe and effective as the identified predicate device, in this case the Cleveland Multiport Catheter (CMC). The CMC design includes a sheath that can be retracted from a stylet to reveal four microcatheters, as described by Vogelbaum et al. [4]. The indication of use of the device is to gain access to the ventricles of the brain for the removal of cerebrospinal fluid (CSF) or to inject

Cytarabine. Safety and efficacy can be evaluated by conducting similar performance tests on the CETCS device that were done on the CMC.

This paper discusses a method to identify the repeatability and backlash distances produced using the manual operation of the CETCS actuation block. The repeatability is a measure of how precise the actuation block is at moving the microneedles a specified distance. The backlash in the system can be characterized as the movement lost in changing direction: deployment to retraction or retraction to deployment. Understanding and identifying these metrics will help determine the amount of compensation we need to account for in the calibration of the system. Our current goal is to stay within 1 mm of the ideal movement.

METHODS

The following experiments evaluated the ability of the actuation block to control the movement of the microneedles as they were deployed and retracted from the main cannula. Measurements of the actual length of a side microneedle and the center microneedle were taken using a caliper, as shown in Figure 3.



Figure 3: Side and center microneedle deployment distance from the main cannula controlled by the actuation block, not pictured.

Repeatability

The sequence of microneedle movements included setting an initial placement of the microneedle and then four subsequent changes in position in increments of 5 mm deployment. Then four additional changes in position were conducted in increments of 5 mm retraction. Measurements were taken at each step and the displacement was noted as: x_j . The displacement was then used to evaluate the repeatability (RP_x) of the microneedle, using equations below:

$$\bar{x} = \frac{1}{n} \sum_{j=1}^n x_j \quad (1)$$

$$l_{x_j} = |x_j - \bar{x}| \quad (2)$$

$$\bar{l}_x = \frac{1}{n} \sum_{j=1}^n l_{x_j} \quad (3)$$

$$S_x = \sqrt{\frac{\sum_{j=1}^n (l_{x_j} - \bar{l}_x)^2}{n-1}} \quad (4)$$

$$RP_x = \bar{l}_x + 3S_x \quad (5)$$

First solving for the sample mean (\bar{x}), n is the number of values in the sample and determine how much the measurements deviate from the average (l_{x_j}). Then we determine the average deviation (\bar{l}_x), which is used to solve for our sample variance among the measurements (S_x). This was used to determine the repeatability (RP_x) of the measurement.

Backlash

For this experiment, we evaluated the displacement of the microneedle, where the direction of motion of the microneedle was either changed from deployment to retraction or retraction to deployment.

RESULTS

Repeatability

Measurements were taken at each position change and recorded. The results were evaluated using Equations 1-5. The average repeatability for the center needles was lower (better) than the side needle.

	Repeatability (mm, n = 6)
Center Deployment	0.33 ± 0.09
Center Retraction	0.33 ± 0.07
Side Needle Deployment	0.59 ± 0.34
Side Needle Retraction	0.98 ± 0.63

Table 1: Average repeatability found in microneedle positioning.

Backlash

For the center and side needle the change in position from deployment to retraction or retraction to deployment did not affect the overall backlash measured. The side needle did experience a higher amount of backlash when there was a change in position than the center needle.

Needle (n = 3)	Deployment to Retraction (mm)	Retraction to Deployment (mm)
Center	0.43 ± 0.02	0.47 ± 0.02
Side	0.94 ± 0.1	0.97 ± 0.16

Table 2: Average backlash results for retraction to deployment and deployment to retraction.

DISCUSSION

We observed a higher mean and variability in the repeatability and backlash measurements that were taken for the side needle versus the center needle. These results indicate that the actuation block has an error of about 1 mm for the side needles and an error of 0.33 mm for the center needle. This could be explained by the greater bend angle and resulting friction of the side needle within the main cannula versus the center needle. Fortunately, the CETCS device can be calibrated to compensate for known backlash of center and side microneedle when there is a change in direction.

ACKNOWLEDGEMENTS

This project is funded by the National Institutes of Health/National Cancer Institute, grant number P01 CA207206- 01.

REFERENCES

- [1] Ostrom, Q.T., et al., *Neuro-Oncology*, **24**(Supplement_5): p. v1-v95, 2022.
- [2] Kang, J.H., Desjardins A., *Neuro-Oncology Practice*, **9**(1): p. 24-34, 2021.
- [3] Elenes, E.Y., et al., *Journal of Engineering and Science in Medical Diagnostics and Therapy*, **4**(1), 2020.
- [4] Vogelbaum, M.A., et al., *Journal of Neurosurgery*, p. 1-10, 2018.

EXTRACTING INHOMOGENEOUS ORIENTATION DISTRIBUTION FUNCTIONS FROM 3D IMAGE DATA OF FIBROUS TISSUES FOR FINITE ELEMENT SIMULATIONS

Adam Rauff (1,2), Michael R. Herron (1,2), Steve A. Maas (1,2), Jeffrey A. Weiss (1,2)

(1) Department of Biomedical Engineering, University of Utah, Salt Lake City, UT, USA
(2) Scientific Computing and Imaging Institute, University of Utah, Salt Lake City, UT, USA

INTRODUCTION

Many biological tissues comprise a fibrous microstructure with a particular organization optimized for a physiological function. This architecture modulates the physical properties of the tissues, including the conduction of electrical signals, diffusion of water and soluble molecules, and mechanical properties. Thus, microstructural information has increasingly been incorporated into computational models of biological tissues [1].

The orientation of the microstructural fibrils is particularly important for the explanation of the anisotropic functions of tissues. This has been extensively shown for a variety of tissues including skin [1], ligaments and tendons [2], myocardium [1], arteries [3] and cartilage [4]. Explicit incorporation of 3D fiber orientation distribution functions (ODFs) such as ellipsoidal or Von-Mises is often used in finite element (FE) modeling of biological tissues [5,6]. These approaches assume a parametric form for the ODF to simplify the representation.

Recently we developed a nonparametric approach to efficiently extract and represent ODFs from 3D image data [7]. The approach is based on the Fourier transform and the Q-ball algorithm. In this work, we developed methods to measure ODFs from image subvolumes and map them onto FE mesh. We developed a user interface in FEBio Studio [8] and extended the finite element software [9] to enable the use of inhomogeneous ODFs in constitutive models. The resulting framework provides a powerful and general approach to represent anisotropy and inhomogeneity in models of fibrous tissues directly from image data.

METHODS

Characterization of fiber orientations: Fibril ODFs were directly extracted from volumetric image with our previously established approach [9]. Briefly, the fast-Fourier transform was applied to the image volume followed by the qball algorithm to the power spectrum. This resulted in an ODF that quantifies the probability density of fibrils along every orientation in space. The ODF was represented by a series

of spherical harmonics (SHs) with a maximum order, L , that allows concise representation of the function using $(L+1)(L+2)/2$ terms.

Implementation in FEBio: Our approach to extracting 3D ODFs from image data was implemented in the FEBio Studio software and further developed for use in constitutive modeling. The Matlab (MathWorks Inc.) code previously developed was ported to C++, replacing the proprietary software with open-source packages and enabling faster speeds. We implemented routines for the import of volumetric image data, and added capabilities for volume rendering and image analysis. The UI allowed the user to specify subvolumes for ODF calculation, with each represented by a separate SH series (Fig 2A).

The ODFs can be mapped to FE discretization within FEBio Studio. The FEBio solver interpolated ODFs to assign to each to a finite element, based on a previously developed Riemannian framework [10]. The resulting ODFs can define the distribution associated with fiber families using a variety of constitutive models available in FEBio [9].

Example applications: The new framework was evaluated using two volumetric image datasets of a collagenous hydrogel. A type I collagen hydrogel was synthesized according to previous experiments [11]. The first dataset was collected with a multiphoton microscope, containing axial slices at $0.5 \mu\text{m}$ apart with lateral resolution of $0.53 \mu\text{m}/\text{pixel}$ encompassing a total volume of $540.0 \times 540.0 \times 351.0 \mu\text{m}^3$. The dataset was median filtered and resampled to an isotropic voxel resolution of $0.75 \mu\text{m}^3$ (Fig. 1). The image demonstrates directional preference along the x-axis in highly noisy data.

The second dataset was collected using focused ion beam scanning electron microscopy (FIB-SEM). The data constituted similar collagen hydrogel at a higher resolution and magnification. This provided a clear example to illustrate the correspondence between the image data and the position-dependent ODFs.

RESULTS

User Interface (UI): The analysis framework was constructed with a UI to facilitate easy use and access to broader research community

(Fig. 2). Image data is directly imported to the modeling pipeline and visualized. The user can add an ODF analysis to the imaging data, revealing the properties dialogue containing parameters of the analysis. That includes the maximum SH order of approximation, the frequency cutoffs of the power spectrum, the number of divisions to image subvolumes, and graphical display settings (Fig. 2Left).

Discretization into image subvolumes and visualization on the image domain: The image analysis resulted in measured fiber ODFs that correspond to each subvolumes, and can be directly visualized in FEBio Studio (Fig. 3). This analysis can be done at various subvolume sizes, and represents increasing specificity of the spatial material inhomogeneity. The ODFs can be visualized as either an intensity colormap over the unit sphere (Fig 3A, B), or additionally as each orientation mapped by probability as radial distance (Fig 3D).

Local ODFs on FIB-SEM dataset: The correspondence between the measured ODFs and the image data can be gleaned from the high resolution FIB-SEM data (Fig 4). The image data, rendered in white, provides high contrast fibrillar structures with varying orientations. The measured ODFs directly correspond with the orientation of collagen fibrils in their subvolume region.

DISCUSSION

This work provides the ability to incorporate inhomogeneous structural information of biological tissues from image data directly into computational models. The fiber ODFs are nonparametric distributions, and thus do not make any prior assumptions about the fiber architecture. The ability to measure this information regionally further provides a high spatial resolution of material properties that is grounded on measures directly from experiments.

The computational framework of analysis was constructed with a UI and integrated into an established modelling software [11]. The need to characterize and analyze fibrous tissues is fundamental to biomechanics. This framework enables others researchers to rapidly adapt this microstructural information into constitutive models. While some of the image analysis was previously published, it was largely inaccessible because of its format and integration into computational models was difficult.

Additional developments are required to enable the effective use of this framework towards the characterization of soft tissues. For instance, nonparametric ODFs introduce increased degrees of freedom to constitutive modeling. Thus, the space of material constants that could fit to constitutive relations is larger. One solution could be to accompany mechanical results with image data, increasing the outcome parameters to regress against and the information about mechanical deformation.

ACKNOWLEDGEMENTS: Funding from NIH R01HL131856 and F31HL154781 are gratefully acknowledged.

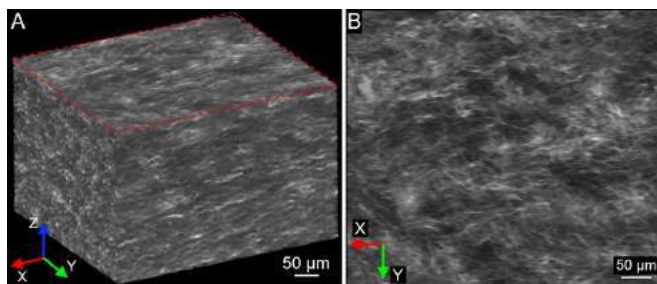


Figure 1: Processed multiphoton Dataset of Collagen Hydrogel. (A) 3D visualization of the image data using FluoRender. The collagen fibrils appear primarily oriented along the x-axis. A red dashed box highlights the first z-slice in the image series. (B) 2D visualization of the first plane. Discrete collagen fibrils can be gleaned with a preferred direction along the x-axis and some noticeable dispersion.

REFERENCES

- [1] Lanir, Y., *J Elast*, 129(1): 2017. [2] Provenzano, P. P., and Vanderby, R., *Matrix Biol*, 25(2): 2006 [3] Gasser, T. C., *J. Roy. Soc.*, 3(6): 2006. [4] Mansfield, J. C., *J. Biomed. Opt.* 13(4): 2008. [5] Holzapfel, G. A., *J. Roy. Soc.* 12(106): 2015. [6] Ateshian, G. A., *J Biomech Eng*, 131(6): 2009. [7] Rauff, A. *et al.*, *IEEE Trans Med Imaging* 41(2): 2021. [8] shorturl.at/cCT04 [9] Maas, S. A., *J Biomech*, 134(1): 2012. [10] Goh, A. *et al.*, *NeuroImage* 56(3): 2011. [11] Labelle, S.A. *et al.*, *AJP Heart Circ. Phys.* 322(5): 2022.

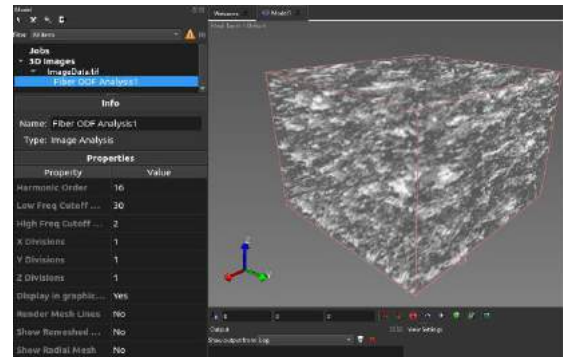


Figure 2: User Interface of Analysis Framework in FEBio Studio. (Left) Model tree demonstrating image data imported directly into a model under “3D images” tab. The image data can then be analyzed, revealing the parameters involved in image analysis. (Right) Rendering of collagen microscopy data (Fig. 1) directly inside FEBio Studio.

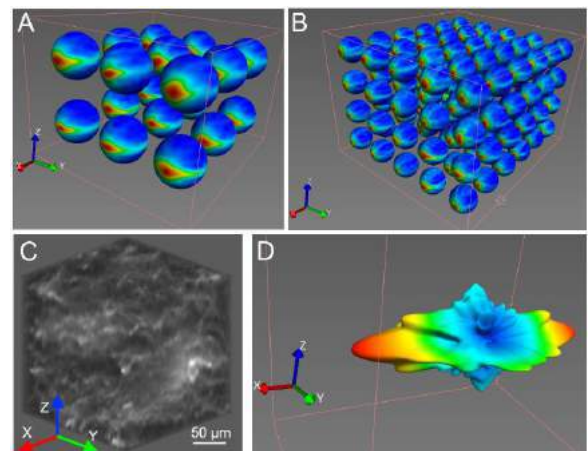


Figure 3: ODF Visualization Within Subvolumes on The Image Domain. (A) Estimated ODFs using subdivisions of 3x3x2 rendered over the original image domain (Fig 2). (B) Graphical display of high resolution of ODFs over the domain, with subdivisions of 6x5x4. (C) Representative subvolume of the original image (Fig 1A). (D) Measured ODF of the subvolume in C, shown in the radial representation.

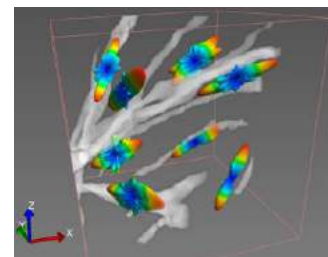


Figure 4: FIB-SEM Image Data Visualized with Measured ODFs. The ODFs are graphed in the radial representation and provide visual correspondence of the approximated ODFs and the original image data containing fibrillar structures.

STRUCTURAL AND FUNCTIONAL HETEROGENEITY OF THE UTEROSACRAL LIGAMENTS IN THE RAT

Joseph G. Thomas (1), Kandace Donaldson (2), Yizheng Zhu (1), Clara Gimenez (2), Raffaella De Vita (2)

(1) Department of Electrical and Computer Engineering, Virginia Tech, Blacksburg, VA, United States
(2) Department of Biomedical Engineering and Mechanics, Virginia Tech, Blacksburg, VA, United States

INTRODUCTION

The uterosacral ligaments (USLs) are the main supportive structures of the upper vagina and uterus within the pelvic floor. Structural changes of the USLs have been shown to contribute to the development of pelvic organ prolapse (POP). Given their anatomical function, the USLs are used as anchoring tissues in the surgical treatment of POP such as the uterosacral ligament vaginal vault suspension [1]. Thus, characterizing the mechanical function of the USLs is a crucial step in identifying the etiology of POP as well as improving corrective surgeries that rely on the USLs to restore the support of prolapsed organs [2]. Animal models can help in studying the functional role of the USLs in POP through *ex vivo* mechanical testing, without the challenges associated with the collection of human tissues [3]. In our lab, we have developed new methods for isolating and mechanically testing rat USLs [4] since rat USLs are relatively easy to acquire and histologically similar to human USLs [5]. We have also observed that rat USLs fail by delamination making the measurement of deformation fields using the digital image correlation method very challenging.

In this study, we propose the use of optical coherence tomography (OCT) during uniaxial testing to obtain volumetric images of the USLs by depth-resolving backscattered light from the tissues [6]. This optical imaging technique allow us to determine the relationship between the mechanical function of rat USLs and through-thickness micro-structural changes that cause delamination and tissue failure. This work serves as a springboard for future developments of OCT-based probes that measure the mechanical integrity of USLs *in vivo* for the prevention, diagnosis, and treatment of POP.

METHODS

Six virgin Sprague-Dawley rat USLs were dissected following recently developed dissection procedures that isolate the ligaments from other pelvic floor organs while maintaining the integrity of the entire ligaments [4]. Ligaments were secured to the linear actuators of a custom-made uniaxial machine by clamping one end of the USLs at the spine and piercing the other end with three needles spaced 3.5 mm at the vaginal attachments. The USLs were preloaded to 5 mN then displaced along their main

in vivo loading directions at a constant rate of 10 $\mu\text{m/s}$ until the stroke limits of the actuators were reached or total tissue failure occurred. Load data were recorded using a 8.9 N-capacity, 0.1% accuracy load cell (FSH00092, Futek Advanced Sensor Technology, Inc., Irvine, CA). A spectral domain optical coherence tomography system (SD-OCT) was assembled with a superluminescent diode (SLD; Superlum, Cork, Ireland; $\lambda = 837 \text{ nm}$, $\Delta\lambda = 54 \text{ nm}$) and a custom spectrometer using a linescan camera (AViVA EM1; Teledyne, Milpitas, CA; 1024 pixel, 78 kHz). The system was mounted above the specimen at a 150 mm working distance with a focused beam of diameter of 60 μm . For volume acquisition, the beam was raster scanned in two lateral dimensions across a 15 mm \times 7.5 mm area on the specimen for 512 \times 512 image pixels in the transverse and loading directions, respectively. The vertical field-of-view (FOV) of the OCT images was approximately 3 mm of optical depth in 513 image pixels. For each specimen, 30 to 40 OCT volumes and color images were recorded with a CMOS camera. Figure 1 shows the color image of the entire USL with the corresponding OCT maximum intensity projection (MIP) image overlaid.

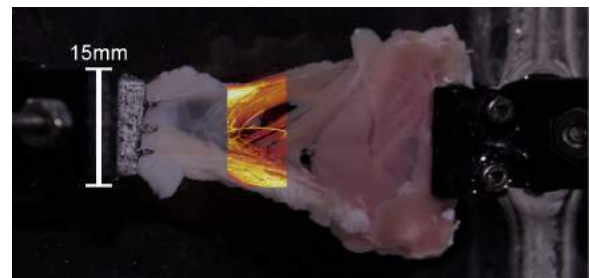


Figure 1: Picture of one rat USL during uniaxial testing with an OCT MIP image overlay.

The typical load-displacement curve of the USL was characterized by the presence of the toe, linear, and failure regions. For one representative specimen, isometric MIP OCT images are displayed for values of the load and displacement in these three regions in Figure 2.

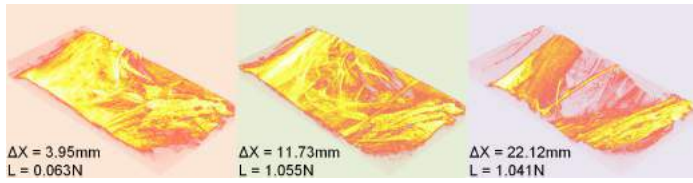


Figure 2: Isometric OCT MIP images at displacements (ΔX) and loads (L) that fall within the toe (orange), linear (green), failure (lilac) regions of the load-displacement curve.

RESULTS

A scalar parameter was extracted from each collected OCT image to describe the bulk tissue structural heterogeneity during mechanical testing. Figure 3 (top) shows depth-coded maps of the highest optical backscatter from *en face* MIP images acquired in the three regions of the load-displacement curve for one specimen. To derive a scalar parameter that represents the heterogeneity of the bulk tissue, a histogram of these MIP depths was computed for each depth-coded image, as shown in Figure 3 (bottom). A mask was used to exclude off-tissue positions in the images from these calculations. The depth-variation parameter, σ , was computed as the standard deviation of MIP depths within all *en face* area of the tissue. To account for inter-specimen variation, the depth variation change relative to each specimen's initial depth-variation parameter, σ_0 , was computed.

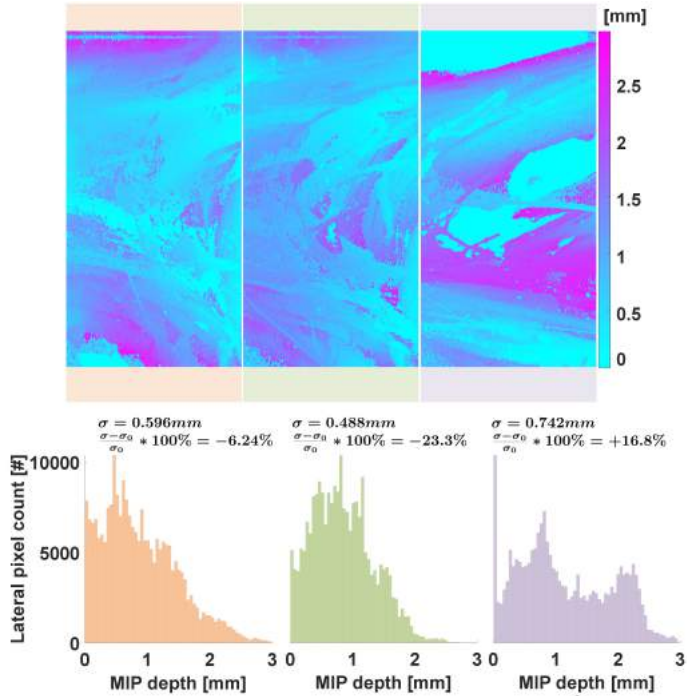


Figure 3: Top: Depth map of optical backscatter from maximum intensity projections. Bottom: Distribution of depths of maximum backscatter. The depth-variation at zero displacement for this specimen was $\sigma_0 = 0.636$ mm

Load versus displacement data measured during tensile testing are presented in Figure 4(a) for the $n=6$ specimens. The depth-variation parameter was also computed for each image during tensile testing, plotted versus displacement in Figure 4(b). The three regions of the load-displacement curve are color-coded. As the displacement increased, the load increased non-linearly in the toe region (orange) while the tissue depth-variation decreased. In the linear region (green), where the load increased linearly with the displacement, the depth-variation remained roughly constant. In the failure region (lilac), following the point of maximum load, a significant increase in depth-variation was recorded as individual micro-structural components of the USLs fail and the load gradually decreased.

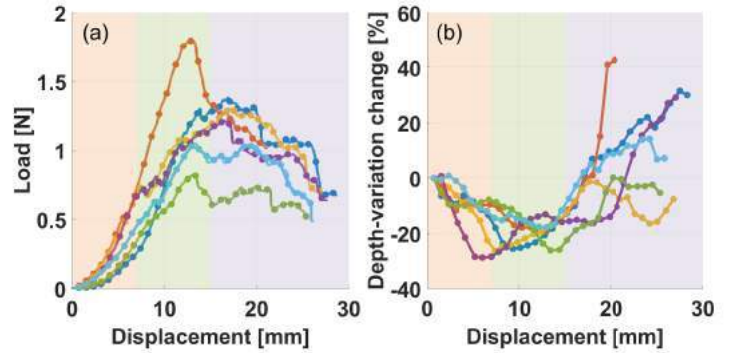


Figure 4: (a) Load-displacement data for USLs ($n=6$) and (b) corresponding depth-variation change data.

DISCUSSION

OCT imaging of the USLs under uniaxial testing allowed for visualization of the complex 3D deformations of the ligaments. The depth-resolving capability of OCT imaging provided new data on the highly heterogeneous structure of the USLs in the rat model. The image-derived depth-variation parameter and the directly-measured load data in all three regions of the load-displacement curves were found to be correlated (Figure 4). In the toe region, the monotonic decrease of the depth-variation parameter was determined by the straightening and alignment of the collagen fibers of the USLs. In the linear region, the depth-variation parameter did not change as the displacement increased; the deformation was homogeneous across the tissue as no major structural changes occurred. In the failure region, individual structural components such as collagen bundles were observed to fail as also reflected in the abrupt decreases in the load/displacement curves. The depth-variation parameter captured these structural changes consistently as it increased significantly in this region.

In summary, the extracted depth-variation parameter serves as a useful parameter to characterize the material heterogeneity of the USLs in the three regions of the load-displacement curve. The correlation between the invasive and contact-based examination of tissue function (i.e., measurement of load and displacement) and the non-invasive and non-contact optical characterization of tissue structure (i.e., measurement of depth-variation parameter) shows promises for the development of OCT-based probes that perform non-contact *in vivo* evaluation of the mechanical integrity of USLs in humans.

ACKNOWLEDGEMENTS

Funding was provided by National Science Foundation Grant No. 1804432. J.G.T. gratefully acknowledges the support of Bradley Fellowship from the Bradley Department of Electrical and Computer Engineering at Virginia Tech.

REFERENCES

- [1] Barber MD et al. *JAMA* 311.10 (2014). ISSN: 0098-7484. DOI: 10.1001/jama.2014.1719.
- [2] Donaldson K et al. *Ann Biomed Eng* 49.8 (2021). ISSN: 1573-9686. DOI: 10.1007/s10439-021-02755-6.
- [3] Baah-Dwomoh A et al. *Applied Mechanics Reviews* 68.6 (2016). ISSN: 0003-6900. DOI: 10.1115/1.4034442.
- [4] Donaldson K et al. *Ann Biomed Eng* (2023).
- [5] Iwanaga R et al. *Int Urogynecol J* 27.11 (2016). ISSN: 0937-3462, 1433-3023. DOI: 10.1007/s00192-016-3008-6.
- [6] Bouma BE et al. *Gastrointest Endosc* 51.4 (2000). ISSN: 0016-5107. DOI: 10.1016/s0016-5107(00)70449-4.

A MATHEMATICAL MODEL OF KIDNEY PODOCYTE RESPONSES TO FLUID SHEAR AND ACTOMYOSIN CONTRACTILITY PREDICTS CHANGES TO KIDNEY FILTRATION IN A MOUSE MODEL OF KIDNEY INJURY

**S. Jiang (1, 2), Y-Y. Huang (1, 3), P. Puapatanakul (4) J. H. Miner (4), F. Alisafaei (5),
H. Y. Suleiman (4), G. M. Genin (1, 2)**

- (1) NSF Science and Technology Center for Engineering Mechanobiology, Washington University in St. Louis, St. Louis, Missouri, USA
(2) Department of Mechanical Engineering and Materials Science, Washington University in St. Louis, St. Louis, MO, USA
(3) Department of Biomedical Engineering, Washington University in St. Louis, St. Louis, MO, USA
(4) Division of Nephrology, Washington University School of Medicine, St. Louis, MO, USA
(5) Department of Mechanical & Industrial Engineering, New Jersey Institute of Technology, Newark, New Jersey, USA

INTRODUCTION

Kidney glomerular diseases result in damage to the kidney's filtration apparatus and often cause chronic kidney disease and kidney failure with no cure [1]. One main reason for them is that the podocyte attachment, especially that of podocyte foot processes, could be disturbed during these diseases [2], and lead to the loss of filtration function of the glomerulus (Figure 1A-C) [3].

The cytoskeleton of the podocytes is well organized to maintain this critical, yet complex structure (Figure 1D) [4], and to maintain the attachment against the changing mechanical environment of these cells. Understanding the force balance inside this environment then became important in fundamental mechanobiology perspective as well as in therapeutic application level.

Based on mathematical model we developed, we hypothesize that stresses on the integrin bonds of these podocytes were the key to their attachment, and it was balanced mainly based on the fluid shear due to the filtration and the actomyosin contraction inside of the cells.

A mouse injury model modulating their blood pressure and contractility is established in the end to verify our prediction about their kidney filtration function which illustrated the potential role of adjusting this balance in the therapy of chronic kidney diseases.

METHODS

The development of the mathematical model first includes the key mechanotransduction components like the contractile actin filaments form the podocyte cell body, the focal adhesion with integrin bonds and the slit diaphragm connecting neighboring foot process (Figure 1E). During the simulation, the force equilibrium is ensured (Figure 2A), and the stability of the integrin bonds can be determined through calibrated relationship with the force on the integrin [5], while a Monte Carlo simulation is carried out to calculate the displacements of each component until a balance is reached.

To test our model results in a mouse injury model. Two sets of techniques were used. Firstly, the sub-cellular structures inside of the podocytes and the foot processes is enables with super-resolution imaging techniques like STORM to check our predictions on cell morphological changes. Then, the filtration function of the mice is evaluated through albumin to creatinine test in the urine, where more albumin in the urine indicates worse kidney diseases, while the mechanical cues were adjusted through blood pressure controlling or myosin function inhibition.

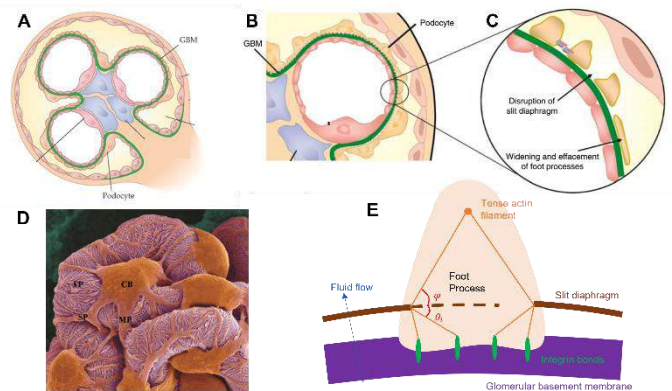


Figure 1: (A-C) Podocytes and their foot processes function in glomerular filtration [3], (D) Scanning electron microscope of healthy podocytes and their foot processes [4], (E) Our simplified model for mechanical transduction in a foot process.

RESULTS

Firstly, our models suggest the existence of linkage between the contractile actin cable, the slit diaphragm and the integrin bonds for the stable attachment of the foot processes (Figure 1E). While this

connection was never observed specifically before, we managed to visualize them using super-resolution imaging of the foot processes, where most actin staining concentrated on the upper side of each foot process, that is the contractile actin cable from the cell body, there are also actin positive signal between the nephrin-labeled slit diaphragm and the integrin on the lower side of the foot process, which we proposed to be responsible for the mechanotransduction and balance between these components (Figure 3A-B).

Then, our simulation results highlight the mechano-responsiveness of the integrin distribution in the foot processes and suggest a potential pathway for changes of the GBM's stiffness (Figure 2B) and changes to blood pressure and fluid flow (Figure 2C) to affect podocyte attachment and function. And the results can be summarized in two predictions that firstly integrins would accumulate on the edges of foot processes to maintain the stable attachment of themselves and that they would move while the foot processes would become narrower due to the increase of either GBM stiffness or fluid shear (Figure 2D). Secondly, it is predicted that the balance of attachment would be broken if fluid shear and cytoskeleton contraction increased beyond a critical point while the foot processes would also be destabilized in the absence of both fluid shear and cytoskeletal contraction at the same time (Figure 2E).

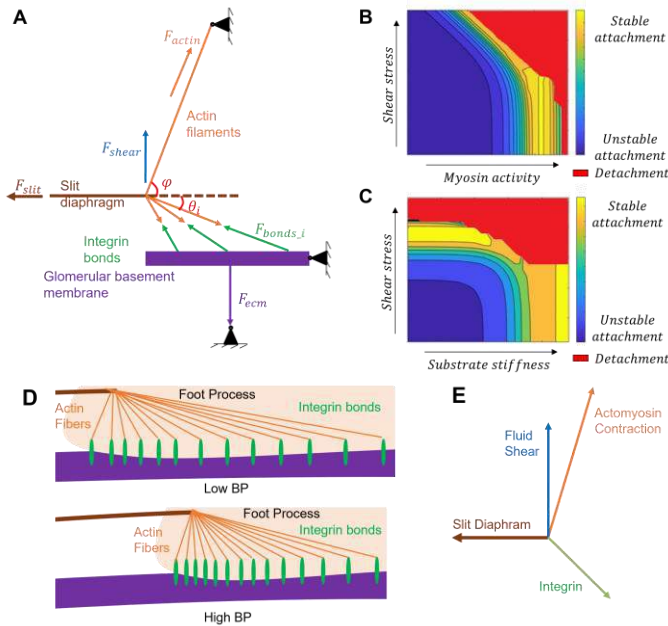


Figure 2: (A-C) Simulation of force balances inside of a foot process, (D-E) prediction of podocyte attachment.

Finally, to verify our predictions from the simulation, we looked into the integrin distribution through super-resolution techniques, and through integrin b1 staining, it is clear that we could notice the concentrated integrin be at the edge of the foot processes (Figure 3A-B) which have also been shown in previous studies [6]. Furthermore, the effect of blood pressure controlling is evaluated to show significant difference (Figure 3C), while proteinuria results reveal the progression of more severe albuminuria in the mice with decreased blood pressure after myosin inhibition, indicating the loss of contractility and fluid shear at the same time did aid the disease progression (Figure 3D).

DISCUSSION

In this project, we successfully modeled the podocyte attachment under varied mechanical properties that simulate physiological and

pathological microenvironment of the glomerulus. And made predictions to podocyte stability and kidney function accordingly. This opened new insight of how mechanical cues could aid or lead to glomerular diseases that have becoming more and more important nowadays.

This work helps us understand the complex interplay between mechanical parameters and the changes during pathological situation that could lead to the effacement and detachment of the podocyte foot processes. The fact that we have coordinated data from the mathematical model and the mouse injury model also highlights the importance of mechanical cues in the development of chronic kidney diseases.

It has potential impact on all kidney disease therapy strategies nowadays, since no mechanical cues were considered before while establishing these therapeutic methods. According to our modeling and experimental results though, the restore of mechanical environments inside of the glomerulus is also needed to achieve the complete cure of chronic kidney diseases. Moreover, different types of disease may have distinct or even opposite mechanical changes so may be beneficial from different regulating strategies.

There's even more to considering as mechanical regulations in the kidney glomerulus as next step: The expansion of capillaries with blood pressure changes, the stable connections between nearby foot processes and more [8]. They may also play an important role in stabilizing the filtration barrier and the filtration function. With increasing understanding of the mechanical cues inside of the glomerulus, we may realize the complete cure of chronic kidney diseases in the future.

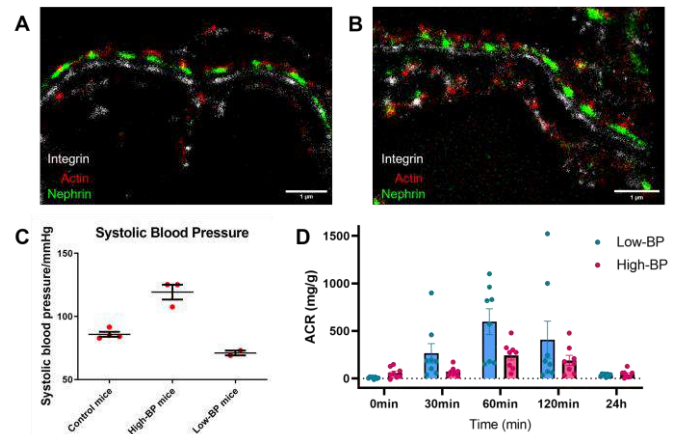


Figure 3 (A-B) Super-resolution imaging of actin linkage and integrin distribution, (C-D) Proteinuria induced in mice model with decreased blood pressure and inhibited myosin function.

ACKNOWLEDGEMENTS

This work is supported by National Science Foundation Center for Engineering Mechanobiology (CMMI 1548571) to G.M.G. NIH grants (R01DK058366, R01DK078314, and R01DK128660) to J.H.M. NIH grant (R01DK131177) to H.Y.S.

REFERENCES

- [1] Levey A S et al, *The lancet*, 379(9811); 165-80, 2012.
- [2] Ebefors K et al, *Frontiers in Physiology*, 12; 689083-689083, 2021.
- [3] Jefferson J A et al, *Kidney International*, 74(1); 22-36, 2008.
- [4] Hu G et al, *Biomedicine & Aging Pathology*, 3(1); 36-42, 2013.
- [5] Elosegui-Artola A et al, *Nature Cell Biology*, 18(5); 540-8, 2016.
- [6] Suleiman H Y et al, *JCI insight*, 2; 2017.
- [7] Endlich N et al, *Seminars in Nephrology*, 32; 327-341, 2012.

MEASUREMENT ERROR ASSOCIATED WITH DECOUPLING OF INSTRUMENTED MOUTHGUARDS

Ryan A. Gellner (1), Mark T. Begonia (1), Matthew Wood (1), Lewis Rockwell (1),
Taylor Geiman (1), Caitlyn Jung (1), Steve Rowson (1)

(1) Department of Biomedical Engineering and Mechanics, Virginia Tech, Blacksburg, VA, USA

INTRODUCTION

Head impact exposure in contact sports has been reported in the literature for years. Head impact sensors characterize both frequency and magnitude of exposure in many studies and are used especially in athlete and military populations. Mouthguard- or retainer-style sensors have become increasingly popular because of their potential to couple directly to the upper dentition and hence the skull [1]. Some sensors perform well in the lab under ideal conditions, for example, a tight fit with the lower dentition clamping the mouthguard in place, but their use by volunteers in the field may differ. This study aimed to determine the effect of introducing small gaps between a boil-and-bite mouthguard-style head impact sensor and the lower dentition of a headform on the sensor outputs compared to a ground truth measurement. The hypothesis was that the mouthguard would become less accurate with increasing gap size due to increased mouthguard movement relative to the headform.

METHODS

A single Prevent Biometrics (Edina, MN) boil-and-bite mouthguard was fit to a 3-D printed dentition according to the manufacturer's instructions for fitting to a typical athlete. Spring clamps provided force for forming the mouthguard to the dentition immediately following boiling. After drying, the mouthguard underwent 96 impacts. A modified medium National Operating Committee on Standards for Athletic Equipment (NOCSAE) headform attached to a Hybrid-III 50th Percentile Male ATD neck was mounted atop a linear slide table; the dentition was attached to the headform in its anatomical location. The tests were conducted at locations and severities described in [2] and [3] using a padded impactor face. Three gap conditions were tested for each combination of location and severity. The gap conditions were created by tightening the bottom dentition to the lower face of zero, one, or three 1.6mm shims stacked on top of one another, resulting in gaps of either

0mm (tight), 1.6mm, or 4.8mm (Figure 1). The mouthguard stayed attached to the upper dentition until the time of impact in all tests. Each test condition included two trials.

Raw data output by the mouthguard sensors were filtered using a custom second-order Butterworth phaseless dual-pass filter and transformed to the headform center of gravity (CG) using rigid body dynamics equations. Based on previous analyses, cutoff frequencies best matching laboratory data for linear accelerometers (350 Hz) and angular rate sensors (250 Hz) were employed to reprocess the mouthguard data. Data collected at the headform CG were filtered at SAE J211 recommended filter cutoff frequencies (1650 Hz for linear accelerometers and 259 Hz for angular rate sensors [4]) and were considered to be ground truth.

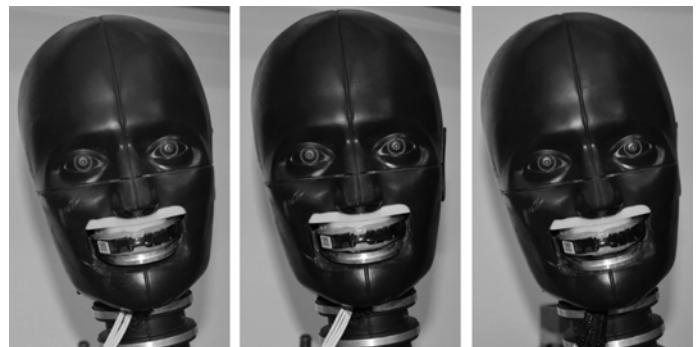


Figure 1: Lower dentition to mouthguard gap conditions from left to right: 0mm, 1.6mm, and 4.8mm.

Headform data collected at the CG were also transformed to the headform teeth location using rigid body dynamics equations. This enabled calculating the relative motion of the mouthguard with respect to the headform. Laboratory data were down-sampled to align with the

mouthguard sampling rate of 3.2kHz. Mouthguard and laboratory signals were shifted such that the first point at or above 4g resultant linear acceleration corresponded to time zero for both measurement sources. Relative resultant linear acceleration was calculated as the difference between mouthguard and headform measurements, as measured at the headform teeth location.

RESULTS

A difference in error between gap conditions was observed (Figure 2). Error relative to headform measurements in peak linear acceleration reported by the mouthguard was as high as 500% in the most extreme cases with the largest gap condition. Impact location also appeared to have an effect, with angled rear (Rearboss) impacts generating lower errors than front and angled front (Frontboss) conditions, even with the largest lower dentition gap.

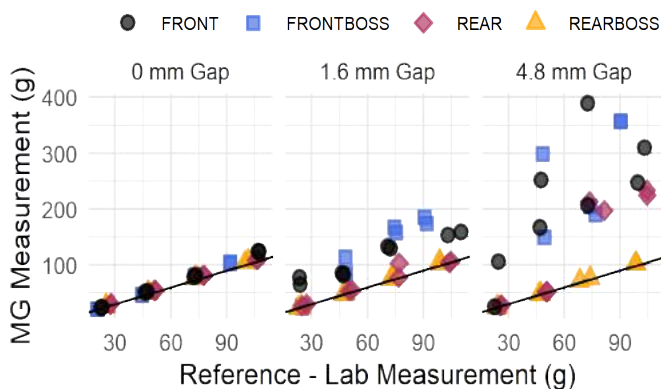


Figure 2: Error in peak linear acceleration reported by the instrumented mouthguard (MG) increased with lower dentition gap size. Differences in performance by impact location were observed. Reference line drawn at a slope of one.

Relative motion artifacts were increasingly recognizable in the mouthguard measurements as impact severity and lower dentition gap increased (Figure 3). These artifacts were observed in both linear and angular measurements.

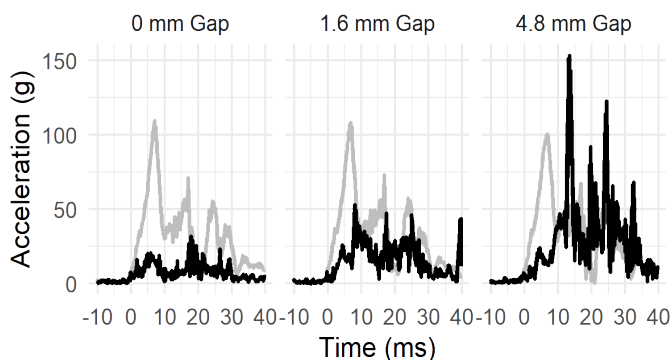


Figure 3: Exemplar traces of resultant linear acceleration at the Front location (100g severity). Relative acceleration (black curves) of the mouthguard increased as lower dentition gap size increased. Lab measurements are shown in gray for reference.

Qualitatively, a majority of the motion artifacts (10-40ms) appeared to have occurred after the true peaks in linear acceleration caused by the

impact (0-10ms), which were easily discernable from the headform measurements. Limiting the peak value output to the first 10ms post-trigger reduced the error in peak linear acceleration reported by the mouthguard (Figure 4).

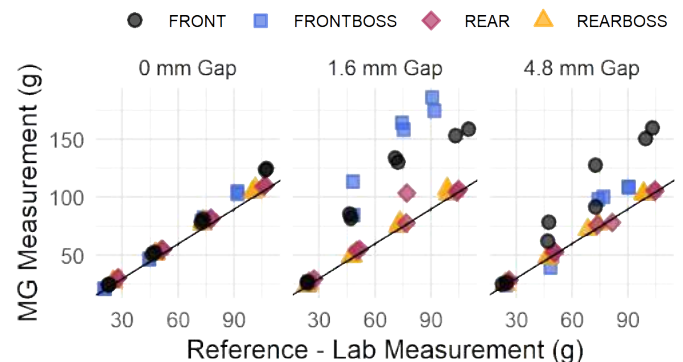


Figure 4: Error in peak linear acceleration reported by the instrumented mouthguard decreased when analyzing peaks occurring only during the time of force applied to the headform (0-10ms post-trigger). Reference line drawn at a slope of one.

DISCUSSION

The fit and retention of instrumented mouthpieces are important to the accuracy of these sensors, and the amount of error introduced into their measurements will vary depending on how they are used on-field. A gap between the lower dentition and mouthguard as small as 1.6mm can affect readings in a laboratory environment. Larger gaps lead to greater errors. Gaps between dentition and mouthguard, representing an impact where an athlete has not clenched his or her jaw, may be present in a number of real-world impacts measured by these sensors and should be considered in mouthguard development and in the interpretation of any studies using these devices.

Error and relative motion differed with impact location, which suggests there may be a directional dependence of the mouthguard for retention when a gap exists. Frontal impacts fared worse, which can be explained by the headform being accelerated away from the inertial position of the mouthguard; rear impacts benefit for the opposite reason.

The mouthguard used in this study performed well during the impact event, even in the highest gap condition; however, the secondary peaks due to mouthguard motion occurred within the data collection window for the mouthguard, which caused erroneously high peak values to be reported. When considering only the 0mm gap condition, this study agrees with previous laboratory analyses of instrumented mouthguard accuracy.

ACKNOWLEDGEMENTS

The authors would like to thank the Institute for Critical Technology and Applied Science at Virginia Tech for their support of this research.

REFERENCES

- [1] Jones, B et al., *Br J Sports Med*, 56:1171-1179, 2022.
- [2] Tyson, AM et al., *J Biomech*, 24:320-326, 2018.
- [3] Keiffer, EE et al., *Ann Biomed Engr*, 48(11):2613-2625, 2020
- [4] Cobb, Bryan R et al., *J Sport Engr and Tech*, 232(2):176-181, 2018

FOCUSED-ULTRASOUND MEDIATED GENE DELIVERY TO BRAIN ENDOTHELIUM WITHOUT BLOOD-BRAIN BARRIER OPENING

Hanwen Fan (1), Mohammadaref Ghaderi (2), Qi Cai (1), Shashank Sirsi (2), Zhenpeng Qin (1,2,3,4)

- (1) Department of Mechanical Engineering, The University of Texas at Dallas, Richardson, TX 75080, USA
- (2) Department of Bioengineering, The University of Texas at Dallas, Richardson, TX 75080, USA
- (3) Department of Surgery, University of Texas Southwestern Medical Center, Dallas, TX 75390, USA
- (4) Center for Advanced Pain Studies, the University of Texas at Dallas, Richardson, TX 75080, USA

INTRODUCTION

The blood-brain barrier (BBB), which is formed by the compact brain capillary endothelial cells (ECs) and junctional protein complexes, prevents the brain's uptake of therapeutic agents from the blood [1]. To overcome this problem, BBB opening by focused ultrasound (FUS) associated microbubbles (MBs) has become an effective method to deliver various therapeutic agents to the brain [2]. It has the advantages of noninvasive, repeatable, and local gene delivery to the brain. However, high acoustic pressure and high concentration of MBs will lead to BBB disruption, which induces an acute sterile inflammatory response in brain tissue [3]. A recent study has reported delivering plasmid DNA to the brain ECs without opening the BBB, called sonoporation [4]. Sonoporation is based on the microbubble cavitation induced by FUS and eventually pore formation on the cell membrane. Non-viral gene delivery to the BBB is a promising approach for brain therapeutics for two reasons. First, BBB dysfunction has been indicated in various neurodegenerative diseases and restoring functional BBB has been shown to restore brain function [5]. Second, gene delivery to BBB offers new opportunities to modify BBB function without opening the BBB and associated side effects.

In this study, we investigated how sonoporation parameters, especially acoustic pressure and microbubble concentration, affect gene transfection and BBB integrity. We found the parameters for gene transfection without opening the BBB. Our results provide guidance for high-efficiency gene delivery into the brain.

METHODS

Cationic MBs are fabricated following reference [4]. Male C57BL/6 mice (8-week-old) purchased from Charles River were anesthetized with isoflurane. A tail-vein catheter was inserted to permit intravenous (i.v.) injections of MBs, plasmids (pcDNA3-luciferase) and fluorescent dye (fluorescein). The heads of the mice were shaved and depilated, and the animals were then placed in a supine position over a

degassed water bath coupled to an MR-compatible small animal FUS system (RK-50; FUS Instruments). Mice received an injection of the conjugated MBs and luciferase plasmid (500 µg per mouse). Sonication applied to the right hippocampus region began immediately after the injection (1.46 MHz, 100 ms burst duration, 1000 ms burst period, 300 bursts).

One day later, to visualize the luciferase expression, the mice were injected with 200 µl D-Luciferin solution (15 mg/ml in PBS) intraperitoneally (i.p.) and were imaged with an IVIS imaging system (Lumina, Series III) after 15 minutes. To assess biodistribution of the gene transfection, mice were sacrificed and their organs (brain, lungs, heart, kidneys, spleen, and liver) were harvested and placed in the solution of D-Luciferin (150 µg/ml) in PBS for 5 minutes. The organs were then imaged using the IVIS imaging system.

To assess BBB integrity after FUS sonoporation, mice received an injection of 100 µl fluorescein dye (330 Da) after the sonication and were perfused with PBS followed by 4% paraformaldehyde after 30 minutes. The brains were fixed in 4% paraformaldehyde for 24 hours at 4 °C, followed by flash freezing and storage at -80 °C. The brains were then mounted with OCT and sectioned using a cryostat into 10 µm thick sections. Sections were imaged on an Olympus slide scanner microscope equipped with a 10x objective.

RESULTS

High acoustic pressure (above 0.3 MPa) has been proven to open the BBB [4]. On the other hand, low acoustic pressure with low MB concentration may not be able to transfect gene plasmids due to weak cavitation. To study how sonoporation parameters affect transfection, we investigated FUS acoustic pressure ranging from 0.1 to 0.6 MPa and the number of MBs ranging from 1×10^8 to 5×10^8 . Data points are represented as black dots in Figure 1A. FUS is applied in the right hippocampus region (red circle in Figure 1B). With extremely high acoustic pressure (0.6 MPa) and a large number of MBs (5×10^8), clear

brain injury was found at the sonication region. With low acoustic pressure (0.1 MPa) and a small number of MBs (1×10^8), there is no luciferase expression in the brain (Figure 1C). Data points with parameter values between these two cases provide results of seeing expression (Figure 1D). Additionally, live imaging shows that there exists a strong luciferase expression signal in the right hemisphere of the brain corresponding to the sonication region (Figure 1B). After harvesting the organs, there is no luciferase expression signal in the organs except the brain. This shows highly specific gene delivery and expression in the brain.

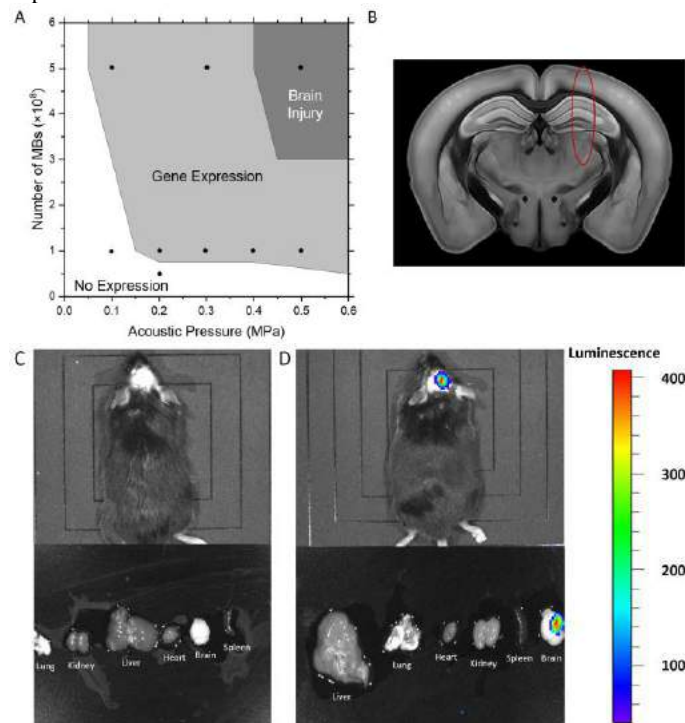


Figure 1: FUS-mediated luciferase plasmid transfection in the brain. (A) Expression efficacy with respect to acoustic pressure and number of MBs. (B) FUS application region. (C) *In vivo* bioluminescent imaging with luciferase expression signal (0.1 MPa, 1×10^8 of MBs). (D) *In vivo* bioluminescent imaging without luciferase expression signal (0.4 MPa, 1×10^8 of MBs)

To test how sonoporation parameters affect BBB integrity, we selected a small molecular dye, fluorescein (330 Da), as a tracer to examine BBB disruption. Figure 2A-B shows that with 0.2 MPa of acoustic pressure and 5×10^8 of MBs, there is an obvious dye leakage in the right hippocampus region with sonication (white arrows). However, when the acoustic pressure or the number of MBs is reduced, we observed no dye leakage, indicating no BBB disruption.

Combining Figure 1A and Figure 2B, there exists an overlap region where the gene is transfected without BBB disruption (Figure 3). In the cases of 0.2 MPa - 1×10^8 and 0.1 MPa - 5×10^8 , the luciferase plasmid is delivered to the brain without opening the BBB. Our ongoing work is to examine whether the plasmid is delivered to brain ECs.

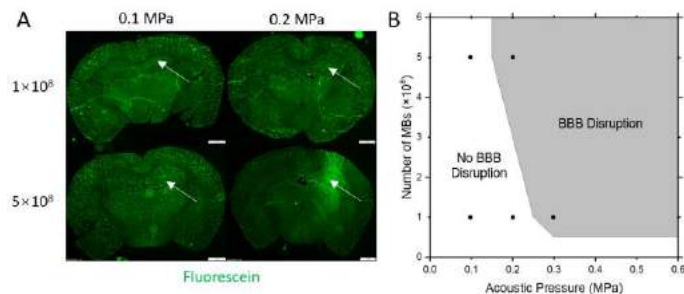


Figure 2: FUS-mediated BBB opening test. (A) Fluorescent imaging of brain sections with different sonoporation parameters (scale bar = 1 mm). (B) BBB integrity with respect to acoustic pressure and number of MBs

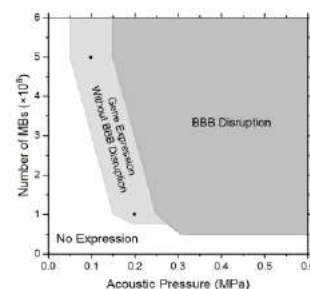


Figure 3: Combination pattern of luciferase plasmid transfection and BBB opening test

DISCUSSION

The development of novel non-invasive gene therapy that modulates brain ECs could significantly improve clinical outcomes for numerous brain disorders. The idea of using MB activation with FUS for local gene delivery to the brain has recently gained traction. Here, we demonstrate that FUS sonoporation can deliver gene plasmid to the brain, and the transfection efficacy depends on sonoporation parameters such as acoustic pressure and MB concentration. Particularly, at optimized conditions (i.e., 0.2 MPa - 1×10^8 or 0.1 MPa - 5×10^8), there is gene expression without BBB disruption. Since BBB integrity is preserved, we will further test the hypothesis that the plasmid is delivered to the brain EC.

ACKNOWLEDGEMENTS

Research reported in this article was supported by the Cancer Prevention and Research Institute of Texas (CPRIT) under award numbers RP190278 and RP210236, and National Institute of General Medical Sciences of the National Institutes of Health under award number R35GM133653.

REFERENCES

- [1] W. M. Pardridge, *Journal of Cerebral Blood Flow & Metabolism*, 32 (11), pp. 1959-1972, 2012.
- [2] K. F. Timbie *et al.*, *Journal of Controlled Release*, 219 pp. 61-75, 2015.
- [3] Z. I. Kovacs *et al.*, *Proceedings of the National Academy of Sciences*, 114 (1), pp. E75-E84, 2017.
- [4] C. M. Gorick *et al.*, *Proceedings of the National Academy of Sciences*, 117 (11), pp. 5644-5654, 2020.
- [5] A. M. Nikolakopoulou *et al.*, (in eng), *J Exp Med*, 218 (4), 2021.

VASCULAR REMODELING DURING LATE-GESTATION PREGNANCY: AN *IN-VITRO* ASSESSMENT OF THE MURINE THORACIC AORTA

Ana I. Vargas (1), Samar Tarraf (1), Chiara Bellini (1), Rouzbeh Amini (1,2)

(1) Department of Bioengineering, Northeastern University, Boston, MA, USA

(2) Department of Mechanical and Industrial Engineering, Northeastern University, Boston, MA, USA

INTRODUCTION

During the nine months of gestation, the maternal body undergoes significant hemodynamic alterations. Such changes are believed to induce structural remodeling of the cardiovascular system [1–3]. During a normotensive human pregnancy, Blood pressure (BP) remains constant, while cardiac output increases (CO), and blood viscosity and peripheral resistance decrease. Combined with the drastic hemodynamic changes, the forces the growing fetus apply on the maternal body cause a burden on the maternal cardiovascular system which can reveal previously undiagnosed cardiovascular problems. Globally, cardiovascular disease (CVD) complicates about 4% of pregnancies [4].

While maternal hemodynamic changes throughout pregnancy have been investigated previously, the changes in the central vasculature during gestation are still unclear. Such a knowledge gap has limited our understanding of the etiology of pregnancy-induced CVD. Towards bridging this knowledge gap, in this study, we aimed to identify biaxial mechanical responses of the murine descending thoracic aorta (DTA) during a normotensive late-gestation pregnancy.

Given the constant BP throughout gestation despite the increase in CO, one could postulate the central vasculature undergoes a remodelling process, while maintaining a homeostatic stress state to accommodate for an increase in blood flow. As such, we hypothesized that DTA wall stress remains unchanged during late-gestation normotensive pregnancies. We also examined whether a murine model mimics clinically measured human data.

METHODS

Pregnant C57BL/6 mice (n=9) at gestation day 18 ± 1 were assigned to the late-gestation group. Nulligravida female mice (n=9) served as the non-pregnant, age-matched controls (10 ± 1 weeks of age). BP measurements were taken using a non-invasive tail cuff system (CODA; Kent Scientific). Mice were euthanized, and the DTA was excised. Samples were mounted onto a custom-made biaxial mechanical testing system, and the passive material properties were measured by performing cyclic pressure-diameter and force-length tests [5]. A four-fiber family constitutive model was fit to

the experimental data via non-linear regression to estimate the constitutive parameters and predict mechanical metrics under *in-vivo* conditions [6]. Additional mice (n=3 for both groups) underwent cardiac echocardiography at the Cardiovascular and Surgical Core, UMass Medical School. Left ventricular volumes at end-diastole and end-systole were derived from m-mode scans. Stroke volume (SV) and heart rate (HR) measurements were used to calculate the CO of each mouse such that

$$CO = \frac{(SV)(HR)}{1000} \quad (1)$$

Data is reported as mean \pm SEM. Unless specified otherwise, Student's t-test was performed to determine statistical significance ($p \leq 0.05$).

RESULTS

In-vivo echo cardiac measurements confirmed up to a 50% increase in CO in late-gestation mice (Fig. 1A). From peripheral BP measurements (Fig. 1B), we did not detect any difference between groups ($p = 0.106$), with systolic and diastolic average values of 118 ± 3 and 89 ± 6 mmHg for control mice and 113 ± 8 and 82 ± 9 mmHg for pregnant mice, respectively.

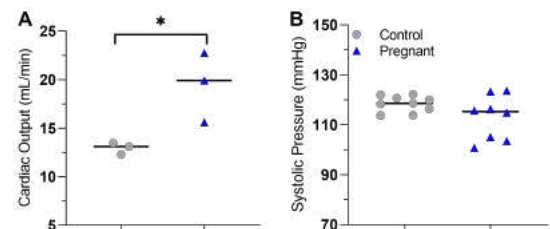


Figure 1: Hemodynamics measurements of late-gestation pregnant mice and age-matched control mice. (A) CO calculated as seen in equation 1. Statistical significance was assessed by Mann-Whitney-Wilcoxon unpaired sample test ($P \leq 0.05$). (B) Systolic Pressure.

As seen in Figure 2, pregnancy was associated with a rightward shift of the stress-stretch curve in both circumferential (Fig. 2A) and axial (Fig. 2B) directions. This shift suggests that DTA tissues in the pregnant group experience a larger stretch at the same amount of applied stress, indicating material softening.

Overall, material softening, without a significant change in BP, led to a larger circumferential stretch at systolic pressure in the pregnant group (data not shown). Concurrently, at group-specific systolic BP, the pregnant aorta was observed to have a greater luminal diameter (Fig. 3A). The increase in diameter accommodates for the significant increase in the CO observed in Fig. 1A.

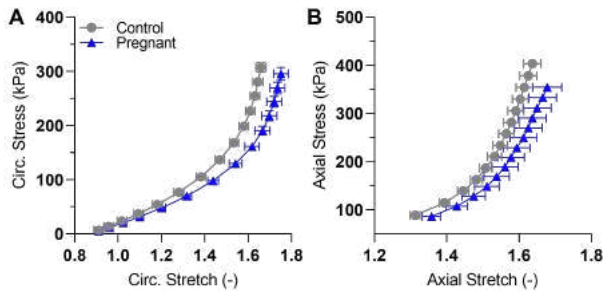


Figure 2: Stress-stretch curves of the DTA of pregnant and control mice for (A) circumferential (Circ.) and (B) axial directions.

At group-specific systolic BP, the intrinsic stiffness of the pregnant aorta was lower than the control aorta in both directions (data not shown. $p = 0.0428$ and $p = 0.0028$, for circumferential and axial directions, respectively). An increase in wall thickness was also observed in the pregnant group (Fig. 3B). However, given the larger luminal diameter at systole in the pregnant aorta (Fig. 3A) and despite no change in pressure observed, aortic distensibility increased during late-gestation (Fig. 3C). Such an increase was coupled by lower structural stiffness of the pregnant tissue. The wall stress, both in the axial and in the circumferential directions, was lower in the pregnant group (Fig. 4).

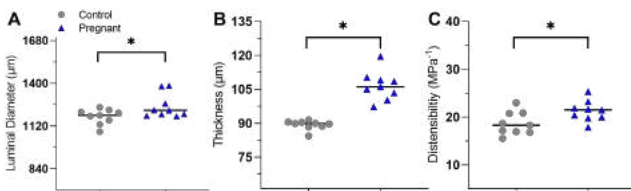


Figure 3: Geometry of the tissue. (A) Luminal diameter and (B) wall thickness were measured at group-specific systolic BP. (C) Distensibility was calculated throughout the cardiac cycle. *For a significant difference of ≤ 0.05

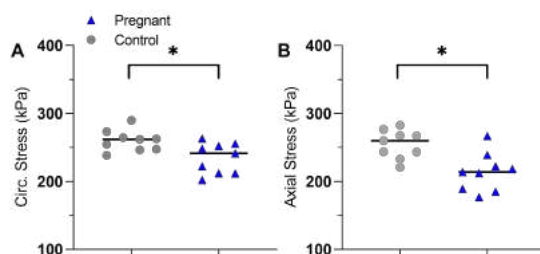


Figure 4: (A) Circumferential and (B) axial wall stress of pregnant and control DTA tissue. *For a significant difference of ≤ 0.05 .

DISCUSSION

With CVD being the leading cause of maternal death in the US, and maternal mortality rates continuing to rise over the years [7, 8], it is crucial to understand the aortic remodeling process that occurs throughout gestation. Herein, for the first time, we report the functional assessment of the DTA from wild-type mice in the late-gestation period, to characterize changes in the intrinsic wall mechanical properties.

Our first important observation was from the non-invasive measurements of BP and CO in the murine model. The pregnancy-induced increases in the murine CO and the lack of change in the pressure are similar to what occurs in normotensive human pregnancies [9]. As such, wild-type mice were deemed appropriate for studying vascular biomechanics during pregnancy.

With no significant changes in the BP during pregnancy, one would intuitively expect that the $\sim 50\%$ increase in CO is caused by an increase in the luminal diameter of the vessel, which is validated by our measurements. Further, we initially hypothesized that the tissue stress would remain unchanged during pregnancy. With an unchanged pressure and increased diameter, for the stress to remain constant, the vessel has to become thicker (the law of Laplace). We also observed such an increase in the wall thickness. In addition, our findings suggest that the DTA experienced material softening both in the axial and in the circumferential directions (Fig. 2). Such softening occurs potentially to accommodate a larger diameter at similar pressure levels during the late-gestation period.

Surprisingly, despite our initial hypothesis, the aortic wall stress did not remain constant — it decreased significantly — in the pregnant group (Fig. 4). Without further analysis of the micro-structure of the tissue, we can only speculate how the remodeling process led to a decrease in the tissue stress. If the remodeling was to avoid excessive stresses, perhaps the lower stress was an “overshoot” response during the shorter period of late-gestation. We did not conduct any test to examine BP or vascular tissue properties during labor and delivery or during the post-partum period. During labor, an increase in BP caused by excessive pain is possible. The reduced stress and the softening of the tissues could also be a mechanism to prevent vascular damage during labor and delivery and/or during the post-partum period. Finally, we did not examine any of the potential changes in the vascular smooth muscle responses during pregnancy. Our observations were limited, as they only pertain to the *passive* response of the tissue, both for the pregnant group and the nulligravida control group.

Our ongoing research is focused on microstructural changes in the vascular tissues during pregnancy. We aim to combine our biaxial mechanical data, with *ex vivo* multi-photon microscopy imaging to investigate the layer-specific micro-structural parameters of both groups. In addition, we will conduct mechanical testing to identify the active properties of vascular smooth muscle between groups.

ACKNOWLEDGEMENTS

Support for this work was provided in part by the National Science Foundation (CAREER 2049088). We thank UMass Medical School, Cardiovascular & Surgical Core for collecting cardiac echocardiographs.

REFERENCES

- [1] Wells S et al. *Can J Cardiol* 38 (2022), S112.
- [2] Pierlot CM et al. *Ann Biomed Eng* 42 (2014), pp. 2058–2071.
- [3] Pierlot CM et al. *Am J Physiol-Heart C* 309 (2015), H1565–H1578.
- [4] Regitz-Zagrosek V et al. *Eur Heart J* 39 (2018), pp. 3165–3241.
- [5] Farra YM et al. *Am J Physiol-Heart C* 320 (2021), H2270–H2282.
- [6] Bellini C et al. *Ann Biomed Eng* 42 (2014), pp. 488–502.
- [7] Creanga AA et al. *Obstet Gynecol* 130 (2017), pp. 366–373.
- [8] Petersen EE et al. *MMWR-Morbid Mortal W* 68 (2019), p. 423.
- [9] Robson SC et al. *Am J Physiol-Heart C* 256 (1989), H1060–H1065.

MATHEMATICAL DYNAMIC MODELING (MADYMO) OF THE MATERNAL PELVIS AND NEONATE FOR SIMULATING SHOULDER DYSTOCIA AND DELIVERY MANEUVERS

J. Iaconainni, M.S. (1), B. Gonik, M.D. (2), M. Grimm, Ph.D. (3), S. Balasubramanian, Ph.D. (1), Anita Singh, Ph.D. (4)

(1) School of Biomedical Engineering, Science and Health Systems, Drexel University, Philadelphia, PA, USA

(2) Department of Obstetrics and Gynecology, Wayne State University, Detroit, MI, USA

(3) College of Engineering and Applied Sciences, University at Albany, Albany, NY, USA

(4) Bioengineering Department, College of Engineering, Temple University, Philadelphia, PA, USA

INTRODUCTION

Shoulder dystocia (SD) is an obstetric emergency that occurs when the neonatal anterior shoulder is impacted behind the maternal symphysis pubis [1, 2]. It affects between 0.2 and 3.0% of vaginal deliveries in the United States [3, 4]. Neonatal brachial plexus palsy (NBPP) is caused by stretching the brachial plexus (BP) beyond its elastic limit and can result in loss of arm function [5]. The BP is a network of nerves that span from the C5-T1 vertebrae and throughout the arms, responsible for sensory and motor function of the arms and hands [6].

During SD, sequential maneuvers are performed by the clinician to alleviate the obstruction with minimal injury to the neonatal BP. The mother starts in the supine position and her legs are in stirrups, which is referred to as the lithotomy position. This is treated as the baseline for the purpose of this study. When SD occurs, the first maneuver attempted by the clinician is suprapubic pressure (SPP), in which force is applied to the soft tissue immediately superior to the symphysis pubis bone [7]. This is in effort to compress the neonatal shoulders under the obstruction.

Forces exerted by the mother and clinician, as well as delivery maneuvers performed to manage SD, contribute to BP stretch. Since these injuries are ethically and technically challenging to study in the clinical setting, computational modeling can be utilized. Previous MADYMO studies have laid a foundation for the application to SD and delivery, however the current study aims to fill the gap by enhancing the biofidelity of existing models.

METHODS

To analyze the BP stretch resulting from various delivery maneuvers used to manage SD, Mathematical Dynamic Models (MADYMO, Siemens, version 2020.2) were developed. The models consisted of a series of rigid body ellipsoids to represent the bony

structures of the 90th percentile neonate and 50th percentile maternal pelvis [8]. The maternal pelvis model is shown in Figure 1 as depicted by the grey ellipsoids and the neonate model is shown in the yellow ellipsoids from the MADYMO geometric viewer.

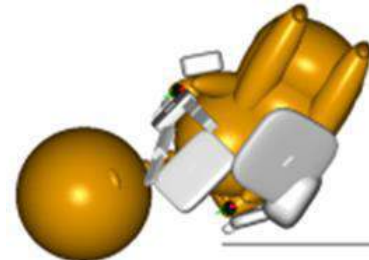


Figure 1: Maternal pelvis (grey) and neonate (yellow) models created from rigid body ellipsoids in MADYMO geometry viewer.

Force-displacement values from an *in vitro* study on neonatal piglet BP were applied to the BP in the model, represented as a 7.5 cm nonlinear spring [9]. The lithotomy position and SPP application were simulated. Endogenous maternal force was measured as the minimum amount of force required to deliver the neonate [10]. Maternal delivery force was applied to the torso of the neonate to simulate contractions and/or Valsalva forces of the uterus. This force was measured by incrementing the force value by 5 N starting at 0 N and observing when the neonate anterior shoulder passes the symphysis pubis. This force value was recorded as the minimum force required by the mother to achieve delivery. BP stretch was measured by the change in length over the original length, as shown in Equation 1, corresponding to the required maternal force in the simulation.

$$\epsilon = \frac{\Delta l}{l_i} * 100 \quad (1)$$

RESULTS

Table 1 shows the results of the baseline lithotomy position with varying magnitudes of SPP. As SPP increased, both required delivery force and BP stretch decreased. This shows a direct relationship between maternal delivery force and BP stretch.

Table 1: Minimum force required by the mother to achieve delivery and brachial plexus (BP) stretch as a result of the lithotomy and suprapubic pressure (SPP) simulations.

Maneuver	Applied SPP Force (N)	Maternal Required Delivery Force (N)	BP Stretch (%)
Lithotomy	0	140	21.52
SPP	40	90	17.97
	100	85	15.74
	140	80	11.26

DISCUSSION

The current study investigates the effects of a SD maneuver, SPP, on the required maternal force and neonate BP. Using models adapted from previous MADYMO studies, SD was simulated, and various forces and maneuvers were applied. The simulated results suggest that increasing SPP force decreases both the required delivery force and BP stretch. SPP is performed to depress and adduct the neonatal shoulders to reduce the obstruction [11].

When 40 N of SPP was applied to the soft tissue of the mother, the required delivery force decreased by 35.7% from the baseline (lithotomy) and BP stretch decreased by 16.5%. With 140 N of SPP, required delivery force further decreased by 42.9% and BP stretch by 47.7%. This shows an inverse relationship between SPP and the required delivery force. Greater expulsive forces acting on the neonate increase the reaction force at the anterior shoulder, therefore increasing BP stretch. In this study, the expulsive forces are the forces generated by the mother, representing contraction or Valsava force. Therefore, there was a direct relationship between the expulsive force and BP stretch observed by the simulations. The observed results align with clinical observation, supporting the biofidelity of the models [12, 13].

The created MADYMO models can allow obstetricians to understand the mechanical effects of various maternal and fetal manipulations on BP stretch and associated injury risk. Future directions include simulating additional delivery maneuvers and utilizing Finite Element models to further advance the computational capabilities [14].

ACKNOWLEDGEMENTS

Funded by Eunice Kennedy Shriver National Institute of Child Health and Human Development of the National Institutes of Health #R15HD093024 and #1R01HD104910-01A1, and National Science Foundation CAREER #1752513.

REFERENCES

- [1] Williams, J. W. et al. New York McGraw-Hill Education Medical, 2018.
- [2] Menticoglou, S. *Int J Womens Health*, vol. 10, pp.723-732, 2018.
- [3] Gherman, R.B. et al. *Am J Obstet Gynecol*, 195(3), pp. 657-672, 2006.
- [4] MacKenzie, I.Z. et al. *Obstet Gynecol*, 110(5), pp. 1059-1068, 2007.
- [5] Chauhan, S.P. et al. *Semin Perinol*, 38(4), pp. 210-218, 2014.
- [6] Leinberry C.F. et al. *Hand Clin*, 20(1), pp. 1-5, 2004.
- [7] Gurewitsch E.D. and Allen, R.H. *Fetal and Maternal Medicine Review*, vol. 17, no. 3, p. 41, 2005.
- [8] Grimm, M.J. et al. *Am J Obstet*, 203(4), pp. 339e331-335, 2010.
- [9] Majmudar, T. et al. *J Biomech*, 128, 2021.
- [10] Buhimschi, C.S. et al. *Lancet*, 358(9280), pp. 470-471, 2001.
- [11] Lok, Z.L. et al. *BMC Pregnancy Childbirth*, 16(1), p. 334, 2016.
- [12] Gurewitsch, E.D. et al. *Am J Obstet Gynecol*, 192(1), pp. 153-160, 2005.
- [13] Dunbar et al. *Clin Anat*, 34(6), pp. 884-898, 2021.
- [14] D'Andrea C.R. et al. *SB3C conference*, p. 208, 2019.

PREDICTING LONG-TERM PATIENT-SPECIFIC OUTCOME OF CARDIAC RESYNCHRONIZATION THERAPY USING A FAST COMPUTATIONAL MODEL

Clara E. Jones (1,2), Derek J. Bivona (3), Kenneth. C. Bilchick (3), Pim J.A. Oomen (1,2)

(1) Department of Biomedical Engineering, University of California, Irvine, Irvine, CA, USA
 (2) Edwards Lifesciences Foundation Cardiovascular Innovation and Research Center, University of California, Irvine, Irvine, CA, USA
 (3) Department of Medicine, University of Virginia, Charlottesville, VA, USA

INTRODUCTION

Cardiovascular disease remains the number one cause of death worldwide. Globally, 1 in 4 deaths in 2020 were attributed to cardiovascular disease. [1] A common complication of heart disease is cardiac dyssynchrony caused by left bundle branch block (LBBB). LBBB initiates adverse cardiac remodeling manifested as left ventricular (LV) free wall dilation and hypertrophy. This can lead to progressive cardiac dysfunction and increased mortality [2]. Cardiac resynchronization therapy (CRT) is a groundbreaking pacing treatment typically offered to patients with LBBB and heart failure to improve LV function. CRT uses biventricular pacing to resynchronize the right ventricle (RV) and LV for more efficient pump function. This process can result in favorable (reverse) LV remodeling, thus lowering LV end-diastolic volume (EDV) [3] and resulting in regression in hypertrophy. However, CRT yields suboptimal results in 30-50% of patients, who then continue to experience the adverse effects of cardiac dysfunction and require additional treatments. [4]

Fortunately, CRT response rates can be improved through patient-centered implementation strategies. In fact, there are several crucial elements that can be optimized for each patient, such as the LV pacing lead location, presence of ischemia, pacing mode, and timing of electrical pacing. The abundance of options make it challenging to identify the optimal CRT configuration during the implantation procedure, even though identification of the best option could improve response to the therapy. Moreover, only short-term outcomes, such as QRS duration and ejection fraction, can be measured during the procedure, even though long-term remodeling is of particular interest.

Based on these considerations, we therefore aimed to develop a patient-specific rapid computational model that can predict strain-based reverse cardiac remodeling following CRT. This model has recently been proven to successfully capture the growth caused by volume overload, pressure overload, LBBB, and CRT in canines [5]. In this study, we demonstrate the feasibility of our novel virtual CRT

simulation framework to predict and optimize long-term remodeling outcome for individual human patients using routine clinical data.

METHODS

Rapid electromechanical model of the heart and circulation

The mechanics of the heart and circulation were modeled using our recently published electromechanical model [5]. In brief, a lumped parameter model was used to model the circulation [6] and the TriSeg method was used to model atrioventricular mechanics [7]. The full-field electrical activation timing estimated by the electrical model was averaged into the 16 AHA segment model for the LV and 5 segments for the RV to link it to the mechanical model. (Fig. 1)

Strain-based growth model

Cardiac growth was modeled using a strain-driven volumetric isotropic growth relationship. Using an evolving growth setpoint, the

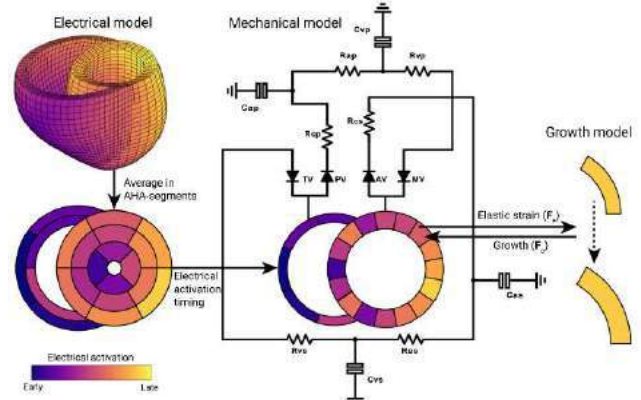


Figure 1: Schematic of the electromechanical framework used to simulate strain-driven cardiac growth following CRT.

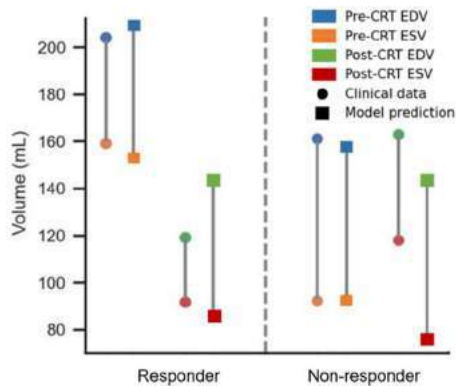


Figure 2: Clinical and simulated LV volumes for the calibration patient (responder) and the validation patient (non-responder).

growth stimulus of each segment was calculated individually. The growth stimulus was defined as the deviation of the maximum elastic circumferential strain throughout the current cardiac cycle ($E_{cc,max}^i$) from the current growth setpoint. The initial setpoint was the maximum circumferential strain at the pre-CRT baseline $E_{cc,max}^{i=0}$, then the setpoint was allowed to evolve based on a moving-average time window of 90 days. The growth stimulus was then entered into a standardized sigmoid growth curve to calculate the incremental growth of each individual segment throughout the simulation.

Model personalization

We personalized our model to two patients treated with CRT (one responder and one non-responder) using routine clinical data. Both patients were female and had non-ischemic heart failure and LBBB. Allometric scaling laws based on body surface area were used to set arterial and venous resistances and capacitances [8]. Heart geometry was derived from cardiac MRI data, and electrical activation timing from 12-lead ECG data. Active and passive constitutive properties were held constant across all simulations, derived from a previous study using canine data [9]. Heart rate was set to directly match the daily heart rate measured by the patients' CRT device.

Calibration and validation of the growth model

The growth model was calibrated for the CRT responder and then validated using the non-responder. The strain-based growth model was calibrated by simulating 6 months of post-CRT cardiac growth and iteratively adjusting the sigmoid parameters to match LV end-diastolic (LVEDV) and end-systolic volume (LVESV). Subsequently, the growth model was validated by simulating 6 months of post-CRT growth for the non-responder using the fitted growth parameters.

RESULTS

We successfully personalized our model to match the pre-CRT states for the two non-ischemic LBBB patients. These two baseline patient models were then used to capture the overall remodeling response to 6 months of CRT pacing, simulated in under 30 seconds on a laptop computer. The calibration growth simulation was able to adequately capture the reduction in LVESV and LVEDV for the responder (Fig. 2). The calibrated model was then able to correctly predict non-response in the other patient, i.e., absence of substantial reduction in LVESV and LVEDV. Post-CRT stroke volumes for both patients were overestimated.

Additionally, we predicted the change in LVEDV (Fig. 3) and LVESV that would occur for each patient with varying lead locations. Interestingly, our model predicted that both patients could have had a

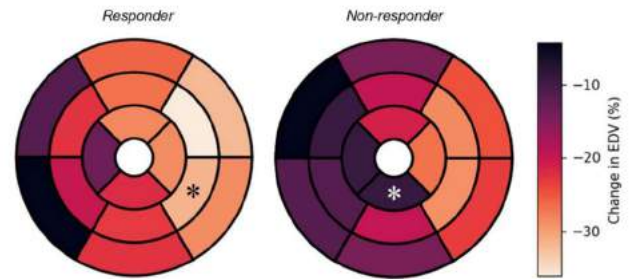


Figure 3: Change in EDV during 6 months of CRT pacing with varying lead locations throughout the 16-segment left ventricle. *Actual lead location selected during implantation

more beneficial degree of reverse remodeling with a different lead location selected. Most importantly, the non-responding patient could have achieved up to a 28% reduction in EDV when pacing from either the mid inferolateral or mid anterolateral segment, thus resulting in a beneficial CRT response.

DISCUSSION

The goal of this study was to create a patient-specific, rapid computational model that can simulate reverse remodeling during CRT. The model was successfully calibrated to data from one patient and able to predict remodeling response for another patient. Moreover, we demonstrated the potential of the model to identify the optimal lead location for individual patients. Most excitingly, our model indicated that a positive response would have been possible for the clinically non-responding patient if a different lead location had been chosen.

The current study has two main limitations. First, hemodynamics, such as blood volume and vascular resistance, were only matched at baseline and held constant throughout the growth simulation. With evolving hemodynamics that match clinical data, the predicted stroke volumes could potentially be more accurate. Second, currently only two case studies were used. We will continue training and testing our model to a larger population of ischemic and non-ischemic LBBB patients to further increase our confidence that this model can predict the reverse remodeling that occurs during CRT, while also potentially determining how ischemia affects prediction accuracy.

By calibrating and validating this framework [5] with data from two non-ischemic CRT patients, we were able to demonstrate the feasibility of our model to predict patient-specific CRT response. This is an important step in creating a valuable clinical tool to identify the best CRT treatment strategy for each patient before clinicians reach the operating room.

ACKNOWLEDGEMENTS

This work was supported by funding from the National Institutes of Health (R01HL159945).

REFERENCES

- [1] Tsao et al., *Circulation*, 145(8):e153–e639, 2022.
- [2] Azevedo et al., *Arq Bras Cardiol*, 106(1):62-9, 2015.
- [3] Sutton et al., *Circulation*, 107:1985-1990, 2003.
- [4] Brignole et al., *Eur Heart J*, 34(29):2281–2329, 2013.
- [5] Oomen et al., *Biomech Model Mechanobiol*, 21: 231–247, 2022.
- [6] Witzenburg et al., *J Cardiovasc Transl Res*, 11:109–122, 2018.
- [7] Walmsley et al., *PLoS Comput Biol*, 11(7):e1004284, 2015.
- [8] Baretta et al., *Philos Trans A Math Phys Eng Sci*, 369(1954):4316–30, 2011.
- [9] Klotz et al., *Am J Physiol Heart Circ Physiol*, 291(1):H403-12, 2006.

SLICK YET STUCK: ELUCIDATING THE UNDERLYING ADHESIVE MECHANICS IN ARTICULAR CARTILAGE

Jamie M. Benson (1) and David L. Burris (1,2)

- (1) Department of Biomedical Engineering, University of Delaware, Newark, DE, USA
(2) Department of Mechanical Engineering, University of Delaware, Newark, DE, USA

INTRODUCTION

As the bearing material of diarthrodial joints, the primary function of cartilage is to support varying loads while sustaining joint lubrication in order to mitigate adhesion and maintain low friction. However, the sound one commonly hears in ‘joint cracking’ is a result of interfacial tension between joint surfaces with sufficient strength to produce an audible noise during contact separation¹. This leads to a contradiction: *low friction* and *high adhesion*. How can cartilage simultaneously exhibit high-lubricity and high-adhesion? Cartilage lubrication has been studied extensively over the past several decades. Yet, there remains a lack of research on cartilage adhesion. The presence of these inherent contradictory mechanisms begs the question: *what is the fundamental role of adhesion in cartilage?* Using instruments unique to this lab, the aim of this experimental study is to quantify these adhesive effects during cartilage contact separation and elucidate the possible implications of adhesion on lubrication and joint biomechanics.

METHODS

Using a coring drill N = 5 full thickness 19mm diameter osteochondral plugs were extracted from the femoral condyles of mature bovine stifles obtained from a local abattoir. Samples were rinsed and stored in 1X PBS containing 1X protease inhibitor at 4°C and tested within 24 hours of extraction. Each sample was subjected to two series of indentation experiments. The first series of measurements focused on retaining interstitial tissue hydration by eliminating dwell times that lead to tissue depressurization. Using a cantilever beam outfitted with a ϕ 6.35mm

borosilicate glass probe, cartilage samples were indented to six randomized indentation depths between 20 and 200 μm , at a 10 $\mu\text{m/s}$ constant indentation rate. After the target deformation was reached the probe immediately retracted at 10 $\mu\text{m/s}$. The second series of measurements focused on systematically varying fluid exudation. Using the same probe, samples were indented to five randomized indentation depths between 20 and 200 μm , at a 10 $\mu\text{m/s}$ constant indentation rate and held for dwell times of 0 s (fully hydrated), 10, 50, 100, 300, 600, and 900s (equilibrium). After each dwell time period, the probe was immediately retracted at 10 $\mu\text{m/s}$. The first series of measurements (effects of indentation depth) were repeated with dry and hydrated silicone on glass, as a measurement of strong adhesion. Data Analysis: The force produced at the cartilage interface is attributed to the culmination of adhesive forces (F_a), solid forces (F_s) and fluid forces (F_f):

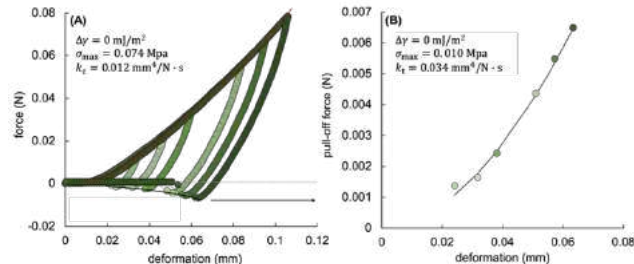
$$F_n = (-1.5\pi \cdot R \cdot \Delta\gamma) + \left(\frac{4}{3} \cdot E_{c0} \cdot R^{0.5} \cdot \delta^{1.5}\right) + \left(\frac{4}{3} \cdot \frac{\dot{\delta} \cdot R^{1.5} \cdot \delta^{1.5}}{k}\right) \quad (1)$$

The probe radius (R) and deformation rate ($\dot{\delta}$) are known variables, while deformation (δ) and pull-off force (F_n) are measured, and work of adhesion ($\Delta\gamma$) and interfacial permeability (k) are fit to Eq. 1. Furthermore, the maximum interfacial tensile stress (σ_{max}) was calculated as a function of the interfacial force (F_n) and the Hertzian contact area (A_c):

$$\sigma = \frac{F_n}{A_c} = \frac{F_n}{\pi \cdot \delta \cdot R} \quad (2)$$

RESULTS

Raw force-deformation data from a representative sample from the first series of measurements is plotted in Fig. 1A. The pull-off force necessary for separation *increased* with indentation depth. The loading curve from the first measurement series was fit to Eqs. 1 and 2 and gave values of 0 mJ/m², 0.074 MPa and 0.012 mm⁴/Ns, for the work of adhesion ($\Delta\gamma$), max interfacial stress (σ_{max}) and



compressive permeability (k_c), respectively (Fig. 1A).

Figure 1: The effects of indentation depth on pull-off force. (A) The loading response was fit to Equation 1 in order to quantify work of adhesion ($\Delta\gamma$) and permeability (k). The work of adhesion and permeability during loading was calculated to be 0 mJ/m² and 0.012 mm⁴/Ns, respectively. Using Equation 2, the maximum interfacial tensile stress (σ_{max}) was calculated to be 0.074 MPa. **(B)** The unloading response was also fit to Equations 1 and 2, and gave work of adhesion, permeability and interfacial tensile stress values of 0 mJ/m², 0.034 mm⁴/Ns and 0.010 MPa, respectively.

The unloading data re-illustrated in terms of positive values (Fig. 1B), was fit and gave values of the work of adhesion ($\Delta\gamma$), max interfacial tensile stress (σ_{max}) and tensile permeability (k_t) as 0 mJ/m², 0.010 MPa and 0.034 mm⁴/Ns, respectively.

Similarly, in the second series of measurements varying dwell time, the pull-off force increased with deformation. The loading curve from the second measurement series, looking at the effects of dwell time, was fit to Eqs. 1 and 2 and gave values of 0 mJ/m², 0.26 MPa and 0.0021 mm⁴/Ns, for the work of adhesion ($\Delta\gamma$), max interfacial stress (σ_{max}) and compressive permeability (k_c), respectively (Fig. 2A). The unloading data re-illustrated in terms of positive values (Fig. 2B), was fit and gave values of the work of adhesion ($\Delta\gamma$), max interfacial tensile stress (σ_{max}) and tensile permeability (k_t) as 0 mJ/m², 0.058 MPa and 0.061 mm⁴/Ns, respectively.

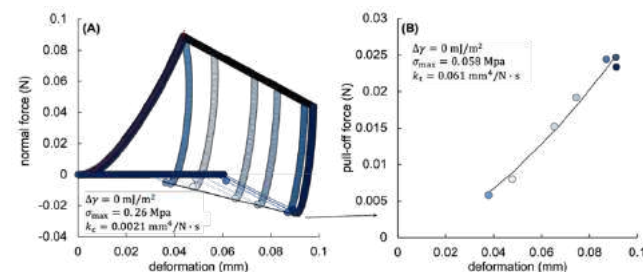


Figure 2: (A) The effects of dwell time on pull-off force. **(A)** The loading response was fit to Equation 1 in order to quantify work of adhesion ($\Delta\gamma$) and permeability (k). The work of adhesion and permeability during loading was calculated to be 0 mJ/m² and 0.0026 mm⁴/Ns, respectively. Using Equation 2, the

maximum interfacial tensile stress (σ_{max}) was calculated to be 0.26 MPa. **(B)** The unloading response was also fit to Equations 1 and 2, and gave work of adhesion, permeability and interfacial tensile stress values of 0 mJ/m², 0.061 mm⁴/Ns and 0.058 MPa, respectively.

Within the silicone on glass contacts, the dry glass on silicone contact resulted in consistent pull-off forces of ~0.0007 N across all deformations. This corresponded to a work of adhesion of ~42 mJ/m², which is consistent with what has been reported in the literature. When the silicone was hydrated, the interface produced zero pull-off forces and zero work of adhesion, which is expected of classically adhesive materials. Comparing the trend of the cartilage to the silicone contacts, it is visually clear that there is a deviation in the behavior of the materials (Fig. 3).

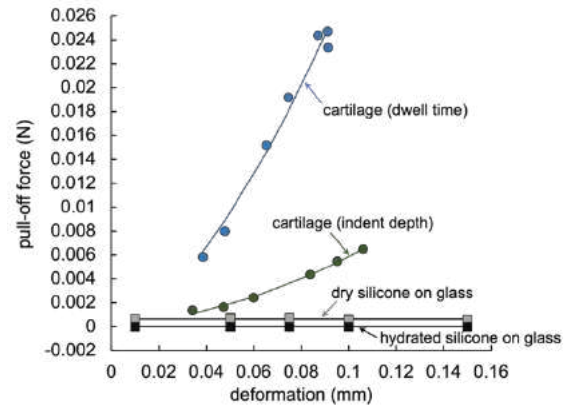


Figure 3: Pull-off forces as a function of deformation. Representative data from the indentation depth and dwell time experimental conditions is plotted with representative glass on silicone datasets under dry and hydrated conditions.

DISCUSSION

This study demonstrates that cartilage exhibits significant interfacial tension. While protected by maximal interstitial hydration (0 sec dwell), cartilage still adhered to the glass probe with appreciable strength to generate detectable pull-off forces. The increased pull-off forces with the increased dwell times indicates that the tissue is exuding fluid, and thus closing the interfacial gaps and increasing contact area. In addition to the zero works of adhesion, the relative permeability observed during the loading and unloading responses also indicate that suction, rather than adhesion, is a dominating force. For both experimental conditions, within each sample, the permeability during loading was comparable, however slightly smaller, than the permeability during unloading. The magnitude of these relative permeabilities suggests that interstitial flow within the tissue was a major contributor to this response. In other words, this suggests that the interface was well-sealed—a requirement for suction. Additionally, the slightly higher effective permeability during unloading is also consistent with the fact that tension expands interfacial and interstitial gaps. This data suggests that suction is driving interfacial tension, creating an interfacial seal and increasing interfacial pressurization needed to drive flow for lubrication.

ACKNOWLEDGEMENTS

This work is supported by the NSF-EAGER (#1937493) and the STLE Jeanie S. McCoy Scholarship

REFERENCES

[1] Kawchuk G. N. *PLoS One*, 2015.

ANISOTROPIC STIFFNESS MEASURED USING A TOROIDAL PROBE IN MESO LEVEL AND CELL LEVEL

J. Li (1), T. Paradis (1), M. Vandadi (2), N. Rahbar (2), K. L. Billiar (1)

(1) Biomedical Engineering, Worcester Polytechnic Institute, Worcester, MA, USA
(2) Civil Engineering, Worcester Polytechnic Institute, Worcester, MA, USA

INTRODUCTION

Characterizing the mechanical properties of cells and biological tissues is of critical importance as the mechanical properties reflect the physiological state and integrity of tissues and may serve as hallmarks of diseases such as cancer, calcification, and atherosclerosis (1,2). While most biological tissues and many cell types are highly mechanically anisotropic, many studies, especially studies in microscale and mesoscale, assume samples to be mechanically isotropic often due to the technical difficulties in measuring anisotropic stiffness of cells and microtissues. This oversimplification does not accurately reflect the mechanical properties of cells and micro tissues and may bias the interpretation in tissue mechanics and mechanobiology.

Indentation is one of the most common methods for measuring mechanical properties of biological tissues and cells. Conventional indenters are equipped with spherical, conical, or pyramidal probes which do not yield information related to mechanical anisotropy. Several recent studies have proposed solutions to this problem. However, these methods require complicated image analysis or samples to be prepared into specific shapes (3,4,5). Moreover, most studies are focused on macro level tissue properties; studies on the mesoscale and cell level are limited. A straight-forward indentation method for the measurement of anisotropic mechanical properties is needed.

Here, we propose a method to measure anisotropic stiffness of microtissues and cells by two indentations in orthogonal directions using our novel toroidal probe. Our preliminary results indicate that this approach is applicable in measuring anisotropic stiffness of aligned tissues and cells. This method will provide researchers with a simple and cost-effective means for measuring mechanical anisotropy of micro-scale samples.

METHODS

The mesoscale toroidal probe tip was designed to be 20 μm in cross-section radius and 100 μm in ring radius, the microscale probe tip

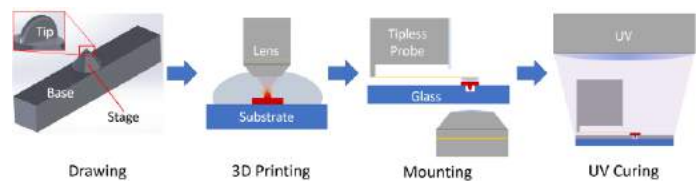


Figure 1. A schematic brief procedure of manufacturing the toroidal probe tip

was designed to be 2 μm in cross-section radius and 10 μm in ring radius. The tip was manufactured using a Naonoscribe GT two-photon 3D printer (Fig. 1). Briefly, the probe tip with supporting stage and base was created in CAD then translated to executable codes with printing parameters optimized for smoothness of the tip surface. A drop of negative photoresist resin was applied onto the cleaned substrate mounted on the device. In the printing, the two-photon laser scans over 3D space according to the code to polymerize the resin at the focal point. After printing, the base was detached from the substrate using a fine tweezer and flipped over under the microscope. A tipless probe was mounted to the nanoindenter (Optics11, Amsterdam), dabbed with UV-curing glue at the end of the cantilever, then lightly touched the bottom of the base. The glue was cured under the UV light for 30 minutes (Fig. 1). The probe was visually inspected using optical and scanning electron microscopy (Fig. 2).

Chicken breast was used for meso-scale indentation study. The sample was dissected and transferred to a 100 mm-petri dish filled with PBS (Fig.3, left). Porcine aortic valvular interstitial cells (PAVICs) were used in cell indentation study. To grow aligned cell monolayers, parallel scratches were made in 35-mm petri dishes, 100,000 cells were seeded. And the cells were cultured for 6 days to form an anisotropic monolayer (Fig.3, right).

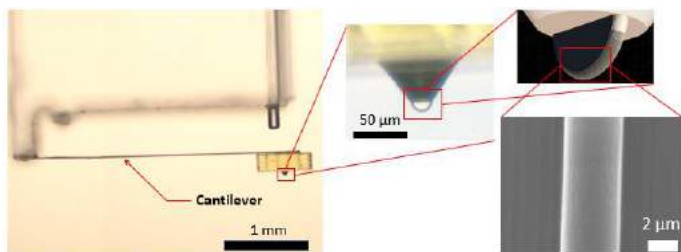


Figure 2. Optical and scanning electron microscopy images of microscale probe and its toroidal tip. The probes were manufactured in accurate size, shape, and smooth surface.

Before indentation, the chicken breast was lightly pressed by a tweezer to avoid floating. Indentation speed was set to be 10 $\mu\text{m/s}$ until 50 μm max indentation depth. For the cell sample, the cell culture media was changed to complete L-15 medium to maintain a stable pH. The cells were aligned to the probe under a Nikon TS-100 inverted microscope. Indentation speed was set to 1 $\mu\text{m/s}$, with 500 nm maximum indentation depth. The force-indentation curves were recorded and fit to the Hertzian model for elliptical contact, in which the effective Young's modulus (E^*) is calculated by

$$E^* = \frac{3F}{4d^{3/2}R_e^{1/2}}f_2^{3/2}(e) \quad (1)$$

where d is indentation, F is force; $R_e = \sqrt{R_1 R_2}$ is the equivalent radius of the probe tip; $f_2(e)$ is an empirical function of the eccentricity of the ellipse (~ 1 for an aspect ratio of 5) (6). Two chicken breasts and one PAVIC monolayer were indented at multiple sites along (0°) and across (90°) the fiber direction. For PAVICs, the indentation data of top 50% stiffness was filtered to rule out the samples affected by substrate effect. Statistical comparisons were made using t-test, $p < 0.05$ is considered significant.

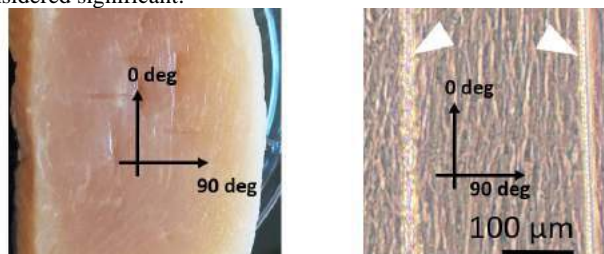


Figure 3. Anisotropic biological materials tested. Left: chicken breast shows clear fiber orientation. Right: PAVICs align in the direction of the scratches (arrowheads) to form an aligned monolayer.

RESULTS

As predicted, chicken breast samples have a higher effective Young's modulus when the long axis of probe is perpendicular to the fiber direction of the chicken breast (90°) compared to the indentation in parallel direction (0°) on both samples ($p < 0.05$). In the two samples, the moduli across the fiber direction were 3.45 ± 2.12 kPa, and 3.70 ± 2.17 kPa, while the moduli at 0° were 2.35 ± 1.27 kPa and 2.17 ± 1.28 kPa (Fig. 4, left).

Similarly, for the indentation test on PAVICs, we found a trend toward higher modulus at 90° (7.22 ± 2.01 kPa) than at 0° (5.84 ± 1.86 kPa) ($p = 0.07$, n.s.) (Fig. 4, right).

DISCUSSION

Measuring the anisotropic properties of biological materials is not readily possible with indentation testing, especially at the cell level. Previous studies trying to resolve this problem are mostly limited to

macro samples, and commonly require high-resolution live imaging to measure the non-uniform strain field or samples of specific shapes (3-5). The one study to date reporting a measure of cell anisotropy using indentation requires live confocal microscopy and inverse finite element analysis (4). Here, we present a method to measure the mechanical anisotropy of cells and tissues by two orthogonal indentations without the need for microscopy or sample of specific shapes which allows for rapid measurement of samples *in vivo*. Importantly, our method can be performed by most of the existing indenters and AFMs at a low cost. The cost of each probe tip is less than \$5 for the mesoscale probe, and \$40 for the micro probe.

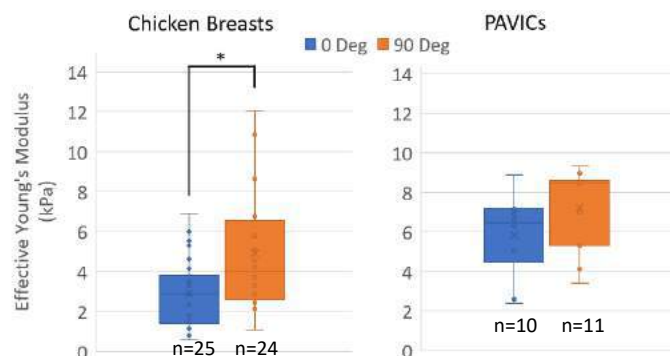


Figure 4. Effective Young's modulus of a chicken breast (left) PAVICs (right) measured in two orthogonal directions (* $p < 0.05$).

In this study, we used chicken breast and PAVICs as the samples. Both samples show higher effective Young's modulus across the fiber direction than along the fiber direction. This result is consistent with previous studies (4,7). While indentation on chicken breast shows significant difference in two directions, the difference is not significant in the case of PAVICs. This may reflect a different degree of anisotropy of PAVICs and chicken breast or simply the low sample size in these pilot tests. Probes of higher anisotropy ratio may be needed for samples with lower degree of anisotropy.

One limitation of this study is that the modulus is calculated based on Hertzian contact theory which assumes materials isotropy and linear elasticity. To our knowledge, there is no analytical solution for the indentation problem on anisotropic materials. In the next step of the study, we plan to apply FE modeling to extract the mechanical parameters based on the indentation curves either with inverse methods or with forward modeling and machine learning.

In conclusion, we created a novel method for measuring anisotropic stiffness of biological samples. This method is simple, cost-effective, and can measure small samples down to the cell level. We expect this method will be of use to researchers in biomechanics, biophysics, and mechanobiology.

ACKNOWLEDGEMENTS

This work was supported by the NSF (CMMI 1761432) and ARMI BiofabUSA (T0137).

REFERENCES

- [1] Chien, S, *Am J Physiol Heart Circ Physiol*., 292(3), H1209-H1224, 2007.
- [2] Goldblatt, Z. E. *et al.*, *Biophys J.*, 118(1), 15-25, 2020.
- [3] Efremov, Y. M. *et al.*, *Sci Rep.*, 9(1), 1-12, 2019.
- [4] Feng, Y. *et al.*, *J Mech Behav Biomed Mater.* 65, 490-501, 2017.
- [5] Fang, S. *et al.*, *Annu. Rev. Biomed. Eng.*, 49(8), 1923-1942., 2021.
- [6] Johnson, K. L., *Contact mechanics.*, 96, 1987.
- [7] Choshali *et al.*, *SB³C2022-241*, 2022.

A MACHINE LEARNING APPROACH TO ESTIMATE SIZE AND LOCATION OF MYOCARDIAL INFARCTION

RR. Mehdi (1), EA. Mendiola (1), R. Avazmohammadi (1,2)

(1) Department of Biomedical Engineering, Texas A&M University, College Station, TX, USA
(2) Department of Mechanical Engineering, Texas A&M University, College Station, TX, USA

INTRODUCTION

Myocardial infarction (MI), due to the blockage of coronary arteries, is a leading cause of death in the US and worldwide [1]. The size of chronic scar in MI adversely affects cardiac function; however, several studies have pointed out that chronic scar formation in MI may remain undiagnosed in a large part of MI incidences [2]. Cardiac scar size and location in MI can be identified using cine cardiac magnetic resonance imaging (CMR) with late gadolinium enhancement (LGE) [3]. LGE imaging based on a gadolinium-based contrast agent identifies matured infarcted regions by bright image intensity. However, LGE has some limitations including accumulation of gadolinium in tissues and prolonged scanning time which limit its scope and safety in time-sensitive clinical applications. Furthermore, the gadolinium-based imaging process may be dangerous to chronic end-stage kidney patients and approximately 20% of the patients who suffer from acute MI also have chronic kidney disease [4]. And, perhaps more importantly, LGE requires CMR which is not a feasible imaging modality at all health centers even in developed countries. Therefore, a less invasive and more feasible method to identify infarct region characteristics will assist in reducing undiagnosed MI cases.

In this work, we developed a machine learning (ML) model to identify the location and extent of infarcted myocardium by employing cardiac strains that are feasibly obtainable from routine CMR scans and very possibly from echocardiography. We implemented a pipeline that takes raw CMR scans and calculates 4D (3D space plus time) strains. The 4D strains were used in the ML as inputs to predict the location and extent of infarct regions. Our results suggest that our framework can learn the relationship between the strains and labeling of infarcts and be used as an efficient and reliable tool to identify infarct regions.

METHODS

The 3-D reconstructed heart geometry from CMR scans was truncated under the valve plane and meshed using quadratic tetrahedral

elements as shown in Fig. 1a. An inverse problem was set up for a biventricular finite element (FE) model to estimate the passive material properties of the infarct and remote regions from the biaxial test result. Organ-level inverse simulations were performed to estimate animal-specific active tension by replicating pressure-volume measurements using inverse modeling. Details of estimating active and passive material properties are described in [5]. We developed a large database of semi-synthetically finite-element heart models covering numerous possibilities of MI region location and shape (Fig 1b). The endocardium surface was pressurized with a pressure wave of maximum amplitude of 7.5 mmHg. The average Green strains were computed at each segment according to American heart association (AHA) segmentation (Fig 1c) in circumferential, longitudinal, and radial directions.

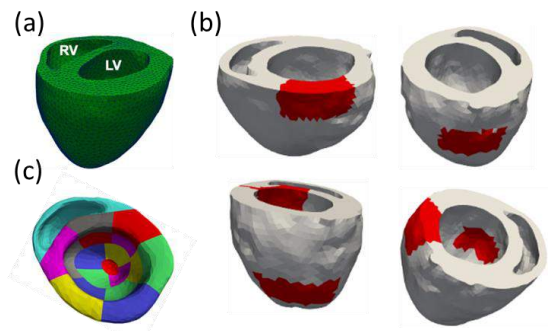


Fig 1 (a) Biventricular FE model (b) Examples of randomly generated infarcts (c) AHA segmentation of the left ventricle.

A 17×3 image was constructed using 17 AHA segments and three anatomical strains (circumferential, longitudinal, and radial) for each segment. This image was provided to the convolutional neural network (CNN) ML model to identify size and location of infarct regions (Fig 2). We built a binary array with the same size of the number of segments

as labels in which 1 is infarct and 0 is non-infarct. Hundred examples with different sizes and locations of infarcts were generated to train the model. Leave-one-out cross-validation technique was utilized to reduce the variance with a limited number of examples. As the number of non-infarct regions was higher than the infarcted regions, the weights imbalance classification was applied, and weights were calculated and distributed at the time of training the CNN model.

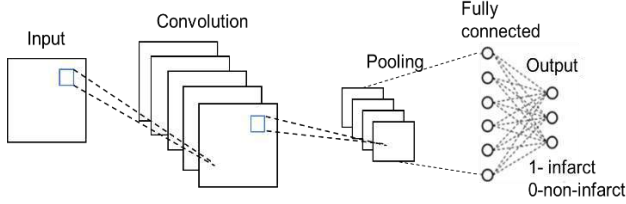


Fig 2: Convolutional neural network model architecture.

The performance of our CNN ML model was evaluated by the following parameters:

$$Accuracy = \frac{TP + TN}{TP + TN + FP + FN}$$

$$Sensitivity = \frac{TP}{TP + FN}$$

$$Precision = \frac{TP}{TP + FP}$$

$$F1 - score = \frac{2 \cdot TP}{2 \cdot TP + FP + FN}$$

Here TP (True Positive) means correctly detected infarct, TN (True Negative) is being identified as correctly detected non-infarct, FN (False Negative) identified infarct when the infarct was present and model did not detect, and FP (False Positive), means infarct was not present, but ML model detected infarct.

RESULTS

The inverse modeling with estimated active and passive parameters and appropriate fiber architecture provided the end-systolic strain as shown in Fig. 3. The ML model utilized these cardiac end-systolic strains in the left ventricle (LV) to locate infarct in the LV. The performance of the ML classifier was demonstrated in the form of a confusion matrix. Our approach accurately classified the infarcted regions from the normal tissues (Fig. 4). We achieved 94.59% accuracy, 0.98, 0.96, and 0.97 sensitivity, precision, and F1-score, respectively.

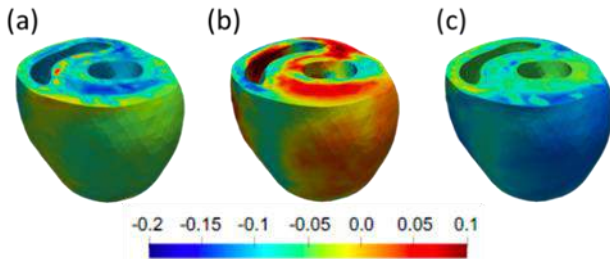


Fig 3: Examples of (a) Circumferential (b) Radial (c) Longitudinal strains.

VALIDATION

We validated our proposed model by comparing the ML predictions with ground-truth measurements by LGE imaging in MI human patients (Fig 5). We used our in-house diffeomorphic image registration to

calculate 4D strains (3D + time) using only short-axis slices. End-systolic strains at each segment of AHA segmentation were provided to the ML model to classify the infarcted region which is compared with the LGE imaging to obtain the accuracy of our model. Our results suggest that ML model can delineate the MI using cardiac strains (from cine CMR or echocardiography) without using a contrast agent which shows the ability of the ML model to provide timely interpretations for clinical follow-up.

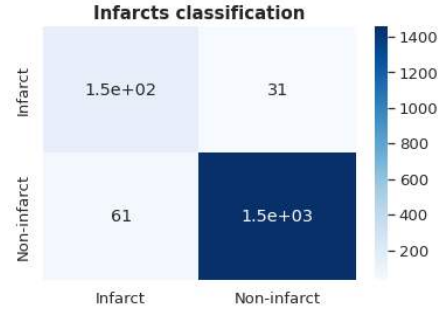


Fig 4: Confusion matrix to locate infarct.

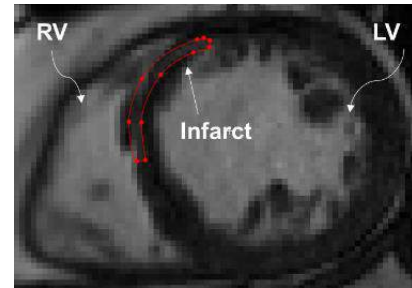


Fig 5: LGE CMR of an MI patient.

DISCUSSION

In this work, we developed a CNN-based ML model to accurately delineate the infarct regions in the LV. For this purpose, the FE simulation-based pipeline was created to mimic the function of the heart (representing the virtual twin of the in-vivo heart) and end-systolic strains were used to train the model. Once the model is trained from the FE simulations at different infarct sizes and locations, it can estimate the infarct regions with high accuracy directly from common imaging modalities, including CMR and echocardiography. Furthermore, we did not use the large dataset of human CMR to train the ML model in contrast to other existing methods that rely on a large CMR database to train the ML. Instead, we used synthetically obtained FE simulations. To the best of our knowledge, this is the first time a ML model to locate infarct location is trained using affordable FE simulations and directly applied to the human images slices. We are currently extending our model to accurately locate infarcts in very small segments and determine their transmural depth.

ACKNOWLEDGEMENTS

RA was supported by the NIH, under grant No. R00HL138288.

REFERENCES

- [1] Bui, A. L. et al., *Nature Reviews Cardiology*, 8(1), pp.30-41, 2011.
- [2] Richardson, WJ et al., *Comprehensive Physiology*, 5, no. 4, 2015.
- [3] Mendiola, EA et al., *The FASEB Journal*, 36, 2022.
- [4] Fox, C. S. et al., *Circulation*, 121(3), pp.357-365, 2010.
- [5] Mendiola, EA et al., *Annals of Biomedical Engineering*, 1-18, 2022.

A THERMODYNAMIC FRAMEWORK FOR SARCOMERE FORMATION IN CARDIOMYOCYTES SPREAD ON MICRO-PATTERNED SUBSTRATES

Ryan J. Coleman (1), Vikram S. Deshpande (2), Patrick McGarry (1)

(1) Department of Biomedical Engineering, University of Galway, Galway, Ireland
(2) Department of Engineering, University of Cambridge, Cambridge, UK

INTRODUCTION

Identification of in-vitro protocols to develop mature cardiomyocytes (CMs) with ordered sarcomeric structures and aligned myofibrils remains a key challenge in the field of cell and tissue engineering [1,2]. An experimental study by Ribeiro et al. [3] reports that human pluripotent stem cells (hPSCs) develop highly aligned sarcomeres when spread on high aspect ratio (7:1) rectangular micro-patterned ligand patches. However, cells spread on square patches do not develop sarcomeres, instead developing unaligned stress fibers (SFs). The mechanism underlying the differentiation of hPSCs to mature CMs as a function of cell aspect ratio is not understood. This deficiency in fundamental understanding presents a significant barrier to the development of robust strategies for cardiac tissue engineering.

We propose a novel thermodynamically based theoretical model for sarcomere and SF formation within a cell. We develop a statistical mechanics framework to simulate the spreading of cells on square and rectangular adhesive patches and quantitatively compare our model predictions to experimentally measured levels of sarcomere formation.

METHODS

We consider that cytoskeletal proteins can exist in three states within a CM: they can be (i) bound as part of a SF, (ii) bound as part of a structured sarcomere, or (iii) unbound within the cytoplasm. Figure 1 shows the corresponding energy landscape; highly structured sarcomeres have a higher ground-state enthalpy than loosely structured SFs. However, sarcomeres generate higher levels of active contractility than SFs.

At steady-state conditions the chemical potentials of all three states are in equilibrium. We derive the chemical potentials to have the following forms: unbound proteins $\chi_U = \frac{\mu_U}{n^R} - T \frac{\partial \Delta S_U}{\partial \hat{N}_U}$, bound SFs

$$\chi_{BF} = \frac{\mu_B}{n^R} - T \frac{\partial (\Delta S_{BF} + \Delta S_U)}{\partial \hat{N}_{BF}}, \text{ and bound sarcomeres } \chi_{BS} = \frac{\mu_H}{n^R} -$$

$T \frac{\partial (\Delta S_{BS} + \Delta S_U)}{\partial \hat{N}_{BS}}$. Change in organizational entropies are computed as ΔS_U , ΔS_{BF} and ΔS_{BS} . n^R is the number of contractile units within a representative volume element (RVE) and T is the cell temperature. Conservation of cytoskeletal proteins within the CM enforces that $\hat{N}_U + \hat{N}_{BF} + \hat{N}_{BS} = 1$, where \hat{N}_{BF} and \hat{N}_{BS} are the fraction of proteins bound in SFs and sarcomeres, respectively, and \hat{N}_U is the fraction of unbound proteins. The areal density of sarcomeres at any point within the cell is given as

$$\hat{n}_S = \frac{\frac{1}{\hat{n}_S} (\xi_1 - \hat{N}_{BF}) (\hat{N}_U + \hat{N}_{BF}) \exp \left(-\hat{n}_S \frac{\mu_H - \mu_U}{k_B T} \right)}{\xi_1 + (\hat{N}_U + \hat{N}_{BF}) \exp \left(-\hat{n}_S \frac{\mu_H - \mu_U}{k_B T} \right)}, \quad (1)$$

where \hat{n}_S is number of sarcomeres in series within a myofibril and ξ_1 is the maximum local concentration of sarcomeres. A similar expression is derived for the concentration of SFs within the cell.

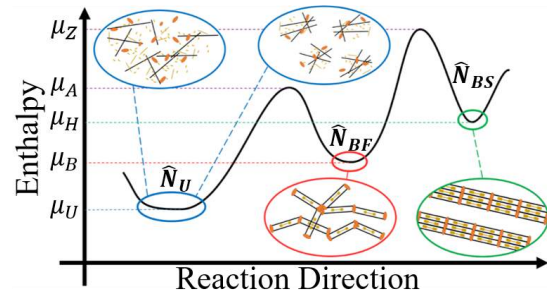


Figure 1: Energy landscape for unbound cytoskeletal proteins, SFs and sarcomeres.

In our statistical mechanics finite element framework, we simulate a cell spreading on a micro-patterned ligand patch by analyzing over two million spread states with incremental deformations between states tested through MCMC walks [4]. For each potential new cell state we calculate the Gibbs free energy, which consists of contributions from sarcomeres, SFs, and the deformed passive cell cytoplasm. Importantly, as the cell spreads and elongates, sarcomere formation results in a reduction in Gibbs free energy. However, such cell elongation results in stretching of the passive hyperelastic cell cytoplasm, resulting in an increase in Gibbs free energy. The potential new spread state is accepted if this energetic competition leads to an overall reduction in Gibbs free energy relative to a reference state. We develop a nested sampling framework to impose a homeostatic constraint such that the mean Gibbs free energy of the ensemble of spread states is equal to the reference state of a suspended cell [5]. Simulations are performed on rectangular ligand patches of aspect ratios 1:1, 3:1, 5:1 and 7:1 for direct comparison with in vitro experiments [3]. Each simulation requires 24 hours using 40 processors using a high-performance machine at the Irish Centre for High-end Computing (ICHEC).

RESULTS

A sample of computed spread cell states are shown in Figure 2 for CMs spread on rectangular ligand patches. Highly aligned dense sarcomere structures are predicted for a cell spread on a 7:1 rectangular patch. In contrast, for a cell spread on a square patch our model predicts a low-density of sarcomeres with low levels of myofibril alignment. Experimental images of Ribeiro et al. [3] are shown for comparison, exhibiting a similar trend to our model predictions.

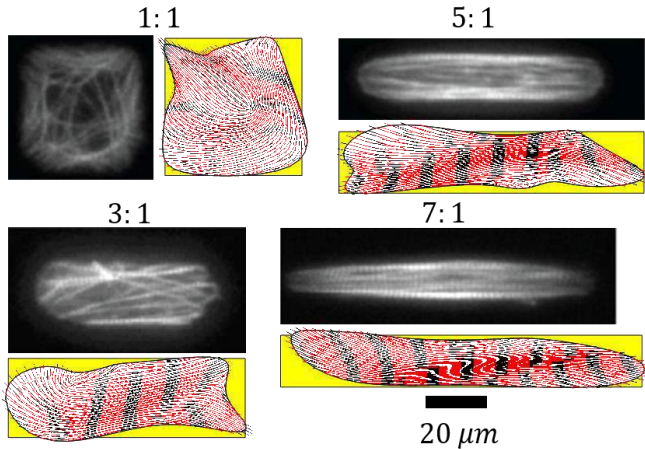


Figure 2: Sample of predicted CM spread states on rectangular ligand patches. All computed states shown are within one standard deviation of the homeostatic free energy. Predicted sarcomere orientations shown by red quivers (thickness of quiver scales with computed sarcomere density). Experimental results adapted from Ribeiro et al. [3] are shown for comparison.

Figure 3A shows that the computed level of sarcomere formation increases with aspect ratio, in agreement with experimental measurements. Figure 3B shows the computed distribution of sarcomere orientations as a function of patch aspect ratio. Again, strong agreement with experiments is observed, with elongated CMs exhibiting higher levels of alignment. Our model uncovers the following mechanism: Gibbs free energy decreases with increasing sarcomere density. Sarcomere areal density exponentially increases with in series units (equation 1), driving an increase in sarcomere length. Such an increase

in sarcomere length is facilitated by elongated cells (e.g. 7:1 rectangle), but not facilitated by isotropically spread cells (e.g. 1:1 square) of a similar spread area.

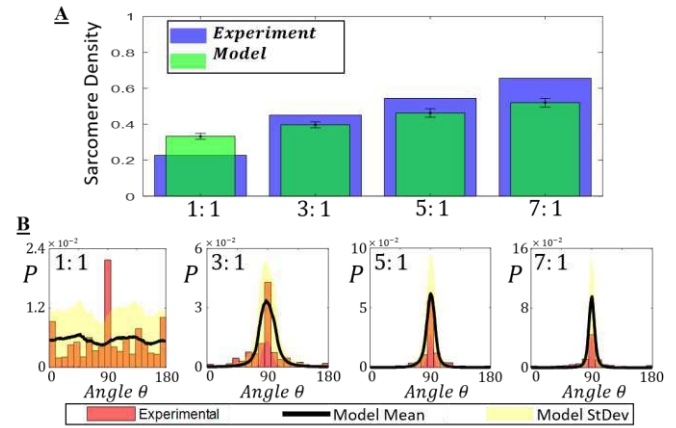


Figure 3: (A) Computed sarcomere density (mean±SD) as a function of ligand-patch aspect ratio. (B) Computed sarcomere distribution (alignment) as a function of ligand-patch aspect ratio. Experimental results (Ribeiro et al. [3]) shown for comparison.

DISCUSSION

We present the first thermodynamically based theoretical model for sarcomere formation in CMs, and we implement this model in a novel statistical mechanics framework to simulate cells spreading on micro-patterned ligand patches. Decreased Gibbs free energy is driven by sarcomere formation as cells spread into highly elongated states. Our model predictions are in strong agreement with the experimental observations of Ribeiro et al. [3]. The mechanism of sarcomere formation uncovered by our model can be used to guide in-vitro strategies to generate mature contractile CMs. As an example, high aspect ratio tissue constructs and electro-spun collagen scaffolds could be designed using our modelling framework to optimize sarcomere formation [6]. Additionally, our model can be used to simulate multi-axial dynamic loading of CMs and cardiac tissue. Optimal dynamic loading regimes to promote sarcomere formation can potentially be identified using our model [7]. Finally, our framework can be implemented into finite element models of a beating heart to predict the influence of a range of pathologies (e.g. hypertension) on remodeling of sarcomeres in vivo [8].

ACKNOWLEDGEMENTS

Science Foundation Ireland (grant 18/ERCD/5481); Irish Centre for High-End Computing.

REFERENCES

- [1] Nunes, S et al., Nat. Methods, 781-787, 10(8), 2013.
- [2] Jacot, J et al., Ann. N. Y. Acad. Sci., 1188(1), 121–127, 2010.
- [3] Ribeiro, A et al., PNAS, 112(41), 12705–12710, 2015.
- [4] Shishvan, S et al., BMBB, 17, 1631–1662, 2018.
- [5] McEvoy, E et al., Biophys. J., 2451-2460, 115(12), 2018.
- [6] Thavandiran, N et al., PNAS, 110(49), 4698-4707, 2013.
- [7] Dou, W et al., Biosens. Bioelectron. 175, 112875, 2021.
- [8] McEvoy, E et al., J Mech Behav Biomed Mater, 113:104074, 2021.

TOWARDS ENHANCED NON-INVASIVE ASSESSMENT OF BLADDER URODYNAMICS - VALIDATION OF DYNAMIC 3D MRI IN A PATIENT-SPECIFIC IN VITRO MODEL OF THE BLADDER

J. Rice (1,2), J. Gwertzman (1), A. Roldán-Alzate (1,2)

(1) Department of Mechanical Engineering, University of Wisconsin - Madison, Madison, WI, USA

(2) Department of Radiology, University of Wisconsin - Madison, Madison, WI, USA

INTRODUCTION

Lower urinary tract symptoms (LUTS) and changes in bladder function occur as individuals age¹⁻³. Patients with LUTS are evaluated through multi-channel urodynamic studies to determine bladder flow and pressure during voiding and filling to gain insight into the progression and severity of symptoms²⁻³. However, these tests are invasive, time-consuming and provide limited flow visualization or insight into anatomical changes as the bladder contracts or expands. To combat this, recent efforts have focused around utilizing MRI to determine bladder volume and flow. Information obtained from MRI can be used to drive computational fluid dynamics (CFD) to analyze flow, pressure, and wall motion³. In either case, validation of these techniques in a bladder-mimicking in-vitro model remains an unmet need. In-vitro flow studies are recognized as the gold standard for flow-based MRI and CFD validation⁴. Using in-vitro models, systematic control of anatomy and flow conditions can be reached. Models can also be evaluated with higher resolution optical imaging techniques, such as particle image velocimetry (PIV).

The aim of this study was to develop an MRI- and PIV-compatible patient-specific, in vitro model of the bladder to validate a real-time volumetric MRI protocol. 3D volumes of the bladder were acquired during voiding and filling tests. Simultaneous acquisition of pressure data at the bladder outlet was obtained. Finally, fluid velocity was measured using 2D phase-contrast (2D-PC) MRI at the bladder outlet to validate the flow rate calculated from 3D dynamic MRI, demonstrating this study as an effective first step towards enhanced validation of novel 3D MRI urodynamics.

METHODS

In this IRB-approved, HIPPA compliant study, a healthy, 37-year-old subject was recruited to void in the scanner during a 3D MRI acquisition. A flexible, transparent in-vitro patient-specific model of the bladder was constructed using a hybrid additive manufacturing process.

The full bladder was segmented from the 3D MRI dataset to produce a stereolithography (STL) model. Using the model, a negative mold was generated representing a larger version of the bladder and printed in two halves using a desktop stereolithography printer (Formlabs, Somerville, MA). A positive bladder “core” was 3D-printed in water-soluble polyvinyl alcohol (PVA) (Ultimaker, Utrecht, Netherlands). The core was placed in the mold where it was cast in silicone and cured. The mold was designed so that the mean thickness of the model wall was 4mm, representing the thickness of the bladder wall⁵. Once the silicone cured, the bladder core was dissolved, leaving an anatomically realistic hollow bladder (Figure 1).

The transparent model was connected to a syringe pump (Chemyx, Stafford, TX). 6.35 mm tubing was connected to the outlet of the bladder representing a urethra. Water was injected or withdrawn from the system at various flow rates to simulate bladder voiding and filling like bladder cystometry⁶. The bladder was placed in a 3.0T MRI scanner (GE Healthcare, Waukesha, WI) where real-time volumetric, and 2DPC, MRI data were acquired. An MRI-compatible, fiber-optic pressure transducer (OPP-M200, Opsens Inc., Québec, CA) was fed into the bladder during MRI acquisitions to obtain pressure measurements during each event (filling and voiding).

MRI and pressure data were analyzed using a custom Matlab script to calculate bladder volumes, pressure, outlet velocity, flow rate and bladder work. 100 sets of images were acquired using volumetric MRI during tests with a time resolution of 1.65 seconds and spatial resolution of 1.0 mm. A semi-automatic segmentation process was used to determine bladder volume. 2DPC MRI data were reconstructed with a time resolution of 1.35 seconds and 1.0 mm spatial resolution. Pressure measurements were acquired at 100Hz, smoothed using a low-pass filter, and resampled to match the time resolution of the volumetric MRI data. The difference in volume at each time was used to approximate volume flow rate and compared to the imposed flow rates.



Figure 1: (A) Schematic of in-vitro fabrication method used to make physical model. (B) Silicone model before dissolving bladder core. (C) MRI- and PIV-compatible hollow bladder flow model (note the model in the anatomical standing position).

RESULTS

Figure 2 depicts in vitro model volumes over time during a voiding (A) and filling (B) event, as well as velocity contours (C) at the outlet of the model during the fastest voiding test. MRI-derived volumes and flow rates agreed within 10% of the flow rates imposed by the pump (Table 1). Flow rate obtained from 2DPC-MRI was 5.58 cm/s, differing from the imposed flow rate by 4.31%.

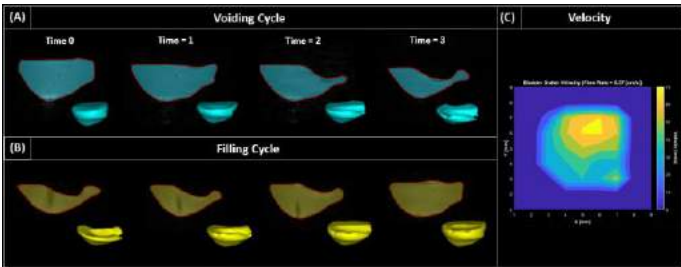


Figure 2: MRI-derived bladder volumes during (A) voiding and (B) filling events. (C) Velocity contours at the bladder outlet derived from 2DPC MRI.

Test	Imposed Volume Change [cc]	Imposed Flow Rate [cc/s]	3D MRI Flow Rate [cc/s]	MRI Volume Change [cc]	Flow Rate Error [%]	Volume Error [%]
Void	150	5.37	5.24	147.7	2.58	1.57
		2.50	2.63	148.6	5.39	0.94
		0.83	0.89	138.7	6.72	7.56
Fill	150	1.67	1.78	154.3	7.34	2.88
		0.83	0.90	140.3	8.00	6.44

Table 1: MRI-derived volume measurements and volumetric flow rates compared to those imposed by the pump during testing.

Figure 3 shows pressure-volume (PV) curves obtained for each voiding and filling test. A pressure drop is seen during voiding while pressure increases are observed during filling. Filling pressure curves exhibited more discrepancy between repeated tests at different flow rates. The work associated with bladder emptying and filling is computed as the integral of the PV-curve. More work output was associated with increased flow rate for both voiding and filling events. Calculated work for each test is summarized in Table 2.

Test	Flow Rate [cc/s]	Calculated Work [millijoule]
Void	5.37	71.75
	2.50	64.82
	0.83	49.70
Fill	1.67	99.72
	0.83	54.24

Table 2: Calculated work output for each voiding and filling event.

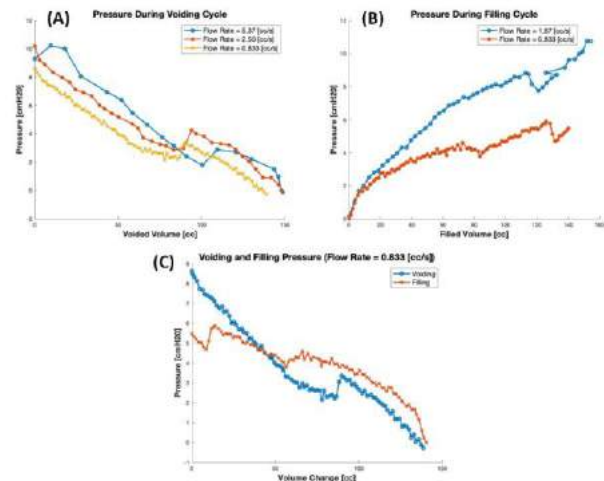


Figure 3: Pressure-volume curves obtained for (A) voiding (B) filling events. (C) Pressure-volume curve for both voiding and filling tests at the same flow rate (0.833 cc/s).

DISCUSSION

Bladder volume during three voiding and two filling tests were successfully calculated from 3D MRI data and used to estimate volumetric flow rate. MRI-derived flow rates agreed with pump flow rate within 10%. As flow rate was decreased, errors between pump and MRI-derived volume and flow rate increased. At lower flow rates there are smaller spatial changes in the model, so distinguishing between true spatial variations becomes difficult near the MRI resolution limit.

Voiding pressure was relatively insensitive to volume flow rate, suggesting that the in vitro bladder may deform similarly regardless of flow rate during emptying. However, this behavior is not seen in filling pressure curves. Higher pressures were associated with higher flow rates, suggesting it takes more effort to deform the model as flow rate increases. Differences between voiding and filling behavior are also observed at the same flow rate (Figure 3c). One explanation may be that the silicone exhibits viscoelastic behavior in response to increased strain rate (i.e higher flow rate). Further experimentation to better understand this behavior is needed.

This modeling pipeline represents a novel technique to systematically assess the validity of experimental MRI in the bladder. MRI-derived volumes can be used to drive CFD simulations to quantify velocity and pressures in 3D. Additionally, this model was designed to be PIV-compatible, and future efforts will focus on its utilization to quantify and validate velocity throughout the bladder, in addition to the localized measurements in the bladder neck reported here. A similar experimental setup can be employed in ex-vivo bladder flow studies, which may represent a more physiologically realistic replication of the bladder and lower urinary tract.

ACKNOWLEDGEMENTS

The authors would like to acknowledge support from the NIH (R01 DK126850-01), GE Healthcare, and Grant Roberts, whose MRI expertise was indispensable during this study.

References:

- [1] Wei JT, et al. J Urol. 2005; 173:1256-1261
- [2] Yao M, Simoes A. StatPearls. 2022
- [3] Pewowaruk R, et al. PloS ONE. 2020;15(11)
- [4] Rutkowski D, et al. J Biomech Eng. 2019;141(12):121004
- [5] Blatt A, et al. J. Urol. 2008;179(6):2275-2278
- [6] Kalayeh K, et al. Investigative Radiology. 2022;10.109

A SLIM, PULSE-DRIVEN MICROFLUIDIC DEVICE FOR INSULIN DELIVERY

Shuyu Zhang (1,2), Rafael V. Davalos (1,2), Anne E. Staples (1,2)

(1) Virginia Tech-Wake Forest School of Biomedical Engineering and Sciences, Blacksburg, Virginia, United States

(2) Department of Biomedical Engineering and Mechanics, Blacksburg, Virginia, United States

INTRODUCTION

Diabetes mellitus is an extremely common condition that affects approximately 500 million people worldwide.¹ Currently, most insulin-dependent diabetic patients rely on syringes or pens that deliver insulin into the subcutaneous fat layer through a macrobore cannula, while others use battery-powered insulin pumps (Figure 1).^{2,3} According to users, both of these treatments can be painful due to the insertion of cannulas.⁴⁻⁸ In addition, insulin pumps are bulky and can interfere with

the tracheal system.¹⁷ Similarly, we have designed our devices in such a way that when gentle physiological pulses are applied, an elastomeric membrane rhythmically collapses and re-expands, changing the flow channel volume, which drives a fluid flow.

METHODS

To fabricate the devices, we have adapted a stereolithographic 3D printing technique to make master molds, which provides higher resolution and reduces time and cost needed to produce each mold as compared to traditional photolithography techniques.¹⁸⁻²¹ Briefly, we design the master mold geometry using CAD software and then print the mold for the pump (flow channel) and reservoir layers using a Formlabs 3B+ 3D printer. We then replica cast a layer of polydimethylsiloxane (PDMS) onto the master molds to make the pump and reservoir layers. For the elastomeric membrane, we spin a thin layer of PDMS onto a silicon wafer using a spin coater. The device layers are bonded together into a multi-layer device with a plasma cleaner. Hollow microneedle arrays with various geometries are fabricated using a Formlabs3B+ 3D printer, following the protocol of Yeung et al. (2019)²² using biocompatible 3D printing resins (Formlabs Clear, Rigid 4000, Surgical Guide, and Tough 2000 resins).

To test the performance of the devices, we have developed a pressurized air-driven apparatus to simulate human pulse. It contains a tunable pressurized air line, a vacuum pump, a 12 V and 1 Amp (?) DC power supply, an Arduino Uno microcontroller, an Arduino control board, a fine-resolution pressure regulator, and a solenoid valve. For the purpose of testing the devices using the pulse simulator, we add an additional device layer made of PDMS containing a pressurized air-filled actuation chamber. The pressure in the chamber is controlled by the pulse simulator. The additional layer is applied over the elastomeric membrane so that fluctuations in the actuation pressure collapse the membrane and drive a flow through the device. Clear Tygon tubing is

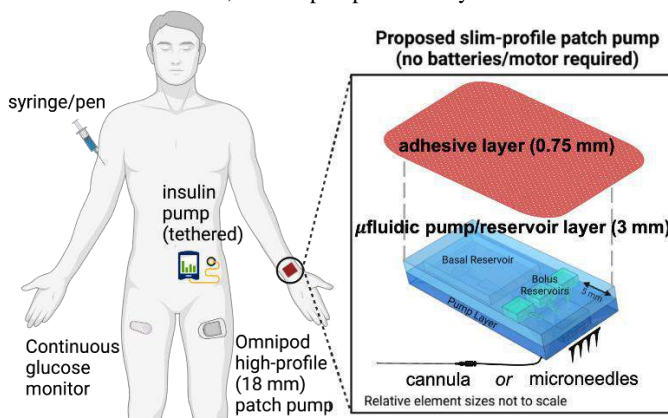


Figure 1. Current insulin delivery methods. Insets: Schematic of our device design (top), and a prototype patch-pump (bottom).

daily activity.^{9,10} These limitations result in reduced patient adherence to prescribed insulin therapy regimens, contributing to diabetes-related hospitalizations.¹¹⁻¹⁶

To remove barriers to insulin adherence, we have developed slim, unpowered microfluidic devices based on principles of insect respiratory systems. Some insects contract their abdomens periodically, which rhythmically collapses tracheal walls and pumps air throughout

connected to the flow channel inlet and outlet, as well as to the actuation channel inlet. To start the testing, a laptop with a simple “blink” Arduino program is connected to the Arduino Uno, which is connected to the DC power supply. The compressed air line and the pressure regulator are gently turned on until the reading on the pressure regulator oscillates between 0 and the desired blood pressure. The vacuum pump is connected to the solenoid valve, which rhythmically switches between the pressurized air and vacuum inlets. The modeled heart rate, or the frequency of the pulse signal, is adjusted in the “blink” program. To start the testing process, the vacuum pump is turned on, and a video is taken to record the time it takes for the fluid-air interface in the inlet tube to travel a predefined distance along the tube.

Devices were tested at 12 physiologically relevant heart rates ranging from 30 to 180 bpm and 7 blood pressures ranging from 75 to 225 mmHg. Devices integrated with reservoirs were tested using the aforementioned pulse simulator at a heart rate of 60 bpm and 100 mmHg, and initial flow rate were measured when the reservoir was fully filled and minimally filled to determine whether the device flow rate would change as the reservoir was emptied.

Additional tests were carried out using a single human subject. Prototype devices were placed on the left radial artery of a seated, X kg, 20-year-old male subject.

RESULTS

A limited number (4) of human subject tests demonstrated the feasibility of pulse-powered flow actuation in prototype devices. (Figure 2D, E). Testing the flow rate produced by the pressurized air pulse simulator, we found that the flow rate across most devices was positively related to the blood pressure (Figure 2B). However, the correlation between the flow rate and the heart rate was not consistent and depended on the device design (Figure 2A). For the integrated device, we have found no statistical difference in the initial flow rate when the reservoir was fully filled and when it was minimally filled (Figure 2C).

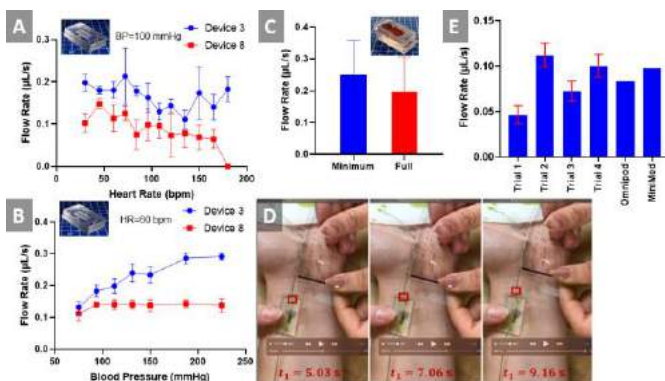


Figure 2: (A,B) Pulse simulator-produced flow rate versus heart rate and blood pressure for two prototype devices. (C) Initial flow rate of integrated device with minimally filled and fully filled reservoirs. (D,E) Human subjects test on the radial artery demonstrated proof of concept.

DISCUSSION

For ideal insulin delivery, we aim to achieve a negative correlation between the flow rate and the heart rate because the user would typically be in vigorous exercise and thus has a reduced glucose level when they are experiencing elevated heart rates.²³ This ideal relationship was achieved by some of our devices (Figure 2A), yet there was significant

variability in the flow rate produced in the same prototype designs for the same conditions. To reduce the variability and further reduce the device profile, we plan to redesign the master mold geometry and fabricate a second generation of devices. For the integrated devices, we have demonstrated that the flow rate does not significantly change as the reservoir is emptied, but we are yet to do further characterizations on these devices.

In conclusion, we have fabricated novel, insect-mimetic microfluidic insulin delivery pumps using stereolithographic 3D printing and soft lithography techniques. We have tested the flow across individual prototype devices using pulse-mimicking pressurized air and a human arterial pulse and shown the feasibility of these devices.

In the future, we plan to integrate more components into the microfluidic pump device, including the microneedle arrays and bolus insulin dose reservoirs, to make a slim, all-in-one patch-pump (as shown in the schematic in Figure 1). To tailor the devices towards specific patients, we will use computational methods including feature extraction and genetic algorithms to optimize the device design.

ACKNOWLEDGEMENTS

This work was partially supported by the Student Engineers' Council (SEC) of Virginia Tech and the Apex Center for Entrepreneurs at Virginia Tech. We would like to acknowledge our undergraduate research assistants Adaliah Dunya, Julia Frederick, Aleksandra Grodzki, Cayla Katz, Jessica Prisbe, and Vedant Shah for their hard work towards the project, as well as alumni Krishnashis Chatterjee, Afreen Khoja, Tyler Kwak, Isabelle Mehochko, Demitria Poulos, Jenna Sims, and Ryan Zolovick for their contributions.

REFERENCES

- [1] Saeedi, P et al., *Diabetes Res. Clin Pract*, 157:107843, 2019.
- [2] Sarkar, S et al., *JAMA Netw Open*, 4(10):e2128782, 2021.
- [3] Umpierrez, GE, and Klonoff, DC. *Diabetes Care*, 41(8):1579-1589, 2018.
- [4] Economidou, SN et al., *Addit Manuf*, 38: 101815, 2021.
- [5] Bolton, CJ et al., *Lab Chip*, 20(15): 2788-2795, 2020.
- [6] Wang, Y et al., *J Mater Chem B*, 8(40): 9335-9342, 2020a.
- [7] Lee, BM et al., *Pharmaceutics*, 12(4): 366, 2020.
- [8] Yang, J et al., *Microsys Nanoeng*, 6(1): 1-14, 2020.
- [9] Payne, FW et al., *J Diabetes Sci Technol*, 13(1): 49-54, 2019.
- [10] Yan, B et al., *IEEE*, 2018.
- [11] Sarbacker, GB, and Urteaga, EM., *Diabetes Spectr*, 29(3): 166-170, 2016.
- [12] Murphy, SL et al., *Natl Vital Stat Rep*, 61(4), 2013.
- [13] Ho PM et al., *Arch Intern Med*, 166(17): 1836-1841, 2006.
- [14] Farsaei S et al., *Prim Care Diabetes*, 8(4): 338-345, 2014.
- [15] Davies M et al., *Diabet Med*, 30(5): 512-524, 2013.
- [16] Kang, H et al., *Diabetes Res. Clin Pract*, 143: 24-33, 2018.
- [17] Chatterjee, K et al., *Bioinspir Biomim*, 16(3): 036004, 2021.
- [18] Wang, WY et al., *Lab Chip*, 20(6): 1153-1166, 2020b.
- [19] Wang, WY et al., *Acta Biomater*, 135: 260-273, 2021a.
- [20] Wang, WY et al., *Front Bioeng Biotechnol*, 9: 187, 2021b.
- [21] Margolis, EA et al., *Lab on a Chip*, 21(6): 1150-1163, 2021.
- [22] Yeung, C et al., *Biomicrofluidics*, 13(6): 064125, 2019.
- [23] Colberg, SR et al., *Diabetes Care*, 36(10): e177, 2013.

MULTIFIBER COMPUTATIONAL MODELING OF HOLLOW-FIBER HEMODIALYZERS

Ruhit Sinha (1), Anne E. Staples (1,2)

(1) Department of Biomedical Engineering and Mechanics, Virginia Tech, Blacksburg, VA, USA
(2) Virginia Tech - Wake Forest School of Biomedical Engineering and Sciences, Virginia Tech, Blacksburg, VA, USA

INTRODUCTION

The median life expectancy for patients on hemodialysis is just 5 years because of the poor performance of artificial kidneys, or hemodialyzers, at clearing uremic toxins from the bloodstream, compared to healthy kidneys. Remarkably, the basic design of hemodialyzers, and their prescribed operating regimens, haven't changed significantly since the hollow fiber dialyzer was introduced in the 1960s. Growing evidence suggests that current dialyzer designs and operating regimens are not optimized for toxin removal¹. But optimizing the clearance performance of hemodialyzers would require a complete understanding of the physics of clearance in hollow fiber hemodialyzer units. Efforts to do so are hampered by the difficulty of modeling flow and transport processes in units that typically contain tens of thousands of fibers. Current models of hemodialyzers either extrapolate the performance of a single hollow fiber² to the entire dialyzer unit or model the unit as a porous medium³. Both approaches neglect critical inter-fiber flow and transport physics.

Here, we develop multifiber 3D finite element (FE) models of hollow-fiber hemodialyzers that capture inter-fiber flow physics for the first time. We use the models to test whether current single-fiber models accurately capture clearance performance for 6 commercially available hemodialyzers.

METHODS

Hemodialyzers are cylindrical units containing thousands of parallel hollow fibers with semi-permeable membranes. Blood flows through the fibers and the dialyzer fluid (dialysate) flows around them in the opposite direction (Figure 1). Toxins are cleared from the blood via diffusion and convection across the fiber membranes. Hemodialyzer performance is expressed in terms of clearance (CL) as defined below.

$$CL = Q_b \frac{c_{in} - c_{out}}{c_{in}} + Q_F \frac{c_{out}}{c_{in}} \quad (1)$$

where Q_b is the blood flow rate, c_{in} and c_{out} are the concentrations of a

toxin in the blood at the inlet and outlet of the fibers, respectively, and Q_F is the ultrafiltration (flow of blood plasma across the membrane into the dialysate) rate.

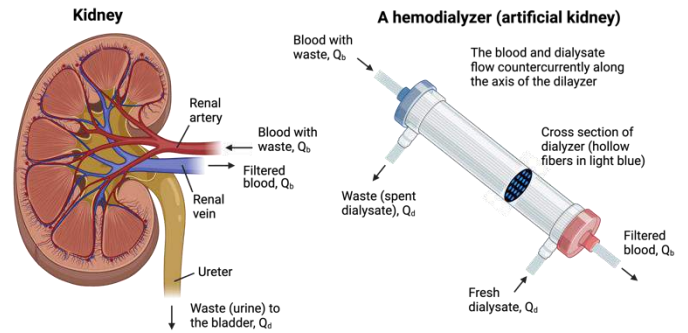


Figure 1: A human kidney and a hollow-fiber hemodialyzer.

We employed a cylindrical-layer domain scaling approach to model clearance in progressively larger 3D FE dialyzer models (Figure 2), developing 1-, 7-, 19-, 37-, 61-, 91-, and 127-fiber models.

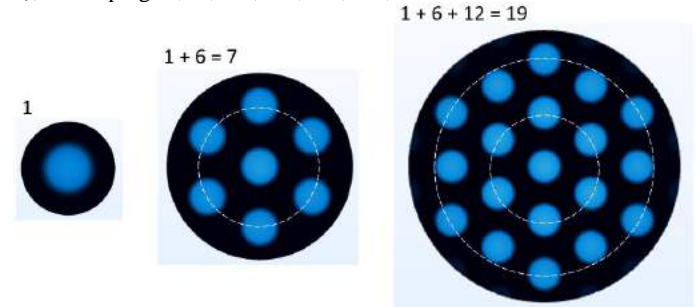


Figure 2: Cross sections of 1-, 7-, 19-fiber hemodialyzer models.

Due to the axisymmetric geometries, we were able to carry out simulations using a one-twelfth section of the models (Figure 3).

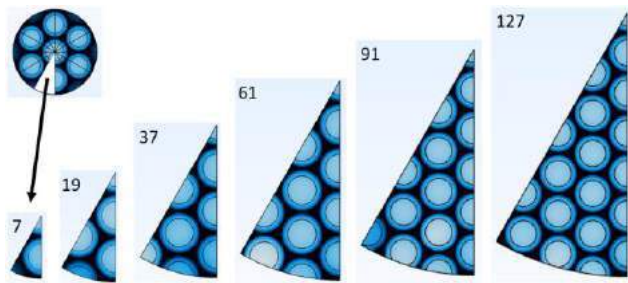


Figure 3: One-twelfth geometry sections used in computations.

For each n-fiber model (n=1, 7, 19, 37, 61, 91, 127), we used the geometric parameters for six different hemodialyzer modules currently available on the market: The Asahi Kasei APS-15S and APS-25SA, Baxter Healthcare CT190G and Syntra 160, and Fresenius Medical Care F60 and Optiflux 180NR modules. The module diameters (D), hollow fiber inner diameter (d), fiber membrane thickness (t), and fiber packing densities (ϕ), defined in Equation (2), where N is the number of hollow fibers in the actual module, are listed in Table 1.

$$\phi = \frac{N(d+2t)^2}{D^2} \quad (2)$$

Table 1: Hemodialyzer module geometries used in the study.

Module	N	D (mm)	d (μ m)	t (μ m)	ϕ (%)
APS-15S	8980	33.5	200	45	68
APS-25SA	16200	45.8	185	45	59
CT190G	12100	35	200	15	53.7
Syntra 160	11580	39	200	30	51.5
F60	9100	40	200	40	44
Optiflux 180NR	11700	48	185	36	34

We used clinically relevant blood (100-500 mL/min) and dialysate flow rates (200-800 mL/min) and solved the 3D Navier-Stokes and convection-diffusion equations, assigning zero-pressure outlet boundary conditions for both the blood and dialysate flows. We neglected ultrafiltration in this study, considering only the diffusive clearance of urea (diffusion coefficients in blood, dialyzer membrane, and dialysate are $[1.75, 0.39, 1.9] \times 10^{-9} \text{ m}^2\text{s}^{-1}$, respectively).

RESULTS

For each of the dialyzer modules considered, the relative clearance of urea (relative to that of the 1-fiber model) decreased as the number

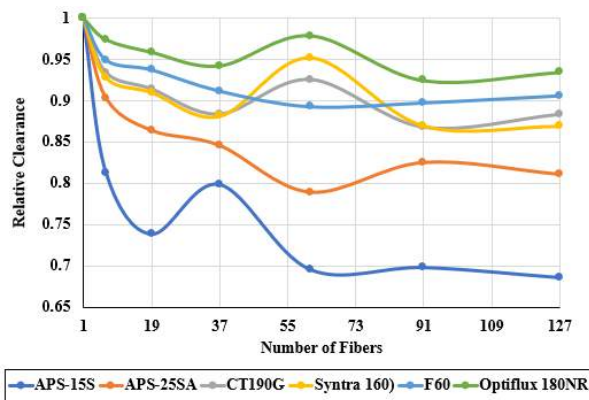


Figure 4: Relative clearances of the 6 commercial dialyzers at $Q_b = 300 \text{ mL/min}$, $Q_d = 500 \text{ mL/min}$.

of fibers in the computational domain increased, saturating at around 127 fibers. The decrease in relative clearance was more pronounced for the modules with higher packing densities, as is evident in Figure 4. Furthermore, the dialysate flow inlet pressure increased with the dialysate flowrate, with the flow becoming turbulent for some values (Figure 5).

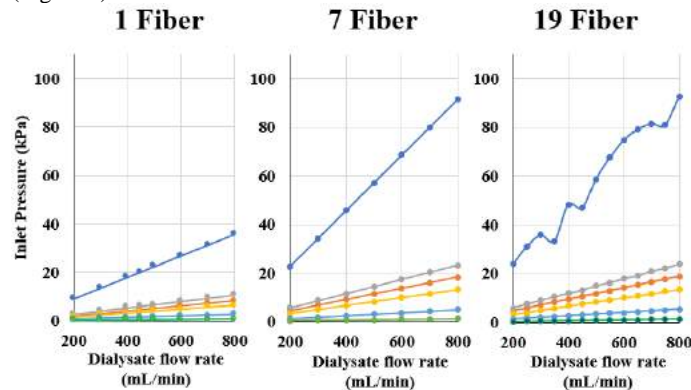


Figure 5: Inlet pressure versus dialysate flow rate.

DISCUSSION

The stabilization of the relative clearance values as a function of the number of fibers in the computational model, for each of the commercially available dialyzers, at around 100 fibers indicates that important features of the inter-fiber dialysate flow and diffusive clearance physics are not captured by less complex models containing fewer fibers. For commercial modules with lower packing densities (the Fresenius Medical F60 and Optiflux 180NR models), the difference in the relative clearances predicted by the 1-fiber and 127-fiber models was relatively minor, less than 10%. This indicates that using standard single-fiber models (e.g., the Krogh cylinder model) to predict the diffusive clearance performance of these modules will give relatively accurate results. But the models with higher fiber packing densities displayed significant differences in the predicted values of urea clearance for the 1- and 127-fibers models, differences of up to 32%. Single-fiber models should be avoided for these models.

The pressure versus dialysate flow rate behavior of the 19-fiber model of the APS-15S dialyzer shown in Figure 5 indicates the presence of turbulence effects. Some of the dialysate streamlines traverse the domain in the radial direction, thus decreasing the average dialysate velocity, and ultimately the clearance, as observed experimentally by Costello et al.⁴ These effects have not been captured by any previous computational model of hemodialyzer.

Because of their ability to capture previously unmodeled features of dialyzer clearance physics, the multifiber hemodialyzer models developed here could be used to improve the designs of hemodialyzers, ultimately impacting millions of patients worldwide. The models could be further improved in the future by including convective clearance physics, and by validation via *in vitro* studies.

ACKNOWLEDGEMENTS

This work was partially supported by the Regenerative Medicine Interdisciplinary Graduate Education Program at Virginia Tech.

REFERENCES

- [1] Eloit, S. & Verdonck, P. Artificial Kidney, Modeling of Transport Phenomena in. *Wiley Encyclopedia of Biomedical Engineering*. 2006.
- [2] Happel, J. *AIChE J.* 1959. [3] Labecki, M., Piret, J. M. & Bowen, B. D. *Chem. Eng. Sci.* 1995. [4] Costello, M. J., Fane, A. G., Hogan, P. A. & Schofield, R. W. *J. Memb. Sci.* 1993.

DEVELOPMENT AND UTILIZATION OF A VASCULARIZED *IN VITRO* PHYSIOLOGICALLY REPRESENTATIVE SKIN TISSUE PLATFORM FOR BURN INJURY INVESTIGATION

S. Brocklehurst (1), N. Ghousafim (2), K. Zuniga (1), D. Stolley (2), M. N. Rylander (2)

(1) Biomedical Engineering
University of Texas
Austin, Texas, USA

(2) Mechanical Engineering
University of Texas
Austin, Texas, USA

INTRODUCTION

There is a lack of burn studies using *in vitro* and *in vivo* models that quantify both time-temperature history and tissue response for short-duration, high-temperature burns, both of which are needed to elucidate mechanisms of burn injury and to develop predictive models [1, 2]. The influence of vasculature embedded within skin on resulting burn injuries has not been adequately investigated. Engineered *in vitro* tissue platforms provide a great system for evaluating burn injury mechanisms [1, 3]. Some previous studies have created skin platforms with embedded vascular networks, however to the best of our knowledge none have been used as models for burn or wound healing research [4]. This paper presents a multilayer vascularized *in vitro* human skin platform to conduct quantitative burn experiments for investigation into the influence of vasculature on burn injuries.

$$\Omega(\tau) = \ln\left(\frac{C(0)}{C(\tau)}\right) = \int_0^\tau A e^{\left(\frac{-Ea}{RT(t)}\right)} dt \quad (1)$$

The Arrhenius model (equation 1) has been widely used for modelling burn injuries to account for the temperature-dependence of damage rates, with the common form assuming irreversible first-order kinetics [cc]. Use of this model allows tissue damage and cell response to be predicted from time/temperature data, assisting heat-based therapies to achieve successful outcomes while minimizing complications due to damage to surrounding tissue [2]. $C(0)/C(\tau)$ is the ratio of the initial cell concentration or tissue strength over that at time τ , the logarithm of which gives the damage parameter Ω . Two process coefficients determine the behavior of the common form of the Arrhenius model (Equation 1), frequency factor A (Hz) and activation energy Ea

(kJ/mol). Each type of tissue damage and cell response is modelled by its own set of coefficients, which must be determined for the temperature range of interest due to the domination of different mechanisms at different temperatures [5].

METHODS

In vitro skin tissue platforms were created by casting collagen I hydrogels bearing human dermal keratinocytes and fibroblasts into a layered structure. Silicone sample holders were made with an open top and a glass slide adhered to the bottom using plasma treatment. A pair of 22 gauge needles were inserted into the holder parallel to each other 5 mm apart. The dermis layer containing fibroblasts was cast into the holder, polymerized in an incubator, then the epidermis layer containing keratinocytes was cast on top. After polymerization of the collagen, removing the needles left well-formed cylindrical channels through the platforms, forming the vasculature. This vasculature was gradually perfused with a suspension of microvascular endothelial cells in a ramping flow scheme, forming a monolayer lining the interiors of the channels

Platforms were subjected to contact burn injury to create to characterize both extracellular matrix damage and the response of cells to thermal stress. A contact burn apparatus was made with a 3 mm diameter cylindrical copper burn tip and a motor with a microcontroller for consistent control of tip position and contact duration. Burn tests were performed with the burn tip heated to 50-100 °C for 3 seconds of contact with the platforms. Cell culture media was perfused through the model vasculature using syringe pumps, configured to impart 2 dyn/cm² of wall shear stress, in both parallel and countercurrent regimes for at least 3 seconds before, during, and 5 seconds after contact burn exposure.

Platforms were treated with a variety of fluorescent stains and imaged with z-stack confocal microscopy 24 hours after exposure. The resulting 3D images show the spatial distribution of this damage throughout the platforms and were used to measure the volumes of damaged regions.

Temperature distributions within platforms during contact burns were modelled computationally in Comsol Multiphysics (5.4a) to obtain a much higher temporal and spatial resolution than could be directly measured. Experimentally determined thermal characteristics of skin platforms and perfused media were used as inputs for this model. The resulting time/temperature histories were correlated with the experimentally determined distributions of tissue damage and cell response to determine which temperature conditions caused which level of damage. Arrhenius process coefficients A and E_a were determined for cell death and collagen ablation that closely predict the experimentally observed tissue damage using the computational temperature model.

RESULTS

Vascularized skin platforms were successfully created, with cells stratified within their respective layers. Endothelial cells form monolayers adhered to the channel walls similar to *in vivo* vessels.

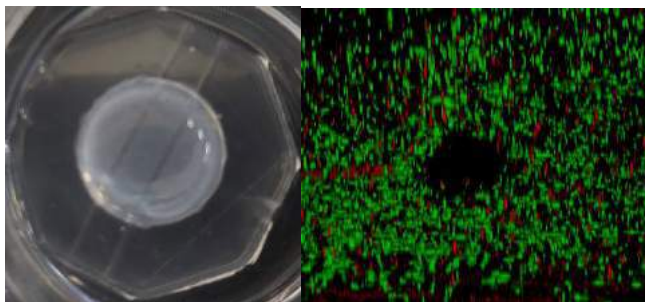


Figure 1 – (Left) Vascularized skin platform in holder (Right) Fluorescent cross-section image down length of channel 48 hours after creation, with minimal deformation

Contact burn injuries resulted in consistent injury to the skin platforms, which were quantified by the volume of damaged regions. Close to the contact point collagen was completely ablated, whereas further out the damage is progressively less severe as evaluated by different stains. The different measurements taken show a range of severities of cell response, and provide a potential means to study how cell fate is determined after burn exposure. Further work is in progress to collect burn injury data with different levels of tissue damage and to determine their governing Arrhenius parameters.

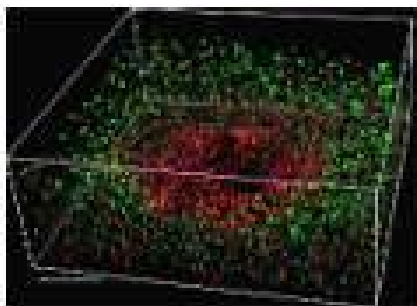


Figure 2- Live/dead (green/red) staining of skin platform 24 hours after contact burning with a 75 °C copper cylinder

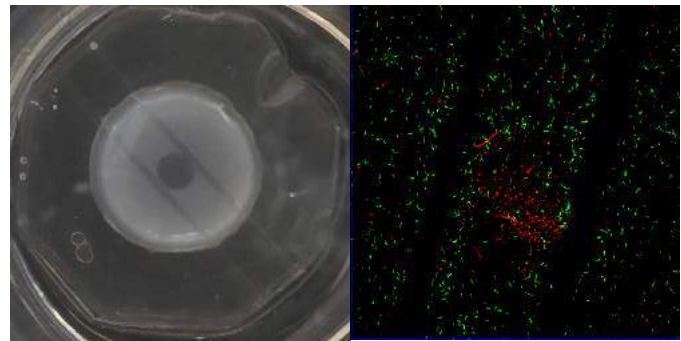


Figure 3 – (Left) Vascularized skin platform in holder after 75 °C contact burn. The edges of the ablated region may make small breaches in channels, 100 °C destroy significant parts of channels (Right) Live/dead (green/red) staining of skin platform 24 hours after 75 °C contact burn, showing cross section of burned region. Intact channels are visible, cell death contained in the center

DISCUSSION

The *in vitro* multilayer vascularized skin tissue platforms created in this project provide a means of quantitatively evaluating the as-of-yet unknown influence of vasculature on burn injury response. Platforms can be created in large quantities with minimal specialized equipment and maintained with minimal labor due to the perfusion of media – essential for the large sample sizes required to determine mechanisms of burn injury. Knowledge of these parameters is needed to elucidate mechanisms of burn injuries and to help drive the parameters of predictive therapeutic models.

ACKNOWLEDGEMENTS

Thank you to Nicholas Fuselier, Alican Ozkan, Leslie Schroder, Steven Pugliese, and Zoe Meyer for their assistance.

REFERENCES

- [1] Ryan, C. M., Parry, I., & Richard, R. (2017). Functional outcomes following burn injury. *Journal of Burn Care and Research*, 38(3), e614–e617. <https://doi.org/10.1097/BCR.0000000000000537>
- [2] Kollias, S., Stampolidis, N., Kourakos, P., Mantzari, E., Koupidis, S., Tsaousi, S., ... Castana, O. (2015). Abdominal compartment syndrome (ACS) in a severely burned patient. *Annals of Burns and Fire Disasters*, 28(1), 5–8.
- [3] Sen, S., Palmieri, T., & Greenhalgh, D. (2015). Review of burn research for year 2014. *Journal of Burn Care and Research*, 36(6), 587–594. <https://doi.org/10.1097/BCR.0000000000000289>
- [4] Kolesky, D. B., Homan, K. A., Skylar-Scott, M. A., & Lewis, J. A. (2016). Three-dimensional bioprinting of thick vascularized tissues. *Proceedings of the National Academy of Sciences of the United States of America*, 113(12), 3179–3184.
- [5] Viglianti, B. L., & Dewhirst, M. W. (2013). Thresholds for thermal damage to normal tissues : An update, 27(4), 320–343.

DELINEATING EFFECTS OF SUBSTRATE STIFFNESS, CHEMISTRY, AND CYCLICAL STRAIN ON LUNG FIBROBLASTS GENE EXPRESSION

Qi Wang (1, 2), Kristan S. Worthington (1), Edward A. Sander (1)

- (1) Roy J. Carver Department of Biomedical Engineering, University of Iowa, Iowa City, IA, USA
(2) Medical Scientist Training Program, Roy J. and Lucille A. Carver College of Medicine, University of Iowa, Iowa City, IA, USA

INTRODUCTION

Pulmonary fibrosis is a hallmark and final consequence of several acute and chronic lung diseases including ventilator induced lung injury and idiopathic pulmonary fibrosis. Although these diseases have distinct etiologies, the outcome is fibrogenesis that leads to impaired pulmonary function. Fibrotic lesions and scarring of the lung connective tissue are a result of alterations in extracellular matrix (ECM) composition and biochemistry. In fibrotic lung tissue, the ECM was found to stiffen from 1-2kPa to ~16.5kPa¹ and contained increased collagen, hyaluronan (HA), and fibronectin.² Cells have various receptors for these ECM molecules that relay mechanical and chemical signals and therefore regulate fibrosis.

Mechanosensing pathways can potentially mitigate lung fibrosis. However, animal models do not allow for isolated study of mechanical or chemical cues. Reductionist cell culture systems are essential for unraveling the molecular mechanisms of the fibroproliferative response and resolution of fibrosis. However, the lung is a dynamic environment in which cells experience cyclic mechanical loading in addition to biochemical and static mechanical cues from the extracellular matrix (ECM). Thus, engineered *in vitro* systems that allows for precise manipulation of mechanical and biochemical cues is needed to advance our understanding of how changes in the ECM influence fibrotic lung disease progression, so that better therapies can be developed.

In this study, photopolymerized hydrogels are used as substrates for the study of cellular responses to ECM alterations. Non-methacrylated monomers can be included in pre-polymer solution to reduce hydrogel stiffness while maintaining relative number of cell binding sites. The composition and concentration of pre-polymer mixtures can also be tuned to yield desired hydrogel biochemistries and stiffnesses, respectively. These hydrogels are also attached to a bioreactor that applies dynamic mechanical loading. The objective is to observe how combinations of cyclic strain, stiffness and biochemical composition differentially modulates fibroproliferative response compared to each stimulus alone.

METHODS

Fabrication of hydrogels: Methacrylated gelatin (GelMA), methacrylated hyaluronan (HAMA) and non-methacrylated gelatin (Gel) were mixed in various concentrations as base materials. Hydrogels were formed via ultraviolet light (1W/cm²), with Irgacure-2959 used at 1% vol as a photoinitiator.

Photo-rheology: Rheology was performed during the photo-crosslinking process using Kinexus Ultra+ (Malvern Panalytical) fitted with an Omnicure S2000 UV light source. Storage modulus during polymerization (G') was fitted to **Equation 1** to determine final storage modulus (G'_{∞}) and polymerization time. Crossover point (t_c) was defined as the point in which storage modulus is greater than loss modulus (G''). Compressive modulus is calculated using the slope of stress-strain curves.

$$G' = G'_{\infty}(1 - \exp[-\alpha(\frac{t}{t_c-1})^{\beta}]) \quad (1)$$

Mechanical Loading: Pre-polymer mixtures were applied to attachments designed for a force bioreactor (ADMET Inc.). Photopolymerization was then performed at pre-determined times, resulting in solid hydrogels attached to bioreactor. These hydrogels were then deformed at 0.2 Hz and 50% strain.

Cell Culture: Normal human lung fibroblasts at low passage number (<P7) were cultured in EMEM + 10% FBS. Cells were allowed to attach on hydrogels overnight before downstream analysis.

Gene expression analysis: RNA extraction was performed using TRIzol lysis followed by ethanol precipitation of aqueous phase and Zymo RNA Clean and Concentrator column. cDNA was then synthesized using Superscript VILO cDNA synthesis kit. qPCR for 30 genes related to mechanosensing and fibrogenesis was then performed using Power SYBR green with primers sequences from Primer Bank.

RESULTS

Compressive moduli were measured after pre-polymers were fully polymerized using polymerization times obtained through photo-

reology. Non-methacrylated gelatin can be added to methacrylated gelatin (GelMA) to decrease hydrogel compressive modulus (**Fig. 1A**). The addition of methacrylated hyaluronan (HA) significantly increased hydrogel modulus (**Fig. 1B**) due to inherent material stiffness.

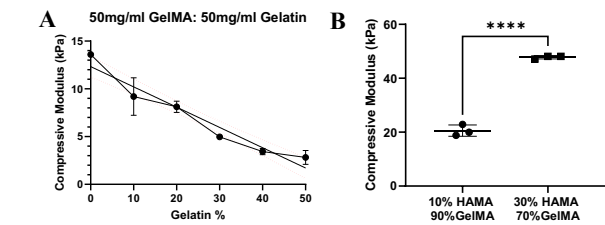


Figure 1: Precise control of hydrogel stiffness
 Mechanosensing and fibrogenesis transcriptomics (**Fig. 2**) suggest that stiffer hydrogel resulted in increased ECM synthesis and turnover and upregulation of fibrotic growth factors and cytokines. However, fibroblasts on a stiff hydrogel with 10% HA and 90% GelMA produced gene expression profile more similar to a softer hydrogel.

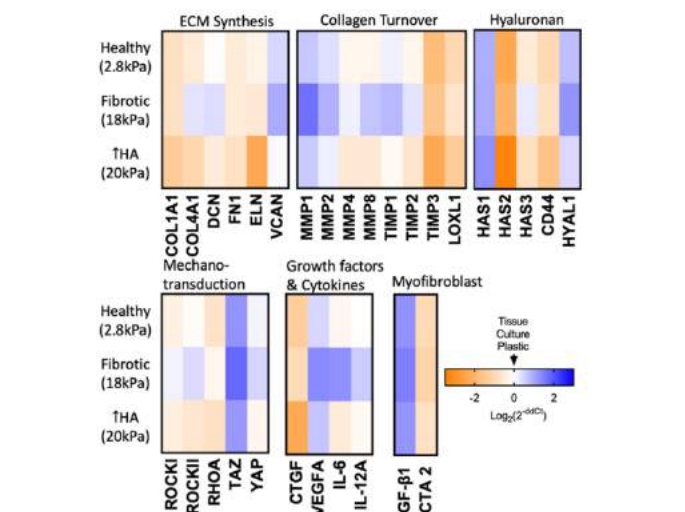


Figure 2: Heatmap of RT-qPCR analysis of lung fibroblasts on static photopolymerized hydrogels. (n=1)
 Cyclical strain was applied to lung fibroblasts seeded on stiff (50 mg/ml GelMA, 13 kPa) hydrogels for 45 minutes or 1 hr. Gene expression analysis (**Fig. 3**) showed that cyclical strain decreased expression of collagen type III (COL3A1), decorin (DCN), and fibronectin-1 (FN1) but increased the expression of elastin (ELN). In addition, there was an increase in matrix metalloproteinase 1 (MMP1) and hyaluronan synthase 2 (HAS2). There was also a decrease in TAZ expression, but a relatively constant expression of YAP compared to cells on static GelMA hydrogels.

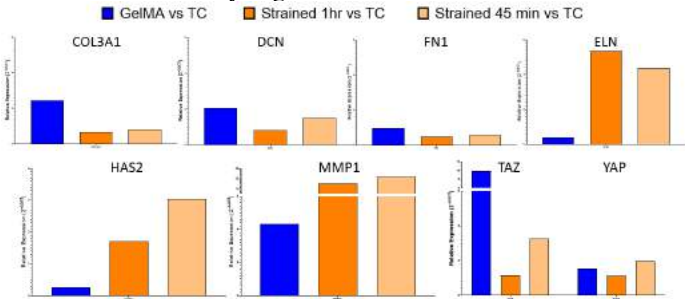


Figure 3: Gene expression of lung fibroblasts on strained GelMA hydrogels. (n=2, y-axis represents relative expression)

DISCUSSION

Our results demonstrate that photopolymerized hydrogel stiffness and biochemistry can be easily controlled. The range of stiffnesses obtained by GelMA, HAMA and Gelatin were within the range of lung tissue stiffness seen in healthy and fibrotic lungs. Inherent cytocompatibility of these hydrogels is also an advantage for this application. Photopolymerized hydrogels composed of GelMA allows for direct cell attachment, an advantage over bulk materials coated with proteins. The addition of gelatin facilitates a wider range of hydrogel stiffnesses than GelMA alone while enabling constant quantity of Arg-Gly-Asp (RGD) binding sites.

Physiologic mechanotransduction throughout the ECM involves a variety of binding sites and proteins with differential effects. For example, vascular smooth muscle cells exhibited opposing responses to substrate stiffening that were dependent on ECM chemistry (laminin, fibronectin or collagen)³. Our results indicate that despite the similar stiffness of hydrogels with HA to “fibrotic” gel, the gene expression profiles of these cells are more similar to those cultured on “healthy” substrates. However, the effects of photopolymerized HAMA on cells needs further investigation as low and high molecular weight HA have differential effects in inflammatory and fibrotic cell response.

Physiologically, lung cells undergo continuous mechanical stimulation, and in some instances, the mechanical stimuli can promote fibrogenesis.⁴ When we applied cyclical strain to lung fibroblasts, ECM deposition, turnover and mechanotransduction gene expression were altered. Interestingly MMP1, which is responsible for degrading collagen I and III, was upregulated, but we also observed a decrease in COL3A1 expression. Increase in type I and type III collagen turnover biomarkers were associated with a greater risk of disease progression in patients with idiopathic pulmonary fibrosis⁵, thus changes in COL3A1 and MMP1 expression prompts further investigation. Decorin has an inhibitory effect on fibrosis, thus decreased expression of DCN indicates a potential profibrotic effect of cyclical strain⁶. In addition, the interaction of fibronectin extra domain A and latent TGF-β1 has been implicated in fibrotic response⁷. Thus, changes we observed in FN1 expression with cyclical strain also suggest further research into fibronectin alternative splicing. Increased elastin has been observed in lungs of bleomycin injured mice and our result is consistent with this observation⁸. HAS2 is responsible for majority of hyaluronan synthesis, and its increased expression suggests cells have increased HA synthesis under cyclical strain. ECM stiffness has also been shown to mechanoactivate YAP/TAZ and promote profibrotic mediators, while decreased TAZ can attenuate fibrotic response⁹. Thus, the decreased expression of TAZ we observed with cyclical strain could potentially indicate a protective effect of strain in fibrogenesis. Inclusion of protein expression studies in the future will help confirm our gene expression results and could help resolve some apparent contradictions. Together, these experiments will address many questions regarding the relative contributions of ECM stiffness, composition, and cyclic mechanical loading to lung fibrosis progression.

ACKNOWLEDGEMENTS

Support for this work was provided by the National Institute of Health (NIH T32 GM007337), Roy J. Carver Department of Biomedical Engineering Research Excellence Fund, and Roy J. Carver Department of Biomedical Engineering Carver Graduate Fellowship.

REFERENCES

- [1] Herrera, J. et al. *JCI Insight* 4 (2019)
- [2] Thannickal, V.J et al. *Am. J. Pathol.* 184, 1643-1651 (2014)
- [3] Sazonova, O.V. et al. *Matrix Biol.* 41, 36-43 (2015)
- [4] Marchionni, A. et al. *Int. J. Mol. Sci.* 22, 6443, 2021
- [5] Jessen, H. et al. *Respir Res* 22, 205 (2021)
- [6] Dong, Y. et al. *J. Immuno Rsrch*, vol 2022 Article ID 1283383
- [7] Klingberg, F. et al. *J Cell Sci* (2018) 131 (5): jcs201293
- [8] Blaauw, M. et al. *Matrix Biol.* (2014) Feb;34:170-8
- [9] Noguchi, S. et al. *Sci Rep* 7, 42595 (2017)

MECHANICAL MODELS OF COLLAGEN NETWORKS FOR UNDERSTANDING CHANGES IN THE FAILURE PROPERTIES OF AGING MOUSE SKIN

Nathan J. Witt (1), Alan E. Woessner (2), Jacob Herrmann (1), Kyle P. Quinn (2), Edward A. Sander (1)

(1) Biomedical Engineering, University of Iowa, Iowa City, IA, USA
(2) Biomedical Engineering, University of Arkansas, Fayetteville, AR, USA

INTRODUCTION

Skin is a heterogeneous, anisotropic, and non-linear tissue whose composition, structure, and mechanical behavior changes with age [1]. With age, nonenzymatic collagen crosslinks accumulate within the dermis, which stiffens collagen fibers and decreases interfibrillar sliding [2]. These crosslinks also interfere with the normal turnover of collagen that occurs over the lifetime of the tissue, such that the dermis weakens as it evolves into a fragmented collagen network [3].

We have been investigating the influence of aging in mouse skin and found an increase in non-enzymatic crosslinking within the dermis. Although crosslinking is generally associated with fiber stiffening, we found that the mechanical response of aged skin during uniaxial stretch was softer, the peak force was lower, and the failure displacements were larger compared to young skin (Fig. 1). In this study, we used computational models of collagen fiber networks to explore how changes in fiber properties and network connectivity might explain our experimental observations of softer mechanical response despite increased crosslinking. Ultimately, we envision that these models will contribute to a better understanding of how to improve skin health with aging.

METHODS

Experiment: Young (16 wk, n=6) and aged (23 mos, n=6) dog-bone-shaped murine skin was mechanically tested in an ADMET bioreactor mounted on a multiphoton microscope (MPM). Samples were preconditioned and then stretched to failure at a rate of 0.2 mm/min while being imaged. MPM image stacks of microstructural collagen were acquired in the center of the gauge region at each mm of displacement. Microstructural measurements of collagen properties, including non-enzymatic collagen crosslinking were also obtained.

Simulation: To better understand age-related differences in the mechanical response of mouse skin, we modeled dermal collagen as crosslinked growth networks that matched the experimental fiber

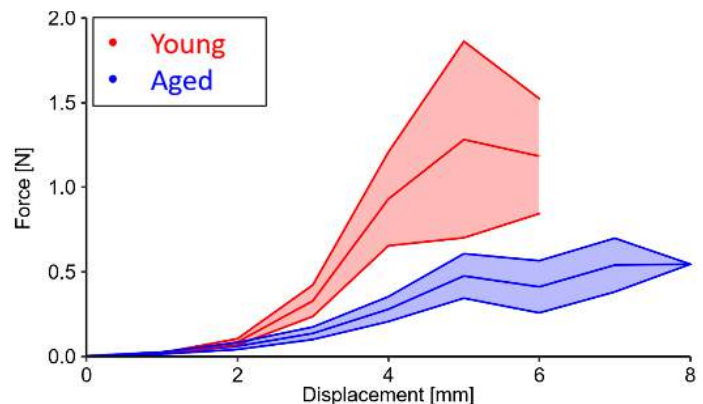


Fig 1. Mechanical responses of mouse skin demonstrate a softer response, lower peak force, and greater displacement with aging.

alignment (i.e., directional variance = 0.77) and fiber volume fraction (25%). We then explored the ramifications of three alterations to the model: (1) introducing age-dependent plastic deformation prior to fiber failure; (2) applying stretch- versus force-based fiber failure rules; and (3) decreasing network connectivity. In these models, the fiber mechanical response is implemented with an exponential force equation [4]. Once a fiber's stretch ratio (λ_{fiber}) exceeds 1.33, plasticity is introduced by incrementally increasing the fiber's reference length. To simulate progressive crosslinking and a reduction in interfibrillar sliding with age, the plastic modulus was increased by two-, three-, or fourfold [2, 5, 6]. Stretch- and force-based failure were implemented by removing fibers that exceeded a stretch ratio of 1.43 or a force of 70 μN , respectively. A decrease in network connectivity was performed by removing 25% or 50% of fibers prior to the simulation. All simulations were conducted in MATLAB under constrained uniaxial stretch to $\lambda_{\text{network}} = 2.0$.

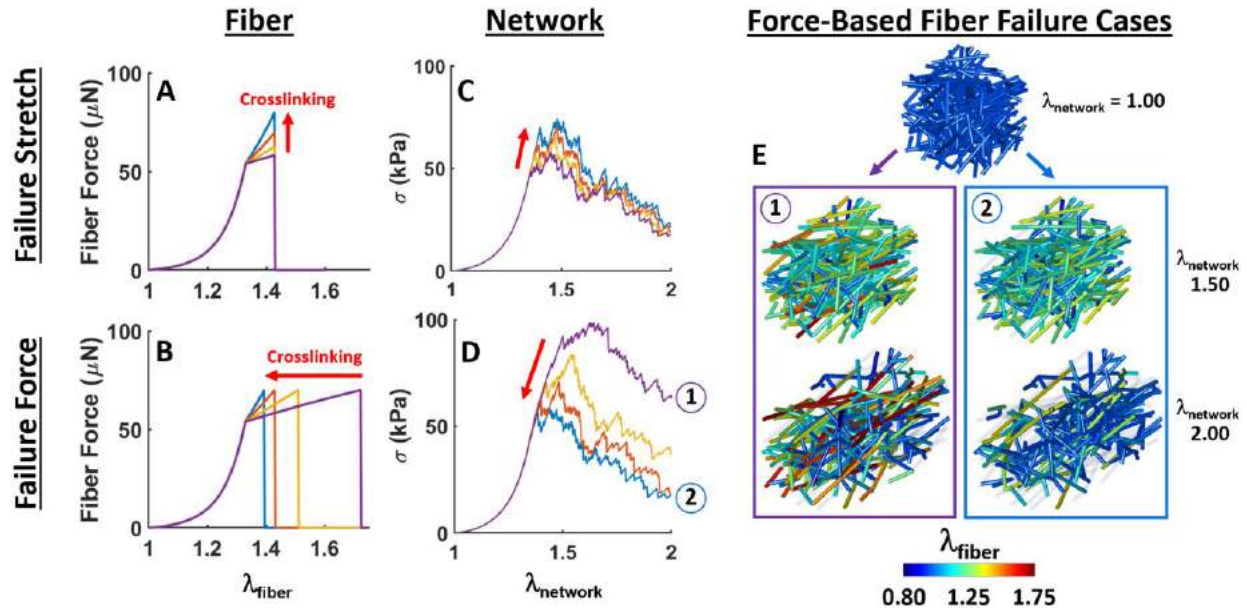


Fig 2. (A) Stretch- and (B) force-based failure rules were investigated in combination with progressively stiffer plastic responses to simulate increased crosslinking. (C) With a stretch-based failure rule, increased crosslinking resulted in higher failure stresses. (D) With a force-based failure rule, increased crosslinking resulted in reduced failure stresses. (E) The network under force-based failure rules demonstrated fewer failed fibers (transparent fibers) with (1) less crosslinking than (2) with more.

RESULTS

Modelling an increase in crosslinking combined with a stretch-based failure rule (Fig 2A) resulted in larger stresses prior to failure (Fig 2C) but did not appreciably alter the stretch at which it occurred. Increased crosslinking with a force-based failure rule (Fig 2B) reduced network stresses and the stretch at failure. (Fig 2D). Additionally, networks with increased crosslinking and a failure force rule experienced fiber breakage earlier in the simulation (Fig 2E2) while younger fibers demonstrated sustained recruitment and elongation (Fig 2E1). In both fiber failure cases, neither method strongly impacted the network's fiber reorganization results (data not shown).

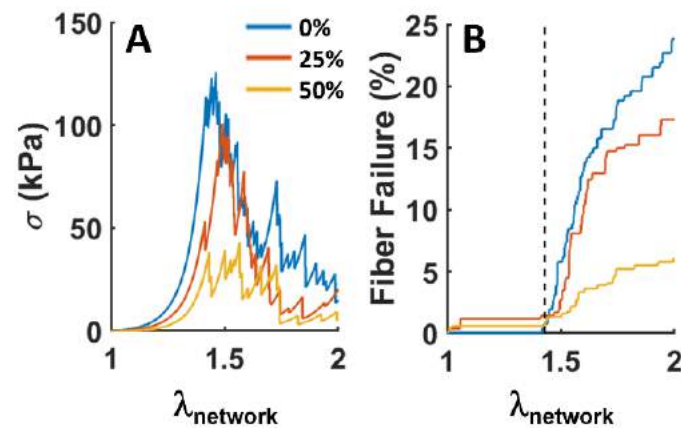


Fig 3. (A) A reduction in network connectivity softened the stress responses and decreased the maximum stresses. (B) Decreasing network connectivity results in a lower percentage of fiber failure. The vertical dashed line indicates the stretch ratio at which fiber failure occurs ($\lambda_{\text{fiber}} = 1.43$). Interestingly, some fibers fail well before the network stretch ratio approaches λ_{fiber} .

Decreasing network connectivity limited the number of stress-bearing pathways, resulting in a softer stress response (Fig 3A) and fewer failed fibers (Fig 3B).

DISCUSSION

Aging within biological tissues, including skin, is a complex process that involves multilayer compositional and functional changes [3]. Our initial investigation explored the counterintuitive experimental results suggesting murine skin mechanically softens with age despite an assumed increase in collagen stiffness. Our results suggest that: (1) increased crosslinking alone does not stiffen networks responses; (2) stretch-based failure increased network stresses with crosslinking while a force-based failure rule elicited a reduction in stresses, but not stiffness; (3) decreasing network connectivity limited stress bearing pathways in the network and lessened the percentage of fiber failure, resulting in a softer stress response. Future work will include progressive aging mechanisms, consideration toward hydrating matrix proteins, and a multiscale perspective on age-dependent fiber-tissue interactions and biomechanics.

ACKNOWLEDGEMENTS

Support for this work was provided by R01 AG056560. Computational resources were provided by the University of Iowa Argon HPC Cluster.

REFERENCES

- [1] Blair, M.J. et al, *Adv Wound Care*, 9(3):127-143, 2020
- [2] Gautieri, A. et al, *Matrix Biol.*, 59:95-108, 2017
- [3] Marcos-Garcés, V. et al, *J Anat.*, 225(1):98-108, 2014
- [4] Witt, N.W. et al, *J Biomech Eng.*, 144(4):041008, 2022
- [5] Depalle, B. et al, *Mech Behav Biomed Mater.* 52:1-13, 2015
- [6] Stammers, M. et al, *J Biol Chem.*, 295(31):10562-10571, 2020

A CONSTITUTIVE-FINITE ELEMENT MODEL OF CYCLIC HEAD ROTATIONS IN THE NEONATAL PIGLET

Ruhit Sinha (1), Qianhong Wu (2), Ji Lang (3), Anne E. Staples (1,4)

- (1) Biomedical Engineering and Mechanics, Virginia Tech, Blacksburg, Virginia, United States
(2) Mechanical Engineering, Villanova University, Villanova, Pennsylvania, United States
(3) Jiangsu Key Laboratory for Design and Manufacture of Micro-Nano Biomedical Instruments, School of Mechanical Engineering, Southeast University, Nanjing, Jiangsu, China
(4) Virginia Tech-Wake Forest School of Biomedical Engineering and Sciences

INTRODUCTION

Repetitive shaking head accelerations are considered to be a central mechanism responsible for traumatic brain injury (TBI) in some cases of abusive head trauma (AHT) in young children.^{1,2} Finite element (FE) head models have been developed to assist with understanding and predicting TBI in pediatric and other populations, but most FE models drastically simplify the structures and mechanics of the pia-arachnoid complex (PAC), a thin layer between the brain and the skull containing connective tissues, vasculature, and cerebrospinal fluid (CSF). Accurately modeling the mechanics of the PAC has been shown to significantly improve the accuracy of FE head model predictions.³ But directly computing the mechanics of the complex structures and CSF in the PAC is often prohibitively computationally expensive.

Here, we implement a new constitutive model of the forces developed in the PAC from cyclic sagittal head rotations in an FE model of the neonatal piglet brain, resulting in a reduced order, multiscale FE neonatal piglet head model. The model allows us to carry out FE simulations of the brain only, and represents the forces the skull and PAC impose on the surface of the brain at a low computational cost. The aim of this study is to carry out a qualitative comparison between the cortical stresses and displacements predicted by the new model and an existing FE head model of the neonatal piglet that uses sophisticated three-dimensional models of the PAC and skull, and to thereby determine the feasibility of this modeling approach.

METHODS

The FE brain model was constructed from a stereolithography geometry file assembled from MRI images of a Göttingen minipig brain.⁴ We added a falx cerebri structure between the hemispheres of the brain in order to capture the correct gross strain behavior. The brain tissue was modeled as a time-dependent Ogden hyperelastic material, following Prange et al.⁵ and using the materials property values from

their Table 2 for 5-day-old porcine tissue. The falx was modeled as a linearly elastic material, following Scott et al.,³ and using the material property values from their Table 7. Following Scott et al.,³ in order to accurately model the mechanics of the PAC, we defined 12 regions on top surface of the brain with different average densities of arachnoid trabeculae (AT), strands of connective fibers that extend between the dura mater lining the inner surface of the skull and the pia mater covering the brain, and used their “low-volume fraction” model distribution values (Figure 1).

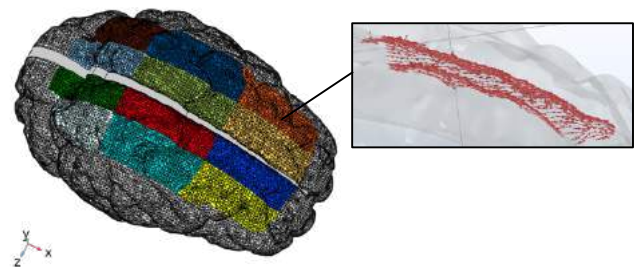


Figure 1: FE model of the neonatal piglet brain. Inset: The shear force the PAC imposes on the brain surface during cyclic head rotations, calculated from the constitutive model.

The constitutive model of the forces developed in the PAC models the AT in a region as uniform strings with constant diameter and spacing. It applies a theoretical model⁶ of the response of a thin fibrous gap to oscillating shearing impacts. In the model, fibers in the gap are displaced in response to relative motion between the brain and the skull in the sagittal plane, while the flow of CSF through the fibers is governed by an effective medium approach and the Darcy-Lapwood-Brinkman model. The key dimensionless parameters that govern the

oscillating shear process are the Womersley number, representing the influence of frequency, the Brinkman number, representing the influence of the porous structure, and the Bingham number, representing the influence of the fiber stiffness.

RESULTS

We compared the predictions of our piglet head model to those of the piglet head model developed by Scott et al.³ Figure 2 shows the stress developed on the top surface of the brain during sagittal head rotations in our model and in Scott et al.'s model. While the brain geometries and rotation conditions are different (Scott et al. carry out constant sagittal plane rotation computations, while our computations are for cyclic rotations), we compare our results at 0° phase angle, which represents the same forcing conditions as constant rotation. We use an angular velocity, ω , of 156.7 rad/s, which is in the range of values that Scott et al. use in their computations. The stress maps are qualitatively similar, with the highest stresses concentrations appearing along the falx and in laterally oriented bands in the mid-anterior region.

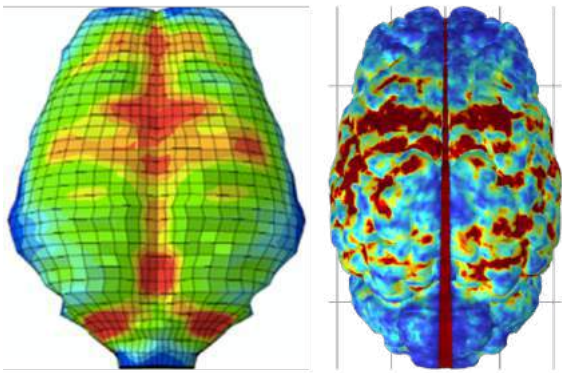


Figure 2: Stress patterns on top surface of brain (right) match qualitative features of those from Fig. 12 of Scott et al.³ (left) for $\omega = 156.7$ rad/s. Left image modified with permission from.³

We then carried out simulations of repetitive shaking head accelerations using our model. Figure 3 shows the von Mises stresses (color map, units: N/m²) and the normalized in-plane brain tissue displacements (black arrows) that develop on the top surface of the brain for a shaking frequency of 3 Hz at 0° and 90° phase angles. The inset of Figure 3 is a close-up of in-plane brain tissue displacement vectors. The magnitudes of the displacements are represented by the lengths of

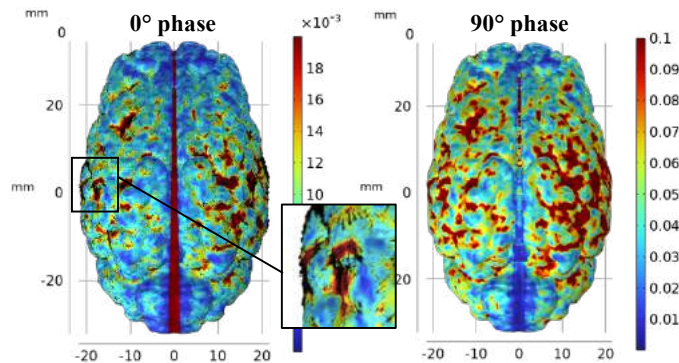


Figure 3: Stress and in-plane displacements on top surface of the brain for $\omega = 28.0$ rad/s and $f = 3$ Hz. Left: 0° phase, Right: 90°.

the arrows. Figure 4 shows the stresses and the displacements that develop for a shaking frequency of 1 Hz. Finally, Figure 5 shows the stresses and displacements that develop for a shaking frequency of 0.5

Hz. All simulations were carried for an angular velocity value of $\omega = 28$ rad/s, a typical value of angular velocity in a pediatric abusive head trauma setting.⁷

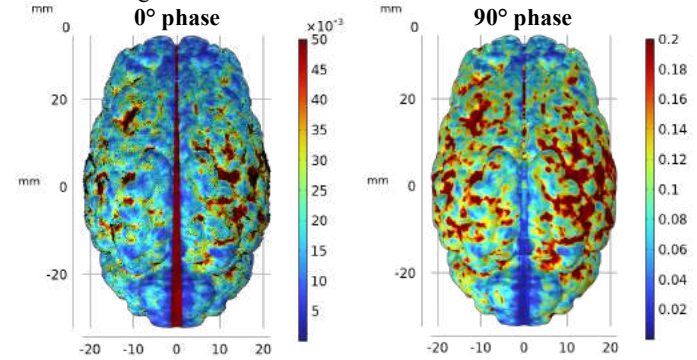


Figure 4: Stress and in-plane displacements on top surface of the brain for $\omega = 28.0$ rad/s and $f = 1$ Hz. Left: 0° phase, Right: 90°.

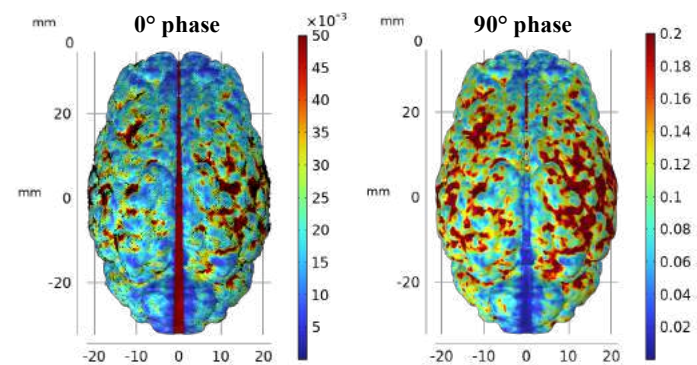


Figure 5: Stress and in-plane displacements on top surface of the brain for $\omega = 28.0$ rad/s and $f = 0.5$ Hz. Left: 0° phase, Right: 90°.

DISCUSSION

We presented a reduced order, finite element head model for the neonatal piglet that aims to accurately represent the forces from the pia-arachnoid complex (PAC) that act on the surface of the brain at a low computational cost via constitutive modeling.

Simulations of cyclic head rotations at parameter values typical of pediatric abusive head trauma predicted that the peak stress on the surface of the brain decreases with increasing shaking frequency, and that peak brain tissue displacements happen at 0° phase angle and are concentrated at the lateral edges of the brain hemispheres.

While the qualitative comparison with an existing piglet head model is promising, extensive validation studies must be carried out in order to further demonstrate the utility of the model presented here.

ACKNOWLEDGEMENTS

This work was partially supported by the Regenerative Medicine Interdisciplinary Graduate Education Program at Virginia Tech and by NSF Grant #2003077. AES thanks B. Coats for helpful discussions.

REFERENCES

- [1] Coats, B et al., *J Neurotrauma*, 34(1):235-247, 2017. [2] Joyce, T et al., *Pediatric Abusive Head Trauma*, StatPearls Pub, 2022. [3] Scott, G et al. *Biomech Model Mechanobiol*, 15(5):1101-19, 2016. [4] thingiverse.com/thing:1696714. [5] Prange, M, and Margulies, S, *J Biomech Eng*, 124:244-252, 2002. [6] Lang, J, Wang, L, and Wu, Q, *Phys. Fluids*, In submission. [7] Prange et al., *J Neurosurg*, 99:143-150, 2003.

TECHNOLOGY FOR RAPID REWARMING OF REFRIGERATED BREAST MILK

Melika. Mehrabi Dehdezi (1), Marissa N. Rylander (1), Christopher G. Rylander (1)

(1) Walker Department of Mechanical Engineering, The University of Texas at Austin, Austin, Texas, United states

INTRODUCTION

Current methods for heating or cooling liquids are unsatisfactory due to the extended timeframe needed for getting a liquid to the desired temperature. For instance, existing technologies for warming breast milk and formula focus on boiling water and causing a phase change in the surrounding bath liquid and transferring heat across a plastic milk bottle to heat the target milk volume. Therefore, the heat is transferred across the insulating plastic leading to poor heat conduction and extended time to warm the milk. Furthermore, there is a need to reach the desired target temperature and maintain the temperature. Current technologies frequently overshoot the target temperature creating dangers for pediatric burns. This creates a vicious cycle of heating and cooling leading to frustration by the user and the target temperature is rarely met. Most baby bottle warmers heat milk to above 80 °C which can degrade the nutritional and immunological properties of the milk [1]. Current solutions are not able to rewarm the milk uniformly due to the lack of stirring [2]. We have developed an easy to use and inexpensive heat exchanger technology which can rapidly heat liquids to the desired temperature. Our technology decreases the heating time needed to warm an 8 ounce bottle of milk from 10-15 min with conventional bottle warmers to only 30 seconds (20 times less) which has enormous psychological benefits by reducing the crying time of a baby and stress inflicted on caregivers. Our technology leverages the on demand hot temperature and steady flow rate of a conventional household water faucet to expedite the heat transfer process when coupled with an efficient and rapid circulation of milk through a novel heat exchanger system. The technology also stirs the milk while warming it so the temperature will be uniform regardless of the bottle's geometry. A primary application for this technology is warming of breast milk which is relevant for households, child development centers, nurseries, and neonatal care facilities in hospitals. We anticipate our technology will enhance the safety and efficiency of warming bottles

for babies and create a better environment for teachers, caregivers, and families.

METHODS

We designed the device based on heat transfer and fluid flow analysis (Fig.1). The technology directly interfaces with a faucet (e.g., kitchen, bathroom, tub etc.) to harness the on-demand heating properties



Figure 1. Warming technology circulates milk via a pump from a bottle directly into a copper coil which is submerged in a bath containing hot water from the faucet. Bottle warming takes about 15 s to warm 8 oz milk bottle from refrigerator temperatures (4 °C) to body temperature (37 °C).

available from the faucet to quickly and uniformly heat a target liquid while also leveraging effective heat transfer from a heat exchanger/high thermal conductivity coil (fig.2A) submersed in a capacitive water bath at the faucet temperature. The device consists of a container housing a high thermal conductivity material heat exchanger which is submerged in a water. Water enters the container from the faucet which is continually run at a hot temperature and is continuously monitored with a temperature sensor (fig.2B). An intake tube that removes liquid to be heated (fig.2C) and circulates it by a diaphragm pump (fig.2D) at a desired flow rate (approx. 4 L/min) to be heated and send it through the previously mentioned heat exchanger coil immersed in heated water (50 °C) in the container. The container has a drain to enable continuous circulation of water by the faucet to enhance heating and enable draining during heating and cleaning. Another tube will return the heated liquid directly to the original liquid container at the desired temperature. Tubing for the intake and exit tubing is made of inert, flexible, food grade material such as silicone. The diameter of the tubing is 0.25 inch. The intake and exit tubes are coupled with the temperature sensor for monitoring temperature of the liquid to be heated so the user knows when the liquid to be heated is at the target temperature. Fluid is circulated through the heat exchanger or coil multiple times to enhance heat transfer and until desired temperature is reached. Copper material of the heat exchanger coil immersed in the water bath has a high thermal conductivity and also possesses antimicrobial properties.

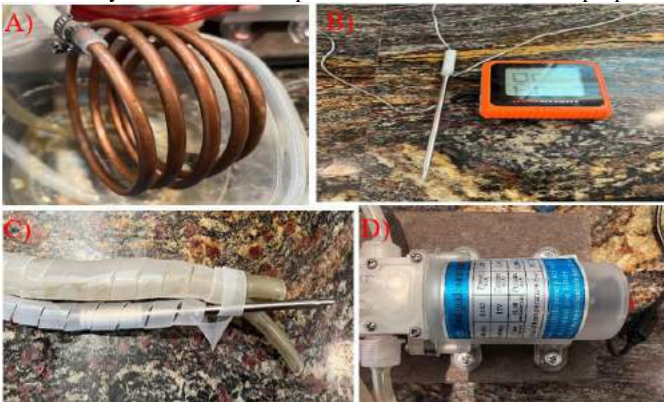


Figure 2. Primary components of the system. A) Copper coil. B) Temperature probe and reader. C) Tube bundle consisting of intake and exit tubes for circulating fluid. D) Pump

RESULTS

Based on our analytical analysis using a transient heat transfer model with geometrical, material, and thermophysical properties of our design, we predict to be able to heat the milk from refrigerator temperature of 4° C to the desired temperature of 37° C in 17.3 seconds (Fig.3). Additionally, we conducted two experimental tests in which the milk was 8 fluid ounces of milk, and the water bath temperature was approximately 50 °C). The results of the experimental tests were close to the analytical results. Compared to traditional bottle warmers which require approximately 5 min to heat refrigerated milk to 37°C, our technology can warm up the breast milk in less than 20 seconds.

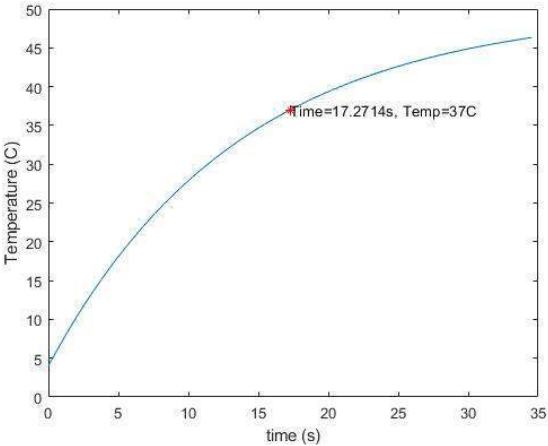


Figure 3. Model Predicted Milk Temperature vs. Time.

Table1. Experimentally Measured Time to Heat Milk

	Initial bath temperature (°C)	Initial milk temperature (°C)	Final milk temperature (°C)	Time (s)
Run 1	51	12	37	13
Run 2	46	3	37	16

DISCUSSION

Compared to traditional methods which rely on heat conduction through the vessel containing the fluid, our technology directly heats the target liquid (milk). Innovations of our technology includes the mixing of milk for generation of a uniform mixture. In further studies, other metals of high thermal conductivity such as aluminum and steel can be considered for the heat exchanger coil. Temperature sensors can be integrated in the system to provide continuous feedback of the temperature in the fluid in the heating container housing the coil or heat exchanger. This allows the user to determine when the faucet temperature has reached the maximum high temperature before initiating the heating process of the target liquid.

REFERENCES

[1] A. Eglash, L. Simon, A. of B. Medicine, ABM clinical protocol# 8: human milk storage information for home use for full-term infants, Revised 2017, Breastfeed. Med. 12 (2017) 390–395.

[2] S. Bransburg-Zabary, A. Virozub, F.B. Mimouni, Human milk warming temperatures using a simulation of currently available storage and warming methods, PLoS One. 10 (2015) e0128806.

BEHAVIORAL IMPAIRMENTS IN REPETITIVE MILD TRAUMATIC BRAIN INJURY

S. Vafadar (1), H. Li (2), S. Assari (1), S J. Ward (2), R F. Tuma (2), K. Darvish (1)

(1) Department of Mechanical Engineering, Temple University, Philadelphia, PA, USA
(2) Lewis Katz School of Medicine, Temple University, Philadelphia, PA, USA

INTRODUCTION

Mild Traumatic Brain Injury (mTBI) is a serious public health issue. There are various causes of mTBI, including blast overpressure, rapid acceleration or deceleration, penetration by a projectile, direct impact, etc. [1]. mTBI often occurs in a repeated fashion over a few minutes to a few months or years, collectively known as Repeated Mild Traumatic Brain Injury (rmTBI) and it may result in prolonged disabilities such as cognitive and motor impairments [2]. There is discrepancy between reports of the behavioral impairments in consequence of rmTBI depending on the injury model, the time of assessing the outcomes after injury, the animal species, and the severity of the injury [3].

We created a repetitive acceleration/deceleration-induced mTBI model for rats and compared sub-acute (20 days after injury) behavioral outcomes in two repetition patterns. Our goal was to see whether there is a cumulative effect in behavioral impairment over time and explore how the results depend on the repetition pattern.

METHODS

A novel rmTBI model in rats was developed based on applying Whole Body Deceleration (WBD) in the dorsal direction (Fig.1a). The anesthetized animal is positioned on a freely sliding carriage and is immobilized. The carriage is accelerated on a track at 4g to the velocity of 12 m/s and is decelerated with about 70g peak deceleration (Fig.1b) after the impact with a hydraulic shock absorber. WBD tests were either repeated 3 times in one day (WBD1) or 4 times in one day and another 4 times after 48 hours (WBD2). Each impact and retraction took about 1s. No direct impact is applied to the head and any TBI is the result of pure linear acceleration.

20 male Sprague-Dawley rats weighing approximately 300 grams were tested for this study. The Institutional Animal Care and Use Committee of Temple University approved all the experimental

protocols. We randomly grouped rats to WBD1 (n=7), WBD2 (n=5), and sham controls (n=8).

Animals were returned to standard housing for 21 days after injury to allow TBI symptoms to develop. The objective of the WBD model is to replicate mTBI in humans as in the case of repeated hits to the head in sports such as football and hockey that cause head acceleration. We used a battery of behavioral tests including Rotarod to assess motor function, Open field (OF) to evaluate anxiety, and Novel Object Recognition (NOR) for memory. These tests were conducted on days 5, 9, 15, and 20 post-injury.

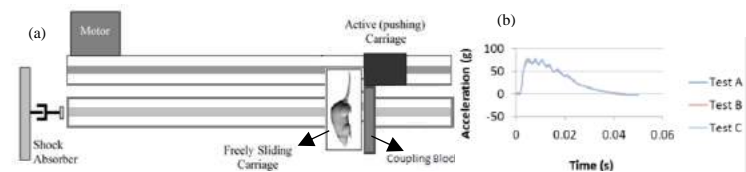


Figure 1-(a) Schematic diagram of the experimental setup with linear impact carriage to study whole body deceleration TBI (WBD). (b) Three representative deceleration pulses are shown that indicate high degree of repeatability

Rotarod tests were conducted with accelerated speed from 4 to 40 rpm with maximum time of 50 s (LE8500, PanLab Harvard Apparatus). The mean latency to fall off the rotating rod and its corresponding velocity for each rat were recorded. The baseline data was recorded on three consecutive days before the injury day (day 0). The highest value for each rat normalized to the preinjury baseline is reported.

We used a large square field (82x82x35.5 cm) with solid walls for OF. The time spent in central zone of the arena was recorded by ANY-maze software for 5 minutes. The recorded times have been normalized as the percent of (time in center zone)/ (total test time).

NOR test consisted of three phases: the habituation phase, the familiarization phase, and the test phase. In the habituation phase,

animal explored the empty open field arena for 5 minutes. The OF test was used as the habituation phase in this study. In the familiarization phase, the animal explored two identical objects located in the arena for five minutes. In the test phase, one of the identical objects was replaced by a novel object and the rat was allowed to explore the familiar and novel objects for five minutes. There was at least 20 minutes between the phases. The exploration time around each object was recorded for each rat. The metric used was discrimination index (DI) defined as the difference in time spent by each rat with the novel and the familiar objects divided by the total time spent exploring both objects in the test phase.

For histological assessment, we used RT-PCR to investigate the brain inflammatory response in day 21 post-injury. We evaluated TLR4 proteins in the prefrontal cortex for both repetitive patterns.

RESULTS

Rotarod results on days 5, 9, 15, and 20 showed 15, 7, 3, and 24 percent decline in performance for WBD1, and 20.5, 27.4, 34.5, 47 percent for WBD2 (Fig.2a). There are significant differences compared to sham on day 5 ($p=0.01$) for WBD1, and days 15 ($p=0.01$) and 20 ($p=0.004$) for WBD2. WBD2 indicated significant change compared to WBD1 in rotarod performance on day 20 ($p=0.04$).

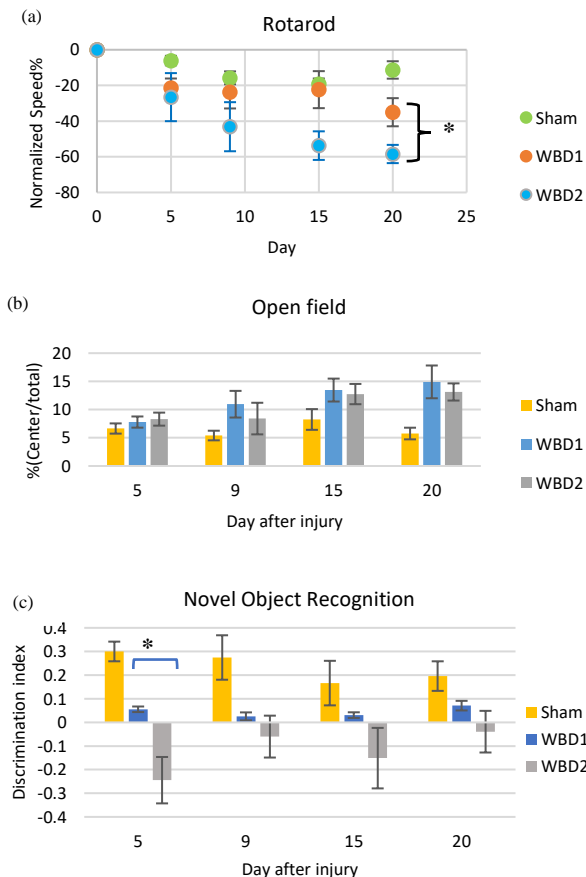


Figure 2- Behavioral test results. (a) Rotarod results show the normalized speed at fall. (b) OF results show the percentage of time spent in the center zone. (c) NOR results show the discrimination index.

OF results showed no significant difference between the two injury patterns (Fig.2b). The results demonstrated significant difference

between each injury and sham on day 20 ($p<0.05$). Injured rats spent more time in the center zone compared to shams.

NOR results detected memory deficit on days 5 ($p<0.01$) and 9 ($p<0.02$) after WBD2 and signs of recovering on day 20 (Fig.2c). For WBD1, NOR showed significant difference on day 5 ($p<0.01$) and 9 ($p=0.03$). The differences were close to significant ($p<0.1$) on day 20 for WBD1, and on days 15 and 20 for WBD2. NOR showed significant difference between WBD2 and WBD1 on day 5 ($p=0.03$).

RT-PCR showed no significant change in TLR4 following both repetition patterns compared to sham groups.

DISCUSSION

In this work, behavioral and histological outcomes were compared in two rmTBI patterns, namely WBD1 and WBD2. We used a novel injury model to replicate rmTBI in rats and evaluated motor function, anxiety and memory following rmTBI.

Rotarod showed much higher differences between WBD2 and sham compared to WBD1 that lasted for 20 days post-injury, i.e., the sub-acute phase. Motor impairment following rmTBI has been reported by some studies in the literature [4]. However, other studies reported no chronic motor deficits detected by rotarod following rmTBI [5].

OF displayed significant changes compared to sham on day 20 for both injuries. Spending less time in the center zone has been known as an indication of increased anxiety in rodents [6]. Some studies report no change [5] or increased anxiety after TBI [6], whereas others find a decreased anxiety-like behaviors [7]. In our study, injured animals compared to sham spent more time in the center zone which can be described as impulsivity or risk-taking behavior [6]. The differences were however not statistically significant.

In NOR, both WBD1 and WBD2 demonstrated significant differences in DI initially and the showed signs of recovery. There are studies that support the sub-acute memory dysfunction caused by rmTBI [5]. Also, WBD2 consistently resulted in more memory loss compared to WBD1.

Histological assessments showed that sub-acute histological changes were not significant. In contrast, in our previous work, we detected significant changes in TLR4 seven days post-injury [8].

In conclusion, the results indicate that the cumulative effect of WBD2 on motor function and memory is more severe than that of WBD1. They also suggest that rmTBI can cause sub-acute impulsivity over time. While no histological difference was found on day 20, behavioral assessments showed measurable differences at this time point. Using a greater number of samples as well as employing more than one type of behavioral test for each function can help to reach to more robust conclusions.

ACKNOWLEDGEMENTS

Funding for this project was provided by the Commonwealth Universal Research Enhancement program (CURE) directed by the Pennsylvania Department of Health under the grant no. 4100077079.

REFERENCES

- [1] Y. Xiong, et al., *Nature Reviews Neuroscience*, 14:128–142, 2013.
- [2] H. M. Bramlett et al., *J Neurotrauma*, 32:1834–1848, 2015.
- [3] B. D. Stemper et al., *Front Neurol*, 7:1–13, 2016.
- [4] R. Mannix et al., *J Neurosurg*, 121:1342–1350, 2014.
- [5] Y. Feng et al., *Front Cell Neurosci*, 15:1–16, 2021.
- [6] L. B. Tucker et al., *Front Behav Neurosci*, 15:1–16, 2021.
- [7] J. Popovitz et al., *Front Behav Neurosci*, 13:1–12, 2019.
- [8] S. Vafadar et al., *IMECE*, 2022

PERFORMANCE COMPARISON OF PORTABLE SUCTION DEVICES

Saketh R. Peri (1&3), Forhad Akhter (2), Robert A. De Lorenzo (1,2,3), R. Lyle Hood (1,2,3)

(1) Department of Biomedical Engineering, University of Texas at San Antonio, San Antonio,
Texas, USA

(2) Department of Mechanical Engineering, University of Texas at San Antonio, San Antonio,
Texas, USA

(3) Department of Emergence Medicine, University of Texas Health Science Center San Antonio,
San Antonio, Texas, USA

INTRODUCTION

Suction devices, also termed aspirators, are powered or unpowered devices employed to remove infectious materials from wounds or fluids from a patient's airway or respiratory support system [1]. It is the first equipment employed in airway management, which is itself the foremost priority when assessing a traumatically injured patient [2]. Airway compromise is the second leading cause of potentially survivable battlefield injuries among US military forces [3, 4]. Unfortunately, many of the commercial portable suction devices have not been scientifically validated for key performance measures relevant to prehospital care [5]. The current ISO 10079-1 standard for performance is for maximum free air flow rate of 20 L/min, which is confusing given the intended use of the device is to suction viscous liquids [6]. This is even more problematic as manufacturers use maximum free air flow rate as the primary reported performance metric, which misleads consumers and overestimates the real-world capability of a given device as instantaneous peak airflow rate can be manipulated to have a higher value than a unit would be able to provide in a sustained fashion. In addition, ISO 10079-1 performance requirements for portable suction devices, "equipment intended for pharyngeal suction shall evacuate 200 ml of simulated vomitus in not more than 10 s" [6]. The standards lay down the requirement for liquid flowrate but does not include requirement for avoiding backflow of liquid into patient's mouth. Suction devices are prone to the risk of having backflow during evacuation, which is a serious risk of infection to patients. Our hypothesis is that a time averaged air flowrate is a better estimate for overall device performance than peak instantaneous air flowrate. Time averaged air flowrate is a metric that provides information of device's capacity to evacuate a certain amount of fluid (liquid or air) in specific time.

To test the hypothesis four (4) portable suction devices were tested to gauge their performances based on the metrics, instantaneous air flowrate, liquid flowrate, and vacuum pressure. The metrics used to

determine the peak instantaneous air flowrate, time averaged air flowrate, real time liquid flowrate during the operation of device, and backflow. All the portable suction devices selected for the testing were the current market leaders and their weight was less than 1.5 kgs.

METHODS

The four (4) portable medical suction devices selected were subdivided into powered and unpowered categories: the Laerdal LCSU 4 & SSCOR Quickdraw were chosen as representative battery-operated suction devices, and Laerdal V-VAC & AMBU RES-QUE were chosen as the manually operated suction devices.

Air flowrate test setup utilized a microelectromechanical system (MEMS) air flow sensor (Omron MEMS Air Flow Sensor - D6F-50A61-000) which was operated against the suction devices to measure the instantaneous air flowrate. All four (4) suction devices were tested using this experimental setup. The suction devices were operated for 30 seconds, where the air flow sensor captures the air drawn by the suction device for a period of 30 seconds at 100 Hz.

The flowrate was calculated by measuring the volume of liquid (water and ISO vomit solution) evacuated by the device from a beaker filled with liquid in a certain time. Simultaneously a pressure transducer was attached to the suction tube tip to measure the vacuum pressure during the suction. The amount of liquid evacuated was measured by tracking real time the weight of the beaker filled with liquid and MATLAB timer to record the evacuation time. All the suction devices were operated until the canister capacity of the respective suction devices were filled.

All suction devices were operated at their respective peak settings. Each device was tested for 5 trials. Manual suction devices were operated by a single operator for 5 trials.

RESULTS

Figure 1 shows the comparison of peak air flowrate, total averaged air flowrate, and peak air flowrate claimed by manufacturer among all the 4 suction devices. The peak air flowrate was the maximum instantaneous air flowrate the device reaches during the operation. The time averaged air flowrate was the total air evacuated by the suction device during the operation of 60 seconds. Figure 2 shows the comparison of liquid flowrates of the 4 suction devices used against two different liquids, water ($\mu = 1$ cp) and ISO vomit solution ($\mu = 22$ cp)[3].

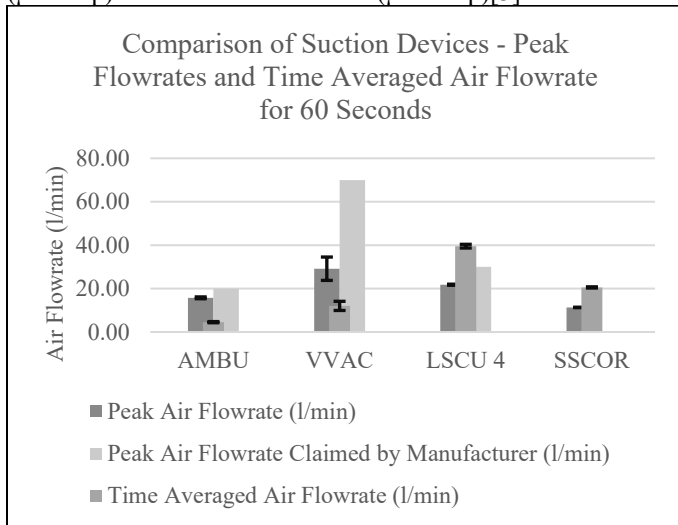


Figure 1: Comparison of Air Flowrate of Suction Devices

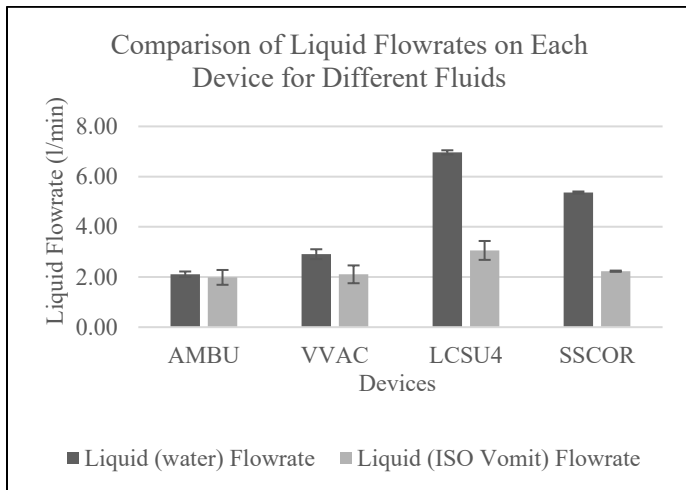


Figure 2: Comparison of Liquid Flowrates of Suction Devices

DISCUSSION

Comparison of total air flowrate and instantaneous flowrate (figure 1) for manual suction devices show that, although the manual suction devices offer high instantaneous flowrate, the time averaged air flowrate for 60 seconds were far less. Peak instantaneous air flowrate is not a meaningful or relevant specification as it cannot provide information on total amount of air drawn by the suction device, which is an implied correlation to the liquid flowrate. Time averaged air flowrate for 60 seconds, is more likely to imply liquid flowrates than peak air flowrate.

Use of the peak/maximum air flowrate metric allows the manually operated suction devices to claim comparable, or even superior, performance to their battery-powered counterparts. As per the data herein, this is untrue and misleading to purchasers and users of these portable suction systems. Based on this data, we recommend time averaged airflow rate as an improved specification for analyzing the performance of the suction device.

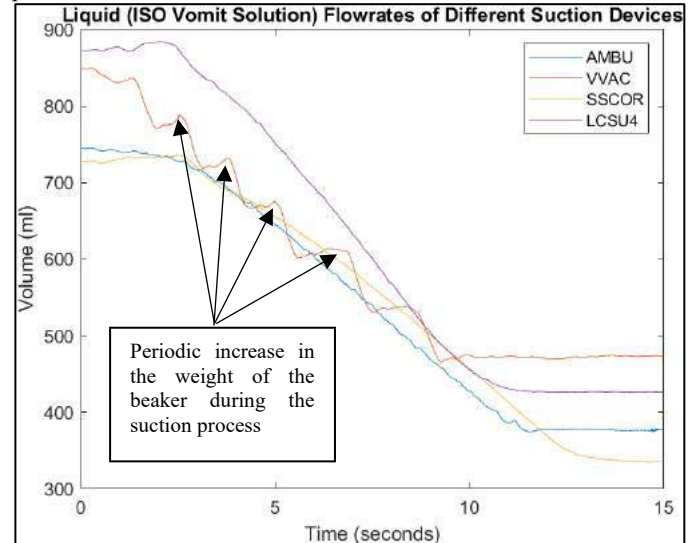


Figure 3: Liquid Flowrate Profile of Suction Devices

The initial observation to the liquid flowrate profiles of all suction devices in figure 3 shows that VVAC manual portable suction device exhibited backflow. As per data from liquid flowrate testing it can be incurred that the liquid evacuated from the beaker was entering back into beaker when performing suction using VVAC portable suction device. This phenomenon can be observed by the periodic increase in weight of beaker. Measured the local minima and local maxima of the peaks observed in the flowrate profile of VVAC suction device to calculate the amount of backflow. The device exhibited a backflow of 2 to 5% for every 100 ml which can lead to serious infections to the patients and it may be dangerous to use these device on patients.

ACKNOWLEDGEMENTS

The authors acknowledge funding support under a Sponsored Project from the Norwegian company Excitus AS towards the investigation of the current portable suction units on the commercial market.

REFERENCES

- Latif, L. and J. Macdonald, *Suction devices*. Anaesthesia & Intensive Care Medicine, 2018. **19**(1): p. 16-19.
- Jain, P., et al., *Airway Clearance Using Suction Devices in Prehospital Combat Casualty Care: A Systematic Review*. Prehospital and Disaster Medicine, 2020. **35**(6): p. 676-682.
- Akhter, F., et al., *Characterization of a novel emergency suction device for combat medics*. Journal of Medical Devices, 2019. **13**(4).
- Eastridge, B.J., et al., *Death on the battlefield (2001–2011): implications for the future of combat casualty care*. Journal of trauma and acute care surgery, 2012. **73**(6): p. S431-S437.
- Peri, S.R., et al., *Portable Medical Suction and Aspirator Devices: Are the Design and Performance Standards Relevant?* 2022. **22**(7): p. 2515.
- Standardization, I.O.f., *ISO 10079-1: 2015, in Medical suction equipment — Part 1: Electrically powered suction equipment*. 2015.

RIGHT VENTRICULAR MYOCARDIUM REMODELING IN PULMONARY ARTERIAL HYPERTENSION IS SEX DEPENDENT

Becky A. Hardie (1), Jessica Huberts (1), Daniela Valdez-Jasso (1)

(1) Department of Bioengineering, University of California, San Diego, La Jolla, CA, USA

INTRODUCTION

Pulmonary arterial hypertension (PAH) is a progressive vasculopathy of the pulmonary arteries that frequently results in right-heart failure and death.^[1] PAH manifests as sustained elevation of pulmonary arterial pressures above 20 mmHg and irreversible vascular remodeling that leads to an overloaded right ventricle (RV).^[1,2] Previous studies with male animal models have shown that elevated RV pressures are associated with increased myocardial stiffness and tissue fibrosis.^[2]

PAH is significantly more predominant in women; modern registries suggest the incidence is 2-4 times higher in women than men.^[3] Despite the high incidence in women, they tend to fare better and survive longer.^[3] The sex-differences in PAH progression are thought to be at least in part due to the effects of sex hormones, specifically 17- β estradiol (E2), the primary female sex hormone in non-pregnant women.^[3,4] Previous studies have demonstrated that E2 improves RV function in rats with PAH and that E2 levels correlate with RV function in healthy post-menopausal women undergoing hormone replacement therapy.^[3] To investigate the tissue-level properties that may lead to a sex dependent RV remodeling, we designed a study using the well-established Sugen-hypoxia (SuHx) rat model of PAH in male, female, and ovariectomized female rats.

METHODS

Animal model. PAH was induced in male, intact-female, and ovariectomized-female (OVX) Sprague-Dawley rats by a 20 mg/kg injection of Sugen 5416, a vascular endothelial growth factor receptor blocker, followed by 3 weeks of hypoxia at 10% oxygen and a further 5 weeks of normoxia. Control animals were kept at normoxia. Hypertension was confirmed by invasive measurements of blood pressure at the inlet of the pulmonary artery with a mean pulmonary arterial pressure greater 20 mmHg.

Tissue preparation. Immediately after hemodynamic measurements, the heart was harvested, flushed, and the RV free wall

excised. A square sample aligned along the apex-to-outflow (AOT) direction was cut from the mid-wall. Side lengths and tissue thickness measurements were taken with calipers prior to testing. Five graphite markers were glued on the epicardium in the center of the tissue to track displacement. The sample was attached to a Bose Electro-Force planar biaxial testing device with 4 custom-made hooks on each side and submerged in 37°C phosphate buffered saline.

Mechanical testing. RV samples were pre-stretched with a 3 g load to ensure complete planar motion and preconditioned with two stretch series of an 8%, a 10%, and a 12% *ex vivo* lengths at 0.2 Hz. Samples were subjected to displacement-controlled biaxial testing with 7 blocks of 15 loading-unloading cycles at 0.5 Hz. The AOT:circumferential stretch ratios were 1:1, 1:0.5, 1:0.25, 1:1, 0.5:1, 0.25:1, 1:1, with a maximum stretch of 10% of the *ex vivo* side-length. The last 3 cycles of blocks 2-6 were point-wise averaged and used for analysis. Pixel positions of the markers were recorded at 200 Hz throughout the test.

Constitutive equations. The locations of the four outer pixels were used to calculate the deformation gradient tensor \mathbf{F} through isoparametric mapping. The Green strain tensor \mathbf{E} was defined with respect to the pre-loaded reference configuration β_1 , and the second Piola-Kirchhoff stress tensor \mathbf{S} was calculated with the deformation gradient tensor.

The myocardium was assumed to be a planar hyperelastic material with the loading curve described by a Fung-type exponential strain-energy function.

$$W(\mathbf{E}) = C(e^{Q(\mathbf{E})} - 1) \quad (1)$$

where

$$Q(\mathbf{E}) = a_1 \mathbf{E}_{11}^2 + a_2 \mathbf{E}_{22}^2 + a_3 \mathbf{E}_{11} \mathbf{E}_{22}. \quad (2)$$

Numerical implementation. Pre-stretches $\{f_1, f_2\}$ were estimated in terms of the experimental stretches Λ_i as:

$$f_1 = \sqrt{\frac{\mathbf{E}_{11}\Lambda_2}{\Lambda_1}} + 1, f_2 = \sqrt{\frac{\mathbf{E}_{22}\Lambda_1}{\Lambda_2}} + 1 \quad (3)$$

and used to map from the stress-free reference state β_0 to the pre-loaded configuration β_1 at the beginning of the test. Experimental data was fit to the model equations and parameter estimation was carried out using the Limited Memory BFGS algorithm with the material parameters $\{C, a_1, a_2, a_3\}$ positive in Python. A strain-energy surface was generated for each animal using the optimized set of parameters and within each group, the set of strain-energy surfaces was point-wise averaged. This averaged surface was used to generate a representative set of parameters for each group and the stress and strain relations from an equibiaxial stretch of 10% was computed.

Statistics. All values are presented as mean \pm standard error and the significance level was set at 0.05 for all statistical tests. Two-factor ANOVA was used to compare thicknesses of the RV samples, with the factors being treatment and sex or, within the female animals, treatment and ovariectomy. Stress-strain relations were compared using three-factor analysis of covariance (ANCOVA) with a log transformation in JMP, with the factors being strain, treatment, and sex when all the data was included or strain, treatment, and ovariectomy within the female animals.

RESULTS

SuHx-treated RV thickness significantly increased compared to control ($p < 0.0001$) and thickness was not dependent on sex ($p = 0.2940$) or the presence of sex hormones (ovariectomy, $p = 0.5442$) [Control-to-SuHx] (Male: 1.39 ± 0.03 mm to 1.82 ± 0.12 mm, Intact Female: 1.32 ± 0.04 mm to 1.86 ± 0.13 mm, OVX-Female: 1.21 ± 0.04 mm to 2.01 ± 0.23 mm). The biaxial mechanical data was closely fit by the Fung-type model with coefficients of determination ranging from 0.81 to 0.99. The RV myocardium was isotropic with no significant difference between the AOT and circumferential stress-strain relations within each group (Figure 1).

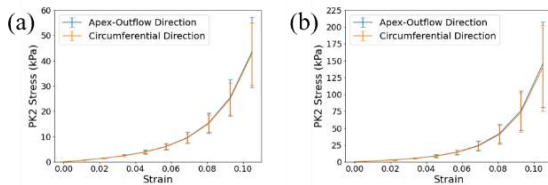


Figure 1: Second Piola-Kirchhoff equibiaxial stress-strain relations from control (a) and PAH (b) RV myocardium from male rats. Data are shown as the mean and standard errors.

There was a significant increase in second Piola-Kirchhoff stress with SuHx-treatment and strain (circumferential direction: treatment, strain, treatment-strain interaction: all $p < 0.0001$), but no difference between the male and female (intact-female and OVX) RV myocardium stress-strain relations ($p = 0.0519$) (Figure 2). Ovariectomized female RV samples were significantly less stiff than intact females ($p = 0.0002$) (Figure 2).

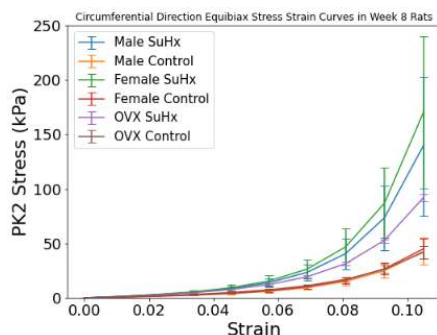


Figure 2: Averaged second Piola-Kirchhoff equibiaxial stress-strain relations for control and SuHx-treated male, intact-female, and OVX-female rats. Data are shown as mean and standard errors.

DISCUSSION

Several prior studies have examined RV remodeling due to pulmonary hypertension (PH) with male animal models, however no studies include female RVs. Prior studies from our lab and Frump *et al.*^[3] have shown sex dependent RV remodeling at the organ, cell, and molecular level. Thus, this work fills an important gap in the PH literature by providing tissue-level properties.

In the SuHx-treated PAH groups, significant RV myocardial thickening compared to normoxic controls is consistent with previous studies.^[2,3] The constitutive model used in this study was able to approximate the experimental data equally well in all the groups. The pre-stretches ranged from 0.9996 to 1.001, indicating that the pre-loaded configuration β_1 from which the tests were run was a slightly deformed version of the stress-free reference state β_0 . In all the control and SuHx-treated groups, the RV was isotropic. Most previous studies have noted that RV tissue is anisotropic, but the degree of anisotropy varies from the AOT direction being stiffer by a factor of 5:1 to the circumferential direction being stiffer by almost 2:1.^[2] Our findings of an isotropic myocardium fall within these ranges, however additional studies of RV myofiber and extracellular matrix orientations are necessary to fully understand the isotropy or anisotropy of the RV.

Although the RV has been studied from both the organ-level and the cell-level in female PAH subjects, these are the first reported tissue-level mechanical properties in intact-female and OVX-female animal models. For the normotensive animals, the stress-strain relations are similar across groups. In SuHx animals, the RV myocardium is substantially stiffer than the control myocardium in both sexes. Interestingly, there is no significant difference in the stress-strain relations when comparing the male group to a female group comprising of intact and OVX female rats. However, when accounting for the presence of sex hormones, our analysis found a significant difference between the two female subgroups. The comparative stiffening of the passive RV myocardium tissue in intact females may explain why premenopausal women are able to preserve cardiac function, such as ejection fraction, by preventing ventricular dilation.

Significant sex differences in organ-level RV function shown in patients and in Frump *et al.*'s study^[3] are not completely captured by our tissue-level RV myocardium mechanical properties. Given our previous studies in male rats where we found significant, anisotropic remodeling of the collagen extracellular matrix with SuHx treatment^[2] and Frump *et al.*'s work suggesting that the ER- α /BMP2/apelin signaling axis is linked to sex differences and RV fibrosis,^[5] in our future studies we will investigate the role played by collagen deposition and reorganization on the extracellular matrix mechanical properties in the absence or presence of estrogen.

ACKNOWLEDGEMENTS

This work was funded by the AHA 16SDG29670010, NHLBI 1R25HL145817-01, and NHLBI 1R01HL155945 – 01.

REFERENCES

- [1] Lai, YC *et al.*, *Circ. Res.*, 115:115–130, 2014.
- [2] Vélez-Rendón, D *et al.*, *J Biomech Eng*, 141:1–8, 2019.
- [3] Frump, AL *et al.*, *Am J Physiol - Lung Cell Mol Physiol*, 308:L873–L890, 2015.
- [4] Liu, A *et al.*, *Hypertension*, 66:1082–1088, 2015.
- [5] Frump, AL *et al.*, *J Clin Invest*, 131:e129433, 2021.

HUMAN IPSC HYDROGEL ENCAPSULATION FOR EFFICIENT PRODUCTION OF EMBRYOID BODIES

Matthew T. Conway (1), Edward A. Sander (1), Kristan S. Worthington (1)

(1) Roy J. Carver Department of Biomedical Engineering, University of Iowa, Iowa City, Iowa, USA

INTRODUCTION

Induced pluripotent stem cells (iPSCs) are autologous, can be attained with minimal invasion, and possess the ability to differentiate into nearly any cell type [1]. Consequently, iPSCs are a popular choice for regenerative cell-based therapies and tissue engineering. Prior to directing iPSCs toward a specific cell lineage, it is a common practice to form them into 3D spheroids known as embryoid bodies (EBs). EBs contain each of the three germ layers (mesoderm, ectoderm, and endoderm) and can be formed through various methods, including spontaneous self-aggregation in suspension, settling in low adhesion round-bottomed wells, and hanging drop culture [2]. EBs can also be generated through the encapsulation of iPSCs within hydrogels, such as alginate, PEGDA, and hyaluronic acid [3-5]. During the encapsulation process, a Rho-kinase inhibitor (ROCKi), Y-27632, is often added help maintain cell viability [3]. Once the encapsulated iPSCs have grown to the desired size, the EBs can either be differentiated within the hydrogel or retrieved from the gel via decapsulation for additional processing. One potential benefit of the hydrogel encapsulation method is that it may offer a means to substantially improve EB generation efficiency over conventional methods, which could benefit pilot scale cell manufacturing or high-throughput clinical or research operations. However, iPSC stemness and differentiation can be impacted by the mechanical environment; and cell responsiveness to the mechanical environment is known to be altered by ROCKi [6]. Here, we investigated how encapsulation of human iPSCs in alginate hydrogels impacts the efficiency and yield of EB formation and whether changes in the mechano-sensing abilities of iPSCs also impacts iPSC viability, stemness, and differentiation in this context.

METHODS

Human iPSC Culture: Human iPSCs sourced from bone marrow CD34+ cells and reprogrammed using Sendai virus (ATCC) at passage 12 were grown to 80% confluency in a 6-well plate coated with cell

basement membrane (ATCC) and using E8 Flex stem cell culture medium (Thermo Fisher). The cells were gently washed with PBS and lifted by adding 1 mL of Accutase (Sigma-Aldrich) and incubated for 7 minutes.

Conventional EB Method: Dissociated iPSCs were centrifuged at 0.2 rcf for four minutes and resuspended to a cell density of 10^5 cells/mL in E8 flex medium containing 20 μ M ROCKi. 100 μ L of the cell suspension was then dispensed into each well of a 96-well low adhesion V-bottom plate (S BIO) to aggregate iPSCs into EBs. Culture medium was changed every two days without ROCKi.

Alginate Gel EB Method: Two hours prior to lifting the cells, a media change was performed with the addition of 10 μ M ROCKi (Stem Cell Technologies). Dissociated iPSCs were then collected, centrifuged, and resuspended in 1 mL of E8 flex with 10 μ M ROCKi, and mixed with 1 mL 1.2% (w/v) alginate (A2033, Sigma-Aldrich) in PBS for a final concentration of approximately 10^6 cells/mL and 0.6% (w/v) alginate. The solution was loaded into a syringe with a blunt 20G needle and added dropwise by hand into a gelling bath containing sterile 100 mM CaCl₂ (Fisher Scientific) in PBS to form 30 spherical alginate beads containing approximately 70,000 cells in each bead (Fig. 1).

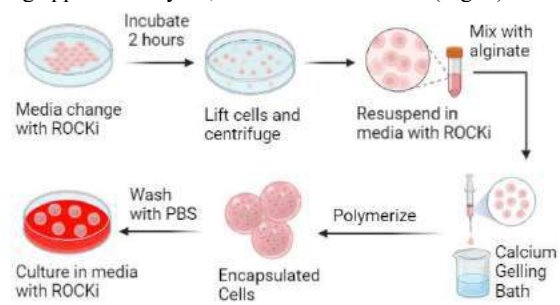


Figure 1: Schematic of method used to encapsulate human iPSCs in alginate hydrogels.

The beads were allowed to fully polymerize in the gelling solution for 5-10 minutes, collected, and washed with PBS two times. Finally, the beads were transferred to a 6 cm dish with E8 flex media containing 10 μ M ROCKi. The beads were cultured for one day before being split into different groups to be grown in different ROCKi concentrations of 0, 10, and 20 μ M over the span of 8 days. Culture medium was changed after three days followed by regular media changes every two days.

Imaging and Analysis: Phase contrast images were collected from each test group on Days 2, 4, and 6 and analyzed for size using FIJI. Eight iPSC encapsulated beads were analyzed from each ROCKi concentration group along with imaging of eight wells containing conventionally generated EBs. Viability staining was performed on Day 8 using NucRed Live 647 and NucGreen 488 ReadyProbes (Invitrogen) according to the manufacturer's instructions. A one-way ANOVA with post-hoc Tukey HSD test was used to determine significance ($p < 0.05$) between test groups on Day 6.

RESULTS

Aggregates cultured in medium containing 10 or 20 μ M ROCKi quickly expanded in size compared to the 0 μ M ROCKi group and formed into EBs (Fig. 2).

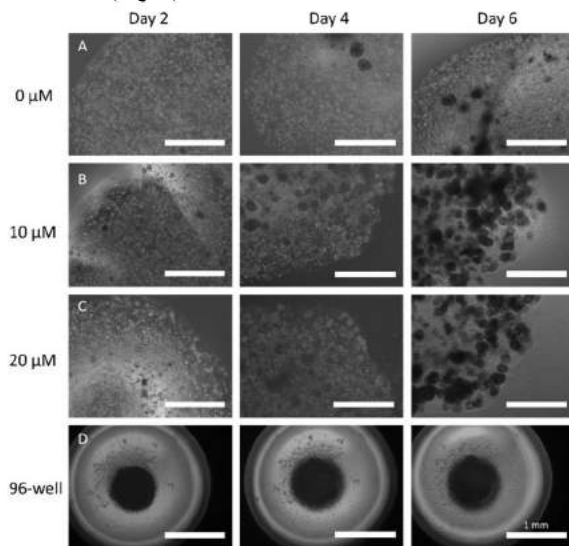


Figure 2: Comparison of methods to produce EBs over 6 days. A) 0 μ M ROCKi. B) 10 μ M ROCKi. C) 20 μ M ROCKi. D) 96-well round bottom plate.

EBs formed in 96-well plates aggregated into a single large spheroid by Day 2. On average, EBs formed in a 96-well plate were approximately 4-8 times larger than those formed in hydrogels (Fig 3.).

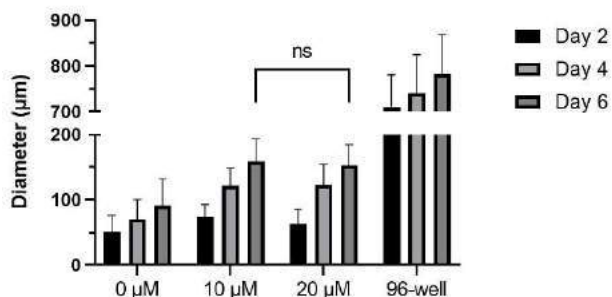


Figure 3: Average diameter of EBs generated using alginate encapsulation method and 96-well method cultured over the span of 6 days (Error bars: \pm SD).

EBs maintained with ROCKi grew to be two times larger than those without ROCKi. Statistical testing showed significant difference in size between the 0 μ M ROCKi group and both 10 and 20 μ M ROCKi groups at Day 6 ($p < 0.0001$), while it was determined that there was no significant difference between the 10 and 20 μ M groups ($p = 0.6098$).

The number of encapsulated EBs within the 10 and 20 μ M group was estimated to contain at least 250 per bead, whereas only 37 EBs were counted within the 0 μ M ROCKi group. Compared to the conventional method, only 96 EBs could be made from the same number of starting cells, but these EBs had a much more consistent size distribution with a coefficient of variation of 11.2% on Day 6, whereas the ROCKi groups of 0, 10, and 20 μ M showed variation of 44.9%, 21.9%, and 21.3%, respectively. To determine the EB formation efficiency, the number of EBs was divided by the number of cells initially used. The encapsulation method using 0 and 20 μ M ROCKi showed an EB efficiency of 0.053% and 0.357%, respectively, whereas the 96-well method produced an efficiency of 0.0001%.

Encapsulated and conventional EBs showed similar distributions of a few dead labeled cells located at the periphery of the spheroids (Fig. 4).

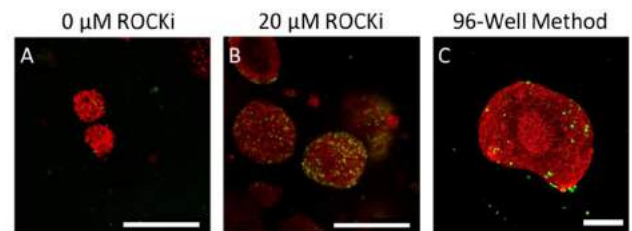


Figure 4: A-B) 20x and C) 10x live (red) and dead (green) staining of EBs on Day 8. Scale Bars: 250 μ m.

DISCUSSION

Generating EBs using the alginate encapsulation method enabled the production of more EBs, but at smaller sizes. Utilizing the 96-well method allowed for the quick generation of large EBs, but at a smaller quantity. It has been shown that consistent sizing of EBs is crucial when differentiating EBs toward specific cell lineages [7]. To make use of the inconsistently sized EBs formed in alginate, precise sorting of EBs would help maximize the yield of viable EBs available to researchers. Increasing the formation efficiency of EBs using alginate encapsulation could lead to improved differentiation protocols to produce cell types with limited sources. Future work involves using a TaqMan hPSC Scorecard Assay and qPCR to determine pluripotency and lineage bias towards any of the three germ layers as a function of method parameters.

ACKNOWLEDGEMENTS

This work was supported by funding from an Iowa NASA EPSCoR Seed Grant.

REFERENCES

- [1] Takahashi, K et al., *Cell*, 131:861-872, 2007.
- [2] Pettinato, G et al. *Stem Cells and Develop.*, 24:14:1595-1609, 2015
- [3] Chayosumrit, M et al. *Biomaterial*, 31:505-514, 2010.
- [4] Nachlas, A et al. *Acta Biomaterialia*, 71:235-246, 2018.
- [5] Wu, S et al. *J. Mater. Chem. B*, 5:3870-3878, 2017.
- [6] Teramura, T et al. *Bioc. & Biophys. R. Comm*, 417:2 836-841, 2012.
- [7] Hwang, Y et al. *PNAS*, 106:40 16978-16983, 2009.

CYCLIC STRETCH RESULTS IN DIRECTIONALLY DEPENDENT RECELLULARIZATION ALIGNED WITH CELLULAR STRESS AVOIDANCE REORIENTATION

Adam W.Y. Ley (1), Eric Slaughter (2), Victor H. Barocas (1), Robert T. Tranquillo (1,2)

(1) Biomedical Engineering, University of Minnesota, Minneapolis, MN, USA

(2) Chemical Engineering & Materials Science, University of Minnesota, Minneapolis, MN, USA

INTRODUCTION

Tissue recellularization is influenced by physiologic mechanical loading conditions. This is especially true for tissues that undergo constant cyclic stretch, like cardiovascular tissues [1]. This affects recellularization, as cyclic stretch impacts cell proliferation [2] and migration velocities [3], while also causing cells to reorient perpendicular to the stretch direction in a behavior known as stress avoidance (SA) [4,5]. The effects of cyclic stretch on directed single-cell migration, however, remains largely uncharacterized. In this work, we analyzed the effects of cyclical uniaxial stretch on the recellularization of an acellular “invasion” region parallel and perpendicular to the direction of stretch. We then conducted a circular statistical analysis on the morphological data to further characterize cells’ migration behavior after 24 hours of cyclic stretch.

METHODS

Glass coverslips were placed on collagen I coated FlexCell UniFlex plates in two configurations, “parallel” and “perpendicular”, (fig. 1). Human dermal fibroblasts were seeded onto the plates at 2,000 cells/mL and incubated with DMEM/F12 with 15% FBS, 100 U/mL penicillin, and 100 U/mL streptomycin at 37 °C and 5% CO₂. Coverslips were removed after 24 hr. “Static” plates were incubated another 24 hr. “Flexed” plates were incubated in a FlexCell FX-5000 tension system with 7% uniaxial tensile strain at 0.5 Hz in a sinusoidal waveform for 24 hr. This protocol resulted in 4 treatments: parallel static, perpendicular static, parallel flexed, and perpendicular flexed.

After the final incubation, cells were fixed in 4% PFA for 15 minutes, permeabilized with 0.1% Triton X-100 for 5 minutes, and stained with 500x Alexa Fluor 594 Phalloidin and 10,000x Hoescht-33342 for up to 3 hours. Imaging was conducted using a BioTek Cytation 3 with fluorescence microscopy capabilities. Fluorescence was captured using TxRed (Ex 586/15 nm, Em 647/57 nm) and DAPI (Ex 377/50 nm, Em 447/60 nm) filter cubes using a 4x objective.

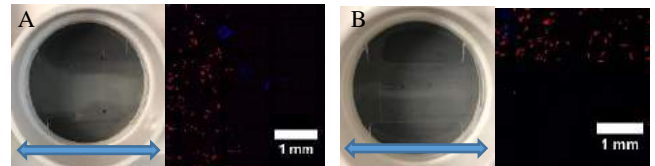


Fig. 1 A. Perpendicular, and B. parallel configurations with resulting cell seeding patterns. Arrows denote stretch direction

Nuclei in the invasion region were counted using Gen5™ Data Analysis Software. The initial location of the coverslip used to identify the border between the initial cellular and acellular regions (hereafter referred to as “edges”) and identify the invasion region. Nuclear counts were normalized by the length of these edges. Single-cell morphology was characterized using a custom MATLAB script that fit ellipses to overlapping F-Actin cytoskeletons and nuclei, recording the centroid and major axis orientation for both structures. Past literature established that cells elongate in the direction of migration [6], and that the nucleus translates to the rear of migrating cells [7]. To approximate migration direction, we subtracted the nucleus centroid from the F-Actin centroid and compared the resulting vector to the major axis angle of the ellipse fitting the F-Actin cytoskeleton. If the difference was less than 90°, migration direction was approximated as the major axis angle. Otherwise, the migration direction was the major axis angle + 180°.

This data was then split based on whether cells were migrating towards or away from the edges. Rayleigh’s test tested for uniformity in the data, and non-uniform data was fit to a von Mises distribution, estimating peak angle, μ , and concentrating parameter, κ . The parameters were compared using Watson Williams and ANOVA tests respectively, grouping the data by migration direction towards or from the edge and the configuration. Finally, a Kuiper’s test was used to compare the migration direction distributions for the aggregate data.

RESULTS

First, we characterized how flexion affected the recellularization of the invasion region and determined if flexion affected parallel and perpendicular recellularization with respect to the stretched direction. Outliers were removed from the data, and the normalized counts were pooled by treatment type. 1-way ANOVA testing on the cell counts indicated significant differences ($p < 0.001$) among the treatment groups. A Tukey multiple comparison test indicated that the flexed experiments exhibited significantly ($p < 0.001$) lower cell counts than static experiments for both parallel and perpendicular configurations, suggesting that flexion results in decreased recellularization. There were also significant differences between the flexed experiments, with flexed perpendicular having lower normalized cell counts ($p < 0.05$). These results indicate that cyclic stretching's effect on recellularization is two-fold: decreasing cell recellularization of the invasion region and causing preferential recellularization orthogonal to the stretching direction. However, this data doesn't elucidate the associated migration. Specifically, the recellularization rates of the two directions could differ if the time scale for reorientation due to SA is much less than the observation time and/or if cell speed depends on orientation relative to the stretching direction. This is pertinent as cells migrating into the acellular region have perpendicular and parallel orientations relative to the stretching direction for the parallel and perpendicular configurations, respectively.

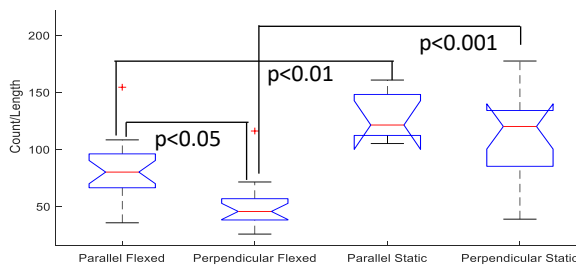


Fig 2. Normalized cell counts categorized by treatment type

Circular statistical analysis of the migration directions were used to better characterize migration behavior. As shown in fig. 3, the flexed experiments resulted in a bimodal distribution of migration directions, whereas static migration angles appeared uniform. Rayleigh's tests conducted on the split data indicated that 22 of the 24 static migration angles were uniformly distributed ($p > 0.05$) and that 23 of the 24 flexed migration distributions were non-uniform ($p < 0.05$). Von Mises fits for the flexed experiments resulted in mean angles and concentration parameters that did not differ significantly ($p > 0.05$). These results suggest after 24 hours of cyclic stretch, cells preferentially migrate nearly orthogonal to the stretch direction at 73° and 253° with $\kappa = 0.517$.

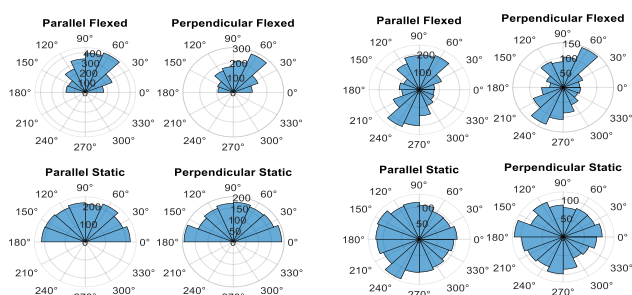


Fig 3. Polar histograms for **A.** ellipse major axis angles and **B.** approximated cell migration direction

Moreover, a Kuiper's revealed no that there were no differences in cell migration direction distributions when comparing the two orientations. However, the test did indicate that the migration direction distributions were different between flexed and static experiments.

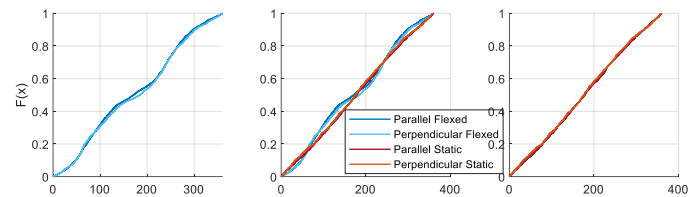


Fig 4. Cumulative density functions for cell migration angles.

DISCUSSION

In this study, we sought to determine how cyclic stretch affects cell migration perpendicular and parallel to the stretching direction and characterize the nature of the migration. Our results indicate that cyclic stretch results both decreased recellularization and induced directionally dependent single-cell cellularization orthogonal to the stretch direction. Recent literature suggests that cyclic stretching can decrease cell proliferation and migration rates [2,3], impacting recellularization. Our results align with these interpretations, but does not separate each factor's effect on observed recellularization. Fitting the data to reaction-diffusion models Fisher-Kolmogorov equation [8] can provide further insight into the impacts of each, and is a potential future direction.

The results from the circular statistical analysis suggests that at 24 hours, migration behavior is symmetric and consistent with observed reorientation behavior due to SA [4,5]. The Rayleigh's tests of uniformity demonstrated that cell migration towards and away from the edges were effectively symmetric. Further, the results of the Kuiper test indicate that the cells undergoing flexion exhibited the same migration patterns irrespective of their initial migration past the edge. These differed from the migration angle distributions of the static tests. These data indicate that at 24 hours, the direction of cell migration closely aligns with observed SA reorientation behavior. This suggests that SA behavior might be responsible for the observed directionally dependent recellularization. Future experiments with more granular timepoints can be used to monitor the onset of this behavior to ascertain the dynamics of the observed direction-dependent recellularization.

In all, our results indicate that flexion reduces recellularization rates and results in directionally dependent recellularization rates. Circular statistical analysis indicates that after 24 hrs, cell migration orientations closely align with cellular SA reorientation behavior, resulting in preferential migration orthogonal to the direction of stretch. Ultimately, the combination of these methods allows for a more thorough analysis linking cell migration behavior with recellularization results and can lead to a better understanding of recellularization dynamics in cyclically-stretched cardiovascular tissues.

ACKNOWLEDGEMENTS

This work was supported by the NIH (T32-HL139431).

REFERENCES

- [1] VeDepo, M et al., *J Tissue Eng*, 8:2041731417726327, 2017.
- [2] Song, J., et al., *Bioscience Rep*, 40(6):BSR20192012, 2020.
- [3] Desai, L., et al., *J Biol Chem*. 285(7):4511-9, 2010.
- [4] Iba, T., et al., *Microvasc Res*. 42(3):245-54, 1991.
- [5] Lien, J., et al., *Sci Rep*, 11(1):14803, 2021.
- [6] Ridley, A., et al., *Science*, 302(5651):1704-9, 2003.
- [7] Zhu, R., et al., *Semin Cell Dev Biol*, 82:41-50, 2018.
- [8] Simpson, M., et al., *J R Soc Interface*, 10(82):20130007, 2013.

A FLUID-SOLID-GROWTH FRAMEWORK FOR SIMULATING PATIENT-SPECIFIC VASCULAR GROWTH AND REMODELING USING CONSTRAINED MIXTURE THEORY

Erica L. Schwarz (1), Martin R. Pfaller (2), Jason Szafron (2), Christopher Breuer (3), Jay D. Humphrey (4), Alison L. Marsden (1,2)

(1) Bioengineering, Stanford University, Palo Alto, CA, USA
(2) Pediatrics, Stanford University, Stanford University, Palo Alto, CA, USA
(3) Regenerative Medicine, Nationwide Children's Hospital, Columbus, OH, USA
(4) Biomedical Engineering, Yale University, New Haven, CT, USA

INTRODUCTION

Understanding the mechanisms by which the hemodynamic environment affects the behavior and evolution of cardiovascular structures has become increasingly central to predictive simulations. Early experiments showed that vascular cells are sensitive to their mechanical environment and seek to maintain homeostatic stress values and have been used as a basis for cardiovascular growth and remodeling (G&R) theory ever since. [1-4]

Early G&R studies treated vascular soft tissue as homogeneous when predicting vascular evolution. However, vascular tissue is made up of a complex mixture of biological constituents that each have specific biomechanical behavior. To more accurately model this behavior, the constrained mixture theory of vascular G&R was introduced to model how turnover of individual constituents drives the evolution of vessels as a whole. [5] Constrained mixture theory proved successful at modeling vascular response to a wide variety of hemodynamic and pathological conditions and has since been adapted to a myriad of applications. [6, 7]

The versatility of constrained mixture theory makes it an attractive framework to integrate into high-fidelity models of patient-specific hemodynamics. Given the ability of computational fluid dynamics to quantify hemodynamic forces in arbitrarily complex geometries, this would significantly expand the ability of constrained mixture theory to predict outcomes in clinically relevant cases. However, the complexity of constrained theory has limited its ability to be adapted to patient-specific frameworks. Previous studies have attempted to circumvent this limitation by using simplifying assumptions, either in the calculation of the hemodynamic fields or in the constrained mixture theory itself, and there has yet to be a full implementation of constrained mixture theory in fully 3D, patient-specific fluid-solid interaction (FSI) simulations.

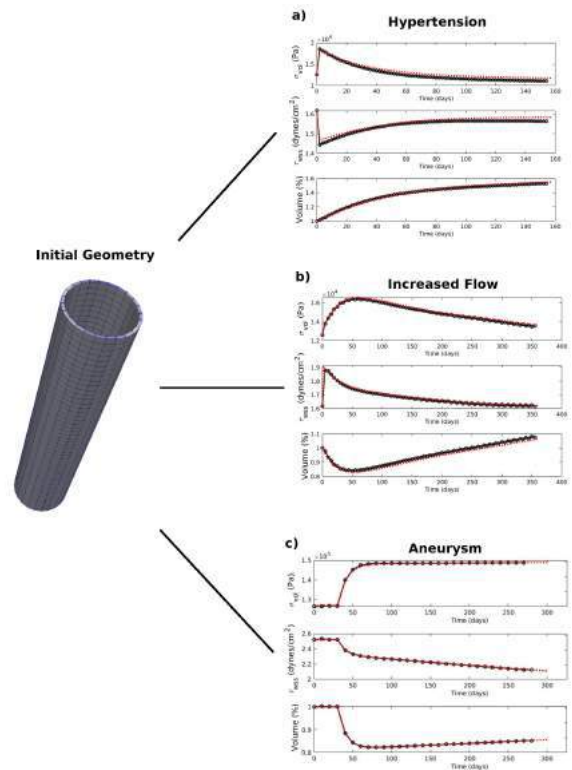


Figure 1: Validation of the FSG framework in a 3D geometry (black line) against reduced order solution (red dotted line).

This work presents the methodology for fluid-solid growth (FSG) framework that utilizes full constrained mixture theory. We validate the performance of this framework against benchmark constrained mixture theory problems and show its ability to simulate arbitrary geometries in the case of standard hypertension, increased flow, and aneurysm formation. This represents the first framework able to simulate constrained mixture theory G&R in complex, fully-3D, patient-specific anatomies.

METHODS

The evolution of the referential mass densities an individual constituents, α , is given as

$$\rho_R^\alpha(s) = \rho_R^\alpha(0)Q^\alpha(s) + \int_0^s m_R^\alpha(\tau)q^\alpha(s, \tau)d\tau \quad (1)$$

where the mass production function, $m_R^\alpha(\tau)$, and the mass survival function, $q^\alpha(s, \tau)$, are dependent on wall shear stress, τ_{wss} , and the volumetric stress, σ_{vol} . The strain energy density at any point in the tissue is postulated to be

$$W(s) = \sum_\alpha \left[\rho^\alpha(0)Q^\alpha \hat{W}^\alpha(\mathbf{F}_{n(0)}^\alpha(s)) + \int_0^s m^\alpha(\tau)q^\alpha(s, \tau)\hat{W}^\alpha(\mathbf{F}_{n(\tau)}^\alpha(s)) \right] \quad (2)$$

τ_{wss} , σ_{vol} , and the current configuration, $\mathbf{F}(s)$, are calculated using coupled fluid-solid interaction. The fluid domain is governed by the Navier-Stokes equations

$$\nabla \cdot \mathbf{v}^f = 0 \quad (3)$$

$$\dot{\mathbf{v}}^f + \mathbf{v}^f \cdot \nabla \mathbf{v}^f = \frac{1}{\rho^f} \nabla p^f + \nu^f (\nabla^2 \mathbf{v}^f + (\nabla \mathbf{v}^f)^T) + \mathbf{f}^f \quad (4)$$

and solid domain is governed by linear momentum balance

$$\text{div} \boldsymbol{\sigma} + \mathbf{f} - \rho \mathbf{a} = \mathbf{0}. \quad (5)$$

To evolve the configuration of the vessel we iterate between the fluid, solid, and *G&R* equations until convergence is reached at each timestep. To keep the evaluation of the solid governing equations tractable, we used the linearized behavior of the vascular material response at each iteration and enforce volume change via a dilation penalty framework where. The Cauchy stress then takes the form

$${}^{n+1}\boldsymbol{\sigma}(s) = -({}^n p(s) + {}^*p)\mathbf{I} + \frac{1}{{}^*J} {}^*\mathbf{F} {}^n \hat{\boldsymbol{\sigma}}(s) {}^*\mathbf{F}^T + \frac{1}{{}^*J} {}^*\mathbf{F} ({}^n \mathbf{C}(s) : {}^*\mathbf{E}) {}^*\mathbf{F}^T \quad (6)$$

$${}^*\mathbf{E} = \frac{1}{2} \left(\left(\frac{\det {}^*\mathbf{F}}{{}^*J} \right)^{2/3} {}^*\mathbf{F}^T {}^*\mathbf{F} - \mathbf{I} \right) \quad (7)$$

$${}^*p = k(\det {}^*\mathbf{F} - {}^*J) \quad (8)$$

where k is a penalty parameter that enforces the volume change to desired accuracy and ${}^n \mathbf{C}(s)$ is the linearized stress response given as

$$\begin{aligned} & {}^n \mathbf{C}(s)_{\alpha\beta kl} \\ &= \frac{4}{{}^n J(s)} {}^n F_{\alpha A}(s) {}^n F_{\beta B}(s) {}^n F_{kP}(s) {}^n F_{lQ}(s) \frac{\partial^2 W(s)}{\partial C_{AB} \partial C_{PQ}} \Big|_{{}^n \mathbf{C}(s)} \end{aligned} \quad (9)$$

RESULTS

This FSG framework was implemented in the SimVascular open-source multiphysics solver (<https://simvascular.github.io/>). Validation was done using a hypertension model where the vessel pressure was raised 40% above its homeostatic value, a increased flow model where flow was increased 20% above its homeostatic value, and an aneurysm model where elastin was degraded by 65%. We used a timestep size of 1 day, 5 days, and 10 days respectively.

In the hypertension model there was an instantaneous increase in σ_{vol} that returned to homeostatic values over the course of the simulation. In the increased flow case there was an instantaneous increase in τ_{wss} accompanied by an instantaneous increase in σ_{vol} triggered by the increased flow condition under constant outlet resistance. τ_{wss} monotonically decreased until homeostatic values were reached. σ_{vol} initially increased due to the τ_{wss} perturbation dominating the change in volume but then decreased after sufficient mediation of τ_{wss} allowed for late-stage volumetric growth. In the aneurysm case, elastin injury was initiated at $t = 30$ days after which vascular dilation progressed resulting in decreasing τ_{wss} . In all cases, the FSG framework results matched the solutions previously produced by reduced order implementations of constrained mixture theory.

DISCUSSION

This study shows that our FSG framework can accurately capture expected constrained mixture results under a variety of hemodynamic conditions, pathological conditions, and simulation timestep sizes. Unlike previous implementations of constrained mixture theory, this framework utilizes the fully 3D forms of the constrained mixture, fluid, and solid governing equations. By doing this, this framework is generalizable to arbitrary geometries including patient-specific models of cardiovascular structures. In addition, it is implemented as part of an open-source computational fluid dynamics solver, SimVascular, providing a open tool for the scientific and clinical communities. This represents a major step forward in the field of vascular simulation and will provide the basis for future studies of patient-specific vascular G&R.

ACKNOWLEDGEMENTS

We gratefully acknowledge the American Heart Association under award number 835662 for providing the financial resources to conduct this research.

REFERENCES

- [1] Rodbard S. *Cardiology* 60.1 (1975).
- [2] Kamiya A et al. *American Journal of Physiology-Heart and Circulatory Physiology* 239.1 (1980).
- [3] Lehoux S. *Biomechanics of Coronary Atherosclerotic Plaque* (2021).
- [4] Davies PF. *Physiological reviews* 75.3 (1995).
- [5] Humphrey J. *Journal of Elasticity* 145.1 (2021).
- [6] Szafron J et al. *Annals of biomedical engineering* 46.11 (2018).
- [7] Latorre M et al. *ZAMM-Journal of Applied Mathematics and Mechanics/Zeitschrift für Angewandte Mathematik und Mechanik* 98.12 (2018).

AN INTRAVASCULAR CATHETER WITH SWITCHABLE FLEXURAL RIGIDITY

D.G. Rucker,¹⁻³ J.W. Osbun,⁴ M.A. Zayed,¹⁻² G.M. Genin²⁻⁴

(1) Vascular Surgery, Washington University, St. Louis, MO, USA

(2) Biomedical Engineering, Washington University, St. Louis, Missouri, United States

(3) NSF Science and Technology Center for Engineering MechanoBiology, Washington University, St. Louis, MO, USA

(4) Neurological Surgery, Washington University, St. Louis, MO, USA

INTRODUCTION

Peripheral arterial disease (PAD) can occur in various vascular beds – including the neurovasculature and the vasculature of the limbs [1]. Atherosclerosis or thrombus formation in the inner lumen of arteries can lead to significant clinical complications, including stroke, acute limb ischemia, wounds, and gangrene. To alleviate these conditions, clinicians need to be able to navigate in the arterial system, locate these areas of obstruction, and administer treatment expeditiously. Endovascular catheterization to facilitate these types of treatments requires steerable and navigating low profile catheters to the diseased arteries [1]. A major limitation of this is catheter kinking, buckling, and herniation during the process of catheter navigation within complex tortuous arteries.

To address this major limitation, our team developed a catheter (the *MultiFlex Catheter*) that can retain flexibility during navigation towards areas of disease, and then subsequently become rigid once in place to facilitate treatment of the area of disease (with stents, angioplasty balloons, or endovascular coils) without catheter herniation or buckling. The design uses a multi-lumen catheter that encases an array of wires; when space between the catheters is suctioned with a syringe, the inner and outer tubes cinch against the wire array and the catheter stiffens [2]. Our objective was to evaluate mechanisms that influence the efficacy of this mechanism. We hypothesized that including expanded polytetrafluoro-ethylene (ePTFE) tape within the outer lumen would aid this change in stiffness by holding the wire array in place during actuation.

We additionally hypothesized that the introduced wrapping styles have varying levels of effectiveness in maintaining the string array's position. Each prototype introduced a unique combination of wrapping method, ePTFE spacing, and width. Modeling the catheter as a cantilever beam with a point load placed at points along its length provides the data to find its maximum and minimum range of flexural rigidity [2]. Image analysis of this modeling allows for the

measurement of angular deflection (1) at the point load and its tangent length to the beam.

METHODS

Resonetics, an engineering and manufacturing company for the life sciences industry, created the prototypes through shaft lamination and complex catheter reflow operations. They were constructed with a reinforced coil within the inner lumen that provides support and a uniform passage for wires. The bifurcated hub located at its port end allows for access to the inner and outer lumen. The catheter without ePTFE wrap securing its string array was assigned as the control, and the remaining catheters were labeled as experimental.

The Various ePTFE tape width and spacing used in either the spiral or banded wrapping method is tabulated and differentiates each prototype based on these variables.

Catheters, which are constructed of pliable composite materials, flex significantly even under relatively light stresses. To precisely measure catheter stiffness, a non-linear formulation of Euler-Bernoulli beam theory is used as the basis for deriving flexural rigidity (2) [3].

A dunk test, which slowly injected air into the outer lumen while it was submerged to observe for leaks in the form of escaping air bubbles, was done prior to collecting data to ensure catheter viability.

Using a clamp on the bifurcation hub, the catheter is pinned horizontally to its background and placed vertically against a perpendicular, flat surface. The photos taken of each prototype in its actuated state, with the addition of a point load along its length, provides the initial imaging data for measuring the angular deflection and tangent length of the moment arm at the point load. Using ImageJ, an image analysis software, these two previously variables are measured to find the flexural rigidity, quantifying the stiffness along the catheter's length.

Angular deflection

$$\theta = \theta_f - \theta_i \quad (1)$$

Non-linear flexural rigidity

$$EI = \frac{PL^2 \sqrt{1 + \tan^2(\theta)}}{2 \tan(\theta)} \quad (2)$$

RESULTS

The ePTFE tape addition to the array successfully demonstrates its ability to secure the wires in place, increasing the stiffness range. The varying flexural rigidity range of each catheter also shows the influence of the wrapping method on actuating ability (Figure 1).

Both prototypes with the tightly wound spiral method showed the highest effectiveness in increasing flexural rigidity. Their ability to retain string array spacing during actuation attributes to this.

Plotting the stiffness range of each prototype in comparison to commercially available catheters and sheaths (Figure 2) also illustrates its potential in peripheral and neurovascular procedures. Each prototype overlaps the Catheter and LEPA Sheaths required flexural rigidity range, showing that the *Multiflex catheter's* wrapping style can be designed for an intended range.

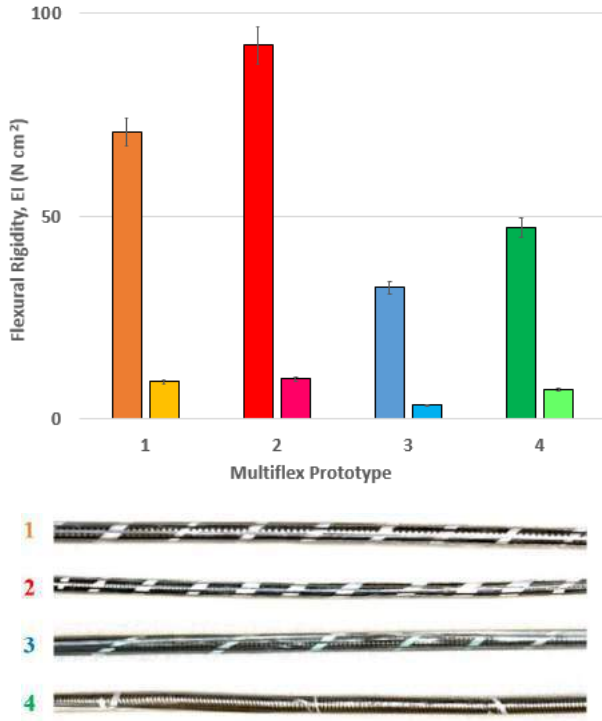


Figure 1: Flexural rigidity range of prototypes based on cantilever beam model testing. Prototype demographic displaying wrapping methods.

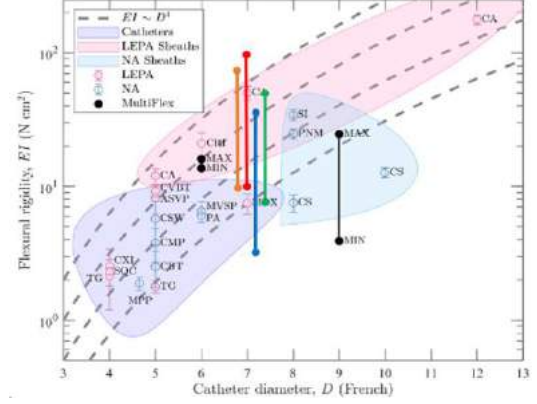


Figure 2: Ashy chart with the addition of prototype flexural rigidity ranges.

DISCUSSION

Overall, the results from conducting the cantilever beam modeling were within range of findings from previous prototype iterations. They also demonstrate the effectiveness of the string array tape addition and how it attributes to the variance in flexural rigidity range based on the wrapping style.

With this testing, there are flaws that allow for inconsistencies in the data. The mass per unit length is not considered in the equations and violates the previous assumption that it is negligible compared to the point load. When moving along the length, the catheter mass must be considered as well because its considerable mass does effect the deflection. The accuracy of its maximum flexural rigidity may have validity because this considerations may be disregarded when the point load is at the maximum distal end, which provided the greatest tangent length and angular deflection. Although, the minimum flexural rigidity and its measurement with respect to specific catheter segments may be inaccurate.

Setting up the experiment for each catheter also introduced a variance that may affect data accuracy. The catheter itself may have not been aligned perfectly horizontal. This influence combined with the variable, innate stiffness of each catheter based on its orientation may affect the point load location measurement and angular deflection.

The limiting factors of image quality and pixilation error during image analysis also played a role. These influences provided room for error when measuring angles and tangent point load length. The angle may not be perfect, and the length may be distorted given the set scale.

ACKNOWLEDGEMENTS

The author thanks Drs. Mohamed Zayed and Guy Genin for guidance in this project, and collaborators within the Engineering and Medical school for their companionship and support. This work was funded by the Cardiovascular Research Innovation in Surgery & Engineering Fellowship.

REFERENCES

- [1] Kokkinidis, D.G. and Armstrong, E.J., 2020. Current developments in endovascular therapy of peripheral vascular disease. *Journal of thoracic disease*, 12(4), p.1681.
- [2] Chandrasekaran V et al. *JMBBM* 113 (2020). OI: 10.7936/nwn0-9a57.
- [3] Hartquist CM et al. *J. Biomech* 119 (2021). DOI: 10.1016/j.jmbbm.2021.104459.

CHARACTERIZATION OF CELLULAR RESPONSE TO ENDOVASCULAR ABLATIVE THERAPIES IN 2D AND 3D

S. Brocklehurst (1), Amin Sabaghan (1), D. Stolley (2), N. Ghousifam(1), E. Cressman(2), D. Fuentes(2), M.N. Rylander(1)

Mechanical Engineering, University of Texas at Austin, Austin,
Texas, USA (1)

M.D. Anderson Cancer Center, Houston, Texas, USA (2)

INTRODUCTION

Curative therapies are not available to greater than 80% of the patient population with hepatocellular carcinoma (HCC). There is a well-recognized need for novel methods that can intricately balance (1) treatment of the disease extent with (2) preservation of liver function and minimize the risk of recurrence and metastasis. Ablation and embolization are the two most common minimally invasive methods used in treating unresectable HCC. These are established therapies with a known survival advantage [1]. Thermally ablative therapies include radiofrequency ablation (RFA) and microwave ablation (MWA) and utilize thermal energy to destroy the disease. Embolization techniques utilize a direct injection of a chemotherapeutic agent or radiation into the hepatic artery with or without lipiodol and a procoagulant material to promote intratumoral retention. Thermoembolization (TE) provides a novel conceptual endovascular approach in which a bolus of acid chloride dissolved in an inert oily solvent delivers an exothermic chemical reaction. Recent investigations of TE indicate that it might offer unique advantages versus current techniques [2]. This approach is unique and combines the benefits of embolic and thermal- and chemical-ablative therapy modalities. The target tissue and vascular bed are subjected to simultaneous hyperthermia, ischemia, and acidic environments in a single procedure.

These complex conditions caused by the injection of acid chloride into the target tissue must be understood thoroughly in order to develop techniques to effectively destroy the intended cancerous tissue without negatively affecting the surrounding parts of the body. Accurate predictions of cell death are important towards these goals, and we have developed and calibrated preliminary mathematical models of the TE procedure using *in vitro* platforms that mimic vascularized liver. Validated cell damage models will accurately estimate the cellular damage as a function of hyperthermia, ischemia, and low pH stress that occurs during TE. The work presented in this paper focuses on the evaluation of how the conditions in the target tissue affect cells cultured

in 2D cell monolayers and 3D collagen platforms in order to develop an appropriate cell damage model.

METHODS

To understand the independent contribution of hypothermia, ischemia, and acidic environments that work in concert during TE, we first isolated the decrease in local pH and localized hyperthermia to determine their individual impact *in vitro* for computational model development. These conditions were later combined to identify any synergistic effects between them. Human hepatocellular carcinoma cell line HEPG2 was cultured in flasks and then passaged and seeded into 96-well plates for use in experiments. Cell survival ratios were determined 24 hours after exposure to hyperthermia and diminished pH using Cell-Titer blue assays. Additional unexposed control plates were measured alongside the exposed samples. The survival ratio was calculated as the ratio of absorbance between exposed and unexposed samples after subtracting the background absorbance observed from an acellular plate. The effect of heat associated with thermoembolization on representative 2D and 3D extracellular matrices was determined as follows:

2D samples: Each plate had 20-25 wells with adherent cells seeded on their bottom surfaces. Plates were placed in an incubator with desired temperature to expose cells to hyperthermia. Cell culture media was removed from cell-seeded plates, and it was replaced with only 40 μ L of media per well to reduce heating times. In order to set the exposure temperature more accurately, one cell-bearing plate was tested simultaneously with a second, acellular plate with the same fluid volumes and a thermocouple placed in the bottom of one well. Temperatures were recorded throughout the exposure. At the end of the experiment, warm media was removed rapidly, then fresh media was added, and the plates were stored in an incubator at 37 for 24 hours. Cells were exposed to temperatures of 43, 45, 47, and 50 °C for 10 to 60 minutes.

3D samples: As we have previously published [3], type I collagen was used to replicate the 3D tissue microenvironment. Collagen was mixed with HepG2 cells at a concentration of 1×10^5 cells/ml and dispensed as 50 μ L aliquots in 96 well plates and allowed to polymerize.

Phosphate-buffered saline (PBS) solutions with added glacial acetic acid were used to expose cells to acidic pH. Solutions with a pH of 6.00, 6.25, 6.50, 6.75, and 7.00 were prepared and passed through sterile filters. Media was removed from each well of a plate, then a timer was started, and 150 μ L of acidified PBS was added to each well. The plate was kept in an incubator for between 10 and 60 minutes, then the acid solutions were removed in the same order they were added. A small pH probe was used to record the pH over time in identical cell-bearing plates. Combined pH and hyperthermia testing were performed using the pH exposure protocol listed above with heated solutions, then placing the plates into cell culture incubators set to 43 or 45 $^{\circ}$ C.

Modified Arrhenius damage models are used to provide a first-order estimate of the cell death resulting from the thermal and acidic pH exposure. Cell kill as a function of exposure to temperature is known to approximately follow an Arrhenius rate process [4]. Here, parameters of the Arrhenius damage model will be considered dependent on the presence of the acid as well. Arrhenius parameters are calibrated to the pathology response observed from *in vitro* cell damage testing. The Arrhenius parameters follow a log-linear relationship [5]. Regardless of the type of damage process being examined, a plot of the activation energy versus the log of the frequency factor that defines the Arrhenius model approximately follows a straight line. This empirical relationship has been measured independently by Wright [6] and He [7] and is used to constrain the damage model under variations in temperature and acidic pH exposure. A constrained optimization formulation is numerically solved to fit model parameters to the cell viability data. The parameters corresponding to the temperature-only data are recovered first. The parameters corresponding to pH are then recovered given the known Arrhenius parameters that fit temperature.

RESULTS

Preliminary *in vitro* testing results have been applied toward the creation of cell death models based on exposure to hyperthermia and acidic solutions. As seen in Fig. 1-A, a steady decline in cell survival was observed during hyperthermia, with the rate of death increasing with higher temperature and longer exposure times.

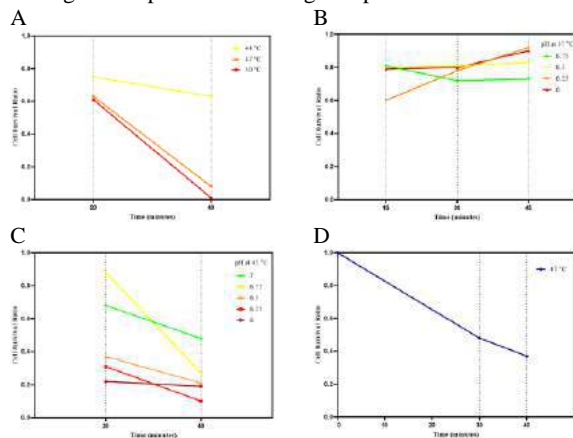


Figure 1 – Experimental viability. A – Hyperthermia exposure in 2D samples B – Acidic pH exposure in 2D samples C – Combined hyperthermia and acidic pH exposure in 2D samples D – Hyperthermia exposure in 3D samples

In the studied range, HepG2 cells in 2D samples are not sensitive to low pH (Fig. 1-B) unless exposed simultaneously to hyperthermic temperature (Fig. 1-C). These results further confirm the benefit of the combined effect of multiple mechanisms of cell injury implicitly to TE. As it is shown in Fig. 1-D, viability of HepG2 cells in 3D samples in response to hyperthermia decreases significantly while its rate decreases over time. Furthermore, it was observed that the 3D samples heat up more slowly than 2D samples and were melted almost completely at 49 $^{\circ}$ C while they had no noticeable melting at 47 $^{\circ}$ C.

A modified Arrhenius damage model was utilized to include both effects of temperature and pH to the cell viability as follows:

$$\Omega = \ln\left(\frac{1}{S}\right) = \int_0^t A \exp\left(-\frac{E_a}{RT + E_a pH}\right) dt \quad (1)$$

Two approaches of Sequential and Joint were used to curve fit the math model to the experimental data are shown in Fig. 2-A and B, respectively. These model fits of the predicted damage vs. measured damage achieve an R^2 values of 0.797831 and 0.7833556 in turn.

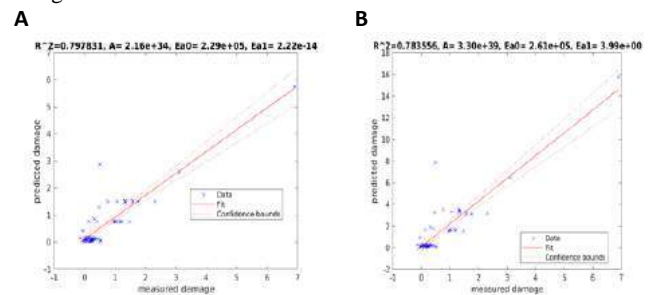


Figure 2 – Fitting of modified Arrhenius model to viability data

DISCUSSION

The work presented in this abstract has successfully broken down the conditions present in the target tissue during TE in separate and combined experiments to observe the resulting cell death. In this way, the contribution of each variable to the therapeutic effect of TE can be quantitatively studied, and the synergistic interactions between multiple conditions can be identified. Initial results demonstrate the feasibility of calibrating a temperature and pH-dependent cell damage model to the observed viability data. Further studies will cross-validate the results to study the prediction accuracy of our cell damage modeling approach.

The results from this study will enable the development and calibration of mathematical models to understand and predict the independent and synergistic effects of hyperthermia and acidic environments caused by TE. Deeper insight into effective delivery of this new therapy will provide valuable knowledge applicable to the treatment of cancers.

ACKNOWLEDGEMENTS

Resources for cell studies were supported by the MD Anderson-Oden Institute-Texas Advanced Computing Center pilot project.

REFERENCES

- [1] Jean-Charles Nault et. al. Journal of hepatology, 68(4):783–797, 2018.
- [2] David Fuentes et. Al. International Journal of Hyperthermia, 37(1):356–365, 2020.
- [3] Özkan, Alican, et al. Frontiers in oncology, 1956, 2021.
- [4] Mark W et. al. International Journal of Hyperthermia, 19(3):267–294, 2003.
- [5] John A Pearce et. al. International Journal of Hyperthermia, 29(4):262–280, 2013.
- [6] Neil T Wright et. al. Journal of biomechanical engineering, 125(2):300–304, 2003.
- [7] Xiaoming He et. al. Critical Reviews in Biomedical Engineering, 31(5&6), 2003.

BIAXIAL MECHANICS OF THE MURINE VAGINA DURING POSTPARTUM HEALING BEFORE AND AFTER ELASTIC FIBER DISRUPTION

Shelby E. White (1), Lily M. Buchanan (2), Niyousha Karbasion (3), Matthew R. Bersi, Ph.D., (3),
Maria Florian-Rodriguez M.D., (4), Kristin S. Miller, Ph.D., (2,4)

(1) Biomedical Engineering, Tulane University, New Orleans, LA, USA

(2) Bioengineering, University of Texas at Dallas, Dallas, TX, USA

(3) Mechanical Engineering and Materials Science, Washington University, St. Louis, IL, USA

(4) Obstetrics and Gynecology, University of Texas Southwestern, Dallas, TX, USA

INTRODUCTION

The vagina is a fibromuscular organ that must undergo significant remodeling to act as a passageway during menstruation, intercourse, and vaginal delivery. The vagina is principally composed of collagen fibers, elastic fibers, and smooth muscle cells. Elastic fibers dictate compliance, constrain collagen undulation, and influence smooth muscle cell phenotypes¹⁻³. Smooth muscle cells are the primary contributor of the active mechanical properties of the vagina, which include contractility and the maintenance of the structural and functional integrity of the vaginal wall⁴. The active contribution of the postpartum rat has previously been characterized uniaxially and is thought to have an increased receptor sensitivity to agonist concentration as compared to the nulliparous vagina⁵. The vagina experiences multi-axial loading in the body, which is not reflected in the previous uniaxial testing. Biaxial extension-inflation protocols are useful tools to evaluate the multi-axial mechanical properties while maintaining the native cylindrical geometry and cell-matrix interactions^{6,7}. Such protocols have quantified the maximum contractile potential and the passive mechanical contribution of the nonpregnant murine vagina⁷. However, how the biaxial active and passive mechanical contributions change during postpartum remodeling is unknown. Therefore, the objective of this study was to determine the active and passive mechanical properties of the murine vagina through postpartum remodeling. A general agonist of potassium chloride (KCl) will be utilized to determine the dose dependent contractile response. Further, elastase digestion will be used to observe potential interactions between elastic fibers and smooth muscle cell contractility.

METHODS

Sample Size A total of n=105 nulliparous (NP) and postpartum (PP) CD-1 mice aged 2–3 months were used within this study (Tulane IACUC approved). **In Vivo Vaginal Pressure Measurements (n=5/ group)** To inform the loading environment for mechanical testing,

intravaginal pressure was quantified with a balloon catheter at the estrus stage in nulliparous mice as well as 24 hours (1D PP), 72 hours (3D PP), 1 week (7D PP), and 2 weeks (14D PP) postpartum^{7,8}. The balloon catheter was inserted into the vaginal canal and PowerLab and LabChart8 software recorded pressure (AD Instruments). **Specimen preparation** A separate cohort of CD-1 mice (n=16/ group; nulliparous at estrus, 1D PP, 3D PP, 7D PP, and 14 D PP) were euthanized via guillotine without anesthesia to preserve SMC function⁷. Immediately after euthanasia, the vaginal tissue was dissected from the cervicovaginal complex and cannulated onto a biaxial extension-inflation device (Danish MyoTechnology; DMT). **Elastase treatment (n=8/ group)** Samples were randomly allocated to either a control (n=8/ group) or elastase treatment (n=8/ group). If allocated to elastase treatment, samples were intraluminally exposed to 15 U elastase digestion for 45 minutes^{6,7}. **Dose response contractility testing** To quantify the smooth muscle contractile potential, varying doses of a general agonist, potassium chloride (KCl), induced vaginal contractions⁹. Isobaric and axially isometric vaginal contractions were first induced with 20 mM of KCl for 5 minutes. The tissue was then allowed to rest for 5 minutes in fresh active Krebs's Ringer Buffer (KRB) Solution. The protocol was then repeated with 30 mM, 40 mM, 50 mM, 60 mM, 80 mM, and 100 mM of KCl. For each KCl dose, the change in outer diameter and axial force was recorded. **Passive mechanical testing (n=16/ group; 8 control, 8 elastase)** To remove calcium from the tissue and hinder the contractile response, the media was replaced with fresh calcium free passive (KRB) solution and the vagina was subjected to 2 mM of Egtazic acid (EGTA) for 30 minutes⁷. To quantify the circumferential and axial 1st Piola-Kirchhoff stress and material stiffness, 5 cycles of pressure-inflation tests (0–15 mmHg) were performed at the physiologic length as well as $\pm 2\%$ the physiologic length⁷. **Data analysis** The axial contractile potential was defined as the difference in the maximum and minimum axial force over the 5-minute period⁹. The passive material stiffness was determined by fitting a linear function

through the 1st Piola-Kirchhoff stress-stretch curve around the physiologic region¹⁰. **Statistical analysis** To determine if concentration of KCl, elastase treatment, and postpartum timepoint influenced contractile potential, 3-way ANOVAs (dose, elastase, timepoint) evaluated changes in axial force and outer diameter, respectively. A 3-way ANOVA (direction, elastase, timepoint) evaluated differences in the circumferential and axial material stiffness.

RESULTS

For the datasets described herein, the Shapiro-Wilks test suggested that the error of the data was normally distributed ($p > 0.05$). **Dose response contractility** A 3-way ANOVA (dose, elastase, timepoint) identified significant differences in the circumferential contractile potential with respect to KCl dose (not shown) ($p < 0.001$), elastase treatment ($p < 0.001$), and postpartum timepoint ($p < 0.001$). Significant interactions were observed among dose and elastase ($p = 0.02$), dose and timepoint ($p = 0.007$), elastase and timepoint ($p = 0.006$), as well as a 3-way interaction among all three variables ($p = 0.002$). An additional 3-way ANOVA (dose, elastase, timepoint) determined significant differences in the change in axial contractile potential with regard to agonist dosage (Figure 1) ($p < 0.001$), elastase ($p < 0.001$), and postpartum timepoint ($p < 0.001$). Significant interactions were noted among dose and elastase ($p = 0.005$), dose and timepoint ($p = 0.009$), elastase and timepoint ($p < 0.001$), and a 3-way interaction among the independent variables ($p < 0.001$). **Stress-Stretch curve** Early postpartum (1D PP) resulted in a leftward shift of the stress-stretch curve, denoting decreased distensibility (not shown). Subsequent postpartum remodeling (3D, 7D, 14D PP) demonstrated increased distensibility, as indicated by a rightward shift (not shown). **Material stiffness** A 3-way ANOVA identified significant differences in the material stiffness with respect to the postpartum timepoint ($p = 0.004$), elastase treatment ($p < 0.001$), and direction ($p < 0.001$). Significant interactions were observed between the postpartum time and elastase ($p < 0.001$), the postpartum time and direction ($p = 0.003$), direction and elastase ($p < 0.001$), as well as the timepoint, elastase treatment, and direction ($p = 0.006$). Posthoc analyses was not conducted due to significant interactions.

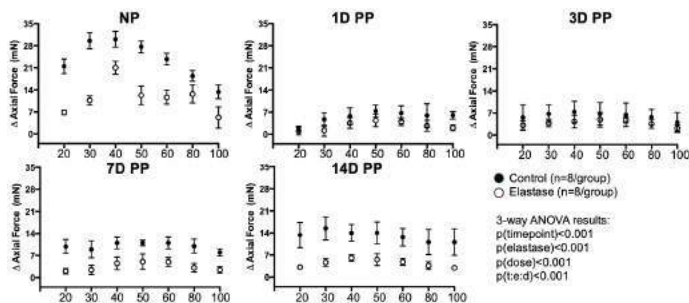


Figure 1: The axial contractile potential in the control (filled) and elastase (outlined) samples of nulliparous mice as well as 1D, 3D, 7D, and 14D postpartum (PP) samples. The dose-dependent contractile response was quantified at 20 mM, 30 mM, 40 mM, 50 mM, 60 mM, 80 mM, 100 mM of potassium chloride (KCl). Data are reported as mean \pm standard deviation.

DISCUSSION

Dose-Dependent Contractile Potential The axial contractile potential decreased in the immediate postpartum timepoint (1D PP) and increased in subsequent timepoints (7D PP, 14D PP; Figure 1). This supported prior results obtained by testing uniaxial strips of rat vaginal

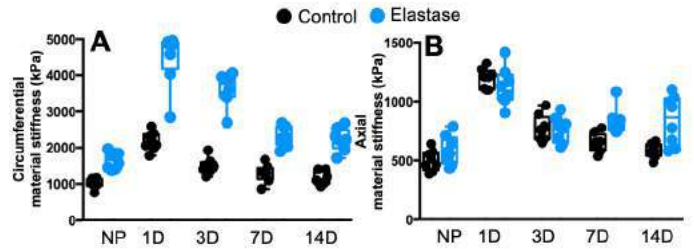


Figure 2: The circumferential (A) and axial material stiffness (B) for control (black) and elastase (blue) samples of nulliparous mice as well as 1D, 3D, 7D, and 14D postpartum (PP) samples. In both directions, the material stiffness increased early postpartum with a subsequent decrease with postpartum remodeling. Elastase increased the material stiffness in the circumferential direction. However, elastic fiber disruption had minimum effect in the axial direction. To best visualize the diminished change, the y-axis for the two directions were optimized to varying scales.

tissue⁵. Additionally, elastic fiber disruption via elastase treatment reduced the axial contractile potential, as evidenced by the decreased change in axial force, respectively compared to control (Figure 1). The demonstrated decrease may potentially be due to disrupted physical interactions between elastic fibers and smooth muscle cells. Similar decreases in vaginal contractility with elastase treatment were observed in CD-1 mice aged 2–6 months¹¹. Furthermore, the elastase induced decrease in contractile potential had a diminished effect in the 1D and 3D PP samples, as compared to the nulliparous, 7D, and 14D PP groups. In the C57BL/B mouse, decreased contractility was observed in the axial direction of the vagina at 4–6 months⁷. This decrease in axial contractility coincided with an increased area fraction of elastic fibers in the axial direction of the C57BL/6 mouse⁷. Taken together, this may suggest the potential for decreased functional elastic fibers in the early postpartum timepoints of 1D and 3D PP. **Material stiffness** In both directions, the material stiffness increased in the early postpartum groups and subsequently decreased in the later timepoints (Figure 2). Previous work in the mouse model suggests a potential burst of elastic fibers in the postpartum vagina¹². However, additional work observed an upregulation of matrix metalloproteinases¹³. These data may indicate time-dependent microstructural remodeling of the postpartum vagina. Future work is needed to better define relationships between mechanical metrics, such as material stiffness, and microstructural composition. **Limitations** Mice do not naturally sustain injuries during birth. Future work should carefully consider variations among the birth canal and fetal size. Quantifying vaginal mechanics through postpartum and with elastase treatment may provide key insights to improve the overall quality of care given postpartum patients in the clinical setting.

ACKNOWLEDGEMENTS

We acknowledge funding from the NSF (CMMI-#1947770; KSM)

REFERENCES

- [1] Murtada, et al., *J of biomechanical engineering*, 128(5) [2] Ferruzzi et al., *Cardiovasc Res* 92 (2) pp 287-295, 2011 [3] Akintunde et al., *J Biomech Eng* 2018. [4] Chen et al., *Int J Mole Med* 25(93) pp 95-104, 2016. [5] Feola et al., *Annals of BioE* 39 pp 549-558. [6] Ferruzzi et al., *Cardiovasc Res* 92 (2) pp 287-295, 2011. [7] Clark et al., *Interface Focus*, 9(4), p. 20190025, 2019. [8] Byers, S et al., *PloS ONE*, 7(4), pp-13-17, 2012. [9] Skoczylas et al., *Reproductive Sciences*, 20(4), 382-390. [10] Wagenseil, J et al., *J of Cardi Transl Res*, 5(3) pp. 264-273. [11] White et al., *SB3C 2022 abstract*. [12] Drewes et al., *Am J Pathol* 2007 170 (2) pp 578-589. [13] Wieslander et al, *J Pelv Med Surg* 2005 11:16

AUTOMATIC MODEL CONSTRUCTION FOR PATIENT-SPECIFIC AORTIC FLOW SIMULATIONS USING GEOMETRIC DEEP LEARNING

Pan Du (1), Delin An (2), Chaoli Wang (2), Jian-Xun Wang (1)

(1) Aerospace and Mechanical Engineering, University of Notre Dame, Notre Dame, IN, USA
(2) Computer Science and Engineering, University of Notre Dame, Notre Dame, IN, USA

INTRODUCTION

Image-based computational fluid dynamics (CFD) modeling has great significance in facilitating clinical diagnosis and treatment planning for cardiovascular diseases (CVD) [1], where the image-segmentation, which involves characterization of cardiac geometries from image data such as computerized tomography (CT) or magnetic resonance imaging (MRI), is one of the essential steps in the process as the resulting geometry directly determines the quality of the subsequent CFD modeling. Manual segmentation has considerable artifacts and is time-consuming [2]. With the rapid development of computer vision and artificial intelligence, a large group of works emerge recently, leveraging machine learning techniques to automate the image segmentation process. Early works use conventional machine-learning methods well-developed for image processing to realize automation. For example, feature descriptors or filters are used to detect edges representing the vessel wall [3-4]. Supervised or unsupervised classifiers are utilized to classify regions according to the gray-scale intensity [5-6]. Those methods require cumbersome pre- and post-processing procedures and yield unsmooth or discontinuous reconstructed surfaces. More recently, deep neural networks (DNN) are adopted to directly map the raw image data to vessel geometry. The most popular approaches are either using 2-D CNNs for each image slice or 3-D CNN that performs 3-D convolution in the volumetric data. Usually, a deformation mechanism will be added to ensure the surface smoothness of the reconstructed geometry [7-8]. Despite the rich literature in this field, those methods are either not fully automated (e.g., require user input of the centerline, requires manual pre- or post-processing) or suffer from surface irregularity, especially for the multi-branch aorta model.

To fill the gap, we proposed an automatic-segmentation model for patient-specific multi-branch aorta which combines a 3-D CNN to encode the image data and graph deformation model where a 2-D CNN is used to extract centerline from image data and a deformation model

is used to transform the template to the 3-D label geometry. We trained and tested our model on the Vascular Model Repository (VMR) which is an open-source database of cardiovascular models [9]. The proposed model features predicting centerline and the aorta geometry simultaneously and proved to have good generalizability across different patients.

METHODS

As shown in Figure 1, the auto-segmentation model consists of two parts: an encoding-decoding 3-D CNN structure (top half of Figure 1) and a graph convolution network (GCN) based deformation module (bottom half of Figure 1).

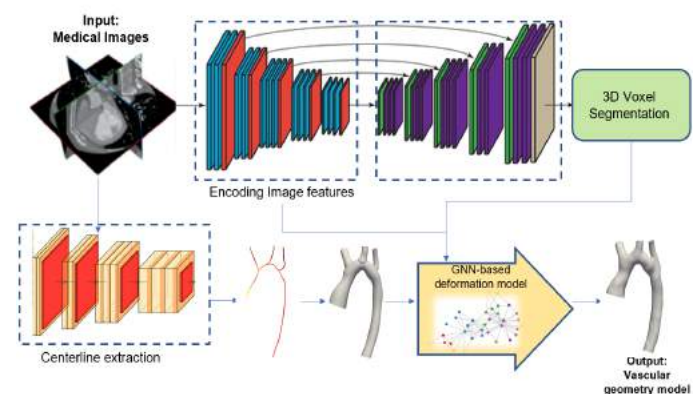


Figure 1: Diagram of the auto-segmentation model

3-D CNN: The 3-D CNN encodes the volumetric image data into the latent space and decodes them back to volumetric data with the same dimension to match the binary voxel segmentation labels (top half in Figure 2). Skip connections are added to avoid severe gradient decay. The input information is volumetric pixels with gray-scale values and

the output is a block of binary volumetric pixels where 1 represents inside the vessel and 0 otherwise.

Graph deformation model: A 2-D recurrent neural network (RNN) is used to extract the centerline of the aorta. The 2-D RNN takes in a sequence of the horizontal image slices in the image data and outputs the centerline point locations as well as the local vessel radius.

The centerline and the radius information are later used to create a synthetic aorta geometry via lofting a non-uniform rational B-spline (NURBS) surface. Then a graph convolutional network (GCNN)-based deformation model is adopted to deform the template to the 3-D label geometry with the guidance of the encoded information from the encoded information of the 3-D CNN.

Loss function

The loss function consists of two parts: the segmentation loss (from the 3-D CNN) and the deformation loss (from the graph deformation model). The segmentation loss is:

$$L_{seg}(I_i, I_o) = \sum_{x \in I_o} (I_o(x) \log(I_i(x)) + (1 - I_o(x)) \log(1 - I_i(x))) + \frac{2 \sum_{x \in I_o} I_{out}(x) I_i(x)}{\sum_{x \in I_o} I_o(x) + \sum_{x \in I_i} I_i(x)} \quad (1)$$

where the I_i and I_o denote the input image and the output binary label image. x denotes the voxel inside the image data.

The deformation loss contains four components: point loss, normal loss, edge loss, and Laplacian loss. The point loss is minimizing the point close distance between the deformed template to the label geometry, which is computed via the bidirectional chamfer distance:

$$L_{point}(G_i, G_o) = \sum_{v_i \in G_i} \min_{v_o \in G_o} \|v_i - v_o\|^2 + \sum_{v_o \in G_o} \min_{v_i \in G_i} \|v_i - v_o\|^2 \quad (2)$$

where v is the vertex of the mesh.

The normal loss promotes the surface normal similarities between the deformed template to the label geometry:

$$L_{normal}(G_i, G_o) = \sum_{v_i \in G_i; v_o \in G_o; v_o = \arg \min_{v_o \in G_o} \|v_i - v_o\|^2} \min_{v_o \in G_o} \|n_{v_i} - n_{v_o}\|^2 \quad (3)$$

where the n_v denotes the normal vector of the vertex.

The edge loss encourages the triangles mesh elements to be uniform:

$$L_{edge}(G_i, G_o) = \sum_{v_i \in G_i} \sum_{u_{v_i} \in N(v_i)} \left| \|v_i - u_{v_i}\|^2 - \mu_o^2 \right| \quad (4)$$

where the $N(v_i)$ denotes the neighborhood of the vertex v_i .

The Laplacian loss ensures the mesh smoothness:

$$L_{lap}(G_i) = \sum_{v_i \in G_i} \left\| v_i - \sum_{u_{v_i} \in N(v_i)} \frac{u_{v_i}}{\|N(v_i)\|} \right\|^2 \quad (5)$$

The total loss is calculated as:

$$L_{total} = \lambda_1 L_{seg}(I_i, I_o) + \lambda_2 L_{point}(G_i, G_o) + \lambda_3 L_{normal}(G_i, G_o) + \lambda_4 L_{edge}(G_i, G_o) + \lambda_5 L_{lap}(G_i) \quad (6)$$

RESULTS

Our model is trained for 10000 epochs on an Nvidia A6000 video GPU. The training time is about 30 minutes per case during which the Adam optimizer is used with an initial learning rate of 0.01. 30 samples are used for training and the performance of the model is evaluated over a set of 5 test samples. The prediction of the centerline extraction and the prediction of the mesh is shown in Figure 2.

The results show great consistency for the centerline. The location of the predicted centerline is very close to the center of the vessel along the streamwise direction for all branches. From the CT data, one can observe the proposed model can also predict meshes very similar to the ground truth segmentation. The average relative L2 norm loss is around 3% averaged over all 5 test samples.

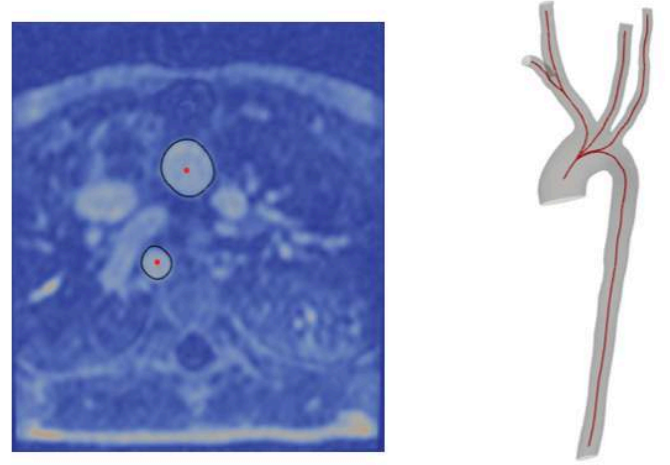


Figure 2: Prediction of the multi-branch geometry and centerline

DISCUSSION

In this work, we established an auto-segmentation algorithm that reconstructs centerlines as well as geometries from raw image data for patient-specific multi-branch aorta structure. The proposed model can accurately predict the centerline of the aorta structure and reconstruct the aorta surface very close to the ground truth. This highlight of this work includes the following: Previous work usually requires manual inputs (e.g., centerline) or pre- and post-process in the segmentation process, whereas the proposed method is fully automatic. There are few work outputs centerlines and the geometry simultaneously and embedded a deformation template to ensure surface smoothness. This work fills the gap and is capable of predicting multi-branch aorta structure. Nonetheless, our model also has the following limitations: The prediction performance will worsen if the input image data has a different orientation. Furthermore, the predicted surface has smoothed out certain geometric details from the ground truth aorta surface. This can be improved by improving the graph deformation model. In general, this work demonstrates how to build a fully auto-segmentation model for multi-branch aorta structures, which massively accelerates the image-segmentation process and can be applied to further uncertainty quantification studies.

ACKNOWLEDGEMENTS

The author acknowledges the funding from the Lucy Family Institute for Data and Society from the University of Notre Dame.

REFERENCES

- [1] Li et al., *IEEE/WIC/ACM*. 2021.
- [2] Patil et al., *IJCSMC* 2.1: 22-27, 2013
- [3] Lindeberg et al., *CVIU*, vol. 67, no. 1, pp. 88--98, 1997.
- [4] Vukadinovic et al., *IEEE T-MI* 29.1: 65-76, 2009
- [5] Zhang et al., *IEEE ICIP*. IEEE, 2014.
- [6] Lu et al., *Magnetic resonance imaging* 36: 180-186, 2017
- [7] Wang et al., *Diagnostics* 12.4 (2022): 967.
- [8] Kong et al., *Medical image analysis* 74 (2021): 102222.
- [9] Wilson et al., *J. Med. Devices* 7(4), 040923, 2013

INVESTIGATING CHANGES IN HEMATOLOGICAL AND HEMORHEOLOGICAL PARAMETERS IN A MOUSE STENT IMPLANTATION MODEL

D. Kokkinidou (1), E. Kaliviotis (1), C. Shammass (2), A. Anayiotos (1), K. Kapnisis (1)

(1) Department of Mechanical Engineering and Materials Science and Engineering, Cyprus
University of Technology, Limassol 3036, Cyprus
(2) Bioanalysis Clinical Laboratory, Limassol 4001, Cyprus

INTRODUCTION

Even though cardiovascular stenting is widely used for the treatment of coronary artery disease, there is little information in the literature on how it can affect the hematological and hemorheological profile. Stent functionality is compromised by complications at the site of implantation, including altered wall shear stresses, disordered blood flow, and device wear and biocorrosion, which may lead to thrombosis and occlusion and in-stent restenosis [1-2]. Presently, most of the work on this issue is based on simplified theoretical models and computational fluid dynamics analysis on local hemodynamics [3], lacking *in vitro* and *in vivo* experimental verification with blood samples. Several studies suggest that red blood cells (RBCs) undergo mechanical and biochemical changes during blood passage through medical devices [4]. This study aimed to evaluate, in an *in vivo* setting, the effects of time-course stenting on hematological and hemorheological parameters that could potentially compromise the device's functionality and longevity.

METHODS

Custom-made self-expanding nitinol stents (Admedes GmbH, Pforzheim, Germany), 0.7 x 3.3 mm in dimension with a closed-cell design and a diamond-shaped pattern, were implanted in male CD1 mice, weighing 40 ± 5 g (Project license: CY/EXP/PR.L9/2019). Operative procedures were performed following the experimental protocol reported by Simsekylmaz et al. 2013 [5], which describes a rapid and accessible procedure of stent implantation in mouse carotid artery. Animals were pre-treated for 48 h with aspirin (75 mg in 250 mL drinking water), which was discontinued 48 h postoperatively. General anesthesia was induced by intraperitoneal injection of 100 mg/kg b.w. ketamine and 10 mg/kg b.w. xylazine.

Whole blood (0.5 - 1.0 ml per animal) was withdrawn from control (healthy, non-stented; n=5) and stented animals at 5- and 10-weeks post-implantation (n=3 per time point). Blood collection was performed by direct cardiac puncture under anesthesia, using citrate-dextrose solution

(Sigma-Aldrich, MI, USA) prefilled syringes at a ratio of citrate-to-blood of 1:9. Hematological measurements were performed using a Sysmex XT-2000i analyzer (Sysmex, Landskrona, Sweden), within 4 hours after blood collection.

RBC aggregation and deformability and blood viscosity were estimated using standard techniques at room temperature (25 ± 0.5 °C). The RBC aggregation was evaluated through a laser-photodiode-based system, the Rheoscan A200 instrument (Rheomeditech, Seoul, Korea). An aggregation index (AI) was used, defined as the ratio between the area under the light intensity/time curve, and the sum of the areas below and above the curve in the first 10 seconds. RBC deformability measurements were performed using the Rheoscan D300 (Rheomeditech, Seoul, Korea). The instrument is based on the principle of a diffraction technique combined with microfluidic rheometry, using a disposable microfluidic chip. In this technique a very low RBC-to-medium volume is perfused through the microfluidic chip, at a varying pressure (vacuum-driven shearing of a thin layer of RBC suspension), causing the cells to deform in an ellipsoidal shape. The elongation index (EI) of the cells is calculated based on the obtained diffraction patterns over a range of shear stresses. Blood viscosity was evaluated through the Brookfield DV2T instrument (AMETEK GB LTD T/A Brookfield, Stadium Way Harlow, Essex) using a cone-plate geometry. All measurements were performed using the same predefined shear rates between 251.2 and 1.4 s^{-1} (higher to lower shear rates).

RESULTS

The effect of stenting on various hematological indices, RBC and white blood cell (WBC) counts, hematocrit (HCT), red blood cell distribution width-coefficient of variation (RDW-CV), and mean corpuscular volume (MCV), is shown in Figure 1. Results are presented as mean \pm standard deviation (SD) along with the physiological range. Even though no statistically significant differences were observed between the tested samples, notable trends were apparent. Our findings showed an increase in RBC counts and slightly elevated HCT levels at

10 weeks post-stent implantation, contrary to a reduction in MCV. These could also account for the higher RDW-CV, demonstrated at the same time point. WBC counts were used for assessing the inflammatory status of healthy (control) and stented CD1 mice. The analysis revealed a rising trend over time suggesting a gradually increasing implant-included inflammatory response. Variations were previously reported between blood sampling sites [6] and data suggest that blood cell counts and indices are found significantly lower in heart blood compared to eye and tail vein withdrawal.

RBC aggregation and deformability, expressed by the indices AI and EI_{max} respectively, are presented in Figure 2. A marked decrease in AI index is observed at 5 weeks, compared to the control case, followed by an elevation at the late stages after stent implantation. Similar behavior is also reported in other *in vivo* studies involving human subjects [7]. RBCs showed decreased deformability in the 10-week sample group, compared to the other two cases. This decreasing trend can be due to biological but also mechanical factors such as the shear stress and the period of exposure to stress, which play a role in the RBC membrane properties and deformability. It is noteworthy that the decreased RBC deformability also corresponds well with the distinct increase in RDW-CV.

The viscosity data are listed in Table 1, as normalized (η^*) with high-shear viscosity (η_∞) values ($\eta^* = \frac{\eta}{\eta_\infty}$). Measurements demonstrate the shear thinning non-Newtonian nature of blood and at shear rates of 15.82 and 44.70 s⁻¹. The results indicate a decreased blood viscosity in stented mice at the more conservative shear rate of 44.70 s⁻¹, particularly at 5 weeks post-implantation. The hemorheological results observed, are in general agreement with the literature. That is the viscosity of blood is negatively affected by increased hematocrit, RBC aggregation, and impaired RBC deformability.

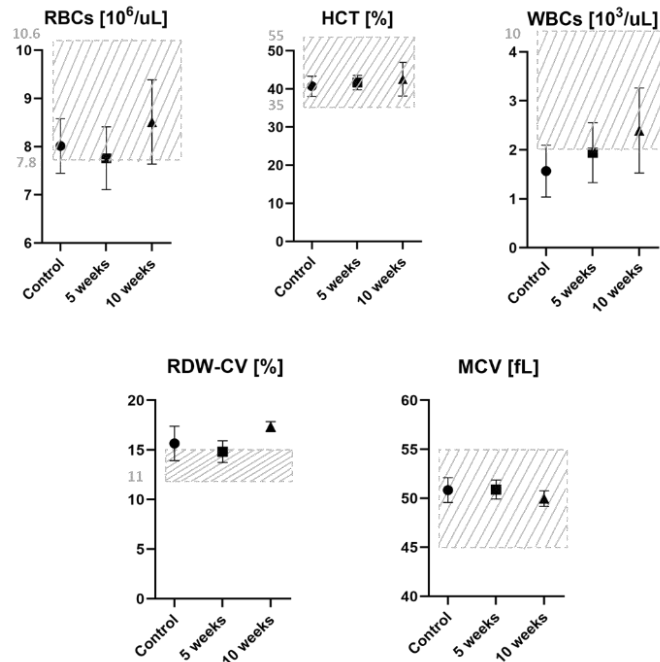


Figure 1: Effects of time-course stenting on hematological parameters. Values are expressed as mean ± SD and the physiological range is indicated with gray-lined boxes.

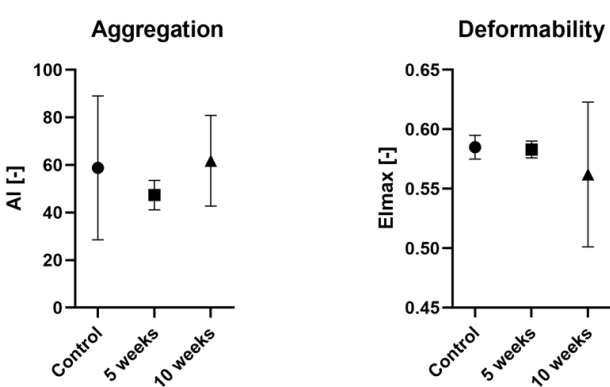


Figure 2: Stent-induced alterations in RBC aggregation and deformability.

Shear rate (s ⁻¹)	Normalized Viscosity η^*		
	Control	5 weeks	10 weeks
15.82	1.9867	2.0338	1.9505
44.70	1.5090	1.3678	1.4748

Table 1: Changes in the normalized viscosity of the samples, measured at shear rates of 15.82 s⁻¹ and 44.70 s⁻¹.

DISCUSSION

The present study showed that various hematological factors and the rheological properties of blood in mice were associated with stent implantation. The preliminary findings in this study agree with the current understanding in hemorheology that the reduction in RBC deformability results in higher viscosity and reduced RBC aggregation [8]. Although the alterations observed in the hematological parameters, and consequently on blood rheology, may be the result of inflammation caused by the stent presence, the physiological consequences in the circulation due to the stent-induced flow changes, need to be further investigated. Cells could be subjected to repeated stresses caused by the complex local flow conditions and interactions with the protruding struts in the flow. Further work on additional flow, geometry, and device parameters is warranted to establish the clinical significance of the trends apparent in the present study.

ACKNOWLEDGEMENTS

The authors would like to thank Microlumen Inc. (Oldsmar, FL, USA) for providing the polymeric tubing used as guiding catheters in the carotid stenting procedures. The work was co-funded by the European Regional Development Fund and the Republic of Cyprus through the Research and Innovation Foundation (Project: INTERNATIONAL/USA/0118/0057).

REFERENCES

[1] Jaryl Ng et al. *Arterioscler Thromb Vasc Biol*;37:2231–2242, 2017.
[2] Wang J et al. *Regen Biomater*.;5(3):177-187, 2018.
[3] P.T.Gamage et al. *Comput. Biol. Med.*, 139;104962, 2021.
[4] David M. Saylor et al. *ASAIO J.* 65(3):207-218, 2019.
[5] Sakine Simsekyilmaz et al. *J Vis Exp.* (75): 50233, 2013.
[6] J A Nemzek et al. *Inflamm Res.* 50(10):523-7, 2001.
[7] Theodor Baars et al. *Microcirculation.* 23(8):637-645, 2016.
[8] Baskurt OK, Meiselman HJ. 29(5):435–50, 2003.

N-ACETYL CYSTEINE RESCUES CHONDROCYTES FROM OXIDATIVE STRESS AND INCREASES THEIR METABOLIC ACTIVITY

Austin C. Jenk (1,2,3), Elisabeth A. Lemmon (1,2,3), Sarah E. Gullbrand (1,3), Robert L. Mauck (1,2,3)

- (1) Department of Orthopaedic Surgery, University of Pennsylvania, Philadelphia, PA, USA
(2) Department of Bioengineering, University of Pennsylvania, Philadelphia, PA, USA
(3) Translational Musculoskeletal Research Center, Corporal Michael J. Crescenz Department of Veterans Affairs Medical Center, Philadelphia, PA, USA

INTRODUCTION

Post-traumatic osteoarthritis (PTOA) is temporally linked to joint injuries, including intra-articular (i.a.) ligament ruptures, fractures, or meniscus tears (1). Despite PTOA representing 12% of all OA cases with incidence rates up to 50% following acute knee injuries, there are still no FDA-approved disease-modifying OA drugs designed to delay or prevent the development of PTOA (2). Absent such intervention, acute knee injuries induce diverse pathologic cascades that result in cartilage degradation (3). One of the main drivers of post-injury cartilage degradation is hemarthrosis, which occurs in 77% of acute knee injuries (4). Blood in the joint results in the rapid initiation of joint damage due to iron deposition and elevated levels of reactive oxygen species (ROS), matrix metalloproteinases (MMPs), and pro-inflammatory cytokines (5). N-acetyl cysteine (NAC) acts as an antioxidant by directly scavenging ROS and indirectly by generating intracellular glutathione (GSH), the body's most abundant antioxidant (6). Previous studies have explored NAC delivery to scavenge ROS in the context of joint injury (6–8). However, these studies focused on systemic or i.a. delivery before or at the time of joint injury, and few have investigated whether NAC administered after injury would retain its ability to delay or prevent cartilage degradation. Indeed, there is a paucity of research regarding NAC's chondroprotective nature and the “window of opportunity” for therapeutic intervention following acute knee injuries (1). Therefore, the goal of this study was to determine whether NAC can prevent chondrocyte apoptosis after oxidative stress and to identify the therapeutic “window of opportunity” for such interventions.

METHODS

An *in vitro* model was used to recapitulate the oxidative stress produced following acute knee injuries. Briefly, articular chondrocytes were harvested from juvenile bovine joints and cultured on tissue-culture-treated polystyrene at 70,000 cells/cm². After 48 h, cells were

treated with 100 μ M H₂O₂ for 0, 2, or 12 h, before NAC was added to 0.5, 2.0, 5.0, or 10.0 mM (without media replacement). Cells were cultured for an additional 12 h following NAC administration before analysis (Fig 1). The oxygen radical antioxidant capacity (ORAC) of NAC was compared to reduced GSH and a Trolox standard (Abcam; ORAC Assay Kit) with values expressed as μ M Trolox Equivalents (TE). To visualize the extent of cell death, live (calcein-AM) and dead (ethidium homodimer-1) (ThermoFisher; LIVE/DEAD™) stained cells were imaged using confocal microscopy (Nikon A1R+; 4x magnification) and cells were quantified using ImageJ. Metabolic activity was determined with a resazurin-based solution (ThermoFisher; AlamarBlue™). Messenger RNA (mRNA) was isolated at the terminal time point and expression of interleukin-1 beta (IL1B), glutathione peroxidase 1 (GPX1), inducible nitric oxide synthetase (iNOS), and glyceraldehyde 3-phosphate dehydrogenase (GAPDH) was determined by quantitative polymerase chain reaction (qPCR), expressed as fold change relative to untreated chondrocytes. Metabolic activity and cell viability analysis was conducted with n=4 biological replicates, and ORAC and qPCR analysis was conducted with n=3 biological replicates. One-way ANOVA was used to compare values amongst groups, and two-way ANOVA was used to compare values between groups and time points. Both were followed with post-hoc Tukey HSD (GraphPad Software, Inc.). Significance was set at p<0.05.

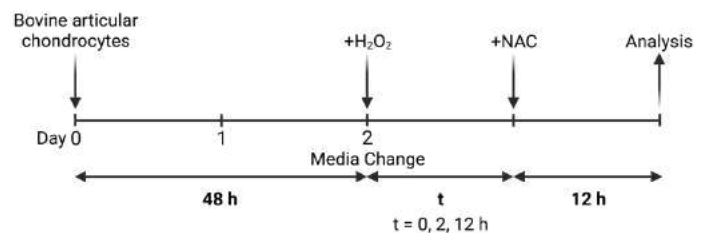


Fig 1: Study design for *in vitro* model of oxidative stress.

RESULTS

In terms of antioxidant potential, 20.0 μ M NAC had a greater capacity to reduce oxygen radicals than 20.0 μ M GSH (had a larger area under the curve) (Fig 2A). The ORAC value for NAC was 17.6 ± 0.46 μ M TE compared to 7.70 ± 0.09 μ M TE for GSH (Fig 2B). When applied to chondrocytes, NAC at 5.0 mM showed no cytotoxicity compared to controls, as indicated by similar calcein-AM/ethidium homodimer-1 staining (Fig 2C-D) and percentage of living chondrocytes (Fig 2G). Following H₂O₂ treatment, the addition of NAC showed a dose-dependent increase in chondrocyte viability with increasing concentration, with 5.0 mM being most effective at preserving chondrocyte viability ($70.1 \pm 16.9\%$ viability with NAC treatment versus $24.6 \pm 7.50\%$ viability in H₂O₂ treated cells) (Fig 2E-G). NAC treatment in the absence of H₂O₂ significantly increased chondrocyte metabolic activity compared to the control (Fig 3A). When cells were treated with H₂O₂ alone, there was a significant reduction in metabolic activity (Fig 3A). This could be rescued with NAC treatment in a dose-dependent manner when NAC was administered at 0, 2, and 12 h (Fig 3A). When treated with 5.0 or 10.0 mM NAC at 2 h, metabolic activity was not significantly different from control cells (Fig 3A). Expression analysis showed that genes associated with oxidative stress, IL1B, GPX1, and iNOS, were all significantly increased in chondrocytes exposed to 100 μ M H₂O₂ (Fig 3B). Treatment with 5.0 mM NAC 2 h after H₂O₂ returned expression levels back to that of chondrocytes in the 5.0 mM NAC control group (Fig 3B).

DISCUSSION

Our data demonstrate that administration of NAC can rescue chondrocyte viability and metabolic activity, as well as regulate the expression of critical genes, after exposure to ROS in an *in vitro* model of oxidative stress. Our data further identify a “window of opportunity” in the therapeutic intervention with antioxidants following an oxidative insult. Specifically, we showed that treatment with NAC within 2 h of injury can reduce the severity of ROS-mediated cell death, maintain normal chondrocyte metabolic activity, and significantly reduce the expression of IL1B, GPX1, and iNOS compared to untreated conditions. While treatment with NAC at 12 h also increased chondrocyte viability and metabolic activity compared to untreated conditions, its efficacy was reduced. This suggests that the optimal “window of opportunity” is within the first 12 h period and that such early intervention with NAC following an acute knee injury may be capable of rescuing cartilage cell health and have implications for the prevention of PTOA. Ongoing studies are extending these findings to a 3-dimensional hydrogel culture model (9, 10) and exploring the delivery of NAC from mechanically-activated microcapsules (10, 11) to prolong residence time and localization following *in vivo* i.a. delivery.

ACKNOWLEDGEMENTS

This work was supported by the National Institutes of Health R01 AR077362 and the Department of Veterans Affairs IK6 RX003416.

REFERENCES

1. Mason, D. *et al.*, *J. Orthop. Res.* 39, 1152–1163 (2021). 2. Brown, T. D. *et al.*, *J. Orthop. Trauma.* 20, 739–744 (2006). 3. Lieberthal, J. *et al.*, *Osteoarthritis Cartilage.* 23, 1825–1834 (2015). 4. Hardaker, W. T. *et al.*, *South. Med. J.* 83, 640–644 (1990). 5. Lyons, L. P. *et al.*, *Osteoarthritis Cartilage.* 29, 471–479 (2021). 6. Nakagawa, S. *et al.*, *J. Orthop. Res.* 28, 156–163 (2010). 7. Riegger, J. *et al.*, *Int. J. Mol. Sci.* 20, 2916 (2019). 8. Kaneko, Y. *et al.*, *Sci. Rep.* 9, 18741 (2019). 9. Mohanraj, B. *et al.*, *J. Orthop. Res.* 36, 2901–2910 (2018). 10. Peredo, A. P. *et al.*, *Biomaterials.* 265, 120255 (2021). 11. Mohanraj, B. *et al.*, *Adv. Funct. Mater.* 29, 1807909 (2019).

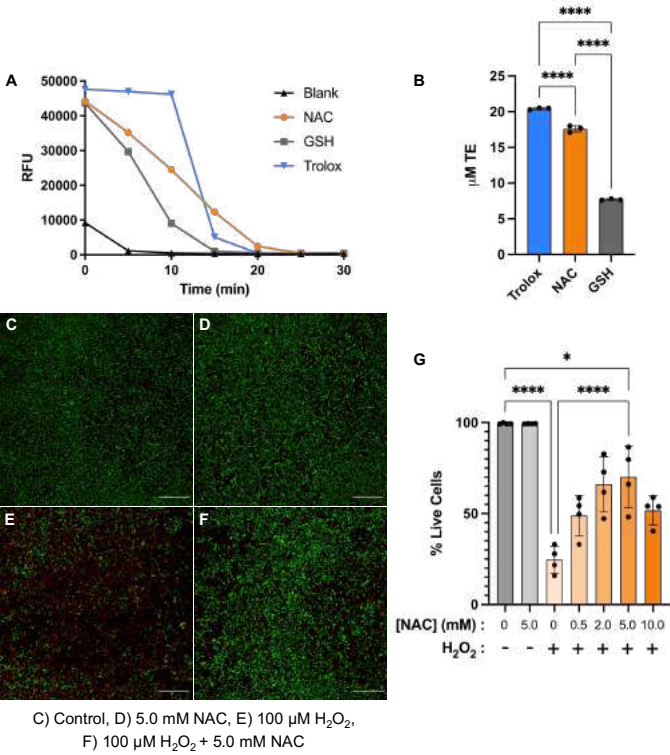


Fig 2: NAC has greater antioxidant capacity than GSH (A-B) (n=3, ****=p<0.0001) and improves chondrocyte viability (C-G) (n=4, scale bar: 500 μ m, *=p<0.05, ****=p<0.0001).

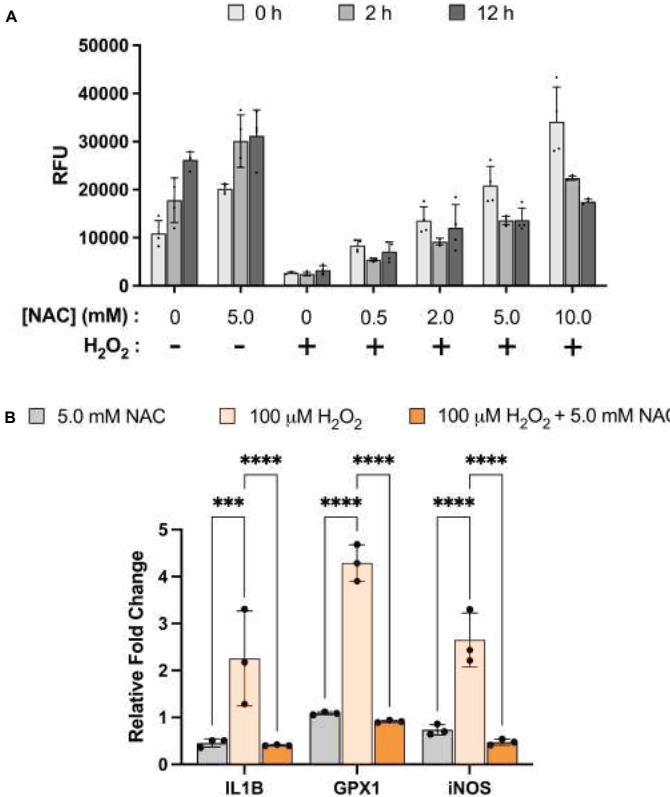


Fig 3: NAC improves chondrocyte metabolic activity (A) (n=4) and reduces the expression of genes associated with oxidative stress (B) (n=3, ***=p<0.001, ****=p<0.0001).

DO AGE AND SEX MATTER IN A 1D SIMULATION STUDY TARGETING ARTERIAL STIFFNESS?

Friederike Schäfer, Jacob Sturdy, Leif Rune Hellevik

Department of Structural Engineering, Norwegian University of Technology (NTNU), Trondheim, Norway

INTRODUCTION

Over the past 20 years, cardiovascular diseases (CVDs) have been the leading cause of death worldwide, additionally the percentage of deaths caused by CVDs has been increasing [1]. CVDs like aneurysm formation and plaque deposition in the arterial wall alter the arteries' material properties. However, arterial material properties are not only altered by disease, but also by lifestyle, diet, and aging [2–4]. A biomarker describing cardiovascular health is local arterial stiffness. Yet, it cannot be measured directly in vivo [5]. Computational modelling approaches may allow non-invasive estimation of local arterial stiffness through inverse methods, but a key challenge are model parameter uncertainties. As some model parameters vary between age and sex groups [6–8], and certain sub-populations may have distinct distributions of these parameter values, model performance may differ between those groups. In this work, we investigated the necessity of considering sub-populations during the development of a 1D-common carotid artery (CCA) model. For each sub-population, we quantified model output uncertainty and identified the input parameters leading to the greatest output variability through a sensitivity analysis.

METHODS

To establish age and sex specific model parameter probability distributions, we identified relevant papers through a structured literature review, extracted parameter values, and computed pooled mean and standard deviations of several input parameters. The inferred distributions were then propagated through a 1D-model of the CCA. In a subsequent sensitivity analysis, we applied polynomial chaos (PC) expansion to attribute model output uncertainties to specific uncertain input parameters.

Structured literature review

The structured literature review was performed by following best practices and guidelines given in the Cochrane Handbook for Systematic Reviews and Interventions [9]. We included articles with the scope of quantifying CCA stiffness in humans. To have representative values for a cross-section of society – all ages, fitness levels, body sizes, and subjects with risk factors – we excluded only non-original studies and studies investigating rare diseases with significant changes in the cardiovascular mechanics. Mean and standard deviation of geometric parameters, pressure values, stiffness measures and the occurrence of risk factors were extracted from 94 publications. Subsequently, a pooled mean and standard deviation was computed for each age and sex group. Due to the lack of knowledge on the underlying probability distribution of each parameter, lower a and upper bound b of a uniform probability distribution were computed based on the pooled mean and standard deviation by $a, b = \mu \pm \sqrt{3} \sigma$.

1D-model of the CCA

The CCA was modelled in 1D as a straight, compliant tube with a thin, homogeneous, linear elastic wall material, shown in Fig. 1. At the inlet, a parabolic inflow with a representative CCA flow rate and waveform was

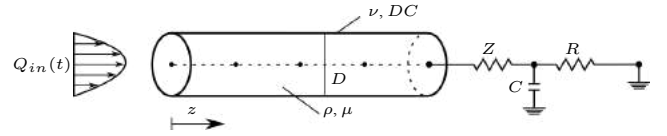


Figure 1: 1D-model of the CCA with a parabolic flow at the inlet and a three-element Windkessel model at the outlet. The eight uncertain parameters are indicated.

imposed [10]. A three-element Windkessel model was coupled to the 1D-model outlet to account for the downstream vasculature's influence on the CCA. The Windkessel model elements are arterial impedance Z , arterial compliance C , and peripheral resistance R .

With the assumption of blood as an incompressible Newtonian fluid, the conservation of mass and momentum are

$$\frac{\partial A}{\partial t} + \frac{\partial(Au)}{\partial z} = 0 \quad (1a)$$

$$\frac{\partial u}{\partial t} + u \frac{\partial u}{\partial z} + \frac{1}{\rho} \frac{\partial p}{\partial z} = \frac{f}{\rho A}, \quad (1b)$$

with the time t , cross-sectional area A , velocity u , fluid density ρ , spatial coordinate z , pressure p , and the frictional force term per unit length f . Fluid-structure interaction was described with the tube law [11]. Uncertain model parameters were C , total arterial resistance $R_{tot} = Z + R$, ρ , μ , Poisson ratio ν , arterial wall thickness h , lumen diameter D , and dilatancy coefficient $DC = (\Delta A/A)/\Delta p$ [2].

Uncertainty quantification and sensitivity analysis

Uncertainty and sensitivity measures were estimated by applying PC expansion [12]. The stochastic model output $Y = f(\mathbf{Z})$, which depends on a vector of independent random variables \mathbf{Z} , can be approximated with a finite number of polynomials p as

$$Y \approx Y_{PC} = \sum_{p=0}^N c_p \Phi_p(\mathbf{Z}), \quad (2)$$

where the expansion coefficients are c_p and the polynomials Φ_p . From the PC expansion, statistical moments and variance based sensitivity measures can be computed analytically.

Global sensitivity measures attribute model output variance to particular input parameters and their interactions. The main Sobol index S_i quantifies the direct contribution of a particular input parameter z_i to total model output variance $\text{Var}[Y_{PC}]$ [13]. It is computed as

$$S_i \approx \frac{1}{\text{Var}[Y_{PC}]} \sum_{p \in A_i} \text{Var}[c_p \Phi_p], \quad (3)$$

where the set A_i contains all basis functions only dependent on z_i . The total Sobol index ST_i quantifies the contribution to output variance of a parameter z_i and all its interactions with $z_{\sim i}$ as

$$ST_i \approx \frac{1}{\text{Var}[Y_{PC}]} \sum_{p \in A_{T_i}} \text{Var}[c_p \Phi_p]. \quad (4)$$

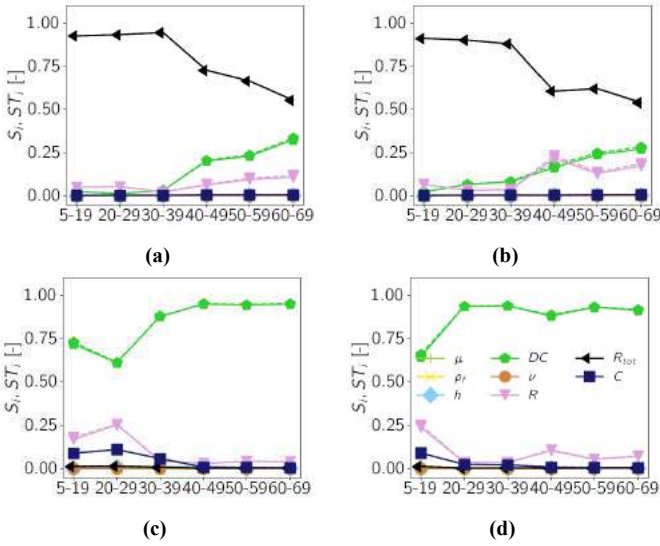


Figure 2: ST_i (dashed line) and ST_i (solid line) at the artery's mid-point and time averaged over the last cardiac cycle for (a) male pressure (b) female pressure (c) male ΔD (d) female ΔD .

RESULTS

The main and total sensitivity indices at the mid-point of the vessel for the eight uncertain parameters are shown in Fig. 2 for each age and sex group. The quantities of interest (QoI) are the pressure (a-b) and the diameter change ΔD (c-d). Values of ST_i (dashed lines) are approximately the same as S_i (solid lines). Regardless of age and sex, pressure is most sensitive to R_{tot} of the Windkessel model. Nonetheless, with increasing age changes the sensitivity structure for pressure such that DC and D contribute to the variance of the model's pressure prediction. For the two youngest age groups, ΔD is sensitive to variations in DC , D , and C , where DC 's value prevails. In the remaining age groups, all sensitivity indices except of DC are approximately zero. Fig. 3 displays the 95% prediction interval for pressure and ΔD for females in their 60s with colored area apportioned to the respective sensitivity index.

DISCUSSION

We conducted a structured literature review to evaluate pooled mean and standard deviations of geometric and material parameters for twelve groupings by age decade (7-19, 20-29, ..., 60-69) and sex. The uncertainty about input parameters based on the inferred population distributions were propagated through a 1D-model of the CCA with a PC expansion method to quantify model output variability and sensitivity.

Ranges for geometric parameters, pressures, and stiffness measures computed from the literature review were in accordance with published reference intervals for a healthy sub-population [7] and a previous summary of literature findings [8].

Since the difference between S_i and ST_i is approximately zero, parameter interactions are not significant in this model. Low sensitivity indices for fluid viscosity and density, arterial wall thickness, Poisson ratio, and Windkessel model compliance indicate that population variability within the applied distribution of these parameters does not influence model output variability. Setting these parameters to reference values will therefore not change model output variance while reducing the number of input parameters. High sensitivity of DC for ΔD suggests that it is possible to infer arterial stiffness in the inverse problem for ΔD .

The mean pressure in the arterial tree is directly determined by the total arterial resistance and mean flow as $R_{tot} = p/Q$. As such the pressure level at each time point is highly sensitive to uncertainties in R_{tot} . The magnitude of the pulse pressure depends on the total arterial compliance. In the 1D-model used in this work, total arterial compliance consists of the compliant vessel and the compliance element in the Windkessel model.

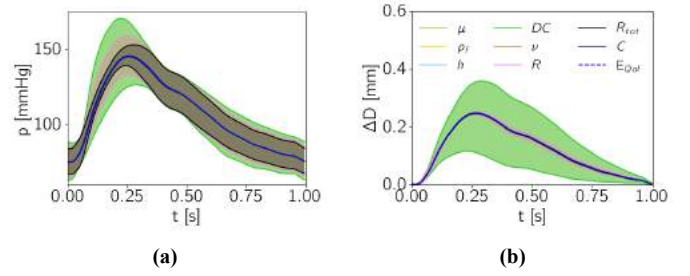


Figure 3: 95% prediction interval and expected value E with sensitivity apportioned to the QoIs of (a) pressure and (b) ΔD for females in their 60s.

DC describes the area compliance and thus, depends on the artery's D . With increasing age decreases DC , which makes the pressure more sensitive to this parameter in the systolic phase of the heart cycle, as seen in Fig 3. However, the current results suggest that the pressure is not sensitive to C . Therefore, further investigations are needed to verify the total compliance distribution between the different elements of this model and their influence on model output variance.

Differences in the sensitivity structure between age groups are apparent, whereas sex differences are not clearly evidenced. Comparison of sensitivity indices in the 20-year old group shows differences for ΔD , however, the studies investigating young males included mainly participants with a high fitness level. Thus, DC in this particular group was higher than from cross-sectional studies which confounds with any difference due to sex alone. Another difference is visible in the ranking of DC and D sensitivities for the pressure in the group aged 40-49 years. If this is due to irregularities in the data from the literature review or if this is a general trend needs to be subject to further investigation.

Summing up, we have performed a literature review to establish pooled mean and standard deviation values for geometric and material parameters of the CCA for twelve age and sex groups. Based on these values, uncertainty quantification and sensitivity analysis using PC expansion was performed on a 1D-CCA model. Results suggest that pressure is most sensitive to R_{tot} , while ΔD is most sensitive to DC . We observe that the sensitivity structure changes between age groups, whereas sex differences are not that distinct (Fig. 2). In a next step, uncertainties in the inlet boundary condition will be considered and the total compliance distribution between the 1D-artery and the Windkessel model and its implications on output variance will be examined.

ACKNOWLEDGEMENTS

The research leading to these results is funded by the Norwegian Financial Mechanism 2014-2021 operated by the National Science Center, PL (NCN) within the GRIEG programme under grant# UMO-2019/34/H/ST8/00624, project *non-invasive iN-vivo assessment Human aRtery wAlls (ENTHRAL, www.enthrall.pl)*

REFERENCES

- [1] World Health Organization. <https://www.who.int>.
- [2] Chirinos JA. *J. of Cardiovasc. Trans. Res.* 5.3 (2012).
- [3] Parati G et al. *Blood Pressure and Arterial Wall Mechanics in Cardiovascular Diseases*. Ed. by Safar ME et al. London: Springer, 2014.
- [4] Vosse F van de et al. *Annu Rev Fluid Mech* 43 (2011).
- [5] Alastruey J et al. *Journal of Biomechanics* 44.12 (2011).
- [6] DuPont JJ et al. *British Journal of Pharmacology* 176.21 (2019).
- [7] Engelen L et al. *Journal of Hypertension* 33.10 (2015).
- [8] Charlton PH et al. *American Journal of Physiology-Heart and Circulatory Physiology* 317.5 (2019).
- [9] Higgins J et al. *Cochrane*. version 6.3 (updated February 2022). Cochrane, 2022. Available from www.training.cochrane.org/handbook. 2022.
- [10] Figueroa CA et al. *Computer Methods in Applied Mechanics and Engineering* 195.41 (2006).
- [11] Sherwin S et al. *Journal of Engineering Mathematics* 47.3 (2003).
- [12] Smith RC. *Computational science & engineering*. Philadelphia: Society for Industrial and Applied Mathematics, 2014. xviii+382.
- [13] Saltelli A et al. Chichester, England ; Hoboken, NJ: John Wiley, 2008. 306 pp.

COMPUTATIONAL MECHANOBIOLOGY MODEL EVALUATING HEALING OF POSTOPERATIVE CAVITIES FOLLOWING BREAST-CONSERVING SURGERY

Zachary J. Harbin (1), Emma L. Vanderlaan (2,3), Sherry L. Voytik-Harbin (2,4), Adrian Buganza Tepole (1,2)

- (1) School of Mechanical Engineering, Purdue University, West Lafayette, IN, USA
(2) Weldon School of Biomedical Engineering, Purdue University, West Lafayette, IN, USA
(3) Indiana University School of Medicine, Indianapolis, IN, USA
(4) Department of Basic Medical Sciences, Purdue University, West Lafayette, IN, USA

INTRODUCTION

Breast cancer is one of the most prevalent cancers in women today, with approximately 287,850 new cases diagnosed yearly in the United States [1]. In recent years, breast-conserving surgery (BCS; otherwise known as lumpectomy) has replaced mastectomy (the removal of the entire breast) as the preferred standard of care for breast cancer. Illustrated in Fig. 1, BCS preserves healthy breast tissue, as surgeons only excise the tumor along with a small margin of healthy tissue, forming a cavity. The resulting tissue cavity induces inflammation, generating a cytokine gradient that induces fibroblast proliferation, collagen deposition, and scar formation. Fibroblast differentiation into myofibroblasts further promotes contraction of the cavity and adjacent tissue, which often leads to breast deformities. Patient-to-patient variability in terms of breast size, tissue composition, and tumor geometry and location affect the outcome. With current techniques, 30% of BCS patients report poor healing and cosmetic outcomes, which can potentially compromise quality of life and self-image [2].

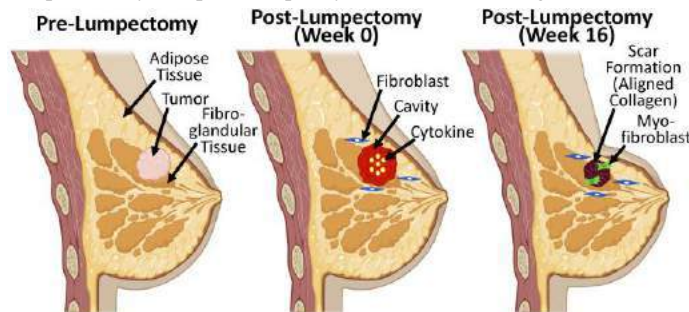


Figure 1: Schematic of breast healing process after BCS.

To overcome these challenges, we are developing a predictive computational mechanobiology model that simulates patient-specific breast healing following BCS. The proposed model has the potential to assist surgeons with better predicting oncologic, healing, and cosmetic outcomes, allowing for a comprehensive individualized treatment plan. Previously, computational models have been developed with a focus on simulating breast cavity healing after BCS [3,4]. These models, which are often informed by patient-specific imaging data (e.g., magnetic resonance and/or surface), emphasize biochemical rather than biomechanical healing processes. The model described in the present work simulates a unique generalized breast geometry using a coupled

biochemical-biomechanical model focused on multi-scale mechanics, including cell contractility and collagen remodeling. Available human clinical data evaluating cavity contraction and data from experimental porcine lumpectomy studies were used for model calibration [5,6].

METHODS

The computational mechanobiological model is a custom C++ solver adapted from previously developed code designed to explore three-dimensional (3D) cutaneous wound healing [7,8,9]. Tissue parameter values from the cutaneous wound model were modified to be breast tissue specific. Additionally, the model was modified to express cellular diffusion as a function of fibroblast speed which is dependent on collagen density (ϕ), and cytokine concentration (c).

Two breast cavity geometries were created in COMSOL (COMSOL Multiphysics, Burlington, MA), with meshing and boundary conditions shown in Fig. 2. The porcine geometry was based on an experimental porcine lumpectomy model used to evaluate surgical outcomes with and without regenerative breast fillers [5]. The human geometry represents a generalized breast cavity based on available clinical data that analyzed cavity contraction in BCS [6].

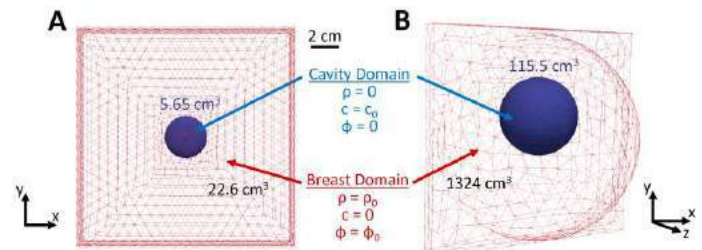


Figure 2: The meshing and initial conditions for the (A) porcine and (B) human breast cavity geometries.

Time-dependent changes in fibroblast (ρ) and collagen densities were informed through the porcine study [5]. Hematoxylin and eosin (H&E) stained cross-sections were analyzed 1, 4, and 16 weeks after surgery in comparison to normal porcine breast tissue. Twenty-five regions ($500 \times 500 \mu\text{m}^2$) spanning each cavity domain were identified and processed in ImageJ (National Institutes of Health, Bethesda, MD), where multiple color balance filters and thresholding were applied to quantify fibroblast density. Average collagen density was measured at each time point by normalizing intensity of fibrous tissue deposition

relative to intensity of normal breast connective tissue. Cytokine decay was based on prior work in the literature [10].

To optimize model biochemical parameters, Gaussian Process (GP) was fitted to the experimental fibroblast and collagen data. To start, five uninformed biochemical parameters ($p_{p,c}$, C_{dpp} , Δ , p_ϕ , and $p_{\phi,c}$) were identified and assigned a broad range of possible values. Using the porcine geometry, the model was then run in COMSOL using parameter combinations determined through the Latin hypercube sampling algorithm. Predictive regression lines for various parameter combinations were then used to find optimum parameter combinations based on root mean square error (RMSE). Optimized parameter values from the GP were then translated directly from the porcine geometry to the human geometry. The mechanobiological model was then fit using a similar methodology. In this case, the mechanobiological model was fit to clinical post-surgical cavity contraction data in terms of the ratio between deformed and original cavity volume (V_s/V_o) [6]. Fitting was done leveraging a separate GP that focused on tuning four uninformed mechanobiological parameters (t_p , $t_{p,c}$, K_t , and $\tau_{\lambda,p}$).

RESULTS

We fitted fibroblast and collagen density data to the biochemical model using the GP and obtained profiles within the standard deviations of the experimental data. These results provided confidence in the robust selection of the biochemical parameters. We then turned our attention to the full mechanobiological model implemented with the human geometry. Using the mechanobiology GP, optimal parameters for the mechanobiological parameters were determined ($t_p = [8.5714E-6 - 1.9286E-5]$ [1/hr], $t_{p,c} = [2.14286 \cdot t_p - 5 \cdot t_p]$ [1/hr], $K_t = [0.2 - 0.328571]$, and $\tau_{\lambda,p} = [0.0388 - 0.14065]$ [hr]). Along with this fit, mechanistic parameter relationships were inferred by evaluating the cavity contraction at 4 weeks over the entire parameter range as shown in Fig. 3. Cavity contraction was heavily dependent on fibroblast force (t_p), with increasing force leading to larger contraction (lower V_s/V_o). Myofibroblast force ($t_{p,c}$) had a similar effect. The rate of plastic deformation ($\tau_{\lambda,p}$) showed larger contraction (lower V_s/V_o) for smaller values of $\tau_{\lambda,p}$ but this effect was less pronounced compared to the fibroblast and myofibroblast force. The saturation of force, parameterized by K_t , had an interesting coupling with the myofibroblast force, with lower K_t leading to more contraction as $t_{p,c}$ increased. In fact, the largest contraction (less than 20% of the initial volume) occurred at the lower end of K_t and upper end of $t_{p,c}$.

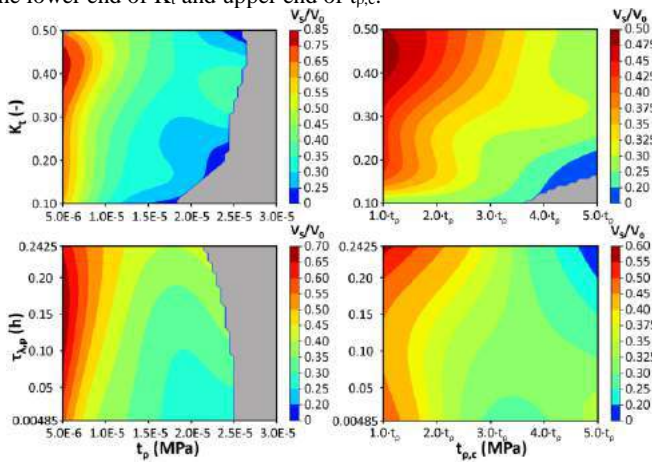


Figure 3: Plots describing the relationship between mechanobiological parameters t_p , $t_{p,c}$, K_t , and $\tau_{\lambda,p}$ on cavity contraction measured as deformed over initial volume (V_s/V_o).

The cavity contraction results from the fully informed computational model are displayed in Fig. 4. Contraction was found to

substantially increase across the first 4 weeks before reaching a steady-state, with the cavity contraction at approximately 36% of the original volume. The local metric of contraction is the plastic volume change (J^p) which decreased over time inside the cavity region while the surrounding tissue was drawn in tension ($J^p > 1$). The severity of this contraction contributed to clear deformation that was visible on the breast surface. By week 16, a visible divot had formed on the breast surface, which is a common outcome of BCS.

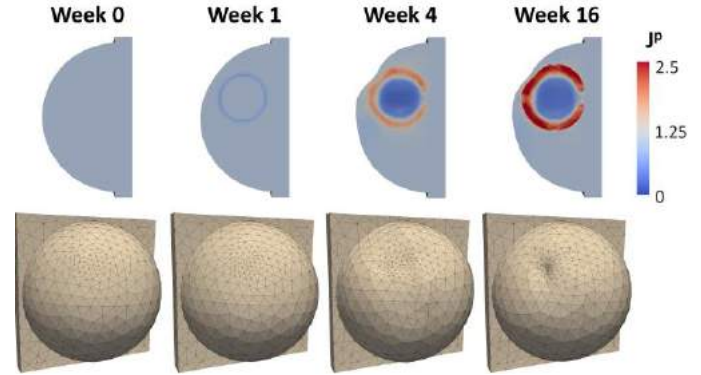


Figure 4: Mechanobiological model outcomes using optimized parameters. Permanent volume change denoted J^p .

DISCUSSION

The presented computational model proved to effectively simulate the breast healing response following BCS, including fibroblast infiltration, collagen remodeling, and breast permanent deformation. By using preclinical porcine data and human clinical data, biochemical and mechanobiology parameters were informed [5,6].

Although previous models of wound healing after BCS have been developed, we advanced these efforts by implementing a detailed mechanobiological model coupled with the nonlinear mechanics of breast tissue, including large plastic deformation and collagen remodeling. The study is not without limitations. A generalized breast geometry rather than a patient-specific geometry was used. Clinically, variables such as breast tissue composition or breast and cavity size can vary from patient to patient, which will be the focus of future model iterations. While we have some detailed data from the porcine model, the human data was more limited. Nevertheless, the mechanistic nature of the model and its fit to porcine and human data are encouraging to explore the design of therapeutic approaches (e.g., regenerative breast fillers), enabling the promise of *in silico* trials for BCS before animal or human subjects are involved.

ACKNOWLEDGEMENTS

This work was supported by NSF CMMI grant (A.B.T.; 1911346), NSF SBIR Phase I award (S.V.-H.; 1913626). E.V. is a trainee of the NIGMS-funded Indiana Medical Scientist/Engineer Training Program (T32 GM077229) and recipient of NIDDK-funded fellowship (T32 DK101000) and Indiana CTSI predoctoral fellowship (UL1TR002529).

REFERENCES

- [1] Key Statistics for Breast Cancer, *American Cancer Society*, 2022.
- [2] Vos, E. et al., *Quality of Life Research*, 27(2), 545–553, 2018.
- [3] Salmon, R. et al., *PloS one*, 10(4), 2015.
- [4] Vavourakis, V. et al., *PloS one*, 11(7), 2016.
- [5] Puls, T.J. et al., *Scientific reports*, 11(1), 1–17, 2021.
- [6] Prendergast, B. et al., *IJROBP*, 74(3), 695–701, 2009.
- [7] Sohutskey, D.O. et al., *Acta Biomaterialia*, 135, 368–382, 2021.
- [8] Buganza Tepole, A. et al., *CMBBE*, 19(1), 13–30, 2016.
- [9] Buganza Tepole, A. et al., *CMBBE*, 314, 46–70, 2017.
- [10] Valeta-Magara, A. et al., *SpringerPlus*, 4(1), 1–11, 2015.

FIBROUS FINITE ELEMENT MODELING OF POSTERIOR SCLERA

Mohammad R. Islam (1), Fengting Ji (1,2), Manik Bansal (1), Yi Hua (1), Ian A. Sigal (1,2)

(1) Department of Ophthalmology, University of Pittsburgh, Pittsburgh, PA, USA

(2) Department of Bioengineering, University of Pittsburgh, Pittsburgh, PA, USA

INTRODUCTION

Scleral collagen fiber mechanics plays an important role in eye physiology and pathology and is therefore of great interest in ocular biomechanics [1]. Of particular interest is understanding how increases in intraocular pressure (IOP) affect the sclera adjacent to the optic nerve head (ONH) in the posterior pole of the eye, and the lamina cribrosa within the ONH (Fig. 1a). Sclera biomechanics has been studied extensively but the role of its three-dimensional (3D) collagen fiber organization is not well-understood. Most computational models assume sclera to be a continuum structure reinforced by fibers, rather than fundamentally a fibrous structure. These models incorporate collagen fibers empirically such that fibers are non-continuous spatially

in 3D and confined into small sub-domains of the model. Hence, current models do not represent the sclera's 3D collagen structure of long fibers that are continuous across regions. For instance, the continuity of fibers from the sclera to the pia or dura is not accounted for in current models.

We present an entirely fibrous finite element (FFE) model of sclera that incorporates scleral collagen fiber bundles, their 3D spatial organization continuous with pia and dura maters, and fiber-fiber interactions. We demonstrate that this model can predict the IOP-induced response of sclera during inflation tests and investigate the nonlinear mechanics of fibrous sclera, pia, and dura regions at the ONH under elevated IOP.

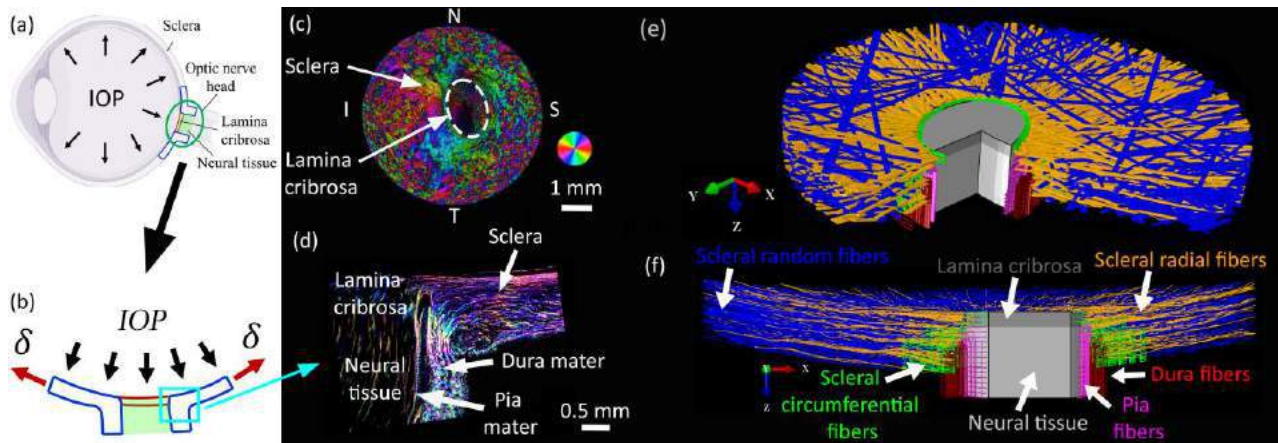


Figure 1. (a) Schematic of eye cross-section with the ONH highlighted and (b) enlarged view of the ONH with boundary conditions. (c) PLM images of coronal sections were used to determine fiber location and orientation. Shown is an example image with in-plane fiber orientation in color. (d) Example sagittal section of another eye corresponding to the region shown in (b). (e) Isometric and (f) sagittal perspective views of the FFE model. (e) shows full bundle widths. (f) shows only bundle centerlines. Longitudinal fiber bundles of the pia and dura are continuous with fibers of the sclera. The colors in (e) and (f) are intended to help compare with conventional tissue definitions.

METHODS

Model geometry: Highly detailed imaging data of a porcine eye from polarized light microscopy (PLM) was used to construct the FFE model of sclera [2]. The model included circumferential, random, and radial fiber bundles in a coronal image (Fig. 1c). The sagittal section (Fig. 1d) shows the continuation of sets of sclera fibers into lamina cribrosa, pia mater, and dura mater regions. The radial and random bundles of the sclera were constructed by tracing the bundles with PLM-matched local orientation from a stack of coronal images (Fig. 1c) and transforming them into a curved assembly using in-house algorithms [3]. Radial fibers, 100 μm away from the anterior side of the sclera along the sagittal direction, were further post-processed to mimic their transition into pia and dura maters like in the sagittal image (Fig. 1d). The circumferential bundles were included in sclera, pia, and dura regions manually with microscopy-based distributions [1,4].

FE modeling: Fibers were modeled at bundle-scale with Timoshenko beams of ellipsoidal cross-section and linear elastic material properties (E_b). The bundle widths were sampled from microscopy images and a constant thickness of 20 μm was used. The lamina cribrosa and neural tissue regions were included as linear elastic continuum structures ($E_{LC} = 0.1 \text{ MPa}$, $E_{NT} = 0.01 \text{ MPa}$) to represent the boundary conditions for the scleral canal region. A surface-based contact algorithm was used to account for the fiber-fiber interactions. The model was subjected to $IOP = 30 \text{ mmHg}$. A displacement boundary condition ($\delta = 0.1 \text{ mm}$) was applied on the periphery of the model to represent radial tension of the sclera due to IOP (Fig. 1b). The boundary of the solid regions and nearby sclera fibers were kinematically coupled. The solution was obtained using the FE solver Abaqus/Explicit.

Validation: The model response was validated against an ex-vivo inflation experiment [5] by calculating IOP-induced peripapillary sclera's (PPS) posterior displacement and scleral canal expansion. The validation was performed by inverse fitting the modulus parameter (E_b) iteratively.

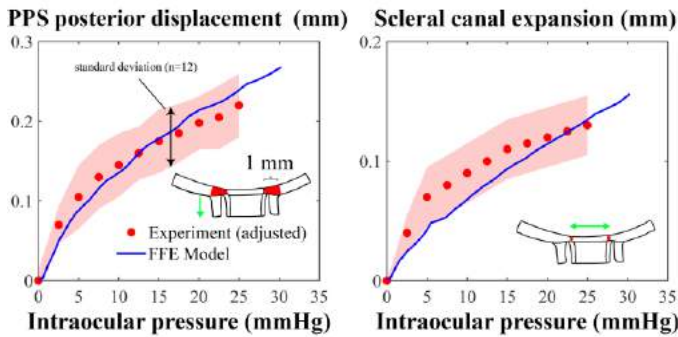


Figure 2. Intraocular pressure effect on (a) peripapillary sclera's (PPS) mean posterior displacement and (b) mean scleral canal expansion as obtained from the FFE model and experiments [5]. The insets indicate the regions used to calculate the average posterior displacement and canal expansion. Experimental data is shifted by 5 mmHg to ensure proper comparison with the model.

RESULTS

Fig. 2 compares the PPS's posterior displacement and scleral canal expansion of the model ($E_b = 8 \text{ MPa}$) with the experiment. The FFE model effectively captured the highly nonlinear variation of posterior displacement and canal expansion with IOP as observed experimentally. Note that the nonlinear response of sclera predicted by our model is a purely geometric effect of its 3D fibrous collagen structure since all the material parameters were linear elastic.

The model displacements along three directions at $IOP = 30 \text{ mmHg}$ are shown in Fig 3. Sclera, lamina cribrosa, and neural tissue

regions undergo relatively smaller in-plane displacement (along superior-inferior and nasal-temporal directions) compared to out-of-plane displacement in the posterior direction. The range of in-plane displacement was -0.1 mm to 0.175 mm whilst the range of out-of-plane displacement was $\sim 0.025 \text{ mm}$ to 0.8 mm . Posterior displacement was the dominant deformation mode of the ONH under elevated IOP [6].

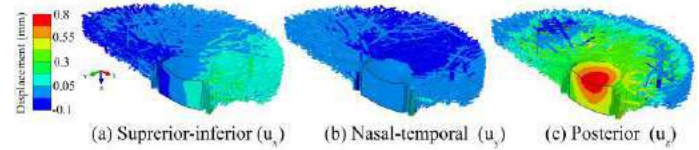


Figure 3. Displacement contour plots of the model: (a) superior-inferior, (b) nasal-temporal, and (c) anterior-posterior directions at intraocular pressure ($IOP = 30 \text{ mmHg}$).

Fig. 4 shows the heterogeneous strain distribution in various fiber bundle groups of the model at $IOP = 30 \text{ mmHg}$. The axial strain varied from -1% to 5% with most fiber bundles showing tensile strains (positive) and longitudinal bundles of Pia and Dura maters showing compressive strains (negative). The circumferential bundles undergo larger strains compared to other groups of fiber bundles.

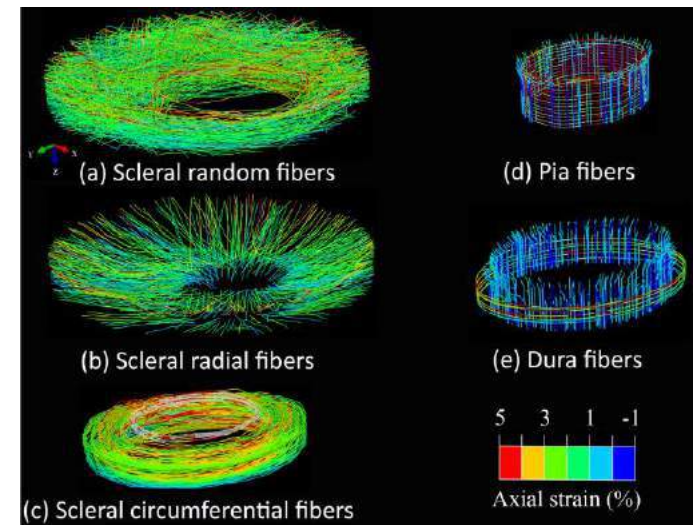


Figure 4. Axial strain contour plots for various fiber bundle groups of the FFE model at $IOP = 30 \text{ mmHg}$.

DISCUSSION

We presented a novel FFE model of sclera and demonstrated its ability to capture the nonlinear deformation of the ONH under elevated IOP entirely based on 3D fibrous collagen structure and a single material parameter. The FFE model allows for direct analysis of fiber-scale mechanics as a function of various fiber groups in sclera, which will help us understand the regional susceptibility of ONH damage in significant detail. Future work will investigate how various fiber groups independently affect ONH biomechanics under elevated IOP.

ACKNOWLEDGEMENTS

Supported in part by NIH R01-EY023966, R01-EY028662, P30-EY008098 and T32-EY017271 (Bethesda, MD), the Eye and Ear Foundation (Pittsburgh, PA), and Research to Prevent Blindness.

REFERENCES

- [1] Boote, C. et al., *Prog. Retin. Eye Res.*, 74, 100773, 2020.
- [2] Gogola, A et al., *IOVS*, 59(12): 4763-4774, 2018.
- [3] Ji, F et al., *Exp. Eye Res.*, 2022 (under review)
- [4] Shin et al., *Curr. Eye Res.* 45(7), 854-863, 2020.
- [5] Pavlatos, E. et al., *IOVS*, 59(8), 3779-3788, 2018.
- [6] Sigal, I. et al., *IOVS*, 52(3):1896-907, 2011.

REDUCED VASCULAR SMOOTH MUSCLE CELL MECHANOADAPTATION IN AN *IN VITRO* MODEL OF CEREBRAL AMYLOID ANGIOPATHY

Samuel F. Boland (1), Patrick W. Alford (1)

(1) Department of Biomedical Engineering, University of Minnesota, Minneapolis, MN, USA

INTRODUCTION

Cerebral amyloid angiopathy (CAA) is characterized by the deposition of the 40 amino acid amyloid beta peptide ($A\beta(40)$) around cerebral blood vessels¹ and is present in more than 80% of Alzheimer's disease (AD) patients². $A\beta(40)$ is highly cytotoxic and gradually leads to vascular smooth muscle cell (VSMC) death³ and hemorrhagic stroke⁴. VSMCs extracted from CAA patients are more contractile than VSMCs from healthy patients⁵ but it is unclear whether this behavior results from exposure to $A\beta(40)$ or instead drives $A\beta(40)$ deposition. Conversely, *in vitro* models of CAA suggest chronic exposure to $A\beta(40)$ reduces contractility in VSMCs⁶, but these methods rely on measurements of cell area to make indirect claims about VSMC contractility. Here we use cellular microbiaxial stretching ($C\mu$ BS) microscopy to benchmark VSMC basal stress and mechanoadaptation in an *in vitro* model of CAA. We hypothesized that VSMCs would display reduced basal stress and reduced mechanoadaptation in an *in vitro* model of CAA and found support for this hypothesis.

METHODS

Substrate fabrication and cell culture. Human umbilical artery VSMCs were incubated at 37 °C and 5% CO₂ in supplemented Medium 199. VSMCs were micropatterned with aspect ratio 1:4 (AR4) on a fluorescent bead-doped polyacrylamide (PA) gel (Fig. 1A) with a Young's modulus of 13.5 kPa as previously described⁷. Cells were incubated in serum-free supplemented Medium 199 24 hours prior to experimentation to induce a contractile phenotype⁸.

***In vitro* cerebral amyloid angiopathy (CAA) model.** To simulate CAA, VSMCs were incubated in supplemented Medium 199 with either 100 nM or 1 μ M $A\beta(40)$ dissolved in DMSO for four days. Cells were incubated in serum-free supplemented Medium 199 with the same concentration of $A\beta(40)$ 24 hours prior to experimentation, resulting in five total days of $A\beta(40)$ exposure.

Cellular Microbiaxial Stretching ($C\mu$ BS). $C\mu$ BS experiments were performed using a custom-built microscope-mounted device (Fig.

1B) to perform traction force microscopy (TFM) on VSMCs micropatterned on a deformable substrate. VSMCs were biaxially stretched at a strain rate of 0.001 s⁻¹ to 0.2 strain in 0.05 strain increments and then returned to 0 strain in 0.05 strain increments (Fig. 2A) at the same strain rate. At each strain increment a brightfield image was acquired of the VSMC and a fluorescent image was acquired of the

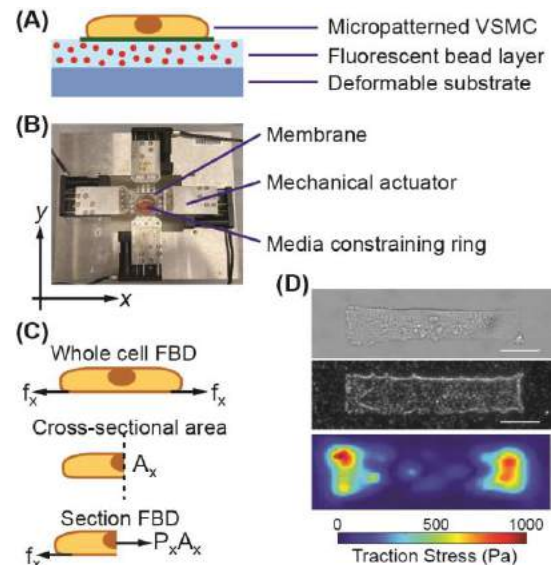


Figure 1: (A) Schematic of micropatterned VSMC. (B) Schematic of $C\mu$ BS apparatus. (C) Free body diagram (FBD) relating cell traction forces f_x to first Piola-Kirchoff stress P_x and cross-sectional area A_x . Adapted from Rothermel et al.⁷ (D) Bright field (top), bead layer (middle), and traction stress map (bottom) for a representative VSMC. Scale bar = 25 μ m.

underlying PA gel bead layer using at TRITC filter (Fig. 1D). Cells were then lysed with SDS, and the gel was imaged again using the same modalities at the location of each cell for each strain.

Traction forces at each strain were calculated using previously described methods⁷. The first Piola-Kirchoff stress, represented by $P_i = f_i/A_i$, where f_i is the total traction force acting in direction i and A_i is the undeformed cell cross-sectional area in the i -axis, was calculated at the mid-plane of the cell (Fig. 1C). Basal stress was defined as the stress produced by the cell before any deformation is applied. First Piola-Kirchoff stress was plotted against applied strain. Slope of the loading phase (0 strain up to 0.2 strain) and unloading phase (0.2 strain down to 0 strain) were calculated by taking the slope of a linear fit to the respective data. Total energy (work) and stored energy were calculated by calculating the area under the P_x vs strain plots during the loading and unloading phases, respectively. Lost energy was calculated by subtracting stored energy from total energy.

RESULTS

VSMCs were strained according to Fig. 2A. Prior to stretch, VSMCs generate a non-zero basal stress. Stress increases with each increasing strain increment up to 0.2 strain and then decreases with each successive step back to 0 strain (Fig. 2C). Stress during the unloading phases is lower than stress in the loading phase in both the x - and y -directions (Fig. 1B). Stress in the y -direction is consistently lower than stress in the x -direction. The P_x vs. strain plots for cells treated with increasing doses of $A\beta(40)$ shift downwards with a statistically significant difference between stresses in untreated VSMCs vs VSMCs treated with 1 μ M $A\beta(40)$ (Fig. 2D). There is no significant difference between the P_y calculations for each strain increment between the three treatment conditions (Fig. 2E). Slope during both loading and unloading phases of the experiment (Fig. 3A), basal stress (Fig. 3B), and both

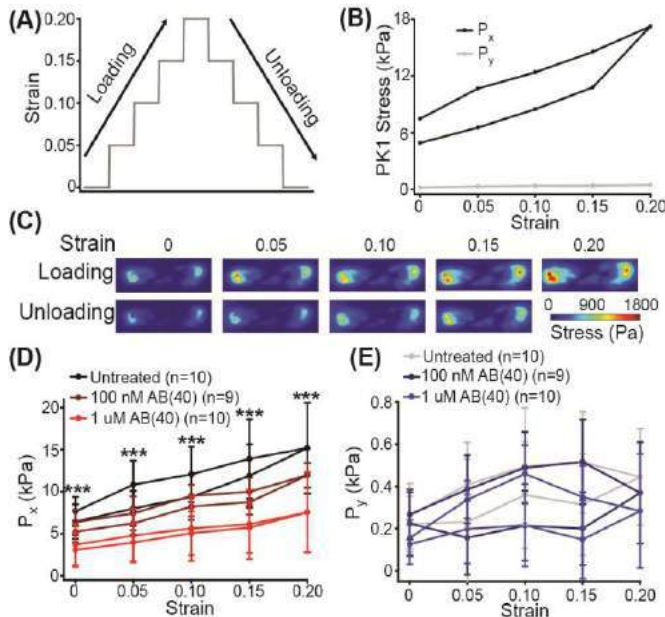


Figure 2: (A) Applied strain protocol for VSMCs. (B) First Piola-Kirchoff stress along x - (P_x) and y -axis (P_y) for a single, untreated VSMC subjected to strain protocol in (A). (C) Corresponding traction stress maps at each strain interval for cell in (B). (D) Mean P_x of untreated VSMCs (black), VSMCs incubated with 100 nM $A\beta(40)$ (dark red), or 1 μ M $A\beta(40)$ (red). $n = 10, 9$, and 10 , respectively. (E) Mean P_y for the same cells in (D). Error bars represent s.d. *** indicates $p < 0.001$.

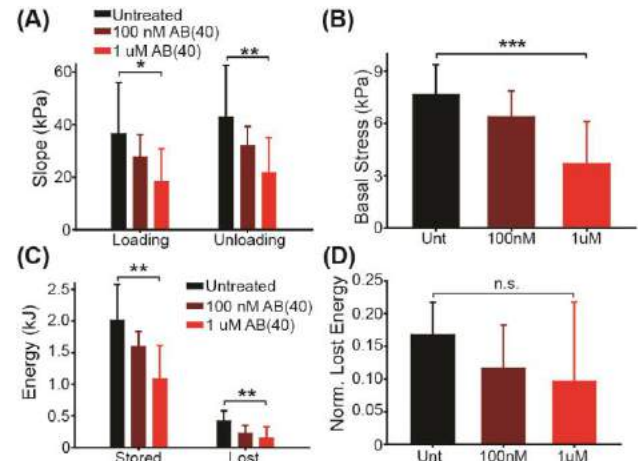


Figure 3: (A) Slope of P_x vs. strain during loading and unloading phases of experiment (B) VSMC basal stress for untreated VSMCs (Unt) and VSMCs treated with either 100 nM $A\beta(40)$ (100nM) or 1 μ M $A\beta(40)$ (1uM). (C) Stored and lost energy for each treatment condition. (D) Lost energy normalized by total energy for each treatment. * indicates $p < 0.05$, ** indicates $p < 0.01$, *** indicates $p < 0.001$, n.s. indicates no significance.

stored and lost energy (Fig. 3C) are all significantly lower in VSMCs treated with 1 μ M $A\beta(40)$ compared to the untreated control VSMCs. When lost energy is normalized to total energy for each condition there is no significant difference across conditions.

DISCUSSION

In this study, we demonstrate that VSMCs incubated with $A\beta(40)$ in an *in vitro* model of CAA generate significantly less stress at every increment of strain when compared to untreated control VSMCs. VSMC stress decreases in a dose-dependent manner when treated with $A\beta(40)$. This finding aligns well with results from similar *in vitro* CAA models, and conflicts with the finding that VSMCs from CAA patients are hypercontractile, suggesting that VSMC hypercontractility in CAA is perhaps a driver of the condition rather than a result of amyloid deposition. Further analysis of data shows that although stored and lost energy decrease in a dose-dependent manner, when lost energy is normalized to total energy in each condition there is no significant difference. This suggests that mechanical hysteresis is conserved in an *in vitro* CAA model. We intend to develop a new predictive model of VSMC contraction in CAA based on our Hill-type active fiber model⁹. Understanding how VSMC contractile function is modified in CAA will help better understand how vascular dysfunction in AD¹⁰ leads to cognitive deficits.

ACKNOWLEDGEMENTS

This work was supported by the National Science Foundation (CMMI-1935834). Portions of this work were conducted in the Minnesota Nano Center, which is supported by the National Science Foundation through the National Nanotechnology Coordinated Infrastructure (NNCI) under Award Number ECCS-2025124.

REFERENCES

- [1] Haglund, M et al., *Acta Neuropathol*, 2006.
- [2] Jellinger, K, *J Neural Transm*, 109:813-836, 2002.
- [3] Vilhjalmsson, D et al., *Exp Mol Pathol*, 2007.
- [4] Winkler, D et al., *J Neurosci*, 2001.
- [5] Chow, N et al., *Proc Natl Acad Sci U S A*, 2007.
- [6] Yun, J et al., *Pathophysiology*, 64-75, 2021.
- [7] Rothermel, T et al., *J Biomech Eng*, 143:1-11, 2021.
- [8] Han, M et al., *Am J Physiol - Cell Physiol*, 2006.
- [9] Win, Z et al., *Biophys J*, 2018.
- [10] Zlokovic, B, *Nature Reviews Neuroscience*, 2011.

VERIFICATION ERRORS IN EULERIAN POWER-LAW HEMOLYSIS MODEL PREDICTIONS IN SIMPLE FLOWS

Mohammad M. Faghih (1), Brent A. Craven (1), M. Keith Sharp (2)

- (1) Office of Science and Engineering Laboratories, Center for Devices and Radiological Health,
United States Food and Drug Administration, Silver Spring, MD, USA
(2) Department of Mechanical Engineering, University of Louisville, Louisville, KY, USA

INTRODUCTION

An empirical power law was originally used to correlate hemolysis with constant shear stress and exposure time in a Couette flow [1]

$$D = \frac{\Delta PfHb}{Hb} \% = C \sigma^\beta E^\alpha \quad (1)$$

where D is the percentage change in plasma free hemoglobin $PfHb$ relative to total hemoglobin Hb , σ is a representative scalar stress, E is the exposure time, and α , β and C are empirical coefficients. This power law has been extrapolated to apply to flows with varying shear and extensional stresses by using a resultant scalar stress [2]. While an improved version of the scalar stress has been proposed with increased weighting of extensional stresses [3], this paper focuses on the errors caused by Eulerian application of a linearized blood damage function with a purely convective transport equation [4]

$$\vec{v} \cdot \nabla D' = (C\sigma^\beta)^{\frac{1}{\alpha}} \quad (2)$$

where \vec{v} is the fluid velocity vector, $D' = D^{1/\alpha}$ is the exposure time-linearized damage index and $S = (C\sigma^\beta)^{1/\alpha}$ is the hemolysis generation source term.

Hemolysis is an inherently Lagrangian mechanism, since hemoglobin release fundamentally depends on the stress history applied to individual erythrocytes. Thus, a Lagrangian formulation of the power-law model analyzes fluid stresses along pathlines followed by the cells. The Reynolds transport theorem, which transforms the Lagrangian form to Eulerian, gives the full source term as $(C\sigma^\beta)^{1/\alpha} \frac{|\vec{v}|}{\bar{v}_s}$, where $|\vec{v}|$ is the local magnitude of the velocity at a specific point and \bar{v}_s is the average velocity along the streamline passing through that point [4]. Comparison with equation 2 shows that the source term in

equation 2 applies only for constant velocity along each streamline. A second issue related to integration of the linearized damage function can be addressed by raising the function to the power α before integration [4]. Therefore, the comparisons to follow will quantify the effect of the Reynolds transformation error only.

METHODS

Eulerian and Lagrangian hemolysis predictions are compared for three geometries: 1) Poiseuille flow, 2) inclined Couette flow, and 3) converging pipe with two different convergence ratios (a/b): 12 mm/4 mm and 12 mm/2 mm (Fig. 1).

The Eulerian prediction follows the common procedure of integrating the flux of hemolysis at the outlet

$$\overline{D_E} = \frac{\sum_{k=1}^l (D'_k)^\alpha Q_k}{\sum_{k=1}^l Q_k} \quad (3)$$

where Q is the flow rate through each two-dimensional element k of the outlet patch and l is the number of elements. The Lagrangian prediction at the outlet is for streamtubes in which the accumulated hemolysis along the streamline central to the streamtube is

$$D_L = \sum_{i=1}^n C \alpha \sigma_i^\beta E_i^{\alpha-1} \Delta E_i \quad (4)$$

where n is the number of exposure time steps, E_i is the exposure time from the beginning of the streamline to the end of the i th exposure step, ΔE_i is the exposure step size, and σ_i is the average scalar stress acting during that exposure step. The total blood damage is found by summing the flux of hemolysis through the outlet

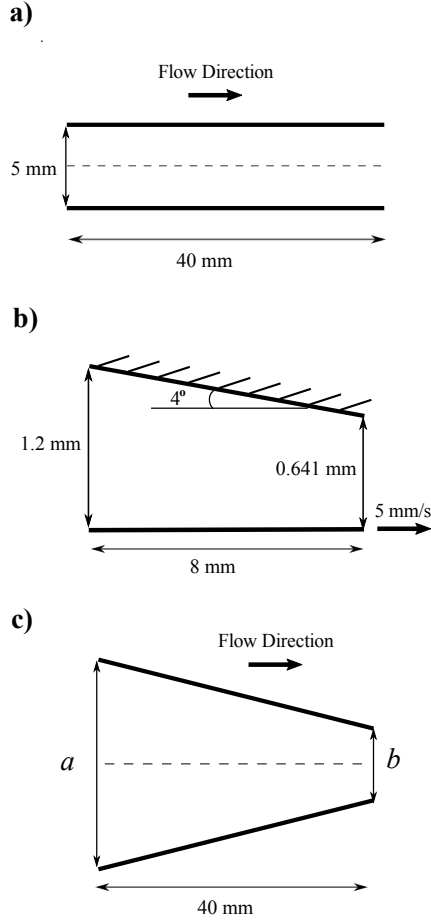


Figure 1: Schematics of the benchmark geometries; a) Poiseuille flow through a straight tube, b) two-dimensional inclined Couette flow with a gradual contraction, and c) flow through a straight, converging tube. Not drawn to scale.

$$\overline{D}_L = \frac{\sum_{j=1}^m D_{L,j} Q_j}{\sum_{j=1}^m Q_j} \quad (5)$$

where j refers to the streamtubes and m is the number of streamtubes.

Empirical coefficients from Song, et al. [5] were used. CFD computations were performed in OpenFOAM and postprocessing was done in Python. Spatial convergence of Eulerian estimates was evaluated with course, medium and fine meshes. Convergence of Lagrangian damage was obtained by increasing the number of streamlines and decreasing exposure step size along each streamline until estimates varied by less than 0.1%.

RESULTS

Results for the four cases are shown in Fig. 2, where the results are multiplied by different factors to make the differences visible on the same plot. The Poiseuille flow has no variation of velocity along streamlines, thus the Eulerian and Lagrangian hemolysis predictions are essentially the same. The inclined Couette flow has moderately increasing velocity downstream, and the Eulerian hemolysis prediction is 8% greater than Lagrangian. The converging tubes have the greatest velocity increase, yielding Eulerian predictions that exhibit 116% and

257% higher values, respectively, compared to the Lagrangian predictions.

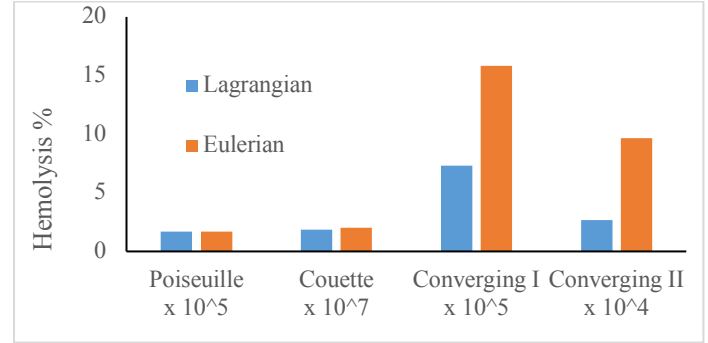


Figure 2: Results from the Lagrangian and Eulerian hemolysis simulations for the four benchmark test cases.

DISCUSSION

These results indicate that variations in velocity cause differences in Eulerian and Lagrangian power-law model hemolysis predictions, with larger variations leading to greater differences. This trend is consistent with Hariharan, et al. [6], who found relatively small differences in Eulerian and Lagrangian predictions in Poiseuille and inclined Couette flows, but did not analyze converging channels. For more complex flows, the differences associated with the error in Reynolds transformation may be even larger.

REFERENCES

- [1] Heuser G, Opitz R. A Couette viscometer for short time shearing of blood. *Biorheology* 17:17–24, 1980.
- [2] Faghih MM, Sharp MK. Extending the Power-Law Hemolysis Model to Complex Flows. *J Biomech Eng* 138:(124504)1-(124504)4, 2016.
- [3] Faghih MM, Sharp MK. Deformation of human red blood cells in extensional flow through a hyperbolic contraction. *Biomech Model Mechanobiol* 19:251–61, 2020.
- [4] Faghih MM, Sharp MK. On Eulerian versus Lagrangian models of mechanical blood damage and the linearized damage function. *Artif Organs* 43:681–7, 2019.
- [5] Song X, Throckmorton AL, Wood HG, Antaki JF, Olsen DB. Computational fluid dynamics prediction of blood damage in a centrifugal pump. *Artif Organs* 27:938–41, 2003.
- [6] Hariharan P, D’Souza G, Horner M, Malinauskas RA, Myers MR. Verification benchmarks to assess the implementation of computational fluid dynamics based hemolysis prediction models. *J Biomech Eng* 137: 094501:1-10, 2015.

PERISTALTSIS ALONE IS INCONSISTENT WITH MEASURED FLOW IN THE PARAVASCULAR SPACE

M. Keith Sharp (1)

(1) Department of Mechanical Engineering, University of Louisville, Louisville, KY, USA

INTRODUCTION

Diffusive or advective transport through brain tissue is important for exchange of nutrients and metabolites and for immune function, while clearance of metabolic waste requires fluid flow. Production of cerebrospinal fluid is thought to occur in the choroid plexus and interstitial fluid at the blood brain barrier of the capillaries, while a number of outflow pathways have been identified, including arachnoid villi and perineural passages in the cribriform plate [1]. It also has been proposed that fluid enters along paraarterial spaces and exits through paravenous spaces (the so-called glymphatic system [2]). Recent measurements have shown oscillatory displacement of the arterial wall and pulsatile flow around the middle cerebral arteries in rats [3]. The pulsatility of the flow logically suggests that the driver of the flow is peristalsis. However, the effectiveness of peristalsis is low for small amplitude of wall motion, as well as for oscillatory wavelength longer than the length of the channel. These recent measurements allow validation of models of paraarterial flow to evaluate the potential that it is driven by peristalsis. Comparison will also be made with alternative driving mechanisms.

METHODS

Mestre, et al. [3] reported the amplitude of normalized artery diameter displacement as 0.008, which gives a radial amplitude of $b = 0.176 \mu\text{m}$ and amplitude ratio $\phi \equiv b/a = 0.004$ in a channel with inner wall radius of $22 \mu\text{m}$ and gap between the inner and outer walls of $a = 44 \mu\text{m}$. They also measured mean flow velocity of $18.7 \mu\text{m/s}$. Ladrón-de-Guevara, et al. [4] reported the spatial root-mean-square oscillatory velocity to mean velocity ratio as 0.53. For a parabolic profile, the ratio of mean to root-mean-square is $5/4$, so the amplitude of the mean oscillatory velocity is estimated as $18.7 * 5/4 = 12.3 \mu\text{m/s}$.

Several mathematical solutions will be applied to model this flow, including peristalsis with and without a longitudinal pressure gradient in parallel-plate [5] and annulus [6] geometries. Both models assume

channel length longer than the oscillation wavelength, which likely overestimates the net flow rate, but is conservative for evaluating the plausibility of peristalsis as the primary driver of flow. Augmentation of mean flow by directional flow resistors is also evaluated in the parallel-plate geometry [7]. In this case, the resistors flex in the direction of blood flow in order to promote forward flow.

RESULTS

Fig. 1 shows the mean velocity normalized by the wavespeed (the maximum velocity that can be caused by peristalsis alone) for four different cases. For the parallel-plate model with no imposed pressure gradient (blue curve), with the measured paraarterial gap amplitude ratio of $\phi = 0.004$ (between the two purple dots on the figure), the mean flow rate is 0.000024. This value (dimensional velocity of $24 \mu\text{m/s}$) is close to the measured value of $18.7 \mu\text{m/s}$. However, the mean oscillatory velocity amplitude is too large at $4000 \mu\text{m/s}$ versus measured $12.3 \mu\text{m/s}$. For amplitude ratio $\phi = 0.00353$, at which the mean velocity is matched, the velocity amplitude is still too large at $3530 \mu\text{m/s}$. At amplitude ratio $\phi = 0.0000123$, the oscillatory velocity is matched, but the mean velocity is insignificant at $0.000227 \mu\text{m/s}$ (black square at the right-hand end of the blue curve).

Pressure has little effect on the flow for large amplitude ratio, but becomes strong as ϕ decreases. The mean and oscillatory velocities are both matched with a dimensional pressure difference of $\Delta p = 1.56 \text{ mmHg}$ at an amplitude ratio of $\phi = 0.0000123$ (black square at the right-hand end of the green curve), where the channel length is taken as $L = 2 \text{ m}$.

The effect of flexing flow resistors (red curve in Fig. 1) approaches zero as ϕ approaches its maximum value, however, the effect increases more quickly with decreasing ϕ than that of a pressure gradient. Mean velocity is matched at $\phi = 0.0000881$, but the oscillatory velocity is too large at $88.1 \mu\text{m/s}$. At a smaller $\phi = 0.0000123$ that matches the

oscillatory velocity, the mean velocity is too low at $2.61 \mu\text{m/s}$. The volume fraction of cylinders for these results is a somewhat arbitrary $\varepsilon_0 = 0.01$. The mean velocity is nearly insensitive to ε at the amplitude $\phi = 0.0000123$ that matches the oscillatory velocity, and a simultaneous match of measured mean and oscillatory velocities is not possible.

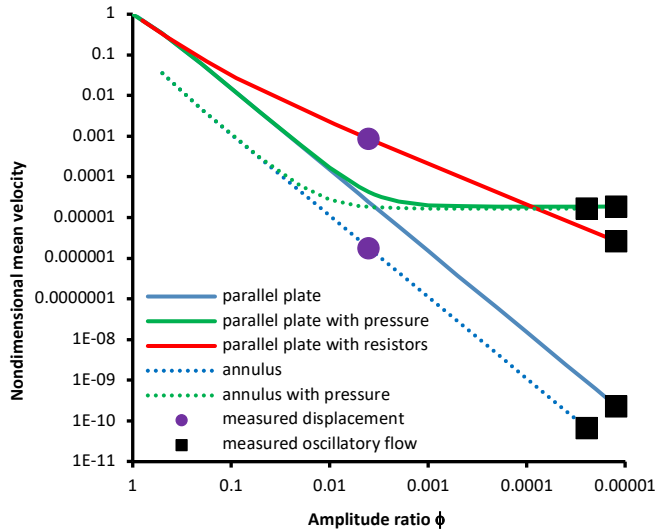


Figure 1: Mean velocity normalized by the maximum peristaltic mean velocity versus wall-amplitude-to-gap-height ratio.

The dotted blue curve in Fig. 1 presents the Wang & Olbricht [6] model for a nonporous annulus with zero pressure difference. The curve confirms that the annular model with oscillating inner wall has less potential for creating mean flow than the parallel-plate model. The purple dot again shows the mean velocity for the measured displacement. For this model, the mean velocity is $2 \mu\text{m/s}$ with an oscillatory velocity amplitude of $2000 \mu\text{m/s}$. For matched mean velocity at amplitude $\phi = 0.01223$, the oscillatory velocity is too great at $6110 \mu\text{m/s}$. For matched oscillatory velocity amplitude at $\phi = 0.0000246$, the mean velocity is only $0.0000756 \mu\text{m/s}$ (black square).

With a pressure difference of 1.54 mmHg added (dotted green curve), both the mean and oscillatory velocities can be matched to measured values (black square at the right-hand end of the curve), at an amplitude ratio of $\phi = 0.0000246$.

For the Mestre, et al. [3] measurements, the ratio of oscillatory to mean velocity is 0.66 . Fig. 2 shows that at the measured displacement of $\phi = 0.004$ (purple dots), the ratios for peristaltic flow without a pressure gradient are too large at 167 and 100 for the parallel-plate and annulus models, respectively. At the measured mean velocity (upper two green triangles), the ratios for peristaltic flow without a pressure gradient are too large at 189 and 327 for the parallel-plate and annulus models, respectively. Where the oscillatory velocity is matched to the measurements (upper two black squares), the ratios are $54,200$ and $163,000$ for the parallel-plate and annulus models, respectively. Indeed, a ratio of 0.66 is approached for the parallel-plate model only as $\phi \rightarrow 1$, and for the annulus model the smallest ratio obtainable is 6.27 for $\phi = 0.5$ (because the artery radius cannot collapse beyond its center). This fundamental characteristic of the performance of peristaltic channels reinforces that the mean flow must be driven by a different mechanism. With the appropriate pressure gradient, in both models the ratio initially rises for decreasing ϕ , but then decreases to 0.66 at smaller ϕ that simultaneously matches mean and oscillatory velocity (black squares overlaid by green triangles). The parallel-plate model with directional

resistors exhibits an asymptotic ratio for decreasing ϕ that is too high at about 4.7 .

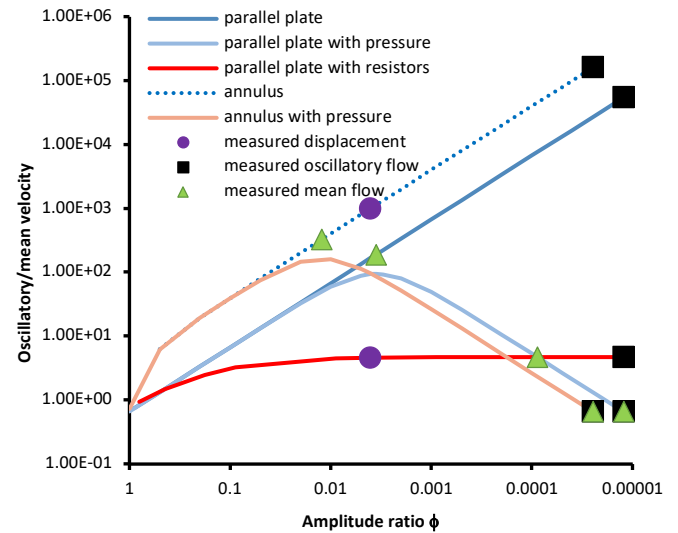


Figure 2: Ratio of oscillatory to mean velocities versus amplitude ratio. This ratio is 0.66 for the Mestre, et al. [2018] measurements.

DISCUSSION

The Mestre, et al. [3] measurements quantified the displacement only of the inner wall of the channel. It stands to reason that the outer wall may also move, which would reduce the effective amplitude ratio. A two orders-of-magnitude reduction in amplitude ratio is necessary to match the oscillatory velocity, but this smaller amplitude ratio drives very limited mean flow. Directional flow resistors increase the mean flow, but not enough to create a simultaneous match of oscillatory and mean velocities. An added pressure difference of about 1.5 mmHg , however, is capable of producing a match of both velocities. Therefore, these models suggest that peristalsis is the driver of the oscillatory flow, but a pressure gradient is necessary to force the mean flow.

REFERENCES

- [1] Hladky SB, Barrand MA. Mechanisms of fluid movement into, through and out of the brain: evaluation of the evidence. *Fluids and Barriers CNS* 11:26, 2014.
- [2] Iliff JJ, et al. A paravascular pathway facilitates CSF flow through the brain parenchyma and the clearance of interstitial solutes, including amyloid beta. *Sci Translational Med* 4(147):147ra11, 2012.
- [3] Mestre H, et al. Flow of cerebrospinal fluid is driven by arterial pulsations and is reduced in hypertension. *Nat Commun* 9:4878, 2018.
- [4] Ladron-de-Guevara A, Shang JK, Nedergaard M, Dh K. Perivascular pumping in the mouse brain: Realistic boundary conditions reconcile theory, simulation, and experiment. *bioRxiv* 2020:07:02:183608, 2020.
- [5] Jaffrin & Shapiro AH. Peristaltic pumping. *Ann Rev Fluid Mech* 3:13-36, 1971.
- [6] Wang P, Olbricht WL. Fluid mechanics in the perivascular space. *J Theoretical Biol* 274(1):52-57, 2011.
- [7] Sharp MK, Diem AK, Weller RO, Carare RO. Peristalsis with oscillating flow resistance elements: A mechanism for retrograde periarterial clearance of amyloid beta from the brain with implications for Alzheimer's disease. *Ann Biomed Eng* 44 (5):1553–1565, 2016.

STRENGTH, STIFFNESS, AND TOUGHNESS OF TENDONS, AND THEIR VARIATION WITH TENDON FUNCTION

Yuxuan Huang,¹ Ulrike G. K. Wegst,² Victor Birman,³ Stavros Thomopoulos,⁴ Guy M. Genin¹

¹NSF Science and Technology Center for Engineering Mechanobiology, Department of Biomedical Engineering and Materials Science, Washington University, St. Louis, MO, USA

²Department of Physics, Northeastern University, Boston, MA, USA

³Department of Mechanical and Aerospace Engineering, Missouri University of Science & Technology, Rolla, Missouri, USA

⁴Department of Orthopedic Surgery, Columbia University, New York, NY, USA

INTRODUCTION

Tendons throughout the body all serve to connect muscle to bone, but their function, structure, and composition vary [1]. Tissue engineering and repair strategies aim to restore function to tendons and joints, including the restoration of strength, stiffness, and toughness. However, debate persists on whether and how these properties vary over tendons throughout the body, including tendons that are sometimes categorized as predominantly energy-storing, such as the Achilles tendon, or positional, such as flexor and extensor tendons [2]. Our objective was to identify target mechanical properties for tendons across the body. Because more compliant springs are typically superior for energy storage, we hypothesized that tendons traditionally classified as energy storing tendons would be less stiff and less strong than positional tendons. We additionally hypothesized that toughness of tendons could be replicated by polymeric scaffolds.

To test these hypotheses, we conducted a comprehensive review of data in the and studied these data in the context of Ashby property charts [3]. Data falsified our first hypothesis, with properties of positional and energy-storing tendons overlapping. Data supported our second hypothesis, with strength, stiffness, and toughness of tendons all overlapping the range of existing polymers.

METHODS

Data collection

We collected tensile test data for various human tendons with the goal of establishing the ranges of their mechanical properties and comparing these properties to each other and to other engineering materials. We found 96 papers reporting data that identified a combination of elastic modulus, ultimate tensile strength, and/or data to estimate the modulus of toughness (area under the stress-strain curve to failure). From these 96 studies, a total of 236 data sets were found.

Modulus of toughness approximation

The modulus of toughness U_T was calculated as:

$$U_T = \int_0^{\varepsilon_f} \sigma(\varepsilon) d\varepsilon \approx \frac{1}{2} (\sigma_y + \sigma_u) \varepsilon_f \quad (1)$$

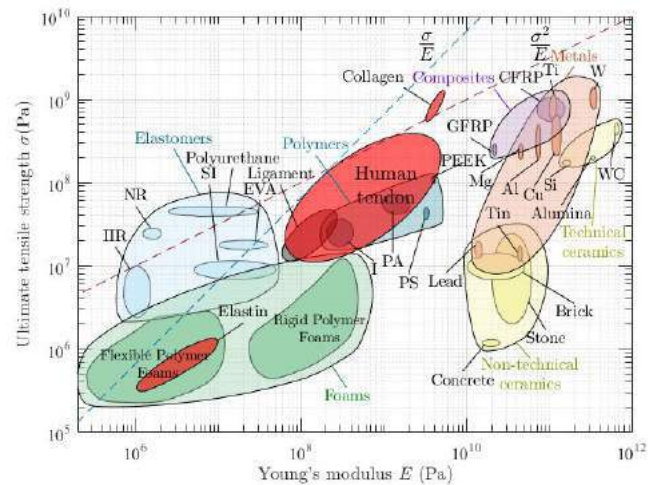


Figure 1: Strength and modulus of human tendon, elastin, and collagen compared to engineering materials. (NR=natural rubber, IIR=“butyl” rubber, SI=silicone, EVA=ethylene vinyl acetate, I=ionomers, PS=polystyrene, PEEK=polyetheretherketone, PA=polyamides, WC=tungsten carbides.)

where ε_f is the failure strain, σ_y is the stress associated with the end of the elastic range, σ_u is the ultimate stress, and the approximation on the right was used when area under the stress strain curve was unavailable, as is common for ductile materials and polymers [4, 5].

Data analysis

Data were synthesized using logarithmic property charts known as Ashby plots [3]. Two dimensional Ashby plots were made using Matlab (The Mathworks, Natick, MA), with logarithmic ellipses drawn around the ranges representing the upper and lower limits of average quantities. Data for engineering and natural materials that were used for comparison were taken from references [6], and [7].

RESULTS

Property charts were drawn for ultimate strength versus Young's modulus (Figs. 1-2) and Young's modulus versus mod-

ulus of toughness (Fig. 3). As expected for a heterogeneous, composite material, the mechanical properties of tendon fell between those of its primary constituent proteins, elastin (lower left of Fig. 1) and collagen (upper right). Energy storage at failure can be compared qualitatively by the dashed line in Fig. 1 representing the ratio σ^2/E . The σ^2/E property line intersecting tendon and ligament also intersects engineering composites and some of the strongest metals, as well as certain elastomers. Collagen fibrils outperform elastin in this metric, with tendon and ligament having values that lie between the two.

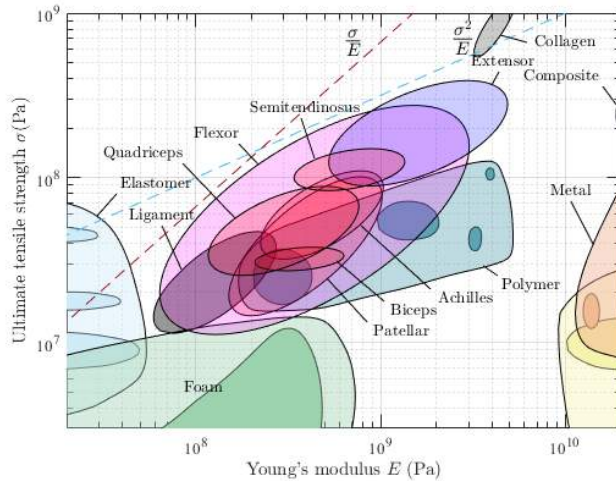


Figure 2: Property differences amongst human tendons.

Although collagen fibers are amongst the toughest of all materials (right side of Fig. 3), comparison to other materials reveals that the toughness of tendon is not remarkable for a material of its stiffness and that its stiffness is not impressive for a material of its toughness. The stiffness and toughness of the tendon are situated near the center of the material's space. Elastomers and certain metals are the toughest; non-technical ceramics such as brick are the least tough. Tendon has toughness on the order of midrange polymers.

DISCUSSION

Comparison of tendon to engineering materials

Individual collagen fibrils are as strong as the strongest metals, but tendon has a complicated composite structure that has a lower strength and stiffness than collagen. Two factors are potential contributors. The first is structure. Tendon and ligament both have a hierarchical structure of type I collagen stretching from the molecular level to the tissue, with nearly 70 percent of the weight of tendon being water [8]. This structure partly accounts for the lower stiffness and strength, but the composition also plays a role. Tendon and ligament consist primarily of type I collagen I and a small amount of elastin, as well as smaller quantities of proteoglycans, glycosaminoglycans, and minor collagens. As a composite of predominantly collagen and elastin, tendon and ligament have strength and stiffness between those of elastin and collagen. The ligament has the same hierarchical type I collagen structure as tendon but contains more elastin and thus, as expected by the rule

of mixtures, has a range of properties that lie in a region situated closer to that of elastin on the Ashby plot than does the range associated with the tendon (Fig. 2).

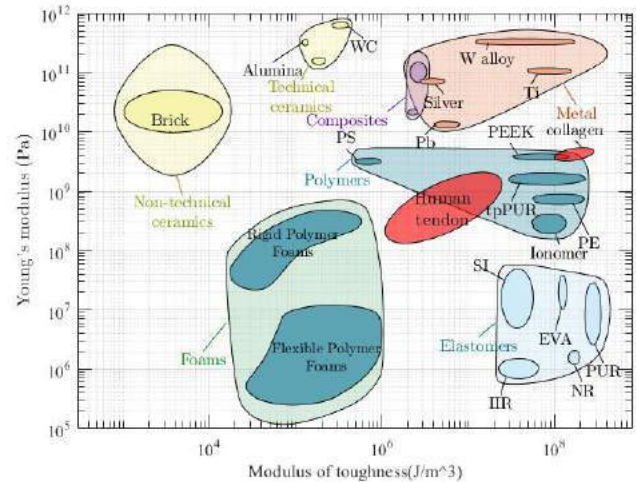


Figure 3: Young's modulus versus toughness Ashby chart.

Comparison of energy storing and positional tendons

A hypothesis to be found in the literature is that tendons fall into two distinct categories: positional tendons and energy storing tendons. Zooming into Fig. 1, Fig. 2 shows a spread of properties for different types of human tendons and ligaments and allows some evaluation of this hypothesis. In Fig. 2, all ligaments and tendons lie within a relatively narrow range of σ/E , indicating that nearly all of these tissues have failure strain in the same order. However, the data appear to falsify this hypothesis, with flexor and extensor tendons spanning the entire range of tendon and ligament properties. Although extensor tendons are the stiffest tendons, the range of values reported for flexor tendons exceeds the range of values reported for all other tendons.

Implications for tissue engineering

Results revealed no significant differences between the mechanical properties of positional and energy storing tendons. Results suggest that a single range of mechanical properties with elastic moduli in the hundreds of MPa range and strength in the 100 MPa range is adequate to replicate the properties of most tendons. These property ranges are achievable with existing engineering polymers, as are the toughness ranges of tendon.

REFERENCES

- [1] LaCroix et al. In: *J Appl Physiology* 115.1 (2013), pp. 43–51.
- [2] Thorpe et al. In: *J Roy Soc Interface* 9.76 (2012), pp. 3108–3117.
- [3] Ashby and Cebon. In: *Le Journal de Physique IV* 3.C7 (1993), pp. C7–1.
- [4] Dieter. In: *ASM Handbook, Vol. 8*. Ed. by Kuhn and Medlin. Materials Park: ASM, 2000, pp. 99–108.
- [5] Jenkins et al. West Conshohocken: ASTM, 1997.
- [6] Wegst and Ashby. In: *Phil Mag* 84.21 (2004), pp. 2167–2186.
- [7] Ashby et al. In: *Proc Roy Soc Lond A* 450.1938 (1995), pp. 123–140.
- [8] Thomopoulos and Genin. In: *Orthopaedic Biomechanics*. Ed. by Winkelstein. Boca Raton: CRC Press, 2012. Chap. 49.

IN VIVO ASSESSMENT OF PASSIVE AND ACTIVE ARTICULAR CARTILAGE STRAIN RECOVERY

Shu-Jin Kust (1), Dana Voinier (2), Kyle D. Meadows (1), Dawn M. Elliott (1), Daniel K. White (2), Axel C. Moore (1)

(1) Department of Biomedical Engineering, University of Delaware, Newark, DE, USA

(2) Department of Physical Therapy, University of Delaware, Newark, DE, USA

INTRODUCTION

Articular cartilage lines the ends of long bones in synovial joints and functions to provide load-bearing and low-friction articulation. These biomechanical functions are largely driven by the poroelastic mechanics (fluid pressurization) of the articular cartilage [1]. Unfortunately, the same poroelastic pressure that leads to load-bearing and lubrication also drives fluid exudation and concurrent tissue strain. In vivo static loading (e.g., standing) produces as much as -30% strain in 60 min. Interestingly, active loading (e.g., walking, knee bends, cycling, running) in vivo produces an initial period of fluid exudation and strain ($\sim -5\%$) [2]; after which, active loading arrests further fluid loss and tissue strain [3]. While static and active loading drive fluid exudation and cartilage strain, static unloading (e.g., lying down) provides recovery, and to date, is the only in vivo mechanism that has been shown to restore hydration and strain.

We hypothesize that active loading is actually a hydration and strain recovery mechanism that has yet to be observed. In this study, we investigate whether active loading (walking) is only an exudation and arresting mechanism or whether it is also capable of recovery. We use magnetic resonance imaging (MRI) to evaluate the in vivo strain of articular cartilage in human knees following: (1) standing (static loading), (2) lying down (static unloading), and (3) walking (active loading).

METHODS

Participants. Following IRB approval, we recruited N=8 asymptomatic young adults to participate in the study. Participant age (29 ± 3 years of age, mean \pm 95% confidence interval), biological gender (4 male, 4 female), and BMI (23 ± 2) were recorded. Up to 5 days prior to MRI scanning, participants were given a wrist worn activity monitor to track the number of steps taken each day (13 ± 5 k steps/day). Knee joint health was assessed using the self-reported Knee Injury and Osteoarthritis Outcome Score (KOOS).

MRI Scanning. Participants arrived at the MRI facility on the day of scanning and were positioned within the scanner (3T

MAGNETOM Prisma, Siemens) with a 15 channel Tx/Rx knee coil around their right knee. Participants were scanned in the following fixed order: (1) baseline, and immediately after (2) 30 min of standing, (3) walking for 10 min at 110 steps per min, (4) 30 min of standing, and (5-8) 12, 24, 36, and 48 min of lying down (**Fig 1**). A proton density weighted turbo spin echo (PD-TSE) was used to assess the morphology and thickness of the articular cartilage. The in-plane resolution and slice thickness were 0.3 and 1.5 mm respectively.

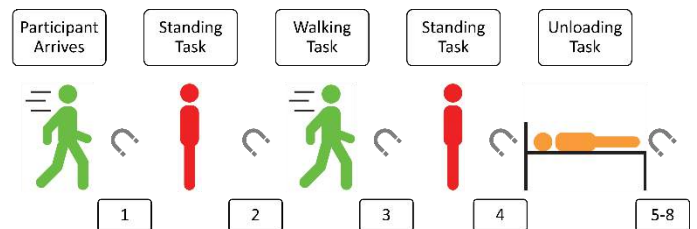


Figure 1: Order of activities (walking – green, standing – red, lying down – yellow). MRI scanning is indicated with the magnet symbol, and the numbering corresponds to the scan number, see section MRI Scanning.

Data Analysis. We calculate cartilage thickness as the tibiofemoral bone-to-bone distance within the medial and lateral compartments, measured within the region of contact. MRI scans were registered to the baseline scan to ensure the same region was measured. We calculate cartilage strain as the change in cartilage thickness divided by the baseline thickness. All values are reported as the mean \pm 95% confidence interval unless stated otherwise.

RESULTS

The average strain in the medial and lateral compartments for 8 participants are shown in **Fig 2A&B**. The baseline strain is set at 0%; we discuss the implications and rationale for this later. After 30 min of static loading (standing), there is a clear thinning of the articular

cartilage to an average -5.0 ± 0.4 and $-5.3 \pm 0.6\%$ strain in the medial and lateral compartments. Following a 10 min walk (active loading), the cartilage thickness recovers 2.3 ± 0.3 and $2.6 \pm 0.6\%$ strain, which directly agrees with our hypothesis that active loading is capable of recovery. Following another bout of static loading to approximately the same strain (-5.4 ± 0.3 medial and $-5.1 \pm 0.5\%$ lateral) the participant lies supine (static unloading), and the cartilage thickness and strain progressively recover. Following the first scan (12 min post standing), the cartilage recovered 1.5 ± 0.6 and $1.1 \pm 1.0\%$ strain in the medial and lateral compartments. Following 48 minutes of unloaded recovery the cartilage recovered 3.8 and 3.6% strain in the medial and lateral compartments.

DISCUSSION

In agreement with prior literature, static loading causes cartilage strain [4] while static unloading causes strain recovery [3]. These dynamics are driven by fluid flow out of and into the articular cartilage [5]. Counter to the existing literature, we have shown that active loading (walking) is not simply an exudative and arresting mechanism [3,6] but also a mechanism of recovery, which we hypothesize is driven by fluid flow back into the articular cartilage. In future work, we will further assess the flow of fluid back into articular cartilage using T2-w imaging.

The implication for activity driven cartilage recovery is significant. While epidemiological studies have documented the chondroprotective nature of joint activity, we have yet to identify the mechanism that provides chondroprotection. The observation that in vivo active loading recovers cartilage strain, and possibly hydration, opens new opportunities for understanding the long term biomechanical and cellular responses to active loading.

This study is not without limitations. The most notable limitation is the resolution of MRI. The PD-TSE sequence had an in-plane resolution and slice thickness of 0.3 and 1.5 mm respectively. Despite this, prior work by our group and others has shown sub-pixel sensitivity and precision when measuring tissue thickness and strain [7]. Furthermore, 0.3 mm is the typical in-plane resolution achieved for 3T MRI of cartilage. While not a limitation, it is important to note a significant deviation in our study design compared to the existing

literature. Prior studies place strict criteria on limiting a participant's activity prior to MRI and ask subjects to arrive early in the morning (e.g., 7:00 AM) and often provide wheelchair transport from the moment of their arrival [8]. The goal of this is to maximize the hydration and thickness of the cartilage. In addition, subjects typically sit or lie down for 45 minutes prior to scanning. While this gives the most realistic case for measuring 0% strain, it does not represent the typical operating strain of daily life. It has been shown that the diurnal strain for cartilage in the knee is $\sim 5\%$ and it is achieved in as little as 3 min of active loading [3]. In this study we evaluate cartilage at its 'operating strain' which we call baseline and define as 0% strain. We then drive the cartilage strain and hydration into a deficit through static loading. This deficit is what allows us to observe the recovery effect of joint activity.

In conclusion, we have shown that active loading is indeed a recovery mechanism for articular strain and has a potentially significant role in maintaining joint health. Furthermore, this finding reveals that the current view of joint activity being an exudative and arresting process (strain and hydration) is incomplete and that activity is a balance between load driven exudation and active recovery. The results of this work will help in developing evidence-based activity guidelines to promote long term cartilage health and potentially delay or prevent the development of osteoarthritis.

ACKNOWLEDGEMENTS

This work was supported by NIH COBRE 2P20GM 103653-06.

REFERENCES

- [1] G.A. Ateshian et al, *J. Biomech.* (2009).
- [2] F. Eckstein et al, *J. Anat.* (2006).
- [3] F. Eckstein et al, *Anat. Embryol.* (1999).
- [4] S. Uzuner et al, *J. Mech. Behav. Biomed. Mater.* (2021).
- [5] R.B. Souza et al, *Osteoarthr. Cartil.* (2014).
- [6] C.S. Paranjape et al, *Sci. Rep.* (2019).
- [7] W. Wirth et al, *Osteoarthr. Cartil.* (2022).
- [8] K.A. Taylor et al, *J. Biomech.* (2018).

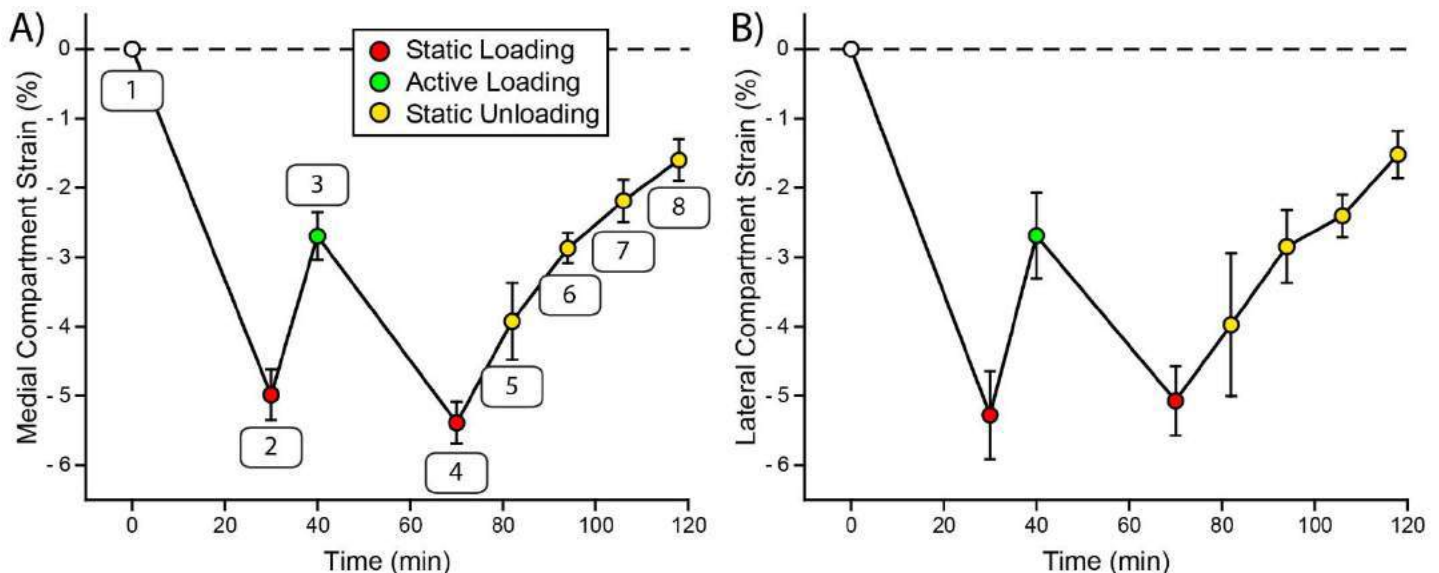


Figure 2: The mean $\pm 95\%$ confidence interval strain are shown for 8 participants in the (A) medial and (B) lateral compartments. The baseline strain is set at 0% (open circle). Static loading (standing) is shown in red, active loading (walking) is shown in green, and static unloading (lying supine) is shown in yellow. Numbers in (A) correspond to the scan numbers in the section *MRI Scanning*.

HEMODYNAMIC PERFORMANCE OF DUAL LUMEN VV ECMO CANNULAS

Louis P. Parker (1), Anders Svensson Marcial (2,3), Torkel B. Brismar (2,3), Lars Mikael Broman (4,5), Lisa Prah Wittberg (1)

(1) Department of Engineering Mechanics, Royal Institute of Technology (KTH), Stockholm, Sweden

(2) Department of Clinical Science, Intervention and Technology, Karolinska Institute, Stockholm, Sweden

(3) Department of Radiology, Karolinska University Hospital and Karolinska Institute, Stockholm, Sweden

(4) ECMO Centre Karolinska, Karolinska University Hospital, Stockholm, Sweden

(5) Department of Physiology and Pharmacology, Karolinska Institute, Stockholm, Sweden

INTRODUCTION

Venovenous extracorporeal membrane oxygenation (VV ECMO) is a life-saving treatment for acute respiratory distress syndrome (ARDS). Blood is drained from the patient's venous network, is oxygenated in an artificial membrane, and returned. Traditionally, this drainage and return of blood from the patient has been achieved with two separate, single lumen, cannulas (SLCs). More recently dual lumen cannulas (DLCs) combining both functions into a single device have become more commonplace.

Recirculation fraction (R_f) is the proportion of oxygenated return blood which is directly drained out before passing through the tricuspid valve thus not contributing to patient oxygenation. Effective VV ECMO cannulation should achieve a low R_f . Another key design objective for ECMO cannulas is to minimize the shear stress that the blood is exposed to. High shear stress is known to increase the risk of coagulation activation (secondary thrombosis/clotting) (Casa et al. 2015) and hemolysis (red blood cell damage) (Leverett et al. 1972). Finally, VV ECMO cannulas should disrupt physiological hemodynamics as little as possible.

Whilst DLCs are thought to have superior R_f performance compared to SLCs, this has not yet been conclusively demonstrated in a direct comparison. The shear stress acting on blood when using DLCs and its impact on native hemodynamics have also not been reported in adults.

METHODS

A patient-averaged model of the adult right atrium (RA) and venae cavae from a previous study was used to model background venous flow (Parker et al. 2022c) (Figure 1). This model was based on four healthy volunteers (3 female) with mean age = 58.3 ± 3.5 yrs, weight = 77.0 ± 11.9 kg and height = 173.0 ± 2.8 cm. Two common DLC designs, the Maquet Avalon Elite® (Getinge, Rastatt, Germany) and MC3 Crescent® (Medtronic International Trading Sàrl, Tolochenaz,

Switzerland) were sectioned, measured and reconstructed, creating accurate 3D models following the same methodology as applied previously to SLCs (Parker et al. 2022b). The measured DLCs were both downscaled to 27Fr, an appropriate size for our patient model, and inserted into the model. To delineate these from the off-the-shelf products we refer to the devices with the prefix “ds” for downscaled.



Figure 1: The patient-averaged 3D model with downscaled 27Fr Avalon dual lumen cannula inserted in baseline position (left). Venous image segmentation from one of the healthy volunteers (middle + right). SVC = superior vena cava, IVC = inferior vena cava, RA = right atrium.

The computational fluid dynamics (CFD) approach followed the same setup as applied in previous investigations (Parker et al. 2022a, Parker et al. 2022c, Parker et al. 2022b). This consisted of a Large Eddy Simulation (LES) with wall-adapting local-eddy viscosity (WALE) model, simulated on a mesh of 10.5-13.3M cells. Blood was modelled as non-Newtonian using the Quemada viscosity model. All venous and cannula walls were assumed to be rigid. All simulations were run on the Tetralith Supercomputer (National Supercomputer Centre, Sweden).

The dsAvalon and dsCrescent were first placed in the optimal position with the reinfusion port directly facing the tricuspid valve location (Figure 1). These were simulated at 2, 4 and 6 L/min ECMO flow. Analyzing flow patterns, we noted a high degree of similarity between the two designs. Therefore, the impact of insertion depth (± 4 cm) and rotation ($\pm 30^\circ$ and $\pm 60^\circ$) was only assessed for the dsAvalon design.

Simulations were run for several cardiac cycles until periodicity was achieved. The velocity, wall shear stress (WSS), R_f and turbulent kinetic energy (TKE), averaged over the final cardiac cycle were analyzed. Pressure probes were also placed in the superior vena cava (SVC), inferior vena cava (IVC) and RA.

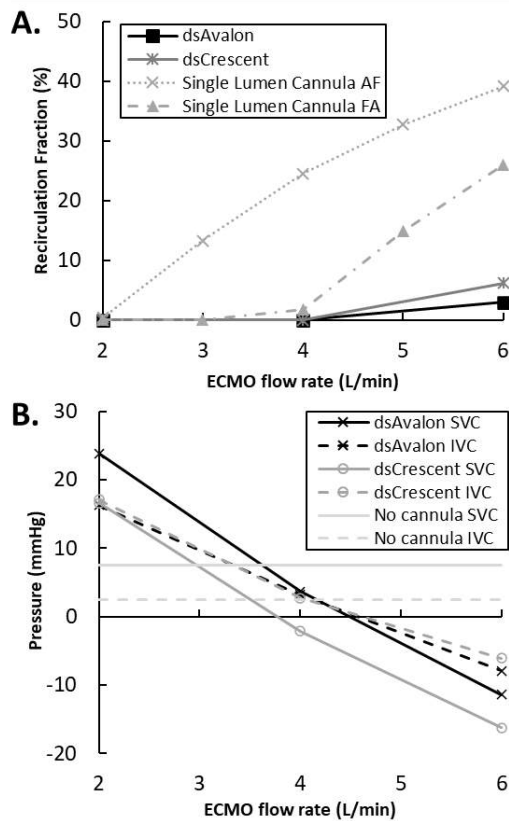


Figure 2: A. Recirculation fraction (R_f) for the downscaled (ds) Avalon and Crescent models. These are compared with previous findings for single lumen cannulas in atriofemoral (AF) and femoroatrial (FA) configuration (Parker et al. 2022b). B. Superior (SVC) and inferior vena cava (IVC) pressures using both the dsAvalon and dsCrescent compared to no cannula.

RESULTS

R_f was low for both DLCs compared to our previous findings with SLCs. Even at high ECMO flow rates R_f remained below 7% (Figure 2A). Caval pressures were abnormally high at low ECMO flow rates for

both DLCs (Figure 2B). As expected, at high ECMO flow rates caval pressures were negative (Figure 2B). Time-averaged WSS (TAWSS) was very high (>475 Pa) at the reinfusion port for both designs at all ECMO flow rates. The focused jet of return blood created regions of similarly high TAWSS (>50 Pa) at the RA wall for all flow rates. R_f did not change significantly with rotation from -60° to $+60^\circ$. Conversely, R_f was highly sensitive to insertion depth. With short insertion depth (-4 cm from baseline), R_f was $>30\%$ at all ECMO flow rates. Under long insertion depth ($+4$ cm from baseline), the increase in R_f was only significant at 6L/min ECMO flow rate (24.0%).

DISCUSSION

The results from this study confirm the widely held belief that DLCs exhibit superior R_f performance compared to SLCs under ideal conditions. The two downscaled designs assessed here both show minimal recirculation even at high ECMO flow rates. The high caval pressures at low ECMO flow rates was an unexpected finding. This likely arises from the significant obstruction caused by the large outer diameter of both DLCs. At low ECMO flow rates, caval drainage is low but return venous flow is impeded from entering the RA. This high caval pressure may provide a possible explanation for the higher incidence of intracranial hemorrhage reported when using large diameter DLCs (Mazzeffi et al. 2019). Both DLC designs feature a highly focused reinfusion port to direct flow towards the tricuspid valve. This creates high TAWSS conditions at the reinfusion port and the RA wall which may cause hemolysis and coagulation activation. Our results also provide practical clinical information. DLCs appear to be highly sensitive to insertion depth where too short an insertion depth is particularly detrimental to R_f performance. Rotation of the devices did not have any significant impact on R_f performance.

ACKNOWLEDGEMENTS

Funded by the European Union (ERC CoG 2022: Project 101045453 - fitsCAN) and Region Stockholm (grant HMT2018). Views and opinions expressed are however those of the author(s) only and do not necessarily reflect those of the European Union or the European Research Council Executive Agency. Neither the European Union nor the granting authority can be held responsible for them. The authors would like to acknowledge the Swedish National Infrastructure for Computing (SNIC) for access to Tetralith (National Supercomputer Centre, Sweden), partially funded by the Swedish Research Council (grant agreement no. 2016-07213).

REFERENCES

- [1] Casa, L. D. C., et al., *Journal of Vascular Surgery*, 61:1068-1080, 2015.
- [2] Leverett, L. B., et al., *Biophys J*, 12:257-273, 1972.
- [3] Mazzeffi, M., et al., *ASAIO journal (American Society for Artificial Internal Organs : 1992)*, 65:674-677, 2019.
- [4] Parker, L. P., et al., *Journal of Engineering and Science in Medical Diagnostics and Therapy*, 2022a.
- [5] Parker, L. P., et al., *Scientific Reports*, 2022b.
- [6] Parker, L. P., et al., *Journal of Applied Physiology*, 132:1167-1178, 2022c.

DEVELOPMENT OF MELT ELECTROWRITING BASED POLYMER HEART VALVE LEAFLETS INFORMED THROUGH FINITE ELEMENT MODELLING

Celia Hughes (1,2,3), Robert D. Johnston (1,2,4), Alix Whelan (1,2), David O'Reilly (3), Evelyn Campbell (3), Caitriona Lally (1,2,4)

- (1) Trinity Centre of Biomedical Engineering, Trinity Biomedical Sciences Institute, Trinity College Dublin, Dublin 2, Ireland
- (2) Department of Mechanical, Manufacturing, and Biomedical Engineering, School of Engineering, Trinity College Dublin, Dublin 2, Ireland
- (3) Structural Heart Division, Boston Scientific Corporation, Galway, Ireland
- (4) Advanced Materials and Bioengineering Research (AMBER), Trinity College Dublin, Dublin 2, Ireland

INTRODUCTION

Aortic stenosis is a prevalent disease of the aortic valve, affecting 5% of people over the age of 65 and carrying a 50% chance of mortality within two years if left untreated [1, 2]. Bioprosthetic heart valve replacements that use porcine or bovine pericardium are most commonly used to treat this disease; however, such devices typically experience premature failure within 25 years due to loss of structural integrity and calcification [3, 4]. In this research, we propose a method to develop bioinspired polymer-based materials to improve leaflet functionality while extending device lifetimes.

Glutaraldehyde-fixed bovine or porcine pericardium currently used in commercial devices does not accurately replicate the complex structure or function of the native aortic valve leaflets, which have a unique tri-layered structure and predominantly circumferentially aligned collagen fibre bundles [5]. In addition, pericardium suffers from structural valve degeneration (SVD), which is the deterioration of the tissue ultimately leading to device failure through stenosis or regurgitation [6]. SVD is known to be exacerbated by glutaraldehyde fixation, which increases tissue stiffness and promotes calcification [7]. Consequently, it is desirable to use a non-calcifying material that can withstand the complex loading environment of a heart valve for an extended period of time, which is the goal of using a polymer-based material inspired by the native aortic valve leaflets.

To better understand the material properties and structure of native leaflets in order to determine the optimum polymer material, extensive work has been performed to establish the material behaviour of individual valve leaflet layers and key microstructural characteristics. Specifically, second harmonic generation (SHG) microscopy was carried out in order to identify local collagen alignment in key locations across fresh porcine leaflets. From this, we can use finite element (FE) modelling and melt electrowriting (MEW) to define and manufacture a polymer material with an optimal, fibre-reinforcement structure that

mimics the structure of native aortic valve leaflets. We have developed an FE framework that informs this MEW fibre reinforcement structure to ultimately form the basis of an idealised polymeric valve leaflet material.

METHODS

An ACURATE neo2™ leaflet geometry was provided by industrial collaborators at Boston Scientific. This leaflet was partitioned into 28 discrete rectangular regions, all ranging from 2.5 to 3.5 mm in both height and width, see Figure 1(b). Constitutive properties of silicone rubber and PCL were informed by relevant literature and applied to a preliminary discrete fibre-reinforced model, based on a 2-layered MEW structure [8, 9]. Tensile behaviour of this PCL-reinforced silicone was then used to calibrate parameters for the anisotropic, fibre-reinforced HGO model implemented in Abaqus CAE [10]. Collagen orientation was imaged by SHG at the commissure and belly regions using a Carl Zeiss 710 NLO microscope, see Figure 1(a). With these images, fibre angles were obtained using ImageJ, defined at these locations in the model, and then extrapolated for the rest of the locations in the leaflet, see Figure 1(b). Half of the leaflet was modelled using symmetrical boundary conditions for computational efficiency, elements around the edge of the leaflet were fixed in all directions, and a pressure of 80 mmHg was applied to the face of the leaflet; see Figure 1(c). Three cases were investigated in order to probe the mechanical contribution of a MEW fibre-reinforcement structure: (i) matrix with no fibres (Neo-Hookean model: $C_{10}=0.3$ MPa), (ii) fibre-reinforced matrix with calibrated parameters (HGO model: $C_{10}=0.3$ MPa, $D=0$, $K_1=0.2$ MPa, $K_2=0.1$, $\kappa=0$), and (iii) fibre-reinforced matrix with stiffer fibres ($K_1=2$ MPa, $K_2=1$).

To assess manufacturing feasibility, MEW structures were printed using a custom-built, in-house printer [11]. One structure was embedded in Ecoflex 00-30 silicone rubber and a second implemented curved fibres in the horizontal direction.

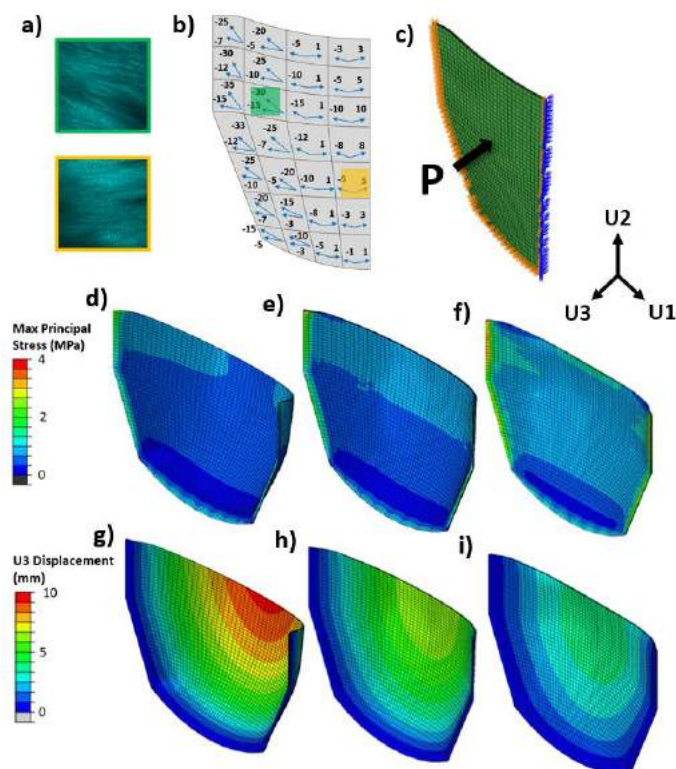


Figure 1: (a) Example SHG images for commissure and belly regions, (b) partitioned leaflet with specified fibre angles relative to the x-axis, (c) leaflet boundary and loading conditions; stress distributions for each considered case: (d) matrix only (max: 1.60 MPa), (e) calibrated fibre reinforcement (max: 1.89 MPa), and (f) stiffer fibres (max: 3.03 MPa); displacement distributions for each considered case: (g) matrix only (max: 9.77 mm), (h) calibrated fibre reinforcement (max: 6.64 mm), and (i) stiffer fibres (max: 4.13 mm)

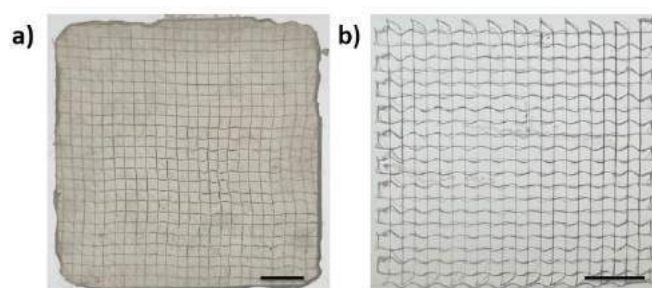


Figure 2: (a) MEW structure embedded in silicone rubber, (b) MEW structure with curved fibres in the horizontal direction. Scale: 5 mm.

RESULTS

A partitioned polymer leaflet model with biologically inspired varying fibre orientations subjected to an applied physiological pressure was successfully simulated. Both the matrix-only and calibrated fibre-reinforced models exhibited similar stress distributions (max: 1.60 and 1.89 MPa, respectively), see Figure 1(d,e). As expected, an increase in stress magnitude was caused when increasing the fibre stiffness (max: 3.03 MPa), see Figure 1(f).

Furthermore, adding a fibre reinforcement structure and increasing fibre stiffness led to notable decreases in leaflet displacement. While the matrix-only model experienced a maximum displacement of 9.77 mm, this decreased after the addition of fibres, with the calibrated model displacing to a maximum of 6.64 mm. Increasing the stiffness of these fibres further impacted the leaflet displacement, bringing the maximum displacement down to 4.13 mm, see Figure 1(g-i).

Showing the feasibility of MEW for this application, two structures were successfully printed: one box structure that was subsequently embedded in silicone rubber, and a second with curved fibres to mimic the impact of collagen crimp, see Figure 2(a,b).

DISCUSSION

While MEW has been shown to be an effective and versatile manufacturing method for the fibre-based reinforcement of materials, there are few frameworks in place to inform MEW using modelling approaches [12]. With a comprehensive understanding of native leaflet structure and properties, computational modelling can be used to minimise the empirical mechanical assessment required during the design and fabrication of MEW constructs, and, importantly, inform an ideal material geometry.

This work has introduced a framework for using FE modelling and SHG imaging to define an optimal fibre-reinforced leaflet material manufactured using MEW for use in prosthetic aortic heart valves. We have demonstrated the impact of fibre reinforcement on an elastomeric material: by adding supporting structures at varying stiffness and orientations, the load-bearing capacity and deformation characteristics of the leaflet under applied loading can be tuned to suit the desired performance. This allows for the complete customisability of the polymer leaflets, allowing us to manufacture a material that can readily emulate native tissue.

We can validate the results of this model by conducting tensile testing of MEW-reinforced elastomeric materials, and further use this model to investigate different MEW reinforcement structures. Additionally, using the information gained from the assessment of porcine leaflets, this model can be compared to native valve tissue to evaluate its performance.

Ultimately, the objective of this work is to develop a methodology to aid with the design and development of new prosthetic heart valve leaflets, ensuring an extended lifetime for these devices. By bringing together knowledge of the native aortic valve leaflets, MEW, and FE modelling, we can define and manufacture these optimal leaflets for future commercial devices.

ACKNOWLEDGEMENTS

This project has received funding from the Irish Research Council and Boston Scientific Corporation, Galway (EBPPG/2020/200).

REFERENCES

- [1] Clark, M et al., *Circ. Card. Qual. Outc.*, 5(5):697-704, 2012.
- [2] Martinsson, A et al., *Circulation*, 131(11):988-94, 2015.
- [3] J. Carroll et al., *Journ. of the Am. College of Cardio.*, 2020.
- [4] Bourguignon, T et al., *Ann. Thor. Surg.*, 100(3):853-59, 2015.
- [5] Sacks, M et al., *Journ. of Biomec.* 42(12):1804-24, 2009
- [6] Dvir, D et al., *Circulation*, 137(4):388-99, 2018.
- [7] Lee, C, *Exp. Op. on Bio. Ther.*, 9(8):1031-42, 2009.
- [8] Spagnoli, A et al., *Applied Sciences*, 9(6):1086, 2019.
- [9] Castilho, M et al., *Scientific Reports*, 8(1):1-10, 2018.
- [10] Gasser, T C et al., *Journ. of Roy. Soc. Int.*, 3(6)15-35, 2006.
- [11] Eichholz, K, Hoey, D, *Acta Biomaterialia*, 75:140-51, 2018
- [12] Saidy, N T et al., *Small*, 15(24):1-15, 2019.

DESIGN, COMPUTATIONAL AND EXPERIMENTAL EVALUATION, AND 3D PRINTING OF PATIENT SPECIFIC STENTS FOR TREATMENT OF PAEDIATRIC AORTIC COARCTATION

Robert D. Johnston^{1,2,5}, Niall Linnane^{1,2,3,4}, Samuel Geraghty^{1,2,5}, Conor O’Keeffe^{1,2}, Shirsha Bose^{1,2,5}, Damien Kenny⁴, Caitriona Lally^{1,2,5}

¹ Trinity Centre for Biomedical Engineering, Trinity Biomedical Sciences Institute, Trinity College Dublin, Dublin, Ireland

² Department of Mechanical, Manufacturing & Biomedical Engineering, School of Engineering, Trinity College Dublin, Dublin, Ireland

³ Royal College of Surgeons, RCSI, Dublin, Ireland.

⁴ Children’s Health Ireland at Crumlin, Dublin 12, Ireland.

⁵ Advanced Materials and Bioengineering Research Centre (AMBER), Royal College of Surgeons in Ireland & Trinity College Dublin

INTRODUCTION

Aortic coarctation has an incidence of 0.3 to 0.6 in 1000 live births, ultimately accounting for 5 to 12 % of all congenital heart disease [1,2]. Currently, neonatal coarctation is treated surgically via a thoracotomy procedure, which involves excision of the narrowed section of the aorta followed by an end-to-end anastomosis. However, for older children and adults, stenting is now the procedure of choice. Although, stenting is associated with low instances of acute complications, there is a risk of hypertension long-term [3]. Currently, due to the small patient cohort and little financial incentive for medical device companies, biliary stents are commonly used off-label in the treatment of aortic coarctation with less than optimum outcomes.

In recent years, research has been carried out into the development of 3D printed metallic stents in an attempt to overcome the disadvantages and shortfall of manufacturing stents in the conventional laser cut manner [4]. Additive manufacturing of metallic stents is a very promising method of creating bespoke stents for paediatric aortic coarctation. Recent studies by McGee et al [5] and by Demir & Previtali [6] have established the manufacturing rules for printing stents using selective laser melting (SLM). 3D printing stents provides an opportunity to create stents that are designed specifically with the patient in mind. Finite element (FE) modelling can act as this precursor to stent manufacturing by establishing what specific design is required in order to achieve maximum lumen gain and at the same time minimize the stress on the host vessel.

Therefore, the objective of this work is to develop a framework to design, experimentally and computationally evaluate 3D printed stents and individual stent units, to assess their performance and ultimately 3D print bespoke stents for patient specific treatment of aortic coarctation.

METHODS

Stent and stent unit design

The biliary Max LD Intrastent (Medtronic, United States) with a diameter = 10mm and strut thickness = 200µm was used for the initial design.

A stent repeating unit was sketched in Abaqus (SIMULIA, Dassault Systèmes) and subsequently wrapped using the wrap mesh plugin. The geometry of the full stent was assembled and then imported into ANSA Beta (BETA CAE Systems, Greece) and segmented into individual units, as shown by Fig. 1.

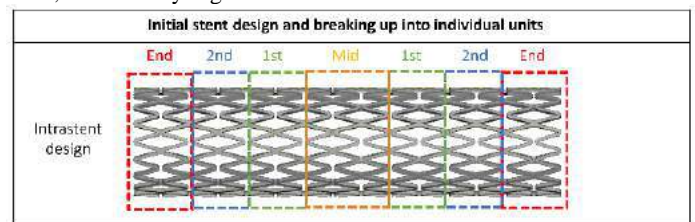


Figure 1: Creating initial intrastent geometry and segmentation of full stent design into individual units.

Computational setup

For the materials, 316L stainless steel was described by an elastic-plastic material model with elastic modulus of 196 GPa, Poisson’s ratio of 0.3 and a yield strength of 375 MPa [7] and printed titanium Ti6Al4V by an elastic modulus of 65.09 GPa, Poisson’s ratio of 0.3 and a yield strength of 663.519 MPa.

Crush tests were simulated by modelling two parallel rigid plates, meshed using SFM3D4 quadrilateral elements. Zero friction and hard contact was assigned between the stent and plates. The bottom plate was fixed, whilst the top plate was assigned a displacement boundary condition corresponding to half the stent diameter (5 mm).

Crimp tests were simulated by assigning a cylindrical coordinate system at the centre of the stent geometry. A radial displacement boundary condition was then applied to simulate the crimping response to a pre-set diameter.

3-point bend tests were simulated according to ASTM standard F2606-08. Three pins were modelled as rigid, with two pins fixed and separated by a span length of 30.30 mm and indented by 6.06 mm by a third centrally placed pin.

3D printing and postprocessing of stents

A Realizer SLM 50 was used to 3D print stent designs (10 mm diameter, 400 μm strut thickness) using Ti6Al4V powder using previously established parameters [5]. A scan and hatching strategy were employed to ensure continuous build-up of the structure. After printing, the stents were post-processed by sandblasting and chemical etching to achieve a strut size of 100 μm .

Crush tests, crimping & 3-point bend tests of printed stents

Each computational setup was also investigated through respective experimental methods. These are detailed as follows:

Crush tests was conducted by compressing the 3D printed stents by two parallel plates as shown by Fig. 3A. Stents were compressed to 50% of their nominal diameter at a compression rate of 3mm/min in accordance with ISO 25539-2 standard.

Crimping and balloon expansion was conducted by firstly crimping the 3D printed stents down to known diameters of 3D printed cylinders using a Machine Solutions Inc. HV 500 crimping tool. After being fully crimped, the balloon from the Express LD stent delivery system was used to expand the crimped stent to its maximum dilation.

3-point bent tests were conducted by the test method outlined in ASTM F2606-8. Like the computational setup, span length and maximum deflection was calculated and used for the test. Stents were pre-loaded to 0.1 N and deflected at a rate of 10 mm/min.

RESULTS

Changing strut dimensions can significantly alter the yield observed in individual units, see Fig. 2A, where locations above 663.519 MPa stress correspond to locations of yield in the 3D printed titanium stents. Stent units with uniform strut dimensions (100 μm) showed no yield when crushed to 50% of their diameter, demonstrating elastic behaviour and the ability to be compressed further before yielding. In our crimping simulations, yielding of the stent material is only observed when crimped to sufficiently small diameters, as shown by Fig 2B. The stent with uniform smaller strut dimensions (100 μm) could be crimped to a smaller diameter without yield. Three-point bend simulations showed Ti64Al stents to be more elastic compared to stainless steel 316L, where the latter showed yielding and consequently significant plastic deformation for the same loading, see Fig 2C.

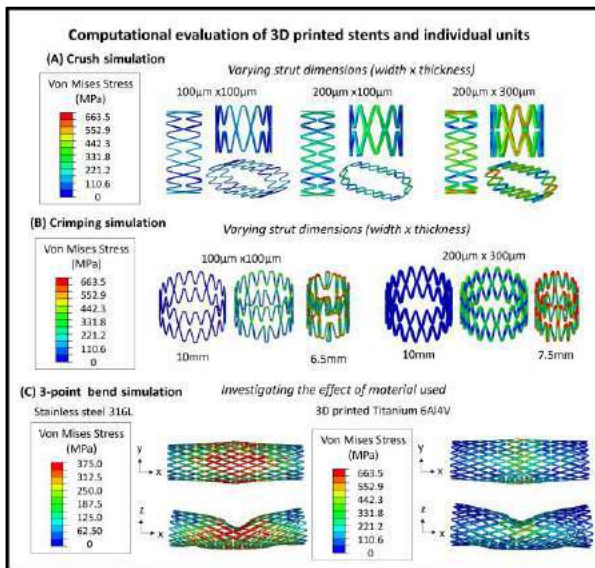


Figure 2: Computational evaluation of the stent and individual units (A) Crush testing simulation of units with different strut dimensions (B) Crimp testing simulation of units with different strut dimensions (C) 3-point bend test of stent with strut size of 200x100 μm with different material assigned

Experimental tests qualitatively validated all our computational simulations. Our post-processed stents (strut thickness = 100 μm) showed an elastic response when crushed to 50% of their diameter, as predicted by our models which showed no yield, see Fig. 2A and 3A. Radial crimping of the 3D printed stent shows the ability to crimp down to a smaller diameter, see Fig 3B(i). Interestingly, the stent shows considerable elastic recoil when crimped to set diameters, see Fig 3B(ii). Furthermore, balloon expansion shows unfolding of the stent geometry without fractures, as shown in Fig 3C. Lastly, 3-point bend experiments agreed with our computational results showing significant yield in the Intrastent and an elastic response in our 3D printed stents, see Fig. 3D

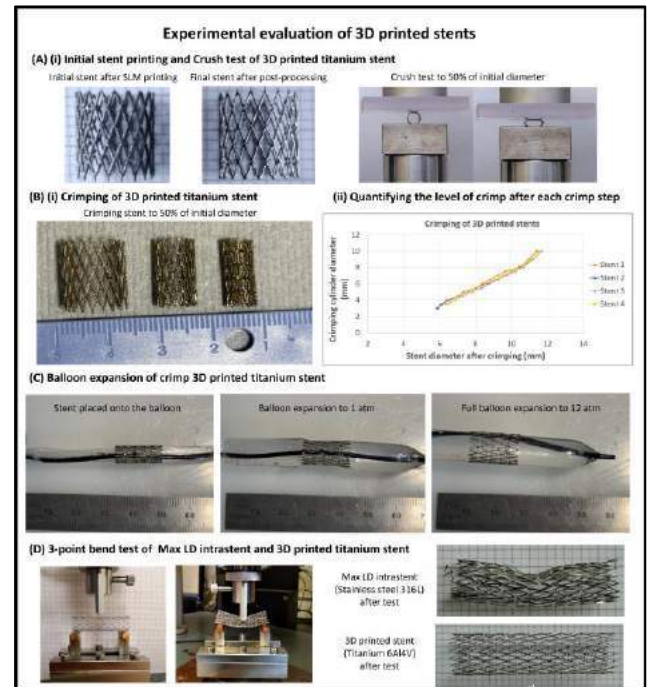


Figure 3: Experimental evaluation of the stent and individual units (A) Initial stent printing and postprocessing with subsequent crush testing (B) Crimp testing of 3D printed stent (C) Balloon expansion of crimped 3D printed stent (D) 3-point bend test of Max LD intrastent made from stainless steel 316L and 3D printed stent made from Titanium 6Al4V.

DISCUSSION

This study shows a feasible framework for creating patient specific stents for treatment of aortic coarctation. Using these virtual simulations and further validation of these using experimental methods, it is possible to estimate the geometry and material-dependent variations in radial strength, crimpability and three-point bend flexibility of the stents, enabling optimization, design, and manufacture of patient specific stents.

ACKNOWLEDGEMENTS

This study is funded by a research grant from Science Foundation Ireland (SFI) under the grant number 12/RC/2278_2.

REFERENCES

- [1] Mai CT et al, Birth Defects Res. 2019 Nov 1;111(18):1420-1435.
- [2] Rosenthal E. Heart. 2005;91(11):1495-1502.
- [3] Morgan et al., JACC, 6, 192-201, 2013.
- [4] V. Finazzi et al., Procedia Struc. Integrity, 15, 16–23. 2019.
- [5] McGee et al, JMBBM,134,2022.
- [6] Demir & Previtali. Mater Design. 119. 338-350. 2017.
- [7] Murphy et al., Ann. Biomed. Eng., 31, 686-691, 2003.

THE NON-AFFINE NETWORK SOLVER PLUGIN: A GENERALIZED FIBER NETWORK MATERIAL MODEL FROM VOLUME AVERAGING THEORY

Ryan R. Mahutga (1), Victor H. Barocas (1), Patrick W. Alford (1)

(1) Department of Biomedical Engineering, University of Minnesota, Minneapolis, MN, USA

INTRODUCTION

Finite element (FE) modeling is the most widely used technique for modeling the mechanical behavior of biological materials. Implicit to the use of FE modeling is the definition of a material constitutive relation describing the behavior of the microstructure of the material. There has been extensive work performed in the development of such constitutive models in the area of biological materials [1–3], with the roots of such material models tracing back to continuum mechanics. Current material models allow us to simulate the behavior of many tissues in many applications, but most material models fall short in two critical areas: failure and growth. As the biomechanics field moves toward understanding the microscopic features of biological tissues that drive failure initiation (e.g. fiber-fiber crosslinking, cell-fiber (integrin) connection, cell-cell adhesion) and growth and remodeling (e.g. cellular mechanotransduction, cellular manipulation and self-assembly of fibers), we need models that describe these features of the discrete microstructure. Thus, we propose a material model derived from the volume averaged stress within a fiber network which we call the Non-affine Network Solver (NaNS). This model allows us to simulate the discrete nature of cells and the extracellular matrix (ECM) including the non-affine nature of deformations within fiber composites and the interactions between constituents.

METHODS

In traditional FE modeling of mechanics, the application of a constitutive relation requires the stress tensor and the elasticity tensor. **The Network Stress Tensor:** Volume averaging theory gives us a convenient way to calculate the average Cauchy stress in a volume as an integral over the domain, or a summation over the fiber elements [4]

$$\begin{aligned}\sigma_{ij} &= \frac{1}{V} \int \sigma'_{ij} dv \approx \frac{1}{V} \sum_e \sigma^e_{ij} v^e \\ &= \frac{1}{V} \sum_e \left(\frac{f^e n_i^e n_j^e}{a^e} \right) (a^e l^e) = \frac{1}{V} \sum_e f^e l^e n_i^e n_j^e \quad (1)\end{aligned}$$

From this equation, we can calculate the volume averaged stress for any arbitrary shaped network provided we know the volume V , the constituent fiber forces f^e , the fiber lengths l^e , and the fiber directions n_i^e . We can also convert this Cauchy stress to the second Piola-Kirchoff using the inverse deformation gradient and the relations $J = V/V_0$ and $l^e n_i^e = L^e F_{ij} N_j^e$

$$S_{IJ} = J F_{Jk}^{-1} \sigma_{kp} F_{Ip}^{-1} = F_{Jk}^{-1} \left(\frac{1}{V_0} \sum_e f^e L^e n_k^e n_l^e \right) \quad (2)$$

where L_0^e is fiber rest length and N_j^e is the unit vector along the fiber axis in the undeformed configuration.

In the solution process for a fiber network, we only need the internal forces at all ‘nodes’ (connections between constituents) to be balanced given the deformation of the microstructural boundary. There are many ways to do this, but for this work, we choose to use a Newton iterative scheme utilizing the internal nodal Jacobian $J_{nm} = df_n/dx_m$ where f_n is the force on the node (i.e. the resultant of all fiber forces acting on the node), and x_m is the nodal coordinate.

The Network Elasticity Tensor: Let us consider the fourth-order material elasticity for our derivation given as

$$C_{IJKL} = \frac{\partial S_{IJ}}{\partial E_{KL}} = 2 \frac{\partial S_{IJ}}{\partial C_{KL}} = 2 \frac{\partial S_{IJ}}{\partial F_{pq}} \frac{\partial F_{pq}}{\partial U_{MN}} \frac{\partial U_{MN}}{\partial C_{KL}} \quad (3)$$

where polar decomposition gives us $F_{pq} = R_{pw} U_{wq}$, and the right Cauchy-Green tensor can be rewritten as $C_{KL} = U_{wK} U_{wL}$. The derivative of deformation with respect to the right stretch tensor can further be evaluated as $\frac{\partial F_{pq}}{\partial U_{MN}} = R_{pw} \frac{\partial U_{wq}}{\partial U_{MN}} = R_{pw} \delta_{qN}$, and the derivative of the right stretch tensor U with respect to the right Cauchy-Green tensor is simply $\frac{\partial U_{MN}}{\partial C_{KL}} = \left(\frac{\partial C_{KL}}{\partial U_{MN}} \right)^{-1} = (U_{MK} \delta_{LN} + U_{ML} \delta_{KN})^{-1}$. Thus, we only need the derivative of stress with respect to the deformation gradient which is given by

$$\frac{\partial S_{JJ}}{\partial F_{pQ}} = \frac{\partial F_{JJ}^{-1}}{\partial F_{pQ}} \left(\frac{1}{V_0} \sum_e f_j^e L_{0i}^e \right) + F_{JJ}^{-1} \left(\frac{1}{V_0} \sum_e \frac{\partial f_j^e}{\partial F_{pQ}} L_{0i}^e \right) \quad (4)$$

where $\partial F_{JJ}^{-1} / \partial F_{pQ} = -F_{JJ}^{-1} F_{QJ}^{-1}$.

Then the final piece is calculating how the fiber forces change with deformation, which we can do using a linear approximation of the fiber assuming that the fiber stiffness is $k = df^e / d\epsilon^e = df^e / d\lambda^e$.

$$\begin{aligned} f_j^e &= k \left(\frac{l^e}{L_0^e} - 1 \right) n_j^e = k \left(\frac{l_j^e}{L_0^e} - n_j^e \right) = k \left(\frac{F_{JJ} L_{0i}^e N_j^e}{L_0^e} - n_j^e \right) \\ &= k (F_{JJ} N_j^e - n_j^e) = k (F_{JJ} - R_{JJ}) N_j^e \end{aligned} \quad (5)$$

So that

$$\begin{aligned} \frac{\partial f_j^e}{\partial F_{pQ}} &= k \left(\frac{\partial F_{JJ}}{\partial F_{pQ}} - \frac{\partial R_{JJ}}{\partial F_{pQ}} \right) N_j^e = k \left(\delta_{jp} \delta_{jQ} - \frac{\partial R_{JJ}}{\partial (R_{pM} U_{MQ})} \right) N_j^e \\ &= k (\delta_{jp} \delta_{jQ} - U_{MQ}^{-1} \delta_{jp} \delta_{MJ}) N_j^e = k (N_Q^e - U_{JQ}^{-1} N_j^e) \delta_{jp} \end{aligned} \quad (6)$$

Dealing with Non-Affinity: The prior derivation for elasticity (Eqs. 3-6) does not account for non-affinity in the network, and is, in fact the exact formulation one would use for linear fibers deforming affinely with the macroscopic domain. To correct for non-affinity, we recalculate the fiber orientation in the undeformed configuration by remapping the fiber vector to the undeformed domain as $N_K^e = F_{Kv}^{-1} n_v^e$ after the calculation of equilibrium stress. This removes the non-affine rotations from the undeformed state to the current stress state allowing for a better approximation of the elasticity at the given deformation state. The choice of boundary behavior (fixed, sliding, periodic) while influencing the non-affine behavior, does not change the volume averaging relation, and can be entirely handled at the microscale.

RESULTS

The network stress and elasticity equations derived above were implemented as part of a material plugin in FEBio3. The non-affine network solver was adapted from [5], and utilizes periodic networks in the calculation of stress and elasticity. We combine the constitutive behavior of a Neo-Hookean solid with the network to simulate a composite fiber network (with fiber behaviors taken from [5]) embedded in a ground matrix, giving an overall stress of

$$\sigma_{ij} = \sigma_{ij}^{NH} + \sigma_{ij}^{net} \quad (7)$$

Two case-study examples for our simulation framework are given in Figs. 1 and 2. In Fig. 1a, we show the cruciform with only the neo-Hookean ground substance. In Fig. 1b, we show the cruciform with the combined neo-Hookean ground substance and a collagen network utilizing the NaNS plugin.

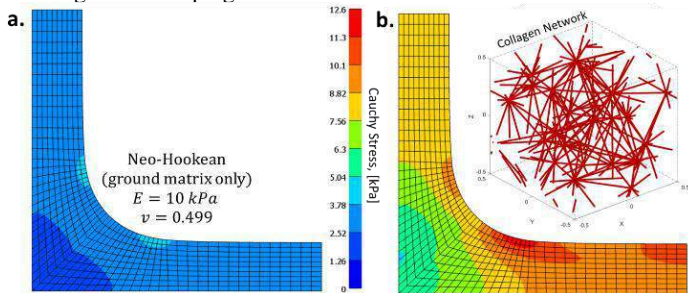


Figure 1: Biaxially stretched cruciform with neo-Hookean ground matrix only (a) and neo-Hookean ground matrix combined with collagen Delaunay networks (b).

In Fig. 2a, we show a cylinder inflation and highlight the heterogeneity present in the NaNS material model. In Fig. 2b, we show the model constituent stresses both within the neo-Hookean ground matrix and the individual fiber constituents of the model. In Fig. 2c, we show histograms of individual fiber stretches for each constituent at varying locations throughout the cylinder thickness.

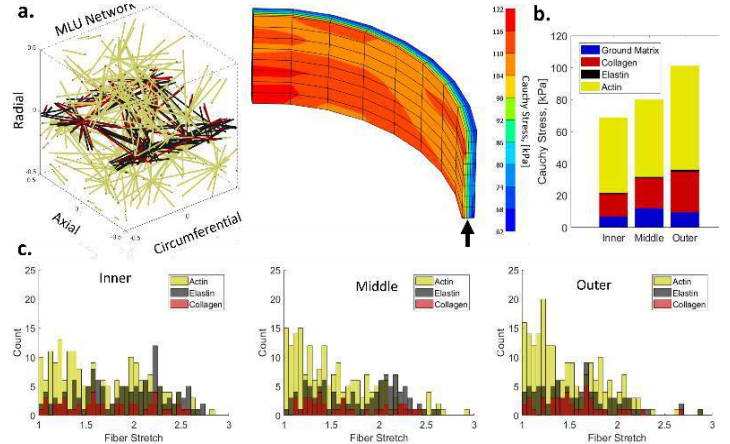


Figure 2. (a). A pressurized cylinder with composite Delaunay medial lamellar unit (MLU) networks. (b). The constituent stresses for each constituent of the MLU model at the arrow. (c). The fiber stretch histograms for each fiber constituent shown in the inner, middle, and outer element of the cylinder at the arrow.

DISCUSSION

This plugin framework is a new implementation of volume averaging theory for multiscale fiber network modeling in FEBio based on [4,5]. The mathematic description of the network elasticity and the novel method for dealing with non-affine deformations within the network are critical features that give us the ability to simulate micro-networks within our FE simulations. Further, the use of a linearized approximation allows us to use a wide variety of fiber constitutive models including structural fiber models and actively contracting fibers. This work is also a first step towards including individual fiber elements in a failure model or in an evolving growth and remodeling model.

Our simulations show heterogeneous stress fields due to the network alignments. In Fig. 1 we use a single network for all elements which has slight alignment preference in the x-direction, which is evidenced by the resulting stress field. In Fig. 2a, we use separately generated MLU networks, which on average have the same properties, but locally have small variations in stiffness and alignment as evidenced by the stress field. Our NaNS plugin not only allows us to break down stresses by constituent (Fig. 2b), but also look directly at individual fiber behaviors (Fig. 2c), which is not possible in other frameworks [1-3].

In terms of the computational resources necessary for this plugin, we examined both computational time and peak memory usage. We saw little change in memory usage, but significant increases in computational time, which is expected given the nature of the plugin. The plugin adds another force balance calculation to each element stress calculation which means it increases the computation time proportional to the number of iterations the micro network requires to converge. In the case of the cruciform, the network is close to affine and requires few iterations to converge, whereas the MLU network is heterogeneous including the structure and fiber types (including active fibers).

ACKNOWLEDGEMENTS The authors acknowledge funding from the NIH under grants R01 HL164800 and R01 NS126762, and funding from the NSF under grant CMMI-156319. Ryan Mahutga acknowledges support from the American Heart Association Post-Doctoral Fellowship (Award 827242).

REFERENCES [1] T.C. Gasser, et al. R. Soc. Interface. 3 (2006) [2] G.A. Holzapfel, et al. J. Elasticity 61 (2000) [3] J.D. Humphrey, F.C. Yin, Biophys. J. 52 (1987) [4] P.L. Chandran, V.H. Barocas, J. Biomech. Eng. 129 (2007). [5] R. Mahutga, V.H. Barocas, J. Biomech. Eng. 142 (2020)

SHEAR-MEDIATED PLATELET ADHESION DYNAMICS AND MULTI-PLATELET AGGREGATION: *IN VITRO* VALIDATED MULTISCALE SIMULATIONS USING COARSE-GRAINED MOLECULAR DYNAMICS AND DISSIPATIVE PARTICLE DYNAMICS

Peineng Wang (1), Yicong Zhu (2), Jawaad Sheriff (1), Peng Zhang (2), Yuefan Deng (2), Danny Bluestein (1)

(1) Department of Biomedical Engineering
Stony Brook University
Stony Brook, New York, U.S.A.

(2) Department of Applied Mathematics and Statistics
Stony Brook University,
Stony Brook, New York, U.S.A.

INTRODUCTION

Platelet adhesion to blood vessel walls and platelet-platelet aggregation in shear flow is essential in initiating the blood coagulation cascade and clot formation in vascular disease processes and prosthetic cardiovascular devices. In adhesion and aggregation, which lead to thrombus formation, platelets undergo complex and rapid receptor-ligand binding such as GPIIb α -von Willebrand factor (vWF) and α IIB β 3-fibrinogen (Fg)- α IIB β 3 bond association and breakage.

We developed a combined Dissipative Particle Dynamics (DPD) - Coarse Grained Molecular Dynamics (CGMD) multiscale model (MSM) to continuously evolve platelet structures, to describe platelet mechanotransduction processes induced by blood flow and synergistically activate platelets, aggregate, and adhere to the blood vessel wall [1]. Our multiscale adhesion model, based on in vitro platelet adhesion kinematics [2], can provide quantified flipping dynamics and comprehensive information on the GPIIb α -vWF bonds acting on the platelets. We expanded our multi-platelet model to a more realistic representation of blood clotting in blood vessel with 250 platelets (124M particles), the first of such effort to integrate multi-physics of thrombus formation at multi-scales [3].

We applied a semi-supervised learning system (SULS) [4], trained with in vitro platelet morphological changes, to overcome a major challenge of analyzing flowing in vitro platelet images and generate accurate inputs for the MSM simulations. We also developed a novel artificial intelligence (AI) inference algorithm that adaptively adjusts multiple timestep (MTS) sizes to underlying biophysical dynamics, achieving 500 \times speedup over fixed timesteps while accurately preserving diverse spatial and temporal occurrences [5].

METHODS

For platelet adhesion, we adapted our deformable CGMD multiscale platelet model to describe flipping over vWF in a channel

with DPD particles at 15-45 dyne/cm² (Fig. 1a). The platelet's bilayer membrane has a total of 67,004 particles, with 16,751 particles designated as GPIIb α receptors, which were redistributed on the membrane according to local membrane curvature (Fig. 1e). The vWF, seeded on a square-lattice 3-dimensional deformable plane with 506/ μ m² density, binds to a GPIIb α receptor and initiates adhesion. The force field between the GPIIb α and the vWF ligand is described by a parameterized hybrid force field combining Morse and Hooke potentials:

$$E_{Adhesion} = E_{Morse} + E_{Hooke} \quad (1)$$

$$E_{Morse} = D_0 \left(e^{-2\alpha(r_{ij}-r_0)} - 2e^{-\alpha(r_{ij}-r_0)} \right) \quad (2)$$

$$E_{Hooke} = k_1(r - r_b)^2 + k_2(r - r_b)^4 \quad (3)$$

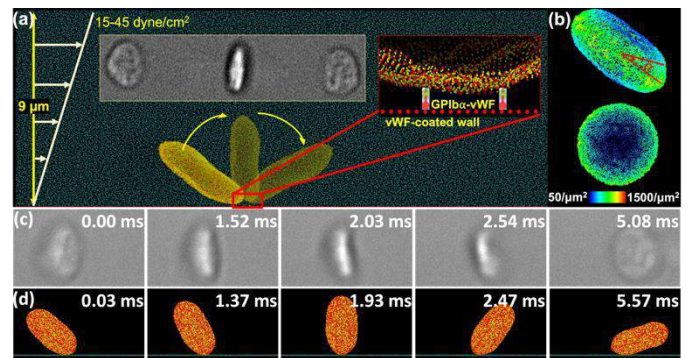


Figure 1. (a) MSM platelet adhesion model. (b) Surface GPIIb α density. (c) In vitro and (d) simulated platelet flipping at 30 dyne/cm².

We reproduced the flipping kinematics as the rotation angle θ during adhesion and validated this model by correlating with microchannel experiments [2], further expanded to 15 and 45 dyne/cm².

We also simulated a large-scale multiscale system of a shear flow-mediated forming thrombus with 250 platelets (124M particles), consisting of 70 flowing and 180 aggregating platelets, and integrated it with our AI-MSM framework (Fig. 2). A microchannel was simulated by a rectangular channel ($391.2 \times 21.3 \times 19.9 \mu\text{m}$) with periodic boundary conditions. The blood vessel walls are modeled with a no-slip boundary conditions with a pressure-driven Poiseuille blood flow between the top and bottom plates. Two blood adhered clots, each with 90 aggregated platelets, formed a $14.6 \mu\text{m}$ stenosis, with aggregation between receptors of the platelets is mediated by the membrane $\alpha\text{IIb}\beta 3$ receptors and Fg, governed by a force field [1].

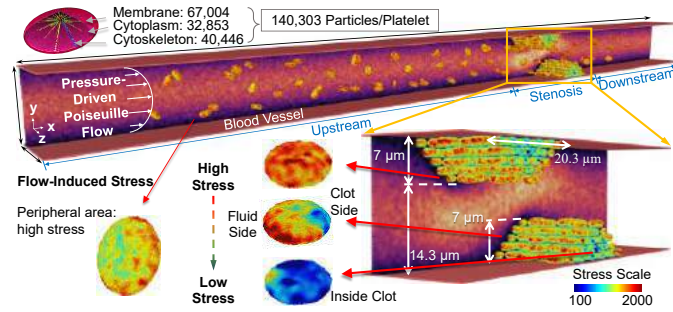


Figure 2. Simulated thrombosis with 124,171,840 particles, involving 70 flowing platelets and 2 thrombi, each with 90 aggregated platelets.

Our AI-MTS algorithm splits the system into two subsystems based on the spatial scales of the underlying components [5]: the macroscopic fluid and the microscopic platelet. By collecting multiple time series properties describing platelet dynamics, we predicted the adaptive timestep sizes and number of jumps via a deep learning framework consisting of (a) 2-stage denoising by moving average and wavelet transform filters to cleanse high-frequency noise in raw data and (b) two RNN-based autoencoders to extract latent features.

RESULTS

Our multiscale model successfully described the biophysical properties for platelet adhesion and thrombus down to nm -length and ps -time scales. Angular velocity $\dot{\theta}$ during platelet flipping was quantified in vitro and in silico under at shear stresses of 15, 30, and 45 dyne/cm^2 (Fig. 3a-d). In vitro, peak $\dot{\theta}$ increases with shear stress, with $\dot{\theta}$ at 30 dyne/cm^2 ($1.618 \pm 0.206 \text{ rad/ms}$, $n=9$) and 45 dyne/cm^2 ($2.086 \pm 0.346 \text{ rad/ms}$, $n=9$) significantly higher than at 15 dyne/cm^2 ($0.688 \pm 0.102 \text{ rad/ms}$, $n=8$, $p<0.05$). The asymmetry in duration between platelet liftoff and reattachment to the vWF layer diminishes with increasing shear stress. For each shear stress level, the simulated θ curve tracks closely to in vitro data when the platelet rotational angle is $\pi/2$.

Our multiscale adhesion model can provide comprehensive information on the GPIIb α -vWF bonds acting on the platelet. At dimensionless time 0, the platelet approaches $\pi/2$ and the total bond force is 800 pN, corresponding to 200 GPIIb α -vWF bonds (Fig. 3e-f). Prior to dimensionless time 0, bond force and numbers decrease proportionally with a decrease in shear stress. Fluctuations observed in the 45 dyne/cm^2 case subsequent to dimensionless time 0 indicate that higher shear stress may be accompanied with wobbling, where bond numbers decrease in a short period, then increase again.

In the thrombus formation system, the position of individual platelets impacts the accumulation of flow-induced stresses: the closer to the blood vessels, the larger stress accumulation as expected (Fig. 2). The periphery zone of the platelets (red) experiences larger stresses than its central area (green/blue). Fluid particles approaching the stenotic section strongly accelerated downward, then redirected upwards after passing the first thrombus, slowing down downstream of the stenotic

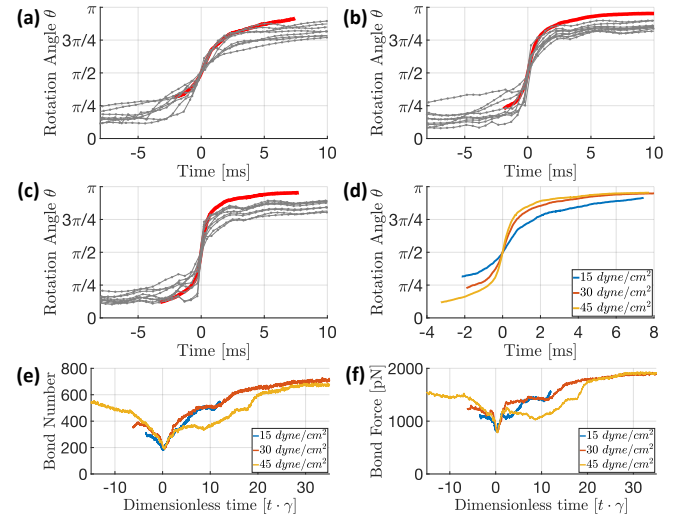


Figure 3. Flipping angle θ from simulations (curves) and in vitro measurements (black dots) at (a) 15, (b) 30, (c) and (d) 45 dyne/cm^2 . (e) Summary of simulated θ , (f) GPIIb α -vWF bond number and (g) force.

section (Fig. 4a). Shear stresses of blood flowing in this system corresponded to its velocity profile, with the highest stresses generally observed upstream of the thrombi (Fig. 4b). We adapted a biomechanics-informed online learning framework (BIOL) to learn platelet dynamics from the ground truth generated in this platelet system and generalize the Jeffery orbit equation (L-JOE) [6]. Validation of L-JOE with platelet rotation at various shear stresses and platelet deformability is ongoing.

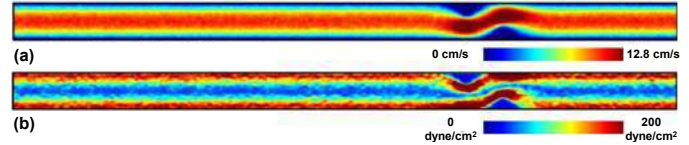


Figure 4. (a) Flow speed and (b) shear stress in the thrombus system

DISCUSSION

We simulated the initial adhesion process of a flowing platelets at several shear stresses, where our results converge towards high-fidelity prediction of flipping dynamics and reveal asymmetry of the adhesion process. We modeled a multi-physics MSM of flow- and platelet-mediated thrombus formation involving 124 million particles and integrated an AI-MTS algorithm for splitting the system and adapting timestep sizes to varying dynamics, with platelet dynamics learned via an online machine learning framework. This MSM approach enables computationally affordable, highly resolved, and validated granular studies of flow dynamics in stenoses, accumulated stress-induced platelet activation, platelet adhesion to vWF-coated vessels, and aggregation of flowing platelets with activated platelets adhered to the vessel walls. This approach will be expanded to simulate thrombosis processes involving several hundred platelets under pathological flow.

ACKNOWLEDGEMENTS

This project was supported by the NHLBI (5U01HL131052, DB) the SUNY-IBM Consortium (88003, YD), and the AiMOS supercomputer.

REFERENCES

- [1] Gupta, P. et al., *Cell Mol Bioeng*, 12: 327-343, 2019.
- [2] Sheriff, J. et al. *Ann Biomed Eng*, 49: 3452-3464, 2021.
- [3] Zhu, Y. et al. in B.L. Chamberlain et al. (Eds.), *ISC High Performance 2021*, LNCS 12728: 237-254, 2021.
- [4] Zhang, Z. et al., *Comput Med Imaging Graph*, 89: 101895, 2021.
- [5] Han, C. et al., *J Comput Phys*, 427: 110053, 2021.
- [6] Zhang, Z. et al. *Front Mol Biosci*, 8: 812248, 2022.

A TALE OF TWO MICE – HYPERTENSION, INFLAMMATION, AND INSIGHTS FROM IMMUNO-MECHANICAL MODELING

Jay D. Humphrey (1), Marcos Latorre (2), Bart Spronck (3)

- (1) Department of Biomedical Engineering, Yale University, New Haven, CT, USA
(2) Center for Research and Innovation, Universitat Politècnica de Valencia, Valencia, Spain
(3) Department of Biomedical Engineering, Maastricht University, Maastricht, The Netherlands

INTRODUCTION

Systemic hypertension is a primary risk factor for myriad cardiovascular, reno-vascular, and neuro-vascular diseases. It compromises health in women and men, and increasingly in children. Hypertension differentially affects vessels across scales – from arterioles to the aorta. Due in part to their strong myogenic capacity, elevated blood pressures lead to an inward remodeling and thickening of arterioles, which increases total peripheral resistance and thus contributes further to increasing the mean arterial pressure. Due in part to their high elasticity, elevated pressures lead to a slight dilatation and thickening of the aorta, which increases its structural stiffness and thus central pulse wave velocity, causing proximal pulse pressure augmentation. In both cases, therefore, disease progression tends to be driven by insidious positive feedback loops. There is a pressing need to understand better the vascular processes, including biomechanical, that drive hypertension.

In this work, we examine hypertensive remodeling of the aorta within the context of compromised mechanical homeostasis. The concept of homeostasis was introduced in the 1920s by the American physiologist W. Cannon and it continues to help us to understand complex biological and physiological responses. Toward this end, we sought to interpret novel data from two mouse models of hypertension within the context of mechanical homeostasis and we sought to use these data to inform a computational modeling framework that is inspired by the concept of mechanical homeostasis. In this way, we sought to discover mechanisms by which homeostasis is lost in certain cases of hypertensive remodeling.

Specifically, we contrasted hypertensive aortic remodeling in C57BL/6J and 129SvEvTac mice, both with comparable levels of induced hypertension. Biaxial data were collected after 2 weeks of hypertension and modeled biomechanically using a novel constrained mixture framework that included both mechano- and immuno-biological contributors to the remodeling.

METHODS

Animal Models. All live animal protocols were approved by the Institutional Animal Care and Use Committee of Yale University. Briefly, adult male C57BL/6J and 129SvEvTac mice were anesthetized and a mini-osmotic pump was implanted subcutaneously on the flank. This pump delivered angiotensin II (AngII) at a rate of 1000 ng/kg/min. Blood pressure was measured using a non-invasive tail cuff, without anesthesia, following 2 weeks of AngII infusion. The mice were then euthanized using an intraperitoneal injection of Beuthanasia-D and the descending thoracic aorta was harvested.

Ex vivo Experiments. The proximal thoracic aorta was cleaned of loose perivascular tissue, then secured on custom drawn glass micro-pipets and placed within a custom computer-controlled test system [1]. Following equilibration of the vessel in an oxygenated Krebs solution at body temperature, specimens were first subjected to a series of vaso-constrictors and vasodilators at a constant pressure (90 mmHg) and in vivo value of axial stretch to assess smooth muscle and endothelial function. Following replacement of the solution with a calcium-free Krebs solution, which ensured a passive mechanical response, the specimens were preconditioned via cyclic pressurization at the in vivo value of axial stretch, then subjected to a series of 7 protocols: cyclic pressurization tests at 3 different values of fixed axial stretch and cyclic extension tests at 4 different values of fixed distending pressure. Pressure, outer diameter, axial force, and axial extension were collected on-line.

Data Analysis. These biaxial data were first fit with a four-fiber family constitutive model using the unloading data from the last cycle of each of the 7 protocols. Unloading data provide information on the elastically stored energy that would be available to work on the fluid during unloading. Specifically, the 8 model parameters in this radially homogenized constitutive relation were determined using a Levenberg-Marquardt method to minimize normalized differences between

theoretically computed and experimentally measured pressures and axial loads. This approach has proven robust in describing bulk mechanical properties of the murine aorta from diverse mice [2].

Next, the data were fit using a similar model, but separately for the medial and adventitial layers. Again, this approach has proven to yield robust descriptions of the material behavior, with the added advantage that it allows one to compute values of wall stress, stiffness, and stored energy in the two primary layers of the wall [3].

Histology and Immunohistochemistry. Following mechanical testing, each vessel was fixed, paraffin-embedded, sectioned, and stained using standard methods – Movat pentachrome to identify the elastic lamellae, fibrillar collagen, glycosaminoglycans, cell cytoplasm, and fibrin, if present. Immuno-stains identified CD45+ leukocytes and CD68+ macrophages.

Computational Modeling. Finally, the associated mechanical data [4] were used to parameterize a “constrained mixture model” for aortic growth (changes in mass) and remodeling (changes in microstructure) that allows one to delineate mechano-biological and immuno-biological contributions to the adaptive or maladaptive responses of the aorta to hypertension [5].

RESULTS

Two weeks of AngII-induced hypertension resulted in similar pressure elevation in the two different mouse models and yet very different aortic remodeling. The descending thoracic aorta in the C57BL/6J mice showed excessive thickening of the wall, both medial and especially adventitial. The latter was characterized by a dramatic deposition of fibrillar collagen. By contrast, the aorta in the 129SvEvTac mice showed a nearly adaptive response to the hypertension, meaning thickening proportional to the pressure elevation. Two important observations appeared to delineate these different responses. First, the C57 aortas exhibited significantly less vasoconstrictive capacity *ex vivo* in response to exogenous AngII than did the 129 aortas, both before and after the 2 weeks of hypertension. Second, the C57 aortas had much greater accumulations of inflammatory cells than did the 129 aortas, and this accumulation was greatest in the adventitial layer wherein the collagen deposition was highest in the C57 aorta.

The bilayered model suggested that wall stress would initially increase in both the medial and adventitial layers of the hypertensive aortas under passive conditions, but that these increases could be greater in the adventitia. Noting that wall stress can be reduced at a fixed pressure during a strong vasoconstriction, the model also suggested that the potentially greater increase in wall stress in the adventitia could be attenuated by vasoconstriction. Hence, model findings were consistent with the hypothesis that a strong vasoconstrictive response of the aorta to exogenous AngII in the 129SvEvTac aortas reduced wall stresses in hypertension, especially in the adventitia, and that this lower wall stress was not sufficient to stimulate inflammatory cell infiltration. A corollary to this hypothesis, therefore, is that a weak vasoconstrictive response in the hypertensive C57BL/6J aortas led to higher wall stresses in the adventitia, which stimulated inflammatory cells.

The computational growth and remodeling model was refined to identify a data-based estimate of wall stress below which there was no inflammation but above which there was inflammation consistent with CD45 and CD68 cells. This threshold-based model was able to capture differential time-courses of change in geometric and mechanical metrics in response to hypertension in the two mouse models.

DISCUSSION

The immune system has evolved to protect against diverse threats, including bacterial, fungal, and viral. Given the importance of this

defense system, it is prioritized – that is, it can over-ride other systems, including those that promote mechanical homeostasis.

Our comparison of hypertensive aortic remodeling across two mouse models, C57BL/6J and 129SvEvTac, revealed that immunological factors tended to dominate in the former, which was characterized by maladaptive remodeling, whereas mechanical factors tended to dominate in the latter, which was characterized by near adaptive remodeling. In particular, CD45+ leukocytes and CD68+ macrophages increased significantly in the hypertensive C57BL/6J aortas but not in the 129SvEvTac aortas. The former also exhibited a gross thickening of the wall and associated reduction in wall stress well below normal. Given that wall stress appears to be a key mechano-regulated quantity in the aorta [6], this suggests that excessive inflammation contributed to the loss of mechanical homeostasis. By contrast, the lower immune cell density in the 129SvEvTac aortas associated with less thickening and a near adaptation consistent with mechanical homeostasis. Our computational growth and remodeling model suggested further that there may exist a stress threshold, above which inflammatory cells are recruited to the adventitia. Such a scenario is consistent with highly stressed fibroblasts increasing chemokine production to recruit the inflammatory cells [7]. There is a related literature suggesting that such fibroblast – immune cell communication often exists, including in AngII infusion models in mice [8].

In summary, the present results reveal a need to understand better what we refer to as immuno-mechanics wherein both infiltrating inflammatory cells and host mechano-sensitive cells play independent and interdependent roles. Single cell RNA sequencing and associated bioinformatics modeling promises to contribute further to our understanding, providing a method to test our computational model-based hypothesis on mechanical stress-mediated cell-cell interactions. Genomics information similarly promises to provide insight into possible genetic modifiers that drove the differences seen in the two different inbred strains of mice.

ACKNOWLEDGEMENTS

This work was supported, in part, by grants from the US NIH (U01 HL142518 and R01 HL155105).

REFERENCES

- [1] Gleason, RL et al., *J Biomech Engr*, 126:787-795, 2004.
- [2] Ferruzzi, J et al., *J Biomech Engr*, 137:031007, 2015.
- [3] Bellini, C et al. *Annl Biomed Engr*, 42:488-502, 2014.
- [4] Spronck, B et al., *J R Soc Interface* 18:20210336, 2020.
- [5] Latorre, M et al. *Proc R Soc Lond A* 477:20200622, 2021.
- [6] Humphrey, JD et al. *Annu Rev Biomed Engr* 23:1-27, 2021.
- [7] Tieu, BC et al. *J Clin Invest* 119:3637-3651, 2009.
- [8] Franklin, RA. *Immunol Rev* 302:86-103, 2021.

MIXED APPROACHES TO NONINVASIVE VENTILATION MASK DESIGN: TRIPHASIC MIXTURE THEORY MATERIAL MODEL CALIBRATION AND GLOBAL FINITE ELEMENT ANALYSIS

Anne D. Zakrajsek (1), Marty O. Visscher (2), Vivek Narendran (3,4) Eric A. Nauman (1)

- (1) Department of Biomedical Engineering, University of Cincinnati, Cincinnati, OH, USA
(2) Skin Pharmaceuticals & Cosmetic Science, University of Cincinnati, Cincinnati, OH, USA
(3) Department of Pediatrics, University of Cincinnati, OH, USA
(4) Perinatal Institute, Cincinnati Children's Hospital Medical Center, Cincinnati, OH, USA

INTRODUCTION

Approximately 2.5 million individuals sustain pressure injuries in acute care facilities per year, resulting in an estimated annual US hospital acquired pressure injury cost exceeding \$26.8 billion [1]. The pediatric population is uniquely vulnerable to pressure injury due to immobility, underdeveloped skin, compromised perfusion, anatomical differences, sensory development status, and medical device intervention [2-4]. Pressure injury prevalence within the pediatric population has been reported as 1-8% overall and as high as 43% in critical care settings [2]. Pressure injuries result in reduced quality of life, morbidity, and increased cost. Goudie et al [5] reported for the pediatric population an average cost of \$20,000 per injury and among ages 1-4 specifically an average cost of \$86,000 per injury for advanced stage pressure injuries.

Medical device related pressure injuries (MDRPIs) are notably more prevalent than those caused by immobility within the pediatric population. Pediatric MDRPI rates range from 40%-80%, with the most common problem areas being external monitoring, oxygen delivery, and airway maintenance devices [6]. Lauderbaugh et al [7] studied the relationship between non-invasive ventilation (NIV) use and pressure injury in hospitalized pediatric patients and found a pressure injury incidence of 7.3% with high mask leak as the only significant contributing factor associated with NIV pressure injury. Masks with a high leak are likely not achieving a proper fit and as such result in a non-uniform pressure distribution over bony prominences. This is especially prevalent in the neonatal intensive care unit where NIV is the preferred intervention over mechanical ventilation.

Several approaches have been taken to evaluate the fit of NIV masks and to determine the effects of custom mask fabrication. Visscher et al [8] evaluated mask fit using 3D surface scans of the face and mask. Duong et al [9] evaluated the feasibility of custom 3D printed CPAP masks and demonstrated improved comfort. Ma et al. [10] developed a system for CPAP interface selection based on a set of anthropomorphic

data points. Most recently, Kamath et al [11] developed a workflow for custom fabrication of neonatal CPAP masks that resulted in lower interface pressures.

These approaches have demonstrated the importance of mask fit through leak and pressure measurement, 3D scanning techniques, and basic pressure distribution analysis, but have yet to incorporate the complex solid mechanics of the skin tissue at the interface. Furthermore, there is no standardization across methods making model validation difficult. The objectives of this research are two-fold: 1.) to calibrate a compressible, neo-hookean, hyperelastic material model of aggregate skin tissue in compression and 2.) to develop a global model of the contact using the resulting material properties. Effectively, a local model of skin tissue mechanics will be coupled with a global model to better elucidate the tissue-mask interaction at NIV interfaces within the neonatal population.

METHODS

Model Calibration

A three-constituent mixture theory model was developed for skin tissue in compression with solid extracellular matrix (*s*), interstitial fluid (*f*), and blood (*b*) constituents. The material properties were calibrated utilizing the *in vivo* plane ended cylindrical indentation tests of the anterior forearm from data obtained by Bader et al [12]. A hyperelastic, compressible, neo-hookean material model with a Hertzian type input was derived resulting in a total Cauchy stress of

$$T_{zz} = -p_0 + \phi^s \kappa J^s (J^s - 1) + \frac{\phi^s \mu}{J^{s/3}} \left\{ (1 + \epsilon_z)^2 - \frac{1}{3} [2(1 - \eta \epsilon_z)^2 + (1 + \epsilon_z)^2] \right\} \quad (1)$$

where κ is the bulk modulus and μ is the shear modulus.

Integration to NIV Mask Finite Element Analysis

An Artec MHT (Artec 3D) scanner was used to capture 3D scans of a Premie HAL S108.100 24-Week Preterm Newborn Skills Trainer

(Gaugard Scientific). Post processing and finite element analysis were completed in COMSOL Multiphysics 6.0 (COMSOL Group). For an initial analysis, a NIV mask was approximated as a hollow cylinder for the purposes of modeling the pressure distribution at the contact interface. The skin was modeled as a single, aggregate layer as the material properties were calibrated in this manner. The mask was modeled as a linear elastic material with a Young's modulus of 2Mpa and a poisson ratio of 0.49 consistent previous analyses of mask fit [10]. The mask approximation was aligned with the nasal bridge via visual inspection. A pressure boundary load applied at the top surface of the mask approximation was varied and von Mises stress, displacement, and contact force were the outputs of interest.

RESULTS

Model Calibration

The compressible, neo-hookean constitutive law with a Hertzian type input resulted in calibrated material properties of 227.7 kPa and 1.04 kPa for bulk modulus and shear modulus, respectively, with a root mean squared error of 0.209 (Figure 1A). The calibrated model was used to investigate capillary occlusion by tracking the volume fraction of blood during quasi-static compression. Assuming that complete capillary occlusion occurs at a blood volume fraction of zero, the corresponding interface pressure can be determined and compared to clinically relevant interface pressures (Figure 1B).

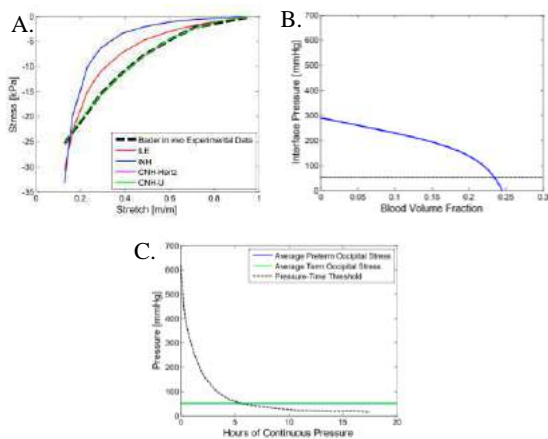


Figure 1. A) Predictive capabilities various material models of *in vivo* skin tissue compression, including compressible, neo-hookean with a Hertzian type input (CNH-Hertz). B) Tracking the volume fraction of blood across a large interface pressure range to elucidate capillary occlusion thresholds. The dashed line represents typical pressures measured at the occiput of a neonate in supine position. C) Comparison of predicted interface pressure to the classic Reswick and Rogers [13] pressure time threshold curve.

Global Model

Consistent with what is observed both clinically in existing models, the finite element analysis results show peak pressure at the nasal bridge as well as elevated pressure near the nasal septum (Figure 2). Peak values are highly dependent on the parameters of the pressure boundary condition, as well as the material model of the skin and mask; however, the results are consistent with those of previous studies [10-11].

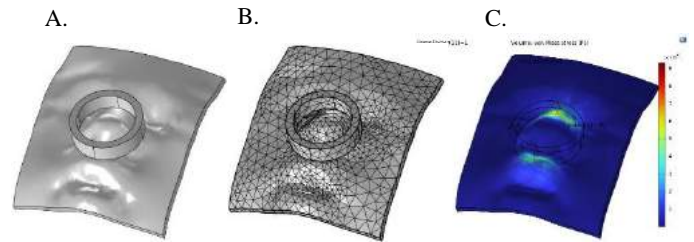


Figure 2. The imported, repaired, and solid geometry conversion (A) of the 3D scan, the mesh (B), and a representative loading case (C) of a 6kPa boundary load resulting in a peak von Mises stress of 9.3kPa at the nasal bridge.

DISCUSSION

The ability to accurately predict the pressure distributions throughout skin tissue at both the micro- and macro-level is critical for both understanding the complex etiology of pressure injury and designing medical devices that prevent iatrogenic injury. Our results show that a triphasic mixture theory derived hyperelastic material model can be used to describe aggregate skin tissue in compression. The use of triphasic mixture theory shows promising results for the ability to track blood flow throughout the deformation of skin tissue to better elucidate capillary occlusion and tissue demise thresholds or even to revisit and refine the classic Reswick and Rogers pressure-time threshold curve [13]. However, the material model was significantly limited by lack of *in vivo* or *ex vivo* compression data, and even further limited when considering the neonatal population. This limitation is especially notable since skin tissue properties are highly dependent on age and site.

The integration of the material model into a global model of a NIV mask interface demonstrated the ability to include skin tissue mechanics at the contact boundary while applying a clinically relevant boundary load condition to the NIV mask. Previous studies have modeled the mask contact with an arbitrary prescribed displacement. This method can be used to better inform commercial and custom mask design. Limitations of this FEA effort include registering the mask placement via visual inspection, an approximation of mask geometry, and limited data on applied mask pressure (strap tension). Future work should consider developing a standardized procedure for capturing interface pressure and applied strap tension such that model validation across studies is feasible.

ACKNOWLEDGEMENTS

This project was supported by the University of Cincinnati Department of Biomedical Engineering.

REFERENCES

- [1] Padula, W. V. et al., *Int. Wound J.*, 16:634–640, 2019.
- [2] Delmore, B et al., *Adv Skin Wound Care*, 32:394–408, 2019.
- [3] Manning, M et al., *Am. J. Crit. Care*, 24:342–348, 2015.
- [4] Schindler, C. A. et al., *Am. J. Crit. Care*, 16:568–574, 2007.
- [5] Goudie, A et al., *J Pediatr*, 136:432–439, 2015.
- [6] Visscher, M et al., *Sci. Rep.*, 4:1–6, 2014.
- [7] Lauderbaugh, D. L. et al., *Respir. Care* 64:1455–1460, 2019.
- [8] Visscher, M. O. et al. *Respir. Care* 60:1536–1547, 2015.
- [9] Duong, K et al., *Eur. Respir. J.*, 7:00632-2020, 2021.
- [10] Ma, Z et al., *Proc Inst Mech Eng H*, 235:44-53, 2021.
- [11] Kamath, A et al., *J. 3D Print. Med.*, 8:22, 2022.
- [12] Bader, DL et al., *Biomaterials*, 4:305-308, 1983.
- [13] Reswick, JB, et al., *Bed Sore Biomechanics*, 301-310, 1976.

A COMPLETE PHYSICS-BASED MODEL FOR THE FULL FLOW MEDIATED DILATION (FMD) RESPONSE

B. Sidnawi (1), B. Zhou (1), S. Santhanam (1), Z. Chen (2), C. Sehgal (2), P. Kaufmann (3), Q. Wu (1)

(1) Department of Mechanical Engineering, Villanova University, Villanova, PA, USA
(2) Department of Radiology, University of Pennsylvania, Philadelphia, PA, USA
(3) Department of Brain Health, University of Nevada Las Vegas, Las Vegas, NV, USA

INTRODUCTION

Brachial artery flow mediated dilation (FMD) is a widely reported phenomenon, based on which the integrity of arterial walls, the ballast of cardiovascular health, is assessed. The appealing aspects about the FMD test are its inexpensiveness and noninvasiveness. After having a pressure cuff wrapped around a subject's upper arm while lying supine, the cuff is inflated to a certain pressure, long enough to cut off the blood flow to the lower arm, thereby collapsing the brachial artery. The cuff is then abruptly deflated, and the arterial diameter response is monitored via ultrasound imaging, until full recovery. Comparing the peak diameter throughout the response, to its baseline value, provides a dilation metric that can serve as a quantitative description for the physical state of the arterial wall. Abnormal FMD levels have been linked to smoking, renal dysfunction, and visceral obesity¹⁻⁴. BAFMD's utility for assessing cardiovascular health and diagnosing cardiovascular diseases has been further established by other studies⁵⁻⁸. Moreover, according to a recent comprehensive review⁹ dedicated to how the virus affects the heart and blood vessels, SARS-CoV-2 has been associated with leaky vessels, pointing to a compromised glycocalyx layer and endothelial function, which therefore suggests that such changes could be picked up by this test.

Based on prior experimental studies on the mechanisms tying vasodilation stimulation to Wall Shear Stress (WSS), our group hypothesized a mechanism by which mechanotransduction is manifested in the FMD response and formulated a mathematical model that successfully reproduced its rising-and-dwelling part^{10,11}. In the current study, and for the first time, a model rooted in first principles is developed to describe the entire FMD response. The parameters arising from the model, and which collectively serve as a quantitative description of the arterial state, were adjusted to produce a response that matched its experimental counterpart extracted from healthy volunteers. The new parameter among those is one that characterizes the arterial

wall's drive for recovery, thereby providing a more encompassing description of the artery's physical state.

METHODS

This paper is based on the same brachial artery FMD tests performed in the Department of Radiology at the University of Pennsylvania for our prior studies¹⁰⁻¹², where 19 data sets were obtained from the FMD response of 12 healthy volunteers aged 23-66. After 5 minutes of blood flow obstruction by means of an inflated pressure cuff wrapped around the subject's upper arm, the cuff is deflated, and the artery is monitored with an ultrasound scanner for the next 5 minutes (Fig. 1). diameter-vs-time data sets were extracted by processing the obtained ultrasound images in MATLAB.

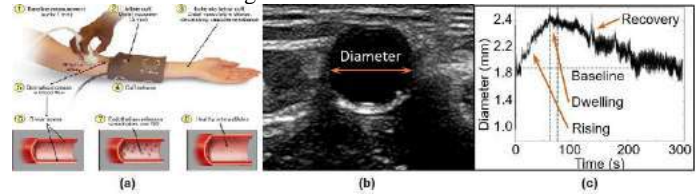


Figure 1: BAFMD test. (a): Ischemic cuff wrapped around the arm for 5 minutes while monitoring the artery. (b) A snapshot of the monitored artery. (c) Monitoring the arterial diameter response after deflating the cuff

The system of equations governing the arterial response is:

$$\frac{\partial^2 u^*}{\partial r^{*2}} + \left(\frac{1}{E^*} \frac{\partial E^*}{\partial r^*} + \frac{1}{r^*} \right) \frac{\partial u^*}{\partial r^*} + \left(\frac{\nu}{E^* r^*} \frac{\partial E^*}{\partial r^*} - \frac{1}{r^{*2}} \right) u^* = 0 \quad (1a)$$

$$\frac{\partial E^*}{\partial t^*} + 2 \ln(10) E^* = 2 \ln(10) [(1 - E_{min}^*) e^{-Bs^*} + E_{min}^*] \quad (1b)$$

$$\frac{\partial s^*}{\partial t^*} = 2 \ln(10) \gamma \left(\frac{\partial^2 s^*}{\partial r^{*2}} + \frac{1}{r^*} \frac{\partial s^*}{\partial r^*} \right) \quad (1c)$$

$$s^*(1, t^*) = \frac{1}{(1 + \delta(t))^3} - 2 \ln(10) \zeta^* \int_0^{t^*} H(\delta(z^*) - \delta_b) \left(\frac{1}{(1 + \delta_b)^3} - \frac{1}{(1 + \delta(z^*))^3} \right) dz^* \quad (1d)$$

Eq. 1a describes the radial displacement field (u^*). Eq. 1b governs the arterial stiffness distribution (E^*) throughout the arterial wall. Eq. 1c describes the diffusion of vasodilation stimulation signal (s^*), elicited by WSS. Eq. 1d is about the modulation of the vasodilation stimulation due to the artery's expansion. E_{min}^* is a measure of the wall's sensitivity to WSS. The maximum value of 1 points to an artery that is indifferent to any sensed level of WSS. B describes the artery's resistance to softening due to an increasing WSS. A higher value signifies a lower resistance. The parameter quantifying the mechanotransduction integrity, γ , indicates how fast the dilation stimulation signal, s , diffuses throughout the arterial wall. ζ^* is the parameter characterizing the arterial propensity for recovery. A higher value results in an earlier and faster recovery.

RESULTS

The values of the parameters E_{min}^* , B , γ , p^* , and ζ^* were optimized to obtain a theoretical response $\delta(t)$ that most closely matched the complete experimental FMD response. A representative comparison is shown in Fig. 2.

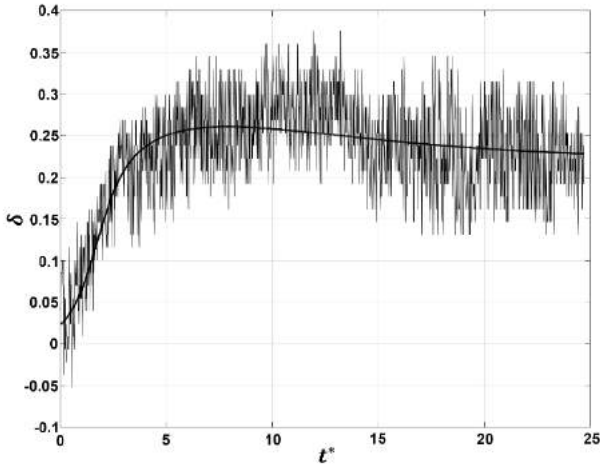


Figure 2: A representative result of matching an experimental FMD response with its theoretical counterpart (solid line)

DISCUSSION

In addition to the initial curvature shift that is a hallmark of mechanotransduction, the recovery phase is also generally well captured, thereby showcasing the first complete physics-based model that can reproduce an entire typical FMD response. While the previous studies focused on the rising-and-dwelling part of the response and managed to reproduce it from more simplified models that were rooted in first principles, this one is extended to include the recovery phase. The result is a unified model that successfully reproduced an entire typical FMD response for the first time. In addition to the parameters previously introduced¹¹, a new one quantifying the artery's ability to recover, arose from the model, hence offering a more detailed description of the arterial physical state. A minimally noisy set of data (Fig. 2) highlighted the model's ability to reproduce a real FMD

response. It is anticipated that the series of studies^{10–12} concluded by the current one, will be foundational for the potential emergence of future clinical noninvasive tools that can provide a comprehensive picture describing an individual's arterial health from a simple ultrasound test.

ACKNOWLEDGEMENTS

Q.W and B. S would like to acknowledge the support of the National Science Foundation under Award No. 1511096 for model development. C.S and Z. C would like to acknowledge the support of the National Institute of Health under Award Number R21 EB005326 for experimental data collection. The capital funding from the College of Engineering and the Mechanical Engineering Department at Villanova University is greatly appreciated.

REFERENCES

1. Stoner, L., Sabatier, M., Edge, K. & McCully, K. Relationship between blood velocity and conduit artery diameter and the effects of smoking on vascular responsiveness. *J. Appl. Physiol.* **96**, 2139–2145 (2004).
2. Celermajer, D. S. *et al.* Cigarette smoking is associated with dose-related and potentially reversible impairment of endothelium-dependent dilation in healthy young adults. *Circulation* **88**, 2149–2155 (1993).
3. Nakamura, T. *et al.* Endothelial vasomotor dysfunction in the brachial artery predicts the short-term development of early stage renal dysfunction in patients with coronary artery disease. *Int. J. Cardiol.* **148**, 183–188 (2011).
4. Hashimoto, M. *et al.* The impairment of flow-mediated vasodilatation in obese men with visceral fat accumulation. *Int. J. Obes.* **22**, 477–484 (1998).
5. McCully, K. K. Flow-mediated dilation and cardiovascular disease. *J. Appl. Physiol.* **112**, 1957–1958 (2012).
6. Birk, G. K. *et al.* Brachial artery adaptation to lower limb exercise training: Role of shear stress. *J. Appl. Physiol.* **112**, 1653–1658 (2012).
7. Pyke, K. E. & Tschakovsky, M. E. The relationship between shear stress and flow-mediated dilatation: Implications for the assessment of endothelial function. *J. Physiol.* **568**, 357–369 (2005).
8. Kaźmierski, M., Michalewska-Włodarczyk, A., Krzych, Ł. J. & Tendera, M. Diagnostic value of flow mediated dilatation measurement for coronary artery lesions in men under 45 years of age. *Cardiol. J.* **17**, 288–292 (2010).
9. Veluswamy, P. *et al.* The sars-cov-2/receptor axis in heart and blood vessels: A crisp update on covid-19 disease with cardiovascular complications. *Viruses* **13**, (2021).
10. Sidnawi, B., Chen, Z., Sehgal, C. & Wu, Q. Characterization of arterial flow mediated dilation via a physics-based model. *J. Mech. Behav. Biomed. Mater.* **107**, 103756 (2020).
11. Sidnawi, B., Chen, Z., Sehgal, C., Santhanam, S. & Wu, Q. On the modeling of mechanotransduction in flow-mediated dilation. *J. Mech. Behav. Biomed. Mater.* **120**, 104606 (2021).
12. Sidnawi, B., Santhanam, S., Sehgal, C. & Wu, Q. On the examination of the viscous response of the brachial artery during flow-mediated dilation. *J. Mech. Behav. Biomed. Mater.* **131**, 105255 (2022).

COMPUTATIONAL ANALYSIS OF HEART VALVE GROWTH AND REMODELING IN PULMONARY AUTOGRAFTS AFTER THE ROSS PROCEDURE

**Elmer Middendorp (1,2), Fabian Bräu (3,4), Frank P.T. Baaijens (1,2), Jay D. Humphrey (5),
Christian J. Cyron (6,7), Sandra Loerakker (1,2)**

- (1) Department of Biomedical Engineering, Eindhoven University of Technology, The Netherlands
- (2) Institute of Complex Molecular Systems, Eindhoven University of Technology, The Netherlands
- (3) Singapore Eye Research Institute, Singapore National Eye Center, Singapore
- (4) Singapore-MIT Alliance for Research and Technology, Singapore
- (5) Department of Biomedical Engineering, Yale University, Connecticut, USA
- (6) Institute for Continuum and Material Mechanics, Hamburg University of Technology, Germany
- (7) Institute for Material Systems Modeling, Helmholtz-Zentrum, Hereon, Germany

INTRODUCTION

Current heart valve replacements are inadequate for young and active patients: mechanical prostheses require lifelong anticoagulant therapy and bioprosthetic valves are prone to structural degeneration. To overcome these limitations, in situ cardiovascular tissue engineering is a promising strategy to create living neo-valves, directly at the functional site by using the regenerative capacities of the host. Currently, inter- and intra-valve variation in tissue formation and scaffold resorption have often been reported during in situ tissue engineering [1], limiting the translation of this technique to the clinic. To overcome these challenges, a deeper understanding of growth and remodeling in (tissue-engineered) heart valves is essential [2].

So far, no studies have reported the establishment of homeostasis in in situ tissue engineered heart valves. However, it is hypothesized that mechanically regulated growth and remodeling (G&R) mechanisms are key players in this process, and similar to mechano-regulated G&R in native cardiovascular tissues to changes in hemodynamic loads [3]. In this study, we therefore developed a computational model to investigate native valvular G&R mechanisms, since more long-term experimental results are available for comparison. We specifically simulated the Ross-procedure (replacing a defective aortic valve with the autogenous pulmonary valve) to investigate if homeostasis can be re-established in these valves through mechanoregulated G&R. Since the specific mechanical homeostatic targets in valves are still unclear, we investigated both stress- and stretch-based homeostasis to determine which of these hypotheses is most likely.

METHODS

Homogenized constrained mixture models can provide valuable insights into growth and remodeling as they can efficiently predict changes in tissue composition and geometry [4]. These models utilize a constituent-specific kinematic split of the deformation gradient tensor (Fig. 1). This split ensures that each different constituent has its own

stress-free configuration and corresponding elastic deformation. Our heart valves were modeled as a mixture of collagen, glycosaminoglycans (GAGs) and elastin.

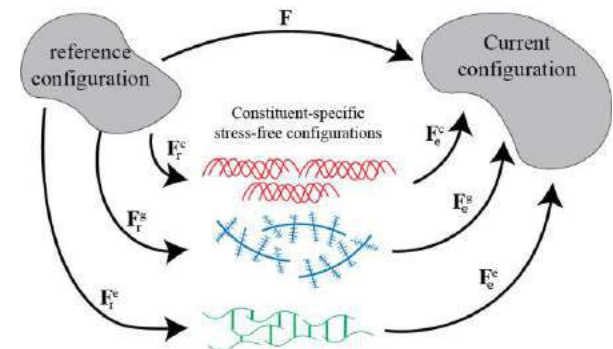


Figure 1: The deformation gradient tensor (F) is split into a inelastic deformation (F_r^i) and an elastic deformation (F_e^i) for collagen ($i=c$), glycosaminoglycans ($i=g$) and elastin ($i=e$).

The stress-free states of collagen and GAGs evolved due to their continuous turnover while elastin degradation and production were assumed to be negligible. The turnover of collagen and GAGs was assumed to be regulated by mechanical cues. When these cues were at their homeostatic level, production and breakdown were balanced. When homeostasis was disturbed, collagen and GAG production changed, which translated into in- or decreases of the constituent mass, and consequently changes in the tissue composition, stiffness and/or volume.

In this work, two different hypotheses were adopted to define this homeostasis: either stress- or stretch-based homeostasis. For stress homeostasis, the production of a constituent was modulated by the normalized differences between the current and the homeostatic stress

levels in that constituent, while for stretch homeostasis, the normalized differences in constituent stretches were used.

To describe the geometry of the leaflet a Gulbulak valve geometry [5] was adopted. First, the diastolic pulmonary pressure was applied to the outflow surface of the leaflet to determine the homeostatic stresses or stretches of the individual constituents. Subsequently, the Ross procedure was simulated by increasing the pressure to systemic diastolic values - either instantaneously or gradually over 1000 days - while the tissue was able to grow and remodel until homeostasis was re-established.

RESULTS

After an instantaneous increase in pressure, assuming stretch homeostasis (Fig. 2b) resulted in more growth in the belly region of the valve and the belly region dilating further compared to assuming stress homeostasis (Fig 2a) resulting in an average increase in thickness of 27% and 43% respectively. This difference in valve morphology can also be appreciated at the tip of the leaflets, which decreased in height more under the assumption of stretch homeostasis. This dilation was initially similar for both types of homeostasis, but valve geometry stabilized earlier in the case of stress homeostasis (Fig 2c) compared to stretch homeostasis (Fig 2e). Finally, the different homeostatic target variables resulted in different tissue compositions in the new mechanical equilibrium (Fig 2d); stress homeostasis resulted in a more collagen-dominated composition while the valve under strain-homeostasis contained more GAGs. Elastin volume fractions were greatly reduced in both valves, due to the lack of turnover and synthesis.

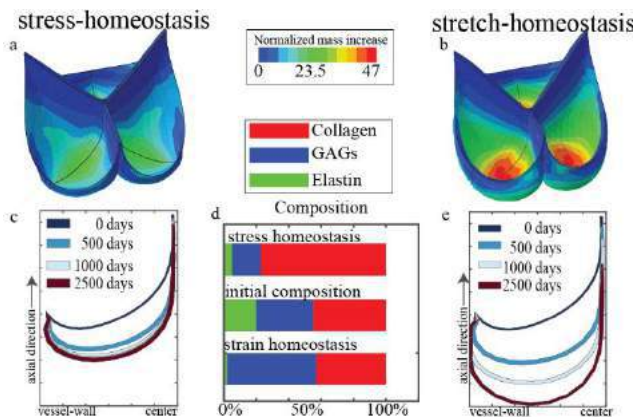


Figure 2: Homeostatic heart valves after growth and remodeling following stress (a) or stretch (b) homeostasis. Time evolution of the mid-section profile of the leaflet for stress (c) and stretch (e) homeostasis, and tissue compositions (d).

Interestingly, under the assumption of stress-homeostasis, a gradual increase in pressure (Fig. 3b) was predicted to induce a more dilated valve geometry with a smaller increase in thickness (38% vs. 43%) compared to valves subjected to instantaneous loading (Fig. 3a). Specifically, the valve dilation almost stabilized within 500 days when an immediate increase in hemodynamic load was imposed (Fig 3c). On the other hand, in the case of gradual increase in blood pressure, this dilation only stabilized after the increase in loading was complete (Fig 3e). Despite these geometrical differences caused by different rates of the blood pressure increase, the composition of the valves was predicted to be nearly identical (Fig 3d).

DISCUSSION

To better understand G&R of native and ultimately also tissue-engineered heart valves, the compositional and geometric changes of

pulmonary autografts after the Ross procedure were analyzed for either stress- or stretch-regulated G&R. An increased hemodynamic load from pulmonary to aortic diastolic blood pressure generally resulted in thickened valves with altered morphologies. The predicted increases in thickness for both stress- and stretch-based homeostasis agreed well with reported data [6,7,8]. In addition, the simulated changes in collagen content under stress-mediated growth and remodeling were more in line with findings from the literature than those under stretch homeostasis [6,7,8], suggesting that stress homeostasis might better describe heart valve growth and remodeling than stretch homeostasis.

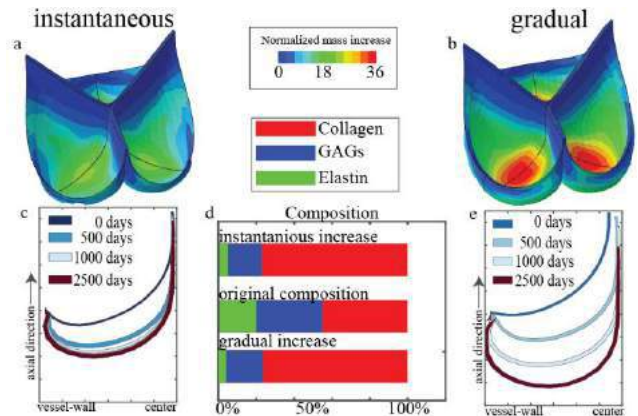


Figure 3: Homeostatic heart valves after growth and remodeling following an instantaneous (a) or gradual (b) increase in pressure. Time evolution of the mid-section profiles of the leaflet for an instantaneous (c) and gradual (e) increase in pressure, and tissue compositions (d).

A gradual increase in pressure resulted in more dilated valves compared to an instantaneous increase in pressure. This was caused by lower tissue stresses throughout the course of G&R under a gradual increase in pressure versus an instantaneous increase, due to the ongoing remodeling response. Consequently, less thickening occurred which, in turn, allowed for more elastic deformation, eventually leading to a more dilated valve morphology.

Altogether, we demonstrated that a G&R response regulated purely by mechanical cues is able to re-establish homeostasis in heart valves after an increase in hemodynamic loads. Furthermore, the predicted changes in composition suggest that stress-based homeostasis is more suitable to describe heart valve G&R in response to changes in diastolic loading. In the future, this model can be extended to understand, predict and ultimately even optimize the development and adaptation of in situ tissue engineered heart valves.

ACKNOWLEDGEMENTS

This project has received funding from the European Research Council (ERC) under the European Union's Horizon 2020 research and innovation program (Grant agreement No. [802967]).

REFERENCES

- [1] Kluin, J et al. *Biomaterials*, 125:101-117,2017.
- [2] Bouten, C.V.C. et al. *Front. Cardiovasc. Med.*, 5:54,2018.
- [3] Szafron, J.M. et al. *Ann Biomed Eng.*, 46:1938-1950,2018.
- [4] Cyron, C.J. et al. *Biomech Model Mechanobiol.*, 14:1389-1403,2016.
- [5] Gulbulak, U. et al. *J Mech Behav Biomed Mater.*, 112:104039,2020.
- [6] Schoof P.H. et al. *Surgery for acquired cardiovascular disease*, 132:1426-1432,2006.
- [7] Mookhoek, A et al. *Journal of Thoracic and Cardiovascular Surgery*, 139:1416-1419,2010.
- [8] Yacoub, M.H. et al. *Eur J Cardiothorac Surg.*, 57:977-985,2020.

INFLUENCE OF WALL SHEAR AND MECHANICAL STRESS ON ATHEROSCLEROTIC ARTERY DISEASE IN HUMAN CORONARIES

Aikaterini Tziotziou (1), Eline Hartman (1), Suze-Anne Korteland (1), Antonius F.W. van der Steen (1), Joost Daemen (2), Jolanda Wentzel (1), Ali C. Akyildiz (1,3)

- (1) Department of Biomedical Engineering, Erasmus Medical Center, Rotterdam, the Netherlands
(2) Department of Cardiology, Erasmus Medical Center, Rotterdam, the Netherlands
(3) Department of Biomechanical Engineering, Delft University of Technology, Delft, the Netherlands

INTRODUCTION

Atherosclerosis in coronary arteries is the main cause of coronary artery disease, also known as ischemic heart disease or myocardial ischemia [1]. The non-homogeneous distribution of atherosclerotic plaques along the coronary tree with varying components hints towards the effect of local risk factors on atherosclerosis [2]. Among such local factors, the biomechanical ones are hypothesized to influence the dynamic progression of plaques over time [3]. The two important biomechanical factors effective in arterial circulation are the wall shear stress (WSS) and the wall mechanical stress (WMS) [4]. WSS is the stress that the frictional force of the blood flow exerts on the endothelial cells on the arterial lumen surface and low WSS is known to be associated with plaque progression [5]. WMS is the structural stress caused by the blood pressure-induced arterial wall stretch and is mainly studied for plaque rupture [6], but not for plaque progression yet. In order to have a comprehensive understanding of the involvement of the biomechanical factors in atherosclerosis, we studied the individual and combined effects of WMS and WSS in healthy and atherosclerotic coronary segments.

METHODS

Study Design

The prospective patient study (IMPACT) was designed at Erasmus Medical Center to investigate the influence of biomechanical factors towards healthy and atherosclerotic plaque tissue progression in coronary arteries [7]. For the study, 40 patients with acute coronary syndrome and at least one non-stented, non-culprit atherosclerotic coronary artery were recruited. The arteries were imaged with near-infrared spectroscopy intravascular ultrasound NIRS-IVUS and optical coherence tomography (OCT) at two time points (baseline and after ~12 months (follow-up time point)) and with CT one month after the baseline imaging [7].

Wall Shear Stress and Wall Mechanical Stress

The 3D coronary lumen geometries necessary for the WSS assessment were constructed from the IVUS data. WSS was computed with Computational Fluid Dynamics (CFD) models and reported previously [7]. Briefly, blood flow was implemented as an incompressible, homogeneous, Carreau fluid. The inlet and outlet flow boundary conditions were prescribed based on the local Doppler flow measurements and the final computed WSS were averaged over a cardiac cycle to obtain the time-average-wall shear stress [7].

For the wall mechanical stress, 2D coronary cross-sectional geometries were obtained from the combined and co-registered IVUS and OCT frames every 0.5mm. IVUS data was used to delineate the lumen and the external elastic lamina (EEL) contours, and OCT data for the lipid-rich necrotic core (LRNC) [8]. A layer of a uniform thickness of 0.15 mm was added around the EEL to account for the adventitia layer [6]. Finite Element Modeling (FEM) was used to compute WMS on the arterial cross-sections due to the intraluminal blood pressure, via ABAQUS software under plane strain assumption. Isotropic, nonlinear, hyperelastic and incompressible material models were used for intima/media, adventitia and LRNC components as reported previously [3,9]. Since the imaged arteries were under blood pressure and not at zero mechanical loading, the backward incremental method [9] was applied to compute the initial stresses, already present in the arteries. Standard intraluminal pressure of 120mmHg was applied and the maximum Max Principal stress was calculated on the peri-luminal region in all forty arteries. Highly calcified regions ($> 90^\circ$) were excluded from the study as they impeded the segmentation of the EEL layer [7].

Sector Categorization and Statistical Analysis

For a local analysis of the data, the coronaries were divided into sectors, where a sector comprised an angle of 45° in the circumferential

directions and a thickness of 1.5mm in the longitudinal direction (Fig.1A). WSS and WMS results were averaged per sector. Vessel wall progression or regression was quantified as the wall thickness and plaque burden (plaque area/ total vessel area * 100%) change between baseline and follow up measurements. The sectors were also categorized as either “diseased with LRNC” (mean wall thickness >0.5mm & NIRS positive), or “diseased w/o LRNC” (mean wall thickness >0.5mm & NIRS negative), or “healthy” (mean wall thickness <0.5mm) (Fig.1B). The association of WSS and WMS on plaque progression was evaluated using Linear Mixed Model analysis in SPSS. WSS and WMS values per sector were divided into tertiles (low, mid and high) per artery for the statistical analyses [7]. A p-value < 0.05 was considered significant.

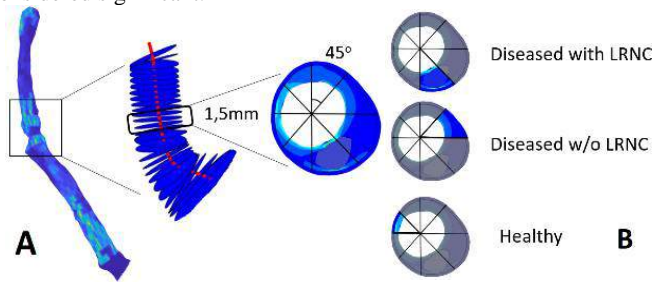


Figure 1: (A) Coronal geometries were split into sectors of 1.5mm thickness, by dividing the cross-sections into 8 sectors in the circumferential direction. (B) Sectors are categorized as healthy or diseased (with or without LRNC) based on 0.5mm thickness threshold.

RESULTS

In total, ~8k sectors were obtained and analyzed from 40 coronary arteries. At the baseline, 65% of the sectors were identified as healthy and 35% as diseased. Of the diseased sectors, 24% contained a LRNC and 76% did not. Over the ~12-month follow-up time period, 52% of the sectors demonstrated atherosclerotic disease progression while 48% showed regression. OCT measurements of the diseased sectors with LRNC revealed thinner fibrous caps in 71% of the cases resulting in supposedly more vulnerable plaque tissue.

According to the statistical analysis, low WSS was statistically significantly associated with increased plaque burden (Δ BP) (Fig.2) and wall thickness change (Δ WT) (data not shown) for all sector types (healthy, diseased w/o and with LRNC), as well as when all sectors combined. This trend was most pronounced for the diseased sectors with LRNC, where low WSS category sectors resulted in almost two-times higher disease progression than the high WSS category sectors.

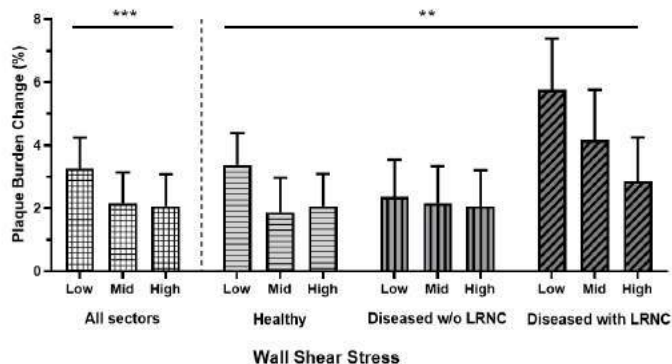


Figure 2: Plaque burden change distribution based on WSS in overall, healthy, diseased with and w/o LRNC sector categories.

The association between WMS and Δ BP (Fig.3), and WMS and Δ WT (data not shown) was similar: healthy sectors with higher WMS demonstrated higher disease progression whereas the opposite was observed for diseased sectors with LRNC.

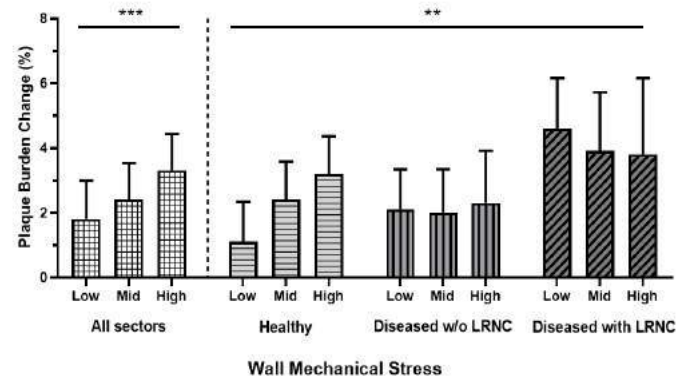


Figure 3: Plaque burden change distribution based on WMS in overall, healthy, diseased with and w/o LRNC sector categories.

The analysis of the combined effect of WSS and WMS on Δ BP and Δ WT revealed that in healthy sectors, the combination of low WSS and high WMS was associated with the highest Δ BP and Δ WT. In the diseased sectors w/o LRNC, the highest plaque progression (Δ BP and Δ WT) was observed in the category of mid WSS and high WMS and in the diseased sectors with LRNC, high and low WMS combined with low WSS were associated with plaque progression.

DISCUSSION

Our findings suggest that the local atherosclerotic disease progression in coronary arteries is not only associated with the well-known WSS, but also with WMS, which has not received enough attention yet. Moreover, our results show that the association of the disease progression with WMS depends on the existing local structural composition. Our findings indicate the importance of biomechanical analysis and local plaque composition assessment for local atherosclerotic disease progression prediction. In the future, studies with larger cohort and multiple follow-up time points are warranted in order to fully understand the association between shear and structural stress with atherosclerosis development over time.

ACKNOWLEDGEMENTS

This project has received funding from the European Research Council, Brussels, Belgium # 310457.

REFERENCES

- [1] Bhatia SK et al., *Springer Science & Business Media*, 2010.
- [2] Diletti R et al., *JACC Cardiovasc Imaging*, 4:774–780, 2011.
- [3] Costopoulos C et al., *Eur Heart J.*, 40:1411–1422, 2019.
- [4] Chatzizisis YS et al., *J American College Cardiology*, 49, 2007.
- [5] Wentzel JJ et al., *EuroIntervention*, 9:989–995, 2013.
- [6] Akyildiz AC et al., *BioMedical Engineering OnLine*, 10:25, 2011.
- [7] Hartman E et al., *J. of Cardiovasc. Trans. Res.*, 14:416–425, 2021.
- [8] Kok AM L et al., *Biomed. Eng. Online*, 15: 48, 2016.
- [9] Akyildiz AC et al., *Computer. Methods in Biomech. and Biomed. Eng.*, 19:771–779, 2016.

CHANGES IN MYOCARDIAL DEFORMATION INDUCES ABNORMALITIES IN VALVULAR DYNAMICS CAUSING MITRAL VALVE REGURGITATION

Tawfik M. Hussein (1,2), Gediminas Gaidulis (2,3), Michael Silverman (3), John N. Oshinski (1,4), Muralidhar Padala (2,3)

(1) Wallace H. Coulter Department of Biomedical Engineering, Georgia Institute of Technology and Emory University School of Medicine, Atlanta, GA, USA

(2) Structural Heart Research and Innovation Laboratory, Carlyle Fraser Heart Center, Emory University Hospital Midtown

(3) Department of Surgery, Emory University School of Medicine, Atlanta, GA, USA

(4) Department of Radiology and Imaging Sciences, Emory University School of Medicine, Atlanta, GA, USA

INTRODUCTION

While myocardial motion plays an important role in driving mitral valve physiology and pathophysiology, the biomechanical interplay between them is not well understood. Hence, the goal of this work was to study how abnormal myocardial deformation induces mitral regurgitation (MR) via quantifying changes in the anterior annular perimeter (AAP), posterior annular perimeter (PAP), and myocardial circumferential strain (Ecc) in MR secondary to an inferior wall myocardial infarction (IWMI), using displacement encoding with simulated echoes (DENSE) [1]. The hypothesis is that an inferior wall MI will cause an increase in Ecc in the regions remote to the myocardial infarct, which will prevent the steep increase in the AAP that is otherwise typically seen in the PAP.

METHODS

A postero-lateral MI was induced in 4 healthy Yorkshire pigs by injecting ethanol into the left circumflex artery (LCX). ECG-gated MRI was acquired in the mid short axis (SA) to measure Ecc at baseline (pre-MI) and 3 months post-MI. The SA images were divided into 3 zones (i.e., infarcted, border, and remote), based on late Gadolinium enhancement images and the AHA 17-segment model (Figure 1). Measured strains were averaged for each zone, and their respective mean and standard deviation were calculated. Finally, the AAP and PAP were calculated at both timepoints from echocardiography, and a correlation coefficient was calculated to assess if the correlation between AAP and peak systolic Ecc in the remote zone was significant.

RESULTS

At 3 months post-MI, PAP significantly increased compared to baseline ($p = 0.037$) whereas the change in AAP was not significant. Additionally, Ecc changed over both timepoints across all three zones, where remote peak systolic Ecc increased by 0.03 ± 0.01 ($p = 0.007$).

Interestingly, AAP was found to correlate with the remote Ecc ($r = 0.91$) but less so with the infarct Ecc ($r = 0.57$).

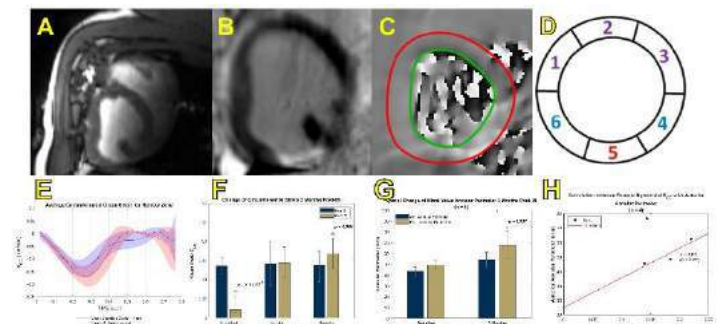


Figure 1: (A) Cine image for orientational reference. (B) Late Gadolinium enhancement image to locate the infarct. (C) Phase SA image of DENSE. (D) AHA 17-segment model for the mid SA image where 1: mid anterior; 2: mid anteroseptal; 3: mid inferoseptal; 4: Mid inferior; 5: Mid inferolateral; and 6: Mid anterolateral. Red denotes infarct zone, blue denotes border zone, and purple denotes remote zone. (E) The mean Ecc and standard deviation ($n = 4$) for the remote zone of the mid SA view; baseline strains are shown in blue whereas MI strains are shown in red. (F) The mean value of peak systolic Ecc and standard deviation for all 3 zones post-MI (left); baseline data shown in navy blue whereas MI data is shown in gold. (G) Change of mitral valve systolic anterior and posterior annular perimeters 3 months post-MI. (H) Correlation between the remote myocardial Ecc with systolic annular perimeter.

DISCUSSION

This work signifies a novel investigation for the impact of myocardial deformation on mitral valve mechanics. The results suggest that increases in remote myocardial strain prevents the increase in the AAP that is otherwise seen in the PAP of an MR. Additionally, while the severity of MR is determined by valvular dynamics, it seems to well-correlate with myocardial deformation. This provides further insights into MR heterogeneity, and thus careful consideration should be taken with respect to animal modeling as well as patient therapy as the location of the infarct will potentially dictate both myocardial and valvular mechanics.

REFERENCES

- [1] Kim, D. *et al.*, Journal of Radiology, 2004, 230(3):862–71.

IDENTIFYING CONTRIBUTORS TO ANEURYSMAL PROGRESSION IN THE MARFAN AORTA USING A CONSTRAINED MIXTURE MODEL

David S. Li (1), Cristina Cavinato (2), Marcos Latorre (3), Jay D. Humphrey (1)

(1) Department of Biomedical Engineering, Yale University, New Haven, CT, USA
(2) Laboratoire de Mécanique et Génie Civil, University of Montpellier, Montpellier, France
(3) Center for Research and Innovation in Bioengineering, Valencia Polytechnic University, Valencia, Spain

INTRODUCTION

Marfan syndrome (MFS), affecting roughly 1 in 5000 births, is caused by mutations to the *FBN1* gene coding the glycoprotein fibrillin-1 [1]. Fibrillin-1 is primarily responsible for the long-term stability of elastic fibers in the aorta, as well as promoting mechanosensing and mechanoregulation of extracellular matrix by mural cells. A major cause of premature death in Marfan individuals is aortic dissection and rupture following the development of thoracic aortic aneurysm, resulting from progressive loss of structural integrity and function in the aorta. It is thus critical to understand the underlying mechanisms in the Marfan aorta for improved diagnosis and patient outcomes.

Experimental studies on animal models of MFS, namely *Fbn1*^{mgR/mgR} and *Fbn1*^{C1041G/+} mice, have allowed for significant advancements in our understanding of MFS. Quantifying changes in histology and biomechanics of thoracic aortas in these mice has revealed marked three-dimensional (3D) damage to elastic fibers along with strong correlations between elastin porosity and elastic energy storage, circumferential stiffness, and luminal diameter [2]. In this study, we focused on modeling aneurysm development the Marfan ascending thoracic aorta (ATA) using a constrained mixture framework [3] to capture recently published experimental data.

METHODS

Experimental characterization

Three stages of MFS disease severity were bracketed using wild-type, *Fbn1*^{C1041G/+}, and *Fbn1*^{mgR/mgR} mice at 60 days of age. Ascending thoracic aortas underwent (1) biaxial testing to compute specimen-specific material properties with a four-fiber family hyperelastic model and (2) two-photon microscopy to quantify microstructural metrics including elastin porosity and engagement of collagen fibers and cells [2]. Standard histology with Movat's pentachrome was then performed to assess fractions of elastin, collagen, and cells in each group.

Mechanobiologically equilibrated constrained mixture model

We aimed to capture experimentally observed changes in a model by investigating the individual roles of compromised elastic fiber integrity as well as lost mechanosensing and mechanoregulation of matrix. The arterial wall was modeled as a mixture of three primary load-bearing constituents that undergo changes in mass and microstructure in response to biomechanical stimuli: elastin-dominated ($\alpha = e$) and collagen-dominated ($\alpha = c$) matrix along with smooth muscle ($\alpha = m$). Each constituent α was governed by a mass density production rate $m^\alpha(\tau)$, removal function $q^\alpha(s, \tau)$, and stored energy density function $\hat{W}^\alpha(s, \tau)$, where s is the current G&R time and $\tau \leq s$ is the time of deposition. We adopted stress-mediated descriptions for production and removal given by

$$\begin{aligned} m^\alpha(\tau) &= m_o^\alpha \left(1 + K_\sigma^\alpha \Delta\sigma(\tau) - K_{\tau_w}^\alpha \Delta\tau_w(\tau) \right) \\ q^\alpha(s, \tau) &= \exp\left(-\int_\tau^s k_o^\alpha \left(1 + \omega \Delta\sigma^2(t) \right) dt\right), \end{aligned} \quad (1)$$

where m_o^α and k_o^α are basal values of production and removal, respectively, $\Delta\sigma = (1 - \delta)\sigma/\sigma_o - 1$ and $\Delta\tau_w = (1 - \xi)\tau_w/\tau_{wo} - 1$ represent normalized stress (σ and τ_w) deviations from original homeostatic targets σ_o and τ_{wo} , and gain-type parameters K_σ^α , $K_{\tau_w}^\alpha$, and ω control the sensitivity of the response. Additionally, δ and ξ model cellular mechanosensing. Material responses were described with constitutive relations

$$\begin{aligned} \hat{W}^e &= c^e (I_1^e - 3) \\ \hat{W}^{m,c} &= \frac{c_1^{m,c}}{4c_2^{m,c}} \left(\exp[c_2^{m,c} (I_4^{m,c} - 1)^2] - 1 \right), \end{aligned} \quad (2)$$

where $\{c^e, c_1^{m,c}, c_2^{m,c}\}$ are material parameters, and $\{I_1^e, I_4^{m,c}\}$ are measures of constituent-specific deformations. Material properties were

assigned from fitting to the histological and biomechanical data with a nonlinear least-squares regression routine.

Aneurysmal dilatation was modeled by prescribing heterogeneous insults ϑ onto an initially uniform cylindrical vessel with axial length l_o , varying spatially according to the expression

$$\vartheta(z_o) = \vartheta_{apex} \exp\left(-\left|\frac{z_o - l_o/2}{z_{od}}\right|^{v_z}\right), \quad (3)$$

where $z_o \in [0, l_o]$, parameters z_{od} and v_z govern the width and boundary softness of the insult region, and ϑ_{apex} is the maximum value of the insult. We modeled compromised elastic fibers by reducing the value of c^e . Dysfunctional mechanosensing was modeled with increases in $\delta = [0, 1]$. Finally, changes in mechanoregulation were modeled by modifying the collagen deposition stretch G^c from its baseline value.

Computational methods

We have previously shown in cases of TAA that the constrained mixture framework can be simplified via the assumption of mechanobiological equilibrium, resulting in a time-independent, computationally efficient approach implemented into the finite element solver FEBio [3]. We used this 3D finite element model consisting of a $1 \times 20 \times 20$ mesh of quadratic hexahedral elements, prescribing individual and combined insults of increasing severity to generate aneurysmal geometries and evaluate key biomechanical metrics related to aortic health such as stored energy and material stiffness. We determined optimal insult parameters by fitting the model-predicted to experimentally-measured quantities using a surrogate management framework algorithm [4].

RESULTS

Performance of individual insult contributors

We initially focused on characterizing the effect of insults to elastic fiber integrity alone. Simulations were run for losses in elastic fiber integrity of 0–84%, in which the stored energy and circumferential stiffness were evaluated in the insult region. We performed similar simulations for compromised mechanosensing (0–15%) and mechanoregulation (0–1.2%), shown in Fig. 1. Insults in elastic fiber integrity accurately captured the decrease in stored energy observed in experimental data. However, no insult alone achieved substantial circumferential stiffening or aneurysmal dilatation (Fig. 2).

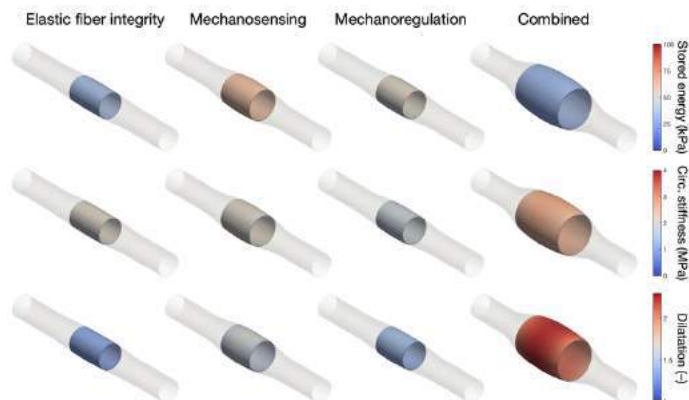


Figure 1: Columns 1-3: individual compromises in elastic fiber integrity, mechanosensing, and mechanoregulation. Column 4: insult with all effects combined. (Top) stored energy, (middle) circumferential stiffness, and (bottom) dilatation are shown in the highlighted central insult region.

Combined insult captures geometric and mechanical properties of aortic aneurysm

In contrast, insults combining optimized values of parameters describing a loss of elastic fiber integrity with simultaneous compromises in mechanosensing and mechanoregulation maintained the desired loss of stored energy while also predicting significantly more circumferential stiffening than isolated insults (Fig. 1). Furthermore, the combined model was able to recapitulate the trends in several trends observed in the experimental data, including lost distensibility, reduced axial stiffness, and increased thickness (Fig. 2).

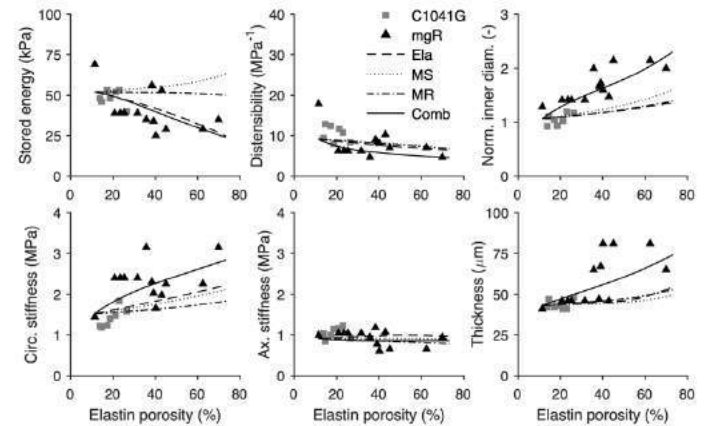


Figure 2: Performance of individual and combined insult models (lines) compared to experimental data (symbols), plotted as a function of elastin porosity measured by two-photon microscopy.

Ela = elastic fiber integrity, MS = mechanosensing, MR = mechanoregulation, comb = combined.

DISCUSSION

We found that while localized defects can give rise to progressive aortic dilatation, the model could only describe the actual data when multiple disease contributing factors co-existed. Given that fibrillin-1 microfibrils not only contribute to elastic fiber homeostasis but also promote smooth muscle cell mechanosensing and mechanoregulation of matrix. Our computational findings are thus consistent with myriad effects of compromised fibrillin-1 in the Marfan aorta. Optimal insult parameters further suggested an early loss of cellular mechanosensing in mild disease relative to loss of elastic fiber integrity, highlighting the importance of inter- and intra-lamellar elastin in the Marfan aorta, which should be further explored in future studies.

The present computational results show that aneurysmal dilatation in MFS results from multiple simultaneous contributors to progressive degeneration of the aortic wall, and mechanobiological models can help to disentangle these contributions.

ACKNOWLEDGEMENTS

This work was supported by grants from the US National Institutes of Health (P01 HL134605, R01 HL146723).

REFERENCES

- [1] Milewicz, DM et al., *Nat Rev Dis Primers*, 7(1):1-24, 2021.
- [2] Cavinato, C et al., *Front Cardiovasc Med*, 16:1904, 2021.
- [3] Latorre, M et al., *PLoS Comput Biol*, 16(10):e1008273, 2020.
- [4] Szafron, JM et al., *Tissue Eng Part C Methods*, 25(10):561-70, 2019.

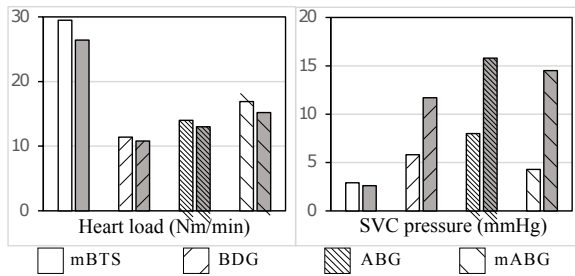


Figure 2: The proposed operation (mABG) in comparison to the earlier ABG, conventional stage-1 (mBTS), and stage-2 (BDG) operations, in terms of the heart load and SVC pressure. Unshaded and shaded bars correspond to the normal and elevated PVR, respectively.

To evaluate the performance of the proposed operation, we use multi-scale CFD simulations [5]. This methodology, which has been extensively used in the past for modeling single-ventricle circulation [2–4], is capable of capturing the local and global response of the patient circulatory system to the proposed operation.

For an apple-to-apple comparison of the proposed operation against other alternatives, we consider three cases in addition to the proposed operation (mABG). Those are 1) the conventional stage-one anatomy with a 3.5 mm modified Blalock Taussig Shunt (mBTS), 2) the conventional bidirectional Glenn (BDG) anatomy with an end-to-side SVC-PA anastomosis, and 3) the original assisted bidirectional Glenn (ABG) [3]. All parameters are kept the same between these cases (including the lumped-parameter network), except for the altered anatomy associated with each operation. We additionally consider normal and elevated pulmonary vascular resistance (PVR) values to model patient response in a normal and worst-case scenario setting.

RESULTS

A comprehensive set of parameters are extracted from these simulations [6, 7], which are not reported here for the sake of space. In what follows, we only focus on the most critical parameters, which are the SVC pressure, heart load, and oxygen delivery.

As shown in Figure 2, the BDG, ABG, and mABG heart workloads are approximately half of that of the mBTS at both PVR. The mABG procedure also has the highest oxygen delivery and aortic oxygen saturation among the four procedures at both normal and high PVR. Most importantly, the present mABG lowers the SVC pressure below the PA pressure. At normal PVR, the SVC pressure in the mABG is lower than that of the BDG despite a significantly higher PA flow rate. At both normal and elevated PVR, the SVC pressure in the mABG is lower than that of the original ABG.

DISCUSSION

The simulation results confirm the advantages of the ABG circulation, including the lower heart load, which is significantly lower than the conventional mBTS operation. Even though the ABG heart load is slightly higher than the BDG due to the shunt flow, that also increases pulmonary perfusion to boost the development of pulmonary circulation in infants undergoing this operation.

As mentioned earlier, the ABG has the highest oxygen delivery among all operations as it has the highest systemic saturation. The higher systemic saturation in the ABG can be attributed to redirecting SVC flow so that it no longer mixes with the oxygenated flow in the atrium to otherwise lower systemic saturation.

The ABG has also the potential to combine the first two open-chest operations performed on single ventricles, thus reducing the total number of operations from 3 to 2. Later transition to stage-2 (i.e., BDG) circulation can simply be accomplished by blocking the shunt via a catheter.

Redundancy is built into the ABG pulmonary circulation as the PA flow is supplied through SVC and shunt. Hence, if the shunt occludes due to thrombosis, the ABG circulation reverts back to the BDG circulation. That is in contrast to stage-1 operation, where shunt blockage is a fatal incident.

The high SVC pressure was one of the major concerns in the ABG procedure that motivated this study. Both previous studies and our study shows that the ABG produces an SVC pressure that exceeds that of the mBTS and BDG at normal and high PVR to a level that may not be tolerated by infants. The proposed modifications in the mABG lowered the SVC pressure to 4.3 mmHg at normal PVR, a value that potentially avoids upper-body edema and SVC syndrome [8].

In contrast to these encouraging outcomes at normal PVR, the SVC pressure remains relatively high at high PVR. That is so since the PA pressure scales with the PVR while the ejector pump pressure recovery does not, resulting in an SVC pressure three times higher than that of a normal PVR. In practice, the PVR of newborns is elevated up to 3-6 weeks, during which a high SVC pressure could create adverse effects [9].

To identify the conditions where the ABG can be safely employed, we have generated a 2D map that allows one to look up the SVC pressure given the PVR and nozzle area (Figure 3). This 2D map, which is obtained using the combination of multidomain CFD simulations and algebraic models [7], permits one to select the right slit thickness (hence, a nozzle area) once the PVR and acceptable SVC pressure are known.

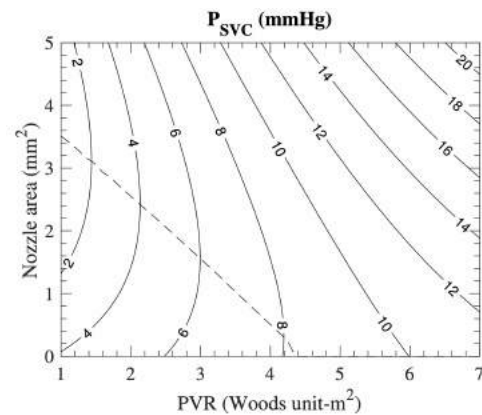


Figure 3: A master chart for selecting the nozzle size if the patient PVR and the highest tolerable SVC pressure are known. The dashed line shows the optimal nozzle area that produces the lowest P_{SVC} .

REFERENCES

- [1] d'Udekem Y et al. *Journal of the American College of Cardiology* 59.13 (2012).
- [2] Moghadam ME et al. *Journal of biomechanical engineering* 134.5 (2012).
- [3] Esmaily Moghadam M et al. *The Journal of thoracic and cardiovascular surgery* 149.3 (2015).
- [4] Verma A et al. *World Journal for Pediatric and Congenital Heart Surgery* 9.2 (2018).
- [5] Moghadam ME et al. *Journal of Computational Physics* 244 (2013).
- [6] Jia D et al. *Journal of Biomechanical Engineering* 143.7 (2021).
- [7] Jia D et al. *Fluids* 7.1 (2022).
- [8] DeCampi WM. *The Journal of thoracic and cardiovascular surgery* 149.3 (2015).
- [9] Glenn WW. *New England Journal of Medicine* 259.3 (1958).

EYE-SPECIFIC MODELING OF EFFECTS OF INTRAOCULAR PRESSURE ON OPTIC NERVE HEAD OXYGENATION

**Yuankai Lu (1), Yi Hua (1), Bingrui Wang (1), Fuqiang Zhong (1), Andrew Theophanous (2),
Shaharoz Tahir (2), Po-Yi Lee (2), Ian A. Sigal (1,2)**

(1) Department of Ophthalmology, University of Pittsburgh, Pittsburgh, PA, USA
(2) Department of Bioengineering, University of Pittsburgh, Pittsburgh, PA, USA

INTRODUCTION

Glaucoma is characterized by progressive degeneration of retinal ganglion cells and their axons. The axon damage is believed to start within the optic nerve head (ONH) [1]. Although the mechanisms leading to axon damage remain not fully understood, a leading hypothesis is that an insufficient oxygen supply within the ONH would contribute to this process [2]. This can happen at any level of intraocular pressure (IOP), and would likely worsen if elevated IOP distorts the vasculature, affecting blood flow [3].

Our goal was a better, more comprehensive, understanding of the effects of IOP-induced deformations on the ONH hemodynamics and oxygenation. Direct examination of this process is extremely complex since measurement of ONH oxygenation in-vivo is not yet possible. Hence, we use 3D eye-specific numerical models to characterize ONH hemodynamics and oxygenation at a baseline IOP and when under subjected to experimentally-derived IOP-induced tissue distortions. Specifically, we focus on the relationship between IOP-induced vessel diameter reduction and the local decrease in oxygen.

METHODS

We reconstructed detailed 3D models of the ONH vessel networks of 3 healthy monkey eyes using histological techniques, as described elsewhere [4]. We also obtained in-vivo IOP-induced ONH deformations from a healthy monkey using optical coherence tomography images and digital volume correlation techniques while IOP was controlled, as reported before [5]. A biomechanics-based technique was used to map the experimentally-derived tissue strains to local vessel distortions. The hemodynamics and oxygenation of the three vessel networks were simulated under deformations from various IOP increases, using the methods reported before [6]. The oxygen fields adjacent to the vessels were compared to the baseline value to determine the effect of IOP-induced mechanical insult to each vessel.

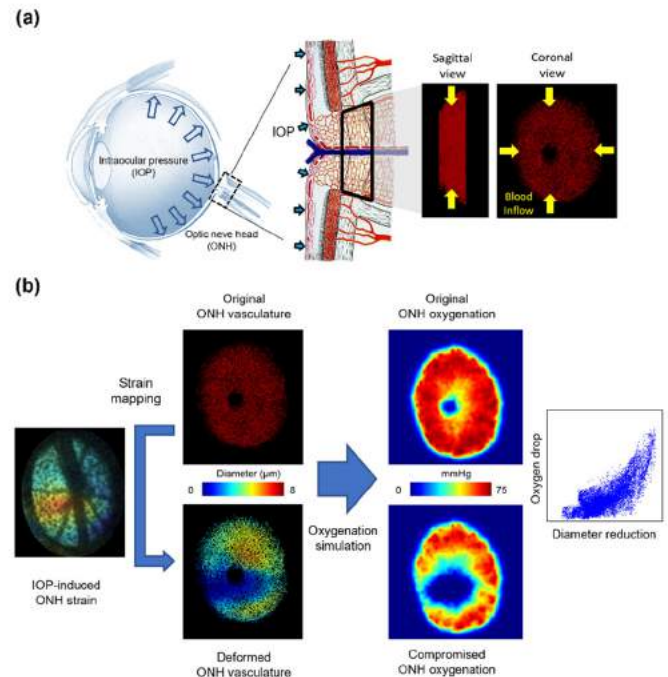


Figure 1: (a) Diagrams of the eye and ONH vasculature (left and middle). An eye-specific model of ONH vasculature (right). Blood inflow was at the periphery from the circle of Zinn-Haller [1] (yellow arrows). (b) Schematic of our analysis process, based on applying experimentally-derived deformations and computing changes in vessel diameter and oxygenation.

RESULTS

ONH oxygenations under different IOP-induced deformations are shown in **Figure 2**. As IOP increases, tissue distortions led to decreased vasculature diameters, and with this to also decreased ONH oxygenation. We analyzed the spatial association between vascular deformation and oxygenation in ONH. There was a positive, nonlinear association between the IOP-induced diameter reduction of each vessel and the decrease in oxygen in the tissues adjacent to the vessel (**Figure 3**). Overall, vessels with larger diameter reductions were more likely to have large oxygen drops. Similar patterns were observed for the two other ONH vessel networks simulated.

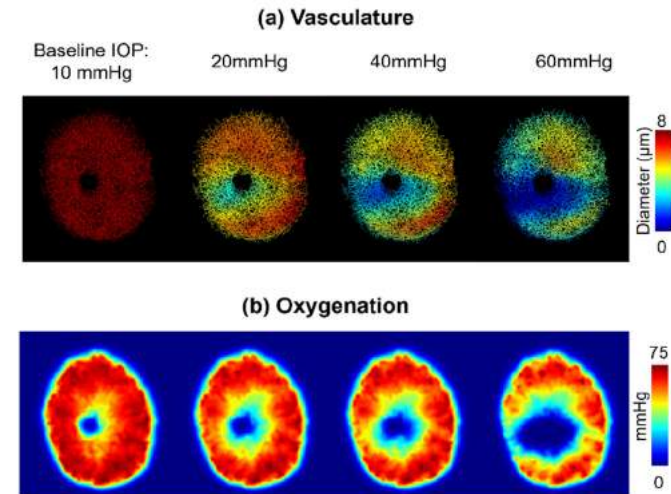


Figure 2: ONH #1 vasculature deformation and oxygenation at different IOPs. The diameters of the vasculature and the oxygenation are both decreasing with IOP elevation. Regions of low oxygenation and vessels with large diameter reduction had similar spatial distributions.

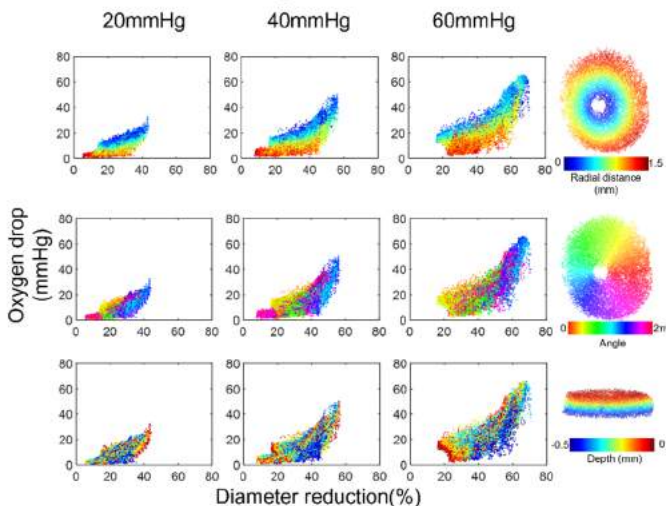


Figure 3: Scatterplots of oxygen decrease and diameter reduction at three IOPs relative to the baseline IOP=10mmHg (columns) of ONH #1. Dots corresponds to capillary segments colored according to the location by: radial distance from the central vessels (top row), clock-hour (middle-row) and anterior-posterior (bottom row). Results show larger decreases in oxygen for more central vessels for a given diameter decrease. The dependence on clock-hour and depth were more nuanced.

The spatial distribution of diameter reductions and oxygen drops relative to the baseline for each vessel are shown in **Figure 3**. For radial direction, the results show a layered structure. The periphery vessels have the smallest oxygen drop under various diameter reductions. The further away from the periphery, the more difficult it is for the vessel to maintain a small oxygen drop under deformation. For angular direction, the angular differences are mainly in the vascular compressions, which are consistent with the angular distribution of the IOP-induced deformation, as expected. For vessels at different depths, the oxygen drops and diameter reductions did not show significant differences.

DISCUSSION

We leveraged 3D eye-specific numerical models to characterize ONH hemodynamics and oxygenation under different IOP-induced deformations. Specifically, we investigated the oxygen drops and diameter reduction of ONH vessels during IOP elevation. Two main findings arise from the work: First, as IOP increases, both oxygen decreases and the diameter reduction of vessels become larger. Second, the peripheral vessels have smaller oxygen drops than the central vessels for various deformations. Below we discuss each of the main findings in detail.

As IOP increases, both the oxygen drops and the diameter reductions of vessels become larger. This can be understood as follows: Increases in IOP led to tissue deformations. The deformations, applied to the vessels result in compromised blood flow, which lead to the oxygenation reduction. This finding supports the hypothesis that elevated IOP alters the hemodynamics and oxygenations within the ONH, which, may contribute to neural tissue injury in glaucoma.

We also observed that peripheral vessels had smaller oxygen drops than central vessels under various deformations. This can be understood by recalling that ONH blood perfusion within ONH is from the periphery, draining through the central retinal vein. When interpreting these results, we must be careful to recall that the ONH vascular system is highly interconnected and therefore that capillary flows are not independent. For instance, we cannot conclude that higher oxygen decreases in more central capillaries for the same diameter reduction implies that they are more sensitive to peripheral capillaries. The results represent an integrated simulation of the whole system, in which blood flows from the periphery to the center. The diameter decreases in the periphery that cause local blood flow decreases likely contribute to the decrease in blood flow and oxygen in the central vessels downstream.

In summary, we used 3D eye-specific models to evaluate the ONH hemodynamics and oxygenations under IOP-induced deformation. Results from this study help understand the mechanisms of the IOP-induced retinal ganglion cell axon damage in glaucoma. Next steps involve expanding the analysis to IOP-induced deformations on other eyes, and eventually on the same eyes from which the vessel network was reconstructed.

ACKNOWLEDGEMENTS

NIH R01-EY023966, R01-EY031708, R01-HD045590, R01-HD083383, P30-EY008098, and T32-EY017271; Eye and Ear Foundation (Pittsburgh, PA); Research to Prevent Blindness (unrestricted grant to UPMC Ophthalmology and Stein Innovation Award to Sigal IA).

REFERENCES

- [1] Quigley, H et al., *Glaucoma Lancet*, 1367-1377, 2011.
- [2] Stefánsson, E et al., *Prog. Retin. Eye Res.*, 24, 307-332, 2005
- [3] Chuangsuwanich, T et al., *IOVS*, 57, 6167-6179, 2016.
- [4] Lee, P. Y. et al., *J. Biomech. Eng.*, 144.6: 061006, 2022
- [5] Zhong, F et al., *Acta biomaterialia*, 143: 72-86, 2022
- [6] Lu, Y et al., *PloS one*, 16.2, e0247641, 2021

SPATIAL MAPPING THE MATERIAL AND STRUCTURAL PROPERTIES OF THE UTERINE FIBROID-MYOMETRIUM BOUNDARY

Daniella M. Fodera¹, Johanna L. Lund-Jackson¹, Shuyang Fang², Arnold Advincula³, Michelle L. Oyen⁴, Kristin M. Myers²

¹Department of Biomedical Engineering, Columbia University, New York, NY, USA.

²Department of Mechanical Engineering, Columbia University, New York, NY, USA.

³Department of Obstetrics & Gynecology, Columbia University Irving Medical Center, New York, NY, USA.

⁴Department of Biomedical Engineering, Washington University in St. Louis, St. Louis, MO, USA.

INTRODUCTION

Uterine fibroids, also known as leiomyomas, affect 70-80% of women by age 50 and account for more than 200,000 hysterectomies in the U.S. annually [1, 2]. Characterized by the non-cancerous growth of tumors in the uterus, fibroids are a common cause of excessive bleeding, infertility, preterm labor, pelvic pain, and other obstetric conditions [3]. While fibroids have been documented to grow as large as 30 cm in diameter, all originate initially as seedling fibroids on the mm scale [4]. Relatively few studies have characterized the mechanical properties of uterine fibroids to date [4-6]. It is well established that uterine fibroids are significantly stiffer than the myometrium using bulk tissue testing approaches, exhibiting both intra- and inter-patient variability, yet no studies have investigated the transition in material properties at the fibroid-myometrium boundary [4-6]. Understanding whether a sharp or gradual change in stiffness exists at this boundary will provide key knowledge in the development of diagnostic tools for the detection and treatment of uterine fibroids. Therefore, this study aims to spatially map the time-dependent material properties of seedling uterine fibroids and their surrounding myometrium at the microscale.

METHODS

In accordance with IRB approval at Columbia University Irving Medical Center (CUIMC), human uterine tissues embedded with fibroids ($n = 13$) were collected from nonpregnant women ($n = 2$) undergoing hysterectomies. Uterine sections were collected at the anterior, fundus, and posterior regions, immediately flash-frozen, and stored at -80°C until further processing. Prior to testing, seedling uterine fibroids on the mm-scale were revealed following careful dissection of uterine tissue. A subset of samples was stained for Masson's Trichrome using standard protocols. Spherical nanoindentation (Piuma, Optics11Life, Amsterdam, NL) was utilized to map the spatial variations of time-dependent material properties of uterine fibroids and patient-matched myometrium. Samples were thawed at 4°C overnight in PBS solution and equilibrated at room temperature for 30 min prior to testing.

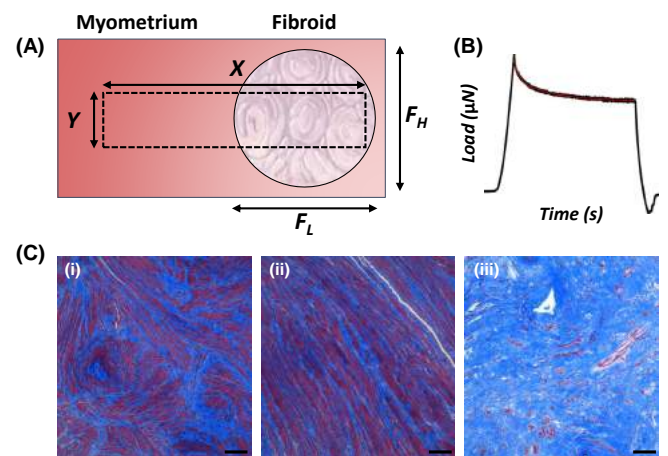


Figure 1: (A) Schematic of testing protocol for the fibroid-myometrium boundary. (B) Representative load relaxation curve generated from nanoindentation testing fit with the PVE model. (C) Histology (Masson's Trichrome) stains of the (i) distant myometrium and (ii) adjacent myometrium, and (iii) fibroid (blue = collagen; red = smooth muscle). Scale bar = 100 μm .

The fibroid-myometrium boundary was tested as a rectangular region shown in Fig. 1A and centered relative to the fibroid's height (F_H). The length (X) of the testing region was equivalent to the full length of the fibroid (F_L) plus a fixed 3 mm of the adjacent myometrium. The height (Y) was equal to $0.4 \cdot F_H$. The distance between indentation points was fixed at 200 μm . Distant myometrium was defined as a region of tissue greater than 5 mm from any visible fibroid; one sample per anatomic region was sampled for each patient ($n = 6$).

Using a spherical probe (50 μm radius), samples were indented to a fixed depth of 4 μm , corresponding to a 5% strain, for 15 s to achieve a load relaxation curve approaching equilibrium (Fig. 1B). Load relaxation curves were fit in Matlab with a combined poroelastic-viscoelastic (PVE) model based on established methods [7-9]. Fitted data points were excluded from the final data set if the load relaxation curve displayed (i) sharp discontinuities, (ii) increasing loads over time, and (iii) ΔP ($P_{\max} - P_{\min}$) less than 0.005. Parameters of stiffness (E), viscoelastic ratio

(E_{∞}/E_0), and intrinsic permeability (k) were determined from the PVE model. Statistical analysis was performed in GraphPad Prism 9.4.0 using a nested one-way ANOVA with significance set at $p < 0.05$.

RESULTS

Structurally, uterine fibroids exhibit increased collagen and decreased smooth muscle content compared to patient-matched myometrium (Fig. 1C). Uterine fibroids are surrounded by dense circumferentially aligned smooth muscle fibers, which is markedly distinct from the distant myometrium displaying random fiber orientation (Fig. 1C).

On the whole, uterine fibroids demonstrate increased stiffness relative to matched myometrium by nearly an order of magnitude (Fig. 2A-B). Yet, notable intra-sample variability in stiffness is exhibited across the fibroid's length without any discerning patterns, ranging from 10^1 to 10^4 Pa. The transition in stiffness values at the fibroid-myometrium boundary does not follow a singular pattern for different uterine fibroids, displaying both sharp and gradual changes in stiffness on the μm -scale (Fig. 2A). Coupled with increased stiffness, uterine fibroids exhibit decreased permeability compared to patient-matched myometrium, indicating that the tissue is less porous (Fig. 2C). On average, no differences between the distant and adjacent myometrium are observed for both stiffness and permeability parameters (Fig. 2B-C). Interestingly, no difference in viscoelastic ratio is evident across all sample groups, with median values ranging from 0.4 to 0.6 (data not shown).

DISCUSSION

Here, a novel dataset representing the time-dependent material properties of seedling uterine fibroids at small length scales is presented. Uterine fibroids are determined to be significantly stiffer and less permeable when compared to patient-matched myometrium, yet they exhibit a large degree of heterogeneity within and across different fibroids regardless of the individual patient. The transition in material properties at the fibroid-myometrium boundary also varies by sample, exhibiting both sharp and gradual changes in stiffness. Such a finding suggests multiple morphological phenotypes may in fact exist for seedling fibroids. Future work will investigate underlying changes in composition and structure for different fibroid phenotypes with immunohistological staining and second harmonic generation imaging.

Further, structural and compositional features at the fibroid-myometrium boundary suggests for the very first time that growing fibroids alter the directionality of muscle fibers for the adjacent myometrium. For this reason, we propose that uterine fibroids impart hoop stresses within the surrounding myometrium that disappear following removal of the fibroid, a hypothesis that can be confirmed with non-contacting extensometry and computational modeling.

A key limitation of this study is the singular focus on seedling uterine fibroids which are often too small to be surgically removed during a myomectomy procedure. Additionally, this study focuses almost entirely on intramural fibroids embedded in the myometrium, yet, fibroids can exist in submucosal, subserosal, and pedunculated forms. As such, future work will investigate the

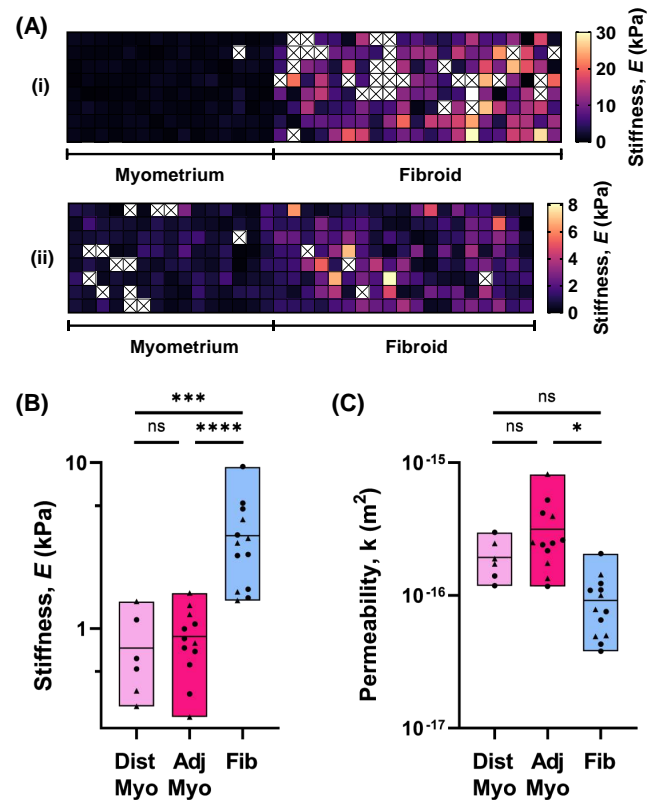


Figure 2: (A) Spatial heatmap of stiffness across the fibroid and adjacent myometrium for two representative samples (i,ii). The distance between each colored square is 200 μm . Squares marked by an [X] indicate points removed due to exclusion criteria. (B) Stiffness and (C) permeability of uterine fibroids and patient-matched myometrium (distant and adjacent). Each symbol represents the median value of all indentation points (10^1 - 10^2) for a given sample. Triangle and circle symbols denote different patients.

material properties of this boundary for larger centimeter-sized uterine fibroids found in different tissue layers of the uterus.

Yet, despite these limitations, the data presented here yield key insights into the mechanical and structural properties of uterine fibroids. Focusing exclusively on a snapshot of uterine fibroids in their seedling stage provides foundational knowledge for improved understanding of uterine fibroid nucleation and growth. In doing so, targeted therapeutic treatments for the removal and prevention of uterine fibroids may be developed.

ACKNOWLEDGMENTS

We would like to thank Dr. Joy Vink for assistance in the collection of uterine tissue at CUIMC. Research was supported in part by the NSF GRFP, Iris Fund, and Eunice Kennedy Shriver National Institute of Child Health Human Development Grant (R01HD091153).

REFERENCES

- [1] Farquhar, C et al. *Obstet Gynecol.* 2002. [2] Wu, J et al. *Obstet Gynecol.* 2007. [3] Bulun, S. *N Engl J Med.* 2013. [4] Jayes, F et al. *PLoS One.* 2019. [5] Jayes, F et al. *Am J Obstet Gynecol.* 2016. [6] Norian, J et al. *Matrix Biol.* 2012. [7] Mattice, J et al. *J. Mater. Res.* 2006. [8] Hu, Y et al. *Appl. Phys. Lett.* 2010. [9] Islam, M et al. *Experimental Mechanics.* 2021.

EFFECT OF SINOTUBULAR JUNCTION SIZE IN TAVR LEAFLET THROMBOSIS AND THE POTENTIAL OF TAV-IN-TAV PROCEDURE: A FLUID STRUCTURE INTERACTION BASED THROMBOGENIC RISK ASSESSMENT ANALYSIS

Symon Reza (1), David Oks (2), Brandon Kovarovic (1), Mariano Vázquez (2), Danny Bluestein (1)

(1) Biomedical Engineering, Stony Brook University, Stony Brook, NY, USA

(2) Barcelona Supercomputing Center, Computer Applications in Science and Engineering, Barcelona, Spain

INTRODUCTION

Transcatheter aortic valve replacement (TAVR), a minimally invasive procedure, has demonstrated superior or noninferior hemodynamic performance compared to surgical aortic valve replacement (SAVR) and became the standard procedure for high and intermediate-risk aortic stenosis patients. However, prosthetic TAVR leaflets are inherently subjected to degeneration, along with calcification and thrombosis [1]. Hence, durability remains as one of the major concerns for TAVR technology. Recently, clinical studies have found evidence of early leaflet thrombosis formation [2] that may be associated with an earlier risk of structural valve degeneration. Therefore, it is important to thoroughly investigate the thrombogenic risk of the TAVR devices with respect to patients' anatomical variability. While choosing a TAVR device, the size of the left ventricular outflow tract (LVOT) and calcium deposits on the LVOT and native leaflets get major attention. However, the sinotubular junction (STJ) size may also affect the hemodynamic performance of TAVR devices and may increase the thrombogenic risk [4]. An analysis of hemodynamic performance and thrombogenic risk of TAVR devices associated with STJ size variability may provide crucial information that can potentially aid the clinicians in optimizing device selection and reduce the risk of leaflet thrombosis and degeneration in the long run.

TAVR has recently been approved for use in low-risk patients. The increasing number of younger and low-risk TAVR recipients, and recent evidence of rapid degeneration of prosthetic valves can potentially lead to the need for another TAVR procedure on top of the first TAVR device. This procedure, known as TAV-in-TAV (transcatheter aortic valve-in-transcatheter aortic valve), is typically performed to address suboptimal outcomes such as aortic regurgitation. However, it is still unknown whether TAV-in-TAV can be a viable solution to early TAVR valve degeneration. Recently, Hoda et.al.[5] performed an in-vitro hemodynamic analysis of different TAV-in-TAV combinations deployed in an idealized geometry and suggested combination-dependent hemodynamic performance. Performance of

TAV-in-TAV may also depend upon factors including the diseased patient-specific anatomy and complex flow domain formed by the native leaflets and two TAVR device prostheses. Conducting a computational hemodynamic performance and thrombogenic risk analysis of different TAV-in-TAV combinations in a patient-specific scenario may provide important insights into the feasibility of TAV-in-TAV procedures and help identify the optimal combination.

METHODS

A patient with a 26 mm LVOT size and 30 mm STJ size was selected. The patient model was then reconstructed from a CT scan. The STJ size was later modified to 26 mm and 34 mm, while the aortic annulus size was kept unchanged (Figure 1a). An

Evolut 26 mm TAVR device was subsequently deployed in 3 virtual patient cases using Abaqus 2019 (SIMULIA, Dassault Systèmes, Providence, RI) following our previous study (Figure 1b) [6]. A 2-way coupled fluid structural interaction (FSI) using an immersed boundary method was then performed on each virtual patient case (using an in-house Multiphysics solver 'Alya', developed in Barcelona Supercomputing Center, Spain) (Figure 1c) [7]. The thrombogenic risk assessment analysis was performed following our previously developed and validated technique (Figure 1d) [8]. In this study, 2 million

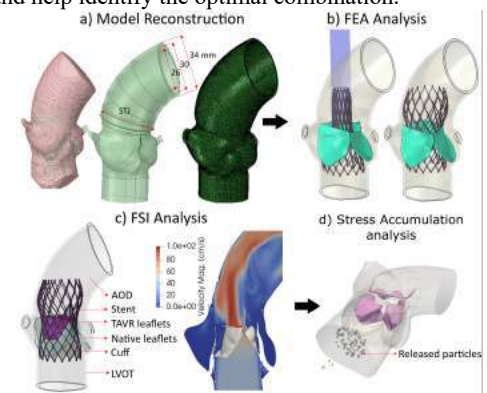


Figure 1: Schematic of the (a) model reconstruction, (b) TAVR deployment, (c) FSI simulation, and (d) particle injection for stress accumulation (SA) analysis is presented

Lagrangian particles representing platelets were injected into the flow over 10 cardiac cycles. Stress accumulation (SA) was computed along each particle trajectory and collapsed into a probability density function (PDF) to compute the “thrombogenic footprint” [8] for each virtual patient case. Additionally, Residence Time (T_R) (Figure 3), Wall Shear Stress (WSS), Transvalvular Pressure Gradient (TPG), and Geometric Orifice Area (GOA) for each model were computed.

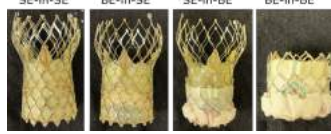


Figure 2: Representations of the considered TAV-in-TAV combinations (SE- self expandable, BE-balloon expandable) [5]

In the second study, four TAV-in-TAV combinations were modeled using Abaqus Explicit 2019 (SIMULIA, Dassault Systèmes, Providence, RI) in a reconstructed patient model based on the two most commonly used self-expandable (SE) Evolut and balloon expandable (BE) Sapien TAVR systems. Subsequently, 2-way coupled fluid structural interaction (FSI) analysis and stress accumulation (SA) based thrombogenic risk analysis were performed for each TAV-in-TAV combinations presented in Figure 2.

RESULTS

26 mm STJ size demonstrated a smaller median GOA (9%), higher median T_R (3%), TPG (35%), WSS (11%), and a larger number of particles with high-stress accumulation (SA) (Figure 4) compared to 30 mm STJ size. 34 mm STJ size had a similar GOA and number of particles with high accumulated stress (AS), higher T_R (4.8 %), TPG (13%), and a lower WSS (12 %) compared to the 30 mm STJ size. (Table 1). However, a higher number of particles experienced SA magnitude of more than 1 Pa.s for models with larger STJ sizes in both sinus and the neo-sinus (Figure 4). Initial results demonstrate TAVR device-specific performance in TAV-in-TAV implantations in a patient-specific model (Figure 5).

DISCUSSION

TAVR subclinical leaflet thrombosis is generated following a complex process including platelet activation at high shear flow caused by a high-velocity jet either through paravalvular leaks or narrowed leaflet opening and platelets aggregation at low shear flow in pockets of space created between the native leaflets and the TAVR prosthesis that promotes blood stasis. In this study, we performed a set of computational analyses starting from finite element-based TAVR deployment in patient-specific models to FSI-based hemodynamic analysis coupled with particle stress accumulation (SA) analysis. SA accounts for the combined effect of shear stress and exposure time that drive platelets beyond their activation threshold and promotes thrombus formation.

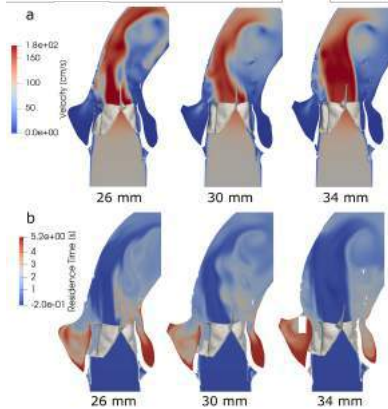


Figure 3: a) Velocity contour, and b) Residence time during peak systole

Using these techniques, we analyzed the effect of STJ size on TAVR performance and associated thrombogenic risk. We also analyzed the feasibility and the best performing TAV-in-TAV combination, that is being considered as a solution to TAVR leaflet thrombosis and degeneration.

The patient model with a 30 mm STJ size-close to the diameter of the upper crown (32 mm) of the 26 mm Evolut device

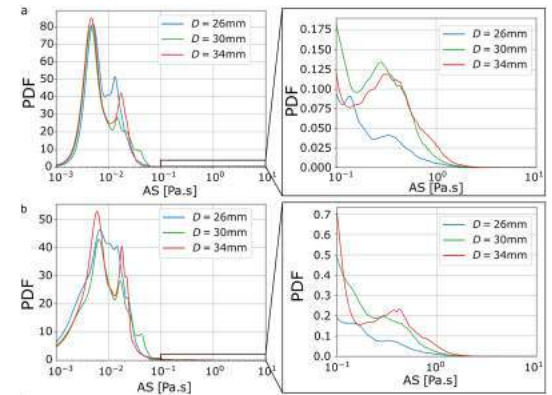


Figure 4: Overall probability density functions (PDF) of stress accumulation (SA) for models with different STJ size in (a) sinus and (b) neo-sinus

demonstrated the best performance with the highest GOA, lowest T_R , TPG, and WSS. The model with 34 mm STJ size had a relatively inferior performance compared to the 30 mm STJ model with a higher T_R and TPG. 26 mm STJ restricted the opening of the upper crown of the TAVR device and caused the smallest GOA compared to 30 mm and 34 mm STJ models. 26 mm STJ model also had the highest TPG and WSS. However, larger room for blood recirculation causes a larger number of platelets to experience high SA for models with larger STJ size. Initial results from the TAV-in-TAV combination analysis demonstrated a device-specific performance. Further investigation is being performed to find the best-performing TAV-in-TAV device combination in a patient-specific basis.

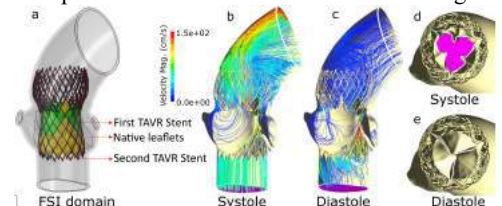


Figure 5: (a) FSI domain of SE-in-SE combination, velocity streamline during (b) systole, and (c) diastole, leaflet opening during (d) systole and (e) diastole

This study presents a thorough computational protocol to analyze patient-specific hemodynamic performance and thrombogenic risk of TAVR devices, shedding light on mechanisms that promote TAVR leaflet thrombosis – addressing a major clinical concern and indicating on potential approaches to mitigate it by informing clinicians how to improve pre-procedural planning in order to minimize the risk of TAVR leaflet thrombosis.

ACKNOWLEDGEMENTS

This project was supported by NIH-NIBIB II-U01EB026414 (DB), the “la Caixa” Foundation (fellowship ID: LCF/BQ/DI18/11660044) from the EU’s H2020 Marie Skłodowska-Curie grant No. 713673, and by the project CompBioMed2 (H2020-EU.1.4.1.3. Grant No. 823712).

REFERENCES

- [1] Sellers, SL et al. *JACC Cardiovasc Imaging*. 2019. [2] Yanagisawa, R et al. *Circ Cardiovasc Interv*. 2019;12:e007349. [4] Nappi, F et al. *JTD*, 12(5), 2020.[5] Hatoum, H et al. *JTCS* 161.2 (2021): 565-576. [6] Bianchi, M et al. *BMMB* 18.2 (2019): 435-451.[7] Oks, D, et al. *IJNMBE* (2022).[8] Chiu, W.C. et al. *Sci Rep* 9, 2946 (2019).

CONSTITUTIVE MODELING OF MOUSE ARTERIES SUGGESTS CHANGES IN DIRECTIONAL COUPLING AND EXTRACELLULAR MATRIX REMODELING THAT DEPENDS ON ARTERY TYPE, AGE, SEX AND ELASTIN AMOUNTS

Keshav A. Kailash (1), Jie Z. Hawes (2), Austin J. Cocciolone (1), Robert P. Mecham (3),
Jessica E. Wagenseil (2)

(1) Biomedical Engineering, Washington University, St. Louis, MO, USA
(2) Mechanical Engineering and Materials Science, Washington University, St. Louis, MO, USA
(3) Cell Biology and Physiology, Washington University, St. Louis, MO, USA

INTRODUCTION

Large artery stiffening is both a cause and consequence of cardiovascular disease and occurs during natural aging. Men and women have different susceptibilities for cardiovascular diseases related to large artery stiffening, such as hypertension and aneurysms, and also have a different timeline for arterial stiffening during aging. One cause of arterial stiffening is a shift in the amount or organization of extracellular matrix (ECM) proteins, including collagen and elastic fibers. Animal models have been used to investigate how changes in ECM proteins are related to arterial stiffening and cardiovascular disease. In particular, elastin heterozygous (*Eln*^{+/-}) mice have ~60% of normal elastin levels, increased arterial stiffness, and hypertension. We previously showed that elastin haploinsufficiency has divergent effects on arterial remodeling with aging that depends on sex [1]. However, we only investigated circumferential mechanical behavior and it is known that arteries are under biaxial loads.

Biaxial mechanical data from mouse arteries has been fitted with 2- or 4-fiber Holzapfel-Gasser-Ogden (HGO) [2] type constitutive models for biomechanical phenotyping in aging and disease. These studies provide insight into how physiological stresses and strains adapt (or not) and possible microstructural explanations for these changes. These models have a built in coupling between fiber and cross-fiber deformation. Dong and Sun (DS) [3] recently proposed a novel constitutive model that does not need a specified number of fiber families and can have varied amounts of deformation coupling. We evaluated the ability of the DS model to fit biaxial mechanical data of *Eln*^{+/-} arteries and interpret biomechanical phenotype changes as a function of age, sex, and ECM alterations in the ascending aorta (ASC) and left common carotid artery (LCC).

METHODS

Animals. Male and female *Eln*^{+/+} and *Eln*^{+/-} mice at 6 and 24 months were used [1]. All animal procedures were approved by the IACUC.

Mechanical Testing. The LCC or ASC was mounted in a pressure myograph. The artery was preconditioned and then pressurized from 0 – 175 mmHg for 3 cycles at different axial stretches and then axially stretched from about 1.0 – 1.8 at 3 different pressures. Unloaded dimensions were measured from cut rings. The experimental stresses were calculated assuming an incompressible cylinder with no shear [1]. **Constitutive Modelling.** Inflation and extension of the artery can be described by the deformation gradient (*F*) and the right Cauchy-Green (*C*) strain tensor. The total strain energy ($\bar{\Psi}$) is the sum of the matrix (*m*) and fiber (*f*) components [2], $\bar{\Psi} = \bar{\Psi}_m + \bar{\Psi}_f$. The matrix is considered an isotropic, Neo-Hookean material,

$$\bar{\Psi}_m = \frac{1}{2} c (\bar{I}_1 - 3), \quad (1)$$

where *c* is a material constant, $\bar{I}_1 = tr(\bar{C})$, $\bar{C} = J^{-\frac{2}{3}} \bar{C}$, $\bar{C} = F^T F$, $J = det F$. The DS fiber strain energy depends on the degree of deformation coupling (medium or strong) and can be described by [3],

$$\bar{\Psi}_{f-medium} = \frac{k_1}{2k_2} \{ \exp [k_2 (\delta_{\parallel} \bar{E}_{\parallel}^2 + \delta_{\perp} \bar{E}_{\perp}^2)] - 1 \}, \quad (2a)$$

$$\bar{\Psi}_{f-strong} = \frac{k_1}{2k_2} \{ \exp [k_2 (\delta_{\parallel} \bar{E}_{\parallel} + \delta_{\perp} \bar{E}_{\perp})^2] - 1 \}, \quad (2b)$$

where *k₁* and *k₂* are material parameters, $\delta_{\parallel} = H(\bar{I}_4 - 1)$, $\delta_{\perp} = H(\bar{I}_{4\perp} - 1)$, where *H* = the Heaviside step function, $\bar{I}_4 = (a_o \otimes a_o) : \bar{C}$ and $\bar{I}_{4\perp} = (a_{o\perp} \otimes a_{o\perp}) : \bar{C}$, where *a_o* and *a_{o⊥}* are unit vectors representing the symmetric mean and perpendicular fiber directions, respectively. The strain terms (\bar{E}_{\parallel} , \bar{E}_{\perp}) are,

$$\bar{E}_{\parallel} = (1 - \zeta)(\bar{I}_4 - 1) \text{ and } \bar{E}_{\perp} = (\zeta)(\bar{I}_{4\perp} - 1), \quad (3a,b)$$

where ζ is a scalar material parameter characterizing the average fiber component in the *a_{o⊥}* direction in an integral sense and ranging within [0,1] for a general planar distribution of multiple fiber families.

$\bar{\Psi}_{f-strong}$ is mathematically equivalent to the 2-fiber HGO model and strongly couples stress in one planar direction to stretch in the perpendicular planar direction. $\bar{\Psi}_{f-medium}$ has less strong deformation coupling. The theoretical Cauchy stress can be determined by,

$$\sigma = 2F \frac{\delta \bar{\Psi}}{\delta C} F^T - pI. \quad (4)$$

Material parameters for the strong and medium forms of the DS model were fitted to the mechanical testing data by minimizing the error between the experimental and theoretical stresses. Results were compared by ANOVA for age, sex, and genotype.

RESULTS

Biaxial mechanical data for the LCC, which is a muscular-elastic artery, has a better fit to $\bar{\Psi}_{f-medium}$ than $\bar{\Psi}_{f-strong}$. The ASC, which is the most elastic artery in the body, has a better fit to $\bar{\Psi}_{f-strong}$ than $\bar{\Psi}_{f-medium}$. Mean R^2 for the best fit model ranges from 0.74 - 0.80 for both arteries. Figure 1 shows material parameters for the best fit models only. For the LCC with medium deformation coupling, sex has a significant effect on all fitted material parameters except ζ , age has a significant effect on k_2 , and genotype has a significant effect on c , k_2 , and ζ (Fig. 1, left). For the ASC with strong deformation coupling, sex has a significant effect on c and k_1 , age has a significant effect on k_2 and ζ , and genotype has a significant effect on all fiber parameters (Fig. 1, right). The results show artery dependent deformation coupling and variation of the matrix and fiber material parameters that depend on artery type, age, sex, and genotype.

Using the fitted material parameters, we calculated the strain energy and biaxial stresses under physiologic loading conditions [1]. The stored strain energy decreases with age in both arteries and also with elastin amounts by genotype in the LCC (Fig. 2). In the LCC, the stresses decrease with elastin amounts and the axial stresses also decrease with age (Fig. 2, left). The stresses in the ASC are maintained across sex, age, and genotype (Fig. 2, right). The results show adaptations in the ASC to maintain stresses and partially maintain strain energy that are not observed in the LCC.

DISCUSSION

Large arteries have varying amounts of cells and ECM that depend on their location and function. Our results suggest that deformation coupling varies by artery type. As the LCC can experience large axial stretch with positioning of the head and neck, medium (as opposed to strong) deformation coupling may protect cells within the wall from excessive circumferential stress. Our results also suggest a higher capacity for remodeling to maintain homeostatic strain energy and stresses in the ASC compared to the LCC. As the ASC receives the entire cardiac output and its energy storage and pulse dampening is critical for cardiac function, this may be necessary to build flexibility into the cardiovascular system and adapt to changes in ECM amounts with aging and disease. The DS model used here allows investigation into changes in matrix and fiber mechanical contributions with artery type, age, sex, and genotype. Future work will investigate how changes in ECM amounts and organization correlate with specific material parameters for a better understanding of the remodeling process.

ACKNOWLEDGEMENTS

This work was partially supported by NSF 1662434, NIH R01-HL-105314, NIH R01-HL-164800, and AHA 19TPA-34910047.

REFERENCES

1. Hawes, J.Z., et al., Am J Physiol Heart Circ Physiol, 2020.
2. Holzapfel, G.A., et al., Journal of Elasticity, 2000.
3. Dong, H. and W. Sun, J Mech Phys Solids, 2021.

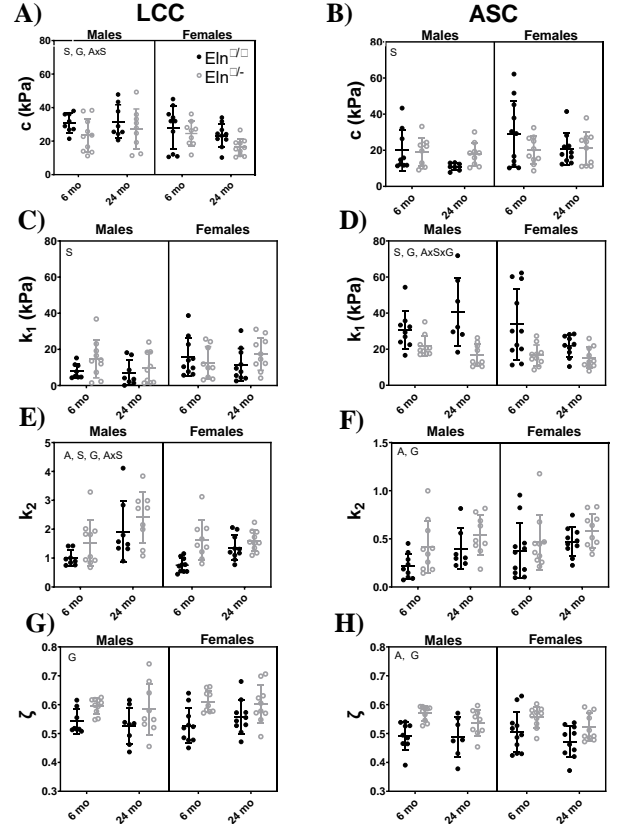


Fig 1. Fitted strain energy constants (Eqs. 1-3) for the LCC (left) and ASC (right). Notation indicates significant differences for age (A), genotype (G), and/or sex (S).

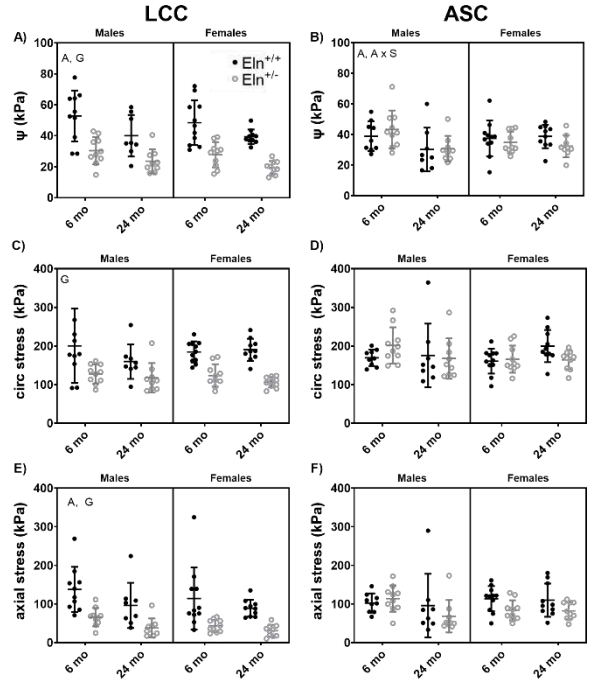


Fig. 2: Predicted ψ (A, B), circumferential (C, D), and axial stress (E, F) under physiologic loads for the LCC (left) and ASC (right). Notation indicates significant differences between groups for age (A), genotype (G), and/or sex (S).

THERMODYNAMICS OF PHASE TRANSFORMATION OF WATER: THEORY AND EXPERIMENTS

Raphael J. Kepecs, Gerard A. Ateshian

Department of Mechanical Engineering, Columbia University, New York, NY, USA

INTRODUCTION

Phase transformations play an essential role in many bioengineering applications, such as evaporation of saliva droplets leading to aerosolization of virus loads [1], or cryo-preservation of cells for medical and research applications [2]. However, theoretical thermodynamic principles, when applied to phase transformations, are limited to reversible processes, implying that these processes undergo very slow phase changes with negligible mass fluxes. Governing equations that remain valid for irreversible phase transformations have not been reported in the standard literature.

In a recent theoretical study [3] we used the framework of reactive mixtures [4] to formulate jump conditions across a phase boundary, which remain valid for irreversible processes. Using the jump condition for the axiom of entropy inequality, we recovered the conventional result that stable phase equilibrium coincides with continuity of temperature, pressure, and free enthalpy across the phase boundary. Moreover, this jump condition led to the novel formulation of a constitutive relation for the phase transformation mass flux,

$$M\bar{\zeta} = - \left[\left[\frac{1}{T} \mathbf{q} \right] \right] \cdot \mathbf{n}^\Gamma / [s], \quad (1)$$

where \mathbf{q} is heat flux, $\left[\left[\frac{1}{T} \mathbf{q} \right] \right] \cdot \mathbf{n}^\Gamma$ is the jump in entropy flux normal to, and across the phase interface Γ , and $[s]$ is the corresponding jump in specific entropy. This relation implies that phase transformations must be accompanied by a jump in absolute temperature T across the phase boundary, consistent with experimental data for the evaporation of liquid water [5]. Recently, we reported encouraging agreement between eq.(1) and experimental data for steady-state water evaporation [3].

The objective of the current study was to validate this theoretical framework against a well-known experiment reported extensively on YouTube [6], where supercooled liquid water in a bottle suddenly freezes (turns to slush) along a rapidly moving front when the bottle is shaken or struck. The initial metastable state of the supercooled water

is explained using this novel theoretical framework. Moreover, the rapid motion of the freezing front (phase boundary) epitomizes the irreversibility of this phase transformation, thus providing an excellent illustration of a common observation which could not be explained from classical thermodynamic principles.

METHODS

The experimental method employed for producing a freezing front in a water bottle was based on various videos posted on YouTube, such as [6]. A sealed natural spring water bottle (330 mL) was placed horizontally in a household freezer for 75 minutes (-30°C). Care was taken to leave the household freezer undisturbed over this duration. The bottle was then carefully taken out, gently turned upright, and placed on a table top. The bottle cap was slowly unsealed and removed to insert a thermocouple (K type, 0.1°C resolution) and measure the temperature at various locations along the height. The bottle was also placed in front of a thermal imaging camera (FLIR ONE Pro-iOS, flir.com) to assess spatial variations in temperature, and a visible light camera as an alternative method of visualizing the moving phase boundary. Phase transformation was initiated by lifting up the bottle by a few centimeters and banging it down lightly against the table top. Thermocouple and thermal/visual imaging measurements were conducted throughout the duration of the phase transformation. In a separate experiment, two holes were drilled in the cap of a water bottle to insert thermocouples, one of which measured the water vapor (v)-air temperature above the water level while the other measured the liquid water temperature halfway along its height, as a function of time, as the bottle was kept upright in the freezer for 70 minutes.

Let the outward normal \mathbf{n}^Γ point upward on the liquid water interface Γ . Based on the axiom of mass jump across the phase boundary Γ [3], the normal velocity of Γ , v_n^Γ , is related to normal velocities v_n^ℓ and v_n^i of the liquid and ice phases, respectively, by

$$v_n^\Gamma = v_n^\ell - M\bar{\zeta}/\rho^\ell = v_n^i - M\bar{\zeta}/\rho^i \quad (2)$$

where ρ^ℓ and ρ^i are the mass densities of liquid water and ice, respectively. Since the liquid water in the bottle remained stationary, we could set $v_n^\ell = 0$ and solve for the phase transformation mass flux $M\bar{\zeta}$ from eq.(2), using measurements of v_n^Γ and knowing that $\rho^\ell \approx 1000 \text{ kg/m}^3$ near freezing temperatures.

RESULTS

When the water bottle was placed upright in the freezer, to allow placement of thermocouples in the v +air pocket, and in the liquid, through the perforated bottle cap, the temperature of v +air dropped more rapidly than that of the liquid water, as shown in Fig. 1. When the temperature of v +air dropped below -5°C , the liquid water eventually froze to a slush, reaching a nearly constant temperature of $\sim 0.2^\circ\text{C}$.

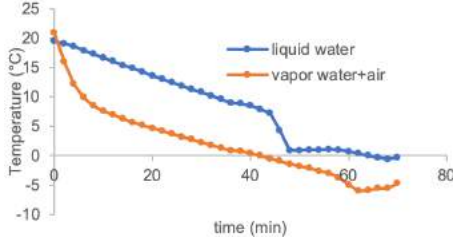


Fig. 1. Temporal temperature variation in liquid water and v +air pocket, in a bottle placed upright in a freezer.

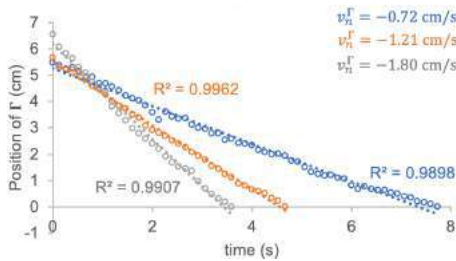


Fig. 2: Velocity v_n^Γ of phase boundary Γ obtained from slope of position vs. time, in bottles initially placed horizontally in a freezer.

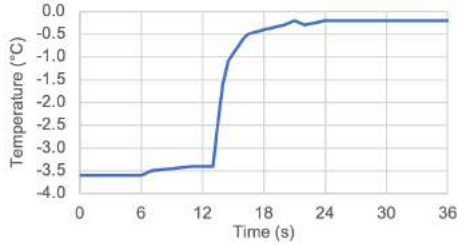


Fig. 3: Temporal evolution of T at a fixed point in bottle, as the liquid-ice phase boundary Γ traveled downward (thermocouple)

When the water bottle was placed horizontally in the freezer, then taken out carefully and banged upright on a table top, the phase boundary Γ traveled downward ($v_n^\Gamma < 0$) along the height of the bottle, with an average velocity of 1.24 cm/s as assessed from measurements on three (Fig. 2). The corresponding phase transformation mass flux, evaluated from eq.(2), would be $M\bar{\zeta} = -\rho^\ell v_n^\Gamma \approx 12.4 \text{ kg/m}^2 \cdot \text{s}$ if all the liquid water had turned into ice; however, the actual value of $M\bar{\zeta}$ is smaller since the liquid water turns into slush (liquid+ice mixture). Thermocouple measurements at $\sim 6 \text{ cm}$ above the base of the bottle was used to capture the temporal temperature variation as Γ travelled across that location (Fig. 3). In this case, the temperature of the supercooled liquid water (-3.6°C) rose to -0.2°C during the phase transformation.

A snapshot of the vertical variation of temperature across Γ in the bottle, obtained from the thermal imaging camera, is shown in Fig. 4.

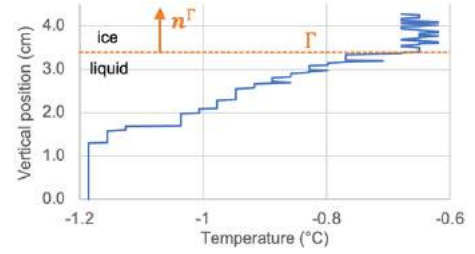


Fig 4. Snapshot of vertical variation of temperature during phase transition, with phase boundary Γ at $\sim 3.4 \text{ cm}$.

DISCUSSION

As discussed in our recent theoretical study [3], metastable phase equilibria ($M\bar{\zeta} = 0$) must satisfy the entropy inequality jump

$$[[1/T]]q^\Gamma \cdot n^\Gamma \leq 0 \quad (3)$$

where $q^\Gamma \cdot n^\Gamma$ is the mean (and continuous) heat flux across and normal to the phase boundary Γ . Familiar stable phase equilibrium is the special case when temperature T is continuous across Γ , thus $[[1/T]] = 0$, satisfying eq.(3) unconditionally. In our experiments, supercooling liquid water below 0°C represents a metastable state where the interface between liquid (ℓ) and vapor water (v) + air must satisfy the above inequality. This relation is satisfied either if the air temperature is lower than the liquid and heat conducts from liquid to vapor water, or vice-versa. Experimental measurements of this study (Fig. 1) demonstrated that the v +air temperature dropped below that of liquid water, as soon as the water bottle was placed in the freezer, and until the water spontaneously froze. Thus, prior to the start of liquid-to-ice transformation, temperatures at the liquid-vapor interface satisfied $[[1/T]] = 1/T^\ell - 1/T^v \leq 0$ in eq.(3). For this upright bottle orientation, the water did not reach a supercooled state prior to freezing (Fig. 1). Nevertheless, we can assume that the temperature variation in horizontal bottles decreased similarly, with the v +air temperature dropping much faster than that of the liquid, with the latter eventually achieving a supercooled state (Fig. 2). This thermodynamic description of the metastable state of supercooled water, as per eq.(3) and experimental measurements of this study, has not been given before.

Since the specific entropy s^ℓ of liquid water is nearly zero at freezing temperatures, we have $[[s]] \approx -s^i \approx 1.22 \text{ kJ/kg} \cdot \text{K}$. Now, eq.(1) may be rewritten in the simplified form

$$M\bar{\zeta} = \frac{1}{s^i} \left(\frac{q_n^\ell}{T^\ell} - \frac{q_n^i}{T^i} \right), \quad (4)$$

where q_n^ℓ and q_n^i represent the heat fluxes normal to Γ , in liquid and ice water, respectively. Since $M\bar{\zeta} > 0$ and $s^i < 0$, this constitutive model would be valid only if $q_n^\ell/T^\ell - q_n^i/T^i < 0$ on Γ , which is indeed satisfied by the temperature gradients (Fig. 4, with $q_n^\ell \approx 0$ and $q_n^i < 0$). Therefore, experimental measurements of this study support our constitutive model in eq.(1), under irreversible conditions of rapid phase transition of water to ice.

ACKNOWLEDGEMENTS

National Institutes of Health (R01GM083925)

REFERENCES

- [1] Netz, RR, *J Phys Chem B*, 2020. **124**(33): p. 7093-7101.
- [2] Pegg, DE, *Methods Mol Biol*, 2015. **1257**: p. 3-19.
- [3] Ateshian, GA, JJ Shim, *arXiv preprint arXiv:2207.14158*, 2022.
- [4] Bowen, RM, *Arch Ration Mech Anal*, 1969. **34**(2): p. 97-127.
- [5] Badam, V et al., *Exp Therm Fluid Sci*, 2007. **32**(1): p. 276-292.
- [6] Hacker, Mr., <https://www.youtube.com/watch?v=kEHdyiBMgAg>.

A METHODOLOGY TO OBTAIN INJURY AND BIOMECHANICAL DATA FROM LIVE SWINE EXPERIMENTATION FOR BEHIND ARMOR BLUNT TRAUMA

**Alok S. Shah (1), Narayan Yoganandan (1), Mary F. Otterson (2), Brian D. Stemper (3),
Joost Op 't Eynde (4), Cameron D. Bass (4), Justin McMahon (5), Robert S. Salzar (5),
B. Joseph McEntire (6)**

- (1) Department of Neurosurgery, Medical College of Wisconsin, Milwaukee, WI, USA
- (2) Department of Surgery, Medical College of Wisconsin, Milwaukee, WI, USA
- (3) Joint Department of Biomedical Engineering, Medical College of Wisconsin, Milwaukee, WI, USA
- (4) Biomedical Engineering, Duke University, Durham, NC, USA
- (5) Center for Applied Biomechanics, University of Virginia, Charlottesville, VA, USA
- (6) Injury Biomechanics and Protection, U.S. Army Aeromedical Research Laboratory, Fort Rucker, AL, USA

INTRODUCTION

The use of body armor has been shown to reduce the risk of penetrating injuries among military personnel and first responders [1], [2]. While the body armor decreases the risk of penetrating injuries, ballistic energy can still be transferred through the protective layers, causing backface deformation, and result in injuries to the underlying tissues [3]. These non-penetrating injuries are referred to as Behind Armor Blunt Trauma (BABT).

The National Institute of Justice (NIJ) Standard-0101.06 is an armor test standard widely used to assess the ballistic resistance of personal body armor [4]. Tests are performed by placing the armor over Roma Plastilina No. 1 clay backing, and targeting is based on test specifications. Assuming there is no penetration of the armor, the performance of the armor is assessed by measuring the residual deformation depth of the clay behind the armor. The pass/fail criteria of the armor are solely based on the maximum allowable backface deformation depth of 44 millimeters (mm) for all test conditions. The 44 mm limit was developed in the 1970s for soft body armor applications using a limited series of ballistic impacts on live goats [5]. Although the standard was initially developed for soft body armor, it has been adopted for rigid body armor assessments. Armor plates can alter the resulting backface deformation characteristics compared to soft body armor, which could alter injury tolerance. The standard also does not account for the differing regional thoracoabdominal tolerances to injuries caused by BABT.

The overall objective of this research program was to develop thoracoabdominal regional injury risk curves by applying a hybrid approach utilizing cadaveric swine, live swine, and post-mortem human subjects to update the legacy standard. The development of new standards will aid in assessing and designing body armor and improve BABT safety against current and future threats. The present study was conducted to demonstrate a BABT experimental methodology using an

impact loading indenter to simulate backface deformation with a live swine surrogate.

METHODS

All experiments were conducted in compliance with the Institutional Animal Care and Use Committee at the Medical College of Wisconsin and the Zablocki Veterans Administration Medical Center. Prior approval was obtained from the Animal Care and Use Review Office (ACURO) of the U. S. Department of Defense.

A live swine of approximately 42 kilograms (kg) was used for the experiment. Trachea tubes and intravenous lines were placed following induction of anesthesia using telazol and xylazine. Pressure transducers were placed in each lung and aorta. One transducer was guided into each lung through the trachea tube. To place the transducer in the aorta, a small incision in the neck was made to isolate a blood vessel routing to the aorta. The blood vessel was clamped on one end to allow for a small incision to be made to insert the transducer. The transducer was sutured and secured to prevent movement and blood loss. The placement of lung and heart transducers was confirmed via C-arm radiographic imaging. The swine was connected to isoflurane ventilation for continuous anesthesia delivery for the remainder of the experiment.

A BABT indenter was designed using high-speed flash x-rays to approximate backface deformation profiles produced in body armor from military relevant ballistic rounds [6]. The indenter was launched at the target region using a gas-driven launching system. A triaxial accelerometer (Endevco 7284, Depew, NY) was mounted within the indenter and hardwired to an external data acquisition system (DTS Slice PRO, Seal Beach, CA). The mass of the instrumented indenter was 240 grams. Data from the indenter accelerometer and pressure transducers were recorded at 500 kilohertz (kHz) sample frequency and filtered at 2 kHz with a four-pole Butterworth filter.

The animal was subjected to a single impact to the left thoracic wall between the third and fourth ribs to target the left lung. The animal was placed in a supine position on a lift table so that the impact site was in line with the exit of the launching system. The animal was kept in a continuous surgical state of anesthesia, and vitals were monitored and recorded for six hours post-impact. Upon completion of the six-hour survival window, the animal was euthanized, and a necropsy was performed.

RESULTS

The animal survived the six-hour survival window post-impact. There was an increase in cardiovascular activity immediately following the impact, but vitals stabilized over the course of the survival window. The impact energy was 349 Joules (J), and the indenter peak acceleration was 3844 G. The acceleration time history of the indenter is shown in Figure 1. A contusion occurred at the impact location, but the skin remained intact.

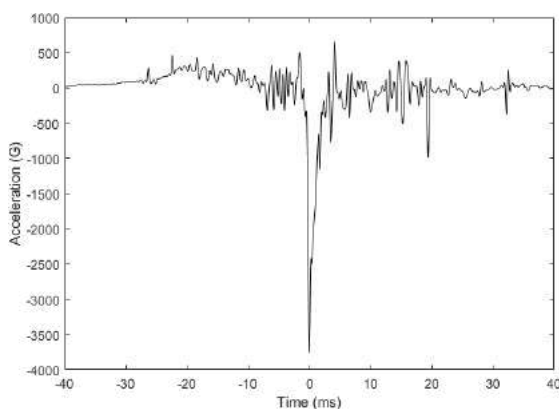


Figure 1: Acceleration-time history of indenter filtered at 2 kHz.

There were fractures at ribs V, VI, VII, and VIII (Figure 2). Additionally, pleural lacerations occurred (not shown). Hemorrhages were seen in the left lung, and lacerations were seen on the lung adjacent to rib VI and VII fractures. Blood aspiration was observed in the right lung (Figure 3). No damage was found in the heart, stomach, liver, spleen, or kidneys.

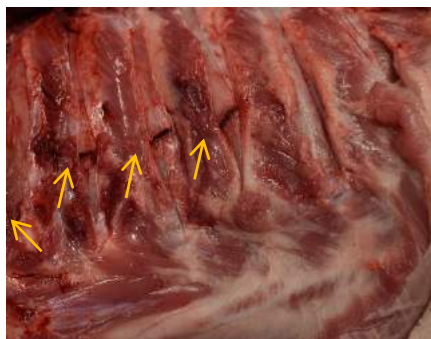


Figure 2: Rib fractures at ribs V, VI, VII, and VIII (left to right).

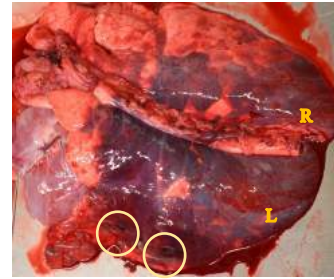


Figure 3: Left lung hemorrhages and lacerations adjacent to rib VI and VII fractures.

DISCUSSION

The overall objective of this research program was to develop injury risk curves for different thoracoabdominal regions for BABT-induced injuries. It should be noted that this study focused on one sample to demonstrate the feasibility of using the experimental methodology. While studies have been conducted using live swine and different types of impactors, this study used an indenter design based on backface deformation data recorded using high-speed x-rays on a human cadaver in an earlier study [6], thus adding relevance to the BABT loading. While not reported herein, preliminary experiments were conducted at the three institutions of the authors of this study with swine cadavers and unembalmed human cadavers to add to the feasibility of using the simulated indenter on different surrogates and at different thoracoabdominal regions. In the current study, the injury severity matched a previous study by Liden et al. [3], who reported similar injuries in the left lung from using a 12-bore shotgun with U.S. No. 1 shot against 12-ply Kevlar 29 [3]. Similar injury patterns have been found in a study evaluating hard body armor [7]. Although other studies have shown similar injury patterns to the lungs, the human thoracoabdominal organs and musculoskeletal systems likely have different tolerances to BABT injuries at the same level of insult. Kunz et al. showed fatalities in swine from BABT simulated impacts to the heart at energy impact levels similar to those used in the present study (>300 J) [8]. It is necessary to perform additional tests at injurious and non-injurious impact loading levels to develop region-specific BABT injury criteria. This experimental methodology allows for targeting different thoracoabdominal regions at varying energy levels.

DISCLAIMER

The views, opinions, and/or findings contained in this abstract are those of the author(s) and should not be construed as an official Department of the Army position, policy, or decision, unless so designated by other official documentation.

ACKNOWLEDGEMENTS

This research was supported by the U.S. Army Medical Research and Development Command contract W81XWH-21-9-0015 and the Department of Veterans Affairs Medical Research.

REFERENCES

- [1] Gondusky, JS et al., *Mil. Med.*, 170:546-549, 2005
- [2] Latourrette, T. *J. Occup. Environ. Hyg.*, 7:557-562, 2010
- [3] Liden E et al., *J. Trauma-Inj. Infect, Crit Care*, 28:145-148, 1988
- [4] Mukasey MB et al., *NIJ Stand. - 0101-16*, pp. 1-89, 2008.
- [5] Hanlon E et al., *Mil. Med.*, 177:333-339, 2012
- [6] Bass CR et al., *Int. J. Occup. Saf. Ergon.*, 12:429-442, 2006
- [7] Gryth D et al., *Mil. Med.*, vol 172, 2007
- [8] Kunz SN et al., *J. Trauma - Inj. Infect. Crit. Care*, 71:1134-1143, 2011

MACHINE LEARNING-BASED REDUCED ORDER MODELLING FOR THE SIMULATION OF BRAIDED STENT DEPLOYMENT.

Beatrice Bisighini(1,2,3), Miquel Aguirre (4,5,1), Baptiste Pierrat (1), David Perrin (2), Stéphane Avril (1)

- (1) Mines Saint-Étienne, Univ Lyon, Univ Jean Monnet, INSERM, U 1059 Sainbiose, 42023, Saint-Étienne, France
 (2) Predisurge, 10 rue Marius Patinaud, Grande Usine Creative 2, 42000 Saint-Etienne, France
 (3) University Tor Vergata, Department of Enterprise Engineering, Via del Politecnico 1, 00133 Rome, Italy
 (4) Laboratori de Càlcul Numèric, Universitat Politècnica de Catalunya, Jordi Girona 1, E-08034, Barcelona, Spain
 (5) International Centre for Numerical Methods in Engineering (CIMNE), Gran Capità, 08034, Barcelona, Spain

INTRODUCTION

Flow diverters are self-expanding braided stents used in the endovascular treatment of intracranial aneurysms [1]. Nowadays, surgeons choose the device based only on their clinical experience and measurements taken on medical volumetric images, acquired shortly before surgery. However, the configuration assumed by these devices once deployed within the parent vessel is not easily predictable. Given the tight timescale, there is a compelling need to develop computational models capable of simulating in real-time the deployment of flow diverters within patient-specific vessels to assist practitioners in the planning and interventional stages.

The mechanical behaviour of braided stents is typically assessed using a finite element (FE) model where beam elements are used to model the wires [2, 3]. However, due to the large amount of degrees of freedom (DOFs) needed to model accurately flow diverters and the necessity to solve the contact with the arterial wall, the computational time required by FE simulations is very high.

Reduced order modelling (ROM) is a family of methods that aim at reducing the computational complexity of numerical problems by approximating their solution. In practice, these techniques, such as the reduced-basis (RB) method, replace the high-fidelity (HF) model with a reduced-order model characterized by a much smaller dimension. ROM methods have been successfully used before in computer-aided surgery, e.g. to model the arterial blood flow and the heart electrophysiology [4, 5] and predict the thrombectomy procedures outcome [6].

In this study, we propose a machine learning (ML)-based ROM scheme for the prediction of the stent deployed configuration. This is achieved using a non-intrusive ROM scheme that combines the proper orthogonal decomposition (POD) algorithm and Gaussian process regression (GPR). The workflow is validated on an idealised intracranial artery with a saccular aneurysm and the effect of six geometrical and surgical parameters on the outcome of stent deployment is studied.

METHODS

Braided stent model. The braided stent is modelled as a tubular net of thin wires with circular cross-section, whose nodal positions are defined through parametric equations. A generic stent is employed in this study, with radius $R_s = 2.6$ mm, length $L = 15$ mm and composed of 48 wires.

Parametric vessel model. The Visualization Toolkit (VTK) software is employed to build the parametric model. The artery is created as a tube with constant diameter D_v around the vessel centerline. The latter is defined using a planar quadratic Bézier curve:

$$\mathbf{B}(t) = (1-t)^2 \mathbf{P}_0 + 2t(1-t) \mathbf{P}_1 + t^2 \mathbf{P}_2, \quad t \in [0, 1], \quad (1)$$

where $\mathbf{P}_0, \mathbf{P}_2$ are fixed and \mathbf{P}_1 is the control point included in the parametrisation. A spherical idealised aneurysm with diameter D_a is then added to the artery model: the sphere centre \mathbf{C}_a is positioned in the middle of the vessel centerline and the relative y -distance is parametrised.

FE simulations of stent deployment. The stent structure is discretised using beam elements and simulations are performed using EndoBeams.jl, an in-house and open-source FE solver [7]. The procedure of stent deployment within an artery is performed as follows: the braided stent is first crimped by imposing a radial displacement to all its nodes, then bent along the vessel centerline and, finally, deployed by releasing it within the artery. Since we are interested in the final deployed configuration of the stent, quasi-static simulations are performed.

HF database. For the creation of the HF dataset, we considered the following parameters:

$$\boldsymbol{\mu}_B = [y_{\mathbf{P}_1}, z_{\mathbf{P}_1}, D_v, D_a, y_{\mathbf{C}_a}, \eta] \quad (2)$$

where η is the stent deployment site along the vessel centerline. A Latin hypercube sampling method is used to generate N_s different values for $\boldsymbol{\mu}_B$; the corresponding artery models are created and a stent deployment simulation is performed within each model. If given the deployment conditions

the stent is well positioned against the vessel wall and does not land inside the aneurysm, the deployment is considered successful from a clinical perspective. Since there is no clinical need to predict the stent configuration after an unsuccessful deployment, these simulations are excluded from the training. Alternatively, the simulation parameters μ_B are substituted with μ_{cl} where, instead of the middle point of the Bézier curve (\mathbf{P}_1) and the stent deployment site (η), the y and z coordinates of N_{cl} points on the positioned stent centerline are used. The μ_{cl} vector components are calculated geometrically from the deployment conditions and no FE simulation is required.

ROM. Once the database is ready, the snapshots matrix \mathbf{S} is built by arranging the high-fidelity solutions \mathbf{u}_h , containing the nodal displacements at the end of the deployment simulation, as columns of a matrix. The POD algorithm consists in performing the singular value decomposition of \mathbf{S} and extracting, based on an optimal algorithm, the first L left-singular vectors. These column vectors represent the RBs of the model and are assembled in the matrix \mathbf{V} . To compute the projection coefficients, a GPR model is used where the predictors are the parameter values μ and the outputs are the coefficients \mathbf{u}_L , computed starting from the high-fidelity solutions as:

$$\mu \rightarrow \hat{\mathbf{u}}_L(\mu) \approx \hat{\pi}(\mu) \quad \text{trained from} \quad (\mu_i, \mathbf{V}^T \mathbf{u}_h(\mu_i)). \quad (3)$$

Once trained, the model is used to predict the projection coefficients for any desired value of the parameters μ^* , i.e., $\hat{\mathbf{u}}_L(\mu^*)$. This allows recovering the full order solution as $\mathbf{u}_p(\mu^*) = \mathbf{V} \hat{\mathbf{u}}_L(\mu^*) \approx \mathbf{u}_h(\mu^*)$.

Evaluation metrics. For the test cases, the ROM results are evaluated against the HF solutions by computing the absolute prediction error at each node of the stent mesh: $E_p = \|\mathbf{u}_p(\mu) - \mathbf{u}_h(\mu)\|$. The accuracy of a single solution can be evaluated as the average error on the mesh nodes (AE_p) while global variables can be computed by averaging these values on the test dataset (AE_p).

RESULTS

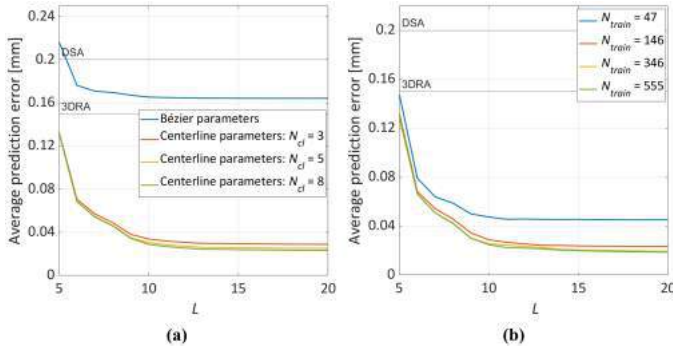


Figure 1: Sensitivity analysis on (a) the predictors used as ML input and (b) the number of training samples.

We started with a dataset with $N_s = 900$ simulations and defined three optimal subspaces with $N_s = \{150, 300, 600\}$. Then, we built four datasets with only the deployment simulations outcomes which are labelled as successful from a clinical perspective, $N_{success} = \{97, 196, 396, 555\}$. We considered a fixed number of samples for testing ($N_{test} = 50$). The spatial resolution of imaging techniques currently used for IAs detection and treatment was considered for evaluating the prediction errors: digital subtraction angiography (DSA) = 0.2 mm, 3D rotational angiography (3DRA) = 0.15 mm. Other imaging techniques show worse spatial resolution.

As visible in Figure 1, the prediction does not benefit considerably by considering a number of RBs greater than 15: in fact, the average prediction error reaches a stable plateau around $L = 15$. It can be noticed in Figure 1(a) that the prediction error is strongly reduced when using μ_{cl}

instead of μ_B : with 3 points along the stent centerline ($N_{cl} = 3$), the average prediction error is 5.65 times lower than when using μ_B . Increasing the number of considered points N_{cl} , the prediction does not improve significantly. We also analysed the influence of the number of train samples on the ROM performance (Figure 1(b)): considering $N_{train} = 146$ instead of $N_{train} = 47$, the average prediction error is 1.92 times lower. No particular improvement is observed when the training set is further expanded.

DISCUSSION

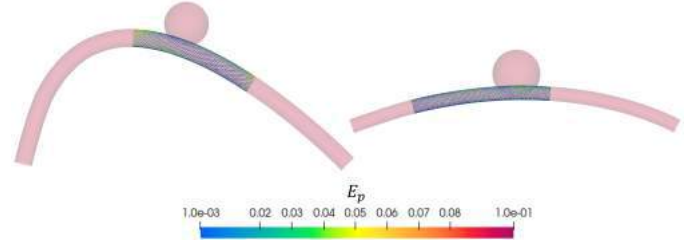


Figure 2: Examples of predicted solution from the testing database.

In summary, using this technique, simulations are achieved within a few milliseconds once the ROM is trained, compared to ~ 1 h required by traditional FE simulations, while retaining the mechanical realism and predictability of the deployed configuration. The impact of these geometrical and surgical parameters on the deployed stent configuration could be predicted accurately even with a low number of RBs (15). As can be seen in Figure 2, the prediction error is evenly distributed and the stent configuration adapts very well to the vessel curvature. The results showed that the GPR is strongly influenced by the input parameters: using the positioned stent centerline (μ_{cl}) as GPR predictors, the average prediction error could be reduced by more than 5 times. With only 47 training samples, we achieved an average prediction error more than 3 times lower than the 3DRA spatial resolution; using 147 training samples, even more than 7 times. This demonstrates the ability of ML and ROM to model the complexity of stent deployment problems.

A limitation of this workflow is the use of a parametric model that reproduces only partially the complexity of patient-specific models: the introduction of more parameters will result in a larger number of bases and thus, require a larger training database. Therefore, specific methods for constructing the training database and alternative ML algorithms need to be considered. A similar scenario could occur by introducing non-rigid arteries. Our current efforts focus on understanding the number of parameters needed to fully describe patient-specific geometries and implementing deformable-wall models within our FE framework.

ACKNOWLEDGEMENTS

This project is carried on in the framework of the MeDiTaTe Project, which has received funding from the European Union's Horizon 2020 research and innovation programme under Grant Agreement 859836.

REFERENCES

- [1] Durso PI et al. *Stroke* 42.8 (2011).
- [2] Ma D et al. *Journal of Biomechanics* 45.13 (2012).
- [3] Zaccaria A et al. *Journal of Biomechanics* 107 (2020).
- [4] Girfoglio M et al. *Medical Engineering and Physics* 107.7 (2022).
- [6] Bridio S et al. *Journal of the Mechanical Behavior of Biomedical Materials* 137.6 (2022).
- [7] Bisighini B et al. *Advances in Engineering Software* 171.6 (2022).

A MULTI CENTER ILIAS REGISTRY BASED DIAGNOSTIC CUTOFF FOR PRESSURE DROP COEFFICIENT IN RELATION TO THE CURRENT PRESSURE AND FLOW ENDPOINTS IN PATIENTS WITH CORONARY ARTERY DYSFUNCTION

Shreyash M Manegaonkar (1), Mohamed A. Effat (2), Tim P. van de Hoef (3), Rupak K. Banerjee (4)

(1) Department of Mechanical and Materials Engineering, College of Engineering and Applied Science, University of Cincinnati, Cincinnati, Ohio, USA

(2) Division of Cardiovascular Health and Disease, University of Cincinnati, Cincinnati, Ohio, USA

(3) Department of Cardiology, Amsterdam UMC location AMC, Amsterdam, The Netherlands

(4) Department of Biomedical Engineering, University of Cincinnati, Veterans Affairs Medical Center, Cincinnati, Ohio, USA

INTRODUCTION

Coronary artery disease (CAD) occurs when the coronary arteries that supply blood to the heart muscle are blocked or narrowed. The combination of epicardial stenosis (ES) and microvascular disease (MVD) resistances cause sequential obstruction of blood flow to the heart muscle [1-5]. The relative contributions of these resistances must be distinguished for guiding the clinical decision-making process that leads to the selection of the most effective treatment protocol [6, 7]. The functional assessment of intermediate coronary stenosis with or without MVD remains a clinical challenge for interventional cardiologists. Current clinical practice frequently uses diagnostic variables like fractional flow reserve (FFR, the ratio of the mean distal coronary and aortic pressure at hyperemia) and coronary flow reserve (CFR; the ratio of coronary flow at hyperemia to that at rest), which are independent measures of intra coronary pressure and flow respectively. They are both susceptible to being confounded by the presence of MVD; thereby, these indices are unable to distinguish between the hemodynamic condition of concomitant ES and MVD [8, 9].

In order to simultaneously detect ES and MVD, we developed a non-dimensional parameter, the pressure drop coefficient (CDP; the ratio of pressure drop (Δp) across a stenosis to distal dynamic pressure), based on fundamental principles of fluid dynamics which combines pressure and flow measurements. The ability of the CDP to distinguish between stenosis and MVD has been examined, and the CDP cut-offs were initially evaluated to determine the various levels of ES severity using a meta-analysis [10-12].

The *objective* of this research is to determine the limiting value of CDP that can distinguish between patients with ES and MVD using patient level pressure-drop and average peak velocity (APV) data from the multicenter international ILIAS (Inclusive Invasive Physiological Assessment in Angina Syndromes) registry. We *hypothesize* that CDP, provides sufficient diagnostic accuracy for assessing the severity of coronary lesions.

METHODS

The data was extracted from ILIAS registry, which has been established on a global multicenter platform, for improved diagnosis of CAD when combined coronary pressure and flow measurements are used in clinical settings. The registry is made up of 20 reputable medical institutions from 7 different countries and all data were prospectively recorded in accordance with the protocols for individual trials. The registry consists of 2,322 patients enrolled and 3,046 assessed vessel data. Informed consent was obtained from all the study subjects who, based on the inclusion and exclusion criteria, underwent exercise testing and myocardial perfusion scans.

Using standard-of-care catheterization techniques such as coronary thermodilution and doppler flow velocity measurement, intracoronary pressure and APV measurements across the ES were obtained. Doppler flow velocity measurement was used to analyze 1,050 arteries. Patients undergoing coronary thermodilution were excluded from the present analysis, because a direct measure of velocity was unavailable for calculating the pressure drop coefficient (CDP).

FFR is defined as the ratio of the mean distal coronary pressure, p_d and aortic pressure, p_a , at hyperemia (Eq. 1).

$$FFR = \left(\frac{p_d}{p_a} \right)_{\text{hyperemia}} \quad (1)$$

CFR is defined as the ratio of coronary flow at hyperemia to that at rest.

CDP is defined as the ratio of trans stenotic pressure drop ($\Delta p = p_a - p_d$) to distal dynamic pressure, which is the product of blood density (ρ), the square of average peak flow velocity (APV) at hyperemia, and a constant value of 0.5 (Eq. 2).

$$CDP = \frac{\Delta p}{0.5 \times \rho \times APV^2}, \text{ (where } \Delta p = p_a - p_d \text{)} \quad (2)$$

The FFR and CFR were regarded as 'positive' for values of 'less than 0.80' and 'less than 2.0', respectively. The diagnostic performance of CDP with FFR and CFR was compared using a Receiver Operating Characteristic (ROC) curve analysis. The area under the curve (AUC) was calculated after the ROC curves were generated using sensitivity and specificity values with the help of R Markdown software (RStudio Team (2022); RStudio: Integrated Development Environment for R. RStudio, PBC, Boston, MA; <http://www.rstudio.com/>). For predetermined and clinically accepted cut off values of CFR = 2.00 and FFR = 0.80, the accuracy of CDP to successfully predict the outcome of FFR and CFR was calculated. For $p < 0.05$, the results were considered statistically significant.

RESULTS

Figure 1 shows the receiver operating characteristic (ROC) curve, used to determine the optimal CDP cut-off value corresponding to $FFR \leq 0.80$. A total of 464 data points satisfied the criterion for $FFR \leq 0.80$. The area under the ROC curve for CDP (Figure 1A), to predict $FFR < 0.80$, equals 0.88 (95% CI: 0.86 to 0.90, $p < 0.001$), with a sensitivity of 83.40% and specificity of 76.76%. For $FFR \leq 0.80$, the equivalent CDP cut-off value was 26.20.

Similarly, the ROC curves for the subgroups with FFR threshold of 0.8 and CFR threshold of 2.0 were plotted. The area under the ROC curve for the subgroup of $FFR \leq 0.80$ and $CFR < 2.0$ was significant at 0.75 (95% CI: 0.70 to 0.79, $p < 0.001$). Additionally, the area under the ROC curve for the subgroup of $FFR > 0.80$ and $CFR < 2.0$ was significant at 0.65 (95% CI: 0.62 to 0.70, $p < 0.001$). Also, the logarithmic correlation of CDP with combined FFR and CFR was found to be significant with $r = 0.75$, $p < 0.001$.

Figure 2 shows the schematic representation of CDP values to predict combined assessment of FFR and CFR. According to Figure 2, for FFR cut-off of 0.80, the CDP range to predict both physiologically insignificant FFR ($FFR > 0.80$) and CFR ($CFR > 2.0$) is between 0 and 15.78, whereas the CDP range to predict physiologically insignificant FFR ($FFR > 0.80$) and significant CFR ($CFR < 2.0$) is between 15.78 and 26.20. Similarly, the range of CDP to predict physiologically significant FFR ($FFR < 0.80$) and insignificant CFR ($CFR > 2.0$) is between 26.20 and 73.77, whereas the group of both physiologically significant FFR ($FFR < 0.80$) and CFR ($CFR < 2.0$) had CDP values greater than 73.77.

DISCUSSION

The CDP, developed based on fundamental principles of fluid dynamics, has the benefit of being a non-dimensional parameter. It accounts for the relationship between pressure drop and flow across the coronary artery dysfunction. As a result, it can determine the status of an ES, with or without concomitant MVD.

This study establishes the range of CDP cut-off values for distinguishing the four possible combinations of ES and MVD based on the established cut-off values of FFR 0.8 and CFR 2.0: 1) 0 to 15.78 indicating absence of both diseases; 2) 15.78 to 26.20 identifying absence of ES and presence of MVD; 3) 26.20 to 73.77 identifying presence of ES and absence of MVD, and 4) $CDP > 73.77$ indicating presence of both diseases. *Therefore, this multi-center trial further strengthens our hypothesis that CDP could be an improved diagnostic index for decision-making in the cardiac catheterization lab.*

Limitations. The outcomes of the study were presumptive as the patient-level data was extracted from a multicenter, international ILIAS registry, and all clinical decisions were made solely using the FFR, which is now the accepted gold standard. A prospective randomized clinical trial of CDP vs FFR is needed to further assess the clinical

outcome of CDP in relation to FFR and confirm the results from this multicenter trial.

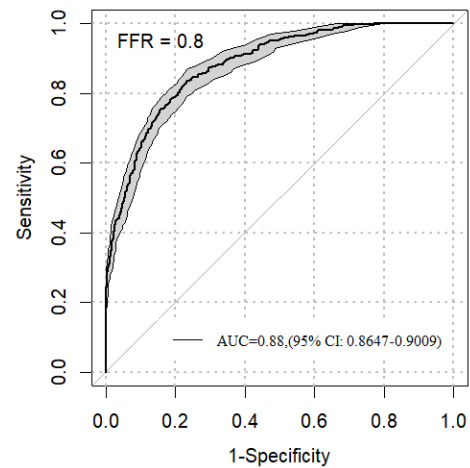


Figure 1: ROC curve for prediction of significant stenosis by CDP with FFR threshold of 0.80

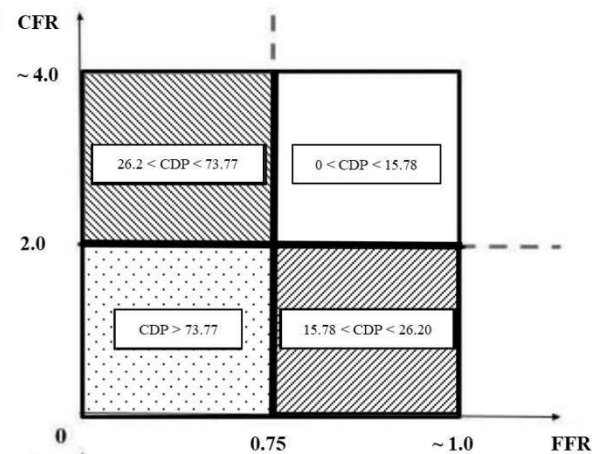


Figure 2: Schematic representation of CDP cutoff for FFR = 0.80 and CFR = 2.0

REFERENCES

- [1] Pijls, N. H. 1993, Circulation, 87(4), pp. 1354-1367.
- [2] Chilian, W. M., 1997, Circulation, 95(2), pp. 522-528.
- [3] Kern, M. J., 2000, Circulation, 101(11), pp. 1344-1351.
- [4] Fearon, W. F. 2004, Circulation, 109(19), pp. 2269-2272.
- [5] Siebes, M. 2004, Circulation, 109(6), pp. 756-762.
- [6] Fearon, W. F. 2003, Circulation, 107(25), pp. 3129-3132.
- [7] Verna, E. 2006, J Cardiovasc Med (Hagerstown), 7(3), pp. 169-175.
- [8] Hoffman, J. I. 2000, Ann Biomed Eng, 28(8), pp. 884-896.
- [9] van de Hoef., 2012, J Mol Cell Cardiol, 52(4), pp. 786-793.
- [10] Kolli, K. K. 2014, Catheter Cardiovasc Interv, 83(3), pp. 377-385.
- [11] Kolli, K. K. 2014, J Invasive Cardiol, 26(5), pp. 188-195.
- [12] Kolli, K. K. 2016, Catheter Cardiovasc Interv, 87(2), pp. 273-282.

POROELASTIC MODEL OF TRABECULAR STRUCTURES IN THE DEVELOPING HEART

Christine Miller Buffinton (1), James W. Baish (2)

- (1) Department of Mechanical Engineering, Bucknell University, Lewisburg, PA, USA
(2) Department of Biomedical Engineering, Bucknell University, Lewisburg, PA, USA

INTRODUCTION

Trabeculation is a dominant feature of the developing heart across organisms. Trabeculation begins at the end of the cardiac looping phase as myocardial evaginations project from the endocardium toward the jelly (mouse E9.5), progressing to a meshlike network between the central open region and the compact wall (Fig. 1), and finally coalescing with the ventricular wall (mouse E14.5) to thicken the compact myocardium. This timeline encompasses the critical chamber formation and outflow tract (OFT) septation stages. Trabeculae clearly increase ventricle mass and compliance, facilitate oxygen exchange, and increase pumping ability. Their prominence and orientation also suggest a substantial impact on flow through the heart and a role in mechanotransduction. Mechanotransduction mechanisms relating hemodynamic loading to responses at the genetic, molecular, and cellular levels are as yet unknown and likely due to a cascade of responses. Computational models can allow parametric studies and help elucidate dependencies, thus supplementing and better focusing experimental measurements.

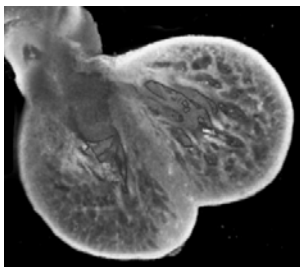


Figure 1: Confocal microscopic image of the ventricles of a mouse heart at embryonic day 12.5 (image width = 1.4 mm)

A major challenge with modeling the trabeculated ventricles is that the pore spaces are numerous and small, but not to the extent that a continuum model averaging over countless microstructures can be naively

applied. Although the complete morphology of the trabeculated ventricles can be determined by, e.g., confocal imaging and 3D reconstruction [1, 2], inclusion of the explicit geometry in computational fluid dynamic (CFD) analysis with two-way fluid-structure interaction (FSI) is computationally-intensive, sensitive to thresholding and segmentation settings in image analysis, and does not allow parameter sensitivity studies.

The goal of this study was to provide a computational framework that can be used to study the effects of hemodynamic loading in the chamber formation and OFT septation stages of cardiac development. We analyzed detailed models of single pores and multiple pore systems to recommend and calibrate appropriate continuum models of poroelastic materials, considering alternative formulations of the continuum model to recommend the simplest model that accurately accounts for inertial and viscous effects within the pores. The continuum model is intended to be suitable for use in a whole-organ model where the explicit model would be computationally impractical. Ultimately, the aim is to provide tools for relating results obtainable from the whole-organ continuum model back to the shear and bending stresses expected in the trabecular structures, these stresses being most relevant to the mechanobiological processes guiding development.

METHODS

This study considered CFD FSI models of the trabecular region on three levels (Fig. 2). The first is an idealized single 3D pore with fluid flow through the pore modeled with the full Navier-Stokes equations and the solid structure governed by linear elasticity. Pore geometry was determined from a study of reconstructed confocal images of E12.5 mouse [2], and inlet pressure chosen to match experimentally measured ventricular blood velocity. Calculations of flow and pressure with finite element analysis (COMSOL) yielded an effective fluid permeability, and parameter studies over inlet pressure and elastic modulus assessed the contribution of poroelasticity.

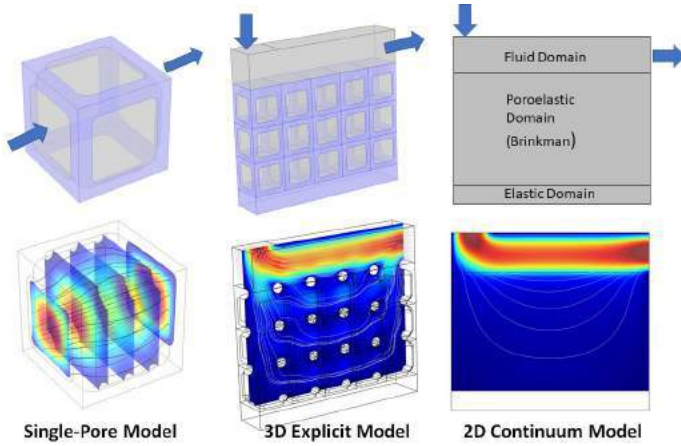


Figure 2. Three levels of model. The single-pore model represents a typical trabecular pore in the developing heart that is surrounded by identical pores (strut diameter=18 μm , pore width=65 μm). The 3D explicit multi-pore model combines several typical pores and exposes the composite structure to an impinging flow from an open domain as might occur where blood in the open center of the ventricular chambers interacts with the heart wall. The 2D continuum model shares the geometry of the multi-pore model, but the porous domain of the wall is now modeled with permeability and stiffness properties that yield the same flow and deformation as obtained from the more computationally intensive multi-pore model.

The second level is an explicit 3D model of a developing heart wall section containing layers of open channel flow, pores, and elastic wall, also analyzed using the full fluid and solid equations (Fig. 2). We examined how free-flowing fluid that impinges on the porous wall from the open chamber of the heart passes through the trabecular spaces. The third level is a 2D continuum model with the same configuration as the 3D explicit model, but replacing the explicit model of the pores with a continuum representation using the Brinkman equation [3]

$$\mu \nabla^2 \mathbf{u} - \frac{\mu}{\kappa} \mathbf{u} = \nabla p \quad (1)$$

relating the average velocity \mathbf{u} , fluid pressure p , and viscosity μ to the effective fluid permeability κ that was determined from the single pore model.

RESULTS

For a rigid structure, the permeability estimated from the single pore model was typically $9 \times 10^{-11} \text{ m}^2$ ($\pm 3\%$) over the range of velocities 4–21 mm/s. Deflection of the pore structure due to elastic effects decreased the permeability by only 17–24%. Solid stress was largest at the junction of the trailing vertical and horizontal struts, with maximum of 250x inlet fluid pressure, while wall shear stress (WSS) was largest on the curved inner cylindrical surfaces of the struts and approximately equal to inlet pressure.

The 3D explicit model showed that most fluid flow was contained in the open channel, with 21% entering the porous region. Half of this flowed through the first pore layer underneath the open channel. Maximum velocity was 1.6 mm/s in the center of the inlet for 1 Pa inlet pressure. Porous layer velocity was small, with increases when flowing through the narrowed regions between trabeculae. Solid stress was largest in the radii at the junction of horizontal and vertical struts, while WSS was largest on the top curved edges of the upper layer of pores (1.6x inlet pressure).

Flow patterns in the 2D continuum model were similar to those of the 3D model, 21% of inlet flow entering the porous region and 1.9 mm/s maximum velocity. The largest fluid velocity in the porous region was near the porous-open interface. The fluid volume entering porous could be matched with $5.4 \times 10^{-11} \text{ m}^2$ permeability. WSS was maximal at the inlet and outlet channel walls. The results were relatively insensitive to changes in Brinkman region elastic modulus and porosity within a reasonable physiological range. A tenfold increase in permeability, from 10^{-11} to 10^{-10} m^2 , caused only a small reduction in maximum stress, a 1.5x increase in maximum flow velocity, and an 18x increase in volumetric flow rate into the porous region.

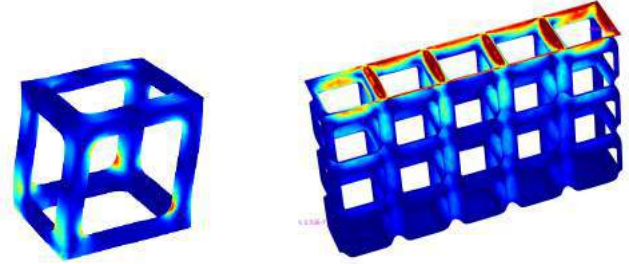


Figure 3. Relative solid stress with deflection in the single pore model (left), and wall shear stress on trabecular struts in the 3D explicit model (right), with maximum values shown in red.

DISCUSSION

In general, we found that the effective fluid permeability based on porosity ϵ was well estimated by the Kozeny-Carman relationship [3]

$$\kappa = \frac{\epsilon^3}{G s_0^2 (1-\epsilon)^2}, \quad (2)$$

where G depends on the shape of the pores and s_0 is the wetted surface area to solid volume ratio. We confirmed that small differences in the estimated porosity and pillar dimensions have a dramatic effect on the effective permeability. The changes in porosity and shape due to elastic deflections, while not negligible, were relatively small and insensitive to the elastic modulus compared to the uncertainties inherent in the initial estimation of the porosity and strut diameter. We also found that the fluid velocity and inertial effects diminish rapidly away from the porous-open interface, which would allow use of the simpler Darcy's equation (Eq. 1 without the first term) deep into the wall, but that the full Brinkman equation was appropriate near the interface where fluid shear stresses are highest and likely produce the strongest mechanotransduction effects.

Results from the single pore model compared favorably to our CFD analysis of image-based reconstructions of sections (150- μm cubes) of trabecular region from E12.5 mouse. These confirm that a small change in strut diameter causes a large change in fluid permeability.

The results of the present study are being used as the basis for model of the entire developing heart where trabecular structure will be represented by an equivalent poroelastic continuum. The simplifications made possible by this study will facilitate an efficient parametric study of congenital defects in the heart flow paths and the resulting solid and fluid stresses.

REFERENCES

- [1] Buffinton, C et al., *Biomech Model Mechanobiol*, 12:1037-1051, 2013.
- [2] Buffinton, C et al., *PLOS ONE*, 12(9):e0184678, 2017.
- [3] Truskey, G. et al., *Transport in Biological Systems*, 2nd ed. Prentice-Hall, 2009.

DESIGN AND CHARACTERIZATION OF A SILICONE VENOUS VALVE MODEL

Matthew S. Ballard (1), Dallin Brimhall (1), Sarah Dayley (1) and Andrew Rasmussen (1)

(1) Department of Engineering, Utah Valley University, Orem, Utah, USA

INTRODUCTION

Venous valves act as a series of miniature pumps to aid blood in returning to the heart from the lower extremities against the pull of gravity. Fluid pressure oscillations from contractions of the skeletal muscles surrounding the vein cause the valves to open to allow forward flow, and to close to prevent backward flow. While venous valves are vital to proper circulation, they are also a known location of the formation of thrombi in the deep veins, a condition known as deep vein thrombosis (DVT). While DVT can lead to pain and swelling, its chief risk is that thrombi can break free and travel through the circulation to ultimately block blood flow to the lungs, giving a condition known as a pulmonary embolism (PE). PE is a leading cause of death in the United States and has been estimated to cause approximately 200,000 deaths annually, which is likely a conservative figure since PE can be difficult to detect and thus is often not recognized [1]. The presence of DVT, PE, or both is also known as venous thromboembolism (VTE). Individuals who experience an extended period of immobility, such as hospital patients and long-haul plane passengers, are especially at-risk for VTE.

Despite the severity and prevalence of VTE, the effect of valve morphology on flow conditions through venous valves has remained largely unknown. Recently, a numerical model was used to investigate the effect of morphological factors such as the stiffness, length and shape of valves on the resulting flow conditions [2]. In this work, we develop and demonstrate a physical silicone model for use in validating the numerical model and in expanding the capability of testing the effect of valve morphology on disease-conducive flow conditions. Specifically, we reproduce the geometrical features and boundary conditions used in the numerical model to compare experimental and numerical findings. We experimentally reproduce results that show how valve stiffness and three-dimensional (3-D) shape affect the ability of valves to allow forward flow and block reverse flow. Further, we introduce particles into flow through the venous valve silicone model to elucidate the effect of valve morphology on disease-conducive factors

such fluid residence time. Results of this study make progress toward providing doctors with the information needed to better identify at-risk patients for whom they should take preventative measures against VTE.

METHODS

The vein and valve geometry used in this study is a simplified venous valve region consisting of a rigid sinus vessel containing water and a flexible bi-leaflet valve taking the shape of two planes intersecting the vessel. Leaflet tips are crescent-shaped with a sinusoidal cutout of depth δ , as shown in Figure 1. A pressure gradient is applied across the vessel by attaching the open ends of the vein test section to water lines at pressures applied using a pressure controller (Elveflow OB1). The model recreates the geometry and conditions previously studied numerically [2], to directly compare to numerical results.

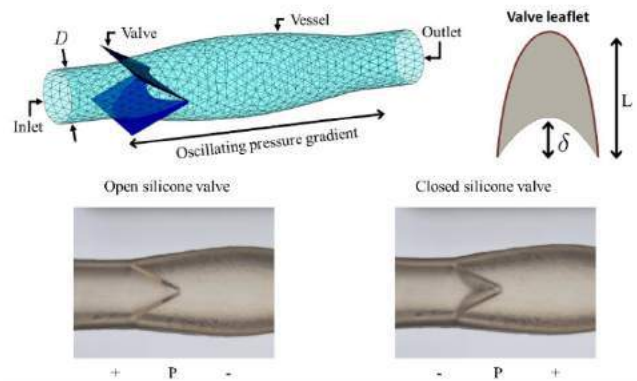


Figure 1: Simplified venous valve model. Bottom images show the silicone venous valve silicone model open (left) and closed (right) due to applied fluid pressure gradients

Parameters varied in this study are the valve length L , depth of the crescent at the valve tip δ , valve thickness, and applied pressure gradient ΔP . Relevant parameters varied in this study are characterized and reported in terms of dimensionless parameters, namely the aspect ratio $A = L/D$, the depth of cut $D_c = \delta/L$, and the dimensionless stiffness K [2,3]:

$$K = \frac{4 k_b}{\pi D^3 \Delta P} \quad (1)$$

The silicone venous valve model is created as a single piece using a molding process. A computer-aided design (CAD) model of the negative of the silicone model is created to give the desired geometry. The CAD model is sliced and then used by a stereolithography (SLA) 3-D printer (Elegoo Mars 3) to create a four-part mold (Figure 2) consisting of a two-part mold for the outer vessel wall and a two-part mold of the inner vessel wall and valve leaflet geometry. Printed molds are post-processed through cleaning with alcohol, followed by post-curing and polishing. Finished molds are coated to prevent curing inhibition of the silicone. Liquid silicone (Smooth-On Ecoflex 00-31 Near Clear) is then degassed and poured into the mold, then cured for 24 hours in a pressure pot at 10 psig.

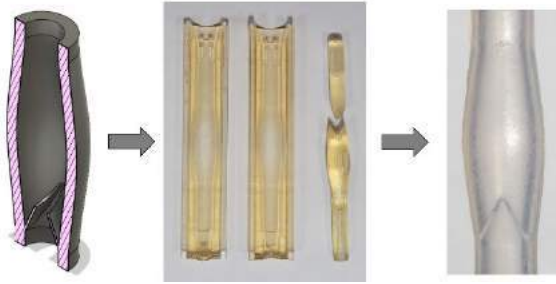


Figure 2: CAD model of geometry used to 3-D print a mold, which is used to create silicone model of vein and valve

In this study, a numerical model is also used to compare experimental and numerical results [2]. Briefly, the numerical model is a fully-coupled 3-D fluid solid interaction (FSI) model using a lattice-Boltzmann method (LBM) [4] for the fluid mechanics, and a lattice spring method (LSM) [5] for the solid mechanics. The LBM and LSM models are fully-coupled via appropriate boundary conditions [3,6].

RESULTS

A numerical model was previously used to study the effect of valve morphology on the ability of venous valves to properly open and close to allow forward flow and block reverse flow [2]. This model showed that valves with low A , low K and high D_c are most effective at allowing forward flow and preventing backward flow, provided that they have enough material to allow for proper closure. For example as seen in Figure 3, numerical simulations showed the effect of D_c and A on the ability of fluid to flow through the valve. Figure 3a shows the resistance that a valve gives to forward flow, normalized by flow resistance in a valve-less vein section. The three curves representing various values of K demonstrate that the resistance to forward flow increases with increasing K . From this plot, it is also evident that forward flow resistance decreases with increasing D_c . Figure 3b shows the normalized conductance of reverse flow with varied D_c and K . Here, significant conductance means that the valve did not close well

enough to block reverse flow. Figure 3b shows that a valve with D_c of about 0.25 or less is predicted to adequately close over a significant range of K , while higher D_c can result in regurgitation since the crescent tip is too deep to adequately close. For $D_c > 0.25$, high K results in increased regurgitation as compared to lower K valves.

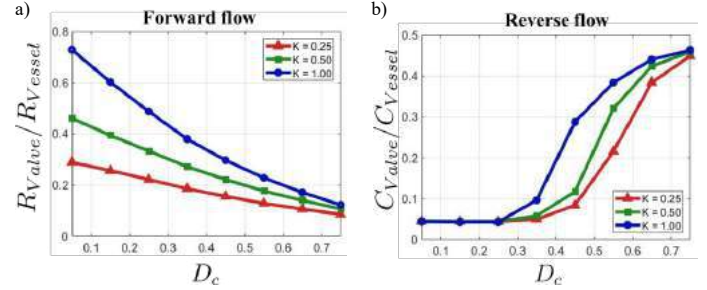


Figure 3: Numerical results to which silicone model will be compared. For constant $A = 1.25$, effect of D_c and K on a) valve resistance to forward flow and b) valve conductance of reverse flow

In this study, we use the silicone venous valve model to reproduce the conditions from the numerical model to reproduce the numerical results, including the plots from Figure 3. This provides additional validation of the numerical model, and demonstrates that the silicone model is designed and operating as expected.

DISCUSSION

Comparing the numerical and physical models not only provides the ability to ensure accuracy of both models, but also allows the two models to complement each other in providing a more complete picture of the behavior of venous valves than either could provide on its own. For example, particles are introduced to flow through the silicone model demonstrated in this study to investigate the residence time of particles in the venous valve region, as well as locations where they tend to adhere to solid surfaces. Additionally, this silicone model can be used to develop and test VTE intervention strategies such as active compression devices. Thus, the use of this silicone venous valve model can provide insight into risk factors that can alert doctors of the need of preventative measures, and can also inform the effective design of preventative technologies.

ACKNOWLEDGEMENTS

We gratefully acknowledge the National Science Foundation (NSF) CMMI 2138836 grant for financial support.

REFERENCES

- [1] G.T. Gerotziakas, M.M. Samama, Prophylaxis of Venous Thromboembolism in Medical Patients, 2004.
- [2] A. Rasmussen, J. Biesinger, M. Ballard, Bulletin of the American Physical Society (2022).
- [3] M. Ballard, K.T. Wolf, Z. Nepiyushchikh, J.B. Dixon, A. Alexeev, Biomech Model Mechanobiol (2018) 1–14.
- [4] S. Succi, The Lattice Boltzmann Equation for Fluid Dynamics and Beyond, Oxford University Press, Oxford, 2001.
- [5] G.A. Buxton, R. Verberg, D. Jasnow, A.C. Balazs, Phys Rev E 71 (2005) 56707.
- [6] A. Alexeev, R. Verberg, A.C. Balazs, Macromolecules 38 (2005) 10244–10260.

REGIONAL HETEROGENEITY IN THE BIOMECHANICS OF HUMAN AORTA

M.Kazim (1), S.Razian (1), D.Varandani (2), M.Jadidi (1)

(1) Department of Biomechanics, University of Nebraska-Omaha, Omaha, NE, United States
(2) Department of Computer Science, University of Nebraska-Omaha, Omaha, NE, United States

INTRODUCTION

Aorta is the largest conduit in the human body that acts as a buffering chamber to distribute blood to the peripheral organs and tissues. It starts as the ascending thoracic aorta as it leaves the left ventricle, travels down the thorax and abdomen, and branches into common iliac arteries. Due to the structural inhomogeneity, varied blood flow, and kinematic constraints on the aortic wall from the spine, different vascular disorders are more prone to occur at certain locations than others. For instance, the aneurysm is more commonly observed at the abdominal aorta (AA) and thoracic aorta (TA). In contrast, calcification is first observed at the AA and iliofemoral artery [1]. Given the important role of arterial mechanical and structural properties on its physiologic and pathophysiologic response, a better understanding of the aorta biomechanics can help explain disease development and progression at specific locations along the aorta and develop improved vascular repair materials and devices.

Prior *in vivo* studies demonstrated that aortic stiffness is greatest at the abdominal aorta and least at the aortic arch [2]. While these studies provided valuable information about the aortic biomechanical environment, they rely on surrogate measures of stiffness and cannot reliably estimate the intrinsic arterial wall properties while accounting for the residual and physiologic deformations [3]. *Ex vivo* techniques, on the other hand, allow for determining the intrinsic anisotropic aortic stiffness and assessing its structure. Comprehensive *ex vivo* analysis of arterial properties along the aortic tree has been carried out in animal models [4]. However, animals differ from humans in many factors, and a comprehensive study of human aorta biomechanics along its length is warranted. Human studies from diverse samples have mostly been centered around one or two locations, such as the abdominal and thoracic region, or compared specimens from different subjects [5]. Our objective in this study was to determine the morphological, structural, and mechanical properties of the aorta and iliac arteries at different

anatomically important locations and study how these properties vary within the arteries of each subject.

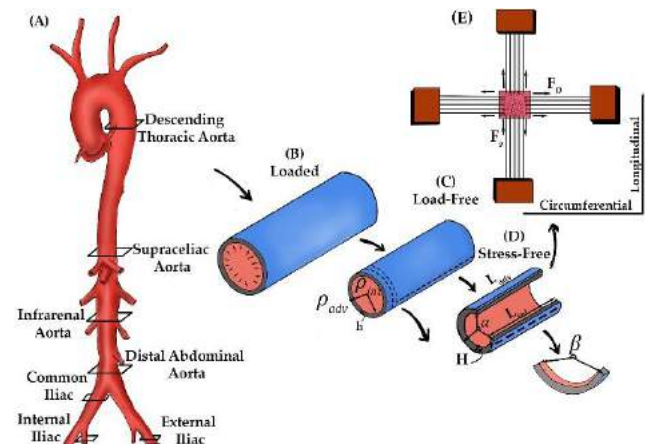


Figure 1: (A) Aorta along the length demonstrating locations used in mechanical and structural analysis. (B) Kinematics of the aorta in the loaded configuration under axial pre-stretch and luminal pressure. (C) The arterial specimen transected from the body. (D) The residual stresses are released when the load-free specimen is cut radially. (E) schematic of planar biaxial testing.

METHODS

We obtained 108 specimens from 20 cadaveric human aortas and iliac arteries (51.8 ± 18.12 years, mean \pm SD) within 24 hours of death. Samples were tested fresh within 12 hours of procurement. First, arteries were dissected from their surrounding tissues, and visual and palpatory analysis was done on the vessels to record the extent and spread of the vascular disease. If the artery did not have significant

calcification along its circumference or blood clots, it was used for further mechanical testing and structural evaluations.

Specimens were cut from the descending thoracic aorta (TA), supraceliac aorta (SC), infrarenal aorta (IFR), distal abdominal aorta (dAA), common iliac (CI), external iliac (EI), and internal iliac (II) arteries (Figure 1). We measured the morphometric characteristics, including the thickness (h), and inner and outer radius of the load-free ring (ρ_{int}, ρ_{adv}), the thickness (H), intimal and adventitial lengths (L_{int}, L_{adv}), and the opening angle of the stress-free cut ring (α), and the opening angle of the stress-free longitudinal strip (β), using a custom-written software in Visual Studio C#.

From each anatomical location, specimens were cut from the lateral region of the wall for mechanical tests. The intrinsic passive mechanical properties of the tissues were determined by applying multi-ratio biaxial protocols using a CellScale BioTester while samples were submerged in 37°C phosphate-buffered saline (PBS).

Samples used in morphometric assessments were fixed in methacarn, dehydrated in ethanol, and embedded in paraffin for histological analysis. Slides were cut from each paraffin block and stained with Movat to assess the Extracellular Matrix (ECM) structure.

Statistical analyses were performed in Jamovi 2.2.5 to investigate the possible differences in the morphological characteristics of the seven anatomical locations. First, we assessed the normality of the data and then used Repeated Measures of Analysis of Variance (ANOVA) or Friedman's nonparametric tests to compare the locations. A p -value <0.05 was considered statistically significant.

RESULTS

We observed that in 30-50 years old aortas, soft plaques were distributed inhomogeneously at the lateral section of IFR till the dAA. In 50-60 years old aortas, we observed soft plaque localizing at the posterior TA extending to the medial and lateral quadrants of SC. Around this age, we also observed calcification at dAA. Subjects older than 60 displayed circumferential disease at the dAA, and plaques at the medial region at CI and II, while EI showed almost no sign of disease.

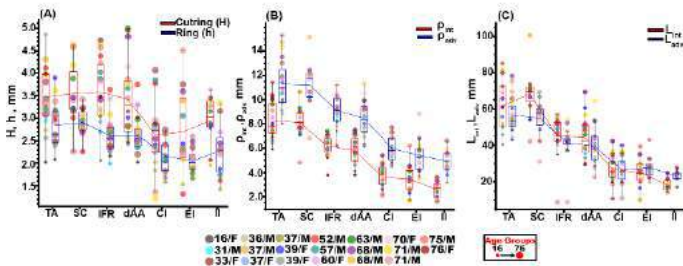


Figure 2: (A) Changes in the load-free ring and stress-free cut ring thickness, (B) decrease in the intimal and adventitial radius of the load-free ring, and (C) stress-free cut ring's length. Boxplots represent the 75th and 25th percentiles, with endpoints of whiskers corresponding to the 5th and 95th percentile. The size of the dots corresponds to the subject's age.

Overall, the inner and outer radius of the load-free ring and stress-free ring length decreased along the aortic length from TA to II (Figure 2). The average load-free thickness remained relatively constant until SC at 2.87 ± 0.4 mm. It remained stable in the abdominal region with a minimal decline till EI and a subsequent increase in II (2.05 ± 0.3 mm to 2.28 ± 0.61 mm). While we observed a gradual decrease in the thickness, radii, and length, statistically, the aortic locations were not different but showed a variation below the common-iliac bifurcation ($p < 0.05$). TA was the only location that differed from IFR and dAA in radius and length ($p < 0.001$). The circumferential opening angle remained

relatively constant at $228.86 \pm 86.60^\circ$, while a difference between locations was only observed after the aortoiliac bifurcation. The longitudinal opening angle, on the other hand, remained constant until IFR at $291.22 \pm 30.57^\circ$ and subsequently decreased in CI.

In terms of mechanical behavior, overall, longitudinally, in younger samples, we observed TA to be more compliant than the other locations. This was closely followed by dAA, IFR, and CI. The circumferential compliance decreased throughout the length of most arteries, and TA was more compliant than other locations (Figure 3).

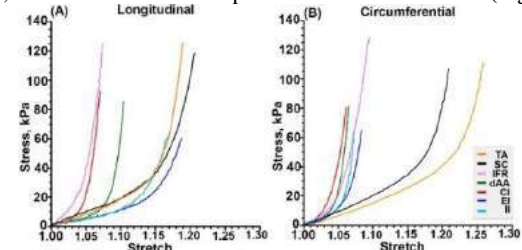


Figure 3: Representative experimental equibiaxial stress-stretch response of a 71-year-old male in the (A) longitudinal and (B) circumferential direction.

Figure 4 shows representative histological images demonstrating changes in the ECM structure throughout the aorta and iliac arteries. We observed that elastin content decreased throughout the length while collagen content increased.

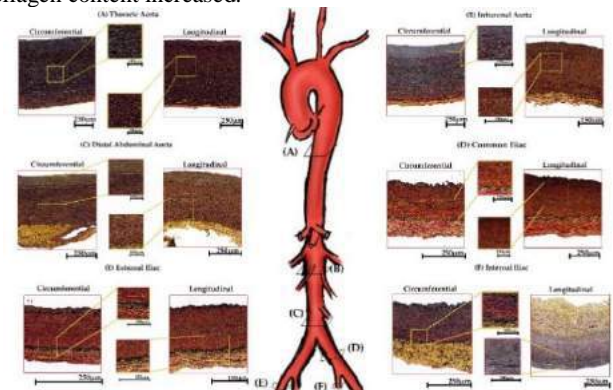


Figure 4: Structural changes along the aorta and iliac arteries of a 37-year-old male subject.

DISCUSSION

Our results demonstrate that there is a difference in the disease formation along different aortic locations, which may have originated from different blood flow conditions, structure, and mechanics along the vessel. The presented data can help better understand the aorta physiology and pathophysiology and inform the development of better repair materials and devices.

ACKNOWLEDGEMENTS

We wish to acknowledge LiveOn Nebraska for their help and support in collecting the blood vessels and thank donors and their families for making this study possible.

REFERENCES

- [1] M. Jadidi *et al.*, *AJPHEART*, 320: H2313–H2323, 2021
- [2] S. S. Hickson *et al.*, *JACC Cardiovasc. Imaging*, 3: 1247–1255, 2010.
- [3] M. Jadidi *et al.*, *Acta Biomater.*, 119, pp: 268–283, 2021.
- [4] X. Guo *et al.*, *AJPHEART*, 2715: 2614–2622, 2006.
- [5] M. Jadidi *et al.*, *Acta Biomater.*, 103: 172–188, 2020

AN *IN VITRO* ASSESSMENT OF EMBOLI TRAJECTORIES WITHIN A PATIENT SPECIFIC MODEL: INVESTIGATION INTO THE INFLUENCE OF THROMBUS SIZE, MECHANICAL PROPERTIES, AND CEREBRAL BLOOD PRESSURE

A. Glynn (1,2), A. Consoli (3), B. Murphy (1,4), R. McCarthy (2), C. Lally (1,4)

- (1) Trinity Centre for Biomedical Engineering & School of Engineering, Trinity College Dublin, Dublin 2, Ireland.
(2) Cerenovus, Galway, Ireland.
(3) Hôpital Foch, Paris, France.
(4) Advanced Materials and Bioengineering Research Centre (AMBER), RCSI & TCD, Dublin, Ireland.

INTRODUCTION

Stroke has a high prevalence in society, affecting 1 in 4 adults over the age of 25 globally [1]. The majority (~87%) of strokes are ischemic in nature, which occur due to a thrombus obstructing blood flow in a cerebral artery. These thrombi can occur *in situ*, or more commonly as emboli [2]. The trajectories of emboli *in vivo* is hypothesized to be influenced by their size, mechanical properties, and cerebral blood pressure [3,4]. Understanding the dynamics of emboli has important implications in the treatment of Acute Ischemic Stroke (AIS), as the final occlusion location of a thrombus is directly associated with the degree of neurological severity experienced by the patient [5]. *In-vitro* simulations of embolic occlusion formation in the anterior circulation can provide critical insights to gain a better understanding of thrombus dynamics in AIS patients.

To date, limited research has been conducted investigating the trajectories of emboli *in-vitro*. Previous *in-vitro* testing has been completed in simplified models, which failed to include the geometry and characteristics of known vessel sites for stroke occurrence [6]. These models also failed to accurately recreate physiological pressure conditions [5] and or to use suitable thrombus analogues [7], limiting the translation of the results.

The deformation patterns of thrombi have been hypothesized to be associated with their composition [11]. Understanding the influence of composition on thrombus deformation may have important implications in the choice of AIS treatment, as thrombi may possess varying responses to different mechanical thrombectomy treatment approaches.

The aim of the present study is to investigate the influence of thrombus size, mechanical properties, and cerebral blood pressure on the trajectory of emboli *in vitro* in patient specific models.

METHODS

A design of experiment (DoE) response surface model, with a central composite design was conducted using Design Expert (Statease®). Three factors were identified for inclusion in the experimental design: thrombus size, mechanical properties, and systolic blood pressure (SBP). The experimental design space was created with a high and low setting, a center point, and two axial points for each factor. This resulted in five different levels for each factor: thrombus size (0.09g, 0.2g, 0.4g, 0.6g, 0.7g), mechanical properties, controlled by varying the composition of red blood cells (RBCs) in the thrombus (5%, 11%, 22.5%, 34%, 40%), and SBP (120mmHg, 130mmHg, 150mmHg, 170mmHg, 180mmHg). 40 runs were completed in total, with a minimum of 2 replicates per run.

Platelet-contracted clot (PCC) analogues with various compositions, determined by the percentage of RBCs used in clot preparation (5-40%), were assembled from ovine blood [8]. Ovine blood was selected as it has been shown to be an appropriate substitute for human blood in coagulation studies [9] and the clot analogues produced following this methodology have been shown to be histologically comparable to human clots [8,10]. The thrombus analogues had a diameter of 9 mm (± 1 mm) and were cut to a pre-defined weight (0.09-0.7g).

An *in-vitro* patient specific silicone model was used to represent the cerebral anatomy. The model consisted of the complete intracranial circulation, including a complete Circle of Willis, anterior and posterior communicating arteries, distal circulation up to M3 segment of the middle cerebral artery, and extracranial circulation, including both carotid, basilar, and vertebral arteries, the aorta and aortic arch, and vessels to simulate femoral access. A glycerol/water blood mimic was

circulated in the model at 37°C, to simulate *in vivo* conditions. The range of SBP between 120-180mmHg was selected based on patient physiological data (n=20) provided by Hôpital Foch (Paris, France). Clots were introduced into the model via the ascending aorta, to simulate embolization from the heart. The distance from the proximal clot face to the Carotid Terminus (mm) was used as a metric to evaluate thrombus embolization after 15-minutes.

RESULTS

Each factor: thrombus size, mechanical properties, and SBP, was found to have a significant influence on the trajectories of emboli *in vitro* ($p < 0.01$). Figure 1 a) & b) shows the significant impact RBC content had on the ability of thrombi to deform and embolize distally. Figure 2 a) displays the linear relationship between SBP and the extent of embolization, independent of clot size and mechanical properties. Smaller thrombi with increased RBC content were more likely to occlude a vessel within the distal vasculature (see Figure 2b). Thrombi with higher RBC compositions, lower weight and under higher physiological pressures embolized further in the *in vitro* model.

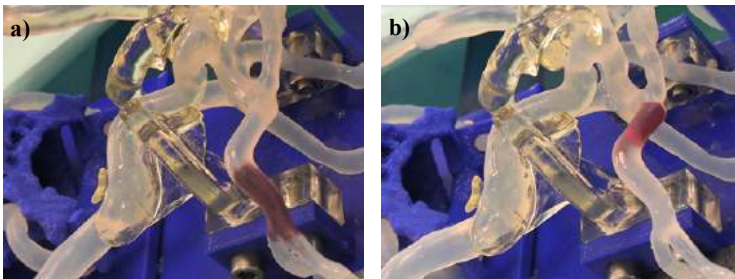


Figure 1: a) 0.2 g clot made from a blood mix with 34% RBC under 130mmHg, b) 0.2 g clot made from a blood mixture with 11% RBC under 130mmHg. These images show the effect of RBC content on the final occlusion location of the same size thrombus.

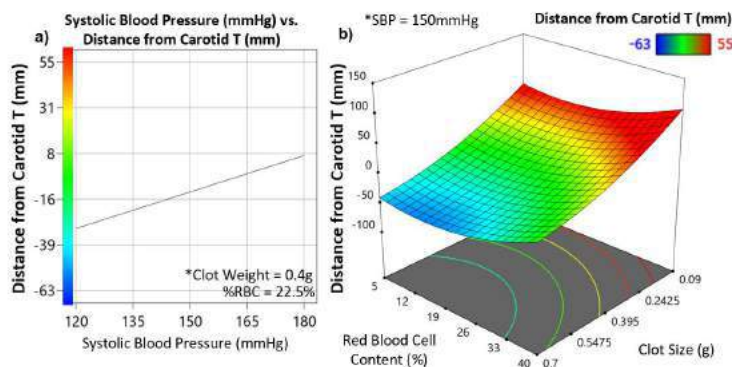


Figure 2: a) Graph displaying linear relationship between SBP (mmHg) and thrombus distance from the Carotid Terminus (mm), b) 3D-heat map showing the effect of RBCs (%) and size (g) on thrombus embolization *in vitro*.

DISCUSSION

The composition of thrombi impacts their mechanical properties, by altering their morphology [8], and thus, their ability to deform and travel distally. Thrombi may be described in various ways based on their composition, one common approach divides thrombi into RBC-rich and fibrin-rich thrombi. In this study, we found that thrombi rich in RBCs were more likely to travel further distally in comparison to fibrin-rich thrombi (Figure 1). These results may be explained by the well reported

associations between composition and mechanical properties [8,12]; where thrombi rich in fibrin have been found to have a greater coefficient of friction, increased stiffness, and higher fracture toughness in comparison to RBC-rich thrombi, which may limit their ability to deform and embolize distally. The fibrin network in thrombi provides mechanical strength to the thrombus, reinforcing its structural integrity [8]. RBC-rich thrombi in comparison, have been shown to have higher tendencies for fragmentation due to their limited fibrin network. We only observed fragmentation during embolization (n=4) in thrombi with medium-to-high RBC content (22.5%, 34% and 40%). Interestingly, all fragmentation events occurred in the same location, the Carotid Terminus. At this location, thrombi experienced tension in two directions via the fluid flow, towards the A1 segment of the anterior cerebral artery and M1 segment of the middle cerebral artery. Overall, our findings suggest that at constant pressure, thrombi with different composition must be of different sizes to create an occlusion in the same location, as a result of their differing mechanical properties.

The deformability of thrombi is also an important factor during retrieval. In AIS treatment, thrombus retrieval is primarily performed via two techniques: stent retrieval (SR) or contact aspiration (CA). The mechanisms by which these devices interact with thrombi differ; SRs aim to achieve interaction of the whole thrombus between struts to optimize retrieval, while CA interacts with the proximal face of the thrombus only to achieve retrieval [11]. It is hypothesized that the appearance of the shape of the thrombi at the occlusion site may be a prognostic factor for the success of retrieving the thrombus with different techniques [11]. However, there is currently much debate surrounding this topic. If the shape of the thrombus can be associated with the mode of deformation during embolization, and in turn used to predict the behavior of the thrombus during retrieval, it could aid selection of the optimum procedural approach. Investigating this link between thrombus shape and mechanical properties is ongoing at our lab. Future work will examine the interaction between the mechanical properties of the thrombus, inferred by its composition, and choice of retrieval technique to better understand this relationship.

In conclusion, as visualization of thrombus embolization *in vivo* is challenging, realistic thrombus analogues combined with representative *in-vitro* models are critical to better our understanding of thrombus dynamics in AIS [12]. These results provide an important insight into the influence of thrombus size, mechanical properties, and cerebral blood pressure on thrombus occlusion dynamics *in vitro*.

ACKNOWLEDGEMENTS

This work has been funded by the Irish Research Council and Cerenovus (EBPPG/2021/66). SBP data provided by Dr Arturo Consoli, Hôpital Foch (Paris, France).

REFERENCES

- [1] World Stroke Organization; Learn About Stroke, 2022.
- [2] Bartels *et al.*, Stroke Rehabilitation, 2016.
- [3] Sporns *et al.*, J Neurointerv Surg., 3(5): 409-41, 2020.
- [4] Nogueira *et al.*, Stroke., 40(2): 516-22, 2009.
- [5] Fahy *et al.*, Ann Biomed Eng., 43(9): 2265-78, 2015.
- [6] Asakura *et al.*, Neuroradiology., 49(3): 243-251, 2007.
- [7] Chung *et al.*, Stroke., 41(4): 647-652, 2010.
- [8] Johnson *et al.*, J Neurointerv Surg., 12(9): 853-857, 2019.
- [9] Siller-Matula *et al.*, Thrombo. and haemo., 100(3): 397-404, 2008.
- [10] Duffy *et al.*, J Neurointerv Surg., 50(5): 1156-1163, 2019.
- [11] Mohammaden *et al.*, J Neurointerv Surg., 1(13): 599-604, 2021.
- [12] McCarthy *et al.*, J Biomechanics., 131: 0021-9290, 2022.

BLOOD FLOW ENERGY PROFILES IN CORONARY ARTERIES PREDICT MYOCARDIAL INFARCTION

**M. Lodi Rizzini (1), A. Candreva (1,2), V. Mazzi (1), C. Chiastra (1),
B. De Bruyne (3), C. Collet (3), D. Gallo (1), U. Morbiducci (1)**

(1) Polito^{BIO}Med Lab, Dept. of Mechanical and Aerospace Eng., Politecnico di Torino, Torino, Italy
(2) Department of Cardiology, Zurich University Hospital, Zurich, Switzerland
(3) Cardiovascular Center Aalst, OLV-Clinic, Aalst, Belgium

INTRODUCTION

The identification of atherosclerotic plaques prone to cause myocardial infarction (MI) is a clinically relevant problem. The anatomical evaluation of coronary lesions still plays a fundamental role in clinical decision making, although a functional approach based on intravascular pressure gradients evaluation, measured in terms of fractional flow reserve (FFR), has emerged as an effective risk assessment tool [1].

Recalling the Bernoulli's principle, the presence of a lumen narrowing within the vessel is not only associated with a translesional pressure drop, but also with intravascular blood flow energy conversion/transformation involving kinetic energy. In the complex scenario of cardiovascular flows, the energy transformation process may also lead to a production of rotational energy [2]. Moreover, the blood pressure gradient caused by lumen narrowing impacts the shear forces acting at the blood-endothelium interface, i.e., the wall shear stress (WSS). In this regard, WSS has been reported to be associated with intravascular flow features [3], with plaque progression and destabilization [4], and ultimately with future MI [5].

Motivated by the fundamental fluid mechanics theory as well as by previous observations [2], here we investigate the capability of blood flow energy profiles in diseased coronary arteries to predict MI within 5 years by applying a recently proposed angiography-based computational fluid dynamics (CFD) strategy [5].

METHODS

Patient population. Patients presenting with MI were retrospectively selected according to three main inclusion criteria: (1) a previous coronary angiography performed between 1 month and 5 years before the event (baseline angiography); (2) a visually recognizable mild stenosed lesion (i.e., less than 50% diameter stenosis) culprit for future MI (FC) at the baseline angiography; (3) at least one additional lesion, non-culprit for the future MI (NFC) in the other major epicardial

vessels. This selection resulted in 80 patients and 188 diseased coronary arteries with 80 FC and 108 NFC lesions.

Vessel reconstruction and computational hemodynamics. The 3D geometry of each coronary artery was reconstructed from two angiographic projections. Then, the discretized governing equations of fluid motion were solved under unsteady-state conditions using the finite volume method, as detailed elsewhere [5].

Myocardial infarction predictors. By using a quantitative coronary angiography (QCA) approach, the lesion segment was identified as the one containing the minimum lumen area (MLA) and delimited by the proximal and distal intersection of the interpolated reference line with vessel area line (Figure 1).

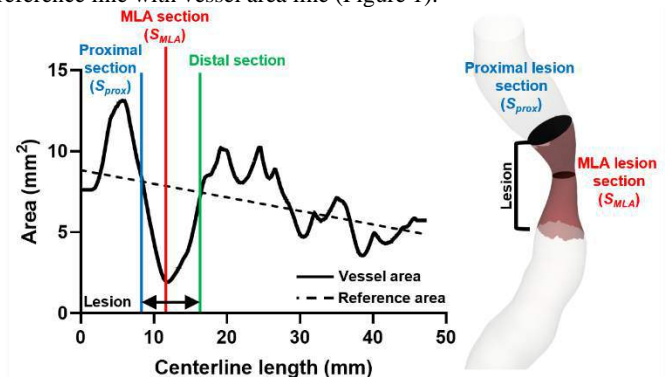


Figure 1. Lesion and sections definition based on QCA.

In addition to the clinically adopted anatomical and functional quantities percentage area stenosis (%AS) and translesional virtual FFR ($\Delta vFFR$), and to the WSS-based quantity topological shear variation index (TSVI, recently emerged as a strong predictor for MI on the same dataset [5,6,7]), blood flow kinetic and rotational energy production in the converging flow segment of the lesion were tested as possible MI

predictors in coronary arteries. Technically, the amount of kinetic energy was quantified in terms of specific kinetic energy (KE_u). The amount of rotational energy was quantified in terms of enstrophy (ε):

$$\varepsilon = \frac{1}{2} |\boldsymbol{\omega}|^2 \quad (1)$$

where $\boldsymbol{\omega}$ is the vorticity vector. Then, the transformation of kinetic and rotational energy within the converging flow segment was quantified in terms of kinetic energy ratio (KER) and rotational energy ratio (RER):

$$KER = \frac{\frac{1}{S_{MLA}} \int_T \int_{S_{MLA}} KE_u dS dt}{\frac{1}{S_{Prox}} \int_T \int_{S_{Prox}} KE_u dS dt} \quad (2)$$

$$RER = \frac{\int_{S_{MLA}} \int_0^T \varepsilon dt dS}{\int_{S_{Proximal}} \int_0^T \varepsilon dt dS} \quad (3)$$

KER and RER quantify the change of kinetic and rotational energy, respectively, occurring between the narrowest section of the vessel (i.e., MLA) with respect to a healthy section (i.e., proximal section), as defined in Fig. 1.

Statistical analysis. Differences between FC and NFC lesions for continuous variables was tested using Mann-Whitney's U test. The area under the curve (AUC) of receiver operating characteristic (ROC) curves and DeLong test was used to assess the predictive power of each variable. Statistical significance was assumed for $p < 0.05$.

RESULTS

The distribution of ε and KE_u averaged over the cardiac cycle is visualized within all vessel and at MLA and proximal section for two representative cases (one FC and one NFC lesion) in Figure 2. In general, FC and NFC vessels presented comparable values of ε and KE_u on the proximal section while FC lesions exhibited markedly higher values of ε and KE_u at the MLA section, compared to NFC lesion.

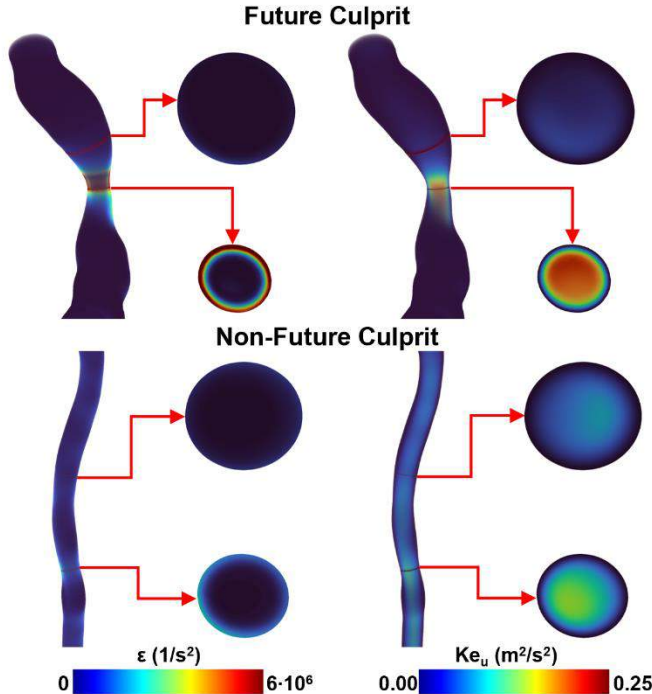


Figure 2: Enstrophy (ε) and specific kinetic energy (KE_u) volume and surface (at proximal and MLA sections) visualization for two explanatory cases (one FC and one NFC lesion).

The analysis highlighted that FC lesions were characterized by significantly higher KER (5.59 [3.59-7.69] vs. 3.37 [2.58-5.13],

$p < 0.0001$) and RER (6.59 [3.92-9.63] vs. 3.67 [2.60-5.16], $p < 0.0001$) values, compared to NFC lesions. From the analysis of ROC curves (Figure 3) it emerged that RER and KER were strong predictors for MI at 5 years (AUC=0.76, 95% CI 0.70-0.83, $p < 0.0001$ and AUC=0.74, 95% CI 0.67-0.81, $p < 0.0001$, respectively). The clinical parameters %AS and $\Delta vFFR$ resulted also significant predictors of MI (AUC = 0.65 95% CI 0.56-0.72, $p = 0.0008$ and AUC = 0.63 95% CI 0.55-0.71, $p = 0.0030$, respectively) though significantly weaker than RER (DeLong test: $p = 0.0042$, $p = 0.0059$, respectively) but not KER (DeLong test: $p = 0.0620$, $p = 0.0519$, respectively). Finally, TSVI emerged as the strongest predictor of MI at 5 years (AUC=0.77, 95% CI 0.71-0.84, $p < 0.0001$), but not significantly stronger than RER and KER (DeLong test: $p = 0.8927$ and $p = 0.2982$, respectively).

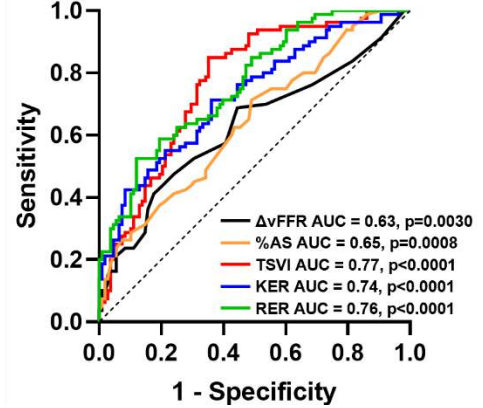


Figure 3: Receiver operating characteristic (ROC) curves for myocardial infarction (MI) prediction.

DISCUSSION

This study compared the predictive power of blood flow energy-related quantity with clinically used parameters and the WSS-based descriptor TSVI, which has been identified as a strong predictor of MI. The main results can be summarized as follow: (1) RER and KER were strong predictors of MI at 5 years; (2) RER was a significantly stronger predictor of MI than clinically used parameters; (3) RER and KER presented a predictive capacity for MI comparable to TSVI.

Blood flow energy conversions/transformations was related to the geometry of the lesion: the converging flow segment imparts a transformation of pressure in kinetic energy ($KER > 1$ in all vessels) and a decrease of pressure ($\Delta vFFR > 0$ in all vessels), consistently with Bernoulli's theorem that links variation of pressure and velocity. The results on rotational energy expand recent observations of abnormal vorticity profiles in diseased coronary arteries [3], providing a direct link with clinical outcome which was previously only inferred.

In conclusion, blood flow energy conversions/transformations in coronary lesions resulted a strong predictor for future MI. These findings encourage further study on blood flow energy transformation using angiography-based CFD models, suggesting the addition of quantitative intravascular flow characterization to $vFFR$ and WSS in the next-generation clinical decision making tools available to interventional cardiologist.

REFERENCES

- [1] Tonino et al., *N Engl J Med*, 360:213-224, 2009.
- [2] Chu et al., *Atherosclerosis*, 273:136-144, 2018.
- [3] De Nisco et al., *Ann Biomed Eng*, 47(2):425-438, 2019.
- [4] Wentzel et al., *Cardiovasc Res*, 96:234-243, 2012.
- [5] Candrea et al., *Atherosclerosis*, 342:28-35, 2022.
- [6] Morbiducci et al., *Ann Biomed Eng*, 48(12):2936-2949, 2020.
- [7] Mazzi et al., *Ann Biomed Eng*, 49(9):2606-2621, 2021.

A PNEUMATICALLY CONTROLLED DEVICE FOR UNIAXIAL AND BIAXIAL CELL STRETCHING

Jue Wang ⁽¹⁾, Aritra Chatterjee ⁽²⁾, Clarisse M. Zigan ⁽²⁾, Alex Chortos ⁽¹⁾, Deva D. Chan ⁽²⁾

(1) Mechanical Engineering,
Purdue University,
West Lafayette, IN, USA

(2) Biomedical Engineering,
Purdue University,
West Lafayette, IN, USA

INTRODUCTION

Adherent cells in several tissues and organ systems such as lungs, arteries, and cartilage undergo cyclic stretch and actively respond to changes in mechanical stimuli, which play an important role in regulating cellular form and tissue function [1]. The ability to mimic the complex, biomechanical environment experienced by cells and tissues *in vivo* is a crucial to better understand variations in tissue properties under stretch and characterize them in disease contexts such as fibrosis. Key requirements in the design of stretching devices for such applications are the abilities to independently control the amplitude and frequency of stretch in orthogonal directions mimicking deformations relevant to biological applications, maintain strain homogeneity in thin planar materials, and be compatible for high resolution optical imaging for real-time data acquisition during experimentation. Existing cell stretchers have some of these features but are limited to either equibiaxial or uniaxial stretching, use large amounts of cell media (increasing expenses), or use out-of-plane actuation that makes real-time imaging difficult [2-4]. To address these limitations, in this work, we have developed and validated a pneumatically controlled cell stretcher with independent control of strain in two directions of a membrane. In-plane actuation geometry allows real-time microscope imaging during actuation. Our biocompatible device is sized similarly to standard 60-mm petri dishes, making it compact and lightweight.

METHODS

The design of the biaxial cell stretcher is depicted in Figure 1-i). Four vacuum cavities generate two-directional stretch, with two opposing cavities connected to a single pneumatic channel to ensure uniform strain in each direction. All cavities (34-mm inner diameter, 64-mm outer diameter) and stretching membrane (0.4-mm thickness) are made of polydimethylsiloxane (PDMS) Sylgard 184 (Dow Corning, USA) with base to cross-linker ratio 17.5:1. The mechanical properties of the PDMS (17.5:1) were characterized by uniaxial testing. Vacuum pressure driven shrinkage of the inner shell of cavities stretches the membrane that is attached to the shell's bottom. Rigid stickers at the edges of the membrane guide the deformation of the membrane to enable uniform strains [2]. The base is made by stereolithography (SLA) 3D printing and cured in an oven at 70°C for 24 hours to ensure

biocompatibility. This base enable mounting on an inverted microscope stage for live-cell imaging. We used uncured PDMS to bond the individual components together. For the control system, an Arduino with MPC4725 is used to generate 0-5V analog signal that is input to an Alicat Electro-pneumatic Transducer (PCD-series) to control the pressure from 0 to 100 psi. By means of vacuum generator (Festo VAD 1/4), the pressure is transferred to vacuum pressure and then connected to the actuator to generate shrinkage of the inner shell of the cavity. The in-plane membrane strains were quantified by tracking fiducial markers on PDMS using a particle tracking algorithm [5]. All materials in contact with culture media were tested separately for biocompatibility. We also tested for biocompatibility of the entire system by performing live-dead staining on 3T3 fibroblasts cultured using DMEM +10% FBS+1% PenStrep inside the cell stretcher system for 24 hours under standard culture conditions (37°C, 95% humidity, 5% CO₂).

RESULTS

Uniaxial tensile tests on the 17.5:1 PDMS membrane measure a Young's modulus of 303.26 ± 11.56 kPa and an elongation at break of 240%. We used these parameters to predict the strain fields on the membrane under different vacuum inputs using Finite Element (FE) simulations by COMSOL (Figure 1h-1j).

We validated the actuation of the stretcher under sinusoidal loading. We compared three cases – uniaxial, equibiaxial and non-equibiaxial loading – and experimentally quantified the in-plane strains in each case. The maximum strain amplitude was maintained to be 7% in each case. From Figure 1e-1g, we observe that the device has a stable and repeatable sinusoidal response to the loading input. Figure 1e indicates the uni-directional stretching in x-axis can cause a heterophase strain change (~2.4%) in y-axis caused by the Poisson ratio of the elastomer membrane. [5] FE simulations shown in Figure 1h shows uniform strain in the middle working area with average E_{11} of 7.1% and E_{22} of 2.2%, corresponding well with experimental measurements. Figure 1f indicates that the stretcher can produce equibiaxial strains when the input air pressure is the same in both channels. Figure 1g demonstrates the stretcher can generate different strain in two directions independently, allowing the investigation of unique phenomena in

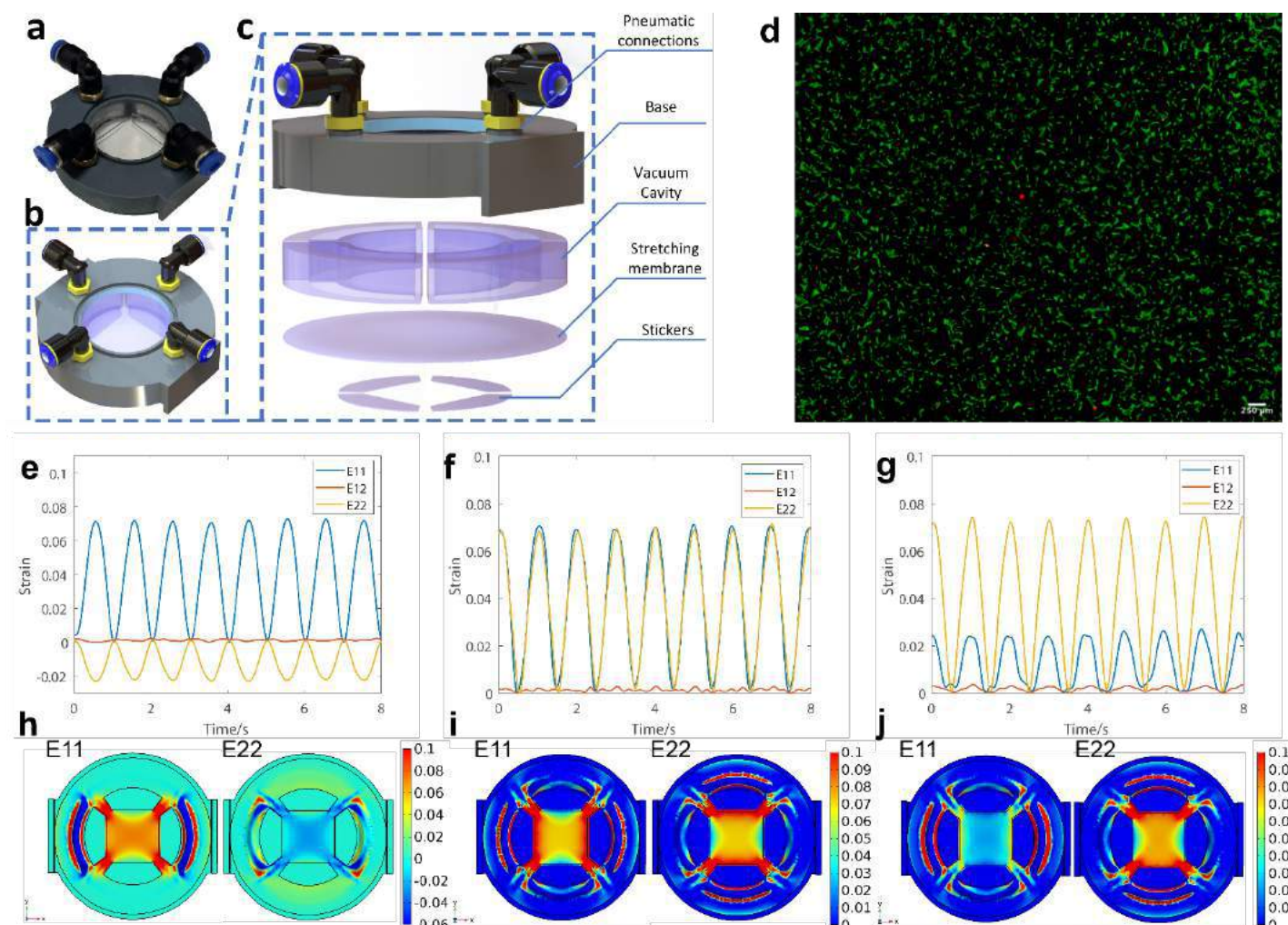


Figure 1: a)-c) Design of the pneumatic bi-axial cell stretcher. a) The practical cell stretcher. b) The 3D model of cell stretcher. c) The exploded diagram of cell stretcher. d) Live-dead assay of cells cultured on the stretcher shows 99% viability after 24 hours. (Green-live cells, red- dead) Scale bar = 250 μm . e)-j) Strain calibration under cyclic multiaxial loading. e) uniaxial stretch. f) equibiaxial stretch and g) non-equibiaxial stretch. All three cases employ sinusoidal loading. h), i) & i) shows the corresponding strain maps using FEA for each case.

mechanobiology. Also, Figure 1i & 1j depicts that FE simulation results that agree with their relevant experimental measurements within 5% error. Finally, 3T3 fibroblasts cultured on the membrane for 24 hours were shown to be 99% viable by live-dead assay as shown in Figure 1d.

DISCUSSION

In this work, we present a novel cell stretching system that enables independent control of orthogonal in-plane strains on a deformable membrane, through which live cell imaging is possible. Uniaxial and biaxial cell stretching devices are useful to quantify cellular response to complex microenvironment during tissue development or disease progression. These devices can provide useful insights in research on tissue engineering, cell and developmental biology, cancer, among other areas. Our strain calibration experiments show that the custom-developed stretching device can provide multiaxial mechanical stimuli. Ongoing efforts are aimed at measuring amplitude and frequency dependent cellular responses under multidirectional stretch using the custom stretching device. We have verified cell viability and biocompatibility in our cell stretching system. The device can also be mounted on a microscope stage, suggesting potential for capturing dynamic cellular responses under mechanical stretch. The controlling

set-up also enables us to simultaneously stretch up to five identical devices which allows for higher-throughput studies. Development of such customizable mechanobioreactors will be crucial in quantifying strain-dependent cell responses [6] under multiaxial cyclic stretch.

ACKNOWLEDGEMENTS

This research was supported by NSF Awards 2149946 and 2120200, as well as startup funding at Purdue University. The authors declare that they have no competing interests.

REFERENCES

- [1] Vogel V. and Sheetz M., *Nature Reviews Molecular Cell Biology*, 7: 265–275, 2006.
- [2] Kreutzer, J et al., *Biomech. Model. Mechanobiol.* 19: 291-303, 2020.
- [3] Ursekar C.P et al., *Plos One*, 9: e90665, 2014.
- [4] Correia Carreira, S et al., *ACS Biomater. Sci. Eng.* 7: 2225-2245, 2021
- [5] Chatterjee A et al. *Biomech Model Mechanobiol.* 21: 553–567, 2022.
- [6] Pendyala M, et al., *PLoS One*, 17: e0267921, 2022.

COMPUTATIONAL FLUID DYNAMICS STUDY TO INVESTIGATE THE IMPACT OF SUDDEN PHYSIOLOGICAL ACTIONS ON CEREBROSPINAL FLUID PRESSURE AND FLOW

Sarah Vandenbulcke (1), Paul Condrón (2,3), Haribalan Kumar (2,4,5), Soroush Safaei (4),
Samantha Holdsworth (2,3), Joris Degroote (6), Patrick Segers(1)

- (1) IBitTech-bioMMeda, Department of Electronics and Information Systems, Ghent University, Ghent, Belgium
(2) Mātai Medical Research Institute, Tairāwhiti-Gisborne, New Zealand
(3) Faculty of Medical and Health Sciences & Centre for Brain Research, University of Auckland, Auckland, New Zealand
(4) Auckland Bioengineering Institute, University of Auckland, Auckland, New Zealand
(5) GE Healthcare, Australia and New Zealand
(6) Department of Electromechanical, Systems and Metal Engineering, Ghent University, Ghent, Belgium

INTRODUCTION

Cerebrospinal fluid (CSF) and the brain tissue pulsate following the cardiac cycle and respiration [1]. These pulsations are caused by volume changes of cerebral arteries and veins and were previously implemented in a computational fluid dynamics (CFD) model of the CSF which, together with windkessel boundary conditions, allowed computing CSF flow and intracranial pressure in line with literature [2].

Less well understood is the impact of sudden venous volume changes, induced by physiological actions such as coughing, on the overall CSF flow. Coughing was observed to cause a rapid rise and fall of intracranial pressure and has been associated with volume variations of cerebral and epidural veins [3]. Previous experimental and computational studies have investigated the impact of sudden physiological actions on the CSF and the surrounding tissues but did only consider simplified geometries or certain parts of the CSF space such as the spinal subarachnoid space (SAS) [4, 5].

Therefore, in this study, the effects of sudden changes in venous volume on CSF pressure and flow are investigated in our CFD modeling framework of the complete cranial and upper spinal CSF circulation. After tuning the model to a newly generated and comprehensive MRI dataset, it was used to evaluate the implementation of sudden physiological actions with the aim to improve our understanding of their impact on the overall CSF circulation.

METHODS

Image acquisition: Under ethics approval, MRI brain images were obtained on a healthy subject using a 3T MRI scanner at the medical research institute Mātai (Gisborne, New Zealand)(SIGNA Premier; General Electric Healthcare, Milwaukee, WI) based in Gisborne, New Zealand. Data collection included whole-brain anatomical T1, T2, and T2 FLAIR weighted images (0.5 mm³ isotropic resolution) and PC-MRI images (axial slices at cervical level (C2) and cerebral aqueduct with

velocity encoding = 9 and 16 cm/s, respectively and 0.7 mm² in plane resolution).

Segmentation and meshing: The 3D geometry of the CSF space was extracted from the anatomical MRI images using the segmentation software Mimics (Materialise, Leuven, Belgium). An unstructured mesh was generated using ICEM (Ansys, Canonsburg, USA) containing 1,445,916 cells.

Model setup: The model was set up using the numerical software Fluent (Ansys, Canonsburg, USA) with boundary conditions based on physiological processes as presented in [2]. Figure 1A depicts the locations of the inlet and outlet boundary conditions in blue and red, respectively. Bulk flow was modeled through a source term in the lateral ventricles, resistors at the arachnoid villi and lymphatic outlets, and 2-element windkessel models at the spinal and interstitium outlet. A total compliance of 0.17 ml/mmHg was considered for all cases distributed over the interstitium (1/3) and spinal (2/3) outlet. Cardiac contraction was assumed to create a pulsatile displacement of CSF in front of the brainstem (arterial 1), which was implemented as a sinusoidal source term with an amplitude of 5.06 ml/s and a frequency of 1Hz. Moreover, brain motion was observed to show an up-and-down piston-like pumping motion in the mid-brain region following the cardiac cycle [6]. This effect was considered by imposing a sinusoidal velocity at the upper wall of the lateral ventricles (arterial 2). Starting from a maximal displacement of 0.03 mm as in [2], the value leading to the best match with subject-specific phase-contrast MRI measurements was determined (= baseline model). The phase-contrast data was analyzed using CFI42 (Circle, Calgary, Canada), across two cross-sections: the cerebral aqueduct and spinal SAS. In contrast to the model in [2], normal breathing was not considered.

Imposing sudden physiological actions: To mimic the effects of coughing, sudden flow changes are numerically introduced in the region of the occipital veins (vein) as a source term by imposing consecutively a positive and a negative gaussian curve as a time signal with an

arbitrarily chosen standard deviation of 0.05s and amplitudes of 5.3 ml (cough 1) and 10.6 ml (cough 2), and a standard deviation of 0.1 s and amplitude of 12.7 ml (cough 3). Finally, a short positive flow peak is mimicked by a positive gaussian curve with a standard deviation of 0.05s and amplitude of 5.3 ml (peak). The corresponding input flows are visualized in figure 2 (input change). The pressure gradients are calculated between a point in the spinal SAS and the lateral ventricles as depicted by Δ_{lv-sas} in figure 1A.

RESULTS

In figure 1, CFD flow rates at a cross-section of the cerebral aqueduct and the spinal SAS are visualized together with subject-specific phase-contrast MRI measurements. The maximal displacement of the ventricles was increased from 0.03 to 0.13 mm to match the measured flow amplitudes, which increased CSF flow at the aqueduct level by a factor 4.6 (figure 1B) and causes the maximal pressure gradient (not plotted here) to go up from 0.4 to 2.4 mmHg/m.

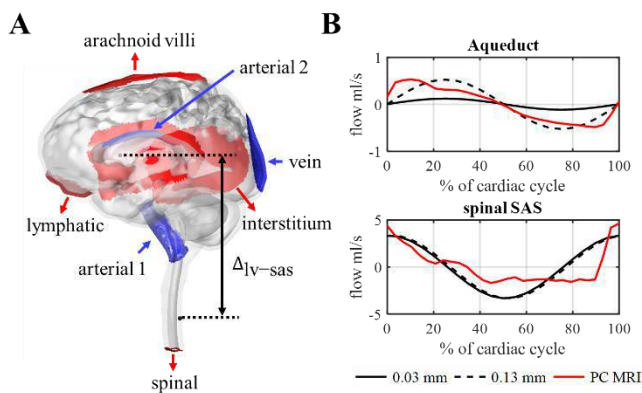


Figure 1: (A) Overview of inlet (blue) and outlet (red) boundary conditions. (B) Comparison of simulation results (maximal displacement of 0.03 and 0.13 mm) to phase-contrast MRI measurements at two cross-sections.

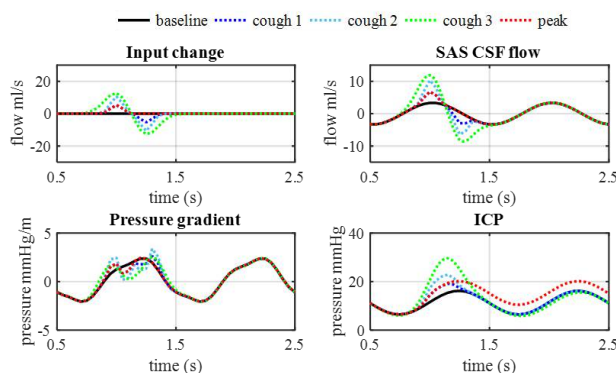


Figure 2: Input flow rates and CFD simulation results of the baseline model, cough 1, 2, 3 and peak for the CSF flow through the spinal SAS, the pressure gradient between the lateral ventricles and the spinal SAS, and the intracranial pressure (ICP).

Figure 2 shows the effects of three physiological actions against the baseline model (0.13 mm) on spinal SAS CSF flow, the pressure gradient between the lateral ventricles and spinal SAS, and the intracranial pressure (ICP). A maximal pressure gradient of 2.6, 3.4, and 2.5 mmHg/m was obtained for cough 1, 2, and 3, respectively, compared to 2.4 mmHg/m for the baseline model. Coughs 1, 2, and 3 cause a brief intracranial pressure elevation of 3.7, 7.5, and 14.2 mmHg,

respectively, above the baseline at time = 1.15s. Meanwhile, a positive peak (peak) results in a maximal pressure elevation of 4 mmHg or 25% which is sustained beyond the peak.

DISCUSSION

Comparison of CFD with in vivo CSF measurements at the level of the spinal SAS and cerebral aqueduct shows that a maximal displacement of 0.13 mm matches the in vivo CSF flow amplitudes (Figure 1). This also leads to a pressure gradient of 2.4 mmHg/m which is better in line with values 0.72 and 2.2 mmHg/m as recorded in patients with idiopathic normal pressure hydrocephalus [7].

Important differences are observed when imposing sudden flow changes (see cough 1, 2, and 3, and peak in figure 2). Simulating cough results in a brief perturbation of the CSF flow and intracranial pressure, whereafter the original conditions are directly restored, as the volume increase is directly followed by an equal volume decrease. In the model, peak pressure appears to linearly increase with input flow magnitude and standard deviation. In vivo studies reported an increase in intracranial pressure of about 35 mmHg in response to a single cough [3], which is more than two times the amplitude reported for cough 3 in this study. In contrast to [3], no decrease in pressure was found after the sudden volume changes.

Meanwhile, a short infusion of fluid results in a slightly higher and long-term elevation of intracranial pressure. Predictions based on 0D model simulations (data not shown) indicate that it might take over 15 minutes before returning to normal intracranial pressure. This delay depends on absorption and compliance parameters imposed through resistor and windkessel boundary conditions.

Importantly, the volume changes increase and disrupt the pressure gradient between the ventricles and the spinal SAS. Whereas these pressure gradients are quickly restored in healthy subjects, we speculate that a CSF flow obstruction might sustain and even increase these pressure differences. Previous studies reported larger spatial pressure gradients in patients with a spinal SAS blockage as in Chiari type 1 malformation and hypothesized that physiological actions such as coughing might drive syrinx progression in patients with Chiari type 1 malformation [4].

In this study, the effects of sudden physiological actions on CSF circulation are investigated in a CFD model of the CSF. This allowed us to evaluate the effects on both intracranial pressure and pressure gradients. Comparison with the literature indicates that accurate modeling of cough requires adequate selection of amplitude and duration of input flow. Moreover, further optimization of inlet and outlet boundary conditions in the baseline model should continue. In the future, accurate modeling of physiological actions can lead to a better understanding of their role in neuro-biomechanical disorders such as Chiari type 1 malformation.

ACKNOWLEDGEMENTS

This work was supported by the Research Foundation Flanders (FWO) and the Kānoa - Regional Economic Development & Investment Unit, New Zealand.

REFERENCES

- [1] Dai, H et al., Front Neurol, 11, 959, 2020
- [2] Vandenbulcke, S et al., Front Bioeng Biotechnol, 10, 2022.
- [3] Williams, B, Acta Neurochirurgica, 59, no. 1: 123-142, 1981.
- [4] Martin B, et al., Fluids Barriers CNS, 6: 17, 2009.
- [5] Bertram C D, J Biomech Eng, 132, no.6, 2010.
- [6] Terem I, Magn Reson Med, 86: 1674-1686, 2021
- [7] Vinje, V. et al., Sci Rep, 9: 9732, 2019.

MECHANICAL CHARACTERISATION OF HUMAN PENILE TISSUES TO INFORM THE DEVELOPMENT OF PRE-CLINICAL TESTBEDS

Shirsha Bose (1,2,3), Majid A. Khorshidi (1,2,3), Robert D. Johnston (1,2,3), Brian Watschke (4), Evania Mareena (5), Daragh Nolan (5), Sean Cooney (5), Caitríona Lally (1,2,3)

- (1) Trinity Centre for Biomedical Engineering, Trinity Biomedical Sciences Institute, Trinity College Dublin, Dublin, Ireland
- (2) Department of Mechanical, Manufacturing & Biomedical Engineering, School of Engineering, Trinity College Dublin, Ireland
- (3) Advanced Materials and Bioengineering Research Centre (AMBER), Royal College of Surgeons in Ireland and Trinity College Dublin, Dublin, Ireland
- (4) Urology, Boston Scientific Corp, Inc, Minnetonka, MN, USA
- (5) Urology, Boston Scientific Corp, Inc, Clonmel Co, Tipperary, Ireland

INTRODUCTION

Erectile dysfunction (ED) is the inability to achieve or maintain erection during sexual activities, affecting approximately 52% of men in the age 40-70 [1] and increasing by 10% for each decade of age [2]. It is one of the most commonly undiagnosed and untreated diseases leading to a poor quality of life for both the sufferer and their partner. Minimally invasive treatment methods such as pharmacotherapy, intracavernous injection, low-intensity shock-wave therapy exist, yet, many men do not respond well to these treatments, often due to underlying health issues such as diabetes or vascular diseases [3]. The only real alternative in such cases is a penile implant [3, 4]. Various penile implants are commercially available, including malleable penile prostheses and, 2- or 3-piece inflatable penile prostheses (IPPs). All of these implants consist of a pair of cylinders which are placed in the corpora cavernosa (CC). The 2- and 3-piece IPPs also consist of a pump (inside the scrotal sacs) while an additional component, reservoir (inside the abdomen), is attached to the 3-piece IPP. In this study, the authors focus on the 3-piece IPP which shows a higher satisfactory rating among consumers [5]. The components of a 3-piece IPP, along with their placements inside the body, are shown in Figs. 1a, b. The pump consists of a button which helps in inflating (erect state) and deflating (flaccid state) the cylinders by passing the fluid stored in the reservoir. The positioning of the IPP cylinders results in non-physiological loading within the CC and tunica albuginea (TA), see Fig. 1b.

Penile biomechanics is a relatively unexplored topic and to-date very few research studies have been performed on mechanical testing of human penile tissues. Timm *et al.* designed an external fixator, with four indenters, which was used to record the force-displacement behaviour of the whole penis [6]. Whilst this was the first mechanical characterization of the whole penis, the indenters created only local deformation on the tissue and hence tissue characterization was limited. A recent study reported the material properties of TA but there was a limitation in the number of specimens and irregular specimen

geometries [7]. Earlier work by Gefen *et al.* [8], using finite element analysis to explore penile mechanics, represented the penis as a linear-elastic material with somewhat arbitrary tissue properties; although it is widely known that soft tissues behave as hyperelastic materials.

There is a lack of available knowledge on penile tissue properties and hence the pre-clinical testbeds (benchtop and computational models) developed to date, do not provide a realistic testing environment [8],[9]. To improve these models, mechanical characterization tests of whole penis and individual penile tissues are necessary. Individual tissue properties are needed to define or identify suitable analogue materials for pre-clinical models, whilst intact penis segment testing can validate them. Such pre-clinical testbeds will ultimately provide a means to improve IPP designs, their surgical implantation and long-term success.

METHODS

Fresh-frozen human penis (distal and proximal) was purchased from ScienceCare, USA, cleaned and segmented into 30 mm segments (Fig. 1c, d). These segments (n=4) were tested between two compression platens (Zwick Testing Machine) with a load cell of 20 N up to 30% deformation in multiple orientations to obtain the whole tissue response. The segments were labelled as S1, S2, S3, and S4, from the distal to the proximal end (see, Fig. 1d).

Following this, these segmented sections were snap frozen to -80°C and subsequently stored at -20°C. After this stage, individual components such as CC, TA and whole urethra encompassed within corpus spongiosum (Ur_CS) were segregated whilst frozen using scalpel and biopsy punches. These tissues were then cryopreserved at -80°C using a tissue freezing media (TFM) until mechanically tested.

Cylindrical specimens were obtained for CC in radial and longitudinal (n=5) directions. CC and CS along with the urethral lumen (Ur_CS) (n=5), were tested under compression up to 50% deformation using a load cell of 5 N. TA (n=5) was tested in tension along both

longitudinal (TA (Long)) and circumferential (TA (Circum)) directions and also in compression (radial direction, TA (Rad)) using a load cell of 200 N. All the tissue testing was performed in phosphate buffered saline at $37 \pm 2^\circ\text{C}$.

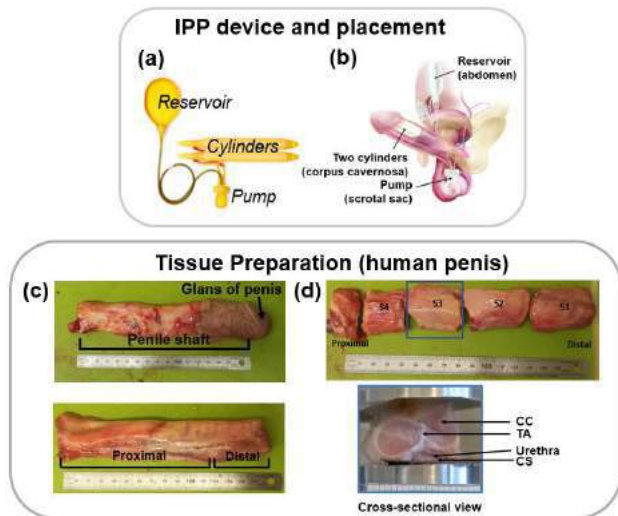


Figure 1: (a) 3-piece IPP device having a pair of cylinders, reservoir and pump [10], (b) the placement of the IPP inside the body [11], (c) Preparation of the tissue by removal of the penile glans and foreskin, (d) Segmenting the penile shaft into 30 mm segments and the cross-section showing the important features of the penis.

RESULTS

The whole penis segments ($n=4$) were tested in multiple orientations: 0-degree and 90-degree up to 30% deformation (Fig. 2a). This whole tissue response will be used to validate the pre-clinical models in future (benchtop and computational models).

The '0-degree' orientation testing was dominated by the buckling of the TA septum whilst the septum had little impact during '90-degree' compression. The levels of force generated ranged 0.15 – 0.6 N and 0.1 – 0.45 N for 0-degree and 90-degree loading, respectively, for deformation up to 30% (Fig. 2b).

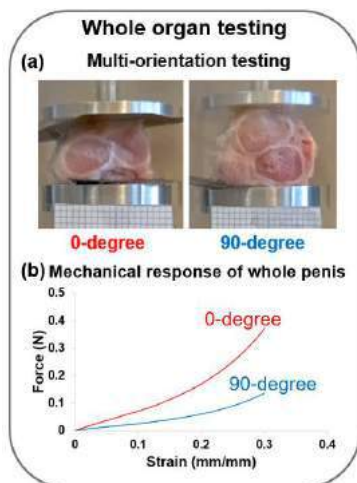


Figure 2: (a) Testing of whole penis representative segment in multiple orientations, (b) Mechanical response in both orientations.

The tissues most affected during IPP inflation/deflation are the CC, TA and urethra along with CS (Ur_CS) (Fig. 3a). Individual tissues were segregated and mechanically tested. CC and Ur_CS are spongy tissues demonstrating very low stiffness initially but showing a stiffening behaviour at higher levels of deformation (Fig. 3b).

TA exhibited stress of approximately two orders of magnitude higher when compared to CC and Ur_CS in compression (at 50% strain). As expected, for tension test, TA in the transverse direction showed a stiffer mechanical response than the longitudinal direction, this could be due to the orientation of the underlying collagen fibers along the circumferential direction (Fig. 3b).

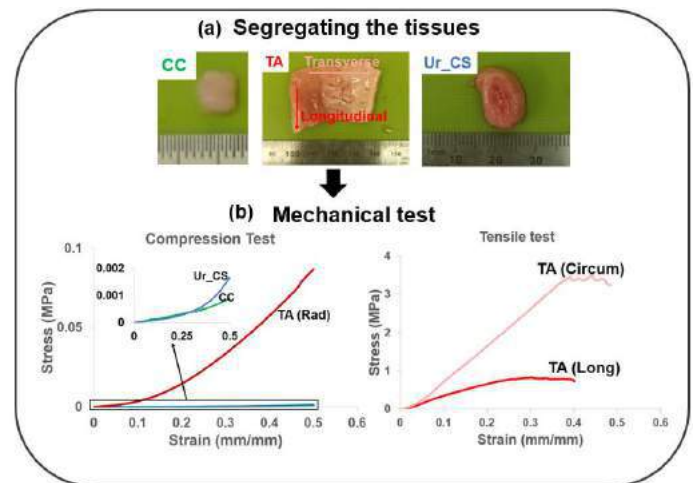


Figure 3: (a) Segregating the whole penis segments into CC, TA and urethra, (b) Mechanical testing of the individual tissues under compression and tension.

DISCUSSION

The whole tissue testing results show that the whole organ tissue is much more deformable than some of the numerical models that have previously been presented in the literature [8].

The segregated tissue results show that TA is much stiffer in tension when compared to the other penile tissues in compression. The material properties obtained from the segregated tissue tests will be used to develop benchtop and computational models in the future. These models can then be validated against the mechanical response obtained from the whole penis segments.

ACKNOWLEDGEMENTS

The authors would like to acknowledge the financial support of Science Foundation Ireland (SFI) under grant number 12/RC/2278_2 and Boston Scientific Limited (Clonmel, Ireland).

REFERENCES

- [1] Ayta, Jet al., BJU Int., 84, 50–56, 1999.
- [2] Ferrini et al., Transl. Androl. Urol., 6, 1, 20, 2017.
- [3] Salonia et al., Eur. Urol., 80, 3, 333–357.
- [4] Bajic, et al., Sex. Med. Rev., 8, 333–337, 2020.
- [5] Bernal and Henry, Adv. Urol., 10–15, 2012.
- [6] Timm, et al., Trans. ASME J. Biomech. Eng., 127, 956–963, 2005.
- [7] Brady, et al., Int. J. Impot. Res., 34, 5, 477–486, 2021.
- [8] Gefen et al., Ann. Biomed. Eng., 28, 6, 619–628, 2000.
- [9] Renterghem K. & Ghazi A., Int. J. Impot. Res., 32, 3, 261–263, 2020.
- [10] Barnard et al., J. Sex. Med., 18, 7, 1156–1166.
- [11] Chou et al., Abdom. Radiol., 44, 2, 739–748.

OPTIMIZATION AND IMPLEMENTATION OF A CAROTID QUANTITATIVE SUSCEPTIBILITY MAPPING SEQUENCE FOR ATHEROSCLEROTIC PLAQUE VULNERABILITY ASSESSMENT

Brooke Tornifoglio (1,2), Sarah McElroy (3), Alan J. Stone (4), Karin Shmueli (5), Caitríona Lally (1,2,6)

- (1) Trinity Centre for Biomedical Engineering, Trinity College Dublin, Dublin, Ireland
- (2) Department of Mechanical, Manufacturing and Biomedical Engineering, Trinity College Dublin, Dublin, Ireland
- (3) MR Research Collaborations, Siemens Healthcare Limited, Frimley, United Kingdom
- (4) Department of Medical Physics and Clinical Engineering, St. Vincent's University Hospital, Dublin, Ireland
- (5) Department of Medical Physics and Biomedical Engineering, University College London, London, United Kingdom
- (6) Advanced Materials and Bioengineering Research Centre (AMBER), Royal College of Surgeons in Ireland and Trinity College Dublin, Dublin, Ireland

INTRODUCTION

The buildup of atherosclerotic plaque tissue within the carotid arteries contributes to approximately 34% of ischemic strokes and is linked to an increased risk of cardiac arrest [1]. While the vessel wall is composed of collagen, elastin, and smooth muscle cells, plaques can be composed of fat, calcium, fibrous tissue, and iron in differing quantities and microstructural arrangements [2,3]. Early identification and treatment is of the utmost importance to avoid stroke-related disability and death caused by carotid plaque. Currently, the percent stenosis, or luminal blockage, is the diagnostic criterion to determine if a patient should undergo surgical intervention [4]. If the plaque occludes the lumen by more than 50-70%, it is deemed vulnerable to rupture. However, this criterion lacks mechanical insight and is becoming more widely accepted to be insufficient [5-8]. Therefore, the implementation of a mechanically sensitive and clinically relevant biomarker is needed.

Quantitative susceptibility mapping (QSM) is a magnetic resonance imaging (MRI) method which can spatially map the magnetic susceptibility of biological tissue [9]. Recent studies have investigated QSM *in vivo* at the carotid bifurcation and showed the ability to differentiate between intraplaque hemorrhage and calcification due to their markedly different susceptibilities [10-12]. Meanwhile, previous work from our lab investigating *ex vivo* arterial tissue identified QSM susceptibility as a promising arterial tissue biomarker, with significant sensitivity to elastin and collagen, the main load bearing component in arterial tissue [13].

This work aims to further translate QSM from *ex vivo* to *in vivo* to assess the potential of this technique for diagnosis of atherosclerosis with a specific focus on mechanically sensitive microstructures like collagen. Through the optimization and implementation of a carotid QSM sequence on two different 3T clinical scanners, Siemens and Philips, the true potential of this methodology will be assessed. Novel insights from this work have the potential to change how current clinical decisions are made.

METHODS

A multi-echo gradient echo (ME-GRE) sequence was implemented at two centers on both a 3T Philips Achieva (Centre for Advanced Medical Imaging, St. James' Hospital, Dublin) and a 3T Siemens Prisma (Trinity Institute of Neuroscience, Trinity College Dublin). Table 1 outlines the sequence parameters. Voxel size, slice thickness, and the impact of a venous saturation band were investigated. One healthy volunteer (male, 29 years old) was recruited and provided written informed consent with ethical approval provided by the St. James' Hospital/Tallaght University Hospital Joint Research Ethics Committee (#2170). The volunteer was imaged at both centers on two different days.

Table 1. Sequence parameters for both scanners. Parameters marked with an asterisk were investigated.

	3T Siemens Prisma	3T Philips Achieva
Sequence	VIBE	THRIVE
Coil	(2) 4-channel special purpose coils	8-channel carotid coil
Field of view [mm]	210 x 210	258 x 258
Orientation	Transverse	Transverse
Slices	28	40
Voxel size [mm]*	0.5 x 0.5; 0.6 x 0.6	0.5 x 0.5; 0.6 x 0.6
Matrix size	448 x 448	480 x 480
Slice thickness*	1.0; 2.0 mm	1.0; 2.0 mm
TEs	2.9, 7.6, 12.3, 17 ms	2.9, 7.6, 12.3, 17 ms
Flip angle	10°	10°
TR	21 ms	21 ms
Bandwidth	580 Hz/Px	430 Hz/Px
Averages	2	2
Saturation band*	ON; Off	ON; OFF
Acquisition time	7 min 38 sec	6 min 25 sec

RESULTS

Figure 1 shows magnitude images of a healthy volunteer scanned on a 3T Siemens Prisma with (A) 0.6 and (B) 0.5 mm in-plane resolution. Figure 2 demonstrates the impact of slice thickness, from 2.0 to 1.0 mm, in a healthy volunteer on both scanners. The influence of the application of a venous saturation band on both scanners in a healthy volunteer can be seen in Figure 3. Red arrows point to (A, C) the signal in the jugular vein and (B, D) lack of signal when the saturation band is applied.

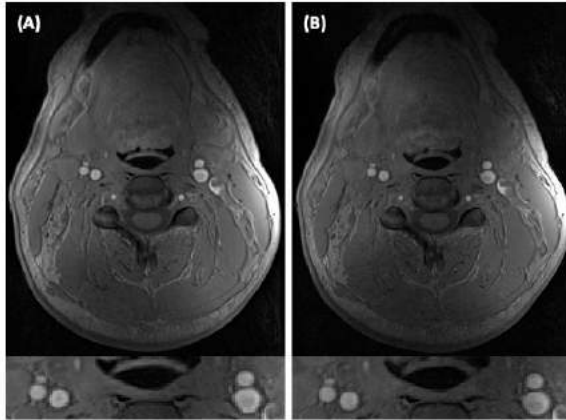


Figure 1. Magnitude images of healthy volunteer scanned on Siemens Prisma with (A) 0.6 and (B) 0.5 in-plane resolution.

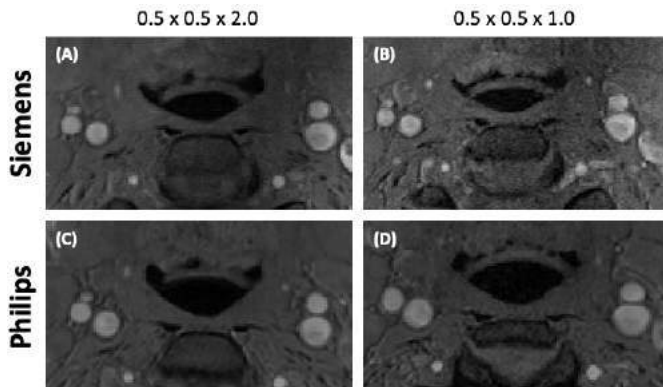


Figure 2. Magnitude images with slice thickness of 2.0 mm (A, C) and 1.0 mm (B, D) for both clinical scanners.

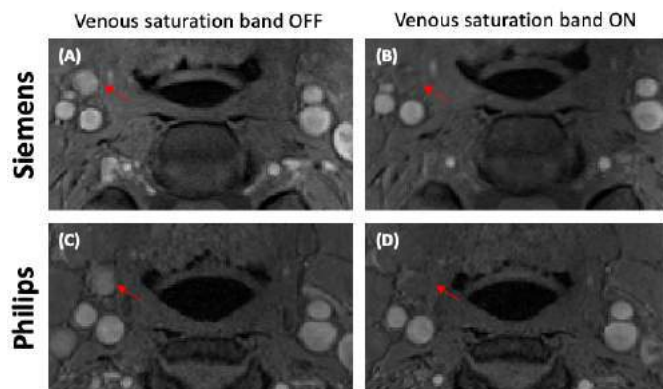


Figure 3. Magnitude images with venous saturation band off (A, C) and on (B, D) for both clinical scanners.

DISCUSSION

A previously reported ME-GRE carotid QSM sequence which was used to investigate calcifications and hemorrhage [12], was repeated on a Siemens scanner (Fig. 1(A)). A higher resolution ME-GRE sequence, with respect to both in-plane voxel size (Fig. 1(B)) and out-of-plane slice thickness (Fig. 2), was implemented on two clinical scanners. To the authors knowledge, this is the first implementation of QSM at the carotids on a 3T Philips Achieva. The influence of a venous flow saturation band was also investigated – with no qualitative advantage or disadvantage observed (Fig. 3).

While higher resolutions are advantageous when imaging at the carotid bifurcation to avoid partial voluming effects on the vessel wall, several issues can arise. Smaller voxel sizes lead to decreased signal and increased noise which can be insufficient for further QSM analysis. This increase in noise can be seen in Fig. 2(B) when compared to Fig. 2(A). Additionally, it has been shown previously that isotropic voxels are generally required for accurate susceptibility maps [14]. Therefore, future work aims to optimize the current sequences further to achieve high resolution and isotropic voxels, while maintaining a sufficient signal-to-noise ratio.

Once the sequence is further optimized, more healthy volunteers will be imaged in both scanners to better establish a multi-center comparison. We will also need to further optimize the processing pipeline. With an optimized sequence and QSM processing pipeline, the final stages of this work will focus on patients scheduled for carotid endarterectomy surgeries. Patients will be imaged prior to surgery to obtain *in vivo* carotid plaque QSM. Their excised atherosclerotic plaques will then be imaged *ex vivo* and mechanically and histologically characterized. By linking *ex vivo* characterization of the mechanical integrity of these tissues with *in vivo* QSM, this work will assess the feasibility of this sequence to yield novel insights into carotid atherosclerosis and plaque vulnerability.

ACKNOWLEDGEMENTS

This project has received funding from the European Research Council 2022 Proof of Concept (VASCOLL). The authors would like to also thank the Centre for Advanced Medical Imaging at St. James' Hospital and Trinity's Institute of Neuroscience for their help with this work.

REFERENCES

- [1] Smith-Bindman & Bibbins-Domingo, *JAMA Network Open*, 4(2):e2036218, 2021.
- [2] Sarty, et al., *Circ*, 89:2462-2478, 1994.
- [3] Sarty, et al., *Circ*, 92:1355-1374, 1995.
- [4] Savastano, L. E., & Seibel, E. J. *Neurosurg*, 64:188-198, 2017.
- [5] Naylor, et al., *Eur J Vasc Endovasc Surg*, 55:3-81, 2018.
- [6] Millon, et al., *J Vasc Surg*, 57:1046-1051, 2013.
- [7] Gimnich, et al., *Curr Atheroscler Rep*, 2022.
- [8] Svoboda, et al., *J Stroke Cerebrovasc Dis*, 31:106262, 2022.
- [9] Wang and Liu, *Magn Reson Med*, 73:82-101, 2015.
- [10] Ikebe, et al., *Magn Reson Med Sci*, 19(2):135-140, 2019.
- [11] Ruetten, et al., *Magn Reson Med*, 84(2): 686-697, 2019.
- [12] Nguyen, et al., *Magn Reson Med*, 84:1501-1509, 2020.
- [13] Stone, et al., *Magn Reson Med*, 86(5):2512-2527, 2021.
- [14] Karsa, et al., *Magn Reson Med*, 84:3206-3222, 2020.

DETERMING THE GEOMETRICAL PROPERTIES OF URINARY BLADDER WALL DURING PASSIVE FILLING

F. Azari (1)

(1) Department of Mechanical Engineering and Materials Science, University of Pittsburgh, Pittsburgh, PA, U.S.A.

INTRODUCTION

Bladder is a hollow muscular organ capable of undergoing massive deformations during filling and voiding. The functionality of this organ decreases with age leading to numerous abnormalities (i.e., cancer, urinary incontinence, interstitial cystitis). Bladder wall undergoes a complex remodeling process as it experiences heterogeneous properties from dome to trigonal area. To aid surgical interventions and pharmacological treatments, a better understanding of the filling behavior is essential [2,3].

Understanding the shape of the bladder is a significant steppingstone to quantifying the deformation amount (i.e., stress vs. strain relation). Previously, biaxial and uniaxial testing of a bladder strip was studied. However, almost no study up to this date analyzed the geometrical properties of the whole bladder under applied pressure. The thickness of a rat's urinary bladder is characterized by a custom inflation setup and microcomputed tomography (micro-CT) scanner.

METHODS

The inflation setup studied the passive filling process of bladders. Each rat's bladder was mounted to a 40mm gauge needle and secured by multiple nuts at the middle of the urethra. The bladders were inflated from 0mmhg to 35mmhg by an automated syringe pump while recording the process with a high-resolution stereo imaging system. Prior to any inflation, bladders were imaged by micro-CT at 0mmhg. The n=5 bladder geometries (P=0mmhg) were reconstructed from scanned slices. After the shape reconstruction, bladder wall thickness was measured by an algorithm (Materialize-3Matics) based on the nearest distance from the luminal body to the abluminal body.

RESULTS

There were N=5 cases analyzed to understand the sharp thickness changes. It was observed that the bladder dome has the highest thickness of around 2.6mm, while the trigonal areas have the least thickness of

0.16 mm. The bladder tends to be stiffer at the initial filling pressure (Figure 1).

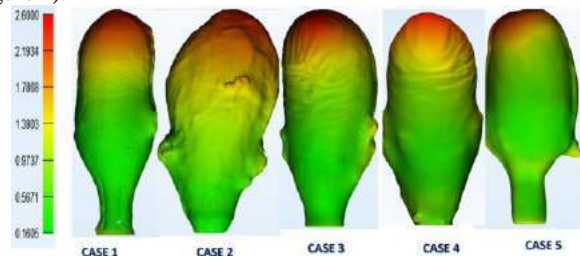


Figure 1: wall thickness color maps, n=5, P=0mmhg

It then expands to relatively uniform thickness, highlighting the bladder colormaps at 17.5mmhg to be very similar to 35mmhg. This is another scientific observation while characterizing the geometrical properties (Figure 2).

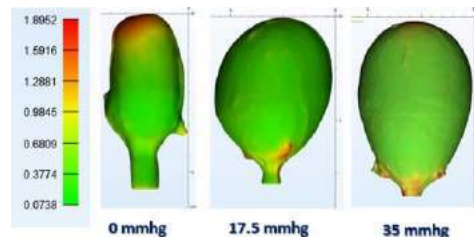


Figure 2: wall thickness color maps during bladder filling up to P=35mmhg, CASE 5

The filling images also demonstrate the areas with the least transparency from the dome towards the bladder body (Figure 3A).

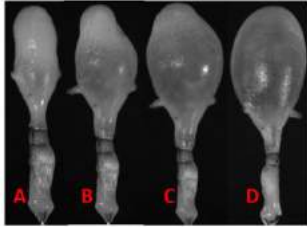


Figure 3: Bladder filling images from stereo cameras, P=35mmhg (D), P=0mmhg (A), CASE 1

The filling process for the bladder (CASE 5) was also recorded and depicted in (Figure 4).

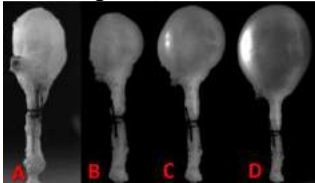


Figure 4: Bladder filling images from stereo cameras, P=35mmhg (D), P=0mmhg (A), CASE 5

DISCUSSION

This study shed some light on the heterogeneity of the bladder wall during the initial phases of passive filling. As depicted in the wall thickness color maps, towards the end of the inflation cycle, the bladder reaches an almost uniform wall thickness of around 0.073mm, much thinner than (p=0mmhg) lowest thickness of 0.16mm. The thickness of the bladder at higher pressures (p=35mmhg) supports the assumptions of [3] that the bladder is a vessel of constant thickness. However, the thickness of the bladder varies regionally at lower luminal volumes [2]. The microstructure of the bladder at the dome is still unknown. The study of [4] assumes types of collagen III coils sit within the extracellular matrix. Parts of the bladder microarchitecture were imaged under an SEM microscope (Figure 5); the complex vasculature highlights the tissue's ability to contract many times during filling and distension while preventing any damage to surrounding blood vessels and organs. Thus, to better understand the thickness variability, the bladder microstructure needs to be understood (Figure 5).

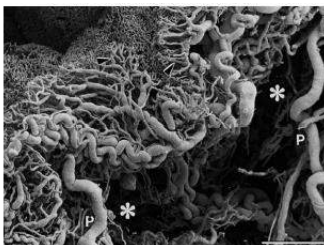


Figure 5: Bladder mucosal microstructure observed under SEM [1] * features the submucosa layer

The passive filling of the bladder wall was drawn from two studies [2] and [3] corresponding to (Figure 6) and (Figure 7), respectively. The pressures ranged from 2 cm H_2O to 4.5 cm H_2O and volumes of 0-50ml had the peak pressures; then they reached a stable pressure of 3.5 cm H_2O [2]. As the pressure increases, the luminal volume also increases nonlinearly (Figure 6).

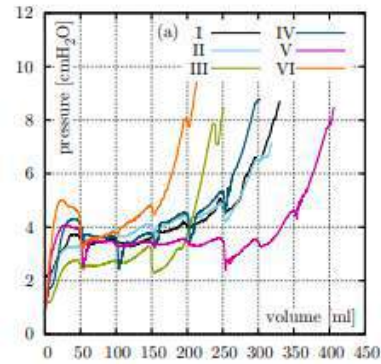


Figure 6: Pressure (cm H_2O) vs volume (ml) graph during pig's bladder passive filling, N=6, [2].

The filling process for mouse bladders is also very stiff, near 200 for the green and red lines with pressure around 2.5mmhg (Figure 7), then the pressure increased to 7.5mmhg-9mmhg for the black and purple lines. The black line is the only different filling case, while the remaining five cases increase in a similar pattern (Figure 7).

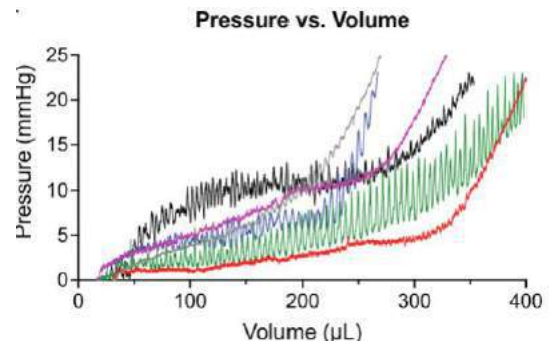


Figure 7: Pressure (mmhg) vs volume (μL) graph during mouse bladder passive filling, N=6, [3]

Additionally, there is a lack of consensus on the reference volume or thickness for the measurements. The study of (Trostorff et al., 2022) [2] extrapolated the thickness between 4.6 and 7.2 mm (porcine bladders) to find the 0% luminal volume. However, in this report, the bladder with zero inflation was assumed to serve as the reference point. This study is limited to the number of samples at intermediate pressure levels (2.5mmhg-8.5mmhg). On the contrary, it clearly depicts the massive regional differences in thickness as the bladder fills. Furthermore, the images from the stereo cameras provide the opportunity to calculate the abluminal volumes of the bladder and quantitatively describe the shape of the bladder during filling.

With the extension of future detailed experiments, the filling process of intact bladder and its correlation to the thickness and luminal volume can be analyzed and compared.

ACKNOWLEDGEMENTS

The author appreciates the support from NIH-1R01AG056944-01A1 Bladder Mucosal Dysfunction During Aging.

REFERENCES

- [1] Hanczar, M. et al (2021). International journal 22(23), 12657.
- [2] Trostorff, R., et al (2022). Journal of the mechanical behavior of biomedical 133, 105347.
- [3] Hennig, G.,etal.(2022).Quantifying Whole Bladder Biomechanics Using the Novel Pentaplanar Reflected Image Macroscopy System.
- [4] Parekh, A.et al. (2010). Journal of biomechanics, 43(9), 1708-1716

MULTISCALE MODEL PREDICTS THE EFFECT OF BETA BLOCKERS ON VENTRICULAR REMODELING IN DOGS WITH EXPERIMENTAL MITRAL VALVE REGURGITATION

J. Bracamonte (1), L. Watkins (2), J. Saucerman (2), J. Holmes (1)

(1) Department of Biomedical Engineering, University of Alabama at Birmingham, Birmingham, AL, USA
(2) Department of Biomedical Engineering, University of Virginia, Charlottesville, VA, USA.

INTRODUCTION

Understanding the triggers and drivers of left ventricular remodeling due to mitral valve regurgitation (MR) is key for the design of therapies for patients with mitral valve disease. This motivated several groups to develop animal models of volume overload and experimental MR, generating a rich body of literature. Consistent with the complex multiscale nature of eccentric hypertrophy, which involves an array of hormonal and mechanical changes, published studies include data on non-invasive imaging, histopathologic assays, and gene microarray analyses. Integrating the wealth of available information to better understand the progression of hypertrophy and design potential therapies requires a holistic approach that incorporates multiple aspects of cellular and organ physiology. We therefore coupled a multicompartimental model of the heart, a lumped model of the systemic vascular circulation, and a logic-based network model of relevant cell signaling pathways to generate a multiscale model of eccentric hypertrophy in the heart. The model was calibrated to reproduce short-term hormonal alterations and long-term ventricular mass increase of dogs after experimental MR by chordal rupture.

METHODS

Ventricular and circulation model

The multi compartmental model of the heart assumed the left and right ventricles to be spherical shells with time-varying elastances (Fig. 1a) and end diastolic and systolic pressure-volume functions defined as:

$$P_{ES} = E(V_{ES} - V_0) \quad (1)$$

$$P_{ED} = A(e^{B(V_{ED}-V_0)} - 1), \quad (2)$$

where E was the end-systolic elastance of the ventricle, V_0 the unloaded volume of the ventricle, and A and B were coefficients describing the exponential shape of the end-diastolic pressure-volume relationship (EDPVR). We assumed equal end-diastolic parameters for both ventricles and set the end-systolic elastance of the right ventricle to 43% of that for the left.

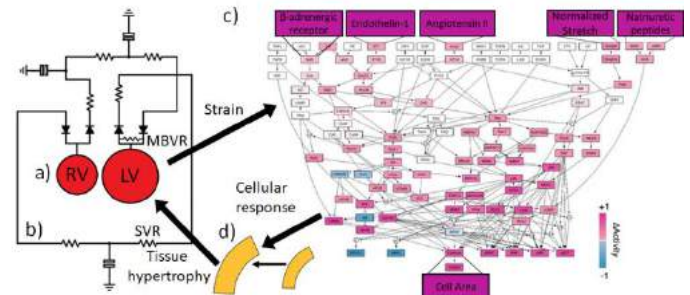


Figure 1. Coupled multiscale model. a) Compartmental model of the heart, b) Lumped model of vascular circulation, c) Network model of cellular hypertrophy pathways, d) Continuum model of tissue growth.

We set parameters for the vasculature circulation model at the values employed by Santamore and Burkhoff [1], except for the stressed blood volume (SBV), systemic vascular resistance (SVR), and mitral valve regurgitant flow resistance (MBVR) (Fig. 1b). SBV, SVR, MBVR, A , B , E and V_0 were fitted from experimental reports of baseline and acute experimental MR from dogs with body weights and regurgitant fractions (RF) ranging between 19-26 kg and 50 and 70% respectively [2,3]. A , B , E and V_0 were adjusted at each growth time-step to maintain fixed material stiffness (stress-strain function) of the myocardium [4]. MBVR was adjusted to keep RF at 60%.

Hypertrophy signaling network model

We incorporated a computational model of the hypertrophy signaling network that integrates many established pathways implicated in cardiac myocyte growth through logic-based differential equations. The network consists of 109 nodes representing hormones and intracellular molecules and 144 reactions (Fig. 1c) [5]. The baseline state was defined by setting all hormonal inputs at an activity level of 0.06 and running the network model until it reached steady state.

Coupling of the multiscale model

At each step, the multicompartamental model and lumped circulation model were solved to simulate one cardiac cycle. The calculated strains were fed to the network model and used to simulate 12 hours of cellular remodeling, producing a normalized Cell Area between 0 and 1. The Cell Area output was used to prescribe the growth of the left ventricle at the organ level. The fiber-direction strain at the baseline and acute states were linearly mapped to the normalized Stretch input of the signaling network so that baseline strain produced a Cell Area of 0.21 (no growth) and maximum strain during acute MR produced a Cell Area of 0.5 (Figure 2a). The Cell Area output was linearly mapped to the growth tensor so that the basal value produced no growth and the predicted mass fold change over 120 days was 1.2. The estimated growth was used to update ventricular properties. All growth was assumed to occur in the fiber direction (Fig. 1d).

Modeling the effect of MR+ β B

β blockade (β B) was simulated by assigning a null maximum value for the β AR network node (β -adrenergic Receptor). Additionally, we imposed decreases in heart rate (HR), systemic vascular resistance (SVR), and pulmonary vascular resistance (PVR), such that they were 95%, 90%, and 84% of their respective values for untreated MR. These were calculated by averaging the reported effect of β B in dogs [6–8].

Cell-signaling network parameter selection

A comprehensive literature review of volume overload by experimental MR and aorto-caval shunt in mammals revealed that under volume overload the renin-angiotensin system and sympathetic nervous systems are activated and circulating concentrations of natriuretic peptide, endothelin-1 and norepinephrine are elevated [6,8]. Within the Network model, these are implemented by increasing the input weights of AngII, NE, BNP, ANP, and ET1 above baseline.

RESULTS

In the coupled model, the simulated MR produced an increase in both normalized stretch network input and circulating hormone levels, triggering rapid growth. That growth reduced peak strain in the compartmental model and the normalized stretch input in the network model by increasing the unloaded volume V_0 . Sufficiently high hormonal input levels could produce enough growth to drive the normalized stretch network input level below its baseline, despite the continued presence of volume overload due to MR (Figure 1a).

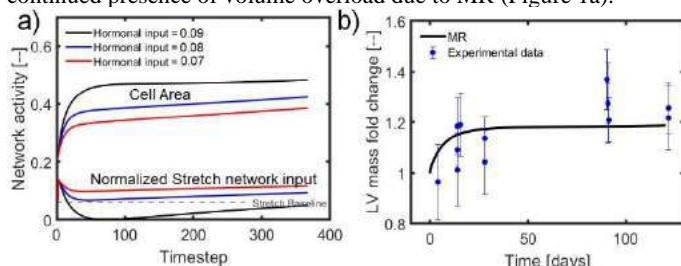


Figure 2. a) Effect of hormonal input (AngII, NE, BNP, ANP, and ET1) on normalized Stretch input and Cell Area. b) Ventricular mass fold change.

Focal adhesion kinase (FAK) is a signaling protein involved in cell adhesion, migration, and growth, which is phosphorylated in response to integrin engagement. Within the network model, FAK activity depends primarily on the normalized Stretch network input and is rather insensitive to other hormonal inputs. Sabri et al. reported that 4 weeks after experimental MR in dogs, FAK phosphorylation drops to 30% of its magnitude on healthy dogs. For the remaining simulations, we therefore chose a hormonal input level that produced similar FAK activity at 28 days as reported by Sabri, and adjusted the Cell Area to ventricular growth mapping function to match experimental data on LV

mass changes during MR in dogs (Fig 2b). When calibrated, the model predicted end-diastolic volumes consistent with experimental data at most time points (Fig 3a). The model estimated a decrease of ventricular wall thickness of 2%, slightly below the average $7 \pm 5\%$ reported in literature. The model also predicted increased activity of p38, JNK, ERK, and AKT during MR relative to control/baseline as reported by Sabri, although the modeled increases were overestimated for JNK and underestimated for AKT (Fig 3b).

Simulations of MR+ β B

In simulations of β B treatment following MR, our model predicted changes of less than 2% in ventricular mass between the MR and MR+ β B, which agrees with the observations of Sabri et al. and Trappanese et al. [7,9] (Fig 3b). In agreement with data on intracellular signaling pathways reported by Sabri et al, β B treatment reversed the depression of FAK signaling associated with MR. Our model also matched the trend of decreased activity of p38, ERK, and AKT with β B treatment but underestimated its magnitude (Fig 3b).

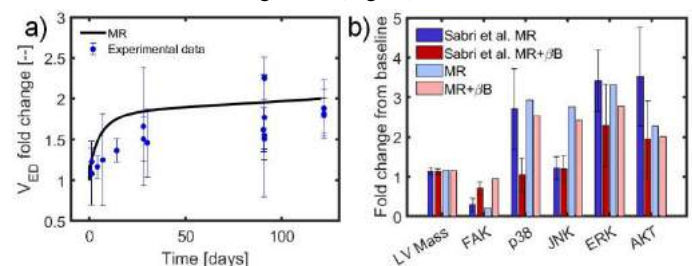


Figure 3. a) Simulated end-diastolic volume fold change vs experimental data. b) Effect of β B on LV mass and hormonal alterations at 4 weeks after experimental MR.

DISCUSSION

We developed a multiscale model of hypertrophy during experimental MR that quantitatively matched data on mass and volume changes over several months and qualitatively matched trends in the activity of several intracellular signaling nodes. Although the model was sensitive to both hormonal inputs and stretch, hormones accounted for most of the growth during simulated MR, because the growth itself reduced stretch below baseline levels after the first ten days. This model result offers a possible explanation for the otherwise paradoxical finding that activation of the stretch-sensitive kinase FAK is reduced rather than increased during experimental MR in dogs [7]. Our model reproduced both this drop in FAK during MR and its recovery following β B treatment, illustrating the promise of multiscale approaches for understanding and designing therapies to modulate hypertrophy. Further work is needed to capture changes in other signaling pathways and to account for the effects of other drugs and combinations.

ACKNOWLEDGEMENTS

This work is supported by the American Heart Association Grant 23POST1026645 (JB) and NIH/NHLBI Grant R01 HL159945 (JH).

REFERENCES

- [1] Santamore, W. and Burkhoff, D. 1991, Am. J. Physiol. Heart Circ. Physiol, 260(1), pp. H146–H157.
- [2] Kleaveland, J. et al. 1988, Am. J. Physiol. Heart Circ. Physiol, 254(6), pp. H1034–H1041.
- [3] Nakano, K. et al. 1991, J Clin Invest, 87(6), pp. 2077–2086.
- [4] Witzenburg, C. , and Holmes, J. 2018, J Cardiovasc Transl Res, 11(2), pp. 109–122.
- [5] Frank, D. et al. 2018, J Mol Cell Cardiol, 121, pp. 180–189.
- [6] Dillon, A. et al. 2012, Journal of Veterinary Cardiology, 14(1), pp. 73–92.
- [7] Sabri, A. et al. 2008, Circ Res, 102(9), pp. 1127–1136.
- [8] Oyama, M. A. 2009, J Small Anim Pract, 50(SUPPL. 1), pp. 3–11.
- [9] Trappanese, et al. 2015, Basic Res Cardiol, 110(1), pp. 1–14.

BUILDING ENTREPRENEURIAL MINDSET: MOTIVATING CURIOSITY, CONNECTIONS, AND CREATING VALUE IN AN ASSISTIVE-DEVICE DESIGN PROJECT.

Joshua A. Gargac (1)

(1) Dr. Carl D. and H. Jane Clay Department of Mechanical Engineering, Ohio Northern University, Ada, Ohio, USA

INTRODUCTION

The Kern Entrepreneurial Engineering Network (KEEN) outlines the 3C's associated with the entrepreneurial mindset (EM) as Curiosity, Connections, and Creating Value. Incorporating EM into curriculum can help students understand the bigger picture, recognize opportunities, and learn from mistakes to create value [1]. Developing these 3C's can equip students with the tools to "build interfaces across tissues, disciplines, and communities." Entrepreneurship is cross-disciplinary in its nature, bringing together multiple skillsets. Students with an EM are willing to explore unfamiliar tissues, disciplines, and communities (Curiosity), identify opportunities to integrate this new knowledge with their existing ideas (Connections), and design products to address the needs of actual people (Creating Value).

Previously a rehabilitative design project was designed and incorporated into a junior-level machine design course [2]. The goal of the original project was to introduce mechanical engineering students to the field of biomechanics. The purpose of this paper is to describe additions made to incorporate entrepreneurial-minded learning (EML). Specifically, the updated project required students to 1) discover the project's motivation by connecting personal passions and everyday objects with client need, (2) build empathy for their clients and develop design ideas using the Wrong Theory Protocol [3], 3) create value by applying course content to design an assistive device, 4) communicate value propositions and design details through formal presentations and design reports, and 5.) consider aspects of curiosity, connections, and creating value through periodic reflections.

METHODS

Mechanical Design 1 is a required course for junior Mechanical Engineering students at Ohio Northern University. The 15-week course covers the theory of machine kinematics and dynamics. Four bar linkages are the focus of the course since they are the most common one degree-of-freedom mechanisms. Throughout the semester, students

applied 3D modeling and MATLAB to design and analyze these mechanisms. The 3 credit hour course had a total enrollment of 53 students across two sections and met for 50-minute lectures three times each week.

A semester-long project was updated to include EML elements during the Fall 2022 semester. The projects were completed in 14 teams with 3-4 students each. A project flow chart is shown in Figure 1.

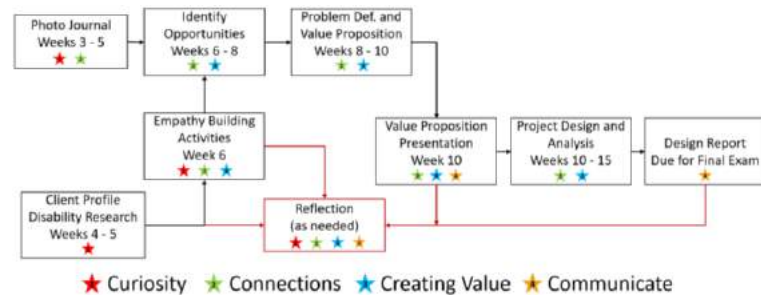


Figure 1: Project flow chart for semester long EML project. The project is not content-specific and could be adapted to any course.

Part 1: Discovery and Connections (Weeks 1 - 5)

The project was not immediately described to the students. Instead, the students discovered the project's goals and motivation over the course of several weeks. To motivate this outcome, each student was required to create a photo journal by taking pictures of 1) objects they interact with every day, 2) activities they enjoy, and 3) products that improved their life through the product's motion. They uploaded these pictures to a Google Jamboard [5] to create a photo journal.

Student groups were formed during the fourth week of the semester. Each group was provided with a client profile detailing an existing medical condition and the challenges associated with daily life

while living with the condition. Each profile was created based on interviews the instructor conducted with real people and an example can be found at this link:

https://drive.google.com/drive/folders/16Eqm_6k_Arbiv4mSrgvbYV_IWE3jY5ov?usp=sharing

Part 2: Identifying Opportunities to Create Value (Weeks 6 - 10)

At the start of the 6th week, the students were provided with the goal of their project: Design an assistive device to create value for their client, but the device must contain a mechanism that can be analyzed with the course content (typically a 4-bar or crank slider linkage).

Lecture meetings during the 6th week were dedicated to project groupwork and focused on building empathy for the client. Project teams met and compared research notes. Students shared their photo journals with their teammates. Using Jamboard, each student added "sticky notes" to the photos with objects or activities that could be good candidates for an assistive device. To address empathy, the students completed the Toronto Empathy Questionnaire [4] and discussed their scores. Finally, the Wrong Theory Protocol [3] was utilized as both an empathy-building and design ideation tool. Reflections were assigned to help the students connect the project and course content to their own passions and interests.

Part 3: Technical Design Work (Weeks 10 - 15)

The project teams were required to apply the course content to design and evaluate the assistive devices. The teams were also required to apply content from previous courses by using computer-aided design tools and completing a stress analysis on their mechanism. To build EM, each student created a concept map to visualize the connections between the client's needs, proposed value proposition, course content, and content from previous courses. The students reflected on the knowledge gaps they would have to address in order to complete the project. A final design report, peer evaluation, and project reflection were due during final exam week.

RESULTS

The project followed the paradigm from Norton's *Design of Machinery* text [6]. Performance and motion goals were defined and linkage dimensions were determined to provide that motion (linkage synthesis). A vector loop equation was used to calculate the spatial orientations of the links with respect to the input link (position analysis). Given an input motion (i.e. motor input), the first and second derivatives were taken to calculate the velocity and acceleration of each link (velocity and acceleration analysis). Joint and inertial forces were then calculated through inverse dynamics (force analysis).

Due dates were scaffolded throughout the semester. Each team presented their problem definition and value proposition during the 10th week of the semester. Next, the teams submitted a memo report describing their synthesis and position analysis during the 11th week of the semester. A velocity and acceleration analysis memo was completed for week 13. Finally, force analysis, stress analysis, and finalized design plans were due as part of the final report at the end of the semester.

Overall, student teams were able to complete the project with periodic guidance from the instructor. Example assistive devices included a wheel chair mounted table (Fig. 2A), a wheel chair lift platform (Fig. 2B), a wheel chair mounted ball launcher (Fig. 2C), and a translating painting easel (Fig. 2D). The scaffolded assignments and in-class work time ensured that each group appropriately applied the course theory to prove the efficacy of their design. The average project score was a $77\% \pm 12.8\%$ with scores varying in value created, design quality, and evaluation strength. Periodic reflections revealed student comprehension of and engagement with the EM concepts.

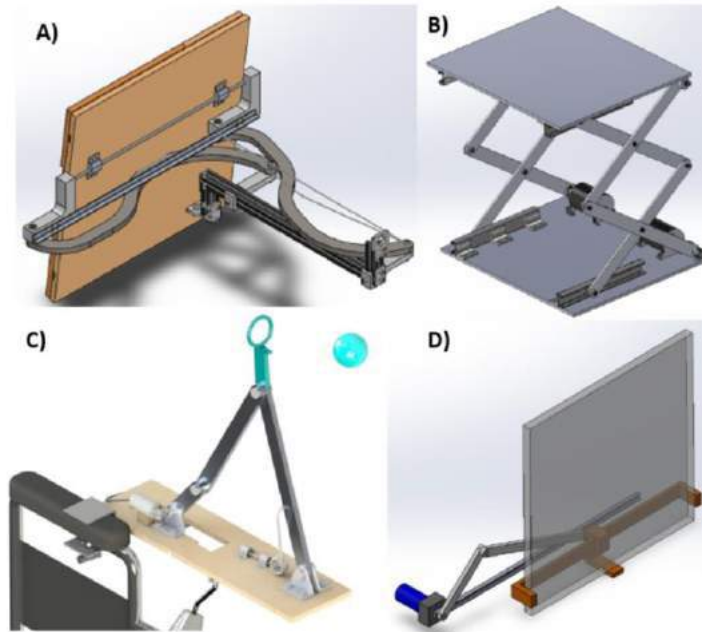


Figure 2: Example student designs include A) a wheel chair mounted table, B) a wheel chair lift platform, C) a wheel chair mounted ball launcher, and D) translating painting easel.

DISCUSSION

Since first described [2], this assistive device project has provided a practical application for vector-based analysis while reinforcing the engineering design process, rigid body dynamics, mechanics of materials, programming in MATLAB, and 3-D solid modeling. The described changes promoted entrepreneur thinking. Instead of a solving well-defined problem, the student teams were asked to think in terms of value creation to determine the best design. Post course surveying revealed that some students struggled with this type of open-ended assignment. However, exposure to open-ended design projects will help prepare the students for future coursework, including the senior capstone design course.

During past iterations, the students were only provided a short, general description of the client. Most recently, the students engaged with longer client profiles developed from interviews with real people. This enabled a greater sense of empathy for their clients than possible before, and anecdotally the students were more motivated to complete the project. Building upon this, the project could be further improved in the future by providing opportunities to interface with the clients and then building prototypes to demonstrate the performance of each device.

ACKNOWLEDGEMENTS

Funding for this project was provided by the Kern Family Foundation for Engineering Unleashed Faculty Development (#2G0132).

REFERENCES

- [1] Kern Entrepreneurial Engineering Network website. Online: <https://engineeringunleashed.com>.
- [2] Gargac, JA. SB3C 2017, Tuscan AZ.
- [3] Svihla, V, et al. ICDC 2020. Albuquerque, NM.
- [4] Toronto Empathy Questionnaire, <https://psychology-tools.com/test/toronto-empathy-questionnaire>
- [5] Google Jamboard <https://jamboard.google.com/>
- [6] Norton, R. *Design of Machinery 6th edition*. McGraw Hill, 2019.

MEASUREMENT OF CLOT ATTACHMENT FORCES TO BIOMATERIALS AND COMPARISON TO A HYPERELASTIC SIMULATION

Jose L. Monclova (1), Sara E. Almasy (1), Nicolas Tobin (1), Vikas Kannojiya (1),
Francesco Costanzo (2), Scott Simon (3), Keefe B. Manning (1,4)

- (1) Department of Biomedical Engineering, The Pennsylvania State University, University Park, Pennsylvania, USA
(2) Department of Engineering Science and Mechanics, The Pennsylvania State University, University Park, Pennsylvania, USA
(3) Department of Neurovascular Surgery, Penn State Hershey Medical Center, Hershey, Pennsylvania, USA
(4) Department of Surgery, Penn State Hershey Medical Center, Hershey, Pennsylvania, USA

INTRODUCTION

Acute ischemic stroke is a leading cause of death and morbidity in the United States [1]. Recent studies suggest that, in addition to embolus morphology, their mechanical properties contribute to complications in clot removal procedures [2,3]. In addition, thrombus adhesion to medical devices is well documented, and computational modeling has accounted for an adhesive behavior of clot-artery interfaces [4,5,6], but the nature of the adhesion has not been characterized. Due to the fragile nature of clots, benchtop experiments that have characterized thrombus behavior have been limited to mainly tensile and compressive work. The goal of this project is to characterize the adhesive tendencies of embolus analogs (EAs) to various biomaterials and endothelial cells as a mechanism for potential complications in thrombus removal.

METHODS

EA Formation Conditions:

To study the effect of EA composition on embolus adhesion to biomaterials, EAs were created using human blood, following approved institutional IRB protocols. Briefly, extracted whole blood was anticoagulated with 0.32% wt. sodium citrate. Blood was separated into red blood cells, platelet rich plasma (PRP), and platelet poor plasma (PPP) via centrifugation. Blood was reconstituted to 214×10^6 platelets per mL. Hematocrit was controlled in EAs by addition of 40% vol. red blood cells to form clots. To counter the effects of the anticoagulant, blood was recalcified with 20 mM calcium chloride (CaCl_2), 15 NIH Unit/mL thrombin from human plasma (BioPharm, Bluffdale, UT, USA), and 100 mM ADP to initiate platelet activation in the blood. Recalcified blood was mixed and injected into custom cylindrical molds that allowed for attachment to biomaterials. Samples were coagulated on acrylic, glass cover slips, and endothelial cells. Blood was allowed to coagulate for 24 hours at 37 °C for EAs to form 14 mm diameter by 10 mm cylindrical specimens. To prepare the endothelial cell lining,

human coronary artery endothelial cells were cultured with human cell media at 37 °C and 5% CO_2 before testing.

EA mechanical testing:

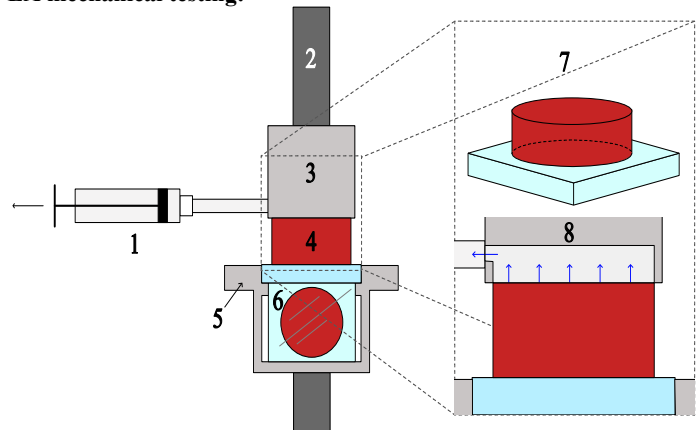


Figure 1: Detachment Instron rig with a 1. syringe applying a suction through 2. a custom suction chamber fixed to 3. the Instron top grip. 4. The cylindrical specimen was fixed to 5. a bottom fixture with 6. a mirror placed at 45° to visualize the bottom of the clot as it detaches. 7. Shows an isometric projection of the clot attached to the biomaterial and 8. shows a zoomed in view of the suction mechanism.

Once EAs were formed, the samples were removed from molds and attached to the bottom plate of a custom rig on a uniaxial load frame (Instron, Norwood, MA, USA) with a 5 N load cell, see **Figure 1**. A suction fixture was used to apply a negative pressure of 200 mmHg to the top surface of the cylindrical specimens to grip the surface, using a custom syringe fixture. Once the suction was applied, the specimen was loaded at a rate of 10% strain per second (based on sample height) until

complete detachment from the bottom plate. From these data, a polynomial of degree 1 was fit to the curve prior to fracture to compute the modulus. The peak stress and strain were recorded. All samples were embedded in paraffin wax for histology and stained with a standard Carstairs protocol to visualize all major clot constituents.

Statistics:

Due to variability in coagulation, clot contraction, and other factors, multiple sources ($n = 6$) were collected with replicates ($n = 6$) tested for each source. For this reason, mean values were computed with standard deviation, and a Kruskal-Wallis analysis of variance was applied to compare means. All data analysis was carried out using MATLAB's multiple comparison function.

Hyperelastic Modeling:

To simulate the experiment, a Neo-Hookean elasticity model was applied to the interior of the clot in an axisymmetric setting. A spring foundation and a displacement-based failure criterion were applied to the bottom surface to simulate the detachment. Finally, surface traction on the bottom and top surfaces were computed. All work was done in COMSOL Multiphysics (Stockholm, SWE).

RESULTS

Preliminary, nominal stress-strain curves, as shown in **Figure 2**, show a tensile-like behavior with nearly linear elastic-like behavior in the loading portion of the curve. Measured moduli were 2.17 ± 0.34 kPa, with a linear R^2 value of 0.92. Maximum nominal stresses at failure were 0.37 ± 0.13 kPa and maximum strains were $14.74 \pm 4.06\%$, meaning the clot elongated 14% before detachment. From the COMSOL simulation in **Figure 3**, a detachment is seen to initiate from the bottom corner of the cylinder and radiate inward, due to a stress concentration near this point. Failure was initiated via a displacement criterion of 0.1 mm. Von Mises stress distribution mapping shows a stress concentration near the corners of the specimen, with fracture stresses similar to those observed in the experiments, roughly 400 Pa. Traction vectors near the fracture also show a slight decrease in the axial force before full clot detachment.

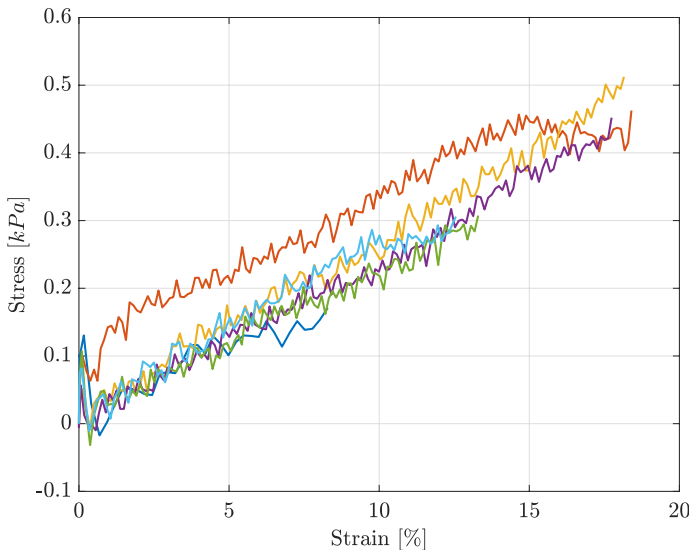


Figure 2: Nominal stress – strain curves for the detachment test with 40% HCT human blood clots on acrylic.

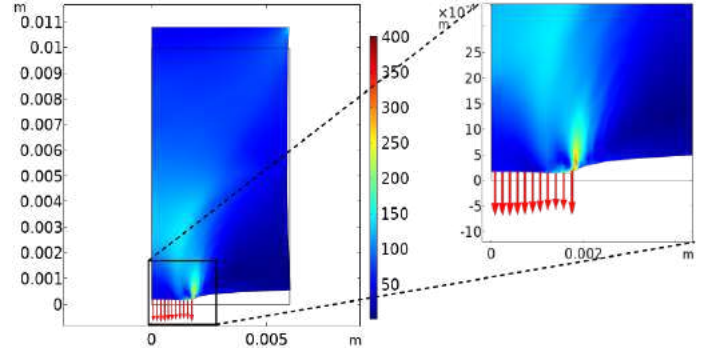


Figure 3: Axisymmetric center view of a hyperelastic Neo-Hookean simulation of clot detachment test with a spring foundation bottom boundary and displacement-based failure criteria at $t = 0.2$ s. The zoomed in panel shows fracture initiating from the bottom corner of the clot and radiating inward. Von Mises stresses shown in Pa, and the red arrows depict tractions on the bottom surface of the clot.

DISCUSSION

Measured moduli were 2.17 kPa, similar to work done by Sugerman et al. [5] This suggests the loading for this test prior to detachment was similar to a standard uniaxial tensile test. Pressure gauges on the aspiration rig confirmed constant pressure at the top of the clot. Nearly linear loading curves also suggest a linear elastic behavior of the material in tension. Previous work by F. Ghezelbash *et al.* has shown a highly nonlinear behavior in compression, attributing this to loading of elastic-like fibrin and viscous-like red blood [7]. In tension, EAs seem to exhibit a more elastic behavior. Furthermore, clots detached at roughly 15% strain, lower than previously reported fracture strains of roughly 40% [8].

The COMSOL hyperelastic model used a spring foundation, allowing for displacement of the bottom surface before fracture, a phenomenon not observed in the experiments. As mentioned, the fracture stresses from the computational model were similar to experimental measurements. However, in the experiments, clot detachment occurred at random from the surface, where the computations showed a constant initiation from the outer corner. The clot deformation is constrained to be incompressible, yet from the testing, fluid leakage was observed clearly. This suggests a different nature than either hyperelastic or viscoelastic, with a tendency of the clot to store fluid. Future work will focus on capturing this porous nature of clots and the uneven detachment of the clot to different surfaces. This work has shown that there exists an adhesive behavior of EAs that has been understudied, and which may play a role in complications for clot removal in thrombectomy surgeries among other scenarios.

ACKNOWLEDGEMENTS

This research was supported, in part, by U.S. NIH HL146921, NSF CMMI-2017805, NIH T32GM108563, an Alfred P. Sloan and a Gates Millennium Scholarship.

REFERENCES

- [1] Murphy, S. *et al.*, *NCHS Data Brief*, 38:4-5, 2017.
- [2] Liu, Y. *et al.*, *J. of Stroke and Cerebr. Diseases*, 29, 2020.
- [3] Boodt, N. *et al.*, *Stroke*, 52:2510-2517, 2021.
- [4] Oyekole, O. *et al.*, *J. Biomech.*, 128:110721, 2021.
- [5] Patki, P. *et al.*, *Int. J. Num. Meth. Biomed. Eng.*, 2022.
- [6] Good, B. *et al.*, *Biomech. Model Mechanobiol.*, 19:761–778, 2020.
- [7] Ghezelbash, F. *et al.*, *J. of Mech. Behavior of Biomed. Materials*, 128, 2022.
- [8] Sugerman, G. *et al.*, *Soft Matter*, 2019.

COMPUTATION FOR BIOENGINEERING AND MECHANICAL ENGINEERING STUDENTS: AN EXPERIENTIAL LEARNING OPPORTUNITY IN NORWAY

Samuel D. Salinas (1), Ana I. Vargas (1), Turner Jennings (2), Sean Harington (2), Mohammad J. Sadeghinia (3), Mojgan Y. Jacobsen (4), Trine Eide (4), Cecilie Udberg-Helle (4), Torill Andersen Eidsvaag (5), Torjer A. Olsen (6), Jonathan Crossen (6), Victorien Prot (3), Bjørn H. Skallerud (3), Rouzbeh Amini (1, 2)

(1) Department of Bioengineering, Northeastern University, Boston, MA, USA

(2) Department of Mechanical and Industrial Engineering, Northeastern University, Boston, MA, USA

(3) Department of Structural Engineering, Norwegian University of Science and Technology, Trondheim, Norway

(4) Kinn Education and Resource Centre, Florø, Norway

(5) Department of Chemistry, University of Bergen, Bergen, Norway

(6) The Centre for Sámi Studies, UiT The Arctic University of Norway, Tromsø, Norway

INTRODUCTION

Global/intercultural learning is an area of interest at Northeastern University. Students are strongly encouraged to participate in activities that foster enhancing intercultural communication skills. In a global learning setup, students can benefit both from the international and transnational aspects of their discipline and from the intercultural and local nuances in the host country. The students are also able to combine critical thinking and problem-solving skills with comparative perspectives and multidisciplinary approaches. Northeastern University has highlighted the following areas as goals for the intercultural learning [1]: *(1) recognize and critically examine their own cultural influences; (2) analyze the connection between the global and the local, and understand how structures, forces, and phenomena shape culture and individual experience; (3) live, learn, and work effectively with people whose backgrounds, experiences, and perspectives are different from their own; and (4) reflect and act with an understanding of the local and global impacts of their decision.*

Dialogue of Civilization (DOC), a faculty-led program at Northeastern University, is one of the mechanisms through which these goals are sought after. During a DOC program, students spend 30 days or more of a summer semester with a faculty leader in locations outside of their main campus. For many students, DOC is an excellent short-term program to obtain international experience. Students are required to complete two courses during this program. The faculty leader(s), with help from local stakeholders, teaches the courses that require closer examination of the problems and their potential solutions in the host country.

Travelling to Paraguay and Argentina for learning Guarani or spending time in Samarkand and Bukhara to examine the history of the silk road in the central Asia seem to be no-brainer ideas for DOC programs. However, at the first look, learning computational skills for mechanical engineering and bioengineering students may not seem to be a skill requiring a global framework. Afterall, everybody can sit at

their computer and write scripts. Nevertheless, as shown in our previous work, even in computational courses, active and experiential learning positively contributes not only to the students' course-specific knowledge but also to their self-efficacy [2,3]. Herein, we have shared our experience of a DOC program in Norway. We aimed to teach important technical skills to students and to stimulate them to think and discuss the cultural and social aspects of engineering and technology in Norway.

PROGRAM DESCRIPTION

We travelled for 31 days in Norway, from mid-May to mid-June in 2022. We chose Norway because its pioneering role in the development and application of computational methods in engineering. For example, Norwegian Computing Center, established in 1952, is one of the World's leading institutions in computational research and provides service for many of the local industries. Our program focused primarily on two courses: Mechanical Engineering Computation and Design (ME 4508) and a special topics class particularly designed for this DOC program (ME4699).

In ME 4508, we introduced the theory of finite element (FE) analysis, focused mainly on the behavior of elastic materials. Heat transfer through conduction and convection was also covered. Students developed scripts in MATLAB and used available commercial FE software. At Northeastern University, ME 4508 is a required course for the Bachelor of Science in mechanical engineering, and an elective course for Bachelor of Science in bioengineering. Specifically for this DOC, we chose applications that were relevant to guest lectures and site visits in Norway. For example, students received lectures from biomechanics experts at the Norwegian University of Science and Technology and then completed a biomechanics project. In addition, they were able to visit sites and see the outcomes of the design and analysis that they learned about in the classroom (Fig. 1). Considering the importance of experiential learning, many of the site visits were

planned for the students to become more familiar as how to apply their knowledge of computational methods in practice.

Besides the industry exposure and engineering aspects of the program, this global experience gave ample opportunities of exposure to a different culture, with a rich history both as it pertains to the modern era as well as to the ancient traditions of Sámi people. The special topics course was focused on the interplay of modern technologies (e.g., green energy) and the rights and traditions of the Sámi people. Although Norway has rich crude oil resources, it has been vibrant and proactive in using other sources of energy such as hydropower, wind power, and wave power. In the realm of social policies, Norway is an interesting and progressive European country and one of the pioneering nations with supportive legislations for women's rights, minority rights, and LGBTQ rights. Nevertheless, Norway, for decades had discriminated against the Sámi people and had unjustly deprived them of owning their ancestral lands as part of the policies of Norwegianization [4]. In the special topic course, the students first learned about the general policies of governance (including education, healthcare, etc.) and the concept of a "welfare state" in Norway. Subsequently, the lectures were focused on the experience of the Sámi people (Fig. 2) and how, for decades, they were displaced from their land. The students also learned about the modern concept of "green colonialism", e.g., the expansion of the wind energy industry into the ancestral lands of the Sámi. For engineering students, who are often used to exact solutions to technical problems, posing open-ended questions in this course seemed to be thought provoking and enriching. Based on the lectures from the local experts and group discussions, students presented their final project for this course on the following topic:

Renewable energy resources (including wind) are often considered as the solution to curb global warming. However, they may have other environmental and social disadvantages. In Norway, for example, they can lead to deposition of micro-plastic beads in protected mountain lakes and/or to stressing and starving reindeer. Another example is the offshore windmills that generate vibrations, changing the marine lifestyle and affecting the fishing industry. While these problems may affect many people, some like Sámi people, who traditionally live outside of urban centers and/or are involved in farming reindeer, may suffer more than others. How can we protect the earth inhabitants (including ourselves) from climate change without marginalizing already disadvantaged groups such as Sámi people?

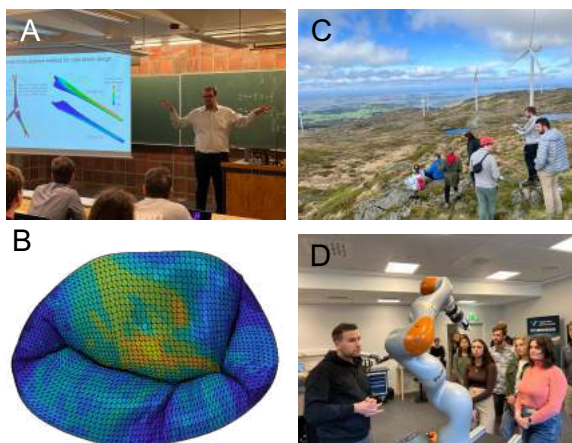


Figure 1: Guest lecturers presented applications of computational techniques in (A) mechanical and (B) biomedical engineering often accompanied by (C and D) visiting the sites where the technologies are used.

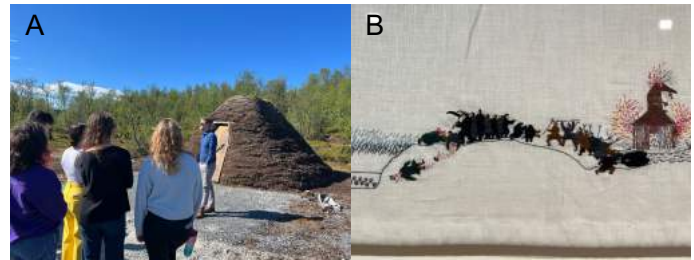


Figure 2: (A) Lectures at Arctic University of Norway (B) history of the struggles of Sámi people in handmade artwork.

STUDENT FEEDBACK AND FUTURE DIRECTION

The student anonymous feedback for this DOC program was overwhelmingly positive. The experiential component of the course was acknowledged by many students. For example, the students were fascinated to learn about heart valve structure and how FE modeling is used in *in-vivo* imaged-based approaches from experts in this field. They felt that a "real-world" example of this approach was extremely relevant and motivating for them when they conducted their own FE project for the course focusing on biomechanics of image-based shapes. They better appreciated the complexity of segmentation and generation of such models. Some of the students' comments are provided here:

- *I want you to know that this trip has had an incredibly positive effect on my life (and for a lot of other people), and I'm so happy that I had this opportunity. This was such a unique experience that I will be talking about for the rest of my life. Thank you so, so, so much for everything. I really can't thank you enough for planning and executing this trip.*
- *Wrapping up this trip, I am very happy with everything we were able to see and do over the past month in Norway. This is the most engaging trip I have ever been on and I will definitely be applying for another dialogue of civilization in the future.*
- *This program has truly been a source of great personal growth as well as great enjoyment for me, and I am so very grateful for having been given the opportunity to participate in it.*

Based on the positive feedback from the students, we intend to continue this program in the upcoming years. For better assessment of the program, we plan to conduct pre-departure and post-departure surveys including self-efficacy assessments [5].

ACKNOWLEDGEMENTS

We thank Northeastern University Global Experience Office (GEO) both for their assistance in the development of this program and for providing Rouzbeh Amini with the Global Experience Faculty Fellowship. Tireless efforts of GEO staff, particularly those of Meisha Swaby and Brigid McMahan, were essential for this program. We also thank Elise Mikkelsen, Cristian Gebhardt, Maria Brandsøy, Rune Knapstad, Guttorm Nygård, Eli Nummedal, Marcin Fojcik, Trond Strømren, and Navid Varasteh for their tremendous support.

REFERENCES

- [1] Global Learning. Retrieved January 5, 2023, from <https://geo.northeastern.edu/about/global-learning/>
- [2] Ham, T. et al. *J Biomech. Eng.*, 140(8), 2018.
- [3] Rezvanifar, SC. et al., *J Biomech. Eng.*, 142(11), 2020.
- [4] Berg, R., *Acta Borealis*, 30(2):154-173, 2013.
- [5] Wigfield, A., *Educ Psychol Rev*, 6(1):49-78, 1994.

CALCIUM SIGNALING IN IN-SITU CHONDROCYTES UNDER DYNAMIC COMPRESSIVE LOADING

Vineel Kondiboyina (1), Timothy Boyer (1), Sandra J. Shefelbine (1,2)

(1) Dept. of Bioengineering, Northeastern University, Boston, MA, USA

(2) Dept of Mechanical and Industrial Engineering, Northeastern University, Boston, MA, USA

INTRODUCTION

Physiological deformation of articular cartilage results in several mechanical, electrical, and chemical stimuli in the chondrocytes. Studies have shown that chondrocytes respond to all these signals by increasing their intracellular calcium concentration. However, the spatiotemporal characteristics of the calcium influx differ based on the cellular environment.

Chondrocytes in explanted cartilage respond relatively quickly (within 5 secs) under static load while cells in 3D hydrogel constructs respond much more slowly (~200 secs). Similarly, with increased mechanical load, about 20% of chondrocytes respond with increased calcium influx but under osmotic loads of 20mOsm, about 35% of cells respond and higher magnitudes of an osmotic shock result in a greater percentage of signaling. These studies demonstrate the importance of the matrix environment as well as the load characteristics on the intracellular calcium signaling in chondrocytes.

Previous studies on load-induced calcium signaling in in-situ chondrocytes utilized slow ramp loads with non-physiological strain rates¹. While the studies using dynamic cyclic loads were done on cells embedded in hydrogels². The response of chondrocytes in their native environment under physiologically relevant cyclic loads has not been studied yet.

In this study, we characterized the calcium signaling response of in-situ chondrocytes (explanted cartilage) under physiological cyclic compressive loads with varying frequency and strain rates. We hypothesized that chondrocytes have strain rate-dependent calcium signaling characteristics compared to no load control conditions.

METHODS

Full-thickness cartilage explants were collected from the femoral condyles of a fresh bovine knee (2-3 weeks old, Research 87, Boylston, MA) using a 6mm biopsy punch. The explants were cut into cylindrical discs of 6mm diameter and 2mm thickness from the articular surface

using a custom cutting tool. The harvested explants were incubated in culture media for three days prior to the experiment.

On the day of the experiment, the cylindrical explants were axially halved and stained with a fluorescent calcium indicator dye solution of 10 μ M CalbryteTM 520 AM (AAT Bioquest) in HBSS with 20mM HEPES for 40 mins at 37°C. The samples were then washed with fresh HBSS for 30 mins at room temperature.

The stained explants were placed in an imaging chamber filled with HBSS with the cut surface facing down. The explants were secured in a custom-built loading device. The loading device was secured on a confocal microscope (Zeiss LSM 800). A schematic of the setup along with the different loading profiles used is shown in Fig 1. A description of the loads can be found in Table 1.

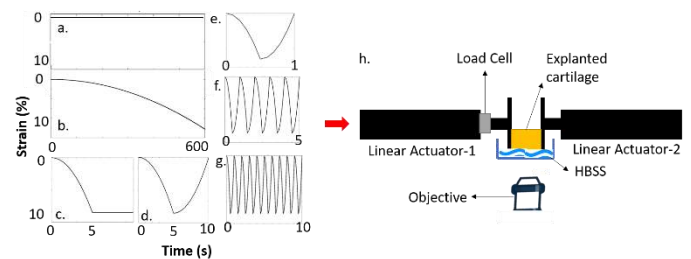


Figure 1: (a-g) Different loading profiles tested (h) Schematic of the custom loading machine

The loading device consists of two linear actuators (Helix Linear Technologies, SMA-8S2.5V-C) that apply equal displacement from both directions, simultaneously during imaging. The resultant load was recorded by a load cell (Loadstar USA, REB7-005M-S). During the test, the loading platens were moved until contact was detected with the explant (threshold: 0.1N). A 10-minute resting period was allowed for the explant to recover from the agitation. Using a 20x objective and 0.8X zoom, a 400 μ m \times 400 μ m area was located along the central axis of

the explant. The imaging area was focused ~30um below the cut surface to avoid imaging damaged cells. The explants were imaged for 10-mins at a frequency of 1.5s under randomized loading conditions (Table 1). A maximum strain of 10% was applied in all conditions.

Calcium fluorescence intensities of the cells were tracked using the Trackmate® plugin in ImageJ. 150-300 cells were tracked per explant sample. A custom-built MATLAB code was used to plot the calcium intensities of the cells and identify responsive cells. A cell was regarded as responsive if it had at least one calcium peak with a prominence greater than 4 times the noise level of the signal¹ and a width of at least 20 seconds. The number of explants tested, and the total number of cells tracked in each case are listed in Table 1.

Table 1: Number of explants and cells analyzed for each loading condition							
Load Condition	Baseline	Slow ramp	Fast ramp and Hold	0.1 Hz x 1 cycle	1 Hz x 1 cycle	1 Hz x 5 cycles	1 Hz x 10 cycles
Time to Peak Strain (s)	-	600	5 (Hold for 600 s)	5	0.5	0.5	0.5
Number of Explants	3	3	3	3	3	3	3
Imaging During/After Load	During	During	During Hold	After	After	After	After
Total Cells Tracked	925	761	691	741	873	877	861

MATLAB (R2019b) Statistical Toolbox was used to perform all statistical analyses. The percentage responsive cells were compared across loading conditions using 1-way ANOVA followed by a posthoc test with Tukey correction (normal distribution and equal sample sizes). The duration of the calcium signal and the distance between consecutive peaks were analyzed using Kruskal-Wallis Test with Tukey-Kramer correction (non-normal distribution and varying sample sizes). An alpha value of 0.05 was used as the threshold for significance.

RESULTS

The percentage of cells signaling increased in all loading conditions compared to the no-load baseline (Figure 2). Further, the percentage of cells responding under 1Hz load (1,5,10 cycles) was significantly greater than the slow ramp group.

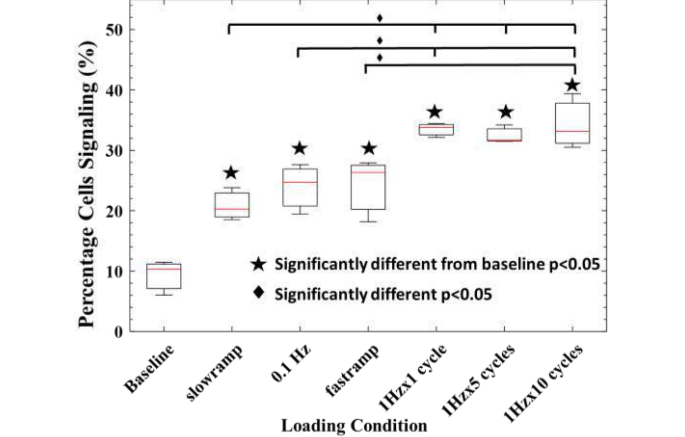


Figure 2: Percentage of cells responding to load with increased calcium fluorescence intensity. The upper and lower boundaries on the box plot represent the 25th and 75th percentile in the data respectively with the median being represented by the red mid-line. The non-outlier extremes in the data are shown by the whiskers.

Similarly, the response percentage of the 1Hz group (1, 10 cycles) was greater than the 0.1Hz group and the 1Hz x 10 cycles group had a

greater response percentage than fast ramp group. No difference in the percentage of responsive cells was found between the slow ramp, fast ramp, and 0.1Hz groups.

The width of the signal was not different between the loaded groups compared to the no-load baseline (Fig 3a). Similarly, the time between consecutive peaks was also not different between the groups compared to the baseline (Fig 3b).

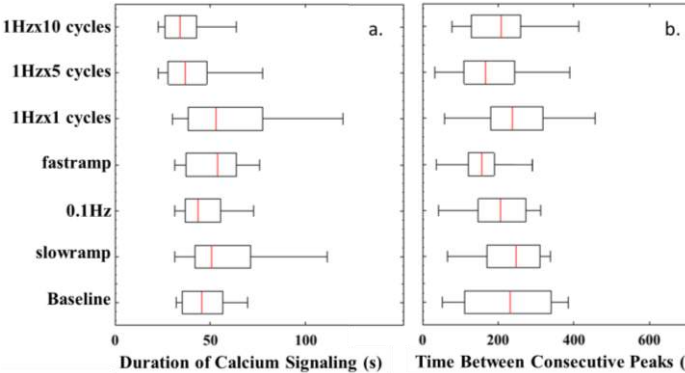


Figure 3: (a) Width of calcium peak (b) Distance between consecutive calcium peaks

DISCUSSION

In this study, the characteristics of calcium signaling in chondrocytes in their native environment were quantified under physiological dynamic compressive loads. An increase in the percentage of cells responding with increased intra-cellular calcium concentration was observed with loading. Further, the percentage response increased with strain rate.

0.1 Hz and fast ramp cases in the current study have similar strain rates during the loading phase. However, 0.1Hz case has an unloading phase preventing fluid flow while fast ramp phase experiences fluid flow induced stress-relaxation after loading. No difference in the percentage response between the groups suggests that sustained fluid flow might not be the driving factor for calcium signaling.

The increase in response between 0.1Hz and 1Hz groups suggests that hydrostatic pressure might be the stimulus that induces calcium signaling in chondrocytes in their native environment. We hypothesize that the increase in matrix hydrostatic pressure causes cell volume changes due to reverse osmosis, which in-turn activates calcium signaling in in-situ chondrocytes.

No effect of the number of cycles on the responsive rate of in-situ cells was found which is consistent with previous findings in hydrogel embedded chondrocytes³.

In conclusion, in-situ chondrocytes respond to physiological loads in a strain rate-dependent manner with an increased number of responsive cells. Signaling profiles, however, are similar across all loading profiles. Future studies will evaluate how hydrostatic pressure induced by the physiological loading of the tissue is transduced into a cellular-level signal.

ACKNOWLEDGEMENTS

This project was funded by NSF grant # 2010010. Imaging was performed at the Center for Imaging Living Systems (CILS), Northeastern University.

REFERENCES

1. Lv M, et.al, *J Orthop Res.* 2018;36(2):730-738.
2. Pingguan-Murphy B, et.al, *J Cell Physiol.* 2006;209(2):389-397.
3. Pingguan-Murphy B, et.al, *Ar Biochem Biophys.*2005;444(1):45-51

DETERMINING HOW VEGFR-2 INHIBITION AFFECTS PHOSPHORYLATION AND FUNCTION IN THE PRESENCE OF MECHANICAL STRAIN

Bronte Miller (1), Michael Heim (1), Bryan Mortimer (2), M.K. Sewell-Loftin (1,3)

- (1) Biomedical Engineering, University of Alabama at Birmingham, Birmingham, Alabama, USA
(2) Heersink School of Medicine, University of Alabama at Birmingham, Birmingham, Alabama, USA
(3) O'Neal Comprehensive Cancer Center, University of Alabama at Birmingham, Birmingham, Alabama, USA

INTRODUCTION

Blood vessel growth is a vital part of development; however, dysregulation of vascular structures is involved in various disease states such as ischemia and cancer. New vessel growth from preexisting vasculature is known as angiogenesis, a key process in tumor progression. When small, a tumor can rely solely on diffusion to receive nutrients and oxygen, but it requires a vascular network to meet increased demand as the tumor grows [1]. Tumors induce an angiogenic signaling cascade which causes nearby vessels to grow towards the mass. Vascular endothelial growth factor (VEGF) and VEGF receptor-2 (VEGFR-2) are common targets when treating cancer due to their essential role in angiogenesis. However, notwithstanding the critical role of VEGF and VEGFR-2 in angiogenesis, these therapies are often insufficient and demonstrate little to no improvement in patient populations [2].

One reason why anti-angiogenic therapies have proven ineffective could be due to VEGFR-2 mechanoactivation, which remains understudied in cancer research. The tumor microenvironment (TME) contains altered mechanics such as increased matrix stiffness, interstitial fluid flow, and strain [1]. Cancer-associated fibroblasts (CAFs) are known to be mechanically-active, distorting the matrix surrounding cells and causing strains [3]. This cellular-induced strain likely affects VEGFR-2 expression and phosphorylation, and previous studies have shown that forces such as matrix stiffness and shear stress can alter VEGFR-2 activity [4, 5]. Different VEGFR-2 tyrosine residues have shown varied phosphorylation patterns depending on mechanical cues, with matrix-bound VEGF stimulation causing prolonged Y1214 phosphorylation [6]. VEGFR-2 inhibition through soluble factors such as SU5416, a drug previously involved in clinical trials, may be insufficient to stop mechanoactivation of the receptor and subsequent blood vessel growth. We hypothesize that endothelial cells exposed to biomechanical stimulation will express altered VEGFR-2 phosphorylation patterns and enhanced angiogenic activity even in the

presence of VEGFR-2 inhibitors. Results from these studies will help address the knowledge gap related to mechanically-driven blood vessel regulation and possibly provide novel targets for anti-angiogenic therapeutic strategies.

METHODS

To study VEGFR-2 phosphorylation patterns, human microvascular endothelial cells (HMECs) received either 3 μ M SU5416 and/or 25ng/ml VEGF in EGM-2 (Lonza) for 72hr. Western Blots analyzed resulting lysates to quantify VEGFR-2 pY1054/Y1059 or pY1214. HMECs also received 25ng/ml VEGF and/or uniaxial strain through FlexCell plates for 0, 5, or 15min. Western Blots analyzed the same VEGFR-2 tyrosine residues. Densitometry was performed using FIJI, and all expression levels were double normalized to β -actin then to total VEGFR-2.

A custom-built, multi-microtissue microfluidic platform was utilized to determine the effect that mechanical stimulation has on angiogenesis [7]. The system has three chambers that can be loaded with matrix and cells, each with its own fluidic lines to permit control over interstitial flow. Flow within devices moved outward from the center chamber to the side chambers, inhibiting soluble factors from diffusing into the center chamber. Tissue chambers were filled with 10mg/ml fibrin gels with the center chamber filled with 1:1 human umbilical vein endothelial cells (HUVECs) and normal human lung fibroblasts (NHLFs). Devices contained either control normal breast fibroblasts (NBFs) or CAFs in the side chambers and were treated with SU5416 or a vehicle controls. Additional experimental set-ups utilized thrombin-coated magnetic beads or cell-free/bead-free fibrin gels. The magnetic beads permit mechanical stimulation of the microtissues without requiring stromal cells. Half of the devices containing magnetic beads were placed above a magnet on a rotating orbital shaker inside the incubator, while the others were kept in a control incubator. Devices were fed for 7 days then were fixed and stained for VE-Cadherin, a

blood vessel marker. Devices were then imaged and processed with FIJI and AngioTool to quantify blood vessel growth.

RESULTS

HMECs show a significant decrease in pY1054/Y1059 and pY1214 with the addition of SU5416, even in the presence of VEGF (Figure 1a). Levels of pY1054/Y1059 increase at 5min with the addition of VEGF; however, the residue appears unaffected by strain (Figure 1b). pY1214 levels increase in HMECs at both 5min and 15min when exposed to strain (Figure 1c). Overall VEGFR-2 phosphorylation can increase due to mechanical strain, and SU5416 can decrease this activity in unstrained conditions.

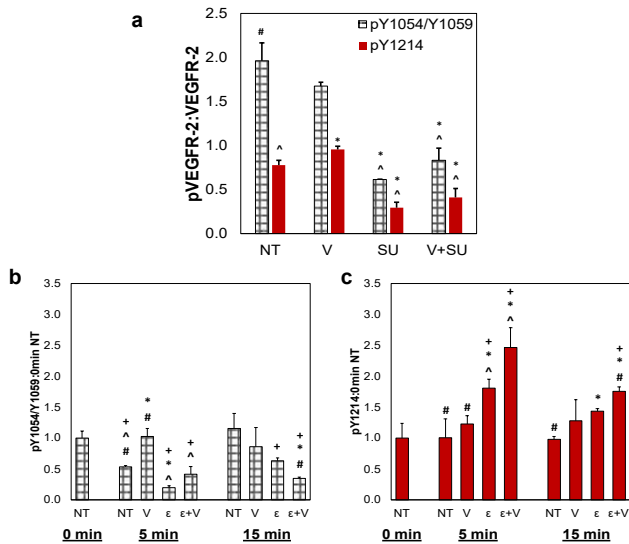


Figure 1: VEGFR-2 phosphorylation in HMECs. (a) HMECs were treated with VEGF (V) or SU5416 (SU) for 72hr.

Western Blots quantified VEGFR-2 pY1054/Y1059 and pY1214. * $p < 0.05$ compared to NT, ^ $p < 0.05$ compared to V, # $p < 0.05$ compared to SU. (b) HMECs were treated with VEGF or strain (ε) for 0, 5, or 15min. Western blots were run on pY1054/Y1059 and (c) pY1214. + $p < 0.05$ compared to 0min NT, * $p < 0.05$ compared to NT at same time, ^ $p < 0.05$ compared to V at same time, # $p < 0.05$ compared to ε at same time. N=3, Avg+SEM.

To examine phenotypic changes due to strains in the TME, microfluidic devices were used to determine how angiogenesis is regulated by mechanical stimulation. HUVECs and NHLFs in the center chamber create a self-assembled, stable vascular network. Fluorescent images were taken showing sprouting blood vessels penetrating the side chambers (Figure 2a,c). Devices treated with SU5416 show increased angiogenesis in chambers filled with CAFs compared to control NBFs (Figure 2b). For devices with magnetic beads in one side chamber, those that experienced mechanical strain induced by the magnetic stimulation of the beads show increased angiogenesis in the bead side chambers compared to devices without the magnet (Figure 2d).

DISCUSSION

In our HMEC line, we decided to analyze Y1214 due to its link to mechanoactivation and Y1054/Y1059, which is necessary for full kinase activity [6, 8]. SU5416 limited chemical activation of both these residues in unstrained environments, and future work will determine if strain is sufficient to restore VEGFR-2 phosphorylation in the presence

of an inhibitor. Furthermore, Y1214 displayed an increase in phosphorylation when treated with strain even without exogenous VEGF, suggesting that certain tyrosine residues are more sensitive to mechanical activity than others. Further research will focus on additional residues.

In our three-chamber microfluidic devices, vessel networks treated with SU5416 grew towards chambers with mechanically-active CAFs compared to NBFs, suggesting that strain is sufficient to promote angiogenesis even with a soluble inhibitor. We also showed that there was an increase in angiogenesis in chambers containing magnetic beads and cultured above a magnetic force, producing matrix strain similar to CAFs. This magnetic bead system fully removes stromal secreted factors that could potentially affect the observed angiogenesis. Overall, this work indicates that mechanically-active environments result in increased angiogenesis, even in the presence of soluble inhibitors. The TME can produce similar mechanical forces, which may be one reason why anti-angiogenic therapies have often proven ineffective in stopping blood vessel development in tumors. Understanding how the TME regulates angiogenesis via mechanical forces and how this process is affected by inhibition is a critical area that requires further investigation to develop effective anti-angiogenic therapies.

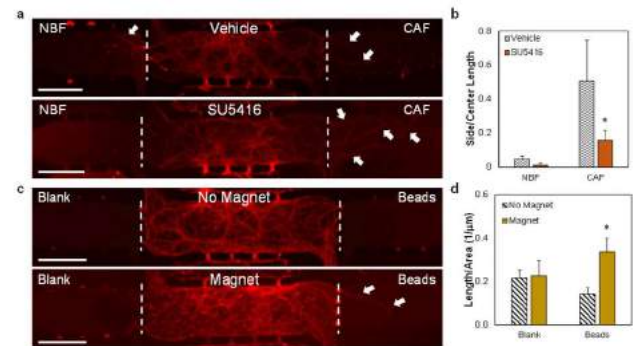


Figure 2: Angiogenesis in a mechanically-active TME model.

(a) Representative images of devices treated with SU5416 or control, stained for VE-cadherin. (b) Graph of angiogenesis in each side chamber. Total vessel length was quantified and normalized to total length in the center chamber. * $p < 0.05$ compared to NBF of same treatment (c) Representative images of a device with and without a rotating magnet, stained for VE-Cadherin. (d) Graph of angiogenesis in side chambers. Total vessel length was normalized to explant area then to center chamber. * $p < 0.05$ compared to Beads of different treatment.

White arrows point to blood vessels. Scale bars = 500μm.

ACKNOWLEDGEMENTS

The authors would like to acknowledge funding for this project: Blazer Fellowship (B.M.); T32-EB023872 (M.B.); R00-CA230202 (M.K.S.L.), IMPACT Award, O'Neal Comprehensive Cancer Center (M.K.S.L.).

REFERENCES

- [1] Zanotelli, MR et al., *Adv Exp Med Biol*, 1092:91-112, 2018.
- [2] Carmeliet, P et al., *Nature*, 473:298-307, 2011.
- [3] Ribatti, D, *Oncotarget*, 7:46668-46677, 2016.
- [4] Jin, ZG et al., *Circ Res*, 93:354-363, 2003.
- [5] LaValley, DJ et al., *Converg Sci Phys Oncol*, 3, 2017.
- [6] Chen, T et al., *J Cell Biol*, 188:595-609, 2010.
- [7] Sewell-Loftin, MK et al., *Lab Chip*, 20:2776-2787, 2020.
- [8] Kendall, RL et al., *J Biol Chem*, 274:6453-6460, 1999.

COMPUTATIONAL ASSESSMENT OF ELASTIN IN A HYBRID MODELLING APPROACH OF ARTERIAL BIOMECHANICS

Yousof MA. Abdel-Raouf (1), Mathias Peirlinck (2), Nele Famaey (3), Patrick Sips (4), Patrick Segers (1)

- (1) Institute of Biomedical Engineering and Technology (IBiTech), Ghent University, Ghent, Belgium
(2) Department of Biomechanical Engineering, Delft University of Technology, Delft, Netherlands
(3) Department of Mechanical Engineering, KU Leuven, Leuven, Belgium
(4) Center of Medical Genetics (CMGG), Ghent University, Ghent, Belgium

INTRODUCTION

Elastin lamellae play a key role in the load bearing function of elastic arteries, especially at lower levels of strain before collagen becomes the major load bearing component, and damage to elastin integrity is associated with diseases in human aortic tissue [1]. With genetic mouse models of aortic dilatation/dissection exhibiting elastin lamellae defects to various extents, we want to better understand the biomechanics of the elastin lamellae. In previous work, we and others assessed the straightening of lamellae as they go from a crimped, wavy configuration at zero luminal pressure, to straight, circumferentially loaded configurations [2,3]. Here, mouse carotid arteries were subjected to quasi-static intra-luminal loading at fixed axial stretches, and two different imaging modalities were used to assess the above criteria. Additionally, Yu et al. hypothesized that the gradient of waviness between the inner lamella and outer ones at an unloaded configuration correlates directly with the homogeneity of the stretch transmurally [3]. Moreover, they observed that as the artery was loaded from this stress-free configuration, lamellar stretch (and therefore load-bearing) begins even before the lamellae are fully unfolded, and that unfolding occurs at the inner lamellae more drastically in comparison to outer ones.

In this study, we propose a hybrid method of modelling the arterial microstructure, where elastin lamellae are modelled discretely as isotropic hyperelastic sheets embedded within a homogenized matrix of fiber-dominant anisotropic hyperelastic material. Data from [2,3] were used to set up the hybrid modelling approach, whereby the three lamellae (henceforth referred to as L1, L2 and L3 for the inner, middle and outer lamella respectively) are considered. Different initial configurations of crimped elastin lamellae, that reflect a waviness gradient between lamellae, are loaded *in silico*. We compare the effect of having three different waviness gradients on lamellar stretch, within each simulation and between simulations.

METHODS

An idealized axisymmetric 3D model of the artery with the initial dimensions of an inner and outer diameter of the unloaded artery reported in [2] was constructed using Matlab. A cross-section of the artery is shown in **Fig. 1** where the solid black undulating lines are the lamellae while the green represents the matrix continuum in which they are embedded. The first elastic lamella was taken to be at an average radius of $R + (\frac{1}{2} \times \text{lamella thickness})$ and with the same β (the amplitude of the undulation) and ω (the frequency of undulation) as the inner wall (R of L1, L2, and L3 is 135, 145, 155 μm). The circular length of the elastin lamella was taken as (s) and the straightness parameter (p) was

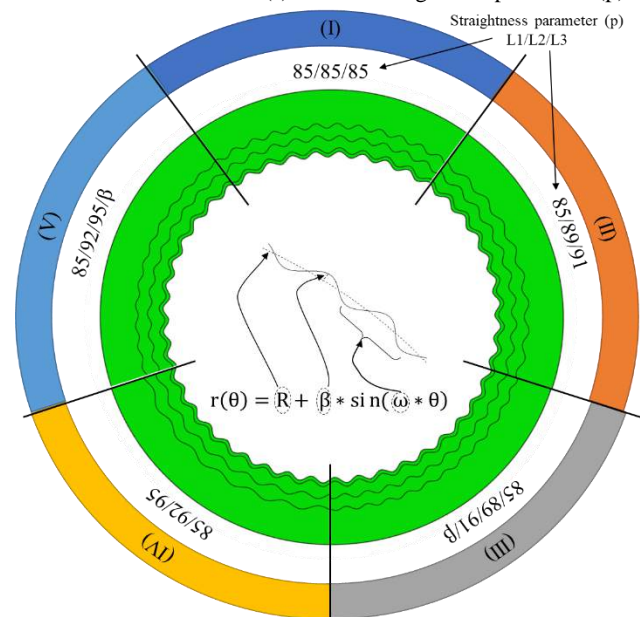


Figure 1 Five configurations of lamellae shown adjacently

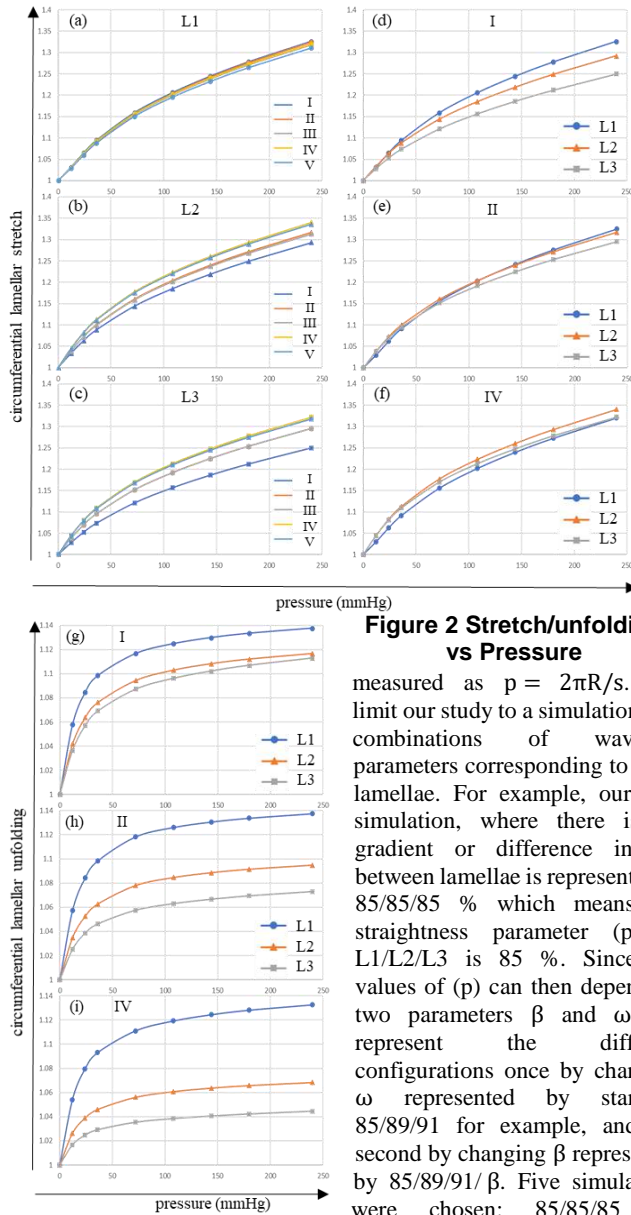


Figure 2 Stretch/unfolding vs Pressure

measured as $p = 2\pi R/s$. We limit our study to a simulation of 3 combinations of waviness parameters corresponding to the 3 lamellae. For example, our first simulation, where there is no gradient or difference in (p) between lamellae is represented as 85/85/85 % which means the straightness parameter (p) at L1/L2/L3 is 85 %. Since the values of (p) can then depend on two parameters β and ω , we represent the different configurations once by changing ω represented by standard 85/89/91 for example, and the second by changing β represented by 85/89/91/ β . Five simulations were chosen: 85/85/85 (I), 85/89/91 (II), 85/89/91/ β (III), 85/92/95 (IV), and 85/92/95/ β (V). **Fig. 1** shows the five configurations chosen, with sections shown adjacent to one another. The sections are color coded to match the plots in **Fig. 2** (a-c). The 2D geometries of the underlying matrix and the elastin lamellae are then extruded into 3D in the axial direction.

In Abaqus/Standard, the underlying matrix is discretized and modelled as C3D6 hexahedral elements in 3D, and the elastin lamellae are modelled as M3D3 triangular membrane elements formed as a sheet. The elements of the lamellae and matrix meshes are coupled using the distributing continuum coupling approach [4], with the master node coupled to nodes within a radius of influence ($3 \mu\text{m}$), and every coupling is given a cubic radial weighting function. The elastin lamellae are defined as neo-Hookean materials while the underlying matrix was defined as an anisotropic Gasser-Ogden-Holzapfel (GOH) material model with 2 fiber families [5]. The matrix was also partitioned into two sets with differing material properties, namely the Media and the Adventitia. While the material properties of the matrix were used from [6], three key assumptions had to be made:

1. Collagen/SMC fibers are defined circumferentially, where the radial directions of these local coordinates were assumed to be distributed along a linear curvature gradient between lamellae, where the circumferential directions of the fibers are biased towards the curvature of the lamella closest to it.
2. Definition of the GOH material properties of the Media in which the elastin lamellae are embedded. We assumed the neo-Hookean component of the GOH model to be zero or negligible. As such, we assume the media's isotropic response to arise from the interaction between lamellae and the underlying matrix.
3. Residual stresses are not taken into account in our model, and that the compression of elastin, along with the tension in the adventitia is not accounted for.

The analysis involves two steps: the first of which an axial stretch of 1.6 is applied, and the second is the static inflation from 0-240 mmHg. Lamellar stretch (**Fig. 2** a-f) is calculated as $(s_{\text{deformed}})/(s_{\text{initial}})$, and Lamellar unfolding (**Fig. 2** g-i) is calculated as $(p_{\text{deformed}})/(p_{\text{initial}})$.

RESULTS & DISCUSSION

A comparison of our simulations demonstrates faint difference in stretch. **Fig. 2** demonstrates two comparisons: (a-c) shows that lamellae L2 and L3 stretch more at higher gradients of (p) . The absence of a toe region confirms the hypothesis in [3] that stretch begins before lamellar unfolding is complete. Additionally, the method of defining (p) plays no role as the simulations (II) and (III) or (IV) and (V) are indistinguishable. Interestingly, a comparison of lamellae within simulations in **Fig. 2** (d-f) shows that a large gradient corresponds to a smaller difference in lamellar stretch. As we increased the gradient from **Fig. 2** (d) to (e) to (f) we see that the L2 and L3 stretch more freely at these higher (p) values. This suggests that the lamellae move somewhat independently of each other. Moreover, the difference in lamellar stretch of L2 and L3 (**Fig. 2** (b), (c)) suggests that the drastic mitigation in L3 stretch arises from its over-constraint, since it is coupled to nodes in the adventitia which are stiffer in the circumferential direction, and so at a wavier configuration, it is less likely to stretch and flatten. Finally, we comment on the similarity between results shown in **Fig. 2** (h) and Fig. 3 (d) in [3], demonstrating that unfolding occurs more drastically at L1 than at L2 and L3. Furthermore, a cursory comparison between our lamellar stretch shown in **Fig. 2** (e) which has the most similar configuration to [3], and Fig. 5 (c) in [3] shows two characteristics of note: 1- That the different lamellae in the artery have similar stretches, confirming that the gradient may play a role in that similarity. 2- The stretch in our model is lower overall. We surmise that this discrepancy can be attributed to our assumption not to incorporate residual stresses, and that the ideal figure of waviness may correspond more closely to a combination of flattened and undulating configuration rather than strictly one or the other. Future work involves reconstruction of 3D synchrotron data obtained in [2] and applying our methodology to investigate lamellar dynamics and further assessment and (experimental) validation of the hybrid approach.

ACKNOWLEDGEMENTS

This research was funded by the Concerted Action Program of Ghent University Special Research Fund

REFERENCES

- [1] Tsamis, A et al., *J R Soc. Interface*, 10, 2013.
- [2] Trachet, B et al., *J R Soc. Interface*, 16, 2019.
- [3] Yu, X et al., *J R Soc. Interface*, 15, 2018.
- [4] Abaqus/Standard User's Manual, Version 6.9
- [5] Gasser, T.C. et al., *J R Soc. Interface*, 3:15-35, 2006.
- [6] Badel, P et al., *MBSM Vol.2:11-17*, 2011.

IMPACT OF THE CORONARY STENT FOOTPRINT ON WALL SHEAR STRESS IN PATIENT-SPECIFIC ARTERIES – ANALYSIS FROM THE SHEAR-STENT TRIAL

I. Shah (1,2), D. Molony (3), K. Crawford (3,4), A. Lefieux (2,4), A. Veneziani (2), H. Samady (3,4)

- (1) Department of Biomedical Engineering, Georgia Institute of Technology, Atlanta, GA, USA
(2) Department of Mathematics, Department of Computer Science, Emory University, Atlanta, GA, USA
(3) Northeast Georgia Medical Center, Gainesville, GA, USA
(4) Emory University School of Medicine, Atlanta, GA, USA

INTRODUCTION

Coronary stenting has become a common technique to treat patients with atherosclerotic plaque build-up in the coronary arteries. Implantation of the stent allows for the restoration of blood flow through the previously stenotic artery. However, once implanted, the presence of the stent frame often causes several additional complications, most common of which are restenosis and thrombosis. These complications are thought to occur due to the altered hemodynamics at the microscopic scale near the stent struts and the lumen wall [1]. Wall shear stress (WSS), which is the frictional force of blood against the lumen wall, has become a critical hemodynamic metric for predicting the likelihood of such complications in patients who have undergone the stenting procedure. Specifically, WSS is known to be significantly altered at the “local” scale (the stent struts) due to the presence of the stent footprint, which may begin the process of restenosis or thrombosis.

In-silico approaches, namely computational fluid dynamics (CFD) simulations, are commonly used for quantifying WSS. When used for predicting the likelihood of stent-induced complications in individual patients, these computational models require the use of patient-specific lumen and stent geometries for the most accurate results [1]. However, many previous approaches do not include the stent footprint, thus providing information only at the “global” scale (the artery) and little information at the “local” scale (the stent struts), where the local scale information is required to accurately assess and predict flow dynamics.

Recent studies have begun including the stent footprint into the patient-specific lumen geometries as well [2]. However, in such instances, the number of cases evaluated becomes severely limited, primarily due to the level of automation required for reconstructing such high-fidelity models. Recently, we have developed a semi-automated reconstruction approach for patient-specific stented coronary arteries that is based on data assimilation techniques and computer aided design (CAD) [3]. The approach allows for a nearly operator-independent reconstruction of patient-specific coronary geometries, which is critical

for analysis of large patient cohorts, especially within the context of clinical trials, i.e., *in-silico clinical trials*.

The objective of this study is to employ the previously developed reconstruction methodology as a part of the SHEAR-STENT clinical trial. A subset of patients was taken ($n = 30$) for analysis, where we focus on the applicability of the reconstruction pipeline for efficiently generating a large cohort of patient-specific arteries for CFD analysis. In addition, we perform an analysis of the same patient cohort without the presence of the stent to evaluate the true impact the stent footprint has on the resulting WSS distribution at a large-scale statistical level. We hypothesize that the presence of the stent footprint causes a statistically significant difference in the WSS distribution, and this difference may be correlated with the vessel curvature and tortuosity.

METHODS

Patient data was obtained from the SHEAR-STENT trial in the form of optical coherence tomography (OCT), intravascular ultrasound (IVUS), and angiography imaging. The trial focuses on evaluating the effects of two drug-eluting stents, the Abbott XIENCE Xpedition and Medtronic Resolute Integrity, on regional plaque response following implantation. The subset of patient data for this study ($n = 30$) was randomly chosen from the total cohort in the clinical trial ($n = 86$).

The previously developed semi-automatic reconstruction approach can be summarized in a few steps. Angiography and OCT imaging were initially used to reconstruct the 3D lumen for each of the patients. OCT imaging was then used to identify stent strut point clouds in a semi-automatic manner, where most of the points are identified automatically with some manual input to fix any errors in the point cloud. A 3D CAD template of the two stents (XIENCE and Resolute) are deformed to the point cloud via an image registration approach [3]. The deformed stent template is then deformed to the 3D lumen via an elastic deformation process. Finally, the stent skeleton is expanded into a 3D structure with the use of Nef-polyhedra, and subsequently imprinted into the 3D lumen via a Boolean operation, resulting in the final patient-specific stented

geometries. Non-stented geometries of the same patient cases were also generated for direct comparison purposes.

All stented and non-stented models were meshed using *ICEM CFD* (ANSYS ICEM 21), with the average mesh size ranging from 2-3 million elements. Steady CFD simulations were performed with the commercial solver *Fluent* (ANSYS 21). The steady approach was used as a surrogate for the time average of the unsteady solution, as the primary objective was to compare the WSS between the stented and non-stented reconstructions using the same CFD approach. Inflow boundary conditions were prescribed with patient-specific constant velocity inlets, and percentage-based flow distributions were prescribed at the outlet. WSS data was calculated and extracted from *Fluent*.

To gain a better understanding of the local hemodynamics at the stent strut level, a series of post-processing steps were performed. Specifically, this involved thresholding the WSS data from the stented simulation such that the region of focus along the lumen geometry was only on the stented area. This was followed by a series of filtering and thresholding steps to remove all WSS data that were not embedded on the lumen wall, such that the focus of the WSS analysis would only be on the endothelium surrounding the stent struts. Finally, these steps for the stented WSS data were also repeated for the non-stented WSS data for comparison purposes. All post-processing was done using the *Visualization Toolkit* (VTK) and *Vascular Modeling Toolkit* (VMTK).

Curvature analysis was performed for the reconstructed arteries using *VMTK*. Individual centerlines were extracted for each case, from which average curvature and tortuosity values were calculated and compared against the difference in WSS between the stented and non-stented models. A slice-by-slice analysis was also performed along four randomly chosen patient cases to have a better understanding of the local average curvature against the local average differences in WSS.

RESULTS

CFD results for five sample cases following filtering of the lumen geometries are shown in Fig. 1. Comparing the WSS distribution between the stent and no-stent models, clear visual differences can be seen. The presence of the stent footprint causes regions of lower luminal WSS as compared to the same regions from the no-stent model. The average WSS was greater in the no-stent model, with an average difference of 0.293 Pa and a standard deviation of 0.086 Pa. Closer inspection of the endothelial WSS also indicates that the WSS is lower in parts of the lumen that correspond to regions of stent malapposition.

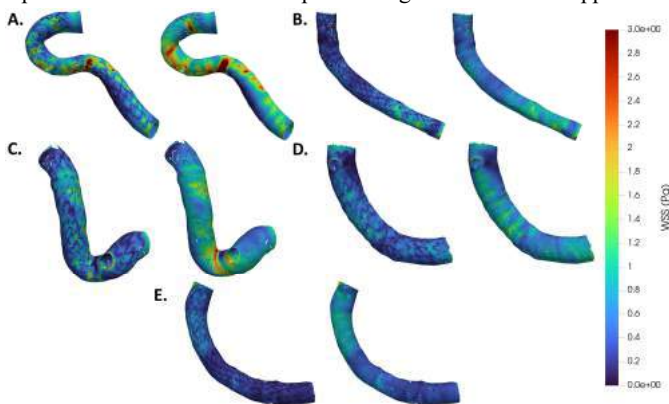


Figure 1. Comparison of WSS between stented (left) and non-stented (right) models for five sample cases (A-E).

The percentage of lumen area exposed to low (less than 0.5 Pa) and moderate (less than 1.0 Pa) WSS was also compared to gain a better understanding of the impact at the microscopic scale (Fig. 2). Both scenarios had statistically significant differences between the models, with the low WSS case showing an especially large discrepancy.

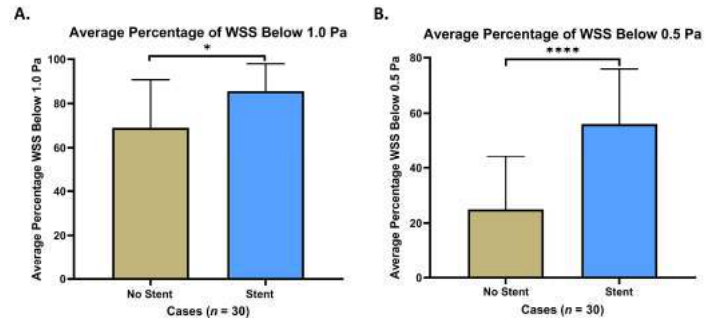


Figure 2. Comparison of the percentage of lumen area exposed to moderate (A) and low (B) WSS between the two models.

Average curvature and tortuosity values for each case are plotted against the difference in percent WSS below 0.5 Pa in Fig. 3. A negative trend is seen with R-squared values of 0.1779 and 0.06061, indicating that the greater the vessel curvature is, the less of a difference is seen in the WSS. Slice-by-slice analysis for the four patient cases also resulted in similar and stronger trends (R-squared values up to 0.6837).

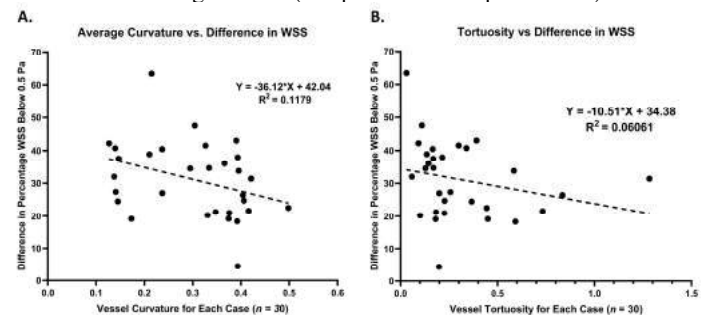


Figure 3. Curvature (A) and tortuosity (B) vs. differences in WSS.

DISCUSSION

In this study, we employ a semi-automatic reconstruction approach for patient-specific arteries to examine the impact of the coronary stent footprint on the WSS at a large-scale, statistical level, which is one of the first to focus on such a large sample size ($n = 30$). The results show that the stent footprint causes a statistically significant impact on the coronary hemodynamics, indicating that the stent footprint must be included in most traditional computational models for accurate WSS analysis. Especially large differences were seen at low WSS thresholds, which may be important in the context of restenosis as it is known to begin developing in regions of lumen wall exposed to low WSS [4]. The curvature analysis indicates that vessel curvature may help determine the need for the stent footprint in simulations, where a potential cut-off value could be determined to see when exactly the stent footprint should be included. A major limitation of the study is that only steady flow simulations were performed, which may ignore the pulsatile nature of flow through the coronaries. Future work includes performing transient, pulsatile CFD simulations for more accurate values, although we expect to see similar, and potentially more significant trends as seen here.

In conclusion, this study shows that the stent footprint causes a significant impact on the WSS. The present study also indicates the feasibility of performing large scale *in-silico* clinical trials in a patient specific manner with the use of automated reconstruction methods.

ACKNOWLEDGEMENTS

Research was supported by the NSF 2012286 (A. Veneziani).

REFERENCES

- [1] Migliori, S., et al., *Med Eng & Physics*, 47:105-116, 2017.
- [2] Bourantas, C., et al., *JACC: Cardio Interventions*, 7:315-324, 2013.
- [3] Lefiux, A., et al., *Cardiovascular Eng & Tech*, 13:517-534, 2022.
- [4] Samady, H., et al., *Circulation*, 124:779-788, 2011.

BIOMECHANICAL FOLLOW-UP AND EVALUATION OF ANEURYSM GROWTH

F. A.M. Garbou (1), O. O. M. Elnamla (1), W. A.K.A. Saber (1), K. B. Kose (1),

(1) Biomedical Engineering Department, Istanbul Medipol University, Istanbul, T^urkiye

INTRODUCTION

Cardiovascular diseases have the highest mortality and morbidity rates. Each year, cardiovascular disease (CVD) is estimated to be the cause of 32% of all deaths worldwide[1]. During blood flow in the circulatory system, the vessel wall is constantly exposed to mechanical forces and can play a role in the development of pathologies if the arterial endothelium morphology is abnormal. In an aortic artery with an aneurysm, these changes may result in a rupture of the endothelium. An accurate pre and post-operative risk of an abdominal aortic aneurysm rupture is an important guide for planning aortic aneurysm repair surgery. Clinical studies have determined the risk with maximum aneurysmatic diameter based on medical imaging technologies. [2] However, it is known that the risk is not necessarily reflected by the maximum diameter alone [3]. Therefore, additional information is required for accurate risk assessment of an aneurysm before and after surgical repair. This study was designed to numerically evaluate the remodeling in aortic aneurysm morphologies and underlying mechanical factors. This study compared the relationship between the changes in aneurysm morphology and hemodynamic parameters in patients who were scanned at regular intervals. In flow visualizations based on virtual aortic models obtained from computed tomography datasets of three different scans, it was determined that the endothelial segments with distinctive changes in wall shear stress (WSS) distribution showed high consistency with the morphological change segments seen in the next periodic scans of the same patients.

METHODS

Five patients diagnosed with thoracic aortic aneurysms and aged between 70-75 were included in the study. Virtual aorta models were created from the CT images of the patients taken at

three-month intervals (Figure 1). Three-dimensional (3D) models were created with VTK algorithms and a model mesh for finite element analysis was created with Simmetrix libraries. Blood flow was simulated by computational fluid dynamics analysis and visualized in Ceetron Analyzer Cloud [4]-[6].

In this study, we focused on WSS visualization, a parameter that cannot be measured in the clinical setting but can be calculated by multi-physics algorithms. Blood was considered Newtonian fluid and boundary conditions were established from case-specific data obtained from the clinic [7]. The initial velocity gradient was obtained from the Doppler ultrasound reports of the patients.



Figure 1: 3D models of the aorta segmented from CT data obtained at regular intervals of the selected patient.

RESULTS

Numerical simulation results were visualized as WSS distribution on the arterial wall. The WSS in the proximal ascending aorta was reported to be up to 1800 ± 100 Pa for patients with aortic aneurysms, while it was reported to be up to 700 for healthy people in the literature. Studies have shown that WSS can alter the material properties of thoracic aortic aneurysms through arterial wall remodeling, making the aortic wall more prone to swelling as shown in the figure which represents the growth segments of the following scan (Figure 2).

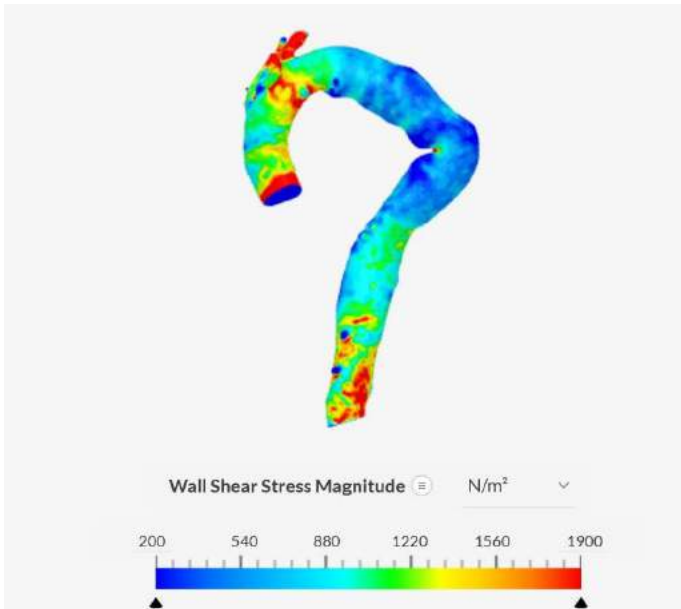


Figure 2: The WSS distribution on the first scan of Patient A.

DISCUSSION

After this preliminary study, it has been observed that the most obvious effect of WSS on the change of endothelium morphology starts from the segments where dramatic decreases in WSS distribution are seen. The numerical analysis results were obtained in line with our hypothesis that shape change rates that may be encountered in the next scan could be predicted. This work was able to present significant findings on the evaluation of studies on aneurysm growth with in-silico methods and it is possible to strengthen it with more scan datasets.

ACKNOWLEDGEMENTS

We thank Dr. Korhan Erkanlı from Istanbul Medipol University Medical School who provided insight and expertise that greatly assisted the research.

REFERENCES

- [1] "Factsheet: Health Inequalities in the EU | EuroHealthNet." <https://eurohealthnet.eu/publication/health-inequalities-in-the->

[eu/?gclid=CjwKCAjw8JKbBhBYEiwAs3sxN5bmjX5SvJkpI3OGbsvR6SI0yiYQPRgqa8rFIDatLS000B0LT85WSxoCABIQAvD_BwE](https://eurohealthnet.eu/publication/health-inequalities-in-the-) (accessed Nov. 04, 2022).

- [2] K. C. Kent, "Clinical practice. Abdominal aortic aneurysms.," *N Engl J Med*, vol. 371, no. 22, pp. 2101–8, Nov. 2014, doi: 10.1056/NEJMCP1401430.
- [3] K. M. Tse, P. Chiu, H. P. Lee, and P. Ho, "Investigation of hemodynamics in the development of dissecting aneurysm within patient-specific dissecting aneurismal aortas using computational fluid dynamics (CFD) simulations," *J Biomech*, vol. 44, no. 5, pp. 827–836, Mar. 2011, doi: 10.1016/J.JBIOMECH.2010.12.014.
- [4] "CEETRON Advanced 3D visualization of CFD and FEA." <https://ceetron.com/> (accessed Jan. 18, 2023).
- [5] "Simmetrix :: Home." <http://www.simmetrix.com/> (accessed Jan. 18, 2023).
- [6] "OpenFOAM." <https://www.openfoam.com/> (accessed Jan. 18, 2023).
- [7] S. E. Razavi, V. Farhangmehr, and N. Zendeali, "Numerical investigation of the blood flow through the middle cerebral artery," *Bioimpacts*, vol. 8, no. 3, pp. 195–200, 2018, doi: 10.15171/BI.2018.22.
- [8] I. Technologies, S. A. Gombe, and T. Supervisor, "43D Visualization and Segmentation of Lungs Using Itk / Vtk / Qt Kopsude 3D Visualiseerimine Ja Segmenteerimine Itk / Vtk / Qt," 2017.

SEX DIFFERENCES IN AXON DYNAMIC BEHAVIOR UNDER AXIAL LOADING AND UNLOADING

C. Zhang (1), S. Ji (1,2)

(1) Department of Biomedical Engineering, Worcester Polytechnic Institute, Worcester, MA, USA
(2) Department of Mechanical Engineering, Worcester Polytechnic Institute, Worcester, MA, USA

INTRODUCTION

Biological sex is a significant risk factor for traumatic brain injury (TBI). However, there has been little attention to sex differences in concussion until recently. Diffuse axonal injury (DAI) is one of most prominent pathologies found in all severities of TBI. At the axonal level, there are significant sex morphological differences as observed in ultrastructure studies (e.g., smaller in microtubule (MT) density and axon cross-sectional area and with fewer MTs than male axons⁵).

To-date, studies on axonal injury are focused on injury triggering mechanisms, such as microtubules (MTs) tear¹, strain concentration around the Ranvier node,² and interaction among various axonal substructures³. These axonal injury models offer valuable insight into the potential causes of heterogenous DAI pathologies. However, no study exists to investigate sex differences in axonal substructural responses.

To facilitate a systematic investigation into sex differences in DAI at the microscale, we have developed a parameterized modeling approach for automatic and efficient generation of sex-specific axon models according to specified geometrical parameters. In this study, baseline female and male axon models in the corpus callosum with random MT gap locations are generated for model calibration and validation. We then report results of sex differences of MT and Ranvier node peak strain amplification and tau protein and neurofilament (NF) failures under a realistic dynamic input generated from a real-world impact simulation that contains both a loading and an unloading phase.

METHODS

Baseline unit female and male FE models of 8 μm in length were developed. The main cytoskeleton components of both axon models include MTs, axolemma, myelin sheath, Ranvier node, MT-associated protein (MAP), tau and NF network. Both models explicitly meshed all

major axonal substructures and adopted their respective averaged geometrical parameters according to the literature, as reported in (Table 1). To maximize geometrical radial symmetry and to facilitate meshing, 7 MTs were retained for a typical female model (1 MT in the center with 6 additional ones to form a one-layered hexagonal pattern), and 13 MTs were retained for a typical male axon (with 6 additional MTs in the second layer), respectively. They reflect the average of 8 and 12 MTs. To avoid ambiguity, they are also referred to as MT7 and MT13 models.

Table 1 | Geometrical features of axonal substructures²⁻⁴

Axolemma radius	# of MTs	MT spacing	MT inner radius	MT outer radius	g-ratio*
200/300 nm	7/13	30 \pm 2.5 nm	7.0 \pm 0.75 nm	12.5 \pm 1.5 nm	0.65 \pm 0.075
MT length	NF	Axolemma thickness	Ranvier node	MT gap length	
4.02 \pm 5.28 μm	Fill remaining space.	8 \pm 0.75 nm	1 μm	0.12 μm	

*g-ratio, the ratio of the inner axonal diameter to the total outer (myelin sheath) diameter

Most axonal substructures were assigned with linear viscoelastic material properties based on the literature. Material properties for the NF were calibrated for both MT7 and MT13 models with a hertz contact experiment to ensure their responses fall within the experimental measurement corridor. With the calibrated NF stiffness, the baseline models were then validated against in-vivo experimental tension dataset⁷ by simulating a quasi-static uniaxial tension experiment (30% peak strain at a rate of 0.17 s^{-1}). MT breakage and Axolemma rupture behaviors were simulated using a strain failure threshold of 50% and 34%, respectively. For tau and NF, a 100% failure threshold was adopted based on relevant literature, above which the corresponding elements would produce a zero-reaction force. Elements after failure

were deleted for subsequent simulation. Baseline models were then used to simulate axonal stretch from a real-world impact. Specifically, a strain history curve (Figure 1a) in the corpus callosum obtained from a previous simulation of a reconstructed real-world head impact using the anisotropic Worcester Head Injury Model V1.0.

Axon dynamic behaviors depend on MT gap configurations. They are quantified by using a bivariate probability strategy. The unit axon model length (L) was used to define a series of discrete “sampling lengths”. Starting from the shortest sampling length (L_s) chosen to be 5% of L , the entire axon model was scanned axially to identify the maximum number of MT gaps (N) falling within the specified length. The pair of parameters, (L_s , N), were then used to characterize the MT gap configuration. For each sex, ten thousand ($N=10,000$) models with baseline geometrical parameters (Table 1) were created, from which the bivariate distribution probability, (L_s , N), was calculated.

For each simulation, 5 axon models were generated for each MT gap configuration with a nonzero probability for each sex. Peak strain amplifications in MT relative to peak input strain were obtained, along with the associated tau and NF failure rates. They were then organized according to the bivariate MT gap configurations to obtain corresponding averaged responses, from which sex differences in responses were compared. All simulations were conducted in SIMULIA Abaqus with the implicit non-linear FEA solver (32 CPUs, 64GB).

RESULTS

For each simulated axon model, we consistently observed MT undulation, regardless of the sex or specific MT gap configurations. They all started near the end of the unloading phase and sustained even after the completion of unloading. The undulation behavior agreed well with TEM findings observed immediately after dynamic stretch injury. Case illustrations are shown in Figure 1.

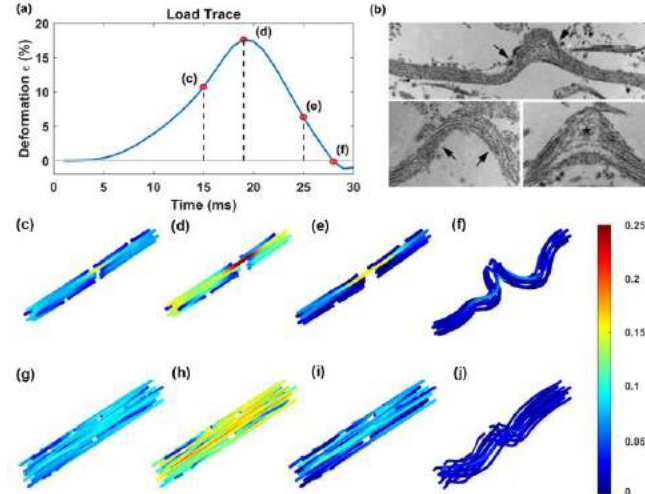


Figure 1: (a) Corpus callosum fiber strain time history as input applied to the axon models. (b) MT undulation in dynamic stretch injury test ⁶; From (c) to (j): MT strain distributions in deformed states at selected time points (as indicated in (a)) for a typical female and male axon model.

With the applied input (peak strain of 18%), none of the MTs or Ranvier nodes in any model exceeded their failure strain thresholds. In general, higher MT strain amplifications occurred when there were more MT gaps within a shorter sampling length for both female and male models. However, peak strain amplifications in the Ranvier node were mostly uniform for both models and were insensitive to the gap configuration. Figure 2a-b report tau and NF failure rate (element

length-weighted percentage of failed elements) progressions over time for a female and a male axon model with their most common MT gap configurations. The male model had a higher tau failure, but the female axon model had a much higher rate for NF failure.

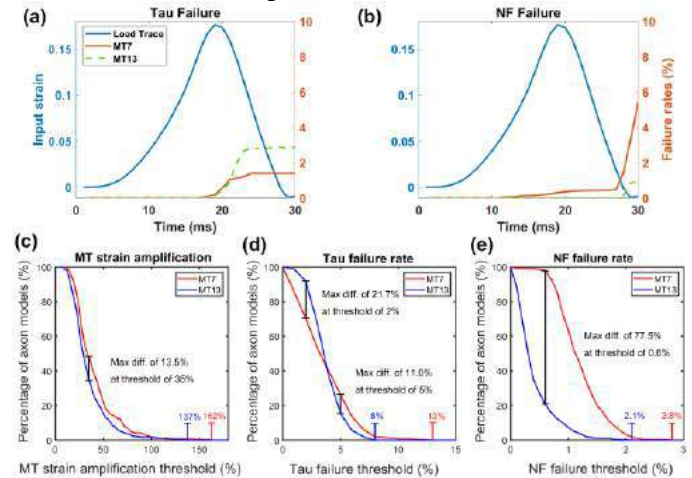


Figure 2: Tau (a) and NF (b) failure rates over time for a female and a male axon (MT7 and MT13, respectively); Percentages of female and male axon models with MT peak strain amplification (c), tau (d) and NF (e) failure rates exceeding a range of thresholds for each sex.

Using a large sample of axon models with random MT gaps for each sex, the percentages of axon models with MT peak strain amplifications exceeding a range of thresholds were compared, as well as those with tau and NF failure rates above a given threshold across their respective value ranges (Figure 2c-e). For MT strain amplification and NF failure, female axon models always had a higher percentage of above-threshold responses across the value ranges. For tau failure, however, the sex difference depended on the threshold value, itself.

DISCUSSION

We find axonal substructural responses in terms of peak strain amplifications in MTs and the Ranvier node as well as NF failure rates in female axons are considerably higher than those in male axons in dynamic tensile loading and unloading. The underlying reason are largely due to the sex-related difference in the cross-sectional number of MTs and the random nature of MT gaps. Both random MT gaps in model and the unloading phase in dynamic tension are critical to reproducing MT undulation as observed experimentally. The study may lead to an improved understanding of sex differences in injury vulnerability at the microscale as well as the biomechanical mechanism of DAI in general.

ACKNOWLEDGEMENTS

Funding is provided by NSF CMMI 2114697. Simulations were conducted using a high-performance computing system acquired through the NSF MRI grant DMS-1337943 to WPI.

REFERENCES

- [1] Peter, S. J. et al., Arch. Biophys. J. (2012)
- [2] Zhu, F. et al., Arch. Phys. J. Neurotrauma 33, 859–870 (2016).
- [3] Montanino, A. et al., Front. Neurol. 9, 1–12 (2020).
- [4] Ahmadzadeh, H. et al., Biophys. J. 106, 1123–1133 (2014).
- [5] Dollé, J. P. et al., Exp. Neurol. 300, 121–134 (2018).
- [6] Yu, W. et al., J. Neurosci. 14, 2818–2829 (1994).
- [7] Ouyang, H. et al., J. Biol. Eng. 7, 1 (2013).

UNDERSTANDING FABRIC FRICTION TO REDUCE THE RISK OF PRESSURE INJURIES IN WHEELCHAIR USERS

Archana Lamsal and Tamara R. Bush, PhD

Mechanical Engineering, Michigan State University, East Lansing, MI, USA

INTRODUCTION

Wheelchair users spend a great deal of time seated and because of this, they have a high risk of developing pressure injuries (PIs). Wheelchair users are particularly prone to PIs on the bottom of their buttocks [1]. Infections, sepsis, and even death can result from PIs which makes PIs a serious health issue [2]. One risk factor that increases the risk of PIs are shear forces (forces parallel to person's tissue) on the buttocks [3]. Shear forces are greater when friction is higher. Lowering the coefficient of friction between the seat and the user's pants, can help reduce the shear forces that a wheelchair user experiences and as a result, decrease PI risk. To achieve this, it is essential to understand the friction at the interface between the seat cushion and the pants. It is also critical to understand how the presence of a deformable foam affects the frictional behavior of these interacting fabrics.

Thus, the goals of this study were: 1) to determine the coefficients of friction of seven commonly worn pant fabrics and two seat cover fabrics and 2) to investigate the effects of a deformable seat cushion on the coefficients of friction between fabrics.

METHODS

The materials and devices used for this research included a seat pan with the ability to tilt from zero degrees (horizontal) to 45 degrees of rearward tilt; a mechanical system called the 'sled' (Figure 1) where different fabrics were attached; a multi-camera motion capture system; and reflective markers. The sled had a cross section of 15 cm x 15 cm and thickness of one centimeter. A test weight of 110N was attached to the sled and the sled system was placed on top of the seat pan with the seat cover attached to it (Figure 1). The friction was determined through monitoring movement of the sled on the tilting seat pan. The seat pan was tilted until the sled system started sliding. Positional data of markers on the sled and the seat pan were obtained using a motion capture camera system with sampling rate of 100 Hz and accuracy < 0.5 mm.

The coefficient of static friction was determined using Newton's second law of motion. The free body diagram of the experimental setup, just before the sled started sliding on the seat pan, is shown in Figure 1 (right). The axis parallel to the inclined surface was denoted as the t-direction (tangent) and that perpendicular to the inclined surface was denoted as the n-direction (normal).

The force balances used to determine the coefficient of static friction (μ_s) are given by Equations 1 and 2.

$$\sum F_t = \mu_s mg \cos(\theta_{\max}) - mg \sin(\theta_{\max}) = 0 \quad (1)$$

$$\mu_s = \tan(\theta_{\max}) \quad (2)$$

Where, F_t was the total force in tangential direction, m was the mass of the sled system, g was the gravitational constant and θ_{\max} was the maximum angle of tilt before the sled started to slide.

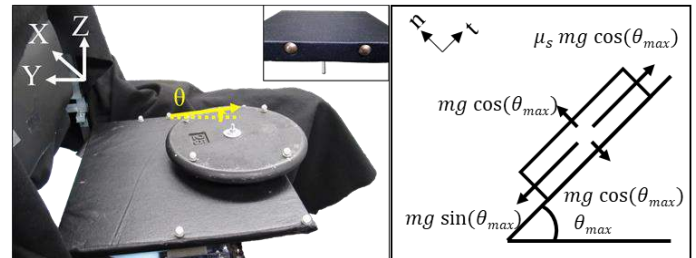


Figure 1. Left: Sled system on seat pan was tilted from horizontal until sliding started. The angle of tilt is denoted by θ . Right: Free body diagram of the sled system just before the sled started to slide on the seat pan, used to calculate coefficient of static friction (μ_s).

Two different seat covers were analyzed; a vinyl seat cover commonly used in wheelchairs and a fabric type seat cover commonly

used in office chairs (referred to as ‘office cover’). Seven different pant fabrics were analyzed (Figure 2).



Figure 2. The fabric structures of all the pant fabrics and seat covers under 50x magnification.

To achieve the second goal, a piece of polyurethane foam with a density of 67 kg/m³ and thickness of 38 mm was secured underneath the seat cover to replicate the effect of an office or wheelchair seating environment. The seat cover was nailed into the wooden seat pan (along the sides) to secure the foam and the seat cover taut. All the data sets were collected for 10 repetitions.

RESULTS

The static coefficients of friction between the pant fabrics and the seat covers; both with and without the foam in the seat pan are presented in Table 1. The office seat cover produced a smaller friction coefficient than the vinyl seat cover for all the pant fabrics - both with and without the foam. With the vinyl seat cover, the women's pull on pants and women's khakis produced the lowest coefficients of friction whereas jeans and basketball shorts produced the highest coefficients of friction. With the office seat cover, the basketball shorts and women's khakis produced the lowest coefficients of friction whereas the sweatpants and jeans produced the highest coefficients of friction. For any given pair of pants and seat cover, the coefficient of friction was consistently larger with the presence of foam in the seat pan than without the foam.

Table 1 Static coefficients of friction (μ_s) between the pant fabrics and seat covers; both with and without the foam in the seat pan. Values in the parenthesis indicate the standard deviation.

Pant material	Vinyl seat cover		Office seat cover	
	Without foam	With foam	Without foam	With foam
Women's pull on pants	0.492 (0.025)	0.548 (0.032)	0.376 (0.029)	0.381 (0.016)
Women's khakis	0.502 (0.016)	0.549 (0.01)	0.343 (0.038)	0.375 (0.029)
Sweatpants	0.539 (0.015)	0.572 (0.021)	0.414 (0.037)	0.449 (0.02)
Men's khakis	0.54 (0.014)	0.555 (0.021)	0.345 (0.03)	0.379 (0.027)
Women's jeans	0.546 (0.018)	0.61 (0.016)	0.428 (0.026)	0.493 (0.039)
Men's jeans	0.585 (0.016)	0.635 (0.017)	0.422 (0.033)	0.486 (0.037)
Basketball shorts	0.59 (0.031)	0.661 (0.042)	0.281 (0.016)	0.308 (0.01)

DISCUSSION

Understanding the frictional properties of the seat interface is important, especially for wheelchair users. Since increased shear forces leads to increased risk for PI formation, identifying material pairings with lower frictional properties could help mitigate this risk.

Fabrics such as men's and women's jeans were not optimal pant choices as they had higher frictional coefficients with both seat covers. Women's khakis produced smaller friction coefficients with both the seat covers and therefore would be considered an optimal fabric choice with the seat covers tested. The lower coefficient of friction demonstrated by women's khakis could be due to the interaction of various factors such as presence of spandex in the fabric, a relatively smooth feel of the fabric (although it was difficult to quantify) and a tight fabric structure woven with a thin yarn as shown by the microscopic images.

The results of this study also documented the complexity of frictional behavior of fabrics. While the basketball shorts demonstrated the largest coefficient of friction with the vinyl seat cover, this fabric also had the lowest coefficient of friction with the office seat cover. This implies that the best fabric choice for friction reduction with a particular seat cover might not be an optimal choice with a different seat cover. Furthermore, there were large differences in the friction coefficients of basketball shorts and women's pull on pants with the vinyl seat cover despite both being made of 100% polyester. These results demonstrate that despite a similarity in the type of material (polyester), there might be differences in other properties such as yarn material, weave, surface finish etc., which also affects friction [4, 5, 6].

The larger coefficient of friction with the vinyl cover was likely attributed to the larger contact area of the vinyl surface as evident from the microscopic images (Figure 2). The vinyl surface comprised of large flat plateaus and smaller valleys which would provide a large contact surface area as opposed to the office fabric which was made of woven fabric yarns. Since vinyl is commonly used in wheelchairs, choosing an alternative seat cover that provides lower frictional coefficients would be beneficial.

The effect of foam should also be considered in regards to the friction at the seat interface as all customized wheelchairs include a foam cushion on the seat pan. The data indicated that the presence of foam underneath the seat cover increased the coefficient of friction for all materials.

The results of this study provide valuable information regarding the friction that occurs between pants and a seat surface. Replacing a traditional vinyl cover with an alternative fabric cover might be beneficial to reduce friction, and therefore reduce shear forces on wheelchair users. While some pant fabrics demonstrated consistent frictional behavior with both seat covers, some fabrics showed vastly different behavior with the two seat covers. Thus, careful considerations should be made while selecting pant fabrics for wheelchair users as well as the cushion material.

ACKNOWLEDGEMENTS

The authors would like to thank Dr. Justin Scott and BDRL for their support during this study.

REFERENCES

1. Mervis and Philips, J. Am. Dermatology, 81:4, 881-888, 2022
2. Bryan C. et al., Arch. of Int. Med., 143:11, 2093-2095, 1983
3. Hanson D. et al., Adv. Skin Wound Care, 23:1, 21-24, 2021
4. Ajayi J., Text. Res. J., 62: 2, 87-93, 1992
5. Ajayi J., Text. Res. J., 62:1, 52-59, 1992
6. Jeddi A. et al., J. of Text. Instit., 79:2, 103-109, 2010

POST-MITRACLIP MITRAL VALVE GRADIENT WITH MITRACLIP G4

Shelley C. Gooden (1), Mani A. Vannan (2), Konstantinos D. Boudoulas (3), Vinod H. Thourani (2), Pradeep K. Yadav (2), Lakshmi P. Dasi (1)

(1) Department of Biomedical Engineering, Georgia Institute of Technology, Atlanta, Georgia, US
(2) Marcus Valve Center, Piedmont Heart Institute, Atlanta, Georgia, US
(3) Division of Cardiovascular Medicine, Wexner Medical Center, Columbus, Ohio, US

INTRODUCTION

Mitral regurgitation (MR) is a prevalent disease, present in 1.7% of the general population and 9.3% of those age 75 and older [1]. The disease occurs when the two leaflets of the mitral valve (MV) do not close properly during systole. For treatment of symptomatic moderate-to-severe or severe MR in patients deemed high-risk for surgical treatment, Abbott's MitraClip transcatheter edge-to-edge repair device may be used. MitraClip is the only FDA approved transcatheter device and one of two transcatheter devices with CE mark. The device clips the two leaflets together to reduce MR, creating a double orifice. The current G4 generation is composed of four sizes with leaflet footprints of: NT, 9x4mm; NTW, 9x6mm; XT, 12x4mm; XTW 12x6mm.

Analyzing MV pressure gradient (MVG), defined as the mean MVG by simplified Bernoulli through diastole measured by continuous wave (CW) Doppler, during the MitraClip procedure is important. Leaving patients with gradients of 5 mmHg or more is undesirable and can lead to iatrogenic mitral stenosis, worsening patient prognosis [2-3]. MitraClip size is expected to impact MVG, and the impact on MVG is especially important in patients with geometries on the border of usage guidelines. However, there is a lack of understanding relations between geometric factors and MVG after clip sizes, as current analyses require full, expansive, patient-specific simulations. The objective of this study is to assess how border-line mitral anatomies and different MitraClip sizes impact MVG.

METHODS

A parameterization method was developed and applied to simplify MV geometries based on annular commissural (CC) and anterior-posterior (AP) dimensions and anterior and posterior mitral leaflet (AML and PML) lengths.

Based on measurements from 3D echo scans of 13 MR patients and guidelines for MitraClip use, six parameterized MV geometries were created *in silico* to capture the borders of MitraClip usage while

remaining reflective of patient MVs. Key measures of the six pre-clip geometries are shown in **Table 1**.

Table 1: Pre-Clip Model Dimensions

Model	CC [mm]	AP [mm]	AML [mm]	PML [mm]
A	26.0	24.0	23.0	10.0
B	28.0	26.0	23.0	10.0
C	28.0	26.0	23.0	10.0
D	30.7	28.7	22.0	10.5
E	32.7	30.7	22.0	10.0
F	37.3	35.3	22.0	11.0

Using an in-house reduced-order clipping simulation, clip placement was simulated to produce post-clip geometries. First, NT with central placement was mimicked. An example of pre- and post-clip geometries is shown in **Figure 1**.

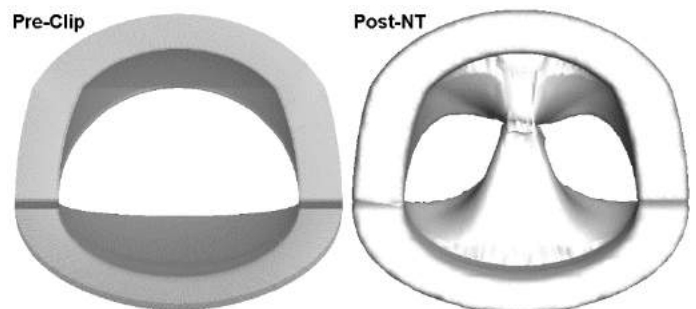


Figure 1: Post- and Post-Clip Mitral Geometries

The pre- and post-clip geometries were 3D printed from rigid ABS for assessment in a left-heart simulator, where the model was placed upstream a bioprosthetic MV in order to maintain proper mitral flow. The simulator was set to physiological conditions of 60 bpm heartrate, 120 mmHg left ventricular pressure, and 5 L/min cardiac output. The working fluid was a 60-40 water-glycerin mixture to mimic the kinematic viscosity (3.88 cSt) and density (1060 kg/m³) of blood. MVG was measured using CW Doppler.

Based on these results, the models with the highest post-NT MVG and the highest post-NT percent increase MVG were reassessed using the other three MitraClip G4 sizes (NTW, XT, XTW) with central clip placement.

The resultant post-clip MVGs were compared against geometric factors to find a meaningful relation.

RESULTS

Post-NT MVG and percent increase MVG are shown in **Table 2**.

Table 2: Post-NT Mitral Valve Gradient and Percent Increase

Model	MVG [mmHg]	Percent Inc MVG [pct]
A	10.8	283
B	6.3	192
C	7.8	318
D	4.5	178
E	3.2	165
F	1.7	109

Since the greatest post-NT MVG was observed with model A (10.8 mmHg) and greatest post-NT percent MVG increase was observed with model C (318%), these models were analyzed with NTW, XT, and XTW. Analyzing the MVG against geometric factors yielded the area product between MVA and MAA to have a meaningful relation. This relation for all model-clip combinations is shown in **Figure 2**.

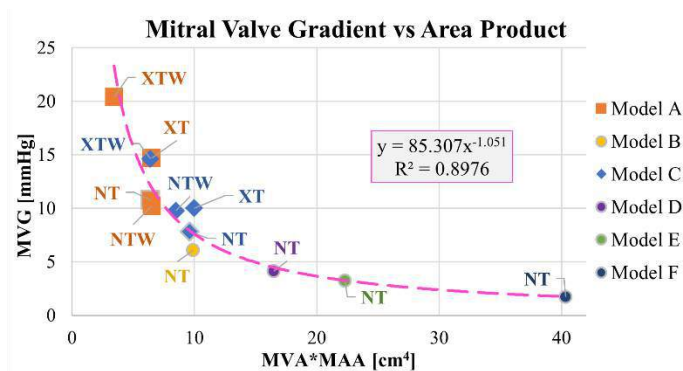


Figure 2: Mitral Valve Gradient vs Area Product

DISCUSSION

Across all configurations assessed, there was a strong power relation between the post-clip MVG and area product, with an R² of 0.90. This relation is expected, as choking off the flow by reducing inlet area (MAA) and outlet area (MVA) area is expected to greatly increase MVG as the velocity increases.

Focusing first on the smallest clip, which is the NT, the MVG had an overall increase with smaller models. Again, this relation is expected. Model A had the greatest post-NT MVG. This is because the conditions of the left-heart simulator were maintained across all configurations assessed, and model A was the smallest model. However, model C had the greatest post-NT percent increase MVG. This may have been due to

how the annular dimensions effect stretching of the leaflet over the orifice when clipped.

Assessing the G4 generation on model A yielded overall expected results. First, the relation between MVG and area product operate on the steeper limb of the relation (**Figure 2**), which is expected since model A is the smallest. The largest clip (XTW) gave the highest MVG followed by the XT. NT and NTW had similar MVG.

Assessing the G4 generation on model C gave similar results, landing a further down the relation curve compared to model A (**Figure 2**). Again, the XTW gave highest MVG. XT and NTW had similar MVG, and NT had the smallest MVG.

One cause of similar post-clip MVG with different clip sizes may be due to how the left-heart simulator is tuned between models, as afterload may have differed in order to maintain the same cardiac output, peak LVP, and overall mitral flowrate waveform. This also serves as a limitation of the study, as keeping these parameters constant between pre- and post-clip configurations does not account for changes in forward flow that comes with MR correction. Another limitation is the rigidity of the left-heart simulator, which is likely the leading contributing factor of sharp MVG increases, especially for smaller orifice models and larger clip sizes. However, these limitations keep conditions similar in order to capture effects of MV size and clip size alone.

Future work includes assessing different clip placement, as location of MitraClip in patients depends on location of the regurgitant lesion. Similarly, multiple clips should be assessed, as well as a combinations of different clip sizes, which is also reflective of clinical practice. Lastly, these results should be compared to *in vivo* data to assess potential of translating findings to clinical practice.

Results from this study show how simplified mitral geometries with *in silico* MitraClip placement can be used to gain insight on how device size and mitral geometry effect MVG. Expanding this work can help guide clip selection to prevent suboptimal MVG outcomes.

ACKNOWLEDGEMENTS

This research was supported by National Institutes of Health (NIH) under Award Number R01HL119824.

REFERENCES

- [1] Benjamin, E.J. et al., *Circulation*, 137:e67-e492, 2018.
- [2] Itabashi, Y et al., *J Cardiol*, 71:336-345, 2018.
- [3] Nishimura, R et al., *J Am Cardiol*, 63:e57-e185, 2014

ULTRASOUND IMAGING TO CHARACTERIZE INFLATED ATHEROSCLEROTIC PLAQUES

**Yasmine Guendouz (1,2), Brooke Tornifoglio (1,2), Sherif Sultan (3,4), Niamh Hynes (3,4),
Cleona Gray (5), Caitríona Lally (1,2,6)**

- (1) Trinity Centre for Biomedical Engineering, Trinity College Dublin, Ireland
- (2) Department of Mechanical, Manufacturing and Biomedical Engineering, School of Engineering, Trinity College Dublin, Ireland
- (3) Western Vascular Institute, Department of Vascular and Endovascular Surgery, University Hospital Galway, National University of Ireland
- (4) Department of Vascular Surgery and Endovascular Surgery, Galway Clinic, Doughiska, Royal College of Surgeons in Ireland and National University of Ireland, Galway affiliated Hospital
- (5) Department of Vascular Surgery, Mater Misericordiae University Hospital, Dublin, Ireland
- (6) Advanced Materials and Bioengineering Research Centre (AMBER), Royal College of Surgeons in Ireland and Trinity College Dublin, Dublin, Ireland

INTRODUCTION

Stroke is one of the leading causes of death and disability worldwide, with 13.7 million strokes in 2016 alone [1]. Large vessel occlusions account for up to 46% of acute ischemic strokes [2]. More specifically, blockage of the carotid arteries accounts for 34% of all ischemic strokes [3]. The rupture of ‘vulnerable plaques’ present in the carotid artery can lead to the obstruction of downstream vessels, consequently blocking blood flow to the brain [4]. Atherosclerosis is a progressive inflammatory disease, initially occurring in the inner layer of the arterial wall. The amount of lumen blockage caused by the cascade of inflammatory events is commonly referred to as the percent stenosis. Clinical decisions for carotid atherosclerosis treatment are primarily based upon this measure [5]; however, there is a growing body of evidence highlighting that vulnerability is governed by plaque composition and morphology, and not simply percent stenosis [6].

Ultrasound imaging is a non-invasive, safe, cheap, low-cost, and fast technique that can provide valuable information on plaques. The American Society of Echocardiography recently recommended the increased use of multimodal ultrasound imaging to gather more information on plaque characteristics [7], highlighting the need to establish better clinical biomarkers for plaque risk assessment using ultrasound. The goal of this study is to investigate *ex vivo* inflation testing of fresh human atherosclerotic plaques using ultrasound imaging. This testing set up, which reproduces physiological loading, facilitates the investigation of plaque mechanical behaviour, and has the potential to yield new insights for ultrasound derived biomarkers which can be assessed *in vivo*.

METHODS

Depending on the surgical technique, excised atherosclerotic plaques can present with large incisions. To circumvent leaks and allow for watertight pressurization, highly deformable balloons were created, and their compliance investigated on native porcine carotid arteries (NPCaA). For balloon fabrication, stainless steel mandrels were dipped in a liquid latex:water solution (3:2) and after >6 hours curing at 37°C, the balloons were removed using lukewarm water. NPCaA were collected from 6-month-old large white pigs and cryopreserved to -80 °C at a controlled rate of -1 °C/min in the presence of a cryoprotectant to preserve mechanical and structural properties. Samples were thawed in a water bath at 37°C on the day of testing and connective tissue was removed prior to inflation, Fig.1(a). NPCaA (n=6) were then inflated both with (n=3) and without (n=3) a balloon inserted in the lumen.

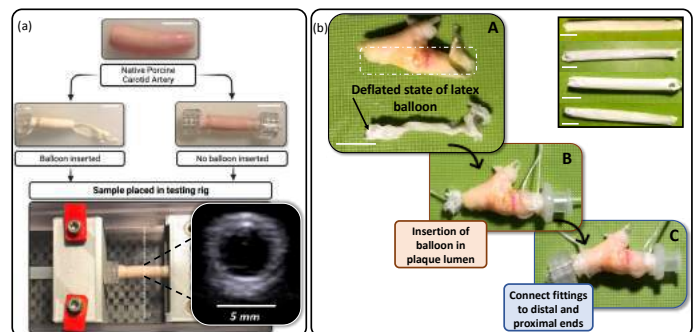


Figure 1: (a) NPCaA and (b) atherosclerotic plaque testing.

Intraluminal pressure was applied using a PID controlled syringe pump in 10 mmHg increments. An in-house inflation testing rig was developed to allow for ultrasound imaging of the pressurized samples up to 120 mmHg. Inflation occurred at room temperature in PBS. An axial stretch of 10% was applied to the NPCaA to reproduce *in vivo* pre-stretch. An ultrasound probe (9L4/12L4, SIEMENS, S2000) was placed above the sample to obtain B-mode scans for each pressure step. Outer diameters were measured using ImageJ and static compliance was calculated for each inflation [8]. For plaque testing, fresh human atherosclerotic plaques (n=6) were collected from carotid endarterectomy surgeries. Samples were cryopreserved and thawed in the same manner as NPCaA. Any lacerations or holes on the plaques were sutured closed using 6-0 polypropylene sutures followed by balloon insertion into the plaque lumen (Fig. 1(b)). After balloon insertion, both the plaques' and balloons' ends were attached to connector fittings. Statistical analysis was performed with Prism 6 statistical software (GraphPad Software Inc., San Diego, California). For compliance measurements, unpaired non-parametric t-tests were performed between the tested NPCaA groups (No Balloon, Balloon) for each sample. Significance was considered when $p < 0.05$.

RESULTS

B-mode scans of cross-sections of an inflated sample without (Fig. 2, top row) and with balloon (Fig. 2, bottom row) at 120 mmHg reveal similar wall expansion. This is further confirmed when comparing compliance measurements between inflations for each NPCaA (Fig. 2(b)). No significant differences were found. Therefore, the mechanical response of NPCaA to intraluminal pressurization is not affected when using this compliant balloon inflation approach.

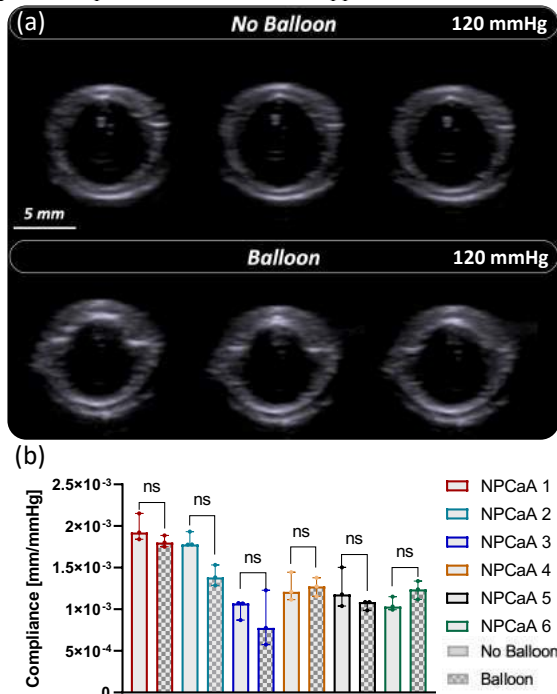


Figure 2: (a) B-mode scans of cross-sections of inflated NPCaA (n=1) without (top row) and with balloon (bottom row). (b) Median compliances of NPCaA (n=6) each inflated three consecutive times with and without balloon.

Using the method presented in Fig. 1(b), human, fresh atherosclerotic plaques were pressurized. B-mode scans of cross sections were obtained, see Fig. 3. A 9L4 probe was used for samples I to IV while a 12L4 one was used for samples V and IV. Bright hyperechoic regions

reveal areas of calcification as seen for sample I. Interestingly, sample V ruptured near the bifurcation where the balloon border can be observed out of the lumen, see Fig. 3.

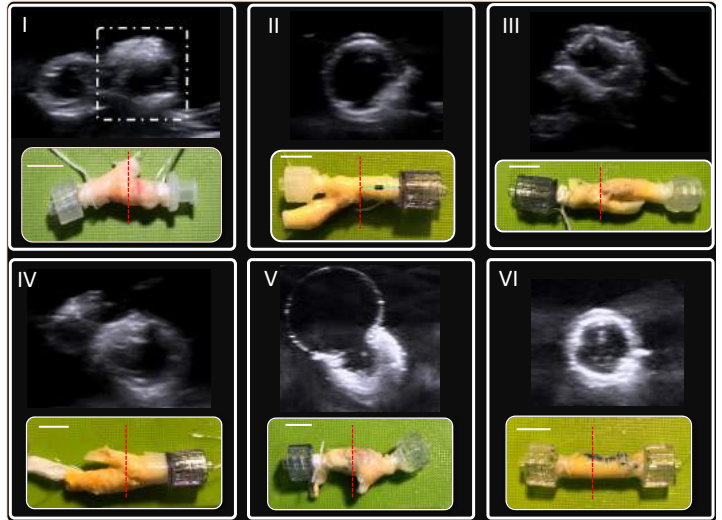


Figure 3: B-mode scans and photographs of plaques (n=6) inflated using the balloon inflation methodology. Red dotted lines show cross sections imaged using ultrasound. Scale bars = 1 cm.

DISCUSSION

A methodology to perform watertight pressurization of excised human plaque samples is presented. NPCaA wall expansion was not significantly influenced by the balloons, with no significant difference between vessel compliance measurements with and without the balloons. This methodology was then used to inflate excised atherosclerotic plaques and obtain ultrasound cross-sections. This *ex vivo* testing setup facilitates *in vivo* physiological loading to be replicated; conditions which are inherently precluded when performing uniaxial or biaxial tensile testing on strips of plaque tissue. This set-up can therefore provide improved fundamental understanding of plaque mechanical behavior and, through parallel ultrasound imaging, identify features that can be translated clinically as biomarkers of vulnerability. Specifically, the potential of intraplaque neovascularization as a vulnerability indicator [9] can be investigated through this *ex vivo* testing rig. This opens the door for future quantitative analyses and investigations between mechanical indicators and plaque features, ultimately improving the clinical management of carotid atherosclerosis.

ACKNOWLEDGEMENTS

This work was conducted with the financial support of the Science Foundation Ireland Centre for Research Training in Digitally Enhanced Reality (D-REAL) under Grant No. 18/CRT/6224. Special thanks to Chief Technical Officer, Gordon O' Brien who helped design the inflation testing rig.

REFERENCES

- [1] Johnson, C et al., *The Lancet Neurology*, 18.5, 439-458, 2019.
- [2] Robert C., et al. *Neurosurgery* 85.suppl_1, S4-S8, 2019.
- [3] Smith-Bindman & Bibbins-Domingo, *JAMA Network Open*, 4(2), 202, 2021.
- [4] Kolodgie et al., *Semin Vasc Surg*, 30, 2017.
- [5] Savastano, L. E., & Seibel, E. J. *Neurosurgery*, 64,188-198, 2017.
- [6] Brinjikji et al., *J Neurosurg*, 124(1):27-42, 2016.
- [7] Johri AM et al., *J Am Soc Echocardiogr*. 33(8):917-933, 2020.
- [8] Hsu S, Kambic H. *Artif Organs*. 21(12):1247-1254,1997.
- [9] Shah et al., *Vasc Med*, 12(4):291-297, 2007.

TOWARDS REAL-TIME PREDICTIVE MODELS OF TRANSCATHETER AORTIC VALVE REPLACEMENT PROCEDURES VIA REDUCED ORDER MODELING

I. Shah (1,3), F. Ballarin (2), A. Veneziani (3,4), L. Dasi (1)

- (1) Wallace H. Coulter Department of Biomedical Engineering, Georgia Institute of Technology, Atlanta, GA, USA
(2) Department of Mathematics and Physics, Università Cattolica del Sacro Cuore, Brescia, IT
(3) Department of Mathematics, Emory University, Atlanta, GA, USA
(4) Department of Computer Science, Emory University, Atlanta, GA, USA

INTRODUCTION

Transcatheter aortic valve replacement (TAVR) has become an increasingly common technique to treat patients with stenotic native aortic valves. As a part of the pre-operative planning strategy for patient-specific TAVR cases, computational modeling has become a critical tool for assessing the risk of post-TAVR complications, namely coronary obstruction and paravalvular leakage [1]. Traditionally, these models involve the use of finite element analysis (FEA) and computational fluid dynamics (CFD) techniques for visualization of the transcatheter heart valve (THV) during and after deployment [2-3]. Such analyses become extremely computationally expensive, as they involve time-dependent simulations of highly nonlinear mechanics that govern the THV stent frame and leaflets, as well as the patient-specific aortic root, native leaflets, and calcium deposits.

Reduced order models (ROM) have been readily used to introduce significant computational advantages as compared to traditional full order model (FOM) simulations (CFD or FEA). ROMs are traditionally divided into two stages, the *offline* and *online* stages. In the offline stage, several hundreds of parameterized FOM simulations are performed to generate a *snapshot* library of solutions. Using model reduction techniques such as the Proper Orthogonal Decomposition (POD) approach, this library is subsequently recycled in the online stage for new parameters of interest which results in a rapidly produced reduced order solution that comes at a fraction of the cost of the FOM [4].

The overarching objective of this study is to develop real-time predictive models of the entire TAVR deployment process with the use of ROMs, predicting both the structural and fluid dynamics of the THV during and after deployment. This involves generating separate ROMs for both the structural and fluid problems, which will then be coupled with appropriate boundary conditions at the fluid-solid interface. Specifically, the focus here is on advancing a previously developed POD-ROM for the structural deformation of the Medtronic Evolut R valve. This includes incorporating the nonlinear elastic properties of the

stent frame, as well as the time-dependent problem within the ROM framework. The goal is to use ROMs such that the computational costs of simulating the deployment of the valve are significantly reduced.

METHODS

For small local deformations, an initial linear elastic constitutive law is prescribed as follows,

$$\nabla \cdot \sigma = F \quad (1)$$

$$\sigma = \lambda(\nabla \cdot u)I + 2\mu\varepsilon \quad (2)$$

$$\varepsilon = \frac{1}{2}(\nabla u + \nabla u^T) \quad (3)$$

where, σ is the Cauchy stress tensor, ε is the strain tensor, F is the external volume force, and λ and μ are the Lamé constants. For larger deformations, nonlinear constitutive laws are required to accurately capture the deformation of the self-expandable nature of the Evolut stent frame. Specifically, a hyperelastic model is implemented, which serves as an initial approximation of the true superelastic properties of the nitinol stent. A Generalized Neo-Hookean form of the strain-energy density function in the following form is used.

$$\psi = \frac{\mu}{2}(I_c - 3) + \frac{\lambda}{2}(J - 1)^2 \quad (4)$$

Here, J is the Jacobian of the deformation gradient, and I_c is the first invariant of the right Cauchy-Green tensor. Boundary conditions (BC) in the form of zero displacement ($u = 0$) were prescribed at the upper and lower edges of the stent frame. The normal stress was also prescribed at a set of 15 points, i.e. $\sigma \cdot n(P_i) = d_i$ for $i = 1, 2, \dots, 15$. More precisely, all possible pairs among the 15 points were obtained, and the vector d_i was defined such that it was oriented along the line connecting two end points of each pair. These BCs are labeled as “force-pair” BCs which idealize the loads applied from the aortic wall on the stent frame and are used to mimic crimping and expansion of the stent (Fig. 1). The steady form of the models were initially used, followed by implementation of the time-dependent hyperelastic problem.

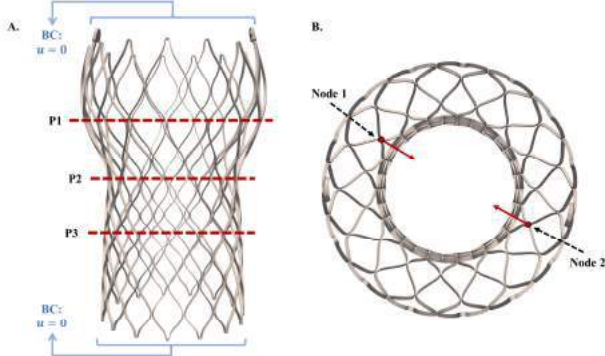


Figure 1. Boundary conditions enforced on Evolut R model.

The offline phase of the framework begins with a series of finite element (FE) simulations of Eq. (1) and (4). The 3D geometry of the Evolut R stent frame was generated in *SolidWorks*, and subsequently meshed using *Netgen* and *MmgTools* (260K elements). The stent frame was modeled with Young's modulus of 50 GPa and Poisson's ratio of 0.33. Using the 15 specified points for the parameterized BCs, a total of 105 FE simulations were performed in the offline stage. For the transient simulations, a semi-implicit approach is used. The time step was defined as 0.01 seconds, and the total time simulated was 0.3 seconds, which approximates the time taken for the stent to undergo deployment.

The online stage of the framework begins with a filtering operation to reduce the redundancy of the generated snapshot library. This is performed via the *Singular Value Decomposition* (SVD), which allows for analysis of the resulting singular values of the snapshot library. A rapid decay in the singular values indicates high redundancy, and that key features of the snapshot library can be captured by a linear combination of those left eigenvectors associated with the largest singular values. These eigenvectors form the reduced order basis, in the sense that the ROM solution reads as

$$u_{ROM} = Wc \quad (4)$$

where W is an $N \times n_{ROM}$ matrix, and c is a vector of coefficients. Following discretization of the governing problem, the FOM leads to a linear system of equations in the traditional form (i.e., $Au = b$, where A is the stiffness matrix and b is the forcing terms). With the POD technique, the ROM solution may then be substituted into the traditional discretization, resulting in the final reduced order system below.

$$W^T A W c = W^T b \quad (6)$$

Here, $W^T A W$ is a matrix that has a size in the range of tens or hundreds of rows, as compared to the traditional stiffness matrix A , which may feature a size in the range of hundreds of thousands or millions. Thus, the savings in computational costs becomes evident.

The entire ROM framework is implemented within *RBniCS*, an open-source model reduction library which is built upon *FEniCS*, an open-source FE library [4]. *RBniCS* allows for the automation of the entire process, from offline stage FE simulations to model reduction and online stage simulations. Results are all visualized in *ParaView*.

RESULTS

Stent crimping and expansion simulations were performed using a new set of force-pair BCs in the online stage. Fig. 2 visualizes the von Mises stress distribution for both linear and hyperelastic stent crimping simulations, and the ROM and FOM solutions were in strong agreement for each. In the linear elastic case, the maximum stress occurs along the same planes at which the BCs are applied (peak stress of 2344.66 Pa). In the hyperelastic case, the stress values are much greater (peak stress of 6948.72 Pa), and the maximum stress occurs adjacent to the nodes at which the BCs are applied. The stress distribution is also significantly more asymmetric in the hyperelastic case.

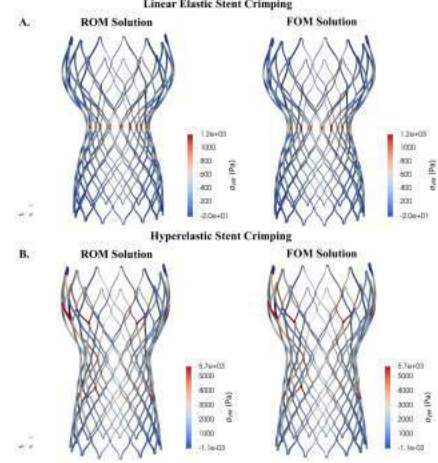


Figure 2. Comparison of ROM and FOM solutions for linear elastic (A) and hyperelastic (B) stent crimping simulations.

Computational details for all simulations are summarized in Table 1. The linear elastic case had a large reduction in time, with the FOM taking 14.82 and the ROM only 1.05 seconds, a 98.25% reduction. In the hyperelastic case, the reduction was from 107.99 to 10.46 seconds with the ROM, a 90.32% decrease. The transient simulations also had a slight decrease (195.50 to 132.83 seconds) with the use of the ROM.

Table 1. Computational details for all simulations.

Simulation	Mesh Size	# of Snapshots	# of FE DOF	# of RB	Wall Clock Time (s)		
					FE	ROM (Online)	ROM (Offline)
Linear Elastic	257671	105	227511	12, 13, 15	14.82	1.045	1556.32
Hyperelasticity	257671	105	227511	20	107.99	19.602	2797.79
Transient + Hyperelasticity	257671	105	227511	20	195.51	132.831	18062.44

DISCUSSION

This study introduces and advances a previously developed POD-ROM framework for rapidly simulating the structural deformation of the Evolut R valve. The ROM framework significantly reduced computational costs in both the linear and nonlinear cases while providing identical results as the FOM, highlighting the effectiveness of the POD approach for such structural problems. Although the reduction in computational time with the transient problem was not as large as the steady cases, this will be improved with the use of more advanced model reduction techniques. Namely, we will implement the discrete empirical interpolation method (DEIM), which is more effective for nonlinear transient problems and will allow for a larger reduction in costs. A major limitation is the lack of a true superelastic model, which is needed to capture the unique material properties of the nitinol stent. Future work involves implementing such a constitutive model, as well as adapting this structural ROM framework for use in real-time simulations of THV leaflet motion during the cardiac cycle. This new framework will then be coupled with a fluid-based ROM for the valve that will allow for real-time fluid-structure simulations following deployment of the THV.

In conclusion, the proposed ROM framework significantly reduces the computational costs of simulating the deformation of the Evolut R, while maintaining the accuracy from traditional FE simulations. Further refinements are underway for the framework to rapidly simulate the full fluid and structural dynamics of the THV following deployment.

ACKNOWLEDGEMENTS

Research was supported by the NSF 2012286 (PI: A. Veneziani).

REFERENCES

- [1] Ribeiro, H. et al., *JACC: Cardio Interventions*, 6:452-461, 2013.
- [2] Anam, S. et al., *J Cardio Translational Research*, 15:834-844, 2022.
- [3] Luraghi, G. et al, *Cardiovascular Eng & Tech*, 10:437-455, 2019.
- [4] Hesthaven, J. et al. *Cert Reduced Basis Meth for PDEs*, 590, 2016.

THE ROLE OF ANNULOPLASTY RING SHAPE AND SIZE ON TRICUSPID VALVE REPAIR

Collin E. Haese (1), Mrudang Mathur (2), Manuel K. Rausch (1,3,4)

- (1) Department of Aerospace Engineering & Engineering Mechanics, University of Texas at Austin, Austin, TX, USA
(2) Department of Mechanical Engineering, University of Texas at Austin, Austin, TX, USA
(3) Department of Biomedical Engineering, University of Texas at Austin, Austin, TX, USA
(4) Oden Institute for Computational Engineering and Sciences, University of Texas at Austin, Austin, TX, USA

INTRODUCTION

Tricuspid valve disease remains a significant source of morbidity and mortality in the United States and worldwide [1]. Current estimates believe nearly 1.6 million Americans suffer from a regurgitant tricuspid valve [2]. The current gold standard surgical treatment for tricuspid valve disease, despite novel inventions in the percutaneous heart valve space, is tricuspid valve annuloplasty. Over the last 30 years of innovation in the medical device community many different annuloplasty ring sizes and geometries have been introduced. However, current clinical guidelines for selection of ring size and shape are not well defined and are primarily motivated by surgeon preference rather than quantitative scientific investigations. We have developed a high-fidelity, subject-specific finite element model of the healthy and diseased human tricuspid valve. The objective of our current work is to utilize the high-fidelity model to quantitatively compare different annuloplasty ring geometries as well as sizes. Specifically, we intend to investigate their effect on three measures of valve competence: 1) coaptation area as a primary measure of valve function, 2) opening angle as a secondary measure of tricuspid valve function, 3) leaflet stresses as a likely measure of mechanobiological stimuli for future valve disease.

METHODS

As mentioned in the introduction, we are going to use our high-fidelity finite element model of the healthy and diseased human tricuspid valve, the Texas TriValve 1.0, to quantify the effect annuloplasty ring size and shape has on valve function [3]. Please find a detailed account of all model specifics in our recent work. In brief, we built an accurate model of the human tricuspid valve from donated healthy human heart valves. To this end, we used data collected in a beating human heart that was rejected from transplantation using an organ preservation system. Thereby, we were able to record transvalvular pressure and displacement boundary conditions at the leaflet-myocardial annular interface as well as dynamic data for

validation using 2D echocardiography. After collecting hemodynamic data from the organ preservation system, we performed mechanical testing of the leaflet and chordae tendineae to derive valve-specific material properties and morphology. This data informed Holzapfel-like hyperelastic constitutive models and an Ogden material law for the leaflets and the chordae tendineae, respectively.

After assembling this valve in conjunction with knowledge from existing literature on placement of the chordae tendineae, we validated an explicit finite element simulation of the valve closure dynamics against our 2D echocardiography recordings. We use the same model to simulate a diseased valve state through asymmetric dilation of the annulus and displacement of the papillary muscles to test the impact of various annuloplasty devices.

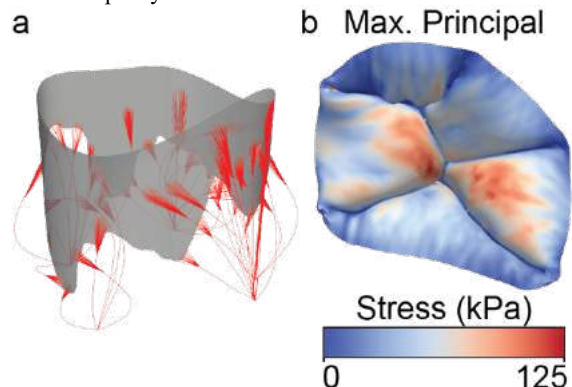


Figure 1: a) Assembly of the healthy Texas TriValve 1.0
b) Cauchy stress of the healthy valve model at end-systole

RESULTS

In Figure 1 we see the results of a baseline simulation of our healthy Texas TriValve. The healthy valve after assembly is depicted in

Figure 1a while Figure 1b shows the valve at end-systole with Cauchy stress overlaid on the closed configuration of the valve. In Figure 2 we see the comparison between the stress state in the healthy valve and the diseased valve as well as the stress induced by five unique annuloplasty rings. For the results presented herein, the diseased annulus was asymmetrically dilated to be 60% larger than the healthy valve. The five annuloplasty rings utilized were the Edwards Lifesciences Carpentier-Edwards Physio, the Cosgrove-Edwards Classic, and the Edwards MC3, as well as the Medtronic Contour 3D and the TriAd 2.0 Adams band, which are all widely available. A uniform nominal ring size of 30 mm was used across repaired valve simulations, which were previously digitized [4]. The predicted deformation and stress state produced by the five rings is heavily dependent on the chosen ring. The Contour 3D appears to produce the lowest level of stress in the leaflets followed by the Physio ring. The Physio and MC3 rings present high levels of stress on the posterior leaflet which is likely due to chordae tethering. The stress on the other leaflets is similar between the MC3, Classic, and TriAd rings.

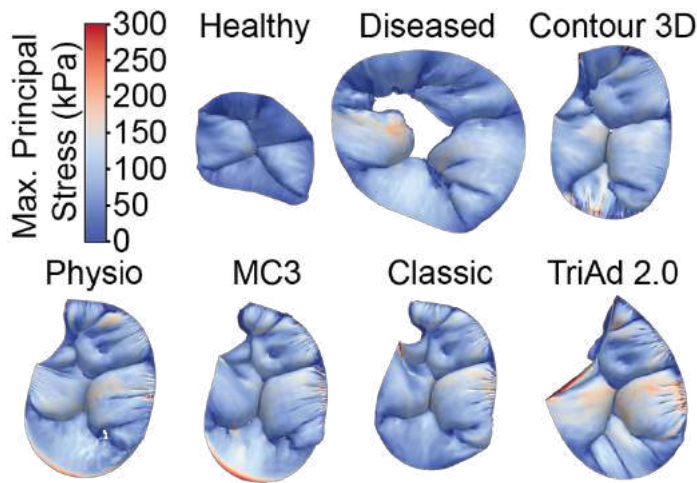


Figure 2: Comparison of the Cauchy stress exhibited by the healthy, diseased, and repaired valves

The comparison of the opening angle between the healthy, diseased, and repaired valves is detailed in Figure 3. The Contour 3D and Physio rings produce a smaller opening angle than found in the healthy valve, while the Classic ring presents a larger opening angle. The remaining rings reproduce an opening angle similar to the one found in the healthy valve. Likewise, Figure 4 illustrates the differences in coaptation area between the various valves. All repaired valves predict a larger coaptation area versus the healthy and diseased valve, suggesting all rings produce competent valve closure. However, between rings the amount of contact area varies substantially. Notably, the TriAd 2.0 generates the largest coaptation area while the MC3 develops the smallest contact area increase.

DISCUSSION

In this current work we used the Texas TriValve to investigate the impact of five different annuloplasty devices on three measures of tricuspid valve function. We found that annuloplasty ring choice impacts all measures of tricuspid valve function. Thereby, we have shown a numerical model such as ours, which is openly available, can be used to gain quantitative insight into choices which have previously been dominated by the personal experience of each surgeon. Please note we are currently working on completing identical comparisons to investigate the role of annuloplasty ring size. We anticipate to present a

total of 180 combinations of simulations to give never-before gained insight into choices of not only device type but also device size. We will apply these combinations on three different valves from three separate patients with various levels of annular disease progression to better represent the larger patient population as seen by clinicians. We are hoping our insight not only improves future device choice but also encourages others to use our open-source valve for similar investigations.

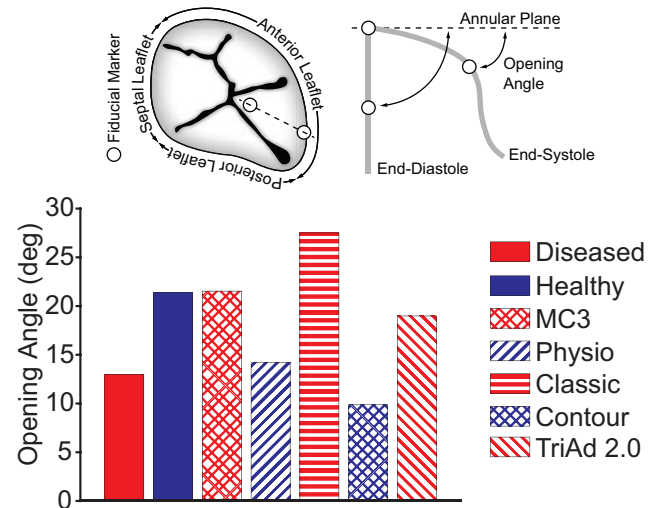


Figure 3: Comparison of the opening angle seen in the healthy, diseased, and repaired valves

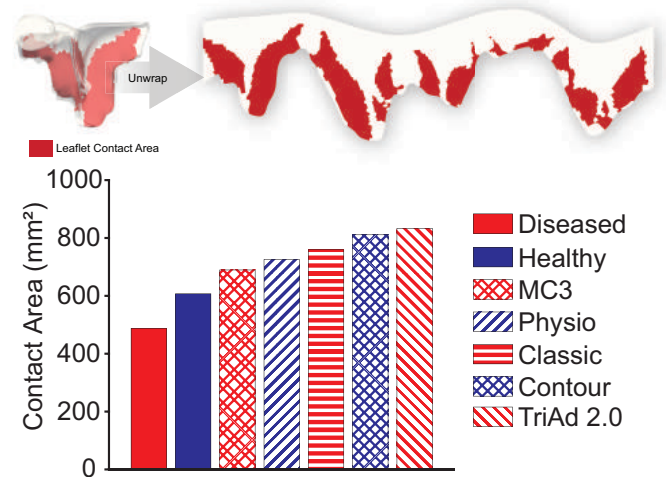


Figure 4: Coaptation area simulated in the healthy, diseased, and repaired valves

ACKNOWLEDGEMENTS

This research was supported by funding from the AHA 18CDA34120028 (to MKR) & 902502 (to MM), as well as NIH R21HL161832 (to MKR) & R01HL165251 (to MKR).

REFERENCES

- [1] Nkomo, V.T. et al., *Lancet*, 368:1005-1011, 2006.
- [2] Nath, J. et al., *JACC*, 43:405-409, 2004.
- [3] Mathur, M. et. al., *Eng with Comp*, 38:3835-3848, 2022.
- [4] Mathur, M. et. al., *Ann of Thor Surg*, 110:1605-1614, 2020.

MICROSTRUCTURE-BASED ESTIMATION OF THE EFFECTIVE STIFFNESS OF CROSSLINKED, EMBEDDED FIBER NETWORKS

Sotirios Kakaletsis (1), Emma Lejeune (2), Manuel K. Rausch (1,3,4)

(1) Department of Aerospace Engineering and
Engineering Mechanics
University of Texas at Austin
Austin, TX, USA

(2) Department of Mechanical Engineering
Boston University
Boston, MA, USA

(3) Department of Biomedical Engineering
University of Texas at Austin
Austin, TX, USA

(4) Oden Institute for Computational Engineering
and Sciences
University of Texas at Austin
Austin, TX, USA

INTRODUCTION

Embedded fiber networks are ubiquitous in nature. For example, soft tissues rely on an embedded fiber network for strength and elasticity. Examples of such tissues include blood clots and myocardial tissue [1,2]. Notwithstanding their omnipresence in nature, there is little literature on the mechanics of these *embedded* fiber networks. That is, most prior work investigates networks in isolation, without considering the mechanics of the embedding matrix and the effects of their coupling. Those few works that considered embedded fiber networks have used either a confined mixture, i.e., continuum, approach (Fig. 1A) or have used discrete network and matrix models with matching discretization between the fibers and the surrounding matrix (Fig. 1C). In the former case, anisotropic, hyperelastic strain energy functions are being used to model both the network architecture and the surrounding matrix and confinement between both constituents is assumed [3]. While computationally inexpensive, this approach does not provide detailed control over the network's microstructure or the coupling between fibers and matrix. The second approach, while accurately representing

the network geometry, requires a very fine mesh, thus leading to a prohibitive computational cost [4].

A possible compromise between these two approaches is the use of a coupling scheme to embed discrete elements in an isotropic solid matrix without the requirement for matching discretizations (Fig. 1B). Thereby, we can inform our model with detailed microstructural information such as the network density, average fiber length, fiber crimp, type of crosslinking and average connectivity number, without requiring a matching mesh for the matrix material. Therefore, the matrix can be modeled with few elements, making this approach computationally highly efficient. Thus, this current study aims to use this fiber embedding approach to better understand embedded fiber networks. Specifically, we are interested in the network parameters that affect the “effective stiffness” of soft tissues.

METHODS

Network geometry. We consider Voronoi-based networks by discretizing a 3D unit domain using the Voronoi tessellation (Fig. 2A). Next, we isolate the cell edges, representing the individual fibers of the

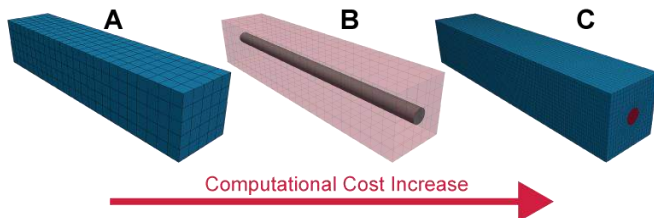


Figure 1: Modeling approaches for embedded fibers. (A) Continuum model. (B) Beam to solid coupling. (C) Full 3D model with matching discretizations.

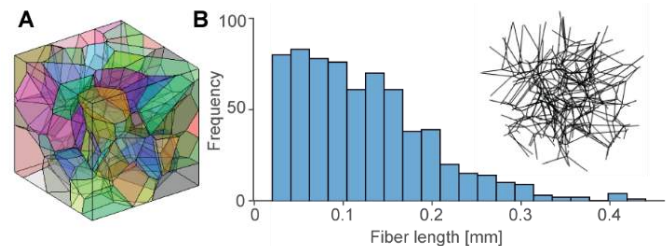


Figure 2: A) Voronoi tessellation of the unit cube. B) Network and fiber length distribution after applying min. length constraints.

network (Fig. 2B). Our pipeline can impose minimum fiber length constraints and generate networks with a target average connectivity $z < 4.0$, representing real semi-flexible polymer applications. To model fiber crimp, we introduce sinusoidal undulations on two normal axes of the cross-section. Finally, our pipeline iteratively removes any dangling or disconnected fibers.

Finite Element Model. We implement a mortar-type finite element method in Abaqus (SIMULIA, Providence, RI) as first described in [3]. We model individual fibers as spatial shear flexible (Timoshenko) beams and the surrounding matrix as an incompressible, hyperelastic material. We enforce the displacement coupling constraint through a Lagrange multiplier field using the penalty method.

RESULTS

To gain initial insight into how the effective stiffness depends on embedded fibers, we first investigate the simple case of a helical beam embedded in an isotropic, incompressible Neo-Hookean matrix under uniaxial extension (Fig. 3A). Note that the beam's cross-section is circular, and its material law is linearly elastic.

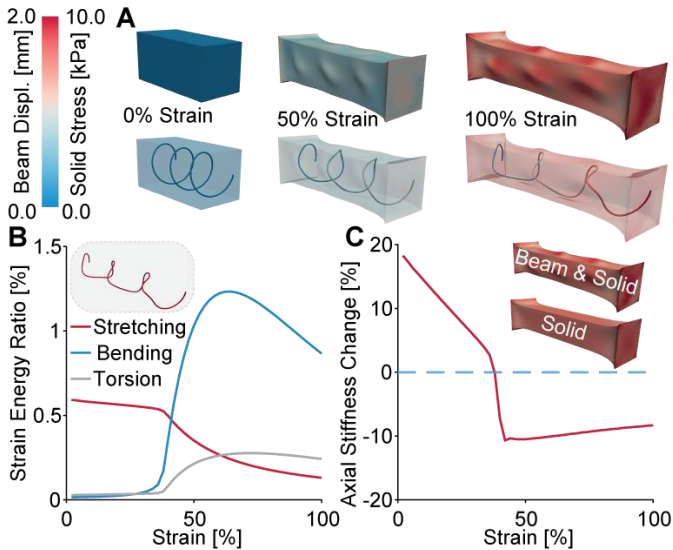


Figure 3: Embedded helical beam example. A) Beam displacement and solid stress fields. B) Beam strain energy components. C) Relative change of the axial stiffness of the embedded, coupled system with respect to the corresponding stiffness of the Neo-Hookean matrix without the embedded beam.

In particular, we examine the strain energy ratios of the beam at each strain level (Fig. 3B). Note that at approximately 40% strain, the dominant strain energy mode transitions from stretching to bending and torsional components. Fig. 3C illustrates the same transition in terms of the effective axial stiffness, as a %-relative change with respect to Neo-Hookean matrix without any embedded elements. Accordingly, even though the axial force always remains higher during the extension for the embedded/coupled model, the corresponding stiffness does not.

Fig. 4 illustrates our preliminary results of a Voronoi-based fiber network under simple shear (up to 40% shear strain), embedded in an isotropic, incompressible Neo-Hookean solid. Here, we introduced sinusoidal undulations of amplitude 5% and 10% of the straight fiber length (Fig 4A, B). In Fig. 4C & D we show that the increase in the undulation amplitude leads to a decrease in the effective shear stiffness.

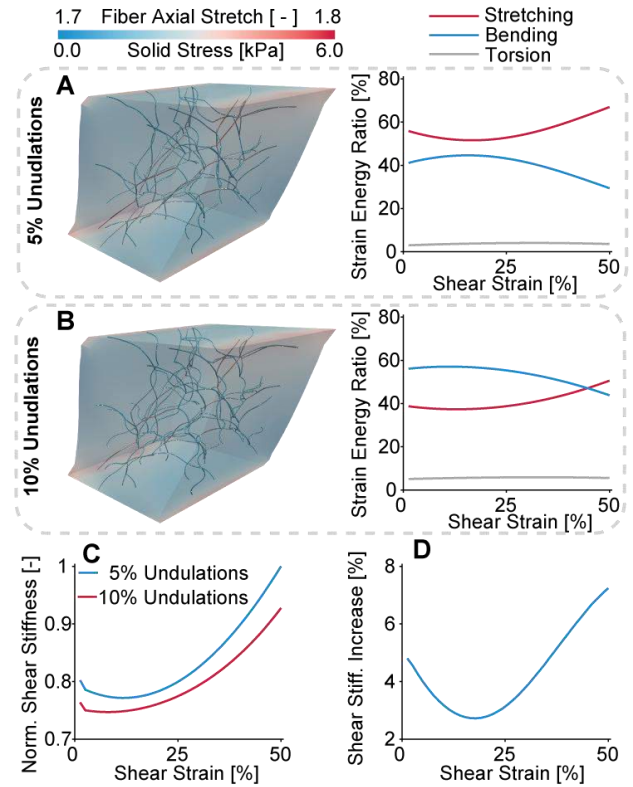


Figure 4: Embedded Voronoi-based networks. A), B) Fiber axial stretch, solid stress and beam strain energy ratios in cases of undulations with amplitude of 5% and 10% fiber length, respectively. C) Normalized shear stiffness for (A) and (B). D) Relative shear stiffness increase.

DISCUSSION

We presented a modeling approach to study the elastic behavior of embedded fiber networks. To this end, we used a coupling approach that allows embedding discrete fibers into an amorphous matrix without requiring matching discretizations. Our approach's main advantage is that we can change a microstructure's architecture without requiring the high computational cost of remeshing and solving a high-density (matching) matrix. For example, this enables investigating the effect of the fiber length, crimp, crosslinking, and fiber axial and bending stiffness on the global, effective stiffness. As we have shown in the example of the embedded helical beam, the fiber-beam kinematics and any instabilities caused by the interface forces may have a significant impact on the apparent stiffness. Furthermore, in the case of the networks, our preliminary results suggest that an increase in fiber crimp/undulations is associated with a decrease in the effective shear stiffness. The latter depends on the dominant beam strain energy component, namely the stretching energy (Fig. 4C, D).

In conclusion, our model is able to capture the effects of microstructural features on the effective stiffness of embedded networks in a computationally efficient manner.

REFERENCES

- [1] Sugerman G et al., *J Mech. Beh. Biom. Mat.*, 115:104216, 2021.
- [2] Kakaletsis S et al., *Acta Biomaterialia*, 123:154-66, 2021.
- [3] Holzapfel, G et al., *Phil Trans Royal Soc A*, 367:3445-3475, 2009.
- [4] Ban, E et al., *J Appl. Mech.*, 83(4): 041008, 2016.
- [5] Steinbrecher, I et al., *Comp Mech*, 66, pages 1377–1398, 2020.

REAL-TIME OPTIMIZATION OF THE TOTAL CAVOPULMONARY CONNECTION VIA REDUCED ORDER MODELING

I. Shah (1,2), F. Ballarin (3), T. Iliescu (4), O. San (5), L. Dasi (1), A. Wei (6), A. Veneziani (2)

- (1) Department of Biomedical Engineering, Georgia Institute of Technology, Atlanta, GA, USA
- (2) Department of Mathematics, Department of Computer Science, Emory University, Atlanta, GA, USA
- (3) Department of Mathematics and Physics, Università Cattolica del Sacro Cuore, Brescia, IT
- (4) Department of Mathematics, Virginia Tech, Blacksburg, VA, USA
- (5) Department of Mechanical and Aerospace Engineering, Oklahoma State University, Stillwater, OK, USA
- (6) Department of Biomedical Engineering, University of Massachusetts Lowell, Lowell, MA, USA

INTRODUCTION

The Fontan surgery is a common palliative treatment operation for children born with single ventricle malformations. The operation involves an artificial connection of the inferior vena cava (IVC) directly to the pulmonary arteries (PA), resulting in a cross-shaped graft known as the total cavopulmonary connection (TCPC). The TCPC allows for unidirectional flow of oxygenated and deoxygenated blood, preventing any mixing of the two in the ventricle. However, the surgery typically provides only short-term effectiveness, and in the long-term, several complications are commonly seen in patients such as pulmonary venous malformations (PAVMs) and exercise intolerance. Optimizing the shape of the TCPC for individualized patient-specific cases has previously shown to limit the severity of these complications.

Within the pre-operative planning strategy for patient-specific Fontan surgeries, computational fluid dynamics (CFD) has often been used to visualize and predict flow dynamics in the TCPC. This analysis, commonly known as surgical planning, allows for the examination of many different TCPC morphologies for the individual patient prior to surgery. This essentially represents a shape optimization problem, where the different potential anatomical connections between the IVC and the PAs results in unique flow dynamics. Traditionally, the most optimal TCPC geometry is determined by two factors: the hepatic flow distribution (HFD), and power loss (PL). Certain thresholds for both hemodynamic factors are known to be correlated with increased risk of post-operative complications, and thus clinicians often quantify these metrics for any potential TCPC geometry to aid in decision-making.

Although surgical planning and CFD simulations are effective in helping optimize the TCPC, the computational costs associated with simulating physiologically accurate conditions (unsteady Navier-Stokes, with time-dependent boundary conditions) becomes extremely expensive. This is especially true for repetitive testing of various patient-specific TCPC options in a trial-and-error manner, which may take several weeks or months to complete for a single patient [1-2].

To this end, many new methodologies have been introduced for reducing the computational costs of fluid dynamics modeling. One such approach is the idea of reduced order models (ROMs), which are a common *model-driven paradigm* used to simplify the governing full order model (FOM). ROMs are traditionally divided into two stages, the *offline* stage, where the computationally expensive FOM simulations are performed, and the *online* stage, where these results are recycled for a rapid, reduced order solution. This approach is in contrast to *data-driven paradigms* which have been more recently popular, such as neural network or artificial intelligence techniques.

The primary objective of this study is to develop an ROM framework using the Proper Orthogonal Decomposition (POD) approach coupled with trust-region optimization methods for real-time optimization of the TCPC geometry. Specifically, the POD-ROM will allow for a significant reduction in the computational costs of simulating finite element (FE) based CFD simulations with the TCPC. This may then be leveraged in the optimization problem for determining the optimal TCPC morphology, where the optimization criteria will be determined by the HFD to the left and right PAs (LPA, RPA).

METHODS

An initial reference geometry of an idealized 2D TCPC is generated, where specific points that dictate the inlet diameters of the superior vena cava (SVC) and the IVC as well as the offset between the two were parameterized as indicated by $\mu_0 \dots \mu_5$ in Fig. 1. Parabolic velocity profiles were prescribed at the inlets for each parameterized case, with the maximum velocity prescribed to be 100 cm/s at the SVC, and 50 cm/s at the IVC. Pressure boundary conditions were employed at the LPA and RPA ($P_{RPA} = 200 \text{ Pa}$, $P_{LPA} = 1000 \text{ Pa}$). 100 FE-based CFD simulations were performed in the offline stage using the parameterized geometries, from which a *snapshot* library of solutions was generated. Both the steady and unsteady forms of the Navier-Stokes equations (NSE) were simulated in each case, each creating separate snapshot libraries.

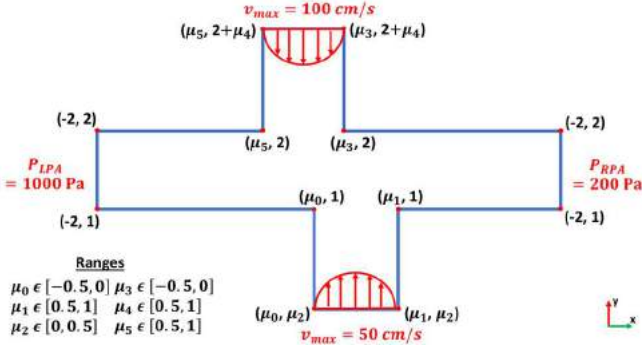


Figure 1: Idealized 2D TCPC reference geometry.

In the online stage of the ROM framework, a filtering step is first performed to reduce the redundancy found in the snapshot library. This is done via the *Singular Value Decomposition* (SVD) technique, which calculates the singular values and eigenvectors of the snapshot matrix. If a rapid decay is seen in the singular values, this indicates that the snapshot library can be well approximated by a small number of eigenvectors that are associated with the largest singular values. These select eigenvectors are then used in the POD approach to form the reduced basis functions. When substituted into the traditional linear system of equations that results from discretization of the NSE via the FE method (i.e. $Au = b$, where A is the stiffness matrix and b is the forcing terms), the final reduced order problem below is obtained [3].

$$W^T A W c = W^T b \quad (6)$$

In this reduced problem, the matrix $W^T A W$ is in the range of tens or hundreds of rows, and when compared to the stiffness matrix A , which is in the range of thousands or millions of rows, the savings in computational costs become evident.

The ROM framework is implemented utilizing the open-source model reduction library *RBniCS*, which automates all the above steps. The framework is then leveraged for the shape optimization problem. The optimization criteria implemented depends on the HFD, such that the TCPC shape optimization problem reads as follows: find a value for μ_0 and μ_5 that minimizes the functional J_{TCPC} under the constraints of the NSE, where J_{TCPC} reads as follows.

$$J_{TCPC} = \left(\int_{LPA} u \cdot n d\gamma - \frac{x}{100} Q \right)^2 \quad (6)$$

Here, μ_0 and μ_5 are the two parameters that directly control the offset between the IVC and SVC, and Q is the inlet flow rate from the IVC, with the fraction in front indicating the desired percentage of flow split from the IVC to the LPA in the optimal TCPC geometry. Specifically, two test cases were simulated, where x was chosen to be 45 and 75, which translates to finding the optimal TCPC morphology such that the HFD_{LPA} is equal to 55% and 25%, respectively. The optimization problem was implemented using the *Py-BOBYQA* library, a Python-based derivative-free trust-region method optimizer [4]. Each iteration of the optimizer calls the online stage, which allows for the real-time calculation of the optimal TCPC geometry. Local and global optimal solutions were calculated for the steady version of the framework.

RESULTS

The local optimal TCPC geometries generated from the ROM framework are shown in Fig. 2 for an HFD_{LPA} value of 55% (left) and an HFD_{LPA} value of 25% (right). In each case, the velocity streamlines are visualized, and the hepatic flow streamlines are shown in yellow. Visualization shows that the distribution of the hepatic flow streamlines match with the intended optimal HFD_{LPA} value that was prescribed in the framework, indicating that the ROM framework was successfully able to produce the optimal offset between the IVC and SVC for the

desired HFD_{LPA} value. The ROM results shown are also identical to FOM simulations with the same offset prescribed in terms of resultant velocities, flow distributions, and pressure contours.

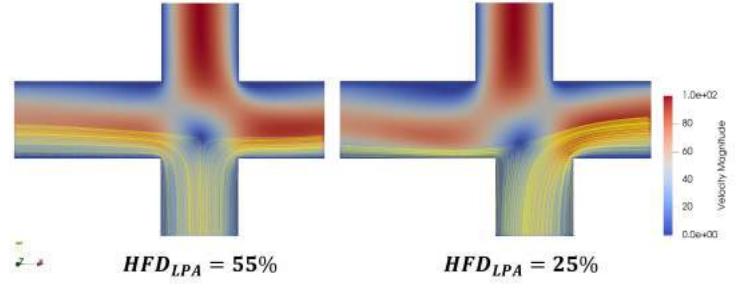


Figure 2: Optimal TCPC geometry for specified HFD values, with hepatic flow streamlines (yellow) from IVC.

The computational details for the optimization simulations via the ROM framework are summarized in Table 1. Both local and global optimal solutions were calculated, where the local solution differed depending on the initial guess chosen for the parameters μ_0 and μ_5 . In terms of computational time, local optimal solutions required approximately 15 minutes to compute, highlighting the real-time nature of the framework to produce the optimal TCPC morphology.

Table 1. Computational details of optimization simulations.

Optimization	Initial Guess	μ_0	μ_5	J	$\ \nabla J\ $	# of Evaluations	Wall Clock Time (min)
Local	[-0.1, -0.1]	-0.1129	-0.1041	3.93E-13	2.40E-05	32	about 15
Local	[-0.4, -0.3]	-0.275	-0.265	2.04E-16	1.70E-08	35	about 15
Global	[-0.49, -0.1]	-0.362	-0.4183	1.17E-17	2.80E-07	300	about 155

DISCUSSION

This study introduces a POD-based ROM framework that is leveraged for real-time shape optimization of an idealized 2D TCPC. The framework resulted in near real-time simulations (under 15 minutes) that were able to produce the optimal TCPC geometry for a desired HFD distribution towards the LPA, all while providing accurate and identical results as compared to traditional FOM CFD simulations. Such an approach may be able to provide critical information in terms of flow distributions and unique hemodynamics to clinicians in a rapid manner, all on local computational facilities. Although the framework shows increasingly promising results in performing this shape optimization of the TCPC, a significant limitation of this study is the use of idealized 2D TCPC geometries. To this end, we have begun adapting this framework towards 3D TCPC geometries, with the goal of eventually employing the framework for patient-specific models. To do this, more advanced shape optimization techniques will be required. Specifically, we are employing the free form deformation (FFD) and radial basis function (RBF) techniques, both of which allow for adaptive mesh morphing. Such techniques will be critical for use in the parameterization of the 3D geometry that occurs during the offline stage, as well as during the optimization problem.

In conclusion, the POD-ROM framework for shape optimization of the TCPC presented in this study allows for the identification of the optimal TCPC morphology for a given HFD value in a near real-time fashion. Further refinements are underway to translate the framework towards more physiologically accurate geometries.

ACKNOWLEDGEMENTS

Research was supported by NSF Project 2012254 (T. I.) – 2012255 (O.S.) – 2012286 (A.V.).

REFERENCES

- [1] Siallagan, D., et al., *J Thorac Cardio Surg*, 155:1734, 2018..
- [2] Yang, W., et al., *J Thorac Cardio Surg*, 143:1086-1097, 2012.
- [3] Hesthaven, J., et al., *Cert Reduced Batsis Methods for PDEs*, 2016.
- [4] Cartis, C., et al., *Optimization*, 71:2343-2373, 2021.

AN INEXPENSIVE, SHARED BIAXIAL DEVICE TO STUDY THE MULTISCALE MECHANICS OF SOFT MATERIALS

Alberto Madariaga (1), Chien-Yu Lin (1), Mrudang Mathur (2), Manuel K. Rausch (1,3,4)

(1) Department of Biomedical Engineering
University of Texas at Austin
Austin, TX, USA

(2) Department of Mechanical Engineering
University of Texas at Austin
Austin, TX, USA

(3) Department of Aerospace Engineering and
Engineering Mechanics
University of Texas at Austin
Austin, TX, USA

(4) Oden Institute for Computational
Engineering and Sciences
University of Texas at Austin
Austin, TX, USA

INTRODUCTION

The field of biomechanics is currently suffering from a reproducibility crisis. That is, biomechanical data on the same tissues often suffer from drastic uncertainty, especially when collected from different groups [1]. This uncertainty partially stems from inherent tissue variability, i.e., inter-subject variability [2]. However, we argue that in addition, the use of differing tissue storing protocols, loading conditions, and testing devices add to the uncertainty. As a result, comparing data between studies is usually difficult, if not impossible [3]. We submit that one critical step toward overcoming the current reproducibility crisis in biomechanics would be the use of the same device among groups – in addition to agreeing on common tissue storage and testing protocols. Our goal was, therefore, to provide such a device. That is, we designed a low-cost biaxial device made of mostly off-the-shelf parts and are planning to make this device openly available. Note, this device is also designed to allow the sample to be loaded and imaged simultaneously with different imaging modalities such as optical coherence tomography (OCT) or 2-photon microscopy. Thereby, the device not only enables the use of shared hardware among research groups, but it also lends itself to new, enriched biomechanical studies in which micro- and macro-properties of tissues can be characterized simultaneously. In summary, our goal is to construct an affordable, planar biaxial device to improve the accessibility of such devices and decrease data variability among groups.

METHODS

The objective of this study is to build a planar biaxial device that is inexpensive, easy to assemble, and composed largely of off-the-shelf parts, as depicted in Figure 1. To this end, the device consists of four linearized motor stages (X-LSM025A-E03, Zaber, Inc., Vancouver, British Columbia, Canada) and two load cells (LSB200, FUTEK, Inc.,

Irvine, California, USA). It employs 3D printable goosenecks to connect the motors and load cells to a rake system (CellScale, Waterloo, ON, Canada) by which the tissues are mounted. The base of the device is 3D printed and may be customized to fit under a variety of imaging modalities and different microscopy.

Furthermore, the setup also contains a mount for a high-resolution camera for digital image correlation (DIC) (UI-308xCP-C, IDS Imaging Development Systems, Obersulm, Germany). Additionally, the device includes a clear acrylic water bath to submerge tissues. The clearness of the bath permits the simultaneous use of DIC from underneath the bath and other imaging modalities from above such as OCT, as shown in

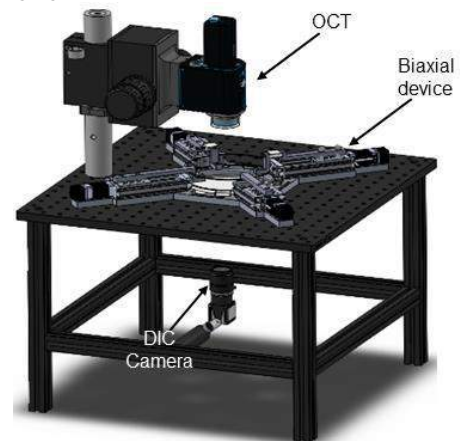


Figure 1. Imaging stage combining a camera for DIC, and an OCT device. Also shown is the miniature biaxial device that can be transferred between this station and a 2-photon microscope.

Figure 1. To hold the device, we built a table consisting of an aluminum breadboard (MB18) held up by a frame composed of 25 mm square construction rails (XE25L24) joined by construction cubes (RM1G), T-Nuts (XE25T1) and, low-profile channel screws (SH25LP38, ThorLabs, Inc., Newton, NJ, USA).

The software is written in LabVIEW (LabVIEW Version 20.0.1, National Instruments, Austin, TX, USA) and enables various loading protocols such as cyclic loading, step loading, stress relaxation, and individual control over each motor.

To test our device, we mechanically tested and imaged two representative soft, fibrous materials: mouse skin and electrospun polymer meshes. To collect the skin samples, we adhered to NIH's Guide for Care and Use of Laboratory Animals and all animal procedures described here were approved by the Institutional Animal Care and Use Committee at the University of Texas at Austin under #AUP-2020-00054. Following the humane sacrifice of the mice via CO₂ inhalation we excised 10 mm x 10 mm square samples of skin. We then speckled the samples with graphite powder for DIC-based strain tracking. Next, we mounted the tissue in our custom biaxial device and performed 20 cycles of preconditioning to 1000 mN and then performed one final equibiaxial loading cycle to 1000 mN. During testing, we halted the displacement, let the tissue stress relax, and then imaged the collagenous microstructure of these samples under a 2-photon microscope (Ultima IV, Bruker, Billerica, MA, USA) via second harmonic generation while being mounted in the device.

To make representative fibrous polymer meshes, we dissolved PCL in an 80:20 mixture of chloroform and dimethylformamide before doping the solution with 0.1 wt% rhodamine-B to create fluorescent fibers. We then used a custom electrospinning setup to spin the solution onto a copper plate at 15 kV, 25 cm distance, and a 20-gauge needle. We then cut out two 10 mm x 10 mm square samples of the meshes and mounted them on our custom device. Next, we again performed 20 cycles of preconditioning to 4000 mN followed by one equibiaxial cycle to 4000 mN. Finally, we imaged the fibrous microstructure of the electrospun meshes using a 2-photon microscope through the fluorescence produced by rhodamine-B.

RESULTS

We built a planar biaxial device for a total cost of \$15,728 and tested its versatility by recording biaxial, DIC, and 2-photon data. Figure 2A-B depicts representative skin (left column) and electrospun mesh (right column) samples mounted in our custom device. In addition, Figure 2C-E illustrates mechanical data collected with our device on both sample types, as well as 2-photon microscope images collected *in-situ*, i.e., while the samples were mounted on our device. From our tests, we found that skin samples exhibited classic nonlinear J-shaped constitutive behavior with more compliance in the cranial direction. While difficult to see from the raw images, fiber orientation analyses of the 2-photon data highlighted a higher orientation probability of collagen in the lateral direction, explaining the observed mechanical anisotropy. Similarly to the mouse skin, the electrospun PCL samples also exhibited nonlinear J-shaped constitutive behavior. However, its behavior was more isotropic. The 2-photon images of the electrospun mesh samples explain this mechanical isotropy by revealing a random fiber orientation. Overall, the device performed flawlessly and, through its simplicity and flexibility, allowed us to test two vastly different materials, while also allowing us to adapt it for use with a 2-photon microscope and DIC.

DISCUSSION

The field of biomechanics is currently dealing with a reproducibility crisis. To address this challenge, we designed a planar biaxial device that is easy to assemble, inexpensive, and composed nearly entirely of

off-the-shelf components. We chose a biaxial device because of its applicability to many soft tissues. In addition, by omitting two motors, this device can readily become a uniaxial testing device. The device's compatibility with multiple imaging modalities will also allow others to study the microstructure of samples *in-situ*. Thereby, the device provides an avenue to investigate the structure-function relationship of a variety of soft fibrous materials. The end-result is a versatile device capable of testing many kinds of tissues under different loading and imaging modes. In addition, commercial biaxial devices cost \$100,000 or more, making them inaccessible to many smaller labs and start-ups. Designing this device for a fraction of the price increases accessibility encouraging the use of the same device among research laboratories, minimizing variability due to device selection.

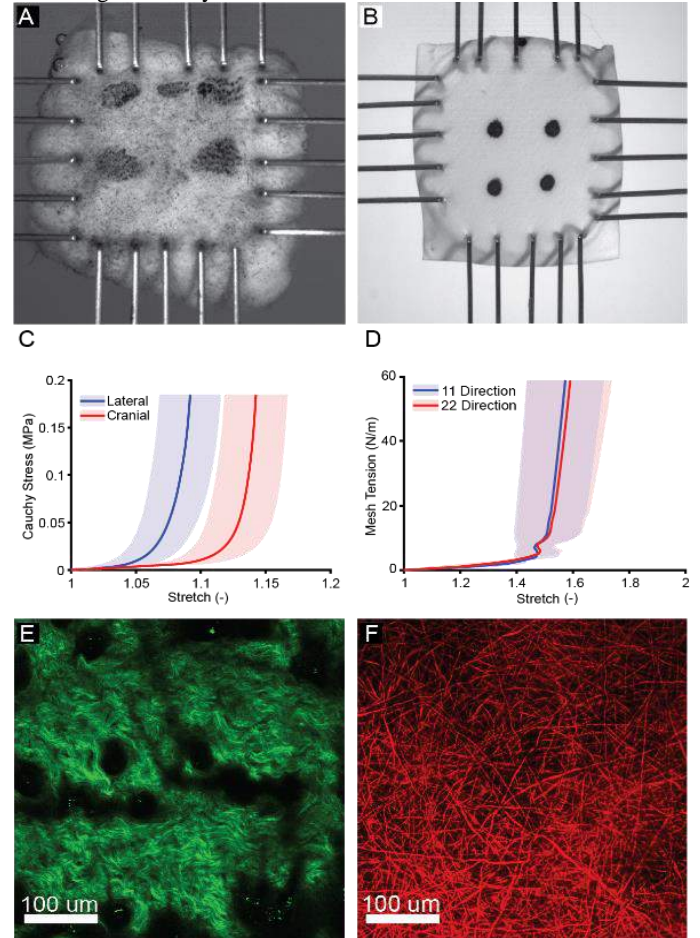


Figure 2. A) Mounted dorsal skin sample from young male mice. B) Mounted PCL electrospun mesh. C) Dorsal male equibiaxial stress stretch graph. D) Electrospun equibiaxial tension stretch graph. E) 2-photon image of mice dorsal skin. F) 2-photon image of electrospun mesh.

ACKNOWLEDGEMENTS

National Science Foundation (NSF) 2127925, 2105175, 2046148, 1916663

REFERENCES

- [1] Polio, S et al., *PLoS One*, 13: e0204765, 2018
- [2] Silver-Thorn, M et al., *IEEE Transaction on Rehabilitation Engineering*, 7: 268-277, 1999
- [3] Ramadan, S et al., *Biomedical Materials*, 12:025013, 2017

CYCLIC LOADING COMPARISON BETWEEN STANDARD ULTRA-HIGH MOLECULAR WEIGHT POLYETHYLENE BLOCKS AND BIOFIDELIC SOLID RIGID POLYURETHANE BLOCKS FOR ASTM PEDICLE SCREW TESTING

Jeremy G. Loss (1), Robb W. Colbrunn (1), Kevin J. Lawson, MD (2)

(1) Lerner Research Institute, Cleveland Clinic, Cleveland, Ohio, USA

(2) Department of Orthopedic Surgery, Ascension Medical Group, Saginaw, Michigan, USA

INTRODUCTION

Current pedicle screw compliance tests rely on ASTM standards to determine the durability of screws. However, ASTM testing is conducted using ultra-high molecular weight polyethylene (UHMWPE), which has a significantly higher density than spinal bones. It has been noted clinically that pedicle screws fail in patients at lower cycles of loading and with different modes of failure than what is seen in the ASTM standard. Conducting ASTM testing in materials with more physiological material properties may generate loading patterns more similar to those seen *in vivo*. In this study we investigated the influence of testing block material properties used in ASTM Standard F1717. We compared four solid rigid polyurethane blocks with differing material properties to the standard UHMWPE blocks. We hypothesized that, using the same loading profile, blocks with material properties more similar to human bone will fail at lower cycles and have different modes of failure compared to the UHMWPE blocks.

METHODS

All testing was completed by Element Materials Technology (Element Materials Technology, Fairfield, OH, USA) at their Cincinnati location. Testing was conducted in two stages and followed the “fatigue test” instructions provided in ASTM Standard F1717 with a constant load ratio (R) of 10. Briefly, compressive loads were applied using a sinusoidal profile where the ratio between the peak load and valley load was 10 (i.e. a peak load of 300 N and a valley load of 30 N). All loading is applied perpendicular to the superior and posterior faces of the blocks. In the first stage, four pairs of ultra-high molecular weight polyethylene (UHMWPE) blocks were made according to Figure 13 in ASTM Standard F1717 for lumbar pedicle screw testing. Each block was instrumented with 6.5 x 40 mm lumbar pedicle screws (Spine Wave, Shelton, CT, USA), and a block set was made by joining two blocks with titanium rods (Fig. 1). Each block set underwent fatigue testing at one of four different loads (250 N, 300 N,

345 N, and 375 N) for a runout of 5,000,000 cycles. Displacement (peak and valley values), Load (peak and valley values), number of cycles before failure, and failure mode (rod fracture, screw fracture, block fracture) were recorded for each set.

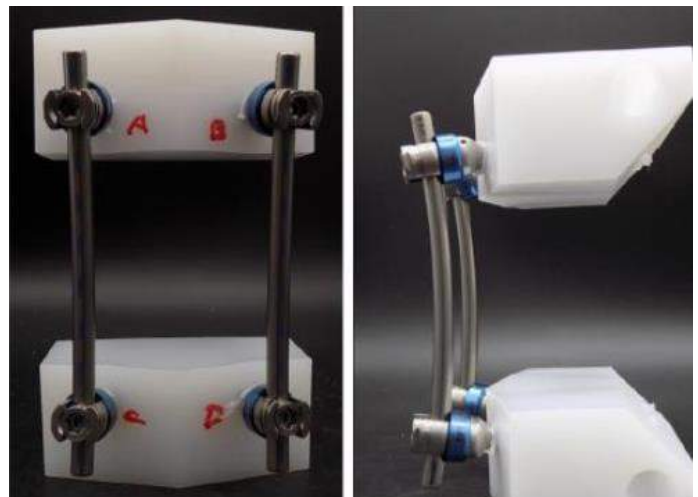


Figure 1: Sample block set featuring two UHMWPE blocks.

For the second stage, four pairs of solid rigid polyurethane foam (non-UHMWPE) blocks were procured from Sawbones (Sawbones, Vashon Island, WA, USA). Three block pairs had varying densities (15 pcf, 20 pcf, and 25 pcf) to simulate different quality of bone. The fourth block pair had a density of 20 pcf with an added 2mm layer of short fiber filled epoxy laminate to simulate the cortical layer of bone. Similar to the first stage, each pair of blocks were instrumented with lumbar pedicle screws and joined with titanium rods. The loading

condition for these four block sets was determined by selecting the largest load applied in the first stage to the UHMWPE blocks that led to runout (i.e. the fatigue testing ran to completion of 5,000,000 cycles). Displacement (peak and valley values), Load (peak and valley values), number of cycles before failure, and failure mode were recorded for each block set.

RESULTS

Table 1 outlines the number of cycles achieved before failure for both the UHMWPE and non-UHMWPE blocks. Based on the results of the first stage, a maximum load of 300 N was selected for the non-UHMWPE block sets in the second stage. Failure in the non-UHMWPE blocks occurred well before failure in the UHMWPE blocks, even though the UHMWPE blocks failed under higher loads.

Table 1: Cycle achieved for each block set prior to failure.

Test Block	Test Load (N)	Cycles
UHMWPE	250	5,000,000
UHMWPE	300	5,000,000
UHMWPE	345	539,430
UHMWPE	375	319,341
25 PCF	300	5,000,000
20 PCF	300	151,501
15 PCF	300	202,610
20 PCF + 2 mm laminate	300	197,078

For all 5 block sets that did not reach runout, mode of failure was rod fracture. The two UHMWPE block sets that failed had their rods break at the head of the pedicle screw while the rod failure in all three non-UHMWPE block sets occurred closer to the middle of the rod (Fig. 2).

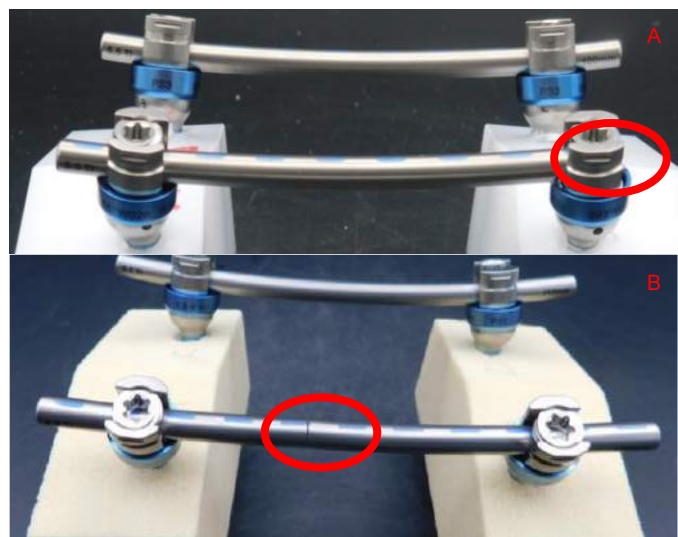


Figure 2. Failure location in the A.) UHMWPE and B.) Non-UHMWPE blocks.

With respect to average displacement of the blocks during fatigue testing, the three non-UHMWPE blocks with varied densities had similar average displacement (7.65 mm for 15 pcf, 7.28 mm for 20 pcf, and 7.28 mm for 25 pcf) to the UHMWPE block tested at 300 N (7.52 mm) (Fig. 3). However, the 20 pcf block with the 2mm laminate had a noticeably larger average displacement (9.34 mm) than the UHMWPE block tested at 300 N.

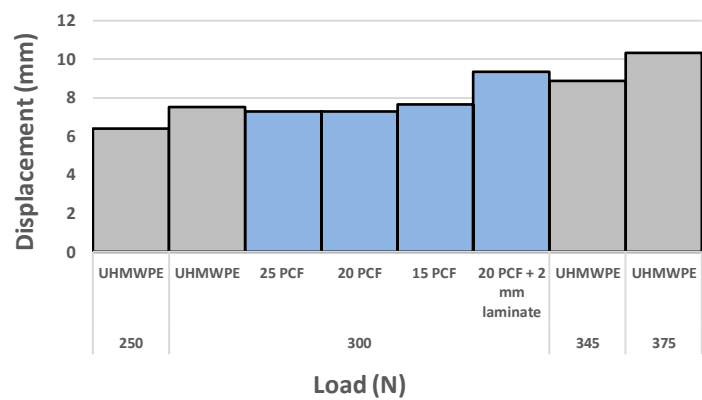


Figure 3. Average displacement during cyclic testing for each block set.

DISCUSSION

Our results indicate that the material properties used for the ASTM testing block influence the failure mode for pedicle screw testing. Focusing on the difference in average displacement, it is hypothesized that the laminate caused a pivot point for the pedicle screw that was not seen in either the UHMWPE or other non-UHMWPE blocks. This pivot point could account for the increased displacement seen in the laminate non-UHMWPE block and support anecdotal clinical findings of screws loosening by gaps formed at the tip of the screw in patients needing revision spine procedures. Based on clinical device failure modes and this biomechanical data, we believe that the substantial material property differences between UHMWPE and vertebral bone affects the loading characteristics and the durability of spinal fixation devices in clinical use. While UHMWPE testing can serve as a comparative measure between devices, the biofidelity may be insufficient to understand in vivo failure modes and loads.

SIGNIFICANCE

The difference in the numbers of cycles prior to failure and in average displacement between the UHMWPE blocks and the solid rigid polyurethane blocks calls into question the biofidelity of using UHMWPE blocks for ASTM pedicle screw testing. Future works can test additional non-UHMWPE blocks to increase sample size, delve deeper into alternative materials for pedicle screw testing, and advise new ASTM guidelines to better understand the strength of pedicle screws within the human body.

ACKNOWLEDGEMENTS

The authors would like to acknowledge SpineWave for supplying the pedicle screws and rods used throughout testing. Partial funding for this project was provided by the Field Neuroscience Institute.

ANATOMICAL LOCATION-SPECIFIC QUANTIFICATION OF TISSUE COMPOSITION OF PERIVASCULAR ADIPOSE TISSUE

D. McClintock (1), E. Flood (2), S.W. Watts (2), W. Jackson (2), S. Roccabianca (1)

(1) Department of Mechanical Engineering, Michigan State University, East Lansing, MI, USA
(2) Department of Pharmacology and Toxicology, Michigan State University, East Lansing, MI, USA

INTRODUCTION

Remodeling of the vascular tunics has been identified as a contributing factor to increased arterial stiffness in aging and hypertension. Arterial stiffness is an independent risk factor for stroke, heart disease, and cognitive decline [1-5]. Although perivascular adipose tissue (PVAT) is recognized as an essential layer of the functioning vasculature, few studies have quantified its composition in health and disease. Here, we introduce the novel idea that the composition of load-bearing constituents in PVAT remodels in hypertension, much like that of the arterial wall.

METHODS

We analyzed the collagen composition of the thoracic aorta and its surrounding PVAT of six Dahl SS rat, half fed a control diet and half fed a high-fat diet. This is recognized as an established model of adiposity-driven hypertension [6]. A 2-photon microscope was used to image the histology samples stained with picrosirius red (PSR) for visualizing collagen. The intensity of each pixel ranged from 0 to 255, correlating with increasing collagen density. To quantify the collagen content in a reliable and reproducible way, we developed a custom algorithm in Python. To consider variations due to the anatomical location, the samples were analyzed using a polar coordinate system, i.e., considering a radial and an angular direction (Fig. 1).

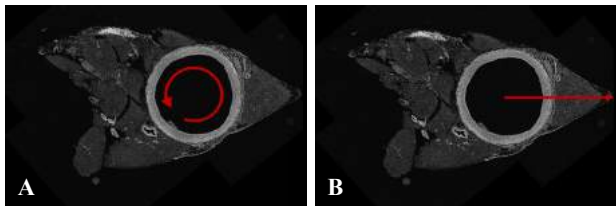


Figure 1: Coordinates based on thoracic aorta geometry A) angular direction, θ B) radial direction, r

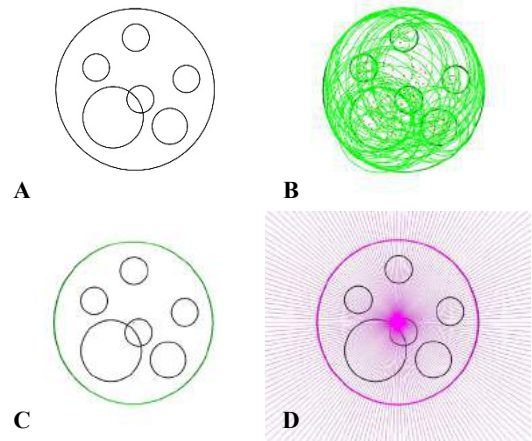


Figure 2: A) Calibration image. B) Circle detection. C) Circle selection. D) Lines for intensity profile every 2 degrees about the aortic center.

Angular zero was set at the symmetry axis of the ventral PVAT strip (Fig. 1B) and radial zero was placed at the geometric center of the aortic lumen (identified using a circle detection function in Python, shown in Fig. 2). Every two degrees about the center of the aorta (Fig. 2D), the intensity profile was recorded in the radial direction and stored in a data frame. This allows us to unravel the arterial wall and represent the data collected in a cartesian reference system (Fig. 3 and 4), representing the angle on the horizontal axis and on the vertical axis the normalized radius calculated as

$$\text{normalized radius} = \frac{\text{radius}}{\text{average lumen radius}} \quad (1)$$

For this study, pixel values equal to or above 100 were identified as collagen, while values of 25 or below were considered background noise. Thus, the lumen radius was identified at each angle as the first pixel with a value at or above 100 (represented by the bold line in **Fig. 3**). The interface between the arterial wall and PVAT at each angle was then identified by, first, taking the derivative over periods of 5 pixels in the radial direction. The derivatives of each angle were then smoothed using a convolution integral. Finally, the interface between the arterial wall and PVAT was located where the largest negative derivative occurred, signifying a large change in pixel value (represented by the bold line in **Fig. 4**).

With the arterial wall and PVAT borders identified, the fractional area of collagen was calculated as the number of pixels with values over 100, over the total of the non-background pixels in each region.

$$\text{fractional area} = \frac{\text{pixels} \geq 100}{\text{pixels} > 25} \quad (2)$$

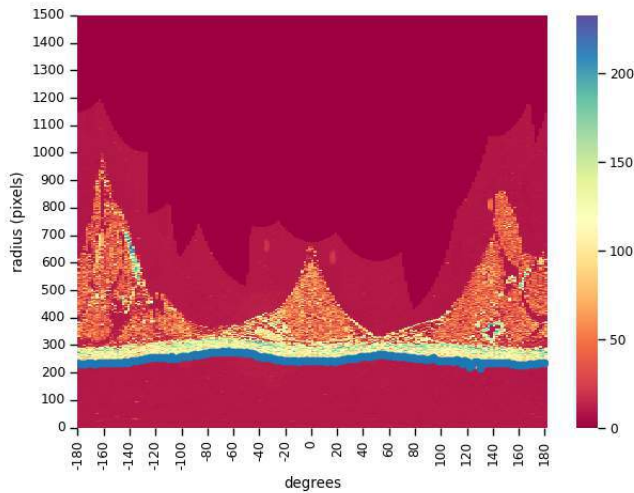


Figure 3: Analysis of the PSR histological image of a representative control diet sample of the thoracic aorta + PVAT with lumen detection.

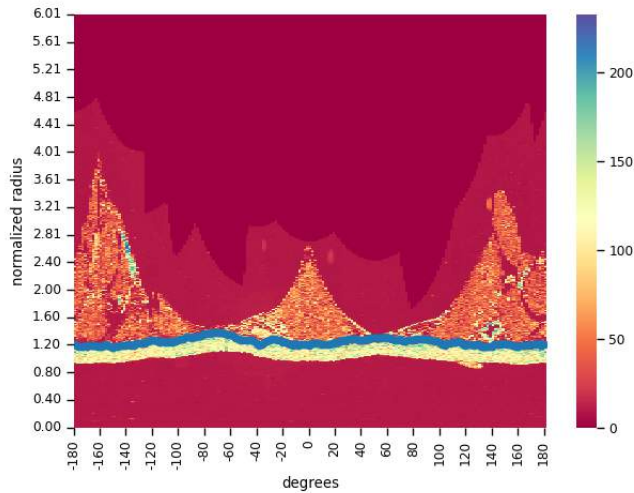


Figure 4: Analysis of the PSR histological image of a representative control diet sample of the thoracic aorta + PVAT with thoracic aorta-PVAT interface detection.

RESULTS

There was no statistically significant difference between the collagen content of the control and high-fat diet thoracic aortas. There was a statistically significant difference between the left dorsal strip of the PVAT between control and high-fat diet samples. These results suggest that there may be location-specific remodeling associated with hypertension in the extracellular matrix of the PVAT surrounding the thoracic aorta.

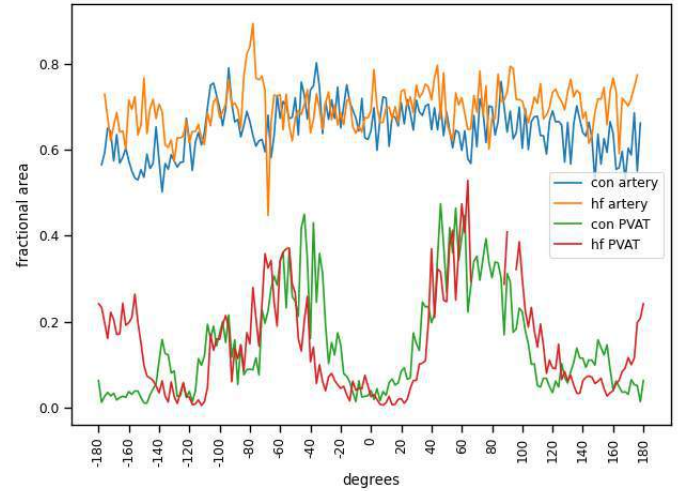


Figure 5: Average fractional area of thoracic aorta collagen and PVAT collagen for three control and three high-fat diet samples.

DISCUSSION

Through the histology image analysis of the thoracic aorta with perivascular adipose tissue, we were able to analyze the distribution of collagen in six Dahl SS samples. Comparing control and high-fat diet PVAT, there was a statistically significant difference in the collagen fractional area of the left dorsal strip. No other significant differences were found with the current small sample size for this study.

ACKNOWLEDGEMENTS

This research was supported by grant number P01HL15951 from the National Heart, Lung, and Blood Institute, National Institutes of Health.

REFERENCES

- [1] Seghal, N et al., *Frontiers in Physiology*, 6:355, 2015.
- [2] Chirinos, J et al., *Journal of the American College of Cardiology*, 9: 1237-1263, 2019.
- [3] Humphrey, J and Tellides, G, *American Journal of Physiology-Heart and Circulatory Physiology*, 316:H169-H182 2019.
- [4] Kaess, B et al., *JAMA*, 308:875, 2012.
- [5] Oh, Y et al., *Circulation Research*, 121:1216-1218, 2017.
- [6] Grobbl, MR et al., *Experimental Mechanics*, 61(1):191-201.

TARGETING THE CHROMATIN REMODELING IN MESENCHYMAL STROMAL CELLS UNDER HYPER OXIDATIVE STRESS FOR MAINTAINING CELL PHENOTYPE AND VIABILITY

Lauren A, Monroe (1,3), Samantha Kaonis (1,3), Neda Kabi (1,3), Abigail Fennell (1), Jack Forman (1,3), Soham Ghosh (1,2,3,4)

- (1) School of Biomedical Engineering, Colorado State University, Fort Collins, CO, USA
(2) Department of Mechanical Engineering, Colorado State University, Fort Collins, CO, USA
(3) Translational Medicine Institute, Colorado State University, Fort Collins, CO, USA
(4) Cell and Molecular Biology Program, Colorado State University, Fort Collins, CO, USA

INTRODUCTION

Mesenchymal stromal/ stem cells (MSC) are one of the most promising candidates for a myriad of cell therapy applications because of their multifunctional regenerative properties. Despite showing promise for numerous preclinical studies, MSC based therapies are not yet a reality for regenerative medicine due their suboptimal outcome at the clinical endpoint. During degenerative disease and aging, the cell niche turns into a microenvironment characterized by hyperoxia produced by high amounts of reactive oxygen species (ROS). Therefore, MSC are exposed to a high amount of ROS in their natural environment in disease and aging, and post implantation in the degenerated tissue. ROS is known to cause cell damage at various cellular compartments including the DNA that can alter the functionality and viability of cells. Using isolated DNA, it was previously reported that upon exposure to the ROS, chromatin remodeling occurs which protects the chromatin over a short timeframe post ROS exposure [1]. However, it is largely unknown what the key regulators are in chromatin remodeling and what effect chromatin remodeling has on the cell phenotype and viability in the longer timeframe. Such information is relevant for understanding the cell functionality in their natural environment and upon implantation in aged and diseased tissues characterized by a high amount of hyper oxidative stress.

In this study our objective is (i) characterize what changes the chromatin of MSC undergoes upon exposure to hyperoxia, (ii) to identify a key molecular regulator of such chromatin level changes and (iii) finding a potential intervention strategy for maintaining cell viability on a longer timeframe upon the ROS exposure. We utilized an *in vitro* model of cell exposure to hydrogen peroxide and confocal microscopy imaging to accomplish the objectives. We hypothesized that the chromatin remodeling complex (CRC) SWI/SNF (SWItch/ Sucrose Non-Fermentable) is a critical component for the chromatin remodeling during the cell exposure to ROS and is a potential target to minimize the chromatin remodeling mediated damage in cells.

METHODS

Cell culture: Human bone-marrow derived passage 4 MSC (Lonza) was used for all experiments. **Characterization of chromatin remodeling:** MSC were stained with Nucblue, a live DNA stain. Cells were exposed to 500 μ M hydrogen peroxide. Subsequently, the MSC nuclei were imaged at a high-resolution using time lapse laser scanning confocal microscopy (Zeiss LSM 980) while cells were maintained in an incubation chamber. An in-house image registration algorithm was created, validated, and applied to calculate the Chromatin Remodeling Index (CRI: unit is pixels) at every pixel, thus providing a spatiotemporal map of chromatin remodeling. The CRI was further averaged over each chromatin region - euchromatin, heterochromatin, and interchromatin to quantify the spatially averaged CRI at different intranuclear domains. **Inhibition of chromatin remodeling:** GSK126 (10 μ M) was used to indirectly block ARID1A and hence, chromatin remodeling through inhibiting EZH2 methyltransferase. **Immunofluorescence:** DNA damage was assessed by an antibody targeting the DNA damage marker γ -H2AX. Cell damage was assessed through the F-actin staining by phalloidin. **Statistics:** T-tests were used for all statistical analysis. Sample sizes are reported in the figures.

RESULTS

First, we wanted to characterize the effect of ARID1A inhibition for 3 days on the MSC phenotype and proliferation. Cell proliferation was found to decrease (Figure 1A) when they were exposed to the pharmacological agent GSK126 indicating ARID1A was inhibited. SWI/SNF CRC including ARID1A is necessary for cell division, specifically during the chromatin condensation in the metaphase and anaphase periods of cell division. However, ARID1A inhibition almost doesn't have any effect on the cell and nuclear phenotype (Figure 1B) and the cell viability (data not included: found by calcein AM and Ethidium Bromide based viability assay). The cytoplasm structure was maintained (Figure 1A) and stress fiber formation was not affected.

Therefore, this data suggests that GSK126 treatment does not affect the MSC phenotype in the prophase period.

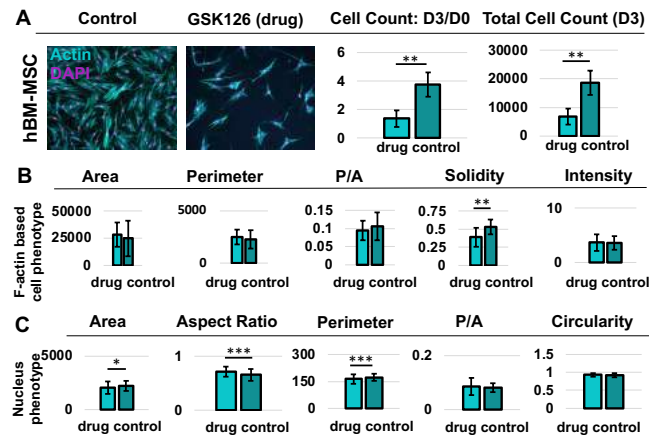


Figure 1. Characterization of cell and nuclear phenotype and the cell proliferation on the application of 10 μ M GSK126 (ARID1A inhibitor). (A) GSK126 treatment decreases cell proliferation. (B) Cell phenotype after GSK126 treatment on day 3. (C) Nuclear phenotype after GSK126 treatment on day 3. * p <0.05, ** p <0.01, *** p <0.0001. Error bars: SD. Based on n > 500 cells/ group.

Next, we visualized the effect of hydrogen peroxide treatment on the nuclear and cell shape. 500 μ M hydrogen peroxide is a physiological level of hyperoxia cells undergo *in vivo*. The Nucblue stained nuclei and time lapse images revealed that nuclei undergo rapid change in their shape and area (Figure 2). The cell shape also changes during this period (revealed from bright field images) because the nucleus is connected to the cytoskeleton through the nuclear envelope. Interestingly, the pretreatment of cells by the inhibition of ARID1A significantly decreases such drastic change in nuclear and cell shape (Figure 2).

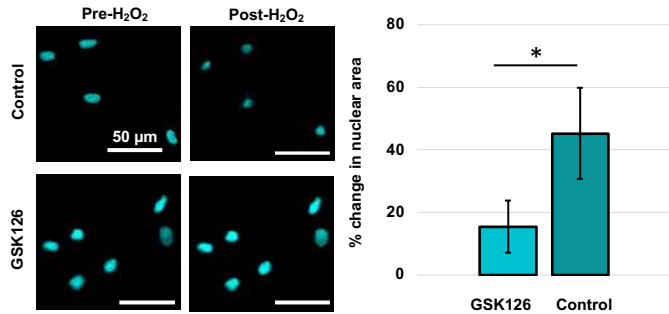


Figure 2. Effect of hydrogen peroxide treatment and ARID1A inhibition on nuclear area change. * p <0.0001. n > 20 cells/ group.

High resolution imaging of the chromatin revealed that hyperoxia causes rapid chromatin remodeling (Figure 3) which starts at around 20 min after H₂O₂ treatment and continues until 80 min in all chromatin regions - heterochromatin (HC), euchromatin (EC) and interchromatin (IC): interface of EC and HC. ARID1A is indeed required for the chromatin remodeling as shown by the spatiotemporal CRI maps (Figure 3A) and CRI values over time in the 3 chromatin regions (Figure 3B). This data reveals that SWI/SNF CRC is required for the chromatin remodeling post exposure to hydrogen peroxide.

Previous studies with isolated DNA suggested that nanoscale chromatin reorganization occurs after DNA damage [1]. We wanted to understand how much DNA and cell damages are incurred after the MSC exposure to 500 μ M H₂O₂ treatment for 90 minutes.

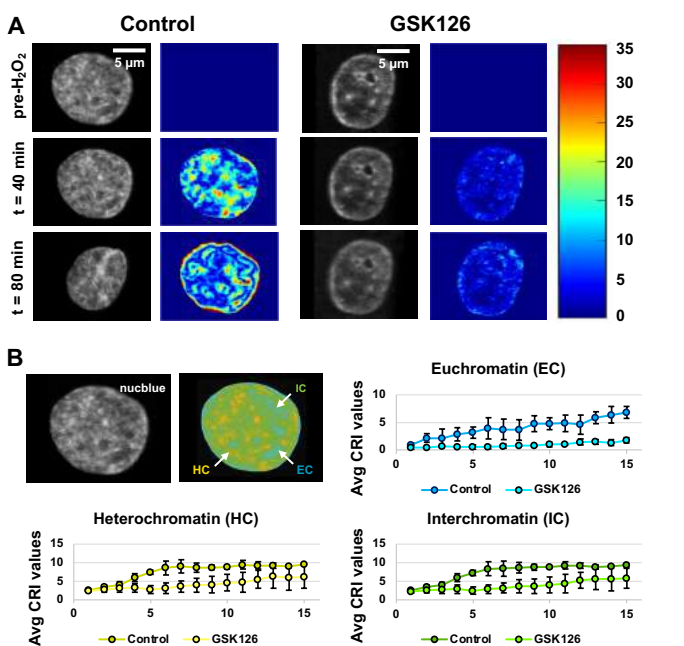


Figure 3. Time lapse visualization of chromatin remodeling and calculation of CRI. (A) MSC nuclei and CRI maps over 80 minutes on 500 μ M H₂O₂ treatment. Color bar indicated the CRI value (unit: pixel). (B) Temporal evolution of average CRI values in each intranuclear domain. Based on n > 4 cells/ group. * p <0.05, ** p <0.01

We found that GSK126 treatment only does not result in DNA damage (Figure 4: control vs GSK126 groups) after 90 minutes of H₂O₂ treatment. Treatment of MSC with H₂O₂ increases the DNA damage after 90 minutes (stronger green signal in H₂O₂ and H₂O₂+GSK126 groups). However, 24 hours after the removal of the H₂O₂ the DNA damage level is same in all groups but cytoskeleton is almost destroyed in H₂O₂ group while it is preserved in the H₂O₂+GSK126 group.

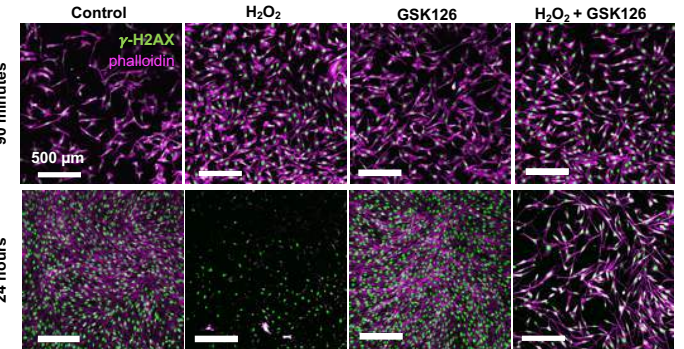


Figure 4. Effect of hydrogen peroxide and GSK126 on the DNA damage in short term (90 minutes after hydrogen peroxide treatment) and longer term (24 hours after 90 minutes treatment of hydrogen peroxide).

DISCUSSION

We identified a key regulator of chromatin remodeling upon hyperoxia using MSC. Our future work will include the pretreatment of MSC with the blocking of chromatin remodeling before the injection of MSC in the degenerated and hyperoxic tissues.

REFERENCES

[1] Liu, B et al., *Curr Genomics*, 13:533-547, 2012.

THE MTOR INHIBITOR RAPAMYCIN DECREASES SUBCHONDRAL THICKNESS AND AFFECTS VARIABILITY IN THE TIBIAL PLATEAU OF COMMON MARMOSETS

Michael D. K. Focht (1), Dennis M. Minton (2,3), Adam B. Salmon (4,5), Adam R. Konopka (2,3), Mariana E. Kersh (1,6)

(1) Department of Mechanical Science and Engineering, University of Illinois at Urbana-Champaign, Urbana, Illinois, USA

(2) Department of Medicine, University of Wisconsin-Madison, Madison, Wisconsin, USA

(3) Geriatric Research and Education Center, William S. Middleton Memorial Veterans Hospital, Madison, Wisconsin, USA

(4) Sam and Ann Barshop Institute for Longevity and Aging Studies, University of Texas Health San Antonio, San Antonio, Texas, USA

(5) Geriatric Research Education and Clinical Center, Audie L. Murphy Hospital, South Texas Veterans Health Care System, San Antonio, Texas, USA

(6) Beckman Institute for Advanced Science and Technology, University of Illinois at Urbana-Champaign, Urbana, Illinois, USA

INTRODUCTION

Osteoarthritis (OA) is a degenerative joint disease characterized by aberrant changes in subchondral bone remodeling (increased subchondral thickness, density, or both) [1]. While there is not a cure for OA, pharmaceutical interventions continue to be explored including the use of rapamycin. Human and animal models of OA demonstrate increased activity of the mechanistic target of rapamycin (mTOR) [2] and inhibition of mTOR by rapamycin can attenuate OA severity in surgical mouse models [3]. However, it is unknown if rapamycin can modify features of naturally occurring OA—the most common form of OA in older humans. Marmosets are small, short-lived non-human primates that develop OA naturally—an ideal model system. The aim of this study was to determine how age and rapamycin treatment affect subchondral bone architecture of the common marmoset knee.

METHODS

Sample Preparation and Imaging: Fifty-five marmosets (31M/24F, mean age = 9.5 ± 4.2 years) were analyzed. They were housed in male-female pairs at the University of Texas Health Science Center at San Antonio and the males were vasectomized. The marmosets were divided into two groups: control ($n = 35$) and rapamycin-treated ($n = 20$). The treated group received 1mg/kg/day of eudragit-encapsulated rapamycin dissolved in yogurt and the controls received empty eudragit encapsulation in yogurt [4]. At necropsy, hind limbs were collected, fixed in 10% neutral buffered formalin, and then stored in 70% ethanol. The knees were micro-CT scanned using a Rigaku CT Lab GX130 (isotropic voxel size = $50 \mu\text{m}$). Study staff were blinded to the treatment allocation and all subject characteristics.

Image Processing: Micro-CT data were binarized using a consistent attenuation threshold and the femur and tibia were separated into individual image stacks in Amira (v2021.2). Anatomical landmarks were used to identify the subchondral regions (Fig 1).

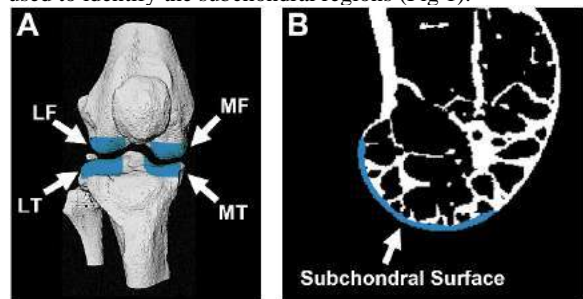


Figure 1: A) 3D micro-CT rendering of a representative marmoset knee (four subchondral surfaces analyzed in blue). L = lateral, M = medial, F = femur, and T = tibia. B) Sagittal view of a femoral condyle (subchondral surface in blue).

The subchondral bone was segmented from the underlying trabecular bone using our previously validated algorithm [5]. Three hydroxyapatite (HA) phantoms were included in all scans and used to convert Hounsfield units to apparent HA density. Three-dimensional thickness and density maps of the subchondral surfaces were created using ImageJ (BoneJ plug-in) [6] and custom MATLAB code (R2021a). Four regions of subchondral bone were analyzed: the lateral and medial condyles of the femur and tibia (Fig 1). The subchondral surfaces were spatially normalized to account for morphological differences between subjects and visualize the average thickness and density for each group.

Statistical Analysis: Kolmogorov–Smirnov tests were used for comparisons. We calculated the median and median absolute deviation (MAD) of thickness and density per subchondral region per subject to measure the central value and variability of the data, respectively. Statistical analyses were done in R with a type one error rate of $\alpha = 0.05$.

RESULTS

Thickness: Rapamycin significantly affected subchondral thickness of the lateral tibia. Specifically, the median subchondral thickness was 11% lower ($p < 0.05$) in the rapamycin-treated marmosets (0.32 mm) than the controls (0.36 mm) (Table 1). The subchondral thickness of the lateral tibia had 38% less variability ($p < 0.01$) in the rapamycin-treated marmosets than the controls. Neither age nor sex had a significant effect on thickness. Local differences in thickness were observed with heat maps of the subchondral surface (Fig 2).

Density: Rapamycin did not affect median subchondral bone density (Table 1). However, subchondral bone density of the medial tibia had 24% more variability ($p < 0.01$) in the treated marmosets than the controls. Neither age nor sex had a significant effect on density.

Table 1: Median and MAD of the thickness and density for the control and rapamycin-treated groups (* p-value < 0.05, ** p-value < 0.01). Lat = Lateral and Med = Medial.

	Bone	Side	Thickness (mm)		Density (mg HA/cm³)	
			Control	Rapamycin	Control	Rapamycin
Median	Femur	Lat	0.39	0.37	619	633
		Med	0.40	0.38	642	665
	Tibia	Lat	0.36	0.32*	606	626
		Med	0.39	0.40	684	717
MAD	Femur	Lat	0.07	0.08	79	75
		Med	0.06	0.06	58	59
	Tibia	Lat	0.08	0.05**	83	78
		Med	0.06	0.06	70	87**

DISCUSSION

Osteoarthritis of the knee is commonly associated with subchondral sclerosis [1]. Thus, thicker and/or denser subchondral surfaces are

indicative of osteoarthritis. Here we used marmosets, a natural aging model of OA, to evaluate the effect of rapamycin on subchondral bone and found that rapamycin decreased subchondral thickness (Fig 2).

Surprisingly, rapamycin only significantly affected subchondral thickness of the lateral tibia. This may be related to the biomechanical usage of the marmoset knee. Marmosets spend much of their time squatting, unlike humans, who are primarily upright while the knee is loaded. During knee flexion, the center of pressure on the femoral condyle varies, whereas tibial loading tends to stay within the same plateau region. We hypothesize that more consistent loading of the tibia could lead to increased bone remodeling as compared to the femur.

One limitation of our study is the sample size ($N = 55$), which does not allow us to fully analyze how age and sex interact with rapamycin treatment. Also, there is some subjectivity with the identification of bony landmarks, from which the subchondral regions are defined. Nonetheless, the ability to co-register the datasets provided a unique ability to visualize the average thickness and density across the entire articular surface and gave insight into the spatial changes in response to rapamycin. Indeed, rapamycin decreased thickness in most regions of the tibial plateau, suggesting a robust response to treatment. Our results show that inhibition of mTOR by rapamycin may prevent OA-related subchondral sclerosis. Continued work using natural animal models of OA, as done here, will lead towards improvements in our understanding of the causes and treatment options for osteoarthritis.

ACKNOWLEDGEMENTS

This work was supported by funding from the National Institutes of Health (R21 AG067464). Marmoset samples were collected at the San Antonio Nathan Shock Center of Excellence in the Basic Biology of Aging in San Antonio, TX, and micro-CT scans were taken at the Beckman Institute in Urbana, IL.

REFERENCES

[1] Felson, DT, *The New England Journal of Medicine*, 354:841-848, 2006. [2] Zhang, Y et al., *Annals of the Rheumatic Diseases*, 74:1432-1440, 2015. [3] Caramés, B et al., *Annals of the Rheumatic Diseases*, 71:575-581, 2012. [4] Tardif, S et al., *The Journals of Gerontology Series A: Biological Sciences and Medical Sciences*, 70:577-588, 2015. [5] Ang, IC et al., *IEEE Transactions on Biomedical Engineering*, 67:924-930, 2020. [6] Doube, M et al., *Bone*, 47:1076-1079, 2010.

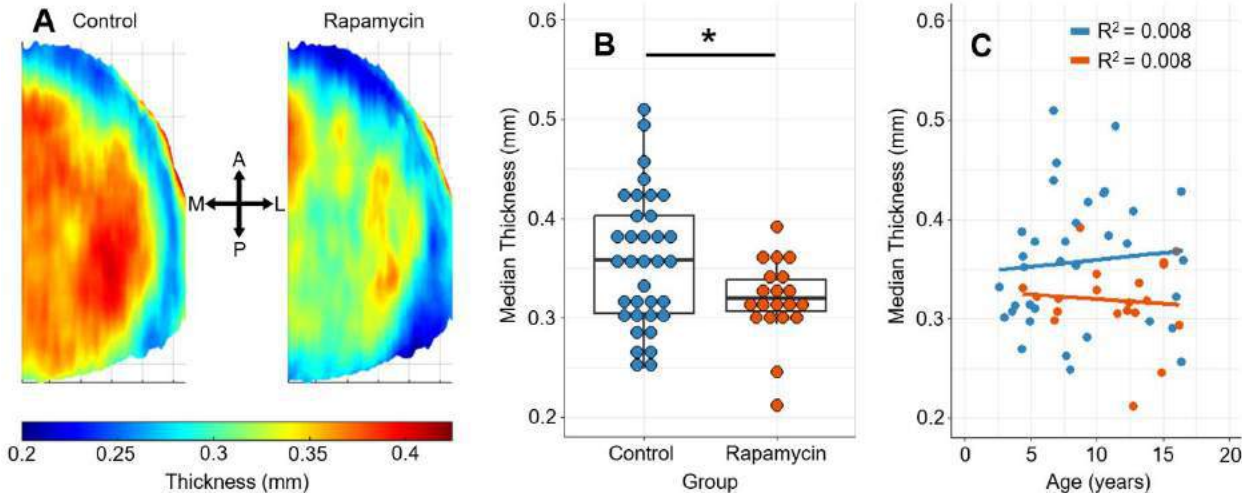


Figure 2: Lateral tibia thickness comparisons for the control and rapamycin-treated groups. A) Mean thickness maps with A, P, M, and L denoting the anterior, posterior, medial, and lateral anatomical directions respectively. B) Box plots with each dot representing the median subchondral thickness of the lateral tibia for an individual marmoset (* p-value < 0.05). C) Scatter plots of median thickness vs. age with lines of best fit for each treatment group.

IT TAKES A VILLAGE: CATALYZING CLINICALLY-DRIVEN UNDERGRADUATE DESIGN PROJECTS AT THE NEXUS OF ENGINEERING, MEDICINE AND BUSINESS

Byron D. Erath, Laurel Kuxhaus

Mechanical and Aerospace Engineering, Clarkson University, Potsdam, NY USA

INTRODUCTION

Design projects offer unparalleled opportunity for students to synthesize their classroom knowledge and wrestle with the unpredictable nature of real-world problems that often involve competing optimization criteria. In essence, design projects are a gateway to useful problem solving in the real world, while simultaneously serving as a meaningful introduction to the research process. For assistive technology concepts to become market-ready solutions, incorporation of engineering, clinical, and business perspectives is essential.

Prior literature has described tools and techniques for identifying clinically-relevant projects that need engineering solutions [1], global student collaborations [2] and the importance of design projects as a vehicle to meet ABET goals. [3]

There are substantial challenges endemic to such 3-way collaborations, particularly at the undergraduate level. For example, at Clarkson University although the graduate health sciences programs encourage (and in some cases require) participation in research, those programs run on a quarter system that is not well-aligned with the undergraduate semester. A further complication is that capstone courses in business programs (such as Engineering & Management) and health sciences have substantially different learning outcomes from those in engineering design courses. This same problem often arises even when organizing design teams from different engineering disciplines.

This abstract presents outcomes from 12 undergraduate design team projects in biomedical engineering that was implemented over 6+ years at Clarkson University. We present strategies for overcoming common obstacles such as those described above, as well effective approaches for catalyzing cross-disciplinary collaborations in undergraduate design projects.

METHODS

Our approach was to create interdisciplinary design teams including undergraduate students in engineering (primarily mechanical engineering, and mostly those enrolled in Clarkson's biomedical engineering minor), students in health sciences (those pursuing PA, PT, or OT graduate degrees), and business to tackle clinically-motivated meaningful design projects to improve quality of life for persons with disabilities. All students earned course credit for their work, whether it fulfilled a major requirement (e.g., capstone design) or an elective requirement. Given critical mass of students and faculty, our process typically ran in parallel with the Mechanical Engineering capstone design courses in which students chose teams and projects near the end of the first semester, with the bulk of project work being done in the second semester. We recruited clinical and business students through faculty networks and email advertisements, including through the University's Honors program. The development of this design strategy was supported by NSF (#1510367, Walking and Talking: Improved Quality of Life Through Enhanced Mobility and Communication; original PI Kuxhaus).

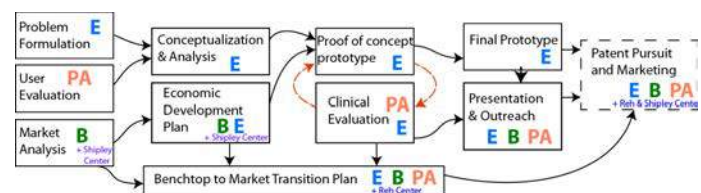


Figure 1: Idealized workflow (E=engineering; B = business; PA = PA/clinical students)

Student teams included at least one clinical student (PT, OT, or PA) and at least one business student to more realistically model the R&D process. In pursuit of the idealized workflow (Figure 1), each team

performed a needs assessment, product ideation and design, and made a prototype, while intertwining clinical relevance, human subject research, and marketing activities throughout. At least one trainee continued the research and development (including refinement) of promising projects; this often included an intensive summer period, with some continuing into the next academic year and one leading to a student's Master's thesis.

RESULTS

The 14 completed end-user identified projects engaged 72 students (at least 47 women and 10 with disclosed disabilities) in the design experience. These projects produced 12 conference publications, two journal articles, and eight provisional patent applications. Five teams were selected as finalists in the Summer Biomechanics, Bioengineering, and Biotransport Undergraduate Design Competition in Rehabilitative and Assistive Devices, with one team winning first place. Over 15 of these undergraduates went to graduate school to pursue bioengineering-related research (e.g., Georgia Tech; Michigan State).

Recurring challenges that appeared to be exacerbated by the interdisciplinary nature of the teams included:

- Scheduling challenges for meetings and work sessions, exacerbated by fluctuating class times common in health sciences curricula and others that use a cohort model (e.g., class times can flex from one week to the next);
- Necessity of IRB training and approval prior to students interacting with end users;
- Emphasis on different deliverables and timelines as required by different disciplinary courses.
- Logistics of interacting with end users, particularly if travel was involved.
- Ideation of *de novo* solutions compared to developing a solution that had previously been described but not implemented.
- Student perception of having to do 'extra' work beyond what was required by their 'own' course (e.g., a Benchtop-to-Market transition plan)
- Projects within a single semester (e.g., without a second-semester continuation) generally did not yield a useful prototype.

DISCUSSION

Our student design teams worked together and the demographic diversity within our teams was greater than that of the University's student population, as expected from [4]. We attribute this to the emphasis on improving quality of life through product design that attracted more diverse students, and that our funded projects offered students more opportunities to interact with end users, present their work, and the possibility of a national conference presentation. We explicitly observed that the SB3C Undergraduate Design Competition was a strong motivator, particularly in years when multiple teams submitted abstracts because only one team per University could be make the finals. We believe that this 'friendly competition' was particularly motivating.

The most developed products came from teams that worked for 2 semesters, and had a team member continue the work (with funded support); this led to additional publications, including two journal papers. An additional benefit of project continuation (beyond offering professional development to trainees) is that this additional product development can set the stage for patents, small business opportunities, and other commercialization (e.g., I-Corps, SBIR/STTR, or NSF PFI proposals).

In many instances, these projects served as gateways to research for students who previously professed disinterest in pursuing a graduate education. Many of the students that ultimately attended graduate

school weren't even thinking of it when they started the projects. Our gains of building confidence in research capability in students may be comparable to those seen by a summer REU program [5], yet do so within the context of the typical academic year and avoid the selection bias inherent in REU programs, which self-select for students predisposed to research pursuit. Future work could study the effect of these team design projects on developing scientific identity and fostering a sense of belonging.

Our students thrived when they established direct personal contact with the end-user (or group) to establish design goals. This helps students gain an appreciation for the challenges faced by the end users (sometimes accompanied by wide eyes during meetings, and intense fervor in group discussions about how to improve quality of life for persons with disabilities).

To optimize student success in such projects, we offer the following recommendations:

- Ensure that all students get some form of course credit for their work (e.g., Independent Study, research, or fulfill a course requirement). If students are using the project to fulfill a course requirement, ensure that deliverables are aligned with an engineering design project and at an appropriate timeline. This may necessitate direct faculty-faculty communication across disciplinary lines, or pedagogically-appropriate alternatives. (For example, we had success in pulling students out of traditional capstone design in some semesters to ensure that prototyping timelines allowed for revisions.) Simply put, over-emphasis on reports can hamper product development.
- Mitigate scheduling challenges by modeling clear expectations that cross-disciplinary meetings often occur outside of 'typical' course hours.
- A meaningful design experience in biomedical engineering requires a design assessment; end users must be involved throughout the process, and students must be coached to integrate the feedback appropriately.
- External support, even if small, can create motivating opportunities for students. (Those with an active NSF award from the Engineering Directorate may apply for Undergraduate Design Supplements, see NSF 19-078)
- Clinically-driven design groups should make IRB training and evaluation an integral part of the instruction/design process prior to project initiation. This could be a significant roadblock at larger institutions.
- "Piggy-backing" off of existing frameworks for integrated design typically lead to more developed prototypes; *de novo* projects come with additional mostly-administrative tasks that are educational for students often at the expense of prototype progress.

ACKNOWLEDGEMENTS

The authors thank their students and colleagues for the education through the years, NSF CBET-1510367 for support of many of these projects, and the SB3C Undergraduate Design Competition for serving as a strong motivator for students.

REFERENCES

- [1] Berry+, *J Biomech Eng.*, 141(12): 121003 (5p.) 2019.
- [2] McCullough+ *J Biomech Eng.*, 141(12): 124503 (8p.) 2019.
- [3] Grimm *J Biomech Eng.*, 142(11): 110802 (6p.) 2020.
- [4] Zhu+ *J Biomech Eng.*, 142(11): 111010 (7p.) 2020.
- [5] George and Domire, *J Biomech Eng.*, 142(11):111012 (8 p.) 2020.

USING BAYES' OPTIMIZATION FOR INVERSE FINITE ELEMENT ANALYSIS OF THE TRICUSPID VALVE IN HYPOPLASTIC LEFT HEART SYNDROME

Colton J. Ross (1), Jaden Norman, Arshid Mir (2),
Harold M. Burkhardt (3), Ming-Chen Hsu (4), Chung-Hao Lee (1)

(1) School of Aerospace and Mechanical Engineering, University of Oklahoma, Norman, OK, USA
(2) Department of Pediatrics, University of Oklahoma Health Sciences Center, Oklahoma City, OK, USA
(3) Department of Surgery, University of Oklahoma Health Sciences Center, Oklahoma City, OK, USA
(4) Department of Mechanical Engineering, Iowa State University, Ames, IA, USA

INTRODUCTION

Computer simulations of the heart valve function are an invaluable tool for research into the progression and treatment of valvular disease. Of particular interest is the potential for individualized simulations for patient-specific care, which requires solving the inverse problem to determine the soft tissue material properties based on the *in vivo* deformations. To date, inverse analysis frameworks have been developed for the aortic and mitral valves [1, 2], yet there remain issues with the clinical translation of these tools due to the computational time or the potential for inaccurate predictions. In these *in vivo* animal models or *ex vivo* beating heart apparatuses, the use of high resolution imaging, fiducial markers, or the implantation of sonocrystals allows the inverse problem to be solved with greater confidence. On the other hand, when using clinical images (e.g., echocardiography) the inverse problem is more challenging due to noise in the segmentation data caused by low resolution images, and the inability to perform a distinct mapping between the simulated and image-segmented surfaces.

As the next step in improving the inverse finite element analysis (iFEA) of the atrioventricular heart valves, we propose the use of Bayesian optimization (BO). Briefly, in the BO method the objective function is considered a "black box" fitted by a posterior distribution. For each iteration of the solver, this distribution is updated and the next query point is selected by a probabilistic selection that balances exploration and exploitation of the search space. This technique is computationally advantageous due to the pre-assessment of each query point. Evidence for the usefulness of BO in complex inverse problems can be found in the fields of fluid mechanics [3] and skeletal muscle biomechanics [4].

In this work, we demonstrate that BO can be used as an efficient solver for the iFEA of the heart valves. Specifically, we evaluate this technique by performing iFEA using medical imaging data of the tricuspid valve (TV) from newborns with hypoplastic left heart syndrome (HLHS).

METHODS

Finite Element Analysis Setup: Echocardiogram images were obtained from newborns with HLHS (IRB#14112), and the images were segmented to obtain the points along the annulus (open and closed valve) and the leaflet free edge (open valve), and a point cloud of the leaflet surfaces (closed valve) (Fig. 1(a)). The annulus and free edge points were imported to MATLAB (MathWorks, Natick, MA) and smoothed using a periodic cubic spline fit. The finite element mesh was then constructed using a "lofted surface" approach, joining the annulus and free edge curves and discretizing the surface into 4-node shell elements (i.e., S4 elements in ABAQUS) (Dassault Systèmes, Simulia Corp., Johnson, RI). The leaflets were also modeled using an isotropic Lee-Sacks material:

$$\psi_{\text{leaflet}} = \frac{c_0}{2}(I_1 - 3) + \frac{c_1}{2}(e^{c_2(I_1 - 3)^2} - 1) - \frac{p}{2}(J - 1). \quad (1)$$

In this model, $c_0=10$ kPa, c_1 and c_2 are the material parameters to be optimized, p is a penalty term to enforce tissue incompressibility (i.e., $J=\det(\mathbf{F})=1$), and I_1 is the first invariant of the right Cauchy-Green tensor ($\mathbf{C} = \mathbf{F}^T \mathbf{F}$, where \mathbf{F} is the deformation gradient).

Due to limitations of the echocardiograms, we were unable to extract the chordae tendineae or papillary muscle locations. To this end, we elected to use a generic representation, with branching chordae inserting to the center and free edges of each leaflet. All chordae were modeled as truss elements (T3D2) with a cross-sectional area of 0.1 mm^2 , and material behaviors following a hyperelastic form:

$$\psi_{\text{chordae}} = c_{10}(e^{c_{01}E_{11}} - 1), \quad (2)$$

where c_{10} and c_{01} are the optimized material parameters, and $E_{11} = (1/2)(F_{11}^2 - 1)$ is the uniaxial chordae strain. Finally, the boundary conditions applied to the model were as follows: (i) a transvalvular pressure

gradient of 30 mmHg; (ii) pinned papillary muscles; (iii) deformation of the annulus based on the segmented image data.

Bayesian Optimization: In our iFEA framework, our goal was to determine the leaflet and chordae material parameters that provide agreement between the shapes of the image-segmented point cloud and the finite element surface. Our objective function was thus formulated as the minimization of the summed Euclidean distances between each segmentation point and the corresponding element centroid (Fig. 1(c), see [1] for additional details). From our preliminary analyses, we determined that the objective function required an additional weighting parameter (w) for the residual of each leaflet (i.e., $\mathcal{F}_{\text{total}} = \sum_{i=1}^3 w_i \mathcal{F}_i$), where $w_{\text{septal}} = 20\%$ and $w_{\text{posterior}} = w_{\text{anterior}} = 40\%$.

The BO-based minimization of \mathcal{F} was implemented in MATLAB via the bayesopt function. The optimization parameters were restricted to the search domains: $c_1, c_{10} \in [0.001, 10]$ kPa, $c_2 \in [1, 20]$, and $c_{01} \in [10, 30]$. Herein, we use this technique for two demonstrations: (i) the verification of the framework using a finite element surface with a known solution with the target leaflet parameters of $c_1 = 0.209$ kPa and $c_2 = 11.65$ uniformly prescribed to all 3 leaflets; and (ii) the prediction of the *in vivo* tissue properties for a representative HLHS newborn, with the chordae and leaflet parameters unique to each leaflet, resulting in a 12-dimensional problem.

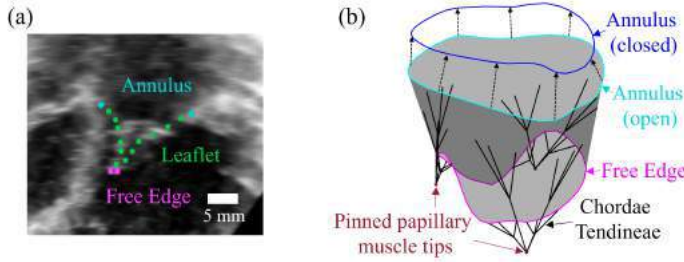


Figure 1: (a) Echocardiogram of the tricuspid valve; (b) the generated finite element mesh

RESULTS

From our verification problem, we found that the BO routine was able to successfully reconstruct the synthetic solution with reasonable accuracy within 100 iterations ($\mathcal{F} = 2.19$ mm, average error of 0.006 mm per point) (Fig. 2(a)). Specifically, the optimized parameters were $c_1 = 0.184$ kPa and $c_2 = 9.73$. Analyzing the residual search space (Fig. 2(b)), we observed that the BO successfully found the global minima despite the presence of several local minima, demonstrating an advantage of the technique.

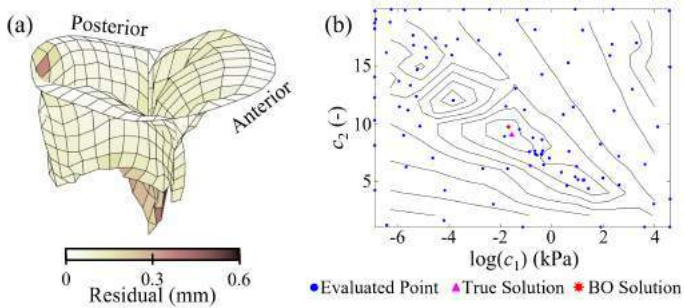


Figure 2: (a) Isometric view of the element-wise errors for the optimized solution to the synthetic problem; (b) a contour plot fitted to the residual history

For the representative patient, the optimized finite element surface yielded a total error of 29.1 mm (average error of 0.081 mm per point) after 100 iterations (Fig. 3(a)), with the final parameters provided in Table 1. With this solution, we observed the posterior leaflet as the stiffest and the septal leaflet was the most extensible, whereas for the chordae this trend was reversed (i.e., septal chordae as the stiffest). For the mechan-

ics metrics, the average von Mises stresses were found as: anterior leaflet, 35 ± 20 kPa; posterior leaflet, 50 ± 26 kPa; septal leaflet, 43 ± 27 kPa (Fig. 3(b)). We also noted minimal regurgitation in the final valve configuration, which was in agreement with the echocardiogram.

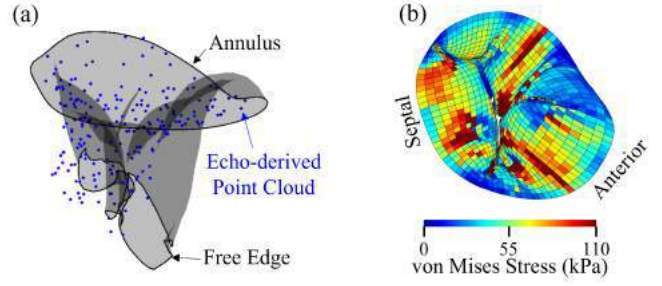


Figure 3: (a) Isometric view of the optimized solution for the representative patient; (b) superior view of the von Mises stresses

Table 1: Leaflet and chordae material parameters from the BO of the representative patient

Parameter	c_1 (kPa)	c_2 (-)	c_{10} (kPa)	c_{01} (-)
TV Septal Leaflet	0.004	19.8	99.30	20.4
TV Anterior Leaflet	0.028	11.5	1.82	11.5
TV Posterior Leaflet	0.774	13.6	0.02	11.5

DISCUSSION

From our preliminary results, we have demonstrated a novel use of BO for iFEA of the tricuspid valve. First, we have shown the method to provide minimal error in retrieving a synthetic solution. Second, the efficiency of the method was evidenced by solutions being obtained within 100 iterations and performed in under 3 hours with batch parallel processing. Third, we have also shown the usefulness of BO for solving high-dimension problems by optimizing the 12-D problem with the representative patient.

It is worth noting that in these preliminary analyses we used low-resolution models (360 leaflet elements) to reduce the computational time; however, this technique may be useful for improving processing times for iFEA while maintaining accurate predictions – a topic of future investigation. Also, we noticed a mismatch of the coaptation line in the simulated surface and the point cloud (Fig. 3(a)). This may be attributed to the inability to accurately reconstruct the chordae geometry from the medical images, which could potentially be remedied by using a functionally equivalent model [5]. While additional progress must be made in iFEA research and medical imaging resolution to address this issue, BO will be a valuable tool for making efficient predictions of the *in vivo* tissue properties.

ACKNOWLEDGEMENTS

We gratefully acknowledge the supports from the Presbyterian Health Foundation, American Heart Association Scientist Development Grant Award (16SDG27760143), and the National Science Foundation Graduate Research Fellowship (GRF 2020307284).

REFERENCES

- [1] Aggarwal A *et al. Biomech Model Mechanobiol* 15.4 (2016). DOI: 10.1007/s10237-015-0732-7.
- [2] Krishnamurthy G *et al. Am J Physiol - Heart Circ Physiol* 295.3 (2008). DOI: 10.1152/ajpheart.00284.2008.
- [3] Cotter SL *et al. Inverse Probl* 25.11 (2009). DOI: 10.1088/0266-5611/25/11/115008.
- [4] Li Y *et al. Comput Methods Biomech Biomed Engin* 24.15 (2021). DOI: 10.1080/10255842.2021.1906235.
- [5] Khalighi AH *et al. Ann Biomed Eng* 47.1 (2019). DOI: 10.1002/abeb.20038. s10439-018-02122-y. Copyright 2023 SB³C Foundation, Inc.

IMPACT OF VIMENTIN INTERMEDIATE FILAMENTS ON 3D MULTICELLULAR DEVELOPMENT AND MORPHOGENESIS

Camille D. Rodriguez (1), Ming Guo (1)

(1) Mechanical Engineering, Massachusetts Institute of Technology, Cambridge, MA, USA

INTRODUCTION

Vimentin intermediate filaments (VIFs) are a type III intermediate filament and the most abundant in mammalian cells. VIFs are known as markers for epithelial to mesenchymal transitions, and evidence has been shown that vimentin expression contributes to cancer metastasis. In 2D analysis, vimentin expression is shown to alter cell mechanics through reorganization of the cytoskeleton and cell-cell adhesion. While it has become increasingly clear that VIFs are important in individual cell behavior, their role in collective cell behavior remains unclear, especially in a 3D environment. A recent study examined vimentin in varying malignant breast cancer cell lines, and found without VIFs there was a decrease in proliferation and directional migration [1]. It has also been recently revealed that vimentin adjusts a collective's mechanical properties by reducing cell-substrate traction and intercellular tension while increasing stiffness in MCF-7 cells [2]. However, both studies were conducted as 2D collectives.

In this work, to elucidate vimentin's role in the development and morphogenesis of multicellular clusters in 3D, cell clusters are embedded in a Matrigel-Alginate interpenetrating gel for growth *in vitro*. Compared to 2D cultures, cells are able to remodel their surrounding matrix appropriately. MCF-7 cells are utilized in this study due to a naturally null vimentin expression, allowing vimentin to be chemically induced. A comparison of morphology, migration patterns, and invasiveness between control (uninduced) MCF-7 cell clusters and induced vimentin clusters was examined. Clusters with induced vimentin had significantly higher instances of protrusions along with an increase in mean square displacement and nuclei velocity.

METHODS

MCF-7 cells with a nuclear localized sequence (NLS) were embedded in a Matrigel-Alginate gel. Using a Matrigel-Alginate mixture for the gel allows for a tunable viscosity and other mechanical properties. The final concentration used for all samples was 4.4 mg/mL

Matrigel, 5 mg/mL Alginate, and 0.043 mM CaSO₄. 10 µL of cell suspension was mixed in when creating the gel. Vimentin expression was induced in MCF-7 cells by adding 5X concentration of Cumate in MEM media.

From single cells, clusters began expanding from roughly 3 cells around day 3 of embedding to about 10 cells around day 7. Clusters were imaged on a confocal microscope on days 3, 6, 7 and 10 to study growth progression.

Using grayscale static images, the area moment of inertia was studied along with an invadopodium count. The area moment of inertia was determined by first finding the area, A , and centroid, d_{xy} , of the cluster body (2) applied to (1).

$$I_p = \int r^2 dA = I_x + I_y \quad (1)$$

$$I_{x,y} \propto d_{x,y}^2 A \quad (2)$$

The ratio (4) compares the calculated area moment of inertia to its theoretical circle, I_{circle} . The larger this value is from 1 the greater it deviates from a perfect circle.

$$C_{2D} = \frac{I_p}{I_{circle}} \quad (3)$$

Migration analysis was conducted on day 7 over 12 hours with a 10-minute frame rate. Tracking the fluorescent nuclei, the mean squared displacement (MSD) was calculated along with velocity trajectories and average velocities. Analysis was on 8 induced and 6 uninduced clusters.

RESULTS

There are clear distinctions on day 7 when comparing induced and uninduced MCF-7 clusters of approximately the same size and cell

count. In Fig. 1A those induced with vimentin have an increase in protrusions from the bulk of the body. Uninduced cell clusters tend to be more rounded, with minimal, if any, protrusions.

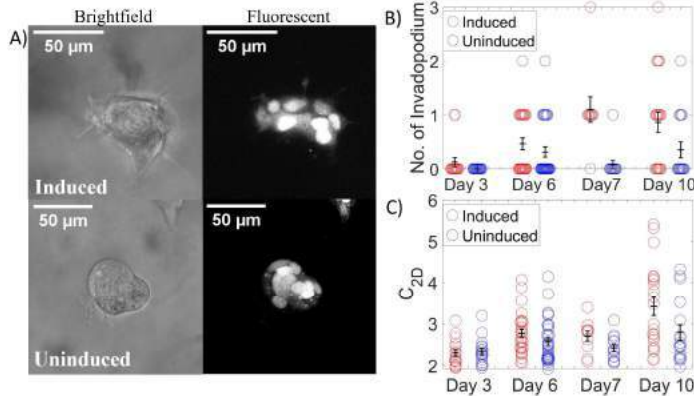


Figure 1: Morphological differences between induced and uninduced cluster. A) Grayscale and fluorescent images of sample clusters. B) Number of invadopodium over increasing days. C) Area moment of inertia coefficient over increasing days. ($n_I = 16, 28, 10, 22$ and $n_U = 18, 32, 13, 17$ with days 3, 6, 7, 10 respectively).

The number of invadopodium would increase in the vimentin induced MCF-7 cells as the days progressed (Fig. 1B). Invadopodium's were classified as having a nucleus leading a protrusion, and the protrusion had a larger length than width. With this classification system the largest number of invasive tips seen in induced clusters was at 3 with an average of about 1. To better quantify the irregular shapes exhibited by the vimentin induced clusters, the area moment of inertia was calculated (Fig. 1C). As the days progressed the deviation of vimentin clusters from a perfect circle (C_{2D} of 1) increased averaging at 3.41 on day 10 whereas uninduced was 2.79 ($p = 0.0403$).

Induced cells within a cluster showed an increase in migratory behavior. While the cells were confined generally to the cluster body, induced cells had an increase in velocity trajectories compared to uninduced cells. In the induced cluster (Fig. 2A), most trajectories have a velocity of 13 μm/h or above, with more instances of velocities around 27 – 31 μm/h and 36 – 40 μm/h. The uninduced cells mainly vary between 4 – 18 μm/h.

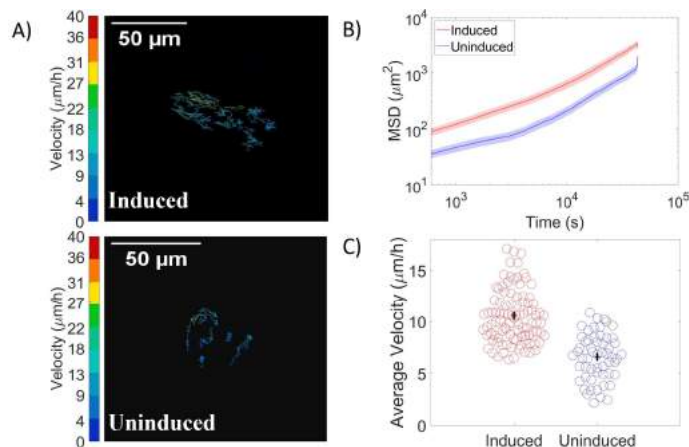


Figure 2: Dynamic differences between induced and uninduced clusters. A) Velocity map of sample clusters. B) MSD of induced clusters. C) Average velocity of induced and uninduced clusters.

and uninduced. C) Average velocities of individual cells within induced or uninduced clusters ($n_I = 98$ and $n_U = 56$).

Additionally, the MSD quantitatively expressed this larger distance covered by the induced cells (Fig. 2B) with an average velocity of 10.56 μm/h. Uninduced cells had an average of 6.59 μm/h ($p = 3.6E - 16$, Fig. 2C).

DISCUSSION

Vimentin expression in MCF-7 3D clusters alters collective behavior. Morphology of induced clusters are more irregular than uninduced. The area moment of inertia quantitatively captures these morphological differences. It considers both cases of filopodia and invadopodium (protrusions) and possible invasiveness of inducing MCF-7 cells. One difference against 2D collective behavior was that uninduced MCF-7 cells had more membrane extensions than induced cells [1]. Indicating a further need to study in a 3D softer, environment. Potentially VIFs are needed to cleave the ECM, thus making them more likely to form extensions or protrusions.

The MSD and velocity trajectories show with vimentin expression individual cells within the collective tend to migrate greater distances and with larger average velocities. Similarly, in 2D MCF-7 analysis it was found that there was weaker cell-cell adhesion thus cells can reorganize within the cluster [2]. However, one key difference is that vimentin expression reduces intracellular motion in 2D [2]. In 3D the nuclei's movement is generally confined within the cluster region but has a significantly more active motion.

The preliminary results indicate clear morphological and dynamic differences when vimentin intermediate filaments are present in clusters. When induced in individual cells, vimentin impacts the collective behavior of 3D multicellular systems. Lending some evidence to the study of vimentin as a marker for early stages EMT or hybrid EMT. With this knowledge there can be a deeper understanding of vimentin's active role in cancer progression, along with other physiological processes such as wound healing.

ACKNOWLEDGEMENTS

A thank you to the Lemelson Minority Engineering Presidential Fellowship at MIT and the Sloan-MIT University Center of Exemplary Mentoring Scholarship for the continuous support.

REFERENCES

- [1] Liu CY, Lin HH, Tang MJ, Wang YK. Vimentin contributes to epithelial-mesenchymal transition cancer cell mechanics by mediating cytoskeletal organization and focal adhesion maturation. *Oncotarget*. 6(18):15966-83. 2015 Jun 30. doi:10.18632/oncotarget.3862.
- [2] Sivagurunathan S, Vahabikashi A, Yang H, Zhang J, Vazquez K, Rajasundaram D, Politanska Y, Abdala-Valencia H, Notbohm J, Guo M, Adam SA, Goldman RD. Expression of vimentin alters cell mechanics, cell-cell adhesion, and gene expression profiles suggesting the induction of a hybrid EMT in human mammary epithelial cells. *Front Cell Dev Biol*. 10. 2022 Sept 19. doi:10.3389/fcell.2022.929495

SUPERPOSITION TESTING ON A FUNCTIONAL SPINAL UNIT WITHIN A MULTI-LEVEL SPINE CONSTRUCT

Callan M Gillespie (1), Robb W Colbrunn (1)

(1) BioRobotics and Mechanical Testing Core
Lerner Research Institute
Cleveland Clinic
Cleveland, OH 44195

INTRODUCTION

Robotic testing of anatomical joints involves deterministic control of a 6 degree of freedom (DOF) joint with a 6 DOF robot. However, in the case of spine testing, the number of DOF is 6 times the number of functional spinal units (FSU). If testing more than 1 FSU, the motion at every level cannot be independently controlled by a 6 DOF robot.

Historically this limitation has meant that robotic spine testing, is typically approached as control of the superior and inferior end points of the spine. This results in the FSU not being uniquely controlled when part of a multi-level spine construct. Consequently, applied kinetics have been limited to pure moment testing where every level of the spine experiences the same torque and all forces are commanded to 0 N.

Given these kinetic limitations, kinematic control has historically been approached in two ways. The **first method** is to align load cells and actuators with an estimate of the spine axis of rotation and use the native load cell and robot/actuator coordinate systems for measuring and controlling motions and loads [1]. This approach does not take into account local vertebra shifts in orientation or translation as a function of spine bending. The **second method**, the *static transform method*, is to control motion based on the location of the middle two vertebra in a spine construct and robot position. A joint coordinate system (JCS) that relates the superior and inferior vertebrae of the middle FSU would be constructed based off the ISB standard [2]. Static transforms are constructed based on the pose of the spine and robot during an initial digitization. These transforms will only account for local vertebra shifts in translation or rotation at the instance of digitization.

The aim of this study was to show that with a **third methodology**, called the *eXactoPOSE method*, it is possible to perform 6-DOF repetitive kinematic control (i.e. superposition testing) on a single FSU within a multi-level construct. This will serve as a stepping stone for future work that will look at how both kinetic and kinematic control of a single FSU interacts with adjacent level motions and loads.

METHODS

A thoracolumbar spine was obtained with T9-L5 intact. L5 was attached to a based mounted load cell while T9 was attached to the robot (Figure 1).

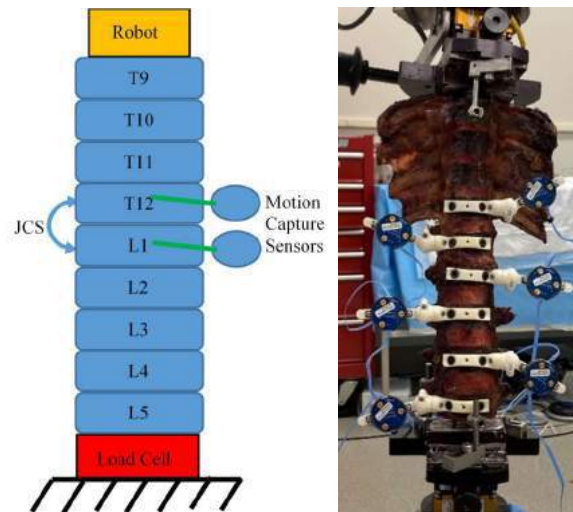


**Figure 1: Left: Schematic of Experimental Setup
Right: Representative Spine Mounted to simVITRO System**

In order to control the T12-L1 FSU within the middle of the spine, two 6-DOF motion capture markers (Optotrak Certus, Waterloo, CAN) were attached to T12 and L1 and a JCS was constructed to describe FSU kinematics. The simVITRO[®] software (Cleveland Clinic, Cleveland, OH) was used to apply 5 Nm of flexion to the spine while minimizing all other torques and forces. The kinematics of the T12-L1 FSU were

recorded during the pure moment tests, low pass filtered at 3 Hz to reduce noise from the motion capture data, and played back at 1/3 speed to improve kinematic tracking when doing superposition testing. Next, a sensor fusion algorithm in simVITRO called eXactoPOSE was used to control only the motion of the T12-L1 FSU. The eXactoPOSE algorithm closes the loop on 6-DOF positions using both the robot and motion capture data. Kinematics were again recorded during these superposition tests.

RESULTS

Figure 1 shows the T12-L1 kinematics based on the eXactoPOSE method from the pure moment vs superposition flexion test. The RMS error of the kinematics in all 6-DOF are given in Table 1, Column 1.

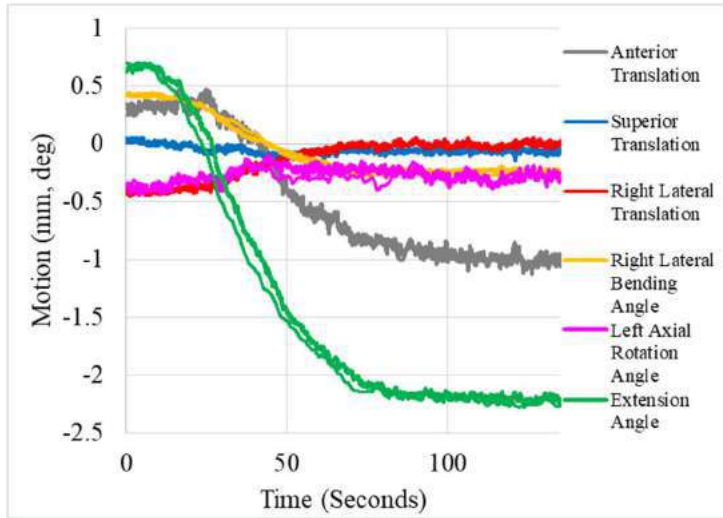


Figure 2: L1-T12 eXactoPOSE Pure Moment vs Superposition Kinematics (superposition kinetics have a thicker line)

It is notable that the static transform method measures different kinematics than the eXactoPOSE method. This is because the static transform method only uses robot motion and ends up being more of a global measure of spine motion rather than a local FSU measure based on motion capture sensors. Further, the static transform method was 1-2 orders of magnitude less repeatable than the eXactoPOSE method when comparing pure moment kinematics to superposition kinematics (Table 1).

Table 1: Root Mean Squared Error (RMSE) between pure moment and superposition test kinematics

Degree of Freedom	eXactoPOSE Method	Static Transform Method	Units
Anterior Translation	0.05	9.34	mm
Superior Translation	0.03	1.50	mm
Lateral Translation	0.03	2.18	mm
Right Lateral Bending	0.03	0.80	deg
Left Axial Rotation	0.04	2.11	deg
Extension	0.15	5.45	deg

Forces when performing the pure moment vs superposition tests were also different. In the pure moment tests all forces/torques are

commanded to 0 load except for flexion torque where 5 Nm is applied to the spine.

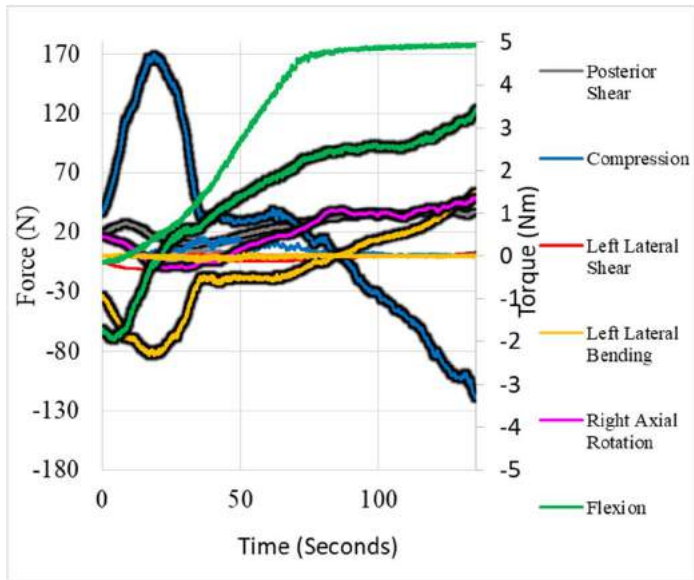


Figure 3: Force Control vs Superposition 6-DOF Kinetics (superposition kinetics have a black border)

DISCUSSION

Comparison of the 5 Nm flexion pure moment test to the T12-L1 superposition test reveals that it is possible to control the 6-DOF kinematics of a single FSU within a larger spine construct. The T12-L1 kinematics are different when looking at the static transform method's kinematics (Table 1) so kinematic reporting in manuscripts should always clarify this distinction. Since the spine has many more DOF than are actively able to be controlled by the robot, an indeterminate system will result where there can be many kinematic or kinetic poses of the superior and inferior vertebra (T9 and L5) that can produce the same pose in the middle of the spine (T12-L1). The static transform method is based on robot position and does not take into account local deformation of the spine, which means that it cannot account for multiple robot positions producing the same kinematics in the middle of the spine. These multiple solutions explain how different positions of the robot (table 1) and different forces (figure 3) can produce the same 6-DOF kinematics at the T12-L1 FSU.

The number of robot positions that could produce identical T12-L1 kinematics is indeterminate given the under-constrained system. Future work will add constraints to limit this solution space by using control laws weighting FSU forces and/or additional FSU kinematics.

Traditionally, cadaver spine testing has been focused on controlling global spine kinetics or kinematics and seeing these affect local kinematics. The authors hope that the ability to fully control an FSU in the middle of a spinal construct will allow researchers to ask meaningful questions about how FSU motion might affect motion both at adjacent levels of the spine and globally over the whole spinal construct. Additional future work will look at controlling compression and shear forces on a vertebra within a spinal construct so that clinicians can better understand the effect of combined loading scenarios on a spine construct.

REFERENCES

- [1] Holsgrove, TP et al., *J Biomech*, 70: 59-66, 2018
- [2] Wu, G et al., *J Biomech*, 35:543-548, 2002

EFFECT OF AGING, SEX, AND GENE (FIBULIN-5) ON THE ARTERIAL STIFFNESS OF MOUSE: 20 WEEKS ADULT MICE WITH FIBULIN-5 KNOCKOUT ARE OLDER THAN 100 WEEKS WILD-TYPE MICE

H. Dong (1,2), J. Ferruzzi (3), M. Liu (1,2), L. Brewster (4), R. Gleason (1,2)

- (1) Department of Biomedical Engineering, Georgia Institute of Technology and Emory University, Atlanta, GA
(2) School of Mechanical Engineering, Georgia Institute of Technology, Atlanta, GA;
(3) Department of Bioengineering, The University of Texas at Dallas, Richardson, TX;
(4) Division of Cardiothoracic Surgery, Department of Surgery, Emory University, Atlanta, GA;

INTRODUCTION

Arterial stiffening is an independent predictor of cardiovascular risk [1]. It is also a key cause of many cardiovascular diseases. For instance, arterial/aortic stiffening could alter the hemodynamics in the aorta, increase the afterload of the left ventricle and ultimately promote myocardial remodeling, dysfunction, and failure [2].

Fibulin-5 (Fbln5) is an extracellular elastin-associated protein that connects to integrins and localizes tropoelastin to microfibrils [3, 4]. Fbln5 deficiency alters arterial microstructures by disrupting the integrity of elastic lamellae [5], which results in elongated and tortuous central arteries [3]. In addition, aging is another dominant risk factor for many cardiovascular diseases. Prior work by Wan et al. [5, 6] and Ferruzzi et al. [7, 8] documented how aging and loss of elastic fiber integrity due to Fbln5 deficiency alters material properties across the central vasculature. However, it is still not fully understood how the Fbln5 and aging influence the intrinsic material property/stiffness of arteries.

Here, we investigated how the aging, sex and Fbln5 gene affect the arterial stiffness of mice, based on a total of 128 biaxial testing samples of mouse arteries by Ferruzzi et al. [7, 8], using the recently developed unified-fiber-distribution (UFD) model for arterial tissues [9, 10].

METHODS

We assumed that arterial tissues are incompressible. The strain energy function of the unified-fiber-distribution (UFD) model can be expressed as [9, 10] $\bar{\Psi} = \frac{1}{2}c(\bar{I}_1 - 3) + \frac{k_1}{2k_2}[\exp\{k_2[\zeta^2(\bar{I}_{4\theta} - 1)^2 + (1 - \zeta)^2(\bar{I}_{4z} - 1)^2]\} - 1]$, where c, k_1, k_2 and ζ are four material parameters, representing the matrix stiffness, fiber initial stiffness, arterial stiffening factor, and circumferential fiber component, respectively. \bar{I}_1 is the 1st invariant of right Cauchy–Green tensor $\bar{\mathbf{C}}$, $\bar{I}_{4\theta} = (\mathbf{a}_{0\theta} \otimes \mathbf{a}_{0\theta}) : \bar{\mathbf{C}}$, and $\bar{I}_{4z} = (\mathbf{a}_{0z} \otimes \mathbf{a}_{0z}) : \bar{\mathbf{C}}$, where $\{\mathbf{a}_{0\theta}, \mathbf{a}_{0z}\}$ are the unit vectors in the circumferential and axial direction, respectively. The UFD model [9, 10] considers the fibers as a unified distribution,

rather than separating the fiber distribution into two/several fiber families. The consideration of a unified distribution for the fibers in the UFD model may be more physically consistent with the real fiber distribution of arterial tissues than existing fiber-family-based models.

We applied the UFD model to a total of 128 biaxial testing samples of mouse central arteries, which were obtained from Ferruzzi et al. [7, 8]. The samples were classified into three pairs (**Table 1**). The values of c, k_1, k_2 and ζ for each sample were obtained by fitting of the cylindrical biaxial testing data. Paired Student's t-tests were used to compare the parameters from different groups. A p -value less than 0.05 was considered to be statistically significant.

Table 1: three pairs of biaxial testing data of mouse arteries. M: male, F: female, 20wk/100wk: 20/100 weeks old, Fbln5^{+/+}: wild-type with fibulin-5 gene, Fbln5^{-/-}: knockout type. ATA: ascending thoracic aorta, DTA: descending thoracic aorta, SAA: suprarenal abdominal aorta, IAA: infrarenal abdominal aorta, and CCA: common carotid artery. Note that Pair-1 and Pair-3 contain a same group type (M-20wk-Fbln5^{+/+}).

Pair	Group type	Specific Location				
		ATA	DTA	SAA	IAA	CCA
Pair-1	M-20wk-Fbln5 ^{+/+}	n=5	n=5	n=5	n=5	n=5
	M-20wk-Fbln5 ^{-/-}	n=5	n=5	n=5	n=5	n=5
Pair-2	F-20wk-Fbln5 ^{+/+}	n=5	n=5	n=5	n=5	n=5
	F-20wk-Fbln5 ^{-/-}	n=5	n=5	n=5	n=5	n=5
Pair-3	M-20wk-Fbln5 ^{+/+}	n=5	n=5	n=5	n=5	n=5
	M-100wk-Fbln5 ^{+/+}	n=6	n=6	n=5	n=6	n=5

RESULTS

The UFD model obtained good fittings (Fig. 1a, b) of the experiments, with $R^2 = 0.9363 \pm 0.0032$ ($n=128$). The results show (Fig. 1c, d) that the arterial stiffening of the mouse with the knockout of the fibulin-5 gene ($Fbln5^{-/-}$) is significantly larger than that of the wild-type ($Fbln5^{+/+}$), for both male (Fig. 1c: $p<0.001$, “All Locations”) and female (Fig. 1d: $p<0.001$, “All Locations”), at each of the five locations (Fig. 1c, d: all $p<0.02$, each “Specific Location”). No statistical difference was found between the male and female groups at all five locations (all $p>0.05$ for each “Specific Location”).

The aging effect (20 vs 100 weeks old) also significantly increases the arterial stiffening of mice (Fig. 1e: $p<0.001$, “All Locations”). As to the “Specific Location”, the arterial stiffening factor of mice at 100 weeks old is notably larger than that of mice at 20 weeks old for most locations (Fig. 1e: $p<0.02$ for each “Specific Location” except ATA).

It is interesting to note that the mouse arterial stiffening of 20 weeks old with fibulin-5 knockout ($Fbln5^{-/-}$) is even larger than that of 100 weeks old with fibulin-5 ($Fbln5^{+/+}$), as shown in Fig. 1f (all $p<0.001$). This indicates that the 20 weeks old mice of $Fbln5^{-/-}$ are even much older than 100 weeks old wild-type mice of $Fbln5^{+/+}$, in the sense of arterial stiffening, based on the assumption that older mice have stiffer arteries.

Another interesting phenomenon is that the arterial stiffening follows exactly the same pattern in terms of locations for male (Fig. 1c) and female (Fig. 1d) mice. For the $Fbln5^{+/+}$ male/female groups (orange bars in Fig. 1c, d), the arterial stiffening factor increases from ATA to DTA, and then decreases to IAA to CCA. For the $Fbln5^{-/-}$ male/female groups (green bars in Fig. 1c, d), the arterial stiffening factor increases from ATA to DTA, and then keeps about the same value among DTA, SAA, IAA, and CCA.

The parameters c , k_1 and ζ also follows similar patterns in terms of locations for male and female mice (not shown here due to limited space). The parameter c decreases from ATA to SSA to CCA for $Fbln5^{+/+}$ groups, while first increases from ATA to SSA, and then decreases to CCA for $Fbln5^{-/-}$ groups. The aging significantly decreases circumferential fiber component (ζ) but has not much effect on matrix stiffness (c) or fiber initial stiffness (k_1). The parameters c , k_1 and ζ were influenced little by the $Fbln5$ gene knockout.

DISCUSSION

Comparison between Fig. 1c and Fig. 1f indicates that the knock-out of $Fbln5$ changes the location patterns but the aging effect does not, despite both aging and the $Fbln5$ knock-out increase the arterial stiffening factor. The specific location patterns may be a result of adaption to the hemodynamic, which suggests that the $Fbln5$ knock-out may also alter the blood flow profile in the arteries.

Ferruzzi et al. [7, 8] showed that the elastic fibers lose some waviness in $Fbln5^{-/-}$ mice with respect to $Fbln5^{+/+}$ controls, while medial collagen was increased in 100 weeks old mice. Therefore both loss of elastic fiber integrity and accumulation of collagen represent micro-structural mechanism for the increased arterial stiffening by $Fbln5$ knock-out and aging.

It should be noted that the 4-fiber family model was applied to the comprehensive and valuable experimental data [7, 8], however, property/stiffness differences have been seldom captured between different groups. The reason could be the overparameterization of the 4-fiber family model which has 8 material parameters, in contrast to the UFD model applied here which has only 4 material parameters but still achieves good accuracy (Fig. 1a, b).

ACKNOWLEDGEMENTS

This study is supported by NIH (R01HL155537 and R01HL142036).

REFERENCES

- [1] D.K. Arnett, G.W. Evans, W.A. Riley, American journal of epidemiology 140(8) (1994) 669-682.
- [2] J.A. Chirinos, P. Segers, T. Hughes, R. Townsend, Journal of the American College of Cardiology 74(9) (2019) 1237-1263.
- [3] T. Nakamura, P.R. Lozano, Y. Ikeda, Y. Iwanaga, A. Hinek, S. Minamisawa, C.-F. Cheng, K. Kobuke, N. Dalton, Y. Takada, Nature 415(6868) (2002) 171-175.
- [4] H. Yanagisawa, E.C. Davis, B.C. Starcher, T. Ouchi, M. Yanagisawa, J.A. Richardson, E.N. Olson, Nature 415(6868) (2002) 168-171.
- [5] W. Wan, H. Yanagisawa, R.L. Gleason, Annals of biomedical engineering 38(12) (2010) 3605-3617.
- [6] W. Wan, R.L. Gleason Jr, American Journal of Physiology-Heart and Circulatory Physiology 304(5) (2013) H674-H686.
- [7] J. Ferruzzi, M. Bersi, S. Uman, H. Yanagisawa, J. Humphrey, Journal of biomechanical engineering 137(3) (2015) 031007.
- [8] J. Ferruzzi, D. Madziva, A. Caulk, G. Tellides, J. Humphrey, Biomech Model Mechanobiol 17(5) (2018) 1281-1295.
- [9] H. Dong, W. Sun, Journal of the Mechanics and Physics of Solids 151 (2021) 104377.
- [10] H. Dong, M. Liu, T. Qin, L. Liang, B. Ziganshin, H. Ellauzi, M. Zafar, S. Jang, J. Elefteriades, W. Sun, R.L. Gleason, Journal of the Mechanical Behavior of Biomedical Materials (2022) 105081.

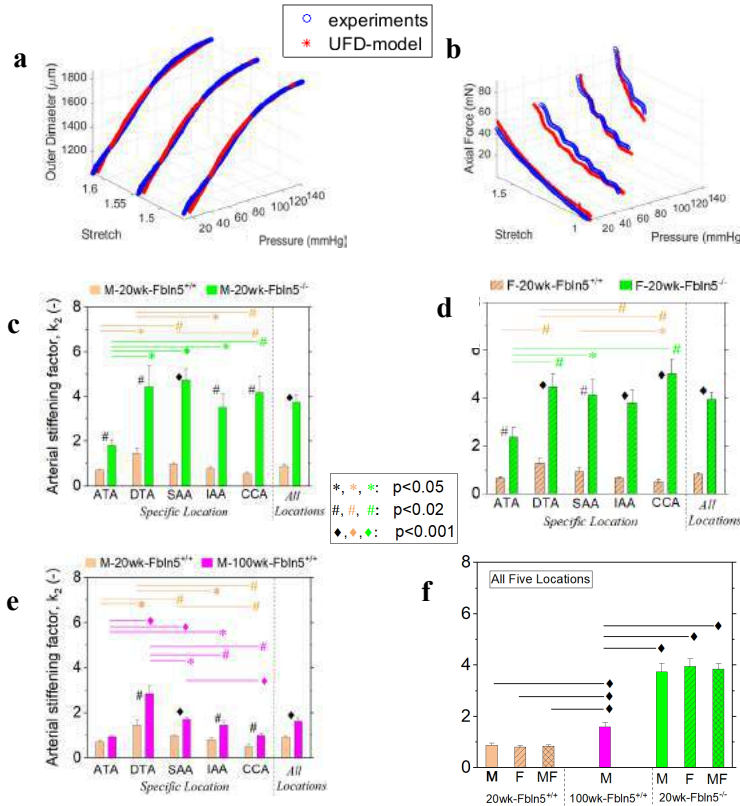


Fig 1. a-b: A representative example of fitting results of Pressure-Diameter relation (a) and Pressure-Axial Force relation (b), based on the unified-fiber-distribution (UFD) model. **c-f:** mean and standard error of arterial stiffening factor (k_2) of male (M) and female (F) mice of 20 weeks (20wk) and 100 weeks (100wk) old, for wild-type ($Fbln5^{+/+}$) and knock-out type ($Fbln5^{-/-}$). **f:** All five locations considered together. ATA: ascending thoracic aorta, DTA: descending thoracic aorta, SAA: suprarenal abdominal aorta, IAA: infrarenal abdominal aorta, and CCA: common carotid artery.

A NON-CONTACT MICROFLUIDIC APPROACH TO DISTINGUISH LARGE EXTRACELLULAR VESICLES FROM IDH1-MUTATED GLIOBLASTOMA CELLS BASED ON STIFFNESS

Mi Ho Jeong (1), Hyungsoon Im (1,2), and Joanna B. Dahl (3)

- (1) Center for Systems Biology, Massachusetts General Hospital, Boston, MA, USA
(2) Department of Radiology, Massachusetts General Hospital, Boston, MA, USA
(3) Engineering Department, University of Massachusetts Boston, Boston, MA, USA

INTRODUCTION

Extracellular vesicles (EVs) are cell-derived, membrane-bound vesicles that carry various biomolecules, such as proteins, nucleic acids, and lipids. They play important roles in cell-to-cell communications as molecular messengers. EVs are also attractive circulating biomarkers for molecular diagnosis of various diseases and carriers for therapeutics. Most published studies have investigated nanoscale EVs and focused on EV biochemical content. There is much less understanding of large microscale EV characteristics and EV mechanical properties.

EV stiffness has been measured using atomic force microscopy (AFM). AFM can differentiate natural EV populations based on stiffness [1], though only nanoscale EVs have been studied and the molecular origins of stiffness differences were not proven. However, pressure build-up inside the vesicles during AFM indentation from substrate adhesion [2] seems to have led to large variability and suspiciously high values of reported EV stiffnesses measured by AFM. We recently introduced a microfluidic technique that measures the effective stiffnesses of large EVs (L-EVs, >1 μm diameter) [3] as a higher throughput and non-contact approach to study L-EV biomechanics.

The objective of this pilot study is to probe the robustness of our microfluidic technique to distinguish between EV populations by comparing stiffness distributions of L-EVs derived from glioblastoma cell lines with expected lipid differences. Thus, this study will investigate the potential of high-throughput microfluidics to distinguish between large EV populations that differ in biomolecular composition.

METHODS

L-EVs were derived from glioblastoma multiforme cell lines (MGG, Gli36) with and without the isocitrate dehydrogenase 1 (IDH1) mutation, which occurs in many GBM cancers and affects lipid metabolism. L-EVs were isolated from collected cell culture media using differential centrifugation (300g for 10 minutes then 2,000g for

20 minutes). L-EV morphology, size distributions, and concentrations were assessed from optical microscopy images.

The microfluidic device that stretched suspended L-EVs consisted of two straight channels (width 1 mm, depth 150 μm) at right angles that generated linear planar extensional flow at the intersection (**Figure 1A**). L-EVs were suspended in a viscified aqueous solution (0.7% w/v methyl cellulose in phosphate-buffered saline, ~65 mPa·s) and injected through one inlet channel (**Figure 1B**). Fluid infusion flow rates were 500 $\mu\text{L hr}^{-1}$ to 1500 $\mu\text{L hr}^{-1}$ (equivalent strain rates ~ 2.8 – 8.3 s^{-1}). L-EV stretching was imaged with a 100 \times objective (Zeiss Axiovert 200M, Prime95B sCMOS camera, 500 frame movies at 40 fps). L-EV stretch was quantified from a strain measure based on the axes of the best-fit ellipse to the detected contour in MATLAB (**Figure 1C**).

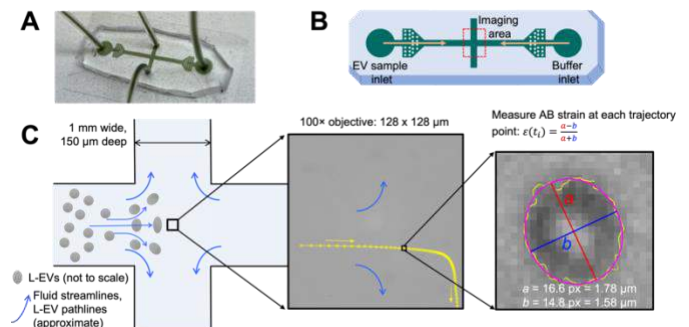


Figure 1: Non-contact microfluidic technique to measure the effective stiffness of microscale large extracellular vesicles. (A) The extensional flow microfluidic device. The channel width is 1 mm. (B) The extensional flow is created by impinging sample and buffer flows. (C) The L-EV strain measurement procedure.

An analytical linear elastic mechanical model of a sphere deforming in planar extensional flow [4] was applied to extract the L-EV's effective shear modulus G from the average strain. Stiffness distributions were statistically compared using classical (two-sided Wilcoxon) and bootstrapping (100,000 iterations) hypothesis tests. 95% confidence intervals of distribution medians and difference in medians was estimated from bootstrap resampling of the data.

Lipidomics analysis of L-EV populations was conducted to determine lipid profiles. Full scan spectra were collected on an LTQ-Orbitrap Velos mass spectrometer in both positive and negative ionization modes. Lipids were identified using the Lipid Mass Spectrum Analysis (LIMSA) v.1.0 software linear fit algorithm, in conjunction with an in-house database of hypothetical lipid compounds. For principal component analysis (PCA), all the lipid portion data was processed using the R program (version 4.0.3).

RESULTS

The diameter of all spherical L-EVs measured for stiffness ranged from 0.65 – 5.7 μm with a sample mean of 2.6 μm and a standard deviation of 0.95 μm . This is within the 1 – 5 μm size range considered for atypically large vesicles. The concentration of L-EVs that were measured for stiffness was $0.4 - 1.2 \times 10^7$ spherical L-EVs per milliliter.

L-EVs derived from Gli36 and MGG cells with the IDH1 mutation had ~20% higher medians than their wild-type counterparts (Figure 2) with a relatively small overlap of the median 95% confidence intervals (Table 1). Hypothesis testing of the difference in medians using the Wilcoxon rank-sum test and bootstrapping yielded p-values < 0.05 for all comparisons (Figure 2, Table 1).

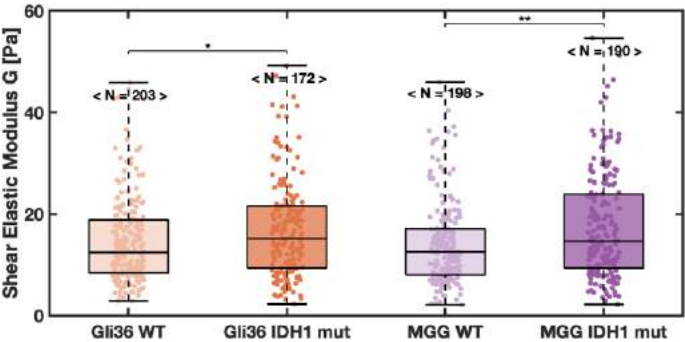


Figure 2: Box plots of stiffness distributions of L-EVs derived from Gli36 and MGG cell lines. Pairwise comparisons were conducted using the two-sided Wilcoxon rank sum test. *p < 0.05, **p < 0.01.

Table 1: Summary of bootstrap hypothesis testing and 95% confidence interval (CI) statistics for comparisons between L-EV stiffness distributions. 100,000 bootstrap iterations were used.

Cell Line	N	95% CI: G Median [Pa]	95% CI: difference in medians [Pa]	Bootstrap Hypothesis Test p-value
Gli36 WT	203	10.79 – 13.89	0.235 – 5.42	0.0145
IDH1 mut	172	13.56 – 17.37		
MGG WT	198	11.52 – 13.76	-0.150 – 4.36	0.03169
IDH1 mut	190	12.78 – 16.73		

Lipidomics showed that the four L-EV populations had different lipid content. In the PCA analysis, the four analyzed samples were in

different quadrants, indicating that the lipid components of each sample showed distinct characteristics. The amounts of phospholipids, a major component of membranes, decreased in both Gli36 and MGG cells with the IDH1 mutation. Larger numbers of unsaturated lipids were decreased in L-EVs from IDH1-mutated cell lines compared to saturated lipids.

DISCUSSION

Our L-EV stiffness and lipidomics data suggest that the stiffening could be related to the changes in lipid compositions of L-EVs. A significant reduction of unsaturated lipids means relatively more saturated lipids in L-EVs from cell lines with IDH1 mutations compared to those from wild-type cell lines. Saturated lipids pack more tightly than unsaturated lipids that contain double carbon bonds, leading to larger attractive intermolecular forces and stiffer biomembranes [5]. Further study is needed to determine if this change in lipid composition is a driving cause of L-EV stiffening with the IDH1 mutation. One such study could be to measure L-EV stiffness variation with distinct levels of the IDH1 mutation such that multiple points along the lipid composition spectrum between wild types and mutant cases are measured. Our results are consistent with recent studies that reported that the IDH1 mutation caused changes in lipid content and lipid order rearrangements in the membranes of internal organelles [6].

The advantages of our microfluidic approach over AFM are higher throughput and non-contact EV deformation. Though further validation of our technique is needed, our L-EV measurements here and in our previous publication [3] match a physical intuition that vesicles are softer than cells. In contrast, several AFM studies reported EV stiffnesses that are several orders of magnitude larger than cell stiffnesses [1]. In our view, approaches both should be used in a complementary manner and further improved to gain a more complete understanding of EV mechanics. Currently, AFM is the only mechanical measurement technique for nanoscale EV mechanical properties, while microfluidics offers an alternative microscale technique.

We are limited to studying microscale L-EVs because our microfluidic technique requires visual measurements of single L-EV deformation from optical microscopy, which is limited by the diffraction of visible light. To improve the size resolution of microfluidics, other imaging modalities (e.g., digital holography) that have a smaller diffraction limit could be used.

Most EV research has focused on smaller exosomes and microvesicles. The L-EVs studied here could be easier to handle and separate due to their large size and the ability to see them easily with conventional optical microscopy. L-EVs likely hold more biomolecular cargo that could make assays more accurate and robust for (large) EV subpopulation characterization. This study may imply that the less-studied L-EVs could also rich multiplex biomarkers for bioanalysis.

ACKNOWLEDGEMENTS

This work was supported in part by National Institutes of Health grants (R21CA217662, R01GM138778 to H.I.). M.H.J. is supported by Basic Science Research Program through the National Research Foundation of Korea (NRF-2021R1A6A3A14039686).

REFERENCES

[1] LeClaire, M., et al., *Nano Sel.*, 2:1–15, 2021.
[2] Vorselen, D., et al., *ACS Nano*, 11:2628–2636, 2017.
[3] Rodriguez-Quijada, C., J.B. Dahl. *Biochim. Biophys. Acta, Gen. Subj.*, 1865:129657, 2021.
[4] Murata, T., *J. Phys. Soc. Jpn.*, 50:1009–1016, 1981.
[5] Israelachvili, J.N., *Intermol. Surface Forces*, Academic Press, 2011.
[6] Lita, A., et al., *Nat. Commun.* 12:614, 2021.

PARTIAL MENISCECTOMY OF THE MENISCAL INNER PART INCREASES THE MENISCAL DEFORMATION AND EXTRUSION

Satoshi Yamakawa(1), Tomoki Ohori(2), Issei Ogasawara(1, 3), Akira Tsujii(1),
Shoji Konda(1, 3), Seira Sato(4), Takashi Kanamoto(3), Ken Nakata(3)

Osaka University Graduate School of Medicine, Osaka, Japan

- (1) Department of Sports Medical Biomechanics
- (2) Department of Orthopaedic Surgery
- (3) Department of Health and Sport Sciences
- (4) Department of Sports Medical Science

INTRODUCTION

The hoop stress is generated in the meniscus under the femoral compression load [1]. At that time, in the mid-substance of the meniscus, the compression and tensile stresses might be generated in the inner part and the outer part respectively like a beam bending situation due to the compression force from bony contact and tensile force from anterior and posterior horns. Based on that prediction, we hypothesized the inner part loss of the meniscus due to the partial meniscectomy may break the mechanical balance of the meniscus and may lead to the deformation and extrusion of the meniscus. Therefore, the aim of the present study was to investigate the effect of the inner part loss of the meniscus on its deformation and extrusion based on the biomechanical test for the radial meniscal tear model using the porcine knee joint.

METHODS

Porcine knees (n=6) were used for the test. The tibia was cut at 5 cm distally from the joint line after removed femur, and the soft tissue around the tibia was dissected down while the medial meniscus (MM) and medial capsule were preserved. The specimen was set at the lower jig of the material testing apparatus (ElectroForce 5500, TA instruments), and a 3 mm diameter indenter was touched down to a 2 mm inner point on the mid-region at the rim of the anterior-posterior length of the MM (Figure 1). As a pre-load, 1 N of compression force was applied to the MM on the specimen, and this configuration was defined as a reference to calculate the meniscus displacement. After recording the reference configuration, the compression force was applied up to 10 N to the MM. During the test, the meniscus motion and deformation were measured by a 3-D motion capture system (V120 Trio, OptiTrack). The markers for the measurement were placed at the meniscus-ligament junction of the anterior and posterior horns, and the mid-point of the meniscus outer surfaces. After the measurement of the intact state, the radial tear with 80% length of the mid-substance width was created from the inner edge at the mid-point of the MM, and the

measurement was repeated. Finally, the MM had been removed a total of 10 mm anterior-posterior length based on the radial tear and it was defined as partial meniscectomy in the present study, and then the measurement was repeated. The meniscus deformation was calculated based on the anterior-posterior length change and it was standardized by reference configuration. The meniscus displacement was calculated based on the reference configuration and it was standardized by the meniscus width in each specimen.

To statistically compare the radial tear and partial meniscectomy groups, paired t-test was performed on the displacement and deformation data.

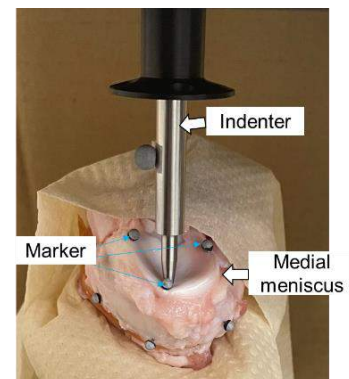


Figure 1 Experimental setup

RESULTS

In the anterior-posterior length change of the MM, the radial tear group showed $0.9 \pm 0.9\%$ and $0.8 \pm 1.3\%$ decrease compared to the intact in response to 1 N and 10 N of compression load, respectively in the radial tear group (Figure 2). The partial meniscectomy group

showed $4.5 \pm 2.0\%$ and $4.3 \pm 2.2\%$ in response to 1 N and 10 N of compression load, respectively, and those decreases were significantly greater than those of the radial tear group.

In the displacement of the meniscus, the radial tear group showed $3.5 \pm 1.7\%$ and $6.1 \pm 2.1\%$ displacement in response to 1 N and 10 N of compression load, respectively. The partial meniscectomy group showed $7.0 \pm 3.9\%$ and $10.7 \pm 2.7\%$ displacement in response to 1 N and 10 N of compression load, respectively, and those values were significantly larger than those of the radial tear group (Figure 3).

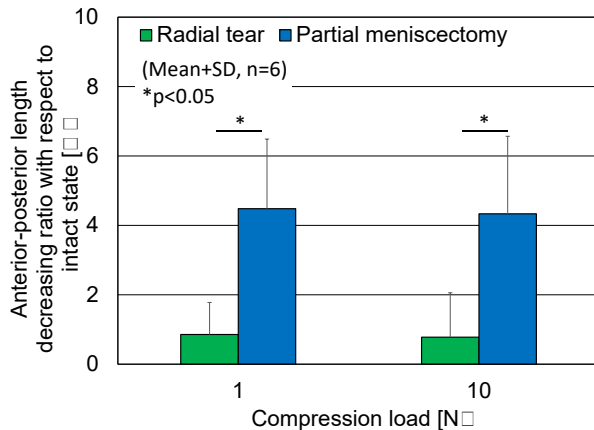


Figure 2 Anterior-posterior length decreasing ratio with respect to the reference configuration in the radial tear and partial meniscectomy groups

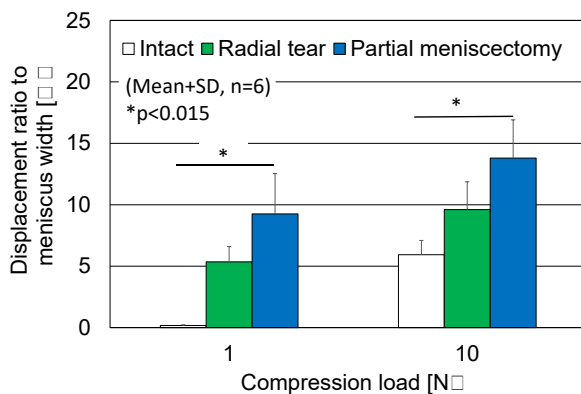


Figure 3 Mid-substance marker displacement ratio to meniscus width in intact, radial tear, and partial meniscectomy groups

DISCUSSION

In the present study, the change of the meniscal motion and deformation due to the radial tear and partial meniscectomy were clearly indicated based on the biomechanical test. As a main result of the present study, the partial meniscectomy generated great anterior-posterior deformation and mid-substance part displacement.

In the anterior-posterior length change, the partial meniscectomy group showed a significantly large decrease compared to applying the radial tear individually. In general, under outward direction loading at the mid-substance of the meniscus from the femur, the ligament of the anterior and posterior horns generate inward direction tensile force to prevent the meniscus extrusion. During that situation, the meniscus deforms like a U or V shape, and this deformation generates tensile and compression stresses at the outer and inner parts, respectively. At the inner part, the tissue is compressed under loading and sustained each

other to keep the structure shape and function. After the radial tear was created, although the same deformation was generated by the loading, the structure still remained and could support each tear side. Therefore, the anterior-posterior length change was small in the radial tear group while the partial meniscectomy group generated a significantly larger change due to the loss of the tissue at the inner part.

The amount of displacement of the mid-substance marker of the meniscus was significantly greater than that of the normal meniscus in both the radial tear and partial meniscectomy groups, although the partial meniscectomy group showed significantly greater displacement than the radial tear group, with approximately 130% and 45% greater than the intact and radial tear groups, respectively. Those results suggested that large V shape deformation due to the loss of the inner part resulted in the large displacement of the mid-substance. That result indicated that individually applying the radial tear affected the displacement compared to the intact state, while the partial meniscectomy more strongly affected the displacement compared to the radial tear individual applied state.

The V shape deformation was led by the bending torque at the mid-substance generated by the ligament tensile force and compression forces from the bone. To estimate the resistance capability to the bending torque at the mid-substance of the meniscus, calculated the cross-sectional secondary moment. In the intact meniscus, the shape of the cross-sectional area at the mid-substance is a triangle. On the other hand, the shape of the remained cross-sectional area after partial meniscectomy is a trapezium (Figure 4). From the ratio of each part between the intact and partial meniscectomized menisci based on the present experimental procedure, the cross-sectional secondary moment decreased by 98% in the partial meniscectomized meniscus compared to the intact meniscus. It is suggested that the weakness to resistance to the bending torque is one of the factors to lead the large V shape deformation in the partial meniscectomized meniscus.

Those results suggested that loss of the inner part of the meniscus led to the abnormal deformation of the meniscectomized part and resulted in its large displacement related to the extrusion. Those results supported our hypothesis based on the bending torque generated by the outward direction loading. Additionally, it is suggested that repairing the inner part for remaining the structure to resist the bending torque is the key to the prevention of meniscus extrusion.

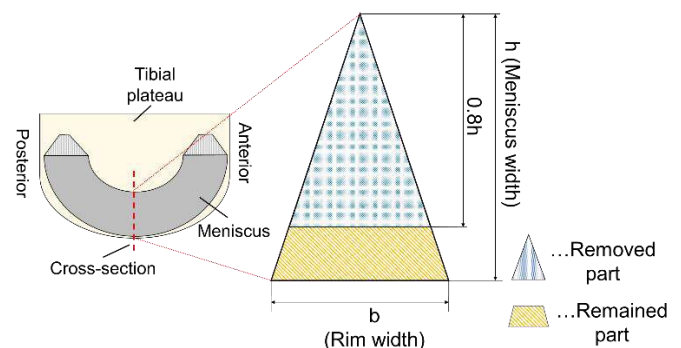


Figure 4 Schematic draw of the cross-sectional area of the mid-substance in the meniscus

ACKNOWLEDGEMENTS

This work was supported by a grant from the Japan Society for the Promotion of Science, JSPS KAKENHI 21K18054.

REFERENCES

- [1] Sharma L, et al, Arthritis Rheum, 58(6): 1716-26, 2008.

NON-CONCUSSIVE HEAD IMPACT KINEMATICS AND BRAIN STRAIN DISTRIBUTION IN COLLEGIATE FOOTBALL

Enora Le Flao (1), Xianghao Zhan (1), Nicholas J. Cecchi (1), Yuzhe Liu (1), Ashlyn A. Callan (1),
Landon P. Watson (1), Collin Pang (1), Gerald A. Grant (2,3,4), Michael M. Zeineh (5),
David B. Camarillo (1,2,6)

- (1) Department of Bioengineering, Stanford University, Stanford, CA 94305, USA
- (2) Department of Neurosurgery, Stanford University, Stanford, CA 94305, USA
- (3) Department of Neurology, Stanford University, Stanford, CA 94305, USA
- (4) Department of Neurosurgery, Duke University, Durham, NC 27710, USA
- (5) Department of Radiology, Stanford University, Stanford, CA 94305, USA
- (6) Department of Mechanical Engineering, Stanford University, CA 94305, USA

INTRODUCTION

To better understand the mechanisms of concussion, head impact sensors such as instrumented mouthguards have been increasingly used in recent years. These devices measure the motion of the skull upon an impact, and researchers have primarily used the peak of the linear and angular acceleration signals to describe the exposure to potentially injurious events [1]. Concussion has been shown to occur in the absence of any high-magnitude singular event [2], but the effects of low-magnitude sub-concussive head impacts on mid- and long-term health remain unclear.

The lack of a strong relationship between head impact exposure and brain injury may be partially explained by the inadequacy of peak kinematics to describe trauma to the brain. In contrast, the amount of strain experienced by the brain, estimated using finite element modeling, has been shown to be a relevant descriptor of injury [3]. However, global measures of strain may not appropriately describe the damage sustained by the various regions of the brain. Therefore, the objective of this research is to describe the regional distribution of brain strains resulting from sub-concussive head impacts.

METHODS

Head acceleration events were collected from collegiate football players during practices and games from 2018 to 2021. The Stanford instrumented mouthguard (MiG2.0) [4], containing a triaxial accelerometer (sampling rate: 1000 Hz) and a triaxial angular rate sensor (8000 Hz), was used to record 200-ms events when the linear acceleration on any axis crossed a 10-g threshold. True head impacts were later classified using a three-step process. First, a deep learning algorithm eliminated events that were likely to result from spurious triggering. Second, the remaining events were reviewed on video and were kept only if they resulted from a direct impact to the head. Third, an author visually analyzed the raw kinematic signals and eliminated the events showing abnormal frequency content and high-magnitude

spikes, which would be indicative of the mouthguard decoupling from the skull or of an electronic issue [5].

For verified head impacts, the kinematics signals were processed with a Butterworth filter at a cutoff frequency of 160 Hz. Angular acceleration was derived, and linear acceleration was transformed to the estimated head's center of gravity. The peaks of the resultant linear acceleration, angular velocity, and angular acceleration signals were extracted as PLA, PAV, and PAA, respectively.

To compute brain strains, we used a deep learning algorithm [6] based on the KTH head and brain finite element model, composed of 4,124 elements divided into anatomical regions with specific material properties [3]. The algorithm used features extracted from the angular kinematic signals to estimate the maximum principal strain (MPS) experienced by each element. The 95th percentile of the MPS (MPS95) was calculated for each impact, as well as the cumulative strain damage measure (CSDM), which represents the percentage of brain volume experiencing strains above a defined threshold (here 15%).

A Shapiro-Wilk test determined that the distribution of the peak kinematics and brain strains was significantly skewed towards low magnitude values. Therefore, the differences in strain between brain regions were examined with a Kruskal-Wallis analysis of variance test with a Dunn-Šidák correction.

RESULTS

Over the duration of the study, acceleration events were obtained from 45 athletes over a total of 1369 player-sessions. Here, we present preliminary results on a subset of 209 verified head impacts, collected from 21 athletes over 77 player-sessions (see an example impact in Figure 1A). For the 209 impacts, the median and inter-quartile range for the PLA, PAV, and PAA were, respectively: 21.07 [14.74 - 26.85] g, 13.25 [10.59 - 16.49] rad.s⁻¹, and 1,135.94 [908.47 - 1,599.85] rad.s⁻².

The median MPS95 for the whole brain was 6.16 [5.06 - 7.75] %. The MPS95 varied across brain regions ($p < 0.001$), with the strains in

the midbrain, grey matter, white matter, and corpus callosum being significantly higher than in the thalamus, brainstem, and cerebellum (Table 1). Overall, the median CSDM was 0% with 18 impacts (8.6% of the dataset) showing element-wise strain over the 15% threshold. For those impacts, the whole brain CSDM ranged from 0.02 to 62.71%; CSDM values for each region are presented in Table 1.

Table 1: Median [interquartile range] of the MPS95 for the 209 verified head impacts and CSDM for the 18 impacts over 0%, for the whole brain and the various regions. The abbreviations in the MPS95 column indicate significant differences between regions.

Brain region	MPS95 (%) (N = 209)	Regional CSDM (%) (N = 18)
Whole Brain (WB)	6.16 [5.06 - 7.75] ^{CC, TH, BS, CL}	6.57 [1.58 - 24.56]
Midbrain (MB)	6.70 [5.87 - 8.40] ^{WM, CC, TH, BS, CL}	6.25 [0.00 - 38.28]
Grey Matter (GM)	6.51 [5.41 - 8.21] ^{WM, CC, TH, BS, CL}	9.88 [2.62 - 33.16]
White Matter (WM)	5.73 [4.64 - 7.02] ^{MB, GM, TH, BS, CL}	4.65 [0.60 - 21.94]
Corpus Callosum (CC)	5.33 [4.33 - 6.91] ^{WB, MB, GM, TH, BS, CL}	2.44 [0.00 - 62.80]
Thalamus (TH)	3.91 [3.19 - 4.99] ^{WB, MB, GM, WM, CC, CL}	0.00 [0.00 - 1.43]
Brainstem (BS)	3.83 [3.09 - 4.92] ^{WB, MB, GM, WM, CC, CL}	0.00 [0.00 - 0.00]
Cerebellum (CL)	2.02 [1.63 - 2.60] ^{All}	0.00 [0.00 - 0.00]

DISCUSSION

In this study, we calculated and described the global and regional brain strains experienced as a result of direct head impacts in collegiate football. The global strains (MPS95) from our sample of 209 impacts (median of 6.16%) were slightly lower than previously reported for collegiate women's soccer headers (8.84%) [7]. While differences may be due to the sport and/or the population, there are also multiple methodological distinctions between the two studies, such as the impact selection process. Here, we visually selected impacts based on the raw kinematics to keep only events that were most likely to represent true head motion. It has been shown previously that sensor decoupling from

the skull results in the overestimation of head kinematics [4], which would result in the overestimation of brain strains. Further analysis is required to determine the effect of signal quality on the magnitude of brain strains.

No other study has reported regional MPS95 values. However, the results from studies reporting regional peak MPS are similar to our findings, with the strain measured in the midbrain and corpus callosum being generally higher than in the thalamus and brainstem [8,9]. Studies involving neuroimaging can elucidate the consequences of these regional variations.

The limitations of the present study include the absence of strain rate. It has been suggested that strain rate is a valuable predictor of brain injury, and future versions of the deep learning model will allow the calculation of this important metric. Additionally, our analyses may benefit from the use of region-specific strain thresholds, as the properties of each brain region differ and they may not respond similarly to strain.

ACKNOWLEDGEMENTS

This work was supported by the PAC-12 Student-Athlete Health and Well-Being Initiative.

REFERENCES

- [1] Le Flao, E et al., *Sports Med*, 52:481–504, 2021
- [2] Beckwith, J et al., *Med Sci Sports Exerc*, 45(4):747-54, 2013
- [3] Kleiven, S, *Stapp Car Crash J*, 51(1): 81-114, 2007
- [4] Liu, Y et al., *Ann Biomed Eng*, 48(11):2580-98, 2020
- [5] Rooks, T et al., *ASME IMECE Proceedings*, 2019
- [6] Zhan, X et al., *IEEE Trans Biomed Eng*, 68(11):3424-34, 2021
- [7] Filben, T et al., *J Biomech*, 128:110782, 2021
- [8] Tiernan, S et al., *Comput Methods Biomech Biomed Engin*, 24(3): 278-88, 2020
- [9] Brooks, J et al., *Neurotrauma Rep*, 2(1):354-62, 2021

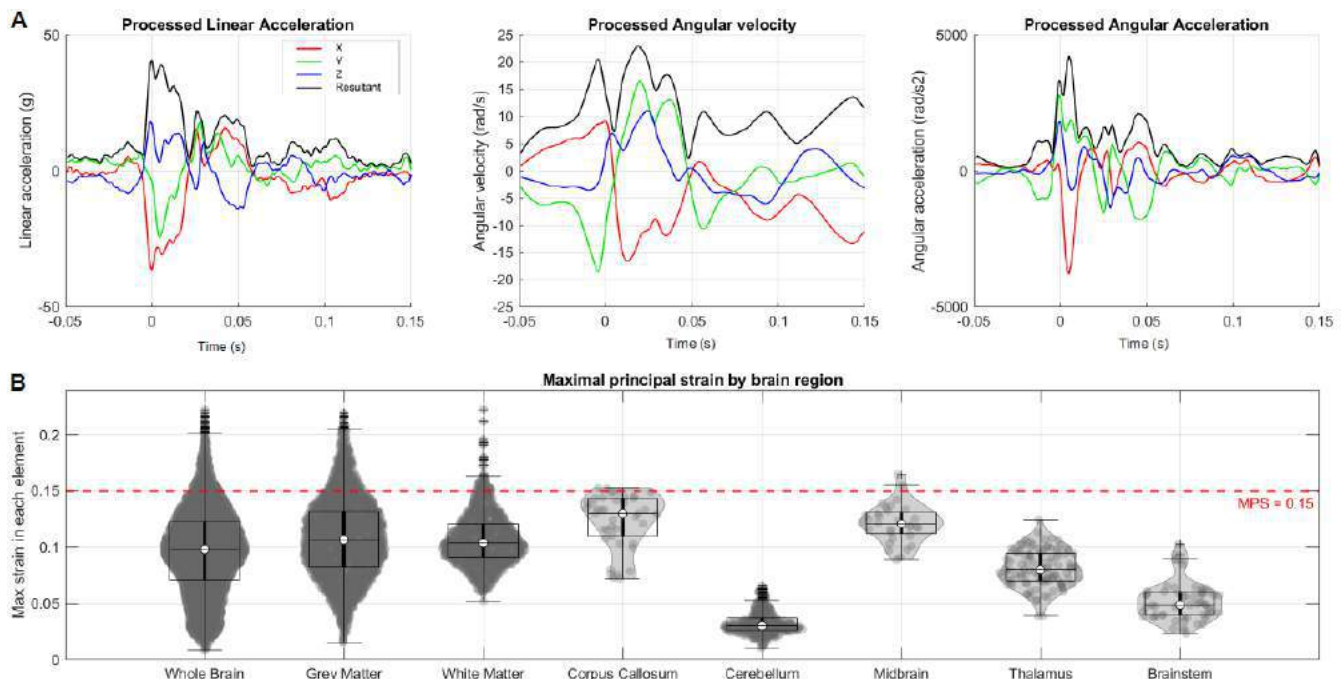


Figure 1: Example of one video-verified direct head impact showing high levels of strain. (A) Processed kinematics; (B) Distribution of the maximal principal strain experienced by each of the 4,124 elements of the brain model. Each region's shade of grey results from the overlapping of multiple individual elements. The horizontal dashed line represents a maximal principal strain value of 15%.

INVESTIGATING ELASTIN FIBER KINEMATICS IN PORCINE EPICARDIAL LAYER WITH LASER SCANNING CONFOCAL MICROSCOPY

Sara R. McMahan (1), Alan Taylor (1), Duc Khang Chung (1), Jiazhu Xu (1), Matthias Peltz (2),
Pietro Bajona (2,3), Yi Hong (1), Jun Liao (1)

- (1) Department of Bioengineering, University of Texas at Arlington, Arlington, TX 76010, USA
(2) Department of Cardiovascular and Thoracic Surgery, University of Texas Southwestern Medical Center, Dallas, TX 75390, USA
(3) Allegheny Health Network-Drexel University College of Medicine, Pittsburgh, PA 15212, USA

INTRODUCTION

Current research increasingly indicates the importance of structural proteins in the function of highly dynamic tissues in the body [1]. Specifically, elastin provides resilience and unique kinematic capabilities to many components within the respiratory and cardiovascular systems. Recently, our lab reported that the epicardial layer, rich in elastin, acts like a prestrained 'balloon' that wraps around the heart and functions as an extra confinement and protective interface for the ventricle [2]. This novel discovery alone indicates the necessity of elastin as an integral component of overall cardiac output. Moreover, these conclusions emphasize the importance of a full biomechanical characterization of the epicardial layer, which has vastly been ignored compared to the myocardial layer. For instance, how the elastin fibers arrange themselves into epicardium interface is still a missing component of our current understanding. Though we now know this intricate fiber network enables a significant dynamic deformation during the ventricular diastolic expansion and systolic contraction, we have limited knowledge on how this is so. To begin answering some of these questions, we designed a custom miniature uniaxial stretcher compatible for imaging under a laser scanning confocal microscope (LSCM) to reveal the epicardial elastin kinematics under mechanical loading. Using this technique will enable us to explore the microstructural arrangement and dynamic behavior of the elastin fibers responsible for maintaining cardiac output.

METHODS

Fresh adult epicardial layer samples were dissected from the porcine left ventricle and sutured to denote the heart longitudinal direction. The epicardial layers were cleaned of most excess muscular tissue (remaining sample ~1 mm thick). The samples were decellularized for 24 hours in 0.1% SDS and rinsed with distilled water overnight to remove any excess detergent. The decellularized samples were treated with glycerol to replace the water content in a gradient

fashion, i.e., 30 minutes in 25% glycerol, 30 minutes in 50% glycerol, 30 minutes in 75% glycerol, and 30 minutes in 100% glycerol. The glycerol has an optical index very close to collagen fibers and thus make the collagenous tissue transparent. Water, on the other hand, has an optical index different from collagen fibers. The mismatched optical index between the water and collagen interface is integral to the imaging process, as the interface dissipates light. This optical behavior causes the hydrated collagenous tissue to appear as an opaque whitish color. The transparency of the tissue sample enables a deeper laser penetration, allowing for LSCM imaging of the 3D elastin fiber matrix.

Glycerol-treated samples were mounted onto a custom-made uniaxial stretcher, which was designed to fit onto a LSCM sample stage for imaging. Markers were used to indicate the position of the sample stretching so deformation could be tracked. One end of the tissue was attached to stationary hooks within the uniaxial stretcher. The other end of the tissue was attached to a movable stand via hooks so that the tissue could be stretched to different strains for LSCM imaging. The following step strains were applied: 0%, 10%, and 20%. These strains were chosen to capture the elastin fiber morphology at the reference state (0%), in the toe region (10%), and in the linear region (20%) of the stress-strain curve. Note that the loading direction for this experiment is along the heart longitudinal direction.

A Nikon LSCM (Nikon A1R HD25) was used for 3D elastin fiber imaging. The tissue was imaged using the CY3 channel, Ex 543 nm to obtain 2D images and z-stacks of the elastin at different tissue strain levels. A small weight was placed on the tissue to ensure a close tissue contact with the glass imaging window that allows confocal laser passing through. Images were further processed in ImageJ to determine waviness ratios among groups, as well as fiber alignment distribution. Mean \pm standard deviation was used to present the experimental data and determine if the parameters were statistically different using one-way analysis of variances (ANOVA). Data was considered significant when $p < 0.05$.

RESULTS

The 3D elastin fiber structure at different step strain levels were captured by LSCM imaging. The real time elastin fiber structure tracking showed unique engagement of fiber kinematics at different stages of the tissue's loading conditions (**Figure 1**). Under 0% strain (**Figure 1A**), fibers appeared closely bundled and wavy, with a significant degree of alignment. Note that the uniaxial loading was conducted along the horizontal direction of the image plane, which was also the longitudinal direction of the epicardium sample. Hence, the elastin fibers in **Figure 1A** indicated an alignment slightly deviating from the circumferential direction of the left ventricle. At 10% tissue strain (**Figure 1B**), the deformation reached to the toe region of the stress-strain curve, i.e., where fiber uncrimping took place. The rotations and realignment of fibers occurred as the tissue was stretched, and a defined, mesh-like structure appeared as each fibers uncrimped and clearly separated from each other. At this stage, the elastin fibers were spread wider in the horizontal loading direction, which was perpendicular to the original overall fiber orientation. While most fibers appeared largely parallel, this strain level initiated the load bearing capabilities of a number of fibers that spanned in the direction normal to the preferred-fiber direction (**Figure 1B**).

Under 20% global tissue strain, fibers showed further mesh-pulling kinematics, in which the alignment shifted from a unimodal to a flattened distribution (**Figure 1C**). The high longitudinal strain appeared to engage even more fibers rotating towards the longitudinal direction. Mesh-like fiber network at 20% global tissue strain showed a taut and stretched morphology, consistent with the fact of tissue stretching was in the linear region of the stress-strain curve. Waviness ratio of elastin fibers under 10% and 20% global strains were smaller when compared to the elastin fibers under no strain.

DISCUSSION

We were able to image elastin fibers under different step strains to reveal the engagement of epicardial elastin fibers in global tissue deformations. At 0% global tissue strain, elastin fibers exhibited a high degree of waviness and fibers bound closely. Elastin fibers appeared relaxed and entangled, resulting in a less distinguished 3D fiber image due to autofluorescence signal disbursement. Under 10% global tissue strain, the elastin fibers were pulled apart and the mesh-like elastin architecture were shown with the 3D reconstructed LSCM image. This uncrimping, fiber rotation and mesh pulling kinematics corresponded well with the mechanical behavior in soft tissue toe region. Additionally, under 20% global tissue strain, elastin fibers indicted more fiber rotation towards the external loading direction with a taught, web-like mesh morphology. The distribution of fiber alignment reflected this fiber dynamic, with the alignment distribution shifting from a unimodal to a flattened distribution. Though there are still many gaps in our understanding elastin kinematics, our approach opens a new avenue to understand the structural mechanism of epicardium under dynamic, complex large deformations that associated with vigorous cyclic pumping of the heart.

ACKNOWLEDGEMENTS

NIH R15HL159599, R01HL157050

REFERENCES

- [1] H. M. Langevin *et al.*, *BMC Systems Biology*, vol. 1, no. 1, pp. 1-12, 2007.
- [2] X. Shi *et al.*, *Journal of the Royal Society Interface*, vol. 16, no. 152, p. 20190028, 2019.

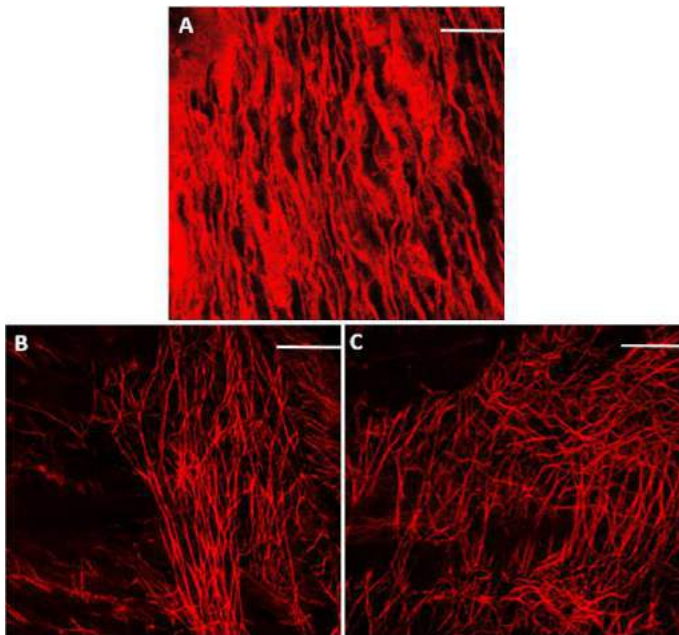


Figure 1: 3D confocal images of elastin fibers undergoing (A) 0% global tissue strain, (B) 10% global tissue strain, and (C) 20% global tissue strain. The uniaxial loading was pull along the horizontal direction of the image plan, which was also the heart longitudinal direction of the epicardium sample.

Scale bar = 100 μ m

PRESTRESS ON NASCENT DESMOSOMES REGULATES ELECTROPHYSIOLOGY OF STEM CELL-DERIVED HEART MUSCLE

Daniel W. Simmons^{1,2}, David R. Schuftan¹, Jingxuan Guo³, Kasoorelope Oguntuyo¹, Ghiska Ramahdita^{2,3}, Mary Munsell¹, Brennan Kandalaf¹, Missy Pear¹, Nathaniel Huebsch^{1,2}

(1) Department of Biomedical Engineering, Washington University, St. Louis, MO, USA
(2) NSF Center for Engineering Mechanobiology, Washington University, St. Louis, MO, USA
(3) Department of Mechanical Engineering and Materials Sciences, Washington University, St. Louis, MO., USA

INTRODUCTION

Cardiomyocytes derived from human induced pluripotent stem cells (hiPSC) are promising tools to predict drug-induced arrhythmias and study inherited diseases, but physiologic immaturity remains a challenge. Compared to hiPSC-derived cardiomyocytes (hiPSC-CM) grown in monolayers, hiPSC-CM within engineered tissues typically show hallmarks of better maturity, as evidenced by more “*in vivo*-like” cell shape, sarcomere architecture and pharmacology. However, mechanisms through which “*in-vivo*-like” cellular organization translates into more mature physiology remain uncertain, making it challenging to devise strategies to accelerate maturation further.

We hypothesized that prestress transmitted across cell-cell contacts is higher in aligned 3D tissues and enhances hiPSC-CM maturation. To test this hypothesis, we developed a double molding approach to replicate high resolution 3D prints into elastomers and leveraged this tool to study how geometrically-determined tissue prestress, together with the presence of desmosome plaques that link cell-cell junctions to intermediate filaments [1], regulates electrophysiology of hiPSC-derived micro-heart muscles (μHM) [2].

METHODS

Devices: μHM are formed by seeding hiPSC-CM into dogbone-shaped molds atop culture substrates. Dogbones consist of square “knobs” (1mm x 1mm) connected by a rectangular shaft (200μm wide, and either 0, 1 or 2mm long). We developed a double molding technique to replicate high-resolution 3D printed features into poly (dimethyl siloxane) (PDMS). Briefly, dogbones were printed in FormLabs ClearResinTM on a Form3 printer. Either agar or alginate hydrogels were formed as negative replicas of the 3D print. Sylgard 184 PDMS was then crosslinked within the gel negatives [2]. Replication fidelity was gauged based on a user-defined “fidelity score” from 1-5 (5 being best).

Cardiomyocyte Differentiation: Wild-type iPSC (WT) were genome edited using CRISPR to induce a homozygous knockout of

plakophilin-2 (PKP2). PKP2^{-/-} and control iPSC were differentiated into hiPSC-CM by manipulating Wnt signaling [3]. hiPSC-CM together with stromal cells were seeded together at a density of 7.5x10⁷ cells/mL (3μL) into PDMS stencils to form μHM with 0, 1 or 2mm shafts.

μHM Phenotyping: Electrophysiology was assessed optically in spontaneously contracting day 15 μHM stained with the voltage sensitive dye BeRST-1 [4]. Ca²⁺ was tracked using GCaMP6f, a genetic Ca²⁺ indicator [5]. Action potential and Ca²⁺ transient waveform morphology were analyzed using open source Matlab pipelines [6].

Saxitoxin (STX) was used as a probe for sodium current (*I_{Na}*), and E4031 was used as a probe for the rapidly rectifying potassium current (*I_{Kr}*). Cellular structure and protein localization were assessed in confocal micrographs of 12μm longitudinal μHM cryosections stained for cell shape (Wheat Germ Agglutinin; WGA), nuclei (Hoescht) and with antibodies against Sarcomeric α-Actinin, sodium channels (Nav1.5) and gap junctions (Connexin 43).

Statistical Analysis: Comparisons amongst groups were made first by ANOVA followed by post-hoc Holm-Sidak test. Comparison between only two groups was performed with two-tailed student *t*-test.

RESULTS

Hydrogel assisted molding replicated 3D printed features into PDMS with high fidelity (**Fig. 1A,B**). Gel ultimate modulus was critical for predicting feature transfer success (**Fig. 1C**). Increased μHM shaft length was hypothesized to increase tissue prestress based on a Comsol model of μHM uniform compaction (**Fig. 2A,B**). Within predicted regions of prestress in μHM shafts, we observed cellular alignment and sarcomere organization (**Fig. 2C,D**). We verified robust nuclear alignment in both control and PKP2^{-/-} μHM (**Fig. 2E**). However, tissue-geometry induced nuclear elongation was reduced in PKP2^{-/-} compared to controls, suggesting that the nascent desmosomes are required for complete transmission of cell-cell junctional stress throughout the cell (**Fig. 2F**).

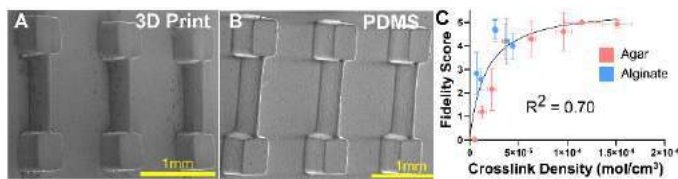


Figure 1: Scanning electron micrographs of (A) stereolithographic 3D prints and (B) PDMS replicas. (C) Hydrogel crosslink concentration regulates replication fidelity.

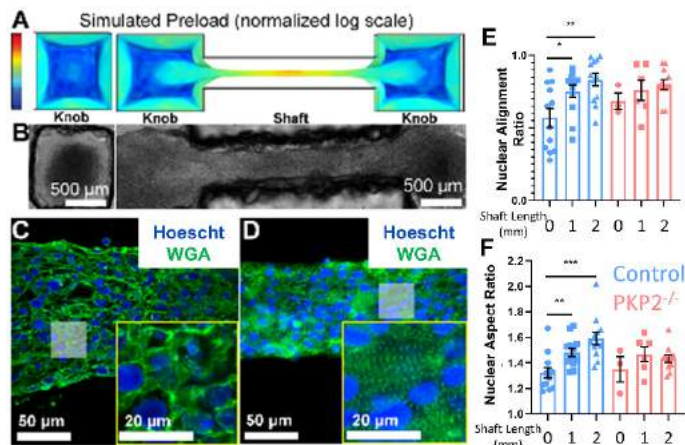


Figure 2: (A) Simulated prestress (Comsol) developed during compaction of μ HM with different shapes. (B) Micrographs of μ HM with either 0mm (left) or 2mm (right) shaft length. (C-D) iPSC-CM in μ HM stained with (C) WGA and (D) antibodies against Sarcomeric α -Actinin (ACTN2). (E-F) analysis of (E) nuclear alignment with respect to shaft, and (F) nuclear aspect ratio, a measure of nuclear deformation in.

Tissue prestress had global effects on electrophysiology (Fig. 3A). Strikingly, studies in day 15 μ HM with the sodium current (I_{Na}) specific probe saxitoxin (STX) suggest that I_{Na} was absent in 3D tissues without geometrically-induced prestress (Fig. 3B). In contrast, E4031-dependent hERG block was not dependent on μ HM geometry. qRT-PCR, immunostaining, and western analysis suggest that changes in sodium channel function triggered by tissue prestress are not directly related to expression of SCN5A, the pore forming subunit of the channel (data not shown). However, there may be changes in trafficking. PKP2^{-/-} μ HM showed much lower electrophysiologic change in response to tissue geometry compared to wild type controls. Although cardiomyocytes in PKP2^{-/-} μ HM exhibited nuclear alignment, these tissues had no response to STX (Fig. 3C).

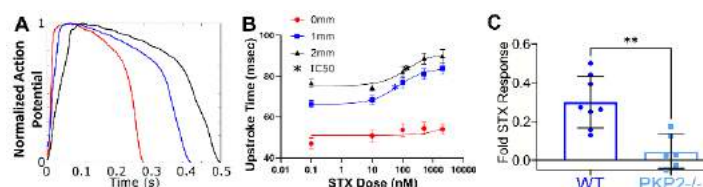


Figure 3: (A) Changes in action potentials in μ HM with different shaft length. (B) Action potential upstroke duration in response to dose of Saxitoxin (STX), a specific sodium channel blocker. (C) Fold response (normalized increase in upstroke duration) to 2 μ M STX in either wild type control (WT) or PKP2^{-/-} μ HM.

DISCUSSION

Our data show that hydrogels can be used to effectively replica mold high resolution 3D prints to create PDMS devices for tissue engineering. Using this technique to modulate tissue geometry/prestress, we observed global effects of tissue prestress on cellular electrophysiology. Pharmacologic studies indicated that a threshold level of prestress is necessary to generate STX-response sodium currents, while other channels such as hERG are less sensitive. This suggests a role for prestress in sodium channel function.

Prior studies performed in 2D micro-patterned cells have suggested that the channel protein $K_{ir2.1}$, encoding rectifying potassium current (I_{K1}), is directly regulated by integrin-ECM adhesion plaques, whereas the sodium channel is less sensitive to the presence of adhesions [7]. Here, we observed direct control over STX-responsive sodium currents by overall tissue geometry. Our finding that PKP2 knockout tissues allowed cardiomyocyte alignment but did not lead to STX-response currents suggest that alignment alone is insufficient to induce functional sodium channels, and instead that mechanical transmission of prestress across cell-cell junctions is critical to this response. While important to cardiomyocyte maturation, other currents, including hERG, appear less sensitive to prestress.

Because the overall levels of transcript and protein encoding SCN5A, the pore forming subunit of the sodium channel, were unchanged across conditions, our findings point to post-translational regulation mechanisms, potentially related to sodium channel trafficking [8] and/or activation, in response to prestress.

Our studies have limitations that will be addressed in future work. First, all-optical analysis of cellular electrophysiology precludes direct measurements of resting membrane potential and the absolute magnitude of the action potential upstroke. Second, our system thus far only allows geometrically-induced changes in prestress. In the future, we plan to address this limitation by dynamically stretching the μ HM. Finally, the resolution of the 3D prints we used in this study was insufficient to reveal whether there are fundamental limits to the resolution that can ultimately be achieved in transferring 3D prints into elastomers using gel intermediates. We are currently studying these resolution limits using 3D prints created by 2-photon photopolymerization on a NanoscribeTM system.

ACKNOWLEDGEMENTS

This work was supported by the Center for Engineering Mechanobiology (CEMB), an NSF Science and Technology Center, under grant agreement CMMI: 15-48571, the American Heart Association (19CDA34730016, TPA970198, PD828938) and the National Institutes of Health, (RO1HL159094).

REFERENCES

- [1] Broussard *et al.* *Cell Tissue Res.* 2015.
- [2] Simmons, *et al.* *BioRxiv*, 2022.
- [3] Lian, *et al.* *PNAS*, 2012.
- [4] Huang, *et al.* *JACS*, 2015.
- [5] Huebsch, Loskill, *et al.* *Tissue Eng. C.* 2015.
- [6] Oguntuyo, Schuftan, *et al.* *Tissue Eng. C.* 2022.
- [7] Sengupta, *et al.* *J Cell.Sci.* 2019.
- [8] Marchal, *et al.* *Circ Res.* 2021.

VISCOELASTIC AND SHEAR MECHANICAL PROPERTIES OF HUMAN HYPERTROPHIED SEPTUM

Katherine M. Copeland (1), Uday Chintapula (1), Alan M. Taylor (1), Duc Khang Chung (1), Yi Hong (1), Kytai T. Nguyen (1), Zhi-Ping Liu (2), Matthias Peltz (2), Pietro Bajona (2,3), Jun Liao (1)

- (1) Department of Bioengineering, University of Texas at Arlington, Arlington, TX 76010, USA
(2) Department of Cardiovascular and Thoracic Surgery, Department of Internal Medicine, University of Texas Southwestern Medical Center, Dallas, TX 75390, USA
(3) Allegheny Health Network-Drexel University College of Medicine, Pittsburgh, PA 15212, USA

INTRODUCTION

Hypertrophic cardiomyopathy (HCM) is often caused by genetic disorders, resulting in abnormal sarcomere, thickening of the heart muscle, and overgrowth of the left ventricular septum. This overgrowth can block the outflow of blood, disrupt the mitral valve coaptation, and increase the mechanical stress experience by the heart. Besides the hypertrophied and disarrayed cardiomyocytes, overexpressed fibrotic collagen alters the septum constitutions and microstructures [1]. As a result, cellular hypertrophy and the fibrotic environment change the mechanical properties of the hypertrophied septum, contributing to the abnormal biomechanical behavior of the septal tissues. For example, previous research showed that the circumferential myocardial shortening of ventricular muscle during contraction often takes place and contributes to the preservation of left ventricular systolic performance in HCM [2]. Due to the thickening of the wall, reduced left ventricular strain is also associated with poor cardiac performance, consequently resulting in heart failure [3]. However, the mechanical properties of human hypertrophied septum are not well investigated. In this study, we performed viscoelastic mechanical tests such as stress relaxation testing and creep testing, as well as shear mechanical testing on human hypertrophied septum obtained from myectomy surgeries and compared with the healthy septum.

METHODS

Hypertrophic septal samples were obtained from the surgical waste of clinical myectomy of the HCM patients (UTSW: IRB STU 082017-072). Patients include both male and female and range in age from 19 years to 71 years. Healthy human septal tissues were obtained from a tissue bank under the same IRB protocol. Septal tissues were then dissected for viscoelastic and shear mechanical tests. Samples prepared for viscoelastic and shear tests were aligned with the longitudinal direction of the septum. For viscoelastic tests, tissue samples were mounted onto the TestResources Universal Testing Machine

(Shakopee, MN) and tested in 1X Phosphate Buffered Saline (PBS). After preconditioning, the following testing protocols were completed: (1) Stress Relaxation: hypertrophied and healthy samples were loaded to 100g and the achieved strain was kept constant while recording the stress decay up to 15 minutes. (2) Creep: hypertrophied and healthy samples were loaded to 100g and kept at this constant load while deformation was continuously monitored up to 15 minutes. (3) Failure test: hypertrophied and healthy samples were loaded until failure (tissue breakage). Each sample was pulled at a rate of 0.5 mm/s. Simple shear testing was performed to assess shearing property of the septal tissues. 3 mm x 3 mm x 3 mm cubed septum samples were mounted onto custom-built steel shear plates with minimal cyanoacrylate. The shear direction is along the longitudinal direction of the septum tissue. The shear plates were then mounted on the TestResources Universal Testing Machine. The samples were subjected to positive and negative shear up to 50% strain with a loading rate of 0.02 mm/s.

RESULTS

We found that the healthy septum exhibited a stress decay similar to most soft tissues, $57 \pm 6.3\%$. On the other hand, hypertrophied septum exhibited a much larger stress decay, $68 \pm 11\%$. Both healthy septum and hypertrophied septum showed a small amount of creep over time. The final creep amount at 15 minutes reached $9.1 \pm 1.0\%$ for healthy septal tissues and $9.8 \pm 4.2\%$ for hypertrophied septum. We also observed that the healthy septum showed a very typical nonlinear concave upward stress-strain relation. However, the hypertrophied septum showed a stress-strain trend that was much less nonlinear. The hypertrophied septum had an initial modulus that was higher than healthy septal tissues, most likely due to the abundant fibrotic collagen associated with HCM. An important observation was that the healthy septum had much higher mechanical strength than the hypertrophied septum (failure stress -

healthy: $2,561 \pm 919$ kPa vs HCM: 494 ± 206 kPa). In the high strain region, the healthy septum was also stiffer than the hypertrophied septum. Both healthy and hypertrophied septum demonstrating a nonlinear shear behavior. The hypertrophied septum appears much stiffer with greater energy dissipation than the healthy septum. The maximum shear modulus of the healthy septal tissues and hypertrophied septum were 100 ± 12 kPa and 250 ± 73 kPa, respectively.

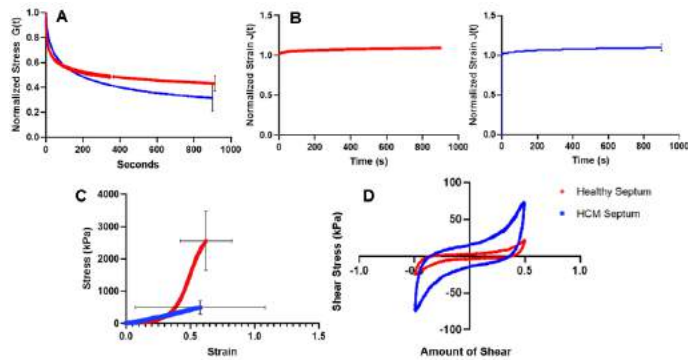


Figure 1: (A) Average stress relaxation curves, (B) Average creep curve, (C) Average stress-strain curves up to tissue failure, and (D) Shear stress-strain curves for human healthy septum (red) and hypertrophied septum (blue).

DISCUSSION

Overall, hypertrophied septum had larger stress relaxation, larger creep, and was stiffer at the initial phase of tissue loading, less nonlinear, less stiff in the linear region, and much weaker in mechanical strength. We also found a stiffer shear behavior and a greater energy dissipation during simple shear test. The stress relation and creep behavior, the failure behavior, and the shear property all reflected the fact that hypertrophied septum had more disorganized fibrotic collagen fibers when compared with the healthy septum. The poorly organized, pathological compositions in hypertrophied septum seemed to lose the benefit of native tissue design and hence exhibited an inferior viscoelastic and shear mechanical behavior as described above. Our viscoelastic and shear mechanical data build a strong foundation to understand tissue behavior of hypertrophied septum and the degree of its deviation from the healthy septum.

ACKNOWLEDGEMENTS

NIH R15HL159599, R01HL157050

REFERENCES

- [1] Varnava et al, Heart 84(5) (2000) 476-482.
- [2] Urbano-Moral et al, Circulation: Cardiovascular Imaging 7(1) (2014) 11-19.
- [3] Hinojar et al, International journal of cardiology 249 (2017) 467-472.

EFFECTS OF DYNAMIC COMPRESSIVE LOADING ON MECHANICAL AND BIOCHEMICAL PROPERTIES OF CHONDROCYTE-EMBEDDED HYDROGELS

Clarisse Zigan (1), Honganh Nguyen (2), Aritra Chatterjee (1), Alex Chortos (2), Deva D Chan (1)

(1) Weldon School of Biomedical Engineering, Purdue University, West Lafayette, Indiana, USA

(2) School of Mechanical Engineering, Purdue University, West Lafayette, Indiana, USA

INTRODUCTION

Articular cartilage found in synovial joints primarily functions to provide a smooth, lubricated surface to facilitate joint movement and load transmission [1]. Chondrocytes, the resident cells of cartilage, maintain and interact with the surrounding extracellular matrix (ECM) to maintain this function. Numerous studies have been conducted with the goal of developing tissue constructs that mimic native articular cartilage by culturing chondrocytes in three-dimensional hydrogels under compression, shear, or articular motion [2-4]. However, the role of specific ECM molecules, like hyaluronan (HA), in mechanical response remains unclear. The ECM is mechanosensitive to loading, therefore affecting tissue mechanical and biochemical properties [5]. By simulating the microenvironment of cartilage, cellular proliferation and ECM composition within hydrogel constructs can be enhanced. The goal of our study is to outline the mechanism of action of HA in chondrocyte-embedded hydrogels in response to compression over 21 days. The primary objective of the first time point (day 1 of loading) is to evaluate the performance of a custom bioreactor system and will be followed by a full three-week study, with more specific outputs.

METHODS

A custom bioreactor (Figure 1) was fabricated using machined aluminum for the base and 3D printed materials for the compression posts. An actuation waveform was created using a programmable logic controller to control the pneumatic cylinder, enabling a set frequency without causing extraneous vibrations or unwanted disturbances to unloaded samples. The system was verified using a displacement gage to compare the heights of individual compression posts and image analysis to compare strains applied to hydrogel constructs.

Human chondrocytes (SW1353, ATCC, passage 4) were seeded at a density of 2×10^5 cells/mL in neutralized type I collagen solution

(4mg/mL RatCol, Advanced Biomatrix) to form cylindrical hydrogel constructs (3.08 ± 0.32 mm \times 6.64 ± 1.35 mm ϕ , mean \pm SD). Following overnight polymerization, hydrogels were moved to a 24-well plate within a custom bioreactor. After 72 hours, hydrogels were subjected to a bout of unconfined, dynamic, uniaxial compression at 10% peak-to-peak strain superimposed on a 1% static offset strain, respectively to the initial dimensions, at a 1 Hz for three hours, based on a duty cycle of one hour of loading followed by one hour of unloaded rest. Separate, unloaded samples were used as free-swelling controls. Two hours after the end of loading, loaded and free-swelling hydrogels were evaluated for change in volume and viscoelastic behavior ($n = 3$), total sulfated glycosaminoglycan (sGAG) content ($n = 3$), or gene expression ($n = 3$).

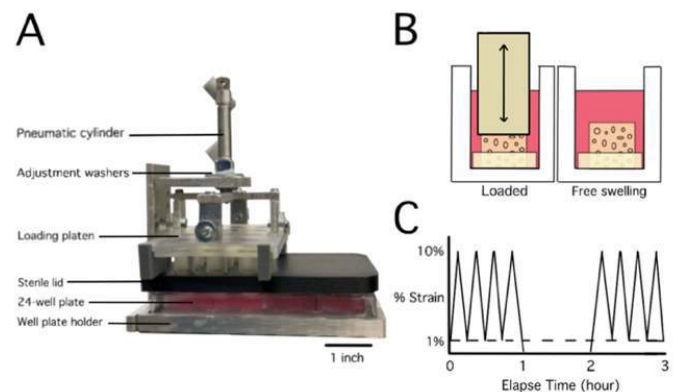


Figure 1: Custom compressive bioreactor. A: Compressive loading device. Loading platen situated over wells and to apply desired load.

B: Illustrative description of hydrogels loaded by the platen versus free swelling (not to scale). C: Schematic showing input parameters.

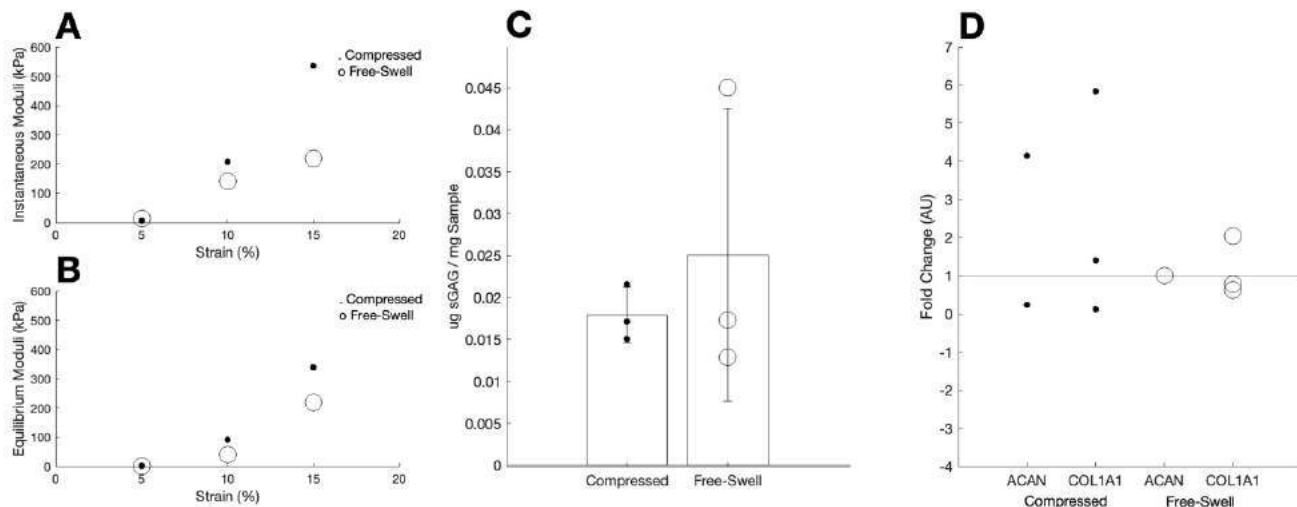


Figure 2: Cyclic compression does not significantly alter mechanical behavior, ECM composition, and gene expression after 1 day in culture.

A: Representative Instantaneous hydrogel moduli (kPa) response, $p > 0.05$ **B:** Representative Equilibrium hydrogel moduli (kPa) response, $p > 0.05$

C: sGAG expression quantified per mg of sample, $p > 0.05$ **D:** Fold changes in gene expression corrected for 18S rRNA, $p > 0.05$

Hydrogels were measured with a caliper to determine volume change. Samples then underwent stress relaxation experiments using an Electroforce 5500 test instrument while remaining hydrated in 1x phosphate buffered saline. Separate hydrogels were weighed and digested in 1mL of 50 μ g/mL Proteinase K solution overnight before sGAG content was measured using a 1,9-dimethylmethylene blue (DMMB) colorimetric assay. RNA was extracted and purified from remaining hydrogels using Qiazol reagent and rapid homogenization. TaqMan®-based qRT-PCR was used to measure expression of aggrecan (*ACAN*), type I collagen (*COL1A1*), and 18S rRNA.

RESULTS

The custom bioreactor was calibrated to ensure consistent loading could be applied, across the well plate and experiments. Post heights were measured using a displacement gauge and found to be statistically similar. To ensure 10% compression could be accurately applied, constructs were created from various materials (PDMS, agarose, and collagen), and compressed by the loading system. Images were taken prior to and during loading to verify the set strain amplitude. Target strain levels could be achieved with less than 1.5% deviation.

Following intermittent loading, hydrogels decreased in volume by $22.7 \pm 6.1\%$ and free-swelling hydrogels decreased in volume by $22.2 \pm 12.9\%$, showing no significance between groups. Stress relaxation tests were used to derive the instantaneous and equilibrium moduli (Figure 2A, 2B). While only one sample was usable from this output group, one can see a general trend where loaded samples have higher response moduli compared to free swelling samples. No significance was observed between the expression of sGAG concentration (Figure 2C) in compressed hydrogels (0.018 ± 0.003 ug sGAG / mg sample) versus free-swelling (0.025 ± 0.017 ug sGAG / mg sample). *ACAN* and *COL1A1* expression was evaluated with respect to the housekeeping gene 18S rRNA. The $2^{-\Delta\Delta C_t}$ method was used for analysis, showing no significant changes in *ACAN* or *COL1A1* relative gene expression levels, though a general trend can be seen in which compressed samples have higher expression (Figure 2D).

DISCUSSION

We observed that a single bout of compressive loading did not produce significant alterations in mechanical behavior, ECM content, or gene expression of chondrocyte-embedded collagen hydrogels. This

is supported by previous dynamic loading studies, which typically do not report significant changes between free-swelling and loaded culture groups until the third week of culture. Significant changes in contraction and moduli levels are not significant between free swelling and dynamic groups until week two of culture [6]. Biochemical metrics also tend to take two weeks in culture prior to demonstrating significances between culture parameters. For example, DNA content begins to differ after 7 days in culture and GAG synthesis begins to show significant differences after 14 days in culture [6]. Additionally, significant changes in *ACAN* and *COL1A1* are not generally observed until 14 days of culture [6-7].

We evaluated the biomechanical and biochemical response of chondrocyte-embedded type I collagen hydrogels after one bout of dynamic compressive loading. As expected, no significant effects are observed yet. Additional time points (3, 7, 14, and 21 days) are expected to yield significant differences of the aforementioned metrics. Future outputs will consist of metabolism-based assays to demonstrate cell viability over a longer period, immunofluorescent staining to highlight the location of ECM molecules, and additional probes specific to hyaluronan (i.e., *HAS*, *CEMIP*, *MMP*, and *HYAL* genes) to provide a fuller understanding of the effects of dynamic loading on HA and associated molecules in articular cartilage growth. Outlining the influence of dynamic loading on HA will be incredibly useful, as little is known about HA's mechanism of action in cartilage, despite gaining acceptance in treatment of cartilage-degenerating diseases [8].

ACKNOWLEDGEMENTS

This research was supported by NSF Award 2149946 and startup funding internal to Purdue. The authors declare no competing interests.

REFERENCES

- [1] Schmidt, T et al., *Arthritis Rheum*, 56(3):882-91, 2007
- [2] Bougault, C et al., *Nat Protoc*, 4(6):928-38, 2009
- [3] Salinas, E et al., *Biofabrication*, 12(4):045010, 2020
- [4] Schätti, O et al., *Eur Cell Mater*, 22:214-25, 2011
- [5] Bian, L et al., *Tissue Eng Part A*, 16(5):1781-90, 2010
- [6] Cao, W et al., *Regen Biomater*, 6(2):9-106, 2019
- [7] Cochis, A et al., *Sci Rep*, 7:45018, 2017
- [8] Ghosh, P et al., *J Rheumatol Suppl*, 43:155-7, 1995

FUNCTIONALIZED PARTICULATE CARRIERS TARGETING ABDOMINAL AORTIC ANEURYSMS UNDER FLOW

Moran Levi (1), Yevgeniy Kreinin (1), Ido Rachbuch (1), Perla Namour (1), Josué Sznitman (1),
Meinrad Gawaz (2), Netanel Korin (1)

(1) Department of Biomedical Engineering, Technion - IIT, Haifa, Israel

(2) Department of Cardiology & Cardiovascular Medicine, School of Medicine Eberhard Karl
University Tuebingen, Germany

INTRODUCTION

Cardiovascular diseases are a group of disorders of the heart and blood vessels and are a leading cause of morbidity and mortality¹. Abdominal Aortic Aneurysm (AAA) is the permanent dilation of the abdominal aorta that is caused by the local weakening of the arterial wall resulting from reoccurring inflammation processes caused by atherosclerosis² and the influence of hemodynamic forces. AAA is typically in fusiform shape and occurs mainly in the infrarenal aorta³ and when exceed 5.5 cm may lead to its rupture and a life-threatening internal bleeding with mortality of approximately 80%. If detected unruptured, patients are treated with either open surgery or endovascular aortic repairs, both comes with major post-operative complications. To date, there are no drug treatments that can inhibit AAA progression⁴.

Here, we study the deposition under physiological flow of particulate carriers coated with a collagen high affinity receptor, glycoprotein VI (GPVI), in *in vitro* models replicating mouse and human AAAs (see Figure 1 and Table 1).

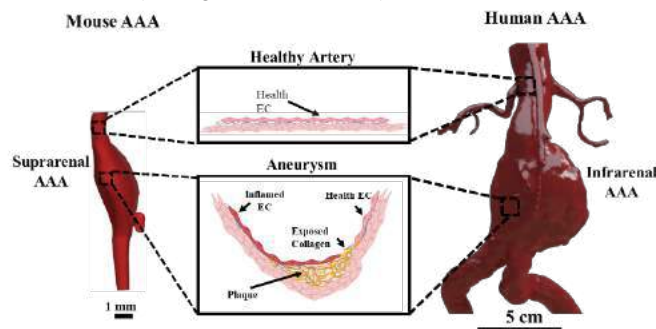


Figure 1 - AAA models - human vs. mouse

	Human	Mouse
Parent Vessel Diameter [mm]	24	1.2
Flow Rate [ml/min]	1000	15
Reynolds number	100	300

Table 1 - Human vs. mouse AAA models properties

METHODS

We fabricated 2 μ m GPVI-coated polystyrene particle carriers and then tested their deposition in an *in vitro* real-size reconstructed mouse and human AAA models. STL files of the mouse and human models were acquired and converted from US or CT angiogram scans (see Figure 1), respectively. The STL files were altered to our needs in SOLIDWORKS and printed out in a 3D printer. The 3D printed models acted as a negative template and then silicone was poured and was allowed to solidify, see Figure 2 for mice AAA model and Figure 3 for the human AAA model. We then coated the models with a type I collagen and cultured endothelial cells (ECs) on their walls. The GPVI particles were then perfused in a closed-circuit perfusion system which mimicked physiological flow conditions (see Table 1). GPVI particle accumulation at the models was observed using fluorescent microscopy. In addition, we used computational fluid dynamics (CFD) simulations to obtain local flow characteristics such as streamlines and wall shear stress (WSS) maps to allow better understanding of the local flow patterns and their correlation with the particle adhesion in the experimental section.

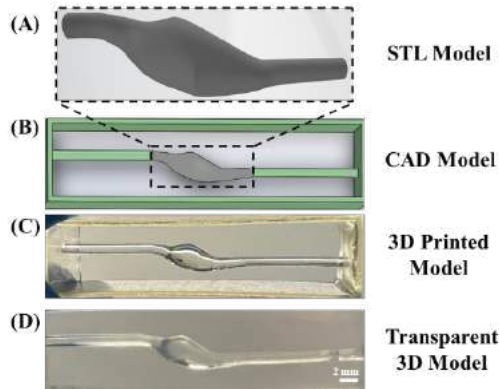


Figure 2 - Fabrication of the *in vitro* real size mouse AAA model. (A) The STL mouse AAA model. (B) The CAD mouse AAA model. (C) The 3D printed mouse AAA model and (D) The ready to use transparent 3D mouse AAA model.

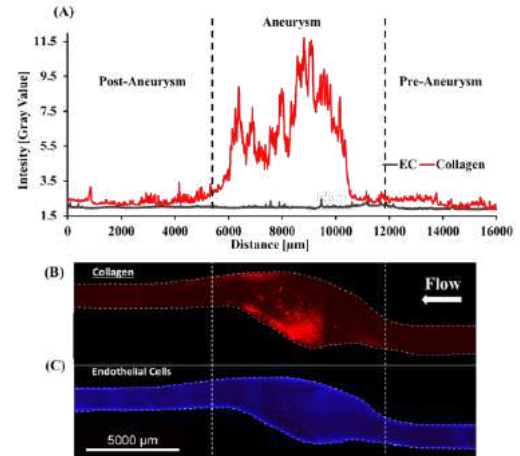


Figure 4 - 2 μ m GPVI-PS Particle deposition inside the collagen and EC coated mouse model. Particles are in red (B) and Blue is DAPI staining for ECs nuclei (C).

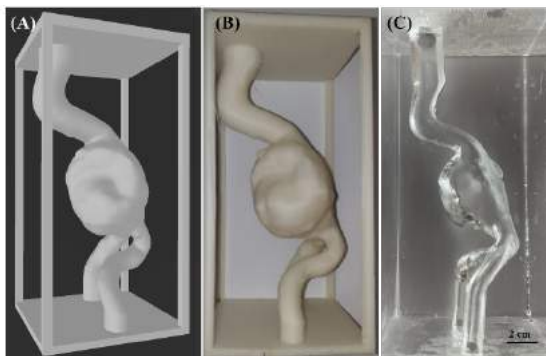


Figure 3 - *In vitro* human AAA fabrication process. (A) CAD model. (B) The 3D printed model and (C) The ready to use transparent 3D human AAA model.

RESULTS

In the mouse AAA model, the results show the enhanced accumulation of the 2 μ m GPVI particles at the collagen coated aneurysm (see Figure 4A&B), and almost no accumulation in the EC coated model (see Figure 4C). We further showed that the 2 μ m GPVI particles adhered at the collagen coated aneurysm region significantly more than the pre- and post-aneurysm regions as can be seen in Figure 4A. This is influenced by the low WSS and the recirculation zone at the aneurysm. However, preliminary results in the human AAA model show no significant difference in the accumulation of the 2 μ m GPVI particles at the aneurysm, pre- and post-aneurysm regions (see Figure 5). This is maybe influenced by the lower WSS levels in human circulation compared to mice throughout the human AAA model.

DISCUSSION

Our results suggest that GPVI particles can serve as drug carriers to target injured/inflamed collagen exposed AAA sites, however it is required to properly engineer the particle size and GPVI density on the surface of the particles in order to accommodate the WSS and the flow patterns in AAA as relevant to human AAAs and circulation.

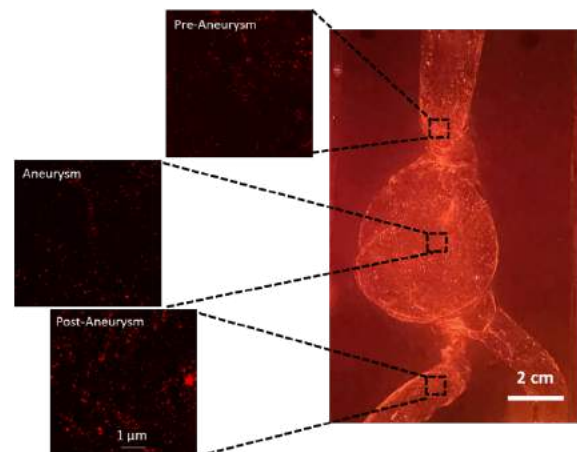


Figure 5 - Preliminary results of 2 μ m GPVI particles deposition in a human AAA model

ACKNOWLEDGEMENTS

This work was partly supported by the Israel Science Foundation (ISF grant # 902/18).

REFERENCES

1. Roth, G. A. *et al.* Global Burden of Cardiovascular Diseases and Risk Factors, 1990-2019: Update From the GBD 2019 Study. *Journal of the American College of Cardiology* vol. 76 2982–3021 (2020).
2. Libby, P. Inflammation in atherosclerosis. *Arterioscler Thromb Vasc Biol* **32**, 2045–2051 (2012).
3. Wang, L. J., Prabhakar, A. M. & Kwolek, C. J. Current status of the treatment of infrarenal abdominal aortic aneurysms. *Cardiovascular Diagnosis and Therapy* vol. 8 S191–S199 (2018).
4. Moll, F. L. *et al.* Management of abdominal aortic aneurysms clinical practice guidelines of the European society for vascular surgery. *European Journal of Vascular and Endovascular Surgery* **41**, (2011).

COMPUTATIONAL STUDY OF ROLE OF ULTRA LARGE VON WILLEBRAND FACTOR IN COVID-19 RELATED THROMBOSIS

Nahid Rahmati (1,2), Nima Maftoon (1,2)

- (1) Department of Systems Design Engineering, University of Waterloo, Waterloo, ON, Canada
(2) Centre of Bioengineering and Biotechnology, University of Waterloo, Waterloo, ON, Canada

INTRODUCTION

The Coronavirus 2019 (COVID-19) pandemic has had a significant impact on global health, causing widespread illness and death. The effects of COVID-19 on the respiratory and vascular systems, specifically the occurrence of thromboembolism in patients, particularly those in the intensive care unit, are particularly concerning. The causes of thromboembolism are suggested to be related to hypoxia, severe inflammation, and immobilization [1]. The underlying mechanisms of thromboembolism in COVID-19 patients are by examining the role of released von Willebrand factor (VWF) multimers, from endothelial cell, which is activated by COVID-19 and facilitates to platelets and leukocyte adhesion to the vessel wall. Additionally, the moderate deficiency of the zinc-containing metalloprotease ADAMTS13, which is responsible for cleaving VWF multimers, in COVID-19 patients has been observed and it leads to the newly released ultra-large VWF (UL-VWF) multimers [2]. A computational model is used to investigate the underlying mechanism of the adhesion process between platelets and VWF multimers that leads to the onset and progression of thrombosis, and also examines the effects of this adhesion process on hemodynamics.

METHODS

In this study, the Lattice Boltzmann Method (LBM) was used to model the blood plasma flow as an alternative to directly solving the Navier-Stokes equations. The open-source LBM code Palabos (Ver 2.0r0) [3] was used to calculate the fluid velocity and density at each Eulerian node of the flow domain.

The goal of the study was to use LBM to provide a better understanding of the flow behavior in the cardiovascular system. Additionally, the coarse-grained spectrin link membrane method was used to model the deformable bodies (red blood cells, platelets, and von Willebrand factor strings) floating in the plasma flow. The method was implemented using the Hemocell open-source code (Ver 2.1) and discretized using triangular elements. The deformation of cells is governed by a set of reaction forces on the nodes of the discretized cell membrane, including stretching and compression, bending, local surface conservation, and volume conservation. The spring stiffness coefficients in these equations were already found and validated for red blood cells and platelets using optical tweezers experiments.

The LBM model of blood and spring-network models of deformable bodies were coupled using the immersed boundary method (IBM) implemented and validated in the Hemocell open-source framework (V2.1) [4]. It is used to model the interaction between the Lagrangian grid of cells and the Eulerian fluid grid, assuming no-slip condition at the solid-fluid interface.

Finally, an adhesive dynamics model, proposed by Hammer and Apte [5], was used to simulate the platelet-von Willebrand factor and von Willebrand factor-von Willebrand factor interactions. This model uses a spring-based model integrated with a probability distribution function that employs a stochastic Monte Carlo method. The adhesion force of the receptor-ligand bond is calculated using the spring model as well as the effective force. The study investigated the adhesion among von Willebrand factor strings, platelets, and endothelial cells.

RESULTS

In this study, we observed that platelets initially stick to stretched and uncleaved UL-VWF multimers that are anchored to the walls of small blood vessels (Figure 1-a). By the end of this initial adhesion phase, the UL-VWF multimers and platelets form a mesh-like structure that captures red blood cells, leading to the gradual formation of a microthrombosis (Figure 1-b). The blood flow near the inlet slows significantly during the initial adhesion phase (Figure 2-a), and since the fluid flow velocity within the microthrombosis drastically decreased, it increased around the microthrombosis due to mass conservation. In addition, RBCs are increasingly caught as the thrombus forms and grows. This leads to the development and thinning of a cell free layer (CFL; the plasma-rich near-wall region without RBC cells). The increased velocity variation within the CFL caused increased velocity variation within the CFL and enhanced the wall shear stress around the microthrombosis (Figure 2-b). This results in a pressure drop of up to 6 times that of normal conditions.

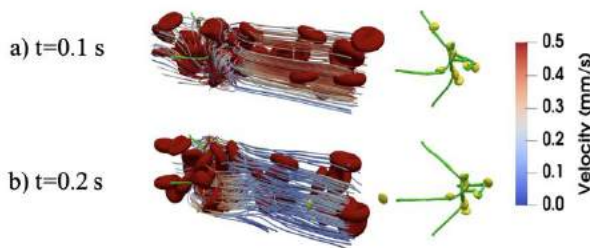


Figure 1: Process of UL-VWF-induced thrombus formation in COVID-19 patients. (a-b)

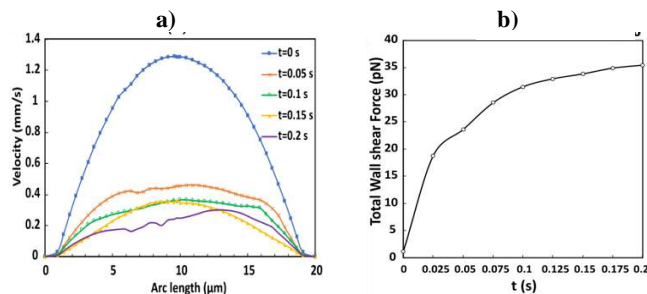


Figure 2: (a) The velocity profile near the microvessel inlet, (b) The total wall shear force (obtained by integration of the WSS magnitude over the entire microvessel surface).

DISCUSSION

Thrombotic complications are estimated to occur in over 30% of critically ill COVID-19 patients in the intensive care unit and 70 to 100% of patients who died from COVID-19 experienced deep venous thrombosis [6].

Our findings demonstrate that the presence of uncleaved UL-VWF tethered to the endothelium contributes to thrombus formation and coagulopathy in COVID-19. The underlying mechanisms responsible for this phenomenon have been quantitatively investigated.

Our results represent that platelets first adhere to unfolded and stretched uncleaved UL-VWF multimers tethered to the microvessel wall. By the end of this initial adhesion phase, the UL-VWF multimers and platelets make a mesh-like trap in which the red blood cells increasingly accumulate to initiate a gradually growing microthrombosis. During the initial adhesion phase, the blood velocity drastically drops, and the wall shear stress is elevated near UL-VWF roots on the wall, and the pressure drops from 1.5 to 6 times compared to no clot situation and healthy condition and at wall locations closest to the thrombosis. As time passes, these trends progressively continue until the microthrombosis is fully developed and the effective size of the microthrombosis as well as flow quantities remain almost constant. While, in a vessel with a constant diameter, the pressure drop in the Poiseuille flow is directly proportional to the average velocity at the vessel inlet, in presence of thrombosis, the situation becomes more complicated because the flow velocity, thrombosis size, and pressure drop all depend on one another.

ACKNOWLEDGEMENTS

The authors acknowledge funding from the Natural Sciences and Engineering Research Council of Canada.

REFERENCES

- [1] Kichloo, A et al., COVID-19 and Hypercoagulability: A Review. Clin. Appl. Thromb. 26, 2020.
- [2] Rostami, M et al., Clinical and Experimental Medicine. 22, 347–357, 2022.
- [3] Latt, J et al., Palabos: Parallel Lattice Boltzmann Solver. Comput. Math. Appl, 81:334-50, 2020.
- [4] Závodszy G et al., Frontiers in physiology, 8: 563, 2017.
- [5] Hammer DA, Apte SM, Biophysical journal. 63(1):35-57, 1992.
- [6] Klok, FA et al., Thrombosis Research. 191:145-147, 2020.

AORTIC WALL STRESS CONCENTRATION AS A PREDICTOR OF TYPE A AORTIC DISSECTION

Christina Sun (1), Tongran Qin (1), Asanish Kalyanasundaram (2), Wei Sun (1),
John Elefteriades (2), and Liang Liang (3)

- (1) Sutra Medical, Lake Forest, CA, USA
(2) Aortic Institute, Yale University School of Medicine, New Haven, CT, USA
(3) Department of Computer Science, University of Miami, Coral Gables, FL, USA

INTRODUCTION

Type A aortic dissection (TAAD) is a lethal disease that, if untreated, has a mortality rate of approximately 1% per hour once aortic dissection has occurred [1]. Increased age, hypertension, smoking, and atherosclerosis could serve as independent predictors of acute TAAD. However, such demographic parameters lack precision and cannot predict when and where the dissection would occur in individual patients. Patients with thoracic aortic aneurysm can undergo elective surgical repair prior to a dissection or rupture. The current risk assessment involves evaluating the aortic diameter, using medical imaging techniques such as computed tomography (CT) or echocardiogram scans, where surgical repair is recommended if the ascending aortic diameter is greater than 5.5 cm. However, studies have shown that aortic size alone does not completely predict type A aortic dissections [2, 3]. As such, indices other than diameter are needed as criteria to predict where an aortic dissection or rupture is likely to occur. In this study, we hypothesize that stress concentration in the aortic wall may lead to TAAD, and stress analysis may be used to predict where TAAD occurs on the aortic wall.

METHODS

We performed engineering analysis on a rare dataset of retrospectively obtained pre-dissection (PreD) with corresponding post-dissection (PostD) and post-repair (PostR) computed tomography (CT) scans from the same 8 patients from the Yale New Haven Hospital database. Each PreD CT scan was performed as part of their care, as dictated by their treating physician, and not for reasons associated with this study.

To obtain the aorta geometry of each patient, the entire aortic root, ascending aorta, aortic arch, and descending aorta, including true lumen, false lumen, and dissection flaps for the PostD state, were manually segmented from the CT scans using 3D slicer. A geometric quad-mesh

was then generated from the segmentations using Hypermesh and offset to mimic the aortic wall.

To obtain the aortic wall stress distribution of each patient, finite element analysis (FEA) was applied using Abaqus. The thickness of the normal wall was assumed to be 2mm, and the thickness of the dissection wall was assumed to be half the normal thickness. Three different values for systolic pressures (16 kPa, 18 kPa, and 20 kPa) were used to simulate normal systolic blood pressure, hypertension stage 1, and hypertension stage 2, as defined by the American Heart Association. Based on the principle of static determinacy [4], given the blood pressure and geometry, the stress distribution of the aortic wall is insensitive to material properties. Thus, the wall stress distribution was obtained by assuming very stiff material properties. The wall stresses at preD, postD, and postR states were collected and analyzed.

RESULTS

To investigate the correlations between the aortic wall stresses and the location of dissection, finite element analysis was performed using the static determinacy principle. Patient-specific geometries in pre-dissection state were used, with systolic pressure of 16 kPa. The mean aortic wall stress in different regions were calculated and compared. It is found that the mean stresses in the ascending aorta (208.25 ± 36.25 kPa), including the aortic root (215.10 ± 44.92 kPa) and the aortic arch (198.43 ± 44.16 kPa), were significantly higher than that of the descending aorta (139.62 ± 17.69 kPa, $P < 0.001$). Moreover, stress concentration regions were defined as greater than 75th percentile peak stress in the aortic wall and identified. As shown in Figure 1, the identified high stress regions based on FEA calculations showed strong correlations with the actual dissection border of the patients at post-dissection stage.

In addition, a more comprehensive patient-specific FEA were performed for different states (PreD, PostD, and PostR), at different systolic pressures (16kPa, 18kPa, and 20kPa). The mean stress and peak

stress at different regions of the aorta were obtained and compared. Five different regions of aorta were identified, which are the root, the ascending aorta (AsA), the aortic arch, the proximal descending aorta (pDsA), and the distal descending aorta (dDsA). As shown in Figure 2 (a), mean stresses increased from PreD to PostD, and decreased after the surgical repair (PostR). The mean stresses at the root, ascending aorta and arch are typically larger than those at the descending aorta. The mean stress increased significantly in the root region from PreD to PostD states under all pressure conditions, which correlates well to the location of dissection. At pressure conditions of 16kPa and 20kPa, the mean stresses in the root decreased significantly after surgical repair. As shown in Figure 2 (b), the peak stresses showed similar trend. The peak stresses in the root, ascending aorta and arch were consistently higher than those in the descending aorta. At the root and ascending aorta regions, the peak stresses increased from PreD to PostD state, which was not significant. On the other hand, the peak stresses decreased significantly from PostD to PostR state.

DISCUSSION

With this dataset of retrospectively obtained PreD and corresponding PostD and PostR CT scans from the same patients, we were able to perform aortic wall stress finite element analysis and compare them between different regions and different states. Our results showed that the high stress region of the aorta in PreD state correlates well with the actual *in vivo* dissection location, which indicates that stress concentration in the aortic wall may serve as a good predictor of TAAD. The mean stresses at the root and ascending aorta increase significantly after dissection occurred and decreased significantly after the surgical repair. This suggests that the mean stress can be useful for the prediction of dissection events, and current treatment plan can effectively reduce the rupture risk of TAAD patients.

This preliminary study has several limitations, such as the uniform wall thickness assumption. These limitations will be resolved in our future work. For example, the wall thickness can be obtained by using both the contrast and non-contrast CT images: the inner wall will be revealed by the contrast CT image, and the outer wall will be revealed by the non-contrast CT image. Our future work also includes machine learning-based FEA [5,6] to facilitate a fast and accurate estimate of aortic wall stress and allow for patient-specific diagnosis and prediction of TAAD.

ACKNOWLEDGEMENTS

This work is supported in part by the NIH grant R01HL158829.

REFERENCES

[1] John Elefteriades, Adam Sang, Gregory Kuzmik, and Matthew Hornick, Guilt by association: paradigm for detecting a silent killer (thoracic aortic aneurysm), *Open Heart* 2015;2:e000169.

[2] Nishimura RA, et al, AHA/ACC guideline for the management of patients with valvular heart disease: Executive summary: A report of the American College of Cardiology/American Heart Association task force on practice guidelines, *Circulation*, 2014.

[3] Linda Pape, et. al, Aortic Diameter ≥ 5.5 cm Is Not a Good Predictor of Type A Aortic Dissection, *Circulation*, 2007.

[4] Minliang Liu, Liang Liang, Haoifei Liu, Ming Zhang, Caitlin Martin, and Wei Sun, On the computation of in vivo transmural mean stress of patient-specific aortic wall, *Biomechanics and Modeling in Mechanobiology*, 2019.

[5] Minliang Liu, Liang Liang, Qing Zou, Yasmeen Ismail, Xiaoying Lou, Glen Iannucci, Edward Chen, Bradley Leshnower, John Elefteriades, and Wei Sun, A probabilistic and anisotropic failure metric

for ascending thoracic aortic aneurysm risk assessment, *Journal of the Mechanics and Physics of Solids*, 2021.

[6] Liang Liang, Minliang Liu, Caitlin Martin, and Wei Sun, A deep learning approach to estimate stress distribution: a fast and accurate surrogate of finite-element analysis, *Journal of The Royal Society Interface*, 2018.

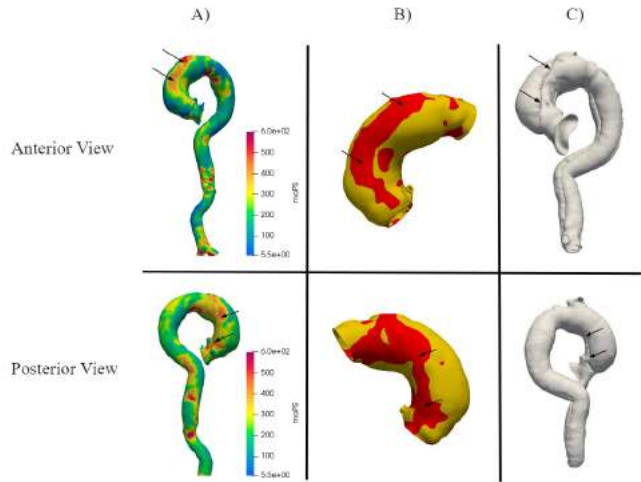


Figure 1: Anterior and posterior views of a representative patient's aorta with A) the PreD stress distribution, B) part of the ascending aorta, where the red region shows the peak stresses larger than 75th percentile, and C) the PostD state. The arrows show areas of stress concentration and the dissection borders.

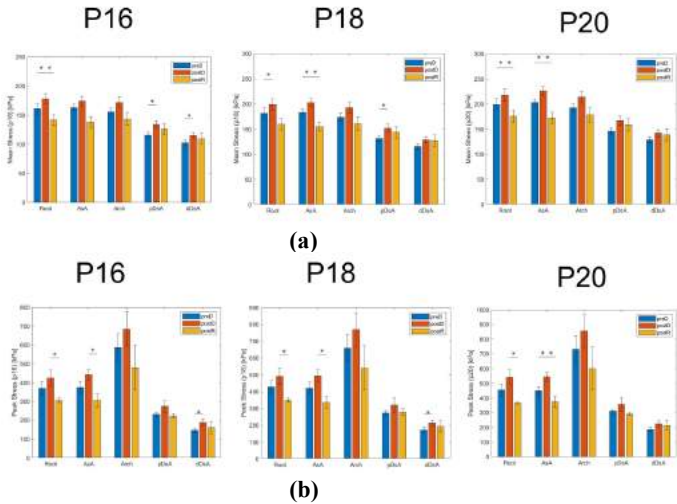


Figure 2: Maximum principal stresses at the root, the ascending aorta (AsA), the aortic arch (arch), the proximal descending aorta (pDsA), and the distal descending aorta (dDsA) at the pre-dissection (PreD), post-dissection (PostD), and post-repair (PostR) states. (a) Mean stress within each region, averaged among all patients; (b). Peak stress within each region, averaged among all patients. Three different values of systolic pressures were applied, which are 16 kPa (P16), 18 kPa (P18), and 20 kPa (P20). The * sign suggests significant differences.

SCAFFOLDED AND ITERATIVE COURSE DESIGN IN A BIOMECHANICS LABORATORY COURSE

S Bansal (1), J Benson (1), S Sullivan (1), and E Corbin (1)

(1) Department of Biomedical Engineering, University of Delaware, Newark, DE, USA

INTRODUCTION

Engineering mechanics, statics, dynamics, and biomechanics courses are prevalent in Biomedical Engineering curricula, and a course to this effect is a core/required class in many BME programs. One method to supplement and enhance student learning is to include a studio or laboratory class in conjunction with a traditional lecture course. The incorporation of team-based learning has shown positive impacts on student comprehension and belongingness [1]. The inclusion of a lab course also allows the teaching team to uniquely address ABET Student Outcomes 5 (an ability to function effectively on a team whose members together provide leadership, create a collaborative and inclusive environment, establish goals, plan tasks, and meet objectives) and 6 (an ability to develop and conduct appropriate experimentation, analyze and interpret data, and use engineering judgment to draw conclusions). These two outcomes are in addition to outcomes 1 (an ability to identify, formulate, and solve complex engineering problems by applying principles of engineering, science, and mathematics) and 7 (an ability to acquire and apply new knowledge as needed, using appropriate learning strategies), which can be assessed during a lecture-based Biomechanics course. Due to the positive impacts of lab-based courses on student learning, we at the University of Delaware have developed a Biomechanics Laboratory Course in parallel with the Biomechanics: Statics class taken by all 3rd year students in our department.

Students self-select into one of three sections (Monday, Wednesday, or Friday) to attend the Laboratory course, which comprises of three modules. Each module focuses on a core mechanics concept and includes hands-on experimentation and data collection, a MATLAB assignment, and a final Lab Report written in a one-page abstract format. Given the importance of computer science in engineering and the importance of strengthening and integrating skills between classes [2], the MATLAB assignments were modified to require students to write a script to analyze their data in addition to figure generation. These last two deliverables (MATLAB and Lab Report) are scaffolded such

that Lab 1 templates are ~85% filled out for students, Lab 2 is ~50% guided, and Lab 3 requires students to develop MATLAB code, figures, and an abstract with minimal instructor input. Grading rubrics are adjusted to reflect the amount of guidance given to students in each Lab Module. In this way, the course is highly scaffolded to allow for skill growth, confidence, and independence.

This course is iterated upon from year-to-year as driven by student feedback. For example, Fall 2022 saw a reorganization of the course schedule as requested by students from the Fall 2021 semester, and we plan adjustment for Fall 2023 given Fall 2022 feedback. In addition to yearly iteration, this course benefits from constant adjustment throughout the week. Indeed, after Monday's class, the teaching team adjusts materials and in-class assignments for implementation on Wednesday, and similarly tweaks material in advance of Friday's section as needed. It is yet to be determined if these sorts of micro-adjustments impact student comprehension and learning outcomes.

Therefore, the purpose of this study is to determine how semester-long scaffolding and weekly iteration impacts student outcomes, both through qualitative and quantitative assessments. Our hypothesis is that scaffolding increases student confidence with writing and coding, and that iteration within weeks (i.e. the difference between sections) has a positive effect on student learning.

METHODS

Student outcomes were measured at the end of the semester via assignment grades and collation of student course evaluations. To explore the impacts of scaffolding, student grades on specific assessments (MATLAB and reports) were compared across modules. To understand the impacts of iteration, course evaluations were analyzed. Evaluation questions of interest to this study included "*The lectures were well organized*", "*This course positively impacted my learning in Biomechanics – Statics*", and questions regarding knowledge of topics covered in this course at the start and end of the

semester. Through these questions, knowledge “growth” was calculated by subtracting the self-assessment at the start of the course from the self-assessment at the end of the course. Lastly, students were asked if they were aware of year-to-year iteration and if that iteration was deemed helpful to the course. One-way ANOVA and Tukey Post-Hoc tests were used to compare student evaluation and final score data across sections and assignment scores across Modules. In addition to these quantitative data, qualitative comments about the course were reviewed.

RESULTS

We saw no differences in final course grades between sections (M: 94.7 ± 3.3 , W: 95.7 ± 2.5 , F: 94.2 ± 2.8 , $p = 0.29$). Assignment grades were similar between Labs 1 and 2 (MATLAB, Lab 1: $49.2/50.0 \pm 1.4$, MATLAB, Lab 2: $48.6/50.0 \pm 2.5$, $p = 0.37$; Report, Lab 1: $90.8/100.0 \pm 5.3$, Report, Lab 2: $89.6/100.0 \pm 5.6$, $p = 0.50$). However, both assignments saw lower scores in Lab 3 (MATLAB, Lab 3: $45.6/50.0 \pm 1.4$, $p < 0.0002$; Report, Lab 3: $86.9/100.0 \pm 6.0$, $p < 0.03$), **Figure 1**.

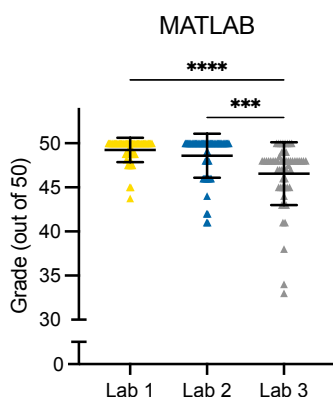


Figure 1: MATLAB grades for all students during each Lab Module.

Student assessment of course organization (scale: 1 – 5, “hardly ever” – “almost always”) increased across sections (M: 4.0 ± 0.9 , W: 4.4 ± 0.6 , F: 4.8 ± 0.4 , $p = 0.003$) although post-hoc testing indicated differences between Monday and Friday sections ($p = 0.002$), only, **Figure 2**.

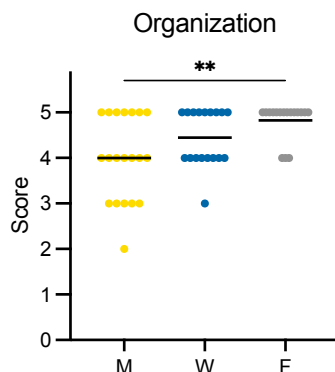


Figure 2: Student assessment of lecture organization by section.

Self-reported impacts of the laboratory course on lecture comprehension (scale: 1 – 5, “strongly disagree” – “strongly agree”) was similarly lowest in Monday’s section and highest in Friday’s section (M: 4.5 ± 0.8 , W: 4.9 ± 0.3 , F: 5.0 ± 0 , $p = 0.006$). Here, post-hoc tests indicate significant differences between Monday and the other two sections ($p < 0.04$), **Figure 3**.

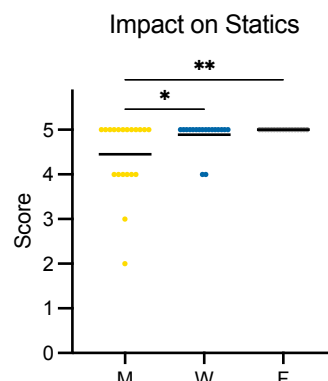


Figure 3: Self-reported student assessment of how lab impacted understanding in lecture by section.

Knowledge growth was consistent across sections (M: 1.6 ± 1.1 , W: 1.5 ± 1.2 , F: 1.4 ± 0.9 , $p = 0.93$). Through all sections, 63.6% of students were aware of the year-to-year iteration of the course and 97.9% of students believe the course benefits from iteration.

DISCUSSION

The lack of differences in final grades between sections indicates that sections were comparable in student achievement. Interestingly, assignment grades across modules suggests that course scaffolding should be adjusted, perhaps by reducing Lab 2’s level of instructor involvement to better prepare students for Lab 3. Even so, students recognized scaffolding and appreciated it, stating, “*I like that [the instructors] eased us into writing an abstract*”, and they appreciated that the course emphasizes “*a few topics very thoroughly*.” In particular, we plan to scaffold the modified MATLAB assignments more deliberately for the Fall 2023 semester. This is in direct response to student feedback, which suggested that while these assignments helped students “*gain a lot of MATLAB skills through this course*”, more explanation and guidance would be helpful in the future.

Regarding iteration, students recognized the adjustments made from year-to-year and believed them to be positive. Impacts of mid-week adjustments were unclear, however. There was a modest increase in perceived lecture organization and impacts on lecture understanding across the week but no change in self-assessment of knowledge gain at the end of the course. These results are inconclusive, but do not indicate any negative repercussions to adjustment. These results also suggest that perhaps macro-scale, semester to semester adjustment is more impactful than mid-week adjustment.

Overall, this course was successful in supporting student learning goals. It helped students gain confidence and skills in MATLAB, writing, teamwork, power tool usage, and dissection. In addition, multiple students reported that the laboratory class “*helped my understanding of [Statics]*” and “*demanding students to be problem-solvers*”, giving students an opportunity to “*feel like a biomedical engineer*”. Going forward, this course will continue to involve assignment scaffolding, which will be adjusted in response to student feedback.

ACKNOWLEDGEMENTS

The authors acknowledge the course TAs for their help with the course.

REFERENCES

- [1] Matalonga, S et al., *IEEE/ACM SECM*, 9-15, 2017. [2] Joll, J et al., *ASEE AM*, 2021.

TRIBOLOGICAL ASSESSMENT OF PVA HYDROGELS AS INTERPOSITIONAL IMPLANT MATERIALS IN THE TEMPOROMANDIBULAR JOINT

Kevin M. Labus (1), Jason P. Kuiper (1), Christian M. Puttlitz (1,2,3)

- (1) Department of Mechanical Engineering, Colorado State University, Fort Collins, CO, USA
(2) School of Biomedical Engineering, Colorado State University, CO, U.S.A
(3) Department of Clinical Sciences, Colorado State University, CO, U.S.A

INTRODUCTION

The temporomandibular joint (TMJ) provides articulation between the mandible and cranium during chewing, communication, and clenching. The TMJ contains of an interpositional articular disc between the mandibular condyle and the fossa of the temporal bone. For advanced TMJ disorders that consist of displacement and degeneration of the articular disc, disc resection is the most common treatment. However, disc resection fails to reduce pain in approximately 25% of patients [1]. The disc plays a critical role in distributing stresses and preventing wear on the joint surfaces. Thus, removing the disc can further disrupt the joint and advance degeneration. Therefore, there is a need for interpositional implants to replace the function of the disc when disc resection is required. Towards this goal, we have characterized the mechanical behavior of the TMJ disc to guide the development of biomimetic materials [2] and identified poly-vinyl alcohol (PVA) hydrogel as an excellent material due its biocompatibility, low friction, and mechanical properties that can be tuned to match the properties of the native disc [3].

The purpose of this study was to assess the wear performance of PVA hydrogels under cyclic loading. We compared three PVA hydrogel variants. PVA hydrogels are traditionally synthesized by mixing PVA with water and applying freeze-thaw cycles. PVA hydrogels have also been synthesized using a dry-cast method without freeze-thaw cycles, and the resulting hydrogels have shown more regular microstructure and lower wear [4]. Additionally, PVA hydrogels may require reinforcement in order to achieve adequate tensile properties. Therefore, wear tests were used to compare freeze-thaw (FT) PVA hydrogels with dry-cast (DC) hydrogels and FT hydrogels with an embedded melt-extruded polypropylene scaffold (FT + scaffold).

METHODS

Three variants PVA hydrogels were synthesized, all with 25% polymer weight content. (1) Freeze-thaw (FT) gels were produced by

dissolving PVA powder in deionized water, pouring the solution in a mold between two glass slides, and applying 6 freeze-thaw cycles, creating an opaque gel. (2) freeze-thaw gels with embedded scaffolds (FT + scaffold) were produced by printing angle-ply polypropylene scaffolds via melt extrusion, embedding them in the PVA solution, and applying the identical freeze-thaw protocol. (3) Dry-cast (DC) gels were produced by dissolving PVA powder in DMSO solvent, pouring the solution in a mold between two glass slides, allowing the solution to dry for 5 days, then rehydrating and rinsing the gels in deionized water, creating a transparent gel.

TMJ fossa cartilage specimens were extracted from sheep euthanized for unrelated studies, potted in a two-part epoxy resin for clamping during wear tests, and frozen until used for testing. Wear tests were conducted by translating the cartilage in a reciprocal sliding motion relative to a stationary hydrogel sheet clamped to the base of a lubricating bath of artificial synovial fluid [5] (Figure 1). Contact area was measured via ink transfer from hydrogel to cartilage under 1 kg mass, and weights were used to apply a constant 100 kPa mean pressure, an estimate for average TMJ pressure during use [6]. Friction forces were measured via an offset torque cell. Three tests of each hydrogel variant were conducted to 100,000 cycles at 1.5 Hz and 8 mm sliding distance, and one DC hydrogel was tested to 1 million cycles. Following the tests, a stylus profilometer was used to measure wear area and surface roughness of the tested hydrogels, tested cartilage, and untested (naïve) hydrogel and cartilage surfaces. Three scans were measured per specimen in the direction across the wear tracks.

RESULTS

The FT hydrogels exhibited a rapid increase in coefficient of friction after about 10,000 cycles (Figure 2). The coefficient of friction also increased over time for the FT + scaffold, but was significantly less than the FT group at 100,000 cycles ($p = 0.04$). The coefficient of friction in the DC group remained steady throughout the tests, including

for the sample tested to 1 million cycles and was significantly less than the FT group at 100,000 cycles ($p = 0.01$).

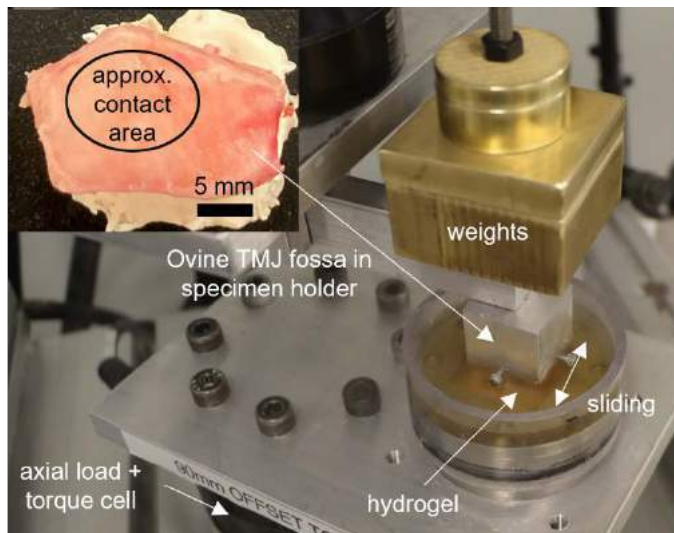


Figure 1: Wear testing setup of ovine TMJ fossa cartilage (articular surface shown in inset) sliding against a hydrogel sheet in an artificial synovial fluid bath.

Profilometry results showed a 5-fold and 15-fold decrease in mean wear area for the FT + scaffold and DC hydrogels, respectively, compared to the FT hydrogels (Figure 3). Differences in post-test hydrogel surface roughness were not significant between hydrogel variants. Mean surface roughness of the naïve hydrogels was four times greater in the FT gels compared to the DC gels. No significant differences in surface roughness were observed on cartilage surfaces between hydrogel groups or untested control cartilage surfaces. Qualitatively, surface damage was not visually observed on the tested cartilage specimens, except for the specimen tested to 1 million cycles, which exhibited minor burnishing.

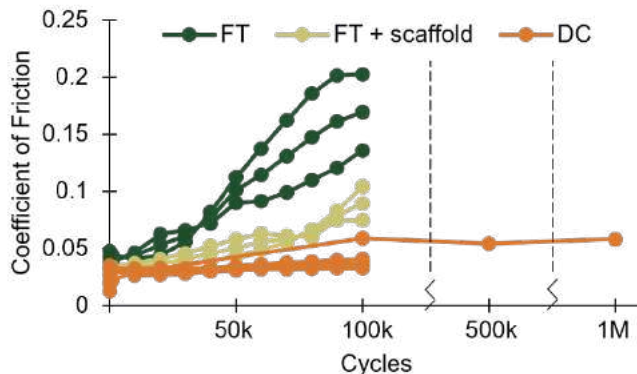


Figure 2: Coefficient of friction results for all specimens.

DISCUSSION

The friction and wear area results demonstrate that the DC PVA hydrogels exhibit greater wear resistance compared to FT PVA hydrogels of the same polymer concentration. This comparative result has been demonstrated previously [4], but the current study was novel in the assessment of PVA hydrogel wear in an environment targeted to the TMJ, including a TMJ-specific load magnitude, and sliding against TMJ cartilage, which consists of fibrocartilage that is structurally

distinct from the hyaline cartilage found in most articular joints. The lower surface roughness measured on the naïve DC gels compared to FT gels may partially explain the improved friction and wear properties.

Compared to the FT hydrogels alone, the embedded scaffold hydrogels resulted in decreased wear and lower friction over time. The scaffolds were not exposed to the tested surface, so the improved friction and wear were likely due to stiffening of the bulk construct properties which would decrease plowing effects. Combining the scaffold-hydrogel composite construct with a DC hydrogel may further improve tribological performance.

Study limitations included a relatively low sample size; however, some statistically significant results were still found. Also, tests were conducted to a fairly small number of cycles. The use of 100,000 cycles was chosen to provide a relatively rapid screening test for hydrogels while still obtaining measurable wear results. Future tests will use a greater number of cycles in order to better estimate the expected lifetime of materials for implantation in the TMJ joint. These results will guide the development of TMJ disc replacements to provide a new treatment option for TMJ disorders.

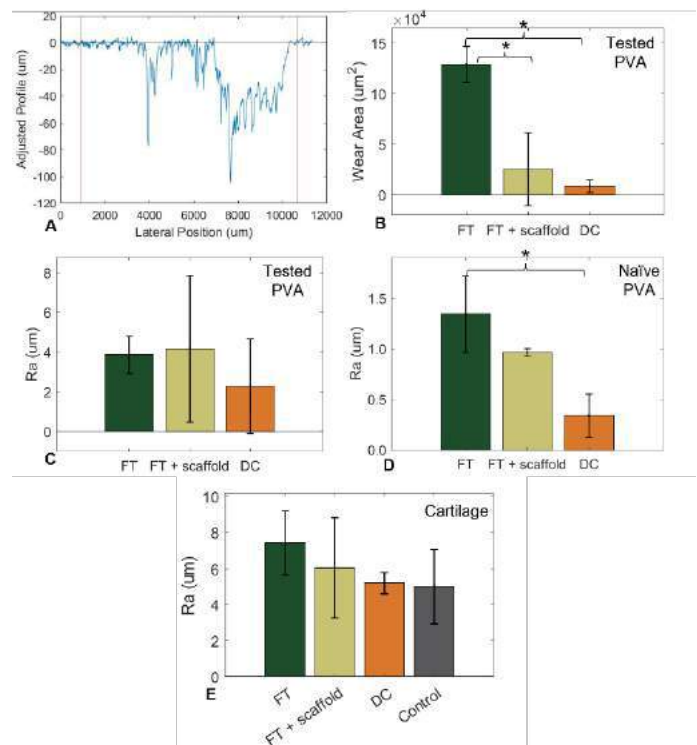


Figure 3: Profilometry results, including (A) example profile curve from a FT specimen, (B) hydrogel wear area, measured as the area above the profile curve, (C) average roughness of the tested hydrogels, and (D) average roughness of the naïve (untested) hydrogels, and (E) average roughness of the cartilage surfaces. Plots show mean \pm standard deviation. * represents $p < 0.05$ from one-way ANOVAs with Tukey post-hoc tests.

REFERENCES

- [1] Ellis, O et al., *J Oral Maxillofac Surg*, 79(12): 2448-2454, 2021
- [2] Labus, K et al., *J Mech Behav Biomed Mater*, 116: 104300, 2021
- [3] Kuiper, J et al., *Frontiers in Physics*, 10:928579, 2022
- [4] Yarimitsu, S et al., *Biosurface and Biotribology*, 2.1:40-47, 2016
- [5] Bortel, E et al., *Lubricants*, 3: 664-686, 2015
- [6] Sagl, B et al., *Frontiers in Physiology*, 10:1165, 2019

CORRELATING BALL DELIVERY PARAMETERS WITH HEAD IMPACT KINEMATICS FOR A COMMON SOCCER HEADING PROTOCOL IN BRAIN INJURY RESEARCH

Keili R. Shepherd (1), David Luke (1), Rebecca Kenny (2), Lyndia C. Wu (1,2)

- (1) Biomedical Engineering, University of British Columbia, Vancouver, BC, Canada
(2) Mechanical Engineering, University of British Columbia, Vancouver, BC, Canada

INTRODUCTION

There is growing concern that repetitive subconcussive soccer headers may cause long-term neurological deficit¹. Given this concern, many studies have investigated brain response (e.g. cognitive function, postural control and blood biomarkers)²⁻⁴ following a bout of controlled soccer headers. These studies often employ a heading protocol using standard sports ball launchers that enable a range of ball delivery speeds and angles. However, study protocols have been highly inconsistent, with ball speeds varying between 6 and 24 m/s⁷. This inconsistency may explain the largely conflicting results from literature, i.e., some studies found neurological changes after heading while others did not^{3,4,8-10}. Additionally, while sports head impact studies typically report head kinematics, as the motion of the head during an impact is deemed one of the most important indicators of brain injury risk¹¹, most controlled soccer heading studies only report ball delivery settings. Our objective is to investigate the influence of ball launch speed, angle, and participant height on ball impact speed and head impact kinematics through analytical modeling and human participant experiments. This information will not only help to standardize future study protocols, but also provide context to past soccer header study results and potentially explain the discrepancies in reported neurological effects of heading.

METHODS

ANALYTICAL MODEL: A 2D analytical model of the soccer ball trajectory in the sagittal plane was used to predict the speed and angle at which the soccer ball impacts the head (horizontal = 0°). Ball velocity was calculated using equation (1)

$$\vec{v}_i = \vec{v}_{i-1} + (\vec{a}_{di} + \vec{a}_g) \times \Delta t \quad (1)$$

where \vec{v}_{i-1} is the velocity of the previous time step, \vec{a}_{di} and \vec{a}_g are the components of acceleration from air drag and gravity, and Δt is the time step (0.001s). The acceleration component from drag was calculated using (2)

$$\vec{a}_{di} = -0.5\rho\vec{v}_i^2 C_D A / m \quad (2)$$

Where ρ is the density of air of 1.2 kgm^{-3} , C_D is the drag coefficient (0.3), A and m are the frontal area (0.0314 m^2) and mass of the soccer ball (0.4 kg), respectively. The inputs to the model were the initial ball speed, the initial launch angle, and the height at which the ball contacted the participant. We simulated three common initial angles of 40°, 45° and 50° and ball speeds between 6-24 m/s, and heights corresponding to those of a 5th and 50th percentile female, as well as a 50th and 95th percentile male¹². The analytical model predictions were verified through ball launching experiments, where ball speeds were determined through video analysis.

HUMAN PARTICIPANT SOCCER HEADING EXPERIMENT:

A ball delivery system (Pro Trainer Ball Machine) was used to deliver balls at initial angles of 45 and 50° and initial speeds between 7 and 13 m/s. Participant testing was done in an indoor, covered space to reduce the effects of wind and weather. Soccer balls were inflated to 0.7 atm. The participant was instructed to perform a standard frontal header (non-jumping) where the ball contacts the forehead. Headers were excluded if the head was rotating in the transvers plane, or if the ball hit the top or side of the head. GoPro cameras (2.7K Resolution, 60 FPS) were used to record each ball launch and verify head impacts. We calculated ball speeds from the experiments through video analysis. The human participant protocol was approved by the UBC Research Ethics Board (H21-00958).

HEAD KINEMATICS MEASUREMENT AND ANALYSIS:

One male participant, with a height of 188cm, was fitted with an athletic boil and bite mouthguard, to which a PCB 356A32 tri-axis accelerometer (2500Hz) and a DTS ARS3 tri-axis gyroscope (2500Hz) were secured via a custom acrylic bite bar. Accelerometer and gyroscope data were filtered using a 4th order lowpass Butterworth filter at 300 Hz and 256 Hz respectively¹³. Linear kinematics were transformed from the mouthguard to the head center of gravity.¹⁴ We

calculated peak linear acceleration (PLA), peak rotational velocity (PRV) and peak rotational acceleration (PRA) from each heading impact.

RESULTS

Figure 1A and 1B show the ball impact speed and angle predicted by the analytical model given varying launch speed, angle, and participant height. We show a reference line at 11.2 m/s, the ball launch speed most commonly used in past studies^{4,8}. In experimental testing, the initial speed of the ball was found to be correlated with dial setting ($r = 0.9612$) (Fig 1C). The average standard deviations of the initial and impact ball speeds for each dial setting were 0.43 m/s and 1.1 m/s. The predicted and measured impact speeds were linearly correlated with Pearson's correlation coefficient $r = 0.8963$ (Fig 1D) and Mean Absolute Error (MAE) of 0.4 m/s.

In the human participant experiment, soccer balls were launched at initial speeds between 7.25 and 12.6 m/s. Entering these velocities into the analytical model generated velocities at impact between 4.5 and 10.2 m/s. Kinematic parameters in the sagittal plane for all trials were plotted as a function of predicted impact speed and angle. A generalized linear model determined that PLA in the superior-inferior direction was linearly correlated with ball speed at time of head impact ($p < 0.05$). No other correlations were statistically significant (Fig 2).

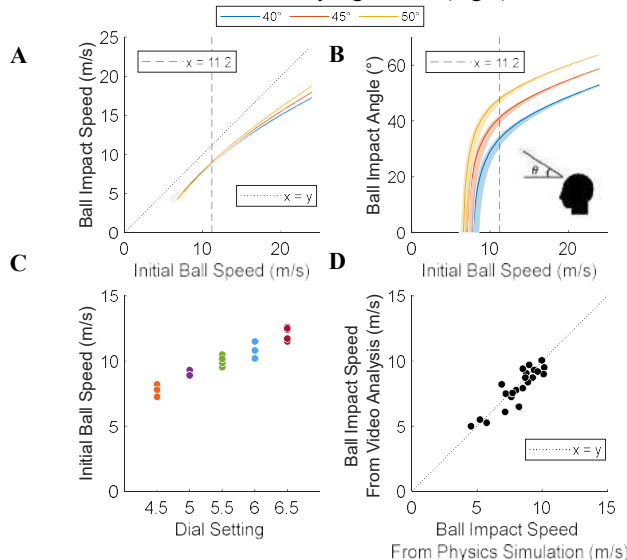


Figure 1: Predicted speed (A) and angle (B) of the soccer ball at the time of head impact for initial launch angles of 40°, 45°, and 50°. Upper and lower limits of shaded regions correspond to heights of a 95th percentile male and a 5th percentile female participant. Correlation between analytical and experimental impact speeds (C). Initial speed of balls launched at each dial setting on the ball delivery system (D).

DISCUSSION

Based on a simple analytical model of the soccer ball's projectile motion, the relationship between initial ball speed and impact speed is close to linear, especially in the range of 6–15 m/s initial speed. Further, the ball impact angle also increases with increasing launch speed. We found that the analytical model was fairly good at predicting impact speeds when compared to speeds determined experimentally ($r = 0.8963$). However, even in a highly controlled environment the initial launch speeds of the ball are variable. The variability is higher for ball speeds at impact, suggesting additional variance likely occurs due to factors such as spin and drag during flight. Also, while ball impact speed

is correlated with inferior-superior linear head acceleration, other components of kinematics are not significantly correlated with ball speed. We found high variability in head kinematics for the same ball launch setting, which may be attributed to subtle changes in the participant's stance and head/neck position. Based on our findings, both ball and head kinematics are variable, which may explain discrepancies in the reported neurological effects of heading. We recommend that future soccer heading protocols measure head kinematics, rather than rely on controlled launching parameters. In addition, future investigations of brain injury risk will also benefit from the design of more repeatable head impact experimental methodology.

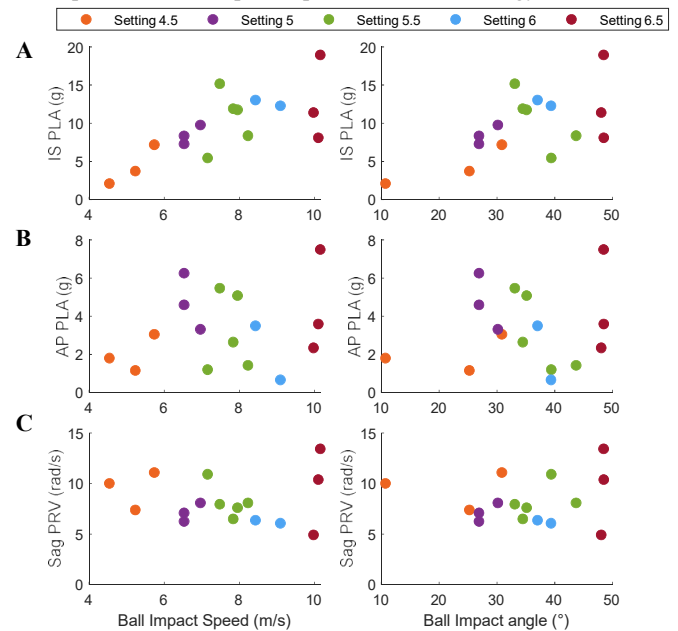


Figure 2: Kinematic parameters obtained from frontal headers as a function of soccer ball speed and angle at the time of head impact. A) PLA in the superior-inferior (Z) direction, B) PLA in the anterior-posterior (X) direction, and C) PRV in the sagittal (Y) plane.

ACKNOWLEDGEMENTS

The authors would like to thank Zaryan Masood and Crystal Zheng for their help with pilot data collection. This study is supported by a CIHR CGS-M award to KRS and an NSERC Discovery Grant (RGPIN-2018-04606).

REFERENCES

- [1] Bunc, G et al., *Med. Arch.*, 71:356–359, 2017.
- [2] Ashton J et al., *Sci Med Footb.*, 5:181–287, 2021.
- [3] Schmitt, D. M et al., *Int. J. Sports Med.* 25:326–331, 2004.
- [4] Huibregtse, M. E., et al. *PLoS ONE* 10:15, 2020.
- [5] Elbin, R. J. et al., *Res. Sports Med.* 23:203–214, 2015.
- [6] Broglio, S. P. et al., *Br. J. Sports Med.* 38:561–567, 2004.
- [7] Harriss, A. B et al., *Sports*, 7:229, 2019.
- [8] Haran, F. J et al., *Int. J. Sports Med.* 34:350–354 (2013).
- [9] Bonke, E. M et al., *J. Sci. Med. Sport*, 24:247–257, 2021.
- [10] Caccese, J. B. et al., *Res. Sports Med.* 26 :64–74, 2018.
- [11] Arrué, P et al., *Front. Bioeng. Biotechnol.* 8, 2020.
- [12] <https://www150.statcan.gc.ca/n1/pub/82-626-x/2012001/t023-eng.htm>.
- [13] Kenny, R et al., *Ann. Biomed. Eng.* 2022.
- [14] Miller, L. E. et al., *J Biomech Eng* 140, 2018.

CLUSTERED LOW SEVERITY IMPACTS MAY LEAD TO CONCUSSIONS

David S. Luke (1), Marko M. Elez (2), Daniel R. Bondi (2), Adam C. Clansey (2), Alexander Rauscher (3), Paul van Donkelaar (4), Lyndia C. Wu (1,2)

- (1) School of Biomedical Engineering, University of British Columbia, Vancouver, BC, Canada
(2) Mechanical Engineering, University of British Columbia, Vancouver, BC, Canada
(3) Department of Pediatrics, University of British Columbia, Vancouver, BC, Canada
(4) School of Health and Exercise Sciences, University of British Columbia, Okanagan, BC, Canada

INTRODUCTION

While concussions were once thought to be caused by single severe impacts, there is growing evidence of repetitive head impact exposure being a predisposing factor. Athletes with a delayed onset of symptoms often have difficulty identifying a single impact that caused their concussion. Indeed, a higher frequency of sports impacts with higher kinematics in a single day have been more likely to lead to a concussion than a lower frequency of impacts with lower kinematics [1]. Furthermore, impacts closer together have resulted in prolonged recovery and higher brain physiology alterations in animal models [2]. A shorter time window between impacts has also been correlated with a higher risk of concussion in athletes [3, 4]. All the evidence suggests that we may have to consider the impact history, and not just a single impact, when identifying the input mechanism for a concussion. However, limited concussion data with impact exposure information are available to investigate the potential interaction between impact severity and timing in concussion risk, especially in female athletes. In the current study, we deployed instrumented mouthguard sensors to varsity women's rugby and men's hockey athletes. Our objective is to characterize head impact exposure on days of diagnosed concussions and examine the relationship between impact magnitude, timing, and injury occurrence.

METHODS

34 UBC Women's Rugby Team (Research Ethics Protocol H21-03824) and 35 UBC Men's Hockey Team (H21-00400) athletes were recruited to wear Prevent Biometrics mouthguard sensors [5] during one and two competitive seasons, respectively (Figure 1). Concussion diagnoses were made by team physicians following the Berlin consensus guidelines [6]. Only impacts captured by the mouthguards that passed a 5g head center-of-gravity (CG) linear acceleration threshold and verified with video review on the day of concussion were included for analysis. Head impacts that led to symptoms were

identified on video by the athletes who sustained the concussion. Impact kinematics were transformed to head CG and low-pass filtered using a 4th-order Butterworth filter at 200Hz. Peak linear acceleration (PLA) and peak angular acceleration (PAA) were computed for each head impact to characterize the impact severity.

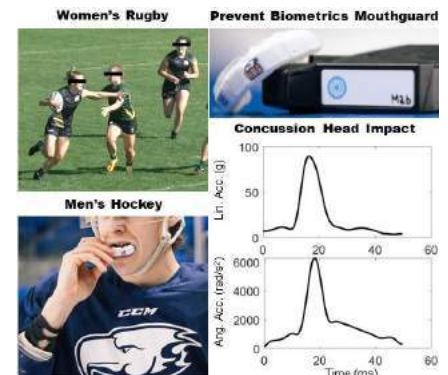


Figure 1: UBC women's rugby and men's hockey. Prevent Biometrics mouthguards capture head impact kinematics.

RESULTS

We collected data from seven women's rugby concussions over one season and four men's hockey concussions over two seasons. One women's rugby player (Athlete 6) and one men's hockey player (Athlete 3) each sustained two concussions within the same season. The number of impacts observed on the day of concussion ranged from 2-35 for women's rugby and from 2-7 for men's hockey. Women's rugby players identified between 1-7 impacts that occurred during play as symptom-inducing, while men's hockey players identified between 1-2. The time between the first and last head impact ranged from less than 1 second-67 minutes for women's rugby and from less than 1 second-114 minutes for men's hockey. The timing and peak linear/angular kinematics of impacts sustained by athletes on the day of their concussion are shown in Figure 2. The peak kinematics of impacts that led to symptoms ranged from 7-31 g and 569-6213 rad/sec² for women's rugby, and from 10-90 g and 459-6288 rad/sec² men's hockey athletes.

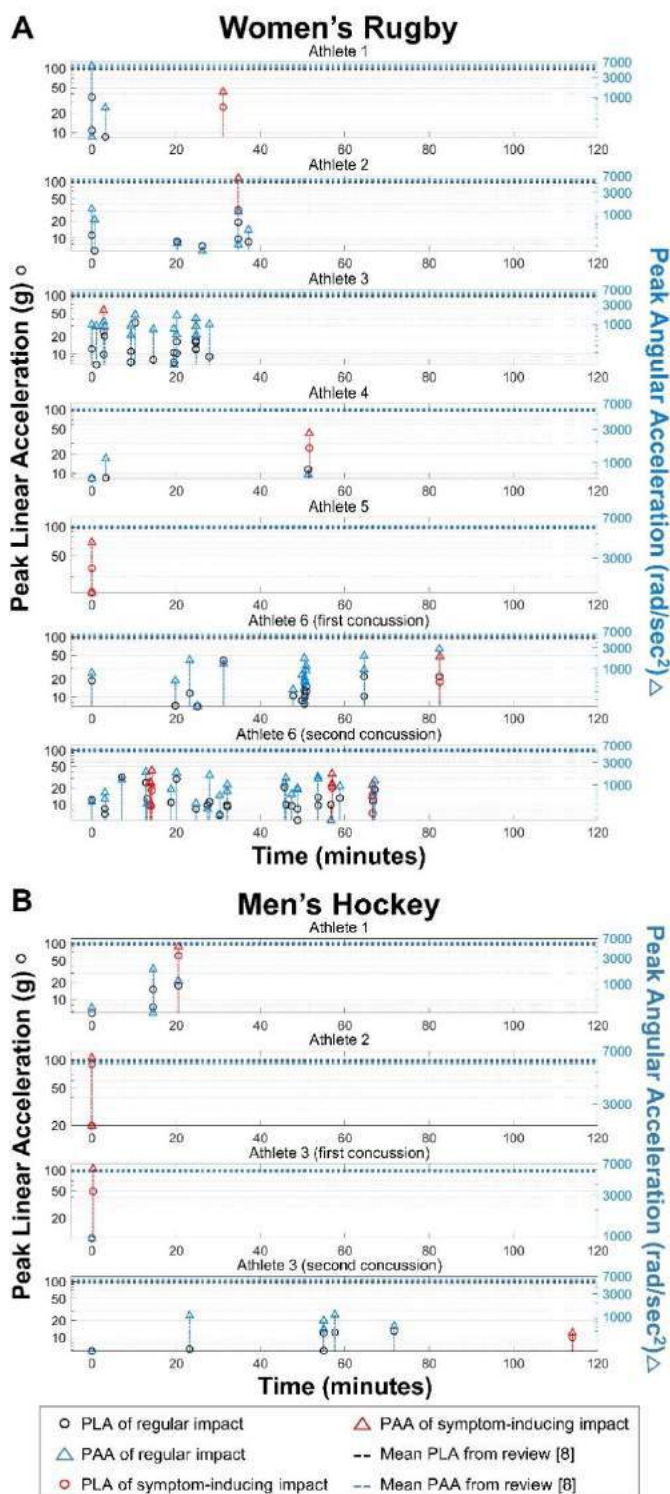


Figure 2: A) Women's rugby and B) men's hockey athletes' head impact exposure on the day of concussion. Black circles and blue triangles represent the peak linear acceleration (PLA) and peak angular accelerations (PAA) of impacts, respectively. Symptom-inducing impacts (red) are highlighted. Mean PLA and PAA for concussion impacts from literature [7] are shown for reference (dashed lines). Time zero is set at the time of the first impact.

DISCUSSION

Most impacts sustained by athletes on days of diagnosed concussions in the current study are mild (<30 g, <3000 rad/s²), including those identified by athletes to be symptom inducing, especially for women's rugby athletes and repeat concussions. In comparison, a 2017 systematic review on wearable head sensor-based concussion kinematics in male athletes reports a pooled mean (95% confidence interval) of 98.7 g (82.4-115.0 g) and 5576 rad/sec² (4584-6970 rad/sec²) [7], and a 2021 systematic review reports mean peak kinematics from concussive sports impacts ranging from 71-145 g and 3379-7951 rad/sec² [8]. Since prior studies mostly applied helmet-based sensors, which may overestimate impact kinematics, additional concussion data collected using mouthguard sensors [9] may help understand the discrepancies in impact kinematics levels.

The impact history, which includes both the number and timing of impacts, has been largely omitted when attempting to determine a kinematic threshold for concussion, but may explain the occurrence of concussion after low severity impacts in the current study. Impacts that were identified as symptom-inducing appear within 20 seconds of another impact in nine of the eleven exposure sets, with six sets having symptom-inducing impacts within 1 second of another impact. This suggests that the timing of these repetitive head impacts may be an integral part of concussion predisposition, and clusters of relatively mild impacts may also be symptom-inducing. Most injury criteria only consider impact severity, and not timing, of the impacts. One previously proposed criterion, Impact Density, considers the severity, timing between, and frequency of impacts [3]. However, Impact Density still relies on the assumption that a single impact can be identified as the concussive event, and only 19 impacts prior to this impact are included in the risk function. With these assumptions, Impact Density could not be calculated for all concussions from the current dataset. In several of our same-day exposure datasets, athletes experienced over 20 head impacts, continued to play after experiencing symptoms and were not able to identify a single event as the cause of the concussion.

In summary, our results demonstrate the possibility that clusters of mild sports head impacts may also be symptom-inducing and lead to concussion diagnoses. This mechanism seems to be at play for the women's rugby concussions and repeat concussions in our study, highlighting potential sex-based differences and increased vulnerability of athletes with recent prior concussions. As such, further development of injury criteria may need to account for this potential mechanism.

ACKNOWLEDGEMENTS

We would like to thank the Canadian Institutes of Health Research, Canada Foundation for Innovation and the Natural Sciences and Engineering Research Council of Canada for funding these ongoing studies. We would also like to thank the UBC Women's Rugby Team and UBC Men's Hockey Team coaches, staff, and players, Prevent Biometrics, and Susan Schmitz of UBC Dentistry for their support.

REFERENCES

- [1] Beckwith, J et al., *Med Sci Sports Exerc.*, 45:737-746, 2013.
- [2] Prins, M et al., *J Neurotrauma*, 30:30-38, 2013.
- [3] Broglio, S et al., *J Neurotrauma*, 34:2675-2683, 2017.
- [4] Stemper, B et al., *Ann Biomed Eng*, 47:2057-2072, 2019.
- [5] Bartsch, A et al., *Annu Int Conf IEEE Eng Med Biol Soc*, 2068-2072, 2019.
- [6] McCrory, P et al., *Br J Sports Med*, 51:838-847, 2017.
- [7] Brennan, J et al., *Sports Med*, 47:469-478, 2017.
- [8] Tierney, G et al., *Sports Biomech.*, 2021.
- [9] Wu, L et al., *Ann Biomed Eng*, 44:1234-1245, 2016.

VORTICITY TRANSPORT IN ANEURYSMS OF THE ABDOMINAL AORTA

Valentina Mazzi (1), Karol Calò (1), Maurizio Lodi Rizzini (1), Ludovica Saccaro (2,3), Diego Gallo (1), Angelo Iollo (2,3), Umberto Morbiducci (1)

- (1) Polito^{BIO}Med Lab, Department of Mechanical and Aerospace Engineering Politecnico di Torino, Italy
(2) IMB, UMR 5251, Université de Bordeaux, Talence, France
(3) Inria - Bordeaux Sud-Ouest, Talence, France

INTRODUCTION

The Abdominal Aortic Aneurysm (AAA) is an unphysiological localized enlargement of the abdominal aortic lumen. The pathogenesis of the AAA is modulated by a complex interplay between systemic, biological, and hemodynamic risk factors. Concerning hemodynamics, local blood flow disturbances have been linked to AAA evolution [1], because they might alter the transport of biochemicals and fluid-wall interactions which are involved in the progression of the disease. In this context, a plethora of hemodynamic quantities has been proposed over the years to provide potential indicators of flow disturbances in relation with aggravating biological events. However, the proposed hemodynamic quantities (1) often fail in describing/extracting fluid structures hidden in the arterial hemodynamic richness and (2) resulted only moderately associated with aneurysmal progression/rupture risk. These still unsatisfactory (both in terms of mechanistic comprehension and clinical translation) results suggest that the richness of fluid structures characterizing AAAs hemodynamics should be explored differently to identify more effective hemodynamic markers/predictor of disease. Starting from the observation that the presence of large-scale vortices with rich dynamics dominates the AAA hemodynamics, here we propose a quantitative analysis of the vorticity in AAAs based on the terms of vorticity transport equation. The final aims are (1) deciphering more clearly the intricate hemodynamics in AAAs, and (2) identifying vorticity-based quantities to be tested as biomechanical markers of the disease. The vortex structures analysis is carried out on patient-specific computational hemodynamics models of AAA characterized by a large anatomical inter-variability.

METHODS

Computational hemodynamics. The 3D geometry of eight AAAs was reconstructed from CT-scan data using the software PRAEVAorta (<https://www.nurea-soft.com>) [2]. The unsteady-state discretized Navier-Stokes equations were numerically solved using the

finite element-based open-source code SimVascular [3], prescribing a flow rate waveform available from literature [4] as inflow boundary condition.

Vorticity transport equation. The AAA velocity data from computational fluid dynamic simulations were used to compute the terms of the vorticity transport equation:

$$\frac{D \boldsymbol{\omega}}{Dt} = (\boldsymbol{\omega} \cdot \nabla) \mathbf{u} + \nu \Delta \boldsymbol{\omega} \quad (1)$$

where \mathbf{u} is the velocity, $\boldsymbol{\omega}$ is the vorticity and ν is the kinematic viscosity. The physical interpretation of eq. (1) is that the material derivative of the vorticity, describing the rate of change of vorticity of the moving fluid particles (left side term), is given by the contribution of a stretching term, quantifying the vortex deformation due to velocity gradients, and of a term quantifying vorticity diffusion due to viscosity (first and second term on the right side, respectively). We consider eq. (1) because vorticity typically develops in terms of vortex tubes which, transported by the local flow, are stretched, tilted, and disrupted in consequence of the local velocity gradients.

Vortex detection. The local vortex *swirling strength* and vortex core line (i.e., the vortex centerline) were adopted to visualize and reconstruct the vortex dynamics within AAAs. More in detail, the swirling strength of a vortex was quantified by computing the absolute value of the imaginary part of the complex eigenvalue of the velocity gradient tensor, while vortex core lines were identified applying the parallel vectors method proposed elsewhere [5].

Interaction of a vortex with the vascular wall. The analysis of the Wall Shear Stress (WSS) topological skeleton, which is composed by WSS critical points (where WSS vanishes) and critical lines (identifying WSS contraction/expansion action [6]), was carried out aiming at exploring how the near-wall vortex structures affect WSS topology on the AAA luminal surface. The WSS topological skeleton features were identified by applying a recently proposed Eulerian-based approach based on the divergence of the normalized WSS [6]:

$$DIV_{WSS} = \nabla \cdot \left(\frac{\tau}{\|\tau\|_2} \right) = \nabla \cdot (\tau_u) \quad (2)$$

where τ_u is the WSS unit vector. Technically, DIV_{WSS} negative values identify WSS contraction regions, while positive values identify WSS expansion regions.

RESULTS

Examples of volumetric maps of vortex stretching and diffusion terms (eq. (1)) are presented in Figure 1 for two explanatory models. The dynamics of the AAA volume-average values of vortex stretching and vortex diffusion (normalized in terms of min-max scaling) along the cardiac cycle are also presented (Figure 1). The two presented explanatory AAA models were selected because model AAAI is characterized by a marked expansion, while model AAAII presents a quasi-physiological blood flow canalization due to intraluminal thrombus formation. The inflow jet in AAAI rolls up into a well-defined vortex ring entering the expansion region due to the presence of the pressure-gradient mechanism. This large vortex ring undergoes stretching and tilting during the systolic deceleration phase (as confirmed by the second peak of vortex stretching time-history in Figure 1B) and dissipates in the AAA sac causing a stirring/mixing effect during diastole. Contrarily, in model AAAII vorticity transport is dictated mainly by the viscous diffusion mechanism.

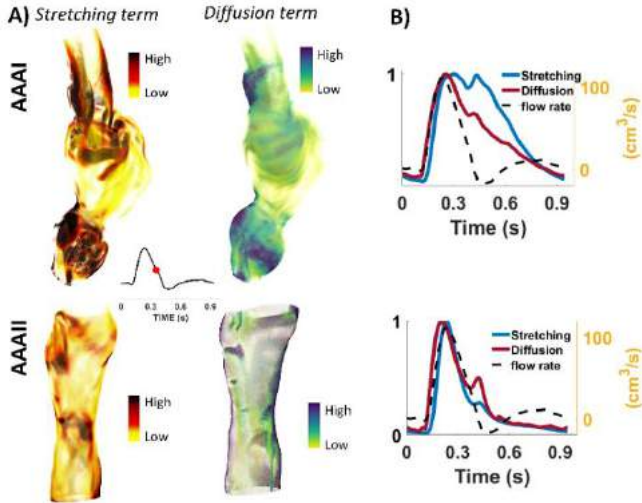


Figure 1: A) Instantaneous volumetric maps at mid-deceleration point and B) time-histories of volume-average values of the vorticity equation terms in two representative AAA models.

The evolution along the systolic deceleration phase of the vortex ring generated as a consequence of model AAAI expansion is analyzed in Figure 2A through the visualization of (1) instantaneous volumetric maps and (2) isosurfaces of the local swirling strength superimposed to the vortex core lines. Contrarily to model AAAI, due to the quasi-physiological geometry, the inflow jet does not roll up into a vortex ring in model AAAII (data not shown).

Finally, the WSS topological skeleton distribution on the luminal surface of AAAI and the sagittal section of velocity field at systolic peak are presented in Figure 2B (vortex core lines are plotted in black to highlight the presence of the vortex ring). It emerges that WSS topological skeleton features are the footprint of the interaction of vortex structures with the AAA wall, with WSS contraction and expansion regions (identified by negative and positive DIV_{WSS} values, respectively) identifying the boundary of the vortex ring on the luminal surface, highlighting flow separation and recirculation regions.

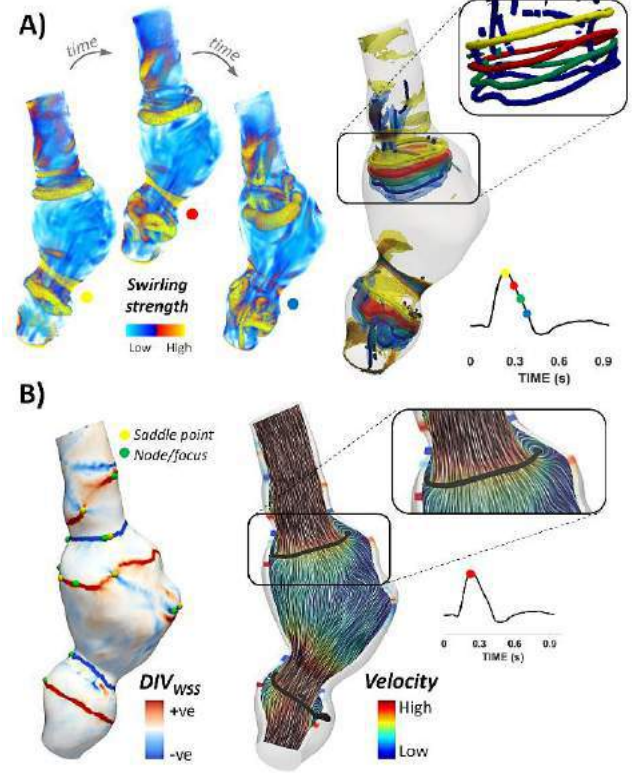


Figure 2: A) Volumetric maps and isosurfaces of the swirling strength and vortex core lines at different times along the cardiac cycle in AAAI. B) WSS topological skeleton and sagittal surface of velocity vector at the systolic peak in AAAI.

DISCUSSION

In this study a quantitative analysis of vorticity transport in computational hemodynamics models of AAA is performed, with the aim to decipher the AAA hemodynamic richness in AAA and the existing link between large-scale vorticity and WSS. A thorough characterization of vortex stretching/tilting and diffusion as well as vortex dynamics within AAAs may represent a useful approach for better elucidating the mechanistic link between organization of intravascular blood flow patterns, shape of the aneurysm, and clinical observations. This is particularly relevant because the transport of vortex structures is expected to be markedly involved in intraluminal thrombus formation, inflammatory mechanisms, as well as platelets dynamics, as it was suggested that platelets are ‘trapped’ inside vortices and when vortices break-up they release the activated platelets that aggregate and/or adhere to the wall [7]. In conclusion, the here vorticity transport-based quantitative analysis may contribute to a deeper understanding of the hemodynamics-driven processes underlying AAA progression, potentially improving risk assessment and the clinical management of AAA patients.

REFERENCES

- [1] Arzani, A et al., *Phys Fluids*, 24(8), 2012.
- [2] Caradu, C. et al., *J Vasc Surg*, 74(1):246-256, 2021.
- [3] Updegrove et al., *Ann. Biomed Eng*, 45(3):525-541, 2016.
- [4] Olufsen, M. et al., *Ann. Biomed. Eng.*, 28(11), 1281–1299, 2000.
- [5] Rothm M. et al., *IEEE Visualization '98*, 143-150, 1998.
- [6] Mazzi, V. et al., *Biomech Model Mechanobiol*, 19:1403-1423, 2020.
- [7] Biasetti, et al., *J. R. Soc. Interface*, 8:1449–1461, 2011.

SENSITIVITY OF PLATELET ACTIVATION IN AN ECMO PUMP DUE TO DIFFERENT MODELLING APPROACHES

Francesco Fiusco (1), Lars Mikael Broman (2,3), Lisa Prahli Wittberg (1)

(1) FLOW, Dept. Engineering Mechanics, KTH Royal Institute of Technology, Stockholm, Sweden
(2) ECMO Centre Karolinska, Astrid Lindgren's Children Hospital, Solna, Sweden
(3) Dept. Physiology and Pharmacology, Karolinska Institutet, Solna, Sweden

INTRODUCTION

Extracorporeal membrane oxygenation (ECMO) is a life-saving therapy used in the critically ill to treat both heart and lung failure. The circuit comprises a membrane oxygenator with heat exchanger, a blood pump to drive the circuit, cannulae to drain and reinfuse the blood to/from the patient and tubing with connectors. Its use is associated with a number of complications, with thromboembolism and hemolytic damage being primary causes of morbidity and mortality by the treatment[1].

It is widely recognized that mechanical stresses play a role in platelet activation, which can be characterized by means of a platelet activation state (PAS)[2]. In this perspective, Computational Fluid Dynamics (CFD) can be a valuable tool to assess the effect of the flow structures on the thrombogenic properties of the various components in different scenarios. Besides assigning appropriate boundary conditions, modeling of these flows requires different assumptions regarding liquid properties or the way the different blood components respond to flow unsteadiness. This work focuses on how the forces considered in Newton's second law influence the particle (platelet) trajectory in a centrifugal blood pump flow. The purpose is to assess the sensitivity and potential effect on the simulation results.

METHODS

In this work, Lagrangian Particle Tracking (LPT) was used to inject 100'000 spherical particles (representing platelets) in an ECMO blood pump (geometry shown in Figure 1) and record their stress history. Thereafter, platelet activation was computed by considering the mechanical dose accumulated along each platelet pathline. The activation state was assessed according to the model by Nobili *et al.*[2]:

$$\frac{dPAS}{dt} = ca \|\tau(\mathbf{x}_i(t), t)\|^{b/a} \mathcal{D}(t)^{a-1} \quad (1)$$

where a, b, c are model constants. \mathcal{D} is the mechanical dose, function of shear stress history:

$$\mathcal{D}(t) = \mathcal{D}(t_0) + \int_{t_0}^t \|\tau(\mathbf{x}_i(t), t)\|^{b/a} dt \quad (2)$$

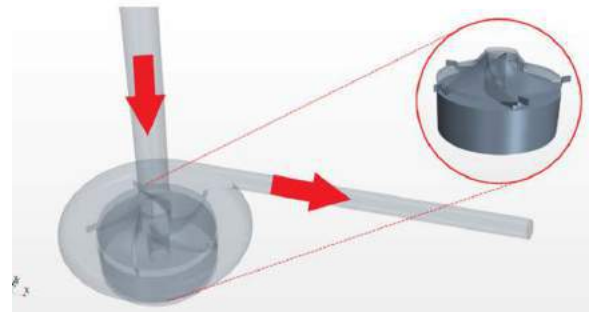


Figure 1: Geometry of the blood pump. Adapted from [3]

The LPT was carried out as a post-processing step on time-resolved 3D volume data produced using the commercial CFD package Star-CCM+, generated by solving the incompressible Navier-Stokes equations with a sliding-mesh approach. Blood was treated as a Newtonian fluid. According to Fuchs *et al.*[4] and Fiusco *et al.*[3], the particle inertia can as a first approximation be neglected, given the small size ($r = 1 \mu m$) and density of the platelets (similar to blood), i.e. Stokes number $< 2E-8$. Thus, the platelets can be considered as passive tracers following the flow, neglecting the forces acting on the platelets.

However, if considering particle inertia, Newton's second law needs to be used to computing the particle velocity:

$$m_p \frac{d\mathbf{v}_p}{dt} = \sum \mathbf{F}_i \quad (3)$$

where m_p represents the mass of the particle, v_p particle velocity and F_i are all the forces acting on the particles. In this work, the following two forces were considered:

- Drag force:

$$D = 6\pi r\mu(\mathbf{u} - \mathbf{v}_p) \quad (4)$$

where μ is the carrier phase viscosity and u is the fluid phase velocity at the particle center.

- Saffmann lift force:

$$L = 1.61d_p^2\sqrt{\rho_f\mu}\frac{(\mathbf{u} - \mathbf{v}_p) \times \boldsymbol{\omega}}{\sqrt{\omega}} \quad (5)$$

where ω is the vorticity of the carrier phase at the particle location.

The impact of these forces on particle trajectories and platelet activation will be studied.

RESULTS & DISCUSSION

In the case neglecting the forces acting on the particle, i.e. the tracer particle case, some typical pathlines are shown in Figure 2.

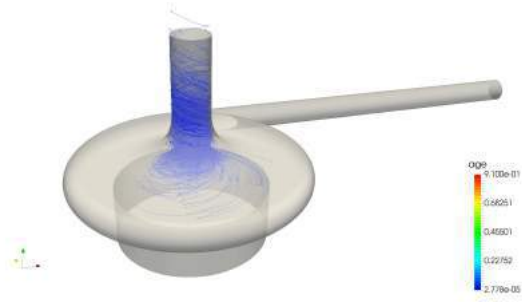


Figure 2: Typical platelet pathlines for the tracer case. Adapted from [3]

As depicted in Figure 2, a backflow phenomenon was observed at the inlet pipe[3]. The distribution of PAS values of the platelets, as illustrated in Figure 3, showed a peak of platelets with moderate PAS levels.

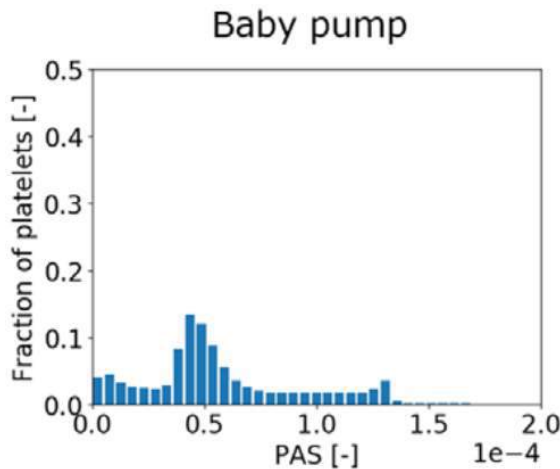


Figure 3: Distribution of platelet activation state (PAS) values for the injected platelets. Adapted from [3]

Given the characteristics of the flow, the question on which parameters play a role on blood damage arises. Thus, the aim of this work is to assess the influence of modelling techniques on the observed behavior of platelets and their activation. For that purpose, a similar analysis as for the tracer particles will be conducted on the case in which particles are subject to lift and drag force. Platelet activation models are usually power laws that are calibrated experimentally. In ECMO pumps the flow situation is such that the stress values fall outside the activation models' calibrated range. However, the models can be used comparatively providing valuable insights regarding the effects on different flow conditions and modelling approaches. In particular, the scope of this work is to assess the sensitivity of both quantities of clinical interest (such as overall levels of platelet activation and their distributions) as well as gain an improved fluid-dynamical understanding of the forces influencing the motion of blood components in a flow field characterized by highly unsteady turbulent behavior. Such knowledge will prove useful to improve the predictive modelling of particle tracking, e.g. to predict areas of high thrombogenic potential, as well as to characterize which phenomena need to be accounted for to correctly compute platelet (and other particles) trajectories.

ACKNOWLEDGEMENTS

The research was funded by the Swedish Research Council (Vetenskapsrådet), Grant no. 2019-04800. The computations were enabled by resources provided by the Swedish National Infrastructure for Computing (SNIC) at the National Computing Centre (NSC) and the Paralleldatorcentrum (PDC) partially funded by the Swedish Research Council through grant agreement no. 2016-07213.

REFERENCES

- [1] Iacobelli R et al. *Scientific Reports* 11.1 (2021). DOI: 10.1038/s41598-021-83157-5.
- [2] Nobili M et al. *ASAIO Journal* 54.1 (2008). ISSN: 10582916. DOI: 10.1097/MAT.0b013e31815d6898.
- [3] Fiusco F et al. *ASAIO Journal* 68.1 (2022). ISSN: 1058-2916. DOI: 10.1097/MAT.0000000000001493.
- [4] Fuchs G et al. *Scientific Reports* 8.1 (2018). ISSN: 20452322. DOI: 10.1038/s41598-018-32247-y.

VALIDATION OF THE COUPLED MOMENTUM METHOD AGAINST A COMPLIANT AORTIC PHANTOM IN A HYBRID MOCK CIRCULATORY LOOP

Francesco Bardi (1,2,3), Emanuele Gasparotti (1), Emanuele Vignali (1), Miquel Aguirre (2), Stéphane Avril (2), Simona Celi (1)

(1) BioCardioLab, Fondazione Toscana “G. Monasterio”, Italy

(2) Mines Saint-Etienne, Université Jean Monnet Saint-Etienne, INSERM, SAINBIOSE U1059, F-42023 Saint-Etienne, France

(3) R&D, PrediSurge, Saint-Étienne, France

INTRODUCTION

Computational fluid dynamics (CFD) is a widely used tool in research to improve the understanding of various cardiovascular diseases. Patient-specific blood flow simulations enable high-resolution visualization of key hemodynamic indicators, such as the wall shear stress. Fluid Structure Interaction (FSI) simulations consider the motion of the vessels, providing a more accurate solution for the blood velocity and pressure fields [1]. However, the computational cost of the standard ALE-FSI method is significantly higher than that of a rigid wall CFD simulation, making it infeasible for the clinical practice. To address this issue, the coupled momentum method for fluid-solid interaction problems (CMM-FSI) has been proposed [2]. In the CMM-FSI approach, the flow domain is kept fixed and the wall is treated as a linear elastic membrane, reducing computational cost while providing similar results when deformations are less than 10%. The aim of this work is to do a rigorous in-vitro validation of the coupled momentum using a flexible thoracic aortic phantom. A novel Hybrid Mock Circulatory Loop (HMCL) was used to replicate different physiological conditions in the flexible phantoms and the gathered experimental data were compared with the results of numerical simulations.

METHODS

A thoracic aortic model was manufactured with a photopolymerization 3D printer (J735 PolyJet, Stratasys) and the printing material was characterized via uniaxial tensile testing using four dumbbell shape samples. Each sample was loaded up to a strain of 0.4, repeating the cycle varying the strain rate from 0.01 to 0.3 s^{-1} . The aortic model was connected to a HMCL system, described in [3, 4] and shown schematically in Figure 1. A physiological flow rate was imposed at the inlet of model with a piston pump, and the outlets were connected to Hybrid-Units that regulate the pressure with a PID controller according to a 3-Element Windkessel model. The Windkessel parameters (proximal resistance R_p , distal resistance R_d , compliance C and ground pressure P_0) were tuned for each outlet to achieve a desired flow split and pressure range. A pressure range of 0-40 mmHg was reproduced. A camera system was synchronized with the piston pump to take images at 100 fps with a resolution of 24 px/mm. The obtained images were segmented, and the contours were extracted to track diameter variation during the cardiac cycle. The CMM-FSI simulation was set up with the CRIMSON software environment [5]. The measured experimental data were used to set boundary conditions; more specifically the same inlet flow rate and outlet pressures were prescribed. The Young's modulus assigned to the aortic phantom was obtained via a linearization of the stress strain curve. A rigid material was assigned to the adapters, whereas the piping to the Hybrid Units were modelled as additional resistors and inductors. Three cardiac cycles were simulated to achieve convergence.

to achieve a desired flow split and pressure range. A pressure range of 0-40 mmHg was reproduced. A camera system was synchronized with the piston pump to take images at 100 fps with a resolution of 24 px/mm. The obtained images were segmented, and the contours were extracted to track diameter variation during the cardiac cycle. The CMM-FSI simulation was set up with the CRIMSON software environment [5]. The measured experimental data were used to set boundary conditions; more specifically the same inlet flow rate and outlet pressures were prescribed. The Young's modulus assigned to the aortic phantom was obtained via a linearization of the stress strain curve. A rigid material was assigned to the adapters, whereas the piping to the Hybrid Units were modelled as additional resistors and inductors. Three cardiac cycles were simulated to achieve convergence.

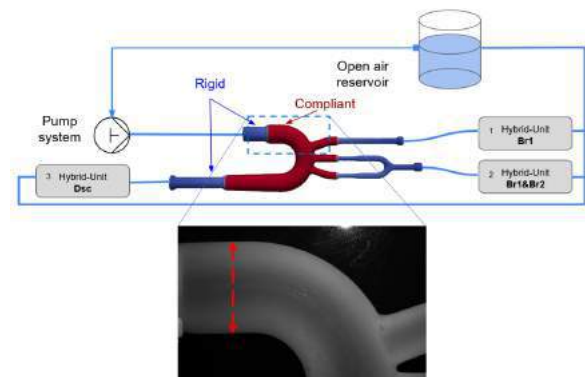


Figure 1: Hybrid Mock Circulatory Loop system. Phantom image with the measured diameter at the aortic root highlighted.

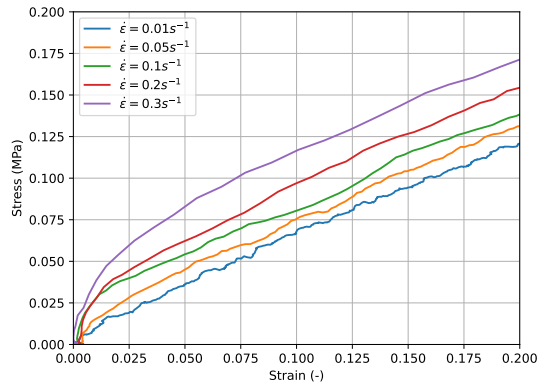


Figure 2: Uniaxial tensile test stress strain curve for different strain rate values.

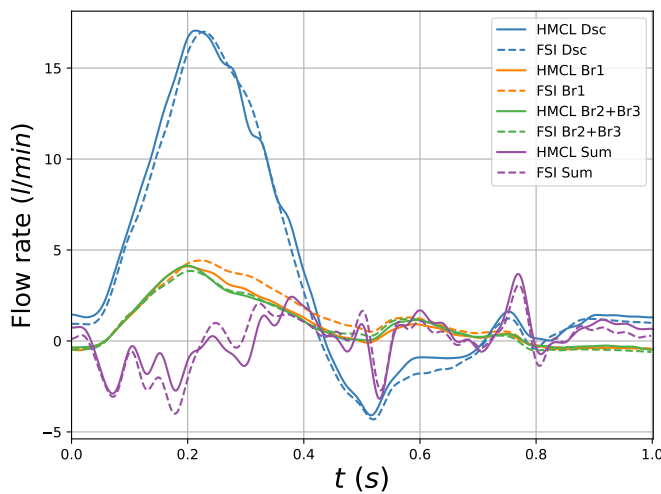


Figure 3: Outlets flow rates. Comparison between the experimental data (HMCL) and the results of the numerical simulation (FSI).

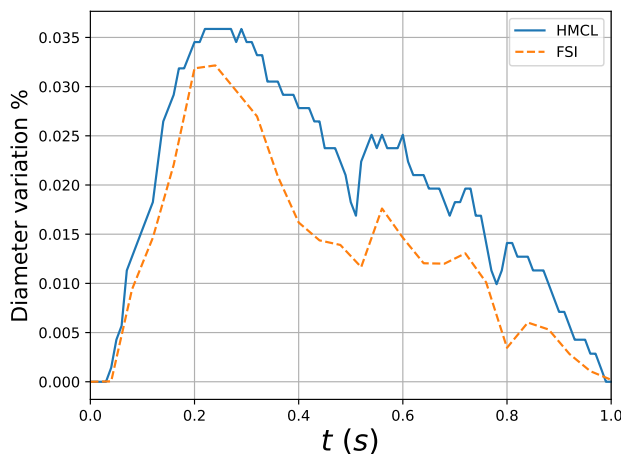


Figure 4: Diameter variation at the aortic root. Comparison between the experimental data (HMCL) and the results of the numerical simulation (FSI).

RESULTS

The stress strain curve of the printing material for the different strain rates is shown in Figure 2. It is evident that the material exhibits a strain rate dependent behaviour. Consequently, evaluating the maximum loading rate of the phantom (Figure 4), we estimated the Young's modulus of 1 MPa, from the stress strain curve corresponding to a strain rate of 0.2 s^{-1} . This Young's modulus was then used for the numerical simulation. Figure 3 shows that there is a good agreement between the measured flow rates at the outlets and the results of the numerical simulation. Moreover, the difference between the sum of the outlets flow rates, and the inlet flow rate (labelled as sum Figure 3) indicates that the total volume variation of the phantom was well predicted. Analogously, the simulation successfully replicated the diameter variation at the middle section of the aortic root (Figure 4).

DISCUSSION

The presented experimental setup can be used to rigorously validate fluid-structure interaction simulation strategies. The obtained data were used to validate the coupled momentum method, as it is attractive due to its low computational cost, when compared to the standard ALE approach. Moreover, the coupled momentum method was previously validated in-vitro only using straight phantoms with only one outlet [6]. In our study we found that the experimental and numerical results were in good agreement, both in terms of flow rates and deformations. Nonetheless, a closer examination revealed some minor discrepancies. Specifically, the flow rate at the first epiaortic branch (Br_1) was overestimated between the systolic peak and the beginning of the diastolic phase. The diameter variation at the aortic root was instead underestimated. These discrepancies could be attributed to the fact that the wall is modelled as a linear elastic membrane, whereas the results of the uniaxial test indicate a strain rate dependent behaviour. In order to better investigate the effects of this approximation, as a future development it would be interesting to repeat the numerical simulation adopting an ALE approach using more realistic material properties.

ACKNOWLEDGEMENTS

MeDiTaTe Project has received funding from the European Union's Horizon 2020 research and innovation programme under Grant Agreement 859836.

REFERENCES

- [1] Mourato A et al. en. *Applied Sciences* 12.16 (2022). ISSN: 2076-3417. DOI: 10.3390/app12168049.
- [2] Figueroa CA et al. en. *Computer Methods in Applied Mechanics and Engineering* 195.41-43 (2006). ISSN: 00457825. DOI: 10.1016/j.cma.2005.11.011.
- [3] Bardi F et al. *IEEE Transactions on Biomedical Engineering* (2022). DOI: 10.1109/TBME.2022.3224581.
- [4] Vignali E et al. *ASAIO Journal* (2022).
- [5] Arthurs CJ et al. en. *PLOS Computational Biology* 17.5 (2021). Ed. by Schneidman-Duhovny D. ISSN: 1553-7358. DOI: 10.1371/journal.pcbi.1008881.
- [6] Kung EO et al. en. *Annals of Biomedical Engineering* 39.7 (2011). ISSN: 0090-6964, 1573-9686. DOI: 10.1007/s10439-011-0284-7.

CELLULAR SIGNAL PROCESSING MACHINERY DURING DIRECTED MIGRATION OF CANCER CELLS

Andrew Mugler (1,3), Bumsoo Han (2,3)

- (1) Department of Physics and Astronomy, University of Pittsburgh, Pittsburgh, PA, USA
(2) School of Mechanical Engineering, Purdue University, West Lafayette, IN, USA
(3) Purdue Institute for Cancer Research, Purdue University, West Lafayette, IN, USA

INTRODUCTION

Directed migration of cancer cells in the tumor microenvironment is a critical step in tumorigenesis, local invasion, and metastasis [1, 2]. The tumor microenvironment imposes multiple, heterogeneous environmental cues on cancer cells [2, 3]. These cues include various chemokines or growth factors such as transforming growth factor- β (TGF- β) and epidermal growth factor (EGF) [4, 5], stiffness and microstructure of the extracellular matrix, and interstitial fluid flow [6-10]. Understanding the underlying mechanisms of directed migration has a profound impact on cancer biology as well as drug discovery to prevent and suppress cancer metastasis.

Because of its importance, the directed migration of cancer cells has been extensively studied [6, 7]. Many of these studies have focused on the relationship between a single environmental cue and corresponding signaling molecules and pathways of migration. Among the environmental cues, chemical cues are the most actively studied. These studies have led to the discovery of several key molecules of the cell. However, these reductionist approaches are not easily translatable to predict migration behavior within the complex tumor microenvironment.

In this study, we will provide our perspective of using a minimal systems approach to understand directed cell migration under complex environmental cues. We have been investigating cancer cell's migratory behaviors by approximating a cancer cell as a system of sub-cellular systems of sensing, signal processing, and actuator, as illustrated in **Figure 1**. We reverse-engineered cancer cell's migratory behavior to construct these sub-cellular systems. The underlying rationale is that directed migration may require sensing, polarization, and motility. A cell's ability to execute these interrelated aspects of directed migration determines its migration performance, including the accuracy, persistence, and speed of migration. Our systems approach enables understanding and prediction of how cells decode complex environmental cues during directed migration.

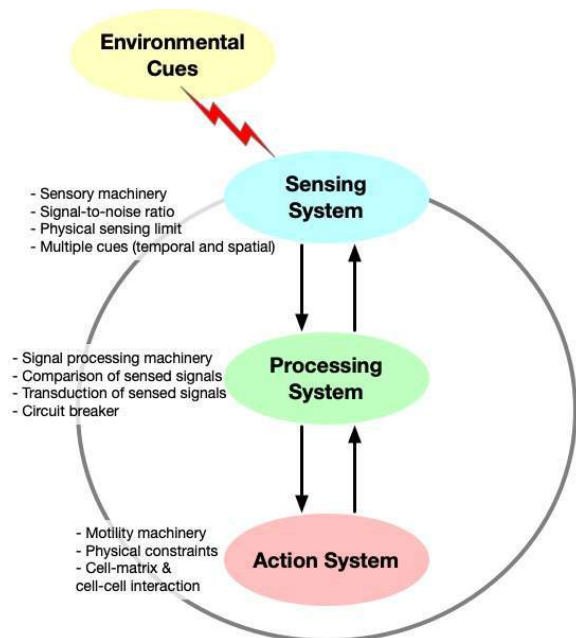


Figure 1: Systems approach to directed migration of cancer cells.

METHODS

We use a combination of experiment and theory to build a systems approach to directed cell migration, as illustrated in **Figure 2**. Experimentally, we employ microfluidic devices designed to subject cancer cells to multiple heterogeneous and simultaneous cues, including chemical gradients and fluid flow. Theoretically, we employ mathematical modeling and computational simulation to validate experimental results and make new predictions.

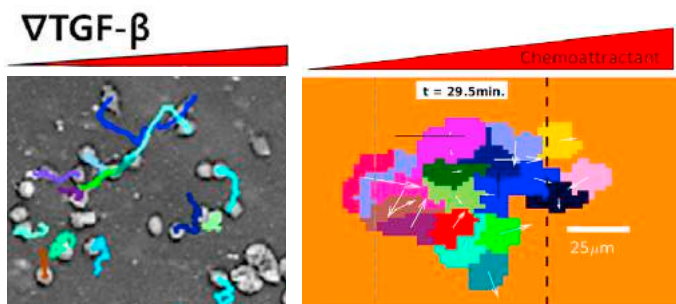


Figure 2: Joint experiment-theory approach employing microfluidics and microscopy, combined with mathematical modeling and simulation.

RESULTS

Several interesting results emerge from our approach when we consider the directed migration of cancer cells subjected to multiple cues. In one example [4], we present cells with two growth factor gradients, TGF- β and EGF. When each cue is presented individually, cells migrate up the gradient, resulting in a positive chemotactic index, CI (red and blue in Figure 3, left). When both cues are presented together, aligned in the same direction, cells no longer migrate up the gradients as strongly, resulting in a lower CI (purple in Figure 3, left). This counterintuitive behavior, known as antagonism, was successfully explained by a model in which the intracellular response pathway to each cue converges at a common point which then leads to migration. The convergence causes saturation of the signaling response when both cues are present. A mathematical model based on this concept successfully reproduced the experimental results (Figure 3, right).

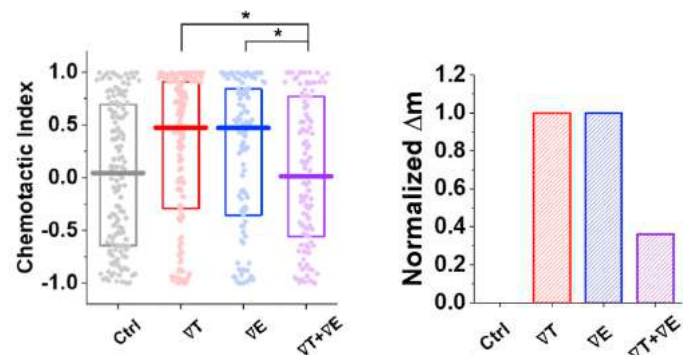


Figure 3: Both experiments and theory exhibit antagonism: the migratory response of a cell to each chemical gradient individually (red, blue) is weaker than its response to both together (purple).

In a second example [8], we also present cells with two cues, but now the cues are of heterogeneous natures: a TGF- β gradient and fluid flow. The first result we find is that these two cues are intrinsically coupled, as the flow necessarily affects the shape of the TGF- β profile. The second result we find is that cells preferentially respond to the gradient over the flow. This is illustrated in Figure 4 (top left), where we see that in the cases where the two cues compete (upper right and lower left corners), the cells migrate in the direction of the TGF- β gradient, not the flow. In fact, as illustrated in Figure 4 (top right), these experimental results can be described by a ternary logic gate, where the three input states are the presence of a cue pointing right (+), pointing left (-), or absent. This logic implies a systems-level circuit that

describes the migratory behavior of the cell and can be used to make future predictions (Figure 4, bottom).

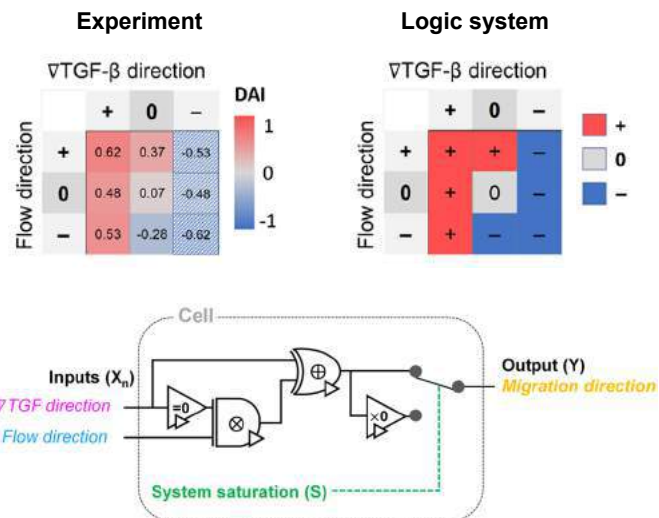


Figure 4: Cells migrate preferentially up a chemical gradient rather than up a fluid flow, and this can be described by a ternary logic gate.

DISCUSSION

Through this framework, we proposed the physical sensing limits, individual and collective sensing, a system capacity of the signal processing, and physical constraints of precision and persistence of cancer cell migrations. All these concepts not only supplement the existing molecular signaling pathways of cell migration but also provide new insights into how cancer cells sense, decode and determine migration direction. This approach and the resulting understanding may lay the groundwork for a unified framework to explain the migration of other cell types in the tumor microenvironment, including endothelial cells during angiogenesis and immune cells during anti-tumor immunity.

ACKNOWLEDGEMENTS

This work was partially supported by grants from the National Institutes of Health (U01 HL143403, R01 CA254110, U01 CA274304, and P30 CA023168) and National Science Foundation (MCB-2134603, MCB-1936761, and PHY-1945018).

REFERENCES

- [1] Worbs T, Hammerschmidt SI, Förster R, *Nature Reviews Immunology*, 17:30-48, 2017.
- [2] Oudin MJ, VM Weaver, *Cold Spring Harbor Symposia on Quantitative Biology*, 030817, 2017.
- [3] Ozcelikkale A, Dutton JC, Grinnell F, Han B, *Journal of the Royal Society Interface*, 14:20170287, 2017.
- [4] Moon H, Saha S, Mugler A, Han B, *iScience*, 24:103242, 2021.
- [5] Roussos ET, Condeelis JS, Patsialou A, *Nature Reviews Cancer*, 11:573-587, 2011.
- [6] Devreotes P, Horwitz AR, *Cold Spring Harbor Perspectives in Biology*, 7:a005959, 2015.
- [7] Welf ES, Haugh JM, *Wiley Interdisciplinary Reviews: Systems Biology and Medicine*, 3:231-40, 2011.
- [8] Moon H, Saha A, Mugler A, Han B, *Lab on a Chip*, advance article doi:10.1039/D2LC00807F, 2023.

4D ULTRASOUND-BASED REGIONAL MECHANICAL CHARACTERIZATION OF ABDOMINAL AORTIC ANEURYSMS USING VIRTUAL FIELDS METHOD

Mirunalini Thirugnanasambandam (1,2), Esther J Maas (1,2), Arjet HM Nievergeld (1,2),
Marc RHM van Sambeek (1,2), Stephane Avril (3), Richard Lopata (1)

- (1) Eindhoven University of Technology, the Netherlands
(2) Catharina Hospital Eindhoven, the Netherlands
(3) Ecole des MINES Saint-Etienne, France

INTRODUCTION

Abdominal aortic aneurysms (AAA) affect 4-6% of the general population and are characterized by a rupture-prone inflated abdominal aorta. Despite decades of biomechanics research aimed at understanding the underlying disease pathophysiology and at identifying the most accurate predictor of rupture, current methods of clinical management of AAAs continue to focus on the maximum diameter threshold (5.5 or 5 cm for male or female patients respectively). Thus, it is crucial to replace clinically impractical techniques with routinely available ones in the AAA biomechanics evaluation protocol. In this study, we utilize the availability of functional ultrasound (US) images from AAA patients, and use it in combination with a modified virtual fields method (mVFM) [1] to estimate patient-specific material parameters. This is only possible due to the ability of 4D US to non-invasively assess AAA wall motion, which inherently contains information about its material behavior.

METHODS

US acquisition

AAA patients were imaged using a clinical US probe in a supine position to acquire 4D-US images at a frequency of 4-8Hz over multiple heartbeats. The image volumes were segmented at diastole and an in-house speckle-tracking algorithm [2] was used to track the inner wall and outer wall over the cardiac cycle. Point clouds generated from this process were fitted with B-spline grids at systolic and diastolic configurations. The two geometries were co-registered by minimizing the distance between neighboring knots in the two grids, and subsequently, the displacement fields of the inner wall and outer wall were generated. Displacement fields of the nodes in the bulk of the AAA wall were evaluated by interpolating between the displacement vectors of their neighbors located in the inner wall and outer wall. An unsupervised, discretized, spline smoother was used to smooth the 3D

deformation field and was post-processed before using it as a replacement for 3D full field deformation data. The overall schematic of the material estimation process is presented in Figure 2.

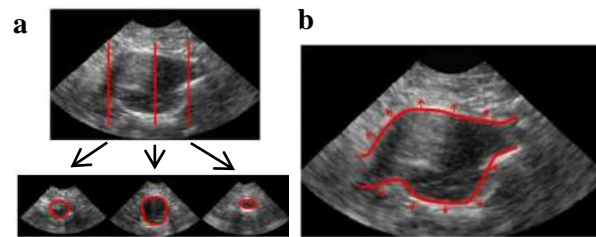


Figure 1a: Automatic segmentation of US images. b: illustration of 3D speckle tracking of the inner wall of AAA.

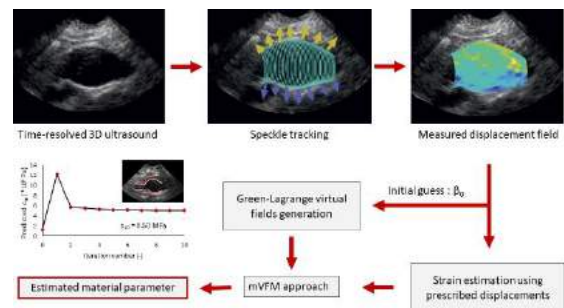


Figure 2: Overall schematic of the material parameter estimation method.

Modified virtual fields method

mVFM combines the strengths of two robust inverse methods – the finite-element model updating (FEMU) technique and the traditional virtual fields method (VFM). While FEMU's iterative nature and VFM's principle of virtual work-based cost function are integrated within mVFM, FEMU's high computational costs and VFM's difficulty in choosing an appropriate test function are both eliminated. Thus, mVFM is able to achieve quick convergence of a problem that is setup automatically.

Two different models of FEA were simulated to implement VFM:

- (1) Strains were evaluated in the current configuration, where the displacement vectors derived from US-based 3D tracking were prescribed to each node.
- (2) Virtual fields were derived automatically using a stressed intermediate configuration where an initial guess for the material parameter was provided. An intraluminal pressure load corresponding to the displacement field was applied, and displacements were prescribed in every boundary where traction was not known.

RESULTS

Using an uncoupled, Neo-Hookean material model with an initial guess of $c_{10}=1.2 \cdot 10^6$ Pa, the predicted material parameter values converged within three iterations when global patient-specific values of c_{10} were sought. Later, the mesh was divided into three regions based on location and presence of AAA as shown in Figure 3a. This led to ten iterations before convergence was achieved while predicting the material model parameters in all three regions.

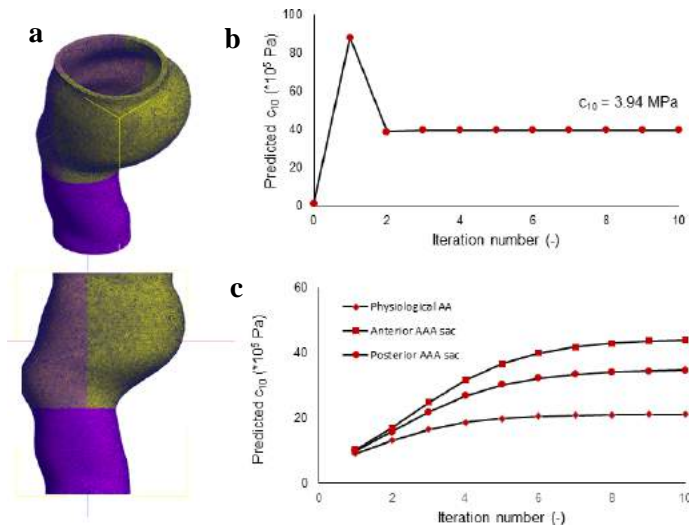


Figure 3a: AAA mesh showing physiological (purple), anterior AAA (yellow) and posterior AAA (orange) wall. Prediction of b: global and c: local values of material model parameters

DISCUSSION

We were able to demonstrate, for the first time, the feasibility of using an innovative combination of 4D US and mVFM to determine unknown constitutive material model parameters in different regions of the AAA. The deformation fields obtained from routine US images were

input into the modified VFM algorithm. FEMU has been previously used to evaluate Neo-Hookean material parameters using US images. However, about two weeks were needed to achieve convergence for one dataset while using a quad core CPU with 32GB RAM [3]. Using mVFM, we were able to achieve convergence within 3 hours while using a 6-core CPU with 16GB RAM. This drastic reduction in computational time suggests the immense potential of our new technique in in-vivo, patient-specific, material characterization, and demonstrates a high translational value.

While performing regional mechanical characterization, it was observed that the anterior AAA sac had a higher shear modulus when compared to that of the posterior AAA sac tissue. It was also seen that non-aneurysmatic abdominal aortic tissue had the least shear modulus when compared to its pathological counterparts. This observation is in line with other studies which investigated the effect of location on AAA tissue properties where anterior wall was found to be the stiffest, compared to the lateral and posterior wall tissue specimens [4].

One of the limitations of our method is the use of simple Neo-Hookean material model to characterize AAA tissue, while it has been proven to be anisotropic. As a next step, the use of more sophisticated material models and local material characterization within the mVFM framework will be evaluated. The latter requires more precise input data [5].

ACKNOWLEDGEMENTS

The authors would like to thank the Dutch Research Council NWO (VIDI 17533) for financially supporting this project.

REFERENCES

- [1] Mei Y et al. Journal of Elasticity, 145, 265-194 (2021).
- [2] van Disseldorp EMJ et al. European Heart Journal. 20(2), 185-191 (2019).
- [3] Wittek, A. et al. Journal of Mechanical Behavior of Biomedical Materials, 58, 122-138 (2016).
- [4] Raghavan ML et al. Journal of Biomechanics, 39(16), 3010-16 (2006).
- [5] van Hal VHJ et al. IEEE Transactions on Ultrasonics, Ferroelectrics, and Frequency Control, 69(2), 604-616 (2022).

A CLOT COMPOSITION DEPENDENT HYPERELASTIC MODEL IN THE SIMULATION OF DIRECT ASPIRATION THROMBECTOMY

K. Bein Snee (1), R. McCarthy (2), P.E. McHugh (1), B. Fereidoonzhad (3), J.P. McGarry (1)

(1) Biomedical Engineering, University of Galway, Ireland
(2) Cerenovus, Galway, Ireland
(3) Biomechanical Engineering Department, TU Delft, the Netherlands

INTRODUCTION

Stroke is the second leading cause of death globally and resulted in over 6 million deaths in 2019 [1]. Acute ischemic strokes (AIS) are most commonly caused by embolic occlusions of a cerebral artery. Mechanical thrombectomy, whereby stent retriever devices are used to remove occluding clots, has revolutionized treatment of AIS [2,3]. However, while complete recanalization of the vessel is achieved in 85% of cases, 80% of AIS patients still suffer long-term disabilities [1]. Clot composition, specifically the red blood cell (RBC) and fibrin fiber content, has been shown to be a key determinant of the success of thrombectomy procedures [2,4,5]. Clot fracture and distal embolization during thrombectomy has been shown to be a significant risk for RBC-rich clots [1,5]. Clinically, fragmentation during thrombectomy leads to multiple clot-removal attempts (passes) and increases the risk of poor long-term patient outcomes [4].

Direct aspiration (DA) is emerging as a promising alternative to stent-retriever devices. In DA, an aspiration catheter is used to apply a negative suction pressure on the proximal end of the clot, with the aim to ingest the clot into the catheter [1,3,4]. Large-bore catheters have recently been developed with the aim of increasing DA efficacy [3,4,6]. However, the influence of catheter design on clinical outcomes, including clot fracture and distal embolization, has not fully been established [6].

In the current study we present the first analysis of the effect of DA catheter design on clot deformation and fracture. We develop a finite element (FE) framework to simulate the aspiration of red blood cell (RBC) -rich clots and fibrin-rich clots. We develop a novel anisotropic material model based on experimental mechanical testing of a range of clot compositions [5]. Our results demonstrate that the success of DA treatment of AIS is highly dependent on catheter diameter and clot composition.

METHODS

In order to develop the first customized FE model of DA, we consider the case of a cylindrical clot which is in direct contact with the catheter at its distal surface, as shown in Figure 1A. Based on a range of devices currently under development, we consider three catheter diameters, 1.2 mm, 1.62 mm and 2.5 mm, while assuming a clot diameter of 3 mm and length 10 mm, based on an M1 occlusion [7]. A negative suction pressure is applied to the clot surface inside the catheter. As the pressure is increased, the model simulates the deformation of the clot into the catheter which is characterized by the length of the aspirated section (u). The critical pressure is defined as the computed pressure required to fully ingest the clot into the catheter.

In order to simulate the clot material, we develop and implement a customized composition-dependent constitutive law [5,8,9] as a user defined material subroutine (UMAT) in the FE software Abaqus. In summary, this anisotropic hyperelastic material law considers non-linear volumetric and isochoric deformation of the RBC components of the clot, in addition to an anisotropic representation of the fibrin network. The volumetric stress is given as

$$\sigma_{vol} = \begin{cases} \kappa_1(J - 1), & |J - 1| \leq |D_{1v}| \\ p_v(J - 1)^2 + q_v(J - 1) + r_v, & |D_{1v}| < |J - 1| < |D_{2v}| \\ \kappa_2(J - 1 - D_{2v}) + (p_v D_{2v}^2 + q_v D_{2v} + r_v), & |J - 1| \geq |D_{2v}| \end{cases} \quad (1)$$

where κ_1 and κ_2 are the bulk moduli at low and high strains, respectively. The parameters p , q and r govern a strain stiffening transition region.

The principal isochoric stress components are given as

$$\bar{S}_i(\bar{\lambda}_i) = \quad (2)$$

$$\begin{cases} \frac{9\kappa_1 G_1}{3\kappa_1 + G_1} (\bar{\lambda}_i - 1), & |\bar{\lambda}_i - 1| \leq |D_{1m}| \\ p_m (\bar{\lambda}_i - 1)^2 + q_m (\bar{\lambda}_i - 1) + r_m, & |D_{1m}| < |\bar{\lambda}_i - 1| < |D_{2m}| \\ \frac{9\kappa_2 G_2}{3\kappa_2 + G_2} (\bar{\lambda}_i - 1 - D_{2m}) + (p_m D_{2m}^2 + q_m D_{2m} + r_m), & |\bar{\lambda}_i - 1| \geq |D_{2m}| \end{cases}$$

where G_1 and G_2 are the shear moduli at low and high strains, respectively. $\bar{\lambda}_i$ are the isochoric principal stretches.

The anisotropic stress tensor in the fibrin network is calculated as $\sigma_{\text{aniso}} = \sum_{i=4,6} \sigma_{fi} \mathbf{a}_i \otimes \mathbf{a}_i$, where the vector \mathbf{a}_i describes the deformed orientation of fiber i . The axial fibre stress is given as

$$\sigma_{fi} =$$

$$\begin{cases} E_{1f}(\lambda_{fi} - 1), & \lambda_{fi} - 1 \leq D_{1f} \\ p_f(\lambda_{fi} - 1)^2 + q_f(\lambda_{fi} - 1) + r_f, & D_{1f} < \lambda_{fi} - 1 < D_{2f} \\ E_{2f}(\lambda_{fi} - 1 - D_{2f}) + (p_f D_{2f}^2 + q_f D_{2f} + r_f), & \lambda_{fi} - 1 \geq D_{2f} \end{cases} \quad (3)$$

where E_{1f} and E_{2f} are the axial tangent moduli of a fibrin fiber at low and high strain, respectively. λ_{fi} is the stretch of fibre i . The total stress tensor is obtained assuming additive decomposition of the strain energy density function.

We first simulate fibrin-rich clots (5% hematocrit (H)) and RBC-rich clots (40% H), with parameter calibration based on experimental testing performed by our group [5]. We then perform a parametric study to investigate the influence of bulk moduli, shear moduli, and fibrin tangent moduli on DA outcomes.

RESULTS

Maximum principal stress distributions for a 1.2 mm catheter diameter are shown in Figure 1B. Computed values for the RBC-rich clot exceed the reported fracture strength for this composition (0.01 MPa [4]). In contrast, computed values for the fibrin-rich clot do not exceed the reported fracture strength (0.045 MPa [4]). This suggests a higher probability of fragmentation of RBC-rich clots during DA.

Our model predicts that RBC-rich clots are aspirated further into the catheter than the fibrin-rich clot at any given sub-critical pressure (Figure 1C). Furthermore, for a 1.2 mm catheter diameter, the critical pressure required to fully ingest RBC-rich clots (165 mmHg) is significantly lower than that for fibrin-rich clots (198 mmHg).

With regards to catheter design, our simulations reveal that the critical pressure required to fully ingest a clot increases as the catheter diameter decreases (Figure 1D). Fibrin-rich clots are fully ingested into the catheter at 198 mmHg, 60 mmHg, and 15 mmHg for catheter diameters of 1.2 mm, 1.62 mm, and 2.5 mm, respectively.

As shown in Figure 1E, a ten-fold increase in the bulk moduli (κ_1 and κ_2) prevents full ingestion of fibrin-rich clots into a 1.2 mm catheter, even when the maximum clinical pressure of 660 mmHg is applied. In contrast, ten-fold increases in shear moduli or in fibrin moduli do not prevent full ingestion of the clot. This suggests that clot compressibility is a key determinant of the success of a DA treatment.

DISCUSSION

Our study presents the first FE analysis of DA thrombectomy. Results reveal that higher aspiration pressures are required to fully ingest a fibrin-rich clot in comparison to a RBC-rich clot. This provides insight into the clinical observation that fibrin-rich clots have a higher probability of failing to be fully ingested during DA [10]. However, our models predict that RBC-rich clots are predicted to have a higher risk of fragmentation and distal embolization due a low fracture strength that is exceeded by the principal stresses in the clot. Clinical studies report that distal embolization presents a higher risk for RBC-rich clots during

stent retriever thrombectomy [5]. Our results suggest a high fragmentation risk will also be encountered during DA. Our investigation of the effect of DA catheter diameter supports suggestions that the use of a large bore catheters will increase the probability of full ingestion while reducing fracture risk [3]. Our finding that clot compressibility significantly influences the probability of full clot ingestion during DA has significant clinical implications. Clot compressibility is highly dependent on the level of contractility that is actively generated in platelets [8]. The use of agents to reduce platelet contractility could be considered as part of an optimized DA protocol. Future model developments will incorporate inelastic clot deformation in order to analyze the influence of dynamic applied pressure as a means of increasing the probability of full ingestion of fibrin-rich clots.

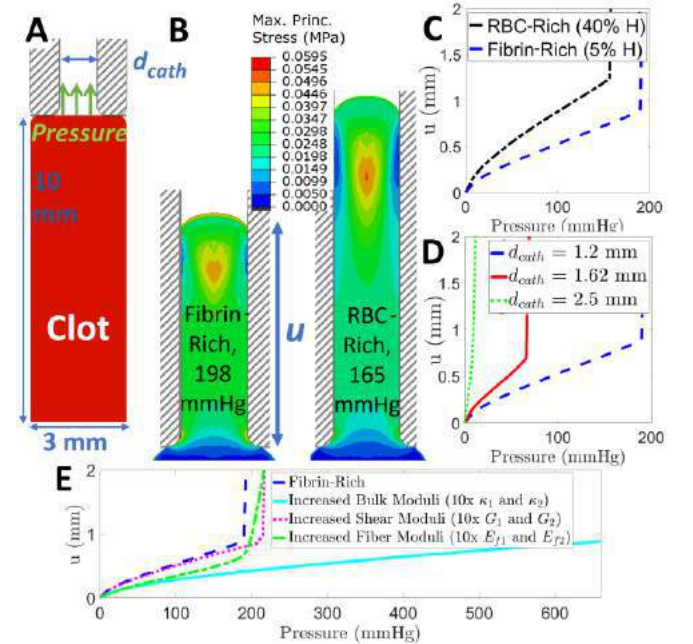


Figure 1: A) FE model of the clot and catheter with diameter d_{cath} . B) Deformation and distribution of maximum principal stress during DA for fibrin- and RBC-rich clots ($d_{\text{cath}} = 1.2$ mm). C) Aspiration length (u) as a function of applied pressure for fibrin-rich and RBC-rich clots. Initiation of full ingestion is characterized by a dramatic increase in slope at a critical applied pressure. D) Influence of catheter diameter on DA of a fibrin-rich clot. E) Parametric investigation on the effect of bulk, shear, and fibrin tangent moduli.

ACKNOWLEDGEMENTS

The research conducted in this publication was funded by the Irish Research Council under grant number EPSPG/2022/379 and the enterprise partner Cerenovus (Neuravi Ltd.).

REFERENCES

- [1] Good, B.C. et al., *BMMB*, 19:761-778, 2020
- [2] Jolugbo, P. et al., *Stroke*, 52:1131-1142, 2021
- [3] Arslanian, R.A. et al., *J NeuroIntervent Surg.*, 11(9):931-936, 2019
- [4] Boisseau, W. et al., *J NeuroIntervent Surg.*, 12(11):1099-1106, 2020
- [5] Fereidoonhezad, B. et al., *Acta Biomater.*, 127:213-228, 2021
- [6] Al Kasab, S. et al., *Neurosurgery*, 91(1):80-86, 2022
- [7] Halama, D. et al., *Diagnostics*, 12(19):2471, 2022
- [8] Fereidoonhezad, B. et al., *BMMB*, 20:1317-1335, 2021
- [9] Fereidoonhezad, B. et al., *J. Biomech.*, 111: 110006, 2021
- [10] Andersson, T. et al., *J Stroke*, 21(1):2-9, 2019

EFFECT OF GAGS ON TENSILE PROPERTIES OF PORCINE CORNEA

H. Hatami-Marbini (1)

(1) Mechanical and Industrial Engineering, University of Illinois at Chicago, Chicago, IL USA
Email: hatami@uic.edu

INTRODUCTION

The cornea is the transparent protective layer of the eye protecting its delicate internal components while refracting incoming light such that it focuses on the retina in the back of the eye. The cornea is responsible for the majority of the eye's total focusing power; thus, distorted or blurred vision could occur when the corneal highly organized microstructure and composition get damaged. The corneal extracellular matrix, i.e., stroma, constitutes about 90% of its thickness and is responsible for its mechanical strength. The stroma primarily consists of collagen fibrils and proteoglycans (PGs). The collagen fibrils dominate biomechanical properties of the cornea in tension and PGs are responsible for corneal compressive properties. PGs are composed of a core protein covalently attached to glycosaminoglycan (GAG) side chains. PGs fill the space between collagen fibers and play an important role in the creation and maintenance of the precise organization and composition of collagen fibrils in the corneal stroma. The primary objective of the present study was to determine the effects of GAGs on the mechanical properties of the cornea.

There are different types of GAGs in the corneal stroma such as chondroitin sulfate (CS), dermatan sulfate (DS), keratan sulfate (KS). KS constitute the majority of the corneal GAGs [1] and its density is altered in different eye diseases. For example, KS GAG density decreases significantly in keratoconus. Furthermore, the cornea loses its mechanical strength in keratoconus [2]. Thus, it is important to determine the possible role that KS GAGs may have in resisting external forces that are applied to the corneal tissue. In the present research, we used keratanase II enzyme to remove KS GAGs enzymatically from porcine corneal samples. We then used uniaxial tensile experiments to determine the mechanical properties of GAG depleted corneal samples and quantified the effect of GAGs on the tensile response of the corneal tissue.

METHODS

Samples preparation. Fresh porcine eye globes were collected from a local abattoir and transported to the laboratory. After removing excess muscles and fat, we excised corneal rings with 2 mm sclera from eyeballs. The thickness of corneal rings was measured by an ultrasonic pachymeter (DGH Technology Inc., PA) and a custom-made double bladed device was used to cut corneal strips in the nasal temporal direction. For the mechanical experiments, the samples were divided into three groups, i.e., control (n=10), buffer (n=10), and enzyme (n=10). Eight additional samples were prepared in each group for GAG content quantification studies.

Enzyme and buffer treatment. 0.1 M sodium acetate buffer solution at pH = 6.0 was prepared. In order to remove KS GAGs (enzyme group), we placed corneal strips in the buffer solution with 0.1 U/ml keratanase II enzyme for 18 hours at 37 °C with gentle agitation. The samples in the buffer group were kept in the buffer solution without the enzyme for 18 hours. Furthermore, control samples were used after dissection.

GAG quantifications: The Blyscan assay (Biocolor Ltd., UK) was used to determine the GAG content of control, buffer treated, and enzyme treated samples. To this end, they were first dried in a desiccator and their dry weight was determined. Then, they were incubated in the buffer solution or enzyme solution for 18 hours and the Blyscan assay was used to determine their GAG content.

Mechanical tests: An RSA-G2 (TA Instruments, DE) tensile testing machine was used to determine the mechanical properties of corneal strips. For this purpose, corneal strips were mounted to the RSA-G2 machine and sandpaper was used at the grips to avoid any sliding. The thickness of corneal strips before the test was brought to 700 μ m to minimize possible hydration effects on tensile measurements [3,4]. A prestress $\sigma_{initial}$ was applied to the samples in order to straighten them and determine their initial length. The length of samples after applying the prestress was used to calculate the engineering strain. The

tensile strain of $\varepsilon = 20\%$ with a displacement rate of 2 mm/min was used to measure the tensile response of corneal strips.

Numerical Analysis: The experimental tensile stress-strain curves were represented using the following relation,

$$\sigma = A\varepsilon^B + \sigma_{initial}, \quad (1)$$

where σ is the tensile stress, A, and B are the unknown constants that were determined by fitting the above equation to the experimental stress-strain data.

Statistical Analysis: The experimental data were reported as mean \pm standard deviation and the analysis of variance (ANOVA) with $P = 0.05$ was done to determine any statistically significant difference between the measurements.

RESULTS

The GAG content studies showed that the GAG content of enzyme treated samples was significantly lower than that of the control and buffer treated specimens ($P < 0.05$). Furthermore, the numerical equation (1) represented the experimental strain-stress curves successfully. The dotted lines in Figure 1 show the numerical fits. The tensile response of control and buffer treated specimens was almost similar without any significant difference. However, GAG depletion caused a significant tensile property softening ($P < 0.05$).

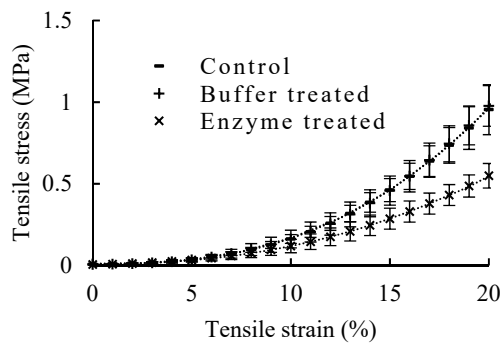


Figure 1: Stress-strain curves obtained from the experimental measurements. The dotted lines represent the numerical fits and the symbols denote the experimental data. The enzyme treated had a significantly softer tensile mechanical response; however, no difference was observed in the tensile response of buffer treated and control samples.

DISCUSSION

The stroma is made up of collagen fibrils that are arranged in an approximate hexagonal packing arrangement. PGs fill the space between the collagen fibrils such that their GAG side chains interact with each other. GAGs are known to have significant role in collagen fibril assembly and their maintenance in a hexagonal lattice arrangement, which is required for corneal transparency [5]. However, there has not been any previous research in characterizing the role of GAGs in tensile properties of cornea. The present work removed KS GAGs from corneal strips and measured the effect of GAG depletion on mechanical properties of porcine cornea.

The tensile modulus of control samples from this study was in agreement with previous studies [6,7]. Figure 1 shows that GAG-depleted corneal strips became soft and their tensile stiffness decreased significantly. In particular, we found that the average maximum tensile stress of enzyme treated samples was 0.55 MPa, which was significantly less than that of the average maximum tensile stress of control samples. This significant reduction in tensile properties could be explained in

terms of a popular hypothesis that GAGs form bridges between collagen fibrils and behave as many tiny yardsticks holding them together, Figure 2. In particular, PGs attach to collagen fibrils by their core proteins while their GAG side chains form interfibrillar duplexes between neighboring collagen fibrils. The GAG quantification studies showed that enzyme treated samples had significantly less GAGs, which implies that the number of GAG bridges between collagen fibrils was significantly less in the enzyme treated samples. If we assume that corneal extracellular matrix behaves as a composite material composed of collagen fibrils that are placed in a PG matrix domain, the removal GAG weakened the matrix domain, which in turn caused the composite domain to show a softer mechanical response, Figure 2.

In conclusion, the present research determined for the first time the structural role of KS GAGs in tensile properties of porcine cornea. The findings are important as they could be used to relate the mechanical changes in disease such as keratoconus to the microstructural changes of the corneal tissue.

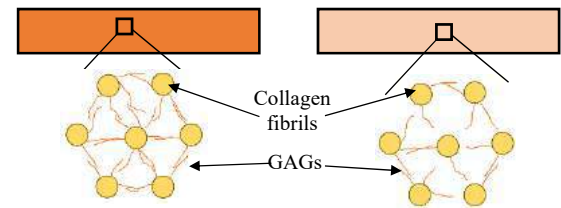


Figure 2: (a) A schematic showing the GAG duplexes exist between the collagen fibrils and b) some of them are removed because of enzymatic digestion of GAGs in GAG-depleted samples. This is hypothesized to be the reason why enzyme treated showed a softer tensile response compared to the control samples.

ACKNOWLEDGEMENTS

The author acknowledges the support in part from NIH-EY030264 and help from members of computational biomechanics laboratory at the University of Illinois at Chicago in conducting this research.

REFERENCES

- [1] Schwend T, Deaton RJ, Zhang Y, Caterson, B, Conrad GW. Corneal sulfated glycosaminoglycans and their effects on trigeminal nerve growth cone behavior in vitro: roles for ECM in cornea innervation. *Invest Ophthalmol Vis Sci*, 2012. 53(13): 8118-37.
- [2] Andreassen TT, Simonsen AH, Oxlund H. Biomechanical properties of keratoconus and normal corneas. *Experimental eye research* 1980; 31: 435-441.
- [3] Hatami-Marbini H, Etebu E. Hydration dependent biomechanical properties of the corneal stroma. *Experimental eye research* 2013;116: 47-54.
- [4] Hatami-Marbini H. Hydration dependent viscoelastic tensile behavior of cornea. *Annals of biomedical engineering* 2014; 42(8): 1740-1748.
- [5] Hassell JR, Birk DE. The molecular basis of corneal transparency. *Experimental Eye Research* 2010; 91: 326-335.
- [6] Wollensak G, Spoerl E., Seiler T. Stress-strain measurements of human and porcine corneas after riboflavin-ultraviolet-A-induced cross-linking. *Journal of Cataract & Refractive Surgery* 2003; 29: 1780-1785.
- [7] Hatami-Marbini H, Jayaram SM. Relationship between initial corneal hydration and stiffening effects of corneal crosslinking treatment. *Journal of Cataract & Refractive Surgery* 2018; 44: 756-764.

EFFECT OF GAGS ON SHEAR PROPERTIES OF CORNEA

H. Hatami-Marbini (1), M.E. Emu (1)

(1) Mechanical and Industrial Engineering, University of Illinois at Chicago, Chicago, IL USA
Email: hatami@uic.edu

INTRODUCTION

The cornea is a collagen-rich connective tissue that transmits light and protects the inner parts of the eye. The cornea is composed of five distinct layers (from top to bottom), epithelium cells, Bowman's layer, stroma, Descemet's membrane, and endothelium. The stroma forms about 90% of the corneal thickness and is responsible for its mechanical properties. The composition and microstructure of stroma are necessary for the corneal function; any change to the highly ordered structure of the stroma could affect corneal shape and curvature, which are necessary for its transparency and refractive function. The corneal stroma is composed of many collagen fibrils with almost uniform diameter that are embedded in a matrix domain composed of small leucine-rich proteoglycans (PGs). Decorin and biglycan are the primary PGs in the corneal stroma. PGs consist of glycosaminoglycans (GAGs) that are attached to a core protein. Chondroitin sulfate, dermatan sulfate, and keratan sulfate are found in the stroma. PG core proteins are important for fibrillogenesis and its regulation. GAGs are negatively charged and attract water molecules inside the corneal ECM; thus, they play an important role in defining the hydration of the cornea [1]. Furthermore, GAG chains could form bridges between neighboring collagen fibrils and influence the mechanical properties of the cornea [2]. In a recent work, we have characterized the effect of GAGs on mechanical properties of the cornea by conducting uniaxial tensile tests [3]. The collagen fibrils are known to be the primary structural elements resisting tensile forces. However, because of the unique microstructure of collagen fibrils in the posterior regions of the cornea, it is expected that the PG matrix defines the shear properties. The primary objective of the present work was to characterize the effect of GAGs on shear properties of the cornea.

The microstructure and composition of the cornea is different through thickness, i.e. the collagen lamellae interweave in the anterior regions while they are parallel to each other in posterior part [4]. Thus,

although shear properties of the anterior region are a function of both collagen fibrils and PGs, GAGs are expected to have a significant role in defining the shear response of posterior layers. In this study, we prepared posterior flaps from porcine cornea and measured their shear response. Then, we used keratanase enzyme to remove GAGs from the posterior layers in order to determine the role of GAGs in defining the shear properties of cornea.

METHODS

Porcine eye globes were collected from a local slaughterhouse and were divided into two groups, control and enzyme. The eyeballs were used to prepare corneal rings from which we obtained posterior flaps. In particular, a DSAEK system was used to excise the anterior part of the cornea from the corneal rings. Then, a circular biopsy puncher was used to obtain 8 mm corneal disks from the remaining posterior region. A pachymeter (DGH Technology Inc., PA) was used to measure the thickness of all posterior disks.

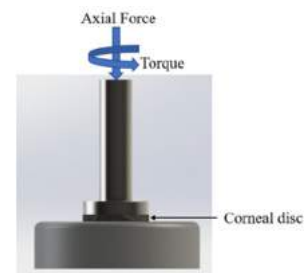


Figure 1. The corneal samples were mounted in a rheometer. Then, an axial force was used to ensure full contact between corneal samples and upper geometry. The shear properties of control and enzyme treated corneal discs were measured as a function of applied compressive stress.

The GAGs were removed from the samples using the procedure that we used before [3]. For this purpose, corneal disks were allowed to complete dry in a desiccator and their dry weight was measured using a digital scale (Mettler Toledo, OH). The dried corneal disks were then immersed in a 0.1 M sodium acetate buffer solution containing 0.1 U/ml keratanase enzyme. The pH of the solution was 6.0 and the samples were kept inside the solution at 37 °C.

The shear response of control and enzyme depleted samples was determined using a rheometer (Discovery HR-2, DE), Figure 1. For this purpose, corneal disks were placed between two parallel surfaces of the machine. We used sandpaper in order to prevent slippage during the oscillatory shear tests. After mounting the samples, we brought down the upper geometry of the rheometer and ensured a full contact between its surface and corneal disks following the procedure that was described in our previous work [5-6]. Then, we used frequency sweep and shear sweep experiments to characterize their shear response. It is noted that in order to determine the shear response of the samples as a function of compressive force, we brought down the upper geometry incrementally and measured the shear response of the samples. The compressive stress was allowed to reach equilibrium between consecutive shear measurements.

RESULTS

The complex shear modulus was computed and plotted as a function of compressive stress in Figure 2. In agreement with previous studies [5], it is seen that the complex shear modulus of posterior flaps increased with increasing the compressive stress. The enzyme treatment significantly decreased the shear modulus of flaps ($P < 0.05$). The difference between the shear modulus of GAG depleted and control samples was dependent on the compressive stress and was reduced with increasing the compressive stress.

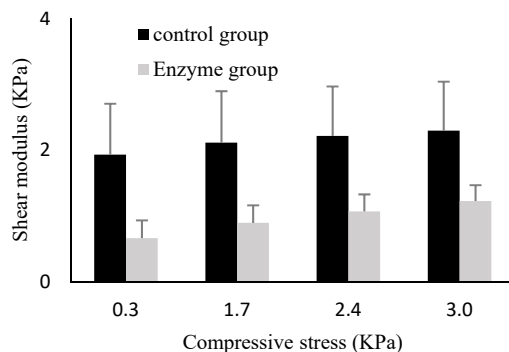


Figure 2. Complex shear modulus of porcine corneal flaps as a function of applied compressive stress. The vertical error bars indicate one standard deviation. A significant reduction of shear modulus was observed because of GAG depletion ($P < 0.05$).

DISCUSSION

The main objective of this study was to investigate the shear properties of enzyme-treated porcine corneal flaps. The shear moduli of both control and enzyme group samples changed nonlinearly with increasing compressive stress. The shear modulus of control samples was similar to porcine corneal shear modulus that was previously found [5-6]. The enzyme-treated flaps showed significantly less strength under shear deformation in comparison with the control flaps, Figure 2. The enzyme treatment reduced the GAG density in the enzyme treated samples; this was confirmed by performing histochemical analysis and immunochemistry (results not shown here). Thus, the number of GAG bridges between adjacent collagen fibril is expected to be less than the ones in the control samples, Figure 3.

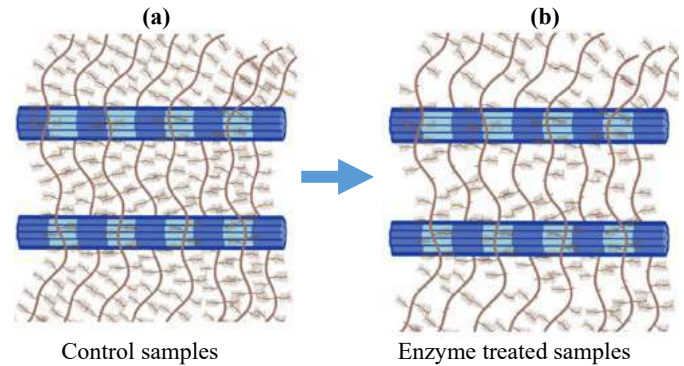


Figure 3. Schematic plots describing the proposed explanation for the softening of shear properties of porcine cornea because of GAG removal. In corneal stroma, the PGs are attached to the collagen fibrils such that their side chains extends out. The GAG sides interact with each other and form structures that behave as tiny ropes attaching neighboring collagen fibrils together. The number of GAG bridges significantly reduces in (b) GAG depleted samples, which is why they showed a softer shear response in comparison to (a) control samples.

With increasing the compressive stress, the shear modulus of samples increased. This is because with increasing the compressive force, collagen fibrils became closer with each other and stronger GAG bridges form between the collagen fibrils. Although we successfully quantified the importance of GAGs in the corneal shear modulus, this study had a number of limitations. First, we did not consider the effect of the breed and age of the pigs. These factors may affect the density of GAGs in the porcine corneal samples and subsequently the mechanical measurements. However, the significant difference between the shear modulus of different sample groups suggest that these effects were not statistically important. Furthermore, because of the scarcity of human donor cornea, we used pig corneas to investigate the effects of GAGs on corneal shear response. In future studies, the human cornea can be used to make a comparison and quantify the similarities and differences between pig and human cornea after GAG removal. Despite these limitations, the present work characterized the effect of GAGs on the shear properties of the cornea as a function of compressive stress.

ACKNOWLEDGEMENTS

The authors acknowledge the support in part from NIH-EY030264

REFERENCES

- [1] Hatami-Marbini H, Etebu E. Hydration dependent biomechanical properties of the corneal stroma. *Experimental eye research* 2013;116: 47-54.
- [2] Lewis, PN, Pinali C, Young RD, Meek KM, Quantock AJ, Knupp C. Structural interactions between collagen and proteoglycans are elucidated by three-dimensional electron tomography of bovine cornea. *Structure*. 2010, 18(2):239-45.
- [3] Hatami-Marbini, H. On mechanical roles of Glycosaminoglycans in tensile properties of the porcine corneal stroma, *Invest. Ophthalmol. Vis. Sci.*, accepted.
- [4] Hatami-Marbini H., Jayaram SM. UVA/riboflavin collagen crosslinking stiffening effects on anterior and posterior corneal flaps. *Experimental Eye Research*. 2018, 176:53-8.
- [5] Hatami-Marbini, H. Viscoelastic shear properties of the corneal stroma, *J. Biomech.*, 2014, 47 (3):723-728.
- [6] Hatami-Marbini, H., Emu, M.E. Effect of corneal collagen crosslinking on viscoelastic shear properties of the cornea, *J Mech Behav Biomed Mater.*, 2022, 133:105300.

KINEMATIC DECOMPOSITION OF A LIVING OCTOPUS: APPLICATION TO SOFT ROBOTIC ASSISTIVE DEVICES

Garrett S. Weidig (1), Brittany Bush (1), Fermin Jimenez (1), Galit Pelled, Ph.D. (1),
Tamara Reid Bush, Ph.D. (1)

(1) Department of Mechanical Engineering,
Michigan State University,
East Lansing, MI, USA

INTRODUCTION

Octopuses are capable of some of the most unique movements, including complex bending and twisting throughout the arm. Because of this, they have been great inspirers in the field of soft robotics [1]. Robotics applications range from grasping tools on assembly lines to being used as a wearable device. However, most existing devices are not able to mimic the full function that can be obtained with an octopus arm. Additionally, methods to quantify three-dimensional (3D) octopus movements (or similar robotic devices) do not exist.

Researchers have largely studied octopus arms and their ability to bend and twist, as those movements had the most influence on the overall posture of the arm [2, 3]. However, the technology and the methods used to capture and analyze these movements were not sophisticated enough to comprehensively define the posture of the arm in 3D. Instead, they focused on measuring movements that were simpler and had fewer degrees of freedom.

One of the simplified movements was bend propagation, where researchers observed bending to be approximately on one plane. Thus, all motion was attributed to either curvature (magnitude of bending toward the suckers) or twist (magnitude of the torsion of the arm). However, this neglected one of the most interesting capabilities of octopus arms: the ability to bend the arm in multiple directions, not just towards the suckers.

In scenarios of sufficiently complex octopus arm movements and in soft robotic applications, the current definitions for octopus movements are not comprehensive enough. There is a need for a new set of complex, kinematic octopus data along with new movement definitions that can better be applied to the octopus and the soft robotics for humans they may inspire. Thus, the goal of this work was to develop a set of methods to fully quantify the complex octopus arm movements, and compare them to results using previous mathematical definitions. In order to do this, 3D movements were collected on a living, swimming octopus.

METHODS

A four-camera underwater motion capture system was used to collect 3D movement data on one arm of a live octopus, species *Octopus bimaculoides*. Five retroreflective markers were adhered along the arm while the octopus was anesthetized in a small tank (Fig. 1a). Once the octopus woke up, it was placed in the larger tank with the motion capture cameras (Fig. 1b). Data were collected at a frame rate of 150 Hz and for as long as all five markers remained on the octopus' arm.

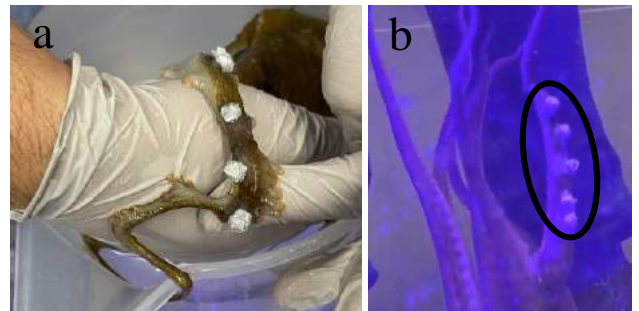


Figure 1. Reflective markers (a) attached to octopus arm while anesthetized and (b) on a free-swimming octopus.

For analysis, the arm was divided into a proximal segment consisting of the first three markers and a distal segment consisting of the last three markers (the segments shared the middle marker). Computations were then made on each segment to describe the overall 3D posture of the arm, which included both curvature and relative rotation between the two segments.

The magnitude of bending (curvature) on a segment was defined as the angle deviation from collinearity of the three markers. Thus, as the arm bent more, the greater the reported curvature for that segment.

The arm was also capable of twisting and ‘out of plane’ bending (bending of one segment on a different plane than another segment). Thus, it was necessary to define the plane on which each segment moved. This was called planar orientation and was done by creating separate, orthogonal local coordinate systems on the proximal and distal segments. Next, rigid body rotation angles (α , β , and γ) were used to measure differences in orientation between the two planes (Fig. 2a). Conceptually, α represented the amount of orientation change of the distal segment in the same plane as the proximal segment. β and γ represented the amount of orientation change of the distal segment in planes perpendicular to the proximal segment (either due to twisting or out-of-plane bending).

In previous studies, only one angle (θ) was used to define this out of plane movement and was attributed to twist only. Twist was measured by the angle between the two normal vectors of the two segments. This previous method was also used in this study to compare to the novel planar orientation method (Fig. 2b).

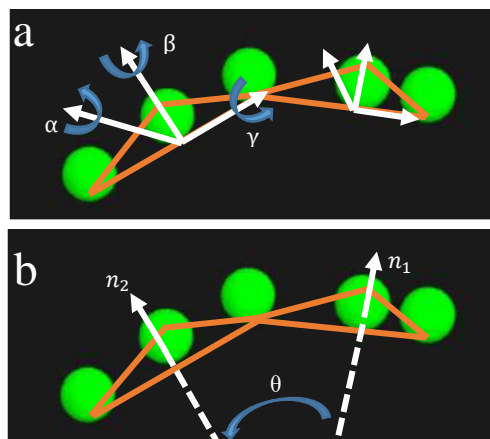


Figure 2. View of markers on octopus arm. (a) Local coordinate systems were created for both segments to determine the three angles of rotation (α , β , and γ) between the two segments. (b) Depiction of prior method used for computing twist in the literature, which is done using the angle (θ) between the two normal vectors on the proximal and distal planes which cannot capture complete 3D motions.

Two key postures were analyzed: simple bending and complex bending. Simple bending occurred when the proximal and distal curvatures were observationally on the same plane (e.g., θ , γ , $\beta \approx 0$ degrees). Complex bending was defined when the proximal and distal curvatures clearly occurred on different planes (e.g., θ , γ , $\beta \neq 0$ degrees). Analysis included computing curvature for the two segments, the angle of twist between the two segments, and the three planar rotation angles between the two segments.

RESULTS

The curvature, twist, and planar rotation angles for the two postures are reported below (Table 1). In the simple bending condition, the proximal and distal segments were curved 27 and 20 degrees, respectively. It was expected that, as reported in the literature, these curvatures occurred on near exact planes (θ , γ , $\beta \approx 0$ degrees) or any out of plane motion would be caused by twist (θ , γ , $\beta \neq 0$ degrees). These data showed that most of the movement of the distal plane occurred on a similar plane as the proximal one, indicated by the largest orientation value having been α . However, the 22 degrees of twisting alone was not comprehensive enough to describe the out of plane motion, since there

were non-zero values for both β and γ , meaning that reported twist (θ) likely had components of both twisting and out-of-plane bending.

Table 1. Analysis of two key postures. Curvature, planar rotation and twist angle results: simple and complex bending cases for a live, swimming octopus. Prior approaches using only θ are missing key pieces of information.

Posture	Prox. Curve	Dist. Curve	α (°)	β (°)	γ (°)	Twist θ (°)
Simple Bending	27	20	28	19	13	22
Complex Bending	33	12	-25	-11	-145	142

*negative sign is rotation in opposite direction based on right hand rule

In the complex bending condition, the bending on the proximal and distal planes were 33 and 12 degrees, respectively. Visually, these curvatures were clearly on two different planes, unlike the simple bending scenario. Using the method of twist in the literature, these planes were separated by 142 degrees. Mathematically, this meant that the two normal vectors were pointing in near-opposite directions. This level of twist at one location was not feasible. Instead, this was a result of the arm bending in more than one direction. Thus, it was clear that θ alone was not comprehensive enough to visualize posture in 3D and that all three orientation angles (α , β , and γ) were required.

DISCUSSION

To the authors’ knowledge, this was the first 3D, marker motion capture study completed with a living, swimming octopus. Two positions were analyzed from its motion: the simple bending condition, which was assumed in previous octopus studies, and a complex bending condition, which was new.

These postures are important and require the appropriate definitions because they are frequented by octopuses and potentially by the devices they inspire. Whether it will be for an orthosis, prosthetic, or on an assembly line, it would not be possible to comprehensively understand the overall posture of an octopus arm in 3D without these kinematic data and new definitions.

The biggest limitation to this study was the number of markers used. Because of the arm’s near infinite degrees of freedom, there was no number of markers that could be used to obtain the true overall posture of the octopus arm. Too many markers would be too heavy for the arm and prohibit movement. Thus, it would be difficult to speculate how many markers would be sufficient for a given arm length. For segmented soft robots with uniform curvature (where curvature values at each point along a given segment remained uniform throughout movement), it would be appropriate to have three markers per segment.

Whether it be an octopus arm grasping for food, or a soft robotic prosthetic being used to open a door, it is crucial to understand the 3D kinematics required for completing a task. In the future, the impact of these novel, kinematic analyses span across better understanding complex movements of the octopus, visualizing soft robotics in 3D, as well as streamlining communication between biologists, roboticists, biomechanists, clinicians, and those who would operate an octopus arm-inspired device.

ACKNOWLEDGEMENTS

This work was supported by NIH grant UF1NS115817 and is under IACUC# PROTO201800092.

REFERENCES

- [1] Laschi, C et al., *Adv Robot*, 26: 709-727, 2012
- [2] Sumbre, G et al., *Nature*, 433: 595-596, 2005
- [3] Zelman, I et al., *Front. Comput. Neurosci.*, 7, 2013

ACTIVE MICROTISSUE ARRAYS FOR PROBING TISSUE RESPONSE TO DYNAMIC CONDITIONING

William P. Cortes (1), Kalyn R. Younger (2), Thao D. Nguyen (2), and Daniel H. Reich (1)

(1) Department of Physics and Astronomy, Johns Hopkins University, Baltimore, MD, USA
 (2) Department of Mechanical Engineering, Johns Hopkins University, Baltimore, MD, USA

INTRODUCTION

The structure of soft collagenous tissues is highly dynamic and mechanoresponsive. Identifying how an applied load induces changes in tissue-level mechanical and structural properties remains challenging. Various active cellular processes occur concurrently with collagen deformation and reorganization in the extracellular matrix (ECM), and these processes and their interactions can depend on loading conditions [1]. Such structural changes in the ECM are widely relevant in physiological, pathological, and bioengineering contexts [1,2]. Thus, a more complete understanding of how loading directs the underlying processes of collagen growth and remodeling is important.

Disentangling the micromechanisms implicated in collagen growth and remodeling and their interactions calls for a versatile, high-throughput experimental platform. Previously, Reich and coworkers developed a magnetic microtissue tester (MMT) to probe the mechanical behavior of sub-millimeter cell/ECM constructs [3,4]. In this device, arrays of cell/ECM microtissues are suspended between pairs of flexible pillars, whose deflection reports the microtissues' contractile force. A magnetic bead affixed to one pillar for each microtissue enables actuation with a magnetic tweezer (Fig. 1A-C) allowing measurement of individual tissues' mechanical properties under dynamic loads. However, due to the construction of the magnetic actuation apparatus, these experiments were constrained to minutes to hours, which limits the ability to study collagen growth and remodeling. Here, we describe the integration of the MMT arrays with a system that provides long-term mechanical stretch of the entire array (Fig. 1D, E), enabling loading conditions compatible with studying growth and remodeling processes (Fig. 1F).

METHODS

MMT. MMT arrays are fabricated in polydimethylsiloxane (PDMS) and consist of over 100 400 μm x 800 μm wells, each containing two flexible posts. An individual microtissue is formed between the posts of each well and contractile forces exerted on the

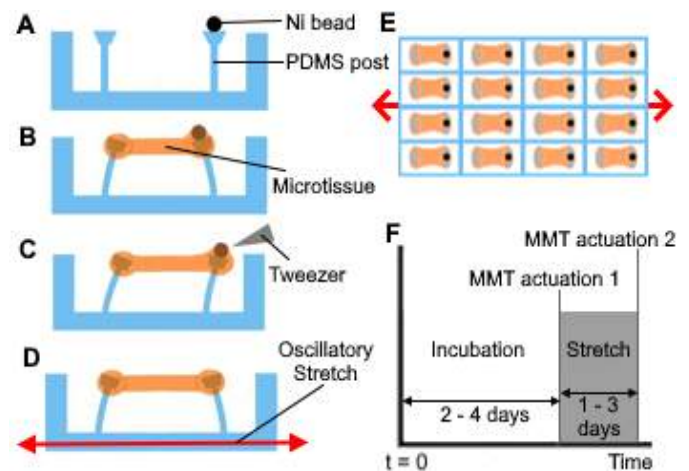


Figure 1. Scheme for long-term loading and mechanical characterization experiment. A) An empty MMT well is seeded with B) a cell-ECM microtissue and C) subjected to a magnetic field via tweezer. D&E) The entire membrane is then subjected to stretch over times much longer than the magnetic measurement. F) Time-course of experiment.

posts are determined from observations of the displacements of the pillar heads. Nickel beads (dia. $\sim 100 \mu\text{m}$) enable magnetic actuation.

Stretching apparatus. A commercial cell-stretcher (STREX 1400) was adapted for MMT arrays. The STREX stretching chambers are PDMS blocks with a 2 cm x 2 cm well with thin bottom membranes. Cells are cultured on this membrane, and the chamber is mounted between two plates, one of which is linearly actuated to produce stretch (Fig 2D). The unit is housed in a CO₂ incubator. Data are collected by unmounting the chamber and imaging the cells.

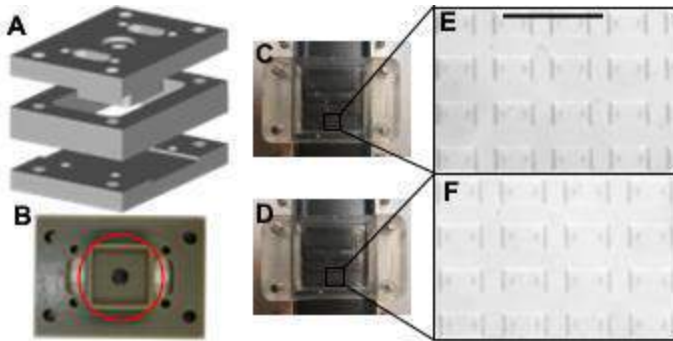


Figure 2. Fabrication of stretching chamber. A) Molds are 3D printed and B) combined with PDMS negatives (circled in red) to produce stretch chambers. C, D) Stretch chambers on the STREX at 0 and 0.16 strain. E, F) Portions of unstretched and stretched MMT array. Scale bar: 2 mm.

Fabrication. PDMS MMT negative molds were replica molded [5] and macroscopic chamber molds were produced via LCD resin 3D printing (Fig. 2A). Final chamber molds were constructed by mounting the negatives to the 3D print (Fig 2B). The final devices were cast in PDMS, yielding stretching chambers with comparable tolerances to the OEM devices, but with MMT elements patterned along the membrane. Fig. 2C, D shows an MMT chamber mounted on the STREX stretcher.

Microtissues. A mixture of Type I collagen ECM-analogue and adult human dermal fibroblasts (nHDFs) was centrifuged into the stretching chamber and incubated following previously described protocols [5]. The cells compacted the ECM, forming dog-boned shaped microtissues after 48 hours incubation.

Mechanical characterization. Microtissues were uniaxially strained by applying a triangular magnetic up-down ramp to the magnetic pillar. The tensile stress-strain relationship was determined by observing the pillar displacements and microtissue geometry via microscopy. Tissue elastic modulus was calculated over the initial 0 – 0.1 strain region of the stress-strain curve. Selected microtissues were probed for active recovery for 5 minutes after magnetic actuation.

Stretching protocol. Microtissue-seeded chambers were subjected to oscillatory stretch (0.1Hz 2-10%), for 24 hours after 48-hour microtissue formation. Tissue stiffness was measured by magnetic mechanical characterization before and after loading

RESULTS

The strain applied to the MMT arrays under stretch was characterized via videos of MMT chambers without microtissues subject to strains up to 0.16 (Fig. 2E, F). The well-to-well variation of the peak strain over the array was $< \pm 0.01$ as determined by measuring the displacement of embedded MMT well walls.

This work represents the first characterization of the active dynamics of nHDF microtissues under magnetic stretching in MMTs. The displacements of the pillars under magnetic stretching of such tissues are illustrated in Fig. 3A. An example of the stress and strain response to magnetic actuation is shown in Fig. 3B, along with the resulting stress-strain loop (Fig. 3C). The microtissue stiffness was comparable to other cell-ECM constructs studied on this platform [3,4]. The stress-strain curves displayed hysteresis during actuation arising from tissue viscoplasticity, followed by a longer-term recovery driven by active force generation of the cells in the tissue [3].

Initial stretching experiments up to 24 h duration have shown that the microtissues remain in good contact with the pillars, retain their characteristic morphology under low-frequency oscillatory strain (0.1Hz 2-10%), and are amenable to magnetically actuated mechanical characterization following loading (Fig. 4). Preliminary results are indicative of stiffness increases compared to unstretched controls.

Further studies of changes in ECM morphology will also be presented. We also note that results to date indicate strain-rate dependence in the dynamic response (Fig. 3C,4); these effects will also be discussed.

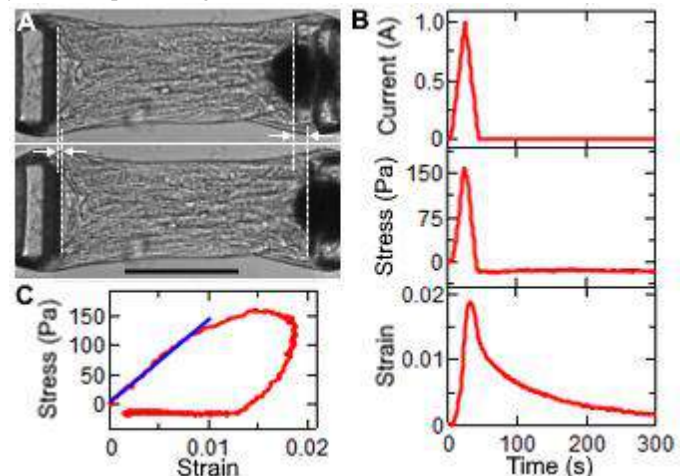


Figure 3. Magnetic actuation of microtissue is used to determine tissue mechanical properties. A) Pillar displacements used to extract mechanical properties. B) Current pulse applied to magnetic tweezer over 40 s. Shown below are the accompanying stress response and applied strain (Initial strain rate: 0.001/s). C) The resulting stress-strain curve (red) and linear fit (blue) over 0-0.01 strain yield an elastic modulus of 15 kPa. Scale bars: 200 μ m.

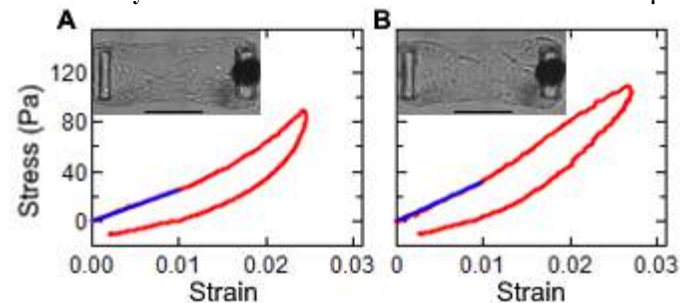


Figure 4. Stress-strain curves A) before and B) after 24 h stretch conditioning, with tissue images inset. The elastic modulus observed was 2.5 kPa and 3.2 kPa respectively (Initial strain rate: 4×10^{-4} /s). These measurements did not probe the active recovery phase. Scale bars in insets: 200 μ m.

DISCUSSION

Here, we describe the construction of an apparatus for applying long-term mechanical stimulation to a microtissue array model. At low oscillatory strain rates, MMTs were shown to be compatible with long-term conditioning via stretch. The fabrication process described can be used to integrate a variety of bio-MEMs architectures with long-term conditioning, and the compatibility of this platform with many standard cell culture assays allows for a wide range of experimental studies that can provide new input for the development of models that relate cellular function and ECM mechanics to the effects of applied loads.

ACKNOWLEDGEMENTS

We acknowledge support from the U.S. National Science Foundation (NSF): CMMI-2032922.

REFERENCES

- [1] Vernerey, F. and Farsad, M. *J Mech Behav Biomed Mater.* 4(8):1683-1699, 2011. [2] Frantz, C. et al., *J Cell Sci.* 123(24):4195-4200, 2010. [3] Zhao, R. et al., *Adv Mater.* 25(12):1699-1705, 2013. [4] Liu, A. et al. *Sci Rep.* 6(1):33919, 2016. [5] Legant, W. et al., *Proc Natl Acad Sci*, 106(25):10097-10102, 2009.

EXPERIMENTAL STUDY OF FLOW-MEDIATED FIBRIN CLOT ACCUMULATION IN PROSTHETIC HEART VALVES

Yevgeniy Kreinin, Moran Levi, Yahel Talmon, Josué Sznitman, Netanel Korin

Department of Biomedical Engineering, Technion - IIT, Haifa, Israel

INTRODUCTION

Heart valve disease is a condition in which one or more of the heart's valves do not function properly. Heart valve replacement surgery has increased the survival rate and quality of life for patients with severe valvular disease. The most common valve to be replaced is the aortic valve, and there are two types of prosthetic heart valves (PHVs) used to replace it: mechanical heart valves (MHVs) and biological heart valves (BHVs) [1]. However, one of the known problems associated with aortic MHVs is valve thrombosis. This is linked to abnormal hemodynamics in MHVs, resulting in high shear stress around the device and low shear zones where clots accumulate [2].

In this study, an *in vitro* fibrin-clot model was developed to study thrombosis in MHVs under relevant hydrodynamic conditions while allowing real-time imaging. 3D-printed aortic valve models were inserted into a transparent glass aorta model and connected to a perfusion system. Fibrin clot formation was initiated via thrombin injection into a fibrinogen solution. Clot accumulation was quantified via image analysis and weight measurements. Results of valves positioned in a normal vs. a tilted configuration showed that clot accumulation correlated with areas of low shear, high residence time, and re-circulating flows, as observed by Computational Fluid Dynamic (CFD) simulations.

METHODS

In Vitro: We developed and built a closed-loop experimental system that enabled volumetric pulsatile flow at a physiological rate simulating an aortic artery flow profile as well as real-time monitoring of the pressures, controlled injection of thrombin, and timelapse imaging of the valves placed in a custom glass aorta model, see Figure 1. For the valve models, we 3D printed MHVs, using an SLA technology 3D printer (Elegoo Mars) and ABS-like resin. The 3D printed MHV and tilted MHV were positioned in the glass aorta model, see Figure 2. A fibrinogen solution was perfused in a

concentration of 0.3[mg/ml], and 1 ml of 31.6 [μ g/ml] thrombin was injected at 1 [ml/hour] rate into the system for clot formation. At the end of the experiments, the model was weighed in order to check the weight of the clots that accumulated on the valve. In addition, the images of the valve surface were analyzed by a custom Matlab® code to estimate the area covered with clots. A comparison was made between two types of implants, a normal implant, and an angled valve implant.

CFD: MHV and aortic root were modeled in SolidWorks®. The models were meshed in ANSYS GAMBIT 21 R1 and the simulations were conducted in ANSYS fluent 21 R1. The blood flow was simulated in a steady state using a Newtonian fluid and incompressible flow. The flow was assumed as laminar based on the clinical data reported by Yamaguchi and Parker [3]. We used a blood viscosity value of 3.5×10^{-3} and blood density of 1080 Kg/mm^3 . Flow path lines and Wall shear stresses were extracted from the simulations.

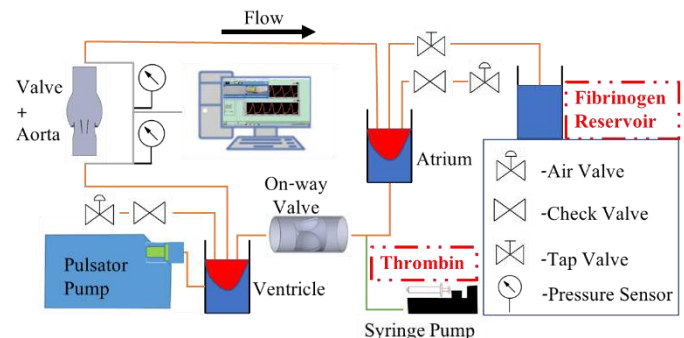


Figure 1: Schematic of the fibrin-thrombin experimental perfusion system

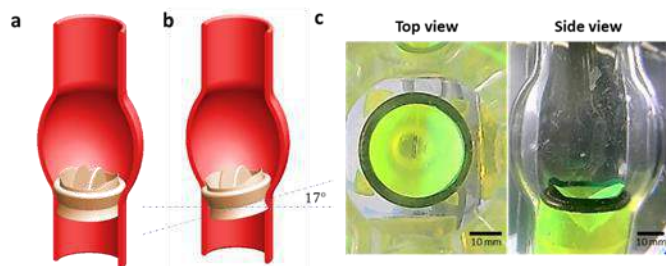


Figure 2: MHV models. (a) CAD illustration of regular orientated implantation of a MHV. (b) CAD illustration of angled-tilted implantation of a MHV. (c) Photo images of the 3D-printed valve in the transparent aorta model during an experiment.

RESULTS

First, as seen in Fig. 3A, under normal conditions clots accumulated in the sewing area around the valve as known to occur in patients [1]. A comparison of the results of clot accumulation between the two configurations revealed that a significantly lower number of clots settled on the angled-orientated valve as compared to the other configuration (Fig.3). Computational fluid dynamics (CFD) analysis, presented in Figure 4 has revealed that the sites of clot accumulation correspond to regions of low shear and stagnation within the flow field. The difference between the clot accumulation can be potentially explained by the CFD results, which indicate that the angled configuration is characterized by less recirculation and stagnation areas, as well as streamlines that suggest increased washing of the sewing areas (Fig.4c-f). Overall, these findings underscore the importance of considering the effects of implantation orientation on clot formation in the design and development of valvular prostheses.

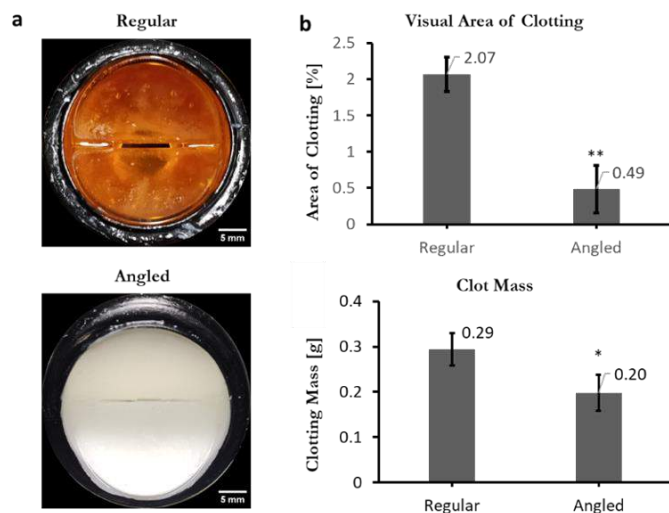


Figure 3: Clot accumulation comparing regular vs. an angled-tilted valve . (a) Image of the regular orientated valve after 60 minutes of perfusion showing clot at the outer ring of the valve (top) compared to the angled orientated valve (bottom). (b) The clot on regular vs. angled oriented valves: the percent of the clot cover area as obtained via image analysis (top) and the corresponding clot mass.

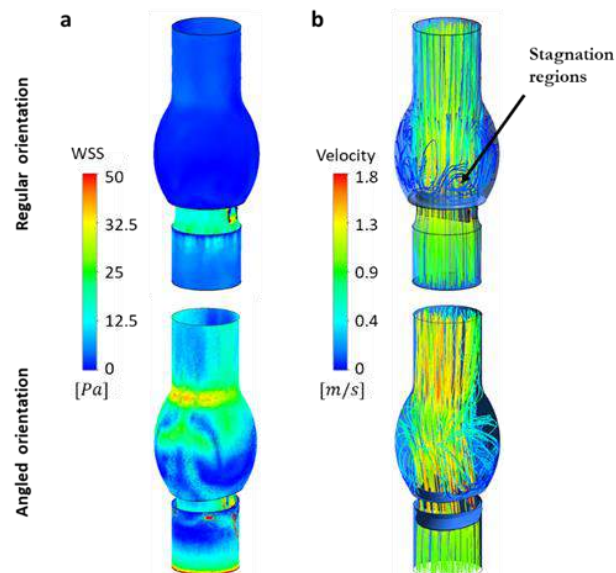


Figure 4: Computational fluid dynamic analysis of flow stasis in a regular vs. an angled oriented valve. (a) 3D CFD WSS in valve (upper-regular, bottom-angled oriented). (b) 3D CFD streamlines in the valve(upper-regular showing stagnation areas, bottom-angled oriented).

DISCUSSION

The results of this study demonstrate the utility of an in-vitro experimental system for monitoring clot accumulation in prosthetic heart valves. The CFD results obtained in this study were found to match the coagulation zones observed in the *in vitro* experiments, providing validation for the use of this method. Notably, the CFD results also revealed that the valve implanted in a rotated manner had better washing around the valve, which was consistent with the results obtained in the *in vitro* experiments. This highlights the potential of this method to provide a better understanding of the clot accumulation processes in prosthetic heart valves as well as study new approaches to reduce thrombosis in MHVs.

ACKNOWLEDGEMENTS

This work was partly supported by a KAMIN grant from the Israel Innovation Authority.

REFERENCES

- [1] G. D. Dangas, J. I. Weitz, G. Giustino, R. Makkar, and R. Mehran, "Prosthetic Heart Valve Thrombosis," *Journal of the American College of Cardiology*, vol. 68, no. 24, Elsevier USA, pp. 2670–2689, Dec. 20, 2016, doi: 10.1016/j.jacc.2016.09.958.
- [2] M. Nobili, J. Sheriff, U. Morbiducci, A. Redaelli, and D. Bluetein, "Platelet Activation Due to Hemodynamic Shear Stresses: Damage Accumulation Model and Comparison to In Vitro Measurements," *ASAIO J.*, vol. 54, no. 1, p. 64, Jan. 2008, doi: 10.1097/MAT.0B013E31815D6898.
- [3] T. Yamaguchi, S. Kikkawa, and K. H. Parker, "Application of Taylor's hypothesis to an unsteady convective field for the spectral analysis of turbulence in the aorta," *J. Biomech.*, vol. 17, no. 12, pp. 889–895, Jan. 1984, doi: 10.1016/0021-9290(84)90002-2.

EXCESSIVE SHEAR RATE, NOT SHEAR STRESS, IS RESPONSIBLE FOR CELL MECHANOLYSIS IN SMALL BORE NEEDLE INJECTIONS

**George Morgan, Lamis Elsawah, Alejandro Esclamado-Cadenas, Amelie Daudet,
Jennifer Frattolin, Daniel Watson, Qian Xu, Nicola Negrini, Adam Celiz, James E. Moore Jr.**

Department of Bioengineering, Imperial College, London UK

INTRODUCTION

There are nearly 3000 ongoing cell therapy clinical trials for over 900 medical indications, and many involve cell injection through small-bore needles. A significant challenge for these therapies is that the passage from the syringe through the needle applies harsh mechanical conditions on the cells. Long term cell survival rates below 5% have been reported [1]. This means that to achieve clinical effectiveness, large volumes of cell suspensions must be injected, perhaps over the course of several extra treatments. Injections can be done very slowly to try to minimize mechanolysis, but this implies steady hands applying carefully controlled forces for perhaps tens of minutes.

There have been efforts to develop hydrogel-based suspension fluids in the hope that they increase survivability. These formulations have shown partial success [2, 3], but the experiments were not done under appropriately controlled conditions or with the requisite fluid mechanical analysis to determine the actual biomechanical conditions that cause cell deaths. Thus, the bioengineering challenge of designing injectors, suspension fluids and injection protocols has remained guesswork. Using a combination of fluid mechanical analysis of prior studies and targeted cell injection experiments, we demonstrate that the shear rate of a flow field is the most appropriate parameter that determines likelihood of cell survival in cylindrical tube flows.

METHODS

A simple, appropriate starting point for analysis of the flow of a cell suspension through a needle is a force balance of a fully developed flow (Figure 1). The force balance applies anywhere in the flow field up to the tube wall. Thus, shear stress is a linear function of radial position. Note that this applies regardless of the fluid properties.

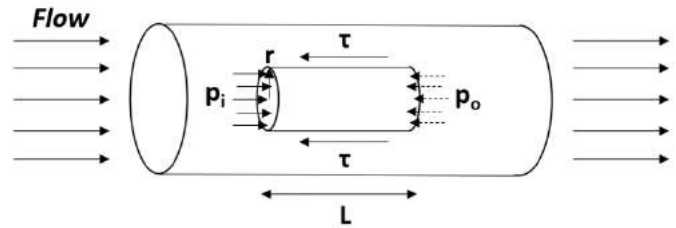


Figure 1. Illustration of force balance for the fully developed flow of a fluid in a cylindrical tube. p = pressure, t = r - z component of shear stress tensor, r = radial coordinate, z = axial coordinate, L = axial length, i = inlet, o = outlet.

$$\tau = r \frac{p_i - p_o}{2L} \quad (1)$$

To obtain the velocity profile (and shear rate), one must specify fluid properties. For Newtonian fluids, the shear rate is proportional to shear stress, and thus also a linear function of radius. For shear-thinning fluids such as blood and most hydrogels, the velocity profile is blunted relative to the parabolic profile indicative of a Newtonian fluid. This gives a nonlinear shear rate profile that varies from a low value in the middle of the tube to a higher value at the wall.

This approach is sufficient for a proper interpretation of the results of Aguado et al. [2], who injected cells suspended in different fluids through small-bore needles. Key aspects of that study in this context include the fact that they used the same flow rate throughout, provided viscous properties of all fluids, and assessed variations in cell viability using a calcein-AM/ethidium homodimer-1 live/dead assay. Cell viability varied from 59% for PBS suspensions to 89% for a crosslinked alginate hydrogel. These data provide a basis for determining if cell viability is better correlated with shear stress or shear rate. A useful

concept for making this determination is the critical radius, r_c , defined as the radial position at which the shear stress or shear rate transitions from below a critical mechanolytic value to higher than the critical value. Cells located within $r < r_c$ are presumed to survive because both shear stress and shear rate increase monotonically with radial position.

We also performed a set of experiments in which Human Umbilical Vein Endothelial Cells (HUVECs) were suspended in Newtonian fluids of different viscosities and injected through small bore needles using a precision controlled syringe pump. Briefly, cells were suspended in room temperature PBS, 2.7% Dextran, 3.9% Dextran, 7.4% Dextran solutions (w/w) (Sigma-Aldrich), at concentrations of 5×10^6 cells/ml. 500 μ L samples of encapsulated cells were loaded into a 10ml glass syringe fitted 30G needles. The flow rate was adjusted to achieve the desired shear rate and shear stress profile combinations. Two sets of experiments were performed: one set in which wall shear stress varied but wall shear rate was held constant, and another in which shear rate varied but shear stress was held constant. Live/dead assays were performed as in Aguado et al. [2].

RESULTS

Analysis of the results of Aguado indicate that cell survival was actually higher when cells were subjected to higher shear stresses. A primary finding of theirs was that cells suspended in the alginate hydrogel showed a significantly higher survival rate than cells suspended in the much less viscous PBS. Because their experiments were done at a consistent flow rate, the pressure drop (and thus shear stress, see Equation 1) for the hydrogel experiments was some 2x the pressure drop in the PBS experiments, based on the rheological properties they reported.

Employing the critical radius concept, we backed out the critical values of both shear stress and shear rate from their various experiments, assuming that all cells within $r < r_c$ survived and all cells $r > r_c$ died. The results indicate that the critical shear stress amongst the experiments varied from 20 to 300 Pa, whereas the critical shear rate was consistently around 20,000 1/s (Figure 2).

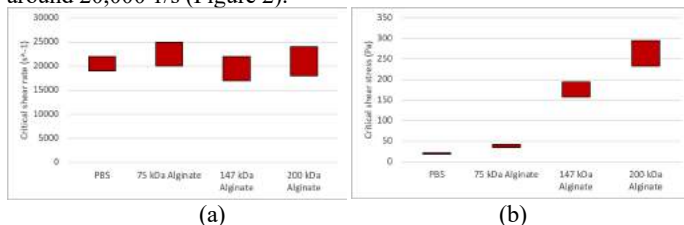


Figure 2. Estimations of (a) critical shear rate, and (b) critical shear stress based on the experimental data of Aguado et al. [2], rheological properties of fluids used and the critical radius concept.

In our own experiments, we controlled for comparisons of the effects of shear rate and shear stress on cell viability. The results indicated a relationship between viability and wall shear rate in which the slope was negative (95% confidence interval). The slope of the relationship with shear stress could not be identified as positive or negative (Figure 3).

DISCUSSION

We sought to determine the most appropriate fluid mechanical criterion that determines mechanolysis of cells during injections through small-bore needles, as might occur during cell therapy administration or bioprinting. Previous studies have provided indications that viability rates do vary with injection rate and fluid composition, but their application to improving injection protocols has been impeded by the

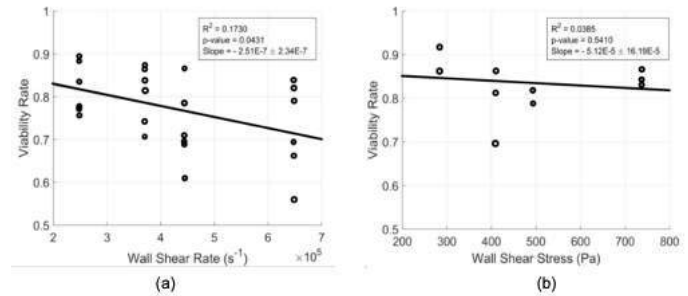


Figure 3. Results from cell suspension needle injection experiments using Newtonian fluids of different viscosities. (a) Data from experiments in which shear stress was held constant and shear rate was varied, showing a relationship with a negative slope (95% CI). (b) Data from experiments in which shear rate was held constant and shear stress was varied, showing an indeterminate slope.

a priori assumption that shear stress is the relevant parameter. Based on previously reported experiments as well as our own, we conclude that excessive shear rate is the appropriate parameter. This information can be applied to designing syringes and injection protocols to minimize the number of cells subjected to these mechanolytic conditions. Note that it is likely that the critical shear rate depends on cell type.

The reason for shear rate being the appropriate criterion is that it represents the relative velocity at which adjacent fluid layers and suspended cells must slide past each other. Even if the cells do not contact each other, that process increases the cell membrane stress several fold, relative to the stress experienced by a single cell in the same shear field [4]. For shear thinning fluids such as alginate hydrogels, the shear rate near the middle of the tube is low due to the plug flow-like conditions and the cells do not have to slide past each other with such high relative velocities.

We have assumed that the fluid composition has no direct effect on cell viability, which is supported by our experimental data (not shown). In the analysis shown in Figure 1, we have assumed fully developed flow. Under most injection conditions, the entry length is a fraction of the needle length. Aguado et al. [2] did show that extensional normal viscous stresses can be high in this entry region, but that measure did not correlate with their viability results. We also note that the damage accumulated by cells during the injection process should not be considered a binary determination of live vs. dead. It is likely that some cells damaged during injection would still stain as “live” but fail to survive long term.

ACKNOWLEDGEMENTS

Funded in part by the Imperial College Confidence in Concept program and the Rosetrees Trust.

REFERENCES

- [1] Smith et al., Stem Cells, 30:785–796, 2012
- [2] Aguado et al., Tissue Engineering Part A, 18(7-8): 806-815, 2012
- [3] Hernandez et al., Macromol. Biosci. 1800275, 2018
- [4] Lac et al., J. Fluid Mech, 573:149–169, 2007

DEVELOPMENT OF A TGFβ2 ELUTING TISSUE ENGINEERED VASCULAR GRAFT WITH TUNABLE DELAYED RELEASE

Katarina M. Martinet (1), Tracey Moyston (1), Stephen C. Balmert (2),
Steven R. Little (1,3,4) Jonathan P. Vande Geest (1,4,5)

- (1) Department of Bioengineering, University of Pittsburgh, Pittsburgh, PA, USA
(2) Department of Dermatology, University of Pittsburgh School of Medicine, Pittsburgh, PA, USA
(3) Department of Chemical Engineering, University of Pittsburgh, Pittsburgh, PA, USA
(4) McGowan Institute for Regenerative Medicine, University of Pittsburgh, Pittsburgh, PA, USA
(5) Vascular Medicine Institute, University of Pittsburgh, Pittsburgh, PA, USA

INTRODUCTION

It is well known that a prominent source of failure for small diameter vascular grafts is compliance mismatch between the native artery and the graft. Clinically used synthetic and autologous grafts tend to be overly stiff compared to the native vessel. This mismatch alters hemodynamic flow in the vessel and contributes to the development of intimal hyperplasia and eventual graft failure [1]. In 2021 there were an estimated 185,000 coronary artery bypass graft (CABG) procedures performed in the US alone [2]. These procedures still have up to a 40% failure rate depending on the graft used [1]. Therefore, this work aims to continue development of a tissue engineered vascular graft (TEVGs) that remains compliance matched throughout host integration.

The Soft Tissue Biomechanics Laboratory has previously developed a compliance matched vascular graft made from layers of electrospun polycaprolactone (PCL) and gelatin. These compliance matched grafts showed improved acute (<28 days) remodeling when compared to stiffer grafts [3]. However, insufficient vascular smooth muscle cell (VSMC) infiltration and degradation of the biopolymer causes the TEVG to become hypercompliant with long term remodeling.

Additionally, our lab has shown that TGFβ2 is a key regulator in VSMC fate. Low concentrations of TGFβ2 have been shown to increase VSMC infiltration into biopolymer grafts, whereas high concentrations of TGFβ2 have been shown to cause an increase in collagen deposition through cellular remodeling [4]. Ideally, TGFβ2 can be incorporated into a TEVG to both maximize initial VSMC infiltration and increase ECM synthesis as the biopolymer degrades to ultimately

minimize scaffold compliance loss. Therefore, the goal of this study is to fabricate Poly(lactic-co-glycolic) acid (PLGA) microparticles (MPs) that exhibit tunable delayed burst release of TGFβ2 and incorporate them into our compliance matched TEVGs.

METHODS

TGFβ2 MPs were fabricated using a water in oil in water (w/o/w) emulsion [5]. Briefly, lyophilized recombinant human TGFβ2 (Peprotech) was reconstituted and added to a PLGA and dichloromethane (DCM) solution. PLGA formulations used in this study can be seen in **Table 1** (Boehringer Ingelheim Chemical). Each formulation has a unique molecular weight and lactic acid to glycolic acid (LA:GA) ratio to alter release kinetics. The mixture was then sonicated to create the primary emulsion and homogenized in a polyvinyl alcohol (PVA) to create the secondary emulsion. Resulting MPs were washed, frozen in liquid nitrogen, and lyophilized.

Scanning electron microscopy (SEM) was used for surface characterization of MPs. To characterize release, MPs were submerged in phosphate buffer solution and bovine serum albumin and spun on a rotary mixer at 37°C for a total of 93 days. Releasate was collected and replenished every 24 hour for the first three days of release and then every three days for the remainder of the study. A TGFβ2 ELISA (R&D Systems) was used to assess protein loading and release.

Gelatin TEVGs were fabricated via electrospinning and MPs were included via electrospraying. The grafts were then genepin crosslinked and SEM was used to confirm successful inclusion of MPs.

RESULTS

The average loading of protein into the MPs can be seen in **Table 1**. All formulations were fabricated using 2.5ng of TGFβ2 and yielded approximately 100mg of MPs and had n = 3 samples.

Table 1: Microparticle formulations and loading.

Formulation	Molecular Weight	LA:GA Ratio	Loading (ng of TGFβ2/mg of MP)
RG503H	24 - 38 kDa	50:50	0.439±0.22
RG504H	38 - 54 kDa	50:50	0.059±0.01
RG653H	24 - 38 kDa	65:35	0.298±0.051
RG753H	24 - 38 kDa	75:25	0.113±0.011

All formulations displayed an initial burst release of TGFβ2 within the first 24 hours. The polymer with the most successful delayed burst release was RG753H which has the highest LA:GA ratio. Delayed release begins around day 60 and was maintained until day 87. These results can be seen in **Figure 1**.

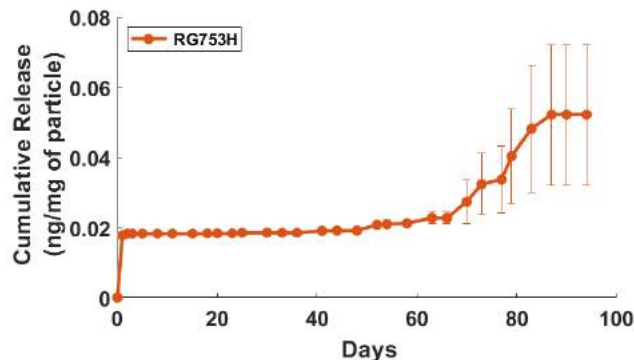


Figure 1: Release profile of RG753H microparticles.

The other formulations displayed either complete burst release within the first 24 hours (RG504H) or constant sustained release over the 93 days (RG503H & RG653H). These release profiles can be seen in **Figure 2**.

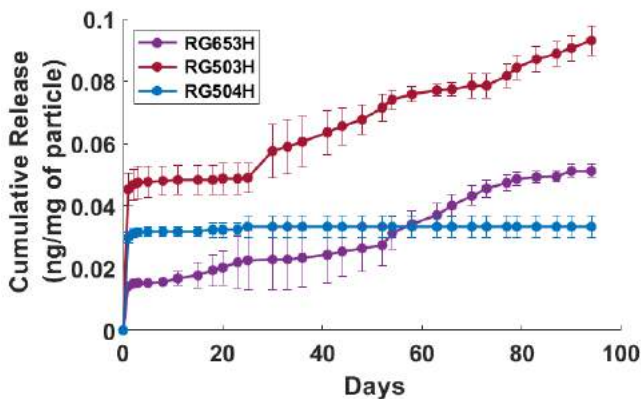


Figure 2: Release profile of TGFβ2 containing microparticle

Electrospraying of MPs yielded a seemingly uniform distribution of particles throughout the scaffold. Successful inclusion of MPs into TEVG scaffolds can be seen in **Figure 3**.

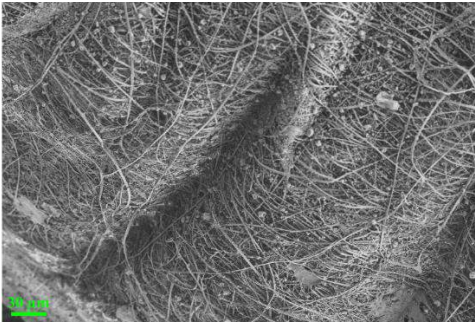


Figure 3: SEM image of TEVG surface with MPs.

DISCUSSION

From our results we have shown that PLGA microparticles can successfully delay the burst release of TGFβ2 for over 50 days as well as create sustained protein release over 90 days depending on the polymer formulation chosen. This delay is sufficiently long to begin TGFβ2 release before scaffold degradation leads to a hypercompliant environment.

As expected, the formulation with the highest LA:GA ratio displayed delayed burst release. This has been demonstrated previously with MPs containing proteins such as BSA and melittin [6]. Surprisingly all other formulations had little to no delayed burst release. This could be due to electrostatic interactions between the polymer and the protein, degradation kinetics of the polymer, encapsulation efficiency, or a variety of other fabrication factors that need to be further studied.

Surprisingly the polymer with the highest molecular weight only demonstrated initial burst release. Usually, polymers made of larger molecules are expected to degrade at a slower rate. It is possible that release from these MPs was below the detection limit of the assay used due to the poor initial loading efficiency.

There were large variations in loading efficiency across the formulations. The encapsulation efficiency of a MP is highly dependent on the unique interaction of PLGA and the specific protein being loaded. Due to this, many studies showcase contradicting correlations between changes in LA:GA ratio and/or molecular weight with encapsulation efficiency [7].

As this work continues we hope to increase the efficiency of release to evaluate the release profiles of the MP containing grafts, evaluate VSMC migration and infiltration *in vitro*, and monitor graft remodeling within a small animal model.

ACKNOWLEDGEMENTS

This research was funded by the NIH 1 R01 HL157017 awarded to JPVG and the Cardiovascular Bioengineering Training Program (T32HL076124).

REFERENCES

[1] Tsao, CW et al., *Circulation* n.d.;**145**:e153–639, 2022.
[2] Hess, CN et al., *Circulation*, 130:1445-1451, 2014.
[3] Furdella, KJ et al., *Acta Biomater*, 123:298-311, 2021.
[4] Ardila, DC et al., *J Control Release*, 299:44-52, 2019.
[5] Jhunjunwala, S et al., *J Control Release*, 159:78-84, 2012.
[6] Rothstein, SN et al., *J Mater Chem*, 21:29-39, 2010.
[7] Su, Y et al., *Drug Delivery*, 28(1):1397-1418, 2021.

ASSOCIATION OF HEMODYNAMIC FORCES WITH PATTERNS OF CORONARY ARTERY DISEASE AND ATHEROSCLEROTIC PLAQUE PHENOTYPES

Diego Gallo (1), Alessandro Candreva (1), Maurizio Lodi Rizzini (1),
Valentina Mazzi (1), Daniel Munhoz (2), Jean Paul Aben (3), Bernard De Bruyne (2),
Claudio Chiastra (1), Carlos Collet (2), Umberto Morbiducci (1)

(1) Polito^{BIO}Med Lab, Department of Mechanical and Aerospace Engineering,
Politecnico di Torino, Turin, Italy

(2) Cardiovascular Center Aalst, OLV-Clinic, Aalst, Belgium

(3) Pie Medical Imaging BV, Maastricht, The Netherlands

INTRODUCTION

An elevated translesional pressure gradient is considered the main biomechanical hallmark of atherosclerotic coronary artery disease (CAD) [1], as it has been associated with plaque destabilization and adverse clinical events [1]. Measurement of the translesional pressure gradient is typically performed in the distal segment of the coronary artery and thus it reflects the cumulative pressure losses along the vessel length [2]. However, focal narrowing can be almost entirely responsible for the pressure loss. Nonetheless, diffuse pressure losses outside angiographic stenotic regions contribute to the total decrease in pressure. The assessment of pullback pressure measurements allows quantifying the distribution of pressure loss [2], promising standardization in the diagnosis of focal vs. diffuse CAD. Besides pressure gradients, wall shear stress (WSS) features are associated with plaque nucleation, progression and destabilization [3], potentially predicting adverse clinical events [4].

In this work, invasive pressure assessment, WSS profiles obtained from angiography-derived computational fluid dynamics (CFD) simulations, and atherosclerotic plaque phenotype characterization based on optical coherence tomography (OCT) were combined to uncover the links between focal vs. diffuse intracoronary pressure gradients, WSS and atherosclerotic plaque features.

METHODS

Study design. 105 vessels presenting with significant flow impairment by distal fractional flow reserve (FFR) ≤ 0.80 underwent assessment of intracoronary pressure gradient and angiography-based 3D reconstruction for WSS analysis. Of those vessels, 51 had OCT pullbacks. Study protocol was approved by local ethics committee.

Pressure pullback measurements. Motorized FFR pressure pullback tracings were acquired using a pullback device (Volcano R100, Volcano Corporation, USA) and used to obtain functional CAD descriptors. Technically, FFR was defined as the lowest ratio between

distal and proximal coronary pressures during hyperemia. An FFR value was extracted from the pressure tracing every 10 mm. The pullback pressure gradient (PPG) was calculated from the FFR pullback curves [2] according to the formula:

$$PPG = \frac{1}{2} \left[\frac{MaxPPG_{20mm}}{\Delta FFR_{vessel}} + \left(1 - \frac{L_{FD}}{L_{TOT}} \right) \right] \quad (1)$$

where $MaxPPG_{20mm}$ was defined as the maximum PPG over a 20 mm length; ΔFFR_{vessel} as the difference between FFR values obtained at the ostium of the vessel and at the most distal anatomical location; the length of functional disease L_{FD} as the length with FFR drop ≥ 0.0015 per mm; the total vessel length L_{TOT} was derived from the motorized pullback pressure tracing. PPG is a non-dimensional continuous quantity, ranging from 0 (diffuse CAD) to 1 (focal CAD) [2].

Quantitative coronary angiography (QCA). Vessel geometries were reconstructed based on 3D QCA from vessel ostium to pressure sensor position, using two end-diastolic frames at least 30° apart (CAAS Workstation WSS software, Pie Medical Imaging, the Netherlands). The lesion was characterized by the percentage area stenosis (%AS) and defined as the coronary segment including the minimum lumen area, delimited proximally and distally by the intersection of the QCA vessel diameter function line with the interpolated reference line (Fig. 1). Within the lesion, the mid lesion segment was delimited on the QCA diameter function line using the 60% relative severity of the minimum lumen diameter as threshold value (Fig. 1).

OCT. Plaque composition analysis [5] was performed acquiring OCT pullbacks of 75 mm length, using Dragonfly OPTIS Imaging Catheter (Abbott Vascular, USA).

Computational hemodynamics. CFD simulations were carried out on the reconstructed 3D vessel geometries using a finite element-based code (CAAS Workstation WSS software, Pie Medical Imaging). In addition to the time-average WSS (TAWSS), the variability of the WSS

contraction/expansion action along the cardiac cycle was quantified by the topological shear variation index (TSVI) [4,6]:

$$TSVI = \left\{ \frac{1}{T} \int_0^T [DIV_w - \overline{DIV_w}]^2 dt \right\}^{1/2} \tag{2}$$

where DIV_w is the divergence of the normalized WSS vector field [4] and T is the duration of the cardiac cycle. On each model, TAWSS and TSVI values were averaged over the mid segment of the lesion.

Statistical analysis. The median PPG value was used to define groups with focal or diffuse disease. The Chi-squared test was used for comparing categorical variables, the Student’s t test (or Mann-Whitney test as appropriate) for continuous ones. Generalized linear models were used to perform regression analyses on continuous OCT variables and PPG- or WSS-based quantities. Logistic generalized linear model was used in case of categorical OCT variables. Odd ratios (OR) per unit increase in the independent variable were obtained from the exponential of the standardized correlation coefficients. A p-value < 0.050 was considered significant.

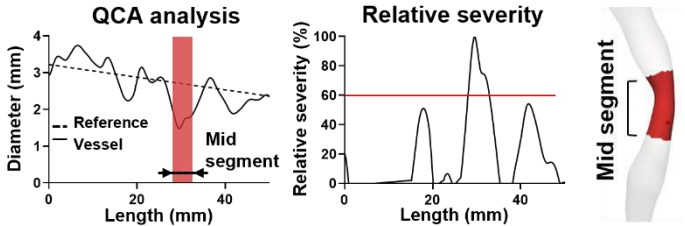


Figure 1: Anatomical definition of the mid lesion segment.

RESULTS

Focal lesions (PPG above the median value of 0.67) had significantly lower FFR, higher %AS, and higher TAWSS and TSVI (Table 1). Both TAWSS and TSVI were associated with PPG (Fig. 2). The association between TSVI and PPG was retained after adjustment for the %AS. OCT-based plaque characteristics of 51 vessels are reported in Table 2. Thin cap fibroatheroma (TCFA) and plaque rupture were more prevalent among focal lesions. PPG was associated with the presence of TCFA (OR 2.85, p=0.029) and plaque rupture (OR 4.94, p=0.002). TAWSS was associated with the presence of macrophages (OR 1.15, p=0.018). TSVI was associated with plaque rupture (OR 1.01, p=0.024) and the presence of cholesterol crystals (OR 1.01, p=0.041).

DISCUSSION

The findings of this study, summarized in Fig. 3, support the hypotheses that: (i) the hemodynamic profile, identified by pressure gradients and WSS-based quantities, is different in patients presenting with focal and diffuse CAD; (ii) the different hemodynamic profile characterizing focal vs. diffuse CAD is associated with different atherosclerotic plaque phenotype; (iii) focal CAD and elevated TAWSS and TSVI are associated with high risk plaque phenotypes at the OCT evaluation; (iv) TAWSS and TSVI represent different hemodynamic cues, as they are associated with different plaque features. Taken together, these findings point towards a synergistic role of pressure gradients and adverse WSS features in the destabilization mechanisms of lesions presenting a focal pressure drop pattern. Thus, the analysis of pressure gradients and WSS profiles appears promising in augmenting diagnosis, risk assessment, stratification, and tailoring preventive therapeutic strategies for CAD patients.

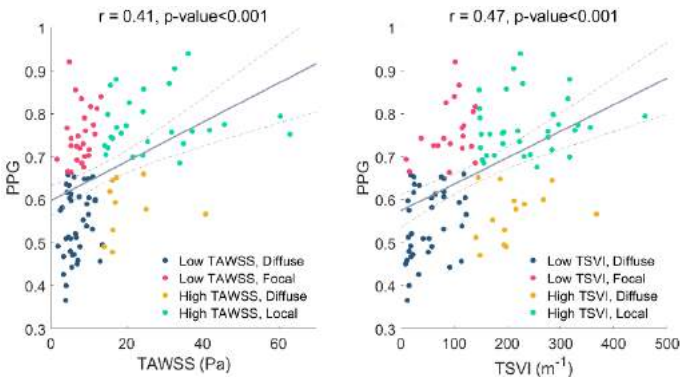


Figure 2: Correlation between PPG vs. WSS-based descriptors.

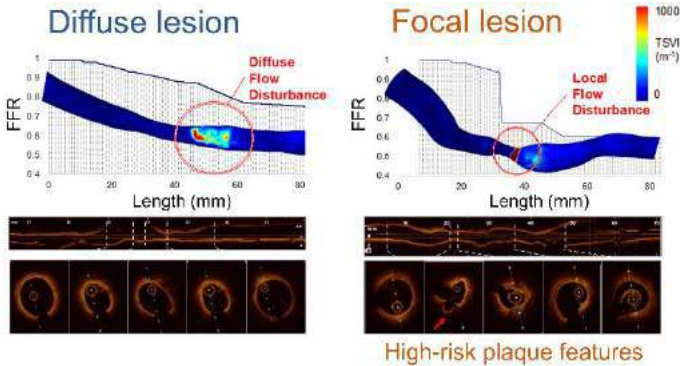


Figure 3: Interplay between coronary hemodynamics and plaque composition in diffuse vs. focal lesions.

Table 1: Functional characteristics of diffuse vs. focal lesions			
	Diffuse (N=53)	Focal (N=52)	p-value (two-sided)
%AS	72.86	83.73	<0.001
FFR	0.75	0.57	<0.001
TAWSS, Pa	7.03	14.78	<0.001
TSVI, m ⁻¹	76.82	163.93	<0.001

Table 2: OCT characteristics in diffuse vs. focal lesions			
	Diffuse (N=38)	Focal (N=13)	p-value (two-sided)
Lipid-rich plaque, n (%)	20 (52.6)	9 (69.2)	0.297
Calcific plaque, n (%)	31 (81.6)	11 (84.6)	0.804
Calcium thickness, mm	0.89	0.90	0.933
Fibrous cap thickness, μm	91.0	61.0	0.005
TCFA, n (%)	5 (13.2)	6 (46.2)	0.013
Plaque rupture, n (%)	7 (18.4)	6 (46.2)	0.048
Macrophage, n (%)	10 (26.3)	4 (30.8)	0.756
Cholesterol crystals, n (%)	14 (36.8)	7 (53.8)	0.282

REFERENCES

[1] Pijls, NH et al., *J Am Coll Cardiol*, 56(3):177-184, 2010.
[2] Collet, C et al., *J Am Coll Cardiol*, 74(14):1772-1784, 2019.
[3] Kumar, A et al., *J Am Coll Cardiol*, 72(16):1926-1935, 2018.
[4] Candreva, A et al., *Atherosclerosis*, 342:28-35, 2022.
[5] Jang, IK et al., *Circulation*, 111(12):1551-1555, 2005.
[6] Morbiducci, U et al., *Ann Biomed Eng*, 48(12):2936-2949, 2020.

NUMERICAL PREDICTIONS OF FLOW-INDUCED HEMOLYSIS: CAN THE ACCURACY OF THE POWER LAW MODEL BE IMPROVED USING CALIBRATED COEFFICIENTS?

Alberto Mantegazza (1,2), Nicolas Tobin (2), Keefe B. Manning (2), Brent A. Craven (3)

(1) Department of Mechanics, Mathematics and Management, Polytechnic University of Bari, Bari, Italy

(2) Department of Biomedical Engineering, Pennsylvania State University, University Park, PA, USA

(3) Office of Science and Engineering Laboratories, Center for Devices and Radiological Health, United States Food and Drug Administration, Silver Spring, MD, USA

INTRODUCTION

Hemolysis is the damage to red blood cells that causes the release of hemoglobin into the plasma. Mechanical hemolysis may occur in blood-contacting medical devices when the red blood cells are exposed to a high level of flow-induced stress for a prolonged time. Historically, the hemolytic potential of a medical device was assessed experimentally. Over the last decade, computational fluid dynamics (CFD) has become more and more used for predicting mechanical hemolysis. The most popular hemolysis model is the stress-based hemolysis model [1], which correlates empirically the release of hemoglobin from red blood cells (RBCs) to the exposure time (t_{exp}) and intensity of fluid-induced shear stress (σ_{shear}):

$$H = Ct_{exp}^a \sigma_{shear}^b \quad (1)$$

H is the relative fraction of plasma-free hemoglobin to the total blood hemoglobin; C , a , and b are coefficients traditionally obtained by statistical regression of data from simplified experiments in Couette-type blood shearing devices where the red blood cells are typically subjected to a uniform-shear laminar flow for a well-defined exposure time [2]. Even though these simplified experiments depart significantly from the working conditions in which real medical devices operate (i.e. turbulence, non-uniform shear stress, highly variable exposure time), such *idealized* coefficients are more than often used to perform numerical hemolysis predictions. As a result, absolute hemolysis predictions using idealized coefficients for the power law model are traditionally inaccurate.

Craven *et al.* [3] developed a novel approach for calibrating the coefficients of the power law model in a real medical device to potentially improve the accuracy of absolute hemolysis predictions. The approach consisted in combining a CFD-based Kriging surrogate model with experimental hemolysis measurements in a real device to determine a set of *calibrated* coefficients that can be used to obtain numerical simulations matching experiments. In theory, these calibrated hemolysis coefficients can be used to predict absolute plasma-free hemoglobin levels for the same device used for calibration but operating at different conditions or in a completely

different device sharing similar design features. The success of this strategy relies on the universality of the power law model and the extent of differences between the device used for calibration and the device of interest. It has yet to be investigated, however, whether calibrated coefficients from one device can be reliably used to predict hemolysis in a similar device.

The aim of the study is to assess the validity of the approach of using calibrated hemolysis coefficients to improve the power law model hemolysis predictions in real medical devices. Experimental hemolysis data in a 1-mm diameter capillary tube [4] were used by Craven *et al.* [3] to calibrate the power law model coefficients. In this study [5], we used the same calibrated coefficients to predict relative and absolute hemolysis levels in the 4-mm diameter FDA benchmark nozzle and compared the results with different experimental hemolysis data [2, 6].

METHODS

Large-eddy simulations (LES) and Reynolds-averaged Navier–Stokes (RANS) simulations of flow and hemolysis were performed for the FDA nozzle benchmark geometry [6] in both sudden contraction and gradual cone orientations (Fig. 1).

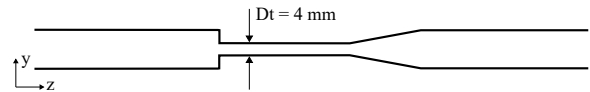


Figure 1: FDA benchmark nozzle in the sudden contraction orientation. The gradual cone orientation is symmetric with respect to the y-axis. Figure adapted from Mantegazza *et al.* [5]

The Eulerian power law model was used for hemolysis simulations [3]:

$$\frac{\partial H'}{\partial t} + (\mathbf{u} \cdot \nabla) H' = (C\sigma^b)^{1/a} \quad \text{SB}^3\text{C2023-371}$$

Copyright 2023 SB³C Foundation, Inc.

where $H' = H^{1/a}$ is the linearized plasma-free hemoglobin fraction and σ is the effective scalar stress defined as the resolved viscous stress. The power law model was tuned using the calibrated set of coefficients from Craven *et al.* [3]: $C = 2.875 \times 10^{-10}$, $a = 0.5$, and $b = 2.65$. Given the solution of Eq. 2, a modified index of hemolysis (MIH_{CFD}) was calculated to directly compare the CFD hemolysis predictions with the experimental data [6]:

$$MIH_{CFD} = 10^6 \frac{\int_A (H\mathbf{u}) \cdot d\mathbf{A}}{\int_A \mathbf{u} \cdot d\mathbf{A}} \quad (3)$$

where \mathbf{u} is the flow velocity and $d\mathbf{A}$ is the area normal vector of the cross-section A where hemolysis is evaluated. Fluid properties and boundary conditions were specified to reproduce the experimental conditions reported by Herbertson *et al.* [6], who measured hemolysis in separate experiments at conditions corresponding to 5 and 6 L/min through the FDA nozzle for both the sudden contraction and gradual cone orientation. The fluid was treated as Newtonian: $\rho = 1040 \text{ kg/m}^3$ and $\mu = 4.24 \text{ cP}$. For all simulations, a laminar fully developed inlet velocity boundary condition was used and a parabolic velocity profile was prescribed as an initial condition throughout the entire domain. A zero-gradient pressure boundary condition and a zero-pressure condition were applied at the inlet and outlet, respectively. For the plasma-free hemoglobin, we imposed $H = 0$ as initial condition and as inlet boundary condition, whereas a zero-gradient Neumann condition was prescribed at the outlet and on the walls. For the RANS simulations, we used the $k - \omega$ SST model with the SIMPLEC algorithm. Time-resolved LES simulations were performed with the PIMPLE algorithm. All computations were performed with OpenFOAM using second-order accurate discretization schemes. The convergence of the steady simulations was assessed by ensuring that the normalized residuals were less than 10^{-10} and by monitoring minimum and maximum values of variables of interest such as inlet pressure and flow rate. Given the flow solution, Eq. 2 for hemolysis prediction was solved using a custom solver previously developed and verified [3].

RESULTS

Absolute hemolysis predictions. Both LES and RANS predicted that the maximum plasma-free hemoglobin concentration (H) was found along the wall of the throat region just downstream of the sudden contraction. Using the calibrated coefficients from Craven *et al.* [3] and the sudden contraction configuration for the FDA nozzle at 5 L/min, we obtained MIH values of 421 and 210 for the LES and RANS, respectively (Fig. 2a).

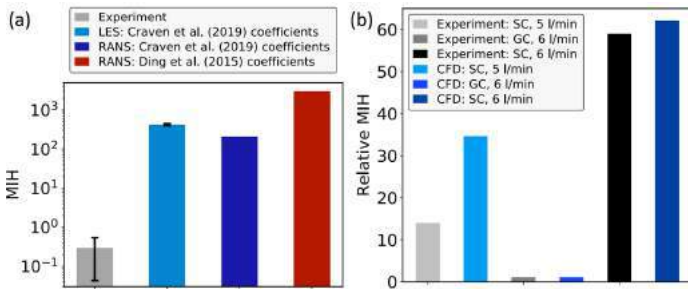


Figure 2: (a) CFD absolute hemolysis predictions for the FDA nozzle in the sudden contraction orientation at $Q = 5 \text{ l/min}$ compared with the experimental data from Herbertson *et al.* [6] and Ding *et al.* [2]. (b) CFD relative hemolysis predictions for the FDA nozzle in the sudden contraction (SC) and gradual cone (GC) orientation at $Q = 5 \text{ l/min}$ and $Q = 6 \text{ l/min}$ compared with the experimental data from Herbertson *et al.* [6]. Figures adapted from Mantegazza *et al.* [5].

This difference is ascribed to the fact LES predicted that some hemolysis is generated by the resolved turbulent viscous stresses in the core of the nozzle throat, while RANS predicted hemolysis generation in the nozzle near-wall region only. However, this CFD absolute MIH difference is negligible as both CFD predictions differ by approximately 3 orders of

magnitude from the experimental data from Herbertson *et al.* ($MIH = 0.292 \pm 0.249$) [6]. To investigate whether using calibrated coefficients improves the accuracy of the hemolysis predictions, we performed an additional RANS simulation with the idealized power law coefficients from Ding *et al.* [2] ($C = 9.772 \times 10^{-7}$, $a = 0.2076$, and $b = 1.4445$) obtained in experiments using simplified Couette-type shearing devices. The CFD simulation using these traditional idealized coefficients yielded an MIH of 2974, which is more than 4 orders of magnitude larger than the experimental data (Fig. 2a) and in error compared to the calibrated RANS simulations by approximately one order of magnitude.

Relative hemolysis predictions. In addition to the sudden contraction (SC) at 5 L/min that we considered for the absolute hemolysis predictions, we performed two additional RANS simulations to test the power law model accuracy of relative hemolysis predictions: gradual cone (GC) orientation at both 5 L/min and 6 L/min. CFD results were compared to experimental data [6]. For both the experiments and CFD, relative MIH was calculated by normalizing the absolute MIH value for each case by the respective MIH value for the GC orientation at 6 L/min. Fig. 2b shows that relative hemolysis numerical predictions generally match experimental results. In fact, CFD correctly predicts the rank ordering of the relative hemolysis levels for all three conditions. For the SC orientation at 5 L/min, the relative MIH from CFD is 34.9 compared to an MIH of 13.9 from the experiments. For the SC orientation at 6 L/min, the CFD relative MIH prediction of 62 is in excellent agreement with the value of 59 from the experiments.

DISCUSSION

Our study showed that reasonably accurate relative hemolysis predictions in the FDA nozzle can be obtained using the power law model in combination with model coefficients (C, a, and b) calibrated for a similar device. This is a valuable result for medical product development because it allows the investigation of the hemolytic impact of small design modifications to an existing device without the need of performing additional *in vitro* experiments. However, highly inaccurate absolute hemolysis predictions were found despite the use of calibrated model coefficients. To be noted, the device-specific calibration approach used in this study improved the absolute hemolysis predictions by one order of magnitude compared to using the traditional empirical coefficients from simplified Couette-type shearing devices with idealized flow conditions. The main reason why the power law model failed to accurately predict absolute hemolysis levels lies in the subtle fluid dynamic differences between the FDA nozzle and the capillary tube used by Craven *et al.* [3] for the calibration of the model coefficients. This is due to the entirely empirical nature of the power law model which does not take into account RBC damaging mechanisms that lead to RBC damage. Thus, the power law model lacks universality and cannot be applied across all operating conditions. To obtain accurate absolute hemolysis predictions, the power law model has to be first calibrated under fluid dynamic conditions that closely match those in the hemolytic regions of the device of interest.

ACKNOWLEDGEMENTS

This work used the Extreme Science and Engineering Discovery Environment (XSEDE), which is supported by National Science Foundation grant number ACI-1548562. The study was funded in part through the NIH NHLBI grant HL146921.

REFERENCES

- [1] Giersiepen M *et al.* *Int. J. Artif. Organs* 15.5 (1990).
- [2] Ding J *et al.* *Artif. Organs* 39.9 (2015).
- [3] Craven BA *et al.* *Biomech. Model. Mechanobiol.* 18.4 (2019).
- [4] Kameneva MV *et al.* *ASAIO Journal* 5 (2004).
- [5] Mantegazza A *et al.* *Biomech. Model. Mechanobiol.* (2022).
- [6] Herbertson LH *et al.* *Artif. Organs* 3 (2015).

ESTIMATING SOLEUS MUSCLE VOLUME BY ANTHROPOMETRIC AND ULTRASOUND-MEASURABLE PARAMETERS

Shabnam Rahimnezhad (1), Karin G. Silbernagel (2), Daniel H. Cortes (1)

(1) Department of Mechanical Engineering
Penn State University
State College, PA, USA

(2) Department of Physical Therapy
University of Delaware
Newark, DE, USA

INTRODUCTION

Muscle volume and its cross-sectional area are essential parameters in estimating the force and strength of young athletes[1], the elderly[2], and patients[3]. Specifically, muscle volume accurately predicts torque [2], and strength[4]. Patients with Achilles tendon injuries suffer from long-term reduction in the gastrocnemius muscle volume (GMV) and soleus muscle volume (SOLV). Reduced muscle volume is related to lower-leg functional outcomes [5]. Therefore, a quick and accessible measurement tool for muscle volume is essential for assessing patient recovery after an Achilles tendon rupture (ATR). Muscle volume can be calculated using 3D imaging techniques such as MRI (Magnetic Resonance Imaging) and 3D ultrasonography (3D US)[6],[7]. However, MRI and 3D ultrasound are expensive and not readily available in many clinical settings. We have previously used parameters from panoramic ultrasound images to accurately estimate the volume of gastrocnemius muscles[8]. However, obtaining spatially-accurate panoramic images of the Soleus muscle is challenging due to its depth, size and shape. Therefore, this study aims to develop a method to estimate Soleus muscle volume from anthropometric parameters that can be easily measured with standard ultrasound equipment.

METHODS

This study was approved by the Pennsylvania State University IRB (STUDY00019121). The current study aims to propose a clinically applicable tool to measure SOLV. For this aim, five healthy participants (three females, two males, age=30.8±1.9, weight=67.6±15 kg, height=167±7 cm), without lower limb injuries or disease, take part in this study. 3T whole-body MRI system (Siemens Prima Fit) was used to gather the imaging data with the following parameters: T1-weighted, time to echo= 3.69 ms, time to repetition= 7.8 ms, and 6 mm slice thickness. Ultrasound panoramic ultrasound data were obtained within 15 days of the MRI test using a SIEMENS (ACUSON P300™) Ultrasound System. Free software 3D Slicer 4.13.0, and Sante DICOM viewer were used to create the volume from MRI images and measure the different parameters (Figure 1- a). The sagittal and cross-sectional area of the Soleus muscle in five participants are normalized and plotted, to examine the possibility of defining a shape factor (The ratio between muscle volume and predictor factors) for this muscle. Furthermore, the

possibility of estimating the soleus muscle volume by measuring the ratio of the Soleus muscle to the Gastrocnemius muscle was examined. Additionally, seven equations to estimate the SOLV involving anthropometric and ultrasound-measurable parameters were considered (Eqs 1-7). The parameters considered are Soleus length (Ls), Maximum axial cross-sectional area (Aa), Maximum sagittal cross-sectional area (As), the thickness of the Soleus muscle at the maximum Aa (t), the thickness of the soleus muscle at a bulging point of the leg (tm), the circumference of a leg (C), the thickness of the fat (tf), half of the circumference of the leg omitting the fat and the skin (Cs), Knee-ankle (Lateral femoral epicondyle, standing - Medial malleolus) distance (Ll). The accuracy of the prediction was evaluated using regression analysis.

$$MVS = a + b (t \times Ls) \quad (1)$$

$$MVS = c + d (Aa \times Ls) \quad (2)$$

$$MVS = e + f \left(Aa \times \frac{As}{t} \right) \quad (3)$$

$$MVS = g + h \left(Cs \times \frac{As}{tm} \right) \quad (4)$$

$$MVS = i + j (Cs \times Ls) \quad (5)$$

$$MVS = k + l (Cs \times Ll) \quad (6)$$

$$MVS = m + n (Cs \times Ll \times tm) \quad (7)$$

Where a, b, c, d, ... m, n are constant parameters obtained from regression analysis.

RESULTS

Figure 1-a shows the volume segmented for the participants in 3D Slicer. Figure 1- b shows the ratio between the soleus and gastrocnemius muscles in different participants. While the soleus muscle is always bigger than the gastrocnemius muscle volumetrically, the ratio between these muscles varies from person to person. The main axes of the soleus muscle with tibia bone in different participants do not have the same angle, therefore to analyze the normalized axial and sagittal cross-sectional area of the muscle, first, the soleus muscles are rotated in all three axes to become aligned. Figure 2 illustrates the normalized area of the soleus muscle in axial and sagittal directions over the normalized length and width.

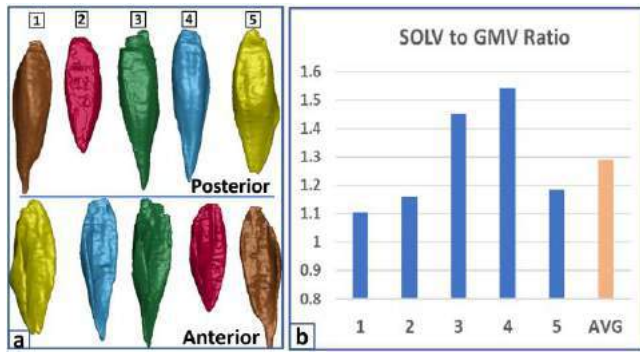


Figure 1: a) Posterior and anterior view of the segmented Soleus muscle, b) Soleus to Gastrocnemius muscle volume ratio

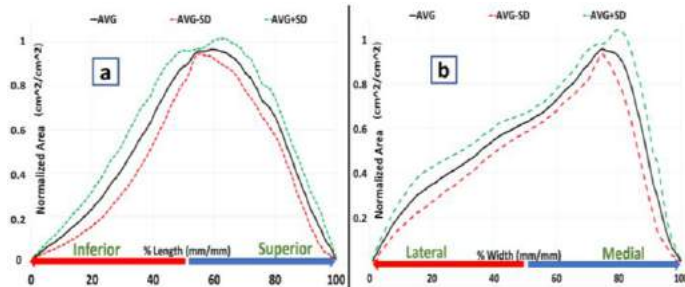


Figure 2: Change of normalized axial area of Soleus over Length percentile, b) Changes of the normalized sagittal area of Soleus over width percentile

The trends for both normalized curves in figure 2 are the same for all the muscles, and these similarities increase the possibility of defining the shape factor for analytical equations to estimate the soleus muscle volume. The maximum axial cross-sectional area of the soleus muscle is around % 50-70, and the maximum sagittal cross-sectional area of the soleus muscle is around % 75-85. After plotting normalized curves, the validity of the equations suggested in the methodology section is studied. Table 1 illustrates the anthropometrical, and parameters measured based on US and MRI-acquired images.

Table 1: Measured parameters

Sob No.	Anthro data		MRI data								US data		
	Ll	C	Vol	Aa	As	t	tm	tf	Cs	Ls	Cs	tf	tm
	(cm)	(cm)	(cm ³)	(cm ²)	(cm ²)	(cm)	(cm)	(cm)	(cm)	(cm)	(cm)	(cm)	(cm)
1	35	35	365.8	22.4	71	3	3.2	0.8	15	31.9	15.3	0.7	3.6
2	33	32	246	17.4	54	2.5	2.5	0.9	13.2	24	13.3	0.8	2.5
3	38.4	38	531.6	30.9	108.3	3.8	3.96	0.6	17.1	33.5	17.4	0.5	3.94
4	35.5	34	401	25.7	84.5	2.9	3.6	0.9	14.2	31	14.7	0.73	3.5
5	37.8	39	620	40.21	125	4.3	4.4	0.4	18.2	30.5	18.4	0.34	4.3

The soleus muscle is a deep muscle and considering the difficulty in following the curvature of the leg while moving the probe on the skin, acquiring the axial panoramic images for this muscle with the US is not convenient for general clinical examination. We did not consider the area of sagittal panoramic images in our analysis while capturing it is not as hard as axial panoramic images. In the first column of table 2, the regression result for suggested equations based on MRI data is demonstrated, and in the second column of table one, the regression results based on the measured parameters in the US are shown.

Table 2: Regression analysis to estimate SOLV

EQUATION	REGRESSION ANALYSIS (MRI DATA)	REGRESSION ANALYSIS (US DATA)
$a + b (t \times Ls)$	a= - 54.881 b= 4.8384 R= 0.9432	—
$c + d (Aa \times Ls)$	c= 38.855 d= 0.47 R= 0.9953	—
$e + f \left(Aa \times \frac{As}{t} \right)$	e= 90.145 f= 0.4625 R= 0.9559	—
$g + h \left(Cs \times \frac{As}{tm} \right)$	g= - 116.77 h= 1.4193 R= 0.9514	—
$i + j (Cs \times Ls)$	i= - 180.9 j= 1.2985 R= 0.8467	—
$k + l (Cs \times Ll)$	k= 57.596 l= 0.2177 R= 0.9746	k= - 330.14 l= 1.3322 R= 0.9642
$m + n (Cs \times Ll \times tm)$	m= 48.24 n= 0.1883 R= 0.9973	m= 24.12 n= 0.1949 R= 0.9785

DISCUSSION

Although in all cases the Soleus muscle, volumetrically, is bigger than the Gastrocnemius muscle, there is not a constant ratio between these two muscles. Since the functionality of these muscles is different, we are hypothesizing the ratio between these muscles is mostly a function of the daily activity and routine exercises, and by knowing the volume GMV, we cannot estimate the SOLV. The normalized axial and sagittal cross-sectional area over normalized length and width shows the same trend in the shape of the muscle, and this increase the possibility of defining the shape factor in analytical equations to estimate the muscle volume. Capturing accurate axial panoramic images for the soleus muscle might not be convenient. It is possible to capture sagittal panoramic images for the soleus muscle, but MRI analysis showed that using the sagittal cross-sectional area does not improve the estimation of the muscle. Also, since the angle of this muscle with the tibia bone varies in different subjects, defining the correct plane for acquiring the sagittal cross-sectional area is not easy. Therefore, this parameter is not included in the US regression analysis. But according to the regression analysis, measuring the circumference of the leg, the thickness of fat, and the thickness of the Soleus muscle on the bulging part of the leg can provide a good estimation for SOLV. A limitation of this study is the deformation of the skin while moving the probe, which can cause an error in measuring the thickness of the fat, also defining the accurate, boundaries for the soleus muscle with the current resolution of the MRI pictures are not easy. In conclusion, this study showed that considering US data and anthropometric parameters of the leg can provide a good estimation of the volume of the soleus muscle.

ACKNOWLEDGMENTS: Research reported here was supported by NIAMS of the NIH under award number R21 AR077282.

REFERENCES

- [1] K. Funato, et al., *Sports Med. Phys., Fitness*, 40(4): 312–318, 2000.
- [2] R. Akagi, et al., *Age Ageing.*, 38(5): 564–569, 2009.
- [3] E. S. Park, et al., *Yonsei Med. J.*, 55 (4):1115–1122, 2014.
- [4] R. Akagi, et al., *Age Ageing.*, 38(5):564–569, 2009.
- [5] G. Eken, et al., *Foot Ankle Surg.*, 27(7): 730–735, 2021.
- [6] M. Miyatani, et al., *Eur. J. Appl. Physiol.*, 86 (3): 203–208, 2002.
- [7] J. I. Esformes, et al., *Eur. J. Appl. Physiol.*, 87(1): 90–92, 2002.
- [8] Sh. Rahimnezhad et al., *SB3C*, 2022.

CLINICAL IMMERSION OF UNDERGRADUATE BIOMEDICAL ENGINEERING STUDENTS: BEST PRACTICES FOR SHORT-TERM PROGRAMS

Emily L. Lothamer (1,2), Katherine R. Moravec (1,2), Amy Hoene (1), P. Mike Wagoner (1), Daniel J. Beckman (1,3), Craig J. Goergen (2,3)

(1) Indiana University Health Methodist Hospital, Indianapolis, IN, USA
(2) Weldon School of Biomedical Engineering, Purdue University, West Lafayette, IN, USA
(3) Indiana University School of Medicine, West Lafayette, IN, USA

INTRODUCTION

Engineering curricula, although functional at delivering technical skills, often fail to impart many vital aspects of a successful engineer [1]. This includes exposure to experiences designed to create a deeper understanding of how these skills translate to real-world impacts [2-3]. While biomedical engineering students often benefit from immersive clinical experiences, especially at the undergraduate level, such opportunities can be difficult to provide due to challenges associated with implementation [4-5]. There is, thus, a need for strategically developed clinical immersion programming within biomedical engineering curricula that contribute to the training of well-rounded students using comprehensive clinical experiential learning.

METHODS

To address this challenge, we designed, implemented, and assessed a two-week cardiovascular clinical immersion program for biomedical engineering undergraduate students from Purdue University. This was accomplished through a partnership with Indiana University Health (IUH) Methodist Hospital and associated branches of IU Health and intentionally structured relationships established between IU Health administration, Purdue University faculty, and an engineering student intern. Since it began in 2014, this yearly program has expanded from five students for one two-week period in May to twelve students total over two separate two-week periods in May and August. To provide equitable program access to the greatest number of biomedical engineering students, we target students finishing their sophomore year and ask for a brief, open-ended application that includes their interest in the program and eventual career goals, with 15-20 students being selected for interviews. This two-phase application process was implemented to allow for multiple interactions with potential participants before deciding on a final group. In most years, thirty or more students apply to the program, demonstrating the demand and interest in clinical immersion programs. From 2014-2022, data was

collected from students via program application materials and open-ended reflections post-program. Repeating motifs in the data were operationalized and quantified to examine pre- and post-program career objectives and common takeaways from participants. This study received a Category IV exemption from Purdue University's IRB based on the use of these data (2022-844).

Student participants hear from clinical specialists employed by medical device companies of several relevant cardiovascular technologies and tour the facilities of IU Health's Simulation Center and 3D Innovations Lab for further exposure to the intersection of biomedical engineering and clinical medicine. Additionally, participants shadow and interact with medical professionals in several clinical departments involved in cardiovascular care throughout the duration of the program. These typically include Cardiology, Cardiothoracic Surgery, Radiology, and Interventional Radiology. Each program runs Monday-Friday for two weeks entirely on-site at the hospital, typically from 7am to 3pm each day. The focus of the first week is preparatory and includes lecture-based components, while the second week centers on active shadowing.

RESULTS

Response data from students who participated in this minicourse suggests that the experience is beneficial by exposing students to a wide variety of careers. While previous studies have shown that participation in a clinical shadowing program does not increase students' likelihood of intending to enter industry [5], our program does provide evidence that students unsure of their future career goals have a better idea of what they want to pursue post-graduation (Figure 1). Of the 55 program reflections we received, 30 indicated both pre- and post-program career objectives. Eleven started as unsure, and of those, five (42%) heavily preferred a specific path after the course. One student started with a pre-med objective and decided against this pursuit during the two-week program, becoming "unsure" as a result of their clinical experiences.

The seven students that ended the program undecided on a career path all stated feeling like they better understood the options available to them (100%). Of the 18 reflections with the same starting and ending career goal, six (33%) indicated in their reflection that they felt more confident in their path, while the remaining twelve (66%) did not discuss this aspect of their program experience. While the participant group composition included a higher-than-representative number of students interested in pursuing medicine, a greater number of undecided students indicated an increased interest in graduate school or industry compared to medicine. This demonstrates that clinical shadowing programs could have the ability to increase the biomedical engineering workforce. Previous data has shown that exposure to shadowing increases desire to attend medical school, so this may hold true for industry and graduate school as well since students see firsthand what careers each path may entail [6].

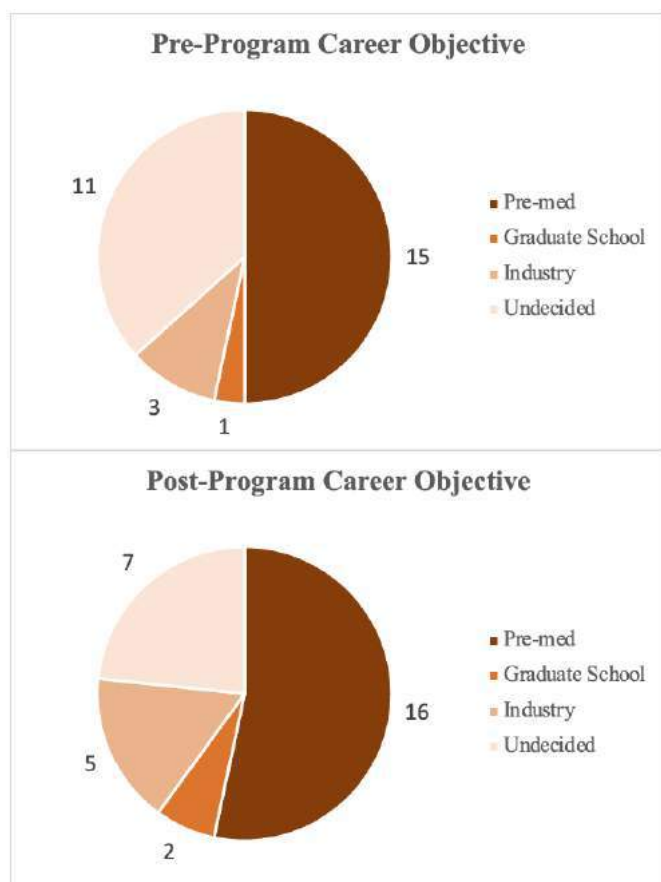


Figure 1: Self-reported career interests before and after program participation for participants between 2014-2021.

We found through our program that the successful organization and implementation of clinical immersion programs is dependent upon 1) close connections with and support from administrative personnel and 2) sustained relationships with clinicians and other medical professionals at the host facility. The support from administrative staff at the host facility is invaluable during the process of scheduling and obtaining clearance for the student participants. Maintaining connections with professionals who have previously participated in the program allow for continued support and the introduction of additional opportunities for future groups. For example, several cardiothoracic

surgeons have given guest lectures and hosted students during operations for multiple years in a row, leading to incredible learning experiences, continuity, and expansion to other clinicians in cardiology and radiology. Within the IU Health program, an engineering student intern is chosen each year from the pool of previous participants. This intern serves as a primary contact for participant selection and program coordination and, although funded through the hospital, focuses on communication with hospital administration and student and clinical program participants. Overall, the coordinated effort of these individuals is crucial to the execution of clinical immersion programs.

DISCUSSION

This experience provides biomedical engineering students at Purdue University with a rare, unique opportunity to gain hands-on access to the clinical environment of a top cardiovascular care center. Students interact with clinicians in cardiothoracic surgery, radiology, cardiology, interventional radiology, and other departments. The course has demonstrated potential to be life-changing for participants, as stated in multiple student reflections upon completion of their two-weeks. Key strategies for success include recruitment of student participants with diverse interests, provision for a funded intern position, developing staff and clinician contacts for year-to-year program constancy, and strategic program scheduling. Overall, both industry-focused and pre-med students alike can benefit from programs like this that give engineering students first-hand knowledge of current success and challenges associated with clinical care. While our program was targeted at undergraduate students, future endeavors could open opportunities to graduate students to benefit a wider group of students.

ACKNOWLEDGEMENTS

Funding for student interns came from Indiana University Health Methodist Hospital.

REFERENCES

- [1] Frank Stefan Becker. Globalization, curricula reform and the consequences for engineers working in an international company. *European Journal of Engineering Education*. 2006; 31:3, 261-272. <https://doi.org/10.1080/03043790600644749>
- [2] Davis, D.C., Gentili, K.L., Trevisan, M.S., Calkins, D.E. Engineering Design Assessment Processes and Scoring Scales for Program Improvement and Accountability. *Journal of Engineering Education*. 2002; 91: 211-221. <https://doi.org/10.1002/j.2168-9830.2002.tb00694.x>
- [3] Dym, C.L., Agogino, A.M., Eris, O., Frey, D.D., Leifer, L.J. Engineering Design Thinking, Teaching, and Learning. *Journal of Engineering Education*. 2005; 94: 103-120. <https://doi.org/10.1002/j.2168-9830.2005.tb00832.x>
- [4] Walker, M., Churchwell, A.L. Clinical Immersion and Biomedical Engineering Design Education: "Engineering Grand Rounds". *Cardiovascular Engineering Technology* 7, 1-6. 2016. <https://doi.org/10.1007/s13239-016-0257-y>
- [5] Kotche M, Felder AE, Wilkens K, Stirling S. Perspectives on Bioengineering Clinical Immersion: History, Innovation, and Impact. *Annals of Biomedical Engineering*. 2020;48(9):2301-2309. <https://doi.org/10.1007/s10439-020-02508-x>
- [6] Langenau, E., Frank, S. B., Calardo, S. J., & Roberts, M. B. (2019). Survey of Osteopathic Medical Students Regarding Physician Shadowing Experiences Before and During Medical School Training. *Journal of Medical Education and Curricular Development*, 6. <https://doi.org/10.1177/2382120519852046>

PRONLONGED SUBCULTURE AND PROGERIN EXPRESSION SENSITIZE VSMCS TO THREE DIMENSIONAL FIBER STRUCTURES

Yu-Yu Hsueh and Pen-hsiu Grace Chao

Department of Biomedical Engineering
National Taiwan University
Taipei, Taiwan

INTRODUCTION

Vascular smooth muscle cells (VSMCs) respond to various environmental signals, such as injury or inflammation, by changing their phenotype to maintain vascular structural and mechanical homeostasis [1, 2]. In vascular aging, VSMC dedifferentiation from the 'healthy' contractile phenotype is accompanied by elastin fiber fracture and excessive ECM deposition, resulting in arterial wall stiffening. The fragmented elastin fibers in the aged tissues also lose their wavy structure, a crucial component of vascular mechanics [3].

Hutchinson-Gilford progeria syndrome (HGPS) is an accelerated-ageing syndrome, caused by expression of the mutated lamin protein, progerin [4, 5]. HGPS patients suffer from atherosclerosis and heart failure, leading to death in their teens [6]. Progerin accumulation in VSMCs leads to altered mechanotransduction and phenotypic changes in mouse models [7]. We previously developed straight and wavy scaffolds to approximate the changes in ECM structure [8]. In this study, we investigate the effects of fiber structure on aging VSMCs, simulated with progerin-expressing VSMCs and prolonged passing [9].

METHODS

Electrospun Scaffold Poly-L-lactide (PLA, 6% in HFP) fibers were co-electrospun with 15% polyethylene oxide (PEO, in ethanol) on a rotating collector. The PEO fibers were removed with water to increase scaffold porosity. Fiber crimp was induced by heat treatment [8]. Materials were coated with polydopamine and type I collagen.

VSMC Culture Cre-LoxP-flanked PGK-neo-4XpA transgenic mice were provided by Dr. Chi Ya-Hui [10]. VSMCs were isolated from 10-week-old aortae via explant cultures. Cells were treated with 1 μ M 4-hydroxytamoxifen (4OHT) at passage 1 (P1) to induce progerin::FLAG production. VSMCs were subcultured to P6 and P9, and seeded on fiber scaffolds at 15,000 cells/cm².

Phenotypic Analysis Cell proliferation was quantified by either cell doubling time or normalized metabolic activity using AlamarBlue

assay according to the manufacturer's protocol. Immunofluorescence staining of phenotypic markers, including alpha smooth muscle actin (α SMA, Sigma), transgelin (SM22, Abcam), and calponin 1 (Abcam), were used to assess percentage of cells expressing these contractile markers.

Statistics Nonparametric Kruskal-Wallis test, Fisher's exact test, and 2-way ANOVA were performed using R.

RESULTS

To establish the effects of prolonged passing and progerin expression on VSMC phenotype, we monitored cell proliferation and phenotypic marker expression in 2D cultures. 4OHT induction resulted in more than 95% cell expressing progerin (data not shown). Population doubling time decreased with serial passing, indicating higher proliferation rate. At the same time, expression of most contractile markers tested reduced with subculture. Overall, prolonged cell passing increased cell proliferation and attenuated contractile marker expression, indicating a change in VSMC phenotype. Progerin induction had only minor effects.

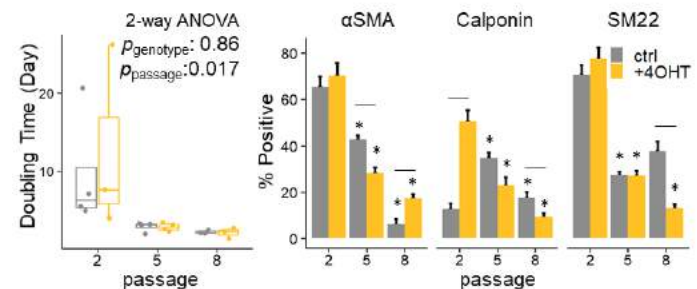


Figure 1 (A) Cell doubling time (B) Proportion of VSMCs staining positive for contractile markers (* $p < 0.05$ vs P2, line: $p < 0.05$ vs indicated groups)

We cultured the dedifferentiated VSMCs on straight and wavy fiber scaffolds for 3 weeks (Fig 2A). P6 VSMCs followed fiber structure in the straight group and had more random orientation in the wavy scaffolds (Fig 2B). Interestingly, P9 VSMCs are more elongated in both fiber groups and exhibited better fidelity to fiber structure. Progerin expression reduced shape conformity to fibers. Immunofluorescence staining of contractile marks found similar reduction with serially passaged cells, and wavy fiber structure increased contractile marker expression. Contrary to the 2D finding, progerin induction reduced phenotypic marker expression (Fig 2A and C).

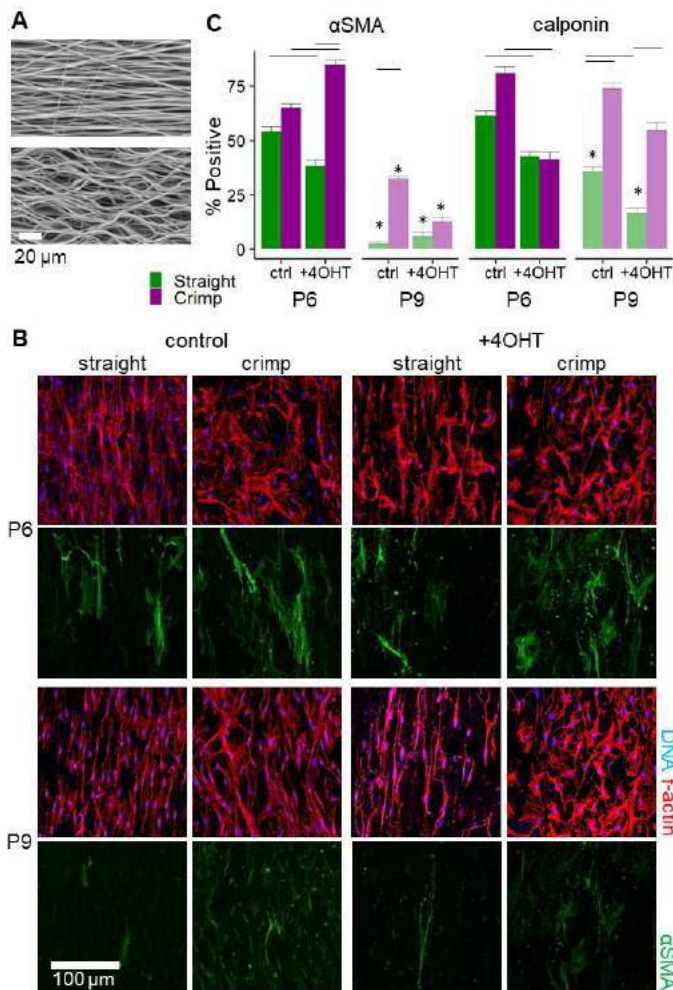


Figure 2 (A) Electrospun fiber structure, visualized by SEM, (B) immunofluorescence images of VSMC morphology and marker expression, and (C) proportion of cells positive for contractile markers.

We also monitored cell metabolic activities as a proxy for proliferation during scaffold culture. Both cell passaging and progerin expression increased VSMC proliferation rate (Fig 3). In P6 control cells, fiber structure did not change VSMC proliferation, while in P6 progerin-expressing cells, the increased proliferation was suppressed by wavy scaffold. For all groups, P9 VSMCs had increased proliferation rate. The effect of progerin expression was minimized but wavy fiber structure significantly reduced proliferation. In conjunction with results from Fig 2, our data indicate significant changes in VSMC phenotype with serial passaging and progerin induction. The wavy fiber structure partially rescues the phenotypic changes in these ‘aged’ VSMCs.

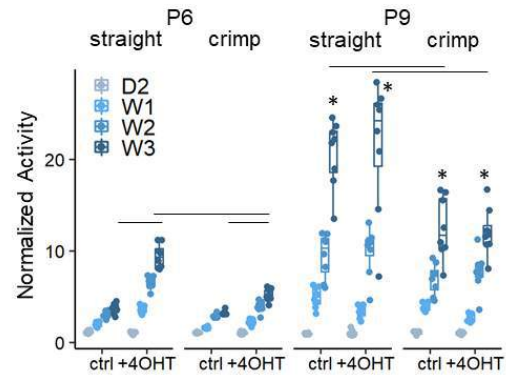


Figure 3 Cell activity, normalized by day 2, from Alamar Blue assay. Culture time had statistically significant effects on cell activity ($p < 0.05$, not shown on figure, Line: $p < 0.05$ in indicated groups at W3, * $p < 0.05$ vs P6 at W3).

DISCUSSION

Increased arterial stiffness is a significant risk factor for atherosclerosis and cardiovascular diseases. While inflammation and endothelial signaling play important roles in its regulation, VSMC manifest the arterial changes by altering its phenotype [2]. This is particularly evidenced by mice with VSMC-specific progerin expression [11]. In this study, we established ‘aged’ VSMCs by prolonged passaging and progerin expression (Fig 1) and investigated the effects of extrinsic structures on VSMC.

In the ‘healthy’ VSMCs (P6 without progerin expression), fiber structure did not change their contractile phenotype. With further passaging or progerin expression, however, VSMCs had decreased marker expression and increased proliferation, yet was able to respond to fiber structure (Fig 2, 3). In preliminary studies, P3 VSMCs was also not sensitive to fiber structure (data not shown). These findings suggest that the intrinsic VSMC contractile phenotype plays a dominant role, and the dedifferentiated cells are more mechanosensitive and plastic [12]. It is interesting to note that while progerin expression had only a minor effect in 2D cultures, its impact in 3D fibrous cultures was more robust. This result is in agreement with the different cell morphologies on the fibrous scaffolds and supports previous findings that progerin disrupts nuclear membrane structure and changes cell mechanotransduction [13]. Overall, we demonstrate that prolonged subculture and progerin expression sensitizes VSMCs to wavy fiber structure to promote a more contractile phenotype. As the crimp structure is lost with aging and disease, our findings suggest the intrinsic and extrinsic changes with aging interact to exacerbate vascular health.

ACKNOWLEDGEMENTS

This work was supported by the National Health Research Institute and the National Science and Technology Council (NHRI-EX110-10910EI, NSTC 110-2221-E-002-011-MY2).

REFERENCES

- [1] Vatner SF+ Frontiers Physio. 2021.
- [2] Frisantiene A+ Cell Signal. 2018.
- [3] Dingemans KP+ Anat Rec. 2000.
- [4] Carrero D+ Dis Model Mech. 2016.
- [5] Eriksson M+ Nature. 2003.
- [6] Gordon LB+ Hutchinson-Gilford Progeria Syndrome. In: GeneReviews. Univ Washington; 1993.
- [7] Coll-Bonfill N+ GeroScience. 2022.
- [8] Chao PG+ Biofabrication. 2014
- [9] Goldman RD+ Proc Natl Acad Sci USA. 2004.
- [10] Wang WP+ Aging Cell. 2020.
- [11] del Campo L+ Aging Cell. 2019.
- [12] Sorokin V+ Frontiers Immuno. 2020.
- [13] Danielsson BE+ Nucleus. 2020.

END-TO-END 3D GEOMETRIC MODEL RECONSTRUCTION OF PELVIC ORGANS BASED ON 3D MAGNETIC RESONANCE IMAGING AND DEEP LEARNING

Hui Wang (1), Xiaowei Li (2), Chenxin Zhang (1), Xiuli Sun (2), Jianliu Wang (2), Jiajia Luo (1)

(1) Biomedical Engineering Department, Peking University, Beijing, China
(2) Department of Obstetrics and Gynecology, Peking University People's Hospital, Beijing, China

INTRODUCTION

Reconstruction of 3D geometric models of pelvic organs based on 3D magnetic resonance imaging (MRI) is a very important and challenging task for computer-aided diagnosis, treatment and prognosis of female pelvic organ prolapse. The 3D geometric model can show the spatial structure of the organ, help the physician visualize the specific shape of the organ, analyze the etiology [1], and provide a good basis for subsequent finite element analysis [2] and surgical planning. Traditional methods usually first manually or automatically segment 2D MRI slices, and then perform post-processing such as 3D geometric model reconstruction and complex geometric repair based on the segmentation results. However, due to the complex shape of the pelvic organs, the traditional methods still have some problems, such as complex manual operations, high workload and long working time.

Deep learning has been widely used in computer vision tasks in the past decade, for automatic natural image classification, detection, and segmentation. There have also been some methods to automatically segment MRIs using deep learning. However, the segmentation results still require manual post-processing to make them conform to the real

3D geometry. In addition, the error tolerance rate of such automatic segmentation method is quite low. Once there is a segmentation error in one slice, the whole structure can be changed significantly, which affects the reconstruction of the 3D geometric model. End-to-end deep learning could directly learn the process "from MRI to the final 3D geometric model". This not only automates the reconstruction process, but also makes it possible to focus on the global structural information of the 3D geometric model, which in turn has a higher error tolerance rate and more realistic reconstruction results.

In this work, we aimed to develop an end-to-end deep learning-based reconstruction technique for 3D geometric model reconstruction of pelvic organs from 3D MRI.

METHODS

Figure 1 shows a proposed architecture for the end-to-end 3D geometric model reconstruction, along with exemplary inputs and outputs. For example, a set of 3D MRIs (where 480×480 is the size of one slice and 18 is the number of slices per set) and a spherical point cloud (uniformly sampled from a spherical 3D geometric model with diameter 1) were used as inputs to predict the 3D geometric model of

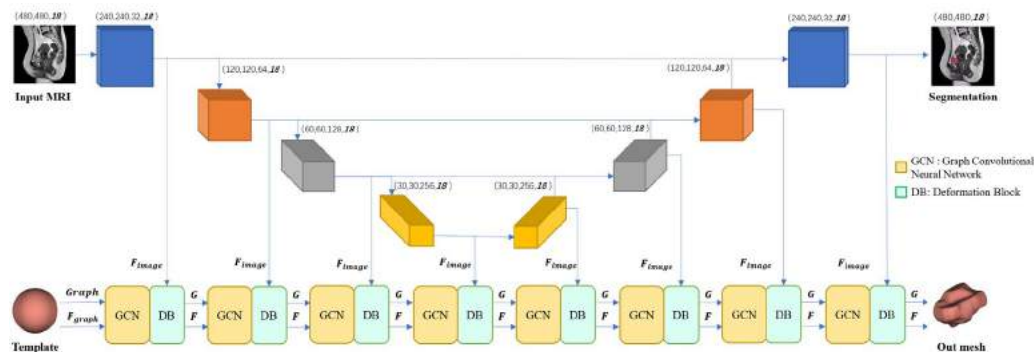


Figure 1: Network architecture.

the pelvic organs. First, a convolutional neural network (CNN) was used to extract layer-specific image features. Then, the spherical point cloud was constructed into a graph, and a graph convolutional neural network (GCN) was used to extract 3D structural features. GCN is a feature extractor for graph data structure, which has been widely used in 3D shape analysis in recent years. It can exchange features between neighboring nodes and eventually return to each node. In addition, a Deformation Block (DB) was designed to integrate image features with 3D structural features and transform spherical point cloud into a new point cloud. This completes a deformation of the point cloud. The above process was repeated eight times to extract deeper and more comprehensive feature information. Finally, the transformed point cloud was generated with the corresponding 3D geometric model of the organ. A manually reconstructed 3D geometric model was used as the ground-truth for the supervised training process.

The detailed structure of the Deformation Block (DB) is shown in Figure 2. A CNN was first used to encode the image information into a 1D vector. Next, each point of the sphere was concatenated with this 1D vector, and a multilayer perceptron (MLP) was used to learn the global features of the point cloud. We concatenate this feature with the 3D structural feature extracted by the GCN. Next, another MLP was used to learn the global changes, and EdgeConv [4] was used to learn the local changes to reconstruct the point cloud. Finally, the PointNet [5] was used to reconstruct the new point cloud.

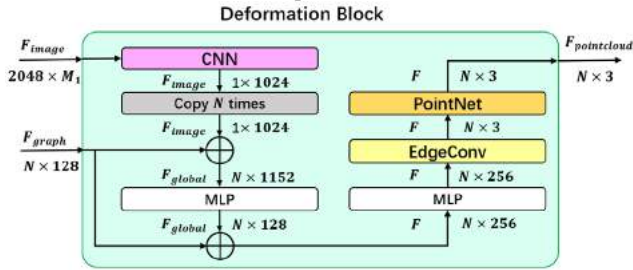


Figure 2: The detailed structure of the Deformation Block.

Several loss functions [6] were used to train our network, including Chamfer distance loss, Edge loss, and Laplacian loss, which were defined as follows.

$$L_{CD} = \sum_p \min_g \|p - g\|_2^2 + \sum_g \min_p \|p - g\|_2^2 \quad (1)$$

where p is the vertex coordinate of the predicted surface mesh, and g is the vertex coordinate of the ground-truth surface mesh.

$$L_{edge} = \sum_p \sum_{k \in N(p)} \|p - k\|_2^2 \quad (2)$$

where $N(p)$ are the neighbor vertices of p .

$$L_{Lap} = \sum_p \|\delta'_p - \delta_p\|_2^2, \delta_p = p - \sum_{k \in N(p)} \frac{k}{\|N(p)\|} \quad (3)$$

where δ_p and δ'_p are the Laplacian coordinates of vertex p before and after deformation.

The overall loss is a weighted sum of all four losses, defined as:

$$L = \lambda_1 L_{CD} + \lambda_2 L_{edge} + \lambda_3 L_{Lap} \quad (4)$$

where $\lambda_1 = 1.0$, $\lambda_2 = 0.01$, $\lambda_3 = 0.1$.

Chamfer distance (CD), Earth Mover's Distance (EMD), PC-to-PC L2 Distance (L2) and PC-to-PC L1 Distance (L1) were used as the evaluation metrics.

We used the Adam optimizer with a learning rate $1e^{-4}$ and a batch size of 2 for training in all experiments conducted. The network was implemented using Python 3.6.0, Pytorch 1.10.0, Dgl 0.7.2, and all experiments were streamlined and executed on an Nvidia Titan RTX graphic card with 24GB of computational memory.

We built a 3D MR dataset with 17 subjects from Peking University People's Hospital. Specifically, the T2 3D sagittal MR data of each subject at rest were used. The spacing of the MR images was 2 mm with a slice thickness of 2 mm. We randomly divided the annotated dataset

into a training set (13 series) and a testing set (4 series). Each training sample contains a source-target pair, where the former is the original 3D MR image and the latter is the corresponding bladder surface mesh. To make the deformation process more reasonable, we first normalized each coordinate value of the real bladder to a range of 0 to 1. Then we moved the geometric center of the original sphere and the geometric center of the normalized real bladder to the origin (0,0,0). To prove the effectiveness of our model, we compared it with two other advanced 3D reconstruction of natural objects, including Pixel2mesh and Pixel2mesh++.

RESULTS

The testing result of the 3D reconstruction with comparison is summarized in Figure 3.

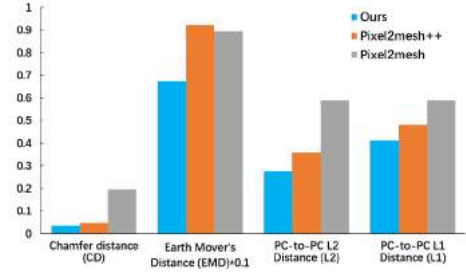


Figure 3: 3D reconstruction performance on the testing set. Smaller metrics better 3D reconstruction results.

In addition, the visualization results of the 3D reconstruction of the bladders of three subjects in the testing set are shown in Figure 4. From the results, our 3D reconstruction results are close to the ground-truth.

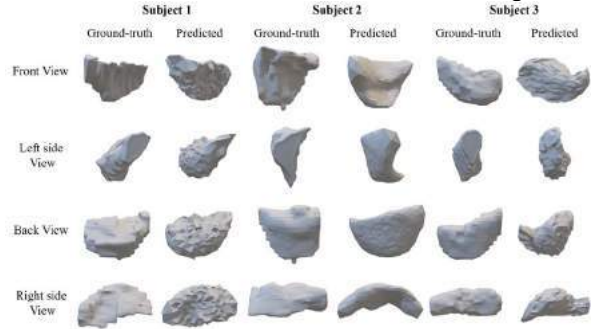


Figure 4: A visual comparison of 3D reconstruction results. Results of different views were compared with the ground truth labeling.

DISCUSSION

This study presents a novel end-to-end deep learning method with the CNN and GCN for fast reconstruction of 3D geometric models of pelvic organs from 3D MRI. Unlike traditional manual methods that are time-consuming and laborious, our method takes only 3 seconds. The experimental results demonstrate that the proposed network has achieved good qualitative and quantitative results in 3D reconstruction of the bladder. In the future, a larger training dataset will be expected to improve the reconstruction process.

ACKNOWLEDGEMENTS

NSFC Grant 31870942, Peking University Clinical Medicine Plus X-Young Scholars Project PKU2020LCXQ017 and PKU2021LCXQ028, PKU-Baidu Fund 2020BD039.

REFERENCES

- [1] Luo et al., *Am J Obstet Gynecol*, 205(4), 2011.
- [2] Luo et al., *J Biomech*, 48(9):1580-1586, 2015.
- [3] Feng et al., *Med Phys*, 47(9):4281-4293, 2020.
- [4] Wang et al., *Acm T Graphic*, 38(5), 2019.
- [5] Charles et al., *CVPR 2017*, 77-81, 2017.
- [6] Chen et al., *Med Image Anal* 2021, 74, 2021.

ENGINEERED COMPOSITE FIBROUS HYDROGELS THAT MIMIC DYNAMIC DEVELOPMENTAL SIGNALS DURING FIBROUS TISSUE DEVELOPMENT

Karen L. Xu (1), Jason A. Burdick (1,2), Robert L. Mauck (1)

(1) Department of Bioengineering, University of Pennsylvania, Philadelphia, PA, USA
(2) Department of Chemical and Biological Engineering, University of Colorado, Boulder, USA

INTRODUCTION

Fibrous tissue (tendon, annulus fibrosus, meniscus) growth and development is exemplified by dramatic transitions from cell rich-disorganized aggregates to ones that are cell-poor but rich in organized extracellular matrix [1]. As such, development of these tissues includes a transition from a state in which information is relayed through cell-to-cell contacts to one governed by cell-to-matrix contacts. Importantly, differential presentation of cell-cell adhesion vs. cell-matrix adhesion cues can regulate cell behavior [2]. Further, forming tissues often use boundaries as mechanical anchorage points against which cell-mediated contraction occurs [3]. Not only are these growth and remodeling events necessary to achieve the final functional form of these fibrous tissues, but these same physical cues can regulate resident cell differentiation and function to drive regional tissue specialization [4]. In a series of recent studies, we queried meniscus development from its point of origin (E15) to postnatal maturity [5,6]. Once the meniscus was identifiable, it consisted of a highly aligned cellular template that spanned from either end of the tibial plateau [6]. During this phase, active cell contraction, mediated by large, organized actin stress fibers, deformed the meniscus cell nuclei. Soon after, nascent extracellular matrix (collagen) was deposited and interwoven between cells. At this stage, the large actin stress fibers began to disappear, and the nuclear deformation relaxed, indicating a transition to force transfer through the ECM rather than through the cell template. As development further progressed, this original cell and ECM templating culminated in an organized ECM separating cells with a differentiated phenotype.

Clearly, there is a dynamic and time-evolving interplay during fibrous tissue development between the cells, their deposited ECM, and forces imposed by other knee structures. How, and to what extent, this crosstalk governs cell function is difficult to study given the complexity of the *in vivo* situation and inability to decouple these cues. To address this, we and others have developed increasingly sophisticated neo-tissue constructs. Most commonly, investigators utilize micropost-based

systems to introduce boundary constraints coupled with cells embedded in collagen or other natural polymers that cells can contract [7]. However, these natural polymers are poorly defined and limit independent exploration of how multiple extracellular inputs, such as mechanics, degradation, and adhesion moiety type, influence cell behavior [8]. To that end, we developed a tunable and dynamic composite fibrous hydrogel system that can undergo both cell-mediated contraction and dynamic phase transitions at defined time points in response to exogenous stimuli.

METHODS

Material Fabrication: Our composite material (**Fig 1**) consists of a continuous phase of acrylated hyaluronic acid (AHA) and a fragmented fiber phase consisting of short RGD-modified methacrylated HA fibers (produced by electrospinning followed by mechanical fragmentation [9]). In this composite material, crosslinking occurs via a Michael

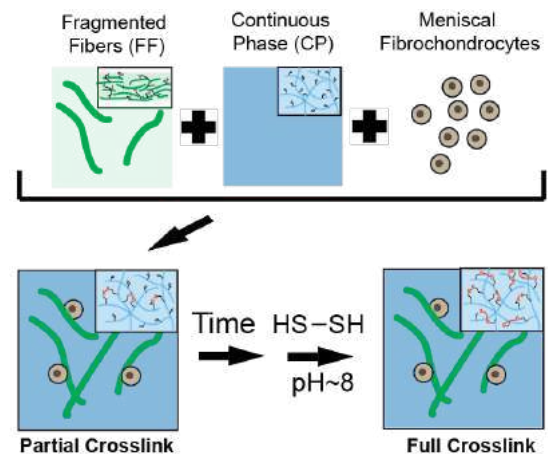


Figure 1: Schematic of material fabrication.

addition reaction with the sequential addition of dithiothreitol (DTT) at a basic pH. **Cell-Mediated Contraction Assays:** Constructs were created by mixing juvenile bovine meniscal fibrochondrocytes with the prepolymer solution, pipetting into circular polydimethylsiloxane (PDMS) molds, and allowing constructs to partially crosslink for 1 hour at pH 8 and 37°C (during which time a specific proportion of the acrylates are consumed, leaving the remaining groups free for subsequent crosslinking steps). To fully crosslink constructs, additional DTT was added at defined time points and allowed to crosslink as above. **Imaging:** Fluorescent fibers and cells were visualized through staining for actin cytoskeleton or CellTracker Red. Viability was assessed via Live/Dead assay. Images were taken of constructs using a brightfield microscope and construct area was quantified using ImageJ. **Statistics:** Contraction studies were repeated 3-5 times for each group and timepoint. Outcomes were compared using one-way ANOVA with Bonferroni posthoc, with significance set at $p < 0.05$.

RESULTS

Initial studies focused on identifying the concentration of the continuous phase (CP) and degree of partial crosslinking required to form a stable gel that is conducive to cell contraction. Partial crosslinking was performed by introducing cells within the prepolymer solution as it began crosslinking. With a 20wt% fragmented fiber (FF) concentration and a 0.7 wt% CP concentration, we observed progressive contraction of 30% over the first day, which increased to 37% by day 3 (Fig 2). Notably, cells transitioned from a rounded to an elongated morphology over this time. Next, to determine the impact of FF concentration, we evaluated contraction over 3 days when FF levels were set at 5, 10, or 20% (with CP held at 0.7 wt%). Results showed that reducing the fiber concentration resulted in a greater extent of contraction (Fig 3A). To determine how cell concentration regulated the rate of contraction, we set the starting cell density at 5, 7, or 10e6 cells/mL. Reducing cell concentration decreased the rate of construct contraction (Fig 3B). Finally, to determine if we could arrest contraction by transitioning the construct from partial to full crosslinking, DTT was added in excess to consume remaining acrylate groups, 2.5 hours after gels were formed (Fig 4). With this full crosslinking, constructs no

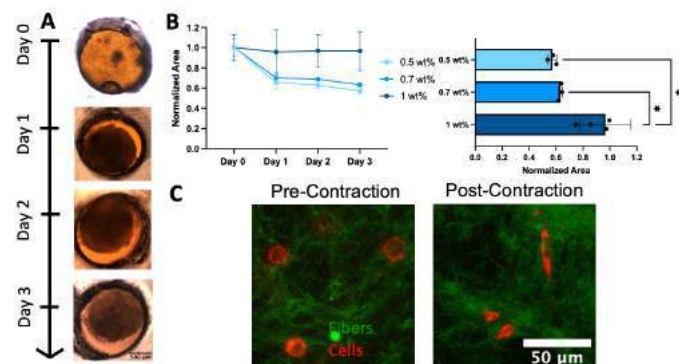


Figure 2: Representative images (A) and quantification of contraction over time (B, left panel) and on day 3 (B, right panel) of construct (0.5, 0.7, and 1wt% CP, 20wt% FF, 10e6 cells/mL). Representative images of cells prior to (C, left panel) and after (C, right panel) contraction. * $p < 0.05$.

longer contracted. Notably, cells within fully crosslinked constructs remained viable throughout all crosslinking steps (Fig 4B).

DISCUSSION

Herein, we describe an engineered composite fibrous hydrogel system in which cell-mediated contraction can be halted in a user-defined manner by dynamic stiffening of the extracellular environment. The partial crosslinking of the acrylate groups in the CP produced a

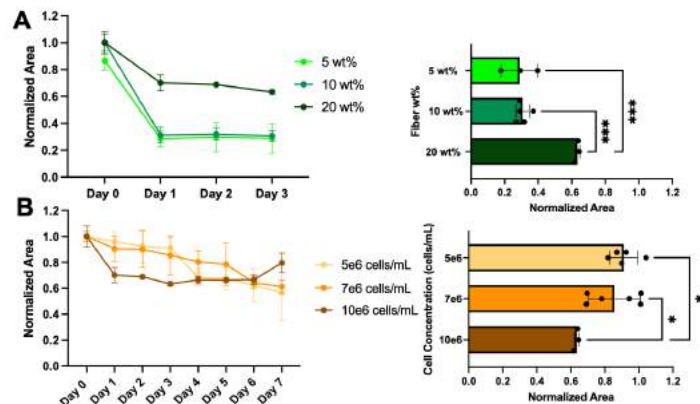


Figure 3: Quantification of contraction of constructs with varying FF wt% (A; 0.7% CP, 5, 10, 20wt% FF, 10e6 cells/mL) and varying cell concentration (B; 0.7% CP, 20wt% FF, 5e6, 7e6, 10e6 cells/mL) over time (left panel) and at day 3 (right panel) * $p < 0.05$, * $p < 0.001$.**

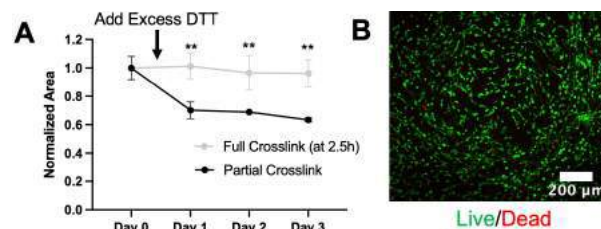


Figure 4: Quantification (A) of construct contraction (0.7 wt% CP, 20wt% FF, 10e6 cells/mL) over time with partial and full crosslinking. (B) Live/Dead imaging of fully crosslinked construct on day 3. ** $p < 0.01$ compared to partial crosslink at same time point.

mesh size that allowed cells to interact with their extracellular environments. Notably, the only adhesive ligands present in the composite were on the FF, which suggests that cells are interacting with and pulling on these fibers to mediate contraction. We also showed that consumption of free acrylate groups could arrest construct contraction, suggesting the opportunity to influence cell contractility by tuning the full crosslinking of the extracellular environment.

Future directions of this work include the introduction of boundary constraints to promote alignment in the forming of neo-meniscus tissues. We will also explore how cell-cell interactions (through introduction of N-cadherin-based moieties) in addition to cell-matrix interactions (RGD moieties) influence cell contraction. Ultimately, these tunable materials will be used to probe molecular signaling and how perturbations to contraction, adhesion, and external physical cues regulate meniscus progenitor cell differentiation. This novel material system will enable exploration of key developmental inputs that guide meniscus formation, providing new insight into regenerative strategies that may be leveraged towards meniscus repair.

ACKNOWLEDGEMENTS

This work was supported by the Center for Engineering Mechanobiology (CMMI 1548571) and the NIH (F30 AG074508, R01 AR056624, and R01 AR075418).

REFERENCES

- [1] Clark et al. *JBJS*, 65(4), 538-547, 1983.
- [2] Cosgrove et al. *Nat. Mater.* 15(12), 1297-1306, 2016.
- [3] Ma et al. *AJP-Cell Physiology*, 323 (6), 1652-1663, 2022.
- [4] Bonnevie et al. *Nat. Biomed Eng.*, 3, 998-1008, 2019.
- [5] Tsinman et al. *ORS Annual Meeting*, 2021.
- [6] Tsinman et al. *FASEB*, 35, 2021.
- [7] Awad et al. *JBM*, 51(2), 233-240, 2000.
- [8] Bell et al. *PNAS*, 76 (3), 1274-8, 1979.
- [9] Davidson et al. *Sci Adv*, 7 (46), 2021

LOCAL NONLINEAR ELASTIC RESPONSE OF EXTRACELLULAR MATRICES

Haiqian Yang (1), Ming Guo (1)

(1) Department of Mechanical Engineering, Massachusetts Institute of Technology, Cambridge, MA, USA

INTRODUCTION

Nonlinear stiffening is ubiquitous in biopolymers [1, 2], including the extracellular matrix (ECM) polymers such as collagen, fibrin and basement membrane [3–5]. In these ECM materials, cells such as fibroblasts and certain types of cancer cells are known to deform and stiffen the matrix [4, 6]. However, the bulk response is the primary focus of existing studies on the nonlinear elasticity of biopolymers [3, 7, 8], while cells embedded in the ECM interact with the matrix locally. For example, a fibroblast in the collagen matrix extends filopodia and pulls on the fibers (Fig. 1A-C), such loading from a cell is localized, and it generates a nonuniform deformation field in the matrix, which is distinct from uniform bulk measurements [9]. How much resistance does a cell feel when pulling on its surroundings, and how does the resistance increase with the force applied?

Here we show experimental results by optical tweezers that the nonlinear response of collagen to a local force deviates from the expectation from the bulk response $k \sim F$, but instead is closer to $k \sim F^{1/2}$, where k is the differential stiffness and F is the force. We find that this weaker power-law relation can be explained by a minimal scaling argument of an effective probe: the observed local nonlinear response is similar to the case of using a larger effective probe (radius R^*) to linearly deform the far-field matrix whose shear modulus is G , and R^* grows as $(\frac{F}{G})^{1/2}$. Surprisingly, this argument suggests $k \sim F^{1/2}$ is a universal relation for local mechanical measurements independent of bulk stiffening behaviors provided that the stiffening is sufficiently strong. Our results highlight the significant differences between nonlinear responses upon local and bulk force applications, relevant to cell-ECM and cell-cell interactions in multicellular living systems.

METHODS

Optical Tweezers Measurements. Microparticles (2 μm , C37278, ThermoFisher, and 4.5 μm carboxylate microspheres, Polyscience) are embedded in the gel prior to polymerization. The laser beam is moved at a constant velocity of 1 $\mu\text{m s}^{-1}$. The relative distance between the laser and the bead is recorded.

Finite Element Simulations. An axial symmetric geometry is used, where a rigid spherical domain of radius R_0 is embedded in a cylindrical matrix of radius $R = 250R_0$ and height $H = 2R$. The lateral surface

of the matrix is fixed and the top and bottom surfaces are traction-free. A series of point forces are applied at the center of the rigid spherical domain and the displacement is recorded. The matrix is modeled as an incompressible material with a free energy function $W_{exp} = \frac{G}{2b} \exp(b(I_1 - 3))$, where G is the linear shear modulus, b is a stiffening parameter, and I_1 is the first invariant of the deviatoric Cauchy-Green deformation tensor. Calculations are also performed with variations of this free energy $W_2 = \frac{G}{2}(I_1 - 3) + \frac{Gb}{4}(I_1 - 3)^2$, and $W_4 = \frac{G}{2}(I_1 - 3) + \frac{Gb}{8}(I_1 - 3)^4$.

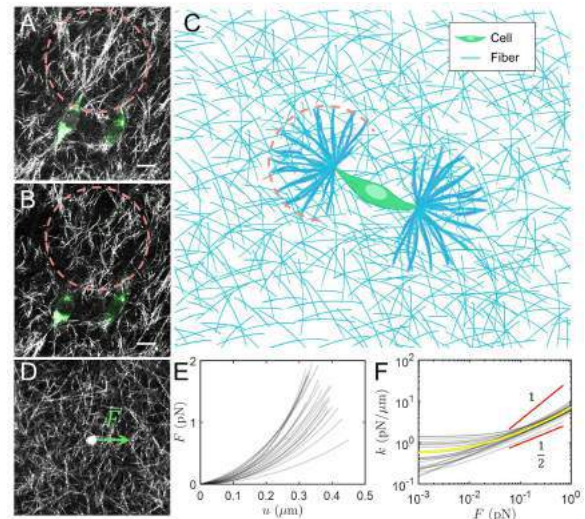


Figure 1: Local nonlinear elastic response. (A) A mouse embryonic fibroblast (green, cytoplasm) within collagen networks (grey). (B) The same cell with one filopodium released. The dashed circle marks the highly deformed region. (scale bar, 10 μm .) (C) The filopodium applies a point force to the matrix and creates a highly deformed zone. (D) A particle (2 μm in diameter) embedded in a 4 mg mL^{-1} collagen gel. A laser trap applies force F . (E) Force F is a nonlinear function of displacement u . (F) Differential stiffness k deviates from the bulk scaling law ($n=23$). The yellow line is the average. SB³C2023-377

RESULTS

Local stiffening in collagen deviates from bulk stiffening. A bead is displaced a distance u from its equilibrium position by an optical force F (Fig. 1D), and the differential stiffness k can be calculated by $k = \frac{dF}{du}$. When we perform this measurement in 4 mg mL⁻¹ collagen gels with 2 μ m-in-diameter beads, we find that the material indeed stiffens with increasing force (Fig. 1E); the differential stiffness k shows a linear regime followed by a nonlinear regime (Fig. 1F). Interestingly, the logarithmic slope in the nonlinear regime clearly deviates from the bulk slope of 1 since the initiation of nonlinear stiffening and ranging 2 orders of magnitude of the applied force ($10^{-2} \sim 1$ pN). A closer examination reveals that the logarithmic slope is about 1/2, suggesting $k \sim F^{1/2}$ (Fig. 1F). To further confirm this behavior, we perform this experiment in collagen gels of different concentrations (e.g. 1.6, 2.4 and 3.2 mg mL⁻¹) with a different particle size (4.5 μ m in diameter); these experiments all show logarithmic slopes close to 1/2 in the nonlinear regime (Fig. 2). Moreover, we perform measurements on fibrin gels. Remarkably, the local nonlinear response of fibrin gels is also close to $k \sim F^{1/2}$ (Fig. 2), regardless of the different bulk stiffening response of collagen and fibrin gels [3, 10]. These results demonstrate the generality of this weak power-law relation $k \sim F^{1/2}$ in local micromechanics measurements.

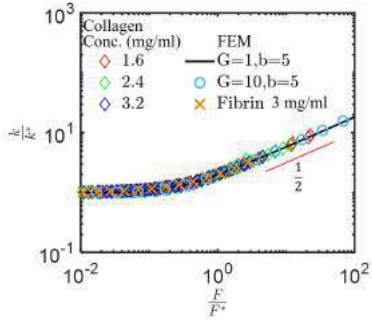


Figure 2: All the experimental and theoretical curves can be collapsed to a single master curve by nondimensionalizing stiffness and force. The master curve shows $k \sim F^{1/2}$ in the nonlinear regime. The characteristic force F^* is defined as the force at which the differential stiffness is twice the linear stiffness.

Increase of effective probe size. To understand this 1/2 power-law relation, we first follow a dimensional analysis of the nonlinear elastic boundary value problem defined in the method section. Considering the force balance, the point force to perturb the particle is balanced by the integral of traction fields on an arbitrary closed surface containing this point force, $F = - \int \sigma_{ij} n_j e_i^1 dA$, where σ_{ij} are the stress components, n_j are components of the surface normal vector and e_i^1 are components of the unit vector along the point force. In the matrix, strain and stress fields decay away from the probe. Although F can be comparably large that nonlinearly deforms the vicinity of the probe, because the strain and stress fields approach 0 at infinity, there must be a closed surface above which the material only undergoes moderate strain, and thus behaves almost linearly. A stress scale on this surface is the linear shear modulus G . Denoting the length scale of this closed surface as R^* , the force balance equation yields $F \sim GR^{*2}$, so R^* scales as $(\frac{F}{G})^{1/2}$. Because the material within this range R^* is more severely deformed and much stiffer than the outside as a result of nonlinear elastic stiffening, effectively we are using a larger rigid particle of length scale R^* to probe the linear matrix surrounding this rigid particle. This yields $k \sim GR^*$ similar to the Stokes-Einstein law. Consequently, the stiffness $k \sim R^* \sim F^{1/2}$ (Fig. 3D). As we examine the profile of displacement in the direction of the applied force in simulation, the direct adjacency of the particle moves with it almost rigidly; indeed, there is a critical length R^* above which the displacement field starts to rapidly decay (Fig. 3B). By perturbing the particle at different forces, we find $R^* \sim F^{1/2}$ (Fig. 3C).

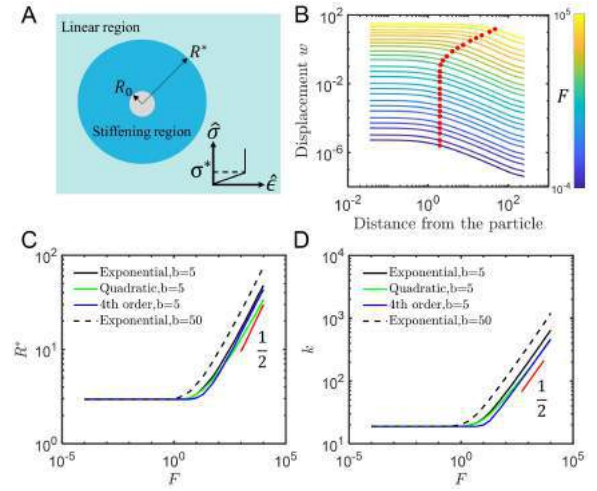


Figure 3: The local stiffening response can be attributed to the growth of an effective probe size R^* . (A) The adjacency of the particle is stiffened over the length scale R^* such that the point force probes the far-field linear matrix with an effective larger size R^* . (Inset) The extreme case is an 'elastic-rigid' simplification. (B) R^* is estimated as the distance when the axial displacement decays to half of that of the particle. (C) Effective probe size R^* grows as $F^{1/2}$. (D) Stiffness k grows as $F^{1/2}$.

DISCUSSION

We report the stiffening relation in bulk no longer holds for localized force applications. Instead, we find the relationship is closer to $k \sim F^{1/2}$ (Fig. 1F). We show that this local response ($k \sim F^{1/2}$) can be explained by introducing an effective probe (radius R^*) that grows with increasing forces (Fig. 3). We, therefore, propose a hypothesis that local forces such as those applied by cells feel the nonlinear elasticity through an effective probe that nonlinearly grows with the applied force. These results may provide insights into understanding cell-cell interactions through ECM, and mechanobiology of complex living systems such as tissues and organs.

ACKNOWLEDGEMENTS

We would like to acknowledge the support from the NIH (1R01GM140108), the MathWorks, and the Jephtha H. and Emily V. Wade Award at the Massachusetts Institute of Technology. M.G. acknowledges the Sloan Research Fellowship.

REFERENCES

- [1] Storm C et al. *Nature* 435.7039 (2005).
- [2] Xu X et al. *Physical Review E* 92.3 (2015).
- [3] Licup AJ et al. *Proceedings of the National Academy of Sciences* 112.31 (2015).
- [4] Han YL et al. *Proceedings of the National Academy of Sciences* 115.16 (2018).
- [5] Li H et al. *Proceedings of the National Academy of Sciences* 118.11 (2021).
- [6] Hall MS et al. *Proceedings of the National Academy of Sciences* 113.49 (2016).
- [7] MacKintosh F et al. *Physical review letters* 75.24 (1995).
- [8] Broedersz CP et al. *Reviews of Modern Physics* 86.3 (2014).
- [9] Burkel B et al. *Soft matter* 13.34 (2017).
- [10] Piechocka IK et al. *Biophysical journal* 98.10 (2010).

BRINGING DISCUSSIONS OF ACCESSIBILITY TO ENGINEERING CLASSROOMS

N. Rich (1), S. Johnson (1), C. Bellini (2)

(1) Tatum Robotics, Hudson, MA, USA
(2) Department of Bioengineering, Northeastern University, Boston, MA, USA

INTRODUCTION

Discussing accessibility and assistive design in engineering classrooms, where students learn product design principles and implementation, keeps disabled groups at the forefront of the students' attention when they develop their ideas.

There exist misconceptions about designing for disabilities among the able-bodied population; namely, that inclusive design is something that able-bodied groups do not benefit from, and therefore an emphasis on inclusive design is unprofitable and only serves the needs of the few.

To alleviate this issue, we aimed to introduce students to inclusive design principles, explain the importance of including disabled groups themselves within research (rather than using disability simulations to envision product needs), and prompt students to design product ideas that consider the objectives of inclusive design.

METHODS

Targeting upper-level undergraduate and graduate bioengineering students, we created a lesson plan that highlighted the essentials of inclusive design, adaptive technology, and assistive technology.

Warm-up. Incorporating the fundamentals of inclusive design (such as text-to-speech tools, large print, easy navigation, the one-fits-one model, etc.) [1] showed students how web-based media often adds features that are meant for accessibility.

Disability models. We discussed the social model of disability (as opposed to the medical model of disability), which defines the limiting factor in a disabled person's life as the obstacles society presents rather than the disability itself. Where the medical model aims to "fix" a person's disability—a task that may not even be possible in most cases—the social model aims to eliminate the societal obstacles that limit the disabled community's access [2]. For example, a person in a wheelchair may struggle not because of the fact they are in a wheelchair at all, but because buildings are inaccessible. The social model focuses on what we can change about our shared environment, rather than what

an individual should go through to assimilate with the able-bodied world at their own personal cost.

Assistive technology (AT). After, we showed examples of positive AT, such as the white cane that blind people use for navigation, or eye-gaze tracking software that people who are nonverbal or have a physical disability that prevents them from accessing other technology. We discussed the qualities of poorly designed AT that did not consider the needs of real people with disabilities. We specifically cited companies that used disability simulations, wherein someone without the target disability simply fakes the disability to test the product (i.e. covering their eyes to simulate blindness) rather than asking a disabled person for their feedback. We emphasized that able-bodied people are unable to make informed guesses about the lived experiences of disabled people; instead, one must ask target users what kind of technology would suit them without making assumptions.

Guest lecturers. First, Tatum Robotics speakers explained their model of development in the disability space. Tatum Robotics is developing technology to make digital media accessible to the isolated DeafBlind community. Tatum Robotics engages with the DeafBlind community at social events and invites DeafBlind individuals to regularly offer their feedback on their devices. All features and designs are informed by the feedback, needs, and desires of the target user.

Secondly, a Deaf guest speaker named Spencer Montan shared his experience and fielded questions from curious students who had never considered the daily problems a Deaf person might encounter. Montan is the Associate Director of the Center on Access Technology at the Rochester Institute of Technology, where he works with students to create AT projects alongside his own innovations.

Debriefing. Once the lecture was over, we had students, in groups, compile lists of problems that they face on a regular basis that some type of innovation could potentially solve. After, groups traded problem statements with one another and picked a problem another group had written to design an innovation that could solve it. This activity was

followed by a class discussion on their proposed solutions, design strategy, and where the inclusive design strategies were utilized within their process.

Students completed a survey before and after the lecture. The survey evaluated how confidently students understood inclusive design, accessibility, and disabled communities. They answered questions on a scale of 1 – 5. Using the de-identified data, we calculated the percent increase in confidence levels for each question, as depicted in Table 1.

RESULTS

The student groups each gave brief presentations to share their final designs and ideation processes. Each idea began with the purpose of solving a fellow able-bodied classmate's frequent struggle, but was then expanded to encompass the needs of disabled communities as well. Discussion with the class about both tools recalled questions about the proposed user interface. All tools could be made further accessible by designing voice command capabilities or large buttons.

Group 1. The first group's idea was a wet pet food dispenser to solve the student problem statement that they struggle to remember to leave food out for their cat, who only eats wet food. The students drafted a product that can, on a timed basis, open packs of wet food automatically and dispense the contents into a dish for the pet. Students explained that while automating this process would be helpful for anyone, the product is especially helpful to people with certain disabilities. Anyone with limited mobility or finger dexterity would benefit from the device. Anyone struggling with memory would also benefit, since one would no longer need to remember exactly when to feed their pet to be a responsible pet owner.

Group 2. The second group addressed the common struggle with trying to open jars. The group's innovation was modeled after existing tools that make opening jars and bottles easier, except this tool had a more enclosed design, meant to keep the tool as safe as possible for those with limited vision as many of the existing tools have exposed parts. The design is meant to best accommodate anyone with arthritis, limited vision, missing limbs, or a lack of finger dexterity. Additionally, able-bodied people would benefit from a tool that could open tight jars independently.

Group 3. The third group aimed to solve the problem of forgetting to call people and return phone calls. Their solution was a service that would make the call for you—if one scheduled a call, they would receive a call at the scheduled time which would then connect them to the receiver upon your answering the call. This service intended to help forgetful students and employees was also thought about through the lens of helping those with cognitive disabilities. Additionally, not having to find the contact information of those called would help those who struggle with finding contacts in their phones due to visual impairments.

DISCUSSION

Both the results of the innovation activity and the increase in confident survey responses attest to the effectiveness of the lecture. Students learned about important standards and exceptional AT used to ensure accessibility for disabled communities. Additionally, by teaching students about how inclusive design improves products' overall usability as well as outcomes for target users and disabled users alike, students demonstrated their understanding through their projects and class discussions highlighting universal design.

In the survey, the question that resulted in the highest percentage increase was about the guidelines for accessible design and development. The 161.25% increase in confident answers for this question after the lecture series was over indicates that, while students

Table 1: Student surveys completed before and after the series, all questions were formatted as “On a scale from 1 to 5, how confidently can you:” with the subsequent question.

Survey Question	Student Evaluation Percent Increase
Define “accessibility” as the term relates to technology and media	28.78%
Give an example of inclusive/universal design	38.21%
Give an example of how accessible technology is used by people with disabilities	38.21%
Give an example of a technological barrier somebody with a disability might face	25.35%
Define the purpose of the Americans with Disabilities Act	98.00%
Explain guidelines for accessible design and development	161.25%
Consider accessibility and universal design during the design process	38.21%
How familiar are you with the accessibility features built into devices?	60.77%

before were unfamiliar with accessibility guidelines in design and development, the lecture made them far more aware. Similarly, the survey results showed a 98% increase in confident student responses to a question about the purpose of the Americans with Disabilities Act (ADA), a landmark moment in American history for disabled individuals. The ADA itself addresses many key points of accessibility design, making it a useful document for engineers to be familiar with.

One strength of this study was the inclusion of a guest speaker from a disability group who is also an expert in assistive design. Including Spencer Montan gave the students exposure to a disabled entrepreneur as well as an environment where spoken language interacts with signed language. Many students had never encountered a Deaf individual before or had never directly interacted with someone through an interpreter. When students asked questions, they were forced to be cognizant of the requirements that accessibility demanded of them, and each student responded positively to the experience.

A limiting factor of the study was time. Ideally, we would have had more time to lecture and would have given more time to students to research, draft, and design their ideas. Additionally, while many students had deafness on the mind when brainstorming ideas because of the guest lecturer's talk, involving experts from other disability groups could only have made the study stronger by exposing students to the experiences of other disability groups.

In conclusion, our study shows that, when given proper attention and nuance, education about disability groups and assistive design improves engineering classrooms by disambiguating community needs, providing steps towards achieving inclusion, and introducing students to ways of life they ordinarily would not be challenged with considering.

ACKNOWLEDGEMENTS

The team is grateful for the Teach Access grant program which provided the funding to Northeastern University for this series, and Spencer Montan and the NTID Center on Access Technology.

REFERENCES

- [1] Clarkson, P, *Inclusive Design: Design for the Whole Population*, 2013
- [2] Shakespeare, T, *The Disability Studies Reader*, 195-203, 2016

THE EFFECTS OF CEREBROSPINAL FLUID AND HYPERELASTIC MODEL ON ANEURYSM WALL VIBRATION USING HIGH-FIDELITY FLUID-STRUCTURE INTERACTION SIMULATIONS

Kei Yamamoto (1), David Bruneau (2), David Steinman (2), Kristian Valen-Sendstad (1)

(1) Department of Computational Physiology, Simula Research Laboratory, Oslo, Norway.

(2) Department of Mechanical and Industrial Engineering, University of Toronto, Ontario, Canada

INTRODUCTION

A cerebral aneurysm is a pathological dilation of an artery in the brain and its rupture is known to be a life-threatening condition. It is estimated that 3-5% of the population harbor aneurysms [1]. Throughout years of biomechanical research, computational fluid dynamics has been used to retrospectively correlate flows and shear stress with rupture status in search of a prospective clinical tool. However, the mechanisms of aneurysm growth and rupture are not fully understood.

Aneurysms produce sounds known as bruits that originate from either transitional blood flow or flow-induced vibration of the aneurysm wall [2]. To use these sounds as a non-invasive way of detecting aneurysms, clinicians have conducted acoustic measurements by placing a transducer on the eyelid [3]. These measurements have revealed a narrow-banded peak in the frequency spectrum, which is indicative of high-frequency vibrations [3]. From a mechanobiological perspective, vibrations have also been proposed as a potential cause of various disorders, such as poststenotic dilatation [4]. Despite this, the vibration of the aneurysm wall is not well studied and only a small number of recent studies have explored this phenomenon.

A recent study from Souche and Valen-Sendstad [5] showed that an aneurysm wall could vibrate at ~ 120 Hz in a high-fidelity fluid-structure interaction (FSI) simulation, which was previously reported *in-vitro* study [6]. This study was, to our best knowledge, the first one to numerically demonstrate the existence of wall vibration in a cerebral aneurysm, but the model included several limitations. In the present study, we focused on the two limitations of that previous study: the lack of response from the cerebrospinal fluid (CSF) surrounding aneurysms, and the lack of non-linearity in the material model. The results of simulations with different models are compared to examine the effects of these two model improvements on the frequency and amplitude of the wall vibration.

METHODS

We considered a single patient-specific geometry of a middle cerebral artery aneurysm, which was previously shown to exhibit weakly unstable flow with a prominent fluid frequency of 100-150 Hz [7] and vibrations in the range of 100-500 Hz [8]. FSI simulations were carried out using a high-

fidelity finite-element solver, turtleFSI [9]. The computational mesh was constructed by the Vascular Modelling Toolkit [10] with roughly 110,000 and 40,000 elements in the fluid and structure domains, respectively. Since the movement of an artery in the brain is restricted by its surroundings, we selected the deformable region to be in the vicinity of the aneurysm sac as shown in Figure 1(a). Prior to performing FSI simulations, a zero-pressure geometry was approximated by inversely applying the deformation obtained in a separate simulation. Inflow was prescribed as Womersley flow using a waveform shown in Figure 1(b) and the pulsatile cerebral perfusion pressure was applied at the fluid-structure interface in the range of 70-110 mmHg.

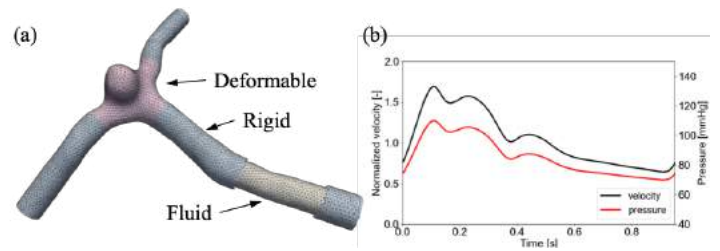


Figure 1: (a) is a computational domain where the part of the structure domain is removed to show the fluid mesh. Only the light red part is deformable. (b) represents waveform of the fluid velocity used at the inlet and the pressure used at the fluid-structure interface.

To account for the damping effects of the CSF on the deformation of the aneurysm wall, we specified the Robin boundary condition to the outer wall of the deformable region with the following formulation [11]:

$$\sigma_s \cdot n_s = -k_s d_s - c_s u_s, \text{ on } \Gamma^s. \quad (1)$$

where σ_s is the stress tensor of the solid, n_s is the outward normal vector at the solid surface, k_s and c_s are the elastic and viscoelastic response of the CSF, d_s and u_s are the deformation and the velocity of the solid, and

Γ^s represents the surface of the solid region. To determine the value for the coefficient k_s , c_s , we conducted a simple numerical experiment where a cylinder was submerged into the fluid with properties of CSF and forced to oscillate by inducing a body force in a very short time period. Based on the result of this numerical experiment and the assumption that the viscosity of CSF has dominant effect to the motion of aneurysm wall, we chose $k_s = 0$ and $c_s = 100 \text{ N} \cdot \text{s}/\text{m}^3$.

For the material model, we used the three-parameter Mooney-Rivlin (MR) model with the following strain energy density function [12]:

$$W = C_{10} (\bar{I}_1 - 3) + (\bar{I}_2 - 3) (C_{01} + C_{11}(\bar{I}_1 - 3)) + \frac{1}{D_1} (J - 1)^2. \quad (2)$$

where three parameters, C_{10} , C_{01} , C_{11} , are calibrated to match the experimental data from Robertson et al. [13]. Compared to the previously employed St. Venant-Kirchhoff (SVK) model, which behaves almost linearly, the MR model has higher non-linearity in its strain-stress relationship, which is more physiologically accurate.

RESULTS

To present a global overview of the deformation of the aneurysm wall, sac-averaged spectrograms shown in Figure 2 were generated following previously published methodology [14]. Here, the same threshold of -42 dB for the color (i.e., power) intensity was applied and the time frame was taken from the second cardiac cycle.

Focusing first on the effects of modelling CSF, a comparison of results with and without damping reveals a noticeable difference in amplitude of vibration. In the case of no damping, frequency bands near 300 Hz persisted throughout the cardiac cycle, but were quickly dampened after systole in the model that included CSF. It is worth noting that these narrow-bands were not completely eliminated with damping; they just have lower power and thus do not stand out as prominently on the spectrograms using these particular dB threshold.

Shifting focus to the effects of hyperelastic constitutive law, the SVK model had relatively higher frequencies than the MR model, notably in the narrow-banded spectrum $\sim 350 \text{ Hz}$ vs $\sim 300 \text{ Hz}$, respectively. Additionally, the amplitude of the vibration increased slightly from the SVK to MR model.

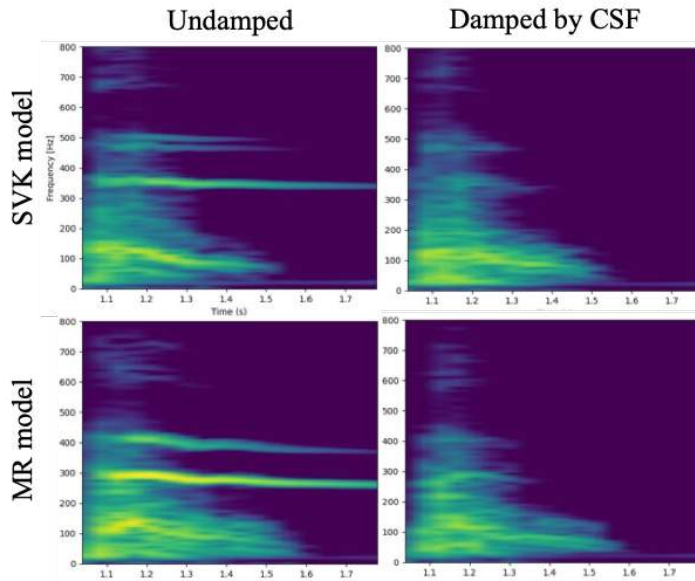


Figure 2: Spectrograms of wall displacements for all the models. The x-axis indicates the time while the y-axis shows the frequency, and the intensity of the color represents the amplitude of the frequency component.

DISCUSSION

To the best of our knowledge, this simulation is the first FSI study to investigate the impact of CSF on the vibration of a cerebral aneurysm. A

key finding was that the inclusion of damping from CSF in the model resulted in a reduction of the post-systolic narrow-band “ringing” that has been previously reported [8]. The narrow-bands were still present but with a decreased intensity, which is in line with clinical observations [2]. It has been observed that transitional flow is responsible for driving wall vibrations after peak systole and during early deceleration. However, the aneurysm sac continues to vibrate even after the flow has become laminar, likely as a result of the sac’s inertia. During the post-systolic phase, the flow instability has ended and the vibrations become free vibrations, not driven by any external forces. Therefore, it is likely that the effect of damping is more significant in the diastolic phase than the systolic phase. This stabilizing effect of CSF was previously shown against perturbations but with a simplified geometry [15]. Since the prominent bands remained in a similar regime with and without damping, it is suggested that the damping force affects the amplitude more than the frequency.

The utilization of a non-linear hyperelastic material model resulted in variations in the amplitude and frequency of the wall vibrations during the cardiac cycle. The amplitude increased and the frequency decreased, indicating that the MR model had a lower effective stiffness compared to the SVK model. Despite these differences, both models predicted similar patterns of prominent vibrations persisting into diastole, indicating that the overall biomechanical impact of the vibrations may be consistent.

In summary, we found that both damping and non-linear hyperelastic model can affect the vibration of the aneurysm wall. However, the locations of vibrations were consistent across different wall/damping models, which suggests that the biomechanical implications of the vibrations may be similar despite differences in their characteristics. The present study, however, only considered one specific geometry and value for the damping coefficient. Therefore, it is not clear how vibrations would be affected in other cases. As a next step, we will apply these improved models to a highly-unstable-flow aneurysm case and conduct a sensitivity analysis of the parameter. One limitation of the present study is that the Robin boundary condition may not fully represent the characteristics of the surrounding CSF, which also acts as an additional mass on the outside of the aneurysm. Another limitation is the uniform wall thickness, as the wall thickness is known to be heterogeneous. Nevertheless, the present work is an important step towards establishing a reliable and robust model of aneurysm vibrations.

ACKNOWLEDGEMENTS

This project is supported by the EU Horizon 2020 SimCardioTest project (101016496) and the Natural Sciences & Engineering Council of Canada Sciences (RGPIN-2018-04649). D.A.B. acknowledges the support of an NSERC Canada Graduate Scholarship. Simulations were performed on resources provided by Sigma2 - the National Infrastructure for High Performance Computing and Data Storage in Norway.

REFERENCES

- [1] Schievink WJ. *N. Engl. J. Med.* 336.1 (1997).
- [2] Aaslid R et al. *J. Neurosurg.* 60.1 (1984).
- [3] Kurokawa Y et al. *Stroke* 25.2 (1994).
- [4] Roach MR. *Am. J. Card.* 12.6 (1963).
- [5] Souche A et al. *J. Biomech.* 145 (2022).
- [6] Balasso A et al. *Biomed. Tech.* 64.3 (2019).
- [7] Khan MO et al. *Am. J. Neuroradiol.* 36.7 (2015).
- [8] Bruneau DA et al. *Biomech. Model. Mechanobiol.* (in press).
- [9] Bergersen A et al. *J. Open Source Softw.* 5.50 (2020).
- [10] Piccinelli M et al. *IEEE Trans. Med. Imaging* 28.8 (2009).
- [11] Moireau P et al. *Biomech. Model. Mechanobiol.* 11.1-2 (2012).
- [12] Rivlin RS. *Proc. R. Soc. London. Ser. A. Math. Phys. Sci.* 243.865 (1951).
- [13] Robertson AM et al. *Ann. Biomed. Eng.* 43.7 (2015).
- [14] Natarajan T et al. *J. Biomech.* 110 (2020).
- [15] Shah A et al. *J. Biomech.* 110 (2020).

A MICROFLUIDIC PLATFORM TO INVESTIGATE TRANSPORT PHENOMENA IN CHEMOKINE GRADIENT ESTABLISHMENT

J. Frattolin (1), D.J. Watson (1), W.V. Bonneuil (1), F. Fasanella Masci (2), M. Russell (3),
B.S. Brook (3), R.J.B. Nibbs (2), J.E. Moore Jr (1)

(1) Department of Bioengineering, Imperial College London, London, United Kingdom
(2) Institute of Infection, Immunity & Inflammation, University of Glasgow, Glasgow, United Kingdom
(3) School of Mathematical Sciences, University of Nottingham, Nottingham, United Kingdom

INTRODUCTION

The innate immune response is facilitated by a range of different antigen-presenting cells, such as dendritic cells, that undergo surveillance of tissues for antigen. When a dendritic cell (DC) encounters antigen within peripheral tissues, its migration to the lymph node is mediated by gradients of chemokines, including CCL21, which is secreted by lymphatic endothelial cells. A fundamental understanding of how these gradients are formed and regulated has yet to be realized. They depend on complex physical and biological interactions, including diffusion, advection, scavenging, as well as extracellular matrix (ECM) and cell binding, among others.

To gain critical insight into chemokine gradient establishment, a microfluidic device was fabricated that allows for the recreation of specific sets of *in vivo* conditions with fine control in a reproducible manner. DC migration can then be analysed in response to known, controllable chemokine gradients, which cannot be achieved *in vivo*.

METHODS

Chip design and fabrication: A microfluidic chip was designed that facilitates the individual assessment of the effects of diffusion, advection, ECM binding and unbinding on chemokine gradients. The chip has a three-dimensional hydrogel region between two fluid channels (Figure 1), with four inlets and a common fluid outlet. Trapezoidal posts keep the hydrogels in place whilst allowing fluid, macromolecules, and cells into and out of the hydrogel. To generate controllable advection across the hydrogel, screw-actuated membrane valves have been placed between the hydrogel region and the fluid outlet [1]. Depending on the configuration of the screw deflections, a range of both positive and negative Peclet numbers can be generated.

The chip implements a “sandwich” hydrogel region, with two narrow outer hydrogels that envelop a central hydrogel. These outer hydrogel channels, made of 5 mg/ml Collagen I hydrogels, provide structure support to the central 1.4 mg/ml Collagen I hydrogel. This

facilitates collagen fiber spacing of 20-30 μm in the central hydrogel region, which we have previously determined to be critical to enable physiological DC migration.

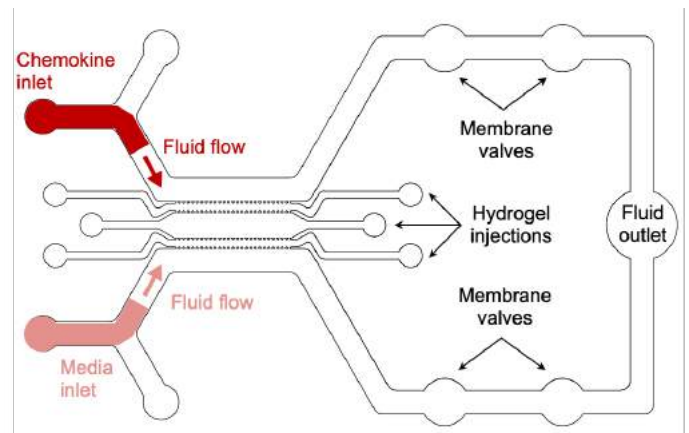


Figure 1: Schematic of the microfluidic chip.

The microfluidic chips were cast with polydimethylsiloxane (PDMS) on a silicon wafer, and then subsequently cured at 80°C. Devices cut and bonded to glass slides using a plasma oxygen generator and baked overnight at 80°C to restore hydrophobicity.

Cell culture: The inguinal and mesenteric lymph nodes were dissected from wild type mice and digested using 0.2 mg/ml Collagenase P, 0.8 mg/ml Dispase and 0.1 mg/ml DNase I. DCs were then isolated from the digested fraction by magnetic cell sorting using the MojoSort Dendritic Cell Isolation Kit (BioLegend, San Diego, CA,

USA) and matured overnight in culture with 200 ng/ml of Escherichia coli LPS.

Live cell imaging: DCs were encapsulated in a 1.4 mg/ml Collagen I hydrogel and injected into the central hydrogel region, after injection and polymerization of the outer collagen hydrogel channels. The chip was transferred to a confocal microscope (Leica Microsystems Ltd, United Kingdom) with a custom environmental chamber for live cell imaging. Syringe pumps were used to deliver 100nM of AF647-conjugated CCL21 at 3 μ l/min. Z-stacks, 60 μ m in height, were acquired continuously every 4-5 s for 80 minutes. After experiment completion, cells were fixed *in situ* with 4% PFA and stained with MHCII, CD11c, and CD86 fluorescent antibodies. This allowed for post-hoc identification and tracking of immature and mature dendritic cells.

RESULTS

A gradient of CCL21 was established across the hydrogel region (Figure 2(a)). A rapid decay in CCL21 concentration was observed across the outer hydrogel region, decreasing from its source concentration of 100 nM to approximately 30 nM. This is owing to the reduced diffusivity of the 5 mg/ml Collagen I hydrogel. A refractive effect at the fluid-gel interface was observed and accounts for the increase in CCL21 concentration at the boundary. In the central hydrogel region, where DCs are encapsulated, a physiological concentration of CCL21 ranging from 30 nM to 5 nM was established [2].

DCs migrated in the direction the chemokine gradient (Figure 2(b)), from left to right. Analysis of the cell tracks indicate a preferential motion of the DCs along collagen fibers, referred to as contact guiding. This creates a persistence at a length scale equal to the size of the collagen fibers. The collagen fibers have a preferential vertical orientation due to the direction of the hydrogel injection, which results in DC migration in both x and y, rather than purely in the x-direction of the chemokine gradient. After experiment completion, cells were fixed and stained *in situ*, and a high-resolution z stack was taken to identify cells' phenotype (Figure 2(c)). Most cells positively stained for CD86, MHCII, and CD11c, indicative of a mature DC phenotype.

DISCUSSION

A novel microfluidic chip was developed that investigates the effects of transport phenomena on chemokine gradient formation, maintenance, and modification, including diffusion, advection, and binding. Work is currently ongoing to quantify chemokine binding to ECM substructures, including glycosaminoglycans, in the developed chip using a novel application of FLIM-FRET. This method can capture the transient binding and unbinding kinetics, which has not been previously realized.

The microfluidic platform described herein will enable an improved understanding of critical immunological processes that aid in protection from infection and drive pathology in a variety of diseases. The resulting quantitative knowledge base can facilitate the development of immunoengineered therapies involving chemokine gradient manipulation.

ACKNOWLEDGEMENTS

The authors acknowledge the support of the Wellcome Trust Collaborative Award 206284/Z/17/Z and the British Heart Foundation Non-Clinical PhD Studentship FS/17/41/32976, which funded this work.

REFERENCES

- [1] Bonneuil, W.V. et al. *AIP Adv.* 12:025121, 2022.
- [2] Luther, S.A. et al. *J. Immunol.* 169:424-33, 2002.

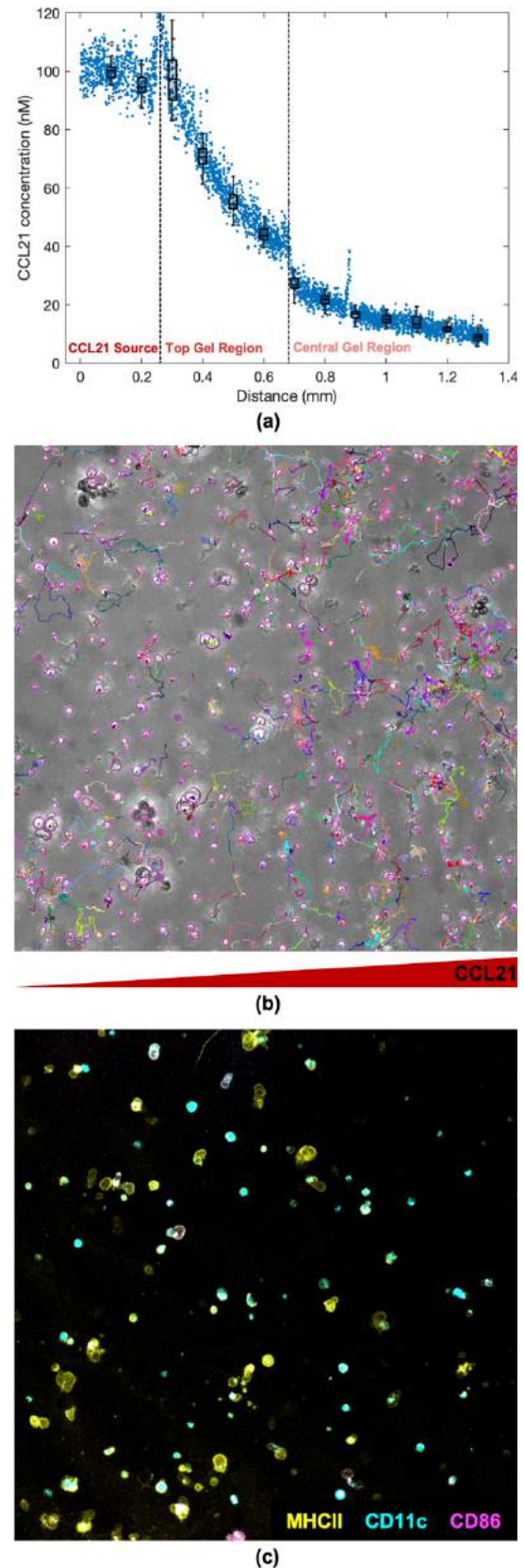


Figure 2: (a) CCL21 concentration across the top half of the chip; (b) DC cell tracks; (c) in-situ stained DCs.

REGENERATIVE REHABILITATION OF MUSCLE DEFECT UNDER MECHANICAL STIMULATION: AN ORGAN CULTURE STUDY

D. Jacho (1), E. Yildirim-Ayan (1) *

(1) Department of Bioengineering, University of Toledo, Toledo, OH, USA

* Corresponding Author: eda.yildirimayan@utoledo.edu

INTRODUCTION

Muscle damage and muscle strain caused by high-force lengthening contractions are among the most common muscle ailments associated with \$50 billion in health care costs annually in the US ^{1,2}. Recovery from a muscle injury or muscle strain includes a series of overlapping processes starting with inflammation and regeneration and subsequently remodeling¹. While physical therapy or mechanotherapy is the first line of non-invasive treatment method for muscle repair³, it is still relatively unclear how mechanical strain applied during mechanotherapy affects the muscle as an organ and cellular responses exposed to the loading. Our preliminary 3D in vitro data showed that mechanical loading exerted on cell-seeded scaffolds can initiate autocrine or paracrine tissue healing via mechanical strain amplitude-dependent manner³. In particular, 12% mechanical strain at 0.1Hz frequency on fibroblast residing within 3D tissue promoted the fibroblast-to-myofibroblast (FMT) differentiation with upregulation of α SMA and increased stress fiber formation³. Further investigation needs to be conducted to understand how supra-mechanical loading, such as 12% mechanical strain, affects the muscle tissue and cellular response using a physiologically relevant platform. Organ culturing can be a superior alternative to the 3D in vitro culturing platform because it maintains the original structural relationship between cells and their interactions. This setup also allows researchers to study the long-term effects of external stimuli.

The structural and molecular changes within the skeletal muscle tissue were analyzed to assess the inflammation and tissue regeneration range upon mechanical loading. To this end, a custom-built ex-vivo muscle organ culture system was used for 21 days to understand how 12% mechanical strain applied to the mouse leg (muscle tissue) affects the cellular response towards regeneration. The unloaded mice legs were used as a control group.

METHODS

Extraction of Mouse legs and Mechanical Stimulation under Organ Culturing Conditions.

Mouse back legs were extracted from 2-month-old mice. Legs were deskinning to expose the skeletal muscle tissue. Then, a longitudinal incision (~2mm) was made on the top lateral of the femur, followed by a blunt separation of the hip bone from the body. Extracted legs were kept in phosphate-buffered saline (PBS) with 3% penicillin-streptomycin on ice.

Following extraction, mice legs were vertically positioned on a computer-controlled custom-built muscle organ culture bioreactor. Legs were gripped-secure from the bottom and top bones to the plates of the bioreactor. A 12% mechanical tensile strain at 0.1 Hz stimulation was applied 4 hours a day for 21 days per our well-established protocols. 50% of new media was replaced every 4-5 days.

Gross Imaging and Scanning Electron Microscopy Analysis

After 21 days of organ culture, legs were extracted from the bioreactor and analyzed through optical imaging. Then, longitudinal incisions were made to remove sections of the tibialis anterior muscle tissue for scanning electron microscopy. Briefly, tissues were washed with PBS and fixed with 4% paraformaldehyde for 30 min. The samples were

dehydrated and in sequential ethanol solutions for 15 min each. Samples were then submerged into sequential ethanol/hexamethyldisilane (HDMS) solutions for 10 min each for image quality enhancement. Finally, samples were dry out overnight, gold-sputter coated and imaged.

Histological Analysis

To further evaluate the fibrotic area, myofiber bundle size, and the number of cells after mechanical stimulation, Masson's trichrome and hematoxylin and eosin staining (H&E) were carried out on the muscle tissues. Briefly, muscle tissues were incubated in 10% formalin after extraction, dehydrated using an ethanol gradient, and cleared with xylene before embedding in paraffin. The paraffin-embedded samples were sectioned at 5um thickness using a microtome and mounted on microscope slides.

Molecular Analysis

The gene expression analysis was performed using real-time PCR to understand the specific molecular changes in the skeletal muscle regeneration and fibrosis processes. Tissues were harvested and analyzed. RT-PCR was performed using TaqMan SYBR Green (Bio-Rad, USA) according to the manufacturer's protocol. The relative gene expression for fold difference between control and stimulated samples was obtained using $\Delta\Delta C_t$ method, and GAPDH as a housekeeping gene. Markers for inflammation, myogenesis, and fibrosis were checked.

Statistical Analysis

Statistical Analysis was conducted using RStudio. Data were analyzed for normalization, and proper statistical analysis was selected. Student's t-test was carried out where appropriate. Symbols on top of each bar profile summarize the student's t-test of at least two independent groups ($P < 0.05$). The data is reported as the mean \pm SE.

RESULTS

Figure 1 shows the gross observations from the control and stimulated legs. The data show significant morphological differences in the integrity of the tissue and a marked increase of H&E staining in the stimulated group. The H&E images showed increased cellularity and that the tissue regions of the stimulated samples were significantly occupied with bridging tissue. Masson's trichrome staining also demonstrated that fibrosis was increased upon mechanical stimulation. The number of cluster cells (area of fibrosis) increased in the stimulated group (Fig.1C). We further investigate myogenesis and fibrosis, figures 2 and 3 show the RT-PCR results for fibrosis markers (α SMA), myogenesis markers (Pax7, MyoD, and Myogenin) and pro and anti-inflammatory markers. The gene expression data demonstrated that 12% strain-stimulated legs significantly enhanced the expression of α SMA almost 3-fold.

Similarly, IL1 β and TNF α (pro-inflammatory) showed a significantly increased expression compared to the control group, while anti-inflammatory markers were downregulated. Additionally, myogenic markers were also upregulated. Pax7, MyoD, and Myogenin increased by 6-, 4-, and 2-fold, respectively, compared to the unstimulated control group.

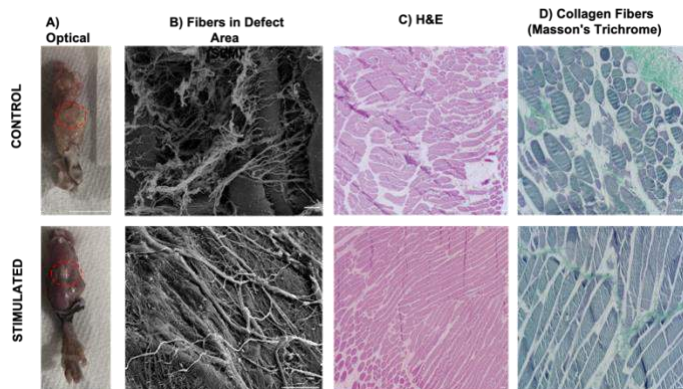


Figure 1. (A) Optical gross images of control and stimulated mice legs, (B) SEM images, (C) H&E staining images, (D) Masson's Trichrome staining images after 21 days of organ culture under mechanical stimulation.

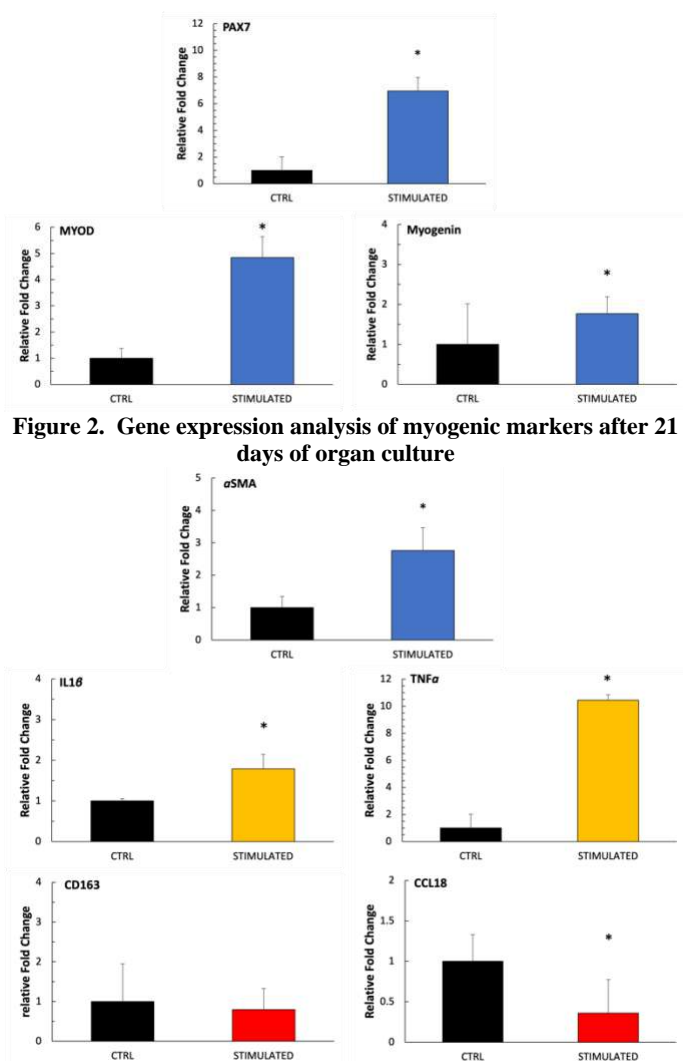


Figure 3. Gene expression analysis of fibrosis, pro- and anti-inflammatory markers after 21 days of organ culture

DISCUSSION

The data presented in this study support our previous 3D in vitro investigations that mechanical stimulation plays a more significant role in understanding the regenerative process of tissues. Muscle tissues exposed to 12% mechanical strain demonstrated an increase in inflammation and regeneration, as seen by the bundle's tissue bridges formed upon stimulation. SEM imaging also reflects fiber diameter and alignment increase, correlating with the increased number of bundle bridges in histology images. PCR also confirmed this by the increased expression of myogenesis and fibrosis markers. Specifically, a decrease in fiber size but not fiber number is characteristic of the downregulation of Pax7, while an increase in myogenic markers enhanced fiber production and marked muscle. These findings suggest that acceleration of the muscle healing process can be achieved through mechanical stimulation.

Moreover, these findings presented here are the first demonstration of a thriving organ culture set up for 21 days while preserving cell viability and molecular changes. Additionally, our results indicate that skeletal muscle regeneration with external stimulation can overcome previous treatments and studies done with conventional setup (2D in vitro) treatments.

In conclusion, our study showed that mechanical stimulation in the form of tensile strain could accelerate the progression of skeletal muscle healing. This process of mechanical stimulation can be further applied with the addition of cell-based therapies for skeletal muscle injuries from laboratory to clinical applications.

REFERENCES

- Passipieri JA, Baker HB, Siriwardane M, Ellenburg MD, Vadhavkar M, Saul JM, Tomblyn S, Burnett L, Christ GJ. Keratin Hydrogel Enhances In Vivo Skeletal Muscle Function in a Rat Model of Volumetric Muscle Loss. *Tissue Eng Part A*. 2017;23(11-12):556-71. Epub 20170414. doi: 10.1089/ten.TEA.2016.0458. PubMed PMID: 28169594; PMCID: PMC6916122.
- Choi YJ, Kim TG, Jeong J, Yi HG, Park JW, Hwang W, Cho DW. 3D Cell Printing of Functional Skeletal Muscle Constructs Using Skeletal Muscle-Derived Bioink. *Adv Healthc Mater*. 2016;5(20):2636-45. Epub 20160816. doi: 10.1002/adhm.201600483. PubMed PMID: 27529631.
- Jacho D, Rabino A, Garcia-Mata R, Yildirim-Ayan E. Mechanoresponsive regulation of fibroblast-to-myofibroblast transition in three-dimensional tissue analogues: mechanical strain amplitude dependency of fibrosis. *Sci Rep*. 2022;12(1):16832. Epub 20221007. doi: 10.1038/s41598-022-20383-5. PubMed PMID: 36207437; PMCID: PMC9547073.

MECHANICAL FAILURE PROPERTIES OF PORCINE ANNULUS FIBROSUS: AN I-PREDICT STUDY

J. Seifert (1,3), A. Shah (2,3), L.L. Frazer (5), N. Yoganandan (2,3), B.S. Shender (4), J.B. Sheehy (4), G. Paskoff (4), T. Bentley (6), D.P. Nicoletta (5), B.D. Stemper (1,2,3)

- (1) Department of Biomedical Engineering, Marquette University & Medical College of Wisconsin, Milwaukee, Wisconsin, USA
- (2) Department of Neurosurgery, Medical College of Wisconsin, Milwaukee, Wisconsin, USA
- (3) Zablocki Veterans Affairs Medical Center, Milwaukee, Wisconsin, USA
- (4) Naval Air Warfare Center Aircraft Division, Patuxent River, Maryland, USA
- (5) Southwest Research Institute, San Antonio, Texas, USA
- (6) Office of Naval Research, Arlington, Virginia, USA

INTRODUCTION

Military aircrew are exposed to elevated loads on their lumbar spine during flights associated with their seating posture, high amplitude accelerations, body-borne equipment, and low frequency vibration ([1-2]). Low back pain in airmen occurs at a higher rate than the general population due, in part, to this loading ([3-4]), in which the intervertebral disc (IVD) annulus fibrosus (AF) is particularly susceptible. Understanding how these loads can damage the AF is important to develop effective mitigation solutions and strategies to reduce injury risk and improve aircrew effectiveness. Finite element modeling can be used to understand injury mechanisms unique to this environment. Modeling enables comprehensive parametric studies to be performed, as occupant and environment related factors within the model can be incrementally changed to elucidate their influence on spine biomechanics. However, accurate mechanical properties of the AF are needed to produce realistic prediction of spine biomechanics. Previous studies used postmortem human subjects (PMHS) to investigate elastic and failure properties of the AF and some inconsistencies among studies regarding the role of different factors in AF biomechanics were noted. For example, some studies reported that AF properties varied between different regions of the disc ([5-8]), whereas others reported no significant regional differences ([9-10]). Elastic modulus (E) was also shown to be dependent on spinal level whereas ultimate tensile stress was independent of spinal level ([9]). One contributor to these inconsistencies across studies may be the quality and type of tissue. PMHS are limited in supply and often of advanced age. Because the AF degrades with age ([11]), previously reported mechanical properties may have been derived from degraded tissue. This can increase variability among specimens/studies in addition to the measured properties not being representative of younger military aircrews. In turn, these factors can all affect the accuracy of a finite element model. An alternative to PMHS are animal models. Hedlund et al ([12]) has shown that porcine cervical spines offer an

acceptable substitute to PMHS lumbar spines due to their anatomical and range-of-motion similarities. In addition to anatomical similarities, young porcine cervical spines are free of age-related degenerative changes making them more applicable to a younger military population. The goal of this study is to characterize elastic and failure properties of the AF across different anatomical regions and levels using a porcine model to determine its applicability for use in modeling efforts of AF damage experienced by aircrew.

METHODS

Fresh porcine cervical spines were acquired from a local abattoir (Johnsonville, LLC). Specimens were refrigerated until the day of testing. All specimens were tested within five days postmortem. On the day of testing, AF test specimens were dissected from C2/3 to C6/C7 IVDs. Each IVD was separated into four anatomical regions: anterior, posterior, and two lateral regions. Test specimens were cut with a scalpel from the outer third of each anatomical region and oriented in the circumferential direction relative to the vertical axis. The targeted width of each specimen was the height of the disc, the targeted length was at least 10 millimeters, and the targeted thickness was approximately one millimeter. Test specimens were then hydrated in a bath of physiologic saline for approximately one hour to ensure uniform hydration levels between specimens. Specimen length, width, and thickness were measured using ImageJ Software (Version 1.53) following hydration and prior to testing. A fine metal mesh was secured to each end of the specimens to prevent slippage during tensile testing and the specimen was mounted in the load frame (ElectroForce 3200, TA Instruments, New Castle, DE) using grips with knurled contact surfaces. Because individual collagen fibers are oriented ± 30 - 45° off the circumferential axis ([13]), and not continuous around the circumference of the AF, care was taken to ensure collagen fibers were clamped on both free ends.

The loading protocol consisted of preconditioning the specimens with five cycles of 20% strain at 0.5 Hz followed by a five-minute recovery. They were then pre-loaded to 0.1 N and held for ten minutes to allow for stress relaxation equilibrium. Finally, specimens were quasi-statically distracted to failure at a rate of 0.005 mm/s. As temperature variations during mechanical testing can affect mechanical properties of spinal tissue [14], specimens were submerged in a saline bath and heated to a constant temperature of 37°C. Force and displacement were measured via a 45-N loadcell (TA Instruments, New Castle, DE) and a linear variable differential transformer (LVDT) internally within the load frame, respectively, at a rate of 5 kHz. Force was converted into stress using the mid-length cross sectional area of the specimen as measured prior to the initiation of the loading protocol and displacement was converted into strain based on the length of the specimen at the 0.1-N pre-load step in the loading protocol. Stress versus strain was subsequently plotted for each specimen. E and ultimate tensile stress and strain for each specimen were then calculated. E was calculated as the slope of the linear region of the stress/strain curve. Ultimate tensile stress and strain were the point at which each specimen reached peak stress. To analyze level and regional based differences, two factor ANOVA tests ($p < 0.05$) were used with a Tukey post hoc test to determine if any significant differences existed.

RESULTS

A total of 79 specimens were tested across five porcine cervical spine IVDs with four anatomical regions per level. It was determined that no difference existed between the right and left lateral regions of the AF ($p > 0.05$), and consequently, lateral specimens were grouped together. All statistical tests analyzing regional based differences were subsequently conducted with three groups: Anterior, lateral, and posterior. Each specimen had an average clamped length of 4.6 ± 1.1 mm, a width of 5.8 ± 1.4 mm, and a thickness of 1.0 ± 0.3 mm.

Ultimate stress was significantly dependent on spinal level ($p = 0.001$), but not anatomical region ($p = 0.8$). C3/C4 had the highest ultimate stress, and the ultimate stress for each level decreased inferiorly and superiorly of this level (Figure 1). Tukey post hoc tests determined that ultimate stress of C3/C4 was significantly higher than C2/C3, C5/C6, and C6/C7.

Ultimate strain was not significantly dependent on spinal level or anatomical regions ($p > 0.05$). The average ultimate strain across all specimens was 0.51 ± 0.16 . While the strains were not dependent on spinal level, it was found that ultimate strain was lowest for C2/C3 (0.45 ± 0.14) and increased slightly each spinal level until peaking at C6/C7 (0.57 ± 0.16).

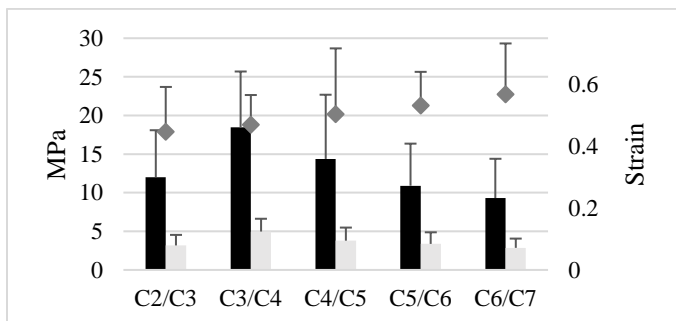


Figure 1: Mean E (black), ultimate stress (light grey), and ultimate strain (grey diamond). Both stress and elastic modulus were determined to be significantly dependent on the cervical spinal level. Error bars display + one standard deviation.

Elastic modulus was significantly different across each of the cervical spinal levels ($p = 0.004$), but not across the anatomical regions of the AF ($p = 0.7$). C3/C4 had the stiffest E, and E for each level decreased inferiorly and superiorly of this level, similar to the ultimate stress behavior (Figure 1). Tukey post hoc tests determined that E of C3/C4 was significantly stiffer than C2/C3, C5/C6, and C6/C7.

DISCUSSION

This study quantified elastic and ultimate tensile mechanical properties of isolated porcine AF specimens. These data are valuable in developing more refined finite element models to predict intervertebral disc mechanics in military environments. These results demonstrated that spinal level is an important factor in the biomechanics of the IVD, but mechanical properties did not vary throughout the different regions of the disc. Level dependent stiffness variation was expected as Stemper et al. had previously reported level-based differences for human lumbar AF ([9]). Compared to the present study, porcine E ranges varied from 9 MPa to 18.5 MPa, they found human AF to have a slightly stiffer response, ranging from 15 MPa to 22 MPa. Their slightly stiffer response may be explained by the difference in test specimen thickness (0.8 mm compared to our 1 mm), as Werbner et al. has shown that thinner specimens, have a stiffer response ([15]). The overall strength of the AF reported in the present analysis was also dependent on level, ranging from 2.86 to 4.97 MPa, which is similar in magnitude (2.25 - 10.30 MPa) to previous studies ([6], [8-9]). Ultimate strain was not dependent on the level or the region, in agreement with previous studies ([9]). With the data generated by these experiments, a more accurate model of the human AF can be created. The elastic and failure properties found can provide valuable information to characterize the dynamic response of the AF, and ultimately, how the forces experienced by aircrews may lead to degradation of the AF. This knowledge will result in a more accurate finite element model of the AF that can be used to better understand degradation of the AF and how to reduce the risk of it occurring to future generation of military aircrews.

ACKNOWLEDGEMENTS

This study was supported by the Incapacitation Prediction for Readiness in Expeditionary Domains: An Integrated Computational Tool (I-PREDICT) program supported by the Office of Naval Research (ONR) through the Medical Technology Enterprise Corporation (MTEC) and Southwest Research Institute (SwRI). Support was also provided by Department of Veterans Affairs Medical Research.

REFERENCES

- [1] De Oliveira et al., *Aviat Space Environ Med*, 76(6):576-80, 2005.
- [2] Mastalerz et al., *Int J Environ Res Public Health*, 19(20): 13413, 2022
- [3] Meucci et al., *Rev Saude Publica*, 49:1, 2015
- [4] Yang et al., *Front Public Health*, 9:744601, 2021
- [5] Ebara et al., *Spine*, 21(4):452-61, 1996.
- [6] Skaggs et al., *Spine*, 19(12):1310-1319, 1994.
- [7] Fujita et al., *J Orthop Res*, 15(6):814-9, 1997.
- [8] Acaroglu et al. *Spine*, 20(24):2690-701, 1995
- [9] Stemper et al., *J Neurosurg Spine*, 21(4):608-13, 2014.
- [10] Holzapfel et al., *Biomech Model Mechanobiol*, 3(3):125-40, 2005
- [11] Singh et al., *Spine*, 34(1):10-16, 2009.
- [12] Hedlund et al., *J Exp Orthop*, 9(1):54, 2022.
- [13] Marchand et al. *Spine*, 15(5):402-10, 1990.
- [14] Bass et al., *Spine*, 32(16):436-42, 2007
- [15] Werbner et al., *J Biomech Eng*, 139(11):111001, 2017

FLUID-STRUCTURE INTERACTION SIMULATIONS IN AN IDEALIZED MODEL OF THE DISSECTED AORTA: RELATION BETWEEN FALSE LUMEN PRESSURE AND OUTFLOW VIA SIDE BRANCHES

Amith Balasubramanya (1), Lise Gheysen (1), Nele Famaey (2),
Joris Degroote (3), Patrick Segers (1)

(1) IBitech, BioMMeda, Ghent University, Ghent, Belgium
(2) Biomechanics Section, Department of Mechanics Engineering, KU Leuven, Leuven, Belgium
(3) Department of Electromechanical, Systems and Metal Engineering, Ghent University, Ghent, Belgium

INTRODUCTION

Patients with Type-B aortic dissection (TBAD) exhibit delamination of the descending thoracic aorta wall distal to the left subclavian artery. In the presence of one or more tears of the intima, a so-called false lumen (FL) is formed in parallel to the effective, true lumen (TL), both separated by a dissected membrane called the intimal flap. In the acute phase, this leads to altered hemodynamics with an in-out flow of blood from the FL. Endovascular treatment of TBAD with a stent graft aims to interrupt the exchange of blood between the TL and FL to enhance FL thrombosis. The long-term prognosis of patients with TBAD largely depends on the extent of thrombosis that can be achieved in the FL, with clinical studies indicating that partial FL thrombosis has a negative impact on the long-term mortality risk in patients [1].

Little is known about the (biomechanical) mechanisms underlying the association between partial FL thrombosis, patient outcome and progression of disease. Some hypothesized that pulsatile inflow through the intimal tears into a lumen with impaired outflow (when there are no re-entry tears) would increase blood pressure in the FL which leads to a higher risk of lumen expansion, dissection and rupture. However, we have previously estimated the direct effect of inflow on FL pressure (arising from dynamic pressure) to be limited to 5mmHg [1]. In addition, aortic side branches sprouting from the FL provide alternative outflow, and may thus prevent pressure build-up within the FL. We also stated that realistic computational fluid-structure interaction (FSI) models accounting for in- and outflow of the false lumen via intimal tears and side branches may help elucidate the pressure build-up within the false lumen and mechanical stresses within the aortic wall [1].

The aim of this study is therefore to setup FSI simulations in a model of an aortic dissection that allows the assessment of impact of the outflow via side branches emanating from the FL on the pressure build-up inside the FL, the transmembrane pressure and aortic wall stresses.

METHODS

An idealized dissection model with an axial length of 60 mm, a dissection length 40 mm and two tears were generated using the in-house geometry and mesh generation tool PyFormex [2]. We define two new parameters called extent of dissection ($s/S = 0.66$) where 's' is the circumference of the FL and 'S' is the total aortic circumference and flap thickness ratio ($t/T = 0.4454$) where 't' is the thickness of the dissected membrane and 'T' is the overall aortic thickness. To the resulting configuration, a side branch with a diameter (d) of 3 mm (~0.1 time the diameter of the aorta) and a length of 15mm was added in the FL resulting in a geometry as seen in Figure 1.

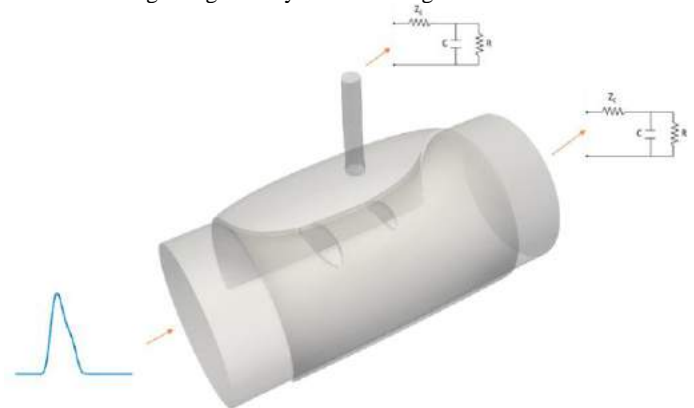


Figure 1: 3D model indicating the fluid model boundary conditions

The resultant structural model was meshed using 151128 linear tetrahedral (C3D4H) elements in Abaqus (Dassault Systems, USA) and the interior lumen was filled with 374592 tetrahedral elements using ICEMCFD (Ansys Inc, PA, USA). A flat velocity profile was prescribed at the inlet [3] and scaled to match a mean flow of 3.87 l/min [4] in the descending aorta. Downstream, 3-element windkessel models (WK)

were imposed and the WK parameters were tuned to achieve diastolic/systolic pressure of 80/120 mmHg. Two cases were considered: one with 5% and the other with 0.5% of the total flow through the side branch. For the soft tissue, a linear elastic model was considered to model the material properties chosen from Delpano [5]. Stiffness of the aortic tissue was 5.39MPa and that of the intimal flap was 0.51MPa. Nodes at the inlet and outlets were fully constrained except for movement along the radial direction. Initial stresses in the structural model without a side branch were determined using the pre-stretch algorithm previously implemented by Famaey [6]. The resulting stresses were mapped to the configuration with side branch using nearest neighbor interpolation using an in-house implemented python script.

The governing fluid equations were solved using the finite volume solver Fluent (Ansys Inc, PA, USA) and structural equations were solved using the finite element solver Abaqus (Dassault Systems, USA). Coupling between the flow and structural solver was performed using the in-house coupling code CoCoNuT [7]. A partitioned FSI simulation where 72 cores were used for the fluid solver and 48 for the structural solver took ~27 hours for four cardiac cycles where a time period of 0.6 seconds for each cardiac cycle was chosen.

RESULTS & DISCUSSION

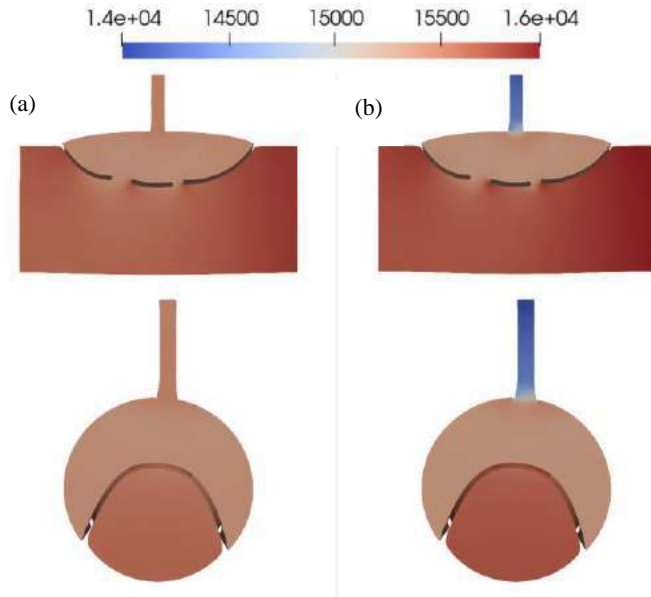


Figure 2: Pressure in Pa at peak systole when (a) 0.5% and (b) 5% of the total flow is prescribed at the side branch with top panels indicating the longitudinal and bottom panels indicating transversal cuts

Since the intention of this study is to assess the impact of outflow via side branches, pressure variation across the TL and FL are studied. As observed from Figure 2, an increased side branch outflow resulted in an increased pressure in the TL at systole, leading to an increased transmembrane pressure difference (TL-FL) of 4.1 mmHg compared to 3.2 mmHg with reduced flow through the side branches. A localized pressure drop is observed in the side branch when there is an increased flow which can be attributed to the reduced resistance value at this outlet.

Maximal principal wall stresses are shown in Figure 3 for the case with increased flow through the side branches. Given the relatively small differences in residing pressure, stress differences between both cases studied are limited. Note that our approach to generate the model leads

to relief of the initial stresses of the intimal flap as the aortic wall delaminates. Stresses on the flap thus remain lower even at peak systole and regions of higher stresses are observed on the outer aortic wall. This is consistent with increased displacement observed in the outer walls compared to the intimal flap, even though flap motion was limited (0.9 mm displacement in the intimal flap at peak systole) and FL volume changes were mainly due to outer wall expansion rather than flap displacements. This can be attributed to increased s/S, high membrane thickness and material stiffness in the configuration. To indicate the influence of material stiffness, Baumler [8] showed that reducing the flap stiffness to 0.02 MPa (currently used stiffness is 0.51MPa) with simplified properties showed flap motion mimicking motion observed in-vivo.

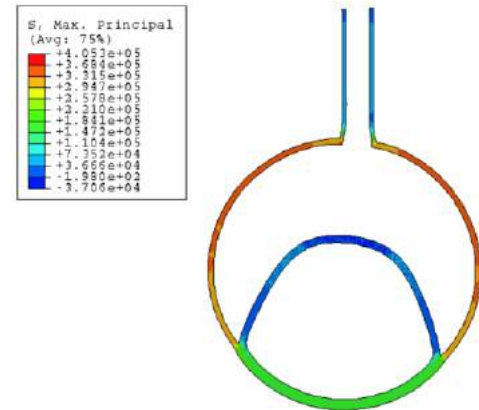


Figure 3: Max principal stresses (Pa) at systole when there is 5% of total flow through the side branch (very similar results were obtained for the other case).

While a partitioned FSI study or even a numerical study that includes variable flow through side branch in the FL has never been studied, there are some limitations which need to be addressed. Even though realistic initial stresses are used, rather simplistic material properties are considered for the flap and the aortic tissue. Nonetheless, we present promising initial results of pressure variation in the TL and FL with variable flow through the side branch. Future work would also include a fully coupled simulation with lower values of (s/S), thinner and less stiff intimal flap in patient-inspired geometries. These additional parametric simulations would give us a broad(er) understanding of geometrical and material influence on pressure distribution for variable outflow through side branches in the FL in vivo.

ACKNOWLEDGEMENTS

This research is funded by the Fund for Scientific Research – Flanders (G029819N and G086917N).

REFERENCES

- [1]Logghe, G et al., *Front. Cardiovasc. Med*, 34:859-871, 2021.
- [2]De Santis et al., *Medical, Biological Engineering, Computing*, 48:371–380, 2010.
- [3]Madhavan, S et al., *BioMed Eng OnLine*, 17:66, 2018.
- [4]Chong, M et al., *Int.J. for Numerical Methods in Biomed*, 36(12):3399, 2020.
- [5]Delpano, V et al., *Computer methods in Biomechanics & Biomedical Engineering*, 23:153-155, 2020.
- [6]Famaey, N et al., *Journal of Applied Mathematics and Mechanics*, 98:2239-2257, 2018.
- [7]Delaisse, N et al., *ECCOMAS 2020 Proceedings*, 2021.
- [8]Baumler, K et al., *Biomech Model Mechanobiol*, 19(5):1607-1628, 2020

IMPACT OF TYPE V COLLAGEN DEFICIENCY ON FIBROBLAST MECHANOSENSING UNDER INFLAMMATORY STIMULATION

N. Patel (1), T. Li (1), J. Duggan (2)
S. M. Kallish (3), K. L. Spiller (1), R. J. Petrie (2), L. Han (1)

- (1) School of Biomedical Engineering, Science and Health Systems, Drexel University, Philadelphia, PA, United States
(2) Department of Biology, Drexel University, Philadelphia, PA, United States
(3) Division of Translational Medicine and Human Genetics, Department of Medicine, University of Pennsylvania Perelman School of Medicine, Philadelphia, PA, United States

INTRODUCTION

Fibroblasts are highly sensitive to the biomechanical and biochemical cues of their residing niche [1]. During wound healing, inflammatory stimuli leads to aberrant collagen remodeling [2], and pro-regenerative stimuli leads to myofibroblast activation, resulting in excessive deposition of collagen I [1, 3]. The fibrotic matrix, in turn, impacts the phenotypic shift of fibroblasts, contributing to a vicious cycle of scar formation [1, 3]. Type V collagen, a minor regulatory collagen, plays a key role in regulating collagen I fibril assembly in vivo [4], and thus, could be a central player in this process. Indeed, atrophic scar formation is a prevalent symptom observed in patients with classic Ehlers-Danlos syndrome (cEDS), a connective tissue disorder caused by the mutation of human *COL5A1* gene [3]. Understanding the role of collagen V in fibroblast mechanosensing can provide new insights into the cell-matrix crosstalk of fibrosis. This study aims to determine how the deficiency of collagen V alters fibroblast response to external inflammatory and mechanical stimuli.

METHODS

Fibroblast culture. Primary normal adult human dermal fibroblasts (ATCC: HDFa) and collagen V mutant cEDS fibroblasts (ATCC: JaySen) were maintained in complete DMEM. To provide inflammatory stimuli, cells were treated with the inflammatory cytokine, TNF- α (20 ng/ml) to simulate M1-macrophage-induced proinflammatory response, or DMEM as a control. CytoSoft gels (Advanced BioMatrix) with Elastic Modulus of 2 kPa (soft) and 64 kPa (stiff) were used to subject fibroblasts to mechanical stimuli. **Immunofluorescence imaging:** Fibroblasts were stained with F-actin/phalloidin (ThermoFisher), and anti-FAK antibodies (ThermoFisher) and imaged (Leica SP8). **Cell-derived matrix (CDM) generation:** Cells were grown on 35 mm glass dishes coated with 0.2% bovine skin gelatin. Upon reaching confluency, L-ascorbic acid was supplemented every 2 days for 14 days. Cells were

denuded and resulting CDMs were stained with Succinimidyl Ester (ThermoFisher) and imaged via a Zeiss LSM700 Confocal Microscope. **AFM-nanoindentation** was applied on the CDMs to measure indentation modulus (in kPa), using a microspherical colloidal tip ($R \approx 5 \mu\text{m}$, $k \approx 0.03 \text{ N/m}$, HQ: CSC38/tipless/Cr-Au, NanoAndMore) and a Dimension Icon AFM (BrukerNano). The loading portion of the resultant force-indentation depth curve was then fit to the finite-thickness corrected Hertz model [5] via least-squares linear regression to calculate the effective indentation modulus, E_{ind} , following our established procedures [6, 7]. **Statistical analysis:** An unpaired two-sample student's *t*-test was used to determine any significant differences in CDM indentation modulus. In all tests, the significance level was set at $\alpha = 0.05$.

RESULTS

The reduced collagen V expression in cEDS cells was confirmed by decreased collagen V staining relative to the normal control (Fig. 1a). Also, cEDS cells showed higher cell density and DAPI staining, indicating loss of collagen V may lead to accelerated cell proliferation. On the soft substrate, both groups expressed low amount of F-actin, and we did not notice substantial morphological differences between the normal and cEDS cells (Fig. 1b). However, when seeded on the stiff substrate, cEDS cells adapted a more elongated morphology. In alignment with this morphological change, the F-actin cytoskeleton also became more aligned along the long axis of cEDS cells. The contrast was further aggravated when cells were stimulated with the inflammatory cytokine, TNF- α (Fig. 1b).

When characterizing focal adhesion formation, we did not detect appreciable changes in FAK expression in the control group with or without TNF- α stimulation, with notable expression along the actin fibers, as shown by zoomed-in green rectangle (Fig. 2). For the cEDS

group, we did not observe any notable differences in FAK expression under normal culture conditions relative to the control. When stimulated with TNF- α , there was a marked decrease in FAK expression along the fibers (Fig. 2). Meanwhile, cell derived matrices (CDMs) from the cEDS fibroblasts developed a significantly higher indentation modulus (Fig. 3a), as well as a denser matrix in comparison to those produced by the normal cells (Fig. 3b).

DISCUSSION

This study highlights the important role of collagen V in the inflammatory phase of wound healing. Studies have shown that collagen V regulates the expression of integrins in human cell lines [8]. While we have not elucidated the role of collagen V in integrin expression patterns yet, this study provides direct evidence on the impact of collagen V loss on altered fibroblast mechanotransduction, as shown by changes in F-actin expression (Fig. 1) and FAK localization (Fig. 2). It is widely known that integrins often serve as direct mechanotransducers and are crucial in regulating downstream biomechanical signals [9]. Our data suggest that despite the low concentration of collagen V in vivo, changes in F-actin dynamics and FAK expression due to the collagen V deficiency may result in the change of types and expression of integrins. This, in turn, would disrupt mechanosensitive pathways that are crucial to tissue homeostasis or pathogenesis, such as YAP/TAZ, Rho/Rock, Notch and Wnt signaling [10, 11]. For example, stimulation with inflammatory cytokines such as TNF- α would further perturb these mechanosensitive pathways, and collagen V could play an important role in mediating the mechano-inflammatory response of fibroblasts, as supported by the altered FAK pattern in TNF- α -treated cEDS fibroblasts (Fig. 2).

When assessing the matrix mechanics of collagen V deficient CDMs, we noticed a marked increase in indentation modulus when compared to the normal group (Fig. 3a). This could be due to altered fibril assembly of the CDM in the deficiency of collagen V. For example, we noticed a porous matrix deposition in the healthy group, while cEDS matrices were denser (Fig. 3b). These observations corroborate the canonical role of collagen V in regulating collagen I fibrillogenesis and limiting aberrant fibril lateral fusion or alignment [4]. Building on our observed impact of collagen V on the CDM at normal conditions, our ongoing studies are further investigating the roles of collagen V in mediating the CDM formed under inflammatory stimuli. Integrating these results with the roles of collagen V in regulating integrin activities, our findings provide a basis to elucidate a new mechanobiological role of collagen V at the cell-fibrous matrix interface under inflammation. This would provide a basis for developing collagen V-based biomaterials to modulate fibroblast immunoresponses and injury-induced fibrosis.

ACKNOWLEDGEMENTS

This work was supported by NSF CAREER CMMI-1751898 and the U.S. Department of Education's Graduate Assistance in Areas of National Need (GAANN) program.

REFERENCES

- [1] Hannan, R.T., et al., *ACS Biomater Sci Eng.* 4:1223-1232, 2018.
- [2] Chou, D.H., et al., *J Immunol.* 156:4354-4362, 1996.
- [3] Witherel, C.E., et al., *Biomaterials.* 269:120667, 2021.
- [4] Wenstrup, R.J., et al., *J Biol Chem.* 279:53331-7, 2004.
- [5] Dimitriadis, E.K., et al., *Biophys J.* 82:2798-810, 2002.
- [6] Chery, D.R., et al., *Acta Biomater.* 111:267-278, 2020.
- [7] Li, Q., et al., *Acta Biomater.* 54:356-366, 2017.
- [8] Zoppi, N., et al., *J Biol Chem.* 279:18157-68, 2004.

[9] Ross, T.D., et al., *Curr Opin Cell Biol.* 25:613-8, 2013.

[10] Martino, F., et al., *Front Physiol.* 9:2018.

[11] Noguchi, S., et al., *Int J Mol Sci.* 19:3674, 2018.

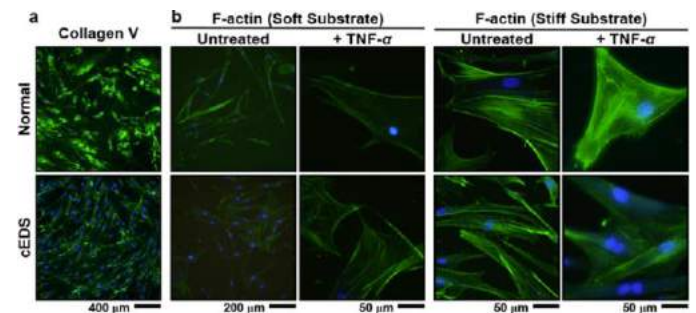


Fig. 1 a) Representative collagen V (green) and DAPI (blue) IF staining of normal and cEDS fibroblasts. **B)** F-actin (green) and DAPI (blue) staining of normal and cEDS fibroblasts seeded on soft, and stiff substrates with or without the treatment of TNF- α for 14 days.

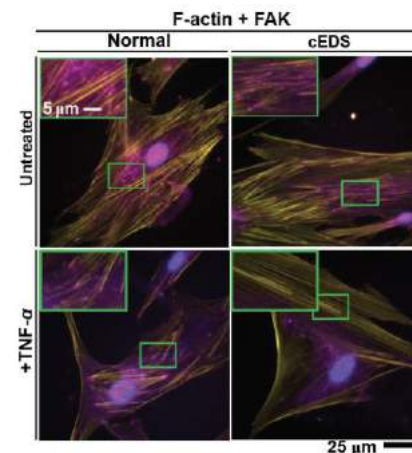


Fig. 2 Representative IF images of F-actin (yellow), FAK (purple) and DAPI (blue) staining of normal and cEDS fibroblasts treated with or without TNF- α (20 ng/ml) for 14 days.

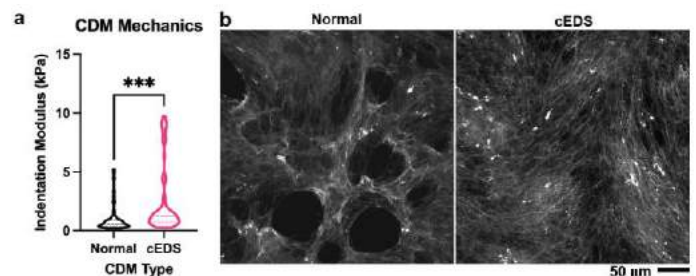


Fig. 3 a) Nanoindentation modulus of cell-derived matrices (CDMs) generated by normal (HDFa) and cEDS fibroblasts without the treatment of TNF- α for 14 days (***: $p < 0.001$). **b)** Representative confocal microscopy images of CDMs without the treatment of TNF- α .

COMPARISON BETWEEN MATERIAL PROPERTIES OBTAINED FROM ULTRASOUND IMAGE BASED INVERSE FE METHOD AGAINST EX-VIVO INFLATION TEST

Hadi Wiputra (1), Sydney Q. Clark(2), Craig J. Goergen (2), Matthew R. Bersi (3), Victor H. Barocas (1)

(1) Department of Biomedical Engineering, University of Minnesota, Minneapolis, Minnesota, USA
(2) Weldon School of Biomedical Engineering, Purdue University, West Lafayette, Indiana, USA
(3) Mechanical Engineering & Materials Science, Washington University, St. Louis, Missouri, USA

INTRODUCTION

Thoracic aortic aneurysms affect 17,000 Americans annually, with a 90% mortality rate when the aneurysm ruptures [1]. When determining the risk of rupture, the ability to account for changes in aortic material property due to its remodeling is important. However, this requires a large amount of data. Various studies have used different imaging modalities in humans to try to estimate aneurysm or aortic wall mechanics *in vivo* [2]. However, there is a lack of data on (1) a set of *in vivo* images that could be used to estimate aortic wall mechanical properties, and (2) the corresponding data on the true mechanical properties of the wall of the same sample *ex vivo* [2].

Wild-type mice infused with angiotensin II (Ang-II) are often used to study the development of thoracic aortic aneurysms. Ang-II increases the pressure within the vessel [2], and the aorta, under abnormally high pressure, will stiffen, thicken, and dilate, increasing propensity to develop an aneurysm and rupture [3]. This model system presents an opportunity to generate the desired data set.

In addition, many studies use population-based, generalized growth parameters and geometry [4]. Yet, due to large variability in complications associated with thoracic aortic aneurysm [5], mouse-specific data would be more valuable. However, difficulty in obtaining non-invasive longitudinal mechanical data impedes efforts in the development of aneurysm growth model on an animal-specific level. Therefore, this study focuses on generating non-invasive mechanical data from ultrasound images in Ang-II infused mouse models, with results validated against biaxial extension-inflation tests [6].

METHODS

The non-invasive mechanical testing method used in the current study is based on inverse finite element (FE) and computational fluid dynamics (CFD) models, fitted to vessel deformation obtained from volumetric ultrasound images, as illustrated in Fig 1. It can be described thusly: first, ultrasound images were obtained from three, 16-week-old mice that had been infused with 1000ng/kg/min Ang-II for 4 weeks,

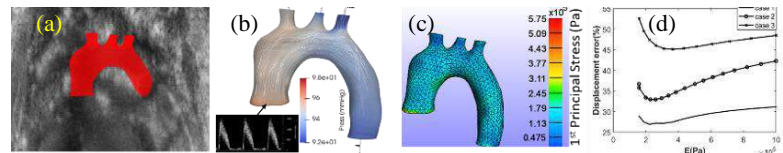


Figure 1: Inverse Finite Element Approach. (a) Aortic wall is segmented and tracked from 4D ultrasound image. (b) CFD is used to determine wall stresses. (c) FE model is used to calculate wall displacement from stresses. (d) Optimal FE stiffness is determined.

during which the aorta was expected to grow and remodel [2]. 4D ultrasound images of the thoracic aorta were obtained from a high frequency ultrasound system (25-55 MHz, Vevo3100, VisualSonics), resulting in approximately 0.03x0.03x0.1mm resolution at 40 frames per cardiac cycle. The ascending and proximal descending thoracic aorta were then segmented, and deformation was tracked over the cardiac cycle with B-spline Fourier-based image registration, as described and validated in [7].

Velocity at the ascending, descending, and the three branches of the aortic arch were obtained by pulsed wave Doppler imaging. Those velocities and the tail cuff pressure of the mice were used to calibrate a resistor-capacitor-resistor (RCR) model of the downstream circulation for CFD (Fig1b), via differential evolution [8]. CFD simulation was then performed with Ansys Fluent to obtain traction forces on the aortic wall.

The traction forces were then used as loads for an FE model of the aortic arch in FEBio. Branch ends had prescribed deformation based on the ultrasound images. Robin boundary conditions were assigned at the outer vessel wall to describe stiffness of the surrounding tissue and loads from CFD applied to the inner vessel wall of the unloaded aortic geometry (Fig1c). The unloaded geometry of the aorta was obtained by gradual reduction of its radius until the computed loaded geometry during systole matched the *in vivo* ultrasound image (Fig1d).

A quasi-incompressible neo-Hookean model was used:

$$W = \frac{\mu}{2}(I_1 - 3) - \mu \ln J + \frac{\lambda}{2}(\ln J)^2$$

$$\mu = \frac{E}{2(1 + \nu)}, B = \frac{\nu E}{(1 + \nu)(1 - 2\nu)}, \nu = 0.45 \quad (1)$$

where W is the strain energy density function, I_1 is the first invariant of right Cauchy-Green deformation tensor, J is the determinant of the deformation gradient tensor, μ is shear modulus, B is the bulk modulus, and ν is the Poisson ratio, taken to be close to incompressible. For the model, the Levenberg-Marquardt algorithm was used to find the optimized parameter value E_{opt} that minimized the disparity between aortic deformation from ultrasound images (\vec{X}_{US}) and FE model (\vec{X}_{FE}), given by the following equation:

$$E_{opt} = \operatorname{argmin}_E (|\vec{X}_{US} - \vec{X}_{FE}(E, \nu)|^2) \quad (2)$$

RESULTS

There exists a neo-Hookean parameter (E) that minimizes the tracked displacement error for the three mice studied (values in Fig 2). The displacement error curves for the three mice maintained the same shapes: the error increases drastically at low E and plateaus at high E as the vessel becomes effectively rigid. The geometrical fit can be observed qualitatively from the ultrasound and FE images in Fig 3a and 3b during diastole and systole, respectively.

Comparison between mechanical testing and FE model is done with the stress-strain curve shown in Fig 3c. The range of stretches displayed (circumferential and axial) were within diastolic to systolic ranges, accounting for additional axial and circumferential pre-stretch. Due to the material model, the FE result is nearly linear with overlapping lines for different λ_z values, in contrast to the four fiber family models, which can isolate the circumferential and axial stiffness.

DISCUSSION

In this study, a linear-based, hyper-elastic material model was used, which is common for inverse FE models [9]. Fiber-based material models, however, are favored in forward FE problems in arteries [10]. Fiber-based material models were also tested but converged to an isotropic matrix with neo-Hookean behavior. This effect likely arises from the small range of strains induced by diastolic to systolic pressure changes, and from the single loading condition (pressurization). The resulting stress-stretch curve could be fitted with linear relationship (Fig 3c).

Comparison between *in vivo* and *ex vivo* material property estimations from the same tissue have been performed previously, but such studies are uncommon [2]. Comparisons are often based on higher resolution CT scans on larger subjects, with errors in the material property estimation ranges of 10-25% [12]. The current study resulted in larger errors despite a similar methodology. However, direct comparisons between the results in this study against the others are difficult to make due to different material models, studied vessels, and image quality. With respect to the image quality, relative to the size of the aorta, the ultrasound image in the current study has ~40% lower resolution than CT scans. An increase in Gaussian noise on the image by 5% can result in increased error of material properties estimation by 1.5% [13], and this effect might not be additive, but multiplicative.

One of the largest uncertainties in the inverse FE approach is the determination of the unloaded geometry or the pre-strain of the *in vivo* geometry [14]. Indeed, the actual *in vivo* axial pre-stretch of the geometry is unknown and is often directly prescribed in modeling studies [11]. Similarly, in this study, the axial pre-stretch was assigned based on the excised unloaded geometry. Increases in the axial pre-stretch would reduce the approximated material stiffness, as the material

needs to be more compliant to ensure that pressure would still cause radial deformation against the pre-tensioned vessel.

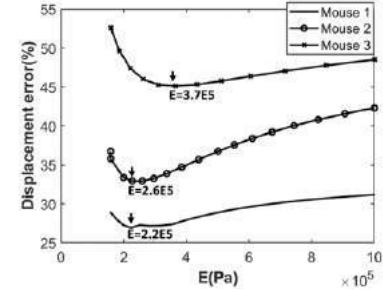


Figure 2: Time-averaged displacement errors (normalized to the maximum displacement) against neo-Hookean parameter E for the three mice studied.

ACKNOWLEDGEMENTS

Funding provided by NIH grants U01-HL139471, R01-HL164800, and R01-HL164800. Computational resources were provided by the Minnesota Supercomputing Institute.

REFERENCES

- [1] Melo, G.E.R. et al., *Semin Thorac Cardiovasc Surg*, 34(1):1-16, 2022. [2] Wang L., et al., *J. Funct. Biomater.*, 13: 147, 2022. [3] Bersi, M.R., et al., *Hypertension*, 67(6): 890-896, 2016. [4] Spittell Jr, J.A., *J. Am. Coll. Cardiol.*, 1(2): 533-540, 1983. [5] Mahutga R., et al., *J. Biomech. Eng.*, 142(11), 2022. [6] Hiratzka F. L, et al., *Circ.*, 121(13):e266-369, 2010. [7] Ferruzzi J., et al., *Ann Biomed Eng*, 41(7), 1311-1330, 2013. [8] Wiputra, H., et al., *Scientific Reports*, 10(1): 1-14, 2020. [9] Storn R., Price K., *J Global Optimization*, 11: 341-359, 1997. [10] Farzaneh, S. O., et al., *Biomech Model Mechanobiol*, 18(1): 137-153, 2019. [11] Cai R., et al., *Comput. Methods in Appl. Mech. Eng.*, 399: 115294, 2022. [12] Cosentino F., et al., *Comput. Biol. Med.*, 109: 70-78, 2019. [13] Narayanan, B., *Sci. Rep.*, 11: 22540, 2021. [14] Maso T., *Front. Physiol.*, 28:292, 2018.

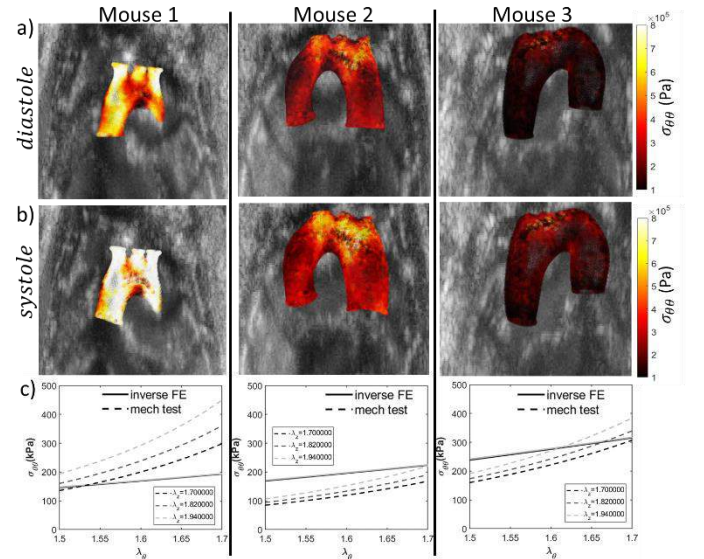


Figure 3a) Circumferential stress ($\sigma_{\theta\theta}$) obtained from FE model at diastole overlaid on ultrasound image. b) $\sigma_{\theta\theta}$ obtained from FE model at systole overlaid on ultrasound image. c) Circumferential stress-stretch ($\sigma_{\theta\theta} - \lambda_{\theta}$) curve of the inverse FE against mechanical test results at different axial stretches ($\lambda_z = 1.7 - 1.94$).

EVALUATION OF THE RELATIVE STIFFNESS OF THE SURGICALLY TREATED RUPTURED AND CONTRALATERAL ACHILLES TENDON DURING HEALING

Sarah Thompson Murray (1), Shabnam Rahimnezhad (2), Dov Bader (3), Cristy French (4), Karin G. Silbernagel (5), Daniel H. Cortes (2)

(1) Department of Kinesiology
Penn State University
State College, PA, USA

(2) Department of Mechanical Engineering
Penn State University
State College, PA, USA

(3) Department of Orthopaedics
Hershey Medical Center
State College, PA, USA

(4) Department of Radiology
Hershey Medical center
Hershey, PA, USA

(5) Department of Physical Therapy
University of Delaware
Newark, DE, USA

INTRODUCTION

Achilles tendon ruptures (ATR) have increased 10-fold in the past few decades[1]. Lower-leg functional deficits include decreased heel-rise height, heel-rise work, reduced plantar flexion strength, and decreased ability of the ankle to generate power[2]. These deficits persist as far out as 14 years after injury[3]. The cause of long-term functional deficits remains unclear and is thought to be multifactorial. Structural changes in the tendon-muscle unit after ATR are strongly related to deficits in plantarflexion function. Specifically, ATR results in long-term tendon elongation, increased tendon area, altered mechanical properties, and reduced calf muscle volume. These structural changes rapidly develop over the first weeks of recovery, slowly progress for a few months after injury, and change very little thereafter. The rapid initial development of muscle and tendon abnormalities coincides with the period of no weight bearing or partial weight bearing of current rehabilitation protocols. Neuromuscular electrical stimulation (NMES) can potentially provide muscle activity and mechanical stimulus to the healing tendon during the first weeks of recovery to minimize the large initial decline. NMES can positively impact several of the factors affecting recovery from ATR and has been successfully applied as part of rehabilitation protocols for knee surgery to preserve muscle volume and strength[4]. Therefore, NMES can potentially attenuate muscle atrophy during the first weeks of recovery after ATR repair surgery. To safely apply NMES, the tensile forces need to be modulated based on the strength of the healing tendon. Unfortunately, there is limited information about the mechanical properties of the Achilles tendon during the early stages of healing (first 4 weeks). Shear wave elastography (SWE) is an imaging method that quantifies the healing tendon's mechanical properties without applying load. It has been shown that the shear modulus measured via SWE is correlated to Young's modulus[5] and the ultimate tensile strength of the tendon[6]. Therefore, the shear modulus can serve as a surrogate property to evaluate the tensile strength of the tendon during the first weeks of healing after an Achilles rupture. This study aims to determine the tendon mechanical properties in the first 12 weeks of healing for patients undergoing surgical repair and a standard rehabilitation protocol.

METHODS

This study was approved by the Penn State University IRB (STUDY00016462). The SWE tests on participants were performed at Penn State Biomechanics and Imaging Lab, and Hershey Medical center. Patients who participated in this research consented before any data collection. All the participants were treated surgically in the same procedure without adding grafts. After surgery, participants received almost the same rehabilitation program, including the use of CAM Walker Boot from week 1, and weight bearing from day 10. To avoid any stress on tendons at the time of performing SWE measurements, the participants laid down on the bed, in a prone position and their legs were on the bed.

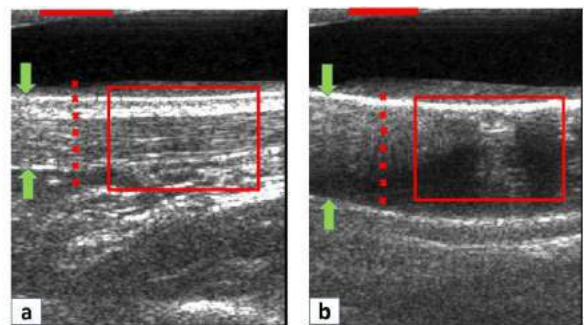


Figure 1: B-mode images of the a) Contralateral healthy Tendon and b) Injured Tendon at week 12

The SWE measurements were obtained by applying light skin compression on desired points, using a handheld transducer. The colored SWE map was provided for each participant by utilizing B-mode imaging. The measurements on a defined ROI window were captured. The shear speed was measured on the surgically treated part of the ATR and the collateral leg on any weeks 2, 4, 6, and 12 after the injury. Figure 1 shows B-mode images of the healthy and injured tendons of one of the participants at week 12. The green arrows illustrate the boundaries of the tendon. The red rectangle shows the region where the speed map was calculated. An ROI of approximately 10x10 mm was used.

diameter was selected inside the tendon to calculate a representative value of the shear wave speed. Each measurement was repeated 5 times. Measurements were taken from both legs to calculate the stiffness ratio. The ankle angle was measured in both the injured and the contralateral legs. The difference in plantar flexion angle of both feet at rest in the prone position was measured as an indication of tendon elongation.

RESULTS

Eleven patients were recruited for this study (4 women and 7 men). The average age was 32.6 y/o. Figure 2 shows the ratio of the stiffness of the injured tendon to the contralateral one in different weeks and the curve fitted on the average of these results. ANOVA analysis resulted in $p = 0.012 < 0.05$, $F = 4.8713$, $F_{crit} = 3.1967$, and this means that time has a significant effect on the stiffness ratio. Figure 3 shows the absolute value of the angle differences in the healthy and injured legs. The ANOVA analysis on results illustrated in figure 3, resulted in $p = 0.418 > 0.05$, $F = 1.0128$, $F_{crit} = 3.41$. Meaning that there is not a significant difference between angles with time.

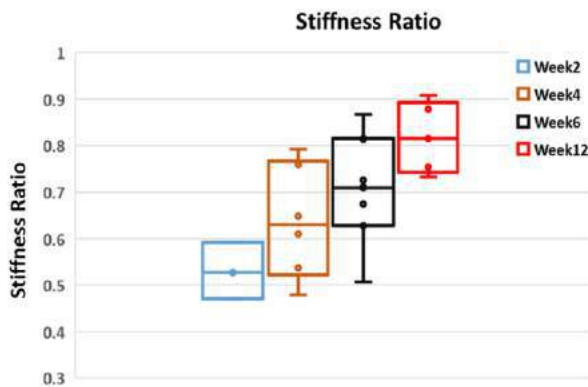


Figure 2: Change of ratio of the Stiffness between the injured leg and the healthy leg

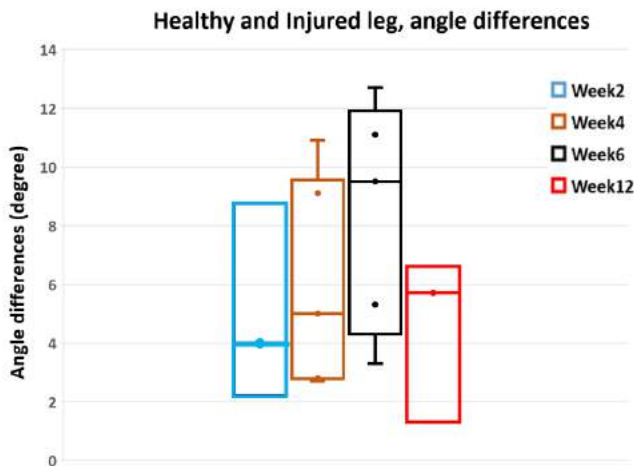


Figure 3: Healthy and Injured leg angle differences

DISCUSSION

The stiffness (shear modulus) ratio illustrated in figure 2, shows the increasing trend as expected for healing tendons. Previous studies have shown that the shear modulus is proportional to the ultimate strength of the tendons[6]. Therefore, the ratio presented here can also be viewed as a percentage of tendon strength re-gained as a function of time after rupture. This information is crucial for the development of rehabilitation techniques.

Week 12 is particularly important in current rehabilitation protocols because it marks the time point when patients are allowed to walk with normal footwear and full weight bearing. Walking forces at the Achilles tendon have been well characterized[7]. Therefore, those values can be taken as a reference for allowable forces at that time point. Using the stiffness ratio, allowable forces can be estimated at earlier time points.

Current rehabilitation techniques prescribe a timeline for increasingly applying a fraction of weight bearing to the injured leg. However, there is no consensus on the timing and amount of load bearing for optimal healing. Inconsistencies in the rehabilitation protocols can potentially contribute to the variability of functional outcomes in this patient population. Information about the strength of the healing tendon can be used in the design of more consistent protocols that would prescribe activities and exercises that would progressively increase the tensile demands of the tendon.

NMES is a technique often used in the rehabilitation of knee injuries and surgeries to prevent quad muscle atrophy. NMES can offer several advantages in the rehabilitation of Achilles tendon ruptures. By controlling the stimulation intensity and position of the pads, the amount of force applied to the healing tendon can be reduced, while still applying a significant contraction to the muscle. The position of the pads can be changed to stimulate the entirety of the calf muscles. This combination of low force and significant muscle contraction cannot be achieved by voluntary contractions. NMES can potentially reduce the variability in current rehabilitation protocols since it doesn't rely on voluntary contraction or percentage of body weight which are very difficult to control.

Mechanical properties of tendons are also important for potential personalized treatment strategies or identification of delayed healing. Achilles tendon ruptures are common in athletes. In this patient population, the timing of the return to activities can play a big role in the athlete's career. Evaluation of the mechanical properties of the healing tendon can inform clinicians and trainers of the best time to return to activities. Similarly, mechanical properties can alert clinicians of delayed healing in patients with risk factors such as diabetes and smoking.

Limitations of this study include that the rehabilitation protocol was not controlled. As mentioned above, surgeons may use rehabilitation protocols that may have subtle differences. Another limitation is the relatively small number of patients recruited for the study.

In conclusion, the stiffness ratio is a mechanical parameter that can be used to estimate tendon strength at the early stages of tendon healing, to guide the design of rehabilitation protocols, and to personalized evaluation of tendon healing.

ACKNOWLEDGMENTS: The research reported here was supported by NIAMS of the NIH under award number R21 AR077282.

REFERENCES

- [1] A. A. Suchak, et al., *Foot Ankle Int.*, 26(11): 932–936, 2005.
- [2] A. Brorsson, et al., *Am. J. Sports Med.*, 46(2): 470–477, 2018.
- [3] J. Heikkinen et al., *J. Bone Jt. Surg.*, 98(2): 85–92, 2016.
- [4] S. Hasegawa, et al., *J. Electromyogr. Kinesiol.*, 21(4): 622–630, 2011.
- [5] T. Haen, et al., *J Mech Behav Biomed Mater.*, 69: 178–184, 2017.
- [6] J. A. Martin, et al., *Ultrasound Med. Biol.*, 41(10): 2722–2730, 2015.
- [7] M. Kharazi, et al., *Sci. Rep.*, 11(5830), 2021.

EVALUATING THE EFFECTS OF COORDINATE SYSTEM SELECTION ON THUMB CARPOMETACARPAL JOINT ANGLES

Adam J. Chrzan (1), Nicole D. Arnold (1), Kevin Chan, M.D. (2), Tamara Reid Bush, PhD (1)

(1) Mechanical Engineering, Michigan State University, East Lansing, MI, USA
(2) Orthopedic Hand and Upper Extremity Surgery, Spectrum Health, Grand Rapids, MI, USA

INTRODUCTION

The human thumb is essential for performing activities of daily living, and accounts for 40-50% of overall hand function [1]. The carpometacarpal (CMC) joint of the thumb, located at the interface of the thumb metacarpal and trapezium at the base of the thumb, is of particular importance because it is capable of complex, multi-planar movement and is responsible for the majority of thumb motions required for task completion [2]. Consequently, loss of CMC motion poses challenges for the completion of activities of daily living.

To determine the three joint angles (flexion, abduction, internal rotation) of the thumb CMC joint using motion capture, two coordinate systems (CSs) are needed: one on the thumb metacarpal, and one on the hand. The dorsum, or back, of the hand is often used because it is accessible and does not interfere with hand motions. By attaching reflective markers to key bony landmarks, cartesian CSs can be established in a variety of ways. Many different CSs on the dorsum of the hand have been used in previous works. The International Society of Biomechanics proposed a standard CS constructed using bony landmarks on the trapezium, but this location is difficult to confirm with surface markers. Some have suggested the use of a pod of rigidly connected markers on the 3rd metacarpal as a more accessible substitute for the trapezium, but the practice is not widely used. The effects of CS choice on thumb CMC motion has not been studied in detail. In particular, the placement of markers used to establish hand dorsum CSs were hypothesized to have a significant effect on motion data outcomes.

Therefore, the goals of this work were to 1) determine the effect of hand dorsum coordinate system choice on thumb CMC joint angle ranges, and 2) identify the most accurate CSs for each of the three joint angles.

METHODS

Motion data were both collected from a custom designed reference system that was used to establish the ground truth alignment of CSs as

well as human participants. All three-dimensional (3D) positional data were gathered using reflective markers and a six-camera motion capture system (Qualysis, Gothenburg, Sweden) at 100 Hz. Each system described below.

A custom axial rotation device (ARD) was used to identify three perpendicular planes of motion (Fig. 1). The ARD consisted of a rigid vertical wall with an aligned marker pod (Fig. 1a) and three additional marker pods, each mounted on a uniaxial bearing (Fig. 1b-d). Bearings were positioned to rotate only about the axes of a cartesian CS on the ARD (Fig. 1a).

Participants placed their hand and forearm flat against the rigid wall of the ARD, aligning it with the ARD. Participants then performed a circumduction motion to move the thumb through its maximum range of motion to examine the impact of hand dorsum CS choice on thumb CMC joint angle ranges. Each participant performed the motion three times and results were averaged. Recruited participants had no history of significant hand injury, hand surgery, or diagnosis of arthritis, were right-hand dominant, and not pregnant. This work was approved by the university (IRB #00006111) and all participants were consented.

A rigid marker pod containing four markers was placed on the thumb metacarpal and individual markers were placed on the ulnar styloid (denoted as U), distal radial tubercle (R), and the distal ends of the 2nd (2) and 5th (5) metacarpals (Fig. 2). A second order zero-phase low-pass Butterworth filter with a cutoff frequency of 6 Hz was applied to all marker data.

Five hand dorsum CSs (RU2, RU5, R25, U25, RU25) were constructed using different combinations of the single markers denoted as R, U, 2, and 5 (Fig. 2). Each was then compared to the three known planes from the ARD. Flexion, abduction, and internal rotation angles were calculated between pairs of CSs using the Grood and Suntay method with modifications by Dabirrahmani and Hogg [3]. Flexion was the rotation about an axis pointing out of the palm, abduction about an axis pointing in the 'thumbs-up' direction, and internal rotation about an

axis pointing from the wrist to the distal end of the fingers (Fig. 2). Thumb CMC angle ranges were calculated between CSs on the hand dorsum and thumb metacarpal. The error of each hand dorsum CS was evaluated as the average difference of the angles resulting from the ARD CSs and hand CSs. CSs with errors closest to zero (positive or negative) were considered more desirable because they had greater alignment with the hand dorsum.

Analysis was performed using MATLAB (MathWorks, Natick, MA). One-way ANOVA tests were used to determine the impact of CS on each of the three joint angle ranges, while pairwise multiple comparisons were done using the Tukey adjustment.

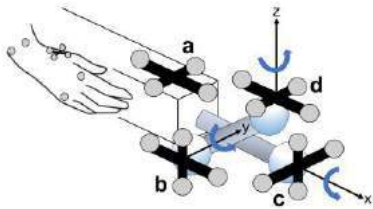


Figure 1: Axial rotation device (ARD). Coordinate systems were established on the ARD aligned marker pod (a), and each of the uniaxially rotating bearing pods (b-d).

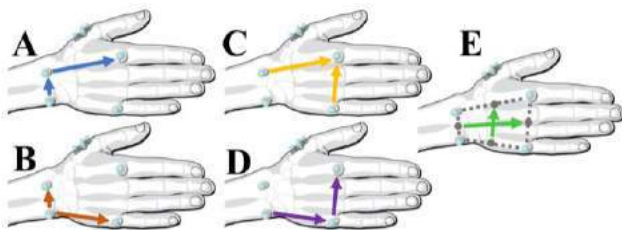


Figure 2: A) RU2, B) RU5, C) R25, D) U25, and E) RU25 hand dorsum coordinate systems constructed using single markers placed on the ulnar styloid, distal radial tubercle, and the distal end of the 2nd and 5th metacarpals. A rigid marker pod was attached to the dorsal surface of the thumb metacarpal.

RESULTS

62 participants (30M, 32F, avg. age = 40.4 years \pm 17.8) performed the circumduction motion, and a subset of 10 participants (4M, 6F, avg. age = 25.6 years \pm 4.7) performed the axial rotation tests with the ARD.

The effect of CS on joint angle ranges (Fig. 3) was significant for all three angles ($p < .01$ for each) – flexion, abduction, internal rotation. Pairwise comparisons revealed three CS pairs that were significantly different for all three angle ranges, three pairs for two angle ranges, and three pairs for one angle range. Only the U25-RU25 pairing was insignificant for all three angle ranges, meaning that all other CS pairs should not be directly compared and that significant differences in motion between studies could be solely a result of CS choice.

The effect of CS on error (Fig. 4) was significant for each axial rotation ($p < .01$ for each), signifying that the most appropriate choice of CS differs depending on the thumb motion that is analyzed.

DISCUSSION

Five hand dorsum coordinate systems were evaluated to identify their effects on thumb CMC joint angle ranges. When performing a circumduction motion, the choice of CS significantly affected each of the angles - thumb CMC flexion, abduction, and internal rotation (Fig. 3). This highlights the need for careful consideration of CS selection, particularly with regard to thumb motion. This is critical as differences in motion could be a result of the CS selection, and not related to any

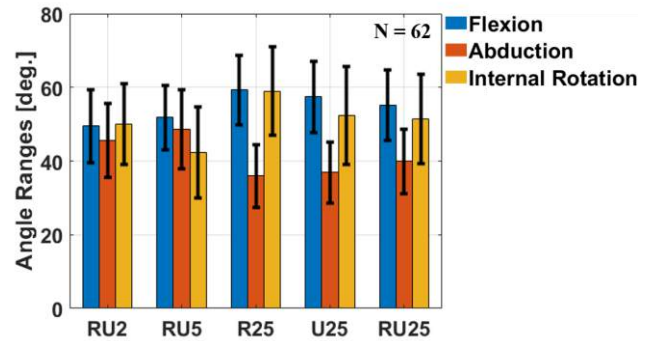


Figure 3: Thumb CMC joint angle ranges during the circumduction motion (N=62) were significantly different across coordinate systems.

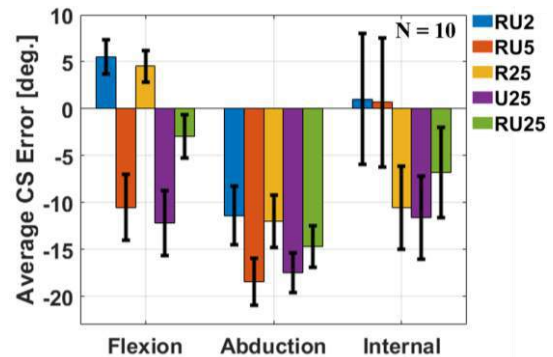


Figure 4: Average coordinate system errors were significantly different across each of the three angles (N=10).

physiological or disease associated changes. This work also provides insight into interpreting past results when comparing studies that utilized different CSs and could be used to adjust angle range numbers for comparison purposes.

Ground truth testing using the ARD showed CS errors differed across all three angles. If only interested in thumb CMC flexion, or if a motion is performed that predominantly utilizes CMC flexion, the RU25 CS would be the most attractive choice because it had the flexion error that was closest to zero ($\sim 2.9^\circ$) (Fig. 4). All CS errors in abduction were $>11^\circ$, but if interested in only abduction, the RU2 CS had the error closest to zero. In internal rotation the RU2 and RU5 had errors of $\sim 1^\circ$ and would both be suitable. Overall, when considering all angles, the RU2 CS had the lowest average error across all three angles, which would make it an appropriate choice for the study of complex, multiplanar thumb motions.

Future work will apply this knowledge to clinically collected data to report accurate findings of results.

ACKNOWLEDGEMENTS

Funding was received from the Spectrum Health – Michigan State University Alliance Grant.

REFERENCES

- [1] Moran, S. L., & Berger, R. A., *Hand Clinics*, 19(1):17–31, 2003.
- [2] Curran, P. F. et al., *Clinical Biomechanics*, 63:63–72, 2019.
- [3] Dabirrahmani, D., & Hogg, M., *Med Eng & Phy*, 39:113–116, 2017.

BIOMECHANICAL ANALYSIS OF A FETAL PULMONARY HEART VALVE REPLACEMENT

Sanchita S. Bhat (1), Katelynne Berland (1), Anna Farnan (1), Katherine Vietmeyer (1), Lakshmi Prasad Dasi (1)

(1) Department of Biomedical Engineering, Georgia Institute of Technology, Atlanta, GA, US

INTRODUCTION

Congenital heart diseases account for nearly one third of all congenital defects, and require surgical repair or medical management [1]. Pulmonary atresia with intact ventricular septum (PA/IVS) is one type of extremely rare congenital heart defect that occurs in 1% of total heart defects [2]. In this defect, the pulmonary valve is underdeveloped and atretic leading to hypoplasia of the right side of the heart and limiting flow through the right ventricle and main pulmonary artery. Many of these patients undergo palliation, but are subject to high risks of morbidity and mortality, eventually requiring heart transplantation or a pulmonary valve replacement [3]. Although these replacements are made from biocompatible materials, they can become dysfunctional, requiring further intervention and multiple surgeries. Attempts have been made to restore normal flow dynamics and allow for remodeling of the heart for biventricular circulation *in utero*, using minimally invasive techniques such as balloon valvuloplasty of the fetal pulmonary valve [4-5]. Performing fetal valvuloplasty can reverse the ventricular hypoplasia and allow a biventricular circulation, but most of these patients will go on to ultimately require postnatal valve replacements over their lifetimes. In an attempt to avoid the aforementioned circumstances, a completely bioresorbable tissue engineered heart valve was developed by our group for percutaneous implantation in the fetus [6]. The unique environment of the fetus and the fetal milieu may serve as an excellent host for tissue engineering concepts, because of the large number of progenitor cells. Our previous fetal tissue engineered heart valve (TEHV) could not be reliably reproduced, due to design challenges with the stent, as well as assembly challenges of mounting the leaflets on the stent frame. Therefore, this study aims to develop an alternative fetal transcatheter pulmonary valve replacement (FTPVR) with a novel sutureless technique to mount leaflets, thus eliminating premature catastrophic failure of valves, for use in endovascular repair *in utero*.

METHODS

Stent design and simulations. A balloon expandable stent frame was designed in-house using 3D CAD Software (Solidworks, Dassault Systems, Vélizy-Villacoublay, France) based on our adult transcatheter aortic valve replacement (TAVR) design, which exhibited improved hemodynamics (**Figure 1**). The stent structure comprised of a large commissural region, with cell regions comprising of the skirt and

leaflet. A commissure-to-commissure strut ensured the stent would not break during crimping and expansion. Computational simulations simulated our resolvable prototype stent made of nontoxic magnesium alloy (WE43) and a cobalt-chromium (Co-Cr, L605) stent for testing in the current study. We established a proof-of-concept design with Co-Cr, commonly used as medical grade stent material for the purposes of this study. The material properties were modeled as described in literature [7,8]. The 150 μm thick stent model was meshed using Altair Hypermesh (Altair Engineering, Troy, MI, USA) and boundary conditions were applied such that the stent was crimped and expanded.

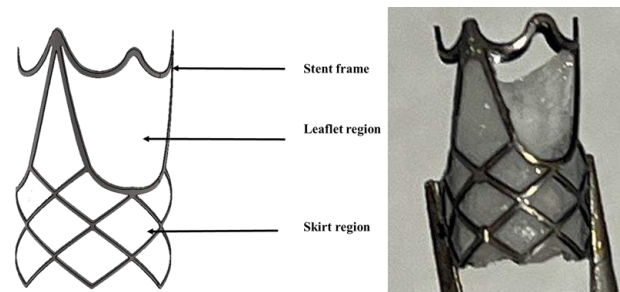


Figure 1: Stent CAD showing different regions of prototype

Valve manufacturing and assembly. Stent prototypes were laser cut using a 5mm tube of Co-Cr in a rotational stage in the OPTEC Femtosecond laser on high setting. To establish the efficacy of manufacturing and testing, a Co-Cr prototype was used. Post manufacturing, the stent prototypes were mounted with polycaprolactone (PCL) leaflets made from 0.75% PCL in chloroform (wt/vol) using an in-house spray coated technique. This was adapted to eliminate point stresses on the sutures that previously held the leaflets, leading to catastrophic failure of the valve. N=3 prototypes were manufactured with Co-Cr and ones with WE43 stents are currently underway.

In vitro performance. We mounted the FTPVR in a custom acrylic test chamber connected in our fetal right heart simulator (FRHS) as shown in **Figure 2**. Two pressure transducers, PI, P2, were placed upstream and downstream of the test valve respectively. A clamp-on flow

transducer recorded forward flow through the system from the FRHS via a LabView (National Instruments Corp, Austin, TX, USA) system. Additional details on the simulator have been previously reported [24]. We employed the following test conditions: 0.5 L/min cardiac output, 70/45 mmHg pulmonary artery pressures, heart rate 140 beats per minute and a working fluid of 60/40 water/glycerin (99% pure glycerin), representative of the fetal pulmonic physiological conditions around the 22 to 24 week gestational period, where the implant typically would take place. The effective orifice area (EOA) was computed using the Gorlin's equation and regurgitant fractions (RF) were calculated as the ratio of the closing volume (CV) and leakage volumes (LV) to the forward flow volume (FV):

$$EOA = \frac{Q}{51.6 \sqrt{PG}} ; RF = \frac{LV + CV}{FV}$$

Q represents the root mean square aortic valve flow over the same averaging interval of the pressure gradient, ΔP.

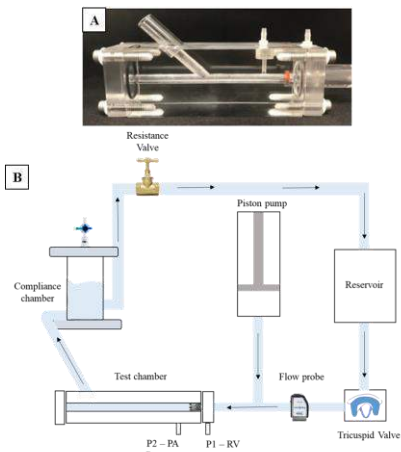


Figure 2: A: Acrylic test chamber and B: FRHS

RESULTS

The maximum stresses were found to be 300 MPa for WE43 alloy and between 877 MPa and 895 MPa for Co-Cr, observed mostly at the struts near the skirt region. The values for high stresses were distributed along the cell shape and within the ultimate tensile strength for both materials, indicating low susceptibility of catastrophic failure.

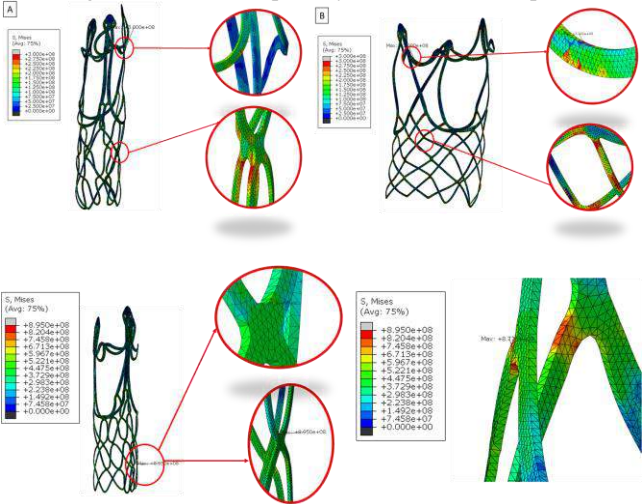


Figure 3: Results of WE43 (top) and Co-Cr (bottom) prototypes

Three trileaflet FTPVRs were successfully tested in the FRHS. On average, the valves had an EOA of 0.10 cm², a mean transvalvular pressure gradient of 5.79 mmHg and a regurgitant fraction of 8.9%. Between the prototypes, each of the measured metrics had a moderate standard deviation with the exception of regurgitation fraction, due to one prototype having higher than average regurgitation.

Prototype	Effective Orifice Area (EOA) (cm ²)	Mean Pressure Gradient (mmHg)	Regurgitation Fraction (%)
FTPVR – 1	0.07	8.07	2.8
FTPVR – 2	0.18	3.84	3.9
FTPVR - 3	0.07	5.48	20.06
Average	0.10	5.79	8.92

Table 1: Results from FRHS experiments

DISCUSSION

In patients who have PA/IVS, treatment may be beneficial, due to the regenerative capacity of the fetal milieu since most postnatal valve replacements that are limited by size and availability. In our preliminary computational simulations, we observed leaflet stresses to be very high at suture points. Since PCL is ductile when it is first manufactured, the high-stress regions will hold until PCL degrades to its brittle state, where suspected failure can happen. To avoid these circumstances, the sutureless method was adopted. This study, for the first time, incorporated a custom *in vitro* setup that mimicked the physiological conditions for a fetus at 22–24-weeks of gestational age. Imposing accurate conditions increases the efficacy of successful valve development. The standard deviations between prototypes were low, with the exception of one prototype having high regurgitation fractions, contributing to higher standard deviations in that metric.

Overall, this indicates the need to further fine tune and streamline the manufacturing protocol. To supplement the efficacy of this FTPVR, a full biomechanical analysis accounting for degradation rates and patterns within various designs is needed, and studies are underway. The hemodynamic characterization of a fetal valve prototype does not account for neotissue growth *in vivo*. The growth of the neotissue along with valve degradation will change its performance. For this, future animal studies are needed to supplement this data.

ACKNOWLEDGEMENTS

The authors want to acknowledge the surgeons at Nationwide Children’s Hospital, Ohio – Dr. Christopher Breuer and Dr. Aimee Armstrong for their continued guidance and support.

REFERENCES

[1] Farmer, D., et al, *Surgical Interv. for Congenital Anomalies*, 2015
[2] Gorla, S.R. et.al, *StatPearls*. 2022
[3] Bautista-Hernandez, V., et al., *Ann Thorac Surg*, 2011.91(2):p.555-60.
[4] Freeman, J.E., et al., *Ann Thorac Surg*, 1993. 56(6): p. 1393-5.
[5] Devanagondi, R., et al., *Pediatr Cardiol*, 2017. 38(2): p. 247-254.
[6] Zakko, J., et al., *JACC Basic Transl Sci*, 2020. 5(8): p. 815-828.
[7] Poncin, P., et al., *Materials & Processes for Medical Devices Conference* 2004, 2005: p. 279-283.
[8] Pang, T.Y., et al *MRS Advances* 6, 54–60 (2021)

FINITE ELEMENTS OF MULTISCALE MIXTURES (FE2M): THEORY, NUMERICAL IMPLEMENTATION, AND ANALYSES OF SIZE EFFECTS

Ashkan Almasi (1), Tim Ricken (2), David M. Pierce (1,3)

(1) Department of Mechanical Engineering, University of Connecticut, Storrs, CT, USA
(2) Institute of Structural Mechanics and Dynamics in Aerospace Engineering, University of Stuttgart, Stuttgart, Germany
(3) Department of Biomedical Engineering, University of Connecticut, Storrs, CT, USA

INTRODUCTION

We present a multi-scale finite element (FE) framework for modeling fluid saturated materials with a porous microstructures. Mixture theory and the theory of porous media both play an important role in many diverse areas of engineering, including the biomechanics of soft tissues (e.g. liver, brain, and cartilage), as well as coupled problems in material science and environmental sciences. The remarkable macro-mechanics of soft tissues derive from the complex micro-mechanics of their constituents, e.g. proteoglycans, collagens, and electrolytic fluid, and their interactions, thus multiscale models arise naturally. To facilitate mechanistic understanding and improved analyses (e.g. of experimental results) of the multi-scale mechanics of soft tissues we aimed to establish a computational framework specific to fluid-saturated, fibrous soft tissues and engineered materials.

We implemented a 3-D multiscale framework within FEBio (Version 3.5.1, University of Utah) combining mixture theory [1] and the FE²-method [2] (i.e. finite elements of multiscale mixtures or FE2M) to solve two-scale, non-linear, coupled, and time dependent boundary value problems (BVPs) for poro-hyperelastic, fluid-saturated porous media. We attached a representative volume element (RVE) of the microstructure at each material point of the macrostructure and performed discretizations of the BVPs on both macro- and micro-scales. After successful implementation of this algorithm in 3-D nonlinear FEs, we investigated the effect of the microstructural RVE size with respect to the macrostructural model.

METHODS

Theory. We write the pull back of the balance of linear momentum of the mixture (from the current to reference configuration \mathcal{B}_{0S}) as

$$\int_{\mathcal{B}_{0S}} \text{Div} (\mathbf{P}_E^S - p \mathbf{F}_S^{-T} J_S) dV_{0S} = \mathbf{0}, \quad (1)$$

where \mathbf{P}_E^S is the first Piola-Kirchhoff solid extra stress, p is the fluid pressure, \mathbf{F}_S and J_S are the deformation gradient and Jacobian of the solid. We

write the corresponding balance of mass of the mixture as

$$\int_{\mathcal{B}_0} \text{Div} [(n^F \mathbf{w}_{FS} + \mathbf{x}'_S) \mathbf{F}_S^{-T} J_S] dV_{0S} = 0, \quad (2)$$

where n^F is the current volume fraction of the fluid, \mathbf{w}_{FS} is the filtration velocity, and \mathbf{x}'_S denotes the velocity of a material point of the solid.

Numerical implementation. To solve the partial differential equations governing the macroscopic BVP, (1) and (2), we used the finite element method twice. We first provide macroscopic quantities, calculated from an intermediate solution of the macroscopic FE model, as boundary conditions (BCs) on the microscopic RVE, i.e. the deformation gradient $\bar{\mathbf{F}}_S$ and the gradient of pressure times the volume fraction of the fluid $\text{Grad}(n^F p)$. After solving the microscopic FE model with these BCs, we evaluate the macroscopic material tangent $\bar{\mathbf{A}}$ and measures $\bar{\mathbf{P}}, (\bar{\mathbf{E}}_S)_S^T \cdot \mathbf{C}_S \mathbf{J}_S, n^F \mathbf{w}_{FS}$ (first P-K stress, Green Lagrange strain rate, right Cauchy-Green tensor, respectively) at each Gauss integration point by a volume averaged solution of the underlying RVE. We perform computational homogenization of an arbitrary microscale quantity \bullet over a RVE or over a representative surface element in order to calculate its macroscopic counterpart $\bar{\bullet}$ following

$$\langle \bar{\bullet} \rangle \approx \frac{1}{V_{0S}} \int_{\mathcal{B}_{0S}} \bullet dV_{0S}, \quad [\bar{\bullet}] \approx \frac{1}{A_{0S}} \int_{\partial \mathcal{B}_{0S}} \bullet dA_{0S}, \quad (3)$$

where V_{0S} and A_{0S} are reference volumes and areas respectively.

Numerical analyses of size effects. We considered single-scale models as benchmark solutions for comparison to corresponding solutions from equivalent two-scale models, see Fig. 1. In Fig. 1 we illustrate the scale separation in the macrostructure, meaning that each cell in a single-scale model is equivalent to an RVE (considering we have periodically repetitive cells). The shaded region in the single-scale model is equivalent to the shaded element in the two-scale model, i.e we solve an RVE for each Gauss point within each element of the macrostructure. To study the size effect we use the same RVE in progressively larger macrostructures, thus increasing the difference in scales, and compare results obtained from single and two-scale models for displacement, stress, and fluid pressure.

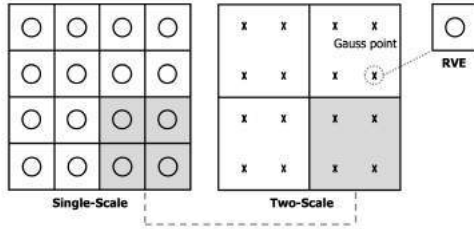


Figure 1: Schematic comparison of single-scale vs. two-scale models.

Single-scale models as benchmark solutions. We considered 3-D square plates with circular holes of length $4L$, $12L$, and $18L$ with $L = 0.4$ mm; thickness $t = 0.04$ mm; and radius of holes $r = 0.04$ mm, see Figs. 2(a)-(c). We subjected the plates to traction $T_x = 10$ MPa and allowed that surface to freely drain. We used a biphasic, neo-Hookean model with properties $E = 100$ MPa, $\nu = 0.3$, $K_d = 1e - 6$ mm⁴/(Ns) and extracted the numerical results at time $t = 1$ s. We used eight-node hexahedral elements for all finite element models.

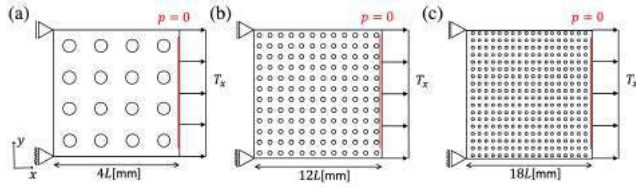


Figure 2: Single-scale finite element models: (a) Macro 1 ($4L \times 4L \times t$), (b) Macro 2 ($12L \times 12L \times t$), and (c) Macro 3 ($18L \times 18L \times t$).

Corresponding two-scale models. We considered 3-D square plates of lengths nL with $n = 4, 12, 18$ and $L = 0.4$ mm, and thickness $t = 0.04$ mm (for the macro-scale models), see Fig. 3(a). We subjected the macro-scale models to the same BCs as the single-scale models above. For the microstructural RVEs we considered a 3-D square plate of length $L = 0.4$ mm and thickness $t = 0.04$ mm with a circular hole $r = 0.04$ mm (using 1160 elements and 1968 nodes and the same material model as above), see Fig. 3(b). We detail the number of nodes, elements, and holes for both single-scale and two-scale (macro-scale) models in Table 1.

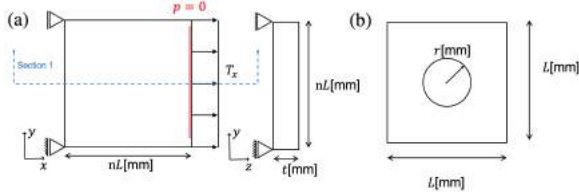


Figure 3: Two-scale finite element models: (a) macro-scale 3-D plate ($nL \times nL \times t$) and (b) micro-scale RVE ($L \times L \times t$).

Table 1: Number of nodes/elements in single- and two-scale models.

		Macro 1	Macro 2	Macro 3
Single-scale	Nr nodes	30,003	155,673	348,141
	Nr elements	18,560	101,376	227,412
	Nr holes	16	144	324
Two-scale	Nr nodes	27	147	300
	Nr elements	8	72	162

RESULTS

In Fig. 4 we show the comparison between single-scale and two-scale models based on volume integrals, considering the traction plus free-draining surface boundary conditions. In Fig. 5 we show the convergence plot in $\|e\|_2$ for fluid pressure ($n = 4, 12, 18$ and $L = 0.4$ mm). For Macro 1, 2, and 3 (Fig. 4(a), (c), and (e)), the results of the total Cauchy stress for our two-scale models showed excellent agreement with the single-scale (benchmark) solutions. As the difference in length scales increases between the macrostructure and the microstructural RVE, the error in the fluid

pressure decreases significantly to 2.8% and 1.6% for Macro 2 (Fig. 4(d)) and Macro 3 (Fig. 4(f)), respectively.

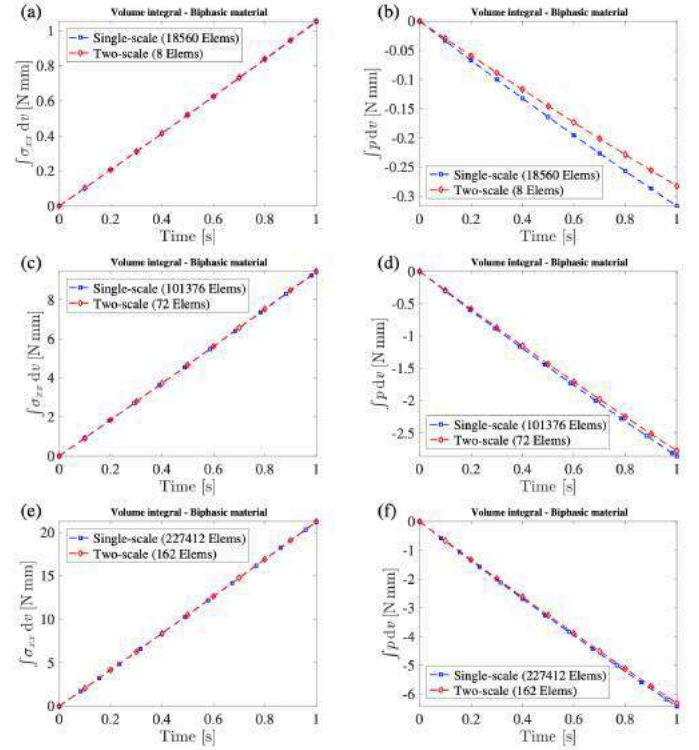


Figure 4: Single- vs. two-scale models based on volume integrals: total Cauchy stress (σ_{xx}) for (a) Macro 1, (c) Macro 2, (e) Macro 3; and fluid pressure for (b) Macro 1, (d) Macro 2, (f) Macro 3.

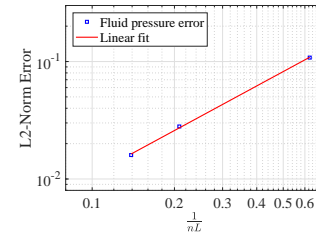


Figure 5: Convergence plot in $\|e\|_2$ for fluid pressure ($n = 4, 12, 18$ and $L = 0.4$ mm). The slope of the regression line is 1.26.

DISCUSSION

We established a 3-D multiscale homogenization scheme for fluid-saturated porous media. Our results demonstrate that size effects do influence results, e.g. distributions of stress and fluid pressure, within our multiscale solutions. However, the size effects are manageable as we can make them arbitrarily small by increasing the difference in length scales between macro- and micro-scale models. As this difference increases, e.g. increasing n in $1/nL$ ($n = 4, 12, 18$), the $\|e_p\|_2$ -norm error decreases with slope 1.26. Our FE2M framework (FE analyses augmented to derive the material behaviors from a distribution of finer scale FE analyses) facilitates studies of engineering materials for applications in biomedical engineering, material science, and environmental sciences. In particular, our FE2M framework is ideally suited to bridge the joint, tissue, and intra-tissue scales for problems in biomechanics, but has not yet been applied to multi-phase, fibrous soft tissues.

ACKNOWLEDGEMENTS

NSF CAREER 1653358; Gerard Ateshian and Steve Maas.

REFERENCES

- [1] Bowen RM. *Int. J. Eng. Sci.* 20.6 (1982).
- [2] Feyel F. *Comput. Methods in Appl. Mech. Eng.* 192:28-30 (2003).

EVALUATING THE USE OF ELASTIC REGISTRATION FOR DETERMINING ATRIOVENTRICULAR VALVE ANNULUS MECHANICS

Devin W. Laurence Ph.D. (1,2), Christian Herz M.S. (1), Silvani Amin B.A. (1), Ana Sulentic B.S. (1),
Patricia Sabin M.S. (1), Andras Lasso Ph.D. (3), Matthew A. Jolley M.D. (1,2)

- (1) Department of Anesthesiology and CCM, Children's Hospital of Philadelphia, Philadelphia, PA, USA
(2) Division of Pediatric Cardiology, Children's Hospital of Philadelphia, Philadelphia, PA, USA
(3) Laboratory of Percutaneous Surgery, Queen's University, Kingston, ON, Canada

INTRODUCTION

Atrioventricular valves regulate the unidirectional blood flow between the atria and the ventricles. These one-way check valves are complex structures that consist of the *leaflets* that seal the atrioventricular orifice, the *annulus* that is the hinge between the leaflets and surrounding cardiac tissue, and the *chordae* that anchor the leaflets to *papillary muscles* in the ventricle wall. The synergistic function of these sub-valvular components is crucial to healthy valve function.

Recent studies have revealed that dynamic annular shape is an important contributor to healthy valve function and patient outcomes [1-2]. More recently, research groups have used *in vivo* data from animal models [3] and patients [4] to extend these findings to consider annulus mechanics. Specifically, these studies used embedded sonocrystals or annular curve fitting techniques to determine annular displacements and kinematic measures (e.g., stretch). However, no study has yet employed deformable image registration to automatically provide annulus deformations with point-to-point correspondence between phases.

Thus, the objective of this study is to explore the use of elastic registration in determining atrioventricular annulus mechanics (e.g., stretch). We leveraged open-source tools in SlicerHeart to define the annulus for one representative tricuspid valve (TV) and custom deformable image registration code to automatically propagate the user-defined annulus throughout the cardiac cycle. This allowed us to evaluate existing approaches for determining annular kinematics and explore the influence of inter-user variability on annulus stretches.

METHODS

This study was performed according to a protocol approved by the Institutional Review Board at the Children's Hospital of Philadelphia.

Image Acquisition: 3DE images of the TV were acquired using EKG gated, Full Volume or 3D Zoom mode. Transthoracic X7 or X5 probes were used with the Philips IE33 and EPIQ 7 ultrasound systems (Philips

Medical, Cambridge, MA).

Annulus Modeling: 3DE images of one patient with hypoplastic left heart syndrome and a Fontan circulation were imported into 3D Slicer using the SlicerHeart extension, and the TV annulus was manually defined using the Valve Annulus Analysis module in SlicerHeart [5]. We considered three phases: end diastole (ED), mid systole (MS), and end systole (ES) (**Figure 1**). Timing of the cardiac cycle was determined by valve position. Three independent observers repeated this process to understand how inter-user variability influenced annulus definition as well as subsequent elastic registration and mechanics-based analysis.

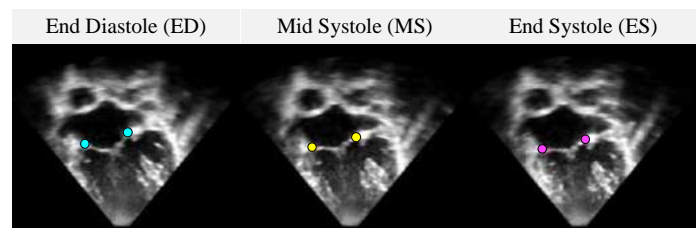


Figure 1. Representative TV annulus during the cardiac cycle.

Elastic Registration: The annulus curve was resampled to 200 uniformly distributed control points. These points were then automatically propagated to the ED and ES phases via custom code using Elastix image registration [6] with frame-to-frame propagation.

Annular Stretch Quantification: The manually generated and automatically propagated annuli for the three cardiac phases were then transformed to cylindrical coordinates (**Figure 2**) and the annulus stretches were computed using two methods. The first “*correspondence*” approach considered the 200 automatically propagated annulus control points as virtual fiducial markers. On the other hand, the second “*fitting*” approach used moving least squares to fit the manually generated annulus point cloud with a periodic curve and

generate 200 uniformly distributed material points [4]. The acquired points from both methods were used to compute the annulus stretch.

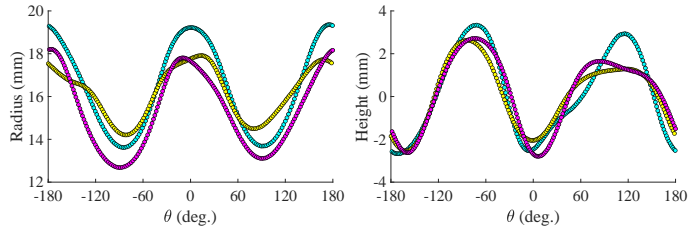


Figure 2. Transformed TV annulus to cylindrical coordinates. Colors indicate the cardiac phase (see also Figure 1).

RESULTS

Inter-User Variability in Annulus Definition: The three independent users produced manually generated annuli with minimal inter-user variability (<1 mm) (Figure 3). The variation was larger for the radius compared to the height.

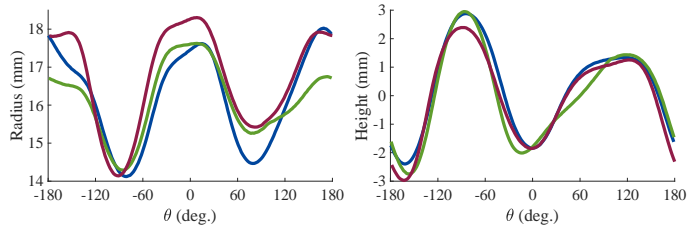


Figure 3. Annulus radius and height for one representative TV repeated by three independent users (denoted by color).

Annulus Stretches Computed Using Correspondence vs. Fitting: Annulus stretches determined via the correspondence and fitting approaches are provided in Figure 4. We noted some similarities with regions of larger discrepancies likely due to limitations in the fitting approach outlined in the Discussion.

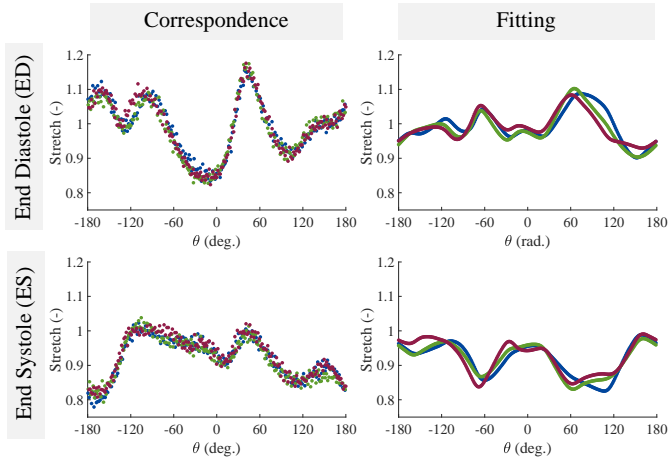


Figure 4. Annulus stretches computed using the correspondence and fitting approaches for three independent users.

Annulus Stretches Computed Using Registration vs. User Definition: The annulus stretches computed using automatically propagated and manually generated annuli are provided in Figure 5. Interestingly, we observed that the relatively small inter-user variability (Figure 3) resulted in substantial variations in the computed annulus stretches. On the other hand, elastic registration led to less variation in the computed annulus stretches for both ED and ES.

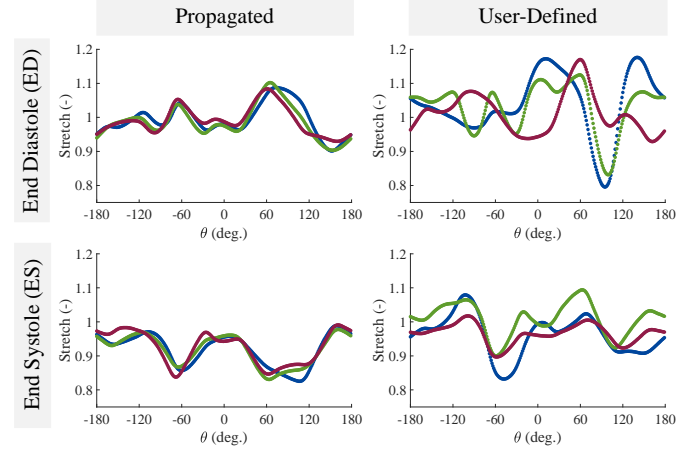


Figure 5. Annulus stretches computed via fitting with the propagated and user-defined annuli for three independent users.

DISCUSSION

In this investigation, we explored the use of elastic registration to support the analysis of atrioventricular valve annulus mechanics. We leveraged open-source tools in 3D Slicer and SlicerHeart to define the TV annulus in MS and custom Elastix image registration code to propagate it to ED and ES. The resulting manually generated annuli and automatically propagated annuli allowed us to compare two methods of computing annulus stretches. Our *primary finding* was that the existing curve-fitting approach resulted in incorrect annulus stretches when compared to our new method that ensures correspondence between cardiac phases. Specifically, lack of correspondence for the existing curve-fitting approach resulted in erroneous annulus stretches for large changes in annulus radius or height. Our *second finding* was that inter-user variability of the user-defined annulus did not strongly influence computed stretches for automatically propagated annuli but led to significantly different stretches for manually generated annuli.

There are several extensions of this work. First, the present analysis can be extended to consider other image registration methods (e.g., ANTs [7]) or emerging deep learning approaches [8]. Second, future animal studies can consider affixing sonocrystals to the atrioventricular valve annulus [3] to experimentally evaluate the accuracy of deformable image registration. Finally, application of these tools can be applied to more effectively understand differences in annular mechanics for normal and dysfunctional valves. We have demonstrated the value of using elastic registration for more accurate determination of annulus mechanics, and future studies should consider more patients for more powerful statistical comparisons.

ACKNOWLEDGMENTS

This work was supported by the Children's Hospital of Philadelphia (CHOP) Pediatric Valve Center (Frontier Grant), the Cora Topolewski Foundation, and NIH 1R01HL153166. DWL was supported by NHLBI T32 HL007915.

REFERENCES

- [1] Grewal J, *et al.*, *Circ.*, 121:1423-1431, 2010.
- [2] Bartels K, *et al.*, *J. Cardio. Vasc. Anesth.*, 28:18-24, 2014.
- [3] Malinowski M, *et al.*, *Ann. Thorac. Surg.*, 106:1804-1811, 2018.
- [4] Ross CJ, *et al.*, *JTCVS Open*, 10:324-339, 2022.
- [5] Lasso A, *et al.*, *Front. Cardio. Med.*, 2384, 2022.
- [6] Klein S, *et al.*, *IEEE Trans. Med. Img.*, 29:196-205, 2009.
- [7] Avants BB, *et al.*, *Med. Image Analysis*, 12:26-41, 2008.
- [8] Herz C, *et al.*, *Front. Cardio. Med.*, 1839, 2021.

PATIENT-SPECIFIC FLAP MOTION, FL FLOW, AND AORTIC STIFFNESS IN ACUTE UNCOMPLICATED TYPE B AORTIC DISSECTIONS USING 4D FLOW MRI AND 2D PC MRI: A PRELIMINARY STUDY

H. Cebull (1), S. Hashemi (2), K. Porte (3), J. Oshinski (1,4), B.G. Leshnower (3), M. Piccinelli (1),

(1) Department of Radiology and Imaging Sciences, Emory University School of Medicine, Atlanta, GA, USA

(2) Cardiovascular Imaging Core, Children's Healthcare of Atlanta, Atlanta, GA, USA

(3) Division of Cardiothoracic Surgery, Department of Surgery, Emory University School of Medicine, Atlanta, GA, USA

(4) Department of Biomedical Engineering, Georgia Institute of Technology, Atlanta, GA, USA

INTRODUCTION

Aortic dissection is a life-threatening condition that is defined by a tear within the aortic wall separating it into a true and false lumen (FL). Stanford type B aortic dissections (TBAD) occur in the descending aorta (DescAo) and can be classified into acute (< 7 days onset), subacute (< 30), and chronic phases (> 30). While some uncomplicated TBAD cases can be medically managed, others fail medical therapy and develop false lumen aneurysms. To prevent rupture, these cases can be treated with thoracic endovascular aortic repair (TEVAR) ideally within the acute and subacute phases to eliminate antegrade false lumen flow and achieve optimal aortic remodeling [1]. Determining which cases will lead to aortic growth remains a challenge due to inadequate methods of dissection characterization and lack of studies within the acute phase. Identifying independent predictors of aortic growth early on would allow early intervention, improving patient outcomes.

Studies aiming to identify unique morphological features of TBAD (e.g., entry tear size, aortic length, diameter, tortuosity) or flow- and thrombus-derived metrics lack consistent findings [2-5]. Some recent studies, however, are showing that FL flow assessments via 2D and 4D flow MRI data may be predictive of adverse complications for patients with TBAD [4,6]. One such study found that systolic antegrade flow greater than 30% and diastolic retrograde flow greater than 80% within the FL identified patients at higher risk for complications [6]. Burris *et al.*, similarly demonstrated that a large percentage of FL diastolic retrograde flow measured at the entry tear is associated with an increased aortic growth rate [4]. Both studies point toward false lumen pressure being the strongest identifier of high-risk cases, but only investigated TBAD cases in the chronic phase when the dissection flap is much stiffer (i.e., less suitable for TEVAR).

Therefore, there is currently an unmet need for a simple, yet thorough assessment of the false lumen particularly in acute TBAD to identify patients that would benefit from early TEVAR. While it is understood the flap distensibility is much larger in the acute phase, it is

poorly quantified and its role in overall FL stiffness and flow is also underexplored. Here, we present a novel, preliminary approach that assesses flap motion in the acute phase using 2D PC-MRI. We also aim to assess FL aortic stiffness and pressure of these acute cases using 4D flow and 2D PC-MRI techniques previously applied to chronic TBAD.

METHODS

Patient Demographics and Data Collection. 2D PC MRI and 4D flow MRI were acquired on five patients (P1-5; 3M/2F) with acute uncomplicated TBAD using a Siemens 3T scanner at Emory University Hospital. We acquired the 4D flow over the entire thoracic aorta region and acquired the 2D data at planes in both the proximal and distal regions of the descending thoracic aorta. Data were analyzed using Siemens 4Dflow (v2.4), Horos (v3.3.6), and Medviso Segment [7]. CTA images from routine clinical acquisition were used to identify and measure the dominant entry tear size (i.e., largest tear), branch locations, and growth. The CTAs were collected at the time of diagnosis and at a one month follow up. We segmented the CTAs using VMTK for visualization of the geometry.

Flap motion. To determine flap motion amplitude, we placed a line on the longest axis parallel to the dissection flap and a perpendicular line that reached from the long axis line to a point on the dissection flap furthest from that line (Fig. 1a) throughout the whole cardiac cycle on each 2D PC-MR image (proximal and distal DescAo). The flap movement was calculated by recording the length of the perpendicular, short axis line at all 20 timesteps. We took the difference between the highest and lowest values in the waveform to find max. flap amplitude.

False lumen flow. False lumen ejection fraction (FLEF), established by Burris, *et al.* [4], was calculated at the dominant entry tear as mean diastolic retrograde flow (mL/s) divided by mean systolic antegrade flow (mL/s) from 4D flow data (Eq. 1). FL_{DR} and FL_{SA} represent false lumen diastolic retrograde and systolic antegrade, respectively. We placed the planes perpendicular to the primary entry tear. 4D flow data

was omitted for P5 due to acquisition errors. Using 2D PC-MRI, FL systolic antegrade and diastolic retrograde flows were measured distal to the entry tear within the descending aorta.

$$\frac{FL_{DR}}{FL_{SA}} = FLEF \quad (1)$$

Pulse wave velocity. We calculated FL pulse wave velocity (PWV) by dividing the length (m) from the ascending aorta 2D PC-MRI acquisition plane to the descending plane by velocity wave propagation time (s) from the ascending aorta to descending within the false lumen (locations of planes in Fig. 1).

RESULTS

From the standard clinical CTA analysis, we found that entry tear sizes ranged from 40 - 132 mm². P1 and P5 exhibited growth at follow-up (no follow up for P4). Due to the substantial growth, P5 underwent TEVAR at 3 months. Analysis of the 4D flow MRI data, revealed that FLEF substantially varied among the four cases (26.125% ± 22.15, Fig. 1a, Table 1).

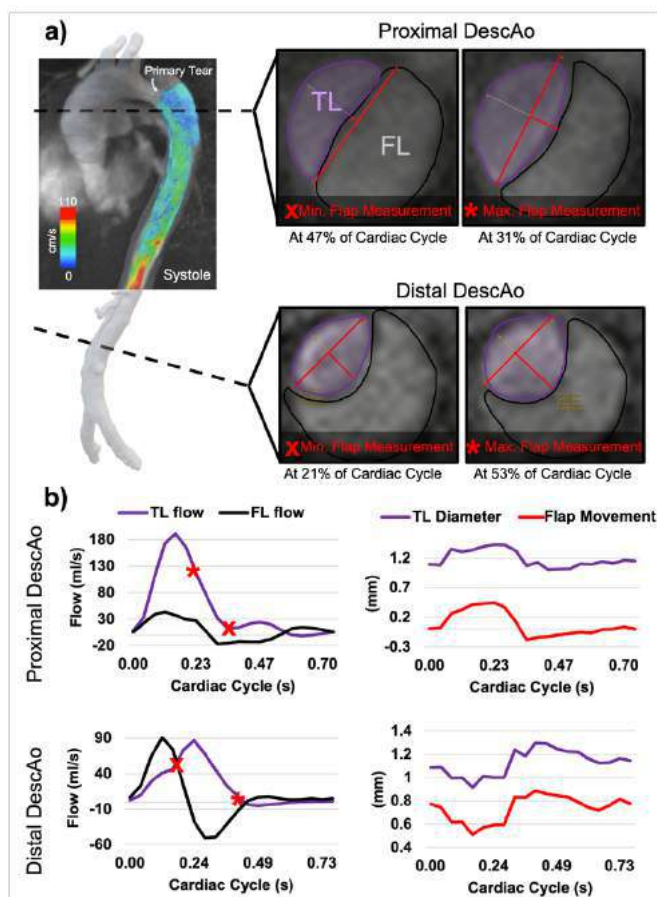


Figure 1: a) CTA segmentation overlaid on 4D Flow MRI of P3. Proximal and distal 2D PC-MRI planes with representative flap measurements (min. (x) and max. (*) locations shown on TL flow); b) 2D PC-MRI-derived flow and flap movement measurements over one cardiac cycle. TL = true lumen; FL = false lumen

From our 2D PC-MRI data, we recorded the peak flap amplitude in Table 1 and generally found that the distal plane yielded lower peak amplitudes. Figure 1 shows example cross-sections from P3 of flap movement over one cardiac cycle. Our FL_{DR} and FL_{SA} and PWV values are reported in Table 1. We observed that patients with higher PWV also had lower flap amplitude.

Table 1: Summary of measured parameters.

PID	CTA	4D Flow	2D PC-MRI		
	ΔD at 1 mo. (mm)	FLEF (%)	Flap Amplitude (mm)	FL _{DR} /FL _{SA} (%)	PWV (m/s)
P1	6	29.6	6.7	42 / 43	--
P2	0	8.3	6.2	63 / 77	3.79
P3	0	56.1	11.5	57 / 49	1.58
P4	--	10.5	8.0	67 / 77	18.14
P5	14	--	5.7	87 / 44	23.45

ΔD = diameter difference; FLEF = false lumen ejection fraction; FL_{DR} = false lumen diastolic retrograde flow; FL_{SA} = FL systolic antegrade flow; PWV = pulse wave velocity

DISCUSSION

This study demonstrates how 2D PC-MRI and 4D MRI flow can be used to investigate *in vivo* FL flow for patients with acute uncomplicated TBAD. Given the preliminary nature of this study and the limited number of patients currently enrolled, we were unable to identify significant trends between FLEF, flap motion, wall stiffness and aortic growth. More patients will be needed to confirm the suitability of these metrics in stratifying uncomplicated TBAD and predict the risk of growth. All our metrics showed a high degree of variability, requiring further investigation and comparison to follow-up measurements as a potential unique study of TBAD progression.

Patient 5 proved to be an interesting case: Based upon findings from Evangelista *et al.*, FL_{DR} and FL_{SA} values for P5 suggested that the patient was at high risk for complications, which was confirmed by the large follow up growth and subsequent TEVAR. We also noted the lowest flap amplitude and highest PWV in P5, suggesting a greater aortic stiffness. On the other end of the spectrum, P3 showed the highest flap amplitude and lowest PWV with no growth at follow-up.

Our long-term goal is to incorporate these into a larger predictive risk model to identify patients with acute TBAD that might benefit from early endovascular therapy. More sophisticated approaches to quantify flap motion will be considered to link the cyclic deformations to local flow features as measured with 2D and 4D Flow MRI.

One limitation of our study is the acquisition of 2D PC-MRI at fixed levels resulting in variable distances from entry tear. The other notable limitation is our small sample size due in part by the difficulty of collecting data from acute TBAD patients.

There are many 4D flow studies and approaches to investigate chronic TBAD. However, standardization and implementation of these methods remains limited. Our current findings demonstrate the potential for methodologies that combine the anatomical assessment provided by CTA analysis with PC-MRI measurements of FL flow and proxies for FL pressure in the acute phase of TBAD. We believe this approach has potential for identifying patients at risk for aortic growth thereby improving the timing of intervention which may result in improved survival for patients with this lethal disease.

ACKNOWLEDGEMENTS

We would like to acknowledge the effort of the healthcare team and the patients willing to participate in this study.

REFERENCES

- [1] Yang, Y., *et al.*, Front Surg, 3;9:852628, 2022.
- [2] Cao, L., *et al.*, Eur J Cardiothorac Surg, 58(4): p. 714-721, 2020.
- [3] Qiu, P., *et al.*, J Thorac Dis, 12(12): p. 7193-7201, 2020.
- [4] Burris, N.S., *et al.*, Eur J Cardiothorac Surg, 1;57(5):896-903, 2020.
- [5] Chu, S., *et al.*, Front Cardiovasc Med, 9; 9: 905718, 2022.
- [6] Evangelista, A., *et al.*, JACC, 79(24), 2022.
- [7] Heiberg, E., *et al.*, BMC Med Img, 10;1, 2010

EFFECT OF GAGS ON TENSILE PROPERTIES OF POSTERIOR CORNEA

M.E. Emu (1), H. Hatami-Marbini (1,2,3)

- (1) Mechanical and Industrial Engineering, University of Illinois at Chicago, Chicago, IL USA
 - (2) Biomedical Engineering, University of Illinois at Chicago, Chicago, IL USA
 - (3) Civil, Materials & Environmental Engineering, University of Illinois at Chicago, Chicago, IL USA
- Email: hatami@uic.edu

INTRODUCTION

The cornea is the outermost part of the eye considered the eye's window. Among five layers, the thickest layer of the cornea is the stroma which forms almost 90% of the corneal total thickness. The corneal stroma is composed of many collagen lamellae. These lamellae are interwoven in the anterior region; however, the amount of their interlacing decreases moving towards the posterior layers such they become almost parallel with respect to each other and form a plywood structure in the posterior region of the cornea [1].

The individual collagen lamellae are made up of thin collagen fibrils that are embedded in a hydrated proteoglycan matrix. The proteoglycans (PGs) are shown to be important for corneal transparency as they determine the hydration of the cornea in vivo conditions. PGs are composed of glycosaminoglycans (GAGs) that are attached to core proteins. The major PGs in the human cornea are decorin, lumican, keratocan, and mimecan that primarily contain keratan sulfate and chondroitin sulfate GAGs. PGs bind to collagen fibrils at specific location by their core proteins [2]. The negatively charged GAG chains of PGs attract charged ions and water molecules inside the corneal stroma by osmosis. The mechanical properties of the cornea depends on hydration [3]. Thus, GAGs are believed to be important in defining the mechanical response of the cornea. They also play a role in preventing neighboring collagen fibrils come together and maintain their hexagonal arrangement [4]. It has been proposed that the interaction between GAG chains creates molecular attractive forces between adjacent collagen fibrils. This model suggest that GAGs are important for the corneal mechanical strength. In a recent work, we showed that removing GAGs from the corneal samples results in a significant softening of corneal mechanical properties [5]. This work is a continuation of our recent research with the primary objective of determining the relation between structural functions of GAGs and the anisotropic corneal microstructure. Here, we prepared corneal strips from the posterior part

of the cornea and used keratanase enzyme to remove keratan sulfate GAGs from the corneal strips. We then performed uniaxial tensile experiments to assess the effect of GAGs on tensile response of posterior flaps.

METHODS

We collected fresh porcine eyes and used a sharp scissor to remove excess tissue and fat. The epithelial layer was removed using the blunt edge of a scalpel. Then corneal rings were excised using a sharp scissor. The thickness of the specimens was measured by a digital pachymeter (DGH Tech.). The corneal rings were dried in the air until the thickness reached about $800\mu m$. Then, the anterior 400 μm part of corneal samples was removed using a DSAEK system. The remaining portion of the cornea was referred to as posterior region and a custom-made double bladed device was used to cut strips. The specimens were divided into two control and enzyme groups.

For the enzyme treatment, the samples were completely dried and were then immersed in sodium acetate buffer solution (0.1M) with keratanase enzyme (KS II, 0.1 U/ml). The pH of the solution was 6.0 and samples were kept in the solution at $37^{\circ}C$ for about 20 hours. This was similar to the method that we used to remove GAGs from full thickness corneal samples in a previous study [5].

All the specimens were tested using ARES G2 uniaxial testing machine. Before testing, the thickness of the corneal specimens was measured. Then, the corneal strips were mounted into the machine using sandpaper at the grips. A tare load was applied to straighten the samples and confirm their firm grip [6]. The corneal strips were stretched to 20% strain at the displacement rate of $2mm/min$. The initial cross-sectional area of the strips was used to calculate the tensile stress from the measured force.

The experimental data were processed and analyzed in Microsoft Excel. Statistical analyses were performed in SAS analytical tool. Shapiro–Wilk test was performed for the normality check of the data while one-way ANOVA was used to determine the possible significance level of difference that existed in the behavior of different groups. P-value of 0.05 was used.

RESULTS

The stress of each group of corneal flaps was plotted as a function of tensile strain in Figure 1. The results suggested that the enzyme treatment reduced the tensile strength of posterior flaps but the effect of GAG removal was not significant at all levels of applied strain. In Figure 2, the tangent moduli were shown at 5%, 10%, 15%, and 20%. The tangent modulus followed a similar trend of tensile stress, i.e., the enzyme treatment did not have a significant effect on the tensile modulus of posterior flaps.

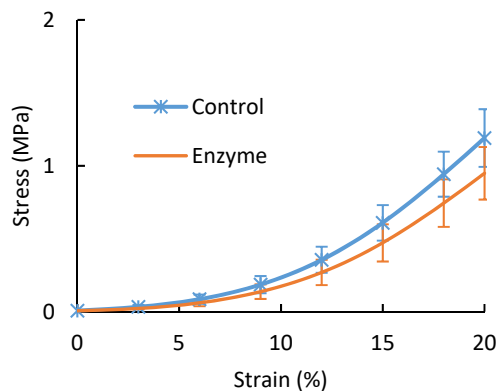


Figure 1: Stress-strain curve of porcine corneal posterior flaps.
The vertical error bar indicates the standard deviation.

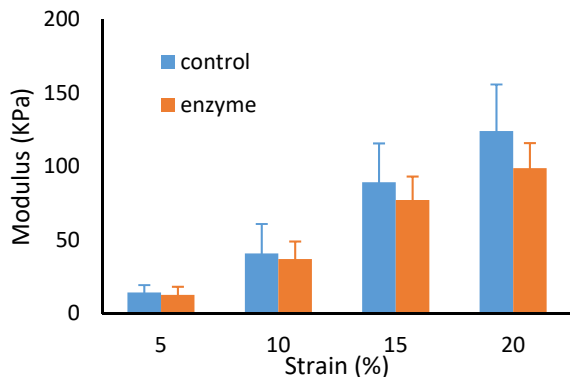


Figure 2: Distribution of tangent modulus of porcine corneal flaps at 5%, 10%, 15%, and 20% strain. The vertical error bar indicates the standard deviation.

DISCUSSION

The main purpose of this study was to characterize the tensile response of enzyme-treated porcine corneal flaps that were prepared from the posterior parts of the cornea. All the stress-strain curves reported in this study (Figure 1) appeared to be nonlinear which was consistent with previous studies characterizing the tensile stress-strain response of the cornea. Although enzyme treated samples had a softer tensile stress-strain behavior compared with the response of control

samples; the difference between the behaviors of two groups was not significant. This was different than our previous finding for the role of GAGs on the tensile response of full thickness cornea [5]. This suggests the importance of the arrangement of collagen lamellae throughout the corneal microstructure. The collagen lamellae lie on top of each other in the posterior regions. In a previous study on characterizing the efficacy of corneal collagen crosslinking treatment, we found no significant tensile property improvement of posterior flaps because of this treatment procedure [6]. The previous imaging studies of the cornea showed that collagen lamellae in the anterior region appeared to be interwoven whereas the ones in the posterior part are parallel with respect to each other. PGs attach to collagen fibrils with their core proteins while their GAG side chains interact with each other and act as a glue connecting the neighboring collagen fibrils together [4]. In enzyme treated sample, the GAG density was significantly reduced because of their enzymatic digestion. Thus, the number of GAG bridges was reduced, which is why the tensile properties of enzyme treated samples were lower compared to those of the control samples. However, the difference was not significant because of the specific arrangement of collagen fibrils in the posterior regions of the cornea. Based on the present experimental study, we propose that collagen fibrils are primarily responsible for tensile properties of the cornea in the posterior regions. However, GAGs become important when collagen lamella interweaving is significant. We are currently conducting additional experimental studies in order to characterize the effect of GAGs on tensile properties of the corneal strips prepared from anterior region to test this hypothesis. The lack of these experiments can be seen as a limitation of the current work. Furthermore, future studies are required to characterize the response of human corneas. Although the tensile properties of human and porcine corneas did not show significant variation [7], human cornea exhibited higher amount of stiffening than the porcine cornea when they were undergone collagen crosslinking treatment.

ACKNOWLEDGEMENTS

The authors acknowledge the support in part from NIH-EY030264

REFERENCES

- [1] Y. Komai, T. Ushiki, The three-dimensional organisation of collagen fibrils in the human cornea and sclera, *Invest. Ophthalmol. Vis. Sci.*, 1991, 32: 2244-2258
- [2] J.E. Scott, M. Haigh, Identification of specific binding sites for keratan sulphate proteoglycans and chondroitin-dermatan sulphate proteoglycans on collagen fibrils in cornea by the use of cupromeronic blue in 'critical-electrolyte-concentration' techniques, *Biochem. J.*, 1988, 253: 607-610
- [3] Hatami-Marbini H, Etebu E. Hydration dependent biomechanical properties of the corneal stroma. *Experimental eye research* 2013, 116: 47-54.
- [4] Lewis, PN, Pinali C, Young RD, Meek KM, Quantock AJ, Knupp C. Structural interactions between collagen and proteoglycans are elucidated by three-dimensional electron tomography of bovine cornea. *Structure*. 2010, 18(2):239-45.
- [5] Hatami-Marbini, H. On mechanical roles of Glycosaminoglycans in tensile properties of the porcine corneal stroma, *Invest. Ophthalmol. Vis. Sci.*, accepted.
- [6] Hatami-Marbini, H. and S.M. Jayaram, UVA/riboflavin collagen crosslinking stiffening effects on anterior and posterior corneal flaps. *Exp Eye Res*, 2018, 176: 53-58.
- [7] Elsheikh, A., D. Alhasso, and P. Rama, Biomechanical properties of human and porcine corneas. *Exp Eye Res*, 2008, 86(5): 783-90.

TOWARD A BIOMECHANICAL MODEL OF AORTIC DEVELOPMENT

Bruno V. Rego (1), Sae-Il Murtada (1), Guangxin Li (2),
George Tellides (2,3), Jay D. Humphrey (1,3)

(1) Department of Biomedical Engineering, Yale University, New Haven, CT, USA
(2) Department of Surgery, Yale School of Medicine, New Haven, CT, USA
(3) Vascular Biology and Therapeutics Program, Yale School of Medicine, New Haven, CT, USA

INTRODUCTION

Despite its vital importance for establishing proper cardiovascular function, the process through which the vasculature develops and matures postnatally remains poorly understood. From a clinical perspective, the ability to mechanistically model the developmental time course in arteries and veins, as well as to predict how various pathologies and therapeutic interventions will alter the maturation process of affected vessels, is vital to improving treatment approaches and long-term clinical outcomes, particularly in pediatric patients suffering from congenital heart disease. Several investigations have uncovered remarkable changes in vessel wall composition, structure, and mechanical properties during postnatal development [1,2]. However, the relative role of mechanoregulation (along with genetic programming/predetermination and other mechanisms) in governing vascular maturation is not well quantified. As a first step toward predictive modeling of vascular development and maturation, there is thus a critical need to synthesize and extend previous insights within a mathematical modeling framework in order to elucidate how (and to what extent) developmental phenomena at the tissue and cellular scales are coupled to the evolving loading conditions on the vessel.

Toward this end, we seek to construct a predictive mechanobiological model that (1) links the tissue-level mechanical loading state to subcellular changes in biosynthetic activity and (2) uses the corresponding age-dependent gene/protein expression information to predict compositional/structural changes within the vessel wall. In the present study, we focused on the development of the murine thoracic aorta and examined the relationship between *in vivo* functional stresses, collagen I and III expression, and observed collagen content over the postnatal developmental time period as well as in maturity.

METHODS

All data for the present study were collected from wild-type C57BL/6J mice, in accordance with protocols approved by the Yale

University IACUC. Following euthanasia, the thoracic aorta was excised from the aortic root to the diaphragm. Biaxial mechanical data were collected at ages of $t = 1.5, 3, 6$, and 14 wk, using methods previously described in [3]. Briefly, vessels were preconditioned and then subjected to three cyclic pressure–distension protocols and four axial force–extension protocols, under age-specific loading conditions. An established four-fiber-family constitutive model [3] was then used to fit the mechanical data for each specimen, which enabled calculation of directional stresses and stretches, tangent stiffness tensor components, and stored elastic energy at configurations corresponding to the age-specific *in vivo* diastolic and systolic states.

Relative expressions of collagen I and III (*Col1a1* and *Col3a1*) were measured via quantitative reverse transcription PCR (qRT-PCR) for mice at $t = 0, 1.5, 3, 6, 9, 12$, and 24 wk of age. PCR data were normalized to 0 wk using GAPDH as a loading control and were interpolated using piecewise cubic Hermite interpolating polynomials (PCHIP) to ensure continuity over the entire time range considered.

Total collagen area within the medial layer was quantified from histological cross sections using custom image analysis software. Collagen area as a function of age was predicted assuming that the rate of production of functional collagen was directly proportional to a weighted sum of the *Col1a1* and *Col3a1* expressions. Specifically,

$$\frac{d}{dt}(A_{\text{col}}) = f_{\text{production}}(t) - f_{\text{removal}}(t) = \xi_I[\text{Col1a1}](t) + \xi_{III}[\text{Col3a1}](t) - f_{\text{removal}}(t), \quad (1)$$

where A_{col} is the medial collagen area, ξ_I and ξ_{III} are coefficients for the contributions of collagen I and III, respectively, to the production function, and $f_{\text{removal}}(t)$ is the removal rate function, which was defined empirically in the present study by treating the removal rates at $t = 0, 1.5, 3, 6, 9$, and 12 wk as free parameters. The removal rate function was constrained to be monotonically decreasing between 0 and 12 wk, and constant afterward. All parameters (8 total) were optimized via least-squares regression to the collagen area data.

RESULTS

Among all the mechanical metrics considered, the ratio between the circumferential stresses at systole and diastole ($\sigma_{\theta,sys}/\sigma_{\theta,dia}$) was found to correlate most strongly with collagen gene expression (Figure 1). The expression of collagen I was mostly closely associated with the age-dependent stress ratio, with both peaking at 2 wk and then dropping sharply by 6–8 wk. Collagen III followed the same trend qualitatively, but exhibited a more sustained expression until 6 wk, subsequently dropping to its mature steady-state value by 9 wk.

The gene expression-driven model of collagen accumulation within the media was able to capture the observed collagen area data well (Figure 2). Notably, model parameter optimization resulted in a ratio of production rate function coefficients $\xi_I:\xi_{III}$ close to 15:85, which is consistent with prior knowledge that the medial layer contains mostly type III collagen. The inferred removal rate function (Figure 2b) suggests that collagen removal is highest at birth, and drops sharply to its mature steady-state value by $t=6$ wk. Accordingly, collagen half-life is likely much shorter in early postnatal development (e.g., 4.5 days at $t=2$ wk vs. 70 days in maturity).

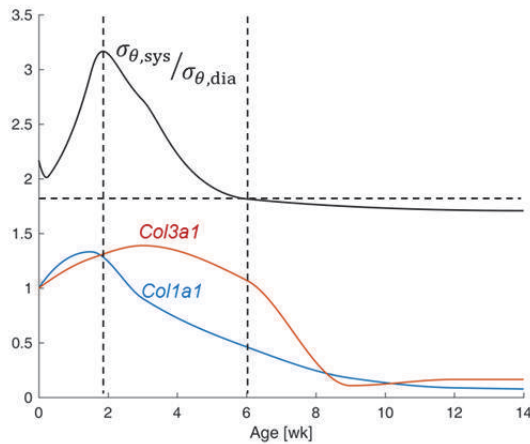


Figure 1: Correlation between the systolic-to-diastolic circumferential stress ratio and collagen gene expression.

DISCUSSION

The present study is a natural extension of previous efforts to describe how vessels alter their size, geometry, internal composition, and matrix architecture during the postnatal development and maturation period [1,2]. Unique to the present study, however, we have explicitly linked tissue-level cyclic mechanical loading patterns to cell-level transcriptional activity, which we used in turn to predict structural growth and remodeling of the collagen network back at the tissue level. This work thus represents an important step in the larger endeavor to construct a predictive multiscale model of vascular development and maturation, which must ultimately be robust to deviations from normal conditions (i.e., pathology, intervention) in order to ensure clinical applicability.

Our results suggest that the production of collagen in the developing aorta is tightly correlated with the *relative* magnitude of loading *over the cardiac cycle*, as quantified by the ratio of circumferential stresses between systole and diastole. While both systolic and diastolic circumferential stresses increase monotonically during development (result not shown), the ratio between them increases from birth to 2 wk and then decreases to its mature value by 6–8 wk, as does collagen expression (Figure 1). This result is consistent with previous studies showing biosynthetic sensitivity of

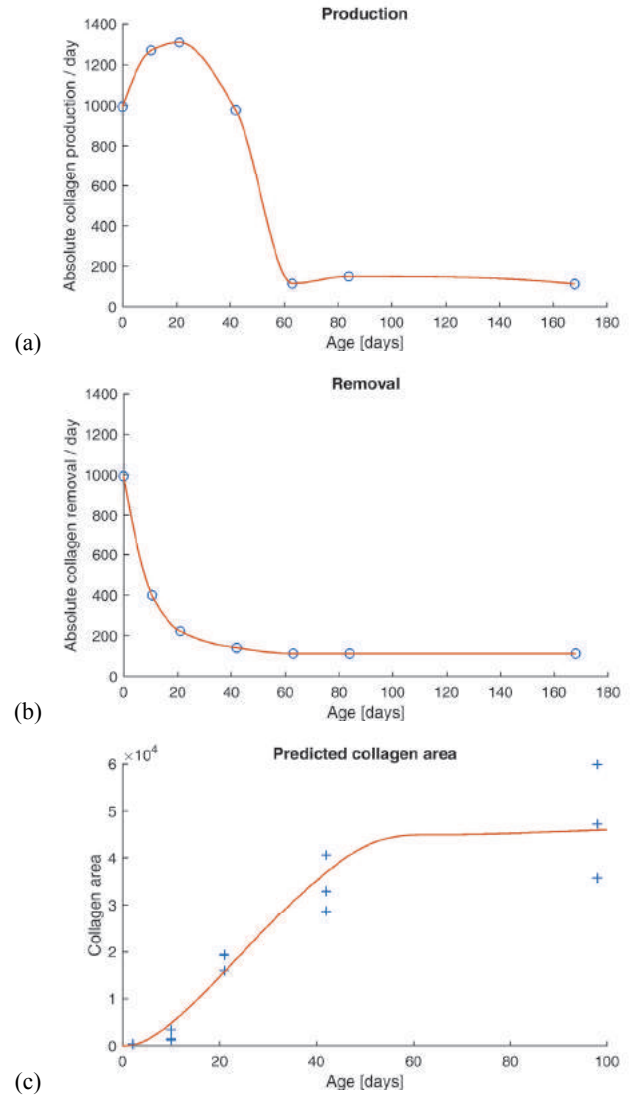


Figure 2: (a) Collagen (I + III) production rate function estimated from *Col1a1* and *Col3a1* expression. Open circles denote ages at which qRT-PCR data was collected. (b) Empirically determined collagen removal rate function. (c) Histological data (blue crosses) used to fit the model, and predicted collagen area (red curve).

vascular smooth muscle cells to the frequency and magnitude of cyclic loading [4]. Moreover, we have shown herein that collagen expression data can be used to predict extracellular collagen accumulation through the inference of associated production and removal rate functions (Figure 2), which themselves have broad implications for mechanobiological studies that include developmental time points.

ACKNOWLEDGEMENTS

This work supported by grants from Additional Ventures (AVCC) and the US National Institutes of Health (R01-HL155105).

REFERENCES

- [1] Gerrity RG, Cliff WJ. *Lab Invest*, 32(5):585-600, 1975.
- [2] Murtada SI, et al. *Dev Dyn*, 250(5):629-639, 2021.
- [3] Ferruzzi J, et al. *Ann Biomed Eng*, 41(7):1311-1330, 2013.
- [4] Gupta V, Grande-Allen KJ. *Cardiovasc Res*, 72(3):375-383, 2006.

ON THE ASSOCIATION OF RUPTURE POTENTIAL INDEX WITH ABDOMINAL AORTIC ANEURYSM GEOMETRIC MEASURES IN PATIENTS UNDER SURVEILLANCE

Juan C. Restrepo-Perez (1), Pratik Mitra (1), Satish C. Muluk (2), Mark K. Eskandari (3), Ender A. Finol (1)

(1) Department of Mechanical Engineering, University of Texas at San Antonio, San Antonio, TX
(2) Department of Cardiothoracic Surgery, Allegheny Health Network, Pittsburgh, PA
(3) Division of Vascular Surgery, Northwestern University School of Medicine, Chicago, IL

INTRODUCTION

The rupture of an abdominal aortic aneurysm (AAA) is a nearly fatal event, carrying an overall mortality rate of 80%. The U.S. clinical standard to assess the need for AAA repair is 5.5 cm of maximum transverse diameter for male patients and between 5.0 cm and 5.4 cm for females [1]. However, wall stress measures have been postulated to be better predictors of rupture risk compared to size alone. To estimate accurately patient-specific wall stress, a subject's intra-aneurysmal blood pressure, wall and intraluminal thrombus (ILT) material properties, and the spatially distributed wall thickness would be needed at the time of clinical imaging. Along with wall stress, an estimate of wall strength can also be used concurrently to assess AAA rupture risk, in the form of a rupture potential index (RPI). Wall strength requires knowing the patient-specific familial history of AAA, sex, local diameter, and the ILT thickness. In addition, AAA geometric measures other than maximum diameter have also been implicated in rupture risk assessment [2].

The present work was performed to accomplish two primary objectives. The first objective was to interrogate the existence of an association between global AAA geometric measures and their growth rate with RPI, and biomechanical deterioration rate in a sample of surveillance AAA models generated from serial computed tomography angiography (CT) images. The second objective was to assess whether there is a relationship between spatially distributed AAA geometric measures with wall stress and RPI in the same aforementioned population sample. We hypothesized that RPI is positively correlated with ILT thickness and ILT volume, and is negatively correlated with wall thickness, AAA wall surface area, and AAA sac volume, in surveillance AAA.

METHODS

We retrospectively acquired images from 23 computed tomography angiography (CTA) exams obtained from seven AAA

patients with at least two CT exams performed at Allegheny General Hospital (Pittsburgh, PA) and Northwestern Memorial Hospital (Chicago, IL), following Institutional Review Board approval at both clinical centers (see Table 1). The CTA images were segmented from the renal arteries to the aorto-iliac bifurcation using a custom in-house MATLAB®-based (MathWorks Inc., Natick, MA) script [3] to generate the point cloud of three contours of interest (lumen, inner wall, and outer wall). Using another in-house code script [4], we generated volume meshes for each AAA model from which triangular surface meshes of the outer wall surface (in the range of 35,000-80,000 elements) were created with ICEM (ANSYS Inc., Canonsburg, PA).

Table 1. Surveillance AAA subject information (F and M refer to patient sex; the time in months is between each CT exam).

Patient	CT	Time (months)	Patient	CT	Time (months)
AAA1 (F)	CT1	-	AAA4 (F)	CT1	-
	CT2	5.3		CT2	13.9
	CT3	10.4	AAA5 (F)	CT1	-
	CT4	6.1		CT2	30.8
	CT5	4.4		CT3	3.9
	CT6	2.4		CT4	6.9
AAA2 (F)	CT1	-	AAA6 (M)	CT1	-
	CT2	15.2		CT2	12.8
	CT3	14.5		CT3	15.7
AAA3 (M)	CT1	-	AAA7 (F)	CT1	-
	CT2	8.4		CT2	12.1
	CT3	11			

Geometric indices were calculated using previously developed in house MATLAB® scripts [2]. The AAA wall thickness was calculated for each surface element based on the known CTA-measured thickness

prior to following a nonlinear elastic membrane analysis (NEMA) method to compute the first principal normal and shear stresses at the wall [5]. The proximal and distal ends of the models were fixed and an intraluminal pressure of 120 mmHg was applied. The wall strength was calculated using the following Eq. (1) proposed by Vande Geest et al [6].

$$\text{Wall Strength} = 72.9 - 33.5 * (\sqrt{ILT} - 0.79) - 12.3 * (NORD - 2.31) - 24 * HIST + 15 * SEX \quad (1)$$

where ILT is the ILT thickness(cm) and NORD is the normalized local diameter (dimensionless) at each node of the surface mesh, HIST is the familial history of AAA (+0.5 for positive familial history; -0.5 otherwise), and SEX is the sex of the patient (+0.5 for male; -0.5 for female).

The RPI for each element of the AAA surface mesh was calculated as the ratio of the first principal normal stress and the wall strength. Absolute and relative growth rates and biomechanical deterioration rate were calculated with the expression proposed by Lindquist et al [7].

RESULTS

Jarque-Bera and Shapiro-Wilks normality tests were calculated with a confidence interval of 95%. Both tests showed that most of the data is not normalized. RPI vs. time for patients with at least 3 CT exams revealed evidence of a positive nonlinear slope. Thus, a Spearman's correlation was used to obtain correlations for each pair of variables. Conversely, a Kolmogorov-Smirnov test was used to examine the normality of the data of each AAA and globally ($n > 1$ M) for the NEMA surface meshes, as it shows all variables are not normally distributed. Further, a Spearman's rank correlation coefficient ρ was calculated for the correlations of ILT thickness and wall thickness with wall stress and RPI for each surface element and globally for all AAA.

The following AAA global geometric measures were used: γ , ratio of ILT volume to AAA sac volume; V_{ILT} , ILT volume; V , AAA sac volume; S , surface area of the AAA wall; and D_{max} , maximum diameter of the AAA.

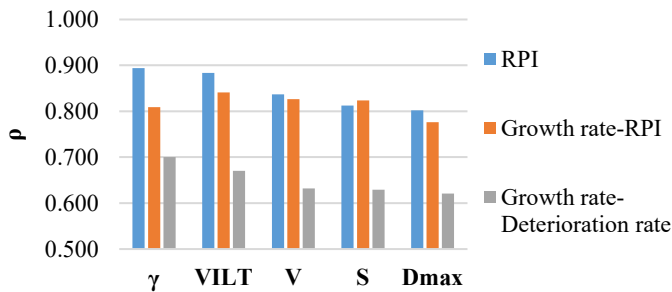


Figure 1. Spearman's rank correlation coefficients for geometric measures correlated with RPI.

The highest Spearman's rank correlation coefficients were 0.894 and 0.883 for γ and V_{ILT} , respectively (see Fig. 1). The maximum correlation between growth rate and RPI was 0.841 (for V_{ILT}) while the lowest was 0.776 (for D_{max}). All correlation coefficients between growth rate and deterioration were at least 10% lower than the correlations between growth rate and RPI.

In Table 2, PS indicates a patient-specific correlation, while Global refers to a correlation generated by the seven patients' data. The AAA spatially distributed geometric measures used were TH, aortic wall

thickness; TT, ILT thickness; NORD, normalized local diameter; GC, Gaussian curvature; and MC, mean curvature.

Table 2. Element based correlations for wall stress and RPI.

	Wall Stress				
	TH	TT	NORD	GC	MC
PS	[-0.7430 0.00087]	[-0.2851 0.47835]	[-0.2262 0.22853]	[-0.2113 0.05009]	[-0.3880 - 0.0845]
Global	-0.4633	0.39592	0.04980	-0.0857	-0.2600
	RPI				
	TH	TT	NORD	GC	MC
PS	[-0.7390 -0.0017]	[-0.1741 0.74486]	[-0.1420 0.29394]	[-0.1520 0.09192]	[-0.3489 - 0.0626]
Global	-0.3891	0.6334	0.19860	-0.0336	-0.2182

The strongest positive correlation for RPI was 0.633 for TT and the strongest negative correlation for wall stress was -0.4633 for TH. NORD and the Gaussian and mean curvatures do not exhibit strong correlations with wall stress or RPI.

DISCUSSION

Surveillance AAAs represent the most clinically relevant population group of this vascular disease, since the standard of care clinical guidelines for interventional repair do not apply due to their relatively small size. Thus, measures characteristic of the AAA size and shape, and biomechanics-based metrics can be used to interrogate which variables are associated with AAA growth.

The correlations presented herein indicate there is a strong association between RPI and growth rates of global size-based geometric measures, with the ratio of ILT volume to AAA sac volume, and the ILT volume being the most important measures. We infer that AAAs under surveillance that grow nonlinearly are associated with a high risk of rupture dependent on the ILT volume present in the AAA sac. Wall thickness and ILT thickness are the two most relevant spatially distributed variables strongly associated with wall stress and RPI. Collectively, this may indicate the need to develop automated image processing methods that can estimate the change in wall thickness and ILT volume and thickness over time.

Some limitations of this study are the relatively small population sample size, the peak systolic pressure, which was assumed the same for all patients due to the lack of patient-specific cuff or intraluminal aortic pressure. In addition, a more balanced number of male and female subjects may offer more insightful inferences on the sex-specific associations of geometric measures with RPI.

ACKNOWLEDGEMENTS

This work was supported in part by National Institutes of Health award R01HL159300.

REFERENCES

- [1] Chaikof, E.L. et al., J Vasc Surg., 67(1):2-77.E2, 2018.
- [2] Raut, SS et al., A Biomed., 41(7):1459-1477, 2013.
- [3] Shum, J et al., Medical Physics, 37:638-648, 2010.
- [4] Raut, SS et al., J Biomech, 48(10), 53:1972-1981, 2015.
- [5] Thiruganasambandam, M et al., PhD Thesis, UTSA, 2018.
- [6] Vande Geest, JP et al., Ann. N.Y. Acad. Sc., 1085:11-21, 2006.
- [7] Lindquist, M et al., J Vasc Surg., 63(6):1434-1442.e3, 2016.

IMAGING AND MECHANICAL CHARACTERISATION OF HUMAN BLOOD CLOT ANALOGUES WITH DIFFERENT COMPOSITIONS AND DEGREES OF CONTRACTION

Rachel Cahalane (1), Janneke M.H. Cruts (1), Ahlam Rachid (2), Kim van Gaalen (1), Heleen M.M. van Beusekom (3), Moniek de Maat (4), Marcel L. Dijkshoorn (5), Nikki Boodt (5,6), Aad van der Lugt (5), Frank Gijzen (1,7)

- (1) Department of Biomedical Engineering, Erasmus Medical Center, Rotterdam, the Netherlands
- (2) Department of Biomedical Engineering, Eindhoven University of Technology, Eindhoven, the Netherlands
- (3) Department of Experimental Cardiology, Erasmus Medical Center, Rotterdam, the Netherlands
- (4) Department of Hematology, Erasmus Medical Center, Rotterdam, the Netherlands
- (5) Department of Radiology and Nuclear Medicine, Erasmus Medical Center, Rotterdam, the Netherlands
- (6) Department of Neurology, Erasmus Medical Center, Rotterdam, the Netherlands
- (7) Department of Biomechanical Engineering, Delft University of Technology, Delft, the Netherlands

INTRODUCTION

Stroke is the 2nd leading cause of death worldwide. Endovascular thrombectomy is the current standard of care for patients with large vessel occlusions. However, these procedures are not effective in up to 40% of the cases [1]. Thrombi causing stroke are diverse in their composition. The main components are red blood cells (RBCs), fibrin, platelets, and white blood cells, and the thrombus composition is an important factor influencing successful recanalization [2]. The exact reason for this is unknown, but it is known that the composition and platelet-driven thrombus contraction affect the mechanical properties of thrombi, which has been postulated to influence the interaction with the thrombectomy device [3, 4, 5]. A pre-interventional estimation of the mechanical properties is hypothesized to aid in selecting the most suitable treatment on a case-by-case basis to improve success rates.

Computed Tomography (CT) imaging is the most commonly used imaging modality for diagnosis of stroke and could therefore potentially be useful to assess thrombus properties prior to the thrombectomy [3]. The purpose of this study is to examine the imaging and mechanical properties of clot analogues with different RBC compositions and degrees of contraction.

METHODS

Blood was drawn by venipuncture from six healthy human donors. Clots were made by reconstituting the platelet rich plasma and RBCs in five different volumetric RBC percentages of 0, 0.5, 2, 5, and 40% in order to span the range of compositions from ex vivo thrombi [2]. Also, clots were made with a low, medium, and high degree of contraction. The effect of platelet concentration on the degree of clot contraction was assessed by varying the platelet concentration in twelve 5% RBC volume clots (n=3 donors). From this, three platelet concentrations were selected to study three distinct degrees of contraction. To assess the extent of thrombus contraction, the weight of each clot was measured

and expressed as a percentage of the weight of the original clotting mixture [5].

To determine the mechanical properties, unconfined compression tests were performed using a custom made compression tester [4]. For this, the clots were cut into 2 mm slices. The samples were 80% compressed, with a compression and retraction speed of 0.2 mm/s (10% strain/s). As a measure for the stiffness, the high strain (approximately final 2%) secant moduli was measured from the slopes of fitted straight lines of the non-linear nominal stress-strain curves [4].

Clinical CT was used to determine the clot imaging characteristics. First, a non-contrast computed tomography (NCCT) was made to study the density. Subsequently, an iodinated contrast agent was added and a scan was made 20 minutes after administering the contrast in order to study the perviousness, which reflects the permeability of a clot. In each scan, three non-overlapping regions of interest with 1 mm diameter were defined in each clot, of which the mean density was measured in ImageJ [6].

The composition of the clot was analysed using histology. Hemotoxylin and Eosin (H&E) and Martius Scarlet Blue (MSB) stain was used to identify the percentage of RBCs using Orbit Image Analysis software.

One-way ANOVA tests were performed to assess whether the differences in clot properties between the clot types are significant. A p-value lower than 0.05 was considered statistically significant.

RESULTS

A non-linear relationship between the platelet concentration and the degree of contraction was observed (Fig.1). To produce clot analogues with distinct degrees of contraction, 30, 90 and 270 x 10³ platelets/ μ L concentrations were selected to create 'high', 'medium' and 'low' degrees of contraction.

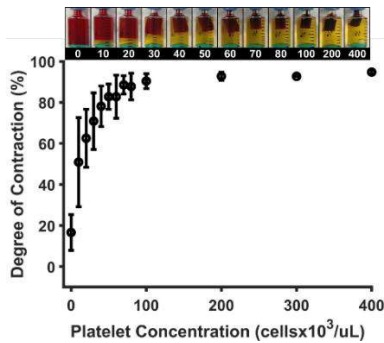


Figure 1: Platelet concentration vs degree of clot contraction.

Figure 2A presents representative images of high, medium and low contraction groups for 2% RBC volume clots. RBC volumes of 0, 0.5, 2, 5, and 40% produced clots with 0.04, 25, 77, 94 and 99% RBC content, respectively ($P < 0.001$) (Fig.2B). There was no significant difference in RBC content of the three contraction groups (high, medium and low) within each clot RBC type (Fig.2B). The degree of contraction significantly increased with increasing platelet concentration within each RBC volume clot group ($P < 0.05$) (Fig.2C).

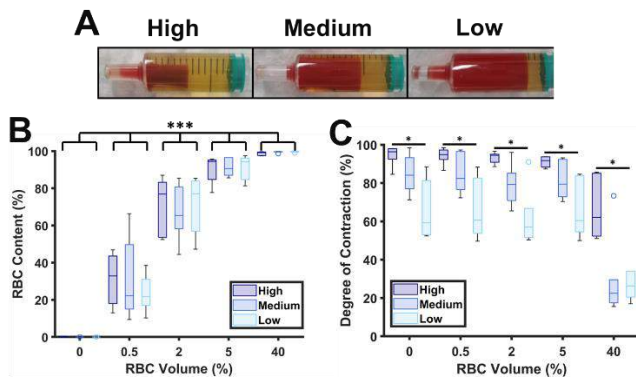


Figure 2: Confirmation of clot analogue composition and degree of contraction. (A) Representative images of a high, medium and low degree of contraction for 2% RBC volume clots. (B) RBC content for each RBC volume and contraction group. (C) Degree of clot contraction for each RBC volume and contraction group.

The compressive stiffness significantly increased with increasing contraction level, regardless of the RBC volume group (Fig.3A). In terms of RBC volume, for high degrees of contraction, the 0, 0.5 and 2% RBC clots had significantly higher stiffness values compared with the 40% RBC group (Fig.3B). In the medium contraction group, 0.05 and 5% RBC clots were significantly stiffer than the 40% RBC clots. There were no significant differences for the low contraction group.

The clot CT density significantly increased with increasing degree of contraction within each RBC volume group (Fig.4A). The clot CT density is also dependent on the RBC content (Fig. 4B). For each contraction group the density tends to increase with increasing RBC content, with significance occurring between the lower and higher RBC groups. Highly contracted clots tend to have higher perviousness values compared with medium and low groups, but not significantly (Fig.4C). There is only a significant difference between the perviousness values of RBC clot groups when they are highly contracted (Fig.4D), with significance occurring between the lower and higher RBC groups.

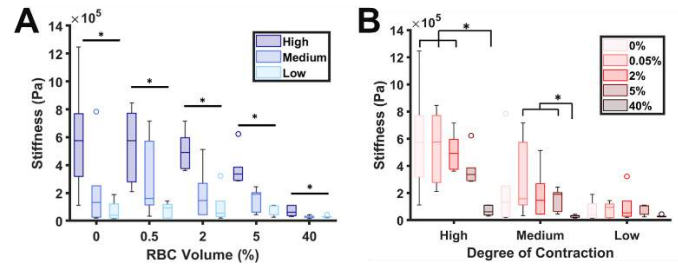


Figure 3: Clot mechanics. (A) Compressive stiffness per RBC volume group. (B) Compressive stiffness per contraction group.

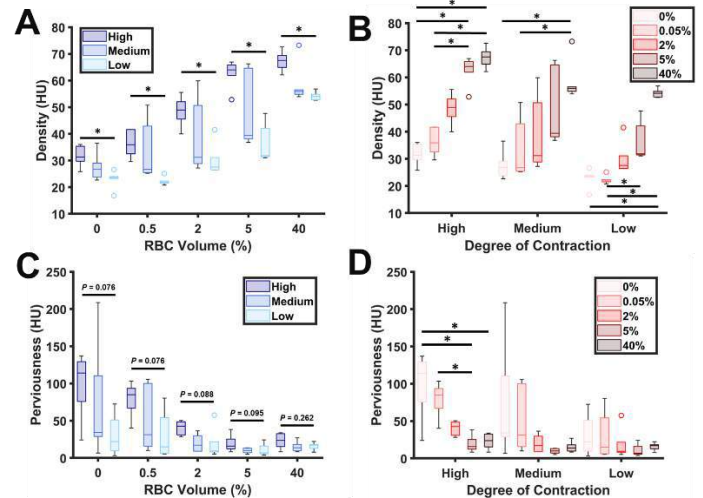


Figure 4: Clot imaging characteristics. (A) NCCT density per RBC group. (B) NCCT density per contraction group. (C) Perviousness per RBC group. (D) Perviousness per contraction group.

DISCUSSION

We successfully produced clots with 5 different RBC contents and 3 different degrees of contraction. Compressive stiffness increased with decreasing RBC content and increasing degree of contraction. This is as expected since clots with a lower RBC content contain a denser network of thicker fibers compared to RBC-rich clots [7], and contraction causes a higher clot compactness [5], both leading to a higher stiffness. We showed that the clot CT density increased with increasing RBC content, which confirms earlier findings [3]. For the first time, we showed that the density also increased with increasing degree of contraction (when the RBC content is unaffected), indicating that the RBC concentration is not the only factor affecting the CT density. It was hypothesized that highly contracted clots would contain denser structures and therefore a lower perviousness compared to less contracted clots; however, the opposite was observed in this study. Furthermore, perviousness values are only affected by RBC volume in the highly contracted group. The implication is that the assessed CT imaging characteristics alone cannot directly characterize a clot's RBC content and degree of contraction, and may therefore not be predictive of the mechanical behaviour.

REFERENCES

- [1] Jansen et al., *BMJ*, 360: k949, 2018.
- [2] Staessens et al., *Haematologica*, 105:498–507, 2020.
- [3] Cahalane, R. et al., *J. Biomech*, 129: 110816, 2021.
- [4] Boodt et al. *Stroke*, 52(8):2510-2517, 2021.
- [5] Johnson S. et al., *J. Neurointerv. Surg*, 12(9): 853-857, 2020.
- [6] Benson, J. C. et al., *J Neurointerv Surg*. 12(1):38-42, 2020.
- [7] Mereuta O, et al., *J Neurointerv Surg*, 13: 906–911, 2021.

EVALUATING MATERIAL MODELS FOR LOW-FREQUENCY MAGNETIC RESONANCE ELASTOGRAPHY OF AGAROSE GELS VIA FINITE ELEMENT SIMULATIONS

Julian A. Rey (1), Kulam N. Magdoom (1,2), Thomas T. Jones (3), Marcial Garmendia-Cedillos (3), Randall Pursley (3), Michal E. Komlosh (1,2), Thomas Pohida (3), Peter J. Basser (1)

- (1) Eunice Kennedy Shriver National Institute of Child Health and Human Development, Bethesda, Maryland, USA
(2) The Henry M. Jackson Foundation for the Advancement of Military Medicine Inc., Bethesda, Maryland, USA
(3) National Institute of Biomedical Imaging and Bioengineering, Bethesda, Maryland, USA

INTRODUCTION

Magnetic resonance elastography (MRE) is an imaging technique used to estimate a tissue's mechanical properties remotely by measuring and analyzing the propagation of elastic body waves through the tissue. MRE of the liver provides a clinically approved assessment to support the staging of liver fibrosis [1]. In this setting, the mechanical waves are commonly produced at 20-200 Hz by an external actuator [1]. Preclinical MRE in animals is typically performed at a higher frequency range (200-1500 Hz) [1]. However, it is important to characterize the mechanical response of tissue at lower actuation frequencies because 1) mechanical properties tend to be frequency dependent, 2) new biomarkers owing to different mechanical phenomena may be available, and 3) body tissues undergo low-frequency displacements due to normal physiological processes which may be altered by disease.

In this study, various material models were employed to analyze and simulate the mechanical response of a cylindrical agarose gel sample to 10 Hz axial actuation. While pressure waves, as opposed to shear waves, are often ignored in MRE, a full viscoelastic inversion method was implemented to ascertain their potential contribution to the displacement field at low frequencies. Finite element method (FEM) models of the MRE experiment were developed to complement the inversion results by predicting the displacement field for a range of pressure and shear wave speeds.

METHODS

A cylindrical sample of 0.12% agarose gel measuring 60 mm in length and 19 mm in diameter contained in a glass vial was used as a tissue phantom for the MRE experiments. The free circular face of the gel was displaced axially by a piston 11 mm in diameter attached to a custom piezoelectric actuator operated at 10 Hz. A pulsed gradient spin echo (PGSE) sequence was used to acquire the 3D MRE data on a 7 T Bruker Biospin scanner. The displacement distribution data were acquired for 0.5 mm isotropic voxels in a 30 x 25 x 25 mm FOV using

a Hadamard encoding scheme with $b = 0$, 250 s/mm², $\delta/\Delta = 1.5/10$ ms, and $TR/TE = 200/16$ ms.

Viscoelastic properties of the sample were estimated using the full algebraic inversion of the differential equation (AIDE) method described in Oliphant et al. [2]. In this method, the displacement field is substituted into the frequency domain formulation of the linear viscoelastic momentum equations assuming an isotropic, locally homogeneous material (Eq. 1)

$$\mu \nabla^2 \mathbf{u} + (\lambda + \mu) \nabla(\nabla \cdot \mathbf{u}) = -\rho \omega^2 \mathbf{u} \quad (1)$$

Here λ and μ are Lamé's first and second parameters, ρ is density, ω is the angular actuation frequency, and \mathbf{u} is the complex-valued displacement at the actuation frequency. Complex-valued parameters λ and μ were estimated at each voxel by algebraic inversion and used to calculate the pressure and shear wave speeds by Eq. 2.

$$c_s = \sqrt{\frac{2|\mu|^2}{\rho(\mu' + |\mu|)}} \quad (2)$$

Above, μ' is the real part of μ . The pressure wave speed c_p can be found by substituting the pressure wave modulus $\lambda + 2\mu$ in place of μ . The full AIDE method was implemented in MATLAB R2022a.

FEM models were developed to predict the dynamic displacement field within the agarose gel phantom when subjected to the experimental loading conditions. The gel was modeled as either a compressible, isotropic linear elastic solid or a biphasic mixture. The biphasic mixture material consisted of a linear elastic solid matrix with pores through which an incompressible fluid phase may flow according to Darcy's law.

A half-cylinder geometry was subjected to sinusoidal axial displacement at 10 Hz on the piston-gel interface. No motion parallel or

perpendicular to the tube walls was permitted. A symmetry boundary condition was prescribed on the remaining flat surface of the half-cylinder. The mesh consisted of 9,216 trilinear hexahedral elements with a maximum side length of 1.87 mm. The model was solved with the dynamic quasi-newton solver available in FEBio.

RESULTS

Axial actuation of the cylindrical agarose sample by a circular piston at 10 Hz produced a nearly axisymmetric displacement field consisting of alternately rotating toroids propagating axially (Fig. 1).

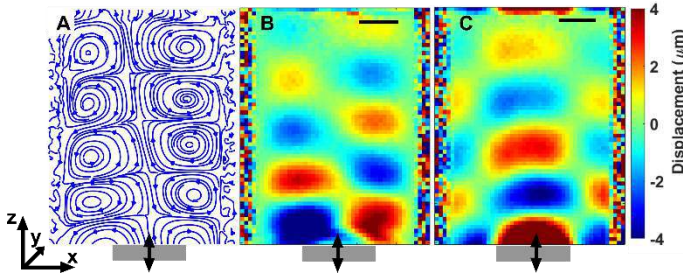


Figure 1: Measured displacement field in a sagittal cross-section. A) Displacement streamlines. B) X-direction displacement. C) Z-direction displacement. Scale bar = 5 mm. The piston is represented by the gray bar at the bottom of each panel moving along the sample axis.

While the X-direction displacement is orthogonal to the propagation direction, indicative of a transverse shear wave, the Z-direction displacement is parallel to the propagation direction, suggesting a longitudinal wave is present. An axially alternating pattern of positive and negative dilatation is apparent near the centerline of the sample (Fig. 2).

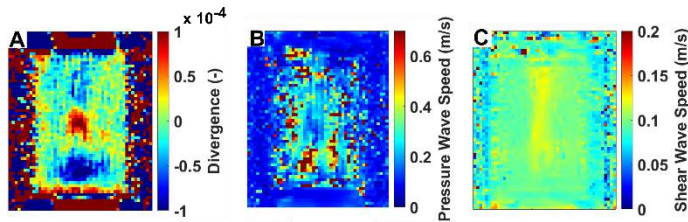


Figure 2: Viscoelastic wave properties derived from the displacement field. A) Divergence of the displacement field. B) Pressure wave speed. C) Shear wave speed.

Algebraic inversion of the viscoelastic momentum equation resulted in a shear wave speed estimate of ~ 0.1 m/s and a pressure wave speed approximately 3 to 6 times greater for many voxels in the sample, although the latter estimate is considerably noisier.

A linear elastic solid FEM model of the MRE experiment showed that in a material with lower compressibility (pressure wave speed = 2.4 m/s) the axial wavelength of the displacement waves is longer than in the experiment. A more compressible material (pressure wave speed = 0.6 m/s) resulted in a displacement field with a shorter axial wavelength, which is more like that observed in the experiment (Fig. 3).

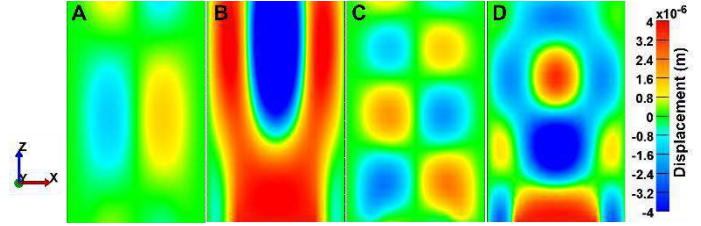


Figure 3: Varying pressure wave speed in solid FEM models. A) X-direction displacement and (B) Z-direction displacement for $c_p = 2.4$ m/s and $c_s = 0.1$ m/s. C) X-direction displacement and (D) Z-direction displacement for $c_p = 0.6$ m/s and $c_s = 0.1$ m/s.

An FEM model of a biphasic material consisting of a solid matrix with fluid-filled pores produced better agreement with the experiment than the linear elastic solid model (Figure 4). The solid and fluid velocities are nearly the same for this material, meaning they tend to move in-phase at this actuation frequency. However, dynamic changes in volume fraction of each phase appear to enable the development of axially shorter displacement waves.

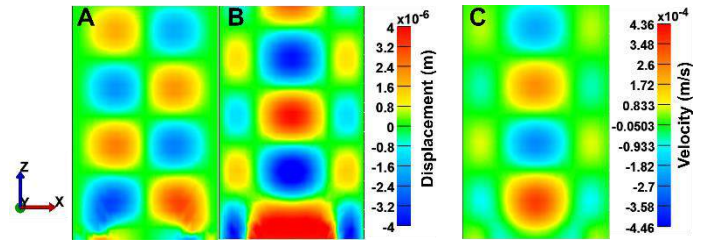


Figure 4: Modeled displacement and velocity fields for a biphasic material. A) X-direction displacement. B) Z-direction displacement. C) Solid and fluid phase velocity (same appearance).

DISCUSSION

This study demonstrates that low-frequency actuation of agarose gel can produce complex displacement fields exhibiting both transverse and longitudinal waves. While the longitudinal wave evident along the centerline of the sample in Fig. 1C may be an example of a “longitudinal shear wave” [3], our viscoelastic inversion (Fig. 2B) and FEM analyses (Fig. 3) suggest that slower pressure wave speeds (0.3 - 0.6 m/s) than typically assumed for tissue (~ 1540 m/s) [1] are present in the sample. The corresponding “compressibility” of the gel is not likely an intrinsic property of the gel constituents since the gel is mostly water but may instead be a consequence of changes in the local volume fraction of fluid. Such poroelastic effects may be relevant at lower actuation frequencies [1], and our biphasic model (Fig. 4) matches the measured displacement field better than the solid model (Fig. 3). The unexpected behavior of the gel at 10 Hz suggests the need to characterize mechanical properties of tissues at low frequencies to better understand their mechanical response to normal physiological loading.

ACKNOWLEDGEMENTS

JAR and PJB were supported by the IRP of the NICHD, NIH; TTJ, MGC, RP, and TP were supported by the IRP of the NIBIB, NIH; MK and KNM were supported by the CNRM under the auspices of the HJF. The opinions expressed herein are those of the authors.

REFERENCES

- [1] Manduca, A et al., *Mag Res Med*, 85:2377-2390, 2021.
- [2] Oliphant, T et al., *Mag Res Med*, 45:299-310, 2001.
- [3] Zhu, J et al. *Appl Phys Lett*, 110, 201101, 2017

QUANTITATIVE ASSESSMENT OF THE ROLE OF CHROMATIN MECHANICS AND ARCHITECTURE IN MONOLAYER CELL MIGRATION

Jack Forman (3,5), Brady Hine (1,2,3), Eric Havenhill (2,3),
Samantha Kaonis (1,3), Soham Ghosh (1,2,3,4)

- (1) School of Biomedical Engineering, Colorado State University, Fort Collins, CO, USA
(2) Department of Mechanical Engineering, Colorado State University, Fort Collins, CO, USA
(3) Translational Medicine Institute, Colorado State University, Fort Collins, CO, USA
(4) Cell and Molecular Biology Program, Colorado State University, Fort Collins, CO, USA
(5) Chemical and Biological Engineering, Colorado State University, Fort Collins, CO, USA

INTRODUCTION

Cell migration is a fundamental process in normal physiology, development and pathology [1]. Cells migrate inside the tissue to maintain the tissue homeostasis and to close the wounds. During development, cells migrate to neo-tissues and for subsequent deposition of the extracellular matrix. Cancer cells migrate through tissues to metastasize. Significant effort has been reported to understand the dynamics of single and collective cell migration in two dimensional and three-dimensional settings using *in vitro* and animal model.

The cell nucleus is emerging as a key mediator of the cell migration and has become a topic of recent interest to both the basic science and clinical research communities [2, 3]. The nucleus is the stiffest organelle in the cell and therefore appears as a limiting factor in cell migration through small pores. Recent discoveries show that cancer cells evolved to squeeze through small pores in tissues by adapting a specific mechanism in the cell nuclear envelope [4]. However, limited understanding exists regarding the role of intranuclear chromatin mechanics and architecture on cell migration, which are often compromised with aging and associated genomic instabilities [5]. The objective of this work is to elucidate how the chromatin mechanics and architecture affect two-dimensional (2D) cell migration using a model of the scratch wound assay with murine embryonic fibroblasts (NIH 3T3 cell line).

Scratch wound assay is a simple technique to understand the mechanism of cell migration. It is easy to control the biochemical and biophysical environment of the cells by changing the substrate chemistry and by adding pharmacological agent to the cell culture medium. We hypothesize that maintaining the nuclear stiffness (chromatin mechanics) and the chromatin remodeling (chromatin architecture) are critical factors for the efficient cell migration. To test this hypothesis, we decreased the nuclear stiffness by the application of a pharmacological agent trichostatin A (TSA) and inhibited the chromatin remodeling using GSK126.

METHODS

Cell culture: NIH 3T3 cells were cultured according to the ATCC protocol. Passage 4 cells were used for all the experiments. Cells were cultured in an ibidi 8 well slides to confluency. These slides have a thin transparent polymer bottom for imaging using an inverted microscope. **Scratch wound assay:** After cells reached confluency, a scratch was made using a 200 μ M pipette tip. DPBS was used to wash the debris. Subsequently, fresh medium was added to the wells. **Cell migration imaging:** Time lapse imaging of the wound closure and cell migration was performed using a live DNA stain – Nucblue to visualize the nucleus and also in the bright field to visualize the cells. The cells were maintained in an incubation chamber during the migration period. The incubation chamber has the environmental control to maintain a physiological condition of temperature, carbon di-oxide concentration and humidity. **Modulation of chromatin mechanics and architecture:** TSA (100 ng/ml) softens the nucleus by HDAC inhibition thus compromising chromatin mechanics. GSK126 (20 μ M) hinders chromatin remodeling by inhibiting EZH2 methyltransferase thus compromising chromatin architecture. Both drugs were added 12 hours before the scratch was made so that drugs are already in effect. Drugs were also added after the wash while adding the fresh medium. **Analysis:** ImageJ was used to track the individual cell nuclei in order to quantify several cell migration parameters such as speed, distance travelled and persistence of migration. The bright field images were used to quantify the wound closure by calculating the area covered by the cells. **Statistics:** ANOVA and post hoc tests was used for all statistical analysis.

RESULTS

The wound closure efficiency of cells was affected by the chromatin softening and by hindering the chromatin remodeling. Figure 1A shows that softened nucleus (TSA treated) and condensed chromatin (GK126 treated) decreases the wound closure efficiency by more than

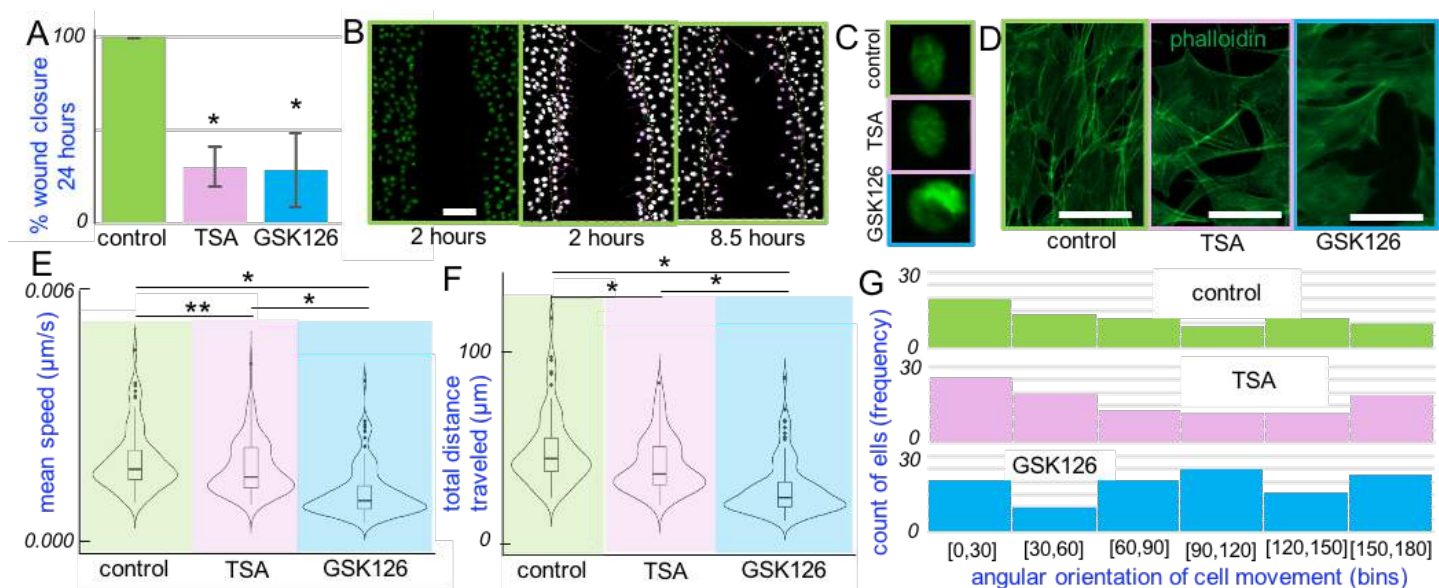


Figure 1. (A) Altering the chromatin mechanics (TSA) and chromatin architecture (GSK126) decreases wound closure efficiency. (B) Live cell imaging and automated tracking shown for a sample control group. Scale: 100 μ m. (C) TSA does not visibly affect chromatin architecture but GSK126 causes chromatin condensation. (D) F-actin structure is not affected by TSA and GSK126. Scale: 50 μ m. (E) Cell speed is drastically decreased by GSK126 but slightly decreased by TSA. (F) Track distance is drastically decreased by GSK126 and significantly decreased by TSA. (G) TSA does not change the migration persistence, but the GSK126 drastically hinders the migration persistence. For all cases, * $p < 0.01$ and ** $p < 0.05$. Data reported based on 3 technical replicates and at least 500 cells.

50% at 24 hours post scratch. In the control group, cells completely repopulate the wound at 24 hours. Figure 1B shows a representative image of cells migrating after the wound is created. Nuclear softening does not visibly affect the chromatin architecture but hindering the chromatin remodeler leads to a condensed chromatin (Figure 1C). The cytoskeletal architecture is not significantly affected by either drug treatment as shown by the F-actin staining Figure 1D. The cell shape is intact and stress fibers are visible in all groups.

Next, we wanted to investigate how softening of the nucleus and the inhibition of chromatin remodeling affects the specific cell migration parameters. Softening of cell slightly decreases the cell speed compared to control but blocking the chromatin remodeling significantly reduces the cell speed (Figure 1E). Similarly, the distance moved by cells significantly decreased by the chromatin softening and drastically decreased by the inhibition of chromatin remodeling (Figure 1G). The persistence of cell migration was calculated by computing the angle between the direction of cell movement and the direction perpendicular to the wound edge, at a given time point (Figure 1G). The distribution of the angular orientation shows that softening of nucleus does not significantly affect the persistence, but inhibition of chromatin remodeling drastically affects the persistence. Note that for a persistent migration, most cells will be oriented at 0° and 180° whereas for non-persistent migration, the cells are least oriented in 0° and 180° angular directions resembling the cells are undergoing mostly a random movement.

DISCUSSION

In this work we show that maintaining an optimal nuclear stiffness and the chromatin remodeling is required for efficient cell migration and wound healing in a two-dimensional plane. Stiff nucleus is known to be a barrier in 3D migration but in 2D context, certain amount of nuclear rigidity is required. This rigidity might be required for maintaining the

mechanical dynamics and force balance inside the cell during the leading edge protrusion and trailing edge contraction. The chromatin remodeling is turning out to be a critical component in several physiological process and our work identifies that plasticity of the chromatin remodeling is required for cells to migrate. It should be noted that none of the pharmacological inhibition affects the cytoskeletal structure. Therefore, the cell migration is primarily affected by an exclusive nuclear mechanical role. Our future work includes the profiling of other cytoskeletal proteins known to be responsible for cell migration so that we can understand if the pharmacological inhibition affects only the nuclear mechanics or also affects the cytoskeletal proteins. Other future works will include experiments with aged cells and cells with compromised nuclei (cancer and laminopathy). Finally, we are currently working to understand how the substrate stiffness plays an additional role in coordination with the nuclear mechanics during the cell migration.

REFERENCES

- [1] Jain et al, *Nat Phys*, 167(16), 2020.
- [2] Lee et al, *Sci Adv*, 7(2), 2021.
- [3] Jones et al, *ASME JBME*, 144(8), 2022.
- [4] Denais et al, *Science*, 352, 2016.
- [5] Phillip et al, *Ann Rev Biomed Eng*, 17, 2015.

AGING INFLUENCES STATIC AND DYNAMIC PROPERTIES OF PRIMARY MOUSE PULMONARY FIBROBLASTS THROUGH CELLULAR SENESCENCE

L. Lee (1), K. Penumatsa (2), M. Guo (1)

(1) Department of Mechanical Engineering, MIT, Cambridge, MA, USA
(2) Division of Pulmonary and Critical Care Medicine, Tufts Medical Center, Boston, MA, USA

INTRODUCTION

Half of all heart failure cases are found within the 6% of the US who is older than 75, and the prevalence of heart failure rises to almost 10% of the population older than 80. With an increasingly aging population estimated to reach 70 million or 25% over the age of 65 by the year 2030, the connection between cardiopulmonary aging and cardiopulmonary diseases becomes increasingly important to investigate [1]. In particular, the strong association between aging and structural and pressure-volume alterations from cardiopulmonary diseases suggests a mechanical difference at the cellular level. A central hallmark of aging lies in the increased presence of senescent cells, which express the phenotype of permanent cell-cycle arrest as proliferation and apoptosis comes to a halt [2]. These issues lead to an impaired ability to repair damaged tissues and an accumulation of unhealthy cells, which can cause a myriad of aging-related diseases.

Cell mechanics of aging and senescence have been investigated for geometric, static, and dynamic differences. Early sampling of cardiomyocytes from deceased human donors aged 17-90 years showed a progressive increase in cell volume but a decrease in cell count [3]. Multiple research groups measured aging cells to be stiffer than younger cells, including monkey vascular smooth muscle cells (VSMCs) [4] and rat cardiomyocytes [5], both measured using Atomic Force Microscopy (AFM). There are studies on cell spread and migration such as the comparison of human dermal fibroblasts in aging [6]. While previous studies focus on specific mechanical measurements, less work has been done to understand how these differences relate to one other. In addition, many cellular-level studies for cardiopulmonary systems focus on structural alterations from VSMCs and cardiomyocytes – knowledge is lacking on the functional differences of fibroblasts in those organs, which lead to the impaired wound healing abilities and other issues.

Because previous works observe mechanical differences in different cellular systems, this study aims to address the comprehensive understanding of how geometric, static, and dynamic properties are

influencing one another in the aging process. In addition, these aims seek to complement current knowledge of cellular mechanics in cardiopulmonary organs by investigating fibroblasts involved in the structural framework of tissues instead of VSMCs or cardiomyocytes. In order to investigate the differences in aging in cardiopulmonary fibroblasts, this study measures cell stiffness, migration, and cell spread area *in vitro* with primary lung fibroblasts isolated from senescence-resistant mice (SAMR1) and senescence-prone mice (SAMP8).

METHODS

Cell Culture and Substrate Preparation. Cells extracted from SAMR1 and SAMP8 mice (Envigo) were cultured at 37°C and 5% CO₂ in Fibroblast Medium (ScienCell) supplemented with 10% fetal bovine serum, 1% penicillin/streptomycin and 1% Fibroblast Growth Supplement. In all experiments, both groups were seeded on glass substrate coated overnight at 2°C with rat tail collagen I (4.06 mg ml⁻¹) diluted to 0.1 mg ml⁻¹ in phosphate buffered saline (PBS).

Optical Tweezers for Cytoplasmic Stiffness. Cell stiffness measurements were conducted by optical tweezers from a well-established method [7]. After cells had adhered to the surface of the substrate, polystyrene particles of diameter 870 nm were introduced into the media and endocytosed overnight. To measure the stiffness, the particles were dragged to the right by optical tweezers for 1 μm at a speed of 1 μm s⁻¹. The displacement of the bead and the resultant force were recorded and the stiffness, defined as the slope of the force-displacement curve, was calculated via linear curve fitting in MATLAB.

Fluorescent Imaging for Cell Spread Area. Cell spread area was calculated from cytoplasm stained using CellTracker CMFDA Green (ThermoFisher) with recommended protocols (1:1000 for 30 minutes at 37°C). The fluorescent images were taken using LEICA 8 confocal microscope on 63x water objective of z-stacks at pinhole 1.00 AU. Using ImageJ, z-stacks were projected onto a 2D image with maximum intensity, and thresholding was applied to obtain the area measurements.

Cell Migration Tracking for Long Time Scales. 2D migration studies were conducted with LEICA 8 confocal microscope on 10x dry objective. Cells were seeded at low density and allowed to spread for two days on the glass substrate, stained with CellTracker CMFDA Green and then placed on the stage at 37°C and 5% CO₂. Same locations were imaged every 5 minutes for a total of 10 hours. The positions of the cells were traced the TrackMate plugin in ImageJ [8], and the analysis of the positions, such as mean squared displacement, moving velocities, and trajectory plotting, were conducted using MATLAB.

RESULTS

Cell Stiffness. Taking samples from SAMR1 (n=5) mice and SAMP8 (n=4) mice, the optical tweezers measurements conclude differences ($p = 0.0025$) in the subject-level means tested against the null hypothesis with the student's t-test (Figure 1). SAMR1 stiffness measured 1.39 ± 0.0931 (SE) Pa while SAMP8 stiffness measured 2.79 ± 0.323 (SE) Pa, showing that the SAMP8 cytoplasm is 2.00 times stiffer than the SAMR1 cytoplasm on average.

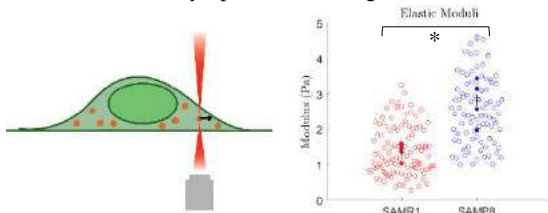


Figure 1: Schematic of optical tweezers (left) and a comparison of elastic moduli of SAMR1 vs SAMP8 cells (right)

Cell Spread Area. The subject-level means tested against the null hypothesis using the student's t-test shows $p = 0.0386$ (Figure 2). SAMR1 spread on $7,296 \pm 737$ (SE) μm^2 while SAMP8 spread on $19,316 \pm 2,320$ (SE) μm^2 . The comparison of the sample means shows that SAMP8 spreads 2.65 times larger on average than SAMR1.

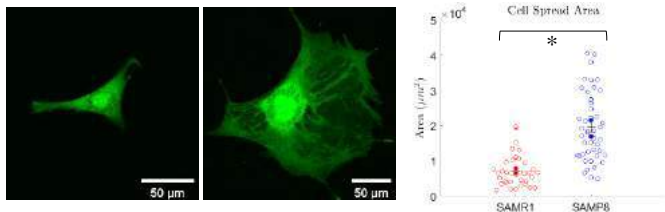


Figure 2: Representative fluorescent images of SAMR1 (left) and SAMP8 (middle) and spread area of SAMR1 vs SAMP8 (right)

Cell Migration in 2D. Preliminary results from cell migration tracking show shorter trajectories in SAMP8 cells compared to SAMR1 cells (Figure 3), and correspondingly, characteristics of its movement such as the mean-squared displacement and the moving velocities of the two are displaying some differences.

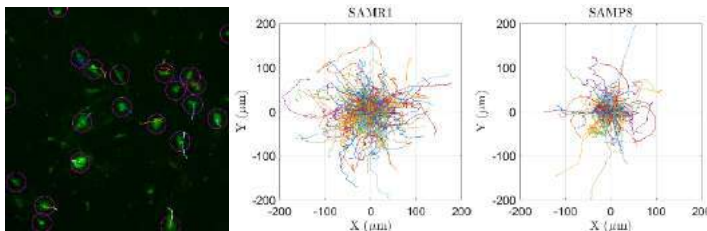


Figure 3: Cell tracking method on ImageJ TrackMate plugin (left) and 10-hour trajectory maps of SAMR1 and SAMP8 (right)

DISCUSSION

Cell Cytoplasm Stiffens. SAMP8 cells showed a twofold increase in stiffness from SAMR1 cells. This is consistent with previous literature that aging stiffens cells and complements other results due to the location the optical tweezers probe. These measurements take place inside of the cell and delineates the overall stiffness of the cells to measure specifically the internal cytoplasmic network of cells. While other studies utilize AFM, Deformable Cytometry, and the like to measure stiffness of the whole cell, this study was able to confirm the stiffening of one area of the cell during the aging process, adding more detail into the understanding of cell stiffening in the aging process.

Cells Seem to Spread More on Glass Substrate. Cell spread area measurements conducted in this study suggests that aging causes more than 2.5x larger spread area, and this observation aligns with the previous results conducted by Park et al. on human dermal fibroblasts [9]. This study contextualizes these numbers against the stiffness measurements to draw correlations between them. With the framework that stiffness and cell spread may be related [10], more work can provide hints toward other physical properties of these cells, such as cell adhesion or growth. In particular, the fundamental size difference of aged versus young cells is especially of interest since both cell groups in this study tend to spread more thinly on the glass substrate than other types of fibroblasts used in cell studies.

Cell Migration Seems Slower and Shorter. Tracking the 2D migration on glass substrate, SAMP8 cells traveled less and more slowly than SAMR1 cells. These results seem to suggest a lower motility in the aging phenotype, which is also observed in other studies. One interesting observation from the preliminary results show anomalous diffusion [11] in the motion of these cells with mean squared displacement slope close to 1.5 (not shown), which are not fully explained in previous works on aging studies.

A Comprehensive Mechanical Study of Aging. This study encompasses a wide variety of mechanical changes in cells due to aging, from the static to the dynamic properties *in vitro*. The different parameters may assess the cellular-level causes into both the structural and functional deterioration of aging in cardiopulmonary organs. While this study contextualizes different mechanical properties of the aging phenotype by measuring cytoplasmic stiffness, cell spread area, and 2D migration, the results are unable to conclude the underlying mechanism behind these changes. Given the three trends observed, the density of cytoplasmic proteins within the cell becomes a question of interest and a possible explanation behind the mechanism of mechanical change.

ACKNOWLEDGEMENTS

National Institute on Aging (R01AG064064)

REFERENCES

- [1] Strait, JB and Lakatta, EG, *Heart Fail Clin*, 8(1):143-164, 2012.
- [2] McHugh, D and Gil, J, *J Cell Biol*, 217(1):65-77, 2018.
- [3] Olivetti, G et al., *Circ Res*, 68(6):1560-8, 1991.
- [4] Qiu, H et al., *Circ Res*, 107:615-619, 2010.
- [5] Lieber, SC et al., *Am J Physiol Circ Physiol*, 287(2):H645-41, 2004.
- [6] Sliogeryte, K and Gavara, N, *Cells*, 8(10):1164, 2019.
- [7] Gupta, SK et al., *Soft Matter*, 15:190-199, 2019.
- [8] Ershov, D et al., *Nature Methods*, 19(7):829-832, 2022.
- [9] Park J-W et al., *Micromachines*, 11(9):801, 2020.
- [10] Guo, M et al., *PNAS*, 114:E8618-E8627, 2017.
- [11] Dieterich, P et al., *PNAS*, 105(2):459-463, 2008.

NOVEL METABOLIC LABELING DEMONSTRATES A CRITICAL ROLE OF DECORIN IN THE ASSEMBLY AND TURNOVER OF CARTILAGE MATRIX

T. Li (1), M. Fan (1), A. Porter (2), B. Kwok (1), C. Wang (1)
D. E. Birk (3), R. V. Iozzo (4), X. L. Lu (2), R. L. Mauck (5), L. Han (1)

- (1) School of Biomedical Engineering, Science and Health Systems, Drexel University, Philadelphia, PA, United States
(2) Department of Mechanical Engineering, University of Delaware, Newark, DE, United States
(3) Department of Molecular Pharmacology and Physiology, University of South Florida, Tampa, FL, United States
(4) Sidney Kimmel Medical College, Thomas Jefferson University, Philadelphia, PA, United States
(5) McKay Orthopaedic Research Laboratory, University of Pennsylvania, Philadelphia, PA, United States

INTRODUCTION

Osteoarthritis (OA) is the most prevalent musculoskeletal disease classified by irreversible degradation of articular cartilage extracellular matrix (ECM), a hydrated composite of collagen II/IX/XI fibrils entrapping the aggrecan aggregate networks [1]. Current reparative and regenerative strategies are challenged by the incomplete understanding of molecular activities of ECM molecules that regulate the matrix assembly and degradation [2]. Our recent study identified decorin, a small-leucine rich proteoglycan (SLRP), in mediating the biomechanical functions of cartilage during post-natal growth [3] and attenuating cartilage breakdown in OA [4]. Specifically, in decorin-null murine model, loss of decorin leads to reduced aggrecan content in both the PCM and bulk territorial/interterritorial matrix (T/IT-ECM), and in turn, chondrocyte in situ mechanotransduction [5]. This impact on aggrecan integrity cannot be directly interpreted by its canonical role in regulating the structure of collagen fibrils [6]. This study thus aims to further delineate the molecular activities of decorin in regulating the aggrecan integrity versus mediating collagen fibril assembly. We investigated the role of decorin in mediating distribution and retention of newly synthesized proteins and glycosaminoglycans (GAGs) using the click-labeling method [7], and at the same time, assessed its impact on the mechanical properties of collagen network via AFM nanoindentation.

METHODS

Explant culture model with metabolic click labeling. Femoral head cartilage explants were harvested from age-matched, 21-day-old (P21) decorin-null (*Dcn*^{-/-}) and wild-type (WT) C57BL/6J mice, and cultured for studying. Explants were first pre-cultured for two days with an additional 1% penicillin-streptomycin, followed by 3 days of metabolic labeling with either 30 mM N-azidoacetyl-galactosamine-tetraacylated (GAL) (1086, ClickChemistryTools) in phenol red deficient high

glucose DMEM or 30 mM L-azidohomoalanine (AHA) (1066, ClickChemistryTools) in DMEM-LM to label for newly synthesized GAGs and proteins, respectively. *Nascent proteoglycans released* into the supernatant were collected daily over a period of 6 days after an overnight wash post-click labeling with 30 mM AZDye 488 DBCO (1278, ClickChemistryTools). Tissues were digested with 2% papain, and the relative release percentage was calculated. *Confocal images* of neo-proteoglycan and proteins were obtained 24 hours following click labeling at the time point of interest to assess the spatial distribution of nascent proteoglycans and proteins (Fig. 1). *AFM-nanoindentation* was applied to quantify the indentation modulus, E_{ind} , of fresh medial femoral condyles of *Dcn*^{-/-} and WT mice in PBS using a microspherical tip ($R \approx 5 \mu\text{m}$, $k \approx 5.4 \text{ N/m}$), following established procedure [3]. To pinpoint the role of decorin in the integrity of collagen network, we quantified the modulus of 1) untreated tissue with native proteoglycans intact, 2) sGAG-depleted via treatment of 0.5 U/ml chondroitinase ABC (chABC) and 500 U/ml hyaluronidase, 3) exogenous decorin-infiltrated (20 $\mu\text{g/mL}$ for 24 hours) for both genotypes. A repeated measure two-way analysis of variance (ANOVA) was applied to compare release at each day and regular two-way ANOVA was applied to compare E_{ind} for each genotype and treatment condition, followed by the Tukey-Kramer multiple comparison to correct for family-wise errors. The significance level was set at $\alpha = 0.05$.

RESULTS

Fluorescence imaging showed clear differences in the distributions of nascent GAGs (Fig. 1a) and proteins (Fig. 1b). From AHA-labeling, at both day 2 and day 6, the nascent proteins were distributed nearly homogeneously throughout the intercellular spacing. In contrast, from GAL-labeling, there was a high concentration of nascent GAGs surrounding individual cells, illustrating preferred localization of newly synthesized proteoglycans in the pericellular spacing. At both time points, we did not observe any salient differences between the WT and

Dcn^{-/-} groups, except for a mildly increase in the GAL-fluorescent signal in the T/IT-ECM at day 6 (black arrowheads). On the other hand, when stimulated by inflammatory cytokine IL-1 β , an increasing percentage of nascent GAGs were released from the explant (Fig. 2). Given that cartilage GAGs are mainly contributed by aggrecan, this evidenced the reduced retention of neo-aggrecan in degenerative cartilage upon inflammatory attacks with the loss of decorin.

Under AFM nanoindentation, *Dcn*^{-/-} cartilage showed significantly lower modulus in comparison to the WT (Fig. 3). Furthermore, removal of sGAGs significantly decreased the cartilage modulus for both WT and *Dcn*^{-/-} groups, albeit the degree of reduction was much greater for the WT group. Meanwhile, infiltration of exogenous decorin significantly elevated the modulus of WT, but not *Dcn*^{-/-} group.

DISCUSSION

This study highlights a crucial role of decorin in regulating the assembly and integrity of articular cartilage matrix. Previously, we have shown that loss of decorin reduces the retention of aggrecan network in cartilage without altering the architecture of collagen II fibrils [3]. It begs the question how does decorin mediate the individual assembly of collagen fibrils and aggrecan network, and in turn, integration of the two. As collagen II is the major protein content of cartilage matrix, the AHA-click labeling shows loss of decorin does not directly impact the assembly of nascent collagen molecules, consistent with our previous observation that the collagen content was not reduced in adult decorin-null cartilage [3]. Meanwhile, we show that the nascent aggrecan is mainly concentrated in the PCM following its biosynthesis, and then, diffuses to the T/IT-ECM (e.g., day 6). Although loss of decorin does not show a clear effect within the 6-day culture duration (Fig. 1), increasing aggrecan fragmentation via IL-1 β leads to accelerated loss of nascent aggrecan (Fig. 2). Thus, the impact of decorin on cartilage matrix integrity is mainly on the retention of aggrecan, and this effect is mainly manifested through the retention of aggrecan within the collagen network.

Comparing the impact of sGAG removal on the moduli of WT and *Dcn*^{-/-} cartilage (Fig. 3), the major impact of decorin was to regulate the contribution of aggrecan to E_{ind} . On the other hand, the differential effects of exogenous decorin indicated a role of decorin in mediating the collagen fibril networks. For WT sGAG-depleted cartilage, decorin was able to elevate E_{ind} , suggesting that decorin could strengthen the collagen network by providing additional physical linkages between collagen fibrils. In contrast, for the *Dcn*^{-/-} group, such effect was minimal. Here, loss of decorin during collagen fibrillogenesis results in disrupted assembly of collagen II fibrils, including altered fibril diameter in the PCM and increased fibril heterogeneity in both PCM and T/IT-ECM [5]. It is thus possible that exogenous decorin is unable to strengthen the altered collagen fibril network. As a result, although the integrity of aggrecan may not be affected in the short duration, this disrupted fibril network is unable to sustain the retention of aggrecan under external instigations. For example, in vivo, the effect of decorin loss is minimal in newborn mice, but increases progressively with age [8]. Here, upon accelerated aggrecan degradation IL-1 β , the effect of decorin loss becomes more apparent. Taken together, our results suggest a crucial role of decorin in mediating the interplay between collagen fibril network and aggrecan network, which is necessary for the maintenance of cartilage integrity, especially upon the fragmentation of aggrecan under inflammation or in disease initiation.

ACKNOWLEDGEMENTS

This work was supported by NIH R01 AR074490.

REFERENCES

- [1] Muir, I. H., In *Adult Articular Cartilage*. 145-214, 1979.
- [2] Heinegård, D., *Int J Exp Pathol*. 90:575-586, 2009.
- [3] Han, B., et al., *ACS Nano*. 13:11320-11333, 2019.
- [4] Li, Q., et al., *Arthritis Rheumatol*. 72:1266-1277, 2020.
- [5] Chery, D. R., et al., *Matrix Biol*. 96:1-17, 2021.
- [6] Douglas, T., et al., *Biomacromolecules*. 7:2388-2393, 2006.
- [7] Porter, A., et al., *ACS Biomater Sci Eng*. 8:2564-2573, 2022.
- [8] McAlinden, A., et al., *Osteoarthritis Cartilage*. 9:33-41, 2001.

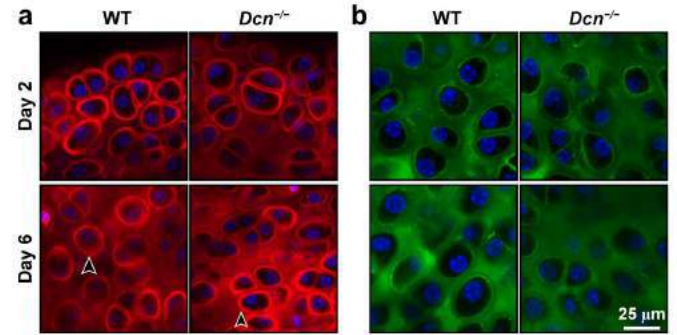


Fig. 1: Confocal click-labeling images of a) newly synthesized GAGs by GAL, and b) newly synthesized proteins by AHA of WT and *Dcn*^{-/-} P21 femoral head cartilage explants at 2 and 6 days post removal of metabolic conditions.

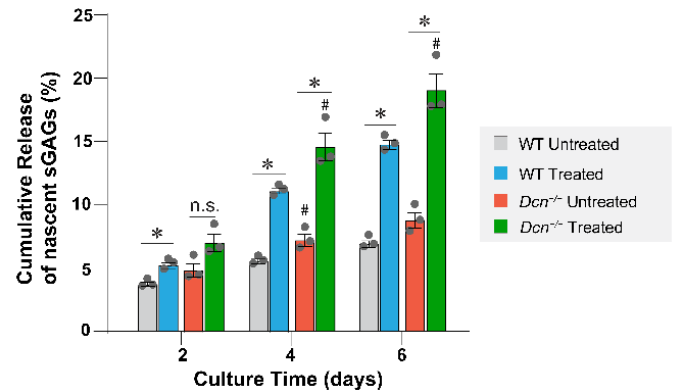


Fig. 2: Daily cumulative release of newly synthesized sGAGs by WT and *Dcn*^{-/-} P21 femoral head cartilage explants in the presence of IL-1 β with respective untreated controls at 2, 4, and 6 days post removal of metabolic conditions (mean \pm S.E.M., $n \geq 3$, *: $p < 0.05$ between each treatment; #: $p < 0.05$ between genotypes).

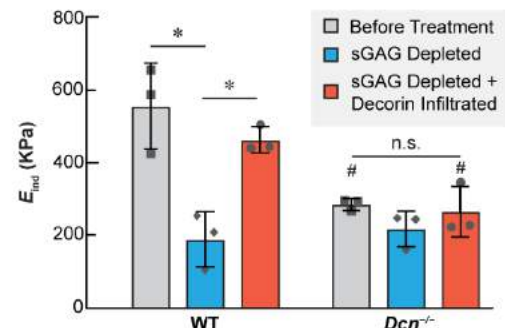


Fig. 3: AFM-nanoindentation modulus, E_{ind} , of medial condyle cartilage from P21 WT and *Dcn*^{-/-} mice subjected to sGAG depletion followed by infiltration of exogenous decorin, and untreated controls (mean \pm 95% CI, $n \geq 3$, *: $p < 0.05$ between each treatment; #: $p < 0.05$ between genotypes; n.s.: not significant).

EVALUATING THE EFFECT OF SOFT TISSUE FORCES ON THE FIXATION MECHANICS OF REVERSE SHOULDER ARTHROPLASTY: A FINITE ELEMENT ANALYSIS DRIVEN BY MUSCULOSKELETAL SIMULATIONS

Jonathan Glenday (1), Benjamin Johnston (2), Fernando Quevedo Gonzalez (1),
Lawrence Gulotta (1), Andreas Kontaxis (1)

(1) Hospital for Special Surgery, NY, NY, USA

(2) Cornell University, Ithaca, NY, USA

INTRODUCTION

Reverse shoulder arthroplasty (RSA) is used to alleviate pain and restore shoulder function to patients with rotator cuff arthropathies [1]. Despite promising clinical results, multiple complications still exist, such as reduced post-operative function, impingement, and glenoid loosening [2]. Numerous cadaveric and computational studies have investigated the fixation of the glenoid, including finite element (FE) analyses conducted to understand the bone-implant fixation [3-5]. Unfortunately, the current FE models in the literature use simplistic loading profiles which are applied to the glenohumeral (GH) joint and do not consider the effect of the multiaxial loads that are typically observed during activities of daily living. Moreover, these models have not considered the loads applied by the soft tissues during these complex movements. Therefore, we sought to use a musculoskeletal model of the shoulder to determine physiological loading conditions and then transfer these loads to a corresponding FE model to holistically evaluate the fixation mechanics at the bone-implant interface. With this approach, we sought to test the hypothesis that including soft tissue forces during FE simulations of an activity of daily living would increase the bone-implant micromotion of RSA.

METHODS

Our computational approach used the outputs of a multibody musculoskeletal model (the Newcastle Shoulder Model – NSM [6]) as the inputs to a corresponding FE model. The NSM, which consists of 6 segments (thorax, clavicle, scapula, humerus, ulnar, and radius), 31 muscles, and 3 ligaments (soft tissues), determined the soft tissue forces and the glenohumeral (GH) joint contact forces of the RSA joint using inverse dynamics and optimization techniques. The FE model then used all the soft tissue and GH joint contact forces as inputs to determine the micromotion at the interface of the implant and resected glenoid on the scapula (Fig. 1). Both the musculoskeletal and FE models were adapted with the glenohumeral anatomy of five patients with rotator cuff arthropathies. The scapula and humerus were reconstructed from pre-operative CT scans and soft tissue attachments were customized to the patient-specific attachment sites. A commercially available RSA system (Comprehensive Reverse Shoulder System. Biomet, Inc., Warsaw, IN) was then virtually implanted into each model. The component placement was verified by a board-certified shoulder orthopaedic surgeon (LG). The musculoskeletal model simulated a single activity of daily living (reaching for an object at head height) and determined the soft tissue and GH joint contact forces throughout the activity, which were then transferred to the matching patient-specific FE models. The GH joint contact forces were applied to the center of rotation (center of the glenoid sphere) and the soft tissue forces on the scapula were applied at their attachment sites (i.e., the same locations as used in the musculoskeletal models). The bone was modeled as a non-homogenous material, with an elastic modulus (E) determined from the pre-operative CT scans using a pooled density-modulus relationship [7]. The glenosphere was modeled as a rigid body and the superior, inferior, and central locking screws and metaglene were modeled as a solid titanium alloy ($E=113.8$ GPa, Poisson's ratio, $\nu=0.3$). The bone-implant interface

was modeled as frictional, with a coefficient of 0.6. The bone was fixed at the medial border of the scapula and at the acromioclavicular joint [4]. For each FE model, we simulated two loading configurations: 1) application of only the GH contact forces (Fig. 1a) and 2) application of both the GH contact forces and the soft tissue forces (Fig. 1b). For each configuration, our primary outcome measure was the bone-implant micromotion (measured in micrometers, μm), which was computed as the difference in displacement between each pair of closest nodes at the bone-implant interface.

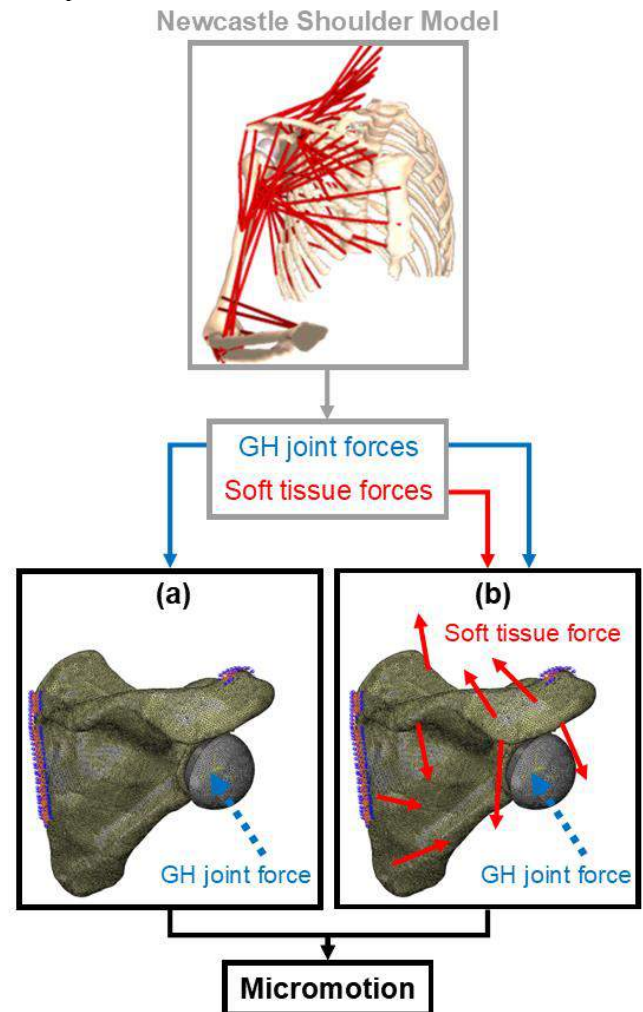


Figure 1: Overview of our computational approach to determine bone-implant micromotion. It used the NSM to predict soft tissue and GH joint contact forces and then transferred these forces to corresponding FE models which used (a) only the GH joint contact force and (b) both the soft tissue and GH joint contact forces.

RESULTS

The net GH joint contact force (reported in bodyweight, BW) exhibited a first, larger, peak of $0.52 \text{ BW} \pm 0.03 \text{ BW}$ at 31% of the cycle and a second, smaller, peak of $0.47 \text{ BW} \pm 0.05 \text{ BW}$ at 65% of the cycle (Fig. 2; top). Within these two peaks, the arm was elevated as it reached for the object at head height. At the first loading peak, the compression and shear forces were $0.49 \text{ BW} \pm 0.04 \text{ BW}$ and $0.17 \text{ BW} \pm 0.06 \text{ BW}$, respectively. In addition, the compression force represented 50% - 92% of the net GH joint contact force throughout the activity.

When only the GH joint contact force was considered, the average peak micromotion varied from $3 \mu\text{m} \pm 1 \mu\text{m}$ (at 33% of the cycle) to $6 \mu\text{m} \pm 2 \mu\text{m}$ (at 73% of the cycle). Conversely, when both the soft tissue and GH joint forces were considered, the peak micromotion ranged from $13 \mu\text{m} \pm 9 \mu\text{m}$ (53% of the cycle) to $18 \mu\text{m} \pm 11 \mu\text{m}$ (79% of the cycle, Fig. 2; bottom). At the instant of the overall peak micromotion, the compression force represented 72% of the net GH joint contact force. This was a 16% reduction compared to the instant of peak GH loading (31% of the cycle).

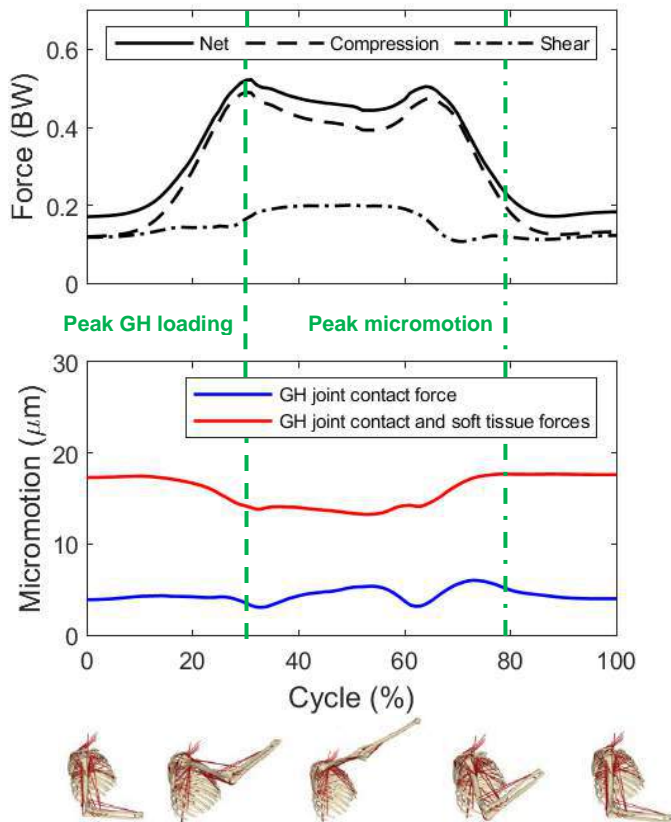


Figure 2: Top: Average GH joint contact forces (in BW) during the activity cycle. Solid line: net GH joint force; dashed line: compression force; and dot-dashed line: shear force. Bottom: Peak micromotion (in μm) at the bone-implant interface during the activity cycle. Blue line: configuration where only GH joint contact forces were considered; red line: configuration where both soft tissue and GH joint contact forces were considered. The dashed green vertical line represents the instant of peak net GH loading, and the green dot-dashed line represents the instant of overall peak micromotion.

DISCUSSION

By simulating an activity of daily living, we found that the instant of peak micromotion did not correspond with the instant of peak GH joint contact force, which has been a commonly used loading scenario for prior FE models of shoulder replacements. From our observations, we postulate that this may be attributed to the changing distribution of the compression and shear forces in the GH joint throughout the activity. For example, the compression force accounted for 88% of the net GH joint contact force at the instant of peak GH loading and 72% at the instant of peak micromotion. Moreover, these changes may also have an interaction with the inherently complex geometry of the scapula.

For both loading configurations, the peak micromotion throughout the cycle was small and within the acceptable limits for bone ingrowth to occur for cementless implants [8]. However, by including the soft tissue forces in the FE models, we observed an average increase in micromotion by 370% across the activity cycle. Thus, our results suggest that the omission of soft tissue forces can lead to an underestimation of the burden placed on the bone-implant interface.

Our study considered a fixed acromioclavicular joint, and this may be a limitation. In our future studies we intend to investigate the impact of the acromioclavicular joint as a non-fixed boundary condition as the muscle forces attached to the acromion may also contribute to the bone-implant micromotion.

In conclusion, by connecting musculoskeletal and finite element models, we found that the peak micromotion during an activity of daily living did not correspond with the instant of peak GH joint loading and that the inclusion of soft tissue forces led to the prediction of increased micromotion. These methodological updates to the FE modelling of shoulder arthroplasty are important as future FE studies should investigate more representative activities cycles, with soft tissue forces, to holistically assess the impact of shoulder biomechanics on the fixation mechanics at the bone-implant interface.

Going forward, we aim to use to our workflow to evaluate the impact of the design and placement of total and reverse shoulder arthroplasty components on both the joint mechanics and implant fixation mechanics of the post-operative glenohumeral joint.

REFERENCES

- [1] Boileau et al. JSES (2006).
- [2] Day et al. JSES (2010).
- [3] Sabesan et al. JSES (2019).
- [4] Bonneville et al. JEO (2022).
- [5] Elwell et al. J Biomech (2017).
- [6] Kontaxis and Johnson. Clin Biomech (2009).
- [7] Morgan et al. J Biomech (2003).
- [8] Jasty et al. JBJS (1997).

AN EULER-LARGANGE APPROACH FOR MODELING PARTICLE-LADEN FLOWS IN BIOLOGICAL APPLICATIONS

Abhilash Reddy Malipeddi (1), Jesse Capecelatro (1), C. Alberto Figueroa (2)

(1) Mechanical Engineering, University of Michigan, Ann Arbor, MI, USA
(2) Biomedical Engineering & Surgery, University of Michigan, Ann Arbor, MI, USA

INTRODUCTION

Fluid mechanics plays a crucial role in numerous physiological processes related to health and disease. Advances in medical imaging, computational power, and mathematical algorithms have made it possible to perform real-time, patient-specific computational fluid dynamics analyses. However, many problems involve complex interactions between fluids and particles of varying mass and size,

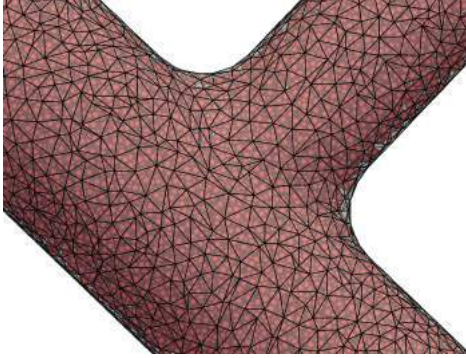


Figure 1: Snapshot from a simulation of a concentrated particle-laden flow through unstructured grid geometry.

which presents challenges in understanding and modeling their dynamics. The goal of this work is to develop a computationally efficient, scalable, physics-based framework for particle-laden biological flows in complex subject-specific geometries (e.g., Figure 1) to enable the next generation of methods for computer-aided diagnostics and disease research. The proposed scheme is based on a volume-filtered Euler-Lagrange formulation of the incompressible Navier-Stokes equations in which particles and fluid are fully coupled, and the finite volume fraction effect of the particles is accounted for explicitly.

METHODS

In the Euler-Lagrange method, the fluid flow governing equations are solved on an Eulerian grid. Particles within the fluid are treated as discrete points, which can interact with the fluid and other particles through the exertion and experience of forces. For cases where the particle mass and volume fraction are small, feedback of the particles on the fluid can be reasonably neglected, leading to "one-way" coupled models. However, to ensure applicability to a wide range of particle-laden flows, we have implemented a fully coupled model, also referred to as a "4-way" coupling in literature. The level of coupling can be easily adjusted depending on the specific problem and desired level of accuracy. These methods and models are implemented within the CRIMSON framework [1], providing a flexible and user-friendly platform for simulating particle-laden flows in patient-specific geometries. The equations are solved using the finite element method. The fluid governing equations shown below are derived from the incompressible viscous flow equations after application of a filtering (averaging) operator. See [2] for a detailed derivation. The volume filtered fluid phase equations take the form

$$\frac{\partial u_i}{\partial x_i} + \frac{1}{\phi_f} \frac{D\phi_f}{Dt} = 0 \quad (1)$$

$$\rho \left(\frac{\partial u_i}{\partial t} + u_j \frac{\partial u_i}{\partial x_j} \right) = - \frac{\partial p}{\partial x_i} + \frac{\partial \tau_{ij}}{\partial x_j} + \frac{1}{\phi_f} f_i^p \quad (2)$$

where the velocity and pressure should be understood to be volume filtered quantities. ρ is the density of the fluid phase, ϕ_f is the volume fraction of the fluid phase, and f_i^p is the momentum source that couples the particles to the fluid phase, which can be understood as the reaction force felt by the fluid due to the drag experienced by the particles. The fluid equations are solved using a stabilized finite element method

which incorporates streamline-upwind/Petrov-Galerkin (SUPG), pressure-stabilizing/Petrov-Galerkin (PSPG) and grad-div stabilizations. This allows for solving advective incompressible flows with equal order elements for velocity and pressure. The equations are solved implicitly and marched in time using a generalized- α method.

The particle dynamics are calculated individually in accordance with the Newton's laws of motion where each particle's position is obtained by integrating the following

$$\frac{d\mathbf{X}_p}{dt} = \mathbf{V}_p, \quad m_p \frac{d\mathbf{V}_p}{dt} = \mathbf{F}_d + \mathbf{F}_c, \quad I_p \frac{d\boldsymbol{\Omega}_p}{dt} = \mathbf{T}_d + \mathbf{T}_c \quad (3)$$

where \mathbf{X}_p is the position of the particle, \mathbf{V}_p is the translational velocity, m_p is the mass, $\boldsymbol{\Omega}_p$ is the angular velocity and I_p is the rotational moment of inertia of the particle. \mathbf{F}_d is the drag force experienced by the particle and \mathbf{F}_c is the force due to collisions with other particles. \mathbf{T}_d is the hydrodynamic torque on the particle and finally \mathbf{T}_c is the collisional torque arising from friction between the interacting particles. Numerous drag models have been developed and used for Euler-Lagrange simulations in the literature. Here we use the drag model put forth by Tenneti [3], which is well suited for the parameter space of problems relevant for biofluid applications:

$$F(\phi, Re_m) = \frac{F_{\text{isol}}(Re_m)}{(1-\phi)^3} + F_\phi(\phi) + F_{\phi, Re_m}(\phi, Re_m) \quad (4)$$

here, F_{isol} is the drag force acting on an isolated sphere moving in an unbounded medium. The remaining two terms are given by

$$F_\phi(\phi) = \frac{5.81\phi}{(1-\phi)^3} + 0.48 \frac{\phi^{1/3}}{(1-\phi)^4} \quad (5)$$

$$F_{\phi, Re_m}(\phi, Re_m) = \phi^3 Re_m \left(0.95 + \frac{0.61\phi^3}{(1-\phi)^2} \right)$$

where ϕ is the particle volume fraction and Re_m the Reynolds number based on particle diameter and mean slip velocity. Particle collisions are modeled using the soft-sphere discrete element method (DEM).

RESULTS

A critical component of the volume filtered Euler-Lagrange scheme is the transfer of physical quantities between the Lagrangian and Eulerian representations. For instance, the particle distribution must be projected onto the finite-element mesh before the governing equations

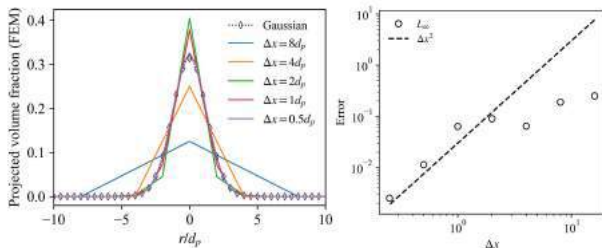


Figure 2: Left: Projected volume fraction due to a single particle at the origin, with increasing grid resolution. Right: Plot showing convergence of the projection procedure employed.

can be solved. For consistency, this process needs to be conservative and convergent. This is achieved via a two-step procedure that decouples particle size from the element size which allows flexibility and gives convergent solutions. Figure 2 shows the convergence plot for the projection process as implemented in the current FEM setting.

Results from preliminary simulations are shown in Figure 3 for a T shaped geometry where the left and right sides of the T are inlets, and the stem is an outlet boundary. Initially, XX particles of RR radius and rho density are uniformly distributed over the volume of the geometry. As the simulation goes on, fluid enters the domain from the inlet faces and particles are carried out of the domain through the outlet.

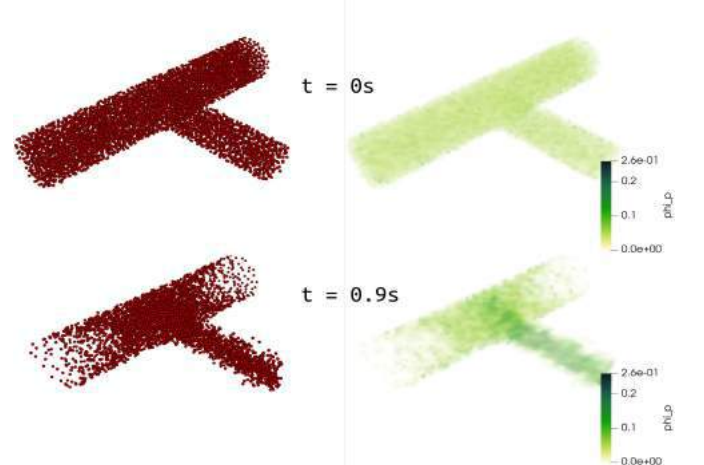


Figure 3: Results from a particle-laden simulation showing distribution of particles in a T-shaped geometry. Top frames show the initial condition and bottom frames shows the state at $t = 0.9s$. Particles are shown explicitly on the left, while the projected particle volume fraction field is shown on the right.

DISCUSSION

We have developed a scalable volume-filtered Euler-Lagrange scheme for the simulation of particle-laden flows on unstructured grids. This method is applicable to a range of biological fluid dynamics phenomena. It involves a Lagrangian to Eulerian projection of conserved quantities for unstructured finite element grids, which is consistent, conservative and convergent. These improvements contrast with existing methods that lacked this combination of qualities. We have presented preliminary results which demonstrate the capabilities of our proposed multiphase flow solver. Further development and validation of the solver is currently ongoing. Our CFD-DEM solver will enable efficient large-scale simulations of particle-laden flows, while retaining important microscale physics. This will provide a versatile tool for computer-aided diagnostic applications. While the CRIMSON framework is specialized for cardiovascular flows, it is easily generalizable to other biofluid applications, and we plan to apply these developments to study particulate flow in the inner ear to aid in the analysis and treatment of benign paroxysmal positional vertigo caused by suspended particles settling in the semi-circular canals.

ACKNOWLEDGEMENTS

Authors acknowledge funding from the Michigan Institute for Computational Discovery and Engineering (MICDE) Catalyst Grant 2021.

REFERENCES

- [1] Arthurs, C. J. et al, *PLoS Comput Biol* (2021) 17(5): e10008881
- [2] Capecelatro, J. and Desjardin, O., *J. Comp. Phys.* 238 (2013) 1-31
- [3] Tenneti, S. et al, *IJMF* 37 (2011) 1072-1092

A DEEP LEARNING APPROACH FOR CARDIAC MODEL CONSTRUCTION FOR CONGENITAL HEART DISEASE PATIENTS

Fanwei Kong (1), Alison L. Marsden (1, 2, 3)

- (1) Department of Pediatrics, Stanford University, Stanford, CA, USA
(2) Department of Bioengineering, Stanford University, Stanford, CA, USA
(3) Department of Mechanical Engineering, Stanford University, Stanford, CA, USA

INTRODUCTION

Congenital heart defects (CHDs) are the most common birth defects and are characterized by abnormal cardiac anatomies that can dramatically impact cardiac functional outcomes. CHD patients often have unique but complex cardiac malformations and anatomical arrangements that warrant patient-specific treatment planning and surgical interventions. Personalized computer models of the heart derived from patient image data can simulate various aspects of cardiac function and can thus model complex clinical scenarios in CHD patients and have demonstrated potential to facilitate personalized treatment planning and decision-making¹⁻². However, prior studies often require prohibitively laborious human effort to generate models that accurately capture CHDs from patient image data, thus limiting large-scale validation studies and clinical translation of this novel paradigm. Therefore, there is a strong need for automated image-based modeling of the heart for CHD patients to support virtual surgery planning in real clinical settings.

Although deep learning (DL) methods have demonstrated immense potential in automatic medical image analysis in the area of whole heart reconstruction and segmentation³, prior approaches were mostly developed to model normal cardiac structures and cannot be generalized to model cardiac malformations seen in CHD patients. For example, our prior work proposed a DL method to deform a *template mesh* of a healthy heart to automate the model generation process for various cardiac simulations⁴. This method thus cannot capture the CHD anatomies that have peculiar cardiac arrangements and topologies that differ significantly from those in the mesh template.

Therefore, we aim to develop an DL algorithm to automatically and efficiently generate cardiac models from image data of CHD patients. Rather than deforming an explicit mesh template, we propose to implicitly represent the shapes of the heart using *signed distance fields* (SDF) learned by neural networks to conveniently capture the unique arrangements and topologies of the cardiac shapes in several

types of CHDs. We then deform the SDFs based on patient image data to reconstruct personalized cardiac models that successfully capture the structural abnormalities.

METHODS

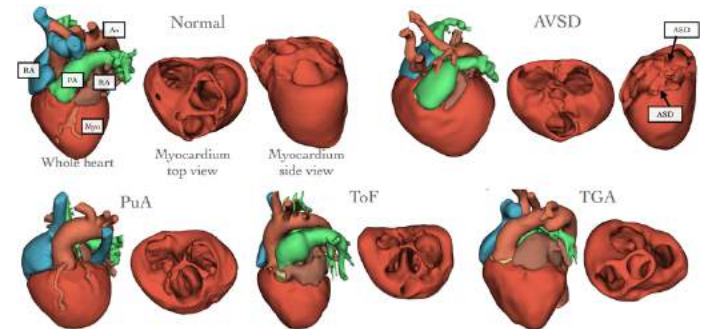


Figure 1: Example segmentations for different CHD types.

Dataset: We considered a few types of CHDs that cause abnormal arrangement and anatomy of heart chambers and great vessels in our study. Namely, we included a total of 51 CT images that covered 29, 14, 12, 5, and 5 instances of ventricular septal defects (VSD), atrial ventricular septal defects (AVSD), Tetralogy of Fallot (ToF), transposition of great arteries (TGA), and pulmonary atresia (PuA), respectively, as well as 5 CT images that do not have the above CHDs. Among those, we used 35 images for training, 4 for hyperparameter tuning, and 12 test images for final evaluation. The 12 test images contain at least 2 images for each CHD type. The CT images were selected from the public imageCHD dataset⁵ which includes ground truth segmentations of 7 cardiac structures including the myocardium (Myo), blood pools of right atrium (RA), left atrium (LA), right ventricle (RV) left ventricle (LV), aorta (Ao), and pulmonary arteries (PA). Fig. 1 shows example segmentations for different CHD types.

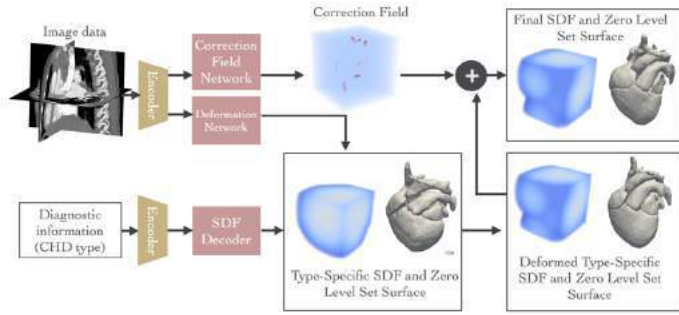


Figure 2: Diagram of the proposed approach

Network Design: Fig. 2 illustrates the proposed algorithm to automatically construct meshes of cardiac structures from CT images of patients with CHDs. We used neural networks as a field function to model SDFs that can represent the shapes of the cardiac structures. Namely, an SDF assigns any point $\mathbf{p} \in \mathbb{R}^3$ a scalar value $s \in \mathbb{R}$, such that $\text{SDF}(\mathbf{p}) = s$, where the magnitude of s represents the distance from \mathbf{p} to surfaces of cardiac structures and the sign represents whether \mathbf{p} is inside or outside. Given the types of CHD that a patient could have, we represented this diagnostic information as a vector containing true or false values, corresponding to whether the patient modeled had those allowable CHD types we chose to include in this study. We then trained multilayer perceptrons (MLP) to model the SDFs of cardiac structures corresponding to the input CHD type. To deform the type-specific SDFs to match the predicted cardiac shapes with patient images, we used convolutional neural networks to extract image features. We then sampled these features at the point locations in the type-specific SDF and then used MLP to predict the corresponding locations on the image data. We further predicted a correction field from the image features to add to the deformed SDFs to more accurately match patient-specific anatomical features that cannot be modeled by simply deforming type-specific cardiac shapes. The final meshes were generated at the 0 level set of the SDFs by the marching cube algorithm.

Network Optimization: Ground truth SDFs of the whole heart constructed from manual segmentations were used to supervise the training of the neural network model. We supervised the accuracy of deformed type-specific SDF both before and after adding the correction field by computing the mean squared error (MSE) between the predicted SDFs the ground truth SDFs. We also minimized the L2 norm of the predicted gradient field to encourage smoother deformation from the type-specific SDFs.

RESULTS

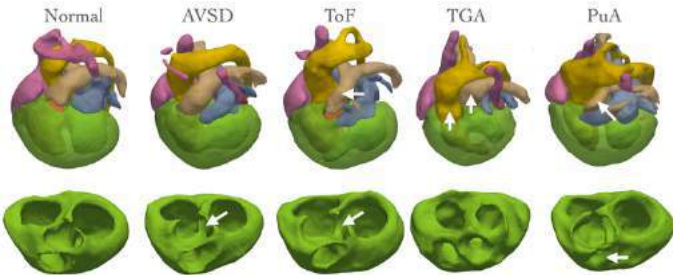


Figure 3: Surface meshes (top row: whole heart; bottom row: myocardium) extracted from the learned type-specific SDFs.

Fig. 3 visualizes the cardiac structures extracted from the automatically learned SDFs corresponding to various CHD types. Our networks were successfully trained to predict SDFs that captured the typical abnormalities given the CHD type as the input, namely, the ventricular septal defects in AVSD, the shifted aortic opening and the

narrowed PA trunk in ToF, the transposed aorta and PA in TGA and the missing PA outlet in PuA.

Table 1 displays the average Dice scores (a similarity index) of the reconstruction results of both the whole heart (WH) and individual cardiac structures for all samples in the testing datasets and for each CHD type, respectively. Our method generally performed better for heart chambers than for great vessels. Fig. 4 visualizes example reconstruction results of our methods for both training and testing samples. The deformation network was able to morph the learned type-specific cardiac shapes shown in fig. 3 to better match the patient image data and the ground truth segmentations. The predicted correction field was able to capture some additional patient-specific anatomical details, such as the vessel branches. Our method produced worse reconstruction for testing samples than for training samples, indicating overfitting and a lack of diversity of the training dataset.

Table 1: Dice scores for different CHD types in the test dataset

	WH	LV	RV	LA	RA	Myo	Ao	PA
Total (n=12)	0.66	0.68	0.60	0.71	0.74	0.66	0.52	0.48
VSD (n=6)	0.73	0.77	0.66	0.80	0.73	0.73	0.62	0.61
AVSD (n=5)	0.59	0.58	0.51	0.62	0.73	0.58	0.41	0.37
ToF (n=2)	0.79	0.82	0.70	0.82	0.82	0.79	0.73	0.75
TGA (n=2)	0.61	0.56	0.47	0.58	0.80	0.62	0.38	0.17
PuA (n=2)	0.68	0.63	0.75	0.59	0.79	0.72	0.68	0.38

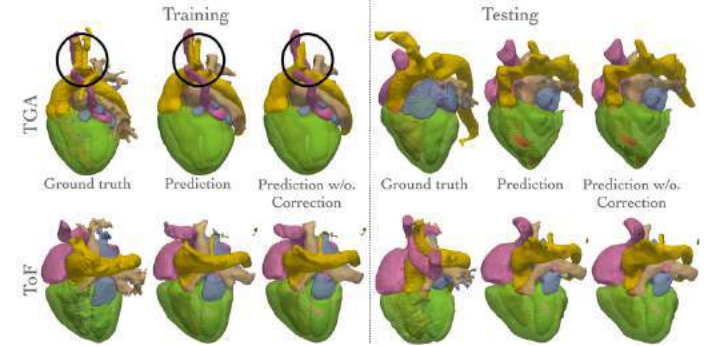


Figure 4: Example reconstruction results compared with ground truth segmentations.

DISCUSSION

Automatic construction of cardiac structures from image data of CHD patients can greatly facilitate patient-specific virtual treatment planning. We have demonstrated preliminary results from a novel DL approach to automatically construct cardiac shapes represented by SDFs from CT images. Compared with prior approaches that were designed for normal cardiac anatomies, our method was trained to capture the different abnormal cardiac anatomies corresponding to various types of CHDs. Our method produced an average WH Dice score of 0.66 on the test dataset, whereas prior methods that model healthy can achieve a WH Dice score of around 0.8-0.9³⁻⁴. This is partly due to the limited number of training images available and the greater diversity of cardiac anatomies both within a single CHD type and across different CHD types. In the future, we will train and evaluate the proposed method using larger datasets and continue to improve the method to produce more accurate reconstructions.

ACKNOWLEDGEMENTS

This work was supported by NSF 1663671, NIH R01EB029362, and NIH R01LM013120.

REFERENCES

- [1] Marsden AL & Feinstein JA, *Curr Opin Pediatr*, 27(5):587-96, 2015.
- [2] Clementel, IV et al., *Prog. in Ped. Cardiology*, 30:3-13, 2010.
- [3] Zhuang et al., *Med Image Analysis*, 58, 101537, 2019.
- [4] Kong F and Shadden SC, *IEEE Trans. Med. Imaging*, 2022.
- [5] Xu X et al., *MICCAI, LNCS*, 12264: 77-87, 2020.

DESIGN AND EVALUATION OF A FLOATING PLATFORM SYSTEM FOR MECHANICAL TESTING OF MESOSCALE GELS AND TISSUES

Tyler G. Tuttle (1), Sarah Calve (1)

(1) Mechanical Engineering, University of Colorado Boulder, Boulder, CO, United States

INTRODUCTION

Measuring the mechanical properties of biological tissue is crucial for understanding healthy physiological and pathological function in many organs. Accurately describing and modeling systems in the fields of biomechanics and mechanobiology hinges on the ability to properly execute mechanical tests. Mechanical tests come in all shapes and sizes, including tensile, compressive, or shear deformations, can be performed uniaxially, biaxially, or even triaxially [1], and apply deformations in temporally linear or sinusoidal patterns, or set deformations followed by constant stresses or strains. All of these mechanical tests come with challenges. The challenges outlined below focus on tensile testing but are applicable to many other types of tests.

When designing a mechanical testing setup, it is necessary to consider the method of force measurement, mounting system, and imaging techniques. Additionally, protocol considerations for testing and post-processing (*i.e.* preload, maximum applied stress/strain, temperature, sampling frequency, choice of reference configuration) must cater to the material/tissue being used and the hypotheses being tested. For force measurement, proper load cell capacity with adequate signal to noise ratio for the intended force range is important, and this can be greatly affected by not only the force measurement system, but the mounting system as well. Mounting systems may include some amount of friction or other off-target forces that need to be corrected in post processing. Other mounting issues may be sample slipping, damage, or imperfect application of the intended deformation. Imaging systems must have the resolving power to measure sample geometry, including cross-sectional area, initial sample dimensions, and amount of applied deformation. Finally, when combining these systems the testing protocol, post processing, and data analysis choices must be thought out thoroughly, as something as simple as choice of reference configuration for the measurement of stretch can drastically impact results [2]. The compounding effects of these challenges contribute to

the variability seen between data of the same tissue, using similar tests, but by separate research groups with different testing setups.

This work aims to address some of these challenges, namely, friction and off-target forces. This is accomplished through the design and validation of a multi-buoy floating platform mechanical testing setup.

METHODS

The design of the mechanical testing system consists of a fibrin gel mounting system, a multi-buoy floating platform, and a bath. Equipment used for testing consisted of a micromanipulator system (FemtoTools FT-RS1002) that allows for application of microscale uniaxial tensile displacements and force measurement. Imaging of the fibrin gels was performed with a confocal microscope (Leica, STELLARIS 5) and a dissecting microscope (Leica, M80).

Mechanical testing was performed on fibrin gels (2 and 4 mg/mL fibrinogen). Fibrinogen-soaked porous polyethylene blocks were glued to laser-cut frames with cyanoacrylate adhesive. The frames were designed with mounting through-holes for M2 threads. Fibrin was polymerized to the blocks in a custom 3D printed mold (Figure 1a) to create mounted fibrin gels for mechanical testing (Figure 1a-b). Gels were approximately 0.7 x 1.4 x 6.6 mm in size.

The multi-buoy floating platform (Figure 1c) was designed with three buoys for stable floating. The front buoy has a raised section with holes, where a stainless-steel wire is glued to allow the micromanipulator to hook to the floating platform. An angled cylindrical extrusion was offset from between the back buoys to hook onto the fibrin gel frame through-holes. The floating platform was designed in SolidWorks, and 3D printed (Stratasys J750) with a photopolymer (VeroClear, Stratasys) that is similar to acrylic.

The bath was designed to contain the floating platform with enough room to apply more than 4 mm displacement to the fibrin gel. Circular arc barriers were designed into the bath floor to hold the

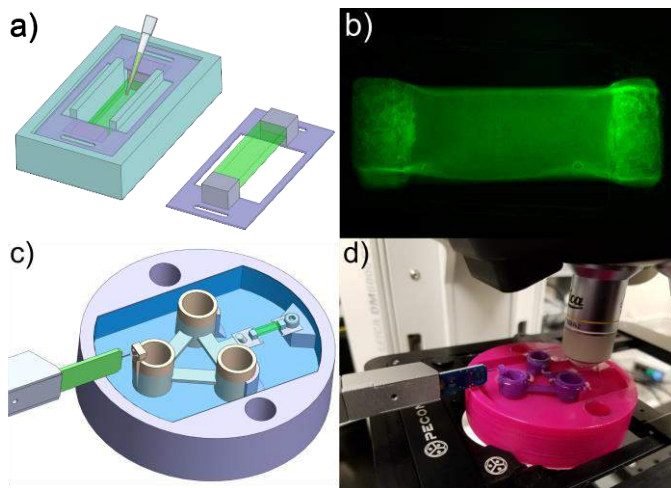


Figure 1. (a) Fibrin gel mold and the resulting frame-block-gel assembly for mechanical testing, (b) representative fibrin gel, (c) model of the multi-buoy floating platform mechanical testing setup showing the force sensor, floating platform, bath, and gel, and (d) an image of the setup in use with the confocal microscope.

floating platform in place while applying no deformation to the fibrin gel. These barriers prevented rotation and translation of the platform without obstructing the application of tensile deformation. A raised M2 threaded hole was used mount the frame to the bath.

The following mechanical testing protocol was used to test the system. The bath was filled with 20 mL of PBS and the fibrin gel frame was mounted to the bath with a M2 screw. The floating platform was hooked into the other end of the frame, and the platform was lowered into the bath. The sides of the frame were then cut and removed to allow application of deformation. The micromanipulator force sensor arm was hooked onto the wire loop on the front buoy of the floating platform. A 100 μ N preload was added to the fibrin gel to ensure engagement of the hook. Stress-relaxation tests were performed in 1 mm increments at 66 μ m/s, with 60 minute relaxation times, to a final displacement of 3 mm. Water (50 μ L) was pipetted into the bath every 5 minutes to minimize evaporation related changes in platform height and PBS osmolarity. Additionally, a test was performed with no fibrin gel attached to evaluate the presence of off-target forces due to inertia or drag from the solution during movement.

RESULTS

The buoy system enabled the combination of mechanical testing with imaging on both a confocal microscope (Figure 1d) and dissecting microscope (not shown). The mechanical testing system captures the stress-relaxation behavior of fibrin gels, and resolves differences in force between gels with different concentrations of fibrinogen (Figure 2a). Mechanical data collected with no sample attached shows a flat signal with noise centered at zero load with a mean \pm standard deviation of 0.01 \pm 0.09 mN. During the movement phase the noise is slightly greater than in the stationary phase, but still centered at zero load (movement: 0.02 \pm 0.13 mN, stationary: 0.01 \pm 0.07 mN).

DISCUSSION

This multi-buoy floating platform mechanical testing setup allowed us to resolve differences in forces measured from same-sized fibrin gels containing different concentrations of fibrin. The zero-centered forces in the no-sample test suggest that there are negligible off-target forces acting from inertia or drag from the PBS. Beyond the investigation of fibrin gel mechanics [3], modified versions of this setup are currently

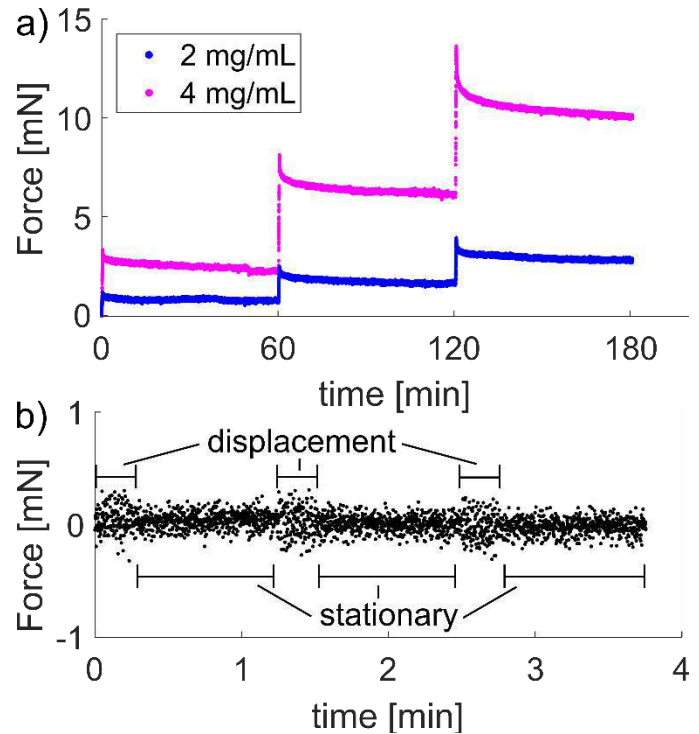


Figure 2. (a) Representative fibrin gel stress-relaxation test force-time data for 2 and 4 mg/mL samples, and (b) shortened stress-relaxation mechanical test with no sample attached demonstrating minimal off-target forces during movement and stationary phases.

being used to study mechanics of uterosacral ligaments, forelimb tendons, and other tissues in our lab. This design has the potential to push forward the field of biomechanics by allowing improved collection of mechanical data for a wide array of tissues and materials.

There are some limitations with the design that are in the process of being addressed. First, evaporation is an irrefutable problem. Proper measurement of force with this system requires a constant height of the floating platform, and some tissues may be susceptible to changes in mechanics or geometry based on changes in solution osmolarity [4]. Both of these issues could be present with excessive evaporation of solution. A second issue is the off-axis application of deformation and force reading. Due to the force sensor attachment being out of the bath and the sample being in the bath, deformation application and force measurement are not colinear with the sample. The amount of error from this problem may be negligible but requires evaluation or a creative redesign of the sensor attachment.

The advancement of the field of biomechanics hinges partially on the ability to improve mechanical testing methodologies. The design presented in this abstract minimizes friction and off-target forces, which is particularly beneficial for studying small organs and tissues.

REFERENCES

- [1] R. Avazmohammadi, et al., *Biomechanics and Modeling in Mechanobiology*. 17 (2018) 31–53.
- [2] S. Wognum, et al., *Journal of Biomechanical Engineering*. 131 (2009) 101018.
- [3] J.M. Jimenez, Tuttle, T.G., et al., *BioRxiv*. (2022) 2022.12.06.519227.
- [4] T.A. Sorrentino, et al., *Journal of Biomechanical Engineering*. 137 (2015).

COMPUTATIONAL SIMULATION OF PATIENT-SPECIFIC BLOOD COAGULATION IN STENT THROMBOSIS

Janneke M.H. Cruts (1), Mohammad Rezeimoghaddam (2), Frans N. van de Vosse (2), Frank J.H. Gijsen (1,3)

- (1) Department of Biomedical Engineering, Erasmus Medical Center, Rotterdam, the Netherlands
(2) Department of Biomedical Engineering, Eindhoven University of Technology, Eindhoven, the Netherlands
(3) Department of Biomechanical Engineering, Delft University of Technology, Delft, the Netherlands

INTRODUCTION

Stent thrombosis is a serious complication that is defined as a thrombotic occlusion of a coronary stent. It has been associated with high rates of morbidity and mortality. Stent thrombosis can be caused by a number of factors, such as injury or endothelial disruption caused by the stent struts, and hypercoagulability of the patient (an increased tendency for the blood to clot) [1]. The efficacy of metallic stents and bioresorbable scaffolds to treat coronary artery stenosis is related to the hemodynamic environment. The struts of these devices disturb the local flow field and induce flow recirculation zones and endothelial damage [2]. Computational work has been utilized to analyze the relation of coronary stents to hemodynamics and platelet aggregation [3]. However, despite the central role of fibrin network formation in thrombosis, limited research has been done on the effect of stent design on coagulation dynamics.

The aim of this study is to improve understanding of the impact of injury induced blood coagulation on stent thrombosis and to identify risk factors that contribute to it, with the ultimate goal of improving stent designs. This will be studied analyzing local hemodynamics together with patient-specific clot formation using computational fluid dynamics (CFD).

METHODS

A biophysical model of a fibrin-rich clot is developed based on the framework presented earlier in Bouchnita et al. [4]. A system of coupled convection-diffusion-reaction (CDR) equations is used to solve the concentration of factor IX and X, prothrombin, thrombin, fibrinogen, fibrin, and fibrin polymer. The production or consumption of each of these agonists is incorporated into the source terms in the CDR equations.

The computational domain consists of a 2D channel (8x1mm) including a stent strut representing a large bioresorbable scaffold (180x157 μm) (Fig.1) [2]. A section of 200 μm of the bottom wall

(indicated in red in Fig.1) serves as a surface flux boundary condition representing a tissue factor (TF) coated surface. The Navier-Stokes equations are used to describe blood flow, in which the blood is considered as a Newtonian fluid. The clot is modeled as a porous medium with the porosity depending on the concentration of fibrin polymer [5]. A velocity inlet was prescribed with an initial wall shear rate of 250s^{-1} . The model is implemented into the computational fluid dynamics software FLUENT 2021 R1.

In order to compare the simulation results with the model of Bouchnita et al. and in vitro experiments of Shen et al. [4, 6], the time for blood clotting initiation near the TF patch while increasing the initial wall shear rate was computed (with a maximum physical time of 1200 seconds). This experiment was mimicked by using the 2D geometry of Figure 1 with a single TF patch, excluding the stent strut. Finally, in the geometry with stent strut a set of cases are studied with 3 different TF patch locations (indicated in Fig.1), with both average healthy and hypercoagulant coagulation parameters for a physical time of 30 minutes. The parameters are taken from the work of Ratto et al., in which an approach to patient-specific modelling was proposed based on conventional thrombin generation tests, allowing for the determination of parameters of a reduced kinetic model [4].

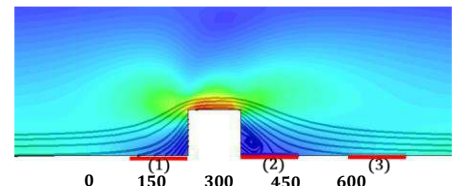


Figure 1: Part of the 2D geometry visualized with a contour plot of the shear rate and streamlines around the stent strut. The 3 tissue factor (TF) patch locations are indicated in red.

RESULTS

The relationship between clotting initiation time as a function of wall shear rate under undisturbed flow conditions is illustrated in Figure 2. We found that the value of the clotting initiation time increases with increasing wall shear rate until a shear rate of 40s^{-1} . Our results are in good agreement with the model results of Bouchnita et al. and the experiments of Shen et al. in which they observed a threshold response at a shear rate of 35s^{-1} and 30s^{-1} , respectively. Above this threshold no clot was formed near the TF patch within the measured time frame.

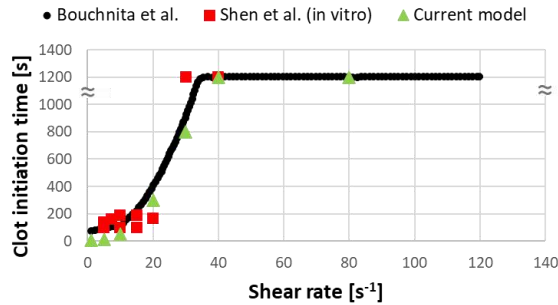


Figure 2: The moment of clotting initiation as a function of the initial wall shear rate for normal pooled plasma. Results of the current model, the model of Bouchnita et al. [4] and experimental results of Shen et al. [6] are shown for comparison.

For the disturbed flow conditions in the presence of a stent strut, the results for the healthy and hypercoagulant plasma are shown in Figure 3. When comparing the impact of the location of the TF patch, we observed that in the healthy case the initiation of clot formation occurred earlier proximal to the stent strut where a denser clot was formed, but a larger clot was observed to form distal to the strut after 30 minutes (Fig. 3A-D). When the TF patch was located after the recirculation zone no fibrin polymer was formed (Fig. 3E-F). In the case of hypercoagulant plasma, it was found that clot formation occurred at a significantly faster rate and resulted in a larger clot compared to the case of healthy plasma (Fig. 3G-J). Also in this case the clot proximal to the strut was denser compared to the clot distal to the strut in which the fibrin was completely spread downstream of the recirculation zone after 30 minutes (Fig. 3H). Even for the hypercoagulant case no clot was observed when the TF patch was located after the recirculation zone (Fig. 3K-L).

DISCUSSION

We successfully implemented a computational model of fibrin-rich clot formation in order to study blood coagulation in stent thrombosis. The largest clots were formed when the wall was damaged right after the stent strut. This phenomenon can be attributed to the presence of the recirculation zone, characterized by a low shear rate of about 5s^{-1} , which allows for prolonged interactions between coagulation factors. When the wall damage occurred proximal to the stent strut a smaller clot was observed, but it exhibited a relatively high concentration of fibrin polymer. This is likely due to the confinement of coagulant factors by the stent strut, leading to the formation of a more concentrated clot. The presence of a high shear rate (250s^{-1}) at the TF patch after the recirculation zone was observed to prevent clot formation in both the healthy and hypercoagulant cases. This outcome was expected from previous understanding of healthy blood flow dynamics.[6] but was previously unknown in the context of hypercoagulability. Results furthermore demonstrated that the clot growth rate and size were increased in a hypercoagulant case compared to a healthy case. This highlights the importance of incorporating patient-specific parameters,

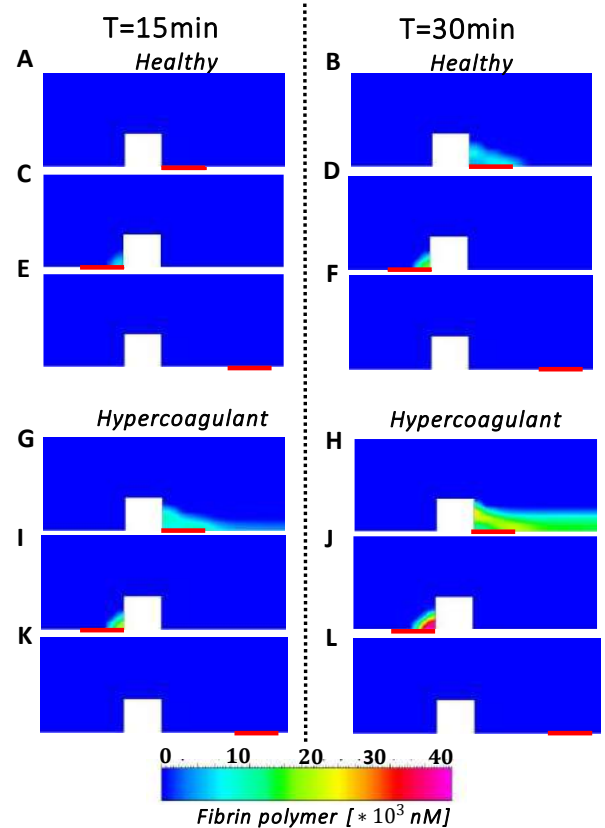


Figure 3: Results of the 2D simulation including a stent strut after 15min. (left) and 30min. (right) for different TF patch locations indicated in red, with (A-F) healthy plasma and (G-H) hypercoagulant plasma.

which is most often not taken into account into computational thrombus formation modeling.

It is important to acknowledge that the current study did not include all coagulation pathways, for instance the protein C pathway, which has been demonstrated to inhibit coagulation at undamaged vessel walls. The absence of this pathway may contribute to the observed formation of a fibrin network along the entire distal side of the strut in the hypercoagulant case (Fig. 3H). We are currently investigating the effects of various stent designs and flow conditions on coagulation dynamics, and future studies will aim to incorporate additional coagulation pathways and examine the formation of platelet plugs.

ACKNOWLEDGEMENTS

The authors acknowledge the EU funded project In Silico World, grant number 101016503.

REFERENCES

- [1] Claessen, B. E. et al., *JACC: Card. Interv.*, 7(10), 1081-1092, 2014.
- [2] Tarrahi, I. et al., *EIJ-D-19-00657*, 186,178-85, 2015.
- [3] Chesnutt, J. K. et al., *Computers in biology and medicine*, 56, 182-191, 2015.
- [4] Bouchnita, A. et al., *PloS one*, 15(7), e0235392, 2020.
- [5] Wufsus, A. et al. *Biophysical journal*. 104(8), 1812-1823, 2013.
- [6] Shen, F. et al. *Arteriosclerosis, thrombosis, and vascular biology*, 28(11), 2035-2041, 2008.
- [7] Ratto, N. et al. *Bulletin of Mathematical Biology*, 83(5), 1-31, 2021.

MECHANICAL STIFFENING OF EXTRACELLULAR MATRIX BY NEUTROPHIL EXTRACELLULAR TRAPS PROMOTES BREAST CANCER PROGRESSION

C.-M. Boghdady (1,2), N. Wong (3), A. Shen (2), E. Solymoss (2), M. de Meo (3), A. Chandrasekaran (1), R. Rayes (3), Y. Chen (1), A. Ghagre (4), A. Ehrlicher (4), L. McCaffrey (2,3,5), J. Spicer (3), P. Siegel (2), C. Moraes (1,2,3,6)

- (1) Department of Chemical Engineering, McGill University, Montreal, Quebec, Canada
(2) Goodman Cancer Institute, McGill University, Montreal, Quebec, Canada
(3) Division of Experimental Medicine, McGill University, Montreal, Quebec, Canada
(4) Department of Bioengineering, McGill University, Montreal, Quebec, Canada
(5) Gerald Bronfman Department of Oncology, McGill University, Montreal, Quebec, Canada
(6) Department of Biological and Biomedical Engineering, McGill University, Montreal, Quebec, Canada

INTRODUCTION

Mechanical stiffness has been shown to play a determining role in tissue fate and function, particularly in cancer, where increases in tissue stiffness are correlated with progression and metastasis [1]–[4]. However, clinical measurements of tissue stiffness in metastatic patient samples do not consistently demonstrate increased zonal stiffness, suggesting that transient stiffening mechanisms may be at play [5]. However, the precise nature of these mechanisms remains unclear.

The extracellular matrix (ECM), primarily composed of type I collagen, is the non-cellular component of tissues and is a significant contributor in determining local mechanical properties. Changes in collagen organization and protein content mediated by fibroblast remodelling have been shown to permanently alter stiffness and scaffold function [1], [2], [6], [7]. Soft tissues require large strains to observe significant strain-stiffening, beyond the typical fibroblast span, suggesting that other transient stiffening mechanisms may be at play *in vivo*.

As part of the innate immune response, neutrophils have the capability of spraying out sticky protein-DNA webs to trap pathogens, termed neutrophil extracellular traps (NETs) [8]. NETosis is significantly affected by the state of the neutrophil population, and in the context of breast cancer, neutrophil populations skew from being primarily mature, high-density neutrophils (HDNs) towards immature, low-density neutrophils (LDNs). NETs formed from LDNs correlate with more aggressive disease progression and poorer prognoses [9], [10].

In this work, we hypothesize that NETosis acts as a transient mechanism for heterogeneously stiffening surrounding tumour matrix. Considering the physical limitation imposed by pore size in 3D biomaterials (Fig. 1 images), NETs are proposed to locally cross-linking and create stiff “hot spots” within the tissue (Fig. 1 schematic). Furthermore, we hypothesize that NETs from disease-associated neutrophil populations (LDNs) increase heterogeneous stiffening and promote breast cancer progression by destabilizing the tumor structure and encouraging metastatic dissemination.

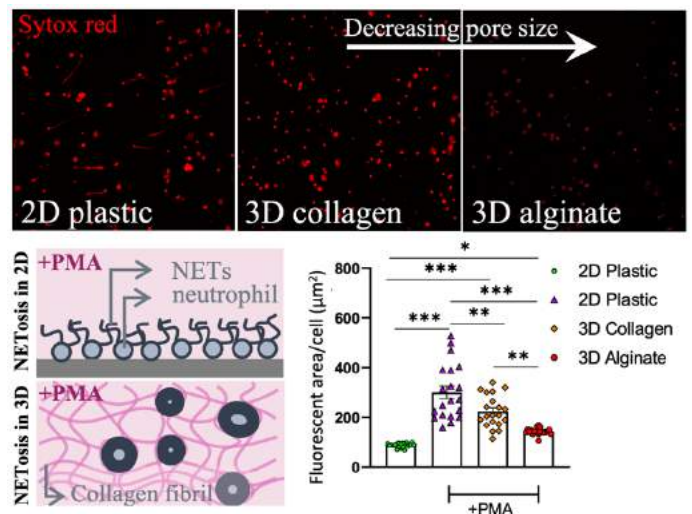


Figure 1: Constriction of NET dispersal with decreasing pore size in 3D matrices as proposed mechanism for heterogeneous stiffening.

METHODS

Either murine or human neutrophils were isolated and induced with phorbol 12-myristate 13-acetate (PMA) to produce NETs *ex vivo* within 3D collagen matrices. Local mechanical properties were assessed by optical magnetic twisting cytometry while bulk properties were quantified by shear rheology.

An inducible 3D breast cancer invasion assay was used to observe effects of NETosis on dissemination and invasion. Spheroids were formed from non-invasive MCF7 breast cancer cells with an inducible Src oncogene, embedded in collagen-NET gels and monitored for varying degrees of invasion. As controls, homogeneously stiffened collagen gels were prepared by glycation to increase cross-linking while maintaining a constant collagen concentration.

RESULTS

In situ NETosis was found to significantly stiffen collagen matrices both locally (Fig. 2A) and in bulk (Fig. 2B). Upon degradation by DNase, gels regain the same stiffness as those not subject to NETosis (Fig. 2A), demonstrating that NETs content are responsible for the observed stiffening. In contrast, the addition of either harvested or purified DNA-containing NETs with or without cell bodies does not result in significant stiffness changes (data not shown). This suggests that NETosis must be triggered *in situ*, and the NET dispersal must be constrained within collagen pores to cause a stiffening effect, likely due to intertwining and crosslinking of the NETs with collagen.

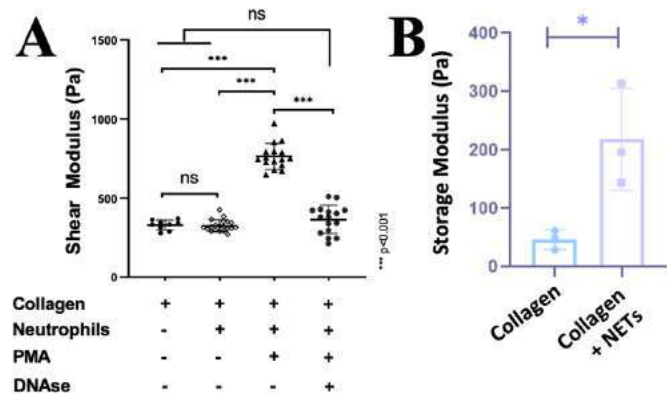


Figure 2: *In situ* NETosis from human neutrophils stiffens 3D collagen matrices (A) locally and (B) in bulk.

Breast cancer spheroids embedded within heterogeneously stiffened collagen matrices by murine NETs exhibited more invasive behaviours with observed dissemination into the surrounding matrix (Fig. 3). Interestingly, LDN NET-stiffened collagen prompted more extensive invasive spheroid behaviour in comparison to HDN NET-stiffened collagen, suggesting a compositional and functional difference between their responses *in vivo*. Invasion was not observed in collagen matrices that homogeneously stiffened through chemical glycation, suggesting that heterogeneous mechanical properties are required for disruption of architecture and inducing invasion.

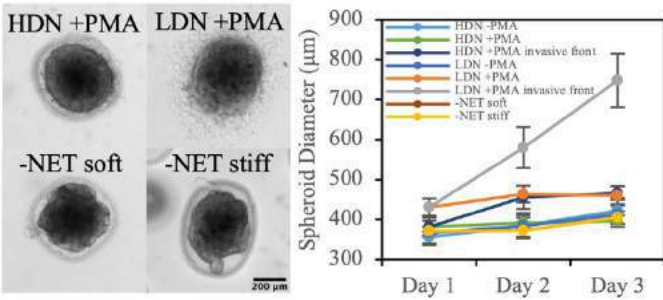


Figure 3: Heterogeneously stiffened collagen by murine NETs promote breast cancer invasion.

DISCUSSION

Together, this *in vitro* study suggests that NETs, particularly those associated with the presence and progression of cancer, may play a previously unsuspected role in transient biophysical regulation of cancer metastasis. Additionally, varying neutrophil populations may produce compositionally and functionally different NETs as part of their contribution in the immune response, affecting breast cancer progression. Future proteomic analyses of purified NET populations may provide significant insight on potentially fundamental differences.

Other studies in cancer have found similar trends of heterogeneity supporting these findings, particularly in the context of stiffness [5], [11], where more aggressive breast cancer spheroids were shown to have stiff hot spots throughout the tissue architecture [5]. This work provides a potential mechanism for transient heterogeneous stiffening in tumors, contributing to better understanding the role of the immune response in breast cancer progression, as well as potentially providing new therapeutic targets to limit progression.

ACKNOWLEDGEMENTS

We gratefully acknowledge support from the FRQNT doctoral award to C.-M.B, the Cancer Research Society (Grant #25227), and the Canada Research Chairs program to C.M.

REFERENCES

[1] Levental, K.R. *et al.*, *Cell*, vol. 139, no. 5, pp. 891–906, Nov. 2009.
[2] Bonnans, C. *et al.*, *Nat. Rev. Mol. Cell Biol.*, vol. 15, no. 12, pp. 786–801, Dec. 2014.
[3] Paszek, M.J. *et al.*, *Cancer Cell*, vol. 8, no. 3, pp. 241–254, Sep. 2005.
[4] Discher, D.E. *et al.*, *Science*, vol. 310, no. 5751, pp. 1139–1143, Nov. 2005.
[5] Mok, S. *et al.*, *Nature Communications*, vol. 11, no. 1, Art. no. 1, Sep. 2020.
[6] Engler, A.J. *et al.*, *Cell*, vol. 126, no. 4, pp. 677–689, Aug. 2006.
[7] Barriga, E.H. *et al.*, *Nature*, vol. 554, no. 7693, Art. no. 7693, Feb. 2018.
[8] Rosales, C. *et al.*, *Front Physiol*, vol. 9, p. 113, 2018.
[9] Arpinati, L. *et al.*, *Cancers*, vol. 13, no. 20, p. 5082, Oct. 2021.
[10] Hsu, B.E. *et al.*, *Cell Reports*, vol. 27, no. 13, pp. 3902–+, Jun. 2019.
[11] Liu, C. *et al.*, *Acta Biomater.*, vol. 131, pp. 326–340, Sep. 2021.

THE IMPACT OF REGULATING THE PLANTARFLEXION AND DORSIFLEXION RESISTANCE OF AN ARTICULATED ANKLE FOOT- ORTHOSIS ON LOWER LIMB KINEMATICS AND KINETICS OF STROKE SURVIVORS DURING AMBULATION.

Oluwaseye P. Odanye (1), Emily E. Steffensen (1), Christopher J. Burcal (2), Aaron D. Likens (1), Elisa S. Arch (3), Brian A. Knarr (1)

- (1) Biomechanics Department, University of Nebraska, Omaha, NE, USA.
- (2) School of Health and Kinesiology, University of Nebraska, Omaha, NE, USA.
- (3) Kinesiology and Applied Physiology, University of Delaware, Newark, DE, USA.

INTRODUCTION

During ambulation, stroke survivors often experience a decreased ability to push off with their ankles due to plantar-flexor muscle weakness [1], and some show a typical dragging of the foot in a foot-drop presentation due to weakness of their dorsiflexors. This ankle muscle weakness results in functional limitations that could cause long-term disability, so assistive devices in the form of orthotics like the Ankle Foot Orthosis (AFO) are recommended for rehabilitative or assistive purposes [2] in affected persons.

AFOs are prescribed to stroke survivors to ensure stability, improve gait, prevent foot drop through the swing phase of gait, and improve their overall functional capacity [3]. Specifically, these devices improve the function of the weak ankle muscles through a sagittal plane resistance to plantarflexion (PF) and dorsiflexion (DF) characteristic also referred to as bending stiffness [2]. This AFO characteristic augments the weak ankle muscle functions, such that AFO PF resistance functions to augment weak dorsiflexors at the initial contact (by ensuring proper loading response) and the swing phase (prevent toe dragging) of the gait cycle, while the DF resistance augments plantarflexor muscles function primarily at the midstance phase of the gait cycle [4]. This DF resistance prevents excess DF at mid-stance ensuring stability as the shank translates anteriorly over the foot at this 3rd rocker [4]. This resistance characteristic is tuned distinctly in 2 AFO categories of the articulated and non-articulated types; the articulated AFO types have the merit of possessing joints through which AFO resistances can be tuned post-fabrication [2].

There exists a constraint in clinically prescribing AFO stiffnesses because of the difficulties in converting laboratory research setup to the clinic [2]. Clinicians are riddled with the challenge of balancing the concerns of ankle and knee instability while deciding on the right stiffness for individual patients. This study looked to further inform clinical AFO prescription by investigating how the independent tuning

of the plantarflexion and dorsiflexion resistance of a 3D-printed articulated AFO coupled with triple action joints impacted the gait of stroke survivors walking over the ground. We hypothesized that increasing the PF resistance will increase the peak ankle DF moment, the knee flexion angle at initial contact, and the ankle angle at initial contact. We also hypothesized that increasing the DF resistance will decrease peak DF angle at stance, peak knee extension moment, and peak positive ankle power at stance, while there will be increased peak ankle PF moment.

METHODS

This study was done in two sessions with a minimum of 1-week interval. We recruited five Subjects (3M and 2F; age: 64.6 ± 5.7 yrs; stroke onset: 6.0 ± 5.2 yrs) who have had a stroke for more than 6 months and could walk independently with or without a walking aid (current AFO users: 2). We customized the articulated AFO's footplate and calf section for each of the subjects by using a 3D scanner in scanning the shank -to- foot of the participants before fitting the image in a predetermined design, which we 3D printed using Polylactic Acid printing material. The printed parts were assembled into the final product with a commercially available mechanical joint for each of the participants (*figure 1, images a-i*). These fabrication processes were done from the first visit till before the second session. At the second session, participants were fitted with their customized AFO and had a 2-minute minimum walking trial to adapt to the new device for each of the analyzed resistance settings. Afterward, they were instructed to walk over inground force plates at their comfortable walking speed in the same direction for 3 trials for each resistance setting. We tested 3PF (PF1-low; PF2-medium; PF3-High) and 3DF (DF1-low; DF2-medium; DF3-High) resistance settings for all participants. We utilized a double randomized set-up between the two-resistance settings group of PF and DF, and within each of the groups for the 3 conditions of low, medium,

and high resistance settings. Data was collected using a 20-camera motion capture system (at 100Hz) and the joint kinematics and kinetic variables were derived in visual 3D software (C-Motion, Inc., Germantown, MD, USA).

Simulation modeling analysis (SMA v11.10.16) for single-case time-series data was used in analyzing the data on a case-by-case basis for each participant for the investigated variables of the peak DF moment, knee flexion angle at initial contact, and the ankle angle at initial contact for the PF resistance settings while it was the peak DF angle at stance, peak knee extension moment, peak ankle positive power at stance, and the peak PF moment for the DF resistance settings.

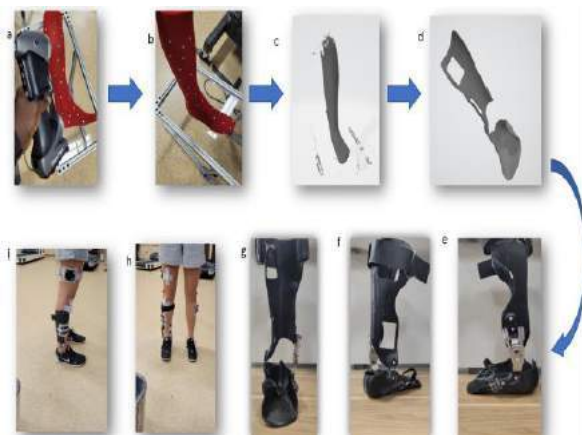


Figure 1: Images (a – i) show the stepwise process for AFO fabrication

RESULTS

There were significant phase changes in some participants when the DF resistances were tuned through DF1, DF2, and DF3. All the participants had significant phase changes ($p < 0.05$) for the peak DF angle at the stance phase of gait when the DF resistance was tuned, while only participants S01, S02, and S05 had significant phase changes for their peak positive ankle power ($p < 0.05$) at the stance phase of gait when the DF resistance was increased from DF1 through DF2 to DF3. The peak knee extension moment and the peak PF moment were not impacted by the DF resistance settings of the AFO ($p > 0.05$).

Tuning the PF resistance through PF1, PF2, and PF3 resulted in significant phase changes in the peak ankle DF moment for participants S01, S04, and S05 ($p < 0.05$) while there were significant phase changes for only participants S01 and S02 for their knee angle (flexion) at initial contact ($p < 0.05$), and the ankle angle at initial contact was significantly impacted by the PF resistance settings in participants S01, S03, and S04 ($p < 0.05$) with a noted increase from PF1 through PF2 to PF3.

DISCUSSION

The findings from this study showed the ability of the articulated AFO with mechanical joints to impact the gait characteristics of stroke survivors by causing significant phase changes when the PF resistance was increased so that participants S01, S04, and S05 experienced an increase in their DF moment. Also, the time series data showed that this DF moment was increased at the loading response phase of their gait, a

finding consistent to that of a pilot study by Kobayashi et al. (2017) [2] where they tested the mechanical properties of a similar triple action joint in an AFO and reported a more normalized DF moment in the heel rocker phase of their participant's gait cycle. This result implies that increasing the PF resistance may optimize the heel rocker phase of the gait cycle, but we cannot be exceedingly certain because the participants responded differently to changing the PF resistance of the AFO device. With increased DF resistance, the SMA showed significant phase shifts with lower mean DF angles in the stance phase of the gait cycle for all the subjects. When stroke survivors have weak plantarflexor muscles, it is imperative to prevent excessive DF during the stance phase of the gait cycle. Our findings showed that the AFO DF resistance settings can prevent this possible excessive DF and complement the weakness in the plantarflexors which could cause increased DF leading to instability.

Importantly, 3 participants had significant phase changes in peak ankle power at the terminal stance with noted decreases when DF resistance was increased. A previous study has indicated that decreased ankle power generation may imply limited propulsion at the 3rd rocker of the gait cycle [3]. Although, our study did not evaluate the propulsion characteristics of the participants we understand that a wrong AFO prescription could impede the optimal gait function of users. Future studies will look to explore the impact of changing AFO resistance characteristics on the propulsive forces of the affected lower limb.

This study is limited in the small sample size recruited, although we looked to complement this in the statistical analysis method and the technique used in AFO fabrication. The technique of fabricating the AFO using the 3D scanning and printing devices enabled ease in centralizing the joint support forces to each participant's sagittal plane in order to minimize frontal and transverse plane movements, while the SMA method revealed phase changes in the compared resistance levels for the individual participants. This method brings visibility to the distinct response of each participant to changing the AFO resistance characteristics especially considering the heterogeneous nature of the stroke population; stroke patients present in clinics as individuals and this study shows how the articulated AFO device with triple action joints systematically changes the kinematic and kinetic properties of stroke survivors. We believe this study structure gives an advantage over studies that utilize statistical methods emphasizing group means.

Overall, this study reinforces the potential of the articulated AFO with triple action joint as a viable assistive device for 'onsite resistance tuning' to aid the clinical prescription of AFOs for stroke survivors. Further investigation with a larger sample size will ensure the development of a standardized prescription mechanism by incorporating the objective and subjective clinical measures of patients.

ACKNOWLEDGEMENTS

Funding for this study was provided by UNO GRACA – 31254.

REFERENCES

- [1] Ju Y et al. *Brain & Neurorehabilitation*, 15:1, 2022, doi: 10.12786/bn.2022.15.e5.
- [2] Kobayashi T et al., *Med Eng Phys*, 44:94–101, 2017, doi: 10.1016/j.medengphys.2017.02.012.
- [3] Kobayashi T et al., *J Biomech*, 75:176–180, Jun. 2018, doi: 10.1016/J.JBIOMECH.2018.04.034.
- [4] S. Tyson S et al., *Clin Rehabil*, 7.10:879–891, Oct. 2013, doi: 10.1177/0269215513486497.

COMPARING THE ELASTIC AND FRACTURE PROPERTIES BETWEEN FIBRIN AND WHOLE BLOOD

Grace N. Bechtel (1), Gabriella P. Sugerman (1), Sapun H. Parekh (1), Manuel K. Rausch (1,2,3)

- (1) Department of Biomedical Engineering, University of Texas at Austin, Austin, TX, USA
- (2) Department of Aerospace Engineering and Engineering Mechanics, University of Texas at Austin, Austin, TX, USA
- (3) Oden Institute for Computational Engineering and Sciences, Austin, TX, USA

INTRODUCTION

Blood clots, or thrombi, are critical to our well-being by playing a vital role in the healing process following vascular injury. However, blood clots – as the source of thromboembolic disease – also lead to significant morbidity and mortality. In fact, thromboembolic disease accounts for 1 in 4 deaths worldwide [1]. Thromboembolic disease follows from blood clots forming and detaching from distant vessels in the circulatory system. Once broken off, these embolized thrombi, i.e., emboli, travel downstream, potentially occluding vital arteries or veins such as those in the heart, lungs, or brain [2]. Because it is the blood clots' ability – or lack thereof – to resist mechanical forces, understanding its mechanics (especially its fracture mechanics) is crucial to our understanding of thromboembolic diseases. Therefore, the mechanical properties of thrombi have been extensively studied. To this end, a large body of literature has used fibrin gels as blood clot mimics [3]. However, blood clots are more complex than fibrin gels, as they are also comprised of platelets and red blood cells.

In our own previous work, we have therefore focused on characterizing blood clots made from whole blood [4,5]. Our current project now aims to bridge the gap between others' past work on fibrin gels and our work on whole blood clot. To this end, we are comparing four critical markers of these materials' mechanics: the tangent modulus as a measure of these materials' elastic properties and strength, work-to-fracture, and fracture toughness to understand their fracture behaviors which contribute to their critical role in thromboembolic disease.

METHODS

We generated blood clots from bovine blood obtained from a commercial service (Lampire Biological Laboratories, PA, USA)

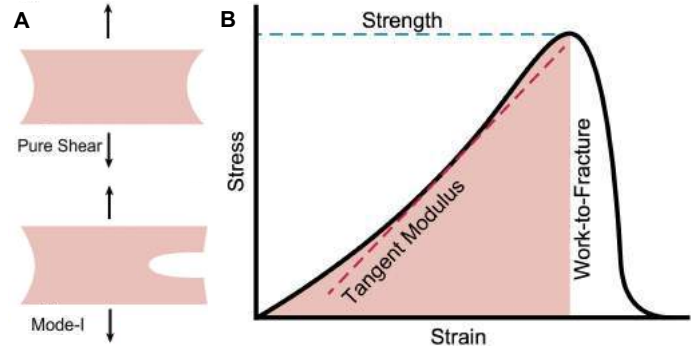


Figure 1: A) Sample geometries for pure shear and mode-I fracture experiments. B) Model stress-strain curve from which a sample's tangent modulus, strength, work-to-fracture, and fracture toughness (not pictured) are computed.

where blood is collected directly into CPDA-1 anticoagulant. We added calcium chloride to a concentration of 20 mM to reverse the anticoagulant and cast samples into a pure shear geometry following prior protocols [6]. We cast fibrin gels into the same pure shear geometry following standard protocols using fibrinogen concentrations of 20, 30, and 40 mg/ml (please note, lower concentrations did not yield testable gels). After 60-minute coagulation or incubation periods, respectively, samples were mounted to our tensile testing machine (Instron, Norwood, MA, USA). We conducted two tests: extension-to-failure in a simple pure shear geometry and extension-to-failure in a mode-I fracture geometry, as shown in Figure 1A. We conducted all tests until failure at a displacement rate of 0.1 mm s^{-1} , corresponding to

a strain rate of 1% s⁻¹. Figure 1B illustrates the definitions of three of our mechanical metrics, while we computed fracture toughness as

$$\Gamma_c = W(\lambda_c)H, \quad (1)$$

where H is the reference sample height and $W(\lambda_c)$ is the strain energy density of the pure shear sample at the fracture stretch λ_c .

Finally, to compare these mechanical metrics between the fibrin and whole blood samples, we conducted two-tailed independent Student's t-tests. We defined differences to be statistically significant for p-values less than 0.05.

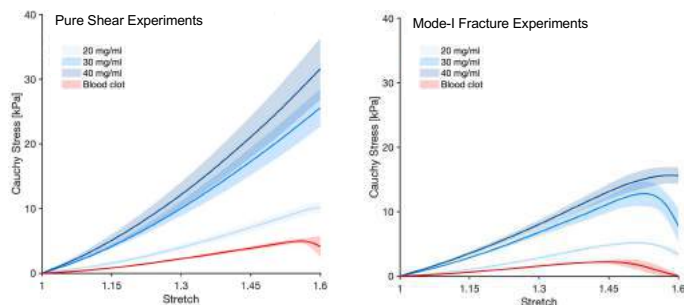


Figure 2: Stress-stretch curves of fibrin gels and blood clots during pure shear and mode-I fracture experiments.

RESULTS

Figures 2 and 3 summarize the mechanical data from our study. Specifically, Figure 2 shows the average (± 1 standard deviation) stress-stretch curves for each sample type studied for both pure shear and mode-I fracture experiments ($n=3$ per group). While variability between samples increased as they neared failure, the fibrin gels consistently had a higher tangent modulus than blood clot, as can be observed qualitatively based on the steeper loading slopes of the fibrin gels in Figure 2.

Figure 3A shows this data quantitatively, as it compares the samples' tangent modulus in the pure shear samples at a stretch of 1.35. From these data, we can see that the fibrin gels are significantly stiffer than blood clot. This holds true for all fibrin concentrations, i.e., 20 mg/ml, 30 mg/ml, and 40 mg/ml. Similarly, Figure 3B summarizes the samples' peak stress before failure, i.e. their strength. Fibrin gels of all concentrations have consistently higher strength than blood clot. On average, fibrin gels can withstand anywhere from two to six times the amount of stress before failing in comparison to blood clot. Furthermore, Figures 3C and 3D show that work-to-fracture and fracture toughness of fibrin gels, regardless of the fibrinogen concentration, are also higher than those of blood clot. Even at a fibrinogen concentration as low as 20 mg/ml, fibrin gels show a work-to-fracture and fracture toughness double that of blood clot. At 40 mg/ml, these values are closer to ten times the magnitude of blood clot.

DISCUSSION

There is extensive literature studying the mechanical behaviors of fibrin gels in an effort to understand blood clots. However, because of significant compositional differences between fibrin gels and blood clots, our work aimed at comparing the mechanical properties between the two. Thereby, we are hoping to bridge the gap between prior work on fibrin and others' – and our work – on blood clot. We chose four mechanical metrics that describe both materials' elastic (tangent modulus) and fracture properties (strength, toughness, and fracture

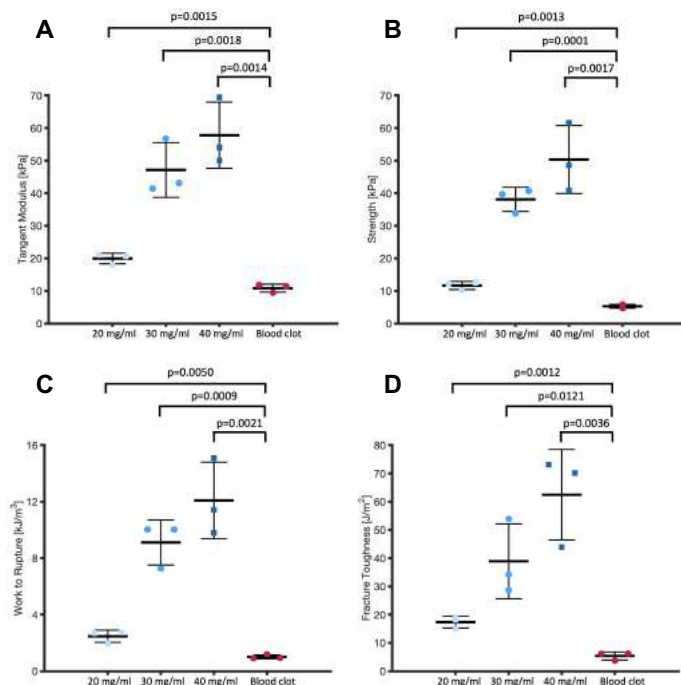


Figure 3: Quantitative comparison of the A) tangent modulus, B) strength, C) work-to-fracture, and D) fracture toughness between fibrin gels and blood clots.

toughness), all of which are critical in understanding clots role in thromboembolic disease. In summary, fibrin gels have a higher stiffness, strength, and show an increased resistance to fracture. These data suggest that using fibrin gels to study the mechanical behavior of blood clots may have to be done with care. That is, the role of platelets and red blood cells in blood clots' mechanics should not be overlooked. For example, recent studies demonstrated that platelets and red blood cells significantly alter a material's behavior [7], which supports the results of our study. Therefore, future work using fibrin gels as blood clot mimics should be careful when interpreting their work. Naturally, our study is subject to limitations. For example, our study used bovine blood, which may differ from human blood. Additionally, for experimental reasons our lowest fibrin concentration exceeds that of human blood. In future work, we aim at overcoming this experimental limitation to include lower fibrin concentrations in our study.

ACKNOWLEDGEMENTS

We acknowledge support from ONR with grant N00014-22-1-2073 and NSF with grants 2046148, 2105175, and 2127925.

REFERENCES

- [1] Wendelboe, A and Raskob, G, *Circ. Res.*, 118:1340-1347, 2016.
- [2] Fuster, V et al., *Circulation*, 70:580-587, 1984.
- [3] Janmey, P et al., *J R Soc Interface*, 30:1-10, 2008.
- [4] Sugerman, G et al., *J Mech Behav Biomed Mater*, 115:104216, 2021.
- [5] Sugerman, G et al. *Soft Matter*, 16:9908-9916, 2020.
- [6] Sugerman, G et al., *Current Protocols*, 1:e197, 2021.
- [7] Van Oosten, A et al., *Nature*, 573:96-101, 2019.

DEVELOPMENT OF A NOVEL POLYMERIC TAVR VALVE – DESIGN OPTIMIZATION AND ADDRESSING TAVR CLINICAL COMPLICATIONS

B. Kovarovic (1), R. Helbock (1), O.M. Rotman (1), K. Baylous (1), M. Slepian (2), D. Bluestein (1)

(1) Biomedical Engineering, Stony Brook University, Stony Brook, NY, USA

(2) Sarver Heart Center, University of Arizona, Tucson, AZ, USA

INTRODUCTION

Transcatheter aortic valve replacement (TAVR) is a minimally invasive alternative to the high-risk surgical approach, in which a stented bioprosthetic valve is deployed inside the failing aortic valve. TAVR is rapidly becoming the standard treatment for aortic stenosis (AS) with favorable hospital stay times, in 2019 the number of TAVR procedures exceeded the surgical standard [1]. TAVR was originally designed to treat severe aortic stenosis (AS) patients who were deemed too high-risk for the invasive surgical approach, but with the widespread adoption of TAVR, recently trails for lower-risk and younger patients were approved in US.

Despite the expansion, TAVR is subject to persistent clinical complications which are primarily a result of the chemically-fixed tissue bioprosthetic valve material. The most precarious complication of TAVR is the unknown *in vivo* durability of the leaflet structures. Bioprosthetic valves have historically been subject to structural valve degeneration (SVD) or intrinsic and extrinsic factors that lead to wear and tear or recalcification of the prosthesis and eventual valve failure [2]. TAVR is hypothesized to be subject to increased rates or faster progression due to damage of the leaflet tissues during the crimping and deployment phases [2]. The tissue material is also subject to promoting thrombosis, which may lead to subclinical leaflet thickening or thromboembolic events.

To address these shortcomings of tissue valve, polymeric valve alternatives currently being investigated. Polymeric technology allows the design of an optimal valve configuration that would exploit the ease, cost-effectiveness, and control of polymer manufacturing. Polymeric valve devices have been attempted since the 1950's but were all subject to limitations of the available material due to the extreme demands on the material. The polymer must be hemocompatible, flexible, and extremely durable (expected to remain functional for 25 years *in vivo*). For polymeric TAVR devices, the main shortcoming is that polymer material is generally not compressible compared to tissue materials, and

therefore the design must reduce the total volume of polymer to allow crimping into reasonable delivery catheter sizes.

The presented study demonstrates the progress and development of our polymeric TAVR device. We began with developing a surgical valve (Figure 1) and with further refinement of the material properties and development of an *in silico* optimization strategy, we are presenting the latest generation polymeric TAVR device, PolyV2 27 mm (PolyNova Cardiovascular Inc, Stony Brook, NY).

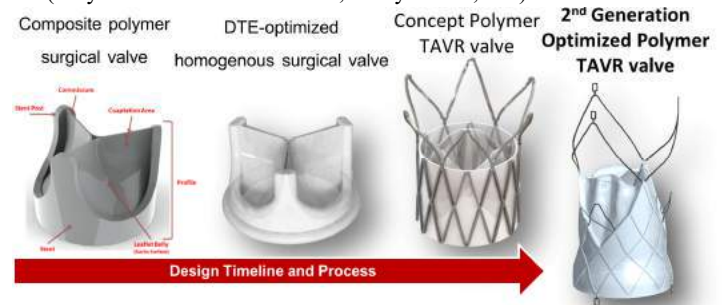


Figure 1: Timeline of polymeric TAVR development to the PolyV-2 design.

METHODS

The PolyV-2 device is based on the progress and success of the cross-linked SIBS based thermoset “Flexamer” material, which recently demonstrated both anti-thrombotic material characteristics [3] and extreme durability while achieving 25 *in vivo* year equivalent 1 billion accelerated wear cycles [4]. The goal of the development and optimization of the PolyV-2 was to generate larger valve sizes, achieve suitable radial anchoring forces, target a 18F delivery catheter, increase the valve performance, and design for “sutureless” molding, allowing the cast of the leaflets and sleeve on the stent frame in a single operation. This sutureless molding helps eliminate the most significant source of manufacturing error, the multi-day hand suturing of the tissue to the

stent frame. The design process was achieved with the use of *in silico* trials, utilizing finite element analysis (FEA, Abaqus 2022, Dassault Systemes, Vélizy-Villacoublay, France), to optimize first the stent frame design, second the leaflet profile, and finally the leaflet thickness.

The self-expandable nitinol stent was designed from an initial cut profile and the heat-treatment/shape-setting steps were simulated to obtain the final profile, which was confirmed with manufacturing of the design. Radial force and crimping study on the open profile (implicit FEA, rigid crimping surface with radial movement, stent with superelastic material and C3D8R elements post convergence study) was used to determine the radial force in the deployment region, both along the axial length of the device and within the deployment diameter range, optimized against the volume of the stent for a lower crimping profile and confirming no plastic deformation at 16F crimp. The leaflet stresses were also simulated (polymer Arruda-Boyce material, C3D8R elements post convergence study) with a typical normotensive aortic pressure waveform over the cardiac cycle.

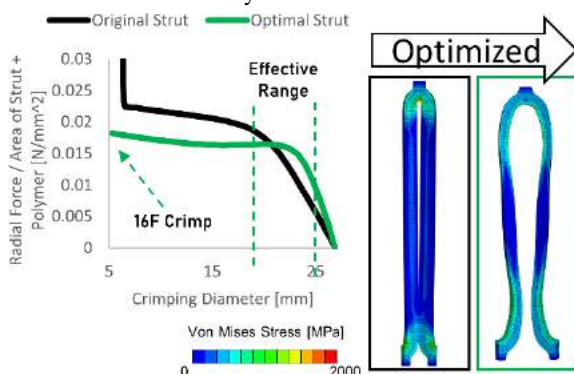


Figure 2: (Left) Radial force normalized to material volume vs the crimping diameter. (Right) Stress distribution of original and optimized strut design.

RESULTS

Optimization of the stent frame is seen in Figure 2 with larger radial force in the deployment range targeted for the device. The final strut design features more curvilinear struts and wider attachment angles to distribute the stresses away from joints. The final stent design does not achieve the radial force of current popular commercial TAVR stents but were confirmed to have comparable anchorage forces while reducing the total stent volume due to the restriction of polymer TAVR valves.

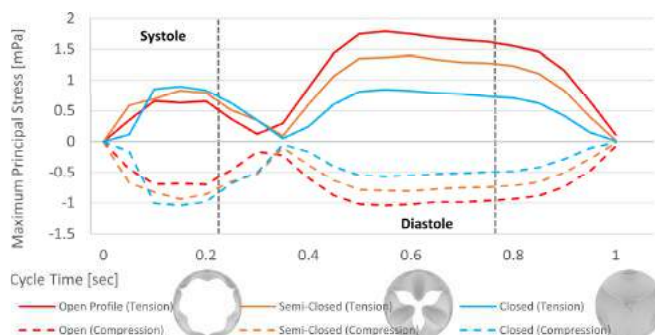


Figure 3: Comparison of maximum principal stresses over the cardiac cycle versus the initial “free-stress” opening profile.

Optimization of the leaflet structures began with first selecting an opening profile of the device allowing the design and selection of the “free-stress” state of the polymer, which is not easily achievable with tissue-based valves. Figure 3 demonstrates the tradeoff of the selection of an open profile for reduced systolic stresses and increased diastolic

stresses, or visa versa for a closed profile. The final profile was influenced by the valve sized and was selected also based on the ability to cast the final design. Lastly, the polymeric design allows the optimization of the leaflet by varying the thickness across the entire leaflet structure to reduce cycle stresses. The cyclic leaflet stresses of the uniform thickness leaflets were extracted and processed in an in-house code that varied the thickness across the leaflets based on the absolute stress magnitude. The new varying thickness profile was simulated again and processed repeatedly to determine the final optimal thickness profile seen in Figure 4 which was able to dramatically reduce the stress magnitude below the fatigue limit of the polymer and reduce material thickness/volume.

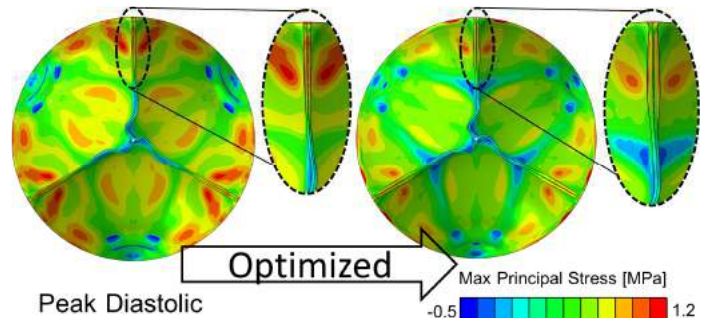


Figure 4: Maximum principal stress distributions of the uniform thickness leaflet (left) versus the non-uniform optimized leaflet (right). Inset highlighting uniformity of the leaflet free edge.

DISCUSSION

Upon casting the initial articles, the hydrodynamic performance of the PolyV-2 design will be measured according to the ISO-5840 standard and benchmarked against other commercial TAVR devices. Accelerated wear testing will begin again to confirm the durability of the new larger size device. With confirmation of performance, acute ovine animal trials will be conducted to begin study of the *in vivo* performance.

Polymeric TAVR technology offers the immense benefits over the intrinsically flawed tissue based TAVR devices currently on the market. Since polymeric valves can be cast in virtually any shape, compared to the uniform stamp-cut and hand-sutured shapes of tissue valves, the design of the leaflets can be optimized and tailored to the anatomy. The PolyV-2 leaflet profile has a unique variable thickness- optimized to reduce the leaflet stresses over the cycle for enhanced durability and improved hemodynamic performance. After finding a suitable material and manufacturing process for polymeric TAVR, proper design is critical to the success of the device. Many devices have failed at this stage and prior to large investments of resources, optimization and simulated trials can be easily conducted so that the subsequent *in vivo* trials are predictable. The PolyV-2 valve was optimized with *in silico* trials and the material was fully tested *in vitro* to develop a design construct with superior hemodynamics and performance mitigating persistent, common complications of current TAV devices.

ACKNOWLEDGEMENTS

NIH-NIBIB Phase II-U01EB012487 (DB); NIH-NIBIB 1U01EB026414-01 (DB). Industry Partners: ANSYS, Simulia LHP.

Disclosure: Author OMR and BK are consultants for PolyNova Cardiovascular Inc. Author DB and MS has an equity interest in PolyNova Cardiovascular Inc.

REFERENCES

- [1] Carroll J, et al. (2020). J Am Coll Cardiol, 24;76(21):2492-2516.
- [2] Rotman O, et al. (2018). Ex Review of Med Devices, 15:11, 771-79.
- [3] Rotman O, et al. (2019). Ann Biomed Eng 47, 113–125.
- [4] Kovarovic B, et al. (2022). JBME. 144(6): 061008.

MODELING THE FRACTURE MECHANICAL PROPERTIES OF LOAD-BEARING SOFT BIOLOGICAL TISSUES

Christopher Miller (1) and T. Christian Gasser (1,2)

(1) Solid Mechanics, Department of Engineering Mechanics, KTH Royal Institute of Technology,
Stockholm, Sweden

(2) Faculty of Health Sciences, University of Southern Denmark, Odense, Denmark

INTRODUCTION

Collagenous soft biological tissues are composed of numerous extracellular matrix (ECM) proteins. Their complex structural arrangement and interaction define their macroscopic material properties. Fibrous collagen is known to be the principal load-bearing ECM constituent. Its hierarchical architecture and deformation mechanisms that act over several length scales, greatly determine observed physical phenomena such as its nonlinearity and time-dependency.

However, our current understanding of soft tissue damage and failure is somewhat restricted, specifically, those multiscale structure-function relationships that give rise to macroscopic fracture behavior are not well known. An improved general comprehension of soft tissue failure could have potentially beneficial implications for the treatment and management of certain pathologies, such as abdominal aortic aneurysms (AAA) in vascular tissue.

The difficulty in discerning such information experimentally has prompted the development of constitutive models. A versatile material description for load-carrying soft biological tissue should therefore incorporate salient microstructural deformation mechanisms and be able to reliably predict complex load-case scenarios. Yet, the computational modelling of damage and failure in materials undergoing finite deformations is a particularly challenging feat, and various approaches have been considered for the tackling of such problems, which can be generally divided into either a continuous or a discontinuous representation of the fracture process.

METHODS

We present an extension of our previous microstructural continuum model that includes proteoglycan-mediated collagen fibril sliding towards capturing the non-linear time-dependent properties of collagenous tissue [1]. It incorporates an interfibrillar failure (fibril pull-out) mechanism and gives rise to physiologically reasonable damage-induced mechanical behaviour across several length scales [2].

A bottom-up approach is followed, whereby the microstructural model is employed in a single-element representation of the modes of fracture. A qualitative description of soft tissue rupture is accordingly attained, to which a transversally isotropic cohesive zone model for the equivalent fracture surface is then calibrated. In doing so, a phenomenological surface-based discontinuous characterization of failure is derived directly from the upscaling of irreversible and dissipative damage mechanisms from the microscale. The constitutive description has been implemented in FEAP (Univ. of California at Berkley, US) using an in-house PUFEM description [3].

Furthermore, a novel crack initialisation criterion has been introduced, whereby the positive definiteness of the intermediate stiffness tensor is evaluated. Specifically, a negative eigenvalue and its associated eigenvector, inform the initialisation of the localisation and its orientation, respectively. Importantly, once a discontinuity is inserted within a particular element, the further accrue of damage within the continuum (bulk) material is switched off. Accordingly, all failure-related (strain-softening) behaviour is encapsulated by the cohesive model.

RESULTS

A number of representative examples were investigated in order to highlight the efficacy of the outlined computational framework. The standard uniaxial tensile test, in which a monotonically increasing load was applied until eventual failure, was evaluated. Additionally, the symmetry-constrained compact tension (symconCT) test was replicated, see Figure 1a. The setup consists of a square excised aorta specimen, clamped between two grips, to which a force/displacement may be applied. A polymer beam inserted above the sample, ensures the rotation of the grips and therefore the propagation of fracture, whilst also ensuring that the crack remains centralized. Such a configuration permits the stable propagation of fracture relative to other tests in the literature, and the consequent investigation of underlying microstructural damage/failure mechanisms.

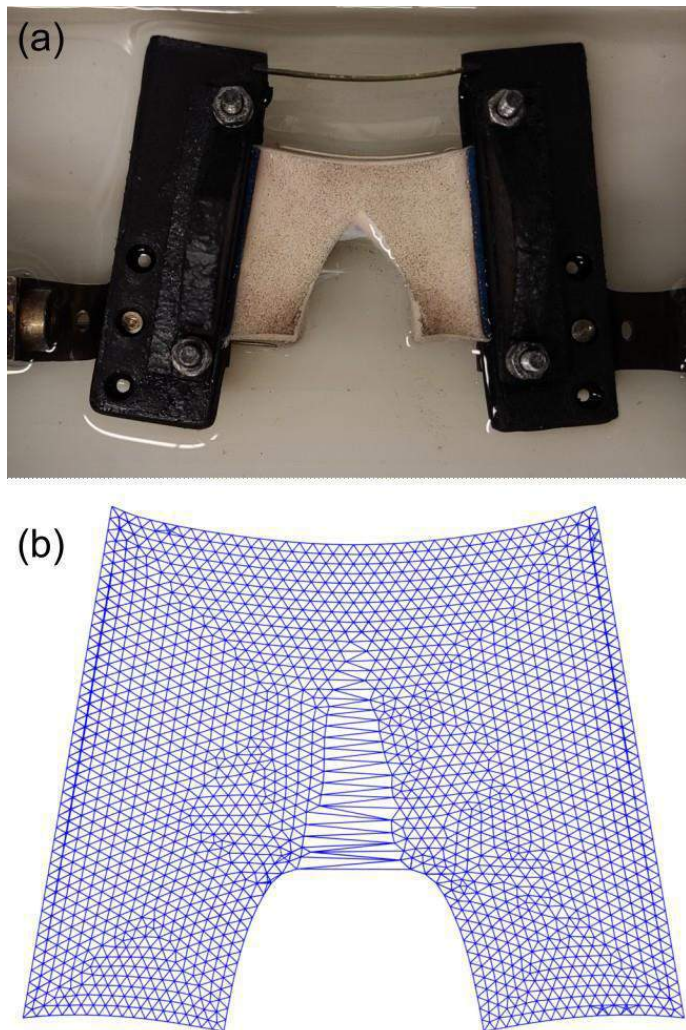


Figure 1: (a) Experimental setup for the symconCT testing of the abdominal aorta, displaying the propagation of a crack through the specimen from an initial notch. (b) Preliminary results relating to the application of the discussed PUFEM constitutive description to the problem, showcasing comparative fracture behavior.

In both cases, qualitatively similar failure behavior was arrived at; both in terms of the resulting force-displacement profile and the path of the discontinuity through the material, see Figure 1b.

DISCUSSION

There is a paucity in the academic and clinical communities' fundamental understanding of soft tissue damage/failure processes at small-length scales. Computational modelling strategies present as a viable tool towards the exploration of hypothesized experimentally informed microstructural mechanisms. Such approaches may advance our view of disease and injury, and could prove a potential pathway towards enhancing patient outcomes.

This work has introduced a constitutive formulation for the study of fracture in collagenous soft biological tissues. A microstructurally informed continuum (bulk) material has been used, and a discontinuous surface-based description of fracture has been qualitatively derived from said model. Both models are implemented within the previously introduced PUFEM formulation, in which the discontinuity is embedded within the bulk material.

Finally, the application of the computational framework to a series of applicable examples demonstrated its suitability for the computational modelling of real-world soft tissue fracture mechanical problems.

ACKNOWLEDGEMENTS

The authors would like to thank Marta Alloisio and Marína Chatziefrimídou for providing experimental data and images in relation to the symconCT test.

REFERENCES

- [1] Miller and Gasser, J Mech Phys Solids., 2021
- [2] Miller and Gasser, J Mech Phys Solids., 2022
- [3] Gasser and Holzapfel, Comput Methods in Appl Mech Eng, 2005

A VASCULARIZED TISSUE MODEL TO INVESTIGATE HUMAN SYNOVIOCYTE – ENDOTHELIAL CELL CROSSTALK IN JOINT HEALTH AND DISEASE

Hannah M. Zlotnick (1), Abhishek P. Dhand (1, 2), Matthew D. Davidson (1), Gabriel J. Rodriguez-Rivera (1), Christopher J. Calo (1, 3), Hannah K. Weppner (1, 3), Laurel E. Hind (1, 3), Jason A. Burdick (1, 3)

(1) BioFrontiers Institute, University of Colorado, Boulder, CO, USA

(2) Department of Bioengineering, University of Pennsylvania, Philadelphia, PA, USA

(3) Department of Chemical and Biological Engineering, University of Colorado, Boulder, CO, USA

INTRODUCTION

The synovium is a connective tissue that is present throughout the knee joint (and all articulating synovial joints). When injured or diseased, the synovium becomes hypervascularized through angiogenic processes (**Fig 1A**). Synovial angiogenesis has been studied most frequently in cases of rheumatoid arthritis (RA), a chronic autoimmune inflammatory disease; however, there is recent evidence to implicate the vascular system in the progression or pathogenesis of osteoarthritis (OA) [1,2], which can occur after joint injury or with age. Within patients with OA, it has been suggested that fibroblast-like synoviocytes (FLS) release the potent angiogenic factor vascular endothelial growth factor (VEGF), which contributes to the increased endothelial cell proliferation and vessel sprouting observed in the synovium [3]. In addition, immune cell populations within the synovium and neighboring tissues may contribute to the angiogenic response. To probe such complex behaviors, *in vitro* models are needed where specific cell populations can be introduced and monitored. In this work, we establish both spheroid and vascularized microfluidic models of the synovium to probe the coordinated signaling of FLS cells and endothelial cells in homeostasis and with OA.

METHODS

Validation of human FLS. FLS (P4 adult human synoviocytes) spheroids (50,000 cells/spheroid) were formed using 96-well U-bottom plates and synoviocyte growth medium. Seven days after spheroid formation, samples (n = 3 / stain) were fixed for whole mount immunofluorescence (lubricin), and fixed, processed, and sectioned for paraffin histology (haematoxylin & eosin). **HUVEC sprouting potential.** Multicellular spheroids consisting of human umbilical vein endothelial cells (HUVECs) and human mesenchymal stromal cells (MSCs) in a 2:1 ratio (1,000 cells/spheroid) were formed as previously described [4]. After 1 day of pre-culture, spheroids were mixed into a norbornene-modified hyaluronic acid hydrogel with adhesive (RGD)

moieties and a matrix metalloproteinase (MMP)-degradable crosslinker. The spheroid-laden gels were cultured in media with VEGF, Sphingosine 1-phosphate (S1P), and phorbol 12-myristate 13-acetate

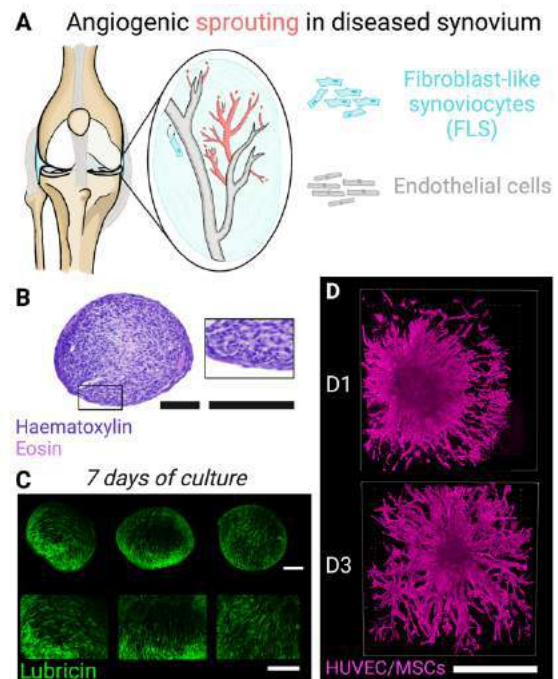


Figure 1: Cellular crosstalk within the synovium. (A) Angiogenic sprouting in the synovium. (B, C) Validation of adult human synoviocytes in spheroid culture. Scale bars = 100 μ m. (D) Sprouting of HUVEC/MSC (labeled actin) spheroids. Scale bar = 400 μ m.

(PMA) for 3 days. **Microfluidic device fabrication.** Microfluidic devices were fabricated as previously described [5]. Briefly, polydimethylsiloxane (PDMS) was poured on silicon masters, and baked for 4 h at 60 °C to create the top and bottom layers of the devices. PDMS rods were formed via extrusion through 23-gauge blunt needles, resulting in lumens ~340 µm in inner diameter. The top and bottom PDMS layers were aligned, and a PDMS rod was inserted through the inner channel of each device. **Endothelialized synovium formation.** FLS (3 million mL⁻¹) were encapsulated in 2 mg mL⁻¹ bovine collagen hydrogels and injected into the hexagonal chamber of the devices. To expedite collagen polymerization, the devices were incubated at 37 °C for 1 h. Post-gelation, the PDMS rods were removed from the devices, permitting the influx of media with HUVECs (20,000 cells/µL). The devices were rotated for 2 h to permit endothelial cell adhesion. **Nascent synovium viability and spreading.** After 4 and 10 days, the nascent synovium tissues (n = 3 / time point) were stained with calcein-AM, and ethidium homodimer-1 to assess live and dead cells, respectively. The calcein-AM images were also used to assess cell spreading using Cell Profiler. **HUVEC retention.** After 4 days, devices were fixed (n = 3), stained with DAPI, and imaged to assess the retention of the HUVECs in the vessel and positioning of synoviocytes. **Statistical analysis.** The mean cell spread areas were compared using a t-test in GraphPad. n = 96-256 cells / device, N = 3 devices / time point. * p < 0.05.

RESULTS

Healthy human FLS self-assembled into a synovium-like tissue when cultured in U-bottom wells. The spheroid tissues developed a thin outer lining a few cell layers thick, as evident by H&E staining (Fig 1B), reminiscent of the synovial intima. Interestingly, the synovial spheroids also developed a shell-like distribution of lubricin along the surface of the tissues (Fig 1C), similar to native synovium that has heightened lubricin expression in the intimal layer.

To verify the sprouting potential of the HUVECs in the presence of a mesenchymal cell population (alike the synovium), spheroids were fabricated that contained both HUVECs and MSCs. After encapsulation in a hyaluronic acid-based hydrogel with adhesive moieties and MMP-degradable crosslinkers, the spheroids began emitting cellular protrusions into the surrounding hydrogel (Fig 1D). Sprouting was observed as soon as 1 day after encapsulation in the hydrogel in the presence of angiogenic factors VEGF, S1P, and PMA.

To enhance the physiologic relevance of the spheroid tissue model, we next fabricated PDMS microfluidic devices containing inner hollow lumens (Fig 2A, B). The lumens were created by injecting a synoviocyte-seeded collagen solution into the device, allowing this solution to gel, and then removing the PDMS rod through the media inlet. The gelation period and subsequent culture did not disrupt synoviocyte viability, as the cells appeared nearly 100% viable after 10 days of culture (Fig 2C). In fact, the synoviocytes significantly spread over time in the collagen gel (Fig 2D). When the lumens were seeded with HUVECs, the HUVECs coated the central channel of the devices, and remained in the channels, as evident 4 days post-seeding (Fig 2E).

DISCUSSION

Our work establishes both self-assembled spheroid and 3D vascularized models of the synovium to investigate joint health and disease. It is currently unknown why and how the synovium becomes hypervascularized during RA and to a lesser extent during OA. To piece apart the complex signaling between the cell types in the synovium, *in vitro* models of varying complexity are needed. We show that human FLS self-assemble into tissues reminiscent of the synovium, with cells on the surface of the tissue preferentially expressing lubricin. Next, mesenchymal cells can be interspersed with HUVECs and surrounded

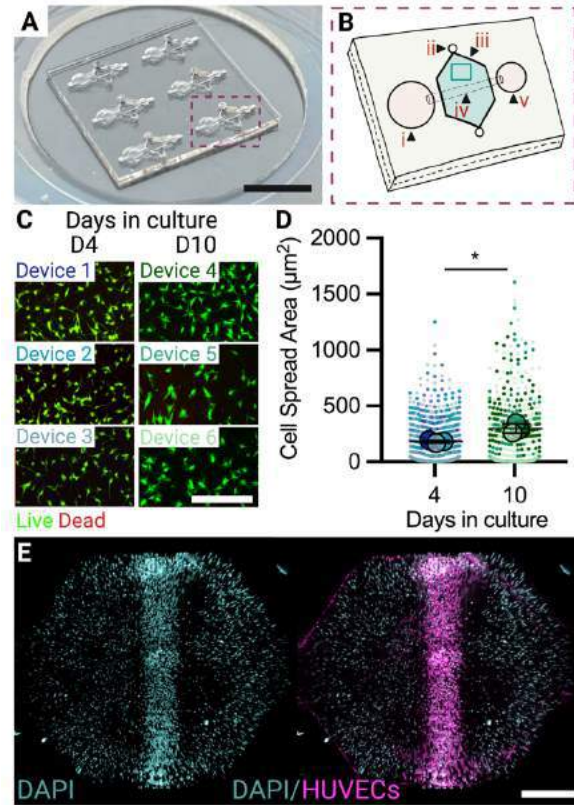


Figure 2. A multicellular vascularized tissue model of the synovium. (A) PDMS microfluidic devices before seeding with cells. Scale bar = 700 µm. (B) Schematic of a single device. (i) Cell culture media inlet. (ii) Collagen gel/synoviocyte inlet. (iii) Zone with collagen gel and synoviocytes. (iv) Endothelialized channel. (v) Cell culture media outlet. (C) Viability within region iii of the device. Scale bar = 200 µm. (D) Cell (synoviocyte) spread area (µm²). *p < 0.05. (E) Endothelialized device. Scale bar = 500 µm.

by a hydrogel matrix to permit sprouting—indicative of disease in the case of RA/OA.

To enhance the physiologic relevance of our model, we utilized a microfluidic device that contained a vascularized channel in the center of an engineered synovium-like tissue. This device is unique to any multicellular synovium model previously created as it enables the investigation of angiogenic sprouting, and FLS – endothelial cell interactions. Ongoing work is exploring the inclusion of diseased synoviocytes, and the impact of disease severity on HUVEC sprouting in this multicellular vascularized tissue model. We are also exploring the addition of exogenous inflammatory factors to the tissues to better understand the interplay between inflammation, angiogenesis, and OA.

ACKNOWLEDGEMENTS

The authors would like to thank the Rhodes Trust, Schmidt Futures, and the Schmidt Science Fellowship.

REFERENCES

- [1] Enomoto, H., *et al.*, Am J Pathol, 162:171-181, 2003.
- [2] Kim, H. R., *et al.*, Int J Rheum Dis, 19:233-240, 2016.
- [3] Haywood, L., *et al.*, Arthritis & Rheum, 48:2173-2177, 2003.
- [4] Qazi, T. H., *et al.*, ACS Biomater Sci Eng, 8(4):1427-1442, 2022.
- [5] Jimenez-Torres, J. A., *et al.*, Adv Healthcare Mat, 5:198-204, 2016.

BULK MATERIAL DENSITY IS ASSOCIATED WITH MECHANICAL RESPONSE OF POLYDIMETHYLSILOXANE AND PORCINE THORACIC AORTIC TISSUE

Pete H. Guelnder (1), Alexandria Trevino (2), Ronald Fortunato (3), Cyrus J. Darvish (1), Emma E. Ahlgren (3), Isabelle K.M. Chickanosky (1), Timothy K. Chung (1), Keshava Rajagopal (4), Kumbakonam R. Rajagopal (1,2), Spandan Maiti (3), Chandler C. Benjamin (2), and David A. Vorp (1,3,5-9)

(1) Department of Bioengineering, University of Pittsburgh, Pittsburgh, Pennsylvania, USA

(2) Department of Mechanical Engineering, Texas A&M University, College Station, Texas, USA

(3) Department of Mechanical Engineering and Materials Science, University of Pittsburgh, Pittsburgh, Pennsylvania, USA

(4) Department of Advanced Cardiopulmonary Therapies and Transplantation, University of Texas Health Science Center at Houston, Houston, Texas, USA

(5) McGowan Institute for Regenerative Medicine, University of Pittsburgh, Pittsburgh, Pennsylvania, USA

(6) Department of Surgery, University of Pittsburgh, Pittsburgh, Pennsylvania, USA

(7) Department of Chemical and Petroleum Engineering, University of Pittsburgh, Pittsburgh, Pennsylvania, USA

(8) Department of Cardiothoracic Surgery, University of Pittsburgh, Pittsburgh, Pennsylvania, USA

(9) Clinical and Translational Sciences Institute, University of Pittsburgh, Pittsburgh, Pennsylvania, USA

INTRODUCTION

An aortic aneurysm forms when the thoracic or abdominal aortic wall weakens and irreversibly expands. The ballooning and expansion are attributed to a gradual loss/breakdown of extracellular matrix (ECM), primarily elastin [1]. Aneurysm rupture caused 9,923 deaths in the US in 2018 [2] and occurs when localized wall stress exceeds wall strength [3]. For this reason, it would be clinically impactful to better understand and predict wall tissue strength for aortic aneurysms.

Protease treatments have been used to alter vascular ECM and to explore its impact on mechanical properties of tissue [4,5]. In general, reduced ECM leads to a less robust tissue. It has also been shown that the density of concrete can be used to predict failure [6]. We conjecture that polymer and aortic tissue behave similarly (i.e., material strength relates directly to density) and hypothesize that a decrease in wall tissue density will result in a decreased strength.

The purpose of this study was to investigate the relationship between experimentally altered density and mechanical properties of polydimethylsiloxane (PDMS) and porcine thoracic aortic tissue.

METHODS

PDMS Specimen Curation: 27 PDMS samples (100mm x 5mm) were curated either at a 10-1 curing ratio (n=11) or at a half-density, 20-1 curing ratio (n=10). Since the 20-1 dilution specimens contain half the amount of curing agent, they are considered half-density of the 10-1 dilution PDMS samples. The samples had their density measured as described below. All samples were uniaxially tensile tested to failure on an Instron (model 5543A, Norwood, MA).

Porcine Specimen Treatment: Freshly excised, intact porcine thoracic aortas were obtained from a local abattoir and cut into longitudinally-oriented rectangular (80mm x 4mm) specimens and submerged in phosphate buffered saline (PBS) overnight. The initial (untreated) saturated mass and volume were measured for each specimen and initial density calculated as described below. The samples

were then submerged in a collagenase (50 mg/mL, n=7) or elastase (0.01 mg/mL, n=7) solution to selectively degrade collagen or elastin, respectively. Sham/control specimens were submerged in pure PBS (n=7). Submerged specimens were then incubated with end-over-end rotation at 37 °C for 24 hours. Post-treatment mass and volume were measured, and density calculated for each specimen following incubation and then uniaxially tensile tested to failure. The stress-stretch curve was used to calculate nominal ultimate tensile strength (UTS) and tangent modulus, and all statistical analysis was performed using an ANOVA with Tukey's post-hoc.

Specimen Density Measurements: Mass (m) of all porcine specimens was measured using a precision balance (PR503, Mettler Toledo, Columbus, OH). The width-length surface area and average thickness were determined from images captured of the specimens prior to testing. Solid volume (V) was calculated from the measured surface area (SA) and average thickness (t) across the specimen (**Equation 1**).

$$V = SA * t \quad (1)$$

Density (ρ) was determined for each specimen before and after enzymatic degradation (**Equation 2**).

$$\rho = \frac{m}{V} \quad (2)$$

Percent density change (before vs. after treatment) for each specimen was calculated.

Material Modeling: Stress/stretch curves were imported for each specimen and analyzed independently (either 10:1 vs 20:1 for PDMS, or sham vs collagenase vs elastase for porcine tissue). These stress stretch curves were fit with a Vorp-Raghavan 2 parameter hyperelastic isotropic material model [7] (**Equation 3**)

$$W = \alpha(I_B - 3) + \beta(I_B - 3)^2 \quad (3)$$

Here I_B is the first invariant of left Cauchy-Green deformation tensor B . The mechanical properties α and β were determined by nonlinear regression analysis.

RESULTS

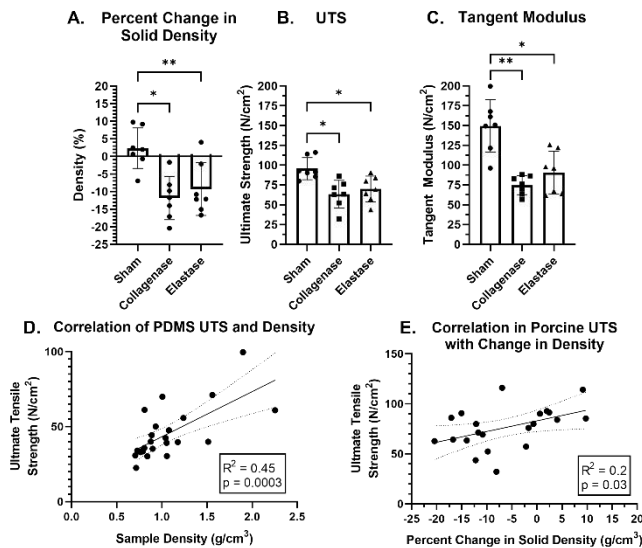


Figure 1: A) Percent change in density of material after proteolytic treatment, B) UTS of protease treated porcine aortas, C) Tangent modulus of protease treated porcine aortas, D) Correlation of PDMS samples comparing UTS and sample density, and E) Correlation of porcine samples comparing UTS and sample density. *p-value < 0.05 and **p-value < 0.01.

The results for the PDMS show a significant difference in solid density between the 10-1 and the 20-1 (1.16 ± 0.44 g/cm³ vs 0.88 ± 0.13 g/cm³, respectively; $p=0.03$). The UTS (55.0 ± 19.5 vs 37.1 ± 8.26 N/cm², respectively; $p=0.002$) and tangent modulus (38.9 ± 14.7 vs 10.5 ± 1.91 N/cm², respectively; $p<0.001$) were both also higher for the 10-1 compared to the 20-1.

The results for the porcine aortic tissue show a significant difference in % change in solid density between sham ($2.3 \pm 5.3\%$) and both collagenase-treated ($-11.8 \pm 5.7\%$, $p=0.005$) and elastase-treated ($-9.2 \pm 6.9\%$, $p=0.011$) tissue (Figure 1A). Parallel differences were also seen for the UTS for the sham (95.70 ± 12.8 N/cm²) and the collagenase (63.5 ± 16.2 N/cm², $p=0.024$) and the elastase groups (69.9 ± 15.2 N/cm², $p=0.03$) as shown in Figure 1B. The tangent modulus also showed similar differences between the sham (149.5 ± 30.7 N/cm²), collagenase (74.8 ± 11.1 N/cm², $p=0.007$) and the elastase groups (90.8 ± 25.0 N/cm², $p=0.025$), as shown in Figure 1C.

Linear regression reveal that density is a significant predictor of UTS in PDMS ($R^2=0.45$, $p=0.0003$) (Figure 1D). Similarly, % change in density is a significant predictor of UTS for porcine thoracic aorta ($R^2=0.2$, $p=0.03$) (Figure 1E).

PDMS material parameters, when fit to the Vorp-Raghavan Model [7] (showed a significant difference from each other Figure 2A). For the α values, the 10-1 dilution (7.6 ± 0.5 N/cm²) was significantly higher than in the 20-1 (3.7 ± 0.1 N/cm², $p<0.0001$). This trend remained for the β values, for the 10-1 (0.5 ± 0.2 N/cm²) were significantly higher than in the 20-1 (0.04 ± 0.02 N/cm², $p<0.0001$).

For the porcine tissue material parameters (Figure 2B) The α values were not different in sham control (9.8 ± 2.7 N/cm²) compared to collagenase-treated (10.8 ± 3.4 N/cm², $p=0.20$) or elastase-treated (6.5 ± 1.2 N/cm², $p=0.68$) specimens. However, there was a difference when comparing the α values of collagenase- (10.8 ± 3.4 N/cm²) and elastase-treated samples (6.5 ± 1.2 N/cm², $p=0.0071$). The β values were different when comparing the sham control (4.8 ± 1.3 N/cm²) with collagenase-treated samples (1.2 ± 0.7 N/cm², $p=0.01$), but no difference compared to elastase-treated samples (2.0 ± 0.3 N/cm², $p=0.10$).

Similarly, there was no difference when comparing collagenase- (1.2 ± 0.7 N/cm²) versus elastase-treated samples (2.0 ± 0.3 N/cm², $p>0.99$).

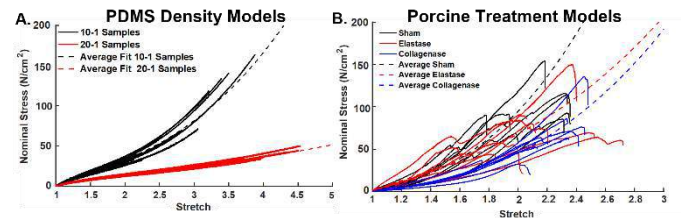


Figure 2: A) Model fit of PDMS samples in a Vorp-Raghavan model, and B) Model fit of protease treated porcine treatments in a Vorp-Raghavan material model.

DISCUSSION

We demonstrated that altering the material density gives insight into the material strength. By using different curing agent concentrations, we were able to successfully perturb PDMS to tune its material density. The 10-1 samples had significantly higher bulk specimen densities, UTS, and tangent moduli. These experimental results are also shown in the model fit of the PDMS specimen. From the model, α is representative of the low-stretch region of the tissue's response and β represents the high-stretch region [8]. The α and β parameters were both significantly larger in high-density (10-1) samples compared to the half-density (20-1) samples. Thus, the high-density samples have stiffer responses in low and high stretch regions than the half-density samples. This observation supports our hypothesis that higher density provides mechanical strength to the sample.

Additionally, we found that altering material density in porcine tissue shows a similar relationship between density and biomechanical failure properties. The experimental tests on the porcine tissue revealed that through proteolytic treatments we can manually manipulate the density to decrease the bulk tissue density, UTS, and tangent modulus, as shown in Figure 1A, 1B, and 1C. Correlation between PDMS strength and density was exhibited here (Figure 1D). Additionally, porcine tissue also exhibits density as a significant predictor of UTS (Figure 1E). The porcine tissue model fit has no difference in α between sham or treatment groups, however, β is significantly higher in sham compared to collagenase. This is corroborated with prior literature[5] as we are reducing the strength of the tissue by removing some collagen from the ECM. Schriebl et al noted the same experimental results in regards to low and high stretch stiffness[9].

This study is limited by assuming that when using collagenase, there is only a reduction in the collagen content. Similarly, we assume when using elastase there is only a reduction in elastin content. Future work will include a ninhydrin and hydroxyproline assay of the treated tissue to quantify the collagen and elastin content in the treated and sham specimen. Future studies will work to measure local densities rather than assign a bulk density value to an entire section of tissue.

ACKNOWLEDGEMENTS

This work was supported by the National Institutes of Health, Award #7R01HL109132-07. PG was supported by the National Science Foundation Graduate Research Fellowship under Grant #1747452.

REFERENCES

- [1] Dobrin, P, et al, *Surgery*, (1988).
- [2] C.f.D Control, WISQARS. 2017.
- [3] Vorp, D, *J. Biomech.*, 2007.
- [4] Berman, A, et al, *Scientific Reports*, 2022.
- [5] Noble, C, et al, *J Mech Behav Biomed Mater*, 2016.
- [6] Murru, P, et al, *Int. J. Pavement Eng.*, 2020.
- [7] Raghavan, M., *J. Biomech.*, 2000.
- [8] Raghavan, M, et al, *Ann Biomed Eng.*, 1996.
- [9] Schriebl, A, et al, *Acta Biomaterialia*, 2015.

INTEGRATION OF FEBIO AS AN INSTRUCTIONAL TOOL FOR UNDERGRADUATE BIOMECHANICS

David Jiang (1), Jeffrey A. Weiss (1,2,3), Lucas H. Timmins (1,2)

- (1) Department of Biomedical Engineering, University of Utah, Salt Lake City, UT, U.S.A
(2) Scientific Computing and Imaging Institute, University of Utah, Salt Lake City, UT, U.S.A
(3) Department of Orthopedics, University of Utah, Salt Lake City, UT, U.S.A

INTRODUCTION

Modern computational modeling & simulation (CM&S) tools have become ubiquitous within the field of biomechanics. CM&S has provided engineers, scientists, and clinicians with new strategies to advance biomedical research, medical device design, and interventional/surgical planning. Moreover, CM&S is recognized by the FDA as central to evaluating device safety and effectiveness [1]. Hence, CM&S has become increasingly important for biomedical engineering trainees. However, medical device consortiums have highlighted barriers to broadly using CM&S, including user expertise, scientific maturity, and cost [2]. To address these limitations, efforts to integrate CM&S as an instructional tool into biomedical engineering curriculums, particularly at the undergraduate level, have been undertaken to promote understanding and application [3].

Initiatives contend that biomedical engineering students should learn computing concepts to improve the educational environment [4]. The introduction and use of computational software that utilizes, for example, finite element (FE) modeling is traditionally taught in graduate-level biomechanics courses due to the advanced nature of the topics. However, CM&S tools have many attractive features that complement standard pedagogical approaches for undergraduate courses in biomechanics and augment student learning and comprehension. Herein, we aimed to develop and implement interactive learning modules developed in the open-source FE software *FEBio* and *FEBio Studio* within our undergraduate biomechanics course and evaluate the effectiveness of this integration in providing a foundation for CM&S to undergraduate biomedical engineering students.

METHODS

Course Overview and Student Participants: *Biomechanics I* is a core (required) course in the undergraduate curriculum in biomedical engineering at the University of Utah. Across 15 weeks, with two 80-minute didactic lectures per week, the course covers topics in continuum

mechanics (e.g., finite deformation kinematics, stress), linearized elasticity, and the mechanical behavior of biological materials. Additionally, this course includes a laboratory component where students perform hands-on experiments to reinforce topics covered in the lecture. In Fall 2022, there were 83 students at the junior or senior level enrolled in the course.

FEBio Learning Modules and Instructional Efforts: We developed and implemented four learning modules that supplemented the course lectures, in-class discussions, assignments, and laboratory exercises. Each module contained self-enclosed lessons that were completed in 90-120 minutes. Across 8 lab sections, with 9-11 students in each section, students were divided into 2-3 person groups. Each group had access to a desktop PC with an Intel® Core™ i7-6700 (3.40 GHz) processor and 16 GB of memory. Modules began with a brief 10-minute lecture by a teaching assistant (TA) to provide clinical/biomedical rationale and describe relevant background information. Next, student groups completed tutorial(s) to construct FE models, including geometry creation, discretization, assignment of boundary conditions, and material selection. In addition, students were provided with pre-built models where they analyzed and interpreted simulation results that reflected concepts from the didactic lectures. At least one TA was always present to provide supplementary instructions, answer questions, and assist with FEBio.

The title and topic of each module are listed in Table 1. Module 1 introduced the basic principles and applications of FE and FEBio, and students simulated simple deformations of a unit cube (e.g., extension, simple shear). For Module 2, students simulated a tensile

Table 1. FEBio Learning Modules

Title
1. <i>Introduction to FEBio:</i> finite deformation kinematics
2. <i>Tensile Testing Simulation:</i> analysis of strain and stress
3. <i>Linearized Elasticity:</i> elastic constants and anisotropy
4. <i>Beam Bending Simulation:</i> verification and validation

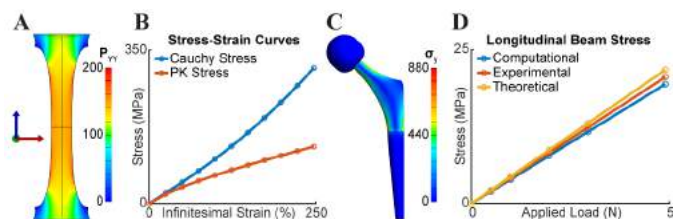


Figure 1. (A) Longitudinal PK1 stress in a dog-bone sample under uniaxial tension, (B) Comparison of Cauchy and PK1 stresses, (C) Von-mises stress in a hip implant, (D) Representative student plot of V&V results via beam-bending experiment.

testing experiment and analyzed the strain and stress predictions (Fig. 1A-B). In Module 3, students investigated material symmetry and elasticity constants (e.g., Young's modulus, Poisson's ratio). Lastly, Module 4 introduced verification and validation (V&V) for a simple beam bending experiment and included a case study on material yielding in the setting of a prosthetic hip implant (<https://grabcad.com/library/hip-prosthesis-1>, Fig. 1C-D).

Student Assessment and Surveys: Following the completion of the tutorial(s) for each module, students completed an assessment to evaluate tutorial effectiveness. In groups, students were given a problem statement and tasked to construct and analyze more advanced FE model(s) that extended concepts and principles from the tutorial(s). The number of attempts each group needed to complete each exercise correctly was recorded. In addition, students were asked to complete questionnaires offered before Module 1 (pre-evaluation), after Module 2 (mid-evaluation), and after Module 4 (post-evaluation; Table 2). Students answered survey questions (Q) 1 and 3 as Yes/No. Q2 and Q4 responses were on a scale of 1 (*strongly disagree, not interested*) to 5 (*strongly agree, extremely interested*). Q5 and Q6 allowed open-ended responses to evaluate module effectiveness and how to improve the educational material. Responses were anonymized. Data are reported as mean \pm standard deviation where appropriate.

Table 2. Student Survey Prompts

	Question
Pre	Q1. Before this course, have you heard of "finite elements/FEA"?
Pre, Mid, Post	Q2. How interested are you in <i>continuing</i> to learn CM&S?
Post	Q3. During this course, have you explored FEBio on your own?
Post	Q4. How effective were the FEBio modules in providing a computational foundation and understanding of theoretical concepts introduced during lectures?
Post	Q5. What was the most beneficial aspect of these modules for you?
Post	Q6. What biomedical applications or diseases would you find most interesting to <i>apply</i> FE to study?

RESULTS

Most students had not heard of FE or FE analysis before the modules, as <35% of students had previously heard those terms. However, as the modules progressed, students became more interested in CM&S (Fig. 2D). The heightened interest coincided with students demonstrating an increased understanding and comprehension of FE model development and use of FEBio (Fig. 2A-C). Not only was there a reduction in the number of attempts across exercises within a module, but fewer attempts were needed as students progressed through the modules. In Module 1, for example, the number of attempts across two exercises decreased from 4.56 ± 2.20 to 2.94 ± 1.64 , while in Module 3,

the number of attempts across three exercises ranged from 1.56 ± 1.33 to 1.80 ± 1.04 . It was encouraging to learn that >60% of students explored FEBio outside of the educational environment and included students exploring user projects in the FEBio Studio model repository. Furthermore, students indicated that the modules integrated well with the didactic lectures and aided understanding of theoretical concepts introduced during lectures (Q4 score: 4.25 ± 0.67 , Fig. 2E). Responses to the open-ended questions (Q5,6) were largely positive, including a few noteworthy statements:

Q5: "... visualizing what we learned in class. Just observing what different deformations looked like helped give context to everything learned in class. Also, getting familiar with real-world tools for solving biomechanics problems was good exposure for third-year BME students."

Q6: "... medical implants in patients. Before this class, I mostly thought of medical device compatibility in the setting of device rejection by the body. However, I should also think about it in the sense of biomechanics. Making sure a medical device does not physically break has to be one of the most important considerations in this field."

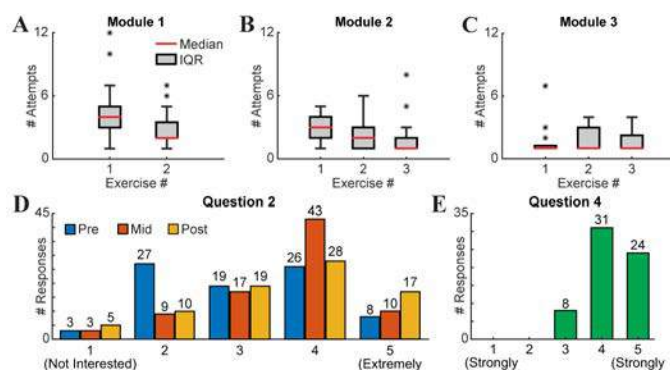


Figure 2. (A-C) Student assessment scores for Modules 1-3. (D-E) Student survey responses for questions Q2 and Q4.

DISCUSSION

Our efforts demonstrate that CM&S can be successfully integrated into an undergraduate biomechanics course and serve as an effective and interactive educational tool. Assessment data indicated that the FE modules increased learning for both course content (i.e., fundamental biomechanics principles) and the application of FE analysis. Importantly, students recognized the advantages of CM&S in evaluating the mechanical behavior of complex systems. The continued integration of CM&S into undergraduate biomedical engineering curriculum holds much promise in training students in modern techniques and tools broadly used in their professional work.

ACKNOWLEDGEMENTS

This research was supported, in part, by the University of Utah - Graduate School's University Teaching Assistantship program, and NIH grants R01GM083925 and U24EB029007.

REFERENCES

- [1] U.S. Food & Drug Administration, "Reporting of Computational Modeling Studies in Medical Device Submissions," 2016.
- [2] MDIC Annual Report, 2021
- [3] Boster, KAS et al., *J Biomech Eng*, 142(11):111008, 2020.
- [4] Harris, TR et al., *Annu Rev Biomed Eng*, 4(1):29-48, 2002.
- [5] Maas, SA et al., *J Biomech Eng*, 134:011005, 2012.

INFLUENCE OF MATERIAL PARAMETER VARIABILITY ON THE PREDICTED CORONARY ARTERY BIOMECHANICAL ENVIRONMENT VIA UNCERTAINTY QUANTIFICATION

David Jiang (1), Caleb C. Berggren (1), Y.F. Jack Wang (1), Jake A. Bergquist (1,2,3), Lindsay C. Rupp (1,2,3), Zexin Liu (2,4), Rob S. MacLeod (1,2,3), Akil Narayan (2,4), Lucas H. Timmins (1,2)

- (1) Department of Biomedical Engineering, University of Utah, Salt Lake City, UT, U.S.A
(2) Scientific Computing and Imaging Institute, University of Utah, Salt Lake City, UT, U.S.A
(3) Nora Eccles Cardiovascular Research and Training Institute, University of Utah, Salt Lake City, UT, USA
(4) Department of Mathematics, University of Utah, Salt Lake City, UT, USA

INTRODUCTION

Advances in medical imaging, computational mechanics, biomechanics, and computing power now provide the ability to perform computational simulations and predict arterial tissue deformations at the patient-specific level [1]. In addition to the model geometry, boundary conditions, and numerical approaches to solve the governing equations, the constitutive relation(s) describing the behavior of the material(s) are required to compute the transmural wall stresses under conditions of interest, which influence the homeostatic and maladaptive mechanobiological processes. While experimental approaches have been developed to characterize the nonlinear, pseudo-elastic, and anisotropic material response of vascular tissue under loading, there is much variability in the employed techniques, ranging from experimental testing protocols to fitting approaches [2]. Furthermore, variability within and across tissue samples leads to uncertainties in the material parameter(s) describing the mechanical properties of vascular tissue. These uncertainties may ultimately propagate to variability in the simulation-predicted mechanical environment.

As simulation results have the potential to influence clinical outcomes (e.g., predict major adverse event), there is a pressing need to provide confidence in simulation predictions and demonstrate that results are reliable and safe prior to clinical adoption. Such confidence in simulation pipelines is marred by uncertainties, which manifest through unaccounted for subject and clinical variabilities that cloud the predictive and prognostic lenses of computer-based modeling. Therefore, the goal of this study was to leverage uncertainty quantification (UQ) techniques to examine the impact of tissue material property uncertainty on the variability in model outputs, namely the predicted stress and strain.

METHODS

Material Parameter Probability Distribution Sampling: Material parameters derived from previous layer-specific mechanical

testing of thirteen human non-atherosclerotic left anterior descending (LAD) coronary artery tissue were employed [3]. Best-fit material parameters for the media and adventitia layers were determined using the microstructurally motivated strain energy function (SEF),

$$W = \mu(I_1 - 3) + \frac{k_1}{k_2} e^{k_2[(1-\rho)(I_1-3)^2 + \rho(I_4-1)^2]} - 1, \quad (1)$$

where μ represents the ground matrix stiffness, k_1 is a fiber “stress-like” parameter, k_2 is a dimensionless parameter, ϕ specifies the angle of circumferential fiber orientation in the circumferential-axial plane, ρ is a measure of fiber dispersion, and I_1 and I_4 are the first and fourth invariants, respectively, of the right Cauchy-Green deformation tensor.

Probability distributions were created for each constitutive parameter in the medial and adventitial layers (10 in total). Material parameters μ , k_1 , k_2 , and ϕ employed gamma distributions to avoid non-physiologic parameters, whereas ρ used a beta distribution. Probability density functions (PDFs) were fit to experimental data via MATLAB (MathWorks, Natick, MA), and defined within *UncertainSCI*, a novel open-source, Python-based UQ software tool [4]. A tensorial distribution (i.e., parameter ensemble), which sampled the entire parameter space and accounted for the interplay between distributions, was created from the 10 PDFs (Fig. 1A).

Idealized Artery Computational Model: A generalized computational model of a human LAD coronary artery was constructed and modeled as a multi-layered, axisymmetric quarter-cylinder ($R_i = 1.59$ mm, $R_o = 2.25$ mm), with a medial and adventitial layer thickness of 0.32 and 0.34 mm, respectively. The SEF defined by Eq. 1 described both layers. Based on a mesh convergence study, the artery was discretized with 8-node hexahedral “brick” elements with 6 elements in the radial direction for each layer. Boundary conditions included: a lumen pressure up to 80 (diastolic) and 120 (systolic) mmHg, fixing the vessel ends, and symmetry boundary conditions to restrict rigid body

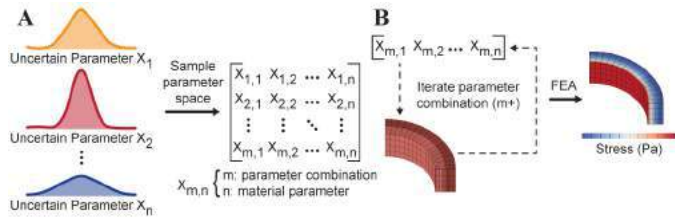


Figure 1: Schematic of UQ integrated into modeling framework. (A) Probability distributions fit to n -material parameters, with m -parameter combinations generated via UncertainSCI sampling. (B) Automated batch-processing scheme created m -number of FE models to predict tissue deformation, strains, and stresses.

motions. The open-source, nonlinear finite element (FE) software *FEBio* (<https://febio.org/>) was used to perform the quasi-static analysis [5]. A batch-processing scheme was implemented via MATLAB to iterate through material parameter combinations derived from the tensorial distribution, creating m -unique input files for FEBio (Fig. 1B). Simulation results were post-processed to evaluate the deformed inner and outer radii, transmural distributions of 1st and 3rd principal stresses (σ_1 , σ_3), and distensibility.

UQ and Sensitivity Analysis: Utilizing UncertainSCI, a parameter-to-model-output emulator was constructed via polynomial chaos expansion (PCE) to approximate the mapping between the SEF parameters (inputs) and FE-predicted principal strains and stresses (outputs). Importantly, the emulator allowed direct extraction of statistics, uncertainty characteristics, and model sensitivity. PCE quality was assessed by quantifying the relative error between PCE approximations and FE-predicted model outputs for orders (p) 1 to 5, over 5 independent PCE runs for each order.

Statistical measures (e.g., mean, standard deviation, coefficient of variance) were calculated directly from PCE output. Sensitivity indices, via first and second-order Sobol indices, were calculated across the SEF parameters to measure the direct contribution of individual parameters (unary interaction) and two-parameter combinations (i.e., binary interaction) to the overall variability in the model output for 1st principal stress. Binary interactions were only evaluated between SEF parameters within each arterial layer.

RESULTS

The number of parameter combinations generated across PCE orders ranged from 21 for order 1 to >3000 for order 5. Evaluation of the relative error and error variability for the 1st and 3rd principal stresses demonstrated that PCE order 2 resulted in error values of <1%, with an error variability of <0.03% across 5 runs. Furthermore, first-order Sobol indices maintained stability at PCE order 2 and higher orders. The FE results from PCE order 2 simulations demonstrated a range of deformed arterial geometries. For instance, vessel diameter, thickness, and distensibility values range from 3.76–4.39 mm, 0.52–0.38 mm, and 5.75–13.88 MPa⁻¹, respectively.

The propagation of material parameter uncertainties to the transmural distribution of 1st principal stress at 120 mmHg yielded standard deviations >40 kPa within the medial and adventitial layers (Fig. 2A). While average stress values and standard deviations decreased radially through each layer, there was an abrupt increase in the standard deviation at the innermost region of the adventitia. Notably, the coefficient of variation in the adventitia was >2× the value in the media, indicating adventitial σ_1 stress values had larger dispersion around the mean (Fig. 2B).

Sensitivity analysis highlighted that the anisotropic material parameters of the adventitia, k_1 , k_2 , ϕ , and ρ accounted for nearly

64.7% of the variance in predicted σ_1 stress (Fig. 2C). Moreover, uncertainty in the stiffness of the adventitial fibers (k_1) alone accounted for >40% of first-order interactions. The stiffness of the ground matrix (μ) for both the media and adventitia had a negligible effect. While unary interactions were dominant (80.8%), binary interactions accounted for 19.2% of predicted σ_1 variance (Fig. 2D). Specifically, binary interactions in the media and adventitia accounted for 5.8% and 13.4%, respectively. In particular, the interaction between the adventitia parameters, fiber angle (ϕ), and dispersion (ρ), accounted for 7.6% of the variance in predicting σ_1 stress.

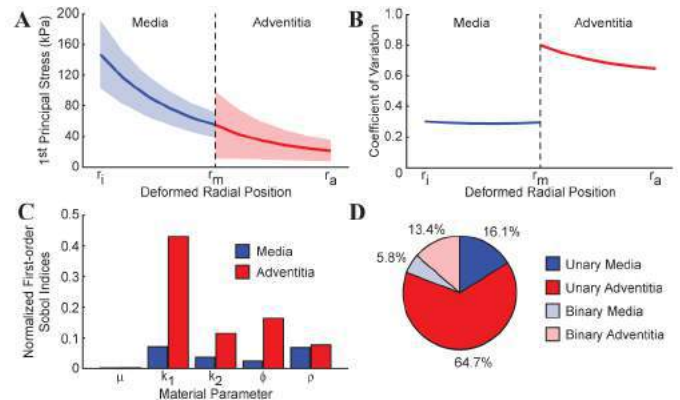


Figure 2: (A) Transmural distributions of 1st principal stress (solid line: Mean, shaded region: ± 1 SD). (B) Coefficient of variation. (C) Normalized first-order Sobol indices (unary interactions) for material parameters in the media and adventitia. (D) Percent variance due to unary versus binary interactions. All data were derived from order 2 PCE analysis.

DISCUSSION

In the present study, we demonstrated the utility of an integrated FE-UQ framework to evaluate the intrinsic uncertainty in material parameters on the variability of the arterial mechanical environment. Our results indicate that the uncertainty in the stiffness of the adventitial fibers, k_1 , drives the variance in FE-predicted stresses. In addition, the pairwise interaction between adventitia fiber angle (ϕ) and dispersion (ρ) had a greater effect on variance in stress than any single parameter in the media. These results highlight not only the importance of accurate measurements of these material parameters to provide confidence in FE-predictions but also the need to acquire considerably more data across tissue samples, including donor/patient age and sex, to obtain improved parameter distributions. Ultimately, these efforts must be integrated into patient-specific modeling frameworks within the clinical setting to promote the safety and reliability of model predictions prior to clinical adoption.

ACKNOWLEDGEMENTS

This work was supported, in part, by the National Institutes of Health grants R01 HL-150608 (LHT), U24 EB-029012 (RSM, AN). The Authors thank Prof. Jeff Weiss and Dr. Steve Maas for their insightful discussions and assistance with the FEBio Software Suite.

REFERENCES

- [1] Taylor, CA et al., *Annu Rev Biomed Eng*, 11:100–134, 2009.
- [2] Ferruzzi, J et al., *Ann Biomed Eng*, 41:1311–1330, 2013.
- [3] Holzapfel, GA et al., *AJP Heart Circ*, 289:H2048–H2058, 2005.
- [4] Narayan, A et al., *Comput Biol Med*, 106407, 2022.
- [5] Maas, SA et al., *J Biomech Eng*, 134:011005, 2012.

A PRELIMINARY IN SILICO STUDY ON THE FLUID DYNAMIC CHANGES WITH CENTRAL VENOUS CATHETER INSERTION

B. Su (1), H. Palahnuk (1), T. Harbaugh (2), E. Rizk (2), S.W. Hazard (2), K.B. Manning (1,2)

(1) Department of Biomedical Engineering, Penn State University, State College, PA, USA
(2) Department of Surgery, Penn State Hershey Medical Center, Hershey, PA, USA

INTRODUCTION

Central venous catheterization (CVC) is a common, albeit invasive, approach to access the central venous system. CVC is often used to deliver sclerotic medications and provides a reliable means by which clinicians deliver large volumes of fluid to critically ill patients. Despite these benefits, its presence as a foreign body within the central venous system can result in thrombosis which may obstruct the fluid flow within the lumen or blood flow within the vessel in which the catheter resides. In addition to the local thrombosis, thromboembolic events arising from the catheter can occur. This feared event can lead to the obstruction of the pulmonary arteries which can be fatal [1]. It is well documented that there are a number of complex biochemical reactions involving soluble factors within the blood that lead to thrombosis however, the hemodynamic parameters also play an important, and often underappreciated, role in the development of thrombosis [2], [3].

Direct measurements of hemodynamic parameters are not conducted routinely in clinical practice. Therefore, computational fluid dynamics (CFD) is widely used to simulate blood flow around the CVC, and the derived hemodynamic parameters are used for analyses. However, CVC numerical studies are very limited in the literature. In the CFD study performed by Peng *et al.*, CVC elevated the wall shear stress (WSS) level and disrupted the blood flow's spiral rotation [2]. Park *et al.* suspected that the increments of time-averaged WSS and normalized transient WSS on the venous lumen should be related to the thrombosis incidence [3]. The tip placement of the catheter may vary in the proximity of the cavo-atrial junction, and De Oliveira *et al.* revealed its effects on the surrounding blood flow in terms of shear stress, recirculation region, and percentage of tip volume with high shear stress level in an idealized right atrium (RA) [4].

The first two studies mentioned above had no RA in the numerical models, and the last one included an idealized RA and the catheter's tip portion only. This study reconstructed an anatomical model based on

patient-specific images, and a double-lumen CVC was inserted along the centerline.

METHODS

The geometry of the anatomical model, including RA, SVC, and IVC, was based on the CT images of a pediatric patient from Penn State College of Medicine (IRB approved), as shown in Fig. 1a. The reconstructed model represents the characteristics of the venous structure. The geometry of the 5 French catheter was segmented from a microCT scan, and the surface was represented by millions of facets in stereolithography (STL) formation in Fig. 1b.

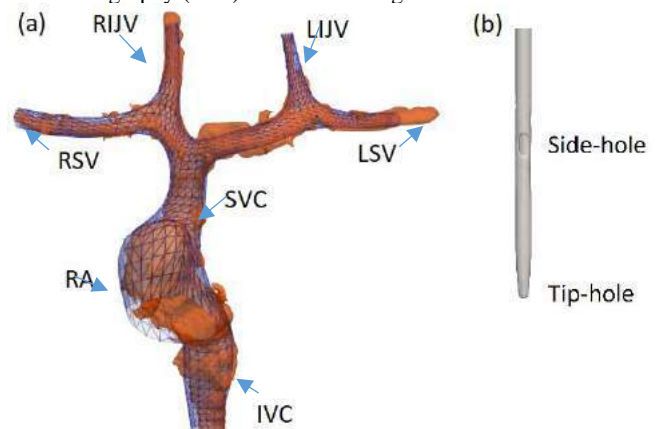


Figure 1: (a): CT image segmentations (orange) and reconstructed model including right internal jugular vein (RIJV), right subclavian vein (RSV), left internal jugular vein (LIJV), left subclavian vein (LSV), SVC, IVC and RA. (b): Double lumen 5 French catheter reconstructed from microCT scan.

The catheter was inserted virtually into the anatomical model along the centerline, as demonstrated in Fig. 2a. Note that the CT scan only

captured images at one-time point, so the numerical model was assumed to be rigid. In this study, the blood was assumed to be an incompressible Newtonian fluid with a density of 1035 kg/m^3 and a dynamic viscosity of $0.0035 \text{ Pa}\cdot\text{s}$, respectively. The numerical models were meshed using cfMesh implemented in the OpenFOAM framework. The numbers of grids in the model with and without the CVC were approximately 4.5 million and 2.6 million, respectively (Fig 2b). Based on the averaged flow rate and the effective SVC diameter, the Reynolds number was about 750, and thus the flow inside the model was laminar. The governing equations were solved using the pimpleFoam solver in OpenFOAM. The flow rates in SVC and IVC were derived from 4D MRI measurements [6], and the cardiac output of the model was assumed to be 5 L/min at a heart rate of 72 beats/min (Fig. 2c).

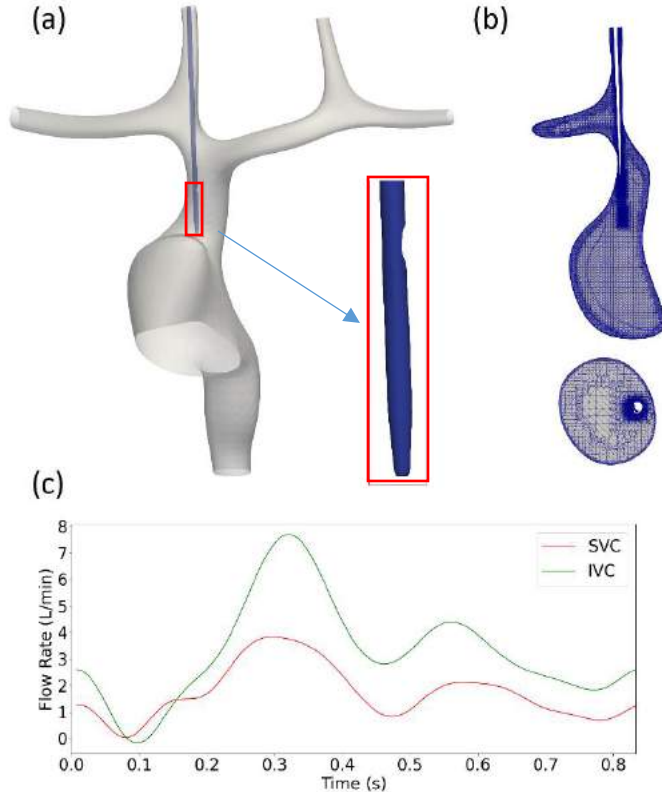


Figure 2: (a): Numerical model with a catheter inserted along the centerline from RIJ to RA. (b): Cross sections of mesh generated using cfMesh. (c): Flow rate profiles in SVC (red) and IVC (green).

RESULTS

Figure 3 shows the time-averaged flow patterns on the cross-sectional plane in the models with and without catheter. The presence of a catheter mainly alters the flow in SVC, and the flow in IVC is not affected. Due to the flow resistance induced by the catheter, the RA region influenced by the IVC flow is slightly larger in the model with the catheter. At the tip and side-hole, the blood in the lumen has zero velocity, as indicated by the contours in Figure 3c.

Figure 4 shows the WSS magnitude elevates at RIJ, owing to the insertion of the CVC. However, the changes in WSS magnitude in other regions are insignificant. The cavities at the tip and side-hole induce low WSS regions ($< 1 \text{ Pa}$), where flow stagnation occurs.

DISCUSSION

In this study, the CVC effects on the flow in the RA and surrounding veins have been simulated. As the catheter tip was placed

near the junction of SVC and RA and its diameter was relatively thin, its influence on RA flow was insignificant in terms of flow patterns and WSS. Instead, the IVC flow dominated the flow in RA and directed the flow in a clockwise direction. This characteristic flow pattern was also observed in the 4D MRI study [7] and thus validated that the simulation results were reasonable. WSS is an important hemodynamic parameter related to thrombosis, its value increased slightly after the insertion of CVC at RIJ, and the potential of thrombosis was altered marginally. However, the flow stagnation and low WSS magnitude at the tip and side-hole could promote the development of a thrombus, which will be thoroughly investigated in future studies. The main significance of this work is establishing the framework for CFD simulations, including CVCs using image segmentation, reconstruction, virtual catheterization, and CFD modeling.

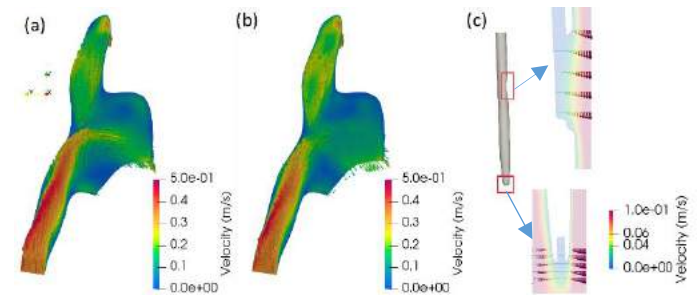


Figure 3: Time-average flow patterns on a cross-sectional plane in the model without (a), with a catheter (b) and detailed flow profiles on the cross sections of tip and side-hole (c).

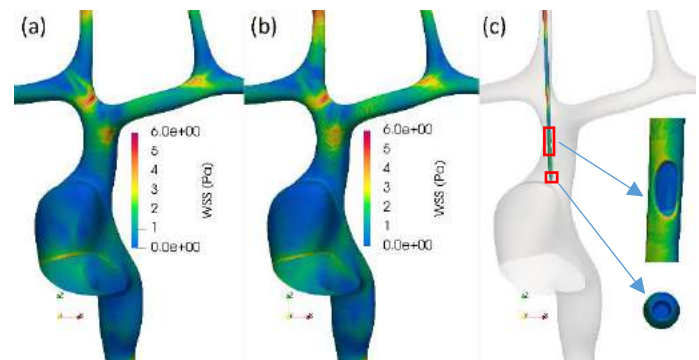


Figure 4: Time-averaged WSS on the numerical model without (a) and with a catheter (b) and contours on the catheter (c)

ACKNOWLEDGEMENTS

The project was supported by the National Center for Advancing Translational Sciences, National Institutes of Health, through Grant UL1 TR002014. The content is solely the responsibility of the authors and does not necessarily represent the official views of the NIH.

REFERENCES

- [1] A. Leung *et al.*, *J. Thromb. Thrombolysis*, vol. 40, no. 3, pp. 363–373, 2015.
- [2] L. Peng *et al.*, *Sci. Rep.*, vol. 7, no. 1, pp. 3–10, 2017.
- [3] M. H. Park *et al.*, *J. Biomech. Eng.*, vol. 142, no. 9, pp. 1–8, 2020.
- [4] D. C. De Oliveira *et al.*, *PLoS One*, vol. 16, no. 2 February, pp. 1–26, 2021.
- [5] C. Bruno *et al.*, *Front. Pediatr.*, vol. 10, no. October, pp. 1–12, 2022.
- [6] L. P. Parker *et al.*, *J. Appl. Physiol.*, vol. 132, no. 5, pp. 1167–1178, 2022.
- [7] J. D. Parikh *et al.*, *PLoS One*, vol. 12, no. 3, 2017,

VISUALIZING THE ORIFICE OF VISCERAL ARTERIES FOR *IN SITU* FENESTRATION OF AAA ENDOVASCULAR STENT GRAFTS

**Cyrus J. Darvish (1), Nicholas P. Lagerman (1), Oldrich Virag (1), Mohammad H. Eslami (4,5),
David A. Vorp (1,2,3,4,6,7,8), Timothy K. Chung (1)**

- (1) Department of Bioengineering, University of Pittsburgh, Pittsburgh, Pennsylvania, USA
- (2) Department of Mechanical Engineering and Materials Science, University of Pittsburgh, Pittsburgh, Pennsylvania, USA
- (3) McGowan Institute for Regenerative Medicine, University of Pittsburgh, Pittsburgh, Pennsylvania, USA
- (4) Department of Surgery, University of Pittsburgh, Pittsburgh, Pennsylvania, USA
- (5) Division of Vascular Surgery, University of Pittsburgh Medical Center, Pittsburgh, Pennsylvania, USA
- (6) Department of Chemical and Petroleum Engineering, University of Pittsburgh, Pittsburgh, Pennsylvania, USA
- (7) Department of Cardiothoracic Surgery, University of Pittsburgh, Pittsburgh, Pennsylvania, USA
- (8) Clinical and Translational Sciences Institute, University of Pittsburgh, Pittsburgh, Pennsylvania, USA

INTRODUCTION

An abdominal aortic aneurysm (AAA) is a common cardiovascular disease which causes the irreversible enlargement of the terminal aorta by more than 50%. AAA can become fatal if ruptured, which makes it the 13th leading cause of death in the US [1]. Surgical intervention can be performed to stabilize the aneurysm and prevent further growth/rupture. There are two methods of intervention: a high-risk open surgical repair or low-risk minimally invasive endovascular aneurysm repair (EVAR) where an endograft is deployed via a catheter inserted through the femoral artery [2]. Nearly 70% of AAA repair cases now use EVAR due to its lower mortality rate; however, roughly 30-50% of patients with AAA are not eligible for EVAR due to geometric constraints [3].

Short aortic neck lengths (< 10 mm) pose compatibility issues for the typical EVAR procedure as it hinders proper stent-graft anchoring and sealing. For aneurysms without an appropriate neck length, fenestrated EVAR (FEVAR) was introduced to extend the anchoring point past the visceral arteries (renal, superior mesenteric, and celiac) with openings for bridging stent-grafts. The EVAR grafts are either surgeon modified or prefabricated according to the patient's anatomy. In either case, fenestrations or holes are created in the graft to allow for bridging stents to be placed and restore blood flow through the visceral arteries. However, extensive planning is required to fabricate fenestrated EVAR (FEVAR) grafts including computed tomographic (CT) imaging and reconstruction, and manufacturing to guarantee precise placement of fenestrations [4].

The Cook Zenith graft (Cook Medical LLC, Bloomington, Indiana) is currently the only FDA approved custom graft on the market. The preparation and manufacturing of this custom graft necessitates a 4-8 week wait period for patients until implantation can occur [5]. The lead time for delivery poses a rupture and death risk for patients that need immediate repair. Katsarygyris et al. reported that ~4% of patients died and ~2% experienced aneurysm rupture before a FEVAR operation

could take place [6]. Alleviating wait times and extensive costs for the FEVAR procedure can improve AAA repair.

The goal of this work is to develop a device to create *in situ* fenestrations (ISF) for off-the-shelf endografts. To perform ISF, it is necessary to detect and visualize the openings of visceral arteries from inside the graft. The purpose of the current study was to develop and validate a prototype to achieve this using fiber optics in an *in vitro* test bench.

METHODS

Summary: Several feasibility studies were performed to assess the ability of evolving prototypes to detect an orifice of an artery. This was achieved by developing a test-bench, stent-graft patch (metal struts with woven polyester fabric), and various media (air and blood) to test whether infrared light in a visceral artery model could be detected with the fiber-optic probe. Additionally, the loss of light intensity was measured and statistically compared between air and water. The device consists of a bundle of fiber optic cables for transmitting light and a camera for real-time visualization of the light. Fiber optic cables consist of thin strands of glass and are used for their ability to transmit light waves long distances. For this experiment, they were used to transmit light from a point source for real time visualization. An infrared light-emitting diode (LED) was used as the light source and connected to an Arduino (Arduino LLC, Boston, MA) for a light intensity of 300 mW at 500 mA. An external computer webcam (Logitech International, Lausanne, Switzerland) was used for visualization because it has a complementary metal oxide semiconductor (CMOS) sensor for detecting infrared light. A separate MATLAB (Mathworks, Inc. Natick, Massachusetts) script was used for visualization.

Fiber Optic Probe Development: A silicone molding technique was utilized to manufacture the fiber optic probe. The advantage of the molding technique enabled the fiber optics to be embedded without the need for additional adhesive. Two halves of the casting mold were

designed on Inventor (Autodesk, San Rafael, CA) and 3D printed using a Form 3 printer (Formlabs Inc. Somerville, MA). Each half cast contained half of the probe longitudinally. The probe was made 7 mm in diameter with six 700 μm fibers (Thorlabs, Newton, NJ) embedded in a 6 mm diameter circular pattern (**Figure 1A**). This number of fibers was chosen to be adequate for an initial feasibility study, size constraints, and minimizing equipment costs. One half of the cast included holes for silicone to be poured into the cast. A 10:1 XPS silicone (Silicones Inc., Woodbine High Point, NC) was poured into the cast chamber and allowed to dry for 24 hours. After sitting, the halves of the cast were separated, and the mold was released.

Experimental Setup: A test bench was designed using Inventor and 3D printed using a Form 3 printer. The test bench was 115 mm long, 60 mm wide, and 80 mm in depth (**Figure 1B**). In the center of the test bench is a half-cylinder mimicking 'inside the lumen' to outer wall to act as half of an aorta. The half cylinder had guiderails to allow for precise movement and tracking of the probe head relative to a 6 mm diameter orifice acting as the opening of an artery. A 5 mm LED emitter at a wavelength of 830 nm infrared (Vishay Optoelectronics, Malvern, PA) was placed into the 6 mm hole. A 10x10 mm piece of Zenith endograft material was cut and attached over the artery orifice using adhesive.

Visualization of the Orifice with Fiber Optics: The free end of each fiber was placed into a 38 mm diameter 3D printed disk in the same pattern as embedded in the probe. The disk is created to allow us to visualize what the probe is detecting (**Figure 1C**). The disk was attached to a tube which connected to the external computer webcam for live capture. The tube created a dark environment to reduce ambient light for better measurement of the light. A MATLAB script was written to capture live images in 3 second intervals. The images were converted to 8-bit grayscale ranging from 0 to 255; 0 being no light detected and 255 being the most intense light. The snapshots were later converted to a graphics interchange format (gif) and the gif would act as a live stream of the probe visualization. The greyscale values of a fixed area from each fiber (**Figure 1D**) were analyzed for average and maximum pixel intensity on ImageJ (National Institutes of Health, Bethesda, MD).

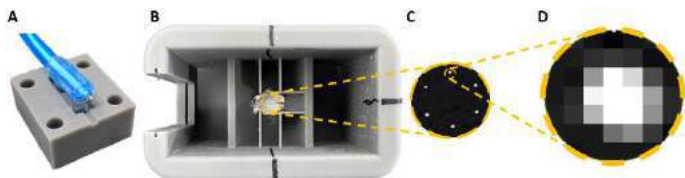


Figure 1. (A) Silicone probe in half of the 3D printed cast with 6 fiber optic wires embedded. The dark blue cables are the fibers, and the gray material is half of the mold cast. (B) Test chamber with endograft material glued over hole opening. (C) Visualization of the infrared light with the probe tip over the center of the opening from the MATLAB code. (D) Fixed area created over an individual fiber for intensity measurement using ImageJ.

RESULTS

The initial prototype successfully detected the orifice within air and blood. When testing in air, the light was transmitted through the fibers and all six fibers detected a maximum pixel brightness value of 255 meaning the artery was successfully detected (**Figure 2B**). The probe was also able to detect light in blood; however, the testing in blood resulted in a statistically significant drop in mean of average intensity from each fiber when compared to air (99.1 ± 10.5 vs. 37.6 ± 12.0 , $p < 0.0001$) (**Figure 2A**). The mean maximum intensity also experienced a significant drop from air to blood (255 ± 0.0 vs. 163.3 ± 71.2 , $p < 0.0346$) (**Figure 2B**). The sweep over the orifice indicated that

the probe could detect edges of the opening. In both air and blood, the feedback was void of an infrared signal when the probe was not over the orifice.

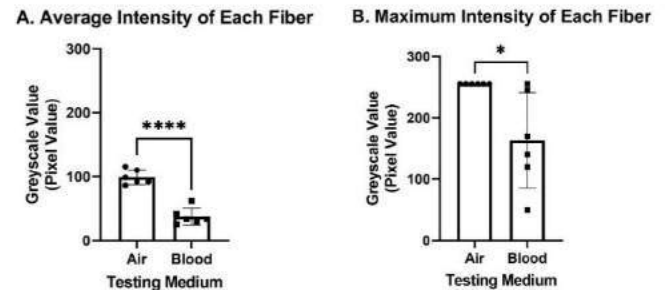


Figure 2. (A) Comparison of the average intensity emitted in the fixed area by each of the six fibers in air and in blood (**** indicates a $p < 0.0001$). (B) Comparison of the maximum intensity visualized from each fiber in air and in blood (* indicates a $p \leq 0.05$).

DISCUSSION

This study revealed that using fiber optics to find a point light source is a viable method of detecting a visceral arterial orifice in both air and blood through the endograft material. This approach highlights the potential for visceral artery detection that could be applied to the development of an ISF device. However, several steps still need to be taken until a clinically viable product can be developed. Future studies will include implementing more fiber optics, determining the feasibility of mechanical fenestration by puncturing the endograft material with a needle once the opening is seen with the fiber optics and creating an *in vitro* AAA phantom model with a pulsatile flow loop and deploying our prototype in the phantom model.

Current methods of ISF are limited; however, several cases have been reported using a mechanical needle, laser, or radiofrequency for fenestration [7]. Shu et al. reported midterm results of an adjustable puncture device used for ISF in thoracic endovascular aortic repair (TEVAR). In this study, several cases using a steerable sheath with an adjustable puncture needle were analyzed. The report found that the adjustable puncture needle demonstrated high technical success with low complications. This study highlighted the successful preservation of aortic arch branches in TEVAR cases and similar methods can be applied to visceral arteries of AAA cases [8].

There are several limitations to this work that need to be acknowledged. The test bench includes a 6 mm hole to act as the artery opening, which is on the larger end of a typical human visceral artery. The test bench also utilizes guide rails that were useful in locating the opening when submerged in blood.

ACKNOWLEDGEMENTS

We would like to thank the Michael G. Wells Pitch Competition hosted by the Innovation Institute at the University of Pittsburgh and grant #NIH R21 HL157646 grant for funding this work.

REFERENCES

- [1] Vorp, D., *J. Biomech*, **40**(9), 1887-1902, 2007.
- [2] Greenhalgh, RM., *THE LANCET*, **364**(9437), 843-848, 2004.
- [3] Li, Y., et al., *Scientific Reports*, **6**(1), 1-12, 2016.
- [4] Cross, J., et al., *J. British Surgery*, **99**(2), 152-159, 2012.
- [5] Swerdlow, N.J., W.W. Wu, and M.L. Schermerhorn, *Circulation research*, **124**(4), 647-661, 2019.
- [6] Katsargyris, A., et al., *E.U. J. Vascular Endovascular Surgery*, **60**(1), 44-48, 2020.
- [7] Glorion, M., et al., *E.U. J. Vascular Endovascular Surgery*, **52**(6), 787-800, 2016.
- [8] Shu, Xiaolong, et al., *E.U. J. Vascular Endovascular Surgery*, **63**(1), 43-51, 2022.

A REVIEW OF THE STATE OF SOFT TISSUE MATERIAL PROPERTY DATA FOR HUMAN BODY MODELING

Justin Scott (1), Nicole Arnold (1), Tamara Reid Bush (1)

(1) Department of Mechanical Engineering, Michigan State University, East Lansing, MI, USA

INTRODUCTION

Finite element (FE) models evaluating internal stresses and strains in the human body's soft tissues are dependent upon realistic soft tissue property inputs. Studies showed that disparities in material properties by less than an order of magnitude can change tissue stresses and strains by up to 70% [1]. Because all soft tissues have a range of reported properties, researchers have described guidelines for using tissue properties in biomechanical models, including sensitivity, verification, and validation studies, allowing for streamlined communication of models' results and their uncertainties [2], [3]. Ideally, personalized data would be used for all human body models, but there are numerous challenges associated with doing so. Recently, two researchers conducted studies in clinical settings to determine personalized tissue properties [4], [5]. Yet, the application of these methods were limited to case studies or small numbers of participants and few body regions.

Several factors have been shown to affect the values of reported material properties. Among the sample or participant characteristics that affect properties are the tissue being *in vivo* or *ex vivo*, from humans or animals, the body region tested, body position, and whether or not participants had disabilities [6]–[8]. Consideration for the experimental setup also has to be given because several types of experimental methods were used to collect load and deformation data from tissue samples, and multiple definitions have been used for load and deformation. Lastly, material model choice has an effect. Early experiments used linear elastic material models, while recent studies characterized tissue using non-linear or viscoelastic materials [9], [10]. Without a method to convert between sets of material property values, there is no standard material characterization for each tissue.

Thus, this work aimed to aggregate material properties reported for muscle, fat, skin, and lumped tissue to categorize them by the source of the sample or participant population, the methods used to measure load and deformation, and material models used to characterize the tissues in an effort to compare and contrast reported results.

METHODS

The authors searched PubMed, Google Scholar, Science Direct, Elsevier, Taylor and Francis Group, Scientific Research, Springer Link, and the Wiley Online Library for studies that described the soft tissue property of both humans and animals. Keywords included in the search were “mechanical properties of human tissue”, “tissue parameters”, “material parameters”, “*in vivo* tissue properties of humans”, “*in vivo* tissue properties of animals”, “*ex vivo* tissue properties of humans”, and “*ex vivo* tissue properties of animals”. The authors found 77 papers to include in this review.

RESULTS

There were 15 studies that included tissue properties from *ex vivo* human tissue. 6 studies included data on muscle, 4 included data on fat, and 7 included data from skin samples. The muscle samples came from the leg, arm, shoulder, and back, while the fat samples were from the abdomen, heel pad, and leg, and skin data were collected from the forehead, arm, neck, back, and abdomen. Each study included a Young's modulus, shear modulus, ultimate stress or strength of the tissue, and/or isotropic material constants.

34 studies were found with data on *in vivo* soft tissue properties from humans. 15 studies included data from muscle, 1 study included data from fat, 12 studies included data from skin, and 8 studies included data from lumped tissues (defined as a homogeneous material of muscle, fat, and skin by lumping the parameters). Differences between the studies included the body region tested, number of participants, position of the body during testing, and whether or not the study included persons with disabilities. Muscle data were collected from the gastrocnemius, gracilis, sartorius, quadriceps, posterior thigh, heel pad of the foot, tibialis anterior, rectus femoris, buttocks, triceps surae, biceps brachii, flexor digitorum profundus, and brachialis. The body region from which the fat data were collected was unspecified. Skin data were collected from the arm, palm, back, shoulder, thigh, and calf.

Lumped tissue parameter data were collected from the buttocks, thighs, and legs. Body positions during these studies included the prone position, supine position, quadruped position, and seated position, while some studies did not report the position in which testing occurred. One study included data from the muscles of persons with disabilities, and one study included lumped soft tissue parameter data from persons with disabilities.

29 studies were found that included data from animals, 20 of which included *ex vivo* animal samples, while 9 included animals *in vivo*. 17 studies included data from the muscles of pigs, frogs, cows, rats, and rabbits. 4 studies included data from the fat of pigs, rats, and sheep. 8 studies included data from the skin of mice, pigs, cows, and rats. Muscle data were collected from the extensor digitorum longus, peroneus tertius, gluteus, semitendinosus, abdomen, tibialis anterior, gracilis, and pelvic and thoracic muscles. The fat samples were collected from the gluteal region, thighs, and legs. Skin samples were collected from the abdomen, posterior hindlimb, back, gluteus, legs, and shoulders.

Several deformation definitions were used in determining material properties with various measurement approaches. Definitions included deflection, strain, stretch, and tensors like the right Cauchy-Green deformation tensor. Measurement methods could be generally described as either measuring internal tissue deformation or external deformation. For internal tissue deformation, techniques such as magnetic resonance imaging and ultrasound were used, while electronic sensors like linear potentiometers and digital calipers measured external deformation.

Material parameters reported from the studies investigating human tissues were determined by the material models used to describe them. 47 distinct relationships were used to determine material properties. Of them, linear viscoelastic models were used in 11 of the studies to describe muscle, fat, skin and bulk tissue. Hyperelastic and viscoelastic terms were used to create models for 6 studies. Purely hyperelastic models were used in 16 studies. 4 studies focused on investigating the differences between multiple material models describing human tissues.

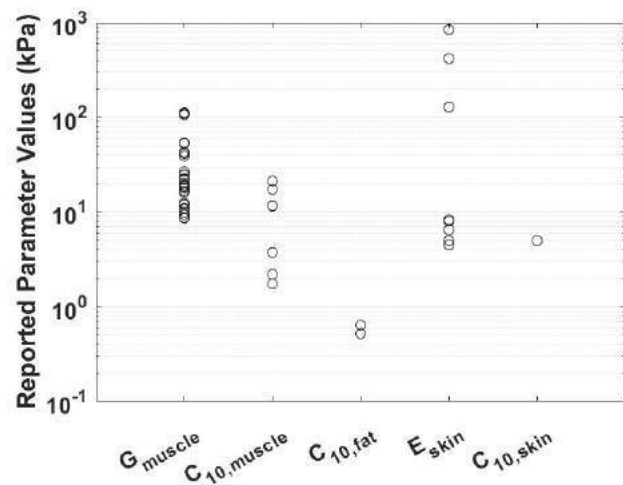


Figure 1. Semilog plot of the parameters reported for human muscle, fat, and skin *in vivo*. All C_{10} parameters are from Neo-Hookean models. The reported properties of muscle span over one order of magnitude, while the properties of skin span over two orders of magnitude.

DISCUSSION

The goal of this review was to collect material properties reported from experiments that studied the soft tissues and categorize them by their inclusion of human or animal data in *in vivo* or *ex vivo* settings, the

method of deformation measurements used, and the material model used, to compare and contrast the properties reported.

The studies showed that factors such as the body position, body region, inclusion or exclusion of persons with disabilities, and method of deformation measurement affect reported properties. As a result, the properties used in models should reflect the conditions of the model itself. For example, material properties from the buttocks in the seated position should be used for a model of the buttocks in the seated position. Inaccuracies in stress or strain predictions due to using inappropriate material properties may not be predictable because the values of material properties varied by up to two orders of magnitude. Examples of this phenomenon included the shear modulus of human muscle ranging from 8 kPa to 100 kPa and the *in vivo* Young's moduli of skin varying from 4.5 kPa to 850 kPa (Figure 1). Because differences within one order of magnitude affected strains by up to 70%, differences of two orders would likely affect strains even more [1]. Model choice is of further importance because there is no readily available method to convert parameters between material models, making comparisons between characterizations with different experimental factors difficult.

In addition to the other factors, whether data were collected *in vivo* or *ex vivo* also affected results. In the human forearm, Young's moduli of skin were at least 10 times larger than in *in vivo* studies (330-99,000 kPa versus 4.5-850 kPa). Because of the gaps between *in vivo* and *ex vivo* material properties, models using properties from the former would likely differ significantly from those using the latter. Whether the data came from *in vivo* or *ex vivo* sources is another factor that must be considered when deciding which material properties models use.

Characterizations of the material properties of soft tissue have grown in both sophistication and scope to describe more tissues from different sources in multiple loading conditions. Before human soft tissue material properties were reported, animal tissue properties were exclusively used in human body models. However, the prevalence of animal studies has decreased as human tissue data have become more widespread. The most recent tests have collected compressive tissue response data on *in vivo* humans, providing more appropriate data for modelers to use in models with compression loads as compared to tensile tests. The progress made in this field over the past several decades has assisted and will continue to assist in the creation of human body models with more realistic stress and strain predictions.

Yet, there are still areas that still need to be explored further. One of these areas is the characterization of soft tissues from persons with disabilities. Though some studies investigated the soft tissue properties of the lower limbs of persons with disabilities, the material properties of other body regions have yet to be explored at all. Until they are, models of persons with disabilities will likely lead to unrealistic predictions of tissue stress and strain.

ACKNOWLEDGEMENTS

This work was funded by National Science Foundation Grant CBET-1603646.

REFERENCES

- [1] Luboz, V. et al, *J Biomech*, 47:2231-2236, 2014.
- [2] Hicks, J.L. et al, *J Biomech Eng*, 137:1-24, 2015.
- [3] Oefner, C. et al, *Med Eng Phys*, 92:25-32, 2021.
- [4] Solav, D. et al, *IEEE Trans Biomed Eng*, 66:2740-2752, 2019.
- [5] Fougerson, P.Y. et al, *J Biomech Eng*, 148:1-8, 2020.
- [6] Moore, C.D. et al, *J Musc. Skel. Neur. Interactions*, 15:32-41, 2015.
- [7] Scott, J. et al, *J Biomech*, 120, 2021.
- [8] Scott, J. et al, *J Mech Behav Biomed Mater*, 110, 2020.
- [9] Maaß, H. and U. Kuhnappel, *Eur Cont Conf ECC*, 2465-2470, 1999.
- [10] Then, C. et al, *Tech. and Health Care*, 15:385-398, 2007.

DEVELOPMENT OF A SCHLEMM'S CANAL "INNER WALL ON A CHIP" FOR HIGH CONTENT BIOMECHANICAL SCREENING

Seyed Mohammad Siadat (1), Jacques A. Bertrand (2), Babak N. Safa (1), Darryl R. Overby (2),
W. Daniel Stamer (3,4), C. Ross Ethier (1)

- (1) Biomedical Engineering, Georgia Institute of Technology/Emory University, Atlanta, GA, United States
(2) Bioengineering, Imperial College London, London, United Kingdom
(3) Ophthalmology, Duke University, Durham, NC, United States
(4) Biomedical Engineering, Duke University, Durham, NC, United States

INTRODUCTION

Glaucoma is the leading global cause of irreversible blindness [1]. Although glaucoma can occur at any level of intraocular pressure (IOP), elevated IOP is a primary risk factor, and is the only treatable risk factor [2]. IOP is largely determined by the resistance to aqueous humor flow generated by the tissues of the conventional outflow pathway, specifically the trabecular meshwork and the inner wall of Schlemm's canal (SC) [3]. In particular, inner wall SC cells play a key role in homeostatic control mechanisms that maintain IOP within a target range [4].

All conventional outflow of aqueous humor crosses inner wall SC cells through micron-sized pores [5]. There are two pore types: trans-cellular "I" pores and paracellular "B" pores [6]. These pores have different sizes and dependencies on IOP, but both may facilitate aqueous humor drainage. Mechanical stretch triggers pore formation [7], and SC endothelium is exposed to significant stretch due to the pressure drop across the inner wall [8], most obviously during giant vacuole formation. It is important to note that pores are not tears or ruptures in the cell, but membrane-delineated structures that are actively formed by SC cells.

The discovery of SC-active agents that exploit and enhance native processes controlling SC hydraulic conductivity could offer novel strategies for IOP control, yet such discovery is impeded by poor assays. Here, we aim to develop a high content *in vitro* mechanobiological assay to assess I-pore formation in subconfluent SC cells exposed to focal stretch delivered by ferromagnetic microspheres. We focus on I-pores since SC cells do not form tight intercellular junctions *in vitro*; thus, methods for high-content screening of B-pores are more challenging.

METHODS

Glass substrates (NuncTM Lab-TekTM chamber slide system) were coated with 0.5 mg/mL biotinylated gelatin cross-linked with 1 unit/mL microbial transglutaminase. Carboxyl ferromagnetic particles (dia. ~5 μ m, Spherotech CFM-40-10) were seeded onto the substrate, followed

by seeding with primary human SC cells (two normal SC cell strains: nSC89 and nSC82 and one glaucomatous cell strain: gSC57; all passage 5 or 6). Pores were detected using fluorescently labeled tracers [9]. Specifically, after 5-7 h of incubation, a first tracer (streptavidin, Alexa FluorTM 488 conjugate) was added to the media for 5 min. The first tracer was then washed away, and a second tracer (streptavidin, Alexa FluorTM 647 conjugate) was added for 20 min, during which time particles were exposed to a magnetic force created by neodymium N52 magnets (D38-N52, K&J Magnetics, Inc.) placed ~0.20 mm (high force; estimated ~1138 pN on each particle), ~0.55 mm (medium force; ~785 pN), or ~0.91 mm (low force; ~435 pN) above cells. The magnets attracted particles to create a local cellular stretch in the basal-to-apical direction in seeded SC cells. In some wells, magnets were not placed above cells as a negative (no force) control.

Cells were fixed, labeled with DAPI and Alexa FluorTM 555 phalloidin, imaged, and analyzed by counting punctate tracer signals that colocalized with particles under cells. The number and area of labelled substrate under I-pores were quantified using custom MATLAB code. I-pores were categorized as Type I (first tracer, i.e., present without magnetic force/stretching) or Type II (second tracer, i.e., present with magnetic force/stretching). We then computed the number and area of Type II pores minus Type I pores (normalized by the number of particles under cells) as an indirect measure of porosity. The number of cells and particles analyzed for each cell strain were: nSC89: 4 wells per force condition; 404 ± 78 cells/well, 106 ± 51 particle/well; nSC82: 4 wells; 71 ± 19 cells/well, 115 ± 39 particle/well; and gSC57: 8 wells; 203 ± 51 cells/well, 130 ± 39 particle/well. Two-way ANOVAs were performed with factors: (i) force level (control, low, medium, high); and (ii) disease state of the cell strains (normal, glaucomatous). Outcome measures were the number and the area of detected pores. When ANOVA indicated a significant factor effect, outcomes were compared pairwise using Tukey's honest significant difference (HSD) test for multiple comparisons. The statistical significance threshold was taken as 0.05.

RESULTS

The fluorescent tracers reached and bound to the substrate at locations not covered by the cells, i.e., surrounding subconfluent cells but also at I-pore sites (Figure 1). Actin microstructure (Figure 1B) was intact at the location of pores detected only by the first tracer (Figure 1C) but was disrupted at some pore locations detected by the second tracer (Figure 1D).

Even in the control wells, where no magnetic force was applied, some pores formed over the microbeads, indicating that the mere presence of the magnetic microbeads under the SC cells was sufficient to induce some I-pore formation (Figure 2). Two-way ANOVA indicated that force significantly affected the number of pores ($F(3,55) = 3.62$, $p = 0.019$); however, the number of pores was not affected by the disease state of the cell strains ($F(1,55) = 0.61$, $p = 0.439$). There was no interaction effect between force and disease ($F(3,55) = 0.92$, $p = 0.439$). Similarly, when considering pore area, force was a significant factor ($F(3,55) = 3.95$, $p = 0.013$), whereas disease state was not ($F(1,55) = 0.01$, $p = 0.906$), and again, no interaction effect was observed ($F(3,55) = 0.43$, $p = 0.733$).

DISCUSSION

Our mechanobiological assay allows assessment of I-pores in SC cells using automated (masked) image processing. In this preliminary study, we showed a correlation between focal magnetically-delivered force and pore formation, with more pores and greater pore area in normal SC cell strains in the high force condition vs. the no force condition. Some pores formed spontaneously (without magnets, i.e., Type I)

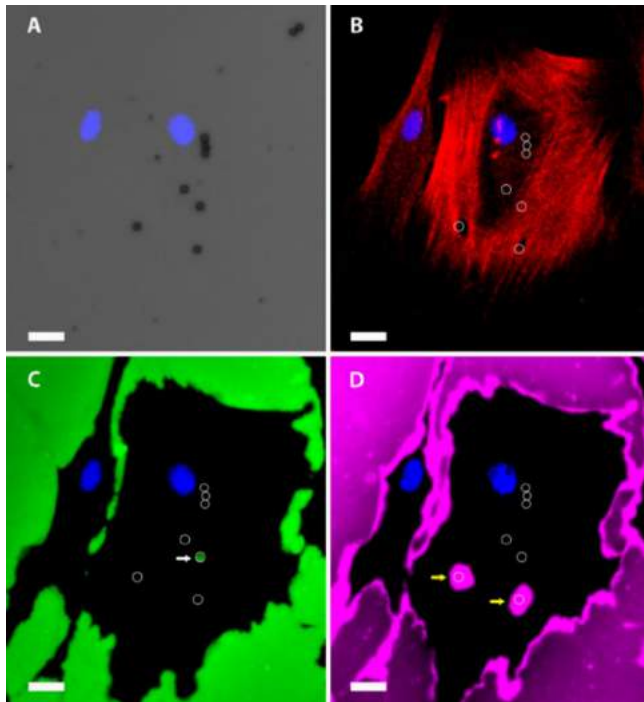


Figure 1: Representative fluorescent micrographs showing I-pores detected by the fluorescent assay colocalizing with magnetic particles under SC cells. (A) Cell nuclei (blue) overlain by brightfield image showing particles (dark spots). Particles are outlined by white circles in panels B-D. (B) F-actin labeling (phalloidin; red). (C) The first tracer (green). White arrow: Type I pore. (D) The second tracer (magenta). Yellow arrows: Type II pores. Note the disruption of the actin network in panel B at the position of Type II pores. Scale bars = 20 μm .

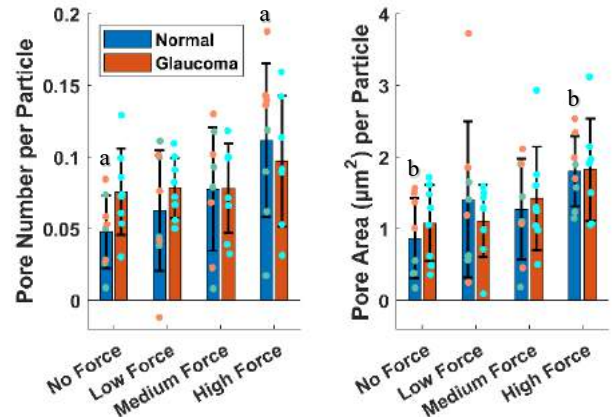


Figure 2: The number (left) and the area (right) of Type II pores minus Type I pores, normalized by the number of particles under subconfluent SC cells. Blue bars indicate normal SC cell strains (nSC89 and nSC82 shown with green and orange points, respectively), while red bars indicate glaucomatous SC cells (gSC57). Data shown as mean \pm standard deviations between wells. ^a and ^b signify differences at $p < 0.05$ by post hoc Tukey's HSD test.

through unclear mechanisms; we hypothesize that intracellular tension within SC cells adhered to the underlying gelatin substrate may cause local stretch over microspheres sufficient to trigger pore formation in some cases.

In glaucomatous cells, I-pores were also detected, and pore number and area showed an increasing trend with applied force by ANOVA; however, pairwise differences between force levels did not reach statistical significance (post hoc Tukey's HSD test, $p > 0.05$). Although based on only a single cell strain, this is consistent with the hypothesis that glaucomatous SC cells are less responsive to local force, perhaps due to their increased cell stiffness [10].

Disruption of actin microstructure only at some Type II pore locations suggests that I-pores form dynamically in our assay. All pores detected only with the first tracer and some pores detected by the second tracer were "closed" at the time of cell fixation, i.e. disruption of actin microstructure was not evident. More complete morphological studies of I-pores formed in this assay are needed and are ongoing.

Significant intra-assay variability was problematic, reduced statistical power, and must be addressed to improve the assay. There was also appreciable inter-well variability in outcomes, perhaps related to the fact that pores were relatively rare, with typically less than 0.1 pore/particle forming (Figure 2). Nonetheless, this assay shows significant potential for screening of agents that may eventually help control IOP in glaucoma patients.

ACKNOWLEDGEMENTS

BrightFocus Foundation CG2020001; NIH 5R21EY033142-02; Georgia Research Alliance (CRE).

REFERENCES

- [1] Heijl, A., *et al.*, *Arch. Ophthalmol.*, 120.10:1268-1279, 2002.
- [2] Weinreb, R., *et al.*, *The Lancet*, 363.9422:1711-1720, 2004.
- [3] Overby, D., *et al.*, *Exp. Eye Res.*, 88.4:656-670, 2009.
- [4] Stamer, W.D., *et al.*, *IOVS*, 52.13:9438-9444, 2011.
- [5] Bill, A., *et al.*, *Acta Ophthalmologica*, 50.3:295-320, 1972.
- [6] Ethier, C.R., *et al.*, *IOVS*, 39.11:2041-2048, 1998.
- [7] Braakman, S., *et al.*, *Exp. Eye Res.*, 127:224-235, 2014.
- [8] Ethier, C.R., *Exp. Eye Res.*, 74.2:161-172, 2002.
- [9] Braakman, S., (Thesis) *Imperial College London*, 2014.
- [10] Overby, D., *et al.*, *PNAS*, 111.38:13876-13881, 2014.

PROTEOMIC CHARACTERIZATION AND METABOLIC LABELING OF A FIBRIN-BASED IN VITRO WOUND HEALING MODEL

Dalton Miles (1), Tyler Tuttle (2), Julian Jimenez (3), Yifan Guo (4), Adrian Buganza-Tepole (3,4), Sarah Calve (2,3)

- (1) Department of Chemical and Biological Engineering, University of Colorado Boulder, Boulder, CO, USA
(2) Paul M. Rady Department of Mechanical Engineering, University of Colorado, Boulder, Boulder, CO, USA
(3) Weldon School of Biomedical Engineering, Purdue University, West Lafayette, IN, USA
(4) School of Mechanical Engineering, Purdue University, West Lafayette, IN, USA

INTRODUCTION

Understanding how extracellular matrix (ECM) properties change over time during the growth and remodeling phase of wound healing has been a goal of biomechanics and engineering research for decades. In particular, understanding the mechanics of heterogeneous materials, such as those found at the interface of healing dermal wounds and healthy tissue, is essential for designing materials that can modulate cell behavior in these environments.[1] In skin, post-wounding, a protein known as fibrinogen is polymerized into a fibrin clot via thrombin cleavage.[2] This fibrin clot provides a temporary matrix that cells use to infiltrate the wound and deposit more permanent ECM.[2] Additionally, fibroblasts and other cell types can differentiate into myofibroblasts and exert contractile forces on the wound to further alter the surrounding matrix.[3] Both behaviors are essential for wound closure, as well as growth and remodeling; therefore, understanding how changes in material properties and mechanical forces interact with these processes is essential for accurately modeling wounds.

Previous work by our lab established parameters for a multiscale model of fibrin gel mechanics with different concentration inclusions (Figure 1).[4] However, multiscale models that capture changes in tissue mechanics during wound healing due to cellular behaviors are lacking. To address this gap, we are developing a model to quantify cellular ECM production cultured in protein gels *in vitro* using a form of metabolic labeling known as bio-orthogonal non-canonical amino acid tagging (BONCAT).[5] Using this technique, newly synthesized proteins (NSPs) can be labeled with an azide moiety that can be reacted with alkynes via a click chemistry reaction, including affinity tags for enrichment of NSPs or fluorescent tags for imaging (FUNCAT).[6] Combining proteomics with BONCAT will facilitate computational modeling of cellular contributions to wound material properties.

METHODS

Fibrin concentrations of 2 or 4 mg/mL were prepared via combining a 1:10 ratio of human fibrinogen to Alexa Fluor (AF) 488 or

AF546 conjugated human fibrinogen with CaCl₂ to a final concentration of 6 mM and 0.002 U thrombin per mg fibrinogen in either Dulbecco's Modified Eagles Medium (DMEM) with cells or PBS. Gels used to measure fibrin material properties were formed between two porous polyethylene blocks that were glued to laser cut polyethylene terephthalate frames using Loctite Super Glue. To ensure consistent geometry, these gels were polymerized in 3D printed 2.5 × 6.6 × 0.75 mm ($w \times l \times h$) molds.

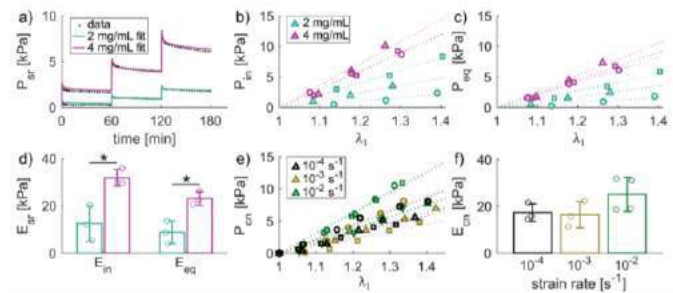


Figure 1: (A) Stress-time response of 2 and 4 mg/mL fibrin gels. (B) Initial stress versus strain. (C) Equilibrium stress versus strain. (D) Tangent modulus from (B) and (C). (E) Stress-strain response of 2 mg/mL fibrin gels with different strain rates. (F) Tangent modulus from (E). Figure from [4].

Two 50 × 50 × 200 μm ($w \times l \times h$) fiducial markers were photobleached on the surface of the fibrin gels 200 μm apart using a Leica STELLARIS 5 confocal microscope and a 10× water-immersible objective. A FemtoTools micromanipulator system was used to apply unidirectional tensile deformations to the fibrin gels with either a custom slider assembly (without a microforce sensor) to observe strain-dependent changes in fibrin network organization via fluorescent

confocal microscopy or a custom floating-platform mounting system with a microforce sensor to measure stress relaxation of the fibrin gels. Collected images were analyzed using a custom tracking script in MATLAB combined with thresholding functions and the OrientationJ plug-in in FIJI. Further experimental details for how parameters were collected and analyzed can be found in [4].

For shotgun proteomics, NIH 3T3 cells were cultured in 2 mg/mL fibrin gels created in 15 μ L Ibidi angiogenesis well plates for 4 days. Samples were then removed from wells with forceps and reduced, alkylated, and digested following a previously published protocol from our lab.[6] Peptides were detected using a Q-Exactive HF-X mass spectrometer (Thermo Scientific). RAW files were searched against the UniProt Mus musculus database supplemented with human sequences for fibrinogen α , β , and γ chains using MaxQuant v.1.6.14.0. Two missed cleavages were allowed per peptide and peptide and protein identifications were filtered at a 1% false discovery rate, determined by comparison to a reverse decoy database generated from the Mus musculus database. Results were further filtered to exclude proteins that were identified by only one unique or razor peptide across all samples, labeled as a potential contaminant by MaxQuant, or identified in only one replicate. Raw intensities were used to determine the percentage of total raw intensity to facilitate intrasample relative quantification. Data analysis was performed in Excel and Prism.

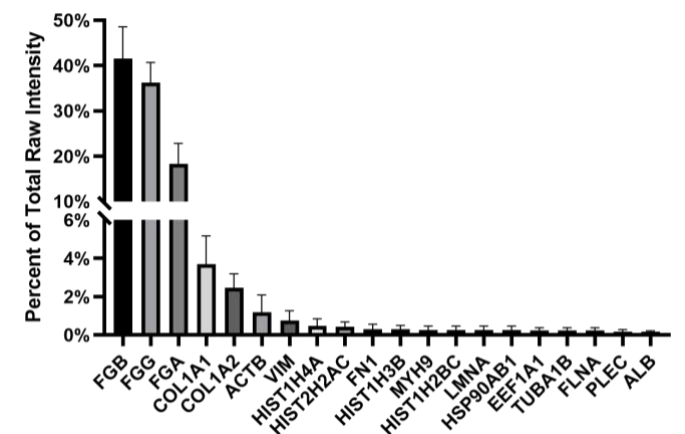


Figure 2: 30 most abundant proteins synthesized by NIH 3T3 cells within fibrin gels relative to fibrin.

For fluorescent imaging of NSPs, NIH 3T3 cells were cultured in 2 mg/mL fibrin gels for 2 days with methionine-free DMEM containing 10% fetal bovine serum, 1% antibiotic/antimycotic, and supplemented with either 20 mM methionine or azidohomoalanine (Aha). Gels were fixed using 4% paraformaldehyde and stained with DAPI (cell nuclei), wheat germ agglutinin-AF555 (glycosylated proteins), and dibenzocyclooctyne (DBCO)-AF647 (azides). Gels were imaged using a STELLARIS 5 confocal microscope and a 10 \times water-immersible objective. Images were processed in FIJI to increase contrast.

RESULTS

Using shotgun proteomics, we identified ECM proteins deposited by NIH 3T3 cells cultured in fibrin gels, including type I collagen α 1 chain (COL1A1), type I collagen α 2 chain (COL1A2), and fibronectin (FN1) (Figure 2). However, because fibrinogen peptides contributed >70% of the total raw intensity signal collected in each sample, lower abundance ECM proteins could not be identified using this technique. Therefore, BONCAT was investigated as a technique to allow separation of NSPs including ECM from the surrounding material as has been previously described and performed in our lab.[6]

The incorporation of the non-canonical amino acid Aha into NSPs by NIH 3T3 cells in fibrin gels was visualized using fluorescent confocal microscopy (Figure 3). Fluorescent signal was found exclusively in cultures containing Aha. There did not appear to be significant reaction between the DBCO fluorophore and the fibrin gel.

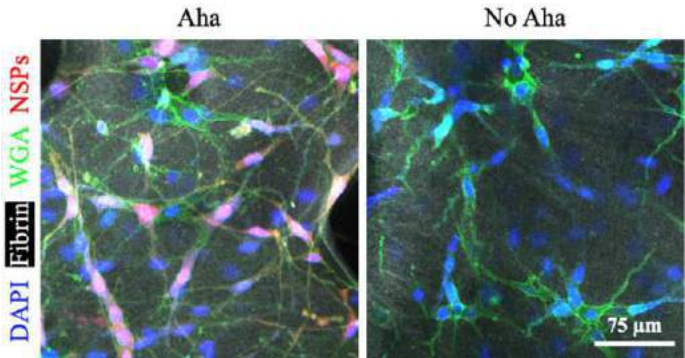


Figure 3: FUNCAT-based visualization of NSPs from NIH 3T3 cells embedded within fibrin gels.

DISCUSSION

While ECM proteins were identified through processing of whole fibrin gels containing cells, the high amount of fibrin peptides from the gel prevented the identification of ECM that 3T3 cells made in lower quantities. To better identify and quantify the ECM directly synthesized by the 3T3 cells, we investigated the utility of BONCAT in protein gels. This has previously been utilized as a means of studying ECM deposition dynamics of cells cultured in non-protein hydrogels but has not yet been used for proteomics of cells cultured in protein-based gel constructs. [6,7]

Fluorescently-labeled ECM was not readily apparent in the collected images but we expect that culturing longer than 2 days will be sufficient to label and visualize ECM NSPs, based on previous hydrogel studies.[6,7] Overall, our findings indicate that more comprehensive proteomics of ECM produced by cells cultured in protein cells will require enrichment techniques such as BONCAT. This technique is effective at labeling proteins in protein gels and will be used to collect more complete proteomics data quantifying ECM production by cells in an *in vitro* wound model. This data will be essential for informing multiscale computational models of wounds that account for cellular behaviors including ECM deposition. This technique can likely be extended beyond fibrin gels to analyze how changing composition due to cellular behaviors alters the mechanical properties of other protein-based constructs that better mimic biological environments.

ACKNOWLEDGEMENTS

This work is supported by NSF 1911346-CMMI and NIH DP2 AT009833 to SC. The authors would like to thank Dr. Robert MacCurdy and Brandon Hayes for assistance with 3D printing gel molds, and the Central Analytical Mass Spectrometry Facility and W.M. Keck Foundation Proteomics Resource for their assistance with mass spectrometry proteomics experiments.

REFERENCES

- [1] Guimarães, CF et al., *Nat Rev Mat*, 5:351-370, 2020.
- [2] Laurens, N et al., *J Thrombosis and Haemostasis*, 4:932-939, 2006.
- [3] Hinz, B et al., *J Invest Dermatol*, 127:526-537, 2007.
- [4] Jimenez, J and Tuttle, T et al., under review at *Acta Biomaterialia*, posted online at BioRxiv: BIORXIV/2022/519227.
- [5] Dieterich, D et al., *PNAS*, 103:9482-9487, 2006.
- [6] Loebel, C et al., *Nat Protoc.*, 17:618-648, 2022.
- [7] Loebel, C et al., *Adv Func Mater*, 30:1909802, 2020.

AN EXPLANT-IN-A-CHIP PERFUSION MODEL FOR *EX VIVO* PRESERVATION OF TISSUE VIABILITY AND FUNCTION WITH APPLICATIONS FOR PERSONALISED MEDICINE IN CANCER

Evangelia E. Zeringa (1), Foivos Chatzidimitriou (1), Ester Reina-Torres (1), Larry O'Connell (1), Beatrice-Cristina Bezdadea (1), Alexandria Mitchell (2), Paula Cunnea (2), Christina Fotopoulou (2), Olivier Pardo (2), Joseph van Batenburg-Sherwood (1), Iain A. McNeish (2), Darryl R. Overby (1)

- (1) Department of Bioengineering, Imperial College, London, United Kingdom
(2) Department of Surgery and Cancer, Imperial College, London, United Kingdom

INTRODUCTION

One of the main challenges across life sciences is the lack of pre-clinical models that mimic the complexity of the tissue microenvironment, which consequently limits the translatability to medical applications. Some of the most promising tools to capture tissue heterogeneity *ex vivo* are explant-based models, because these maintain the 3D architecture and cell diversity found within the native tissue microenvironment. However, larger explants that capture a significant portion of the microenvironment rapidly die in static culture due to insufficient oxygen and nutrient delivery by diffusion to the explant core [1]. To overcome the limitations of diffusion-dominated transport, we developed a fluidic platform having a microchannel that holds the explant within a specially designed constriction (Figure 1). The shape of the constriction is designed to achieve “self-sealing” between the explant and channel walls [2]. It is hypothesised that this self-sealing eliminates flow around the explant (known as peri-fusion) and thereby drives advective flow and nutrient delivery through the explant (perfusion), which preserves the viability and function of large (>1 mm) explants, ideally over several days for *ex vivo* drug screening and analysis.

METHODS

To investigate the effectiveness of tissue self-sealing, we examined the flow-pressure relationship of 2 mm mouse liver explants within the microchannel using an actuated reservoir, a pressure sensor and flow sensor. To improve self-sealing, we added a poly-lysine (PLL) adhesive coating to the microchannel wall. We measured tissue viability based on ATP levels and efficacy of perfusion based on the fluorescent

intensity of particles in sample lysates following perfusion in platforms, with and without the adhesive coating. In order to fully validate the platform and its use in *ex vivo* specimen perfusion, a peri-fusion platform with a cylindrical chamber that allows flow around the explant was used as a control case (Figure 1). Tissue viability via measurement of ATP levels was compared between fresh, perfused explants, perfused and statically cultured mouse liver tissue samples after 3 and 6 days. To assess the quality of intra-vasculature perfusion, we perfused mouse liver tissue explants with a fluorescently labelled breast cancer cell line (MDA-MB-231). To explore the potential of this platform in cancer-related drug assays, mouse and human omental tumour specimens from disseminated ovarian cancer were also perfused for 2 days and stained with haematoxylin and eosin (H&E). Immunohistochemistry stainings for WT1 (ovarian tumour marker), cleaved caspase-3 (CC3 – apoptosis marker) and Ki67 (proliferation marker) were also performed.

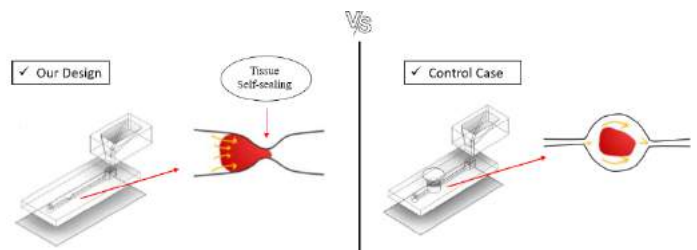


Figure 1: Schematic visualization of the fluidic platform with constriction for perfusion of explants and the control platform used for peri-fusion of explants.

RESULTS

The hydraulic resistance of mouse liver explants when they were properly loaded within the walls of the constriction was on the order of 2 mmHg/nl/min consistent with predictions from Darcy’s law based on reported values of liver permeability [3]. In contrast, resistance measures lower than 0.0005 mmHg/nl/min were expected when liver explants were not properly sealed within the constriction or when there was a functional peri-fusion route. Viability markers were elevated in liver explants perfused in PLL-coated microchannels, having an average ATP level of 167 ± 72 pM/mg protein compared to 92 ± 57 pM/mg protein in uncoated microchannels ($p<0.05$, $n=3$ samples each). The average quantity of fluorescent tracer microparticles recovered from perfused explants was higher with the PLL coating versus without, but this difference did not achieve statistical significance ($p>0.05$, $n=3$). ATP levels were higher in perfused relative to peri-fused and static cultured samples with 137 ± 77 , 52 ± 26 and 42 ± 22 pM, respectively after 3 days and 72 ± 24 , 43 ± 21 and 22 ± 16 pM, respectively after 6 days, but were significantly less than fresh samples with 835 ± 124 pM ($p<0.0001$, $n=3$). Infused red fluorescently labelled MDA-MB-231 breast cancer cells localised with the vascular network within the explant, identified based on GFP expression in endothelial cells (Figure 2). The H&E staining depicted tissue structure and WT1 enabled the identification of tumour regions for ovarian cancer. Perfused mouse omental tumour specimens exhibited lower levels of CC3 and higher levels of Ki67 compared to the peri-fused and statically cultured explants (Figure 3.A). Similarly, human omentum tumour explants showed reduced CC3 and preserved histology after 2 days of perfusion versus peri-fusion (Figure 3.B).

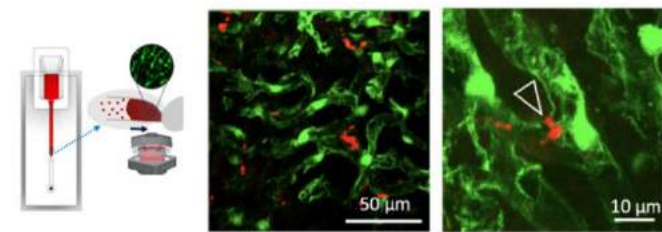


Figure 2: Confocal imaging on cryosections of red fluorescently tagged MDA-MB-231 breast cancer cells perfused in the green vasculature of liver tissue from Tie2-GFP mouse.

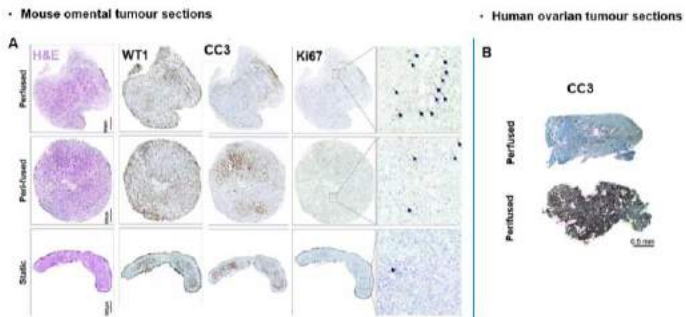


Figure 3: A. H&E, WT1, CC3, and Ki67 stainings on mouse omental tumour sections for three different culture conditions (perfusion, peri-fusion and static culture) after 2 days. B. CC3 staining on human omentum tumour sections for two different culture conditions (perfusion, peri-fusion) after 2 days.

DISCUSSION

The quality of self-sealing of the tissue explant within the constriction plays a critical role by limiting peri-fusion (i.e., flow around the explant) and driving per-fusion (i.e., flow through the explant). The significantly higher values of hydraulic resistance when explants were properly seated within the constriction demonstrate effective self-sealing and minimisation of peri-fusion. The improved viability and greater tracer retention with perfusion, which may be enhanced further by coating the microchannel with PLL, reveals that perfusion achieves effective nutrient delivery to the explant core necessary to support viability. The developed platform facilitates the preservation of viability of ex vivo explants over several days. Future work to extend this platform to human tumour specimens will be performed for *ex vivo* drug screening and analysis.

ACKNOWLEDGEMENTS

We acknowledge funding support for a PhD studentship to Evangelia E. Zeringa from the Imperial-CRUK Convergence Science Centre and grant support from CRUK DRCMDP-May21\100013. We also acknowledge the support provided by the technical staff from the Department of Bioengineering and Experimental Cancer Medicine Centre (ECMC), Department of Surgery and Cancer, Imperial College. Human tumour samples were provided by the Imperial College Healthcare Tissue & Biobank. Other investigators may have received samples from these same tissues. The research was supported by the National Institute for Health Research (NIHR) Biomedical Research Centre at Imperial College Healthcare NHS Trust and Imperial College London.

REFERENCES

1. Helmlinger, G., et al., *Nature medicine*, **3**(2): p. 177-182, 1997.
2. Overby, D.R., et al. *WIPO*, WO 2021/185873.
3. Levick, J.R., *Q J Exp Physiol*, **72**(4): p. 409-37, 1987.

COMPUTATIONAL MODELING OF ARTERIAL GROWTH AND REMODELING INCLUDING MECHANOSENSITIVE NOTCH SIGNALING

Jordy van Asten (1,2), Marcos Latorre (3), Cansu Karakaya (1,2), Frank Baaijens (1,2), Cecilia Sahlgren (1,2,4), Tommaso Ristori (1,2), Jay Humphrey (5), Sandra Loerakker (1,2)

(1) Department of Biomedical Engineering, Eindhoven University of Technology, The Netherlands
(2) Institute of Complex Molecular Systems, Eindhoven University of Technology, The Netherlands
(3) Center for Research and Innovation in Bioengineering, Universitat Politècnica de València, Spain
(4) Faculty of Science and Engineering, Biosciences, Åbo Akademi, Turku, Finland
(5) Department of Biomedical Engineering, Yale University, New Haven, CT, USA

INTRODUCTION

Arteries are known to grow and remodel in response to mechanical stimuli to maintain mechanical homeostasis [1]. This process has been captured in various computational models [2,3]. Notwithstanding the valuable insights gained by these models, their approach has been predominantly phenomenological, ignoring the complex cellular mechanisms underlying growth and remodeling. As such, these models do not allow for the investigation of pathological mutations or targeted interventions involving these cellular mechanisms. To overcome this, cell signaling models can be coupled to growth and remodeling models to obtain a more mechanistic understanding of arterial growth and remodeling [4,5] and optimize and inspire medical therapies.

One of the key signaling pathways in vascular development and homeostasis is the Notch signaling pathway in vascular smooth muscle cells [6]. This pathway involves the interactions between membrane-bound Jagged or Delta-like ligands and Notch receptors of neighboring cells. Numerous studies have indicated a strong influence of Notch signaling on smooth muscle cells behavior, including growth and remodeling [7]. Moreover, Notch has been identified as mechanosensitive, as it is affected by the strains experienced by smooth muscle cells [8,9]. Together, this makes Notch a strong candidate to be an important player in mechano-regulated arterial growth and remodeling.

Here, we developed a multiscale computational framework (Fig. 1) to gain a deeper understanding of the role of Notch and Notch interventions in mechano-regulated growth and remodeling of arteries in response to hypertension.

METHODS

Our multiscale framework combines the widely adopted constrained mixture model for growth and remodeling [2,3] and a previously developed mechanosensitive Notch signaling model [9,10]. Briefly, the constrained mixture model captures the mechanics and

turnover of three structurally significant arterial constituents: collagen, smooth muscle, and elastin. The Notch model simulates interactions between receptors and ligands of the Notch pathway with a system of ordinary differential equations and accounted for the influence of smooth muscle strain on Notch signaling.

The coupling between these models is achieved as follows. The strains calculated in the constrained mixture model serve as input for the Notch model where they regulate the production of Notch receptors and Jagged ligands. In turn, the Notch activity predicted by the Notch model is assumed to regulate collagen synthesis and smooth muscle cell proliferation in the constrained mixture model as informed by in vitro data. In addition to this Notch contribution, a phenomenological contribution, capturing mechanisms other than Notch, is considered, controlling the production and removal of tissue constituents based on deviations in intramural stress and wall shear stress (Fig. 1).

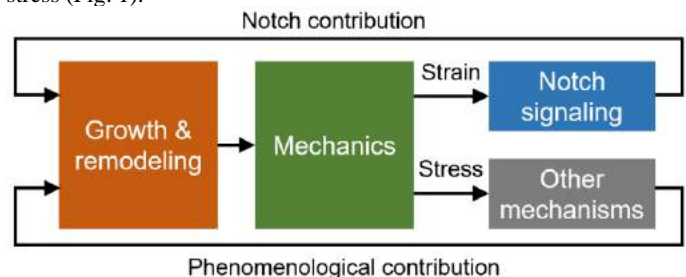


Figure 1: schematic overview of the multiscale model

RESULTS

We first showed that our multiscale framework combining Notch-regulated and phenomenologically driven growth and remodeling can capture in vivo arterial adaptation in hypertension (Fig. 2). We imposed a pressure profile similar to the one observed in a previous in vivo study

[11] (Fig. 2A). This increase in pressure caused an increase in both circumferential strain and intramural stress. The former resulted in a decrease in Notch activity, while the latter affected the phenomenological contribution to growth and remodeling. Combined, these mechanisms resulted in an increase in collagen and smooth muscle densities (Fig. 2B,C) and, consequently, a thickening of the arterial wall (Fig. 2D) aimed at restoring the stress and strain toward their homeostatic values. The model was able to capture changes in density and thickness similar to previous *in vivo* findings [11]. This was achieved by fitting the parameters of the phenomenological contribution, while the Notch parameters were based on our *in vitro* experiments. Thereby, we demonstrated that a combination of specific mechanistic and phenomenological stimuli can describe *in vivo* arterial adaptation. Our results further suggest that Notch may contribute to arterial thickening in hypertension primarily by inducing smooth muscle cell proliferation (Fig. 2C). Other mechanisms, here captured in the phenomenological contribution, are required to capture the full remodeling response (Fig. 2B,C), emphasizing the need to account for multiple mechanisms and pathways.

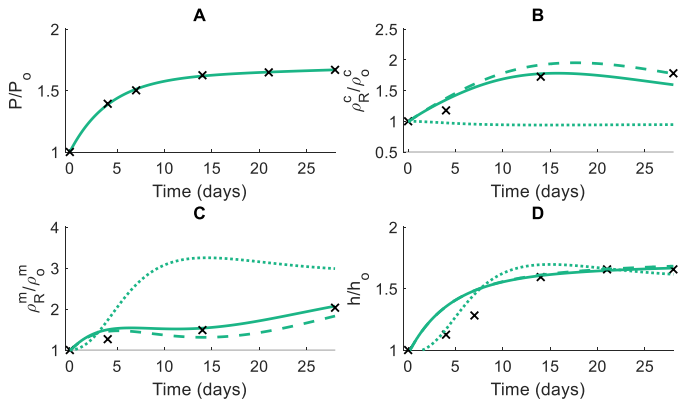


Figure 2: time courses of pressure (A), normalized mass densities of collagen (B) and smooth muscle (C) and wall thickness (D) under hypertension for the phenomenological, Notch, and combined models. Crosses represent *in vivo* data [11].

The inclusion of Notch as a mechanistic regulator of growth and remodeling enabled us to investigate the effects of interventions to Notch on the geometry and composition of hypertensive arteries. We simulated the introduction of either soluble or immobilized Jagged ligands to smooth muscle cells, common methods of Notch manipulation [12]. Our model predicted that soluble Jagged, assumed to inhibit Notch signaling, can decrease collagen density (Fig. 3B) and increase SMC proliferation (Fig. 3C) especially in the short term. Thickness was affected only marginally (Fig. 3D). In contrast, immobilized Jagged, assumed to enhance Notch activity, was predicted to increase collagen production (Fig. 3B) and lower SMC proliferation (Fig. 3C), again predominantly in the short term. A small increase in thickness was also observed (Fig. 3D). Together, these results suggest that Notch interventions can alter both arterial geometry and composition in hypertension.

DISCUSSION

Our multiscale computational framework provides a step forward in the development of more mechanistic descriptions of growth and remodeling by considering Notch signaling, a key mediator of vascular homeostasis. The adopted approach, combining a phenomenological and a mechanistic Notch contribution to regulate growth and

remodeling, enabled us to isolate and investigate the role of Notch. Our results indicate that a more detailed understanding of growth and remodeling may be gained by integrating individual pathways within phenomenological growth and remodeling models.

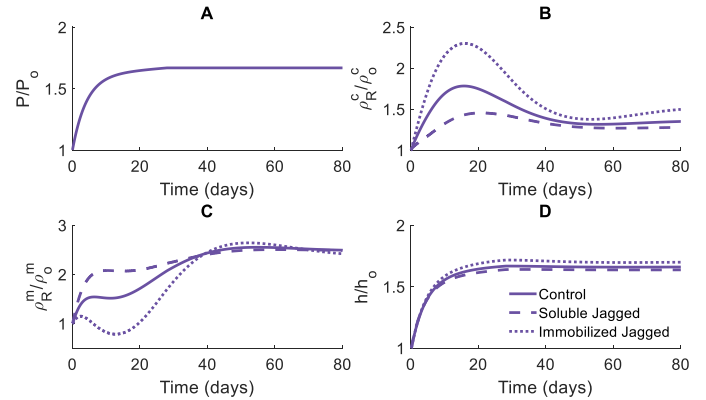


Figure 3: time courses of pressure (A), normalized collagen (B) and smooth muscle (C) mass densities and wall thickness (D) in hypertension with soluble and immobilized Jagged ligands.

By including a mechanistic Notch contribution, the model enabled the investigation of the consequences of Notch interventions for arterial growth and remodeling. Simulations predicted that soluble or immobilized Jagged ligands can be used to change arterial geometry and composition, especially in the short term. This may have promising applications in situations where it would be beneficial to (temporarily) control arterial growth and remodeling such as in vascular tissue engineering.

To further refine the model, future studies should focus on collecting more detailed, context-specific (*in vivo*) data on the effects of Notch signaling on arterial growth and remodeling. The inclusion of other relevant signaling pathways and their crosstalk with Notch should also be considered.

In conclusion, our model points at Notch mechanosensitivity as a key mechanism in arterial growth and remodeling, and it may provide a platform to efficiently optimize current methods in vascular tissue engineering and thereby accelerate clinical translation.

ACKNOWLEDGEMENTS

This project was funded by the European Research Council (ERC) under the European Union's Horizon 2020 research and innovation programme (Grant agreement No. 802967 and 771168) and by the Marie-Sklodowska-Curie Global Fellowship (grant number 846617).

REFERENCES

- [1] Humphrey JD et al., Hypertension, 52:195-200, 2008.
- [2] Humphrey, JD & Rajagopal, KR, Math Models Methods Appl Sci, 12(3):407-430, 2002.
- [3] Valentin, A et al., Phil Trans R Soc A, 367:3585-3606, 2009.
- [4] Irons et al., Ann Biomed Eng, 49:1701-1715, 2021.
- [5] Aparicio P et al., J Biomech, 49:2321-2330, 2016.
- [6] Gridley, Development, 134:2709-2718, 2007.
- [7] Baeten, JT & Lily, B, Adv Pharmacol, 78: 351-382, 2017.
- [8] Morrow, D et al., Am J Physiol Cell Physiol 289: C1188-C1196, 2005.
- [9] Loerakker, S et al., PNAS, 115(16):E3682-E3691, 2018.
- [10] Boaretto, M et al., 112(5):E402-E409, 2015.
- [11] Bersi, MR et al., J R Soc Interface 14: 20170327, 2017.
- [12] Zohorsky, K & Mequanint, K, Tissue Eng Part B Rev 27:383-410, 2021

THE ASSOCIATION BETWEEN CLOT PRESENTATION ON CT, BIOLOGICAL COMPOSITION, AND MATERIAL PROPERTIES: IMPLICATIONS FOR PRE-TREATMENT IMAGING BIOMARKERS

TaJania D. Jenkins (1,2), Briana A. Santo (1,2), Shiau-Sing K. Ciecierska (1), Tatsat R. Patel (1,3), Debanjan Mukherjee (4), Adnan H. Siddiqui (1,3), Vincent M. Tutino (1,2,3)

- (1) Canon Stroke and Vascular Research Center, Buffalo, NY, United States
(2) Department of Pathology and Anatomical Sciences, University at Buffalo, Buffalo, NY, United States
(3) Department of Neurosurgery, University at Buffalo, Buffalo, NY, United States
(4) Department of Mechanical Engineering, University of Colorado, Boulder, Boulder, CO, United States

INTRODUCTION

Approximately 800,000 people in the America have a stroke every year. Towards better classification and outcome prediction, researchers have investigated if pre-treatment (mechanical thrombectomy) computed tomography (CT) imaging can indicate the biological properties of the problem clot. Specifically, several studies have aimed to find robust predictors of whether the clot can be easily retrieved during thrombectomy, using CT angiography and non-contrast CT images. However, the limited physical and biological interpretability of radiomics has hindered clinical application, which is an ongoing challenge across many domains. Understanding the relationship between clot presentation on CT imaging, the biological composition of the clot, and the mechanical properties of that that tissue, will help us better understand CT-based radiomic biomarkers.

To this end, we performed a multi-modal analysis on fabricated clot analogues. In order to determine how biological clot composition is related to the clot's mechanical properties (which effect how well it can be retrieved) and the clots presentation on CT imaging (for radiomic-based biomarkers), we varied fibrin-platelet (FP) and red blood cell (RBC) compositions and subjected each sample to microCT imaging, uniaxial stretch and compression testing. Numerical simulations of the clot tissue using the identified Elastic modulus will then performed to model the clots interaction with thrombectomy devices.

METHODS

Develop Thrombus Analogs: To make clots, we followed [1], but used human blood, enriched the clots for white blood cells (WBCs – to mimic clinical samples), and incubated of clots in a rotator during formation. Citrated, human whole blood was centrifuged (1500g, 15 min) to isolate RBCs, plasma, and buffy coat. WBCs were isolated and concentration was computed using the Countess 3 Automatic Cell Counter (Thermo Fisher). Analogs were prepared by combining RBC and FP isolates in fixed proportions of RBC (0%, 20%, 40%, 60%, 80%,

and 95%), and a fixed volume of WBCs was added (concentration=10⁶/mL). To induce coagulation, CaCl₂ was added, and clots were incubated (1 h, 37°C). Clots were stored overnight at 4°C, transferred to neutral formalin for 24 h, and later stored in 70% ethanol.

Tissue Processing and Imaging: Clots were stained with Lugol's iodine solution (50%, 24 hours) and imaged using the ScanCo μ CT 100 at 4.9 μ m resolution, 90 kV, 155 μ A. Following microCT imaging, clots were de-stained (3X 70% ethanol washes, 24 hours) and prepared for histology. Samples were embedded in paraffin, cut 4 μ m thick, mounted on clear glass slides, and H&E stained. Brightfield whole-slide images were collected at 40X magnification.

Image Analysis: MicroCT images of clots were segmented and quantified using 3D slicer (www.slicer.org). Image processing included application of a bottom-hat transform to remove background signal, global mean-based thresholding to segment the clot region, and use of the Segment Statistics module to compute first order statistics (e.g., mean Hounsfield units, HU). Clot component percent composition (%RBC, %FP, and %WBC) on H&E stained slides was calculated as previously described using Orbit Image Analysis (www.orbit.bio).

Mechanical Testing: Approximately 10 mL of clot of each composition was trimmed to a cylinder measuring 1x6 mm (for stretching) or 1x1 mm (for compression). Uniaxial compression and stretching was done over 10s on a Mark-10 ESM 1500 while load and distance were recorded. A Load-%Elongation graph was created.

RESULTS

% RBC of Clots is Related to Higher Intensity in CT: For analogs of increasing %RBC input as per our protocol, observable increases in clot HUs and RBC composition on histology were apparent (Figure 4A). To define the relationships between protocol %RBC, microCT mean and standard deviation HUs, and %RBC on histology, we completed regression analysis. We found that for every additional 10% RBC input to an analog, the analog's mean CT intensity increased

by ~146 units ($R^2=0.795$, $p=0.017$ [significance defined as $p<0.05$], Figure 4B). Histological %RBC was also found to trend positively with protocol %RBC ($R^2=0.915$, $p=0.003$, Figure 4C). Interestingly, the standard deviation in HUs was greatest for analog of ~60% RBC ($R^2=0.850$, $p=0.038$, Figure 4D). This finding makes sense given that a 50% RBC clot must also be 50% FP, and thus has the greatest composition and textural heterogeneity. The relationship between microCT mean HU and histological %RBC was similar to that of microCT HU and protocol %RBC. For every 10% increase in histological %RBC, microCT mean HUs increased by ~146 units ($R^2=0.877$, $p=0.006$, Figure 4E).

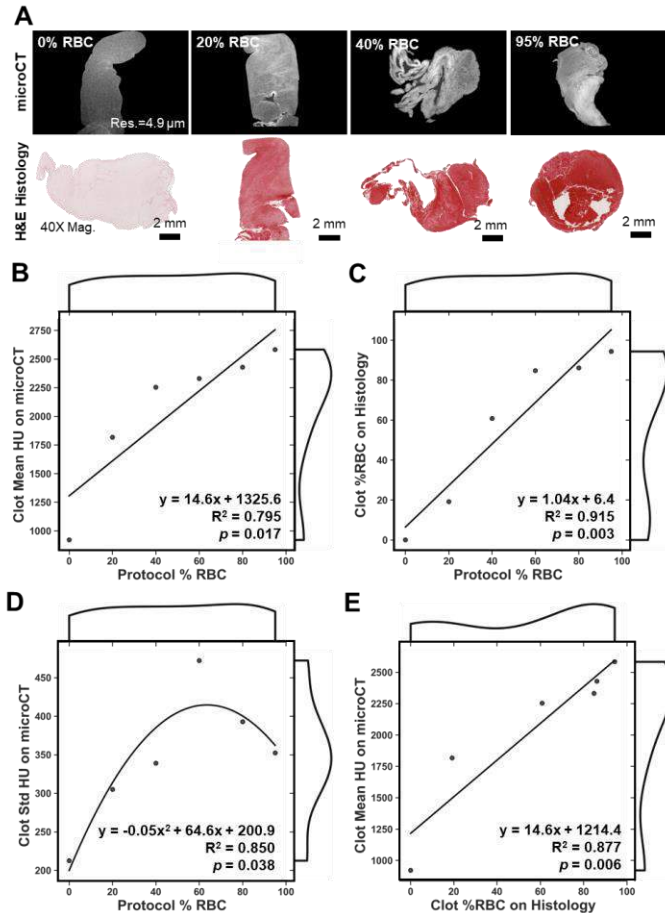


Figure 1: Association of Clot microCT imaging, H&E histology, and % composition calculation. A). Paired CT and histology show RBC portions are associated with higher intensity. B-E). Linear and polynomial correlation plots showing the relationship between clot % RBC and HU from microCT.

% RBC Related to Elastic Modulus (E): Uniaxial compression and stretch testing of clots of varying % composition demonstrated how biology effects the tissues material properties. Here, 0% RBC clots (Figure 2A) withstood the highest stress ($E=0.74$ MPa, Figure 2B), 20% RBC clots (Figure 2C) withstood the second highest stress ($E=0.19$ MPa, Figure 2D), and 40% RBC clots (Figure 2E) withstood the least stress ($E=0.16$ MPa, Figure 2F). A polynomial relationship between the protocol % RBC and the E of each clot was demonstrated ($R^2=1.00$, Figure 2 G).

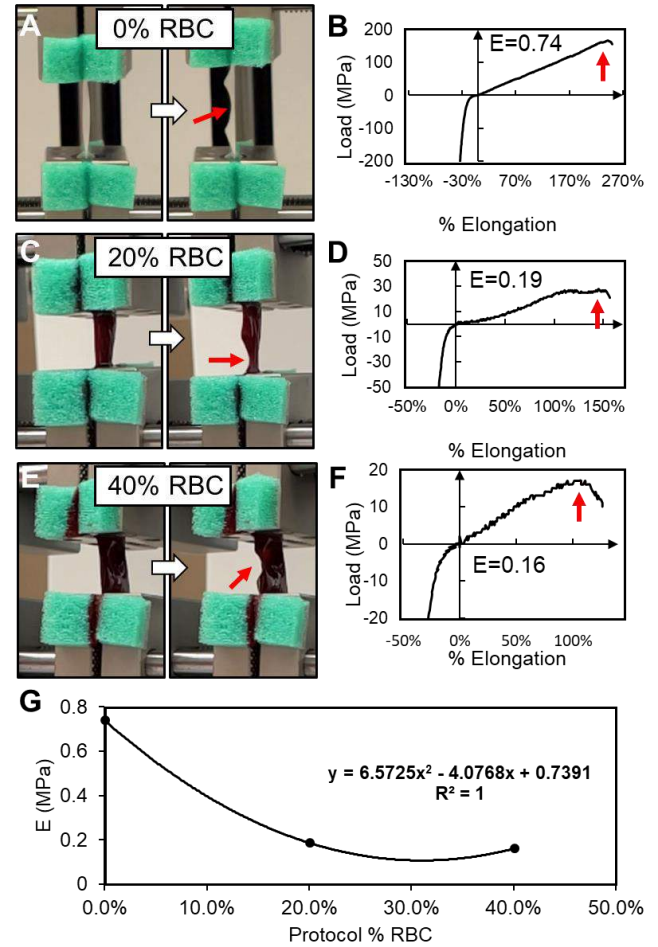


Figure 2: Mechanical testing of clot tissue. A-B) 0% RBC clot test and stress-strain curve. C-D) 20% RBC clot test and stress-strain curve. E-F) 40% RBC clot test and stress-strain curve. G). Correlation plot showing relationship between E and % RBC.

DISCUSSION

In summary, we were able to build statistical models to define the relationships between analog protocols, and CT and histological modalities, that can be validated in future work predicting on resected stroke clots. Our CT and histology results demonstrate that RBCs contribute to higher HU regions in clot tissue, which is consistent with prior studies [3]. Furthermore, the elastic modulus of these clots (range of 0.16 MPa to 0.74 MPa), is also in line with previous reports of thrombotic (stroke and carotid endarterectomy) material in humans [4]. In the future, numerical simulation and benchtop testing will be used to determine if the makeup of a clot, and thus its stiffness, effect its ability to be retrieved via mechanical thrombectomy.

ACKNOWLEDGEMENTS

We thank the Histology Core Laboratory and Optical Imaging and Analysis Facility at the University at Buffalo.

REFERENCES

- [1] Duffy et al., J. Neurointerv. Surg., 2016.
- [2] Mousavi et al., J. Royal Soc. Interface, 2021.
- [3] LaGrange et al., Front. Neurol., 2022.
- [4] Chueh et al., Am. J. Neuroradiol., 2011.

BLADDER WALL STRESS IS LOWER IN FEMALE COMPARED TO MALE IN A MURINE MODEL OF EX-VIVO FILLING

Eli Broemer (1), Pragya Saxena (2), Nathan R. Tykocki (2), Sara Roccabianca (1)

(1) Mechanical Engineering, Michigan State University, East Lansing, MI, USA
(2) Pharmacology & Toxicology, Michigan State University, East Lansing, MI, USA

INTRODUCTION

The urinary bladder is a highly distensible organ capable of accommodating large volumes of urine at low pressures. An idealized spherical pressure vessel is the often-used model for mechanical analysis of the bladder. Studies have shown that bladder mechanical behavior can be affected by aging or disease such as diabetes [1, 2]. There are substantial differences in lower urinary tract anatomy and physiology between the sexes, which can affect bladder function. However, the effect of biological sex on the mechanical properties of the bladder has surprisingly received little attention. Thus, investigating sex as a variable in bladder function is crucial to understand its possible effects on disease progression [3].

In this study, a novel method has been used for analyzing bladder filling in 3D to assess the differences between male and female mouse bladder mechanical behavior. Researching how sex influences filling mechanics is part of understanding the basic functioning of the organ. Furthermore, it will allow improved bladder health care for patients on an individual basis.

METHODS

EXPERIMENTAL SETUP 23 C57BL/6 animals were included in the study, 14 males and 9 females, for comparison. Mouse bladders were extracted, cleaned, and mounted on a cannula connected to a pump and pressure transducer. A custom testing device was built to allow multiple views (i.e. top, left, right, front, & back views) of the organ to be imaged throughout filling (**Figure 1**). The bladder was empty when mounted, submerged in 37°C saline, and then filled at a rate of 30 $\mu\text{L}/\text{min}$ until a measured inner pressure of 25mmHg was reached.

A camera captured the bladder throughout the pressurization. Camera and pressure recordings were synchronized, so that images and pressure measures were collected at the same instant. The output was a video of the experiment at 10 frames/sec, and a spreadsheet of bladder pressure where each measure corresponds to a frame in the video.

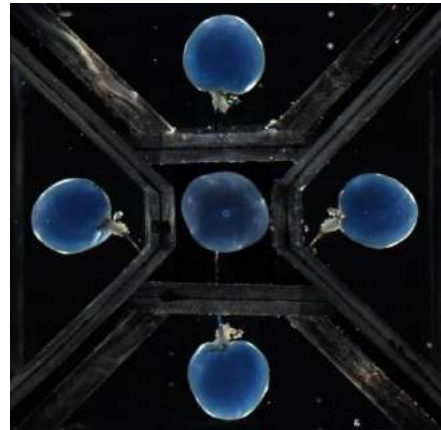


Figure 1: Experiment setup. Bladder is mounted in the center (viewed from the top), and is surrounded by 4 mirrors which show front, back, left, & right views of the tissue.

IMAGE PROCESSING The data was processed with python. Custom code locates tissue boundaries and segments bladder silhouettes from the top, left, and front views (**Figure 1**) in each frame. First, a region of interest was selected in the final frame with the Paint.NET software. Within the region of interest, a Canny algorithm [4] is used to locate the tissue boundaries of each view (**Figure 2A**). In short, the brighter soft tissue in contrast to the dark background creates a sharp gradient along its edge—the result is a line denoting the bladder edge.

The edge line is not guaranteed to be a closed curve (**Figure 2A**), so an Open Curve Filling algorithm was developed [5]. This algorithm seeds a pixel at the center of the bladder view, and then pixels “grow” outwards in all directions until an edge is hit. In directions which are open (i.e., no edge will be found) the algorithm draws a connection

between the two nearest edges. The result is a solid silhouette of the bladder view (**Figure 2B**). These silhouettes are used to generate a 3D reconstruction of the bladder at each time point in the experiment (4D).

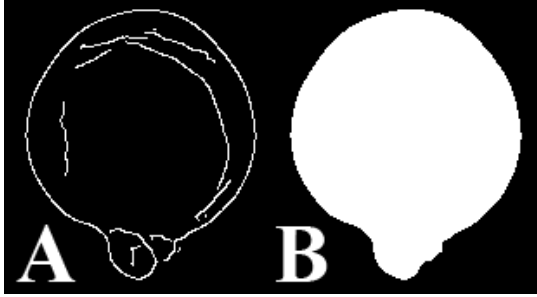


Figure 2: Segmentation of bladder front view. A) Output of Canny edge detection. B) Output of Open Curve Fill algorithm.

MESHING A 3D solid shape is created by the space carving method [6]. The method begins with a primitive rectangular prism, and then the two side views (**Figure 1**) are used to cut away from the primitive in the direction normal to their plane. The top view is then used to form the final shape by carving in the Z direction. However, in this case, the top view is mapped along the entire height of the bladder.

Finally, the voxel (3D pixel) representations of the tissue were transformed into surface meshes (**Figure 3 left**). The marching cubes algorithm [7] was employed for this step. The final result gave a set of bladder meshes at every time point imaged, which have a corresponding internal pressure measure that may be used for mechanical analysis.

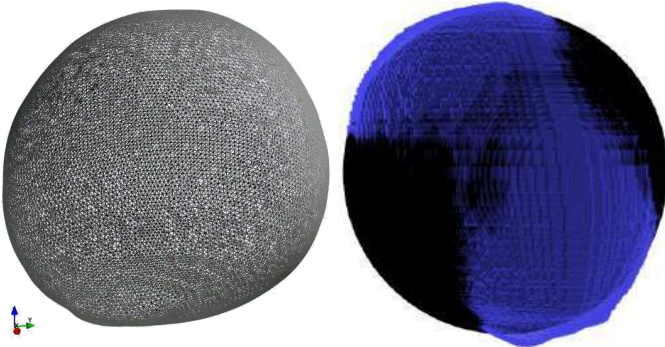


Figure 3: 3D bladder reconstruction. Left) Surface mesh of bladder used for least squares fitting. Right) Least squares fitted sphere (black) superimposed on 3D voxel bladder shape (blue).

SPHERICAL MODEL

The bladder volume was approximated as a sphere via least squares fitting. (**Figure 3 right**) Spherical fitting allows the bladder be modeled as a thin walled spherical pressure vessel with an assumption of isochoric deformation. It follows that we can calculate spherical Cauchy stress (σ) and spherical stretch λ as

$$\sigma = \frac{P * r}{2 * t} \quad (1)$$

$$\lambda = r/r_0 \quad (2)$$

where, the internal pressure P , was obtained via pressure transducer, sphere radius r was obtained from the least squares fitting, r_0 represents the radius for a reference configuration at null internal pressure, wall

thickness t was measured by a researcher when the bladder was at max capacity, and estimated throughout the experiment using the isochoric assumption.

The stress and stretch state was calculated throughout filling from empty to max capacity for each bladder. Bladders were grouped based on sex and stretch was averaged within groups at 1mmHg pressure intervals between zero and maximum pressure. Statistical t-test was used to compare group averages of stress and stretch at max pressure. Results were graphed and significant differences were highlighted where $P < 0.05$ (**Figure 4**).

RESULTS

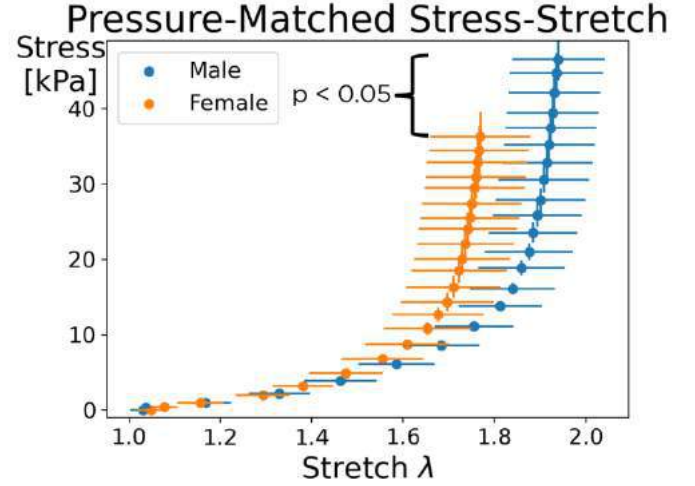


Figure 4: Pressure averaged stress-stretch curves for male and female bladder filling modeled as an idealized spherical pressure vessel. Standard errors shown.

Mechanical behavior between male and female groups was compared (**Figure 4**). At equal pressures, female bladders showed significantly lower wall stress. Smaller stretch was also observed in the female group, but the difference was not significant.

DISCUSSION

The methods described here were used to model bladder filling as a spherical pressure vessel. The differences in mechanical behavior of the mouse bladder shown here due to sex have not been reported before. This information is important for providing context for biomechanical studies. Specifically, considering sex as a variable is important in characterizing bladder function since it does play a role as shown here.

ACKNOWLEDGEMENTS

This work was supported by the National Institutes of Health (grant numbers K01DK103840, R01DK119615, NIH P20DK127554).

REFERENCES

- [1] Smith, P et al., *Am J Physiol Regul Integr Comp Physiol*, 302:R577-R586, 2012.
- [2] Philypov IB et al., *NeuroUrol Urodyn*, 41:1670-1678, 2022.
- [3] Clayton JA et al., *Nature*, 509:282-283, 2014.
- [4] Canny, J, *IEEE Trans Pattern Analysis*, 8:679-714, 1986.
- [5] Broemer, E, *Github Inc.*, github.com/broemere/ccarvv, 2021.
- [6] Kutulakos, KN et al., *Int J Comput Vision*, 38(3):199-218, 2000.
- [7] Lewiner, T et al., *J Graphics Tools*, 8(2):1-15, 2003.

INVESTIGATION OF BIOEFFECTS FROM MICROBUBBLE AND FOCUSED ULTRASOUND ASSISTED BLOOD BRAIN BARRIER DISRUPTION

Jane J. Song (1), Payton J. Martinez (1), Kang-ho Song (1), Jenna Steiner (3), Adam Green (2), Nataile Serkova (3), Mark A. Borden (1)

(1) Biomedical Engineering, University of Colorado Boulder, Boulder, Colorado, USA
(2) Pediatric Oncology, University of Colorado Anschutz Medical Campus, Aurora, Colorado, USA
(3) Radiology, University of Colorado Anschutz Medical Campus, Aurora, Colorado, USA

INTRODUCTION

The development of therapeutics is limited by its ability to localize and be delivered to the site of interest. Among all drug delivery techniques to the central nervous system, the brain is notorious for low drug penetration due to a structure known as the blood brain barrier (BBB). The BBB is maintained by a population of cells, including endothelial cells, astrocytes, and pericytes collectively called the neurovascular unit (NVU), which regulates passage into the brain. Classes of drugs which are developed to treat central nervous system disorders are severely limited since molecules that are large (over 400 Daltons), highly polar and hydrophilic are prohibited from passively diffusing across the barrier. Among the current methods aiming to bypass the BBB, focused ultrasound (FUS) and microbubble assisted blood brain barrier disruption (BBBD) has proven to be one the safest noninvasive methods to guide the delivery of drugs past the BBB and into the parenchyma [1, 2]. Microbubbles (MBs) are ultrasound contrast agents ranging from 1-10 μ m in diameter which oscillate in an event known as cavitation in an acoustic field. Mechanical forces generated from cavitation are able to pry apart tight junctions between endothelial cells creating fenestrations along the blood vessel endothelium. This procedure has been demonstrated irreversibility and success in targeted delivery to the site of interest with millimeter precision and relative safety [3].

A caveat is that inflammation can be triggered in response to BBBD known as the sterile inflammatory response (SIR), recruiting microglia and catalyzing inflammatory cascades (Figure 1). Occurring shortly after disruption, damage associated molecule proteins can be upregulated along with the activation of the inflammatory pathways such as NF κ B [4, 5]. Despite molecular characterizations, little work has been done investigating the degree of inflammation that can occur between BBBD and the onset of SIR dubbed the “therapeutic window”. As the intensity of BBBD can be manipulated through mechanical index (MI), a measurement of ultrasonic energy delivered, and microbubble volume dose (MVD), a dose unifying parameter of microbubbles being injected [6], the objective of our study is to establish the boundaries of the therapeutic window by modulating these

parameters in order to be able to more accurately predict the degree of SIR occurring after disruption.

METHODS

Lipid films were prepared with a 90:10 ratio of lipid 1,2-Distearoyl-sn-glycero-3-phosphocholine (DSPC) and a PEG40S emulsifier. Lipid films were hydrated at 65°C for 40 minutes with sterile 1x PBS and diluted to a final concentration of 2 mg/mL. After rehydration, films were sonicated using a 20 kHz probe, cooled to room temperature (25°C) and re-sonicated with perfluorobutane gas to produce polydisperse microbubble concentrations. Microbubbles were differentially centrifuged down to diameters of 3 μ m and distribution and concentration sizes were measured using the Beckman Coulter Multisizer 3 counter. After successful isolation, microbubbles cakes were stored at 4°C and used within a week to avoid major distribution and concentration changes.

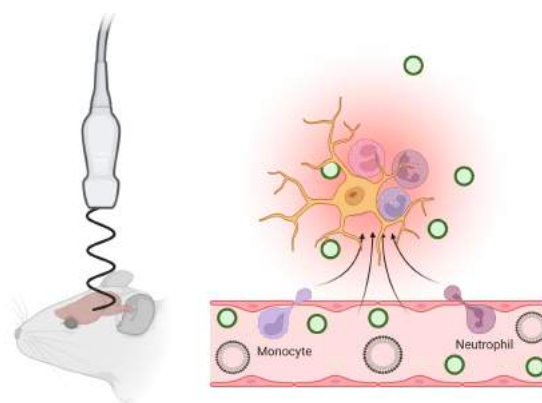


Figure 1: Recruitment of inflammatory markers (SIR) following microbubble-assisted blood brain barrier disruption (BBBD).
Copyright 2023 SB³C Foundation, Inc.

To establish the boundaries of the therapeutic window 5 MVD values were chosen ranging from lowest (0.01 $\mu\text{l/kg}$) to highest concentration (40 $\mu\text{l/kg}$) of microbubbles, these values are indicated in Table 1. All tests for MVDs were performed with a MI of 0.5. CD-1 mice were initially imaged with a 9.4T MRI scanner on the T2 weighted channel to determine correct anatomical targeting of the striatum. MRI coordinates were then transferred to a focused ultrasound machine (RK50, FUS instruments) where mice were retro orbitally injected with a Gadolinium based contrast agent (gadobenate dimeglumine, 4mmol/kg) and sonicated under these conditions: 1.5 MHz pulse frequency, 0.5MI, 0.615 MPa peak negative pressure (accounting for 20 percent skull attenuation), 10 ms pulse length, 1 Hz pulse repetition frequency, and a 5 minute sonication time. Directly after FUS treatment, animals were imaged with a T1+CE MRI where BBBD could be visually confirmed with gadolinium enhancement.

RESULTS

For our BBBD experiments, the mouse striatum was chosen due to its largest anatomical presence and ease of resectability. An MVD of 40 exerted the greatest degree of disruption evident through the intense gadolinium contrast enhancement shown (Figure 2). Interestingly, we observed that disruption occurred at a dose as low as 0.10 A MVD of 0 was selected as a control against BBBD with no visible gadolinium enhancement indicative of barrier impermeability. A linear trend of BBBD is observed over a range of MVDs measured arbitrary units of intensity. To a lesser extent this is also demonstrated in Song KH et al [6].

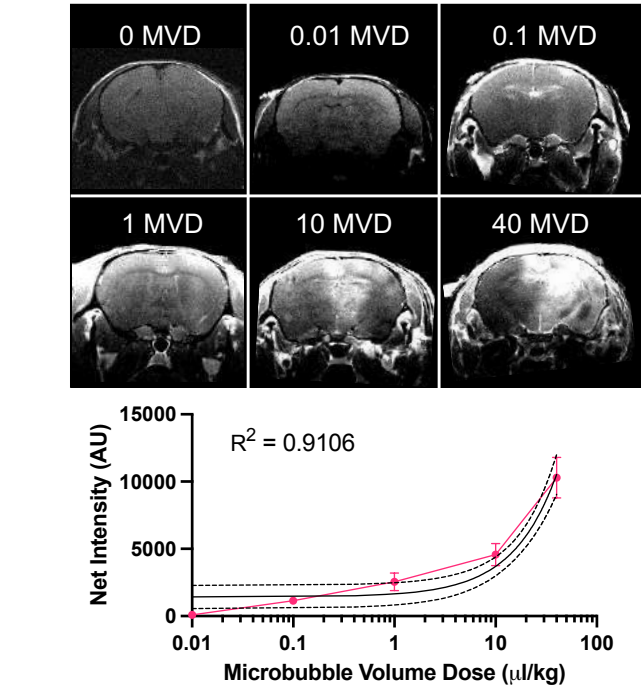


Figure 2: Gadolinium contrast enhancement of BBBD. The solid black indicates a best fit curve with the dashed lines above and below representing 95 percent confidence intervals. X-axis is shown as a logarithmic scale of microbubble doses. R squared values represents disagreement between the best fit line and experimental data

Table 1: Experimental groups

	Mechanical Index	Microbubble Volume Dose
Group 1	0.5	0.01
Group 2	0.5	0.1
Group 3	0.5	1
Group 4	0.5	10
Group 5	0.5	40

DISCUSSION

Preliminary results of this study highlight a relationship between our tested MVD values and MI which can be manipulated to influence the degree of BBBD. At higher MB concentrations of 40 and 10 MVD, larger gadolinium extravasation was observed as compared to the contralateral hemisphere which experienced no FUS treatment. Previous work in microbubble pharmacokinetics have shown that concentration decays exponentially immediately after injection [7] , supporting the case that higher MVDs contribute to longer persistence therefore allowing for more circulating microbubbles to participate in BBBD. This is observed in works of McMahon et al. where similarly, greater doses of microbubbles lead to greater BBBD and thus greater sterile inflammatory responses [8]. Interestingly, at MVDs as low as 1 and 0.1 MVD, slight disruption was detected via gadolinium contrast enhancement when measured against contralateral controls, exceeding our expectations for was what the lowest possible MVD at 0.5 MI to achieve successful disruption. Future work will aim to test more mechanical indices with MVDs and analyze transcriptomic changes at the level of RNA to assess gene regulation in response to the disruption.

Commercial brand microbubbles such as Definity and Optison are commonly used to test clinical doses of microbubble concentrations for BBBD, however, these are manufactured as polydisperse MB populations which may contribute to batch-to-batch variability. Using monodispersed MBs to calculate microbubble gas fractions allows us to measure the concentration of MBs systemically delivered more rigorously. This can be especially advantageous for future directions aiming to gauge or anticipate the amount of inflammation incurred by disruption by exploring various microbubble volume doses tested with different experimental mechanical indices. Currently, there is no method that aims to completely define the therapeutic window by manipulating MVD vs MI which measures the time between disruption and the severity and onset of SIR. Creating a wide range of parameters will create a more defined therapeutic window in which an immune response can be predicted, giving key insights into the safety of blood brain barrier disruption for future clinical translation.

ACKNOWLEDGEMENTS

This work was funded through NIH (RO1CA239465)

REFERENCES

- [1] Hynynen K et al. *Radiology* 220.3 (2001).
- [2] Song KH et al. *Theranostics* 8.16 (2018).
- [3] Jaratlerdsiri W et al. *Cancer research* 78.24 (2018).
- [4] Kovacs ZI et al. *Proceedings of the National Academy of Sciences* 114.1 (2017).
- [5] Kovacs ZI et al. *Theranostics* 8.17 (2018).
- [6] Song KH et al. *Theranostics* 7.1 (2017).
- [7] Navarro-Becerra JA et al. *ACS Biomaterials Science & Engineering* 8.4 (2022).
- [8] McMahon D et al. *Theranostics* 7.16 (2017).

BIOMECHANICAL IMPROVEMENTS IN GAIT WITH CARBON-FIBER ORTHOTIC INSOLE FOR POST-OPERATIVE TIBIOTALAR ARTHRODESIS PATIENTS

Adam J. Bradshaw (1), Austin J. Carcia (1), Colin R. Smith (1), Thomas O. Clanton (1),
Scott Tashman (1)

(1) Department of Biomedical Engineering, Steadman Philippon Research Institute, Vail, CO, USA

INTRODUCTION

Despite the high success rate of tibiotalar arthrodesis (TTA) for patients with degenerative ankle arthritis, many patients still experience functional limitations during daily activity, including reduced sagittal ankle range of motion, plantarflexion moment and power, and increased gait asymmetry [1,2]. Several consumer orthotics and footwear options are available to TTA patients, including rocker-bottom shoes, heel lifts, and solid ankle cushion heels, though none have been shown to restore normal gait biomechanics [3]. Recently, carbon-fiber plates inserted into high-performance running shoes to increase longitudinal bending stiffness have been shown to increase running economy, up to 3% [4]. To our knowledge, no studies have been performed investigating the use of carbon-fiber orthotic insoles for TTA patients.

This study aimed to determine whether a 3-layer carbon-fiber orthotic insole could improve gait biomechanics for TTA patients. Our central hypotheses were that 1) gait asymmetry in joint kinematics and kinetics, 2) ground reaction force (GRF) at heel strike, and 3) muscular activation would each be reduced in TTA patients while wearing the orthotic insole device.

METHODS

Seven participants (2 females; age: 55 ± 9.9 years; weight: 84.7 ± 19.9 kg; height: 1.78 ± 0.11 m) who were at least 29 months removed from single-leg total ankle fusion surgery (mean 77.1 ± 27.9 months) were recruited from the patient population at The Steadman Clinic (Vail CO). This study was IRB-approved and all subjects gave their written informed consent prior to data collection. Three footwear conditions were evaluated, each in standardized shoes: a control condition with no orthotic (NO), a regular orthotic condition (RO, Fig. 1b), and a stiffened orthotic condition (SO, Fig. 1c). To create the SO condition, a compressible foam wedge was inserted behind the middle and bottom layers of the device, providing increased resistance to compression of the orthotic.

Gait analysis was performed in each condition on a split-belt instrumented treadmill with a 16-camera motion-capture system and surface EMG at two different walking speeds: a self-selected pace (Normal: 1.01 ± 0.11 m/s), and a speed that was 20% faster (Fast: 1.22 ± 0.13 m/s). Twenty-six retroreflective markers were placed on the shoes, legs, hips, and trunk of each participant for motion capture. Participants were fitted bilaterally with wireless EMG sensors on their medial gastrocnemius.

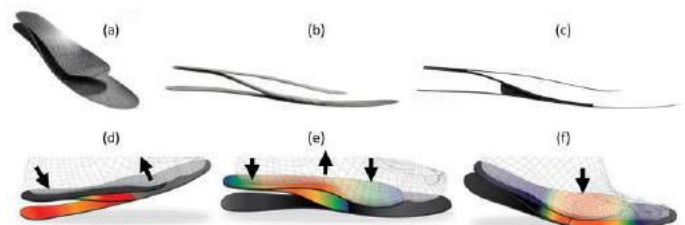


Figure 1: (a) Oblique view of the 3-layer carbon-fiber orthotic insole (OI). (b) Lateral view of regular orthotic (RO). (c) Lateral view of stiff orthotic (SO) achieved using foam wedge. (d-f) A simulated loading response by the OI during stance, showing energy management function.

Nine gait cycles were selected as representative of each condition for analysis, and statistical tests evaluating the effect of the orthotics were performed independently for the Normal and Fast walking speeds. All kinetics, kinematics, and EMG data were normalized to 0 to 100% of stance phase and filtered with a zero-phase low-pass fourth-order 6Hz Butterworth filter. Joint moments and powers were normalized to the product of each participant's height and weight, and ground reaction forces were normalized to weight. Paired t-tests using Statistical Parametric Mapping (SPM) were implemented in MATLAB using

open-access SPM1D functions to assess the effect of each orthotic condition on the data of the affected leg [5]. Gait asymmetry was quantified using a symmetry ratio of affected versus contralateral leg swing time, as a percentage of cycle time [6].

RESULTS

SPM paired t -tests showed statistically significant reductions in ankle plantarflexion moment (Fig. 2a), knee extension moment (Fig. 2b), and gastrocnemius activity (Fig. 3a) during midstance (~30-70% stance) in the SO condition when compared to the control. Significant effects were still seen in the RO condition compared to the control, though to a lesser degree than SO. Significant reduction in impact force (Fig. 3b) occurred at heel-strike (0-10% stance) in the SO condition, though not in the RO condition. Non-parametric paired t -tests showed significant reductions in gait asymmetry at both walking speeds for the SO condition, decreasing gait asymmetry by between 1.1% and 2.6% across all comparisons.

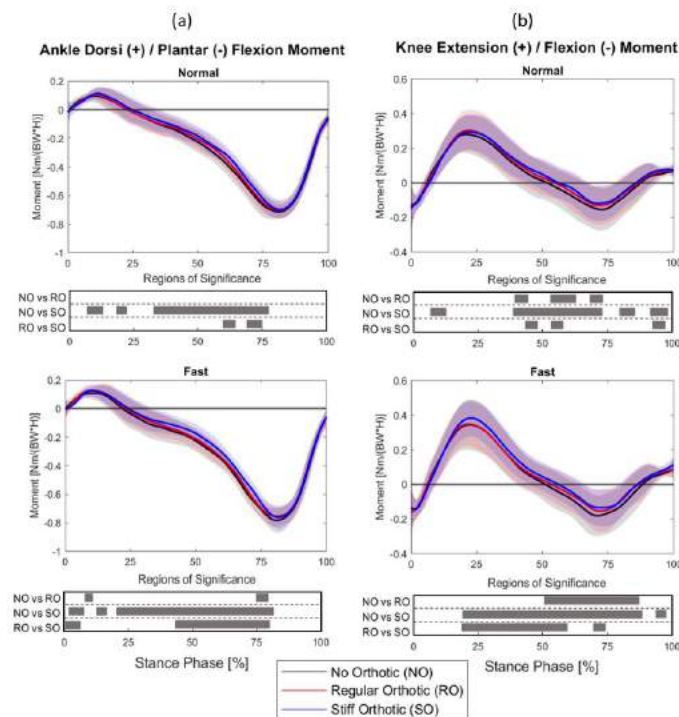


Figure 2: (a) Mean sagittal ankle moment and (b) mean sagittal knee moment of affected leg during gait. The shaded areas indicate one standard deviation from the mean across all subjects. Shaded blocks below the curves indicate regions of significant difference between the conditions ($p < 0.05$), based on the SPM paired t -tests.

DISCUSSION

The stiff orthotic (SO) condition showed the most statistically significant changes in gait compared to the control. Reductions in sagittal knee and ankle moments and gastrocnemius muscle activity during mid-stance suggests savings in muscular effort for the participants. Ground reaction forces were also reduced at heel-strike in both orthotic conditions, indicating a level of energy absorption by the orthotic device at impact. The SO condition, with the additional foam wedge inserted between the carbon-fiber spring system, acts as a better shock absorber than the carbon-fiber on its own, dampening the impact of the foot at heel-strike. Vertical GRFs were also reduced in terminal

stance in both RO and SO as compared to the control, near the point of peak push-off force, indicating that the energy absorbed at heel-strike was not released at toe-off. Previously discussed reductions in knee and ankle moments and gastrocnemius EMG indicate the energy may have been returned during mid-stance instead, although the viscoelastic properties of the foam may lead to overall loss of some of the energy absorbed at impact, resulting in less energy returned overall. Lastly, reductions in patient gait asymmetry in the SO condition can be seen as a positive impact of the device. Further research is needed on the optimal stiffness of the orthotic device, and on patient comfort and quality of life with long-term use.

No options are available to ankle fusion patients that can restore normal gait biomechanics post-surgery. Though this study only investigates the effects of an orthotic device on a small sample size, significant results in important gait metrics are promising for future tibiotalar arthrodesis patients.

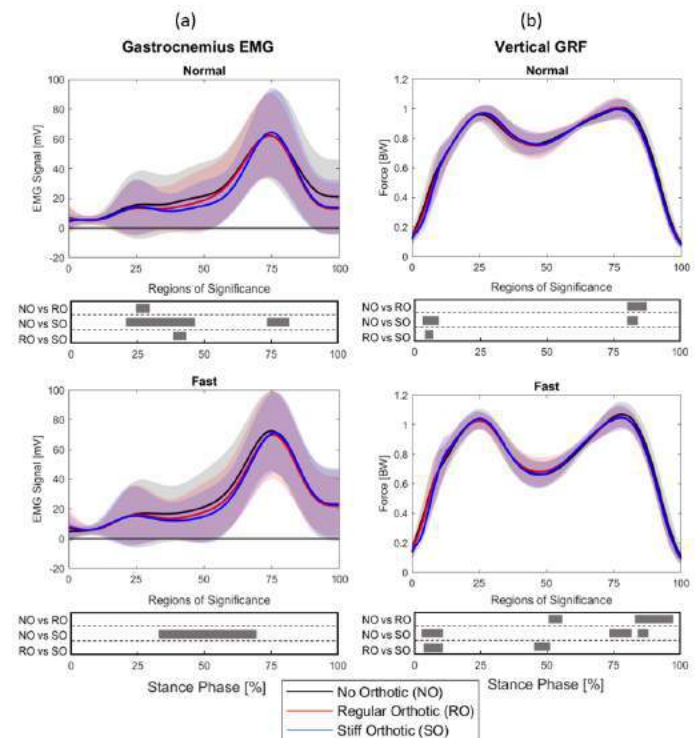


Figure 3: (a) Mean gastrocnemius EMG and (b) mean vertical ground reaction force (GRF) of affected leg during gait. The shaded areas indicate one standard deviation from the mean across all subjects. Shaded blocks below the curves indicate regions of significant difference between the conditions ($p < 0.05$), based on the SPM paired t -tests.

ACKNOWLEDGEMENTS

Financial support and devices received from SubioMed, Inc.

REFERENCES

- [1] Abdo, R. V., et al. *Foot & Ankle*, 13(6):307-12, 1992.
- [2] Piriou, P., et al. *Foot Ankle Int.*, 29(1):3-9, 2008.
- [3] Jones, D. A., et al. *J Foot Ankle Surg*, 55(1):5-8, 2016.
- [4] Ortega, J. A., et al. *Sports Med*, 51(5):873-894, 2021.
- [5] Pataky, T. C. *J. Biomech*, 43(10):1976-1982, 2010.
- [6] Patterson, K. K., et al. *Gait & Posture*, 31(2):241-246, 2010.

ELASTIC FIBERS CONFER TENSILE STIFFNESS TO THE DORSAL MESENTERY, DRIVING BUCKLING MORPHOGENESIS OF THE SMALL INTESTINE

Elise A. Loffet, John F. Durel, Hyunjee Lim, Richard Kam, Nandan L. Nerurkar

Department of Biomedical Engineering, Columbia University, New York, USA

INTRODUCTION

Buckling has emerged as a core mechanism shaping a broad range of tissues during embryonic development [1]. However, integration of tissue mechanics with underlying cell behaviors and molecular cues has been limited. Looping of the small intestine – the process by which the initially straight intestinal tube is bent into tightly packed loops within the body cavity – is among a handful of examples of buckling morphogenesis where the underlying biological cues have begun to be revealed [2]. Differential elongation rates between the initially straight intestinal tube and the dorsal mesentery – a thin membranous tissue attaching the tube to the dorsal body wall – result in buckling of the gut into loops as the slowly elongating mesentery compresses the rapidly elongating tube [3][2]. The resulting wavelength and curvature of intestinal loops can be fully predicted from experimental measurement of growth rates, geometry, and mechanical properties of the gut and the mesentery [3]. Effectively, the mechanical properties of the mesentery determine how differential growth between the two tissues is converted to compressive forces that buckle the tube. Here, we focus on looping of the chick small intestine to understand how tissue stiffness is controlled during buckling morphogenesis.

The biological effectors involved in the mechanical properties of the mesentery remain largely unexplored. More broadly, the biological basis of tissue stiffness during embryonic development has received far less attention than other aspects of the mechanics of morphogenesis, such as regulation of acto-myosin activity [4] or cell migration [5]. In this study, we observed that changes in mechanical properties of the mesentery during the looping process correlate with changes in the expression of genes related to extracellular matrix (ECM), and elastic fibers in particular. Focusing on the functional role elastic fibers in looping, we enzymatically depleted elastin in the mesentery to observe the effects on tensile properties of the mesentery.

METHODS

Bulk RNAseq was carried out on mesentery tissues from White Leghorn chicken embryos (*gallus gallus*) embryos at embryonic day (E) 8, 12, and 16. Fastq files went through quality control (FastQC), residual adapter cleaning (cutadapt), genome alignment (hisat2) and read counting (htseq2). Subsequent analyses were done using R using package DESeq2 for differential expression and clusterprofiler for Gene Ontology analysis.

Elastase treatment: samples were incubated in PBS + 0.1 mg/ml SBTI (Sigma-Aldrich) and elastase (Elastin Products Company) for 4h at 37°C under agitation.

Immunostaining: Fixed samples were cryosectioned (16 μ m) and immunostained for elastin (Millipore Sigma MAB2503) [2]. Sections were counterstained with DAPI, mounted in and imaged using a LSM880 confocal microscope (Zeiss).

qPCR: Total RNA was extracted using RNeasy mini kit (Qiagen) ND reverse transcribed using SuperScript III Reverse Transcriptase (Life Technologies). Real-time quantitative PCR was performed using a C1000 thermocycler (Biorad) with a Sybr green mix kit (Applied Biosystems). The relative expression of the gene of interest was measured by the $2^{-\Delta\Delta C_t}$ method and normalized for the housekeeping gene ACTB.

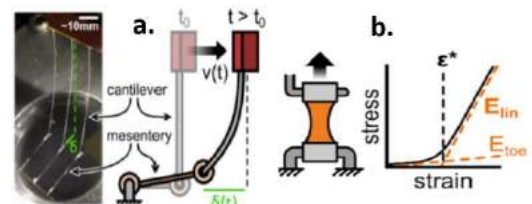


Figure 1: Mechanical testing of mesentery

Mechanical testing of the mesentery was performed in uniaxial tensile testing on a custom micromechanical tester [2]. 1 mm wide

samples were hooked to a tungsten cantilever attached to a linear actuator, stretching the sample (fig 1.a.). Fluorescent dyes placed on the tissue and tungsten cables were used to measure strain. Bi-linear curve fits were applied to quantify the toe-region modulus E^{toe} , the linear region modulus E^{lin} , and the transition strain ϵ^* (fig.1.b.).

RESULTS

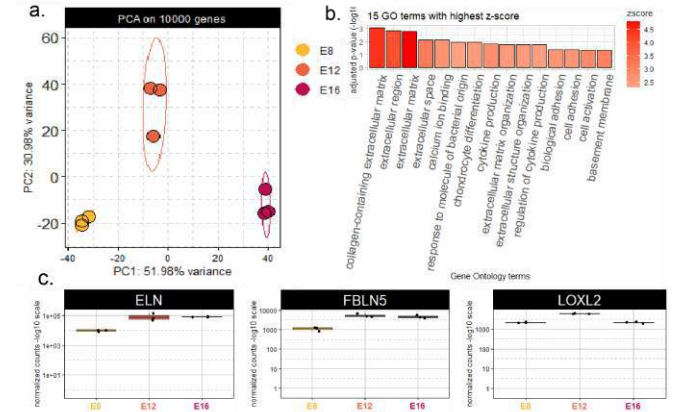


Figure 2: Bulk RNAseq of mesentery at E8, E12 and E16. a. Principal Component Analysis b. 15 Gene Ontologies with highest z-score (up-regulation association score) at E12 vs E8 c. Boxplots of gene expression for ELN, FBLN5 and LOXL2

Principal Component Analysis (PCA) showed significant difference between the three time points (fig 2.a.). Gene Ontology analysis of differentially expressed genes showed an upregulation of several ontologies related to ECM gene expression (fig 2.b.). Upregulated genes included collagen genes, as well as genes involved in elastic fiber formation: ELN (tropo-elastin), FBLN5 (fibulin-5) and LOXL2 (lysyl-oxidase, a cross-linking enzyme) (fig 2.c.).

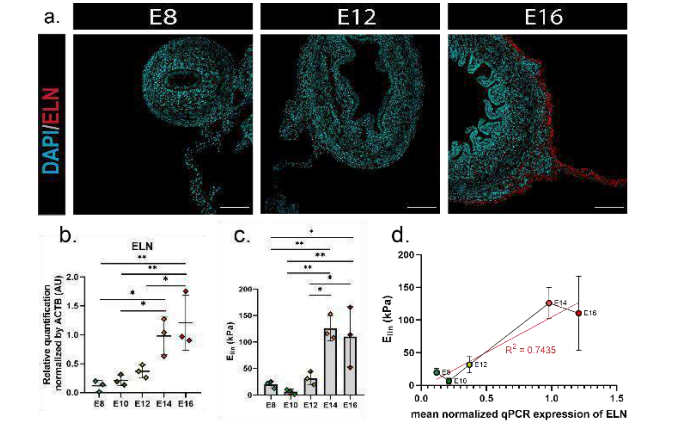


Figure 3: Elastin and the buckling the gut tube. a. Immunofluorescence staining for elastin and DAPI on E8, E12 and E16 sections (scale bar = 100µm) b. qPCR for ELN in the mesentery at E8 to E16 c. Linear modulus for mesenteries at E8 to E16 d. Correlation of Elin and qPCR expression of ELN in the mesentery from E8 to E16.

Immunostaining revealed a progressive increase in elastin staining from E8 to E16, in the outside wall of the gut tube and in the mesentery (fig 3.a.). In untreated embryos, the linear modulus of mesentery tissue increased from E8 to E16 (fig 3.c.), correlating with qPCR expression for ELN (fig. 3.b) at these same time points ($R^2=0.7435$) (fig 3.d.). We did not measure a significant change in toe modulus or transition strain.

We treated mesentery and gut tube segments with 0, 2 or 4 U/mL of elastase for 4 hours at 37°C (fig. 4.a.). Controls showed no significant cell death or loss of collagen network and content. The treatment resulted in a down-regulation of the linear modulus at 2 and 4 U/mL (fig. 4.b.), but no significant difference in transition strain or toe modulus (data not shown).

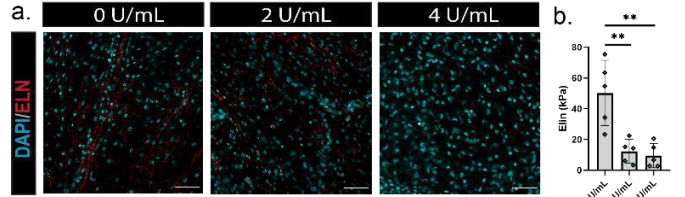


Figure 4: Elastase depletion. a. Whole-mount immunofluorescence staining for elastin and DAPI on control and elastase-treated mesenteries (scale bar = 50 µm) b. Linear modulus.

DISCUSSION

In this study, we show that elastic fiber formation is closely associated with looping of the small intestine and that elastin depletion changes the mechanical properties of the mesentery.

Enzymatic digestion has been used to probe mechanical contributions of elastic fibers in a range of adult tissues, revealing some behaviors shared by the mesentery in the present study. For example, elastase treatment reduced linear modulus of the mesentery as it does in several tissues [6][7], and in synthetic matrices [8]. Elastase treatment has also been shown to result in lower capacity to withstand load, resist fatigue loading, and recover after loading in equine ligament [9]. However, disparities between our findings and those from other tissues may help explain the physical mechanism by which elastic fibers resist elongation of the mesentery to drive looping. Unlike porcine ligamen and human inter-vertebral disc, which experience a reduction in toe modulus as well [6][7] and an increase in transition strain for the intervertebral disc [7], the mesentery experiences an ~80% reduction in the linear modulus with no changes in toe modulus or transition strain. One explanation may be that elastin in the mesentery functions primarily to permit load transfer across stiff collagen fibers, and removal of elastin attenuates the influence of collagen in the linear region, where conventionally it is thought to dominate the properties of adult connective tissues. This is supported by the observation that elastase treatment increases the Poisson’s ratio of the mesentery (not shown), which has been suggested to reflect a reduction of load transfer between fibrous components in a matrix [10].

Altogether, our data shows that elastic fibers play a previously unappreciated role in resisting passive stretching of the mesentery, in turn contributing the compressive forces that buckle the intestinal tube into loops. Future work will aim to address the underlying mechanisms, and to ask whether tissue tension regulates elastic fiber deposition to provide feedback controls on looping of the intestine.

ACKNOWLEDGEMENTS

This work was supported by R01 DK131236 (NLN).

REFERENCES

[1] Nelson. J Biomech. Eng. 138, 021005 (2016); [2] Savin+ Nature 476, 57–62 (2011) ; [3] Nerurkar+ PNAS. 114, 2277–2282 (2017); [4] Kasza+, Curr. Opin. Cell Biol. 23, 30–38 (2011); [5] Barriga+. Nature 554, 523–527 (2018); [6] Henninger+ J Orthop. Res. 31, 1226–1233 (2013); [7] Smith+ Ann. Biomed. Eng. 36, 214–223 (2008); [8] Black+ J. Appl. Physio. 98, 1434–1441 (2005); [9] Godinho+ Acta Biomater. 123, 187–196 (2021); [10] Picu+. Journal of Biomechanical Engineering vol. 140 (2018).

ELUCIDATING THE LONGITUDINAL IMPACT OF SOLID MECHANICS ON ATHEROSCLEROTIC PLAQUE IN PATIENT-SPECIFIC CORONARY ARTERIES

Jeremy L. Warren (1), Clark A. Meyer (1), Heather N. Hayenga (1)

(1) Department of Bioengineering, University of Texas at Dallas, Richardson, TX, United States

INTRODUCTION

In 2020 the CDC reported that approximately one in five deaths were attributed to cardiovascular disease (CVD) from 1999-2020 [1], [2]. In particular, coronary artery disease (CAD), also called atherosclerosis, accounted for roughly 55% of CVD-attributed deaths in 2020 alone, making it the leading cause of death across all CVD [2]. CAD is an inherently complex and heterogeneous disease wherein fatty plaque forms and accumulates within the artery wall. It is known that the growth and progression of plaque in coronary arteries is largely influenced by low or oscillatory wall shear stress at the luminal interface which causes inflammation [3], increased leukocyte transendothelial migration [4], and low-density lipoprotein (LDL) transport across the endothelium [5]. What is less known is how solid mechanics within the lesion augments atherosclerosis. Untreated plaque growth results in luminal narrowing which impairs blood flow hence, increasing the chance of adverse ischemic events downstream of the blockage. Moreover, a narrowed morphology results in large mechanical stresses in the cap and shoulder of the plaque, causing a sudden and life-threatening biomechanical failure known as plaque rupture [6]. However, the unpredictable nature of plaque rupture makes it difficult to clearly identify the magnitude or threshold of the mechanical stresses or strains that cause rupture. Therefore, we investigated how artery wall mechanics influence plaque growth pre-rupture. To do so, we use patient-specific data and in-silico methods to correlate the biomechanics of real-patient arteries with morphological features of plaque remodeling over 6 months. The outcomes of this work will further the current understanding of mechanically mediated plaque growth with implications in personalized treatment to minimize disease progression.

METHODS

Current imaging modalities such as coronary angiography and virtual histology intravascular ultrasound (VH-IVUS) are utilized to diagnose plaque severity and uncover locational and compositional features.

Recently, we published our work on an automated algorithm that is capable of using patient-specific VH-IVUS images and coronary angiography data to generate volumetric 3D meshes of coronary arteries for in-silico biomechanical modeling [Figure 1] [7]. Utilizing the model and in collaboration with a medical center, Emory University, we processed a 16-patient dataset of paired VH-IVUS and angiography images at baseline (BL) and 6-month follow-up (FU). MATLAB was used to generate the meshes and extract image derivable features.

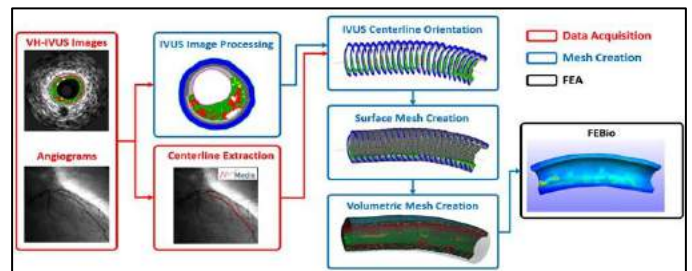


Figure 1. Simplified mesh generation flowchart.

Mesh Reconstruction and FEA. We used our reconstruction algorithm to generate straight meshes using BL patient data. Each mesh comprises quadratic 10-node tetrahedral element shapes with edge length of approximately 0.2mm. This mesh resolution is suitable to accurately represent semi-fine details present in the VH-IVUS images. Subsequent finite element analysis (FEA) simulations were performed using the open-source FEBio FEA software. Patient-specific blood pressure were applied to luminal surfaces. Nonlinear Neo-Hookean material model was utilized with heterogeneous literature-derived material properties pertaining to each plaque constituent. Mean elemental effective stress and strain corresponding to each pair of BL and FU VH-IVUS image was calculated from the FEA results.

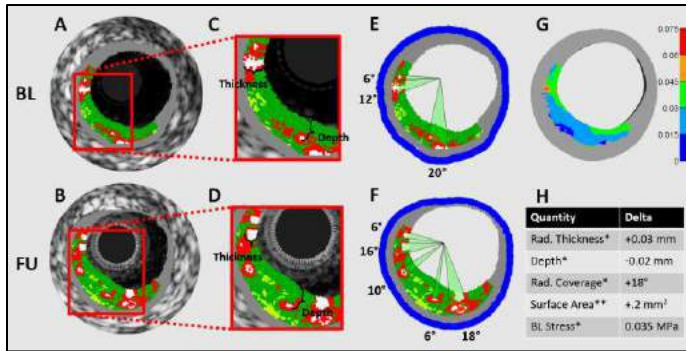


Figure 2. Image-derivable features and FEA.

A,B) Original BL and FU VH-IVUS. C,D) Plaque thickness and depth. E,F) Radial coverage. G) FEA stress. H) Calculated differences.

Image-derived features. A separate automated script analyzed every pair of BL and FU VH-IVUS images and extracted image-derivable features. These features include surface area, radial coverage, radial depth, and radial thickness of each plaque constituent [Figure 2]. The difference between BL and FU is then calculated between for use in the following analysis.

RESULTS

Preliminary results using 13 of the 16 patient datasets ($n = 842$ images) suggest that larger changes in plaque area between BL and FU occur at low-mid eff. stresses whereas smaller changes in surface area occur at mid-high eff. stresses [Figure 3A]. Similar patterns for radial coverage and radial thickness of the plaque arise as well. These patterns were not restricted to the global dataset as local changes within a single artery also exhibit a similar relationship [Figure 3B].

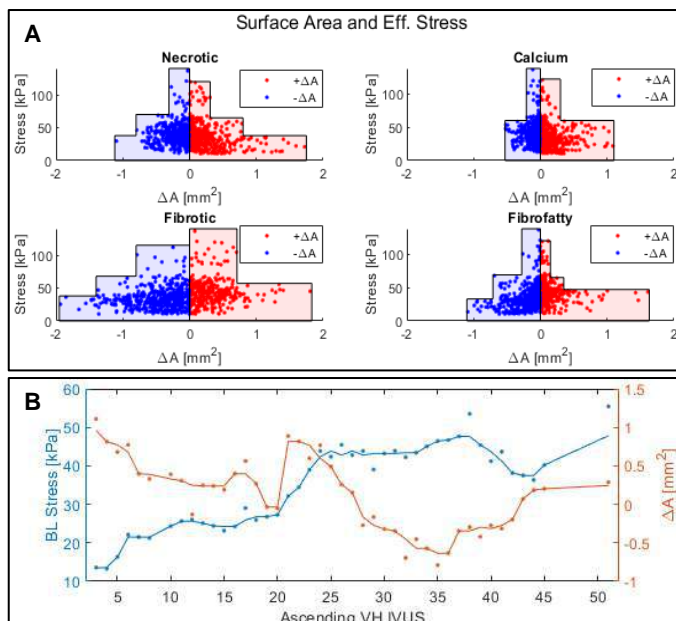


Figure 3. Mechanically mediated changes in plaque area.

A) Results for the global dataset, y-axis effective stress in kPa, x-axis change in area in mm². B) FEA results for necrotic tissue in a representative patient, x-axis VH-IVUS ascending image index, left y-axis effective stress in kPa, right y-axis changes in area in mm².

DISCUSSION

Our preliminary results corroborate the work by Samady et al. which found that low hemodynamical WSS correlated with increased plaque volume over a 6-month period [8]. It is thought that endothelial cells lining the lumen must be in a constant state of motion to maintain healthy cell-cell connections between them and minimize transport of leukocytes or LDL into the wall. Similarly, smooth muscle cells (SMCs) inside the artery wall responsible for remodeling the extracellular matrix can be negatively impacted by lower stresses. Pathological remodeling via SMCs has been replicated during in-vivo experiments. SMCs in low stretch conditions (0-10%) were found to proliferate less than those under large stretch conditions [9]. Taken together, this suggests a mechanobiological remodeling paradigm largely influenced by the mechanics felt at the cellular level. Yet, we do see some instances where it is the stress distribution rather than the magnitude that drives volume changes [Figure 4]. Further investigation is needed to quantify these relationships, but initial results indicate mechanobiological remodeling.

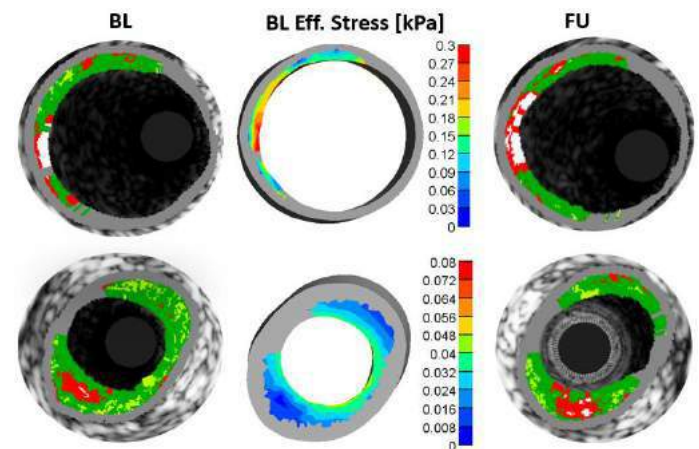


Figure 4. Similar volume change, different stresses. The necrotic core (red) had a similar change in volume between both pairs of BL and FU images. However, stress magnitudes were vastly different.

ACKNOWLEDGEMENTS

Authors gratefully acknowledge funding for this work provided by the American Heart Association (17SDG33400239), the National Heart, Lung, And Blood Institute of the National Institutes of Health (NIH) under Award Number R01HL136776, and the Louis Stokes Alliances for Minority Participation program. The content is solely the responsibility of the authors and does not necessarily represent the official views of the NIH. Emory University (ClinicalTrials.gov; Identifier: NCT00576576) for the data set used in this study. Vascular Mechanobiology Lab at UTD for providing opportunity to work on this research through the guidance of Dr. Hayenga, the lab director.

REFERENCES

- [1] CDC WONDER Online Database, 2022.
- [2] C. W. Tsao et al, *Circulation*, 145:8, 2022
- [3] S. Sheikh et al, *Blood*, 8:2828–2834, 2003
- [4] R. Bhui et al, *PLoS Comput Biol*, 13:5, 2017
- [5] M. Dabagh et al, *Am J Physiol Heart Circ Physiol*, 2009
- [6] J. Ohayon et al, *Am J Physiol Heart Circ Physiol*, 2008
- [7] J. L. Warren et al, *Front Med Technol*, 4, 2022
- [8] H. Samady et al, *Circulation*, 124:779–788, 2011
- [9] L.-E. Mantella et al, *Vasc Cell*, 7:7, 2015

CHANGES IN THUMB FORCE DUE TO OSTEOARTHRITIS

Nicole D. Arnold (1), Adam J. Chrzan (1), Kevin Chan, MD (2), and Tamara Reid Bush, PhD (1)

(1) Department of Mechanical Engineering, Michigan State University, East Lansing, MI, USA

(2) Department of Orthopedic Hand and Upper Extremity Surgery, Spectrum Health, Grand Rapids, MI, USA

INTRODUCTION

Osteoarthritis (OA) has been shown to be a debilitating musculoskeletal disease with significant degradation of the joints [1]. One of the most common locations of hand OA has been reported to be at the base of the thumb, or the carpometacarpal (CMC) joint. The CMC joint was also reported to be the most painful joint when compared to other joints of the hand [2]. Additionally, CMC OA has been shown to affect 67% of women over the age of 55 [3]. As a result, those impacted by CMC OA suffered from increased thumb pain which led to movement and strength limitations in the hand, including reduced force production. Because of the loss of hand and thumb strength, people had difficulties carrying out activities such as opening and closing containers, gripping and picking up objects, and lifting heavy items.

There are several surgical procedures to treat thumb CMC OA, however no procedure has been proven to be superior to the rest. Studies have evaluated the effectiveness of a surgery via patient questionnaires and clinical measurement devices. Clinical measurement devices, such as the dynamometer and pinch gauge, do not isolate the force produced by the thumb. Additionally, there are limited data reported on isolated thumb force generation following surgery. Relying on these clinical metrics have led to a gap in data gathered on the thumb. To determine how effective surgical treatment is for those with thumb CMC OA, we must understand not only the motion abilities, and the reduction of pain, but also the abilities to generate force post-surgery.

Thus, the purpose of this research was to determine the isolated forces generated by the thumb pre and post-surgery at two time points, 3 months and 6 months post-surgery, in those with thumb CMC OA in order to assess what strength has been restored.

METHODS

Our study included 10 female participants (average age 62.1 ± 8.9 years) (IRB# 2021-148). Of the 10 participants, a ligament

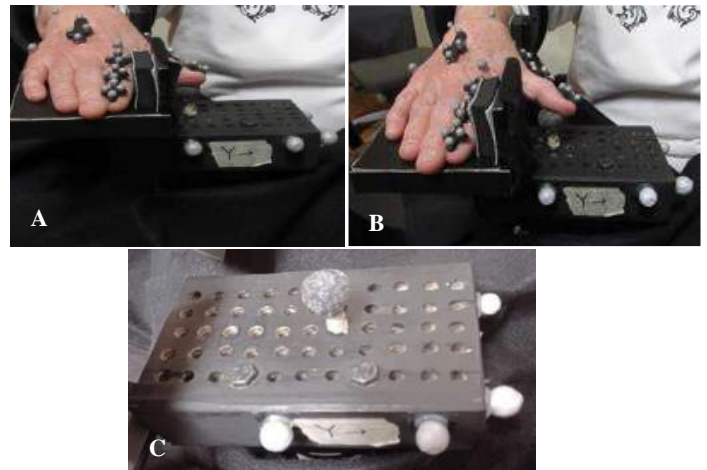


Figure 1: A) Participant performing a push at 0° of wrist supination. B) Participant performing a pull at 0° of wrist supination. C) A wooden block was mounted on the load cell with equally spaced holes where participants place the peg.

reconstruction with tendon interposition (LRTI) surgery was performed on 7 right hands and 3 left hands. Participants were of various ages: one 40-year-old, four between 50 and 59, three between 60 and 69 and two between 70 and 79. Participation in this study was voluntary. Each participant was consented, tested prior to their surgery, 3- and 6-months post-surgery. Participants sat in a chair with their back against the seat, their elbow extended, arm adducted with their hand and forearm on a custom testing device that was located on a table. The custom testing device restricted movement of the forearm and wrist allowing

individuals to focus on performing thumb force (Figure 1) and was adjustable to accommodate both right- and left-handed participants. The device included a wooden block mounted on a load cell (AMTI, Watertown, MA). The block had an array of holes spaced, approximately 12.7 millimeters apart, into 5 rows and 11 columns (Figure 1C). Force data sets were collected at 200Hz. Participants performed two trials of a thumb push and pull in 0° of wrist supination (Figure 1A and 1B, respectively). A push was described as the thumb pushing the peg “downward” or “into the ground”. A pull was described as the thumb pulling the peg in toward the index finger. Participants were instructed to execute each push and pull on the peg with their thumb positioned at a “close”, “far” and “comfortable” position. The close position was described as a position of the peg in the closest hole to the hand in which the pad of the thumb could grip the peg. The far position was described as the location of peg in the farthest hole away from the palm. And finally, the comfortable position was the most comfortable peg location selected by the participant. Each location (close, far, or comfortable) the participant was instructed to exert maximum force during each push and pull on the peg.

RESULTS

The maximum thumb pull and push forces in the comfortable position at 0° of wrist supination are presented in Figures 2 and 3., respectively. The trends shown in both figures for the comfortable position were similar to what was seen in the close and far and 90° wrist

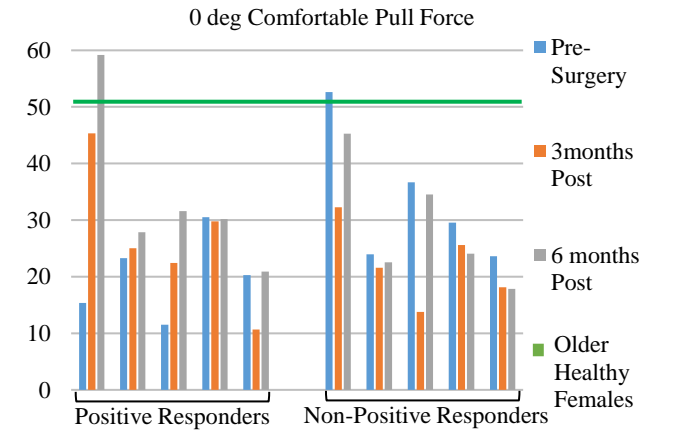


Figure 2: Maximum pull force in the 0° wrist for CMC OA females (n=10) in the comfortable position. In green is the average maximum comfortable pull force for older healthy females.

orientation for those positions. As shown in each figure, a subset of participants each showed a positive response or non-positive response post-surgery. Nearly half of the participants reduced the amount of thumb force at 3 months post-surgery. However, some participants increased force at each time point. At 6 months post-surgery, some participants had similar or less favorable results at 6 months post-surgery, compared to pre-surgery. On each respective plot, the green line shows the average older healthy (OH) female thumb force. One participant surpassed OH female thumb pull force at 6 months post-surgery. Two participants reached or surpassed OH female thumb push force at 6 months post-surgery. Additionally, at each time point the pull force was the larger force generated as compared to push, no matter the peg location or wrist position.

DISCUSSION

In this study, force data were collected for 10 female participants both before and two time points following surgery for thumb osteoarthritis. The reason for most individuals to have this surgery is for pain reduction. Nearly all participants did experience a reduction in pain. However, little attention has been given to understanding the specific changes with force generation after the thumb surgery. Our data suggests that there is a mixed response to force generation after CMC

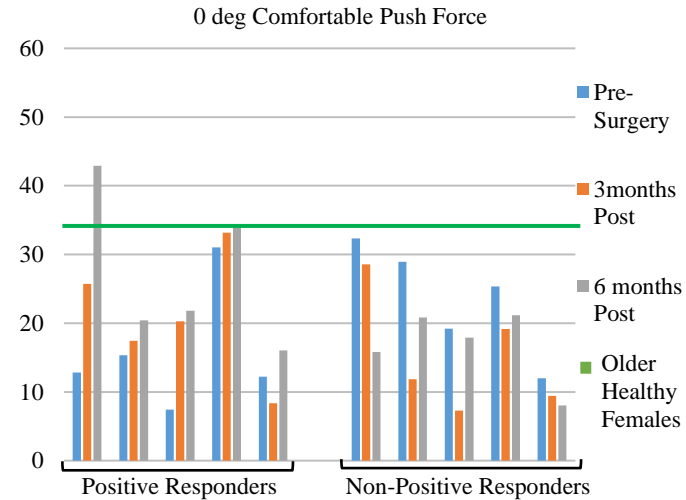


Figure 3: Maximum push force in the 0° wrist for CMC OA females (n=10) in the comfortable position. In green is the average maximum comfortable push force for older healthy females.

OA surgery. Ideally, each patient would reach the point of full strength, preferably to the level of a healthy adult in the same age range. Although, there were some participants who did reach the force generation level of a healthy older adult, most who improved did not improve to that magnitude, but they did increase in comparison to their pre-surgery abilities. However, others had force generation abilities that were reduced as compared to their abilities before the surgery.

It should be noted that compliance with therapy was not monitored, and the participants were only tracked to the 6-month point, so further improvement could occur beyond our measurement term.

There is a great deal more to study with regard to the biomechanics associated with thumb function particularly after surgical intervention.

ACKNOWLEDGEMENTS

This work was supported by the Michigan State-Spectrum Alliance Grant.

REFERENCES

[1] Clynes, MA et al., Aging Clin Exp Res, 31:1049–56, 2019.
[2] Dickson, RA et al.,
[3] OA Prevalence & Burden Osteoarthritis Prevention and Management in Primary Care. 2019.

AGE- AND SEX-BASED SKULL THICKNESS DISTRIBUTION FOR PREDICTING SKULL FRACTURE PATTERNS IN YOUNG INFANTS

Yousef Alsanea (1), Timothy Dixon (1), Tagrid Ruiz-Maldonado (2), Brittany Coats (1)

(1) Mechanical Engineering, University of Utah, Salt Lake City, Utah, USA
(2) Pediatrics, University of Utah, Salt Lake City, UT, USA

INTRODUCTION

Child maltreatment is the second leading cause of death in infants less than 1 one year of age [1]. Early identification is critical to the prevention of adverse outcomes, but child abuse in young infants is still highly under-detected. Skull fractures are common in both accidental and abusive head trauma and provide a unique opportunity to assess the validity of caretaker histories of infant trauma based on fracture initiation sites, fracture lengths, and level of complexity [2].

Skull thickness distribution influences skull fracture patterns [3], but the effect of age and biological sex in early development on skull thickness distribution have not been reported. The objective of this study was to develop an imaging pipeline for high-resolution, three-dimensional maps of skull thickness, and use this pipeline to compare distributions between male and females from birth (newborn) to 4 months of age. Similarity metrics were created to determine the need for sex-based anatomical templates for fracture simulation, as well as to identify appropriate age-divisions for those templates. These methods and data will lead to universal anatomical templates for skull fracture simulation, as well as form the foundation for a patient-specific modeling pipeline.

METHODS

IRB approval was obtained to review CT images of 300 healthy infant (<12 months of age) skulls from Primary Children's Hospital at the University of Utah. Serial stacks of axial and coronal images were aligned in MATLAB using DICOM image position alignment and an iterative closest point (ICP) algorithm. Cranial bone segmentation, identification of suture locations, and thickness extraction at more than 12,000 sites across the infant skull were performed using a custom python script (Fig.1).

To compare skull thicknesses at similar relative locations, despite differences in head shape and size, one subject within each age group (0-4, 5-8, 9-12 months) was selected as a template. The skull

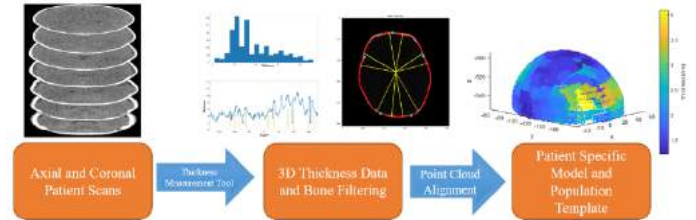


Figure 1. Imaging pipeline for high-resolution skull thickness comparison across age and sex.

distribution in each subject was then fit to their respective template using ICP. Thickness was average across 132 discrete regions (Fig.2) representing approximately 22-39 locations in 4 cranial bones (right and left parietal, occipital, and frontal bones). 44 subjects < 4 months of age (21 female, 23 male) were selected from the dataset to evaluate changes in skull thickness distribution in early development.

The effect of age and sex was evaluated for each cranial bone using a two-way ANOVA with repeated measures, correlations of thickness with age by gender, and one-way ANOVAs that controlled for location. Moran's I and Geary's C spatial analyses were performed for each subject to identify trends in global and local skull thickness spatial clustering, respectively (Eq. 1, 2).

$$I = \frac{N \sum_i \sum_j w_{ij} (x_i - \bar{x})(x_j - \bar{x})}{W \sum_i (x_i - \bar{x})^2} \quad (1)$$

$$C = \frac{(N-1) \sum_i \sum_j w_{ij} (x_i - x_j)^2}{W \sum_i (x_i - \bar{x})^2} \quad (2)$$

The spatial weight matrix w_{ij} was calculated with an exponential function $w_{ij} = \exp(-r_{ij}/r_c)$ consisting of the Euclidean distance between two locations r_{ij} and the average distance between all locations within a cranial bone r_c .

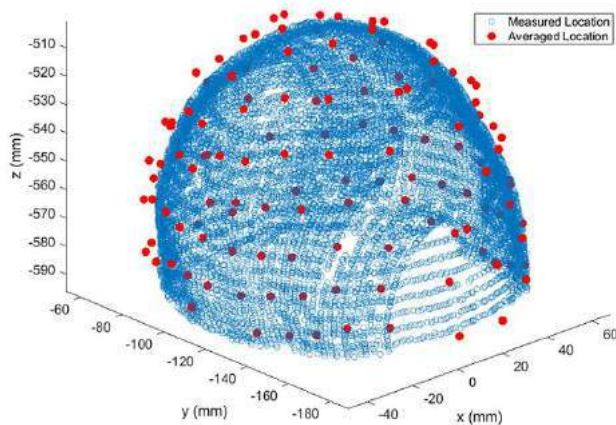


Figure 2. Skull thickness was measured at over 12,000 locations on each skull (blue) and averaged over 132 locations (red) for comparing age and sex.

A similarity metric was developed to identify similar patterns of skull thickness distribution among the subjects. Briefly, this metric calculated and summed distances between ranked-ordered thickness locations for pairwise comparisons of all subjects. Data were normalized by the distance sums of non-ranked ordered locations. A similarity score of 0 indicates perfect similarity between regions of high and low thickness across the bone. Similarity was assessed for four groupings of data (all subjects; sex; age; sex/age combination).

RESULTS

Infant ages were either < 1.25 months of age (newborn) or 3-4 months of age (infant). Occipital and frontal bones were significantly thicker than parietal bones for both ages and sexes ($p < 0.001$, **Fig. 3**). Male occipital and frontal bones were significantly thicker than female bones at birth ($p < 0.0001$), while parietal bones were equal across sex. Increased thickness between newborns and infants was significantly more pronounced in females than males for all bones ($p < 0.001$). In fact, male skull thickness had no significant correlation of thickness with age between 0-4 months old, except for parietal bones which had a weak positive correlation ($r < 0.12$, $p < 0.001$).

Moran's I and Geary's C spatial analysis found positive correlations of skull thickness in most infants (88%), primarily on the parietal bones (**Fig. 4**). Similarity scores ranged from 1.72-3.18 across all groupings. In general, males and infants had similarity scores nearly identical to those when all data was combined, particularly for the parietal and frontal bones. However, separating by females and newborns improved similarity in skull thickness patterns by 7-8%. Further refinement by age and sex improved similarity in all groups by 3-10% in male infants and newborns and by 13-20% in female infants and newborns, respectively.

DISCUSSION

The high-resolution imaging pipeline and skull thickness comparison in this study illustrates distinct changes in skull thickness with age that are dependent on biological sex and cranial bone. Female skulls are thinner at birth, but grow rapidly and are thicker than males by 3-4 months. Areas of thicker and thinner regions of the skull are most unique in female newborns compared to other groups, and suggest that predictions of skull fracture may also be unique in this population.

The early development data from this study illustrates age- and sex-dependent changes in skull thickness distribution, and suggests the need for unique skull geometry templates between male and female

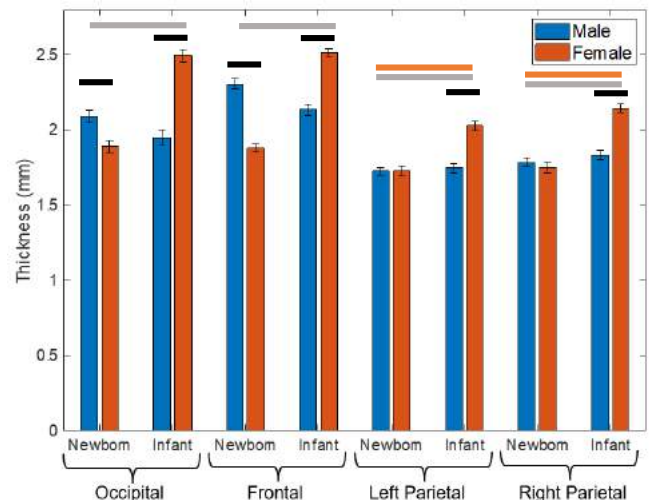


Figure 3. Skull thickness categorized by bone and age in male and female. Solid black, gray, and orange bars indicate significant differences ($p < 0.001$) for sex, age for females, and age for males respectively.

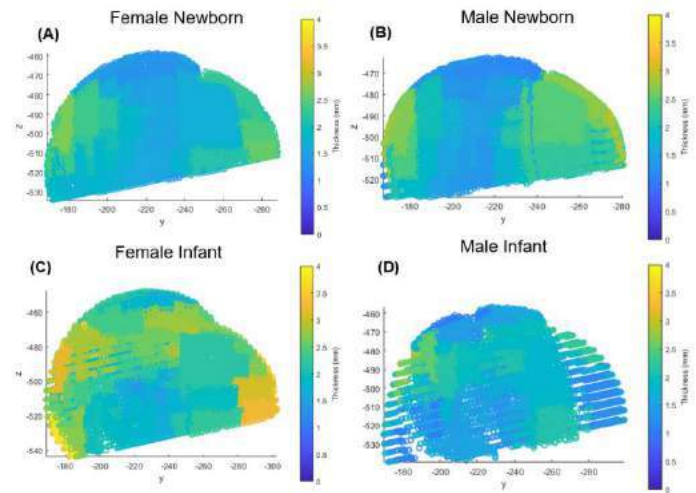


Figure 4. Contour plots of skull thickness illustrating skull thickness changes with age and sex.

newborns and young infants to accurately predict skull fracture patterns from head impact. Given large variations within the studied population, patient-specific modeling may be required. Data analysis on older infant populations is currently underway to identify if similar trends exist for infants up to 12 months of age. Once complete, these data will establish anatomical standards for simulations of head trauma in this rapidly developing age group.

ACKNOWLEDGEMENTS

This research was supported by 2016-DN-BX-0160 and 2020-75-CX-0014 provided by the National Institute of Justice. The opinions, findings, and conclusions are those of the authors and do not necessarily reflect those of the Department of Justice.

REFERENCES

- [1]. US Department of Health and Human Services, 2020
- [2] Ruiz-Maldonado T. et al. *Pediatr. Res.*, 2022
- [3] Weber, W. *J. Legal Med*, 1985

DEEP LEARNING FRAMEWORK FOR STRESS STRAIN ANALYSIS OVER POINT CLOUD

Jia Lu, Nishant Sundaravaradan

Department of Mechanical Engineering, The University of Iowa, Iowa City, IA, USA

INTRODUCTION

We introduce a deep learning framework for image-driven analysis. The method is presented in the context of membrane bulge inflation test recorded by Digital Image Correlation (DIC). The DIC data provides a point-cloud representation of the surface and a one-to-one correspondence between points in different configurations. In conventional approaches, one usually extracts a deforming mesh from the point-clouds, conducts mechanical analysis on the mesh, and when needed, transfers data between the mesh and point-clouds. The transformation of geometric presentation and data transfer between geometric models entail approximations and are known sources of system error. Moreover, the workflow typically involves the use of multiple software, which is burdensome, to say the least. In the new paradigm, all analyses are conducted on a single platform, and directly over the point-cloud. This is achieved by using deep learning as the sole computation platform. In what follows, we demonstrate the new platform using an example of aneurysm tissue test.

METHODS

Figure 1 shows the DIC point-clouds of an aneurysm tissue sample at two configurations. The lower, Ω_0 , is the reference configuration. The upper, Ω , produced by the application of a transvers pressure, is the current configuration. Since point-to-point correspondence between the configurations has been registered by the DIC software, the tasks here are 1) to compute the surface strain, 2) to determine the stress field in the current configuration (the reference configuration, which was slightly pressurized, is assumed stress-free), and 3) to analyze the stress-strain behavior. We will focus on tasks 1 and 2 herein. For these tasks, the analysis consists of three steps: 1). construct an implicit continuous presentation of the surface; 2). derive a smooth mapping between the reference and the current configurations; and 3). perform stress analysis in the current configuration. All steps are accomplished in the deep learning framework. Steps 1 and 2 use neural network (NN) regression,

and step 3 employs a stress solver developed in physics informed neural network (PINN) [1].

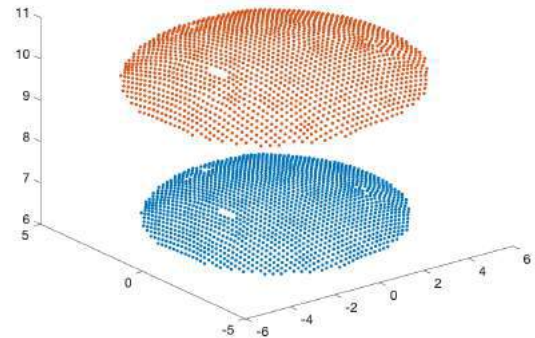


Figure 1. Point clouds at two configurations. Blue: reference. Red: current. Length unit: mm

Step 1: Implicit continuous representation. For computing geometric features such as surface tangent, we need a continuous parameterization of the surface. To this end, the point-cloud is fitted to itself via NN regression. For the example considered here, since the geometry is dome-like, we fit the z-coordinate to a function of (x, y) , resulting in the surface form $(x, y, z(x, y))$. Geometric entities such as surface tangent can be readily computed from this form. Missing points (due to glare, for example) may also be inserted by NN prediction. The step also serves as an intrinsic smoothing process.

Step 2. Deformation mapping. The reference cloud is mapped to the current cloud by NN regression. We seek a function $\Phi: \Omega_0 \mapsto \Omega$ by minimizing the loss function $\sum (x_i - \Phi(X_i))^2$. The outcome is a smooth mapping in the NN function space. The surface deformation gradient can be obtained directly via automatic differentiation.

Step 3. Stress analysis. We leverage the property of static determinacy to find an equilibrium stress field in the current configuration. Following [2], we solve a (linear) elastic membrane problem using a fictitious elasticity model with high Young's modulus. The ensuing stress solution is expected to be a close approximation of the true stress field while the displacement solution is immaterial. The high stiffness ensures that the displacement is small and hence the deviation from the current geometry is negligible. The membrane problem is then solved in the PINN framework, which minimizes the total potential in the NN function space.

RESULTS

Continuum Model. To illustrate the utilities of the continuum parameterization, a surface tangent vector is computed at every point and the vector field is shown in Figure 2. A four-layer NN (one input layer + 2 hidden layers of 20 neurons each + one output layer) was used in this computation. The training took ~30 seconds.

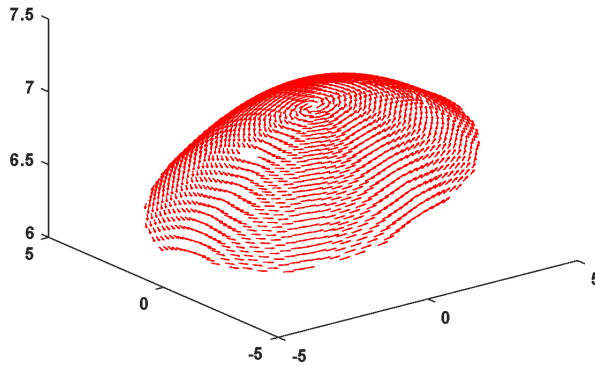


Figure 2. Tangent vector field derived from NN parameterization.

Mapping. Figure 3 shows the predicted current point cloud (red) via NN regression, superposed on the original points (blue). Clearly, the point positions were recovered accurately (the mean deviation is ~0.02 mm). The same NN configuration as in step 1 was used. The computation took ~60 seconds.

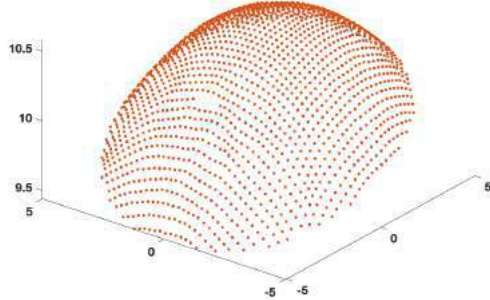


Figure 2. Predicted point-cloud (red) superposed on the original cloud (blue)

Strain. Figure 4 illustrates the contour of strain norm. The strain was computed directed from the gradient field made available by NN automatic differentiation.

Stress. The surface tension (stress resultant over the wall thickness) obtained from PINN computation is shown in Figure 5. The NN used in this analysis contained three layers with 100 neurons in the hidden layer. The computation took ~4 minutes to complete. The stress distribution compares well with finite element results reported elsewhere [3].

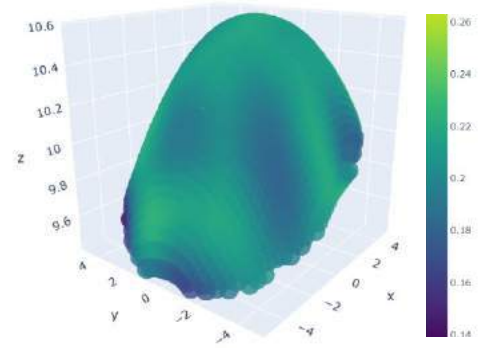


Figure 4. Contour of the strain norm.

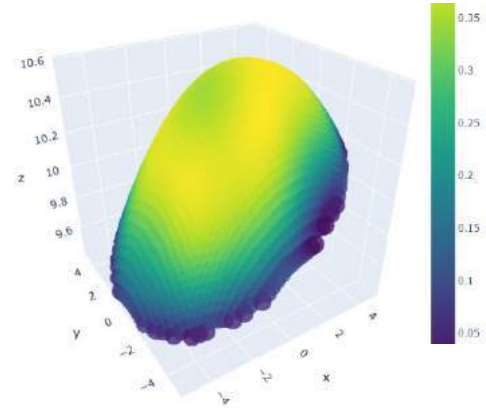


Figure 5. Contour of the norm of surface tension (N/mm)

DISCUSSION

We have demonstrated a deep learning framework for extracting full field strain and stress information from DIC point cloud. The neural network provides a unified paradigm (namely optimization) to address seemingly different tasks, enabling us to solve the problems in a single framework. For some individual tasks (for example stress analysis), the computational efficiency is inferior to finite element method at this moment. However, the entire workflow is much simpler and requires nearly zero user interference. The input to the analysis is a point cloud, and there is no need to introduce solid model or mesh or elaborated finite difference schemes. Continuum representations, which is indispensable for finite element type computations, is furnished naturally by NN. In principle, the techniques presented here are applicable to 3D image-based biomechanical analysis.

ACKNOWLEDGEMENTS

The work was supported by US Department of Education grant ED#P116S210005.

REFERENCES

- [1] Karniadakis, George Em, et al. Nature Reviews Physics 3:422-440, 2021.
- [2] Lu, J et al. Comp. Meth. in Applied Mech. and Eng., 308:134-150, 2016.
- [3] Davis, F. M. Davis, et al..Biomech Model Mehanobiology, 14 (5), 967-978, 2015.

FINITE ELEMENT MODELING OF C-SECTION SCARS AND SCAR DEFECTS

Adrienne K. Scott (1), Erin M. Louwagie (2), Kristin M. Myers (2), Michelle L. Oyen (1)

(1) Biomedical Engineering, Washington University in St. Louis, St. Louis, MO, United States

(2) Mechanical Engineering, Columbia University, New York, NY, United States

INTRODUCTION

Uterine rupture is an inherently biomechanical process associated with high maternal and fetal mortality [1]. A cesarean section (C-section) scar increases the risk of uterine rupture in a subsequent pregnancy due to failure of the tissue in the scar region [1]. It is well known that vertical scars along the sagittal plane in the uterus further increase the risk of uterine rupture. For this reason, vertical incisions are avoided unless needed for emergency situations and low transverse incisions are used instead. An additional complication that may lead to increased risk of uterine rupture is the presence of an isthmocele, or a defect in the uterine wall at the site of a previous C-section scar [2]. As the rate of C-sections continues to increase [1], it is critical to understand the mechanisms leading to uterine rupture with a trial of labor after C-section (TOLAC) during a subsequent pregnancy.

Although some risk factors have been identified, there is currently no reliable model to predict uterine rupture. Furthermore, to the best of our knowledge, no one has previously examined the risk of uterine rupture with C-section scars with a biomechanical approach. Finite element (FE) modeling of the uterus and the scar tissue may present a promising method to further understand and predict uterine ruptures. To work towards this goal, our objective is to first generate a mechanical model of the uterus to examine how the scar positioning (vertical versus transverse), material properties of the scar, and the presence of a defect influence uterine tissue mechanics.

METHODS

A representative model of a uterus and cervix (Fig. 1A) was

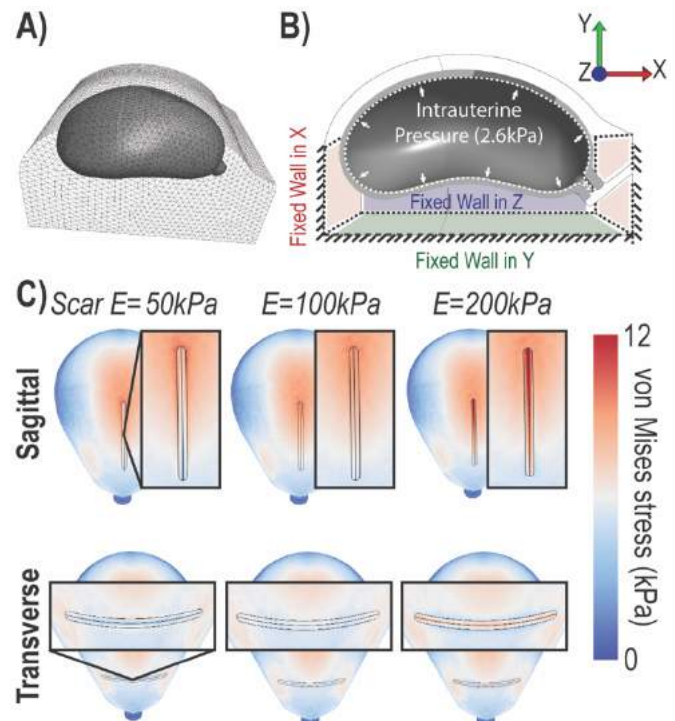


Figure 1: Geometries of the abdomen, uterus, cervix, and C-section scars were A) meshed and B) modeled in FEBio with an applied intrauterine pressure (2.6kPa), while the abdomen walls were fixed in the X, Y, Z directions. C) Heat maps of von Mises stress were generated and showed increased stress with sagittal scars compared to transverse scars with the same material properties.

generated by averaging uterine dimensions acquired from MRI images of five at-term pregnant patients and constructing the geometries in Solidworks [3,4]. Additionally, scar tissue and scar defects were also included in the Solidworks model along with a surrounding abdomen tissue. Dimensions of the scar tissue (e.g., length) and defect size (e.g., width, depth) were based on average measurements found in literature [2,5,6]. The abdomen, uterus, cervix, and scar geometries with and without defects were discretized into elements using Hypermesh (Fig. 1A). Meshed geometries were imported into FEBio and modeled as a nearly incompressible (Poisson's ratio $\nu = 0.48$) neo-Hookean elastic material. The Young's modulus (E) of the abdomen and the uterus were set to 100 kPa, while the midline of the scar region was varied (50 kPa, 100 kPa, 200 kPa). The Young's modulus of the remaining scar tissue was calculated by a linear interpolation between the midline value and the surrounding uterine tissue. The boundary conditions and a physiological intrauterine pressure (2.6 kPa) [7] were applied as shown in Fig. 1B. A finite element analysis was performed using FEBio to generate heat maps of von Mises stress.

RESULTS

When varying the stiffness of the midline of the scar region, the von Mises stress increased in the scar region with increasing scar stiffness, as expected (Fig. 1C). The magnitude of the von Mises stress was greater for all sagittal scars compared to the respective transverse scar with the same Young's modulus (Fig. 1C). Models in which the scar properties matched the surrounding tissue properties validated the boundary conditions and demonstrated the expected null-response. Literature was reviewed to determine the average dimensions and geometry of patient scar defects and a defect was incorporated into the model of the low transverse scar (Fig. 2). Preliminary results show elevated stress in the defect region of the scar compared to the low transverse scar without the defect.

DISCUSSION

The modeled stress distributions of the sagittal and transverse C-section scars were consistent with clinical observations, since the von Mises stress was higher on sagittal scars compared to transverse scars and it is well known that there is an increased risk of uterine rupture in sagittal scars compared to low transverse scars. Incorporating a defect in the model will allow us to further understand how this complication may lead to increased stress in the scar region and tissue failure.

While the results are promising, this simplified study includes several limitations. The model assumes all tissues can be represented as a neo-Hookean material and other materials, such as a fibrous material, may be more representative of the uterine and scar tissue. Additionally, we chose a Young's modulus range of 50-200 kPa, but in the future more accurate measurements of material properties of uterine tissue could be incorporated into the model. This model also did not account for spatial variation of material properties in the uterine tissue. While there was a spatial variation of material properties of the scar tissue, we assumed that the greatest change in the elastic

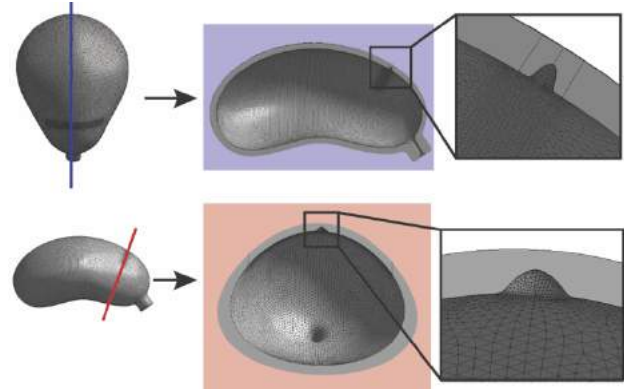


Figure 2: A representative isthmocele, or scar defect, geometry was determined from measurements reported in literature [2] and was included in the low-transverse scar model to understand how a scar defect alters uterine mechanics.

modulus was at the midline of the scar tissue, which may not accurately represent the spatial variation of material properties in C-sections scars. Therefore, future work is needed to characterize the material properties and spatial variation of material properties of uterine tissue and C-section scars. Lastly, the modelled geometry only represents the average dimensions of five patients. In the future, the geometry of the uterus could be varied within the bounds of patient dimensions to understand the role of uterine geometry.

Overall, the results motivate a future parametric study which not only varies the material properties of the scar, but also the geometry of the uterus (e.g., thickness of the uterine wall) and the geometry of the defect (e.g., depth). By understanding what parameters influence the strain and stress distributions in the uterine tissue, we could identify potential risk factors for uterine rupture to be considered for patient specific planning for TOLAC. In summary, the agreement of the preliminary model results with clinical observations suggests mechanical modeling of the uterus with C-section scars presents a promising method to evaluate the risk of uterine rupture.

ACKNOWLEDGEMENTS

The authors acknowledge the NIH T32 Postdoctoral Training Grant in Regenerative Medicine (T32 EB028092).

REFERENCES

- [1] Schepker, N et al., *Arch Gynecol Obstet*, 291:1417-1423, 2015.
- [2] Savukynne, E et al., *Medicina*, 57:1091, 2021.
- [3] Louwagie, E.M. et al., *PloS one*, 16:e0242118, 2021.
- [4] Rajasekharan D et al., Summer 2020 Undergrad Project-Late Pregnancy Uterus Model, 2020.
- [5] Naji, O et al., *Ultrasound in obstetrics & gynecology*, 39:252-259.
- [6] Kan, A, *The Surgery Journal*, 6:98-103
- [7] Wheeler ML, Oyen ML, *Front Physiol*, 11:524, 2020.

MECHANOREGULATION OF CADHERIN EXPRESSION IN A 3D CO-CULTURE

Vaishali Bala (1), Faith Muriuki (1), M. K. Sewell-Loftin (1,2)

- (1) Department of Biomedical Engineering, University of Alabama at Birmingham, Birmingham, Alabama, USA
(2) O'Neal Comprehensive Cancer Center, University of Alabama at Birmingham, Birmingham, Alabama, USA

INTRODUCTION

The presence of biomechanical crosstalk between different components of the tumor microenvironment (TME) is known; however, there is a gap in understanding these mechanobiological interactions and their role in regulating tumor progression [1]. Previous work from our laboratory has shown that endothelial cells can be mechanically stimulated to promote angiogenesis in a 3D *in vitro* model via interactions with cancer-associated fibroblasts (CAFs) [2, 3]. CAFs are stromal cells that inherently have pro-tumorigenic and pro-angiogenic properties, allowing tumor growth and subsequent progression [4]. We have shown that CAFs have higher mechanical activity than patient-matched normal breast fibroblasts (NBFs); in other words, the CAFs generate larger microstrains that induce distortions to the matrix of the TME compared to normal fibroblasts. The current project focuses on investigating the biomechanical behaviors of CAFs as regulators of cell-cell crosstalk TME, specifically in the growing vascular network.

Previous work has identified cadherins as mechanosensors that are responsible for communication between cell types. For example, competition between neural cadherin (N-Cad) and vascular endothelial cadherin (VE-Cad) is essential in regulating tumor vasculature stability [5]. Moreover, heterotypic cadherin bonding between endothelial cells and smooth muscle cells has been linked to controlling vascular growth. As smooth muscle cells also demonstrate high mechanical activity or contractility levels, we hypothesize that heterotypic N-Cad/VE-Cad bonds may form between CAFs and endothelial cells to control blood vessel growth or stability in the TME. To investigate this, our studies focused on characterizing changes in cadherin expression levels for CAFs, NBFs, and a human microvascular endothelial cell line (ATCC, HMEC-1, CRL-3243). We hypothesize that the mechanical behaviors of stromal cells directly impact the expression of cadherins.

METHODS

Human microvascular endothelial cells (HMECs), cancer-associated fibroblasts (CAFs), and normal breast fibroblasts (NBFs) were tested for protein levels of VE-Cad and N-Cad using standard Western blot procedures. Briefly, the sample lysates were collected with HALT Protease and Phosphatase Inhibitor Cocktail (Thermo Scientific, no. 78441) in RIPA buffer. Samples were run in 8% SDS-PAGE resolving gels before transfer to PDVF membranes for blocking with 5% milk in TBST. Membranes were incubated overnight at 4°C in primary antibodies for N-Cad (CST, 13116, 1/1000) or VE-Cad (Abcam, ab33168, 1/1000) diluted in TBST. Membranes were next incubated with secondary antibodies for detection with ECL (Thermo Scientific, no. 32106). The blots were imaged in a LI-COR Odyssey XF Imaging System. FIJI software was used to calculate the intensity of bands for specific cadherins relative to the intensity of β -Actin.

We utilized a previously developed *in vitro* 3D microtissue model to investigate crosstalk between the fibroblasts and HMECs [2]. We cultured HMECs, CAFs + HMECs, or NBFs + HMECs in 3D fibrin gels (10mg/mL) at a 1:1 ratio for seven days before fixing and staining the cells for analysis of N-Cad (Abcam, ab19348, 1/500) or VE-Cad (Abcam, ab33168, 1/500). Both CAFs and NBFs are tagged with GFP; DAPI was used as a counterstain to determine total cell content in each sample. An epifluorescence inverted microscope (Olympus, IX-83) was used to image the samples and provide a 100 μ m z-stack; a maximum intensity z projection was generated for each sample. FIJI software was used to calculate the average size of positive staining for specific cadherins relative to the total cell area, as shown by DAPI. All samples were run in triplicate, with results reported as average plus SEM.

RESULTS

In 2D single cultures, HMECs exhibited the highest VE-Cad expression (Figure 1a), while the NBFs exhibited the highest N-Cad ex-

pression (Figure 1b). Significantly lower levels of VE-Cad were observed in both fibroblast lines compared to HMECs. In 3D co-cultures, the samples with CAFs + HMECs displayed the highest N-Cad and VE-Cad levels visually (Figure 2a). Quantifying these images, results demonstrated that there was significantly less N-Cad and VE-Cad in HMECs alone compared to the CAFs + HMECs and NBF + HMECs samples. In addition, it was observed that the CAFs + HMECs co-culture sample had significantly higher levels of N-Cad than the NBFs + HMECs co-culture (Figure 2b).

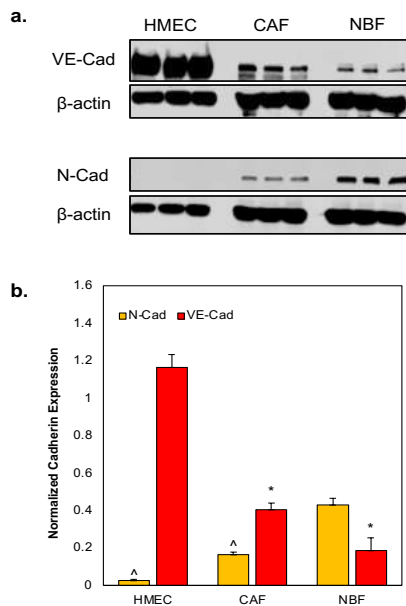


Figure 1: Analysis of Cadherin Expression in 2D. (a.) Representative Western blot images of N-Cad and VE-Cad expression in a single culture of HMECs, CAFs, or NBFs. All samples run in triplicate. (b.) Quantification of cadherins from the Western blot images, shown as expression relative to β-actin, a loading control. Averages + SEM. N=3; * p < 0.05 vs. HMEC, ^ p < 0.05 vs. NBF.

DISCUSSION

Our results indicate that the endothelial cells (HMECs) show undetectable levels of N-Cad in 2D studies but may express N-Cad when cultured in 3D microtissues. Studies show that once the endothelial monolayer reaches maturation at confluency, the levels of N Cadherin decrease in a 2D culture [6]. The cadherin interactions in a 2D monoculture are homotypic in nature. Our results indicate that the fibroblasts express VE-Cad in 2D; while unexpected, this could be due to the origin of the CAFs and NBFs from a breast cancer patient. Recent studies have highlighted that while it was previously thought only endothelial cells express VE-Cad, vascular mimicry and aggressive tumors demonstrate aberrant VE-Cad expression [7]. We next moved to 3D microtissue models and co-cultures to better understand the cadherin interactions between the different cell types. The addition of fibroblasts to the microtissue models increased the observed levels of both N-Cad and VE-Cad. The CAFs + HMEC samples demonstrated the highest levels of both cadherin types. This could be partially due to the activated, myofibroblast-like phenotype of CAFs and that it might lead to heterotypic cadherin interactions.

Future studies will utilize shRNA to genetically inhibit mechanotransduction pathways in the CAFs before analyzing N-Cad and VE-Cad expression levels in both single and co-culture. Additionally, we will utilize a 3D microtissue model design for studies of vascular systems to investigate the expression patterns of N-Cad and VE-Cad in HMECs and fibroblasts to determine if heterotypic cadherin bonds are forming. Results from our studies will elucidate how mechanobiological crosstalk occurs between cell types to regulate the vasculature and TME.

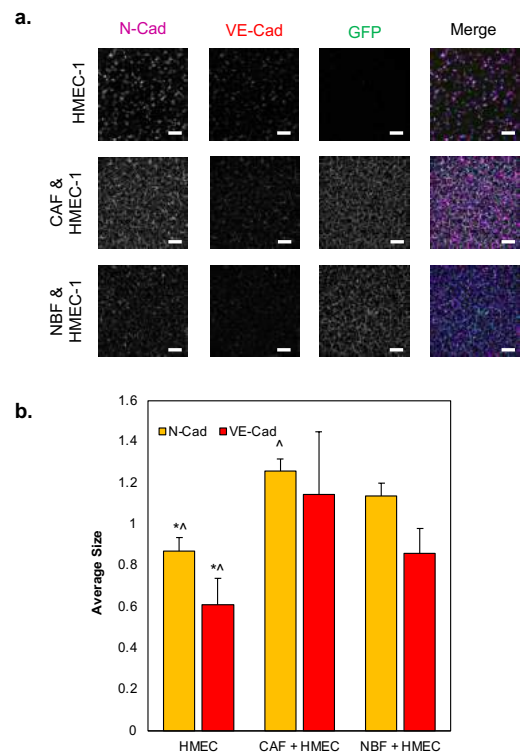


Figure 2: Expression of Cadherins in 3D Microtissue Models. (a.) Representative images from single and co-cultures of N-Cad and VE-Cad in a 3D microtissue model. Scale bar = 200μm. (b.) Quantification of cadherin expression in stained, co-culture 3D microtissue model. Averages + SEM. N=3; *p < 0.05 vs. CAF + HMEC, ^p < 0.05 vs. NBF + HMEC.

ACKNOWLEDGEMENTS

We wish to acknowledge funding for this project: R00-CA230202 (M.K.S.L.), IMPACT Award, O'Neal Comprehensive Cancer Center (M.K.S.L.), and Blazer Graduate Research Fellowship (V.B.).

REFERENCES

- [1] Zanotelli, MR & Reinhart-King CA. *Adv Exp Med Biol*, 1092:91-112, 2018.
- [2] Sewell-Loftin, MK et al. *Sci Rep*, 7:12574, 2017.
- [3] Sewell-Loftin, MK et al. *Lab Chip*, 20:2776-2787, 2020.
- [4] Augsten M. *Front Oncol*, 4:62, 2014.
- [5] Navarro, PN et al. *J Cell Biol*, 140:1475-1484, 1998.
- [6] Ferreri DM, et al. *Cell Commun Adhes*, 15:333-349, 2008.
- [7] Delgado-Bellido et al. *Mol Cancer*. 16:65, 2017.

THE MECHANICS AND MORPHODYNAMICS OF 3D MIGRATING CANCER CELLS

Bo Sun (1)

(1) Department of Physics, Oregon State University, Corvallis, OR, USA

INTRODUCTION

Cell shape is linked to cell function. The significance of cell morphodynamics, namely the temporal fluctuation of cell shape, is much less understood.

METHODS

Here we study the morphodynamics of MDA-MB-231 cells in type I collagen extracellular matrix (ECM). We systematically vary ECM physical properties by tuning collagen concentrations, alignment, and gelation temperatures. We also compare individual and collective invasion of the cells.

RESULTS

We find that morphodynamics of 3D migrating cells are externally controlled by ECM mechanics and internally modulated by Rho/ROCK-signaling. We employ machine learning to classify cell shape into four different morphological phenotypes, each corresponding to a distinct migration mode. As a result, we map cell morphodynamics at mesoscale into the temporal evolution of morphological phenotypes. We characterize the mesoscale dynamics including occurrence probability, dwell time and transition matrix at varying ECM conditions, which demonstrate the complex phenotype landscape and optimal pathways for phenotype transitions. Morphological phenotype transitions also facilitate cancer cells to navigate non-uniform ECM such as traversing the interface between matrices of two distinct microstructures.

DISCUSSION

we demonstrate that 3D migrating cancer cells exhibit rich morphodynamics that is controlled by ECM mechanics, Rho/ROCK-signaling, and regulate cell motility. Our results pave the way to the functional understanding and mechanical programming of cell morphodynamics as a route to predict and control 3D cell motility.

ACKNOWLEDGEMENTS

The work is supported by Department of Defense award W81XWH-20-1-0444 (BC190068), the National Institute of General Medical Sciences award 1R35GM138179, and National Science Foundation PHY-1844627. The results shown in the presentation are obtained from collaborative works with authors in reference 1 and 2.

REFERENCES

- [1] Morphodynamics facilitate cancer cells to navigate 3D extracellular matrix, Christopher z Eddy, Helena Raposo, Aayushi Manchanda, Ryan Wong, Fuxin Li, Bo Sun, Scientific Reports, 2021, 11:20434
- [2] The mechanics and dynamics of cancer cells sensing noisy 3D contact guidance, Jihan Kim , Yuansheng Cao, Christopher z Eddy, Youyuan Deng, Herbert Levine, Wouter-Jan Rappel, Bo Sun, Proceedings of the National Academy of Science, 2021, 118 (10) e2024780118

A COMPUTATIONAL MODEL FOR THE ROUGHNESS OF CORONARY AND CEREBRAL ARTERY STENOSIS AND TREATMENT FOR DIABETES MELLITUS DISEASE

S. Piskin (1)

(1) Department of Mechanical Engineering,
Faculty of Engineering and Natural Sciences,
Istinye University
Istanbul, Turkey

INTRODUCTION

Cardiovascular diseases (CVD) are still major threats to human health since they are the leading cause of death in western countries. Atherosclerosis occurs generally in carotid and coronary arteries and is a type of CVD related to hypertension, diabetes, high levels of cholesterol, smoking, oxidative stress, and age [1]. Atherosclerosis in coronary artery disease (CAD) or carotid artery disease is treated by implementing a stent through interventional cardiology or by deploying a bypass graft through open-heart surgery. Diabetes mellitus (DM) is one of the most common comorbid conditions in patients with coronary artery disease, which is important in determining the severity of the disease, treatment strategy, and the prognosis of patients [2].

Computational hemodynamics (CH) is an in-silico methodology to plan the coronary artery bypass grafting (CABG) or predict the short term or long-term effects of the treatment. Wall shear stress (WSS) is a prominent biomarker that can be predicted by CH and is related to the patency of the graft or the stenosed artery after the revascularization operation. But it is still controversial if high, low, oscillating or any other derivative of WSS causes restenosis of the artery or closure of the CABG. There are many ongoing clinical and computational studies to find out the possible correlations. The computational hemodynamics of CABG for DM patients is not a well-studied field even though the high number of the patient cohort. Another important factor on the hemodynamics is the roughness of the surface of the artery [9] or the graft. In the healthy left anterior descending (LAD) coronary artery, surface roughness has recently been characterized [3-4]. But, the effect of roughness on the hemodynamics has not been well characterized. It may cause a substantial change in the WSS distribution. Here, we analyze and compare the DM patients' flow dynamics to healthy control using a computational model. We also aim to find out the effects of wall roughness on the WSS for the DM patient model.

METHODS

Two different in silico models have been generated and simulated using computational fluid dynamics (CFD). For simplicity and isolate the geometrical contribution into the hemodynamics, idealized coronary artery models have been designed. Figure 1 shows the geometry of the coronary artery with mild stenosis. The roughness of the wall is assigned zero (0) for the smooth artery surface and 0.001m (height) for the rough wall.

Three-dimensional (3D) continuity and steady-state Navier-Stokes (NS) equations (Equations 1 and 2, respectively) have been solved using commercially available computational fluid flow solver ANSYS Fluent (ANSYS Inc, PA, USA). The inlet boundary condition has been assigned a velocity profile and the outlet boundary has been assigned a pressure outlet. Artery geometry has a length of 30mm and a diameter of 5mm based on the typical size of the artery [5]. The wall roughness height has been assigned as $0.5 \cdot 10^{-4}$ mm and the roughness coefficient has been set as 0.5 based on the assumption of uniform roughness.

$$\nabla \cdot \mathbf{u} = 0 \quad (1)$$

$$\rho \mathbf{u} \cdot \nabla \mathbf{u} = -\nabla p + \nabla \cdot [\mu(\nabla \mathbf{u} + (\nabla \mathbf{u})^T)] \quad (2)$$

where \mathbf{u} is the velocity vector, p the pressure, t the time, ρ and μ the density and the dynamic viscosity of the blood, respectively. Besides NS equations, the standard $k - \epsilon$ model was included to simulate the turbulence. The transport equations for the $k - \epsilon$ model are given in Equations 3 and 4.

$$\frac{\partial}{\partial t}(\rho k) + \frac{\partial}{\partial x_i}(\rho k u_i) = \frac{\partial}{\partial x_j} \left[\left(\mu + \frac{\mu_t}{\sigma_k} \right) \frac{\partial k}{\partial x_j} \right] + G_k - \rho \epsilon \quad (3)$$

$$\frac{\partial}{\partial t}(\rho\epsilon) + \frac{\partial}{\partial x_i}(\rho\epsilon u_i) = \frac{\partial}{\partial x_j} \left[\left(\mu + \frac{\mu_t}{\sigma_\epsilon} \right) \frac{\partial \epsilon}{\partial x_j} \right] + C_{1\epsilon} \frac{\epsilon}{k} G_k - C_{2\epsilon} \rho \frac{\epsilon^2}{k} \quad (4)$$

where x_i and x_j the spatial coordinates, k the turbulence kinetic energy, ϵ the rate of dissipation of turbulence kinetic energy, μ_t the turbulence viscosity, $\sigma_k (=1.0)$ and $\sigma_\epsilon (=1.3)$ the turbulent Prandtl numbers for k and ϵ , respectively, G_k the generation of turbulence kinetic energy due to the mean velocity gradients, and $C_{1\epsilon} (=1.44)$ and $C_{2\epsilon} (=1.92)$ are constants. μ_t and G_k are computed by Equations 5 and 6, respectively.

$$\mu_t = \rho C_\mu \frac{k^2}{\epsilon} \quad (5)$$

where $C_\mu (=0.09)$ is a constant, and

$$G_k = \mu_t S^2 \quad (6)$$

where S is the modulus of the mean rate-of-strain tensor, defined as $S = \sqrt{2S_{ij}S_{ij}}$. Viscosities are taken $3.5 \cdot 10^{-3}$ Pa·s and $6.8 \cdot 10^{-3}$ Pa·s [6-7] for healthy subject and diabetes mellitus patients, respectively. Densities are assigned 1060 kg/m^3 for both groups.

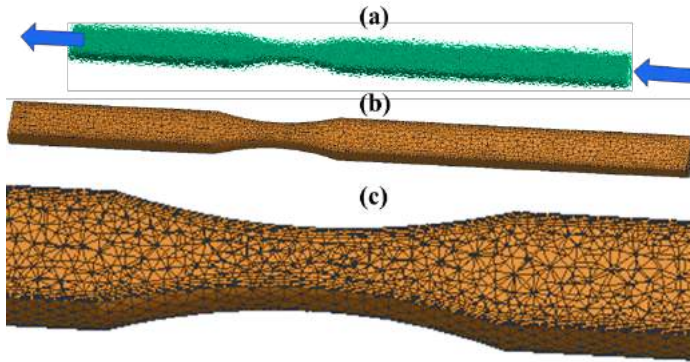


Figure 1: (a) Coronary artery model geometry with representative wall roughness and inlet and outlet boundary conditions, (b) Three-dimensional mesh with boundary layer at the proximity of the wall (c) Zoomed in view of the mesh around the stenosis zone.

CFD simulations have been run until the convergence of u_x , u_y , u_z , p , k and ϵ variables to an iteration error of 10^{-5} .

RESULTS

WSS distribution of the cases has been shown in Figure 2. WSS is higher at the proximity of the wall compared to the center of the artery for all cases: healthy control, DM patient and rough and smooth wall. Pressure distribution is verifies the physiology of linear pressure drop (not shown in the figure).

Table 1 presents the spatially averaged WSS (SAWSS) for all cases: healthy control, DM patient and rough and smooth wall. The wall roughness has been studied parametrically with respect to the roughness height and the corresponding SAWSS values have been presented in the corresponding table. Wall roughness value for the nominal case has been taken from the literature [3-4]. The other two heights represent hypothetical artery sickness, stent or vascular graft surfaces. They were simulated to analyze the possible treatment or medical device designs.

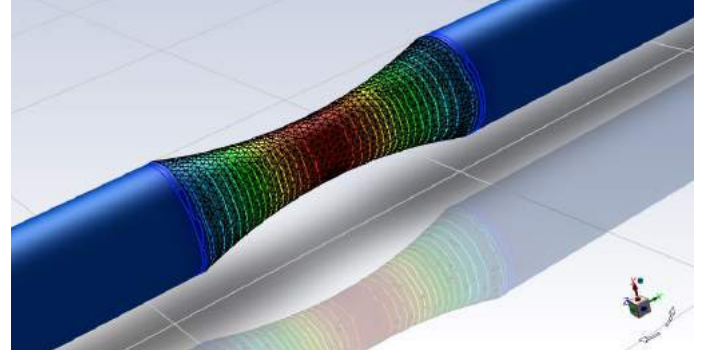


Figure 2: Wall shear stress distribution for the healthy case around the stenosis zone.

Table 1: Spatially averaged wall shear stress (SAWSS) values for all cases.

SAWSS	Healthy (Pa)	Diabetes Mellitus (Pa)
Smooth wall	107	175
Rough wall ($=3 \cdot 10^{-6} \text{ m}$) [3]	107	175
Rough wall ($=3 \cdot 10^{-5} \text{ m}$)	108	176
Rough wall ($=3 \cdot 10^{-4} \text{ m}$)	92	157

DISCUSSION

Diabetes mellitus patients may have substantially different blood viscosity levels compared to a healthy cohort. When they have the comorbidity with coronary artery or carotid artery stenosis, extra care is necessary for their cardiovascular disease treatments. Here, we have investigated the hemodynamics characterization of lumen or medical device roughness using an in-silico model for these patients. Preliminary results of our study show that the natural wall roughness does not cause any SAWSS change for neither DM patients nor healthy subjects (Table 1). But when the wall roughness is around $3 \cdot 10^{-4} \text{ m}$, the SAWSS decreases moderately, around 15% for healthy cases and 10% for DM patients. After deployment stents can have and cause roughness [8]. Actually, these roughness values can be possible by designing novel stents or bypass grafts. Decreasing the WSS values around the stenosis region could help to improve the outcome of interventions or surgical operations. The study is at its early stage with limited simulations. The simulations are planned to be improved using real coronary or carotid artery geometries and real surgery scenarios. But the results suggest that the WSS can be changed using surface roughness for DM patients.

ACKNOWLEDGEMENTS

We acknowledge the following two fundings which supported this research: Istinye University BAP project with an ID of 2019B1 and Marie-Sklodowska Curie Actions Individual Fellowship funded by European Research Executive Agency with an ID of 101038096. This project has received funding from the European Union's Horizon 2020 research and innovation programme.

REFERENCES

- [1] Avgerinos, NA et al, *Ann. Biomed. Eng.*, 47:1764–1785, (2019).
- [2] Alexandrovna BN et al, *Coronary Artery Bypass Grafting in Patients with Diabetes Mellitus: A Cardiologist's View*, 2017.
- [3] Burton HE et al, *Cardiovasc. Eng. Technol.*, 8:41-56, 2017.
- [4] Burton HE et al, *Appl. Bionics. Biomech.*, 2019.
- [5] Dodge JT Jr et al, *Circulation*, 86:232-46, 1992.
- [6] Hochmuth RM et al, *Annu. Rev. Physiol.*, 49:209–219, 1987.
- [7] Irace C et al, *Diabetes Care*, 37: 488-492, 2014.
- [8] Syaifudin A et al, *Bio-Med Mater. Eng.*, 25: 189-202, 2015.
- [9] Owen DG. et al, *J. R. Soc. Interface.*, 17:20200327-20200327, 2020

PROBING LUNG FUNCTION AT HIGH SPATIOTEMPORAL RESOLUTION VIA CRYSTAL RIBCAGE

Rohin Banerji^{1†}, Gabrielle N. Griffo^{1†}, Linzheng Shi¹, Dylan Smolen¹, Rob LeBourdais¹, Johnathan Muhvich¹, Cate Eberman¹, Bradley Hiller², Jisu Lee², Kathryn Regan¹, Siyi Zheng¹, Sue S. Zhang¹, John Jiang¹, Riley Pihl², Katrina Traber², Giovanni Ligresti², Joseph P. Mizgerd², Bela Suki¹, Hadi T. Nia^{1*}

(1) Department of Biomedical Engineering, Boston University; Boston MA.

(2) Pulmonary Center, Boston University School of Medicine; Boston MA.

(†) These authors contributed equally to this work

INTRODUCTION

The lung is a mechanically active and highly dynamic organ, being exposed to cyclic deformations from a combination of respiration and pulsatile blood flow. The addition of the air-liquid interface makes it one of the most complex organs to probe in real-time at the subcellular level. Being continuously exposed to mechanical, biological, and immunological stresses, the lung is the site of many pathologies such as primary and metastatic cancers, pneumonia, fibrosis, and obstructive diseases. Understanding the complex and dynamic function of the lung in health and disease requires characterization of structure and function at high spatial resolution to capture molecular and cellular dynamics, and at high temporal resolutions to resolve respiration-circulation dynamics such as vascular transport and cellular trafficking.

Current imaging modalities such as MRI/CT lack the spatiotemporal resolution needed to resolve dynamic events such as alveolar deformation, capillary flow, and cellular activities. Histological analysis is commonly used to visualize a snapshot of the fixed lung tissue at subcellular resolution, however, dynamic biological and physical information relevant to respiration-circulation and cellular motility are lost. Recent intravital microscopy approaches are capable of imaging microcirculation dynamics in a limited region of the lung surface at high spatial resolution through a glass window placed over an opening in the ribcage. However, these methods do not allow normal respiratory function in the imaged region as the lung is immobilized against the glass using glue or suction thereby interfering with respiration at the region of interest. Furthermore, being limited to a small region of imaging, these approaches do not capture the lung heterogeneities (e.g., apex vs. base differences) and cannot track dynamic events outside the window of imaging.

METHODS

We developed and validated a transparent ribcage, termed “crystal ribcage” to visualize and mechanistically probe the real-time dynamics

of a functioning lung at high optical resolution. Our platform is composed of a ventilated and perfused *ex vivo* mouse lung housed in a transparent crystal ribcage (Fig. 1). The crystal ribcage is a biocompatible shell with a shape that recapitulates the native mouse ribcage to provide near-*in vivo* boundary conditions for the lung to slide against during ventilation and perfusion. We designed the crystal ribcage based on μ CT scans of the mouse lung, which was specific to the age and strain of interest. The physics, biology and immunity of the *ex vivo* ventilated, perfused, and viable whole lung is preserved at near *in vivo* physiological conditions.

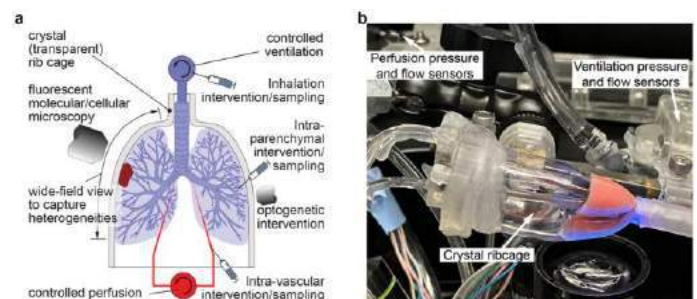


Figure 1 | Development and validation of a novel crystal ribcage and its integration into imaging platform.

RESULTS

Multiscale probing of the lung in health and disease: Utilizing the spatiotemporal resolution that this platform offers over nearly the entire surface of the lung, we, for the first time, mapped the spatial heterogeneities of alveolar deformations in healthy lungs, and quantified the alteration in alveolar deformation in multiple pulmonary pathologies such as cancer, pneumonia, and fibrosis. The large field of view provided by the crystal ribcage, combined with a novel

computational platform, allowed us to probe the lung micro-physiology in response to respiratory and circulatory pressures at multiple scales, from the whole lung down to the alveolar, capillary, and single cell scale.

We utilized LungEx to probe alveolar deformation and heterogeneities in health and key pulmonary diseases including pneumonia, fibrosis, and lung metastases with different growth patterns. We, for the first time, imaged the functional mouse lung at multiple scales starting at the whole lung level (Fig. 2a, f, k, p, u) and the lobe level (Fig. 2b, g, l, q, v), and down to the alveolar level (Fig. 2c, h, m, r, w). At all these scales, the images were acquired over a physiological range of alveolar pressures of 3, 7, 12, and 18 cmH₂O.

Next, we probed how the alveoli are remodeled by early-stage metastatic tumor. We observed much denser tumors in the case of the MMTV tumors reflected in the organ (Fig. 2f), lobe (Fig. 2g), and alveolus levels (Fig. 2h). Interestingly, in nodular growth pattern (Fig. 2i), we observed much smaller strain values (i.e., very stiff) intratumorally compared to the infiltrative tumor with similar diameters (Fig. 2n). Intriguingly, due to the “pushing” effect of the nodular tumor, alveoli remained distended even at low alveolar pressures (Fig. 2j), while the alveoli in the infiltrative tumors change diameters with pressure similar to those far from the tumor (Fig. 2o).

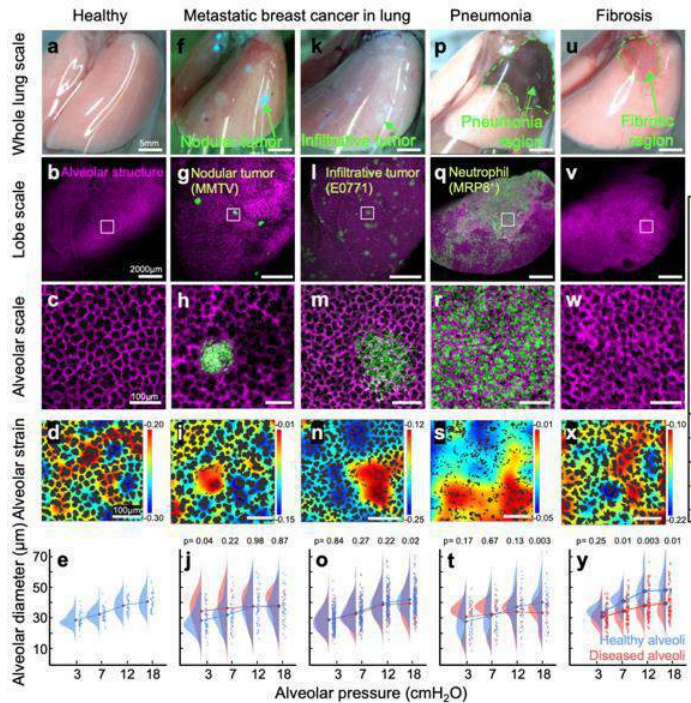


Figure 2. The crystal ribcage allows multi-scale analysis of lung micromechanics in health and disease.

Next, we probed the remodeling of single alveoli by pneumonia. We used a left lobar model of bacterial pneumonia (*Streptococcus pneumoniae* serotype 3, Sp3) induced in MRP8-mTmG reporter mice, where the MRP8+ cells (neutrophil dominant) express green fluorescent protein (GFP) in the cell membrane. The whole-lung level imaging through the crystal ribcage shows the hepatized left apex (Fig. 2p), densely packed with MRP8+ neutrophils at both the lobe (Fig. 2q) and alveolar scales (Fig. 2r). Surprisingly, the alveoli that were affected by pneumonia showed equal or even greater stiffening compared to nodular tumors (Fig. 2s,i). We also observed more heterogeneities in alveolar diameter, not only in the infected areas, but in the alveoli adjacent to them (Fig. 2t). Finally, we applied the bleomycin model of lung fibrosis

on Col1a1-Cre-mTmG reporter mice. Lung cells of this transgenic mouse are labeled tdTomato and those with an active Col1a1 promoter become GFP-labeled upon tamoxifen administration. By taking advantage of the whole lung fluorescence, we identified dense fibrotic patches in the alveolar structure imaged using tdTomato and fibroblast aggregates using GFP (col1a1-mTmG).

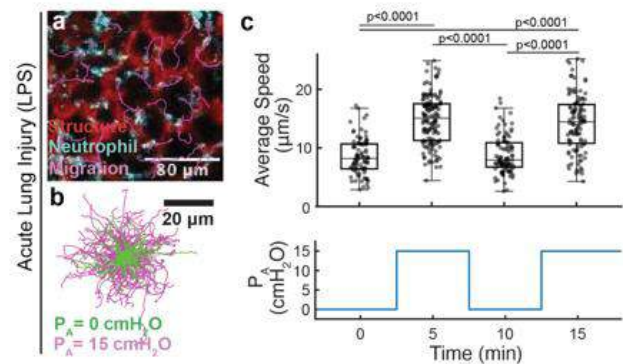


Figure 3. Mechanosensitivity of neutrophils to hydrostatic pressure.

Mechano-immunity of the lung: Neutrophils traffic into the lung in response to injury and infection. While neutrophil responsiveness to shear stresses and cyclic pressure has previously been reported, we show that migration of neutrophils in the lung is highly dependent on hydrostatic vascular pressure, in the absence of perfusate flow and shear stresses (Fig. 3). By real-time tracking of neutrophils at vascular pressure of 0 and 15 cmH₂O under no flow conditions and a constant alveolar pressure of 7 cmH₂O, we found that neutrophils were substantially more migratory and traveled a longer distance over 5 minutes at higher perfusate pressures (Fig. 5).

DISCUSSION

We have presented the development, validation, and several key applications of the LungEx platform for multiscale imaging of the whole, functional mouse lung in real-time. Whereas previous methods (i) do not resolve micro-scale features (such as in MRI, CT), (ii) provide no temporal resolution, lose the 3D architecture and functional air-liquid interface (such as in histology), or (iii) lack respiratory motion within a small field of view (such as in intravital microscopy), the crystal ribcage supports multiscale and high spatiotemporal resolution imaging of the whole organ with near-*in vivo* boundary conditions to capture dynamic functions of the lung simultaneously over almost the entire surface of the lung. We have applied LungEx to image a wide range of lung dynamic (dys)functions at multiple spatial scales including alveolar deformation and elasticity, capillary distensibility, cellular deformation, trafficking and migration of immune cells, and vascular transport. We demonstrated the capabilities of LungEx in health and pathologies such as nodular and infiltrative lung metastases, pneumonia, acute lung injury, and pulmonary fibrosis. Furthermore, this transformative platform offers a wide range of applications to mechanistically probe pathophysiologies relevant to the lung parenchyma such as in emphysema, adenocarcinoma, ventilation-induced lung injury, and dysfunction of blood and lymphatic vessels in aging and lung transplantation.

ACKNOWLEDGEMENTS

We acknowledge NIH DP2HL168562 Award, Beckman Young Investigator Award, Neurophotonics Center, and Center for Multiscale Translational and Mechanobiology.

INFLUENCE OF MULTIDIRECTIONAL LOADING ON MENISCUS WEAR BEHAVIOR

Kate J. Benfield (1), Katherine J. Fors (2), Trevor J. Lujan (2)

(1) Biomedical Engineering Doctoral Program, Boise State University, Boise, ID, USA
(2) Department of Mechanical & Biomedical Engineering, Boise State University, Boise, ID, USA

INTRODUCTION

The menisci are fibrocartilaginous tissues that facilitate smooth articulations and attenuate 45-75% of loads across the knee joint.¹ Through overuse and mechanical wear, the menisci become prone to degeneration – a retrogressive breakdown of the fibrous network.² This degeneration affects nearly 20% of people over 50 years of age, and over 55% of people over 70 years of age.² As degeneration progresses, microstructural changes to the fiber network occur, resulting in pain, joint instability, restricted physical activity, and increased likelihood of developing knee osteoarthritis.³ Given the high prevalence of meniscal degeneration, the characterization of meniscal wear behavior is vital to understanding the pathomechanics of joint degeneration, yet no study has characterized the mechanical wear behavior of meniscus tissue.

Mechanical wear within the knee joint is a system response that is dependent on the contact conditions of interfacing surfaces. Numerous in-vitro wear studies of artificial joints have shown that unidirectional motion promotes fiber orientation and hardening along the principal fiber direction, while multidirectional motion creates an environment of continually changing shear (cross-shear), leading to accelerated wear debris.⁴⁻⁶ Similar to polyethylene components in artificial joints, meniscus tissue has a complex and highly organized fibrous network and experiences multidirectional motions during daily activities, and could therefore be susceptible to accelerated wear due to cross-shearing. The objective of this study was to characterize the wear behavior of bovine meniscus subjected to repeated multidirectional and unidirectional contact with bovine articular cartilage.

METHODS

Specimen Preparation: Cartilage plugs (n = 6) were extracted using a drill-press and custom corer from the femoral surface of one skeletally mature bovine femur. Each cartilage pin was 4 mm in diameter and composed of the cartilage layer and approximately 8 mm

of subchondral bone used for mounting (**Fig. 1A**). The medial meniscus from the same bovine specimen was harvested and packed in cellu-clay. Following our previously published methods,⁷ the meniscus was cut into 2 mm thick layers to serve as the “plate”. The most superficial layers of these strips were used for six experiments: unidirectional loading (n = 3) and multidirectional loading (n = 3). Custom-made tooling was utilized to cut each meniscal strip (25 mm x 10 mm) (**Fig. 1B**), and to flatten the natural curvature of the meniscus to allow for a uniform plate surface. Specimens were wrapped in gauze soaked in 0.9% saline solution and frozen. On the day of mechanical wear testing, each sample was thawed for 1 hour (21°C).

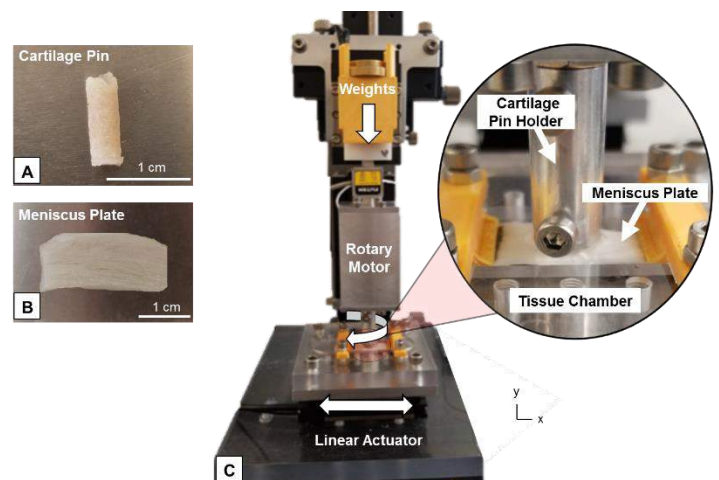


Figure 1: Pin-on-plate system for A) femoral cartilage pin and B) flat bovine meniscus plate. C) Two-axes of motion enable multidirectional loading (white arrows) to create cross-shear between the pin and plate in the tissue chamber.

Mechanical Wear Testing: A custom built pin-on-plate device applied unidirectional and multidirectional loading conditions by simultaneously spinning and translating the cartilage pin relative to the meniscus plate (**Fig. 1C**). For each of the six experiments, the meniscus plate was first clamped into the test chamber and immersed in 0.9% saline solution while the cartilage pin was rigidly fixed to the test apparatus via set screws. To ensure proper loading along the principal fiber direction, the meniscus plate was aligned so that the longitudinal fibers were parallel to the x-axis. Using weights, a 3.5 N vertical load was applied between the cartilage and meniscus corresponding to approximately 67% of physiological stresses during walking.⁸ For the unidirectional loading condition, the meniscus specimen oscillated linearly at a rate of 4 mm/s along the longitudinal fiber orientation (4 mm stroke). For the multidirectional tests, this exact protocol was used, except that the cartilage pin was also spinning at a rate of ~0.5 Hz, thus creating a perpendicular component to the translational motion (cross-shear) (**Fig. 1C**). For each specimen, the thickness of the meniscal tissue was measured for 10,000 cycles using a linear encoder (accuracy = 1 μm). Linear wear was recorded as the displacement of the meniscal tissue over the duration of testing. Following testing, each specimen was imaged using a light microscope (Leica DM750) to visualize the worn meniscus surface. The effect of loading condition on linear wear was assessed using an independent t-test in SPSS ($p < 0.05$).

RESULTS

The multidirectional loading condition showed greater meniscal tissue displacement within the wear region-of-interest than unidirectional loading (**Fig. 2A-B**). Steady-state wear was achieved for multidirectional ($R^2 = 0.94$) and unidirectional ($R^2 = 0.92$) loading after an initial 1000 cycles (run-in). The menisci had average steady-state wear rates of $0.016 \mu\text{m}/10^3\text{-cycles}$ and $0.012 \mu\text{m}/10^3\text{-cycles}$ for multidirectional and unidirectional loading, respectively (**Fig. 2C**). Overall, the application of multidirectional loading increased the linear wear of meniscus by 30% relative to unidirectional loading (**Fig. 2C**), a significant increase ($p = 0.013$).

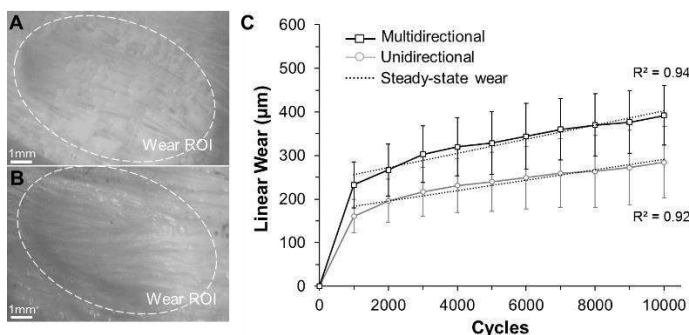


Figure 2: Wear behavior of bovine meniscus subjected to A) unidirectional and B) multidirectional contact conditions. C) Linear wear is greater for multidirectional motion relative to unidirectional x-axis motion ($p = 0.013$).

DISCUSSION

Given the high prevalence of meniscal degeneration, characterizing meniscal wear behavior is vital to understanding disease pathomechanics. While prior studies have evaluated the coefficient of friction in meniscus tissues ($0.09 - 0.25$)⁹, and the mass wear rate of bovine knee articular cartilage ($52 \pm 0.24 \mu\text{g}/\text{m}^3$)¹⁰, no study to our knowledge has quantified the wear behavior of meniscal tissue. This study characterized bovine meniscus wear behavior under varying contact conditions using a pin-on-plate test system. To our knowledge,

this is the first study to evaluate the influence of multidirectional loading on mechanical wear within meniscus tissue, or any soft tissue.

Our results show that the application of multidirectional loading significantly increases the steady-state wear rate of bovine meniscus tissue by nearly 30% (**Fig. 2C**). These results follow a similar trend to those observed during wear testing of polyethylene components in artificial joints. Marrs et al., determined that multidirectional motion led to greater wear versus unidirectional motion in polyethylene,¹¹ however their wear rates were nearly 3x greater than the wear rates observed in the present study. Additionally, our results can be compared to a prior cartilage-on-cartilage study. Northwood et al., applied 30,000 cycles of unidirectional and multidirectional motion between a bovine articular cartilage pin and cartilage plate and found a 60% increase in surface roughness for the multidirectional case.¹² This is consistent to our results as increased surface roughness may potentially lead to more material wear debris being removed from the surface. Furthermore, we observed that the worn meniscal surfaces of the unidirectional cases appeared to have more pronounced fiber alignment and hardening within the wear region of interest (**Fig. 2A**) than the reoriented fibers of the multidirectional case (**Fig. 2B**). This indicates that the cross-shear phenomena, observed in polyethylene⁵, may also exist in meniscal tissue. Consequently, daily activities associated with cross-shear may be detrimental to the structural integrity of meniscus tissue, thus potentially leading to greater risk of degeneration. For example, stair climbing creates multidirectional joint motions, and is associated with nearly two times greater risk of meniscal degeneration.¹³

A principal limitation of this study is that the measured wear may be caused by material wear, creep, or a combination of the two. This challenge can be overcome through the use of a load-soak control (axial loading only) to determine the linear displacement due to creep and swelling.¹⁴ Additionally, plate specimens were independent of meniscus region (anterior, central, posterior) which could have influenced mechanical wear behavior. Future experiments are planned to apply varying loading magnitudes to 100,000 cycles within different meniscus regions to better understand the regional wear behavior under multidirectional and unidirectional contact conditions.

In summary, we have shown that meniscal wear is dependent on contact motion, which suggests that activities associated with cross-shearing could increase the risk of tissue degeneration. This study provides a basis for measuring meniscus wear and important joint system responses that are essential to developing mechanistic theories that describe and predict the pathomechanics of meniscus degeneration.

ACKNOWLEDGEMENTS

This project was supported by NIH (NIAMS 1R15AR075314-01).

REFERENCES

- [1] Shrive et al., Clin Ortho Relat Res. 1978. (131):279
- [2] Englund et al., J. Med. 2008. 359(11)
- [3] Englund et al., Rad Clinics. 2009. 47(4)
- [4] Korduba et al., Wear. 2011. 271(9-10)
- [5] Turell et al., Wear. 2003. 255(7-12)
- [6] Bragdon et al., Proc Inst Mech Eng 1996. 210(3)
- [7] Wale et al., JBE. 2021.
- [8] Majd et al., Colloids and Sur. 2017. (4)
- [9] Link et al., Clin Biomech 2020. (79)
- [10] Hossain et al., JMBBM. 2020. (109)
- [11] Marrs et al., J Mats Sci. 1999.
- [12] Northwood et al., Clin Biom. 2007. 22(7)
- [13] Snoeker et al., J Ortho Spts Phys Ther. 2013. 43(6)
- [14] Warburton et al., J Ortho Res. 2018. 36(4)

DEVELOPMENT AND VALIDATION OF A SMART SCREWDRIVER (SSD) FOR SPINE SURGERY

Allison M. Tanner (1), Daniel Jacobson (1), Alexander W. Hooke (1), James S. Fitzsimmons (1,2), Chunfeng Zhao, M.D. (1,2), Brett A. Freedman, M.D. (1,2)

(1) Biomechanics Core, Mayo Clinic, Rochester, MN, USA
(2) Department of Orthopedic Surgery, Mayo Clinic, Rochester, MN, USA

INTRODUCTION

Spinal fusion is prescribed to treat spinal deformity and instability resulting from a variety of indications, such as spine fracture, degenerative disks, severe scoliosis, or stenosis [1]. As technologies in spinal surgeries have advanced, so have recommendations for spinal fusion, resulting in an increased frequency of fusion surgery [1],[2].

A critical demand for all fusions is implant fixation, which relies primarily on anchors that connect to bone. Trabecular bone screws, such as pedicle screws, are the most common anchors used in fusion surgeries. Achieving optimal screw fixation is crucial, especially in osteopenic or osteoporotic patients. Failure of screw fixation such as screw migration, loosening, or pullout can lead to severe complications such as fusion non-union, unstable spine segments, or even neurological injury that increases the likelihood of revision surgery. According to data from 2002 to 2009, mechanical complications of implanted devices was the most common primary diagnosis for all revision fusions [3].

Though many factors affect screw fixation strength, peak insertion torque is known to be a key determinant [4]. Over-torquing can cause the screw to strip in trabecular bone, while low insertion torque implies a missed opportunity for greater fixation strength and higher risk of complications following surgery. Currently, surgeons rely on intuition and feel to determine when a screw has been appropriately tightened, but optimal torque is a quantitative property that is not reliably discerned by the surgeon's hand and varies based on bone quality, trajectory, and screw design. A comprehensive study found surgeons stripped screws more frequently than biomechanical researchers with no surgical experience (48% vs 18%), and for researchers and surgeons with high stripping rates, an augmented screwdriver that indicated when optimal torque had been reached reduced stripping rates [5].

We have characterized three phases of cancellous bone screw insertion (**Fig. 1**). The initial goal of this project is to develop a device to conduct extensive experimentation studying the correlation between torque value in phase 1, torque slope in phase 2, and percentage of total

torque in phase 3 with varied bone quality and screw size using both foam and cadaveric bones. This data will be used to develop an algorithm which can predict peak torque based on initial phase 3 torque, therefore determining optimal torque to achieve strong screw insertion.

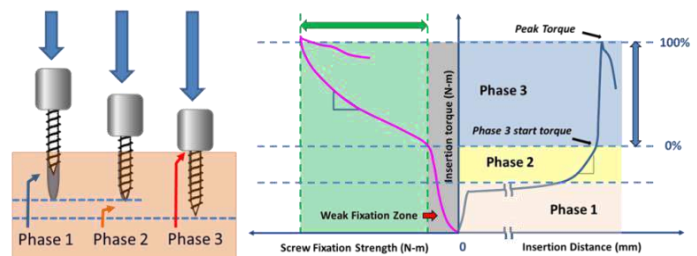


Figure 1: Characterization of screw insertion mechanics and relation between insertion torque and screw strength.

Because of the inconsistency in successful screw fixation, and evidence suggesting that real-time quantitative indicators of optimal fixation improve surgeon performance, there is a need for a tool that can be used in a surgical setting to assist with determination of optimal fixation. Therefore, the ultimate goal of this work is to develop an intelligent, instrumented screwdriver which measures insertional torque and can provide algorithmic predictions of bone strength and implant failure.

METHODS

Device Design

A custom benchtop device was designed and constructed to insert screws into foam bones or vertebral bodies with controlled parameters, while collecting data characterizing the insertion torque profile (**Fig. 2**).

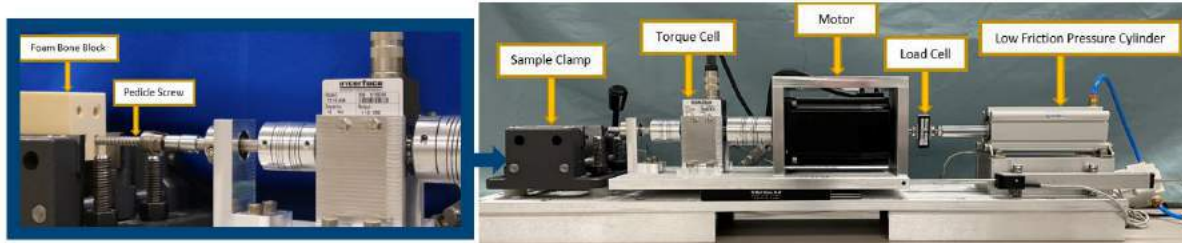


Figure 2: Smart Screwdriver Device (SSD).

The device consists of an electropneumatic regulator connected to a low friction pressure cylinder, which provides a constant, axial force when the device is in operation. A load cell (Transducer Techniques, Model: MLP-100, 100lbs) connected to the pressure cylinder measures and reports force. The end-effector of the device is rotated using a motor, and a torque transducer (Interface Force Measurement Solutions, Model: T2-10-A3A, 10Nm) measures insertion torque as the screw is driven into samples. A custom LabVIEW program allows the user to specify insertion distance, rotation speed, and axial force.

Data Collection

Data was collected on foam bones intended to mimic both osteoporotic and healthy bone (Synbone PCF 12.5 and PCF 20 Cell, respectively) using a 40mm pedicle screw. Screws were inserted with an axial force of 15N at a speed of 5rpm until the surrounding foam bone stripped, or the head of the screw was sunk into the foam bone. Insertion parameters were selected based on values measured from an instrumented screwdriver and load cell as a spine surgeon drove screws into similar foam blocks.

Foam bone samples were tapped and pre-drilled using appropriately sized clinical tools and clamped such that the pre-tapped hole was directly in line with the path of the screw as attached to the end-effector of the device (Fig. 2). Initial testing and validation of the device sought to ensure that reasonable torque profiles were acquired and could be used to detect differences between foam bone densities.

RESULTS

The healthy bone surrogate stripped at a higher peak torque than the osteoporotic bone surrogate (2.1 Nm and 0.76 Nm, respectively), which stripped prior to entering phase 3 of the expected torque profile (Fig. 3). Torque per 90° screw rotation was also assessed (example, Fig. 4), which shows torque increases across individual turns and isolates turns in which bone was stripped.

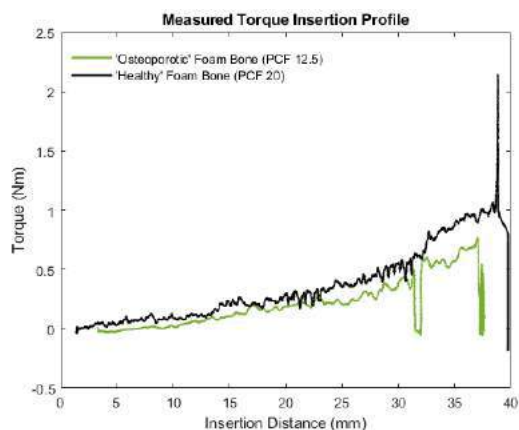


Figure 3: Torque insertion profile of a 40mm pedicle screw for PCF 12.5 Cell and PCF 20 Cell foam bones (Synbone).

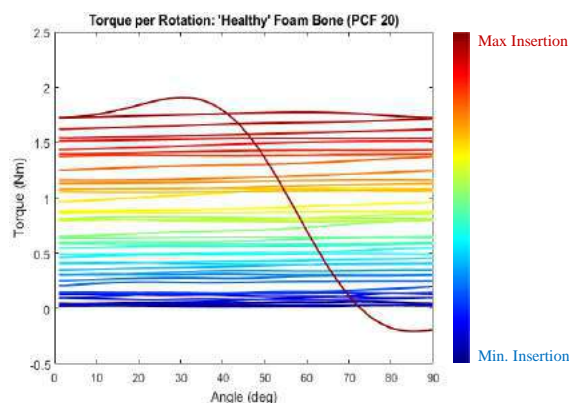


Figure 4: Torque per 90° screw rotation. Colors indicate insertion depth (mm). Torque increases steadily until the final turn, where the sharp drop-off in mid-rotation indicates stripping.

DISCUSSION

There are many variables affecting screw fixation strength and failure, one of which is the person inserting the screw. One recent study compared screw tightness and stripping between surgeons and biomechanical researchers and demonstrated that the surgeons stripped screws at a higher rate [5]. This may indicate that mechanical training is a factor in optimal screw fixation. Successful development of an SSD that has been well-trained by machine learning and AI could help eliminate human error.

Initial data collections using the SSD are promising. Torque profiles vary between foam bones of different densities, and higher values are required to strip “healthy” bone than “osteoporotic” bone, consistent with clinical trends. Bone stripping can be isolated to a single screw rotation.

Additional data will be collected on varying foam bones and pedicle screws to increase sample power and develop algorithmic predictions of stripping torque. Once collection on foam bones is complete, data will be collected using vertebrae from cadaveric specimens. Finally, engineering design will move to development of a handheld device that could feasibly be used in a surgical setting, as opposed to a benchtop device.

ACKNOWLEDGEMENTS

This project was supported by the Mayo Clinic Department of Orthopedic Surgery in conjunction with the Wendel Foundation and the Mayo Clinic Biomechanics Core.

REFERENCES

- [1] Martin, B et al., *SPINE*, 44:369-376, 2019.
- [2] Rajaei, S et al., *SPINE*, 37:67-76, 2012.
- [3] Rajaei, S et al., *The Bone and Joint Journal*, 96-B:807-816, 2012
- [4] Ab-Lazid, R et al., *J of Mech Behav of Bio Mat*, 40:354-361, 2014
- [5] Fletcher, J et al., *J of Ortho Surgery and Research*, 16:1-9, 202

MICROMECHANICAL MODEL OF MECHANOSENSITIVE COLLAGEN TISSUES

Kalyn G. Younger (1), William Cortes (2), Daniel H. Reich (2), Thao D. Nguyen (1)

(1) Mechanical Engineering, Johns Hopkins University, Baltimore, MD, United States

(2) Physics and Astronomy, Johns Hopkins University, Baltimore, MD, United States

INTRODUCTION

The mechanical behavior of soft collagenous tissues is largely influenced by the reinforcing collagen fiber microstructure. The anisotropic collagen microstructure can remodel in response to changes in mechanical loading, which can dramatically alter the mechanical properties of the tissues and the mechanical environment of the resident cells. It is important to study the remodeling mechanisms of collagen tissues to understand the pathophysiology of various connective tissue diseases. We hypothesize that the collagen structure actively changes in response to mechanical stimuli through concurrent processes of collagen deposition and degradation and that the rates of these processes are altered by collagen mechanochemistry, mechanosensitive collagen production, and cellular contraction. In prior studies, we developed micromechanical models of collagen tissues to investigate the role of collagen mechanochemistry and mechanosensitive collagen production in remodeling the collagen fiber structure and tissue growth.[1,2] We found that stress inhibition of enzymatic degradation and stimulation of collagen production can explain many phenomena, including remodeling the anisotropic collagen structure along the directions of the maximum principal stress and the development of stress homeostasis.

The goal of this study is to investigate the effect of mechanical loading on the active behavior of the cells. Our approach uses a model 3D microtissue system, self-assembled on a magnetically actuated two-pillar system (μ TUG), to investigate these cell-collagen interactions and effects of mechanical loading.[4] The micropillar support allows for measurement of the active cellular contraction, while the magnetic tweezer allows for mechanical testing of the microtissue under a controlled stress rate. Digital image analysis is applied to measure the local two-dimensional (2D) strain field.

To analyze the mechanical measurements for mechanical properties of the collagen structure and active behavior of the cells, we developed a micromechanical model for the mechanical behavior of the microtissue. The micromechanical model includes the elastic behavior

of the anisotropic collagen structure and the anisotropic active behavior of the cells. To describe mechanosensitive cellular contraction, we assume concurrent polymerization/depolymerization of actin filaments, where the polymerization rate increases with the fiber stress.[3]

In this paper, we will briefly summarize the model and describe an initial model validation by comparing to μ TUG experiments measuring the stress-strain behavior of the microtissue to load-unload tests.

METHODS

Mechanical characterization: To validate our model we considered previous studies of Liu et al. [4] of microtissues composed of bovine pulmonary artery smooth muscle cells (SMCs) in model collagen/fibrinogen matrix. In this prior study, microwell array devices (μ TUGs) were fabricated from poly(dimethylsiloxane) (PDMS) via replica molding. One of the two micropillars in each well was affixed with a 100 μ m nickel sphere for actuation by magnetic tweezers. Microtissues were seeded in the μ TUG arrays from SMC-collagen/fibrinogen mixtures at a density of \sim 300 cells per microwell. Over the course of 24-48 hours microtissues self-assembled on the pillars. During tissue formation, the cells contracted and compacted the extracellular matrix (ECM) causing the pillars to deflect. The deflection of the pillars was measured via phase-contrast imaging [4] and used to calculate the baseline active stress $\sigma_0 = 5.1$ kPa.

Uniaxial quasi-static load-unload tests were performed on individual microtissues by actuating the magnetic pillars via magnetic tweezers. The tissues were stretched using a magnetic force of 25-35 μ N over 120 s and then unloaded to nominally zero stress at the same rate. The passive mechanical behavior of the ECM was directly measured with the same stretching protocol on tissues treated with Triton X-100 for 10 min, to lyse the cells.[4]

Micromechanical constitutive model of microtissue: We conceptualize the microtissue as an anisotropic network of wavy collagen fibrils arranged in an isotropic matrix that represents the

nonfibrous extracellular matrix materials and passive mechanical behavior of the cells. The wavy collagen fibers are modeled as planar sinusoidal elastica, with initial crimp angle $\Theta(\mathbf{X})$, subjected to a horizontal force, which causes the fibers to unbend and stretch axially. The axial stretch, $\lambda_f(\mathbf{X})$, and deformed crimp angle $\theta(\mathbf{X})$ can be determined as described by Comninou and Yannas [5]. The strain energy density of the fiber is given by, [1]

$$U_f = \int_0^1 \left[\underbrace{\frac{E\beta D^2}{2} (\theta(\bar{X}_1) - \theta(\bar{X}_1))^2}_{U_{bend}} + \underbrace{\left[\frac{E}{2} (\lambda_f(\bar{X}_1) - 1)^2 \right]}_{U_{axial}} d\bar{X}_1, \quad (1)$$

Where E is the fiber axial modulus, β is the bending stiffness of the fiber cross-section, and D is the collagen diameter. The contractile cells exert a force on the collagen fibrils in their environment. The active stress of an actin filament is described by a Hill-Type law given in [2],

$$\sigma_{sf}(\theta) = \sigma_{\max} f(\lambda_\theta) g(\dot{\lambda}_\theta), \quad (2)$$

where σ_{\max} is the isometric contraction of an actin filament and $f(\lambda_\theta)$ and $g(\dot{\lambda}_\theta)$ describe the strain sensitivity and rate sensitivity of the contractile stress. We assume the cellular component of the tissue can be described by an anisotropic network of stress fibers that undergo concurrent polymerization and depolymerization in response to stress. Furthermore, we assume that the rate of polymerization increases with the fiber stress. This process is incorporated into the model as a kinetic equation for the fiber volume fraction. [3]

$$\frac{d\phi_{sf}(\theta)}{dt} = (k_0^f + k_1^f \sigma_{sf}(\theta, \lambda_\theta, \dot{\lambda}_\theta)) \phi_{am} - k_d \phi_{sf}(\theta) \quad (3)$$

Finally, we assume that active stress of the cells and passive stress of the extracellular matrix add to give the tissue stress response,

$$\sigma = \frac{1}{\pi} \phi_{sf} \int_{-\pi/2}^{\pi/2} \sigma_{sf}(\theta) \rho_{sf}(\theta) \mathbf{a} \otimes \mathbf{a} d\theta + \frac{1}{\pi} \phi_{cf} \int_{-\pi/2}^{\pi/2} \frac{\partial U_f}{\partial \lambda_\theta} \frac{1}{\lambda_\theta} \rho_{cf}(\theta) \mathbf{F} \otimes \mathbf{F} d\theta + \phi_m (\mu \mathbf{B} - p \mathbf{I}), \quad (4)$$

where ϕ_{sf} , ϕ_{cf} , and ϕ_m are volume fractions, ρ_{sf} and ρ_{cf} are angular distributions of fibers, \mathbf{a} is the deformed orientation of the fibers, σ_{sf} is the active stress generated by the stress fiber. We applied the model to simulate the uniaxial tensile tests of the microtissues (Fig. 1C-D).

RESULTS

We fit the scaled isometric contraction $\phi_{sf} \sigma_{\max} = 0.2$ kPa to the baseline stress of the microtissue and use the parameters of $f(\lambda_\theta)$ and $g(\dot{\lambda}_\theta)$ determined in a prior study.[3] We used $\beta = 0.02$ and initial crimp angle $\Theta_0 = 29^\circ$ determined in a prior study [1] and fit the axial modulus $E = 1.2$ MPa (Fig.1C). These results are used to validate the model response in Fig. 1D. This preliminary result shows that the model can recapitulate the loading curve for the untreated tissue. The model accurately predicted the modulus at small strain but overestimated the peak stress. In contrast, the model produced a poor fit for the Triton treated cells. Experiments showed that the Triton treated tissues also exhibited a small baseline stress $\sigma_0 = 1.6$ kPa caused by tissue compaction, which we neglected. The small baseline stress may have straightened the collagen fibers, such that subsequent stretch produced a linear stress-strain response. Fig. 1E shows the model prediction of the reorientation of stress fibers towards the loading direction.

DISCUSSION

This study proposed a model for the investigation of the interaction of mechanosensitive stress fiber evolution and the non-linear properties of the ECM in 3D microtissues. The current model demonstrates how physically derived parameters can describe the mechanical response of

the microtissues. The model has some limitations. First, the model neglected the effects of tissue compaction and the viscoelastic behavior of the collagen structure. Consequently, the model cannot reproduce the hysteresis of the unloading response. The viscoelastic response of the collagen needs to be coupled with the contractile dynamics of the cells to investigate the shielding by the cells of the viscoelastic effects.

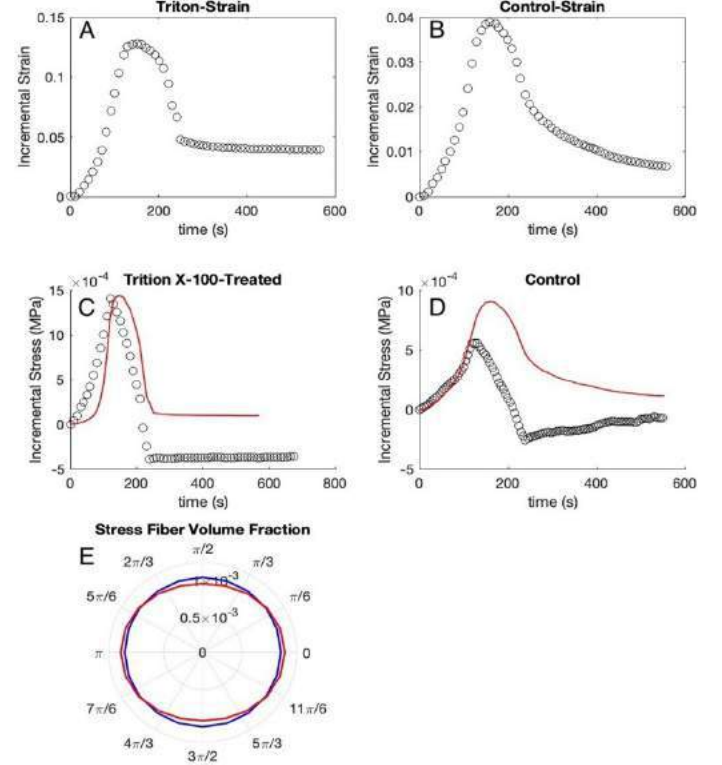


Figure 1: (A-B) Measured strain of Triton-treated and untreated tissue. (C) Model fit of the stress response of Triton-treated tissue. (D) Model prediction of the stress response of the untreated tissue. (E) Loading caused the initially isotropic stress fibers (blue) to align in the loading direction (red). Data in A-D from [4].

We also assumed an initial isotropic distribution of the collagen and stress fibers. However, confocal imaging of the matured tissues before loading revealed that the collagen and stress fibers exhibited a dominant axial orientation. To account for tissue maturation, we will incorporate the anisotropic collagen and actin fiber structure and the cell-mediated tissue compaction of the matured tissue.

In future studies, we apply a viscoelastic extension of the model to investigate the effect of strain rate on cell response. Furthermore, we will extend the model to include a fiber-level description of collagen remodeling and the effects of strain inhibition of collagen degradation and strain stimulation of collagen production.

ACKNOWLEDGEMENTS

Supported by National Science Foundation Grant CMMI-2032922

REFERENCES

- [1] Tonge, T. K. et al., *Biophysical journal*, 109(12):2689-2700, 2015.
- [2] Jia, Z. et al., *J Mech Behav Biomed Mater*, 98:96-107, 2019.
- [3] Obbink-Huizer C et al., *Biomech Model Mechanobiol*, 13(1):227-236, 2014
- [4] Liu A.S. et al., *Sci Rep*, 6:33919, 2016
- [5] Comninou M et al., *J Biomech*, 9:427-433, 1976.6

RETROPUBIC TROCAR TEMPORAL CHARACTERISTICS BETWEEN EXPERT AND NOVICE SURGEONS

Md A. Arif (1), Austin Bachar (2), Gregory W. King (1), Gary, Sutkin (2), Antonis P. Stylianou (1)

(1) School of Science and Engineering, University of Missouri – Kansas City, Kansas City, MO, USA

(2) School of Medicine, University of Missouri – Kansas City, Kansas City, MO, USA

INTRODUCTION

The Retropubic Midurethral sling (MUS) procedure is the most common surgical treatment for stress urinary incontinence. During the procedure, a sharp trocar is used to place the sling beneath the urethra. The trocar is blindly navigated through the vaginal canal, cephalad to the pubic symphysis and finally exiting the body above the pubic bone. This path is adjacent to the urethra and bladder and near the iliac blood vessels and the bowel. Surgeons must rely on haptic feedback from the trocar as it makes contact with the surface of the suprapubic bone. Failure to guide the trocar correctly can lead to several complications including bladder and urethral perforations (4.9%), bowel perforation (0.1%) and injuries to major blood vessels (2.0%). Error rates among novice surgeons are higher in comparison to experts [1-2].

Successful trocar passages depend on correct navigation of the trocar through the retropubic space using a series of discreet steps. The discreet steps of the procedure can be defined as: Stage 1: trocar tip from incision to pubic bone contact, stage 2: trocar tip from first contact to the most cephalad point of the pubic bone, stage 3: trocar tip from most cephalad point to the most ventral point of the pubic bone, stage 4: trocar tip from the most ventral point of the pubic bone to the exit point. Novice surgeons are instructed to advance the trocar in an anterior/cephalad direction until the trocar makes contact with the pubic bone, then aim for the exit point right above the pubic symphysis and about 2 cm lateral to the body midline while continuously maintaining contact with the pubic bone.

The objective of this study was to investigate trocar temporal and spatial characteristics during simulated MUS procedures between expert and novice surgeons.

METHODS

Three expert surgeons with experience performing and teaching at least 100 retropubic MUS procedures and three novice surgeons with no experience performing the procedure participated in this study.

Simulated MUS procedures were performed on a surgery simulator described previously [3]. Briefly, three simulation models were created by segmenting the pelvic bones and organs, and 3d printing the pelvic bone structure from MRI of three patients with urinary stress incontinence. The open space in the simulator was filled with thermoballistic gel to provide the haptic feedback associated with trocar passage through soft tissue. The biofidelity of the simulator was investigated previously [3].

Participants used a Gynecare TVT trocar with the mesh tape removed connected to a Gynecare TVT introducer (Ethicon Inc, Somerville, NJ). The introducer was fitted with a 3d printed rigid body that included seven 8 mm reflective motion capture markers. Reflective markers were also mounted on the simulation model and all markers were tracked with 12 motion capture cameras connected to the OptiTrack Flex 13 motion capture system. The marker trajectories were sampled at 120 Hz through the Motive software (NaturalPoint Inc, Corvallis, OR). Each participant performed 15 trocar passes. The order of simulation models used and the order of patient's side passage was randomized.

Multibody kinematics models were created in ADAMS (MSC Software Corp, Santa Ana, CA). These models included the 3d geometries of the surgery simulators and the trocar. Major blood vessels and the bladder geometries were segmented from the MRI and overlaid in the multibody model by aligning the pelvic geometry using least squares fit. Landmark oriented planes corresponding to the end of stages 2,3, and 4 were also added to the model (Figure 1). Motion capture data from the experimental trials on the simulators was used as an input to drive the kinematic analysis. For each trial, the outputs of the kinematic analysis were the trocar tip location, the time intervals for each of the four stages, contact and penetration of the trocar into the bladder or the major blood vessels. Passage of the trocar posterior to the pubic symphysis was also noted.

Linear mixed models were used to analyze the data. Significance was set at $p < 0.05$. All statistical analysis was done in SAS 9.4 (SAS Institute Inc, Cary, NC).

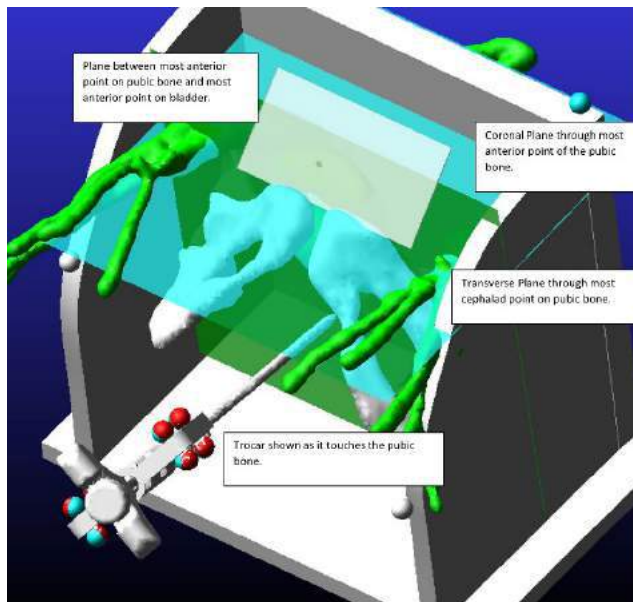


Figure 1: Multibody used for kinematic analysis. Includes the surgery simulator, trochar, and landmark planes.

RESULTS

Experts completed 27 error free passes and 18 passes where the trochar penetrated the bladder (40%). While novices completed 18 error free passages, 4 passes where the trochar penetrates the bladder and 23 passes where the trochar passed anterior to the pubic symphysis resulting in an overall error rate of 60%. Trocar tip trajectories were significantly different between error free passes and bladder error passes in the anterior-posterior and caudal-cephalad directions for both left and right trocar passages. These trajectory difference existed when comparing the total trocar trajectories (whole procedure) and when comparing only in stage 3 (which is the stage when bladder penetration can happen). Incidence of anterior trocar passage error was significantly higher in novice surgeons for both left and right passes. Anterior error passes had significantly altered trocar tip trajectories in all directions.

A mixed model was used to decompose total trocar path variation and the results indicate that 14% of the variation was attributed to experts while 45% was attributed to novice surgeons.

Temporal characteristics were analyzed by stages and shown in figure 2. Since anterior trocar error passages do not have stages 2,3, and 4, those trials were excluded from this analysis. There was no significant difference in stage 1 duration between error free posterior passages and anterior error passages.

DISCUSSION

Results indicate that monitoring the kinematics of the trochar handle can provide insight into the types of errors that can occur during the blind passage of the trochar in MUS procedures. In particular, during stage 3, the cephalad excursion of the trochar was smaller in bladder error trials compared to error free trials.

Bladder error for the expert surgeons was 40% which is slightly higher with previous studies looking at error ratios from the OR. Bladder error for the novice surgeons was 20% but this rate may not be indicative of the true error because anterior pass error trials are not

included in this calculation. Novices had 23 anterior pass error trials out of 45 trials performed. The overall error (bladder plus anterior) for the

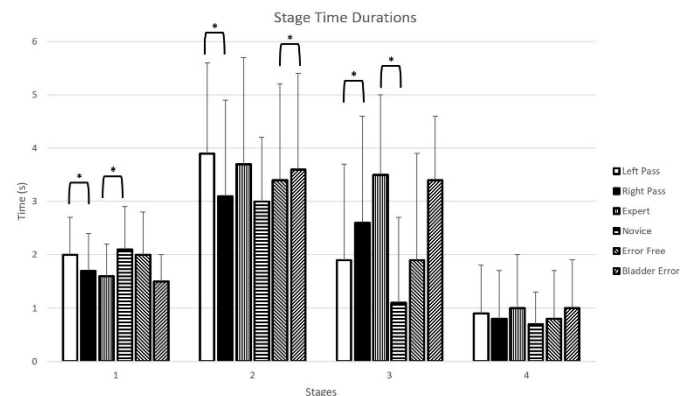


Figure 2: Trocar temporal characteristics by stage.

novices was 60%. This is the first time that anterior error passages were observed in the MUS procedure. This is attributed to the fact that most previous studies looked at surgery outcomes post-surgery. Since anterior passages are in fact a complete failure in terms of MUS placement, they would have been addressed in the OR by repeating the trocar pass until a posterior placement is achieved. In our study, participants were allowed to perform the procedure without an attending surgeon correcting and guiding their passes therefore we were able to observe this error. In our study, inexperienced surgeons seemed to have a hard time navigating the trocar cephalad to the pubic bone after initial contact with the pelvis.

Path trajectory variation was higher for the novices indicating that they are not able to follow a consistent trocar path between trials. Overall differences between experts and novices indicate that experience is a major factor in successfully placing the sling without complications such as bladder perforation.

This is the first study that incorporated motion capture to track the trocar instrument during the MUS procedure. Monitoring the temporal and kinematic characteristics of the trocar provides insight into the types of errors that can occur and can also provide insight into proper education of young surgeons. Methods used in this study can also be implemented for monitoring sling placement in the OR thus reducing preventable surgical errors. The surgical simulator and real time trocar motion monitoring can also be used in an educational setting so that young surgeons can acquire the necessary skills for performing the MUS procedure.

ACKNOWLEDGEMENTS

Funding for this study was provided by the National Institute of Biomedical Imaging and Bioengineering.

REFERENCES

- [1] Blaivas, J.G., et al., *Safety considerations for synthetic sling surgery*. *Nat Rev Urol*, 2015. **12**(9): p. 481-509.
- [2] Linder, B.J. and Elliott, D.S., *Synthetic midurethral slings: roles, outcomes, and complications*. *Urol Clin North Am*, 2019. **46**(1): p. 17-30.
- [3] Arif, M.A., et al., *Retropubic trocar modified with a load cell to verify contact with pubic bone*. *Surgery*, 2022. **172**(3): p. 1024-1028.
- [4] Oliphant, S., et al., *Teaching the Retropubic Midurethral Sling Using a Novel Cadaver and Model-Based Approach*. *Cureus*, 2017. **9**(5): p. e1214.

CHANGES IN ELASTIN STRUCTURE AND EXTENSIBILITY INDUCED BY HYPERCALCEMIA AND HYPERGLYCEMIA

C. Yang (1), A. S. Weiss (2,3,4), A. Tarakanova (1,5)

- (1) Department of Biomedical Engineering, University of Connecticut, Storrs, CT, USA
- (2) Charles Perkins Centre, The University of Sydney, Sydney, NSW, Australia
- (3) School of Life and Environmental Sciences, The University of Sydney, Sydney, NSW, Australia
- (4) Sydney Nano Institute, The University of Sydney, Sydney, NSW, Australia
- (5) Department of Mechanical Engineering, University of Connecticut, Storrs, CT, USA

INTRODUCTION

Elastin is a key component of elastic fibers which endow many important tissues and organs, from arteries and veins, to skin and heart, with strength and elasticity. Due to its intrinsic long life and low turnover rate, damage in elastin induced by pathophysiological conditions, such as hypercalcemia and hyperglycemia, accumulates during biological aging and in aging-associated diseases, such as diabetes mellitus and atherosclerosis. Prior studies have shown that calcification induced by hypercalcemia deteriorates the function of aortic tissues. Glycation of elastin is triggered by hyperglycemia and associated with elastic tissue damage and loss of mechanical functions via the accumulation of advanced glycation end products. Yet, molecular mechanisms associated with these processes are still poorly understood. To evaluate the effects on elastin's structural conformations and elasticity by hypercalcemia and hyperglycemia at the molecular scale, which is yet unknown, we perform classical atomistic and steered molecular dynamics simulations on tropoelastin, the soluble precursor of elastin, under different conditions, based on our previously established all-atom model. We characterize the interaction sites of glucose and calcium and associated structural conformational changes. Additionally, we find that elevated levels of calcium ions and glucose hinder the extensibility of tropoelastin by rearranging structural domains and altering hydrogen bonding patterns, respectively. Overall, our investigation helps to reveal the behavior of tropoelastin and the biomechanics of elastin biomaterials in these physiological environments.

METHODS

The starting structure of tropoelastin was chosen from our previous work based on human tropoelastin isoform 2 [1], where the molecule has been well equilibrated by REMD simulations. Atomistic classical MD simulation of wild type (WT) tropoelastin was performed using the Gromacs simulation package, for a total running time of 1000 ns.

Simulations of tropoelastin in calcium, glucose and mixed solution were studied. Topology and force field parameters were assigned from the CHARMM36m protein parameter set for elastin and from the CHARMM36 sugar parameter set for α -D-glucose and calcium. Domains 10-19 of tropoelastin were spliced from the same starting structure of the whole molecule to perform steered MD simulations, as these domains are chiefly involved in elastin's elasticity. The α -carbon of the last residue in domain 19 was fixed, and the α -carbon of the first residue in domain 10 was pulled at a velocity of 50 m/s and a force constant of 1000 kJ mol⁻¹ nm⁻² along the axis parallel to the length of the molecule. To investigate the specific role that calcium ions and glucose play in altering mechanical properties of tropoelastin and the correlation between such variations and calcium/glucose concentrations, we introduced calcium ions with a concentration range of 100 mM, 750 mM, 1000 mM, 1500 mM to 2000 mM, to represent hypercalcemia, and glucose with a concentration range of 246 mM, 493 mM, 738 mM, 985 mM to 1969 mM, to represent hyperglycemia, with tropoelastin only as the control. We set up three replicates for each condition. All modeling used in-house and Gromacs scripts.

RESULTS

Compaction of elastin's structure and depletion of hydration waters results in a higher modulus of elasticity in calcium solution. In the mechanical pulling simulation, we find a significant increase in elastic modulus (Fig 1). With more calcium ions present, it becomes increasingly harder to pull the molecule at the same strain. Notably, the phase-wise deformation patterns become more pronounced in the presence of higher calcium concentrations, as seen in the corresponding snapshots presented. Such distinct deformation patterns point to calcium-induced stiffness. To examine the role of each domain in this phase-wise deformation pattern, we analyze dissociation profiles of protein-protein hydrogen bonds formed within each domain. Interestingly, compared with the dissociation profiles of hydrogen

bonds of the control, the presence of calcium ions encourages the formation of a larger number of more stable hydrogen bonds formed by each domain, especially in domains 10, 11, 12, 14, pointing to roles for calcium ions in stabilizing hydrogen bonds formed within the protein for increasing global molecular stiffness.

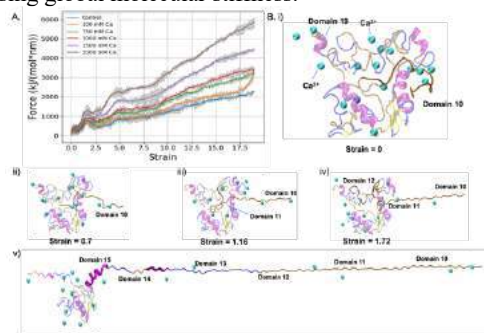


Fig 1. Calcium effects on tropoelastin mechanics. (A) Force vs strain curves in the presence of various concentrations of calcium. (B) Snapshots of tensile tests at various strains, (i-v).

Replacement of hydration water and viscosity conferred by glucose yields altered mechanical properties. We examine the number hydration waters within a shell radius of 2.2 Å and 3.2 Å, in the presence of glucose and in the control. The former shows a reduced number of hydration waters that can be attributed to competing hydrogen bonding between protein and glucose replacing interactions with water. This bonding behavior also influences the mechanical properties of tropoelastin (Fig 2). With a higher concentration of glucose, the elastic modulus increases. The phase-wise deformation patterns observed in tropoelastin with 1969 mM glucose are more discernible compared to the control. We believe such distinct deformation patterns to be the consequence of hydrogen bonding between glucose and tropoelastin. To examine the role each domain plays in this phase-wise deformation pattern, we also analyze dissociation profiles of hydrogen bonds formed within the protein by each domain. Our findings suggest the supporting roles of domains 10-14 in resisting deformation; the earlier dissociation pattern compared to control and tropoelastin with 1000 mM calcium ions, however, suggests the increased elastic modulus and overall stiffness are not likely due to increased intramolecular bonding, but instead, is associated with intermolecular hydrogen bonding between glucose and protein.

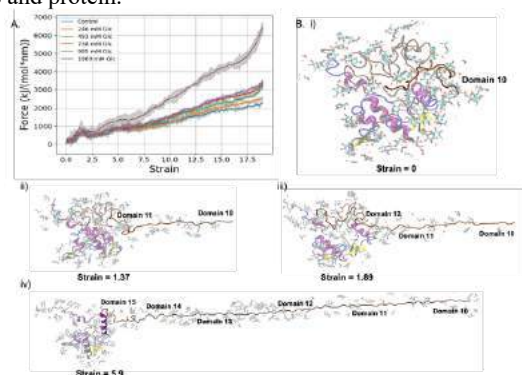


Fig 2. Glucose effects on tropoelastin mechanics. (A) Force vs strain curves in the presence of various concentrations of glucose. (B) Snapshots of tensile tests at (i) Strain = 0, (ii) Strain = 1.37, (iii) Strain = 1.89, (iv) Strain = 5.9, tropoelastin + 1969 mM glucose.

The addition of calcium in the presence of glucose induces linear alterations in mechanical profiles. Due to the heterogeneous conformations identified in response to calcium and glucose coupling

effects, different intramolecular contact maps for various conditions are found (two shown, Fig 3A). As the hydration water number in both nearest hydration shells shows a nearly linear decrement as the calcium concentration increases (data not shown), we would expect there to be a clear linear change in mechanical profiles. However, when glucose concentration dominates, the addition of calcium only shows significant difference between tropoelastin with 738 mM glucose + 100 mM calcium and tropoelastin with 738 mM glucose + 200 mM calcium, and a slight difference between tropoelastin with 738 mM glucose + 200 mM calcium and tropoelastin with 738 mM glucose + 400 mM calcium (Fig 3B). It is possible that changes due to the relatively small increase in calcium concentration are not discernible in steered MD simulations, and glucose may block calcium from interacting with the protein, as observed in the case of MD simulation of tropoelastin with 738 mM glucose + 400 mM calcium.

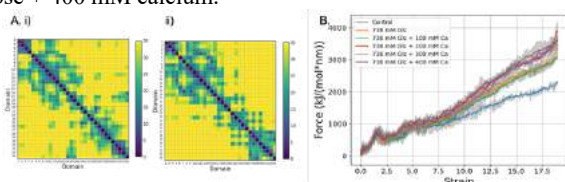


Fig 3. Calcium and glucose coupling effects on tropoelastin structure and mechanics at glucose concentration 738 mM. (A) Residue-wise contact maps showing intramolecular interactions in 738 mM glucose and (i) 100 mM calcium or (ii) 200 mM calcium. (B) Mechanical profiles of control and various calcium/glucose concentrations.

DISCUSSION

The introduction of different combinations of glucose and calcium to tropoelastin yields nonlinear variations in protein conformations, since these solvents invoke divergent changes to the molecule's structural rearrangement, namely, structural collapse by calcium, and structural dissociation by glucose. Interestingly, we find that when glucose concentration dominates, protein dynamics do not exhibit a correlation over a range of calcium concentrations, possibly due to a higher number of conformational degrees of freedom that arise from the molecular flexibility promoted by glucose binding.

From a macroscopic perspective, our findings provide insights into diseases of elastin of genetic origin. For instance, elastin gene deletions in Williams Syndrome result in reduced expression of functional elastin and an altered deposition of elastin in skin. Given reports of occasional childhood hypercalcemia in Williams Syndrome, there are, nevertheless, contradictory observations of the phenotype of accompanied arterial stiffness. Our findings may point to a general recovery through reversible calcium binding, and support a general model where other calcium-binding molecules are needed to achieve persistent vascular calcium binding. It may also be that elastin attracts calcium through persistent binding, and that this persistence is locked in by resident calcium-binding proteins such as fibrillin-1. Overall, these studies have implications for uncontrolled, persistent hypercalcemia and hyperglycemia, where we hypothesize changes in biomechanics and adverse physiological consequences due to stiffening on a larger scale, still to be probed, particularly in the vasculature where functional elasticity is needed.

ACKNOWLEDGEMENTS

This research was supported by NSF, grant 2145759 and utilized XSEDE, which is supported by NSF.

REFERENCES

[1] Tarakanova, A et al., PNAS 115:7338-7343,2018.

THE GENERATION OF SYNTHETIC GEOMETRIC DATASETS FOR FLOW CHARACTERIZATION IN THE CAROTID BIFURCATION

Retta El Sayed (1,2), Paul Klein (2), John N. Oshinski (1), Tiziano Passerini (2)

- (1) Department of Biomedical Engineering, Georgia Institute of Technology & Emory University, Atlanta, GA, United States.
(2) Cardiovascular Physiology and Flow Team, Siemens Healthineers, Princeton, NJ, United States.

INTRODUCTION

Previous studies in the literature have linked geometric features of the carotid bifurcation to the prevalence of hemodynamic disturbances resulting in vessel wall thickening and atherosclerosis [1,2]. A common approach to finding a mechanistic explanation of the effect of geometry on flow is based on computational fluid dynamics (CFD) simulation. Patient-specific CFD requires two key pieces of information: geometric boundary conditions and flow boundary conditions which include input flow and outlet pressure [3]. Geometric boundary conditions are generally defined through a laborious process including segmentation and meshing. Flow boundary conditions can be derived from phase-contrast magnetic resonance imaging. The solution of the CFD problem typically involves long processing time and high computational power. To date, these factors have limited the use of CFD in clinical decision-making.

Due to the complex dependency between geometry and flow in the carotid bifurcation, there is a need in the field for mechanistic studies on larger datasets to better identify geometrical risk factors. *Therefore, the aim of this work is to conduct a CFD study on a large set of realistic, synthetically generated carotid bifurcation geometries based on previously published geometric features such as the bifurcation angle, common carotid (CCA) radius, internal carotid artery (ICA) bulb area expansion, tortuosity, and inlet flow condition.* We choose wall shear stress (WSS) as a measure of disturbed blood flow [1], and we analyzed the relationship between WSS in the carotid bifurcation and various geometric features.

The gold standard WSS values are derived from three-dimensional, three-directional, ECG gated, time-resolved, phase-contrast magnetic resonance imaging (4D Flow MRI). 4D flow MRI will be used as qualitative validation for the data generation and simulation method [4].

METHODS

A total of 250 synthetic carotid bifurcations were generated and CFD simulations were conducted. The geometries included two main populations, healthy and diseased models with varying degree of stenosis in the ICA representing atherosclerosis. One healthy volunteer (27-year-old female) underwent an MRI scan for validation. Pre- and post-processing was conducted in python and ParaView.

Geometric Data Generation: each bifurcation geometry is represented by bifurcating vessel centerlines; each centerline point is associated with the radius of an inscribed sphere centered in the point. The envelope of the inscribed spheres was computed as a triangulated mesh and used as geometric boundary conditions for CFD simulations. A literature search was conducted to extract realistic geometric features to generate the synthetic carotid bifurcation (Table 1) [1,2].

Table 1: Parameters with corresponding ranges used to generate synthetic carotid artery:

Parameter	Ranges Used
CCA diameter	4.3 - 7.7 mm
ICA bulb: CCA Diameter Ratio	1.2 - 2.5
Bifurcation angle	31.2° - 97.6°
ICA angle	1.8° - 62.7°
ICA tortuosity	0.006 - 0.521

ICA: CCA Diameter Ratio	0.52 - 1.04
ECA: CCA Diameter Ratio	0.50 - 1.10
ECA: ICA	0.63 - 1.39
Inlet mean Velocity	20 - 40 cm/s
Stenosis	25% - 80%

For each generated geometry, flow boundary conditions were assigned as mean inlet flow and flow split at the carotid bifurcation, these were also varied as in **Table 1**.

Fluid Simulation: We adopted a fast, graphics processing unit- (GPU-) accelerated CFD solver using the lattice Boltzmann method (LBM) and previously validated [5]. This supports automatic selection of optimal spatial and temporal resolutions for accuracy and stability. Additionally, an average value of the velocity and WSS was calculated at every cross-section and associated to the corresponding centerline point. The main region of interest in this work was the expansion region in the bulbar segment of the ICA.

Solution Validation: To validate our method, we generated a carotid bifurcation based on a healthy volunteer that underwent an MRI scan including black blood vessel wall scan and 4D flow MRI scan. The black blood scan was used to extract geometric features for synthetic geometry generation while the 4D flow MRI scan was analyzed using EnSight to compare the velocity profile to the CFD solution.

RESULTS

An example of synthetic carotid bifurcation is seen in **Figure 1** (left). The computed flow field has a good qualitative agreement with the flow field derived from the healthy volunteer scan, with very similar velocity profiles across multiple cross-sections in the carotid geometry.

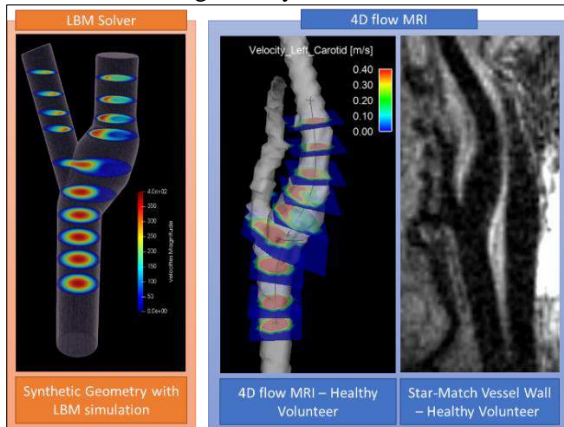


Figure 1. An example of a synthetic carotid bifurcation based on measurements from Vessel Wall Black blood MRI with LBM simulation (orange background) compared to a healthy volunteer 4D flow MRI scan with multiple cross-sections displayed in EnSight.

Analysis of the geometric features and WSS measurements on the full database of synthetic geometries is shown in **Figure 2**. WSS is highly dependable on geometric features including radius, flow, cross-sectional area and bifurcation angle. Normal geometries can be clearly separated from abnormal geometries.

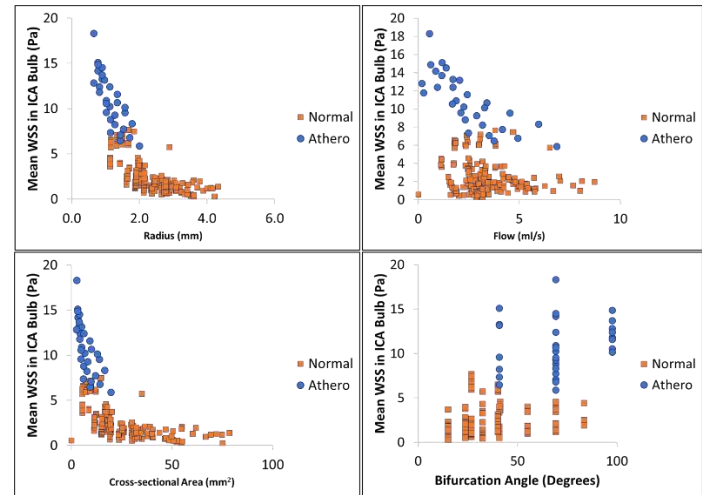


Figure 2. The effect of radius, inlet mean flow, cross-sectional area, and bifurcation angle on the mean WSS in the ICA bulbar segment in normal and stenosed geometries.

DISCUSSION

In this work, we were able to generate synthetic geometries of carotid bifurcation to assess the effect of different geometric features on flow disturbance. Few limitations of this method are that all simulations were done for steady flow conditions rather than pulsatile. Additionally, the averaging of the WSS around the cross-section contour does not allow studying localized flow disturbance. The longer-term goal of this work is to generate richer data sets including more variation in geometry and flow conditions, as well as more detailed descriptors of local flow patterns. A regression model will then be defined using machine learning techniques to elucidate the complex effect on local flow features of geometric measurements of the carotid bifurcation. The model will allow the assessment of disturbed flow in patient-specific anatomical models of the bifurcation, without the need for time consuming CFD analysis.

The concepts and information presented in this paper are based on research results that are not commercially available. Future commercial availability cannot be guaranteed.

ACKNOWLEDGEMENTS

This material is based upon work supported by the National Science Foundation Graduate Research Fellowship Program under Grant No. 1937971 (El Sayed). Any opinions, findings, and conclusions, or recommendations expressed in this material are those of the author(s) and do not necessarily reflect the views of the National Science Foundation.

REFERENCES

- [1] Lee, SW et al., *Stroke*. 39:2341-7, 2008.
- [2] Thomas, JB et al., *Stroke*. 36:2450-6, 2005.
- [3] Gharahi, H et al., *Int J Adv Eng Sci Appl Math*. 8:40-60, 2016.
- [4] Markl, M et al., *J Magn Reson Imaging*. 36:1015-36, 2012.
- [5] Nita, I et al., *Comput Math Methods Med*. 355:928-39, 2020.
- [6] Itu, L et al., *J Appl Physiol*. 121: 42-52, 2016.

POLYFEM: FINITE ELEMENT SOLVER FOR COMPLEX BIOMECHANICS PROBLEMS

Pranav Jain (1), Liam Martin (2), Zachary Ferguson (1), Torkan Gholamalizadeh (3), Faezeh Moshfeghifar (4),
Kenny Erleben (4), Steven Abramowitch (2), Daniele Panozzo (1), Teseo Schneider (5)

(1) Courant Institute of Mathematical Sciences, New York University, New York, New York, United States

(2) Department of Bioengineering, University of Pittsburgh, Pittsburgh, Pennsylvania, United States

(3) 3Shape ApS, Copenhagen, Denmark

(4) Department of Computer Science, University of Copenhagen, Copenhagen, Denmark

(5) Department of Computer Science, University of Victoria, Victoria, British Columbia, Canada

INTRODUCTION

The simulation of many complex, biological problems has been addressed using existing commercial finite element software packages (e.g., AnsysTM, ABAQUSTM, and NIKE3DTM) or open-source solvers like FEBio (University of Utah). However, many common biomechanics problems cannot be addressed or cause significant investments of time due to human-in-the-loop parameter tuning, especially in the presence of contact forces. These problems generally include some combination of very large deformations, deformations that occur quickly, contact between multiple deformable bodies, irregular geometries, and/or extremely soft and/or highly heterogeneous materials in terms of stiffness. End-users often have to make compromises related to the physics of the problem, the geometry, or the mesh to achieve a solution. Fortunately, the recent development of novel, smooth contact models and the corresponding interior point solvers address many of these compromises.

PolyFEM, a C++ FE library implementing Incremental Potential Contact (IPC), is one such solver. Implementing IPC into the solver allows for robust and accurate time-stepping and guarantees intersection- and inversion-free solutions to simulations that are undergoing large deformations and large time steps. We aimed to compare the usability of PolyFEM and compare it to the well-established biomechanics FE approaches (FEBio 3.0) using problems with published solutions to evaluate its utility in challenging scenarios common in biomechanics.

METHODS and RESULTS

We compared each of the solvers in four head-to-head comparison tests, 1) the FEBio test suite, 2) the FEBio validation paper [1], 3) three material high-energy contact, 4) simulation of hip and jaw movements. Each set of simulations is designed to compare the capabilities of the two solvers to determine their strengths and limitations.

First Benchmark. The test suite is a set of examples that outline the features of FEBio, including static, dynamic, and contact simulations. A group of 18 problems was selected from the test suite and simulated using both solvers. The selected simulations are a mix of static (with and without contact) and dynamic problems. Depending on the type of simulation, displacement, stress, and simulation time were collected and compared. Of the 18 selected simulations, 9 were static and involve contact. The other 9 were dynamic. We noticed that both FEBio and PolyFEM produce similar results, but PolyFEM, in general, takes more time to simulate. For example, consider the simulation *co07* (Figure 1). This simulation was of a curved plane being pushed into and then dragged across a block. Both the materials are modeled as Neo-Hookean (curved plane: $E = 10$ kPa, $\nu = 0.0$, $\rho = 1.0$; block: $E = 1.0$ Pa, $\nu = 0.45$, $\rho = 1.0$). No friction is involved. Figure 1 shows the initial and final configuration of the simulation. The computation time for FEBio is 12.1 seconds, while PolyFEM takes 585.2 seconds. We observe similar results in most other tests. Note that the FEBio TestSuite is carefully tuned to work best for FEBio; PolyFEM works without any manual tuning of the simulation. Including this tuning, time may make the overall runtimes more similar.

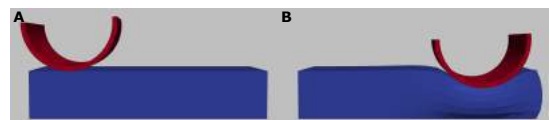


Figure 1: Simulation result of *co07* from FEBio TestSuite. A) configuration at $t = 0$ and B) final configuration.

Second Benchmark. Our second set of comparisons was based on the validation paper released by FEBio, which compares the results of FEBio to analytical results, and results generated with ABAQUSTM and NIKE3DTM [1]. This paper outlines ten simulations and compares the results between

the three solvers. In the “upsetting of an elastic billet” simulation from this work, a 1 mm x 1 mm x 0.1 mm elastic billet (meshed with 40x40x1 hexahedral elements) is compressed to 60% of its initial height between two rigid surfaces. A limitation of PolyFEM is that there was no way to use rigid bodies therefore these rigid surfaces were simulated as extremely stiff deformable bodies. This example was chosen as it is a good example of contact-driven deformation with an easily interpretable outcome measure. Using a quarter symmetry assumption, only one-quarter of the elastic billet is simulated. The billet is modeled as a Mooney–Rivlin material ($C_1 = 1$ MPa, $C_2 = 10$ MPa, $K = 10$ GPa), Figure 2A. The outcome measure of this simulation is the maximum lateral displacement of the elastic billet.

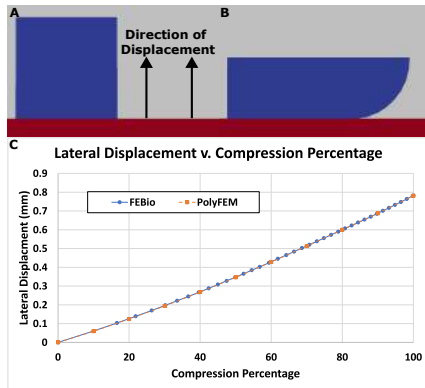


Figure 2: Figure showing the displacement of the elastic billet caused by the compression of the two rigid surfaces. A) Elastic billet at the beginning of the simulation, B) elastic billet fully compressed, C) Plot comparing the lateral displacement of the billet due to compression.

We were able to replicate seven of the ten simulations from the validation paper published by FEBio, the only exclusions were the simulations that are not possible in PolyFEM based on the current feature set [1]. In the example case, the solvers agreed on the lateral displacement of the top of the billet to the thousandths of a millimeter (0.781 mm, Figure 2) The simulation was significantly faster when conducted in FEBio when compared to PolyFEM (3 v. 56 seconds).

Third Benchmark. The third comparison test was developed to emphasize the difference in contact algorithms and human-in-loop optimization differences between the solvers. These differences are apparent when considering contact between two very soft materials. First, we generated three geometries using Houdini (v19.5.388). A dodecahedron (planet) and a rectangular prism consisting of two different materials, a relatively soft material (jello), which was encased by a relatively rigid outer material (mold). All three materials are modeled as neo-hookean materials (planet: $E = 100$ kPa, $\nu = 0.4$, $\rho = 5000$ kg m⁻³; jello: $E = 500$ kPa, $\nu = 0.4$, $\rho = 1000$ kg m⁻³; mold: $E = 100$ GPa, $\nu = 0.4$, $\rho = 1000$ kg m⁻³). The bottom face of the mold was fixed in all three directions. The planet was dropped onto the top face of the jello accelerated by gravity.

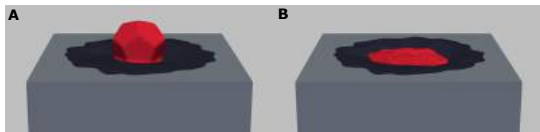


Figure 3: Frames from simulation of the high energy collision between two very soft materials (Planet = Red, Jello = Black, Mold = Gray). A) Approximate time in the simulation where FEBio failed. B) Point in the simulation where the planet has deformed the most.

The simulation of the planet falling onto the jello emphasized the capabilities of the contact algorithm used by PolyFEM. FEBio was unable to finish this simulation and failed due to an inverted element around the time of initial contact (Figure 3A).

Fourth Benchmark. Next, we assessed the performance of PolyFEM when using patient-specific models of the human body. We used the hip

and jaw FE models from the LibHip and Open-Full-Jaw repositories [2, 3]. The anatomical structures are assumed homogeneous and modeled using Neo-Hookean material (hip bone: $E = 17$ GPa, $\nu = 0.30$; hip cartilage: $E = 12$ MPa, $\nu = 0.45$; teeth: $E = 2$ GPa, $\nu = 0.3$; periodontal ligament: $E = 68.9$ MPa, $\nu = 0.45$; jaw bone: $E = 1.5$ GPa, $\nu = 0.30$). We set up pseudo-stance and biting scenarios for the hip and jaw models, respectively [2, 3]. As PolyFEM’s contact algorithm checks for potential contact between each object at every timestep there is no need for manual tagging of contact interfaces. Some simulations from this test were unable to be replicated by FEBio. Specifically, in the case of the biting simulation, FEBio fails to converge due to an inverted element in the extremely soft ligamentous tissue. Otherwise the simulations were nearly identical between PolyFEM and FEBio. Additionally, we benefit from the adaptive P -refinement option in PolyFEM and assign *Tet10* elements to the soft tissues to increase the simulations’ accuracy.

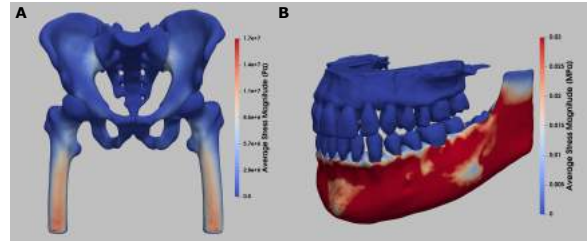


Figure 4: The von Mises stress distribution in the human hip (A) and jaw (B) in response to pseudo-stand and biting scenarios.

DISCUSSION

This study demonstrates that PolyFEM produces results matching those from FEBio for previously published simulations based on solid, hyperelastic materials. This provides important verification of the solutions provided by PolyFEM. Further, this study demonstrates that PolyFEM offers solutions to problems that are challenging for other solvers involving contact. Finally, this study demonstrates the utility of PolyFEM in solving patient-specific models in biomechanics. Thus, this alternative solver is very suitable for solving many problems in biomechanics where geometric nonlinearities are common.

It is important to note that at this stage of development, PolyFEM lacks many of the features available for other solvers. These include a user interface (PolyFEM uses a JSON setup file and Paraview for post-processing), a wide array of materials, shell and rod elements, a rigid body solver, tied-contact, a multi-physics platform, and optimization for parallel performance. However, it has a high potential for biomechanical simulation due to its higher automation and robustness. In addition, one limitation of using a barrier potential for contact is that the simulation cannot have interpenetrating surfaces in its initial configuration. This will need to be considered when creating meshes from segmented medical images. The upside of this limitation is the higher robustness and the guarantee that there will be no penetrations in all timesteps.

While PolyFEM is early in its development, it currently provides verified solutions for hyperelastic materials that are consistent with FEBio, and it is capable of simulating challenging problems in biomechanics where other solvers fail. It is also open-source and publicly available. Future work will aim to implement many of the aforementioned features to provide more options for the biomechanics community to implement it as another tool in their workflows.

ACKNOWLEDGEMENTS

We acknowledge funding from NSF 2053851, NSERC DGEER-2021-00461, RGPIN 2021-0370, and Horizon2020 MSCA grant No.764644.

REFERENCES

- [1] Maas SA et al. *J Biomech Eng* 134.1 (2012).
- [2] Moshfeghifar F et al. *Comput Meth Prog Bio* 226 (2022).
- [3] Gholamalizadeh T et al. *Comput Meth Prog Bio* 224 (2022).

DEVELOPMENT OF A SYSTEM FOR MEASURING AORTIC VALVE DEFORMATION USING DIGITAL IMAGE CORRELATION

Alexander W Hooke¹, Christopher Noble², David Morse², Melissa Young², Amir Lerman²

(1) Biomechanics Core, Mayo Clinic, Rochester, MN, USA

(2) Department of Cardiovascular Medicine, Mayo Clinic, Rochester, MN, USA

INTRODUCTION

The demand for transcatheter aortic valve replacement (TAVR) aortic valve replacement continues to outpace that of standard surgical intervention.[1] While TAVR valves were originally intended only for treatment of elderly patients or those deemed too high risk for open heart surgery, their utilization has shifted to include lower risk and younger patients, increasing the call for improved TAVR durability.

As valve materials, geometry, and designs are studied to heed this call, the ability to thoroughly quantify the strain and stress on valves' leaflets is crucial to both understand the currently available commercial valves' performance and develop next generation of bioprosthetic heart valves. The combination of its non-invasive nature and its high temporal and spatial resolutions make three-dimensional digital image correlation (DIC) an excellent candidate to measure valves' functional mechanics. Similar measurements of aortic replacement valves have been performed by Abbasi et al. [2] and Stanova et al. [3], with promising results. The objective of this project was to expand on their techniques, improve compatibility with a larger number of valve types/models, improve the resolution of DIC measurements, and create an overall robust DIC system to support bioprosthetic valve research.

METHODS

Hardware & Software

A test set up was created consisting of a custom-fabricated optically clear acrylic tank, 2 peristaltic pumps, 2 pressure transducers, and an interchangeable set of chamber dividers that enabled the valve to be mounted at different orientations relative to the camera. A pair of GOM Aramis 12M SRX cameras (Carl Zeiss GOM Metrology GmbH, Braunschweig, Germany), mounted with a stereo angle of 20°, with Titanar 75 mm lenses were mounted atop a custom test rack and held rigid to the tank after calibration with a standoff distance of 620mm, resulting in an image scale of 28.9 pixel/mm (Figure 1). All DIC

analyses were performed using the Aramis Pro 2018 software (Carl Zeiss GOM Metrology GmbH, Braunschweig, Germany).

Valves

An assortment of TAVR valves were tested including: the Edwards Sapien 9300TF, the Medtronic Core Evolut, and the Medtronic EvProPlus as well as custom, in-house fabricated valves made from fixed porcine pericardium. These valves were tested before and after undergoing 200 million cycles of simulated wear using a TA Durapulse 4-station heart valve test instrument. Two retrieved, ex vivo TAVR valves were also tested.

Patterning

Patterning of the valves required consideration and compromise of several factors including: their state of wetness, the adherence of the pattern to the material, ability to withstand endurance testing, inaccessibility of some valve surfaces due to their geometry, and permanence of staining prohibiting patterning corrections. The selected balance of these factors resulted in a patterning technique of aerosolized India ink to create contrast on the tissue's white surface for the



Figure 1: Test set up with camera mount on left atop test rack and acrylic chamber on right equipped with angled mount.

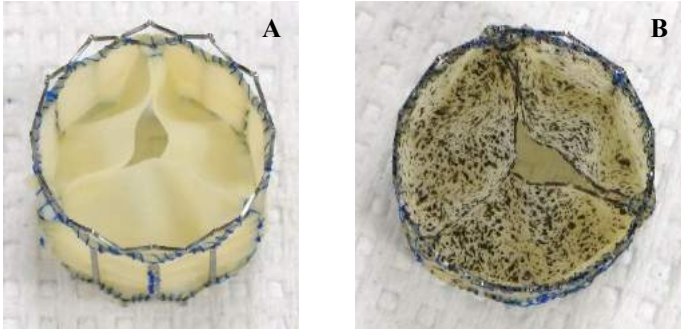


Figure 2: Custom-built TAVR valve A) unpatterned and B) patterned with aerosolized India Ink with typical feature size.

commercially available valves and aerosolized methylene blue stain for the ex vivo. For the in-house fabricated valves, patterning was done on sheets of the pericardium material prior to their assembly into valves, yielding a more complete pattern coverage over all valve surfaces. These techniques resulted in a minimum attainable feature diameter size of 0.24-0.41mm (7-12 pixels), seen in Figure 2.

Calibration

The system was calibrated using a vendor-supplied calibration panel (model CP20/55x44, Carl Zeiss GOM Metrology GmbH, Braunschweig, Germany) with the panel in the water-filled tank during acquisition of all calibration images. The resulting calibration consisted of a measuring volume of 80mm wide x 60mm high x 40mm deep with a calibration deviation of 0.1 pixels (3 μ m).

Noise Floor

An unloaded valve remains open in its resting state and when loaded by peristaltic pump there is an oscillation in the valve's load and displacement. These conditions made an accurate determination of the system's noise floor challenging. To achieve a noise floor measurement, a vent was opened on the aortic side of the valve, resulting in the valve shutting under the static and steady atmospheric pressure. This loading was recorded to determine the in-plane and out-of-plane noise floor.

Testing

The two chambers were filled with distilled water. Valves were mounted in a silicone ring, creating a seal around their perimeter, then press fit into a polycarbonate tube separating the two chambers. Each valve was tested using the chamber's flat mount, enabling measurement on the broad, belly surface of all leaflets and the areas approaching the perimeter annulus, as well as the chamber's angled mount, enabling measurement of individual leaflet's central surface near the central

leaflet intersection. The mounting tube's fixture included a rotary bearing, allowing rotational adjustment of the region of the valve seen by the cameras such that each leaflet could be visible when using the angle mount. Load was applied to the valves via peristaltic pumps, decreasing the pressure behind the valve through altering the pump flowrate. Images, aortic pressure, and ventricular pressure were recorded at 64Hz. For most valves and conditions, pressure differentials of 60mmHg, 80mmHg, and 120mmHg were produced across the valve via control of the pumps.

Analysis Parameters

A subset size of 30 pixels and step size of 15 pixels was used for all deformation analyses. The primary outcome measures included principal technical strain and displacement with a reference value taken at the minimum pressure under which the valve would be closed.

RESULTS & DISCUSSION

The system results in a virtual strain gauge (VSG) size of 1.0mm with a noise floor estimate of 0.02mm in-plane and 0.07mm out of plane. The deformation of the commercial TAVR valves tested showed mean displacements on the leaflet bellies of 0.7-1.1mm compared to 0.3-0.8mm in the Abbasi study. [2]

The presented system can continue to be improved. While the current patterning technique is largely successful, speckle resistance to fade under wear, adherence, and the minimum feature size can all still be improved. Additionally, a more robust valve orientation adjustment method would enable more surface of the leaflets to be measured and both the pressure measurement and pump control can be improved to yield more precise control over the load applied to the valves.

Future studies using these techniques will include the analysis of a phantom sample for uncertainty evaluation, a pre- and post- wear analysis on a set of custom TAVR valves, and validation of valve finite element modeling.

ACKNOWLEDGEMENTS

Support provided by: NIH Grant K99HL161272-01A1, the Mayo Clinic Career Development Award in Cardiovascular Diseases Research Honoring Dr. Earl H. Wood, the HH Sheikh Hamed bin Zayed Al Nahyan Program in Biological Valve Engineering, and the Mayo Clinic Biomechanics Core.

REFERENCES

1. Leon, M.B., et al., New England Journal of Medicine, 2016. 374(17): p. 1609-1620.
2. Abbasi, M., et al., Journal of Biomechanics, 2018. 76: p. 27-34.
3. Stanova, V., et al., Euro Intervention, 2019. 15(7): p. 581-585.

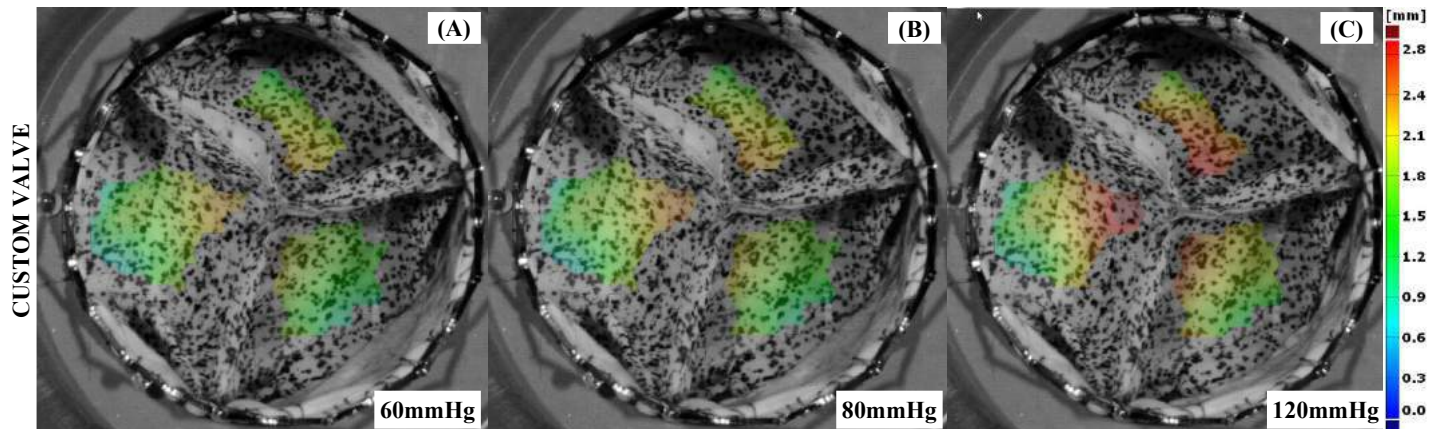


Figure 3: Surface displacement of a custom-built TAVR valve at 3 different loads: A) 60mmHg, B) 80mmHg, and C) 120mmHg

EFFECTS OF WILDLAND FIRE SMOKE EXPOSURE ON AIRFLOW AND PARTICLE DEPOSITION IN THE MOUSE RESPIRATORY TRACT

Matthew J. Eden (1), Jacqueline Matz (1), Chiara Bellini (1), Jessica M. Oakes (1)

(1) Department of Bioengineering, Northeastern University, Boston, MA, USA

INTRODUCTION

The occupational health hazards associated with being a wildland fire fighter (WLFF) remain largely unknown, in spite of growing evidence that wildland fire smoke (WFS) inhalation may affect the function of both pulmonary and extrapulmonary organs. Epidemiological data is challenging to acquire in the WLFF population due to the sporadic nature of wildland fire events, varying length of employment, and because WLFFs are constantly mobile. To compliment limited epidemiological data, animal models are valuable tools for ascertaining the health effects of repeated WFS exposure.

We recently developed a mouse model to investigate the cardiopulmonary health implications following repeated WFS exposure¹. To design our exposure protocol, we leveraged 1-D dosimetry modeling to equate the smoke particle mass deposited on the lungs of our mouse model to that of a WLFF with a mid-length career, normalized by their respective lung surface areas. Following exposure, we experimentally assessed alterations in pulmonary health through functional and structural measurements. Herein, we integrate experimental measurements into a high-fidelity computational fluid-particle dynamics (CFPD) framework to understand how WFS induced changes in pulmonary function impacts airflow and particle transport in the mouse upper airways.

METHODS

Recording of breathing waveforms. Smoldering Douglas fir smoke (DFS) at a mass concentration of 22 mg/m³ was generated with a custom-built apparatus, consisting of a quartz-tube furnace mounted onto a linear actuator^{2,3}. Whole-body barometric plethysmography was used to monitor breathing patterns in male *Apoe*^{-/-} mice when exposed to either filtered air (e.g., normal breathing) or DFS (N = 5). Following 15 minutes of exposure, breathing waveforms were collected to extract respiratory rate (RR) and tidal volume (TV). Their minute volume (MV) was then calculated as: $MV = RR * TV$.

Mouse Airway Geometry Construction. A male *Apoe*^{-/-} mouse was anaesthetized and whole-body imaged using a μ CT scanner (SkyScan 1276, Bruker BioSpin Co.). The open-source software SimVascular⁴ was then used to manually segment and create the mouse airway geometry, shown in Figure 1.

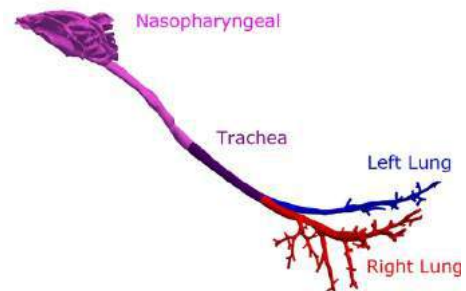


Figure 1: Male *Apoe*^{-/-} mouse airway model

Airflow Simulation and Particle Tracking. Airflow in the mouse airway geometry was modeled using the incompressible Navier-Stokes equations and numerically solved with SimVascular's finite element solver svFSI. A steady Dirichlet boundary condition was applied to the nostrils, at the average MV measured during either normal breathing or DFS exposure. A constant zero pressure boundary condition was applied at all outlets since the bronchial tree extended to approximately the same generation in each lobe.

An in-house Lagrangian particle tracking solver was used to model the transport and deposition of spherical smoke particles in the mouse respiratory tract⁵. A particle's position was updated using a reduced form of the Maxey-Riley equation, which accounts for viscous drag, Brownian diffusion, and gravitational sedimentation. We simulated particle sizes of 100, 150, and 200 nm, since the majority of DFS

particle mass falls within this range¹. We assumed particles were noninteracting and do not impact the flow field.

Table 1: Exposed respiration conditions, * $p<0.05$

	RR (breaths/min)	TV (mL/breath)	MV (mL/min)
Air	404 ± 8	0.30 ± 0.02	122 ± 8
DFS	83 ± 10*	0.34 ± 0.05	27 ± 4*

RESULTS

Mice exposed to DFS experienced a significant decline in MV when compared to air-exposed mice ($p<0.05$), which was driven by a stark reduction in RR (Table 1). This resulted in a 4.5x decrease in volumetric flow rate in the DFS exposed model, compared to normal breathing. The flow fields are similar between the left and right nasal passages (Figure 2, A1-A2 & B1-B2). Distal of the nostrils, most of the mass flux is concentrated at the floor of the nasal cavity, with little mass flux in the olfactory region (B1-B2). Consequently, we anticipate few particles being transported to this region. A small jet of high fluid velocity is observed at the glottis due to its smaller cross-sectional area (C1-C2). The flow split between the right and left lung is 73 and 27%, respectively, for both DFS and normal breathing (D1-D2).

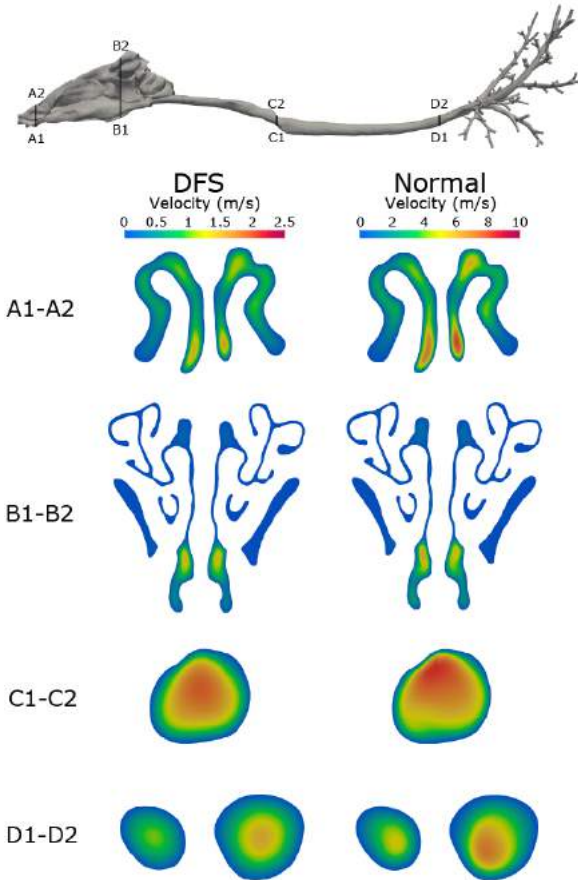


Figure 2: Cross-section velocity profiles from CFD results

Particle deposition in the size range considered in this study is notably dependent on breathing conditions, with normal breathing mice on average exhibiting a deposition percentage 146% greater than the DFS group (Figure 3). Deposition in the nasopharyngeal region is effectively constant over the particle sizes considered for the DFS exposed group, however, there is a notable decrease in deposition in the upper respiratory tract (URT) for 200 nm particles, compared to the

other two sizes. In the normal breathing group deposition is relatively constant across the 150 and 200 nm particle sizes, while there is a substantial decrease in deposition in the URT between 100 and 150 nm.

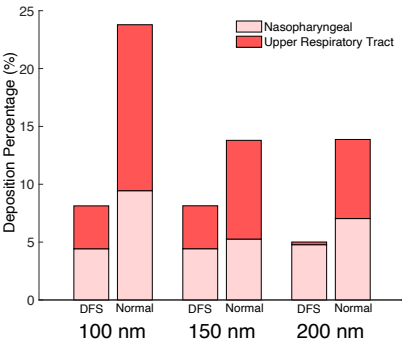


Figure 3: Particle deposition fraction at varying sizes

DISCUSSION

To date, the non-accidental occupational health risks posed to WLFFs remain poorly understood. Mouse models serve as an effective surrogate for studying the health consequences following repeated WFS exposure. Regional deposition of smoke particulates impacts how toxins are cleared, retained, or translocated from the lung, thereby affecting their overall toxicity. Thus, the deposition patterns of inhaled particulates are important to consider when interpreting the health consequences following exposure. In this study, we leveraged plethysmography and particle size measurements to computationally investigate how DFS exposure impacts airflow and particle transport in the mouse respiratory system.

Consistent with previous studies, we found that exposure to biomass smoke causes a significant decrease in the mouse minute volume⁷. This reflex may be triggered by sensory irritants found in DFS. We found that deposition patterns in the mouse respiratory tract are dependent on the ventilation rate, in agreement with Kolanjiyil et al. (2019)⁸. Therefore, breathing measurements are critical for accurately calculating particle deposition, particularly when the treatment may alter respiration. Lastly, our CFPD results show that regional deposition percentages can be sensitive to particle size. This is likely due to size-dependent contributions from the mechanisms by which particles deposit in the lungs, mainly sedimentation, impaction, and diffusion.

In conclusion, we developed a mouse airway model to enable high-fidelity CFPD simulations. We found regional and cumulative deposition of smoke particulates to be dependent on the particle size and breathing conditions. Future work will focus on implementing physiologically-inspired boundary conditions to investigate the effects of WFS-induced remodeling on airflow and particle deposition.

ACKNOWLEDGEMENTS

This study was supported by DHS/FEMA: EMW-2017-FP-00446 and NIH/NIEHS: R01E5033792. We'd also like to thank Michelle Williams at Ohio State University's Small Animal Imaging Core.

REFERENCES

[1] Eden, M. J. et al., *Sci Total Environ*, 160609, 2022.
[2] Einbrodt, H. J. et al., *J Fire Sci*, 2(6), 427-438, 1984.
[3] Garg, P. et al., *Int J Wildland Fire*, 31(1), 14-23, 2021.
[4] Updegrove, A. et al., *Ann Biomed Eng*, 45(3), 525-541, 2017.
[5] Oakes, J. M. et al., *J Biomech*, 49(11), 2213-2220, 2016.
[6] Hsieh, T. H. et al., *Aerosol Sci Technol*, 31(5), 358-372, 1999.
[7] Hargrove, M. M. et al., *Inhal Toxicol*, 31(6), 236-247, 2019.
[8] Kolanjiyil, A. V. et al., *Respir Physiol Neurobiol*, 260, 82-94, 2019.

STEM CELL-DERIVED EXOSOMES PROMOTE CELL HOMING AND ANGIOGENIC DIFFERENTIATION FOR DENTAL PULP REGENERATION

Venkateswaran Ganesh (1,2), Piedad C. Gomez-Contreras (1), Henry L. Keen (3), Kyungsup Shin (4), James A. Martin (1,2), Dongrim Seol (1,4)*

- (1) Department of Orthopedics and Rehabilitation, University of Iowa, Iowa City, Iowa, USA
- (2) Department of Roy J. Carver Biomedical Engineering, University of Iowa, Iowa City, Iowa, USA
- (3) Iowa Institute of Human Genetics, University of Iowa, Iowa City, Iowa, USA
- (4) Department of Orthodontics, University of Iowa, Iowa City, Iowa, USA

* Correspondence: dongrim-seol@uiowa.edu

INTRODUCTION

Carries and trauma compromise pulpal regeneration demanding an endodontic intervention to restore overall tooth health. Current endodontic interventions of replacing damaged pulp with synthetic filling such as calcium hydroxide paste (CHP) and mineral trioxide aggregate (MTA) *via* root canal therapy have proven successful against early bacterial protection and dentin bridge formation. However, bacterial leakage overtime into healing pulp, poor cohesive strength, cost, and longer setting time highlight the need for a novel dental restorative offering improved patient outcomes [1,2]. Preserving the biosensing ability of tooth through vital pulp therapy have proven successful in younger population, and a cell homing strategy can recruit endogenous dental pulp stem cells (DPSCs) residing in the pulp tissue to the damaged site in need of repair. Exosomes, bioactive vesicles constantly shed by cells can serve as both biomarker and drug with detailed profiling of its content for reversing disease pathophysiology [3,4]. We hypothesized that exosomes would stimulate dental pulp regeneration by promoting DPSC recruitment and subsequent angiogenic differentiation. The aim of this study was to characterize DPSCs-derived exosomes (DPSC-Exos) and evaluate the effect of DPSC-Exos on *in-vitro* cell homing, proliferation and angiogenic differentiation for pulpal regeneration. We further examined the profile of exosomal microRNA (miRNA) for validating exosome effects.

METHODS

Characterization of DPSCs and DPSC-Exos: Incisor pulps from two New Zealand White rabbit cadavers were harvested to isolate DPSCs and establish its lineage-specific differentiable ability; angiogenesis and odontogenesis. Exosomes were isolated under growth media condition. The characterization of exosomes was confirmed by Exo-Check™ exosome antibody array (System Biosciences) which included 8 positive markers (CD63, epithelial cell adhesion molecule (EpCAM), annexin A5 (ANXA5), tumor susceptibility gene 101 (TSG101), flotillin-1 (FLOT1), intercellular adhesion molecule 1 (ICAM), programmed cell death 6 interacting protein (ALIX), and CD81), a negative control (cis-golgi matrix protein (GM130)), 2 positive controls (+ ctrl) and blank. Exosome morphology was imaged using scanning electron microscopy (SEM), and cellular exosome uptake was evaluated

by a PKH67 uptake assay (Sigma-Aldrich) according to the manufacturer's instructions. The size distribution and concentration of DPSC-Exos were analyzed by nanoparticle tracking analysis (NTA).

***In-vitro* effects of DPSCs-Exos:** Initial cytotoxicity screening was performed to select optimal concentration of exosomes with varying concentration of exosomes (low (Exo-L): 5×10^7 /ml, medium (Exo-M): 5×10^8 /ml, high (Exo-H): 5×10^9 /ml) prior to cell proliferation assay using CellTiter 96® Aqueous One Solution (Promega). Transwell® plates with an 8 µm pore (Corning) was used for a migration assay, and the number of migrated cells was stained with Calcein AM (Thermo Fisher Scientific) after removing non-migrated cells. RNAs were isolated from DPSCs treated with DPSC-Exos for real-time polymerase chain reaction (RT-PCR) with probes of key angiogenic markers including vascular endothelial growth factor A (VEGFA), Fms-related tyrosine kinase 1 (FLT1), and platelet and endothelial cell adhesion molecule 1 (PECAM1).

miRNA profiling via Next-Generation Sequencing (NGS): To quantitate known small RNAs and to identify novel miRNAs, we used the Nextflow-based workflow nf-core/smrnaseq (version v1.1.0, <https://github.com/nf-core/smrnaseq>) as a small-RNA sequencing analysis pipeline. To determine differential expression, a model incorporating all the experimental factors was created, and Wald tests were used to compute statistical metrics. To identify novel miRNAs, sequence read files (fastq) from samples in the same group were first concatenated together then ran through the same nf-core/smrnaseq workflow with the miRDeep2 software used for novel miRNA identification. The results from miRDeep2 were filtered to include only potential novel miRNAs.

RESULTS

Characterization of DPSCs and DPSC-Exos: Multi-differentiation potential of DPSCs was validated by both endothelial tube formation and alizarin red staining. DPSCs formed capillary-like formation (Fig. 1A) and apparent calcium deposit (Fig. 1B) in angiogenic and odontogenic induction medium, respectively. Isolated DPSC-Exos were confirmed by exosome markers with ANXA5, TSG101, FLOT1, ICAM, ALIX, and CD81 (Fig. 1C). Exosomes had morphologically a spheroid shape with approximately 100 nm-diameter (Fig. 1D and F)

and $11.6 \times 10^{10}/\text{ml}$ concentration (Fig. 1F). PKH67-stained exosomes were effectively taken up by DPSCs cultured under exosome-depleted media condition (Fig. 1E).

In-vitro effects of DPSCs-Exos: Cytotoxicity test revealed that the cells were less damaged in concentrations of $5 \times 10^7/\text{ml}$ and $5 \times 10^8/\text{ml}$ in comparison with higher concentration ($5 \times 10^9/\text{ml}$) (Fig. 2A). Cell proliferation assay with preselected exosomal concentrations ($5 \times 10^7/\text{ml}$ and $5 \times 10^8/\text{ml}$) demonstrated an anabolic effect of DPSC-Exos in $5 \times 10^8/\text{ml}$ (Exo-M) (Fig. 2B). In the migration assay, the number of migrated cells was dramatically increased in exosome-treated groups, especially $5 \times 10^8/\text{ml}$ (Exo-M) (Fig. 2C and D). In addition, DPSCs treated with DPSCs-Exos showed significant increases in the mRNA levels of angiogenic markers, VEGFA, FLT1, and PECAM1 when cultured with angiogenic induction medium (Fig. 2E).

miRNA profiling: A total of 474 mature and 254 hairpin miRNAs were discovered (Table 1). Interestingly, *ocu-miR-146a-3p*, *ocu-miR-199a-3p*, *ocu-miR-122-5p*, *ocu-miR-221-3p*, *ocu-miR-143-3p*, *ocu-miR-24-3p*, and *ocu-miR-21-5p* were detected over 100,000 total reads. *miR-146a-5p* and *miR-122-5p* function as negative regulation of inflammatory response [5] and positive stimulation of cell proliferation [6], respectively. Regulation of nitric oxide pathway and extracellular signal-regulated kinase (ERK) / mitogen-activated protein kinase (MAPK) signal pathways by *miR-199a-3p* and *miR-21-5p* can involve in promoting angiogenesis [7,8]. Additionally, 88 novel miRNAs were identified (data not shown).

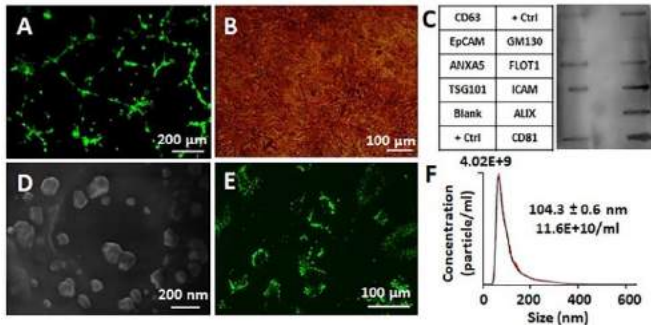


Figure 1. Characterization of rabbit dental pulp stem cells (DPSCs) and DPSC-derived exosomes (DPSC-Exos). (A) Endothelial tube formation at day 10. (B) Alizarin Red staining at day 20. (C) Exosome antibody array. (D) Scanning electron microscope (SEM) images. (E) PKH67 exosome uptake assay with DPSCs. (F) Size distribution and concentration of DPSC-Exos via nanoparticle tracking analysis (NTA). Reproduced with permission [9]. Copyright 2023, MDPI.

DISCUSSION

The objective of this study was to demonstrate the potential of DPSCs-Exos on pulpal regeneration. Exosome treatment significantly improved cell migration/homing, proliferation and angiogenic differentiation *in-vitro*. Through NGS, the profiled miRNAs can be functionally categorized to confirm its efficacy in dental pulp regeneration. For *in-vivo* efficacy of DPSC-Exos, we plan to use a partial pulpotomy animal model, which can mimic clinical conditions in human (Figure 3). In conclusion, our exosome-based cell homing and angiogenic differentiation strategy has a significant therapeutic potential for dental pulp regeneration.

ACKNOWLEDGEMENTS

This research was supported by the National Institute of Dental and Craniofacial Research (NIDCR) of the National Institute of Health (NIH) under award number 1R03DE030515-01.

DISCLOSURE

The authors declare that there is a potential intellectual property regarding data presented here.

REFERENCES:

[1] Desai *et al.*, *J. Endod.*, 35(4):475-480, 2009.
[2] Parirokh *et al.*, *J. Endod.*, 36(3):400-413, 2010.

[3] Zhang *et al.*, *Osteoarthr. Cartil.*, 24(12):2135-2140, 2016.
[4] Raposo *et al.*, *J. Cell Biol.*, 200(4):373-383, 2013.
[5] Yang *et al.*, *FEBS Lett.*, 585(6):854-60, 2011.
[6] Zhou *et al.*, *Aging*, 12(24):25528-46, 2020.
[7] Joris *et al.*, *Arterioscler. Thromb. Vasc. Biol.*, 38(10):2345-2357, 2018.
[8] Eulalio *et al.*, *Nature*, 492(7429):376-381, 2012.
[9] Ganesh *et al.*, *Int. J. Mol. Sci.*, 24(1): 466, 2023.

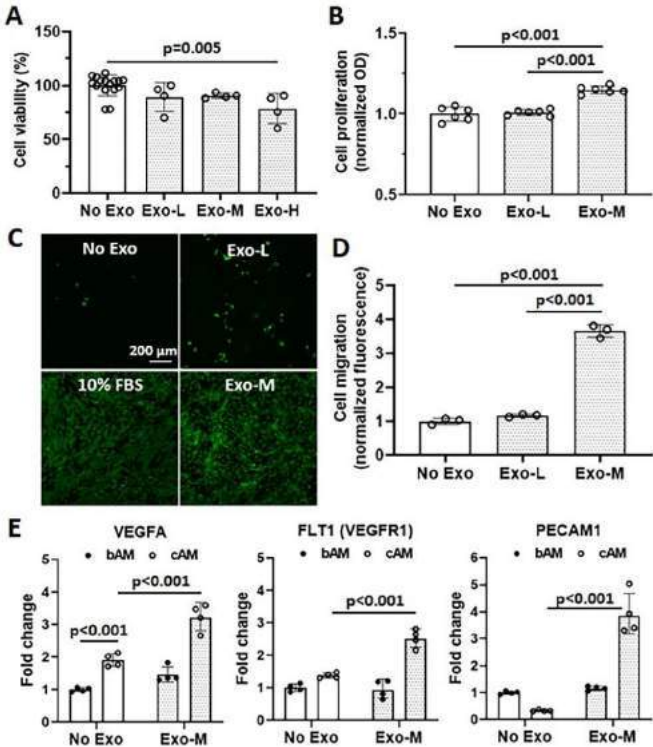


Figure 2. Effects of DPSC-Exos on cell toxicity, proliferation, migration, and angiogenesis. (A) Cytotoxicity assay at 24 h (n = 4-16). (B) Cell proliferation assay at day 4 (n = 6). (C and D) Cell migration assay (n = 3). (E) Gene expression of key angiogenic markers (n = 4). Exo-L: $5 \times 10^7/\text{ml}$, Exo-M: $5 \times 10^8/\text{ml}$, Exo-H: $5 \times 10^9/\text{ml}$. Reproduced with permission [9]. Copyright 2023, MDPI.

Table 1. List of top 10 mature and hairpin microRNAs (miRNAs).

Mature miRNAs	Total read counts	Hairpin miRNAs	Total read counts
ocu-miR-146a-5p	296,149.6	ocu-miR-214	20,367.4
ocu-miR-199a-3p	217,998.9	ocu-miR-503	10,826.0
ocu-miR-122-5p	190,513.3	ocu-miR-199a-1	5,689.2
ocu-miR-221-3p	185,003.3	ocu-miR-199a-2	5,687.8
ocu-miR-143-3p	143,493.5	ocu-miR-23b	5,641.1
ocu-miR-24-3p	137,071.1	ocu-let-7b	5,052.3
ocu-miR-21-5p	122,765.1	ocu-miR-142	3,211.0
ocu-miR-92a-3p	61,986.4	ocu-miR-34a	2,377.4
ocu-miR-23b-3p	49,175.0	ocu-miR-146a	1,816.3
ocu-miR-27b-3p	47,342.7	ocu-let-7i	1,375.5

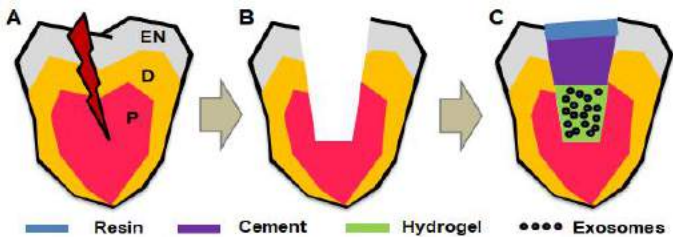


Figure 3. Schematics of pulp regeneration in a rabbit partial pulpotomy model. (A) Irreversible infected or inflamed pulpitis, (B) Class V cavity with partial pulpotomy, (C) Injection of DPSC-Exo with hydrogel. EN: enamel, D: dentin, S: pulp. Reproduced with permission [9]. Copyright 2023, MDPI.

IMPACT FORCES OF DIVISION 1 COLLEGIATE OFFENSIVE AND DEFENSIVE AMERICAN FOOTBALL PLAYERS USING PRACTICE SLED

Sloan Kanat (1), Ryan Harth (1), William Burghardt, PhD (2), Tamara Reid Bush, PhD (1)

(1) Department of Mechanical Engineering, Michigan State University, East Lansing, MI, USA
(2) Department of Intercollegiate Athletics, Michigan State University, East Lansing, MI, USA

INTRODUCTION

The NCAA reports a steady increase in the number of collegiate American football players from 40,000 in 1981 to over 70,000 players in 2013 [1]. As the number of players increases in the sport, so has the number of injuries. A study analyzing collegiate football players through 2002-2020 reported .89 injuries per year which correlates to 1.17 per 100,000 participants obtaining a sports-related structural injury [2]. Additionally, the study found that the majority of players injured were on defense or offense at the time of injury, as opposed to being on special teams [2].

Repeated head trauma, even minor traumas that may not be recognized as a moderate or severe traumatic brain injury (TBI), can lead to chronic traumatic encephalopathy (CTE). CTE is brain degeneration that occurs after repeated head trauma. CTE symptoms can be latently onset making it harder to diagnose until later in life. One study found 87% of a sampled population of ex-football players (n=202 players) had evidence of CTE [2]. CTE can lead to mood disorders in younger populations and cognitive impairment in older populations [3]. With the sport of football growing every year, the risk of more individuals experiencing CTE also increases.

Previous research has focused on measurement of direct head and helmet impacts. Although an important measure, direct helmet impacts do not provide the ability to look at the force transference when the impact occurs elsewhere on the body, for example to the torso. Since it is clear that the potential for head injury exists with tackle football, it is equally important to quantify and understand the magnitude of forces that occur to the body with a “hit”, particularly with regard to a torso hit. Using this information, hit technique can be analyzed for both efficiency and safety.

The goals of this study were to quantify the impact force of a football hit from different stance points (2, 3, and 4 point stances). This data will help to bridge the gap between direct head impact and transference impacts to other regions of the body.

METHODS

This study investigated 15 Michigan State University male football players and obtained the forces they exerted on a practice sled (IRB Approval #00007331). Players had an average age of 19.29 years with a standard deviation of 1.43 years and were exclusively offensive and defensive linemen. A Bertec force plate was mounted on a practice sled and a blocking pad was secured on top of the system. The measurement system was hit by the player and then was pushed up the rails as the player advanced forward. Force data perpendicular to the sled (Z direction) were collected at a sample rate of 1000 Hz during a simulated hit (Fig. 1). Anthropometric measurements of each player were also recorded.



Figure 1. Mounting of the force plate with green blocking pad secured. Z-direction was labeled to show the direction of recorded force.

The players began the hit in one of three different stances: 2-point, 3-point, and 4-point (Fig. 2); the stance selection was randomized. Each player completed two trials in each of the stances.

The hit against the force plate was broken up into three sections. The impact was defined as the largest recorded force immediately after contact with the force plate was made. After the initial contact, the players continued to push the sled until it reached the end of the track. Two parameters were developed to analyze these data 1) average drive force and 2) a drop-off force. The force recorded from the time the sled began to move until the end of the track was averaged to obtain the drive

force. The drop-off force occurred between the impact and the beginning of the drive force. The measured force decreased rapidly after the initial impact and before the drive force began.



Figure 2. Demonstration of a player in A) a 2-point stance, B) a 3-point stance, C) a 4-point stance

RESULTS

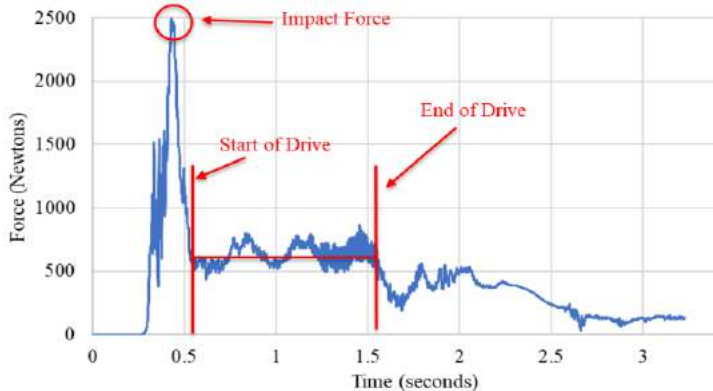


Figure 3. Characteristic example of force generated by a player performing a hit on the sled.

Figure 3 demonstrates the impact force, or the peak force immediately after contact with the force plate was made. It also demonstrates the start and end of the drive force. After the initial impact force, the drop-off force was calculated for each player (Fig. 4). This drop-off force signifies a decrease in the applied force against the force plate before the player begins to drive the sled forward.

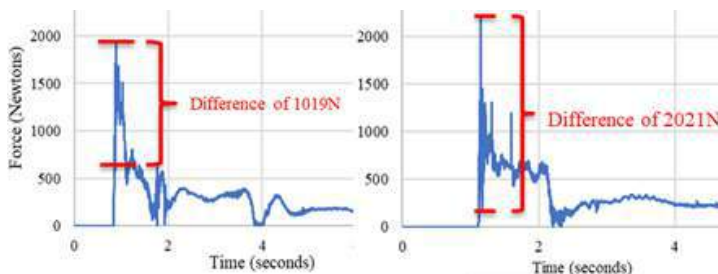


Figure 4. Demonstration of the drop-off values. The graph on the left shows a player with a much smaller drop off value than the player in the graph on the right.

As seen in Figure 5, when examining a set of five players who were in the same height (300-305cm) and weight ranges (87.5-89.8kg) two of the five players had a maximum impact force below the average and the other three were above the average.

The stance in which the maximum impact force occurs varies between players (Fig.6). The percentages (33% in 2-point, 27% in 3-point, 40% in 4-point stance) show the number of players that achieved the maximum impact in the corresponding stances.

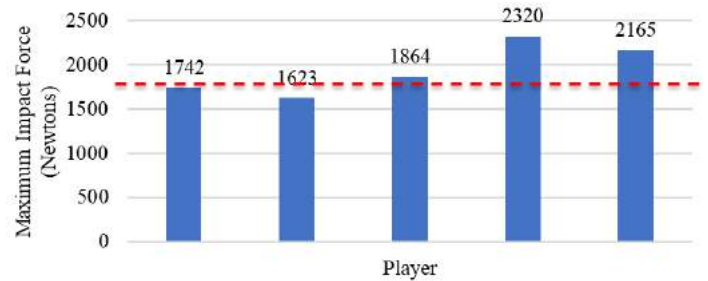


Figure 5. Maximum impact force values for 5 players with similar height and weight. The red line indicates the average impact force across players.

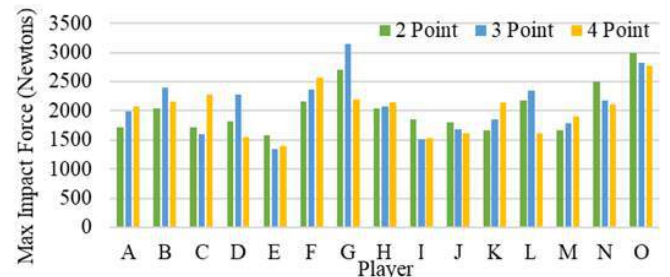


Figure 6. Maximum impact force in each stance.

DISCUSSION

This study quantified the forces exerted by football players during a hit on a practice sled across different tackle stances.

The impact values represent the maximum value delivered by the football player. These would also represent the force that the player was applying to their opponent and can be used for consideration in force transmission as it relates to head trauma. This research provides a better understanding of the force profile that is seen when an “initial hit” is being applied to the players during the initial drive between offensive and defensive players.

In terms of the stance, for some players, the stance affected the impact force applied to the sled, whereas others, the stance has little influence on the force generated. Our data also indicates that estimating the force generated by a player just by their height or weight is problematic. In our sampling of players with similar height and weights, there was a differential force of ~700N in the maximum impact force.

While there was substantial research regarding impacts directly to players helmets, there is limited data regarding the force exerted at the initial impact of a body hit after the whistle is blown to start a play. The data presented here demonstrates the ability to gather force data and analyze it from multiple aspects of a tackle, including impact force, drive force and drop-off force.

Future work for this study will look at the mechanics of the transference of forces from a hit to the chest up through the neck and to the head. It will also look at differences in teenage versus adult impacts to determine the influence of the weight of the player and the muscle distribution to the transference of forces to the head during impact.

REFERENCES

- [1] NCAA. Student-Athlete Participation 1981-82-2012-13. NCAA Sports Sponsorship and Participation Rates Report, 2014
- [2] Boden, BP et al., American Orthopedic Society for Sports Medicine 2022
- [3] Mez, J et al., JAMA, 318(4):360–370, 2017.
- [4] Gatt. CJ et al., *The American Journal of Sports Medicine*, 25(3):317-321, 1997.

GROWTH AND REMODELING IN SPARSE AND SEMI-SPARSE TISSUES: BRIDGING THE GAP BETWEEN THE CONSTRAINED MIXTURE MODEL AND ESHELBY'S INCLUSION

Ryan R. Mahutga (1), Elizabeth D. Shih (1), Patrick W. Alford (1)

(1) Department of Biomedical Engineering, University of Minnesota, Minneapolis, MN, USA

INTRODUCTION

The field of computational growth and remodeling (G&R), and computational mechanobiology has largely been driven by constrained mixture models [1]. These models work well for many tissues, particularly those with dense, homogeneous microstructures [2,3]. However, tissue compositions vary widely between organs, and in disease. For example, the anterior cruciate ligament (ACL) has a much lower density of cells than the aorta. While the aorta does tend to have dense, organized cellular substructures, it is quite common to see apoptosis and reductions in cellularity in diseases like aneurysm.

The foundation of many models of growth and remodeling is tensional homeostasis. Tensional homeostasis assumes that cells attempt to modify themselves and their environment to return to a homeostatic state of stress. In tissues with low or reduced cellularity, stresses can be concentrated near cells, which could change the remodeling process. In this work, we propose a model based on strain concentration factors allowing us to bridge between the constrained mixture assumption and Eshelby's inclusion [4,5]. This allows us to model growth and remodeling in cell-sparse tissues like the ACL, and through the time-course of disease like aneurysm.

METHODS

Tissue Material Behavior: For this model we assume tissues are made up of an incompressible mixture of constituents including an extracellular ground matrix given by

$$W^g = C_1(I_1 - 3) \quad (1A)$$

where W^g is the strain energy density, C_1 is the neo-Hookean material parameter, and I_1 is the first strain invariant of the right Cauchy-Green tensor, an extracellular collagen fiber component given by

$$W^c = k_1 \left[\exp \left(\alpha \left(\lambda^2 + \frac{2}{\lambda} - 3 \right) \right) - 1 \right] \quad (1B)$$

where W^c is the collagen strain energy density, k_1 is the collagen fiber modulus, and α is the collagen fiber nonlinearity, and a cellular component having both active and passive properties given by

$$W^m = C_a \left[\left(\frac{\lambda}{\lambda_a} \right)^2 - 1 \right] + k_2 \left[\exp \left(\beta \left(\lambda^2 + \frac{2}{\lambda} - 3 \right) \right) - 1 \right] \quad (1C)$$

where W^m is the cellular strain energy density, C_a is the active contraction parameter, λ_a is the minimum active contraction stress, k_2 is the cellular fiber modulus, and β is the cellular fiber nonlinearity.

The total stress within the tissue is given in terms of the mass fractions and the strain concentration factors in 1D as

$$\sigma_{11} = S^{cell} \varphi^m \sigma_{11}^m + S^{ecm} (\varphi^c \sigma_{11}^c + \varphi^g \sigma_{11}^g) \quad (2A)$$

Where σ_{11} is the total averaged stress, S^{cell} is the 1D cellular strain concentration factor, $\varphi^h = m^h / \sum_h m^h$ is the mass fractions of each constituent, h, subject to $\sum_h \varphi^h = \varphi^m + \varphi^c + \varphi^g = 1$, σ_{11}^h is the constituent stress as calculated from the remotely applied boundary conditions (i.e. calculated like the constrained mixture model), and S^{ecm} is the extracellular matrix strain factor calculated to make the total strain factor stress equivalent to the constrained mixture stress.

Based on previous work in our lab, a good functional form for the 1D strain concentration factor is based on an exponential weighting of the mass fraction with the Eshelby strain factor

$$S^m = \exp(-\kappa \varphi^m) [S^{Eshelby} - 1] + 1 \quad (2B)$$

Where $S^{Eshelby}$ is the Eshelby strain factor, which is a function of cell aspect ratio (diameter to length) and cell stiffness relative to the extracellular matrix stiffness [5].

Growth and Remodeling: Growth and remodeling is applied similarly to conventional constrained mixture models with the addition of a strain factor. In our model, collagen turns over and cells and the ground matrix do not. The evolution of collagen mass is

$$m^c(t) = m^c(0)Q(t) + \int_0^t \dot{m}^c(t, T) dt \quad (3A)$$

where $m^c(0)Q(t)$ is the survival of the initial mass at time t, $\dot{m}^c(t, T)$ is the change in mass of collagen (which is deposited at time T and exists at the current time t). The change in collagen mass is broken down as an exponential decay and an addition related to the cellular stress level

$$\dot{m}^c(t) = \begin{cases} -k^d m^c(t) + \dot{m}^\alpha & \text{if } \sigma^m(t) \leq \sigma_\infty^m \\ \dot{m}^\alpha + \dot{M}(\sigma^m(t) - \sigma_\infty^m) & \text{else} \end{cases} \quad (3B)$$

where k^d is the decay time constant for masses existing prior to time t , \dot{m}^α is the basal deposition rate for mass deposited at time t , \dot{M} is the cell stress dependent deposition rate, and σ_∞^m is the target cell stress. Collagen is further assumed to be deposited at a pre-defined stretch so the mass additions are made at length $L^c(t) = L(t)/\lambda_{dep}$. Because of the inclusion of deposition stretch, the masses are tracked individually, the differential equations are solved using forward Euler, and integrals evaluated using a simple Riemann sum.

1D Examples: To demonstrate this new G&R framework, we apply two simple 1D cases: 1. a bar at fixed length and 2. a bar under controlled stress. One could think of these cases loosely representing growth and remodeling of cell sparse tissues during 1. the period following tendon or ligament reconstruction or grafting and 2. normal growth of the tendon or ligament with the body during development.

RESULTS

Remodeling of a 1D Bar at Fixed Length: During remodeling of a bar at a fixed applied length, we see an instantaneous spike in stress following the application of stretch (after the Basal remodeling phase), which is recovered, as one might expect. All constituents experience a spike in stress, which is recovered with the remodeling of collagen (Fig. 1). As the cell strain factor increases (Fig. 1A), we get more collagen remodeling, which results in lower ECM stresses overall (Fig. 1B). When we decrease the magnitude of stretch, we see a dip in the stresses for all constituents, and we still see lower overall stresses on the ECM in cases of increasing strain factor.

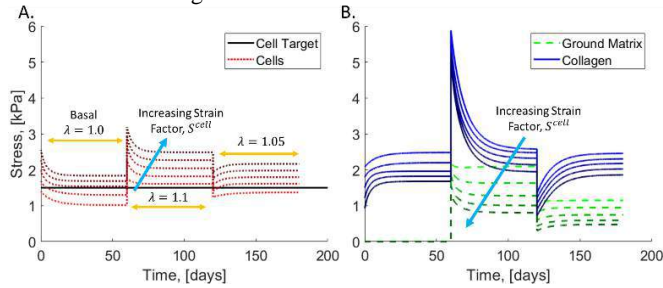


Figure 1. A. Cellular stresses and **B.** extracellular matrix stresses during stretch-controlled remodeling using different strain factors.

During the stretch phase, we further see increases in collagen mass fraction which accompanies decreases in ground matrix and cell densities (Fig. 2A). The result of this decrease in cellular mass fraction is an increase in strain factor (Fig. 2B). Further, the higher the initial strain factor, the more collagen is added, the lower the cell mass fraction, which results in larger increases in the remodeling strain factor creating a positive feedback loop. When, the stretch is reduced, we see decreases in collagen content, which correspond to increases in ground matrix and cell content, and leads to lower cell strain factors.

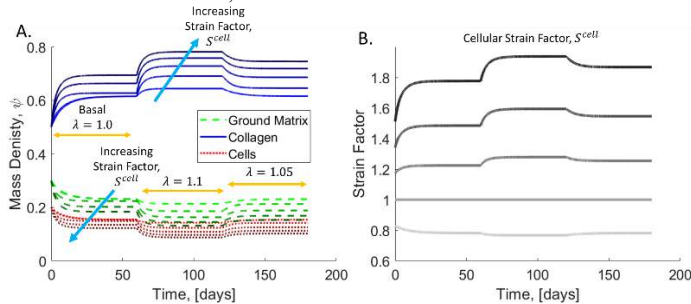


Figure 2. A. Mass fraction evolution of constituents during remodeling and **B.** Evolution of the cellular strain factor during remodeling.

Remodeling of a 1D Bar under Controlled Force: Under an increase in applied stress (following the Basal phase), the cell stress increases along with the ground matrix, while the collagen remodels to lower stress (Fig. 3). When the stress is decreased, the cell stress and ground matrix stress slowly decrease, while the collagen stress increases. Similarly to the controlled stretch, an increase in cellular strain factor resulted in higher cell stress which results in lower ECM stress (Fig. 3).

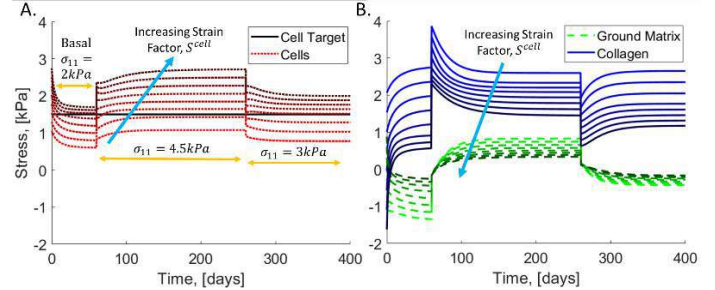


Figure 3. A. Cellular stresses and **B.** extracellular matrix stresses during stress-controlled remodeling using different strain factors.

The bar grows with increased stress and shrinks with reduced stress, as one might expect (Fig. 4A). In addition, higher strain factor results in more growth with higher stress, and more contraction with lower stress (Fig. 4A). When the stress is increased, the collagen density increases while the ground matrix and cell content decreases (Fig. 4B). When the stress is decreased, the collagen content decreases while the ground matrix and cell content increase (Fig. 4B).

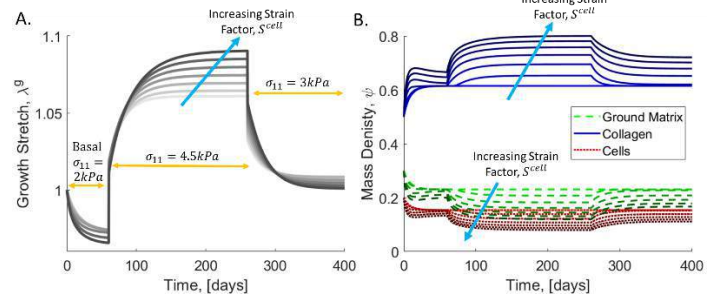


Figure 4. A. Growth under sustained stress, and **B.** mass fraction evolution of constituents during remodeling

DISCUSSION

Growth and remodeling in cell-sparse tissues is a significant challenge with current computational tools [1,2,3]. To try to understand how cell sparsity might influence G&R, we have created a new framework based around the definition of strain factors allowing us to span from the single inclusion of Eshelby to the fully parallel assumptions of the constrained mixture model. Our model shows that as tissues become more sparse, the cellular stresses increase leading to increased collagen deposition, which results in lower overall ECM stress. The increase in collagen content drives down the cell content which increases the strain factor. Thus, this creates a positive feedback loop where the addition of more matrix results in higher strain concentration on cells, which results in more remodeling.

ACKNOWLEDGEMENTS

The authors acknowledge funding from the National Science Foundation (CMMI-156319) and from the National Institutes of Health (R01-NS126762). Ryan R Mahutga acknowledges support from an American Heart Association Postdoctoral Fellowship (Award 827242).

REFERENCES

- [1] J.D. Humphrey, K.R. Rajagopal, Math. Model. Methods Appl. Sci. 12 (2002) [2] I. Karsaj, J.D. Humphrey, Mech. Mater. 44 (2012) [3] M.Y. Emmert, et al. Sci. Transl. Med. 10 (2018) [4] J.D. Eshelby, Proc. R. Soc. A 241 (1957) [5] J.P. Marquez, et al., Biophys. J. 88 (2005)

TOWARDS MODELING ACUTE ISCHEMIC STROKE: IN VITRO EXPERIMENTS AND SIMULATIONS OF BLOOD FLOW AND MEAN ARTERIAL PRESSURE IN AN ARTIFICIALLY CLOTTED CEREBROVASCULAR MODEL

**Saurabh Bhardwaj (1), Brent A. Craven (2), Jacob E. Sever (1), Francesco Costanzo (1,3),
Scott D. Simon (4), Keefe B. Manning (1,5)**

- (1) Department of Biomedical Engineering, Pennsylvania State University, University Park, PA, USA.
- (2) Office of Science and Engineering Laboratories, Center for Devices and Radiological Health, United States Food and Drug Administration, Silver Spring, MD, USA
- (3) Department of Engineering Science and Mechanics, Pennsylvania State University, University Park, PA, USA
- (4) Department of Neurosurgery, Penn State Hershey Medical Center, Hershey, PA, USA.
- (5) Department of Surgery, Penn State Hershey Medical Center, Hershey, PA, USA.

INTRODUCTION

The life-threatening medical condition known as acute ischemic stroke (AIS) occurs when a blood clot lodges in the cerebral vasculature and restricts blood flow to the brain. A number of previous studies have been performed to examine cerebral hemodynamics [1-7], primarily focusing on measuring regional blood flow. The severity of AIS is largely determined by the location and the extent to which emboli become trapped in the cerebral vasculature. Elucidating the underlying causes and therapy of AIS requires quantifying blood flow, pressure, and embolus migration in the cerebrovascular, which are extremely challenging to measure in AIS patients. The goal of our research is to develop and validate a computer model for predicting the hemodynamics and the migration and lodging of emboli in complex anatomical models of the cerebrovasculature.

METHODS

As reported by Bhardwaj et al. [8], a representative anatomical model of the aorta and cerebral vasculature is used in this study (Fig. 1). The model was designed by United Biologics (Irvine, CA, USA) based on patient medical image data from several sources (e.g., the NIH Visible Human Project, patient-specific CT data). The *in vitro* model is made of silicone with an elasticity that is representative of human arteries. A corresponding computational model of the *in vitro* model is created by reconstructing high-resolution 3D micro computed tomography (μ -CT) scans (Fig. 2). Using the 3D reconstructed model, computational fluid dynamics (CFD) simulations are performed using the open-source computational continuum mechanics library, OpenFOAM.

The working fluid in the experimental flow loop that is being modeled is a solution of water (60% by weight) and glycerol (40% by weight) that has a density and dynamic viscosity similar to blood [9] (1.09 g/mL and 3.98 cP, respectively). The inlet flow was ensured to be fully developed by connecting an additional tube of 900 mm in length to the model inlet. By adjusting clamps on the outlet tubing downstream of the pressure and flow rate measurement sites, the regional flow distribution to the different arteries was tuned to match available data in the literature [10-11]. This resulted in a regional flow distribution

in which 73.2% of the fluid flowed through the descending aorta and 26.8% was distributed to the other arteries branching from the aortic arch. The *in vitro* stroke condition was achieved by clamping right middle cerebral artery (RMCA), right posterior artery (RPCA) and right access port using forceps.

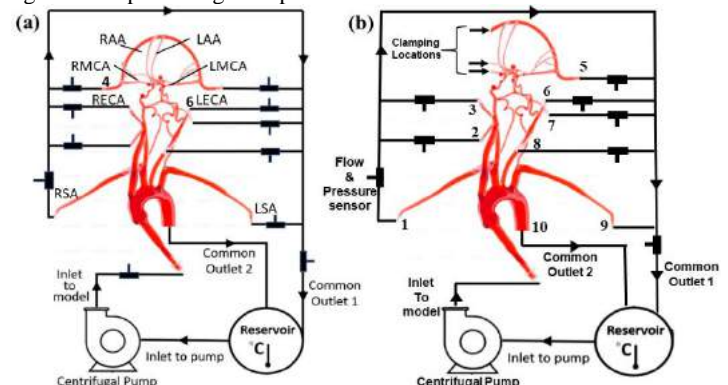


Figure 1: Circulatory flow loop illustrating (a) the experimental setup for normal physiological conditions and (b) the locations of cerebral artery clamps that are used to mimic a stroke condition. The flow rate and pressure are measured during steady flow at the numbered cerebrovascular outlets. Here, LSA and RSA are left and right subclavian arteries, LECA and RECA are the left and right external carotid arteries, LMCA and RMCA are the left and right middle cerebral arteries, and the LAA and RAA are left and right anterior arteries.

Figure 2 depicts the CFD models for the normal and stroke conditions (clamping RMCA, RPCA and right access port). The boundary conditions were chosen to correspond to the *in vitro* experiments. To obtain fully developed flow entering the inlet to the ascending aorta at a flow rate of 5.17 L/min, a steady, uniform inlet velocity was applied to the extended inlet. On the walls, which were assumed to be rigid, a no-slip velocity boundary condition was imposed. At the inlet, a zero-gradient pressure condition was used, and fixed static pressure boundary conditions were specified for all outlets. The outlet pressure values were determined by

iteratively performing simulations to match the measured flow rate in each outlet in the experiments to within $\pm 10\%$.

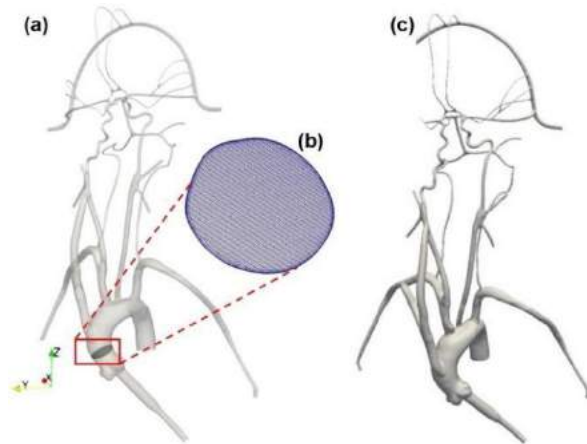


Figure 2: (a) 3D reconstructed computational model of the corresponding *in vitro* cerebrovascular model for normal physiological conditions with (b) a cut plane in the aortic arch to illustrate the mesh, and (c) the CFD model for the stroke condition.

RESULTS

Table 1 summarizes the volumetric flow rate (L/min) and pressure (mmHg) data recorded at the various arterial outlets in the experiments. The superior arteries originating from the aortic arch receive 26.8% of the overall flow rate entering the model and 73.2% of the fluid flows through the descending aorta. For the stroke condition, when there is no flow from outlet 4, the change in arterial pressure and volumetric flow rate were also measured.

Table 1: Flow rate (L/min) and mean arterial pressure (mmHg) obtained from *in vitro* experiments in normal and stroke conditions at the inlet and outlets.

Location	Flow Rate (L/min)		Pressure (mmHg)		% Diff	
	Normal	Stroke	Normal	Stroke	Flow Rate	Pressure
Inlet	5.16	5.15	84.91	84.15	-0.19	-0.90
1	0.197	0.206	83.84	83.24	4.57	-0.72
2	0.199	0.212	82.56	81.21	6.53	-1.64
3	0.154	0.161	83.93	82.52	4.55	-1.68
4	0.143	0	82.11	-	-	-
5	0.147	0.149	83.43	80.34	1.36	-3.70
6	0.157	0.159	83.51	79.23	1.27	-5.13
7	0.189	0.188	83.9	80.78	-0.53	-3.72
8	0.185	0.185	83.83	79.24	0.00	-5.48
9	0.331	0.322	80.31	78.44	-2.72	-2.33

The experimental measurements reveal that the pressure at all of the outlets reduces for the stroke condition. As seen in Table 1, the flow rate through the right artery outlets, as well as outlets 5 and 6, increases to compensate for the blocked flow caused by the stroke. Figure 3 depicts the pressure and velocity distribution for the stroke condition from CFD. A comparison of pressure and volumetric flow rate between the normal and stroke conditions reveals that the mean pressure at all of the outlets reduces in the stroke condition, as observed in the experiments.

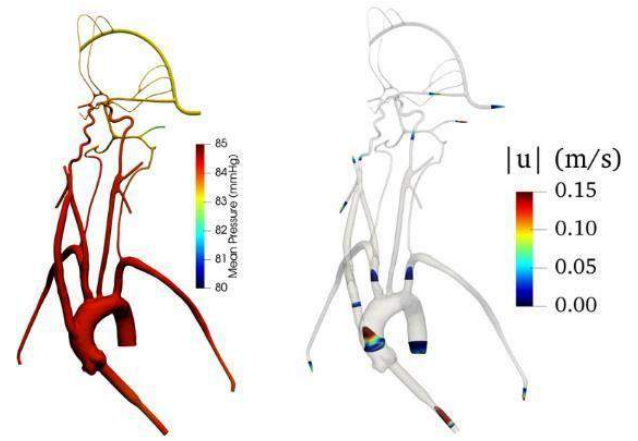


Figure 3: (a) Mean pressure contours and (b) profiles of mean velocity at various sections in the anatomical cerebral vascular model from CFD for the stroke condition.

DISCUSSION

In order to investigate flow and embolus migration and lodging in the brain, this work aims to create a realistic *in vitro* experimental model and a corresponding computational model of the cerebral vasculature. To validate the accuracy of the flow predictions, pressure and flow rate measurements were acquired and corresponding CFD simulations were performed. Overall, the CFD simulations compare reasonably well with the experiments. The aortic arch flow pattern in the current study is similar to that reported by Numata et al. [12]. The transient flow field found in the aortic arch in our work has also been reported in other studies [13-16]. Future work will investigate the migration and lodging of emboli in this cerebrovascular model.

ACKNOWLEDGEMENTS

This work was partially supported by the NIH NHLBI through Grant HL146921. Some details of this study are reported in a preprint posted to bioRxiv (<https://doi.org/10.1101/2023.01.13.523948>). This abstract contains recycled and adapted material from this bioRxiv preprint.

REFERENCES

- [1]. Giller et al., J Neuroradio, 11 :177- 182, 1990. [2]. Gur D. et al., Stroke, 13:750- 758, 1982.
- [3]. Gur D. et al., In vest Radio, 20:672-677, 1985.
- [4]. Ito M. et al., Neuroradiology, 23:63-74, 1982.
- [5]. Norrving B. et al., Stroke, 13: 155- 162, 1982.
- [6]. Uemura K. et al., J Comput Assist Tomogr, 64:677, 1982.
- [7]. Yonas H. et al., Stroke, 15:443-450, 1984.
- [8]. Bhardwaj S. et al., biRxiv, doi: 10.1101/2023.01.13.523948, 2023
- [9]. Li, Z., and C. Kleinstreuer., Med. Eng. Phys., 27(5):369–382, 2005.
- [10]. Migliavacca, F., et al., J. Biomech., 39(6):1010–1020, 2006. [11]. Taylor, C. A., et al., Comput. Aided Surg., 4(5):231–247, 1999.
- [12]. Numata, S. et al., Eur. J. Cardio-Thorac. Surg., 49(6): ezv459, 2016.
- [13]. Cheng Z, et al., Med Eng Phys., 36(9):1176-84, 2014.
- [14]. Miyazaki S, et al., Heart Vessels, 32(8):1032-1044, 2017.
- [15]. Vinoth, R. et al., The Proceedings of the International Conference on Sensing and Imaging. ICSI 2017. Lecture Notes in Electrical Engineering, Springer, Cham., 506, 2019.
- [16]. Eslami P, et al., J Biomech Eng., 141(10):1045011–8, 2019.

QUANTIFYING THE EFFECT OF FEMORAL COMPONENT INTERNAL ROTATION ON LIGAMENT FORCES FOR TOTAL KNEE ARTHROPLASTY WITH VARUS TIBIAL

Jonathan Glenday, Jonathan Vigdorchik, Peter Sculco, Cynthia Kahlenberg, David Mayman, Eytan Debbi, Joseph Lipman, Timothy Wright, Fernando Quevedo Gonzalez

Hospital for Special Surgery, NY, NY, USA

INTRODUCTION

One of the main goals of total knee arthroplasty is to achieve a well-balanced knee that will provide appropriate kinematics, stability, and longevity [1]. Modern TKA techniques, like kinematic alignment, avoid soft tissue manipulations and achieve balance of the knee through appropriate component placement that replicates the native knee anatomy [2]. After component placement, surgeons evaluate knee balance by applying varus and valgus stresses to the knee, typically in full extension and in 90° of flexion, to determine the constraints provided by the different ligaments. While biomechanical research typically focuses on the effect of varus/valgus component alignment in the frontal (i.e., coronal) plane on joint mechanics and balance [3], little attention has been paid to component alignment in other planes. As such, while the axial (internal/external) rotation of the femoral component can directly impact knee balance in flexion, its effect on the soft tissue forces, particularly in the context of alignments which replicate the native coronal orientation, remains unclear. Furthermore, the connection between this intraoperative knee balance assessment and knee function during daily activities also remains unclear. Therefore, we asked two questions: (1) what is the effect of internally rotating the femoral component to match the tibial coronal alignment in flexion on the intraoperative ligament forces? (2) How do these intraoperative ligament forces relate to functional ligament forces during gait?

METHODS

We adapted a generic multibody dynamic musculoskeletal model of the lower limb [4], developed in OpenSim [5] to calculate subject-specific ligament forces and tibiofemoral kinematics and kinetics (Fig. 1). The model included 44 Hill-type muscle-tendon units spanning the leg. The affected knee of the generic model was replaced by a six degrees-of-freedom (DOF) tibiofemoral joint and a 6 DOF patellofemoral joint, using the Joint and Articular Mechanics (JAM) toolbox (<https://simtk.org/projects/opensim-jam>) [3]. This formulation uses 12 non-linear spring bundles to represent the principal knee ligaments, patellar tendon, posterior capsule, and iliotibial band. This formulation models the ligaments as non-linear, tension-only springs, with a slack region where the ligament could stretch without generating force and a linear region, where the ligament force was proportional to its change in length. In addition, the JAM formulation uses an elastic foundation model to determine the joint contact forces in the knee.

We adapted the generic model by introducing the subject-specific anatomy and motion capture markers from the third Grand Challenge Competition to Predict In Vivo Knee Loads [6]. This dataset included pre- and postoperative CT-scans and motion analysis data of five gait trials from a 63-year-old female with an instrumented TKA.

Next, in the coronal (frontal) plane, we virtually implanted the tibial component in 5° varus and the femoral component in 5° valgus to represent an extreme deviation of the components from the mechanical axes of the bone whilst maintaining a neutral hip-knee-angle alignment. For the axial rotation of the femoral component, we considered two scenarios: (1) the component oriented parallel to the epicondylar axis (2) the component internally rotated by 5° to match the varus alignment of the tibial component.

For the JAM toolbox's elastic foundation model, we discretized the articular surfaces of the femoral component and tibial insert using

triangular elements with an edge length of 1 mm, which was reported to be adequate for musculoskeletal simulations [7]. The femoral component was assumed rigid, and the tibial insert was modeled as linear elastic ultra-high molecular weight polyethylene (UHMWPE) with an elastic modulus of 463 MPa and a Poisson's ratio of 0.46. Similar to prior studies [3], we reduced the stiffness of the tibial insert by a factor of 10 to improve simulation convergence.

We considered a single definition of the ligament properties across based on the default knee position. Ligament stiffness was obtained from literature and the slack length of each bundle was calculated using the resting length at 0° of knee flexion and the corresponding reference strains [3].

For both varus alignments, we reproduced the intraoperative varus/valgus assessment by performing passive forward dynamic simulations at 0° (full extension) and 90° of knee flexion with an applied tibial compression of 50 N and 10 Nm of varus torque and valgus torque. Subsequently, we used the Concurrent Optimization of Muscle Activation and Kinematics algorithm [3] to simulate the five gait trials provided in the dataset. For both the varus/valgus assessments and the gait simulations, our primary outcome measure was the force of the medial and lateral collateral ligaments (MCL and LCL, respectively) and the posterior cruciate ligament (PCL).

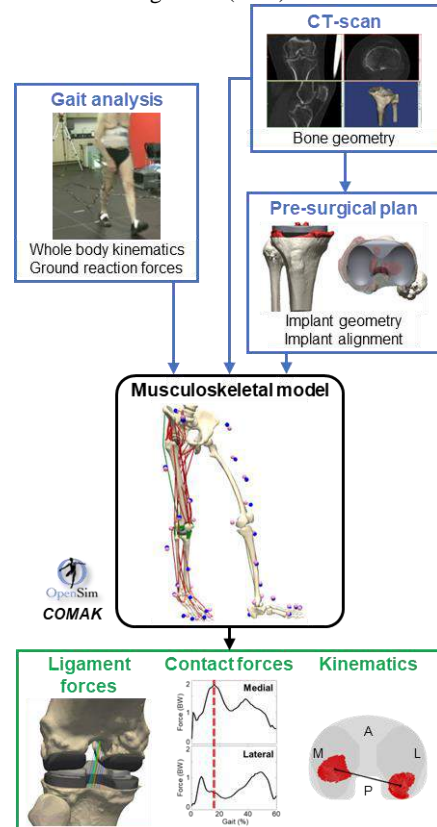


Figure 1: Overview of the musculoskeletal simulations used to predict TKA joint mechanics.

RESULTS

During the simulated intraoperative varus/valgus assessments (Fig. 2), femoral component internal rotation decreased the MCL force at 90° flexion (0 N vs. 102 N for the valgus assessment). Conversely, femoral component internal rotation resulted in negligible change of the LCL force at full extension and a small decrease at full extension at 90° flexion (6 N vs. 1 N for the varus assessment). Femoral component rotation also resulted in a large increase of the PCL force, which was greater at 90° flexion than full extension (278 N vs 630 N across both assessments).

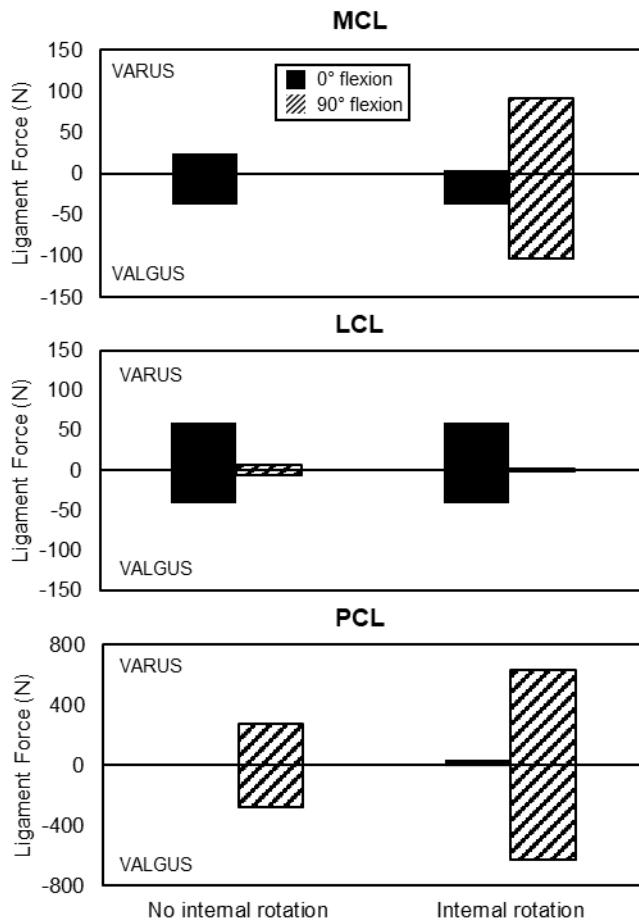


Figure 2: Bar graphs of the MCL (top), LCL (middle), and PCL (bottom) forces for the varus/valgus assessments performed at 0° and 90° of flexion for the varus alignment without (left) and with matching (right) femoral component internal rotation. Ligament force is reported as a positive value for the varus assessment and as a negative value for the valgus assessment.

During gait, femoral component internal rotation increased the MCL force, especially at late stance, when the knee flexion was at its greatest (Fig. 3, top). Femoral component internal rotation resulted in a small decrease in LCL force throughout stance (Fig. 3, middle). Conversely, femoral component internal rotation resulted in a large increase in PCL force throughout stance (Fig. 3, bottom). These changes in ligament forces during gait due to the femoral component internal rotation followed the trends observed during the simulated intraoperative assessments.

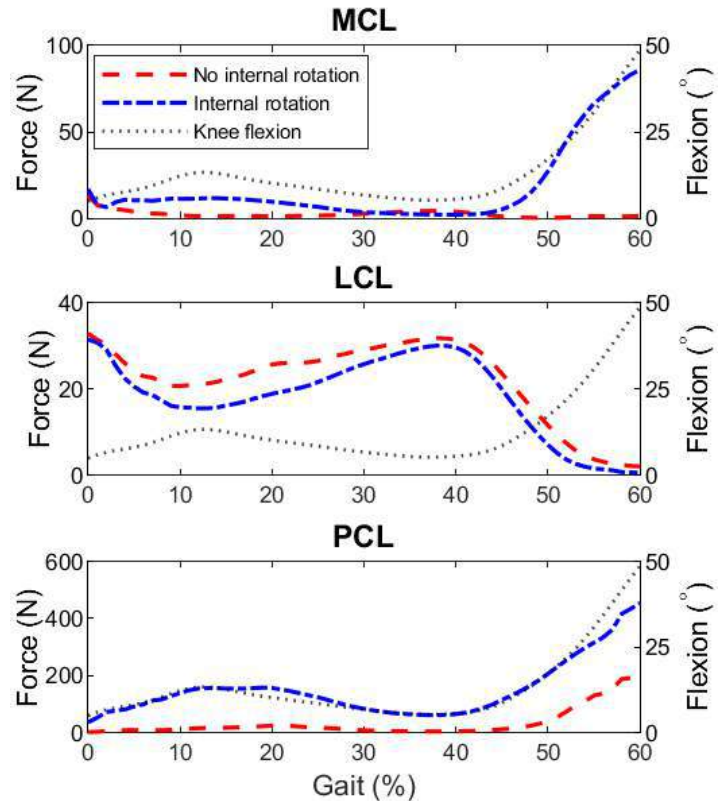


Figure 3: MCL (top), LCL (middle) and PCL (bottom) forces during the stance of a gait trial.

DISCUSSION

Using the predictions from our musculoskeletal simulations, we observed that the effect of femoral component position on the functional ligament forces during gait were consistent with the changes observed during the simulated intraoperative varus/valgus assessments. In this way, the MCL force increased during late stance when the femoral component was internally rotated, which was consistent with the increase in ligament force that occurred at 90° flexion of the varus/valgus assessments. Similarly, the increase in PCL force observed for the varus/valgus assessment at 90° flexion was reflected by larger PCL forces throughout stance, while the small reduction in LCL forces during simulated intraoperative assessments led to a small reduction in the LCL forces during gait. These changes could have implications for knee kinematics and stability. Future studies should aim to investigate how these coronal and axial plane deviations of the implant alignment can affect the fixation mechanics at the bone-implant interface.

REFERENCES

- [1] Bourne et al., *Clin Orthop Relat Res* (2010).
- [2] Blakeney et al., *Knee Surgery, Sport Traumatol Arthrosc* (2019).
- [3] Smith et al., *Biomech Eng* (2016).
- [4] Arnold et al., *Ann Biomed Eng* (2010).
- [5] Delp et al., *IEEE Trans. Biomed. Eng* (2007).
- [6] Fregly et al., *J Orthop Res* (2011).
- [7] Smith et al., *Comput. Methods Biomech. Biomed. Eng.* (2018).

EXTRACELLULAR MATRIX COMPOSITION AND VISCOELASTICITY ARE LONGITUDINALLY HETEROGENEOUS IN TENDON

Hannah M. Larson (1), Olivia J. Ward (1), Sarah Calve (1)

(1) Paul M. Rady Department of Mechanical Engineering, University of Colorado, Boulder, CO, USA

INTRODUCTION

Tendons perform a critical function in the body by connecting and transmitting forces from muscle to bone. The extracellular matrix (ECM), composed of a three-dimensional network of macromolecules, provides tendons with the mechanical structure necessary to bear loads and assists in cellular communication and biochemical regulation. The material structure of tendon ECM can be viewed as a fiber-reinforced composite comprised of load bearing *fibers* of type I collagen and elastin embedded in a *matrix* of ECM constituents including proteoglycans (PGs) and glycosaminoglycans (GAGs), with an interface where fibers and *matrix* bond. Canonically, in composites, the *matrix* is responsible for binding the material and transmitting stresses between load bearing fibers.

The hierarchical structure of collagen, from the molecular scale to fibril, fiber, and fascicle scales, drives the characteristic stress-strain response of tendon. However, the mechanism of load transfer between and within hierarchical levels is unknown [1]. Previous studies aimed at characterizing the multiscale mechanics of collagen are limited by the removal of fibrils and fibers from physiological boundary conditions at insertion sites and/or without the surrounding *matrix*. Furthermore, the role of *matrix* ECM in mature tendon mechanics is not clearly defined, though PGs have been shown to impact fiber recruitment [2]. Much of the previous work that aimed to define the effect of *matrix* ECM was limited by the use of enzymes, which can cause off-target effects due to lack of substrate specificity.

The objective of this study was to define how collagen fiber mechanics are altered by the surrounding ECM composition. Specifically, we investigated the distribution of PGs and GAGs longitudinally across tendon. Further, we examined how ECM heterogeneity along the length of the tendon impacts collagen fiber deformation. Investigating the effect of relative ECM composition on the collagen mechanical response will contribute to the knowledge of

how fibers share loads in tendon, illuminating how and when individual fibrils stretch and recover from applied forces.

METHODS

The extensor capri radialis longus tendon, a forelimb positional tendon, was harvested with muscle and bone insertions preserved from adult C57Bl/6 mice and kept hydrated in PBS throughout experiments.

Mechanical testing was performed using a Femtotoools micromanipulator system (FT-RS1002) and microforce sensor probe (FT-S100000) attached to our lab's custom designed floating-platform mounting system [3]. Tendon samples (N=2) were held at insertion sites and displaced at 1%/s to a set force of 80,000 μ N at the beginning of the linear stress-strain regime (previously found to be 15% of average failure force), then held for 10 minutes to allow the force to equilibrate. Samples were imaged using an Olympus FVMPE-RS twin laser multiphoton system and a 25 \times (NA = 1.05) FV30-AC25W truResolution water-immersible objective at a digital zoom of 3. Collagen was visualized using second harmonic generation (SHG) (Figure 1A-1A'). Five *x*-positions equidistant along the length of the tendon were selected to probe the fiber mechanical response. At each *x*-position a fiber, below the surface of the tendon, was selected and two region of interest (ROI) lines were placed perpendicular across the fiber 20 μ m apart (Figure 1A'). A sequence was then performed to 1) take an initial image of the tendon (Figure 1A); 2) ablate each ROI line, effectively cutting the fiber without disturbing surrounding tissue; and 3) image the strain recovery of the ablated fiber segment from 100 ms after ablation to 300 s after ablation. To ensure no effect on the order in which *x*-positions were ablated, each sample was tested in opposite order (proximal to distal, or distal to proximal). Image sequences were processed using FIJI to calculate average fiber segment length immediately after ablation (L1) and after 300 s (L2) to compare with the ROI length (L0). These values were used to calculate the change in length after load is removed, or strain recovery (Equation 1).

$$\epsilon_{\text{recovery}} = \frac{L_{\text{final}} - L_{\text{initial}}}{L_{\text{initial}}} \quad (1)$$

To view the distribution of *matrix* ECM throughout the tendon, tendon samples (N=3) were fixed in 4% PFA and immunohistochemically stained. Hyaluronic acid (HA), a non-sulfated GAG, was stained using hyaluronic acid binding protein (HABP) with AF555 conjugated streptavidin and a subset of PGs containing sialic acid and *N*-acetylglucosaminyl residues were stained using AF647 wheat germ agglutinin (WGA). Samples were imaged using a STELLARIS 5 confocal microscope (Leica) and an Apochromatic 10× (NA = 0.40) water-immersible objective with a digital zoom of 0.75. Image stacks of the full tendon length and depth were acquired and processed using FIJI (NIH) to view as a maximum z-projection.

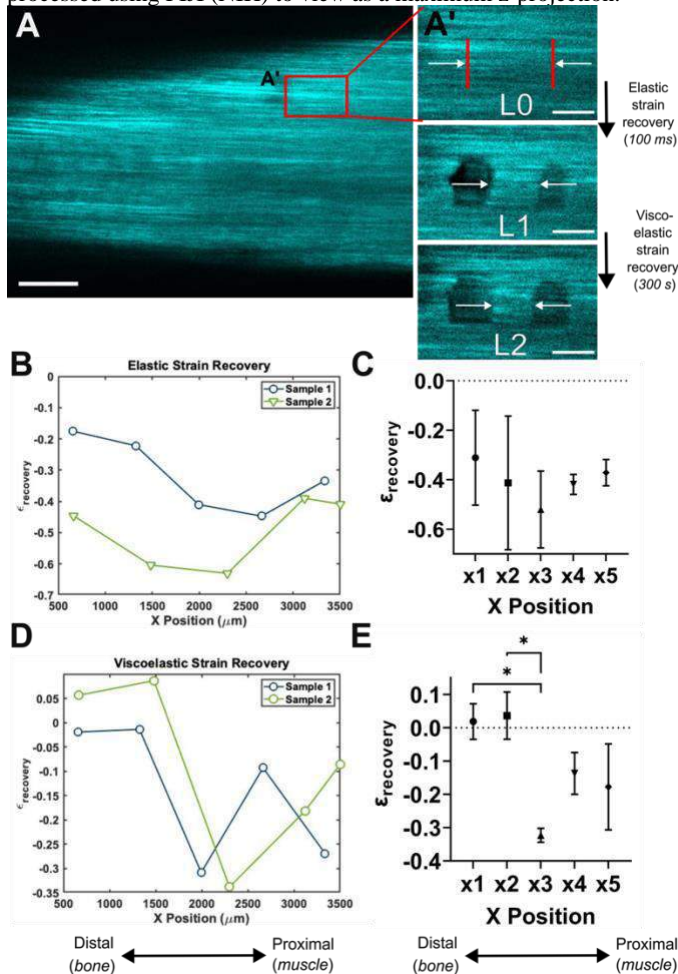


Figure 1: Mechanical perturbation of collagen fibers *in situ*. A) Representative SHG image within tendon subsurface (scalebar = 25 μm). A') Zoom inset of ROI lines defining 20 μm fiber segment (L0), fiber segment length after 100 ms (L1), and fiber segment length after 300 s (L2) (scalebar = 10 μm). B) Individual data points for elastic strain recovery with *x*-position. C) Mean +/- SD for elastic strain recovery. D) Individual data points for viscoelastic strain recovery with *x*-position. E) Mean +/- SD for viscoelastic strain recovery.

RESULTS

The elastic, or instantaneous, strain recovery varied with *x*-position along the length of the tendon, irrespective of the order in which

positions were ablated (Figure 1B). Broadly, *x*-positions near insertion ends appeared to experience less strain recovery than central positions; however these differences were not significant. (Figure 1C). The viscoelastic, or time-dependent, strain recovery also varied with *x*-position (Figure 1D). In both samples, the two *x*-positions closest to the distal bone insertion experienced no strain recovery in the 300 s of imaging after ablation, whereas the three *x*-positions nearest the proximal muscle insertion did experience viscoelastic strain recovery in this period. Similarly, the central point on the tendon (*x*3) experienced significantly more viscoelastic strain recovery than the two distal positions near the bone, as determined by a one-way ANOVA with significance of *p*<0.05 (Figure 1E).

Immunohistochemical staining intensity also varied along the length of the tendon. HABP fluorescence was greatest at the distal bone insertion side of the tendon through the center, indicating greater amounts of HA in those regions (Figure 2A). WGA fluorescence was also greatest at the distal end of the tendon, indicating higher concentrations of PGs in that region compared to lower staining intensity in the proximal side of the tendon (Figure 2B).

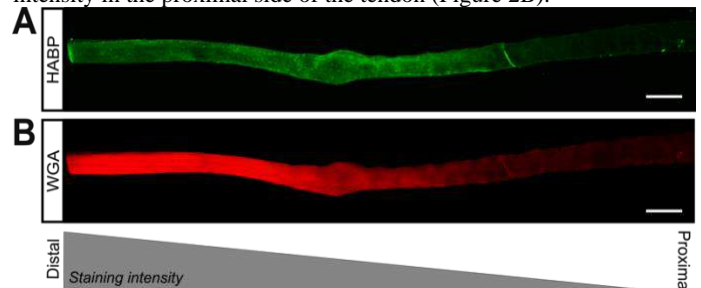


Figure 2: Representative confocal images of immunohistochemical staining. A) Hyaluronic acid binding protein (green). B) Wheat germ agglutinin (red). Both scalebars = 250 μm.

DISCUSSION

In this work, we demonstrated that both collagen fiber strain recovery and the distribution of PGs and GAGs were heterogeneous along the length of tendon. Near the bone insertion, tendons exhibited greater amounts of PGs and GAGs than on the muscle insertion end, as shown by immunofluorescence. In *x*-positions that had high amounts of HABP and WGA fluorescence, no viscoelastic recovery was seen in ablated collagen fibers. This result suggests that PGs and GAGs support interfibrillar sliding, thereby reducing the amount of time it takes for a fiber under strain to recover to initial length. We found that elastic strain recovery was greatest in the central tendon region, which may result from differences in macroscopic strain across the tendon. This study leveraged the regional differences in ECM distribution found in tendon to investigate the effect of varied ECM composition on load transfer from the bulk tissue to collagen fiber. Further, laser ablation offered the unique ability to probe fiber mechanics *in situ* and observe mechanical behavior within physiological boundary conditions. Additional studies will further these findings by comparing regional fiber-scale strain recovery with macroscopic strain across the tendon, as well as using mouse models that vary in PG and GAG composition in tendon. Overall, these findings indicate a potential role of PGs and GAGs in regulating stretch and viscoelasticity at the fiber scale.

ACKNOWLEDGEMENTS

This work was supported by NIH T32 AR080630 to H.L. and NIH R01 AR071359 to S.C.

REFERENCES

- [1] Zitnay, J. L. et al., *J Orthopaedic Res*, 36(12):3093-3104, 2018.
- [2] Beach, Z. M. et al., *J Orthopaedic Res*, 40(11):2546-2556, 2022.
- [3] Jimenez, J. M., et al, *bioRxiv*, 10.1101/2022.12.06.519227, 2022.

A CONSTITUTIVE MODEL THAT INCORPORATES A MICROSTRUCTURAL MECHANISM OF HOMOGENIZING TRANSMURAL STRESS DISTRIBUTIONS IN ARTERIES

Taisiya Sigaeva (1), Yanhang Zhang (2)

(1) Department of Systems Design Engineering, University of Waterloo, Waterloo, Ontario, Canada.

(2) Department of Mechanical Engineering and Department of Biomedical Engineering, Boston University, Boston, Massachusetts, USA.

INTRODUCTION

Designed by nature to be strong, flexible, and resilient, arteries are constantly adapting to changing environments and seeking to maintain stable and balanced mechanobiological states across different length scales [1]. At the tissue level, it is believed that cells relentlessly work to alter vascular microarchitecture and thus ensure mechanical homeostasis, or the state at which mechanical stresses are kept constant at some target value across the arterial wall [2]. Despite the vital role of homeostasis in vascular functions, the exact microstructural mechanisms enabling it are still unknown.

The primary load-bearing microstructural components commonly identified for arterial walls are: 1) an isotropic ground substance, 2) elastic fibers which enable artery recoiling and respond to mechanical loads linearly, and 3) wavy collagen fibers that resist deformations in a stiff and nonlinear manner when straightened. In material models, collagen fibers are usually considered to enable an anisotropic and nonlinear response of the arterial wall, while the contributions of elastic fibers and a ground substance are simply combined to be represented by the isotropic neo-Hookean solid (e.g., [3]). However, only a fraction of collagen fibers are known to engage during a normal cardiac cycle [4], while most of the load is carried by elastic lamellae (EL), a structure represented by concentric layers of wavy sheets made of elastic fibers (Fig. 1a) [5]. Importantly, in addition to the load-bearing function, the function of maintaining homeostasis through vascular adaptations is also attributed to EL [5].

The recent study [6] used microscopy to observe how concentric layers of EL unfold and deform during inflation and extension of the artery (Fig. 1a). One important finding was that EL layers closer to the inner wall of the artery are wavier than EL layers further away from it. Because the inner regions of the artery experience more deformations due to blood pressure, such structural heterogeneity essentially relieve these regions from excessive stresses and can be directly linked to homeostasis. There are no existing models of EL capable of capturing such behaviour, and, in this study, we propose a novel model for this structure using the concepts of worm-like-chain elasticity [7]. We then utilize this model to demonstrate how EL structural heterogeneity can homogenize transmural stress distributions.

METHODS

Worm-like chain-fiber model: Wavy EL layers consist of elastic fibers; for simplicity, it is assumed that global EL waviness matches the elastic fibers waviness. Each elastic fiber is represented by a worm-like chain (WLC) of length L_c with end-to-end distance x (Fig. 1b). Because elastic fibers are extensible, the ratio x/L_c describes both unfolding and stretching, or simply the chain deformation. The chain force F required to unfold/stretch such fibers from the referential state x_0/L_c is shown in Fig. 1c and found from the relationship [7]

$$F = \frac{kT}{L_p} \left[\frac{x}{L_c} + \frac{1}{4 \left(1 - \frac{x}{L_c} - \frac{F}{K_0} \right)^2} - \frac{1}{4} - \frac{F}{K_0} \right]. \quad (1)$$

Here k and T are the Boltzmann constant and the absolute temperature, while L_p and K_0 are unknown constants which define, respectively, the toe region and the linear behaviour of elastic fiber-chains upon straightening. Notably if we assume $K_0 \rightarrow \infty$, we will obtain an inextensible version of the WLC model with the chain deformation x/L_c used for unfolding only and with $F \rightarrow \infty$ as $x \rightarrow L_c$. This version of the model will be used to model collagen fibers as it was successfully done before [8].

Loaded artery kinematics: A loaded artery is modelled as a two-layered non-linearly elastic cylindrical annulus undergoing internal inflation and axial extension described by the following deformation field [3]:

$$r = r(R), \quad \theta = \Theta, \quad z = \lambda_z Z. \quad (2)$$

Here λ_z is the axial stretch, coordinates $\{r, \theta, z\}$ and $\{R, \Theta, Z\}$ are used to describe the deformed and reference configurations, respectively. The incompressibility condition allows for the solution of $r = r(R)$ explicitly and to express the deformation gradient \mathbf{F} . Further, the principal invariants can be derived as $I_1 = \text{tr} \mathbf{C}$ and $I_{4,j} = \mathbf{M}_j \otimes \mathbf{M}_j : \mathbf{C}$, where $\mathbf{C} = \mathbf{F}^T \mathbf{F}$ and \mathbf{M}_j describe a unit vector along a fiber family j . To link the kinematics of individual fiber-chains defined via (1) with the bulk kinematics for a fiber family j , the following relation is used:

$$(x/L_c)_j = (x_0/L_c)_j \sqrt{I_{4,j}}. \quad (3)$$

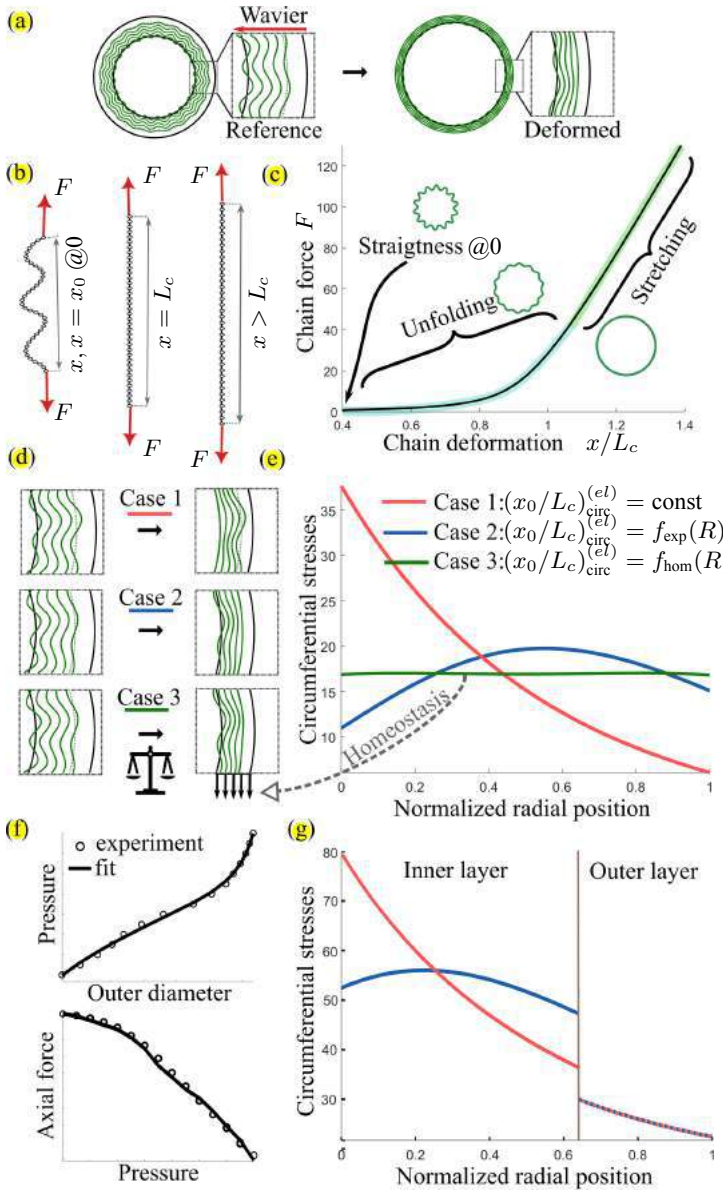


Figure 1: (a) Deformations of EL layers in arteries [6]; (b) WLC model of an EL's elastic fiber and (c) chain force-deformation curve; (d-e) isolated EL transmural circumferential stresses for three cases of structural heterogeneity $(x_0/L_c)^{(el)}_{\text{circ}}$; (f) model fit to the actual experimental data [6] and (g) the resulting transmural stress distributions.

Loaded artery material: It is assumed that the arterial wall consists of the ground substance (gs), circumferential and axial fiber families of elastic fibers (el) representing EL in the inner layer and four fiber families of collagen fibers (clg) in the outer layer. The strain energy density function is then given by

$$\Psi = \Psi^{(gs)} + \Psi^{(el)} + \Psi^{(clg)} \quad (4)$$

with the neo-Hookean term $\Psi^{(gs)} = \mu(I_1 - 3)/2$ and the terms for elastic and collagen fiber families $\Psi^{(el)}$ and $\Psi^{(clg)}$ expressed via chain forces (1) along an individual fiber family j as $\Psi_j = (\gamma \int F(x) dx + \Psi_{rep})_j$. Here μ is the shear modulus, γ is the fiber density and Ψ_{rep} is a repulsive energy term to ensure no stresses in the reference configuration [8].

Solution and Fitting: With (4), the constitutive law is derived as

$$\sigma = -p\mathbf{I} + \mathbf{F} \left[2 \frac{\partial \Psi}{\partial \mathbf{C}} \right] \mathbf{F}^T, \quad (5)$$

where p is the Lagrange multiplier and \mathbf{I} is the identity tensor. When used with the equilibrium equations $\nabla \cdot \sigma = 0$ and boundary/interface conditions, the internal pressure and axial force can be expressed as functions of the geometry and unknown material constants (4). Then, the model can be fitted to the experimental data from [6], from which the unknown material constants can be determined [3]. Importantly, (4) allows to directly

incorporate the structural heterogeneity observed in EL [6] (Fig. 1a) via the initial elastic fiber straightness $(x_0/L_c)^{(el)}_{\text{circ}} = f(R)$, defined as a function of the radial position.

RESULTS

Circumferential EL term: First, we investigate the behaviour of the term from (4) associated ONLY with the EL's circumferential elastic fiber family. Reduced circumferential stress distributions are plotted in Fig. 1e for three cases with everything the same but the structural heterogeneity $(x_0/L_c)^{(el)}_{\text{circ}} = f(R)$. Case 1 represents the homogeneous distribution of fiber waviness across the wall $(x_0/L_c)^{(el)}_{\text{circ}} = \text{const}$ (Fig. 1d). For this case, high stresses are observed on the inner surface of the artery and lower stresses on the outer surface, with a significant gradient across the wall (Fig. 1e). Cases 2 and 3 are somewhat similar heterogeneous cases $(x_0/L_c)^{(el)}_{\text{circ}} = f(R)$ (Fig. 1d) that both immediately demonstrate the reduced gradient in the stress distributions due to non-uniform EL waviness (Fig. 1e). The difference is that Case 2 is experiment-based $(x_0/L_c)^{(el)}_{\text{circ}} = f_{\text{exp}}(R)$ [6], while the heterogeneity distribution $(x_0/L_c)^{(el)}_{\text{circ}} = f_{\text{hom}}(R)$ for Case 3 is optimized to produce nearly constant circumferential stresses representing the homeostatic state (Fig. 1e). Now, with the new understanding of how the circumferential EL fiber family behaves outside of the model (4), it can be studied how it interacts with the other load-bearing microstructural components. For simplicity, only Cases 1 and 2 are retained.

Experimental data fitting: The two-layer model of the artery that includes contributions from all identified load-bearing microstructural components (4) was successfully fitted to the experimental data from [6]. The fitting was very similar for the homogeneous Case 1 and the experiment-based heterogeneous Case 2 (Fig. 1f). In contrast, at the physiological deformation state, the corresponding transmural stress distributions in the inner layer (where EL layers are defined) were quite different (Fig. 1g.) As in Fig. 1e, there is a significant stress gradient for the homogeneous EL structure $(x_0/L_c)^{(el)}_{\text{circ}} = \text{const}$, while the heterogeneous EL structure $(x_0/L_c)^{(el)}_{\text{circ}} = f_{\text{exp}}(R)$ results in more uniform stresses.

DISCUSSION

This work proposes a novel approach to include EL layers into the material description of the artery using the extensible worm-like-chain model. It allows to directly include the microscopically observed structural heterogeneity of EL layers $(x_0/L_c)^{(el)}_{\text{circ}}$ and robustly fit the experimental data [6]. Similarly to residual stresses [3], EL structural heterogeneity homogenizes the transmural stress distributions. However, it has a more evident connection to the arterial microstructure and is also capable of producing a homeostatic stress state (Fig. 1e, Case 3). Hence, the proposed model has a potential to improve our understanding of vascular pathways to maintaining homeostasis and it clearly demonstrates the importance of accounting for EL and its structural heterogeneity in constitutive modelling of arteries.

ACKNOWLEDGEMENTS

T.S. and Y.Z. acknowledge, respectively, the funding from the Natural Sciences and Engineering Research Council (DG RGPIN- 2021-02643) and from the National Heart, Lung, and Blood Institute (2R01 HL098028).

REFERENCES

- [1] Humphrey J. *Cell Biochem. Biophys.* 50.2 (2008).
- [2] Spronck B et al. *J. Biomech. Eng.* 141.9 (2019).
- [3] Holzapfel GA et al. *J. Elast.* 61.1 (2000).
- [4] Lillie M et al. *J. Biomech.* 45.12 (2012).
- [5] Wolinsky H et al. *Circ. Res.* 20.1 (1967).
- [6] Yu X et al. *J. Roy. Soc. Interface* 15.147 (2018).
- [7] Hillgärtner M et al. *J. Biomech.* 80 (2018).
- [8] Kuhl E et al. *J. Mech. Phys. Solids* 53.7 (2005).

ANALYSIS OF A NEW SOCKET BASED REFERENCE FRAME FOR ANKLE ROLLOVER-SHAPE FOR TRANSTIBIAL PROSTHESES

David Herlihy, BS¹, John Chomack, MS², Jason Maikos, PhD²

(1) Narrows Institute of Biomedical Research and Education, Inc., Brooklyn, NY, USA
(2) Department of Veteran Affairs New York Harbor Healthcare System, New York, NY, USA

INTRODUCTION

For individuals with transtibial limb loss, the ankle roll-over shape (ARS) model describes the rocker-like movement of the prosthetic foot-ankle complex during stance. It is typically calculated as the transformation of the center of pressure (COP) into a shank-based coordinate system, which creates an arc that forms the ARS. Believed to be a critical mechanism for efficient walking, an ideal ARS reduces step to step transition work [1] and enables the exchange of kinetic and potential energy as described by the Inverted Pendulum Walking Model [2]. Asymmetries are common with prosthetic gait. Models have shown that the vertical center of mass (COM) excursion can be attributed almost entirely to step length and ARS rocker radius [2]. Using the ARS model, we can gain insight into how categories of prosthetic feet influence prosthetic gait symmetry. A prosthetic foot should be designed to achieve the appropriate ARS, while prosthetic alignment positions the resulting arc with the ideal orientation [3]. We hypothesize that the traditional method of calculating ARS is dependent on prosthetic alignment and is an inaccurate method to determine ARS for individuals with transtibial limb loss. Ultimately, this can negatively impact foot design and alignment guidance. The purpose of this study was to calculate ARS parameters using a modified Socket Coordinate System (CS) that controls for prosthetic alignment as to further optimize the design and alignment of prosthetic feet.

METHODS

ARS is determined by transforming the center of pressure data in stance to a planar coordinate system. The resultant trajectory is then fit using a quadratic circular regression, resulting in a circular fit that follows Equations 1 and 2.

$$R = \sqrt{(COP_x - x_0)^2 + (COP_y - y_0)^2} \quad (1)$$

$$\theta = \tan^{-1} \left(\frac{COP_y - y_0}{COP_x - x_0} \right) \quad (2)$$

R defines the arc radius, while the arc center is given by x_0 and y_0 (Eq 1). These parameters are then normalized by the participant's height. θ defines the angle between the arc center and the COP progression along the arc. θ_0 and θ_e define the initial and end points of the arc. The traditional ARS analysis uses the Shank CS (Fig 1A), calculated by the following steps.

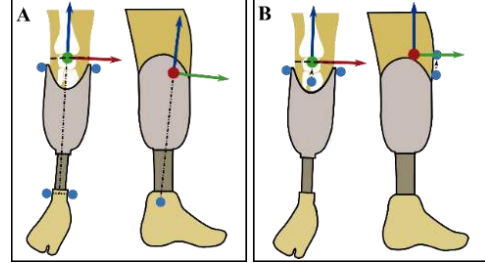


Figure 1: A) Shank and B) Socket CS Visualization

- 1) Calculate the functional knee axis.
- 2) Project the midpoint between the medial and lateral knee markers onto the functional knee axis: this is the CS origin.
- 3) Find midpoint between the medial and lateral ankle markers.
- 4) The Y axis is determined by the line from the distal ankle center point to the proximal knee center.
- 5) The X axis is determined by the plane of best fit between the two joint centers and the lateral ankle and knee markers.
- 6) $\hat{X} \times \hat{Y}$ defines the Z Axis

The modified CS, the Socket CS, uses only socket markers in its calculation (Fig 1B), detailed below.

- 1) Calculate the functional knee axis – defining the Z axis.
- 2) Project the midpoint between the medial and lateral knee markers onto the functional knee axis: this is the CS origin.

- 3) A marker placed on the tibial tuberosity is projected to the height of the knee center landmark to create a virtual landmark. The line between these two landmarks defines the X Axis.
- 4) $\hat{Z} \times \hat{X}$ defines the Y Axis.

The comparison between the Shank and Socket CS was performed for 24 participants, on three different categories of prosthetic feet: Energy Storing and Returning (ESR), Articulating (ART) ESR, and powered (PWR) ESR. Each participant was fit with each type of foot in a randomized order and given separate, 1-week acclimation periods. Following each acclimation period, participants underwent a biomechanical gait evaluation. Motion and force data were collected using an optical motion capture system (Qualisys, Goteborg, Sweden) and force platform system (AMTI, Watertown, MA). Additionally, ten individuals without limb-loss (controls) completed the same biomechanical assessment. The data was then processed using Visual 3D (C-Motion Inc.) and a custom MATLAB (The MathWorks Inc.) script. Independent T-tests were then used to determine significant differences ($p < 0.05$) in three key analyses (A1-A3): A1 and A2 assessed the differences between feet and between experimental and control groups in the Shank CS and the Socket CS, respectively; A3 compared the ARS parameters of the feet between the Shank and Socket CS.

RESULTS

Figure 2 is a visual representation of the average ARS for each foot and controls in both the Shank and Socket CS. Visual differences between the ARS for experimental and control groups were present in all three feet in the Shank CS. However, when removing the influence of alignment using the Socket CS, the ARS of the three feet aligned to the controls. This is confirmed in Figure 3, where the five ARS parameters are shown. Tables 1-3 highlight the significant differences in all key analyses.

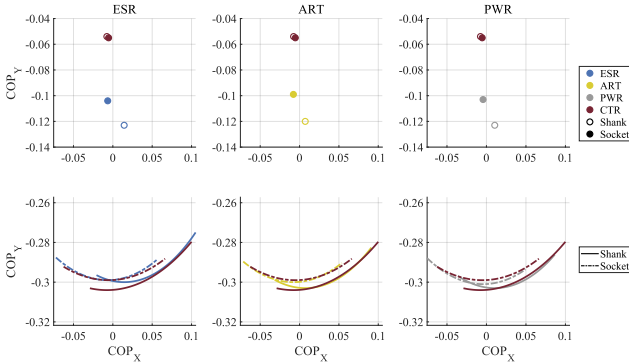


Figure 2: Shank and Socket CS ARS Comparison

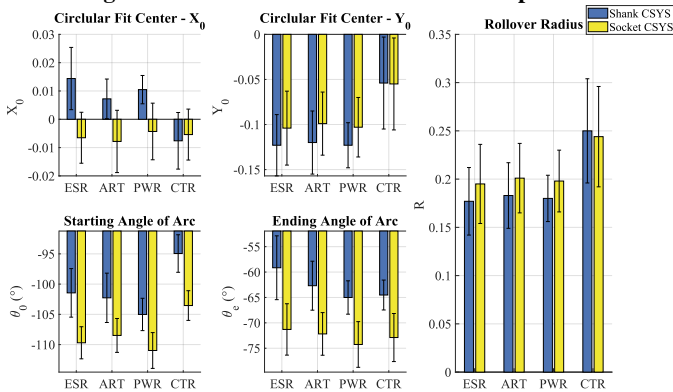


Figure 3: Shank and Socket CS ARS Parameters Comparison

Table 1: Shank CS P-Values (A1)

Parameters	ESR-ART	ESR-PWR	ART-PWR	ESR-CTR	ART-CTR	PWR-CTR
X Center	0.01	0.12	0.07	0.00	0.00	0.00
Y Center	0.75	0.97	0.74	0.00	0.00	0.00
Radius	0.58	0.77	0.72	0.00	0.00	0.00
Start Angle	0.50	0.00	0.01	0.00	0.00	0.00
End Angle	0.04	0.00	0.06	0.02	0.27	0.69

Table 2: Socket CS P-Values (A2)

Parameters	ESR-ART	ESR-PWR	ART-PWR	ESR-CTR	ART-CTR	PWR-CTR
X Center	0.66	0.43	0.25	0.74	0.53	0.77
Y Center	0.67	0.89	0.74	0.01	0.01	0.00
Radius	0.63	0.84	0.75	0.01	0.01	0.00
Start Angle	0.14	0.13	0.01	0.00	0.00	0.00
End Angle	0.52	0.04	0.11	0.40	0.67	0.44

Table 3: Shank and Socket CS Comparison P-Values (A3)

Parameters	ESR	ART	PWR	CTR
X Center	0.00	0.00	0.00	0.61
Y Center	0.10	0.06	0.03	0.97
Radius	0.11	0.09	0.04	0.81
Start Angle	0.00	0.00	0.00	0.00
End Angle	0.00	0.00	0.00	0.00

The alignment differences were largely found in x_0 and θ_e in the Shank CS analysis (Table 1), whereas the Socket CS normalized these values to the controls (Table 2). Also, there were several differences in x_0 , θ_0 , and θ_e between feet in the Shank CS analysis (Table 1), but only two differences in θ_0 and θ_e between ART & PWR and ESR & PWR respectively (Table 2). In Table 3, comparing ARS parameters from the Shank and Socket CS analyses, θ_e and θ_0 were found to be significantly different for all groups between CSs. x_0 also varied between CSs for all three feet. The control group's x_0 held constant. The PWR was the only group to see a significant difference in y_0 and R .

DISCUSSION

Using the Shank CS reference frame, key differences in ARS parameters were found. However, those variances were not found in the alignment neutral Socket CS, suggesting that prosthetic alignment was the driving force behind the ARS shape, not the foot type. Additionally, when the Shank and Socket CS analyses were performed on control participants, the only differences found were in starting and ending angles (θ_0 and θ_e). This difference was caused by the rotation of the Socket CS compared to the Shank CS and is consistent across all groups. Otherwise, the ARS parameters of the control group were constant between CSs, demonstrating that differences found in the experimental group were due to alignment effects, not by a change in CS. Radius (R) and Arc Center Height (y_0) were only found to change between CSs in the PWR group. It is hypothesized that the PWR device is aligned to optimize powered push-off rather than ARS. While the ESR and ART feet are aligned for low energy step to step transitions, the PWR foot is aligned to take advantage of the powered push-off, an effect not captured in the ARS analysis. The PWR's difference from ESR and ART in θ_e and θ_0 , respectively, also hints at this alignment adjustment. Future analyses can compare the changes in alignment priority (powered push-off vs. ARS) and the effects on step-to-step transition work. This would be useful in determining the trade off in changing the rollover radius compared to maximizing power output in late stance.

ACKNOWLEDGEMENTS

This work was supported by a DoD OPORP grant (W81XWH-17-2-0014). We would also like to acknowledge our collaborators at Walter Reed National Military Medical Center.

REFERENCES

- [1] Adamczyk, P et al., *J Exp Biology*, 209:3953-3963, 2006
- [2] Gard, S et al., *J Prosthet Orthot*, 13:64-67, 2001
- [3] Hansen, A et al., *Prosthet Orthot Int*, 27:89-99, 2003

PATIENT-SPECIFIC PREDICTIVE SIMULATION OF transcATHETER EDGE-TO-EDGE REPAIR IN HUMANS WITH MITRAL REGURGITATION

Natalie T. Simonian (1), Sneha Vakamudi (2), Mark J. Pirwitz (2), Alison M. Pouch (3), Joseph H. Gorman, III (3), Robert C. Gorman (3), and Michael S. Sacks (1)

- (1) James T. Willerson Center for Cardiovascular Modeling and Simulation, The Oden Institute and the Department of Biomedical Engineering, University of Texas at Austin, Austin, TX, USA
(2) Ascension Texas Cardiovascular, Austin, TX, USA
(3) Gorman Cardiovascular Research Group, Smilow Center for Translational Research, Department of Surgery, Perelman School of Medicine, University of Pennsylvania, PA, USA

INTRODUCTION

Mitral regurgitation (MR) is a highly prevalent cardiac disease affecting approximately 2% of the United States population. MR is typically categorized into two broad groups each covering a wide range of etiologies. Degenerative MR (DMR) is caused by primary myxomatous degeneration of the mitral valve (MV) tissue. In contrast, functional MR (FMR) is an insufficiency of an otherwise normal MV secondary to ischemic or non-ischemic cardiomyopathy and the associated left ventricular dilatation. MR of either type is also a major prognostic factor of mortality, with even mild MR increasing the risk of mortality by 17% in patients with ischemia but no MR [1]. Furthermore, MR remains severely undertreated despite its deadly outcomes, even in patients with low comorbidity, suggesting a critical need for treatment planning optimization [2].

Transcatheter edge-to-edge repair (TEER) techniques are significantly safer options for MV repair compared to traditional surgical approaches and have thus broadened the eligible patient cohort for MR treatment. However, the long-term durability and efficacy of TEER has been unpredictable especially when compared to surgical undersized ring annuloplasty or guideline-directed medical therapy, with major randomized controlled trials reporting diametrically opposite outcomes. These inconsistencies have largely been attributed to the vast heterogeneity of the MR patient population and have generated prolific inquiry into image-based predictive markers of TEER success [3]. However, the clinical utility of these markers has not been demonstrated in practice. Therefore, there remains an urgent, unmet clinical need for *quantitative, patient-specific* treatment optimization techniques that account for the highly variable patient population and combinatorial nature of TEER.

Advances in real-time 3D echocardiography (rt-3DE) have enabled the acquisition of high-resolution MV images over the entire cardiac cycle using standard-of-care imaging techniques. Thus, we have developed a patient-specific MV simulation pipeline *based strictly on*

preoperative, standard-of-care imaging to predict post-repair MV functional behavior.

METHODS

First, we developed a finite-element model of the full, patient-specific MV apparatus. Since the MV chordae tendinae (MVCT) are not visible on rt-3DE, we quantified the left ventricular MVCT origins and MVCT insertions on the MV leaflet from 5 CT-imaged excised human hearts. From this data, we determined a normalized MVCT insertion map which guided the distribution of MVCT on the leaflets for each patient (Fig. 1B). Next, we obtained rt-3DE images of the MV from 10 patients who underwent TEER with MitraClip (Abbott Inc.). Half the patients presented with mixed or DMR, and half with FMR. For each patient, we segmented the end-diastolic (ED) and end-systolic (ES) leaflet geometries from preoperative rt-3DE images and meshed both states using triangular shell elements. Additionally, we segmented all identifiable MVCT origins from rt-3DE images and tracked them from the ED to ES states. To produce the final MV apparatus model, we used the insertion distribution map to place 160 MVCT on the patient-

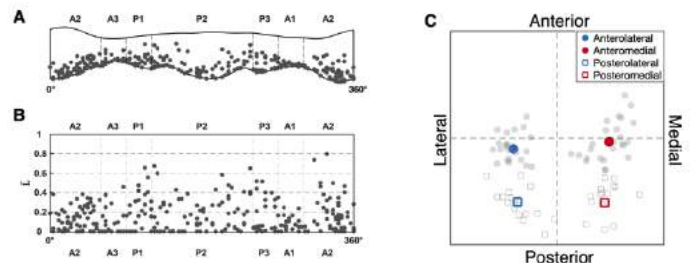


Figure 1: (A) All MVCT insertion points on an averaged MV leaflet geometry (B) MVCT insertion density map on a normalized MV leaflet grid (C) MVCT origin positions relative to normalized MV annular centerlines.

specific ED leaflet geometry and connected each insertion to its nearest segmented MVCT origin using truss elements (Fig. 2).

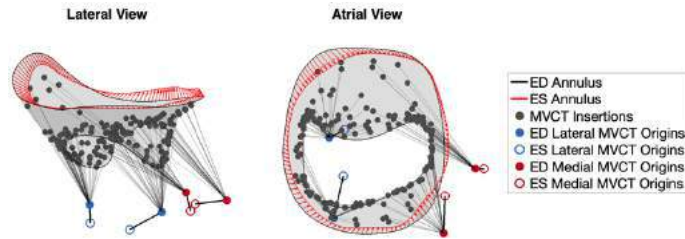


Figure 2: Full patient-specific MV apparatus, with unbranched MVCT and boundary conditions.

In order to model MV closure, we set ED to ES annular and MVCT origin displacements as Dirichlet boundary conditions, assigned an established structural model for the human MV leaflet and an Ogden model for human MVCT, and applied a ventricular pressurization in Abaqus 6.14 [4,5]. Given that patient-specific material properties are impossible to obtain from rt-3DE imaging, we calibrated the model by adjusting MV leaflet and MVCT prestrains such that the l^2 -norm between the simulated and segmented preoperative ES geometries was minimized. First, we iteratively updated the MVCT prestrain until the mean change in l^2 -norm was less than 5%. Next, we divided the MV leaflets into three zones (MVCT insertion zone, anterior clear zone, posterior clear zone), and iteratively updated the prestrain in each zone using fininsearch in MATLAB to the same convergence criterion. We utilized this fully calibrated MV model to simulate MV repair scenarios by implementing 3D MitraClip models onto the MV leaflets (Fig. 3).

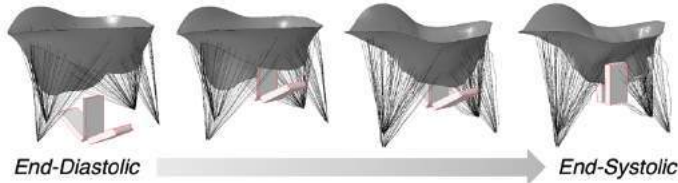


Figure 3: Predictive TEER simulation progression with full patient-specific MV apparatus.

RESULTS

Our anatomical analysis of the excised human hearts quantitatively demonstrated that most MVCT insertions are located near the free edge of the MV leaflets (Fig. 1A), and that the majority of MVCT origins are shifted towards the posterior side of the LV wall (Fig. 1C). In all postoperative simulations, the mismatch between the predicted and segmented ES geometries was less than 1 mm. Furthermore, the predicted MV leaflet strain fields showed close correspondence in both the circumferential and radial directions and captured local variation in deformation across the MV leaflets (Fig. 4). Additionally, we analyzed the circumferential and radial MV leaflet strains for all 10 patients and noted considerable heterogeneity in preoperative deformation in both material directions, with no obvious patterns when grouped by etiology (Fig. 5). There is also substantial variation in MV annular orifice area, though the FMR MVs tend to be slightly larger, likely due to the underlying mechanism of LV dilatation ($10.09 \pm 3.17 \text{ cm}^2$ DMR, $13.58 \pm 3.45 \text{ cm}^2$ FMR, $p > 0.05$).

DISCUSSION

Given the complexity and inadequacy of current stratification methods for patient selection in MR treatment, there is a clear need for quantitative, patient-specific methods of predicting MV repair outcomes preoperatively using readily available clinical data. In this

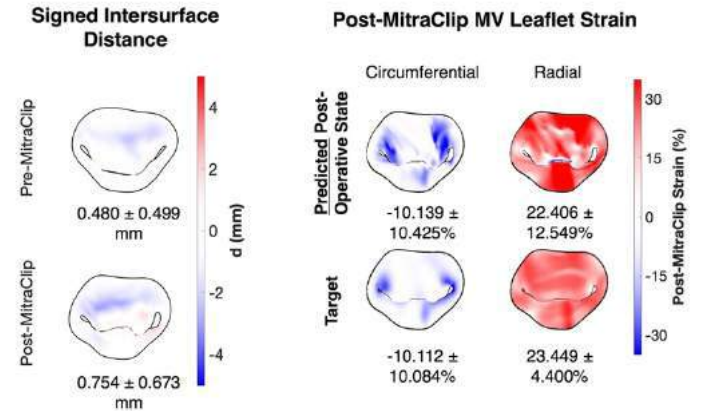


Figure 4: Preoperative calibration and postoperative prediction results for a representative TEER case, showing close correspondence between the target and predicted geometries and deformation fields.

study, we have developed an anatomically faithful, patient-specific full MV apparatus model and a *predictive MV repair simulation pipeline based solely on preoperative standard-of-care imaging*. We have demonstrated the capacity of this pipeline to predict postoperative MV geometry and deformation with close agreement to segmented data. Additionally, we observed large variation in preoperative deformation in our patient cohort, highlighting both the fundamental challenge that underscores MR treatment planning and the importance of a patient-specific approach for optimization of TEER outcomes.

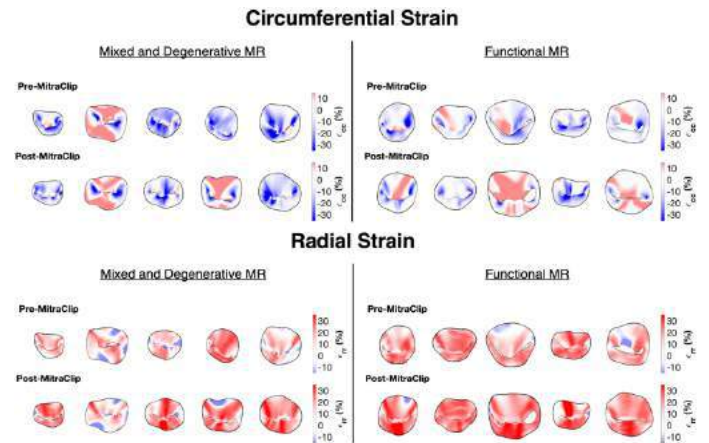


Figure 5: Circumferential and radial strain fields before and after TEER for the full patient cohort. There is wide variation in deformation amongst the patients, even those with the same type of MR, underscoring the need for patient-specific treatment planning.

ACKNOWLEDGEMENTS

The authors gratefully acknowledge funding from National Institutes of Health grant no. R01 HL073021 to MSS and RCG and American Heart Association grant no. 23PRE1018120 to NTS.

REFERENCES

- Perrault L, et al. J Thorac Cardiovasc Surg. 2012;143(6):1396–403.
- Iung B, et al. Circulation. 2019;140(14):1156–69.
- Salvatore T, et al. Frontiers Cardiovasc Medicine. 2021;8:585415.
- Zuo K, et al. J Mech Behav Biomed. 2016;62:607–18.
- Rego BV, et al. Int J Numer Meth Bio. 2018;34(12):e3142.

COMPARISON OF SOME NOVEL 1D IMPLEMENTATIONS OF HYPERELASTIC ARTERIAL MODELS WITH 3D APPROACHES FOR A CYLINDRICAL TEST CASE

Jacob Sturdy (1), Friederike Schäfer (1), Aleksander Sinek (1,2), Mateusz Mesek (1,2), Marek Rojczyk (2), Wojciech P. Adamczyk (2), Bartłomiej Melka (2), Ziemowit Ostrowski (2), Ryszard Bialecki (2)

(1) Department of Structural Engineering, Norwegian University of Science and Technology, Trondheim, Norway
(2) Department of Thermal Technology, Silesian University of Technology, Gliwice, Poland

INTRODUCTION

The physics of flow of blood through the cardiovascular system constitute a strongly coupled fluid-structure interaction, and consequently many aspects of the functional and dysfunctional physiology may be determined by the relationship between the deformation of the vessels and the pressure and flow generated by the heart. Numerous numerical methods and computational models of fluid-structure interactions (FSI) in blood vessels have been reported. The most general approaches solve the full fluid and solid mechanics within an anatomically detailed and realistic geometric model of some portion of the vascular system; however, solving these for dynamic problems in 3D domains is computationally demanding, thus a 1D approach based on several simplifying assumptions has seen wide application for simulation of large networks of blood vessels.

While previous works have compared 1D and 3D simulations to our knowledge this has been limited to cases where the arterial wall is modelled as a linear elastic material, yet in 3D solid mechanics advanced hyperelastic material models including multiple fiber components have been shown to be much better suited to describe the behavior of the arterial wall tissue [1]. Some works have developed 1D versions of such models [2, 3], but to our knowledge no comparison of such 1D models with comparable 3D-FSI simulations has been reported. We have developed new 1D implementations of several hyperelastic materials and present here a comparison of several 1D models and 3D models of an idealized cylindrical arterial geometry.

METHODS

In 1D arterial pulse wave propagation models, the tube law or compliance model relates the radius at a given point in the artery to the blood pressure at the same point. The most widely employed tube law is based on assuming linear elasticity and a thin walled cylinder [4]. However, due to the relatively large deformations and nonlinear stress-strain relationship of the arteries, nonlinear hyperelastic models are generally applied in studying the solid mechanics of arterial tissue [1]. We consider 3 hyperelastic constitutive laws defined by a strain energy function Ψ in terms of the Left Deformation Tensor \mathbf{C} or the Green Strain tensor \mathbf{E} . The first strain energy density approximates linear elasticity and is referred to as the Isotropic Elastic Model

$$\Psi = \frac{1}{2} \lambda (\text{tr } \mathbf{E})^2 + \mu \mathbf{E} : \mathbf{E}. \quad (1)$$

where $\lambda = \frac{\nu E}{(1+\nu)(1-2\nu)}$, $\mu = \frac{E}{2(1+\nu)}$ are Lamé parameters in terms of the Young's modulus E and Poisson ratio ν . The second is a NeoHookean material

$$\Psi = \frac{\mu}{2} (I_1 - 3) - \mu \ln J + \frac{\lambda}{2} (\ln J)^2 \quad (2)$$

where $I_1 = \text{tr}(\mathbf{C})$ and $J^2 = |\mathbf{C}|$.

Finally, the Holzapfel-Gasser-Ogden material is one of the most accurate models for characterising the deformation of arterial wall tissue

$$\begin{aligned} \Psi = & \frac{c}{2} (I_1 - 3) - c \ln J + \frac{k_1}{2k_2} \sum_{\alpha} (\exp(k_2 \langle E_{\alpha} \rangle^2) - 1) \\ & + \frac{K_0}{2} \left(\frac{J^2 - 1}{2} - \ln J \right) \end{aligned} \quad (3)$$

with $E_{\alpha} = \kappa (I_1 - 3) + (1 - 3\kappa) (I_{4\alpha} - 1)$ and $I_{4\alpha} = \mathbf{a}_0 \mathbf{C} \mathbf{a}_0$ with \mathbf{a}_0 specifying the fiber direction and κ fiber dispersion. The parameter c represents the stiffness of tissue matrix while the parameters k_1 and k_2 determine the contribution of the fibers, and K_0 is the bulk modulus.

We follow the approach of Mehta et al. [5] to implement a tube law based on each of these strain energy functions. This is a quasi-static approximation and assumes that the principal directions of stress are aligned with the local cylindrical coordinate system of the vessel and that axial deformation is constant throughout the cross section. Then the equilibrium equations are

$$\frac{\partial}{\partial R} \frac{\partial \Psi}{\partial \lambda_R} + \frac{1}{R} \left(\frac{\partial \Psi}{\partial \lambda_R} - \frac{\partial \Psi}{\partial \lambda_{\Theta}} \right) = 0 \quad (4)$$

which may be evaluated to find a second order differential equation for $r(R)$ by substituting $\lambda_R R = r$ and $\lambda_{\Theta} = \frac{r}{R}$. Together with the internal (p_i) and external pressure (p_e) a boundary value problem may be formulated with boundary conditions $\frac{\partial \Psi}{\partial \lambda_R} (R = R_{i,e}) = \lambda_{\Theta} P_{i,e}$. We solve this numerically using the `solve_bvp` routine from `scipy` [6].

We compare the solution produced by this 1D approach with the solution produced by FEBio [7, 8] for equivalent 3D models using the same hyperelastic constitutive laws. The idealized artery was modelled as cylinder. The wall was meshed with 32 angular sections, 8 layers and 32 longitudinal sections. The inner radius was 2.654 mm and the thickness was 0.3 mm. No deformation was allowed at the ends of the cylinder. The fluid domain was meshed using a hexahedral butterfly mesh with square elements extending to 70% of the internal radius and 5 transitional layers to the boundary. A parabolic inflow profile was imposed, and pressure

was imposed at the outlet. Backflow and tangential stabilization was also employed at the outlet. For the isotropic elastic and Neo-hookean materials $E = 0.7\text{MPa}$ and $\nu = 0.49$ were used. The Holzapfel-Gasser-Ogden material parameters were $c = 0.3\text{MPa}$, $k_1 = 20.9\text{kPa}$, $k_2 = 56.5$ and $K_0 = 1.5e7$. The fiber direction was assumed to be 30 degrees relative to the axial direction. The density of the wall and fluid was set to 1000kg/m^3 for all cases. For the fluid simulations, a Newtonian fluid with shear viscosity of $0.001\text{Pa} \cdot \text{s}$ and bulk viscosity of 0.01 was employed.

RESULTS

The deformation of the inner and outer wall at the midpoint of the cylinder is shown in Figures 1-3. We see good agreement between 1D and 3D results across the models.

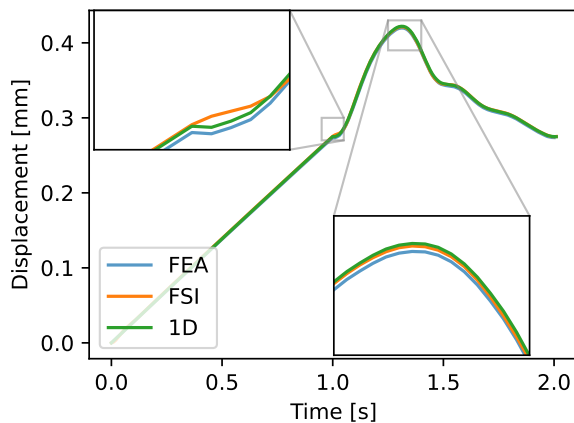


Figure 1: Deformation of inner wall at mid length for an Isotropic elastic material Eq. (1)

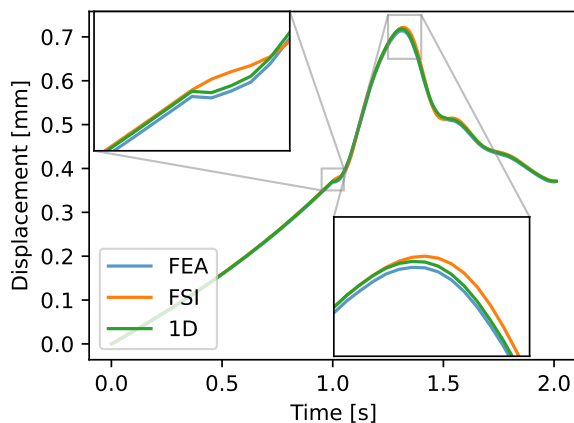


Figure 2: Deformation of inner wall at mid length for a Neo-hookean material Eq. (2)

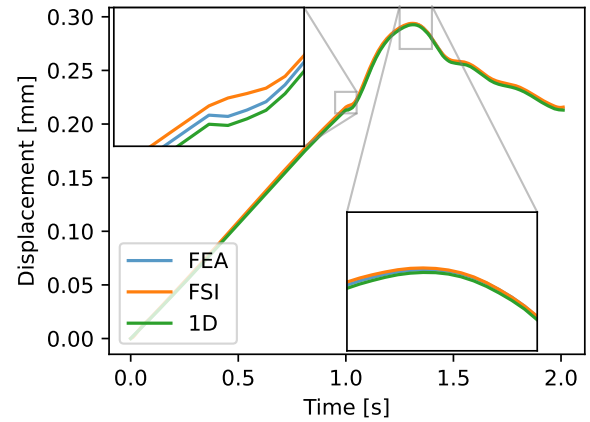


Figure 3: Deformation of inner wall at mid length for a Holzapfel-Gasser-Ogden material Eq. (3)

DISCUSSION

The good agreement of the 1D approach introduced here suggests that further integration of these approaches into 1D pulse wave propagation models of the vascular system may provide an efficient method for simulating blood flow and pressure dynamics while representing the vessel wall with state-of-the-art constitutive laws that can account for multi-component effects. The comparison only considered an idealized vessel geometry, and further comparisons using asymmetric geometries must be evaluated. Additionally, here homogeneous material parameters were assumed, but in the physiological case variations in material properties are expected. Future work should investigate how the 1D axisymmetric assumption performs when such variations are present. Additionally, as we conducted this work to verify and validate our 1D approach to solving deformation, we did not conduct a detailed comparison of the fluid structure interaction results with the flow and pressure gradient in the 1D domain. The comparison of 3D-FEA and FSI suggests for the present problem that the deformation depends only on the pressure, which is imposed at the outlet; however, in more complex geometries where the boundary conditions may be somewhat less dominant, discrepancies between 1D and 3D fluid mechanics may be significant. Yet, the previous comparisons [4] showed that for many quantities of interest, if the geometry and solid mechanics are in agreement then the fluid flows and pressures will also be within reasonable agreement between 1D and 3D models.

ACKNOWLEDGEMENTS

The research leading to these results is funded by the Norwegian Financial Mechanism 2014-2021 operated by the National Science Center, PL (NCN) within GRIEG programme under grant# UMO-2019/34/H/ST8/00624, project *non-invasive iN-vivo assessment Human aRtery wAlls (ENTHRAL, www.enthrall.pl)*

REFERENCES

- [1] Gasser TC et al. *Journal of The Royal Society Interface* 3.6 (2006). DOI: 10.1098/rsif.2005.0073.
- [2] Coccarelli A et al. *Biomech Model Mechanobiol* (2021). ISSN: 1617-7940. DOI: 10.1007/s10237-021-01437-5.
- [3] Seyed Vahedein Y et al. *Biomech Model Mechanobiol* (2019). ISSN: 1617-7940. DOI: 10.1007/s10237-019-01163-z.
- [4] Xiao N et al. *International Journal for Numerical Methods in Biomedical Engineering* 30.2 (2014). ISSN: 2040-7947. DOI: 10.1002/cnm.2598.
- [5] Mehta S et al. *International Journal of Non-Linear Mechanics* 144 (2022). ISSN: 0020-7462. DOI: 10.1016/j.ijnonlinmec.2022.104031.
- [6] Virtanen P et al. *Nature Methods* 17 (2020). DOI: 10.1038/s41592-019-0686-2.
- [7] Maas SA et al. *Journal of Biomechanical Engineering* 134.1 (2012). ISSN: 0148-0731. DOI: 10.1115/1.4005694.
- [8] Shim JJ et al. *Journal of Biomechanical Engineering* 134.1 (2012). ISSN: 0148-0731. DOI: 10.1115/1.4043031.

REDUCED POSTNATAL LOADING AFTER SCIATIC NERVE RESECTION IMPAIRS ACHILLES TENDON GROWTH AND MATURATION

Talayah A. Johnson (1), Natalie Fogarty (1), Alisia Lin (1), Tonia K. Tsinman (1), Xi Jiang (1),
Eiki Koyama (3), Lin Han (2), Josh R. Baxter (1), Robert L. Mauck (1), Nathaniel A. Dymnt (1).

(1) McKay Orthopaedic Research Laboratory, University of Pennsylvania, Philadelphia, PA, USA

(2) Drexel University, Philadelphia, PA, USA

(3) Children's Hospital of Philadelphia, Philadelphia, PA, USA

INTRODUCTION

Mechanical forces during embryonic and postnatal development are vital for successful limb and musculoskeletal tissue formation and maturation. Load bearing tissues such as tendons can respond to mechanical loading events to maintain tensional homeostasis. For example, tenocytes respond to altered loading by fine tuning the formation and degradation of extracellular matrix proteins [1]. Both excessive and insufficient loading are implicated in the disease etiology of tendons. Overuse tendinopathies, which commonly involve the Achilles tendon, account for 7% of musculoskeletal disorders in the US [2]. The most common treatment options are physical therapy and surgery. Manipulation of mechanical loads through implementation of rehabilitative loading exercises promotes repair processes that may culminate in improved restoration of normal tendon structure and function [3]. While loading has been shown to influence tendon composition in adults and healing tendons, it is less clear how mechanical forces influence Achilles tendon growth during early postnatal stages. Understanding the role of mechanical loading on developmental processes of tendon growth can 1) help to understand tissue optimization during development of healthy tendons and 2) provide mechanistic insight to guide new therapeutic treatments for adult tendon healing.

In the Achilles tendon, rapid tissue growth occurs in early postnatal stages. Growth of the Achilles is predominantly governed by cell proliferation and extracellular matrix (ECM) production. Here, we performed sciatic nerve resection (SNR) in neonatal mice (surgery performed on postnatal day 1 (P1)) to explore how a reduction in postnatal loading impacts Achilles tendon growth and how mechanical force affects extracellular matrix production during this critical time window. We hypothesized that reduced mechanical loading of the hindlimb after SNR would result in reduced growth and development of the Achilles tendon, and that this would be evidenced by changes in morphology and mechanical properties.

METHODS

All animals and procedures were approved by UPenn's IACUC. Unilateral left sciatic nerve resection (SNR) was performed on postnatal day 1 (P1) in male and female CD1 mice with evaluation on postnatal day 42. Gait Analysis. The CatWalk XT system was used to measure gait parameters in SNR and control mice at postnatal day 42. MicroCT. Excised hindlimbs from each group of mice were scanned on a Scanco μ CT45 scanner to measure tibia length. Biomechanical Testing. Achilles tendons were dissected, cross-sectional area was measured using a custom laser device, placed in custom grips, preconditioned, and loaded to failure (0.1%/sec). Structural and material properties were calculated using custom MATLAB scripts. Cryohistology. Hindlimbs were harvested, formalin-fixed, embedded in OCT, and cryosectioned (8 μ m) in the transverse plane using Cryofilm 2C. Fluorescent imaging with a nuclear counterstain followed by brightfield imaging with toluidine blue staining was performed. Image Analysis. Achilles tendon cross-sectional area and cell density were quantified using Fiji. Statistics. Gait parameters between SNR and control groups were compared via one-way ANOVA with Tukey's HSD post-hoc comparisons ($p < 0.05$). SNR limb vs. contralateral limb were compared via paired t-tests for all other assays ($p < 0.05$).

RESULTS

SNR resulted in sustained impairments in gait. CatWalk XT analysis on post-natal day 42 was used to assess changes in gait parameters that would inform hindlimb loading patterns. SNR mice exhibited sustained gait perturbations, including a >30% reduction in maximum stride intensity and a >70% reduction in paw print width, a hallmark of sciatic denervation ($p < 0.0001$, **Figure 1**).

Reduced loading from SNR resulted in muscle atrophy and bone shortening. Gross microscopic images revealed signs of marked muscle atrophy (red arrow, **Figure 2A**) of the posterior hindlimb muscles. The Achilles tendons also appeared smaller, with reduced birefringence. (**Figure 2A**). This model system has been shown previously to affect

bone growth, which led us to investigate differences in tibia length. We confirmed, as shown previously [4], via micro-computed tomography (μ CT) that the tibias in SNR limbs were shorter compared to injured contralateral limbs ($p<0.05$, **Figure 2B**).

Cross-sectional area, cell density, and mechanical properties were impaired following SNR procedure at P1. Histomorphometric analysis showed that Achilles tendon cross sectional area (CSA) was significantly decreased in the SNR limbs ($p<0.05$, **Figure 3**). The total number of cells per cross section was also reduced ($p<0.05$) while there was an increasing trend for cell density ($p=0.08$) in the SNR group. To further examine the role of early postnatal loading in Achilles tendon growth and maturation, we performed uniaxial tensile testing to failure. The failure force, stiffness, and modulus were all significantly reduced in the Achilles tendon of the SNR limb ($p<0.05$, **Figure 4**), with a decreasing trend in maximum stress ($p=0.1$).

DISCUSSION

The role of physiologic mechanical loading in maintaining Achilles tendon homeostasis is well established and aberrant loading conditions can lead to disease, such as overuse tendinopathy. The importance of applied loading to Achilles tendon during periods of active cell proliferative- and matrix-driven growth are less studied. Using a SNR model, we found persistent gait alterations with posterior muscle atrophy and tibia shortening, which is consistent with previous findings [4]. We also found that the reduced loading had profound effects on the growth and maturation of the Achilles tendon. The marked reduction in postnatal loading produced tendons with smaller cross-sectional area and increased cell density. These structural changes corresponded with reduced stiffness, failure force, modulus, and failure stress. The reduced tendon cross-sectional area with a trending increase in cell density suggest that matrix production was predominantly affected in the SNR group. However, future studies will investigate cell proliferation changes in this model system. Interestingly, both structural and material properties were reduced, even with the changes in cross-sectional area, suggesting a deficit in the quality of tissue produced, a finding that will be investigated further in future studies.

ACKNOWLEDGEMENTS

This work was supported by NIH R01 AR075418 and P30 AR069619.

REFERENCES

[1] Wang JH, et al, *J Biomech.* 2006; [2] Rutland M, et al, *N Am J Sports Phys Ther.* 2015; [3] Langberg H, et al, *J Phys.* 1999 [4] Killion CH, et al, *Mol. Biol. Cell.* 2017.

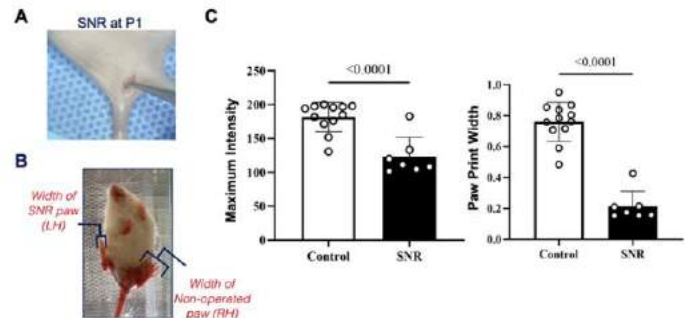


Figure 1: Gait perturbations following sciatic nerve resection. A) Intraoperative images of the operated hindlimb. **B)** Representative image of reduced paw width in SNR mice at P42. **C)** Average maximum intensity of left hindlimb strides and paw print width of control and SNR P1 mice measured via the CatWalk XT gait analysis system on post-natal day 42.

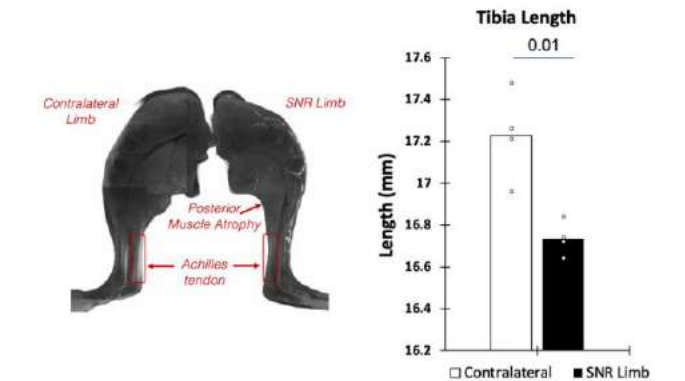


Figure 2: Postmortem images showing posterior muscle atrophy and differences in Achilles tendon morphology in the SNR limb compared to the contralateral limb B) Reduced tibia lengths in the SNR limb compared to the contralateral limb.

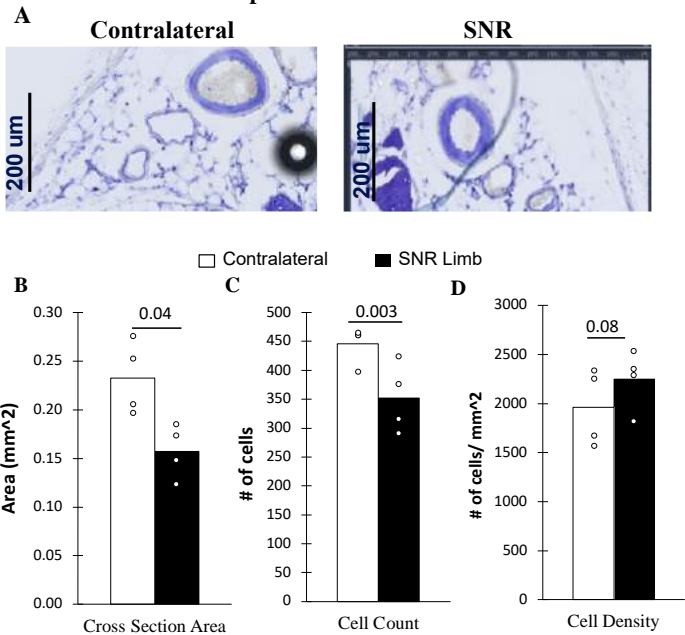


Figure 3: Reduced loading induces histological alterations in the SNR limb. A) Toluidine blue staining of Achilles tendon cross sections in the contralateral (left) and SNR limb (right). **Histological analysis of B) cross sectional area, C) cell count, and D) cell density.**

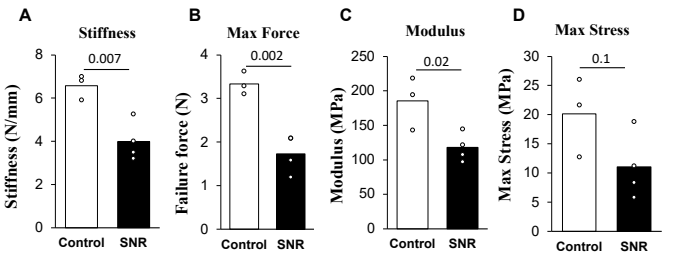


Figure 4: Mechanical testing of the Achilles Tendon showing reduced A) Stiffness, B) Max force, C) Modulus, and D) Max stress for SNR mice.

PASSIVE MECHANICS OF DEEP AND SUPERFICIAL HUMAN FEMALE PELVIC FLOOR MUSCLES

Megan R. Routzong (1,3), Justin Dubik (2), Raffaella De Vita (2), Marianna Alperin (3), Pamela A. Moalli (4), Steven D. Abramowitch (1)

- (1) Department of Bioengineering, University of Pittsburgh, Pittsburgh, PA, USA
(2) Department of Biomedical Engineering and Mechanics, Virginia Tech, Blacksburg, VA, USA
(3) Department of Obstetrics, Gynecology, & Reproductive Sciences, University of California San Diego, La Jolla, CA, USA
(4) Department of Obstetrics, Gynecology, & Reproductive Sciences, University of Pittsburgh, Pittsburgh, PA, USA

INTRODUCTION

The human female pelvic floor consists of skeletal muscles and connective tissues that work synergistically to mechanically support the pelvic organs (including the urethra, vagina, and rectum) and to facilitate physiologic functions (including urination, childbirth, and defecation). The term pelvic floor muscles (PFMs) is used to refer to many different pelvic skeletal muscles. The levator ani (LA) are the largest and most studied, but the term can also include the coccygeus (posterior/superior to the LA) and superficial perineal muscles (inferior to the LA). The PFMs remodel during pregnancy, must stretch extensively to accommodate vaginal childbirth, and their dysfunction has been associated with the development of pelvic floor disorders.¹⁻³ Their mechanical behavior impacts and is impacted by all of these processes and conditions, yet little is known about the passive mechanics of the human female PFMs.

Existing studies have focused on the LA and both the muscle and muscle fiber bundle level have been evaluated.^{4,5} One study found differences with age evaluated by comparing older and younger women, but the other did not see a correlation with age within a postmenopausal cohort. However, the PFMs have only been evaluated in a limited number of studies, and these studies did not include superficial perineal muscles. Therefore, we aimed to characterize the passive mechanical behavior of deep and superficial PFMs from female human cadavers.

METHODS

PFMs were dissected from fresh-frozen female cadavers obtained from Anatomy Gifts Registry with approval from the Committee for Oversight of Research and Clinical Training Involving Decedents at the University of Pittsburgh. These dissections were carried out by exposing the superficial muscles, moving posteriorly towards the coccyx; exposing the posterior surfaces of the deep pelvic floor muscles; removing the pelvic viscera except for the most distal portions that are attached to the PFMs; separating the superficial perineal muscles from

the bony pelvis; and separating the LA from the bony pelvis and pelvic sidewalls. This resulted in the removal of the pelvic floor *en bloc*, which was frozen in saline soaked gauze at -20°C. These samples were frozen *en bloc* because the dissection of the pelvic floor and the harvest of individual muscle samples was substantially time consuming and muscle orientations could more easily be maintained if harvested immediately before mechanical testing.

Samples were moved to a refrigerator to thaw two days prior to mechanical testing and then finished thawing at room temperature immediately prior to tissue harvest. During and following harvest and leading up to testing, samples were kept hydrated by periodically spraying them with 1x phosphate buffered saline. Individual PFMs were isolated. Muscle samples included the left and right ischiocavernosus (IS), bulbocavernosus (BC), transverse perinei (TP), and LA. Due to size and shape, some PFMs could not be tested whole. Such samples were divided into sections cutting with the orientation of the fibers and along natural breaks between fibers when present to create samples of sufficient size while minimizing variations in the sample's width.

The length, width, and thickness of each sample were measured before and after mechanical testing. Length and width were measured via digital calipers, and thickness via laser micrometer. Samples were dyed blue and speckled with white spray paint to allow for regional, non-contact strain measurements via 3D digital image correlation (DIC). This DIC system included two CCD cameras (Basler ace acA2440-75µm, Basler Inc., Exton, PA) that captured high resolution images of each specimen during testing (**Figure 1**). Tensile tests were performed with an Instron uniaxial testing system equipped with a 50 N load cell at a rate of 0.1 mm/s (after a 0.1 N preload) until failure or tearing at the clamps.

Data from the DIC system and Instron were aligned and noise reduced with a MATLAB script. The DIC system calculates heterogeneous strains across a manually selected region using the speckle pattern to track deformation (**Figure 1**). The strain values used

were an average over a small circular sub-region (diameter < 1 mm) selected based on the best speckle visibility and how long it remained within the field of view. Stress was calculated using the Instron's load data and the widths and thicknesses measured before testing. The resulting stress-strain curves were sampled at specified stress values and compared across muscles.⁶ Lagrangian strains in both the main *in vivo* loading direction (axial strain) and perpendicular to the loading direction (transverse strain) were evaluated.

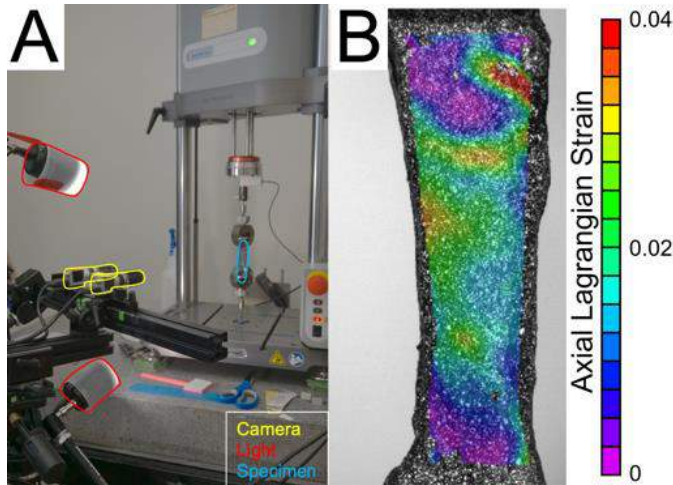


Figure 1: An image depicting A) the mechanical testing and DIC system setup and B) an example DIC image and strain map.

RESULTS

The PFM of 8 donors were included in this study (white, age 64.8 ± 9.1 years, BMI 25.4 ± 4.7 kg/m²). During testing, it was noted that the LA samples were the largest, while the IS samples were the thinnest. In terms of width, the TP samples were the most non-uniform (being more triangular-shaped than the other PFMs), and the IS appeared to have the most consistent widths throughout the sample.

Note that the data shown here only includes 4 samples of each muscle type as analyses are still in progress. In the toe region, the LA and TP experienced the highest axial strains, while the IS exhibited the lowest (**Figure 2**). Additionally, the TP axial strains had the greatest variability, encompassing almost all of the other PFMs' values. In the transverse direction, the LA experienced remarkably larger strains than the superficial PFMs and the greatest variability by a large degree.

DISCUSSION

This study quantified the mechanical behavior of superficial and deep human female PFMs. This adds to existing levator ani data from a small number of studies, but also introduces a novel assessment of local strains using DIC methods. Additionally, this study generated mechanical data for the previously uncharacterized superficial PFMs.

The LA demonstrated axial behavior more similar to the superficial muscles than expected. They are considered to be much larger contributors to the mechanical support of the pelvic organs than the superficial PFMs, but that difference isn't apparent based on this passive behavior. This idea would likely be better reflected in the structural properties. Though LA can be divided into multiple distinct muscles (e.g., iliococcygeus), they were evaluated together in this analysis, which could have contributed to the large variability in LA transverse strains. Furthermore, the axial strains of the superficial PFMs were not as similar as expected. While the TP and BC had comparable axial strains at lower stress values, their distributions grew more divergent

with increasing stress, potentially due to the distinct geometry of the TP.

Studying female PFM biomechanics is difficult, especially in living women, due to the PFMs often having complex geometry and being located deep enough in the body to make biopsy or minimally invasive investigation challenging. Therefore, cadaveric PFM data is quite valuable, though still rare. We observed that non-uniform muscle structure further complicates the resulting mechanical behavior and quantifications. Many samples were embedded with pockets of fat, creating regions of lower muscle fiber density. Fibers in regions like this would tear, but the tissue as a whole would recover and stress would continue to increase. This occurred quite frequently throughout our testing, particularly in LA samples, which was also the PFM that experienced the greatest transverse strains. However, this is not well documented in the literature. Further evaluation of and a system for quantifying these events may need to be conducted.

This study provides important insight into the passive mechanical behavior of superficial and deep female PFMs. Moreover, resulting material property data can be used in finite element simulations of the female pelvic floor to improve models that incorporate the superficial perineal muscles in addition to the more commonly simulated LA.

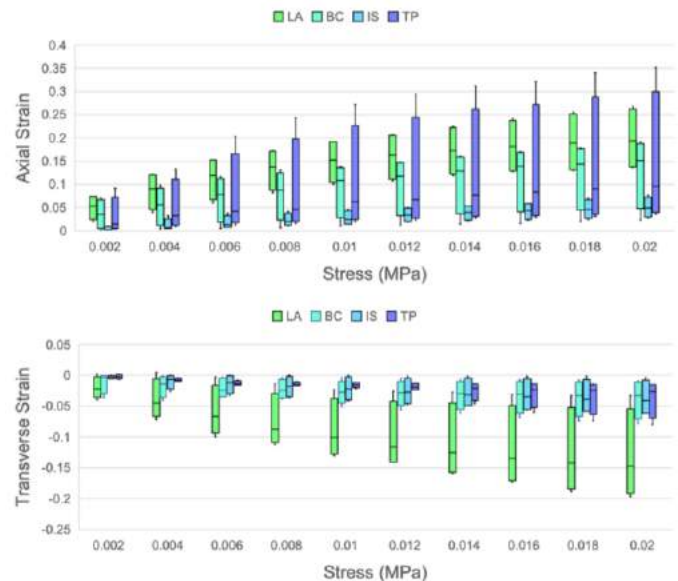


Figure 2: Axial (top) and transverse (bottom) strains for each PFM at specified stress values representative of the toe region of the stress-strain curves.

ACKNOWLEDGEMENTS

We thank those who donated their bodies to Anatomy Gifts Registry to contribute to the advancement of education and research.

We acknowledge funding from the National Science Foundation: M.R. from Graduate Research Fellowship Program Grant #1747452 and J.D. and R.D. from Grant #1929731. Opinions, findings, and conclusions/recommendations are those of the author(s) and do not necessarily reflect the views of the National Science Foundation.

REFERENCES

- [1] Rieger, MM et al., *Am J Obstet Gynecol*, 226(5):708.e1-e13, 2022.
- [2] Routzong, MR et al., *Interface Focus*, 9(4):2019011, 2019.
- [3] Kepenekci, I et al., *Dis Colon Rectum*, 54(1):85-94, 2011.
- [4] Nagle, AS et al., *J Biomech*, 47(2):583-586, 2014.
- [5] Burnett, LA et al., *J Biomech*, 98:109436, 2020.
- [6] Donaldson, K et al., *Ann Biomed Eng*, 2023.

OBESITY AFFECTS THE BIOMECHANICS OF THE POSTERIOR KINETIC CHAIN DURING MANUAL LIFTING

Sergio A. Lemus (1), Mallory Volz (2), Francisco Beron-Vera (1), Mitchell Hurtado (1), Eduard Tiozzo (3), Arlette Perry (4,5,6) Thomas M. Best (2,7,8), Francesco Travascio (1,7,9).

- (1) Department of Mechanical and Aerospace Engineering, University of Miami, Coral Gables, FL
- (2) Department of Biomedical Engineering, University of Miami, Coral Gables, FL
- (3) Department of Physical Medicine and Rehabilitation, University of Miami, Miami, FL
- (4) Department of Kinesiology and Sport Sciences, University of Miami, Coral Gables, FL
- (5) Laboratory of Clinical and Applied Physiology, University of Miami, Coral Gables, FL
- (6) School of Education and Human Development, University of Miami, Coral Gables, FL
- (7) Department of Orthopaedics, University of Miami, Miami, FL
- (8) UHealth Sports Medicine Institute, Coral Gables, FL
- (9) Max Biedermann Institute for Biomechanics at Mount Sinai Medical Center, Miami Beach, FL

INTRODUCTION

One out of three adults are obese in the United States [1]. Obesity is considered a major health issue that constantly appears as contributor to musculoskeletal injuries in the workplace [2-4]. Particularly, workers with elevated body mass index (BMI) are more susceptible to injuries affecting the posterior kinetic chain [5-7]. Despite this escalating problem, recommended weight limits (RWL) for manual lifting tasks are still designed based on average body weight individuals as per National Institute of Occupational Safety & Health (NIOSH) guidelines [8]. The recommended NIOSH lifting equation (RNLE) calculates RWL with the objective of safely regulating energy expenditure and musculoskeletal loads during manual lifting [9]. However, the adverse effects of elevated BMI on the prevalence of musculoskeletal injuries in manual workers are not considered in designing lifting tasks that account for a major portion of activities demanded from manual work occupations. As a result, the present study measured and compared parameters associated to the biomechanics of the posterior kinetic chain in individuals with different BMI categorization while performing manual lifting activities at the RWL. We hypothesize that the execution of manual lifting at RWL would produce forces and moments in L5-S1 above biomechanical safety limits for obese individuals.

METHODS

30 people were enrolled. Subjects were stratified into groups of 10 for 3 BMI classifications based on the definitions of the World Health Organization [10]: normal weight ($18.5 \leq \text{BMI} \leq 24.9$), overweight ($25 \leq \text{BMI} \leq 29.9$), and obese ($\text{BMI} \geq 30$). Individuals standing in front of a box were required to move it from the floor to a table 30" high. Four repetitions of this lift were performed with rest allotted in between lifts. A 'freestyle' lifting technique was allowed. The geometrical setting of the task is represented in Figure 1.

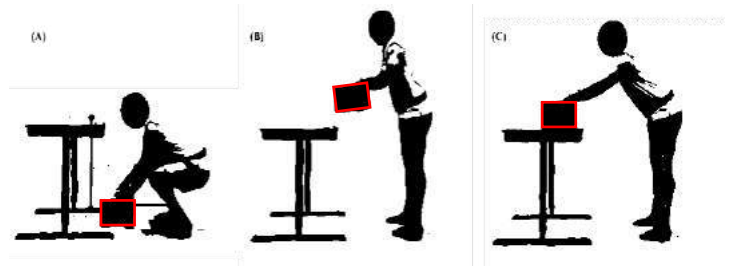


Figure 1: Geometrical setting for experiment divided in three stages: (A) Initial lifting phase. (B) Maximum height. (C) Deposit phase

The weight of the box was calculated to be equivalent to the RWL as defined in the revised NIOSH lifting equation:

$$\text{RWL} = \text{LC} \times \text{HM} \times \text{VM} \times \text{DM} \times \text{AM} \times \text{FM} \times \text{CM} \quad (1)$$

Body biomechanics was evaluated via a ViconNexus® Motion Capturing System integrating eight MCam cameras and two Kistler force plates. Thirty-nine reflective markers were placed on subjects according to Vicon's Plug-in Gait Full Body (PIGFB) model [11]. Kinematic data and ground reaction forces were collected at 500 Hz, processed with the PIGFB biomechanical model, and were enhanced by a previously validated custom spinal specific BodyBuilder® plug-in [12]. Data post-processing provided three parameters associated to the biomechanics of the lumbosacral joint: anterior-posterior (A/P) force, axial compression force, and bending moment. A two-way ANOVA compared these parameters across BMI classification and gender, and linear regressions investigated potential correlations between these parameters and BMI.

RESULTS

BMI classification significantly affected all L5-S1 forces and moment parameters as per the two-way ANOVA analysis: A/P shear force ($p \leq 0.001$), compression force ($p = 0.002$), and bending moment ($p = 0.016$). Linear regression models helped understand the relationships between BMI and L5-S1 forces and moments: A/P shear force ($R^2 = 53.19\%$, $p \leq 0.001$), compression force ($R^2 = 46.60\%$, $p \leq 0.001$), and bending moment ($R^2 = 31.02\%$, $p = 0.002$). Notably, more than half of obese individuals exceeded the shear safety limit, showing that clinically elevated BMI affects the biomechanics of the posterior chain. Forces and moment values for L5-S1 are represented in Figure 2 and listed in Table 1.

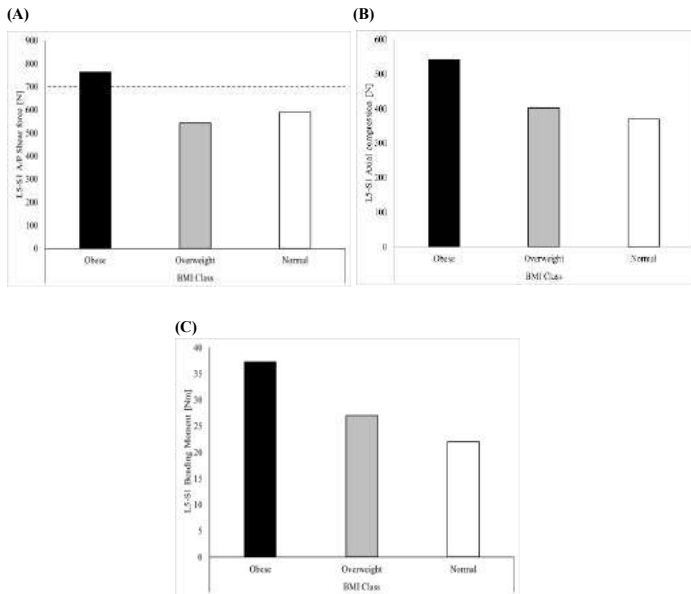


Figure 2: Values of biomechanical stress and moment classified per BMI: (A) A/P shear force on L5-S1, safety limit line at 700 N. (B) Axial compression force on L5-S1. (C) Bending moment on L5-S1.

		Normal (n=10)	Overweight (n=10)	Obese (n=10)	Subtotal (n=30)	P-Value
A/P Shear Force	Subtotal (n=30)	589.2	543.2	763.5	633.4	0.001*
	Group	B	B	A		
Axial Compression	Subtotal	369.0	402.3	542.4	436.6	0.002*
	Group	B	B	A		
Bending Moment	Subtotal	22.1	27.0	37.3	29.1	0.016*
	Group	B	B	A		

Table 1. Peak forces and moment for L5-S1 versus BMI. Marginal means for BMI classifications are grouped using a Fisher Pairwise comparison. A p-value for the ANOVA test comparing each biomechanical variable with BMI class is also reported, with (*) indicating statistically significant difference.

DISCUSSION

Our previous research showed that 80% of obese individuals exceeded physiological stress safety limits during manual lifting [13]. Moreover, previous investigations had identified a need to consider physical attributes when calculating RWL [14-16]. However, to the authors' best knowledge, this is the first study evaluating the degree to which the RWL guarantees the L5-S1 biomechanical safety limits for both axial and A/P shear spinal forces. Biomechanical stresses is the most understudied cause that links obesity and occupational musculoskeletal injuries in the posterior chain [17]. Specifically, L5-S1 is the most common location of degenerative spinal pathology and most highly correlated with injury [18-20].

In the present study, the magnitudes of these L5-S1 parameters were significantly dependent on BMI group. Figure 2 illustrates the differences in L5-S1 A/P shear force in reference to the safety limits: the A/P shear force of the obese group surpassed the safety threshold (700 N) proposed by Gallagher [21] by 9 percent. Overall, the relationship between L5-S1 shear spine loads and BMI when lifting at RWL confirms our hypothesis: spine loads in obese individuals exceed biomechanical safety limits under specific loading conditions when compared to overweight and average weight individuals. Furthermore, BMI also affected the L5-S1 peak bending moment ($p = 0.016$): values for obese subjects were 30 percent larger than overweight individuals and 65 percent larger than normal individuals. Our results agree with those reported by Corbeil et al, where peak moments at L5-S1 were up to 60 percent larger for obese individuals [22]. Overall, these results provide a groundwork for future studies to consider physical characteristics in coefficients for the RNLE. Such efforts could help to reduce the risk of biomechanical stresses to the posterior chain and lead to a reduced rate of lower back injury among manual laborers.

ACKNOWLEDGEMENTS

Study supported by UM-PRA-2022-3243 award from The University of Miami.

REFERENCES

- [1] Ogden, C.L., et al., *NCHS Data Brief*, (82):1-8, 2012.
- [2] Cowan, DN, et al., *Occup Med (Lond)*, 61(4):247-52, 2011
- [3] Humphreys, SL, *Bariatric N and Surgical P Care*, 2(1): 3-6, 2007.
- [4] Toivanen, AT, et al., *Rheumatology (Oxford)*, 49(2): 308-14, 2010.
- [5] Ostbye, T, et al., *Arch Intern Med*, 167(8):766-73, 2007.
- [6] Schmier, JK, et al., *Scand J Work Environ Health*, 32(1):5-11, 2006.
- [7] Gu, JK, et al., *J Occup Environ Med*, 58(4):335-43, 2016.
- [8] Waters, TR, et al., *U.S. Dept of Health*, 94(110), 1994.
- [9] Waters, TR, et al., *Ergonomics*, 36(7):749-76, 1993.
- [10] *World Health Organ Tech Rep Ser*, 894: 1-253, 2000.
- [11] Davis, RB, et al., *Human Movement Science*, 10(5):575-587, 1991.
- [12] Eltoukhy, M, et al., *J Orthop*, 13(3):210-9, 2016.
- [13] Lemus, SA, et al., *PLOS ONE*, 17(12): e0278858, 2022.
- [14] Barim, MS, et al., *Applied Ergonomics*, 74:67-73, 2019.
- [15] Corbeil, P, et al., *Applied Ergonomics*, 74:124-133, 2019.
- [16] Singh, D, et al., *Work*, 51:337-348, 2015.
- [17] Pollack, et al., *Injury Prevention*, 13(5):297-302, 2007.
- [18] Granata, KP, et al., *Ergonomics*, 42(9):1187-1199, 1999.
- [19] Coenen, P, et al., *J of Occup Rehabilitation*, 23(1): 11-18, 2013.
- [20] Hoozemans, MJM, et al., *Ergonomics*, 51(7):1053-1063, 2008.
- [21] Gallagher, S, et al., *Clin Biomech*, 27(10):973-8, 2012
- [22] Corbeil, P, et al., *Human F and Ergonomics*, 57(1):958-961, 2013.

LYMPH NODE CONDUIT MODELLING OFFERS INSIGHT INTO THE ROLE OF FLUID FLOW IN ANTIGEN DEPOSITION

**Daniel J. Watson (1), Willy V. Bonneuil (1), James Marshall (1), Peter Xie (1), Thomas Adam (1),
Jennifer Frattolin (1), Matthew J. Russell (2), Francesca Fasanella Masci (3), Angela E. Goode
(4), Shafa Balaram (1), Alexandra E. Porter (4), Anil A. Bharath (1), Bindi S. Brook (2), Robert J.
B. Nibbs (3), James E. Moore Jr (1)**

(1) Bioengineering Dept, Imperial College London, United Kingdom
(2) School of Mathematics Sciences, Nottingham University, United Kingdom
(3) School of Infection and Immunity, Glasgow University, United Kingdom
(4) Dept of Materials, Imperial College London, United Kingdom

INTRODUCTION

Adaptive immunity and peripheral tolerance depend on antigen recognition within the lymph node. This process is essential to the development of a robust immune response to harmful pathogens. Dysfunction in this process can lead to immunodeficiency as well as autoimmune disorders. There are two mechanisms by which antigen can arrive at the lymph node. Firstly, it can be captured by dendritic cells within the tissues and carried into the lymph node. Secondly, it can be directly sampled from afferent lymph by resident dendritic. Previous works have shown that small molecular weight antigens can rapidly enter the lymph node parenchyma via the conduit system [1][2]. The conduit system is a series of pathways through the lymph node comprised of bundles of collagen fibers enclosed by fibroblastic reticular cells (FRC).

It is unclear what processes drive this transport and the mechanisms responsible will inform the factors effecting the deposition of antigen within the lymph node. If fluid flowing through the conduit system predominantly carries antigen by advection, then the deposition of antigen will be dictated by the upstream lymphatic flow. Conversely, if this process is driven by diffusion, then the antigen will travel in all directions within the network and its deposition will depend on the conduit network structure. Understanding this process will allow the design and development of vaccines and anti-inflammatory interventions which are optimized to inhibit or encourage antigen recognition by effecting the mechanical process of deposition. This work sort to study this transport by combining FIB-SEM images of the conduits with *in silico* models of the fluid flows and mass transport within the conduit system.

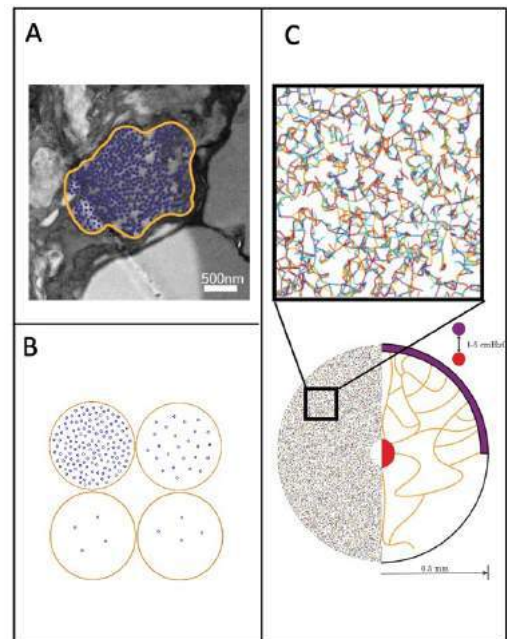


Figure 1: A) An example FIB-SEM image with the fibers and FRC indicated. B) An example idealized geometries with differing fiber densities. C) An example node-scale conduit network with the model setup indicated on the left and an inset revealing the structure.

METHODS

FIB-SEM images were taken of the conduits within murine lymph nodes. The walls and fibers were segmented and idealized to produce many different cross-section geometries, see Figure 1.A and B. 2D fluid solvers were used to calculate the fluid velocity distribution over these geometries in order to estimate the fluid resistance of a conduit section. A series 1D lattice networks representing the conduit system of an entire lymph node were generated with a 15° periodic symmetry, see Figure 1.C.

These networks were constructed with constraints on the minimum and maximum nodal index, edge length and the density. The individual sections of these networks were given properties derived from the 2D study. A circular region in the center was used to represent the high endothelial venules and an outer region was chosen to represent the subcapsular sinus. By imposing a pressure difference between these region the flow rates through the conduit could be found. These flow rates were used by 1D advection-diffusion solvers to calculate the transport of an antigen, presented at the subcapsular sinus, through the system, see Figure 3.

RESULTS

The relationship between flow and resistance was found to be fairly predictable, for individual cross sections between area fractions of 0.5-0.9. Comparing antigen transport between a zero flow model and one that would maximize flow – conduit density 50%, 0.9% cross-sectional area-fraction and 3 μm diameter [3]. The maximum difference in antigen concentration, during 15 minutes of exposure, was less than 0.01%.

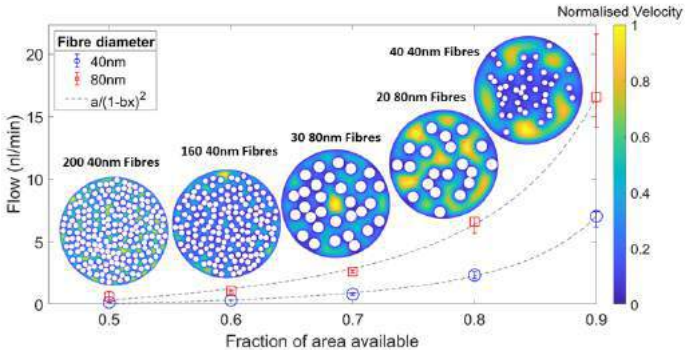


Figure 2: Normalized fluid velocities and flows for a 1 cmH₂O /cm gradient for differing area fractions and fiber diameters, insets show example geometries.

DISCUSSION

Wherever possible assumptions were made that would maximize the effect of flow. However, for all models considered, no significant effect of flow on the transport of antigen could be established. While flow is present within the lymph node conduit system, it is not sufficient to affect the transport of antigens. Work is underway to explore the role of the network structure such as anisotropy and small-world property, as well as the role of anomalous diffusion within and without the conduit system.

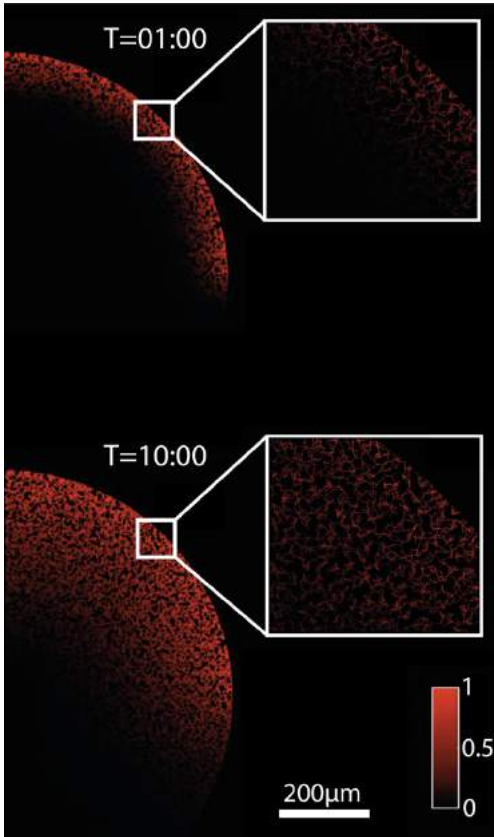


Figure 3: Lymph node scale model shows the normalized concentrations of a 70kDa antigen introduced to the subcapsular sinus at 1 & 10 minutes post exposure. Insets show fine structure.

ACKNOWLEDGEMENTS

This work was funded by the Wellcome Trust Collaborative Award 206284/Z/17/Z.

REFERENCES

[1] Sixt M et al. *Immunity*. 22:19-29, 2005
[2] Roozendaal, R et al., *Int Immunol*, 20:1483-7, 2008.
[3] Kelch, I.D. et al *PLoS Biol*, 17, 2019

FUNCTIONAL DIFFERENCES IN HUMAN AORTIC VALVE INTERSTITIAL CELLS FROM PATIENTS WITH VARYING CALCIFIC AORTIC VALVE DISEASE

R. Tuscher (1), A. Khang (1), T. West (1), G. Ferrari (2), M. Sacks (1)

(1) Willerson Center for Cardiovascular Modeling and Simulation, Biomedical Engineering,
University of Texas, Austin, TX, USA
(2) Department of Surgery, Columbia University, New York, NY, USA

INTRODUCTION

Calcific aortic valve disease (CAVD) is a progressive disease of the aortic valve (AV) in which the aortic valve develops calcium deposits that gradually stiffen the valve [1]. For severe CAVD and aortic stenosis, patients must receive an AV replacement, either a mechanical valve or a bioprosthetic valve [1]. Currently, there is no pharmaceutical treatment for CAVD [1].

A crucial risk factor for CAVD is a congenital valve defect known as bicuspid aortic valve (BAV) [1], [2]. BAV is present in roughly 1-2% of the population and is characterized by the development of an aortic valve with two leaflets rather than the physiological three [2]. BAVs are around twice as common in men as women [2]. Despite the relatively low abundance of BAV in the general population, this defect is present in roughly 50% of patients undergoing AV replacement for aortic stenosis [2].

The leaflets of both TAV and BAVs consist of collagen, elastin, and glycosaminoglycans, which is maintained by contractile cells known as aortic valve interstitial cells (AVICs) [1]. AVICs mechanically sense the microenvironment of the AV with actin stress fibers [1]. In CAVD, the contractility of the AVICs may increase due to pathological activation. Activated AVICs recruit α -smooth muscle actin (α SMA) to stress fibers, leading to increased contractile function. These AVICs may then transition into an osteoblast-like state and deposit calcium into nodules which gradually stiffens the AV.

The microenvironment of BAVs contains pathological strains and disorganized protein structure, especially in the Raphe region. AVICs experiencing atypical strains may rapidly progress into a diseased phenotype [2]. The native activation of AVICs originating from CAVD patients is used to study the functional differences between BAV and TAV. It is not known whether BAVICs are intrinsically more activated than TAVICs, or whether differences in disease progression originate from the different microenvironments of the AV types.

METHODS

The AVICs were assessed in full 3D method for both global and local changes in basal cell characteristics.

Cell Extraction and Culture: Human AVICs were obtained from CAVD patients with TAV and BAV undergoing AV replacement. AVICs from the Raphe region of BAVs were studied (RBAVs), as well as from the BAV non-Raphe region (NRBAV), from a calcified region of a TAV (CTAV), and from a non-calcified region of a TAV (NCTAV). The AVICs were grown in 3D PEG hydrogels with CRGDS adhesive peptides and MMP-degradable crosslinkers, interspersed with 0.5 μ m fluorescent markers as previously described [3].

3D Imaging: A confocal microscope was used to image individual cells randomly selected from the gels in their Normal (N) state and Inactivated (I) state, which is the addition of Cytochalasin-D (CytoD), a drug which depolymerizes stress fibers [3].

Marker Recovery and Displacement: The basal tonus, or intrinsic contractility, of the AVICs was measured using 3D-TFM. The markers were recovered and tracked from Normal to Inactivated (CytoD treatment) with FM-Track [3]. AVIC surface meshes were computed by cell-recognition and surface smoothing.

Data Analysis: The AVIC surface meshes were reconstructed using spherical harmonic shape fitting as previously described [4]. This technique condensed the 3D geometry of the membrane into a spherical harmonic series. Stretches and displacements at the tip of the protrusion were computed for each AVIC experimental group.

RESULTS

Total AVIC Shape Change: All AVICs expanded outward to some capacity in the I state relative to the N state (Fig. 1). Spherical harmonic analysis was used to reconstruct the AVIC surface meshes. The resultant spherical harmonic coefficients represent the contribution of each term in the spherical harmonic series. Only coefficients of order

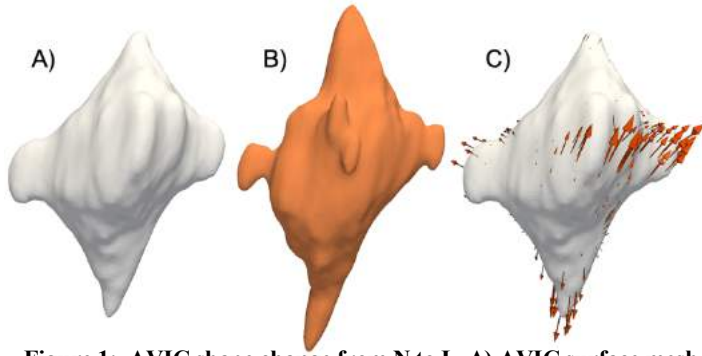


Figure 1: AVIC shape change from N to I. A) AVIC surface mesh reconstruction in the Normal state. B) AVIC surface mesh reconstruction in the Inactivated state. C) Surface displacements representative of AVIC deformation.

ten and below were shown to contribute to functional shape change. The difference of these coefficients from N to I was computed for each group. NCTAVs were found to have the highest magnitude of change and NRBAVs were found to have the lowest magnitude of change (Fig. 2). Additionally, different directions of deformation were assessed for trends in polarity of the AVICs. TAVICs were found to have similar magnitudes in two principal directions, while BAVICs deformed in primarily one direction.

AVIC Protrusion Displacement: AVICs have been shown to have piston-like deformation, in which the tip of the protrusion relaxes radially outward from the AVIC surface. The largest magnitude of displacement occurs at the protrusion tips (Fig. 1C). The displacements at the surface tip of the protrusion were computed for each experimental group (Fig. 3A). NCTAVs had the highest magnitude of displacement at the protrusion tips. The protrusion tip deformation shared the same trend as total shape change in which the group with the most displacement was NCTAV, followed by CTAV, RBAV, and lastly NRBAV (Fig. 3A).

Sex-Specific Distinctions: Female AVICs were found to have higher displacements on average than male AVICs (Fig. 3B).

DISCUSSION

The basal contractility of AVICs from varying disease states of CAVD has been shown to differ between experimental groups and sexes. The implications of this finding are in the contractile stress fibers of the AVICs, the extent of AVIC activation, and recruitment of α SMA to those stress fibers.

Results of both the spherical harmonic analysis and protrusion displacement analysis show the same trend in which TAVICs are more natively contractile than BAVICs. Of the TAVICs, NCTAVs had the highest displacements at the protrusion tips, indicating the highest basal contractility. The next highest basal contractility was measured to be the CTAVs, followed by the RBAVs. The least contractile group was found

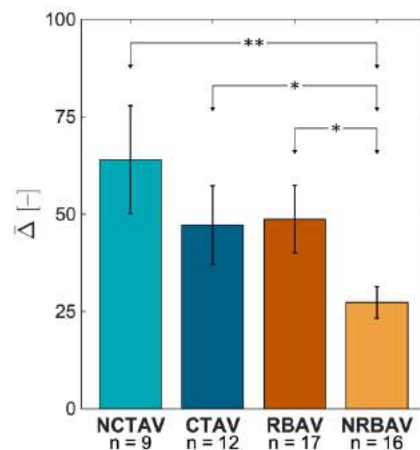


Figure 2: Mean magnitude of change in spherical harmonic coefficient from N to I states.

* P-value < 0.05; ** P-value < 0.005

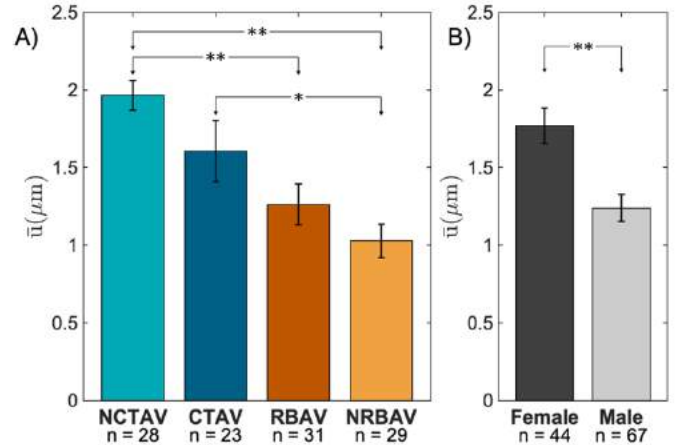


Figure 3: Mean displacements at the protrusion tip. A) AVICs from TAVs and BAVs. NCTAVs have the highest displacements at the protrusion tips. B) Females on average have higher displacements at protrusion tips than males.

* P-value < 0.05; ** P-value < 0.005

to be the NRBAVs. On average, TAVICs were found to be more activated than BAVICs. Diseased TAVICs may have a higher contraction strength than BAVICs due to this pathological activation, which can be speculated to be because of increased α SMA recruitment.

In addition, AVICs from BAVs were shown to form stress fibers differently than AVICs from TAVs. Based on findings that TAVICs basal contractility was primarily in one direction and BAVIC basal contractility was in two directions, a possible explanation is that TAVICs form stress fibers that align in two directions, while BAVICs form stress fibers that align in one direction. The minor direction(s) of deformation occur because of compensatory isovolumetric effects, not inactivation of stress fibers from CytoD. The results of this study suggest that the cells from TAVs and BAVs behave differently in the same microenvironment. This finding in consideration with the prior finding that TAVICs are more contractile suggests that the rapid disease progression in BAVs could be due to microenvironmental effects on the AVICs, not intrinsic activation of BAVICs.

Sex-specific functional differences were observed, namely that female AVICs experience greater magnitude of protrusion displacement (Fig. 3B). This finding agrees with published findings that female VICs have higher basal levels of α SMA than male VICs [5]. The interplay between the prevalence of BAVs in males and the higher activation of female AVICs is a direction of future research.

In TAVs, CAVD development may begin in AVICs, while in BAVs CAVD develops first from the microenvironment, not the AVICs. Overall, this study is the first to compare excised human AVICs for functional differences in varying CAVD states. The findings that there are sex specific differences is crucial to understanding the disparity of disease and possible need for distinct treatment.

ACKNOWLEDGEMENTS

The author would like to acknowledge Dr. Ferrari for providing access to the excised human AVICs.

REFERENCES

- [1] Lerman, DA, et al. *European Cardiol Rev* 10:108-112 (2015).
- [2] Braverman, AC, et al. *Curr Prob Cardiology* 30:470-522 (2005).
- [3] Lejeune, E, et al. *Software* 11:100417 (2020).
- [4] Khang, A, et al. *Acta Biomater* IP:1-16 (2022).
- [5] Aguado, BA, et al. *Circulation* 145:513-530 (2022).

A NEURAL NETWORK FINITE ELEMENT APPROACH FOR HIGH-SPEED CARDIAC PRESSURE-VOLUME SIMULATIONS

Shruti Motiwale (1), Wenbo Zhang (2), Michael S. Sacks (1,2,3)

- (1) James T. Willerson Center for Cardiovascular Modeling and Simulation, Oden Institute, University of Texas at Austin, TX, USA
(2) Department of Mechanical Engineering, University of Texas at Austin, TX, USA
(3) Department of Biomedical Engineering, University of Texas at Austin, TX, USA

INTRODUCTION

Comprehensive patient-specific computational models continue to be developed for cardiac simulations of health and disease [1-3]. However, due to the complex multiphysics and multiscale nature of cardiac biomechanical function, traditional finite element methods remain prohibitively slow for clinical applications. Furthermore, reduced order models are not ideal for clinical applications due to the loss of detail and potential loss of accuracy, especially for patient-specific clinical applications.

To meet the requirements of speed as well as accuracy, we have developed and utilized a novel neural network finite element (NNFE) approach for soft tissue simulations that can produce simulation results within clinically relevant timeframes [4]. The NNFE approach is a physics-based approach for rapid simulations that uses the neural network (NN) to represent the nodal displacements, and finite elements to map the displacement output from the NN on the problem domain, as well as to enforce boundary conditions and perform numerical integrations. In other words, this approach does not rely on data generated from physical experiments or simulations for training, rather, the NNFE model is trained to learn the governing PDE. In this work, we present a feasibility study using an extension of the NNFE approach towards complete organ level cardiac simulations to predict the P-V loop responses of the left ventricle, accounting for active contraction and transmural fiber distributions.

METHODS

The left ventricle was represented as a prolate spheroid as a first step scenario and was discretized with unstructured tetrahedral elements. The basal plane was constrained to in-plane motion only, one point on the basal plane was completely fixed, and an adjacent point was constrained radially, while pressure was applied to the inner surface. Fiber distributions were described by a rules-based approach to approximate the -60 to 60 degree transmural gradient (Fig 1). The

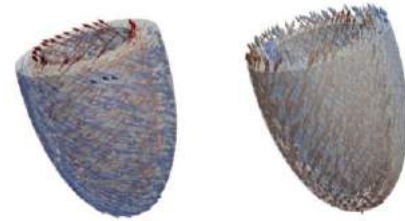


Figure 1: Fiber orientations in the myofiber and sheet directions respectively.

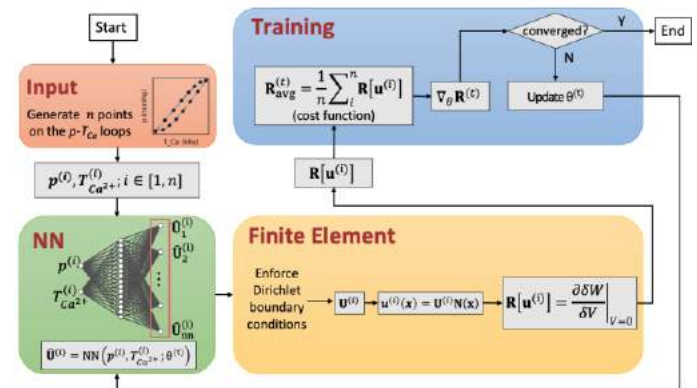


Figure 2: The NNFE training pipeline

passive mechanical properties of the myocardium were modeled with an incompressible transversely isotropic Fung-based hyperelastic material model, and the active contraction was modeled as an additional stress based on the Hunter-McCulloch-Ter Keurs model with minor

modifications. The material constants were taken from an ovine heart model [1]. Briefly, the weak form of the governing PDE is

$$\delta W(\mathbf{u}, \delta \mathbf{u}) = \int_{\Omega_0} \left(\frac{\partial \Psi}{\partial \mathbf{E}} + \mathbf{S}_{act} \right) : \delta \mathbf{E} d\Omega - \int_{\Gamma_0} \mathbf{T} \cdot \delta \mathbf{u} d\Gamma = 0 \quad (1)$$

where, $\mathbf{u} = \mathbf{UN}$ is the displacement field over the domain Ω , \mathbf{U} are the nodal displacements and \mathbf{N} are the basis functions, $\delta \mathbf{u} = \mathbf{VN}$ is the virtual displacement field and \mathbf{V} are the virtual nodal displacements, Ψ is the strain energy density function describing the passive behavior of myocardium, \mathbf{E} is the Green-Lagrange strain tensor, \mathbf{S}_{act} is the 2nd Piola-Kirchhoff active contraction stress and \mathbf{T} is the traction vector. The residual of the governing PDE is

$$R = \frac{\partial \delta W}{\partial \mathbf{v}} \Big|_{\mathbf{v}=0} = 0 \quad (2)$$

The NNFE model was setup to take pressure p and active contraction $T_{Ca^{2+}}$ as the input and predicted the nodal displacements \mathbf{U} in the output layer (Fig 2). In addition, the NN had one hidden layer with 16 neurons. We trained the NN by minimizing the residual of the governing PDE (Eq. 2, Fig 2) using the first-order gradient based optimization algorithm Adam [5] along with learning rate scheduling. Moreover, while our previous approach utilized a reduced order model [6] to train the neural network, no model order reduction was required in this approach, the NNFE model was trained over the full order model. We trained the model over two pressure-volume (P-V) loops and predicted the P-V relationship for a third loop. We compared the results of the NNFE model against an identical simulation setup in FEniCS [7].

RESULTS

The NNFE model predicted the displacement and the corresponding PV loop (Fig. 3). The mean nodal error between the NNFE solution and the FE solution was 2.32×10^{-2} mm, with a standard deviation of 4.53×10^{-2} mm (Fig. 4). The trained NNFE model could accurately produce the twisting experienced by the left ventricle under active contraction. The trained NNFE model took 2-3 seconds for producing the results for each state, whereas FEniCS took 10-20 min.

DISCUSSION

We presented a novel NNFE approach to produce the active contractile behavior of a left ventricle under a given PV loop. Although the NNFE method does take longer to train, this is not a limitation, as the NN only needs to be trained once over a range of boundary conditions. Once trained, the NN can produce results for any boundary condition within the training range without a need for retraining. Consequentially, the NNFE approach is well-suited for many-query problems, such as patient-specific surgical planning, where one needs to solve very similar problems repeatedly with only small changes to the inputs. For such applications, the training can be done in advance, and when presented with the patient-specific data, rapid simulation results can be produced with the trained model.

Our results demonstrate the first application of the NNFE approach for a biomedical application at an organ level. We will use this model to study the effect of infarcts in different locations of the ventricle on cardiac behavior. We are also working on extending this method to study the effects of inotropy on cardiac behavior by varying the slope of the end systolic P-V relationship. Our results represent a small but an important first step towards a digital twin. In the future, geometry and material property variations will be included. While still in its early stages, this approach paves the pathway for high-speed patient-specific clinical simulations.

ACKNOWLEDGEMENTS

NIH R01 HL073021 and Platform for Advanced Scientific Computing (Swiss Federation).

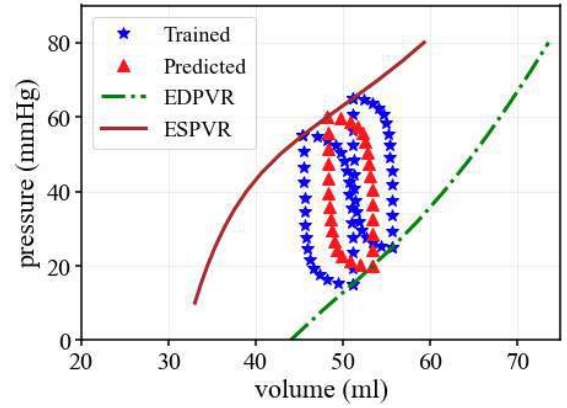


Figure 3: The NNFE model was trained on two PV loops and predicted the third loop. The trained NNFE model took 2-3 seconds for producing the results for each state, whereas FEniCS took 10-20 min.

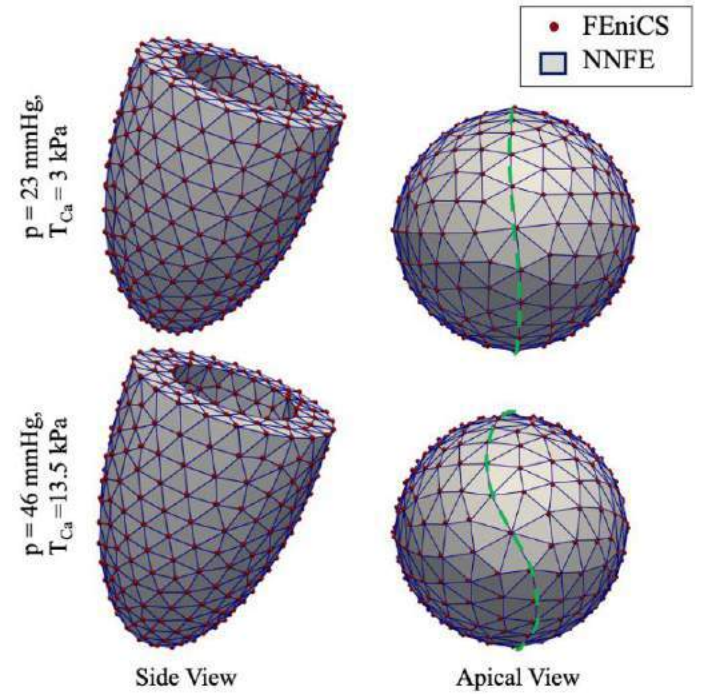


Figure 4: Two points on the P-V loop as produced by the NNFE method (wireframe) overlaid with FEM solution (dots). The NNFE method can accurately capture the twisting, as highlighted with the dotted centerline in the apical view. The mean nodal error between the NNFE solution and the FE solution was 2.32×10^{-2} mm, with a standard deviation of 4.53×10^{-2} mm.

REFERENCES

- [1] Liu H, et al., Scientific Reports 11.1 (2021): 1-15.
- [2] Krishnamurthy A, et al., J Comput Phys 244 (2013): 4-21.
- [3] Corsini C, et al., Comput Methods Biomech Biomed Engin 17.14 (2014): 1572-1589.
- [4] Sacks M, et al., J Biomech Eng 144.12 (2022).
- [5] Kingma DP and Ba J, arXiv:1412.6980 (2014).
- [6] Zhang W, et al., 19th USNCTAM, Austin, TX.
- [7] Logg A., et al., Automated Solution of Differential Equations by the Finite Element Method, Springer (2012).

MULTI-MODAL ANALYSIS OF INTRACRANIAL ANEURYSMS TO EXPLORE THE RELATIONSHIP BETWEEN WALL ENHANCEMENT, PHENOTYPE, INTERNAL STRESS, AND INTRASACCULAR HEMODYNAMICS

Jay P. Shah (1), Sricharan S. Veeturi (2), Nandor Pinter (2), Ammad A. Baig (2), Munjal Shah (3), Tatsat R. Patel (2), Adnan H. Siddiqui (2), Vincent M. Tutino (1,2,3,4)

(1) Department of Biomedical Engineering, University at Buffalo, Buffalo, NY, USA

(2) Department of Neurosurgery, University at Buffalo, Buffalo, NY, USA

(3) Department of Mechanical Engineering, University at Buffalo, Buffalo, NY, USA

(4) Department of Pathology and Anatomical Sciences, University at Buffalo, Buffalo, NY, USA

INTRODUCTION

Intracranial aneurysms (IAs) are weak bulging spots in the cerebral vasculature, that when ruptured, are associated with high mortality and morbidity rates. Currently, the rupture risk of a newly-discovered IA is evaluated based on its size at the time of imaging and the clinical parameters of the patient. Yet, IA size is subjective, and 49% of all ruptured IAs are small [1]. Recently, vessel wall enhancement (VWE) has emerged as a potential imaging biomarker for IA risk stratification. This is a phenomenon where higher signal intensity is observed on contrast enhanced MRI (CE-MRI) compared to a baseline non-enhanced MRI (NE-MRI). Aneurysms exhibiting VWE have been shown to be more unstable and prone to rupture [2]. However, the underlying pathobiology of VWE is poorly understood.

Past studies have shown that VWE is associated with aberrant intra-aneurysmal flow and wall forces, which could lead to disequilibrium in the IA wall, thus potentiating its growth or rupture. To estimate the forces being exerted on the IA wall, tools such as computational fluid dynamics (CFD) and finite element analysis (FEA) are used. In this study, we sought to investigate the underlying relationship between VWE, physical forces in the IA wall and the histopathology of the aneurysm. To this end, we used intraoperative imaging obtained during aneurysm clipping to identify different wall phenotypes (i.e., atherosclerotic, normal, and thin-walled regions), and performed patient-specific FEA and CFD to quantify hemodynamics and wall stresses in the IA tissue. We then quantified the differences in hemodynamic forces and wall stress between different wall phenotypes.

METHODS

We retrospectively collected MRI scans of patients who had undergone VWE imaging protocol at our center and were treated using surgical clipping (Study 00004370). Intraoperative videos taken during microsurgical clipping were used to identify the frame where the IA was best visualized. From this image, different IA wall phenotypes were

quantified (here, purple crimson/pinkish = ‘Normal’, dark red = ‘Thin’, and tan/whitish/yellowish = ‘Thick/atherosclerotic’) using an objective and automated image processing pipeline as described previously [3]. We used a previously-developed pipeline to generate 3D maps of normalized VWE for each case using a combination of time-of-flight MRA and CE-MRI [4] (see workflow in Figure 1). The signal intensity on the IA sac in the CE-MRI image was normalized to the average intensity in the corpus callosum of the same CE-MRI scan (Equation 1).

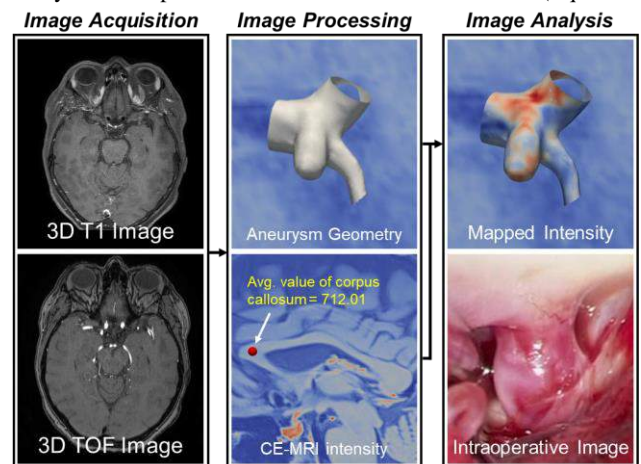


Figure 1: Workflow for 3D mapping of VWE – We register the T1 CE-MRI and TOF MRA image. We compute the average intensity at the genu of corpus callosum and use it to normalize the mapped intensity. We compare mapped VWE intensities of different wall phenotypes observed on intraoperative imaging.

$$CC_{ratio} = \frac{\text{Avg. Intensity of Aneurysm Sac}}{\text{Avg. Intensity of CC}}$$

Next, we used the segmented MRA image to perform CFD and FEA. CFD was performed as described in previous studies [5]. For FEA, we used a uniform wall thickness of 86 μm and a uniform pressure of 100 mm Hg. We computed the sac averaged normalized wall shear stress (WSS) and sac averaged von mises stress. We then analyzed the median VWE intensity, hemodynamic quantities and stress values in regions of different wall phenotypes.

RESULTS

Two patients who received VWE MRI scans were treated using surgical clipping. For both cases (Case 01 and Case 02), a sufficient proportion of the total sac area was visible on intraoperative imaging. Of note, Case 01 had the top of the dome covered entirely during the intraoperative video. For Case 01, thick regions showed the maximum intensity of 0.865. Normal regions had an intensity of 0.824 which was less than the thick regions. The least intensity values were for thin regions of 0.748.

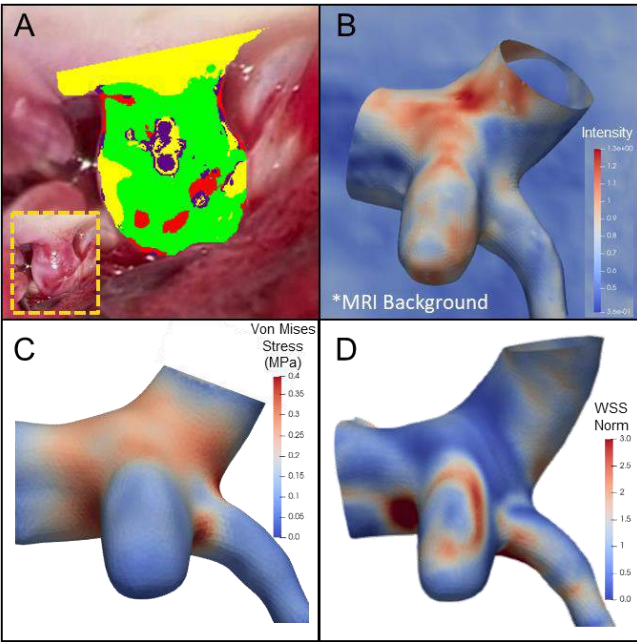


Figure 2: Aneurysm presentation, imaging quantification, and stress calculation for Case 01. Qualitatively, we observed a spatial relationship between the wall phenotype on intraoperative imaging (A), the VWE intensity (B), Von Miese stress from FEA (C), and WSS_{Norm} from CFD (D).

For case 02, thick regions showed the intensity of 1.04. For thin and normal regions, the intensity was slightly lower (1.02 and 0.9856, respectively). In case 02, the highest intensity was shown by thick regions, as in Case 01, but the normal regions had the lowest intensity. Thin regions intensity was higher than that in the normal regions.

From CFD analysis, we found that in Case 01, thick atherosclerotic regions had a lower normalized wall shear stress (WSS_{Norm}), higher relative residence time and a higher negative wall shear stress divergence (WSSD). However, in Case 02, we observed that this trend was reversed where thick, atherosclerotic regions had high WSS_{Norm} and low RRT. However, WSSD was still negative in thick regions.

Through our FEM analysis, we found that thick regions consistently had higher stress values in the IA wall as compared to the thin and normal regions in both Case 01 and Case 02.

Table 1: Median VWE, hemodynamic and stress values in different IA wall phenotypes as observed on intraoperative videos

	Thin Wall	Normal Wall	Thick Wall
Case 01 (Percent Wall)	9.3%	68.3%	14.0%
Norm. VWE Intensity	0.748	0.824	0.865
WSS _{Norm}	1.427	1.154	0.578
RRT (Pa ⁻¹)	0.056	0.069	0.140
WSSD (Pa/m)	-221.35	-381.74	-586.62
Von Mises Stress (MPa)	0.109	0.142	0.153
Case 02 (Percent Wall)	16.6%	53.8%	26.3%
Norm. VWE Intensity	1.020	0.986	1.04
WSS _{Norm}	0.1822	0.325	1.438
RRT (Pa ⁻¹)	1.466	0.810	0.182
WSSD (Pa/m)	47.587	289.995	-966.34
Von Mises Stress (MPa)	0.245	0.270	0.302

DISCUSSION

In the current multi-modal analysis of IA wall phenotypes, we found that thick regions observed on intraoperative images had higher VWE intensity. Past histopathological studies have also found similar trends. A study by Matsushige et al. found that IAs exhibiting focal VWE had an intraluminal thrombus at the location of VWE [6]. Furthermore, we found that the thick regions had a lower WSS_{Norm}, higher RRT and higher negative WSSD. Previous studies exploring the relationship between hemodynamics and intraoperative wall appearance found that low WSS and high RRT were related to recirculation zones in the IA, which could promote lipid deposition and atherosclerosis [7]. We also found that the thick regions had a higher negative WSSD in both cases. WSSD is indicative of the orientation of WSS vectors and the stretch force on the wall. A higher negative WSSD promotes contractile forces in the IA tissue that could promote thicker walls with atherosclerosis [8]. Finally, through FEA we consistently found that thinner regions in the IA sac had higher values of stress which could lead to damage of mural cells and hence thinner wall.

There are several limitations to this study which we are currently addressing. Firstly, our sample size of n=2 was too small for statistical analyses. Secondly, the 3D geometry of the IA was manually oriented to match the intraoperative videos which can introduce subjectivity.

ACKNOWLEDGEMENTS

Funding for this work was provided by the Brain Aneurysm Foundation. We thank UB's Center for Computational Research for providing high-performance clusters for our simulations.

REFERENCES

1. Froelich, JJ et al., World Neurosurg, 91: 260-265, 2016.
2. Edjlali, M et al., Radiology, 289: 181-187, 2018.
3. Veeturi, SS et al., J Cardiovasc Dev Dis., 9: 424-435, 2022.
4. Veeturi, SS et al., Diagnostics, 11: 1742-1753, 2021.
5. Veeturi, SS et al., R Soc Open Sci., 8, 2021.
6. Matsushige, T et al., World Neurosurg., 127: e578-e584, 2019.
7. Cebal, J et al., Am J Neuroradiol., 40: 510-516, 2019.
8. Suzuki, D et al., J of Biomech Sci and Engg., 23: 762-767, 2002.

QUANTITATIVE RAMAN MEASUREMENT OF CARTILAGE COMPOSITION VIA TISSUE PHANTOM CALIBRATION

Erik Ersland (1), Dev Mehrotra (2), Mark W. Grinstaff (2), Brian D. Snyder (3), Mads S. Bergholt
(4), Michael B. Albro (1,2)

(1)Mechanical Engineering, Boston University, Boston, MA, USA

(2)Biomedical Engineering, Boston University, Boston, MA, USA

(3)Department of Orthopaedics, Beth Israel Deaconess Medical Center, Boston, MA, USA

(4)Center for Craniofacial & Reversative Biology, King's College London, London, UK

INTRODUCTION

Osteoarthritis (OA) is a common and debilitating disease caused by the breakdown of articular cartilage. The composition of healthy articular cartilage is optimized for its mechanical performance, comprised of water and negatively charged sulfated glycosaminoglycans (GAG) constrained by a fibrous type-II collagen network (COL). Early-stage cartilage degeneration is characterized by changes in the composition of the tissue—notably loss of sulfated GAG and/or tissue swelling—contributing to mechanical softening, followed by more severe erosion of the collagen network. Biochemical assays and histological staining have long served as gold standards for characterizing cartilage composition in response to pathologic degeneration or treatment [1]. However, these methods are sample destructive—as such, they are incompatible with clinical assessments or repeated-measure analysis of compositional changes in ex vivo and in vivo pre-clinical investigations.

Raman spectroscopy is an inelastic light scattering technique that yields a non-destructive, quantitative, point-wise optical fingerprint of a tissue's molecular building blocks (amides, sulfates, carboxylic acids, and hydroxyls), thus allowing recognition of the predominant molecular constituents of articular cartilage: GAG, COL, and H₂O. In our prior work, we established the capability of optical biomarkers derived from Raman probe-based measures to correlate with the composition (GAG, H₂O) and mechanical properties of articular cartilage tissue specimens, thus establishing the potential of Raman to be used as a novel tool for non-destructive assessments of cartilage health in pre-clinical and clinical investigations [2]. However, Raman biomarkers are defined in spectral intensity units, and as such, provide only semi-quantitative assessments of tissue composition.

In the current study, we explore the capability of using compositional tissue phantoms to convert acquired relative Raman biomarkers from cartilage tissue specimens to absolute biochemical concentration values. Tissue phantoms are composed of hydrogels with prescribed ratios of the key constituents of cartilage and used to generate

a high-quality training data set that converts non-linear, relative Raman biomarker measures into absolute biochemical concentrations of GAG, COL, and H₂O. This conversion algorithm is validated with an in vitro model system, whereby live cartilage explants are monitored in response to a range of biochemical compositional changes akin to those present in early OA, consisting of—1) GAG depletion induced by media supplementation of the catabolic cytokine interleukin-1 α (IL-1 α) [3], and 2) cartilage swelling induced by culture in the absence of the corticosteroid dexamethasone (DEX) [4]. Phantom-calibrated quantitative Raman measures are compared to standard assay techniques for validation.

METHODS

Explant Culture: Cylindrical disks ($\varnothing 3 \times 2$ mm) of deep zone cartilage were harvested from immature bovine femoral condyles. Explants were cultivated in high glucose DMEM (1mM Na pyruvate, 50 μ g/mL L-proline, 1% PS/AM antibiotic/antimycotic, 50 μ g/mL ascorbate-2-phosphate, 0.1% BSA) \pm DEX (100nM) to induce a variable degree of tissue swelling and \pm IL-1 α (50ng/mL) to induce a variable degree of GAG depletion. After 0, 6, 10, or 14 days of culture, explants were subjected to Raman, mechanical (compressive Young's modulus [E_Y], and biochemical analysis (H₂O content and DMMB-measured GAG content). Additional groups were cultured for 15 days without IL-1 α , followed by IL-1 α for subsequent 6 days in an attempt to induce GAG depletion after significant swelling.

Phantom production: GAG (bovine trachea chondroitin sulfate; Sigma) and hydrolyzed collagen (gelatin from bovine skin; Sigma) powders were mixed at prescribed ratios in PBS in Eppendorf tubes to produce 25 phantoms with every combination of 5 concentrations of GAG (0%, 2.5%, 5%, 7.5%, and 10%), 5 concentrations of collagen (0%, 5%, 10%, 15%, 20%), and corresponding H₂O (H₂O%=100%-GAG%-COL%) (fig 1d). Tubes were mixed at 10-30 RPM (56°C) for 3 hours, followed by casting 50 μ L of each phantom into an aluminum sample pan for Raman analysis.

Raman Spectroscopy: Raman spectra of explants and phantoms were acquired via a commercial RIP-RPB-785 probe (Ocean Insight), a 785nm fiber-coupled laser (Innovative Photonic Solutions), and a QEPro spectrometer (Ocean Optics). The spectral fingerprint range (800-1800cm⁻¹) was preprocessed and subjected to a multivariate least-squares linear regression model to calculate the relative contribution, or ‘scores’ of the predominant cartilage constituents (GAG, COL, and H₂O) using equation: $\text{Cartilage}_{\text{spectra}} = \text{GAG}_{\text{score}} * \text{GAG}_{\text{REF}} + \text{COL}_{\text{score}} * \text{COL}_{\text{REF}} + \text{H}_2\text{O}_{\text{score}} * \text{H}_2\text{O}_{\text{REF}}$, where **GAG_{REF}** **COL_{REF}** **H₂O_{REF}** are the spectra of purified reference chemical [2] (Fig 2a,b). The areas under the OH and CH₂ peaks in the Raman high-wavenumber region was measured to yield two additional metrics related to tissue hydration and organic content, respectively.

Phantom Calibration: The concentration of each constituent was estimated using a 2D polynomial curve-fit of two Raman metrics using the Matlab curve fitting toolbox (poly22 sfit object). A representative curve-fit it depicted in Fig 2D. Raman scores were selected by minimizing model error against known constituent concentrations in phantoms. Model performance was then validated against assay-measured GAG and H₂O contents in cultured explants.

RESULTS

Explant model: The following explant trends were observed (Fig 1A-C): For +Dex/-IL1 α , explants exhibited only modest changes in GAG, H₂O, and EY over time. For -Dex/-IL1 α , explants increased H₂O and lost EY over time. For +Dex/+IL1 α , explants lost GAG & EY but increased H₂O over time. For -Dex/+IL1 α , explants exhibited a further loss of GAG & EY and increased further in H₂O over time. These different treatment groups were able to produce explants with a wide range of compositions (Fig 1D), which allowed for assessment of the phantom conversion function over a wide range of compositional states.

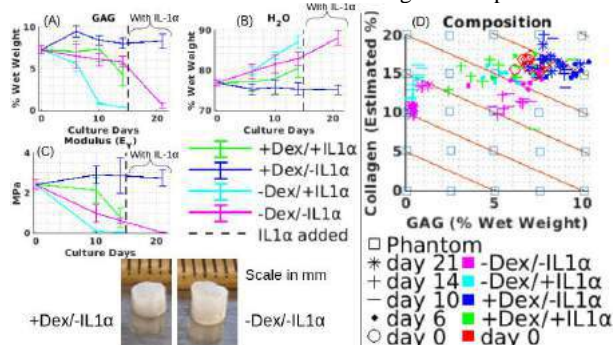


Figure 1:(A) GAG content, (B) H₂O content, and (C) EY of treated explants over time. The dashed line at day 15 is when IL-1 α was added to groups previously cultured without it. (D) Composition of all explants in terms of GAG and estimated collagen content.

Diagonal orange lines are isolines of equal H₂O concentration.

Raman phantom conversion: The spectral contribution of cartilage constituents generally reflected their concentration in the tissue—e.g., a lower GAG score observed for IL-1 α treated explants (Fig 2A&B) and higher OH area observed for -Dex explants (Fig 2C). Raman biomarker scores exhibited moderate-to-strong correlation with direct assay measures ($R^2=0.77$ to 0.84 ; Fig 3A-C). After phantom training set conversion, Raman was able to predict real concentration with a high degree of accuracy (Fig 3D-E). The 95% confidence interval for GAG was $\pm 2.5\%$ - 2.3% of the assay measured value. Similarly, the 95% confidence interval of H₂O estimation was $\pm 2.2\%$ - 3.1% . by correcting for cross talk from overlapping spectra, as seen in the improved R^2 .

DISCUSSION

This work advances a novel Raman assay platform for achieving non-destructive quantitative measures of cartilage biochemical composition. The in vitro cultivation of cartilage explants serves as a unique model

to explore the ability of phantom-trained Raman measures to accurately predict concentrations of biochemical constituents in cartilage for a wide range of degenerative states, where the relative proportions of GAG, COL, and H₂O vary in the tissue. The temporal application of Dex depletion and/or IL-1 α exposure, allows for a parametric variation of combined tissue swelling and GAG depletion serving to test the technique’s ability to measure the degenerative modes observed in OA pathology. Our phantom-training set provides a mapping function that converts Raman biomarker scores to highly accurate measures of the concentration of biochemical constituents in cartilage, as evidenced by tight 95% confidence intervals when comparing predictions to direct assay measures of GAG and H₂O. In the future, we aim to further compare predictions of COL to assay measures.

This platform can serve as a standardized analytical tool to non-destructively quantitatively measure the composition of cartilage in response to degeneration and treatment across a range of preclinical and clinical R+D model systems, spanning from ex vivo explant studies, to in vivo animal studies, to RCT clinical trials. Clinically, quantitative Raman monitoring of patients can be performed arthroscopically for measures of cartilage composition in patients, allowing for earlier and more precise determination of tissue pathology and evaluation of tissue response to treatment.

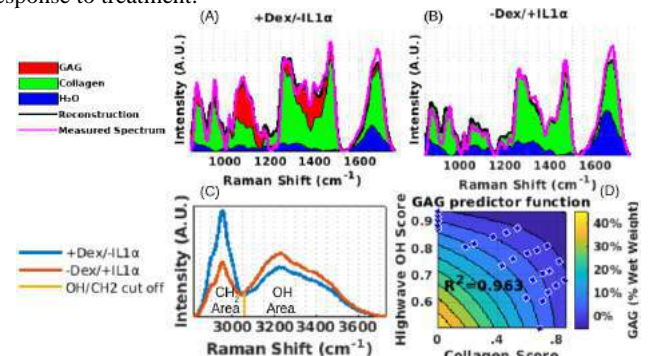


Figure 2: Representative stacked area plots of Raman fingerprint spectra for (A) +Dex/-IL1 α and (B) -Dex/+IL1 α groups. (C) Representative high-wavenumber spectra from the same. (D) 3D contour plot of Raman corrector function predicting GAG.

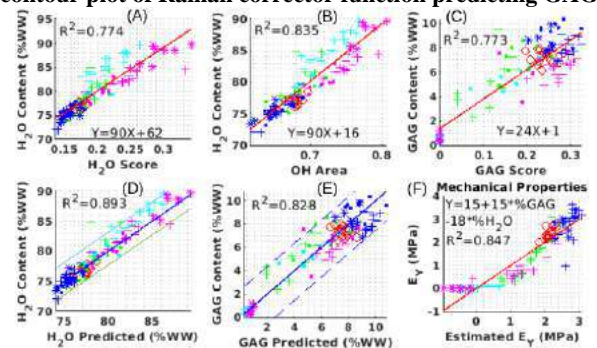


Figure 3: (A-E) Correlation of Raman metrics to biochemically measured composition before and after phantom correction. (F) Shows the correlation of mechanical properties to Raman estimates of GAG and H₂O concentration.

ACKNOWLEDGEMENTS: This work is supported by the NIH (AR081393), Arthritis Foundation, Musculoskeletal Transplant Foundation, and Boston University MSE Innovation Award.

REFERENCES : [1]Waldstein, W et al., J orthop Res., 34(1):135-40, 2016 [2] Kroupa+2021 J Orthop Res. 40(6):1338-1348 [3] McNulty+2013 J Orthop Res,31(7):1039-45. [4] Durney+2019 J Biomech Eng, 141(2):021004..

AN ANTHROPOMORPHIC, ACTUATED WRIST FOR ACHIEVING BIOMIMETIC MOTION OF A ROBOTIC HAND

Jonathan M. Rooney (1), Samantha T. Johnson (2), Chiara Bellini (3)

(1) Department of Mechanical Engineering, Northeastern University, Boston, MA, USA

(2) Tatum Robotics, Hudson, MA, USA

(3) Department of Bioengineering, Northeastern University, Boston, MA, USA

INTRODUCTION

A functionally accurate artificial hand has long been a major focus for roboticists, and critical to that goal is a robotic wrist that can match the human wrist for strength and range of motion. The wrist provides the hand with the majority of its flexibility, allowing for a much finer degree of positioning than is achievable with the shoulder and elbow joints alone. As such, a robust artificial wrist that can achieve most or all of the natural wrist's range of motion is an invaluable development for prosthetics, anthropomorphic or surgical robotics, and other areas where human-like motions would be desirable.

The difficulty of replicating the human wrist lies in its complexity. The wrist proper, consisting of the eight carpal bones and associated anatomy, has two degrees of freedom (DoFs): flexion/extension of the palm, and radial/ulnar deviation (abduction/adduction) of the hand. Additionally, the wrist joint is commonly understood to include the distal heads of the radius and ulna, which add pronation/supination as a third DoF. The precise ranges of motion of these DoFs vary from individual to individual; average values for each are given in Table 1. Achieving these values is not in itself prohibitive; indeed, a standard 3-axis gimbal can approximate or even greatly exceed the natural wrist's range of motion. However, active actuation of such a design poses challenges for maintaining an anthropomorphic footprint, especially for applications where strength and durability are key design factors.

As such, most prosthetic wrists currently on the market are single-DoF devices that include only pronation/supination, either actively or passively actuated. More advanced prostheses, such as the Fillauer Four Function Wrist, incorporate flexion/extension or ab/adduction, but these almost always employ passive friction joints which are externally actuated—typically by the user's other limb or by the environment—and can be locked to pre-position the hand for a given task [1]. Fully actuated devices that can match the natural wrist's three degrees of freedom are more commonly encountered in industrial or research settings, but are typically large, heavy, and deferential to function over

form. Devices such as the Omni-Wrist III achieve a biomimetic range of motion via multi-axis motion platforms rather than a more naturalistic gimbal [2], but the complex linkage structures of these wrists pose challenges for presenting an anthropomorphic form factor. Our project's goal is to address each of these shortcomings, developing a strong, durable three-DoF wrist that is actively actuated and conforms to the anthropomorphic appearance needed for prosthetics and humanoid robotics. Our primary motive is to support the work by Johnson *et al.* in developing a robotic hand to communicate with DeafBlind individuals using tactile American Sign Language (ASL) [3]; however, we hope the resulting wrist can serve as a flexible platform for applications with similar requirements.

METHODS

The wrist was designed to achieve at minimum the range of motion given in Table 1, and to do so via self-actuation. The actuators used are Dynamixel servomotors, chosen for their flexibility, speed, ease of control, and low cost. All structural components are 3D-printed in nylon. To achieve the required degrees of freedom, the wrist uses three joints arranged in series: first pronation/supination, then ab/adduction, and finally flexion/extension just below the end effector (Fig. 1A).

To accommodate cable pass-through, the pronation/supination joint (Fig. 1B) uses an internally driven ring gear. A lower support plate holds the drive motor, a single Dynamixel XL330-M077-T, and provides an attachment point for the wrist to a base; an upper plate houses the ring gear and connects to a forearm structure. A needle-roller thrust bearing between the two support plates supports transverse loads, and a central shoulder screw-ball bearing assembly connects the plates and supports lateral loads. The support plates are slotted to accommodate a 12mm-diameter cable bundle through 180° of motion, and a 3:8 gear ratio allows the joint to rotate 180° in 1.1 seconds (chosen to achieve a speed of 1 letter per second with the Tatum ASL hand). The joint is located 130mm below the next joint axis, chosen to center the

rotation roughly halfway down the average forearm; a shorter or longer distance could be used if required.

The ab/adduction and flexion/extension joints (Fig. 1C) each form one yoke of a modified universal joint structure, with the central crosspiece designed to approximate the structure of the eight carpal bones. To match the natural wrist's centers of rotation, the crosspiece separates the joint axes by 20mm. Both joints ride on ball bearings for free movement, and the crosspiece is hollow to allow for cable pass-through into the end effector. The joints are Bowden cable-driven using nylon-coated steel wire rope, running through surgical spring guides to remotely mounted Dynamixel XC330-M288-T motors. The cables for the ab/adduction joint terminate in the crosspiece, with their spring guides anchored in the forearm; the flexion/extension cables form a continuous loop through the base of the end effector itself, with their spring guides anchored in the crosspiece. This staging of the joints completely decouples the axes from each other, allowing the wrist to rotate in any one axis without affecting the rotation of the other two.

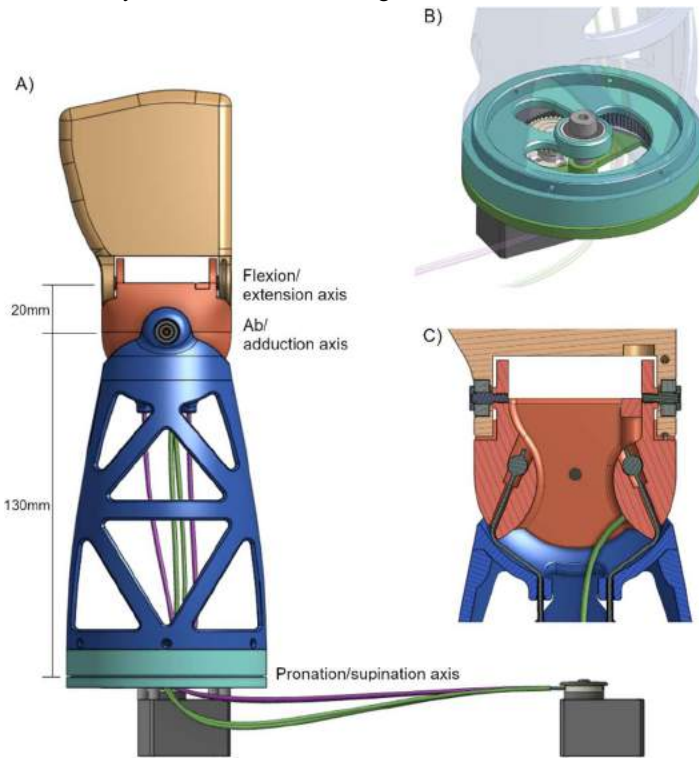


Figure 1: (A) Overview of the proposed wrist, with separation between axes indicated. (B) Detail of pronation/ supination joint, showing gearing and cable passthrough. (C). Section through crosspiece, showing cables and spring guides for the flexion/extension and ab/adduction joints.

RESULTS

As the wrist was designed to support the development of a robotic hand that can communicate in tactile ASL, validation trials with DeafBlind individuals constituted a valuable performance metric. These trials consist of the user holding the back of the robot's hand while it signs letters, allowing them to feel its motions. Results were very promising: the users achieved a letter recognition rate upwards of 90% (N=5), indicating that the wrist's motions felt comparable to those of a natural wrist.

Objective testing was also performed to validate the wrist's range of motion and durability. The wrist exceeded its motion targets in

flexion, abduction, and pronation/supination, but failed to achieve its targets for extension and adduction (see Table 1). To assess durability, each joint was run through its full range of motion in two-second intervals. The gear-driven pronation/supination joint proved durable, readily performing 10,000 cycles and showing no signs of wear. The cable-driven joints, however, each lasted roughly 5,000 cycles before the cables frayed to the point of breaking. The tactile ASL end effector uses two wrist motions each for the letters g, h, j, p, q, y, and z, which collectively have an estimated English frequency of 11% [4]; with a 5,000-cycle lifespan, we would thus expect the hand-wrist unit to form roughly 23,000 letters before servicing was required.

Table 1: Typical ranges of motion for the natural wrist [1], along with those achieved by the designed wrist

Motion	Range of motion		
	Natural wrist	Designed wrist	Percent difference
Flexion	75°	94°	+25.3%
Extension	75°	73°	-2.7%
Abduction	20°	37°	+85.0%
Adduction	45°	37°	-17.8%
Pronation	76°	90°	+18.4%
Supination	85°	90°	+5.9%

DISCUSSION

We feel that the designed wrist successfully captures human motions in all three axes and represents a strong foundation for further refinement. One priority is to improve the range of motion for extension and adduction; minor mechanical alterations should be sufficient. The other major priority is improving the durability of the cable-driven axes, as the estimated 23,000 letters is insufficient for lasting use. Potential solutions include smoothing edges to reduce concentrated stresses, experimenting with lubrication and material selection to reduce friction, or increasing cable diameter. Additionally, future trials will assess the wrist's exerted force in comparison to that of a human wrist, as concrete force measurements would be useful for generalizing the wrist as a platform for various end effectors.

Despite these ongoing focuses, the design shows promise towards an anthropomorphic, actuated wrist that can mimic natural motions. Through further iterations, we hope to increase the wrist's durability in order to stand up to day-to-day wear on a prosthetic or humanoid robot. With the success seen in trials with DeafBlind users, our proposed wrist shows great potential for achieving proper biomimetic functionality in an anthropomorphic form factor; additional generalizations would make it usable as a multi-purpose wrist platform for humanoid robotics.

ACKNOWLEDGEMENTS

We would like to thank Tatum Robotics for commissioning this project, along with Northeastern University and the Institute for Experiential Robotics at NEU for their ongoing development support.

REFERENCES

- 1] Bajaj, N. M. et al., *IEEE Trans Robot*, 35:261-277, 2019.
- 2] Sofka, J. et al., *IEEE Trans Aerosp Electron Sys*, 42:718-725, 2006.
- 3] Johnson, S. T. et al., "A Low-Cost, Open-Source Robot Hand-Wrist System for Tactile-ASL Based Communication for the Deaf Blind", 2021.
- 4] Grigas, G., *Int Ling*, 1:18-32, 2018.

MICROMECHANICAL RESPONSE OF FIBROUS NETWORKS SUBJECTED TO FAR FIELD AND LOCAL CONTRACTILE FORCES

Ashutosh Mishra (1), Hamed Hatami-Marbini (1)

(1) Department of Mechanical and Industrial Engineering, University of Illinois Chicago, Chicago, Illinois, USA, Email: hatami@uic.edu

INTRODUCTION

The primary structural component of wide number biological and non-biological materials is a network of randomly interconnected semiflexible cross-linked fibers. These random fibrous networks can be found in non-living materials such as paper, cloth and in the biological materials such as cytoskeleton and soft tissue [1]. These random structures in biological materials provide the structural integrity and facilitate cellular movement [2]. One such biological material made up of random fibers is the extracellular matrix (ECM) which is ubiquitous in all tissues and organs. The ECM is made-up of multiple macromolecules namely the proteoglycans and fibrous proteins such as collagen, elastins, fibronectins, and laminins [2]. The collagen among others is the most abundant fibrous protein and can be found in the ECM of cornea, cartilage, tendons, and ligaments providing strength, facilitating tissue development, cell migration, and cell adhesion, playing a vital role in multiple physiological processes such as the fibrosis and wound healing [4].

One of the striking feature of these biological random networks, which is not found in synthetic networks, is the nonlinear strain stiffening behavior, wherein the stiffness of the network increases with increase in applied strain. A number of studies over the years have shown the presence of residual stresses or the prestress in biological networks. For instance, the presence of prestress in arteries is important for maintaining the state of homogenizing strain and providing reinforcement [5], or the prestress realigns and straightens collagen fibers in ECM towards the direction of the applied force. The fibrous networks under prestress behave differently than the relaxed networks. In particular, the prestress is known to stiffen or soften the networks under extension or compression and thereby affecting their mechanical response [6-7].

In addition to the far-field force and internal prestress, the biological networks could also experience local contractile forces applied by the shape changing contracting cells resulting into local

stresses and deformation field. Studies have shown that these local forces can give rise to prestress in networks, which in turn play a role in remodeling the network architecture and facilitating long-range displacement propagation [8][9]. It would be interesting to combine the two effects namely the prestress and local contractile forces and study the mechanical response of the random fibrous network as it can provide better insights into the mechanical behavior of biological networks and understanding the cell mechanosensing, long-range displacement propagation, and cell-matrix interactions.

METHODS

A 2D model is created from a regular triangular lattice network of size $W \times W$, fiber length l_0 and connectivity 6. The biological networks are subisostatic structures and their connectivity is often between 3 and 4. Thus, the triangular lattice network is diluted by removing fibers with the probability of $1-P$ until the connectivity is under the Maxwell's threshold value of 4. P is the probability of fibers that are present in the networks. In this work, we use networks with average connectivity of about 3.3, which is comparable to the typical connectivity of collagen networks. The fibers in the network are modeled as athermal planar beam elements having circular cross-section with area A , elastic modulus E and moment of inertia I . The axial modulus μ and bending modulus κ of the fibers are $\mu=EA$ and $\kappa=EI$, respectively. The dimensionless bending rigidity is defined as $\bar{\kappa} = \kappa/\mu l_0^2$ and is considered to be 10^{-4} in this study unless stated otherwise. Furthermore, the fibers in the network are meshed into multiple elements to capture the deformation of the fibers accurately.

First, the effect of prestress on the shear response is studied. To analyze the network under prestress (ϵ_{ps}), the network is uniaxially stretched or compressed by displacing the nodes at the top horizontal boundary either vertically upwards or downwards. The nodes at the bottom horizontal boundary are fixed. Then, the shear strain is applied by displacing the nodes at the top horizontal boundary following the

procedure stated in our previous work [7-8]. A finite element software is used to obtain the solution and displacements of all nodes. The shear stress is then calculated by dividing the sum of forces in the fibers intersecting the top horizontal edge by W . The differential shear modulus $K = d\tau/d\gamma$ is calculated using shear stress-strain curves, where τ is the shear stress and γ is the applied shear strain.

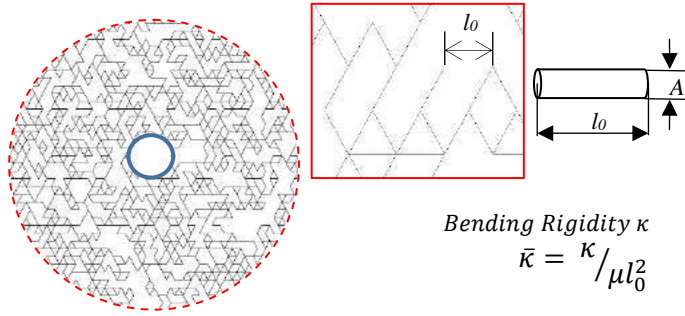


Figure 1: Random fibrous network generated from regular triangular lattice with fibers removed from the center to include the contractile cellular forces

To study the effects of local contractile forces, fibers are removed from a circular region with radius r from random fiber networks, Figure 1. The size effects are curtailed by selecting the radius r such that the ratio of W/r is greater than 40. Next, the cellular contraction forces are applied by isotropically displacing the nodes at the boundary of the empty central circular domain radially inward while keeping the nodes at the network boundary constrained at their respective position. The contraction of 25% in increments of 5% is applied. To track the propagation of displacements within the fibrous networks, the radial displacements U_R vs the radial distance R is plotted and the data is fit to the following equation [9].,

$$U_R = AR^{-n} + BR^n \quad (1)$$

The unknown variables A , B , and n are found using a nonlinear least square fitting algorithm.

RESULTS

The differential shear modulus of the network under applied shear strain for different values of prestress studied on network without the central inclusion region is shown in Figure 2. It is seen that the nonlinear variation of shear modulus is a function of the applied prestress. Furthermore, the radial displacement U_R as a function of radial distance R is plotted in Figure 3(a) for networks with a contractile local force. It is seen that the radial displacement significantly decreases with increasing the distance from the center of the network. The rate of decay n depends on the amount of contractile force and applied prestress. Figure 3(b) shows dependence of the decay rate n as a function of contractile deformation. It is noted that $n=1$ is the displacement decay rate that is obtained from the classical linear elasticity theory.

DISCUSSION

The results here clearly show that the shear modulus and the onset of strain-stiffening is a function of applied axial prestress to the networks, Figure 2. When the applied axial prestress is tensile, the shear modulus is observed to increase proportional to the magnitude of prestress. However, the shear modulus is observed to decrease with compressive prestress. This indicates that the shear modulus of networks become stiffer with the prestress extension and softer during the prestress compression. This behavior is because prestressing the

network reorients fibers in the direction of (or away from) loading thereby increasing the shear response in tension (or decreasing it in compression). With increasing the local contractile deformation, the displacement is seen to propagate further in the networks, Figure 3. The possible mechanisms for such behavior are compression weakening and fiber reorientation [9]. These are interesting findings and lay the foundation for ongoing investigations where combined effects of prestress and local contraction on the fibrous networks are investigated, aiding us in better understanding of interesting mechanical response of fibrous biological networks such as ECM and cytoskeleton.

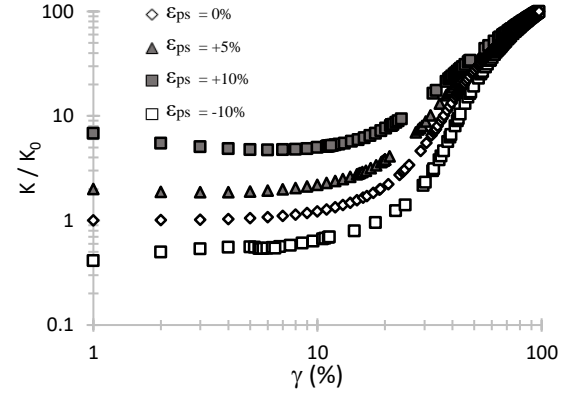


Figure 2: The effect of axial prestress strain ϵ_{ps} on the normalized differential shear modulus where K_0 is the initial shear modulus.

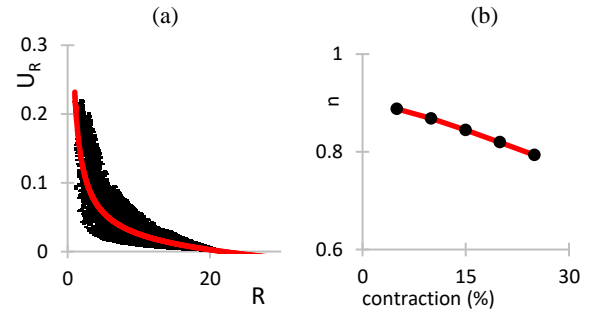


Figure 3: (a) Radial displacement U_R vs radial distance R . The solid line is the numerical fit that is obtained from equation (1); this figure is plotted for 20% contraction. (b) The change in the values of n in equation (1) with changing contraction percent.

ACKNOWLEDGEMENTS

The authors would like to acknowledge the ACER computational resources at UIC.

REFERENCES

- [1] Broedersz C. P. et al., Rev. Mod. Phys., 86, 3, 995–1036, 2014.
- [2] Alberts B, et al., Molecular Biology of the Cell. 4th edition, New York: Garland Science; 2002.
- [3] Hatami-Marbini H. et al., Exp. Eye Research, 116, 47–54, 2013.
- [4] Li B. et al., J of Tissue Viability, 20, 4, 108–120, 2011.
- [5] Destrade M. et al., J of Theoretical Biology, 303, 93–97, 2012.
- [6] Vahabi M. et al., Soft Matter, 12, 22, 5050–5060, 2016.
- [7] Hatami-Marbini H. et al., Biophysical J, 120, 3, 527–538, 2021.
- [8] Hatami-Marbini H. et al., International J of Solids & Structures 228, 111045, 2021.
- [9] Grimmer P. et al., J of Biomechanical Engg, 140, 4, 2018.

INTERSTITIAL CHEMOKINE GRADIENTS AND DENDRITIC CELL MIGRATION DURING INFLAMMATION

**Matthew J. Russell (1), Francesca Fasanella Masci (2), Willy V. Bonneuil (3), Daniel J. Watson (4),
Jennifer Frattolin (4), James E. Moore Jr. (4), Robert J. B. Nibbs (2), Bindi S. Brook (1)**

(1) School of Mathematical Sciences, University of Nottingham, Nottingham, UK

(2) School of Infection & Immunity, College of Medical, Veterinary and Life Sciences, University of Glasgow, Glasgow, UK

(3) KTH Royal Institute of Technology, Stockholm, Sweden

(4) Department of Bioengineering, Imperial College London, London, UK

INTRODUCTION

The main role of dendritic cells (DCs) lies at the interface between the innate and adaptive immune systems. DCs are antigen-presenting cells: upon encountering an antigen while patrolling tissue, they capture and process the antigen and then migrate to a lymph node where they present the antigen, material to T cells. In order to migrate, DCs move up gradients of the chemokines CCL21 and CCL19, the two ligands of the receptor CCR7 that is expressed on the surface of DCs.

We present a mechanistic model of CCL21 gradient formation and DC migration within the interstitium during and after an inflammatory challenge. The model accounts for diffusion and advection of CCL21, binding of CCL21 to extra-cellular matrix (ECM), CCL21 cleavage by DCs, binding of CCL21 to CCR7 on DCs, random motion of DCs (modelled as diffusion), DC maturation, and haptotactic migration in response to CCL21 gradients. We simulate inflammation by varying parameters (representing certain biological processes, such as the rate of DC maturation) thought to take significantly higher values in inflammation compared to homeostasis.

Model parameter values are obtained from the literature where possible, including our previous works [1] and [2]. For the remaining unknown parameters we either infer their values from preliminary experimental data (in particular, specifically designed cleaving assays) or we perform simulations over a wide range of parameter values, allowing us to assess the sensitivity of key model outputs with respect to these parameters.

METHODS

Our model consists of a system of 7 coupled PDEs governing the dynamics of CCL21 and DCs in the interstitium. These are supplemented

with boundary conditions that impose chemokine and cell concentrations or fluxes at blood vessel (b.v.) and lymphatic vessel (l.v.) boundaries. For brevity, in (1) we show only the dimensionless equations governing the concentrations of unbound full-length chemokine, C_u , and mature DCs with ECM-bound chemokine bound to their CCR7, ϕ_{C_b} . The latter are the subset of DCs that migrate up local bound CCL21 gradients.

$$\partial_t C_u = \nabla^2 C_u - \mathbf{P} \mathbf{e}_u \cdot \nabla C_u - \alpha^+ \bar{E} C_u + \alpha^- C_b \quad (1a)$$

$$- N_{R7} \beta^+ C_u \phi_m + \frac{\bar{\phi}}{C} N_{R7} \beta^- \phi_{C_u} - \sum_{\ell=i,m} \gamma_{u,\ell} \phi_{\ell} C_u,$$

$$\partial_t \phi_{C_b} = \nabla \cdot (D_{\phi_{C_b}} \nabla \phi_{C_b}) - \nabla \cdot (\chi_b \phi_{C_b} \nabla C_b) + \alpha^+ \bar{E} \phi_{C_u} \quad (1b)$$

$$- \alpha^- \phi_{C_b} + \frac{C}{\bar{\phi}} \beta^+ C_b \phi_m - \beta^- \phi_{C_b}.$$

The haptotaxis term in (1b), $-\nabla \cdot (\chi_b \phi_{C_b} \nabla C_b)$, is of Keller-Segel form [3, 4] and models how DCs move up gradients of chemokine concentration. A number of variants of the Keller-Segel model can be found in the literature; see e.g. [5]. The Péclet number Pe , which is defined as the ratio of advective and diffusive fluxes, characterises the strength of the interstitial flow that advects unbound and soluble CCL21.

For simplicity, we consider the system (1) in one spatial dimension. We impose a flux of immature DCs (ϕ_i) into the interstitium from the b.v., and assume that migrating mature DCs (ϕ_{C_b}) move into the l.v. as soon as they reach it. All other types of DC have zero flux across the b.v. and l.v. boundaries. We assume unbound full-length chemokine (C_u) has (dimen-

sionless) concentration of unity at the l.v., and concentration zero at the b.v..

Initially, all parameters are set to their homeostasis values and simulations are run until a steady state is reached. Then a state of inflammation is simulated by increasing the immature DC ingress rate and DC maturation rate (Figure 1A). We also allow for a lag between the onset of inflammation and the increase in the DC ingress rate. This is to account for effects seen in preliminary experiments on the rat small intestine [personal communication, Nibbs RJB (2020)], data we used to estimate a number of homeostasis parameter values. When the period of inflammation ends, parameters are set back to their homeostasis values.

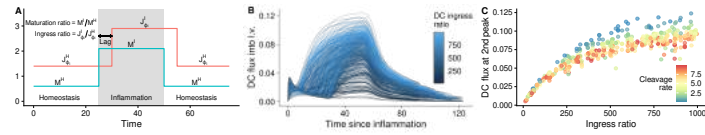


Figure 1: A: An illustration of the homeostasis–inflammation cycle and the corresponding changes in parameter values and ratio definitions. B: DC flux into l.v. for $Pe = -5$. C: DC flux into l.v. at the 2nd peak in panel B vs. ingress ratio, coloured by cleavage rate

RESULTS

We ran 600 simulations each for $Pe = \pm 5$. The flux of DCs into the l.v. for simulations with $Pe = -5$ is shown in Figure 1B, and Figure 1C shows how the DC flux at its 2nd peak depends on both the ingress ratio and cleavage rate. For each simulation, the delay in onset of the inflammation ingress rate, the cleavage rate, and the inflammation values for the immature DC ingress rate and maturation rate are drawn randomly. We then used Sobol indices to quantify the relative impact of the varied parameters on key outputs of the model. For example, Figure 2A shows how, for interstitial flow in either direction, the total number of cells that migrate into the lymphatic vessel over an entire simulation depends most significantly on the value of ingress ratio, with the other parameters playing smaller roles. Interestingly, the cleavage rate appears to have little effect when interstitial flow is towards the l.v. ($Pe < 0$), but its influence is stronger for opposite flow ($Pe > 0$). Figure 2B–E give a qualitative picture of how migrating cell numbers depend on parameter values to complement the Sobol indices: here we see that the total number of migrating cells increases with ingress ratio, which cannot be determined from Sobol indices alone.

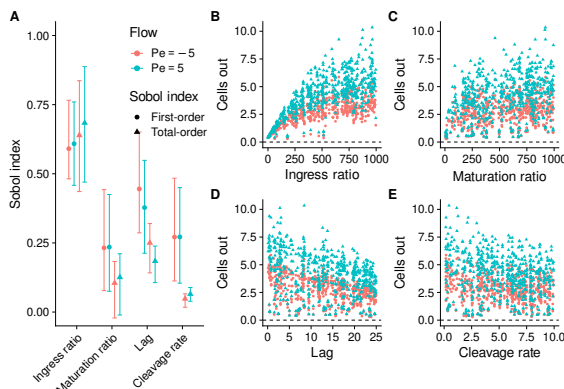


Figure 2: The influence of parameters on the total number of DCs that migrate into the lymphatic vessel. A: Sobol indices quantifying the relative impact of each parameter. B–E: Scatter plots of the total number of cells for each simulation vs. parameter values

To assess the qualitative effects of the unknown parameters on the spatial concentration profiles of ECM-bound CCL21 and migrating DCs we

ran another ensemble of simulations, with all combinations of the minimum and maximum parameter values in the previous ensembles, along with a range of Pe values representing different interstitial flow speeds and directions (Figure 3). In the homeostatic steady state, we observe that increased cleavage rate has a qualitatively similar effect on the bound CCL21 gradient as a reduction in Pe (Figure 3A). By the end of inflammation, spatial profiles for different parameter values reveal interactions between parameters (Figure 3B). For example, increasing the ingress ratio from 2 to 1000 significantly amplifies the effects of cleavage, whereas increasing the maturation ratio by the same amount has somewhat the opposite effect.

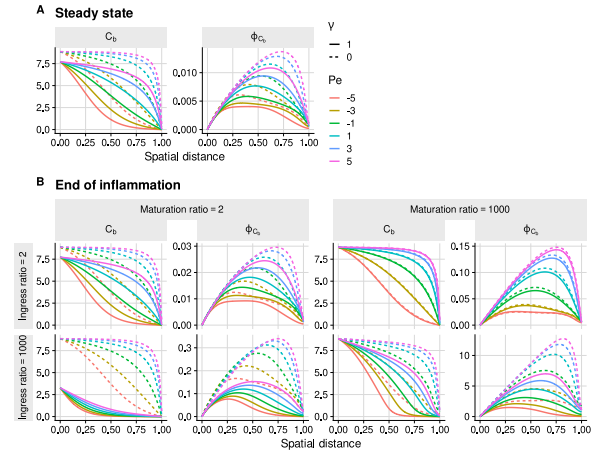


Figure 3: Spatial concentration profiles of ECM-bound CCL21 and migrating DCs

DISCUSSION

We have developed a mechanistic model of CCL21 gradient formation and dendritic cell migration towards lymphatics via haptotaxis and have evaluated their response during and after inflammation. For some parameter values that are not readily available we performed model simulations over a wide range of parameter values, and used sensitivity analysis to quantify the effects of parameters on biologically relevant model outputs such as the total number of DCs that migrate into the l.v.. Analysis of the spatial concentration profiles of ECM-bound CCL21 revealed that stronger flow towards the l.v. and a higher cleavage rate can have similar qualitative consequences on the bound CCL21 gradient. Furthermore, we found that the effect of CCL21 cleavage can depend strongly on the values of other parameters.

A first peak in DC flux across the l.v. during inflammation is to be expected, but the appearance of two peaks might not be (Figure 1B). However, this has been observed experimentally in inflammation of the rat small intestine.

Although we have included a number of biological processes in our model, it has a number of limitations, including: restricted to a 1D domain; DCs treated as a continuous density rather than individual agents; neglecting the effects chemotaxis according to soluble CCL21 gradients and chemokinesis.

ACKNOWLEDGEMENTS

Support from the Wellcome Trust Collaborative Award 206284/Z/17/Z.

REFERENCES

- [1] Jafarnejad M et al. *The Journal of Immunology* 199.7 (2017).
- [2] Kalogiros DI et al. *Frontiers in immunology* 10 (2019).
- [3] Keller EF et al. *Journal of theoretical biology* 26.3 (1970).
- [4] Keller EF et al. *Journal of theoretical biology* 30.2 (1971).
- [5] Hillen T et al. *Journal of mathematical biology* 58.1 (2009).

TRACKING THE RESPONSE OF A SUSTAINED DYNAMIC COMPRESSION DEVICE IN AN OVINE TARSAL FUSION MODEL

Erin E. Estrada (1), Jeremiah T. Easley (1), David L. Safranski (2), Dave Latt (3),
Naohiro Shibuya (4), Christian M. Puttlitz (1), Ben C. Gadowski (1)

- (1) Colorado State University, Fort Collins, Colorado
(2) Enovis Foot & Ankle, Atlanta, Georgia
(3) University of Arizona, Tucson, Arizona
(4) Veterans Memorial Hospital, Temple, Texas

INTRODUCTION

Charcot neuroarthropathy of the foot is a common degenerative disorder that occurs in patients with longstanding neuropathy due commonly experienced in diabetic patients. This progressive disease leads to severe deformities of the foot and limits a person's ambulatory capacity. Surgery is often the only therapeutic option and involves osteotomies to realign the bones of the foot and fusion with an intramedullary (IM) device to stabilize the arch. Success of this treatment depends on the ability of the device to obtain and maintain compressive force across the tarsals throughout the healing process. Commonly employed static devices experience loss of compressive forces due to bone resorption (often 3-5 mm) combined with patient weight-bearing[1], [2], which can lead to non-union, the need for revisional surgery, and even amputation. To address these issues, a sustained dynamic compression midfoot fusion device was developed using a pseudoelastic nickel titanium (NiTi) element. This NiTi element is housed within a titanium outer body and has been designed to contract up to 4mm thereby applying sustained dynamic compression across the fusion site despite bone resorption and/or joint settling. Human clinical studies have demonstrated the ability of dynamically compressive devices to continuously adapt to bone resorption[3], however, to our knowledge, there is currently no large animal model for tarsal arthrodesis and implant response to bone resorption. Therefore, this study investigated the use of a sustained dynamic compressive device designed to maintain bone-on-bone contact and compression between the tarsals throughout the healing process and alleviate the complications experienced that result from bone resorption and device loosening in a large animal (ovine) model. The aim of this study was to investigate the ability of a sustained dynamic compression IM nail to adapt to bone resorption across the tarsal joints in ovine models with normal bone quality and diminished bone quality induced by the placement of an external fixator.

METHODS

This study utilized 32 skeletally mature Rambouillet Cross ewes due to comparable anatomy and physiology of the ovine metatarsal and tarsal bones to those of humans. Animals were randomly allocated into 4 treatment groups with 8 animals in each group as outlined in **Table 1**.

Table 1: Animal Allocation and Treatment Groups

Group 1 (n=8)	Dynamic nail, 4-mo, partially unloaded with external fixator
Group 2 (n=8)	Dynamic nail, 4-mo, no unloading
Group 3 (n=8)	Dynamic nail, 8-mo, partially unloaded with external fixator
Group 4 (n=8)	Dynamic nail, 8-mo, no unloading

Approval for the surgeries performed on these animals was granted by the Colorado State University Animal Care and Use Committee (Approval No. #1199) and in accordance with the Animal Care and Use Review Office (Approval No. # PR191551). Surgery was performed under general anesthesia and aseptic conditions. Groups 1 and 3 underwent surgery to place an external fixator spanning from the tibia to the distal end of the metatarsus to unload the hock joint for one month prior to nail implantation[4]. The fixator was removed immediately prior to the implantation of the nail. The dynamic IM nail was inserted through the calcaneus and advanced to span the calcaneus-tarsus-metatarsus complex and fixed using transverse screws (**Figure 1**).



Figure 1: Radiograph of implanted dynamic nail.

Serial radiographs were taken every four weeks to track bone resorption and/or joint settling (**Figure 2**).

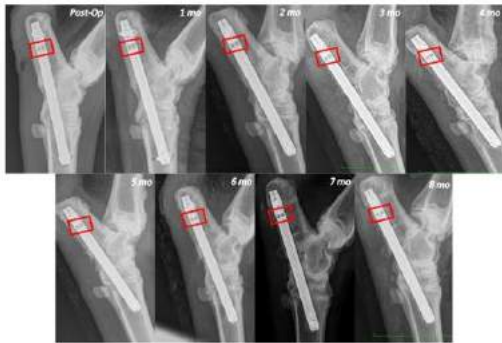


Figure 2: *In vivo* radiographs were taken at the time of device implant and every four weeks until sacrifice. Outlined regions indicate the gap over which device compression occurred.

The animals were allowed to move freely, eat ad libitum, and were sacrificed at either 4 or 8 months post-implantation. Using the radiographs that were taken throughout the course of the study, each image was analyzed using ImageJ software. The measurements taken from each image were scaled with reference to the diameter of the nail which was identical in each animal.

RESULTS

Over 8 months, an average of 2.17mm (SD=0.51) of device compression occurred in group 1, 2.31mm (SD=0.37) in group 2, 2.13mm (SD=0.67) in group 3, and 1.57mm (SD=0.42) in group 4 (**Figure 3**).

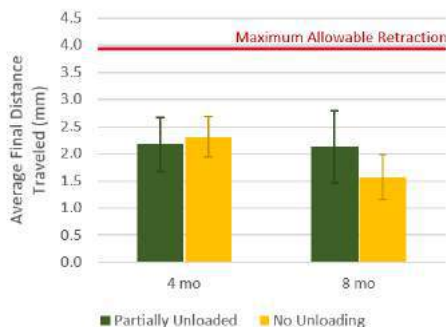


Figure 3: Average total retraction distance experienced by each treatment group.

The majority of compression occurred between the time of implant and 4 months post-op. Additionally, all of the animals experienced ≤ 4 mm of resorption, and none of the nails reached the maximum 4mm travel distance, even after 8 months *in vivo* (**Figure 4**).

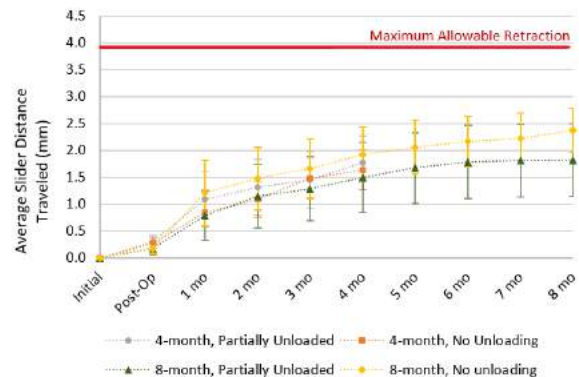


Figure 4: NiTi element retraction distance tracked as a function of time in each animal.

DISCUSSION

Sheep are widely considered to be one of the most valuable translational models to study bone and cartilage remodeling due to their size and biological healing responses, both of which resemble humans. They also allow for full size medical devices to be researched *in vivo* while experiencing similar mechanical forces. The animals tolerated the procedure well and recovered rapidly post-implantation with no signs of infection or other complications. Evaluating the resorption experienced across a joint can help determine whether the joint is experiencing sustained compression throughout the fusion process. The data gathered suggest this novel nail may be a viable option for achieving sustained compression across the hock joint in an ovine model. These data additionally support the idea that this NiTi element is capable of accommodating resorption patterns typical of clinical patients with deteriorated bone quality brought on by conditions such as Charcot neuroarthropathy.

ACKNOWLEDGEMENTS

The U.S. Army Medical Research Acquisition Activity, 820 Chandler Street, Fort Detrick MD 21702-5014 is the awarding and administering acquisition office. This work was supported by the Assistant Secretary of Defense for Health Affairs, through the Peer Reviewed Medical Research Program under Award No. W81XWH-20-1-0677. Opinions, interpretations, conclusions, and recommendations are those of the author and are not necessarily endorsed by the Department of Defense. In conducting research using animals, the investigators adhere to the laws of the United States and regulations of the Department of Agriculture.

REFERENCES

- [1] A. Eschler, et al., *Injury*, vol. 45 Suppl 1, pp. S38-43, 2014.
- [2] D. A. Butt, et al., *The Bone & Joint Journal*, vol. 97-B, no. 6, pp. 809–813, 2015.
- [3] K. Dupont, et al., *GJOR*, vol. 1, no. 5, pp. 1–8, 2019.
- [4] B. C. Gadowski, et al., *Journal of Biomechanics*, vol. 47, no. 12, pp. 2836–2842, 2014.

Fisetin TREATED HUMAN BONE MARROW ASPIRATE CONCENTRATE RAPIDLY REDUCES SENESCENCE SIGNATURES

Jacob B. Singer (1), Haruki. Nishimura (1), Yoichi Murata (1), Sealy Hambright (1), Chelsea S. Bahney (1), Sudheer Ravuri (1), Johnny Huard (1), Marc J. Philippon (1)

(1) Center of Regenerative and Personalized Medicine at the Steadman Philippon Research Institute, Vail, CO, USA

INTRODUCTION

Human bone marrow aspirate concentrate (hBMAC) is a readily available source of mesenchymal stem cells (MSCs) that is a common regenerative medicine treatment for various orthopedic applications. Senescence is a cell fate characterized by the loss of metabolic function, proliferative capability, and increased resistance to apoptosis which leads to tissue decline. Fisetin is a naturally occurring flavonoid with demonstrated senolytic activity through the targeted elimination of senescent cells. The purpose of this study was to investigate the therapeutic effect of fisetin on senescence in bone marrow derived MSCs (BM-MSCs) and hBMAC. We hypothesized that fisetin would decrease senescence in both hBMAC and cultured BM-MSCs, which we posit may improve the quality of the hBMAC orthobiologic product. The utilization of fisetin to improve patient derived products requires a therapeutic index. Here, we demonstrate that 50 μ M of fisetin was able to reduce senescence signatures in BM-MSCs and hBMAC in as little as 2 hours.

METHODS

BM-MSCs were obtained from ATCC used for *in vitro* experiments to determine dose and time course. BM-MSCs were cultured in normal growth media (Low Glucose DMEM, 10% MSC FBS, 1% Penicillin/Streptomycin, and 10 ng/mL FGF). Cells were treated with 50 μ M of the senescence inducing agent etoposide for 24 hrs then treated with 50 μ M of fisetin for 24hrs. Senescence was determined using the β -gal staining kit (Cell Signaling Technology) and further verified using the senescence stain C12FDG staining via flow cytometry (Sigma-Aldrich). Cells were pretreated with Bafilomycin for 1hr prior to C12FDG

staining for 1hr then washed, collected, and analyzed with a Guava EasyCyte flow cytometer. Gene expression was determined for senescence transcripts *p21*, and inflammatory transcripts *IL-1 β* and *IL-6* via qPCR. For hBMAC, samples were obtained from our clinic (**IRB#2020-50**). To confirm the efficacy of fisetin treatment for reduction of senescence; the combination of four different time-courses (0, 2, 6, 24 hrs) and four dose concentrations of fisetin (0, 20, 50, 100 μ M) were investigated. All the data points are presented as the mean \pm standard deviation (SD). Statistical significances were calculated based on one-way analysis of variance (ANOVA) and p-value < 0.05 was considered significant.

RESULTS

β -gal staining confirmed senescence induction with 24 hr etoposide treatment (50 μ M) that could be rescued by 24 hr etoposide treatment (50 μ M) (**Fig. 1A**).

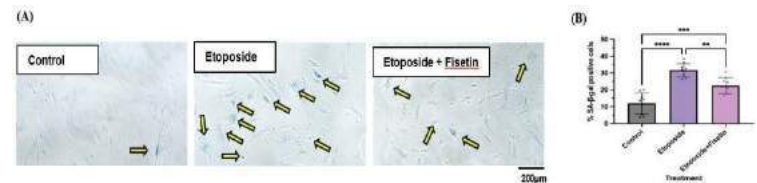


Figure 1. Senescence induction and Fisetin treatment using human bone marrow derived mesenchymal stem cells

(A) Microscopic images of β -gal staining, (B) % SA- β -gal positive cells

Senescence induction by etoposide and reduction with fisetin in BM-MSCs was further confirmed by flow cytometry analysis using C12FDG staining highlighting the C12FDG assay as a valid detection method of senescence (**Fig. 2A**). qPCR analysis demonstrated elevated gene expression of the senescence marker *p21* as well as proinflammatory markers *IL-1B* and *IL-6* (**Fig. 2B**) indicating the efficacy of fisetin on reducing these specific markers (**Fig. 2B**).

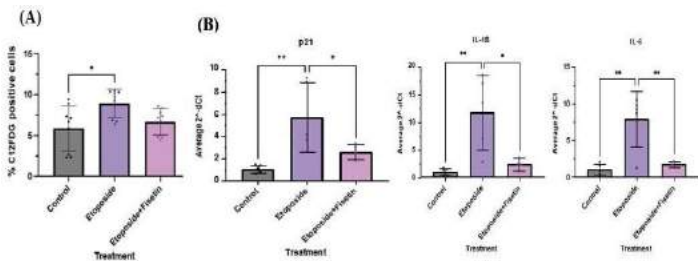


Figure 2. Senescence induction and Fisetin treatment using BM-MSCs
(A) Delta % C12FDG positive cells using flow cytometry, (B) qPCR after after senescence induction (50 μ M of Etoposide, 24hr) with or without Fisetin treatment (50 μ M, 24hr). Mean \pm SD. Significant different: p< * 0.001, p< ** 0.0001, p< *** 0.001, p< **** 0.0001

We next tested senolytic efficacy in hBMAC which contains MSCs to see if senescence signatures could be reduced with senolytic drugs in a dose and time dependent manner. Interestingly, it was found that 50 μ M fisetin treatment of hBMAC could be an effective therapeutic dose capable of reducing senescent cell number within 2 hrs (**Fig. 3**). It was also interesting that 50 μ M did not significantly alter senescence reduction capability or increase cell death between 20 μ M and 100 μ M after 2 hrs (**Fig. 3A**) suggesting that higher doses of fisetin could be safe and tolerable. The time course also revealed a decrease in C12FDG cells even though there was no significant difference between 2, 6, or 24 hr time points (**Fig. 3B**).

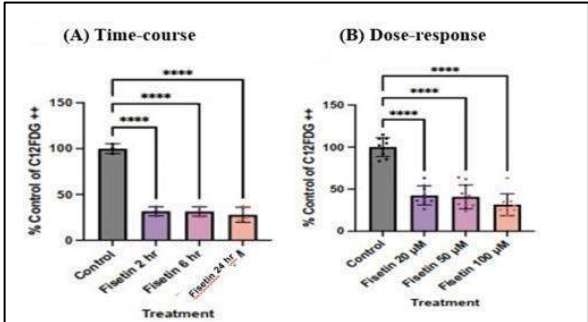


Figure 3. Fisetin treatment on human bone marrow aspirate concentrate
(A) Time-course experiment with 50 μ M Fisetin.
(B) Dose-control experiment with 2 hr Fisetin treatment.
Mean's. Significant different: p< **** 0.0001

DISCUSSION

Aging is the progressive physiological change that leads to the decline of fundamental biological functions and the onset of numerous age-related pathologies. Orthobiologics, specifically hBMAC has garnered significant attention for its regenerative properties and ability to help delay the onset of osteoarthritis. Here, we used BM-MSCs as a proxy for cell specific effects of senolytic treatments that target a fundamental property of aging, senescence. Our overarching goal was to link the therapeutic effect of fisetin on BM-MSCs and compare the outcomes through an *ex vivo* experiment and apply it to an upcoming *in vivo* experiment in a preclinical rat model of OA. FDA regulations regarding supplementation of specific drugs like fisetin applied to hBMAC presence a burden on an exciting, easily accessible source of a depleted senescent hBMAC product. Through our upcoming *in vivo* rat study, we hope to understand the translational aspects of our *in vitro* toxicity dose experiments to reveal why there is a wide range of efficacy of fisetin (0, 20, 50, 100 μ M) with no significant difference in the cell death. This could imply a large therapeutic index of fisetin in a biological setting. Understanding the metabolic process of fisetin will help bring treatments of this senolytic drug to life as we understand the optimal therapeutic effect in different biological specimens and cell types.

The ability to enhance hBMAC therapy in a timely and safe manner is important for the future therapies of orthobiologics. As we look to personalize medicine, fisetin treatment of hBMAC over a 2hr treatment course can improve the product given to patients. An *in vivo* rat study will be conducted via an osteoarthritis model to confirm these preliminary results and reveal the efficacy of this therapy in a biological setting.

ACKNOWLEDGEMENTS

We gratefully thank the Hart Foundation for their support of this collaborative research.

REFERENCES

- [1] Mullen M., et al. *bioRxiv*: 2022.2011.2015.516580.
- [2] Gao X., et al. *Orthopaedic Journal of Sports Medicine*.
- [3] Han Y., et al *Cells* **8**: 886.
- [4] Jeon OH., et al *Nature medicine* **23**: 775-781.
- [5] Choi SW., et all *Evid Based Complement Alternat Med* **2012**: 810563.
- [6] Didomenico C.D., and Bonassar, L.J., *Osteoarthritis Cartilage*. 26: 1438-1446.

TAILORING THE RELEASE PROFILE OF A SMALL MOLECULE AGONIST TO STIMULATE HEDGEHOG SIGNALING DURING TENDON-TO-BONE INTEGRATION

J. Marcelin (1), R. Madi (1), T. Kamalidinov (1), X. Jiang (1), S. Assi (1), D-H. Kim (1), S. Keith Lang (1), R. L. Mauck (1), A. Kuntz (1), N. Dymant (1)

(1) Department of Orthopaedic Surgery, University of Pennsylvania, Philadelphia, PA, USA

INTRODUCTION

Tendon injuries frequently occur at the tendon-to-bone insertion site (i.e., enthesis) and tendon-to-bone repair often leads to disorganized scar tissue formation [1]. The hedgehog (Hh) signaling pathway is a critical regulator of enthesis fibrocartilage formation and maturation during growth and development [2-4]. Thus, this pathway is a promising target for improving tendon-to-bone repair by promoting the formation of a functionally graded zonal enthesis.

We previously demonstrated that stimulation of the Hh pathway via genetic activation or systemic Hh agonist injections promoted tendon-to-bone attachment formation following anterior cruciate ligament reconstruction (ACLR) [5]. Due to the important role of Hh in many tissues within the body [6], there is a need to develop localized therapies to avoid off-target effects while still effectively leveraging this pathway to improve repair outcomes. Therefore, we developed an electrospun scaffold release system containing various concentrations of SAG, a small molecule Hh signaling agonist, for use in the promotion of tendon-to-bone integration.

The objectives of this study were to incorporate SAG into the scaffold, measure the scaffold properties after incorporation, define the *in vitro* release profile and bioactivity of SAG, and determine whether these scaffolds could locally stimulate the Hh pathway and promote tunnel integration in a bilateral transverse tibial tunnel (TTT) surgical model.

METHODS

Scaffold Fabrication: A PCL solution (35 wt%) was prepared in DMF/THF with the Hh agonist (SAG) at different concentrations (0, 0.001, 0.01, 0.1 mg/ml). The solution (2mL) was spun from an 18G needle at 15kV onto a rotating mandrel (8 m/s, 2.5 ml/hr).

SEM: Fibril alignment and fibril diameter (100 fibrils per sample) were measured using the OrientationJ plugin in FIJI from images acquired on an FEI Quanta 600 ESEM.

Mechanics: Scaffold strips (1x20mm) were cut longitudinally,

weighed, and cross-sectional area was measured using a custom non-contact laser device. Strips were preconditioned and loaded uniaxially at 1%/s until failure (Instron 5542). Structural and material properties were calculated from the resulting load-deformation curves.

SAG Release Study: All animals and procedures were approved by Institutional IACUC. Both blank and SAG-infused scaffolds were placed in culture media (DMEM, 5% FBS, 1% pen/strep) in 50 ml tubes covered in aluminum foil on a shaker at 37°C for 28 days. The conditioned media (CM) was collected every other day by removing one half of the volume, which was replaced with fresh media, on days 1, 2, 4...28, and then frozen at -80°C. Bone marrow stromal cell (bMSC) cultures were prepared by flushing the bone marrow from femurs and tibias of four 6-week-old CD1 mice. These cells were expanded and then passaged into 24-well plates. CM collected on days 2, 8, 16, or 26 from each scaffold were delivered to the bMSCs for 4 days. RNA was collected from the treated cells and qPCR was conducted for the downstream Hh gene, *Gli1*, to determine the extent to which SAG released from the scaffolds induced downstream Hh activity. CM samples were compared to 3nM or 300nM of SAG added directly to the culture media.

Tunnel Integration Study: TTT surgeries were performed on 12 mice to test the effect of SAG release on Hh activity and tunnel integration. This procedure was utilized as a simpler, higher throughput model than the ACLR model we used previously [1,5]. Graft tail tendons were harvested from mice and a sterile scaffold was added to the graft bundle. A transverse tibial tunnel was drilled in the metaphysis using a 27G needle. The graft with the scaffold was passed through this tunnel and the samples were assessed on day 14 post-surgery.

Mineralized Cryosectioning, qPCR, and Imaging: Limbs were fixed, embedded, sectioned undecalcified with cryofilm. The medullary canal was microdissected from tissue sections for qPCR. On adjacent sections, alkaline phosphatase (AP) staining was imaged fluorescently on a Zeiss Axio Scan.Z1. AP area was normalized to the area of the

medullary canal and quantified.

Statistical Analysis: Fiber diameter, scaffold mechanical properties, and *in vivo* qPCR and AP activity were compared via one-way ANOVA ($p < 0.05$). Gli1 expression from *in vitro* release was compared via two-way ANOVA with Sidak's post-hoc tests ($p < 0.05$).

RESULTS

SAG incorporation affected fiber alignment but not diameter of electrospun PCL scaffolds: Using the OrientationJ plugin to measure fiber alignment from SEM images, we found that SAG incorporation reduced the overall fiber alignment ($SD_{\text{blank}} = 15.8^\circ$, $SD_{0.01} = 19.1^\circ$, $SD_{0.001} = 25.3^\circ$, $SD_{0.1} = 26.6^\circ$) in the scaffold (Fig. 1C). However, fiber diameters of the SAG scaffolds were not significantly different from the blank scaffold (Fig. 1D).

SAG incorporation increased maximum stress but not modulus: Even though the implanted PCL scaffold will be stress-shielded by the tendon grafts, we wanted to measure the effect of SAG inclusion on mechanical properties of the scaffold as mechanical changes may impact the release profile. We found that SAG incorporation did not alter modulus (Fig. 2A) but did increase maximum stress (Fig. 2B) in the highest concentration (0.1mg/ml) group compared to blank scaffolds.

Delivery of conditioned media to bMSCs increased Gli1 expression in a dose- and time-dependent manner: As expected, we found a significant increase in Gli1 expression with 3nM (2-fold) and 300nM (70-fold) added directly to the media ($p < 0.05$, Fig. 3A) vs control media. Additionally, Gli1 expression increased in the SAG scaffolds in a dose- and time-dependent manner ($p < 0.05$) (Fig. 3B). Gli1 expression did not change with time in the blank scaffolds and the expression levels were comparable to the control media (C in Fig. 3A). Gli1 expression was significantly higher for all SAG concentrations (0.001, 0.01, and 0.1 mg/ml) compared to blank scaffolds in CM collected on day 2, with expression levels being comparable to 300nM media for the 0.01 and

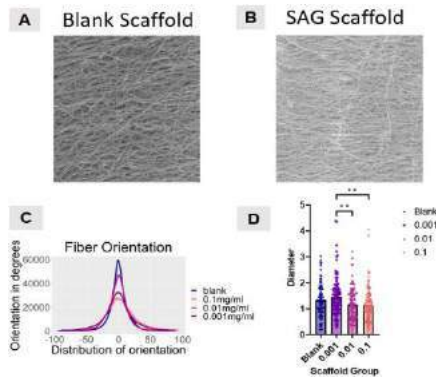


Figure 1: SEM of blank (A) vs. SAG (B) scaffold. Fiber orientation (C) and diameter (D) measurements.

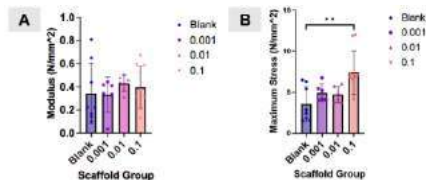


Figure 2: Modulus (A) and maximum stress (B) values from uniaxial stress relaxation and failure tests of PCL scaffolds. ** $p < 0.01$.

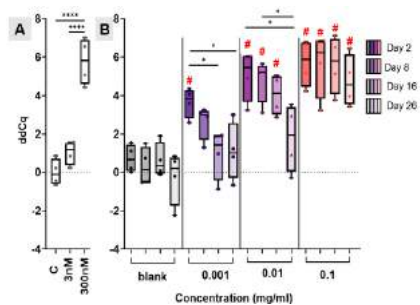


Figure 3: Gli1 ddCq for controls (A) and blank vs the different concentrations of SAG at the four timepoints (B). ** $p < 0.0001$, * $p < 0.05$; # $p < 0.05$ vs. blank.**

0.1 mg/ml scaffolds. Interestingly, while Gli1 expression remained elevated in the 0.1 mg/ml SAG scaffold for CM collected out to day 26 ($p < 0.05$), both the 0.01 and 0.001 mg/ml groups saw reduced Gli1 expression with time of CM collection, which resulted in 0.01 mg/ml at day 26 and 0.001mg/ml at days 8, 16 and 26 not being statistically different than blank scaffolds (Fig. 3B). These results indicate that the 0.1mg/ml SAG scaffold released a sufficient amount of SAG over a 26-day period to maintain activated Gli1 expression in bMSCs.

Localized delivery of SAG to the bone tunnels increased Gli1 activity and alkaline phosphatase activity: To determine the local effect of Hh agonist released from scaffold on nearby cells in an *in vivo* setting, we microdissected tissue within the medullary canal, including the surgically drilled tunnel (Fig. 4A), from cryosections using a needle and performed qPCR. There was an increasing trend in Gli1 expression in the 0.01 and 0.1 mg/ml scaffolds compared to the blank scaffolds at post-operative day 14 (Fig. 4B). To assess whether SAG release increased fibrocartilage and bone mineralization, we measured alkaline phosphatase (AP) activity in the medullary canal and bone tunnel. We found that the 0.1 mg/ml group had significantly greater AP activity compared to blank scaffold ($p < 0.05$, Fig. 4C).

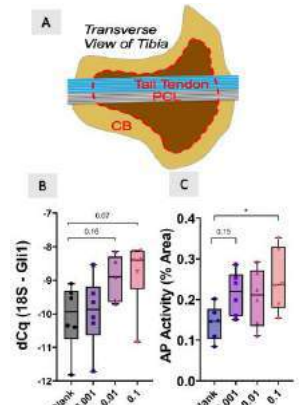


Figure 4: Schematic representation of the TTT (A) including the area (red dotted line) used to calculate Gli1 gene expression (B) and AP activity (C).

DISCUSSION

In this study, we incorporated the small molecule Hh signaling agonist, SAG, into electrospun PCL scaffolds and found that these scaffolds could release SAG *in vitro* and *in vivo* while maintaining bioactivity. The SAG incorporation had a dose-dependent effect on fiber orientation (Fig. 1B) producing an increase in maximum stress but not modulus of the scaffold (Fig. 2). The *in vitro* release profile was dose dependent with CM from the 0.1 mg/ml concentration stimulating sustained, elevated expression of Gli1 in treated bMSCs (Fig. 3), whereas the other doses saw reductions in Gli1 expression to baseline levels by the end of the one-month release experiment. When the scaffolds were inserted within the bone tunnels of a TTT *in vivo* model, the 0.01 and 0.1 mg/ml groups resulted in an increasing trend in Gli1 expression (Fig. 4B). The SAG scaffolds also showed an increasing trend in AP activity, with the 0.1 mg/ml group having significantly greater AP activity than blank scaffolds (Fig. 4C), indicative of increased fibrocartilage and bone mineralization within the bone tunnel regions. This result is consistent with our previous work using systemic injections of a Hh agonist [5]. Future studies will apply the SAG-delivering scaffolds in our more clinically-relevant, yet lower throughput, ACLR model to improve the tendon-to-bone integration processes.

ACKNOWLEDGEMENTS Work supported by NIH R21 R21AR078429, P30AR069619, R01AR076381, and F31AR079840 (TK).

REFERENCES [1] Kamalitinov, T et al., *JOR*, 2020 [2] Lu, H et al., *Annu. Rev. Biomed. Eng.*, 2013 [3] Liu, C-F et al., *PLoS One*, 2013 [4] Dymont, N et al., *Dev Biol*, 2015 [5] Kamalitinov, T et al., *bioRxiv*, 2022 [6] Ingham, P et al., *Nat Rev Genet.*, 2011.

DEPTH-MAP IMAGE BASED INFLATION TEST FOR MECHANICAL CHARACTERIZATION OF SOFT MATTER

Rahul L. Maurya (1), Yash K. Shrivastava (2), Dr. Samarth S. Raut (1)

- (1) Department of Mechanical, Materials and Aerospace Engineering, Indian Institute of Technology Dharwad, Dharwad, Karnataka, India.
(2) Department of Information Technology, Manipal University Jaipur, Jaipur, Rajasthan, India.

INTRODUCTION

Mechanical characterization of soft tissue is very important for studying etiology and risk/factor of assessment. A typical biomechanical material model relates strain tensor (deformation) to the stress tensor (mechanical loading). Analysis of the deformation of 3D surface leads to strain assessment. Previously reported work have made valuable progress with certain assumption or simplifications with inputs ranging from medical images [1] [2] and experimental biaxial testing method [3]. Especially for thin membranes inflation tests are attractive experimental methods [4, 5]. Inflation tests have been applied to variety of soft tissues and polymers earlier however capturing the deformation as well as particle trajectory correctly has remained a challenge. Hence, here we report a method to estimate strain by combining established techniques in computer vision and computational mechanics with inputs about deformation captured in form of recently popular portable hardware for depth map and RGB images. Gelatin membrane samples were used in this prototype.

Non-contact method of strain assessment for mechanical characterization with reliable tracking of entire trajectory of the fiducial markers using depth map images provided by stereoscopic camera is presented here. It is especially suitable for curved samples as biaxial or uniaxial testing methods introduce errors due to flattening of the sample. Robust, flexible, and mathematically sound approach of Bezier surface technique is aptly implemented for strain tensor estimation.

METHODS

The setup for inflation testing here demonstrates the method to quantify the mechanical property of elastic/flexible material ranging from silicone rubber or nitrile sheets to Elastic 3D printed sheets to biological tissues like fetal membranes with adequate accuracy. The membrane

size can easily vary from 20 mm to 100 mm because of its modular design for the experimental test set-up. A 3D camera with resolution of (RGB + depth) to map the inflated surface by capturing the number of fiducial marks made on the surface of the quasistatically inflated membrane over the timestep of around 30 frames every second.

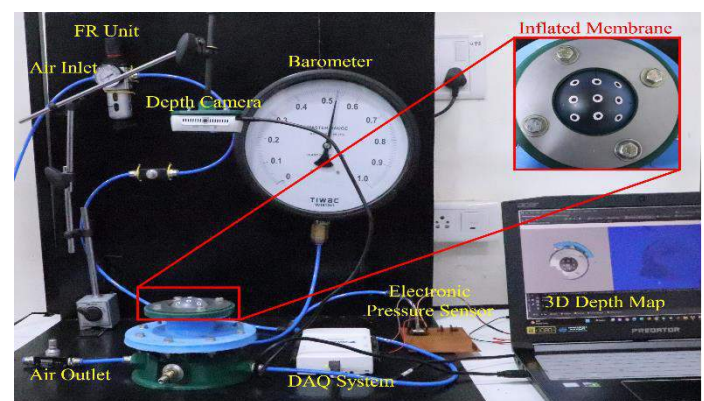


Figure 1: Illustration of the experimental setup, the depth map image, and the normal RGB image displayed on the computer.

Material preparation: To prepare the gelatin sheet/membrane we have taken the bovine (type b) gelatin powder. We mixed 2 tablespoons of water into 2 tablespoons of gelatin powder and allowed to bloom for 30 sec. After that it was heated in water bath for 4 minutes until it melted completely. Then precaution was taken to the air-bubble if any, and then carefully measured volume of this liquid gelatin gel was poured into Petri dish of 80 mm diameter and allowed it to solidify for 5 hours.

Inflation testing and position tracking: The required pressure chamber for inflation setup is designed for up to 10 bar capacity and fabricated by additive manufacturing to optimize the manufacturing cost and maintain the setup's modularity. Air is compressed using an air compressor (1.5 hp, 24L, 8 bar pressure). Proper precautions in design of set-up minimize the air leakage. Nine fiducial marks of approximate diameter of 2 mm each are created on the membranes such that those are located on corners, mid-points, and center of a rectangular region. The depth camera (Intel Realsense D435i) captures the position of the fiducial mark. Fiducial mark detection algorithm locates the markers in the image space and, at the same time, pressure is recorded by using electronic Pressure sensor (AMS-5818-0600_D) of inside the chamber is also taken on every time step by the NiDAQ to the computer (Figure 1). The membranes were pressurized up to 1 bar pressure gradually and de-pressurized; from this experiment, we recorded the position of each fiducial mark due to inflation over time. Bezier surface patch was defined using marker location. (Figure 2)

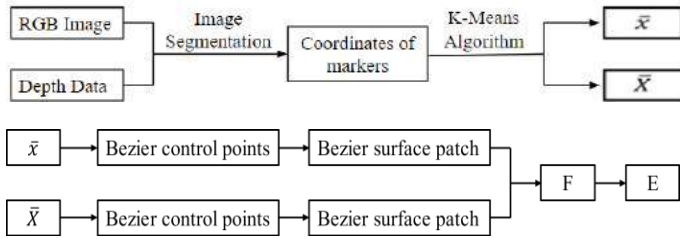


Figure 2: Schematic representation of strain evaluation process

RESULTS

From this point cloud data extracted from the depth map image and RGB images, using k-mean clustering algorithm we classified the trajectory of the individual 9 fiducial markers (refer Figure 3 a) located at corners, mid-point of edges, and center of a rectangular zone of a membrane. Here, we only consider first and last frame for simplicity.

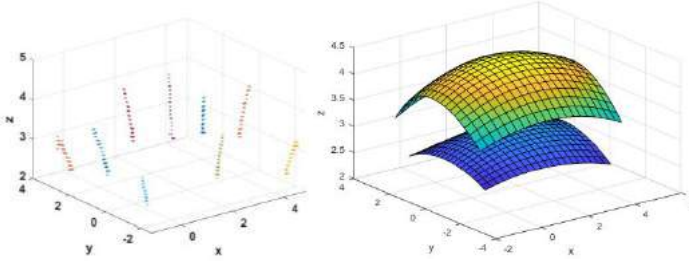


Figure 3: Experimentally observed trajectories of fiducial markers (left, 3a) and visualization of gelatin sheet in reference (undeformed) and in current configuration (deformed) based on bi-quadratic Bezier surface interpolation (right 3b).

For coordinates in the reference configuration (i.e., undeformed state) and the current configuration (i.e., deformed state) we have fit the bi-quadratic Bezier surface (refer Figure 3b).

The deformation gradient tensor, \mathbf{F} , describes the deformation of an object. In the context of a Bezier curve, the partial derivative of the curve with respect to its parameter (u and v) (equation (1)), is used to calculate deformation gradient \mathbf{F} . The composite derivative (equation (2)) is then used to calculate the Lagrange strain tensor, \mathbf{E} (equation (3)), which describes the deformation of the object.

$$\frac{\partial}{\partial u} b^{m,n}(u, v) = m \sum_{j=0}^n \sum_{i=0}^{m-1} (b_{i+1,j} - b_{i,j}) B_i^{m-1}(u) B_j^n(v) \quad (1)$$

$$F_{ij} = \frac{dx(u,v)}{d\mathbf{x}(u,v)} \quad (2)$$

$$\mathbf{E} = \frac{1}{2} [\mathbf{F}^T \mathbf{F} - \mathbf{I}] \quad (3)$$

Where, b represents Bezier control points, u and v are parameters and $B_i^{m-1}(\cdot)$ is Bernstein polynomial. The results were compared with the manual calculations for the strain along two approximated orthogonal directions at the central point by fitting a second order curve and measuring the length of the curved 3D segment.

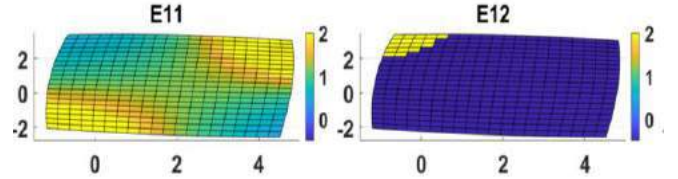


Figure 4: Lagrange strain spatial distribution

DISCUSSION

As seen in the plots above the strain distribution was more or less constant with minor errors reflecting along the peripheral region.. Possible reasons could be the positional error of the markers and curvature as the corner region that compromises marker shape as detected by the camera above. Especially with the more or less isotropic behavior of the material with all radially symmetric boundary conditions (at gripper) the membrane element is expected to be in equibiaxial stress state which would reflect similar values for E11 and E22 strain with the basis vector directions assumed to be along sides of the rectangular zone under consideration. Spatial variation of strain is also observed to be minimal and shear strain E12 is as expected for this specific geometry, loading, and material.

Here we have demonstrated the use of a fiducial mark detection algorithm to capture the deformation in the membrane by using a depth camera and 3D mapping of the membrane surface every instance, while inflation/deformation can tell us more about the fiber orientation and their basic crystallography. Using this device, we can characterize the mechanical properties of various flexible/elastic materials and biological tissues. We have performed this experiment to get the mechanical properties of gelatin tissue membrane and have verified with their standard material properties. Minor air bubble presence in gelatin sheets is ignored in this work. Also, it is targeted that more dense markers will be tracked in future during deformation for better resolution and accuracy for application to complex geometry and materials.

ACKNOWLEDGEMENTS

Valuable insight and help received from Mr. Avinash Kumar K. M. during planning and fabrication of experimental set-up are appreciated. This work was funded by SERB-SRG (Dept. of Science and Technology, Govt. of India) grant SRG/2020/002513 and SGNF funding IITDh/R&D/SGNF/6.46/2021-22/018 by IIT Dharwad.

REFERENCES

- [1] Raut SS et al, Proceedings of the ASME 2013 Summer Bioengineering Conference. Volume 1B, 2013.
- [2] Taniguchi et. Al, Ann Vasc Dis. 2014; 7(4): 393–398.
- [3] Sacks Journal of Elasticity 61, 199 (2000)
- [4] Schulze-Bauer et al, AJP Heart Circ. Physio. Volume 282 Issue June 2002 Pages H2427-H2440
- [5] Elsheikh et al, J R Soc Interface. 2005 Jun 22; 2(3): 177–185.

A LATTICE-BOLTZMANN FLUID-STRUCTURE INTERACTION FRAMEWORK FOR THE INERTIAL TRANSPORT OF BIOPARTICLES IN MICROFLUIDIC DEVICES

Alberto Mantegazza (1), Dario De Marinis (1), Marco D. de Tullio (1)

(1) Department of Mechanics, Mathematics and Management, Polytechnic University of Bari, Bari, Italy

INTRODUCTION

In the last two decades, significant advancements in the field of microfluidics allowed the development of diagnostic or therapeutic devices for bioparticle separation and focusing. In the context of multiphase flows in microchannels, inertial microfluidics has become a very attractive separation method because it does not require any external force to sort cells or bioparticles and has a high throughput. When the channel Reynolds number is in the range 10-100, the particle lateral migration is affected by competing forces: the shear-gradient lift force due to the curvature of the velocity profile and the wall-lift force resulting from the interaction between the particle and the microchannel walls. Reliable fluid-dynamic models are essential to effectively design such microfluidic devices for biomedical applications and to be able to sort cells according to the user needs. In this perspective, the Lattice-Boltzmann Immersed-Boundary (LB-IB) method has emerged as an interesting technique to treat the transport of rigid and deformable objects in a fluid flow [1, 2]. In the traditional LB method, the fluid pressure and density are linearly proportional. In the case of flow conditions typical of inertial microfluidics, in which a large pressure difference may be present between the inlet and outlet of the separation device, this means that fluid density would increase linearly in the streamwise direction. In this flow regime, this is a non-physical density increase that does not satisfy the fluid incompressibility condition.

With the goal of providing an accurate investigation of bioparticle transport in inertial flow regimes to design microfluidic cell-sorting devices, we aimed at developing a fluid-structure interaction (FSI) framework based on a fully-incompressible LB method for particle-resolved simulations.

METHODS

We developed an FSI framework in which the BGK-Lattice-Boltzmann (BGK-LB) method was used to solve the Navier-Stokes equations coupled with a spring-network surface-based model for structure dynamics by means of an Immersed-Boundary (IB) technique to describe the evolution of rigid and deformable bioparticles for $Re = 10 - 100$.

The fluid evolution was modeled on a three-dimensional computational lattice (D3Q19). Here, 19 distribution functions $f_i(\vec{x}, t)$ ($i = 0, \dots, 18$)

representing particles at position \vec{x} , time t , and flowing with velocity \vec{e}_i are transported using the forced Boltzmann equation:

$$f_i(\vec{x} + \vec{e}_i \Delta t, t + \Delta t) - f_i(\vec{x}, t) = -\frac{\Delta t}{\tau} [f_i(\vec{x}, t) - f_i^{eq}(\vec{x}, t)] + \Delta t \vec{F}_i \quad (1)$$

where τ is the relaxation time, which is related to the fluid kinematic viscosity according to $\nu = c_s^2 (\tau - \frac{\Delta t}{2})$, being $c_s^2 = 1/\sqrt{3}$ is the reticular speed of sound. To ensure the full incompressibility of the LB method and simulate flows driven by large pressure differences, an approximated equilibrium distribution function f_i^{eq} ($i = 0, \dots, 18$) was defined as [1]:

$$f_i^{eq}(\vec{x}, t) = \omega_i \left[\frac{1}{c_s^2 \rho_0} p + \frac{1}{c_s^2} (\vec{e}_i \cdot \vec{u}) + \frac{1}{2c_s^4} (\vec{e}_i \cdot \vec{u})^2 - \frac{1}{2c_s^2} \vec{u}^2 \right] \quad (2)$$

The forces generated by the presence of the body onto the fluid (\vec{f}_{lb}) were taken into account in the forcing term \vec{F}_i ($i = 0, \dots, 18$) [1]:

$$\vec{F}_i = \left(1 - \frac{1}{2\tau} \right) \omega_i \left[\frac{\vec{e}_i - \vec{u}}{c_s^2} + \frac{(\vec{e}_i \cdot \vec{u})}{c_s^4} \vec{e}_i \right] \cdot \vec{f}_{lb} \quad (3)$$

with weighting factors $\omega_0 = 1/3$, $\omega_{1-6} = 1/18$, and $\omega_{7-18} = 1/36$. Finally, we computed fluid pressure and velocity as the moments of the distribution functions: $p = c_s^2 \rho_0 \sum_i f_i$, $\vec{u} = \sum_i f_i \vec{e}_i + \frac{\Delta t}{2} \vec{f}_{lb}$.

Bioparticles were considered as a collection of Lagrangian inertial markers immersed in the Eulerian fluid lattice. The IB method was used to enforce the immersed structure boundary conditions onto the flow field. Following de Tullio *et al.* [3], a moving-least-squares reconstruction with a 27-point support domain was used to build a transfer function and make the Lagrangian mesh markers and Eulerian lattice nodes interact. The FSI time advancement was performed following a weak-coupling strategy. Given the fluid field at the time instant t , hydrodynamic stresses are evaluated on the Eulerian fluid lattice and transferred to the Lagrangian markers using the IB method. The internal stresses of the immersed body are evaluated by computing the elastic response modeled by a spring-network model [3].

The Newton equation of motion was solved using an implicit discretization

scheme to predict the immersed body position, velocity, and acceleration. Finally, the volume force \vec{f}_{lb} resulting from the immersed body kinematics was transferred back to the Eulerian fluid lattice nodes and used to compute the forcing term (Eq. 3) of the Boltzmann equation (Eq. 1).

RESULTS

Fluid dynamic and structural solver validation. To validate the LB method, we simulated the flow of an incompressible Newtonian fluid between two infinite parallel plates at different $Re = [1; 10; 100]$. A pressure inlet boundary condition was prescribed according to Poiseuille's theory, whereas a reference pressure was imposed at the outlet. No-slip condition was used at walls; periodicity was imposed on the third direction. A parabolic velocity profile was set as initial condition throughout the entire domain. Simulations were performed on an Eulerian grid of dimensions $(N_x, N_y, N_z) = (1, 216, 10000)$. Given the set of parameters $\tau = 1$, c_s^2 , and Re , the resulting maximum Mach numbers for current Eulerian grid were $Ma = [0.002; 0.02; 0.2]$. We reported CFD results at $Re = 100$ and $Ma = 0.2$, which is the worst-case scenario for the LB method (Fig. 1a). The velocity profile computed using the LB methods is fully developed in the streamwise direction and it is in excellent agreement with the analytical solution predicted by Poiseuille's theory at all longitudinal locations. The same result was obtained for the simulations at lower Re numbers. Despite the significant pressure difference imposed as boundary condition ($\Delta P/P_{out} = 10\%$), the fluid density remained constant over the length of the computational domain confirming that the equilibrium distribution function defined in Eq. 2 ensures fluid incompressibility.

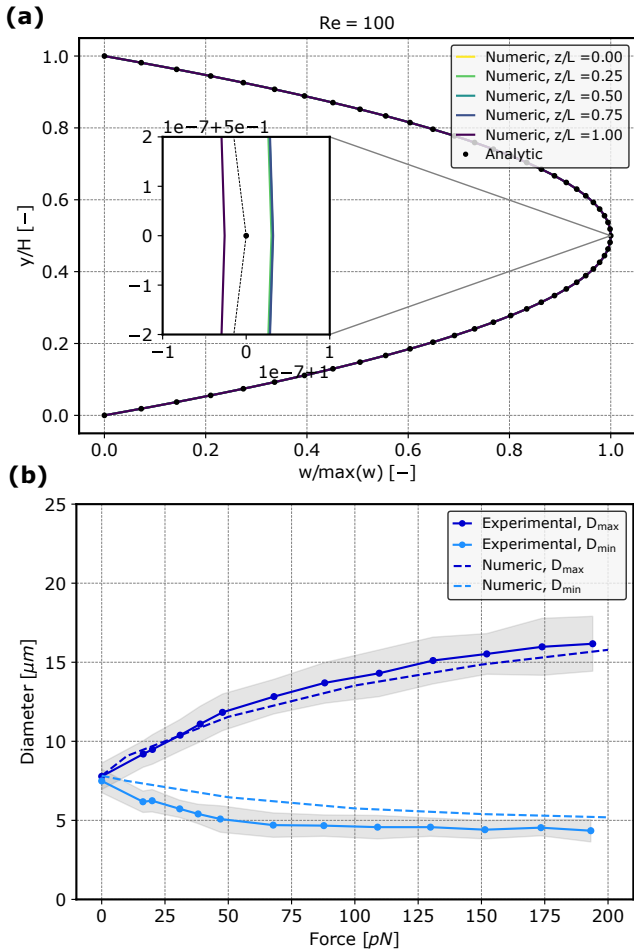


Figure 1: (a) Normalized velocity profile at different locations along the streamwise direction for $Re = 100$. Numerical results are compared to the analytical solution from Poiseuille's theory. (b) Minimum and maximum RBC diameter as a function of the stretching force compared to the experimental data reported in [4].

For the validation of the structural solver, we simulated the stretching of a red blood cell (RBC), when it is subjected to a tensile force. The model for the RBC membrane proposed by Fedosov *et al.* [4] was used in all computations. A triangular mesh with $N_v = 4932$ nodes was used to discretize the RBC surface. An external tensile force in the range $0 - 200$ pN was prescribed as boundary condition. The computations were independent of the viscous properties of the RBC membrane and the fluid because the RBC stretching was measured after convergence to the steady deformed configuration. Fig. 1b shows that the simulated RBC diameters agree very well with the optical tweezers stretching data [4].

Transport of bioparticles in a spiral microfluidic device. To show the capabilities of the proposed framework, we simulated the transport of two bioparticles in a spiral microfluidic device in the presence of inertia ($Re = 20$ and Dean number ≈ 5). A velocity inlet boundary condition was prescribed according to Poiseuille's theory, a reference pressure was imposed at the outlet, and no-slip wall condition was used elsewhere. The curved microchannel (hydraulic diameter $D_h = 33.3$) was treated as an obstacle using the Bouzidi interpolation condition. Simulations were performed on a grid of dimensions $(N_x, N_y, N_z) = (1500, 1600, 50)$. Particles with a diameter $D_p = 0.15D_h$ and a density $\rho_P = 1.1\rho_{fluid}$ were injected and tracked across the entire length of the device. The trajectories of the particles released at the same time instant and at two different transversal locations are displayed in Fig. 2. It is possible to appreciate the inertia-driven lateral migration of particle A that starting from the center of the microchannel, where it flows with a velocity higher than particle B, is eventually focused on the external side of the spiral.

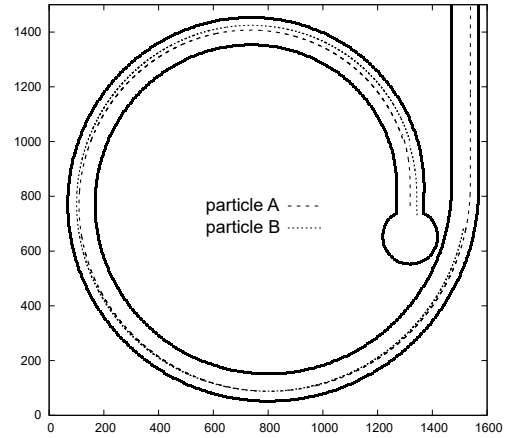


Figure 2: Particle trajectory in the spiral microchannel.

DISCUSSION

In this study, we developed an FSI framework suitable for the inertial transport of bioparticles in microfluidic devices using a fully-incompressible LB method. The framework can be used to reliably predict the flow field in microchannels at $Re = 10 - 100$ and the deformation of soft bioparticles. Preliminary investigations on a spiral microfluidic device confirmed that the fully-incompressible LB-IB method is appropriate for the investigation of inertial microfluidic phenomena that can help to design microfluidic devices for cell-sorting applications.

ACKNOWLEDGEMENTS

The study was part of the project "Tumor Immunotherapy by Nanotechnology (TITAN)" funded through the grant PON ARS01_00906.

REFERENCES

- [1] Guo Z *et al.* *Phys. Rev. E* 65 (4 2002).
- [2] Coclite A *et al.* *Comput. Math. Appl.* 80 (12 2020).
- [3] de Tullio MD *et al.* *J. Comput. Phys.* 325 (2016).
- [4] Fedosov DA *et al.* *Comput. Methods Appl. Mech. Eng.* 199 (29 2016).

COMPUTATIONAL AND EXPERIMENTAL BASED GUIDANCE FOR PERSONALIZED IMPLANT SELECTION AND ALIGNMENT IN REVERSE TOTAL SHOULDER ARTHROPLASTY

Colin R. Smith (1), Rony-Orijit Dey Hazra (1), Alex Brady (1), Matthew T. Provencher (1), Peter J. Millett (1), Scott Tashman (1)

(1) Steadman Philippon Research Institute, Vail, CO, USA

INTRODUCTION

Rotator cuff arthropathy is common in the aging population and has debilitating effects on shoulder function. The most successful treatment for this combined muscle and joint pathology is Reverse Total Shoulder Arthroplasty (RTSA), which medializes the glenohumeral center of rotation to increase the deltoid moment arms to compensate for rotator cuff deficiency. Unfortunately, post-operative shoulder strength and range of motion (ROM) deficits can limit patients' ability to perform activities of daily living. Furthermore, scapular notching is a common complication caused by impingement between the humerus and inferior glenoid.

Technological advancements in virtual planning and patient specific instrumentation enable surgeons to precisely perform RTSA surgeries. However, personalized implant selection and alignment remains a critical challenge to maximize outcomes. The purpose of this study was to assess the predictive capacity of a patient-specific modeling framework to plan RTSA surgeries and investigate the influence of RTSA parameters on range of motion (ROM) and deltoid muscle function.

METHODS

Two shoulder cadavers were CT scanned after which RTSA was virtually planned (Arthrex VIP) and surgically performed. Passive adduction, abduction, scaption, and flexion ROM were measured using a KUKA robot for 9 configurations of glenosphere lateralization (0, 4 mm), inferiorization (0, 2.5 mm), and humeral spacer thickness (0, 6, 9 mm). Then an actuated cable system was used to load the deltoid to measure the force required to abduct from 30-50° for 8 configurations of

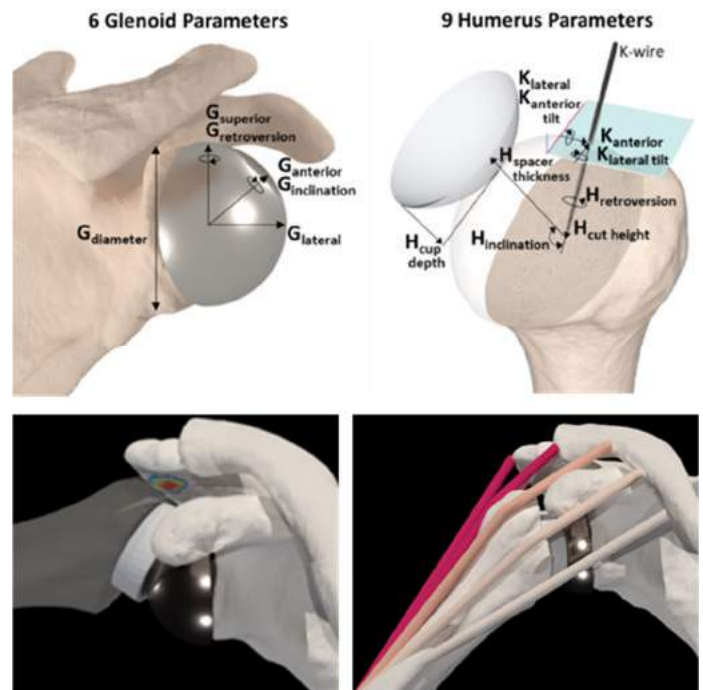


Figure 1: (top) The RTSA procedure was parameterized such that it could be performed virtually. Computational models were created for two specimens from CT scans to virtually assess the influence of RTSA on impingement (bottom left) and deltoid force (bottom right).

glenosphere lateralization (0, 4 mm) and humeral spacer thickness (0, 6 mm) and inclination angle (135, 155°). Computational models were constructed in OpenSim-JAM [1] for both specimens by segmenting the CT scans and identifying attachment points for nine deltoid paths.

Virtual RTSA surgeries were performed where 1000 different combinations of 6 glenosphere and 9 humerus parameters were randomly selected. Passive ROM simulations predicted the elevation angle where bone impingement occurred. Muscle driven simulations predicted the deltoid forces to abduct from 0° to 80° and corresponding glenosphere contact pressures and forces. To evaluate the predictive capacity of the model, the Pearson correlation coefficient (R) was computed between the simulation predictions and cadaver measurements of passive ROM for each RTSA configuration. The influence of RTSA parameters on the predicted ROM and peak deltoid force was ranked by computing the correlation (R) across all 1000 models.

RESULTS

The average errors in the predicted passive ROM were smallest in adduction (2°) and greatest in flexion (17°), with a strong correlation between the simulation predictions and experimental measurements ($R=0.97$). The peak predicted deltoid forces varied by more than 50 N across the 1000 virtual RTSA configurations and exhibited similar magnitude to the experiments and the same trend with increasing abduction angle (Fig 2).

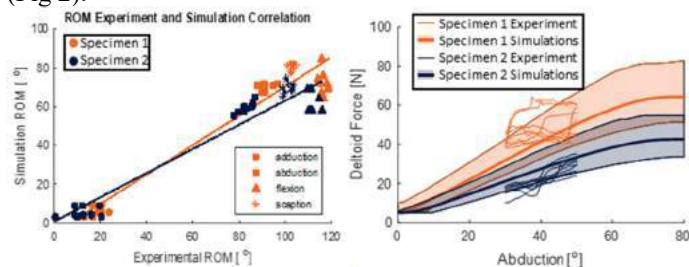


Figure 2: (left) Comparison of measured and predicted passive ROM. (right) The experimental measurements of deltoid force for 8 RTSA configurations generally remained within the 5-95 percentiles of the simulation predictions for 1000 RTSA configuration

In the simulation sensitivity analysis, glenosphere lateralization ($R=0.5$) and inferiorization ($R=0.1$), as well as humeral inclination ($R=0.5$) showed the strongest influence on passive abduction ROM.

The peak predicted deltoid force during abduction was strongly negatively correlated with glenosphere inferiorization ($R=-0.7$) and positively correlated with glenosphere lateralization ($R=0.2$), humeral spacer thickness ($R=0.2$), and inclination ($R=0.2$). The magnitude of the peak glenosphere contact force was also strongly negatively correlated with glenosphere inferiorization ($R=-0.4$).

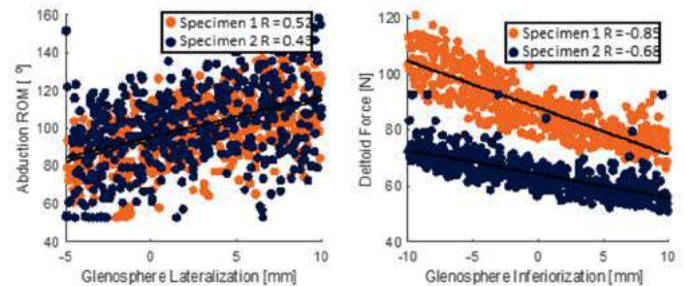


Figure 3: Scatterplots of all 1000 virtual RTSA surgeries. (Left) Lateralizing the glenosphere increased passive abduction ROM. (Right) Inferiorizing the glenosphere decreased the peak deltoid force required to abduct the humerus.

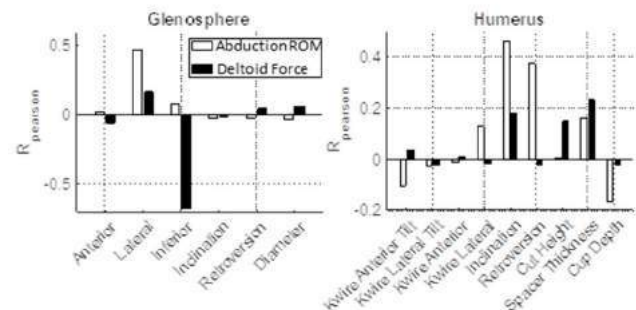


Figure 4: The Pearson correlation coefficients averaged across both specimens representing the relative influence of the RTSA glenosphere (left) and humerus (right) parameters on the predicted passive abduction ROM and peak deltoid force.

DISCUSSION

The model predictions of impingement free ROM and deltoid force generally agreed with the cadaver experiments. In both the experiments and Monte Carlo simulations, the alignment and design of the RTSA implants had large influence on functional metrics, demonstrating that surgical planning and execution has important implications for patient outcomes. Glenosphere lateralization and inferiorization increased the ROM in nearly all directions, however inferiorization decreased the deltoid force while lateralization increased the deltoid force required to abduct the humerus. Humeral inclination increased the ROM in abduction and scaption but decreased the ROM in adduction and flexion as well as increased the deltoid force. These tradeoffs agree with the trends found in previous cadaver studies [2] and demonstrate the importance of including impingement and muscle function considerations in virtual planning for RTSA.

ACKNOWLEDGEMENTS

RTSA implants and surgery plans and partial funding for RDH fellowship were provided by Arthrex

REFERENCES

- [1] <https://simtk.org/projects/opensim-jam>
- [2] Nolte et al., *J Shoulder Elbow Surg* 30:1817–1826, 2021.

THE RELATIONSHIP BETWEEN IMBALANCE SYMPTOM AND CARDIAC PULSATION INDUCED MECHANICAL STRAIN IN THE BRAINSTEM AND CEREBELLUM FOR CHIARI MALFORMATION TYPE I

Mohamad Motaz F. Al Samman (1), Alaaddin Ibrahimy (2), Blaise Simplicite Talla Nwotchouang (3), John N. Oshinski (4), Daniel L. Barrow (5), Philip A. Allen (6), Rouzbeh Amini (7), Rafeeqe A. Bhadelia (8), Francis Loth (7)

(1) Department of Bioengineering, Northeastern University, Boston, Massachusetts, USA

(2) Department of Biomedical Engineering, Yale University, New Haven, Connecticut, USA

(3) Department of Biomedical Engineering, The University of Akron, Akron, Ohio, USA

(4) Radiology & Imaging Sciences and Biomedical Engineering, Emory University School of Medicine, Atlanta, Georgia, USA

(5) Department of Neurosurgery, Emory University, Atlanta, Georgia, USA

(6) Department of Psychology, University of Akron, Akron, Ohio, USA

(7) Department of Mechanical and Industrial Engineering, Department of Bioengineering, Northeastern University, Boston, Massachusetts, USA

(8) Department of Radiology, Beth Israel Deaconess Medical Center & Harvard Medical School, Boston, Massachusetts, USA

INTRODUCTION

Chiari malformation Type I (CMI) is characterized by cerebellar tonsillar descent and crowding of neural structures at foramen magnum [1, 2]. Imbalance is a symptom that affects nearly half of CMI patients and is thought to be caused by damage to neural tracts in the hindbrain [1, 2]. Paul et al. reported sensory loss related to the dorsal column in 19 of 71 CMI patients (~27%) through physical examination and 29 (~40%) of these patients reported loss of balance [1]. Milhorat et al. reported 189 of 364 CMI patients (~52%) experienced poor equilibrium [2]. Similar findings have also been reported by other researchers [3]. These studies suggest possible damage to the neural circuitry pertaining to balance, and postural controls.

The goal of this study is to examine the relationship between CMI imbalance and cardiac-induced strain on the vestibulospinal tract (VST) using displacement encoding with stimulated echoes magnetic resonance imaging (DENSE MRI). Reflexive postural adjustment of the head and body results from the vestibular system influence on skeletal muscular tone ensuring coordination between different muscle groups through the lateral and medial vestibulospinal tracts (lVST, mVST) [4]. We hypothesize that CMI subjects with imbalance have higher strain on VST than those without imbalance.

METHODS

Participants: 35 adult (5 males, 30 females) CMI subjects and 25 (8 males, 17 females) healthy adult controls were scanned at Emory University School of Medicine between 2017 and 2022 under a protocol approved by the institutional review board. All participants signed a written consent before enrollment in the study [5]. Symptomatology was collected by interviewing CMI subjects at the time of presurgical scan using approved questionnaires [5]. Based on self-reported symptoms regarding balance, CMI subjects were divided into two subsets, CMI with imbalance (n = 15, 2 males, 13 females), and CMI without imbalance (n = 20, 3 males, 17 females).

Image acquisition used in this study was described in our previous publications [5]. Briefly, sagittal T1 and T2 weighted images of the brain were acquired using a PrismaFit 3T MRI scanner (Siemens Healthcare, Erlangen, Germany) employing a 20-channel head coil. DENSE MRI scans were acquired in the midsagittal plane using a 2-dimensional (2D) spiral cine technique and peripheral pulse unit gating with spatial and temporal resolution. Pixel size was 0.9 x 0.9 mm, and the slice thickness was 8 mm.

Due to the proximity of lVST and mVST at vestibular nuclei and in the cervical spinal cord, we employed two regions of interest (ROI) boxes for both tracts in the midsagittal plane and referred to them as the vestibulospinal tract (VST) (Fig. 1). The rostral VST (rVST) box was placed at the start of the tract (~3–4 mm anterior to the posterior aspect of the pontomedullary junction to ensure ROI placement on tissue and not on the cerebrospinal fluid), and the caudal VST (cVST) was placed at the center of the spinal cord at the level of C1/C2.

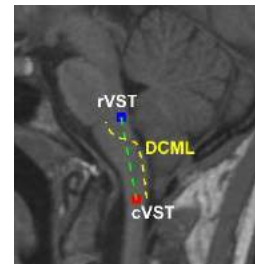


Fig. 1: Location of the region of interest (blue and red boxes) on an anatomical MRI of a CMI patient at the midsagittal plane. The route of DCML was depicted with the dashed yellow line.

The tissue motion of rVST and cVST was traced over the cardiac cycle and the path was illustrated in Fig. 2. This displacement can be decomposed to rigid body motion and lengthening/strain that VST experiences over the cardiac cycle.

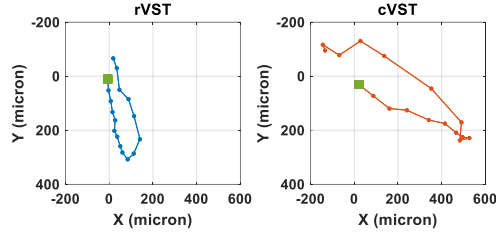


Fig. 2: Brain tissue motion path of rVST and cVST for one CMI subject (green box is starting point).

The 2D displacement field image was analyzed in the midsagittal plane. The local strain distribution along the line connecting the two ROI boxes was computed as it follows: a set of boxes along each line comprised of the average of 1 voxel on the line, and the two voxels adjacent to it (1x3) were determined. The coordinates of the ROI boxes, and the length of the line connecting them change throughout the cardiac cycle. The length of the line between the two boxes spaced seven voxels apart was calculated using equation (1) for each specific location along the line. Subsequently, the maximum lengthening and strain were computed using equations (2) and (3) respectively, to obtain strain distribution along the line. This definition of the lengthening and strain considers the tissue in tension only (no compression) as the undeformed configuration is unknown. Since the length of the lines among subjects was different, the one-to-one comparison of each calculated *localized* strain and the subsequent averaging were deemed impossible. As such as, averaging of the *localized* strains were made not based on the actual distance on the line but based on the relative distance from the caudal end. In particular, the relative distance was chosen in 5% increments from the caudal end, and the corresponding *localized* strain data were averaged for each increment (location) for each participant. Subsequently, the mean distributions were calculated based on the aligned *localized* strains. The average of a given increment was not computed for cases with missing subject data.

Statistical Analysis: were performed using MATLAB. Independent samples *t*-test was used to compare the maximum strain in controls, and CMI with and without imbalance. Comparisons with *p*-values of less than 0.05 were considered significant. Strain values were reported as mean \pm standard deviation.

EQUATIONS

$$d(t) = \sqrt{(X_{rVST} - X_{cVST})^2 + (Y_{rVST} - Y_{cVST})^2} \quad (1)$$

$$L = d_{max} - d_{min} \quad (2)$$

$$\epsilon_{max} = \left(\frac{L}{d_{min}}\right) * 100 \quad (3)$$

RESULTS

The local strain distribution values were typically 1–3% (Fig. 3). In general, the mean strain showed higher values caudally. The mean strain along VST in CMI ($1.97 \pm 0.64\%$) was not significantly different ($p = 0.128$) from that of the controls ($1.63 \pm 0.61\%$). The mean local strain along VST in CMI with imbalance ($1.97 \pm 0.71\%$) was not significantly different ($p = 0.996$) from that of CMI without imbalance ($1.97 \pm 0.60\%$).

DISCUSSION

We demonstrated that cardiac-induced strain distribution along the VST in CMI patients was not significantly higher than that of the controls. We also found no significant difference between the strain distribution along the VST in CMI patients with and without imbalance. The lack of statistically significant difference in the present study between strain in CMI subjects with and without imbalance could imply

that the magnitude of the observed cardiac-induced strain was too small to cause substantial damage to the tissue.

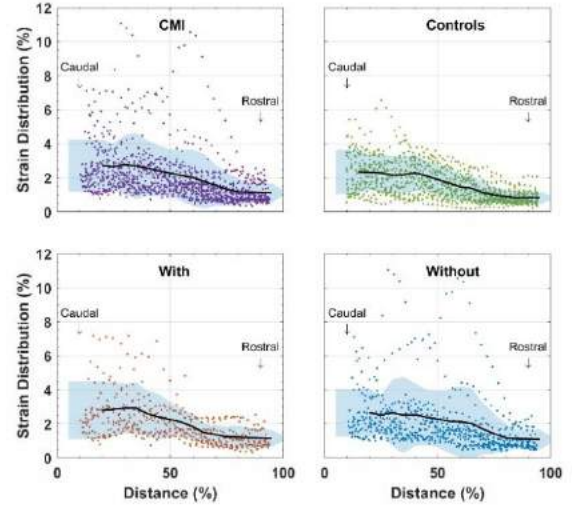


Fig. 3: Localized strain along VST of each participant for controls and CMI subjects with and without imbalance. Caudal and rostral ends are marked. The solid black lines and the shaded blue areas represent the mean and standard deviation, respectively.

We also computed strain along other neurological tracts/peduncles pertaining to balance such as superior and inferior cerebellar peduncles and found no significant difference between the strain in CMI subjects with imbalance as compared to those without. Investigating the relationship between symptom and activity-related (such as coughing or Valsalva maneuver) brain tissue strain may be necessary to explain CMI symptomatology. We believe that tissue strain analysis during a physiological activity is the future direction of this research.

This study has several limitations. First, only the first two-thirds of each cardiac cycle are reliable due to a reduction in signal-to-noise ratio caused by T1 decay [5]. Therefore, rVST and cVST positions at the end of the cycle do not match the start location (Fig. 2). Second, the assumption that DCML tract experiences similar strain as the VST due to their proximity may not be true for all subjects (Fig. 1). The reason for adopting such an assumption was that we did not expect an abrupt change in the displacement gradient within a few voxels, and, as such, we assumed that the DCML strain should be similar to that of the VST.

CONCLUSION

In summary, cardiac-induced strain distributions along VST were not significantly different between CMI and controls, neither between CMI with and without imbalance. As such, investigating activity-related strain may better explain the altered balance function in CMI subjects.

ACKNOWLEDGEMENTS

The authors would like to thank Conquer Chiari and the National Institutes of Health, NINDS R15 (Grant No. 1R15NS109957-01A1) for providing funding for this research work.

REFERENCES

1. Paul, K.S., et al., J Neurosurg, 1983. **58**(2): p. 183-7.
2. Milhorat, T.H., et al., Neurosurgery, 1999. **44**(5): p. 1005-17.
3. Sommers, B.N. and B.L. Davis, Gait Posture, 2021. **88**: p. 280-285.
4. Haines, D.E. and G.A. Mihailoff, *Fundamental neuroscience for basic and clinical applications*. Fifth edition. ed. 2018.
5. Nwotchouang, B.S.T., et al., Ann Biomed Eng, 2021. **49**(6): p. 1462-1476.

FABRICATION AND MECHANICAL CHARACTERIZATION OF DIRECT INK WRITE 3D PRINTED METHACRYLATED HYALURONIC ACID CERIUM OXIDE SCAFFOLDS

Aritra Chatterjee ⁽¹⁾, Jordan Turner ⁽²⁾, Jonathan Banks ⁽²⁾, Joan Adebawale ⁽²⁾, Deva D. Chan ⁽¹⁾,
Juana Mendenhall ⁽²⁾

(1) Biomedical Engineering,
Purdue University,
West Lafayette, IN, USA

(2) Department of Chemistry,
Morehouse College
Atlanta, GA, USA

INTRODUCTION

Degenerative joint disease (DJD) affects more than 30 million adults in the United States. The disease causes the breakdown of articular cartilage which is responsible for bearing loads from body weight, and the loss of this cartilage can result in loss of the underlying bone and cause defects. The use of 3D printed biomaterials with therapeutic properties to mitigate diseased or damaged articular cartilage shows promise in developing novel materials for regenerative tissue engineering applications [1]. Mechanical properties and geometric factors such as porosity are important functional parameters of such engineered cartilage scaffolds [2]. Hyaluronic acid is a natural polysaccharide used as a hydrogel, which is a water-soluble polymer to create 3D structures. Cerium Oxide (CeO) nanoparticles are known as free radical scavenging species that can protect chemical bonds and biological entities by capturing reactive oxygen species (ROS). In this study we have fabricated 3-d printed scaffolds composed of varying polymers such as poly-vinyl-caprolactam (PVCL), methacrylated hyaluronic acid (MeHA), Pluronic F127, the photo-crosslinker Irgacure, (CeO), and varying concentrations of water. We also characterized these scaffolds using mechanical testing and FTIR spectroscopy.

METHODS

Hydrogels composed of varying polymers such as 5.63g poly-vinyl-caprolactam (PVCL), 5.75 g Methacrylated Hyaluronic Acid (MeHA) 3 mL Pluronic F127, 0.85 g of the photo crosslinker Irgacure, 18 μ L cerium oxide and varying concentrations of water were mixed in ice baths for 2 hours at 1100 rpm, replacing the ice every 30 minutes (Fig 1a). The Pluronic acid in samples required the produced solutions to be stored in the fridge or an ice bath when not in use. An Allevi 1 Bioprinter was used for the 3d printing. Each sample was printed using .6-layer height using a 4-layered lattice 3D file. The printer was auto calibrated before each print, and adjustments for temperature were done in increments of .5 degrees Celsius while adjustments for pressure were done in increments of 2 PSI. The samples were analyzed for their physical properties. pictures were taken at the time of printing and were compared to pictures at later time frames (Fig 1b). A Fourier

Transformed Infrared (FTIR) spectroscopy and microscopy was used to identify the chemical functional groups and analyze the distribution of the chemical composition throughout the sample (Fig 1c, d). The compositional make-up of the printed scaffolds is provided in Table 1. For mechanical characterization, the scaffolds were subjected to unconfined compression using bench-top mechanical testing set-up (Electroforce 3230). Scaffolds were compressed in orthogonal direction to the printing plane at a displacement rate of 1mm/s and an initial pre-load of 1 N was applied prior to testing to ensure uniform contact [3]. The contact areas of the porous scaffolds were calculated using image processing in FIJI. Data from the compression tests at 7% strain, were used to calculate elastic modulus by calculating the slope of the stress-strain curve in a linear region of the curve (Fig 1e) [4].

RESULTS

Our results show that samples such as MPV2010 (100 μ L H₂O) and MPV 2010 (300 μ L H₂O) took longer to dry (about 5 days) compared to those that lacked water such as MPV2010 (no H₂O). The inclusion of water also required lower pressure, 35 PSI as compared to 41 PSI for MPV 2010, for printing. Scaffolds such as MPV2010 (100 μ L H₂O) required higher printhead temperatures compared to samples such as MPV2010 (without water). We also observed that consecutive prints can result in thinner prints even when using the same settings. Pluronic F127 being thermosensitive, crosslinks the solution to a solid at higher temperatures. Thus, when not in use sample solutions were kept in a cooler filled with ice. FTIR measurements also showed that there is a more uniform distribution of material in samples containing water than in those without (Fig 1c, d). Compression modulus of the scaffolds varied within the range of 1-9 MPa across different specimens, with altered composition and cross-linking. We observed significant changes in the elastic modulus of the scaffolds subjected to different crosslinking intensities (10,15 and 20%) across HA scaffolds with different Cerium oxide content (Fig 1 f). Further, we found that the addition of CeO significantly increased the elastic modulus of the MPV 2010 scaffolds (Fig 1 g). Also, the addition of water can influence the mechanical properties of these scaffolds.

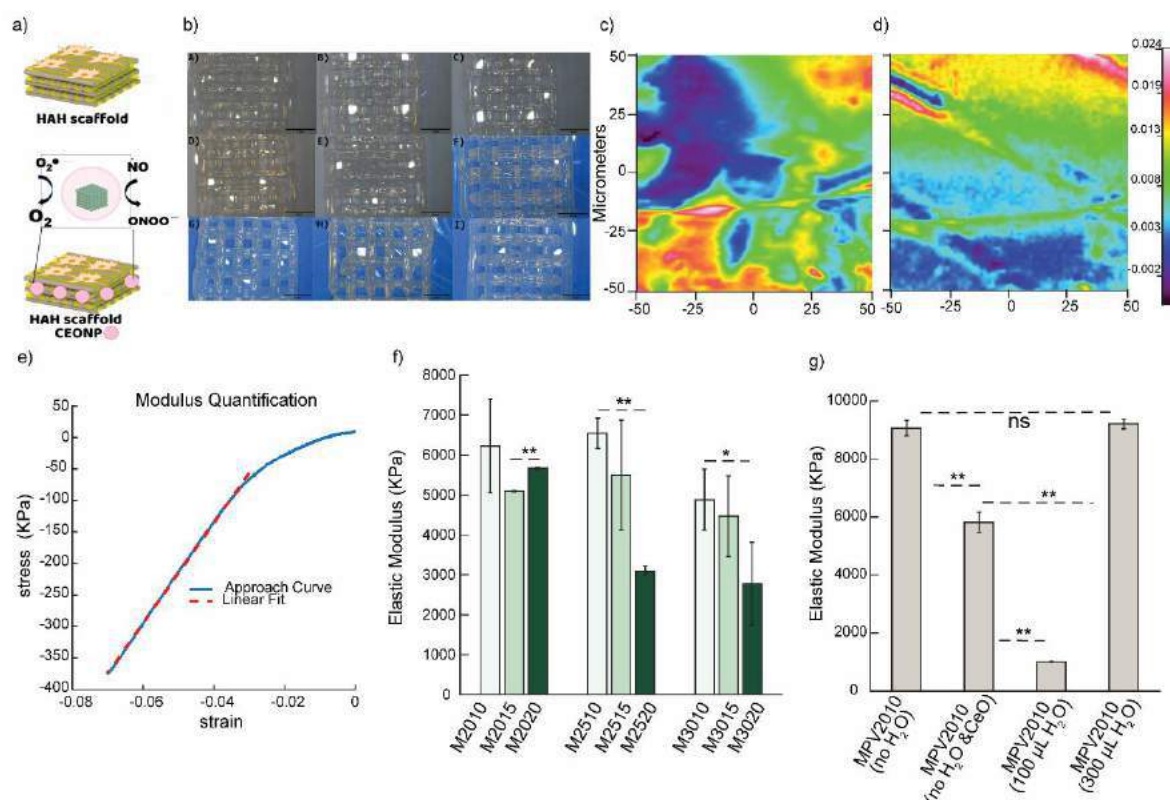


Figure 1: a) Schematic of a multi-layered scaffold containing CeO nanoparticles. b) Bright field microscope images of samples M2010 (A), M2015(B), M2020 (C), M2510 (D), M2515 (E), M2520 (F), M3010 (G), M3015 (H), M3020 (I). c & d) FTIR pictures of samples M2515 (C), and sample MPV2010 (100 µL) H₂O (D). e) Measurement of scaffold modulus from the compression stress-strain curves. f and g) Variation in compressive modulus of 3d- Printed scaffolds with varying composition and water concentration.

Table 1: Compositional make-up and sample porosity of 3-d printed scaffolds.

Hydrogel name	Cerium oxide (mg)	Pluronic (ml)	UV Cross-linking %-duration	Porosity (%)
M2010	2	1	10%-20 s	88.33
M2015	2	1	15%-20 s	59.89
M2020	2	1	20%-20 s	61.21
M2510	2.5	1	10%-20 s	68.11
M2515	2.5	1	15%-20 s	84.69
M2520	2.5	1	20%-20 s	86.84
M3010	3	1	10%-20 s	67.72
M3015	3	1	15%-20 s	58.62
M3020	3	1	20%-20 s	76.38
MPV2010 (no H ₂ O & CeO)	0	1	10%-10 s	57.23
MPV2010 (no H ₂ O)	2	3	10%-10 s	64.45
MPV2010 (100µL H ₂ O)	2	3	10%-10 s	52.06
MPV2010 (300µL H ₂ O)	2	3	10%-10 s	52.69

DISCUSSION

Our results showed that the inclusion of water decreased the required pressure for a successful print and increased the printhead temperature. This is important for integrating cells, as the increased temperature approaches human body temperature it will foster proliferation-friendly environments. The material from scaffolds containing water is more evenly distributed which also alters their mechanical properties. These scaffolds are also environmentally sensitive and show altered responses under temperature change. Current efforts are aimed investigating wait times required for printing samples to ensure consistency of prints and utilizing varying quantities of CeO or MeHA to investigate their influence on print settings and exploring methods of drying samples that contain water. We would like to test for consistency of mechanical properties in each group over a larger sample population and compare the bulk mechanical properties with micro scale properties using an Atomic Force Microscope.

ACKNOWLEDGEMENTS

The authors would like to thank NSF and EMBRIO for funding the research efforts and Jazzmin Owens for helping with scaffold fabrication.

REFERENCES

- [1] Kim, Y et al., *J Functional Biomaterials* , 13:34, 2022.
- [2] Xiao Y et al. *Tissue Engineering* , 19:5 403-412, 2013.
- [3] Bittner S.M. et al. *Acta Biomaterialia*, 1742-7061,2019.
- [4] Lee D et al. *Springer*, 1-21, 2018.

NO STRINGS ATTACHED: PREDICTING TRICUSPID VALVE COAPTATION WITHOUT *IN VIVO* CHORDAL GEOMETRY

Mrudang Mathur (1), Vijay Dubey (1), Manuel K. Rausch (2,3,4)

- (1) Department of Mechanical Engineering, UT-Austin, Austin, TX, USA
(2) Department of Aerospace Engineering and Engineering Mechanics, UT-Austin, Austin, TX, USA
(3) Department of Biomedical Engineering, UT-Austin, Austin, TX, USA
(4) Oden Institute for Computational Engineering and Sciences, UT-Austin, Austin, TX, USA

INTRODUCTION

Tricuspid valve leakage is a significant contributor to morbidity and mortality. That is, when the tricuspid valve does not seal completely, retrograde leakage through the valve reduces ventricular efficiency and induces volume-overload and cardiac remodeling. Together, reduced forward flow with adverse remodeling of the right ventricle leads to exercise intolerance and, when untreated, to heart failure and ultimately death. Methods to treat the tricuspid valves are plentiful and include surgical approaches and – recently – also transcatheter approaches. However, regardless of invasiveness, all current methods are suboptimal with recurrence rates of leakage at least as high as 15-30%, some worse [1]. Reasons for the ineffectiveness are multi-fold. Here we focus on the complexity of the valve apparatus which makes standardization of surgeries and medical devices difficult. Among those complexities are large inter-subject variations in valve geometry. For example, only about 54% of patients actually have a three-leaflet valve, while all other patients have either 2, 4, or even 5 leaflets [2]. We submit that a patient-specific approach to treating the tricuspid valve may overcome some of today's methods' ineffectiveness. Toward this end, we and others have tried to develop patient-specific models of the tricuspid valve with which patient-specific preclinical planning may be possible. Unfortunately, this is an entirely non-trivial challenge. For example, patient-specific data from routine clinical examinations is limited to 3D echocardiography without detailed information on tissue properties and – very importantly – information about the complex subvalvular apparatus, which is invisible to 3D echocardiography. In our current work, we are adapting the work by Sacks' group on the mitral valve to the tricuspid valve. Specifically, we are implementing a modeling approach in which we can replace the (unknown) subvalvular chordal apparatus with a virtual pressure field that we inform through a mapping procedure between 3D echocardiography-derived images of the valve at end-systole and end-diastole. Here, we describe our preliminary findings.

METHODS

To predict tricuspid valve coaptation in the absence of the true, *in-vivo* chordal geometry, we use a hyperelastic shape-matching framework [3]. That is, we build a material-point correspondence between the valve geometries at end-diastole (ED) and end-systole (ES) without explicitly modeling the chordae tendineae.

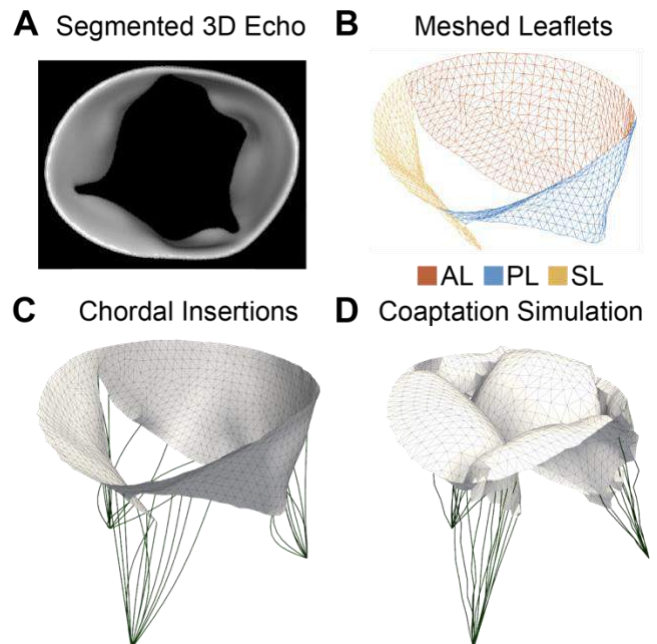


Figure 1: “Synthetic” imaging-based valve modeling pipeline

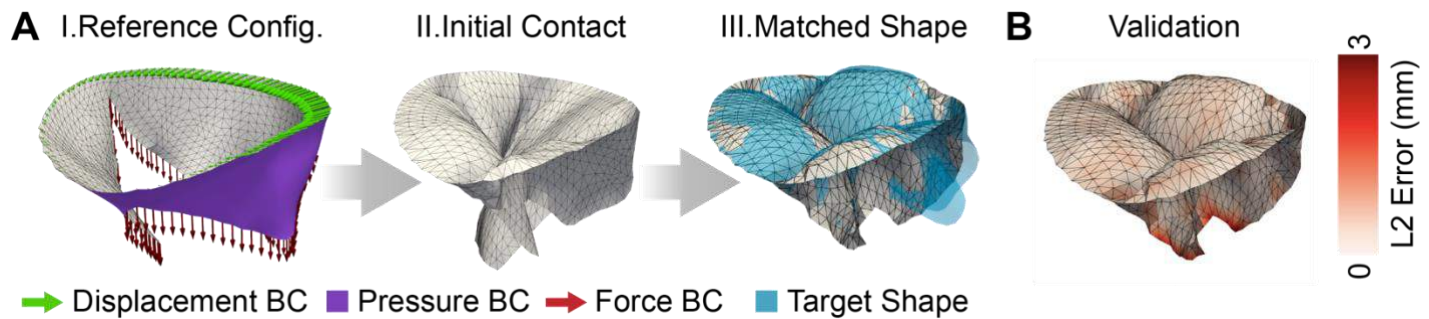


Figure 3: (A) We successfully simulate valve coaptation without explicitly modeling the chordae tendineae. (B) The error in displacements is minimal at the leaflet centers

“Synthetic” Imaging-based Tricuspid Valve Model

We first create a “synthetic” imaging-derived finite element model of the human tricuspid valve. Specifically, from 3D ultrasound data, we segment the tricuspid valve leaflet surfaces using MATLAB (v2021b, MathWorks, Natick, MA) at ED and ES, see **Figure 1A**. Next, we fit spline surfaces to our segmentation at ED and create a finite element mesh in Cubit (Coreform, Orem, UT), see **Figure 1B**. We then define papillary muscle heads from which chordae tendineae originate and insert into the ventricular surface of the leaflets based on existing literature, see **Figure 1C**. Furthermore, we manually adjust chordal insertion sites and lengths to ensure leaflet coaptation that matches the segmentation at ES, similar to our previous work [4]. Next, we assign ultrasound-derived displacements to the annulus and a literature-derived transvalvular pressure to the leaflet surfaces. Finally, we quasi-statically load the valve in Abaqus/Explicit (Dassault Systèmes, Providence, RI) to simulate leaflet coaptation, see **Figure 1D**. As a result, we create a “synthetic” finite element model with which we establish our shape-matching framework.

Hyperelastic Shape-Matching Framework

To begin the shape-matching process, we consider the coapted “synthetic” valve to be our target ES geometry. That is, we morph the segmented ED geometry to match this shape. To this end, we first remesh the ES geometry in MeshLab (ISTI, Pisa, Italy) to smooth out any discontinuities, see **Figure 2A**. Next, we sample the space surrounding the ES geometry and identify the shortest distance to the leaflet surface for each sample point, see **Figure 2B**. This distance map, or shape field, allows us to penalize any mismatch between the ED and ES geometries, as detailed below.

To simulate leaflet coaptation, we delicately balance a downward force in place of chordal tension, annular displacements, and a generic transvalvular pressure. Furthermore, we ensure shape accuracy through penalization from the shape field. That is, we penalize a shape mismatch by applying an incremental pressure load to the ED surface that is proportional to its distance from the target ES surface. Moreover, we

generate an analytical expression for this shape field by encoding its components through a 3D Discrete Cosine Transform, similar to Rego et al. Furthermore, we implement this in Abaqus/Explicit through the VDLOAD subroutine.

RESULTS

We use the hyperelastic shape-matching scheme to successfully morph the ED geometry to that of the ES state, see **Figure 3A**. Specifically, we establish initial contact of the leaflets by balancing annular displacements, the chordal-mimicking force, and generic transvalvular pressures. We then activate our shape field to ensure a close match in geometries. Specifically, we observe an average nodal error of 0.39 ± 0.455 mm between the target and simulated shape, see **Figure 3B**.

DISCUSSION

In conclusion, we successfully adapted a method first proposed by Rego et al, for the tricuspid valve. That is, we are able to identify a virtual pressure field that replaces the chordal apparatus of the tricuspid valve. We do so, through a mapping between 3D echocardiography-derived geometries of the tricuspid valve at end-diastole and end-systole. This pipeline will allow us to conduct patient-specific simulations of the tricuspid valve that are built solely on 3D echocardiography data even in the absence of imaging-based data on the subvalvular chordal apparatus. Naturally, this approach is prone to several potential errors and inaccuracies. Our next step will be to conduct the procedure on a virtual 3D echocardiography image that we create using the Texas TriValve 1.0, a high-fidelity model that we have previously developed, published, and made openly available. Knowing its true deformation throughout the cardiac cycle, we will have the means to quantify the errors we accrue using the above-described approach. If successful, we will expand our preliminary study to actual patient data and evaluate its usefulness in preprocedural planning. Specifically, we aim to predict the outcomes of clinical procedures based on pre-operative images and compare them to post-operative images of the same procedure. We hope that through this work, we will aid surgeons and interventionalists in improving clinical outcomes and providing patients with improved health and quality of life.

ACKNOWLEDGEMENTS

AHA 18CDA34120028 (to MKR) & 902502 (to MM), as well as NIH R21HL161832 (to MKR) & R01HL165251 (to MKR). We would also like to thank Prof. Michael Sacks for the helpful discussion.

REFERENCES

- [1] Taramasso, M et al, *JACC Cardiovasc Interv*, 12(2):155-165, 2019.
- [2] Hahn, R et al. *JACC Cardiovasc Imag*, 14(7), 1299-1305, 2021.
- [3] Rego, B et al., *Int J Numer Method Biomed Eng*, 34(12):e3142, 2018. [4] Mathur, M et al., *Eng Comput*, 38:3835-3848, 2022.

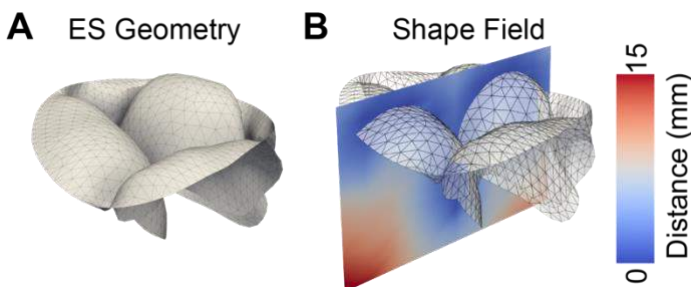


Figure 2: Space surrounding (A) the smoothed geometry at end-systole (ES) is sampled to build a (B) shape field around the leaflet surfaces

A COMPUTATIONAL FRAMEWORK FOR SURGICAL PLANNING OF PULMONARY ARTERY STENOSIS REPAIR IN TETRALOGY OF FALLOT PATIENTS

Alessia Di Nardo (1), Leslie Louvelle (2), David A. Romero (1), Matthew Doyle (1), Thomas L. Forbes (3), Cristina H. Amon (1,2)

- (1) Mechanical and Industrial Engineering, University of Toronto, Toronto, Ontario, Canada
(2) Institute of Biomedical Engineering, University of Toronto, Toronto, Ontario, Canada
(3) Division of Vascular Surgery, Department of Surgery, Peter Munk Cardiac Centre, University Health Network, University of Toronto, Toronto, Canada

INTRODUCTION

Tetralogy of Fallot (ToF) is a congenital heart defect present in 1 of every 3600 births [1]. A characteristic feature of ToF is stenosis of the pulmonary arteries, leading to obstruction of the right ventricular outflow tract. This defect can be repaired surgically through the incision and patching of the pulmonary arteries. However, due to differences in pulmonary artery anatomy, treatment and surgical strategies may vary between patients [2]. Additionally, vessel patches can be made out of multiple synthetic and biological materials [3].

In recent years, methods such as finite element analysis have been used to evaluate the local mechanical environment within regions of the cardiovascular system. Mechanical parameters are known to influence remodelling of the vessel over-time [4] and may have important implications for long-term clinical outcomes within this patient population. In previous work conducted by our group [5], a computational framework to simulate the surgical repair of pulmonary artery stenosis has been developed. This framework was also used to compare the mechanical consequences of using different patch materials in different repair locations (Table 1). This same framework, which is described below, will also be employed in the present work.

Table 1: Summary of Patch Materials and Repair Locations

Patch Materials	Surgical Repair Locations
<ul style="list-style-type: none">• Dacron• PTFE• Porcine Xenopericardium• Human Pericardium	<ul style="list-style-type: none">• INF+MPA (Infundibulum and Main Pulmonary Artery)• MPA (Main Pulmonary Artery)• MPA+LPA (Main Pulmonary Artery and Left Pulmonary Artery)

METHODS

Research Ethics Board approval was received at the Hospital for Sick Children, Toronto, Canada (REB #1000026285). Patient-specific computational meshes were then generated from MRA imaging for three post-operative patients using manual segmentation methods in SimVascular (www.simvascular.org) [6].

The virtual surgery methodology that was developed aimed to computationally replicate the stenosis repair procedure. This was accomplished in three main steps:

1. Cardiopulmonary Bypass Simulation (Depressurization)

Firstly, a zero-pressure geometry was generated to replicate the changes that occur to the vessel as a result of intraoperative cardiopulmonary bypass conditions. This simulation step was developed using the methods proposed by Raghavan et al [7], and was performed using ANSYS APDL (ANSYS Inc, Somerset) and MATLAB (MathWorks, Natick, MA).

2. Virtual Patch Creation

An incision and patch were then defined within MATLAB. A patch mesh was generated and exported to Autodesk MeshMixer (Autodesk Inc., San Rafael, CA) where it was post-processed and combined with the zero-pressure geometry.

3. Return of Blood Flow Simulation (Pressurization)

Finally, the return of blood flow was simulated for the patched geometry by applying a uniform pressure of 6000 Pa (45 mmHg) to the walls of the vessel using ANSYS Mechanical.

RESULTS

Following virtual surgery, the mechanical environment within the repaired vessels was assessed. The average Von Mises stress was compared between patch locations as well as between the patch materials (Figure 1) both visually and using Friedman statistical tests with Dunn post-hoc analysis. It was shown ($p < .001$) that significant differences existed in average stress between models featuring different patch materials. It was also observed that lower levels of average Von Mises stress were seen in models featuring synthetic patch materials (Dacron and PTFE) than in biological patch materials (porcine xenopericardium and human pericardium).

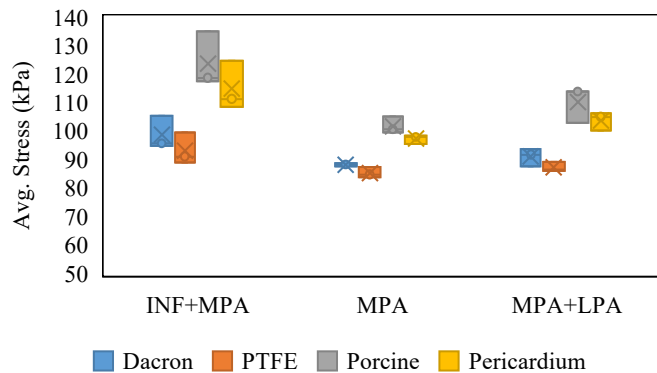


Figure 1: Average Von Mises stress for three patients with stenosis repair occurring at three different locations with four patch materials.

Using the methodology proposed above, it was also possible to visualize the stress distribution within the patched vessels (Figure 2). Regions of high stress are observed at the suture line, between the two materials.

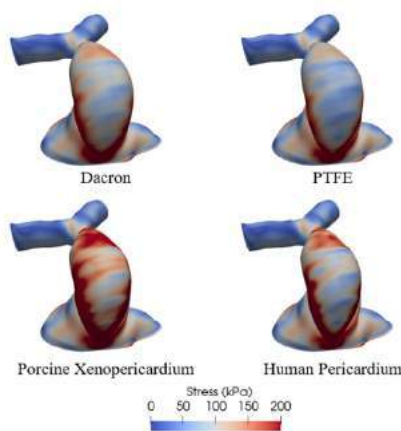


Figure 2: Resulting stress distributions for Patient 3 in a single patch location (INF+MPA) following virtual surgery.

DISCUSSION

The mechanical consequences of pulmonary artery patching have previously been studied using virtual surgery and computational simulation. However, these studies have been limited by factors such as

the use of idealized vessels [3] or the investigation of a single patch location and material [8]. The methods proposed here allowed for the comparison of four patch materials across multiple stenosis locations for multiple patient geometries. It was observed that relative patch material performance, in terms of average stress, was the same across the locations and patient geometries included. This suggests that certain materials may be better suited for patch repair from a mechanical perspective, however, the long-term clinical consequences of these mechanical differences should be assessed in larger, longitudinal studies.

The goal of the present work is to continue to develop our understanding of the relationship between patch parameters and mechanical indices through the inclusion of additional patients. A larger patient cohort will allow us to investigate the influence of patient-specific geometric parameters on patch mechanical performance. Computational methods, such as those presented in this work, may aid in the generation of patient-tailored surgical planning tools in which different repair options can be compared.

ACKNOWLEDGEMENTS

This work was supported by the Natural Sciences and Engineering Research Council (NSERC), the Ted Rogers Centre for Heart Research, and the Labatt Family Heart Centre Innovation Fund.

REFERENCES

- [1] C. Apitz, G. D. Webb, and A. N. Redington, "Tetralogy of Fallot," *Lancet*, vol. 374, no. 9699, pp. 1462–1471, 2009.
- [2] V. J. da Silva Nina, "Surgical Repair of Stenotic Pulmonary Arteries in Tetralogy of Fallot," *Intech*, vol. 32, no. July, pp. 137–144, 2013.
- [3] S. S. Lashkarinia, S. Piskin, T. A. Bozkaya, E. Salihoglu, C. Yerebakan, and K. Pekkan, "Computational Pre-surgical Planning of Arterial Patch Reconstruction: Parametric Limits and In Vitro Validation," *Ann. Biomed. Eng.*, vol. 46, no. 9, pp. 1292–1308, 2018.
- [4] Y. Han, K. Huang, Q. P. Yao, and Z. L. Jiang, "Mechanobiology in vascular remodeling," *Natl. Sci. Rev.*, vol. 5, no. 6, pp. 933–946, 2018.
- [5] A. Di Nardo, L. Louvelle, D. A. Romero, M. Doyle, T. L. Forbes, and C. H. Amon (in press), "A Comparison of Vessel Patch Materials in Tetralogy of Fallot Patients using Virtual Surgery Techniques," *Ann. Biomed. Eng.*, 2023.
- [6] A. Updegrove, N. M. Wilson, J. Merkow, H. Lan, A. L. Marsden, and S. C. Shadden, "SimVascular: An Open Source Pipeline for Cardiovascular Simulation," *Ann. Biomed. Eng.*, vol. 45, no. 3, pp. 525–541, 2017.
- [7] M. L. Raghavan, B. Ma, and M. F. Fillingner, "Non-invasive determination of zero-pressure geometry of arterial aneurysms," *Ann. Biomed. Eng.*, vol. 34, no. 9, pp. 1414–1419, 2006.
- [8] S. S. Lashkarinia, G. Coban, B. Kose, E. Salihoglu, and K. Pekkan, "Computational modeling of vascular growth in patient-specific pulmonary arterial patch reconstructions," *J. Biomech.*, vol. 117, p. 110274, 2021.

ASSOCIATION BETWEEN RESISTANCE TO CEREBROSPINAL FLUID FLOW AND CARDIAC-INDUCED BRAIN TISSUE MOTION FOR CHIARI MALFORMATION TYPE1

Saeed Mohsenian (1), Alaaddin Ibrahimy (2), John N. Oshinski (3), Blaise Simplicie Talla Nwotchouang (4), Rafeeqe A. Bhadelia (5) Daniel L. Barrow (6), Rouzbeh Amini (7) and Francis Loth (7)

- (1) Department of Bioengineering, Northeastern University, Boston, Massachusetts, USA
- (2) Department of Biomedical Engineering, Yale University, New Haven, Connecticut, USA
- (3) Radiology & Imaging Sciences and Biomedical Engineering, Emory University School of Medicine, Atlanta, Georgia, USA
- (4) Department of Biomedical Engineering, The University of Akron, Akron, Ohio, USA
- (5) Beth Israel Deaconess Medical Center, Department of Radiology, Harvard Medical School, Boston, Massachusetts, USA
- (6) Department of Neurosurgery, Emory University, Atlanta, Georgia, USA
- (7) Department of Mechanical and Industrial Engineering, Department of Bioengineering, Northeastern University, Boston, Massachusetts, USA

INTRODUCTION

Chiari Malformation Type 1 (CMI) is a disorder anatomically characterized by descent of the cerebellar tonsils greater than 5 mm below the foramen magnum (FM) [1] causing pressure on the spinal cord. CMI patients experience signs and symptoms such as severe headaches, neck pain, unsteady gait, poor hand coordination, numbness and tingling of the hands and feet, dizziness, difficulty swallowing, sometimes accompanied by gagging, choking, and vomiting, and speech problems, such as hoarseness. However, some patients meeting the anatomic criteria of CMI have minimal to no symptoms while some others have typical CMI symptoms without meeting the anatomic criteria.

Because of altered brain morphology, CMI patients have more resistance to cerebrospinal fluid (CSF) motion compared to healthy subjects [2]. To quantify the CMI patients' resistance to CSF, a hydrodynamic property called *longitudinal impedance* (LI) is defined as the ratio of pressure harmonic to flow harmonic at the same frequency. To obtain the *integrated longitudinal impedance* (ILI), which represents the overall CSF resistance, the resulting LI is integrated from 1 to 8 Hz. Also, CMI patients have increased tissue motion in the cerebellum and brainstem [3].

In the present study, we examined the interaction of CSF motion and brainstem/cerebellum tissue displacement to understand the possible correlation between these factors.

METHODS

The MRI exams were acquired at Emory University under an IRB-approved research protocol. Thirty-two CMI patients (x male, x female) and eighteen healthy subjects (x female, x male) were analyzed by

determining ILI and displacement in the brainstem and cerebellum. All patients had the cerebellar tonsillar position (CTP) greater than 5mm.

To calculate ILI, axial T2 weighted images were used with axial slice thickness 0.9 mm and pixel spacing 0.85 mm to segment the subarachnoid space into a 3D model of CSF space that extends from the FM to an axial plane 60 mm caudal to the FM (near C3 or C4).

ANSYS ICEM CFD was used to generate the computational mesh for the CSF space. Depending on the shape and size of the flow geometry, A time-dependent velocity inlet boundary condition based on the subject-specific MRI flow measurements was specified at the inlet and a zero-pressure boundary condition was assumed at the flow outlet. No slip (zero velocity) boundary conditions were specified at the walls. The commercial finite volume solver *Ansys Fluent* was used to run computational fluid dynamics (CFD) simulations of CSF motion. ILI was calculated using an internally-developed MATLAB program.

To quantify brain tissue motion, another internally-developed MATLAB program was employed (DENSEPro) which utilized DENSE phase images to compute the average displacement of the brain tissue over the cardiac cycle [4]. A 30 mm² circular region of interest (ROI) was automatically identified in sections with the greatest amount of displacement or principal strains to obtain a more homogeneous representation of maximum displacement and principal strain in each brain region. The decision to use 30 mm² was based on the previous findings, which showed that DENSE MRI requires approximately 80 averaged voxels to provide a reliable displacement measurement [4]. The average of the peak displacements within each circular area for all brain regions was used to determine the maximum displacement in each circular area (Figure 1).

Statistical analysis were performed using Excel. The linear regression analysis was used to examine the correlation between ILI and maximum displacement at the cerebellum and brainstem.

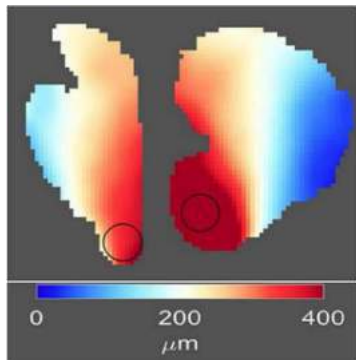


Figure 1: Two-dimensional Eulerian displacement maps of the brainstem and the cerebellum of a CMI subject [4]

RESULTS

Figures 2 and 3 depict maximum displacement at the brainstem and cerebellum versus ILI for CMI and healthy subjects. These figures show a significant correlation between the ILI and displacement at the cerebellum in CMI subjects. The result of the regression test shows a significant correlation between ILI and maximum displacement at the cerebellum of CMI subjects, $r=0.75$, $p=6.77 \times 10^{-7}$. However, the results of the regression test show that no correlation exist between the ILI and maximum displacement at the cerebellum for healthy subjects, as well as maximum displacement at the brainstem for both CMI and healthy subjects.

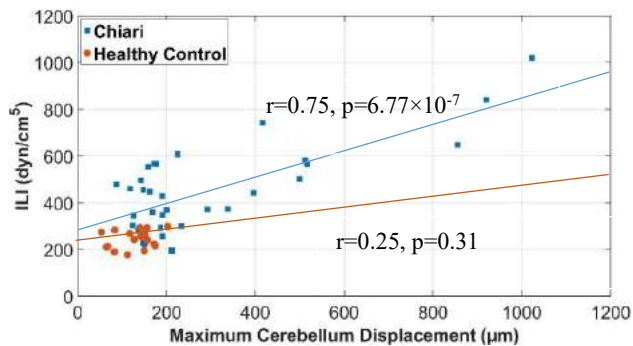


Figure 2. ILI versus maximum tissue displacement at the cerebellum for Chiari subjects and healthy controls.

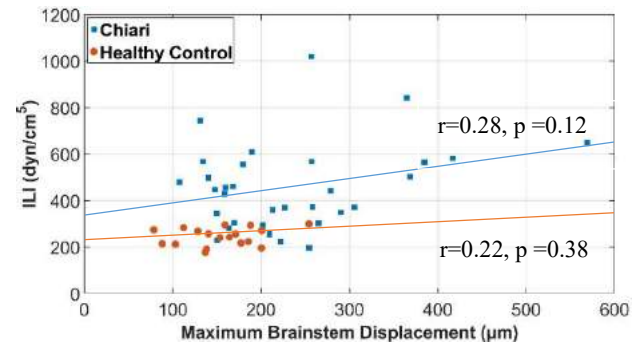


Figure 3. ILI versus maximum tissue displacement at the brainstem for Chiari subjects and healthy controls.

DISCUSSION

The present study examines the effect of two different parameters, including CSF flow resistance and cardiac-induced brain tissue motion for thirty-two CMI patients and eighteen healthy controls. Subjects with CMI have tonsillar herniation which often results in an increase in resistance to CSF motion between the cranium and spinal canal. The magnitude of ILI provides a quantitative measure of this resistance to CSF flow. ILI and brain tissue motion have both been shown to be elevated for CMI subjects [2, 3]. Thus, we postulated that there was a connection between resistance and tissue motion. However, the results of this study demonstrates that this postulation is only true for the correlation between ILI and cardiac induced brain tissue motion for CMI patients in the cerebellum and not in the brainstem. Since, patients with Chiari malformation, have CTP greater than 5 mm below the FM, the tonsils of the cerebellum in CMI patients herniate to the spinal canal and leading to an increase in the CSF flow resistance. On the other hand, since the cerebellar tonsils are in direct contact with CSF flow in the spinal canal, their displacement increases. Therefore, CMI patients show strong correlation between CSF flow resistance and displacement at the cerebellum. This phenomenon can explain the elevated cerebellum displacement in CMI patients compared to healthy subjects. Also, no correlation was found between ILI in both cerebellum and brainstem displacements of healthy controls.

As the resistance to CSF flow in spinal canal and maximum displacement at the cerebellum are significantly correlated in CMI patients, we explored how this relationship might change at higher displacement values. Therefore, we performed regression tests for the ILI and maximum displacement at the cerebellum for the values greater than 150 μm , 200 μm , and 250 μm to find out the correlation of these parametes at higher motion. The results showed that at higher values of displacements, the relationship between ILI and displacement at the cerebellum is stronger (Table 1).

Table 1. Correlation between ILI and maximum displacement at the cerebellum for CMI cases

	p-value	r
Maximum displacement at the cerebellum		
Total CMI cases	6.77E-07	0.75
Greater than 150 μm	9.94E-06	0.77
Greater than 200 μm	4.73E-04	0.82
Greater than 250 μm	1.16E-03	0.86

Elevated brain tissue motion has been associated with elevated brain tissue strain [3, 4] and may imply nerve damage. Thus, understanding the underlying biomechanics present in cardiac induced brain tissue motion/strain could help further understand how various clinical symptoms arise. While ILI clearly plays a role in the unsteady pressure environment within the spinal canal, the relationship between ILI and tissue motion requires further study.

ACKNOWLEDGEMENTS

The authors would like to thank Conquer Chiari and the National Institutes of Health, NINDS R15 (Grant No. 1R15NS109957-01A1) for providing funding for this research work.

REFERENCES

[1] Milhorat et al., *Neurosurgery.*, 44(5):1005–1017, 1999.
[2]Ibrahimy et al., *J. of Biomech. Eng.*, 143 (5), 051003, 2020.
[3] Pahlavian, et al., *J. of Biomech. Eng.*, 140: 2018.
[4] Nwotchouang, B., *Ann. of Biomed. Eng.*, 49: 1462–1476, 2021.

MATERIAL PARAMETRIC ANALYSIS OF POLYPROPYLENE DURING A CONTACT SENSITIVE SIMULATION OF A BALL BURST TEST OF A PROLAPSE MESH

Madeline Hackett (1), Teseo Schneider (2), Zachary Ferguson (3), Daniele Panozzo (3), Denis Zorin (3), Pamela Moalli (1), Steven Abramowitch (1)

- (1) Department of Bioengineering, University of Pittsburgh, Pittsburgh, PA, USA
(2) Computer Science Department, University of Victoria, Victoria, BC, CA
(3) Computer Science Department, New York University, New York City, NY, USA

INTRODUCTION

Pelvic organ prolapse is a condition that results from a loss of support to the pelvic organs. As many as 10% of women will seek surgical repair of this condition in their lifetime [1]. Repair with polypropylene mesh provides the greatest likelihood of a long-term, successful repair. However, these devices have been associated with unacceptable complication rates. Our work has shown that devices with a higher stiffness are associated with a more pronounced host response compared to those with a lower stiffness, suggesting that this response is, in part, driven by mechanical interactions between the device and the host.

Pelvic organ prolapse mesh devices are manufactured from thin, knitted polypropylene filaments. The differences in mechanical behavior across devices largely result from different knit patterns. Our recent data show significant regional variation in the host response, which indicates that mesh-host mechanical interactions must be studied at the level of individual pores if not filaments [2].

Simulating textiles such as polypropylene mesh at the level of filaments is challenging because they undergo large deformations with significant filament-filament interactions (contact and sliding). Recent developments in finite element modeling have now made it possible to simulate these interactions for devices undergoing large deformation. This study aims to utilize Incremental Potential Contact (IPC) implemented in the finite element solver PolyFEM to determine if the force-displacement relationship of a polypropylene mesh undergoing a ballburst test can be predicted from a simulation that includes local filament interactions with large deformations [3].

METHODS

The geometry of Restorelle™, a popular prolapse repair mesh, was captured using a SkyScan 1272 microCT system at 80kV, 125μA, 6.15μm pixel size, 180° rotation, and no filter. The images were thresholded to create a rough 3D geometry (3DSlicer, slicer.org) where individual filaments could be easily visualized, however the exported mesh fused adjacent filaments at areas of contact. To account for this, the exported mesh was imported into Blender (blender.org; v.3.3.1), where a series of circles with the same diameter as the filaments were manually fit to the geometry in 3D space and lofted to create a smoothed geometry of individual filaments within a single pore. An array modifier was then used to create multiple pores from this geometry, thereby resulting in a complete representation of Restorelle's geometry. Individual filaments were discretized into 104,906 tetrahedral elements using Houdini (sideFX, Inc.; v. 19.5) and a custom-written plugin to interface with the meshing software fletwild [4]. A triangular surface mesh (3,960 triangles) obtained from a CAD model of the ballhead that was used in the experiment provided the ballhead geometry. The simulations were performed in PolyFEM, a finite element solver that incorporates an incremental potential contact implementation for robust and accurate high order elastodynamic FE simulations that do not suffer from intersections or inverted Jacobians [3,5,6]. Boundary conditions were assigned to match the experiment with the deformable mesh device fixed around its circumference and the ballhead displaced as a rigid body along the vertical direction (methods depicted in Figure 1). A Neo-Hookean material model was selected for polypropylene. Since the material stiffness of polypropylene can vary depending on

the specific blend, Young's moduli of 0.896, 1.1, 1.3, and 1.55 GPa were assigned based on the range of values reported in the literature [7]. A Poisson's ratio of 0.425 was used for each simulation. The contact force on the ballhead was plotted versus the displacement for each simulation and compared among themselves and to experimental results. The experimental results were previously published and are represented by a force-displacement curve from N= 4 samples.

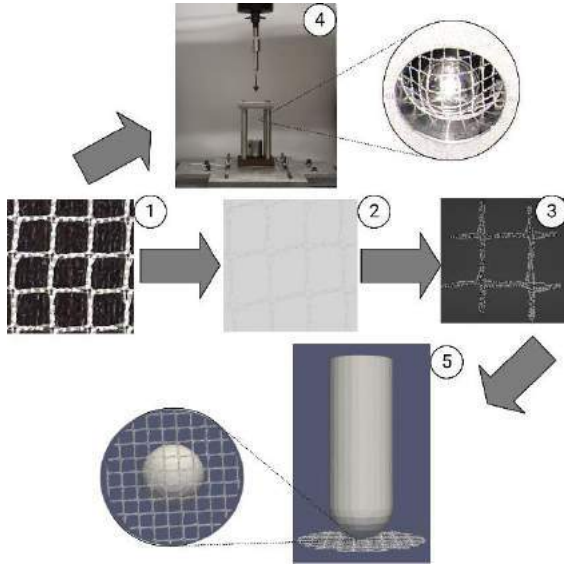


Figure 1: Workflow diagram where 1) is an image of Restorelle, 2) is a shadow projection of the Restorelle during microCT, 3) is the segmentation, 4) is the experimental setup of a ball burst test and 5) is the simulation of a ball burst test

RESULTS

The resulting simulations all demonstrated a nonlinear force-displacement response that was consistent with the experimental data. In addition, all simulations were intersection-free and there were no issues with element inversion. As expected, the predicted force-displacement relationship demonstrated stiffening behaviour with increases in Young's moduli. The predicted curve for a Young's modulus of 1.1 GPa provided the best match to the experimental data (Figure 2).

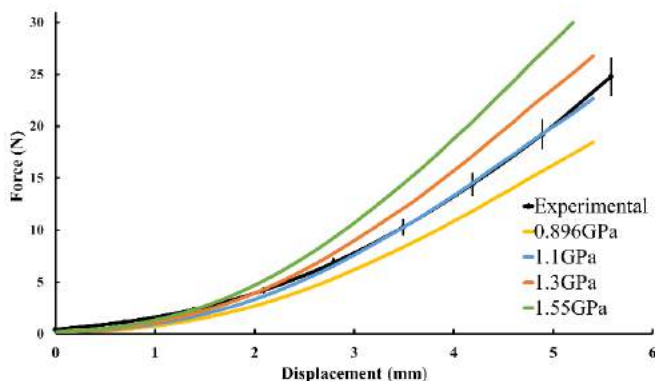


Figure 2: Resulting force-displacement curves compared with experimental data (mean±SD, n=4)

The greatest differences between the simulated and experimental data for the other curves exist primarily at larger displacements; however it is notable that all curves show similar differences in the low displacement behavior with respect to the experimental data (Figure 2). As expected for a ballburst test, stress concentrations appear near the tip of the ballhead and along mesh filaments with local variation within the filaments (Figure 3). The solving times for the simulations was in the range of 41.45 to 56.99 hours with stiffer simulations solving faster (Machine 1: AMD Ryzen 9 5950X, 16 cores at 4.9GHz, 2667 MT/s, 128 GB Machine 2: Intel Core i9-10980XE, 18 cores at 3.0 GHz, 3200 MT/s, 256 GB; no GPU acceleration used).

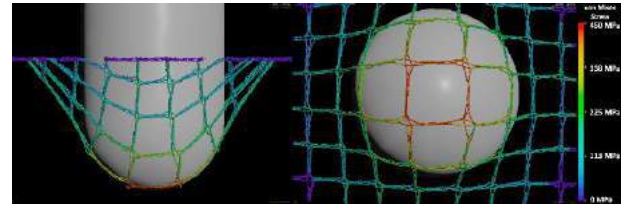


Figure 3: Simulated von Mises stresses in the mesh device as viewed from two perspectives

DISCUSSION

This study demonstrates the feasibility of simulating filament-level mechanical interactions for a textile, namely a pelvic organ prolapse repair device, undergoing large deformations. By validating this approach for a known experimental result, further research comparing mesh devices and modeling their interactions with tissue can be pursued. It should be noted that we have used a hyperelastic neohookean representation of material behavior in this study. While the resulting stresses of a neohookean material for large deformations was likely providing a reasonable approximation of plastic deformation, this methodology cannot be used to make predictions about the plastic behavior in this material. Future work will aim to improve the material model to account for systematic discrepancies between the simulation and experiment (i.e. forces at low displacements). It is possible that the latter may be related to the coefficient of friction, which was not considered in this study but will be in the future. In addition, we are planning to perform mechanical testing of individual filaments that can be isolated from these devices to determine if the measured Young's modulus matches that predicted here (i.e. 1.1 GPa).

ACKNOWLEDGEMENTS

NIH R01 HD097187-01, NSF 2053851, NSF 1835712, NSERC DGEER-2021-00461, RGPIN 2021-0370, and Horizon2020 MSCA grant No.764644

REFERENCES

- [1] Wu *et al.*, *Am J Obstet Gynecol.*, 2011.
- [2] Knight *et al.*, 2018.
- [3] Schneider *et al.*, *PolyFEM*, 2019.
- [4] Hu *et al.*, *TOG*, 2020.
- [5] M. Li *et al.*, *par.nsf.gov*, v.39(4), p. 20, 2020.
- [6] Feola *et al.*, *Int Urogyn J*, v.24(4), p. 559, 2013.
- [7] Jones, *Engineering Materials 1*, 2005.

MUSCLE ERR-GAMMA OVEREXPRESSION MITIGATES THE MUSCLE ATROPHY AFTER ACL RUPTURE

Aiping Lu (1), Katie Sikes (2), Ping Guo (1), Matthieu Huard (1), Kelly Santangelo (2), Scott Tashman (1), Vihang A. Narkar (3), Johnny Huard (1*)

- (1) Steadman Philippon Research Institute, Vail, CO. USA
- (2) Colorado State University, Fort Collins, CO. USA
- (3) Institute of Molecular Medicine, McGovern Medical School at the University of Texas Health Science Center, Houston, TX. USA

INTRODUCTION

Anterior cruciate ligament (ACL) reconstruction is the 6th most common orthopedic procedure performed in the United States (1,2). ACL injury leads to altered knee joint function, significantly increasing the risk of developing knee osteoarthritis. There is substantial evidence to suggest that muscle weakness contributes to adverse outcomes after ACL injury/reconstruction (3). Despite efforts to improve rehabilitation methods, current strategies often fail to restore pre-injury muscle strength in ACL-injured limbs. Our team has identified that estrogen-related receptor gamma (ERR γ) is a crucial regulator of paracrine angiogenesis in skeletal muscle (4). Selective over-expression of ERR γ in skeletal muscle (Err-gamma transgenic mice, TG) activates a robust paracrine angiogenic gene program involving myofibrillar induction and secretion of a battery of angiogenic factors resulting in promotion of muscle vascularization (4). The goal of this study was to determine if ERR γ -driven muscle angiogenesis can mitigate muscle atrophy after ACL injury by comparing TG mice to age-matched wild-type (WT) littermate control mice using a mechanically induced ACL injury model.

METHODS

Animals: 12 week old male and female TG and WT mice obtained from Dr. Narkar's laboratory were used for this study. The mechanically induced ACL rupture was conducted by our collaborators, Dr's Santangelo and Sikes at Colorado State University, who have specialized equipment for and prior experience with this injury model. The ACL rupture was performed on the right leg, and the left leg was used as non-injured control. The mice were euthanized four weeks after injury. The muscle tissues were harvested and the gastrocnemius muscle (GM) mass was flash-frozen in liquid nitrogen-cooled 2-methylbutane, and cryo-sectioned. The myofiber cross-sectional area (CSA) was measured based on the H&E staining on the GM muscle of TG and WT mice. **Cell Isolation and Myogenic Differentiation Assay:** Muscle progenitor cells (MPCs) from TG and WT mice were isolated using a modified preplate technique (5) and myogenic differentiation was performed by replacing the proliferation medium with fusion medium (DMEM with 2% FBS). The MPCs were isolated from TG and WT control mice and the diameters of myotubes were measured based on desmin staining after myogenic differentiation. H&E staining was performed on 10 μ m cryosections from GM according to the

manufacturer's instructions. Immunohistochemical staining and muscle force: It has been reported that ACL injury promotes muscle fibrosis (8). To assess fibrosis, the number of PDGFR α (fibrogenic cell marker) + cells were counted in the skeletal muscle samples. Muscle sections were fixed with 4% paraformaldehyde. PDGFR α and desmin staining were performed as previously described (6). To assess muscle performance, we measured the isometric torque of the anterior crural muscles in TG and WT mice as previously described (7). The number of PDGFR α + cells and the diameter of myotubes were counted and measured using ImageJ software. Statistical analysis: All results are presented as mean \pm standard deviation (SD). Means from ACL injured and non-injured of WT and TG mice were compared using Student's t-test, with a significance value of $p < 0.05$.

RESULTS

Muscle-specific ERR γ activation mitigated muscle fiber atrophy after ACL rupture. As expected, mean muscle fiber size was reduced in gastrocnemius muscles (GM) from the ACL-injured limbs of WT mice compared to the contralateral, uninjured limb (Fig. 1A and Fig. 1B left plot, $p < 0.01$). Conversely, there was significant difference in the average size of muscle fibers between ACL-injured and control limbs for the TG mice (Fig. 1B right plot, $P > 0.05$). We also observed that the muscle fibers in TG mice were significantly smaller than WT muscle fibers (Fig. 1B right, $P < 0.01$), due to a greater percentage of slow-twitch muscle fibers in muscles from the TG mice. Desmin staining demonstrated significantly decreased myotube diameter in the MPCs isolated from WT mice after ACL injury (Fig. 1C, D, $p < 0.01$). However, this ACL injury-induced myotube atrophy was not observed in TG MPCs after ACL injury (Fig. 1C, D). Taken together, these results indicated that ERR γ overexpression in the muscle prevented muscle fiber atrophy after ACL rupture. Muscle-specific ERR γ activation ameliorated muscle function loss after ACL rupture. Muscle torque testing revealed that muscle strength was significantly decreased in the ACL injured limbs in both male and female WT mice compared with non-injured limbs (Fig. 2A, male, 2B, female, 2C, $p < 0.01$). Strikingly, after ACL injury, the hindlimb muscles in TG mice were resilient to atrophy, as muscle function was similar in the ACL-injured and control limbs (Fig. 2. A, B and D). Muscle-specific ERR γ activation prevented fibrogenic cell expansion within skeletal muscle after ACL rupture. The number of PDGFR α + cells was significantly higher in the WT muscle

compared to TG muscle after ACL injury (Fig. 3A and B, $p<0.05$). In summary, those results demonstrated that muscle-specific ERR γ activation mitigated muscle atrophy and appears to reduce or prevent muscle fibrosis after ACL injury.

Figure 1:

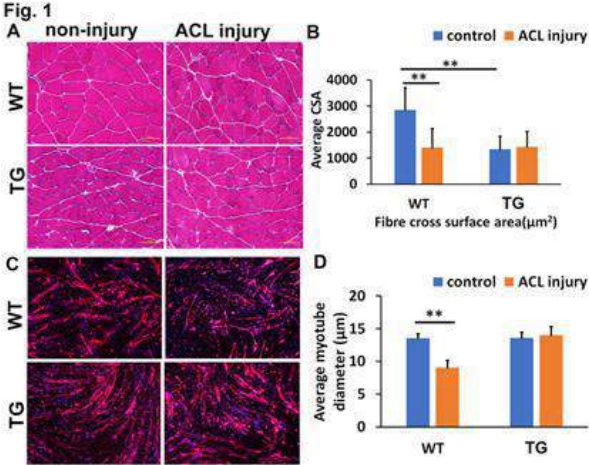


Figure 2:

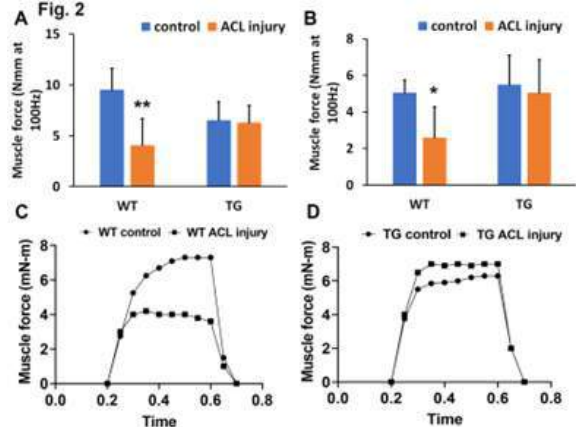
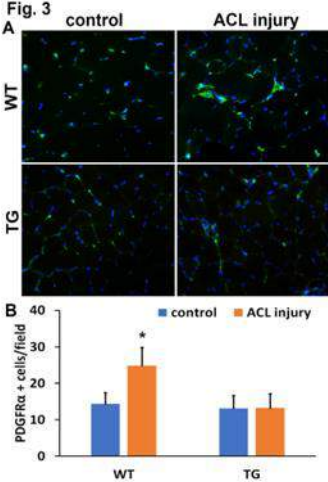


Figure 3:



DISCUSSION

Skeletal muscle is adversely affected by the ACL injury and recovery (even after reconstruction surgery) is often limited by muscle weakness. In the murine ACL injury model, muscle weakness is correlated with a reduction in angiogenesis and accumulation of fibrosis. It has been reported that ERR γ expression in the skeletal muscle directly correlates with vascular density, and ERR γ is highly expressed in well-vascularized muscle beds (4). This evaluated whether ERR γ overexpression can prevent muscle weakness after ACL injury, and if so whether this preventive effect would be potentially linked to increased muscle angiogenesis. We observed that the TG mice with muscle specific ERR γ activation have the capacity to mitigate muscle atrophy, as evidenced by the maintenance of muscle fiber size and muscle function after ACL injury. It is known that exercise induces muscle angiogenesis, and regular physical activity has been considered a therapeutic modality for preventing aging-related muscle wasting. Although exercise is the primary method for alleviating muscle weakness, many patients cannot achieve the exercise intensity that is necessary to prevent or reverse muscle atrophy. ERR γ belongs to the nuclear receptor superfamily, which are excellent ‘druggable’ targets with unique ligand-binding pockets that facilitate selective and specific drug design. Thus, future development of pharmaceuticals targeting ERR γ could provide a safe and effective therapy for improving outcomes after ACL injury and potentially other musculoskeletal disorders.

ACKNOWLEDGEMENTS

This work was supported by the National Institutes of Health (grant # R21 AR075997).

REFERENCES

1).Lubowitz, J.H., et al., Arthroscopy, 2011. 27(10). 2).Buller, L.T., et al., Orthop J Sports Med, 2015. 3(1). 3).Nawasreh, Z., et al., Am J Sports Med, 2017. 45(5). 4).Narkar, V.A., et al., Cell Metab, 2011. 13(3). 5) Gharaibeh, B., et al., Nat Protoc, 2008. 3(9). 6) Aiping Lu, et al., Sci Rep, 2020. 27;10(1):7075. 7) Aiping Lu, et al., Hum Mol Genet, 2014. 15;23(18).8) Christopher S Fry, et al., Orthop Res. 2017, 35(9).

AN INVERSE FE METHOD TO QUANTIFY THE RELATIONSHIP BETWEEN MECHANICAL PROPERTIES AND RESIDUAL STRESSES IN THE MYOCARDIUM

Manoj Ghosh (1), Marissa Grobbel (1), Lik Chuan Lee (1), and Sara Roccabianca (1)

(1) Department of Mechanical Engineering
Michigan State University
East Lansing, MI, United States

INTRODUCTION

Residual stress distributions are a common and characteristic trademark of soft biological tissues, especially in the cardiovascular system [1]. Residual stresses have been shown to have a potential protective effect in healthy tissue, however this beneficial effect can be hindered in disease [2]. As a way to estimate the residual stress distribution, the opening angle experiment has historically been the golden standard in soft tissues of the cardiovascular system, including the left ventricle (LV) [1][3]. Furthermore, while the effect of opening angle has been investigated on the *in vivo* stress state for arteries and the myocardium [4], how the existence of residual stresses affects material parameters estimation has not been studied yet. In this study, we considered how the opening angle affects parameters estimation in the case of a uniaxial tensile test on ring-shaped samples [5]. We have developed an inverse finite element (FE) approach to investigate the relationship between the opening angle and material parameters in the LV, associated with uniaxial mechanical testing.

METHODS

We developed an inverse FE parameter estimation protocol that is briefly outlined here. All FE analysis in this study have been performed in FEBio 3.0, following a modified approach to what previously described in [6]. All material parameters estimations have been performed by pairing FEBio 3.0 with Matlab R2022a.

1) *Development of a reference model for an opening angle equal to 96°.* A FE model of the stress-free configuration of a representative LV was created (**Fig. 1**). This specific model had a value of the opening angle of 96°. To generate the geometry of the model we used a solid arc tool for the LV tissue, the pins were modeled as rigid bodies, and all solid elements were meshed using hex8 elements. We used a sliding node-on-facet contact model between the pin surface and the tissue during the

simulated mechanical test. A defined strain energy density was employed to describe the myocardium, as follows

$$W = c(\exp k(I_1(\mathbf{C}) - 3) - 1) + U(K, J). \quad (1)$$

Here $I_1(\mathbf{C})$ is the first invariant of right Cauchy-Green tensor $\mathbf{C} = \mathbf{F}^T \mathbf{F}$ and $J = \det \mathbf{F}$. The material parameters used were the same as in the continuum model (i.e., $c = 50$ Pa and $k = 2$). The value of bulk modulus K was 1000 Pa to simulate a semi-incompressible material.

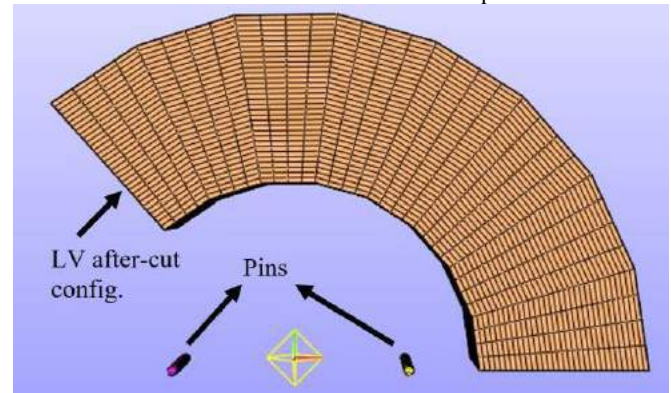


Figure 1: Stress free ring model used for simulations. The tissue is shown in orange and pins are purple and yellow.

2) *Calculation of a pseudo-experimental force-deflection curve.* Using this geometry and material specifications, we created a reference force-displacement dataset for a value of the opening angle of 96°, as follows. First, we applied a deformation to “close” the model based on the closed geometry calculated using a continuum mechanics analytical approach (to ensure an equilibrated condition) [4]. During this step the pins were

fixed. At this simulation point, we identified the elements that where part of the symmetry plane after the opening angle closure. For the specific reference system considered here, this plane can be identified by all points having the x-coordinate equal to zero. Second, a displacement of 2 mm was applied to one of the pins to simulate the mechanical test. We calculated the pseudo-experimental force during the test as the summation of the product of the x-stress by the surface area for all elements part of the symmetry plane. We also calculated the corresponding deflection as the average x-displacement of all elements part of the symmetry plane. This resulted in the force deflection curve shown in Fig. 2.

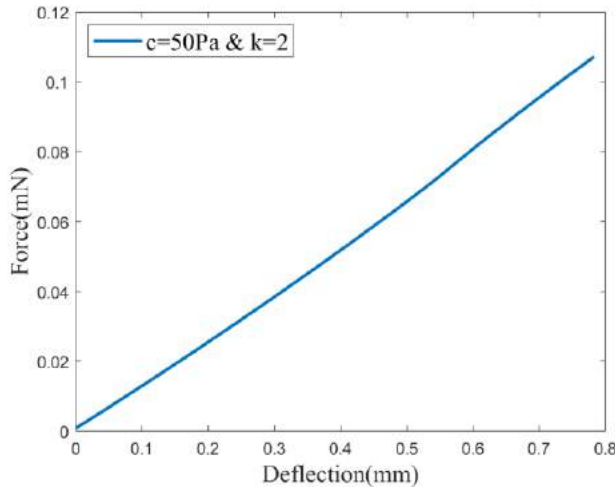


Figure 2: Force distribution during the ring test.

3) *Development of FE models for a set of opening angle values.* Following the same procedure described in point 1, we created 3 more FE models corresponding to opening angles equal to 30°, 60°, 120°. These models where then employed as numerical models to be compared to the pseudo experimental dataset created in point 2. For each model we calculated the numerical force-deflection curve, starting with a set of initial material parameters.

4) *Inverse parameter estimation by interfacing FEBio and MATLAB.* We used MATLAB to perform the parameters optimization. We developed a custom code to interface FEBio and MATLAB and we used the function 'fminsearch' to optimize the material parameters as a function of the opening angle. The error used in the optimization process was the root mean square difference between the pseudo-experimental force-deflection curve and the numerically calculated one for each value of the opening angle. The output was the optimized values for the parameters c and k for which the force displacement plot best-described the pseudo-experimental results.

RESULTS

Table 1 represents the estimated values of c and k for different opening angles that best-fitted the pseudo-experimental dataset. In Fig. 3 (a) and (b) we show the material parameters c and k as a function of the opening angle, respectively. In these results we also include the values we used as reference, i.e., opening angle equal to 96°.

Opening angle	c (Pa)	k
96	50	2
30	92.370	1.917
60	68.503	2.003
120	33.938	2.587

Table 1: Best-fitting values for the material parameters c [Pa] and k , calculated for different values of the opening angle

As a validation we have performed the material parameter estimation for this model as well, which returned the original values. Our parametric study seems to suggest there is as strong inverse linear correlation between the opening angle and the estimated value of c ($R^2 = 0.9925$). Whereas, we could not identify a clear correlation between the opening angle and the material parameter k . moving forward we will explore the possibility of a non-linear correlation, by performing more parametric analysis.

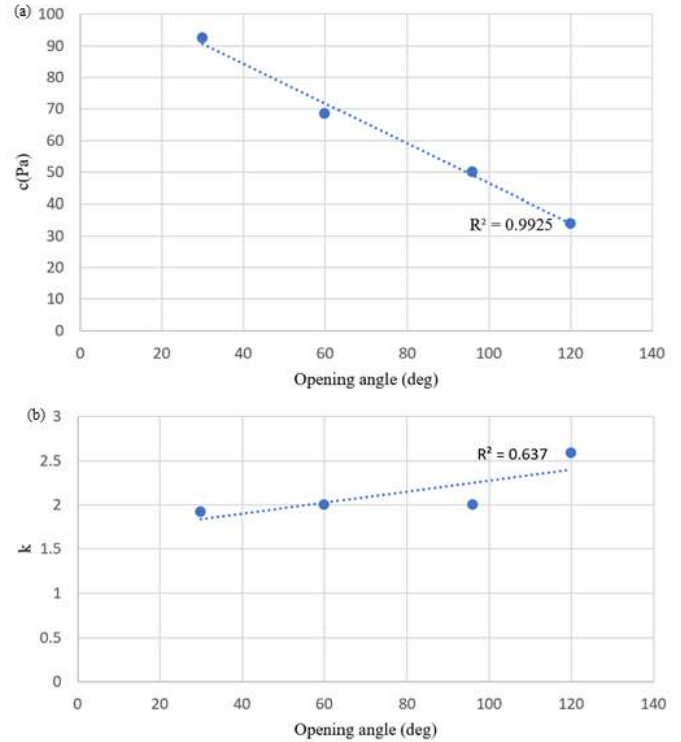


Figure 3. Material parameters c (a) and k (b) as a function of the opening angle. Also shown, the linear correlation as well as the corresponding values of R^2 .

DISCUSSION

We developed an inverse FE parameter estimation protocol to investigate the relationship between material descriptors and residual stress distribution magnitude. We have also performed a parametric study employing a pseudo-experimental reference force-deflection curve. What we found is that the value of the opening angle affects significantly the material parameter estimation. Indeed, we have observed a strong inverse linear correlation between the opening angle and the value of c . In future, we will use the protocol shown here to model experimentally collected datasets.

ACKNOWLEDGMENTS

Projected funded by NSF CMMI GRANT #1933768 (SR).

REFERENCES

- [1] J.H. Omens et. al. Circulation Research, 1990
- [2] Liu SQ et.al. Journal of Biomechanical Engineering, 1989
- [3] C. J. Chuong, et. al. Frontiers In Biomechanics, 1986
- [4] M.R. Grobbel, et. al. Exp Mech, 2021.
- [5] Shazly T,et. al. Exp Mech, 2015.
- [6] R.R. Mahutga et. al. Exp Mech 2021

CARTILAGE CONTACT PRESSURES DURING WALKING ARE RELATED TO T2 RELAXATION TIMES IN PATIENTS WITH KNEE OSTEOARTHRITIS

**Benjamin D. Bernarding (1), Austin J. Carcia (1), Adam J. Bradshaw (1), Johnny Huard (1),
Scott Tashman (1), Lauren E. Watkins (1), Colin R. Smith (1)**

(1) Steadman Philippon Research Institute, Vail, Colorado, USA

INTRODUCTION

Osteoarthritis (OA) is a leading cause of disability in the aging population and is associated with progressively worsening cartilage degeneration, pain, and loss of joint function [1,2]. The loading environment experienced by knee articular cartilage is an important factor in maintaining tissue homeostasis and also plays an important role in the initiation and progression of OA. In this study, we investigated relationships between simulated cartilage contact pressures during walking and MRI measures of cartilage degeneration in patients with mild-severe knee OA.

METHODS

Twenty-one patients with mild to severe tibiofemoral OA (65 ± 8 years, BMI 26 ± 5.1 kg/m², Kellgren-Lawrence Grade II-IV, 11 female) were included in this study. Data was acquired as part of an ongoing IRB-approved clinical trial (NCT04210986). For each subject, the most symptomatic knee was scanned on a 3T MRI system (SkyraFit, Siemens Healthineers USA). A double echo in steady state (DESS) sequence was used for cartilage segmentation and a multi-echo spin echo (MESE) sequence was used to calculate cartilage T2 relaxation times (6 echoes, range 16-96 ms). The patellar, femoral, and tibial cartilage were manually segmented from the DESS images using Mimics (Materialize) and registered to T2 relaxation time images generated using MapIt software. The average T2 relaxation times were calculated for the medial and lateral tibial cartilage, distal portions of the medial and lateral femoral cartilage, trochlear groove of the femoral cartilage, and patellar cartilage. At the same visit, motion capture and ground reaction forces were measured as participants walked at 1 m/s on

an instrumented treadmill (Bertec). A lower extremity musculoskeletal model with a detailed knee joint including explicit representations of fourteen ligaments as well as tibiofemoral and patellofemoral articular contact was scaled to each subject based on segment lengths calculated from a static motion capture trial [3]. Muscle driven simulations of walking were performed using the COMAK simulation routine to predict cartilage contact pressures using the open-source OpenSim-JAM framework [4]. Inverse dynamics was used to calculate the knee flexion and adduction moments. The predicted contact pressure maps on the medial and lateral tibial plateaus and femoral condyles, and also between the trochlear groove and patella, were averaged spatially and temporally over the stance phase. Spearman correlation coefficients were calculated between the average T2 relaxation times and average stance phase contact pressures for the tibiofemoral cartilage and patellofemoral cartilage areas, as well as overall joint adduction and flexion moments.

RESULTS

In regions of tibiofemoral contact, the mean cartilage contact pressure on the medial tibial plateau throughout the stance phase of walking was negatively correlated with the medial tibial cartilage T2 values ($\rho = -0.47$, $p = 0.03$, Figure 1), while the lateral plateau did not show a significant correlation ($\rho = 0.12$, $p = 0.60$). Similar correlations were observed for maximum pressures. Medial femoral T2 values were significantly positively correlated with mean lateral contact pressures ($\rho = 0.44$, $p = 0.04$). The knee flexion and adduction

moments were not significantly correlated with the medial or lateral tibial or femoral T2 values.

In regions of patellofemoral contact, the mean and maximum patellofemoral contact pressures were significantly positively correlated with mean patellar T2 relaxation times ($\rho = 0.47$, $p = 0.04$ and $\rho = 0.57$, $p < 0.01$ respectively). A correlation plot for the mean patellofemoral contact pressure is provided in Figure 2. There were no significant relationships between contact pressures and femoral T2 values, nor between patellar or femoral cartilage T2 values and knee flexion and adduction moments.

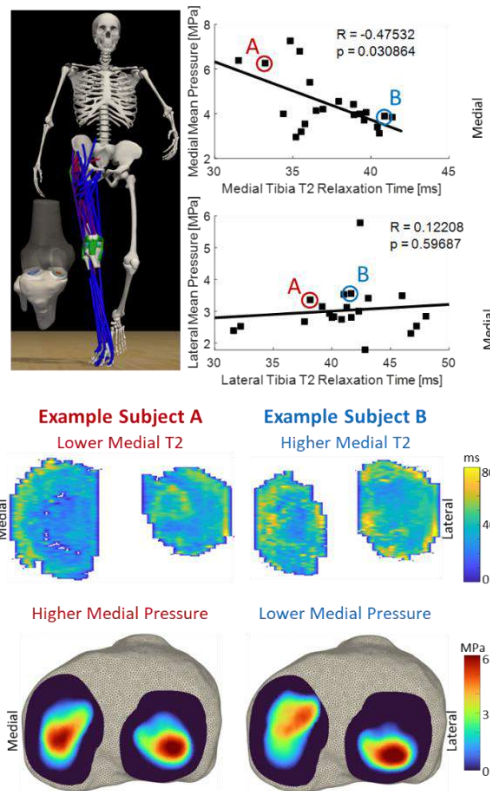


Figure 1: Cartilage contact pressures were estimated using a lower extremity musculoskeletal model with muscle-driven simulations of walking. Predicted contact pressures were negatively correlated with T2 relaxation times for the medial tibia. Representative T2 maps and contact pressure maps are shown.

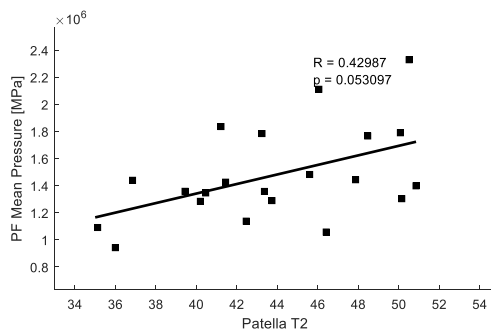


Figure 2: Patellar cartilage contact pressures were significantly positively correlated with T2 relaxation times.

DISCUSSION

OA patients with more severe cartilage degeneration on the medial tibial plateau, as indicated by higher T2 values, demonstrated gait mechanics resulting in lower medial tibial cartilage contact pressures. Conversely, patients with more severe cartilage degeneration on the patella demonstrated higher contact pressures. These differences may reflect different regional pain responses or the limited ability of patients to unload the patellofemoral cartilage on a fixed speed treadmill. Relationships were less pronounced between articular contact pressures and femoral cartilage T2 relaxation, which could be related to more spatially distributed loading patterns across the femoral cartilage surface during movement. There has been mixed information in the literature regarding patterns of cartilage contact pressure and cartilage thickness and T2 relaxation times, though most have been limited to regions of tibiofemoral contact [5,6]. Further work is necessary to investigate these connections in more detail across the joint.

Importantly, the knee flexion and adduction moments exhibited no correlations with cartilage T2 relaxation times. Together, these results demonstrate the important role for musculoskeletal simulations that predict cartilage loading patterns across the joint in OA research.

We plan to incorporate the patient-specific cartilage geometries into the musculoskeletal model for whole-joint modeling of patterns of cartilage loading and degeneration over time. A further longitudinal analysis on the sub-population with early OA at collected follow-up timepoints will be needed to discern whether the unloading of the medial compartment observed in the present study is a cause of cartilage degeneration or instead a local pain response. Additionally, it will be important to examine the role of cartilage thinning in relationships between contact patterns and T2 relaxometry measures.

Overall, significant relationships between articular contact pressure patterns during walking and cartilage composition were observed in individuals with knee OA. Measures of cartilage quality and joint loading provide complimentary information that may be useful in monitoring disease progression and efficacy of disease-modifying interventions.

ACKNOWLEDGEMENTS

This work was supported by the United States Department of Defense Contract # N00014-19-C-2052.

REFERENCES

1. James et. al. *Lancet*. 392: 1789-1858, 2018
2. Menon J. and Mishra P. *Osteoarthr Cartil*. 26(4): 480-484, 2018
3. Lenhart et al. *Ann Bio Eng*. 43(11): 2675-2685, 2015
4. <https://simtk.org/projects/opensim-jam>
5. Miereles et al. *PLOS One*. 12(11): e0187583, 2017.
6. Van Rossom et al. *PLOS One*. 12(1): e0170002, 2017.

IMPROVED IN VIVO MEASUREMENTS OF OUTFLOW FACILITY IN MICE BY ACCOUNTING FOR THE TIME-VARYING EFFECTS OF ANAESTHESIA

Michael Madekurozwa (1), Nicholas Tolman (2), Simon W. John (2), Darryl R. Overby (2),
Joseph van Batenburg-Sherwood (1)

(1) Bioengineering, Imperial College London, London, United Kingdom

(2) Ophthalmology, Columbia University Irving Medical Center, New York, NY, United States

INTRODUCTION

Glaucoma is a leading cause of blindness globally and the major risk factor is elevated intraocular pressure (IOP). The fluid mechanics of the drainage of aqueous humour from the eye determine the IOP, lowering of which is the sole therapeutic target for glaucoma treatment. Therefore, accurate measurements of aqueous humour (AH) dynamics are critical for the development of improved treatments to inhibit progression of sight loss in glaucoma patients.

AH is actively pumped from the ciliary processes into the space behind the iris, then flows through the pupil into the anterior chamber (AC). From there, AH drains across specialized ‘outflow tissues’ with a hydrodynamic resistance, thereby generating the IOP. An increase in the resistance, or equivalently a decrease in the conductance, C (known as outflow facility), is responsible for the IOP elevation in glaucoma.

Due to the financial and ethical difficulties associated with human or non-human primate models, the mouse model is a key tool for glaucoma research. Optimized experimental methods for perfusion of *ex vivo* enucleated eyes to accurately measure C are well established [1]. However, detailed methods for *in vivo* measurements vary widely, and reported values of C *in vivo* vary across a wide range. As an example, two studies that both used the same perfusion method and C57BL/6J mice reported 5.8 [4.7, 7.0] nl/min/mmHg [3] and 19.5 [17.4, 21.6] nl/min/mmHg [4], a difference more than 300%, which is way beyond what would be expected due to random sampling or small differences. There is thus an urgent need for a precise and repeatable method to measure C in mice *in vivo*.

We posit that a major source of variation is the time-dependent changes to aqueous humour dynamics that occur under anaesthesia. Here, we propose a new approach to address this issue and carry out a series of experiments to evaluate how it affects the measurement precision. In order to evaluate repeatability, we compare values measured by two different researchers in two different institutions.

METHODS

The intraocular pressure is determined by a mass balance on AH known as the Goldmann equation, which can be written in the form

$$S\{t\} = \frac{Q_{in}\{t\} - Q_u\{t\}}{C\{t\}} + P_{ev}\{t\} \quad (1)$$

where the braces indicate potential dependence on time due to the effects of anaesthesia. $S\{t\}$ represents the spontaneous intraocular pressure, $Q_{in}\{t\}$ is (AH) inflow, $Q_u\{t\}$ pressure-independent outflow, $P_{ev}\{t\}$ is episcleral venous pressure and $C\{t\}$ is outflow facility. It is assumed that Q_{in} , Q_u and C do not to change with pressure, $S\{t\}$.

In a perfusion, the AC is cannulated and an additional flow rate $Q\{t\}$ is introduced to the anterior chamber, which in turn changes the pressure from $S\{t\}$ to $P\{t\}$, hence

$$P\{t\} = \frac{Q\{t\} + Q_{in}\{t\} - Q_u\{t\}}{C\{t\}} + P_{ev}\{t\} \quad (2)$$

Subtracting Equation (1) from Equation (2) and rearranging yields

$$Q\{t\} = C\{t\}(P\{t\} - S\{t\}) \quad (3)$$

The term $S\{t\}$ can be interpreted as the IOP that would exist in the same animal under anaesthesia in the absence of perfusion. Although $S\{t\}$ cannot be directly measured, it can be accurately inferred via repeated measurements of $Q\{t\}$ at a single pressure S_0 , interlaced between measurements at different $P\{t\}$ values. $C\{t\}$ can be estimated at each time point or by regression under the assumptions that $C \neq f\{t\}$. This approach ‘corrects’ the estimated pressure-drop driving outflow by accounting for time-dependent changes. Our ‘Corrected method’ compares to the ‘Typical method’, which implicitly treats $S\{t\}$ as constant.

We carried out multiple studies with humidity controlled iPerfusion systems [2], and isoflurane anaesthetized C57BL/6J mice. For the purpose of comparison, we consider a fold increase in Precision of the Corrected Method based on the 95% margin of error (ME) for relevant parameters:

$$\text{Precision Increase} = \frac{\text{Typical method ME}}{\text{Corrected method ME}} \quad (4)$$

Statistics were carried out using the log-transform of C which has previously demonstrated to be appropriate [1]. Results are converted back into the linear domain and reported as mean [95% confidence interval].

RESULTS

We first considered both methods with data from N=16 independent eyes perfused by MM at Imperial College, to evaluate the effect on Precision. The average facility was 6.9 [5.9, 8.1] nl/min/mmHg with the Typical method vs 5.9 [5.4, 6.6] nl/min/mmHg with the Corrected method, a 1.8-fold increase in Precision (Eq. 4).

We then compared the measured C in contralateral eyes of N=9 different mice, which has been shown in *ex vivo* models to be similar. For the Typical method, we found a percent difference between the two eyes of 7 [-19,41]%, compared to 0 [-12, 15]% for the Corrected method (Figure 1). This corresponds to a 2.2-fold increase in Precision.

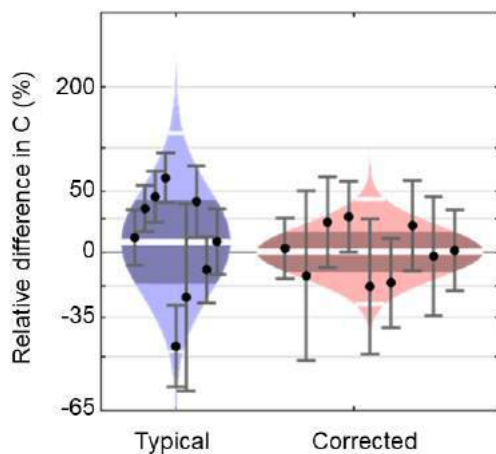


Figure 1: Cello plots [1] comparing the relative difference in C between untreated contralateral eyes for the Typical and Corrected approaches. Each data point represents an animal and error bars indicate 95% confidence intervals. The distributions show the estimated log-normal distribution, with the wide central line indicating the geometric mean. The dark band indicates the 95% confidence interval on the mean and the thin white lines indicate the range covered by the mean $\pm 2SD$.

To further evaluate the value of the approach, we then measured the effect of Netarsudil, a compound known to increase outflow facility. We treated one eye of N=9 mice with Netarsudil solution, with the untreated contralateral perfused with acting as a control. The Typical method predicted an increase of 61 [-4,172]% which is only borderline statistically different from zero at a significance level of 0.05 ($p=0.07$, paired t -test). By contrast, the Corrected method predicted an increase of 36 [13,64]% ($p=0.005$, paired t -test). This significant improvement corresponds to a 3.5-fold increase in Precision (Figure 2).

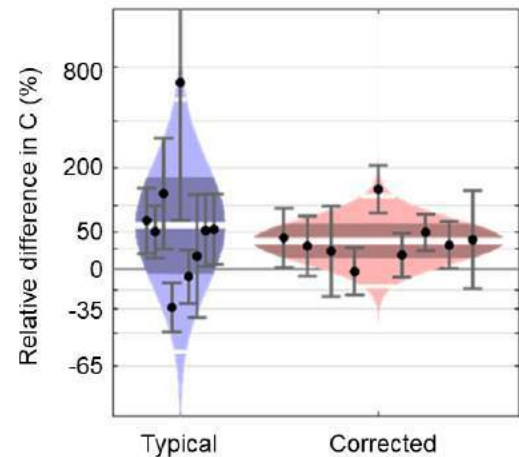


Figure 2: Cello plots [1] comparing the relative difference in C between Netarsudil and untreated contralateral eyes for the Typical and Corrected approaches. See Figure 1 for a description of the statistics visualized.

Finally, to demonstrate repeatability, the average facility in N=16 independent eyes was measured on different perfusion systems at Columbia University by NT. Using the Corrected method, we found an average C of 5.9 [4.6,7.5] nl/min/mmHg (compared to 5.9 [5.4, 6.6] nl/min/mmHg from MM at Imperial).

DISCUSSION

We described and demonstrated a new ‘Corrected’ method for improved measurements of *in vivo* outflow facility in mice. Across a range of experiments, we found that for the same experimental data, the proposed method increased precision by ~2 fold or more, effectively halving the uncertainty on the measurements. For a given sample size, this would provide more confidence on results, or equivalently would allow fewer animals to be used to achieve the same statistical power.

We carried out similar measurements on the same mouse strain at two institutions in order to identify if the measured values were repeatable, which was the case. This adds further confidence to the value of the method.

In addition to this improved analysis method, our measurements used a humidity chamber to inhibit evaporation from the eye, which has been demonstrated to be a source of over-estimation of facility in *in situ* postmortem perfusions [2].

Finally, it is interesting to note that the current values of facility are similar to, but marginally higher than those found in the same strain using *ex vivo* and postmortem perfusions (4.3 nl/min/mmHg & ~4.2 nl/min/mmHg respectively [2]).

In conclusion, our new method seems to effectively account for time-dependent changes in AH dynamics, thereby increasing the precision of *in vivo* measurements of C in mice.

ACKNOWLEDGEMENTS

This work was funded by an Imperial College London Presidents scholarship (MM). We also acknowledge funding support from the BrightFocus Foundation (G2015145 and G2020-003).

REFERENCES

- [1] Sherwood, J.M. et al, *PLoS One*,
- [2] Madekurozwa, M. et al, *Experimental Eye Research*, 220, 109103, 2022
- [3] Lopez, N.N. et al, *Experimental Eye Research*, 164:95-108, 2017
- [4] Zhang, D. et al., *J Gen Physiol*, 119 (6): 561–569, 200

RHEOLOGICAL CHARACTERIZATION OF COLLAGEN-HYALURONIC ACID CO-GELS FOR 3D CELL CULTURE

Jared A. Tucker (1), Benjamin L. Clarke (2), Victor K. Lai (3)

- (1) Department of Applied Materials Science, University of Minnesota-Duluth, Duluth, MN, USA
(2) Department of Biomedical Sciences, University of Minnesota, Duluth, MN, USA
(3) Department of Chemical Engineering, University of Minnesota-Duluth, Duluth, MN, USA

INTRODUCTION

Collagen hydrogels have been used for many applications from tissue engineering to cell culture. The robustness of the collagen protein as well as the diversity of uses within tissues allows for many applications within cell culture. Hyaluronic acid (HA) is another common glycosaminoglycan that resides within many tissues. Current hydrogel cell cultures commonly use collagen as the base protein, and some studies have been conducted showing the stability of Col-HA gels at varying HA concentrations [2]. Increasing HA concentration has been found to lower gel stability, but little work has been done to show how varying HA molecular weight (MW) affects the gel mechanical properties, such as storage modulus (G') and loss modulus (G'') [3]. Many cells, such as macrophage cells, respond to changes within the mechanical environment of their ECM by their adhesion proteins, such as adherons or integrins [4]. Thus, studies involving the characterization of cell behavior in 3D gel matrices must consider the gel culture's physical stiffness and stability and how it will affect the cells. Macrophage cells specifically have been demonstrated to exhibit differing phenotypes, generally called M1 and M2 activation. These activations correspond with inflammatory and anti-inflammatory responses respectively. Previous work has shown that HA MW within the extracellular matrix (ECM) can influence the phenotyping of the macrophage cells, however, in this work, the effect of HA MW on the *mechanical* properties of the hydrogel was not considered [5]. Gel stiffness is a key variable for cell culture as macrophages have been seen to adjust behavior through means of mechanotransduction between the macrophage integrins and the ECM [4]. The goal of this work is to characterize the effects of collagen concentration and HA MW on the mechanical properties of the hydrogel, with eventual application on macrophage activation and behavior in this 3D cell culture. The creation of this gel will also lend itself to the future study of macrophage interaction with pathogenic bacteria, such as *Borrelia Burgdorferi*.

METHODS

Collagen-Hyaluronic Acid Gel Synthesis

To form the various samples needed for the characterization, PureCol® type I bovine collagen (Advanced Biomatrix, Carlsbad, CA) dissolved in acid at a concentration of 3 mg/mL was added to six individual sample wells in a 12-sample well plate. To get the desired final concentrations of 1.8 mg/mL, 2.1 mg/mL, and 2.4 mg/mL, the following volumes in Table 1 were used. Once all necessary portions were added, the gels were stirred and allowed to gel in an incubator at 37°C for 35 minutes until completely gelled for a total sample volume of approximately 2 mL per gel.

Table 1: The volumes volume and mass of the components used for the formation of pure collagen and Col-HA gels

Component:	1.8 mg/mL	2.1 mg/mL	2.4 mg/mL	2.1 mg/mL-20k	2.1 mg/mL-500k	2.1 mg/mL-15M
Collagen (μL)	1200	1400	1600	1400	1400	1400
10x PBS (μL)	450	250	100	250	250	250
MEM (μL)	150	150	150	150	150	150
0.1M NaOH (μL)	170	200	230	200	200	200
NaHy (mg)	-	-	-	4.2	4.2	4.2

For the Col-HA co-gels, a similar process was used at a constant collagen concentration of 2.1 mg/mL. Sodium hyaluronate (NaHy) (Lifecore Biomedical LLC, Chaska, MN) at molecular weights of 20 kDa, 500 kDa, and 15,000 kDa was added to each sample. The total solution was mixed in centrifuge tubes and pipetted into six individual samples in the well plates for each MW. These samples were allowed to gel in the same conditions as previously described.

Rheological Characterization

The gel properties were measured on the Anton Paar MCR 72 rheometer (Anton Paar GmbH, Graz, AT) using a 25 mm parallel plate. Both measuring surfaces had fine-grit sandpaper adhered to them to reduce any possibility of slippage, as demonstrated in previous studies [5]. The rheometer was calibrated with the sandpaper to eliminate any

introduced error. An amplitude sweep from 0.1 to 100% strain was conducted on several test samples to determine the linear viscoelastic range (LVE). Once this was determined, the samples were measured by a frequency sweep at 1% strain, ranging from 0.5 rad/s to 10 rad/s, which was in the LVE and was demonstrated in other collagen gel rheology work [6]. The resulting G' and G'' graphs were analyzed to find the mean values for both properties. The resulting values were analyzed by ANOVA and Tukey-HSD t-test for statistical significance as well as linear regression to determine if a linear trend was present.

RESULTS

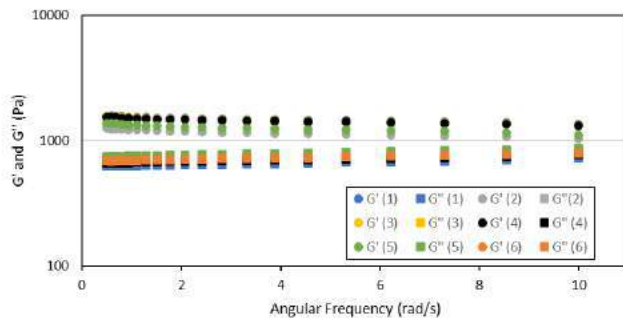


Figure 1: A representative chart with the resulting G' and G'' plots for all six replicates of the 1.8 mg/mL collagen sample.

Figure 1 shows an example of the data collected from a single hydrogel sample using the frequency sweep from 0.5 rad/s to 10 rad/s on the rheometer. Given that G' is greater than G'' for the gel, it can be classified as a viscoelastic solid, which is expected given the polymerization of the collagen within the system.

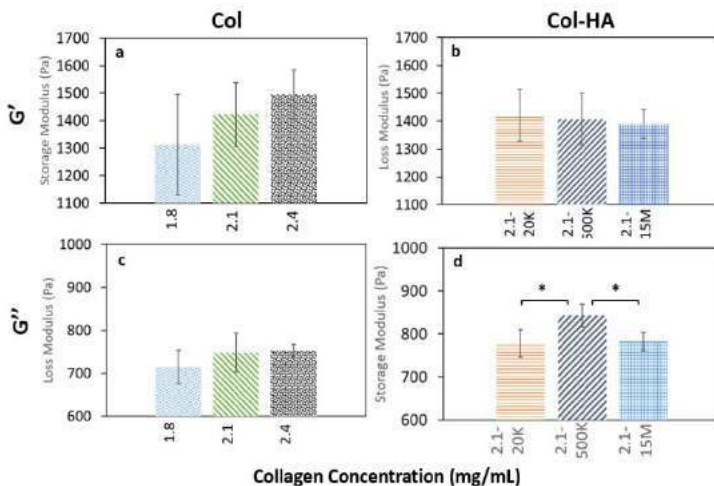


Figure 2: (a) The mean G' values for the 3 collagen concentrations. (b) The mean G' values for the Col-HA co-gels concentrations. (c) The mean G'' values for the 3 collagen concentrations. (d) The mean G'' for the Col-HA co-gels. (n=6 for each group, error bars represent 1 standard deviation). * represents statistical significance with $p < 0.05$ using the Tukey-HSD test.

Figure 2(a) displays the mean values that were determined from the frequency sweep for the storage moduli. While an increasing trend in G' was observed with increasing collagen concentration, no statistically significant differences were found using ANOVA and the Tukey-HSD t-test. Linear regression of the results at different concentrations yielded

an R^2 value of 0.985. This result offers the potential of a linear relationship between collagen concentration and G' . From Figure 2(b), no significant differences were found correlating the MW of HA with storage modulus, although a slight downward trend is observed and had an R^2 of 0.83.

Both the loss modulus results pictured in figure 2(c) and figure 2(d) were much lower in magnitude than the storage moduli. No significant change was found from the t-tests for the collagen concentration samples. For the Col-HA samples, the large spike in G'' for the 500 kDa sample resulted in statistically significant differences when compared to both the 20 kDa and 15,000 kDa samples, with p-values of 0.004 and 0.005 respectively. The large spike in G'' at 500k MW is unexpected and can be further studied.

DISCUSSION

The linear trend with G' increasing is expected as there will be more collagen within the system to polymerize into a stiffer gel. As the collagen polymerizes at 37°C, the greater concentration allows for more available molecules to be added to the actively growing chain. The effects of collagen concentration on the final MW of the collagen itself is unknown; however, it is expected that higher MW of both HA and Col within the gel should increase both G' and G'' . Previous work has shown that in a polymer matrix, increasing MW of the system aids in the construction of a denser polymer network, which will increase G' [7]. However, for the purposes of our Col-HA gel network, it acts more as a bimodal or polydisperse MW distribution, so direct changes in the MW of one of the components will have less direct effect. Any high MW chains that are dissolved in the liquid portion of the hydrogel will also act as a thickener for the system, increasing the G'' and viscosity.

For the purposes of the cell culture gels, relatively low concentrations of the biopolymer matrix are needed. Once cell culture in these gels begins and the cell behavior is studied, the desired gel G' can be fine-tuned using this linear correlation. As the initial data shows, the increase in HA molecular weight does not greatly affect the G' of the system, although it did have an impact on the loss modulus. In the findings here, there is no statistically significant difference between G' at the varying MWs, however, there is a slight decrease overall as MW increases. The initial interpretation is that the collagen network provides the solid structure and is thus less affected by changes in the MW of the HA. The HA is likely contained in the liquid portion of the gel since it does not polymerize itself unless crosslinked. Thus, it will increase the viscosity of the liquid and raise G'' . Why this trend does not correspond with the 15,000 kDa sample warrants further study. As the MW of the HA does not give an observed change in the G' this offers more confidence in future studies of macrophage activation within the gels. Any changes within the macrophage phenotyping would likely not be due to gel stiffness changes and more reasonably could be associated with the HA MW.

ACKNOWLEDGEMENTS

This work is funded by the University of Minnesota – Duluth's office of the Executive Vice Chancellor for Academic Affairs New Collaboration Grant.

REFERENCES

- [1] Luttseva, E. A. et al., *Tsitologiya*, 58(6):467-75., 2016
- [2] Kreger S. T. et al, *Matrix Biol.*, 28(6):336-346, 2009
- [3] Meli, V. S. et al., *Sci. Adv.*, 6(49):eabb8471, 2020
- [4] Chen, S. et al., *Acta Biomater.*, 7(2):644-652, 2011
- [5] Rayahin, J. E. et al., *ACS Biomater. Sci. Eng.*, 7:481-493, 2015.
- [6] Lou, J. et al., *Biomaterials*, 154:213-222, 2018
- [7] Carrero, K. et al., *Polymers*, 14(17):3683, 2022

PRE-OPERATIVE FUNCTIONAL CHARACTERIZATION OF AORTIC NECK IN ABDOMINAL AORTIC ANEURYSMS AND ITS ASSOCIATION WITH TYPE I ENDOLEAK FOLLOWING EVAR PROCEDURE

A. Forneris (1,2), A. Satriano (2), R. A. Beddoes (2), R. D. Moore (1,3), E. S. Di Martino (1,2)

- (1) Department of Biomedical Engineering, University of Calgary, Calgary, AB, Canada
(2) R&D Department, ViTAA Medical Solutions, Montreal, QC, Canada
(3) Division of Vascular Surgery, University of Calgary, Calgary, AB, Canada

INTRODUCTION

Endovascular aneurysm repair (EVAR) has become the primary procedure for the management of abdominal aortic aneurysms (AAA). While less invasive when compared to an open repair, EVAR procedures are associated with negative outcomes and complications that may lead to re-intervention or death [1,2]. Endoleaks are common complications of EVAR procedure. Type I endoleaks occur when a proper sealing between the stent and the artery is not achieved at the aneurysm neck (type Ia) or at the iliac arteries (type Ib) and have been linked to negative clinical outcomes. The pre-operative characterization of AAAs from CT images has been the focus of many studies aimed at predicting the presence of type I endoleaks and poor outcomes [3,4]. These studies mainly looked at the assessment of morphological features of the aneurysm neck to define risk factors associated with post EVAR type I endoleaks. Diameter, length, angulation and conicity are examples of morphological features of the neck that have been extensively investigated and associated with the development of type Ia endoleaks. Anatomical neck features that represent guidelines listed in the recommended instructions for use (IFU) of stent manufacturers are part of current clinical practice. These anatomical features, however, ignore the characterization of the aortic tissue and its suitability for a successful sealing. For this reason, many EVAR procedures still result in negative outcomes despite being performed under IFU, with studies reporting conflicting results when looking at the effect of adherence to IFU on overall negative outcome and mortality [5-7], clearly highlighting the shortcomings of a purely anatomical evaluation.

In the context of AAAs, aortic hemodynamics and aortic wall deformability are known to have an important role in understanding the progression of arterial disease as well as providing an insight into regions of structural weakening in the aorta [8-11].

This retrospective study proposes a non-invasive functional characterization of the aortic neck tissue from pre-operative ECG-gated multiphase CT images by means of a combined in-vivo strain and

hemodynamic analysis and explores the association between the functional characterization and the post-EVAR outcomes for a population of AAAs.

METHODS

The study focused on population of sixteen AAA patients (n=16) enrolled to participate in a CHREB-approved protocol consisting of pre-operative multiphase CT imaging, post-operative follow-up imaging as well as follow up imaging at 12 months or more.

The aortic wall and lumen were segmented and reconstructed from CT images. In-vivo strain analysis was performed with the in-house ViTAATM software by means of a surface mesh of the aortic wall used as 3-D feature-tracking model to measure nodal displacements on successive images throughout the cardiac cycle. The in-vivo strain was obtained from the nodal displacements, therefore no assumption on constitutive model was needed [9,12].

Computational Fluid Dynamic (CFD) simulations were performed on patient-specific geometries of the aortic lumen to obtain a hemodynamic assessment in terms of Time Averaged Wall Shear Stress (TAWSS).

Finally, the presence and amount of intraluminal thrombus (ILT) for each patient was determined by measuring the ILT thickness as the distance between the aortic wall and lumen geometries.

The aortic neck was isolated by defining a region 15 mm below the lower renal artery along iso-length chords defined on the wall surface (*Figure 1*). The functional characterization of the aortic neck was achieved by combining the three obtained variables into one surrogate index of Regional Aortic Weakness (RAW) designed to simultaneously capture areas of disturbed blood flow (low TAWSS), elevated strain and thick ILT [11,13].

Statistical analysis was performed by using a two-sample t-test to investigate associations between neck properties and post-operative outcome (significance for p-value < 0.05).

RESULTS

The AAA study population ($n = 16$, age 72 ± 6 years, 93.75% males) had a mean maximum aortic diameter of 51.6 ± 9.3 mm.

Two patients in the study (12.5%) developed type I endoleak shortly after EVAR procedure as assessed during post-operative imaging, with one patient needing immediate endoleak treatment. The anatomy of the aortic neck was assessed pre-operatively in terms of neck conicity (expressed as difference between the distal diameter and the proximal diameter of the neck), angulation and diameter. The patients who developed a type I endoleak presented significantly higher conicity when compared to the patients that did not develop a type I endoleak (18.22 ± 8.99 mm versus 1.68 ± 2.52 mm, $p = 0.001$), while both neck diameter and angulation did not show significant difference for the two groups (26.74 ± 1.22 mm versus 24.23 ± 2.82 mm, $29.62 \pm 7.37^\circ$ versus $29.23 \pm 11.50^\circ$).

From the pre-operative functional characterization of the aortic neck, the patients who developed a type I endoleak presented significantly higher median RAW index at the neck region when compared to the other cases (4.83 ± 0.16 versus 4.15 ± 0.69 , $p = 0.01$).

During post-operative follow-up imaging the presence of early type II endoleaks was also reported for six patients (37.5%). The early type II endoleaks eventually resolved resulting in no additional treatment and aneurysmal sac reduction. Interestingly this sub-group presented a neck region with significantly higher median TAWSS (1.01 ± 0.36 versus 0.71 ± 0.16 , $p = 0.05$) and lower median RAW index (2.84 ± 0.69 versus 4.00 ± 0.42 , $p = 0.004$) when compared to the group of patients that did not develop an early type II endoleak.

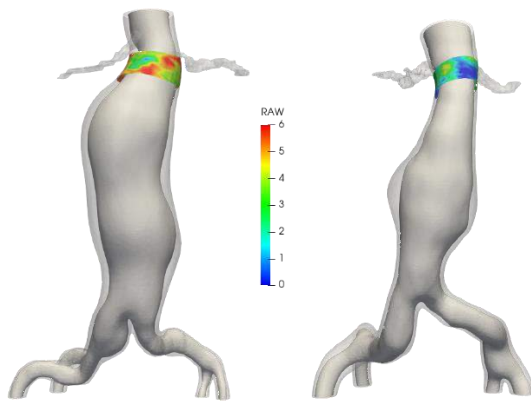


Figure 1: example of two AAA geometries in the study population showing the aortic wall (transparent), aortic lumen and renal arteries. The isolated aneurysm neck is also shown with the distribution for the RAW index for a case of high RAW (right) and a case of low RAW (left).

DISCUSSION

The present study proposes a combined CFD and in-vivo strain analysis approach to achieve the functional characterization of the aortic neck for a population of AAA patients selected to receive EVAR. Despite the procedure being performed following IFU, a type I endoleak was found in two patients during post-operative follow-up imaging. While the conicity of the aortic neck was significantly higher for the

two mentioned cases, it was within threshold according to IFU. Additional anatomical analysis of the aortic neck did not show significant differences for the two analyzed groups (i.e. presence versus absence of type I endoleak). However, after performing the functional characterization of the aortic neck using the RAW index, significant differences were found between the two groups. Patients developing type I endoleak showed higher RAW index at the neck region as indicative of a weaker aortic tissue unlikely to provide a suitable landing zone to achieve correct sealing (Figure 1).

Six patients in the study population showed evidence of early type II endoleak during post-operative imaging. Type II endoleaks may be due to the retrograde flow from collateral aortic branches. Interestingly, the group of patients who developed an early type II endoleak presented lower RAW index and higher TAWSS at the neck region. This finding suggests that a good neck region characterized by unaltered flow conditions could provide an ideal sealing therefore resulting in a reduced pressure in the aneurysm that drives the retrograde flow from collateral branches. For the cases under analysis the early type II endoleak eventually resolved without the need for re-intervention and sac reduction was achieved, supporting the idea that endoseal had been achieved. This association between excellent landing zone seal related to high tissue strength and Type II endoleak has not been previously reported.

Despite being limited to a small patient cohort, the functional assessment of the aneurysm neck provided a useful insight into post-operative complications for patients who received EVAR procedure under IFU. Present results show the potential of the proposed approach to support clinical decisions and improve the management of AAAs.

ACKNOWLEDGEMENTS

This work was supported by ViTAA Medical Solutions and Mitacs through the Mitacs Accelerate Program.

REFERENCES

- [1] Powell, JT et al., *BJS*, 104:166-78, 2017.
- [2] Yei, K et al., *JAMA Netw Open*, 5:e2212081, 2022.
- [3] Banno, H et al., *Ann Vasc Surg*, 81:154-62, 2022.
- [4] Zuidema, R et al., *Eur J Vasc Endovasc Surg*, 64:475-88, 2022.
- [5] Walker, JP et al., *J Vasc Surg*, 60:546, 2014.
- [6] Antoniou, GA et al., *J Vasc Surg*, 71:1415-31, 2010.
- [7] Hahl, T et al., *J Vasc Surg*, 76:699-706, 2022.
- [8] Di Martino, ES et al., *Med Eng Phys*, 43:647-55, 2001.
- [9] Satriano, A et al., *J Biomech*, 48:354-60, 2015.
- [10] Zambrano, BA et al., *Ann Biomed Eng*, 44:1502-14, 2016.
- [11] Forneris, A et al., *Front Cardiovasc Med*, 8:631790, 2021.
- [12] Satriano, A et al., *BMC Cardiovasc Disord*, 18: 76, 2018.
- [13] Forneris, A et al., *J Vasc Surg Cases Innov Tech*, 6:172-6, 2020.

SENSITIVITY OF FINITE ELEMENT MODELS TO RELATIONSHIP BETWEEN T₂ RELAXATION AND MODULUS IN ARTICULAR CARTILAGE

Alexander A. Donabedian (1), Deva D. Chan (1)

(1) Weldon School of Biomedical Engineering, Purdue University, West Lafayette, Indiana, United States

INTRODUCTION

Osteoarthritis (OA) is one of the leading causes of disability in later adult life and consumes 1-2.5% of the gross national product in the USA¹. Degeneration of cartilage in the knee is a hallmark sign of OA and its progression varies greatly between patients. Although finite element (FE) modeling can be tailored to individual patients, critical barriers still hinder FE-based, specific-patient care for the highly heterogeneous disease.

Previous FE models identify regions of high strain or failure within tissue to predict potential areas at risk for degeneration and OA progression.² However, because the mechanical characterization of cartilage and other joint tissues is not often performed within those specific patients, material properties found in the literature are implemented for these tissues. Although several noninvasive techniques exist to characterize tissue ultrastructure, constitutive models used in FE analysis are often simplified due to the complex and heterogeneous material properties of tissues, potentially affecting the predictive ability of patient-specific models.

Recently, we proposed using quantitative magnetic resonance imaging (MRI) to implement elastic heterogeneity in an FE model of articular cartilage using data from the Osteoarthritis Initiative (OAI).³ A linear correlation between T₂ relaxation times and elasticity was found by Nissi et al.⁴ Based on this relationship, our T₂-refined FE model estimated a higher maximum first principal stress and shear strain where high T₂ values were located compared to a model with homogeneous material properties. The regional MRI Osteoarthritis Knee Score (MOAKS) of each patient, dependent on the size of cartilage loss, showed a significant correlation to the number of elements exceeding a threshold of 0.5MPa.

Although we found that a T₂-refined FE model held promise for prediction of regions of future cartilage degeneration, the linear correlation between T₂ relaxation times and material properties is based on a single study with limited human data. Additionally, the correlation

developed by Nissi et al, may not hold for patients outside their study. Therefore, the objective of this work is to determine the degree to which our T₂-refined FE models are sensitive to the assumed relationship between T₂ relaxation times and modulus in articular cartilage.

METHODS

Models of articular cartilage were created using publicly available data from the OAI.³ Three subjects, one classified as having minimal OA (Kellgren-Lawrence (KL) grade = 2) whereas the others showed no sign of OA (KL = 0), were used. Segmented images from the OAI were used to define subject-specific cartilage and menisci regions of interest, which were meshed into hexahedral elements, as in a previous study.⁵

Material properties were assigned to each element using a voxel-to-element mapping based on the T₂ map of each subject.³ T₂ relaxation times negatively correlate to the elastic properties of human tissue and the linear relationship is defined in Eq. (1).⁴ This correlation determined the elastic values in each element within the model. An expected dynamic modulus and span of T₂ relaxation times in human cartilage were used as the inputs to the simulation. A baseline simulation of each subject implemented a dynamic modulus of 1-8 MPa and T₂ relaxation times of 15-75 ms.³

$$E_D = \left(\frac{-3.5}{3} \times 10^5 \right) T_2 + 9.75 \times 10^6 \quad (1)$$

Average motion and loading from a walking gait cycle were applied to the model and the estimated measures of stress and strain were evaluated using FE analysis from FEBio Studio version 2.0.

The sensitivity between the inputs and predicted outputs was analyzed by incrementally changing the maximum and minimum elastic values in the model until a 10% variation from the baseline parameters was reached. These adjustments were first manipulated to change the slope relationship between T₂ relaxation times and the dynamic modulus. Then, the dynamic modulus was shifted while maintaining the

same slope correlation to T_2 values. The maximum first principal stress and shear strain were recorded in each simulation and plotted against its deviation from the baseline predicted outputs.

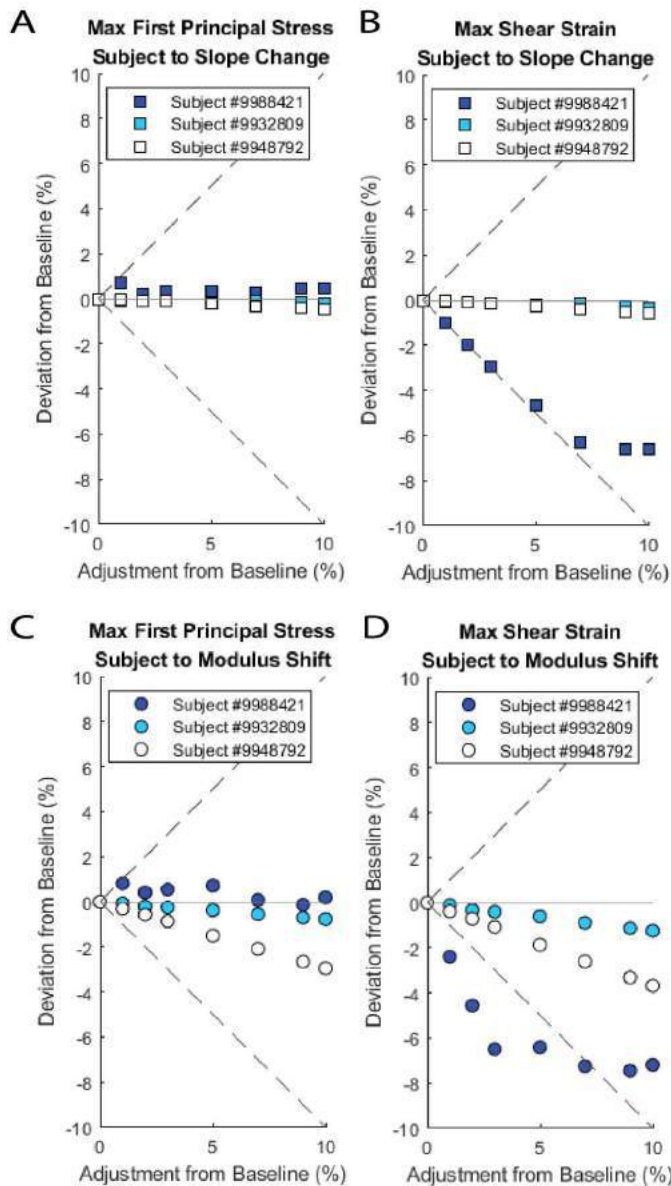


Figure 1: Percent changes in maximum first principal stress and shear strain due to a slope change (A, B) and dynamic modulus shift (C, D)

RESULTS

T_2 relaxation times were used to create elastically heterogeneous, subject-specific models of the knee. The model's sensitivity to changes in the T_2 to modulus relationship was evaluated by altering the slope and intercept from 0 to 10% of the previously published correlation.³ Deviations in the predicted maximum shear strain and first principal stress from the baseline study are shown in Figure 1. A dashed line is presented to visualize a one-to-one ratio between a change in parameters to the model outputs. The estimated maximum first principal stress does not show a sensitivity to a change between the input relationships. All subjects showed a less than $\pm 1\%$ deviation from the baseline outputs

due to a slope change between T_2 values and the dynamic modulus. Similarly, all subjects showed a less than $\pm 3\%$ change in max first principal stress due to a dynamic modulus shift.

The predicted maximum shear strain in each parametric adjustment shows a larger variability. The maximum shear strain differs by less than -1% in two subjects due to the slope relationship change; however, the third subject shows a one-to-one correlation until a -7% deviation is reached. This subject also shows up to a -8% difference from the baseline simulation due to a dynamic modulus shift whereas the others show a linear correlation with varying magnitudes.

DISCUSSION

In this study, a sensitivity analysis was performed on T_2 -refined FE models of articular cartilage. The maximum first principal stress and shear strains were recorded due to incremental parametric adjustments from a baseline simulation. The maximum first principal stress in each test did not deviate far from the initial simulation since the applied load stayed consistent between tests. The elastic values substituted into the constitutive equations resulted in larger changes in max shear strains across the subjects with varying degrees in magnitude. This work informs us that the estimated results are impacted by various aspects of the model in addition to the input relationships.

For the three subjects, a FE model of articular cartilage was created with customized geometry and material properties. Nodes were fixed on the proximal and distal surfaces of the femoral and tibial cartilage respectively to best emulate biological boundary conditions. A rigid body was applied to simulate loads experienced during an average walking cycle as well as constraints to mimic a walking motion. To our knowledge, a method to uniformly constrain articular cartilage models across different subjects does not exist. Therefore, the initial position of the rigid body was manually placed which enabled the model to converge to a solution. Consequently, the initial position of each subject-specific model varied slightly. This manual positioning alongside differing geometries could have induced differences in the model's sensitivity across the patients.

The range of elastic parameters that enabled the simulation to run to completion limited our study. Reducing the dynamic modulus below 1MPa and implementing the large loads experienced while walking produced deformations that were not feasible to estimate in a reasonable amount of time.

In future studies, we may develop a new method to constrain our model that is consistent across any type of geometry. Further research also aims to define a subject-specific relationship between T_2 relaxation times and material properties as well as other quantitative MRI techniques such as diffusion tensor imaging. Work pairing MRI with cartilage morphology enables more advanced subject-specific FE models aimed to accurately represent cartilage degeneration.

ACKNOWLEDGEMENTS

This work was supported by the National Science Foundation award 2149946. The author would like to thank Nathan Lampen for creating the T_2 -refined FE models.

REFERENCES

- [1] Leifer, V et al., *Osteoarthritis and Cartilage*, 30:10-16, 2022.
- [2] Mononen, M et al., *Scientific reports*, 6:1-14, 2016.
- [3] Lampen, N et al., *J Orthop Res*, 1-12, 2022.
- [4] Nissi, M et al., *Osteoarthritis and Cartilage*, 15:1141-1148, 2007.
- [5] Rodriguez-Vila, B et al., *CMBBE*, 20:1543-1553, 2017.

MULTISCALE SIMULATIONS SHOW ROLE OF DIFFUSE DAMAGE IN ANOMALOUS FIBER REALIGNMENT

Jacob S. Merson (1), Catalin R. Picu (1), Mark S. Shephard (1)

(1) Department of Mechanical Aerospace and Nuclear Engineering, Rensselaer Polytechnic Institute, Troy, NY, USA

INTRODUCTION

Neck and back pain impacts 30-50% percent of the population in their lifetime and costs an estimated 30 billion dollars per year [1]. One source of this pain is the highly innervated Facet Capsular Ligament (FCL). The FCL is primarily made from type I Collagen, and reorientation of the collagen fibers has been linked to neuron activation i.e., pain. Collagen fiber alignment varies by spinal region with patches of aligned fibers in the cervical region [2].

Experiments have shown that under some loading conditions, fibers in one region of the ligament rapidly reorient away from the mean fiber orientations in a process called Anomalous Realignment (AR). These AR events have been shown to coincide with the initiation points of observable macroscale rupture. Although significant efforts have gone into the detection and measurement of AR in rat and human FCLs, the micromechanical cause of AR remains unknown [3, 4].

This work explores three hypotheses for the cause of AR in the FCL. Namely, AR is caused by 1) material inhomogeneity caused by the aligned collagen patches in the cervical FCL, 2) localized material instabilities, 3) diffuse damage. We employ a concurrent multiscale method that affords monitoring the fiber micromechanics while constructing tissue scale models directly from biological imaging data.

METHODS

Multiscale Finite Element Method. We will briefly outline the concurrent multiscale procedure that we use and has been implemented in MuMFiM (www.github.com/SCOREC/mumfim). For a complete treatment we refer the reader to [5]. Our two-scale method is based on the FE2 method originally developed by Feyel and others for modeling composite materials.

On the macroscale we seek to solve the static equilibrium equation using an updated-Lagrangian finite element method. This requires a constitutive response function for the Cauchy stress and 4th-order tangent material stiffness tensor. Rather than providing an analytical response function, the constitutive response is computed from a second finite element solution of a representative volume element (RVE) made up from discrete fibers. This

decomposition is shown in figure 1. RVEs must be large enough to have behavior of the continuum scale. A guideline for RVE sizes for 3D fiber networks is provided in [6]. This coupling methodology requires there is a strong scale separation meaning that the physical size of the RVE must be at least an order of magnitude smaller than the size of the macroscale mesh elements.

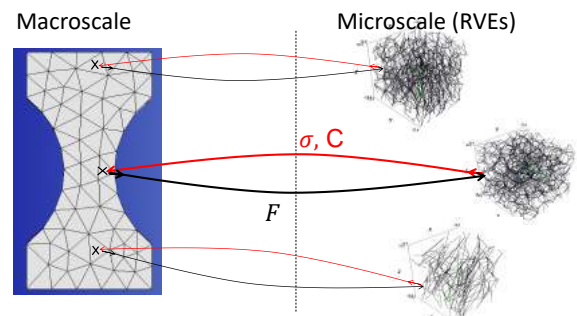


Figure 1: Graphical representation of hierarchical coupling methodology. The black lines represent the transfer of the deformation gradient F to the microscale RVEs. Red lines represent the transfer of the Cauchy stress and tangent material stiffness to the macroscale. This coupling occurs at every macroscale integration point.

Network Generation. To generate the networks, a Delaunay triangulation is created from seed points which are distributed in a uniform random distribution in a domain with an edge length L_g . Fibers are modeled by truss elements placed along the edges of the Delaunay triangulation. For the aligned cases, an isochoric affine deformation is applied (rotations and deformations). Any fibers with a length, l_f , which is less than $1/100$ of the mean segment length, l_c , are removed by merging the two fiber end nodes into a single node that is placed at the mean nodal location weighted by the connectivity. The resulting network is trimmed to a final size with edge lengths L .

For these networks density is quantified as the total fiber length per

volume $\rho = l_{\text{tot}}/V$. This is related to the volume fraction as $\phi = \rho A_f$. Fiber properties and volume fraction follow [7] are selected such that the macroscale stress/strain curve matches a 2mg/mL collagen.

To quantify the level of alignment in the loading direction, the second Legendre polynomial, $P_2 = \frac{1}{2} \langle 3\cos^2(\theta) - 1 \rangle$ is used. This yields a measure that ranges from $-1/2$ for all fibers oriented orthogonal to the loading direction to 1 where all fibers are perfectly aligned in the loading direction.

To promote instabilities, we also produce a diluted network. Construction of diluted networks proceeds similarly to the base networks, however fibers are randomly selected for deletion until the desired mean fiber connectivity is obtained. To aid in the numerical solution of these unstable networks, we do not delete any fibers that have nodes that have a connectivity which is less than or equal to a threshold. In this paper, we use a threshold connectivity of 6 and a mean connectivity of 7.5. The initial number of seed points is varied to ensure that the density remains constant between the dilute and undilute cases.

Diffuse Damage. Based on the load-displacement curves of Rat FCLs we expect that the initial ligament damage is primarily of the diffuse type. To model diffuse damage, we reduce the fiber stiffness to 10% of the original stiffness when the homogenized RVE stress surpasses a threshold value. In this paper, the threshold stress is chosen such that damage starts to develop at $\sim 10\%$ strain. We expect this value is artificially low, however it provides a reasonable trade off for computational cost in these exploratory models.

Macroscale Model. The macroscale model is constructed using the geometry of the cervical FCL sample reported in [2]. The finite element discretization has 63,821 linear tetrahedron elements. At each integration point of the macroscale mesh, a network orientation is selected based on an orientation field. The orientation field is constructed from a Gaussian random field with a correlation length of 0.35 mm as reported in [2]. To obtain a set of orientations that is uniformly distributed along the unit circle, we use inverse transform sampling to obtain a uniform distribution and map the result to angles between 0 and 2π . The orientation field is constant through the ligament thickness which is small and roughly approximates the plane stress condition.

To match the bone attachment, of the FCL, the left and right surfaces shown in figure 2 are fixed and displacement boundary conditions are applied in the loading direction. The top and bottom surfaces have traction free boundary conditions.

Anomalous Realignment. Anomalous realignment is detected using the vector correlation method and thresholds defined in [3]. This method is designed to work on 2D image data. To obtain an “image” from our model that is comparable to the experimental data, we first take a slice of the top surface of the model and use the “ResampleToImage” filter in Paraview with 100 by 100 pixels which provides approximately one pixel per mesh element.

RESULTS

Table 1 summarizes each test condition which corresponds to our original hypotheses for the cause of anomalous realignment. Here we see that AR is detected when diffuse damage is present. However, it is not detected when there is both diffuse damage and patches of oriented fibers.

Table 1: Summary detection of anomalous realignment with various test cases.

network with patches of aligned collagen (H1)	network with reduced connectivity (H2)	network with failure (H3)	AR
X			N
	X		N
		X	Y
	X	X	Y
X		X	N

The white lines in figure 2 enclose the domains where AR is detected for a model with diffuse damage undergoing $\sim 13\%$. These lines are superimposed onto P_2 field of the ligament at the same strain, plotted on the undeformed configuration. The regions of detected AR correspond to a localization band where fibers are more aligned in the loading direction than in the surrounding material.

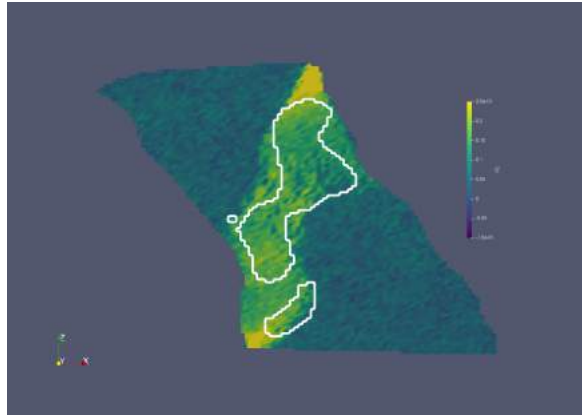


Figure 2: Plot of the P_2 field for a FCL undergoing $\sim 13\%$ strain with diffuse damage. The white lines enclose the regions where AR was detected.

DISCUSSION

This work applies a novel computational approach to understanding the micromechanical causes of AR in the FCL. We see that material inhomogeneity in the form of aligned patches of collagen fibers, and increased microstructural instabilities produced from diluted networks do not allow AR to develop in the FCL. However, when diffuse damage is included in the model AR is detected at similar levels to those observed in experiments. This matches well with experimental observation that AR location is predictive of the locations of visible ligament rupture.

Most interestingly, we also see that when our model contains both patches of aligned collagen fibers and diffuse damage, we no longer see AR develop at the levels of strains that were analyzed. We suspect that the inhomogeneity is delaying the onset of AR and we are continuing to investigate this phenomenon.

When AR does develop, we see that the location visibly correlates to a localization band in the P_2 field where the fibers become more strongly aligned in the loading direction. This is the result of diffuse damage causing a softer region in the material where fibers must reorient into the loading direction to carry the applied load.

ACKNOWLEDGEMENTS

This work was supported in part by the National Institutes of Health (NIH) through Grant No. U01 AT010326-10. This research used resources of the Center for Computational Innovation at Rensselaer Polytechnic Institute.

REFERENCES

- [1] Singh S et al. *Clinical Biomechanics*. SI: Central Nervous System (CNS) Injury Biomechanics 64 (2019).
- [2] Ban E et al. *Journal of Biomechanical Engineering* 139.7 (2017).
- [3] Quinn KP et al. *Journal of Biomedical Optics* 14.5 (2009).
- [4] Quinn KP et al. en. *Journal of Biomechanics* 43.10 (2010).
- [5] Merson J. Ph.D. dissertation. Troy, NY: Rensselaer Polytechnic Institute, 2021.
- [6] Merson J et al. en. *International Journal of Solids and Structures* 206 (2020). tex.ids: mersonSizeEffectsRandom2020.
- [7] Chan VWL et al. en. *Computer Methods in Biomechanics and Biomedical Engineering* 22.2 (2019).

SUSTAINED-RELEASE LOSARTAN FROM PEPTIDE NANOFIBERS PROMOTES CHONDROGENESIS

Kohei Yamaura (1), Nicholas A. Sather (2), Anna Metlushko (2), Haruki Nishimura (1), Radoslav Z. Pavlović (2), Sealy Hambright (1), Sudheer K. Ravuri (1), Marc J. Philippon (1, 3), Samuel I. Stupp (2), Chelsea S Bahney (1, 4), Johnny Huard (1)

- (1) Center for Regenerative and Personalized Medicine, Steadman Philippon Research Institute. Vail, Colorado, USA
- (2) Simpson Querrey Institute for BioNanotechnology. Northwestern University, Chicago, Illinois, USA
- (3) The Steadman Clinic. Vail, Colorado, USA
- (4) The Orthopaedic Trauma Institute, University of California, San Francisco (UCSF). San Francisco, California, USA

INTRODUCTION

Osteoarthritis (OA) is a disease in which there is an irreversible loss of articular cartilage that affects approximately 240 million people worldwide [1]. The TGF- β 1 inhibitor, losartan, can improve cartilage repair by promoting hyaline rather than fibrous cartilage tissue regeneration [2]. However, there are concerns about side effects associated with oral administration and short retention within the joint following intra-articular injections. To facilitate local and sustained intra-articular losartan delivery, we modified the peptide composition of our previously published PA nanofibers [3] to achieve an injectable nanofiber formulation that can bind and slowly release losartan. The aims of this study are to characterize the release kinetics of losartan from two different PA nanofiber compositions followed by testing pro-regenerative bioactivity on chondrocytes. We hypothesize that the PA nanofiber chemistry can be modified to achieve sustained release of losartan over a two-week period and promote chondrocyte proliferation and chondrogenesis *in vitro*.

METHODS

A total of eight nanofiber formulations were prepared by combining four different losartan potassium doses (0, 0.5, 5, and 50 mg/mL) and two PA molecules with opposite charge. First, we tested the impact of electrostatic interactions on nanostructure morphology and release kinetics of the negatively charged losartan molecule from either a positively (K) or negatively (E) charged PA nanofiber over the time course of 2 weeks.

Subsequently, the various losartan nanofibers were co-cultured in 0.4- μ m semipermeable transwell over the ATDC5 chondrocyte cell line in a 24-well plate. Total of 12 groups were divided by losartan dose (0, 0.5, 5, and 50 mg/mL) and presence/absence of positively charged K or negatively charged E nanofibers. Cell proliferation was evaluated longitudinally at 24 hours, 5 days, and 14 days after losartan nanofiber

treatment using the non-destructive PrestoBlue assay. To access the regenerative potential of these nanofibers in an OA pathology, ATDC5 chondrocytes were primed with interleukin (IL) -1 β (10 ng/ml) for 24 hours [4]. The glycosaminoglycans (GAG) assay was used to evaluate proteoglycan production following treatment with the nanofibers. Gene expressions of chondrocyte-related markers (*Il6*, *Mmp13*, *collagen X*, *collagen II*, *aggrecan (acan)*, and *Tgf- β 1*) were evaluated 14 days after treatment using quantitative real-time PCR.

All plots and statistical comparisons were made using GraphPad Prism version 9.4.0 (GraphPad Software, La Jolla, CA, USA) with statistical significance again set at $p < 0.05$.

RESULTS

In TEM imaging, we observed similar fiber length distributions (~200-2000 nm) for K-PA and E-PA nanofibers both with and without losartan (**Figure 1A-D**). Both nanofibers offered a sustained release profile but that negatively charged E-PA nanofibers released losartan at approximately twice as fast as the positively charged K-PA nanofibers (**Figure 1E**).

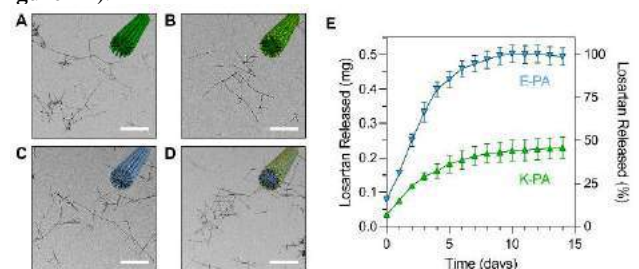


Figure 1: Structure and release profile of losartan sustained release nanofibers.

No cytotoxicity was observed in any of the treatment groups (**Figure 2**). We found that both positively and negatively charged PA nanofibers significantly increased cell numbers at all time points compared to no nanofibers at each losartan dose.

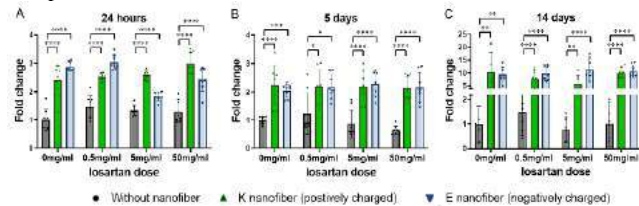


Figure 2: Nanofibers promote cell proliferation in a losartan-independent fashion.

We first confirmed that, in our hands, 24 hours of IL-1 β (10 ng/mL) leads to reduced GAG production (**Figure 3A**). Subsequently, significant increase in GAG production was observed with the positively charged K-PA nanofibers alone or when dosed with low (0.5 mg/mL) or moderate (5 mg/mL) losartan compared to controls without losartan or nanofibers (**Figure 3B**).

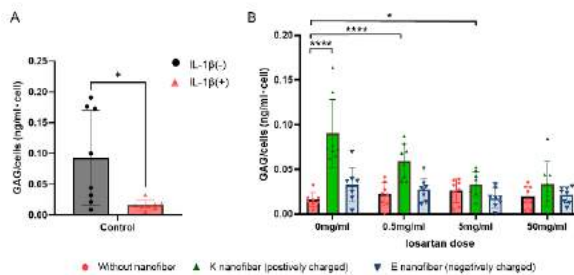


Figure 3: Positively charged nanofibers with low doses of losartan promote GAG production.

The positively charged K-PA nanofibers themselves significantly suppressed *il6* expression, and this stayed low, but not significantly different with the addition of losartan (**Figure 4A**). Conversely, K-PA nanofibers did not significantly change *mmp13* expression, but increasing doses of losartan resulted in a dose dependent decrease in expression of both the metalloproteinase (*mmp13*) and hypertrophy (*col10a1*) marker (**Figure 4B-C**). A pro-regenerative response was stimulated by the addition of K-PA nanofibers, as evident by the significantly increased expression of *col2a1* and *acan* (**Figure 4D-E**). Bioactivity of the losartan as a TGF β antagonist was further confirmed by showing a dose-dependent decrease in *tgfb1* expression with increasing losartan delivery (**Figure 4F**).

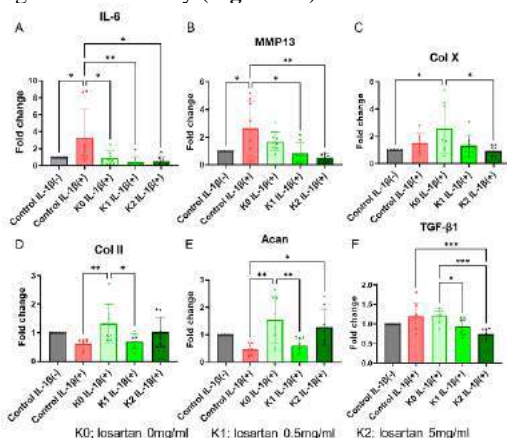


Figure 4: Positively charged nanofibers have pro-regenerative impact on OA-induced chondrocytes.

DISCUSSION

The results of this study showed that slower sustained release of losartan was achieved with our designed PA nanofibers, especially in the positively charged K-PA nanofibers. This result suggests that in addition to hydrophobic encapsulation, positively charged nanofibers supported an electrostatic interaction with the negatively charged losartan that enhanced the binding affinity between the peptide amphiphile molecules and the drug.

The results of this study also showed that PA nanofibers, of either charge, significantly increased chondrocyte proliferation. Self-assembled PA nanofibers have been reported to maintain chondrocyte morphology and promote cell division by encapsulating chondrocytes [5]. As for ECM production, the results of this study showed that positively charged K-PA nanofibers without losartan and with low (0.5 mg/mL) to moderate (5 mg/mL) losartan significantly increased GAG production for OA cells. This result may suggest that positively charged K-PA nanofibers may provide more effective ECM production ability due to their electrical complementarity with GAGs, considering the characteristics of negatively charged GAGs [6].

Positively charged K-PA nanofibers with low (0.5 mg/mL) to moderate (5 mg/mL) doses of losartan also significantly suppressed *il6* and *mmp13* expression. Interestingly, positively charged K-PA nanofibers without losartan did not suppress the expression of *mmp13*, whereas it significantly increased the expression of *col10a1*, a marker of hypertrophic chondrocytes. The results suggested that low doses of losartan, but not PA nanofibers, had an effective inhibitory effect on hypertrophic differentiation and inflammation of chondrocytes in the OA cell model. In addition, our study showed *tgfb1* was significantly inhibited by the positively charged K-PA nanofibers with low (0.5 mg/mL) to moderate (5 mg/mL) doses of losartan.

Taken together the results of this study suggest that the positively charged K-PA nanofibers bound with moderate (5 mg/mL) losartan can have a pro-regenerative phenotype in OA-activated chondrocytes by inhibiting *tgfb1* expression. This therapeutic strategy for articular cartilage repair using losartan sustained release PA nanofibers may provide a safer and more efficient treatment compared to oral administration or intra-articular injection of losartan.

ACKNOWLEDGEMENTS

We gratefully thank the Shannon Foundation for their generous support of this collaborative research.

REFERENCES

- [1] Nelson A.E., *Osteoarthritis Cartilage*, 26: 319-325, 2018.
- [2] Utsunomiya H., et al. *Am J Sports Med*, 48: 974-984, 2020.
- [3] Lewis J.A., et al. *ACS Biomater Sci Eng*, 6: 4551-4560, 2020.
- [4] Deng Z., et al. *J Orthop Translat*, 29: 30-41, 2021.
- [5] Kisiday J., et al. *Proc Natl Acad Sci USA*, 99: 9996-10001, 2002.
- [6] Didomenico C.D., and Bonassar, L.J., *Osteoarthritis Cartilage*, 26: 1438-1446.

A CHEMO-MECHANO-BIOLOGICAL MODEL OF CARTILAGE IN FEBIO: STUDIES OF PATHOLOGICAL LOADING, HOMEOSTATIC ADAPTATION AND BIO-CHEMICAL TREATMENTS

Muhammed M. Rahman (1), Paul N. Watton (2), Corey P. Neu (3),
David M. Pierce (1,4)

- (1) Department of Mechanical Engineering, University of Connecticut, Storrs, Connecticut, USA
(2) Insigneo Institute for in silico Medicine and Department of Computer Science, University of Sheffield, Sheffield, UK
(3) Department of Mechanical Engineering, University of Colorado Boulder, Boulder, Colorado, USA
(4) Department of Biomedical Engineering, University of Connecticut, Storrs, Connecticut, USA

INTRODUCTION

Osteoarthritis (OA) is a debilitating disease of synovial joints, including degeneration and loss of articular cartilage, that impacts nearly 20% of people in the US alone and affects quality of life through pain, functional limitations, lost earnings, anxiety, and depression. Mechanical stimuli are essential for chondrocytes (the cells within cartilage) to maintain healthy cartilage. Chondrocytes express chemicals (e.g. cytokines, growth factors, collagenases, and aggrecanases) in response to pathological loading, i.e. overloading (e.g. trauma) and reduced loading (e.g. immobilization) [1]. These biochemical species promote production or degradation of structural constituents, e.g. collagen and proteoglycan. Existing investigations on effects of mechanical loading on cartilage—including both *in vitro* experiments with human cartilage and *in vivo* animal models—fall short of true human physiological relevance [2]. Additionally, current mathematical models of signaling pathways lack mechanical effects while biomechanical models lack the chemical effects [3]. In particular, the concept of homeostatic adaptation, wherein tissues/cells receive pathological loading for prolonged periods of time, is understudied and poorly understood.

Leveraging our coupled chemo-mechano-biological framework for cartilage [4], we investigate interactions among intra-tissue mechanics and cell-driven mass/volume changes mediated by cytokines and chemical species. In this study, we: (1) implement our framework in 3-D, nonlinear finite elements using FEBio (U. of Utah, USA), (2) elucidate homeostatic adaptation to pathological stimuli during immobilizing, (3) simulate cartilage undergoing injury, immobilization, and treatments (with/without active growth factors). Specifically, we simulate applications of suramin, recently proposed as a treatment for OA and cartilage degeneration [5].

METHODS

Constitutive model. We utilize our established constitutive model of cartilage to predict tissue and intra-tissue mechanics under deformation [6].

Anisotropic growth. We employ anisotropic, through-thickness volume growth (TVG) to model degeneration and thinning of cartilage [7].

Mechanical stimuli - homeostasis and adaptation. We consider that pathological levels of mechanical stimuli cause perturbations to tissue-homeostasis. They drive a signaling pathways biochemical model using a stimulus function $f_S(\sigma_i(\tau), \sigma_{i,hom}^L(\tau), \sigma_{i,hom}^H(\tau))$ that is a function of mechanical stimuli ($\sigma_i(\tau)$) and salient homeostatic thresholds ($\sigma_{i,hom}^L(\tau), \sigma_{i,hom}^H(\tau)$) with L/H representing immobilizing/overloading, and $i \in \{sh, 1\}$ representing maximum shear and first principal stresses, respectively. The function f_S is well-shaped (see Fig. 1(a)) and adapts with time (τ) (see Fig. 1(b)) to reflect adaptation of homeostatic thresholds.

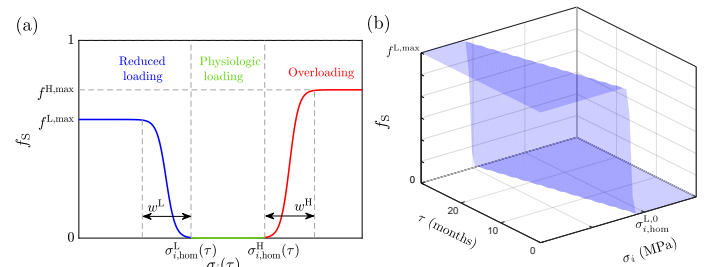


Figure 1: The mechanical stimuli function (a) ranges from reduced loading to overloading region, and (b) adapts pathological stimuli.

We define a piecewise continuous stimulus function f_S as,

$$f_S = \begin{cases} f_S^{L,max}, & \text{if } \sigma_i(\tau) < \sigma_{i,hom}^L(\tau) - w^L \\ f_S^L, & \text{if } \sigma_{i,hom}^L(\tau) - w^L \leq \sigma_i(\tau) < \sigma_{i,hom}^L(\tau) \\ 0, & \text{if } \sigma_{i,hom}^L(\tau) \leq \sigma_i(\tau) < \sigma_{i,hom}^H(\tau) \\ f_S^H, & \text{if } \sigma_{i,hom}^H(\tau) \leq \sigma_i(\tau) < \sigma_{i,hom}^H(\tau) + w^H \\ f_S^{H,max}, & \text{if } \sigma_i(\tau) \geq \sigma_{i,hom}^H(\tau) + w^H \end{cases}, \quad (1)$$

where f_S^L, f_S^H are sigmoidal functions, w^L, w^H control the width of sigmoidal transition regions, $f_S^{L,max}, f_S^{H,max} \in (0, 1]$ are constants. During

normal physiological loading, the tissue is in homeostasis and $f_s = 0$.

The (lower) homeostatic threshold $\sigma_{i,\text{hom}}^L(\tau)$ adapts during immobilizing ($\sigma_i(\tau) \leq \sigma_{i,\text{hom}}^L(\tau)$) as,

$$\sigma_{i,\text{hom}}^L(\tau) = \begin{cases} \sigma_{i,\text{hom}}^L(\tau = 0), & \text{if } \tau \leq \tau_{\text{del}}^L \\ \left(\int_{\tau-\tau^L}^{\tau} \sigma_i(\tau) d\tau \right) / \tau^L, & \text{if } \tau > \tau_{\text{del}}^L \end{cases}, \quad (2)$$

where τ_{del}^L represents a time-delay for homeostatic adaptation to begin and τ^L is a temporal averaging period for adaptation of homeostatic thresholds.

Biochemical signaling pathways. During pathological loading, the stimulus function is activated ($f_s > 0$) and drives the conversion of latent pro-inflammatory cytokines $\hat{c}_{\ell p}$ and latent growth factors $\hat{c}_{\ell \beta}$ to active forms \hat{c}_p and \hat{c}_β , respectively. Activated cytokines, in turn, upregulate collagenases \hat{c}_{ca} and aggrecanases \hat{c}_{ag} that degrade collagen \hat{m}_{co} and proteoglycan \hat{m}_{pg} , respectively. TIMPs \hat{c}_i inhibit collagenases and aggrecanases naturally, and suramin \hat{c}_{sm} prevents their uptake by cells in many tissues, cf. [5]. With the evolution of \hat{m}_{co} and \hat{m}_{pg} , cartilage thickness and intra-tissue stresses changes, and thus, the mechanical stimuli evolve.

Numerical studies. We implement our chemo-mechano-biological framework in FEBio. We exercise our model considering a single, linear hexahedral element representing cartilage, and apply boundary conditions simulating unconfined compression. We complete three studies: (i) homeostatic adaptation during joint immobilization, (ii) treatment with suramin during immobilizing following injury, and (iii) treatment with suramin and growth factors during immobilizing following injury. We predict the chemo-mechano-biological evolution of cartilage over 24 months.

RESULTS

(i) Homeostatic adaptation during joint immobilization. We performed simulations varying $\tau^L = 5, 10$, and 15 months to fit experimental data on cartilage thinning during immobilization over 24 months [8], see Fig. 2. Before immobilizing ($\tau < 0$), cartilage is in homeostasis, i.e. the evolution of all constituents is in equilibrium and $f_s = 0$. At $\tau = 0$, we begin immobilizing such that the current maximum shear stress is less than the lower homeostatic threshold, i.e. $\sigma_{sh} \leq \sigma_{sh,\text{hom}}^L$ and thus f_s increases. Adaptation of homeostatic thresholds to pathological loading follows depending on time averaging period τ^L following (2), see Fig. 2(a). The upper threshold $\sigma_{sh,\text{hom}}^H$ for physiologic loading remains fixed. As the lower homeostatic threshold $\sigma_{sh,\text{hom}}^L$ adapts towards the current maximum shear stress σ_{sh} , f_s approaches zero, see Fig. 2(b). Active growth factors and pro-inflammatory cytokines increase when f_s is elevated in the beginning, but goes back to zero once f_s returns to zero, see Fig. 2(c). With $\tau^L = 15$ months, numerical results for the evolution of cartilage thickness fit experimental data obtained *in vivo*, see Fig. 2(d).

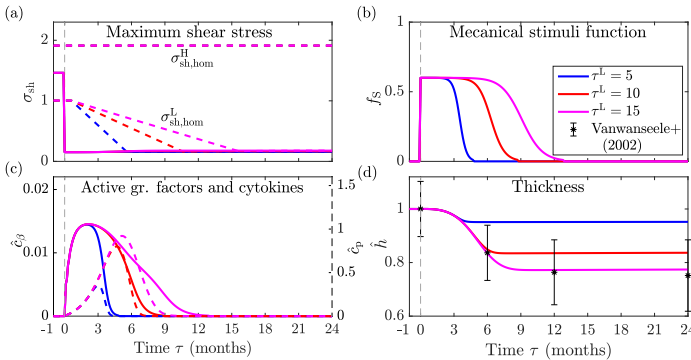


Figure 2: Evolution of intra-tissue mechanics as cartilage evolves during immobilizing with varying time averaging τ^L : (a) maximum shear stress (solid and dashed lines represent current stress and homeostatic thresholds resp.), (b) mechanical stimuli function, (c) activated biochemical species (solid and dash lines represent active growth factors and pro-inflammatory cytokines, resp.), and (d) cartilage thickness.

(ii) Treatment with suramin during immobilizing following injury. We performed simulations of healthy cartilage experiencing a high-impact injury at $\tau = 0$ month, followed by immobilizing for six months. Post injury,

cartilage receives treatments with suramin for 6, 12, 18, and 24 months. Cartilage loses functional collagen and living chondrocytes due to injury. The loss of chondrocytes causes latent growth factors to drop initially, but then increase thereafter due to activation of growth factors during immobilizing, and finally reach equilibrium as immobilizing ends after six months. Cartilage thickness recovers modestly to 77% and 78% if suramin is applied for six and 24 months, respectively (results not shown).

(iii) Treatment with suramin and growth factors during immobilizing following injury. We repeated the simulations in study (ii) but with different applications of active growth factors, i.e. maintaining constant level of $\hat{c}_\beta^{\text{const}} = 0.01, 0.02$, and 0.03 . After 24 months, cartilage thickness is 87% with $\hat{c}_\beta^{\text{const}} = 0.03$ compared to 77% without growth factors (Fig. 3(a)). With the application of active growth factors, chondrocytes promote production of structural constituents and proliferation. Total type II collagen recovery is 32% (Fig. 3(b)) and living chondrocytes are almost fully recovered during highest concentration of applied active growth factors and suramin (Fig. 3(c)). Latent growth factors also see a seven-fold increase with treatment versus without active growth factors (Fig. 3(d)).

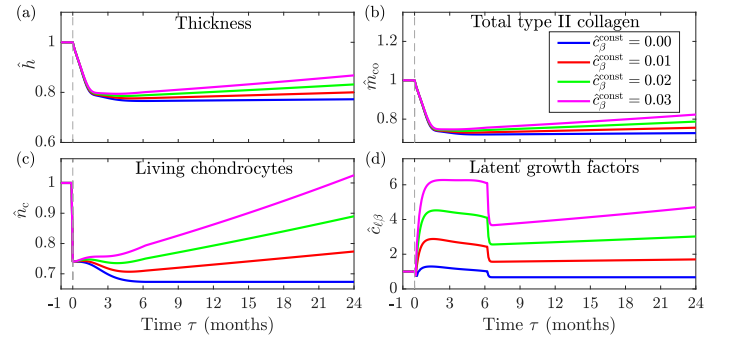


Figure 3: Cartilage evolving in injury and recovery with suramin for different dose of active growth factors. (a) Thickness, (b) Total type II collagen, (c) Living chondrocytes, and (d) Latent growth factors.

DISCUSSION

We implemented our chemo-mechano-biological framework for cartilage, including complex chemical and mechanobiological mechanisms resulting from pathological mechanical loading, into FEBio to facilitate 3-D finite element simulations. Our simulations illustrate the novel features of adaptation to pathological mechanical stimuli using two parameters, a time delay and a time averaging period, and successfully fit thinning of cartilage measured experimentally [8]. Our predictions show that the use of suramin alone to treat OA or thinning of cartilage after injury and immobilization may be ineffective. However, additional predictions indicate that the use of growth factors in addition to suramin may provide significant recovery of cartilage thickness after injury.

Limitations and outlook. We considered only a subset of known signaling pathways [9]. In studies (ii) and (iii), we considered growth factors as a combination of numerous growth factors in cartilage, although some may result undesired changes to homeostasis. We aim to leverage our chemo-mechano-biological framework in FEBio for patient-specific analyses, enabling advanced understanding of pathological changes due to biomechanical factors, improved clinical diagnostics and therapies, and new methods for non-invasive diagnosis and pre-/post-operative decisions.

ACKNOWLEDGEMENTS

NSF 1662429.

REFERENCES

- [1] Goldring MB et al. *Arthritis Res. Ther.* 11 (2009).
- [2] Halloran JP et al. *Ann. Biomed. Eng.* 40 (2012).
- [3] Baker M et al. *J. Math. Biol.* 75 (2017).
- [4] Rahman MM et al. (2022). DOI: 10. 2139/ssrn. 4247860.
- [5] Wiedemar N et al. *Antimicrob. Agents Chemother.* 64 (2020).
- [6] Pierce DM et al. *Biomech. Model. Mechanobiol.* 15 (2016).
- [7] Grytsan A et al. *Materials* 10 (2017).
- [8] Vanwanseele et al. *Arthritis Res. Ther.* 4 (2002).
- [9] Fang T et al. *Int. Orthop.* 45 (2021).

A NEURAL NETWORK-FINITE ELEMENT APPROACH FOR MULTIBODY CONTACT IN SOFT BIOLOGICAL MATERIALS

Christian L. Goodbrake (1), Michael S. Sacks (1)

(1) Willerson Center for Cardiovascular Modeling and Simulation, Oden Institute, University of Texas, Austin, Austin, TX, USA

INTRODUCTION

Simulations of biological mechanical evaluation and system function such as micro-indentation of cells and heart valve closure often rely on accurate simulation of highly nonlinear elasticity with multi-body contact. Additionally, for simulations over time, such as the simulation of an entire cardiac cycle, or simulating disease progression, these contact problems must be solved many times on the same domain with varying boundary conditions. The computational expense of these simulations is a severe bottle neck of digital twin models, since these simulations must be solved as subroutines in a larger, more complicated model. We present a novel technique for the rapid simulation of friction-free contact between soft bodies, represented using Non-Uniform Rational B-Splines (NURBS). This method, which we call the neural network finite element (NNFE) method, utilizes neural networks to learn the equilibrium configurations of multi-body systems under a chosen family of boundary conditions by directly minimizing the system's potential energy. Because this technique learns solutions directly from the system's energy functional rather than pre-computed solutions, it does not rely on previously known solutions to generate results.

Contact was incorporated through a variationally consistent energy penalty, which exactly enforces contact in the limiting case. We demonstrate that this approach generates a neural network capable of rapidly and accurately predicting the equilibrium configurations of systems of several deformable bodies in contact. Once trained, this network accepts specific problem data, such as boundary conditions, body force fields, or the relative positioning of the bodies, as input, and produces equilibrium configurations corresponding to that problem data as outputs. Additionally, the time required to compute these solutions is front loaded into the training of the network, so the trained network produces solutions in the time required to compute a single forward pass through the network, typically on the order of milliseconds. Furthermore, by representing bodies using NURBS

functions, we can ensure solutions of any degree of desired smoothness a priori while accurately capturing any complex geometry present in our own system.

METHODS

Building on our previous work on neural network finite element approaches in soft tissue modeling in [1], we seek to train a neural network to predict equilibrium solutions to a parameterized family of nonlinear elasticity problems involving multi body contact. Summarizing our previous method, we construct a neural network whose inputs are these parameters, and whose outputs are the degrees of freedom of a finite element discretization of our PDE problem. This network therefore assigns a finite element solution to each set of parameters. However, before training, the output of this network are nonsense, with no relation to the PDE, or the input parameters. We therefore use features of solutions to this partial differential equation to train the network.

We do this by sampling from the parameterized family of PDE problems, creating a set of training protocols. The neural network is then applied to these parameters, producing a set of trial configurations. The total potential energy of these configurations is computed, and through automatic differentiation, the gradient of this energy with respect to the neural network's weights and biases computed. This gradient is then used to minimize this total energy by adjusting the network's weights and biases, training the network to predict solutions with minimal potential energy, the defining feature of stable equilibria.

By itself, merely computing the potential energy of a multi body system by summing the energies of each individual body will not enforce contact between these bodies, resulting in predictions involving interpenetration. We incorporate contact by defining a surface-surface interaction energy between bodies. For each pair of bodies, Ω^i and Ω^j , we define a contact energy contribution Π_c :

$$\Pi_c = \frac{k}{2} \int_{\partial \Omega^i} \langle -g^{(j)} \rangle^2 dA + \frac{k}{2} \int_{\partial \Omega^j} \langle -g^{(i)} \rangle^2 dA$$

where $g^{(i)}$ is the signed distance from the boundary of body Ω^i , and $g^{(j)}$ similarly, the angled brackets being the Macaulay bracket, replacing negative arguments with 0, and k an appropriate constant controlling the strength of the contact force. This energy vanishes when the bodies do not interpenetrate each other, and increases as the depth of penetration increases. Thus this energy imbues each body with an expelling force, ejecting other bodies from its interior, this force increasing as k increases. In the limit as k approaches infinity, the equilibrium solutions of this weakened problem will approach the contact constrained problem exactly. Such an energy contribution is added for each pair of bodies to the total energy, and our network is trained as before. Computing this energy in a differentiable and just-in-time compilable way required writing custom python NURBS code in Google's JAX framework. This software was written carefully to avoid dynamic memory allocations or indefinite loop, so that it could be just-in-time compiled to make training feasible.

RESULTS

We applied this approach to several test contact problems involving rigid indentation, where geometric parameters of the indenter are taken as inputs to the network, and the control points and weights of the NURBS discretized domain as the output. The first of these involved rigid spherical indenters, with the radius and the depth of indentation being the geometric parameters trained over (Figure 1).

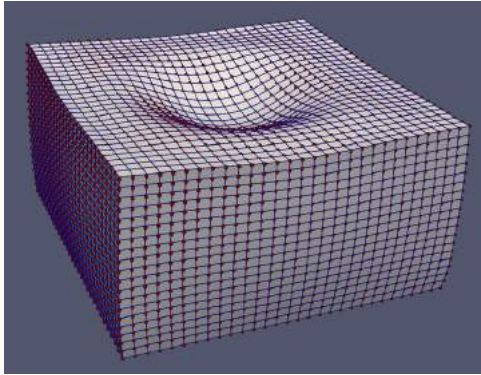


Figure 1: Validation solution (blue wire frame) compared with NNFE prediction (red vertices). NNFE solutions required .0023 to .0026 seconds to compute. The spherical indenter is not shown so as not to obstruct the view of the indentation.

Secondly, we modified this problem by changing the indenter geometry to a cone rather than a sphere, and trained over the tip angle, and depth of indentation. Because our initial NURBS discretization does not allow sharp features, the contact in the very near proximity of the indenter tip is not captured. However, by inserting knots into the knot vectors at the point of contact, NURBS allows for the capture of sharp features (Figure 2). Training a network on this new discretization produces sharp deformations at the point of contact.

Finally, we construct a toy problem involving a rectangular flap impinging on a rigid wall, which serves as a stand-in for heart valve leaflet contact. The solutions to these problems feature large displacements and rotations, features that cause difficulties in traditional finite element implementations, since displacements and rotations do not generate strain energy.

In these simulations, the difference between the NNFE predictions and the ground truth solutions were very small. However, the primary advantage is the minimal run time, as reported in Figure 1.

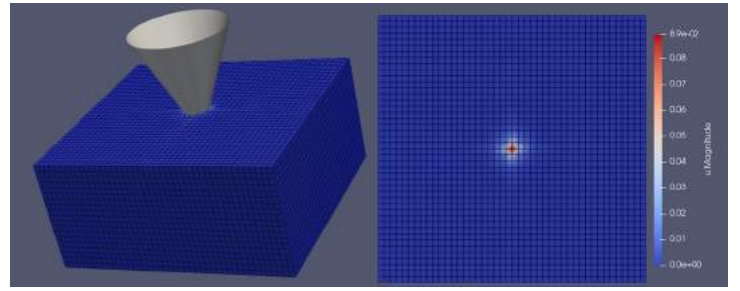


Figure 2: Repeated knots for at the center allow for the localization of sharp features caused by a conical indenter. (Here displacement magnitude is shown, with blue corresponding to 0 and red to the maximum indentation depth .

DISCUSSION

We see that the trained network is capable of rapidly predicting equilibrium solutions of the family of problems used to train the network, in a fraction of the time that a conventional solution methodology requires. Therefore, in the many query setting, or in the low-computational power setting, these neural network models can produce accurate results where traditional solution methods would be infeasible due to their high computational time and power demands.

This allows these NNFE models to be incorporated into, for instance, digital twin models, where they are run several times as a subroutine. Conventional finite element techniques would be infeasible in this setting, because the time they require is two to three orders of magnitude greater than that required by the NNFE predictions. Because these models are incorporated into digital twins as subroutines, they will be run many times, and as such, the runtime of traditional FE techniques accumulates to an unacceptable level.

These NNFE predictions are also useful for inverse problems where many forward solutions must be computed. These inverse problems require the computation of a solution and its gradient with respect to a set of parameters, but the primary computational cost is dramatically concentrated in the forward solve, because the gradient can be computed with a single linear solve using the adjoint method. Therefore, these NNFE models can be used to solve these inverse models much more quickly than the traditional FE models.

Further, in a clinical setting, where patient specific data is necessary to produce accurate simulation results, these trained NNFE models can reduce the computational demands of these models to the point where these simulations can be run in the office during a patient consultation. The hardware required to run the NNFE simulations is significantly more common than that for traditional FE simulations, allowing these trained NNFE models to be deployed in a clinical setting, where high performance computing resources are not available, allowing high fidelity patient specific simulation of heart valve function to be used in real time.

ACKNOWLEDGMENTS

The authors are grateful for the support provided by NIH 1F32HL162423-01 to C. Goodbrake, and NIH R01 HL073021, and NIH R01 HL142504, and the Platform for Advanced Scientific Computing (Swiss Federation) for support.

REFERENCES

- [1] Sacks, M. S., Motiwale, S., Goodbrake, C., and Zhang, W. (October 17, 2022). "Neural Network Approaches for Soft Biological Tissue and Organ Simulations." ASME. J Biomech Eng. December 2022; 144(12): 121010. <https://doi.org/10.1115/1.4055835>

EFFECT OF STANDARDS-BASED GRADING ON THE COURSE GRADE DISTRIBUTION IN A BIOMECHANICS COURSE

Kenneth J. Fischer (1,2), Christopher J. Fischer (2,3),

- (1) Mechanical Engineering, University of Kansas, Lawrence, KS, USA
(2) Bioengineering, University of Kansas, Lawrence, KS, USA
(3) Physics and Astronomy, University of Kansas, Lawrence, KS, USA

INTRODUCTION

The standard midterm and final exam evaluation model creates a high-stakes environment on a few exams that is detrimental to poor test-takers and learners that require more time to master the material. My Basic Biomechanics course had relied on three (3) midterm exams over 3 broad topic areas and a comprehensive final exam. A poor grade on the first exam often 1) limited the final grade in the course, and 2) seemed to discourage learners from continuing to learn/master the material. The only opportunity for re-testing was on the comprehensive final—a separate grade. I believed an alternative form of evaluation may improve outcomes and implemented standards-based grading.

Overview of Standards-Based Grading and Pros/Cons:

Standards-based grading [1,2] is assessing mastery for each learning objective (LO) in a course, with multiple opportunities to demonstrate that mastery. Competency or mastery is demonstrated on exam problems for each LO. There are more exams, so there are more opportunities to demonstrate competency. Students do not get exam grades, but earn points for successfully demonstrating competency in the LOs.

The advocates for standard base grading believe it creates a more equitable learning environment and students are given clear learning targets and rubrics so that they can then use those to master the content in the course. In addition, students are not penalized for early shortcomings or failure as long as they have sufficient chances to study and demonstrate competency. Theoretically standards-based grading encourages and facilitates a deeper learning of the content.

There are detractors for standards-based grading, because it does place essentially based the course grade almost solely on exam problems for the LOs, as assessments of competency. Homework, or what I prefer to call practice, for the LOs is typically not included in the grade.

However, because of the greater number of exams, and the mindset that exams are opportunities to earn points, the test-pressure and anxiety is likely reduced for most students. Some educators also have concerns that giving multiple opportunities to show competency creates a mindset that students should expect to get a do-over.

Standards-Based Grading at KU and my Biomechanics Course:

Let me give you some context about the use of standards-based grading at the University of Kansas in science and engineering. The department of physics began using standards-based grading several years ago in the calculus-based physics courses and has since expanded its use. The goal was to reduce the drop, withdraw, and failure rates in the courses, and physics did see improvement. A few people in engineering, including myself, heard about his approach and adopted it.

My prior course and exam structure only allowed for one additional opportunity on some learning objectives on the final exam. That was an additional (not replacement) grade, so it did not eliminate earlier poor scores. So, in hopes of reducing the D's and F's in the course, I implemented standards-based grading in Fall 2019.

METHODS

Implementation of Standards-Based Grading:

I based the structure of standards-based grading heavily on prior work in physics. Students were given with nearly twice as many opportunities to demonstrate mastery than points required to earn the maximum score for an LO (one point for each problem successfully completed). The approach includes seven (7) exams during the semester, plus an optional final exam with two questions per learning objective. The course has nine (9) learning objectives related to biomechanics concepts including knowledge of anatomy, tissue and cell properties, and analysis approaches including statics, single joint dynamics, inverse dynamics, tissue mechanics and cellular mechanics.

The Table 1 indicates how many opportunities the students had to show competency in each learning objective on individual exams and in total. The last two rows are most important, comparing the total number of opportunities per objective to the total points required to obtain the highest score (called the S-score) for each objective.

Table 1: Learning Objective Problem Distribution by Exam.

Number of Questions from each Learning Objective per Exam									
Exam	Objective								
	1	2	3	4	5	6	7	8	9
Exam 1	3	3							
Exam 2	1	1	2	1					
Exam 3		1	1	1	2	2			
Exam 4	1		1	1	1	1	2	1	
Exam 5	1	1		1	1	1	1	2	
Exam 6	1	1	1	1	1	1	2	2	3
Exam 7	1	1	1	1	1	1	1	1	3
Final Exam	2	2	2	2	2	2	2	2	2
Total	10	10	8	8	8	8	8	8	8
Points for S-score=5	6	6	5	5	5	5	5	5	4

Note that students had to earn the majority of available points to get the maximum S-score in all objectives, except LO9, for which there was the least amount of time for mastery. The maximum S-score was 5, and the minimum S-score was 1. The LO points were related to S-score through Table 2. The geometric average of the S-scores, s_i , determined the overall course score, S , per Equation 1. Note that there are 10 scores in the geometric average and for my course, the 10th “objective” was attendance and submission of an in-class activity. This course does have required active in-class student work on relevant example problems.

Table 2: Converting Learning Objective Points to S-scores

Category	Grade (S_i)				
	5	4	3	2	1
Objective 1 # of Correct Problems (Points)	6	5	4	3	<3
Objective 2 # of Correct Problems (Points)	6	5	4	3	<3
Objective 3 # of Correct Problems (Points)	5	4	3	2	<2
Objective 4 # of Correct Problems (Points)	5	4	3	2	<2
Objective 5 # of Correct Problems (Points)	5	4	3	2	<2
Objective 6 # of Correct Problems (Points)	5	4	3	2	<2
Objective 7 # of Correct Problems (Points)	5	4	3	2	<2
Objective 8 # of Correct Problems (Points)	5	4	3	2	<2
Objective 9 # of Correct Problems (Points)	4	3	2	1	<1
In-Class Activities not submitted*	0-2	3	4	5	>5

$$S = (s_1 \times s_2 \times s_3 \times s_4 \times s_5 \times s_6 \times s_7 \times s_8 \times s_9 \times s_{10})^{1/10} \quad (1)$$

The course grade was determined from the overall course score, S , using cutoff scores in Table 3.

Table 3: Course Grade Assigned from the Course Score, S .

Score	Course Grade
$S \geq 4.6$	A
$3.9 \leq S < 4.6$	B
$2.6 \leq S < 3.9$	C
$1.6 \leq S < 2.6$	D
$S < 1.6$	F

These grade cut-off scores were previously developed by the physics instructors, and I did not alter them. Some, perhaps non-standard approaches in this course with standards-based grading was the opportunity for partial credit (partial LO points for substantially correct work) and the opportunity for extra credit points that could be applied/distributed to any combination LOs prior to the final exam.

The Analysis of Standards-Based Grading:

To determine the effect of standards-based grading on student performance, the course grades for my last three offerings of the course in the traditional exam scheme were compared to the grades with objective base grading (Fall 2019, 2021, 2022). Because Fall 2020 had hybrid course delivery, exams were online, and academic misconduct was apparent, that semester was excluded.

RESULTS

In terms of student perception, they generally indicate preference for the standards-based grading approach, though it is harder for them to predict or understand their grade (standing) early in the course. I generally tell students they are doing OK if they are earning about half of the available points for the LOs. Each semester, some students earned a grade of A without taking the final exam.

As noted earlier, the hope was that the standards-based grading would reduce the D's in the F's in the course. What the data actually show is that standards-based grading increased the A's in the course and decreased the B's (and perhaps slightly decreased C's). The D+F rate was unchanged (Table 4). The sample size is obviously small (3 data points before and after standards-based grading), and the differences are not statistically significant.

Table 4: Average Percentage of Letter Grades Before and After Implementation of Standards-Based Grading.

	Traditional	Standards-Based
A's =	34.4%	42.4%
B's =	32.3%	25.8%
C's =	25.8%	24.2%
D's & F's =	7.5%	7.6%

DISCUSSION

I noted that low-performing students did not complete extra credit assignments. I hypothesize that low-performing students may lack time (or bandwidth) to improve their competency/mastery, whether because they are trying to balance education and work or simply because they are struggling in multiple courses.

From the instructor perspective, there are some challenges with the standards-based grading approach. Standards-based grading requires more exams and more exam problems. Also, for this course, the end of the semester has 3 exams (last LO exam #6, comprehensive exam #7, and the final exam) in quick succession (each about one week apart). Exams can be written in advance, but grading and returning of exams must still be done quickly. The grading of each LO exam problem is more efficient, since the outcome/score for each exam problem is binary (or has few levels) in terms of score. However, providing constructive feedback can still be time-consuming.

So, is standards-based grading effective? Not necessarily in the way I expected, but it does appear to help and motivate some students to improve their understanding of course materials, their performance on exam problems, and, thus, their grades. Is standards-based grading worth the effort? Because the student learning appears to be positively affected, the current plan is to continue this approach in the basic biomechanics course.

REFERENCES

- [1] Spencer, K. (2012). Education Digest, 78(3).
- [2] Wormeli, R. (2011). Educational Leadership, 69(3), 22-26.

CELL-SCALE MEASUREMENTS OF TISSUE VISCOELASTICITY USING THERMOREPONSIVE MECHANOSENSORS IN ENGINEERED TUMOR MODELS

Benjamin E. Campbell (1), Stephanie Mok (1), Christina-Marie Boghdady (1,2), Nikita Kalashnikov (1), Luke McCaffrey (3), Christopher Moraes (1,2,3,4)

(1) Department of Chemical Engineering, McGill University, Montreal, Quebec, Canada
 (2) Department of Biological and Biomedical Engineering, McGill University, Montreal, Quebec, Canada
 (3) Goodman Cancer Research Center, McGill University, Montreal, Quebec, Canada
 (4) Division of Experimental Medicine, McGill University, Montreal, Quebec, Canada

INTRODUCTION

Viscoelasticity describes materials that exhibit both elastic and time-dependent viscous behaviors in response to stress, resulting in stress relaxation and viscous creep under load. While it is well established that matrix stiffness is influential for tissue form and function, matrix viscoelasticity has recently emerged as a key driver in tissue spatiotemporal organization[1]. Furthermore, as cells are the sensors and effectors of mechanical response, it is important to understand how these properties change at cellular length-scales within engineered 3D tissues. Measurements at these scales relevant to cells cannot currently be predicted using bulk mechanical testing methods or sub-cellular optical spectroscopy techniques[2],[3]. To address these limitations, we extend the use of our previously described thermoresponsive hydrogel microdroplet stiffness sensors [2] to measure viscoelastic parameters. These mechanosensors swell at hypothermic temperatures to exert local stresses, and by characterizing, measuring, and modelling expansion time dynamics, we demonstrate the ability to make highly local measurements of tissue viscoelasticity.

METHODS

Fluorescent microspherical hydrogel droplets are fabricated in Poly-n-isopropylacrylamide (NiPAAm) in an oil-water emulsion as previously described, producing sensors 10-50um in diameter that compact at temperatures above 32°C, and can be coated with Type I collagen to allow incorporation into engineered tumor spheroid models [2], [4]. Rapidly cooling the microtissues below 32 °C causes the sensors to expand at a rate commensurate with tissue viscosity.

Since conventional measurements of viscoelasticity require application of a known stress to a deforming tissue, we first needed to measure the stresses generated by the sensors during expansion. Sensors were embedded in polyacrylamide gels of known mechanical properties in their collapsed state. Sensor expansion in these gels, in combination with finite element modelling allowed us to measure stress as a function

of sensor size and actuation stroke length (Fig. 1A, B). This information was then used to simulate sensor expansion in Kelvin-Voigt models of viscoelasticity, for which the two parameters E and τ are parametrically swept (Fig. 1C, D). Matching these characteristic expansion profile libraries to experimental measurements allowed us to obtain two-parameter measurements of tissue viscoelasticity.

Tumor models with randomly distributed embedded sensors were generated by passive confinement in micro-pocket devices[5], using three differentially invasive breast cancer cell lines: non-invasive T47D cells, invasive MDAMB-231 cells, and engineered MCF7 cells that can overexpress Src upon induction, and invade on demand.

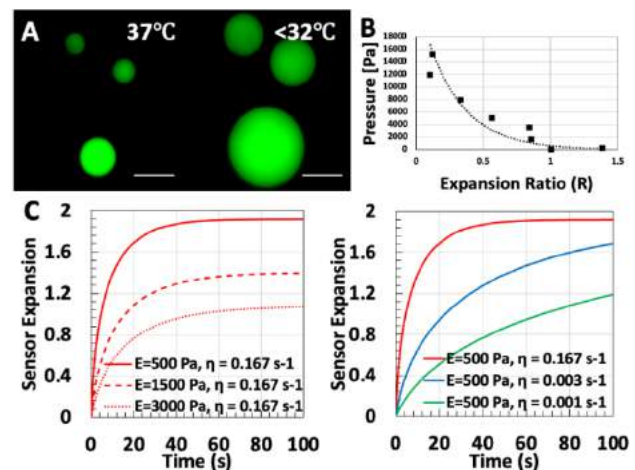


Figure 1: A - Sensors imaged under epifluorescence in their compacted and expanded states (Scale bar 50um). B - Stress-sensor stroke length relation. C - Modelled sensor expansion profile independently controlled by E and η/τ in Kelvin-Voigt model.

RESULTS

We first confirmed that in linear elastic materials such as polyacrylamide gels, expansion completed within seconds of the applied temperature change (data not shown). We then compared measurements in live and fixed T47D tissues, and showed that as expected, viscoelastic characteristics of the tissues were dissipated on fixation, which behaved more elastically and exhibited substantial stiffening due to protein cross linking (Fig. 2).

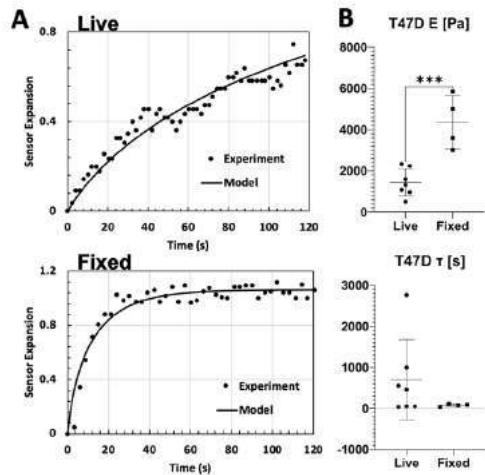


Figure 2: A - Example fitting of model to experimental data for T47D spheroids in live and fixed conditions. B - Young's modulus (E) and time constants (τ) in live and fixed T47D spheroids

We then evaluated viscoelasticity within tumor models of differentially invasive cell lines. Both non-invasive T47D and invasive MDAMB-231 spheroids exhibit similar local stiffnesses, but the time constants of sensor expansion are consistently lower in the invasive tissue, even in regions of similar stiffness (Figure 3), suggesting that internal local fluidity is a characteristic of quiescent tumors.

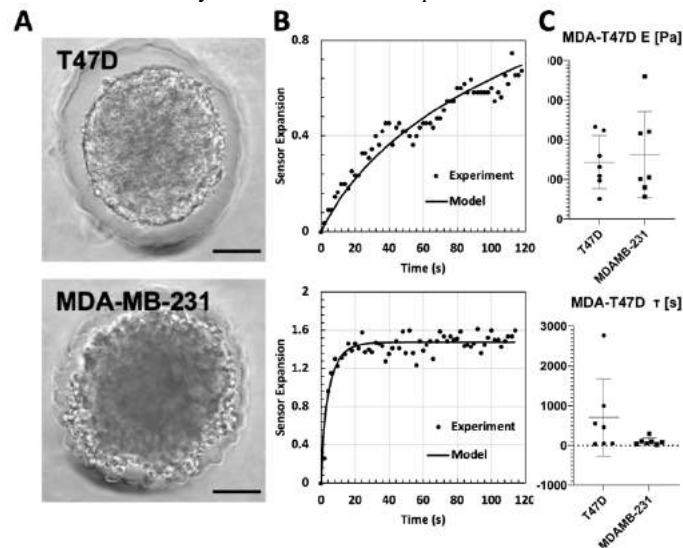


Figure 3: A - Representative images of T47D and MDAMB-231 spheroids. B - Corresponding sensor expansion profiles. C - Young's modulus (E) and time constants (τ) of sensors actuated in invasive (MDAMB-231) and non-invasive (T47D) spheroids.

Because comparisons between the MDAMB-231 and T47D models may capture more than invasive potential, we engineered an MCF7 cell line to overexpress Src upon induction with doxycycline. Consistently, inducing a tissue to invade reduced local viscous properties, while maintaining similar elastic properties (Figure 4).

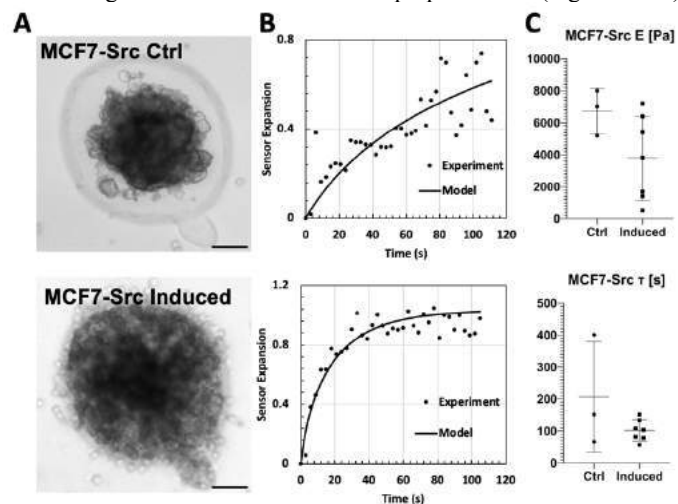


Figure 4: Figure 3: Young's modulus (E) and time constants (τ) of sensors actuated in inducibly invasive MCF7 spheroids.

DISCUSSION

These cell-sized mechanosensors demonstrate that spheroids with different invasive potentials showed highly distinctive internal viscoelastic characteristics, where invasive spheroids (MDAMB-231 and MCF7-Src) display rapid strain responses to stress, compared to non-invasive spheroids (T47D and MCF7-Ctrl) which have more varied viscoelastic responses including a much slower, more viscous deformation profile. These findings are consistent with recent literature evidence demonstrating that individual invasive cancer cells exhibit significantly less viscous behaviors to normal healthy cells [6] and in response to a passive viscous surrounding matrix, non-invasive tissues exhibit high levels of invasion[1]. Ultimately, changes in tissue viscoelasticity affects how those cells perceive their mechanical environment over time and thus, the ability of these sensors to quantify the viscoelastic properties as experienced by cells permits investigation of how mechanics and cell behavior interact.

ACKNOWLEDGEMENTS

This work was supported by funding from the Canadian Cancer Society (Grant Nos. 704422 and 706002) and the Canadian Institutes for Health Research (Grant No. 01871-000) to C.M. and L.M., the Natural Sciences and Research Council of Canada (NSERC) Discovery grants (RGPIN-2022-05165) and the Canada Research Chairs in Advanced Cellular Microenvironments to C.M.

REFERENCES

- [1] Elosegui-Artola, A et al., *Nat. Mater.*, 22:117-127,2023.
- [2] Mok, S et al., *Nat. Commun.*, 11:4457,2020.
- [3] Serwane, F et al., *Nat. Methods.*, 14:181-186, 2017.
- [4] Campbell, BE et al., *Methods Mol. Biol.*, 2614:237-246, 2023
- [5] Zhao, L et al., *Biofabrication.*, 11:045013, 2019.
- [6] Xie, Y et al., *J. Mech. Behav. Biomed. Mater.*, 91:54-58, 2019

EFFECT OF AORTIC CURVATURE ON BIOPROSTHETIC AORTIC VALVE PERFORMANCE

B. Vogl (1), R. Gadhav (1), Z. Wang (2), A. Chavez Ponce (3), A. El Shaer (3), M. Alkhouli (3), H. Hatoum (1)

(1) Department of Biomedical Engineering, Michigan Technological University, Houghton, MI, USA

(2) Department of Mechanical and Aerospace Engineering & SIMCenter, The Ohio State University, Columbus, OH, USA

(3) Department of Cardiovascular Medicine, Mayo Clinic, Rochester, MN, USA

INTRODUCTION

Aortic stenosis (AS) is the most common valvular heart disease in developed countries and is a major cause of heart failure¹. A treatment approach for AS can be accomplished by replacement of the diseased valve with a bioprosthetic transcatheter aortic valve or surgical aortic valve. The performance and durability of these bioprosthetic valves have been related to postoperative mean transvalvular pressure gradient (ΔP).

Echocardiography (ECHO) and catheterization (CATH) modalities are used to measure ΔP non-invasively and invasively, respectively, leading to differences in measurements. These discrepancies are a result of the different measurement locations for each modality in the pressure recovery zone. ECHO measurements do not account for pressure recovery unlike CATH measurements. Several attempts have been made (clinically, computationally, and experimentally) to quantify pressure recovery and to understand its effect on postoperative ΔP measurements. Attempts have also been made to modify the simplified Bernoulli equation to account for pressure recovery as a function ascending aorta size².

Despite the aforementioned efforts, pressure recovery assessment of physiological diameter, shape, and three-dimensional curvature of the ascending aorta and aortic arch is still lacking. In this study, we aim to assess PR in physiological 3D aortic arches to determine their effects on valve performance.

METHODS

A 23mm SAPIEN 3 Ultra (Edwards Lifesciences, Irvine, CA) was hemodynamically assessed in a pulse duplicating left heart flow loop simulator under various combinations of cardiac conditions (**Table 1**)

Table 1. Cardiac Conditions.

Blood Pressure (mmHg)	Cardiac Output (L/min)	Heart Rate (bpm)
120/80, 140/80	3, 5	60, 80

The aortic chambers used had identical root dimensions but with 3 different aortic arch geometries; with 2 distinct physiological 3D aortic arches that will be referred to throughout this abstract as “Curvature 1” and “Curvature 2” and with a straight downstream tube (without aortic arch). All the models had the same aortic root dimensions (same annulus size, sinus dimensions, and sinotubular junction (STJ) dimensions). The aortic arch geometry was based on the work by Boufi et al³. A schematic of all the models is shown in **Figure 1**.

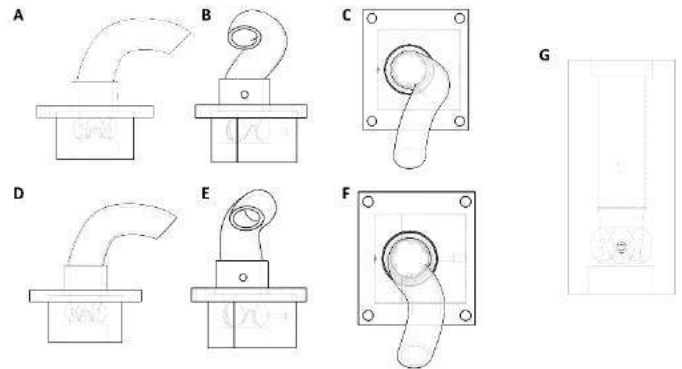


Figure 1. Schematics of the 3 aortic models: (A – C) Curvature 1 model, (D – F) Curvature 2 model and (G) straight model.

All pressure measurements were taken with Millar Pressure Catheters (Millar, Houston, TX) and with a Validyne pressure sensor (Validyne Engineering, Northridge, CA) set to monitor the aortic pressure constantly. The measurements were made incrementally along the aortic model with an interval of 0.2cm from the ventricular pressure port to the valve leaflet tips and 0.5cm from the leaflet tips to the end of the model. In all the models, the position of 0cm corresponds to the most

upstream measurement taken at the same axial position as the ventricular pressure port. Peak flow for each measurement occurred when flow was maximum (peak systole), this time point was used to select the instantaneous pressure for each axial position. The peak ΔP , defined as the difference between the ventricular pressure measurement (0cm) and each subsequent axial position, was calculated for all models at each cardiac condition.

RESULTS

The pressure as a function of axial distance at the different cardiac conditions is plotted in **Figure 2A** and **2B** for the models with aortic arches. Results from the pressure measurements are plotted starting from upstream of the valve and ending downstream of the valve after the aortic arch. As the valve opens, pressure decreases until it reaches the vena contracta (VC), where it is at its minimum. After passing the VC, pressure gradually rises until the start of the aortic arch. This rise in pressure marks the beginning of PR. At the arch, pressure begins decreasing until the middle of the arch. After passing the middle of the arch, the pressure starts increasing gradually marking the beginning of a second PR zone. The pressure follows a general trend for both models, where PR zones occur after the valve and at the aortic arch. This trend is independent of the cardiac condition, but the measured pressures do change with different conditions. At a pressure of 140/80mmHg, an upward shift of the pressure curve is observed for both models. There is less pressure loss after the aortic valve and aortic arch for the 3L/min condition for both models. At a heart rate of 80bpm the resulting pressure curve has a slight downward shift compared to the default 120/80mmHg and 60bpm condition for Curvature 1 model, whereas no shift in the curve is present in Curvature 2 model.

The pressure as a function of axial distance at the different cardiac conditions is plotted in **Figure 2C** for the straight model. Results from the pressure measurements are plotted starting from the upstream of the valve and end downstream of the valve. The straight model pressure curves follow the general trend where only one PR zone occurs after the aortic valve. The trend in the straight model is also independent of the cardiac condition, but the measured pressures do change with the different conditions.

DISCUSSION

In this study, we evaluated PR in three different aortic models which had the same aortic root dimensions but different aortic arch geometries. The models with aortic arches had two distinct PR zones, the first after the VC and the second after the main curvature of the aortic arch, whereas in the straight model, only a single PR zone was present after the VC.

The PR phenomenon has been well described in literature: as the blood leaves the aortic valve towards the STJ and ascending aorta, a decrease in blood velocity and kinetic energy occurs. As a result, pressure starts recovering and potential energy increases. When the blood flow reaches the aortic arch, a change in the velocity profile of the fluid occurs. The faster moving fluid in the aorta is pushed towards the outer wall of the aortic arch due to its higher inertia⁴. In addition, as the fluid passes through the bend, centrifugal forces cause a difference in pressure at the inner and outer bend, causing the formation of a recirculation zone containing Dean vortices⁵. These vortices cause the kinetic energy of the fluid to change, resulting in an energy loss downstream which is represented by a pressure loss.

The general trend of pressure recovery in all the models was independent of the cardiac condition used. Instead, the individual pressure measurements at each axial position that make up the pressure curve depended on the cardiac condition. At a pressure of 140/80mmHg, the same changes in energy are occurring in the 3 distinct aortic models,

but the overall pressure of the system has increased. At a lower cardiac output of 3L/min, lower pressure drops occurred at the aortic valve and aortic arch. This is due to a reduction of kinetic energy from lowering the cardiac output, which is dependent on velocity. As a result of this lower kinetic energy, there is less energy loss due to viscous losses, turbulent losses, and flow separation losses. An increase in heart rate to 80bpm appeared to have little effect on the resulting pressure measurements. The work of Rozenman et al.⁶ shows that an increase in heart rate up to a certain level (150bpm) leads to a decrease in pressure gradient. The magnitude of this decrease depends on cardiac output and aortic valve area.

In this study, we illustrated the differences in PR between distinct aortic curvatures and a straight aorta. This highlights the potential inconsistencies in invasive pressure drop measurements, especially when there is no guideline for optimal commercial catheter placement. Patient specific studies are warranted in order to investigate the impact of catheter position for an accurate assessment of valve performance, and the effect of aortic arch size and angle on valve performance.

ACKNOWLEDGEMENTS

We would like to acknowledge the DeVlieg Foundation, the Blue Cross Blue Shield of Michigan Foundation, the Institute of Computing and Cybersystems at Michigan Technological University, and the Health Research Institute at Michigan Technological University.

REFERENCES

- [1] Nkomo, V., *The lancet* 368.9540 (2006): 1005-1011
- [2] Baumgartner, H., *JACC* 33.6 (1999): 1655-1661
- [3] Boufi, M., *Eur. J. Vasc. Endovasc. Surg.* 53.5 (2017): 663-670
- [4] Caro, Cambridge University Press, 2012
- [5] Dean, R., *Lond. Edinb. Dublin philos. mag.* 4.20 (1927): 208-223
- [6] Rozenman, *Catheter. Cardiovasc. Interv.* 11.5 (1985): 533-538

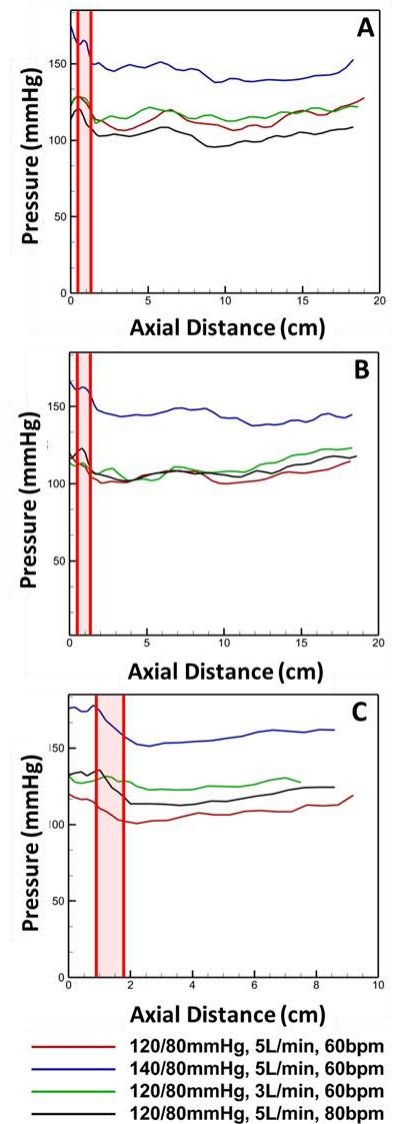


Figure 2. Variations of pressure measurements as a function of axial distances at the selected time points at peak systole for curvature 1 (A), curvature 2 (B) and straight (C) aortic models. The shaded regions represent the location of the valve.

A COMPUTATIONAL ASSESSMENT OF STROKE PREDICTORS AFTER TRANSCATHETER AORTIC VALVE REPLACEMENT

B. Vogl (1), Z. Wang (2), A. Chavez Ponce (3), A. El Shaer (3), M. Alkhouli (3), H. Hatoum (1)

- (1) Department of Biomedical Engineering, Michigan Technological University, Houghton, MI, USA
(2) Department of Mechanical and Aerospace Engineering & SIMCenter, The Ohio State University, Columbus, OH, USA
(3) Department of Cardiovascular Medicine, Mayo Clinic, Rochester, Minnesota, USA

INTRODUCTION

Transcatheter aortic valve replacement (TAVR) is a standard therapeutic approach for patients with severe aortic stenosis (AS). A major postoperative concern with this procedure is the risk of stroke. In fact, the Placement of Aortic Transcatheter Valves (PARTNER) II Trial, reports the incidence of ischemic stroke as 5.5% at a two-year clinical end point¹. Atherosclerosis of the aortic arch has been identified as a significant predictor of stroke. Results of the Rotterdam Study² have shown a strong association between aortic stiffness and atherosclerosis. Veulemans et al.³ has shown an increased rate of stroke in patients with horizontal aortas greater than 51°. It may be possible that aortic geometry influences the development of stroke in patients who have undergone TAVR.

The aim of this study is to assess how aortic arch geometry influences the hemodynamic parameters that are associated with the development of stroke after aortic valve replacement. We hypothesize that stroke after TAVR is more likely to occur in patients with certain geometric and hemodynamic properties in the aortic arch.

METHODS

Contrast-enhanced computed tomography (CT) images of patients who did and did not (control group) have a stroke after TAVR were obtained from Mayo Clinic under an IRB approved protocol. Patient selection criteria was based on age and sex. The CT images were imported into Mimics Research 23.0 (Materialise, Belgium) and segmented to generate patient-specific 3D digital models of the aorta with the brachiocephalic artery (BCA), left common carotid artery (LCCA), left subclavian artery (LSCA), and calcium. The aortic root (aortic annulus to sinotubular junction (STJ)) was removed from the models in order to isolate the effect of the aortic geometry in our analysis. Geometrical measurements of the aorta and main branching arteries were performed using 3-Matic 15.0 (Materialise, Belgium).

All simulations were calculated using STAR-CCM+ (Siemens, Inc., Germany). Large eddy simulations (LES), which has the capability to resolve the wall regions that contain a wide range of scales of flow motion from both temporal and spatial domains, was adopted in our study. It can directly resolve the large scales of turbulence everywhere in the computational domain and model those small-scale motions in the near-wall region. The wall-adapting local-eddy viscosity (WALE) sub-grid scale model was used to account for the effects of small eddies on the resolved flow. The all y^+ treatment method is used to resolve the flow within the near-wall region. This method combines the high y^+ wall treatment for coarse meshes and the low wall y^+ treatment for fine meshes, which gives similar results to the low y^+ treatment as $y^+ \leq 1$ and to the high y^+ treatment for $y^+ \geq 30$. In addition, it is also designed to produce reasonable results within the buffer layer (i.e., $1 < y^+ < 30$) for intermediate meshes. The working fluid has a density of 1060 kg/m³ and a kinematic viscosity of 3.5cSt. In this study, 25 prism layers with a growth ratio of 1.3 were generated in the near-wall region and the first layer thickness is 2e-6m. The maximum wall y^+ value was around 0.0684, which provides sufficient resolution for LES results.

The boundary conditions (e.g., flow and pressure data) adopted in this study were obtained from the literature published by H.J. Kim⁴. Briefly, those data were derived from a lumped parameter heart model and 3-element Windkessel models which was used with the curved aortic model along with a typical straight one under pulsatile physiological conditions. The cardiac output was 3.4 L/min, the heart rate was 88 beats per minute. **Figure 1** illustrates the boundary conditions applied in the computational study for the control model. The hemodynamic parameters of interest were helicity and the volume averaged velocities during peak systole.

RESULTS

The geometry measurements of the aorta, main branching arteries, and calcium for the control and stroke patients are shown in **Table 1**.

The percent total calcium volume (with respect to the total model volume) was higher in the stroke patients than in the control patients. The ostium areas of the LSCAs and LCCAs were similar between the control and stroke patients, but the ostium area of the BCAs was higher in the stroke patients than those of the control. Interestingly, we observed an attachment of the LCCA to the BCA superior in position to the BCA ostium, only in the stroke patients. The STJ area was similar amongst all the patients.

Table 1. Geometry measurements of the control and stroke patients.

Geometric Parameters	Control 1	Control 2	Control 3	Stroke 1	Stroke 2	Stroke 3
Percent total Calcium Volume (%)	0.21	0.25	0.00	1.19	0.94	0.24
STJ Area (mm ²)	662.23	532.67	684.13	508.16	438.51	734.81
Descending Area (mm ²)	434.69	432.88	724.27	227.93	306.21	537.71
Brachiocephalic Ostium Area (mm ²)	160.56	157.8	230.99	409.22	312.87	592.15
Left Subclavian Ostium Area (mm ²)	61.10	96.94	141.78	70.11	73.48	108.91
left Common Carotid Ostium Area (mm ²)	158.33	123.81	241.01	191.73	119.89	200.63

The volume averaged velocities during peak systole for the control and stroke patients are shown in **Figure 2**. Velocity was not found to be a factor of difference between control and stroke patients.

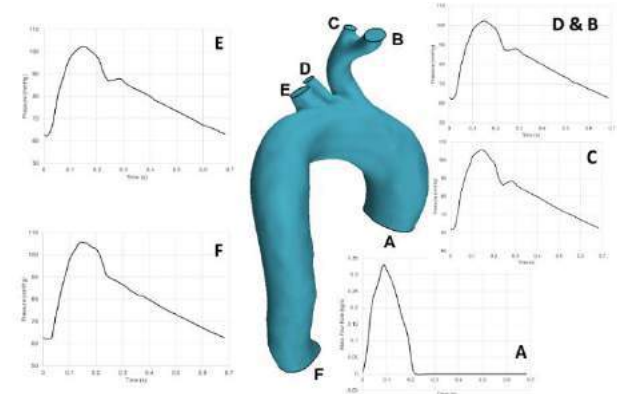


Figure 1. Inlet and outlet boundary conditions, where (A) is the inlet located at the STJ, (B, C) are the BCA outlets, (D) is the LCCA outlet, (E) is the LSCA outlet, and (F) is the descending aorta outlet.

Helicity for a complete cardiac cycle for the control and stroke patients is shown in **Figure 3**. Positive and negative helicity was present during systole before returning to about zero during diastole for all the patients. Helicity was mainly positive for Stroke 1, Control 1 and Control 2. Fluctuations in helicity were present in Stroke 2 but not in any other patient.

DISCUSSION

In this study we have investigated the effect of aortic arch geometry on local flow hemodynamics to better understand and predict stroke after TAVR using LES. A non-uniform trend of hemodynamic parameters (velocity and vorticity) was observed amongst the patient population. However, geometrical measurements showed marked differences in BCA ostium area and the percent total calcium.

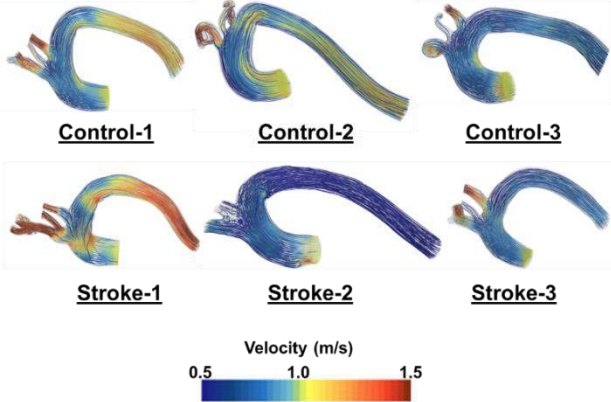


Figure 2. Volume averaged velocities during peak systole for the control and stroke patients.

Deployment of a TAV requires the use of a catheter. While guiding the device into position and expanding it, there is the possibility for the TAV, catheter, and accessory guidewires to interact with the aortic wall and native valve leaflets. This interaction may cause dislodgment and embolization of calcium into the branching arteries. A 2-vessel branching pattern, where the LCCA originated from the BCA otherwise known as a bovine arch, was observed in only the stroke patients. This aortic arch variant has been well documented and is quite common. We have observed that the stroke patients, all of whom have this variant in this study, also have increased BCA ostium areas compared to the control patients. Given this increase in area, we believe it makes embolization of calcium from TAVR procedure far easier than if the artery ostium area were smaller.

It has been reported that lower levels of helicity are associated with vascular stiffness⁵. Results of the Rotterdam Study have shown a strong relationship between aortic stiffness and atherosclerosis². Increased levels of atherosclerosis in the aortic arch are associated with an elevated risk of stroke. Mukherjee et al.⁶ has shown that helical flows may be an important factor for facilitating transport of embolic particles.

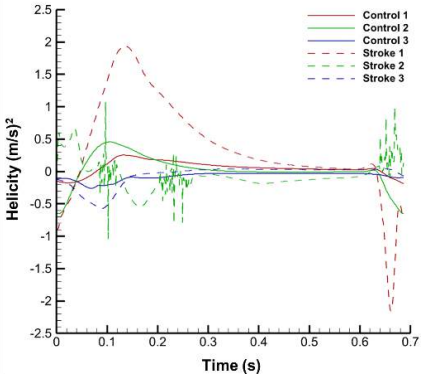


Figure 3. Helicity for a complete cardiac cycle for the control and stroke patients.

In this study we have demonstrated the feasibility of using LES to predict TAVR related stroke. We have observed a trend in the stroke patients where an aortic arch variant is present. Further investigations using a larger patient cohort are warranted to better understand its role and prevalence in this study.

REFERENCES

- [1] Leon MB, *NEJM*, 2016; 374(17): 1609-1620
- [2] Nicole M, *Stroke*, 2001; 32(2): 454-460
- [3] Veulemans V, *Catheter. Cardio. Interv.*, 2020; 96(7): 1511-1519
- [4] Kim HJ, *Ann Biomed Eng*, 2009; 37(11): 2153-2169
- [5] Reisner D, *American Thoracic Society*, 2016; A3949-A3949
- [6] Mukherjee D, *Theor. Comput. Fluid Dyn.*, 2016; 30(1): 23-39

WAVY MICROCHANNELS SUPPRESSED PERSISTENT CELL MIGRATION

Ze-Hao Lin and Pen-Hsiu Grace Chao

Department of Biomedical Engineering
National Taiwan University
Taipei, Taiwan

INTRODUCTION

Extracellular matrices (ECM) with collagen and elastin are often organized in parallel and wavy bundles in dense connective tissues. The wavy architecture varies as a function of location within the tissue microenvironment, with amplitude ranging from 1-15 μm and wavelength from 20-50 μm [1-3]. Reduced fiber curvature surrounding tumor stroma is associated with tumor cell invasion and poor prognosis [4, 5]. Studies propose that the straight fibers increase cancer cell metastasis, however, the underlying mechanism behind cell migration in wavy structure is still unclear.

Persistent cell migration requires defined front-rear polarity which is mediated by the cytoskeleton and focal adhesion [6, 7]. Microtubule and its post-translational modification/stabilization are major regulators of polarity formation and migration [8, 9]. We have previously reported that wavy morphology changes nuclear structure and phenotype [10, 11]. In this study, we investigate the role of wavy structure in MSC migration and the underlying mechanisms.

METHODS

Microfabrication Microchannels with agarose side walls and fibronectin-coated PDMS substrate were generated by micromolding [12]. All channels were 15 μm wide with 10 μm -tall side walls. The wavy pattern was composed of arcs with the inner radius of 7.5 μm at 60 μm wavelength.

Cell Culture Mesenchymal stem cells (MSCs) were seeded at a density of 4,000 cells/ cm^2 in the microchannels for 4 hours before the start of live imaging. Actin cytoskeleton was labeled with SPY555-Actin (Spirochrome) and nuclei were labeled with SPY505-DNA (Spirochrome). Cells were treated with DMSO or 2 μM tubacin (Cayman) for 3 hours prior to live imaging.

Imaging and Analysis For live-cell imaging, cells were imaged every 10 minutes for 5 hours in a stage-top incubator on an inverted

fluorescence microscope using a 20x objective (Tokai-Hit and Nikon). For fixed samples, filamentous actin was labeled with Alexa Fluor 568 phalloidin (Invitrogen) and nuclei were labeled with DAPI (Sigma). Microtubule network was labeled by total α -tubulin and acetylated α -tubulin (Sigma and Abcam), and imaged using confocal microscopy (Leica SP8). Cell migration was tracked by monitoring the centroid location of nuclei using a custom Matlab program. Migration speed was defined as the total length of migration path normalized by time. Migration persistence was calculated as the net nuclear displacement divided by total path length [13]. Nuclear shape change was defined by the maximum difference of the elliptical Fourier analysis index during migration [14].

Statistical Analysis Data figures and statistical analysis were made using R 4.0.3 software. All statistical comparisons were analyzed using the nonparametric Kruskal-Wallis tests.

RESULTS

To determine the influence of wavy structure on MSC migration, we fabricated open microchannels with straight and wavy shapes. Cells conformed to the microchannels and the wavy structure led to wavy cytoskeletal organization and deformed nuclei (Fig. 1, 2). Wavy cells had short and discrete stress fibers and straight cells assembled stress fibers along their entire length in a continuous network. Microtubules in general followed cell structure, with a dense network near the nucleus. This network colocalized with acetylated tubulin, a marker for stable microtubules. Live imaging revealed a more persistent migration by the straight cells, while the wavy cells had more frequent changes in direction, leading to smaller displacement over time (Fig. 2). Quantifying nuclear translocation with time revealed that cells in wavy channels had reduced migration speed and persistence compared with straight cells, indicating that the wavy cells had suppressed motility and persistent polarization (control group, Fig. 3). This reduction corresponds with increased nuclear shape dynamics during migration.

Microtubule-mediated cell polarization involves the formation of stable microtubule network near the centrosome [9, 15]. We thus deduced that the wavy cells were less persistent due to increased microtubule dynamics. By suppressing tubulin deacetylation with the small molecule inhibitor tubacin, we hypothesized that the increased microtubule stability would enhance persistent migration. Contrary to our hypothesis, increasing microtubule stability further suppressed wavy cell persistence, while having no effect on migration speed or in the straight cells (Fig 3). Further exploration of nuclear shape change during migration found tubacin treatment significantly suppressed nuclear shape changes in the wavy cells.

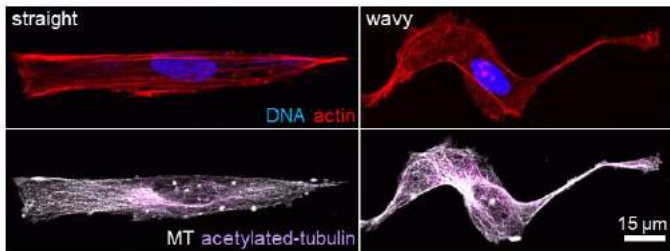


Figure 1 Representative MSC morphology in the microchannels

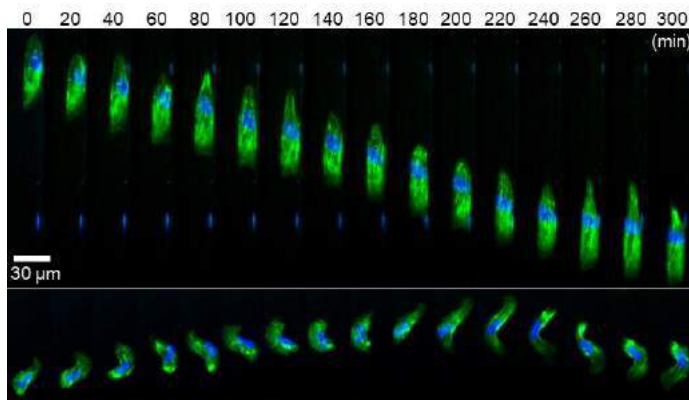


Figure 2 Time series of MSCs migrating in straight and wavy microchannels (blue-nuclei, green-actin)

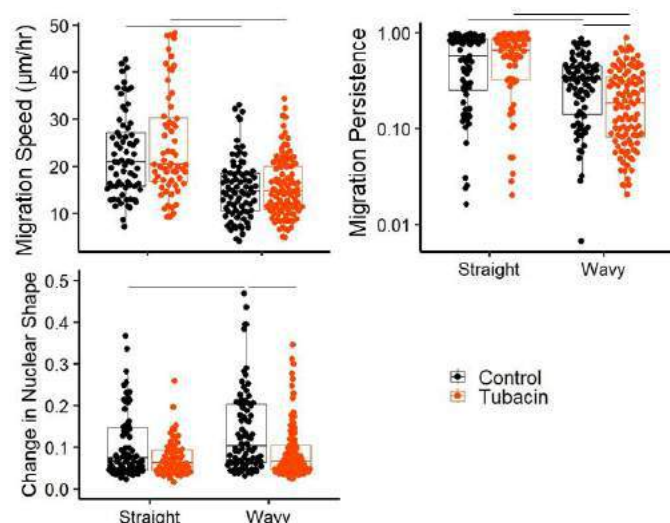


Figure 3 Effect of increasing microtubules stability via tubacin on cell migration and nuclear shape (Line: $p < 0.05$ between the indicated groups, $n = 63-102$)

DISCUSSION

Using mostly microcontact printed or nanotopographic substrates, previous studies have found decreased cell motility and persistence in wavy topography, corresponding with metastatic ability of cancer cells [2, 16]. In this work, we investigate the migration changes in 3D structures. Different from previous reports, cells exhibit wavy morphology in our system, with significant changes in actin and nuclear structure, but similar reduction in motility and persistence (Fig 1 and 3, [2, 4, 17]). This reduction is accompanied by more frequent changes in migration direction (data not shown). We also observe significantly increased nuclear dynamics during wavy cell migration, suggesting that nuclear restriction may contribute to the reduction in motility (Fig 2 and 3, [18]). As the establishment and stability of cell polarization controls migration [7, 8], we investigate the role of microtubule stabilization on wavy cell motility and persistence. Contrary to our hypothesis, increasing microtubule stability by tubulin hyperacetylation reduces wavy cell migration persistence, with no effects on motility (Fig 3). At the same time, nuclear shape change is attenuated with tubacin treatment in the wavy cells. These results suggest that tubulin hyperacetylation stabilizes nuclear structure and suppressed migration persistence in the wavy cells. It is not clear if the change in nuclear shape dynamics is due to altered microtubule structure, nucleus-microtubule engagement, or chromatin organization. It also does not explain the underlying mechanism behind low motility and persistence in wavy cell migration. Together, our results show that wavy cells have changed cytoskeletal organization, with lower motility and persistence, and tubulin acetylation is not involved in the regulation. Our system recapitulates the physiological and pathological structures in 3D connective tissues and permits mechanistic investigations of cancer metastasis and wound healing. Future studies will focus on investigating the role of actin-based cell polarity, focal adhesion dynamics, centrosome positioning, and nuclear restriction on cell migration in wavy channels.

ACKNOWLEDGEMENTS

This work was supported by the National Health Research Institute and the National Science and Technology Council (NHRI-EX110-10910EI, NSTC 110-2221-E-002-011-MY2).

REFERENCES

- [1] Jan NJ, et al. *Exp Eye Res.* 2018;172:159.
- [2] Fischer RS, et al. *Proc Natl Acad Sci USA.* 2021;118:e2021135118.
- [3] Spiesz EM, et al. *Acta Biomater.* 2018;70:281.
- [4] Alkmin S, et al. *Acta Biomater.* 2019;100:92.
- [5] Conklin MW, et al. *Collagen Alignment as a Predictor of Recurrence after Ductal Carcinoma In Situ.* *Cancer Epidemiol Biomarkers Prev.* 2018. p. 138.
- [6] Zhang J, et al. *Proc Natl Acad Sci USA.* 2014;111:16383.
- [7] Petrie RJ, et al. *Nat Rev Mol Cell Biol.* 2009;10:538.
- [8] Gunderson GG, Bulinski JC. *Proc Natl Acad Sci USA.* 1988;85:5946.
- [9] Witte H, et al. *J Cell Biol.* 2008;180:619.
- [10] Huang B-L. 2020.
- [11] PG C, et al. *ICBME.* 2019.
- [12] Kang G, et al. *Lab Chip.* 2009;9:3236.
- [13] Gorelik R, Gautreau A. *Nature Protocols.* 2014;9:1931.
- [14] Diaz G, et al. *Comput Biomed Res.* 1989;22:405.
- [15] Bance B, et al. *J Cell Sci.* 2019;132.
- [16] Provenzano PP, et al. *BMC Medicine.* 2006;4:38.
- [17] Zhang D, et al. *Biofabrication.* 2022;14:024102.
- [18] Denais CM, et al. *Science.* 2016;352:353.

A NOVEL SELF-SEALING DIALYSIS PORT

Jacob M. Wright (1), Alan I. Benvenisty (2), Kenneth R. Nakazawa (2), Marina de Cos (1), Kirk N. Campbell (1), Eric G. Lima (3), Evren U. Azeloglu (1,4)

- (1) Nephrology, Department of Medicine, Icahn School of Medicine, New York, NY, USA
(2) Department of Surgery, Icahn School of Medicine, New York, NY, USA
(3) Mechanical Engineering, The Cooper Union, New York, NY, USA
(4) Pharmacological Sciences, Icahn School of Medicine, New York, NY, USA

INTRODUCTION

A functional renal system is vital to remove waste from blood and maintain organ homeostasis and physiological functions. Chronic kidney disease affects 37 million American adults¹. Currently, there are two treatments options: dialysis or transplantation, which are necessary when >85-90% of kidney function is lost. Kidney transplantation is less restrictive to lifestyle compared to dialysis, and has an over 80% five-year survival rate². However, there is a huge shortage of organs for transplantation due to unavailability of donors leading to a widening gap between the percentage of patients on the waiting list and the percentage of transplanted patients. Indeed, only 20,161 kidney transplants were performed in 2016 out of the 100,000 patients on the waiting list¹. As a result, dialysis remains a life-saving treatment for these patients.

Hemodialysis is the most common type of dialysis, with approximately 90% of dialysis patients undergoing this treatment². The disadvantage of hemodialysis is its high costs, with a total spending of \$28 billion in 2016². Notably, in 2011, 1.4% of US end stage renal disease (ESRD) patients on Medicare accounted for 7.2% of the overall Medicare spending³. During hemodialysis treatment, blood is drawn from the patient and transferred to a dialysis machine via a vascular access, usually an arteriovenous (AV) fistula, with a 14- or 15-gauge needle. There are several complications associated with vascular accesses such as aneurysm, infection, damage, and uncontrolled bleeding. Due to these risks associated with incorrect cannulation, vascular access complications limit treatment opportunities outside of the clinic setting, such as at home since it would require self-cannulation by patients.

To address this issue, improve patient lifestyle, and reduce complications associated with vascular access, we developed a prototype access port, called Safe Entry Port for AV fistulae (SEAL), that integrates well with fistulae, guides self-cannulation, and prevents aneurysms with minimal risk of back-bleeding and infections (Figure 1). Initial *in vitro* prototype testing on an artificial closed loop circuit

demonstrated that cannulation of the device can be safer and simpler, potentially reducing vascular damage, infection and enhancing durability.



Figure 1: SEAL Device and Valve (Raw & TiN/Ag Coated)

METHODS

We optimized the device design for 3D printing via direct metal laser sintering of Ti-6Al-4V *in silico*. We also evaluated variations on valve parameters to ensure smooth operation. Printing was performed by Protolabs®. Self-sealing capabilities of the colinear valve were confirmed using a mock circulation system via a peristaltic pump (Cole-Palmer Masterflex C/L® Model 77120-62) and a hydrostatic pressure gradient. Device valves were treated and evaluated *in vitro* for biofouling to determine valve antimicrobial properties using bacterial spreading area and bacterial turbidity assays. The system was fatigue tested to determine smooth operation of valve overtime and the force required to displace the valve. A micro linear actuator (Progressive Automations, Model:PA-07-1-5) was mounted to a 10 lbs. load cell (Transducer Techniques, Temecula, CA, MLP-10-CO). The load cell was connected to a data acquisition system (DAQ, National Instruments, Austin, Texas, SCB-68), which in turn was connected to a computer running LabVIEW® (National Instruments, Austin, Texas) for data processing and transfer.

A clinical-like *in vivo* model was developed by surgically creating an arteriovenous fistula in the forelimb of a sheep and implanting the device under the skin and on top of the fistula.

RESULTS

In repeated cannulations of the device during *ex vivo* simulations with 14-15G dialysis needles, the peak force required to engage the valve recorded in our dialysis fatigue cycling simulation was 0.1605 ± 0.000018 N (Figure 2). Furthermore, the colinear valve smoothly opened for continuous flow through the needle guide (Figure 3). The valve descended to its closed position when the needle was withdrawn, immediately blocking flow through the channel. Antibacterial TiN/Ag coated valves showed greater bacterial growth resistance than raw and polished titanium valves in both assessments (Figure 4). The device was implanted under the skin and on top of a mature fistula (Figure 5). 10 days after implantation, *in vivo* cannulation assessment of the sheep access was performed twice a week for 3 weeks with a 14G dialysis needle. Blood flow into the dialysis needle and bleeding after the needle was removed was noted. The fistula was accessed through the device and upon removal of the needle there was no back-bleeding or hematoma that may normally occur with a fistula after treatment.

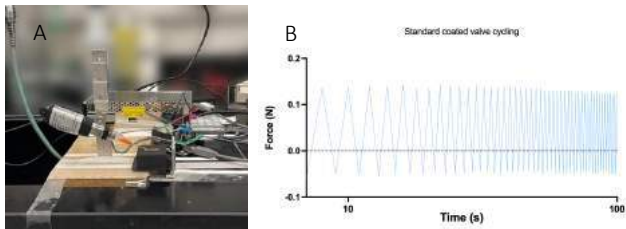


Figure 2: Cannulation cycling test apparatus equipped with linear actuator and load cell (A). Force measurement of needle cannulation of device and valve displacement (B).

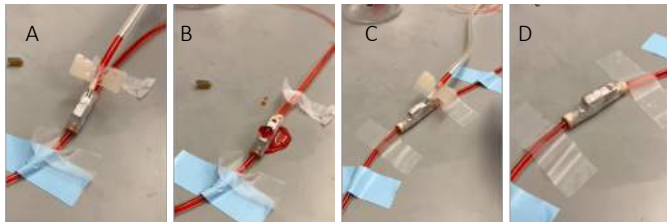


Figure 3: In vitro simulation of SEAL with no valve scenario. (A) Cannulation. (B) Needle Removal without valve. (C) Cannulation. (D) Needle Removal with valve.

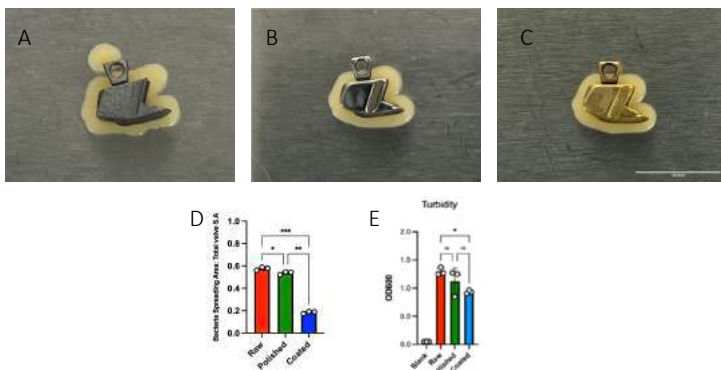


Figure 4: *S. aureus* bacteria growth assay. Bacterial Spreading area on valve: Raw (A), Polished (B), Coated (C). Spreading area ratio to valve surface area (D). Bacteria turbidity growth assay in TSB inoculated with contaminated valves (E)

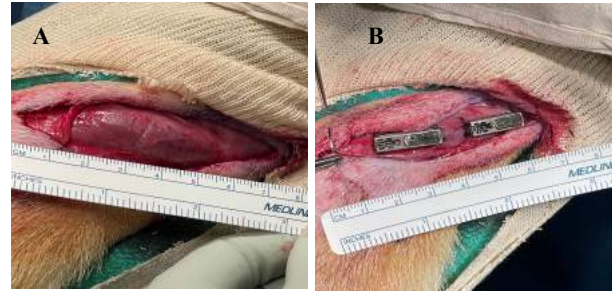


Figure 5: AV Fistula matured for 12 weeks (A). Implanted SEAL devices (B).

DISCUSSION

The SEAL device is engineered to integrate directly over a fistula via an external metallic foam and to utilize an internal colinear valve that uses the tensile energy of the subcutaneous tissue to self-seal the channel immediately following needle removal. SEAL provides guided cannulation for 14-gauge dialysis needles. The device, therefore, has the potential to make treatment initiation easier and to provide a safer method of cannulation. Easier and safer cannulation can give patients and caregivers more comfort for treatment options in the home setting, which are known to yield better outcomes due to the possibility of more frequent treatments and reduced visits to centers that carry additional social contact risks. SEAL was shown to reduce back-bleeding due to its unique valve-needle interaction. The device is durable and withstood 14 years of *in vitro* cannulations. In addition to this durability, the valve only requires about a tenth of a newton to allow access to the underlying fistula wall. The coated valve was shown to significantly prevent bacterial biofilm growth when compared to raw and polished valve samples. Lastly, *in vivo* cannulation showed that the device allowed access to blood flow in a developed fistula and that the valve occluded blood flow through the device and needle site without the need to apply pressure for long periods. SEAL has the potential to change the future of dialysis treatments and improve the quality of life for dialysis patients due the reduction of complications and freedom to have in home treatments.

ACKNOWLEDGEMENTS

We would like to thank Mount Sinai Innovation i3 Genesis award funding and hemodialysis nurse Brian E. Libed for his time and effort.

REFERENCES

- [1] Foundation NK. Kidney Disease: The Basics 2022 [updated May 24, 2022; cited 2022 July 28, 2022]. Available from: <https://www.kidney.org/news/newsroom/fsindex#:~:text=1%20in%203%20adults%20in,of%20death%20in%20the%20U.S.>
- [2] Francisco UoCS. The Kidney Project - Statistics 2019.
- [3] Liu FX, Walton SM, Leipold R, Isbell D, Golper TA. Financial implications to Medicare from changing the dialysis modality mix under the bundled prospective payment system. *Perit Dial Int.* 2014;34(7):749-57. Epub 20141007. doi: 10.3747/pdi.2013.00305. PubMed PMID: 25292402; PMCID: PMC4269500.

TENDON OVERLOAD USING A RODENT MODEL OF SYNERGIST ABLATION LEADS TO MECHANICAL DEGENERATION

Lily M. Lin (1), Ellen T. Bloom (1), John M. Peloquin (1), Michael H. Santare (2), Justin Parreno (1,3),
Karin G. Silbernagel (4), Dawn M. Elliott (1)

- (1) Biomedical Engineering, University of Delaware, Newark, Delaware, United States
(2) Mechanical Engineering, University of Delaware, Newark, Delaware, United States
(3) Biology, University of Delaware, Newark, Delaware, United States
(4) Physical Therapy, University of Delaware, Newark, Delaware, United States

INTRODUCTION

Tendon homeostasis is maintained by a balance between the magnitude and duration of mechanical loading and a disruption in this balance can lead to tendon degeneration. Tendon degeneration is a widespread pathology and current treatments are not consistently effective due to an incomplete etiological understanding of the disorder. Additionally, tendon disorders are typically asymptomatic until later stages when pain or rupture occur, making it difficult to determine mechanisms underlying the initiation and progression to degeneration. Therefore, animal models of altered loading are needed.

Most animal models cause tendon degeneration by overuse, such as treadmill running. [1] However, many tendon disorders are related to overloading, not overuse, thus, we recently established a rodent overload model of synergist ablation (SynAb) where the Achilles tendon was resected, overloading the synergist plantaris tendon, without increasing the number of loading cycles. [2,3] We showed multi-scale structural changes associated with tendon overload, such as an increased cross-sectional area (CSA) from MRI, increased fibril diameter and density from Scanning Electron Microscopy (SEM), and increased cell density and decreased collagen alignment from histology. While these outcomes suggest tendon degeneration, it was unclear whether the degeneration was induced exclusively from structural changes, since some of the parameters could be either adaptive or degenerative. As such, it was necessary to evaluate functional changes of tendon following overload, as a decrease in stiffness and strength is a key hallmark of tendon degeneration. Therefore, the objective of this study was to investigate the mechanical changes induced by tendon overload. We hypothesized that there would be a decrease in mechanical properties would decrease 8 weeks post-surgery indicating tendon degeneration.

METHODS

Bilateral plantaris tendons from 7-month-old female Long Evans rats were randomly assigned to three groups: SynAb (Achilles tendon resected to overload plantaris tendon), Sham Control (incision made but Achilles not transected), and Intact Control (n=6 tendons/group). At 8 weeks post-surgery, rats were sacrificed and stored in a -20°C freezer until the day of testing. Each rat was thawed at room temperature and the plantaris tendons were dissected. The tendon sheath was removed by sectioning off 150µm of the tendon surface using a freezing stage microtome. CSA was measured across the tendon midportion using a laser displacement device.

Mechanical Testing and Data Acquisition: Each tendon was gripped and placed in a bath solution containing 8% SPEG and mounted on a custom uniaxial device. [4,5] The sample was preloaded to 5mN (0.5g) to establish the reference length and preconditioned for 5 cycles between 0 and 5% strain. Testing included 1) a ramp and hold at 25% strain for 10 minutes, unloaded to reference length for a 15 minute

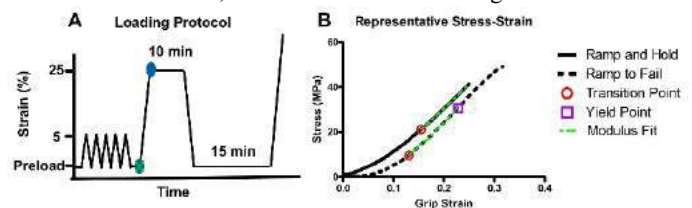


Figure 1: A) Mechanical testing protocol included Ramp & Hold and Ramp to Failure B) Representative stress-strain curve showing mechanical parameters of interest

recovery, and 2) ramp to failure (Fig 1A). All loading and unloading rates were 1%/s.

Data analysis: Stress was calculated by dividing the force by the CSA and strain (ϵ) was calculated by dividing the change in grip-grip displacement by the initial reference length. The stress-strain curves were analyzed for transition point, yield point and linear region modulus (Fig 1B). [6] The transition point was defined as the end of the toe region and beginning of the linear region. The yield point was calculated first by fitting a cubic smoothing spline using the *csaps* function in MATLAB and finding the first zero crossing point of the second derivative. Yield point was only calculated in the Ramp to Failure because the Ramp & Hold did not always reach a detectable yield point. A nonlinear exponential constitutive model was fit to the stress-strain curve up to the yield point to obtain the transition strain (p), transition stress (q), and linear region modulus (E):

$$\sigma = \begin{cases} A * (\exp(B\epsilon) - 1), & |\forall \epsilon \leq p \\ E * (\epsilon - p) + q, & |\forall \epsilon > p \end{cases} \quad (1)$$

Percent stress relaxation was calculated by dividing the stress at the end of the stress relaxation period by the peak stress.

Non-parametric t-tests were performed between the Intact and Sham groups and there was no difference between the groups for any of the parameters, so they were combined as one Control group to compare with the SynAb group. Differences in material properties were analyzed using Mann-Whitney t-tests. All material properties were compared between treatment groups and the linear region modulus and transition point were additionally compared between Ramp & Hold and Ramp to Failure.

RESULTS

The modulus in SynAb was 54% lower than Control in the Ramp & Hold and 47% lower in the Ramp to Failure ($p < 0.05$), but there were no differences in modulus between ramps (Fig 2A). There were no differences in the transition strain between the treatment groups or loading ramps ($p > 0.6$, Fig 2B). The transition stress in SynAb was 41% lower than Control during the Ramp to Failure ($p = 0.02$) but was not significantly different during the Ramp & Hold ($p = 0.2$, Fig 2C). The transition stress in the Control was 52% higher during the Ramp & Hold

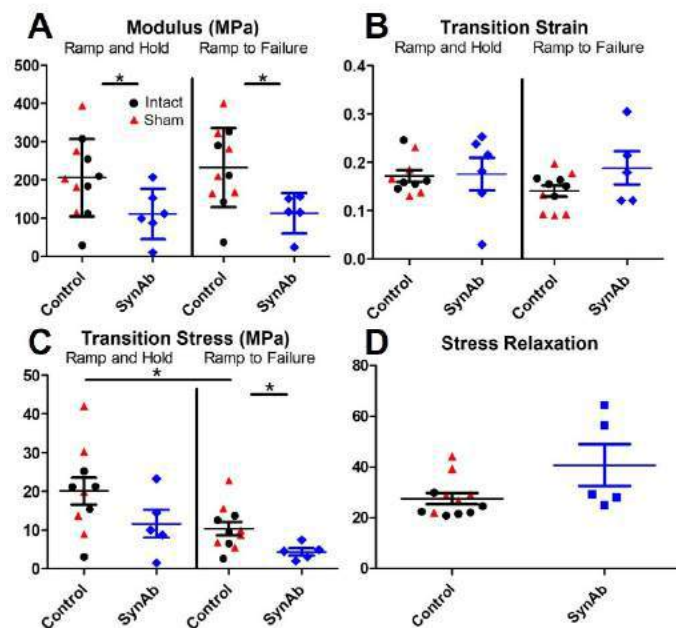


Figure 2: A) Modulus, B) Transition strain, C) Transition stress, and D) Stress relaxation. Where * indicates $p < 0.05$,

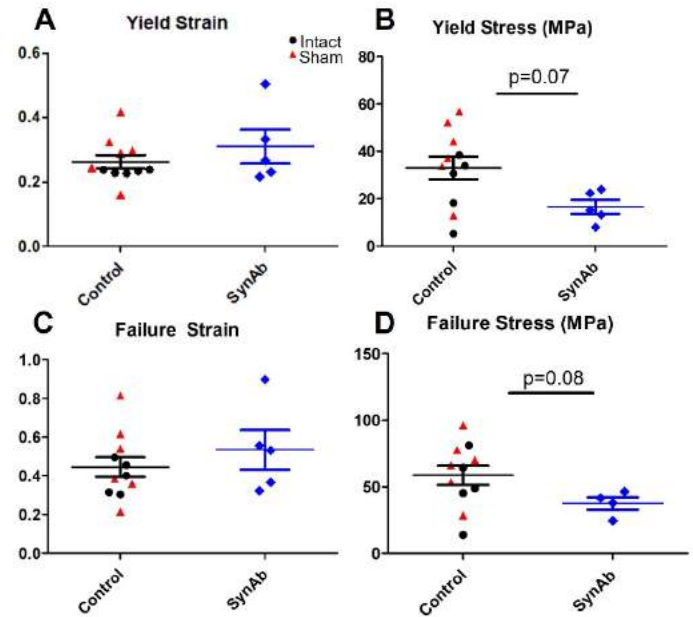


Figure 3: A) Yield strain, B) Yield stress, C) Failure strain, and D) Failure stress. Where * indicates $p < 0.05$

than the Ramp to Failure ($p = 0.03$). There was no significant difference in stress relaxation between treatment groups ($p = 0.1$, Fig 2D).

Yield strain and failure strain were not statistically different between the treatment groups, however, the SynAb yield stress was 52% lower than Control ($p = 0.07$) and the SynAb failure stress was 65% lower than Control ($p = 0.08$, Fig 3).

DISCUSSION

This study showed degenerative mechanical changes following 8 weeks of tendon overload from synergistic ablation in a rat model. Specifically, we observed a decrease in modulus in the SynAb group indicating that increasing mechanical load from SynAb impairs mechanical function. The decrease in modulus could be caused by the observed decrease in matrix organization and collagen alignment from our previous work using the SynAb model. [2,3] The yield stress and failure stress also decreased, with trending significance, likely due to the limited sample size.

The mechanical and structural outcomes in our SynAb overload model are similar to the outcomes observed in overuse treadmill running models. [1] Although both model types cause a degenerative change in mechanical and structural properties, the mechanisms leading up to this degenerative state and the clinical manifestations (rupture versus painful tendinopathy) may be different. Therefore, we will use the SynAb model of tendon overload in future work to explore these potential mechanisms and the progression of these degenerative changes.

ACKNOWLEDGEMENTS

Funding for this research was provided by NIH/NIAMS R01 AR080059-01 & NIH F31 AR078005-02

REFERENCES

- [1] Hast, M et al., *Bone Joint Res*;3:193–202.2014
- [2] Bloom E., et al. *ORS Abstract 2022*
- [3] Lin L., et al. *BMES Abstract 2022*
- [4] Bloom, E., et al. *Biomed Eng*;49:1058–1068. 2021
- [5] Szczesny S, et al. *Acta Biomater*;10(6):2582–90. 2014
- [6] Lee, A, et al. *J Orthop Res*; 37(8):1827–1837. 2019

MECHANICAL PROPERTIES OF PORCINE IRIS STROMA USING MICRO-INDENTATION: THE EFFECT OF TEMPERATURE AND HYDRATION

F. Sebastian (1), G. Bailey (1), V. Kondiboyina (1), S. Dorairaj (2), R. Amini (1)

(1) Department of Bioengineering, Department of Mechanical and Industrial Engineering,
Northeastern University, Boston, MA, USA
(2) Department of Ophthalmology, Mayo Clinic, Jacksonville, FL, USA

INTRODUCTION

Glaucoma is the leading cause of irreversible blindness worldwide, affecting roughly 80 million people [1]. Two major types of glaucoma are categorized by the angle between the iris and the cornea: primary open-angle glaucoma and primary angle-closure glaucoma (PACG). In PACG, the iris bows anteriorly thus blocking the outflow of aqueous humor. The resulting increase in intraocular pressure in the eye could potentially lead to blindness. Previous experiments have shown that the stiffness of the iris in patients with history of PACG is higher than those of healthy subjects [2,3]. Due the importance of iris mechanical properties in the pathophysiology of PACG, experiments such as micro indentation have been used to quantify such properties *ex vivo* [2, 4]. Given the varying experimental environments used in these studies, we aimed to identify how factors such as keeping samples in phosphate-buffered saline (PBS) solution or conducting the experiments in room temperature (RT) versus physiologically relevant 37°C affects the iris stromal mechanical properties. We hypothesized that the samples submerged in 37°C PBS would have significantly different elastic modulus compared to the other groups.

METHODS

Porcine eyes (N=9) were harvested within a 24-h period from 6-month-old pigs (4 male, 5 female). The irides were excised and their posterior surfaces were attached to a flat surface using a biocompatible adhesive. Three irides were used for 3 experimental groups: 1) sprayed with PBS, 2) submerged in RT PBS, and 3) submerged in 37°C PBS. The iris from each group was then indented in 6 clockwise points from 1 to 11 o'clock (Fig. 1). A spherical indenter (Mach-1, Biomomentum, Canada) with 0.5mm diameter was used to indent the iris at 0.005mm/s. Once the surface of the iris was identified, the thickness was recorded, and the tissue was indented to 0.15mN. The sample was then left in that same environment for 20 minutes before being submerged in 37°C PBS. The indentation procedure was repeated for each iris.

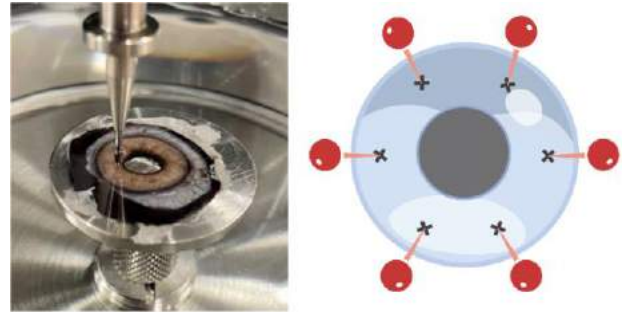


Figure 1: Example of indentation experiment (left) with the indentation points marked on the schematic (right).

The resulting load-displacement data were used to calculate the elastic modulus (E) using the method provided by Dimitriadis et al. [5]:

$$F = \frac{16E}{9} R^{1/2} \delta^{3/2} [1 + 1.133\mathcal{X} + 1.283\mathcal{X}^2 + 0.769\mathcal{X}^3 + 0.0975\mathcal{X}^4], \quad (1)$$

where F is the indentation force, R is the indenter radius, δ is the indentation depth and the constant \mathcal{X} is defined as

$$\mathcal{X} = \sqrt{R\delta}/h, \quad (2)$$

where h is the sample thickness. Dimitriadis et al. established this approach for the indentation of soft biological tissues with finite thickness bonded to a substrate using a spherical indenter. Additionally, since most biological samples can safely be assumed to be incompressible, the Poisson's ratio (ν) was set at 0.5 in our calculation.

Using the *fminsearch* function in MATLAB (MathWorks, Natick, MA), we determined the elastic modulus that minimized the error between the experimental force-displacement data and that of Eq. 1.

Statistical analyses were performed in R (R Core Team). The homogeneity of variance for each group was determined using the Levene's test. A two-way ANOVA and Tukey post hoc test were used to identify relationships between the groups where $p < 0.05$ was considered significant. All data are reported in the format of mean \pm standard deviation.

RESULTS

An example of load-displacement plot that was fitted with Eq. 1 is shown in Fig. 2. For this typical example, the R^2 of the fit was 0.92. The R^2 for all fitted parameters ranged between 0.51 and 0.97.

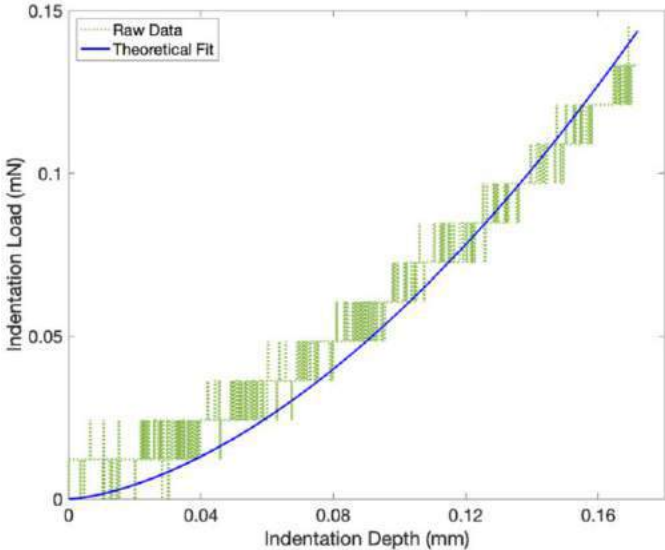


Figure 2: Load-displacement plot showing the raw data in green and fitted line in blue.

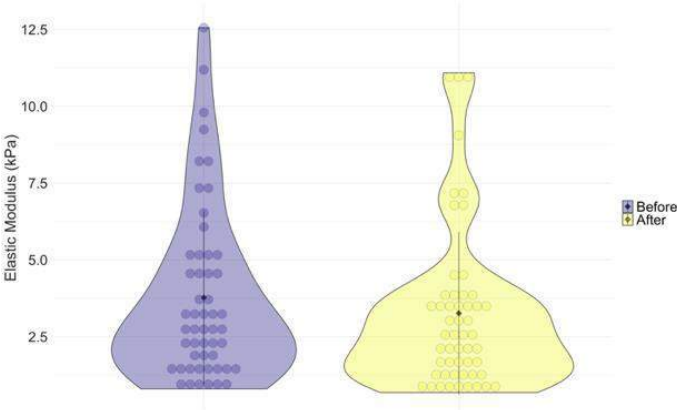


Figure 3: Distribution of iris elastic modulus for the before and after environments with the mean marked with a black diamond.

The moduli of initial experiments in the different environments were 4.29 ± 2.60 , 3.73 ± 3.03 , 3.35 ± 2.89 kPa, for groups 1, 2, and 3, respectively. The respective moduli after all samples were submerged in 37°C PBS were 4.66 ± 3.27 , 2.98 ± 2.51 , and 2.13 ± 1.13 kPa. We found that the data was not normally distributed when lumped together

and in the individual groups, but they had equal variances in both instances. We found no statistical difference between the lumped before and after conditions from the ANOVA as seen in Fig. 3. There was, however, a significant difference between the group interactions. The Tukey post-hoc test revealed there was no significant difference between any of the groups except for group 1 and group 3 ($p=0.02$).

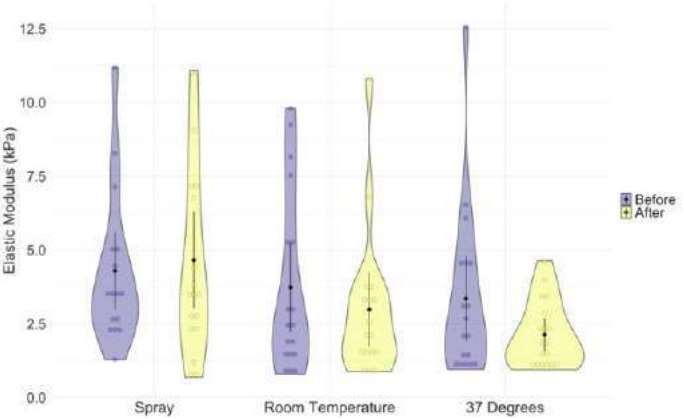


Figure 4: Distribution of iris stiffness data, E, for each group with the mean marked with a black diamond.

DISCUSSION

Our hypothesis was not supported since our study indicates that the mechanical properties of iris stroma may not change significantly whether the samples are tested in room temperature or in 37°C in the given timeframe. We could not make any reliable conclusions about the difference in environmental salinity despite there being a significant difference in the stiffness of irides that were sprayed by PBS and those that were submerged in 37°C PBS. The insignificance in stiffness between the initial environment and the final environment in any of the groups muddies our abilities to make a strong conclusion regarding how the tissue is kept hydrated.

We stipulate that with a larger sample size we might be able to observe the difference being negligible across all methods of hydration. We ran a power analysis with a large effect size (0.5), and it showed that for a 95% confidence interval and power of 0.8, N would have to be at least 25. The increased sample size could also potentially lead to a normalized distribution of data.

Accordingly, the biggest limitation in our study was the small sample size. Despite being able to collect multiple data points per iris, we believe having more irides per sample group would behoove us in drawing more obvious conclusions. This study furthers our understanding on how to obtain reliable characterization of the mechanical properties of irides that may be exposed to prolonged environmental factors.

ACKNOWLEDGEMENTS

Funding for this study was provided in part by BrightFocus Foundation. Schematic created with BioRender.com.

REFERENCES

[1] Tham, YC et al. *Ophthalmology* 121(11):2081–2090, 2014
[2] Narayanaswamy, A. et al. *Invest Ophthalmol Vis Sci* 60(7):2690–2695, 2019
[3] Pant, AD et al. *Invest Ophthalmol Vis Sci* 59(10):4134–4142, 2018
[4] Whitcomb, JE et al. *Exp Eye Res* 93(4):475–481, 2011
[5] Dimitriadis, EK et al. *Biophys J*, 82(5):2798–2810, 2002

TOMOGRAPHIC X-RAY PARTICLE TRACKING VELOCIMETRY AND POSSIBLE APPLICATIONS IN BIOLOGICAL FLUID DYNAMICS

Jason T. Parker, Simo A. Mäkiharju

Mechanical Engineering, UC Berkeley, Berkeley, CA, USA

INTRODUCTION

Studying biological fluid flows outside of their natural environment introduces uncertainty compared to true in-vivo measurements. Boundary conditions, material properties, and scale in an artificial environment differ from a true biological environment. These challenges make in-vivo measurement techniques particularly valuable. Recent developments in laboratory-scale X-ray particle tracking velocimetry (XPTV) [1–3] present an opportunity for non-invasively measuring biological flows with comparatively high spatiotemporal resolution.

Tomographic- and stereo-XPTV (TXPTV and SXPTV) capture all three velocity components in 3D space (3D3C), and will soon be able to supplement ultrasound and magnetic resonance imaging (MRI) as an in-vivo measurement option. For example, MRI's voxel resolution, $O(0.1 - 1 \text{ mm}^3)$, and temporal resolution, $O(100 \text{ ms})$, [4–6] could in many cases be surpassed with TXPTV and SXPTV. 3D ultrasound scans have limited penetration depth that must be balanced with spatial resolution. Scans often take a few seconds and thus have limited temporal resolution.

The experiments presented herein are a proof-of-concept showing that TXPTV is currently able to capture velocity measurements at 2 Hz with a voxel resolution of $4 \text{ }\mu\text{m}$, a marked improvement in spatial resolution over the state of the art and alternative techniques. There is room for future improvement to TXPTV that will increase temporal resolution and reduce radiation dose. Naturally, one of the concerns with X-ray measurement techniques in biological applications is the absorbed radiation dose. Approximate absorbed dose calculations are provided in the Methods section.

We hope to introduce these techniques to the biological fluid dynamics community as a uniquely capable measurement option that will see rapid improvement over the next few years. For example, the TXPTV measurements presented here are an order of magnitude faster than Mäkiharju et al. [3].

METHODS

Tomographic X-ray Particle Tracking Velocimetry (TXPTV) is used to measure the 3D3C velocity of Poiseuille pipe flow and a rising Taylor bubble. A model of the experiment can be seen in figure 1. Experiments are

conducted in pure glycerine to minimize the entrance length considering the pipe length is only 15 cm. Glycerine also retards the rise of the Taylor bubble so we can resolve its motion. For the pipe flow the glycerine is pumped at a constant 0.0950 mL/min flow rate by a Harvard Apparatus Pump 33 DDS syringe pump ($Re = 8.8 \times 10^{-4}$), well within the Stokes viscous flow regime. For the Taylor bubble, 0.5 mL of air is injected into static fluid ($Re = 0.014$). The 6.35 mm (0.25 in.) inner diameter pipe is rotated at 720 dps for the pipe flow and 1080 dps for the Taylor bubble. Alternatively, one could rotate the source-detector pair to keep the object static. In this setup, though, we are limited to keeping the source-detector pair static. SXPTV requires no rotation if multiple source-detector pairs are used.

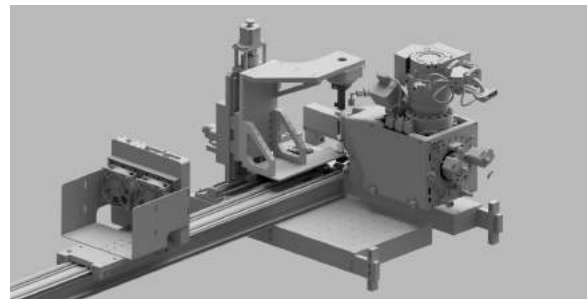


Figure 1: The X-ray imaging setup for Poiseuille pipe flow. A pipe is secured to a rotation stage in front of the Metaljet E1+ X-ray source.

A Metaljet E1+ liquid metal X-ray source is set to operate at 160 kV and 700W; projections are captured with an XC-Thor photon counting detector at 1 kHz. The source-to-detector distance (SDD) and source-to-object distance (SOD) are 521.5 mm and 56.5 mm, respectively, yielding a field of view that is 2.17 cm wide by 0.28 cm tall. In both experiments $O(50 \text{ }\mu\text{m})$ diameter tungsten-coated hollow carbon microsphere (CW) particles – developed by Parker and Mäkiharju in [1] – are used as tracer particles. These particles generate better contrast than other available particles, reducing the necessary exposure time, thereby increasing temporal resolution and

reducing radiation dose.

An approximate dose can be obtained using the Beer-Lambert law, which calculates the number of entrained photons, and thus the deposited energy, in a material of a given thickness for a given incoming X-ray source.

Table 1 shows the calculated dosage in 10 cm^3 blood and soft tissue if the Metaljet E1+ X-ray source is used to capture 1 sec worth of data (equivalent to a two-exposure measurement at 720 dps rotation). The 10 cm^3 represented the exposed volume assuming the same field of view as is used here and assumes a 16.5 cm depth. NIST X-ray attenuation coefficients and densities based on ICRU-44 materials are used to calculate these dosages. In reality, a much larger area would be exposed for a biological scan, reducing the equivalent dose. Furthermore, different approaches such as SXPTV could be taken to reduce the exposure time, which will be reserved for the Discussion section. These equivalent doses should be taken to be a vast overestimate of the real equivalent dose a subject would experience. Nevertheless, these dosages are equivalent to approximately six full-body CT scans [7].

Table 1: The equivalent dose in 10 cm^3 of three ICRU-44 materials calculated with the TXPTV settings used in this study.

Material	Dose (mGy)
Average Annual	6.2
Blood	125
Soft Tissue	126

RESULTS

The measured Poiseuille pipe flow profile can be seen in figure 2. The data show qualitative agreement with the theoretical profile, although the peak velocity is underestimated. There is also substantial spread in the data that could be due to particle localization error. A rudimentary particle tracking code is used to process the data and is an area for future improvement. The data suggest that erroneous particle tracks are the root cause for the slower measured velocity profile.

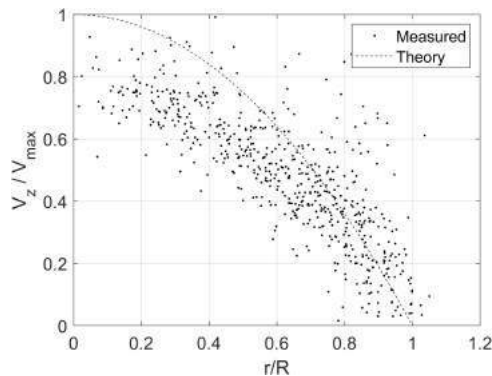


Figure 2: The Poiseuille pipe flow velocity profile measured with TPXTV. The flow rate is 0.0950 mL/min for a maximum speed of 0.01 cm/s.

The streamlines measured from the rising Taylor bubble can be seen in figure 3. Due to the limited FOV, only the flow atop the Taylor bubble was measured. Interestingly, it is possible to reconstruct the flow environment with TXPTV. We can, for example, reconstruct the Taylor bubble in 3D as it moves through the FOV. This capability could potentially be used in tandem with velocimetry to identify patient/specimen-specific morphology.

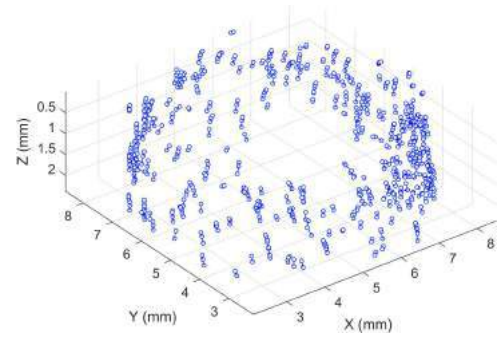


Figure 3: Short streamlines of the flow atop a Taylor bubble, captured over the course of six reconstructions (2 sec), i.e. frames.

DISCUSSION

These experiments demonstrate the potential of TXPTV as a non-invasive 3D3C flow measurement tool in opaque media applications in a laboratory environment. The spatiotemporal resolution in this study is an order of magnitude better than previous TXPTV measurements, indicating that rapid improvement is possible in the near future. The next step is to apply TXPTV to flow systems that are otherwise difficult to observe. Non-invasive 3D3C flow measurement techniques are of high value for in-vivo biological fluid dynamics applications such as hemodynamics. TXPTV experiments such as those done here offer a nearly three order of magnitude improvement in spatial resolution compared to MRI and the fundamental limit to temporal resolution (detector frame rate) is much higher than MRI. TXPTV could complement or, in certain situations, be substituted for MRI measurements.

While the dosage for TXPTV may currently be comparatively high, techniques such as SXPTV can dramatically reduce the exposure time. The temporal resolution for SXPTV would not be limited by the object rotation speed, but instead by the detector frame rate. Using the same procedure as above, the equivalent dose drops to 0.5 mGy for 10 cm^3 of blood and soft tissue with SXPTV. These are, again, overestimates of the actual equivalent dosage. SXPTV can also be achieved with limited-angle rotations of the object, which is not attempted here.

In-lab TXPTV is presently able to measure optically opaque biological systems in-vivo, offering the potential to observe biological flows with unprecedented spatiotemporal resolution.

ACKNOWLEDGEMENTS

We gratefully acknowledge the support of NSF EAGER award #1922877 program managers Ron Joslin and Shahab Shojai-Zadeh, and the additional support provided by the Society of Hellman Fellows Fund.

REFERENCES

- [1] Parker JT et al. en. *Experiments in Fluids* (2022). DOI: 10.1007/s00348-022-03530-6.
- [2] Parker JT et al. en. *Measurement Science and Technology* 33.5 (2022). ISSN: 0957-0233, 1361-6501. DOI: 10.1088/1361-6501/ac4c0d.
- [3] Mäkiharju SA et al. en. *Experiments in Fluids* 63.1 (2022). ISSN: 0723-4864, 1432-1114. DOI: 10.1007/s00348-021-03362-w.
- [4] Ooij P van et al. en. *Journal of Magnetic Resonance Imaging* 38.4 (2013). eprint: <https://onlinelibrary.wiley.com/doi/pdf/10.1002/jmri.24051>. ISSN: 1522-2586. DOI: 10.1002/jmri.24051.
- [5] Zhang J et al. *Journal of The Royal Society Interface* 19.186 (). Publisher: Royal Society. DOI: 10.1098/rsif.2021.0751.
- [6] Wang J et al. en. *Granular Matter* 24.4 (2022). ISSN: 1434-7636. DOI: 10.1007/s10035-022-01271-1.
- [7] en. Section: Cancer. 2010. URL: <https://www.health.harvard.edu/cancer/radiation-therapy>. Copyright 2023 SB3C Foundation, Inc.

QUANTIFICATION OF EMBOLUS TRANSPORT TO THE BRAIN FROM CAROTID STENOSIS SITES

Ricardo Roopnarinesingh (1), Neel Jani (2), Michelle Leppert (3), Debanjan Mukherjee (1)

(1) University of Colorado-Boulder, Boulder, CO, USA
(2) University of Wisconsin-Madison, Madison, WI, USA
(3) University of Colorado School of Medicine, Aurora, CO, USA

INTRODUCTION

Embolic stroke accounts for a majority of all ischemic stroke patients with some studies categorizing up to 60% of these cases as Embolic Stroke of Undetermined Source (ESUS) [1]. Current ability to identify embolic stroke etiology are limited and improvement can lead to increased treatment efficacy and reduced recurring stroke events [2]. Carotid arteries are one major source of stroke, where build up of atherosclerotic plaques can create thromboemboli that move into the cerebral arteries. Carotid endarterectomy (CEA) is a procedure commonly used for severe cases of carotid atherosclerosis to remove plaque buildup. Specifically, CEA is indicated when a patient has a North American Symptomatic Carotid Endarterectomy Trial (NASCET) severity greater than 70% in the ipsilateral carotid along with corresponding symptoms such as transient ischemic attacks (TIA) according to the American Heart Association (AHA) guidelines. CEA is considered if the patient has a severity between 50% and 69% along with symptoms but is not required [3]. It is commonly thought that emboli directed into the Circle of Willis (CoW) will cause ipsilateral embolic events but there have been known cases where emboli cause contralateral cerebral stroke events. Although contralateral events are less frequent, these cases contribute to the inherent difficulty in disambiguating stroke etiology. With both carotids being suspect to combinations of severe and non-severe levels of plaque buildup, the source of ambiguity in contralateral events could lead to a patient who would benefit from receiving a CEA not being qualified per the AHA guidelines. There is currently a lack of understanding in how patients with carotid disease may experience contralateral embolic events in various levels of carotid stenosis. Here, we present an *in silico* study analyzing how different combinations of varying carotid stenosis may present contralateral embolic events and how the altered hemodynamics with the introduction of a stenosis can affect embolus transport.

METHODS

Image-Based modeling: A patient-specific model was created from the aortic arch to the CoW using the open-source program Simvascular [4, 5]. This patient had a complete CoW anastomosis with healthy

(non-stenotic) carotid arteries. Stenosis were computationally applied to each carotid artery using this healthy patient segmentation model by manually decreasing the diameter of the carotid bulb area to the corresponding NASCET severity. The stenosis degrees were categorized into three non-severe NASCET scores of [10%, 25%, 40%], and three high-moderate/severe NASCET scores of [50%, 70%, 85%]. These severity ranks were paired to where one carotid would have a non-severe stenosis and the other would have a high-moderate/severe stenosis for both the left and right carotid arteries. This totaled to 18 different models each with a unique pair of non-severe and high-moderate/severe stenosed carotids. The modeling of these differing severities can be seen in Figure 1.

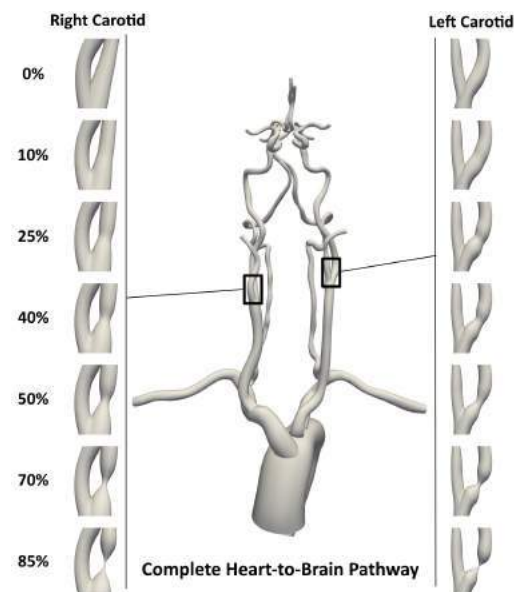


Figure 1: Patient-specific heart-to-brain pathway with varying applied left and right stenosis modifications of the carotid arteries. [4]. SB³C2023-497
Copyright 2023 SB³C Foundation, Inc.

Hemodynamics simulation: Hemodynamics across the aorta-CoW model was simulated using a stabilized finite element method for incompressible Navier-Stokes equations implemented in SimVascular [5]. Blood was assumed to be a Newtonian fluid with viscosity 4.0 cP and bulk density 1.06 g/cc. A validated pulsatile flow profile with a cardiac cycle of 0.83 seconds was applied to the aorta inlet [6]. Downstream vascular beds were accounted for by applying resistance boundary conditions to the outflow vessels of the model. These resistance values were acquired by calculating a total arterial resistance and distributing this resistance proportionally to each outflow artery based upon target flow divisions. 65% of the flow was set to exit the descending aorta [7]. The six cerebral artery outflows were split based upon data reported in [8]. The remainder flow was assigned to the subclavian and external carotid arteries based on their cross-sectional area [9]. The resistance values remained the same across all 18 models to see how flow patterns differed solely due to introduction of the stenosis.

Embolus Transport: Embolus transport was modeled using a custom modified version of the Maxey-Riley equation [10]. These modifications included adding near-wall shear gradient lift forces, particle collisions with the walls of arteries, and elasto-hydrodynamic effects near-wall [4]. Particles were given the mechanical properties of thrombo-emboli [11] and an embolus size of 500 μ m. The emboli were assumed to be spherical particles with a one-way coupled fluid interaction. For each model, approx. 5,500 emboli were released along the artery wall (mimicking release from plaque wall) from the stenosis surface to model plaque emboli. Cardiac emboli were also modeled by releasing emboli from the inlet of the aorta to see how different combination of stenosis severities may affect the pathway of cardiogenic emboli to the CoW.

RESULTS

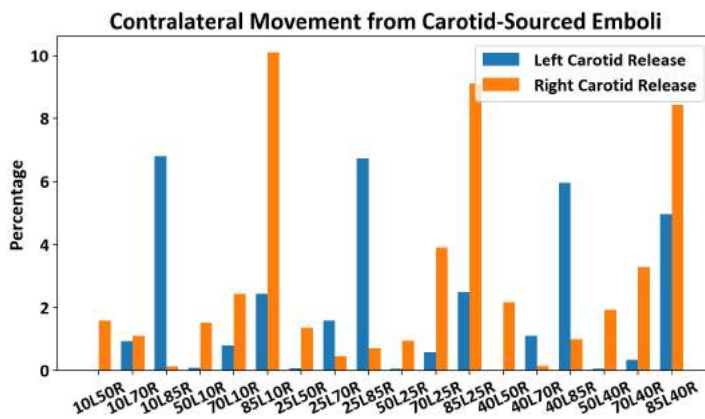


Figure 2: Proportion of emboli that distribute contralaterally. Emboli are released from both the left carotid and the right carotid arteries for each stenosis model of differing severity.

Embolus distribution was computed as the percentage of particles that exit each of the six outlets of the CoW. Figure 2 presents the proportion of emboli that distributed contralaterally into the CoW from the respective carotid in each stenosis model. Each model is labeled by their combination of left-right severity respectively (i.e. 10L50R corresponds to the model with a 10% left carotid stenosis and a 50% right carotid stenosis). Each model produced a non-zero contralateral distribution, meaning that all combinations of severe and non-severe stenosis show the potential for contralateral occlusions. The largest proportions of contralateral movement were found in the models with 85% stenosed carotid, where contralateral movement was highest from the non-severe carotid release. These models had a contralateral proportion between 6% and 10% which was much higher than the other releases that were mostly between 0.5% and 4%. Additionally, distribution fractions for cardiogenic emboli were computed. These distributions were acquired to inform how emboli from the heart would be influenced by the altered hemodynamics due to presence of a stenosis. The distribution of cardiac emboli across all models averaged 55% and 45% (standard deviation of 4.78%) for the left and right hemi-

spheres respectively. Cardiogenic emboli are not strongly directionally influenced by the presence of stenosis and distributions were marginally affected by the stenosis severity, indicating that significant number of emboli travel across the communicating vessels of CoW for these models.

DISCUSSION

Our investigation implemented a patient-specific embolus transport model to characterize embolus transport contralaterally from the left and right carotid arteries in the presence of varying degrees of stenosis. Altered hemodynamics to the CoW cause differing embolus transport patterns due to the stenosed carotids. Specifically, the CoW is supplied with blood flow through three arteries: the left internal carotid (L.ICA), the right internal carotid (R.ICA), and the basilar artery. Since all models have same total cerebral blood flow, Figure 4 illustrates how the proportion of flow through each of these three arteries changes with respect to stenosis severity. Models with high severity could see up to a 30% decrease in flow through the stenosed ICA, wherein the less stenosed carotid and basilar artery compensate with increased flow rates. The increased compensatory flow can in turn drive contralateral movement of emboli from the mild-moderate stenosis sites, while preventing contralateral transport of emboli from the severe stenosis sites. Communicating vessels of the CoW such as the anterior communicating artery (AcoA) will facilitate these contralateral movement, which needs further quantification in future works. Likewise, cardiogenic embolus distribution has a consistent trend across stenosis severity due to compensatory flow from the basilar artery as observed from our simulations. Ultimately, these cases of contralateral movement present difficulties in disambiguating embolus source that can lead to inconsistent recommendations for procedures such as CEA.

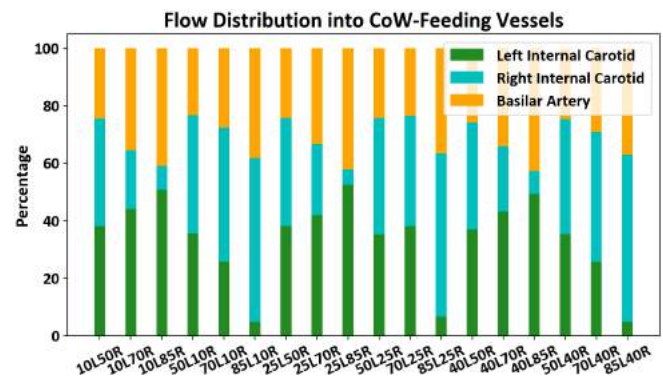


Figure 3: Proportion of flow rate through each of the three arteries feeding the CoW: the left internal carotid artery (L.ICA), the right internal carotid artery (R.ICA) and the basilar artery (BA).

ACKNOWLEDGMENTS

This work is supported by the NIH award R21EB029736. We utilized resources from the CU Boulder Research Computing Group, supported by NSF (awards: ACI-1532235, ACI-1532236), CU Boulder, and Colorado State University.

REFERENCES

- [1] Ferro J. *Lancet Neurol.* 9.11 (2010).
- [2] Ntaios G. *J. Am. Coll. Cardiol.* 75.3 (2020).
- [3] Jose B. *Stroke* 29.2 (1998).
- [4] Mukherjee D. *Ann. Biomed. Eng.* 46.8 (2018).
- [5] SimVascular. URL: <http://simvascular.github.io/>. (2020).
- [6] Olufsen M. *Ann. Biomed. Eng.* 28.11 (2000).
- [7] Carr I. *Am. J. Physiol.-Heart C.* 305.5 (2013).
- [8] Macdonald M. *Physiol. Meas.* 36.7 (2015).
- [9] Zamir M. *J. Biomech.* 25.11 (1992).
- [10] Maxey M. *Phys. Fluids* 26.4 (1983).
- [11] Mukherjee D. *J. Biomech. Eng.* 138.8 (2016).

OPTIMIZATION OF LIPID NANOPARTICLES FOR LOCALIZED MRNA DELIVERY IN FRACTURE REPAIR

Anna Laura Nelson^{1,2}, Chiara Mancino⁵, Josh Choe⁴, Gianluca Fontana⁴, Johnny Huard¹, William Murphy⁴, Francesca Taraballi⁵, Nicole Ehrhart², Chelsea Bahney¹⁻³

- (1) Lynda and Mitch Hart Center of Regenerative and Personalized Medicine, Steadman Philippon Research Institute (SPRI), Vail, CO, USA
(2) School of Biomedical Engineering, Colorado State University, Fort Collins, CO, USA
(3) University of California, San Francisco, San Francisco, CA, USA
(4) University of Wisconsin Madison, Madison, WI, USA
(5) Houston Methodist, Houston, TX, USA

INTRODUCTION

The long-term goal of this project is to develop an injectable and translational mRNA delivery platform specifically designed to localize therapeutic expression within a fracture site. Approximately 15 million fractures occur annually in the United States with 10-20% of fractures resulting in delayed healing or non-union.^{1,2} There are currently no pharmaceutical approaches approved to accelerate fracture healing or to treat non-unions. Current standard of care for non-unions involves surgical intervention to enhance stability and/or to promote regeneration through bone grafting. Delivery of mRNA is an attractive strategy recently popularized by the novel coronavirus vaccine that delivers genetic material without genomic integration.³ Liposomes have been frequently employed for the delivery of mRNA to combat limitations seen with mRNA stability; however little mRNA work has been completed in the field of orthopaedics. Recently, localized gene delivery has shown to be therapeutically efficacious in healing a large osseous segmental defect through having a scaffold delivering modified BMP-2 mRNA.^{4,5} In this study we aimed to test various mRNA delivery platforms specifically for fracture healing, including lipid nanoparticles (LNPs) complexed with Firefly luciferase mRNA. We hypothesize that the fully translational and injectable-based LNP therapeutic will sufficiently prolong transfection efficacy in order to be used for orthopaedic applications as tested in our murine tibial fracture healing model.

METHODS

LNPs have previously been found to encapsulate various genetic material and were assembled using microfluidic technology producing scalable and reproducible nanoparticles. Two different LNPs were tested involving the same synthesis steps, yet phospholipids MC3 and SM-102 were used separately during synthesis. All *in vitro* studies were performed using the ATDC5 chondrocyte cell line. Transfection kinetics and efficiency were studied using Firefly mRNA (TriLink Biotechnology) as a reporter gene and mRNA was isolated at various timepoints following delivery. Firefly luciferase (FFLuc) was used to measure the level of transfection and inflammatory markers (*IL-1 β* , *TNFA*) were used to assess platform interference with fracture healing. All of the procedures listed in this study were approved by our Institutional Animal Care and Use Committee (IACUC) and ARRIVE guidelines will be followed in reporting *in vivo* results. Delivery platforms were tested *in vivo* using a murine tibial fracture model stabilized with an intermedullary rod and all mRNA platforms were injected into

the fracture callus 6 days following fracture induction, within the fibrovascular phase of murine fracture healing. IVIS imaging was used to locate and quantify firefly luciferase protein. RNA was isolated from the fracture callus to measure inflammatory and osteogenic genes using qRT-PCR.

RESULTS

LNPs have previously been reported to deliver mRNA *in vitro* yet have not been studied *in vivo* for fracture repair applications.⁶ To determine LNP's capabilities for transfecting a fracture callus, mRNA encoding for FFLuc was delivered in BM-MSCs testing for luciferase expression and metabolic activity. Significantly more transfection efficacy resulted when delivering FFLuc mRNA encapsulated in SM-102 LNP's as compared to MC3 LNPs (**FIG 1A**). No significant differences were found in metabolic activity using either MC3 or SM-102 LNPs (**FIG 1B**). Biodistribution study revealed that no significant differences were found in luciferase expression between treatment groups in any of the organs tested, except in the fracture callus (**FIG 2**). *In vivo* transfection efficacy and kinetics of LNPs over 10 days post-injection into the fracture callus revealed that SM-102 LNPs had prolonged transfection kinetics over the MC3 LNP group (**FIG 3**). RNA isolated from fracture callus suggested that SM-102 does not interfere with fracture repair (**FIG 4**).

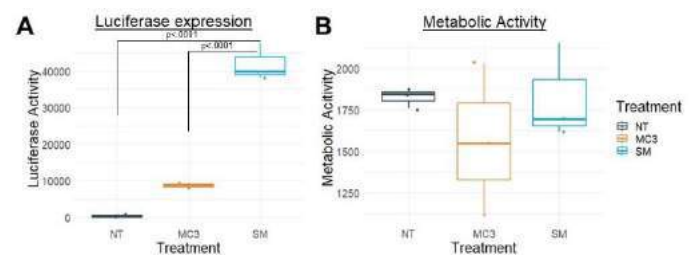


Figure 1 (Above) A). Transfection efficacy of mRNA delivery platforms, MC3 and SM-102 LNPs, *in vitro*. **B).** No differences in metabolic activity were noted.

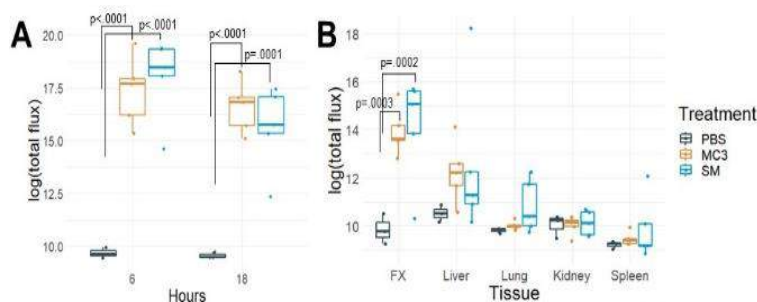


Figure 2 (Above) A. Quantification of IVIS images. **B.** Biodistribution study shows minimal off-target distribution when delivering Firefly luciferase mRNA using various delivery platforms.

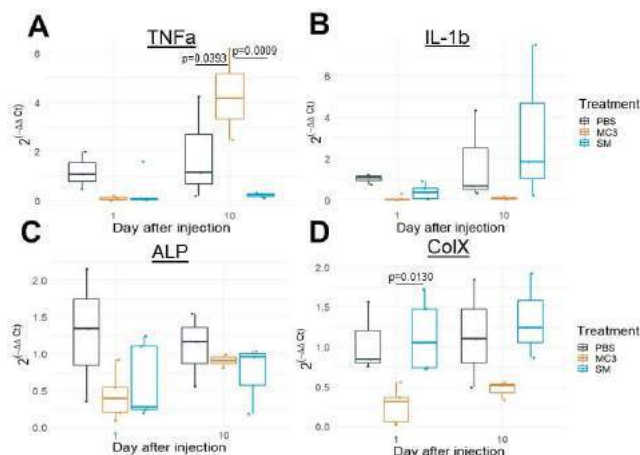


Figure 4 (Above) qRT-PCR analysis of RNA isolated from fracture callus shows reduced inflammatory response (A-B) for SM-102 and suggests that LNPs do not interfere with fracture repair (C-D).

DISCUSSION

There exists an unmet clinical need to stimulate bone regeneration through a non-surgical delivery platform. In order to combat the precedence of non-union and delayed healing in fractures, we are developing an injectable-based mRNA therapeutic using engineered LNPs to deliver mRNA locally to the site of the fracture callus. In this study, we aimed to develop a fully translational and localized mRNA delivery platform to improve therapeutic mRNA delivery for fracture repair. Here we show, for the first time, that SM-102 LNPs has the capabilities to extend and prolong mRNA transfection up to 10 days following injection with significantly more expression over PBS control up to 7 days. This LNP system can be utilized to deliver an osteogenic promoting mRNA transcript which shows that it does not interfere with fracture healing or promote an inflammatory response on its own.

ACKNOWLEDGEMENTS

We gratefully acknowledge support from the Musculoskeletal Regeneration Partnership Fund by Mary Sue and Michael Shannon.

REFERENCES

- 1). The Burden of Musculoskeletal Diseases in the United States. (2010). American Academy of Orthopaedic Surgeons, 247.
- 2). Giannoudis, P. V., et al. (2005). Injury 36 Suppl 3, S20-27.
- 3). Sultana, N. et al. (2017) Mol Ther 25, 1306-1315.
- 4). De La Vega, R., et al. (2022). Science Advances. 8(7).
- 5). Zhang, W. et al. (2019). Tissue Eng Part A. 25(1-2):131-144.
- 6). Molinara, R. et al. Adv Mater. (2018), 1702749.

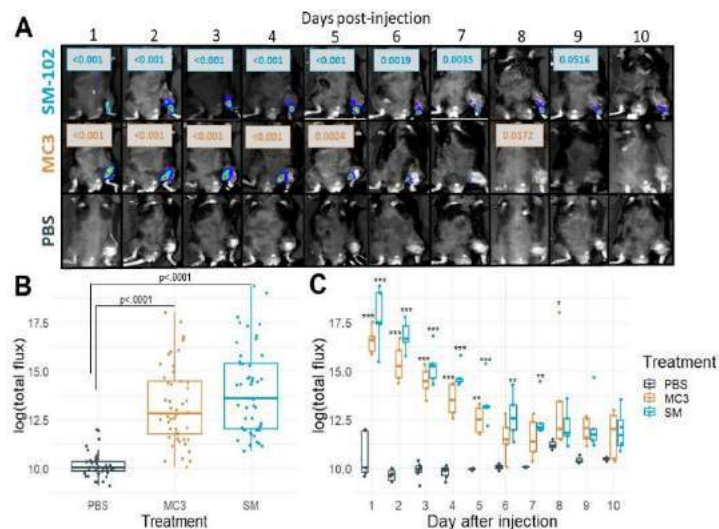


Figure 3 (Above) A. IVIS images over 10 days post-injection. **B.** Quantification of IVIS images all together and **C).** by day.

INTEGRATION OF DEEP NEURAL NETWORKS AND FINITE ELEMENT METHOD FOR BIOMECHANICAL ANALYSIS OF THE AORTA

Liang Liang (1), Minliang Liu (2), Wei Sun (3)

- (1) Department of Computer Science, University of Miami, Coral Gables, FL, USA
(2) Department of Biomedical Engineering, Georgia Institute of Technology, Atlanta, GA, USA
(3) Sutra Medical Inc, Lake Forest, CA, USA

INTRODUCTION

Machine learning (ML) techniques, especially deep neural networks (DNNs), have been developed to build surrogates of finite element analysis (FEA) and computational fluid dynamics (CFD) in a variety of applications, with the goal of speeding up the computations. In our previous studies related to thoracic aortic aneurysm (TAA), we developed DNNs for aortic wall stress analysis [1], steady-state hemodynamic analysis [2], and inverse estimation of material properties [3], which all perform much faster than traditional methods.

ML techniques have a fundamental limitation: ML model output may have large errors if the input is out of the distribution (OOD), i.e., very different from the training samples. For data-driven applications, such as image classification, this OOD issue is unavoidable [4].

In this study, we integrate the finite element method (FEM) and DNNs for forward and inverse analysis of human aorta, which guarantees the accuracy of the final output. Our contributions include: (1) a Pytorch implementation of FEM for aortic wall deformation and stress analysis, (2) five types of DNNs for aortic wall large deformation prediction, (3) integration of DNNs and FEM for aortic wall deformation and stress analysis, and (4) integration of DNNs and FEM for inverse estimation of hyperelastic material properties.

METHODS

Using the Pytorch library, which is an open-source library for implementing DNNs, we implemented FEM for aortic wall deformation and stress analysis. We have validated our implementation by comparing it with Abaqus, and the discrepancy is negligible. As shown in Figure 1, it has a modular design and therefore supports different material models and geometries. The basic finite element is similar to C3D8 in Abaqus, which unitizes selective-reduced-integration technique to handle volumetric-locking issue that may be present for nearly-incompressible materials. The optimizer uses a quasi-newton method that needs the hessian (i.e., stiffness) matrix. Since Pytorch has

auto-differentiation ability, all of the differential calculations are done automatically by using Pytorch functions. Given the material parameters and zero-pressure geometry as the inputs, the goal of the FEM is to compute the aorta geometry at the target blood pressure by minimizing the total potential energy [5].

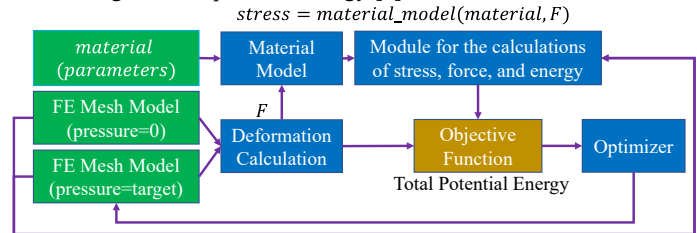


Figure 1: The Pytorch-implementation of FEM for aortic wall stress and deformation analysis.

In this study, we use the well-known GOH material model $\Psi = C_{10}(\bar{I}_1 - 3) + \frac{k_1}{2k_2} \sum_{i=1}^2 [\exp\{k_2[\kappa \bar{I}_1 + (1 - 3\kappa)\bar{I}_{4i} - 1]^2\} - 1] + \frac{1}{D} [\frac{J^2 - 1}{2} - \ln J]$, which has five material parameters $\{C_{10}, k_1, k_2, \kappa, \theta\}$.

To build ML-surrogate models (i.e., DNNs), we created a dataset of 342 shapes using statistical shape models of the zero-pressure geometries, similar to our previous approach [1]. By inflating the 342 zero-pressure geometries with 125 sets of material parameters from zero pressure to the systolic pressure (18KPa assuming hypertension), we obtained a large dataset for training and testing DNNs. The dataset is further divided into a training set including 50% of the shapes and 80% of the material sets, a validation set including 10% of the shapes and 10% of the material sets, and a test set including 40% of the shapes and 10% of the material sets.

We developed five types of DNNs to serve as ML-surrogate models, to predict the aorta geometry at the systolic pressure. Given a predicted aorta geometry from a DNN, we use the FEM method to

calculate the stress distribution on the aorta. The baseline DNN is a simple multilayer feedforward DNN (a.k.a. MLP). We adapted the MeshGraphNet [6] for our application, which is a state-of-the-art graph neural network to simulate mesh deformation. We implemented a U-Net to predict the aorta deformation, which is originally proposed for image segmentation [7]. We designed a TransNet based on the Transformer architecture that is originally proposed for natural language processing [8]. Finally, we designed a novel W-Net whose weights are determined by another network.

We conducted two experiments of ML-surrogate: (1) fixing the material set (using the mean material), and then training and testing the DNNs to predict the deformation given the zero-pressure geometry; and (2) using all the material sets and shapes, and then training and testing the best DNN from (1) to predict the deformation given the zero-pressure geometry and material parameters.

Integration of DNNs and FEM for forward computation: the output from a DNN serves as the starting state for the FEM. The idea is simple, but it won't work if FEM directly uses the DNN output because FEM assumes the starting state is in force-equilibrium that is not guaranteed by the DNNs. We modified the FEM optimizer to handle this issue.

Integration of DNNs and FEM for inverse estimation of material properties: similar to the forward task, to inversely estimate the material properties, we could simply re-define the inputs and outputs of a DNN and use the DNN-predicted material properties as the initial solution for a FEM-based inverse method. In this study, we show another way of integrating DNNs and FEM for inverse estimation of material properties: a DNN can serve as a smoothness constraint to estimate inhomogeneous material properties of the aortic wall, i.e., $m(x) = DNN(x)$ where m is a material parameter and x is the location of a point on the aortic wall. The predicted material parameter m will be one of the inputs to FEM (Figure 1). Because the FEM is implemented in Pytorch, backpropagation can be utilized to find the optimal values of the material parameters, such that the loss function is minimized: $loss = \frac{1}{N} \sum_i \|f_i^{internal} - f_i^{external}\|^2$ where $f_i^{internal}$ is the internal force (from stress) and $f_i^{external}$ is the external force (from pressure) on the node- i of the aortic wall mesh model that has N nodes. The $loss$ is a function of the material parameters and the weights of the DNN.

RESULTS

MRSE (mean root square error, unit: mm) measures the difference between the predicted geometry and true geometry at the systolic pressure. APE (absolute percentage error) measures the difference between the predicted and true peak von-mises stresses. Avg stands for average over the test samples.

Table 1: DNN Performance in Experiment-1.

	MRSE (avg)	MRSE (max)	APE (avg)	APE (max)
W-Net	0.0108	0.2728	3.00%	51.11%
TransNet	0.0192	0.9579	3.71%	>100%
U-Net	0.0436	1.1368	16.03%	>100%
GraphNet	0.0730	4.8231	>100%	>100%
MLP	0.1210	1.9514	20.22%	>100%

Table 2: DNN-FEM-Integration Performance in Experiment-1.

	MRSE (avg)	MRSE (max)	APE (avg)	APE (max)	Time (avg)	Time (max)
W-Net	0.0003	0.0009	0.04%	0.11%	1.65%	3.13%
TransNet	0.0003	0.0009	0.04%	0.11%	1.36%	3.11%
U-Net	0.0003	0.0009	0.04%	0.11%	1.47%	3.54%
GraphNet	0.0003	0.0009	0.04%	0.11%	3.05%	8.89%
MLP	0.0003	0.0009	0.04%	0.11%	2.46%	6.37%

Table 3: DNN Performance in Experiment-2.

	MRSE (avg)	MRSE (max)	APE (avg)	APE (max)
W-Net	0.1072	2.6715	>100%	>100%

Table 4: DNN-FEM-Integration Performance in Experiment-2.

	MRSE (avg)	MRSE (max)	APE (avg)	APE (max)	Time (avg)	Time (max)
W-Net	0.0002	0.0032	0.02%	0.11%	1.47%	9.89%

Note: the computation does not converge for 3.65% of the test samples and therefore those are excluded.

Table 5: DNN-FEM-Integration Performance for The Inverse Task

MLP	C_{10}	k_1	k_2	κ	θ	loss
none	27.03%	15.35%	24.88%	3.64%	1.26%	0.2066
4-128	0.97%	0.66%	1.23%	0.14%	0.01%	0.0053
4-256	0.46%	0.27%	0.50%	0.06%	0.01%	0.0027
4-512	0.56%	0.32%	0.34%	0.06%	0.01%	0.0023
6-128	0.24%	0.15%	0.37%	0.03%	0.01%	0.0026
6-256	0.23%	0.12%	0.25%	0.02%	0.01%	0.0016
6-512	0.57%	0.34%	0.37%	0.07%	0.01%	0.0019

note: the table shows the percentage error of each estimated parameter. "none" means DNN is not used. "m-n" indicate the DNN (i.e., MLP) has m hidden-layers and each hidden-layer has n units. The computation takes about 1 to 2 hours for each DNN model.

As shown by Table 1 and 3, the maximum peak stress errors of the DNNs are unacceptably large for some samples in the test set, indicating the OOD issue. As shown by Table 2 and 4, DNN-FEM-Integration has negligible errors and minimal time cost, compared to FEM.

As shown by Table 5, the DNN-FEM-Integration was able to recover inhomogeneous material properties, and the loss could serve as the indicator for model selection.

DISCUSSION

This study demonstrates that the integration of DNN and FEM can resolve the OOD issue of the data-driven ML-surrogates. It also shows that DNNs can serve as spatial smoothness constraint for the estimation of inhomogeneous material properties (ex-vivo) of the aortic wall.

ACKNOWLEDGEMENTS

This work is supported in part by the NIH grant R01HL158829.

REFERENCES

- [1] L. Liang, et. al, A deep learning approach to estimate stress distribution: a fast and accurate surrogate of finite-element analysis, Journal of The Royal Society Interface, 2018.
- [2] L. Liang, et. al, A feasibility study of deep learning for predicting hemodynamics of human thoracic aorta, Journal of biomechanics, 2020.
- [3] M. Liu, et. al, Estimation of in vivo constitutive parameters of the aortic wall using a machine learning approach, Computer Methods in Applied Mechanics and Engineering, 2019.
- [4] J. Chen, et. al, Adversarial robustness study of convolutional neural network for lumbar disk shape reconstruction from MR images, SPIE Medical Imaging: Image Processing, 2021.
- [5] Javier Bonet and Richard Wood, Nonlinear Continuum Mechanics for Finite Element Analysis, Cambridge University Press, 2010.
- [6] Tobias Pfaff, et. al, Learning mesh-based simulation with Graph Networks, ICLR, 2021.
- [7] Olaf Ronneberger, et. al, U-Net: Convolutional Networks for Biomedical Image Segmentation, MICCAI. 2015.
- [8] Ashish Vaswani, et. al, Attention Is All You Need, NeurIPS, 2017.

A NOVEL STRAIN ENERGY-BASED METHOD TO DYNAMICALLY STIMULATE THREE-DIMENSIONAL CELLULAR CONSTRUCTS

Amevi M. Semodji (1), Faith R. Wilder (2), Anamaria G. Zavala (2), Sean M. Howard (2),
Gunes Uzer (2), Trevor J. Lujan (2)

(1) Biomedical Engineering Doctoral Program, Boise State University, ID, USA

(2) Department of Mechanical & Biomedical Engineering, Boise State University, Boise, ID, USA

INTRODUCTION

Mechanical loads can stimulate growth and healing in soft tissue, and numerous studies have investigated this mechanobiological response *in vitro* using 3D scaffolding materials such as collagen or polyurethane. Yet, the physical mechanism that governs this response under complex in-vivo loading conditions remains unknown. This knowledge gap has hindered efforts to develop more effective therapies for soft tissues injuries that are responsible for 15 million hospital visits every year in the U.S. [1]. One intriguing theory is that cell mechanosensing is regulated by a material's strain energy [2].

Strain energy is a scalar measure of deformation in biological and nonbiological materials. It can be decomposed into hydrostatic energy that relates to volume change, and distortion energy that relates to shape change. Energy-based theories are reliable in predicting structural changes in materials. For example, hydrostatic energy is predictive of cortical bone remodeling [3] while distortion energy theory is an excellent predictor of failure in ductile materials [4]. Strain energy has the potential to create a unifying theory to predict cellular responses to any loading configurations (e.g. tension, compression, biaxial, triaxial), something that has not been possible using stress-based and strain-based mechanisms, but the lack of accurate experimental methods to apply targeted strain energy levels makes the investigation difficult.

Bioreactors can apply mechanical loads on 3D cellular constructs to study the resulting mechanobiological response. They often apply simple uniaxial loads (tension or compression) or more physiological complex loads (e.g., biaxial, triaxial), but no mechatronic control system has been developed to apply targeted strain energy levels, which is needed to hopefully develop a unifying theory to predict cellular response to mechanical loads.

The objective of this work was to develop a novel automated method to apply targeted energy levels to 3D constructs undergoing dynamic mechanical stimulation. The accuracy of the method will be verified with 3D constructs subjected to simple and complex loads.

METHODS

A custom biaxial bioreactor (Fig. 1) was previously created by our group to simultaneously apply tensile and compressive loads to cell-seeded constructs [5]. In brief, it consists of a tissue chamber where a specimen is clamped for testing, and each of its two axes uses an electromagnetic actuator for motion and a 1.0N-load sensor.

Two LabVIEW programs were developed. The first program optimized the force input to apply a user-specified strain energy under cyclic stimulation (Fig. 2), and the second program used the optimized input force to apply the targeted strain energy for a user-specified number of stimulation cycles and days. Strain energy was normalized to volume to compute strain energy density. Strain energy density W can be computed as the area under the characteristic stress-strain curve (Fig. 2), where σ and ϵ denote engineering stress and strain, respectively.

This area can be computed numerically using the trapezoidal numerical integration technique (Fig. 2). Additionally, the energy can be decoupled into its hydrostatic and distortion components using a numerical method previously developed and validated by our group [6]. Energy optimization is performed iteratively using a modified version of the secant root-finding algorithm (Fig. 2).

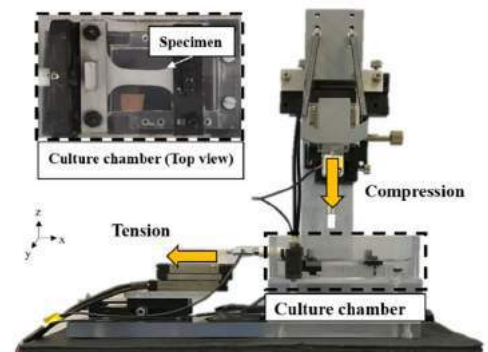


Figure 1: Biaxial tension - compression bioreactor

Method verification. Polyurethane foam samples were cut into dog bone shape, hydrated, then clamped inside the tissue chamber of the bioreactor. Samples were subjected to one of 3 loading conditions ($n=3$ per group): uniaxial tension (T), uniaxial compression (C), and biaxial

compression-tension at equal magnitudes (CT). A single targeted strain energy density of 100 J/m^3 was prescribed to the samples in all loading cases based on preliminary studies that show that this energy results in physiologically relevant tensile strains (2-5%) [7]. For each sample, the energy-optimization program was run first to determine the necessary input force, which was then entered in the force-

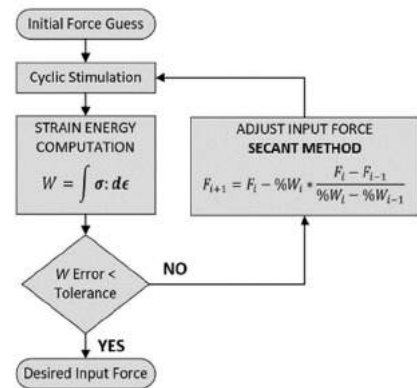


Figure 2: Novel energy optimization method

control program to stimulate the sample for 30 minutes at a 1 Hz-frequency. Correction factors of ~5% were applied to the forces in the biaxial loading case to account for frictional effects. The steady state energy was then computed and compared to the target energy to calculate accuracy (measured – target) and percent error. A one-way ANOVA and Tukey-HSD post-hoc was performed to detect differences in energies between loading configurations.

Application to cell-seeded constructs. To verify that our method did not accelerate cell death, it was applied to a cellular construct subjected to biaxial CT. Murine fibroblasts (Sigma Aldrich) were acquired, plated, allowed to grow in an incubator until confluency, and collected for seeding using standard protocols [7]. 3 polyurethane foam samples (DSM Biomedical) were cut into a dog bone shape, sterilized, seeded with 10^6 cells per sample, and statically cultured for 24 h.

The bioreactor (Fig. 1) was sterilized and placed inside the incubator for stimulation. After the static culture, one cellular construct was clamped inside the tissue chamber of the bioreactor and submerged with growth medium. The novel method was applied to dynamically stimulate the cellular construct in CT at a 1Hz-frequency, for 8 h per day, for 2 days, and at a total target energy of 100 J/m^3 . Two constructs stayed unstimulated inside the incubator to serve as controls. All constructs were analyzed with an XTT cell proliferation assay (Cayman) to determine metabolic activity using standard protocols. In brief, XTT solutions were added to sectioned-out middle regions of the constructs and left to incubate for 2 hours. The solutions were then collected and placed in a spectrophotometer (Fisher-Sci). Absorbance values were read at 450 nm and normalized to scaffold-only controls.

RESULTS

The novel method accurately applied the target energy with a percent error less than 5% (table 1) and with an average of about 6 iterations to convergence (Fig. 3A). To reach the target energy, the specimens required forces of $0.12 \pm 0.003 \text{ N}$ in T, $0.24 \pm 0.015 \text{ N}$ in C, $0.11 \pm 0.006 \text{ N}$ in CT-tension, and $0.16 \pm 0.007 \text{ N}$ in CT-compression. These resulted in strain values of $2.34 \pm 0.02\%$ in T, $7.45 \pm 0.49\%$ in C, $1.05 \pm 0.1\%$ in CT-tension, and $6.38 \pm 0.20\%$ in CT-compression. Additionally, the numerical method successfully decoupled the energy in the constructs and revealed a significant difference in distortion and hydrostatic energies in the combined loading case compared to the simple loading cases (Fig. 3B). Furthermore, the method preserved cell

activity in the fibroblast-seeded construct with an absorbance reading of about 11% higher than control samples.

Table 1: Average accuracy in applied energy per loading condition

	T	C	CT
Target Energy (J/m^3)	100	100	100
Actual Energy (J/m^3)	104.6	101.1	101.5
Percent Error (%)	4.55	1.11	1.49

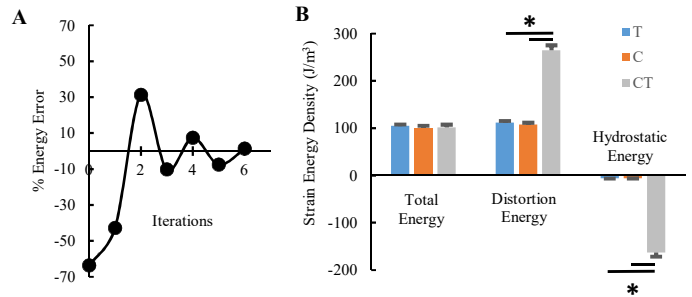


Figure 3: A) Energy optimization iterations. B) Total, distortion, and hydrostatic energies per loading condition (* $p < 0.05$).

DISCUSSION

This work presents a novel experimental methodology to apply targeted levels of strain energy to 3D constructs. The method accurately applied the selected target energy to acellular constructs that underwent similar total energy levels but significantly different distortion energy levels (Fig. 3B). Additionally, the method did not accelerate cell death in constructs that were subjected to a biaxial CT loading configuration.

Interestingly, negative hydrostatic energies were computed in the constructs in all loading conditions (Fig. 3B). This supports previous findings that large Poisson's ratio materials like polyurethane foams display negative hydrostatic energies [6]. Several soft tissues such as ligaments and tendons are also known to display unusually large Poisson's ratios [8]. This phenomenon has been explained by fluid exudation in those materials during loading [6, 8].

Several notable challenges were overcome in the development of this innovative method. For example, consistently optimizing energy regardless of loading condition required changes to the traditional secant method (Fig. 2) and implementation of load-limiting safeguards. The biaxial loading case required load correction factors that were determined analytically to alleviate the effects of additional friction resulting from the simultaneous tension-compression loading. These changes contributed to improving the rate of convergence of the method and making it fully automated. This new method will finally allow the investigation of new energy-based theories to predict cell responses to any loading configuration and potentially confirm that distortion energy is the driving factor for cellular changes in simple and complex loads.

ACKNOWLEDGEMENTS

Funding kindly provided by grants NIH NIAMS #1R15AR075314-01 & NIGMS #P20GM109095.

REFERENCES

- [1] Herzog, L et al, *Orth J Sports Med*, 5:1, 2013.
- [2] Panzetta, V et al, *PNAS*, 116:22004-22013, 2019.
- [3] Mercuri, E et al., *Med Eng & Phys*, 38:904-910, 2016.
- [4] Von Mises, R, *News from Societies of Sciences*, 1:582-592, 1913.
- [5] Everingham, J et al, *WCB*, 2018.
- [6] Semodji, A et al, *SB3C*, 2021.
- [7] Joshi, S et al, *J Orthop Res*, 26:1105-1113, 2007.
- [8] Swedberg, A et al., *J Biomech*, 47:3201-3209, 2014.

FREQUENCY OPTIMIZATION OF A NOVEL SKIN BLOOD FLOW TRANSDUCER

Georgia E. Robles (1), Christopher M. Francis (2), Saeed I. Latif (3), David A. Nelson (1)

- (1) William B. Burnsed, Jr. Department of Mechanical, Aerospace, and Biomedical Engineering,
University of South Alabama, Mobile, Alabama, United States
(2) Dept of Physiology and Cell Biology and Center for Lung Biology, University of South Alabama,
Mobile, Alabama, United States
(3) Dept of Electrical and Computer Engineering, University of South Alabama, Mobile, Alabama,
United States

INTRODUCTION

There are a number of conditions for which it would be useful to have information about the rate of blood flow in the skin. These include detection of asymptomatic Peripheral Artery Disease (PAD), assessing healing of diabetic ulcers and other wounds, management of Raynaud's Disease, and identification of certain emergent conditions (heat stroke, shock). There is no fast, simple method for obtaining quantitative measures of skin blood flow however.

REFLO (Rapid Electromagnetic Flow) is a novel technology for noninvasive measurement of the blood flowrate in the microcirculation of the skin. The method utilizes the relationship between flowrate and tissue temperature increase during exposure to radio frequency (RF) energy in the 15 – 40 GHz range. At those frequencies, heating is superficial and can produce measurable increases in skin temperature, without affecting deeper tissues or organs. It has been shown that the rate of surface temperature increase is a function of the rate of blood flow in the underlying dermal vasculature.

We are developing a prototype REFLO device for measuring skin blood flow. The system incorporates a low-power RF transmitter and a handheld transducer to simultaneously heat the skin and measure the temperature response. As the depth of RF penetration is a function of wavelength, the transmitter frequency is a critical design variable. For example, energy penetration to a depth less than that of the dermal plexus may compromise measurement sensitivity. The depth and magnitude of the energy absorption in the skin depends on many factors, including the frequency and power density of the incident RF energy, and the thickness of the

dermal layer. The objective of this study is to determine the extent to which the magnitude and depth of heating are functions of (i) frequency, and (ii) power density. The results will enable optimization of frequency and exposure duration and allow development of a device and measurement protocol.

METHODS

RF energy absorption was simulated using xFDTD software (Remcom, State College, PA). The heterogeneous tissue models (one-dimensional) consisted of four tissue layers: Stratum Corneum (SC), Epidermis (ED), Dermis (D) and Hypodermis (HD) (Figure 1).

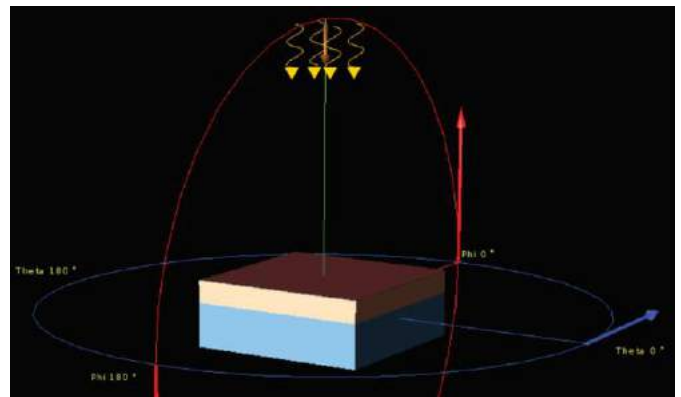


Figure 1: The four layer computational skin model with incident sinusoidal plane wave of various frequencies used to calculate electric fields and SAR values.

Dielectric values for each tissue were determined at frequency according to a Cole-Cole permittivity model. Exposures were far-field, continuous waves with power densities $P=100, 250, \text{ and } 500 \text{ mW/cm}^2$ and frequencies 15, 25 and 35 GHz. The resulting specific absorption rate (SAR) values were then used alongside a thermal solver based on the Pennes Bioheat equation to calculate the corresponding temperature increases as a function of time.

RESULTS

Figures 1 and 2 show surface temperature increases for a range of blood flowrates for incident power density of 250 mW/cm^2 . Results are shown for operating frequencies of 15 and 35 GHz.

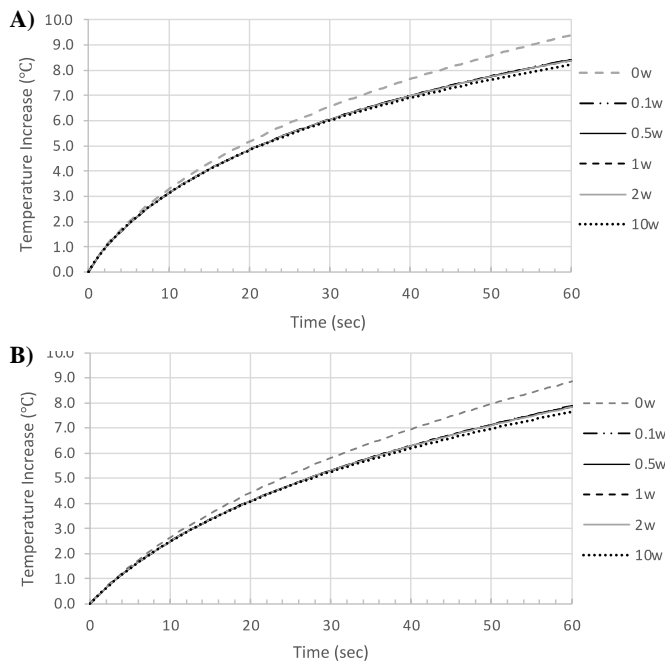


Figure 2: Surface temperature increases for varying perfusion rates over 60 sec heating period under exposure to 15 (A) and 35 (B) GHz with power density 250 mW/cm^2 . Base perfusion rate (w) 0.5 ml/s/ml

The surface temperature increase is important to device performance and safety. Both 15 and 35 GHz bring about similar surface temperature increases at 250 mW/cm^2 . At extremely low perfusion rates there is sufficient sensitivity to blood flow rate, but a greater degree is necessary to differentiate between mid and high level perfusion rates. The results presented here will be used to determine the impact on measurement performance and optimize device parameters.

DISCUSSION

A simple, one-dimensional model of RF absorption in skin is presented. Both 15 and 35 GHz are viable frequency options shown by the similar surface temperature increase curves.

Frequency is an important design consideration not only from a functional standpoint but will also determine the cost point of the device. Using a RF frequency lower than 35 GHz may offer an opportunity to reduce the cost of a device. Hardware costs for amplifiers in particular tend to be quite high for frequencies above 35 GHz. Hence the optimization of the operating frequency may be important to the success of the technology.

Efforts are currently being made to increase the sensitivity of the device to mid to low range perfusion rates. We are currently in the process of testing a prototype on human subjects

ACKNOWLEDGEMENTS

This work was supported by a grant from University of South Alabama, Office of Research and Economic Development, and by the Alabama Space Grant Consortium.

REFERENCES

- [1] Nelson, D. *et al* 2018 *Physiol. Meas.* 39 045001 DOI10.1088/13616579/aab4d4
- [2] Walters, T., Ryan, K., Nelson, D., Blick, D., & Mason, P. (2004). Effects of blood flow on skin heating induced by millimeter wave irradiation in humans. *Health Physics*, 86(2), 115-120. <http://doi.org/10.1097/00004032-200402000-00001>

STUDYING THE MECHANICAL REFERENCE DOMAIN OF THE HEART FOR CARDIOVASCULAR BIOMECHANICS

John Sayut (1), Javiera Jilberto Vallejos (1), Sandra Hager (2), Mia Bonini (1), Marc Hirschvogel (2), David A. Nordsletten (1,2,3)

(1) Biomedical Engineering, University of Michigan, Ann Arbor, Michigan, USA

(2) Department of Cardiac Surgery, University of Michigan, Ann Arbor, Michigan, United States

(3) School of Biomedical Engineering and Imaging Sciences, King's College London, London, United Kingdom

INTRODUCTION

Computational biomechanics is a valuable tool for understanding the physiology and potential impact of treatment in cardiovascular disease. Biomechanical modeling is known to predict the outcome of currently available surgical procedures and found to inspire novel procedures [1]. The knowledge gleaned from computational cardiovascular biomechanics can improve understanding of disease development and progression [2].

A continual challenge in these analyses is that medical imaging of cardiovascular structures, while providing significant detail on a patient's anatomy, occurs under arguably unknown cardiovascular loading conditions. In the context of the heart, blood pressure pressurizes the myocardium, introducing loads concomitant with unknown residual stresses [3]. Additionally, the surrounding pericardium, diaphragm, lungs and rib cage introduces additional uncertainty, challenging our interpretation of the loading state of the heart.

Several works have been introduced to address these challenges in cardiac mechanics. To understand the unloaded state, researchers have used inverse mechanics methods to define the impact of the assumed reference domain in the mechanical response [4] [5]. Additionally, a modified updated Lagrangian formulation (MULF) method has been utilized for model order reduction, shown to develop an accurate approximation of the unloaded state for specific applications [6]. For the challenge of residual stresses, researchers have found that including prestrain has a substantial overall impact on cardiovascular mechanics [3] [7]. The impact of epicardial force has been investigated through phenomenological boundary energy terms [8].

Despite these advances, we still must quantify the uncertainty and fidelity of these techniques in providing information about the unloaded state of the heart. In this abstract, we explore how uncertainty in external loads impact the accuracy and efficacy of cardiac biomechanics. This is done through using a simplified in silico analysis, showing how uncertainty in external loads can significantly impact the estimation of reference domains and strains. We then examine this in vivo, considering 3 patient-specific models, which examine how different interpretations of epicardial loads impact our assessment of cardiac mechanics.

METHODS

To study the impact of uncertainty in the cardiac load state, we explore two modeling systems. In the first, a simplified two dimensional geometry is exposed to a no-penetration spring condition, whereby force is linearly increased (with stiffness k_{wall}) with normal displacement (see Fig 1A). Pressurizing the interior of the model, provides a loaded state influenced by internal and external loads. Two methods of inverse mechanics are considered: a direct inverse approach [9] as well as the MULF method [6], examining their efficacy at predicting the load free reference domain – as well as additional loading geometries in the case of the direct inverse method. We then explore the significance of the no-penetration parameter, k_{wall} , and its influence on predicted reference domains. Lastly, we consider how adding additional load states could help provide determination of k_{wall} .

Extending this analysis to the human heart, we consider (n=3) patient-specific heart models created from dynamic computed tomography imaging. Examining the motion, we compare the normal displacement distributions observed in normal cardiac filling from end-systole to end diastole (Fig 2A). We then explore how joint estimation of external loads and inverse mechanics (across multiple states) could provide insight into the biomechanics of the heart and its external loading state. For both studies, simulations were conducted in CHeart [10]. Forward mechanical simulations were solved as described in [11]. reference domain estimates using direct inverse mechanics follows the techniques described in [9], and the MULF approach follows the technique introduced in [6].

RESULTS

In the case of the in silico two dimensional test, we found that inverse mechanics shows that significant uncertainty in the assumed boundary conditions generate significant differences in the estimated reference domain geometry. Figure 1D below shows the normalized root mean squared error (RMSE) between simple geometry points on the true reference mesh for different assumed boundary conditions. To normalize, we divide each RMSE value by the error between the original cylinder and the reference domain developed when $k_{wall} = 0$. The graph shows significant error between an inverse mechanics problem with no boundary conditions and an inverse mechanics problem with the correct boundary conditions.

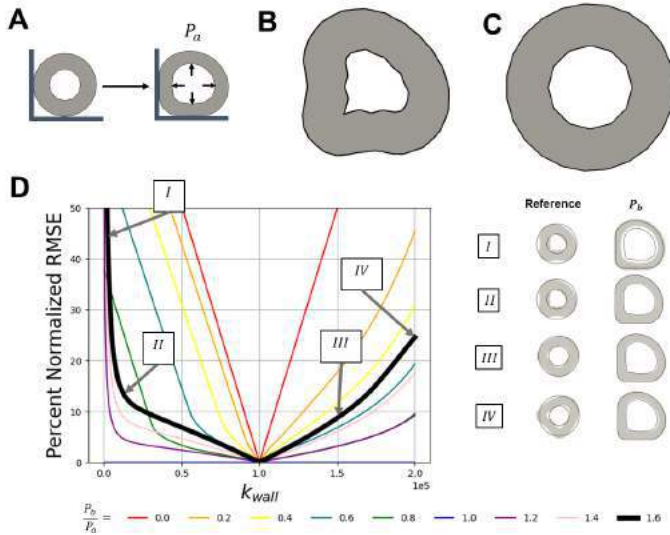


Figure 1: A - Depiction of the mechanical test. B - Reference domain geometry of the cylinder found without epicardial force. C - Reference domain geometry of the cylinder found using accurate epicardial force. D - Graph of RMSE between ground truth and test data for different no-penetration parameter values, with different ratios between the primary and secondary pressure constant as denoted in the legend. In the visualizations, the black outline denotes the ground truth simulation, and the grey cylinder denotes the k_{wall} value specified by the arrow.

In the forward simulations from end-systole to end-diastole, we captured the geometry of an inflated surface and to study the significance of epicardial force. We compare the cardiac epicardium of the end-systole configuration to the imaged end-diastolic epicardium. By doing so, we see the geometric differences due to many factors, one being the boundary conditions exerted on the heart. Figure 2A compares the difference in nearest-neighbor distance from the modeled end-diastolic state and the imaged end-diastolic state for each patient. Figure 2B compares the reference domain generated by the direct inverse and MULF methods from an example patient biventricular model. This case exhibits similar concave behavior to the simple case, depicted in Figure 1B.

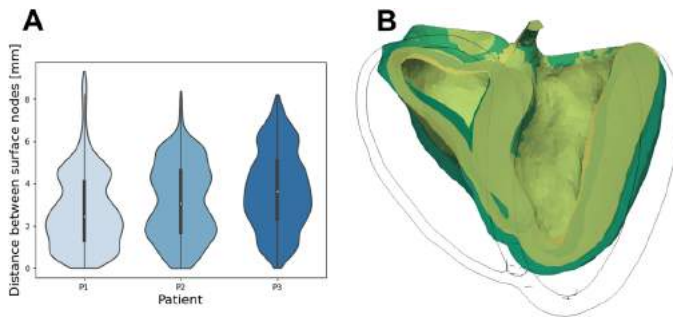


Figure 2: A - Absolute nearest-node distance between an inflated end-diastolic and an imaged end-systolic epicardial surface for patient-specific data. B - Example reference domain geometries in three dimensions without boundary conditions. Green volume indicates the direct inverse method geometry and yellow volume indicates MULF method geometry. The black outline indicates the original model.

DISCUSSION

This study shows that in a two-dimensional test problem, the mechanical reference domain can be located with a reasonably accurate assumption about the boundary conditions on the heart. In our test case, we find a dis-

tinct minimum at the correct boundary condition when comparing between a wide variety of secondary pressure constant values. This means that through appropriate solvers, data routinely collected in the clinic could be utilized for approximating patient-specific boundary conditions, although the complexity of such conditions would increase significantly from the test case. We also see in this test that for a small change in pressure constant, the error of the result will remain relatively low - if we imprecisely estimate the epicardial force. Depending on the relationship of these parameters in vivo, and the accuracy requirements of the biomechanical calculations in question, weaker boundary condition estimations may be sufficient. Biomechanics researchers can better apply computational resources for personalized heart mechanical performance by understanding the assumptions and limits of different math methods used to quantify and represent the reference domain.

In the case of the biventricular surface analysis, we see significant differences in epicardial node distance in the different patients. This indicates that the epicardial force on each patient's heart may be highly variable. It's important to note that in this exploratory data, we ignore diastolic muscle contractions, which would also contribute to the heterogeneity we see. Regardless, the substantial differences show that consideration of cardiac boundary conditions would require patient-specific calculations and may play an important role in modeling.

ACKNOWLEDGEMENTS

We would like to acknowledge funding from the National Science Foundation Graduate Research Fellowship under Grant No. DGE-1841052.

REFERENCES

- [1] Marsden AL et al. *Current Opinion in Pediatrics* 27.5 (2015). ISSN: 1040-8703. DOI: 10.1097/MOP.0000000000000269.
- [2] Zhang Y et al. en. *Annals of Biomedical Engineering* 44.9 (2016). ISSN: 0090-6964, 1573-9686. DOI: 10.1007/s10439-016-1628-0.
- [3] Genet M et al. *Journal of Biomechanics* 48.10 (2015). ISSN: 00219290. DOI: 10.1016/j.jbiomech.2015.03.012.
- [4] Nordsletten D et al. *Progress in Biophysics and Molecular Biology* 104.1 (2011). ISSN: 00796107. DOI: 10.1016/j.pbiomolbio.2009.11.001.
- [5] Nikou A et al. en. *Computer Methods in Biomechanics and Biomedical Engineering* 19.16 (2016). ISSN: 1025-5842, 1476-8259. DOI: 10.1080/10255842.2016.1183122.
- [6] Schein A et al. en. *Advanced Modeling and Simulation in Engineering Sciences* 8.1 (2021). ISSN: 2213-7467. DOI: 10.1186/s40323-021-00203-7.
- [7] Wang HM et al. en. *Biomechanics and Modeling in Mechanobiology* 13.1 (2014). ISSN: 1617-7959, 1617-7940. DOI: 10.1007/s10237-013-0488-x.
- [8] Asner L et al. en. *Computer Methods in Applied Mechanics and Engineering* 314 (2017). ISSN: 00457825. DOI: 10.1016/j.cma.2016.08.002.
- [9] Hadjicharalambous M et al. *Biomech Model Mechanobiol* 20.4 (2021). ISSN: 1617-7959, 1617-7940. DOI: 10.1007/s10237-021-01464-2.
- [10] Lee J et al. en. *SIAM Journal on Scientific Computing* 38.3 (2016). ISSN: 1064-8275, 1095-7197. DOI: 10.1137/15M1014097.
- [11] Miller R et al. *Frontiers in Physiology* 12 (2021). ISSN: 1664-042X. DOI: 10.3389/fphys.2021.716597.

A COMPARATIVE STUDY ON THE DIFFERENCE IN ARTERIOVENOUS FISTULA CFD SIMULATIONS BASED ON GEOMETRY LENGTH

Kaitlin M. Southern (1), Fatemeh Bahmani (1), Veeranna Maddipati (2), Stephanie M. George (1)

(1) Department of Engineering, East Carolina University, Greenville, NC, US
(2) Internal Medicine, Brody School of Medicine, East Carolina University, Greenville, NC, US

INTRODUCTION

Over 15% of U.S. adults suffer from chronic kidney disease (CKD), which over time can progress to end-stage renal disease (ESRD). ESRD is characterized by extremely impaired renal function that can lead to death if unaddressed [1]. Treatments for ESRD include replacement therapy by hemodialysis, peritoneal dialysis, and kidney transplantation [2]. Hemodialysis requires the surgical creation of an arteriovenous fistula (AVF) to allow for increased blood flow through a dialysis machine and back to the right side of the heart [3].

Fistulas are created by surgically connecting an artery and a vein. The most common of these is the radiocephalic fistula, created by anastomosing the end of the cephalic vein to the side of the radial artery. Even though fistula formation is a common and an effective treatment it has been suggested as a risk factor for developing pulmonary hypertension (PH) [3]. Between 30 – 50% of ESRD patients can develop pre-capillary PH, which is associated with increased pulmonary artery pressures and resistance and can lead to eventual heart failure [2].

Considerable work has been completed using computational modeling to visualize flow patterns in AVFs, however there is conflicting evidence pertaining to the underlying cause of the development of pulmonary hypertension and the involvement of AV fistula flow rates. By modeling fistula hemodynamics metrics, this study may offer insight to physicians about AVF monitoring, which may lead to early surgical interventions to prevent the development of pulmonary hypertension. This improvement would cause fewer incidences of pulmonary hypertension and overall enhance the quality of life for those suffering with this condition. The objective of this preliminary study is to construct and compare AVF computational fluid dynamics models with geometry length variations. The length of the patient specific AVF will be shortened as a parameter in the study, and the effect will be examined. Evaluation of the simulation results with a more simplified

geometry could provide a model with fewer mesh elements, reduced computational cost, and a more efficient simulation.

METHODS

Patient inclusion criteria are as follows: patients must be over the age of 18, have an arteriovenous fistula actively being used for dialysis, have been diagnosed with PH by right heart catheterization (RHC), have no contraindications for MRI, have not been diagnosed with connective tissue disease, and do not have advanced left heart disease. The study has been approved by the Institutional Review Board (UMCIRB19-000708). Magnetic resonance (MR) imaging was performed with a Siemens Aera 1.5 Tesla MR machine. A total of 22 images (slice thickness of 8 mm and pixel spacing of 1.61 mm) were captured to obtain geometry in the proximal arterial and venous segments of the fistula. With the patient in the supine position, time varying velocity data, captured through the midplane of the AVF, was gathered using phase-contrast (PC) scans at 30 time points along the cardiac cycle (6 mm slice thickness and 1.77 mm pixel spacing). During the same imaging session, similar data were acquired for the pulmonary artery, as well as clinically standard cardiac measures. Patient files were anonymized prior to processing. MR images were imported into Mimics 20.0 (Materialise, Belgium) for model creation. A thresholding technique was used to segment the anatomical geometry captured in each MR slice and the “Calculate 3D” function was used to create a three-dimensional model of the highlighted region.

The model was then exported to 3-matic 15.0, where perpendicular cross-sectional cuts were created to define the inlet and outlets. A second geometry model was created by cutting the length of the proximal artery and proximal vein as shown in Figure 2. The length of the model was determined by multiplying the diameter of the proximal artery by 12. The 3-matic files were uploaded into ANSYS Workbench

22.1 (ANSYS Inc., USA) for discretization. Meshed using tetrahedral elements, the original and trimmed models were comprised of approximately 2.6 and 1.5 million elements, respectively. Orthogonal quality and skewness metrics were used to assess mesh quality [4].

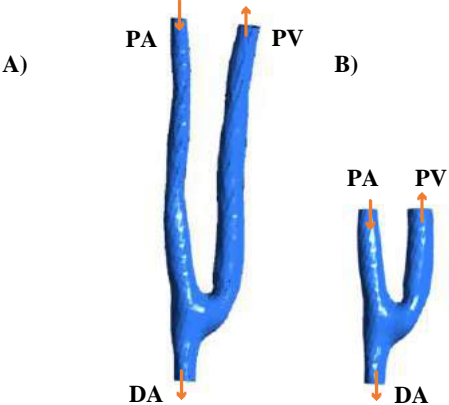


Figure 2: Three-dimensional AVF models. A) original (6.8 cm) B) trimmed (3.6 cm). PA = pulmonary artery (inlet), PV = pulmonary vein (outlet), DA = distal artery (outlet).

Blood was characterized as an incompressible, Newtonian fluid with viscosity of 3.2 cP and density of 1060 kg/m³ [5]. The distal artery and proximal vein were assigned relative pressure-based outlets at 0 Pa. The inlet, or proximal artery, boundary condition was defined by the patients-specific flowrate waveform from the MR data. The MRI waveform was created with in house MATLAB files to crop and isolate cross sections of the AVF from the MRI, segment the AVF cross sections across 30 timesteps in the cardiac cycle, and lastly multiply the segmented AVF cross section images with the phase part of the images to calculate fluid velocity. A rigid wall assumption and no slip boundary conditions at the wall were also applied. A double precision, second order, transient flow pressure-based solver was used for CFD analysis. Simulation time duration was calculated by multiply the RR interval, which is the time elapsed between two consecutive R waves of a QRS signal from an ECG, by three to achieve three full cardiac cycles.

RESULTS

The results only include one patient to date. By RHC, the patient had a mean AVF flow rate, mean pulmonary arterial pressure, and pulmonary capillary wedge pressure of 1.97 L/min, 46.5 mmHg, and 19 mmHg, respectively. Velocity streamline contours (Figure 2) and WSS measurements at peak systole (Table 1) are shown below.

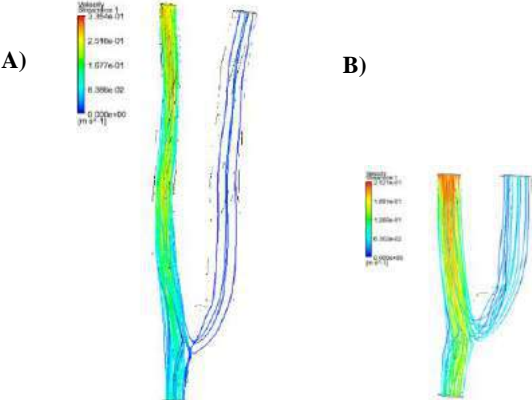


Figure 2: Velocity streamline of blood flow through the patient specific arteriovenous fistula at peak systole. The average inlet velocity was 17.6 cm/s. A) Original model. B) Trimmed model.

Table 1: Wall shear stress measurements at peak systole. Areas of low WSS were found along the proximal vein outlet.

Model	Minimum WSS (Pa)	Maximum WSS (Pa)	Distal Artery Area (cm ²)
Original	0.0006552	28.96	0.1652
Trimmed	0.0004122	24.44	0.1611

The original patient specific AVF model was seen to have relatively higher WSS values than the trimmed model. On the contrary, higher velocity values at peak systole were seen, specifically at the distal artery, for the trimmed model, 17.33 cm/s compared to 14.20 cm/s. The reduced vessel area of the distal artery of the trimmed model, seen in Table 1, can possibly explain the higher velocity, based on flow conservation.

DISCUSSION

Hemodialysis accounts for over 64% of renal replacement therapy plans for ESRD patients and requires the creation of an arteriovenous fistula [3]. While dialysis can work indefinitely to prolong patient’s lives, recent studies have suggested connections between fistula creation (size/shape) and the development of pulmonary hypertension.

Based on the results from the preliminary study, the trimmed model is potentially a viable option for a simplified AVF geometry. Similar flow patterns and WSS trends are present when comparing the two geometry models. However, additional quantitative measures of flow features should be considered. Furthermore, it is unknown if the observed difference in WSS is clinically or physiologically significant. Using a simplified geometry would allow for more rapid time to CFD solutions with minimal impact on the results [6]. These results are exploratory, only represent intermediate steps in the project, and do not provide any clinical value. Future work will include: 1) comparing computational AVF results to computational models of the pulmonary artery from the same patient and 2) examining the impact of fistula banding to control cardiac output and stress on the vessel walls.

There are many limitations to this study. The most evident being the small patient sample size, particularly due to difficult patient recruitment during the COVID-19 pandemic. The results presented include data from only one patient, which limits statistical interpretation of results. Additionally, the computational approach relies on several assumptions. Despite these limitations, a simplified *in-silico* approach could provide more accurate results with reduced computational cost. Overall, modeling fistula hemodynamics may elicit a link between fistulas and pulmonary hypertension; thus, identifying key monitoring parameters. Improved monitoring will allow physicians to intervene; thereby, preventing the development of pulmonary hypertension.

ACKNOWLEDGEMENTS

The authors would like to thank Constantin B. Marcu, MD for image acquisition. This work was supported in part by the Division of Research, Economic Development, and Engagement and Undergraduate Research and Creative Achievement Award, East Carolina University.

REFERENCES

[1] Webster, A et al., *The Lancet*, 389:1238-1252, 2017.
[2] Yigla, M et al., *Seminars in Dialysis*, 19:353-357, 2006.
[3] Quencer, K and Arici, M, *American Journal of Roentgenology* 205:726-734, 2015.
[4] Morris, P et al., *Heart (British Cardiac Society)*, 102:18-28, 2016.
[5] Sigovan, M et al., *Annals of Biomedical Engineering*, 41 (4): 657-658, 2013.
[6] Marshall, L., *Applied Math Modeling Inc.*, 2010.

IDENTIFIABILITY OF POROELASTIC MODEL PARAMETERS USING UNIAXIAL TENSION DATA: ROLE OF 3D STRAIN AND UNLOADING

John M. Peloquin (1), Dawn M. Elliott (1)

(1) Biomedical Engineering, University of Delaware, Newark, DE, USA

INTRODUCTION

Computer simulations of biological systems are attractive because a model constructed from experimental data can make predictions for complex physiologic conditions that are not experimentally accessible. However, extrapolating a model to conditions different from those used to construct it risks substantial error. Fits of model parameters to data are often non-unique because the data does not fully constrain the parameter values. The parameters are then *non-identifiable* and may perform excellently in the conditions used for model fitting, but cannot be assumed to generalize to novel conditions [1]. Because parameter identifiability is independent of goodness-of-fit, it must be verified separately. To address the lack of tools to verify identifiability in biomechanics, we recently developed open-source software for this purpose (github.com/jpeloquin/spamneggs), and found that confined compression stress relaxation tests do *not* provide identifiability for commonly used nonlinear poroelastic models [2].

In this study, we now turn our attention to uniaxial tension. Whereas confined compression is essentially a 1D test due to the confinement chamber, uniaxial tension has the potential to provide 3D data if the transverse (λ_y) and through-thickness (λ_z) strain ratios are measured as well as the longitudinal stress (σ_{xx}). This is almost never done. Most analysis is 1D. Sometimes, λ_y is reported, yielding 2D data. Nevertheless, we recently found that uniaxial tension of knee meniscus in a loading-unloading cycle with 3D strain revealed new aspects of how tension affects meniscus volume and fluid flow [3]. Here, we hypothesized that 3D data and unloading would also improve parameter identifiability for a constitutive model of meniscus tissue. The objective of this work, therefore, was to quantify and compare parameter identifiability for a poroelastic model of meniscus in four variations of the uniaxial tension stress relaxation test with increasing richness of the data: (1) loading ramp and hold with 1D data (σ_{xx}); (2) same + 2D data (σ_{xx} and λ_y); (3) same + 3D data (σ_{xx} , λ_y , and λ_z); and (4) same + unloading, unloaded recovery, and 3D data (σ_{xx} , λ_y , and λ_z).

METHODS

Global sensitivity analysis was used with FEBio finite element simulations to generate synthetic data for analysis of parameter identifiability in each of the 4 test variants. Axes, specimen dimensions, and output variables are defined in Fig 1a. Tension was applied in x, representing tension in the meniscus' circumferential fibers (Fig 1b). The simulated test protocol consisted of a loading ramp to 6.4% strain at 0.1 mm/s, a loaded hold (stress relaxation) for 600 s, unloading at 0.1 mm/s to 0% strain, and unloaded recovery for 1800 s (Fig 2a), matching our experimental work [3]. Analysis of test variants 1–3 used only the ramp and hold portions of the output.

Meniscus tissue was modeled as a poroelastic mixture of a Holmes–Mow (HM) solid, toe–linear fibers, and constant permeability (7 parameters total) [4,5]. Each material parameter was varied using 3-level full factorial sampling spanning the full range of literature values [4–7], generating 2,187 simulations. Borrowing techniques from genomics, parameter effects were quantified as “sensitivity vectors”, Pearson correlation coefficients between the parameter and each output variable at each time point. The uniqueness of each parameter's effect on the output variables, and hence its identifiability, was quantified for each test variant using cluster analysis and eigenvector analysis of the matrix of sensitivity vectors, with eigenvalues > 1% of the variance considered significantly nonzero, indicating practical identifiability.

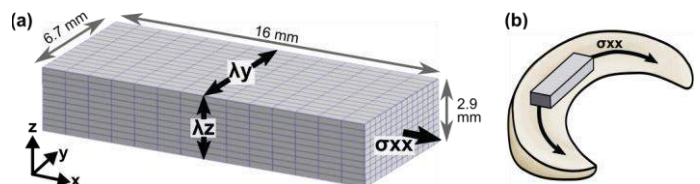


Figure 1: (a) Simulated specimen dimensions and output variables. (b) Relationship of simulation to meniscus physiology.

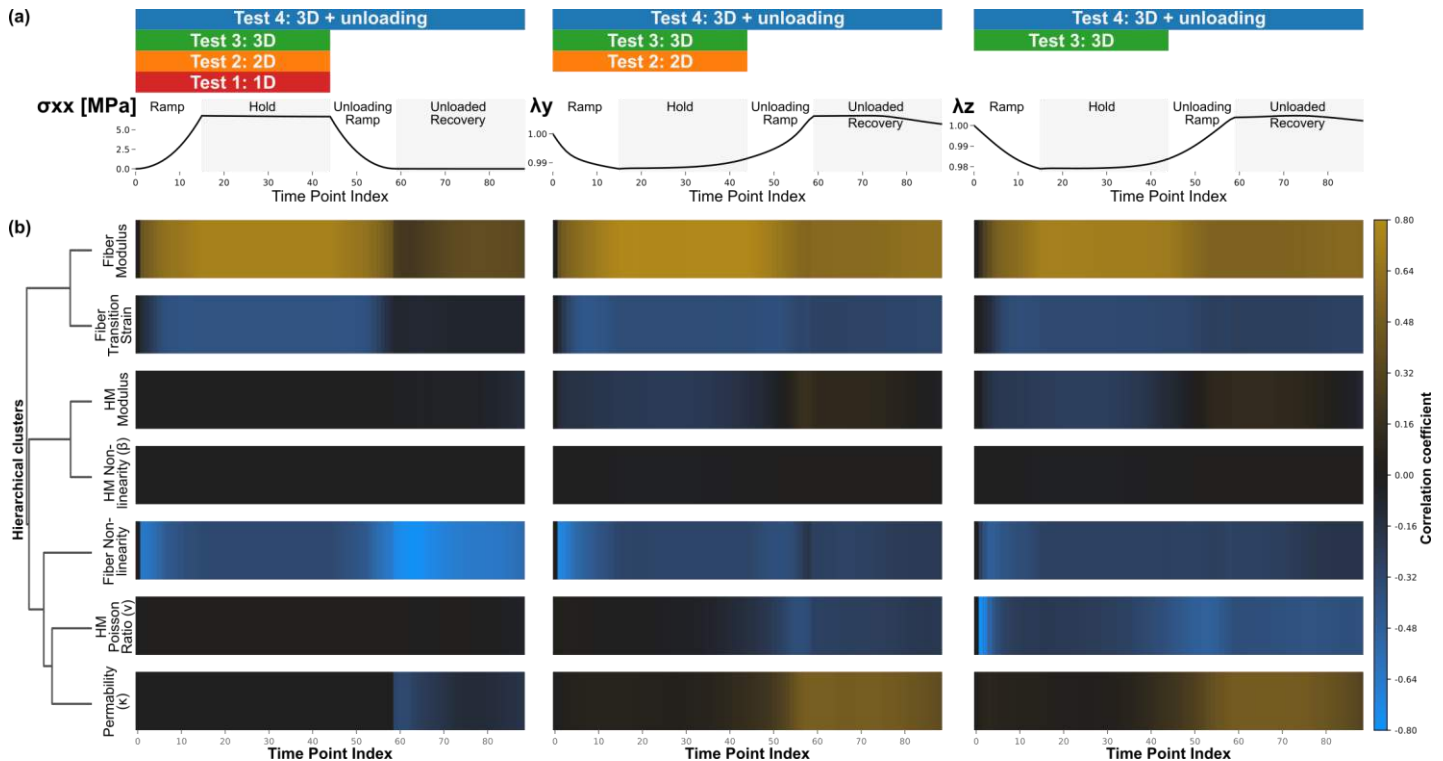


Figure 2: Parameter effects. (a) Representative simulation output. (b) Sensitivity vectors (correlation coefficients, r , between each parameter and each output variable (σ_{xx} , λ_y , & λ_z) across time and their cluster analysis (dendrogram, left). Subsets of this plot (top-edge labels) show parameter effects for the three test variants that used only the loading ramp and hold and a subset of variables.

RESULTS

The sensitivity vectors for test 4 (3D + unloading) showed that most parameters had distinctive effects on σ_{xx} , λ_y , and λ_z (Fig 2b). HM Poisson ratio (ν) appreciably affected only λ_y and λ_z , with little impact on σ_{xx} . Both ν and permeability (κ) had little effect on the loading ramp and hold, with their effects largely confined to unloading. Fiber modulus and transition strain were very similar in their effects. HM nonlinearity (β) had almost no effect. Parameter effects on λ_y and λ_z were slightly different, mostly with respect to ν and, more subtly, κ .

Eigenvector analysis, which also considers identifiability problems due to redundancy of multiple sensitivity vectors in combination, showed that identifiability suffered with the simpler test variants. Test 1 (loading & σ_{xx}) had only 3 eigenvalues > 0 , indicating that it only constrained 3 degrees of freedom in parameter space (Fig 3a). Adding λ_y data (test 2) yielded 5 eigenvalues > 0 (Fig 3b), and adding λ_z (test 3) yielded 6. Unloading was also beneficial as suggested by the unloaded-centric sensitivities for ν and κ , increasing the share of variance belonging to eigenvectors 2 through 6, aiding identifiability.

DISCUSSION

Use of 3D measurements (measuring both λ_y and λ_z) and unloading in uniaxial tension greatly improved identifiability of the nonlinear poroelastic model compared to simpler tests. Use of σ_{xx} and loading alone (test 1) only constrained 3 degrees of freedom, which is sufficient to fit the 3 fiber properties. Experienced modelers sometimes use 1D uniaxial tension data only to fit fiber properties, obtaining the other parameters from confined compression [e.g., 4], which is partly justified by the present results. However, confined compression does not constrain ν [2], so at least λ_y is needed in the uniaxial tension test.

With 3D data and unloading (test 4), uniaxial tension robustly supports identifiability of all parameters except HM nonlinearity (β). Confined compression did not allow identification of β either [2]; the parameter is in fact irrelevant with commonly used values for volume

strain < 30 –50% and may be ignored in most circumstances. When including 3D data but without unloading (test 3), all six relevant parameters are technically identifiable, but smaller eigenvalues 2–6 mean fit uncertainty will be larger (Fig 3c). Overall, these results demonstrate that 3D data is required to identify nonlinear poroelastic model parameters in uniaxial tension, and use of unloading data will further improve parameter identifiability.

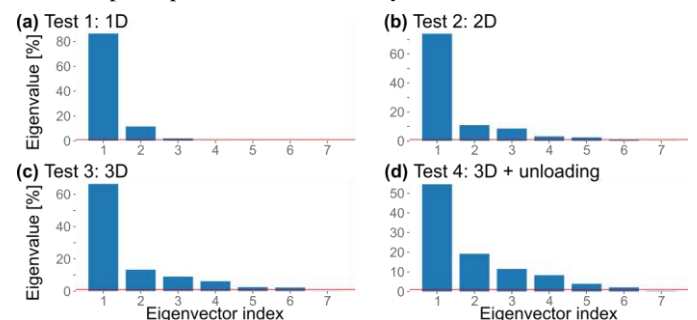


Figure 3: Eigenvalues of the parameter sensitivity vectors for each test variant. Larger eigenvalues indicate better identifiability.

ACKNOWLEDGEMENTS

NIH R01AR050052, P20GM139760, R01AR054620.

REFERENCES

- [1] Apgar, J et al., *Mol bioSyst* 6:1890–1900, 2010.
- [2] Pelloquin, J et al., SB3C 2022.
- [3] Pelloquin, J et al., *J Biomech Eng*. Submitted Jan 2023.
- [4] Upton, M et al., *Biomech Model Mechanobiol* 5: 140–149, 2006.
- [5] Tissakht, M., et al., *J Biomech* 28: 411–422, 1995.
- [6] Danso, E et al., *J Biomech* 48: 1499–1507, 2015.
- [7] Pelloquin, J et al., *J Biomech Eng* 138: 021002, 2016.

A NOVEL IMAGE-BASED COMPUTATIONAL FRAMEWORK TO EVALUATE THE MATERIAL PROPERTIES OF ARTERIAL TISSUE FROM HIGH-RESOLUTION MAGNETIC RESONANCE IMAGE DATA

Y.F. Jack Wang (1), Samer S. Merchant (1), Edward W. Hsu (1), Lucas H. Timmins (1,2)

(1) Biomedical Engineering, University of Utah, Salt Lake City, Utah, USA
(2) Scientific Computing and Imaging Institute, University of Utah, Salt Lake City, USA

INTRODUCTION

Atherosclerotic plaque rupture is responsible for a majority (>60%) of acute coronary syndromes (ACS), which affect millions of people each year [1]. These pathologic events are a significant problem, not only because of their frequency but also due to the challenge of stratifying risk for plaque rupture. Recent advancements in imaging techniques, such as intravascular ultrasound, offer methods to reliably identify high-risk plaques characterized by thin fibrous caps (<65 μm) and large necrotic cores [1]. However, the use of imaging for the prediction of plaque rupture has been proven not accurate. In particular, studies have shown that most high-risk plaques leading to ACS undergo rapid progression preceding the event, and they only precipitate an ACS if associated with sudden progression [2]. As a result, to improve clinical management decisions, plaque rupture risk-stratification strategies must move beyond image-based morphologic markers.

Plaque rupture is the direct result of material failure of the atherosclerotic tissue due to applied mechanical loads. Characterization of material properties of the arterial tissue and plaque constituents with *in vivo* imaging techniques holds tremendous promise in risk-stratifying coronary lesions. Ultrasound elastography and palpography have the potential to identify high-risk plaques. Nevertheless, their clinical impact has been limited due to the oversimplified assumptions for the analysis, including infinitesimal strain and uniform wall thickness. There remains a critical need to characterize the nonlinear and hyperelastic material behavior of the coronary environment. Accordingly, this study aimed to develop a novel image-based computational framework to evaluate the material properties of arterial tissue utilizing high-resolution magnetic resonance (MR) image data, which has the potential to be extended for *in vivo* imaging modalities.

METHODS

High-resolution Magnetic Resonance (MR) Imaging: MR imaging data were collected on excised healthy porcine carotid arteries

($n = 5$). A straight segment $\sim 35\text{mm}$ in length was cut from each specimen and then mounted to a custom MR-compatible apparatus that allowed controllable biaxial loading of the tissue during image acquisition. The device was connected to a height-adjustable saline fluid reservoir for pressurization, with an inline pressure transducer monitoring the lumen pressure. Using a T2-weighted TurboRARE sequence, MR images of the tissue were collected at axial stretch ratios of $\lambda_z^{\text{in vivo}} \pm 0.1$ at static pressure loads of 40, 80, and 120 mmHg (Bruker Biospin 7T MRI). In each sequence, 15 images across the center 10 mm region of the tissue were acquired over a 10×10 mm field-of-view (FOV) with an isotropic resolution of 80 μm (Fig. 1 A-B).

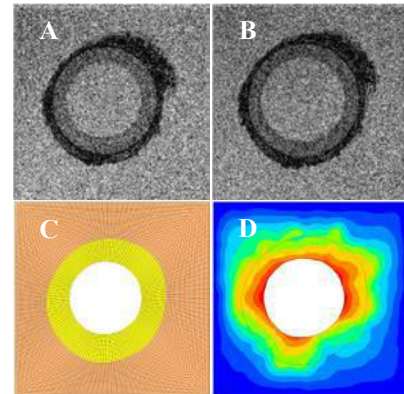


Figure 1: MR images of a porcine carotid artery at (A) $P = 40 \text{ mmHg}$ and (B) $P = 120 \text{ mmHg}$. (C) Template (unloaded) FE model constructed from A. (D) Deformed geometry and displacement magnitude derived from Hyperelastic Warping.

Deformable Image Registration: From the MR images, the strain fields across the deformation states were derived using a

deformable image registration technique termed Hyperelastic Warping [3]. This technique determined the deformation map that best aligned a “template” to a “target” image, where image data corresponded to MR data acquired at distinct lumen pressures. A finite element (FE) model was constructed that corresponded to the template image. The artery wall borders were manually segmented from the MR image (MATLAB, MathWorks, Inc). An outer buffer region, with dimensions of 10×10 mm, was added to provide tethering. The geometry was discretized with linear hexahedral elements (ANSA, BETA CAE Systems). To evaluate the impact of the constitutive model on the proposed framework, the arterial wall was described by either an isotropic or anisotropic strain energy function (SEF). The isotropic SEF (neo-Hookean) took the form,

$$\Psi_{iso} = C_1(I_1 - 3), \quad (1)$$

where C_1 is the material stiffness constant, and I_1 is the first invariant of the right Cauchy-Green deformation tensor. The anisotropic model featured a microstructurally-motivated SEF, which took the form,

$$\Psi_{aniso} = \mu(I_1 - 3) + \frac{k_1}{k_2} e^{k_2[(1-\rho)(I_1-3)^2 + \rho(I_4-1)^2]} - 1, \quad (2)$$

where μ describes the ground matrix stiffness, k_1 and k_2 capture the fiber stiffness, ρ is a measure of fiber dispersion, and I_4 is the fourth invariant of the right Cauchy-Green deformation tensor that describes two fiber families arranged symmetrically around the vessel [4]. The outer buffer region was defined as a compressible, neo-Hookean solid. Applied boundary conditions included pressure on the lumen surface and full constraint of the outer edges of the buffer region. Warping was performed in *FEBio Studio* (www.febio.org), and the first principal strain (E_1) fields were evaluated [5].

Material Parameter Optimization: A forward FE model, identical to the Warping model (Fig. 1C), was constructed and analyzed to quantify strain fields under loading. To determine SEF material parameters, the material parameter optimization module in *FEBio Studio* was employed to identify coefficients that minimized the difference between the forward FE and Warping model strain fields. The objective function was defined as,

$$e = \sum_{i=1}^N [(E_1^{FE} - E_1^{HW})_i^2], \quad (3)$$

where N is the element number and superscripts *FE* and *HW* denote the FE and Warping-determined values, respectively.

RESULTS

Hyperelastic Warping was successfully implemented to derive strain fields from MR images across static pressure loads from 40 to 120 mmHg. A representative Warping-derived strain field from the MR images shown in Fig. 1 A-B is presented in Fig. 2A. Across the 5 imaged tissues and 12 MR slices analyzed, it was observed that elements located on the inner arterial wall had larger deformation than those on the outer wall. For example, in the representative analysis, elements on the inner wall and outer wall had first principal strains of 0.102 ± 0.005 and 0.042 ± 0.009 , respectively (Fig. 2A).

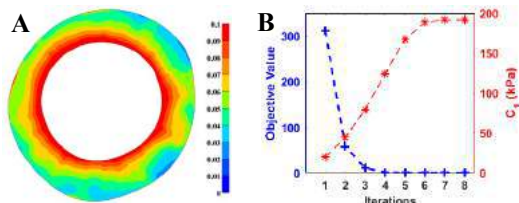


Figure 2: (A) Warping-derived first principal strain (E_1) field. (B) Representative objective function reduction as the material coefficient C_1 in the isotropic constitutive model was optimized.

Analysis of the optimization data indicated a reduction in the objective function value as best-fit material parameters were determined, with final objective values (e_{final}) of 0.24 ± 0.27 across all analyses (Fig. 2B). The best-fit material coefficients for the isotropic and anisotropic SEF when analyzing the center MR image slices across the 5 tissue samples are presented in Table 1. Variability across tissue samples (i.e., inter-sample variability) was evident. In addition, variability was observed when analyzing different MR slices from the same tissue sample (i.e., intra-sample variability). In one tissue sample, the isotropic material parameter, C_1 , ranged from 501.53 to 596.06 kPa across image data acquired in the proximal, central, and distal FOV. In that same sample, the anisotropic SEF parameters μ , k_1 , and k_2 had ranges of 3.81-12.20 kPa, 34.15-71.10 kPa, and 28.72-143.71, respectively. Lastly, analyzing image data across varying axial stretch ratios from the same tissue sample demonstrated that the framework could detect a stiffening of the tissue. For example, at axial stretch ratios of 1.8 and 1.9, the anisotropic SEF parameters μ , k_1 , and k_2 were 4.32 kPa, 34.43 kPa, and 18.58 and 7.65 kPa, 24.08 kPa, and 4.94, respectively.

Table 1: Estimated material coefficients

SEF	Coefficient	Value	e_{final}
Isotropic	C_1	424.66 ± 147.50 kPa	0.10 ± 0.09
Anisotropic	μ	6.16 ± 2.74 kPa	0.14 ± 0.14
	k_1	51.01 ± 14.93 kPa	
	k_2	14.75 ± 8.34	

DISCUSSION

In this study, we present an innovative approach to estimate arterial material properties directly from imaging data. Utilizing healthy porcine carotid arteries, we demonstrated the success and robustness of the framework by determining the material coefficients in isotropic and anisotropic SEFs for hyperelastic materials. Importantly, the derived material parameters demonstrate agreement with published reports on coefficients derived from experimental biaxial mechanical testing [4,6]. Moreover, intra-sample variations in the material parameter values observed across different locations and axial stretch ratios comply with previous observations [7]. We recognize that the presented framework must be validated across samples by comparing Warping-derived material coefficients to values derived from “gold standard” mechanical testing results, and these investigations are ongoing. Future studies that integrate this computational framework with clinical imaging modalities of coronary tissue have the potential to characterize the material properties of diseased arteries and examine their predictive values to risk-stratify human coronary lesions.

ACKNOWLEDGEMENTS

This research was supported, in part, by funding from the National Institutes of Health (R01 HL150608, LHT). We thank Dr. Stewart Yeoh at U of Utah’s Small Animal Imaging Core for the help on the MR image acquisition. We appreciate the *FEBio* development team for the assistance on Hyperelastic Warping and optimization modules.

REFERENCES

- [1] Virmani, R et al., *J Am Coll Cardiol*, 47(8 Suppl):C13-8, 2006.
- [2] Stone, GW et al., *N Engl J Med*, 364(3):226-35, 2011.
- [3] Veress, AI et al., *J Biomech Eng*, 124(6):734-41, 2002.
- [4] Holzapfel, GA et al., *AJP Heart CP*, 289(5):H2048-58, 2005.
- [5] Maas, SA et al., *J Biomech Eng*, 134:011005, 2012.
- [6] Karimi, A et al., *Proc Inst Mech Eng H*, 227(2): 148-161, 2013.
- [7] García A et al., *Med Eng Phys*, 33(6):665-676, 2011.

ASSESSING TRANSMURAL MYOCARDIAL PERFUSION IN HEALTHY AND DISEASED PIGS USING MULTI-SCALE COMPUTATIONAL MODELING

Victoria E. Sturgess (1), Alyssa Taylor-LaPole (2), Cooper M. Warne (3), Hamidreza Gharahi (4), Elaleh Rahbar (5), Johnathan D. Tune (3), Daniel Beard (6), C. Alberto Figueroa (1,4)

- (1) Department of Biomedical Engineering, University of Michigan, Ann Arbor, Michigan, USA
(2) Department of Mathematics, NC State University, Raleigh, North Carolina, USA
(3) Department of Physiology and Anatomy, University of North Texas, Fort Worth, Texas, USA
(4) Department of Surgery, University of Michigan, Ann Arbor, Michigan, USA
(5) Department of Biomed. Eng., Wake Forest University School of Medicine, Winston-Salem, North Carolina, USA
(6) Department of Molecular & Integrative Physiology, Ann Arbor, Michigan, USA

INTRODUCTION

There is a pressing need to understand perfusion and metabolic activity across the myocardium in health and disease. Metrics such as coronary flow can give a global view of myocardial perfusion and oxygen delivery. However, perfusion hemodynamic and metabolic patterns vary transmurally from the epicardium (outer-most layer) and the endocardium (inner-most layer). This local variation across the myocardium can be attributed to transmural differences in intramyocardial pressure. Transmural differences in hemodynamics and perfusion are key to understanding myocardial ischemia, which is more likely to occur in the endocardium than the epicardium [1]. Further, it is important to understand how transmural hemodynamics and regional perfusion change in response to risk factors such as obesity, which have previously been linked to disorders such as coronary microvascular disease and cardiac ischemia [2].

In this work, we studied transmural myocardial perfusion by combining two different multi-scale models: (1) a 1D nonlinear model of aortic flow and pressure and (2) a three-layer lumped parameter model (LPM) of myocardial perfusion. These models will be applied to study a control (lean) and a diseased (obese) Ossabaw porcine model. Each animal model is supported by a rich set of experimental data including aortic, ventricular, and coronary hemodynamics. The models are calibrated to match the available data for both pigs. In doing so, we are able to gain insight into quantities not readily available through experiments, such as flow waveforms in representative vessels in the endocardium and epicardium regions.

METHODS

Experimental Data: Two anesthetized Ossabaw pigs were used: a lean subject (34.1 kg), and a disease model of heart failure with preserved ejection fraction (HFpEF) (68.4 kg), obtained by a combination of high fat diet for 14 weeks and cardiac pacing for 4 weeks [3]. Pressure was measured in the left ventricle (LV) using a pressure-

volume transducer and in the descending aorta (DA) using a fluid filled transducer. Body weight, heart weight, cardiac output, and left anterior descending (LAD) coronary flow rates were collected for each pig (Figure 1). Microspheres were injected into the left atrium. Samples of the LV wall were divided into three equal layers and the number of microspheres in each layer was measured to estimate the relative perfusion ratios of the endocardium, midwall, and epicardium.

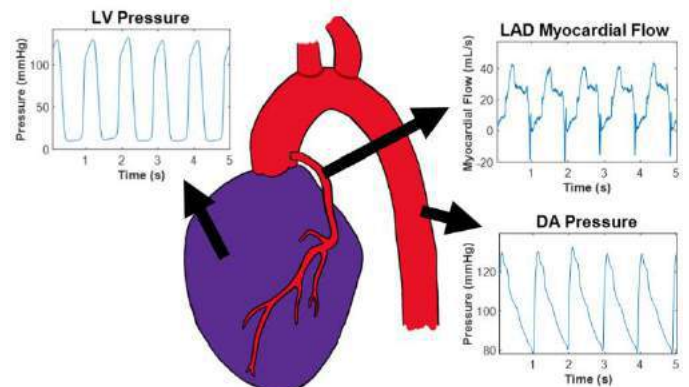


Figure 1: Experimental data included myocardial flow in the LAD and pressure recordings in the LV and descending aorta (DA)

Computational Models: A 1D nonlinear model of arterial pulse wave propagation was used to estimate ascending aorta (AA) pressure [4]. Then, a three-layered LPM of myocardial perfusion was used to study transmural flow [5,6].

- **Model 1:** The 1D model of pulse wave propagation requires an inflow waveform and impedance-based boundary conditions. A simplified aortic valve model was developed to iteratively estimate aortic inflow from the available LV pressure. Information on vessel diameters was obtained from a CT study. Circumferential stiffness

values were defined as a function of vessel radius using available literature data [7]. Stiffness values, aortic valve resistance, and vessel radii were iteratively adjusted to fit DA pressures while maintaining stroke volumes given by the experimental data.

Model 2: An LPM of myocardial perfusion with three parallel components representing the endocardial (ENDO), midwall (MID), and epicardial (EPI) layers of the heart was considered. Input data for this model are: LAD flow, AA pressure, LV pressure, and ENDO/EPI and ENDO/MID microsphere perfusion ratios. Parameters specifying resistance and relative compliance between the three layers (Figure 2) were iteratively adjusted to fit the available data.

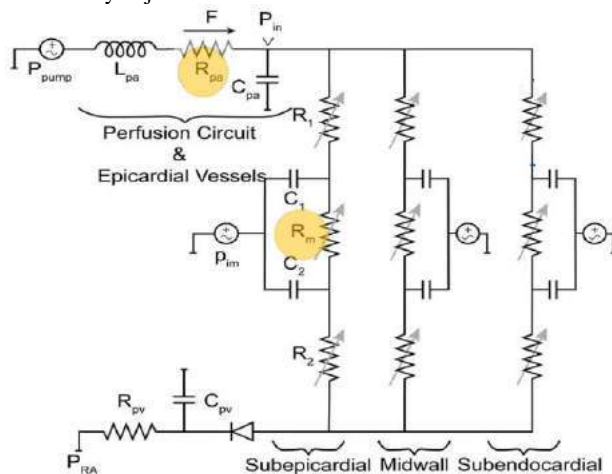


Figure 2: Three-layered LPM of myocardial perfusion. R_{pa} and R_m (highlighted in yellow) are two of the adjusted parameters.

RESULTS

Using the 1D flow solver with a simplified aortic valve model, we successfully estimated AA and DA pressures given the available data on LV pressure, cardiac output, stiffness, and vascular geometry (Figure 3). Computed DA pressures (dashed red line) matched well the experimental DA pressures (purple solid line).

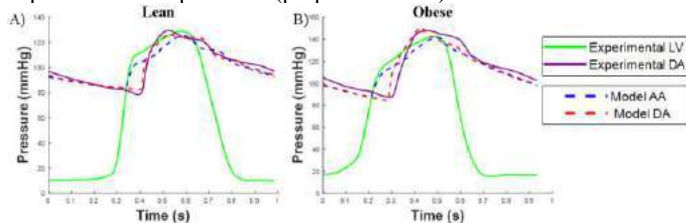


Figure 3: Results from 1D Model for (A) a lean pig and (B) an obese pig. Experimentally pressures shown with solid lines: LV (green) and DA (purple) pressure. Model results are shown with dashed lines: AA (blue) and DA (red) pressure.

Although lean and obese pigs had similar heart rates, mean blood pressure, and ENDO/EPI ratios, other quantities such as cardiac output, stroke volume, and average coronary flow rate were approximately two times larger in the obese pig. The fit of myocardial flow calculated by the LPM to the experimental data is shown in Figure 4 A-B, whereas transmural variations in flow are shown in Figure 4 C-D. For the lean pig, the computed EPI and ENDO mean flows were 9.00 and 8.89 ml/min (orange and blue lines, respectively). For the obese pig, computed EPI and ENDO mean flows were 18.25 and 17.33 ml/min. Both animals show high diastolic endocardial flow and a noticeable negative endocardial flow during late systole.

DISCUSSION

A 1D nonlinear model of arterial pulse wave propagation was used to estimate AA pressure by implementing a simplified aortic valve model and imposing the available LV pressure data. Model results of DA pressure were compared to known experimental data. This method was successful in producing realistic AA pressure waveforms while matching the expected stroke volumes.

Using the LPM of myocardial perfusion we simulated myocardial flow patterns while matching the available LAD flow waveforms and the measured ENDO/EPI and ENDO/MID ratios. Our myocardial flow patterns also reproduce previous work in showing that the endocardial layer experiences significant back flow in late systole [5, 6, 8].

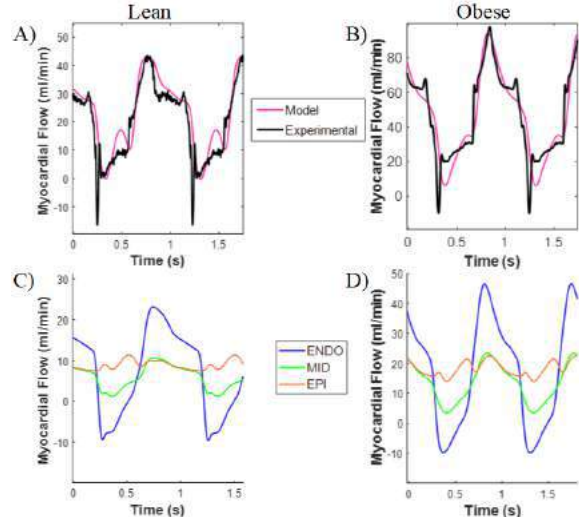


Figure 4: (A-B) LAD flow in Lean (A) and Obese (B) pigs- experimental data (black) and LPM model results (pink). (C-D) Computed endocardial (blue), midwall (green), and epicardial (orange) flows in lean (C) and obese (D) pigs.

Further, this work shows similar flow patterns between a lean and an obese pig with similar ENDO/EPI ratios, despite the obese model having an approximately double coronary flow rate compared to the lean model. A key limitation of this study is that we only explored one lean and one obese animal, with similar ENDO/EPI ratios. Future work is required to explore transmural flow differences in more diseased models, particularly in animals with low ENDO/EPI ratios. However, this work does suggest that the LPM myocardial model can be used to understand transmural flow patterns in models of obesity.

ACKNOWLEDGEMENTS

We gratefully acknowledge support from R01-HL158723 and R01-HL162633.

REFERENCES

- [1] Algranati, D et al. *Am J Physiol Heart Circ Physiol*, 300(3):H1090–H1100, 2011.
- [2] Bagi, Z et al. *Curr Vasc Pharmacol*, 12(3): 453–461, 2014
- [3] Tune et al. *Basic Res. Cardiol*, 117:50, 2022.
- [4] Olufsen, M et al., *Ann Biomed Eng*, 28:1281–1299, 2000.
- [5] Gharahi, H et al., *J Physiol*, 600:1913–1932, 2022.
- [6] Mynard, J and Smolich, J, *Am J Physiol Heart Circ Physiol*, 311: H11–H23, 2016.
- [7] de Beaufort, H et al. *Eur J Vasc Endovasc Surg*, 55(4): 560–566, 2018.
- [8] Fan, L et al. *Front. Physiol.*, 12, 2021.

EVALUATION OF HYPERTENSION AND INTRALUMINAL VASCULAR INJURY ON THE BIOMECHANICS OF THE MURINE FEMORAL ARTERY

J. Caleb Snider, Ph.D. (1), Zachary Tentor (2), Yujun Xu (1), Matthew R. Bersi, Ph.D. (1)

(1) Department of Mechanical Engineering and Materials Science
Washington University in St. Louis
St. Louis, Missouri, USA

(2) Department of Chemistry
University of Virginia
Charlottesville, VA, USA

INTRODUCTION

Peripheral artery disease (PAD) is a pervasive condition which is commonly undiagnosed but affects approximately 13% of the Western population aged over 50 years [1]. Individuals experiencing PAD commonly present with claudication (pain while walking) or critical limb ischemia, significantly reducing health-related quality of life. Major risk factors for PAD include diabetes mellitus and atherosclerosis, which exacerbate inward vascular remodeling and result in impaired blood flow to the extremities [2]. While complications from PAD may go undetected, the effects of diseased endothelium and excessive inflammation can accumulate over time and initiate different cell populations to alter vascular structure [3,4]. Thus, it is feasible that vascular adaptation depends on both vessel wall composition and type of injury, which may require different approaches to address healing.

In this study, we sought to characterize the remodeling of murine peripheral arteries in response to two types of vascular injury: 1) an angiotensin II (AngII) infusion model of hypertension [5] and 2) intraluminal mechanical injury [6]. We first characterized biaxial wall mechanics in the femoral artery and compared its behavior to that of another transitional artery – the common carotid. Initial comparisons revealed lower stored energy and axial stretch in femoral compared to carotid arteries, with stored energy correlating with vascular elastin content. Next, we observed differential remodeling of the femoral artery following hypertension and intraluminal injury. Namely, following AngII infusion, femoral arteries demonstrated minor, yet detectable, remodeling whereas after intraluminal injury, drastic alterations in meaningful metrics of vessel function (axial stretch, stored energy, and stiffness) were observed. As both wall structure and the type of injury influence vascular remodeling, it is important to assess the remodeling of transitional arteries under similar disease conditions to better understand the biomechanical factors contributing to PAD progression.

METHODS

Animal Models - Hypertension was induced in 11-13 week old, male, WT mice by Ang II infusion (490 ng/kg/min) for 14 days. Intraluminal mechanical injury of femoral arteries was performed in 21-23 week old *Rag1*^{-/-} animals through insertion of a 0.38 mm straight spring wire into the common femoral artery. The wire was left in place for 1 minute to denude and dilate the artery, and the arteriotomy was sealed via cautery following removal of the wire. Either 14 or 28 days after injury, femoral and carotid arteries were excised, cleaned of perivascular tissue, and prepared for biaxial mechanical testing.

Biaxial Mechanical Testing – Vessels were cannulated onto a custom computer-controlled mechanical testing device [7]. Specimens were placed in Hanks buffered physiologic solution and underwent 4 preconditioning cycles at approximately the *in vivo* axial stretch. Following estimation of the unloaded geometry and *in vivo* axial stretch, vessels were subjected to 3 cyclic pressure-diameter protocols (10 to 140 mmHg at 95%, 100%, and 105% of the *in vivo* axial stretch) followed by 4 cyclic axial force-length protocols from 0 to f_{\max} (with $f_{\max} = 5.5$ mN for femoral arteries and 15 mN for carotid arteries) at constant pressures of 10, 60, 100, and 140 mmHg. Axial load and vessel geometry were continuously recorded throughout the testing protocols for material parameter identification using the constitutive equation W :

$$W(\mathbf{C}, \mathbf{M}^i) = \frac{c}{2}(I_c - 3) + \sum_{i=1}^4 \frac{c_1^i}{4c_2^i} \left\{ \exp \left[c_2^i (IV_c^i - 1)^2 \right] - 1 \right\} \quad (1)$$

Here, W is used to model the contribution of an isotropic elastin and four families of locally parallel collagen fibers to the transmurally averaged material properties of the aortic wall. Material metrics of stress and stiffness can then be computed from first and second derivatives of W , respectively, with respect to an appropriate measure of strain.

Structural Characterization – Tested arteries were sectioned and histologically stained with AlexaFluor™ 633 Hydrazide to label elastic fibers. Vessel geometries were visualized by optical coherence tomography (OCT) volumes acquired using a commercially available system (Ganymede; Thorlabs, Inc.) with a center wavelength of 930 nm and an index of refraction of $n = 1.38$. Cross-sectional images from each vessel were used to calculate wall thickness based on radial projections from the inner to outer wall. Quantitative image analysis was performed using an adapted custom MATLAB script [8].

Statistical Analysis – Mechanical metrics were compared using either a Student's t-test for the AngII studies or one-way ANOVA for the intraluminal injury studies, respectively, with post-hoc Tukey HSD test for multiple comparisons.

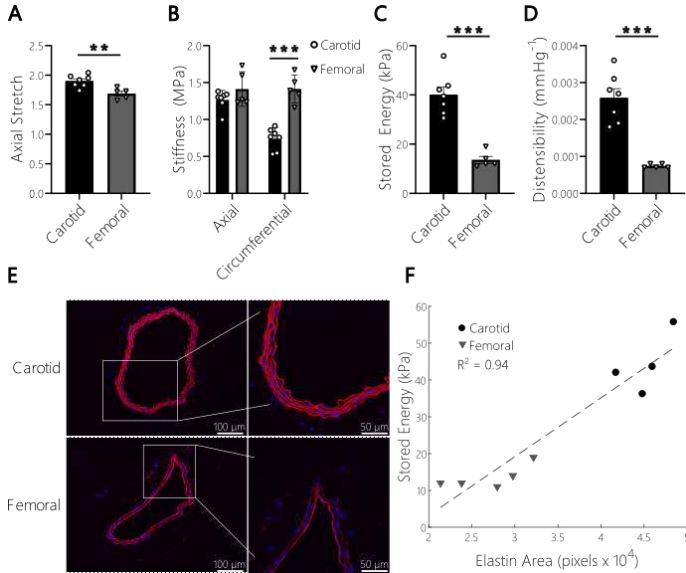


Figure 1: (A-D) Axial stretch, stiffness, stored energy, and distensibility of healthy carotids and femoral arteries. (E-F) Correlation of vascular elastin area and stored energy.

RESULTS

Biomechanical properties of carotid and femoral arteries are shown in Fig. 1A-D. Femoral arteries have a lower *in vivo* stretch and higher circumferential stiffness at 100 mmHg compared to carotid arteries ($p < 0.01$ and $p < 0.001$, respectively). Additionally, stored energy density and distensibility were both lower in femoral arteries ($p < 0.001$) than in carotids. Since we observed differences in circumferential vessel properties, we next quantified elastin area and observed a strong correlation between energy storage and vascular elastin content in these two arteries ($R^2 = 0.94$, Fig. 1E-F).

Mice were treated with AngII for two weeks to induce hypertensive vascular remodeling. While AngII-treated femoral arteries exhibited slightly decreased range of distension over physiological pressures and a left-shifted force-length curve (Fig. 2A, B), stiffness and stored energy values were similar to that of control vessels (Fig. 2C, D).

Following intraluminal mechanical injury, femoral arteries exhibited excessive remodeling and significant biomechanical alterations. In particular, overdistention injury led to increased vessel diameter and a significant loss of distensibility. These pronounced effects were observed as early as 2 weeks after injury and progressively worsened at 4 weeks after injury (Fig. 3A). Furthermore, injured vessels failed to elongate more than 10% before reaching f_{max} , indicative of pronounced axial remodeling (Fig. 3B). Energy storage dropped exponentially and was correlated with increasing vessel wall cross-sectional area, as measured by OCT (Fig. 3C).

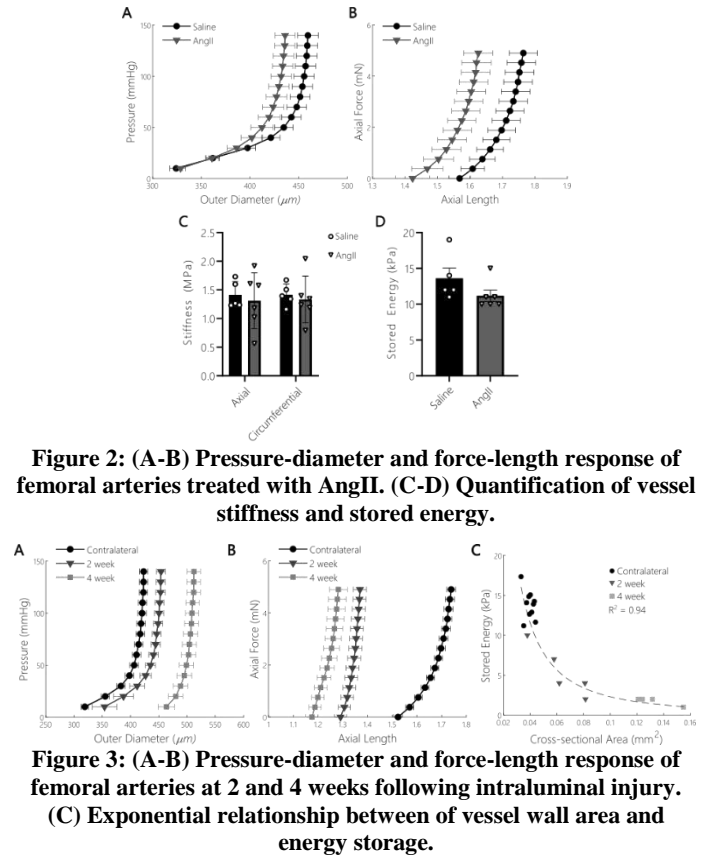


Figure 2: (A-B) Pressure-diameter and force-length response of femoral arteries treated with AngII. (C-D) Quantification of vessel stiffness and stored energy.

Figure 3: (A-B) Pressure-diameter and force-length response of femoral arteries at 2 and 4 weeks following intraluminal injury. (C) Exponential relationship between vessel wall area and energy storage.

DISCUSSION

Incomplete knowledge of the progression of vascular remodeling associated with PAD has limited the development of strategies to effectively improve the quality life for affected individuals. Current management strategies – particularly revascularization surgery to improve critical limb ischemia – warrants further investigation into the relationship with peripheral vessel remodeling [9]. Here, we utilized two models associated with the development of PAD, hypertension and intraluminal injury. To our knowledge, this is the first report of biaxial testing of murine femoral arteries, so we compared their mechanics to well-characterized carotid arteries [10]. Since the femoral arteries are more peripheral than carotids, they appear to have less need for storing energy to propel blood flow. Thus, minimal alterations in vessel behavior were observed in response to AngII-induced hypertension. However, following obliterative intraluminal injury, significant remodeling and neointima formation resulted in drastic alterations to vessel wall mechanics. These findings demonstrate the need to carefully consider both the primary driver of vessel injury (hypertension vs. mechanical injury) as well as the structure of the vessel wall (little vs. moderate elastin) and motivates a continued investigation into how these transitional arteries remodel under various conditions of interest.

ACKNOWLEDGEMENTS

This work was supported, in part, by NIH grant R00 HL146951 to MRB

REFERENCES

- [1] Morley, RL et al., *BMJ*, 360:j5842, 2018.
- [2] Mani, AM et al., *Int J Mol Sci*, 23(18):10715, 2022.
- [3] Bauersachs, R et al., *Cardiovasc Ther*, 2019:8295054, 2019.
- [4] Lin, S et al., *Front Pharmacol*, 13:1078047, 2022.
- [5] Daugherty, A et al., *JCI*, 105(11):1605-1612, 2000.
- [6] Sata, M et al., *JMCC*, 32(11):2097-2104, 2000.
- [7] Gleason, RL et al., *JBME*, 126(6):787, 2004.
- [8] Snider, JC et al., *Circ*, 143:1317-1330, 2021.
- [9] Campia, U et al., *Am J Med*, 132(10):1133-1141, 2019.
- [10] Bersi, MR et al., *Int J Adv Eng Sci Appl Math*, 4(4):228-240, 2013.

USABILITY OF LOW-COST 3D VISUALIZATION SHARING INTERFACES FOR CARDIOVASCULAR BLOOD FLOW DYNAMICS DATA

Zainab Husain (1,*), Noah Egnatis (1,*), Karol Calò (2), Diego Gallo (2), Umberto Morbiducci (2), Peter Coppin (3), David A. Steinman (1)

(1) Biomedical Simulation Lab, University of Toronto, Toronto, Canada
(2) The Department of Mechanical and Aerospace Engineering, Politecnico di Torino, Torino, Italy
(3) Perceptual Artifacts Lab, Ontario College of Art and Design University, Toronto, Canada
*Co-first authors

INTRODUCTION

Easy access to explore-able blood flow data (i.e., data that can be quickly visualized and adjusted to the user's liking) is crucial for the task of bridging technical gaps between communities and involving researchers from different disciplines in cardiovascular research. Especially when viewing complex 3D flows, and potentially multiple complementary flow properties simultaneously (e.g., isosurfaces and streamlines), it is beneficial, and often necessary, for the viewer to be able to alter the visualization independently, such as adjusting the camera angle and altering the plotting thresholds. Designing visualizations to allow for real-time interaction increases the viewer's agency [1] and more closely mirrors the medical data viewing experiences of clinically oriented research collaborators such as radiologists and medical imaging specialists [2].

While robust engineering 3D visualization tools such as Paraview can be used interactively, setup requires multiple steps, including the downloading of large data files and software; and the data interaction requires familiarity with the software's often-dense interface [3]. Researchers more familiar with medical imaging software can find this challenging or time-consuming [2] and, as a result, it is more commonplace to share 3D visualizations with these researchers as static 2D images due to ease of access (e.g., 2D screenshots through email), at the cost of the user's agency. Certain academic journals such as the Journal of Fluid Mechanics have very recently provided solutions to this problem through cloud-hosted Jupyter notebooks [4]. These solutions involve their own trade-offs, such as the fees associated with cloud-based hosting services and the resulting data size limits. The goal of this pilot usability study was to understand the practical trade-offs of free or minimal-cost strategies for sharing 3D flow visualizations, using helical flow in the aorta as an example use-case [5].

METHODS

An aortic helicity visualization was created from 4D phase-contrast MRI data, and was shared using 3 free or low-cost techniques: a Google Colab notebook, a Docker contained notebook, and a Flask webpage

[<https://github.com/Biomedical-Simulation-Lab/web-viz>]. Biomedical engineering researchers with varying computational/programming skill levels were surveyed after accessing data through each technique. Each technique was evaluated on ease of setup and interactivity for the user, and ease of deployment for the visualization developer (i.e., the authors). The data was preprocessed in Paraview, where velocity streamlines and local normalised helicity (LNH) values were computed and saved as VTK unstructured grid files (*.vtu) files. All techniques utilized the PyVista Python library as their visualization basis.

Technique 1: Google Colab: Google Colab is a type of Jupyter notebook hosted on Google's cloud servers. For setting up shareable visualizations on Colab, the developer must store the data in an online storage service (in our case, GitHub) and simply specify the data location within the notebook. This method is quick and free to deploy but is mainly suitable for lightweight datasets due to the processing limitations available on the free version of Colab.

From a user perspective, a visualization created on Colab can be accessed through a web-link and requires no software setup on the user's local computer. The visualization is displayed as a static 2D image that can be rapidly updated by the user after changing the parameter variables (view angles, LNH threshold, streamlines on/off) directly in the PyVista notebook's displayed code.

Technique 2: Docker (Containerized Notebook): Python visualization scripts typically require installation of dependent libraries and require the user to set up their computational environment. As well, running a Jupyter notebook on a local computer can result in hardware related graphics errors for 3D rendered objects. For this reason, it is considered best practice to run local notebooks within a container environment (here, we used Docker) to standardize visualization rendering for different computers and increase stability [6]. To set up the Docker visualization the developer is required to have knowledge of container-based development, such as creating Docker images (containing the notebook and the data) and pushing the images to Docker Hub.

For the user, this technique requires the most setup time and technical skill, requiring the installation of Docker software, and using terminal commands to start the container before the notebook can be viewed. In our survey example, participants adjusted parameters by editing the notebook code as in the Colab technique. However, the Docker technique has the added benefit of 3D object rotation, as the customizability of Docker allowed us to specify the necessary 3D graphics back-end libraries. There was no cost associated with this method.

Technique 3: Flask Web-page: Flask is a Python framework that can be used to build web applications. Utilizing a web-page to display visualizations requires all of the knowledge of the previous two techniques plus knowledge required to develop a web application (familiarity with HTML and JavaScript) and to deploy the application through a chosen cloud server (e.g. Heroku, AWS). For our survey example, the application was hosted on the Heroku cloud platform for a monthly cost of \$5 USD which would cover up to 1000 hours of usage/month.

The user is able to access the visualization through a web-link, rotate the object in 3D, and use intuitive widgets (e.g. sliders, check boxes) for changing thresholds or turning visualization elements on/off.

Table 1: Summary table of visualization techniques for developer (top) and user (bottom).

	Colab	Docker	Flask
Ease of development	Easy	Intermediate	Advanced
Cost for sample dataset	Free	Free	Priced
Rendering location	Server	Local	Server
User setup	Web link	Software download	Web link
Interface	Notebook	Notebook	HTML Webpage
Threshold adjusting	Editable code	Editable code	HTML widgets
Object rotation	replotable 2D	Mouse rotatable 3D	Mouse rotatable 3D

Survey Design: Study participants ranged in educational level from Master’s and PhD students, to postdocs and professors. Each participant was surveyed on their prior experience using the data exploration tools. Participants described their familiarity in 4 skill areas (Python, notebooks, terminal commands, and Docker) by categorizing themselves as either Novice (never used this tool), Beginner (occasionally used this tool) and Experienced (comfortable using this tool) for each of the skills. Ease of setup and interactivity was rated for each method on a 0 to 5 Likert scale, with 0 indicating inability to access the data, 1 indicating extreme difficulty and 5 indicating extreme ease. Participants were also asked their overall likelihood of using each method (unlikely, maybe, likely).

RESULTS

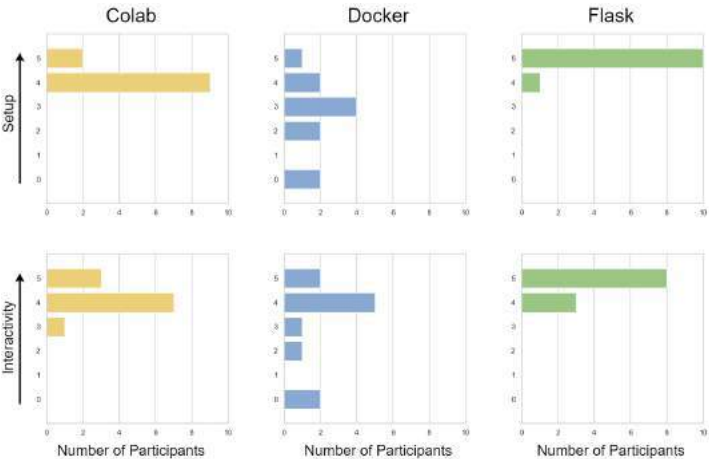


Figure 1: Survey results of setup and interactivity ratings for each data sharing technique.

Participants were generally Experienced at using Python, and Beginners at using notebooks and the terminal commands. Only 1 participant had prior experience using Docker. During the survey, all 11 participants were able to access visualizations shared through Flask and Colab. 2 participants were not able to access visualizations through Docker on their personal laptops due to technical challenges during installation. Flask had the highest average ratings for both ease of setup and interactivity. Docker had the lowest ratings for both categories. However, when asked their likelihood of using each data sharing method, only 4/11 responded likely to use Colab, compared to 7/11 for Docker and 11/11 for Flask.

DISCUSSION

One key question of interest for this study was to compare the preference of mouse rotate-able 3D objects in comparison to a 2D image that can be re-plotted by the user, the latter a low-tech solution which still allows some interactivity. However, the lack of interactive rotatability was reported as the main drawback to Colab by participants during the post survey discussion. While 3D objects do exist in some libraries available in Colab, 3D support is currently unstable and, in particular, is not recommended for dense meshes. We surmise that Google Colab could be a quick and preferred solution for rapid and low-cost sharing between colleagues, but not until there is stable 3D rendering support.

Initial setup of Docker containers was inconvenient for computer beginners due to difficulty installing and configuring on non-Unix based systems. This technique is well suited for situations involving processor-heavy visualizations and limited budget, as all computations are done locally rather than on a server. This places requirements on the user to have a suitable personal computer, which could be a viable option for motivated users for continued use.

Overall, users had a strong preference for quick setup time and rotatable 3D plots, as demonstrated by the clear popularity of the Flask web-page technique. The visual simplicity of the web-page displaying only the data plot and control widgets was also noted as a benefit by participants in comparison to the notebook/code interface, despite that fact the many users were themselves coders. This method also provides a high degree of customizability, and server hours can be scaled up as required. Indeed, during the Flask portion of the survey, multiple users accessing simultaneously caused server failure initially, and participant access had to be staggered. The estimated number of simultaneous users is therefore important to consider when determining computational resources to allocate for a web-page. This method would be the optimal solution for users with minimal technical background, and is a use case where it may be worth investing the extra time, money and effort for the developer.

For this pilot usability study, we desired to have all participants together online, hence it was limited to biomedical engineers due to the scheduling challenges for hospital-based clinical users. Lessons learned from this study will inform future testing with clinical users around the Flask web-page method, and consideration of the cost-benefit of more customizable paid cloud hosted notebook services, such as the Journal of Fluid Mechanics’ use of CoCalc [4].

ACKNOWLEDGEMENTS

This work was supported by a grant to DAS from the Natural Sciences and Engineering Research Council (RGPIN-2018-04649). ZH was also supported by a Barbara and Frank Milligan Fellowship.

REFERENCES

[1] Quam DJ et al., J Biomech Eng 2015;137(3).
[2] Temor L et al., Int J Comput Assist Radiol Surg 2022;17(6):11431154.
[3] Schroeder W et al., The vis toolkit. New York: Kitware, 2006.
[4] Meneveau C and Caulfield CP, J Fluid Mech 2022;952.
[5] Morbiducci U et al., Biomech Model Mechanobiol 2011;10:339–355.
[6] Merkel D, Linux J 2014;2014(239).

EFFECTS OF GLAUCOMA AND OPTIC NERVE CRUSH ON THE BIOMECHANICAL BEHAVIOR OF MOUSE ASTROCYTIC LAMINA CRIBROSA

A. Korneva (1), E. Kimball (1), T.V. Johnson (1), S. Quillen (1), M.E. Pease (1), T.D. Nguyen (2),
H. Quigley (1)

(1) Wilmer Eye Institute, Johns Hopkins University, Baltimore, MD, USA
(2) Department of Mechanical Engineering, Johns Hopkins University, Baltimore, MD, USA

INTRODUCTION

Elevation of intraocular pressure (IOP) in human and animal eyes deforms ocular tissues. The level of IOP is a risk factor in glaucoma, which is a chronic disease resulting in neurodegeneration of retinal ganglion cells followed by vision loss. Traumatic optic neuropathy, which occurs due to an acute injury to the optic nerve, also results in the neurodegeneration of retinal ganglion cells. The process of neurodegeneration is similar between chronic glaucoma and optic nerve injury. Furthermore, neuroprotection studies in animal models were similarly effective in nerve crush and elevated IOP models [1].

The purpose of the study is to compare these two models of retinal ganglion cell neurodegeneration in their biomechanical behavior of the astrocytic lamina cribrosa (AL). For the glaucoma mouse model, we used the microbead model of chronically elevated IOP [2]. For the traumatic optic neuropathy model, we performed optic nerve crush (ONC) in mice. We calculated the strain response to acute IOP elevations of the AL, and the evolution of the strain response 3 days to 6 weeks after the ONC or glaucoma.

METHODS

All experimental procedures were approved and monitored by the Johns Hopkins University School of Medicine Animal Care and Use Committee. Adult (5-8 month old) mice fluorescent in all cells were studied (heterozygous from crossing C57BL/6-Tg(CAG-EGFP)10Sb/J Jackson #003291 and C57BL/6J). One group of mice was subjected to ONC to model mechanical nerve injury, and another was subjected to the microbead injection model of glaucoma. Unilateral ONC was performed for 5 seconds with cross-action forceps, approximately 1 mm behind the eye globe. Unilateral microbead injection was performed to raise the IOP as in [1]. Mice were euthanized and their eyes were enucleated 3 days and 6 weeks after one of the surgical procedures. The fellow eyes of the microbead-injected eyes were used as control specimens. Sample sizes are in Table 1.

Mechanical testing was performed on enucleated eyes as previously described by raising the IOP from 10 to 30 mmHg [3,4]. Briefly, the anterior chamber of the eye was cannulated with a needle connected to fluid reservoir column. The microscopy system consisting of 2-photon laser source, Zeiss laser scanning microscope 710 was used to collect fluorescence signal from all cells expressing enhanced GFP in the AL. Two consecutive z-stacks were captured at 10 mmHg for calculation of errors. One of the stacks was warped (applied 3D strain) to later process and calculate the average absolute strain (E) error as $\sum(\sqrt{((E_{\text{applied}} - E_{\text{calc}})^2)})/N$ for every sample. A third z-stack at 30 mmHg was captured after 15 min equilibration. Post-processing of images and DVC algorithms were used [3-5]. After removing decorrelated data [3,4], the Green-Lagrange strains were calculated from the displacement gradients. Strain was calculated in the Cartesian coordinate system (E_{xx} , E_{yy} , E_{xy}), with x =nasal-temporal and y =inferior-superior axes, and in the cylindrical coordinate system (E_{rr} , $E_{\theta\theta}$, $E_{r\theta}$), and E_{zz} with z =optic nerve axis. The in-plane principal strains: maximum (E_{max}), minimum (E_{min}), and shear (γ_{max}) were calculated as well. The outer perimeter of the AL was traced by an ellipse. Specimen-average strain of the AL refers to the average of strain at all points within the outer ellipse of the AL. Central strain refers to the average of points within a central ellipse whose diameter equal half of the concentric outer ellipse's diameters. Peripheral strain refers to the average of points within the elliptical ring between the outer and central ellipses. Unpaired Student's t -tests were performed for statistical comparison of strain between two groups, with the significance level $p \leq 0.05$.

RESULTS

Specimen-average strain in 3-day glaucoma specimens was compared to the strain in control specimens. Glaucoma 3-day $E_{xx} = 0.046 \pm 0.028$ and $E_{\theta\theta} = 0.063 \pm 0.035$ tended to be greater than control $E_{xx} = 0.029 \pm 0.024$ and $E_{\theta\theta} = 0.030 \pm 0.028$, but the comparisons were

not statistically significant. Six weeks later, $E_{xx} = 0.025 \pm 0.008$ and $E_{\theta\theta} = 0.028 \pm 0.024$ in the 6-week glaucoma group were lower than in the 3-day glaucoma group and similar to the control group. The comparison of $E_{\theta\theta}$ between the 6-week glaucoma and the 3-day glaucoma groups was statistically significant ($p=0.03$, $n=8$ per group). The comparisons of other strain components were not significant.

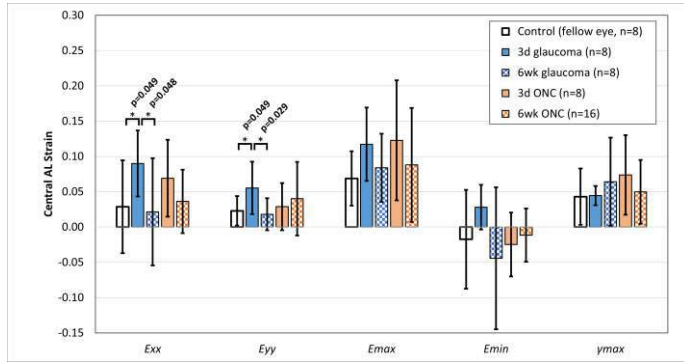


Figure 1: Bar graph of the Central Strain. E_{xx} and E_{yy} were greater in the 3-day glaucoma group compared to the control and the 6-week glaucoma groups. d=days, wk=weeks. * p -value ≤ 0.05 from Student's t -tests. Mean \pm stdev.

Table 1: Strain averaged in the central ellipse of the AL. Unpaired comparisons performed with Student's t -test, with significance level 0.05. * p -value ≤ 0.05 vs. control group. # p -value vs. 3-day glaucoma group. Mean \pm stdev.

	Control (n=8)	3-day glaucoma (n=8)	6-week glaucoma (n=8)	3-day ONC (n=8)	6-week ONC (n=16)
E_{rr}	0.025 ± 0.030	$0.066 \pm 0.038^*$	$0.016 \pm 0.043\#$	0.045 ± 0.045	0.031 ± 0.041
$E_{\theta\theta}$	0.027 ± 0.052	$0.080 \pm 0.044^*$	$0.024 \pm 0.054\#$	0.053 ± 0.039	0.045 ± 0.052
E_{xx}	0.029 ± 0.066	$0.090 \pm 0.047^*$	$0.022 \pm 0.076\#$	0.069 ± 0.054	0.036 ± 0.045
E_{yy}	0.023 ± 0.021	$0.055 \pm 0.037^*$	$0.018 \pm 0.023\#$	0.029 ± 0.033	0.040 ± 0.052
E_{zz}	0.005 ± 0.023	-0.001 ± 0.013	0.003 ± 0.030	0.016 ± 0.021	0.002 ± 0.023
E_{max}	0.069 ± 0.039	0.117 ± 0.052	0.084 ± 0.048	0.123 ± 0.085	0.088 ± 0.081
E_{min}	-0.017 ± 0.070	0.028 ± 0.032	-0.044 ± 0.101	-0.025 ± 0.045	-0.012 ± 0.038
γ_{max}	0.043 ± 0.040	0.045 ± 0.014	0.064 ± 0.063	0.074 ± 0.056	0.050 ± 0.045

Strains were averaged in the center of the AL. The central strain of 3-day glaucoma specimens were compared to the central strain of control specimens. Central strain calculated in the cylindrical coordinate system, E_{rr} , $E_{\theta\theta}$, and in the Cartesian coordinate system, E_{xx} , E_{yy} , were statistically greater in the 3-day glaucoma group compared to the control

group (Figure 1, Table 1). The maximum and minimum principal strains in the central region of the AL, E_{max} and E_{min} , tended to be greater than control, but the comparisons were not statistically significant (Table 1). Six weeks later, central E_{rr} , $E_{\theta\theta}$, E_{xx} , and E_{yy} , in the 6-week glaucoma group were lower than in the 3-day glaucoma group and similar to the control group. The comparison of central E_{rr} , $E_{\theta\theta}$, E_{xx} , and E_{yy} , between the 6-week glaucoma and the 3-day glaucoma groups were statistically significant ($p < 0.05$, $n = 8$ per group).

Specimen-average strain in 3-day ONC specimens was compared to the strain in control specimens. ONC 3-day $E_{xx} = 0.065 \pm 0.055$, $E_{\theta\theta} = 0.067 \pm 0.047$ tended to be greater than control $E_{xx} = 0.029 \pm 0.024$ and $E_{\theta\theta} = 0.030 \pm 0.028$, but the comparisons were not statistically significant. Six weeks later, $E_{xx} = 0.031 \pm 0.032$ and $E_{\theta\theta} = 0.037 \pm 0.040$ in the 6-week ONC group were lower than in the 3-day ONC group and similar to the control group. The comparisons of these strain components, E_{xx} and $E_{\theta\theta}$, between the 6-week ONC and the 3-day ONC groups were not statistically significant. Central and peripheral strain in the 3-day ONC group and in the 6-week group were compared to the respective strain in the control group. The central and peripheral strain components after ONC were similar to the central and peripheral strain components in the control group.

DISCUSSION

The strain response of the AL to IOP was greater in the 3-day glaucoma group compared to the control specimens. This was statistically significant in the central region of the AL. Six weeks later, the strain response in the glaucoma specimens became similar to the strain response of the control specimens. These results were similar to our previous findings in mice of a different genetic background [3]. In this mouse model of glaucoma, astrocytes lose the connections to their peripheral basement membrane at the sclera within 3 days. These connections were re-established 6 weeks later [6]. Studies using the rodent glaucoma model of IOP elevation reported similar structural changes in astrocyte structure [7,8]. This transient change in the astrocyte structure may contribute to the transient changes in the strain response. The increase in the strain of the AL seen in the glaucoma eyes at 3 days were not present in ONC specimens, neither 3 days nor 6 weeks after ONC. The limitation of the ONC procedure is the high variability in the degree of neurodegeneration across samples. Nevertheless, our findings suggest that the effect on the AL strain response with 3-days of glaucoma model is not primarily due to axon degeneration in the optic nerve head. Axon loss due to ONC does not significantly alter the mechanical response of the astrocytic network in the AL.

ACKNOWLEDGEMENTS

This work was supported by National Institutes of Health grants from the National Eye Institute, R01EY02120 and the Center Core Grant P30EY01765.

REFERENCES

- [1] Welsbie, D.S. et al., *Proc Natl Acad Sci* 110:4045-4050, 2013.
- [2] Cone, F. et al., *Exp Eye Res* 99:27-35, 2012
- [3] Korneva, A. et al., *J R Soc Interface* 17:173, 2020.
- [4] Korneva, A. et al., *Acta Biomater* 2022.
- [5] Bar-Kochba, E. et al., *Exp Mechanics* 55:261-274, 2015.
- [6] Quillen, S. et al., *PLoS ONE* 15:8: e0238104, 2020.
- [7] Sun, D. et al., *J Comp Neurol* 516:1-19, 2009
- [8] Tehrani, S. et al., *PLoS ONE* 11:11 :1-22, 2016.

AUGMENTED REALITY VISUALIZATION OF BIOMECHANICAL WALL STRESSES ON ABDOMINAL AORTIC ANEURYSMS USING ARTIFICIAL INTELLIGENCE

Timothy K. Chung (1), Nathan L. Liang (4,5), David A. Vorp (1,2,3,4,6,7,8)

- (1) Department of Bioengineering, University of Pittsburgh, Pittsburgh, Pennsylvania, USA
(2) Department of Mechanical Engineering and Materials Science, University of Pittsburgh, Pittsburgh, Pennsylvania, USA
(3) McGowan Institute for Regenerative Medicine, University of Pittsburgh, Pittsburgh, Pennsylvania, USA
(4) Department of Surgery, University of Pittsburgh, Pittsburgh, Pennsylvania, USA
(5) Division of Vascular Surgery, University of Pittsburgh Medical Center, Pittsburgh, Pennsylvania, USA
(6) Department of Chemical and Petroleum Engineering, University of Pittsburgh, Pittsburgh, Pennsylvania, USA
(7) Department of Cardiothoracic Surgery, University of Pittsburgh, Pittsburgh, Pennsylvania, USA
(8) Clinical and Translational Sciences Institute, University of Pittsburgh, Pittsburgh, Pennsylvania, USA

INTRODUCTION

Abdominal aortic aneurysm (AAA) is a condition where the terminal aorta begins to dilate more than 50% of the arteries original size [1]. AAA will continue to grow until the diameter reaches a maximum diameter (5.0 cm for women or 5.5 cm for men) or a patient experiences rupture. However, the maximum diameter criterion has been reported to have a high false positive rate, as many aneurysms below the threshold experience rupture events (~13-23.4% have been reported [3].

There are two central hypotheses that have been investigated to understand AAA rupture: 1) The aneurysm wall or material begins to weaken, and rupture occurs within a normal range of systolic blood pressure (120 mmHg), or 2) an elevated wall stress due to hypertensive systolic blood pressure exceeds the aneurysm wall. Interrogation of material properties of aneurysmal tissue and intraluminal thrombus (ILT) have been performed to develop material models. The previously developed material models have been incorporated into computational models to assess the biomechanical wall stresses of patient-specific AAA. These techniques are often reserved biomechanics experts and are inaccessible in a clinical setting but may potentially provide greater insight for clinicians to assess patient aneurysms than the current standard of care using the maximum diameter criteria.

The advent of widely available artificial intelligence software packages/toolkits and hardware (cloud-based computing and graphics processing units) present a viable pathway to enable stress-analysis into a clinical setting. In previous work, an artificial intelligence framework was developed to predict wall stresses using trained machine learning (ML) models from automatically segmented medical images using a trained convolutional neural network (U-NET), **Figure 1** [3]. However, the major limitation was the low sample size ($n = 10$), and the limitation of the ML training approach that incorporated the testing dataset.

This study presents an expansion of the stress-prediction ML training approach and incorporates a rendering pipeline to visualize the biomechanical wall stresses of patient-specific AAA using an augmented reality system,

the Microsoft HoloLens 2 (Microsoft Inc., Redmond, WA, USA). A recent push of creating a visualization layer to interact with data (metaverse) has garnered interest for the potential to use a combination of approaches to maximize the utility of medical imaging and biomechanics. This approach may enable clinicians without biomechanics expertise to view the wall stresses on patient aneurysms without adding significant time to their clinical workflow.

METHODS

A total of 274 deidentified patient medical images from a larger cohort was delivered by the Health Research Record Request (R3), an honest broker service provided by the University of Pittsburgh Department of Bioinformatics. The computed tomography (CT) images were manually segmented to extract the lumen and aneurysm wall. The point-clouds from the segmented images were used to create a computational mesh that included three distinct regions (aneurysm wall, lumen, and ILT). Computational wall stress analysis was performed

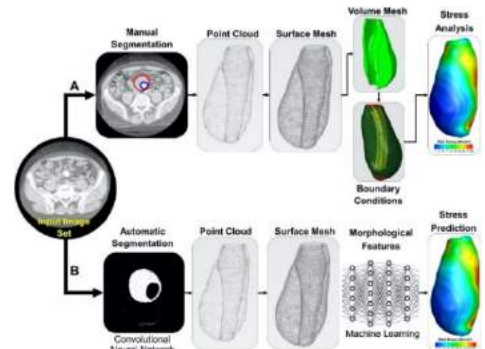


Figure 1: A) Tradition stress analysis pipeline for stress analysis and B) automatic segmentation and wall stress prediction using AI.

using Abaqus Standard (Dassault Systemés, France) using a well-established methodology using material models for the ILT and aneurysm wall [4, 5]. The results from the wall stress analysis were served as the ground truth dataset for the development of the ML model. Machine Learning Approach to Predict Wall Stresses: A custom data preparation MATLAB (MathWorks Inc., Natick, MA) script was used on the entire cohort that included various clustering and labeling methods developed in a previous study [3]. This included computing a neighborhood of principal curvature values, computing the ILT thickness, and retrieving the position of a node relative to the origin of the aneurysm surface placed at (0, 0, 0) in Cartesian coordinates. The last column of the prepared dataset was the computed nodal Von Mises wall stress. The training and testing datasets were split 75% (n = 206 patients) and 25% (n = 68 patients) randomly. Various ML models were selected for training to include ‘representative’ models tree-based, ensemble boosted trees (XGBoost), and neural networks. After the models were trained, the testing dataset was input into the model and compared to the ground truth wall stress values by computing the RMSE, R^2 , and Pearson statistics of a linear fit for each model to assess performance. To understand the effect of certain variables, ILT thickness was removed and neighborhood of principal curvatures in attempts to reduce the number of total variables used in the model. Augmented Reality Pipeline for Visualization: The predicted wall stresses and base geometry from the nodal positions in Cartesian coordinates were used to render a 3D model that can be visualized in the HoloLens 2 system. The total number of nodes were reduced to 20,000 and the wall stress predictions were and ‘baked’ into a rendered 3D model and exported into the cloud for visualization. The embedded software application in the HoloLens 2 app was used to visualize and interact with a patient’s AAA.

RESULTS

The representative trained ML models were tested, and the results were tabulated (Table 1). The highest performing model was the

Table 1: Reporting average wall stresses, RMSE, R2, and linear trendline slope of stress predictions vs. ground truth.

Model Name	Avg Stress N/cm²	RMSE	R²	Slope
Ground Truth	2.65 ± 5.63	-	-	-
Linear Regression	3.21 ± 5.13	3.41	0.56	0.80
Bagged Trees	3.28 ± 5.72	3.16	0.70	0.93
Coarse Trees	3.28 ± 5.84	3.34	0.67	0.93
Neural Network	3.33 ± 5.86	3.23	0.70	0.95
Boosted Trees	3.16 ± 5.40	2.99	0.69	0.88

neural network that had an R^2 closest to 0.70 and a slope of 0.95 of a linear fit that underestimated the wall stresses by 5% overall. It can also be qualitatively seen that the wall stress predictions for the neural network best mimicked the heat map of the ground truth wall stress analysis (Figure 2). The poorest model was the linear regression model (non-ML) that failed to provide any of the banding found in the ground truth models. It was also found that the residual plots (not shown) pertinent to using all variables

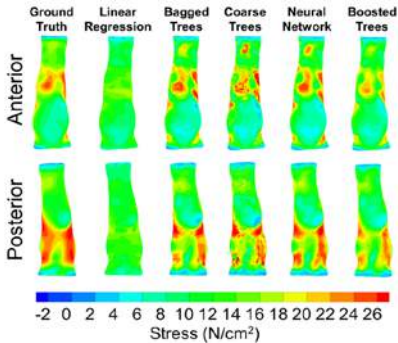


Figure 2: Anterior and posterior views of the ground truth stress map and the predicted wall stress maps from trained ML models.

performed better than the models trained without ILT thickness and node neighbors of principal curvatures with respect to RMSE, R^2 , and slope from a linear fit. The wall stress predictions took on average of 2 seconds with an additional 3 seconds for the rendering pipeline to be performed using a local workstation with an NVIDIA (NVIDIA Inc. Santa Clara, CA USA) A5000 GPU.

DISCUSSION

This study presented the expansion of wall stress predictions by increasing the number of patient cases by 20-fold for training (n = 206). The current study was able to predict the wall stresses using an unseen testing dataset (n = 68) with relatively high accuracy when compared to the ground truth results from traditional stress analysis. However, the best performing model, the neural network still underestimated the wall-stresses by 5% on average. In addition to wall stress predictions, a method to render and view 3D stress maps in HoloLens 2 was also created for potential future use for clinicians to assess a patient’s aneurysm. Previous studies have developed physics-based neural-network approaches to compute stresses in models [6] with high accuracy to investigate a wide range of organs. The potential to generalize an approach may enable such systems to be used for all types of systems within the body (cardiovascular, organ, musculoskeletal, etc.). Although this type of approach is appealing, a reliance remains on experimentally validated biomechanical behavior of such systems within the body that must be continually explored and evaluated. Accelerating biomechanics with AI may provide augmented reality systems the necessary engine for adoption into the clinic without the need for engineering expertise.

There are limitations to the presented study. The number of cases increased but still underestimated the overall stress at each point within the surface of the aneurysm. The expansion of the 3D image-reconstruction using various deep learning techniques was not presented but remains necessary for confirming the accuracy of wall stress predictions directly from CT images. It is unclear whether 206 patient cases are sufficient for training, or if an increased sample size is required to improve overall accuracy of the model. After a suitable sample size for training is found, an expedited feedback process to re-run stress analysis on newly developed material models from experimental measurements may allow for continual updates to the ML stress prediction models.

Future work will expand on the previously trained 3D image classification model from the ground truth manually segmented images from this study. Additional datasets will be incorporated to understand the effect of increasing the sample size with accuracy of the stress prediction models. Lastly, the technology and ability to view the biomechanical wall stresses on patient-specific aneurysms will be tested by clinicians to receive critical feedback with regards to the methodology presented in this study.

ACKNOWLEDGEMENTS

This study was supported by University of Pittsburgh Clinical and Translational Science Institute (via the National Institutes of Health through Grant Number UL1TR001857), Center for Medical Innovation at the University of Pittsburgh Swanson School of Engineering Pilot Award, Pittsburgh Super Computing Neocortex, and NVIDIA Hardware grant. We would also like to acknowledge Jason Lee, Sean May, Christian Hangey, and Aakash Kottakota, undergraduate research interns funded by the Swanson School of Engineering and the University of Pittsburgh Office of the Provost.

REFERENCES

[1] Vorp, D *J Biomech*, 40:1887-1902, 2009. [2] Kontopodis, N et al., *fsurg*, 3, 2016 [3] Chung, T et al., *J apples*, 10, 2022. [4] Wang, D et al., *JVS*, 36:598-604,2002. [5] Vande Geest, J., *J Biomech*, 39:1324-1334, 2006. [6] Zhang, W et al, *J CMA* 394, 2022.

BIAXIAL CONTRACTILITY OF THE MURINE CERVIX WITH ELASTIC FIBER DEFICIENCY

Mari J.E. Domingo (1), Avery G. Franques (2), Qinhan Zhou (3) Kristin S. Miller, PhD (3,4,5)

- (1) Department of Biomedical Engineering, Tulane University, New Orleans, LA, United States
- (2) Department of Cell and Molecular Biology, Tulane University, New Orleans, LA, United States
- (3) Department of Bioengineering, University of Texas at Dallas, Dallas, TX, United States
- (4) Department of Mechanical Engineering, University of Texas at Dallas, Dallas, TX, United States
- (5) Department of Obstetrics and Gynecology, University of Texas Southwestern Medical Center, Dallas, TX, United States

INTRODUCTION

Preterm birth, defined as fetal delivery before 37 weeks gestation, affects 11% of births globally [1]. Cervical insufficiency is a form of spontaneous preterm birth marked by premature dilation and shortening of the cervix. While the etiology of cervical insufficiency is unknown, improper elastic fiber and smooth muscle cell (SMC) remodeling may contribute [2, 3]. Cervical SMCs are critical to maintain contractile behavior and cervical shape [4]. Multiple proteins, such as Fibulin-5 (*Fbln5*), are involved in proper elastic fiber formation which allows the cervix to stretch and recoil [5]. In the vagina and blood vessels, disruption of elastic fibers resulted in lower contractility [6, 7]. However, the relationship between elastic fibers and SMCs in the cervix remains unknown. Therefore, the objective of this study is to leverage the cervixes of *Fbln5* global knockout mice to quantify multiaxial contractility.

METHODS

Animal Care. 28 nulliparous C57BL6 x 129SvEv female mice aged 3–6 months at estrus were used (Tulane IACUC approved). Mice were divided into groups based on genotype wherein $n=10$ mice were wildtype (WT) controls with both copies of the *Fbln5* gene, $n=10$ were heterozygous (HET) mice with one copy of the *Fbln5* gene, and $n=8$ were knockout (KO) mice with *Fbln5* deficiency. ***In Vivo* Contractility.** To determine *in vivo* contractile behavior, transcervical measurements were taken in WT ($n=5$), HET ($n=5$), and KO ($n=3$) female mice at estrus. Mice were anesthetized with 2% isoflurane mixed with 100% oxygen. A 2F Millar catheter was inserted into the vaginal canal until the cervix was reached. The presence of phasic contractions indicated proper placement in the cervix. The catheter was equilibrated in the cervix for five minutes, followed by five minutes of recording in which the baseline pressure, contractile pressure, and contraction frequency were measured (Fig 1A). **Specimen Preparation.** A separate group of mice ($n=5$ /genotype) at estrus were sacrificed via guillotine to

preserve SMC viability. The cervix was dissected from the reproductive tract and cannulated onto a biaxial extension inflation device in Krebs' Ringer Buffer (KRB). The estimated physiologic length was determined following the assumption that soft tissues seek to preserve a constant force over a range of physiologic pressures [9]. Five cycles of preconditioning were performed to achieve consistent and repeatable results [7, 8]. SMCs were preconditioned by inducing contractions with 20 mM of potassium chloride (KCl). ***In Vitro* Contractility.** After SMC preconditioning, the bath was replaced with fresh KRB, and the tissue was equilibrated for 10 minutes. Next, 10 mM of KCl was added to the bath, and the tissue contracted for five minutes. The changes in outer diameter and axial force were recorded. After five minutes, the bath was replaced with fresh KRB, and the tissue was equilibrated for five minutes. This process was repeated for KCl doses of 15–100 mM. **Data Analysis.** Circumferential contractility was determined as the change in outer diameter from the resting to the contracted state. Axial contractility was defined as the change in force measured by the force transducer. **Statistical Analysis.** For the statistical analysis described herein, the Shapiro-Wilks test indicated that the error of the data was normally distributed. Statistics were performed by hypotheses. Paired t-tests determined differences between the *in vivo* baseline and contractile pressure within each genotype. Next, a one-way ANOVA evaluated the effect of the *Fbln5* genotype on the *in vivo* baseline pressure, contractile pressure, and contractile frequency, followed by Tukey's post hoc test. To determine if the concentration of KCl and *Fbln5* genotype influenced contractility, a two-way ANOVA (dose, genotype) evaluated changes in outer diameter and axial force. Post hoc t-tests with Bonferroni corrections were utilized when appropriate.

RESULTS

***In Vivo* Contractility.** The paired t-tests determined the maximum contractile pressure significantly increased from the baseline pressure in the WT ($p=0.007$) and HET ($p=0.029$). However, there was no

significant difference between the baseline and maximum contractile pressure in the KO group. A one-way ANOVA showed significant baseline pressure differences ($p=0.02$) between genotypes. Post hoc testing showed that the KO baseline pressure (6.73 ± 2.90 mmHg) was significantly lower than the HET (12.1 ± 1.58 mmHg) baseline (Fig 1B). No significant differences were identified in maximum contractile pressure or frequency.

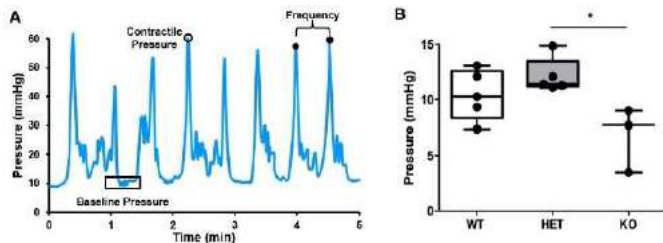


Figure 1: *In vivo* cervical contractility. (A). Representative recording of *in vivo* pressure measurements. Average pressure between contractions determined the baseline pressure (black box). The peak of each contraction (black open circle) was averaged to determine the maximum contractile pressure. Time from peak to peak determined the frequency of contraction (black closed circles). (B). Mean *in vivo* baseline pressure in the WT ($n=5$), HET ($n=5$), and KO ($n=3$) cervix. The KO cervix (6.7 ± 2.9 mmHg) was significantly ($p=0.02$) lower than the HET (12.1 ± 1.5 mmHg) but not the WT (10.4 ± 2.2 mmHg).

***In Vitro* Contractility.** A two-way ANOVA identified significant differences in circumferential contractility with respect to genotype ($p<0.0001$) but not KCl concentration. Post hoc tests showed no significant differences in circumferential contractility between the WT and HET samples. Circumferential contractility significantly decreased in the KO cervix versus the WT cervix for all doses except 10 mM ($p<0.01$ for 15 mM and 60–80 mM, $p<0.001$ for 20–50 mM, and $p<0.05$ for 100 mM) (Fig 2A). Additionally, circumferential contractility significantly decreased in the KO cervix versus the HET cervix for all doses of KCl ($p<0.01$ for 10 and 100 mM and $p<0.001$ for 15–80 mM). A two-way ANOVA (genotype, KCl concentration) detected differences with axial force ($p<0.0001$) (Fig 2B). Post hoc testing showed a significant decrease in contractility ($p<0.05$) between the HET and KO cervix at 15 mM KCl. No other significant differences in axial force were detected. All samples exhibited spontaneous phasic contractions once mounted on the device.

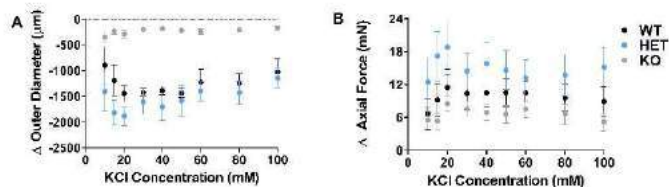


Figure 2: *In vitro* KCl dose response contractility results for the WT (black), HET (blue), and KO (grey) cervix ($n=5$ /group). (A). Circumferential contractility, measured via the change in outer diameter, significantly decreased in the KO cervix compared to the WT cervix ($p<0.01$ for 15 mM, 60–80 mM, $p<0.001$ for 20–50 mM, and $p<0.05$ for 100 mM). Additionally, circumferential contractility decreased in the KO cervix compared to the HET cervix ($p<0.01$ for 10 and 100 mM and $p<0.001$ for 15–80 mM). No significant changes were detected between the WT and HET cervix. (B). The HET cervix increased axial force significantly ($p<0.05$) compared to the KO cervix at a KCl dose of 15 mM dose. No other significant changes were detected.

DISCUSSION

This study investigated *in vivo* and *in vitro* contractility of the murine cervix with varying *Fbln5* genotypes. The cervix exhibits phasic contractions with a significant pressure difference in the WT and HET. The lack of significant changes in the *in vivo* KO contractile pressure may suggest a potential interaction between elastic fiber components, such as *Fbln5*, and SMC modulation from the contractile to the synthetic phenotype. Studies in the vagina showed decreased contractile-associated proteins with *Fbln5* deficiency. [7] Further, previous work suggests that elastin, the main component of elastic fibers, is a regulatory phenotypic modulation cue in vasculature [10]. Contractile-associated genes in arterial SMCs are also significantly downregulated in elastin knockout mice [11].

Additionally, the *Fbln5* KO cervix had the lowest contractile behavior *in vivo* and *in vitro*, suggesting matrix composition and properties may influence contractile behavior. Similarly, decreased contractility was observed in the *Fbln5* deficient vagina compared to the wild-type control [7]. Further, primary cervical SMCs obtained from patients with cervical insufficiency showed decreased contractility when exposed to soft matrix. [3] Studies in vasculature suggest that a decrease in elastic fiber formation leads to increased stiffness, contributing to a lower contractile potential [6, 12]. Further studies are needed to investigate the material properties of the KO cervix.

Similar to the murine vagina, direction-dependent contractile behavior was observed. There was a significant decrease in circumferential contractility in the KO cervix but not axial contractility. The murine cervix of nulliparous CD-1 mice presents with greater axial contractility compared to circumferential [8]. Further, in the murine vagina, increased elastin area fraction along the axial direction coincides with a greater contractile response in the axial direction compared to the circumferential [13]. This may suggest a direction-dependent organization of elastic fibers and cervical SMCs.

This study is not without limitations. The cervix is heavily influenced by gestation and hormones. While investigating cervical contractility throughout gestation is of interest, initial studies in the nulliparous state must first be completed to have a baseline understanding of cervical function and microstructural composition. Further studies employed to understand the relationship between elastic fiber composition and contractility in the cervix will improve our understanding of cervical insufficiency and spontaneous preterm birth.

ACKNOWLEDGEMENTS

This work was funded by NSF Early Faculty CAREER Development Award CMMI-1751050 (KSM).

REFERENCES

- [1] WHO, Preterm Birth, 2022.
- [2] Leppert, PC et al., *Am. J. Obstet. Gynecol.*, 157(5):1134–1139, 1987.
- [3] Vink, JY et al., *Reprod. Sci.* 28, 237–251, 2021.
- [4] Vink, JY et al., *Am J Obstet Gynecol.* 215(4):478, 2016.
- [5] Leppert, PC, et al., *Am J Obstet Gynecol.* 142(2):179–182, 1982.
- [6] Murtada, SI, et al., *J Biomech Eng.*, 138(5):051008, 2016.
- [7] Clark-Patterson, GL et al., *Sci Rep.* 11 20956, 2021.
- [8] Conway, CK et al., *Ann Biomed Eng.*, 49 1974–1887, 2021.
- [9] Vanloon, P et al., *Biorheology*, 14 181–201, 1977.
- [10] Karnik, SK et al. *Development.* 130(2):411–423, 2003.
- [11] Espinosa, G et al., *J Biomech Eng.*, 136(2):021030, 2014.
- [12] Ferruzzi, J et al., *J Biomech Eng.*, 137(3):0310071–03100714 2015.
- [13] Clark, GL et al., *Interface Focus*, 920190025, 2019.

LAMINA CRIBROSA BEAM INSERTIONS. THE HUMBLE HEROES OF THE LAMINA – SCLERA INTERPLAY

Fengting Ji (1), Hua Yi (2), Ian A. Sigal (1,2)

(1) Department of Bioengineering, University of Pittsburgh, Pittsburgh, PA, USA

(2) Department of Ophthalmology, University of Pittsburgh, Pittsburgh, PA, USA

INTRODUCTION

The lamina cribrosa (LC) is a specialized structure in the posterior pole of the eye that supports the retinal ganglion cell axons as they exit the globe on their way to the brain [1]. The LC biomechanical support is necessary to withstand the forces and deformations caused by intraocular pressure or other mechanical challenges. The ability of the LC to support the neural tissues is intrinsically dependent on the much stronger surrounding peripapillary sclera. While much has been learned about the LC, the peripapillary sclera and the crucial interplay between them [2], far less is known about the LC beam insertions through which these two tissues interact. Studies of the LC-sclera simplify the interface between the tissues as a smooth continuum surface, ignoring that the LC beam insertions are discrete with complex shapes [3].

Using recently developed microscopy tools we obtained detailed information on the LC and sclera. Inspecting the LC-sclera interface it is readily visible that the LC insertions are complex, and that they vary greatly in shape. Some insertions resemble the wide roots of old trees, whereas others look much thinner (**Fig. 1**). These shapes suggest that the LC insertions likely also vary in how well they can satisfy the mechanical demands of the LC-sclera interface. **Our goal was to characterize LC beam insertion shape in sheep, pig, monkey and human.** We test the hypothesis that the LC insertion width and insertion angle vary between species (**Fig. 2**). In addition, we present the early stages of the development of a direct fiber-based finite element method to model the mechanics of the LC insertions. We use this tool to evaluate the biomechanical consequences of the differences between insertions.

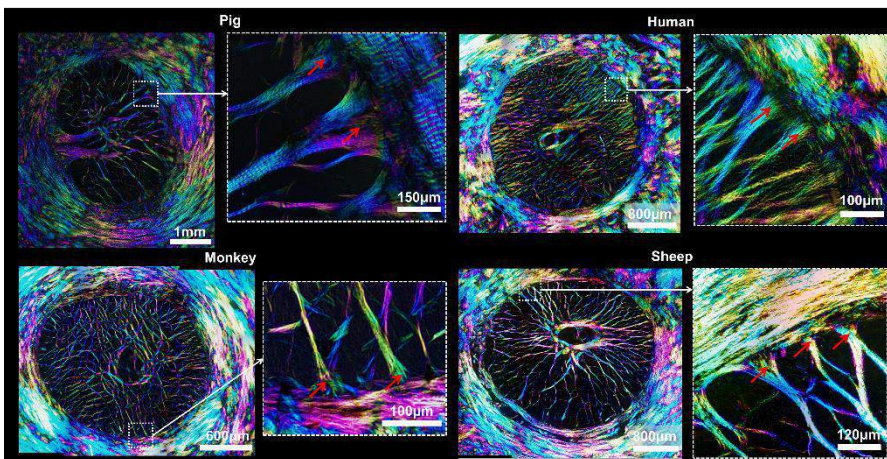


Figure 1: Instant polarized light microscopy images of LC and sclera of eyes from the four species. For each species a close-up is shown to illustrate typical insertions.

METHODS

Sample preparation: two monkey eyes, three sheep eyes, two human eyes, and three pig eyes without known abnormalities were fixed. The LC and peripapillary sclera were trephined and cryosectioned coronally. From each eye, three sections located close to the LC midplane were selected for analysis.

Imaging: Sections were imaged with instant polarized light microscopy (IPOL) with a 10x strain-free objective (Olympus, Tokyo, Japan, 0.66µm/pixel) [4]. Because of the lower collagen density the LC region often appears darker than the sclera. We therefore acquired images with various exposures to allow clear visualization of both tissues. Mosaics with 10% overlap were used to image whole sections. IPOL images reveal local collagen orientation and density in each pixel which helps visualize the LC beam and canal collagen structure.

Insertion quantification: We measured two parameters of each insertion: width and angle. Width was measured at the edge of the scleral canal. Angle was between the LC beam and the tangent of the sclera canal. Insertion angles range from 0 to 90°, with 90° being an LC insertion perpendicular into the canal wall. The parameters were measured from lines drawn manually using Fiji. Calculations were done in MATLAB v2022 (MathWorks, Natick, MA, USA).

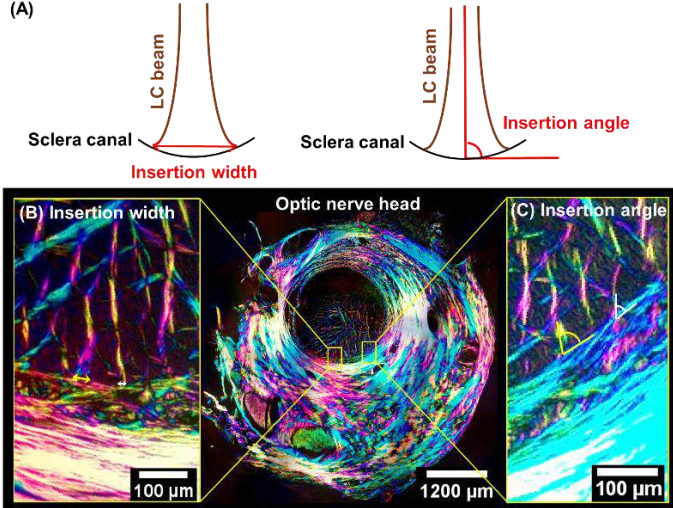


Figure 2: (A) Diagrams showing the definition of (left) insertion width and (right) insertion angle. (B,C) Example images of monkey ONH illustrating insertions of different widths or angles.

Statistics: Linear mixed effects models, accounting for autocorrelations between measurements from the same sections, eyes and species, were used to assess if the parameters of insertions were associated with species.

Finite element analysis: We built two models to simulate two pig insertions with different shapes, one was straightly inserted into the canal while the other one was wide and spread (Fig. 3). The models were built using the direct fiber modeling technique as described elsewhere [5]. Briefly, we manually traced on IPOL images two groups of fibers representing the LC beam and sclera canal. The fibers were discretized with linear truss elements (T3D2) of circular cross-section and linear elastic material properties. Fiber overlaps were resolved using an iterative algorithm that refined and displaced them, resulting in discrete, interwoven realistic-looking fibers.

To compare the difference in the mechanical responses of the two insertions, a 15% equi-biaxial expansion was simulated on both models. Fiber-fiber interactions were incorporated using general contact to prevent fiber interpenetration. The solution was obtained using Abaqus/Explicit. We compared the stress responses of the two models.

RESULTS

Figure 3 shows the direct fiber modeling results of the two pig LC insertions with different shapes.

Figure 4 shows the distributions of insertion widths and angles of the four species across all eyes. Insertion widths were significantly different between all species ($p < 0.001$), with widths (mean \pm SD, μ m) in human (55.28 ± 27.07), sheep (95.40 ± 49.09), pig (137.02 ± 79.91) and monkey (27.58 ± 16.11).

Insertion angles of sheep and pig were larger than monkey and human ($p < 0.05$), with angles (mean \pm SD, $^\circ$) in human (70.74 ± 14.4), sheep (76.43 ± 11.66), pig (74.28 ± 14.17) and monkey (70.88 ± 16.06). No difference was detected in insertion angles between sheep and pig, and monkey and human.

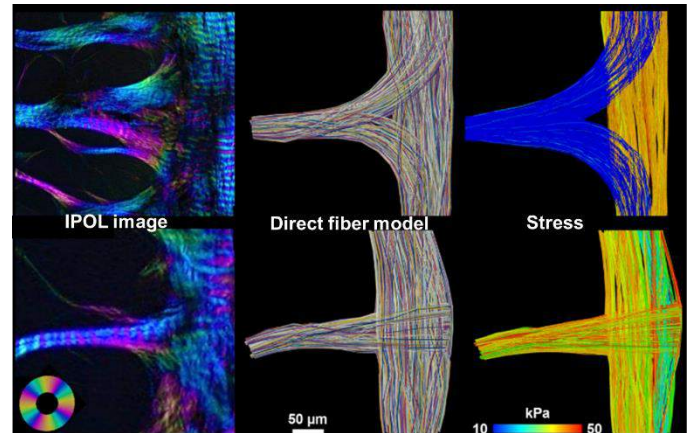


Figure 3: A comparison of the mechanical response between a spread and wide insertion (top row) and a straight and narrow insertion (bottom row). Direct fiber models (middle column) were created by tracing collagen fibers on IPOL images (left column). The stress responses of fibers under 15% equi-biaxial stretch are shown (right column). The insertion with spread and wide LC beam bears substantially less load (lower stress) than the other one, illustrating that LC insertion shape has a large effect on the local sensitivity to IOP.

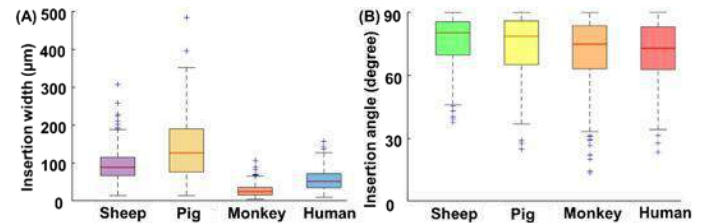


Figure 4: Box plots of (A) insertion widths and (B) insertion angles of each species. There were significant and large differences in insertion widths between species.

DISCUSSION

We present the first characterization of LC insertion width and angle. The discrete LC beam insertions could mean that the interaction between LC and surrounding load-bearing tissue is nonlinear and discontinuous over the canal, with forces concentrated in some regions. Different shapes of insertions can represent different levels of robustness of the LC periphery. The differences could result in different species susceptibilities to glaucomatous damage. Future work involves extending the numerical models to include a wider diversity of insertions and boundary conditions. Further work is also necessary to understand the potential consequences of differences in angle.

ACKNOWLEDGEMENTS

Supported by NIH R01-EY031708, R01-EY023966, P30-EY008098 and T32-EY017271 (Bethesda, MD), the Eye and Ear Foundation (Pittsburgh, PA), and Research to Prevent Blindness (unrestricted grant to UPMC, and Stein innovation award to Sigal IA).

REFERENCES

- [1] Sigal I A. IOVS, 50(6): 2785-2795, 2009.
- [2] Downs J C et al., *Experimental eye research*, 93(2): 133-140, 2011.
- [3] Lee K M et al., *PLoS One*, 9(12): e114935, 2014.
- [4] Lee, PY et al., *Experimental Eye Research*, 217: 108967, 2022.
- [5] Ji F et al., *BioRxiv*, 2022. bioRxiv 2022.11.20.517259

HEAD KINEMATICS IN STOCK CAR RACING: QUANTIFYING DIFFERENCES BETWEEN TRACKS

**Sophia R. Zoch (1,2), Logan E. Miller (1,2), Cole M. Binder (2), Destiny R. Mason (1,2),
John P. Patalak (3), Matthew G. Harper (3), Jillian E. Urban (1,2), Joel D. Stitzel (1,2)**

- (1) Virginia Tech-Wake Forest School of Biomedical Engineering & Sciences, Winston-Salem, NC, USA
(2) Dept. Biomedical Engineering, Wake Forest School of Medicine, Winston-Salem, NC, USA
(3) National Association for Stock Car Auto Racing, Incorporated, Daytona Beach, FL, USA

INTRODUCTION

There is an inherent risk of injury in auto racing due to high speeds and risk of collisions. With significant improvements to safety, severe brain injury in motorsports has significantly decreased [1]. A retrospective analysis of all National Association for Stock Car Auto Racing (NASCAR) data between 2002 and 2008 found that concussion occurred in 27 of the 274 (9.9%) impacts selected for numerical simulation [2]. In addition to the risk of concussion resulting from crashes, drivers also experience perturbations under normal racing conditions, however further research is necessary to understand the neurocognitive effects of these perturbations [3]. Previous studies have examined the application of earpieces instrumented with tri-axial accelerometers in motorsport but have differing conclusions [4,5]. Mouthpiece sensors have been used in football, soccer, and hockey to examine head acceleration events (HAEs), including direct head impacts. However, mouthpieces have not been widely used to study HAEs in motorsports. Examining these events can help inform driver safety systems and mitigate HAEs. Thus, this study aims to characterize HAEs experienced during professional racing across tracks using an instrumented mouthpiece.

METHODS

Six drivers in the NASCAR Cup Series were outfitted with custom mouthpiece sensors containing a tri-axial accelerometer and an angular rate sensor for 20-minute practice sessions at seven different tracks. Track names were assigned based on track type: short track (ST, n=4), intermediate (I, n=1), superspeedway (SS, n=1), and road course (RC, n=1). Mouthpiece data was excluded from analyses if a driver did not wear their mouthpiece for the entire duration of the practice session. The mouthpiece sensors recorded linear acceleration and rotational velocity at 200 Hz, and kinematic data was transformed to the head center of gravity using subject-specific transformation matrices. Time-synchronized video was collected at each practice session to segment

the kinematic data on a per-lap basis. After segmentation, a 100-point moving average filter was calculated and subtracted from the data to remove periodicity associated with movement around the track to obtain “adjusted” data. This process is demonstrated in Figure 1. The adjusted resultant data was then calculated from the adjusted component data. Peak resultant kinematics were compared across drivers at each track. Summary statistics were quantified by number of laps (n), peak resultant linear acceleration (PLA), peak resultant rotational velocity (PRV), and peak resultant rotational acceleration (PRA) for laps. Lap data with a lap time, PLA, PRV, or PRA greater than the 95th percentile (%ile) were excluded from analysis.

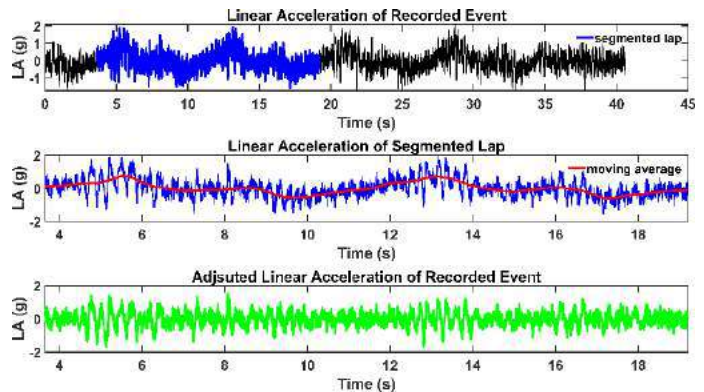


Figure 1: Process for obtaining “adjusted” kinematic data.

Six separate one-way ANOVA (analysis of variance) tests were conducted to determine statistically significant differences between peak kinematic data across tracks and track types using SAS (Cary, NC). Pairwise t-tests were subsequently performed to determine which track types differed. Using driver, track, and track type as categorical

variables, preliminary statistical analyses exploring them as predictors for peak head kinematics were performed in SAS using simple linear regressions. Finally, mixed effects models were prepared to determine whether the driver added random variance in head motion for tracks and track types.

RESULTS

The mouthpiece sensors recorded 506 complete laps at seven tracks. After excluding laps recorded by the mouthpiece when the driver was not wearing the device ($n=19$), summary statistics for PLA, PRV, and PRA were computed. Median (95th %ile) PLA, PRV, and PRA for all laps excluding laps with invalid mouthpiece data were 1.16 (1.77) g, 0.78 (1.57) rad/s, and 7.90 (18.0) rad/s², respectively. Summary statistics were computed by track and track type as shown in Figures 2 and 3. Track RC1 has the greatest median PLA, PRV, and PRA and is the only track identified as a “Road Course”, thus road courses also had the largest magnitude peak head kinematics. Track ST4 had the lowest magnitude median peak kinematics.

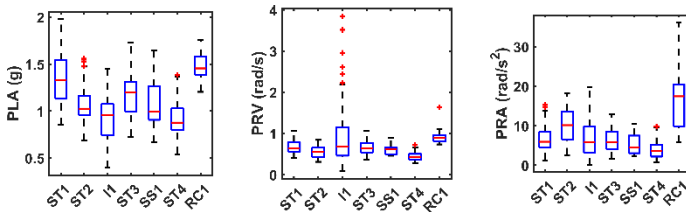


Figure 2: Peak resultant linear acceleration (left), rotational velocity (middle), and rotational acceleration (right) per lap across tracks.

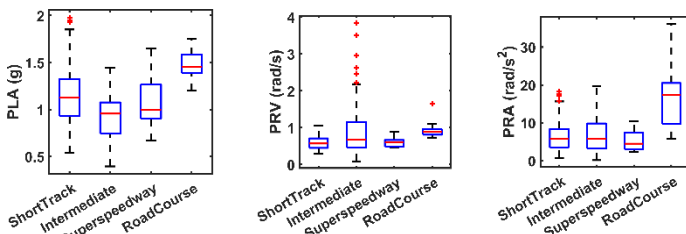


Figure 3: Peak resultant linear acceleration (left), rotational velocity (middle), and rotational acceleration (right) per lap across track types.

From the ANOVA tests, a significant difference ($p < .0001$) in PLA, PRV, and PRA was observed across the seven tracks and four track types. The road course (track RC1) had significantly greater PLA and PRA than the other track types. Additionally, the road course had significantly greater PRV than short tracks ($\Delta=0.34$ rad/s) and the superspeedway (track SS1, $\Delta=0.32$). The intermediate track (track I1) had significantly greater PRV than the superspeedway ($\Delta=0.38$ rad/s) and the short tracks ($\Delta=0.32$ rad/s). However, the short tracks had significantly greater PLA than intermediate tracks ($\Delta=0.22$ g). The linear regressions showed a significant association between track and PLA ($p=.0065$), PRV ($p<.0001$), and PRA ($p=.0174$) and between track type and both PRV and PRA ($p<.0001$). The mixed effects models showed significant differences in peak head kinematics between drivers at the intermediate track (I1), PRA at short tracks (ST2, ST3, ST4), and PLA at track ST3 between drivers.

DISCUSSION

The objective of this study was to quantify differences in peak resultant head kinematics experienced by NASCAR drivers during

practice laps. Previous work has shown differences in peak lap kinematics between drivers and tracks [6]. The “Intermediate” track type had the lowest magnitude median PLA, the “Short Track” track type had the smallest magnitude median PRV, and the “Superspeedway” track type had the smallest magnitude median PRA. Track type analysis is limited as Intermediate, Road Course, and Superspeedway types comprised of one track as opposed to the four tracks identified as Short Tracks.

Despite the significant association between PRA and driver via linear regression, there were not any significant differences in PLA and PRV across the six drivers. This may suggest that while each driver has some variations in their safety system (e.g., HANS vs. Hybrid, seat design), the performance of the systems to reduce linear motion of the head do not significantly differ.

Findings from this study show that peak resultant head kinematics are influenced by the type of track. Particularly, peak kinematics at the Road Course were significantly greater than the other track types. This can potentially be explained by the elevated presence of rumble strips on road courses and turning both left and right. When racing on a road course, the car’s outside tires go often pass over the rumble strips or other track edge markers at high speeds. It was also found that peak resultant rotational velocity at the intermediate track differed from the other three track types. The distance between the driver’s helmet and foam in the head surround may influence the differences in head kinematics. However, further investigation of component data is needed to determine the mechanisms behind the differences in head kinematics.

ACKNOWLEDGEMENTS

The authors would like to thank the drivers for their participation in the study and acknowledge all members of the research team who assisted with data collection.

REFERENCES

- [1] Patalak J et al., *Traffic Inj Prev*, 20(6):588-594, 2019.
- [2] Somers JT et al., *Stapp Car Crash J.*,55:49, 2011.
- [3] Filben TM et al., *Traffic Inj Prev*, 23(sup1):S38-S43, 2022.
- [4] Knox T. *SAE Technical Paper*, 2004.
- [5] Salazar RS et al. *SAE Int J Passeng Cars-Mech Syst*. 1(2008-01-2978):1367-1381, 2008.
- [6] Miller LE et al., *J Biomech Eng*, 145(3), 031006, 2022.

ENDOTHELIAL NUCLEAR MORPHOLOGY IS INCREMENTALLY SENSITIVE TO SHEAR STRESS MAGNITUDE AND DIRECTIONALITY

Jaideep Sahni (1), Mehwish Arshad (2), Peter D. Weinberg (2), Ryan M. Pedrigi (1)

(1) Department of Mechanical and Materials Engineering, University of Nebraska-Lincoln, Lincoln, NE, USA

(2) Department of Bioengineering, Imperial College, London, UK

INTRODUCTION

Vascular endothelial cells form the inner lining of arteries and are exquisitely sensitive to shear stress magnitude and directionality [1]. Unidirectional shear stress at an average physiologic magnitude promotes a healthy endothelial phenotype, while multidirectional shear stress at a low magnitude promotes a dysfunctional phenotype. Although there are many mechanisms by which endothelial cells transduce shear stress into a biological response, a principal one that has received little attention is changes in nuclear morphology. The endothelial cytoskeleton is connected to the nucleus to allow load transmission that directly regulates gene expression [2] by causing nuclear deformation [3]. Different shear stress conditions likely deform endothelial nuclei differently and promote different behaviors. Yet, little work has characterized this relationship. Since local arterial segments around bifurcations and highly curving arteries contain a range of shear stress conditions from low and multidirectional to high and unidirectional [1], it is critical to understand how incremental changes in these conditions affect drivers of endothelial functions to better predict diseases such as atherosclerosis. Therefore, in this study, we quantified nuclear area and aspect ratio over a range of shear stress conditions using an orbital shaker model. We found high correlations with two shear stress metrics previously associated with atherogenesis.

METHODS

Cell Culture. Human umbilical vein endothelial cells (HUVECs) were seeded at passages 4-7 into 6-well culture plates with type I collagen at 40,000 cells/cm². Experiments were run one day after seeding with 2.41 ml of media per well to give a medium height of 2.5 mm. In each experiment, well plates were either subjected to orbital flow or static conditions (control) for 72 h. Orbital flow was induced using an orbital shaker, which moves the culture plate in a planar circular orbit of 5 mm radius, and rotating it at 120, 250, or 350 RPM within a humidified incubator at 37°C and 5% CO₂.

Staining and Imaging. After orbital flow, cells were fixed in 4% paraformaldehyde in PBS for 10 mins and then incubated with 10 μ M DAPI for 2 min. Cell layers were imaged with a Zeiss LSM 800 confocal microscope using a 10x objective and tile scan from the center to periphery of each well. Images of the DAPI stain were automatically processed to quantify nuclear area and aspect ratio using a custom script in ImageJ. These metrics at each radial location of all cell layers under orbital flow are reported relative to their average value at each radial location of the static controls seeded at the time of each experiment.

Computational Fluid Dynamics. Star CCM+ was used for all flow simulations. A single well of a 6-well culture plate was represented as a cylinder with a height of 10 mm and radius of 17.4 mm. The culture medium had a height of 2.5 mm at rest and the remaining space was filled with air. The geometry was discretized using a structured cylindrical mesh with 360,000 grid elements. A no-slip condition was imposed at all walls and surface tension was neglected. The top surface of the cylinder was defined as a pressure outlet. The dynamic viscosity and density of the medium were 0.78 mPa.s and 1003 kg/m³, respectively, whereas the dynamic viscosity and density of air were 0.0187 mPa.s and 1.1115 kg/m³. All three orbital velocities used in the cell experiments were simulated: 120, 250, and 350 RPM. The primary output was the instantaneous wall shear stress (WSS) vector at each element on the base of the well at each time increment over one complete revolution. This was used to calculate magnitude of the mean WSS (MagMeanWSS) and oscillatory shear index (OSI).

Statistics. Quantities are reported as mean \pm standard deviation. Normality was determined by a Shapiro-Wilks test and either a two-tailed *t*-test or Mann Whitney U test was performed. Multiple comparisons were accounted for using a Holm-Bonferroni correction. To quantify the linear association between nuclear morphology and WSS metrics, a Spearman's rank correlation coefficient (ρ) was computed. For this test, a Bonferroni correction was used. An adjusted *p*-value of less than 0.05 was considered statistically significant.

RESULTS

Endothelial nuclear area and aspect ratio were highly dependent on the shear stress condition (Figure 1A-B). Nuclear area (relative to controls) in the central one third of the radius of cell layers, where low and multidirectional shear stress is present, exhibited a significant increase from controls (1.00 ± 0.02) with values of 1.03 ± 0.01 at 120 RPM and 1.05 ± 0.02 at 250 RPM (Figure 1C). In the peripheral one third of the radius of cell layers, where high and unidirectional shear stress is present, nuclear area significantly decreased compared to controls (1.00 ± 0.02) with values of 0.95 ± 0.02 at 120 RPM ($p = 0.0007$), 0.94 ± 0.01 at 250 RPM ($p < 0.0001$), and 0.90 ± 0.01 at 350 RPM ($p < 0.0001$). Nuclear aspect ratio at these angular velocities showed an inverse trend to area (Figure 1C). The most significant changes compared to controls (1.55 ± 0.02) were seen at the periphery with values of 1.62 ± 0.02 at 250 RPM ($p < 0.0001$) and 1.68 ± 0.02 at 350 RPM ($p < 0.0001$). Note that 350 RPM could only be assessed at the periphery of cell layers due to the central portion being nearly devoid of medium.

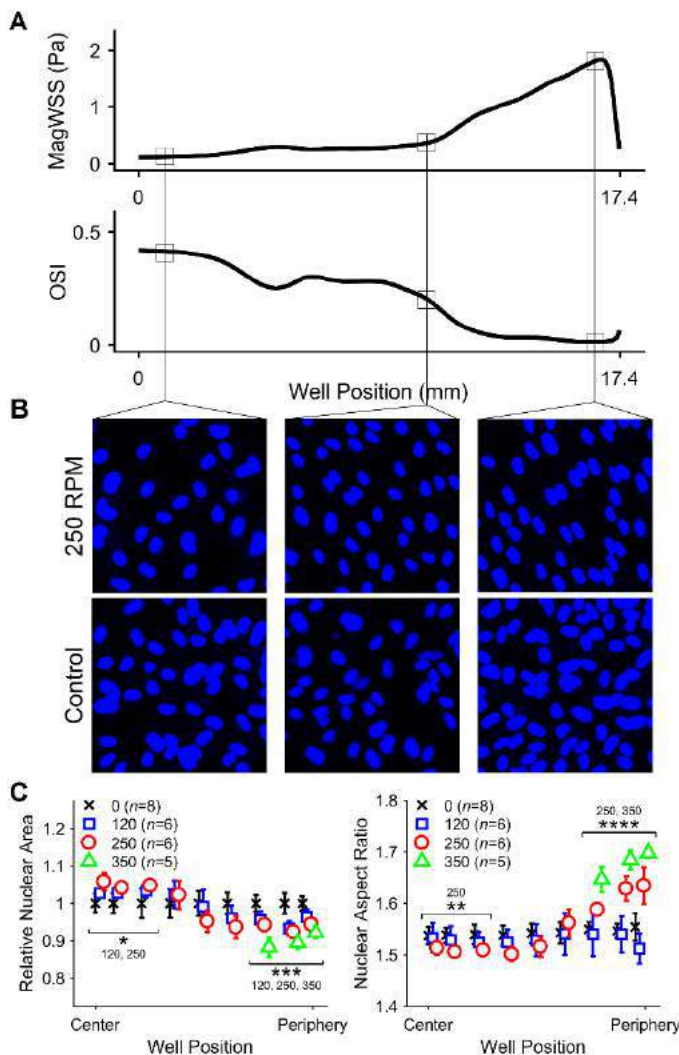


Figure 1: (A) Plots of MagMeanWSS and OSI from center to periphery of a CFD-simulated culture well on an orbital shaker at 250 RPM. (B) Images of endothelial nuclei at three radial locations (top) after 72 h at 250 RPM and (bottom) static conditions (control). (C) Plots of nuclear area and aspect ratio relative to the mean of static controls over each culture well from center to periphery.

We next evaluated how shear stress magnitude (MagMeanWSS) and directionality (OSI) separately associated with nuclear area and aspect ratio. Nuclear area exhibited a high negative correlation with MagMeanWSS of -0.74 ($p = 0.0007$) and a high positive correlation with OSI of 0.8 ($p < 0.0001$). Nuclear aspect ratio showed an inverse trend of a high positive correlation with MagMeanWSS of 0.9 ($p < 0.0001$) and high negative correlation with OSI of -0.81 ($p = 0.009$) (Figure 2).

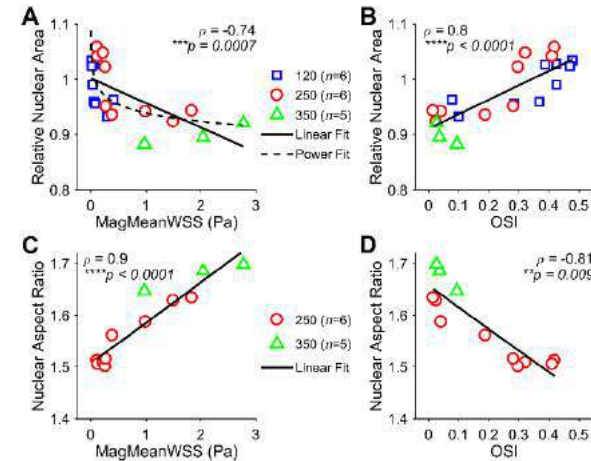


Figure 2: (A, B) Endothelial nuclear area as a function of (A) MagMeanWSS and (B) OSI. (C, D) Endothelial nuclear aspect ratio as a function of (C) MagMeanWSS and (D) OSI. Data points were averaged over all cell layers (indicated by n) for each orbital velocity (120, 250, and 350 RPM) at each duration and radial position in the well (because no statistical difference in nuclear aspect ratio was seen at 120 RPM compared to controls, these data were removed from the correlation calculations). The black line represents a best-fit line (solid) and power (dashed) function across all data points to visualize the trend.

DISCUSSION

To our knowledge, this study is the first to characterize changes in nuclear morphology over a range of WSS conditions that are similar to those found around bifurcations and the inner curvature of highly curving arteries, including with a similar range of WSS magnitudes (e.g., MagMeanWSS ranged from 0.01 to 2.8 Pa) and directionality (e.g., OSI ranged from 0.01 to 0.48). We also demonstrated high correlations (positive and negative) between these endothelial behaviors and WSS metrics of magnitude and directionality, which indicated a strong ability of these metrics to predict endothelial function. These findings demonstrate the sensitivity of the endothelium to incremental changes in WSS over a range of conditions, which may be leveraged to aid in predicting arterial function and dysfunction. In addition, these findings suggest that the susceptibility of an arterial segment to atherosclerosis has a similar level of high sensitivity to the blood flow condition that may be important in determining, not just initiation, but also progression to different plaque phenotypes.

ACKNOWLEDGEMENTS

We gratefully acknowledge that this work was supported, in part, by grants from the AHA (19CDA34660218), NSF (CMMI-1944131), and NIH (R21EB028960).

REFERENCES

- [1] Sahni, J et al., *J Mech Behav Biomed Mater.*, 137:105545, 2023.
- [2] Anno, T et al., *Biochem Biophys Res Commun.*, 424:94-9, 2012.
- [3] Kurby, TJ et al., *Nat Cell Biol.*, 20:373-381, 2018.

UNDERSTANDING MECHANOTRANSDUCTION OF THE DISTAL COLON AND RECTUM BY MULTISCALE AND MULTIMODAL COMPUTATIONAL MODELING

Amirhossein Shokrani (1), Ashkan Almasi (1), Bin Feng (2), David M. Pierce (1,2)

(1) Department of Mechanical Engineering, University of Connecticut, Storrs, CT, USA
(2) Department of Biomedical Engineering, University of Connecticut, Storrs, CT, USA

INTRODUCTION

Irritable bowel syndrome (IBS) is a common reason why patients visit gastroenterologists, with the main complaint of chronic visceral pain [1]. Mechanotransduction, the process of transducing visceral mechanical stimuli into action potentials by sensory nerve endings in distal colon and rectum (colorectum), plays a central role in visceral pain associated with IBS [2]. Thus, investigating the biomechanical behavior of the colorectum can lead us to better understanding of the generation of pain. We and others have made many significant findings experimentally by investigating both the biomechanics of the colorectum and the neural encoding functions of colorectal afferents.

Siri et al. [3] revealed significant mechanical heterogeneity in the colorectum in all three curvilinear directions: longitudinal, circumferential, and radial. They took the distal 30 mm of the colorectums from mice, divided these evenly into three 10-mm-long segments (colonic, intermediate, and rectal), and completed both biaxial mechanical extension tests and opening-angle measurements with each of these segments. They also presented evidence that the submucosa is load-bearing layer of the colorectum that undergoes elevated mechanical stresses. Feng et al. [4] systematically studied the neural encoding function of colorectal afferents by single-fiber recordings. They tested the afferent endings using three distinct mechanical stimulations: circumferential stretch, punctuate probing, and mucosal shearing. Based on the response profiles they measured experimentally, they functionally characterized colorectal afferents into five major subtypes wherein four of them are mechanosensitive subtypes. Guo et al. [5] completed a recent anatomical study using optically clearing that allowed systematic quantification of afferent fiber densities within different layers of the colorectum. Their results revealed that the colonic submucosa contains a significantly higher density of afferent fibers relative to the other sublayers. The focal presence of afferents in the submucosa strongly suggests their nociceptive roles [6].

In this study we aimed to establish a multiscale computational framework which leverages finite element (FE) simulations of the colorectum to predict the patterns of afferent-ending spikes induced by mechanical loading, i.e. simulations of the mechanotransduction process in the colorectum that causes chronic pain.

METHODS

Experimental evidence. We utilized previous evidence from our experiments on mouse colorectums including the biomechanics [3,6,7] and both the encoding function [4] and the intra-tissue morphology of colorectal afferents [5].

Finite element model. We developed a macroscopic FE model that accounted for tissue mechanical heterogeneity in longitudinal, radial, and circumferential directions, see fig. 1(a). In the FE model, we considered colorectum as a three-layered, incompressible, hyperelastic continuum with embedded collagen fibers [8]. We meshed the geometry

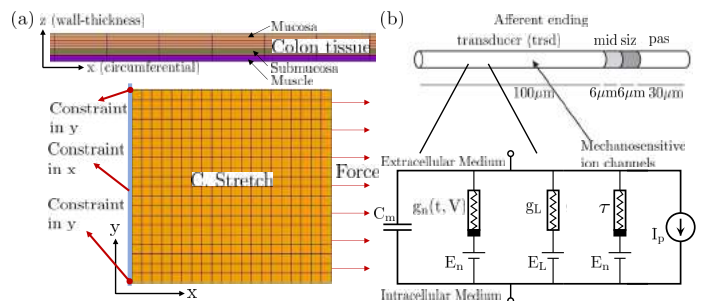


Figure 1: (a) Representative finite element model of a segment of the colorectum undergoing uniaxial, circumferential stretch. (b) Schematic of our Hodgkin–Huxley-type model of action potential generation in the colorectal afferent endings, including mechanosensitive ion channels.

using eight-node hexahedra and applied boundary conditions modeling a uniaxial extension test consistent with previous experiments, i.e. we applied a linear ramp in force to generate uniaxial extension. To prepare for further analyses we extracted representative deformation gradients and Cauchy stress tensors from the submucosal layer of the colorectum as a function of time. We completed all finite element simulations using FEBio (University of Utah).

Morphology of nerve fibers. We quantified the morphology of nerve fibers within submucosa using our second harmonic generation (SHG) images [5] and custom image processing tools. We extracted individual afferent fiber morphologies from confocal image stacks. We then represented these complex data as a series of piece-wise cylinders (diameter = 1 μm) using a custom program [8]. We returned these fiber morphologies to their (stress-free) reference configurations from the deformed configurations required to perform the SHG imaging (i.e. 20 mmHg internal pressure) [5]. To complete this mapping, we established a finite element model of the three-layered colorectum and estimated the inverse deformation gradient.

Micromechanics of nerve fibers. We derived the local mechanical stress/strain profile along the entire length of arbitrary afferent endings embedded in the colorectal wall using a custom program. We depicted the curved nerve fibers as separate microscopic cylinders embedded within a continuous fibrous matrix [8]. Specifically, we used the results of our finite element simulations of the bulk colorectum undergoing uniaxial extension (deformation gradient and Cauchy stress tensors from the submucosal layer of the colorectum as a function of time), pushed the morphology of the afferent ending into the current configuration and then calculated the local membrane tension acting on the surface of the afferent ending.

Generation of action potentials. We used our custom, mechanosensitive neural membrane model to simulate the encoding of afferent stress/strain into action potentials from the local membrane tension along the surface of the afferent ending. We calibrated our neural membrane model to produce results consistent with the experimental data measured from single fibers [4]. Specifically, we utilized the equations established by Feng et al. on the rule of NaV1.6 ion channels and mechanosensitive ion channels in spike initiation at stretch-sensitive colorectal afferent endings. Thus, the deformation and stress derived from FE analysis drove the spike initiation and propagation [9]. We performed all the simulations of action potentials generated by afferent endings using NEURON (Yale University).

RESULTS

Macro- and micro-mechanics of tissue stress distribution. We used a global Cartesian coordinate system to align the FE results with the (assumed) embedded nerve fibers. We traced a representative nerve fiber to demonstrate our modeling framework, see Fig. 2(a). We completed a FE simulation a specimen of colorectum undergoing uniaxial extension, see Fig. 2(b). Using the results from this simulation we predicted the local mechanical conditions acting on the embedded axons embedded within the macroscopic fibrous tissue, see Fig. 2(c). We assumed that the stress and strain distributions acting on each piece-wise cylinder responded uniformly to loading of the bulk colorectum.

Action potential generation pattern. We simulated the response of a single, representative afferent ending during the uniaxial extension test performed experimentally (wherein the total force increases linearly from 0 to 61.8 mN. In Fig. 3 we show the experimental measurement of the action potential (Fig. 3(a)) versus our prediction of the membrane potential (Fig. 3(b)). The result from simulation compares favorably with the experimental results: the initiation time of the action potential spikes and increasing frequency of spikes are consistent between the experiment and the prediction. Moreover, the shape of the spike plotted in Fig. 3(b) is consistent with spikes measured experimentally.

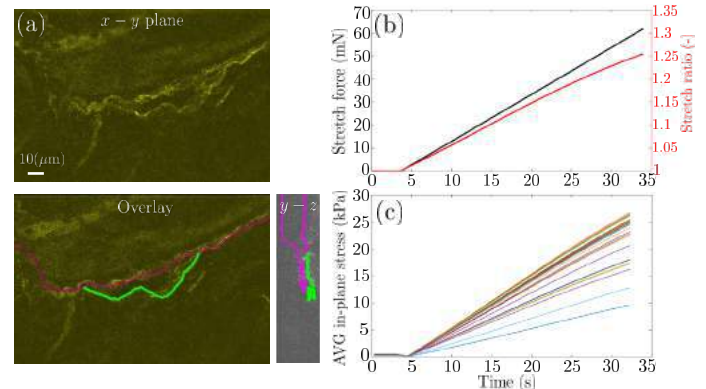


Figure 2: (a) Representative SHG image of and afferent ending in the submucosa and nerve fiber trace (green). (b) Applied circumferential force on the bulk colorectum and the resulting stretch ratio. (c) Resulting average shearing stresses acting on each piece-wise cylinder representing the afferent ending.

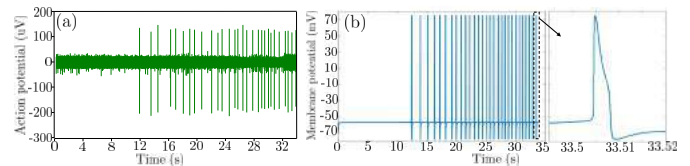


Figure 3: (a) Representative experimental measurement of colorectal afferent endings activated by circumferential stretching (0-170 mN at 5 mN/s). (b) Corresponding prediction of action potential propagation pattern in colorectal afferent endings.

DISCUSSION

We utilized our experimental results to establish a novel multimodal and multiscale computational framework enabling us, for the first time, to investigate mechano-transduction in the distal colon and rectum. Each step of our framework is driven by experimental data. We show a representative example demonstrating mechano-transduction within colorectum, the main cause of IBS-related pain. We aim to complete sensitivity analyses of our modeling framework and assess the relative importance of fiber location, orientation, and curviness on the resulting neural encoding function. Future analyses of the colorectum may help to identify key components triggering neural responses to visceral mechanical stimuli in both health and disease.

ACKNOWLEDGEMENTS

National Institutes of Health 1R01DK120824-01.

REFERENCES

- [1] Feng, B., et al., *American Journal of Physiology-Gastrointestinal and Liver Physiology* (2012) **302** (10), G1085. [2] Pasricha, P. J., et al., *Chronic abdominal and visceral pain: theory and practice*. CRC Press: 2006. [3] Maier, F., et al., *Journal of the mechanical behavior of biomedical materials* (2021) **113**, 104116. [4] Feng, B., and Gebhart, G. F., *American Journal of Physiology-Gastrointestinal and Liver Physiology* (2011) **300** (1), G170. [5] Guo, T., et al., *American Journal of Physiology-Gastrointestinal and Liver Physiology* (2021) **320** (4), G644. [6] Siri, S., et al., *American Journal of Physiology-Gastrointestinal and Liver Physiology* (2019) **317** (3), G349. [7] Siri, S., et al., *American Journal of Physiology-Gastrointestinal and Liver Physiology* (2019) **316** (4), G473. [8] Zhao, Y., et al., *Journal of the Mechanical Behavior of Biomedical Materials* (2022) **127**, 105083. [9] Feng, B., et al., *Journal of neurophysiology* (2015) **113** (7), 2618.

SUB-MILLIMETER STIFFNESS GRADIENTS WITHIN 3D PRINTED COMPOSITE SCAFFOLDS FOR OSTEOCHONDRAL TISSUE ENGINEERING

Kevin N. Eckstein (1), A. Camila Uzcategui (2), John E. Hergert (2), Sarah A. Schoonraad (3),
Stephanie J. Bryant (2,3), Robert R. McLeod (2,4), Virginia L. Ferguson (1,2)

- (1) Department of Mechanical Engineering, University of Colorado at Boulder, Boulder, CO, USA
- (2) Materials Science and Engineering Program, University of Colorado at Boulder, Boulder, CO, USA
- (3) Department of Chemical and Biological Engineering, University of Colorado at Boulder, Boulder, CO, USA
- (4) Department of Electrical, Computer & Energy Engineering, University of Colorado at Boulder, Boulder, CO, USA

INTRODUCTION

Regenerative tissue scaffolds are often designed with functional gradients in chemistry and mechanical properties. Mechanical property gradients enable control of mechanical cues delivered to encapsulated cells. By spatially controlling scaffold stiffness, cell behavior (*e.g.* extra-cellular matrix secretion) may be influenced to recapture native tissue organization.¹ Additionally, an implant that mimics the local tissue stiffness may better integrate with surrounding tissue and improve treatment outcomes.

Controlling mechanical gradients is especially desired in osteochondral tissue engineering. Osteochondral tissue engineering aims to treat defects in articular cartilage that, if left untreated, lead to osteoarthritis. By replacing damaged tissue with a spatially graded tissue engineering scaffold, we seek to regenerate both cartilage and underlying bone and recapture the native organization of articular cartilage. Recently, we demonstrated control over mechanical stiffness by incorporating a load-bearing 3D printed structure within a soft ($E = 25 \text{ kPa}^2$) cell scaffold that featured a stiff bone-regenerative region and a softer cartilage-regenerative region.^{2,3}

Here, we designed stiffness gradients within the cartilage region of an osteochondral scaffold to mimic depth-dependent deformation patterns of articular cartilage⁴ and provide spatially controlled mechanobiological cues to cells. We verified these gradients via experimental testing of digital light processing (DLP) 3D printed, stiff hydrogel micro-truss structures at high ($\sim 10 \text{ }\mu\text{m}$) resolution.⁵ We also present a novel method for verifying sub-millimeter mechanical gradients in composite tissue scaffolds by combining X-ray microscopy (XRM) imaging during compression testing to evaluate regional stiffnesses within a composite osteochondral scaffold.

METHODS

Design and Finite Element Analysis (FEA): Unconfined compression of two selected designs (Fig. 1.b,c) was modeled with

finite element analysis (FEA) in Abaqus CAE while considering non-linear geometric effects. Models used linear elastic material properties ($E = 32 \text{ MPa}^5$, $\nu = 0.45$) contained 310k and 767k second-order tetrahedral elements with hybrid formulation in single (*i.e.*, uniform) and bilayer structures, respectively. Strut diameter in the uniform structure was iteratively varied to establish the influence on structural stiffness, E_{struct} (Fig. 1.a). Using this relationship, we designed a stiffness gradient in the “cartilage” layer that ranged from 0.75-1.0 MPa (Fig. 1.c). The bottom “bone” layer of the bilayer design (Fig. 1.c) used vertical pillars to maximize stiffness and structural efficiency.

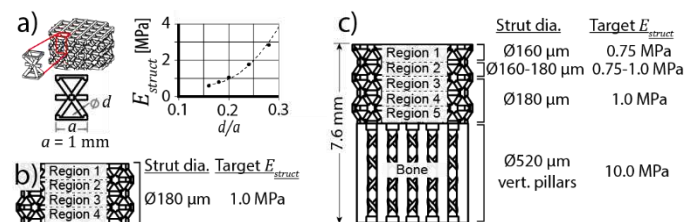


Figure 1: a) Relationship between strut thickness d/a and stiffness; b) uniform structure with consistent stiffness; c) bilayer structure with a gradient in stiffness incorporated in the top “cartilage” region.

Fabrication and materials: Structures were fabricated using our custom DLP printer, described in detail previously.⁵ Materials included an acrylate-based resin, poly(ethylene glycol) diacrylate with pentaerythritol tetrakis(3-mercaptopropionate) (PEGDA:PETMP), and the photoinitiator diphenyl(2,4,6-trimethylbenzoyl) phosphine oxide (TPO). A thermal initiator, 2,2'-Azobis(2-methylpropionitrile) (AIBN) was introduced for post-processing cure. Structures were then mechanically tested (see below) before being stained with iodine (1 wt% Lugol's iodine, 29% water, 70% ethanol) to increase X-ray opacity. Structures were infilled with a poly(ethylene glycol)-based pre-polymer

solution² and photopolymerized to form composite structures (Fig. 2.b,d).

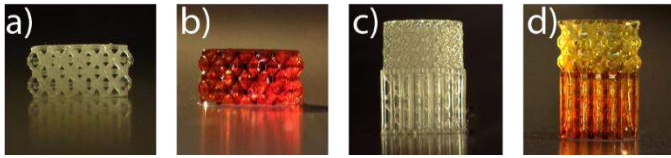


Figure 2: Fabricated structures; a) uniform structure without infill; b) composite uniform structure stained with iodine; c) bilayer structure without infill; d) composite bilayer structure stained with iodine.

Combined Mechanical Testing and X-ray Microscopy (XRM): The regional mechanics of fabricated structures were measured from unconfined compression testing while XRM imaging. Unconfined compression testing was performed to 12% strain (MTS Insight II). The same structures were imaged in undeformed and deformed (10% strain) states using XRM (Zeiss Xradia 520 Versa; 4 \times , 80kV, 7W, 2s exposure; 201 images, 5 μ m voxel size) to measure regional deformations. Average stress, from stress-strain curves, and regional and global strain measurements during XRM imaging allowed estimation of regional stiffness within each structure (Figs. 3, 4).

RESULTS

The uniform structure design was predicted by FEA to have uniform stiffness of $E_{struct} = 1.0$ MPa (Fig. 4.a). Mechanical testing of the empty structure resulted in 10% higher stiffness than predicted by FEA with $\sim 10\%$ variation between regions (Fig. 4.b). However, infilling scaffolds with hydrogel led to a $\sim 25\%$ decrease in global stiffness with greater variability of regional stiffness values.

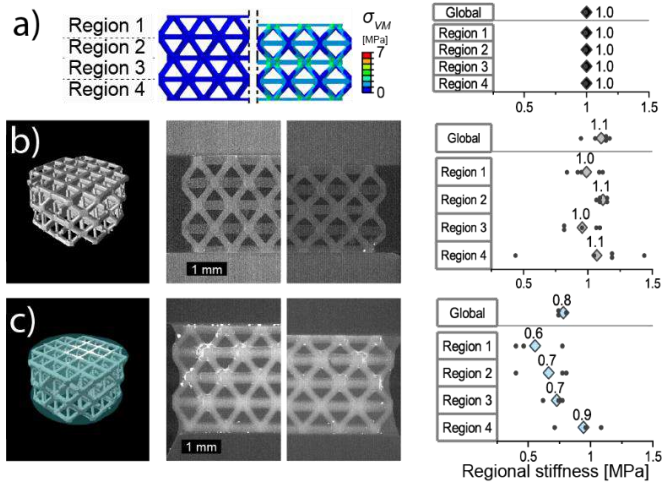


Figure 3: Uniform structure results. a) FEA predictions with von Mises stress visualized; b) empty structure and c) infilled composite results. From left to right in b) and c): 3D XRM rendering, 2D cross-sections of deformed and undeformed states, and regional stiffness.

FEA of the bilayer gradient structure design predicted that the structural stiffness increased with depth in the cartilage region and that the bone region roughly attained the desired stiffness of ~ 10 MPa (Fig. 5.a). Mechanical tests confirmed the cartilage region gradient in the empty structure (Figure 5.b), while the infilled bilayer structure also possessed a stiffness gradient in the cartilage region but that was generally lower than that of the empty structure (Figure 5.c).

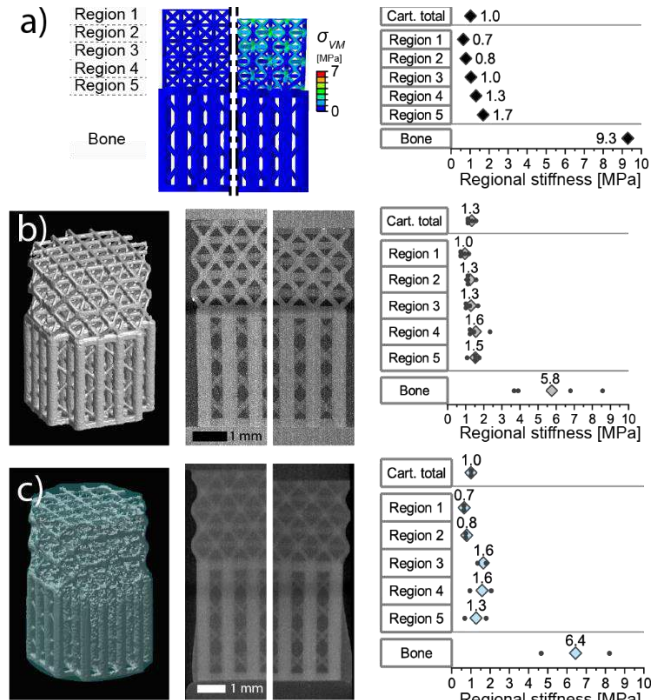


Figure 4: Bilayer structure results. a) FEA predictions with von Mises stress visualized; b) empty structure and c) infilled composite results. From left to right in b) and c): 3D XRM rendering, 2D cross-sections of deformed and undeformed states, and regional stiffness.

DISCUSSION

We successfully fabricated bilayer composite scaffolds for osteochondral regeneration that featured a cartilage region with graded stiffness and an underlying bone region. The regional stiffnesses were characterized at a resolution of approximately 0.5 mm and were similar to our target stiffness. Evaluating the uniform structure demonstrated that the infilled, composite scaffolds had lower average stiffness and greater variability between regions as compared to empty structures. We speculate that the iodine stain that was needed to visualize infilled structures degraded the 3D printed material and led to a lower composite stiffness. Also, swelling stresses from the infilled gels may have introduced local buckling that we observed in the deformed micro-trusses and contributed to variability of regional strains.

The presented bilayer structure may improve upon osteochondral tissue engineering implants through its incorporation of multiple mechanical gradients. Additionally, the presented method of combining XRM imaging with unconfined compression is a useful tool to evaluate gradients in composite scaffolds on a sub-millimeter scale. Through improved mechanical characterization, regenerative implants may be further optimized to improve treatment outcomes.

ACKNOWLEDGEMENTS

Supported by NIH R21/R33 HD090696 and NIH 1R01AR069060

REFERENCES

- [1] Aziz, A.H. et al., *J. Tissue Eng. Regen. Med.*, **13**, 946–959 (2019).
- [2] Schoonraad, S.A. et al., *Biofabrication* **13**, (2021).
- [3] Eckstein, K. et al., SB3C virtual presentation (2021).
- [4] Guilak, F. et al., *J. Orthop. Res.* **13**, 410–421 (1995).
- [5] Uzcategui, A. C. et al., *Adv. Eng. Mater.* **20**, 1800876 (2018).

EXPERIMENTAL AND COMPUTATIONAL ANALYSIS OF THE INJECTION-INDUCED MECHANICAL CHANGES IN THE SKIN MICROENVIRONMENT DURING SUBCUTANEOUS INJECTION OF BIOLOGICS

Yingnan Shen (1), Sameep R. Shah (1), Kejie Zhao (1), Bumsoo Han (1, 2, 3)

(1) School of Mechanical Engineering, Purdue University, West Lafayette, IN, USA
 (2) Weldon School of Biomedical Engineering, Purdue University, West Lafayette, IN, USA
 (3) Purdue Institute for Cancer Research, Purdue University, West Lafayette, IN, USA

INTRODUCTION

Biologics, pharmaceutical products derived from biological origin, are emerging because of higher efficacy and lower toxicity than synthetic drugs. These drugs include recombinant proteins, antibodies, vaccines, blood components, and reprogrammed cells [1-4]. In 2021, eight of the top 10 selling drugs are biologics [5]. However, the effective delivery of biologics is still challenging due to the large molecular weights and the sensitive molecular structure to the environmental condition. Intravenous delivery may be effective, but it typically needs hospital care and professional administration, drastically increasing the treatment cost [6]. Thus, subcutaneous (SQ) injection has been considered a promising delivery route because it can be self-administered [7]. One of the most critical drawbacks, however, is that pain and discomfort are induced during SQ injection. This injection-induced pain and discomfort (IPD) pose significant huddles for the broader use of biologics, the design of injection devices and drug formulations, and the quality of patient's life [8-10].

However, the mechanism of the IPD is not well understood yet. To assess the impact of SQ injection, current studies rely on pain intensity scales which include the faces pain scale (FPS), the numerical rating scale (NRS), the verbal rating scale (VRS), and the visual analogue scale (VAS) [11, 12]. However, these measures of FPS, NRS, VRS, or VAS are subjective and often lead to inconclusive measures. Thus, the identification of quantitative biomarkers of the IPD is highly desirable for the design of formulation and SQ injection protocols of biologics to minimize the IPD.

Thus, we hypothesize that the SQ injected induces changes in the mechanical microenvironment of the skin tissue, which in turn stimulate nociceptor neurons in the dermis. To test this hypothesis, we develop a tissue engineered SQ injection platform and quantify the changes in the tissue's mechanical microenvironment both experimentally and computationally. The results are further discussed to identify potential markers for the IPD.

METHODS

SQ Injection Simulation System

An experiment method named cell image deformetry (CID) was used to measure the spatiotemporal deformation of engineered tissue construct (ETC) during the injection of model biologics. The CID method was also described in our previous work on tissue deformation during freezing [13]. A schematic of the experimental platform constructed for CID is shown in **Fig. 1**. The platform consists of an

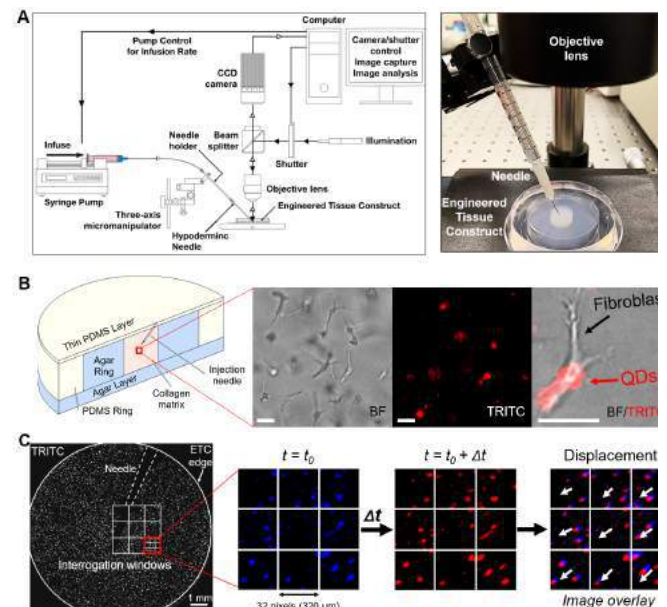


Figure 1: Engineered SQ injection model to mimic injection-induced tissue deformation.

injection system, an imaging system, and ETCs. The imaging system includes a fluorescence macro/microscope (MVX10, Olympus, PA) equipped with a CCD camera (Aqua, QImaging, CA). The injection system includes a syringe pump (NE 1000, New Era Pump Systems, NY) which controls the injection flow rates. The ETC was constructed by seeding and culturing quantum dot-labeled dermal fibroblasts at 2×10^5 cells/ml in type I collagen matrix (6 mg/ml), as shown in Fig. 1B. During the injection, the ETC was imaged under a fluorescence microscope to track the location of QD-labeled cells. These time-lapsed images were cross-correlated to determine the displacement rate first. These displacement rates were further integrated to determine total displacement, as shown in Fig. 1C.

Computational Methods

We used a multi-physics coupled computational framework to simulate the variation in the ETC microenvironment brought by the SQ injection and to further predict the surface and internal three-dimensional distribution of interstitial fluid pressure (IFP) and matrix stress fields. The tissue is considered as poroelastic biphasic material with nonlinear elastic deformable porous solid and interstitial fluid saturated pores. The framework integrates interstitial fluid flow, tissue deformation, and mechanics based on finite deformation hyperelasticity to model the nonlinear response. The computational domain is discretized using an unstructured 3D tetrahedral mesh with extremely fine elements close to the needle and injection location in the ETC. A transient study simultaneously numerically solves the governing equations using the MULTifrontal Massively Parallel sparse direct (MUMPS) solver in COMSOL Multiphysics 5.4.

RESULTS AND DISCUSSION

Fig. 2A shows the displacement rate vector field measured by the CID method when distilled water is injected at a rate of 1.2 ml/min into ETC. The injection site is noted with the dot, and the injection direction is indicated with the arrow. Notable tissue deformation occurred in the first 0.2 s since the start of injection, during which the local displacement rate reached above $800 \mu\text{m/s}$ in the region around the injection site. Although the magnitude of the displacement rate substantially reduced at 0.3 and 0.4 s, the size of the deformed tissue continues to enlarge. The total displacement field provided in Fig. 2B shows the localized deformation around the injection site with a displacement larger than $160 \mu\text{m}$. This result demonstrates the injection induces significant tissue deformation around the injection site.

Computational analysis of the injection-induced deformation of ETC is shown in Fig. 3. It simulates the water injection at 1.2 ml/min. The top view of the computational result can be compared with the experimental measurements. Similarly, significant tissue deformation occurred in the first 0.2 s around the injection site of the computational model, and the size of deformed tissue continues to enlarge at 0.3 and

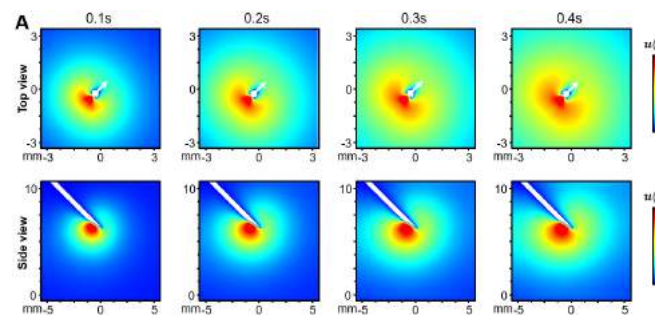


Figure 3: Computational estimation of the injection-induced tissue deformation. Top and side views.

0.4 s. The side view of the computational result provides information on the tissue deformation at the vertical cross-section of ETC. The significant deformation beneath the needle tip, as well as the expansion of the deformed tissue area, is clearly exhibited by the side view. Both the experimental and computational results show larger tissue deformation along the injection direction than in the perpendicular direction. Further computational analysis on the interstitial fluid pressure and matrix stress suggests that both IFP and equivalent matrix stress fields are more localized close to the injection site. The maximum IFP and stress reach 68 and 90 kPa, respectively, at 2.5 ml/min (data not shown). The stress distribution in the tissue is mostly under 25 kPa.

The present study demonstrates that SQ injection causes distinct spatiotemporal changes in the mechanical microenvironment. This study suggests that the mechanical microenvironment changes are thought to activate nociceptors and induce pain, which can be compared with different types of mechanical stimuli studied on the responses of nociceptors.

ACKNOWLEDGEMENTS

This study was partially supported by a grant from NSF (MCB-2134603), the Purdue University Center for Cancer Research (P30 CA023168), and a Program Grant from the Purdue Institute of Drug Discovery.

REFERENCES

- [1] Shanmugaraj, B. et al., *Pathogens* **2020**, 9 (2), 148.
- [2] Charoenphol, P. et al., *Acta biomaterialia* **2018**, 73, 64-80.
- [3] Grilo, A.; Mantalaris, A., *Trends in biotechnology* **2019**, 37, 9-16.
- [4] Li, Y. et al., *Acta Biomaterialia* **2019**, 95, 73-90.
- [5] Urquhart, L., *Nature Reviews Drug Discovery* **2022**, 21 (4), 251.
- [6] Tetteh, E. K.; Morris, S., *Health Economics Review* **2014**, 4 (1), 26. DOI 10.1186/s13561-014-0026-2.
- [7] Jones, G. B. et al. *Science Translational Medicine* **2017**, 9 (405).
- [8] Aronson, R., *Diabetes technology & therapeutics* **2012**, 14 (8), 741-747.
- [9] Heise, T. et al, *Diabetes, Obesity and Metabolism* **2014**, 16 (10), 971-976. DOI 10.1111/dom.12304.
- [10] Chen, M.-C. et al, *Acta biomaterialia* **2015**, 24, 106-116.
- [11] Yoshida, T. et al., *Modern Rheumatology* **2019**, 29 (6), 949-953.
- [12] Nash, P. et al., *Rheumatology and therapy* **2016**, 3 (2), 257-270.
- [13] Teo, K. Y. et al, *Journal of Biomechanical Engineering* **2010**, 132 (3), 031003. DOI 10.1115/1.4000875.

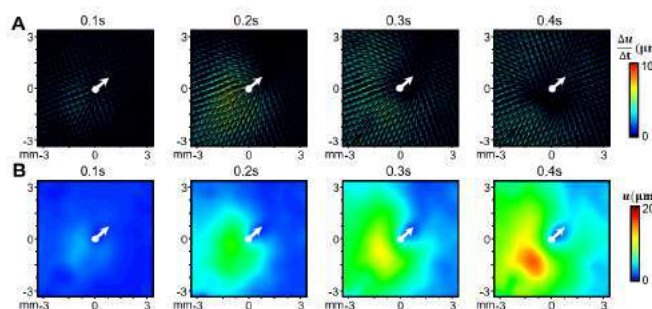


Figure 2: Injection-induced tissue deformation measured by CID measurements.

MACROPHAGE SIGNALING ALTERS FIBROBLAST RESPONSES TO MECHANICAL LOADING

McKenzie E. Sup (1), Min Kyu M. Kim (2), Lee Song (2), Beth Ashinsky (2), Jieon J. Kim (2),
Stavros Thomopoulos (1,2)

(1) Department of Biomedical Engineering, Columbia University, New York, NY, USA
(2) Department of Orthopedic Surgery, Columbia University, New York, NY, USA

INTRODUCTION

The application of excessive levels of mechanical loading has long been accepted as a cause of tendon pathology. More recently, however, evidence is emerging that inflammation also plays a critical role in the initiation and progression of tendinopathy [1]. It remains to be understood how mechanical and inflammatory environments of tendon disease interact with and affect one another; however, there is evidence that inflammatory cytokines such as *IL1 β* can regulate this interaction [2]. Macrophages have been shown, depending on their activation state, to regulate both inflammatory and anti-inflammatory activity of nearby cells, and to stimulate cell proliferation and matrix deposition [3,4]. Additionally, macrophages have been identified in early tendinopathy, abundantly after acute injury, and persistently throughout long-term tendon healing [5,6]. Recent studies have also shown that mechanical loading can regulate macrophage function, but the role of macrophages in tendon mechanoresponsiveness is unknown [7]. Therefore, we investigated the role of macrophage signaling in altering tendon fibroblast (TF) responses to mechanical loading using an *in vitro* loading model. We hypothesized that stimulation of TFs with conditioned media from M1-activated macrophages would cause TFs to be hyper-responsive to mechanical stimulus, accelerating intracellular injury response pathways in an effort to reinforce their cytoskeletal structure and ECM against further loading.

METHODS

Macrophage isolation and culture: Bone marrow was isolated from femur and tibia of 2-month-old C57BL/6 mice. Macrophages were differentiated by culturing bone marrow aspirate in RPMI complete medium with 10% FBS and 1% penicillin/streptomycin, supplemented with 20% L929-conditioned medium (LCM) containing M-CSF. After 5 days of culture, macrophages were seeded into 6-well plates. The following day, macrophages were polarized to M1 phenotype by LPS and IFN- γ stimulation for 24 hours. Then, stimulation media was

replaced with fresh cytokine-free macrophage media. 24 hours later, the media was harvested from the activated macrophages, to be added to TFs.

Tendon fibroblast isolation and culture: TFs were isolated from the tail tendons of 2-month-old C57BL/6 male and female mice by collagenase digestion in a shaking incubator. The cells were seeded on fibronectin-coated silicon elastomer PDMS stretch chambers (STB-CH-04, STREX Co., Osaka, Japan) at passage 2, and then serum starved with 1% fetal bovine serum (FBS) media to synchronize cell cycle phase 24 hours prior to conditioned media treatment and onset of loading. To assess the TF response to macrophage paracrine signaling, conditioned media (CM) harvested from M1-activated macrophages and filtered with a 0.2 μ m syringe filter. TFs were first washed with PBS, and then immediately received a media treatment of equal parts fibroblast medium (media with 10% FBS and 1% penicillin/streptomycin) and M1-macrophage CM. Control media treatment consisted of equal parts fibroblast culture medium and macrophage culture medium.

In Vitro Loading Model: Scaffolds were allowed to equilibrate for 1 hour prior to beginning of the loading protocol. Control scaffolds underwent a mock protocol of preparation for loading prior to being return to static culture in the same incubator. Loaded fibroblasts were subjected to 24 hours of cyclical tensile strain at a magnitude of 7% strain and a frequency of 0.5 Hz, using the STB-1400 STREX cell stretch system (STREX Co., Osaka, Japan).

Outcome measures: For gene expression results, cells were lysed and RNA was isolated immediately after the completion of loading. RT-qPCR was then performed for genes related to fibroblast mechanoresponse, inflammation, and tenogenesis. For imaging experiments, cells were fixed with 10% formalin for 15 minutes prior to immunostaining with alpha smooth muscle actin (α SMA), and DAPI (nuclei). Images were taken at 20x magnification using Zeiss Apotome.

RESULTS

TFs responded to treatment with M1 CM by upregulating *Il6* and *Cox2* gene expression after 24 hours (Figure 1). The increase in α SMA gene expression was not statistically significant, however, α SMA immunostaining was more intense and more homogenous 24 hours after M1-CM treatment (Figure 3).

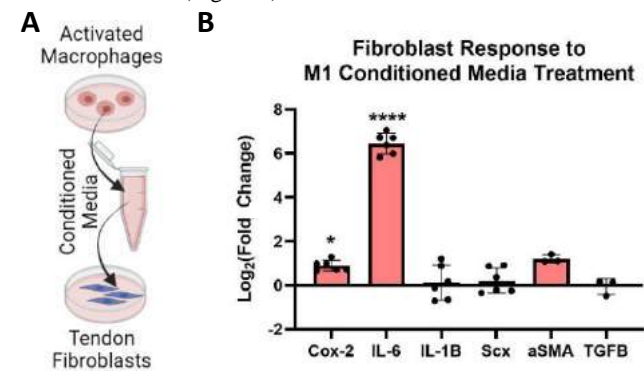


Figure 1: A) Schematic for M1-CM stimulation of tendon fibroblasts and B) Gene expression responses to treatment (*indicates $p<0.05$, ****indicates $p<0.001$, paired t-test with Holm-Sidak correction). Fold changes were relative to TFs with control media.

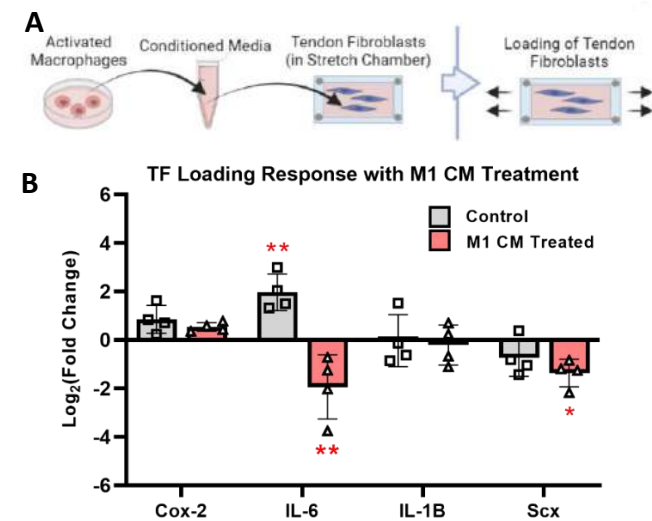


Figure 2: A) Schematic of experimental design (*indicates $p<0.05$, **indicates $p<0.01$, paired t-test with Holm-Sidak correction). B) IL-6 increased with loading in control TFs, but decreased with loading in M1-CM-treated TFs. Fold change is relative to unloaded control-media cells for the control group, and unloaded M1-CM treated cells for the M1-CM treated group.

When fibroblasts cultured in M1-CM were subjected to mechanical loading, they responded differently than fibroblasts in control media. Instead of upregulating *Il6* expression, as unstimulated fibroblasts did, M1-stimulated fibroblasts downregulated *Il6* expression in response to loading (Figure 2). In addition, *Scx* did not change in response to loading in fibroblasts with control media, but significantly decreased in response to loading in fibroblasts treated with M1 CM (Figure 2). α SMA staining revealed increased formation of stress fibers in response to loading compared to TFs in static culture (Figure 3). No clear

difference was noted between loaded TFs treated with M1 CM and loaded TFs in control media.

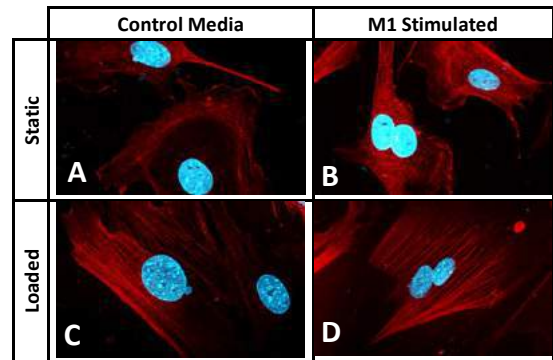


Figure 3: TFs were fixed and stained with α SMA (red) and DAPI (blue) after 24 hours of A) static culture with control media, B) static culture with M1 CM, C) loading with control media, and D) loading with M1 CM.

DISCUSSION

This study established the potential of M1 macrophage signaling for regulating TF responses to mechanical loading. Interestingly, treatment of TFs with M1 CM resulted in an opposite *Il6* response to loading, compared to control media-treated TFs. While this did not reflect the hyper-responsive reaction to mechanical loading that we expected, further studies will be necessary to determine the functional significance behind the change in *Il6* response. *Il6* has been reported to have either pro-inflammatory or anti-inflammatory effects in tendon, and its effects appear to be context dependent [8]. *Il6* has also been shown to regulate matrix deposition and increase collagen production, but can contribute to the formation of excessive scar [9,10]. Thus, negative feedback of *Il6* levels may be a protective mechanism by the TFs, in effort to maintain ideal expression levels for injury response and tissue homeostasis. Additionally, *Scx* was downregulated in the M1-CM-treated TFs, but not in the control-media TFs. Because *Scx* is known to initiate the expression of mechanically-activated genes, this may be further evidence of a protective response against overloading [11]. Future studies will investigate mechanoresponsive pathways in M1-CM treated TFs to determine the mechanism(s) behind the altered response to loading, as well as to investigate for altered patterns of ECM production. In addition, further investigations will be performed to identify the specific components present in the M1 CM that are responsible for inducing the altered mechanoregulation observed in this study.

ACKNOWLEDGEMENTS

The study was supported by NIH R01-AR062947. Schematic figures were created with Biorender.com.

REFERENCES

[1] Arvind V. et al., *Front. Bioeng, Biotechnol*, 9, 1-16.103389, 2021.
[2] Archambault J. et al., *J Orthop Res.*, 20(1):36–39, 2002.
[3] Koh TJ. et al., *Expert Rev Mol Med.*, 13:e23, 2011.
[4] de la Durantaye M. et al., *J Orthop Res.*, 32(2):279–285, 2014.
[5] Millar NL. et al., *AM J Sports Med.*, 38(10):2085–209, 2010.
[6] Sugg KB. et al., *J Orthop Res.*, 32(7):944–951, 2014.
[7] Maruyama K. et al., *Inflamm Regen* 39:3, 2019.
[8] Scheller J. et al., *Biochim Biophys Acta*, 1813: 878–888, 2011.
[9] Liechty KW. et al., *Cytokine*. 12: 671–676, 2000.
[10] Andersen MB. et al., *J Appl Physiol* (1985). 110: 1549–1554, 2011.
[11] Nichols AEC et al., *BMC Cell Biol*. 19, 14, 2019.

SIMULATION OF REPAIR ON A DYNAMIC PATIENT-SPECIFIC LEFT ATRIOVENTRICULAR VALVE MODEL

Stephen Ching (1), Christopher Zelonis (1), Christian Herz (1), Patricia Sabin (1), Muhammad Nuri (2), Yan Wang (3), Andras Lasso (4), John Moore (5), Terry Peters (6), and Matthew A. Jolley (1,3)

- (1) Jolley Lab, Department of Anesthesia and Critical Care Medicine, Children's Hospital of Philadelphia, Philadelphia, Pennsylvania, USA
- (2) Division of Cardiothoracic Surgery, Children's Hospital of Philadelphia, Philadelphia, Pennsylvania, USA
- (3) Division of Cardiology, Children's Hospital of Philadelphia, Philadelphia, Pennsylvania, USA
- (4) Laboratory for Percutaneous Surgery, Queen's University, Kingston, Ontario, Canada
- (5) Archetype Medical Inc., London, Ontario, Canada
- (6) Robarts Research Institute, Western University, London, Ontario, Canada

INTRODUCTION

Each year, 2100 children are born with an atrioventricular canal (AVC) in the United States [1]. Among children with Down Syndrome, this defect is even more prevalent – 40% of those with cardiac disease have AVCs. Patients with complete atrioventricular canals (CAVC) have a single atrioventricular valve that spans across both ventricles. Surgical repair attempts to divide the single valve into two valves including a mitral-equivalent left atrioventricular valve (LAVV). With current repair techniques, LAVV failure requires reintervention in up to 40% of patients [2-4]. Further, reintervention results are poor with more than a quarter of patients who undergo reintervention requiring two or more reoperations [4, 5].

The development of 3D echocardiographic (3DE) based valve modeling tools have been used to make high quality analyses of cardiac structures, allowing precise, quantitative comparison of normal valves to dysfunctional valves, greatly improving the understanding of the 3D structural correlates of adult valve dysfunction [6]. The application of image-derived modeling for physical simulation has potential to allow investigators to better understand treatment options for patients with failing LAVVs. Therefore, there is a need for a platform to test and evaluate repair strategies before treatments are performed on a patient. Current 3D printed models are static and lack a dynamic component necessary for evaluating the success of repairs to these valves. Dynamic simulations have already been developed for mitral and tricuspid valves; therefore, it is the goal of this study to adapt these prior workflows for simulating and assessing different repair strategies for LAVVs [7,8].

METHODS

This study protocol was reviewed and approved by the Children's Hospital of Philadelphia institutional review board.

Patient Selection and Image Acquisition: Patients who had underwent AVC repair and high-quality (3DE) imaging were queried from an

existing institutional database. One case of a regurgitant LAVV was identified: a 21-year-old female with moderate LAVV regurgitation originating centrally from a residual cleft in the neo-anterior leaflet. 3DE images were previously existing and acquired via transesophageal 3DE on a Philips Epiq system (Philips Medical, Cambridge, MA).

Leaflet Segmentation and Mold Generation: The selected Digital Imaging and Communications in Medicine (DICOM) files were imported into 3D Slicer (www.slicer.org). The annulus was defined in mid-systole and late-diastole using Annulus Analysis module in SlicerHeart [9]. Mid-systole is defined as the median time frame between the first frame when the valve is closed and the last frame when the valve is closed in a cardiac cycle. Late-diastole is defined as the frame before systole where the leaflets have not yet coapted and individual leaflets are still visible. The leaflets are then manually segmented using the Valve Segmentation module. Lastly, a mold of the atrial profile of the leaflets is created and the locations of the papillary muscle tips are recorded.

Silicone Model Creation: We create a silicone model to emulate valve physiology that include leaflets, chordae, papillary muscles, and the surrounding myocardium. A composite of silicone (Ecoflex, Smooth-On Inc., Macungie, PA) and nonwoven gauze is painted onto the 3D printed valve profile to create the leaflets. Gauze is added to give the silicone tensile strength and to prevent sutures from dehiscing under hemodynamic loading. Additionally, six frayed Dacron threads are imbedded in the silicon to simulate the chordae tendineae. The Dacron thread then runs through a 3D-printed patient-specific papillary muscle post that is made using the papillary muscle data recorded from the 3DE. The ends of the threads attach to tunable keys that can be used to adjust the tension of the chordae. The myocardium is modeled using silicone (Dragonskin, Smooth-On Inc, Macungie, PA) that has been injected into a 3D printed mold containing a hinge-point-apparatus. The hinge-point-apparatus is used for defining the valve annulus and enforcing the hinge

point. Once the silicone has cured, the entire apparatus is fixed between two 3D printed flanges (Fig. 1a).

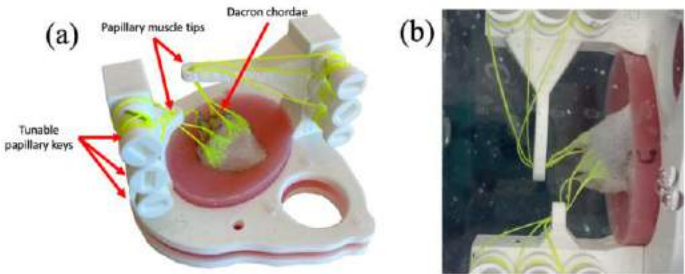


Figure 1: a) Silicone valve model schematic, b) silicone valve model in pulse duplicator.

Simulated Repair: Four identical silicone valves are constructed and presented to an attending cardiothoracic surgeon to perform a different surgical valve repair on each. The strategies employed were an annuloplasty where the annular circumference between the anterolateral commissure and the posteromedial commissure was reduced by 10%, a second annuloplasty where the circumference was reduced by 20%, an Alfieri stitch between the neo-anterior leaflet and the mural leaflet, and a closure of the residual cleft in the neo-anterior leaflet (Fig 2).

Pulse Duplicator: The assembled valve apparatus is then mounted in a two-chamber dynamic simulator (Archetype Biomedical Inc, London, Ontario, Canada) which can replicate patient heart rate, stroke volume, and pressures at the time of image acquisition (Fig. 1b). Performance and regurgitation of the simulated valve are visualized using a transesophageal echo probe with EKG gating and colored Doppler.

Analysis: Image data recorded from the pulse duplicator is imported into 3D Slicer, and the leaflets are segmented in mid-systole for analysis. The four different repair strategies are compared via common clinical metrics: billow height, tenting height, mean trans-valvar pressure gradient, and regurgitant orifice area. Billow height and tenting height are defined as the distance normal to the least-squares annular plane to the highest and lowest points on the leaflets, respectively. The regurgitant orifice area is calculated using a custom shrink-wrapping algorithm on the resulting leaflet segmentation [10].

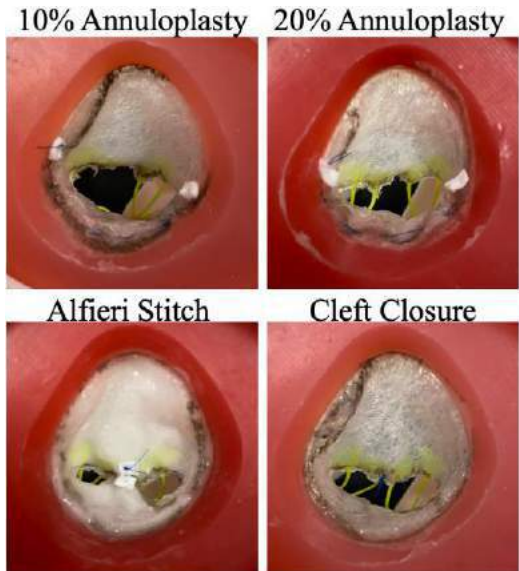


Figure 2: Simulated repairs on four identical LAVVs.

RESULTS

The resulting valves were mounted in the pulse duplicator and patient physiological loads were applied. The 3DE measurements and segmentation data are provided in Table 1.

Billow height and mean gradient pressure were consistent across all models except for the Alfieri stitch repair which resulted in a stenotic valve. The tenting height is increased in all repaired models; this is a product of mural leaflet immobility. Overall, closure of the partial cleft in the neo-anterior leaflet produced the valve with the smallest regurgitant orifice area.

Table 1: Comparison of repair strategies

Valve Model	Tenting Height (mm)	Billow Height (mm)	Mean Gradient (mmHg)	Regurgitant Area (cm ²)
10% Annuloplasty	17.7	3.1	4	1.1
20% Annuloplasty	12.2	3.4	5	0.72
Alfieri Stitch	18.0	3.3	17	0.75
Cleft Closure	17.0	2.2	5	0.37

DISCUSSION

This study has provided a first approach to using dynamic physical modeling for comparing different repair strategies in patient-specific LAVV models. These methods provide powerful opportunities for medical training and preoperative planning. This is especially true for congenital heart diseases where anatomies are highly heterogeneous and treatment options are variable. The work of this study sets the groundwork for a platform for testing and evaluating treatment options for atrioventricular valves. With further development and experimentation using more samples, this system has the potential to simulate the function of complex valve morphologies under physiological loads. This workflow can also continue to be built out with more valves, including CAVCs, and more complex interventions in the future.

There is no concluded best repair method in this study as there is no comparison to a control model or a ground truth. Limitations in this work include variability in the manufacturing workflow. For example, the silicone may have been painted onto the leaflet with varying thickness between each valve model. Additionally, the valvar and sub-valvar apparatuses have been vastly simplified in this study. Future work includes research into enhanced manufacturing techniques that allow for much more precise control over leaflet thickness such as 3D printing in tissue mimicking materials. Further, the manufactured heart valves will need to be validated against a ground-truth patient 3DE.

ACKNOWLEDGEMENTS

This work was supported NIH R01HL153166, The Cora Topolewski Fund at the Pediatric Valve Center at CHOP, and the CHOP Pediatric Valve Frontier Program.

REFERENCES

[1] Mai, C.T., et al., *Birth Defects Res*, 111:1420-1435, 2019.
 [2] Ho, D.Y., et al., *Ann Thorac Surg*, 110:969-978, 2020.
 [3] Suzuki, K., et al., *J Am Coll Cardiol*, 32:1449-1453, 1998.
 [4] Stulak, J.M., et al., *Ann Thorac Surg*, 87:1872-1877, 2009.
 [5] Prifti, E., et al., *J Card Surg*, 28:756-763, 2013.
 [6] Lee, A.P., et al., *Circulation*, 127:832-841, 2013.
 [7] Ginty, O.K., et al., *Int J Comput Radiol Surg*, 14:1227-1235, 2019.
 [8] Boone, N., et al., *Proc SPIE*, 113152E, 2020.
 [9] Lasso, A., et al., *Front Cardiovasc Med*, 9, 2022.
 [10] Van Overveld, K., et al., *Vis Comput*, 20:362-379, 2004.

RIGHT VENTRICULAR GLOBAL LONGITUDINAL STRAIN AND VENTRICULAR DYNAMICS IN PATIENTS WITH PULMONARY HYPERTENSION

Alexandra M. Janowski (1), Scott Visovatti (2), Raymond L. Benza (2), Rebecca R. Vanderpool (2)

(1) Department of Biomedical Engineering, The Ohio State University, Columbus, OH, United States

(2) Division of Cardiovascular Medicine, The Ohio State University, Columbus, OH, United States

INTRODUCTION

Right ventricular (RV) function strongly associates with mortality in patients with pulmonary arterial hypertension (PAH). Survival is associated with right ventricular function rather than pulmonary vascular resistance or PA pressure.^{2,3} Optimization of RV assessment is an identified priority in PH clinical research.^{1,4} Echocardiography and cardiac magnetic resonance (CMR) imaging are both used to quantify RV function but CMR can be used to reliably obtain quantitative information about RV shape, size, and remodeling.⁵ A current unmet clinical need is the identification of clinically meaningful imaging features that clearly distinguishes between normal and abnormal RV structure and function.

Right ventricle global longitudinal strain has been shown to associate with outcomes in PH and is typically measured via echocardiography⁶. Measures of strain help to provide insight into the biomechanics of the RV (diastolic stiffness) and function. Changes in ventricular dynamics during ejection and filling may associate with the biomechanics of the RV. We hypothesize RV strain will be different in advanced RV dysfunction and the aim of the study was to evaluate RV strain and instantaneous strain rates throughout the cardiac cycle from CMR images in patients with pulmonary hypertension.

METHODS

Participants were identified from The Ohio State University CMR PH registry and included if they had four chamber (4CH) CMR images and right heart catheterization (RHC) data (n = 85). Participants were split based on hemodynamics into PH groups: No PH (mPAP < 20mmHg), PH-LHD (mPAP ≥ 20 mmHg, PAWP ≥ 15 mmHg), and Pre-capillary PH (mPAP ≥ 20 mmHg, PAWP < 15 mmHg). Diastolic elastance (E_{ed}) was calculated by fitting the curve $P = \alpha(e^{V^{\beta-1}})$ using pressure and volume data from RHC and CMR. Participants were into low and high E_{ed} groups based on the median E_{ed} value (0.28).

From the 4CH cine images, the right ventricular area was manually segmented throughout the cardiac cycle using MATLAB (**Figure 1A**).

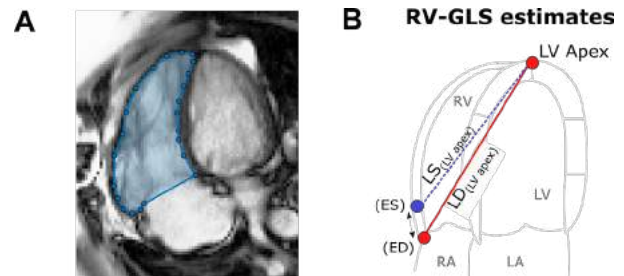


Figure 1: Methods to estimate RV strain. A) Segmentation of the right ventricle (blue area). B) The lateral tricuspid valve point and LV apex was used to estimate the length of the RV. RV global longitudinal strain was calculated as the difference between the end-diastolic length (LD) and end-systolic length (LS).

To estimate RV-GLS, the lateral tricuspid valve and LV apex landmarks were selected at end diastole and end systole (**Figure 1B**). RV-GLS was estimated as the difference in length from the lateral tricuspid valve point to either the LV apex or RV insertion point from end diastole (LD) to end systole (LS) (**Equation 1**).

$$RV_{GLS} = \frac{(L_D - L_S)}{L_D} \quad (1)$$

The segmented areas were plotted as a function of time and repeated a total of three cardiac cycles (**Figure 2A**). The derivative of the area was used to obtain ejection (linear decreasing area, negative derivative) and filling (linear increasing area, positive derivative) phases (**Figure 2B**). The filling phase was split into passive filling (early diastole) and active filling (late diastole). The ejection rate, passive filling rate and active filling rate were determined by fitting a linear line to the identified regions. Statistics were calculated in R. Pearson's correlations were used to obtain correlations. A p-value of 0.05 was used to determine significance.

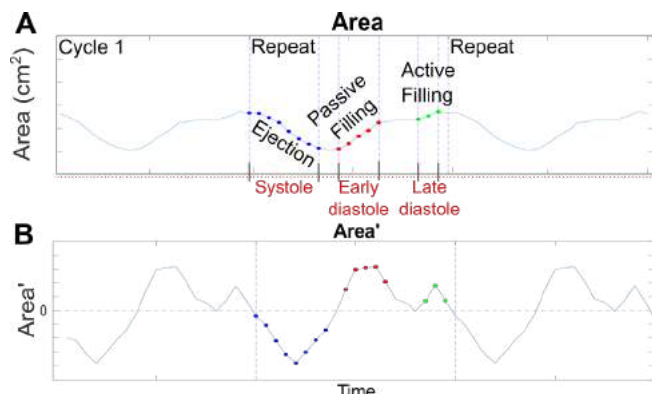


Figure 2: Methods to estimate RV ejection and filling rates. A) Area as a function of time for three cardiac cycles. B) Area gradients were used to identify linear ejection (negative) and filling phases (positive). The filling phase was split into the passive filling (early diastole) and active filling (late diastole).

RESULTS

From the $n = 81$ participants, 56.8% had pre-capillary PH, 29.6% had PH-LHD and 13.5% had no PH based on RHC hemodynamics (Table 1). Participants with PH had increased RV end diastolic pressures (RVEDP) and systolic pressures (RVSP) compared with no PH. PH-LHD had increased RVEDP when compared to pre-capillary PH and no PH participants.

Table 1: Cohort characteristics

	No PH N = 11	PH-LHD N = 25	Pre-capillary PH N = 49
mPAP (mmHg)	16 ± 3	$45 \pm 12^*$	$38 \pm 13^{\dagger}$
PAWP (mmHg)	9 ± 4	$22 \pm 5^*$	$10 \pm 4^{\dagger}$
RVSP (mmHg)	30 ± 8	$71 \pm 22^*$	$61 \pm 21^*$
RVEDP (mmHg)	7 ± 3	$20 \pm 5^*$	$11 \pm 6^{\dagger}$
Ejection Rate (cm^2/s)	-39.8 ± 14.3	-32.2 ± 11.3	-33.4 ± 16.9
Passive Filling Rate (cm^2/s)	33.3 ± 12.4	32.05 ± 19.0	35.8 ± 21.7
Active Filling Rate (cm^2/s)	48.7 ± 20.3	36.2 ± 15.6	40.5 ± 24.0

* $P < 0.05$ vs No PH, $\dagger P < 0.05$ vs PH-LHD

In the PH-LHD and pre-capillary PH groups, PVR was increased, RVEF was decreased and RV-GLS was less negative (decreased movement) compared to no PH (Figure 3A-C). Despite similar RV-GLS and RVEF, PH-LHD group had increased diastolic elastance compared to pre-capillary PH (Figure 3D). There were no significant differences in ejection rate, passive filling rate or active filling rate between PH types (Table 1).

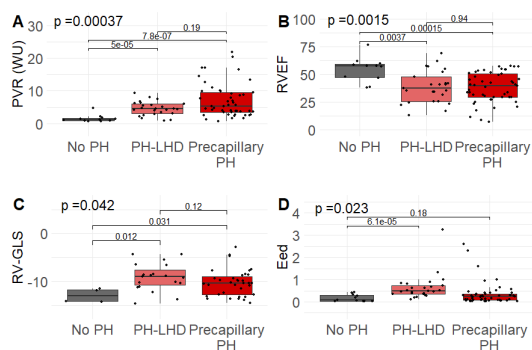


Figure 3: Increased RV diastolic stiffness in PH-LHD. Participants with pulmonary hypertension (PH-LHD and pre-capillary PH) have increased PVR (A), decreased RVEF (B) and less negative RV-GLS (C) compared to no PH. D) PH-LHD had increased diastolic elastance (Eed) compared to no PH and pre-capillary PH.

The RV ejection, passive filling and active filling rates significantly correlated with RV-GLS (Figure 4A&B). Eed correlated with active filling ($r = -0.27$, $p = 0.014$) but not ejection ($r = -0.18$, $p = 0.11$) or passive filling ($r = -0.16$, $p = 0.14$). When split based on high and low Eed, participants with high Eed had decreased ejection rates (Figure

4C), no difference in passive filling rates (Figure 4D), and decreased active filling rates (Figure 4E) compared to low Eed.

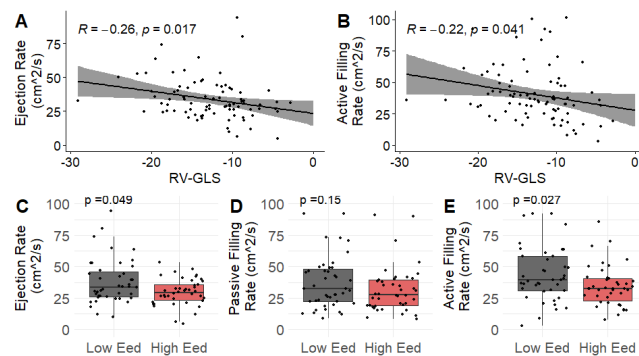


Figure 4: Ejection and active filling rates as a function of RV-GLS and RV diastolic elastance (Eed). RV-GLS significantly correlates with ejection rate (A) and filling rate (B) but not passive filling (not pictured). When split by median diastolic elastance (Eed: 0.28), participants with high Eed had decreased ejection rate (C), no difference in passive filling (D) and decreased active filling rates (E) compared to low Eed.

DISCUSSION

Right ventricular dynamics can be quantified from four chamber CMR images using RV ejection and filling rates. Participants with pulmonary hypertension (PH-LHD and pre-capillary PH) had less dynamic ventricles (less negative RV strain) and more RV dysfunction compared to participants with no PH. The PH-LHD group had increased end-diastolic elastance compared to the other groups but similar RV-GLS and RV function as the pre-capillary PH group. Ejection and filling rates did not associate with PH type but were correlated with RV End-diastolic elastance. The filling phase was split into passive filling (early diastole) and active filling (late diastole)⁷. RV diastolic stiffness might not be as much of driving factor for the passive filling rate because ventricular pressure and strain is less compared to late diastole and active filling. Patients with increased ventricular stiffness (high Eed) have increased end-diastolic pressure that could be contributing to decreased active filling rates compared to low Eed. More investigations into the changes in ventricular stiffness and the biomechanics of the ventricle are needed to understand the altered ventricular dynamics from pulmonary hypertension.

ACKNOWLEDGEMENTS

Research reported in this poster was supported by AHA Career Development Award (19CDA34730039) and the OSU Division of Cardiovascular Medicine.

REFERENCES

- Lahm T, et al., *Am J Respir Crit Care Med*. 2018;198:e15–e43.
- van de Veerdonk MC, et al., *Journal of the American College of Cardiology*. 2011;58:2511–9.
- van de Veerdonk MC, et al., *Chest*. 2015;147:1063–1071.
- Kiely DG, et al., *Pulm Circ*. 2019;2045894019841990.
- Alabed S, et al., *Curr Cardiovasc Imaging Rep*. 2020;13:30.
- Lu, K. J. et al., *Echocardiography* 32, 966–974 (2015).
- Wessels, J. N. et al., *Eur Respir J* 59, 2101454 (2022).

A THERMODYNAMIC FRAMEWORK FOR THE EVOLUTION OF SARCOMERES IN CARDIOMYOCYTES SUBJECTED TO DYNAMIC LOADING

Ryan J. Coleman (1), Vikram S. Deshpande (2), Patrick McGarry (1)

(1) Department of Biomedical Engineering, University of Galway, Galway, Ireland
(2) Department of Engineering, University of Cambridge, Cambridge, UK

INTRODUCTION

Identification of in-vitro protocols to develop mature cardiomyocytes (CMs) with sarcomeric structures and aligned myofibrils remains a key challenge in the field of cell and tissue engineering [1]. Physiologically sarcomeres consist of ordered actin-myosin (AM) bounded by Z-bands. Active contractility is generated through AM cross-bridge cycling. Titin proteins connect M-bands to Z-bands. Sarcomeres spontaneously beat in mature CMs [1, 2, 3].

Similar to sarcomeres, stress fibers (SFs) actively generate tension through AM cross bridge cycling. However, SFs are unstructured and do not contain Z-bands or titin, consequently SFs generate lower levels of tension than sarcomeres [4, 5]. SFs are found throughout the cytoplasm of naïve cardiomyocytes (CMs) and human pluripotent stem cells (hPSCs)-CMs. Sarcomeres evolve from highly aligned SFs during differentiation to a mature CM phenotype. The in vitro study of Dou et al. [6] shows that application of dynamic biaxial stretching significantly increases sarcomere formation in comparison to static controls. However, the mechanism by which dynamic loading leads to increased sarcomere formation and a mature CM phenotype is poorly understood. A new understanding of the role of mechanical loading in sarcomere formation would represent a significant contribution to the field of cardiac tissue engineering, in addition to advancing the current clinical understanding of the pathogenesis of cardiac hypertrophy.

In the current study we propose a novel dynamic theoretical formulation for the remodeling of sarcomeres and SFs. Our analyses uncover a thermodynamic basis for the relationship between dynamic loading and sarcomere formation, including the key energetic role of titin in this complex process. Our model is shown to correctly predict that application of 20% dynamic stretching at 1 Hz results in a three-fold increase in sarcomere density compared to static control, as observed in vitro [6].

METHODS

In our thermodynamic framework, evolution and remodeling of sarcomeres and SFs is driven by differences in chemical potential of bound proteins in sarcomeres and SFs, and that of unbound proteins. Enthalpies of proteins in their ground states are represented as μ_U , μ_{B0} , and μ_{H0} , with activation barriers μ_A , and μ_{Z0} highlighted in Figure 1.

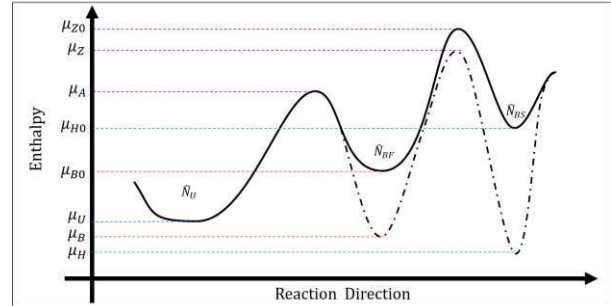


Figure 1: Energy landscape for cytoskeletal unbound cytoskeletal proteins, SFs and sarcomeres, highlighting enthalpies in their ground state (solid curve), in their standard state (dashed curve), and activation barriers.

Through dynamic loading, standard enthalpy changes such that the enthalpy of SFs at any point is calculated as,

$$\mu_B = \mu_{B0}(1 + \beta \tilde{\epsilon}^2) - \Omega \sigma_F(1 + \tilde{\epsilon}). \quad (1)$$

Here, $\tilde{\epsilon}$ is strain within an SF, β is a non dimensional constant governing growth of in series SFs and sarcomeres, Ω is a constant representing volumetric density of functional units at a point, and σ_F is maximum isometric SF tension. The enthalpy of sarcomeres at any point is calculated as,

$$\mu_H = \mu_{H0}(1 + \beta \tilde{\epsilon}_S^2) - \Omega \sigma_S(1 + \tilde{\epsilon}_S) + (1 - \kappa)\Delta\mu_H + \Phi_T - W_T, \quad (2)$$

where, $\tilde{\epsilon}_S$ is strain within a sarcomere, and σ_S is maximum isometric sarcomere tension, κ is a normalized term representing level of alignment of the underlying SF network, and $\Delta\mu_H$ is the maximum penalty when the SF network is isotropic. The activation enthalpy, which affects the rate of sarcomere growth, is given as $\mu_Z = \mu_{Z0} - \kappa\Delta\mu_Z$. Under dynamic loading, titin is stretched between Z- and M-bands, resulting in an internal elastic strain. We assume a titin elastic modulus, κ_T , such that titin strain energy is given as $\Phi_T = \frac{1}{2}\kappa_T\Omega\tilde{\epsilon}_T^2$, and induced work due to titin stretching is given as $W_T = \frac{\partial\Phi_T}{\partial\tilde{\epsilon}_T}\tilde{\lambda}_T$, where $\tilde{\lambda}_T$ and $\tilde{\epsilon}_T$ represent titin stretch and strain respectively.

The evolution of unbound cytoskeletal proteins into sarcomeres, $\hat{\eta}_{SU}$, is given as:

$$\frac{\partial\hat{\eta}_{SU}}{\partial t} = \omega_{SU} \frac{\hat{N}_U + \hat{N}_{BF}}{\hat{n}_S} \left(1 - \frac{\hat{N}_{BF} + \hat{N}_{BS}}{\xi_1}\right) \exp\left(\hat{n}_S \frac{\mu_U - \mu_Z}{k_B T}\right) - \omega_{SU}\hat{\eta}_S \exp\left(\hat{n}_S \frac{\mu_H - \mu_Z}{k_B T}\right), \quad (3)$$

where ω_{SU} is a rate constant, \hat{n}_S is sarcomere concentration in series, ξ_1 is peak sarcomere concentration at a point, and $k_B T$ is Boltzmann's constant and absolute temperature respectively, noting that protein conservation is maintained between unbound functional units, SF, and sarcomeres respectively, where $\hat{N}_U + \hat{N}_{BF} + \hat{N}_{BS} = 1$.

Sarcomere formation in parallel, $\hat{\eta}_{SF}$, due to reorganization of bound aligned SF proteins, and is driven towards thermodynamic equilibrium such that:

$$\frac{\partial\hat{\eta}_{SF}}{\partial t} = \omega_{SF} \frac{\hat{N}_U + \hat{N}_{BF}}{\xi_1} \frac{\xi_1 - \hat{N}_{BF} - \hat{N}_{BS}}{\hat{n}_S} \left(\frac{\xi_0}{\hat{N}_U \xi_0 - \hat{n}_F \hat{\eta}_F}\right)^{\frac{1}{v_S}} \exp\left(\hat{n}_S \frac{\mu_B - \mu_Z}{k_B T}\right) - \omega_{SF}\hat{\eta}_S \exp\left(\hat{n}_S \frac{\mu_H - \mu_Z}{k_B T}\right), \quad (4)$$

where ω_{SF} is a rate constant, \hat{n}_F is the concentration of SFs in series, and ξ_0 is peak SF concentration at a point. Total generation of sarcomeres is then expressed as; $\frac{\partial\hat{\eta}_S}{\partial t} = \frac{\partial\hat{\eta}_{SU}}{\partial t} + \int_{-\pi/2}^{\pi/2} \frac{\partial\hat{\eta}_{SF}}{\partial t} d\theta$.

Aggregation of SFs in parallel, $\hat{\eta}_{FU}$, is solely motivated by available unbound cytoskeletal proteins, driven towards thermodynamic equilibrium of unbound and bound SF species such that:

$$\frac{\partial\hat{\eta}_{FU}}{\partial t} = \omega_{FU}\hat{N}_U \left(\frac{1}{\hat{n}_F} - \frac{\hat{\eta}_F}{\xi_0}\right) \exp\left(\hat{n}_F \frac{\mu_A - \mu_U}{k_B T}\right) - \omega_{FU}\hat{\eta}_F \exp\left(\hat{n}_F \frac{\mu_B - \mu_A}{k_B T}\right), \quad (5)$$

where ω_{FU} is a rate constant. It is also necessary to consider SF loss due to sarcomere recruitment, as highlighted in Eq.(4), thus total SF generation and disassociation is expressed as $\frac{\partial\hat{\eta}_F}{\partial t} = \frac{\partial\hat{\eta}_{FU}}{\partial t} - \frac{1}{v} \frac{\partial\hat{\eta}_{SF}}{\partial t}$, where v is a scalar relating optimal length of sarcomeres and SFs.

In our framework, we simulate a cardiomyocyte that spreads to a steady-state geometry and is then subjected to biaxial dynamic loading to a nominal 20% at 1Hz for a period of 10 hours. Results are compared directly to the in vitro observations of [6].

RESULTS

Figure 2A shows the evolution of SFs and sarcomeres in a cell subjected to 20% biaxial dynamic loading and a cell under static conditions. Dynamic loading leads to the reorganization of proteins in aligned SFs so that they form structured sarcomeres. This process occurs due to the stretching of titin during dynamic loading which reduces the standard enthalpy of sarcomeres. Under static conditions titin is not stretched and the energetic barrier to convert SFs to

sarcomeres is prohibitively high. Figure 2B shows the alignment and concentration of SFs and sarcomeres for static and dynamic cases. Figure 2C shows the computed chemical potential of SFs, sarcomeres and unbound species as a function of orientation. Again, positive differences in chemical potential due to titin stretching along the long axis of the cell drives the ongoing formation of sarcomeres. Figure 2D shows that model predictions of increased sarcomere concentration due to dynamic loading are in reasonable agreement with experimental measurements [6].

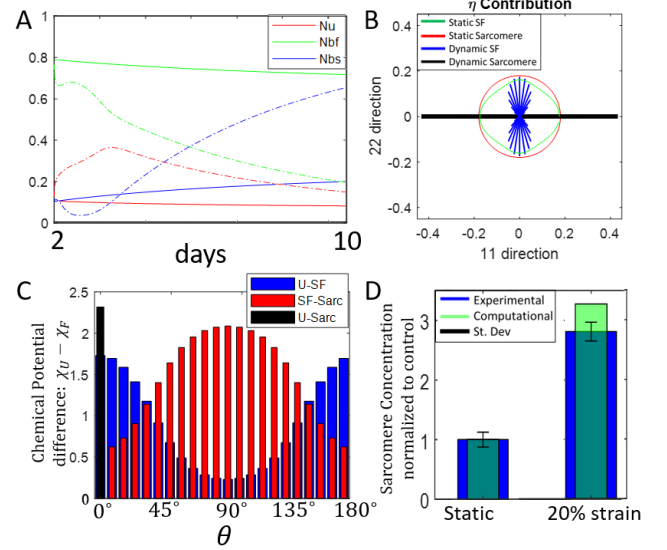


Figure 2: A) Dynamic evolution of protein concentration for static control (solid lines), and biaxial dynamic loading (dashed lines). B) Stress fiber and sarcomere orientation and concentrations following 10 days of cyclic loading. C) Difference in chemical potential between dynamic states after 10 days. D) Computed sarcomere concentration (normalized by static control level) following 10 days of dynamic loading, with comparison to experimental data [6].

DISCUSSION

The key finding that emerges from our novel thermodynamic framework is that stretching of titin during applied dynamic loading of CMs results in a reduction in the standard enthalpy of sarcomeres, which drives the remodeling of cytoskeletal proteins from SFs to sarcomeres. Our model predicts that application of a dynamic biaxial stretch of 20% at 1 Hz results in a three-fold increase in sarcomere concentration. This prediction aligns with the in vitro measurements of Dou et al. [6]. Our model suggests that titin knock-out experiments will lead to reduced sarcomere formation and increased SF formation under dynamic loading, as observed in vitro [7]. The dynamic remodeling framework will also be extended to simulate hypertrophy due to altered mechanical loading of the myocardium [8].

ACKNOWLEDGEMENTS

Science Foundation Ireland (grant 18/ERCD/5481)

REFERENCES

- [1] Jacot, J et al., Ann. N. Y. Acad. Sci, 1188(1), 121–127, 2010.
- [2] Sakamoto, K et al., Scientific Reports 11(1), 1–12, 2021.
- [3] Rodriguez, AG et al., Biophys J, 101, 2455–2464, 2011.
- [4] Bartoo, M et al., J. Muscle Res, 14:5, 14(5), 498–510, 1993.
- [5] Lucas, S et al., Exp. Neurol, 95(1), 142–154 1987.
- [6] Dou, W et al., Biosens. Bioelectron. 175, 112875, 2021.
- [7] Van der Ven et al. J Cell Sci, 113(8), 1405–1414, 2000.
- [8] McEvoy, E et al., J Mech Behav Biomed Mater, 113:104074, 2021.

TRANSMEMBRANE HYDROSTATIC PRESSURE DIFFERENTIALS AS A BIOPHYSICAL BASIS FOR AIR-LIQUID INTERFACE DIFFERENTIATION

Chen Li (1), Tanvi A. Javkar (2), Syeda S. Z. Zaidi (3), John W. Hanrahan (3), Alex Gregorieff (2), Christopher Moraes (1)

- (1) Chemical Engineering, McGill University, Montreal, Quebec, Canada
(2) Pathology, McGill University, Montreal, Quebec, Canada
(3) Physiology, McGill University, Montreal, Quebec, Canada

INTRODUCTION

Biological cells can be differentiated to have specialized functions to build realistic *in vitro* cell culture models. The methods to achieve this are typically based on chemical stimulation with multiple differentiation factors and steps^{1,2}, but can also incorporate biophysical cues such as subjecting cells to specific forces^{3,4}, or combinations of these signals by engineering specific tissue microenvironments.^{5,6} Air-liquid interface (ALI) is a well-established cell culturing method required to differentiate epithelial cells towards functional phenotypes, and allows scientists to generate realistic barrier-based tissue and organ models for research purposes.^{7,8} For example, ALI is used to differentiate tracheobronchial cells to closely mimic human airway architectures for drug screening⁹ or studying lung diseases.¹⁰ Despite common use of ALI for many applications, the precise drivers of differentiation that underlie this approach remains unknown. This lack of knowledge creates additional challenges: ALI differentiation typically requires long multi-week cultures, and the challenges of handling porous *Transwell* inserts make ALI culture less robust than required for industrially scaled-up high-throughput applications.¹¹ Hence, understanding the mechanism driving ALI epithelial differentiation could allow us to develop more flexible and robust tissue process control strategies, scale up the fabrication process of *in vitro* cell culture models, and potentially help reveal and target the mechanisms underlying epithelium formation during fetal development.

ALI consists of culturing cells on a porous membrane, while allowing them to access nutrient-containing culture media through the membrane and exposing the top surface of cells to air. When these ALI conditions were recreated by growing epithelial cells on a media-soaked hydrogel and exposed to air from the top surface, surprisingly the expected ALI differentiation did not occur. Therefore, we hypothesized that the innate hydrostatic biophysical pressure difference created by ALI across the epithelial barrier might play a critical role in epithelial differentiation

and its variability in regular ALI culture due to handlings and evaporation causes the current lack of reproducibility in ALI differentiation.

METHODS

A transepithelial hydrostatic pressure device was built to subject the cell layer to a pressure differential, while maintaining cells at standard submerged culture (Figure 1). This new culture setup removes the confounding effects of an air-liquid interface, such as differential oxygenation, while manipulating and precisely controlling the small hydrostatic pressure differentials that are often unintentionally created by ALI culture in a standard *Transwell* inserts.

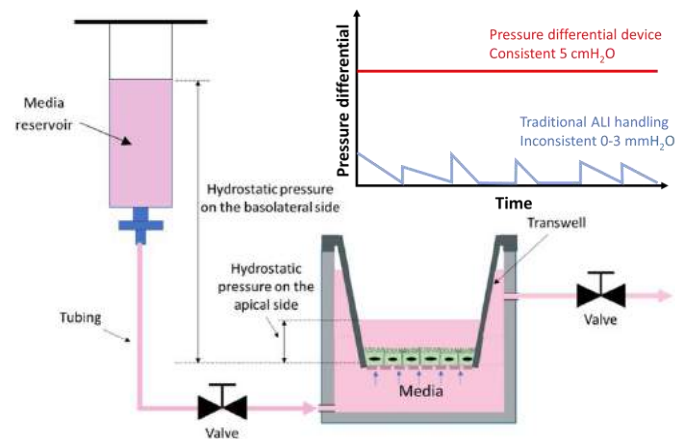


Figure 1. Transmembrane hydrostatic pressure differential device. A raised media reservoir connected to the well induces a constant hydrostatic pressure to the basolateral surface of epithelial layer.

Primary human bronchial epithelium (HBE) and human intestinal organoid were cultured in this device to analyze the effect of pressure differential on different types of epithelial cells. HBE were cultured in 4 different conditions over 3 weeks: Control (regular submerged culture), ALI, pressure differential (5 cmH₂O), and double-sided pressure (increased pressured on both basolateral and apical surface). Epithelial histology sections were then used to compare HBE samples stained with hematoxylin and eosin (H&E).

RESULTS

Histology sections of HBEs are shown in Figure 2 and top views of intestinal organoid grown on *Transwell* inserts in Figure 3.

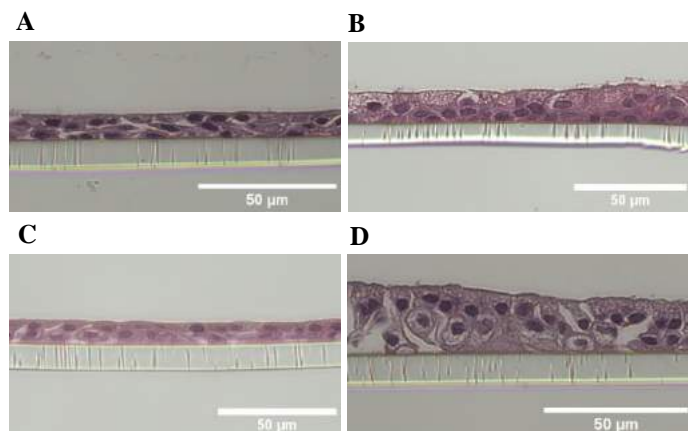


Figure 2. Human bronchial epithelial monolayers grown on *Transwell* inserts cultured for 3 weeks in 4 different conditions: (A) Submerged, (B) ALI, (C) Double-sided pressure, and (D) Pressure differential. Scale bar 50 µm.

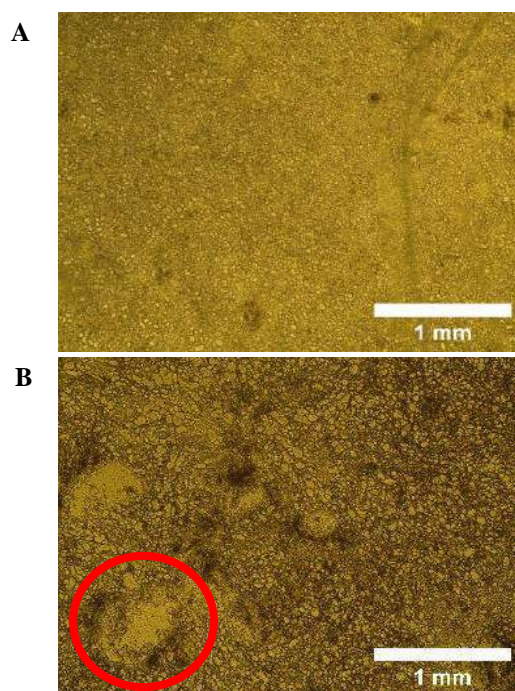


Figure 3. Human intestinal organoid grown on *Transwell* inserts cultured in (A) regular submerged condition and (B) pressure differential device for 14 days. Red circle indicates potential lumen formation.

The observed thicker HBE membrane obtained from pressure differential device (Figure 2D) compared to control condition (Figure 2A) indicates the formation of pseudostratified columnar epithelium which was previously obtained only through ALI culture as shown in Figure 2B. HBE membrane under increased hydrostatic pressure on both apical and basolateral surfaces (Figure 2C) maintained its original thickness similar to control condition. Thus, the formation of pseudostratified columnar epithelium was due entirely to transepithelial pressure differentials rather than an absolute increase of pressure on basolateral surface. Interestingly, the formation of cilia, another marker of airway epithelium differentiation, was only observed in the ALI cultures.

Similarly, human intestinal organoids cultured in the pressure differential device drives heterogeneous growth (Figure 3B) compared to the regular submerged culture (Figure 3A). The heterogeneity of the pressurized tissue suggests differentiation towards specialized cell types and even possible formation of lumens as indicated by red circle. Differentiation profiles arising from various differential hydrostatic pressure treatments are currently being determined.

DISCUSSION

Preliminary results in using this device show significant improvements in phenotypes associated with differentiation for multiple cell lines including primary lung cells and miniature gut tissue. These initial results are very promising as it demonstrates how pressure differential underlies ALI differentiation and can be isolated to precisely control different differentiation features of epithelial cells such as thickening of the monolayer or formation of cilia. Thus, regulating hydrostatic pressure could be a good strategy to control epithelial cell differentiation as it provides an easier, more robust, and more consistent method and thus rendering possible the scale up of differentiation procedure as opposed to ALI cultures. Furthermore, this finding might thus be the key in determining the differentiation mechanism since it could be used as a “filter” condition during genetic analysis. Upon comparison with the full ALI condition, the specific and critical genes involved in differentiation will likely be more apparent compared to the existing genetic analysis of ALI differentiation. This differentiation mechanism behind pressure differential could even potentially play an important role during fetal development in which air is also absent.

ACKNOWLEDGEMENTS

We gratefully acknowledge project funds from the CQDM Quantum Leap program, the NSERC Discovery Grant (RGPIN-2022-05165) and the Canada Research Chairs in Advanced Cellular Microenvironments to C.M.

REFERENCES

- [1] Czyz, J. et al., *Differentiation* 2001, 68 (4), 167–174.
- [2] Behfar, A. et al., *FASEB J.* 2002, 16 (12), 1558–1566.
- [3] Dado, D. et al., *Regen. Med.* 2012, 7 (1), 101–116.
- [4] Altman, G. H. et al., *FASEB J.* 2002, 16 (2), 1–13.
- [5] Luo, W. et al., *Langmuir* 2008, 24 (21), 12129–12133.
- [6] Bratt-Leal, A. M. et al., *Biotechnol. Prog.* 2009, 25 (1), 43–51.
- [7] Jiang, D. et al., *Lung Innate Immunity and Inflammation* 2018; pp 91–109.
- [8] Pezzulo, A. A. et al., *Am. J. Physiol.-Lung Cell. Mol. Physiol.* 2011, 300 (1), L25–L31.
- [9] Lenz, A.-G. et al., *Am. J. Respir. Cell Mol. Biol.* 2014, 51 (4), 526–535.
- [10] Upadhyay, S. et al., *Toxicol. Sci.* 2018, 164 (1), 21–30.
- [11] Choi, K.-Y. G. et al., *Front. Cell. Infect. Microbiol.* 2020, 10.

VIRTUAL TENSILE TEST EXPERIMENTS TO RECONCILE THE MESO- AND MICRO-SCALE MECHANICAL PROPERTIES OF THE LUNG PARENCHYMA

E. Dimbath (1), L. de Castro Brás (2), S. George (3), A. Vadati (3)

- (1) Department of Biomedical Engineering, Duke University, Durham, NC, USA
(2) Department of Physiology, East Carolina University, Greenville, NC, USA
(3) Department of Engineering, East Carolina University, Greenville, NC, USA

INTRODUCTION

Many respiratory system pathologies can disrupt lung function by altering the mechanical properties of the parenchyma. Computational models can provide a non-invasive and patient-specific approach to understanding the mechanics of breathing and the effects of heterogeneous damage distribution on lung function. The geometry and spatial scale of *in silico* models are essential in creating realistic models that produce accurate and reliable results. Similarly, it is vital to consider the accuracy of the constitutive mechanical behavior used to model tissue behavior. Many computational models have been developed for the lung at various spatial scales, while morphological studies combined with increased computing power have allowed for model expansion to smaller length scales. Yet, the wide range of experimental techniques and reported constitutive models for lung tissue at different length scales can lead to uncertainty when utilizing such material properties in computer modeling. Hence, reliable alveolar stiffness values are essential when using multiscale models that incorporate the mechanical properties of the parenchyma.

To compare the mechanical properties of tissue reported across length scales from different studies, the differences in experimental protocols should be considered. Also, other factors, such as tissue preparation technique and loading rate, may affect the reported stiffness values. Thus, reconciling the reported stiffness values of lung tissue across spatial scales may give insight into how well the reported stiffness values represent lung tissue behavior across different scales. As the emergent mesoscale mechanical properties of the parenchyma depend on the microscale properties of the alveolar tissues, reported values at the microscale must be accurate before they can be used in meso- and macro-scale lung models.

Hence, this study aims to use *in silico* modeling to compare, reconcile, and resolve the differences reported in lung tissue mechanics at different length scales. Specifically, the objective of this research is to utilize computational modeling for the purpose of studying whether

the emergent mechanical properties of lung tissue at the mesoscale, based on micro-scale mechanical testing data, can be reconciled with the experimental data reported at the mesoscale.

METHODS

A finite element (FE) analysis was performed at the mesoscale by assigning microscale-based properties to alveolar septa based on previously reported *in vitro* and *in situ* experiments. The 3D geometry comprised an array of alveoli represented by truncated octahedra [1]. The geometry modeled the tissue slices used in the uniaxial tension testing of Birzle et al. [2]. SolidWorks 2022 (Dassault Systems, France) was used to build the geometry where each truncated alveoli had the average dimensions of a rat alveolus as measured by Cavalcante et al. [3]. The geometry was imported to COMSOL Multiphysics v6.0 for FE analysis (COMSOL Multiphysics, MA, USA). The entire structure had overall height, width, and depth dimensions equal to the average dimensions of lung tissue slices used for uniaxial tension testing in Birzle et al. [2], and was simulated for up to 80% strain. The FE model was meshed using 2.2 million quadratic tetrahedral elements.

Mechanical properties at the microscale were taken from the results reported by two different research groups that determined the mechanical behavior of rat lung tissue using atomic force microscopy (AFM) and *in situ* mechanical testing, respectively [4], [5]. The emergent properties from the FE analysis were then compared to mesoscale data from a study that utilized a comprehensive approach to determine the mechanical behavior of rat parenchyma [2] and reporting the strain energy density function below:

$$\varphi = c(I_1 - 3) + \frac{c}{\beta} \left(I_3^{-\beta} - 1 \right) + c_1 (I_3^{-\frac{1}{3}} I_1 - 3)^{d_1} + c_3 (I_3^{\frac{1}{3}} - 1)^{d_3} \quad (1)$$

Where I_1 and I_3 are invariants of the right Cauchy-Green deformation tensor, c_1, c_3, d_1 and d_3 are material constants that characterize the

isochoric and volumetric elastic response of the tissue, and c and β define Young's modulus E and Poisson's ratio ν as:

$$E = 4c(1 + \nu) \quad (2)$$

$$\nu = \beta / (1 + 2\beta) \quad (3)$$

Additionally, based on a study by Birzle and Wall [6], the standard linear solid viscoelastic model was added to the microscale hyperelastic constitutive models to account for the effect of rate of loading [6]. The viscoelastic stress (σ_q) of the standard linear solid model was determined by the equation:

$$\sigma_q = 2n_1\dot{\gamma}_1 \quad (4)$$

Where n_1 is the viscosity and is related to the stiffness (G_I) and relaxation time (τ_1) by $n_1 = G_I \tau_1$. Also, $\dot{\gamma}_1$ is the strain rate. This visco-hyperelastic model of the alveolar tissue was used to determine the emergent mesoscale behavior of the tissue.

RESULTS

The tensile test simulation results (Figure 1) from the visco-hyperelastic model [5] showed reasonable agreement with the reported mesoscale data [2] at strains between 0.0-0.3. Specifically, the simulated curve based on the work of Perlman and Wu [5] showed slightly lower stiffness compared to the reported mesoscale behavior model below ~28% strain. Above 30% strain, the disagreement between the simulated microscale-based curve and the mesoscale dataset increased.

The mean error was determined for each simulated case concerning the reported mesoscale data to quantify the difference in the resulting stress-strain curves. Overall, the visco-hyperelastic microscale model [5] showed the lowest mean error compared to the mesoscale data across all strains (error of 39%) with an even lower error (error of 26%) when only accounting for strains of up to 40%. Conversely, the AFM-based microscale model [4] resulted in a larger mean error overall (error of 61%) with a larger mean error in lower strain ranges (error of 94%) than over the whole strain range of the experiment.

DISCUSSION

In this study, we utilized computational modeling to investigate whether the emergent mechanical properties of lung tissue at the mesoscale, based on micro-scale mechanical testing data, can be reconciled with the experimental data obtained using mesoscale tensile testing. We picked two of the most comprehensive and high-fidelity mechanical testing datasets published by other researchers for the purpose of this study: the microscale data reported by Perlman and Wu [5] and the mesoscale multimodal data of Birzle et al. [2]. An additional comparison to a linear model based on the AFM experiments of Melo et al. [4] was also made for comparison purposes. Overall, the comparative study successfully reconciled the mechanical properties of lung tissue across micro- and mesoscales when comparing the microscale study of Perlman and Wu [5] to the mesoscale data reported by Birzle et al. [2]. By comparing the emergent properties of simulated microscale-based models to the material behavior reported at the mesoscale, this research further confirmed the reasonable accuracy of the mechanical behavior reported for lung tissue in both experimental studies. Furthermore, this study showed that FE modeling could be used as an informative and guiding tool to investigate and potentially resolve the differences in reported lung tissue mechanical properties across spatial scales.

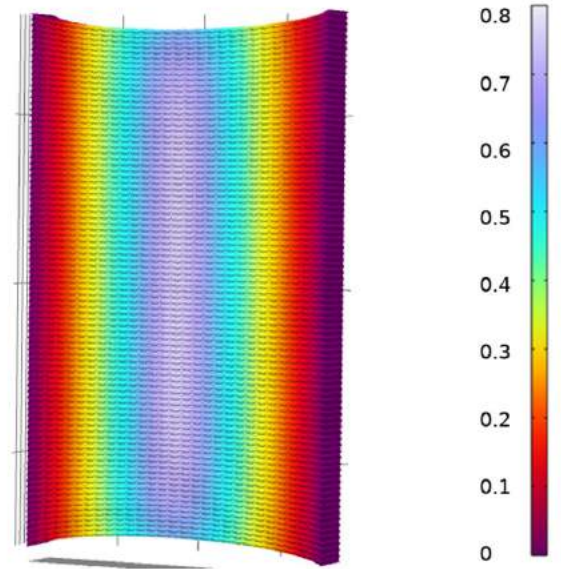


Figure 1: Strain distribution in the uniaxial tension model of 3D model at maximum displacement. The microscale constitutive models are applied to the walls of the truncated octahedra.

ACKNOWLEDGEMENTS

This material is based on the work supported by the National Science Foundation under award # 2034964. The authors acknowledge Research Computing at The University of Virginia for providing computational resources and technical support that have contributed to the results reported within this publication. URL: <https://rc.virginia.edu>. The material in this publication is based upon work supported in part by the National Science Foundation under the ACCORD Grant (Award #: 1919667). Any opinions, findings, conclusions, or recommendations expressed in this material are those of the author(s) and do not necessarily reflect the views of the National Science Foundation.

REFERENCES

- [1] E. Denny and R. C. Schroter, "Viscoelastic Behavior of a Lung Alveolar Duct Model," 2000.
- [2] A. M. Birzle, C. Martin, S. Uhlig, and W. A. Wall, *J Mech Behav Biomed Mater*, vol. 94, pp. 126–143, Jun. 2019, doi: 10.1016/j.jmbbm.2019.02.019.
- [3] F. S. A. Cavalcante et al., *J Appl Physiol*, vol. 98, no. 2, pp. 672–679, Feb. 2005, doi: 10.1152/jappphysiol.00619.2004.
- [4] E. Melo et al., *Tissue Eng Part C Methods*, vol. 20, no. 5, pp. 412–422, May 2014, doi: 10.1089/ten.tec.2013.0325.
- [5] C. E. Perlman and Y. Wu, *Am J Physiol Lung Cell Mol Physiol*, vol. 307, no. 4, p. L302, Aug. 2014, doi: 10.1152/ajplung.00106.2014.
- [6] A. M. Birzle and W. A. Wall, *J Mech Behav Biomed Mater*, vol. 94, pp. 164–175, 2019, doi: 10.1016/j.jmbbm.2019.02.024.
- [7] A. M. Birzle, C. Martin, L. Yoshihara, S. Uhlig, and W. A. Wall, *J Mech Behav Biomed Mater*, vol. 77, pp. 754–763, Jan. 2018, doi: 10.1016/j.jmbbm.2017.08.001.

THE ROLE OF THE POSTERIOR CRUCIATE LIGAMENT ON FEMORAL ROLLBACK IN MEDIAL CONGRUENT TOTAL KNEE ARTHROPLASTY: A COMPUTATIONAL STUDY

Reza Pourmodheji (1), Jacob M. Hirth (1), Brian P. Chalmers (2), Cynthia A. Kahlenberg (2), William J. Long (2), Geoffrey H. Westrich (2), David J. Mayman (2), Peter K. Sculco (2), Timothy M. Wright (1), Carl W. Imhauser (1)

(1) Department of Biomechanics, Hospital for Special Surgery, New York, NY, United States
(2) Adult Reconstruction and Joint Replacement, Hospital for Special Surgery, New York, NY, United States

INTRODUCTION

Total knee arthroplasty (TKA) with medial congruent (MC) polyethylene designs has shown increased clinical utilization with satisfactory clinical outcomes over the last several years [1]. The goal of this design is to reproduce the medial pivoting behavior of the native knee through a more constrained medial compartment allowing posterior sliding of the lateral femoral condyle with flexion [2]. This design employs a standard cruciate-retaining femoral component with the option of retaining the posterior cruciate ligament (PCL).

The role of PCL and whether it should be retained in medial congruent TKA is controversial [3]. Arguments in favor of PCL retention cite more physiological knee kinematics [4]. One desired aspect in PCL-retaining TKA is achieving femoral posterior translation of the native knee, also referred to as femoral rollback, through a range of knee flexion [5]. In contrast, those who advocate sacrificing the PCL cite inconsistency in femoral rollback with retention of the PCL [6]. Therefore, we developed a computational framework to quantify the role of the PCL in the kinematics of medial congruent TKA. We posed the following research question: How does the absence of the PCL affect the posterior translation of the medial and lateral femoral condyles through a range of knee flexion from 0 to 90°? We hypothesized that resecting the PCL reduces posterior translation of the medial and lateral femoral condyles.

METHODS

Computational models derived from 10 independent cadaveric left knees (five male, five female; mean age: 63.7±10.5 years) were virtually implanted with an MC TKA tibial insert (12 mm) and cruciate retaining (CR) femoral component (Persona, Zimmer-Biomet, Warsaw, IN). The computational modeling pipeline utilized the multibody dynamics framework and has been published previously [7]. The tibial bearing surface of the MC design has a conforming feature on the anterior aspects of the medial and lateral compartments while the posterior

aspects are less conforming laterally than medially (Fig. 1a). The model development pipeline consists of the following four steps: (1) segmenting and reconstructing the entire femoral and tibial bony geometries in 3D from computed tomography scans (Fig. 1a); (2) creating an anatomical coordinate system for the knee joint [8] (Fig. 1b); (3) positioning implants according to manufacturer recommendations including 9 mm posterior-referencing femoral bony cuts, 9 mm of tibial bony cut with 5° of slope; and (4) incorporating ligament models based on their anatomical insertions (Fig. 1b).

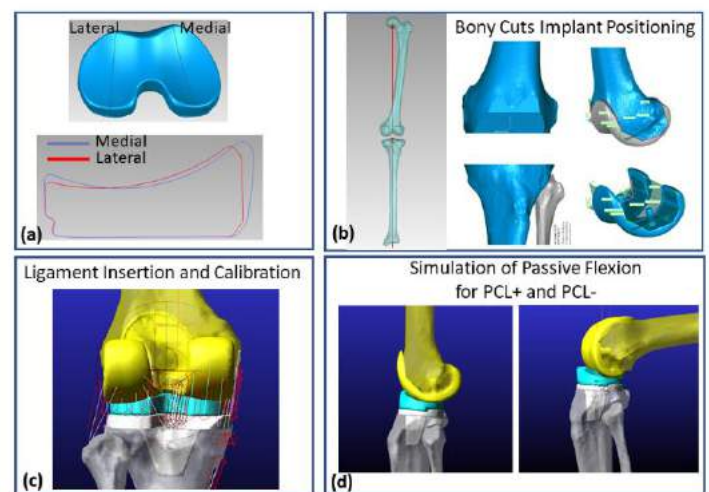


Figure 1: Computational workflow in modeling medial congruent TKA with simulated PCL retention (PCL+) and resection (PCL-).

The ligament models consisted of 33 line-elements describing the collateral and capsular ligaments and the PCL. The PCL consisted of seven line elements with three elements and four elements representing the posteromedial (PM) and anterolateral (AL) bundles, respectively. The nonlinear, tension-only force-elongation response of each ligament was represented with a power function and population mean structural properties taken from the literature. Slack lengths were defined using a previously published optimization algorithm [7].

We modelled two conditions: PCL-intact (PCL+) and PCL-deficient (PCL-). For both conditions, the knee was flexed through a range of motion from 0° to 90° under 500 N of compression representing a common clinical test of passive flexion. Simulations were conducted using a multibody dynamics software package (MSC Software; Adams 2021-4, Hexagon, Stockholm).

Outcome measures were the difference in anterior-posterior (AP) translation between 0° and 90° of flexion for both the medial and the lateral femoral condyles with anterior translation of the femoral condyle designated as positive. A Kolmogorov-Smirnov test ($p < 0.05$) revealed that our data were not normally distributed; therefore, we reported medians and quartiles. To compare the AP translation of the medial femoral condyle for the PCL intact and PCL deficient conditions and the lateral femoral condyles for these same two conditions, we used a nonparametric Wilcoxon signed-rank test ($\alpha = 0.05$).

RESULTS

AP translation of the medial femoral condyle for the PCL intact and PCL deficient conditions were small, differing by a median of 0.8 mm (Fig. 2a). In contrast, the AP translation of the lateral femoral condyle was a median of 4.1 mm greater for the PCL intact condition compared to the PCL deficient condition (Fig. 2b) ($p = 0.002$).

DISCUSSION

We found that the lateral femoral condyle translated posteriorly with the PCL intact but did not when the PCL was deactivated. In contrast, the PCL had minimal effect on the AP translation of the medial femoral condyle. Therefore, our hypothesis was partially accepted. Similar to our findings, Most et al. [9] reported greater rollback of the lateral femoral condyle compared to the medial femoral condyle in an in vitro robotic study of cruciate retaining TKA. They also reported femoral rollback of 10 mm on the lateral side with PCL retention, which corroborates our findings.

The design of the medial congruent bearing surface likely contributes to the greater posterior translation of the lateral femoral condyle compared to the medial femoral condyle when the PCL is retained. The less conforming lateral bearing surface with a larger radius of curvature than the medial bearing surface (Fig. 1a) provides less constraint to the lateral femoral condyle, allowing a higher range of AP translation.

The magnitude of rollback of the lateral femoral condyle was variable even with retention of the PCL. Thus, medial congruent TKA does not guarantee rollback even with retention of the PCL. In contrast, posterior femoral translation was always minimal in absence of PCL.

Although there was femoral rollback laterally with the PCL retained, the femoral rollback varied among knees ranging from -9.9 to 16.2 mm. This variability in femoral rollback agrees with previous findings [5]. Like standard cruciate retaining implant designs, soft tissue balance and PCL anatomy can have a substantial effect on femoral rollback. Possible anatomical explanations for this heterogeneity are variations in the femoral insertion of the PCL. Since the PCL is highly anisometric through a range of flexion [10], small variations in femoral insertion anatomy may have a strong influence on the magnitude of force carried

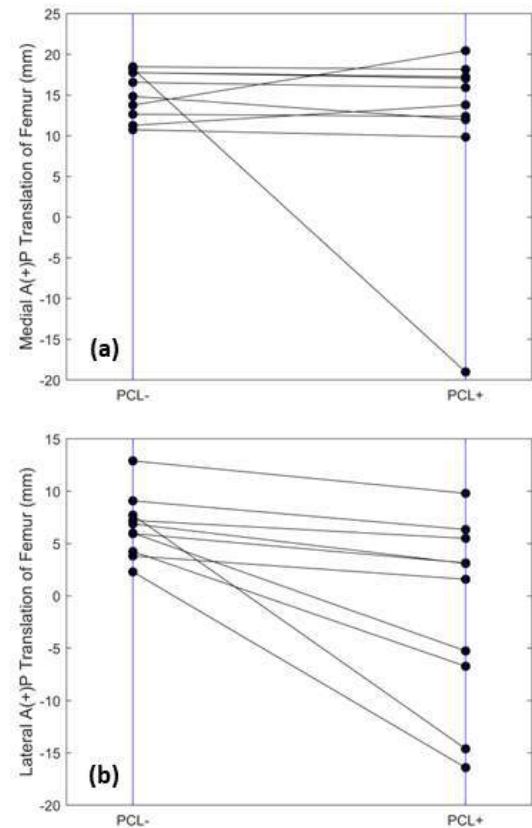


Figure 2: The AP translation of the medial (a) and lateral (b) femoral condyles from 0° to 90° of flexion with PCL intact (PCL+) and PCL deficient (PCL-). Each pair of black dots connected by a solid black line represents an individual knee model.

by the PCL as the knee flexes, which will, in turn, impact the amount of femoral rollback.

In conclusion resection of the PCL has minimal impact on rollback of the medial femoral condyle in MC TKA, likely due to the greater conformity of the medial tibial bearing surface. In contrast, resection of the PCL abolishes rollback of the lateral femoral condyle, while retention of the PCL leads to variable femoral rollback. Our findings support clinical observations of difficulty in achieving predictable femoral rollback with retention of the PCL in MC TKA.

ACKNOWLEDGEMENTS The Clark and Kirby Foundations.

REFERENCES

- [1] Frye, B. M. et al., *Arthroplast. Today.*, 7:243-249, 2021.
- [2] Gray, H. A. et al., *J Orthop. Res.*, 38:1753-1768, 2020.
- [3] Scott, RD et al., *J Arthroplasty*, 23:605-608, 2008.
- [4] Horiuchi, H. et al., *J Arthroplasty*, 27:1196-1202, 2012.
- [5] Nozaki, H. et al., *Clin. Orthop. Relat. Res.* 404:308-314, 2002
- [6] Mahoney, O. et al., *J Arthroplasty*, 9:569-578, 1994.
- [7] Elmasry, S. et al., *J Arthroplasty*, 34:981-986, 2019.
- [8] Grood, E. S., & Suntay, W. J. *J. Biomech. Eng.*, 105:136-144, 1983
- [9] Most, E. et al., *Clin. Orthop. Relat. Res.* 410:101-113, 2003
- [10] Jeong, WS. et al., *Arthrosc. -J. Arthrosc. Relat. Surg.*, 26:1333-1339, 2010.

CHARACTERIZING NATURAL FREQUENCIES OF THE HYBRID III AND NOCSAE HEADFORMS

Kristin J. Dingelstedt and Steven Rowson

Biomedical Engineering and Mechanics
Virginia Tech
Blacksburg, VA, USA

INTRODUCTION

Anthropomorphic test device (ATD) headforms are used to study different head impact scenarios. Two popular ATD headforms are the Hybrid III and the National Operating Committee on Standards for Athletic Equipment (NOCSAE), though they have structural differences [1-2]. The Hybrid III headform was developed for automotive safety testing, modeled after an average American man. It consists of an aluminum shell with a hollow brain cavity for instrumentation and is covered with a vinyl skin. The NOCSAE headform was designed for the evaluation of protective athletic gear, modeled after an American football player. It is constructed with a nylon shell, filled with glycerin, and covered with urethane [2]. Both headforms have been shown to have biofidelic biomechanical responses, and each has been used extensively to study sports-related head impacts, where they perform very similarly in impact scenarios typically seen in helmeted sports [1].

While these headforms are used to understand the behavior of the human head in different impact events, little research has been done on fully understanding their dynamic properties, especially the natural frequencies. All systems have natural frequencies at which they vibrate in the absence of any driving forces. If a time-varying external load is applied to a system, and its frequency is equal to any of the system's natural frequencies, resonance will occur. This causes the system to oscillate at high amplitudes, causing abnormally large deflections of the system. Understanding the natural frequencies of headforms used in impact testing is important because the head will behave differently depending on the characteristics of the impact [1]. Gurdjian et al. [3] hypothesized that awareness of natural frequencies is useful for shorter-duration impacts ($t < 5$ ms), because these impacts have a broader frequency spectrum which can cause resonance frequency excitation and skull deformation, potentially due to relative motion between the brain and the skull. Therefore, in impact testing, it is important to consider frequency content, since the results from these types of impact

scenarios can be influenced by the dynamic response of the headform [3].

In previous attempts to characterize the dynamic properties of the human head, various modal testing techniques have been done to identify the natural frequencies using different methods to vibrate human cadaver skulls [3-4], polymer skull models [5], and human skulls *in vivo* [6]. Many of these tests used modal impact hammers to excite the skulls. However, there are no data describing the dynamic responses of the Hybrid III and NOCSAE headforms. By determining the natural frequencies of these headforms in a similar manner, they can be compared against published values [3-6] to determine which one captures the most accurate vibrational response.

METHODS

Experimental modal analysis uses excitation and response signals to identify natural frequencies and other dynamic characteristics of a structure, so modal testing methods were used to identify the natural frequencies of the two headforms. A 50th percentile male Hybrid III headform and a medium NOCSAE headform were attached to a 50th percentile Hybrid III neck and mounted to a stationary plate. To collect linear acceleration data, which served as the response signals, the headforms were instrumented with 3 linear accelerometers at their respective centers of gravity. An Impulse Force Test Hammer (PCB Piezotronics, Model 086C04 (Depew, NY)), hereafter referred to as simply an impact hammer, was used to provide the excitation force to the headforms. A stainless-steel tip of hard stiffness was used on the impact hammer, as it was capable of providing impacts up to 400 N and covered a broad frequency range of 0-5 kHz.

A “roving hammer” test approach was used, where the accelerometers remained fixed and the headforms were struck with the impact hammer at several locations, ensuring that the impact durations were between 1-3 ms. Five locations were identified for frontal impacts, with each location being impacted a total of 4 times. The same was done

for temporal impacts (Figure 1). Multiple locations were selected in an effort to excite various possible modes in the headforms, as natural frequencies can vary with location. The data were not filtered to avoid the possibility of missing any important frequencies. A custom-written MATLAB (MathWorks, Natick, MA) code was used to calculate the desired metric of natural frequency. The force signal from the impact hammer and the acceleration signals from the headforms' accelerometers were transformed from the time domain into the frequency domain using a Fast Fourier Transform (FFT). Then, the Frequency Response Function (FRF) was calculated, which is the ratio of the response signal to the excitation signal in the frequency domain. When the FRF is plotted, the frequencies that correspond with each peak are the natural frequencies. The results for the Hybrid III and NOCSAE headforms were compared with each other and against published values [3-6].



Figure 1. Experimental setup of the Hybrid III headform (left) and the NOCSAE headform (right), which were each marked with 5 frontal and 5 temporal targets to impact with the tip of the impact hammer.

RESULTS

In both the Hybrid III and the NOCSAE headforms, most of the natural frequencies were observed between 1000-2000 Hz. For certain impacts, there were natural frequencies as low as 700 Hz. More research needs to be conducted to determine the potential effects of impact duration and location on natural frequencies to gain a fuller understanding of the dynamic characteristics of different headforms.

DISCUSSION

The natural frequencies of both headforms fall within the ranges seen in existing published values (Table 1). This is an encouraging result, as it suggests that these headforms behave similarly to the human head regarding their dynamic behaviors.

Table 1. Published natural frequency values associated with various modes in different types of skulls.

	Human cadaver skull filled with silicon gel [3]	Dry human cadaver skull [4]	Polystyrene skull model [5]	Human skull <i>in vivo</i> [6]
1 st Mode (Hz)	313	1385	1410	972
2 nd Mode (Hz)	600	1777	1790	1230
3 rd Mode (Hz)	880	1883	1888	1532

When performing impact testing, it is important to be aware of these characteristics, because when resonant frequencies occur due to the head experiencing a loading at or near one of its natural frequencies, it can be more easily deformed. This makes the head more vulnerable to certain impacts, regardless of their magnitudes. By understanding the intrinsic characteristic of two popular ATD headforms, informed decisions can be made in test environments to determine which one will best capture the frequency response of the head depending on the impact scenarios.

REFERENCES

- [1] Cobb, B.R. et al., *Journal of Sports Engineering and Technology*, 230(1):50-60, 2016.
- [2] Kendall, M et al., *Journal of Sports Engineering and Technology*, 226(3-4):260-265, 2012.
- [3] Gurdjian, E.S. et al., *Journal of Biomechanics*, 3(3):239-247, 1970.
- [4] Khalil, T.B. et al., *Journal of Sound and Vibration*, 63(3):351-376, 1979.
- [5] Huang, B.W. et al., *Life Science Journal*, 6(4):15-22, 2009.
- [6] Håkansson, B et al., *Journal of the Acoustical Society of America*, 95(3):1474-1481, 1994.

SURROGATE MODELS FOR PRESSURE GRADIENTS IN CORONARY ARTERY STENOSES

Elizabeth R. Livingston (1), Siddhartha Srivastava (1), Krishna Garikipati (1,2),
C. Alberto Figueroa (3,4)

- (1) Department of Mechanical Engineering, University of Michigan, Ann Arbor, MI, USA
(2) Department of Mathematics, University of Michigan, Ann Arbor, MI, USA
(3) Department of Biomedical Engineering, University of Michigan, Ann Arbor, MI, USA
(4) Department of Surgery, University of Michigan, Ann Arbor, MI, USA

INTRODUCTION

Narrowing or stenosis in the coronary arteries, the vessels that supply blood to the heart, can lead to serious adverse effects such as heart attack and death. Fractional flow reserve (FFR), a measure of stenosis severity, is the pressure gradient across a stenosis under maximum flow. This metric is determined via an invasive and technically challenging procedure. Developing a computational method to estimate FFR avoids risks associated with this procedure; however high-fidelity (3D) models (e.g., Navier-Stokes) are computationally expensive and impractical for real-time diagnosis. An alternative is to use low fidelity models such as those based on 1D nonlinear theory that are computationally inexpensive.

In previous studies, 1D nonlinear theory was shown to produce relatively low errors compared to 3D theory for multiple types of pulsatile flows in non-stenosed vessels. [1] However, the 1D theory assumes that the pressure is constant over a tubular cross section and that the velocity is an average over the cross-section. Therefore, the lateral velocity components and contributions from the in-section pressure gradient of the 3D model are lost. In scenarios where lateral velocity components are triggered by the stenosis, making the flow patterns more complex, 1D theory is not equipped to capture these complexities and thus the parameter of interest for diagnosis, the axial pressure gradient (a surrogate of the FFR) is not accurate, as shown in Figure 1. In this project, we aim to develop a reduced order model (ROM) capable of accurately describing the complexities of flow across a coronary stenosis.

METHODS

In this study, we consider an analysis-based discovery of a ROM by applying assumptions to the 3D Navier-Stokes equations. High-fidelity data is required to verify the results of this approach. The high-fidelity results are generated using the CRIMSON software. [2] We start with idealized pipes with a constant circular cross-section and a single

cosine shaped restriction defined in Equation 1, a schematic representation is in Figure 2. This specific stenosis profile has often been used in studies of pressure gradient models. [3] Multiple boundary value problems were generated with varying degrees of restriction, stenosis half lengths, and inlet flows. A small sample of these boundary value problems is shown in Figure 3.

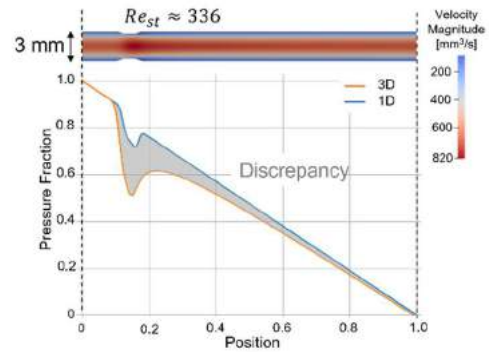


Figure 1: The inaccuracy of existing low dimensional models (1D) in capturing the pressure drop across a mild stenosis; this discrepancy is highlighted in gray.

$$R = R_0 - \frac{\delta}{2} \left(1 + \cos\left(\frac{\pi z}{z_0}\right) \right) \quad (1)$$

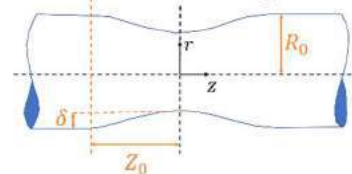


Figure 2: An idealized stenosis geometry with a cosine profile.

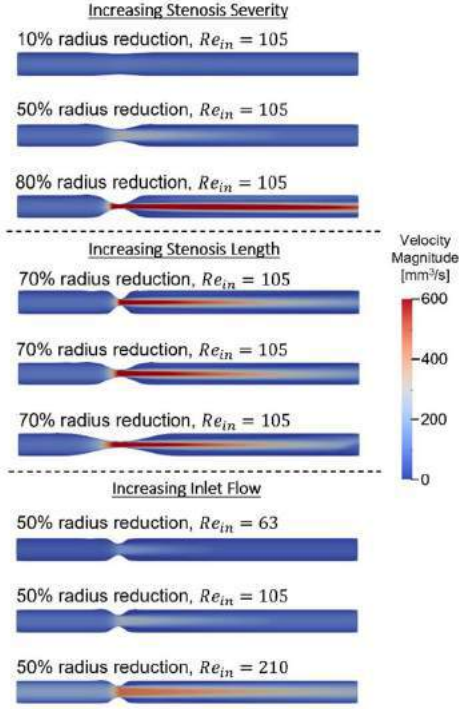


Figure 3: A sampling of the data generation of idealized stenoses. Examples are presented for increasing stenosis severity by increasing the percent diameter reduction, the length of the stenosed region, and increasing the inlet flow.

While our model does not rely on a specific profile, it can be useful to have an explicit mathematical expression for the geometry when developing a reduced order model. We develop a reduced order model by simplifying the full 3D incompressible Navier-Stokes equations in cylindrical coordinates using axisymmetric assumptions. The area averaged form of these equations may be used to relate the pressure gradient to the changes in the axial velocity as shown in Equation 2.

$$\frac{\partial \bar{p}}{\partial z} = \rho \frac{\partial \bar{u}_z^2}{\partial z} + \frac{2\mu}{R} \frac{\partial u_z}{\partial r} \bigg|_R + \mu \frac{\partial^2 \bar{u}_z}{\partial z^2} \quad (2)$$

As a modeling approximation, we assume that the axial velocity as a function of radial and axial positions, r and z , satisfies separation of variables, as shown in Equation 3.

$$u_z(z, r) = \hat{u}_z(z, \hat{r}) = W_z(z)W_r(\hat{r}) \quad (3)$$

We proceed to identify a reduced order model for these area averaged. When substituting in this separation and averaging over the area, we consider the normalized radial position, \hat{r} and expand the radial component of the separation, $W_r(\hat{r})$, in terms of a basis. We apply this to Equation 2 as well as the constant flow rate, Q . From this flow rate equation, we can solve for the separated function $W_z(z)$ and substitute it back into Equation 2 to achieve the final ROM shown in Equation 4.

$$\frac{\partial \bar{p}}{\partial z} = -\frac{2\rho Q^2}{\pi^2 R^5} \frac{\partial R}{\partial z} \gamma_1 + \frac{\mu Q}{\pi R^4} \gamma_2 + \frac{6\mu Q}{\pi R^4} \left(\frac{\partial R}{\partial z} \right)^2 - \frac{2\mu Q}{\pi R^3} \frac{\partial^2 R}{\partial z^2} \quad (4)$$

In this model, the data from multiple boundary value problems may be combined into a linear system and regression is used to solve for the scalar coefficients γ_1 and γ_2 . Data used for this model may have varying geometries and inlet flows, however, there cannot be a laminar separation bubble in the diverging section of the stenosis. This would change the shape of the velocity profile, invalidating our assumption that the axial velocity satisfies separation of variables.

RESULTS

Table 1 shows best fit values for the scalar coefficients γ_1 and γ_2 found using 90 boundary value problems where there was no laminar separation bubble.

Table 1: Coefficients of Equation 5 determined from the data

γ_1	-2.46
γ_2	-54.13

A sample comparison of pressure gradients for two different boundary value problems using these coefficients in Equation 4 is shown in Figure 4. The pointwise error along z was determined between the CFD solution and the ROM. The average error across all problems in the dataset was 0.012.

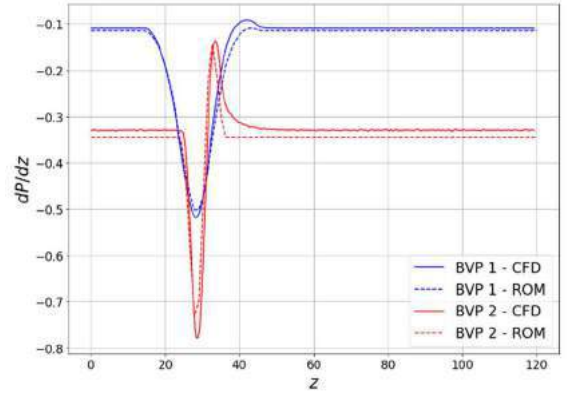


Figure 4: Prediction of the ROM compared to CFD results for a geometric profile not used to fit the model (BVP 1 is a 30% diam. reduction, $Z_0 = 15$ mm, and $Q_{in} = 250$ mm³/s, BVP 2 is a 10% diam. reduction, $Z_0 = 5$ mm, and $Q_{in} = 750$ mm³/s).

DISCUSSION

The model we have discovered is similar to existing models for the pressure drop across a stenosis. However, in our approach, no assumptions were made in deriving our ROM regarding a specific geometric profile for the stenosis. This is an improvement on existing models; however, it is still limited by the assumption that the velocity profile satisfies separation of variables along radial and axial directions. Therefore, this model is only applicable to non-separated flows.

Further exploration is required, relaxing the separation of variables assumptions to obtain a model in which the radial velocity profile can change along the length of the vessel. Alternatively, several data-driven approaches could be used to discover new ROMs. For instance, system identification could be used on a library of candidate operators, inspired by our analytical model, to discover a new ROM. A key component in this approach is stepwise regression, which is used to eliminate terms until the Pareto front is reached. Traditional surrogate modeling approaches like neural networks may also be considered, however, these do not provide an interpretable model.

ACKNOWLEDGEMENTS

This work was supported by the Clare Boothe Luce graduate fellowship, XSEDE allocation BIO220054, and NSF Grant STTR 2151555.

REFERENCES

- [1] Xiao, N et al, *Int J Numer Meth Biomed Eng*, 30(2):204-231, 2013.
- [2] Arthurs C et al, *PLOS Comput Biol*, 17(5):e1008881, 2021.
- [3] Young D et al, *J Biomech*, 6(4):395-410, 1973.

ADAPTIVE CHANGES IN THE BAT'S SHOULDER ANATOMY ALLOW FOR REPETITIVE OVERHEAD MOTIONS

Iden Kurtaliaj (1), Jennifer Kunes (1), K. Michael Rowley (2,3), Lynn Ann Forrester (1), Mikhail Golman (1), Guy M. Genin (4), Sharon M. Swartz (2), Stavros Thomopoulos (1)

- (1) Department of Biomedical Engineering, Columbia University, New York, NY, USA
(2) Department of Ecology, Evolution, and Organismal Biology, Brown University, Providence, RI, USA
(3) Department of Kinesiology, California State University East Bay, Hayward, CA, USA
(4) Department of Mechanical Engineering and Materials Science, Washington University, St. Louis, MO, USA

INTRODUCTION

In humans, the glenohumeral joint enables the greatest mobility in the human body, at the expense of its stability. The bony anatomy between the proximal humerus and glenoid cavity of the scapula has minimal constraints, thus humans are able to perform a wide range of overhead motions. Stability in the joint is largely provided by soft tissues such as the rotator cuff and the labrum. Unfortunately, repetitive overhead motion leads to rotator cuff injuries that affect millions of people in the US each year [1,2]. Bats, however, have evolved to perform repetitive overhead motion in order to achieve flight. Their survival depends on performing these motions across a relatively long lifespan without injury [3,4]. To gain insight into strategies that might inform improved treatment, we therefore investigated the structure and function of the bat rotator cuff. In this study, we performed comparative anatomy to better understand the functional advantages of the bat shoulder versus that of the mouse, a similarly-sized quadrupedal animal. We hypothesized that the anatomy of the bat glenohumeral joint would differ from that of the mouse in ways that are consistent with improved stability.

METHODS

Sample preparation: All animal procedures were approved by the Columbia and Brown University Institutional Animal Care and Use Committees. Shoulders harvested from adult (12 weeks) C57BL6/J mice (n=5) and *C. perspicillata* bats (n=5) were dissected then fixed in three different positions: full shoulder extension ("P1"), intermediate ("P2"), and full shoulder flexion ("P3"). To consistently identify the angle between the scapular spine and the humerus for each fixation position, gait (mouse) and flight (bat) analyses were used. **MicroCT Imaging:** Samples were scanned at 55 kV peaks with 145 mA intensity, and 19.3 μ m resolution (Skyscan 1272, Bruker). **Anatomical Measurements:** Images were reconstructed (NRecon, Skyscan), and bone parameters measured (Skyscan CT Analyzer). The scapular linear

index was determined as the ratio of scapular width to length. Supraspinatus and infraspinatus linear indices were calculated using the length from the medial aspect of the spine to the superior or inferior angle. Glenoid retroversion was measured via the anterior facing angle between the body of the scapula and the glenoid face on the axial cross section. Supraspinatus outlet area was measured as the area posterior to the coracoid, inferior to the acromion, and within the acromial arch. Supraspinatus clearance, measured as the vertical distance between the humeral supraspinatus insertion and the bottom face of the acromion, was measured for each sample at each of the three positions. Glenoid curvature was measured using the circle tool in ImageJ to create the best fit circle. The arc length of the glenoid was calculated using the angle from the superior to the inferior glenoid rim. **Modeling:** Using a mathematical model based upon our imaging of the enthesis of mouse and bats, we predicted how strength, stiffness and toughness of the tendon enthesis would vary with loading direction and the bony ridge abutting the enthesis [9]. Simulations considered 20 linear elastic, brittle fibers of thickness $w = 10 \mu$ m and spacing $s/w = 1.5$ abutting a cylindrical bone ridge of aspect ratio $B/A=1$ (mouse) or $B/A=0.4$ (bat). Strength, stiffness, and toughness were normalized against idealized scenario where tightly packed fibers ($s/w = 1$) were pulled to failure uniaxially at 90° (Fig. 3). **Biomechanics:** Humerus and supraspinatus muscle and tendon units were dissected from adult (8 weeks) C57BL6/J mice (n=10) and *C. perspicillata* bats (n=5). To determine cross-sectional area of the tendon, microCT scanning was performed at 55 kV peaks with 145 mA intensity, and 6.5 μ m resolution (Skyscan 1272, Bruker). Following scanning, samples were preconditioned by being sinusoidally loaded from 0.05 to 0.2 N for 5 cycles then allowed to rest for 2 minutes, before being strained until failure in tension at 0.1 %/s. **Statistical Analysis:** All data are shown as mean \pm standard deviation. Statistical analysis was performed for all experiments using unpaired t-tests with Welch's correction (GraphPad Prism 7). The threshold for statistical significance was defined at $p < 0.05$.

RESULTS

Bony Anatomy: The scapular index and infraspinatus index were both significantly larger in bats than in mice, while the supraspinatus index did not differ (Fig. 1a). Supraspinatus-acromion clearance increased when moving from full shoulder flexion to extension (i.e., from P3 to P2 to P1) in both bats and mice. However, the supraspinatus outlet area was significantly greater in bats compared to mice (Fig. 1b). The glenoid was retroverted in bats and anteverted in mice. Glenoid curvature and arc length were significantly higher in bats than in mice. **Tissue level mechanics:** The supraspinatus tendon cross-sectional area was significantly larger in bats compared to mice (Fig. 2). Mechanical testing revealed that mouse supraspinatus tendons were significantly stronger (i.e., higher maximum failure stress) and significantly stiffer (i.e., higher modulus) compared to bats (Fig. 2). There was no difference in toughness between the two groups (Fig. 2). **Modeling:** Simulations suggested that the strength and stiffness of the supraspinatus tendon attachment are greater for the bat's flatter humeral head than for the mouse's more circular humeral head (Fig. 3). The higher strength associated with the bat was maintained over a broad range of loading angles, while toughness was slightly reduced, particularly at very low abduction angles.

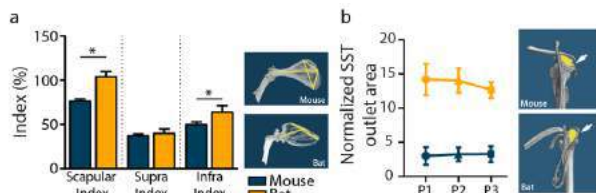


Figure 1. (a) Scapular, supra. and infra. indices (b) Supraspinatus outlet area (yellow) normalized by attachment

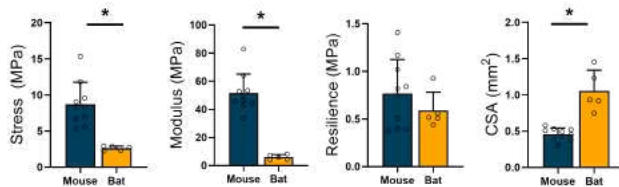


Figure 2. Material properties of supraspinatus tendons

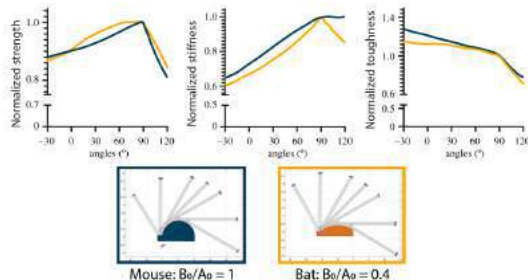


Figure 3. Modeling suggested that the flatter bat humeral head may increase strength and stiffness relative to the mouse.

DISCUSSION

Comparison of the glenohumeral joints of two similarly-sized species (i.e., bats and mice) suggested functional adaptations of bat shoulder anatomy in relation to the demands of flight.

Bony anatomy adaptations: The bat's enlarged scapular and infraspinatus indices imply changes to muscle size and orientation. The supraspinatus index, however, was conserved across species. Because the infraspinatus and supraspinatus stabilize quadrupedal gait, the bat's

enlarged infraspinatus index suggests a larger role for the infraspinatus in the bat's glenohumeral stability. This also hints at adaptation to relieve stress on the supraspinatus. Similarly, the larger supraspinatus outlet in the bat provides more space for the supraspinatus to pass under the coracoacromial arch to prevent supraspinatus shoulder impingement commonly seen in overhead-throwing athletes [5]. Although the glenoid was anteverted in mice, it was retroverted in bats, analogous to the retroverted glenoids reported in high-level overhead-throwing athletes [6]. This may enable more rotation of the joint while limiting capsular tension. The bat glenoid was more concave, encapsulating more of the humeral head when compared to mice. In addition, the bat had a larger glenoid arc length and articulating surface area with the humeral head, thus providing more stability while maintaining mobility.

Tissue level adaptations: Bat supraspinatus tendon cross-sectional area was significantly larger than that of mice, consistent with previous measurements of supraspinatus-acromion clearance and outlet area. While bat supraspinatus tendons were weaker when compared to mice, as indicated by significantly lower maximum failure stresses and significantly lower stiffness, resilience and toughness was similar between the two groups. In bats, the supraspinatus attachment (i.e., the greater tuberosity of the humerus) protrudes laterally to the humeral head, seemingly forming a secondary articulation with the acromion. Due to this enlarged tuberosity, the supraspinatus tendon forms an L-shape as it inserts into the scapular fossa. This adaptation may be to optimize strength over a wider range of motion, as seen by the large energy absorption experienced relative to its lower maximum failure stress and modulus values.

Modeling: The idea of the bat's deeper glenoid providing more stability is consistent with shoulder instability patients, who present with loss of glenoid concavity and a flatter glenoid morphology [8]. Our modeling revealed potential reasons why the humeral head shape at the supraspinatus tendon attachment may affect stability. The models suggested that flatter attachment in bats relative to mice leads to increased strength over a wide range of motion, enabling bats to perform high stress flight by optimizing strength over a wider range of motion than needed for walking. The mechanical energy needed to dislocate the humeral head increases with concavity of the glenoid and stiffness of the rotator cuff tendons: compression of the convex humeral head into the concave glenoid fossa stabilizes the shoulder. Dislocation requires displacing the humeral head laterally over the glenoid lip, with a force that increases with tendon stiffness. The energy required for this displacement is thus directly related to the shape of the glenoid. In the case of the bat, where the glenoid is deeper and more concave, more energy is required for shoulder dislocation.

Implications for rotator cuff repair. From the clinical perspective, adaptations in the bat provide insight into reshaping of the anatomy in surgical repair. Future studies of the bat rotator cuff muscles will further test these hypotheses about passive stabilization of the shoulder and rotator cuff repair techniques to decrease supraspinatus stresses.

ACKNOWLEDGEMENTS

This work was supported by NIH (R01-AR055580).

REFERENCES

- [1] Sher, J et al., *J Bone Joint Surg Am*, 77(1):10-5, 1995
- [2] Galatz, L et al., *J Bone Joint Surg Am*, 86-A:219-24, 2004
- [3] Martorelli, J et al., *Ecol Evol*, 9(1): 703–722, 2019
- [4] Bahlman, J et al., *Bioinspir. Biomim.*, 8 016009, 2013
- [5] Smith, C et al., *J Am Osteopath Coll Radiol*, 7(3):5-14, 2018
- [6] Borsa, P et al., *Sports Med*, 38(1):17-36, 2008
- [7] Willems, W. et al., *J. Normal and Pathological Anatomy of the Shoulder* 3–14, 2015.
- [8] Di Giacomo, G. et al., *Shoulder & Elbow* 10.1302/2058-5241.3.180028, 2018.
- [9] Golman, M. et al., *J R Soc Interface* 18(185):20210421, 2021.

TIME-DEPENDENT MATERIAL PROPERTIES OF NONHUMAN PRIMATE UTERINE LAYERS THROUGH GESTATION

**Daniella M. Fodera¹, Echo Z. Xu², Shuyang Fang², Ivan Rosado-Mendez^{3,4}, Timothy Hall³, Helen Feltovich^{3,5},
Michelle L. Oyen⁶, Kristin M. Myers²**

¹Department of Biomedical Engineering, Columbia University, New York, NY, USA

²Department of Mechanical Engineering, Columbia University, New York, NY, USA

³Department of Medical Physics, University of Wisconsin-Madison, Madison, WI, USA

⁴Department of Radiology, University of Wisconsin-Madison, Madison, WI, USA

⁵Department of Obstetrics & Gynecology, Mount Sinai, New York, NY, USA

⁶Department of Biomedical Engineering, Washington University in St. Louis, St. Louis, MO, USA

INTRODUCTION

The uterus plays a critical role in establishing and maintaining pregnancy, undergoing dramatic growth and remodeling from embryo implantation to labor and birth [1]. In order to support these basic reproductive processes, the uterus is composed of three tissue layers that are structurally and functionally distinct: (i) the endometrium-decidua, the innermost layer that forms the maternal-fetal interface (ii) the myometrium, the thickest layer composed of smooth muscle interwoven with collagen fibers, and (iii) the perimetrium, the outermost serosal layer [1]. Although the uterus performs critical biomechanical functions, few studies have investigated the mechanical properties of the gravid uterus [2-3]. A complete absence of data exists for mid-gestational time points due to ethical limitations surrounding human uterine tissue collection. Therefore, we propose using a nonhuman primate model (Rhesus macaque) to assess mid-gestation uterine changes given known similarities in anatomy and pregnancy physiology [4]. The purpose of this study is to characterize the time-dependent micro-mechanical properties of the nonhuman primate (NHP) uterus at nonpregnant (NP) and three pregnant (PG) time points: early 2nd (E2), early 3rd (E3), and late 3rd (L3) trimesters.

METHODS

NHP uterine tissue was collected from Rhesus macaques following a total hysterectomy for the following groups: NP (n = 2), E2 (n = 2), E3 (n = 2), and L3 (n = 2). Uterine specimens contained all three tissue layers and were sampled from the anterior region (Fig. 1A). Samples were flash-frozen on dry ice and stored at -80°C until testing. This protocol was approved by the University of Wisconsin Institutional Animal Care and Use Committee (IACUC). To investigate the qualitative distribution of smooth muscle and collagen in all three uterine layers, uterine cross-sections were fixed in 10% formalin, paraffin-embedded, sectioned to a thickness of 5 µm, and stained for Masson's trichrome.

Prior to mechanical testing, samples were sectioned into separate tissue layers, swelled at 4°C overnight in PBS solution, and equilibrated at room temperature for 30 min. Spherical nanoindentation (Piuma, Optics11Life, Amsterdam, NL) was utilized to determine the time-dependent material properties of the NHP uterine layers. Using an indenter with a probe radius of 50 µm and cantilever stiffness of 0.19 N/m,

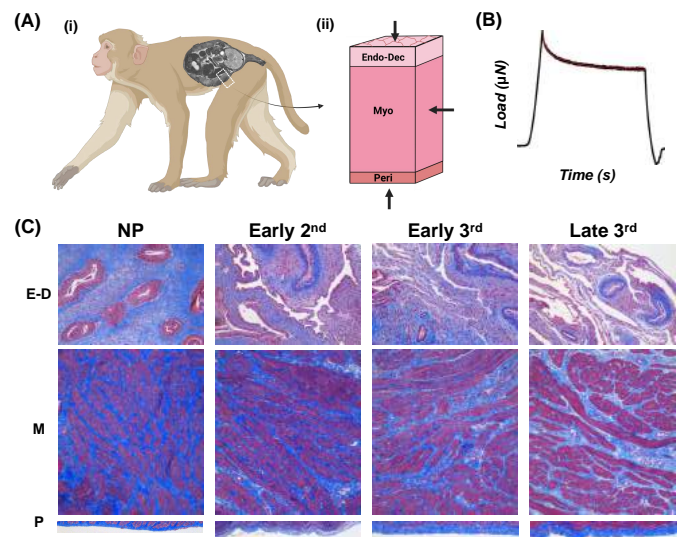


Figure 1: (A) Schematic of a (i) pregnant Rhesus macaque and (ii) uterine cross-section containing all three tissue layers. Arrows indicate the directionality of nanoindentation testing. (B) Representative load relaxation curve (black line) generated from nanoindentation testing fit with the PVE model (red line). (C) Histology (Masson's trichrome) of uterine layers (E-D = endometrium-decidua; M = myometrium; P = perimetrium) for NP, E2, E3, and L3 groups (blue = collagen; red = smooth muscle). Scale bar = 200 µm.

samples were indented to a fixed depth of 4 µm for 15 s, corresponding to a 5% strain, to achieve a load relaxation curve approaching equilibrium (Fig. 1B). The distance between indentation points was fixed at 200 µm. At least 150 indentation measurements were taken for each sample. Load relaxation curves were fit in MATLAB with a combined poroelastic-viscoelastic (PVE) model based on established methods [5-7]. Parameters of stiffness (E), viscoelastic ratio (E_{∞}/E_0), and intrinsic permeability (k) were determined. Statistical analysis was performed in GraphPad Prism 9.4.0 using a nested one-way ANOVA with significance set at a 95% confidence level. P-value symbols follow a standard GraphPad (GP) style (* $p \leq 0.05$, ** $p \leq 0.01$, *** $p \leq 0.001$) with an added

distinction for trends ($^{\#}p \leq 0.1$).

RESULTS

Distinct structural changes are evident for all uterine layers as a result of pregnancy (Fig. 1C). The endometrium-decidua exhibits the greatest degree of remodeling, marked by a shift in collagen content, an increase in the number and size of blood vessels, and the transformation of glandular epithelium morphology into a saw-toothed appearance in pregnancy. Similarly, the myometrium undergoes a significant increase in size during pregnancy through hyperplasia and hypertrophy of smooth muscle fibers. Lastly, the perimetrium, a layer exclusively composed of collagen, appears to thicken in pregnancy, with clear differences observed across all gestational time points.

Differences in the material properties of the NHP uterus are demonstrated for NP and PG tissue layers across gestation (Fig. 2). Notably, the endometrium-decidua is the least stiff layer of the uterus, by nearly one to two orders of magnitude, regardless of PG state (Fig. 2A). Relative to the myometrium, the perimetrium exhibits variable trends within each gestational time point and nonpregnancy, with the greatest differences detected for E2 and L3 trimesters (Fig. 2A). The perimetrium is the only layer of the uterus that stiffens in pregnancy, with tissue in the L3 trimester demonstrating increased stiffness relative to NP, E2, and E3 groups. No change to myometrium stiffness is observed as a result of pregnancy (Fig. 2A).

For all uterine layers, regardless of PG state, viscoelastic ratio ranges from 0.4 to 0.6 (Fig. 2B). For all PG time points, the endometrium-decidua exhibits a decreased viscoelastic ratio relative to both the myometrium and perimetrium, a trend not observed in nonpregnancy (Fig. 2B). No changes in viscoelastic ratio are observed for and between the myometrium and perimetrium in pregnancy (Fig. 2B). Permeability shows variable trends for all tissue layers across NP and PG groups, ranging from 10^{-15} to 10^{-17} m^2 (Fig. 2C). The NP endometrium-decidua appears less permeable than the NP myometrium, yet this difference is not statistically significant for any PG time points (Fig. 2C).

DISCUSSION

Here, we uncover the transformation of structural and material properties for the NHP uterus in pregnancy with the unique inclusion of mid-gestational time points. This robust dataset collected via nanoindentation contributes to a key knowledge gap in pregnancy biomechanics due to insurmountable ethical boundaries in humans. Specifically, this dataset, together with qualitative histology results, highlights drastic differences in structure, composition, and stiffness across the endometrium-decidua, myometrium, and perimetrium in pregnancy. Surprisingly, the perimetrium is the only uterine tissue to exhibit clear stiffening relative to NP and early gestational time points, mirroring changes in thickness to this layer.

A key limitation of this study is the relatively small sample size per group ($n = 2$), making it difficult to conclude whether differences, or lack thereof, are truly representative of each NP and PG group or are subject to individual animal variability. Moving forward, we plan to address this by including additional samples. It is also important to note that the NP endometrium-decidua and perimetrium exhibit the greatest degree of individual variability in stiffness values amongst all tissues tested, a likely product of menstrual cycle fluctuations. Yet, despite these limitations, the data presented here yield key insights into mid-gestational changes that occur for all three uterine layers. Characterizing baseline changes that occur throughout pregnancy in a physiologically comparable animal model is foundational to better understanding and predicting healthy and disordered alterations in human gestation.

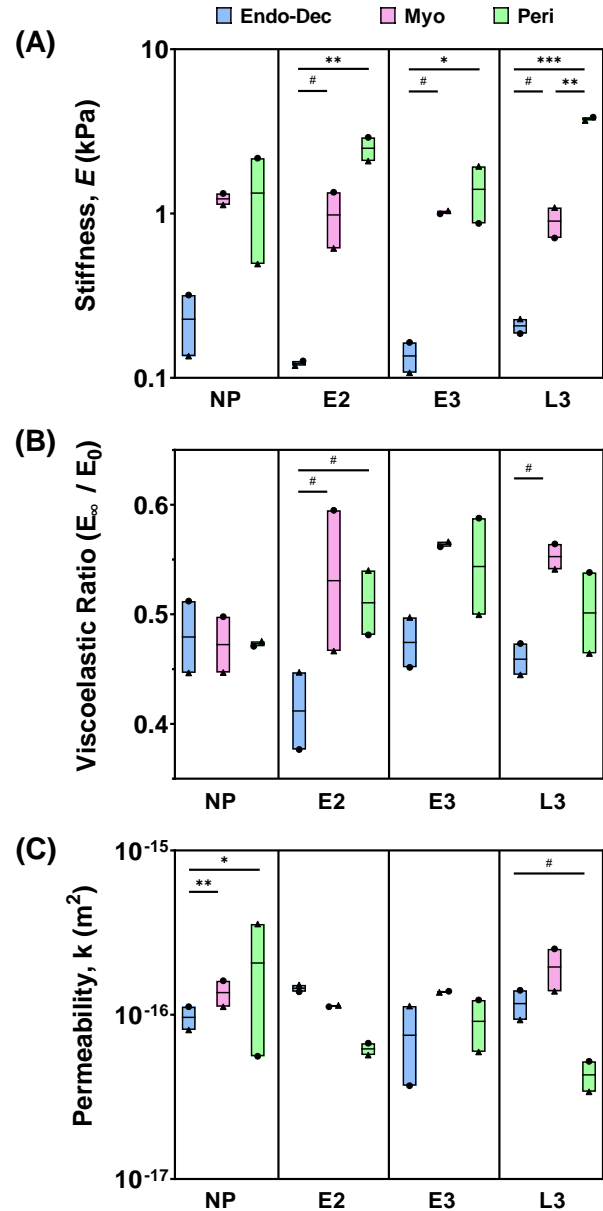


Figure 2: (A) Stiffness, (B) viscoelastic ratio, and (C) permeability of NP, E2, E3, and L3 NHP uterine layers. Each symbol represents the median value of all indentation points ($10^1 - 10^2$) for a given sample, with triangles and circles indicating different animals.

ACKNOWLEDGMENTS

The research was supported in part by the Iris Fund, the Eunice Kennedy Shriver National Institute of Child Health Human Development Grant R01HD072077 to TH, IRM, HF, and KM, and the Office Of The Director, NIH Award P51OD011106 to the Wisconsin National Primate Research Center, University of Wisconsin-Madison.

REFERENCES

- [1] Leveno et al. *Williams Obstetrics* 26e. 2022.
- [2] Abbas et al. *Hum Reprod.* 2019.
- [3] Fang et al. *Ann Biomed Eng.* 2021.
- [4] Stouffer and Woodruff. *ILAR J.* 2017.
- [5] Mattice, J et al. *J. Mater. Res.* 2006.
- [6] Hu, Y et al. *Appl. Phys. Lett.* 2010.
- [7] Islam and Oyen. *Exp Mech.* 2021.

DEVELOPMENT OF A FINITE ELEMENT BIRTHING MODEL TO ASSESS PELVIC FLOOR BIOMECHANICS

M. Mounzer (1), A. Singh, Ph.D. (2), S. Balasubramanian, Ph.D. (1)

- (1) School of Biomedical Engineering, Science and Health Systems, Drexel University, Philadelphia, PA, USA
(2) Bioengineering Department, College of Engineering, Temple University, Philadelphia, PA, USA

INTRODUCTION

Due to ethical constraints of conducting birthing injury studies in pregnant women, computational birthing simulations have been developed to assess the involved structures and forces [1]. However, current models suffer from oversimplified pelvic floor geometry. Therefore, the objective of this study was to create detailed finite element (FE) models of a female bony pelvis with pelvic floor muscles, and a fetal head to simulate birthing.

METHODS

Retrospective MRI images from a female subject (age 25-39 years) was obtained from an open-source database [2]. The geometry of the pelvic floor muscles, namely puborectalis, pubococcygeus, iliococcygeus, coccygeus, and obturator internus were segmented using 3D Slicer (Slicer), an open-source medical image processing software (Figure 1.). Post-processing of these segmented geometries was done in Fusion 360 (Autodesk, San Rafael, CA) to promote uniformity in order to generate quality meshes. Hexahedral meshes of the segmented geometries were created using HyperWorks (Altair Engineering, Troy, MI), and integrated with an existing hexahedral FE model (1031 elements) of the female bony pelvis. A fetal head and skull model was adapted from an open-source license: Position and Personalize Advanced Human Body Models for Injury Prediction (PIPER) project. The 1.5-year-old PIPER head and skull FE model (available at piper-project.org/downloads) was meshed into a hexahedral FE model (3144 elements) and scaled down to the dimensions of a 50th percentile fetus. Material properties and ligamentous structures for the pelvis will be added to create a more biofidelic model for birthing simulations, and therefore can properly assess pelvic floor stresses and strains on muscles and connective tissues.

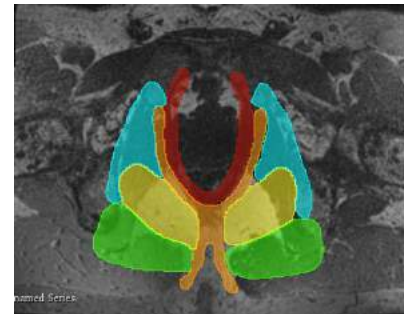


Figure 1: Segmented pelvic floor from MRI-scan slices using 3D Slicer. (Red: Puborectalis, Orange: Pubococcygeus, Yellow: Iliococcygeus, Green: Coccygeus, Blue: Obturator Internus).

RESULTS

High-quality FE model of the pelvic floor muscles were created (271 out of 294 elements have a Jacobian greater than 0.7) and integrated with the FE model of the female bony pelvis (Figure 2). The FE model of the fetus head was positioned within the pelvis to simulate birthing (Figures 3, 4). The Jacobian matrices for bony structures such as the fetal skull and pelvis can be ignored due to the rigidity of bone as compared to soft tissue structures (total element size: 5491).

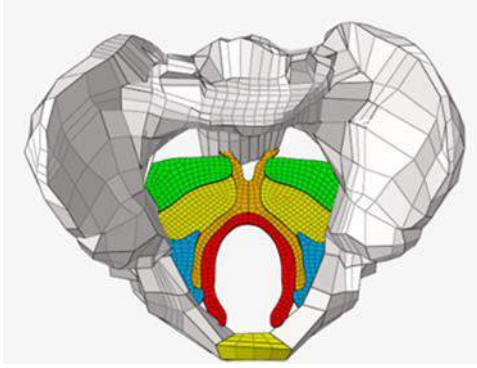


Figure 2. Hexahedral meshed FE models of the bony pelvis and pelvic floor muscles using HyperWorks (Red: Puborectalis, Orange: Pubococcygeus, Yellow: Iliococcygeus, Green: Coccygeus, Blue: Obturator Internus, White: Bony Pelvis, Yellow: Pubic Symphysis).

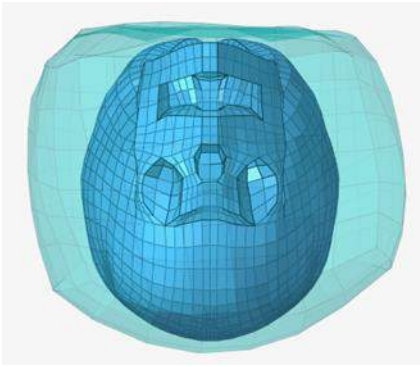


Figure 3. Hexahedral mesh of the fetal head (turquoise) and fetal skull (blue).

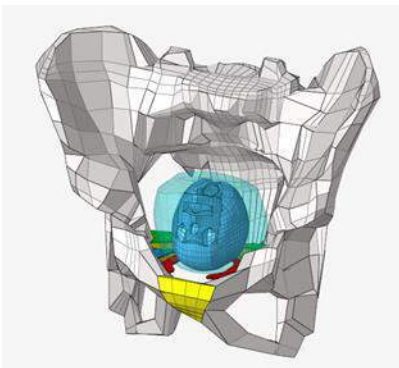


Figure 4. Combined hexahedral FE models with fetal head and skull placed in the occipito-posterior position.

DISCUSSION

Maximum stretch ratios can range from 1.6 to 3.5 and occur at the inner posterior-medial portion of the puborectalis [3]. Furthermore, occipito-posterior (OP) fetal positions result in a greater stretch of the

levator ani than compared to occipitio-anterior position. However, due to variability between muscles and connective tissue comprising the pelvic floor, birthing simulations are necessary to validate appropriate locations of maximum strain of the levator ani muscle. Therefore, parametric simulations are needed to correlate fetal position to maximum stretch ratios of specific pelvic floor muscles.

ACKNOWLEDGEMENTS

Dr. Sriram Balasubramanian, Dr. Anita Singh, and fellow researchers at the Orthopedics Biomechanics Laboratory and the Office of Undergraduate Research

REFERENCES

- [1] M. P. L. Parente, "Biomechanics of the pelvic floor during vaginal delivery," ProQuest Dissertations Publishing, 2008.
- [2] A. S. Fortuin, B. W. Philips, M. M. van der Leest, M. E. Ladd, S. Orzada, M. C. Maas, and T. W. Scheenen, "Magnetic resonance imaging at ultra-high magnetic field strength: An in vivo assessment of number, size and distribution of pelvic lymph nodes," PLOS ONE, vol. 15, no. 7, 2020.
- [3] L. Hoyte et al., "Quantity and distribution of levator ani stretch during simulated vaginal childbirth," American journal of obstetrics and gynecology, vol.199, no. 2, pp. 198.e1–198.e5, 2008, doi: 10.1016/j.ajog.2008.04.027.

GELATIN HYDROGEL POLY-E-CAPROLACTONE 3D PRINTED COMPOSITE BIOMATERIAL CHARACTERIZATION FOR MENISCAL TISSUE ENGINEERING

Anthony J. El Kommos (1), Gabi Schwartz (1) , Andy J Morejon (2)

Department of BioMedical Engineering, University of Miami, Coral Gables, Florida, U.S.A (1)
Department of Mechanical and Aerospace Engineering, University of Miami, Coral Gables, Florida, U.S.A (2)

INTRODUCTION

Meniscal Traumatic Injury is the most prevalent orthopedic injury among adults with approximately 700,000 procedures performed annually in the United States alone according to AAOS data. Further the economic impact of such injury is a multi-billion-dollar annual economic market. As such significant research efforts are being undertaken to improve upon the surgical repair and regeneration of menisci[3].

Current techniques to repair the menisci involved arthroscopic surgical intervention using sutures to reintegrate the torn tissue to the intact tissue. However given the interior avascular nature of the menisci white zone tears offer little in the way of regeneration. As such said injuries are dealt with via meniscectomy are partial or complete in which the tissue is excised and removed. However as the menisci plays a crucial role in maintaining joint function, via lubrication, load bearing, and joint congruency, these procedures are incomplete in restoring joint health and function[3].

As such meniscal alternatives have been developed to offer improved post-surgical outcomes. Implantable devices such as the Menaflex and CMI have been developed. These devices are porous collagen type1 based implants impregnated with GAGs that are trimmed to fit the current defect. These implants are resorbable and typically integrate and resorb into the body over a period of 8-12 weeks post-surgery.

Collagen based meniscal implants have seen varied success within the field. However further improvement upon the properties of Collagen based implants relative to native meniscal tissue is still desired regarding structural integrity, hydraulic permeability, bio composition, and aggregate modulus.

Previous efforts at our lab have been taken to characterize and assess the various properties of native meniscal tissue in relation to transport properties, tissue composition, micro and macro architecture, and viscoelastic behavior under compression, tension, and shear loads.

Utilizing data previously gathered our goal is to begin to recapitulate the behavior of native meniscal tissue. In the development of a composite biomaterial for meniscal tissue engineering.

METHODS

Hydrogel Formation

A 15% Gelatin A wt/vol solution (Sigma-Aldrich 300 Bloom) was prepared by dissolving GelA in PBS at relevant concentrations and dissolving the solution in a heated water bath at 80C. The solution was then cross-linked utilizing a Glutaraldehyde solution diluted with PBS to maintain consistent osmolarity. To achieve varied molar ratios of GelA:GA, various concentrations of GA solution were used, and all samples were cross-linked for 1 hour prior to being thrice rinsed in distilled water and then allowed to swell for 12 hours to reach osmotic equilibrium. Following the swelling period, the samples were removed, patted dry to remove excess moisture and weighed, yielding wet weight. The samples were then placed in a fume hood uncovered and allowed to completely dehydrate for a period of 24 hours and weighed again, yielding dry weight.

Degree of Swelling was then calculated using the following formula.

Equation 1:

$$\frac{Wt_{wet} - Wt_{dry}}{Wt_{dry}} = \text{Degree of Swelling}$$

Stress Relaxation

Unconfined compression stress relaxation was performed on a hydrogel sample utilizing a UniVert Uniaxial testing machine by CellScale. Hydrogel samples were prepared using the protocol in a 6 well plate. Volume was controlled to ensure the total sample height would not exceed 3mm, while molar ratios of GelA:GA were maintained. Samples were allowed to swell to osmotic equilibrium for a period of 12 hours prior to testing. Samples were excised using a 10 mm hole punch and measured for thickness. Samples were then placed on the center of the UniVert platen above an affixed piece of sandpaper (800 grit) to prevent slippage of the sample. The sample was then preloaded to 0.1N and PBS was filled into sample holder. The sample was then compressed at a rate of 0.003 mm/s to 10% and held for a period of 4 hours. Following this hold phase, the sample was compressed and held at 20% using the same protocol.

3D Printing

PCL filament was utilized on a FDM 3D printer at a nozzle temperature of 140C and a bed temperature of 33C. Various patterns and configurations will be utilized and assessed for mechanical properties.

RESULTS

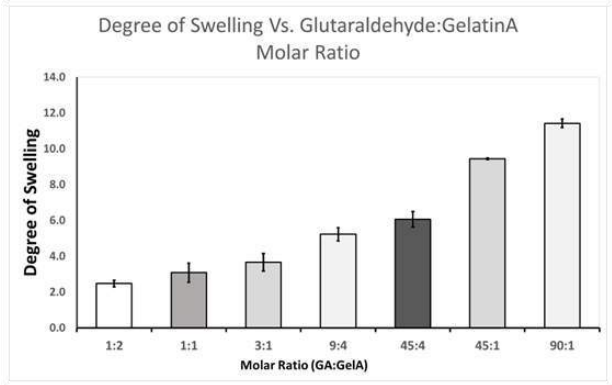


Figure 1 Degree of Swelling relative to Molar Ratio GelA:GA

ANOVA						
Source of Variation	SS	df	MS	F	P-value	F crit
Between Groups	84.0442	6	14.00737	75.43307	7.47E-10	2.847726
Within Groups	2.599697	14	0.185693			
Total	86.6439	20				

Table 1 ANOVA analysis of Degree of Swelling Data

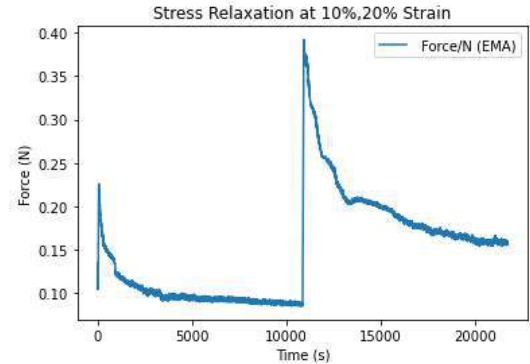


Figure 2 Stress Relaxation Data for GelA:GA hydrogel at 45:4 Molar Ratio

DISCUSSION

While our research and development is still in its’ early phases, initial tests show statistically significant control of swellability in hydrogel formation. Allowing for the fine tuning of osmotic behavior in the hydrogel portion of the composite material. Allowing for control of the matrix portion of the composite material.

Further the stress relaxation behavior of the hydrogel alone follows the behavior exhibited by native meniscal tissue in that, a steep decrease followed by a gradual leveling off to equilibrium force. Consistent with stress-relaxation behavior exhibited by Standard Linear Solid Models.

In turn the integration of PCL printed reinforcement grids will need to be tested under similar protocols to determine the overall enhance effect of the composite material. As well as the relative mechanical properties too native meniscus tissue.

When assessing PCL on its’ own it is found to have a Young’s Modulus of 3.89 MPa with native Meniscus tissue being on the order of 2-5 MPa. While PCL alone exhibits good stress-relaxation behavior our goal is to determine if the composite of PCL and the hydrogel matrix can improve upon the properties relative to native tissue[4].

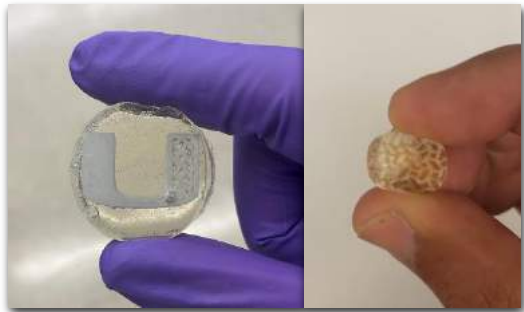


Figure 3 Composite BioMaterials using GelA hydrogels and PCL 3D prints.

Further as such this could provide the basis for generating tissue engineered articular cartilage scaffolds to replace static synthetic materials while improving the efficacy of natural materials alone.

ACKNOWLEDGEMENTS

Research is being funded by the Novel Meniscus Grant GR011307 in accordance with the University of Miami.

REFERENCES

[1] Briscoe, J. (2019). Viscoelastic properties of tissue engineered constructs. In Tissue Engineering (pp. 147-162). Academic Press.

[2]Mao, J., Bao, Y., Tang, J., & Wang, J. (2018). Mechanical properties and viscoelastic behavior of articular cartilage: A review. Materials Science and Engineering: C, 88, 681-698.

[3]Morejon, A., Norberg, C. D., De Rosa, M., Best, T. M., Jackson, A. R., & Travascio, F. (2021). Compressive properties and hydraulic permeability of human meniscus: relationships with tissue structure and composition. Frontiers in bioengineering and biotechnology, 8, 622552.

[4]Song, J., et al. (2019). A Meniscal Tissue Engineering Strategy Using a Glutaraldehyde Cross-Linked Gelatin A Scaffold. International Journal of Molecular Sciences, 20(16), 3849.

[5]Zuo, X., et al. (2018). Fabrication of Meniscal Scaffold Using 3D Printing and Characterization of Mechanical and Histological Properties. Journal of Tissue Engineering and Regenerative Medicine, 12(4), e2124-e2133.

CHANGES IN VISCOELASTIC MECHANICAL PROPERTIES AND GENE EXPRESSION IN RAT ACHILLES TENDON DUE TO TREADMILL RUNNING DEPEND ON EXERCISE INTENSITY AND DURATION

Margaret K. Tamburro (1), Kelsey A. Bonilla (1), Snehal S. Shetye (1), Thomas P. Leahy (1),
Jeremy D. Eekhoff (1), Daniel C. Farber (1), Louis J. Soslowsky (1)

(1) McKay Orthopaedic Research Laboratory, University of Pennsylvania, Philadelphia, PA, USA

INTRODUCTION

Despite high prevalence of Achilles tendinopathy,¹ the effect of exercise on tendon properties that influence prevention, development, and treatment of Achilles tendon pathology remain unclear. Clinically, patients with a variety of exercise histories, ranging from sedentary individuals to elite athletes, present with Achilles tendon pathology.² In animal models, where exercise can be investigated as a controlled variable, effects of exercise on tendon range from anabolic effects including improved tendon mechanical properties³ and increased collagen type I gene expression⁴ to catabolic effects including reduced mechanical properties and damaged collagen fibrils.⁵ Accordingly, to leverage exercise as a tool for Achilles tendinopathy treatment and prevention, the contributions of exercise intensity and duration to exercise-induced tendon changes must be better understood. Using an *in vivo* rat Achilles tendon model, our objective was to define intensity- and duration-dependent effects of treadmill running exercise on mechanical properties, cell morphology and density, and gene expression. We hypothesized that exercise would induce tendon changes in an intensity-dependent manner whereby increased exercise intensity would increase: resistance to mechanical fatigue, tenocyte density, and expression of genes associated with tendonous anabolism with changes most notable after prolonged exercise duration.

METHODS

Study Design: Sixty Sprague Dawley rats ~10 weeks of age (300-350 g) were randomized into six groups (n = 10/group) corresponding to exercise duration (4 or 8 weeks) and intensity: Low (cage activity), Moderate (running 1 hour/day 5 days/week at 10 m/min, 0° incline), or High (running 1 hour/day 5 days/week at 20 m/min, 10° incline). Rats assigned to Moderate and High groups participated in two weeks of treadmill acclimation prior to initiation of the exercise protocol.

Following sacrifice at either 4 or 8 weeks, tendons were harvested bilaterally and randomly assigned to mechanical, histological, and gene expression analyses. All analyses were performed blinded to experimental group. **Mechanical Analysis:** Tendons were prepared, and cross-sectional area was measured as described⁶ (8 mm gauge length). Mechanical assessment was performed with a viscoelastic testing protocol (preconditioning, stress relaxation at 9% strain, and sinusoidal frequency sweep at 0.1, 1, 5, and 10 Hz) followed by a ramp (1% strain/s) to 30 N with subsequent fatigue cycling (5 N to 30 N at 1 Hz). Images were captured during the ramp for optical strain measurement. **Histological Analysis:** Ankles were fixed, decalcified, and embedded in paraffin using standard techniques.⁶ Tendons were sectioned sagittally at 7 μ m, stained with Hoechst 33342, and imaged at 20X magnification. Three regions (1000 x 2000 pixels, 1 at the insertion, 2 in the midsubstance) per tendon were analyzed with a custom thresholding protocol to quantify cell density and nuclear circularity (0 = line, 1 = circle, ImageJ, Bethesda, MD). **Gene Expression:** RNA was isolated from Achilles tendons using TRIzol (ThermoFisher, Waltham, MA). RNA was converted to cDNA (WT PLUS Kit, ThermoFisher), run on a ClariomTM S Rat Transcriptome Array 1.0 (ThermoFisher), and assessed with Transcriptome Analysis Console Software (ThermoFisher, ≥ 1.5 -fold change, 0.1 false discovery rate). **Statistics:** For histological and mechanical analyses, outliers, identified with the ROUT method (Q = 0.1%), were excluded, and differences were assessed for each timepoint with one-way ANOVAs for exercise intensity and Tukey's post hoc tests.

RESULTS

Mechanical Analysis (Fig. 1): After 4 and 8 weeks of exercise, no significant differences were observed in stiffness or modulus for tendons exercised at different intensities (Fig. 1A-B). However, after 4

weeks, viscoelastic mechanical properties were different between tendons in Moderate and High groups. Tendons from the High group demonstrated increased stress relaxation, decreased dynamic modulus at all frequencies, and increased phase shift at 0.1, 1, and 5 Hz compared to tendons from the Moderate group (Fig. 1C-I, 10 Hz data not shown). After 8 weeks, differences between Moderate and High groups resolved but differences between Low and Moderate and Low and High groups emerged. Compared to tendons from the Low group, Moderate and High group tendons had decreased percent relaxation (Fig. 1C). While there were no differences in dynamic modulus at any frequency, Moderate group tendons had decreased phase shift at 0.1, 1, and 5 Hz compared to Low group tendons (Fig. 1D-I). Similarly, compared to Low group tendons, High group tendons demonstrated decreased phase shift at 0.1 Hz and a trend toward decreased phase shift at 1, 5, and 10 Hz. There were no changes in fatigue properties due to exercise intensity (data not shown).

Histological Analysis (Fig. 2): Changes in cellular density and nuclear circularity at the tendon insertion (data not shown) and midsubstance (Fig. 2A-E) were not detected between intensity groups.

Gene Expression (Table 1): With 4 weeks of exercise, differences in gene expression were observed between Low and High groups, including differential expression of several ribosomal RNA transcripts. After 8 weeks of exercise, differences in gene expression occurred between all groups. The highest number of differentially expressed genes was observed between Low and High groups, including genes involved in the regulation of inflammation (Table 1).

DISCUSSION

This study demonstrated dose-dependent changes in mechanics and gene expression of the rat Achilles tendon in response to treadmill running as a form of mechanical loading. Specifically, results indicate that the tendon exercise response is intensity- and duration-dependent; in this model, exercise-intensity induced viscoelastic mechanical changes manifest at 4 weeks and resolve by 8 weeks. Mechanical changes in rat Achilles tendon after treadmill running are known to vary based on exercise duration,⁷ and our results suggest that the nature and time course of such changes is exercise intensity-dependent. Exercise intensity did not influence fatigue properties, but resistance to fatigue at higher load limits should be explored as this may better resemble repetitions of challenging physiologic loading scenarios, such as jumping and landing, which are high risk for Achilles tendon injury. Surprisingly, exercise did not impact tendon cellularity or nuclear shape which may indicate an ability of existing resident tendon cells to maintain homeostasis at the intensities examined. Gene expression was impacted by exercise intensity, concordant with findings in mouse Achilles tendon.⁸ Despite mechanical differences between Moderate and High groups at 4 weeks, gene expression differences were only detected between Low and High groups, which may indicate that early matrix changes are not driven by gene expression changes, additional gene expression changes occur transiently before 4 weeks, or a combination thereof. Gene expression differences at 8 weeks may reflect compensatory adaptations to exercise-induced cell and matrix changes. Future studies of gene expression will incorporate unbiased approaches to continue to elucidate the impact of exercise intensity and duration on the rat Achilles tendon transcriptome. Moreover, to further clarify the relationship between exercise and tendon health, future work will include additional exercise durations and intensities as well as exercise in pre- and post-injury contexts.

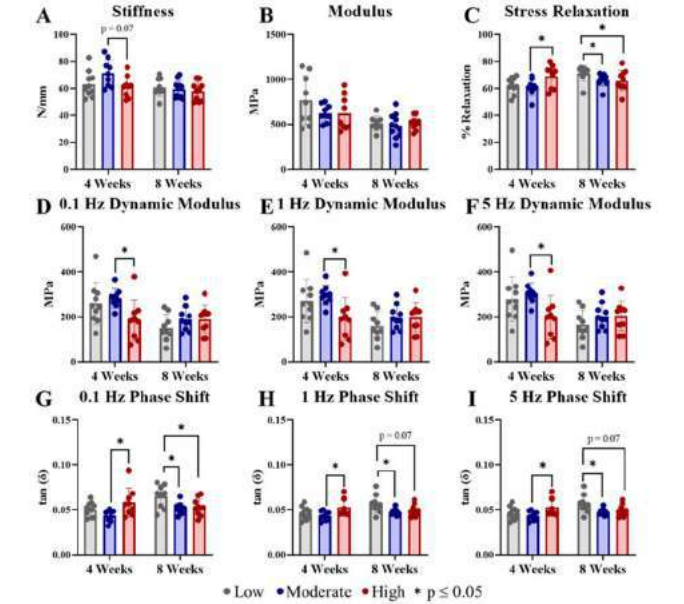


Figure 1: Exercise intensity does not influence tendon stiffness (A) or modulus (B). Differences between Moderate and High intensity exercise groups emerge in viscoelastic properties after 4 weeks but resolve after 8 weeks (C-I). Differences between Low and Moderate as well as Low and High groups emerge after 8 weeks of exercise in percent relaxation (C) and phase shift (G-I).

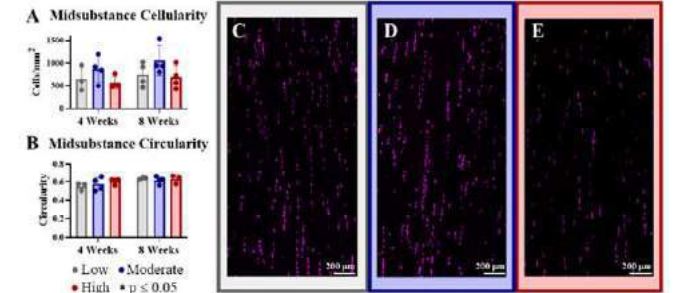


Figure 2: Cellularity (A) and nuclear circularity (B) in the midsubstance region were not altered by exercise (C- Low, D- Moderate, E- High at 8-week timepoint).

Table 1: Intensity (L-Low, M-Moderate, H-High) and duration of treadmill running exercise influence gene expression. Lower intensity exercise is considered baseline for fold change.

Fold Change < 1.5 1.5-2 > 2	4 Weeks		8 Weeks	
	L vs H	L vs M	M vs H	L vs H
	Rpl17, Rpl13, Rpl13, Rpl19, Rpl20, Rpl213, Rpl26, Rpl39, Rpl37a, Rpl37a-ps1, Nsmc1, Mcpt10, Polr2f, Stk33, RGD1565131, RGD1563124, LOC100909911, LOC100360290, LOC100364509, LOC100910336, RGD1566136, LOC100360679, Rpl18	LOC102554798, Srm4, Cxcl1, Il6, Selp, Rnd1	Fhl1	Ilfb1, Il18, Famb151b, Chtf8, LOC100362067
	Sor11, C1orf15, D12u2, LOC102547628, Dicer1, Cyp7b1, Arl13b, Zfp800, Tui1, Paup3, Atf2, Cpnd1, Chrb3, Lnc55, Dhsl1, Pna1, RGD1563049	Mest, Kctd21, Atrbkl1, Chtf8, Cept1, Bet1, Pdcl1, LOC100911365	Ints12, Pdcl1, LOC100911365	Selp, Rad1, Sele, Cxcl1, Btg2, Cks1l, Ntbl, Epc2l1, Pex3, Ccaa2, T3dg, Tret1, Btg3, LOC684828, LOC684681, LOC691918, RGD1560464

ACKNOWLEDGEMENTS

We thank the Penn Genomic and Sequencing Core, Penn Bioinformatics Core (John Tobias), Ryan Leiphart, and Elias Mohammad. Funding support was provided by the OREF and Penn Center for Musculoskeletal Disorders (NIH/NIAMS, P30 AR069619).

REFERENCES

[1] Chiodo CP et al., *JAAOS*, 2010. [2] Józsa L et al. *AJSM*, 1989. [3] Rooney SI et al. *JAP*, 2017. [4] Heinemeier KM et al. *J Physiol*, 2007. [5] Fung DT et al. *JOR*, 2009. [6] Leahy TP et al., *AJSM*, 2022. [7] Chen M et al., *JBME*, 2020. [8] Zhang J et al., *PloS One*, 2013.

UNDERSTANDING CILIARY WAVEFORMS THROUGH OPTIMIZATION

Louis G. Woodhams (1), Philip V. Bayly (1)

(1) Mechanical Engineering and Materials Science
Washington University in St. Louis, St. Louis, MO, USA

INTRODUCTION

Cilia and flagella are slender organelles that move fluid or propel cells through fluid. Proper ciliary function in human beings is essential for clearing mucus in airways, circulating cerebrospinal fluid in brain ventricles, and transporting eggs along fallopian tubes. Those with ciliopathies such as primary ciliary dyskinesia suffer from chronic infections of the sinuses and bronchi, male and female infertility, and a 50% chance of *Situs inversus* – a condition which affects organ locations in the body due to improper function of embryonic nodal cilia, which establish asymmetry in the embryo through fluid flow.

Though the internal structure of cilia and flagella is now well known – the microtubule-based axoneme consisting of 9 outer doublets and a central singlet pair interconnected by radial spokes and circumferential links – the exact mechanism of beating remains poorly understood [1]. The motor protein dynein hydrolyzes ATP to drive a one-way sliding force between adjacent outer doublets, but the question remains as to how these nanomotors are coordinated, or if they are coordinated, to create the propulsive waveforms observed in cilia. Are the activation patterns prescribed by a signal (like spark distribution in an internal combustion engine)? Is there a feedback mechanism based on curvature or sliding? Or is the beating driven purely by mechanical instabilities [2]? Finally, it has been shown that dynein distributions along the length of the axoneme are not uniform, so how do these distributions affect ciliary function.

To answer questions about ciliary beating, there is a long-established practice of mathematical modeling dating back to Machin [3]. This approach typically involves the creation of a hypothetical model and comparing the behavior of that model with observed ciliary behavior to establish the plausibility of the model. In the current work, we approach the mathematical model as an optimization problem – given an objective and a set of constraints, how would the cilium evolve to be as effective and efficient as possible?

METHODS

We applied kinematic optimization to the waveform using resistive force theory. The tangent angle as a function of arclength, $\tilde{\theta}(s)$, was represented as a complex polynomial:

$$\tilde{\theta}(s) = a_1 s + ib_1 s + a_2 s^2 + ib_2 s^2 + \dots \quad (1)$$

A beat cycle is created by rotating the complex tangent angle function through 2π radians in complex space and projecting the complex function values onto the real plane:

$$\theta(s, t) = \text{real}(\tilde{\theta}(s) \cdot e^{i2\pi\omega t}) \quad (2)$$

The beat shape $x(s)$ and $y(s)$ coordinates are reconstructed by integrating the cosine and sine of the tangent angle, respectively, along the arclength of the cilium. The forces along the length of the cilium are calculated using resistive force theory with tangent and normal components taken from experimental values [4]. Total forces in the x -direction (parallel to the undeformed cilium) and y -direction (perpendicular to the undeformed cilium) as a function of time were calculated by integrating the x and y components of the force along the cilium, respectively. To calculate the effective propulsion during one cycle, the impulse of the stroke was calculated by integrating the force with respect to time [5].

For the optimization, the objective function was taken to be either the impulse in the x -direction ('flagellar' beating) or y -direction ('ciliary' beating). Optimization of the polynomial coefficients a_i, b_i of Eq. 1 was carried out in Matlab using the function *fminsearch()* (2021b, Natick, Massachusetts: The MathWorks Inc.). A penalty term was added to avoid excessive curvature in the optimized waveforms.

RESULTS

Optimizing the waveform for transverse propulsion yields asymmetric shapes that bear striking resemblance to those observed in cilia (Fig. 1). This waveform is optimized to propel fluid horizontally to the right. It should be noted that running the optimization multiple times with randomized initial parameters led to different optimized results as the algorithm is attracted to local optima. Without a penalty term associated with curvature, unrealistically contorted shapes emerge (not shown). Excessive curvature penalties lead to shapes that are insufficiently propulsive (not shown). A polynomial order of 3 (for the complex tangent angle function) was found to be sufficient to capture complicated beat shapes. In many cases, increasing polynomial order has minimal impact on the optimized waveform.

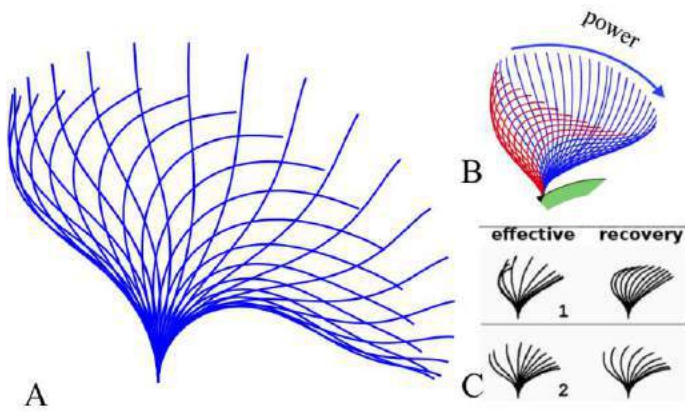


Figure 1: Waveform optimized for transverse propulsion
(A) Waveform produced through optimization. (B) *Chlamydomonas* waveform in Newtonian fluid [6] (C) Effective and recovery waveforms traced from human airway cilia [7]

Optimizing the waveform for axial propulsion yields symmetric shapes such as that shown in Fig. 2A. This waveform is optimized to propel fluid horizontally to the right. There is a wide variety of shapes observed in sperm propulsion. The current process is capable of producing results similar to some of these shapes, such as the one shown in Fig. 2B.

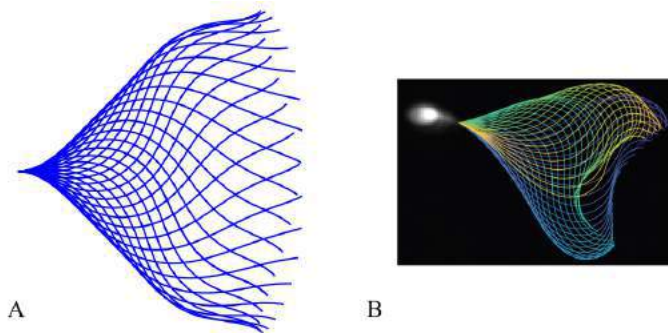


Figure 2: Waveform optimized for axial propulsion
(A) Waveform produced through optimization. (B) Human sperm waveform traced using computer-aided sperm analysis [8]

DISCUSSION

We find that kinematic optimization yields waveforms similar to those observed in cilia, especially for transversely propulsive beating shapes of short (5-15 μ m) cilia such as those of *Tetrahymena* [5], *Chlamydomonas* [6], and human airway cilia [7]. The current work leverages highly-simplified models of fluid behavior and cilia shape; added complexity may be necessary to capture the beating shapes of longer or more intricate structures, such as sperm flagella.

A limitation of the current work is that it is an optimization only of the beat shape, without taking into account a physical model of the mechanics of ciliary beat generation. We are currently working on incorporating this type of optimization into a model of ciliary beating that accounts for bend generation by inter-doublet sliding forces. We hope the results of such an optimization could lead to a better understanding of dynein activity and distribution within the axoneme.

Another future application of this work is extending the optimization to arrays of cilia. Arrays of cilia are known to beat with a temporal propagation pattern known as a metachronal wave [9]. This work could lead to a better understanding of not only why cilia beat with the shapes that they do, but what gains in efficiency and effectiveness might be gained from fine-tuning the metachronal propagation rate.

ACKNOWLEDGEMENTS

The work was supported by NSF grant no. CMMI-1633971 and the Children's Discovery Institute.

REFERENCES

- [1] Brokaw, C.J., *Cell motility and the cytoskeleton*, 66(8),425:436, 2009.
- [2] Woodhams, L. G., Shen, Y., & Bayly, P. V., *Journal of the Royal Society, Interface*, 19(192), 20220264
- [3] Machin, K.E., *Journal of Experimental Biology*, 35,796:806, 1958
- [4] Bayly, P.V. *et al.*, *Biophysical Journal*, 100(11), 2716–2725, 2011
- [5] Soh, A.W.J., Woodhams, L. G. *et al.*, *Molecular biology of the cell*, 33(11), br18, 2022
- [6] Qin, B. *et al.*, *Scientific Reports*, 9190, 2015
- [7] Sears, P. K. *et al.*, *American Journal of Physiology-Lung Cellular and Molecular Physiology*, 304:3, L170-L183, 2013
- [8] Gallaher, M.T. *et al.*, *human reproduction*, 34(7), 1173-1185, 2019
- [9] Elgeti, J., & Gompper, G., *Proceedings of the National Academy of Sciences*, 110(12), 4470:4475, 2013

PROMOTION OF CHRONIC WOUND HEALING BY ALIGNED FIBER SCAFFOLDS: MODELING AND MODEL VERIFICATION

Yin-Yuan Huang (1,2,4), Xiangjun Peng (1), Chengli Li (4), Kunkoo Kim (4), Peilun Hu (4), Chun-Yi Yang (4), Pengchao Ma (4), Yuxuan Huang (1,2), Shumeng Jiang (1,3), Chengqing Qu (1,3), Farid Alisafaei (1,5), Xiumei Wang (4), Guy M. Genin (1,3)

- (1) NSF Science and Technology Center for Engineering Mechanobiology, Washington University in St. Louis, St. Louis, MO, USA.
- (2) Department of Biomedical Engineering, Washington University in St. Louis, St. Louis, MO, USA.
- (3) Department of Mechanical Engineering and Materials Science, Washington University in St. Louis, St. Louis, MO, USA.
- (4) School of Materials Science and Engineering, Tsinghua University, Beijing, China.
- (5) Department of Mechanical and Industrial Engineering, New Jersey Institute of Technology, Newark, NJ, USA.

INTRODUCTION

Chronic wounds and ulcers often set off a cascade that culminates in amputation of a limb. This is particularly common in patients with diabetes mellitus: 6% of diabetes patients suffer from foot ulcers [1-2]; 65-75% of these heal, but the majority of the rest require amputation [3].

Many efforts to improve these poor healing outcomes focus on tissue engineered scaffolds that promote ingrowth of the myofibroblast cells needed for wound healing and the repair of microvasculature that, in the case of diabetic patients, is damaged by hyper-glycemia. To overcome the latter, angiogenic factors such as KLT peptide are of interest in the literature [4]. However, assisting the ingrowth of myofibroblasts onto a chronic wound from the surrounding diabetic tissue remains a critical challenge [5-6]. Our objective was therefore to develop tissue engineered technologies to facilitate the ingrowth of myofibroblasts over a diabetic wound.

The healing grafts we focused on fibrin gels, which have been studied for some time in the literature [7]. Based upon recent observations of the role of mechanical anisotropy on activation of myofibroblasts [8], we hypothesized that fibrin gels could be structured to facilitate myofibroblast ingrowth by providing cells with anisotropic mechanobiological cues.

METHODS

To test our hypothesis, we developed isotropic and aligned electrospun fibrin gel scaffolds, and tested them in an animal model of chronic diabetic wound healing. Results were interpreted through a random walk model of cell ingrowth.

Fibrin scaffolds: Aligned fibrin scaffolds were synthesized by electrospinning and compared to isotropic fibrin scaffolds. To separate mechanobiological and angiogenic factors, KLT peptide was engrafted onto the fibrin in some experiments using the KLT has self-assembly motif (Fig. 1a).

Characterization: scanning (SEM) and transmission (TEM) electron microscopy (TEM) was used to verify alignment of the fibrin in the

scaffolds. Human umbilical vein endothelial cells (HUVECs) cultured on each type of scaffold were imaged using confocal immunofluorescence microscopy to ensure that scaffolds supported angiogenesis.

Animal model: Animal protocols were approved by Institutional Animal Care and Use Committee (IACUC) at Tsinghua University. Adult (36 week) male Sprague-Dawley rats were treated with streptozotocin for 3 days to induce diabetes, then subjected to a square or rectangular wound (20x20 or 25x15 mm²) on the back. Immediately afterwards, isotropic or aligned fibrin gels, with or without KLT peptide were applied and healing results compared to controls (no scaffold). To model the human wound contracture (weak relative to the rat), contracture was restrained by a poly(methyl meth-acrylate) frame sutured beyond the wound periphery. Wound ingrowth was monitored as a function of time by computing the dimensions of the outer wound boundary as delineated by hand from the steepness of the color gradient. Wound height and width time courses were computed from these data.

Mathematical model: We developed a two-dimensional random walk model of cell migration to interpret experimental data and quantify the effects of scaffold alignment and KLT peptide. In the model, the spatial concentration $\varphi(\vec{r}, t)$ of healed wound area was dominated by migration of myofibroblasts and thus followed a diffusivity equation:

$$\frac{d\varphi(\vec{r}, t)}{dt} = \vec{\nabla} \cdot [\mathbf{D}(t)\vec{\nabla}\varphi(\vec{r}, t)] \quad (1)$$

where the migration coefficient tensor $\mathbf{D}(t)$ is diagonal in the axes of the fibers, with components $D_{\parallel}(t)$ and $D_{\perp}(t)$ parallel and perpendicular to the fibers, respectively, including both activation and steadily increasing terms:

$$D_{\parallel}(t) = a_{\parallel} \tanh(t/t_0) + b_{\parallel}t \quad (2)$$

$$D_{\perp}(t) = a_{\perp} \tanh(t/t_0) + b_{\perp}t \quad (3)$$

Dirichlet boundary conditions were used on the borders of the wound.

Hypothesis testing: We estimated $D_{\parallel}(t)$ and $D_{\perp}(t)$ from the experimental data using finite difference approximations if Eq. (1) and

a genetic algorithm. We hypothesized that the model would predict the data, and that the time constants for activation would be independent of healing scaffold, while the wound healing constants a_{\parallel} , b_{\parallel} , a_{\perp} , and b_{\perp} would vary with scaffold type.

RESULTS

SEM images (Fig 1b) analyzed using ImageJ (Fig 1c) revealed that fibrin in “aligned” scaffolds had a tighter orientation distribution than fibrin in “isotropic” scaffolds. KLT treatment roughened fiber texture (Fig. 1b). TEM images (Fig 1d) revealed that the cross-sections of isotropic gel fibers were varied due to their skew with respect to the sectioning plane, and that KLT treatment resulted in a porous structure and increased fiber diameters, likely indicating that KLT peptide was distributed not only on the surface but also within the interior of fibers.

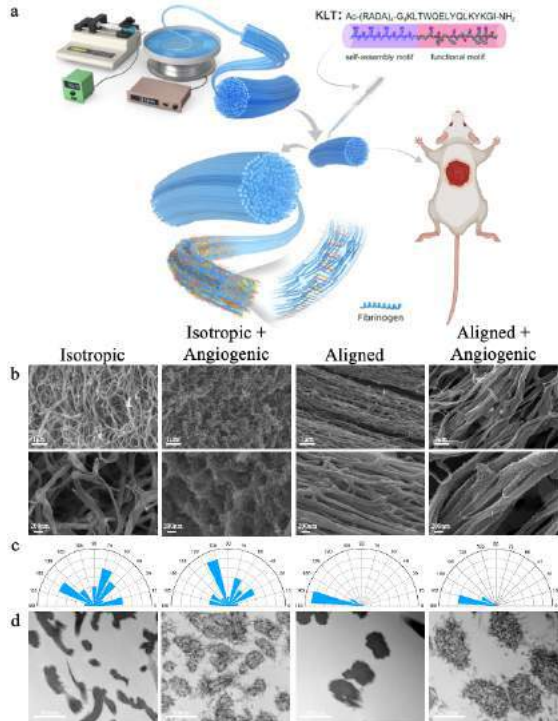


Figure 1: Material Synthesis and Characterization. a. Material synthesis protocol. b. SEM images of scaffolds (top scale bars: 1 μ m; bottom: 200 nm). c. Analysis of fiber orientation based on SEM images. d. TEM images of scaffolds (scale bars: 0.5 μ m).

Confocal microscopy images showed HUVECs cultured for two days on aligned scaffolds to be more uniformly distributed than HUVECs cultured for two days on isotropic scaffolds. After five days of culture, HUVECs formed the expected lumen-like structures needed for eventual vessel formation (Fig 2). These were more prominent and numerous in scaffolds treated with KLT, indicating that KLT had angiogenic effects *in vitro*.

In diabetic rat models *in vivo*, wound healing was fastest in aligned fiber scaffolds, with speed greatest along the fiber direction (Fig 3a-b). The dimensions of the wound parallel and perpendicular to the fiber directions were measured and their evolution over time was fit to the wound healing model.

From the parameters of the fitted model, the effects of the scaffolds on wound healing could be deduced. The migration coefficients for all scaffolds reached activation within one week, and the time constant was insensitive to the scaffold type (Fig. 3c). For isotropic scaffolds, the migration coefficients reached a plateau that did not change with KLT treatment. For aligned scaffolds, the migration coefficients were higher parallel to the fibers than they were perpendicular to the fibers, and

increased steadily over two weeks. KLT treatment accelerated wound healing on these scaffolds.

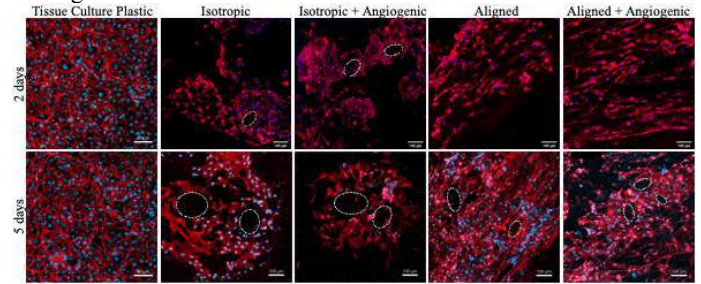


Figure 2: Confocal immunofluorescence images of HUVECs cultured on scaffolds for 2 or 5 days (scale bars: 100 μ m).

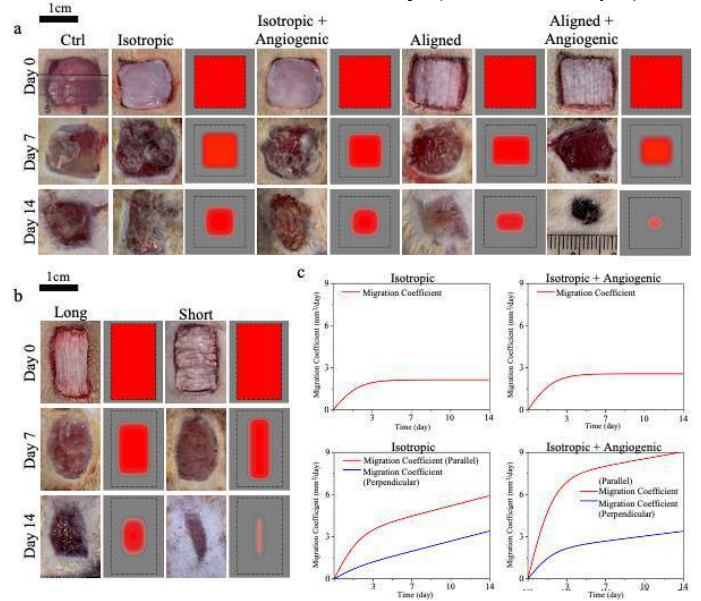


Figure 3: Wound healing model and *in vivo* experiments. a. Square wound. b. Rectangular wound. c. Fitted migration coefficients.

DISCUSSION

Consistent with the results of others, cells migrated faster parallel to fibers [11-12]. Results indicate that this effect can be used to enhance healing on large wounds in diabetic rat models. Consistent with our hypothesis, effects of anisotropy and KLT angiogenic factors were synergistic, with anisotropy leading to an increase in migration coefficient over time, and KLT leading to an increase in migration coefficient immediately following the onset of activation. Results point to a promising technique for enhancing healing of large-scale wounds.

ACKNOWLEDGEMENTS

XM acknowledges funding from National Natural Science Fdn of China (32271414, 82201521), National Key R&D Program of China (2020YFC1107601), Foshan-Tsinghua Innovation Special Fund (2020THFS05) and Tsinghua Precision Medicine Fdn (2022TS001).

REFERENCES

- [1] CDC. National Diabetes Statistics Report website.
- [2] Vadiveloo et al, *Diabetologia*, 2018, 61(12): 2590-7.
- [3] Zhang et al., *Annals Med*, 2017, 49(2): 106-16.
- [4] Okonkwo et al, *Int J Mol Sci*, 2017 Jul 3;18(7):1419.
- [5] Li et al., *Mol Therapy-Nuc Acids*, 2021, 24: 554-78.
- [6] Tartaglia et al, *Int J Mol Sci*, 2021, 22: 5104.
- [7] Liang et al, *ACS Nano* 2021, 15:2687-12722
- [8] Mondrinos et al, *Sci Adv*. 2021, 7:eabe9446.
- [9] Yang et al, *Bioactive Mat*, 2022, 8: 529-544.
- [10] Xia et al, *Int J Nanomed*. 2020, 5:6631-6647.
- [11] Wang et al, *Bioactive Mat*, 2022, 11:206-217.
- [12] Estabridi et al., *ABME*, 2018, 46: 392-403.

PARTICULATED ECM BIOMATERIAL INKS ENABLE 3D BIOPRINTING OF OSTEOCHONDRAL IN VITRO MODELS WITH MULTI-SCALE ARCHITECTURE

Juliet O. Heye (1), Shannon A. Blanco (1,2), Jeanne E. Barthold (2), Emily Y. Miller (1), Corey P. Neu (1,2)

(1) Biomedical Engineering Program, University of Colorado Boulder, Boulder, CO, USA
(2) Paul M. Rady Department of Mechanical Engineering, University of Colorado Boulder, Boulder, CO USA

INTRODUCTION

Articulating joints are susceptible to injury and degenerative diseases like osteoarthritis (OA), which afflicts millions of people in the United States [1]. High-throughput testing of disease pathogenesis and new therapeutics is essential to eliminate excessive animal testing and reduce failure in clinical trials of treatment candidates. While there has been recent progress in the development of *in vitro* models, such as tissue-on-chip technology, there is still a need for a reliable miniaturized joint model that can be used to advance new disease treatments.

A critical first step in producing realistic joint models is the recapitulation of tissue-specific cell and extracellular matrix (ECM) behavior. ECM-derived biomaterials can be utilized as they contain essential components that influence cell behavior. In contrast to solubilized ECM, which consists of enzymatically-digested ECM in liquid form [2], particulated ECM preserves both the biochemical and structural micro-architecture of ECM. Tissue particles can be packed into a hydrogel base to achieve a biomaterial with both practical and biomimetic macro-scale properties [3].

The inclusion of ECM microparticles increases viscosity without compromising extrudability, resulting in an ideal biomaterial for 3D bioprinting. Extrusion bioprinting is the most common type of 3D bioprinting due to its versatility and affordability [4], and can produce complex multi-ink structures for various *in vitro* models. The packing density of microparticles and choice of hydrogel base material enables tuning of macro-scale biomaterial properties, such as stiffness. For *in vitro* joint models, the ability to apply physiologically-relevant load is essential in recapitulating joint movement.

In this study, we present hyaluronic acid-based particulated ECM biomaterial inks for both bone and cartilage tissue, with rheological and mechanical characterization. Furthermore, 3D extrusion bioprinting of our ECM inks is demonstrated to produce two proof-of-concept osteochondral *in vitro* models, including applied compression.

METHODS

Bone tissue was sourced from human donors under 35 years old (AlloSource, Centennial CO). Cartilage tissue was sourced from porcine animals within 48 h of slaughter. Tissues were pulverized using a liquid nitrogen cryo-mill and sorted via a micro sieve stack to isolate microparticles 40-100 μm in diameter (Electron Microscopy Sciences, Hatfield PA). Cartilage microparticles were decellularized in 2% sodium dodecyl sulfate (SDS) for 8 h at 37°C, and in 0.1% DNase for 3 h to remove xenogeneic cellular and genetic material. Microparticles were flash frozen in liquid nitrogen, and lyophilized. Biomaterial ink formulations consisted of 10mg/mL hyaluronic acid (HA) (~20% thiolation) packed with either 0.72g/mL bone microparticles or 0.2g/mL cartilage microparticles to achieve equivalent consistency/extrudability. Biomaterial inks were thoroughly mixed between two syringes attached by a custom luer lock connector with cross hairs. HA and particles crosslinked via disulfide bonding [5].

Rheological properties were measured using a Flow Procedure with a steady state flow step setting on a Rheometer (AR-G2, TA Instruments), with 8mm diameter plates in stiff bearing mode and a gap distance of 800 μm . A room temperature shear sweep was performed within 5 mins of mixing, with shear rates from 0.01 to 250 s^{-1} with no normal force, a pre-shear rate of 10 for 10 s, and zero velocity (**Fig 1C**).

Mechanical properties were assessed using unconfined compression testing on a Bose ElectroForce 5500 system. Molded cylindrical biomaterial ink constructs were polymerized for 30 min at 37°C and compressed to a strain of 40% of the initial height (0.1% per second) for quasi-static loading following 0.1 N pre-load. Compressive modulus was calculated by measuring the slope of the linear portion of the stress strain curve, between 30% and 40% strain (**Fig 1D, Fig 1E**).

Biomaterial inks were 3D printed on a multi-nozzle pneumatic extrusion printer with 20 G or 18 G nozzles (BioX, Cell Ink Life Sciences). Bone ink was extruded with 45-65 kPa pressure at a rate of

12 mm/s, and cartilage ink with 60-80 kPa at 12 mm/s (**Fig 2A**). An osteochondral plug scaffold was printed with 50% infill density (**Fig 2B**). Pre-stained particle inks were 3D printed into a molded Sylgard 184 polydimethylsiloxane (PDMS) tissue-on-chip model (**Fig 2C**) and imaged using confocal microscopy (**Fig 2D**). A cartilage ink construct was loaded on the PDMS chip, and the cross section was imaged via confocal microscopy during compression with a micro-actuator. Deformation microscopy was used to compute construct strains using deformed and undeformed images (**Fig 2E**) [6].

RESULTS

We achieved extrudable and particulated ECM biomaterial inks for both bone and cartilage tissue, and demonstrated 3D printability of these inks suitable to create osteochondral *in vitro* models. Rheological measurements indicate shear-thinning behavior of bone and cartilage biomaterial inks (**Fig 1C**). Unconfined compression testing demonstrated a compressive modulus of 741 kPa for the bone ink and 39 kPa for the cartilage ink (**Fig 1D, Fig 1E**).

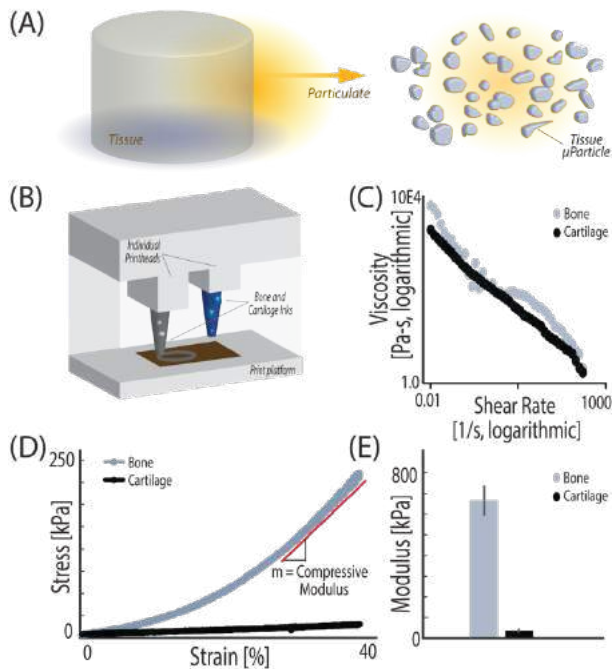


Figure 1: Particulated ECM inks demonstrate shear-thinning and biomimetic mechanical properties. (A) Tissue is cryo-milled into microparticles. (B) Particulated ECM inks can be extrusion 3D bioprinted. (C) Rheological data (n=6) demonstrates shear-thinning behavior. (D) Compressive modulus was calculated from the slope of the linear portion between 30% and 40% strain. (E) Compressive modulus (n=6) for bone and cartilage inks.

Both bone and cartilage inks were easily extruded through pneumatic-based bioprinting (**Fig 2A**). A proof-of-concept osteochondral plug was successfully printed with sequential bone and cartilage inks (**Fig 2B**). Bone and cartilage inks were also 3D printed side-by-side into a proof-of-concept PDMS chip (**Fig 2C**), in which two types of media could flow past the bone versus cartilage ink. The osteochondral chip was imaged using confocal microscopy, revealing a distinct interface between pre-stained bone (DAPI) and cartilage (Ghost Dye) particles (**Fig 2D**). Finally, strain calculated via deformation microscopy showed spatially-dependent mechanical signaling within a compressed cartilage ink construct loaded into a PDMS chip (**Fig 2E**).

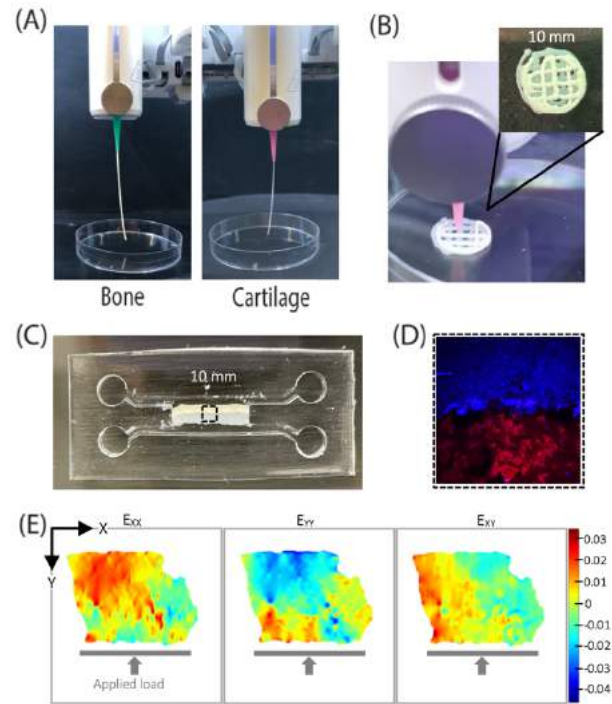


Figure 2: Bone and cartilage inks can be 3D printed to form osteochondral *in vitro* models. (A) Extrusion of bone and cartilage inks. (B) 3D printed osteochondral plug with top layer bone and bottom layer cartilage. (C) Bone (top) and cartilage (bottom) inks printed into PDMS chip. (D) Confocal imaging of tissue-on-chip interface showing bone (top, blue) and cartilage (bottom, red) particles. (E) Deformation microscopy of cross-section of compressed cartilage ink construct.

DISCUSSION

This work provides macro-scale rheological and mechanical characterization and 3D printing demonstrations of novel bone and cartilage particulated ECM biomaterial inks. Previous work showed that as packing density increased in the microparticle cartilage ink, compressive modulus rapidly increased up to 300 kPa [3]. As such, it is expected that this cartilage ink could reach physiologically relevant stiffness under load. Furthermore, we have seen a similar relationship between packing density and compressive modulus of the bone ink (not shown). We have previously shown that cartilage microparticles preserve ECM micro-architecture and biochemical factors, promoting infiltration of chondrocytes and chondrogenic phenotype [3]. Additional studies further support microparticle-guided cell differentiation [7]. Follow-up studies will assess cellular interaction with bone microparticles and explore cellular responses to biomaterial inks. Ultimately, we aim to recapitulate the structure and function of osteochondral tissues to produce realistic *in vitro* joint models.

ACKNOWLEDGEMENTS

This work was supported by grant CDMRP W81XWH-20-1-0268. We also acknowledge AlloSource for providing donor bone tissue.

REFERENCES

- [1] Xu, Y et al. *Sci. Rep.*, 11:1-10, 2021.
- [2] Pati, F et al., *Nat. Commun.*, 5:1-11, 2014.
- [3] Barthold, J et al., *Adv. Funct. Mat.*, 31:2103355, 2021.
- [4] Gu, Z et al., *Asian J. of Pharm. Sci.*, 15:529-557, 2020.
- [5] Barthold, J et al., *Biofab.*, 14:025021, 2022.
- [6] Ghosh, S et al., *Cell Rep.*, 27:1607-1620, 2019.
- [7] Yin, H et al., *Acta Biomater.*, 77:127-141, 2018.

ACL INJURY AND JOINT INSTABILITY LEADS TO MENISCAL HYPERTROPHY IN A SKELETALLY IMMATURE PORCINE MODEL

Jacob D. Thompson (1), Margaret E. Easson (1), Danielle Howe (1), Lauren V. Schnabel (2),
Jeffrey T. Spang (3), Brian G. Pietrosimone (4), Matthew B. Fisher (1,3)

- (1) Joint Department of Biomedical Engineering, North Carolina State University and University of
North Carolina at Chapel Hill, Raleigh, NC, USA
(2) Department of Clinical Sciences, North Carolina State University, Raleigh, NC, USA
(3) Department of Orthopaedics, University of North Carolina at Chapel Hill, Chapel Hill, NC, USA
(4) Department of Exercise and Sport Science, University of North Carolina at Chapel Hill, Chapel
Hill, NC, USA

INTRODUCTION

There are an increasing number of anterior cruciate ligament (ACL) injuries in pediatric athletes compared to adults [1]. While some call for conservative treatment for younger patients, nonoperative treatment leads to knee instability and low return to sports rates [2]. Furthermore, an increased number of meniscal injuries and tears are found with delayed ACL reconstruction even by 6 weeks after surgery [2,3]. These meniscal injuries in the pediatric population could occur at the time of ACL injury or occur over time due to altered joint motion and loading. A previous *ex vivo* study in skeletally mature human cadavers found ACL transection (ACLT) increased joint laxity and force contribution of secondary stabilizers in the knee, such as the medial collateral ligament (MCL)[4]. Previous work in the skeletally immature porcine model also demonstrated similar results in laxity and tissue force changes after ACLT, with the medial meniscus also acting as a stabilizer under injured biomechanics [5]. Long-term degenerative changes, such as radiographic knee osteoarthritis, have also been linked to joint instability and meniscal hypertrophy [6]. However, there is little *in vivo* data detailing long-term degenerative changes in the knee after ACL injury in skeletally immature patients. Therefore, the objective of this study was to evaluate the long-term impact of ACLT on knee function and meniscus structure remodeling in a juvenile porcine model. We hypothesized that joint laxity would increase after ACL injury, along with in altered tissue loading and remodeling of the menisci.

METHODS

Seven female juvenile (3-months) Yorkshire crossbreed pigs underwent a unilateral arthroscopic ACLT and a sham incision on the contralateral joint. All animals were bred at the North Carolina State University Swine Education Unit, and all experimental protocols were approved by the NC State IACUC. Twelve weeks after surgery, hind limbs were imaged using a 3.0-T Siemens MAGNETOM Skyra MRI system (T2 SWI sequence, voxel size 0.5x0.5x0.8mm). Meniscal

measurements were then taken for both medial and lateral menisci from the MRI scans. Specifically, the height and width of the anterior and posterior regions of the meniscus near the attachment sites and the height and width of the central region of the meniscus were recorded. Anterior and posterior heights were recorded in the sagittal plane and the central height and width was recorded in the frontal plane. The animals were euthanized, hindlimbs collected, and stifle (knee) joints stored at -20°C in saline-soaked gauze.

Then, stifle joints were biomechanically tested using a robotic testing system (Kuka, SimVtro) with a universal force-moment sensor. Anterior-posterior loads (80 N) and compressive loads (120 N) were applied at 60° of flexion in force control mode and the kinematic paths were recorded. The kinematic paths were then repeated for the intact joint and after removing the capsule, ACL (or any scar remaining), medial collateral ligament (MCL), lateral collateral ligament (LCL), posterior cruciate ligament (PCL), medial meniscus (MMEN), lateral meniscus (LMEN), medial femoral condyle (MCON), and the lateral femoral condyle (LCON). Each tissue contribution to maximum anterior and compressive loading was determined by the principle of superposition. Joint laxity was recorded as the anterior-posterior tibial translation (APTT) during anterior loading and the anterior tibial translation (ATT) during compressive loading. Differences in APTT and ATT were compared between sham and injured legs using paired t-tests. Multiple paired t-tested were used to detect differences between tissue forces with Holm-Sidak correction. Linear regression analysis was performed to compare interlimb differences in posterior horn height and central width to interlimb differences in axial compressive force in the medial meniscus. Significance was set to $\alpha=0.05$ overall for each analysis.

RESULTS

Total ACL transection led to significant destabilization of the knee joint during applied anterior drawer and axial compression. APTT

(Figure 1A) and ATT (Figure 1B) of the joint increased by approximately 3-fold ($p<0.0001$) and 7-fold ($p<0.0001$) in ACLT joints compared to the sham-operated joints, respectively.

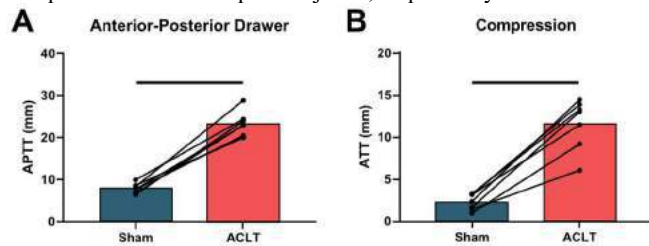


Figure 1: ACL transection (ACLT) led to joint destabilization 12 weeks after injury. (A) Anterior-posterior tibial translation (APTT) under applied AP drawer. (B) Anterior tibial translation (ATT) under applied compression. Bars indicate $p<0.0001$.

In the sham-operated joints, the ACL was the primary stabilizer during anterior loading (Figure 2A). However, in ACLT joints, the ACL resultant force dropped by 99% (adj $p<0.0001$) and the load was distributed across several different tissues. Most strikingly, the capsule anterior force increased by 23 N (adj $p=0.01$) and the medial collateral ligament increased by 57 N (adj $p=0.0002$). Changes in the medial and lateral meniscus were minor (<10 N). Under compressive loading in the sham-operated joint, the compressive forces were largest in the medial and lateral femoral condyles, followed by the medial and lateral menisci (Figure 2B). ACLT joints had drastic shifts in forces during compressive loading, mainly between direct cartilage contact of the femoral condyles on the tibia and the forces transmitted through the menisci. The compressive forces in the medial and lateral menisci increased by 50 N and 22 N in the ACLT joints compared to sham controls (adj $p=0.004$ and adj $p=0.10$, respectively). An opposite shift occurred in the medial and lateral condyles, where the force decreased by 29 N and 45 N (adj $p=0.03$ and adj $p=0.01$, respectively).

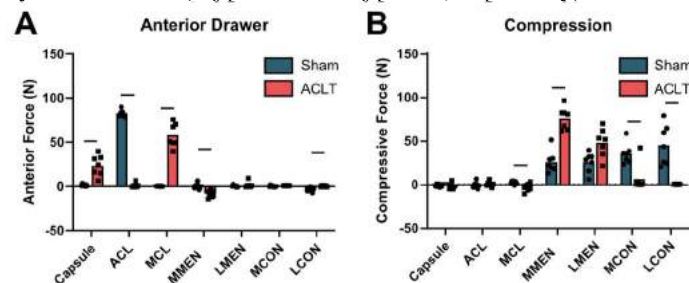


Figure 2: ACL transection (ACLT) impacted the loads carried by tissues under applied joint loading. (A) Anterior force carried by tissues under applied anterior drawer in sham and injured joints. (B) Compressive force carried by the tissues under the applied compression. Bars indicate $p<0.05$ between sham and ACLT.

Meniscus anatomical features were also impacted by ACLT, with a 22% increase in the posterior height in the medial meniscus ($p=0.02$), but not the lateral meniscus ($p=0.79$) (Figure 3A). The medial and lateral central width increased by 14% and 13% in the ACLT joints compared to the sham-operated contralateral joints ($p=0.02$ and $p=0.01$, respectively) (Figure 3B). The interlimb difference in medial meniscus central width was positively associated ($r^2=0.71$; $p=0.02$) with the interlimb difference in axial compressive force carried by the medial meniscus under compressive loading (Figure 3C). However, the change in medial meniscus central width was the only factor that associated with the change in medial meniscus axial compressive force. Changes in medial meniscus posterior height ($p=0.73$) and width ($p=0.80$) did not associate with compressive force changes, despite the statistically significant increases in posterior horn height.

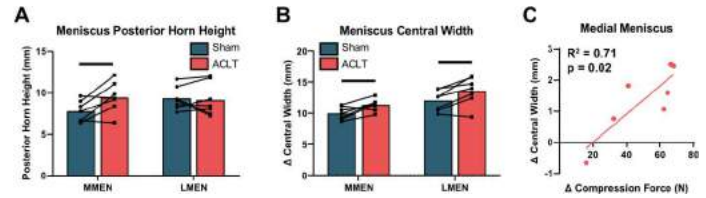


Figure 3: ACL transection (ACLT) led to structural remodeling of the menisci. (A) Posterior height of the medial and lateral menisci. (B) Central width of the medial and lateral menisci. (C) The difference in medial meniscus central width versus the difference in compressive force (relative to sham-operated controls) under compressive loading. Statistical results from the linear regression are shown in the graph corner. Bars indicate $p<0.05$.

DISCUSSION

This study confirmed our hypothesis that ACLT led to a major increase in joint laxity and shift in tissue forces under biomechanical loads as well as an increase in meniscal hypertrophy in the skeletally immature knee joint. The increase in APTT nearly 3-fold between injured joints and sham-operated joints in this study is consistent with previous *ex vivo* findings of an increase (2.7-fold) in APTT in a 6-month pig immediately following ACLT [5]. The shift in tissue function during anterior loading in ACLT joints indicates that the medial collateral ligament acts as the primary stabilizer under an applied anterior load, which is similar to other *ex vivo* findings in human cadavers [4]. While under compressive loads, the medial and lateral menisci become primary stabilizers instead of the cartilage-cartilage contact of the condyles, likely due to the excessive ATT. The meniscal hypertrophy described in this work is similar to meniscal hypertrophy found in an adolescent guinea pig model after ACLT [7]. Meniscal hypertrophy has also been linked to knee osteoarthritis and cartilage degeneration, which is known to be more likely in a patient who has torn their ACL and undergone ACL reconstruction [8]. Therefore, the medial meniscus hypertrophy and shift in compressive forces could be indicative of a higher risk of long-term cartilage degeneration and incidence of post-traumatic osteoarthritis (PTOA). Effect sizes were large between sham and ACLT joints, but larger sample sizes could uncover more subtle changes. Having longer-term data would also prove beneficial for looking at cartilage degeneration and associating early and late degenerative changes. Overall, ACL injury in the skeletally immature joint results in instability, which in turn, causes abnormal meniscus remodeling. Identifying the impact of ACL injury on tissue forces and structural remodeling in growing subjects can lead to a better understanding of secondary tissue injury rates and inform clinical treatments for ACL injuries in young patients.

ACKNOWLEDGEMENTS

We would like to thank the NC State College of Veterinary Medicine and Laboratory Animal Resources for their contributions to this work. Funding provided by UNC Thurston Arthritis Research Center and NIH (R01 AR071985, F31 AR077997). Additional funding provided by the National Science Foundation (DGE-1746939).

REFERENCES

- [1] Zbrojkiewicz, D et al., *Med J Aust.*, 208(8):354-58, 2018.
- [2] James, E et al., *Am J Sports Med.*, 49(14):4008-4017, 2021.
- [3] Anderson, A et al., *Am J Sports Med.*, 43(2):275-281, 2015.
- [4] Kanamori, A et al., *J Orthop Sci.*, 5(6):567-571, 2000.
- [5] Cone, S.G. et al., *J Biomech.*, 101:109636, 2020.
- [6] Xu, D et al., *Osteoarthritis Cartilage*, 29(10):1426-1431, 2021.
- [7] Du, G et al., *Am J Sports Med.*, 44(3):652-663, 2016.
- [8] Nakata, K et al., *Arthroscopy*, 24(3):285-291, 2007.

QUANTIFICATION OF TUMOR BIOPHYSICAL HETEROGENEITY THROUGH MECHANICAL AND ULTRASTRUCTURAL ANALYSIS

**Bradley J. Mahaffey (1), Zachary P. Fowler (1), Zoe Lung (1), Vivien Dang (3), Neha Anil (1),
Marco Munoz (1), Joseph Chen (1,2)**

(1) Department of Bioengineering, University of Louisville, Louisville, KY, USA
(2) Department of Pharmacology and Toxicology, University of Louisville, Louisville, KY, USA
(3) Department of Neurosurgery, University of Louisville, Louisville, KY, USA

INTRODUCTION

Glioblastoma (GBM) is the most aggressive, invasive, and lethal form of cancer in the CNS of adults, carrying a median survival of 15 months and a 5-year survival of ~5%. This poor prognosis is due in part to its resistance to standard treatment – surgical resection followed by radiation and oral chemotherapy. Recent work has demonstrated that intratumor heterogeneity plays a critical role in therapy resistance by mediating tumor adaptation through biophysical and microenvironmental cues¹⁻⁴. Within this heterogeneous tumor, GBM can be separated into two distinct regions: a core and a rim. The core is hypercellular and hypoxic while the rim is sparse and permissive to cell invasion. Further, within these two regions are a diverse set of biomolecular and biophysical signals that underlie GBM evolution and therapy resistance. As recent work has focused on the biomolecular changes in these regions, much less attention has been paid towards the biophysical differences, which have been shown to be significant regulators of GBM malignancy. The elucidation of these factors is critical to identify the key biophysical regulators of GBM progression, adaptation, and therapy evasion. In this work, we investigate the mechanical and ultrastructural characteristics of the tumor ECM in patient matched GBM core and rim tissue. We hypothesize that tumor core and rim exhibit unique mechanical and ultrastructural signatures that correlate with patient prognosis.

METHODS

AFM was performed on 50 μm sections of GBM patient-matched tissue in order to quantify their mechanical stiffness. 20

$\mu\text{m} \times 20 \mu\text{m}$ force maps with 16x16 pixel resolution (256 force curves) were generated across three regions of each section. The Hertzian model, with a Poisson's ratio of 0.5, was then applied to determine the elastic modulus of the samples. SEM was used to characterize tissue ultrastructural differences of control and decellularized tissue. Histological quantification methods were employed using ImageJ. Combination treatment with ionic detergent (0.1% SD) and nuclease (DNase I) was utilized for removal of cellular material with adequate retention of the ECM constituents⁵ hyaluronic acid (HA) and tenascin-C, which was confirmed with immunofluorescence (IF) imaging. Chemical fixation with 1% glutaraldehyde and osmium tetroxide and subsequent sputter coating as SEM preparation.

Porosity Index Equation

$$\text{Porosity Index} = \frac{\text{Void Area}}{\text{Total Area}} \quad (1)$$

RESULTS

The AFM analysis of various patient matched samples provided results in the range of expectation for GBM tissue stiffness⁶. Our sample pool included a non-neoplastic, epileptic control and non-GBM gliomas as metrics for the prognostic implications of the study. Additionally, our prognostic metrics for each of these patients show that the overall survival of GBM patient 1723 was 235 days and our neurofibromatosis patient was 1199 days, thus providing an approach to determine mechanical and ultrastructural signatures that may be present in poor prognosis patients. AFM revealed (Figure 1: A/B) that the GBM patient 1723 exhibited a stiff core (384.8 Pa) and a soft rim

(177.8 Pa) while the neurofibromatosis patient showed a surprising opposite trend with the rim being stiffer (core: 553.5 Pa; rim: 679.8 Pa). Porosity analyses showed an intuitive trend with stiffer regions having lower porosity and softer regions having increased porosity (Figure 1: C/D). IF quantification showed that in GBM, there is more hyaluronic acid (HA) in the core when compared to the rim, while tenascin-C is more prominent in the rim. In the neurofibromatosis patient, there is higher HA and tenascin-C content in the rim. These changes suggest a role for HA in stiffening the matrix.

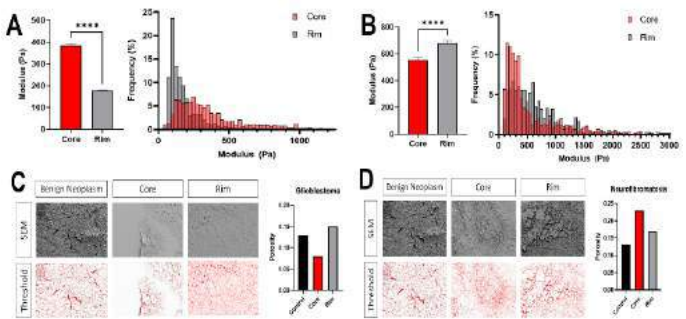


Figure 1: AFM quantification of GBM patient 1723 (A) and Neurofibromatosis patient 1707 (B) core and rim sections alongside a benign non-neoplastic control with porosity quantified. SEM imaging of 1723 (C) and 1707 (D) core and rim sections.

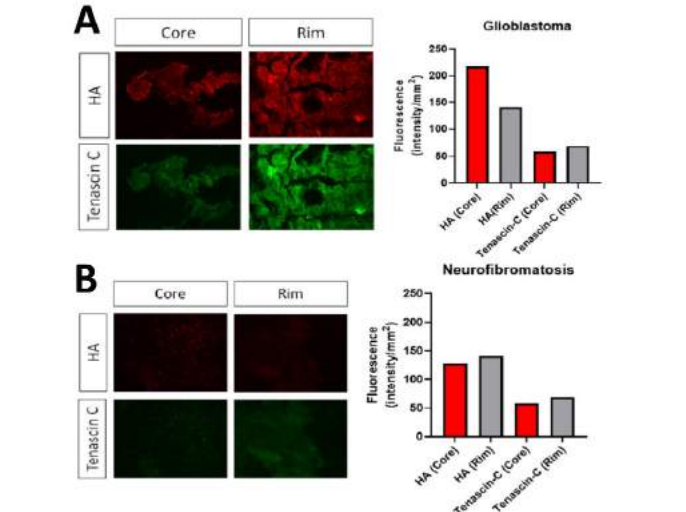


Figure 2: IF imaging of GBM patient 1723 (A) and Neurofibromatosis patient 1707 (B) for the common ECM proteins, hyaluronic acid and tenascin-C with quantification of mean intensity per unit area.

DISCUSSION

In this work, we have provided evidence of a unique biophysical profile in GBM core and rim. This, when taken with the rest of our patient cohort, has demonstrated implications for prognostic outcomes. The mechanical stiffness of the extracellular matrix in these samples have indicated that a hypoxic, hypercellular, necrotic core of greater stiffness is providing a pro-malignant environment that may promote

phenotypic shifts that lead to increased invasiveness and therapy resistance. This, coupled with more compliant rim mechanics, allows for enhanced migration potential and thus seeding of new tumors elsewhere, leading to the poor outcomes of these GBM patients. Regarding the improved survival for the neurofibromatosis patient, we speculate that this is due, in part, to the reduced permissiveness of its rim, limiting the migration potential invasive cells and preventing them from leaving the tumor as effectively. Our results represent the first study of GBM mechanical heterogeneity with patient match tissue to our knowledge and provide a novel connection for tumor biophysics and prognosis.

Currently, through our collaboration with our university hospital, we have acquired 30 patient samples, 9 of which have succumbed to disease, and plan to evaluate additional samples to strengthen the prognostic connections of our study. With a more cohesive look at the progression of this disease from a mechanical standpoint, new therapeutic interventions may be unveiled. From our data, it is suggested that one method may be to soften the core and explore potentially reduced mesenchymal phenotypic changes. Moreover, due to the lowered rim porosity shown here for GBM, allowing for avenues of escape for infiltrating cells, another treatment option may be to target matrix degrading processes in the rim region. We recognize our sample size is expanding, and due to the dismal prognosis of GBM, we expect it to increase in the coming months and provide further evidence for this mechanical connection to tumor mechanics and outcomes.

ACKNOWLEDGEMENTS

The authors gratefully acknowledge the Huson Imaging & Characterization Laboratory at the University of Louisville and the KY INBRE.

REFERENCES

- [1] M. Greaves et al., *Nature* 481, 306 (2012).
- [2] R. J. Gillies et al., *Nat Rev Cancer* 12, 487 (2012).
- [3] A. Marusyk et al., *Nat Rev Cancer* 12, 323 (2012).
- [4] T. A. Yap et al., *Sci Transl Med* 4, 127ps10 (2012).
- [5] M. Narciso et al., *Front Bioeng Biotechnol* 10, 832178 (2022).
- [6] Y. A. Miroshnikova et al., *Nat Cell Biol* 18, 1336 (2016).

IN SILICO INVESTIGATION ON STROKE RISKS FROM LEFT VENTRICULAR ASSIST DEVICE

Sreeparna Majee (1), Akshita Sahni (1), Erin E. McIntyre (2), Jay D. Pal (3), Debanjan Mukherjee (1)

(1) Paul M. Rady Department of Mechanical Engineering, University of Colorado Boulder, Boulder, CO, USA
(2) Division of Cardiothoracic Surgery, University of Colorado, Anschutz Medical Campus
(3) Department of Surgery, University of Washington, Seattle

INTRODUCTION

Left ventricular assist device (LVAD) is a key treatment modality for advanced heart failure (HF) patients. Circulation support using LVAD can improve overall quality of life and reduce mortality for HF patients. However, post implant complications such as ischemic stroke, pump thrombosis, and aortic insufficiency adversely impact the efficacy of LVAD treatment. Prior studies [1] report post-LVAD implant stroke occurrence chances in the range of 10-40%. There can be numerous factors contributing to this complication, originating from altered state of hemodynamics and coagulation due to attachment of LVAD [2]. Prior works have studied LVAD-driven hemodynamics with varying graft angles, and estimated thrombotic risks [3]. In a previous work, we have reported hemodynamics as function of LVAD outflow graft angles and flow pulsation [4]. However, a lack of understanding about factors involving actual embolus transport to the brain by the flow driven by an LVAD hinders comprehensible understanding of post-implant stroke risks in these patients. To address this challenge, here we present an in silico approach to generate a stroke risk descriptor based on computational thromboembolus transport analysis. We use this approach to investigate stroke risk variation with LVAD outflow graft surgical anastomosis.

METHODS

Image-Based modeling of anatomy: A patient-specific vascular network comprising the aortic arch and branch arteries extending up to the iliofemoral arteries was obtained from computed tomography (CT) images [4, 5]. An image-based geometric modeling procedure was devised for virtual surgical placement of an LVAD outflow graft. The angle between the final pathline for the graft, and the pathline for aorta, were varied across a set of 9 different parametric graft anastomoses, referred to as: (1) perpendicular to the aorta (*Inc90*); (2) 45° towards the aortic valve (*Inc45*); and (3) 45° towards the aortic arch (*Inc135*) together with graft anastomosis angled: (1) 45° right of the heart (*AziNeg45*); (2) perpendicular to the coronal plane (*Azi0*); and (3) 45° left of the heart (*Azi45*). These 9 configurations are noted in Figure 1.

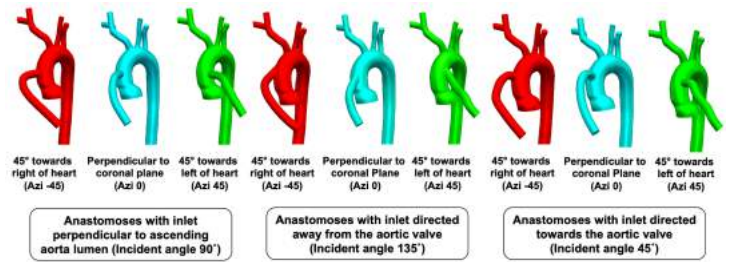


Figure 1: Generating a virtual family of LVADs [4]

Hemodynamics simulation: Hemodynamics across the 9 LVAD outflow graft models was simulated using a stabilized finite element method for incompressible Navier-Stokes equations using SimVascular. Blood was assumed to be a Newtonian fluid with a bulk density of 1.06 g/cc, and viscosity of 4.0 cP. Three-element Windkessel boundary conditions at each outlet of the computational domain were computed based on assumed target flow distribution across each outlet obtained from existing literature [4, 6]. Flow was driven by assigning a uniform (over time) flow-rate of 4.9 l/min at the LVAD outflow graft inlet face, mapped onto a parabolic profile across the face.

Embolus transport: Embolus transport was modeled using a custom modified version of the Maxey-Riley equation [7], leading to a one-way coupled fluid-particle interaction model. The emboli were assumed to be spherical particles, with diameter 1.0 mm. Embolus interactions with vessel wall were resolved using a custom algorithm based on signed distance fields, using a contact restitution of 0.75. The resulting simulations were used to obtain the distribution of emboli entering the aortic arch from the LVAD outflow graft. Two sets of embolus distribution fraction were computed: (a) distribution towards the cervical vessels leading in to the brain; and (b) accumulation at the aortic root near the dysfunctional aortic valve.

RESULTS

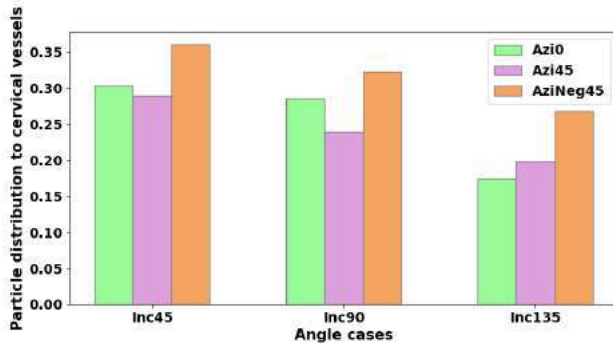


Figure 2: Fraction of embolic particles moving through the LVAD to the cervical vessels for each variation.

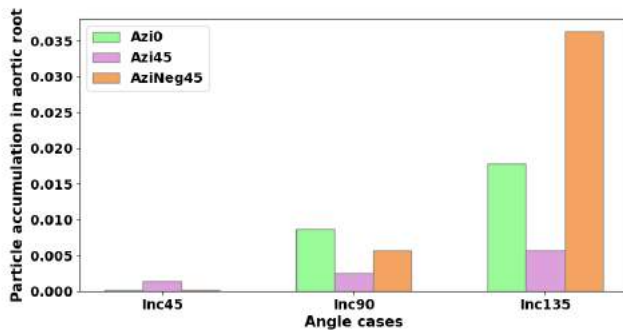


Figure 3: Fraction of embolic particle accumulation near aortic root for each variation.

We present data from $\approx 5,000$ different thromboembolism scenarios for each of the 9 LVAD anastomosis models as described earlier. For each model, the distribution fraction for 1 mm thromboemboli reaching the cervical vessels leading towards the brain are presented in Figure 2. From the data, we observe that LVAD graft anastomosis angle towards/away from the valve has a notable influence on embolus transport towards the brain, with graft angle 45° towards aortic valve transporting a higher percentage of emboli towards the cervical vessels, followed by 90° and 135° . Moreover, the anastomosis angle right/left of the heart on the coronal plane (*Azi* angles) is also observed to have a smaller but notable influence on embolus transport towards the brain. This anastomosis angle has been less commonly investigated in prior studies. Figure 3 presents the fraction of emboli accumulating below the outflow graft anastomosis site at the aortic root for each of the 9 LVAD graft models considered. The results indicate that the fraction accumulation at the root is significantly lower compared to the distribution to the cervical vessels. However, we note that out of the thromboemboli reaching the cervical vessels, a fraction of these actually make it further to the cerebral arteries. When compared accordingly, the accumulation of emboli at the aortic root as shown in Figure 3 is a significant number. We further observe that unlike in Figure 2, the extent of thromboembolus accumulation increases with increasing values of *Inc* angles, with the highest accumulation being for *Inc135*. These distributions are further illustrated by comparing the embolic particle ensemble transport against the flow patterns generated by the LVAD outflow graft jet impingement against the aortic wall [4]. In Figure 4, we present two time instances which show the initial and final embolus locations in the LVAD models with the three *Inc* and 45° right of the heart (*AziNeg45*). The higher velocity profile of model *Inc45* in the aortic root region pushes the particles towards the cervical region whereas the development of flow stasis in the aortic root for *Inc90* and *Inc135* causes accumulation of particles near the aortic root.

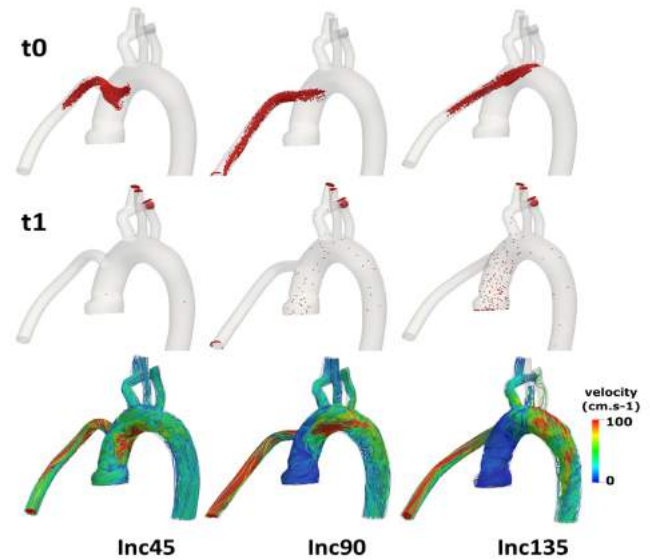


Figure 4: Snapshots of initial and final particle trajectory and velocity profiles for LVAD models with the three inclination angles and *AziNeg45*.

DISCUSSION

Here we have characterized thromboembolus dynamics in the aorta with an attached LVAD outflow graft, towards developing an in silico stroke descriptor. The jet impingement from the LVAD graft at different inclination angle informs aortic hemodynamics, and subsequent embolus transport and stroke risk. The minimum potential for embolic ischemic stroke is when the LVAD attachment is at an angle *Inc135Azi0*, and maximum at an angle *Inc45AziNeg45*. Transport of emboli entering from the LVAD outflow graft towards the cervical vessels enhances stroke risk. Additionally, the development of a stasis region for higher inclination angles can cause embolus accumulation in the aortic root. Due to intermittent opening of aortic valve (not considered here), these accumulated particles can reach the brain causing stroke. Prior works have reported that stasis in the aortic root region is prone to thrombogenicity, leading subsequently to stroke. Our work presents initial data showing a second mechanism by which the aortic root region influences stroke - embolus accumulation originating from LVAD flow. This can lead to significant advancements in accurate pre-surgical assessment of stroke risks as function of LVAD anastomosis. One limiting factor is the small number of cases considered, and more patient/anastomosis cases need to be considered for further statistical analysis and hypothesis testing

ACKNOWLEDGEMENTS

This work was partly supported by a University of Colorado Anschutz-Boulder (AB) Nexus Research Collaboration Grant (DM, JDP); and an NIH R21 award R21EB029736 (DM). We utilized resources from the University of Colorado Boulder Research Computing Group, supported by NSF awards ACI-1532235, ACI-1532236, the University of Colorado Boulder, and Colorado State University.

REFERENCES

- [1] Harvey L et al. *The Annals of thoracic surgery* 100.2 (2015).
- [2] Eckman PM et al. *Circulation* 125.24 (2012).
- [3] Aliseda A et al. *ASAIO Journal (American Society for Artificial Internal Organs: 1992)* 63.1 (2017).
- [4] Sahni A et al. *medRxiv* (2022). DOI: 10.1101/2022.06.17.22276555.
- [5] Updegrave A et al. *Annals of Biomedical Engineering* 45.3 (2017).
- [6] Repository OM. 2020.
- [7] Mukherjee D et al. *Annals of biomedical engineering* 46.8 (2018).

ACELLULAR ECM POWDER PROVIDES LATERAL INTEGRATION AND STRUCTURAL AND CELLULAR SIGNALING IN A 12-MONTH GOAT IMPLANT

Jeanne E. Barthold (1), Juliet Heye (2), Kaitlin McCreery (2), Katie Bizzaza (3), Jeremiah Easley (3), Ben Gadomski (3), Corey P. Neu (1,2)

(1) Department of Mechanical Engineering
University of Colorado at Boulder
Boulder, CO, USA

(1) Biomedical Engineering Program
University of Colorado at Boulder
Boulder, CO, USA

(3) Preclinical Surgical Research Laboratory
Colorado State University
Fort Collins, CO, USA

INTRODUCTION

Osteoarthritis (OA) is a degenerative joint condition commonly found in the knee joint that is triggered by events (e.g. mechanical insult) that lead to a cascade of cartilage degradation. OA is difficult to treat with current biomaterials and eventually leads to total joint arthroplasty. The specific composition of cartilage layers – primarily comprised of type II collagen, proteoglycans, and water – enables the tissue to provide excellent joint lubrication and facilitate load transmission during normal movement^[1]. The loss of cartilage due to disease or overuse leads to an inability for the remaining tissue to lubricate joints properly when exposed to mechanical loading. The lack of blood flow, nano-scale pore size, and the inability of the joint to heal on its own make articular cartilage a important example of the need for native structure to provide proper function in engineered scaffolds.

To treat cartilage defects, a variety of interventions exist, but each have limitations and drawbacks, and successful cartilage regeneration remains an unmet need in medicine. Microfracture is one surgical treatment for cartilage defects, and involves creating small fractures in the underlying subchondral bone to access progenitor cells in the marrow and fill the defect with a blood clot leading to a fibrocartilaginous repair^[2]. Allografts are a gold-standard treatment for cartilage repair^[3,4], but are unfortunately highly limited on the availability of donor tissue.

To address the donor availability limitations, we previously studied the use of full-thickness acellular porcine grafts in an *in vivo* cartilage defect model, and found that the implants suffered from poor recellularization^[5]. To improve integrative cartilage repair, we developed a new granulated extracellular matrix-based biomaterial where acellular tissue is first ground into a powder, and then combined with a unique chemistry to enable crosslinking at body temperature. The polymerized scaffold contains highly-packed particles near or

exceeding a percolation threshold, where the particle network dictates the modulus under compression, approaching native tissue mechanics^[6]. Here, we adapted the technology into a syringe delivery device to evaluate efficacy *in vivo*. Our device – *NatruLage* – is ‘flowable’ to deliver densely-packed ECM tissue particles, which enables forming and shaping after delivery before a temperature-induced crosslinking via thiol-functionalized hyaluronic acid. Here, we show proof-of-concept efficacy in a large animal (goat) model of a critical-sized cartilage defect, compared to microfracture, at 12 months post-surgery. The work presented here uses extensive cartilage and bone structural- and cell-level analyses to evaluate repair functionality, efficacy, and integration.

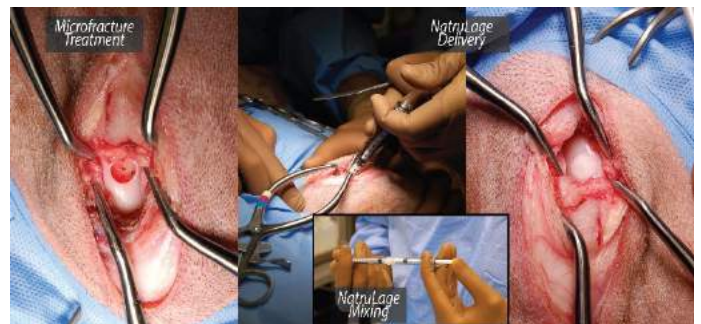


Figure 1: *NatruLage* (shown on the right) is applied to one knee in the surgical suite after mixing. The contralateral limb is left untreated as microfracture control (shown on the left).

METHODS

Decellularized Tissue Particles: Porcine tissue was sourced from a local butcher within 48 hours of slaughter. The articular cartilage was

collected from the knee with a scalpel, taking care not to include calcified tissue. Tissue was pulverized in a liquid nitrogen freezer mill (Qiagen), decellularized in 2% SDS for 8 hours at 37°C plus 0.1% DNase for 3 hours, rinsed, lyophilized, and size sorted to 100-250 μ m using a vibrational sieve. **Thiolating hyaluronic acid:** Glucuronate carboxyl groups on hyaluronic acid (HA) were replaced with thiol groups following previously established protocols [7]. Briefly, HA (MW 100 kDa) was dissolved at 10 mg/ml in degassed milliQ water. DTP was added to the solution, the pH was lowered to 4.5 and then EDC was added. The pH was maintained between 4.5-5 for 50 minutes. Next, DTT was added, and the pH was raised above 8.5 to stir overnight. After 24 hours, the pH of the solution was lowered and the solution was dialyzed (10 kDa membrane cutoff, Spectrum Labs) in an HCl solution +/- 100 mM sodium chloride for 12 changes in a sealed chamber with continuous nitrogen gas. HA thiolation was 20% (thiolated mmols/unthiolated mmols). **NatruLage Formation:** Lyophilized HA was dissolved in sterile DPBS (Hyclone) to make a 20 mg/ml HA solution, neutralized and loaded into a 1 mL syringe, then sealed. In a separate syringe, prepared tissue particles were mixed with DPBS at a ratio of 0.4 g/ml and sealed. **Surgical Protocol:** We created a critical-sized chondral defect in the load-bearing region of the medial condyle (6 mm diameter, 2.5 mm deep) of 11 goats. After drilling 4 holes in the bone marrow, syringes were attached to each other using a custom luer lock connector and mixed back and forth ~30 times until the material ran smoothly. The final mixture had an HA concentration of 10 mg/ml and particle concentration of 0.2 g/ml. The *NatruLage* material was injected into the defect region in one knee, smoothed to match the cartilage surface, and the joint was immediately closed (Figure 1). In the contralateral knee, the joint was closed following drilling of the defect. 12 months later, the goats were sacrificed for analysis.

Joints were opened and 10 mm plugs extracted (including repair tissue with surrounding native tissue). Matrix deposition, structural repair efficacy, integration and cellular migration is assessed using histology where half of the extracted tissue was fixed and embedded in PMMA. Sections were stained with Goldner's trichrome and Toluidine Blue (Indiana University).

A Keysight 5500 atomic force microscopy (AFM) system was used to evaluate the surface roughness, friction coefficient, compressive modulus, and to map the topography of surface structures in repair and native cartilage. All measurements were taken on the articular surface. A cantilever with known geometry was used (silicon nitride pyramidal tip, 20 nm radius), and the cantilever stiffness was calibrated to 0.12 N/m. High resolution contact mode scan was collected at 0.5 ln/s with an applied normal force of 20 nN to generate detailed topography, raw deflection, and lateral voltage signals of surface features in each region. From the averaged topography image of each region, surface roughness was obtained using Gwyddion software. Finally, independent force-spectroscopy curves were acquired with a setpoint force of 12.6 nN and a speed of 5 μ m/s. Force-displacement curves were fit to the Hertzian linear elastic model.

RESULTS

Structural analyses using histological staining indicates full defect filling in joints treated with *NatruLage*, compared to microfracture (Figure 2). Additionally, we observe lateral (structural) integration between the native tissue and the repair material in both bone and cartilage layers. A fibrous integration zone that is often observed at the boundary between a repair (graft) tissue and surrounding cartilage was not observed. Furthermore, cells migrated within and populated throughout the entire *NatruLage* repair material by 12 months. Initial macroscale evaluation and ICRS II scoring parameters indicate evidence of improved tissue organization and defect fill in the

NatruLage repair (n=5), and additional analysis is ongoing to evaluate repair efficacy of *NatruLage* compared to microfracture.

We measured lower adhesion in the *NatruLage* repair, as compared to microfracture and native tissue (n=5 in each treatment). Surface roughness was increased between native tissue and both repair groups, but the *NatruLage* surface roughness was slightly lower compared to microfracture. Using AFM, we measure frictional values similar to the surrounding native cartilage in the *NatruLage* repaired joints (n=5 of each treatment).

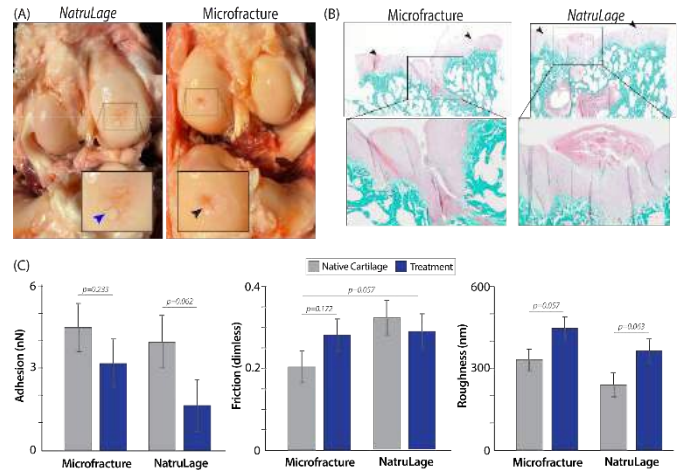


Figure 2: Acellular ECM powder contributes to improved structural integration and surface mechanics. (A) Repair and surrounding tissue is removed for analysis after 12 months. (B) Histological repair shows lateral integration (arrows indicate repair margins) and structural repair in each treatment. (C) *NatruLage* had lower adhesion than native or microfracture tissue, similar frictional profile to the surrounding native tissue, and slightly increased surface roughness.

DISCUSSION

In this work, we evaluated a new ECM particle-based articular cartilage repair material by applying the material to a critical-sized defect in the medial condyle of goats, and evaluating the repair efficacy 12 months later, compared to native tissue and the contralateral microfracture repair. We demonstrate that *NatruLage* is able to adhere to and integrate with native tissue without the use of an adhesive such as fibrin glue. While analysis and evaluation is ongoing, in a subset of 5 animals, we observe that the material enables cell migration throughout the repair, promotes cartilage tissue organization, facilitates smooth lateral integration in both bone and cartilage zones, and demonstrates evidence of improved surface functionality (friction and adhesion) from the microfracture repair. *NatruLage* promotes integration to surrounding tissue, cell migration into the construct, and previous *in vitro* work has shown that the material promotes tissue-specific cell phenotypes.

ACKNOWLEDGEMENTS

CDMRP/DoD W81XWH-20-1-0268.

REFERENCES

- [1] F. Guilak, R. J. Nims, A. Dicks, et.al, *Matrix Biology* **2018**.
- [2] R. Dorotka, et. al, *Osteoarthritis Cartilage* **2005**, 13, 655.
- [3] H. El-Rashidy, et. al., *Journal of Bone and Joint Surgery* **2011**.
- [4] M. Hevesi, et. al, *Cartilage* **2021**.
- [5] T. Novak, et. al, *Tissue Eng Part A*, **2016**.
- [6] J. E. Barthold et. al, *Adv Funct Mater* **2021**.
- [7] D. Eng, et. al, *Acta Biomater* **2010**.

COMPARING FIVE METHODS TO IDENTIFY FRACTURE TOUGHNESS OF SOFT TISSUES

Matthew J. Lohr (1), Manuel K. Rausch (1,2,3)

- (1) Department of Biomedical Engineering, University of Texas at Austin, Austin, Texas, USA
- (2) Department of Aerospace Engineering and Engineering Mechanics, University of Texas at Austin, Austin, Texas, USA
- (3) Oden Institute for Computational Engineering and Sciences, University of Texas at Austin, Austin, Texas, USA

INTRODUCTION

Modeling the behavior of soft tissues is challenging in general. Even more challenging is modeling the *fracture* behavior of soft tissues, as the field of soft tissue fracture is still evolving and includes obstacles that exceed the capabilities of linear fracture theory. There are some methods available to quantify the fracture toughness of materials, which is a measure of a material's resistance to fracture; however, there is no agreed-upon method that is ideal for quantifying this measure for soft tissues. The objective of our current work is to compare five methods of extracting fracture toughness from mode-I fracture experimental data. First, we will use an energetic approach (E1) that goes all the way back to Rivlin [1]. Second, we will use a modified version of this approach that supplements Rivlin's method with finite element (FE) simulations in Abaqus (E2). Third, we will calculate the J-integral that, in this context, is equivalent to fracture toughness, also from FE simulations in Abaqus (J1) [2]. Fourth, we will calculate the J-integral directly from experimental data collected via digital image correlation (DIC) images of mode-I fracture experiments (J2) [3]. Lastly, we will use a FE approach using a cohesive zone (CZ) in Abaqus [4].

METHODS

To collect the data needed to calculate the fracture toughness of blood clot, we performed pure shear and mode-I fracture tests on blood clot samples. An illustration of pure shear and mode-I loading is shown in Figure 1. We collected force-displacement data from both samples and identified the critical displacement (u^*) at which crack propagation began for the mode-I samples. The energetic approach (E1) we use comes from [1], viz.

$$G_c = W(u^*)H, \quad (1)$$

where G_c is the sample's fracture toughness, W is the strain energy density for a pure shear sample of blood clot at the critical displacement u^* , and H is the height of the sample. For this method, we averaged nine

sets of pure shear force-displacement data. We calculated the strain energy density of this averaged data set using the u^* for each mode-I sample to calculate G_c for each mode-I sample.

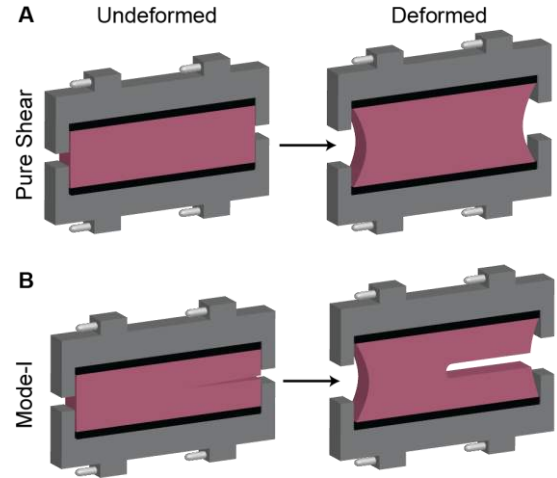


Figure 1: (A) Undeformed and deformed configurations for pure shear loading of blood clot. (B) Undeformed and deformed configurations for mode-I loading of blood clot.

An alternative approach to this energetic method (E2) is to create pure shear data using sample-specific material parameters to create sets of force-displacement data that are more representative of a specific mode-I sample, rather than using averaged data from pure shear tests of other clots. To this end, we performed an inverse FE analysis to fit hyperelastic material parameters to each mode-I clot sample in its elastic regime, which we assume to be 90% of its critical displacement. Specifically, we used a one-term Ogden model, which we have found

to be suitable for blood clot [5]. The methodology for identifying Ogden parameters for blood clot is given in [6]. After identifying the Ogden parameters, we created FE models in Abaqus of the pure shear experiment with sample-specific Ogden parameters for each mode-I experiment. We then calculated W from the force-displacement data and calculated G_c for each sample using Equation (1). Figure 2A illustrates our approaches E1/E2 and shows exemplary force-displacement data as used to calculate G_c .

For methods (J1 and J2), we computed the J-integral as a path-independent contour integral defined as

$$\int_{\Gamma} (W dy - \mathbf{t} \frac{\partial \mathbf{u}}{\partial x} ds), \quad (2)$$

where \mathbf{t} is the traction vector, $\frac{\partial \mathbf{u}}{\partial x}$ is the spatial derivative of the displacement vector with respect to the x-direction, and ds is the differential arc length of the contour. To calculate the J-integral (J1) using Abaqus's built-in function, we created a 2D FE mesh of the mode-I experiment with a highly refined region ahead of the crack tip to capture the nonlinear deformations of the clot. This allowed us to perform contour integration along multiple paths to calculate G_c and ensure the J-integral was path independent. Illustrated in Figure 2C is a FE mesh with a stress field typical of a mode-I sample as well as multiple J-integral contours. We also calculate the J-integral directly from DIC data fully forgoing the use of FE simulations (J2). Here again, we computed the J-Integral along multiple contours, see Figure 2D. Finally, for the CZ approach (CZ), we used the same geometry as in the Abaqus J-integral approach, but we modified the mesh to contain a single layer of cohesive elements along the crack path as seen in Figure 2B. To identify parameters of the bilinear traction-separation law for the cohesive elements, we ran forward simulations of the CZ model and minimized the error between the force-displacement curve and critical displacement of the experiment and simulation using a least squares approach in MATLAB. For all methods, we used plane stress and incompressibility assumptions and sample-specific Ogden parameters previously identified in our inverse analysis. [6].

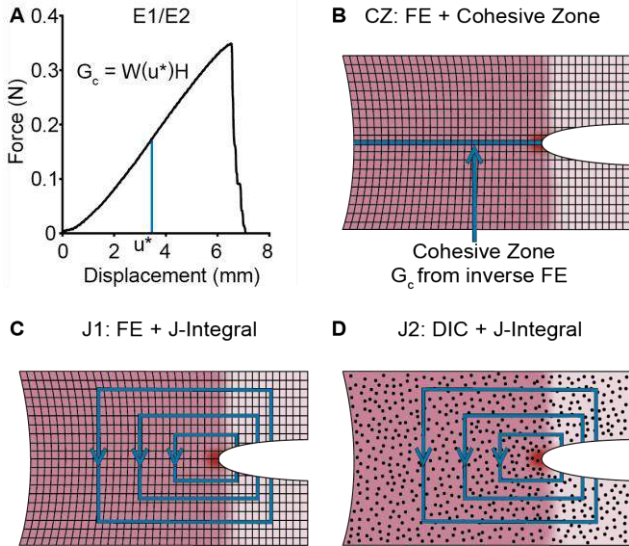


Figure 2: Illustrations of our five methods. (A) E1/E2: A exemplary set of force-displacement data and critical displacement (u^*) used in calculating G_c for a mode-I sample. (B) CZ: Illustration of a FE cohesive zone mesh and a depiction of a stress field typical of mode-I samples, with a stress concentration located at the crack tip. (C) J1: Illustration of a FE mesh and contours used in calculating the J-integral in Abaqus. (D) J2: Illustration of a speckled sample used in DIC, along with J-integral contours.

RESULTS

Figure 3 shows force-displacement data for three pure shear and mode-I samples, along with DIC images of stress fields corresponding to the black circles on the force-displacement plots. Figure 4 shows the calculated G_c for each method. The CZ method, energetic approaches, (E1) and (E2), and Abaqus J-integral (J1) give similar results for G_c , unlike the DIC J-integral (J2).

DISCUSSION

There is no gold standard in measuring G_c for soft tissues, but the fact that four of the five methods give values in similar ranges is promising. A limitation of the current work is that many assumptions went into building the models used, namely the plane stress assumption and the use of 2D models. Future studies should explore the discrepancies between methods and identify a method that is consistent across various fracture experiments for blood clot and other soft tissues.

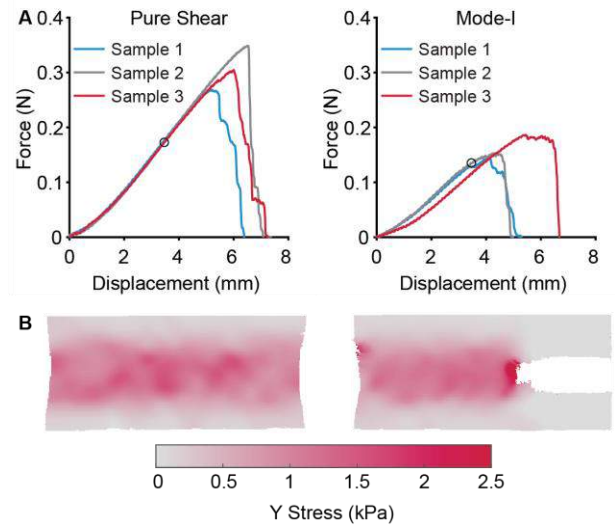


Figure 3: (A) Force-displacement plots for pure shear and mode-I loading of blood clot. (B) Digital image correlation-based stress fields for a pure shear and mode-I sample corresponding to the black circles from the force-displacement plots.

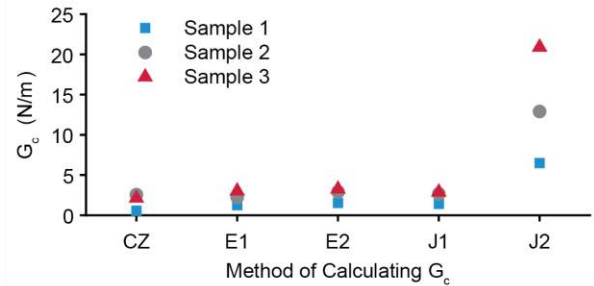


Figure 4: Comparison of G_c values for each method.

REFERENCES

1. Rivlin, R. S. et al. *J. Polym. Sci.* 10:291–318, 1953.
2. Baranwal, A. et al. *Theor. Appl. Fract. Mech.* 118:103253, 2022.
3. Gonz  les, G. L. G. et al *Theor. Appl. Fract. Mech.* 90:14–21, 2017.
4. Bhattacharjee, T. et al. *J. Mech. Behav. Biomed.* 28:37–46, 2013
5. Rausch, M. K. et al. *J. Elast.* 129:125–144, 2017.
6. Lohr, M. J. et al. *Philos. Trans. R. Soc.* 380: 20210365, 2022.

DYNAMIC RESPONSE CHARACTERIZATION OF SHEEP LYMPHATIC PUMPING DURING GROWTH AND REMODELING

Young Jae Ryu (1), Sophia Mavris (2), Zhanna Nepiyushchikh (2), Rudolph L. Gleason, PhD (1,2), J. Brandon Dixon, PhD (1,2),

(1) The George W. Woodruff School of Mechanical Engineering, Georgia Institute of Technology, Atlanta, GA, USA.

(2) The Wallace H. Coulter Department of Biomedical Engineering, Georgia Institute of Technology, Atlanta, GA, USA.

INTRODUCTION

The lymphatic system provides vital physiologic functions by maintaining fluid and protein homeostasis through a network of conduits, actively transporting interstitial fluid from tissues and organs back to the venous system^{1,2}. Interstitial fluid is collected and transported by collecting lymphatics vessels, which contract to drive lymph through one-way valves embedded in the channel¹. Lymphatic dysfunction results in excessive and debilitating fluid build-up in the extremities, known as lymphedema². Lymphedema that results from acute damage to the lymphatic system is deemed secondary lymphedema (SL) and affects 1 in 1000 Americans². SL puts patients at risk of extenuating sequelae including cardiovascular diseases if left untreated or undertreated.

Treatment of SL is informed by our limited understanding of basic structure-function relationships that govern lymphatic physiology. Our group and others have demonstrated remarkable insights to features (i.e., contractile dynamics and passive vessel stiffness) that influence lymphatic pumping across vessel networks^{3,4}. However, there is less data regarding growth and remodeling (G&R) of the lymphatic vasculature in development, growth, wound healing, and disease. These adaptation processes are strongly implicated in the delayed onset of lymphedema after cancer treatment⁵.

In this study, we employed a large-animal experimental model relevant to human physiology to encapsulate the growth and remodeling of lymphatic vasculature in an injury. In humans, gravity is the primary mechanical load that the lymphatic system must overcome⁵. Such load is absent in small animal model. The study of lymphatic remodeling in large animals is an essential step to translate small-animal findings to species more influenced by gravitational effects. We implemented our novel ligation model on sheep subjects where the influence of gravitational loading is greater especially in the hind limbs. The aim of this study is to validate a model that captures the dynamic response to growth and remodeling of lymphatic networks post-acute injury.

METHODS

12 sheep subjects were randomly assigned to three groups with separate termination times, defined as two, four, and eight weeks (n=4 for each group) post-surgery. Prior to the surgical procedure, each sheep underwent initial near infrared (NIR) functional lymphatic imaging of lymphatic vessels in both hind limbs. After imaging, ligation of the collecting lymphatic vessel was performed in a randomly selected hind limb. The ligation surgery was performed approximately 5cm above the hock between the proximal and distal aspects of the limb where a vein is located. During the surgery, one of the two parallel lymphatic vessels was transitively occluded with an ~1cm long excision of the vein, while the other hind limb received a sham surgery with no excision. The limb that received ligation surgery is hereafter termed the remodeled leg, while the leg with the sham operation is the control. Follow-up NIR functional imaging was conducted on each sheep immediately prior to takedown at the assigned group endpoint.

During each imaging session, an NIR lymphatic tracer (IRPEG40), a fluorophore dye conjugation developed in manner similar to a previously described method⁵, suspended in 0.5ml of sterile saline was injected over the course of 10 seconds into the lateral aspect of the mid hind limb centered 10cm proximal to the hock. A second injection of the same dose of IRPEG40 was given in the dorsal aspect of the hind limb 5cm distal to the hock. A 300 mW 785nm laser diode (Thorlabs) provided excitation light to the hind limb about 10cm above the surgical site. A Pixis 1024B back-illuminated charge coupled device camera (Princeton Instruments) with bandpass filter was positioned over the surgical site to capture fluorescence emission from the dye transported by the lymphatics from the site of injection. NIR images of dynamic fluorescence transport were captured at a rate of one frame per second for five minutes.

Two distinct metrics of lymphatic function were evaluated from the images using our previously developed method⁶: packet frequency (PF) and packet transport (PT). PF was evaluated by tracking the

average time between fluorescence peaks within a region of interest traced over lymphatic vessels during imaging. PF correlates to frequency of lymphatic contraction. PT was calculated by integrating the average intensity from the start to end of each fluorescence peak. PT denotes transport by intrinsic contraction and is given in relative peak fluorescence units (RFUs).

The significance of differences between control and remodeled limbs was determined using the paired t test for each time point with $P < 0.05$ indicating statistical significance. Additionally, separate paired t tests were conducted to compare pre-surgery and takedown values from the two-, four-, and eight-weeks groups.

RESULTS

At two weeks post-surgery, PF significantly increased in remodeled limbs relative to pre-surgery values and PT significantly decreased in remodeled limbs relative to control limbs. Mean PF increased from 1.657 min^{-1} to 2.899 min^{-1} (Figure 1a). Mean PT in the control limb was 42248 RFUs whereas the mean packet transport in the remodeled limb was 8371 RFUs (Figure 2a). It is important to note that three sheep data was collected due to unquantifiable PT measurements for one sheep trial in the two-weeks cohort. No further statistical significance was found in the two-weeks group. At four weeks post-surgery, no significant differences were observed either between control and remodeled limbs or between pre-surgery and takedown values. The four-week group demonstrated high variability in PF, packet amplitude, and PT. The eight-week group saw significant increase in mean PF from a pre-surgery value of 1.929 min^{-1} to 3.142 min^{-1} (Figure 1c). High variability of the packet amplitude was noted throughout the entire scope of the experiment, limiting the statistical significance of results.

DISCUSSION

In the two-weeks cohort, the increase in PF in conjunction with a significant decrease in PT demonstrates that lymphatic vessels are contracting more frequently but with less efficiency. Reduced PT is indicative of less fluorescent tracer traveling through the lymphatic vessel, which strongly suggests a compensatory response to the injury. Post-injury, lymphatic vessels sustain a higher load. Increased contractile frequency is expected because increased loads have previously been shown to increase frequency³. While a decrease in PT was observed, the exact mechanism remains uncertain; we hypothesize that it may be driven by a decrease in ejection fraction and lymphatic pumping efficiency.

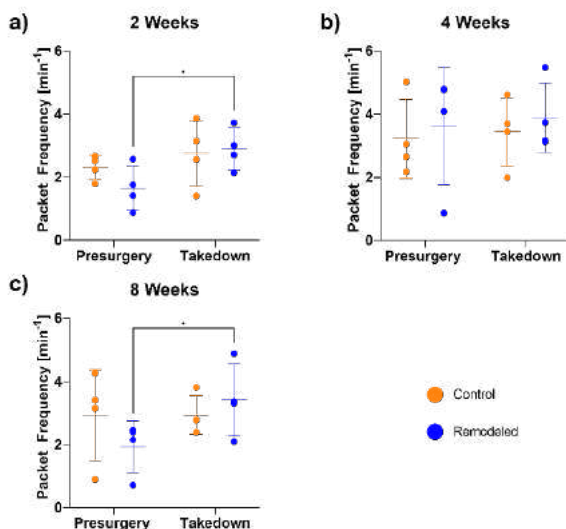


Figure 1: Packet frequency plots comparing the control and remodeled legs over three termination times

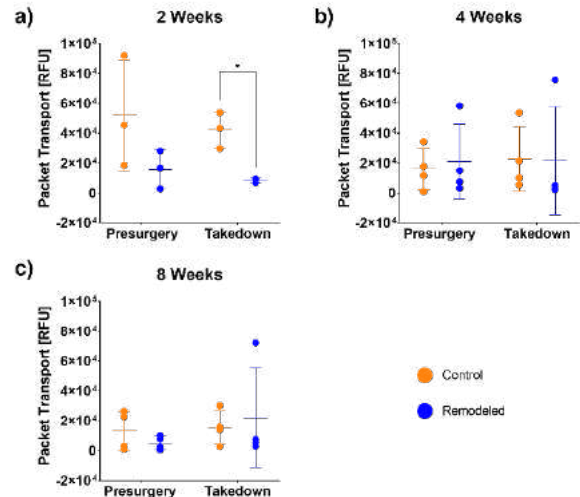


Figure 2: Packet transport plots comparing the control and remodeled legs over three termination times

After sustaining an injury, the lymphatic system must compensate for the barrier to lymph flow to the veins. In this study, we observe lymphatic pump dynamic changes to show that unique physical adaptation processes occur post-trauma. As the load on the lymphatic vessel increases and a barrier to lymphatic flow is in place, the rate of lymphatic pumping increases to maintain fluid balance. An increase in contractile frequency in injured leg at eight weeks post-surgery may suggest longer-term contractile response to the altered physiology.

Functional response to injury is important in maintaining fluid homeostasis, and thus the compensatory mechanisms of growth and remodeling are critical. While our experiment demonstrates that there exists a unique response to injury to compensate for altered lymphatic loads, further study is required to ascribe volumetric insights from changes in contractility. Nevertheless, a comprehensive study of lymphatic contractility through NIR imaging is indispensable tool to study growth and remodeling.

ACKNOWLEDGEMENTS

We respectfully acknowledge the support from the National Institutes of Health (award number 1R01HL152152).

REFERENCES

1. Breslin, J. W. *et al.* Lymphatic vessel network structure and physiology. *Compr. Physiol.* **9**, 207–299 (2019).
2. Kayiran, O., De La Cruz, C., Tane, K. & Soran, A. Lymphedema: From diagnosis to treatment. *Turkish J. Surg.* **33**, 51–57 (2017).
3. Caulk, A. W., Nepiyushchikh, Z. V., Shaw, R., Dixon, J. B. & Gleason, R. L. Quantification of the passive and active biaxial mechanical behaviour and microstructural organization of rat thoracic ducts. *J. R. Soc. Interface* **12**, 20150280 (2015).
4. Kornuta, J. A. *et al.* Effects of dynamic shear and transmural pressure on wall shear stress sensitivity in collecting lymphatic vessels. *Am. J. Physiol. - Regul. Integr. Comp. Physiol.* **309**, R1122–R1134 (2015).
5. Nelson, T. S. *et al.* Lymphatic remodelling in response to lymphatic injury in the hind limbs of sheep. *Nat. Biomed. Eng.* **4**, 649–661 (2020).
6. Weiler, M. J., Cribb, M. T., Nepiyushchikh, Z., Nelson, T. S. & Dixon, J. B. A novel mouse tail lymphedema model for observing lymphatic pump failure during lymphedema development. *Sci. Rep.* **9**, 1–15 (2019).

ALTERING METABOLIC COST FUNCTION OF PULMONARY ARTERIES TO UNDERSTAND HEMODYNAMIC RESPONSE TO PAH

Haritha N. Mullagura (1), C. Alberto Figueroa (2,3), Seungik Baek (1)

- (1) Department of Mechanical Engineering, Michigan State University, East Lansing, MI, USA
(2) Section of Vascular Surgery, Department of Surgery, University of Michigan, Ann Arbor, MI, USA
(3) Department of Biomedical Engineering, University of Michigan, Ann Arbor, MI, USA

INTRODUCTION

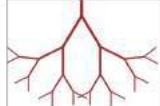

Pulmonary arterial hypertension (PAH) is a complex disease associated with a chronically elevated pulmonary arterial pressure. The onset and early progression of PAH can be traced to changes in the morphometry and structure of the distal vasculature. Coupling hemodynamics with vessel wall mechanics is crucial for understanding pathology at distal vasculature to study PAH. Accordingly, the goal of this study is to provide a multiscale modeling framework that embeds the essential features of arterial mechanics coupled with the PAH hemodynamics within an arterial network characterized by an extension of Murray's law. This framework will be used to establish the homeostatic baseline characteristics of a pulmonary arterial tree in a normotensive and hypertensive case. An iterative homeostatic optimization, which integrates a metabolic cost function minimization, the stress equilibrium, and hemodynamics, is performed. The results are compared with diverse literature data on morphometry, structure, and hemodynamics of pulmonary arteries for normotensive and hypertensive cases. The developed framework demonstrates a potential for advanced parametric studies and future pathophysiological modelling of PAH.

METHODS

The arterial network is assumed to be symmetric in the radial direction with constant mass fractions of the wall constituents. The two cases studied are the normotensive arterial network and hypertensive arterial network. A slow timescale is used to formulate the long-term vascular adaptations and homeostatic maintenance, while a fast timescale is used to formulate the hemodynamics over a cardiac cycle [1]. The slow-time hemodynamics in the arterial tree is computed using Poiseuille flow for each vessel, the flow conservation and pressure continuity for each bifurcation, and boundary conditions at the tree inlet and outlets. These two timescales are then coupled to formulate fluid-

solid growth (FSG) governing equations. The fluid solid interaction solution for one vessel is then extended for the entire geometry to solve for hemodynamics of the open arterial network with the given inlet and outlet boundary conditions. We estimate the baseline homeostatic optimization characteristics by using an extension of Murray's law for an individual normotensive vessel. The total metabolic energy consumption is optimized for the entire arterial network, while mean hemodynamics variables are computed by iteratively updating the geometries from the metabolic optimization. For the hypertensive case, then the cost optimization function (Eq. 1) is modified by incorporating data of PAH arterial thickness and clinically measured inlet hemodynamics. The effect of altering the metabolic cost function on hemodynamic response is studied and compared to normotensive case.

Table 1: Summary of the two cases of the arterial tree framework.

Parameter	Case 1	Case 2
Geometry	Symmetric Arterial Tree Inlet BC: Mean Flow  Outlet BC: Terminal Pressure	Symmetric Arterial Tree Inlet BC: Mean Flow  Outlet BC: Terminal Pressure
Mass Fraction of the Wall Constituents (Elastin, Smooth Muscle Cells and Collagen)	Constant across the Arterial Tree	Constant across the Arterial Tree
Tension	Normotensive	Hypertensive

$$C(R; \bar{p}^s, q^s) = \vartheta^{blood} \pi R^2 + \frac{8\mu q^s}{\rho_f \tau_{iud} \pi R^4} + 2\pi(1 - \phi_f) \bar{p}^s R^2 \frac{\sum_i \vartheta_i v_i^i}{\sum_i v_i \sigma_\theta^i} \quad (1)$$

RESULTS

Hemodynamics and morphometric results of the two cases are presented below for 19 bifurcations, considered here as generations starting at the third bifurcation from the main pulmonary artery. Input flow & terminal pressure are compared for normotensive and hypertensive arterial network (Fig. 1 & 2). Diameter distribution compared to reported data of large vessels (Fig. 3 & 4) in normotensive and PAH case [2,3,4].

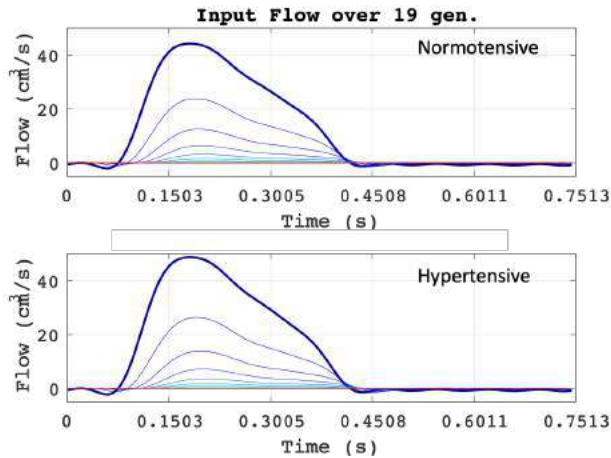


Figure 1: Input flow across arterial tree for the two cases.

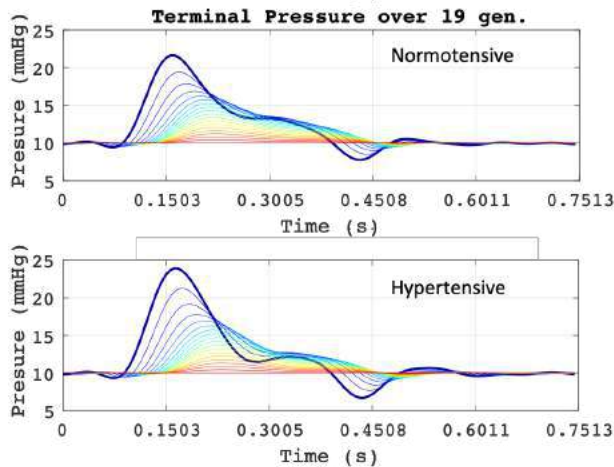


Figure 2: Terminal pressure across arterial tree for the two cases.

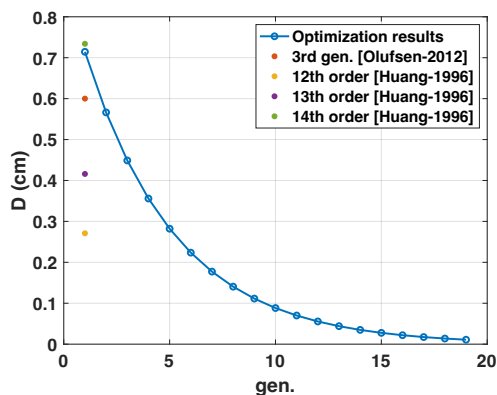


Figure 3: Normotensive homeostatic optimization diameter results plotted against generation number.

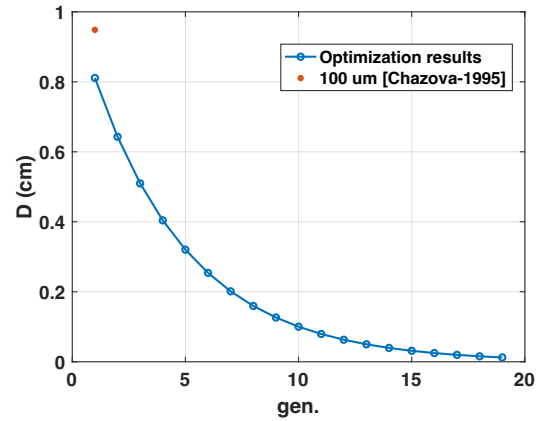


Figure 4: Hypertensive homeostatic optimization diameter results plotted against generation number.

DISCUSSION

We illustrated the utility of our homeostatic optimization framework on examples of normotensive and hypertensive pulmonary trees representing small- to intermediate-size vessels (0.01 to 0.5 cm) of the pulmonary vasculature. The results were presented in terms of the morphometric, and hemodynamics characteristics of the vessels in the tree. Employing our time-scale separation framework, the results of the homeostatic optimization were used to obtain the pulsatile hemodynamics using Womersley's analytical solution.

The morphometric results of the optimization have a direct impact on the pulsatile hemodynamics of the pulmonary tree. Using the developed framework, we demonstrated the impact of metabolic cost optimization on hemodynamics (Fig. 1 & 2). Although the input flow has minimal change, the terminal pressure has a significant change, replicating the hemodynamics of PAH. The increase in diameter of arterial vessels for hypertensive case (Fig. 4) is incoherent with the theory that homeostatic optimization thickens the vessels in PAH.

ACKNOWLEDGEMENTS

This work was supported by the National Institute of Health under Grant U01 HL135842.

REFERENCES

- [1] V. Filonova, H. Gharahi, N. Nama, S. Baek, C. Alberto Figueroa, and C. A. Figueroa, *Arxiv.org*, pp. 1–35, 2020
- [2] Olufsen MS, Hill NA, Vaughan GDA, et al. *J Fluid Mech* 705:280–305, 2012
- [3] Huang W, Yen RT, McLaurine M, Bledsoe G. *J Appl Physiol* 81:2123–2133, 1996
- [4] I. Chazova, J. E. Loyd, V. S. Zhdanov, J. H. Newman, Y. Belenkov, and B. Meyrick, *American Journal of Pathology*, vol. 146, pp. 389–397, 1995.

BLADDER BIOMECHANICS - FILLING AND VOIDING

Juan Pablo Gonzalez-Pereira (1,2), Cody J. Johnson (2), Wade A. Bushman (3), Shane A. Wells (2), Alejandro Roldan-Alzate (1,2,4)

- (1) Mechanical Engineering, University of Wisconsin-Madison, Madison, Wisconsin, United States
(2) Radiology, University of Wisconsin-Madison, Madison, Wisconsin, United States
(3) Urology, University of Wisconsin-Madison, Madison, Wisconsin, United States
(4) Biomedical Engineering, University of Wisconsin-Madison, Madison, Wisconsin, United States

INTRODUCTION

Current methods to evaluate the lower urinary tract (LUT) are invasive but more importantly, do not offer dynamic anatomical evaluation of the LUT and specifically the bladder during filling and voiding^[1-3]. The dynamic study of the LUT, through MRI, has been shown in previous studies, which have demonstrated that MRI can provide both static and dynamic high fidelity 3D images of the bladder^[1,3]. Therefore, the aim of this study is to implement an MRI protocol that allows the comprehensive assessment of the bladder biomechanics during filling and voiding.

METHODS

In this HIPAA compliant, IRB-approved study, a healthy male was equipped with a condom catheter prior to the MRI scanning session. All scans were performed on a clinical 3T scanner (Premier, GE Healthcare, Waukesha, WI), using a high-density flexible surface coil array (AIR Coil, GE Healthcare). A dynamic acquisition was performed using Balanced Steady State Free Precession (BSSFP) imaging with a temporal resolution of 1.66 seconds, generating a total of 100 time steps per scan. A total of 9 scans were taken for filling (approximately 30 minutes worth of MR images) and a single scan for voiding (approximately 3 minutes). 15 minutes prior to the MRI scans, 1/3 of a single weight-based dose (0.1 mmol/kg) of gadolinium-based contrast was hand injected intravenously to enhance the visualization of bladder deformation during filling and voiding as well as volumetric displacement and bladder sphericity over time. Images were imported into MIMICS (Materialise, Leuven, Belgium), where the bladder lumen was segmented to obtain 3D renderings (Figure 1 and 2).

Bladder lumen volumes were then used to calculate volumetric flow rate throughout the whole filling and voiding event by calculating the volume change over time. For filling, data from 9 scans was analyzed. Due to the low filling rates, one time phase from each scan was taken to analyze volumetric changes of the bladder. For voiding,

the entirety of the scan was analyzed but only the phases where emptying of the bladder was observed were segmented.

The bladder can be approximated as a sphere where the largest radius can be measured from dome to bladder neck (base). The surface area of the bladder lumen was acquired from the bladder renderings at each time point. This was later compared to the surface area of a perfect sphere with the same volume as the bladder lumen using equation (1). This ratio is the sphericity index where values approaching 1.0 indicate an approximation to a perfect sphere^[4].

$$\text{Sphericity Index} = \frac{\text{Surface Area of Perfect Sphere}}{\text{Surface Area of Bladder Renderings}} \quad (1)$$

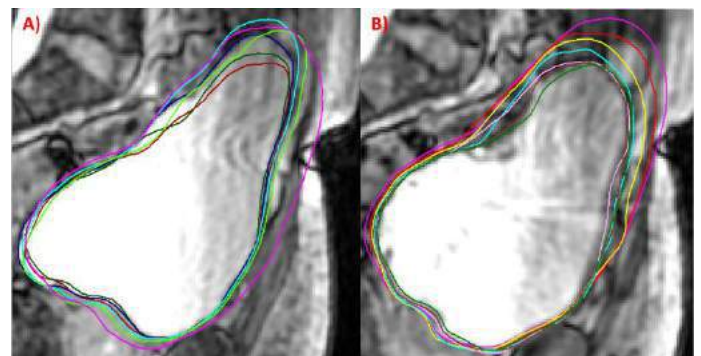


Figure 1: Contour lines of bladder lumen segmentations at different time points during A) filling (t_0 = red, t_1 = green, t_2 = blue, t_3 = light green, t_4 = cyan, t_5 = pink) and B) voiding events on a sagittal view.

Alongside the sphericity index the distance from the center of pubic symphysis (PS) to the dome, trigone, and lateral portions (left and

right) of the bladder were measured to determine the axes of eccentricity of the bladder while filling.

RESULTS

A methodology to evaluate and characterize biomechanics of the entirety of bladder during filling and voiding in a human subject was successfully implemented. Figure 2 shows the filling rate, voiding rate, volume measurements over time alongside analytics for filling and voiding. Filling analytics include total filled volume (TFV), post filling volume (PVF), and maximum and average filling rates (Q_{max} and Q_{avg} respectively). Voiding analytics include total voided volume (TVV), post void residual (PVR), as well as maximum and average voiding rates (Q_{max} and Q_{avg} respectively).

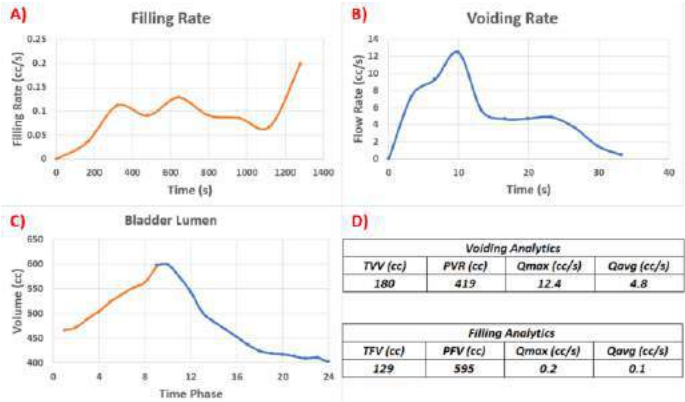


Figure 2: Filling and voiding rates (A and B respectively), bladder lumen volumes (C) during filling (orange) and voiding (blue), and filling and voiding analytics (D).

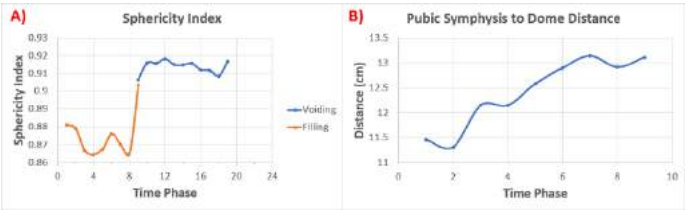


Figure 3: Sphericity Index measurements (A) during filling (orange) and voiding (blue) along with the distance between the center of the PS to the dome during filling (B).

Bladder lumen volumes increase constantly during filling as shown in figure 2C. Filling rates are displayed in figure 2A, displaying variations that range from 0.025 cc/s to 0.05 cc/s but with an average filling rate of 0.1 cc/s as shown in figure 2D. As voiding commences the bladder volumes decrease following voiding rate trends, displaying Q_{max} 10 seconds after the subject started voiding as shown in figure 2B. Bladder lumen volume before filling imaging started is 498 cc and reaches 595 cc after 1280 seconds (21.3 minutes) for the last time phase in the filling scans. During the voiding scan, bladder lumen volumes range from 598 cc to 419 cc and the slope of the bladder volume curves can be directly related to voiding rates.

Sphericity Index was calculated for filling (orange) and voiding (blue). The sphericity index shows different behaviors in filling and voiding but are not disjointed as shown in figure 3A where both seem to join in phase 9. The sphericity index displayed general asymmetry in the bladder during filling as shown in figure 3A having a maximum value of 0.903 right before the voiding scan and a minimum value of 0.864 at time phase 4. During filling, the PS distance to the dome

increases constantly while the sphericity index varies significantly. This indicates changes in the other axes of the bladder. During voiding, the sphericity index increases and reaches a maximum value (0.918) close to the time phase of Q_{max} and then decreases to pre-void values.

DISCUSSION

This non-invasive, novel MRI-based technique, allows for the quantitative assessment of the bladder biomechanics during filling and voiding during a single scanning session under an hour. Current diagnostic methods fail to completely characterize bladder biomechanics. Correspondingly, measurements of volumetric flow rate, TVV, TFV, PVR, PFV and sphericity index were able to be obtained during in a single session in the scanner. Sphericity index provides insight on bladder shape and how uniformly the bladder deforms during filling and voiding. When filling scans began, the bladder was partially filled. As the scans progressed, the dome of the bladder showed the first signs of displacement as shown in figure 3B. Afterwards, the sphericity index decreased which means the bladder became less spherical. This indicates that the bladder did not fill uniformly for that period. This occurs again during time phase 3 and 4 where the distance between the PS and the dome of the bladder stayed the same but the sphericity index curve displays an inflection point. This inflection point may indicate that other regions of the bladder were expanding during these time phases. During voiding, the sphericity index matches the behavior of the voiding rates until reaching Q_{max} , then it decreases slowly until returning to a pre-void index close to the end of the voiding state.

CONCLUSIONS

With this novel technique, we were able to non-invasively capture in-vivo filling rates and characterize the filling of the human bladder without the use of catheterization (urodynamics) or perturbation on the abdomen (ultrasound). Current methodologies have lacked the ability to capture low flow voids and filling. This shows the ability of this novel methodology to characterize diverse bladder biomechanical aspects during any filling or voiding event. This subject's voided volume is close to be deemed unreliable for urodynamic studies as the voided volume was close to 150 cc. Nevertheless, our methodology allows us to analyze low flow events such as filling and low volume voids. Thus, demonstrating necessity for patient specific, non-invasive methodologies to analyze bladder biomechanics during filling and voiding.

MRI protocols have proven to be an invaluable and versatile imaging modality that can be used to characterize anatomical and functional information of the LUT dynamically in a safe, accurate, and reproducible way. Future work will be aimed at using this novel methodology to deepen the comprehension of bladder biomechanics during filling and voiding, and better understand how different diseases affect bladder biomechanics.

ACKNOWLEDGEMENTS

The authors would like to acknowledge GE Healthcare and support from the NIH (R01 DK126850-01).

REFERENCES

[1] R. Pewowaruk *et al.*, *PLoS ONE*, 15(11), 2020, doi: 10.1371/journal.pone.0238404.
[2] Li Y, *et al.*, *Urology*. Published online 2021. doi: 10.1016/j.urology.2021.09.005
[3] L. E. Anzia *et al.*, *Abdominal Radiology*, vol. 46, no. 4, 2021, doi: 10.1007/s00261-020-02808-9.
[4] R. Rorato, *et al.*, *Eng Geol.* 2019;254:43-53. doi: 10.1016/j.enggeo.2019.04.006

EFFECT OF ACOUSTIC RADIATION FORCE AND MICROBUBBLE SIZE PARAMETERS ON $\alpha_v\beta_3$ INTEGRINS-TARGETING IN MICROVESSEL PHANTOMS

Jair I. Castillo (1), J. Angel Navarro-Becerra (1), Federico Di Ruzza (2), Mark Borden (1)

(1) University of Colorado Boulder, Boulder, CO, USA

(2) University of Rome Tor Vergata, Rome, Italy

INTRODUCTION

Ultrasound molecular imaging (USMI) using targeted microbubbles (MBs) is a promising technique for assessing endothelial phenotypes. USMI has shown promising results to visualize targets that are usually associated with angiogenesis, thrombosis, and inflammation [1]. For example, angiogenesis is a crucial contributing factor that could potentially predict tumor growth and cancer progression. Targeted MBs include biomolecular ligands that bind specifically to endothelial receptors. These targeted MBs are injected into the body where they flow through the entire vasculature and their accumulation in the endothelial wall via cell-mediated adhesion is observed using ultrasound. However, more research is necessary to improve specificity and efficiency of MB targeting, here we used the RGD/ $\alpha_v\beta_3$ (ligand/receptor pair). It is known that acoustic radiation force (F_{rad}) increases the number of polydisperse RGD-MBs adhered to cells [2]. Moreover, it has been demonstrated that the combination of size-selected microbubbles with specific frequencies increases the microbubble displacements [3]. Therefore, we hypothesize that the F_{rad} can increase the number of monodisperse RGD-MBs attached to $\alpha_v\beta_3$. The main goal of this work aims to study and elucidate the role of ARF and MB parameters on the targeting of RGD-MBs using an in vitro $\alpha_v\beta_3$ -coated microvessel phantom. The use of F_{rad} in combination with MBs using buried-ligand architecture, represents a potential strategy to enhance the adhesion specificity and efficiency at the target site by matching the ultrasound pulse frequency to the MB resonance frequency. The goal of this work was to study the

effect of MB monodispersity on targeting specificity and efficiency for RGD-MBs to an in vitro $\alpha_v\beta_3$ -coated microvessel.

METHODS

Labeled polydisperse and 2 μm size- isolated MBs (DBPC/DSPE-PEG(5000)/DSPE-PEG(2000)-PDP/Vybrant DiI) attached with the peptides RGD and RAD, target and control ligand respectively, were synthesized with a buried-ligand architecture [4]. A mechanical centrifugation method was utilized to isolate the MBs into a monodisperse distribution [5]. To analyze the MBs targeting, monodisperse MBs were pumped at 1 mL/h in an $\alpha_v\beta_3$ -coated microvessel phantom, with a diameter of 200 μm , and pushed using the UlaOp ultrasound system in B-mode imaging. In addition, the MBs were manipulated using F_{rad} at 3 MHz, 20 cycles or 7 MHz, 47 cycles; 6.7 μs pulse length, 0.15 MHz PRF, and 133 kPa PNP. The number of peptide molecules bound to the MBs was measured by using a BCA assay. The effect of US frequency (3 vs. 7 MHz) and MB concentration (1×10^5 to 1×10^8 MB/mL) on F_{rad} targeting was evaluated. Finally, we compared the adhesion efficiency to polydisperse MB populations. Finally, z-stack pictures of 10 different sections of the phantom were taken using bright and fluorescent contrast. The attached MBs to the microvessel wall were counted and the amount of MBs attached per mm^2 was estimated. In all cases, specificity was estimated as the subtraction of nonspecific isoform control RAD-MBs from the targeting ligand RGD-MBs.

Equations

To calculate the adhesion efficiency of MBs attached to the phantom wall, the following equation was used:

$$\text{Adhesion Efficiency (\%)} = \frac{\# \text{ MBs attached}}{\# \text{ MBs interaction zone}} \times 100 \quad (1)$$

The # MBs interaction zone = $(Q \times t \times [\text{MBs}]) + (V \times [\text{MBs}])$, where V is the microvessel volume (mL), [MBs] is the concentration of MBs (MBs/mL), Q is the flow rate (mL/min) and t is the insonation time (min).

RESULTS

It was observed that the greatest MB adhesion occurred at 7 MHz and was dependent on MB concentration. Remarkably, the data shows that specificity was maximized at a concentration of 1×10^6 MB/mL, whereas at higher concentrations (1×10^7 to 1×10^8 MB/mL), there was a greater number of nonspecific interactions (Fig. 1A). Also, the adhesion efficiency for RGD-MBs decreased from 97% to 13%, for monodisperse and polydisperse populations at 10^6 MBs/mL, respectively (Fig. 1B).

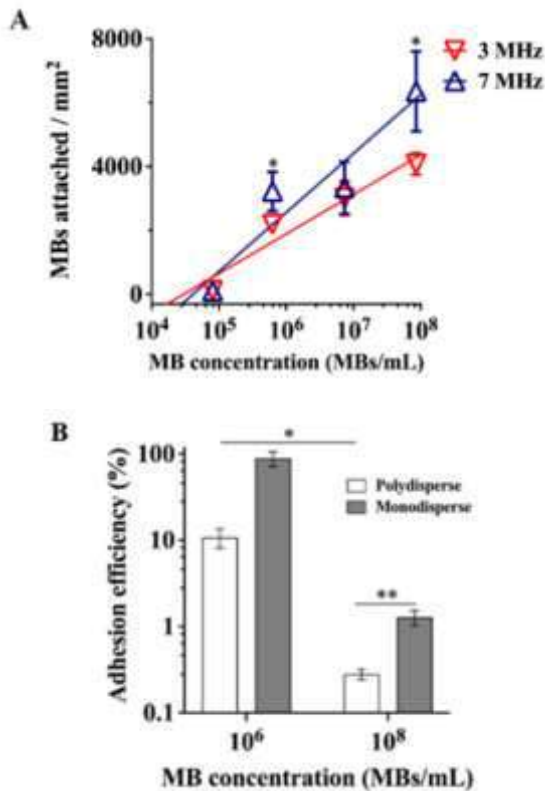


Figure 1: A) Specific RGD-MBs targeting with varying concentrations and frequencies ($*p \leq 0.05$, $R^2 \geq 0.90$). B) Dependence of specific RGD-MBs adhesion efficiency on the MB size distribution ($*p < 0.05$ and $**p < 0.005$). Data represent the mean \pm standard deviation for 3 independent experiments.

DISCUSSION

The combination of US and MB parameters plays a key role in maximizing the adhesion efficiency and specificity of F_{rad} ultrasound targeting of buried-ligand MBs using the RGD/ $\alpha_v\beta_3$ ligand/receptor pair. The density of receptors on the microvessel internal surface represent an important feature to achieve successful MB targeting, specificity, and adhesion efficiency. However, as the MB concentration increased, the nonspecific interactions increased as well, resulting in low specific adhesion efficiency. The data suggest that this behavior could be attributed to the presence of secondary acoustic radiation forces, due to the high number individual MBs bumping into each other at high concentrations and making them dislodge from their binding site. In our study, MB concentration was optimized at $\sim 10^6$ MBs/mL. Furthermore, we also elucidated that the use of monodisperse MBs increases the adhesion efficiency by 8-fold when compared with polydisperse MBs at the same concentration. The results of this study provides a deeper understanding of the MBs behavior under ultrasound and flowing conditions inside a microvessel phantom. This is relevant to the field as we could be a step closer in using a widely-available, low-cost and minimally invasive method of detecting different pathologies in the endothelium with ultrasound technology and ultrasound contrast agents.

ACKNOWLEDGEMENTS

This work was funded by the NIH award R01CA239465.

REFERENCES

- [1] Borden, M. A., Zhang, H., Gillies, R. J., Dayton, P. A., & Ferrara, K. W. (2008). A stimulus-responsive contrast agent for ultrasound molecular imaging. *Biomaterials*, 29(5), 597-606.
- [2] Zhao, S., Borden, M., Bloch, S. H., Kruse, D., Ferrara, K. W., & Dayton, P. A. (2004). Radiation-force assisted targeting facilitates ultrasonic molecular imaging. *Molecular imaging*, 3(3), 15353500200404115.
- [3] Supponen, O., Upadhyay, A., Lum, J., Guidi, F., Murray, T., Vos, H. J., ... & Borden, M. (2020). The effect of size range on ultrasound-induced translations in microbubble populations. *The Journal of the Acoustical Society of America*, 147(5), 3236-3247.
- [4] Borden, M. A., Zhang, H., Gillies, R. J., Dayton, P. A., & Ferrara, K. W. (2008). A stimulus-responsive contrast agent for ultrasound molecular imaging. *Biomaterials*, 29(5), 597-606.
- [5] Feshitan, J. A., Chen, C. C., Kwan, J. J., & Borden, M. A. (2009). Microbubble size isolation by differential centrifugation. *Journal of colloid and interface science*, 329(2), 316-324.

CLASSIFICATION-BASED SUPER-RESOLUTION RECONSTRUCTION IN CMR TO QUANTIFY FOUR-DIMENSIONAL MYOCARDIAL STRAINS IN MICE

Tanmay Mukherjee (1), Sakthivel Sadayappan (2), Reza Avazmohammadi (1,3,4)

(1) Department of Biomedical Engineering, Texas A&M University, College Station, TX, USA

(2) Department of Internal Medicine, University of Cincinnati, Cincinnati, OH, USA

(3) J. Mike Walker '66 Department of Mechanical Engineering, Texas A&M University, College Station, TX, USA

(4) Department of Cardiovascular Sciences, Houston Methodist Academic Institute, Houston, TX, USA

INTRODUCTION

The diagnostic efficacy of organ-level metrics such as the ejection fraction is challenged by the multifaceted nature of structural heart diseases [1]. The functional assessment of cardiac function through the mechanistic quantification of left ventricular (LV) motion is growing in prevalence. In particular, the imaging-based analysis and subsequent characterization of the global longitudinal strain (GLS) strains has been shown to be a strong early-stage marker for cardiac diseases in comparison with traditional volumetric metrics [2]. Despite their merits, such organ-level strain measurements fail to quantify the regional characteristics of LV function accurately. The LV exhibits complex four-dimensional (4D) deformation with remarkable transmural variations, thus confounding the accuracy of regional strain calculations and effectuating variability. The characterization of continuous 4D regional deformation offers excellent potential in establishing a complete LV structure-function relationship. Despite advances in medical imaging, the assessment of 4D continuous myocardial deformation remains vastly under-explored. In this work, we propose a classification-based super-resolution reconstruction (CSRR) framework to improve the characterization of myocardial strains. The CSRR framework combines sets of arbitrarily aligned anisotropic low-resolution cardiac magnetic resonance (CMR) scans to produce a high-resolution field of pixels to generate a 4D map of myocardial motion.

METHODS

The framework is divided into three modules, (i) the classification module, (ii) the interpolation module, and (iii) the registration module. Our objective was to categorize each tissue class, assign pixels from the image set of the low-resolution (LR) acquisitions, and generate query points over a global Euclidean space in the high-resolution (HR) grid. The endocardial and epicardial contours were drawn semi-automatically using Segment version 3.0. Our module assigned pixels to various regions of interest by converting the point clouds into convex hulls and

combining the 2D contours into 3D surfaces. The 2D contours were resampled longitudinally through Delaunay triangulation and smoothed through the application of radial basis functions to mitigate the effects of pixel spacing anisotropy on the segmentation quality in 3D reconstruction. The segmented LR images, along with the information describing the desired HR scan, were passed on to the interpolation module. The HR scan was defined either as an unstructured grid via a global interpolation scheme. Given the anisotropy in pixel distribution and to accommodate arbitrary orientations of LR images, scattered data interpolation was used. The region-specific pixel sets and a combined package comprising parameters such as the resampling ratios, the reference image index, and the segmented contours were passed on to the registration module. A diffeomorphic demons algorithm [3] was implemented to perform non-rigid image registration. The pixel displacements in the Cartesian frame of reference were used to calculate the Green-Lagrange strain tensor and were then transformed into clinically relevant anatomical coordinates. Scans at various orientations describing different views of the LV are desirable inputs for the CSRR framework. Imaging was performed in one diabetic mouse ($n = 1$, 6 months old) using a 7T Bruker Avance III HD scanner with a 72 mm quadrature proton volume coil (Bruker BioSpin MRI GmbH). A set of eight short-axis (SA) and five long-axis (LA) slices orthogonally sampled between the anterior and inferior walls of the LV were captured (Fig. 1A), and the combined stack was subjected to CSRR (Fig. 1B).

RESULTS

The reconstructed LV is shown across an arbitrary plane sampled perpendicular to the SA planes (Fig. 2A). Strains are reported for LV models reconstructed using standard imaging SA images only (standard imaging) and CSRR models. Since only eight LR SA slices were used in the sampling process, the standard LV model was hampered considerably by the slice thickness (Figs. 2A). Whereas in CSRR, the pixel distribution increased from $140 \times 140 \times 8$ to $280 \times 280 \times 220$.

Consequently, any number of planes could be sampled (Fig. 1B) without being restricted to the orientation of the original LA scanning planes. Reconstruction was vastly improved using CSRR with a clear distinction between the high-contrast blood pool and the relatively low-contrast myocardial tissue (Fig. 2A).

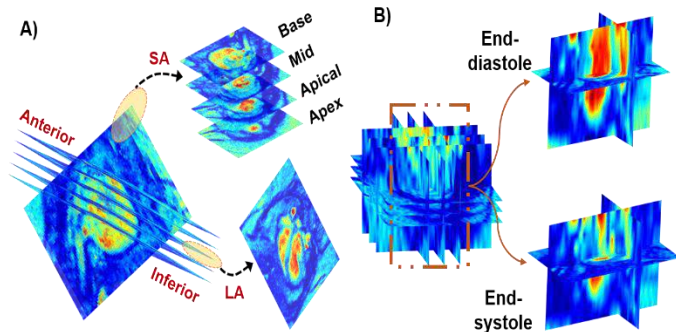


Figure 1: A) Enhanced imaging protocol with 8 SA, 5 orthogonally sampled images B) CSRR of the image stack at end-diastole and end-systole

At end-systole, regional epicardial strains using CSRR showed varying degrees of contraction between the base and the apex, with apical shortening exceeding the other regions. Although qualitative similarity in strain distribution was observed between the two methodologies, there was a significant difference in the peak strains. Specifically, for the standard model, there was a significant presence of positive longitudinal strains despite global LV shortening (Septal; SA stack only, $E_{ZZ} = 0.7342$ vs. CSRR, $E_{ZZ} = 0.4985$. Lateral; SA stack only, $E_{ZZ} = 0.5146$ vs. CSRR $E_{ZZ} = 0.3126$). Also, the regional circumferential shortening seen in CSRR was recapitulated in the conventionally reconstructed model with similar differences in peaks. However, there was an abundance of non-physical transmural strains, which were suppressed by CSRR (Fig. 2B).

DISCUSSION

Standard functional imaging is often limited to 7-9 SA planes with an optional LA or four-chamber view. The resulting pixel set is heavily anisotropic, which impediments accurate strain calculations. The LV exhibits twisting during systolic contraction, resulting in significant ‘through-plane’ deformation with corresponding ‘in-plane’ mechanical adjustments. These deformations translate as ‘out-of-plane’ pixel motions that are not captured by traditional CMR imaging of the LV [4]. We hypothesized that a CSRR-based methodology combining scan planes of varying orientations would considerably reduce pixel spacing, thereby improving strain calculations. The pixel spacing using CSRR was increased to about 25 times the original acquisition. Through this nearly isotropic pixel set, apical and endocardial shortening was captured more accurately, and a majority of myocardial features were preserved. The inadequacy of temporal resolution in standard CMR images results in sharp gradient changes between time points, thereby producing errors in frame registration. A strong correlation was noted between sharp image gradients and the generation of non-physical strains, which necessitate regularization. A by-product of regularizing the image registration process was the underestimation of strains, especially at the tissue-pool interface of the endocardium. In the absence of this regularization, notable variations were observed between the conventionally reconstructed strain representation, with pronounced differences in both the peak values and the patterns. In this study, we presented a novel and comprehensive analysis of 4D myocardial

deformation through the CSRR framework. The framework offers a translational tool that leverages combined CMR acquisitions and tissue classification strategies to improve LV reconstruction with minimal noise and artifacts. A detailed representation of 4D myocardial strains was made possible with such analysis, offering the potential to establish a continuous 4D LV structure-function relationship as a standard practice.

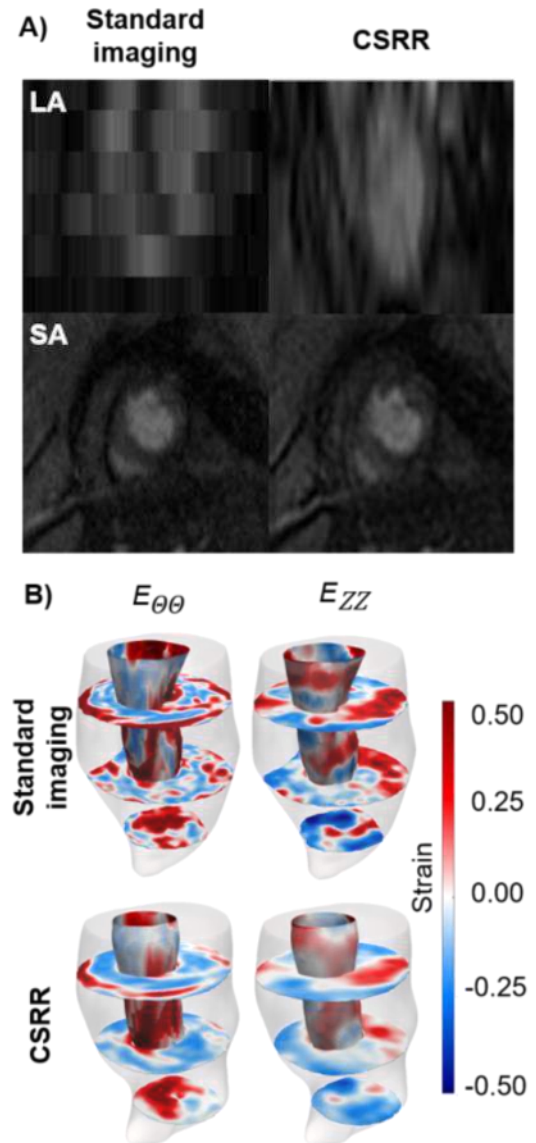


Figure 2: A) Reconstruction of the LA and SA image-planes B) Circumferential ($E_{\theta\theta}$) and longitudinal (E_{zz}) strain calculations

ACKNOWLEDGEMENTS

This work was supported by the National Institutes of Health (K99HL138288 to R.A.).

REFERENCES

- [1] Wehner, G. J. et al. European Heart Journal 41(12), 1249-1257 2020.
- [2] Kalam, K. et al. Heart. 100(21), 1673-1680 2014.
- [3] Vercauteren, T. et al. Neuroimage 45(1), 561-572 2009
- [4] Pedrizzetti, et al. J. of Cardio. Mag. Resonance 18(1), 2016

GROWTH AND REMODELING OF THE PULMONARY ARTERIAL TREE FOR EVOLUTION OF PULMONARY ARTERIAL HYPERTENSION

Jason M. Szafron (1,2,3), Weiguang Yang (1), Jeffrey A. Feinstein (1), Marlene Rabinovitch (1,2,3), Alison L. Marsden (1,2,3)

(1) Department of Pediatrics, Stanford University, Stanford, CA, USA

(2) Cardiovascular Institute, Stanford University, Stanford, CA, USA

(3) Maternal Child Health Research Institute, Stanford University, Stanford, CA, USA

INTRODUCTION

In pulmonary arterial hypertension (PAH), vessels throughout the pulmonary arterial tree alter their geometry and composition in response to hemodynamic and biological stimuli. This remodeling increases pulmonary vascular resistance (PVR), which in turn increases afterload on the right ventricle, leading to heart failure and death [1]. Changes in mechanobiological stimuli alone are sufficient to induce PAH, where increased flow can drive altered endothelial cell behavior in response to increased wall shear stress (WSS) and induce an endothelial-to-mesenchymal transition that narrows distal vessels and contributes to progressive increases in PVR [2]. As such, tracking WSS development in PAH is critical to monitoring disease progress. Yet, WSS is difficult to measure and is typically simulated using modeling approaches from computational fluid dynamics (CFD). Studies tracking WSS changes with disease severity using CFD have shown distinct differences in behavior of large and small caliber vessels, where larger vessels have decreased WSS and smaller vessels have increased WSS [3]. Though these studies are useful in tracking mechanobiological stimuli at single time points, there is a need for simulating disease progression over time for each patient and incorporating both the structural and geometric changes that accompany remodeling to better identify potential interventions. To this end, we have developed a modeling framework using constrained mixture theory growth and remodeling principles combined with a morphometric tree model of the pulmonary arterial tree to simulate vascular evolution in PAH.

METHODS

To simulate growth and remodeling of the vasculature in pulmonary arterial hypertension, we used Strahler diameter-defined morphometric trees [4] to simulate a reduced order model of the mouse pulmonary arterial tree (**Figure 1**). Poiseuille flow conditions were assumed, and resistances were calculated for vessel geometries that were fit to match the total PVR to that of the murine pulmonary tree [5].

Biomechanical behavior of the large pulmonary arteries was taken from biaxial experiments on murine vessels [6]. To simulate loading for the tree, we then found mass fractions and material parameters in a four-fiber family constitutive model for each vessel order that allowed for

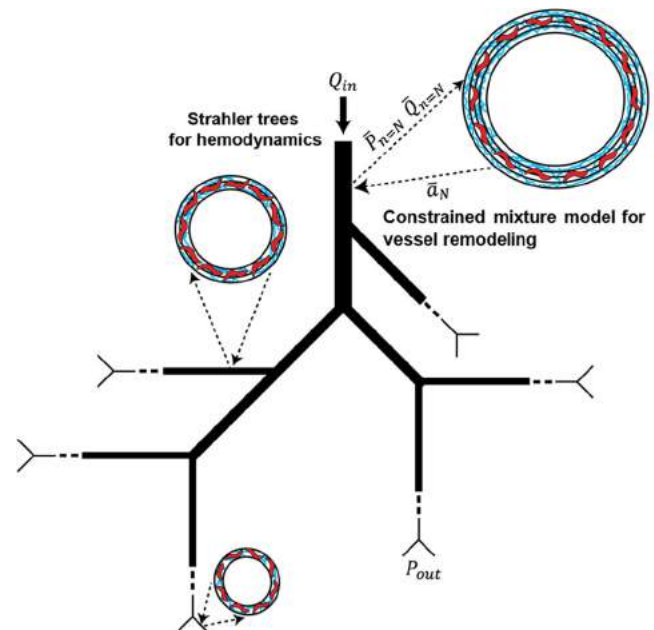


Figure 1: Schematic of the modeling approach for evolution of the pulmonary arterial tree. Strahler diameter-defined morphometric trees were simulated with inlet flow boundary Q_{in} and outlet pressure boundary condition P_{out} . Each order of vessels was represented by a constrained mixture model and remodeled in response to averaged hemodynamics from vessels across the order.

maintenance of the homeostatic vessel diameter when using average pressure loads \bar{P}_n from each order n . A constrained mixture theory growth and remodeling framework was adopted to simulate the adaptation of the vessels to changes in hemodynamic loads and with combinations of maladaptive remodeling stimuli [7]. Average flows \bar{Q}_n and average pressures in each order \bar{P}_n were updated at each time step with solution of the flow equations in the morphometric tree and average radii at each order \bar{a}_n was updated to satisfy the mechanical equilibrium equation with the updated loads. Loads and radius were then iteratively exchanged until convergence, and the model continued to march forward in time. Maladaptive remodeling stimuli were chosen to represent biological processes that have been associated with PAH, and stimuli were added sequentially to understand their net effect on changes in geometry and mechanobiological stimuli that contribute to PAH.

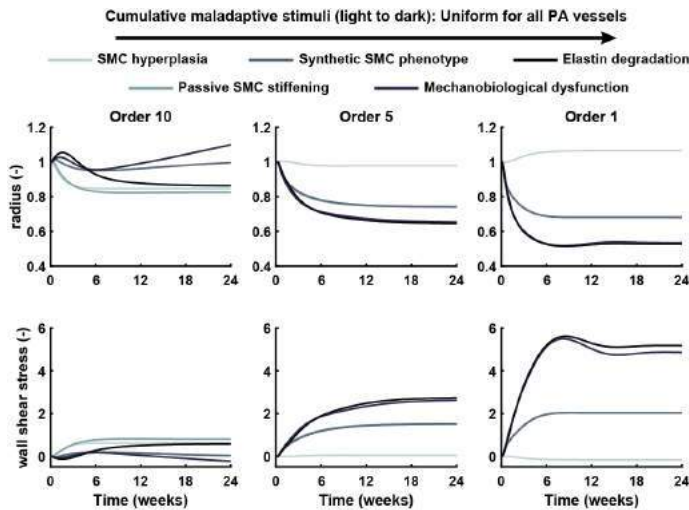


Figure 2: Changes in luminal radius and wall shear stress with maladaptive stimuli driving vascular remodeling. Combinations of stimuli related to multiple biological pathways induced greater dilatation of the proximal vessels and narrowing of the distal vessels as observed in clinical pulmonary arterial hypertension.

RESULTS

With our coupled modeling framework, we simulated the development of PAH in response to several types of cumulative maladaptive remodeling stimuli applied uniformly across the PA tree (**Figure 2**) consisting of: smooth muscle cell (SMC) hyperplasia represented by increased mass density production of SMCs, passive SMC stiffening given by an increase in the material parameter associated with SMC mechanical behavior, conversion to a synthetic SMC phenotype modeled as a decrease in the mass fraction of SMCs contributing to active contraction, mechanobiological dysfunction simulated as a decrease in the gains that mediate production of SMCs and matrix in response to WSS and intramural stress, and elastin degradation modeled as a decrease in elastin mass fraction over time.

With the addition of SMC hyperplasia alone, changes in radius were contrary to those in PAH, where the proximal vessels narrowed, and the distal vessels dilated. Further addition of SMC stiffening allowed for narrowing of both the proximal and distal vessels with more narrowing of the distal vessels and a corresponding greater increase in WSS. Altering the phenotype of SMCs in the modeling framework and decreasing the mechanobiological gains, in combination with the previous stimuli, then led to increases in the proximal vessel radius and greater narrowing of the distal vessels, as is seen moderate and severe

PAH [3]. However, addition of elastin degradation did not further contribute to a PAH-like phenotype, as it caused proximal vessel narrowing and had modest effects on distal vessel narrowing.

For each of these cases, we also simulated the evolving inlet pressure corresponding to the right heart afterload (**Figure 3A**). Each simulated combination of maladaptive stimuli led to increases in pressure, and those simulations with a greater degree of distal narrowing tended to exhibit larger fold increases in pressure. Variation of PVR at the end of the time course with applied changes in active tone from SMCs were performed to illustrate a loss of vasodilatory capacity, which could contribute to long-term disease progression with vasodilator therapy (**Figure 3B**). In the cases with the greatest increases in PVR and pressure, reduction of active tone to zero resulted in less than a 5% decrease in PVR.

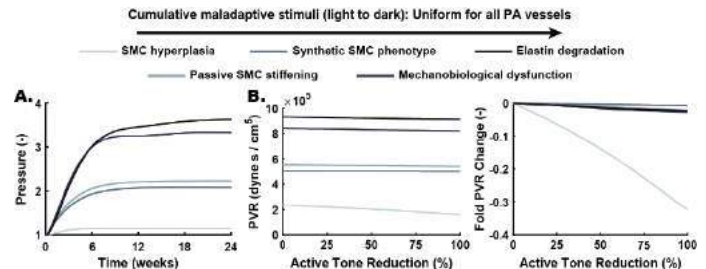


Figure 3: (A) Changes in inlet pressure corresponding to right heart afterload with combinations of maladaptive remodeling stimuli. With additional stimuli, pressure tended to increase indicating more severe disease. (B) Changes in pulmonary vascular resistance (PVR) with simulated decreases in active tone at the end of remodeling. PVR increased with additional maladaptive stimuli and the ability to reduce PVR was lost with maladaptation.

DISCUSSION

PAH is a progressive disease with poor response to current treatments [8]. Computational modeling tools can be used to better understand the mechanisms underlying progression and identify new potential treatments. However, prior modeling approaches lacked the ability to simulate long-term changes in geometry and hemodynamics. In this work, we demonstrate a new framework that incorporates relations for biological mechanisms of maladaptive pulmonary arterial remodeling. Our approach allows for simulation of changes in clinical metrics and includes mechanobiological stimuli that are known to drive adverse changes in pulmonary cell phenotypes. With additional validation, this model could be used to predict the development of PAH in patients and identify novel interventions.

ACKNOWLEDGEMENTS

The authors greatly appreciate funding support from the Parker B. Francis Fellowship Foundation and the Stanford Maternal Child Health Research Institute Pilot Grant Program. This work was supported in part by a training grant from the National Heart, Lung and Blood Institute (1T32HL098049) to the Stanford Cardiovascular Institute.

REFERENCES

- [1] Abman, S.H. et al., *Circulation*, 132:2037-2099, 2015.
- [2] Shinohara, T., et al., *Circulation*, 146:A10270-A10270, 2022.
- [3] Yang, W., et al., *Biomech Model Mechbio*, 18:779-796, 2019.
- [4] Jiang, Z.L., et al., *J Appl Physio*, 76:882-892, 1994.
- [5] Champion, H.C., et al., *Am J Physio*, 278:H8-H15, 2000.
- [6] Ramachandra, A.B., Humphrey, J.D., *J Biomech*, 84: 18-26, 2019.
- [7] Latorre M., et al., *Int J Eng Sci*, 141:35-46, 2019.
- [8] Lajoie, A.C., et al., *Lancet Resp Med*, 4:291-305, 2016.

RAMAN PROBE PREDICTS CARTILAGE FUNCTIONAL MECHANICAL PROPERTIES BETTER THAN OARSI SCORE AND MRI T2* Mapping

Masumeh Kazemi (1), Chenhao Yu (1), Farida Korna (1), Dev Mehrotra (1), Erik Ersland (1), Juncheng Zhang (1), Thomas P. Schaer (2), Julie B. Engiles (2), Mark W. Grinstaff (1), Brian D. Snyder (3), Mads S. Bergholt (4), Michael B. Albro (1)

- (1) College of Engineering, Boston University, Boston, MA, USA
(2) Department of Clinical Studies New Bolton Center, School of Veterinary Medicine University of Pennsylvania, Kennett Square, PA, USA
(3) Department of Orthopedics, Beth Israel Deaconess Medical Center, Boston, MA, USA
(4) Center for Craniofacial & Reversative Biology, King's College London, London, UK

INTRODUCTION

Osteoarthritis (OA) is an incapacitating, chronic disease, characterized by the progressive degradation of articular cartilage. The structure and composition of articular cartilage are optimized for its mechanical performance. It is comprised of water (70-80% of wet weight) and negatively charged sulfated glycosaminoglycan (GAG, 5-15% wet weight) constrained by a fibrous network of type-II collagen (COL, 5-20% wet weight) that provides tribological material properties essential to support applied joint loads and to maintain a nearly frictionless shear interface between articulating joint surfaces. OA initiates with loss of GAG followed by COL network derangement, which increases hydraulic permeability and decreases cartilage stiffness. Promising therapies to treat OA include disease-modifying drugs that mitigate or reverse cartilage degeneration and chondro-regenerative tissue engineering platforms that recapitulate the composition and structure of healthy hyaline cartilage. The development of disease-modifying OA therapies is impeded by a lack of non-destructive clinical assessments of cartilage composition and mechanical properties. Histopathology scoring (OARSI, Mankin grades) serves as an *ex vivo* 'gold standard' for the evaluation of cartilage degeneration and recently has been shown to predict changes to functional tissue properties in early OA [1]. However, these assessments are invasive, destructive, and incompatible with repetitive clinical monitoring. Evidence-based evaluations of the utility of OA therapies should be predicated on measuring biomarkers that reflect OA pathophysiology and portray the structure and composition of regenerated or neo-cartilage repair tissue relevant to its function. Image-based assessments (radiographs and magnetic resonance imaging (MRI; dGEMRIC, T1rho, T2*)) are biased toward late-stage OA pathology and are only moderately correlated with quantitative assessments of the tissue's material properties [2]. MRI measurements of cartilage composition and structure may also be affected by lack of consistency, signal-to-noise ratio (SNR), and insufficient image resolution. Therefore, robust methods capable of

measuring changes in the functional properties of damaged cartilage are required for advancing OA treatment.

Raman spectroscopy is an inelastic optical light scattering technique that can provide a quantitative, point-wise optical fingerprint of a tissue's molecular building blocks (amides, sulfates, carboxylic acids, and hydroxyls), thus allowing recognition of the predominant molecular constituents of articular cartilage: GAG, COL, and H₂O. In our prior work, we developed a Raman arthroscopic needle probe and real-time spectral analysis platform capable of measuring specific compositional biomarkers of hyaline cartilage that reflect the health and function of articular cartilage [3]. In this work, we aim to further advance this platform by investigating the capability of our Raman probe to assess the composition and material properties of cartilage using a unique *ex vivo* early-stage OA model system, consisting of bovine femoral condyles that present with focal chondral lesions, akin to those observed in patients in response to joint trauma. The capability of Raman-derived biomarkers to predict the functional mechanical properties of articular cartilage is compared to histopathological OARSI scoring and compositional T2* MRI mapping.

METHODS

Tissue specimens: Bovine specimens were harvested from medial femoral condyles of twelve skeletally mature bovine knees: six healthy condyles (HC) exhibited no macroscopic degeneration (Outerbridge grade (OB0), and six condyles exhibited a ~Ø15mm focal chondral lesion site (LS; OB2) within the load bearing region, but no macroscopic degeneration (OB0) in the surrounding lesion peripheral sites (LPS). Rectangular osteochondral blocks (~5x5x5mm) were sectioned from the HC (N=37), LS (N=32), and LPS (N=35) regions for analysis. **Raman analysis:** The Raman platform consisted of an NIR diode laser (ex=785nm, 500mW, B&W Tek), fiber-coupled spectrograph (QEPro, Ocean Optics), and needle probe with a 2mm sapphire ball lens [2]. Raman spectra were acquired with the probe lens in gentle contact with

the chondral surface over 30s acquisition time. The spectral fingerprint range (800-1800cm⁻¹) was preprocessed and subjected to a multivariate least-squares linear regression model to calculate the relative contribution of the predominant cartilage constituents (GAG, COL, and H₂O) to the composite cartilage Raman spectra (Equation 1).

$$\text{Cartilage spectra} = \text{GAG}_{\text{score}} * (\text{GAG}_{\text{REF}}) + \text{COL}_{\text{score}} * (\text{COL}_{\text{REF}}) + \text{H}_2\text{O}_{\text{score}} * (\text{H}_2\text{O}_{\text{REF}}) \quad (1)$$

where GAG_{REF}, COL_{REF}, and H₂O_{REF} are the component spectra of purified reference chemicals for each ECM constituent. In the high wavenumber region (2700-3800cm⁻¹), the area under the OH peak (OH area) represents tissue hydration [4]. **Property measurements:** The elastic modulus of the chondral layer for each tissue block was derived by indentation using a Ø3mm spherical indenter and the slope of the loading curve (Hertzian). The central Ø3mm chondral core of each block was sub-punched and GAG content was determined by DMMB assay. **OARSI histological scores:** The OARSI scores (grade×stage) were assessed by a board-certified pathologist on Saf O sections for a random subset of tissues from all analyzed regions (N=30). **MRI measurements:** MRI examination was performed using a 9.4T Bruker BioSpec MRI scanner to obtain T2* relaxation times for an additional 2 healthy and 2 lesion-afflicted condyles. Condyles were subsequently sectioned into blocks and subjected to Raman and mechanical analysis (N=42 blocks total). The imaging protocol included 3D fat-suppressed with gradient echo (GRE) sequences followed by TR/TE=29.74/2.94 ms, flip angle=15, FOV=50x50mm, matrix=250×250, spatial resolution=0.2x0.2mm, and slice thickness=1mm utilizing six echoes for the mono-exponential fit. T2* relaxation times were mapped for the full cartilage thickness and coregistered with the position of each sectioned block. T2* was also measured for the topmost 200µm of cartilage to maintain consistency with the ROI achieved via depth of tissue sampling from the Raman probe [3].

RESULTS

The multivariate regression model accounted for 91±1.5% of the variation in composite Raman spectra. Compared to healthy bovine specimens (HC), tissue from the specimen with lesions was degraded as evidenced by significantly reduced GAG content and elastic modulus within both LS (OB2) and LPS (OB0) (p<0.001; Fig 1A-C).

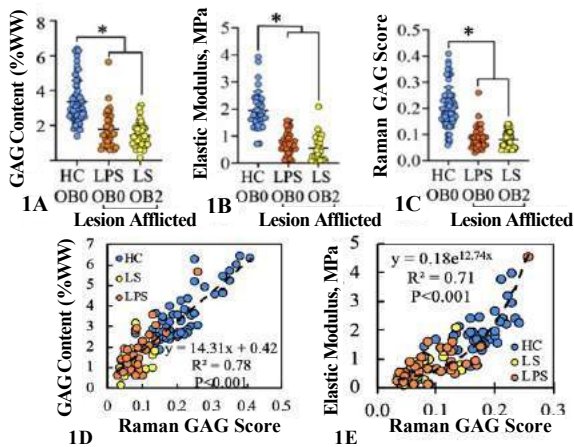


Fig 1: (A) GAG content, (B) elastic modulus, and (C) Raman GAG score for healthy cartilage (HC), lesion sites (LS), and lesion peripheral sites (LPS) of cartilage blocks. Raman GAG score vs (D) assay-measured GAG content and (E) elastic modulus, *p<0.001.

Raman GAG scores predicted 78% of the variation in GAG content and 71% of the variation in elastic modulus (p<0.001; Fig.1D&E). Raman GAG scores accounted for a significantly greater percentage of variation in modulus than OARSI (78% vs 54%; p<0.05; Fig 2A&B). Similarly, Raman biomarkers accounted for a significantly greater percentage of variation in modulus than T2* relaxation times. (62% vs

33%; p<0.001; Fig 3A&C). The utilization of a linear set of multiple Raman biomarkers (GAG score and OH area) improved predictions of modulus (62% to 67%, Fig 3D).

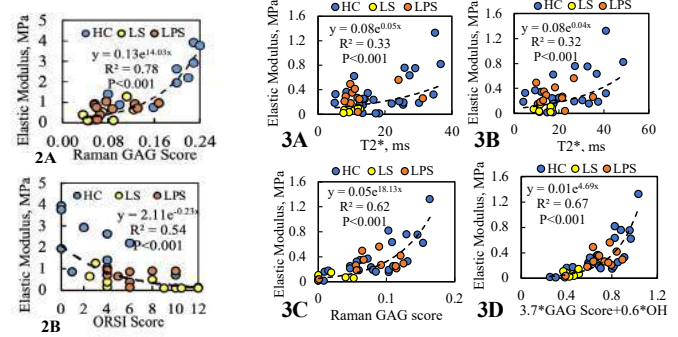


Fig 2: (A) Raman GAG score vs elastic modulus for cartilage blocks. (B) OARSI score vs elastic modulus for cartilage blocks.

Fig 3: Elastic modulus vs measured T2* relaxation time for (A) full cartilage thickness and (B) topmost 200 µm of cartilage. Elastic modulus vs (C) Raman GAG score and (D) linear combination of GAG score and OH area.

DISCUSSION

GAG “scores” derived from multivariate regression spectral analysis represent the relative contribution of GAG to the composite Raman spectra of cartilage using the Raman probe platform. The GAG score accounted for 78% of the variation in the measured GAG composition and predicted 71% of the variation in the elastic modulus of tissue over a range of cartilage morphologies, including intact (OB0) and focal chondral lesions (OB2). OARSI histopathology scoring, the gold standard for *ex vivo* assessment of cartilage pathology, only predicted 54% of cartilage mechanical properties after injury. Compositional T2* MRI assessments, the state-of-the-art for clinical diagnostics of cartilage, only predicted 33% of properties.

Notably, Raman GAG scores revealed depleted GAG content that predicted cartilage softening where there were no visual macroscopic lesions. As such, Raman spectra can arthroscopically “optically biopsy” cartilage and quantify the relative contribution of key biochemical constituents that serve as biomarkers for determining cartilage composition, structure, and material properties in normal and pathological tissue, and in response to chondroprotective and/or chondroregenerative treatments.

This work supports the use of Raman spectroscopy as a research platform to objectively assess the efficacy of emerging OA therapies across the hierarchy of *in vitro*, *in vivo*, and clinical model systems. Raman arthroscopy can also serve as a transformative clinical platform for discrimination of healthy versus degraded tissue, diagnosing early OA, and guiding clinical treatment courses. This study shows that Raman arthroscopy, a low-cost, minimally invasive, fast, and portable diagnostic platform, has the potential to complement other state-of-the-art and emerging OA diagnostic platforms, such as compositional MRI, in portraying changes in cartilage composition, structure, and material properties.

ACKNOWLEDGEMENTS

This work is supported by the NIH (AR081393), Arthritis Foundation, Musculoskeletal Transplant Foundation, and Boston University Materials Science & Engineering Innovation Award.

REFERENCES

[1] Waldstein+ 2016, JOR., 34 (1). [2] Li X+ 2011, Magn Res Imag. 29(3). [3] Kroupa+ 2021, JOR., 40(6). [4] Unal+ 2019, OA&C, 27(2).

PATIENT-SPECIFIC PULMONARY HYPERTENSION SIMULATIONS IN SICKLE CELL DISEASE PATIENTS, A VISCOSITY MODEL STUDY

Fatemeh. Bahmani (1), Alex Vahdati (1), Veeranna Maddipati (2), Stephanie M. George (1)

(1) Department of Engineering, East Carolina University, Greenville, NC, USA

(2) Internal Medicine, Brody School of Medicine, East Carolina University, Greenville, NC, USA

INTRODUCTION

Sickle cell disease (SCD) is a genetic blood disorder caused by an amino acid substitution in the beta globin chain of the hemoglobin. The abnormal molecule hemoglobin S formed by this mutation polymerizes when deoxygenated. The polymerization of HbS is key to the formation of sickled shape red blood cells. Sickle cell disease can lead to hemolysis, chronic inflammations, pain, infections, cardiovascular complications, chronic anemia, vaso-occlusion and increased mortality. Pulmonary hypertension (PH) is among the complications caused by sickle cell disease. [1] Pulmonary hypertension is defined as mean pulmonary artery pressure ≥ 20 mmHg. Pulmonary hypertension is divided into 5 different categories and the pulmonary hypertension due to chronic hemolytic anemia including sickle cell disease is categorized in group 5 (miscellaneous effects) in the updated classification by World Symposium on Pulmonary Hypertension (WSPH). [2, 3]

Pulmonary hypertension has a prevalence of 10% in patients with sickle cell disease and sickle cell disease patients with pulmonary hypertension are at higher risk of morbidity compared to patients who do not have pulmonary hypertension. [4]

Although non-invasive methods such as echocardiography and clinical imaging via magnetic resonance (MR) and computed tomography (CT) are used as techniques to diagnose pulmonary hypertension, physics-based models could be used as powerful tools to quantify the hemodynamics and vasculature mechanics of pulmonary artery and better understand the mechanism of disease progression.

Due to increased hemolysis, whole blood viscosity in sickle cell disease patients is lower compared to normal. [5] Fluid flow analysis of pulmonary hypertension is addressed by several studies (Tang et al. and Kheyfets et al.). Kong et al., Zambrano et al. and Pearce et al. have performed fluid structure interaction simulation of pulmonary hypertension. Rabidou et al. have studied pulmonary hypertension in sickle cell disease but the impact of altered blood viscosity on hemodynamics in sickle cell disease has not been explored. In this study

we have used computational fluid dynamics to study the effect of altered blood viscosity in sickle cell disease patients. The CFD results are then compared with the results from fluid structure interaction simulations to assess improvement of the results. Wall mechanical parameters are also predicted from FSI simulations.

METHODS

Of the four subjects' data included in this study, one (Subject 1) did not have pulmonary hypertension, a control subject, and the other three subjects (2, 3, 4) had pulmonary hypertension. Subjects 1 and 2 had sickle cell disease, the others did not. MR images were gathered on a Siemens Espree (subject 1) 1.5 T or Siemens Aera 1.5 T model MR scanner (subjects 2, 3, and 4). The patient specific pulmonary artery geometries were reconstructed using the segmentation techniques in Mimics 20.0 (Materialise, Inc.; Plymouth, MI) and further postprocessed in SolidWorks 2017 (Dassault Systems; Waltham, MA). The solid models were then imported into ANSYS Workbench (ANSYS Inc.; Canonsburg, PA) where the arterial wall thickness was added in Spaceclaim and the computational mesh was generated. Ansys Fluent and transient structural modules were used to perform computational fluid dynamics and coupled fluid-structure interaction simulations. Geometry and mesh sizes for all four subjects are listed in Table (1). MRI data from patient and control subjects indicate larger diameter of main pulmonary artery in subjects who have pulmonary hypertension.

Table 1: Geometry and mesh properties of subjects 1-4

Subject	Diameter (cm)	Area (cm ²)	Fluid mesh no. of elements	Fluid mesh size (mm)	Structural mesh No. of elements	Structural mesh size (mm)
1	2.69	5.70	1270974	0.35	155190	0.65
2	4.03	12.76	1023147	0.7	211049	1
3	3.62	10.29	1234915	0.5	164041	0.9
4	3.58	10.06	1238648	0.5	164651	0.9

Figure (1) shows the velocity waveforms used as the inlet boundary conditions for subjects 1-4. Also as shown in Figure (1) measured volumetric flow rate is lower in PH subjects.

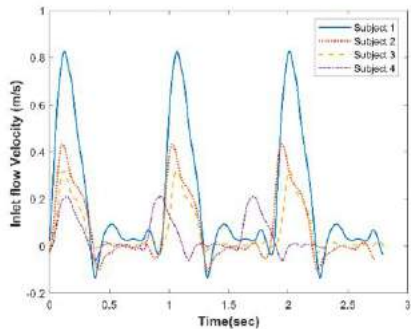


Figure 1: Inlet velocity waveforms for subjects 1-4

CFD SIMULATION RESULTS

Results discussed in this section are from CFD simulations using the rigid wall assumption. Blood density was taken to be 1060 kg/m3. Contours of wall shear stress are presented in Figure (2) for subjects 1 and 2.

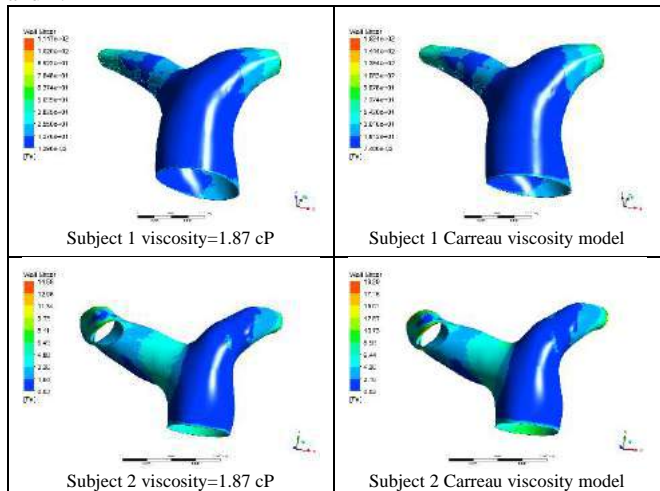


Figure 2: Wall shear stress contours in main, left and right pulmonary arteries at peak systole of 3rd cycle, CFD simulations

Values of maximum wall shear stress (WSS) for subjects 1-4 are shown in Table (2). In these simulations constant viscosity of 1.87 cP is assumed for SCD subjects (1, 2) and 3.5 cP for non-SCD subjects (3, 4). Simulations with Carreau viscosity model were also carried out for all four subjects to compare with constant viscosity results.

Table 2: Maximum WSS of subjects 1-4 for two viscosity models at peak systole of 3rd cycle, CFD simulations

Subjects	Constant viscosity	Maximum WSS (Pa) at Constant viscosity	Max WSS (Pa) at Carreau viscosity model
1 (SCD)	1.87 cP	114.714	162.438
2 (SCD/PH)	1.87 cP	14.578	19.294
3 (PH)	3.5 cP	23.913	23.356
4 (PH)	3.5 cP	13.214	13.228

Wall shear stress values obtained using Carreau viscosity model in sickle cell disease subjects are higher than constant viscosity model but closely match the values in subjects without sickle cell disease.

Maximum wall shear stress is substantially higher is subject 1 who does not have pulmonary hypertension compared to other subjects.

FSI SIMULATION RESULTS

In the FSI simulations blood viscosity was taken to be 1.87 cP for sickle cell disease subjects (1, 2) and Carreau viscosity model was used for subjects without sickle cell disease (3,4). The arterial wall was assumed to behave as a linear elastic solid with density of 1200 kg/m3, elastic modulus of 2 MPa and Poisson ratio of 0.48. [6]

Results are presented here for FSI simulations of subjects 1-4. Data in Table (3) is a summary of fluid flow and structural analysis results as obtained from FSI simulations for subjects 1-4.

Table 3: Results from FSI simulations of subjects 1-4 at peak systole of 3rd cycle

Subjects	Viscosity	Maximum WSS (Pa)	Maximum Total Deformation (mm)	Maximum Stress (MPa)
1 (SCD)	1.87 cP	116.105	1.8252	0.11494
2 (SCD/PH)	1.87 cP	12.7068	0.97273	0.035268
3 (PH)	Carreau	24.2988	0.23	0.014797
4 (PH)	Carreau	13.364	0.1235	0.0077651

Subject 1 who does not have PH has smallest main pulmonary artery diameter and highest inlet flow rate. Simulations results show largest value of wall shear stress and maximum total deformation and stress for subject 1. Subject 2 suffers from both SCD and PH and has the largest diameter. Maximum inlet flow rate of this subject is approximately half of that of subject 1. Therefore subject 2 is experiencing lowest value of wall shear stress among four subjects. Total deformation for this subject is about half of subject 1 and maximum stress is also less than half of subject 1. Subjects 3 and 4 arteries are almost of the same size and inlet flow rate of subject 3 is about 1.5 times of subject 4. So higher values of wall shear stress, total deformation and mechanical stress are observed in subject 3 compared to subject 4.

DISCUSSION

MRI data reveals larger main pulmonary artery diameter and lower volumetric flow rate in PH subjects. Our results confirm lower values of WSS reported in PH subjects [7]. According to CFD simulations, constant viscosity results are closer to Carreau viscosity model results in non-SCD subjects compared to SCD subjects. Maximum WSS values from FSI and CFD simulations are in good agreement using the same viscosity model for each subject. So CFD simulations with much lower computational time yield good approximation of the coupled fluid-structure interaction simulation. The FSI simulations could be further improved by using a more accurate value for the arterial wall modulus of elasticity of subject 1 who does not have pulmonary hypertension.

ACKNOWLEDGEMENTS

This work was supported by East Carolina University’s Department of Engineering. Special thanks to Dr. Bogdan Marcu, Dr. John Cahill, and Jake Rabidou.

REFERENCES

- [1] Stuart, Marie J. et al, The Lancet 364.9442, 1343-1360, 2004.
- [2] Simonneau, Gérald, et al., European Respiratory Journal 53.1, 2019.
- [3] Wood, Katherine C et al., Heart 106.8, 562-568, 2020.
- [4] Parent, Florence, et al., N Engl J Med, 365.1 (2011): 44-53.
- [5] Prohaska C. et al, Adv. In PH, vol. 46, pp. 46-53, 2021.
- [6] Zambrano, Byron A et al., Journal of biomechanics 68: 84-92, 2018.
- [7] Tang, Beverly T et al., Pulmonary circulation 2.4: 470-476, 2012.

RAMAN SPECTROSCOPIC PROBE PREDICTS THE COMPOSITION AND FUNCTIONAL MECHANICAL PROPERTIES OF THE INTERVERTEBRAL DISC

Chenhao Yu (1), Masumeh Kazemi (1), Farida Korna (1), Erik E. Ersland (1),
Mark W. Grinstaff (1), Thomas P. Schaer (2), Mads S. Bergholt (3), Edward J. Vresilovic (4),
Brian D. Snyder (5), Micheal B. Albro (1)

- (1) College of Engineering, Boston University, Boston, MA, USA
(2) Department of Clinical Studies New Bolton Center, School of Veterinary Medicine University of Pennsylvania, Kennett Square, PA, USA
(3) Center for Craniofacial & Reversative Biology, King's College London, London, UK
(4) Department of Biomedical Engineering, University of Delaware, Newark, DE, USA
(5) Department of Orthopedics, Beth Israel Deaconess Medical Center, Boston, MA, USA

INTRODUCTION

The intervertebral disc is responsible for maintaining and distributing large multiaxial spinal loads. The structure and composition of the healthy IVD are optimized for this mechanical performance. The IVD is comprised of a collagen (COL)-rich, fibrous outer annulus fibrosus (AF) ring that surrounds a glycosaminoglycan (GAG)-rich, gel-like nucleus pulposus (NP). The osmotic response to the anionic sulfated GAG of the NP, in conjunction with the restraining tensile properties of the AF, allow the multiaxial spinal loads to be distributed through pressurization of the interstitial fluid in the NP extracellular matrix (ECM). In response to aging and injury, the IVD undergoes detrimental changes to its composition and structure. Notably characterized by a significant loss of GAG and consequently pressurization of the NP which leads to structural breakdown in the AF as the loading is altered from predominantly tension to compression within the AF.

As there is known association between disc degeneration and low back pain, the leading cause of years lived with disability in the US and around the world [1], there are emerging pharmacological and biomaterial therapies aimed at rescuing the composition and material properties of the IVD to restore its mechanical function. However, the ability to uniformly assess the efficacy of treatments that preserve and/or regenerate the IVD is burdened by a lack of standardized biomarkers that can be applied across the spectrum of *in vitro*, *in vivo* and clinical testing platforms. Conventional biochemical and histological assays for composition are destructive, obviating repeated measures and clinical assessment.

Raman spectroscopy is an inelastic light scattering technique that provides a non-destructive, quantitative, optical fingerprint of the molecular building blocks of key molecular constituents in the ECM of articular cartilage: GAG, COL, and H₂O. We recently demonstrated the capability of a Raman spectroscopic to perform high precision assessments of the composition of articular cartilage both *in vitro* and *in vivo* with extremely high correlation to the articular cartilage mechanical properties [2,3].

In the current study, we examine the capability of our Raman spectroscopy to assess the composition, as well as its correlation to mechanical properties, for IVD specimens in health and disease. Assessments are performed using an *in vitro* model system of isolated bovine IVDs subjected to enzymatic degenerative treatment to model compositional changes that are manifest in IVD degeneration.

METHODS

Twenty seven IVDs were isolated from six skeletally mature bovine oxtails and frozen until testing. The cartilage end plate was excised exposing the NP and AF. For an initial batch of 15 disks, Raman measures initially were performed on the center of the NP and at three positions within the AF to differentiate between the spectral properties of these tissue regions. These IVDs were subsequently subjected to an enzymatic degeneration treatment, consisting of incubation in PBS supplemented with 2mg/mL trypsin at 21°C. To prevent IVD swelling during digestion treatment [4], IVDs were confined between two meshed acrylic plates. A polymer filter was inserted used between the IVD and meshed plate to inhibit tissue herniation into mesh holes (Fig 1).

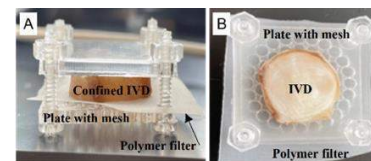


Fig 1. (A) Side view of IVD which is confined between two acrylic plates to restrict swelling during enzyme treatment regimens. (B) Top view of IVD with a polymer filter between IVD and mesh plate to inhibit tissue herniation into mesh holes.

IVDs were subjected to trypsin exposure for 0, 10, or 21 hours (N=5 IVDs per time point). Subsequently, each disk was subjected to

Raman probe analysis in the NP, which was subsequently axially cored via a Ø7mm biopsy punch and subjected to confined compression testing for the aggregate modulus. Mechanical testing consisted of three successive ramps of 5% applied strain (0.5µm/s), followed by 2 hour stress relaxation periods. An additional batch of twelve IVDs were subjected to trypsin exposure for 0 (N=8), 10 (N=2), or 21 (N=2) hours, after which, the NP was cored and subjected to biochemical analysis for water content (gravimetrically) and GAG content (DMMB assay).

Raman analysis: The Raman probe consisted of a NIR diode laser (ex=785nm, 500mW, B&W Tek), fiber-coupled spectrograph (QEPro, Ocean Optics), and needle probe with a 2mm sapphire ball lens [2]. Raman spectra were acquired with the probe lens in gentle contact with the disk surface over a 30s acquisition time. The spectral fingerprint range (800-1800cm⁻¹) was preprocessed and subjected to a multivariate least-squares linear regression model to decompose the Raman spectra to calculate the relative contribution of the predominant cartilage constituents (GAG, COL, and H₂O) to the composite cartilage Raman spectra (Equation 1).

$$\text{Cartilage}_{\text{spectra}} = \text{GAG}_{\text{SCORE}} * (\text{GAG}_{\text{REF}}) + \text{COL}_{\text{SCORE}} * (\text{COL}_{\text{REF}}) + \text{H}_2\text{O}_{\text{SCORE}} * (\text{H}_2\text{O}_{\text{REF}}). \quad (1)$$

where GAG_{REF}, COL_{REF}, and H₂O_{REF} are the component spectra of purified reference chemicals for each ECM constituent [2].

RESULTS

The cumulative spectral contribution of the extracellular matrix constituents by multivariate regression accounted for 94% of the variation in the IVD composite spectra (Fig.2B). Raman-derived biomarkers reflected the biochemical composition of the IVD, as marked by higher Raman GAG and H₂O scores in the NP, relative to the AF (Fig 2D&E). In response to trypsin exposure, NP regions IVDs exhibited a trend of decreased Raman GAG score with digestion time (Fig 3A). For these specimens, Raman GAG score predicted 60% of the variation in aggregate modulus (Fig 3B, p<0.001). For the second experiment of digested IVDs, the NP further exhibited a trend of increased Raman H₂O score with digestion time (Fig 3D). For these specimens, Raman GAG score predicted 80% of the variation in the assay-measured NP GAG content (Fig 3E) and 89% of the variation in the NP H₂O content (Fig 3F).

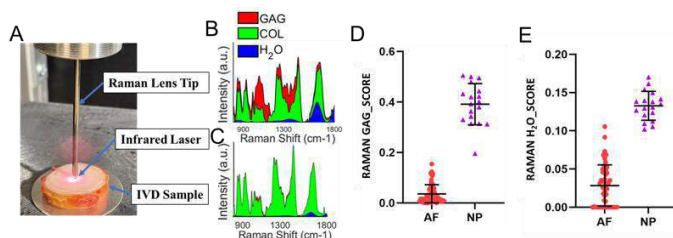


Fig 2: (A) Raman probe in contact with IVD. Representative 2D stacked area plot of contribution of GAG, COL, and H₂O to IVD Raman spectra in (B) NP and (C) AF. (D) Raman GAG score and (E) H₂O score in NP and AF.

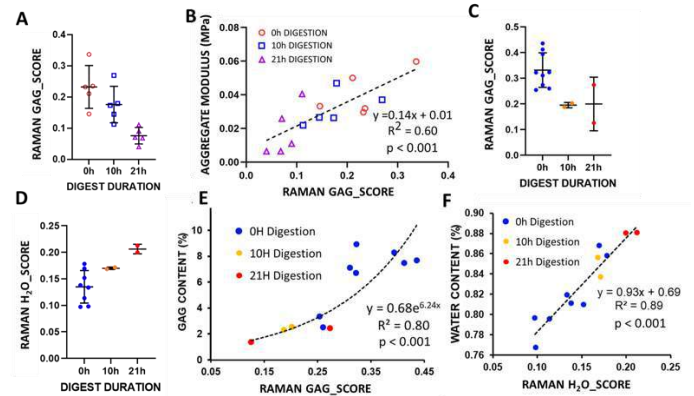


Fig 3: (A) Raman GAG score with trypsin digestion. (B) Correlation of Raman GAG score vs aggregate modulus. (C) Raman GAG score, and (D) Raman water score with trypsin digestion. Correlation of (E) Raman GAG score vs GAG content, and (F) Raman H₂O score vs H₂O content.

DISCUSSION

Results establish the capability of our Raman probe to achieve non-destructive measures of the composition and mechanical properties of IVD tissue specimens. Raman assessments are predicated on a spectral analysis that yields ECM-specific biomarker scores, which reflect the contribution of ECM constituents to underlying acquired Raman spectra. The Raman GAG score accounted for 80% of the variation in the assay measured GAG content and 60% of the variation in the aggregate modulus of the NP. The Raman H₂O score accounted for 89% of the variation in the measured water content. The ability of Raman analysis to faithfully characterize IVD tissue composition was further supported by differential analysis of NP and AF tissue regions, whereby Raman biomarkers depict the GAG and water rich composition of the NP in contrast to the collagen-rich makeup of the AF. These measures support the use of benchtop Raman probes to serve as a novel research tool for rapid, non-destructive, repeated-measure assessments of IVD composition and material properties. Here, Raman can serve as a standardized objective measure of IVD degeneration and treatment response across a heirarchy of preclinical model systems, spanning from *in vitro* explant tissue studies to *in vivo* animal investigations, thus helping to guide new therapies into the clinic.

ACKNOWLEDGEMENTS: This work is supported by the NIH (AR081393), Arthritis Foundation, Musculoskeletal Transplant Foundation, and Boston University Materials Science & Engineering Innovation Award.

References

[1] Wu et al. Ann Trans Med 2020, 8(6): 299-313. [2] Kroupa et al. J Orth Res 2022, 40(6): 1338-48. [3] Jensen et al. Optics Letters 2020, 45(10): 2890-3. [4] Urban et al. Connect Tissue Res 1981, 9(1): 1-10.

LATE TRIGGERING OF TAGGED MRI FOR MEASUREMENT OF IN VIVO BRAIN DEFORMATION DURING HEAD ROTATION

Yuan-Chiao Lu (1), Andy Knutsen (1), Ahmed Alshareef (1), Wen-Tung Wang (2), Joy Mojumder (2), Jerry L. Prince (3), Philip Bayly (4), John A. Butman (2), Dzung L. Pham (2,5)

(1) Center for Neuroscience and Regenerative Medicine, Henry M Jackson Foundation for the Advancement of Military Medicine, Bethesda, MD, USA

(2) Clinical Center, National Institutes of Health, Bethesda, MD, USA

(3) Electrical and Computer Engineering, Johns Hopkins University, Baltimore, MD, USA

(4) Mechanical Engineering and Materials Science, Washington University in St. Louis, MO, USA

(5) Radiology and Radiological Sciences, Uniformed Services University, Bethesda, MD, USA

INTRODUCTION

Tagged magnetic resonance imaging (MRI), a noninvasive approach for quantifying motion *in vivo*, has been previously applied to evaluate brain deformation in live human subjects during head rotation at low accelerations [1,2]. This approach uses a custom device designed to support and constrain the head motion of a human subject with an MRI scanner, facilitating the acquisition of repeated motions to build up the image data (Fig. 1a). Releasing a latch initiates a passive head rotation about the inferior-superior axis towards the left shoulder [2] (Fig. 2a). A rapid deceleration is caused by a padded stop after rotating about 32 degrees.

Two different approaches have previously been proposed to trigger the MRI tagging pulse and initiation of the scan acquisition. Standard triggering applies the tags and acquires the scan when the head rotation is initiated [1]. This approach suffers from inconsistent data due to its high sensitivity to variations in head kinematics. Because tagged MRI can require over 124 repetitions of the head rotation to obtain 3-dimensional (3D) data [2], such variations are highly likely to occur. To remedy this problem, a double trigger (DT) approach has been proposed [2], that applies tag lines when the motion is initiated, but only begins to acquire images near the end of the rotation. This approach has the advantage of realigning the data just before impact, increasing robustness to variations in the head kinematics. In this work, we propose a late trigger (LT) approach, which triggers both the tagging and acquisition near the end of the head rotation. An advantage of this approach over DT is that tag fading [3] is potentially reduced since the tag application is delayed. In addition, a limitation in the tagging scanner software limits the acquisition window (the duration of the scan following acquisition) to be equal to the time between the tagging trigger and the scan trigger when they are not equal. The LT does not suffer from this limitation, allowing for the acquisition of longer time histories (~2x time range) to characterize the brain deformation.

METHOD

MRI scanning was performed on a 3T Siemens mMR Biograph. To evaluate and optimize the tagged MRI acquisition, a gel phantom was used in lieu of the human subject. A homogenous phantom of Sylgard 527 silicone dielectric gel was fabricated with a 1:1.25 base:catalyst ratio (645 grams and 805 grams, correspondingly) [4]. The cylindrical gel-container was firmly fixed to the device. The angular position for each rotation was measured in real-time by an angular position sensor [2]. The LT applied a single trigger to initiate the SPAMM tagging acquisition at 25 degrees (impact is at 32 degrees). We first applied 8 rotations for each tag line direction, repeated twice. Secondly, we applied 4 rotations per tag line direction at reduced temporal resolution. For all phantom scans, images with two orthogonal tag line directions for measuring x and y displacements were acquired in an axial slice at the middle of the gel (Fig. 1b and 1c). Motion was tracked between image frames using harmonic phase (HARP) analysis with the shortest-path refinement algorithm [5]. Lagrangian strain tensors were computed from the displacement vectors.

Four healthy male adults (age: 38.8 ± 10.3 years) with no traumatic brain injury history were recruited (2 adults using DT with 4 rotations per tag line direction, and 2 adults using LT with 2 rotations per tag line direction). Note that the reduced number of rotations using LT was performed to increase subject comfort by reducing the number of phase encodes (PE) from 24 to 16. A third tag line direction on the sagittal plane was added in human scans to investigate the 3D motion, tracked using the HARP-FE method [6] (Fig. 2b-d).

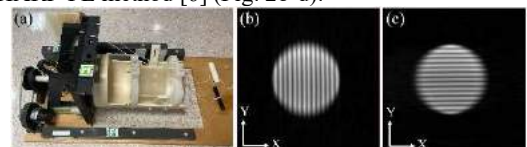


Figure 1: (a) The head rotation device; (b&c) Axial plane with anterior-posterior and right-left tag lines of the gel phantom.

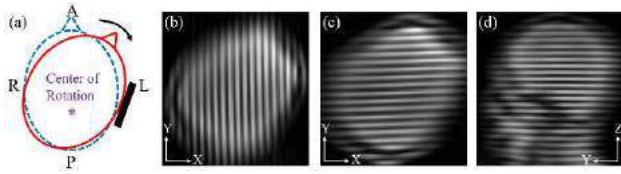


Figure 2: (a) Schematic of head at rest (dotted blue line) and stop (solid red line) positions; (b&c) Axial plane with anterior-posterior and right-left tagging lines of a subject; (d) Sagittal plane with anterior-posterior tagging lines of a subject.

RESULTS

The peak angular acceleration was $282.3 \pm 5.8 \text{ rad/s}^2$ ($N=80$ rotations) for the gel phantom and $236.3 \pm 75.2 \text{ rad/s}^2$ for the human subjects ($N=372$ rotations). In-plane maximum principal strain (E_1), maximum shear strain (G_{\max}), and the area fraction (AF) of E_1 greater than 0.02 were computed for the gel phantom (Fig. 3-5) and the human brain (Fig. 6-7). The E_1 maps of 5 time points around peak E_1 values of gel phantom with 8 rotations for each tag line direction were illustrated in Fig. 3. The repeatability test showed that the differences of the peak 95th percentile E_1 and G_{\max} between every two repeated scans for DT and LT were less than 5% in the first 150 minutes of data acquisition, while the differences of peak AF were less than 3%, indicating high reproducibility of the experiment (Fig. 4). When using 4 rotations, the differences of the measurements between DT and LT also showed a good match (Fig. 5). However, due to the lower stiffness of the phantom compared to human brain, this resulted in a somewhat under sampled measurement.

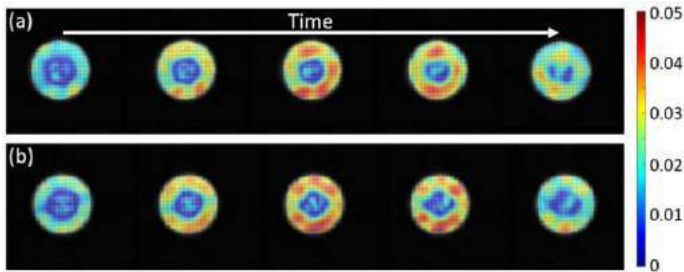


Figure 3: E_1 maps of 5 time points during the time of impact for gel phantom with 8 rotations for each tag line direction: (a) DT with 24 PE; (b) LT with 24 PE.

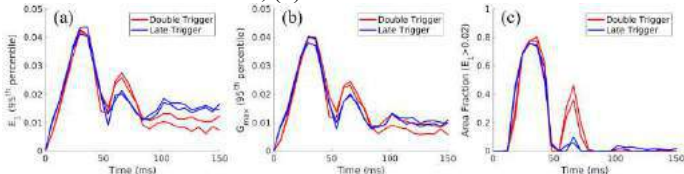


Figure 4: Gel phantom with 8 rotations for each tag line direction: (a) E_1 (95th %ile); (b) G_{\max} (95th %ile); (c) AF of $E_1 > 0.02$. TR = 6 ms.

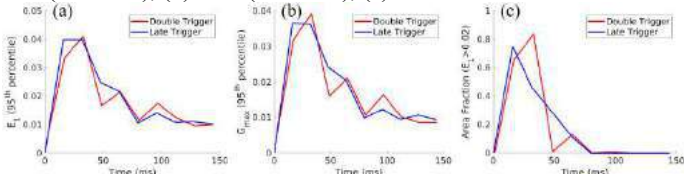


Figure 5: Gel phantom with 4 rotations for each tag line direction: (a) E_1 (95th %ile); (b) G_{\max} (95th %ile); (c) AF of $E_1 > 0.02$. TR = 15.96 ms.

For a subject scanned using DT, a total of 124 rotations was needed, while for a subject scanned using LT and fewer PE required 62 rotations. The temporal resolution was 18.06 ms for DT scans and was 19.52 ms for LT scans. Distributions of in-plane E_1 over time of one

axial image are shown in Fig. 6. Time histories of E_1 , G_{\max} , and volume fraction (VF) had similar patterns within 50 ms during the time of impact, indicating the feasibility and reproducibility of the LT with 16 PE approach vs. DT with 24 PE (Fig. 7).

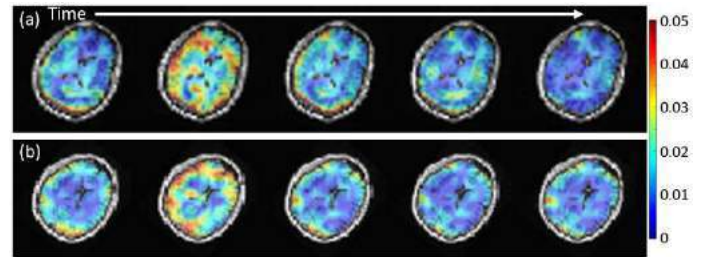


Figure 6: E_1 maps over time of 2 different human subjects: (a) DT with 24 PE (124 rotations per subject); (c) LT with 16 PE (62 rotations per subject). The second frame corresponds to the impact time.

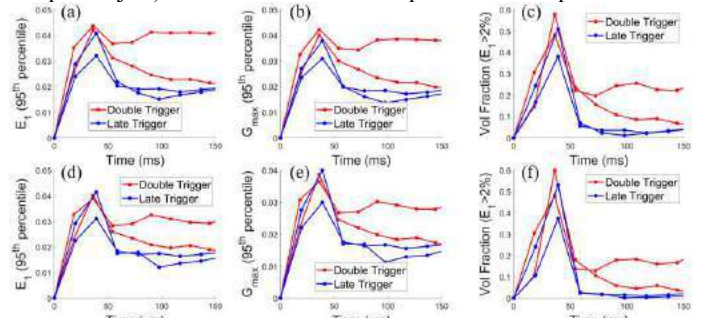


Figure 7: Human brain response in 4 different subjects: (a) E_1 (95th %ile); (b) G_{\max} (95th %ile); (c) VF of $E_1 > 0.02$. Top row: cortical gray matter. Bottom row: white matter. Each line represents one subject.

DISCUSSION

We evaluated a new acquisition approach using LT, which provided comparable results vs. DT in phantom experiments. The LT approach was successfully applied in human subjects in combination with a reduced number of rotations. The reduced rotations could save data acquisition time and reduce the fatigue of repeated neck rotation during MR scans. Lower residual strains following impact were visible, potentially a result of reduced tag fading and lower number of rotations. One limitation is that when using reduced number of rotations, temporal resolution was also slightly reduced. Investigation of strain patterns of these approaches on the same subjects and additional optimization of MR sequence parameters merit further study.

ACKNOWLEDGEMENTS

This work was partially supported by grant NIH U01 NS112120, the Department of Defense in the Center for Neuroscience and Regenerative Medicine, and the intramural research program of the NIH Clinical Center. The opinions and assertions expressed herein are those of the authors and do not reflect the official policy or position of the Uniformed Services University of the Health Sciences or the Department of Defense.

REFERENCES

- [1] Bayly, P et al., J. Neurotrauma, 22: 845-56, 2005.
- [2] Knutsen, A et al., J. Biomechanics, 47: 3475-81, 2014.
- [3] Axel, L et al., Annu. Rev. Biomed. Eng., 4:321-47, 2002.
- [4] Ireland, J et al., Mech. Eng. & Mat. Sci. Ind. Study, 24, 2016.
- [5] Liu, X et al., IEEE Trans Med. Imag, 29:1560-1572, 2010.
- [6] Gomez, et al., IEEE Trans Biomed Eng, 66: 1456-1467, 2018.

A 3D PARTICLE TRACKING STUDY ON THE BLOOD RESIDENCE TIME IN A CEREBRAL ANEURYSM UNDER DIFFERENT INFLOW CONDITIONS

Huang Chen (1), Roya Kamali (1), Thangam Natarajan (1), Satheesh Kumar Harikrishnan (1),
Lakshmi Dasi (1)

(1) Department of Biomedical Engineering, Georgia Institute of Technology/Emory University,
Atlanta, GA

INTRODUCTION

Flow stagnation and the resulting high blood residence time are related to the severity of diseased arterial flow and the risk of thrombosis. As a non-invasive treatment for cerebral aneurysms, flow-diverting stents have been used to increase blood residence time and thus induce thrombus formation in the aneurysm sac [1]. Accurate quantification of the residence time in the aneurysm is crucial in assessing the effectiveness of the treatment. In this experimental work, we used time-resolved 3D particle tracking velocimetry (PTV) with a particle trajectory extension algorithm to quantify the blood residence time in a patient-specific cerebral aneurysm model. The effects of different inflow pulsilities on the residence time were studied after validating the method against more traditional pseudo particle tracking, which based on 3D velocity data. Results have shown that the highly pulsatile inflow causes a large variation and a significant increase in the mean blood residence time.

METHODS

The patient-specific PDMS (Sylgard 184, Dow Corning) flow phantom used in this study is shown in Fig. 1. The geometry was based on patient-specific CT image data, and the phantom was made by the lost core casting method. The aneurysm dome width is about 15mm, and the vessel diameter is 5mm.

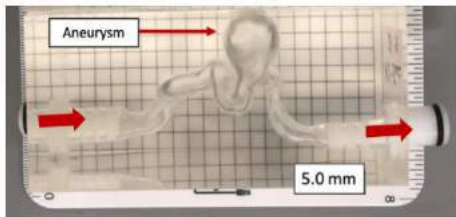


Figure 1: The patient-specific cerebral aneurysm flow phantom.

The inflow to the model was generated by a computerized piston pump (Shelley Medical CompuFlow 1000) and monitored using a flow probe (Transonic Systems Inc.) at the inlet. Three waveforms with different pulsatility used in the study are shown in Fig. 2 and tabulated in Table 1. The patient-specific waveform was based on healthy adult measurement data [2]. The Pulsatility Index (PI) at 70 beats per minute is defined as:

$$PI = (\text{Max flow rate} - \text{Min flow rate}) / (\text{Mean flow rate}) \quad (1)$$

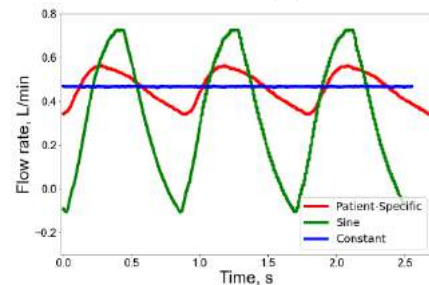


Figure 2: Three waveforms with different pulsatility indices.

Table 1: Mean, Max flow rates and PI for three waveforms.

	Constant	Patient-Specific	Sinusoidal
Mean flow rate (L/min)	0.47	0.46	0.33
Max flow rate (L/min)	0.47	0.56	0.73
PI	0	0.48	2.54

The four-camera 3D PTV setup is shown in Fig.3. Particles were illuminated by a thick (~10mm) laser volume that covered the entire aneurysm sac and part of the inlet and outlet vessels. To ensure zero image distortions, a Urea-Glycerin-Water mixture was used as the blood analog, which matched the viscosity of the blood ($\nu=3.5\text{cSt}$) and the refractive index of the PDMS rubber ($n=1.48$). During the experiment,

the flow phantom was placed in an optical box filled with the same solution. The particle traces viewed by the four cameras are shown in Fig. 4. The images were recorded at 1,200 fps and for about three cardiac cycles. Data was processed in DaVis 10, and particle trajectories at different time steps were obtained using Shake-the-Box (STB) algorithm [3].

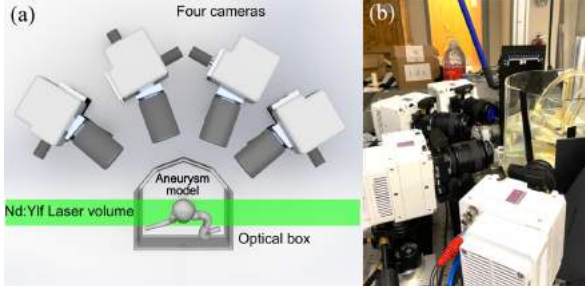


Figure 3: Four-camera 3D PTV setup.

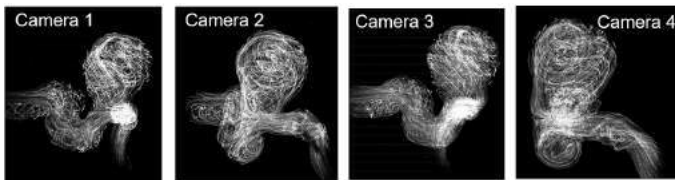


Figure 4: Particle traces viewed by four cameras from different angles.

RESULTS

Sample particle tracks color-coded by the velocity magnitude are shown in Fig. 5a. Unfortunately, the particle tracks generated from STB cannot be used directly to calculate the residence time due to the limited lengths of the tracks. As shown in Fig. 5b, most of the track lengths are less than 100 timesteps, not enough to follow a particle from the entrance to the exit. Moreover, many particles disappear or reappear in the aneurysm sac. To enable direct quantification of residence time, we employed a particle trajectory extension algorithm discussed in [4], which used adjacent particles' movements to extrapolate the missing particle's location to the next time step. The trajectory extension algorithm was applied forward and backward in time to ensure the particles could be traced continuously in the measurement domain. Figure 5c shows the length distributions after trajectory extension. The average length has increased drastically to over 100 timesteps.

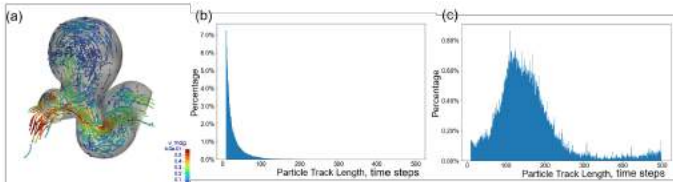


Figure 5: (a) A sample particle track. Particle track length distributions (b) before and (c) after trajectory extension.

The mean residence times in the aneurysm sac for all three waveforms are shown in Fig. 6. The curves were obtained by setting the residence time for all particles to zero at $t=0$ and calculating the average age of the particles in the sac for all subsequent time steps. As a result, the mean residence time at $t=0$ is zero and increases gradually until a stable value is reached. For the constant inflow, the mean residence time in the sac plateaus around 0.27s, about 32% of a cardiac cycle length. The mean residence time for the patient-specific waveform varies slightly during a cardiac cycle, and the mean value for the three cycles is 0.31s, slightly higher than the constant inflow case. The mean residence time oscillates significantly for the sinusoidal waveform,

reaching near 0.7s. The mean residence time for the sinusoidal case is 0.40s, considerably higher than the other two cases.

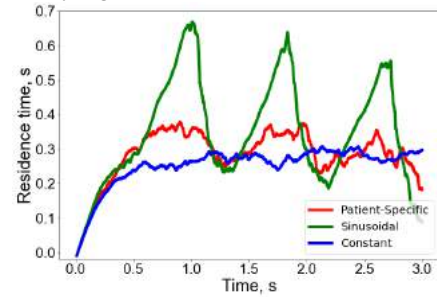


Figure 6: Mean residence time in the aneurysm sac for three waveforms

To validate the accuracy of this new method, a more traditional 3D pseudo particle tracking study was carried out for comparison. First, 3D time-resolved velocity fields were reconstructed based on the original particle tracks [5]. Then, massless particles were continuously seeded at the inflow and tracked through time based on the velocity data, a method called pseudo-tracking. The tracking would stop once a particle exited the domain or reached the boundary of the model. The mean residence time can be calculated later using the same method for the PTV data. The comparisons between these two methods for two different flow waveforms are shown in Fig. 7. Results have shown good agreements between the two methods, and the pseudo-tracking method generates slightly higher residence times.

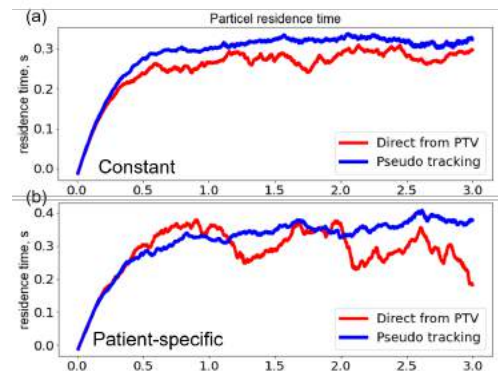


Figure 7: Residence time comparisons between two methods for (a) constant and (b) patient-specific waveforms.

DISCUSSION

The effects of different inflow pulsatility indices on the residence time in a patient-specific aneurysm was studied experimentally using 3D time-resolved particle tracking velocimetry. A method based on a particle trajectory extension algorithm has been developed to directly quantify the blood residence time based on the 3D particle tracks. Results have shown that increased pulsatility increases the residence time in the aneurysm sac, and the mean residence time varies with the pulsatile inflow. The accuracy of the method has been validated by comparing it with pseudo-particle tracking.

ACKNOWLEDGEMENTS

This study was supported by NIH grant no. R21 EB033960.

REFERENCES

- [1] Sfyroeras G, et al., *J. Vasc. Surg.* 56(3), 2012
- [2] Ford M, et al., *Physiol. Meas.* 26(4), 2005
- [3] Schanz D, et al., *Meas. Sci. Technol.*, 24(2), 2012
- [4] Jeronimo M, et al., *Exp. Fluids* 60(4), 2019
- [5] Agarwal K, et al., *Exp. Fluids* 62(4), 2021

TELOCOLLAGEN INJECTABLE SIGNIFICANTLY IMPROVES SUPRASPINATUS TENDON MECHANICAL STRENGTH AFTER FULL-TENDON TEAR IN RATS

Alexandra A. Silverman, MS (1), Nicolo Rossi, MD (2), Jeffrey A. Paten, PhD (1), Mark A. Randolph, MAS (2), Luke S. Oh, MD (2,3), Jeffrey W. Ruberti, PhD (1)

- (1) Bioengineering, Northeastern University, Boston, MA, USA
(2) Plastic Surgery Research, Massachusetts General Hospital, Boston, MA, USA
(3) Orthopaedic Sports Medicine, Rothman Orthopaedics, Winter Garden, FL, USA

INTRODUCTION

Rotator cuff tears are extremely common, difficult to heal, and can significantly impair a patient's quality of life. The rotator cuff is a group of muscles and tendons attached to the humeral head, assisting with shoulder motion and stability. The tendons primarily comprise type I collagen, organized into a hierarchy of fibrils, fibers, and bundles. The intermolecular cross-linking and organization of the collagen is responsible for the tendon's tensile strength and ability to bear and transmit forces. These forces, in turn, can further strengthen the tendon by recruiting more collagen monomers and protecting against enzymatic degradation [1,2].

During the tendon healing process, cells are recruited to synthesize collagen and other extracellular matrix (ECM) molecules which form fibers that are then remodeled and organized. Unfortunately, tendon repair is a complex and slow process. Many patients are unable to fully heal, even after surgical intervention, and tendon retear is common [3]. To improve tendon healing and strength, many bioengineering therapies are currently being explored, such as extracellular patches, stem cells, and growth factors. Collagen-based therapies primarily comprise xenogeneic atelocollagen, where the potentially immunogenic collagen telopeptides have been cleaved, but no significant conclusions have been drawn from clinical trials [3]. We hypothesize this is due to the lack of telopeptides. During collagen fibril formation, telopeptides form covalent cross-links with adjacent collagen molecules, increasing the speed of collagen fibril self-assembly and providing strength. Atelocollagen molecules only associate via hydrogen bonding, resulting in a weaker structure [4]. We hypothesize that telopeptides (present in telocollagen) are essential for tendon repair, strength, and function.

The aim of this study was to address the deficiencies in current atelocollagen therapies by comparing the healing capabilities of telocollagen, atelocollagen, and saline injection treatments after a full-thickness rotator cuff tear in a rat model. We hypothesize that active

telocollagen will home to the damaged tissue, undergo fibrillogenesis in the path of load, and cross-link with the tendon, resulting in increased mechanical strength when compared to atelocollagen and saline.

METHODS

Telocollagen, Atelocollagen, and Saline Injection Preparation. To create atelocollagen, 3mg/mL rat telocollagen (Advanced Biomatrix) was incubated with 0.03 mg/mL pepsin for 3 days, and then salted out to remove pepsin. Atelocollagen was confirmed by assessing its polymerization kinetics [5]. Telocollagen and atelocollagen solutions were concentrated to 10 mg/mL and a saline solution was created. All treatments were sterile, kept at pH 3, and had a final concentration of 1X Penicillin-Streptomycin and 0.9% sodium chloride. Single-dose syringes were prepared and kept at 4°C until injection.

Trackable Collagen Preparation. Azidohomoalanine (Aha), a noncanonical amino acid that can replace methionine and subsequently be fluorescently labeled with click chemistry, was used to create trackable collagen [6]. RAT2 fibroblast cells were cultured at 37 °C with 5% CO₂ with complete media comprising DMEM with 4 mM L-glutamine, 4.5 g/L glucose, 1 mM sodium pyruvate, 10% fetal bovine serum, 0.5 mM L-ascorbic acid, antibiotic, and antimycotic. On day 16, 500 µM Aha was added to cell media and incubated for 48 hours. Then, cells were fixed and stained with Click-iT DIBO Alexa Fluor 488 and confocal microscopy was performed. We attempted to extract this trackable Aha-collagen [4]; however, we were unable to achieve this within the timeframe of this study.

Tendon Detachment and Repair. 36 male adult Sprague-Dawley rats underwent bilateral detachment and transosseous repair of the supraspinatus tendon [7]. Each shoulder received a series of three injections (either 3 saline, 3 atelocollagen, or 3 telocollagen) in the subacromial space. Injections occurred immediately after surgery, postop day 7, and postop day 14. Animals were euthanized at either 30-

or 60- days post-surgery, and for each shoulder, the humerus and supraspinatus tendon were collected. For each treatment group and healing time (saline-treated, atelo-treated, telo-treated, day 30 and day 60), 8 tendons were used for mechanical testing and 4 were used for histologic scoring. Control rats that were weight-matched for day 30 and day 60 rats did not undergo surgery and tendons were used for mechanical testing.

Mechanical Testing. Following established protocols for rat supraspinatus mechanical testing [7], the tendon's cross-sectional area was measured using a 670 nm laser and the humerus was potted with polymethyl methacrylate. Tendons were loaded into the ElectroForce 5500 mechanical tester and submerged in 37°C 1X phosphate buffered saline. They underwent preconditioning, stress relaxation test, frequency sweep, and quasistatic ramp to failure. Load at failure, failure stress, percent relaxation, and stiffness were calculated. The stress-time curve was fitted to Equation 1 to determine τ_1 and τ_2 .

$$E = E_0 + E_1 e^{-x/\tau_1} + E_2 e^{-x/\tau_2} \quad (1)$$

RESULTS

Mechanical testing results are shown in **Figure 1**. 30 days post-surgery, telo-treated tendons had the largest cross-sectional area which remained constant from day 30 to day 60. Conversely, the area of saline-treated and control tendons significantly increased ($p=0.03$) from day 30 to day 60. After 60 days, atelo-treated tendons had the lowest area which was significantly less than control tendons ($p=0.02$) and slightly less than saline-treated tendons ($p=0.33$).

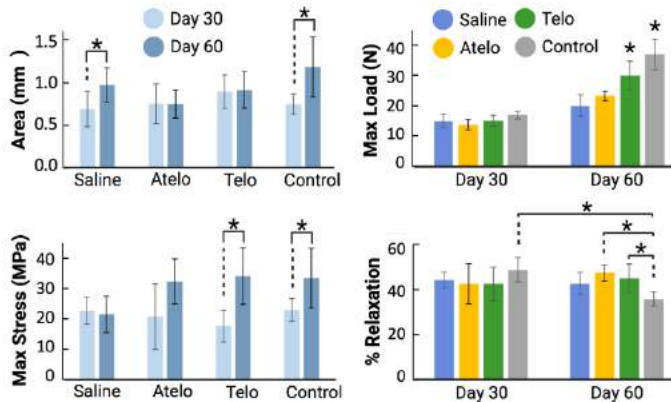


Figure 1: Results of mechanical testing. Data shown as average \pm standard deviation, asterisks represent statistical significance ($p < 0.05$)

On day 30, there was no significant difference in maximum load between experimental tendons, and by day 60, all tendons could withstand significantly more load than day 30 ($p < 0.02$). 60 days post-surgery, telo-treated tendons could withstand significantly more load than atelo-treated ($p=0.025$) and saline-treated tendons ($p < 0.01$) but less than control tendons ($p=0.02$). When normalized for cross-sectional area, the tensile strength significantly increased for only telo-treated and control tendons ($p < 0.03$) over time, and by day 60, and these tendons could withstand the same maximum stress ($p > 0.9$).

The percent relaxation for control tendons significantly decreased ($p=0.005$) from day 30 to 60 and was lower than atelo-treated ($p=0.015$), telo-treated ($p=0.001$), and saline-treated tendons ($p=0.06$) on day 60. Control tendons were significantly stiffer ($p < 0.0001$) than all experimental groups on day 60. No significant differences were found for τ_1 , and control tendons had a significantly higher τ_2 ($p=0.03$) than telo-treated tendons on day 60.

While we did not successfully extract Aha-collagen to inject in our animals, we successfully induced its production in cell culture. **Figure 2** shows that Aha-collagen incorporated into cell-synthesized ECM throughout the depth of the culture and was successfully labeled with DIBO Alexa Fluor 488. This bio-orthogonal collagen reporter will be critical to assess telocollagen treatment in the future.

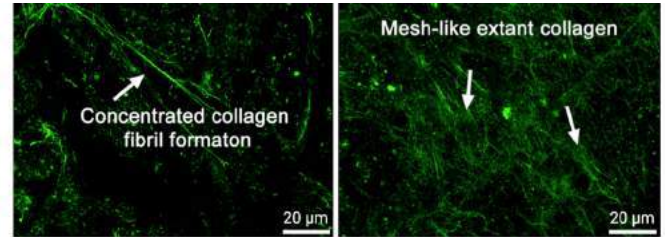


Figure 2: Confocal microscopy of RAT2 cells. Aha-collagen (green) incorporates into collagen fibrils in the extracellular matrix.

DISCUSSION

These results demonstrate that our low-dose telocollagen injectable treatment significantly improves tendon strength and healing within 60 days when compared to saline and atelocollagen treatments in a rat model of a full-thickness supraspinatus tendon tear and surgical repair. Telo-treated tendons formed a larger amount of weak tendon within 30 days post-surgery which strengthened and further organized over time, by day 60, telo-treated tendons could withstand significantly more load than atelo-treated and saline-treated tendons. This suggests that lysyl oxidase-mediated cross-linking begins between day 30 and 60. Additionally, saline-treated tendons had the same tensile strength on day 30 and day 60, suggesting that the tissue formed between day 30 and day 60 was not load-bearing and likely not cross-linked.

The Ruberti Lab has previously demonstrated that strain alone can drive the organized assembly of Type I collagen monomers [8], monomers home to and incorporate with existing collagen fibrils under load [2], and monomers incorporate with existing collagen in cell culture [5]. To determine if our collagen injectable incorporated with the healing tendon, we created trackable Aha-collagen, but were unable to extract it and use it in this study. We plan to conduct future research with Aha-collagen to track the fate of our injectables. Ultimately, these results provide a possible materials-based mechanism for tendon healing and suggest that telocollagen is “active” during the repair process; without telopeptides, collagen treatments are likely not capable of creating a stable, long-lasting, or mechanically robust repair.

ACKNOWLEDGEMENTS

This work was funded by the American Shoulder and Elbow Surgeons.

REFERENCES

- [1] Siadat, S. et al., *Adv in Exp Med & Biol* 1348:45-103, 2021
- [2] Siadat, S., *Northeastern University Dissertation*, 2020
- [3] Deprés-Tremblay, et al., *J Shoulder Elbow Surg* 22:2078-2085, 2016
- [4] Darvish, D., *Materials Today Bio* 15, 2022
- [5] Siadat, S. *Macromolecular Bioscience* 22, 2022
- [6] Mirigian, L. et al., *Connect Tissue Res* 55:403-410, 2014
- [7] Gimbel, J. et al., *J of Biomechanics* 37:739-749, 2004
- [8] Paten, J. et al., *ACS Nano* 10:5027-5040, 2016

IN VIVO MULTISCALE MEASUREMENTS OF SOLID STRESSES IN PRIMARY AND METASTATIC TUMORS

Sue Zhang¹, Rachel Passaro¹, Kathryn Regan¹, Muhamed Hadzipasic^{1,3}, Gabrielle Grifno¹, Siyi Zheng¹, Logan O'Connor¹, Vinson Chu¹, Sung Yeon Kim¹, Jiarui Yang¹, Rohin Banerji¹, Kavon Karrobi¹, Darren Roblyer¹, Mark Grinstaff^{1,2}, Hadi T. Nia^{1,*}

(1) Department of Biomedical Engineering, Boston University, Boston, MA
(2) Department of Chemistry, Boston University, Boston, MA
(3) Department of Neurosurgery, Massachusetts General Hospital, Boston, MA

INTRODUCTION

Solid stress, defined as the mechanical force generated and transmitted by the solid components of a tumor, is a newly identified physical hallmark of cancer with crucial consequences for tumor progression and treatment response¹. Cells sense solid stresses directly and indirectly via mechanosensitive interactions such as cell-extracellular matrix (ECM) and cell-cell adhesions, activation of tensile-responsive ECM proteins, and nuclear deformation. Solid stress causes the compression of blood and lymphatic vessels which contributes to hypoxia and impedes drug delivery, affects T-cell trafficking and infiltration, promotes invasiveness of cancer cells, stimulates tumorigenic pathways, and induces neuronal damage. Targeting solid stress, when combined with standard-of-care anti-cancer treatments, prolongs survival in preclinical studies and is currently being evaluated in clinical trials²⁴ with promising outcomes. While some of the pathophysiological consequences of solid stresses in tumors are now better known, the direct cellular responses to solid stresses and the molecular pathways that are directly activated by them are not fully understood. This is due mainly to a lack of appropriate tools to measure the solid stresses that individual single cancer cells experience *in vivo*, where the complexities of tumor microenvironment are present.

Despite the recent progress in measuring solid stresses *ex vivo* and *in vitro*, *in vivo* measurement of solid stress in tumors is an unmet need. An *in vivo* measurement of solid stress with high spatiotemporal resolution would allow deeper insight into the origins and consequences of solid stresses. In addition, the existing methods to measure solid stresses in murine and human tumors are at the tissue scale and lack the spatial resolution to measure the stresses that individual tumor cells experience. These existing methods are also invasive, typically performed at terminal points, and lack the capabilities for longitudinal monitoring of solid stresses. Furthermore, the existing methods are limited to reporting 1-D and 2-D profiles of solid stresses and do not

provide the 3-D distribution of solid stress as a tensor, which is necessary to describe the anisotropy and heterogeneities of stresses. Therefore, it is critical to develop a method to non-invasively monitor *in vivo* solid stresses at high spatiotemporal resolution across the length scales from the cellular to the tissue scale.

METHODS

Fluorescent PAMs were fabricated (tissue-scale: $397 \pm 69 \mu\text{m}$, cellular-scale: $28.7 \pm 18.2 \mu\text{m}$) and conjugated with fibronectin. For primary breast cancer, mammary intravital windows were implanted on female FVB/NJ mice and PAMs were co-injected with MCA-M3C-H2B-dendra2 cancer cells into the mammary fat pad. Two-photon microscopy (2P) and optical coherence tomography (OCT) was used to image *in vivo* cellular- and tissue-scale PAMs, respectively (Fig. 1). For lung metastasis experiments, PAMs and cancer cells were co-injected via tail-vein. After ~4 weeks, the lung was extracted and imaged using 2P and confocal microscope. Procedures were approved by BU IACUC. Finite-element modeling was used to translate stress-induced deformation to solid stress.

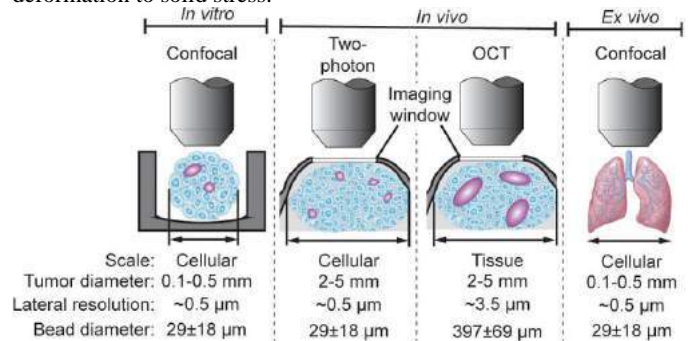


Figure 1. a, Multi-scale intravital microscopy to estimate solid stress in primary and metastatic tumors from the same cancer cells.

RESULTS

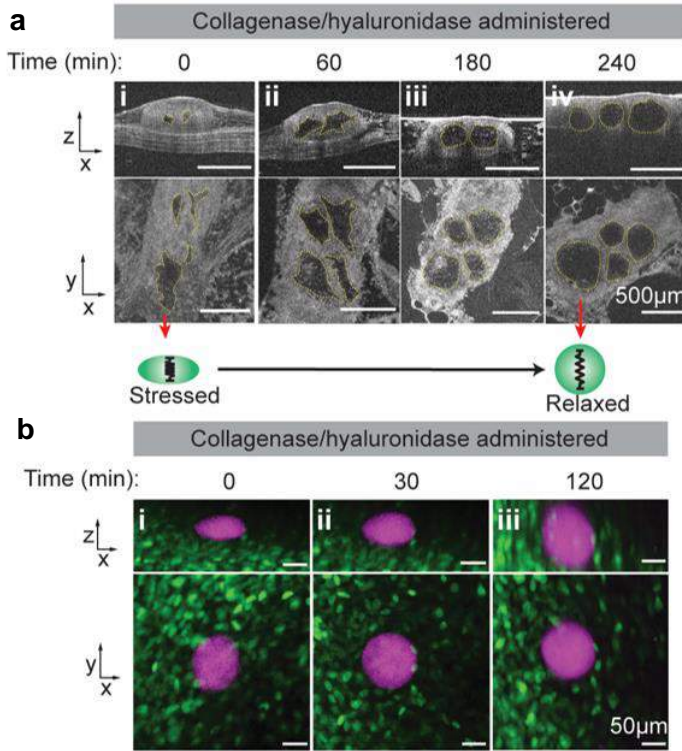


Figure 2. Validation of solid stress measurement at the cellular and tissue scales *in vivo*. a, Relaxation of solid stresses at the tissue scale was demonstrated by enzymatic treatment (collagenase/hyaluronidase) of the tumor *in situ* post-euthanasia and imaging of the beads.

Using intravital microscopy of deformable PA beads, we quantified solid stresses in *in vivo* murine tumors at the cellular and tissue scales in 3-D (Fig. 2). Tumors with cellular-scale beads were formed separately from tumors with tissue-scale beads. We measured the bead aspect ratios after pushing them through 25G and 23G needles (for cellular and tissue scale, respectively) used for tumor injections and our analysis shows that the beads exhibited an aspect ratio of approximately 1 before injecting them into mice. When PA beads are injected into the mammary fat pad without cancer cells and immediately imaged, the aspect ratios of the beads are 1.26 ± 0.10 , suggesting that the baseline mechanical stress applied to the spheres by surrounding normal tissue is much smaller than the deformation measured in the presence of tumors. 5-7 days after injecting the PA beads and MCA-M3C-H2B-dendra2 cancer cells into the mammary fat pad of mice, we observed unexpectedly dramatic deformations in the PA beads with an aspect ratio of 3.41 ± 0.59 (mean \pm STD, N=4) *in vivo* at the tissue scale measured via OCT (Fig. 3a), and aspect ratio of 1.87 ± 0.42 (mean \pm STD, N=3) *in vivo* at the cellular scale measured via two-photon microscopy. Thus, we next sought to determine if the deformation was plastic (irreversible) or elastic (reversible), and if the beads were still intact or broken. To investigate this, we used enzymatic dissociation of the tumor as an effective method to relax the intratumoral solid stresses to observe the relaxation of the highly deformed PA beads to their original stress-free geometry. For the *in vivo* setting, we used a solution

of collagenase and hyaluronidase immediately post-euthanasia *in situ*, and longitudinally imaged the relaxation of the solid stress reflected by a change in the geometry of the PA beads using two-photon microscopy and OCT.

We report the first *in vivo* measurement of intratumoral solid stresses in primary and metastatic settings in mice, and report the unexpected finding that solid stresses experienced at the cell level is significantly lower than that at the tissue level. Our method equips cancer researchers with a multi-scale tool to better understand the spatiotemporal evolution of cancer biophysics and will further inform the discovery of new therapeutic strategies that sensitize cancer cells to solid stresses to e cell death.

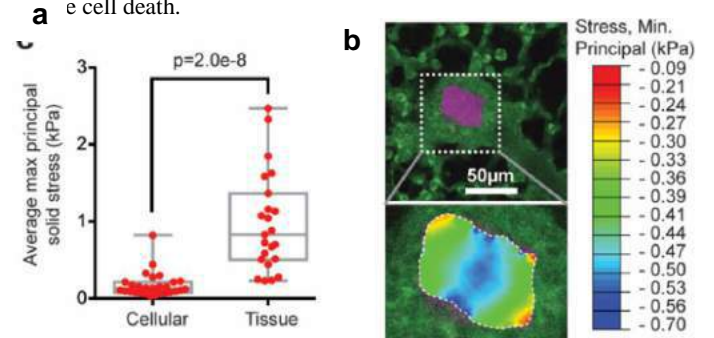


Figure 3. (a) Scale-dependence of solid stress *in vivo* (mean \pm STD, unpaired t-test). (b) Deformed PAM (magenta) in lung microvasculature (green).

The principal solid stress at the tissue scale (0.978 ± 0.64 kPa) was significantly higher (6x) than that of the cellular scale (0.172 ± 0.15 kPa) (Fig. 3a). This was unexpected, as stress (force normalized by area) does not depend on the scale of measurement in homogeneous and linear materials. This finding implicates the presence of potential biophysical mechanisms that dissipates solids stress at the cellular scale and protect tumor cells against lethally high solid stresses. Imaging of lung micrometastasis revealed that cellular-scale PAMs are arrested at the arteriole-capillary junction. Through imaging the deformation of PAMs in the microvessels, we quantified the stresses that single cancer cells experience inside lung microvasculature during metastasis (Fig. 3b).

DISCUSSION

We report the first *in vivo* measurement of solid stresses in mouse models of primary breast cancer and breast cancer lung metastasis. There are four (i-iv) key advantages of our method over existing methods. (i) Longitudinal monitoring of the solid stress, as opposed to the terminal point measurements in existing methods, is critical to characterize the role of solid stress in tumor progression and treatment response. We demonstrate this capability by longitudinally monitoring the stress relaxation *in vivo*. (ii) Our *in vivo* method allows multi-scale measurement of the solid stresses. (iii) Our method affords a measurement of the full magnitude and direction of solid stresses. (iv) Finally, our method accounts for solid stress exerted by surrounding normal tissues since tumors are retained *in situ* and are not excised.

ACKNOWLEDGEMENTS

We acknowledge NIH DP2HL168562 Award, Beckman Young Investigator Award, Neurophotonics Center, and Center for Multiscale Translational and Mechanobiology.

EPIGENETIC TREATMENTS RESTORE NUCLEAR ARCHITECTURE IN CARDIOMYOCYTE CULTURES

Stephanie E. Schneider (1), Adrienne K. Scott (1), Corey P. Neu (1,2)

- (1) Mechanical Engineering, University of Colorado Boulder, Boulder, CO, U.S.
(2) Biomedical Engineering Program, University of Colorado Boulder, Boulder, CO, U.S.

INTRODUCTION

The integrity of the cell nucleus is a function of structural stability involving proteins found in the nuclear envelope and maintenance of genomic architecture. A loss of nuclear integrity presents structurally as an abnormal nucleus morphology, and impacts downstream mechanotransduction events as well as chromatin organization and containment. Alterations in the physical environment such as an increase in stiffness or perturbations in applied mechanical force, impact nuclear structural integrity and cellular differentiation [1,2]. This can result in architectural disruption of the nucleus both along the nuclear envelope (i.e. nuclear wrinkling or increased nuclear area) and disorganized spatial localization of heterochromatin domains as seen in disease states such as cancer and cardiac fibrosis [1].

Force transmission from the environment to the nucleus is modulated through the cytoskeletal network, nuclear envelope, and nuclear lamina. Maintenance of nuclear architecture at the nuclear periphery involves interactions between the chromatin and nuclear lamina. Along with the fibrous network of Lamin A/C and Lamin B proteins, epigenetic modifiers help to organize and support the physical tethering of the chromatin to the nuclear periphery [1].

Previous work from our laboratory has demonstrated that H3K9me3 plays a crucial role in maintaining the cardiomyocyte (CM) phenotype and changes to substrate stiffness, and tissue stiffening disrupts the spatial organization of H3K9me3 and influences the cellular differentiation of CMs [3]. Additionally, we have shown substrate stiffness alters nuclear strains in the actively contracting CMs with cells on stiffer substrates having altered intranuclear strain [4]. Our objective of this study was to determine the extent to which the presence of H3K9me3 protects the structural integrity of the nucleus in the CM. We hypothesized that the restoration of H3K9me3 and chromatin spatial organization using epigenetic treatments could aid in decreased cellular differentiation, and provide structural support necessary for force transmission. To assess this, we exposed CM cultures to substrates of

varying stiffness and inhibitors of epigenetic modifiers to examine the effects on nuclear architecture and organization.

METHODS

Substrate Preparation: 3.5cm² ibidi dishes were coated with Sylgard 527 PDMS at two ratios (A:B), 1:1 (Soft, healthy model) and 1:4 (Stiff, diseased model). A 100µm PDMS layer was deposited uniformly across the culture area. PDMS coated dishes were degassed and cured overnight at 80°C. 24 hours prior to the tissue harvest, dishes were sterilized, plasma treated, and coated with Geltrex overnight at 37°C. **Cell Culture:** Primary cardiac cultures were derived from embryonic (E18.5) H2b-eGFP mice (Jax# 00609). Embryonic hearts were isolated and digested in an enzymatic cocktail at 37°C with gentle agitation. Cardiac co-cultures were plated at a concentration of 1x10⁶/mL in 3.5cm² dish on different substrate stiffnesses (Soft or Stiff) for 4 days. Medium changes occurred on day 1 and 2 along with epigenetic treatments. To study restoration of the healthy phenotype, only cells plated on Stiff substrates received epigenetic treatments. On day 4, cultures were fixed with 4% PFA. **Epigenetic Treatments:** Cardiac cultures were treated with inhibitors of epigenetic modifiers: ML324 (5µM), GSK343 (2µM), or DMSO (0.1%, vehicle control). ML324 is the KDM4 inhibitor which should lead to an increase of the methylation of H3K9. GSK343 is an Ezh2 inhibitor which disrupts the methylation of H3K27. **Microscopy/Immunofluorescence:** All samples were stained with Phalloidin Texas-Red (561nm) and conjugated H3K9me3-640R (633nm). Endogenous GFP signal allowed for visualization of the nucleus without secondary labeling. Using a Nikon A1R confocal, z-stacks of each nucleus were collected with an oil immersion objective at a resolution of 0.08µm/pixel. **Image Analysis:** Max intensity z-projected stacks were created in ImageJ and analyzed using a custom MATLAB code. Peripheral enrichment (PE) was calculated as the ratio of the normalized fluorescent intensity of the performed on max intensity z-projected images.

RESULTS

Primary cardiac cultures were plated on Soft (13kPa) and Stiff (140kPa) PDMS substrates of similar stiffness to that of healthy and diseased cardiac tissue, respectively (Figure 1). With confocal imaging, we observed an increase in PE of H2b-eGFP and H3K9me3 fluorescent intensity in CMs on Soft PDMS with DMSO compared to the Stiff PDMS with DMSO. This confirmed that DMSO did not influence nuclear architecture and reproduced previous studies from our lab [3]. To test if we could restore the PE of H3K9me3 in cardiomyocytes, we treated cardiac cultures with ML324 and GSK343. We observed an increased in H3K9me3 towards the nuclear periphery in ML324 treated cultures (Figure 1).

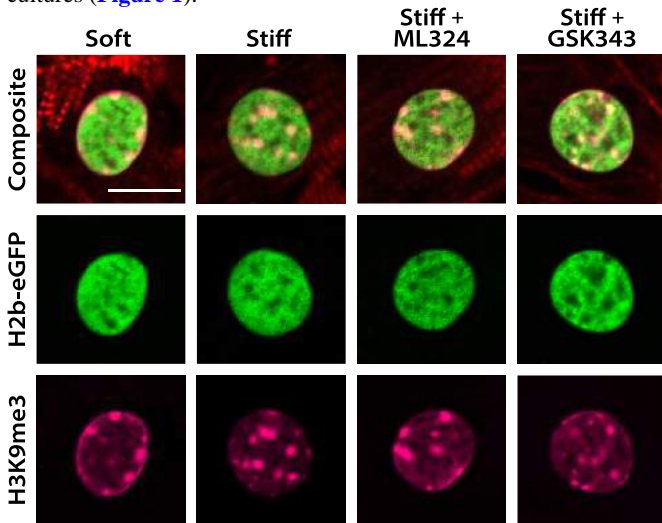


Figure 1: Epigenetic treatment of cardiac cultures impacts nuclear organization in cardiomyocytes. Representative image slices of nuclei from cardiomyocytes (CMs) on Soft (13kPa) and Stiff (140kPa) substrates with epigenetic treatments, ML324 or GSK343. Localization of H3K9me3 of CMs on Stiff PDMS substrates treated with 5 μ M ML324 appeared to have similar localization of H3K9me3 at the nuclear periphery as CMs cultured on Soft PDMS substrates. Soft and Stiff cultures include DMSO (vehicle control). Scale bar = 10 μ m.

After quantifying our observations with a custom MATLAB code, we confirmed that CMs on Stiff substrates had decreased PE levels compared to CMs on Soft substrates as previously shown [3]. Surprisingly, we observed an increase in H2b PE for CMs cultures on Stiff substrates that were also treated with ML324 or GSK343 (Figure 2A). Examining the PE of H3K9me3, we found the PE of CMs on the Soft substrate increased compared to the CMs cultured on the Stiff substrate (Figure 2B). CMs treated with ML324 showed an increase in PE of H3K9me3 compared to CMs on the Stiff substrates, suggesting that the ML324 treatment rescues the PE levels of CMs cultured on Stiff substrates. Other studies have observed an increase in H3K9me3 with a decrease in H3K27me3 levels with the treatment of GSK343 [5]. However, no increase in H3K9me3 PE was observed with GSK343 (Figure 2B). To examine if the changes in H3K9me3 PE were due to increased H3K9me3 throughout the nucleus, we counted H3K9me3 foci. While we still observed an increased number of H3K9me3 foci on Stiff PDMS, ML324 or GSK343 treated CMs displayed a decreased shift in the distribution of foci (Figure 2C).

DISCUSSION

Previous work has shown that culturing CMs on Stiff substrates not only drives the loss of the cardiomyocyte phenotype, but also a

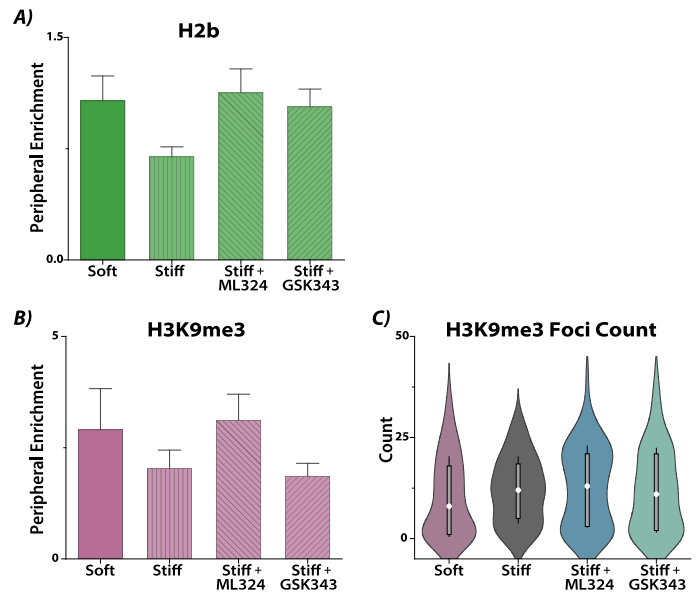


Figure 2: CMs treated with ML324 or GSK343 have increased peripheral enrichment (PE) and altered H3K9me3 organization. A) PE levels of H2b for CMs on Soft PDMS and Stiff PDMS treated with 5 μ M ML324 and 2 μ M GSK343 were elevated compared to CMs on Stiff PDMS. B) PE of H3K9me3 displayed a trending increase in CMs on Stiff PDMS treated with ML324 similar to CMs on Soft PDMS. Error bars = s.e.m. C) The distribution of H3K9me3 foci was affected by substrate and epigenetic treatments, ML324 and GSK343. Box = 25th to 75th percentile, \pm s.d., circle = median. N = 3 animals, n>20 nuclei per treatment.

change in the nuclear architecture [3]. We have also previously linked this change in nuclear architecture to cardiac disease states in which there is an altered mechanical environment (e.g. cardiac hypertrophy). This most recent work shows preliminary evidence that epigenetic treatments can restore the nuclear architecture of CMs cultured on Stiff substrates (diseased model) to that of the nuclear architecture of CMs plated on Soft substrates (healthy model). While we expected an increase in H3K9me3 in the nucleus due to the decrease in the demethylase inhibitor, KDM4, it was unclear how the treatment would alter nuclear architecture in terms of H3K9me3 spatial organization. Finding that the epigenetic treatment restores PE of H3K9me3 and H2b could indicate a cellular state similar to that of the CMs on the Soft substrates. Gene expression analysis for key markers of cardiac maturation can be used to validate the (de)differentiation with the epigenetic treatments. Future work involving GSK343 and H3K27me3 will examine potential causes of the increased PE of H2b. Finally, how restored levels of H3K9me3 and H2b around the nuclear periphery aids in improving structural integrity will be examined through live cell imaging of actively contracting CMs. Using deformation microscopy [4], results will be evaluated to examine the extend that increased H3K9me3 provides structural support leading to decreased intranuclear strains during cellular contraction.

ACKNOWLEDGEMENTS

This work was supported by funding from the NIH and NSF.

REFERENCES

- [1] Gauthier, B. et al., *Int J Mol Sci.*, (14)72-81, 2021. [2] Nava, M. et al., *Cell*, 4:800-817, 2020. [3] Seelbinder, B. et al., *Nat BME*, 5:1500 16, 2021. [4] Ghosh, S. et al., *Cell Rep.*, (5)1607-1620, 2019. [5] Scott, A. et al., *bioRxiv*, doi: <https://doi.org/10.1101/2022.10.23.513439>.

MECHANICAL REGULATION OF LUMEN GROWTH

**Wenhui Tang (1), Anqi Chen (2), Jessie Huang (3,4), Darrell N. Kotton (3,4), Shengqiang Cai (5),
Ming Guo (1)**

- (1) Department of Mechanical Engineering, MIT, Cambridge, MA, US
(2) Department of Applied Physics, Harvard University, Cambridge, MA, US
(3) The Pulmonary Center and Department of Medicine, Boston University School of Medicine, Boston, MA, US
(4) Center of Regenerative Medicine of Boston University and Boston Medical Center, Boston, MA, US
(5) Department of Mechanical and Aerospace Engineering, University of California, San Diego, La Jolla, CA, US

INTRODUCTION

Many organs or tissues exist lumens, and reach to certain sizes during development and maturation. Understanding the development and growth of lumen holds the key for disease modeling and future functional regeneration of distal organs with lumen. While the chemical regulations, such as water and ions transportation are well understood [1], the mechanical regulation of lumen growth and the equilibrium luminal size remain relative unknown.

METHODS

Alveolosphere Model. To study the mechanical regulations of lumen growth, we use a human lung alveolosphere system cultured in 3D in Matrigel (FIG. 1a) [2-3]; this system contains a monolayer of human induced pluripotent stem cells (iPSC)-derived alveolar epithelial type II cells (iAEC2s) and exhibits a spherical lumen. These iAEC2s cells express a global transcriptome and ultrastructure that resemble primary adult Alveolar epithelial type 2 (AT2) cells, thus serving as an *in vitro* model of AT2-related human lung development and diseases. The lumen grows bigger during the growth of alveolospheres and eventually appear an equilibrium luminal size.

Mechanical Force balance. Since the alveolosphere is highly spherical, tension should be dominant in preserving the shape. Therefore, Laplace's law must be satisfied [3],

$$\Delta P = P_o - P_i = \frac{2\sigma}{R} \quad (1)$$

where ΔP is the hydrostatic pressure difference between inside and outside of lumen, σ is surface tension, and R is alveolosphere radius. Hydrostatic pressure difference caused by surface tension.

Water Transportation. The hydrostatic pressure difference caused by higher luminal ion concentration drives passive water transport from inside lumen to outside, while the osmotic pressure difference drives passive water transport from outside into lumen. Together, the net water transport is from outside into lumen: $J_w =$

$\Lambda_w(\Delta\pi - \Delta p)$, where Λ_w is the cell layer permeability. Therefore, our simplified volume conservation equation becomes

$$dR/dt = \Lambda_w(\Delta\pi - \Delta P) \quad (2)$$

Which tells that the change rate of radius is related to the osmotic pressure difference and hydrostatic pressure difference.

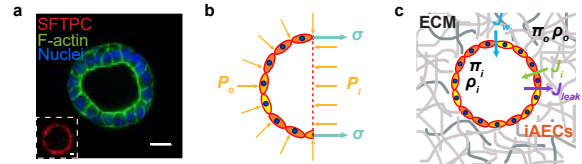


Figure 1: Force balance and water & ions transport in human iPSCs derived lung iAEC2s.

RESULTS

To measure the evolution of $\Delta\pi - \Delta p$ during lumen growth, we perform osmotic compression by adding PEG300 (1.0-2.0v/v%) outside the lumen. Interestingly, we observe that when the hyperosmotic shock π_s is not too large, the size of alveolosphere will decrease first and then increase, which suggests a minimum radius during this process. When the π_s is too large, the alveolosphere lumen will collapse, and therefore the tension becomes compression within the cell layer (Fig. 2). In Eqn. (2) when the minimum size radius is reached, we have $\Delta\pi = \Delta p$ (Fig. 3a). As we analyze the change of $\Delta\pi$ during this process (Fig. 3b), we find that for osmotic pressure difference $\Delta\pi$, it suddenly decreases by a value of π_s after hyperosmotic shock is added. Afterwards, the sphere shrinks and ion concentration increases, resulting in the increase of osmotic pressure. The osmotic pressure difference will increase until the minimum radius is achieved when $\Delta\pi = \Delta p$, and at this moment the radius reaches to a minimum.

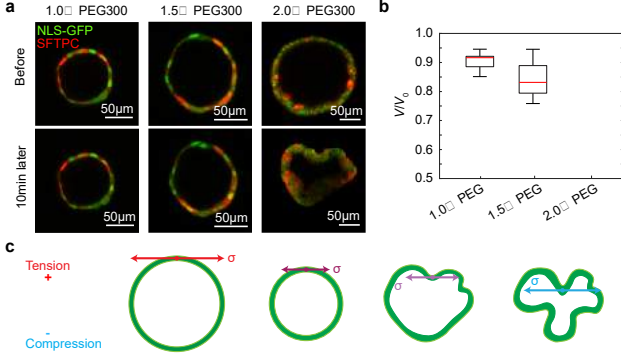


Figure 2: Alveolosphere morphology and force change after osmotic compression.

To relate the lumen radius change with initial osmotic and hydrostatic pressure difference $\Delta p_0 - \Delta \pi_0$, we integrate the volume conservation equation over time

$$R_0 - R_{min} = \Lambda_w \left(\frac{1}{2} t_{min} (\Delta p_0 - \Delta \pi_0 + \pi_s) \right) \quad (3)$$

Rearrange the above the equation, we have

$$\Delta \pi_0 - \Delta p_0 = -\frac{2}{\Lambda_w t_{min}} (R_0 - R_{min}) + \pi_s \quad (4)$$

where the original osmotic pressure difference minus hydrostatic pressure difference $\Delta \pi_0 - \Delta p_0$ can be calculated by measuring t_{min} , $R_0 - R_{min}$, hyperosmotic shock π_s . The measurement of a series $\Delta \pi_0 - \Delta p_0$ with different alveolosphere radii is shown in Fig. 3c-d. Indeed, we find that $\Delta \pi_0 - \Delta p_0$ decreases as the radius of alveolosphere increases. When $\Delta \pi_0 - \Delta p_0$ reaches 0, the alveolosphere stops growing. This indicates a maximum lumen size for alveolospheres system $R_{max} \sim 150 \mu m$, which is consistent with the size of largest alveolosphere range that we observe.

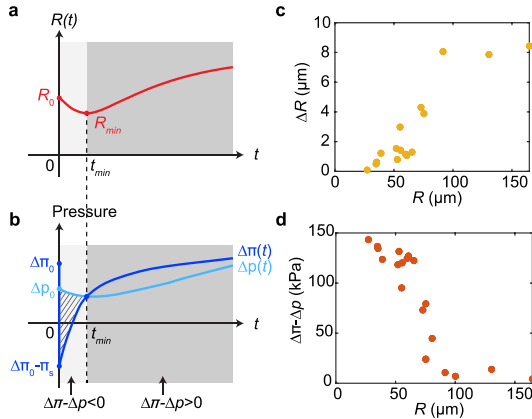


Figure 3: The difference between osmotic pressure and hydrostatic pressure evolution with growth measured by osmotic compression.

To measure the cell layer tension and thus calculating hydrostatic pressure difference, we use micropipette aspiration method (Fig. 5) [5]. At steady state, the cell layer tension can be calculated by Laplace's law,

$$\sigma = \frac{\Delta p}{2} \frac{R_p R}{R - R_p} \quad (5)$$

where the suction pressure is when the tongue length is equal to the micropipette radius R_p and R is the radius of alveolospheres at that time point. The elastic modulus of cell layer can be measured based on [6],

$$\Delta P = \frac{2\pi}{3} E \frac{L_p}{R_p} \phi \quad (6)$$

From the experimental data, we find that the surface tension is $\sim 20 \text{ mN/m}$, corresponding to $\Delta P \sim 10 \text{ kPa}$. The elastic modulus of cell

layer is $\sim 876 \text{ Pa}$. Using this method, we can measure the evolution of cell layer tension, hydrostatic pressure difference, as well as cell layer elastic modulus during the lumen growth.

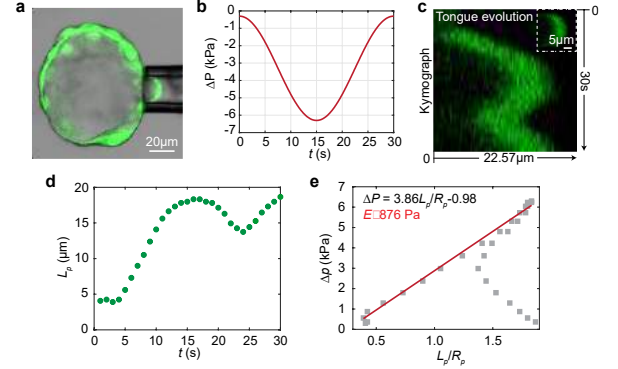


Figure 4: Tension evolution with the growth of alveolospheres.

Furthermore, with this mechanical understanding, a phase diagram explaining how mechanical factors together regulate the equilibrium size is shown in Fig. 5. Pumping ions regulates the osmotic pressure difference, while the cell layer tension regulates the hydrostatic pressure difference. When osmotic pressure equals hydrostatic pressure, an equilibrium lumen size will be reached. As tension in cell layers increases, the equilibrium luminal size decreases; as the pumping ion speed or pump density increases, the equilibrium luminal size will increase.

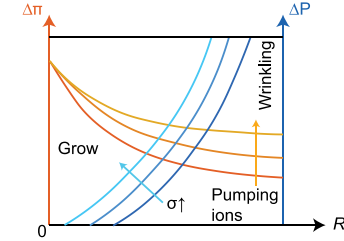


Figure 5: Phase diagram of the mechanical and chemical regulations of lumen growth.

DISCUSSION

To summarize, we study the mechanical regulations of lumen growth and understand the equilibrium luminal size using a human iPSCs-derived alveolosphere system. We find that hydrostatic pressure, osmotic pressure, and cell layer tension together regulate the lumen growth: as lumen grow bigger, $\Delta \pi - \Delta P$ decreases; when $\Delta \pi - \Delta P$ becomes zero, the lumen reaches to maximum size. These findings are essential for understanding other luminal developmental processes as well, such as the budding process of intestinal organoids.

ACKNOWLEDGEMENTS

The authors would like to acknowledge the support from National Institute of General Medical Sciences grant no. 1R01GM140108, and MathWorks.

REFERENCES

- [1] Sanchez, AT et al., *Cells& Dev*, 168:203724, 2021.
- [2] Jacob, A et al., *Cell Stem Cell*, 21(4):472-488, 2017.
- [3] Tang, W et al., *Nat Phys*, 18:1371-1378, 2022.
- [4] Dasgupta, S et al., *Proc Natl Acad Sci U.S.A.*, 115(21):E4751-4757, 2018.
- [5] Hochmuth, RM, *J Biomech*, 33(1): 15-22, 2000.
- [6] Theret, DP et al., *J Biomech Eng*, 110(3):190-199, 1988.

EXAMINATION OF THE COUPLED MOTION OF THE LUMBAR FUNCTIONAL UNIT DURING DYNAMIC MOTION

Matthew R. MacEwen (1), Rebecca E. Abbott (2), Victor H. Barocas (1), Arin M. Ellingson (2)

(1) Biomedical Engineering, University of Minnesota-Twin Cities, Minneapolis, MN, USA
(2) Rehabilitation Medicine, University of Minnesota-Twin Cities, Minneapolis, MN, USA

INTRODUCTION

Low back pain (LBP) is a debilitating condition that is currently listed as the leading cause of disability globally.¹ As a result, the ailment has a high cost both from a health and a socioeconomic perspective. The inability to adequately localize the pain source in LBP and the complexity of the lumbar region necessitates kinematic understanding of lumbar vertebrae to better understand mechanically induced LBP. The functional unit exhibits coupled motion patterns dependent on anatomic variability such as bone morphology, ligament rigidity/laxity, and muscular strength.² Bony morphology contributes predominantly to off axes motion and can be highlighted by measuring the proximity of the facet joints that make up the functional unit of the spine. The degree motion coupling can be understood through an instantaneous helical axes (IHA) approach to generate rich temporal, three-dimensional measures of spinal motion.³⁻⁶ Identifying the instance when coupling is initiated during motion is critical to understanding the behavior of the spine under load and abnormalities due to pathology. The lax zone of motion has been shown to highlight the region of minimal kinematic impedance by the bone morphology, ligament rigidity/laxity, and muscular strength and its end points can act as an aggregate measure of where the resistance of motion begins.⁷⁻⁸ This work aims to investigate coupled motion patterns observed within the L4-L5 functional unit of the spine by quantifying helical axis orientation and facet joint proximity of the segment throughout motion.

METHODS

Seven lumbar spines (age 61 ± 17 yrs; 5 male) were obtained by the University of Minnesota Anatomy Bequest program and screened for spinal abnormalities. The L4 and L5 segments were osteoligamentously isolated and four 1mm tantalum beads were embedded into the transverse processes and vertebral bodies for each vertebra. The spinal units were each imaged with a CT scanner utilizing a B60 kernel scan sequence to enable high contrast between the surrounding tissue and the

bone (Siemens Biograph PET/CT, Germany). To prepare the bone for kinematic testing, the superior and inferior portion of the segments were potted in polymethyl methacrylate and care was taken to insure proper alignment of the L5 vertebrae. Each specimen was then loaded into calibrated Spine Kinetic Simulator (8821 Biopuls, Instron, USA). Retroreflective makers were rigidly drilled into the vertebral bodies of the specimen to be recorded via optical motion capture at 100Hz (MX 40, Vicon Motion Systems, Centennial, CO). Each of the embedded beads were digitized to ensure proper bone model transformation. Pure moments of up to 7Nm were applied to the segment for axial rotation, flexion/extension, and lateral bending at 0.015Hz for 3 cycles of preconditioning and 1 cycle for data analysis.

Mimics Software (Materialise NV, Leuven, Belgium) was used to segment the CT images into bone models. The tantalum beads positions were recorded and their relationships to the anatomic landmarks located on adjacent surfaces of each endplate established within the CT coordinate system. The spine tester and optical motion capture data underwent a spatial frequency analysis to establish lowpass Butterworth cutoff frequencies and were filtered at 15Hz and 6 Hz, respectively and were time-synchronized. Kinematic data was transformed to the anatomic landmarks using a custom MATLAB code that utilized the digitized beads to link the CT and optical motion capture coordinate systems.

The fourth cycle was isolated and lax and stiff zones were determined by the zero-load extrapolation process as outlined in Crawford et al.⁸ The linear regions of the hysteresis curve were calculated via linear regression, and the fit was extrapolated to zero load where the corresponding moments were recorded. (Figure 1) These points act as the boundary between the lax and stiff zone. Helical axes were calculated over a 0.42Nm increment for all directions of bending.³⁻⁴ The axes were categorized based on the zone and its alignment to the L5 coordinate system computed. The kinematics were applied to the bone models of one specimen (37F) via a custom MATLAB

program and the proximity maps of the facet surfaces generated by calculating the minimum Euclidean distance between the facet surfaces of L4 and L5. The percent change was dynamically calculated.

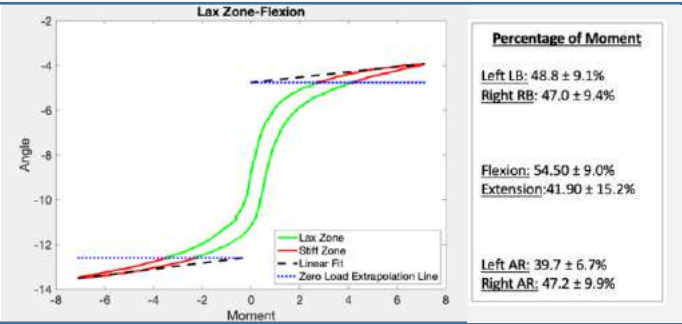


Figure 1: Lax Zone-Stiff Zone calculation: Lax zone of the hysteresis curve shown in green, and the stiff zone shown in red. The lax zone's percentage of the applied moment reported across all specimens.

RESULTS

Figure 2 displays the helical axes for one specimen during a flexion extension movement. The average orientation was calculated across all specimens for each motion. The helical axes were better aligned with the primary anatomical axes within the lax zone when compared to the stiff zone for all motions. Figures 3 and 4 display the proximal data of each facet surface on L5 for axial rotation.

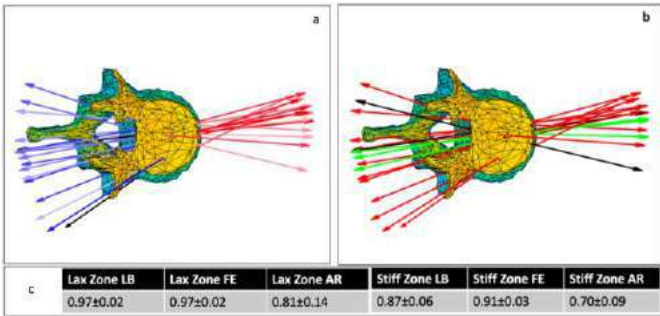


Figure 2: Helical Axes: (a) Dynamic helical axes during an induced lateral bending movement. Flexion is shown in red and extension in blue. (b) Helical axes binned by zone location. Green is within lax zone and red is within stiff zone. (c) Average orientation of helical axes across specimens. A value of 1 indicates a pure hinge joint

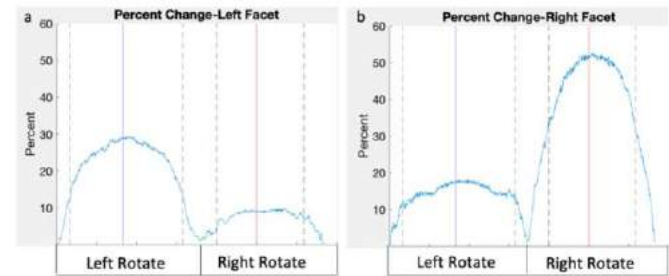


Figure 3: Dynamic percent change in proximity within the facet joints for axial rotation: (a) Left facet surface on L5. (b) Right facet surface on L5. Dashed lines indicate lax zone boundaries and the blue and red lines indicate max applied moment

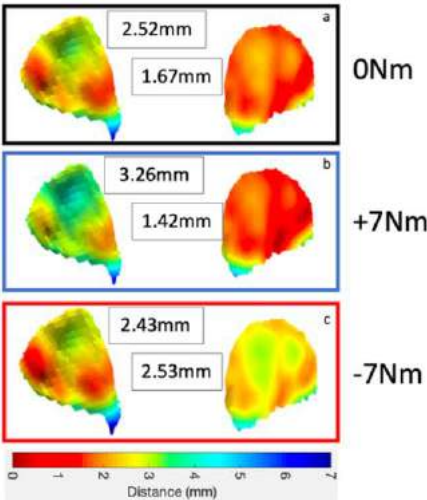


Figure 4: Proximity maps of the facet surfaces of L5 during axial rotation from the posterior perspective: (a) Proximity under zero applied load. (b) Proximity under 7Nm rotating left. (c) Proximity under -7Nm rotation right. Averages shown.

There is a decrease in facet joint spacing on the contralateral joint while the ipsilateral joint space increases. The percent change in proximity is larger for the expanding joint when compared to its compressed counterpart. The lax zone was the smallest percentage of the applied moment for axial rotation and flexion had the largest (Figure 1)

DISCUSSION

The helical axes indicate that the stiff zones of all the applied moments exhibit a higher degree of coupling when compared to their lax zone counterparts. Axial rotation exhibited the most coupling due to the facet joints limiting motion.² The unequal percent change of proximity between left and right facets during axial rotation showcases that the contralateral joint will plateau in its compression while the ipsilateral joint will be forced to expand in a different plane. Flexion lacks this bony influence from the facet joints and would be restricted only by soft tissue.² This resulted in the largest lax zone of all the applied moments. The lax zone shows potential at predicting the bony influence in axial rotation, as the proximity changed the most rapidly during that zone. Some limitations of this study are the lack of active musculature driving the motion, and the quasi-static application of the moment prevents momentum from affecting the trajectory of the motion. Going forward, we plan on applying the proximity map analysis to all the specimens and generate dynamic pressure maps within the joint. We also want to implement a stiffness matrix analysis for each specimen to further quantify the coupling of the L4-L5 functional unit.

ACKNOWLEDGEMENTS

This work was supported by the National Institutes of Health (U01AT010326).

REFERENCES

[1] Andersson, G., et al., Lancet 354:581-85, 1999, [2] Panjabi MM., et al., Orthop Clin North Am, 1977 [3] Woltring, H.J. et al. J. of Biomechanics 18, 5 379-89, 1985 [4] Spoor, C.W. et al J Biomechanics 13, 1980 [5] Ellingson, A. M. et al. J. Biomechanics 48, 2015 [7] Hanlon, A. et al., J. Biomechanical Engineering [8] Crawford, NR. J Spinal Disorders, 1998 Sharma, M., et al, Spine 20:4, 1995

REDUCED SENSOR SET FOR ASSESSMENT OF HAND POSTURE

Ranjith Madhana-Gopal (1), Sara E. Wilson (1,2)

(1) Mechanical Engineering, University of Kansas, Lawrence, Kansas, USA

(2) Bioengineering Graduate Program, University of Kansas, Lawrence, Kansas, USA

INTRODUCTION

Instrumented gloves that can capture hand posture are useful in simulation and training for a variety of clinical applications. For example, in obstetrics training, a glove that can capture hand posture, coupled with pressure sensors, can be used to assess forces applied by the physician. Forces during delivery that are too high have the potential to lead to brachial plexus injuries. In previous work, such a set of instrumented gloves were created using inertial measurement units to capture finger segments and palm orientation and pressure sensors on the fingertips [1]. A low profile is an important feature of such instrumented gloves, so using sensors on only some finger segments is preferable. As such, this work will examine whether it is possible to have sensors on only the palm and distal phalanx of each finger and whether, from that data, the proximal phalanx orientation can be predicted.



Figure 1. Sensors were affixed the palm and proximal and distal phalanx of each finger. The goal of the research was to determine if the distal phalanx orientation could predict the proximal phalanx orientation for an array of motions and orientations.

METHODS

With the approval of the human subjects committee of the University of Kansas and consent of the participants, hand posture data was collected on five subjects performing flex-extension and abduction-adduction in four hand orientations (palm down, palm up, thumb up (shake), and finger tips up (high five)) for both hands. Electromagnetic sensors (Trakstar, Northern Digital) were affixed to the palm and proximal and distal phalanxes of the fingers and proximal and distal phalanx of the thumb. These sensors can return position and orientation of the sensor. The joint centroid of each segment was digitized using an additional sensor and an array of four points around the joint. Due to a limited number of sensors available, data from the index finger and thumb were collected in a separate data collection from the other three fingers. Both the left and right hands were assessed.

Rotation of each segment was assessed relative to palm rotation. The palm was designated as orientation 2, the proximal phalanx as orientation 3, and the distal phalanx as orientation 4. Rotation of the proximal phalanx relative to the palm was designated as $2R_3$ and rotation of the distal phalanx relative to the palm was designated as $2R_4$. $2R_4$ data was plotted against $2R_3$ and a linear regression was performed between the two measures to examine if there was a consistent relationship between the segment postures (Figure 2). These linear regressions were performed for each subjects, for each hand orientation and each motion, for the three rotational axes (x, y, and z)

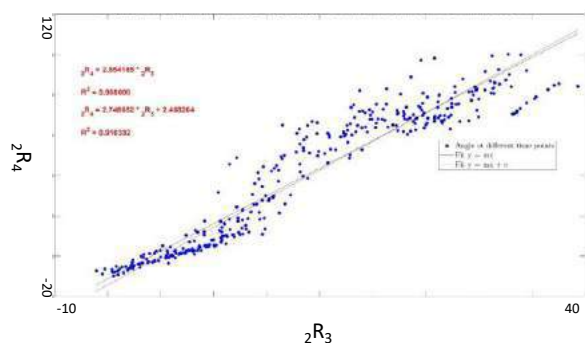


Figure 2 Linear regression of flexion-extension in the palm down orientation for one subject for the index finger for rotation along the primary direction of rotation for flexion-extension. Linear regression was assessed both with a fixed intercept of zero and with a non-zero intercept.

RESULTS

Examining flexion-extension motion it was found that the rotation of the distal segment was 2.81 times that of the proximal segment in the primary direction of rotation with an average r^2 of 0.91 (Figure 3).

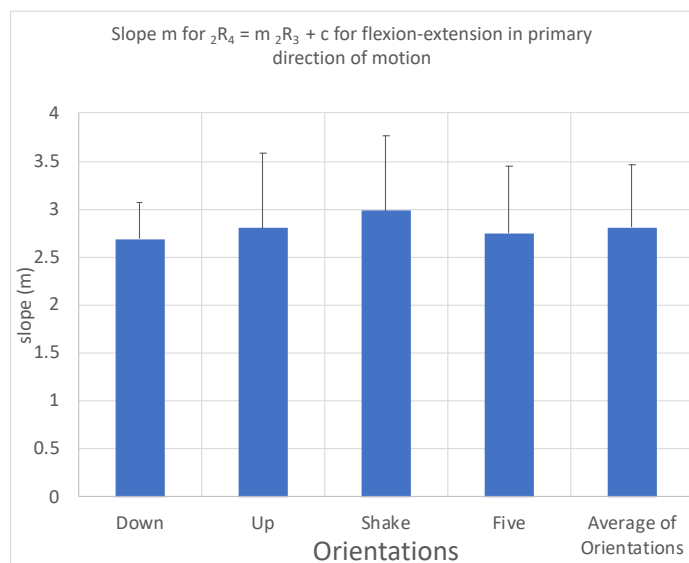


Figure 3 The slope of the linear regression between $2R_4$ and $2R_3$ for the four orientations in flexion-extension across 5 subjects was relatively consistent with an average of 2.81 and an average r^2 of 0.91.

Unlike flexion-extension, where we saw almost 3 times the rotation of the distal phalanx to the proximal phalanx, in abduction-adduction of the index finger, the distal phalanx rotated 1.08 times that of the proximal phalanx with an average r^2 of 0.88 (Figure 3).

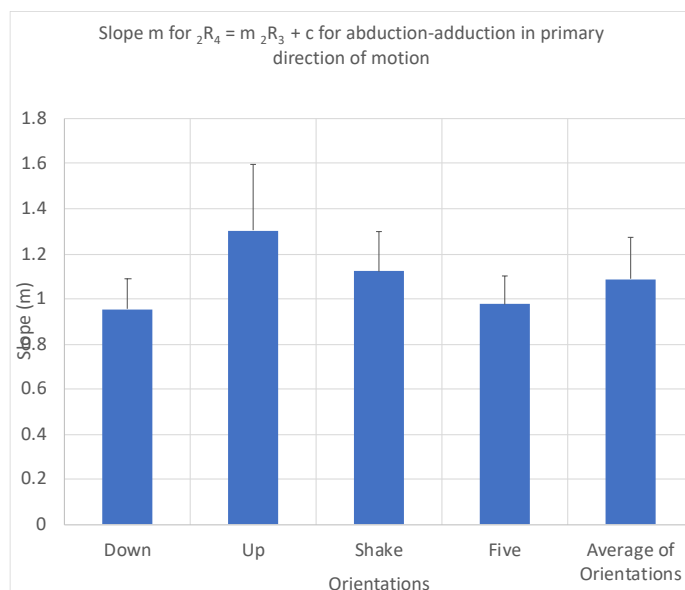


Figure 3 The slope of the linear regression between $2R_4$ and $2R_3$ for the four orientations in abduction-adduction across 5 subjects was relatively consistent with an average of 1.09 and an average r^2 of 0.88.

Unlike the index finger, the relationship between the two segments for the thumb has found to be less consistent. For the flexion-extension, the distal segment rotated 1.54 times the proximal segment with an average r^2 of 0.75 and for abduction-adduction the distal segment rotated 1.05 times the proximal segment with an average r^2 of 0.74. This may reflect the more complex motion of the thumb relative to the other fingers.

DISCUSSION

The findings in this study demonstrate that it is possible to predict proximal segment orientation in the fingers from a sensor located on the most distal segment. As might be expected there is close to a one-to-one correlation between the abduction-adduction of the proximal and distal segments of the index finger and thumb but much greater rotation of the distal segments in flexion-extension, particularly in the index finger. Future work will continue to examine the remaining fingers and to examine more complex motions.

REFERENCES

- [1] Hodes, A., 2015. The Design and Validation of a Force and Bending Moment Sensing Device (Thesis). University of Kansas.

Mechanosensitivity of Naïve and Pro-inflammatory Macrophage Polarization upon Extravasation in 3D Musculoskeletal-like Tissue

P. Babaniamansour¹, D.Jacho¹, A.Rabino², R.Garcia-Mata², E. Yildirim-Ayan^{1*}

(1) Department of Bioengineering, University of Toledo, Toledo, OH, USA

(2) Department of Biological Sciences, University of Toledo, Toledo, OH, USA

* Corresponding Author: eda.yildirimayan@utoledo.edu

INTRODUCTION

Nearly 35 million musculoskeletal injuries are reported each year only in the United States (1). Innate immune cells are critical regulators in musculoskeletal (MSK) tissue regeneration. Among the innate immune cells, macrophages are key elements that can polarize toward pro-inflammatory or -healing phenotypes which can further hinder or promote tissue regeneration (2). Physiotherapy or “mechanotherapy” is a therapeutic approach that introduces forces to activate certain molecular signaling pathways that promote tissue repair. Mechanotherapy through regulating macrophages can be promising for musculoskeletal tissue repair, however, specificity and timeliness are the challenges. Utilizing the amplitude and frequency of the mechanical stimulation can make the therapy more macrophage-specific (3). So far, the role of mechanical strain modalities on macrophage polarization on 2D surfaces was investigated. This research used the comprehensive methodology to decipher the macrophage lineage commitment of naïve (M0) and proinflammatory (M1) macrophages encapsulated in 3D tissue analog exposed to different amplitudes of mechanical strain. The result of this study will shed light into the macrophage mechanome which can be adapted to mechanotherapy research.

METHODS

Synthesizing Macrophage-laden 3D Tissue Analogs and Mechanical Loading Application

First, the human pro-monocytic cell line U937 RPMI 1640 medium, Then, the U937 monocyte cells were treated with 100 ng/mL of phorbol 12-myristate 13-acetate (PMA) for 24 hours to be differentiated to naïve macrophages (M0). The cells were further cultured within the media supplemented with 20 ng/ml interferon gamma (IFN γ) and 100 ng/ml lipopolysaccharide for 24 hours to polarize to M1. To mimic the extravasated macrophages within the musculoskeletal tissue, the M1 and M0 macrophages were encapsulated within a separate neutralized 3mg/ml collagen type-1 solution using our established protocols (4). Then, macrophage-laden 3D tissue analogs were deposited into the mechanical loading apparatus as shown in Figure 1. Following 24-hour incubation, the various mechanical strains with 3%, 6%, or 12% amplitudes, and 0.1 Hz frequency were applied to the 3D tissue analog for 2 hours a day for a period of 7 days.

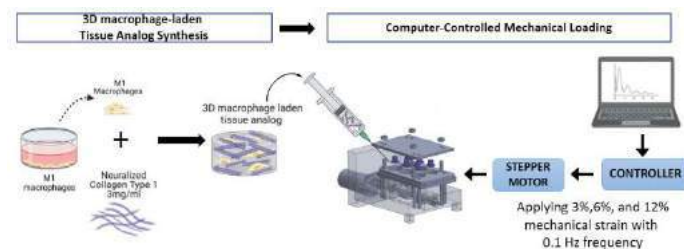


Figure 1. Schematic representations of synthesizing macrophage-laden 3D tissue analog, and mechanical loading of the tissue analog.

Structural Changes in 3D Macrophage-laden Tissue upon Mechanical Loading: M0-laden tissue and M1-laden tissue analogs exposed to various mechanical strain amplitudes were analyzed by scanning electron microscopy (SEM) images and Masson’s trichrome staining analysis to understand how fiber diameter and porosity changes with the mechanical loading and different macrophage phenotype.

Macrophage Polarization within 3D Tissue Analog upon Mechanical Loading: The quantitative real-time polymerase chain reaction (RT-qPCR) was used to perform gene expression fold change analysis of several genes to quantify different responses of the macrophages encapsulated in collagen to different mechanical stimulation modalities. The relative gene expression for fold difference was quantified using the $\Delta\Delta C_t$ method.

RESULTS

The structural changes in M0- and M1-laden 3D Tissue:

M1-laden tissue analog demonstrates higher porosity and smaller fiber diameter when exposed to 3% mechanical strain.

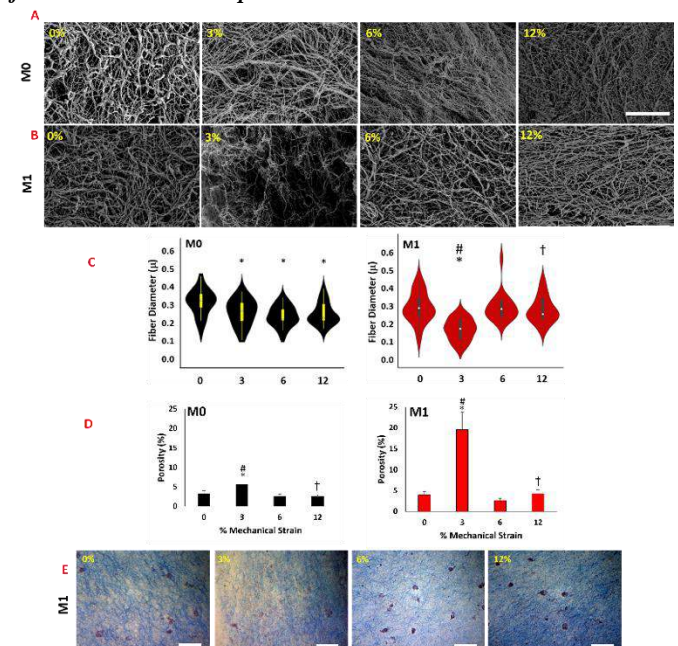


Figure 2. The SEM images of (A) M0- and (B) M1-laden 3D matrix (C) The changes in fiber diameter and (D) The changes in porosity upon mechanical loading, (E) Shows the Masson’s trichrome staining of M1-laden collagen. The scale bar= 10 μ m.

Figure 2 (A) and (B) show that increasing the mechanical strain on M0-laden collagen matrix and M1-laden collagen matrix results in higher fiber alignment. Figure 2C represents the random porosity percentage in M0-laden collagen while higher porosity in M1-laden collagen matrix exposed to 3% mechanical strain. Figure 2D shows that M0-laden

collagen matrix exposed to various amplitude of mechanical strain did not show any different fiber diameter. However, M1-laden collagen matrix exposed to 3% mechanical strain has smaller fiber diameter compared to other strain groups. Figure 2E represents the Masson's trichrome staining of M1-laden collagen constructs which shows the lower fiber density in the scaffolds that are exposed to 3% mechanical strain which further confirms the higher porosity observed in Figure 2D and smaller fiber diameter in Figure 2C.

Early Mechanoresponse of M0 and M1 Macrophages and Phenotypic Changes upon Mechanical Loading:

c-Fos is an early mechanoresponsive gene activated by the external mechanical stimuli. Figure 3 shows c-Fos (early mechanoresponsive gene) expression increased with the increased mechanical strain amplitude for both M0 and M1 macrophages. The highest expression was observed for hyper-mechanical strained group (12%).

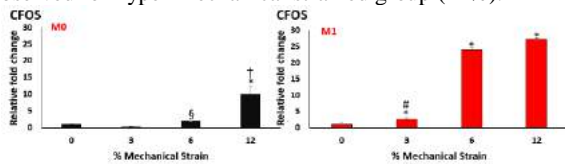


Figure 3. The effect of various amplitude of mechanical strains on relative fold change of c-Fos gene.

Following confirming the external mechanical loading was translated into cellular responses, the polarization state of M0 and M1 macrophages were assessed. Figure 4 and 5 demonstrate the relative fold-change of pro- and anti-inflammatory genes for M0 and M1 macrophages upon various mechanical strain exposure.

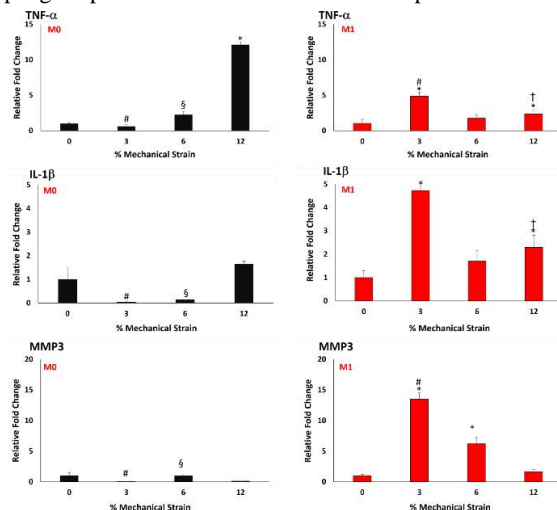


Figure 4. The relative fold change of pro-inflammatory genes in both M0 and M1 macrophages exposed to various mechanical strains.

Figure 4, in M0 macrophages, the expression of the pro-inflammatory gene (TNF-α, IL-β) were highest at 12% mechanical strain. Also, in M1 macrophages the expression of TNF-α, IL-β and MMP3 at 3% mechanical strain is significantly higher than other strain groups. While, the increased expression of TNF-α, IL-β, and MMP3 is the hallmark of the inflammation, the polarization of macrophages toward prohealing phenotype can be recognized through upregulation of anti-inflammatory markers.

Figure 5 shows that anti-inflammatory markers (IL-10, CD163 and CCL18) upregulated at hyper-mechanical strain in M0 macrophages while it increased at 6% in M1 macrophages.

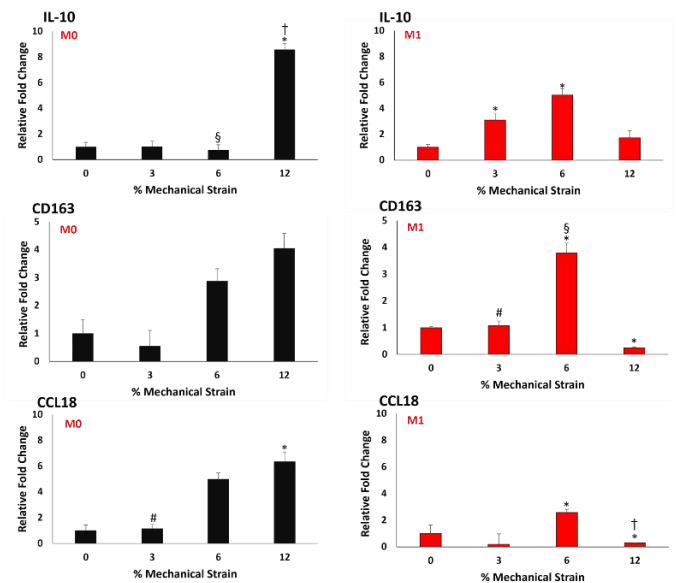


Figure 5. The relative fold change of anti-inflammatory genes in M0 and M1 macrophages exposed to various mechanical strains.

Overall, the data suggested that there is differences in mechanosensitivity of M0 and M1 cells after extravasating within 3D tissue and exposed to even same mechanical strain loading amplitude. For M0, anti-inflammatory genes upregulated with the increased mechanical strain. For M1 macrophages, while 3% mechanical strain pushed M1 cells differentiation into pro-inflammatory lineage, 6% mechanical strain upregulated the anti-inflammatory gene expressions.

DISCUSSION

This research highlighted the different responses of M0 and M1 macrophages to the same amplitude of mechanical strain. M0 macrophage encapsulated in 3D tissue analog demonstrated upregulation of both inflammatory and anti-inflammatory markers at 12% mechanical strain. M1 macrophages encapsulated in 3D tissue analog demonstrated highest upregulation of inflammatory genes at 3% mechanical strain. Furthermore, the higher porosity and smaller fiber diameter observed in M1 macrophages exposed to 3% mechanical strain can be attributed to the upregulation of inflammatory marker MMP3. Moreover, 6% mechanical strain led to upregulation of anti-inflammatory markers in M1 macrophages which suggests that 6% mechanical strain may offset the inflammatory properties of M1 macrophages. This study showed that the modulation of macrophages toward specific phenotype depends on amplitude of mechanical strain. The knowledge from this research can be used to suggest therapeutic window in mechanotherapy exercises.

REFERENCES

1. Wu F, Nerlich M, Docheva D. Tendon injuries: Basic science and new repair proposals. EFORT open reviews. 2017;2(7):332-42.
2. McWhorter FY, Chung T, Liu WF. Modulation of macrophage phenotype by cell shape. Proceedings of the National Academy of Sciences. 2013;110(43):17253-8.
3. Huang C, Schaden W, Orgill D, Ogawa R. Mechanotherapy: revisiting physical therapy and recruiting mechanobiology for a new era in medicine. 2013;19(9):555-64.
4. Subramanian G, Stasuk A, Elsaadany M, Yildirim-Ayan E. Effect of uniaxial tensile cyclic loading regimes on matrix organization and tenogenic differentiation of adipose-derived stem cells encapsulated within 3D collagen scaffolds. Stem cells international. 2017;2017.

EFFECT OF EXCITATION DIRECTION AND FREQUENCY ON REGIONAL DYNAMIC DEFORMATION OF THE HUMAN BRAIN

Ruth J. Okamoto (1), Jordan D. Escarcega (1), Ahmed Alshareef (2), Curtis Johnson (3), Philip V. Bayly (1,4)

(1) Mechanical Engineering and Materials Science, Washington University, St. Louis, MO, USA
(2) Henry M. Jackson Foundation for the Advancement of Military Medicine, Bethesda, MD, USA
(3) Biomedical Engineering, University of Delaware, Newark, DE, USA
(4) Biomedical Engineering, Washington University, St. Louis, MO, USA

INTRODUCTION

Magnetic resonance elastography (MRE) provides a non-invasive way to measure dynamic deformation of soft tissue in the brain caused by external motion of the skull [1,2]. MRE images capture displacement data that is typically processed to estimate tissue mechanical properties, but this data can also be used to estimate wave motion, strain, and energy propagation in the human brain [2–5].

We have recently shown that the ratio of strain energy (SE) to kinetic energy (KE) computed from MRE displacements depends strongly on both excitation direction and frequency[6]. Lateral excitation induces primarily left-right head motion and rotation about the long axis of the neck (“no” neck rotation); whereas occipital excitation induces anterior-posterior head motion and rotation in the sagittal plane (“yes” nodding). We found that the SE/KE ratio was consistently higher for lateral excitation. While brain deformation during MRE is very small, our finding suggests that lateral impacts may cause larger amplitude strains than occipital impacts for a given impact energy, consistent with recent measurements on human cadaver brains [7] and with computational models. In this work, we extend our approach to evaluate regional relationships between deformation and head motion and show how these relationships are influenced by frequency and excitation direction.

METHODS

Thirty-two human participants (16 M, 16 F; age 21-68 Y) were scanned using a Siemens Prisma 3T MRI scanner at Washington University in St. Louis. After standard anatomical images were acquired, skull vibrations were induced at 20, 30, 50, 70, and 90 Hz by acoustic pressure waves generated by an active driver (Resoundant®, Rochester, MN) and transmitted by a deformable actuator at the back of the skull (occipital) or the right temple (lateral); one excitation direction per participant. Phase-contrast images were obtained using an EPI sequence [5] (imaging volume: 240 x 240 x 132 mm, 3 mm isotropic

voxels) with harmonic motion encoding gradients (MEG) and 4 phase offsets.

T1-weighted and T2-weighted anatomical images of each participant were processed using a multi-atlas segmentation that was then registered with MRE image volumes [5]. The segmentation was used to classify voxels into five brain regions of interest: cortical gray matter (CGM), cerebral white matter (CWM), deep gray matter (DGM), cerebellum and brainstem. Mean shear storage moduli (G') for each region were estimated from high-resolution MRE shear moduli maps and corresponding segmentation of six participants scanned at the University of Delaware with occipital excitation at 30, 50, and 70 Hz with regional segmentation data [5]. Regional values of G' were linearly extrapolated to 20 and 90 Hz.

MRE phase images were processed to obtain 3D complex-valued harmonic displacements throughout the brain. Total displacement fields \mathbf{u} were separated into rigid body (bulk) displacement, $\bar{\mathbf{u}}$; and wave displacement fields $\hat{\mathbf{u}}$. Components of the three-dimensional deviatoric strain tensor, $\boldsymbol{\epsilon}_{dev}$, were calculated from the spatial derivatives of $\hat{\mathbf{u}}$. Time-averaged kinetic energy density, W_k [J/m³], was computed from tissue density ($\rho = 1000$ kg/m³), velocity \mathbf{v} and its complex conjugate \mathbf{v}^* at each image voxel and kinetic energy, KE in each brain region was summed:

$$W_k = \frac{1}{2} \left(\frac{1}{2} \rho \mathbf{v} : \mathbf{v}^* \right) \text{ where } \mathbf{v} = i\omega \mathbf{u} = i(2\pi f) \mathbf{u} \quad (1a)$$

$$KE = \sum_{i=1}^n V W_k \quad (1b)$$

where f is the excitation frequency in Hz, $V = 2.7 \times 10^{-8}$ m³ is the volume of each image voxel, and n is the number of voxels in each region.

Deviatoric strain energy density, W_s [J/m³], was computed at each voxel using the corresponding regional G' , $\boldsymbol{\epsilon}_{dev}$, and its complex conjugate, $\boldsymbol{\epsilon}_{dev}^*$ and strain energy in each brain region was summed:

$$W_s = \frac{1}{2} \left(G' \boldsymbol{\epsilon}_{dev} : \boldsymbol{\epsilon}_{dev}^* \right) \quad (2a); \quad SE = \sum_{i=1}^n V W_s \quad (2b)$$

We also computed the mean values of W_k and W_s within each region, denoted by \bar{W}_k and \bar{W}_s respectively, for each participant to account for

variation in the size of the brain and brain regions between participants. To explore the relationship between motion and deformation, we also computed the dimensionless ratio SE/KE within each region for each participant at each frequency.

RESULTS

Estimated values of G' for each region as a linear function of frequency are shown in Figure 1. Consistent with previous studies [8,9], the brainstem and DGM were stiffer than CWM, while CGM and the cerebellum were softer. Stiffness of all regions increased with frequency, approximately doubling from 20 – 90 Hz.

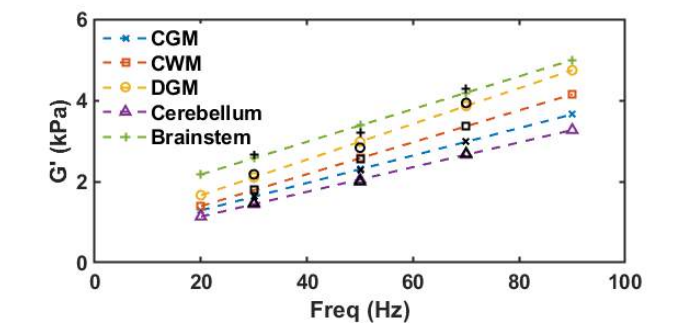


Figure 1: Shear storage modulus G' estimated from high-resolution MRE of six participants at the University of Delaware [5]. Dashed lines indicate linear fit as a function of frequency and extrapolated, black symbols show mean values used for linear fit.

The fractions of the total brain volume in each region were similar for the six high-resolution MRE studies and the participants scanned at Washington University, shown in Table 1.

Table 1: Brain regions and imaged brain volume (mean \pm 1 SD) for 32 participants

Region	Fraction of brain volume	Volume (cm ³)
CGM	44 \pm 3 %	550 \pm 71
CWM	38 \pm 3 %	473 \pm 51
DGM	5.0 \pm 0.2 %	56 \pm 5
Cerebellum	11 \pm 0.2 %	140 \pm 5
Brainstem	1.5 \pm 0.2 %	19 \pm 2
Total		1240 \pm 118

The regional values of \bar{W}_k , \bar{W}_s and SE/KE are shown in Figure 2. \bar{W}_k is larger for occipital excitation than lateral excitation in all regions (Fig. 2a, d); this is expected due to the greater amount of bulk motion observed in occipital excitation than lateral excitation [5]. The regional SE/KE ratios are larger for lateral excitation than occipital excitation at all frequencies and decrease with frequency, particularly in the regions of the cerebrum For occipital excitation, the SE/KE ratio is largest for the brainstem at all frequencies; for lateral excitation, the SE/KE ratio is largest for the brainstem at 20 and 30 Hz, but largest for the cerebellum at 50 – 90 Hz.

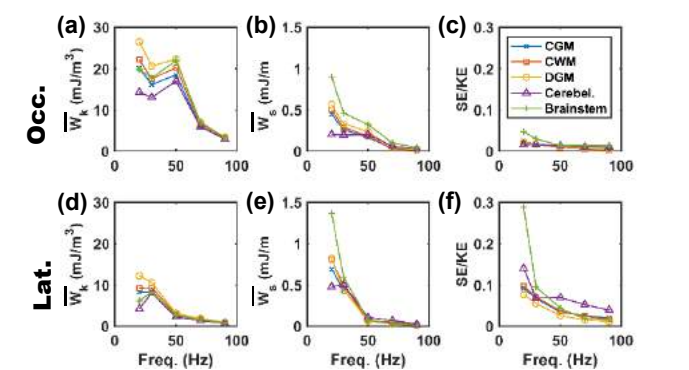


Figure 2: Regional estimates of energy quantities for occipital excitation (top row, N=16, 8M/8F) and lateral excitation (bottom row, N=16, 8M/8F). Mean values of \bar{W}_k (a,d), \bar{W}_s (b,e), and SE/KE (c,f) are plotted at each excitation frequency.

DISCUSSION

Similar to our findings for SE/KE of the entire brain, regional values of SE/KE are larger for lateral excitation than occipital excitation. The decrease in SE/KE ratio with frequency is less pronounced for the cerebellum than for other regions. This suggests that the cerebellum may be more vulnerable to impacts that contain high frequencies than other region.

In this study, regional values of G' were estimated from young adult subjects, but our study population included some older participants who are expected to have softer brain tissue properties [10]. Future work includes using additional high resolution MRE data to obtain age and sex matched tissue properties.

ACKNOWLEDGEMENTS

This research was supported by NIH grant U01 NS112120.

DATA AVAILABILITY

The imaging data used in this study are available for download from the Brain Biomechanics Imaging Resource website : <https://www.nitrc.org/projects/bbir/> [5]

REFERENCES

- [1] Sack, I et al., *NMR Biomed*, 21, 265–271, 2008
- [2] Yin, Z et al., *Top Mag Res Img*, 27(5), 305–318, 2018.
- [3] Clayton, EC et al., *J R Soc. Interface*, 9, 2899–2910, 2012
- [4]Okamoto, RJ et al., *J Exp Neurosci*, 13, 117906951984044, 2019.
- [5] Bayly, PV et al., *Ann Biomed Eng*, 49, 2677–2692, 2021.
- [6] Okamoto, RJ et al., *J Biomech Eng*, in review.
- [7] Alshareef, A et al., *J Neurotrauma*, 37, 1546–1555, 2020.
- [8] Zhang, J, et al., *J Biomech*, 44: 1909–1913, 2011.
- [9] Hiscox, LV et al., *Hum. Brain Map*, 41: 5282–5300, 2020.
- [10] Hiscox, LV et al. *Neuroimage*,232: 117889, 2021.

IMPACT OF BLOOD PRESSURE ON CORONARY AND SINUS FLOW DYNAMICS AFTER AORTIC VALVE REPLACEMENT

B. Vogl (1), S. Lilly (2), V. Thourani (3), M. Alkhouli (4), B. Lindman (5), H. Hatoum (1)

(1) Department of Biomedical Engineering, Michigan Technological University, Houghton, Michigan, USA

(2) Department of Cardiovascular Medicine, The Ohio State University, Columbus, Ohio, USA

(3) Department of Cardiovascular Surgery, Marcus Valve Center, Piedmont Heart Institute, Atlanta, Georgia, USA

(4) Department of Cardiovascular Medicine, Mayo Clinic, Rochester, Minnesota, USA

(5) Structural Heart and Valve Center, Division of Cardiovascular Medicine, Vanderbilt University Medical Center, Nashville, Tennessee, USA

INTRODUCTION

Aortic stenosis (AS) affects 5%–10% of the elderly population and is expected to double by the year 2050¹. Currently, aortic valve replacement (AVR) is the only effective therapy for AS. Transcatheter AVR (TAVR) emerged as a less invasive alternative to surgery with less morbidity and quicker recovery, though surgical AVR (SAVR) is still performed in many patients.

Despite the procedural success of AVR, up to 40% of patients experience death, rehospitalization (principally for heart failure), or poor quality of life 1 year after AVR. In two large patient cohorts, Lindman et al.^{2,3} found that lower systolic and diastolic blood pressures—in the range that is currently recommended as the optimal target in blood pressure (BP) guidelines³—are independently associated with an increased cardiovascular mortality. The reasons for this association are still unclear. We have previously shown that BP is an important factor in maintaining an adequate epicardial coronary flow to prevent myocardial ischemia⁴. Lindman et al.^{2,3} have speculated that having a prosthesis in the aortic root may alter flow in the sinuses, thereby potentially requiring a higher BP to have adequate epicardial coronary flow. Studies have shown that the implantation of a bioprosthetic valve alters the sinus flow dynamics and may compromise or obstruct coronary access, leading to potential impairment of coronary perfusion. However, there are no studies investigating the effect of BP on sinus and coronary flow dynamics after AVR.

The aim of this study is to investigate the effects of BP on sinus and coronary flow dynamics after AVR. We hypothesize that higher BPs will have a stronger, more positive, effect on the flow dynamics in these regions as opposed to lower BPs. We propose using a PIV approach to test this hypothesis.

METHODS

The sinus and coronary flow dynamics of a 25mm Magna Ease (Edwards Lifesciences, Irvine, California), 29mm Evolut R (Medtronic,

Minneapolis, Minnesota) and 26mm SAPIEN 3 (Edwards Lifesciences, Irvine, California) were assessed in a pulse duplicating left heart flow loop simulator at various BP conditions. The flow loop consists of a fluid reservoir to store a blood analog (water-glycerin, 60-40% in volume), a mechanical mitral valve separating the fluid reservoir and pump, a bladder pump controlled by an in-house LabView program, an idealized aortic model, a compliance chamber to simulate arterial distensibility, a gate valve to control the aortic flow, a pinch valve to control the total coronary flow, and ultrasound clamp-on flow rate sensors (Transonic Systems Inc., Ithaca, NY) to measure the flows before the valve and in the total coronary branch. A schematic of the flow loop is shown in **Figure 1**.

The cardiac conditions used were BPs of 100/60mmHg and 160/60mmHg, a heart rate of 60bpm, and a cardiac output of 5L/min.

The total CF was set to 4–5% of the cardiac output which results in a range of 200–250mL/min. In addition, the total CF was set at a BP of 120/80mmHg and was left to vary based on the different BP conditions.

Particle image velocimetry (PIV) was performed to assess the flow dynamics of the sinus and coronary for each

of the valves. The blood analog was seeded with rhodamine B particles. Time-resolved PIV images of the sinus and coronary were taken for

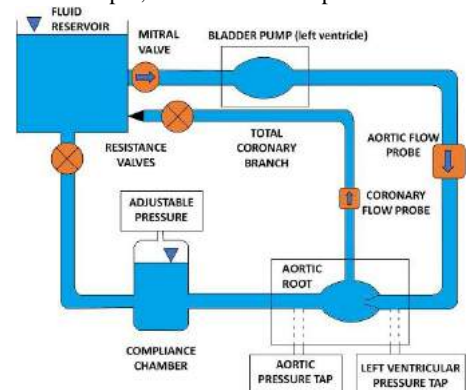


Figure 1. Left heart flow loop with a total coronary flow connection

each valve using a temporal resolution of 4000Hz. Velocity vectors were calculated using DaVis PIV software (DaVis 10; Lavisvision, Göttingen, Germany). The velocity information was extracted and used to calculate the vorticity(ω). Different vector scales were used for the sinus and coronary regions, 1.8 and 0.6, respectively.

RESULTS

Velocity vectors and vorticity contours for each valve at acceleration, peak systole, deceleration, early diastole, and late diastole, are shown in **Figures 2-4**. Note that the purpose of this study is to investigate sinus and coronary flow dynamics at different blood pressure conditions, not to compare performance between each valve.

There were no observable differences in vortex formation at acceleration, deceleration, and late diastole for the Magna Ease. Though, vorticity magnitude is elevated in the coronary with a BP of 160/60mmHg. At peak systole, a small anticlockwise vortex formed towards the back of the sinus which is present only for the 160/60mmHg condition. At early deceleration, two large opposing vortices formed in the center of the sinus, promoting flow into the coronary from both sides of the sinus in the 160/60mmHg. However, these vortices are not present in the 100/60mmHg condition, where flow into the coronary comes from only the back half of the sinus.

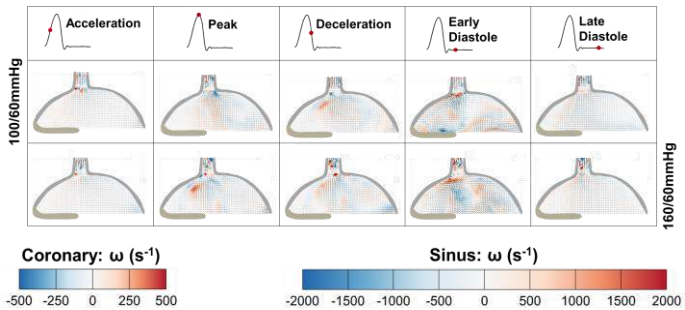


Figure 2. Velocity vectors and vorticity contours at different phases in the cardiac cycle for the Magna Ease.

There were no observable differences in vortex formation at acceleration, and late diastole for the SAPIEN 3. Strong vortices are present throughout the sinus at peak systole and deceleration only at a BP of 160/60mmHg. However, at early diastole a large clockwise vortex surrounded by several smaller anticlockwise vortices is present only at a BP of 100/60mmHg. Furthermore, it appears that this large vortex causes less flow to enter the coronary which is reflected by the decrease in velocity vector size in this region compared to the vectors at a BP of 160/60mmHg.

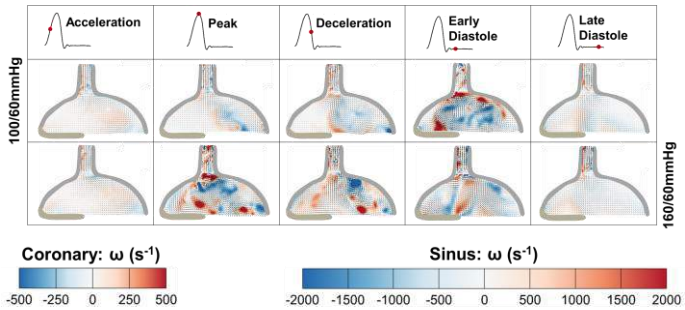


Figure 3. Velocity vectors and vorticity contours at different phases in the cardiac cycle for the SAPIEN 3.

A shadow was present in the back side of the sinus during imaging for the Evolut R, causing incorrect velocity vector calculations in this region which have been removed in **Figure 4**. There were no observable differences in vortex formation at acceleration, peak systole, deceleration, and late diastole for the Evolut R. Though, velocity vector length is moderately longer at some phases for a BP of 160/60mmHg. During early diastole, there is a large clockwise vortex along the right side of the sinus for both BP conditions, but the strength of the vortex is elevated at a BP of 160/60mmHg.

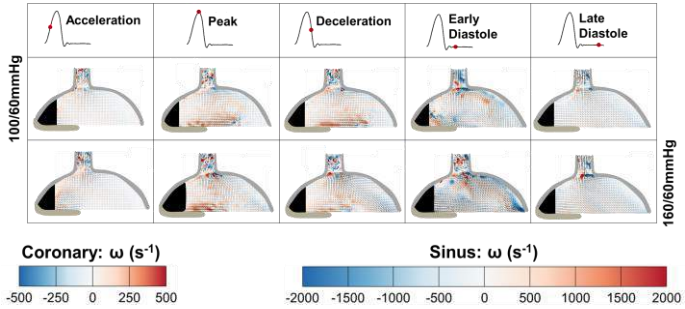


Figure 4. Velocity vectors and vorticity contours at different phases in the cardiac cycle for the Evolut R. The black region represents the location of a shadow present in the sinus.

The timeseries data was divided into systolic and diastolic phases; average velocity was then calculated in the coronary for both BP conditions (**Table 1**). An increase in velocity was observed when increasing the BP from 100/60mmHg to 160/60mmHg regardless of the phase. From systole to diastole, a minor increase in velocity was observed for some of the valves at the different BP conditions.

DISCUSSION

In a previous study, we have reported the effect of BP on maintaining adequate epicardial coronary flow after AVR⁴. We found that higher BPs, not lower, had elevated levels of epicardial coronary flow. Herein, a similar result was observed where an increase in coronary velocities were observed regardless of the cardiac phase.

It has been reported that vortices generated in the sinus play a role in supplying blood to the coronaries⁵. We observed differences in sinus vortices during certain phases of the cardiac cycle for each valve. In addition, it appears that vortices were often more present and encouraging of flow into the coronary at the higher BP.

In this study, we have investigated the effect of BP on sinus and coronary flow dynamics for different bioprosthetic aortic valves using PIV. We observed minor differences in vortex formation, vorticity, and coronary velocities. Currently, we are investigating more combinations of systolic and diastolic BPs, as well as different heart rates.

REFERENCES

[1] Lindman, B., *Circulation* 143.15 (2021): 1455-1457
[2] Lindman, B., *J Am Heart Assoc.* 8.21 (2019): e014020
[3] Lindman, B., *Circ Cardiovasc Imaging.* 10.7 (2017)
[4] Vogl, B., *Catheter. Cardiovasc. Interv.* 99.4 (2022): 1214-1224
[5] Rubenstein, D., *Academic Press* (2015)

CALCIFIED PLAQUE HAS A LOCAL EFFECT ON THE DISSECTION BEHAVIOR OF HUMAN AORTAS

Carly L. Donahue (1), Ruturaj Badal (2), Victor H. Barocas (1)

(1) Department of Biomedical Engineering, University of Minnesota, Minneapolis, MN, USA
(2) Department of Mechanical Engineering, University of Minnesota, Minneapolis, MN, USA

INTRODUCTION

Acute aortic dissection (AAD) is a life-threatening condition in which a tear is initiated in the wall of the aorta, allowing blood to enter and further separate the layers, propagating the tear and creating a false lumen. Nearly 18% of patients who experience AAD die before reaching the hospital [1]. Mortality rates for hospitalized AAD patients are 21% in the first 24 hours and 45% at 30 days [1].

Improving patient outcomes from these lethal events is largely dependent on screening high-risk patients. The most prevalent comorbidities of AAD include hypertension, aneurysm formation, and aortic calcification [2,3]. A recent study [3] used CT angiograms to identify the location of calcifications in AAD patients. They found that the nearest calcification was on or slightly distal to the initiating intimal tear in 60-88% of cases, depending on tear location within the aorta. These results suggest that calcifications have a local effect on the aorta's propensity for dissection.

The mechanics of aortic dissection have been extensively studied using both experimental and computational techniques. Notably, Kozuń et al. correlated peel experiment findings and histological classifications to demonstrate that the progression of atherosclerosis decreased the average delamination strength of the aortas [4]. However, the local mechanical implications of calcifications on aortic dissection remain unknown. The current work correlates calcification location from micro-CT analysis to the local mechanical behavior observed during peel tests to assess the hypothesis that calcifications have a local effect on the delamination strength and behavior of aortas.

METHODS

Sample Preparation: Three human cadaveric aortas (73F, 75M, 86F) were obtained (Anatomy Bequest Program, U of Minnesota) and stored in a 1XPBS solution at 4°C. Excess connective tissue was removed and rectangular strip samples with widths of approximately 5 mm were cut from the vessel wall (Fig. 1A). Samples were cut either in

the circumferential or longitudinal direction. A total of 115 samples were collected, 22 of which were identified as thoracic aorta samples with a calcification detected by the micro-CT and 23 of which were identified as non-calcified samples. Discrepancies between calcification identification performed visually and with the micro-CT were not included. Each sample was marked with horizontal stripes across the width and thickness using a tissue marker. Distances between each mark were measured to aid in mapping the micro-CT results to the local mechanical behavior.

Micro-CT Analysis: Samples were laid flat on a foam stage, sprayed with 1XPBS to keep them hydrated, and scanned with an average resolution of 95.5 μm (NSI, Rogers, MN). Scans times were ~6 minutes. Image analysis was performed using MATLAB's image processing toolbox. Vessel wall and calcification were segmented using Otsu's thresholding method [5], identifying the location and volume of the calcifications within samples (Fig. 1B).

Mechanical Testing: Incisions were made in the center of the media at one end of each rectangular strip to initiate peel propagation. Both "arms" of the incised sample were clamped, loaded onto a uniaxial testing machine (MTS, Eden Prairie, MN) equipped with 10N load cells, and pulled at 10 mm/s (Fig. 1C). Grip force vs. position was recorded. Peel tension was calculated as the force divided by the sample width. The experiment was video recorded to allow for mapping between the mechanical and micro-CT results.

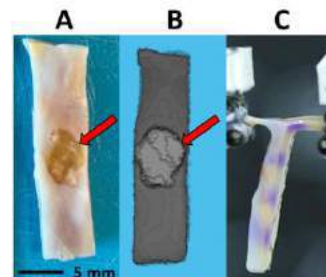


Figure 1: A) Human aorta sample with calcification (arrow). B) 3D rendering of micro-CT image. The vessel wall has been made partially transparent for visibility of the calcification (arrow). C) Aorta sample mounted for peel test.

Data Analysis: All 22 calcified thoracic samples were computationally segmented into three regions: 1) >2mm before the calcification (control), 2) <2mm before the calcification, and 3) calcification region which started at the calcification front and extended 2mm distal to the lesion. Regional minima, maxima, means, and slopes were calculated for samples and compared with paired t-tests. A Bonferroni correction set the p-value cutoff for 95% confidence at $p = 0.05/3 = 0.016$.

RESULTS

The tension required to peel through the sample varied across regions demonstrating a local effect of the calcification (Fig. 2). Fig. 3 shows the average minima, maxima, means, and slopes for each region. The difference between the minimum values for region 2 and regions 1 and 3 were significant ($p = 0.0049$ and $p = 0.0104$, respectively), demonstrating a rise in the minimum peel tension approaching a calcification and a drop in that minimum tension adjacent to a calcification. There were no significant differences in the maximum or means between the three regions.

Slopes were calculated by fitting a linear model to peel tension vs. actuator displacement for each sample. Slopes varied greatly, but tended to be positive in the regions before calcifications and negative in the calcified region. The slope in the calcification region was significantly different from the control region furthest from the calcification ($p = 0.0089$).

In addition to comparing local properties, we also compared 23 samples that did not have any signs of plaque or calcification buildup with the 22 calcified samples. The calcified samples had a mean peel tension of 33.4 N/m, significantly higher than the non-calcified samples, 25.1 N/m ($p < 10^{-6}$). Additionally, the standard deviation of the peel tension within the samples (a measure of mechanical heterogeneity) varied greatly between the two groups. The calcified samples had an average standard deviation of 8.919 N/m, again significantly higher than that observed in the non-calcified samples, 4.86 N/m ($p = 2 \times 10^{-6}$).

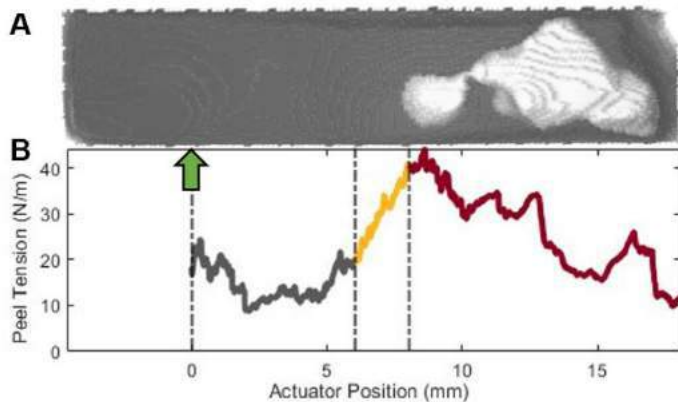


Figure 2: A) 3D rendering of sample micro-CT image. The vessel wall (dark grey) has been made slightly transparent for visibility of the calcification (white). B) Local peel tension mapped to its location within the sample shown above. The curvature is divided into regions: >2mm before the calcification (grey), <2mm before the calcification (gold), and on the calcification (maroon). Peeling started at the green arrow.

DISCUSSION

The results demonstrate that calcifications in the vessel wall have a local effect on the tension required to delaminate the aorta. In general, the peel tension of samples with calcifications exhibited a “rise and fall” behavior, suggesting that calcifications might have an initially

protective effect against peel propagation, but might result in a more brittle failure event when the yield strength is exceeded. This trend is demonstrated in the peel tension graph in Fig. 2 and is captured by the rise and fall of the local minima and the slope turning from positive to negative when the peel front hits the calcified region (Fig. 3).

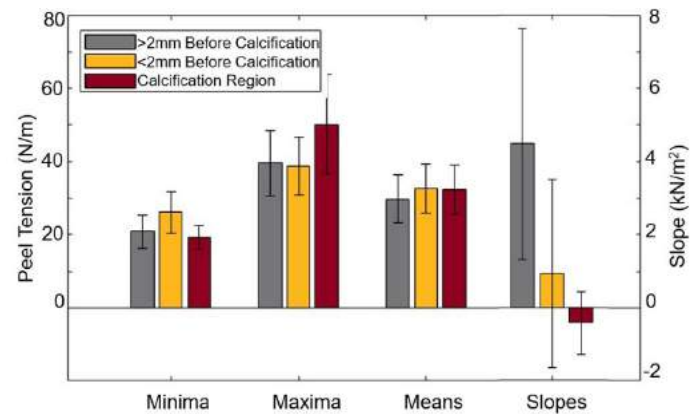


Figure 3: Average regional minima, maxima, and means for peel tension (N/m), and slopes (kN/m²). Error bars are 95% confidence intervals.

The “rise and fall” behavior caused the average peel tension for each calcified sample to be significantly higher than the non-calcified samples. Interestingly, this contradicts the findings of Kozuń et al. who found that atherosclerotic progression reduced average peel tension [4]. In their study, however, Kozuń et al. peeled through the intimal-medial or medial-adventitial interfaces of the aortic samples, while we peeled through the media. This discrepancy could explain the differences in observed trends. Average peel tensions of non-calcified samples agreed with previous studies [6].

The micro-CT is only able to distinguish dense calcifications from the surrounding vessel wall tissue. As a result, “soft plaques”, which likely have an effect on the peel strength, went undetected. This limitation at least in part explains the highly heterogeneous mechanical behavior observed even outside of the calcification regions and the significant increase in peel tension heterogeneity (measured by the standard deviation of each sample) of calcified samples compared to non-calcified samples.

In conclusion, this study demonstrates that calcifications have a local effect on the peel tension and is, to our knowledge, the first to correlate media peel tension mechanics to CT imaging, a modality routinely used in clinical monitoring and diagnostics and thus potentially valuable in assessing aortic wall failure risk.

ACKNOWLEDGEMENTS

This work was supported by AHA Predoctoral Fellowship 23PRE1019931 and NIH grants R01-HL164800, U01-HL139471, and T32-HL139431. We thank Amanda Devos and the Visual Heart Lab for aid in data collection, Hadi Wiputra for aid in image processing, Weihua Guan for statistical expertise, and the anonymous organ donors of the Anatomy Bequest Program for making this work possible.

REFERENCES

- [1] Melvinsdottir, I et al., *Eur J Cardiothorac Surg*, 50:1111-1117, 2016.
- [2] Obel, L et al., *Circ*, 146:1903-1917, 2022.
- [3] Yang, C et al., *PLoS One*, 14(7):e0219461.
- [4] Kozuń, M et al., *J Mech Behav Biomed Mater*, 79:292-300 (2018).
- [5] Otsu, N, *IEEE Trans. Syst. Man Cybern*, 9:62-66, 1979
- [6] *J Mech Behav Biomed Mater*, 133:105340, 2022.

DEVELOPING A PERFUSION OPTIMIZATION FRAMEWORK FOR SYNTHETIC VASCULATURE IN BIOFABRICATION APPLICATIONS

Zachary A. Sexton (1), Karthik Menon (2), Lazaros Papamanolis (1), Alison Marsden (1,2,3)

- (1) Department of Bioengineering, Stanford University, Stanford, CA, USA
(2) Department of Pediatrics (Cardiology), Stanford University, Stanford, CA, USA
(3) Institute for Computational and Mathematical Engineering and Cardiovascular Institute,
Stanford University, Stanford, CA, USA

INTRODUCTION

A major obstacle impeding engineered tissues and organs is the lack of vasculature. At clinically relevant cell densities, functional tissues create significant metabolic demand requiring robust nutrient/oxygen delivery and waste removal. Because engineered tissues often do not have a pre-existing vascular model to incorporate, techniques in synthetic vascular generation have emerged as ways to improve perfusion strategies of fabricated tissue constructs [1].

These computer-generated vascular networks typically rely on combinations of morphometric data and simplified fluid dynamics and demonstrate qualitatively biomimetic topologies to native vasculature. Constrained constructive optimization (CCO) is one popular method for generating synthetic vasculature relies on adequate constraint assignments governing assumptions about vascular scaling, bifurcation angles, and cost function parameters [2]. However, the performance of CCO synthetic vasculature at perfusing living matter remains unclear. Current CCO cost function optimization is dedicated to minimizing blood volume during vascular construction; thus, there is no guarantee that synthetic vasculatures thoroughly perfuse volumes of interest.

To address this, we leverage derivative-free a optimization framework previously developed in our lab for more accurate generation of synthetic vasculature towards target functional perfusion metrics [3]. To inform our optimization we leverage multi-fidelity computational fluid dynamics (CFD) and perfusion modeling to estimate oxygen saturation within tissue volumes.

METHODS

We consider a cube bioreactor volume requiring synthetic vasculature. Models are created using CCO methods through custom scripting and model building tools available in the open-source package, SimVascular. The topology of generated synthetic vasculature is dependent on global parameters including Murray's law and bifurcation angle constraints as well as search, length, and radius exponents [4]. In general, our optimization problem can be expressed as a black-box system of the following form:

$$\begin{aligned} & \underset{\xi}{\text{minimize}} J(\mathbf{u}; \xi) \\ & \text{subject to} \quad \begin{aligned} & N(\mathbf{u}; \xi) = 0; \\ & \mathbf{M}(\mathbf{u}; \xi) \leq 0; \quad 0 < \xi < 1 \end{aligned} \end{aligned} \quad (1)$$

These design parameters (ξ) as well as the pressures and velocities (\mathbf{u}) together are used to satisfy our objective-function, $J(\mathbf{u}; \xi)$, which is an integral metric of tissue volume at ischemic risk. $N(\mathbf{u}; \xi) = 0$ represents the multi-scale equations governing blood flow and diffusion through a porous medium. The pressures, velocities, and design parameters are also explicitly constrained $\mathbf{M}(\mathbf{u}; \xi) \leq 0$. Diffusion modeling is governed by the single-compartment Darcy model:

$$\begin{aligned} & \mathbf{w} + K \nabla p = 0 \\ & \nabla \cdot \mathbf{w} = \beta_{source}(p_{source} - p) - \beta_{sink}(p - p_{sink}) \end{aligned} \quad (2)$$

Here K and w are the permeability tensor and Darcy velocity, respectively. The pressures (p) are obtained from solutions the hydraulic circuit equations governing the fluid domain of the vascular network. β represents the conductance of flow entering and exiting the tissue domain through sources and sinks along the vessels of a vascular network. The Darcy model shown in (2) is solved using a finite-element implementation. To optimize this expensive black-box problem (1), we use the surrogate management framework (SMF) method which relies on surrogate searching and objective-function polling steps to converge upon a given grid resolution threshold [3].

RESULTS

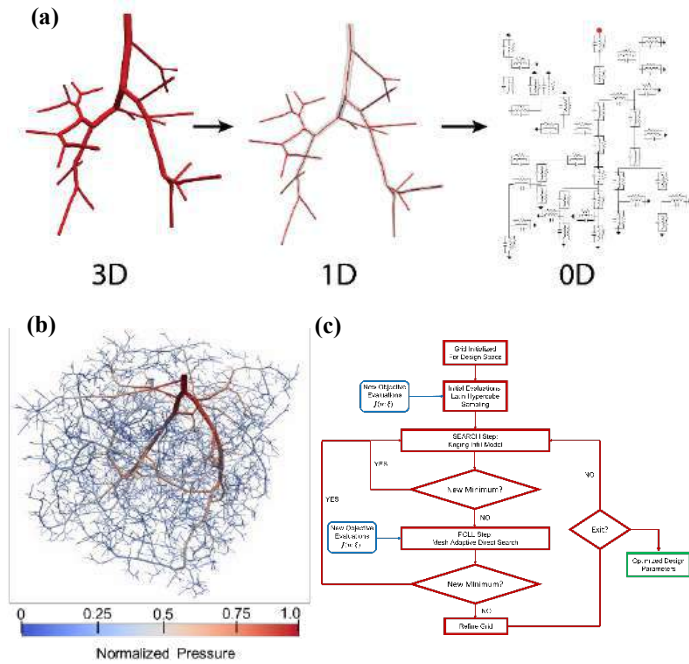


Figure 1: (a) schematic overview for obtaining the hydraulic circuit equations to solve for flows and pressures starting with 3D mesh geometries, 1D centerline extraction, and finally discrete 0D circuit components (b) synthetic vascular network generated within the cube perfusion volume showing normalized pressure distribution obtained from 0D circuit model solution (c) schematic overview of SMF optimization framework. During initialization and POLL steps the objective-function is evaluated

An automated framework for synthetic vascular generation, flow and perfusion simulation has been developed for use within an SMF optimizer. This involves successful generation of reduced order models from initial vascular meshes into circuit representations (Fig. 1a). This forms a set of “0D” differential algebraic equations which are solved with our open-source svZeroDSolver. Obtained pressures are linearly interpolated along vessel segments (Fig. 1b) and used to set the source and sink pressures in the tissue mesh for subsequent perfusion simulation. These steps are repeated for each objective-function evaluation throughout the SMF optimization routine (Fig. 1c).

DISCUSSION

This work presents a framework for generating synthetic vasculature towards more rigorous functional perfusion targets by further optimizing for global constraints including Murray’s law and bifurcation angle constraints as well as search, length, and radius exponents. Overall, this work aims to provide more reliable vascular networks perfusing future engineered tissues by identifying design parameters minimizing ischemic regions. Preliminary work has been undertaken to create a framework for automated SMF optimization which will be used in future work to determine optimal design parameters for convex bioreactor volumes.

ACKNOWLEDGEMENTS

This work is supported by the NSF GRFP and Additional Ventures Cures Collaborative. High performance computing resources were provided by the Stanford Research Computing Center.

REFERENCES

- [1] Guy A et al. *IEEE Transactions on Biomedical Engineering* 67:1650-1663 (2020). DOI: 10.1109/TBME.2019.2942313
- [2] Schreiner W et al. *IEEE Transactions on Biomedical Engineering* 40.5 (1993). DOI: 10.1109/10.243413.
- [3] Verma A et. *Optimization and Engineering* 21:1487-1536 (2020). DOI: 10.1007/s11081-020-09483-1
- [4] Zhou Y et al. *Physics in Medicine and Biology* 44.12 (1999). DOI: 10.1088/0031-9155/44/12/306.
- [5] Papamanolis L et al. *Annals of Biomedical Engineering* 49.5 (2021). DOI: 10.1007/s10439-020-02681-z.

METHOD OF APPLYING TWIST TO COMPLEX FEMOROPOPLITEAL ARTERY DEFORMATIONS IN A FINITE ELEMENT STUDY

Ali Ahmadi (1), Anastasia Desyatova (1)

(1) Department of Biomechanics, University of Nebraska-Omaha, Omaha, Nebraska, USA

INTRODUCTION

The femoropopliteal artery (FPA) is the main artery of the leg that maintains blood supply to the lower limb's tissues. One of the main disease modalities of FPA is a peripheral arterial disease (PAD) which manifests as an atherosclerotic lesion that reduces blood flow to the downstream tissues. PAD is among the most expensive vascular diseases to treat, mainly because of the high rate of reconstruction failures that require reintervention [1–3]. One of the reasons for the high prevalence of PAD and poor treatment outcomes can be the complex mechanical deformations that FPA undergoes during everyday activities, which have been characterized in detail using a perfused human cadaver model previously [4]. Severe deformations of FPA can contribute to its high intramural stresses and strains that may cause arterial injury with the initiation of the disease or restenosis after the treatment. FPA intramural stresses due to leg bending were quantified on separate deformation modalities by [5,6], but there is still a lack of understanding of the combined effect of twist and bending on the FPA stresses. In this study, a method of applying twist in addition to complex bending deformations was proposed and evaluated using one FPA.

METHODS

Model. Finite element analysis using Abaqus 2017 (Simulia, Dassault Systemes) was performed to evaluate the effects of combined twist and bending. Centerline FPA in straight and acutely bent leg positions for a 71-80 year-old-group from [7] was adopted for this study. Here, FPA was modeled as an annular section with 6.0 mm internal diameter and 1.5 mm thickness extruded along the centerline in the straight limb position (180°), scaled with the inverse of longitudinal pre-stretch of 1.10. Soft, highly compressible surrounding tissues were modeled around the FPA as an annular cross-section extruded along the same centerline. Tissue properties were selected using a parametric study to ensure FPA in the bent position matches with the bent centerline. FPA was modeled using the New-Hookean model with $C_{10}=167$ kPa. The

FPA and surrounding tissue parts were meshed with linear hexahedral elements, and time increment was set to keep the kinetic energy below 5% of the internal energy to maintain quasi-static simulation.

Boundary conditions. Boundary conditions were applied in three steps: 1) prestretch, 2) twist, and 3) bending and compression. Prestretch was calculated as a displacement from the scaled-down straight centerline to the CT centerline in the straight position and applied to one end of the artery while the other end remained pinned. Centerlines in the straight (180°) and gardening (60°) postures from [7] were used as bending and compression boundary conditions. Twist deformation along the centerline for the same cadaveric FPA is shown in Figure 1 (black markers).

After prestretch step, the twist deformation was applied to 9 locations along the centerline with the highest values of the twist (Figure 1, red markers) by imposing a rigid body constraint on the FPA's outer surface sections. Constraining only the outer surface allowed to maintain some through-wall compressibility of the artery during bending and compression. Twist was applied to each of the twist sections' reference points in the local coordinate system aligned with the rotation of the twist section. Next, bending deformation was applied to the stiff catheter part around the surrounding tissues that was led from the straight to the bent configuration according to the displacement difference in bent and straight centerlines.

RESULTS

The proposed computational model was able to realistically portray complex deformations of the FPA during the acute bent leg. Figure 2 demonstrates maximum principal strains in the FPA in the unstretched (A) and prestretched (B) configurations, with applied twist deformations (C), and with bending and compression deformations applied (D) as the last step. Regions of strain concentration after applying bending deformations were found to be highly non-uniform. High strains and stresses were localized to the segments with acute

kinks, i.e., near the Adductor Hiatus (AH) and in the popliteal artery (PA) below the knee (Figure 2D). However, it was found that some sections did not fully transform twist deformation after bending deformation (Figure 1, blue markers).

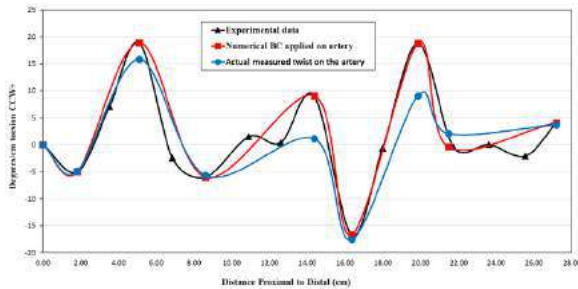


Figure 1: Twist along the FPA length (black, experimental; red, applied BC in the model, blue: measured twist at the end of bending step).

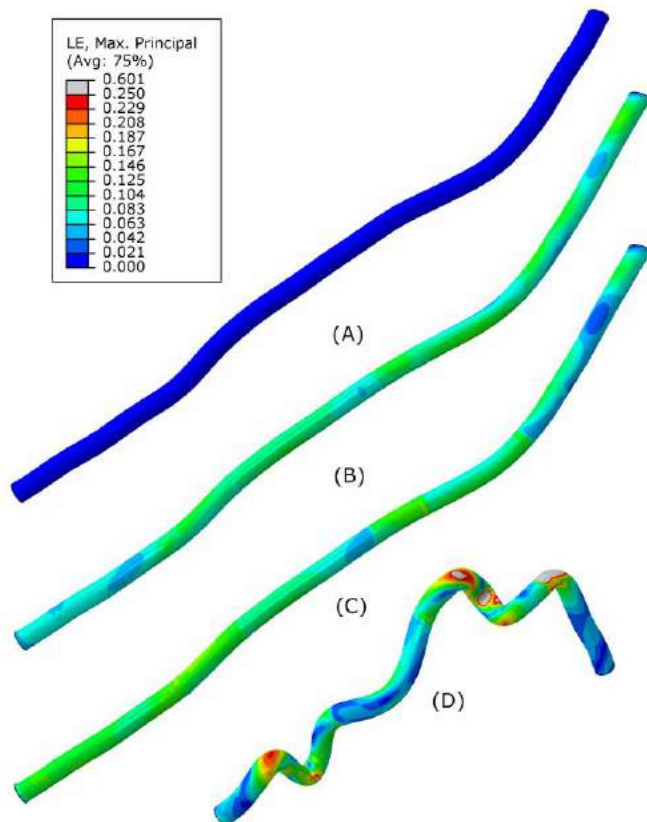


Figure 2: FPA model, demonstrating shape and maximum principal strains of (A) unloaded FPA without residual prestretch, (B) prestretched, (C) with twist applied, and (D) with combined deformations at 60° limb flexion.

DISCUSSION

A model with combined limb-flexion induced deformations was developed using rigid rings to apply twist in addition to a guiding catheter and surrounding tissues to apply bending and compression. Like a previous study that only included bending and compression deformations [8], this study has confirmed highly heterogeneous stress

and strain distribution with high concentrations at the AH and PA below the knee area. These locations are also highly prone to atherosclerotic disease [8] which shows there might be a relation between high strains/intramural stresses and atherosclerotic disease of FPA.

While the study presents a way to include twist in the simulation of combined bending-compression deformation of the FPA, it should be viewed in the context of its limitations. First, twist was applied through the inclusion of rigid rings. These rings introduce artificial localized stress concentrations and limit deformations of the FPA in the vicinity of the rings. Care must be taken to place the rings away from the regions of high kinking, so it is not artificially limited. Second, only one FPA geometry with the simplified material model was used here. A more realistic material model and additional cases of FPA deformations would improve the fidelity of the obtained results.

ACKNOWLEDGEMENTS

This work was supported by the NHLBI HL125736.

REFERENCES

- [1] M. Schillinger, S. Sabeti, P. Dick, J. Amighi, W. Mlekusch, O. Schlager, C. Loewe, M. Cejna, J. Lammer, E. Minar, Sustained benefit at 2 years of primary femoropopliteal stenting compared with balloon angioplasty with optional stenting, *Circulation*. 115 (2007) 2745–2749.
- [2] M.S. Conte, D.F. Bandyk, A.W. Clowes, G.L. Moneta, L. Seely, T.J. Lorenz, H. Namini, A.D. Hamdan, S.P. Roddy, M. Belkin, S.A. Berceli, R.J. DeMasi, R.H. Samson, S.S. Berman, Results of PREVENT III: A multicenter, randomized trial of edifoligide for the prevention of vein graft failure in lower extremity bypass surgery, *J. Vasc. Surg.* 43 (2006) 742–751.e1. <https://doi.org/10.1016/J.JVS.2005.12.058>.
- [3] A.W. Bradbury, D.J. Adam, J.D. Beard, T. Cleveland, J.F. Forbes, F.G.R. Fowkes, I. Gillespie, C. V. Ruckley, G. Raab, H. Storkey, Bypass versus angioplasty in severe ischaemia of the leg (BASIL): multicentre, randomised controlled trial, *Lancet*. 366 (2005) 1925–1934. [https://doi.org/10.1016/S0140-6736\(05\)67704-5](https://doi.org/10.1016/S0140-6736(05)67704-5).
- [4] W. Poulson, A. Kamenskiy, A. Seas, P. Deegan, C. Lomneth, J. MacTaggart, Limb flexion-induced axial compression and bending in human femoropopliteal artery segments, *J. Vasc. Surg.* 67 (2018) 607–613.
- [5] A. Desyatova, W. Poulson, P. Deegan, C. Lomneth, A. Seas, K. Maleckis, J. MacTaggart, A. Kamenskiy, Limb flexion-induced twist and associated intramural stresses in the human femoropopliteal artery, *J. R. Soc. Interface*. 14 (2017). <https://doi.org/10.1098/rsif.2017.0025>.
- [6] C. Gökgöl, S. Schumann, N. Diehm, G. Zheng, P. Buechler, In vivo quantification of the deformations of the femoropopliteal segment: percutaneous transluminal angioplasty vs nitinol stent placement, *J. Endovasc. Ther.* 24 (2017) 27–34.
- [7] A. Desyatova, J. MacTaggart, R. Romarowski, W. Poulson, M. Conti, A. Kamenskiy, Effect of aging on mechanical stresses, deformations, and hemodynamics in human femoropopliteal artery due to limb flexion, *Biomech. Model. Mechanobiol.* 17 (2018) 181–189.
- [8] J.K. Watt, Origin of femoro-popliteal occlusions., *Br. Med. J.* 2 (1965) 1455.

IMAGE DRIVEN SIMULATION OF HEMODYNAMICS AROUND A DYNAMIC CLOT IN VIVO

Chayut Teeraratkul (1), Timothy J. Stalker (2), Maurizio Tomaiuolo (3), Debanjan Mukherjee (1)

(1) Paul M Rady Department of Mechanical Engineering, University of Colorado Boulder, Boulder, CO, USA
(2) Department of Medicine, Thomas Jefferson University, Philadelphia, PA, USA
(3) Wills Eye Hospital, Philadelphia, PA, USA

INTRODUCTION

Clot formation is an essential physiological response to injury, while pathological clotting (thrombosis) is the leading cause of stroke and other major cardiovascular diseases. Complications occur when clots grow to occlude a key vessel or embolize, causing occlusion in distal vessels. Quantitative characterization of flow-induced clot mechanical behavior under realistic hemodynamic forces is key to discerning disease etiology. Advances in *in silico* methods enables highly resolved simulation of local flow environment around clots. Realistic clots have highly arbitrary shapes and are observed to deform dynamically under hemodynamic forces. However, existing *in silico* methods are often limited to idealized or static clot geometries [1, 2]. Intravital microscopy is a molecular-based fluorescence imaging technique which enables quantification of hemostatic response in animal models through high-resolution time-ordered image sequences [3, 4]. Leveraging intravital microscopy, we present an image segmentation methodology that obtains dynamic clot configuration during the clotting process *in vivo*. These clot configurations are used to inform *in silico* simulations of flow and flow-induced forces, to quantitatively characterize clot mechanics and dynamic flow environment in the clot neighborhood *in vivo*.

METHODS

Automatic clot domain segmentation: Intravital microscopy images of clot formation in mouse cremaster arterioles are obtained from a laser injury experiment (Fig. 1a). High-frequency noise artifacts in the images are filtered through a combination of a median filter and a Gaussian filter using the open-source image processing library OpenCV [5] (Fig. 1b). The filtered images are segmented based on pixel intensity using a k-means clustering method implemented in the Python library scikit-learn [6], and the pixels comprising the clot boundary are obtained (Fig. 1c). The extracted clot boundary is represented as a smooth BSpline curve using the open-source library NURBS-Python [7] and imposed onto a computational grid. This segmentation workflow is repeated for each frame of the image stack (Fig. 1d).

In-silico modeling of flow around dynamic thrombi: Local hemodynamics around the dynamic clot is simulated using a fictitious domain

stabilized finite element formulation [1]. The clot interior is assumed to be a heterogeneous porous domain, and resisted flow inside the clot is modeled using a Brinkman equation for flow inside porous media [8]. Blood plasma is assumed to be Newtonian with a bulk density of 1 g/cc, and viscosity of 4 cP. The inlet flow is assumed to be parabolic, with the centerline flow velocity experimentally measured to be 1.3 mm/s.

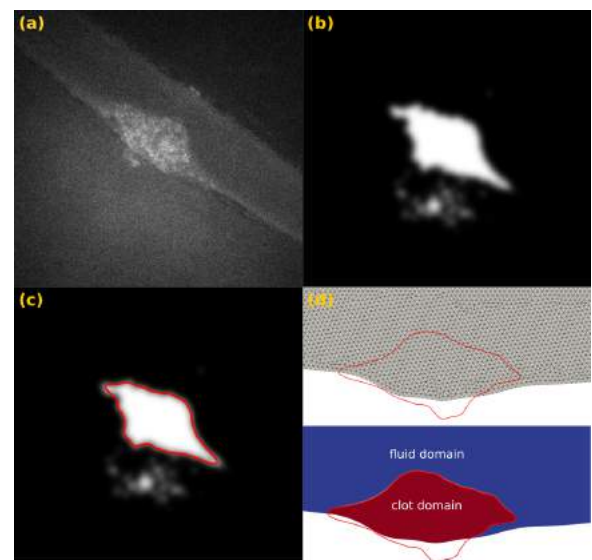


Figure 1: Schematic of the *in vivo* to *in silico* workflow: (a) image frame obtained microscopy experiment; (b) filtered image removes noise content; (c) identified thrombus boundary using ; (d) imposed thrombus boundary as a fictitious domain on the computational grid.

RESULTS

In this work, we demonstrate that our coupled *in vivo* to *in silico* method enables quantification of thrombus stability *in vivo*. Specifically, we used

our framework to analyze microscopy data of the hemostatic plug formed in a wild-type (WT) mouse compared to that formed in a DiYF variant mouse. DiYF variant mice are genetically modified mice that are observed to have hindered clot retraction behavior [9, 10]. The spatiotemporally varying clot configuration is automatically extracted from the intravital microscopy images and is directly coupled with the *in silico* flow simulation. The resulting flow velocity field, clot kinematics, and hemodynamic loading on the clot, for the WT and DiYF variants are presented in Fig. 2 and Fig. 3 respectively. Here, hemodynamic loading is quantified as surface-averaged traction force from blood flow acting on the clot boundary. The results show a greater clot volume, higher level of occlusion, and subsequently higher hemodynamic loading in the WT variant compared to the DiYF variant. Both variants exhibit a critical hemodynamic load at which the clot starts to “yield” (see time **T2** in Fig. 2 and Fig. 3). At this critical hemodynamic load, WT variant clot is observed to stretch laterally along the flow direction without a significant drop in thrombus area, indicating clot deformation and stretching that relieves the hemodynamic load but does not fragment and embolize. This point is identified by the sharp drop in the clot aspect ratio (Fig. 2c). Conversely, after the critical hemodynamic load, DiYF variant clot area sharply decreases (Fig. 3a). This corresponds to a sharp loss of mass, which in turn signifies clot embolization, as also observed in the experimental images.

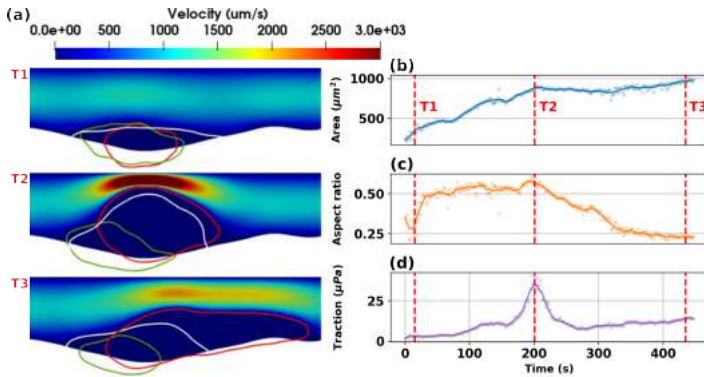


Figure 2: Wild-type variant clot dynamics and corresponding hemodynamic loading: (a) velocity field at initial size, maximum size, late time configuration; (b) thrombus area over time; (c) thrombus aspect ratio over time; (d) surface averaged traction force over time.

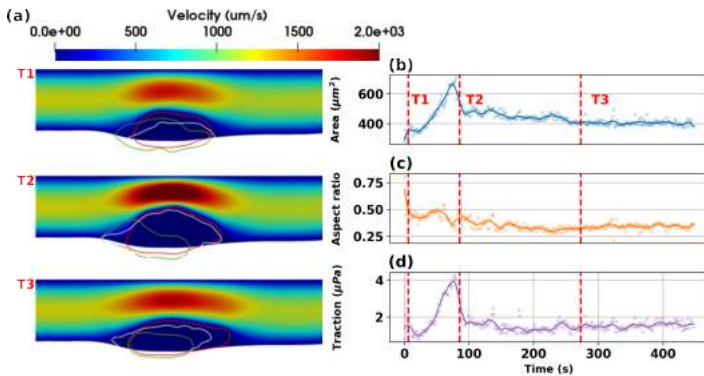


Figure 3: DiYF variant clot dynamics and corresponding hemodynamic loading: (a) velocity field at initial size, maximum size, late time configuration; (b) thrombus area over time; (c) thrombus aspect ratio over time; (d) surface averaged traction force over time.

DISCUSSION

Our custom *in vivo* to *in silico* workflow enables quantitative characterization of clot mechanics and dynamic flow environment in the *in vivo*

clot neighborhood - information that is not otherwise available from intravital imaging alone. Here, we establish this using two illustrative simulation cases - a wild-type (WT) and diYF variant of genetically modified mice. Specifically, the DiYF variants are known to have defective clot retraction, which can result in loosely packed, potentially weaker clot. Fig. 2d and Fig. 3d show a significant decrease in critical hemodynamic load between the WT and DiYF case which is consistent with our understanding of DiYF variant clot. Furthermore, clot mechanical behavior and deformation in response to hemodynamic forces, can be quantified based on this coupled *in vivo-in silico* approach. Specifically, at the time of critical hemodynamic load, a sharp decrease in clot aspect ratio signifies that the clot sustains more stable deformations along the flow. In contrast, sharp decrease in clot volume corresponds with flow mediated fragmentation. This space-time varying force-response mechanical behavior is condensed into a time-envelope plot as shown in Fig. 4. The figure indicates that WT variant with normal retraction properties grew a larger clot sustaining a greater hemodynamic loading (that is, a bigger bounding box in the envelope curve) compared to the impaired retraction behavior in DiYF variants.

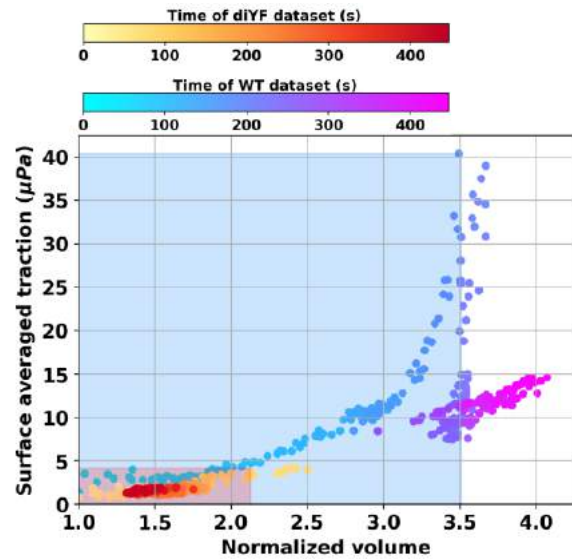


Figure 4: Clot volume vs surface averaged traction for both wild-type and diYF variants, indicated as a time-envelope of the dynamic force-deformation behavior combined with growth/embolization.

ACKNOWLEDGEMENTS

This work utilized resources from the CU Boulder Research Computing Group which is supported by NSF (awards ACI-1532235 and ACI-1532236), CU Boulder, and Colorado State University.

REFERENCES

- [1] Teeraratkul C et al. *Bio. Mech. Mechan.* 20.2 (2021).
- [2] Zheng X et al. *PLOS Computational Biology* 16.4 (2020).
- [3] Welsh JD et al. *Blood* 124.11 (2014).
- [4] Stalker TJ. *Platelets* 31.4 (2020).
- [5] Bradski G. *Dr. Dobb's Journal of Software Tools* (2000).
- [6] Pedregosa F et al. *Journal of Machine Learning Research* 12 (2011).
- [7] Bingol OR et al. *SoftwareX* 9 (2019).
- [8] Durlofsky L et al. *Physics of Fluids* 30.11 (1987).
- [9] Stalker TJ et al. *Blood* 124.11 (2014).
- [10] Tomaiuolo M et al. *Blood* 124.11 (2014).

A NEW APPROACH TO CHARACTERIZE TRABECULAE CARNEAE STRUCTURES USING HIGH-RESOLUTION HUMAN HEART IMAGES

Yasamin Seddighi (1), Keith Bartels (2), Hai-Chao Han (1)

(1) Department of Mechanical Engineering, The University of Texas at San Antonio, San Antonio, TX, USA

(2) Southwest Research Institute, San Antonio, TX, USA

INTRODUCTION

Trabeculae carneae are irregular muscular structures in the heart that cover the endocardial surfaces of both ventricles. Although these trabeculae account for a significant portion of human ventricular mass, their role in the ventricular function is not well understood [1,2]. Reports have shown that the trabeculae structure changes in pathological (e.g., ventricular noncompaction) and physiological (e.g., pregnancy and anemia) conditions [3]. However, the trabeculae carneae are difficult to resolve in clinical cardiac imaging modalities (e.g., echocardiogram and MRI imaging) in vivo due to their small sizes and there is no report of an effective approach to characterize the complex trabecular structure. Therefore, the objective of this study was to acquire high-resolution ex-vivo CT images of human hearts that capture the detailed trabeculae structure and to use 3D image processing and analysis to characterize that structure.

METHODS

Human heart explants were obtained from the South Texas Blood and Tissue Center (San Antonio, TX) after being de-identified and consents for research from the donors' families were obtained in accordance with Institutional Review Board (IRB) requirements. To prepare for CT imaging, heart chambers were filled with a Loctite® Tite foam which provided structural support to prevent the collapse of the chambers and has low density to provide good contrast to the tissue. Each heart was imaged inside a container surrounded by cotton balls to prevent direct contact with the container and reduce movement during scanning. CT-scans were performed using a GE v|tome|x m240 cone-beam micro-focus X-ray CT imaging system. Scanning parameters (tube voltage, beam-hardening filters, scan times, etc.) were determined so that high-resolution (voxel size near 70 microns) were obtained. Scan times of approximately 30 minutes provided images with relatively high signal-to-noise ratio (SNR).

The 3D CT images were imported into MATLAB for 3D visualization and image processing. A combination of custom tools and MATLAB built-in functions were used to automate the measurement of the length and cross-sectional area of the trabeculae.

In the first processing step, the trabeculae structure was isolated from the endocardium by removing the myocardial wall from the left ventricle (LV) (Figure 1a & b). Two layers of voxels were added to the top edge of the initial binary image (bw_1) to close the ventricular chamber and form a void representing the volume of the apex of the LV (Figure 1c). Then, this closed ventricular volume was filled (Figure 1d) and the volume obtained from subtracting bw_1 from the filled chamber gave the lower ventricular volume (Figure 1e). Finally, voxels of the outer edge of the LV chamber were identified and all voxels (0 and 1) within the chamber volume were flipped to obtain the trabeculae structure T (Figure 1f).

After smoothing the outer edges of T, MATLAB was used to find the 3D skeleton (S) of the binary image T. The branch points of the S were removed to separate the branches of the skeleton segments CC_s [4]. However, some larger trabeculae are connected to multiple small trabeculae and thus are broke into multiple short segments. To resolve this issue, thinner trabeculae segments were removed by an iterative process using morphological operation "opening" with a spherical structuring element (SE) of increasing radius R ($R=1, 2, \dots$). In each iteration, "opening" with a given R was applied to T and the resulting image was subtracted from T to obtain T_R . T_R is the reduced structure containing partial or full segments of the trabeculae with maximum inscribed sphere smaller than SE of radius R. This process is repeated for SEs with increasing radii. For a given branch segment, since the cross sections varies along its length, as the radius of the SE increases, the portion of the segment in T_R grows until it contains more than one CC_s (CC_s of its own and neighboring segments) in the N^{th} iteration. Then, the desired configuration representing this trabecula segment is the one obtained at iteration N-1 which is the largest cut (volume) of the

segment that contains only one CC_S. The segment was labeled and stored as an individual segment for further measurement and the skeleton of the segment was removed from the skeleton structure S. After all branching segments are removed, the isolated large trabecular segments having only one CC_S within their volume were labeled and stored as a single trabeculae segment.

After all trabeculae and corresponding skeletons were separated and labeled, the length and central cross-sectional area of all the trabeculae were measured. For each trabecular segment, a second order polynomial curve (p) was fit to its skeleton voxels. The length of each trabecula was determined as the curve length of p between its intersection points with the trabecular surface. The normal plane at the midpoint of the curve p was determined and the trabecular voxels intersected by the normal plane were used to determine the cross-sectional area.

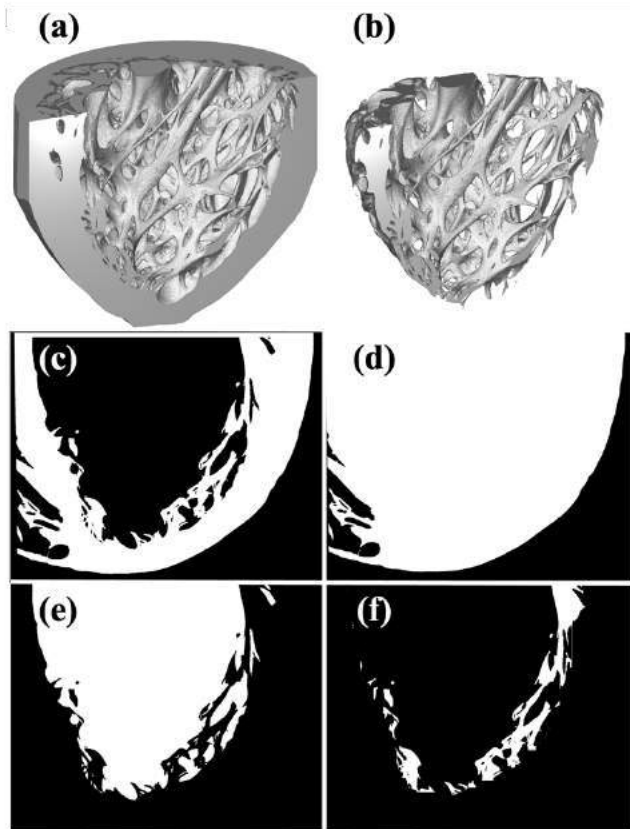


Figure 1: Schematic illustration of the process of removing endocardium from (a) 3D image of human LV to get the (b) isolated trabeculae structure. (c) LV chamber enclosed at the top, (d) LV with void filled, (e) LV chamber after subtracting initial image from (d), (f) isolated trabeculae structure.

RESULTS

Three human hearts have been scanned and all scans successfully captured the fine structure of trabeculae carneae. The rendered volume representation of the LV showed 3D images containing trabeculae structure (Figure 1a).

The segmented trabeculae structure of one heart was analyzed to measure the length and thickness of the free running trabeculae. Our results showed that central trabeculae area varies between 0.004 mm² and 2.43 mm² and trabeculae length ranges from 0.22 mm to 7.00 mm

at the apex of the current LV model (Figure 2). The majority of the trabecula lengths and areas are in the range of 0.22-2 mm and 0.004-0.6 mm², respectively.

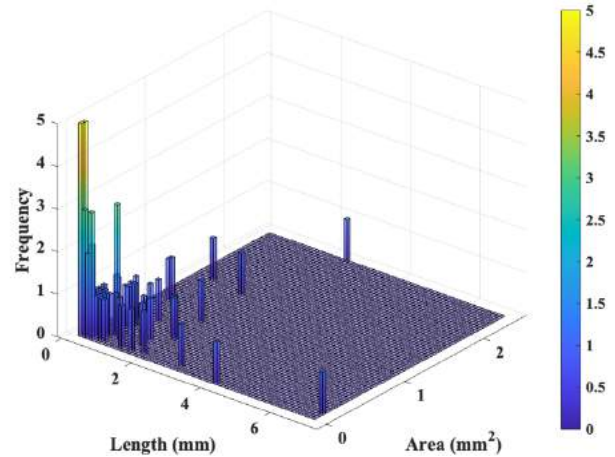


Figure 2: Length and cross-sectional area distribution of the trabeculae carneae at the apex part of the LV

DISCUSSION

A new method to acquire high resolution CT images of the human heart was presented. The method captures the small and complex trabecular structure. Automated 3D algorithms were used to segment and characterize the complex structure of the trabeculae carneae.

There are limitations in this study that could be addressed in future studies. First, the trabeculae carneae structure of only one heart was analyzed with this method. Second, this method cannot automatically distinguish between trabeculae carneae, papillary muscle and chordae tendineae and thus requires manual separation/identification.

Despite limitations, this study provides the groundwork of a new method to automatically capture trabeculae structure that can be used to develop the detailed heart models in future studies. Additionally, characterizing the trabeculae structure in different pathological conditions may shed light on the trabeculae carneae function.

ACKNOWLEDGEMENTS

This study was supported by a grant from the Office of Vice President for Research, Economic Development, and Knowledge Enterprise at the University of Texas at San Antonio and by the Advisory Committee for Research at Southwest Research Institute.

REFERENCES

- [1] Fatemifar F. et al., *J Biomech Eng*, 141(2):021007, 2019.
- [2] Fernández-Golfín C. et al., *J Cardiovasc Med (Hagerstown)*, 10(11):827-33, 2009.
- [3] Halaney DL. et al., *J Biomech Eng*, 139(3):0310121, 2017.
- [4] Stauber M, Müller R., *Bone*, 38(4):475-84, 2006.

ANALYZING REAL WORLD HEAD IMPACTS USING THE BRAIN SIMULATION RESEARCH PLATFORM

Ritika R. Menghani (1), Reuben H. Kraft (1,2,3)

- (1) Department of Mechanical Engineering, The Pennsylvania State University, State College, Pennsylvania, USA
- (2) Department of Biomedical Engineering, The Pennsylvania State University, State College, Pennsylvania, USA
- (3) Institute for Computational and Data Sciences, The Pennsylvania State University, State College, Pennsylvania, USA

INTRODUCTION

Mild Traumatic Brain Injury (mTBI) is a public health concern and often seen in contact sports. As per the CDC in 2019, 15% of US high school students self-reported a concussion in the past 12 months[1]. With the help of instrumented mouthguard sensors, it is now possible to measure and record head kinematics of a player during an impact. The head impact data can be used to determine brain injury metrics to determine to assess the severity of the impact. Several research groups are now using sensor data to run finite element simulations to estimate these metrics. In this study, 500 impacts obtained from Prevent biometrics, some of which were identified as severe head impacts, were analyzed using the brain simulation research platform to test if the 95th percentile Maximum Principal Strain (MPS-95) can accurately identify the severe impacts.

METHODS

Impact Dataset: In this study, 500 head impacts collected by Prevent biometrics were analyzed using the brain simulation research platform. A keyword titled “CHECK_ENGINE” was assigned to all the impacts that were visually determined to be severe impacts. A total of 31 impacts were listed as “CHECK_ENGINE” and the others were treated as though they were non-injurious.

Brain Simulation Research Platform: All simulations were carried out on the brain simulation research platform which is a brain modeling service that can simultaneously run several finite element simulations of a brain mesh. The platform uses a finite element modeling code called FEMTech which has been developed to carry out the simulations using a non-linear explicit

dynamics scheme. FEMTech has been tested against brain experiments in literature and the validation results are available on the platform at <https://brainsimresearch.io/validation>.

Finite Element Model: All 500 impacts were run on the platform using a hexahedral mesh of the brain that includes sulci and gyri (Figure 1). The geometry of the brain corresponds to a male individual head model that scaled to match the dimensions of the 50th percentile male model. The brain was modeled using hyper-viscoelastic material properties obtained from [2]; the parameters used have been listed in Table 1.

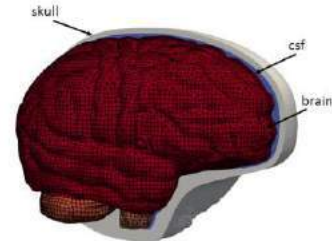


Figure 1: Brain mesh used to simulate the 500 impacts.

Table 1: Material properties used in the simulations.

Part	Model	Properties
Skull	Rigid/Elastic[2]	$E=15\text{GPa}$, $\nu=0.22$, $\rho=2000\text{ kg/m}^3$
CSF	Hyper-elastic[3]	$K=22\text{MPa}$, $G=50\text{kPa}$, $\rho=1040\text{ kg/m}^3$
Brain	Hyper-viscoelastic[2]	$G_1=320\text{kPa}$, $\beta_1=10^6/\text{s}$, $G_2=78\text{kPa}$, $\beta_2=10^5/\text{s}$, $G_3=6.2\text{kPa}$, $\beta_3=10^4/\text{s}$, $G_4=8\text{kPa}$, $\beta_4=10^3/\text{s}$, $G_5=0.1\text{kPa}$, $\beta_5=10^2/\text{s}$, $G_6=3\text{kPa}$, $\beta_6=10^1/\text{s}$, $\nu=0.49999$, $\rho=1040\text{ kg/m}^3$

RESULTS

By plotting the MPS-95 on the x-axis and categorizing the “CHECK_ENGINE” cases on the y-axis, the relationship between severity of the impact and strain can be evaluated. According to the findings in Figure 2, there seems to be no obvious relation between 95th percentile MPS and visible symptoms of a head injury.

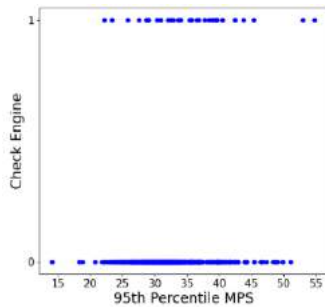


Figure 2: Check Engine vs 95th Percentile MPS; no obvious correlation can be seen in this dataset.

The severe cases were further studied by plotting all the MPS-95 vs time curves. MPS-95 curves for the brain often exhibit two peaks[4]; hence these plots have been color-coded based on whether it is apparent if the highest peak has been reached. The green plot shows two peaks and a decline in the trend indicating that it has likely reached the peak. The yellow plot is cut off at what may be the peak but it is uncertain. The red plot is truncated before the second peak is even hit, leaving the possibility of it being larger. Amongst all 31 severe cases, 8 appear to have reached the peak (green), 4 may have reached the peak (yellow) and 19 were cut off too early (red).

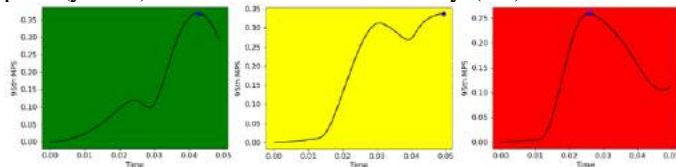


Figure 3: 95th Percentile Maximum Principal Strain vs Time for three "CHECK_ENGINE" cases.

DISCUSSION

In this study, 500 head impact kinematics collected by Prevent Biometrics were analyzed using the brain simulation research platform. Some of these impacts were considered severe and listed as such based on the symptoms that the players exhibited after the impacts, as reported by the sensor company. MPS-95 was computed for each impact to test if it can identify the severe impacts. Based on these results, there is no clear difference in the MPS-95 values between both kinds of impacts, which was unexpected as strain has been thought to relate to head injury in literature[5].

Upon further examination of the severe impacts, it was identified that more than half the cases did not conclusively hit a peak. A possible theory is that larger brain strains may have been missed and that MPS-95 is a better indicator of impact severity than what the results currently show. This is also supported by

some other research that discuss the importance of the recording time window of the kinematics for an impact[4], [6].

Another limitation of the study is that the severe cases were identified as the ones that had visible symptoms of a head injury, which may introduce error and result in cases that were severe but went undetected due to the lack of symptoms. A more reliable approach to distinguish between severe and non-severe cases would be to use a sideline cognitive testing such as the ImPACT test[7]. That data can then be compared with similar brain injury metrics to test for a correlation. Such a study is planned and will take place in the near future.

ACKNOWLEDGEMENTS

This work has been supported by the NSF under award number 1846059. We would also like to thank Prevent Biometrics who have supplied the impact data.

REFERENCES

- [1] “Traumatic Brain Injury / Concussion | Concussion | Traumatic Brain Injury | CDC Injury Center,” Nov. 14, 2022. <https://www.cdc.gov/traumaticbraininjury/index.html> (accessed Nov. 20, 2022).
- [2] S. Kleiven, “Predictors for traumatic brain injuries evaluated through accident reconstructions,” *Stapp Car Crash J*, vol. 51, pp. 81–114, Oct. 2007, doi: 10.4271/2007-22-0003.
- [3] C. Zhou, T. B. Khalil, and A. I. King, “A New Model Comparing Impact Responses of the Homogeneous and Inhomogeneous Human Brain,” *SAE Trans.*, vol. 104, pp. 2999–3015, 1995.
- [4] S. Ji, S. Wu, and W. Zhao, “Dynamic characteristics of impact-induced brain strain in the corpus callosum,” *Brain Multiphysics*, vol. 3, p. 100046, 2022, doi: 10.1016/j.brain.2022.100046.
- [5] T. Wu, M. Hajiaghameh, J. S. Giudice, A. Alshareef, S. S. Margulies, and M. B. Panzer, “Evaluation of Tissue-Level Brain Injury Metrics Using Species-Specific Simulations,” *J. Neurotrauma*, vol. 38, no. 13, pp. 1879–1888, Jul. 2021, doi: 10.1089/neu.2020.7445.
- [6] Y. Liu *et al.*, “Time window of head impact kinematics measurement for calculation of brain strain and strain rate in American football,” *Ann. Biomed. Eng.*, vol. 49, no. 10, pp. 2791–2804, Oct. 2021, doi: 10.1007/s10439-021-02821-z.
- [7] “ImPACT Concussion Test | ImPACT Applications,” Jul. 12, 2017. <https://impactconcussion.com/> (accessed Jan. 19, 2023).

A THREE-NODE ROTATION-FREE KIRCHHOFF-LOVE SHELL FORMULATION FOR CARDIOVASCULAR APPLICATIONS

L. Shi (1), Y. Chen (1) V. Vedula (1)

(1) Department of Mechanical Engineering, Columbia University, New York, NY, USA

INTRODUCTION

Kirchhoff-Love shell formulations are often used to model the biomechanical response of thin structures such as heart valves, skin, and cartilage that undergo finite nonlinear deformation. Shell formulations are also computationally efficient as they substantially reduce the size of the problem compared to 3D solid elements, making them a popular choice for many biomechanics applications. The Kirchhoff-Love shell formulation considers both membrane and bending strains but typically requires both translational and rotational degrees of freedom to resolve the bending strains. On the contrary, rotation-free shell formulations retain only the three translation degrees of freedom at each node, thus further reducing the problem size compared to formulations involving rotations. However, these formulations require additional element treatment or isogeometric analysis, limiting their utility to patient-specific modeling and simulation [1, 2].

We present a novel 3-node rotation-free thin shell formulation for incompressible and compressible hyperelastic materials, implemented in an open-source finite element solver, *svFSI*. Our work is based on the rotation-free formulation developed by Stolarski et al. [1] for St. Venant-Kirchhoff material. We extend the methodology for general hyperelastic materials while also satisfying the plane stress condition. We derive multiple 3D constitutive models in compressible and incompressible forms, including the isotropic (neo-Hookean and Mooney-Rivlin) and anisotropic (Gasser-Ogden-Holzapfel (GOH) and Lee-Sacks) hyperelastic models, routinely employed in cardiovascular biomechanics applications.

We validated the formulation by comparing the model results against analytical solutions for a beam under uniaxial tension and a plate subjected to a transverse pressure load for both compressible and incompressible materials. We also simulated the mechanics of a patient-specific aortic valve subjected to a physiological transvalvular pressure gradient.

METHODS

In this Kirchhoff-Love shell formulation for finite deformations, we split the Green-Lagrange strain tensor into the membrane and bending components. The standard 3-node triangular element shape functions are used for discretization that eliminates membrane locking, typically observed in higher-order shell formulations [1]. Computing the variation of the membrane strain tensors on each element of the triangular mesh is straightforward. However, to accurately account for the bending strain of an element, a complete quadratic polynomial is used to represent a patch of elements in the neighborhood of the main element (Fig. 1) and is used to evaluate the element curvature tensor [1].

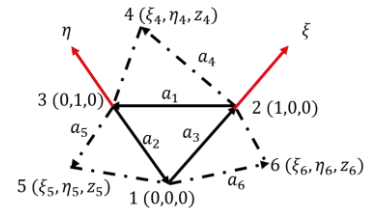


Figure 1: A patch of elements in the neighborhood of the main triangular element is used to resolve bending strains. [2]

The governing weak form of the shell formulation in the reference configuration is given by, [2]

$$\int_{A_0} [\rho \dot{\mathbf{u}} \cdot \delta \mathbf{u} + n^{\alpha\beta} \delta E_{\alpha\beta}^m + m^{\alpha\beta} \delta E_{\alpha\beta}^b - \mathbf{f}_{ext} \cdot \delta \mathbf{u}] dA = 0 \quad (1)$$

where \mathbf{u} is the displacement, $\dot{\mathbf{u}}$ is the acceleration, h is the shell thickness, A_0 is the area of the shell surface in the reference configuration, $n^{\alpha\beta}$ and $m^{\alpha\beta}$ are the stress resultants obtained by integrating the 2nd Piola-Kirchhoff stress tensor ($S^{\alpha\beta}$) through the thickness as,

$$n^{\alpha\beta} = \int_{-h/2}^{h/2} S^{\alpha\beta} d\tau, \text{ and } m^{\alpha\beta} = \int_{-h/2}^{h/2} \tau S^{\alpha\beta} d\tau, \quad (2)$$

with $\alpha, \beta = 1, 2$ denoting the in-plane curvilinear components of the shell mid-surface, and E^m and E^b are the membrane and bending components of the Green-Lagrange strain tensor, respectively.

The stress tensor for incompressible materials is derived by satisfying the plane stress condition and can be expressed by

$$S^{\alpha\beta} = 2 \frac{\partial W}{\partial C_{\alpha\beta}} \quad (3)$$

where W is the free-energy density, and $g_{\alpha\beta}$ is the covariant metric tensor of a shell layer in the current configuration. The compressible stress tensor is obtained by iteratively solving for the off-plane component of the right Cauchy-Green deformation tensor (C_{33}) to satisfy the plane stress condition using the Newton method [2]. The stress tensor can be derived by the standard 3D stress equation, $S^{ij} = 2 \frac{\partial W}{\partial C_{ij}}$, but the right Cauchy-Green deformation tensor $\mathbf{C} = C_{ij} \mathbf{G}^i \otimes \mathbf{G}^j$ here is expressed in the metric coefficients form, where \mathbf{G}^i is the contravariant base vector in the reference configuration.

Here, we apply the above formulation for four hyperelastic constitutive models, including the neo-Hookean, the Mooney-Rivlin, GOH, and the Lee-Sacks valve models [3, 4]. The expressions for the 2nd Piola-Kirchhoff stress tensor for each of these material models are shown below (Eq. 4) in incompressible form as,

$$\begin{aligned} S_{NH}^{\alpha\beta} &= \mu(G^{\alpha\beta} - J^{-2}g^{\alpha\beta}) = \mu S_{I_1}^{\alpha\beta} \\ S_{MR}^{\alpha\beta} &= c_1 S_{I_1}^{\alpha\beta} + c_2 J^{-2}(G^{\alpha\beta} - G_{\gamma\delta} g^{\gamma\delta} g^{\alpha\beta}) + c_2 J^{-2} G^{\alpha\beta} \\ S_{GOH}^{\alpha\beta} &= \mu S_{I_1}^{\alpha\beta} + 2a_f(g_{\gamma\delta} A_f^{\gamma\delta} - 1) \exp[b_f(g_{\gamma\delta} A_f^{\gamma\delta} - 1)^2] [\kappa S_{NH}^{\alpha\beta} + (1 - 3\kappa) A_f^{\alpha\beta}] \\ &\quad + 2a_s(g_{\gamma\delta} A_s^{\gamma\delta} - 1) \exp[b_s(g_{\gamma\delta} A_s^{\gamma\delta} - 1)^2] [\kappa S_{NH}^{\alpha\beta} + (1 - 3\kappa) A_s^{\alpha\beta}] \\ S_{LS}^{\alpha\beta} &= a S_{I_1}^{\alpha\beta} + 2a_0 \mu b_1 (g_{\gamma\delta} G^{\gamma\delta} - 3) \exp[b_1(g_{\gamma\delta} G^{\gamma\delta} - 3)^2] S_{NH}^{\alpha\beta} + 2a_0 (1 - \mu) b_2 \chi (g_{\gamma\delta} A_f^{\gamma\delta}) (g_{\gamma\delta} A_f^{\gamma\delta} - 1) \exp[b_f(g_{\gamma\delta} A_s^{\gamma\delta} - 1)^2] A_f^{\alpha\beta} \end{aligned} \quad (4)$$

where $A_i^{\alpha\beta} = A_i^\alpha A_i^\beta$ is the directional tensor, $g^{\alpha\beta} = g_{\alpha\beta}^{-1}$, $G_{\alpha\beta}$ is the covariant metric tensor of a shell layer in the reference configuration, $G^{\alpha\beta} = G_{\alpha\beta}^{-1}$, $J^2 = \det[g_{\alpha\beta}] / \det[G_{\alpha\beta}]$.

RESULTS

A uniaxial tension simulation is performed to test the ability of the presented shell models to solve the membrane-dominated problem. In this case, a rectangular incompressible strip with length \times width \times thickness = $9 \times 3 \times 0.3 \text{ mm}^3$ is pulled by a force as shown in Fig. 2. For the neo-Hookean model: the elasticity modulus = 0.3 MPa. MR model: $c_1=4 \text{ MPa}$ and $c_2=8 \text{ MPa}$. GOH model: $a_4=10 \text{ MPa}$, $b_4=5$, $a_6=30 \text{ MPa}$, $b_6=5$, and μ changes from 0 to 1/3. Lee-Sacks model: $a=0.1 \text{ MPa}$, $a_0=3 \text{ MPa}$, $b_1=0.3$, $b_2=1$, and κ changes from 0.5 to 1. The fiber directions for the GOH model are shown in Fig. 2, and the fiber is along $+30^\circ$ for the Lee-Sacks model. The displacement curves of the upper edge vs. pressure for different materials are shown in Fig. 2, where dashed lines represent the analytical solutions.

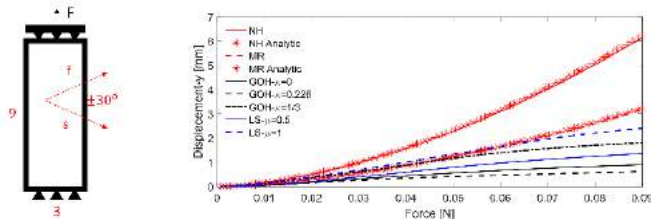


Figure 2: Displacement-force curves of various constitutive models for a clamped force-controlled uniaxial tension simulation.

A clamped plate under pressure simulation is used to test the ability of the presented shell models to capture the membrane and bending deformations together. In this case, a rectangular plate with length \times

width \times thickness = $20 \times 20 \times 1 \text{ mm}^3$ is clamped with fixed boundaries, and a uniform distributed pressure is exerted on the whole plate (Fig. 3). The plate is modeled as either an incompressible or compressible (Poisson's ratio=0.3) shell. For the neo-Hookean model: elasticity modulus = 0.3 MPa. MR model: $c_1=4 \text{ MPa}$ and $c_2=8 \text{ MPa}$. GOH model: $a_4=10 \text{ MPa}$, $b_4=5$, $a_6=30 \text{ MPa}$, $b_6=5$, and $\mu=0.226$. Lee-Sacks model: $a=0.1 \text{ MPa}$, $a_0=3 \text{ MPa}$, $b_1=0.3$, $b_2=1$, and $\kappa=0.5$. The fiber directions for the GOH model are shown in Fig. 2, and the fiber is along $+45^\circ$ for the Lee-Sacks model. The displacement curves of the center node vs. pressure for different materials are shown in Fig. 2, where dots represent the analytical solutions.

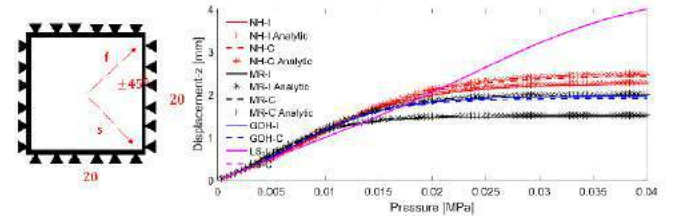


Figure 3: Displacement-pressure curves of various constitutive models for a clamped plate under pressure.

A patient-specific trileaflet aortic valve is created from CT data. (Fig. 4a) For each leaflet, one edge is fixed where the leaflet is attached to the aorta, and the other is left free. The leaflets are modeled as incompressible neo-Hookean material with an elasticity modulus of 1.25 MPa, shell thickness of 0.4mm, and density of 0.001kg/m³. A realistic transvalvular pressure gradient is applied on the ventricular side of the leaflets, and a penalty-based contact algorithm is applied between the leaflets. The opening and closing states of the aortic valve are shown in Figs. 4c and 4d.

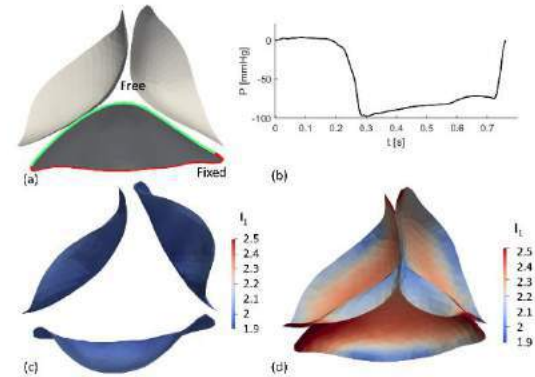


Figure 4: The patient-specific aortic valve under real pressure. (a) FEA model (b) pressure curve (c) opening state (d) closing state. Color denotes the first invariant of the right Cauchy-Green deformation tensor \mathbf{C} .

DISCUSSION

Our results demonstrate a reasonable agreement between model predictions and analytical data (Figs. 2 and 3). The patient-specific aortic valve also opens and closes as expected. In the future, we intend to expand the capabilities of the present shell formulation for performing vascular and valvular fluid-structure interaction (FSI) simulations.

ACKNOWLEDGEMENTS

We acknowledge computing resources from Columbia University's Shared Research Computing Facility – Ginsburg HPC.

REFERENCES

- [1] Stolarski H, et al. IJNME 95.9 (2013): 740-770. [2] Kiendl J, et al. CMAME 291 (2015): 280-303. [3] Gasser TC, et al. JRSI 3.6 (2006): 15-35. [4] Lee CH and Sacks SM. Struct Mech. (2016) 365-381.

HEART RATE IMPACT ON PLAQUE DEPOSITION AT THE CAROTID ARTERY BIFURCATION

Ramita Sajankila¹, Esha Navaneethakrishnan¹, Elvan Dogan, MS¹, Amir K. Miri, PhD¹

¹Department of Biomedical Engineering
New Jersey Institute of Technology
Newark, New Jersey, USA

INTRODUCTION

Atherosclerosis, caused by plaque buildup in the arteries, has been the primary cause of heart disease and 50% mortality rate of all deaths in the United States [1]. It has been shown that when an artery splits into two different counterparts, there is an increased chance of plaque materials' deposition near the bifurcation area [2]. The wall shear stress and blood flow rate in an artery have been shown to directly impact the atherosclerotic plaque build-ups at the bifurcation of an adult artery, where a lower wall shear stress results in a higher plaque formation rate [3]. We need to understand the mechanisms of plaque deposition in the arteries to improve our treatments. In this work, we will perform one case study to quantify the effects of cardiovascular exercise intensity on the rate of plaque deposition near the bifurcation area of the carotid artery by using the ANSYS (FLUENT software) simulation and theoretical modeling to analyze a 3D model of artery's blood flow. The increased wall shear stress and maximum blood flow velocity through the carotid artery during the intense exercise model were used to validate the model. The results of this work can be used for further modeling a potential treatment for such patients.

METHODS

The numerical tool ANSYS FLUENT (Canonsburg, PA) was used to simulate a selected geometry of carotid artery bifurcation (Patient, Ref. [5]). The GrabCAD package was used for this study. Geometry, meshing, boundary conditions, and other elements were identified in the simulation, except for the rate of blood flow into the inlet of the artery (**Figure 1**). Our first case was a blood flow of ~ 120 beats per minute (BPM, heart rate), representing moderate cardiovascular exercise. Our second case was a flow of 180 BPM to represent intense exercise such as running [4]. The fluid flow is considered to be laminar Carreau flow, with a density of 1060 m³/kg. The geometrical parameters of the ANSYS simulation are listed in **Table 1**. The right CCA mean diameter and the ICA mean diameter refer to the dimensions of the bifurcated artery geometry that was used for the purposes of this study, i.e., to observe the intensity of cardiovascular exercise on plaque deposition near the bifurcation area.

The problem information is summarized as:

Table 1: Properties and Parameters from Ref. [5]

Parameter	Value
Right CCA mean diameter (5)	6.52 mm
ICA mean diameter	5.11 mm
External carotid artery (ECA) diameter	1.42 mm

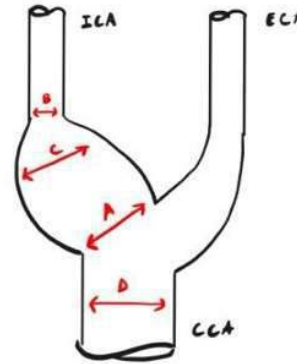


Figure 1: Geometry of 3D carotid artery bifurcation

The governing equations of the mathematical problem are listed below.

Navier Stokes Equation

$$\rho \left(\frac{\delta u}{\delta t} + u \cdot \nabla u \right) \quad (1)$$

$$-\nabla p + \mu \nabla^2 u \quad (2)$$

Continuity Equation

$$\nabla \cdot u = 0 \quad (3)$$

Boundary Conditions

$$v_{\text{wall}} = 0 \quad (4)$$

The mathematical descriptions for the two cases were adapted from a model proposed by Sinnott et al., outlining the flow model of a bifurcated artery through a grid-free method [6].

Case I - 120 BPM:

$$v_{inlet}(t) = 0.5 \sin [4\pi(t + 0.0160236)] : 0.5n < x < 0.5n + 0.218 \quad (5)$$

$$v_{inlet}(t) = 0.1 : 0.5n + 0.218 < n < 0.5(n + 1) \quad (6)$$

$$n = 0, 1, 2, \dots$$

Case II - 180 BPM:

$$v_{inlet}(t) = 0.5 \sin [4\pi(t + 0.05235)] : 0.33n < x < 0.33n + 0.1453 \quad (7)$$

$$v_{inlet}(t) = 0.1 : 0.33n + 0.1453 < n < 0.33(n + 1) \quad (8)$$

$$n = 0, 1, 2, \dots$$

RESULTS

The results of the ANSYS simulations of blood flow through both the moderate and intense exercise models are displayed below.

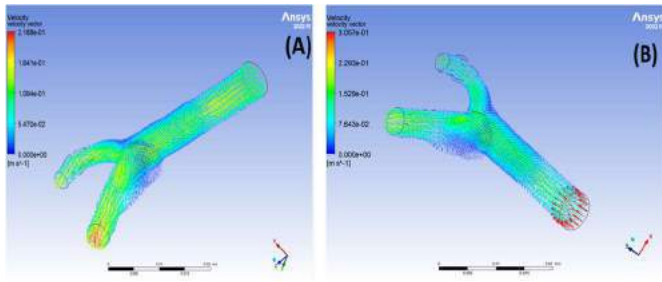


Figure 2: Velocity profile of carotid artery for the two cases: (A) 120 BPM and (B) 180 BPM

The maximum velocity observed in the moderate exercise ANSYS model is 0.2188 m/s. The maximum velocity observed in the intense exercise ANSYS model is 0.3057 m/s.

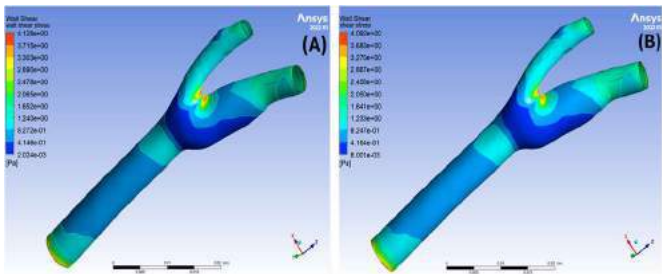


Figure 3: Wall shear stress of carotid artery for the two cases: (A) 120 BPM and (B) 180 BPM

The minimum wall shear stress observed in the moderate exercise ANSYS model is 2.024e-3 Pa. The minimum wall shear stress observed in the intense exercise ANSYS model is 8.001e-3 Pa. v_f for 120 BPM and 180 BPM was found from

ANSYS simulations to be 0.109 m/s and 0.159 m/s respectively.

DISCUSSION

The aim of this study is to observe the extent of the decrease of the rate of plaque formation over time in an artery when subjected to intense versus moderate exercise. As suggested by the results, it can be determined that the maximum velocity of the blood through the carotid artery at 180 BPM was higher than that of the artery at 120 BPM (**Figure 1**). Additionally, the minimum shear stress values at 180 BPM were also significantly increased in comparison to the 120 BPM model (**Figure 2**). Both of these results from the ANSYS FLUENT simulations indicate that the intense exercise model should showcase a lower rate of plaque formation over time. A higher shear stress of the blood on the wall of the artery theoretically results in any plaque that is formed being “washed” off by the blood moving at a higher velocity inside the arteries in the 180 BPM model. Therefore, this demonstrated an approximate decrease in the rate of atherosclerosis due to intense exercise. Such results can be interpreted to suggest that higher intensity cardiovascular exercise, such as sprinting or intense cycling, for example, is increasingly efficient at preventing atherosclerosis than lower intensity exercise, such as walking. Furthermore, these results support a trend between an increased heart rate due to intense exercise and a lower risk of cardiovascular disease due to a reduced atherosclerotic plaque buildup over a given period of time. Regarding future directions, it may be useful to create multiple simulations of identical arteries at varying heart rates including plaque deposition, which would then may be used to compute the rate of plaque formation for each simulation in order to mathematically demonstrate a relationship between the rate of atherosclerosis formation to that of exercise intensity.

REFERENCES

- [1] Lusis, A J, *Nature*, 407(6801), 233–241, 2000.
- [2] Bharadvaj, BK, et al, *J Biomechanics*, 15, pp. 349-362, 1982.
- [3] Genuardi, L, et al, *Cardiology Journal*, 28(2), 321–329, 2021.
- [4]. Kosowski, M, et al *Medicina*, 58(6), 717, 2022.
- [5] Krejza, J, et al, *Stroke*, 37(4), 1103–1105, 2006.
- [6] Sinnott et al., *Fifth International Conference on CFD in the Process Industries*, 1-6, 2006.

A PREDICTIVE MODEL FOR THE COVERAGE OF WOUNDS BY SKIN GRAFTS

Haomin Yu (1,2), Mohammad Jafari (3), Yuan Hong (1,2), Jacob Sandler (1,2), Guy M. Genin (1,2), Farid Alisafaei (1,3)

- (1) NSF Science and Technology Center for Engineering Mechanobiology, Washington University, St. Louis, Missouri, United States
(2) Department of Mechanical Engineering and Materials Science, Washington University, St. Louis, Missouri, United States
(3) Department of Mechanical Engineering, New Jersey Institute of Technology, Newark, New Jersey, United States

INTRODUCTION

Burns, diabetic ulcers, and infection lead to 8.2 million Americans suffering from chronic wounds every year¹. Split-thickness skin grafting is a method widely used in plastic surgery to treat such wounds². The procedure begins with the use of a dermatome to harvest a graft of healthy epidermis with a thin layer of dermis (Fig. 1A). The graft is cut into a meshwork of slits then stretched to cover a larger wound (Fig. 1B). Prediction of the area of wound coverage, S_{final} , is critical for surgical planning, and is typically done using the following formula for the expansion ratio, R_{exp} :²

$$R_{exp} = \frac{S_{final}}{S_{initial}} = 1 + \left[\frac{L^2}{4d(L + g)} \right] \quad (1)$$

where $S_{initial}$ is the initial area of the graft, and d , g , and L are the parameters of the skin graft meshing protocol (Fig. 1C). The term within the brackets is known in reconstructive surgery as the meshing ratio.

Equation (1) is derived by approximating the stretched graft as expanding into a configuration in which the slits become squares and the tissue ligaments do not stretch.³ The equation also ignores the material properties of the skin. However, the sliced skin ligaments do stretch to a degree, and the slits can adopt more complicated shapes in the stretched graft (Fig. 1B). Our objective was therefore to improve tools for surgical planning of split thickness thin grafting by validating and improving upon Equation (1).

We hypothesized that improving upon the predictions of shapes adopted by the opened slits would improve the estimate of the expansion ratio R_{exp} . To test the hypothesis, we created a finite element model of elastic skin grafts, all of which had the differing meshing patterns but the same meshing ratio, and compared the results to Equation (1) and to a new estimate of R_{exp} that we derived. model and change the length of the cut and verify our hypothesis by comparing the expansion ratio.

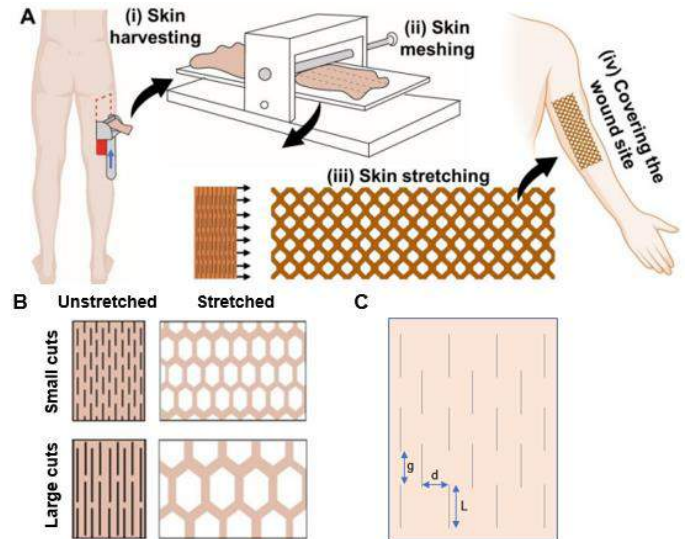


Figure 1: Split thickness skin grafting involves (a) harvesting, and (b) meshing prior to transplantation. Meshing is defined by the parameters shown in (c).

METHODS

Model derivation: To improve upon Equation (1), we rederived the formula by assuming that skin grafts stretch into the shapes shown in Figure 1. The skin was treated as incompressible and plane strain conditions were assumed. Treating each cut as a square after stretching, and considering a unit cell within an infinite sheet of skin, the revised version of Equation (1) was derived using straightforward geometric considerations:

$$R_{exp} = 1 + \left[\frac{L^2}{4d(L+g)} \right] \left(1 - (4 - 2\sqrt{2}) \frac{d}{L} + \sqrt{2} \frac{g}{L} \right) \quad (2)$$

Finite element analyses: A 2D finite element model of a complete graft material was created in the Abaqus finite element package (Dassault Systèmes, Vélizy-Villacoublay, France). The model began with a sheet of elastic material that was slit with prescribed values of the meshing parameters d/L and g/L (Fig. 2). The left and bottom boundaries were assigned symmetric boundary conditions, and the right boundary was displaced to a stretch of 12. The skin was modeled with an incompressible Ogden Model. Plane strain, quadratic interpolation elements were used. Standard convergence tests were performed, and convergence was achieved with meshes that had on the order of 120,000 degrees of freedom.

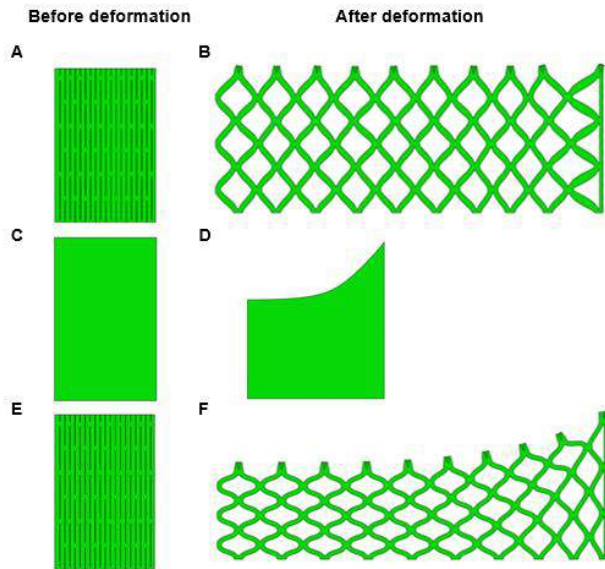


Figure 2: Finite element analysis results with linear and nonlinear Ogden models.

RESULTS

When the material undergoes large deformation, the linear analysis will lead to inaccurate results and the simulation is shown in Fig. 2A and B.

To compare the expansion ratio from formula (1) and formula (2), we used different parameter groups, which means at least one of d , g , and L was changed. The results are shown in Fig. 3A. The red bars mean the ratios are calculated by formula (2) and the blue bars represent the ratios calculated through formula (1). There is a big difference about ratios in group 5 and group 7. The parameters in these two groups show some similar points: (1) L has multiple relationships with d and g . (2) g has multiple relationships with d . In groups 2 and 3, blue bars are higher than red bars and d is greater than g in both groups. In group 7, the ratios are 3 from formula (1) and 3.47 from formula (2), and when the displacement is going to the maximum figure, the expansion ratio is 3.31 as the top point in the blue line in Fig. 3B and is closer to 3.47. In group 8, the ratio is 3.05 that shown in the red bar, and the ratio is calculated by the formula (1) is 3. These two ratios are very close and the maximum ratio in this group is 2.97 by simulation and shown as the peak point on the red line in Fig. 3B.

To verify the factor that affects the area expansion in our model, we created a cut-free skin model (Fig. 2C) and measured the expansion ratio of the skin with different magnitudes of deformation. The expansion ratio is constant as 1, which is shown as the purple line in Fig. 3B. The area of this model does not change after the stretching,

which demonstrates that the area change in our model is independent of the displacement.

We next applied this model to the skin with cuts and measured the area changes to study if the cut size and number affect the expansion ratio. The orange line shows the result with a model which simulates cuts changed to square (Fig. 2A and B) and the red line is the result of the Ogden model with small cuts in Fig. 3B. We can discover that the ratio in the small cuts Ogden model is always smaller than that in the linear model. When we use the big cuts with the Ogden model, the result is shown as the blue line in Fig. 3B. The ratio in this model is always larger than that in the model with small cuts.

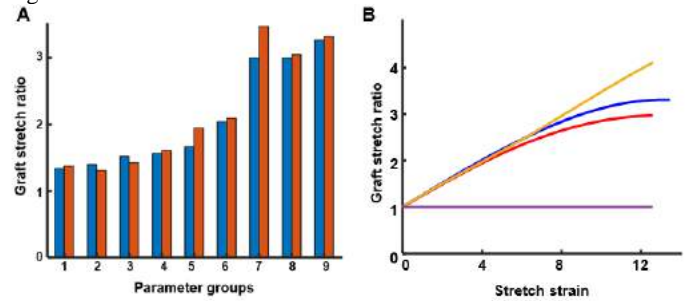


Figure 3: The relationship between graft stretch ratio and displacement in different material models.

DISCUSSION

Skin is an elastic material with rubber-like material properties, an aspect that previous studies overlooked, leading to the assumption that each cut would become a perfect square when stretched at large deformations. Our analysis results show that in this case, the expansion ratio is greater than the result of the formula (1). Formula (2) will get a result closer to the simulation. When using the hyperelastic model for analysis, the analysis results are much smaller than those for linear materials. When using a small cut, the simulation result is lower than that of Equation (1). When using a large cut, the simulation results are higher than the results of formula (1). The formula (2) we spit out is also based on the cut becoming a perfect square after stretching. So, our formula cannot be completely consistent with the simulation results. But our results are closer to those of software analysis in large cut and linear analysis.

ACKNOWLEDGEMENTS

This work was funded by the National Science Foundation Science and Technology Center for Engineering Mechanobiology.

REFERENCES

1. Sen, C. K. Human Wound and Its Burden: Updated 2020 Compendium of Estimates. *Advances in Wound Care* vol. 10 281–292 Preprint at <https://doi.org/10.1089/wound.2021.0026> (2021).
2. Vandeput, J. J., Tanner, J. C. & Boswick, J. Implementation of Parameters in the Expansion Ratio of Mesh Skin Grafts. *Plast Reconstr Surg* **100**, (1997).
3. Hong, Y. *et al.* Mechanobiology of Fibroblast Activation in Skin Grafting. doi:10.1101/2022.10.12.511903.

MULTISCALE BIOMECHANICS ACROSS SCALES: MICROMECHANICS AND NONLINEAR VISCOELASTICITY OF THE NUCLEUS PULPOSUS IN INFLAMMATION

Timothy D. Jacobsen (1,2), Gerard A. Ateshian (1,3), Nadeen O. Chahine (1,2)

- (1) Department of Biomedical Engineering, Columbia University, New York, NY, USA
(2) Department of Orthopedic Surgery, Columbia University, New York, NY, USA
(3) Department of Mechanical Engineering, Columbia University, New York, NY USA

INTRODUCTION: Disc degeneration is characterized by elevated levels of pro-inflammatory cytokines [1]. Inflammatory stimulation of intervertebral disc nucleus pulposus (NP) can lead to a catabolic breakdown of disc extracellular matrix (ECM), acting as a positive feedback of further loss of tissue integrity and inflammation [2]. Using gain and loss of function approaches, we have also shown that actomyosin contractility mediates the effects of TNF α -stimulation on cell biomechanics and ECM biochemistry (GAG content) [3]. In the current study, we investigate the role of increased cell actomyosin contractility, with the RhoA activator drug, CNO3, on micro- and macroscale biomechanical properties of NP explants. We investigated changes in compressive micro-scale properties with atomic force microscopy (AFM) to determine local properties (point modulus) and spatial mapping of moduli (fast force mapping). We also examined viscoelastic response of NP explants to unconfined compression and modeled the behavior using nonlinear reactive viscoelasticity [4]. We hypothesize that inflammatory-induced changes to NP tissue biomechanics are driven by a loss of GAG content and that increasing contractility can mitigate the degradative effects of inflammatory stimulation of the NP micro- and macro- mechanics.

METHODS: NP Explant Culture: NP explant tissue punches were isolated from bovine caudal IVDs and cultured in 24 well-plates in a swelling restricted culture system [3]. Treatment: NP explants were cultured in one of the following groups for 14 days: (1) untreated, (2) 10ng/ml TNF α , (3) 1 μ g/ml CNO3, or (4) 1 μ g/ml CNO3 + 10ng/ml TNF α (n=5-7 per group). Stress Relaxation and Nonlinear Reactive Viscoelasticity: Cylindrical samples were subjected to 5 ramp-and-hold displacement profiles of 5% compression, for a total compression of 25%. To determine viscoelastic properties, stress relaxation data was fit to a Nonlinear Reactive Viscoelasticity model which models a solid material using a combination of strong and weak bonds. Strong bonds

are unbreakable and account for the elastic response of a material while the weak bonds break and reform into a stress-free state and account for the time-dependent non-linear response to loading. Both strong and weak bonds were modeled as uncoupled (nearly incompressible) neo-Hookean materials. Breaking and reforming of weak bonds was modeled using a Malkin relaxation function with a bond recruitment function dependent on distortional strain. The model computation and curve fitting of experimental data was performed using FEBIO. The resulting material parameters μ_e and μ_a (shear moduli of the strong and weak bonds, respectively), τ_1 and τ_2 (shortest and longest relaxation times constants), and F (recruitment function) were compared between groups. Atomic Force Microscopy (AFM): Explants were cryosectioned and samples were tested at specific points (point modulus) in the inner and outer part of the explant using an Asylum MFP-3D BIO AFM with spherical tip probes. Fast force mapping (FFM), a deflection-controlled feedback technique in which the AFM probe is oscillated at sub-resonance frequency, was also used to acquire maps of local elastic moduli and topography over 120x120 μ m regions. Curves were fitted to a Hertzian model to determine distribution of elastic moduli. Biochemical assays: Explant papain digests were assayed for GAG and collagen content using DMMB and OHP assay, respectively, and reported normalized to wet weight. Statistics: Data was analyzed by ANOVA with Fisher LSD post-hoc (GraphPad), with p<0.05 significant. Pearson correlations were used to identify relationships between biomechanical properties and biochemical content.

RESULTS: AFM: At the microscopic scale, TNF α stimulation significantly decreased the AFM point modulus of NP explants vs. untreated. (Fig 1A). FFM of explants showed qualitative differences in topography of interior and exterior areas of the NP explant (Fig 1B), however there were no significant differences in median modulus or surface roughness with location (not shown). Median modulus of TNF α

treated samples also significantly decreased vs. untreated (Fig 1C) in analysis of fast force mapping changes. Co-treatment of the NP explants with CN03+TNF α partially increased the median elastic modulus (FFM) compared to TNF α group (Fig 1C).

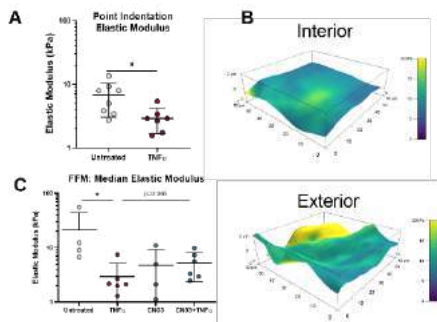


Figure 1: (A) AFM point modulus of untreated and TNF α explants. (B) FFM maps from interior and exterior locations of NP explant. (C) Median elastic modulus from FFM. * $p < 0.05$.

Model Results: At the macroscopic scale, nonlinear reactive viscoelasticity yielded excellent fits, with an average $R^2 = 0.96$ across all groups (Fig 2A). The dependence on distortional strain in the relaxation time τ_2 and recruitment F are shown in Fig 2B. Analysis of the parameter curve fit between groups demonstrated that TNF α did not have a significant effect on any of the viscoelastic model parameters (Fig 3). However, treatment with CN03+TNF α resulted in a significant increase in strong (μe) and weak (μa) bond moduli, and in relaxation time τ_2 compared to TNF α group (Fig 3). **Biochemistry:** While no significant between-group effects were observed in GAG and collagen content, significant relationships between biomechanical and biochemical properties were observed. At the microscale, AFM point modulus was significantly correlated with collagen content ($p = 0.019$, Pearson $r = 0.59$) and had a trend for correlation with GAG content ($p = 0.063$, Pearson $r = 0.47$). At the macroscale, elastic μe was also significantly correlated with collagen ($p < 0.0001$, Pearson $r = 0.92$) and GAG ($p = 0.007$, $r = 0.76$) content. Bond μa exhibited a trend in correlation with collagen ($p = 0.058$, Pearson $r = 0.59$) and GAG content ($p = 0.08$, Pearson $r = 0.55$). Both μe and μa were inversely correlated with water content, given the significant correlations found between water and collagen (Pearson $r = -0.93$) or GAG (Pearson $r = -0.70$).

DISCUSSION: The goal of this study was to evaluate biomechanical changes in NP explants with TNF α stimulation, to advance the understanding on extracellular matrix changes associated with a pro-inflammatory stimulus in NP tissue. Microscale analysis of point modulus using AFM demonstrated a significant loss in compressive properties with TNF α treatment. This was further verified by the results of fast force mapping that pointed to presence of a narrower distribution of compressive properties along with lower median modulus of TNF α treated explants. These findings are consistent with our prior findings of decreased GAG content and Alcian blue staining in TNF α treated explants [3]. Interestingly, the current study, found that point modulus was correlated with GAG and collagen content in the interior but exterior of the explant, which may undergo ECM disruption at periphery of the explant during longer term tissue culture. Treatment of NP explants with the RhoA activator, CN03, resulted in ~2 fold increase in explant microscale elastic modulus, however these levels remained below properties of untreated explants. Our prior studies showed that CN03 counteracted NF- κ B and downstream catabolic signaling [3], however that does not appear to fully protect the microscale biomechanics of the NP.

To examine effects on viscoelastic responses, we also curve fitted the stress relaxation test results to a nonlinear reactive viscoelasticity model, using a new numerical scheme developed by Ateshian and colleagues [4]. The bovine NP explants behaved nonlinearly with each additional stress relaxation step, consistent with prior IVD biomechanics studies [5]. In this model, weak bond recruitment was included as a function of distortional strain to achieve a good curvefit of the experimental data. In the model, strong bonds impart the elastic response while weak bonds break and reform into a stress-free state in response to loading. The process of bonds breaking and reforming is modeled as a reaction where loaded bonds are the reactants and bonds reformed into a stress-free state are the products of a reaction. The reaction is triggered by the evolving state of loading. The state of stress in strong bonds is a function of the total strain in the material, whereas the state of stress in weak bonds is based on the state of strain relative to the time that these bonds were reformed. We found that the relaxation time τ_2 of the reduced relaxation function needed to depend on the distortional strain to achieve good curve fits, further underscoring the nonlinear viscoelastic response of untreated NP tissue. We also modeled a distortional strain dependent recruitment function of the weak bonds. While the strong and weak bond moduli of the NP did not change significantly with TNF α , treatment with CN03+TNF α significantly increased the elastic and bond moduli, as well as relaxation time constant, suggesting that effects of CN03 are affecting both the elastic and viscous responses of NP tissue, which appear to be dependent on tissue water content. Future studies will examine detailed analyses of effects of CN03 on collagen and water content in NP, and examine contributions of CN03 alone on ECM biomechanics.

ACKNOWLEDGEMENTS: Funded in part by NIH R01AR069668 and R01AR077760, and R21AR080516.

REFERENCES: [1] Le Maitre, C et al., *Arth Res Ther*, 2005. [2] Millward-Sadler, S et al., *Arth Res Ther*, 2009. [3] Hernandez, P et al., *Science advances*, 2020. [4] Ateshian et al, *J Biomech Eng*, 2023. [5] Boxberger et al, *J Biomech*, 2009.

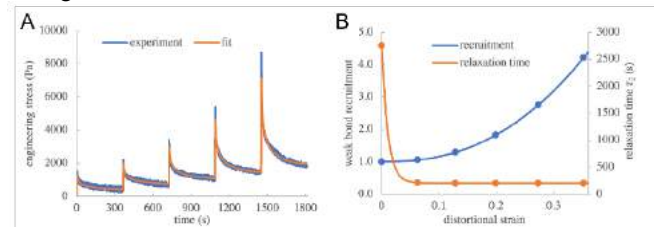


Figure 2: Experimental and model curvefit. (b) Dependence of weak bond recruitment F and τ_2 on distortional strain.

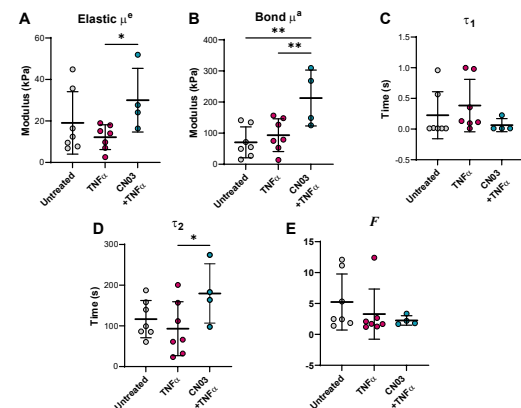


Figure 3: Parameters from nonlinear reactive viscoelasticity analysis. * $p < 0.05$ and ** $p < 0.001$.

MULTISCALE COMPUTATIONAL MODELING OF *TGFBR1/2* KNOCK-OUT IN ADULT MOUSE AORTAS

Ana C. Estrada (1), Linda Irons (1), Jay D. Humphrey (1,2)

(1) Department of Biomedical Engineering, Yale University, New Haven, Connecticut, USA
(2) Vascular Biology and Therapeutics Program, Yale School of Medicine, New Haven, Connecticut, USA

INTRODUCTION

Vascular smooth muscle cells (VSMCs) are critical for the proper functioning and maintenance of the aorta, and dysfunction of VSMCs is responsible for the development of thoracic aortic aneurysms and dissections. Dysfunction of VSMCs is accompanied by changes in intracellular signaling, including altered gene expression and protein activation, as well as tissue-level growth and remodeling (G&R) of the affected vessels. Among the most critical signaling pathways in VSMCs is the TGF- β pathway, which acts through downstream Smad2/3 and MAPK signaling and is responsible for collagen synthesis and remodeling [1].

To better understand the role of TGF- β signaling on vascular G&R, our collaborators developed a conditional knock-out (KO) of TGF- β Receptor 1 (*Tgfr1*) and Receptor 2 (*Tgfr2*) in VSMCs of adult mice, with the KO initiated at 11 weeks of age. They found that while the KO decreased p-Smad2/3 activity, there was no significant change in the morphology of the vessels. However, when the vessels were perturbed with exogenous angiotensin II (AngII) infusion, they developed dissections, demonstrating an underlying vulnerability caused by the KO. The purpose of the present computational study is to understand how *Tgfr1/2* KO can lead to vulnerable but initially stable vessels. We used a multiscale G&R framework, which combines cell-level network modeling and tissue-level constrained mixture modeling, to simulate and analyze the effect of *Tgfr1/2* KO.

METHODS

We used a logic-based network modeling approach to capture the intracellular signaling of VSMCs. Interactions between species within the network were modeled using normalized hill-type functions for activation or inhibition. We built the network model by consolidating relevant signaling pathways reported in the literature. The model in this

study builds on the models used in Irons et al. 2022 [2] and Estrada et al. 2021 [3], and it includes added detail in the TGF- β signaling pathway. In total, the network model consists of 133 nodes and 210 reactions.

To capture tissue-level changes, we used a constrained mixture G&R model for a single-layered vessel previously developed by our group [4]. The G&R model accounts for changes in mass density production and removal of individual constituents, namely smooth muscle cells, collagen, and elastin. The model then integrates these mass densities over time to calculate the inner radius and thickness of the vessel under changes in hemodynamic load, such as blood pressure or flow. Using the method described in Irons et al. 2021 [5], we coupled the network to the G&R model by mapping the key inputs and outputs between the models. We mapped the network circumferential stress and wall shear stress inputs to the calculated change in circumferential stress and wall shear stress from the tissue-level model. We then calculate the mass density production and removal from the steady-state activation of relevant network outputs. The mean activation of collagen mRNA drives collagen mass density production, while mean MMP activation drives removal. Similarly, the network proliferation and apoptosis outputs drive smooth muscle cell mass density product and removal, respectively. We further mapped the contractility output of the network to the active stress calculation in the tissue-level model.

We optimized the wild-type material parameters of the G&R model and the Hill parameters of the network model using a nonlinear least-squares algorithm. We then simulated *Tgfr1/2* KO by gradually reducing the maximum activation of both TGF- β 1 and TGF- β 2 network nodes to 0.4 (where values are normalized to [0,1]) over the course of five simulated days and imposing a mild 15% pressure increase, as reported in the experimental data. To test vulnerability, we further perturbed the model by 1) increasing the pressure to 40% over baseline,

2) adding exogenous AngII as network input, and 3) combining the pressure and AngII perturbations. For each condition, we calculated the relative change in inner radius and wall thickness compared to the wild-type model at its baseline blood pressure (14kPa). We then analyzed the individual activation of network species after each perturbation to determine those with the greatest change compared to the KO alone.

RESULTS

We initialized the coupled G&R model using the mean reported dimensions and material properties of ascending thoracic aortas from wild-type mice in the experimental study and optimized the remaining parameters such that the model would 1) remain stable under constant hemodynamic load and 2) achieve a new homeostatic state with a 15% increase in pressure load. KO of the TGFR1/2 nodes with the optimized parameters resulted in no change to the inner radius and a 15% increase in thickness one week post-KO, consistent with the experimental data. We then performed a qualitative comparison of 68 individual network nodes and their corresponding transcripts from single-cell RNA sequencing performed in the experimental study. The coupled model accurately predicted changes in 55 of the 68 species, corresponding to 81% model accuracy.

To better understand vulnerability, we perturbed the optimized model by increasing the pressure by 40% or by stimulating the network with exogenous AngII, as well as a combined insult. Increased pressure led to wall thickening but mild changes to inner radius, while exogenous AngII infusion enhanced the wall thickening for each applied pressure condition. Comparing the network species with the greatest change from KO alone, we saw that mechanoregulation decreased with each perturbation but lysosome-related species, such as LAMP1/2, MITF, and Dishevelled (Dsh), a key protein in the Wnt/ β -catenin pathway, increased. The activation of these lysosome-related species suggests that these VSMCs may be shifting towards a more degradative phenotype, which has been previously implicated in the development of aortic dissections [3,6]. In order to test if the Wnt/ β -catenin pathway was a primary driver of remodeling due to pressure or AngII infusion, we next simulated inhibition of the Dsh node (based on [7]) during both pressure and AngII perturbations. We found that Dsh inhibition led to attenuation of the wall thickening comparable to that of KO alone (Figure 1), as well as reduced lysosomal activity.

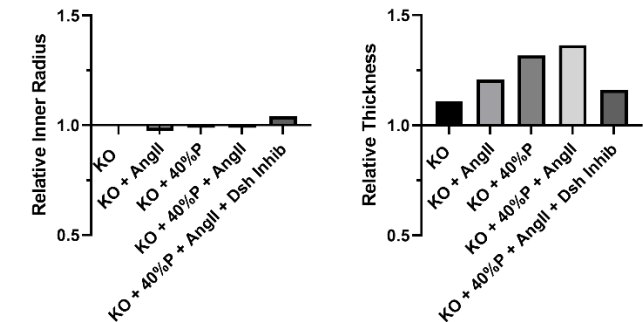


Figure 1: Bar graphs showing the relative change in inner radius and thickness due to TGFR1/R2 KO, and KO combined with AngII infusion, pressure (P) increase, and Dsh inhibition

DISCUSSION

Using a multiscale G&R approach, we built a model of conditional *Tgfr1/2* KO in vascular smooth muscle cells. Our model incorporates a detailed network model of intracellular signaling coupled to a tissue-level constrained mixture model of vascular G&R. Despite a perturbation in a key pathway for cell and tissue maintenance, the KO vessels remain stable but vulnerable under baseline hemodynamic load. Both stability and vulnerability of these vessels highlight the necessary role of feedback between the network and G&R models. Feedback between the scales allows the coupled model to regulate changes in signaling and remodeling, such that mild perturbations in hemodynamic load and signaling lead to adaptive homeostatic responses, consistent with prior studies [2]. Gradual KO of the TGFR1/2 nodes yields changes in inner radius and wall thickness consistent with our experimental data. Additionally, the model captures a qualitative increase or decrease in 55 of 68 intracellular nodes compared to single cell RNA-sequencing data. For the signaling comparison, we assumed that changes in transcript expression correlate with changes in protein activity, acknowledging that the correlation is not guaranteed to be 1:1.

We then saw that increases in pressure had a greater independent effect on the thickness of vessels in the KO model, while exogenous AngII enhanced the G&R response for each pressure condition. Both perturbations resulted in increased activation of the Wnt/ β -catenin signaling pathway, which is also associated with activity of lysosome-related species, but this effect was attenuated by disrupting Dishevelled signaling. Experimentally, the KO causes a disruption in extracellular matrix structure and cell-matrix interactions. The concurrent increase in degradative activity within a disrupted matrix could be a potential mechanism for the vulnerability of the KO vessels.

ACKNOWLEDGEMENTS

This work was supported by: NIH R01 HL146723 (and associated Diversity Supplement), U01 HL142518, P01 HL134605.

REFERENCES

[1] Humphrey, J, *J Vasc Res*, 50:1-10, 2013.
[2] Irons, L et al., *BMMB*, 21:1339-1355, 2022.
[3] Estrada, A et al., *PLoS Comp Biol*, 17: e1009683, 2021.
[4] Valentin, A and Humphrey, J., *Philos Trans R Soc A*, 367:3585-3606, 2009.
[5] Irons, L et al., *Ann Biomed Eng*, 49:1701-1715, 2021.
[6] Li, G et al., *J Clin Invest.*, 130:1233-1251, 2020.
[7] Liu, C et al., *Medicine in Drug Discovery*, 8:100066, 2020.

NOVEL MAGNETIC RESONANCE IMAGING PHANTOMS FOR INVESTIGATING SKULL-BRAIN MECHANICS

Joy Mojumder (1), Suhas Vidhate (2), Yuan-Chiao Lu (1,3), Ahmed Alshareef (3, 4), Curtis L. Johnson (5), Dzung L. Pham (1,6), John A. Butman (1)

(1) Department of Radiology and Imaging Sciences, National Institute of Health, Bethesda, MD, US

(2) Intuitive Surgical, Inc., San Francisco, CA, US

(3) Center for Neuroscience and Regenerative Medicine, Henry M. Jackson Foundation, Bethesda, MD, US

(4) Department of Mechanical Engineering, University of South Carolina, Columbia, SC, US

(5) Department of Biomedical Engineering, University of Delaware, Newark, DE, US

(6) Radiology and Radiological Sciences, Uniformed Services University, Bethesda, MD, US

INTRODUCTION

Traumatic brain injury (TBI), caused by rapid brain tissue deformation in response to sudden linear and angular accelerations of the skull, is a serious health condition that affects both military and civilian populations. However, the mechanisms linking mechanical insult and neurological injury, more specifically how skull motion is transmitted to brain motion during TBI, are not well understood. Recent work has highlighted that injury to the interface between the brain and skull is a relatively common consequence of TBI [1]. Methods to non-invasively probe the biomechanics of the brain and skull have been developed using magnetic resonance imaging (MRI) [2]. Test objects with known boundary conditions are, however, required to validate the ability to accurately characterize the biomechanical relationship between skull and brain. Prior work on biomechanical MRI phantoms have focused only on simulating the brain [3], mostly the deformation of the brain. However, the motion of brain relative to the skull has not been investigated yet. Here, we developed two skull-brain phantom models that can be used to evaluate skull-brain mechanics using tagged MRI. A key feature of these phantoms is the presence of slots that can be used to represent marrow in the skull.

METHODS

Two different biofidelic brain phantoms, namely, skull brain phantom (SBP) models, were developed using a cylindrical container: 1) SBP with attached (fixed) boundary (SBPa), where the container contains only a gel-based brain simulant that sticks to the container wall and 2) SBP with unattached (free) boundary (SBPu), where the simulant does not completely fill the container and is surrounded by a layer of water between stimulant and the container wall. The fabrication of these two models were divided into two steps, namely the mold and gel fabrication process. In the mold fabrication process, two identical cylindrical molds (outer diameter 5 inches, inner diameter 4 inches and length 8 inches) were 3D printed for both SBP models. The inside of the

mold represents the brain region whereas the cavities inside the wall represent marrow within the skull (**Figure 1a**). This design was chosen because in standard MRI acquisitions, bone provides almost no signal, but marrow inside the bone can provide excellent signal. However, the amount of marrow is not uniform throughout the skull. In both models, the bottom end cap had protrusions to fix the gel in the mold at that end, while the gel was kept free at the top end. To make it air-tight, the mold end was covered with a silicone gasket followed with an acrylic endcap tightened by nylon screws. A complete fabricated mold is shown in **Figure 1b**. A luer valve is added at SBPu model for adding water and removing bubbles from the mold.

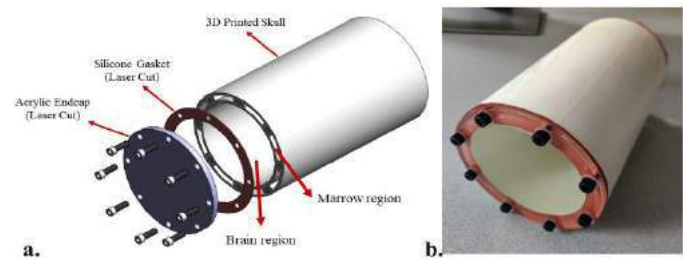


Figure 1: a) Schematic of SBP mold and b) Fabricated mold

The gel fabrication process of these phantom models was modified based on previously reported methods [3]. Polyacrylamide (PAA) gel was used as a brain tissue simulant due to its easily tunable material properties, room temperature fabrication and high level of transparency for optical access. Briefly, 140.0 g of acrylamide (purity $\geq 98.0\%$) was dissolved in 1400 mL deionized water while stirring moderately to generate a 10% (weight/volume) solution. After the acrylamide was fully dissolved, 2.34 g of *N,N'*-methylenebis (acrylamide) (MBA, purity 99%) was added slowly while stirring the solution. Once the solution was homogenized, 1.22 g of ammonium persulfate was added to initiate

the crosslinking of the two monomers of acrylamide. Finally, upon the addition of 2.49ml of *N,N,N',N'*-tetramethylethylenediamine (TEMED, purity 99%), the solution was poured immediately into the molds following the addition of TEMED. For the SBPa model, the PAA solution was directly poured in the 3D skull and was allowed to cure and adhere to container wall, creating a fixed wall boundary condition. For the SBPu model, the PAA solution was first poured into an intermediate cylindrical mold (outer diameter 5 inches, inner diameter 3.75 inches and length 8 inches) with the inner surface covered with a Teflon tape, preventing gel from adhering to the cylinder wall. Once PAA gel was cured, it was then transferred to the 3D printed skull (inner diameter 4 inches), leaving a gap between the gel and the cylinder wall. Since water is widely used as an artificial cerebrospinal fluid, the gel of SBPu model was filled with water using a syringe through luer valve at least 1 hour before scanning. The water between the PAA gel and the cylinder wall created the free boundary condition in the SBPu model.

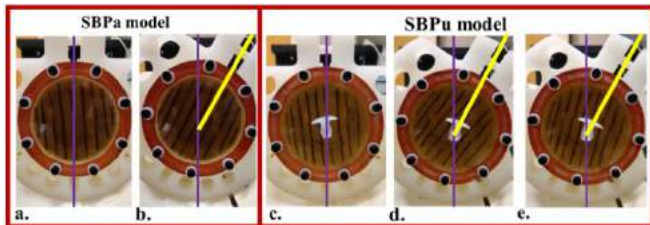


Figure 2: Neck rotation experiment performed on 2 SBP models. a) and c) showing 0° rotation (Purple line) representing resting position, whereas b) and d) showing 32° rotation (Yellow line) representing the position of impact, for SBPa and SBPu, respectively. e) representing the motion of gel in SBPu shortly after impact.

The head motion investigated in this study was neck rotation (rotation within the axial plane) using a previously described custom MRI-compatible device [4] used to constrain the motion of the head (or phantom), thereby facilitating a repeatable acceleration event within the MRI scanner. After the phantom was rigidly coupled to the head cradle using a strap, a cord was pulled to release a latch allowing an offset counterweight causing the head cradle to rotate clockwise at about 32° rotation (Figure 2). At that angular position, the counterweight impacted a padded stop (1/4" Sorbathane pad), which caused a rapid deceleration of the head cradle and phantom. An angular position sensor (Model MR338, MICRONOR, CA, USA) was coupled to the axis of rotation of the head cradle to provide measurements of angular position, velocity, and acceleration over time at 0.85 ms temporal resolution.

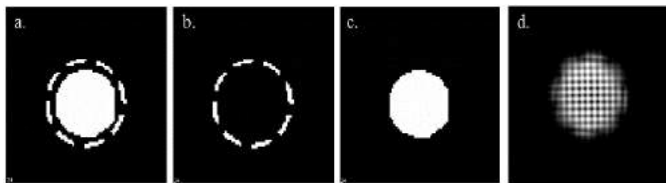


Figure 3: a) Mask region, b) marrow region, c) brain region and d) tagged image of SBP.

The tagged MRI study was performed using a 1.5 T Siemens Aera MR scanner. Data was acquired using a 1–1 Spatial Modulation of Magnetization (SPAMM) tagging pulse followed by 2D cine gradient echo acquisition using two axial acquisitions with orthogonal tag directions and the following acquisition parameters: FOV = 240×240 mm, matrix = 24×160, slice thickness = 8 mm, TR/TE = 3.18/1.68 ms and tag spacing = 8 mm. A single axial slice was acquired at approximately the middle of its long axis.

All MRI data processing was performed in MATLAB R2020a (MathWorks, MA, USA). A mask of the hydrogel portion of the phantom was created using ITK-Snap by registering the FLAIR image rigidly to the first frame of the tagged MRI data and applying the transformation matrix to the mask (Figure 3). Harmonic phase (HARP) analysis [4] with HARP refinement was performed to measure the displacement vectors between each frame and the first frame. Image axes were oriented with respect to the scanner. The maximum principal strain (MPS, largest eigenvalue of strain tensor) was analyzed from Eulerian strain tensors computed from the displacement vectors.

RESULTS

Video capture of both SBP models marked with vertical black lines showed significant rigid body motion in the SBPu at impact compared to the SBPa (Figure 2). The strain in the brain region for the SBP model in the neck rotation experiment was qualitatively similar to the results from an established sylgard phantom [5]. The MPS distribution for both SBP models at 9 different time points are shown in Figure 4. While in both models the strain was observed higher near the wall, the strain was quantitatively higher in the SBPa model (0.014) than the SBPu model (0.010) at the point of impact shown by the yellow box in Figure 4.

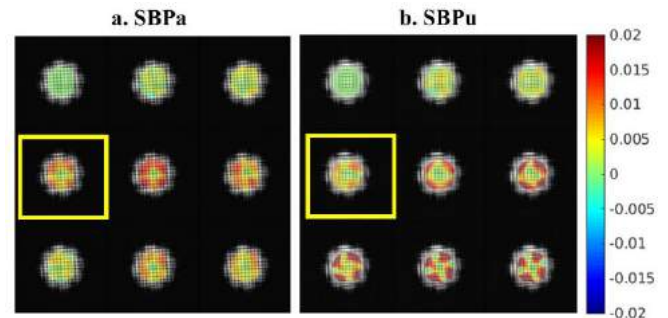


Figure 4: Maximum principal strain shown for SB Phantom with attached wall (a) and unattached wall (b) at first 9 time points (left to right). Yellow square represents the timepoint of impact.

DISCUSSION

The effect of impact forces was studied using two different phantom models and the results suggests that at the point of impact, the strain is larger with a fixed boundary. The lack of attachment to the container wall lessened the effect of impact force on brain in SBPu model. However, at later times after impact, strains were increased in the SBPu model due to a torsional wave originating at the fixed bottom boundary and propagating back and forth in the PAA gel. These models can be developed further by incorporating fat-water emulsion in the skull slots as a simulant for brain marrow.

ACKNOWLEDGEMENTS

This work was partially supported by grant NIH U01 NS112120, the Department of Defense in the Center for Neuroscience and Regenerative Medicine, and the intramural research program of the NIH Clinical Center through the Bench-to-Bedside program. The opinions and assertions expressed herein are those of the authors and do not reflect the official policy or position of the Uniformed Services University of the Health Sciences or the Department of Defense.

REFERENCES

1. Turtzo, LC et al, Brain Commun, 2(2): fcaa143, 2020.
2. Yin Z, et al Magn Reson Med, 80(6):2573-2585, 2018.
3. Knutsen, A.K. et al, J of Mec Beh of Bio Mat, V 138, 2023.
4. Knutsen, A.K. et al, J Biomech, 3475-81, 2014.
5. Knutsen, A.K. et al. Comp Bio for Med. pp 169–183, 2013.

DEVELOPMENT AND CHARACTERIZATION OF A LOW INTENSITY VIBRATIONAL SYSTEM FOR MICROGRAVITY STUDIES

Omor M. Khan (1), Chess Necessary (2), Maximilien DeLeon (3), Mary Farach-Carson (3), Elizabeth Blaber (4), Danielle Wu (3), Aykut Satıcı (1), Gunes Uzer (1).

(1) Mechanical and Biomedical Engineering, Boise State University, Boise, Idaho, U.S.A

(2) Space Tango, State, U.S.A

(3) Diagnostic and Biomedical Sciences, University of Texas Health Houston, Houston, Texas, U.S.A

(4) Biomedical Engineering Department, Rensselaer Polytechnic Institute, Troy, New York, U.S.A

INTRODUCTION

Microgravity related missions are becoming increasingly prominent in the current development of the space industry. With the increasing number of manned missions to the International Space Station (ISS) and the development of commercial space travel, it is important to address the various implications that arise in these microgravity environments. One such issue is the significant bone loss and decreased bone density observed in astronauts during extended periods of microgravity [1]. This bone loss, if left unchecked, can have severe consequences for the health and functionality of astronauts, as well as the success of future microgravity missions.

One promising solution to this problem is the use of low intensity vibration (LIV) as a countermeasure. Studies have shown that low intensity vibration can stimulate bone formation and improve bone density in both normal and microgravity conditions [2], [3]. However, the use of low intensity vibration in microgravity environments has been limited due to the lack of suitable bioreactors capable of providing the necessary stimuli.

Therefore, the goal of this study was to develop a vibrational bioreactor specifically designed for use in microgravity conditions. This bioreactor will be used on Space Tango's CubeLab platform [4] and enable the study of the effects of low intensity vibration on cells in microgravity, and potentially lead to the development of new therapies and treatments for use in space and other microgravity environments.

METHODS

This section describes the design and characterization of the vibrational bioreactor. The goal of this study was to create a bioreactor capable of achieving a target vibration acceleration of 0.7g at a frequency of 90 Hz, a signal regime we have shown to improve the growth rate and productivity of cells under simulated microgravity conditions [5]. We focused on three key components of the bioreactor: (1) the linear guide used to mount the payload and restrict the motion to

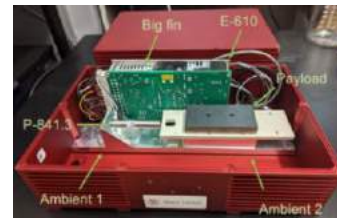


Figure 1 Thermal experiment setup

single dimension, (2) the characterization of the transducer used to induce vibration, and (3) the design of the well plates used to study the diffusion of a tracer molecule in the culture medium to ensure adequate medium change during the microgravity mission.

CubeLab Platform is a modular customizable laboratory developed by Space Tango that is designed for microgravity research on the ISS. It is a compact, self-contained laboratory that can be used to conduct a wide range of experiments in microgravity. We utilized the CubeLab 9U with a volume of 550 cubic inches.

Linear Guides are tested for their size and precision. Both the N drylin® N pre-loaded prism carriage and the Schneeberger NK1 2-95 were vibrated at 90Hz, 0.7g. Both linear guides are also compared to a regular roller guide used in the laboratory. The LIV is applied to a 1 kg steel payload for 20 minutes, and the acceleration is recorded through the MEMSIC CXL04GP3 accelerometer.

Transducer generates the mechanical vibrations that stimulate cells. Heat generated by the transducer can increase the temperature of the cell culture and negatively affect cell growth. To investigate this, thermocouples were used to track the temperature increase of the whole setup over the course of the vibration in a CubeLab. The transducer for this LIV bioreactor was selected as the PI-841.3.S0 from Physik Instrumente and the E-610 is its controller / amplifier. (Figure 1).

CubeWells Cells in culture require regular exchanges of media to maintain optimal growth conditions. In this study, we also aimed to investigate the speed of media exchange in the vibrational bioreactor. A customized microplate designed by Space Tango (will be referred as

CubeWells) and was initially filled with 8mL of water along with stereolithography (SLA) printed scaffolds encapsulated in hydrogels to mimic cellular constructs that will be used in the cell culture experiments (5x5x5mm). A simulated new medium—a mix of water and Royal Blue Icing Color dye—is pumped into the CubeWells at a rate of 0.9 mL/min. The media exchange is observed using a high-speed camera (1000fps, Photron FASTCAM MINI UX50) to see the diffusion of the dye and the movement of fluid in the CubeWells over the course of 5 minutes. Diffusion was quantified at five locations (Figure 4).

RESULTS

Linear Guides The results of the vibration experiment showed that the Schneeberger NKL 2-95 linear guide outperformed the N preloaded prism carriage by showing a consistent 1-axis acceleration over the 20 minutes of LIV. Although the Schneeberger guide is larger in size, it demonstrated a lower standard deviation for all axes when compared to the N preloaded prism carriage. Both guides can reach the targeted 0.7g in the direction of motion. However, when comparing the acceleration values in the other axes, the N preloaded prism carriage had more acceleration in both x and z, 0.4g and 0.1g respectively, compared to the Schneeberger guide.

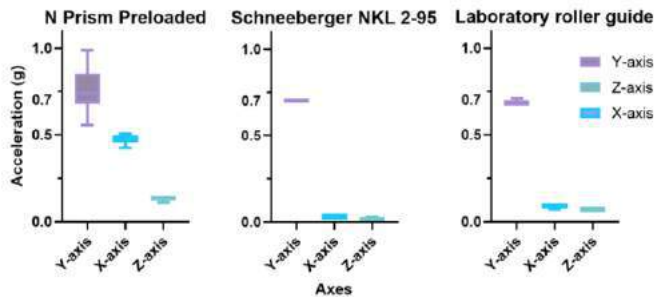


Figure 2 Linear guides acceleration values over 20-minute LIV

Transducer Shown in Figure 3, the results of the thermal experiment on the actuator and controller setup during vibration indicated that the temperature of the system remained within safe limits for cell growth. The highest temperature recorded within the CubeLab was above 50 degrees Celsius, which was recorded at the controller. However, the ambient temperature of the air around the payload was less than 28 degrees Celsius over the course of the vibration. This suggests that the heat generated by the actuator and controller was dissipated effectively and that the temperature of the cells was not affected by the vibration.

CubeWells The results100% (8mL) media exchange indicated that after 3 minutes, the new media had reached the middle of the CubeWell, and after 5 minutes, 80% of the new media had reached the bottom of the microplate (Figure 4Error! Reference source not found.). dye over time, we were able to determine the diffusion of the new media in the microplate. The results showed that following the media change a recirculation would be required to completely exchange media for all of the scaffolds.

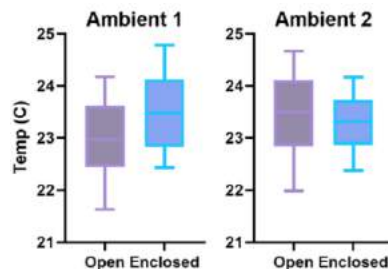


Figure 3 Temperature range of the ambient air inside the CubeLab during 25-minute of LIV

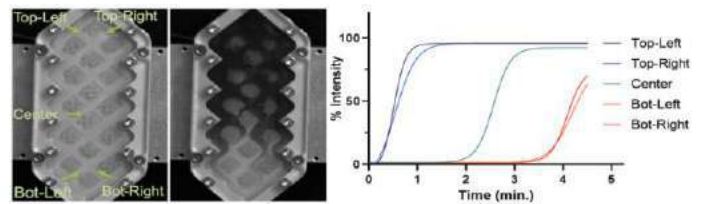


Figure 4 Diffusion rate of 5 locations in the CubeWell during 5-minute pump of new media

DISCUSSION

The results from this study suggest that the Schneeberger NKL 2-95 linear guide is more suitable for applications requiring precise and controlled vibration in a single axis with an acceleration of 0.7 g, while the N preloaded prism carriage may be more suitable for applications requiring multi-axis vibrations. The thermal data collected in this experiment provides information on the thermal behavior of the actuator and controller during vibration, useful for optimizing future bioreactors and evaluating safety and thermal load. The results showed that the temperature inside the bioreactor remained safe for cell growth and cells were not affected by the thermal behavior of the system. Finally, the results of the diffusion study showed that old media can be exchanged remotely 5 minutes with the current CubeWell design, however, additional re-circulation is needed for providing optimal media diffusion for cell growth. These results can be used to improve the design and operation of future vibrational bioreactors.

Overall, our study has provided valuable insights into the design and operation of an LIV bioreactor. This research could be used as a foundation to optimize the design of future bioreactors and provide a better understanding of microgravity's effect on cell growth. Further studies can be done to optimize the design and characterization of the bioreactor, such as finding the optimal vibration parameters for different types of cells and evaluating the bioreactor's performance under varying conditions such as temperature, humidity, and dissolved gas concentration.

ACKNOWLEDGEMENTS

This study was supported by, AG059923, NSF1929188 and, NSF 2025505

REFERENCES

- [1] M. Stavnichuk, N. Mikolajewicz, T. Corlett, M. Morris, and S. V. Komarova, "A systematic review and meta-analysis of bone loss in space travelers," *Npj Microgravity*, vol. 6, no. 1, Art. no. 1, May 2020, doi: 10.1038/s41526-020-0103-2.
- [2] A. LeBlanc *et al.*, "Bisphosphonates as a supplement to exercise to protect bone during long-duration spaceflight," *Osteoporos. Int.*, vol. 24, no. 7, pp. 2105–2114, Jul. 2013, doi: 10.1007/s00198-012-2243-z.
- [3] L. Steppe, A. Liedert, A. Ignatius, and M. Haffner-Luntzer, "Influence of Low-Magnitude High-Frequency Vibration on Bone Cells and Bone Regeneration," *Front. Bioeng. Biotechnol.*, vol. 8, p. 595139, Oct. 2020, doi: 10.3389/fbioe.2020.595139.
- [4] "CubeLab," *Space Tango*. <https://spacetango.com/cubelab/> (accessed Jan. 12, 2023).
- [5] M. Thompson, K. Woods, J. Newberg, J. T. Oxford, and G. Uzer, "Low-intensity vibration restores nuclear YAP levels and acute YAP nuclear shuttling in mesenchymal stem cells subjected to simulated microgravity," *Npj Microgravity*, vol. 6, no. 1, p. 35, Dec. 2020, doi: 10.1038/s41526-020-00125-5.

MODEL FOR HEAT CONDUCTION IN VAPORIZABLE ENDOSKELETAL DROPLET IN RESPONSE TO X-RAY PHOTON ABSORPTION

William N. Frantz (1), David H. Thomas (2), Mark A. Borden (1,3)

- (1) Biomedical Engineering Program, University of Colorado – Boulder, Boulder, Colorado, USA
- (2) Department of Radiation Oncology, University of Colorado – Anschutz, Aurora, Colorado, USA
- (3) Department of Mechanical Engineering, University of Colorado – Boulder, Boulder, Colorado, USA

INTRODUCTION

In cancer treatment, radiation therapy (RT) utilizes high-energy radiation to destroy cancer cells. Each year, more than half a million patients being treated in the United States receive radiation therapy [1]. Administering effective treatment to these patients is heavily reliant on accurately delivering radiation to the patient. Current methods rely on CT scans taken anywhere from days to weeks before the treatment. However, due to weight loss or tumor shrinkage in the time between imaging and treatment, and organ motion during treatment, this is not a fully accurate representation of the radiation delivered to the patient [2-4]. Serious side effects can arise from delivering radiation to healthy tissue, including nausea, radiation fibrosis and radiation pneumonitis, vomiting and diarrhea, or rectal bleeding and incontinence.

To avoid these effects, the radiation distribution within a patient can be measured in a method known as radiation dosimetry. *In vivo* dosimetry is currently possible using a variety of equipment; however, they are limited by their inability to measure in real time and collect information at a single point [5,6]. Currently, no method allows for real time 3D dosimetry mapping for radiation therapy. One proposed method to create such 3D dosimetry is X-ray acoustic computed tomography (XACT). This methodology utilizes the X-ray acoustic (XA) effect, which describes an acoustic wave emitted because of heat expansion by a target that has absorbed X-rays. However, this methodology is prone to issues in the signal-to-noise ratio (SNR) for endogenous targets, inhibiting its ability to translate clinically. By introducing a contrast agent to increase the SNR, the clinical efficacy of XACT can be drastically improved, shown in Figure 1a.

Recently, novel vaporizable endoskeletal droplets (VEDs) have been shown to increase the acoustic response to near-infrared photons during the photoacoustic effect. These droplets are primarily composed of liquid perfluorocarbon (FC) but have a solid hydrocarbon (HC) core, which allows for tunability of the vaporization temperature [7]. When

heated, interfacial mixing between the HC and FC phases facilitates vaporization of the droplet, resulting in a volumetric expansion of up to 125 times its original size [8]. To better understand the resulting temperature of the droplets when exposed to X-ray, we developed a model of the heat conduction through the droplet and into the surrounding water prior to vaporization. Using the model, we aim to determine the theoretical required dose and dose rate to vaporize the droplets.

METHODS

The model consists of three spherical domains, as shown in Figure 1b: a HC core with radius R_h , a FC shell with radius R_f , and a semi-infinite domain of water. The droplets are assumed to have radial symmetry.

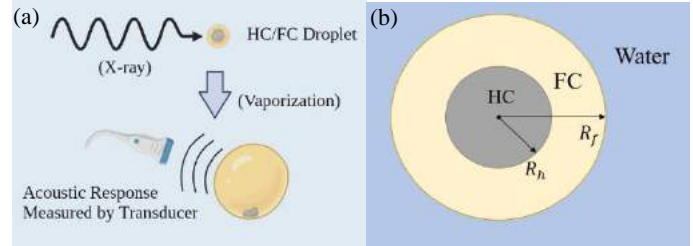


Figure 1: (a) Schematic of contrast-enhanced XACT (b) Schematic of VED used in model, with hydrocarbon (HC), perfluorocarbon (FC), and water domains.

To model the conduction of heat, Fourier's law modeling one-dimensional heat conduction along the radius was implemented for each domain (Eqs. 1-3).

$$\frac{dT}{dt} = \frac{k_h}{r^2} \frac{d}{dr} \left(r^2 \frac{dT}{dr} \right) + Q \quad \text{for } 0 \leq r \leq R_h \quad (1)$$

$$\frac{dT}{dt} = \frac{k_f}{r^2} \frac{d}{dr} \left(r^2 \frac{dT}{dr} \right) \quad \text{for } R_h \leq r \leq R_f \quad (2)$$

$$\frac{dT}{dt} = \frac{k_w}{r^2} \frac{d}{dr} \left(r^2 \frac{dT}{dr} \right) \quad \text{for } R_f \leq r < \infty \quad (3)$$

For the model, it was assumed that heat was generated only in the HC core, given by Q in units of W/m^3 . The thermal diffusivity, k_i , where i indicates the domain, was defined as the thermal conductivity, α , divided by the product of the density, ρ , and specific heat capacity, \hat{C}_p , (Eq. 4) [9].

$$k = \frac{\alpha}{\rho \hat{C}_p} \quad (4)$$

Table 1 provides a summary of the values used to determine the thermal diffusivity of the three domains. For the model, the HC used was eicosane, due to improved vaporization compared to other HCs [10].

Table 1: Summary of the values used for thermal conductivity, density, specific heat capacity, and resulting thermal diffusivity.

	$\alpha [W m^{-1} K^{-1}]$	$\rho [kg m^{-3}]$	$\hat{C}_p [J kg^{-1} K^{-1}]$	$k_i [m^2 s^{-1}]$
HC	0.42	789	2133	2.50×10^{-7}
FC	0.50	1630	1087	2.82×10^{-7}
H ₂ O	0.61	1000	4186	1.47×10^{-7}

The following boundary conditions were implemented: using a semi-infinite ‘far-field condition’, water is 32°C far from the droplet (Eq. 5); at the interface between domains i and j , there is equivalent heat transfer (Eq. 6) and temperature (Eq. 7); all domains have an initial condition of 32°C (Eq. 8).

$$T(r \rightarrow \infty) = 32^\circ C \quad (5)$$

$$-k_i \left. \frac{dT_i}{dr} \right|_{r=R_i} = -k_j \left. \frac{dT_j}{dr} \right|_{r=R_i} \quad (6)$$

$$T_i|_{r=R_i} = T_j|_{r=R_i} \quad (7)$$

$$T(t = 0, r) = 32^\circ C \quad (8)$$

Applying the boundary conditions and the initial condition, the steady state solution was obtained for a value of Q such that the middle of the HC core was 33°C, which is the droplet’s observed temperature of vaporization. Using the value of Q , a corresponding dose rate, DR , was estimated (Eq. 9)

$$DR = \frac{Q}{\rho} \quad (9)$$

The total dose, D , to raise the HC by 1°C (the range of vaporization temperature for eicosane droplets) is determined by utilizing the heat capacity of the material (Eq. 10) [11].

$$D = \frac{\Delta T}{\hat{C}_p} \quad (10)$$

RESULTS

From the steady state solution, a heat map was produced for the VED, shown in Figure 2. From the steady state calculations, it was determined that a dose rate of around 85 Gy/s and a total radiation time of around 25 seconds is needed to bring the HC core to its observed vaporization temperature.

As a more representative solution to the heat conduction of an ideal droplet, a transient solution was calculated using an initial temperature of 37°C (shown in Figure 3) and a dose rate of 24 Gy/min, which is the highest achievable clinical dose rate of standard LINACs.

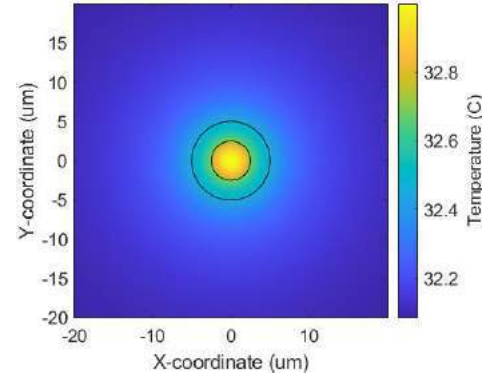


Figure 2: Steady state heat map of eicosane endoskeletal droplet with the HC core and FC shell outlined in black.

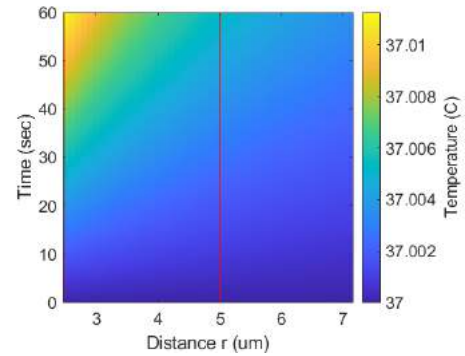


Figure 3: Transient heat map of eicosane endoskeletal droplet with the HC core and FC shell labeled in red vertical lines.

DISCUSSION

The results presented here indicate a large dose rate will be needed to raise the temperature of the droplet by 1°C. Using a more clinically relevant dose rate indicates an expected smaller increase in temperature of the HC, necessitating precise control of the vaporization temperature of the droplets. These findings highlight the need for a high-Z material that can more efficiently convert X-ray to heat, as well as the possible use of FLASH-RT, which is a novel type of RT that delivers high dose rates (> 40 Gy/s) [12]. Future models will explore these materials as dyes within the HC phase and their impact on the amount of heat generated per dose, as well as quantify in more detail the complexities of the interactions between X-rays and the droplets.

ACKNOWLEDGEMENTS

This research is funded by NIH Grant 1R21EB032911-01.

REFERENCES

- [1] Smith, BD et al., *J Clin Oncol*; 28(35):5160-5165., 2010
- [2] Height, R et al., *J Med Imaging Radiat. Oncol.*, 54(5), 497-504. 2010
- [3] Shimohigashi Y et al. *Radiat Oncol Lond Engl*. 12(1):61, 2017
- [4] Houweling AC, et al. *Phys Med Biol*. 62(8):3051-3064, 2017
- [5] Nyeng TB et al. *Acta Oncol*. 54(9):1467-1473. 2015
- [6] Essers M, Mijneer BJ. *Int J Radiat Oncol Biol Phys*. 43(2):245-259. 1999
- [7] Shakya G, et al. *Sci Adv*. 6(14). 2020
- [8] Kripfgans OD, et al. *Ultrasound Med Biol*.;26(7):1177-1189. 2000
- [9] Truskey, G., et al. Transport phenomena in biological systems. 2004
- [10] Shakya, G., et al. *Langmuir*, 38(8), 2634-2641, 2022
- [11] Khan, F. M., & Gibbons, J. P. Khan's the physics of radiation therapy. Lippincott Williams & Wilkins. 2014
- [12] Lin, B., et al. *Front in Onc*, 1890., 2021

PIN LOOSENING IN EXTERNAL FIXATION: A FINITE ELEMENT ANALYSIS TO DEVELOP AN OVINE BONE TRANSPORT MODEL

Michael J. Poland (1), Yunzhi Peter Yang (2), Jeremiah T. Easley (1), Jeffrey Young (2), Holly L. Stewart (1), Chloe Brekhus (1), Christian M. Puttlitz (1), Benjamin C. Gadowski (1)

(1) Mechanical Engineering, Colorado State University, Fort Collins, CO, United States

(2) Orthopaedic Surgery, Stanford University, Stanford, CA, United States

INTRODUCTION

Segmental defect repair remains a primary challenge in orthopedics. Bone transport distraction osteogenesis (DO) is a common surgical approach to bridge long bone critically sized defects. An osteotomy is performed adjacent to the defect to create a bony segment. The segment is then stabilized with external fixation and transported at 1 mm/day until it has crossed the bone gap (Figure 1B). After completion of distraction, the bone often must remain stabilized for more than six months. Consequently, long-term external fixation can lead to complications, such as pin loosening. The breakdown of the pin-bone interface can be attributed to an interplay of mechanics and pin-site infection. For example, increased pin flexion, caused by a weak construct, can irritate the bone and lead to increased infection risk. Conversely, infection at the pin site can weaken the bone, leaving it vulnerable to degradation from the pin [1]. Pin configuration A (Figure 2) was used in an ovine bone transport pilot study, but pin loosening resulted in premature termination of 2 sheep. The aim of this study was to optimize the external fixation construct to minimize stress at the pin-bone interface using finite element (FE) ovine metatarsal bone transport models.

METHODS

Computer Simulation

FE software (ABAQUS/Standard 2020) was used to model ten unique external fixator configurations. An approximated sheep metatarsal was modeled with elastic material properties ($E=18\text{GPa}$, $\nu=0.265$) and as a hollow cylinder with 7mm and 18mm inner and outer diameters, respectively. All external fixation components were modeled as stainless steel ($E=200\text{GPa}$, $\nu=0.3$), and all interfaces were modeled as tie constraints (Figure 1A). A 200N compressive force was applied to the superior surface of the simulated metatarsal at a 20° posterior-anterior angle to mimic the walking conditions of a sheep [2]. Rotation and displacement were constrained in all directions at the distal face of

the distal bone with an encastre boundary condition. Linear, hex elements were used to model the bone segments (1446 elements), pins (2100 elements), and frame (19538).

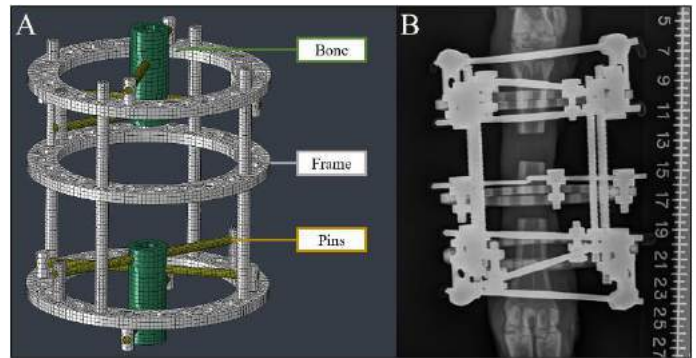


Figure 1: (A) Finite element model of simulated sheep metatarsal (green), external fixation frame (white), and fixation pins (yellow). (B) Radiograph of sheep metatarsal during the bone transport phase.

In Vivo Study

The results of the FE simulations informed the *in vivo* external fixator design where lower stress at the pin-bone interface indicated better performance. Pin configuration F was then used on two skeletally mature female ewes (IACUC #KP 1579). Pin pilot holes were drilled 0.1mm smaller than the pin core diameter. An osteotomy was performed to create a 2cm transport segment and a 3cm distraction gap. Seven days after the operation, distraction began at a rate of 1mm/day for 30 days followed by a consolidation period of 180 days. Biweekly radiographs were taken and analyzed for signs of loosening, such as radiolucency around each pin. Bandages were changed, pin sites were cleaned, and

the leg was palpated to check for loosening twice per week throughout the latency and distraction periods and once per week throughout consolidation. After sacrifice, micro-computed tomography (μ CT) analyses were used to measure the final pin site diameters in each specimen using the following parameters: Voltage: 70kVp, current: 114 μ A, integration time: 500ms.

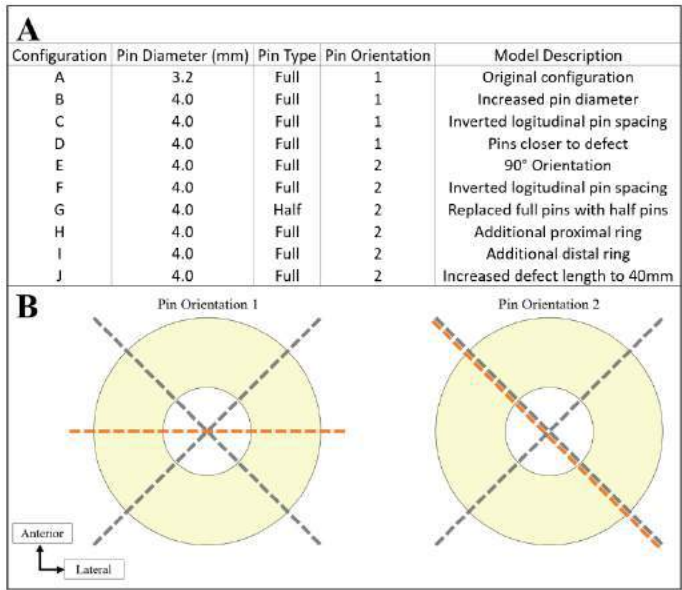


Figure 2: (A) Descriptions of the modeled fixation configurations. (B) Graphical representation of pin placement in a sheep metatarsal cross section

RESULTS

Computer Simulation

Maximum von mises bone stress (MVMBS) was approximately 25% lower for 4.0mm configurations when compared to 3.2mm configurations (Figure 3). Compared to configuration A, the use of 4.0mm half pins increased MVMBS by 40%. Moving pins closer to the defect resulted in the third highest MVMBS value at 34MPa. No other configuration altered bone stress by more than 7%. Maximum von mises pin stress (MVMPS) decreased by at least 52% in all models except for configuration G.

In Vivo Study

In vivo configuration F manual palpation demonstrated no qualitative signs of pin loosening throughout the duration of the study (217 days) in either sheep. In one animal, however, post-sacrifice micro-CT measurements showed a pin hole diameter expanded by an average of 2mm across one pin site. No other pin site in the configuration F animals had a measured diameter expansion larger than 0.2mm. Manual palpation of configuration A animals showed significant loosening after 30 days in 2 animals, and they were terminated early. Micro-CT measurements showed an average expansion of at least 3.5mm across all measured pin sites.

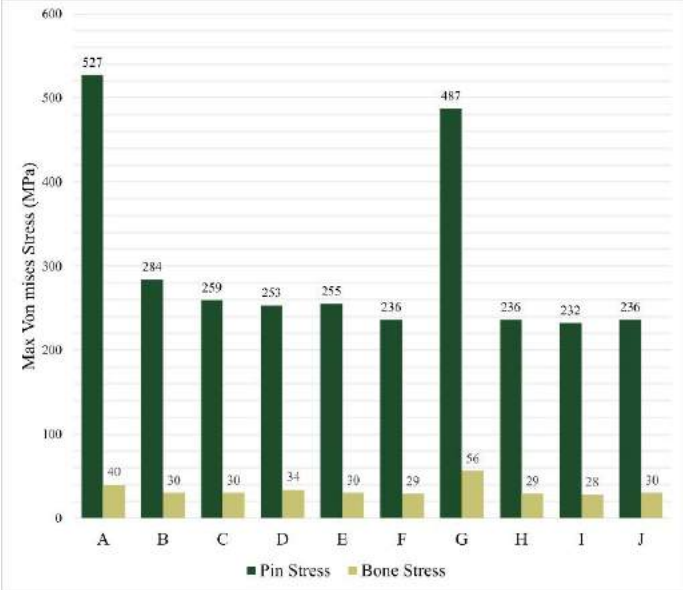


Figure 3: Pin and bone maximum von mises stress for each configuration

DISCUSSION

Pin diameter had the biggest impact on VMBS and VMPS, and further configuration modifications only marginally altered the stresses. The use of half pins in place of full pins erased any benefit of larger pin diameter. However, half pins only have one insertion point per pin and should be considered if infection is believed to be the main cause of loosening. Configuration D resulted in the third highest bone stress. This result is surprising because previous studies have shown that moving pins closer to the defect can increase fixation stability [3]. Therefore, this result may suggest that fixator stability and stress at the pin-bone interface are not always directly related. Configuration F was chosen for use in the *in vivo* study because it both resulted in low stresses at the pin-bone interface and had a higher axial pin spacing, decreasing the chance of fracture upon insertion. Stress may have been further reduced by increasing the pin diameter beyond 4.0mm, but the use of pin diameters greater than 30% of the bone diameter is not advised [3]. A larger *in vivo* sample size would be needed to investigate if the expanded diameter of the single configuration F pin site was a result of fixation mechanics. While it is believed improved fixation mechanics improved the outcome of the *in vivo* study, improved pin site cleaning may have also contributed to pin site longevity. High bone transport associated skin tension [3], tissue viscoelastic properties, and true anatomic geometry are not accounted for in this FE study. A future study could expand on this work by evaluating more configurations and loading conditions. Long-term ovine pre-clinical studies designed to improve the bone quality and rate of healing in bone transport patients would improve with better pin site longevity. The resulting external fixation construct from this work may be an effective model for future ovine DO studies.

REFERENCES

[1] Ferreira N, et al. Strategies Trauma Limb Reconstr, 7(2):67, 2012
[1] Gadowski B, et al. J Orthop Res, 36(3) 921-929, 2017
[2] Fragomen A, et al. HSS J., 3(1):13-29, 2007

COMPARING APPROACHES TO ESTIMATE FAILURE STRENGTH OF SUTURED PATCHES USED IN PEDIATRIC CARDIAC SURGERY

Shannen B. Kizilski (1,2), Dominic P. Recco (1,2), Lauren E. Marshall (1), Nicholas E. Kneier (1),
Patrick D. Earley (1), Peter E. Hammer (1,2), David M. Hoganson (1,2)

(1) Department of Cardiac Surgery, Boston Children's Hospital, Boston, MA, USA
(2) Harvard Medical School, Harvard College, Boston, MA, USA

INTRODUCTION

Patch augmentation of the aorta is a critical component of several pediatric cardiac surgical procedures, including repair of aortic coarctation with hypoplastic arch and the Stage I Norwood procedure for single ventricle palliation. During these procedures, an incision is made in the native aortic tissue and an autologous or commercial tissue patch is sewn in with a running suture line to achieve the targeted vessel geometry. Tissue-based patches are preferred for these reconstructions due to their ability to conform to the desired curvature and to better preserve aortic compliance; however, these materials are not as strong as synthetic alternatives and can be vulnerable to dilation or failure if used under inappropriate loading conditions.

Prior studies have characterized the mechanical behavior and failure properties of conventional patch materials, including pulmonary homograft, autologous pericardium, and various fixed pericardium products [1-3]. These studies typically report the ultimate tensile strength of the patch, determined through uniaxial tests of dogbone-shaped samples. While this type of test is well established and straightforward to perform, it does not reflect a realistic loading scenario for a surgical patch, which will be sewn into aortic tissue and pulled in all directions under a pressure load. Standard and bulge inflation tests better address the loading configuration, but they usually do not evaluate the sutured patch-aorta interface, which represents the weakest region of the patch.

In this study, we evaluated the failure strength of two common patch materials [4]: thick-patch pulmonary homograft (cryopreserved, cadaveric adult main pulmonary artery) and CardioCel Neo (fixed bovine pericardium) using three different test modalities. Unsutured and sutured patch samples were tested uniaxially to identify the effect of the suture line on failure strength, and patches were sewn into a porcine aorta to compare uniaxial failure strength to burst strength.

METHODS

Patch Materials

Each test modality was conducted for three different patch materials: porcine pulmonary artery, pulmonary homograft, and CardioCel Neo (Fig. 1). Due to known similarity between porcine and human large artery mechanics, porcine pulmonary artery was tested to supplement the limited pulmonary homograft sample size [5]. Samples were harvested from fresh, adult whole-heart specimens (Lampire Biological Laboratories, Pipersville, PA). Homograft is the preferred patch material for neonatal arch reconstruction, but its safety in older patients is not well documented. Two 30x30mm patches were retrieved from discarded OR scraps (LifeNet Health, Virginia Beach, VA, and Artivion, Kennesaw, GA). CardioCel Neo (LeMaitre, Burlington, MA) comes in a 0.3mm-thick sheet and is advertised to be stronger than the aorta and suitable for great vessel reconstruction. Two 50x80mm patches were retrieved from discarded OR scraps. All tissue was stored in normal saline at 4°C until use.

Uniaxial Failure Strength

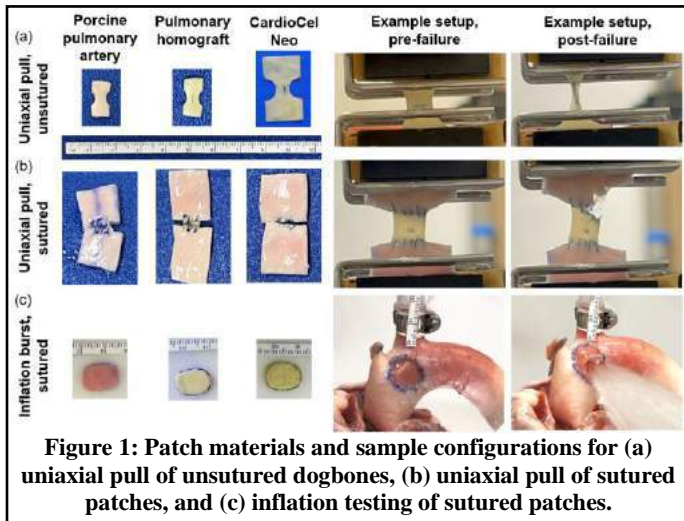
Uniaxial testing was conducted on both unsutured dogbone samples and sutured squares using a single-column Instron. Displacement was set to 10mm/minute, and force was recorded with a 50N load cell. Samples were held by 250N pneumatic clamps with sandpaper. Membrane tension at failure was calculated using the undeformed patch width for both sample types.

Unsutured Dogbone Samples

Ultimate tensile strength of the patch materials was assessed through uniaxial pull to failure of dogbone samples (Fig. 1a). Three axially aligned dogbones were cut from the porcine pulmonary artery to capture failure strength along the weaker direction of the vessel. Two dogbones were cut from each homograft patch for a total of four samples. Samples from both of these materials were prepared as

7.5x15mm strips with an 8mm punch used to create the narrowed central region.

For the CardioCel Neo, there was enough material available to prepare four dogbone samples from each of the two patches (n=8). Due to the significantly higher strength of this material, samples were cut to 15x25mm for increased grip area, and the punch was used to reduce the central region to <4mm width. Sample lengths were recorded as the distance between the grips after the samples were mounted and the Instron jogged to show 0.01N load.



Sutured Square Samples

To minimize the patch material needed for each sutured sample, 7.5x7.5mm squares were cut and sutured on either end to 15x15mm squares of porcine aorta (Fig. 1b). The 7.5mm edge length allowed 4 bites of a running 5-0 Prolene suture to be made into both the patch and the aorta with roughly 1.75mm bite spacing and 2mm bite depth. The two tabs of aorta were clamped into the Instron, and the mode of failure was recorded. Suture line failure was defined as either the patch or the aorta having suture pull-through from the needle holes into the edge of the suture line. Needle hole failure occurred when the patch or the aorta tore internally, originating at a stretched needle hole. Patch rupture was defined as a tear beginning at the free edge of the patch or internally without any continuity with the needle holes or suture line.

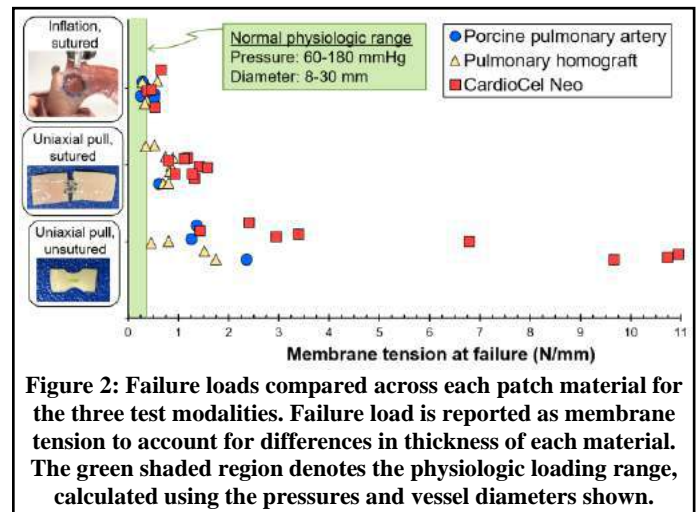
Inflation Burst Strength

To assess the importance of the loading state in patch failure, a series of inflation tests were conducted on patches sewn into porcine aorta models (Fig. 1c). For each patch material, a new porcine heart and aortic arch were prepared. An 11x15mm window on the anterior aspect of the arch was excised using an 11-blade scalpel. A sample of the same dimensions was cut from the patch material and sewn in using the same running 5-0 Prolene suture line as described in the previous section. T

A barbed fitting was clamped into one head vessel for connection to a pressure transducer. Another barbed fitting at the descending aorta connected to a saline bag, which was used to apply an impulse of pressurized water into the system. The other head vessels and the aortic root were clamped with curved forceps. A ruler was attached to the cannulated head vessel for diameter reading at the instant before failure, measured from recorded video. Peak pressure before failure was recorded. Changes to patch and aortic dimensions were used to estimate wall thinning at maximum pressure, and Law of Laplace was used to calculate failure stress. Failure was categorized using the same convention as in the uniaxial suture tests.

RESULTS

Failure strength, expressed as membrane tension, is compared across each patch material and test modality in Fig. 2. Uniaxial dogbone testing yielded the highest strength measurements for each of the materials, with the CardioCel Neo nearly an order of magnitude stronger than the homograft and porcine pulmonary artery. Inclusion of a suture line led to much lower failure loads across all materials, and testing in a pressurized environment led to lower strength measurements than in the uniaxial setup. Under burst testing, all CardioCel Neo failures occurred via suture line failure in the aortic tissue, leaving the patch fully intact. Three of the four homograft failures occurred at needle holes within the patch. Several inflation failures occurred within the adult physiologic loading range.



DISCUSSION

Mechanical strength of cardiovascular patch materials is of significant interest to surgeons as they reconstruct high-pressure vessels like the aorta, but most mechanical tests fail to evaluate the suture line, which is bound to be the weakest element of the patched repair. Our testing demonstrated a significant reduction in failure strength when a suture line was added to three different patch materials. None of the samples with a suture line failed far above the physiologic loading range, suggesting that aggressive control of postoperative blood pressure is essential for patient safety until wound healing begins. A next step for this study is to evaluate how different suture techniques can improve suture line strength.

ACKNOWLEDGEMENTS

The authors would like to thank Professor Tommaso Ranzani and graduate students Jacob Rogatinsky and Leah Gaeta at Boston University for providing access to, and assistance with, the Instron system used for uniaxial testing in this study.

REFERENCES

- [1] Neethling, WML et al., *Interact Cardiovasc Thorac Surg*, 26:985-992, 2018.
- [2] Desai, A et al., *J Mech Behav Biomed Mater*, 79:53-63, 2018.
- [3] Seebacher, G et al., *Artif Organs*, 32(1):28-35, 2007.
- [4] van Beynum, IM et al., *World J Pediatr Congenit Heart Surg*, 12(4):487-491, 2021.
- [5] de Beaufort, HWL et al., *Eur J Vasc Endovasc Surg*, 55(4):560-6, 2018.

NONLINEAR AND ANISOTROPIC MECHANICAL RESPONSE OF FISH SKIN

Sean T. Harrington (1), Frederick Sebastian (2), Rouzbeh Amini (1,2)

(1) Department of Mechanical and Industrial Engineering, Northeastern University, Boston, Massachusetts, USA

(2) Department of Bioengineering, Northeastern University, Boston, Massachusetts, USA

INTRODUCTION

In recent years, fish skin bandage substrates have been proven to be a viable treatment for severe burn victims [1]. It has been postulated that fish skin holds many nutrients that promote tissue regrowth in the epidermis [1]. It has been shown that the cellular responses (including gene expression and protein synthesis) in a wide range of cells depend on the mechanical stiffness of the extracellular matrix [2]. In the realm of wound healing, important processes, such as the migration and proliferation of the epidermal cells, heavily depend on the mechanical microenvironment in which the cells reside [3]. As such, to improve wound healing, identifying a favorable mechanical microenvironment is essential. Since the recent evidence have shown fish skin to be a promising burn dressing that improves wound healing, one could postulate that the mechanical response of the fish skin is like that of the native tissue. In this study, we aim to examine the feasibility of using a biaxial mechanical testing device to evaluate the mechanical responses of the fish skin. If this method deems appropriate, we will compare the results to human skin tissue in the future, to determine if the mechanical properties of the fish skin are a contributing factor to its proven performance as a burn dressing.

METHODS

Fish sample of haddock were acquired from a local fish market specializing in sale of freshly caught fish (John Mantia & Sons, Boston, MA). The skin samples were excised from the fish carcass (unknown sex) and stored in phosphate buffered saline (PBS) solution while the rest of the testing apparatus was set up. Storing in isotonic PBS was chosen because of the

similarity between the osmolarity of fish skin, and that of human skin [4].

The samples were then loaded into our custom-built biaxial testing apparatus [5] as shown in Fig. 1. Careful attention was taken to the sample orientation in relation to the anatomical direction of the fish body. In particular, axis 1 of the device was aligned with the dorsal-ventral (back-to-belly) direction of the fish body, and axis 2 of the device was aligned with the anterior-posterior (head-to-tail) direction of the fish body.

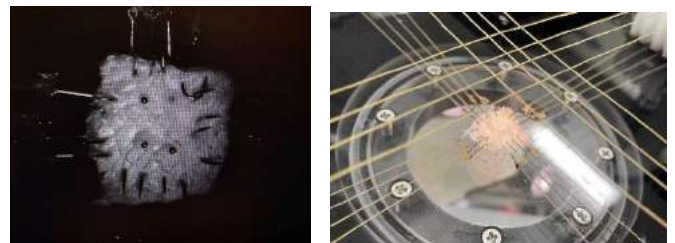


Figure 1: Biaxial Test Setup. Camera view depicting sample and four fiducial markers on the left, and testing apparatus with suture lines used to pull the tissue on the right.

The sample was then loaded under five loading protocols (Table 1) to allow for proper fitment of a constitutive model to the data. Nine preconditioning cycles were applied to each sample. The cross-sectional area of the sample in each axis were measured and denoted as A_0 for stress calculations. The positions of the four fiducial markers (Fig. 1), as well as the load applied to each axis, were recorded for each test.

Table 1: Loading protocols used in the biaxial testing.

Protocol Number	Axis 1 Stress	Axis 2 Stress
1	120 kPa	40 kPa
2	100 kPa	60 kPa
3	80 kPa	80 kPa
4	60 kPa	100 kPa
5	40 kPa	120 kPa

An internally developed image processing MATLAB script was utilized to obtain the positions of the fiducial markers at each timestep of the experiment. The positional data were then used to calculate the Green-Lagrangian Strain tensor \mathbf{E} [6].

$$\mathbf{E} = \frac{1}{2}(\mathbf{C} - \mathbf{I}) \quad (1)$$

where \mathbf{C} is the right Cauchy-Green deformation tensor. The load f_i at each timestep, in each direction i , was obtained from the load cells. Together with the cross-sectional area of the sample in each direction, the normal components of the First Piola-Kirchoff Stress tensor \mathbf{P} were calculated:

$$P_{11} = \frac{f_1}{A_o} \quad P_{22} = \frac{f_2}{A_o} \quad (2)$$

and the second Piola-Kirchoff Stress tensor was defined as

$$\mathbf{S} = \mathbf{F}^{-1}\mathbf{P} \quad (3)$$

with \mathbf{F} being the deformation tensor. After visual examination of the experimental data for the second Piola-Kirchoff stress versus the Green-Lagrangian strain, a Fung-type constitutive model identical to those of other biological tissues with similar responses was adopted [7]. The strain energy density function for this model was defined as

$$W(\mathbf{E}) = \frac{k}{2}(e^{\beta_1 E_{11}^2 + \beta_2 E_{22}^2 + \beta_3 E_{11}E_{22}} - 1) \quad (4)$$

where β_1 , β_2 , β_3 , and k are material parameters, obtained after fitting all five protocols simultaneously to the experimental data using MATLAB *fminsearch* function.

RESULTS

The stress-strain response of the fish skin was similar to the non-linear behavior of many collagenous human tissues (Fig. 2). In particular, the tissue displayed a toe-region where a small amount of stress led to a large deformation. However, the tissue became stiffer as the strain increased.

Further, the tissue response was highly anisotropic. Across all protocols, visual examination of the mechanical responses showed that the fish skin samples were much stiffer in the dorsal-ventral direction as compared to the anterior-posterior direction. In the first protocol, the stress on both directions were equal. In this protocol, the strain in the anterior-posterior direction was positive; however, the dorsal-ventral axis experienced negative strain, due to the Poisson's effect. The non-linear exponential Fung-type model fitted this single experiment reasonably well with the R^2 value of 0.98.

DISCUSSION

In this study, our goal was to identify if using a biaxial mechanical testing device is a feasible approach for quantification of the fish skin. We observed that this approach is indeed applicable to the fish skin. In our future work, we aim to increase the number of our samples, so that a meaningful comparison between our data and those published for human skin may be possible.

An anecdotal conclusion from our preliminary observation is that for greater effectiveness as a bandage substrate, it is perhaps advisable that the fish skin be oriented in a way such that the head-to-tail axis of the fish skin aligns with the axis of the most movement of the patient.

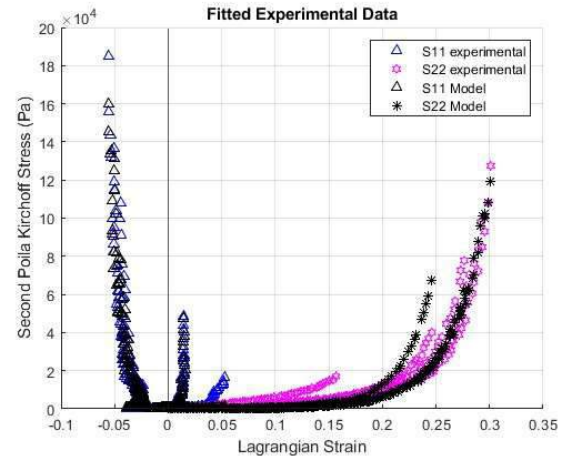


Figure 2: Biaxial mechanical response of the fish skin. S_{11} plotted in blue, S_{22} plotted in magenta along with the fitted constitutive model plotted in black.

Another important observation from our experiment was how similar fish skin behaves in comparison to an-isotropic human tissues. Fung-type model has been widely used as a phenomenological model in predicting the response of human soft tissue. As shown in Fig. 2, the constitutive model had an excellent fit with an R^2 metric of 0.98.

In summary, we observed that fish skin has a nonlinear and anisotropic mechanical response, qualitatively similar to those of human tissues. How similar the micromechanical environment of fish skin is to that of human skin needs to be identified in the future studies. Further research can also be performed to quantify microstructural architecture of the fish skin and its potential similarities to that of human native tissues.

REFERENCES

- [1] Lima, EM, *Plasts Reconst Surg* 147.5 (2021): 1189-1198.
- [2] Engler, AJ, et al. *J. Musculoskelet Neuronal Interact* 7.4 (2007): 335.
- [3] Wang, Y, et al. *Burns* 38.3 (2012): 414-420.
- [4] Lin, MQ, et al. *LWT-Food Sci Technol* 31.1 (1998): 27-32.
- [5] Khoiy, KA et al. *J. Biomech Eng* 138.10 (2016).
- [6] Tadmor, EB., et al. Cambridge University Press, 2012.
- [7] Khoiy, KA, *J. Biomech Eng* 140.9 (2018).

MECHANICAL CHARACTERIZATION OF PORCINE TRICUSPID VALVE ANTERIOR LEAFLETS OVER TIME: APPLICATIONS TO EX-VIVO STUDIES

Julia Clarin (1), Dominique Dang (1), Lucas Santos (1), Rouzbeh Amini (1,2)

(1) Department of Bioengineering, Northeastern University, Boston, MA
(2) Department of Mechanical Engineering, Northeastern University, Boston, MA

INTRODUCTION

The tricuspid valve (TV) relies heavily on the mechanical behavior of its leaflets to ensure unidirectional blood flow and prevent regurgitation in the pulmonary side of the heart. Tricuspid regurgitation (TR) occurs when the leaflets fail to properly coapt, causing backflow of blood into the right atrium and reduced efficiency of the right ventricle. TR increases strain on the heart and can accelerate the development of serious heart conditions such as progressive right heart failure if left untreated [1]. Furthermore, high operative mortality rates and contrasting opinions on surgical approaches severely limit treatment options for over 1.6 million people in the US affected by tricuspid regurgitation [1]. The lack of safe and effective treatment options for TR highlights a critical need to better understand the complex relationship between TV biomechanics and function.

Recent approaches to characterize TV biomechanics include biaxial mechanical tests, ex-vivo experiments [2, 3] and computational simulations [4, 5]. We have previously investigated porcine TV biomechanics in our ex-vivo beating heart system [3]. Such a system enables us to isolate the mechanical behavior of the TV leaflets in whole hearts without requiring dissection of the valve apparatus, while also reducing the need for live animal studies. Ex-vivo experiments, however, often require relatively lengthy sample preparation and setup procedures. For example, preparation of whole-heart samples for our ex-vivo TV experiments may take up to 5 hours on average. Because the mechanical behavior of the tissue is essential to the experimental outcomes, preparation procedures must be performed efficiently to minimize degradation and maintain tissue integrity.

While tissue storage conditions (e.g., fresh versus previously frozen conditions) have been more extensively studied [6], the effect of preparation and setup time on the mechanical properties of the tissue has not been determined in TV leaflets. Therefore, we characterized the mechanical properties of the anterior tricuspid leaflet (ATL) over a relevant time scale to validate the accuracy of our fresh tissue experiments using the ex-vivo beating heart system. We evaluated porcine ATL mechanics by performing a series of biaxial mechanical tests over 5 hours. We hypothesize that the mechanical properties do not significantly change at our time scale.

METHODS

Healthy porcine hearts ($n=7$, approximately 6 months old) were obtained from Animal Biotechnologies (Tyler, TX, USA) within 24–36 hours of harvesting. To preserve freshness, hearts were shipped in chilled phosphate-buffered saline (PBS) and used immediately upon arrival. Tissue specimens were prepared immediately upon receiving the fresh tissue following procedures described in our previous publications [6–8]. Briefly, the ATL was excised from the heart with directional integrity maintained. ATL thickness was recorded as the average of five measurements. A square specimen (7.6×7.6 mm) was prepared from the center of the leaflet, and four glass markers were placed within the test region to quantify in-plane deformation using digital image correlation.

Specimens were mounted onto a custom biaxial tensile machine such that the radial and circumferential directions aligned with both axes [6–8]. Specimens were submerged in a PBS bath during testing to mimic physiological osmolarity and prevent tissue swelling [8]. The PBS bath and tissue specimens were kept at room temperature (21°C) to recreate the ex-vivo testing environment.

Based on our most recent ex-vivo beating heart tests (data not shown), the average time to run an experiment, from time of receipt to data collection, was approximately 5 hours. Thus, we performed biaxial mechanical testing over a period of 5 hours to capture potential changes in ATL mechanical properties that may occur during our experiments. Initial testing ($\text{time}=0$) began immediately after specimen preparation, and the following five tests were spaced out by 1-hour intervals. Specimens remained submerged in the room-temperature PBS bath in an unloaded state between tests.

Biaxial data were collected at all six time points using procedures consistent with our previous publications [6–8]. For this analysis, a stress-controlled equibiaxial loading protocol was used with a target stress of 120 kPa to ensure full engagement of collagen fibers and mimic physiological loading conditions on the ATL in a healthy heart [8, 9]. Positional data obtained from tracking the fiducial markers were used to determine the deformation gradient tensor and calculate the Green-Lagrange strain tensor. The cross-sectional area of the specimen and the forces applied by the actuator were also recorded. SB³C2023-582
Copyright 2023 SB³C Foundation, Inc.

tuators were used to then calculate the normal stresses in the radial and circumferential directions, represented by the first Piola-Kirchhoff stress tensor. Further details on stain and stress calculations can be found in our previous publications [6–8].

To provide a comparative measure of stiffness, the upper tangent modulus (UTM) was obtained by fitting the post-transitional linear region of the equibiaxial response curve (60–120 kPa) using a least-squares approach in MATLAB (Mathworks, Nantick, MA, USA). The circumferential upper tangent modulus (UTM_C) and radial upper tangent modulus (UTM_R) were defined as the slope of the fitted lines in the radial and circumferential directions, respectively. As described previously, the physiological stress on the ATL during systole was estimated to be 85 kPa using Laplace's law for a healthy mean right ventricular pressure of 25 mmHg [7]. Hence, the corresponding radial and circumferential strains at an estimated systolic stress of 85 kPa were obtained for physiological comparison.

Results were subjected to a one-way analysis of variance (ANOVA) to isolate the effect of time on the mechanical response of the ATL ($p \leq 0.05$). Radial and circumferential results were compared for each time point with a paired student's t-test ($p \leq 0.05$). Results are presented as mean \pm standard error of the mean (SEM).

RESULTS

The mean mechanical response of the ATL (mean thickness = $360 \pm 81 \mu\text{m}$) was determined using equibiaxial test data from all specimens ($n = 7$) at each of the six consecutive time steps. The mean mechanical response is represented by the averages of the first Piola-Kirchhoff stress and Green strain curves shown in Figure 1. Visual examination of the overall biaxial mechanical response does not reveal any major differences in radial or circumferential directions with increasing time (Fig. 1).

Mean radial and circumferential UTMs are shown for all time points ($t=0$ –5 hours) in Figure 2a. As previously described, the average stress on the ATL during systole was approximated to be 85 kPa in a healthy heart [7]. Thus, the corresponding strain at stress = 85 kPa represents an approximate physiological systolic strain, as shown in Figure 2b.

A one-way ANOVA revealed that mean UTM and physiological strain did not significantly change over time in either the radial or circumferential directions for the 5-hour test period. The overall mean UTM showed that specimens were significantly stiffer in the circumferential direction ($11.3 \pm 0.98 \text{ MPa}$) compared to the radial direction ($2.29 \pm 0.20 \text{ MPa}$) for $p \leq 0.05$. A similar effect was observed in ATL strains corresponding to the estimated systolic stress, in which mean radial strain ($27.6 \pm 2.9 \%$) was found to be significantly larger than mean circumferential strain ($7.37 \pm 0.85 \%$) for $p \leq 0.05$.

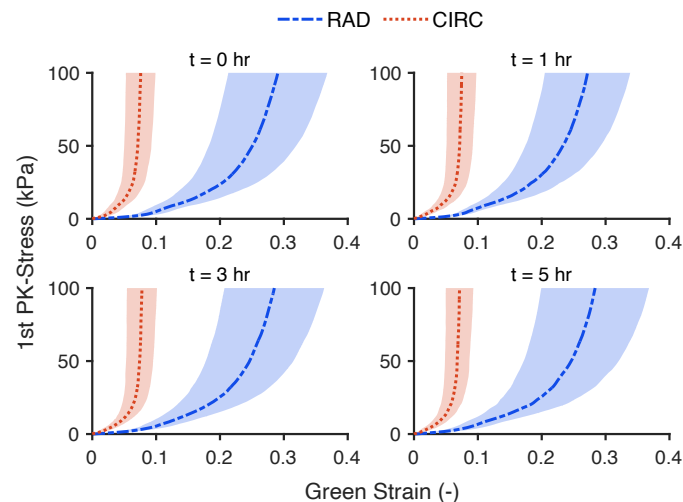


Figure 1: First Piola-Kirchhoff (PK) stress vs. Green strain average curves ($n = 7$) remained consistent in the radial (RAD) and circumferential (CIRC) directions for all time points (only four are shown for visual purposes). Shaded regions indicate SEM.

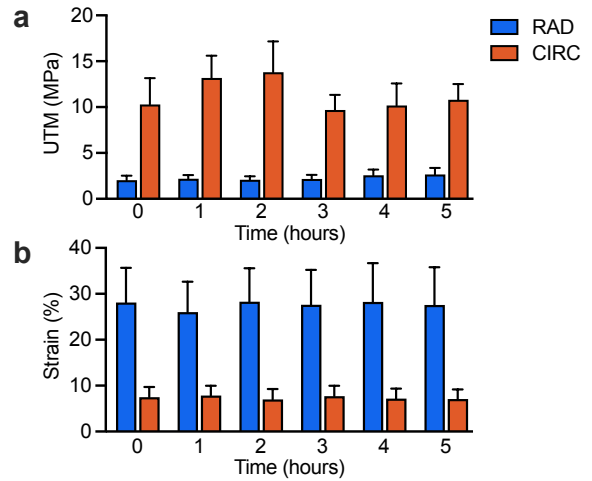


Figure 2: Mean (a) UTM and (b) estimated systolic strain did not significantly change in the radial (RAD) and circumferential (CIRC) directions over five hours ($p \leq 0.05$). Error bars show SEM.

DISCUSSION

Equibiaxial loading of the porcine ATL resulted in an anisotropic and nonlinear mechanical response that was stiffer in the circumferential direction, consistent with previous studies [7–9]. Importantly, there was no significant difference in the mean mechanical response of the leaflets over the course of five hours, as described by the UTM fitting in the radial and circumferential directions. The UTM was chosen as a measure of ATL stiffness to capture the mechanical response of the fully-engaged collagen fibers at physiological stresses. ATL strains corresponding to an estimated systolic stress value (85 kPa) further showed no significant change over five hours. Collectively, these observations support our hypothesis that the mechanical responses of the TV leaflets remain unchanged at a short time scale of five hours, especially as it pertains to ex-vivo setups [3, 7].

Despite our results, we must acknowledge potential changes in mechanical properties of our samples prior to experiments due to shipping time and conditions (in chilled PBS). In a previous study, we investigated the effect of short-term PBS storage on porcine ATLs that were obtained immediately after hearts were harvested. We found that two-hour submersion in PBS had no effect on the mechanical properties, as evaluated with equibiaxial testing [8]. As such, we expect the changes in the mechanical properties due to short storage in chilled PBS during the shipment to be minimal. Further, we did not characterize the ATL microstructure over time. Therefore, our results only indicate that the tissue-level mechanical response is not affected at a time scale relevant to our ex-vivo beating heart experiments.

Consistent with our proposed hypothesis, we observed that the mechanical response of the anterior tricuspid leaflet does not change significantly over a period of five hours. Thus, the outcome of ex-vivo studies that require sample preparation and manipulation up to five hours remain reliable.

ACKNOWLEDGEMENTS

Funding for this project was provided in part by the National Science Foundation (CAREER 2049088).

REFERENCES

- [1] Mangieri A et al. *Circ Cardiovasc Interv* 10 (2017).
- [2] Jaworek M et al. *ASAIO J* 63 (2017).
- [3] Khoiy KA et al. *J Biomech Eng* 138 (2016).
- [4] Lee CH et al. *Biomech Model Mechanobiol* 14 (2015).
- [5] Laurence DW et al. *Int J Numer Methods Biomed Eng* 36 (2020).
- [6] Salinas SD et al. *J Biomech* 98 (2020).
- [7] Khoiy KA et al. *J Biomech Eng* 138 (2016).
- [8] Salinas SD et al. *Bioengineering* 6 (2019).
- [9] Jett S et al. *Data Br* 21 (2018).

TOWARDS HIGH SPATIOTEMPORAL RESOLUTION BLOOD FLOW VELOCITY FIELD MAPPING FOR MICE: A VALIDATION STUDY

Mingyi Tang (1,2), David A. Steinman (1,3), Craig A. Simmons (1,2,3)

- (1) Department of Mechanical & Industrial Engineering, University of Toronto, Toronto, ON, Canada
(2) Translational Biology & Engineering Program, Ted Rogers Centre for Heart Research, Toronto, ON, Canada
(3) Institute of Biomedical Engineering, University of Toronto, Toronto, ON, Canada

INTRODUCTION

Mouse models offer many advantages in studying the contribution of hemodynamic forces to cardiovascular disease development, notably the simplicity of genomic manipulation to generate models of human diseases without other confounding variables [1], and the opportunity to follow the different stages of disease development in the same mouse. However, mice pose a significant challenge for blood flow studies that aim to quantitatively map flow patterns, because common flow imaging methods (e.g., pulse wave Doppler or MRI) provide only bulk velocity estimates [2] or velocity data with low temporal resolution, i.e., maximum velocity in mice is ~1 m/s with heart rate ~5-10 times faster than in humans [3], [4]. A quantitative, non-invasive medical imaging method to map blood flow velocity fields in mice would enable preclinical studies that are not possible currently, leading to new insights into disease mechanisms and treatments.

An alternative flow quantification method that can achieve non-invasive velocity field mapping is ultrasound image velocimetry (UIV) which applies particle image velocimetry (PIV) techniques to ultrasound images to track blood speckle or contrast agent displacement. In this way, UIV can produce instantaneous two-dimensional velocity fields. Both in vitro validations and in vivo studies have been previously conducted for UIV of human cardiac flow [5] but not yet in mice due to temporal resolution limitations in conventional ultrasound imaging. To capture images at higher frame rates, a commercially available imaging mode known as ECG-gated kilohertz visualization (EKV) is available, in which sub-sections of the targeted field of view (FOV) are scanned from different cardiac cycles and then combined into one image for each time point. This can produce higher temporal resolution (up to 10,000 fps) than conventional real-time ultrasound (maximum ~1,000 fps) without compromising image spatial resolution. This imaging mode has been used to capture fast-moving cardiac tissue in mice [6] but has yet to be used for UIV of mouse blood flow; it is therefore necessary to perform validation studies to test if UIV

can provide accurate velocity field information. As a first step to this end, the work presented here focuses on the validation of the technique using in vitro and in silico experiments with linear speckle or particle displacement.

METHODS

In Vitro Experiments: A straight fluidic channel with a circular cross-section was fabricated using high strength agar. The diameter of the channel was 1.2 mm, similar to that of mouse aortas. A blood mimicking fluid consisting of nylon particles with diameters of 5 μm [7] were used to produce speckle patterns in ultrasound imaging. Flow experiments were conducted by providing cross-sectional mean flow velocities between 14 mm/s and 550 mm/s (peak velocities 28 mm/s and 1100 mm/s, respectively) using a syringe pump. The ultrasound images were acquired using the Vevo 3100 (FUJIFILM VisualSonics Inc.) system with a 30 MHz linear array transducer. The ultrasound beam was oriented in two different directions to capture any angle dependency in flow imaging: perpendicular (Fig. 1A) and at a 60-degree angle (Fig. 1B) to the flow direction. The frame rate of EKV was varied between 1,000 to 10,000 fps. Velocity fields were measured from the EKV images using the MATLAB toolbox PIVlab [8]; a multipass approach was chosen with interrogation window (IW) sizes 180×180 px and 90×90 px with 50% overlap (for a FOV of 1440×316 px).

In Silico Experiments: In parallel to the in vitro experiments, in silico experiments were also conducted to understand and verify the effect of EKV reconstruction on UIV measurements in a controlled manner. Synthetic particle images with Gaussian intensity profiles were generated using PIVlab. Particle diameter was 25 ± 4 px and the image size was 800×600 px. The velocity field was linear at a 45° angle from the vertical image axis (Fig. 2); the horizontal and vertical (equivalent to the lateral and axial directions with respect to the ultrasound beam, respectively) components of particle displacement were both 3 px/frame. For EKV image reconstruction, each image sub-section (or

image strip) consists of particles from consecutive frames, thus particle movement is preserved within the region of the strip; however, particles *between* two neighboring strips are not correlated. The strip sizes were chosen to be 600 px in height, and the strip width ranged from 5 to 160 px. A smaller strip width corresponds to a higher EKV frame rate during ultrasound imaging. For PIV, a multipass algorithm was used, and the IW sizes were 160×160 and 100×100 px with a 50% overlap.

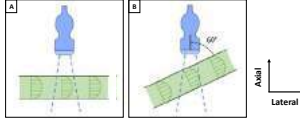


Figure 1: In vitro experiment setup when (A) the ultrasound beam was perpendicular and (B) at a 60° angle to the flow direction.

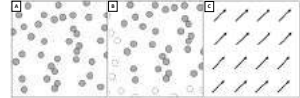


Figure 2: An illustration of the flow field displacements for the in silico experiments showing (A) particles in one frame vs. (B) particles in the next frame (the hollow circles represent new particles introduced due to non-zero displacement) after (C) a linear displacement at a 45° angle from the vertical (axial) axis.

RESULTS

In the in vitro experiments, speckle movement was captured for all flow speeds tested, including higher values close to physiological velocities in mouse aortas (Fig. 3); the higher the flow speed, the higher the required frame rate. To assess the accuracy of the UIV flow fields at different EKV rates, measured lateral (Fig. 4A) and axial (Fig. 4B) velocity components near the image strip edges were compared to ground truth values (based on pump settings) and UIV measurements of B-mode images. The results for a true cross-sectional mean lateral velocity of ~62 mm/s (Fig. 4A) and a mean axial velocity of ~14 mm/s (Fig. 4B) were chosen for demonstration because the velocities are small enough such that speckle movement could be captured by B-mode images (~300 fps) for comparison. The quantitative results show that as EKV frame rate is increased, the lateral velocity values obtained from PIV is increasingly underestimated, while axial velocity values remain relatively constant (i.e., greater errors for lateral velocity components at higher frame rates). The in silico data showed similar trends: a decrease in image strip width (equivalent to higher EKV frame rate) resulted in an increase in lateral velocity underestimation (Fig. 4C). This suggests that the effect of image strip width in EKV images is the main contribution to the observed bias error. The effect of strip width is then further highlighted in Fig. 5 using a heat map of in vitro UIV fields, in which the magnitude of lateral velocity vectors drops at the strip edges.

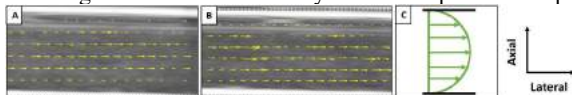


Figure 3: In vitro UIV flow fields for average cross-sectional velocities of (A) 400 mm/s and (B) 550 mm/s for EKV images captured at 8000 fps. The vector fields show that speckle movement was captured, with larger velocity vectors near the tube axis and smaller vectors near the walls; this qualitatively follows (C) the expected flow field which is lateral with a parabolic profile.

DISCUSSION

The validation results showed that although EKV images can capture speckle movement, using UIV for these images results in bias error for lateral velocity components. Due to EKV image reconstruction, there is a discontinuity of particles or speckles at the edges of each image strip. As a result, there is also a discontinuity in

lateral velocity magnitude. This effect is mainly due to the loss of matching particles or speckles at the edges of each strip: when particle lateral velocity is non-zero, foreign particles will be introduced at the strip edges at each time step. When there is a loss of matching particles between two IWs, the PIV cross-correlation peak is skewed towards zero displacement, introducing a bias error [9]. In the current study, when the IW size and particle displacements are fixed, as EKV frame rate increases (i.e., image strip width decreases), more strips and strip edges will appear in a single IW, introducing more foreign particles at each time step and thus increasing the loss of matching particles between frames. This explains the reason for increased lateral velocity underestimation as EKV frame rate is increased. In contrast, since the image strips are always oriented to be along the axial direction, there is no loss of axially moving particles, and thus the axial velocity components are insensitive to EKV frame rate.

To correct the bias error introduced by EKV reconstruction, the PIV cross-correlation function could potentially be multiplied by a weighting function based on the degree of particle/speckle loss prior to correlation function peak evaluation [9]. Upon implementation of bias correction in future work, further in vitro and in vivo studies will follow to eventually establish the techniques for mouse blood flow imaging.

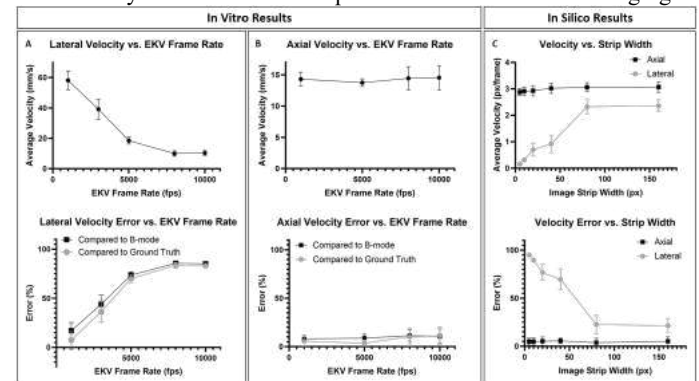


Figure 4: Measured in vitro velocity (near image strip edges) and its error vs. EKV frame rate for a true (A) lateral mean velocity of 62 mm/s and (B) axial mean velocity of 14 mm/s. (C) Measured in silico axial and lateral velocity components and the error vs. strip width. The data is presented as mean±SD; N=20.

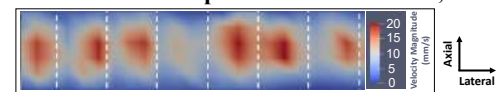


Figure 5: Heat map of the UIV lateral velocity magnitude obtained using EKV images (in vitro at 3000 fps); the values drop at the image strip edges (indicated with white dotted lines). The true cross-sectional average velocity is ~30 mm/s.

ACKNOWLEDGEMENTS

This work was funded by Canadian Institutes of Health Research Project Grant PJT-165817.

REFERENCES

- [1] Rosenthal, N. et al., *Nat Cell Biol*, 9:993-999, 2007.
- [2] Anavekar, N. S. et al., *J Cardiol*, 54:347-358, 2009.
- [3] Lotz, J. et al., *RadioGraphics*, 22:651-671, 2022.
- [4] van Doormaal, M. A. et al., *J R Soc Interface*, 9:2834-2844, 2012.
- [5] Nyrnes, S. A. et al., *JASE*, 33:493-503, 2020.
- [6] Castellán, R. F. P. et al., *Ultrasound Med Biol*, 46:167-179, 2020.
- [7] Ramnarine, K. V. et al., *Ultrasound Med Biol*, 24:451-459, 1998.
- [8] Thielicke, W. et al., *J Open Res Softw*, 9:12, 2021.
- [9] Westerweel, J., *Meas Sci Technol*, 8:1379-1392, 1997.

DEVELOPMENT OF AN ARTIFICIAL TEMPOROMANDIBULAR JOINT DISC REPLACEMENT AND SURGICAL STRATEGY

Jason Kuiper (1), Ryan Dobbs (2), Jeremiah Easley (3) Christian Puttlitz (1,3,4), Kevin Labus (1)

(1) Department of Mechanical Engineering, Colorado State University, Fort Collins CO, U.S.A

(2) Saddle Rock Institute, Aurora, CO, U.S.A

(3) Department of Clinical Sciences, Colorado State University, Fort Collins, CO, U.S.A

(4) School of Biomedical Engineering, Colorado State University, Fort Collins, CO, U.S.A

INTRODUCTION

The temporomandibular joint (TMJ) is the articulation between the cranium and mandible and is necessary for chewing and communication. The TMJ contains a fibrocartilaginous disc, which acts to reduce friction and distribute contact forces throughout joint motion. Muscular and skeletal disorders of the TMJ complex are common and are often indicated by TMJ pain. Pain in the TMJ is estimated to effect 11.2 to 12.4 million U.S. adults according to a study conducted in 2018 [1]. Of those suffering from TMJ pain, 42% report high pain intensity, which can significantly impact quality of life to a degree similar to depression and heart attacks [2,3]. Disc excision is considered a gold standard treatment for advanced TMJ disorders [4] but has resulted in the conversion to total joint replacement in 11.7% of patients [5]. Unfortunately, there are no artificial TMJ disc replacements currently approved for human use, despite their promise as an intermediate treatment for TMJ disorders. We suggest that a robust artificial TMJ disc replacement will arrest joint degradation following disc excision and prevent the need for further surgical intervention. To this end we have performed a mechanical characterization of the ovine TMJ disc [6] and assessed the suitability of polyvinyl alcohol (PVA) hydrogels for TMJ disc replacement [7]. The results of these experiments suggest that PVA hydrogels are a promising candidate for TMJ disc replacement due to their compressive stiffness similar to the native disc, high toughness, and low friction. However, PVA hydrogels require tensile reinforcement to mimic the native tensile elastic moduli. Thus, the purpose of this study was to evaluate scaffold-based reinforcement of PVA hydrogels and to develop an implant design and surgical strategy for TMJ disc replacement.

METHODS

Tensile Reinforcement

Polypropylene (PP) angle ply scaffolds with a 300 μ m fiber diameter were created using a melt extrusion 3D printer. Scaffolds were

created with the following fiber angle (from primary loading direction) and center-to-center fiber spacing: 45° - 1.4 mm (n=6), 20° - 1.4 mm (n=6), 10° - 1.4 mm (n=5), 20° - 1.2 mm (n=6), and 20° - 1.0 mm (n=5). A melt electrowriting (MEW) 3D printer was also used to produce scaffolds (n=5) with a fiber diameter of 74 ± 4 μ m, fiber angle of 20°, and fiber spacing of 150 μ m. All scaffolds were embedded in a 25% PVA hydrogel and molded between two glass slides through six freeze-thaw cycles. One group (n=6) of tensile testing samples was also made from PVA alone. Dog-bone shaped tensile testing specimens were cut from the molded sheets using a scalpel and cutting guide. Physical measurements of each sample were taken using digital calipers. Testing coupons were preconditioned with 20 cycles to 0.08% strain followed by a uniaxial tensile test to failure at a rate of 0.08 strain/s. The sample elastic moduli were calculated using the tensile stress-stretch data. All tested groups were compared using a one-way ANOVA with post-hoc Tukey test, and results with $p < 0.05$ were considered significant.

Implant Design

Two implant attachment methods were assessed through uniaxial tensile testing. Sheets of 25% PVA hydrogel were affixed to a 3D printed substrate using a titanium plate and screws (n=7), or by a cross suture pattern (n=6) (Figure 1). Samples were subjected to a uniaxial tensile test to failure, and construct failure stress was calculated as the peak applied load divided by the sample cross sectional area. Failure

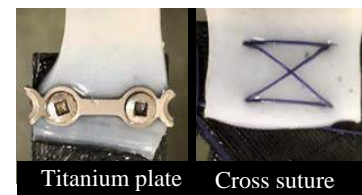


Figure 1: Implant attachment methods on testing fixtures.

stresses were compared using a t-test, a $p < 0.05$ was considered significant.

An iterative approach to implant design and surgical development was used to identify a final implant design candidate. Patient specific artificial TMJ disc implants were designed based on a computed tomography scan of the ovine TMJ, molded from 25% PVA using a 3D printed mold, and implanted in the corresponding ovine cadaveric TMJ by human and veterinary maxillofacial surgeons (all subjects were scanned and sacrificed as part of an unrelated study). Surgeons provided feedback about each design, which was then integrated in the next design iteration until a final implant design was approved.

RESULTS

Tensile Reinforcement

A summary of tensile testing results is provided in Figure 2. All hybrid constructs exhibited increased tensile elastic moduli in comparison to PVA alone. Hybrid melt extrusion scaffolds exhibited elastic moduli within the range of published values for the TMJ disc. The elastic modulus generally increased with a decrease in scaffold fiber spacing or fiber angle.

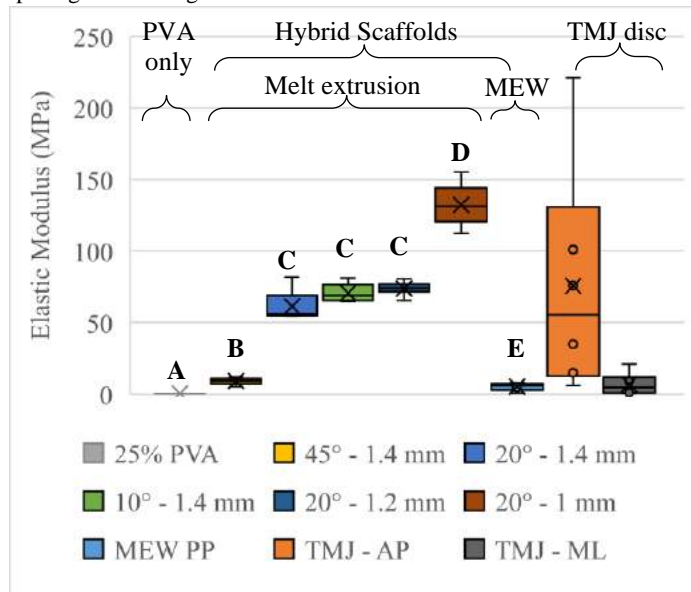


Figure 2: Comparison between the hybrid PVA-PP constructs, PVA alone, and native TMJ discs in the anteroposterior (AP) and mediolateral (ML) directions. Groups that share a letter were not significantly different. TMJ disc data were combined from multiple published sources [6, 8-12].

Implant Design

The failure stress of the PVA hydrogel samples attached using a cross suture pattern was $0.14 \text{ MPa} \pm 0.01 \text{ MPa}$ (mean \pm standard deviation), which was significantly less ($p < 0.001$) than the failure stress of the PVA hydrogels attached using a titanium plate: $0.23 \text{ MPa} \pm 0.02 \text{ MPa}$.

A finalized implant geometry (Figure 3) includes a 2 mm thick superior-lateral flange for attachment to the zygoma, and a 2 mm thick inferior-lateral flange for attachment to the mandibular condyle. Titanium maxillofacial reconstruction plates are used to secure these flanges using 1.9 mm diameter titanium screws. The shape and size of the TMJ disc component is modeled using the shape of the mandibular condyle. All implant sections are molded contiguously with the attachment flanges.

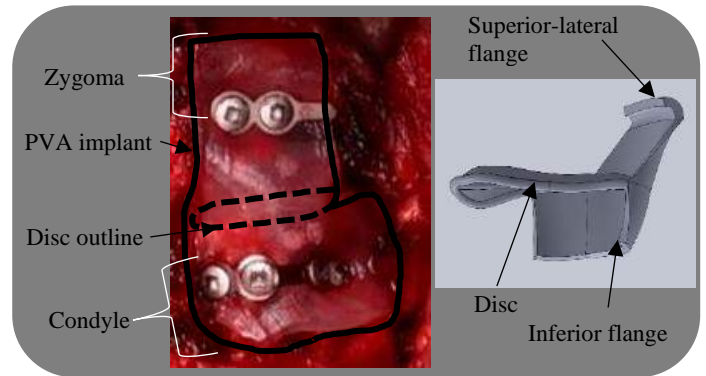


Figure 3: (left) Implanted TMJ disc replacement, and (right) 3D model of corresponding implant.

DISCUSSION

Tensile reinforcement of PVA hydrogels using 3D printed angle ply scaffolds increased the tensile moduli of the construct and allowed for more sensitive tuning of the anisotropic tensile elastic moduli within the range of published values for the TMJ disc across species [6, 8-12]. Using this technique, a mechanically mimetic scaffold can be created to match the anisotropic tensile behavior of the native TMJ disc.

The titanium plate attachment method was superior to the cross suture pattern in terms of failure stress. However, the failure stress of these attachment methods was far below the measured values for a 25% PVA hydrogel ($2.97 \text{ MPa} \pm 0.62 \text{ MPa}$) [7] which suggests that there is a large stress concentration at the implant attachment site. Further refinement of the implant attachment method will be directed toward reducing this stress concentration.

We have developed a patient specific PVA hydrogel TMJ disc implant that is easy to install through a translatable lateral surgical approach. However, rigorous preclinical assessment of these artificial TMJ disc replacement constructs is still necessary. Long term *in-vivo* experiments, paired with *ex-vivo* characterization of PVA hydrogel wear and fatigue properties are needed to predict the *in-vivo* lifetime of a non-degradable TMJ disc replacement. Experiments to investigate high-cycle wear on the artificial disc and strain life of the implant attachments are underway. An *in-vivo* pilot experiment in sheep is also in progress to assess the impact of an PVA hydrogel TMJ disc replacement compared to disc excision alone (current clinical standard). The goal of this pilot experiment is to evaluate the implants and their impact on the TMJ cartilage, chewing pattern, and diet over six weeks.

REFERENCES

- [1] Slade, G. and J. Durham, *Committee on Temporomandibular Disorders (TMDs): From Research Discoveries to Clinical Treatment*. 2020.
- [2] Durham, J. et al., *J Dent Res*, 95(10): p. 1147-54. 2016.
- [3] Velly, A.M. et al., *Pain*, 152(10): p. 2377-2383. 2011.
- [4] Dimitroulis, G., *Aust Dent J*, 63 Suppl 1: p. S79-S90. 2018.
- [5] Ellis, O.G. et al., *J Oral Maxillofac Surg*, 79(12): p. 2448-2454. 2021.
- [6] Labus, K. et al., *J Mech Behav Biomed Mater*, vol. 116, p. 104300, 2021.
- [7] Kuiper, J. et al., *Frontiers in Physics*, 10:928579 2022.
- [8] Kalpakci, K.N et al., *J Dent Res*, 90(2): p. 193-8. 2011.
- [9] Beatty, M.W et al., *J Biomed Mater Res*, 57(1): p. 25-34. 2011.
- [10] Detamore, M.S. and Athanasiou, K.A., *J Biomech Eng.*, 125(4): p. 558-65. 2003
- [11] Wang, X.D. et al., *J Dent Res*, 93(11): p. 1170-6. 2014.
- [12] Wright, G.J. et al., *J Biomech*, 49(16): p. 3762-3769. 2016.

COMPUTATIONAL MODELING OF MACHINE PERFUSION OF THE HUMAN LIVER VASCULATURE

Daniel Emerson (1), Yoed Rabin (1), Levent Burak Kara (1)

(1) Department of Mechanical Engineering, Carnegie Mellon University, Pittsburgh, PA, USA

INTRODUCTION

Transplantation is the primary treatment option for people with severe liver diseases. One major barrier to liver transplantation is the absence of methods to properly store, transport, and transplant livers. The most commonly used method in liver preservation is static cold storage (SCS), where the organ is kept on ice, and preservation of the liver is limited to less than 12 hours [1]. Improvement to liver preservation techniques would help make liver transplantation more widely available and improve transplantation outcomes [2].

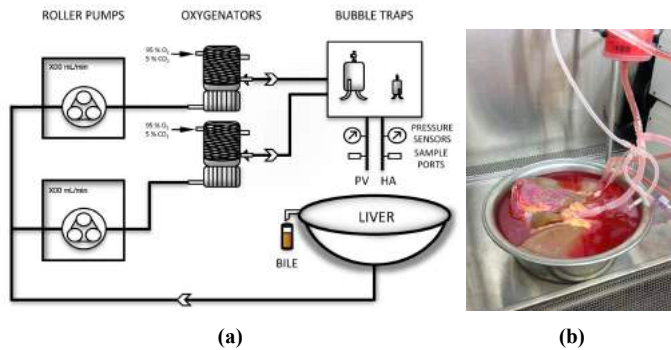


Figure 1: Schematic (a) and experimental apparatus (b) for subnormothermic machine perfusion from [3].

Development of new cryopreservation protocols is a highly complex multi-step process, requiring machine perfusion at varying temperatures, as well the loading and unloading of different cryoprotective agents (CPA). A schematic and experimental apparatus for machine perfusion at a fixed temperature is depicted in Fig. 1. Accurate computational models of the human liver would help researchers explore the complex cryopreservation design space, without the challenges and expenses associated with procuring real human livers. Researchers have created anatomical [4–6] and algorithmic [7–9] models of the liver vasculature. Both existing anatomical and algorithmic models have been primarily evaluated on their ability to match morphological metrics such as mean vessel length and diameter. None of [4–9] consider fluid flow through individual vessels of the liver, entering via the portal vein and out the hepatic vein. To this end, we aim to create a framework to generate variably complex models of the human liver and automatically simulate the perfusion of said models. It is important that our models behave consistently regardless of depth, and perfuse similarly to real human livers.

METHODS

Super Lobules: At a microscopic level, the liver consists of approximately one million highly regular collections of functional hepatocyte cells called lobules [10, 11]. Since it is not feasible to model the liver vasculature to this level of detail, we introduce the concept of a super lobule (SL): a collection of lobules which we model with a single lumped resistance. In our model we assume all super lobules to be of uniform volume and resistance. The notion of a super lobule allows us to create models of various depth that behave similarly by accounting for the contribution of its constitutive vessels with the assigned lumped resistance.

Space Colonization Algorithm: To generate the vascular structure of the liver, we build upon the space colonization (SC) algorithm introduced in [12, 13] where leaf venation and tree structures are generated with a biologically inspired iterative process. We utilize additions made to the algorithm in [14] to ensure the vessels explicitly reach the super lobules and trim non-critical vessels from the network. We make further modifications to the algorithm for modeling vascular trees. For example, we run the algorithm twice: first to generate known primary vessels in the portal and hepatic veins, and second to build the vascular network from this intermediate initialization to the super lobules.

Resistance Network: To simulate the flow through our vascular model, we consider a simple electrical analog model, where voltage and current are analogous to pressure and flow rate [15]. We model the resistance of each blood vessel according to the Hagen-Poiseuille equation. The Hagen-Poiseuille model is commonly used in simplified models of vascular flows in the liver [4, 6, 7, 16]. We can assign each vessel a resistance according to Hagen-Poiseuille with its radius and length. After prescribing pressure boundary conditions at the inlet and outlet, we can solve for the pressures and flows at every node and vessel in the model respectively. This is done by constructing a linear system of equations of the form $\mathbf{A} \cdot \mathbf{x} = \mathbf{b}$. There are three equations used to construct the coefficient matrix \mathbf{A} . First, we consider Ohm's law ($\Delta P = QR$); the pressure drop across all vessels and super lobules. Next, we consider Kirchhoff's current law ($\sum Q_{in} - \sum Q_{out} = 0$) at all nodes except the two boundary nodes. Finally, we enforce the boundary conditions as constant pressures at the inlet and outlet. The flows and pressures in \mathbf{x} are solved using an LU decomposition of the sparse asymmetric coefficient matrix \mathbf{A} .

While we can compute the resistance of a vessel based on its geometry, we do not have a deterministic way to compute the resistance of the super lobules R_{SL} to give our model the desired overall flow rate. We use the bisection method and repeatedly solve linear system with various values of R_{SL} and fixed pressure boundary conditions until our solution converges to the desired model flow rate.

Simulated Machine Perfusion: Using our complete model, we can visualize how CPA concentration varies through the model over time. At each time step, the inlet flow rate is multiplied by the time step to determine the volume of the fluid added. In each vessel the concentration of incoming fluid is combined with the concentration of the fluid already in the vessel, weighted by their respective volumes to determine the new concentration of a given vessel. Excess fluid is passed to downstream vessels according to ratio of cross sectional areas.

RESULTS

We consider the machine perfusion experiment detailed in [3] and pictured in Fig. 1. The portal vein (PV) inlet pressure is set to 5.8mmHg while the hepatic vein (HV) outlet pressure is left at 0mmHg. The steady flow rate at the inlet is 767mL/min. The initial diameter for both PV and HV is set to 15mm. The dynamic viscosity of the CPA is set to 3.5cP.

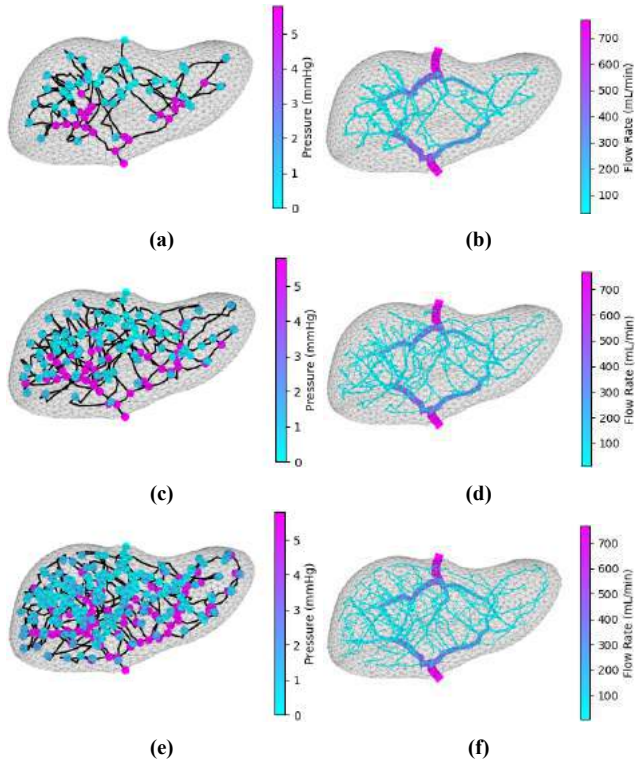


Figure 2: Nodal pressures (a,c,e) and vessel flow rates (b,d,f) for models with 25, 50, and 100 super lobules, respectively.

Results from simulations on models of varying depth can be seen in Fig. 2. We can observe consistency in the partition of flow across models of various depths. Models with more super lobules can provide more fine scale pressure and flow information throughout the liver, at increased computational cost, as detailed in Table 1. SC time refers to the amount of time to generate the vasculature with the space colonization algorithm. Matrix solve refers to the length of time to solve the linear system of equations once, and bisection solve refers to the total time to determine the model R_{SL} value by repeatedly solving the linear system.

Table 1: Model complexity based on number of super lobules.

# SL	SC Time (s)	Matrix Solve (s)	Bisection Solve (s)
5	9.21	0.00113	0.04
10	9.25	0.00265	0.08
25	11.72	0.0136	0.45
50	12.38	0.0427	1.32
100	20.36	0.158	5.03
250	60.21	0.896	27.65

We can also validate our models by examining how the model populates with CPA during simulated machine perfusion. Fig. 3 visualizes the perfusion of the liver, where red represents pure blood that is being displaced, and blue represents pure CPA that is pumped into the model. The color is interpolated between red and blue for vessels with mixed concentrations. We can note that in Fig. 3(b), the majority of small vessels have been populated with CPA, with the exception of a vessel in the top right corner. This observation can be seen in models of all depths, and matches well with what we known from machine perfusion experiments on real human liver. Perfusion of the liver is not a linear process and outermost regions, specifically the narrow, upper right portion of the liver take a disproportionately long time to fully populate with CPA.

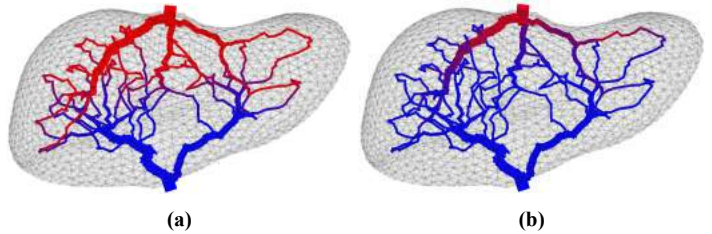


Figure 3: Concentration of vessels in 25 SL model at (a) 50% and (b) 80% total concentration of CPA.

DISCUSSION

Overall, this work presents a novel adaptation and application of the space colonization algorithm to generate models of the human liver. All previous algorithmic models of the liver [7–9] have been generated using constrained constructive optimization [17]. With our notion of super lobules, we can create models of variable depth and fidelity, that all meet global pressure and flow boundary conditions. This approach allows the end user to trade model fidelity for computational cost depending on their needs. Furthermore, we observe that models of various depths behave consistently with each other, and in comparison to observations from experiments on real human livers, as opposed to the morphological validation seen in most prior works. It is also important to note the modeling simplifications made in this work. We simply consider steady Hagen-Poiseuille flow, we do not allow fluid to perfuse across vessel walls into the tissue of the liver, and we maintain a constant viscosity throughout the simulation. Nevertheless, this model serves as a preliminary step in the much larger goal of creating a computational model on which researchers can investigate and develop new cryopreservation protocols.

REFERENCES

- [1] Vries RJ de et al. *Nature Biotechnology* 37.10 (2019).
- [2] Giwa S et al. *Nature Biotechnology* 35.6 (2017).
- [3] Bruinsma B et al. *Am. Journal of Transplantation* 14.6 (2014).
- [4] Debbaud C et al. *IEEE Trans on Biomed. Engineering* 58.1 (2010).
- [5] Peeters G et al. *Journal of Anatomy* 230.3 (2017).
- [6] Ma R et al. *Intl. J. for Num. Methods in Biomed. Eng.* 35.9 (2019).
- [7] Guy AA et al. *IEEE Trans. on Biomedical Engineering* 67.6 (2019).
- [8] Talou GDM et al. *Scientific Reports* 11.1 (2021).
- [9] Jessen E et al. *arXiv preprint arXiv:2202.04406* (2022).
- [10] Felmlee DJ et al. *Hepatology* 67 (2018).
- [11] Lorente S et al. *Scientific Reports* 10.1 (2020).
- [12] Runions A et al. *ACM SIGGRAPH 2005 Papers*. 2005.
- [13] Runions A et al. *NPH* 7.63-70 (2007).
- [14] Ulu NG et al. *Journal of Visual Languages & Computing* 31 (2015).
- [15] De Pater L et al. *Med. Electronics and Biological Eng.* 2.2 (1964).
- [16] Hamarneh G et al. *Comp. Med. Imaging and Graphics* 34.8 (2010).
- [17] Karch R et al. *Computers in Biology and Medicine* 29.4 (1999).

FSGE: A COMPUTATIONAL MODEL FOR EQUILIBRATED CARDIOVASCULAR FLUID-SOLID-GROWTH INTERACTION

**Martin R. Pfaller (1), Marcos Latorre (2), Erica L. Schwarz (1), Fannie M. Gerosa (1),
Jason M. Szafron (1), Jay D. Humphrey (3), Alison L. Marsden (1)**

(1) Pediatrics, Stanford University, Stanford, CA, USA

(2) Center for Research and Innovation in Bioengineering, Universitat Politècnica de València, València, Spain

(3) Vascular Biology and Therapeutics Program, Yale School of Medicine, New Haven, CT, USA

INTRODUCTION

In cardiovascular problems, growth and remodeling (G&R) is commonly triggered mechanically through fluid-structure interaction by a combination of pressure-induced intramural stress and flow-induced wall shear stress [1]. For example, it was hypothesized that G&R plays a key role in saphenous vein graft failure after coronary artery bypass graft surgery [2].

The constrained mixture theory describes mechanisms that drive G&R, capturing the different rates of turnover and material properties exhibited by individual constituents of the tissue [3]. However, this approach can be computationally expensive due to the need for tracking constituent configuration and perturbation history. This limitation was overcome by the recent concept of mechanobiologically equilibrated G&R [4]. This rate-independent theory can compute evolving homeostatic states efficiently by enforcing mechanical and mechanobiological equilibrium without the need to track the history of deposition and removal or to integrate evolution equations.

Previous implementations of the equilibrated constrained mixture model relied on an assumed form for intramural stress and flow-induced wall shear stress. To predict disease progression, we propose to combine fluid-structure interaction and G&R in a novel fluid-solid-growth (FSGe) framework using the mechanobiologically equilibrated constrained mixture theory, hence enabling efficient three-dimensional FSG simulations for patient-specific geometries.

METHODS

Our FSG model is implemented in our open-source multiphysics finite element solver svFSI (available at github.com/SimVascular/svFSI). In the following, we briefly outline the ingredients of our FSG framework. We solve the incompressible Navier-Stokes equations to obtain velocity and pressure inside the blood vessel. We pass local fluid pressure and wall shear stress to our 3D finite strain solid G&R model at the fluid-solid interface. As the solid model, we use a fast and efficient formulation of the constrained mixture theory that assumes that each G&R state is mechanobiologically equilibrated [4]. The shear-to-intramural gain ratio controls the relative importance of wall shear stress and intramural stress stimuli. Both fields are coupled in a partitioned scheme for separating the fluid and solid time scales (seconds vs. weeks).

Fluid: Incompressible Flow

Blood flow in the fluid domain is modeled by the incompressible Navier-Stokes equations,

$$\rho \frac{\partial \mathbf{u}}{\partial t} + \rho(\mathbf{u} \cdot \nabla) \mathbf{u} - \nabla \cdot \boldsymbol{\sigma}(\mathbf{u}, p) = \mathbf{0}, \quad (1)$$

$$\nabla \cdot \mathbf{u} = 0, \quad (2)$$

where \mathbf{u} and p are fluid velocity and pressure, respectively, with Cauchy stress tensor $\boldsymbol{\sigma}(\mathbf{u}, p) = \mu(\nabla \mathbf{u} + \nabla \mathbf{u}^T) - p\mathbf{I}$, density ρ , and dynamic viscosity μ . We calculate wall shear stress $\boldsymbol{\tau}_w$ as

$$\boldsymbol{\tau}_w = \boldsymbol{\sigma} \mathbf{n} - ((\boldsymbol{\sigma} \mathbf{n}) \cdot \mathbf{n}) \mathbf{n}, \quad (3)$$

with normal vector \mathbf{n} .

Solid-Growth: Equilibrated Constrained Mixture

We use a fast and efficient formulation of the constrained mixture theory that is based on the assumption that each G&R state is mechanobiologically equilibrated [5]. This rate-independent formulation eliminates time-dependency and directly predicts grown and remodeled states for given external loads and boundary conditions. Following the rule-of-mixtures, the solid Cauchy stress is calculated from constituent contributions as

$$\boldsymbol{\sigma}_h = \sum_{\alpha}^{e,c,m} \phi_h^\alpha \hat{\boldsymbol{\sigma}}_h^\alpha - p_h \mathbf{I}, \quad (4)$$

with Lagrange multiplier p_h , where subscript h refers to evolved homeostatic variables, and evolved mass fractions ϕ_h^α , namely elastin- and collagen-dominated matrix as well as smooth muscle. Our equilibrated stimulus function yields

$$\frac{\sigma_{Ih}}{\sigma_{Io}} - 1 = K_{\tau\sigma} \left(\frac{\tau_{wh}}{\tau_{wo}} - 1 \right), \quad (5)$$

with shear-to-intramural gain ratio $K_{\tau\sigma} \geq 0$, where subscript o refers to original homeostatic variables. The stimuli are intramural stress σ_I and wall shear stress magnitude τ_w , computed as

$$\sigma_I = \frac{\text{tr} \boldsymbol{\sigma}}{3}, \quad \tau_w = \|\boldsymbol{\tau}_w\|. \quad \text{SB}^3\text{C2023-586}$$

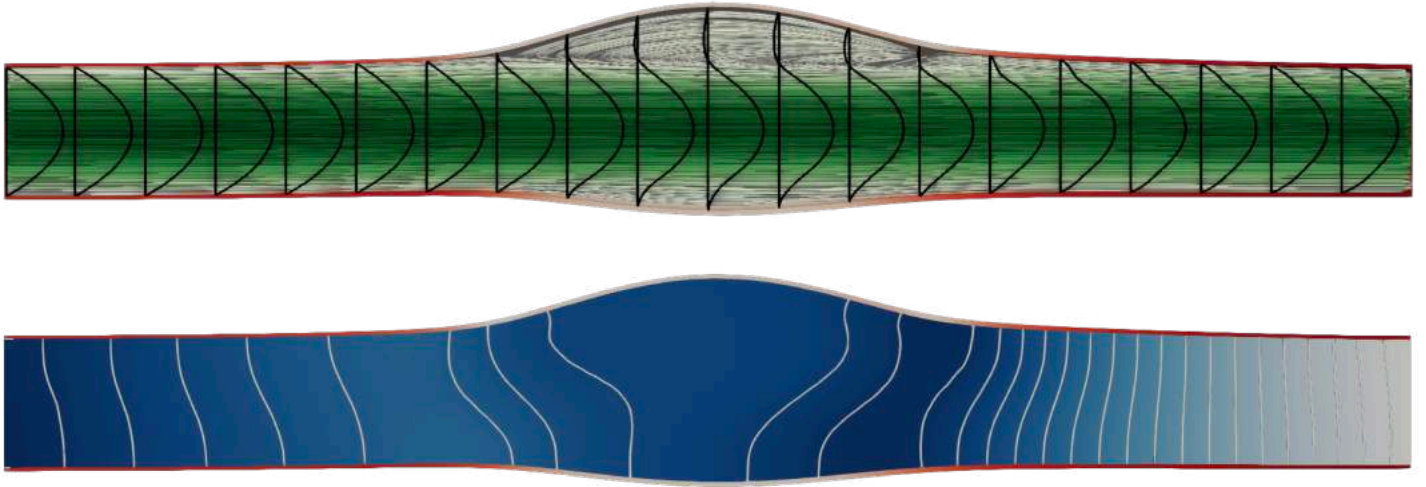


Figure 1: Velocity (top) with streamlines (green) and flow profiles (black) and pressure (bottom, blue), both with wall shear stress (red) in an asymmetric aneurysm (flow is from left to right).

Interaction: Partitioned Coupling

We couple fluid field \mathcal{F} and solid-growth field \mathcal{S} in a partitioned manner. We iterate between the fields, coupled by the interface displacements \mathbf{d}_{k+1} , until a convergence criterion $\|\mathbf{r}_k\|_2 \leq \epsilon_0$ is fulfilled:

$$\text{Update: } \tilde{\mathbf{d}}_{k+1} = \mathcal{S} \circ \mathcal{F}(\mathbf{d}_{k+1}), \quad (7)$$

$$\text{Residual: } \mathbf{r}_{k+1} = \tilde{\mathbf{d}}_{k+1} - \mathbf{d}_{k+1}. \quad (8)$$

We compare different methods to initialize the displacements \mathbf{d}_{k+1} in a new coupling iteration k . In the simplest case, we use a Gauß-Seidel scheme

$$\mathbf{d}_{k+1} = \tilde{\mathbf{d}}_k. \quad (9)$$

However, this coupling scheme is unstable for $K_{\tau\sigma} > 0$. The coupling scheme can be stabilized with static relaxation:

$$\mathbf{d}_{k+1} = \omega \tilde{\mathbf{d}}_k + (1 - \omega) \mathbf{d}_k, \quad 0 < \omega < 1. \quad (10)$$

While improving numerical stability, this coupling scheme typically converges slowly and is highly dependent on the choice of the relaxation parameter ω . A much more efficient scheme is obtained by dynamically choosing ω_k in each iteration k , e.g., through Aitken relaxation [6]:

$$\begin{aligned} \mathbf{d}_{k+1} &= \omega_k \tilde{\mathbf{d}}_k + (1 - \omega_k) \mathbf{d}_k, \\ \omega_k &= -\omega_{k-1} \frac{(\mathbf{r}_{k-1})^T (\mathbf{r}_k - \mathbf{r}_{k-1})}{(\mathbf{r}_k - \mathbf{r}_{k-1})^T (\mathbf{r}_k - \mathbf{r}_{k-1})} \end{aligned} \quad (11)$$

While easy to implement, Aitken relaxation can use only information from one previous coupling iteration. The Interface Quasi-Newton Indirect Least Squares (IQN-ILS) method can use information from up to q previous coupling iterations [7]:

$$\mathbf{d}_{k+1} = \mathbf{d}_k + \mathbf{W}_k \mathbf{c}_k + \mathbf{r}_k \quad (12)$$

$$\mathbf{V} = [\mathbf{r}_{k-1}, \mathbf{r}_{k-2}, \dots] \quad (13)$$

$$\mathbf{W} = [\Delta \tilde{\mathbf{d}}_{k-1}, \Delta \tilde{\mathbf{d}}_{k-2}, \dots] \quad (14)$$

We obtain the coefficients c_k by solving the minimization $\min_{c_k} \|\mathbf{V}_k \mathbf{c}_k + \mathbf{r}_k\|_2$ using QR-decomposition.

RESULTS AND DISCUSSION

The computational cost of our FSGe coupling scheme is comparable to a fluid-structure-interaction simulation with a hyperelastic solid material. We compare our coupled FSGe method to G&R models with different fluid approximations for pressure and wall shear stress [5, 8]. Our examples include aneurysmal formation (see Fig. 1), stenosis formation, and distortions of blood flow. We demonstrate the speed and robustness of our FSGe method for various Reynolds numbers and shear-to-intramural gain ratios. Simplified fluid dynamics in cardiovascular G&R models can provide a good approximation in many scenarios. However, we show that local fluid dynamics can significantly influence the long-term G&R state in blood vessels.

ACKNOWLEDGEMENTS

This work was supported by NIH Grants K99HL161313, R01HL139796, R01HL159954, the Additional Ventures Foundation Cures Collaborative, and the Stanford Maternal and Child Health Research Institute.

REFERENCES

- [1] Figueroa CA et al. *Computer Methods in Applied Mechanics and Engineering* 198.45-46 (2009). DOI: 10.1016/j.cma.2008.09.013.
- [2] Khan MO et al. *Journal of Cardiovascular Translational Research* 14.4 (2020). DOI: 10.1007/s12265-020-09982-7.
- [3] Humphrey JD et al. *Mathematical Models and Methods in Applied Sciences* 12.03 (2002). DOI: 10.1142/s0218202502001714.
- [4] Latorre M et al. *Biomechanics and Modeling in Mechanobiology* 17.5 (2018). DOI: 10.1007/s10237-018-1041-8.
- [5] Latorre M et al. *Computer Methods in Applied Mechanics and Engineering* 368 (2020). DOI: 10.1016/j.cma.2020.113156.
- [6] Küttler U et al. *Computational Mechanics* 43.1 (2008). DOI: 10.1007/s00466-008-0255-5.
- [7] Degroote J. *Archives of Computational Methods in Engineering* 20.3 (2013). DOI: 10.1007/s11831-013-9085-5.
- [8] Latorre M et al. *Biomechanics and Modeling in Mechanobiology* 21.3 (2022). DOI: 10.1007/s10237-022-01562-9.

3D PASSIVE STRAIN MAPPING OF THE EMBRYONIC ZEBRAFISH HEART

Alex L. Gendernalik (1,2), David Bark (1,2)

(1) School of Biomedical Engineering, Colorado State University, Fort Collins, CO, USA
(2) Pediatrics Hematology Oncology, Washington University School of Medicine, St. Louis, MO, USA

INTRODUCTION

Congenital heart defects affect 1% of newborns, often with devastating consequences. However, the causes are poorly understood and only 20% have a known genetic etiology. Altered mechanical signaling or mechanotransduction may be one key contributor. The mechanical environment is spatially and temporally dynamic as the heart begins to function before it is fully formed through a complex coordination of processes. Abnormal mechanical feedback from the hemodynamic environment can lead to defective development of heart structures such as the chambers and trabeculae. We propose that the mechanical properties of the developing heart tissue play a fundamental role in the distribution of stress and the subsequent formation of heart structures. We use a novel technique to quantify the mechanical properties of the embryonic zebrafish heart through forced pressurization. Additionally, we develop strain maps to determine colocalization of strain or stiffness with early cardiac structures. Using this technique, we determine the conditions and material properties necessary for proper structure development.

METHODS

Zebrafish Embryo Production and Morpholino Treatment – Zebrafish were raised according to university IACUC guidelines. Adult *Tg(flk:mcherry)* and *Tg(myl7:eGFP)* transgenic zebrafish were crossed to produce embryos with fluorescent endocardium and myocardium, respectively. Embryos were incubated in E3 egg medium and 0.003% PTU to inhibit pigment formation. Embryos were removed from E3 media at the appropriate stage (2- or 3-days post fertilization) and transferred to media containing 30 mM or 40 mM 2,3-butanedione monoxime (BDM) for 2- and 3-day old embryos, respectively. BDM inhibits myosin ATPase to halt heart contractions. For RBC depletion experiments, Gata1 morpholino with sequence 5'-CTGCAAGTGTAGTATTGAAGATGTC-3' was injected at the 1-4

cell stage (approximately 8 ng in 1 nL injection volume) [1]. RBC depletion was confirmed at 1-day post-fertilization.

Pressurization and Imaging– Glass cannulas with tips pulled to ≤ 10 microns were used to puncture the zebrafish embryo skin and vasculature in the sinus venosus region. After cannulation, pressure was increased in 0.5 mmHg increments and 3D images were acquired using an upright confocal microscope at each pressure step.

Myocardial Strain Analysis – 3D image slices were segmented, aligned, and converted to 3D geometry using custom written code. Deformations were extracted and converted to Green-Lagrange strains using the unpressurized 3D heart image as a reference. Strains were mapped and analyzed in Paraview.

Finite Element Analysis – Finite element analysis was performed with custom code to estimate material parameters that best matched stress and strain observed during experiments. Boundary conditions were set such that the ventricular outlet was fixed, and the atrial inlet was allowed to deform.

RESULTS

Pressure vs. Normalized Volume plots (fig. 1) show that stiffness generally increases from two to three days post-fertilization. Strain was generally evenly distributed; however stiff focal points were present along the inner curvature of the ventricle. The atrium showed stiff areas at the inlet and atrio-ventricular junction. Strain patterns were observed in the ventricle at 2 days that were not present at 3 days. Finite element analysis shows that material parameters are on the order of 10 kPa. Morpholino knockout of RBCs resulted in strain patterns more similar to 2-day old persisting throughout development.

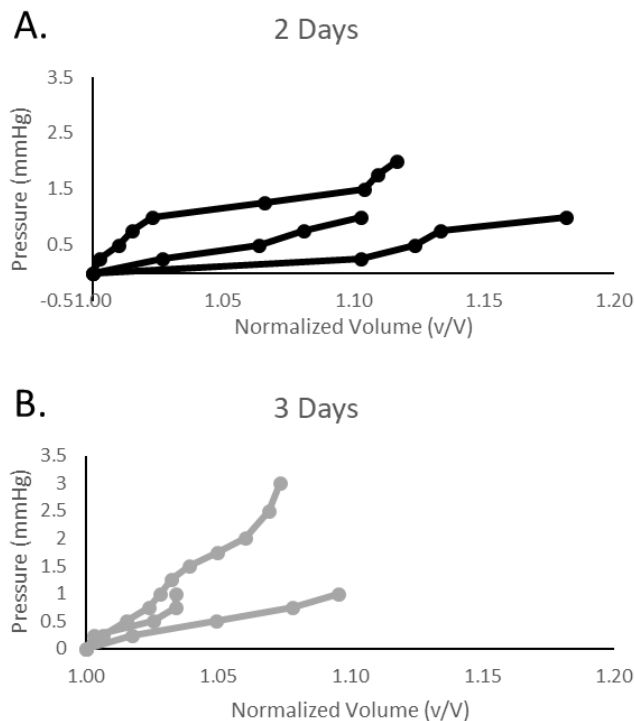


Figure 1: Pressure vs. Normalized volume (v/V) for 2-day (A) and 3-day (B) old zebrafish hearts.

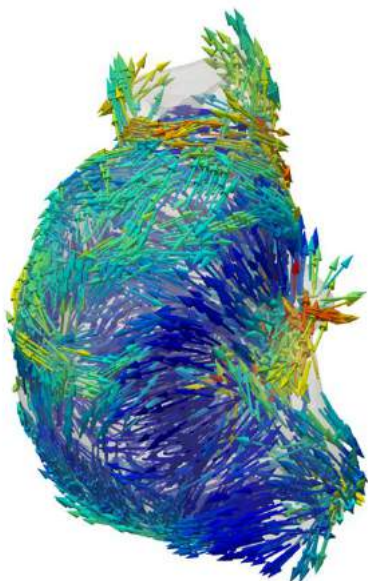


Figure 2: 3D representation of strain magnitude (color) and direction for a 2-day old zebrafish ventricle.

DISCUSSION

We have developed a technique to visualize embryonic heart stiffness in 3D and determined a strain energy density function that represents

the material properties at 2- and 3-days post-fertilization. Additionally, using our strain mapping technique, we have located regions of high and low stiffness and have shown that these regions colocalize with areas of morphological changes or structure formation. Specifically, the ventricle inner curvature, AVJ, and atrial inlet were stiffer than the surrounding tissue at both 2 and 3-days. Patterns of ventricular stiffness observed at 2 days were no longer present at 3 days. During this period, structures such as trabeculae are forming. This suggests that trabeculae or hypertrophy of the ventricle helps to distribute deformation evenly across the ventricle.

ACKNOWLEDGEMENTS

We thank the Washington University zebrafish facility, the Garrity lab at Colorado State University, and our collaborators at London Imperial College.

REFERENCES

[1] Galloway, J et al., *Dev. Cell* 8:109-116, 2005.

CHATGPT AND THE FUTURE OF EDUCATION IN BIOMEDICAL AND MECHANICAL ENGINEERING

Sara E. Wilson (1,2)

- (1) Mechanical Engineering, University of Kansas, Lawrence, Kansas, USA
(2) Bioengineering Graduate Program, University of Kansas, Lawrence, Kansas, USA

INTRODUCTION

In November 2022, ChatGPT (<https://chat.openai.com/chat>), an AI (Artificial Intelligence) powered chatbot, was released by the company OpenAI. ChatGPT allows users to create generate text, code, and mathematical solutions using simple text based prompts. Across academic institutions, concern has been raised about the impact of this tool on academic integrity¹⁻³. In this paper, I will examine the potential impact of ChatGPT on academic misconduct in engineering and strategies that can be implemented to encourage learning and academic integrity.

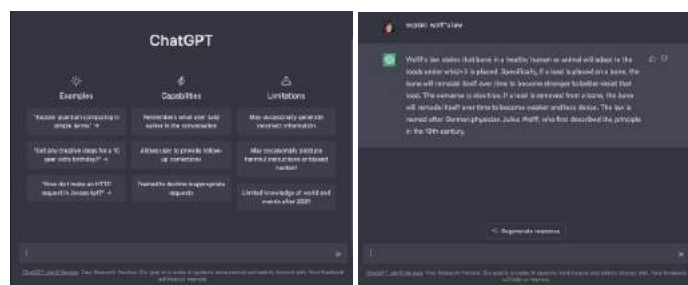


Figure 1 The chat GPT interface allows users to type in a simple text prompts and receive unique, real-text responses that would not be detectable by plagiarism checking software.

METHODS

To assess the impact ChatGPT currently has on biomedical and mechanical engineering education, a range of writing, problem solving, and coding assignment prompts were input into ChatGPT. The responses were assessed using rubrics. For writing, the AACU Value Rubric for Written Communication was used to assess responses⁴. For problem solving, the AACU Value Rubric for Quantitative Literacy was used to assess responses⁵. The rubrics assess competency across

different elements based on levels from benchmark (1) to Capstone (4). It is expected that a freshman student might be at a benchmark level (1) and should progress to capstone (4) at the completion of an undergraduate education. For computer code, a new rubric was created using these same four level across the categories of context (does the code address the prompt assignment?), code functionality and errors (does the code function without errors?), and commenting.

RESULTS

On a 1 to 4 scale, the writing samples generated by chatGPT scored a 2.7. Overall the writing samples had good grammar and addressed the writing prompt appropriately. The essays had generally good structure and a logical flow. The main weakness of chatGPT responses was in the use of literature citations. In general, the citation were few and many statements that should have been supported by a citation were not. Additionally the papers chatGPT chose to cite were fictitious. They looked like real papers and cited real journals but the papers cited could not be found on PubMed or Google Scholar.

For problem solving, ChatGPT scored between 1.3 and 3.2 on the value rubric. More advanced problems scored the lowest while simple math problems scored higher. For this exercise, ChatGPT did not get any math problem fully correct and even made mistakes on a basic differential equations problem for which there are functional solvers on the internet.

ChatGPT did the best at generating correct answers with coding assignments. In this work, coding assignments were presented in the prompt for C++ and Matlab. The average rubric score was 3.5. ChatGPT generated correct code for most of the lower level problems. ChatGPT made some errors in problem interpretation. It also placed functions improperly in the code in one problem. Finally, while

ChatGPT included commenting in the response, the commenting was sometimes sparse.

DISCUSSION

The use of ChatGPT by students to circumvent assigned homework in the classroom is a concern for engineering. From the findings here it is clear that ChatGPT (as it currently exists) could be used to generate writing assignments and code and to a lesser extent solved problems. This would be particularly true for lower level courses. There are several AI detectors currently being developed that can help to detect bot-created text. However these detectors are limited and a few small wording changes can make them fail to detect. Over time it is expected that AI-chatbots will continue to improve and it may be an arms race for the detectors to keep up.

To discourage chatbot use and to promote learning a number of strategies can be employed. The first of these is to talk about expectations and ethics in the classroom³. Another tool is create assignments that are not easily solved with chatbots. Assignments that have several levels, iterations of revisions, and scaffolding of work would be less conducive to chatbot solutions. Watkins suggests that one could even bring chatGPT into the classroom and have students examine the quality of responses and how they should be improved³. ChatGPT's AI is built off of materials on the internet, so more original and unique problems may also be less prone to chatbot answers. One can also move work to within the classroom (rather than homework) or ask for multimedia submissions rather than just code or written text². For my programming classes, I already do this by asking not just for code but also for flowcharts and video presentations of the code. Finally, one can discourage chatbot use by rethinking how points are assigned and grades are assessed.

As someone who teaches a freshman coding course, chatGPT is a serious concern. For my course, I am restructuring homework assignments and using in person grading to not only assess whether students have functional code but also do they understand the code they have submitted. In person grading will be time consuming, but will also allow for personal contact with students that may help with retention.

It is expected that AI will continue to evolve and chatbots will become more sophisticated very quickly. It will be interesting to examine if these scores improve even in the next few months before the SB3C conference. Other AI-driven tools are also coming online and we can expect this landscape to change rapidly.

REFERENCES

1. Gleason N. ChatGPT and the rise of AI writers: how should higher education respond? THE Campus Learn, Share, Connect. Published December 9, 2022. Accessed January 4, 2023. <https://www.timeshighereducation.com/campus/chatgpt-and-rise-ai-writers-how-should-higher-education-respond>
2. McMurtrie B. Teaching Experts Are Worried About ChatGPT, but Not for the Reasons You Think. The Chronicle of Higher Education. Published December 13, 2022. Accessed January 4, 2023. <https://www.chronicle.com/article/ai-and-the-future-of-undergraduate-writing>
3. Watkins R. Update Your Course Syllabus for chatGPT. Medium. Published December 19, 2022. Accessed January 4, 2023. https://medium.com/@rwatkins_7167/updating-your-course-syllabus-for-chatgpt-965f4b57b003

4. VALUE Rubrics - Written Communication. AAC&U. Accessed January 19, 2023. <https://www.aacu.org/initiatives/value-initiative/value-rubrics/value-rubrics-written-communication>
5. VALUE Rubrics - Quantitative Literacy. AAC&U. Accessed January 19, 2023. <https://www.aacu.org/initiatives/value-initiative/value-rubrics/value-rubrics-quantitative-literacy>

GLUTARALDEHYDE CROSSLINKING OF COLLAGEN IS A TIME DEPENDENT REACTION ON THE ORDER OF 24 HOURS

Kimberly R. Kroupa (1), CV Sise (2), Jason Fan (1), Sinisa Vukelic (1), Gerard A. Ateshian (1,2)

(1) Department of Mechanical Engineering, Columbia University, New York, NY, USA
(2) Department of Biomedical Engineering, Columbia University, New York, NY, USA

INTRODUCTION

Glutaraldehyde (GTA) is a well-known chemical crosslinker, widely used in the stabilization of collagenous biomaterials. Its applications vary from the production of heart valves and vascular grafts [2,3], to immobilization of enzymes [4] and proteins for histochemistry and microscopy. This widespread applicability has motivated several efforts to characterize GTA mechanisms [studies on GTA and collagen, E], yet the chemical reactivity of GTA is not yet fully understood.

The primary reaction of GTA with collagen is accepted to be between the aldehyde groups of GTA and epsilon-amino groups of lysine or hydroxyprolines of collagen, resulting in the formation of quaternary pyridinium (PYD)-type crosslink. [4,5]. As such, in our lab, GTA has been used as a tool used to study collagen crosslinks in cartilage, where PYD-type crosslinks are most prevalent, as a model of cartilage pathology and osteoarthritis treatment.

Specifically, our previous work sought to identify and quantify changes in a Raman peak identified as being related to PYD crosslinks, introduced by GTA treatment of proteoglycan (PG) depleted cartilage explants [7,8]. These changes were then correlated to the increase in equilibrium Young's modulus E_Y induced by GTA, to yield new insights into the characterization of cartilage crosslinks. However, this method was limited by the high fluorescence background introduced by GTA, which overwhelmed the Raman cartilage signal only 30 minutes after exposure [10]. Further, it was observed that measurement of the modulus E_Y varied across a treatment group, according to how long after GTA exposure the samples were mechanically tested.

Together, these observations suggest that the reaction of GTA with collagen is time dependent. To examine this reaction and characterize its time constant, cartilage explants were digested of their proteoglycan content, leaving behind a nearly pure type II collagen matrix. These specimens were then treated with GTA for 120 s then washed. Repeated stress relaxation and cyclic strain tests, and confocal microscopy were employed to characterize the reaction over a period of 24 hours.

METHODS

Sample Preparation: Cylindrical cartilage explants were harvested from the condyles of four immature bovine knee joints (\varnothing 5 mm). Middle and deep zones were microtomed, resulting in a thickness of 2.71 ± 0.1 mm. Explants were digested of proteoglycans (PGs) using the protocol in [1]. PG depletion was verified using a DMMB assay.

GTA Treatment: Samples were exposed to 25mL of 0.2% GTA, prepared in phosphate buffer saline (PBS), for 2 min, then washed with 50 mL PBS for 5 mins.

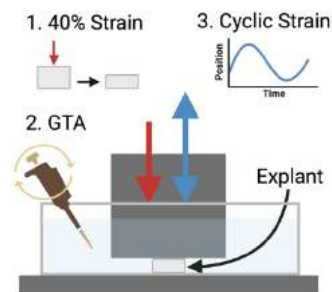


Figure 1. PG-depleted cartilage explants are subjected to 40% strain, allowed to equilibrate, then 1% strain cyclic compression before and after GTA exposure.

Dynamic Testing: The stress relaxation protocol above was performed. After testing, the sample was allowed to recover, then compressed to 40% strain at $1 \mu\text{m/s}$, and again allowed to equilibrate for a minimum of 3 hours, resulting in a tare load of approximately 12 grams. Subsequently, a cyclic compressive strain of 1% was then applied onto

Confocal Imaging: Samples were treated with GTA, then sliced into 1 mm thick sections, submerged in PBS, and imaged on an Olympus Confocal microscope (laser 473 nm, 20 us/pixel, 1024×1024) at 5 min increments for 30 min, then 30 min increments up to 24 hours.

Stress Relaxation Testing: Explants were treated with GTA as outlined above, then tested immediately, 1, 2, and 24 hours after exposure in unconfined compression, by stress-relaxation test (10% strain at $0.5 \mu\text{m/s}$, 1800 s relaxation). Young's modulus E_Y was calculated from equilibrium load, displacement and sample geometry [10].

the specimen using a sinusoidal profile at a frequency of either 0.025 Hz (n=3) or 0.05 Hz (n=1) for 3 cycles, 15 minutes apart (Fig. 1). Samples were exposed to 25 mL of 0.2% glutaraldehyde for 2 minutes, then washed with PBS, all while held under constant compression at 40% strain in the testing apparatus. The cyclic compressive loading regimen detailed above was repeated immediately after treatment, then in 15-minute intervals, followed by 30-minute intervals, and so on, for 24 hours. Dynamic modulus was assessed as the difference from equilibrium tare load at 40% strain to maximum load during cyclic compression, normalized by the surface area of the sample and prescribed strain of 1%.

RESULTS

After enzymatic digestion of the explants, results of the DMMB GAG assay verified that 98% of PGs had been removed from the tissue, resulting in a nearly pure collagen type II matrix. Modulus E_Y prior to GTA treatment was found to be 36.9 ± 2.9 kPa. Preliminary confocal

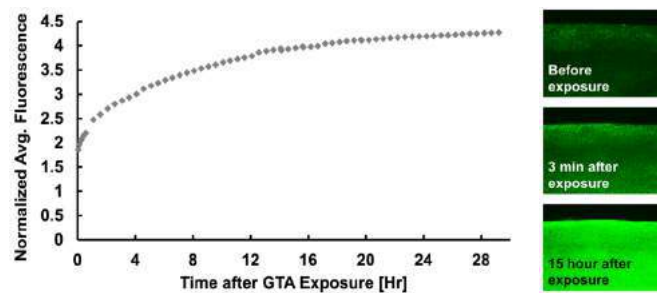


Figure 2. (Right) Normalized average fluorescence of sample over >24h after exposure to GTA. (Left) Confocal images of representative sample before GTA, and 3min and 15h after. microscopy data used showed a monotonically increasing average fluorescence after exposure to GTA, before plateauing at 24 hr (Fig. 2). Repeated measurements of E_Y and corresponding sample height h after GTA exposure showed an increase in E_Y and decrease in h after the first test. Both values then remained constant (Fig. 3, Right).

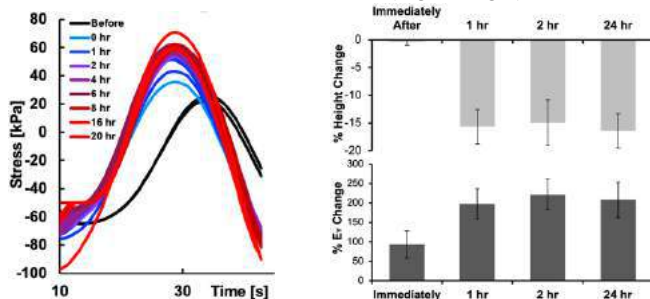


Figure 3: (Left) Representative sample showing stress vs. time curves for 1% strain cyclic compression tests at 0.025 Hz over 24 hours. Smoothed. (Right) Sample height and E_Y repeated measurements after GTA treatment of PG-depleted cartilage over 24 hours. The height of the same did not recover after the first test. E_Y reached a final value at ~2 hours (n=4).

For each sample and corresponding set of cyclic strain tests, load-time curves were obtained and converted to stress-time curves using the axial surface area of the specimen (Fig. 3, Left). After GTA treatment, the maximum force exerted on the platen by the sample increased. The dynamic modulus was then calculated and plotted as a function of time after exposure to GTA, for both the 0.025 Hz and 0.05 Hz frequencies (Fig. 4). The dynamic modulus increased with time until 16 hours, when it began to plateau. The dynamic modulus was higher at the higher frequency of 0.05 Hz.

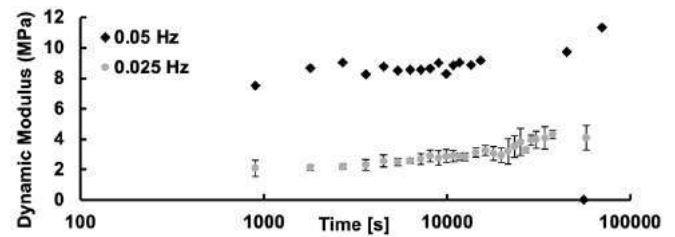


Figure 4: Dynamic modulus as a function of time for both frequencies: 0.025 Hz and 0.05Hz, on a logarithmic time scale. Average and standard deviation for 0.025 Hz (n=3) is shown.

DISCUSSION

The results of this study indicate that the reaction of GTA with collagen is time dependent, on the order of 24 hours, after exposure to GTA for only 120 s. Fluorescence, as measured with confocal microscopy (Fig. 2, Right), indicated that until 24 hours the compound will continue to form new bonds in the collagen Type II matrix, thus increasing the overall fluorescent signal of the sample. The increasing stress seen in Fig. 3, Left, indicates the sample is stiffening, as the same strain of 1% over time elicits a larger force exerted by the tissue, onto the platen. E_Y repeatability tests indicated that the modulus continued to stiffen until the second test at 2 hrs, then reached a final value. However, importantly height was not recovered after the first test (Fig. 3, Right). A change in height was also seen in the full load-time data for the cyclic testing. At later time points, >5hrs, when the platen moved upwards, the load exerted by the sample on the platen would frequently drop to zero (data not shown here). This indicates the sample height does not recover quickly, or at all, even at low strain values. Compression of the sample, as with these mechanical tests, may increase the proximity of binding sites on the bound GTA and collagen, speeding up the reaction, and causing the sample to crosslink completely while in a compressed state, unable to recover its original height.

Together, these observations suggest that the reaction of GTA with collagen is time dependent, where bound GTA continues to induce crosslinks with other GTA molecules and the collagen matrix, even after excess GTA has been washed away. To investigate if this reaction is producing mainly intermolecular crosslinks, or simply lengthening the GTA polymer chains between existing bound GTA, measuring resistivity to the enzyme collagenase could be used, as was done by Cheung et. al [9] in aqueous type I collagen. A reversible binding model can also be developed, to characterize this reaction and the type of bonds formed during it.

The dynamic modulus of GTA treated PG-depleted explants also increased on a similar time scale, reaching a maximum and final value around 24 hours (Fig. 4). The modulus was greater at the higher frequency. This, as well as increases in stress equilibration time of the PG depletion samples after GTA treatment, indicates that GTA could be changing the viscoelastic response of the tissue as well. In future work, this can be explored further with testing at additional frequencies, or with mathematical modeling.

ACKNOWLEDGEMENTS

The authors acknowledge support from NIH 5R01AR073289.

REFERENCES

- [1] Schmidt+ *J Orthop Res*, 1990
- [2] Wang+ *Int J Artif Organs*. 16(7): 530-6, 1993.
- [3] Broom+ *Thorax*. 34(2): 166-76, 1979.
- [4] Migneaul+ *Biotechniques*. 37(5): 790-6, 2004.
- [5] Hardy+, *J. Chem Soc., Perkin Trans. 1*. 2282-88, 1979.
- [7] Rich+, *J. Mol Biol*. 3(5): 483-IN4, 1961.
- [8] Myllyharju et al., *Trends Genet*. 20: 33-43, 2004.
- [9] Cheung+ *Connect Tissue Res*. 10(2): 201-16, 1982.
- [10] 5. Cigan+ *J Biomech*, 6, 2014.

CONFORMAL ABLATION OF ATHEROSCLEROTIC PLAQUE BASED ON MULTI-ELECTRODES AND NSGA II

Hongying. Wang, Ruizhe, Hou, Shiqing. Zhao, and Aili. Zhang

Department of Biomedical Engineering
Shanghai Jiao Tong University
Shanghai, China

INTRODUCTION

Atherosclerosis is a leading cause of mortality and morbidity worldwide. The plaque underneath the intimal will block the blood flow. The ablation of the whole plaque and intimal would cause restenosis. A novel radiofrequency balloon catheter with the integration of surface electrodes and cooling water inside the balloon was proposed, which could ablate the plaque while sparing the intima[1]. However, the plaque morphology varies in different lesions and patients [2]. Achieving precise conformal ablation of plaques with different morphologies while sparing the intimal is the key to achieving long-term patency of arteries and avoiding restenosis as much as possible.

For conformal ablation, optimization of the expandable and compliant electrode configuration design[3, 4] and multiple ablations with overlapping single-needle probe placements[5] are proposed in the radiofrequency ablation of tumors. However, the needle could damage the intimal and the combination of the multiple ablation session takes a long time, not suit for the endovascular ablation of plaque.

To achieve conformal ablation of atherosclerotic plaques underneath the intimal in a short time (~ 2 min), a conformal ablation strategy was developed with a numerical model and the non-dominated sorting genetic algorithm (NSGA II). The numerical model calculated the ablation results and was input into the algorithm. NSGA II searches the optimal parameter set, including the voltages of multiple electrodes, and the velocity and temperature of the coolant, by minimizing the thermal damage in the non-plaque region, especially the intimal region, and increasing the ablation coverage rate as far as possible.

METHODS

Numerical model: As shown in Figure 1, an annulus with thickness and inner diameter of 0.05mm and 2.9mm is used to simulate the balloon catheter, and the cooling water circulates inside the catheter. 12 electrodes were embedded in the outer wall of the catheter evenly, and the artery and the surrounding tissues are located outside the catheter.

Based on the clinical imaging data[6], the plaque was enclosed by four arcs, whose angle range from 91.7° to 154.8° and the thickness ranges from 0.83mm to 2.63mm, and the corresponding circumferential length ranges from 3.73mm to 11.15mm.

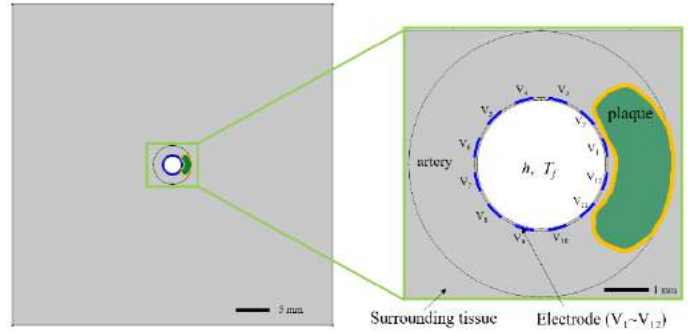


Figure 1: The two-dimensional geometric model for simplified calculation of strip multiple electrodes.

The quasi-electrostatic field equation (1) and the heat transfer governing equation (2) were used.

$$\nabla \cdot (\sigma \nabla V) = 0 \quad (1)$$

$$\rho c \frac{\partial T}{\partial t} = \nabla \cdot (k \nabla T) + \sigma (\nabla V)^2 \quad (2)$$

where V is the potential of tissue, σ and k are the electrical and thermal conductivity, respectively.

The convective condition was applied to the inner wall of the catheter

$$q = h(T_w - T_f) \quad (3)$$

where T_w and T_f are the temperature of the inner wall of the balloon catheter and the cooling water, respectively. h is the convective heat transfer coefficient is the function of velocity ($V/\text{m}\cdot\text{s}^{-1}$) and temperature (T/K) based on empirical correlation. In each electrode, the potential, V , is set to be $V_1 \sim V_{12}$. When one electrode isn't used, the insulation boundary condition is used. The initial temperature is set to

37 °C, and the outer surface of the phantom is set as thermal insulation to simulate *in-vivo* thermal treatment. The electrical and thermal properties of the artery and the catheter are the same as in the study [1].

NSGA II: NSGA II was chosen to search the optimal parameters (including $V_1 \sim V_{12}$, V_f , and T_f) for the ablation of different plaque morphologies with the merit of good performances in global optimization and fast convergence. The detailed algorithm flowchart is shown in Figure 2.

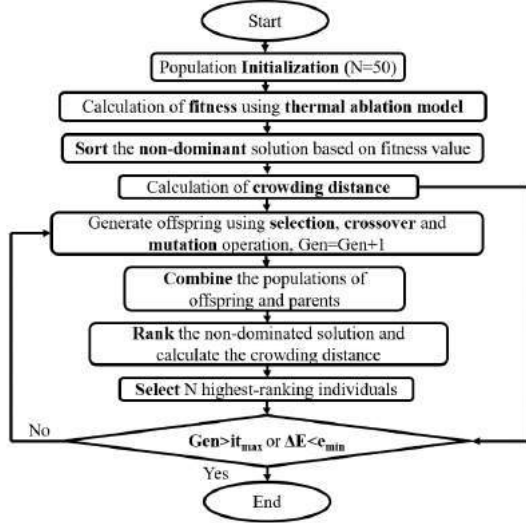


Figure 2: Algorithm flowchart for determining the optimal parameter set ($V_1 \sim V_{12}$, V_f , and T_f).

RESULTS

The optimal parameters were obtained and the optimized ablation results were good using the combination of multiple electrodes and NSGAII optimization (Fig.3). The over-ablation rate of intimal (ablation of intimal to the whole intimal) was 0% ~ 16.05%, the overall over-ablation rate (the area of over-ablation to the area of the plaque) was 2.52% ~ 9.60% and the coverage rate was 75.68% ~ 92.47% (see Table 1). The average values of the over-ablation of rate intimal, overall over-ablation rate, and coverage rate were 6.67%, 4.95%, and 84.92%.

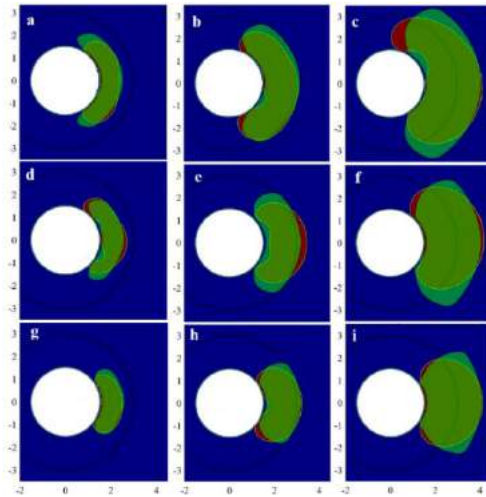


Figure 3: The optimized ablation results for different plaque morphologies (a ~ i). The green region, red region, and blue region

represent the plaque, ablation area, and surrounding tissue.

Table 1: The three ablation indexes for different plaque morphologies.

Plaque	Parameters ($V_1 \sim V_{12}/V$, $T_f/^\circ\text{C}$, $V_f/\text{m}\cdot\text{s}^{-1}$)	over-ablation rate of intimal	Overall over-ablation rate	coverage rate
a	[24,4,27,N,N,N,N,N,N,0,24,5,9,4,8]	12.46%	3.00%	79.20%
b	[24,3,29,N,N,N,N,N,N,27,0,0,8,8,8]	6.85%	3.80%	88.40%
c	[26,32,44,N,N,N,N,N,N,N,16,0,9,21,5,4]	4.50%	5.03%	83.05%
d	[8,25,0,N,N,N,N,N,N,12,35,21,3,8,6]	2.07%	9.60%	86.75%
e	[13,0,N,N,N,N,N,N,N,N,N,N,43,30,7,4,2]	0	8.30%	75.68%
f	[9,0,N,N,N,N,N,N,N,N,N,N,23,21,29,5,5,4]	12.34%	4.56%	85.13%
g	[0,20,N,N,N,N,N,N,N,N,N,N,27,2,7,5,6,6]	0.84%	2.52%	84.78%
h	[33,6,N,N,N,N,N,N,N,N,N,N,0,26,6,5,9]	4.92%	4.95%	92.47%
i	[27,21,N,N,N,N,N,N,N,N,N,N,5,0,36,5,8]	16.05%	2.83%	88.83%

Note: N indicates that the corresponding electrode is not selected as the working electrode.

DISCUSSION

It demonstrates that the conformal ablation of atherosclerotic plaques with different irregular morphologies in a short time could be realized by the combination of multiple electrodes and NSGA II. The over-ablation rate is lower than 10% and the coverage rate was larger than 75% in the nine cases. In the future, the optimal strategies will be assessed with more different plaque morphologies and verified by the experiments. In addition, a three-dimensional model that takes into account the heterogeneity of different plaques will be developed to provide more precise guidance for the conformal ablation of atherosclerotic plaque clinically.

ACKNOWLEDGEMENTS

This work was supported by the National Science Foundation of China under Grants 51890892.

REFERENCES

- [1] Zhao, S. *et al.*, *Biomed Eng Online*, 19:44, 2020.
- [2] Stary, H. C. *et al.*, *Arteriosclerosis and Thrombosis*, 14:840-856, 1994.
- [3] Hanks, B. *et al.*, *Journal of Medical Devices*, 12:2018.
- [4] Wang, Z. *et al.*, *IEEE Trans Biomed Eng*, 64:699-705, 2017.
- [5] Yu, P. *et al.*, *2021 the 3rd International Conference on Intelligent Medicine and Health*, 8-14, 2021.
- [6] Iwakiri, T. *et al.*, *Atherosclerosis*, 225:359-62, 2012.

DIFFUSION MRI CHARACTERIZES MICROSTRUCTURAL CHANGES OF THE CERVIX DURING PREGNANCY

Noel Naughton (1), Amir Ostadi Moghaddam (1), Mariana Kersh (1,2,3), Sanmi Koyejo (4), Amy Wagoner Johnson (1,2,3,5), and Bruce Damon (1,6)

- (1) Beckman Institute for Advanced Science and Technology, University of Illinois, Urbana, IL, United States,
(2) Department of Mechanical Science and Engineering, University of Illinois, Urbana, IL, United States,
(3) Carle Illinois College of Medicine, University of Illinois, Urbana, IL, United States,
(4) Computer Science Department, Stanford University, Palo Alto, CA, United States,
(5) Carle R. Woese Institute for Genomic Biology, University of Illinois, Urbana, IL, United States,
(6) Stephens Family Clinical Research Institute, Carle Health, Urbana, IL, United States

INTRODUCTION

The collagen microstructure of the cervix remodels during pregnancy to accommodate its biological function. As pregnancy progresses, collagen fibers become more disorganized, and, consequently, the cervix softens. Abnormal or early remodeling, however, can lead to preterm birth (PTB). PTB affects approximately 1 in 10 babies and has costly and long-term health consequences [1]. Methods of characterizing collagen organization in cervix tissue have the potential to predict the risk of PTB more accurately and earlier, allowing for timely medical interventions. Currently, cervical length serves as the gold standard for predicting risk of PTB despite its low positive predictive value [2]. Thus there is a need for improved methods for assessing collagen microstructure of cervix.

Second-Harmonic Generation (SHG) microscopy is a well-established technique for acquiring high-resolution images of the tissue microstructure but its clinical application has been limited due to its invasive nature [3]. In contrast, diffusion-weighted MRI (dMRI) is non-invasive and sensitive to changes in tissue microstructure [4], however, the relationship between collagen organization and dMRI metrics is not well established. Here we combine SHG imaging with simulations of diffusion MRI to explore the ability of dMRI to capture collagen remodeling due to pregnancy.

METHODS

Sample preparation. Cervices of 12-week-old Sprague Dawley rats were harvested and stored at -80C (two non-pregnant, two 15-days pregnant, two 17-days pregnant, and three 21-days pregnant). Excised tissue was thawed, embedded in optimal cutting temperature (OCT) compound, and cryosectioned transversely at mid-cervix (-20C). OCT was washed after sectioning and samples imaged immediately.

SHG imaging. A femtosecond laser (MaiTai DeepSee, Newport Corporation, USA), centered at 780 nm, illuminated the cervixes and a confocal microscope (Zeiss LSM 710, Germany) acquired 3D images of the samples

using a 40× 1.2 NA water-immersion objective. Two quantitative parameters, spherical variance (SV) and average out-of-plane fiber orientation (Φ), described the volumetric images. Briefly, Φ quantifies the average orientation of the collagen fibers relative to the imaging plane (the plane perpendicular to the cervical canals) and SV represents the dispersion of the collagen fibers in 3D, with values between 0 (unidirectional) and 1 (dispersed). Detailed descriptions of imaging and image quantification protocols are available in [3].

Diffusion MRI (dMRI) simulations. SHG image stacks (N=86) were binarized into a 3D volume consisting of collagen fibers and interstitial water domains. dMRI experiments were simulated by solving the Bloch-Torrey equation over the domain using the lattice Boltzmann method [5]. The collagen domain was modeled as not contributing to the dMRI signal (due to its low T2). A diffusion coefficient of 2.0 $\mu\text{m}^2/\text{ms}$ was used. dMRI scans consisted of a PGSE sequence with 64 directions, gradient duration of 10 ms, gradient spacing of 4 ms, and a b-value of 400 s/mm^2 . For each sequence, a non-diffusion weighted simulation was also performed. Both diffusion tensor imaging (DTI) and spherical harmonics (SH) approaches to analyzing the dMRI signal were considered [4]. The diffusion tensor was computed using custom Python code along with radial (RD) and mean diffusivity (MD), and fractional anisotropy (FA). Spherical harmonic coefficients up to degree four were computed using the pyshtools Python package.

RESULTS

A comparison of the simulated dMRI experiments for pregnant and non-pregnant cervixes shows a statistically significant ($p < 0.01$) difference in fractional anisotropy (FA), which is a measure of the degree to which water diffusion is restricted in one direction but not in others (Fig. 2a). Pregnant cervixes exhibit lower FA, indicating remodeling of the collagen fibers in the cervical tissue to be more disorganized. Structural metrics of

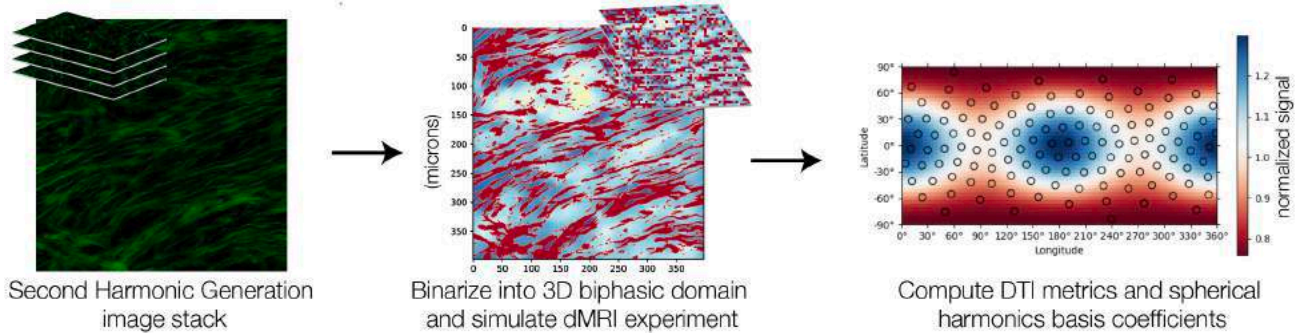


Figure 1: Overview of the simulation process. SHG image stacks (left) are binarized into 3D domains over which a dMRI experiment is simulated by solving the Bloch-Torrey equation, resulting in a map of the microscale signal distribution within the cervix tissue (center). The dMRI experiment is repeated in 64 directions from which DTI and spherical harmonic (SH) representations of the signal are computed. SH provides a model-free representation of the dMRI signal distribution on a sphere (right).

collagen orientation measured from SHG images are also correlated with FA. Both spherical variance (Fig. 2b) and average out-of-plane fiber orientation (Fig. 2c) have inversely proportional relationships with FA demonstrating that dMRI metrics are sensitive to structural variations in the collagen fiber orientations.

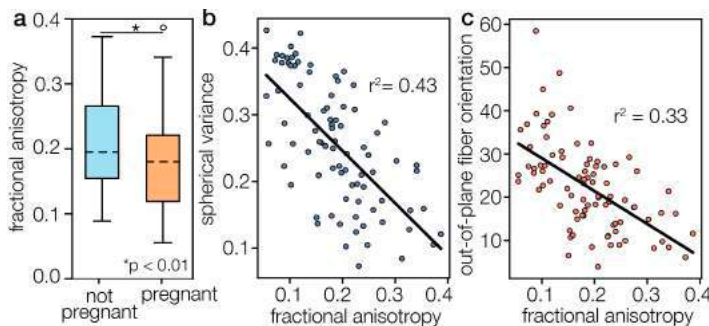


Figure 2: (a) Significant differences in fractional anisotropy (FA) exist between pregnant and non-pregnant rat cervix. FA also correlates with the structural parameters of (b) spherical variance and (c) average out-of-plane fiber orientation measured from SHG images.

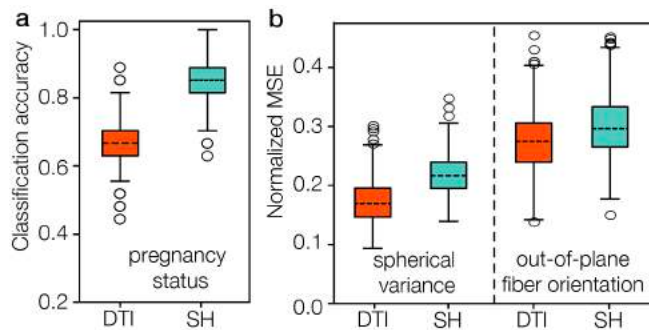


Figure 3: (a) Box plot of the performance of a logistic regression classifier trained to distinguish pregnant or non-pregnant status. Two classifiers were trained, one using traditional DTI metrics and the other using spherical harmonics (SH) coefficients. (b) Normalized mean-squared error of a linear regression model trained to predict spherical variance and out-of-plane fiber orientation. Models using both DTI metrics and SH coefficients were explored with the SH-based models outperforming the DTI-based models.

We next consider if dMRI can distinguish between pregnant and non-pregnant stages. A logistic regression classifier was trained to distinguish pregnancy status (Fig. 3a). Training was performed using 80% of the simulation data and model performance was evaluated on the remaining 20% of data. To generate a robust measure of model accuracy, each model was trained and evaluated 500 times with the training and testing data randomly

shuffled each time. Two types of models were trained. The first model used DTI metrics (FA, MD, RD, λ_1 , λ_2 , λ_3) while the second model used the spherical harmonics coefficients. Testing revealed that using only the first 9 coefficients yielded the best performance. All data were normalized to zero mean and unity variance prior to training. The SH-based model exhibits better performance, with a mean accuracy of 84% while the DTI-based model achieved an average accuracy of 66%. A similar training process using Ridge regression was utilized to predict spherical variance and out-of-plane fiber orientation (based on measurements from the SHG data) from the dMRI data (Fig. 3b). Again both a DTI-based and SH-based model were trained with the SH-based model achieving lower normalized mean-squared error in both cases.

DISCUSSION

Diffusion MRI of human [6] and mouse [7] cervix during pregnancy has shown FA decreases throughout pregnancy, which is in keeping with our results. In contrast to these previous studies, this study focuses on mechanistically establishing the ability of dMRI to reveal structural changes in cervix tissue during pregnancy due to collagen remodeling. By relating the simulated dMRI results with structural metrics of collagen organization, it establishes that FA is sensitive to structural features of collagen such as spherical variance and out-of-fiber orientation. It further shows that both DTI and more advanced models of dMRI such as those based on spherical harmonics offer specificity to these structural features. Additional data collection will enable the use of machine learning techniques to further refine estimates of microstructure from diffusion MRI. Establishing a non-invasive approach to quantitatively evaluate collagen structure *in vivo* during pregnancy may yield novel clinical diagnostic and staging tools for treating a range of pregnancy complications, in particular pre-term birth.

ACKNOWLEDGEMENTS

Funding provided by the Beckman Postdoctoral Fellowship Program.

REFERENCES

- [1] WHO. <https://www.who.int/news-room/fact-sheets/detail/preterm-birth>. 2022.
- [2] Feltovich H et al. *American journal of obstetrics and gynecology* 207.5 (2012). ISSN: 0002-9378.
- [3] Ostadi Moghaddam A et al. *Acta Biomaterialia* 140 (2022). ISSN: 1742-7061. DOI: 10.1016/j.actbio.2021.12.025.
- [4] Alexander DC. *Visualization and processing of tensor fields*. Springer, 2006.
- [5] Naughton NM et al. *Physical Review E* 102.4 (2020).
- [6] Qi W et al. *American journal of obstetrics and gynecology* 224.1 (2021).
- [7] Chatterjee A et al. *Scientific reports* 11.1 (2021).

EFFECTS OF CONDITIONAL SV40-T IMMORTALIZATION ON HUMAN RETINAL PROGENITOR CELL DIFFERENTIATION

Qi Wang (1), Jessica A. Cooke (2), Budd A. Tucker (2), Kristan S. Worthington (1, 2)

(1) Roy J. Carver Department of Biomedical Engineering, University of Iowa, Iowa, USA
(2) Institute for Vision Research, University of Iowa Carver College of Medicine, Iowa, USA

INTRODUCTION

Retinal progenitor cells (RPCs) are multipotent cells fated to develop into neural retinal cell types such as retinal ganglion, horizontal, amacrine, bipolar, and photoreceptors. Although RPCs are not known to be present in the adult mammalian retina, culturing them *in vitro* is important for screening therapeutic molecules, developing retinal cell therapies, and characterizing cellular mechanisms involved in retinal disease and regeneration. Immortalized RPCs originating from prenatal rodents are commercially available, but these animals do not have the same composition and distribution of cells within the retina compared to humans.¹ Although RPC differentiation from human pluripotent stem cells is well established, the differentiation process is cost-, labor-, and time-intensive (~30 days). In addition, achieving sufficient quantities of RPCs is challenging because the RPC stage is inherently transient; RPC proliferation slows substantially within 1-2 weeks as mature retinal cell types emerge.²

There is a critical need for readily accessible human RPCs that are capable of prolonged proliferation while retaining the ability to further differentiate into mature retinal cell types. The most common way to achieve prolonged proliferation in culture is to reprogram, or “immortalize” cells by genetically altering the cell to upregulate replication. However, this effect is quasi-permanent, and thus has been shown to reduce differentiation capacity, since maturation and proliferation are typically mutually exclusive.³ As an alternative to this traditional approach, our objective in this research paper is to generate and characterize a conditionally immortalized human RPC line that enters prolonged proliferation in the presence of a small molecule stimulus, then differentiates towards mature retinal cell types when the stimulus is removed. To accomplish this, we transduced human induced pluripotent stem cells (iPSCs) with a Tet-On SV40-T expression system, which is designed to cause inhibition of cell cycle regulators in the presence of tetracycline. The transduced iPSCs were differentiated to RPCs before being exposed to tetracycline, then phenotypic stability

and proliferative ability were characterized during subsequent passaging using principal RPC markers.

METHODS

Cell Culture and Transduction. Human iPSCs derived from a patient with no known ocular disease were cultured on ATCC cell basement membrane coating in mTeSR with primocin and were fed daily until transduction. DNA plasmids and lentiviral vectors were prepared by Vector Builder according to the simplified schematic in Fig. 1. iPSCs were transduced at an MOI of 1 and transduced cells were subsequently selected by adding puromycin and hygromycin to the culture media.

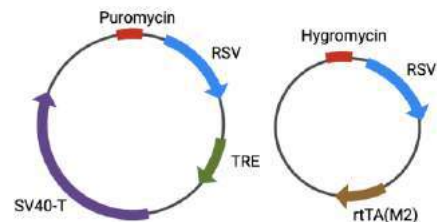


Figure 1: Simplified design of plasmids delivered by lentivirus.

Left: a ubiquitous promoter, RSV, is upstream of a tetracycline-inducible promoter (TRE), which drives expression of SV40-T, a known inhibitor of cell cycle suppressors. **Right:** RSV drives expression of a tetracycline-dependent transcription factor (rtTA), which, in the presence of tetracycline, binds to the TRE promoter to activate transcription of SV40-T.

RPCs Differentiation and Culture. iPSCs were differentiated into RPCs until Day 30 using a previously published protocol.² Briefly, iPSCs were dissociated into single cell suspensions using

accutase. Single cells were then aggregated to form embryoid bodies (EBs) using low adhesion v-bottom plates. EBs were cultured in mTeSR on Day 0 and slowly transitioned to neural induction media over 3 days. On Day 6, 1.5nM BMP4 was added to the media. On Day 8, retinal organoids (RO) were plated with the gradual addition of FBS. FBS was then gradually removed until Day 15 to allow for RO detachment. Transition to retinal differentiation media began on Day 16 and FBS was gradually increased until Day 22. On Day 22, 1X Glutamax was added. On Day 25, 100μM Taurine was added. This media was continued until Day 30 and used in subsequent culture maintenance and studies of RPCs. RPCs were separated into three experimental group after Day 30: RO, no dox (monolayer culture), and dox (monolayer culture). Doxycycline, which is in the tetracycline family was added to media (1μg/ml) for the dox group to induce SV40T expression. Dox group cells were then cultured for 10 passages before removal of dox (no dox P10 RPCs) to assess if dox removal has an impact on RPC gene expression and maturation.

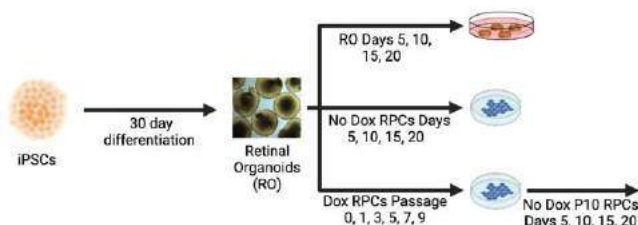


Figure 2: Schematic of experimental groups and timepoints.

Gene Expression of RPCs. RNA was collected at Day 30 of differentiation and every other passage (P1, P3, P5, P7, P9) for dox group or every 5 days for no dox groups (Days 5, 10, 15, 20). cDNA was synthesized using Superscript VILO cDNA kit. IDT PrimeTime standard primers were used to assess gene expression of PAX6, SOX2, CHX10, and Ki67, in conjunction with PrimeTime® Gene Expression Master Mix.

Immunostaining and Confocal Imaging. Immunostaining was performed at the same time points as the gene expression study. Briefly, cells were seeded in chamber slides and fixed with 4% PFA for 30 minutes, followed by 3x10 minute washes with 1X PBS + 0.001 vol % Tween. Primary antibodies were diluted at 1:100 in immunoblock buffer consisting of sodium azide, Triton-X, BSA and donkey serum and incubated overnight at 4°C. This was followed by 5 more 1X PBS + Tween washes and 2hr incubation at 25°C with secondary antibodies diluted at 1:1000 in immunoblock buffer. Finally, the slides were washed 3 times and mounted using ProLong™ Gold with DAPI.

RESULTS

Qualitatively, we observed that transduced cells exposed to doxycycline were able to be passaged up to ten times, while cells in the no dox group were far less proliferative and thus were not passaged throughout the experiment. qPCR analysis (**Figure 3**) demonstrated that expression of SOX2, PAX6, and CHX10 (early retinal markers) decreased after dissociation into monolayers during culture. SOX2, PAX6, and CHX10 were also quickly lost during early passage in the Dox RPC group. Although Ki67 (a marker of proliferation) is relatively constant in ROs and no Dox RPCs, passaging of RPCs led to decreased Ki67 expression over time.

Preliminary immunostaining of SOX2, PAX6, CHX10, and Ki67 did not show protein expression in most retinal organoid time points and Dox RPCs passages. Some Ki67 seemed to be present for ROs at

Day 30 of differentiation (RO Day 0) and for Dox RPCs at P3 (**Figure 4**). In addition, some expression of Chx10 was observed in late passage (P9) Dox RPCs.

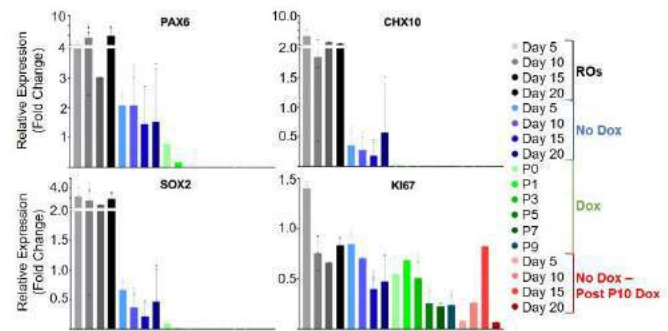


Figure 3: Gene expression analysis of RPC markers.

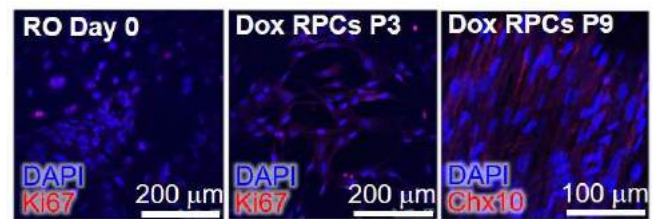


Figure 4: Immunostaining of RPC markers

DISCUSSION

RT-qPCR analysis revealed that after 30 days of differentiation from iPSCs, the RPCs expressed markers SOX2, PAX6, CHX10, and Ki67 indicating they were fated to develop into neural retinal tissue. The expression of Ki67 indicates ability of RPCs to proceed to active cell division. Its presence throughout late passages of Dox RPCs group indicates the possibility of sustained culture of these cells when conditionally immortalized. The co-expression of CHX10 and PAX6 is only present in neural retinal progenitor cells and thus the lost expression of these genes in Dox RPCs during early passages indicates that addition of doxycycline may not facilitate preservation of the retinal progenitor cell state.

Since immunostaining did not show expression of SOX2, PAX6, CHX10 and Ki67, future studies will include positive controls to ensure that the immunostaining protocol and chosen antibodies are functional. If positive controls do show staining of these markers, the differentiation protocol will be continued to a later time point before RPCs are dissociated into monolayer culture and doxycycline is added. Otherwise, the immunostaining protocol and antibodies will be revised.

In the future, experiments will also be performed to compare current data with control iPSCs that were not transduced. This will allow for assessment of leaky expression of SV40-T, which could affect the way iPSCs progress through differentiation. Other retinal cell markers will also be included to further characterize cell phenotype after doxycycline exposure.

ACKNOWLEDGEMENTS

This work was supported by funding from the University of Iowa: Old Gold Scholarship and the Office of the Vice President for Research.

REFERENCES

- [1] Grünert U et al., *Prog Retin Eye Res*, Feb 5:100844, 2020.
- [2] Fligor CM et al., *Methods Cell Biol*, 159:279-302, 2020
- [3] Ikbale E et al., *Data in Brief*, 6: 696-699, 2016

FUNCTIONALIZED NANOWIRES SUCCESSFULLY LOAD AND SUSTAIN RELEASE OF NGF

Molly E. Czachor (1), Joel A. Finbloom (2), Nafisa A. Elghazali (2), Darnell L. Cuylear (2), Kevin O. Rivera (2,3), Tejal A. Desai (2,4), Chelsea S. Bahney(1,3)

(1) Center for Regenerative and Personalized Medicine, The Steadman Philippon Research Institute (SPRI), Vail, CO, USA

(2) Department of Bioengineering and Therapeutic Sciences, University of California, San Francisco (UCSF), San Francisco, CA, USA

(3) Department of Orthopaedic Surgery, Orthopaedic Trauma Institute, University of California, San Francisco (UCSF), San Francisco, CA, USA

(4) Center for Biomedical Engineering, Brown University, Providence, RI, USA

INTRODUCTION

Fractures are one of the most common injuries worldwide with an estimated 178 million new fractures a year and 445 million prevalent fractures leading to billions of dollars in healthcare cost annually.¹ While most bone injuries regenerate well, 10-15% of normal fractures demonstrate impaired healing in the form of delayed- or non-union.^{2,3} Non-union rates increase to 50% of fractures when coupled with vascular damage or a high co-morbidity burden.⁴ Clinically, these non-unions are difficult and costly to treat as physicians are reluctant to intervene until 6-9 months without radiographic evidence of bone formation. There are currently no pharmacological agents approved to accelerate fracture healing or treat non-unions.³ Standard of care for addressing non-unions is surgical intervention to increase biomechanical stability and/or implantation of bone graft to promote healing. Injectable therapies are an exciting alternative to surgically implanted biologics for fracture healing. However, the translation of effective osteoinductive therapies remains challenging due to the need for safe and effective drug delivery. As such, there is an unmet clinical need for a controlled, localized, and non-surgical drug delivery system to treat bone fractures. Our objective is to engineer injectable polycaprolactone (PCL) nanowires loaded with beta nerve growth factor (β -NGF) to promote fracture repair.

METHODS

PEGDMA microrods were first fabricated to be used to demonstrate feasibility of the experiments. The microrods were fabricated as previously described through a process of photolithography.⁵ Prior to photolithography, the PEGDMA macromer was adjusted to have a 75% or 90% concentration to examine if the polymer network density affected protein loading efficiency and release. Following fabrication, the microrods were allowed to passively adsorb β -NGF protein for 30 hours in 4°C.

After loading, the microrods were spun down and the supernatant was collected to analyze NGF loading efficiency. This was done using a μ BCA assay and measuring the amount of NGF in the supernatant. NGF loading levels were calculated based on the depletion of NGF (eq 1) where X_i is quantity of drug added initially and X_t is amount of protein in the supernatant after 30 hours.

$$\text{Loading efficiency \%} = \frac{X_i - X_t}{X_i} * 100 \quad (1)$$

Nanowires were fabricated from polycaprolactone (PCL) polymers using a nano-templating technique.^{6,7} An anodized aluminum oxide (AAO) substrate with controlled pore size formed the template for nanowire formation. A PCL film was cast onto a glass substrate and heated to above melting temperature while in contact with the AAO template. This caused rapid nanowire formation into the AAO pores via capillary action. Following templating and cooling, nanowires were purified by membrane detachment and selective AAO etching with sodium hydroxide. Once released, the nanowires were sonicated, filtered, purified, and stored at 4°C as a suspension in water.

To functionalize the nanowires, a layer-by-layer (LbL) electrostatic assembly approach previously published was used.^{6,7} The PCL nanowires bear a strong negative charge following the alkaline etching method used in the fabrication process. Due to this negative charge, chitosan (positive charge) was used as the first layer to make positively charged nanowires. Chitosan was dissolved at 10 mg/mL in 0.25% Acetic Acid and incubated at 37°C for 15 minutes to fully dissolve. The solution was diluted in LbL buffer (25 mM HEPES, pH 7, 20 mM NaCl, 0.025% AcOH) to make a 2mg/mL chitosan stock solution. The nanowires were then reconstituted at 1 mg/mL in LbL buffer, and an equal volume of chitosan solution was added while sonicating. After 10 seconds of sonication, the nanowire-chitosan solution was removed and shaken at room temp for 30 minutes. The

solution was then centrifuged and washed with water. The nanowires now had a positive charge, and a subsequent layer of heparin (negative charge) could be added. First, β -NGF was loaded onto the heparin by incubating β -NGF solubilized in pH 6 sodium acetate buffer and heparin together at a 1:2 mass ratio for 30 minutes. The heparin-NGF solution was then added to the chitosan-nanowire solution at a 1:1 volume ratio and shaken at room temperature for 30 minutes. The nanowires were then resuspended in 500uL sodium-acetate pH6 buffer and 500uL of 2mg/mL chitosan in sodium acetate pH6 buffer was added. The solution was shaken for 15 minutes, spun down, and washed with sodium acetate pH 6 buffer. The nanowires were then spun down and supernatant was collected to analyze NGF loading efficiency using the same μ BCA assay as was done with the PEGDMA microrods.

RESULTS

First, PEGDMA microrods were fabricated and used to demonstrate feasibility of the release kinetic experiment. It was shown that the macromer concentration did not significantly affect loading efficiency (Fig 1A). The microrods were able to load over 2000ng of β -NGF (Fig. 1A), however less than 2% of the total protein was released over 168 hours (Fig 1B). This was later found to be due to physiochemical interactions between the protein and the microrods.

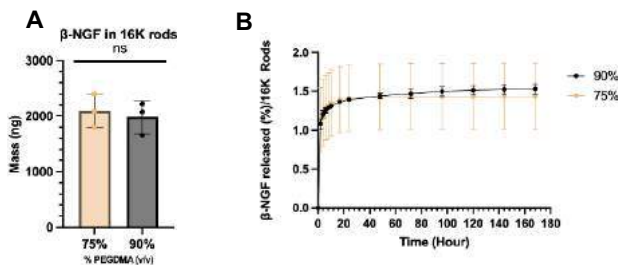


Figure 1: (A) Mass of β -NGF loaded into 16K microrods. (B) Percent release of β -NGF from PEGDMA microrods (n=3) over 168 hours.

To achieve a more linear release of NGF we next aimed to test whether PCL nanowires could be engineered with improved release kinetics. Nanowires were fabricated through a process of nano-templating (Fig 2). The nanowire width was controlled by the pore size of the AAO mold, while the length of the nanowires was controlled by varying the thickness of the polymer film. PCL nanowires were formed through capillary action after melting the PCL polymer and detached using sodium hydroxide. Nanowires with lengths ranging from 2-20 μ m have been fabricated, and a width of 200 nm has been consistently used thus far. PCL nanowires were functionalized through a layer-by-layer electrostatic assembly technique.



Figure 2: Polymeric nanowire fabrication technique. Nanowires are fabricated using an anodic aluminum oxide (AAO) template.

The same release experiment was performed with the PCL nanowires. The nanowires were able to successfully load 5 μ g of β -NGF with upwards of 75% efficiency and sustained first order release of the β -NGF over 8 days (Fig 3A). This data was generated using only a single layer of chitosan, further tuning of the NGF release kinetics to become more linear can be achieved by adding multiple layers of the electrostatic polymers⁶ (Fig 3B).

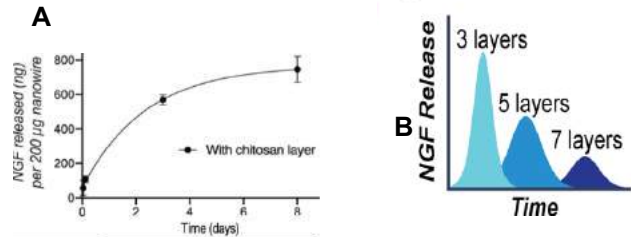


Figure 3: (A) 5 μ g NGF/mg was loaded with 75% efficiency onto nanowires followed by a single layer of chitosan. Sustained first order NGF release was observed over 8 days ($R^2 = 0.999$). (B) Hypothesized relationship of LbL layers and NGF release rates

DISCUSSION

Our results show that we can fabricate PCL nanowires, successfully load them with β -NGF, and deliver a sustained release. We were able to load 2.5 times more NGF on the nanowires compared to the PEGDMA microrods. This allows more NGF to be released locally into the fracture callus. Additionally, the ability to sustain first order release of the NGF over 8 days on the nanowires compared to the small amount released from the microrods shows that we were able to engineer a controlled delivery of this therapeutic.

While our results shown here are a good first step to addressing the clinical unmet need for a controlled and localized delivery system to treat bone fractures, these nanowires need to be further studied. Our next steps will be to add additional LbL layers to test the relationship between the number of LbL layers and NGF release rates. This will allow us to tune our nanowires for a more controlled release at specific timepoints during fracture healing. Following additional release kinetic studies, we will verify that the NGF released from the nanowires maintains bioactivity. This will be done using the canonical bioactivity test for NGF, the TF1 erythroblast cell proliferation assay.

In conclusion, the ability to deliver a therapeutic biologic to promote fracture repair without surgical intervention is the next step in fracture healing. Our developed nanowires can effectively load and release NGF in a controlled and localized way showing that this could be the next step to minimize delayed and non-unions.

ACKNOWLEDGEMENTS

The study was supported by National Institutes of Health through NIGMS (R01AR077761-01A1 Bahney).

REFERENCES

- [1] G. B. D. F. Collaborators, Global, regional, and national burden of bone fractures in 204 countries and territories, 1990-2019: a systematic analysis from the Global Burden of Disease Study 2019. *Lancet Healthy Longev* 2, e580-e592 (2021).
- [2] Giannoudis, P. V., Dinopoulos, H. & Tsiridis, E, *Injury*, 36 Suppl 3:S20-27, 2005.
- [3] Kostenuik, P. & Mirza, F. M., *Journal of orthopaedic research*, 35:213-223, 2017.
- [4] Dickson, K. F., Katzman, S. & Paiement, G., *Contemp Orthop*, 30: 489-493, 1995.
- [5] Ayala, P., Lopez, J. I. & Desai, T. A., *Tissue engineering. Part A*, 16:2519-2527, 2010.
- [6] Zamecnik, C. R., Lowe, M. M., Patterson, D. M., Rosenblum, M. D. & Desai, T. A., *ACS Nano*, 11:11433-11440, 2017
- [7] J. A. Finbloom, B. Demaree, A. R. Abate, T. A. Desai, Networks of High Aspect Ratio Particles to Direct Colloidal Assembly Dynamics and Cellular Interactions. *Adv Funct Mater* 30, (2020).

CONTACT MECHANICS BASED FORMULATION TO EXAMINE THE ROLE OF CELLULAR ADHESIONS IN EPITHELIAL MECHANICS

M. Talukder (1), S. Kale (1,2)

(1) Department of Mechanical Engineering, Virginia Tech, Blacksburg, Virginia, USA
(2) Center of Soft Matter and Biological Physics, Virginia Tech, Blacksburg, Virginia, USA

INTRODUCTION

Epithelial tissue is one of the four major tissues in our bodies that covers all the internal and external surfaces and lines body cavities. Mechanical behavior of epithelial tissues coupled with the biochemical signaling is important in several physiological processes such as morphogenesis and wound healing as well as in pathological condition including cancer invasion. Understanding epithelial rheology is also necessary from a materials point of view for applications including organ-on-a-chip [1] and organoids [2]. The mechanical behavior of epithelia is governed by the complex multiscale architecture spanning subcellular to supracellular length scales. The dynamics of the subcellular constituents introduce complex time-dependent mechanical response of epithelia. On biologically relevant longer timescales, cortical tension and cellular adhesions that connect cellular mechanics control tissue mechanics, remodeling, and fracture behavior [3].

Several modeling approaches have been proposed to model the longer timescale epithelial mechanics governed by capillary forces and adhesion, vertex models [4, 5] being the most prominent approach. In vertex models, cell-cell adhesion is boiled down to an effective negative contribution to the cellular surface tension on lateral faces in contact. However, topological changes including fracture in the cellular network are introduced as additional rules in the model [6]. Consequently, the role of adhesion in epithelial remodeling, especially when the tissue undergoes fracture and neighbor exchanges, is not entirely clear from a modeling point of view. We address this gap here by developing a theoretical and computational framework that explicitly captures the cell-cell adhesion using a contact mechanics-based formulation. We demonstrate the effectiveness of the approach in examining formation of confluent tissues and mechanical response to external loadings.

METHODS

Morphological examination of epithelia has revealed that epithelial monolayers produce polygonal packings in confluent tissues with

polyhedral cell shapes [7]. Taking advantage of this observation, similar to a vertex model, we represent each cell by a deformable contour on a 2D space signifying the apical or basal surface as shown in Figure 1. The polyhedral shape of the cells is implicitly captured by introducing the cell height, h , as a model parameter. This description is accurate for a confluent tissue without the significantly higher computational burden of a 3D model [8], while the cylindrical shape approximation is less accurate for sparse tissues.

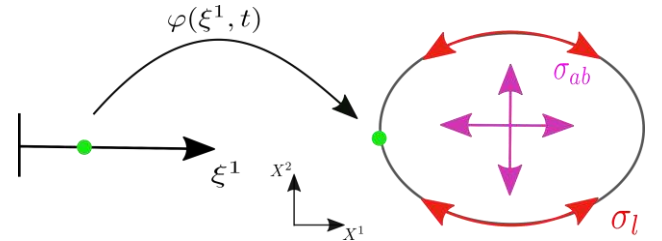


Figure 1: Kinematics of the deformable contour model of cell where φ maps points from 1D parametric domain to 2D physical domain of cell contour. Here, σ_{ab} and σ_l are the cortical tensions on the apicobasal and the lateral surfaces.

To formulate the model and obtain governing equations, we resort to Onsager's variational principle which provides a systematic approach to develop models for dissipative dynamics of soft biological materials involving coupled physical processes [9]. According to this variational framework, the dynamics of the system is governed by the balance of energetic and dissipative forces as well as the external forces. The forces are derived from potentials which account for all the relevant contributions from the underlying physics of the system. In this model, the power terms are due to apicobasal cortical tension, and cortical tension on the lateral surface of the cell. The energetic contributions include relatively weak bending stiffness of the cell contour to penalize

sharp corners by penalizing curvature. The adhesion between two cells is captured using the following form of the Morse potential

$$\varphi(g_n) = D \left\{ \left[1 - \exp\left(\frac{g_{min}-g_n}{l}\right) \right]^2 - 1 \right\}, \quad (1)$$

where g_n is the separation distance, D is the work of adhesion, g_{min} controls the minima location, and l controls the width. We follow the two-half pass algorithm [10] to capture cellular interactions. We include the dissipation from cortical viscosity and friction with surroundings.

The governing equations are obtained by extremizing the Lagrangian formed by all energetic, dissipative, and power terms with cell volume constraint. To discretize the extremized problem temporally, we use backward Euler method and to discretize it spatially, we use cubic B-spline finite elements. The key parameters of the model are cortical tension on apicobasal surface, σ_{ab} ; cortical tension on lateral surface, σ_l ; bending stiffness of cellular contour, k_b ; work of adhesion, D ; internal viscosity due to relaxation of actomyosin cortex, η_{int} ; external viscosity, η_{ext} .

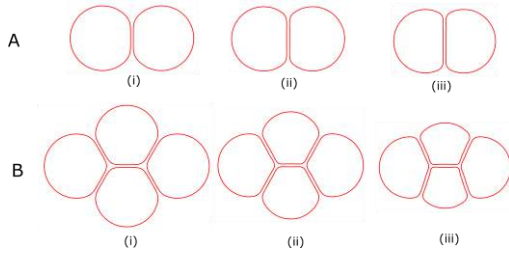


Figure 2: Variation of equilibrium shapes with work of adhesion. Equilibrium shapes of (A) cellular doublet and (B) quadruplet at (i) $D = 0.25$ (ii) $D = 0.5$ (iii) $D = 0.75$.

RESULTS

To test the implementation of adhesion algorithm, we examine the equilibrium shapes formed by a cell doublet and a quadruplet. In both cases, we initialize the simulation by placing 2 and 4 circular cells respectively close to each other, such that they are within the interaction range of the potential. The cells interact through adhesion until they reach the equilibrium states as shown in figure 2. The increase in contact area with increasing work of adhesion is correctly captured by the model in both cases. The normalized parameters used for all the following simulations informed by representative properties of epithelia are $\sigma_{ab} = 1.0$, $\sigma_l = 1.0$, $k_b = 0.01$, $D = 0.5$, $l = 10.0$, $g_{min} = 0.1$, $\eta_{int} = 0.4$, and $\eta_{ext} = 0.5$.

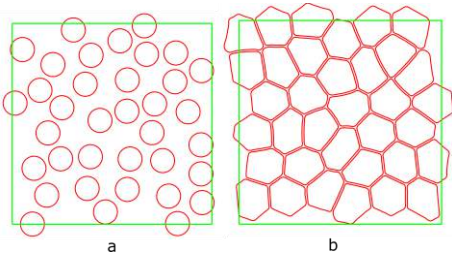


Figure 3: Generation of confluent tissue from disparate cells (a) initial configuration of randomly placed circular cells (b) confluent tissue generated from the initial configuration.

To generate a confluent tissue, we initially generate a distribution of cells with initial radius of 0.6 in a biperiodic box of size 10 using random sequential addition with mutual exclusion to avoid overlap (Figure 3A). The cells are then expanded to increase the apical area until confluency with area fraction close to 1. The adhesive interaction between cells naturally results in a polygonal packing (Figure 3B). The

process involves two steps. First, cells are allowed to increase in volume at a fixed cell height to reach confluency. The cell heights are then allowed to relax such that the configuration reach the steady state.

Finally, we investigate the response of the confluent tissue to different loading conditions imposed by changing the size of the biperiodic box. The loading is applied at a rate slower than other relaxation timescales of the model. For a tissue subjected to uniaxial stretching (Figure 4A), we observe that the cells are first stretched similar to the overall stretch imposed on the tissue. However, at sufficiently higher stretch ratios, the cell-cell adhesion is compromised to form fracture in the tissue (Figure 4A-iv). A qualitatively similar behavior is observed for a confluent tissue subjected to equibiaxial loading (Figure 4B). The biperiodic box boundary conditions play an important role to avoid any boundary effects in these representative element simulations.

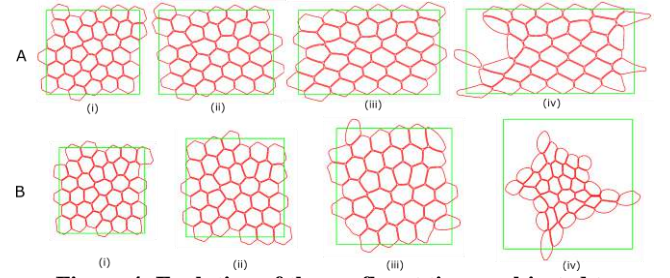


Figure 4: Evolution of the confluent tissue subjected to different loadings. (A) State of the tissue at the stretch ratio of (i) 0.108 (ii) 0.364 (iii) 0.678 (iv) 0.993 after a uniaxial stretch was applied at the rate of 0.033 in the horizontal direction. (B) States of the tissue at the stretch ratio of (i) 0.059 (ii) 0.215 (iii) 0.431 (iv) 0.603 after an equibiaxial stretch was applied at the rate of 0.033.

DISCUSSION

We have presented here a 2D deformable model where the cell contour acts as an active surface interacting with adjacent cells through adhesion potential. The contact formulation used to implement the cellular adhesion is shown to capture equilibrium configurations of multicellular assemblies. Importantly, the cellular rearrangements including fracture are naturally captured in the model without resorting to any rules for topological transitions. Thus, the modeling framework provides a promising way to examine the role of adhesion in epithelial remodeling events. Having demonstrated the capabilities of the model, we intend to investigate the role of the adhesion potential in governing cellular rearrangements and tissue fracture.

ACKNOWLEDGMENTS

We acknowledge the support from ICTAS, and the Mechanical Engineering department at Virginia Tech.

REFERENCES

- [1] Huh, D et al., *Science*, 328:1662–68, 2010.
- [2] Ebrahimkhani, M et al., *iScience*, 24:102505, 2021.
- [3] Khalilgharibi, N et al., *Nat. Phys.*, 15:839–47, 2019.
- [4] Fletcher, A et al., *Biophys. J.*, 106:2291–2304, 2014.
- [5] Alt, S et al., *Philos. Trans. R. Soc. Lond. B*, 372 (1720), 2017.
- [6] Sato, K et al., *Frontiers in Physics* 9, 2021.
- [7] Nagai, T et al., *Philos. Mag. B*, 81:699–719, 2001.
- [8] Arroyo, M et al., *CISM book series*, 577:287–332, 2017.
- [9] Torres-Sánchez, A et al., *PLoS Comput. Biol.*, 18:e1010762, 2022.
- [10] Sauer, R et al., *Comput. Meth. Appl. Mech. Eng.*, 53:369–95, 2013.

FORCE DIRECTION IS DIFFERENT FROM FIBER DIRECTION AT THE ANTERIOR CRUCIATE LIGAMENT ATTACHMENTS IN PORCINE KNEES

D. Ishii (1), S. Koseki (1), S. Sato (1), H. Fujie (1)

(1) Graduate School of System Design, Tokyo Metropolitan University, Minamiosawa, Hachioji, Tokyo

INTRODUCTION

The anterior cruciate ligament (ACL) has two types of insertions to the bone, namely direct and indirect insertions. The direct insertion is composed of fibrocartilage whose amount is greater at the femoral insertion than at the tibial insertion^[1]. It has been suggested that the difference in fibrocartilage amount was related to ACL force, although the details have not been clarified. For a better understanding of the mechanical function of the ACL insertions, it is crucial to analyze the ACL force on the insertions. Previous studies have also investigated the magnitude and direction of the ACL force during joint motion^[2-5], but the direction of force was determined with respect to the tibial plateau and sagittal plane^[3-5]. In this study, the direction of the ACL force was determined with respect to the attachment surface.

METHODS

Ten immature porcine knee joints were used; five for femoral and the remaining 5 for tibial analyses. A previous study reported that the porcine ACL has three bundles; the antero-medial (AM), intermediate (IM), and postero-lateral (PL) bundles^[6]. The AM bundle is located anterior to the tibial attachment of the lateral meniscus while the IM and PL bundles are located posterior to the attachment in the porcine knee. Therefore, in this study, we defined the fiber bundle consisting of the AM bundle as 'long fiber' and the fiber bundle consisting of the IM and PL bundle as 'short fiber' (Figure 1).

Each knee joint was fixed to the 6-DOF robotic system^[7] (FRS-2015, Technology Services) at full extension, 60°, and 90° of flexion. The ACL force in response to an anterior tibial load of 100 N was analyzed under the assumption of superposition, following a previously reported method developed by one of the co-authors^[2].

After the tests, the tibia for femoral analysis was disconnected from the clamp of the robotic system, and a metal rod having a sharp needle tip was fixed to the clamp. The needle tip was controlled to 3-dimensionally digitize 10 points randomly selected in the femoral

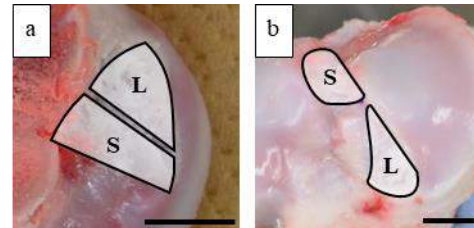


Figure 1: Femoral (a) and tibial (b) attachments of the long fiber (L), and short fiber (S) of the porcine ACL. Scale bar is 10 mm.

attachment areas of the long and short fibers, respectively. Principal component analysis was performed to determine the first, second, and third principal components from the 10 points' coordinate data for the attachment of each fiber. The planes of the long and short fiber attachments were obtained from the first and second principal components, while the directions of the attachments were determined from the third principal component under the assumption that the planes can be represented by 2D flat planes. In addition, the plane and direction of the entire femoral attachment were determined via principal component analysis from the total 20 coordinate data. The elevation was defined as the angle between the attachment direction and the sagittal plane of the femur, while the deviation was defined as the angle between the projection of the attachment direction onto the sagittal plane and the anterior direction of the femur, and both the angles were determined. Similar analysis to the femoral attachments were performed for the tibial attachments. The elevation angle between the attachment direction and the tibial transverse plane, the deviation angle between the projection of the attachment direction onto the transverse plane and the tibial anterior direction were determined.

Finally, the elevation angles of the ACL force between the ACL force direction and femoral and tibial attachment plane were determined.

In addition, the deviation angles of the ACL force between the projection of the ACL force direction onto the entire femoral and tibial attachment planes and a line perpendicular to the resident's ridge^[8,9] for the femoral side and a line found inside the ACL tibial attachment for tibial side (Figure 1) were determined. Statistical analysis was performed to analyze significant changes in the elevation and deviation angles of the ACL.

RESULTS

The attachment directions of the long and short fibers were completely different from fiber orientation, except for the tibial attachment of the short fiber (Figure 2). In those attachments, the attachment directions were tilted away from the ACL fiber direction.

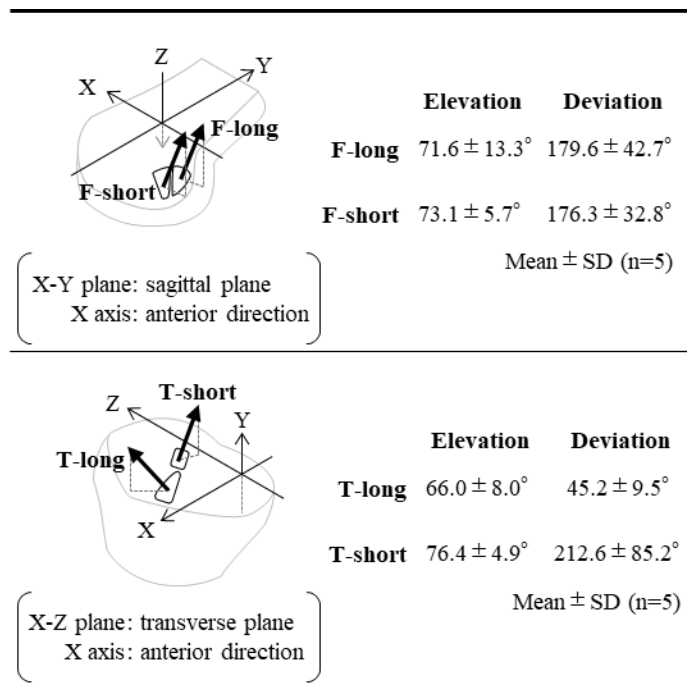


Figure 2: Elevation and deviation angles of the attachments of the long and short fibers of the ACL. The elevation angles are represented with respect to the femoral sagittal plane (x-y plane) and tibial transverse plane (x-z plane), while the deviation angles are represented with respect to the femoral and tibial anterior direction (x-axis).

The elevation angle of the ACL force was less than 10 degrees except for the tibial attachment of the short fiber (Figure 3). The elevation angles were significantly decreased with flexion on the tibial side ($p < 0.05$ in one-way ANOVA), while a contrast tendency was observed on the femoral side. Note that the elevation angle at the tibial attachment of the long fiber was negative at 90° of flexion.

The deviation angles of the ACL force were significantly increased with flexion on the femoral and tibial sides ($p < 0.05$ in one-way ANOVA). The angles varied more on the femoral side than on the tibial side.

DISCUSSION

Previous studies indicated that the elevation angle of the ACL force was approximately 40 degrees from the femoral sagittal plane and the tibial transverse plane^[3-5]. The present study clarified that the

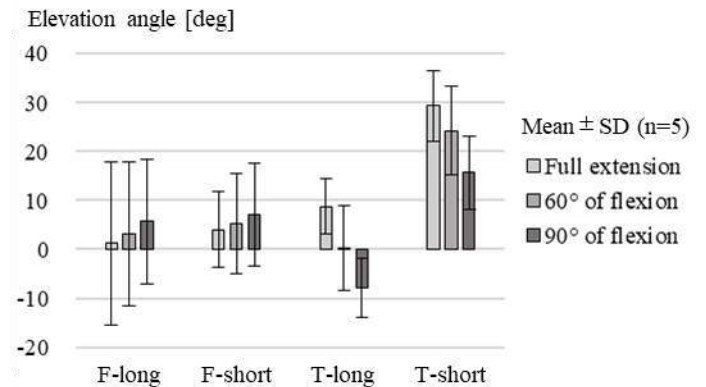


Figure 3: Elevation angle between the ACL force and the femoral and tibial attachment planes of the long fiber and the short fiber.

elevation angle of the ACL fibers from the attachment planes is less than 10 degrees and sometimes can be negative, except for the tibial attachment of the short fiber. Interestingly, the attachment directions were tilted away from the ACL fibers in those attachments. These results imply that the ACL force is transmitted to the femur and tibia not only through their attachments' area but also via bony-contacts of the fibers near the attachments as shown in Figure 4. We believed that this is the reason for the negative elevation angles observed in the present study. It is suggested that the bony-contacts of the ACL fibers play important roles in the structure generation and overall functions of the ACL insertions.

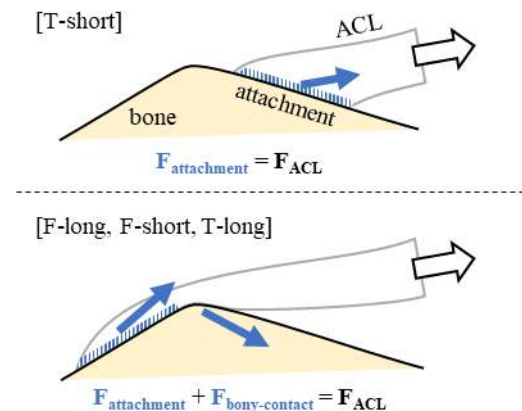


Figure 4: Schematic drawings of force application patterns in the ACL attachments. Direct transmission in the tibial attachment of the short fiber (upper) and indirect transmission in the other 3 attachments (lower).

REFERENCES

- [1] Beaulieu ML et al., *J Orthop Res*, 33(12): 1811-1817, 2015.
- [2] Fujie H, et al., *KSSTA*, 19(S1): S47-S53, 2011.
- [3] Fujie H, et al., *J. Biomech Eng*, 117(1): 1-7, 1995.
- [4] Livesay GA, et al., *Ann Biomed Eng*, 23: 467-474, 1995.
- [5] Li G, et al., *Acta Orthop*, 77(2): 267-274, 2006.
- [6] Tantisrichaenokul G, *KSSTA*, 22: 961-971, 2014.
- [7] Kimura K, Fujie H, *Transactions of the JSME*, 81(826): 1-12, 2015.
- [8] Hutchinson MR, et al., *Arthroscopy*, 19(9): 931-935, 2003.
- [9] Sasaki N, et al., *Arthroscopy*, 28(8): 1135-1146, 2012.

ESTABLISHMENT OF A VALIDATED FINITE ELEMENT FRAMEWORK TO PREDICT THE 3D, PATIENT-SPECIFIC ARTERIAL MECHANICAL ENVIRONMENT

Caleb C. Berggren (1), Y.F. Jack Wang (1), Lucas H. Timmins (1,2)

(1) Department of Biomedical Engineering, University of Utah, Salt Lake City, Utah, USA
(2) Scientific Computing and Imaging Institute, University of Utah, Salt Lake City, Utah, USA

INTRODUCTION

Acute coronary syndrome (ACS) events remain the highest cause of death worldwide [1]. These clinical events primarily originate from atherosclerotic plaque rupture, with recent clinical data indicating that ACS is preceded by rapid plaque progression [2]. As such, there is great clinical need to predict rapidly progressing coronary atherosclerosis. Recent imaging advancements (e.g., intravascular ultrasound; IVUS) allow for the identification of plaque characteristics [3], yet current methods for predicting coronary artery disease (CAD) progression and ACS events that rely solely on imaging are insufficient.

As the local biomechanical environment plays a central role in coronary atherosclerosis development and progression, coronary plaque mechanics may provide an alternative metric to improve clinical prediction of CAD progression and ACS events. Data from patient-specific models has shown increased mechanical stress in vulnerable plaques compared to stable and non-ruptured lesions [4,5]. Although insightful, these models possessed several assumptions that may impact their clinical utility and were not validated. To advance the prognostic abilities of coronary artery computational modeling, it is essential that robust, accurate, and validated modeling strategies are established. Such validation has proved challenging and, to date, has not been performed.

To advance the clinical utility of biomechanics for managing patients with advanced coronary disease, this study aimed to develop and validate an IVUS-based finite element (FE) model to evaluate the patient-specific solid mechanical environment.

METHODS

IVUS Image Acquisition A 6-9 month old porcine carotid artery sample (Animal Technologies, Tyler, TX) was cut to ~30 mm in length and mounted on a custom biaxial mechanical testing device. The device allowed interrogation of the artery with an IVUS catheter (Philips Core Mobile, Eagle Eye Platinum) without impacting tissue loading. Prior to image acquisition and tissue loading, the vessel was preconditioned in

the circumferential and axial directions over 10 cycles to a maximum pressure and axial stretch ratio of 180 mmHg and 1.8, respectively. An axial stretch ratio of 1.5 was applied, and the vessel was pressurized to 2 mmHg to prevent vessel collapse. IVUS images were acquired via a pullback in the central 15 mm of the vessel at approximately 0.5 mm increments (Fig. 1A). In the center of the imaging volume during the pullback (i.e., at 7.5 mm along the pullback), IVUS images were collected at static pressures of 20-120 mmHg in 20 mmHg increments. (Fig. 1A). Subsequently, the applied pressure was returned to 2 mmHg and the pullback and image acquisition was completed. Following the acquisition, image data were spatially co-registered with the aid of a fixed reference object not contacting the vessel but within the imaging frames.

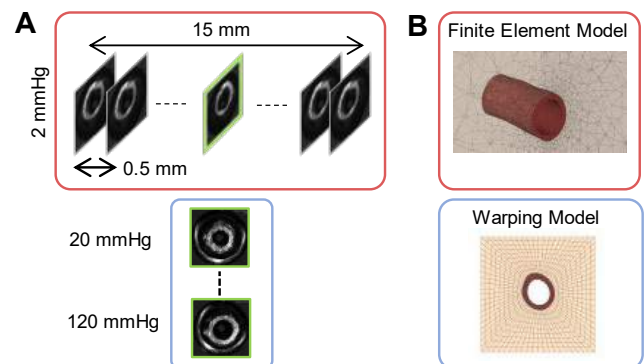


Figure 1: Image acquisition strategy (A) and model reconstructions (B) for finite element (red boxes, model shown with axial cut plane) and warping (blue boxes) models.

Experimentally-Derived Artery Strain Fields Hyperelastic Warping was employed to quantify tissue deformation from the acquired IVUS image data at lumen pressures of 2 (template image) and 120 (target image) mmHg [6]. The geometry was created from the IVUS-derived lumen and outer vessel boundaries extracted from the template image, and a perivascular (PV) tissue region was added for tethering (Fig. 1B). Domains were discretized with linear hexahedral elements. The artery was described as an incompressible neo-Hookean material (70 kPa shear modulus), and the perivascular tissue as a compressible, neo-Hookean material ($E = 50$, $\nu = 0.3$). Boundary conditions included an applied lumen pressure and fixing of the outer borders of the model (i.e., PV boundary) in all directions. Hyperelastic Warping was implemented via the warping module within the FEBio software suite [7] to determine the experimentally-derived strain field.

3D Forward FE Computational Model Lumen and outer vessel boundaries were extracted from all images acquired in the IVUS pullback at 2 mmHg (unloaded geometry). Surfaces were fit to the boundaries to define the artery model volume (Geomagic, 3D Systems). A block of PV tissue was added and encompassed the vessel (Fig. 1B). The artery and PV regions were meshed with linear tetrahedral elements (GibsonCode, TetGen), and were described by the same material properties as noted above. Applied boundary conditions included a lumen pressure of 120 mmHg, fixing the ends of the vessel and the PV outer surfaces in all directions. Data were post-processed to evaluate the FE-predicted strain field.

Data Analysis First principal Green-Lagrange strain (E_1) values were compared between the experimentally-derived (warping) and FE-predicted models. At 2 circumferential locations (0, 180°), strain data were extracted at 5 points through the thickness in the radial direction and absolute and percent differences were assessed.

RESULTS

First principal Green-Lagrange strains from both modalities demonstrated patterns characteristic of vascular tissues under loading, with higher principal strains at the lumen surface that decreased through the vessel wall. FE-predicted strains qualitatively agreed well with warping-predicted strains, as the locations of maximum and minimum strains occurred in similar spatial locations (Fig. 2A). Mean arterial strains were 0.29 ± 0.86 and 0.34 ± 0.73 for warping and FE models, respectively. Evaluating the data in more focal regions further confirmed the agreement between the FE-predicted and warping-derived strains. At 0° circumferential position, for example, FE-predicted strains decreased from 0.40 to .288 through the wall thickness, and the warping-derived strains decreased from 0.38 to 0.22. At the

180° circumferential position, transmural strain values for the FE-predicted and warping-derived ranged from 0.39 (inner) to 0.26 (outer) and 0.34 to 0.27, respectively (Fig. 2B).

DISCUSSION

Herein, we present a combined experimental-computational pipeline to validate FE predictions of the 3D coronary artery biomechanical environment under physiologic loading. Results demonstrate an agreement in the magnitude and location of maximum and minimum first principal Green-Lagrange strains between the FE-predicted and warping-derived methods. Moreover, agreement in transmural distributions of strain were observed between the two modalities. We acknowledge that the computational framework neglects several modeling considerations, such as the lack of pre-strain, only including 1 layer of the vessel, and isotropic material properties. Nevertheless, this study lays the foundation for future validation efforts that can incorporate a microstructurally-motivated strain energy functions for anisotropic materials. Indeed, FE model validation is critical to providing confidence in computational simulations and their integration into the clinical setting to guide patient management. These advances may enhance the prognostic capability for rapid plaque progression and ACS events.

ACKNOWLEDGEMENTS

This research was supported by the National Institutes of Health (R01 HL150608) and the American Heart Association (23PRE1019455).

REFERENCES

- [1] World Health Organization, "Disease Burden and Mortality Estimates", 2018.
- [2] Stone, GW et al., *New Engl J Medicine*, 364:226-235, 2011.
- [3] Yabushita, H et al., *Circulation*, 106:1640-1645, 2002.
- [4] Teng, Z et al, *Circulation Cardiovasc Imaging*, 7:461-470, 2014.
- [5] Brown, AJ et al., *Circulation Cardiovasc Imaging*, e004172, 2016.
- [6] Veress, A et al., *J Biomech Eng.*, 124:734-741
- [7] Maas, S et al., *J Biomech Eng*, 134(1):011005, 2012.

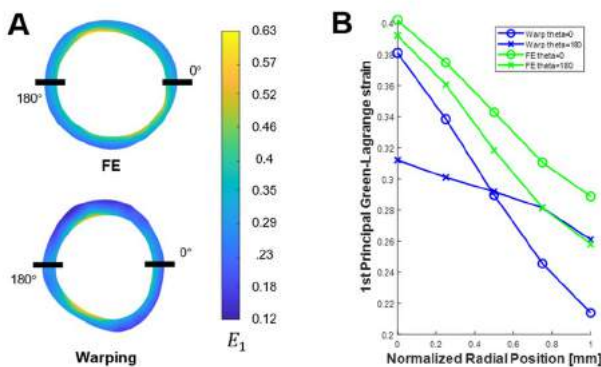


Figure 2: Warping- and FE- derived strain fields at 120 mmHg (A). Transmural strains at 0 and 180 degrees (B).

PLASTICITY AND AVALANCHE FAILURE IN COMPUTATIONAL MODELS OF PULMONARY COLLAGEN-ELASTIN FIBER NETWORKS

Jacob Herrmann (1), Yuqing Deng (2), Béla Suki (2)

- (1) Roy J. Carver Department of Biomedical Engineering, University of Iowa, Iowa City, Iowa, USA
(2) Department of Biomedical Engineering, Boston University, Boston, Massachusetts, USA

INTRODUCTION

The lungs must withstand dynamic stretch associated with breathing and deep inspirations, accommodating a wide range of gas volumes from 1.2 L residual volume to over 6.0 L total lung capacity (TLC) in humans. Failure to sustain stretch and rupture of lung parenchyma cause enlarged airspaces and reduced surface area of the blood-gas interface, leading to ventilation-perfusion mismatching, gas exchange deficiency, and difficulty in breathing. Mechanical failure of the lungs is associated with emphysema progression, pneumothorax, barotrauma in diving-related injuries, and overdistension in ventilator-induced lung injury.

The structural integrity and mechanical function of the lungs depend on the organization of extracellular matrix proteins elastin and collagen, which exist as fibers crosslinked into an elastic network. Elastin fibers are taut under normal prestressed conditions, yet highly distensible—like a spring. Collagen is up to 100- to 1000-fold stiffer than elastin, yet wavy or tortuous at low lung volumes—like a string. Together, collagen and elastin form string-spring pairs that exhibit low stiffness at low stretch ratios and high stiffness at high stretch ratios [1].

A network of string-spring pairs may provide the lung with elastic recoil at low lung volumes as well as strain-stiffening to protect against overdistension at high lung volumes. However, it is unknown how microscale collagen-elastin interactions and network dynamics determine the emergence of TLC and the ability of lung parenchyma to withstand enormous volume change without yielding and failure. Previously, we collected experimental data of tensile testing in individual collagen fibers isolated from bovine lung tissue. In this study, we simulated equitriaxial stretching of elastin-collagen networks imbued with mechanical properties from our experimental data. We hypothesized that (1) no elastin fibers would fail before collagen fibers, and (2) no collagen fibers would fail or plastically deform before total lung capacity.

METHODS

A 3-dimensional network geometry mimicking a cube of lung parenchyma was constructed as a tessellation of truncated octahedra, each loosely representing an alveolus. Each edge (42,748 total) of the structure was represented by a parallel elastin-collagen fiber pair, permanently crosslinked with other fibers at each node (22,069 total). The initial structure was considered the resting configuration of the network with no stress at the boundary faces or internal prestress. Accordingly, every elastin fiber was assigned a rest length equal to its initial length, and every collagen fiber was assigned a rest length greater than its initial length. Elastin fibers were assigned a linear force-extension relationship, with failure occurring at 200% extension. Collagen fibers were assigned polynomial force-extension relationships designed to recapitulate a gradual recruitment “toe-heel” response followed by linear elasticity. Collagen fiber rest lengths were sampled from a microscopy-based waviness distribution [2]. Collagen stiffness was sampled from a log-normal distribution between 100- to 1000-fold stiffer than elastin. Strain thresholds for collagen plasticity and failure were randomly sampled from normal distributions, and plasticity was modeled by successive increases in rest length.

Incremental equitriaxial stretch was applied to the network by controlled displacement of nodes at the boundaries on all 6 faces. After each incremental stretch, the equilibrium configuration of the internal nodes was computed by numerically minimizing the sum of net force magnitudes acting on each node. Plasticity modifications to collagen fiber rest lengths—for fibers exceeding their respective plastic thresholds—were applied before each incremental stretch. Fiber failures were evaluated iteratively before each incremental stretch, such that the next stretch increment was not applied until no further failure events were detected. Network stresses were computed as the sum of force components normal to the boundary surface divided by the boundary face area. Pressure was approximated by the average normal stress across all 6 faces.

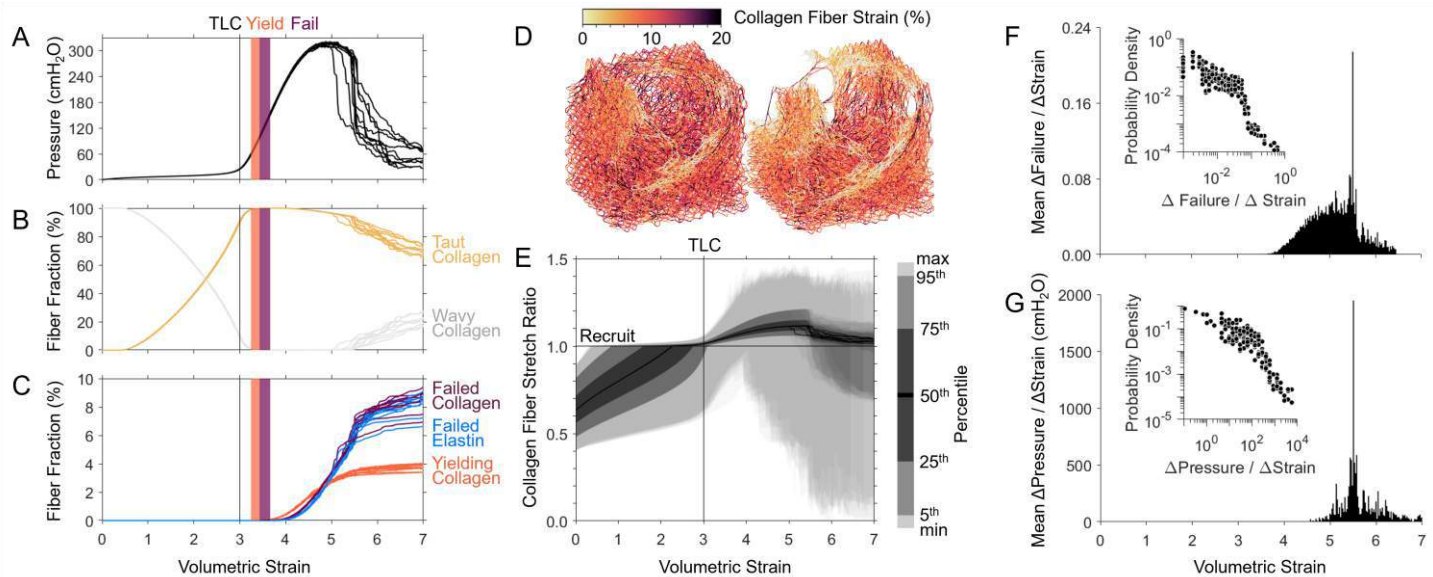


Figure 1: Summarized results from 10 collagen-elastin fiber networks during equitriaxial stretch. Shown at each incremental volumetric strain: (A) macroscale pressure, (B) fraction of collagen fibers recruited into a taut stress-bearing role from a wavy relaxed state, and (C) fraction of fibers plastic deformed or failed. Vertical bars indicate total lung capacity (black), onset of collagen yielding (orange), and onset of collagen failure (purple). (D) Example network during progressive rupture at volumetric strains 5.8 (left) and 6.2 (right). (E) Distributions of collagen fiber stretch ratios at each strain increment. (F) Average incremental fiber failure and (G) pressure drop at each strain increment, and (insets) probability density distributions on bilogarithmic scales.

RESULTS

Figure 1 shows macroscale stresses and microscale fiber status during simulated equitriaxial stretching of 10 collagen-elastin fiber networks. All simulations demonstrated an initial phase of fiber alignment, elastin extension, and gradual collagen recruitment. Collagen fiber recruitment initiated at 0.36 ± 0.04 volumetric strain. A strain of 3.00 was considered to represent TLC at 91.0 ± 0.5 % collagen recruitment and 26 ± 1 cmH₂O pressure. TLC was preceded by a strain-stiffening transition at 2.80 strain and 77.5 ± 0.4 % collagen fiber recruitment. Collagen fiber plasticity initiated at 3.33 ± 0.07 volumetric strain with 99.5 ± 0.3 % collagen recruitment and 78 ± 13 cmH₂O pressure. The onset of collagen yielding was followed shortly by the onset of fiber failure at 3.56 ± 0.08 strain, 99.9 ± 0.1 % collagen recruitment, and 129 ± 18 cmH₂O pressure.

In general, elastin fiber failure lagged collagen fiber failure (Fig. 1C). The first elastin failure occurred 5.8 ± 4.5 iterations after the first collagen failure, corresponding to an additional 3.8 ± 3.0 % increase in volumetric strain and 32 ± 25 cmH₂O (27 ± 23 %) increase in pressure. Despite a relatively gradual accumulation of fiber failure, tissue failure occurred by avalanches in nearly all simulations (Fig. 1A), with a sudden decrease in stress (Fig. 1G) accompanying a cascade of fiber failures (Fig. 1F) initiated at one location or in close proximity and propagating across the network (Fig. 1D). When collagen fiber properties for stiffness, plasticity, and failure were homogenous, failure events were more uniformly distributed throughout the tissue and failure was graceful rather than catastrophic (data not shown).

DISCUSSION

The string-spring model of collagen-elastin interactions in the lung implies that the functional role of collagen is primarily protection against overstretch of delicate parenchymal structures [1]. In this study, inflation of lung parenchyma was simulated by equitriaxial stretching of an idealized collagen-elastin fiber network representing a small alveolar region. The model's TLC emerged at 3.0 volumetric strain with

strain-stiffening and nearly 90% collagen fiber recruitment. Compared to humans with 6-L TLC and 2-L functional residual capacity (FRC), the networks' initial zero-strain state might plausibly approximate FRC, albeit neglecting prestress. The onset of fiber damage and failure in the network occurred at pressures similar to those reported as thresholds for barotrauma and development of emphysema [3],[4].

Collagen fibers recruited throughout inflation to TLC (Fig. 1B) limit the stretch imposed on each string-spring pair as the bulk tissue inflates beyond the range of quiescent breathing. Once the collagen fiber in a string-spring pair becomes recruited, additional inflation of the bulk tissue results in almost no additional stretch of the pair until the vast majority of collagen fibers have been recruited (Fig. 1E). No collagen began yielding before over 99% of fibers were recruited, and only after collagen failure initiated did elastin fibers begin to fail. The probability density of incremental fiber failures and pressure drops exhibited approximately power-law distributions (Fig. 1F), similar to avalanches in airway recruitment [5] and arterial dissection [6].

In conclusion, computational modeling of collagen-elastin fiber networks supports the primarily protective role of wavy collagen as a "safety net" for lung parenchyma, and furthermore highlights power-law behavior during failure. Collagen plasticity may confer additional longevity—without plasticity, the networks are more likely to fail catastrophically, and at lower strains.

ACKNOWLEDGEMENTS

Supported by NIH U01 HL139466 and the Carver Charitable Trust.

REFERENCES

- [1] GN Maksym, JHT Bates. *J Appl Physiol* 82(1):32-41, 1997.
- [2] S Bou Jawde et al. *J R Soc Interface* 18(183):20210594, 2021.
- [3] HP Nennhaus et al. *Arch Surg* 94(1):136-141, 1967.
- [4] MS Malhotra, HC Wright. *J Pathol Bacteriol* 82:198-202, 1961.
- [5] B Suki et al. *Nature* 368(6472):615-618, 1994.
- [6] X Yu et al. *Sci Adv* 6(21):eaaz1173, 2020.

CHARACTERIZING THE BIAXIAL MECHANICAL PROPERTIES OF SKELETAL MUSCLES OF THE MOUSE HINDLIMB

Katherine R. Knaus (1), Rebecca Hardie (1), Jessica Huberts (1), Daniela Valdez-Jasso (1)

(1) Department of Bioengineering, University of California San Diego, La Jolla, CA, USA

INTRODUCTION

Exercise prescription to increase muscle strength and function boosts mobility linked to positive health outcomes but is currently limited by the gap in knowledge of underlying biological mechanisms. This includes how skeletal muscle tissue state [1] – muscle mechanical, metabolic, and plastic capacity – mediates transduction of external exercise stimuli to the biological regulators of strength and remodeling. Muscle tissue state exhibits disparate changes during remodeling, but the contributions of underlying structural and mechanical heterogeneity to the gradients of tissue state changes are not well understood.

Multiscale structural organization of muscle's mechanical constituents is an important determinant of tissue state. Mechanical performance depends on both macro scale properties, including fascicle architecture and tendon morphology [2], and microscale properties, including fiber size and extracellular matrix composition [3]. Muscles exhibit nonuniform tissue displacements that can arise from morphological and material heterogeneity, demonstrated by computational modeling [4], suggesting that structurally determined muscle mechanical behavior could dictate the cell-level mechanical cues arising from a prescribed exercise. Understanding how changes in tissue state will affect the physiologic response to a given exercise requires an understanding of how both muscle morphology and material properties dictate the driving mechanical stimuli.

Mice have long been used as an experimental model to elucidate biological mechanisms, as the capability of genetic manipulation makes them ideal for study of gain or loss of function *in vivo*. Recent advances in experiment models of murine exercise have introduced possibilities to study muscle remodeling response to loading [5]. Computational modeling has the exciting potential to derive mechanistic insight from these murine models by exploring how differences in muscle tissue state give rise to variable mechanical cues. Such an approach would require characterizing both the structure and material properties of mouse hindlimb muscles engaged by the exercise paradigm.

Studies characterizing skeletal muscle mechanical properties are span many species, muscles, and scales [6] and of these, studies of murine muscle do not characterize tissue properties independent of whole muscle structure. Biaxial characterization of porcine muscle has been demonstrated to effectively characterize skeletal muscle stiffness [7], with potential to consider contribution of constituents that would reflect anisotropic changes in tissue state. Similarly characterizing mouse hindlimb muscle is difficult due to the animal size, but important in understanding the influence of variable tissue state characteristics when using murine models of exercise. Therefore, the goal of this work is to develop a method to characterize the anisotropic properties of murine hindlimb skeletal muscles

METHODS

All experiments were performed with the approval of the Animal Care and Use Committee at the University of California San Diego. Two six-month-old female C57BL/6 mice were anesthetized until cessation of breathing followed by cervical dislocation to ensure death. Immediately post-mortem the right and left biceps femoris posterior (BFP) muscle was harvested (Fig. 1A). This hamstring muscle was chosen as its superficial location allowed it to be isolated from other muscles of the hindlimb without damaging the tissue and its wide shape enabled a square sample of continuous muscle tissue to be excised. In the excised samples, muscle fibers were oriented in the longitudinal direction (length = 7.50 ± 0.76 mm). The axis in this direction was called the along-fiber axis while the perpendicular axis oriented in the transverse direction (width = 7.70 ± 0.58 mm) and called the cross-fiber axis. To robustly measure thickness, five measurements were taken within the center region of the sample using calipers (thickness = 1.78 ± 0.06 mm). Muscle samples were stored in a solution of 30mM butanedione monoxime (BDM) in phosphate-buffered saline (PBS) for approximately 60 minutes. Samples were removed from solution and five graphite markers were glued on the surface. Four custom-made

hooks were placed on each side of the sample (Fig. 1B) and mounted in the pulley system (Fig. 1C) of a Bose Electro Force planar biaxial testing device (TA Instruments, New Castle, DE). While kept in a temperature-controlled bath of PBS; markers on the surface of the sample were brought into the visual field of the optical tracking system for computing the deformation gradient tensor. The samples were preloaded equally to 2.5 g to align them with the suture and pulley-system and thus secure a two-dimensional mechanical test. The mechanical testing consisted of 10% stretch-controlled biaxial tests at 0.5 Hz with biaxial ratios of $x_1:x_2 = 1:0.5, 1:0.25, 1:1, 0.5:1, \text{ and } 0.25:1$, all recorded after 15 cycles of preconditioning each [8].

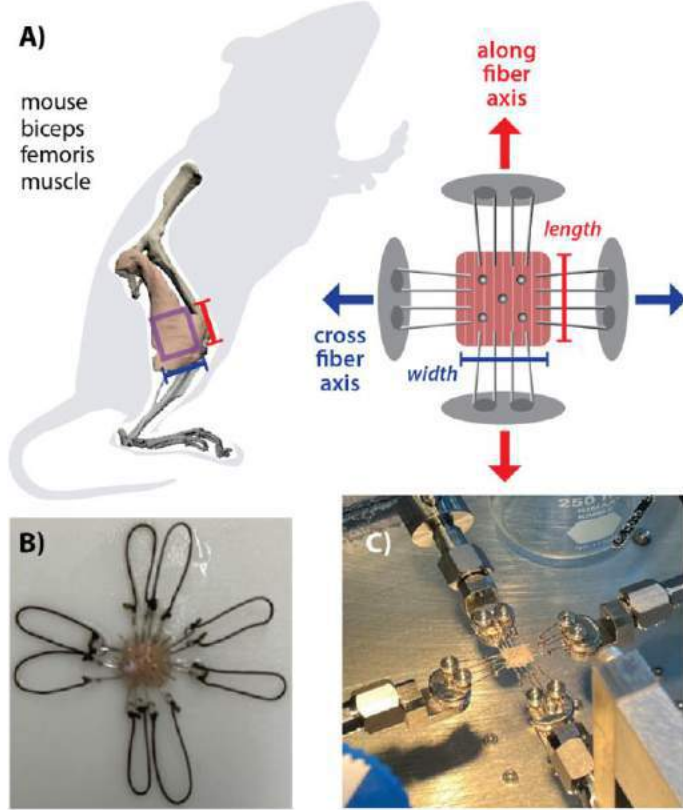


Figure 1: Biaxial testing setup for mouse hindlimb muscle tissue.

Biaxial loads and pixel coordinates of the outer four material markers on the surface of the sample were used to compute stress and strain components with respect to the along and cross fiber axes to characterize the mechanical properties of the mouse BFP muscle. Forces were normalized by the cross-sectional area of the samples to compute the first Piola-Kirchhoff (PK) stress tensor. The reference configuration was the preloaded state of the samples at 2.5g, post-preconditioning, prior to the equibiaxial cycles. From the marker positions, the outer four markers were used to compute the deformation gradient tensor throughout the biaxial test by interpolating displacement gradients relative to the tare-loaded reference state at the center of a bilinear Lagrange finite element. The last three cycles of each biaxial loading protocol were averaged to compute the representative loading and unloading curves (Fig. 2A).

Only the loading curves were used for the constitutive analysis. The Green strain tensor and the 2nd PK stress tensor were calculated using the deformation tensor and 1st PK stress tensor. Shear components were assumed to be negligible, so differentiating a strain-energy function with respect to the Lagrangian-Green strain yielded the 2nd PK

stress in the principal axes. The strain-energy function chosen was a 2D Fung-type constitutive equation [8]:

$$W(E_{11}, E_{22}) = c(e^{a_1 E_{11}^2 + a_2 E_{22}^2 + a_3 E_{11} E_{22}} - 1) \quad (1)$$

The four model parameters θ for each specimen were obtained via the least-squares method through the loading cycles (Fig. 2B). The goodness of fit for each specimen was determined from the coefficient of determination.

RESULTS

Mouse hindlimb muscle tissue exhibited anisotropic mechanical properties when subjected to biaxial loading conditions. Although peak stresses differed between the biceps femoris muscles tested, all samples exhibited greater stiffness in the along fiber direction than in the cross fiber direction (Fig. 2A). The 2D Fung model provided a reasonable fit to the experimental data (Fig. 2B) with R^2 values ranging 0.83-0.97.

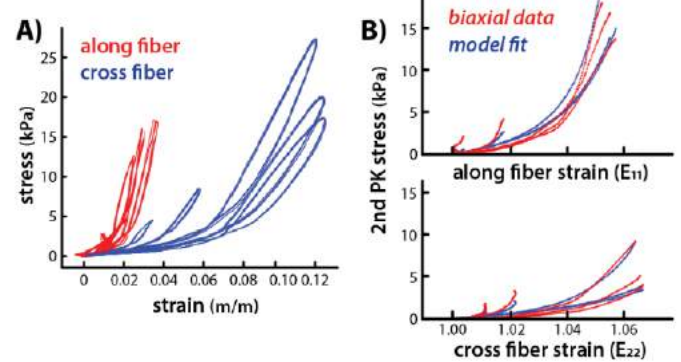


Figure 2: Representative biaxial loading curves and model fitting

DISCUSSION

These findings demonstrate an effective approach for using biaxial testing to characterize the anisotropic mechanical properties of a mouse hindlimb skeletal muscle. The greater stiffness along the fiber direction compared to across the fibers observed here is similar to what has been shown previously with biaxial testing of pig hindlimb muscles [7] and uniaxial testing of rabbit hindlimb muscles [9]. This method is currently limited to mouse hindlimb muscles from which a rectangular sample of continuous muscle tissue with a minimum length and width of 5mm can be excised. This method provides a means to characterize how muscle mechanical properties vary as a function of tissue state determined by intrinsic factors, such as sex and age, and extrinsic factors, such as exercise and diet. Such measurements will provide necessary contextual data to murine exercise models to understand the transduction of mechanical cues driving remodeling responses and will provide important inputs to computational models of mouse muscle contraction.

ACKNOWLEDGEMENTS

This work is supported by the Wu Tsai Human Performance Alliance and the Joe and Clara Tsai Foundation.

REFERENCES

- [1] Lawrence, R, et al., *Physical Therapy*, 101, 2021.
- [2] Zajac, F, *Cri Rev Biomed Eng*, 17(4):359-411, 1989
- [3] Lieber, L, et al., *J Physiology*, 599(16):3809-23, 2021
- [4] Knaus, K, et al., *J Biomech*, 130:110877, 2022
- [5] Murach, K, et al. *J Appl Physiol*, 129(3):516-21, 2020
- [6] Binder-Markey, B et al., *J Biomech*, 129:110839, 2021
- [7] Wheatley, B, *Frontiers Physiol*, 11, 2021
- [8] Vélez-Rendón, D, et al., *J Biomech Eng*, 141(9):091011, 2019
- [9] Morrow, D, et al, *J Mech Behav Biomed Mat*, 3(1):124-29, 2010

INVESTIGATING THE FREQUENCY-DEPENDENT SKULL-BRAIN MOTION TRANSMISSIBILITY THROUGH MR ELASTOGRAPHY

F. Rezayaraghi (1), E. Triolo (2), C. Neher (1), M. Kurt (1,2)

(1) Department of Mechanical Engineering, University of Washington, Seattle, WA, USA

(2) The Biomedical Engineering and Imaging Institute, Icahn School of Medicine at Mount Sinai, New York City, NY, USA

INTRODUCTION

Traumatic brain injury (TBI) is a leading cause of death and disability¹, but the mechanisms involved in its pathology remain unclear. It is currently not completely understood how motion is transferred from the skull to the brain, and there are many different models proposed for this mechanism². Quantifying the relative motion at the skull-brain interface will improve computational TBI models used by researchers and inform the design of protective equipment. One in-vivo measurement technique of relative skull-brain displacement is Magnetic Resonance Elastography (MRE)³, which is a non-invasive imaging technique. Standardization and development of better MRE actuators and methods of motion detection in the brain during MRE is important to maintain an acceptable octahedral shear strain-based signal-to-noise ratio (OSS-SNR)⁴, which is highly dependent on vibrational amplitude. Additionally, it has been shown that quantitative values of MRE, i.e., the magnitude of the complex shear modulus estimate ($|G^*|$), are sensitive to changes in OSS-SNR⁵, so MRE without acceptable vibration can present a challenge of both image quality, and elastogram accuracy. Previous work has simultaneously measured brain and skull motion using MRE⁶, and used an array of accelerometers embedded in a mouthguard to measure skull kinematics⁷. In this work, we aim to develop a measurement system that can accurately measure skull motion under MRI, and use it to understand the transmissibility of motion from the skull to the brain during MRE across a range of frequencies.

METHODS

Sequence and Processing Description: Whole brain coverage MRE⁸ at 2.5mm³ isotropic resolution with 16 phase offsets was performed at three frequencies on one healthy human subject using a Siemens 3T Prisma MRI scanner with a 48-channel head coil (Siemens Healthineers), and a custom pneumatic actuator. In order to capture wavefield images such that we can obtain a higher frequency response

resolution later down the post-processing pipeline, three custom MRE sequences were developed and utilized. The first used an effective encoding frequency of 40Hz (2 abutting 20Hz encoding gradients, TR=8013 ms, TE=113 ms, GRAPPA=3), and the second, an effective encoding frequency of 50Hz (2 abutting 25Hz encoding gradients, TR=6400 ms, TE=93 ms, GRAPPA=3). Settings were adjusted on the MRE hardware between each scan to not only apply the correct frequency, but also to adjust for decreases in vibration amplitude that occurs at higher applied frequencies. For processing, the difference was taken between the two phase images captured with opposite encoding directions, unwrapped using SEGUE⁹ and manual phase unwrapping, before being multiplied by the MENC value to obtain displacement in microns. We then performed a 16 point FFT on the displacement data to obtain the brain's frequency response with resolution half that of the effective encoding frequency. Using Freesurfer 7.0, a T1 structural scan of the subject was segmented into the whole brain, cerebellum, and corpus callosum (CC). Average frequency response was then calculated for each of these regions.

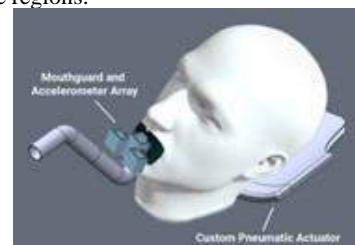


Figure 1.Figure 1. Visualization of experimental setup; custom MRE actuator pillow, mouthguard, and accelerometer array

Mouthguard and BIOPAC Accelerometers: To estimate skull kinematics, three MRI-safe, tri-axial accelerometers (TSD109C2-MRI, BIOPAC, Goleta, CA) were embedded in a 3D-printed mouthguard

array and attached to a boil-and-bite mouthguard that was fitted to the subject (Fig. 1). Accelerometers were offset in 3D to enable the calculation of rotational velocity from three sets of tri-axial linear acceleration data.

Calculation of the skull's motion parameters: Linear acceleration of the skull was recorded using the accelerometers. Rotational kinematic components of the skull and the linear kinematics of the center of gravity (CoG) of the head were unknowns that were calculated in the following analysis. We assumed the skull to be a rigid body which let us use equations (1-3) for each accelerometer^{7,10}.

Considering the position of the accelerometers with respect to the head and the predefined coordinate system, x, y, and z components represent the left-right (LR), superior-inferior (SI), and posterior-anterior (PA) directions, respectively. In these equations, three components of the linear acceleration of the CoG of the head (a_x^{CG} , a_y^{CG} , a_z^{CG}), angular velocities (ω_x , ω_y , ω_z) and angular accelerations (α_x , α_y , α_z) produced 9 unknowns. By solving equations 1-3 for each accelerometer, in which r_x , r_y , and r_z are the distance vector components from accelerometers to the CoG of the head, we found the unknowns at each timepoint.

$$a_x^{MG} = a_x^{CG} + (\alpha_y r_z - \alpha_z r_y) + (\omega_x(\omega_y r_y + \omega_z r_z) - r_x(\omega_y^2 + \omega_z^2)) \quad (1)$$

$$a_y^{MG} = a_y^{CG} + (\alpha_z r_x - \alpha_x r_z) + (\omega_y(\omega_z r_z + \omega_x r_x) - r_y(\omega_x^2 + \omega_z^2)) \quad (2)$$

$$a_z^{MG} = a_z^{CG} + (\alpha_x r_y - \alpha_y r_x) + (\omega_x(\omega_x r_x + \omega_y r_y) - r_z(\omega_x^2 + \omega_y^2)) \quad (3)$$

These linear accelerations and angular velocities are harmonic signals and can be written in the frequency domain using Fourier transformation. We calculated the FFT amplitudes of the angular velocity and linear acceleration at the CoG of the skull. FFT amplitudes of the displacement of the whole brain and its substructures were extracted from MRE images. To calculate the normalized transformation matrix of the angular velocity and linear acceleration for the brain, CC, and cerebellum, we divided the FFT amplitudes of the brain region displacement to the FFT amplitudes of the angular velocity and linear acceleration at the CoG in the dominant motion direction, and then normalized them. To elaborate more, during the MRE scan, the head was vibrated in the AP direction. Although there was vibration and consequently linear and rotational acceleration in other directions, the dominant linear acceleration was in the AP direction and the dominant rotational velocity was around the LR axis. We did these analyses for three different time ranges and to calculate the final normalized transformation matrix.

RESULTS

From the displacement in the brain calculated using MRE, the whole brain moves on average between 20-40 microns in AP direction

as shown in Fig.2. with the corresponding displacements shown in the frequency domain. In both transfer functions, in all regions, the first harmonic occurs at the frequency of 40 Hz and 75 Hz for encoding frequencies of 40 and 50 Hz, respectively (Fig.2). In the MRE vibration frequency of 40 Hz, a second harmonic is observed at the frequency of 80 Hz for the brain and the two other substructures.

DISCUSSION

In this study, we examined the relationship between the motion of the brain (which was estimated from MRE images) and the kinematics of the skull (through accelerometer-derived linear kinematics of the head). This relationship can give us further insights into the brain-skull dynamics. The displacement of the brain is almost the same for both vibration frequencies with a slightly higher value at 50 Hz. Considering the normalized transformation matrices, we observe a higher bandwidth for the vibration frequency of 50 Hz. This might be due to a better penetration of 50 Hz to the brain, which could be creating super harmonic motion at higher amplitudes compared to 40 Hz due to nonlinear effects. In the vibration frequency of 40 Hz, we observed a second harmonic with a relatively lower amplitude. In this encoding frequency, CC has the lowest amplitude in the rotational velocity normalized transformation matrix which might be correlated with its location in the brain. MRE waves attenuate as they move toward the deep regions of the brain, such as CC, which might cause less motion in these regions. Repeating these experiments for more encoding frequencies and analyzing the results for more regions of the brain, can improve our understanding about the broadband transmissibility between the skull and the brain, which could lead to a better understanding of TBI biomechanics.

ACKNOWLEDGEMENTS

We acknowledge funding support from NSF CMMI 1953323 and NSF CMMI 2145512

REFERENCES

- [1] Hyder, A et al., *NeuroRehabilitation*, 22(5), 341–353, 2007.
- [2] Zhou, Z et al., *Biomechanics and modeling in mechanobiology*, 18(1), 155–173, 2019.
- [3] Yin, Z et al., *Magn Reson Med*, 80: 2573– 2585, 2018.
- [4] McGarry, et al., *Phys Med Biol*, 201.
- [5] Murphy, et al., *PLoS One*, 2013.
- [6] Diano, A et al., 2022.
- [7] Badachhape, A et al., *Journal of Biomechanics*, Volume 73, Pages 40-49, 2018.
- [8] Johnson, C. L. et al., *Magn Reson Med*, 70: 404–412, 2013.
- [9] Karsa & Shmueli, *IEEE Trans Med Imaging*, 2019.
- [10] Camarillo, D et al., *Annals of biomedical engineering*, 41(9), 1939-1949, 2013.

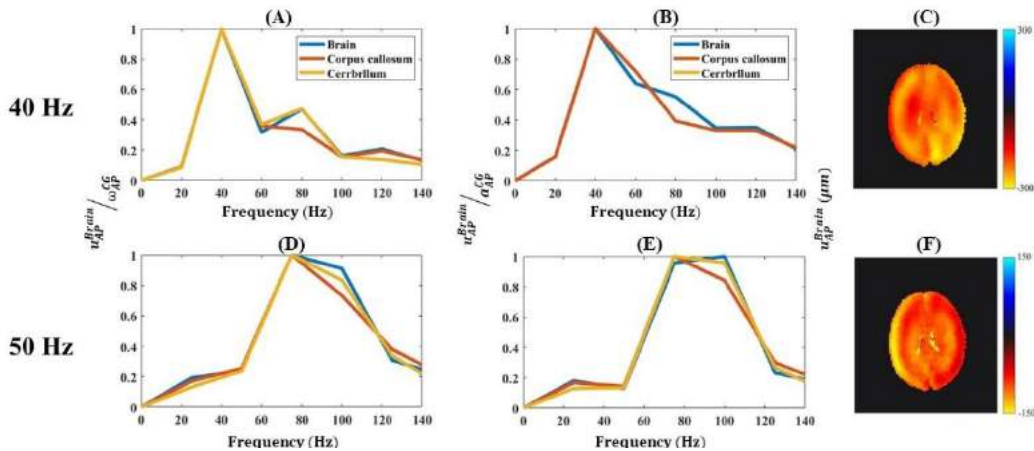


Figure 2. Figure 2. Normalized skull-brain motion transmissibility for 40 Hz (A-C) and 50 Hz (D-F). The transfer functions between the brain displacement and the skull rotational velocity (A, D), skull linear acceleration (B, E) are depicted for the dominant motion.

INVESTIGATING THE ROLE OF ECCENTRIC INLET CONDITIONS ON HEMODYNAMIC RESULTS AT DIFFERENT STAGES OF ANEURYSM GROWTH

Federica Galbiati (1,2), Emanuele Vignali (3), Katia Capellini (3), Claire Morin (2), Stéphane Avril (2), Emiliano Costa (1), Simona Celi (3)

(1) RINA Consulting SpA, Viale Cesare Pavese 305, 00144 Rome, Italy
(2) Mines Saint Etienne, INSERM, SAINBIOSE U1059, F-42023, Saint-Étienne, France
(3) BioCardioLab, UOC Bioingegneria, Fondazione Toscana Gabriele Monasterio, Massa, Italy

INTRODUCTION

Ascending thoracic aortic aneurysm (aTAA) is a life-threatening condition whose etiology is still unknown, but the link between altered aortic hemodynamics and aTAA development is widely recognized. In particular, alterations induced by the presence of a bicuspid aortic valve (BAV) with consequent eccentricity of aortic inlet flow seems to play a role in the highest prevalence of aTAA cases in these patients, compared to subjects with a tricuspid aortic valve (TAV) [1]. In the state of the art, different groups have focused on the analysis of TAV and BAV influence on aortic hemodynamics by using patient specific geometries and inlet conditions [1,2]. However, perspective studies that investigate the evolution of hemodynamics patterns in presence of TAV or BAV phenotypes concurrently with aTAA progression are still limited.

Therefore, the main goal of this study is to investigate the role of inlet conditions eccentricity in the hemodynamics results at different stages of aTAA, accounting different configurations of TAV and BAV.

METHODS

The model representing different stages of a growing aneurysm in a virtual patient is built upon statistical shape analysis and Radial Basis Function morphing technique and has already been used in previous studies [3]. In this preliminary study, we consider two different geometries representing a baseline healthy aorta (A_{00}) and one stage of aTAA growth (A_{05}) (**Figure 1**). In particular, the baseline and the final stage of aTAA growth geometries are obtained by segmenting clinical CT datasets. The segmentation is performed by using the 3DSlicer software.

Transient computational fluid dynamics simulations are performed using Ansys Fluent (Ansys Inc.) pressure-based solver with 2-nd order schemes. The fluid domain is discretized with approximately 700 000 polyhedral elements. Blood is modeled as incompressible and Newtonian, with $\rho = 1060 \text{ kg/m}^3$ and $\mu = 0.00345 \text{ Pa}\cdot\text{s}$. The k- ω SST model is employed to account for turbulence.

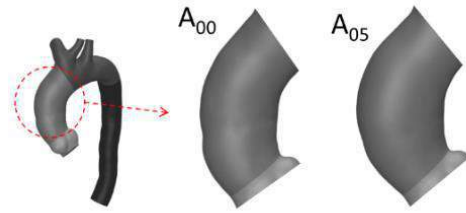


Figure 1: Aorta segmentation with baseline and intermediate aTAA growth stage

PISO algorithm is used for pressure-velocity coupling and convergence is assured at every time step by reducing normalized residual of continuity, k and ω by 10^{-4} and of velocity by 10^{-6} . Outflow pressure boundary conditions are defined applying a 3-elements Windkessel model at each outlet, tuned to have a systolic-diastolic pressure of (120-80) mmHg. Windkessel parameters are computed so as to depend only on systolic-diastolic pressure and outlets dimensions. Since these values are equal for all the geometries, the same Windkessel parameters are imposed at each simulation [4,5]. In order to prescribe a time-space variant inlet velocity boundary, allowing to reproduce TAV or BAV aortic inlet condition, a specific user-defined function is implemented by considering the physiological data of Cao *et al.* [6]. In particular, an elliptic area is identified on the aortic valve plane, resembling the valve orifice. A paraboloid velocity profile is imposed inside the ellipse, while everywhere else velocity is set equal 0 as follows:

$$v_{in}(t, x, y) = \begin{cases} \frac{2 Q(t)}{\pi a_x a_y} \left(1 - \frac{x^2}{a_x^2} - \frac{y^2}{a_y^2}\right) & \text{if } \left(\frac{x^2}{a_x^2} + \frac{y^2}{a_y^2}\right) \leq 1 \\ 0 & \text{elsewhere} \end{cases} \quad (1)$$

where a_x , a_y are the ellipse semi-axis and x , y are the coordinates in a reference system centered in the center of the ellipse and aligned with its axis. $Q(t)$ is a prescribed volumetric flow rate waveform that resembles a physiological flow over a cardiac cycle (**Figure 1a**). All the simulations run for 7 cycles to achieve periodic fully developed solutions. For the result analysis, only data from the last cycle are considered.

Two different cases for the inlet conditions are here considered: a centered inlet condition ($a_x = 10.75$ mm, $a_y = 8$ mm) that describes a TAV patient and one type of eccentricity ($a_x = 6.7$ mm, $a_y = 5$ mm), reproducing a BAV patient. The corresponding inlet velocity profiles at peak systole are shown in **Figure 1b**. Either TAV or BAV inlet conditions are applied at each stage of aneurysm growth to evaluate hemodynamics evolution.

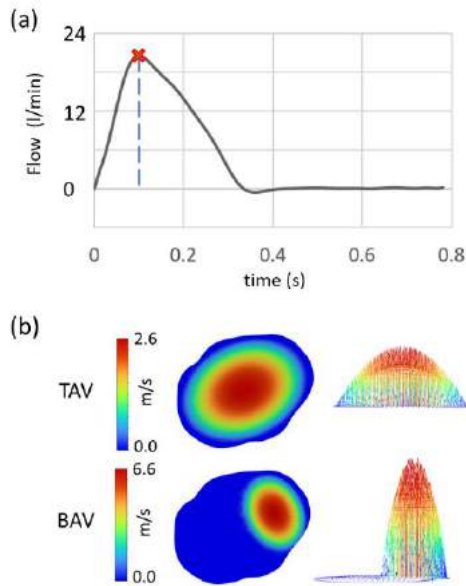


Figure 2: Flow rate profile used in the definition of inlet velocity (a), with highlighted the peak systole instant, with TAV and BAV inlet velocity profiles at peak (b).

RESULTS

Figure 3 shows an example of how the eccentricity of inlet flow and the presence of a bulge due to a growing aneurysm may affect the hemodynamics in the aorta. Observing velocity streamlines at peak systole we can see how the growing aneurysm has a negligible impact on the flow pattern, as A_{00} (**Figure 3a,b**) and A_{05} (**Figure 3c,d**) are compared. On the other hand, the inlet flow eccentricity has a huge impact on both velocity magnitude and flow recirculation. This is consistent with the fact that, having the same flow rate, the maximum velocity at the inlet in the BAV case is 2.5 times higher with respect to the TAV case due to the lower orifice area (**Figure 2b**). When dealing with cardiovascular pathologies, one of the main variables of interest are the Wall Shear Stress (WSS). **Figure 3e-h** shows the effects of eccentricity on the values of WSS in the ascending aorta at peak systole. As an estimation of the effects of eccentricity on WSS, **Table 1** reports the time averaged value of the area-weighted average WSS for the ascending aorta, where the aTAA bulge is observed. Consistently with the velocity increase, average WSS are ~2.5 times higher in presence of eccentricity for both the considered geometries. Both in BAV and TAV case a 7% increase in the average WSS can be observed in the aneurysmatic geometry, compared to baseline.

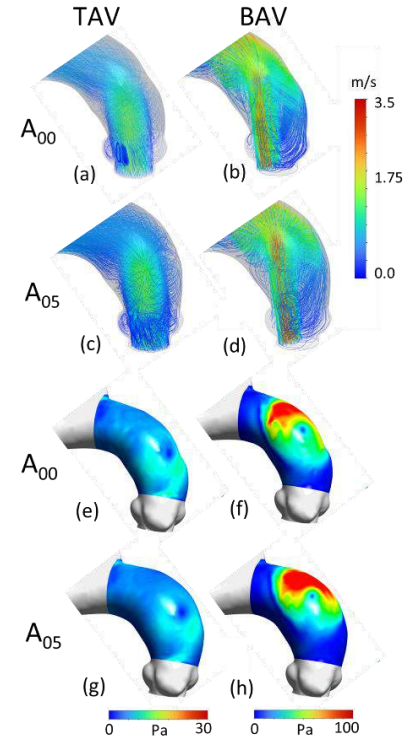


Figure 3: Streamlines of velocity (a-d) and WSS (e-h) at peak systole in the ascending aorta for the TAV (a,c,e,g) and BAV (b,d,f,h) analyzed cases, in A_{00} (a,b/e-f) and A_{05} (c,d/g,h) configurations.

Table 1: Time averaged values of area-weighted average WSS in case of centered (TAV) or eccentric (BAV) inlet flow, for both baseline and aneurysmatic geometries.

	TAV	BAV
A_{00}	2.98 Pa	7.41 Pa
A_{05}	3.18 Pa	7.91 Pa

DISCUSSION

In this study we investigated the effects that an eccentric inlet velocity profile has on aortic hemodynamics. In particular, TAV and BAV configurations have been considered and correspondent inlet conditions have been applied to evaluate hemodynamics in a virtual patient at different stages of aneurysm growth. The jet flow from our eccentricity model is the main responsible for higher velocities and WSS, as a consequence of impingement of the aortic wall, in agreement with previous findings [1,2], thus highlighting the necessity to account for the eccentric inlet flow when modeling aTAA hemodynamics.

ACKNOWLEDGEMENTS

This project received funding from the Marie Skłodowska-Curie grant agreement MeDiTATe project no 859836.

REFERENCES

- [1] Jayendiran, R et al., *J Biomech.*, 110:109954, 2020
- [2] Youssefi, P et al., *J Biomech Eng.*, 140(1): 011002, 2018.
- [3] Capellini, K et al., *J Biomech Eng.*, 140(11): 111007, 2018.
- [4] Pirola, S et al., *J Biomech.*, 60:15-21, 2017.
- [5] Boccadifuoco, A et al., *Comput Fluids.*, 165:96-115, 2018.
- [6] Cao, K et al., *World J. Cardiovasc. Dis.*, 5:129-140, 2015

PREDICTIVE GROWTH ANALYSIS OF ABDOMINAL AORTIC ANEURYSMS UNDER SURVEILLANCE USING GEOMETRIC MEASURES

Pratik Mitra (1), Juan C. Restrepo-Perez (1), Satish C. Muluk (2), Mark K. Eskandari (3), Ender A. Finol (1)

- (1) Department of Mechanical Engineering, University of Texas at San Antonio, San Antonio, TX
(2) Department of Cardiothoracic Surgery, Allegheny Health Network, Pittsburgh, PA
(3) Division of Vascular Surgery, Northwestern University School of Medicine, Chicago, IL

INTRODUCTION

A confined enlargement of the aorta that mainly develops below the renal arteries is known as an abdominal aortic aneurysm (AAA). An 80% overall mortality rate makes AAA a socially significant cardiovascular disease. The clinical management of AAAs consists of assessing their maximum diameter using an ultrasound or computed tomography (CT) examination. The accepted thresholds for surgical/endovascular repair in the United States are a maximum diameter of 5.5 cm for men and 5.0 - 5.4 cm for women with a growth rate of 1 cm/year [1]. Furthermore, it is challenging to identify the normal growth pattern because of non-linearity associated with the change in diameter over time. To this end, the maximum diameter-based criterion has been challenged in recent findings [2] and alternative metrics have been proposed to assess the risk of rupture during AAA surveillance. These include growth rate, AAA volume, AAA wall surface area, and tortuosity. Growth rate appears to be an important metric for the clinical management of small-diameter AAAs [2]. In the present work, we estimated 12 geometric measures from longitudinal CT scans of AAA subjects under surveillance and assessed their ability to predict AAA growth rate using an exponential model.

METHODS

CT images in a DICOM format acquired retrospectively from 7 AAA subjects under surveillance were used as input to AAASc (an in-house MATLAB®-based semi-automated segmentation script) to create binary masks. Using the latter as input to AAAMesh (another in-house MATLAB®-based script for meshing), volume meshes were created for each AAA at each imaging follow-up (30,000-90,000 quadratic hexahedral elements). AAASc and AAAMesh validation were previously described in [3] and [4], respectively. Each AAA subject had multiple follow-ups performed during surveillance, which resulted in 23 CT scans obtained from Northwestern Memorial Hospital (Chicago, IL) and Allegheny General Hospital (Pittsburgh, PA) in

accordance with established Institutional Review Board guidelines. Patient consent was unnecessary since the review was retrospective and using existing medical records.

Growth rates

The exponential expression presented in [6] was used to calculate AAA growth rate according to Eqs. (1) and (2),

$$g = (e^{12r} - 1) \times 100 \quad (1)$$

$$r = \frac{1}{t} \ln \frac{X^{followup}}{X^{baseline}} \quad (2)$$

where $X(.)$ is the geometric measure, t is the time interval between consecutive scans in months, r is the logarithmic growth factor, and $g(.)$ is the growth rate of the measure. The Spearman's rho correlation coefficient was used to quantify the strength of the correlation analysis with growth rate, where a coefficient in the range of 1.00–0.90, 0.90–0.75, 0.75–0.50, 0.50–0.25, and 0.25–0.0, corresponds to a very high, high, moderate, weak, and no correlation, respectively [6].

Exponential AAA growth model and growth prediction

All geometric measures were examined to assess their ability for growth prediction using Eq. (3) [5, 6],

$$Y = \alpha \cdot e^{\beta t} \quad (3)$$

where Y is the measure or prediction, α is the mean value of the measure, and β is the mean value of growth rate. The follow-up measure can be

obtained using $T = \frac{\ln \frac{X^{baseline}}{\alpha}}{\beta}$ and $X^{follow-up} = \alpha \cdot e^{\beta(t+T)}$ where T represents how many months have passed since the aneurysm was last surveilled.

Table 1. Geometric measures used to predict growth rate.

V	AAA sac volume (mm ³)
V _{ILT}	Volume of intraluminal thrombus (ILT) contained within the AAA sac (mm ³)

D_{\max}	Maximum transverse diameter of the AAA sac (mm)
DDr	Maximum diameter to neck diameter ratio
S	Vessel surface area (mm ²)
T	Tortuosity
γ	Ratio of AAA ILT volume to AAA sac volume
H	Height of abdominal aorta (mm)
H_{sac}	Height of AAA sac (mm)
L	Centerline length of abdominal aorta (mm)
L_{sac}	Centerline length of AAA sac (mm)
DHr	Diameter-Height ratio; DHr is an expression of the fusiform shape of the AAA sac

RESULTS

As seen in Table 2, very high correlations were obtained for V vs. D_{\max} ($r = 0.97$), γ vs. V_{ILT} ($r = 0.91$), and L vs. S ($r = 0.90$) correlations for non-linear growth rate. V_{ILT} exhibited a high correlation with D_{\max} ($r = 0.89$), but had no correlation with T, H_{sac} , and L_{sac} ($r = 0.04$, $r = 0.11$, $r = 0.08$), respectively. D_{\max} was highly correlated with S ($r = 0.86$) but had no correlation with H_{sac} and L_{sac} . T has weak correlations with all measures except L ($r = 0.41$).

Table 2. Correlations of geometric measures using non-linear growth model.

Measure	V	V_{ILT}	D_{\max}	DDr	S	T	γ
V	1						
V_{ILT}	0.88	1					
D_{\max}	0.97	0.89	1				
DDr	0.65	0.52	0.65	1			
S	0.86	0.75	0.83	0.54	1		
T	0.29	0.04	0.30	0.62	0.44	1	
γ	0.71	0.91	0.73	0.44	0.60	-	1
H	0.37	0.45	0.37	0.14	0.72	0.16	0.40
H_{sac}	0.08	0.11	0.07	0.38	0.05	0.11	0.34
L	0.60	0.57	0.59	0.34	0.90	0.41	0.48
L_{sac}	0.12	0.08	0.10	0.34	0.10	0.22	0.29
DHr	0.71	0.58	0.72	0.48	0.42	0.36	0.39

To identify a growth curve that could predict AAA growth rates, growth curves were calculated using Eq. (3) for D_{\max} and V. Figures 1(a) and 1(b) show the exponential distribution of the growth based on these geometric measures, where the data was normalized with respect to the baseline measure ($t = 0$). The justification for using only these measures to predict growth rate is that the correlation of D_{\max} vs. V exhibited the highest correlation coefficient of all measures correlated. The non-linear growth model shows that both D_{\max} and V lie within one standard deviation of the mean for nearly all 23 data points derived from the serial CT scans.

DISCUSSION

AAA growth rate was estimated using a non-linear model and geometric growth analysis was performed successfully using an exponential function. There is considerable evidence that growth rate plays a significant role in predicting rupture risk in small AAAs. Aneurysm sac volume was postulated to be a useful metric for predicting risk of AAA in earlier investigations [2].

In the present work, we demonstrated the application of an exponential growth curve for maximum diameter and sac volume. For these, $\alpha = 1.08 \pm 0.08713$ for normalized D_{\max} and 1.20 ± 0.226 for normalized volume. Noteworthy is that α was calculated by using the

mean of the maximum diameters for all patients, while β was calculated as the growth rate using the first-order time derivative. Likely due to the relatively small population sample, which had 2-6 follow-up CT scans at 6-month intervals, the non-linear growth rate equation was not a good fit for the exponential model compared to [6]. Our results show a good agreement with the non-linear exponential model described in [5]. The exponential growth model presented herein could be used to make informed predictions of future AAA growth with as little as two CT scans during the surveillance period. Additional serial imaging data with a larger population sample is needed to corroborate the accuracy of the model.

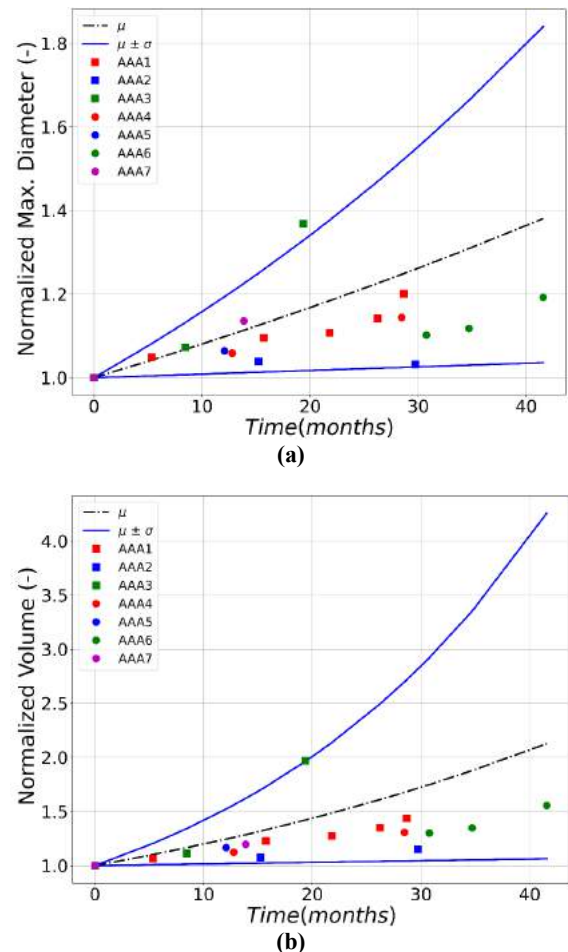


Figure 1. The exponential functions of (a) D_{\max} and (b) V, which are the best predictors of growth for the seven AAAs.

ACKNOWLEDGEMENTS

This study was supported in part by NIH award R01HL159300.

REFERENCES

- [1] Chaikof, E.L., et al., *J of Vascular Surgery* 67(1):2-77.e2, 2018.
- [2] Siika, A., et al., *European J of Vas & Endovas Sur* 50(3):P390, 2015.
- [3] Shum, J et al., *Medical Physics*, 37:638-648, 2010.
- [4] Raut, S.S., et al., *J Biomech* 48(10):1972-1981, 2015.
- [5] Martufi, G., et al., *J of Vascular Surgery* 58(3):748-755, 2013.
- [6] Akkoyun, E., et al., *Comp and Prog in Biomech* 208:106256, 2021.

REACTION KINETICS IN ELECTROOSMOTIC FLOW DRIVEN MICROFLUIDIC DEVICE FOR DETECTION OF ANTIGEN

Israel O. Ajiboye (1), Rupak K. Banerjee (2)

(1) Department of Mechanical and Materials Engineering, College of Engineering and Applied Science, University of Cincinnati, Cincinnati, Ohio, USA

(2) Department of Biomedical Engineering, College of Engineering and Applied Science, University of Cincinnati, Cincinnati, Ohio, USA

INTRODUCTION

Antibodies (Ab) are a critical component in biotechnology and medicine as molecular recognition tools for diagnostic immunoassays or therapeutic applications [1]. Screening antibodies in relation to specific antigens (Ag) are imperative for an accurate diagnosis of disease and the development of vaccines [2]. The antigen-capturing activity of antibodies depends on the immobilization strategy. The antigen to be captured can be driven either by pressure or electrohydrodynamics. Electrohydrodynamic flows, such as electroosmotic flow (EOF), have advantages in microfluidics as they do not require mechanical pumps operating at higher pressures. Instead, EOF is driven by an external electric field under atmospheric conditions where the flow rate is directly proportional to the applied electric field [3]. In previous studies, we developed a numerical model and experimentally designed and tested a microfluidic device for efficient separation of fluorescence-tagged magnetic microbeads (mMBs) driven by EOF [3,4].

The *objective* of this study is to develop a numerical model of antibody-antigen reaction kinetics in EOF. As the Ag approaches the leading edge of the capture zone (the region in the channel wall (Fig. 1A) where the mMB-Ab complex is immobilized), the antibody-antigen complex (mMB-Ab-Ag) is formed and immobilized (Fig. 1B), as the Ag flows downstream in the microchannel.

METHODS

Following governing equations for EOF were derived based on assumptions by Krishnamoorthy et al. [5] and Comandur et al. [6].

- Conservation of mass: $\nabla \cdot \mathbf{V} = 0$ (1)
- Conservation of momentum: $\rho D\mathbf{V}/Dt = -\nabla p + \mu \nabla^2 \mathbf{V} + \mathbf{f}_e$ (2)
- Coulomb force: $\mathbf{f}_e = \rho_e \mathbf{E}$ (3)
- Poisson's equation: $\nabla^2 \phi = 0$ (4)
- Electric field: $\mathbf{E} = -\nabla \phi$ (5)

where \mathbf{V} represents the fluid velocity, ρ is the fluid density, μ is dynamic viscosity, ϕ is the applied potential, ϵ is the permittivity of fluid, and \mathbf{E} is the applied electric field. The momentum equation (eq. 2) includes the Coulomb force (eq. 3) exerted by the external electric field. The pressure drop term is zero because a constant pressure was maintained at the inlet and outlet of the channel during EOF. Poisson's equation (eq. 4) was then coupled with the momentum equation (eq. 2). The electric field in the channel was solved using Equation 5.

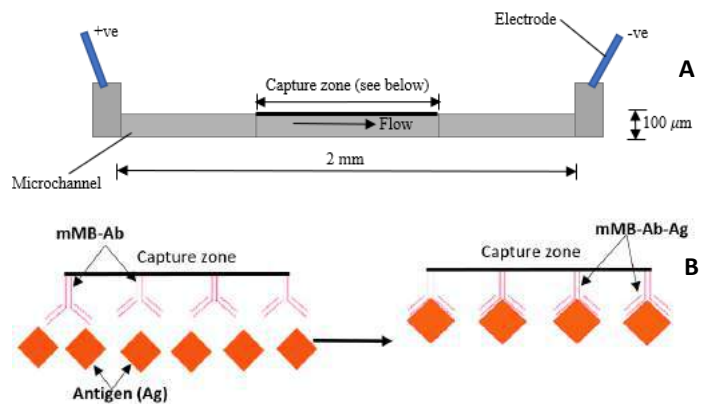


Figure 1: Schematic diagram of A) microchannel with capture zone, B) capture of Ag with immobilized mMB-Ab.

For the chemical reaction at the capture zone, a biomolecular, irreversible reaction (eq. 6) with a forward rate constant, k_f , and a negligible backward rate constant, k_r , was considered. The governing equation of the chemical reaction between the reactants is given in the Equation 7:



$$\frac{DC_i}{Dt} = D_i \frac{\partial^2 C_i}{\partial x^2} \pm k_f C_A C_B, \text{ where } i = A, B, C \quad (7)$$

where D_i and C_i are the diffusion coefficients and species concentration of A, B, and C, respectively. The negative sign corresponds to the depletion of reactants A and B, while the positive sign represents the formation of product C. Samples A and B can be replaced by any Ag and mMB-Ab. The process of anchoring the mMB-Ab molecules to a specified microchannel surface must maintain a balance between the need to reliably attach the mMB-Ab to the surface and keep them in a biologically active molecular conformation with high accessibility for capturing Ag from the solution [7]. Previous study has shown magnetophoretic separation in EOF using a magnetic field generated by a miniaturized magnet, and the capture efficiency of the mMB-Ab was evaluated [3]. In current formulation, the normalized surface density of mMB-Ab was specified at the capture zone of the microchannel, and the Ag was driven by an electric field.

Numerical Formulation. The size of the microchannel is length: 2 mm and height: 100 μm (Fig. 1A). The Ag is injected at the inlet of the channel and approaches the immobilized mMB-Ab at the capture zone (Figs. 1A and 1B). The length of the capture zone is 800 μm . A 2D computational geometry was developed (CFD-GEOM; ESI-CFD Inc., Huntsville, AL). Structured meshing was used with 9528 cells with an aspect ratio of 1.

The boundary conditions for driving the EOF, i.e., zeta potential ($\zeta = -95.6$ mV) and Debye layer thickness ($\lambda_D = 0.1$ μm), were applied to the walls of the microchannel. Based on the experimental data, a normalized surface density of the mMB-Ab at the capture zone is specified along with the concentration of Ag at the inlet. A surface reaction is applied for immobilized mMB-Ab. The surface reaction involves kinetic binding between mMB-Ab (exclusively on the surface quantified by a concentration expressed in moles/ m^2) and Ag in fluid volume (quantified by a concentration in moles/liter). Table 1 lists properties used in calculation.

Table 1: List of properties

Parameter	Value
Fluid density (ρ)	997 kg/ m^3
Dynamic viscosity (μ)	8.6×10^{-4} Pa.s
Relative permittivity (ϵ_r)	78.8
Rate constant (k_f)	10^7 L mol $^{-1}$ s $^{-1}$

RESULTS

Figure 2 shows that the mMB-Ab vs time plot at the leading edge of the capture zone remained the same for the first 0.2s and got depleted as the Ag entered the capture zone. At about 0.5s, the Ag in fluid got fully consumed by the immobilized mMB-Ab at the leading edge. Consequently, mMB-Ab-Ag is formed and remained immobilized at the surface.

Figure 3 shows the depletion with time of the mMB-Ab and mMB-Ab-Ag formation at the midway and trailing edge of the capture zone. The Ag concentration at the capture zone is very low. This is because any Ag that is near the wall reacts immediately with the mMB-Ab on the wall. This results in a near-zero concentration of the Ag at the wall while mMB-Ab still exists sufficiently.

DISCUSSION

A novel method was developed to capture electrohydrodynamics driven Ag by immobilized functional mMB-Ab at the channel surface for microfluidic immunoassays. This study found that the leading edge of the reaction shifts along the capture zone as the Ag reaches the

surface and mMB-Ab is fully consumed. The study suggests that rapid Ag detection can be achieved using this approach. This platform technology can lead to the development of a portable device for the detection of target cells, pathogens, and biomolecules.

Limitation. A capture zone binding surface was defined based on previous study [3], with a specified normalized concentration representing the immobilized mMB-Ab. In other words, Equation 1-7 can be simultaneously solved instead of sequential processing of Equation 1-5, followed by Equation 6-7.

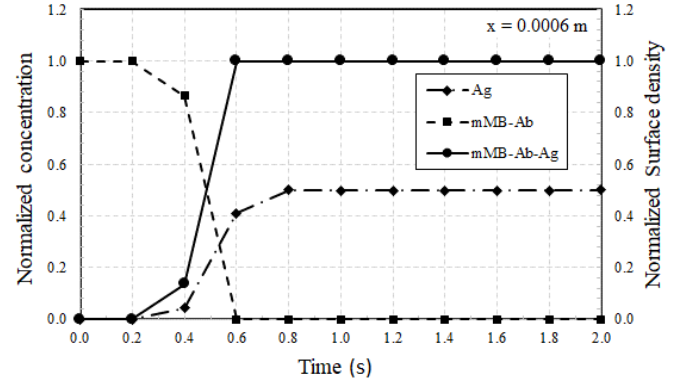


Figure 2: Normalized concentration of Ag and surface density of mMB-Ab, and mMB-Ab-Ag at the leading edge of the capture zone for an electric field of 150 V/cm.

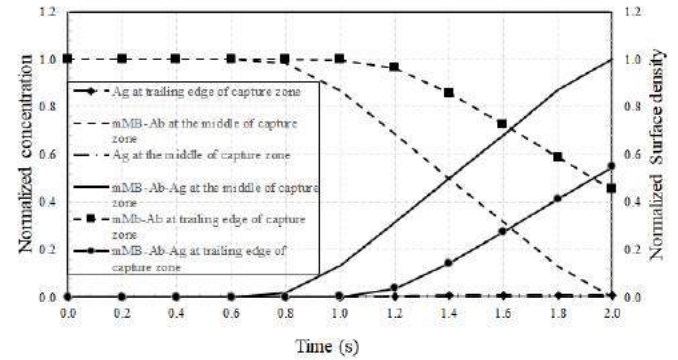


Figure 3: Normalized concentration of Ag and surface density of mMB-Ab, and mMB-Ab-Ag at the middle and trailing edge of the capture zone for an electric field of 150 V/cm.

ACKNOWLEDGEMENTS

This research was supported by the National Institute for Occupational Safety and Health through the University of Cincinnati Education and Research Center Grant #T42OH008432.

REFERENCES

- [1] Reis, P. B et al., *Frontiers in molecular biosciences*, 9.
- [2] Qi, C et al., *Biomedical microdevices*, 8(3), 247-253.
- [3] Das et al., *Journal of Biomechanical engineering*, 137(5).
- [4] Das et al., *J. of Micromechanics and Microengineering*, 26(5), 055013.
- [5] Krishnamoorthy et al., *Microfluidics and Nanofluidics*, 2(4), 345-355.
- [6] Comandur et al., *J. of Micromechanics and Microengineering*, 20(3), 035017.
- [7] Ren, C. L et al., *Journal of colloid and interface science*, 294(2), 482-491.

DEEP LEARNING ENHANCES MICRO-COMPUTED TOMOGRAPHY IMAGE RESOLUTION OF MURINE FEMURS

Michael A. David (1), Tillman James (2), Douglas J. Adams (1)

(1) Department of Orthopedics, University of Colorado, Aurora, CO, USA
 (2) Department of Electrical & Systems Engineering, Washington University in St. Louis, St. Louis, MO, USA

INTRODUCTION

Diagnosing, surgical planning, and research for bone diseases are often performed using the gold-standard imaging technique of X-ray Computed tomography (CT). CT imaging enables high-resolution 3D imaging and reconstruction of bone to visualize and quantify aspects of cortical and trabeculae compartments. The highest resolution CT imaging available requires a long acquisition time, which increases the incidence of motion artifact, radiation dose, and cost. As such, a need exists to develop novel techniques for acquiring high-resolution CT images without compromising the accuracy of bone evaluation.

Deep learning (DL), a subset of artificial intelligence, might provide a computational way to maximize image spatial resolution and overcome CT limitations. DL is capable of generating high-resolution (HR) CT images from standard images that are routinely acquired at lower resolution (LR) [1]. A limited number of studies have demonstrated the feasibility of DL techniques for CT to improve the imaging of trabecular bone clinically [2] and preclinically [3]. However, DL's limitations to resolving smaller morphometric features on the length scale of intracortical porosity remain unknown. Likewise, other model frameworks, such as U-Net [4], could provide increased accuracy in this realm [3] given success in other image-based machine learning tasks. Furthermore, while standard metrics are used to evaluate DL models for image enhancement/quality, namely, structural similarity index (SSIM) and peak-signal-to-noise ratio (PSNR), whether these metrics translate to the conservation of bone morphology, textures, and quantitative metrics across resolutions remains unclear.

Thus, this study aimed to develop a DL model with U-Net framework capable of generating micro-CT (μ -CT) high resolution (HR) images from low resolution (LR) of mouse femurs even within small sample sizes. We hypothesized that DL-generated images would display enhanced image quality and preserve bone morphometry like HR compared to LR.

METHODS

Femurs and μ -CT. 16 femurs from 16 week old Diversity Outbred mice were imaged via μ -CT at 70 kVp and 200 μ A with 3 frame averages to obtain lower (20 μ m voxel) and higher (10 μ m voxel) spatial resolution (1000 and 2000 projections, respectively), while maintaining the same digital registration within a fixed Cartesian reference frame (i.e., x-y-z coordinates). 3D image arrays were converted to DICOM and subsequently into NIFTI format for developing DL model in Python coding language; python packages of Nibabel, Scikit-learn, Scipy, and PyTorch were used. Briefly, NIFTI files were imported and then exported as 2D images from a single imaging plane (traverses the femur entire length; Fig. 1), up-sampled via bilinear interpolation, and then grayscale normalized (max and min of entire training images).

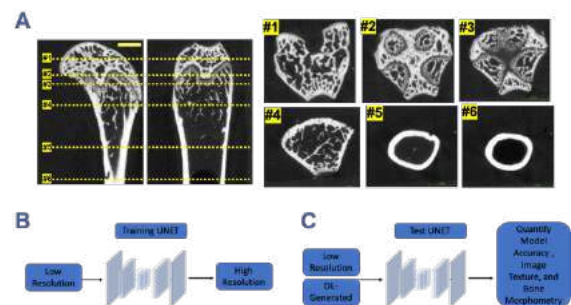


Fig. 1: (A) Example μ -CT images used to develop the DL model, showing the breadth of bone microarchitecture structures through the femur. (B) Schematic of DL training using UNET framework and paired low to high resolution images. (C) Schematic of testing pipeline used to evaluate differences in a trained model accuracies, bone morphometry, and image metrics between low resolution and DL-generated images.

Model Development and Evaluation: A total of 6000 images from 15 femurs (400/femur) were used for training/validation/test process (3375/1125/1500 images, respectively). One femur and the corresponding 2D images (400) were set aside as an external test set. A DL model with a standard U-Net framework was trained for 300 epochs using a 0.001 learning rate, batch size of 5, Adam optimizer, and mean squared error loss function on a GPU (~8hrs; A100-SXM4-40GB; Google Colab Pro). Model accuracy was assessed using PSNR and SSIM. To test the impact of different images (real or predicted) on standard μ CT (morphology) and image metrics (contrast and texture), 2D images from the test set were processed through BoneJ and Texture Analyzer plugins in ImageJ. BoneJ calculated the bone area fraction (i.e., bone area/total area; BA/TA) and thickness. Texture Analyzer calculated the image contrast and entropy.

Statistics. Confidence interval calculations and one-way ANOVA were performed to identify differences in bone and image metrics among groups. Significance was set at $p < 0.05$, and Bland-Altman plots were generated to visualize the differences.

RESULTS

The DL model could enhance the LR toward the HR based on qualitative (Fig. 2A) and quantitative DL metrics (Fig. 2B; test set PSNR mean = 38.4; test set SSIM mean = 0.92). The model could modestly resolve the smallest pores in the cortex and distal growth plate that can be seen in high resolution (Fig. 2A). Qualitatively, the DL-generated image appears to be denoised (Fig. 2A). Quantitatively, DL-generated and LR images have different image contrast and entropy to HR while having comparable BA/TA and thickness (Fig. 2C); except LR has increased thickness. Further, the DL-generated images had reduced confidence intervals for all metrics compared to LR; except DL images, entropy intervals were increased. On the external test, similar findings were seen in the DL-generated images and metrics as an internal test set (not shown); the model had decreased PSNR and SSIM as the images traversed from the cortical midshaft to the femoral head.

intervals = solid lines) highlight the differences in bone and image metrics between LR and HR (LR-HR; blue circles) and between DL generated and HR (DL-HR; red stars).

DISCUSSION

The present study trained a DL model with U-Net framework that successfully enhanced the resolution of μ -CT images of mouse trabecular bone and cortical boundaries and porosities. The DL model transforms an image as acquired via μ -CT at a comparatively low resolution to a virtual “higher” resolution. This study’s DL model, demonstrated with serial images from just 16 femurs, confirms and extends the use of DL techniques for enhancing image resolution in standard laboratory preclinical settings that utilize μ -CT imaging. Our DL model has shown improvement compared to another study that used deep convolution neural network frameworks in mice tibiae scanned via μ -CT (PSNR = 28.6; SSIM = 0.64)[3]. Advances in the current model might be due to differences in model framework, sample sizes, and bone microarchitecture. Similar to previous studies, our DL model was challenged by the smallest porosity in the cortex and spongiosa. Ongoing work aims to improve the DL model’s ability to resolve finer detail/smaller porosities and lacunae by increasing the number and variation of training images. Ultimately, it will be critical to determine the bounds and limitations of DL’s models to reveal features in CT images that are typically considered lost to lower image resolution.

In conclusion, this study demonstrates the initial success of using DL models to enhance standard μ -CT in murine femurs. Translation of these DL approaches to the clinical setting may provide improved image quality without changes in imaging protocol.

ACKNOWLEDGMENTS

This research was funded by grants from NIH (R01AR070879 and R01AR073346).

REFERENCES [1] Yang+ *IEEE* 2019; [2] Guha+ *SPIE* 2020; [3] Jhuboo+ *EUSIPCO* 2022; [4] Ronneberger+ *arxiv* 2015

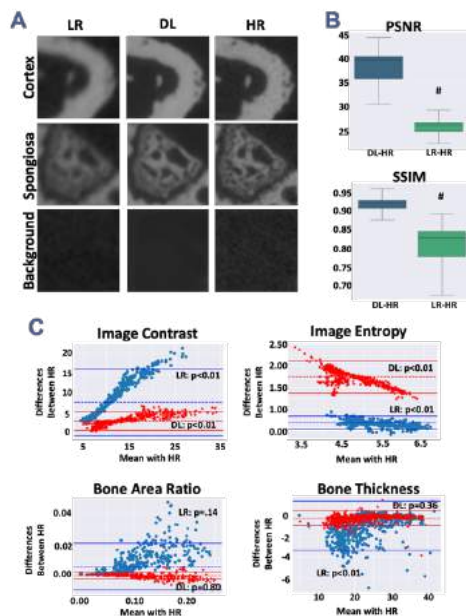


Fig. 2: (A) Representative μ -CT images showing DL-generated HR images from LR (# = $p < 0.05$). **(B)** PSNR and SSIM box plots of training test set between DL and HR (DL-HR) and LR and HR (LR-HR). **(C)** Bland-Altman plots of training test set with overlaid statistical metrics (mean difference = dashed line; 95% confidence

HISTOPATHOLOGY OF CAPSULE AND CARTILAGE PREDICT ELBOW BIOMECHANICS VIA MACHINE LEARNING

Michael A. David (1), Spencer P. Lake (2)

(1) Department of Orthopedics, University of Colorado, Aurora, CO, USA

(2) Department of Mechanical Engineering and Materials Science, Washington University in St. Louis, St. Louis, MO, USA

INTRODUCTION

Trauma to the elbow can lead to a debilitating disease of post-traumatic joint contracture (PTJC) in the afflicted joint and is associated with a loss of range of motion (ROM) and elbow function.¹⁻⁵ Elbow PTJC, most commonly manifesting as a decreased joint extension, is thought to be largely driven by the fibrotic changes to the anterior joint capsule and degenerate changes to other (e.g., cartilage) tissues.¹⁻⁵ Recent evidence has demonstrated that elbow PTJC is a whole-joint disease involving the anterior and posterior regions of the joint and multiple tissues (e.g., capsule, ligaments, cartilage).¹⁻⁵ Traditionally, histopathology is used to study cellular level details that can give rise to biomechanical changes measured *in vivo* and/or *ex vivo*. Unfortunately, it remains challenging to directly predict biomechanical function using only features observed in histological analysis; such predictive relationships could be used as diagnostic and prognostic biomarkers. Consequently, novel methods are warranted to integrate data from multiple tissues and data sources to establish predictive relations to study and treat elbow PTJC.

Machine learning (ML) is a rapidly evolving technique using computer-derived mathematical models that learn to accomplish tasks and find relationships between and within data. ML algorithms can be used to find predictive relationships between a set of inputs (in this case, histopathology scores) and outputs (i.e., elbow ROM). Recently, SHapley Additive exPlanations (SHAP) values have been used to glean insight into important input parameters that impact the model accuracy. Typically, a limiting factor in ML model development is the amount of data used for training; while oftentimes expensive and time-consuming to obtain, large datasets often yield improved accuracy of model predictions. Uniquely, our group has access to a historical database of histology and biomechanical data from several previous studies that used a preclinical animal model of elbow PTJC. Thus, this study aimed to develop predictive ML models linking histology features to elbow

range of motion, and to identify the most important parameter for predicting features of joint disease.

METHODS

Animals, Biomechanical Testing, and Histopathology: Data for ML model development was derived from prior studies using our group's rat elbow injury model of PTJC, histological scoring, and biomechanical testing (Fig. 1A)¹⁻⁵. Experimental groups included controls (i.e., age-matched uninjured and contralateral limbs) and injured rats with either no treatment, physical therapy (varying degree of immobilization + treadmill), or drug therapy (two dosing strategies of simvastatin or losartan) (Fig. 1B), which were assessed at 42- or 84-days post-injury. For ML model development, the input was histology scoring (e.g., cell counts and tissue thickness), and the output was a post-mortem biomechanical measure of elbow ROM. Our rat injury model leads to varying extents of ROM deficits at different timepoints post-injury and following different interventional treatments (Fig. 1B).

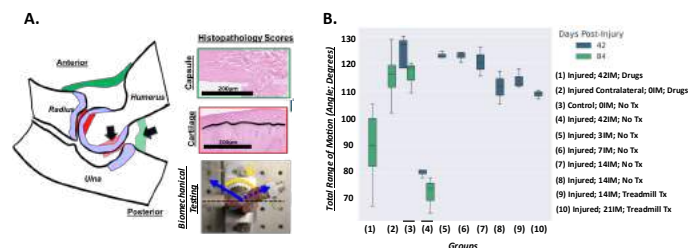


Fig. 1: (A) Schematic of a midsagittal section of the rat elbow used for histopathology scoring. Cellular and tissue evaluation by a pathologist was performed on the capsule and cartilage. Elbow range of motion was determined through *ex vivo* flexion-extension testing. (B) Previous data from our group's PTJC model highlight study groups and breadth of ROM used for model development.

Model Development and Evaluation: To predict elbow ROM, we used paired histological (averaged 3 sections/elbow) and mechanics data to evaluate multiple ML regression algorithms (n=58 elbows; 75/25 train/test ratio): Linear (LR), Support Vector (SV), Decision Tree (DT), Random Forest (RF), K-Nearest Neighbor (KNN), XGBoost (XGB), and one-dimensional Convolutional Neural Network (CNN). Model accuracy was assessed using R^2 values, absolute error, mean squared error, and root-mean-squared error. All model development was performed in Python coding language hosted on Google Colab; python packages of Scikit-learn and Scipy were used. SHAP values were used to identify key input parameters important for model accuracy. Pearson correlation analysis was used to evaluate correlations between input parameters and elbow ROM.

RESULTS

Correlation analysis revealed both negative and positive correlations between histology scores and elbow joint mechanics (Fig. 2). Overall, ML models were able to predict the elbow ROM from histological scores but with moderate accuracy (Fig 3A and B). Notably, RF and XGBoost consistently outperformed other models as assessed by all model metrics, albeit Linear and Support Vector models were also accurate. Absolute SHAP values identified a range of important histological parameters for predicting elbow range of motion (Fig 3C); the posterior capsule appeared to be consistently identified by all models as important.

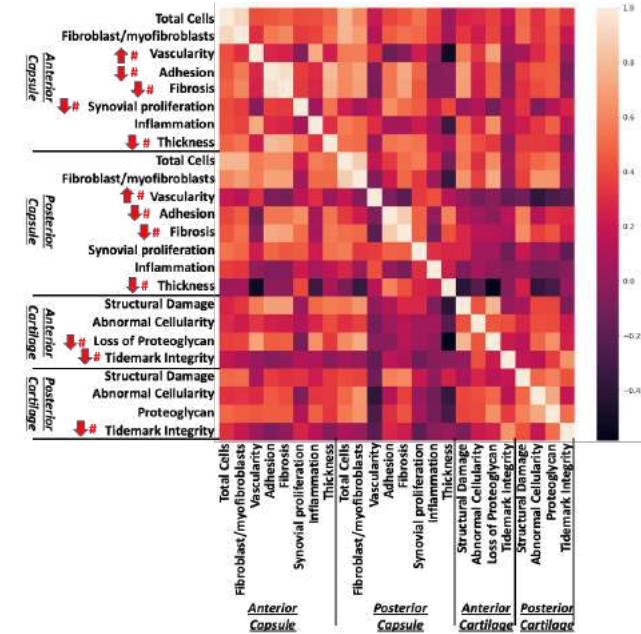


Fig. 2: Heatmap of Pearson correlation R^2 values for histological metrics; data that significantly correlated with elbow ROM shown as either negatively or positively correlated (arrows).

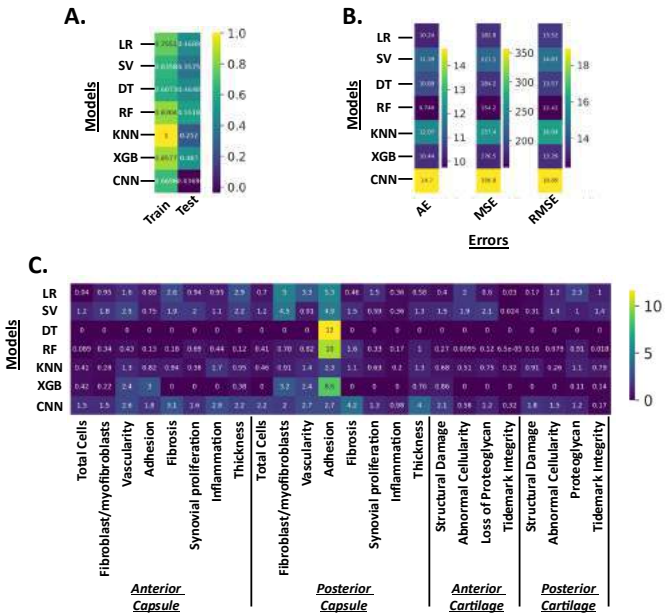


Fig. 3: (A) Heatmap highlighting R^2 values for train and test sets for each model. (B) Heatmap of model absolute error (AE), mean squared error (MSE), and root mean squared error (RMSE). (C) Heatmap of absolute SHAP values highlights the importance of different histological metrics in predicting elbow ROM.

DISCUSSION

This study demonstrated that ML models could predict elbow ROM from histopathology scoring of the capsule and cartilage with moderate accuracy. Each ML model performed to different accuracies, but Random Forest and XGBoost yielded the most accurate models (R^2 of ~0.47). Importantly, SHAP values gave insight into which histology parameter was key for the model. Interestingly, the posterior capsule was the most important tissue for prediction, particularly for thickness, adhesions, and fibroblasts/myofibroblasts. While these key parameters have been identified through previous preclinical and clinical studies, the larger impact of the posterior capsule over the anterior capsule is intriguing and requires further interrogation. ML models agnostically confirmed our intuition of elbow PTJC biology (i.e., important role of capsule tissue) while synthesizing vast information.

While the results of this first study to develop predictive ML models in the context of elbow PTJC are exciting, there is room for model improvements and next steps. For example, increasing the sample size to test the robustness of our model would be a critical step. We have access to additional paired elbows in our historical database; ongoing/future studies will enable even further increase in sample sizes. In addition, including more histological features and other evaluation metrics that are currently under development in our group (e.g., magnetic resonance imaging and computed tomography) might yield insights about novel relationships between multi-modal data.

In conclusion, ML models predicted elbow ROM from histopathology scoring of soft tissues. Ultimately, improving and expanding the use of ML for studying elbow PTJC might yield clinically relevant predictive relationships and lead to novel therapeutic strategies.

ACKNOWLEDGMENTS

This research was funded by grants from NIH (R01 AR071444).

REFERENCES [1] Dunham+ *CORR* 2018; [2] Dunham+ *JBJS* 2019; [3] Reiter+ *JBME* 2019; [4] David+ *ORS* 2021; [5] Reiter+ *Dissertation* 2021

A TESTABLE MECHANISM FOR FORCE GENERATION AND MAINTENANCE IN THE TONIC SMOOTH MUSCLE

Suzanne E. Stasiak (1), Dhanajay T. Tambe (2), Hari Krishnan Parameswaran (1)

(1) Department of Bioengineering, Northeastern University, Boston, MA
 (2) Department of Mechanical, Aerospace, and Biomedical Engineering University of South Alabama, Mobile AL

INTRODUCTION

Tonic smooth muscle (SM) regulates a wide range of vital body functions ranging from breathing, blood flow, vision, and reproductive functions, among others. Yet, despite its overwhelming importance in human health, the mechanisms that underlie force generation and maintenance in the SM remain poorly understood. Tonic SM can generate and maintain the force for durations over an hour. This force maintenance ability is currently attributed to a hypothetical state in the actin-myosin cycle of the SM, called the "latch phase," where myosin dephosphorylates but remains bound to actin^{1,2}. In the past 40 years, no study has been able to show experimental evidence that the latch state exists in the SM. Yet, this unproven concept is currently used to understand and interpret physiological data in diseases of the SM and taught in textbooks as *the* mechanism for force maintenance in SM. Here, we hypothesize that force generation and maintenance in the SM emerges as a result of a force-based mechanism where each cell in a confluent ensemble of SM cells use their contractile force to trigger Ca^{2+} release and force generation in other SM cells.

METHODS:

We measured cytosolic Ca^{2+} oscillations and force generated by human bronchial smooth muscle cells. Human bronchial smooth muscle cells were used for all experiments in this abstract. SM cells were serum starved for at least 24hrs prior to measurements.

RESULTS

Confluent SM cells build networks of cell-cell interactions as they constrict: Exposure to a contractile stimulus evokes cytosolic Ca^{2+} oscillations in the smooth muscle³. The period of these oscillations encodes the strength of the applied stimulus. Increasing dose of contractile stimulus leads to faster oscillations^{3,4}. Conversely, exposure to a muscle relaxant leads to reduction in oscillation frequency⁵. In a

recent study, we found that the Ca^{2+} oscillations in a connected ensemble of SMCs synchronize over a period of ~1 minute⁶. The time course of establishing synchrony in Ca^{2+} oscillations also corresponds to the time taken by the SM to generate steady state force⁷. Our analysis of Ca^{2+} oscillations in confluent ensembles showed that SMCs build dynamic networks of cell-cell interactions as they constrict (**Fig.2**). Isolated SM cells do not form such networks and isolated SM cells do not synchronize their Ca^{2+} oscillations⁶

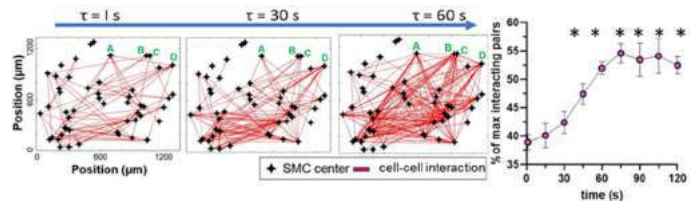


Figure 1 SM cells build dynamic cell-cell interaction networks as they constrict. The number of interacting cell-pairs increase and reach a maximum of 55% of max possible cell pairs. Isolated cells do not synchronize their Ca^{2+} oscillations

Cell-cell interactions persist in the force maintenance phase:

To test whether cell-cell interactions play a role in the force maintenance phase of the SM contraction, we used monolayer stress traction microscopy⁹ to measure the *contractile moment* (M_{ii}) of each cell in a confluent ensemble of SM cells arranged in 300mmx100mm rectangular pattern. M_{ii} is a scalar quantity which indicates the strength of the contractile dipole of an SMC¹⁰. Measurements were made every 30 seconds for a period of 15 minutes. The time traces of M_{ii} for each cell in the ensemble is shown in **Fig.2A**. All cells in the connected ensemble contract in response to 10 μM histamine and the force generated by the cell reaches its maximum at ~1 min and levels off as

the cell enters the force maintenance phase. We *hypothesized* that If each SMC in the ensemble was maintaining tension independent of other cells through the “latch” or similar intracellular mechanisms^{1,11}, *fluctuations* around the steady state value of M_{ii} during the force maintenance phase ($t=5$ mins to 15 mins) should be uncorrelated, random noise. To test this hypothesis, we fit a polynomial curve to each M_{ii} trace to find the mean trend and isolated fluctuations in M_{ii} for each cell. The cross-correlation matrix is shown in **Fig. 2B** We find that fluctuations in contractility of SMCs in a confluent ensemble are strongly correlated, indicating that the SMCs are interacting with each other in the force maintenance phase.

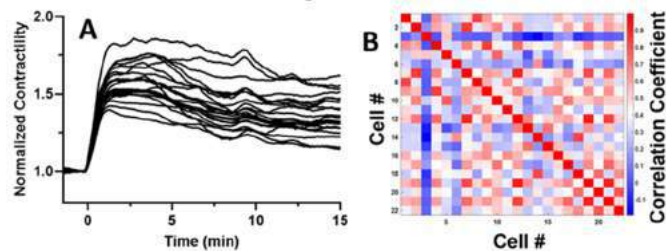


Figure 2 (A) We examined the fluctuations in force in a confluent, ensemble of SM cells during the force maintenance phase of the contraction ($t=5$ mins to 15 mins). (B) We found that the fluctuations in force for individual cells in the ensemble are strongly correlated with each other. This shows that in a connected ensemble of SM cells, the cells are not maintaining tension independent of each other, using mechanisms that are intrinsic to each cell. Rather, the cells are interacting with each other during the force maintenance phase of the constriction.

SM cells can use their force to trigger force generation in other SM cells: One of the first steps in the chain of reactions that lead to force generation in the SM cell is the hydrolysis of membrane bound PIP2 to form IP3 and DAG. Here, we show that PIP2 can be hydrolyzed by a shear stress consistent in magnitude with stress exerted by a SM cell.

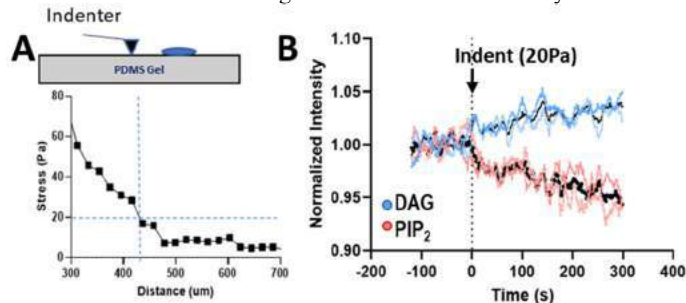


Figure 3: (A) We used an indenter to create a strain field on the collagen coated substrate. The indenter was positioned to apply ~20 Pa shear stress to an isolated SM cell. (B) The mechanical signal leads to an increase in DAG (blue) and a decrease in PIP2 (red). The black lines are average over $N=2$ trials. This data shows that PIP2 hydrolysis can be triggered by stress transfer from cell to cell.

We have confirmed that that the same applied stress leads to Calcium release and force generation in smooth muscle. We have also tested potential confounding effects of stretch activated Ca^{2+} channels by blocking their activity using Gadolinium. We found that that the stress-induced hydrolysis of PIP2 operates independently of stretch activated Ca^{2+} channels.(data not shown due to space constraints)

Mechanical signaling between SM may be sufficient for force maintenance in the tonic SM

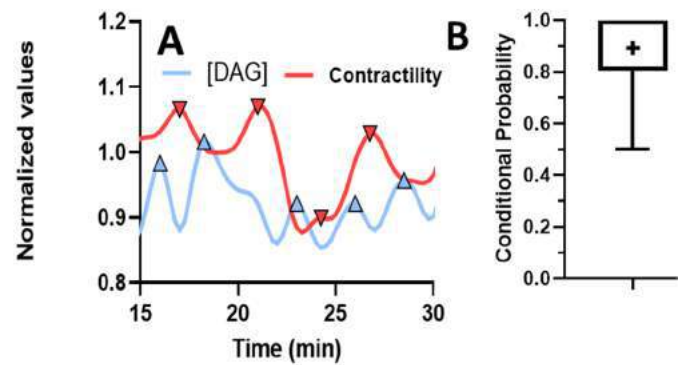


Figure 4: During the force maintenance phase of an SM contraction, we calculated the conditional probability for the following sequence of events to be triggered in an SM cell: (1) Contractility of a cell decreases (2) PIP2 hydrolysis (Fig3) is triggered in that cell (3) The contractility of that cell increases. Measurements were made in 21 cells in a confluent ensemble. Overall, the probability that our proposed mechanism was triggered in SM cells in the force maintenance phase was 0.89 ± 0.17

Taken together, the results we present here indicate that force maintenance in the tonic Smooth muscle is an emergent phenomenon driven by mechanical interactions between SM cells. Further testing using inhibitory compounds is underway.

DISCUSSION:

Dysfunction in the smooth muscle including asthma and hypertension affect over 20% of the world’s population. In the US alone, the cost burden of these diseases exceeds \$200 billion dollars annually. Despite their overwhelming importance to human health, the mechanisms by which SM generated force and maintains it are not well understood. The current dogma holds that force generation in the SM is regulated solely by intracellular molecular mechanisms. In contrast, we propose that force generation and maintenance in the SM is a emergent phenomenon where SM cells use their force to regulate cytosolic Ca^{2+} oscillations and force in other SM cells.

ACKNOWLEDGEMENTS

This work was enabled by NSF CAREER award 2047207 (HP)

REFERENCES

1. Dillon, et al. *Science* **1981**, 211, 495–7.
2. Hai, et al. *Am. J. Physiol.* **1988**, 254, C99–106.
3. Perez, et al. *J. Gen. Physiol.* **2005**, 125, 535–553.
4. Thurley, K. et al. *Sci Signal.* 2014 24;7(331)
5. Bai, Y. et al. *Respir. Res.* **2006**, 7, 34.
6. Stasiak, et al. *Sci. Adv.* **2020**, 6, eaba1149.
7. An et al. *Biochem. Biophys. Res. Commun.* **2009**, 382, 697–703.
8. Stasiak, et al.. *Sci. Adv.* **2020**, 6, eaba1149.6.
9. Tambe et al. . *Nat. Mater.* **2011**, 10, 469–475.
10. Butler, et al.. *Am. J. Physiol. Cell Physiol.* **2002**, 282, C595-605.
11. Murphy, et al. *Can. J. Physiol. Pharmacol.* **2005**, 83, 857–64.

COMPARISON OF LEFT VENTRICULAR FUNCTION ESTIMATED FROM INVERSE FINITE ELEMENT MODELING USING 3D ECHOCARDIOGRAPHIC AND MAGNETIC RESONANCE IMAGES

Chenghan Cai (1), Lei Fan (1), Jenny S. Choy (2), Ghassan S. Kassab (2), Lik Chuan Lee (1)

(1) Department of Mechanical Engineering, Michigan State University, East Lansing, MI, USA
(2) California Medical Innovations Institute, San Diego, California, CA, USA

INTRODUCTION

Three-dimensional echocardiography (3D ECHO) and magnetic resonance (MR) imaging are frequently used to evaluate heart functions in clinic. Magnetic resonance images have higher spatial resolution and are widely regarded as the gold standard for cardiac imaging. Conversely, while of 3D ECHO images as a lower spatial resolution than MR images [1], it is easier and cheaper to acquire. Many studies have used inverse finite element (FE) modeling with either 3D ECHO or MR images to estimate the contractile stress of the heart and quantify left ventricular (LV) function. A recent study has found that (LV) geometrical quantities such as, volume and ejection fraction estimated by these two imaging modalities are different [2]. It remains, however, unclear whether the contractile stress (contractility) estimated from inverse FE modeling based on these two imaging modalities are different. To address this issue, we develop an inverse FE modeling framework based on animal-specific LV geometries and volumes from 3D ECHO and MR images acquired from the same normal swine model to investigate if there are differences in LV function estimated based on these two imaging modalities. Specifically, we seek to determine whether there is a correlation of the contractility estimated based on 3D ECHO with those estimated from MR images.

METHODS

All experiment data were collected following the national and local ethical guidelines. Both MR and 3D ECHO images were acquired from seven normal swine model using a Siemens MR images scanner (Malvern, PA) and an iE33 ultrasound system (Philips, Andover, MA) with an X3-1 transthoracic transducer, respectively. Two-dimensional (2D) and 3D ECHO images were acquired with the animal placed in the supine position. The LV endocardial and epicardial surfaces were segmented from the MR and 3D ECHO images associated with the end-diastolic (ED) time point using MeVisLab (MeVis Medical Solutions AG) (**Fig. 1A**) and TomTec Imaging Systems GmbH (Philips Healthcare, Andover, MA) (**Fig. 1B**), respectively. The LV volume waveform in each case was obtained by calculating the volume of endocardial surfaces at all time points in a cardiac cycle. The 3D LV wall volume was reconstructed from the endocardial and epicardial surfaces (**Fig. 1C**) and meshed using tetrahedral elements. Myofiber orientation was prescribed to be helical with a transmural linear variation starting from a helix angle of 60 degrees at the endocardium to -60 degrees at the epicardium (**Fig. 1D**).

The computational framework consisting of a FE LV model is developed where the functional relationship between pressures and volumes is obtained by minimizing a Lagrangian function consisting of LV cardiac wall tissue potential energy function and terms associated with the enforcement of constraints on **1**) fixed end on the base, **2**) Robin-type boundary condition on the epicardial surface, and **3**) cavity volume. Total stress of the myocardium is decomposed into an active and passive component. Passive and active mechanical behaviors of the LV are described by Fung-type strain energy function and a modified time-varying elastance model, respectively. Active contractile stress P_a is determined from the second Piola-Kirchhoff stress tensor that is defined by the myofiber direction.

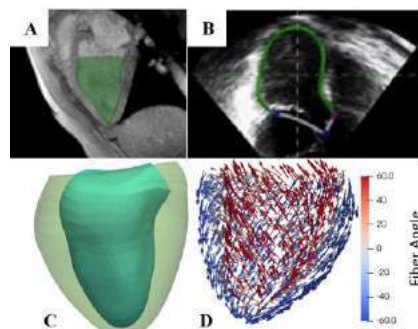


Figure 1: (A) MR images; (B) 3D ECHO of LV; (C) endocardial and epicardial surfaces of the LV segmented from 3D ECHO image; (D) myofiber direction prescribed for inverse FE modeling.

The LV geometry (based on ED) was unloaded with backward displacement method. Passive parameters are then manually adjusted to match the pressure and volume measured at ED point. In the inverse FE modeling framework, the regional contractile stress is optimized until the model predicted pressure-volume loop (PV loop) match with the experimental measurements. Since LV pressure cannot be acquired from imaging techniques, the same LV pressure waveform from a healthy swine is used in all cases. All computational frameworks are implemented using the freely available open-source library FEniCS. Optimization in the FEniCS-adjoint uses inverse FE framework to minimize the difference between simulation and experimental measurements [3].

RESULTS

Fig. 2 shows a comparison of the regional wall thickness, PV loops, regional, global contractility and active tension estimated from 3D ECHO and MR images. Myocardial wall is thicker in basal area whereas thinner in apex in both 3D ECHO and MR images (**Fig. 2A**). The largest difference in wall thickness estimated from 3D ECHO and MR images is located at the apical lateral (#16). The model predicted PV loops from inverse FE modeling show good agreement with the respective experimental measurements from 3D ECHO and MR images (**Fig. 2B**). The percentage difference between measurement and simulation data is less than 10% for volume and pressure in all cases. Mean regional contractility in each AHA region over 7 cases (**Fig. 2C**) was larger based on MR images than that based on 3D ECHO. The peak value of regional contractility (**Fig. 2C**) and time to peak contractility (**Fig. 2D**) are consistent between 3D ECHO and MR images in basal (#1-6) and apical regions (#13-16). Region 9 has the largest difference over 16 regions in both contractility (37%) and time to peak contractility (25%). Maximum contractility estimated from 3D ECHO images (279 mmHg) is larger than that estimated from MR images (227 mmHg) (**Fig. 2E**). The comparison of active tension waveform (**Fig. 2F**) is consistent with maximum contractility, which is 265 mmHg in 3D ECHO and 215 mmHg in MR image. LVEDV and LVESV estimated from 3D ECHO are positively correlated to those estimated from MR images with 0.327 and 0.315 for their gradients, respectively (**Fig. 2G**). The R-value for EDV and ESV are 0.731 and 0.453, respectively, which means EDV has strong positive linear association and ESV has small positive linear association. Correlation expresses a positive linear relation of active tension between 3D ECHO and MR images with a gradient 0.474 (**Fig. 2H**), showing higher active tension based on the geometry and volume from 3D ECHO than MR images in the same animal. Contractility shows a strong positive linear association with R-value is 0.843. **Fig. 2 G-H** shows positive gradients for regional distribution of wall thickness and active tension between 3D ECHO and MR images in LV. The difference in volume segmented from two imaging techniques does not affect the model predicted contractile function.

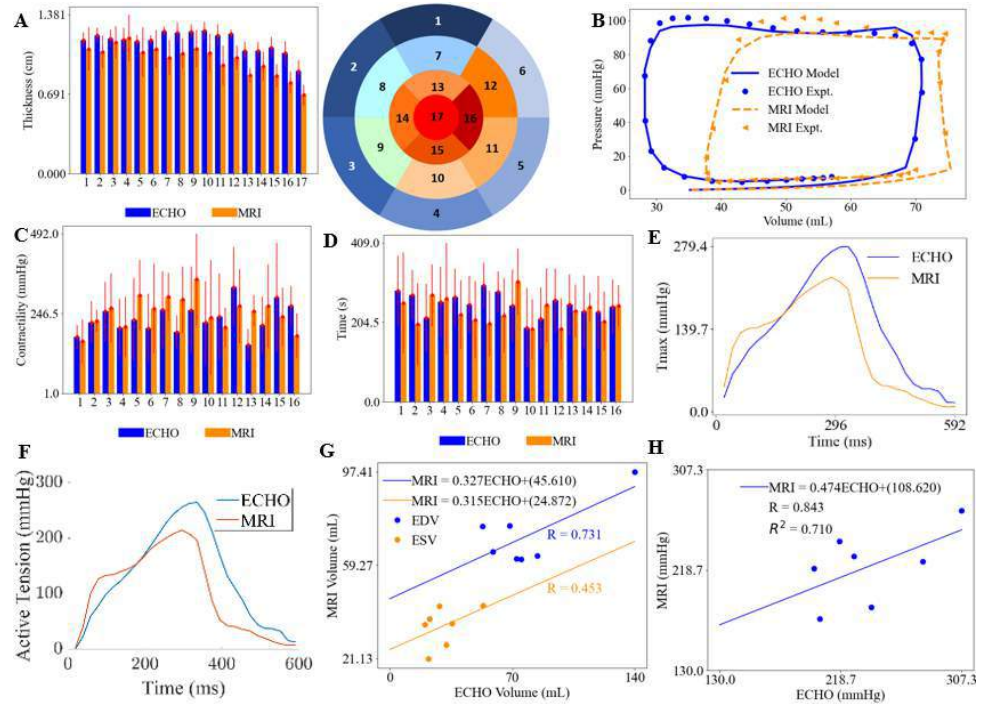


Figure 2: Comparison of (A) regional wall thickness of the LV and AHA Segments for each region; (B) Model predicted and experimentally measured PV loops; (C) regional maximal contractility and (D) time to peak contractility; (E) global contractility and (F) active tension estimated from 3D ECHO and MR images. Correlation of (G) end-diastolic volume (EDV) and end-systolic volume (ESV) and (H) contractility estimated from 3D ECHO and MR images.

DISCUSSION

In this project, an animal-specific inverse FE modeling framework was developed to estimate myocardial contractility in the LV based on 3D ECHO and MR images. To understand the relationship between 3D ECHO and MR images, the regional distribution of wall thickness segmented from images, LVEDV, LVESV, regional and global contractility and active tension predicted from inverse FE modeling were compared. The key findings from this study are as follows. **First**, ESV and EDV estimated from 3D ECHO are larger than that estimated from MR images with a positive correlation gradient 0.315 and 0.327. **Second**, global contractility and active tension estimated based on 3D ECHO is slightly larger than those estimated from MR images with a linear correlation gradient 0.474. The peak of regional contractility is comparable based on 3D and MR images. These findings shows that there is correlation in volumes based on the geometries segmented from 3D ECHO and MR images, and model predicted LV contractility is comparable based on 3D ECHO and MR images. There are some limitations in this work 1) the pressure measurements are not animal-specific, 2) the myocardial strain of the LV is not considered in the model.

ACKNOWLEDGEMENT

This work was supported by the National Institute of Health (R01 HL160997) and American Heart Association Postdoctoral Fellowship (AHA835298)

REFERENCES

- [1] Zhao, D. et al., J. *Front. -Sys. Com.*, 9, 2021
- [2] Herman, F. M. et al., *JASE. -Qua.of lef.*, 12, 2022.
- [3] Henrik, F. et al., *Int J Numer Method Biomed Eng. -Eff. Est.*, 6, 2018

BIOMECHANICAL FOLLOW-UP AND EVALUATION OF ANEURYSM GROWTH

F. A.M. Garbou, O. O. M. Elnamla, W. A.K.A. Saber, K. B. Kose (1),

(1) Biomedical Engineering Department, Istanbul Medipol University, Istanbul, T^urkiye

INTRODUCTION

Cardiovascular diseases have the highest mortality and morbidity rates. Each year, cardiovascular disease (CVD) is estimated to be the cause of 32% of all deaths worldwide[1]. During blood flow in the circulatory system, the vessel wall is constantly exposed to mechanical forces and can play a role in the development of pathologies if the arterial endothelium morphology is abnormal. In an aortic artery with an aneurysm, these changes may result in a rupture of the endothelium. An accurate pre and post-operative risk of an abdominal aortic aneurysm rupture is an important guide for planning aortic aneurysm repair surgery. Clinical studies have determined the risk with maximum aneurysmatic diameter based on medical imaging technologies. [2] However, it is known that the risk is not necessarily reflected by the maximum diameter alone [3]. Therefore, additional information is required for accurate risk assessment of an aneurysm before and after surgical repair. This study was designed to numerically evaluate the remodeling in aortic aneurysm morphologies and underlying mechanical factors. This study compared the relationship between the changes in aneurysm morphology and hemodynamic parameters in patients who were scanned at regular intervals. In flow visualizations based on virtual aortic models obtained from computed tomography datasets of three different scans, it was determined that the endothelial segments with distinctive changes in wall shear stress distribution showed high consistency with the morphological change segments seen in the next periodic scans of the same patients.

METHODS

Five patients diagnosed with thoracic aortic aneurysms and aged between 70-75 were included in the study. Virtual aorta models were created from the CT images of the patients taken at

three-month intervals (Figure 1). Three-dimensional (3D) models were created with VTK algorithms and a model mesh for finite element analysis was created with Simmetrix libraries. Blood flow was simulated by computational fluid dynamics analysis and visualized in Ceetron Analyzer Cloud [4]-[6].

In this study, we focused on WSS visualization, a parameter that cannot be measured in the clinical setting but can be calculated by multi-physics algorithms. Blood was considered Newtonian fluid and boundary conditions were established from case-specific data obtained from the clinic [7]. The initial velocity gradient was obtained from the Doppler ultrasound reports of the patients.



Figure 1: 3D models of the aorta segmented from CT data obtained at regular intervals of the selected patient.

RESULTS

Numeric

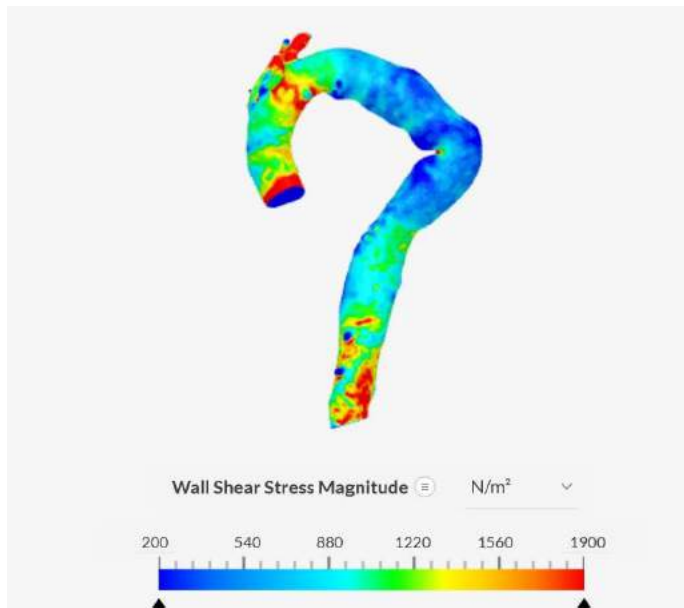


Figure 2: The WSS distribution on the first scan of Patient A.

DISCUSSION

After this preliminary study, it has been observed that the most obvious effect of WSS on the change of endothelium morphology starts from the segments where dramatic decreases in WSS distribution are seen. The numerical analysis results were obtained in line with our hypothesis that shape change rates that may be encountered in the next scan could be predicted. This work was able to present significant findings on the evaluation of studies on aneurysm growth with in-silico methods and it is possible to strengthen it with more scan datasets.

ACKNOWLEDGEMENTS

We thank Dr. Korhan Erkanlı from Istanbul Medipol University Medical School who provided insight and expertise that greatly assisted the research.

REFERENCES

- [1] “Factsheet: Health Inequalities in the EU | EuroHealthNet.” https://eurohealthnet.eu/publication/health-inequalities-in-the-eu/?gclid=CjwKCAjw8JKbBhBYEiwAs3sxN5bmjX5SvJkpI3OGbsvR6SI0yiYQPRgqa8rFIDatLS000B0LT85WSxoCABIQAvD_BwE (accessed Nov. 04, 2022).
- [2] K. C. Kent, “Clinical practice. Abdominal aortic aneurysms,” *N Engl J Med*, vol. 371, no. 22, pp. 2101–8, Nov. 2014, doi: 10.1056/NEJMCP1401430.
- [3] K. M. Tse, P. Chiu, H. P. Lee, and P. Ho, “Investigation of hemodynamics in the development of dissecting aneurysm

within patient-specific dissecting aneurismal aortas using computational fluid dynamics (CFD) simulations,” *J Biomech*, vol. 44, no. 5, pp. 827–836, Mar. 2011, doi: 10.1016/J.JBIOMECH.2010.12.014.

- [4] “CEETRON Advanced 3D visualization of CFD and FEA.” <https://ceetron.com/> (accessed Jan. 18, 2023).
- [5] “Simmetrix :: Home.” <http://www.simmetrix.com/> (accessed Jan. 18, 2023).
- [6] “OpenFOAM.” <https://www.openfoam.com/> (accessed Jan. 18, 2023).
- [7] S. E. Razavi, V. Farhangmehr, and N. Zendeali, “Numerical investigation of the blood flow through the middle cerebral artery,” *Bioimpacts*, vol. 8, no. 3, pp. 195–200, 2018, doi: 10.15171/BI.2018.22.
- [8] I. Technologies, S. A. Gombe, and T. Supervisor, “43D Visualization and Segmentation of Lungs Using Itk / Vtk / Qt Kopsude 3D Visualiseerimine Ja Segmenteerimine Itk / Vtk / Qt,” 2017.

NUMERICAL AND COMPUTATIONAL ANALYSIS OF ARTERY STRESSES CONSIDERING ACTIVE CONTRACTILITY

N. Goulbourne, Y. Li

Aerospace Engineering, University of Michigan, Ann Arbor, MI, USA

INTRODUCTION

Balloon angioplasty with stent deployment is an effective invasive therapy to treat atherosclerotic arteries. Vascular injury during balloon angioplasty with stent deployment is hypothesized to be the trigger of neointimal hyperplasia and phenotype change and migration of smooth muscle cells, which can lead to the subsequent restenosis of stented arteries. There are numerous research efforts focused on the optimization of balloon and stent design in an effort to reduce artery wall trauma, where the artery is treated as a passive material. Computational simulations have evolved as an attractive tool to study the mechanical performance of the artery, balloon, stent, and atherosclerotic lesion rupture over the last decade. Holzapfel et al. developed nonlinear strain-energy functions for characterizing the biomechanical response of arterial tissues and plaque during normal physiological loading and for simulating balloon and stent procedures [1,2]. Buffinton et al., Gastaldi et al., and Conway et al. studied the effects of plaque material, geometry, and stenting approach for artery bifurcation during stent angioplasty [3-5]. Other researchers have focused on the influence of the balloon configuration on the deployment of the stent and resulting wall response. There have also been numerical model results reported for fissuring, rupture, and dissection of the plaque and artery during the balloon angioplasty procedure. In all of these studies, the artery is modeled as a passive hyperelastic material and smooth muscle contractility is neglected. In the current work, we investigate the impact of this assumption on calculating artery and plaque wall stresses due to overstretch loadings.

We present a new coupled chemo-mechanical model to describe the active viscoelastic response of smooth muscle rich tissue in the arterial walls (media layer). The constitutive model is used in a thick walled arterial model to investigate the effects of smooth muscle contraction on artery stresses and quantify the role of active viscoelasticity in the mechanical response. Though previous simulations have shown that viscoelastic effects are minimally

important in the normal pulsatile response of healthy arteries for timescales on the order of a few seconds, our results show that the active viscoelastic behavior has a non-negligible effect on artery wall stress when longer timescale are considered. The current work focuses on the artery being overstretched on longer timescales for example during interventional surgical events.

METHODS

To model the mechanical performance of the artery wall being overstretched during events with time scales on the order of minutes we employ a two-layer thick wall model for the artery (the intima layer is assumed structurally negligible) and a three-layer thick wall model for the artery-plaque complex. The media layer consists of densely packed smooth muscle cells and the adventitia is collagen rich. Based on these characteristics, both layers of the artery are treated as incompressible and anisotropic; the plaque is considered isotropic. A comparison of the artery wall and plaque stresses for both active and passive materials was analyzed. Supra-physiological internal pressures and imposed diameter changes are prescribed as mathematical inputs to the model. Neither interventional tools such as catheters, balloons, nor stent deformation are modeled explicitly.

Accurate simulations of artery wall stresses are a valuable tool in designing medical devices and providing guidelines for surgical interventions. Reference [6] found that normal calcium oscillation of smooth muscle cells hardly affect artery mechanical behavior (3D cylinder simulations on an axisymmetric ring) for normal blood pressure cycles (period of one second). Medical and surgical interventions, however, are on longer timescales where the material viscoelastic response may be non-negligible and worth detailed consideration. The time of balloon inflation in balloon angioplasty procedures is from around half a minute to over one minute, which is on the same timescale as smooth muscle viscoelasticity.

The media layer model considers the active viscoelastic properties of the smooth muscle tissue. The adventitia is modeled as an anisotropic layer using an existing exponential form and an isotropic symmetric plaque layer is incorporated using Yeoh's model. Three types of plaques for various degrees of artery stenosis are considered in this work. The surrounding tissue is modeled as an outer pressure for a constant calcium concentration in the smooth muscle cells. The model material parameters are calibrated for swine common carotid artery. The wall and plaque stress distributions and corresponding deformations are calculated for healthy and diseased arteries for imposed displacements and tractions. The current findings are based on a ring model, so it is expected that further refinement of the results will occur for full 3D cylinder simulations – an aspect of future work.

The new strain energy function for the media layer is

$$\Psi_m = \frac{\mu_p}{2}(I_1 - 1) + \frac{k_1}{2k_2} \left(\exp(k_2(I_f - 1)^2) - 1 \right) + O_{imp}(AMP + AM) \frac{\mu_f}{4} \left(\frac{I_f}{I_f^v} - 1 \right)^2 \quad (1)$$

The strain energy function for the adventitia layer takes the following exponential form to describe the fiber reinforced anisotropic material

$$\Psi_a = \frac{\mu_{pa}}{2}(I_1 - 1) + \sum_{i=4,6} \frac{k_{a1}}{2k_{a2}} \left(\exp(k_{a2}(I_i - 1)^2) - 1 \right) \quad (2)$$

where μ_{pa} , k_{a1} , are modulus like material constants for the matrix and fiber, respectively, k_{a2} is a material constant for the fiber. Plaque is treated as an isotropic material and takes the form of the Yeoh model ($n=3$ in the current work)

$$\Psi_p = \sum_{i=1}^n C_{i0} (I_1 - 1)^i \quad (3)$$

where C_{i0} are material coefficients. The second Piola-Kirchhoff stresses for the media, adventitia, and plaque layers are obtained by taking appropriate derivatives of the strain energy density function in Eqs.1-3. We obtain the following expressions for the stress

$$\begin{aligned} \mathbf{S}_m &= \mu_p \mathbf{I} + \left[2k_1 \left(\exp(k_2(I_f - 1)^2) \right) (I_f - 1) + O_{imp}(AMP + AM) \mu_f \left(\frac{I_f}{I_f^v} - 1 \right) \right] \mathbf{M} \\ \mathbf{S}_a &= \mu_{pa} \mathbf{I} + 2k_{a1} \sum_{i=4,6} \left(\exp(k_{a2}(I_i - 1)^2) (I_i - 1) \right) \mathbf{M}_i \\ \mathbf{S}_p &= [2C_{10} + 4C_{20}(I_1 - 3) + 6C_{30}(I_1 - 3)^2] \mathbf{I} \end{aligned} \quad (4)$$

The parameters for the media layer are calibrated from isometric and isotonic tests. Parameters for the adventitia layer are for swine carotid artery and properties for the plaque are taken for human carotid artery (i.e. in the absence of experimental data for swine carotid artery plaque).

RESULTS

We calculate the stress distributions of the plaque-artery as functions of the normalized thickness and time for cellular (soft), hypocellular (mixed), and calcified (hard) types of plaque for the low activation level with a calcium concentration of 120 nM. Ramped displacement protocols are applied from $t_1 - t_2$, and the displacement held fixed from $t_2 - t_3$. Figure 1 shows the stress distributions for a stenosis ratio of 40% with and without considering active viscoelastic properties of smooth muscles (cellular plaque case). For the active case, the radial stresses increase to the peak values from $t_1 - t_2$ and then eventually go to the new steady state at t_3 , whilst the circumferential stress increases from $t_1 - t_2$, and continually increase $t_2 - t_3$, reaching a maximum at t_3 . For the passive case, stresses increase from $t_1 - t_2$ and are unchanged afterwards. The results show that active contractility of the media influences the mechanical responses of the plaque during artery overstretch.

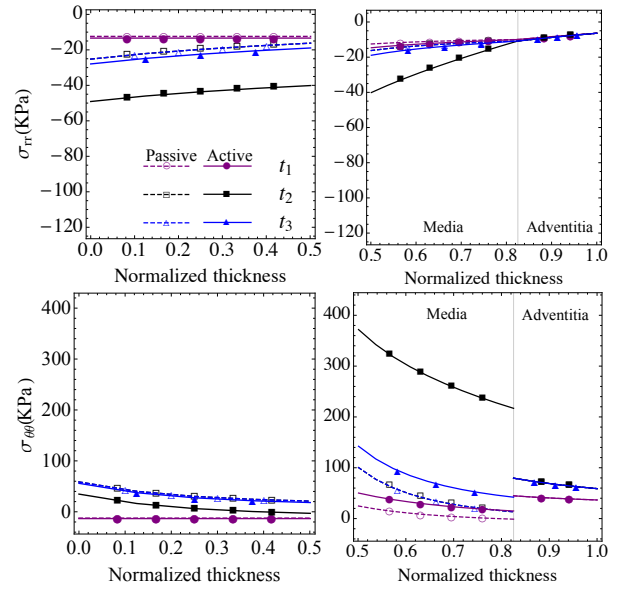


Figure 1. Stress distributions in the artery-plaque composite as a function of the normalized thickness. Active properties are denoted by the solid curves and passive properties given by the dashed curves (the legend applies for plots in the same row).

DISCUSSION

The results show that the magnitude of the stresses increases with plaque stiffness and for softer plaques there is greater cross-over viscous effects due to the interface coupling with the active viscoelastic media. When considering active viscoelasticity of smooth muscle tissue during artery overstretch, larger compression values in the plaque are predicted, which means that viscous effects are in fact non-negligible relative to the passive case.

ACKNOWLEDGEMENTS

This work was made possible by the National Science Foundation.

REFERENCES

- [1] Bergmann, G et al., *J Biomech*, 34:859-871, 2001.
- [1] Gasser, T. C., Holzapfel, G. A., *Computational Mechanics* 40, 47-60, 2006.
- [2] Holzapfel, G. A. et al., *Journal Of Elasticity And The Physical Science Of Solids* 61, 1-48, 2000.
- [3] Buffinton, C. M., Ebenstein, D. M., *Cardiovascular Engineering and Technology* 5, 244-260, 2014.
- [4] Conway, C. et al., *Annals of Biomedical Engineering* 42, 2425-2439, 2014.
- [5] Gastaldi, D. et al., *Biomechanics and Modeling in Mechanobiology* 9, 551-561, 2010.
- [6] Murtada, S.-I., Holzapfel, G. A. et al., *Journal of Theoretical Biology* 358, 1-10, 2014.

HIGH AORTIC DIAMETER VARIATION IS ASSOCIATED WITH TURBULENT-LIKE FLOW CONDITIONS IN POST-NORWOOD PATIENTS

Vivian Tan (1), Ankavipar Saprungruang (2), Brandon Peel (2) Christopher K. Macgowan (3),
David J. Barron (4), Shi J. Yoo (2), M. Owais Khan (1)

(1) Department of Electrical, Computer, and Biomedical Engineering, Toronto Metropolitan University, Toronto, ON, Canada

(2) Department of Diagnostic Imaging, Hospital for Sick Children, University of Toronto, Toronto, ON, Canada

(3) Division of Translational Medicine, Hospital for Sick Children & Department of Medical Biophysics, University of Toronto, Toronto, ON, Canada

(4) Division of Cardiovascular Surgery, The Hospital for Sick Children, University of Toronto, Toronto, ON, Canada

INTRODUCTION

Hypoplastic left heart syndrome (HLHS) is a complex congenital heart defect in which the aorta and the left heart is underdeveloped, limiting systemic circulation. HLHS can be fatal if left untreated [1]. In children with severe HLHS, treatment involves multi-stage surgical palliation of the heart. The stage I, also known as the Norwood procedure, is performed during the neonatal period and consists of complex aortic reconstruction and incorporating the pulmonary artery (PA) augmentation with a surgical patch [2].

Despite significant improvements in surgical techniques, Norwood surgery remains a high-risk procedure [3]. A key factor is the sub-optimal reconstruction of the neo-aortic geometry and resultant disturbed hemodynamics that may play a factor in post-surgical complications (e.g., neo-aortic arch obstruction or aneurysm).

The goal of this study was to characterize the neo-aortic hemodynamics in patients who had undergone stage I Norwood palliation. Specifically, we focused on four representative patients with a range of neo-aortic arch geometries and used computational fluid dynamics (CFD) to evaluate abnormal hemodynamics in the neo-aorta.

METHODS

Clinical Data: MRI scans of four patients were acquired from an existing database at the Hospital for Sick Children who had previously undergone stage I and II procedures (see Table 1). Along with MRI, all patients received phase-contrast MRI (PC-MRI) at the ascending aorta, which was used to obtain inflow waveform for CFD simulations.

Table 1: Clinical characteristics of patients

	Patient 1	Patient 2	Patient 3	Patient 4
BSA (m ²)	0.57	0.50	0.59	0.53
HR (bpm)	81	104	116	103
Q _{inflow} (mL/s)	56	39	32	34

BSA=Body Surface Area; HR=Heart Rate; Q_{inflow}=Inlet flow rate.

CFD Simulations: The open-source SimVascular software package was used to reconstruct 3D aortic model from MRI, which were meshed into ~4 million tetrahedral elements with three boundary layers. Inflow rate at the neo-aorta was assigned based on PC-MRI derived flow waveforms. Flow through each outlet was characterized by the three-element Windkessel model with parameters adjusted through an automated approach to match the flow divisions determined by Murray's Law. CFD simulations were performed with 10,000 timesteps/cardiac cycle, run for 4 cycles to wash out initial transients.

Geometric Analysis: *Vascular Modeling Toolkit* (vmtk.org) was used to compute a range of geometric parameters, such as torsion, curvature, and diameter along the length of the aorta. Diameter was normalized to the inlet diameter to allow for inter-patient comparisons. All subsequent analyses are based on normalized diameter. Linear regression was performed for diameter vs. distance data to determine the line of best fit to the data.

Hemodynamic Analysis: CFD simulations were post-processed to compute three hemodynamic parameters: wall shear stresses (WSS), oscillatory shear index (OSI), and spectral power index (SPI). While the former two are standard hemodynamic parameters, SPI is a recently-proposed parameter that quantifies the extent of "turbulence-like" (high-frequency blood flow instabilities) in cardiovascular flows using a frequency-based approach [4]:

$$SPI = \frac{\sum_{n=n_c}^{+\infty} |Y[n\omega_0]|^2}{\sum_{n=1}^{+\infty} |Y[n\omega_0]|^2} \quad (1)$$

where $|Y[n\omega_0]|$ represents the Fourier transform of the velocity signal, ω_0 is the angular frequency of the signal, and n_c is the cut-off frequency. The cut-off frequency was set to 25Hz [4].

RESULTS

Hemodynamic Analysis: Figure 1 shows SPI maps that highlight regions of turbulent-like disturbances in the neo-aorta. Patient 3 and 4

had notably higher SPI in aortic arch and descending aorta compared to Patient 1 and 2. The velocity signals (see Figure 1 inset) taken from the descending aorta also show high-frequency flow instabilities likely induced by abnormal aortic arch geometry upstream.

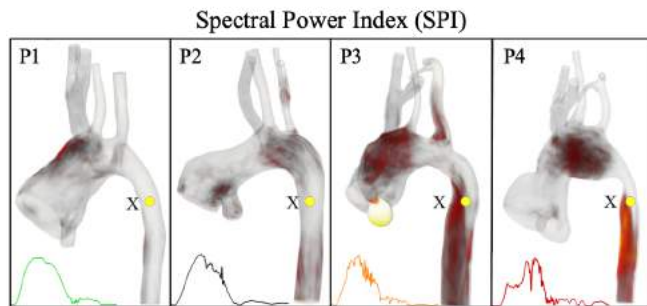


Figure 1: Spectral Power Index (SPI) volume rendered maps showing regions of high-frequency disturbances. The inset shows velocity signal in descending aorta marked with X and a yellow circle.

Geometric Analysis: Figure 2A shows normalized diameter along the length of the aorta, and a best fit line from ascending aorta to mid-descending aorta (corresponds to X in Figure 2). Patient 1 had very high correlation coefficient, which indicates a smooth transition from ascending to descending aorta. Patient 2 and 3 showed mild deviation while Patient 4 had the highest deviation from the linear line. Figure 2B shows maximum diameter deviation from the linear fit line.

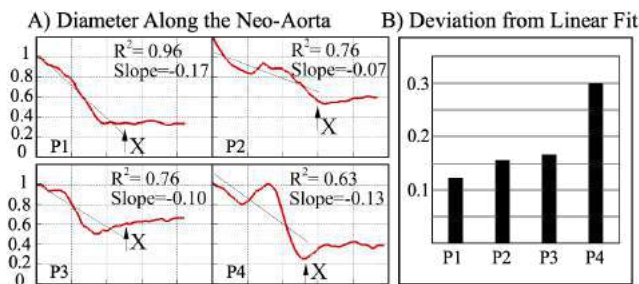


Figure 2: A) Normalized diameter along the length of the aorta and the line of best fit. B) Maximum relative diameter deviation from the linear fit line.

There was a high correlation between normalized maximum diameter deviation and SPI ($R^2=0.98$, Figure 3). No correlation was found between other hemodynamic parameters (i.e., WSS and OSI) and maximum diameter deviation.

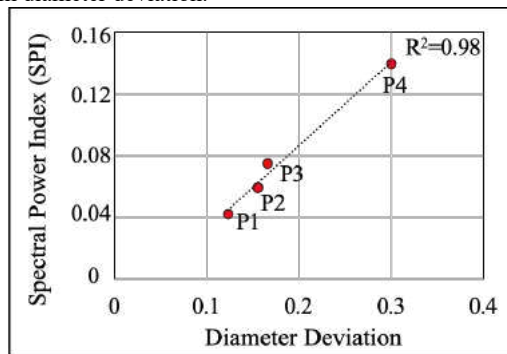


Figure 3: Correlation between maximum relative diameter deviation and spectral power index (SPI).

DISCUSSION

Inefficient aorto-ventricular interactions are recognized factors in heart failure in HLHS children post-surgery. In this study, we have demonstrated that sub-optimal aortic arch geometry is associated with turbulent-like flows that are hallmark of various vascular pathologies (e.g., stenosis, aneurysms), and similarly, may contribute to neo-aortic complications, such as aortic coarctations.

We have introduced a novel parameter, namely, diameter deviation, to quantify the changes in aortic diameter compared to linear fit line, which is conceptually similar to coefficient of determination. Previous studies have used standard deviation of aortic diameter; however, standard deviation can be misleading since aorta may taper in healthy cases even with no surgical interventions [5]. In contrast, diameter deviation is not impacted by natural tapering of the aorta since it compares the local diameter against a linear fit line.

The two conventional hemodynamic parameters (i.e., WSS and OSI) evaluated in this study showed no correlation with diameter deviation. This is not surprising since both OSI and WSS were originally designed to quantify low-frequency oscillatory flow in atherosclerotic-prone regions. In contrast, SPI showed distinct regions of turbulent-like flows in the aortic arch. These turbulent-like flows are known to induce proliferative and inflammatory endothelial gene expressions compared to non-turbulent flows [6] and thus, may be implicated in neo-aortic pathologies.

Previous studies have focused on quantifying energy losses in neo-aorta using 4D Flow MRI [5]; however, those parameters are only able to quantify non-turbulent contribution and neglect turbulent-flow contributions characterized by high-frequency signals. In addition, those parameters are dimensionalized, and thus, make it difficult to perform inter-patient comparison. In contrast, SPI not only quantifies high-frequency instabilities as a proxy of turbulent kinetic energy but also provides a non-dimensional value, both of which allow for inter-patient comparisons.

There was a strong correlation between diameter deviation and SPI. These findings highlight that the presence of turbulent-like flow in the neo-aorta could be due to sub-optimal aortic reconstruction. This has important implications for surgical intervention. For example, surgeons tend to oversize the patch to support growth; however, having a large patch can be a double-edged sword since oversized patches could induce abnormal flow conditions (e.g., similar to P4). Previous studies have shown that native neo-aortic tissue can grow to compensate for a smaller patch, and will likely grow optimally to match hemodynamic demand. Hence, future studies should use optimally designed, patient-specific patches that minimize pathological blood flow in neo-aorta.

ACKNOWLEDGEMENTS

MOK acknowledges support from NSERC Discovery Grant and Banting Research Foundation Discovery Award. VT acknowledge support from Office of the Vice-President, Research, and Innovation at Toronto Metropolitan University.

REFERENCES

- [1] Roeleveld, P.P. et al., *Cardiology in the Young*, 28(11): 1275–1288, 2018.
- [2] Ishino, K. et al., *The Journal of Thoracic and Cardiovascular Surgery*, 117(5): 920-930, 1999.
- [3] Barron, D. et al., *The Lancet*, 374.9689: 551–564, 2009.
- [4] Khan, M.O. et al., *Journal of Biomechanics*, 52: 179–182, 2017.
- [5] Schafer, M. et al., *Journal of Thoracic and Cardiovascular Surgery*, 162 (6): 1791-1804, 2021.
- [6] Aoki, T. et al., *Acta Neuropathologica Comm.*, 4(1): 1-14, 2016.

SIMULTANEOUS MEASUREMENTS OF TEMPERATURE AND BLOOD PERFUSION RATE DURING SURFACE COOLING TO EVALUATE COOLING PENETRATION IN HUMAN SHOULDER REGION

Jacob Lombardo, Md Jawed Naseem, Liang Zhu

Department of Mechanical Engineering, University of Maryland Baltimore County, Baltimore, Maryland, USA

INTRODUCTION

Shoulder injuries, including rotator cuff tears and tendonitis, have affected more than 600,000 patients each year in the US, and surgical repair is an effective treatment.¹ After the surgery, doctors recommend placing a cooling pad on the skin near the surgical site to reduce inflammation and to alleviate pain.²⁻³ However, cooling penetration depth is greatly affected by the unknown local blood perfusion rate. Uneven cooling on the surgical site are factors contributing to the discontinuous use of the cooling device by patients.

In this study, we performed experiments on volunteers to record temperatures and blood perfusion on skin surface under a cooling pad. The experimental data were used as inputs to a whole-body heat transfer model to extract heat transfer coefficients and dependence of blood perfusion on local temperature. Finally, tissue temperature fields were simulated to evaluate whether cooling penetrates into the repair site in the shoulder region.

METHODS

A commercially available cooling device was evaluated in this study. Shown in Figure 1, it consists of a container with good insulation, a pump to induce water circulation, and a cooling pad suitable for cooling on the shoulder. The cooling pad was wrapped on the shoulder of a human volunteer in a sitting position. An elastic belt was used to ensure good physical contact to the skin and an aluminum sheet was attached to the cooling pad to generate even cooling to the skin surface. A Laser Doppler Flowmeter (LDF, BLF-21D, Transonic System Inc., Ithaca, NY, USA) with a flat probe was used to estimate the local blood perfusion rate. The LDF gives a value with an arbitrary unit (AU); however, it can be used to evaluate local blood perfusion changes at a specific skin location during the cooling process.

Three healthy volunteers were recruited to this study with local IRB approval. The LDF probe was attached to the skin, then, the cooling pad was wrapped on the shoulder region of the volunteer. A thermistor bead sensor (0.8 mm dia., T-View system, Alpha Technics, Irvine, CA) was attached to the center of the cooling pad on the upper arm to measure the temperatures before and during cooling. Ice-water

mixture ($0.11 \pm 0.03^\circ\text{C}$, $n=3$) was circulating through the cooling pad and the total cooling time was 20 minutes. The oral temperature of the volunteers were also recorded before ($36.6 \pm 0.2^\circ\text{C}$, $n=3$) and after the cooling ($36.8 \pm 0.2^\circ\text{C}$, $n=3$).

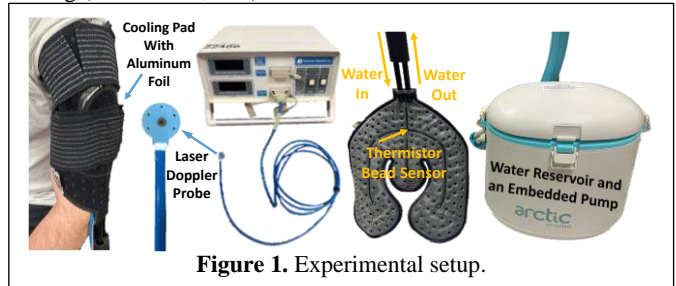


Figure 1. Experimental setup.

A physical model based on realistic measurements of a volunteer was generated. As shown in Figure 2, the body (70 kg and 1.78 m tall) consists of the brain, the internal organs, and the muscle for the rest of the body. The cooling pad is attached to the shoulder region. The thermal resistances due to convection and radiation with the surrounding air are lumped as an overall heat transfer coefficient h_{air} ($9.57 \text{ W/m}^2\text{K}$). The boundary condition of the cooling pad is also lumped as an overall heat transfer coefficient h_{water} , which will be determined from the measured temperatures during the cooling.

The Pennes bioheat equation⁴ is used to model both the steady state and the transient temperature fields of the body as

$$\rho_t c_t \frac{\partial T_t}{\partial t} = k_t \nabla^2 T_t + \omega_t \rho_b c_b (37 - T_t) + Q'''_{met,t} \quad (1)$$

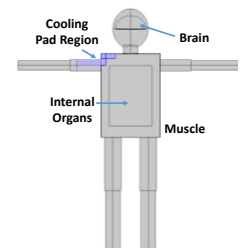


Figure 2. A model of a human body.

where ρ is density, c is specific heat, k is thermal conductivity, ω is blood perfusion rate, and Q'''_{met} is metabolic rate. Both the blood perfusion rate and metabolism are coupled and assumed decreasing as temperature drops, using the following expressions:

$$\omega/\omega_0 = Q'''_{met}/Q'''_{met,0} = A^{(37-T)/10} \quad (2)$$

where subscript 0 refers to baseline value at 37°C. The coefficient A in Eq. 2 will be determined from the measured blood perfusion rate. All the simulations were carried out by COMSOL software.

RESULTS

Tables 1 gives the physical and physiological properties needed in the model. The air temperature, T_{air} , was recorded as 22.5°C. The baseline local blood perfusion rate and the metabolism used in the simulation are shown in Table 1.

Table 1 Physical and physiological properties⁵

Properties	Brain	Internal organ	Muscle	Blood
k , W/mK	0.52	0.52	0.52	0.50
ρ , kg/m ³	1060	1060	1060	1060
c , J/kg K	3800	3800	3800	3800
ω , 1/s	0.009	0.0021	0.00053	
Q'''_{met} W/m ³	9225	2460	535.5	

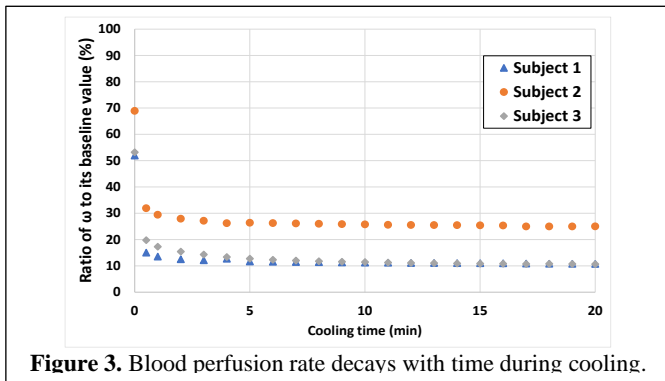


Figure 3. Blood perfusion rate decays with time during cooling.

Figure 3 gives the decaying trends of the blood perfusion rate measured by the LDF probe. The data were fitted with Eq. 2 to determine the unknown parameter A . The skin temperature was 34°C initially, then it decreased to ~27°C after the cooling pad was attached, leading to a blood perfusion rate as 50%-70% of the baseline value. After 20 minutes of cooling, the blood perfusion rate decreased to ~10%-30% of the baseline value. The determined values of A were similar among the three volunteers, varying from 1.45 to 1.9, suggesting blood perfusion decreases by 50-70% for every 10°C temperature reduction in tissue, based on Eq.2.

The recorded transient temperatures in the volunteers are shown by the symbols in Figure 4. Note that water temperatures in the reservoir only increased slightly during the cooling, by less than 0.5°C. The skin temperatures were around 27°C before water circulation, then decreased steadily to 3-5°C after 20 minutes of cooling. The experimental data were used as inputs to the simulation. While adjusting the h_{water} value (160-280 W/m²K), one obtains the best match between the experimental data and simulation predictions.

The final task of this study is to simulate the transient temperature distribution based on the recommended cooling setting by the manufacturer. The water in the reservoir should be ice-water mixture ($T_{water}=0^\circ\text{C}$) and the cooling time is set as 20 minutes. Figure 5 illustrated the baseline temperature contours (left), showing the maximal temperature of 37.3°C occurring in the brain and internal organ. After 20 minutes of cooling, one can see significant cooling penetration to the deep shoulder region (middle panel of Figure 5).

The transient temperature distribution along the vertical line in the upper arm region is also plotted in Figure 5 (right). The results show a relatively uniform temperature distribution inside the tissue

before the cooling, varying from 33°C at the skin to 36.5°C at the center. Once the 0°C water is circulating in the cooling pad, temperature decreases rapidly. Cooling penetration depth depends on the targeted temperature. If the targeted temperature is 27, 30, 33, or 35°C, then the penetration depth will be 19, 21, 29, or 35 mm, respectively. Considering that rotator cuff tear occurs at a relatively superficial region (just below the skin layer, <15 mm), it is highly likely that the surgical site and its vicinity can be cooled below 27°C.

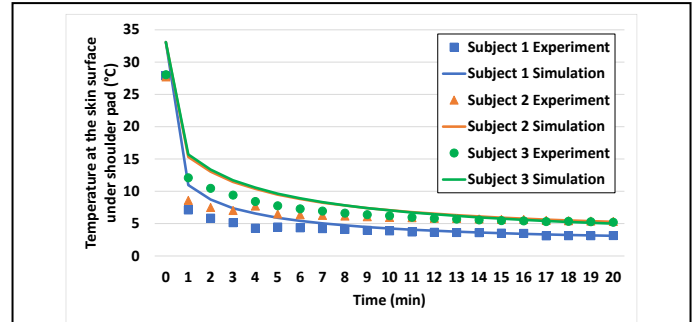


Figure 4: Recorded temperatures by the thermistor bead sensor (symbols) and the simulation using an adjustable h_{water} .

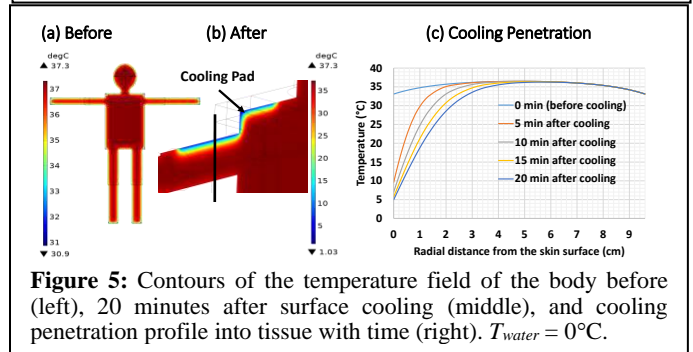


Figure 5: Contours of the temperature field of the body before (left), 20 minutes after surface cooling (middle), and cooling penetration profile into tissue with time (right). $T_{water} = 0^\circ\text{C}$.

DISCUSSION

The current study provides simultaneous measurements of temperature and blood perfusion rate at the skin surface of the shoulder region of human volunteers, leading to extraction of physical and physiological parameters needed to simulate temperature fields. The extracted parameters are within the range of normal physiology, and they are used to improve accuracy of theoretical simulations of tissue temperature fields under a cooling pad. Based on the simulation results, the model predicts a cooling penetration depth (<27°C) as 19 mm to the deep tissue region when ice-water mixture serves as the coolant. This penetration depth should be sufficient to reach the surgical repair site of rotator cuff tears or tendonitis and its surrounding tissue region (~15 mm in depth). Effective cooling may temporarily reduce nerve activity via disrupting the transmission of pain signals.²⁻³ This would be a cost-effective approach to decrease the usage of pain-killer medications, thus addressing the opioid epidemic crisis currently affecting many patients in the US.

ACKNOWLEDGEMENTS

This study was supported by an NSF S-STEM grant (DUE1742170).

REFERENCES

- [1] Yamaguchi, K. www.aaos.org/AAOSNow/2011/Jan/cover/cover1/
- [2] Bech et al., *Physiotherapy Canada*, 67(1):48-55, 2015.
- [3] Dhavalikar et al., *Journal of Exercise Science and Physiotherapy*, 5(1): 24-29, 2009.
- [4] Pennes, H. *Journal of Applied Physiology*, 1:93-122, 1948.
- [5] Caporale et al., *BMES Paper* #36-4007, 2022.

FRACTURE RISK PREDICTION USING FINITE ELEMENT MODELING IN A CANINE MODEL OF OSTEOSARCOMA

Chloe R. Brekhus (1), Kevin M. Labus (1), Bernard Seguin (2), Christian M. Puttlitz (1), Benjamin C. Gadowski (1)

(1) Department of Mechanical Engineering, Colorado State University, Fort Collins, CO, USA
(2) VCA Central Victoria Veterinary Hospital, Victoria, BC, Canada

INTRODUCTION

Pathological fractures due to bone metastases are a common occurrence for patients with advanced cancer [1]. Fracture rates are highest among those with multiple myeloma (43%), breast cancer (35%), and prostate cancer (19%) [1]. Typical treatments for such lesions include radiotherapy and various types of internal fixation, such as intramedullary nails or plates [2]; unfortunately, fracture risk in these patients is often uncertain, and doctors are forced to decide treatment plans based on visual observations of tumor size and location [2]. One way to quantify this risk is by creating patient-specific computational finite element (FE) models, which can be used to better advise doctors whether surgical intervention is necessary. The purpose of this study was to develop and validate a finite element technique to predict fracture risk using a canine radius model.

METHODS

Eight healthy radii (5 left and 3 right) were taken from canine patients euthanized for unrelated reasons. In the distal region of each radius, a cylindrical osteotomy with 25 mm radius was created to remove half of the bone width at the thinnest point and model the effect of a sarcoma, after which the samples underwent computed tomography (CT) scans with 1 mm slice resolution. For mechanical testing, samples were allotted to one of three loading conditions: three samples in cantilever bending (B1-3), three in torsion (T1-3), and two in compression (C1-2). Bending and compression samples were potted for fixation at the proximal end of the bone, while torsion samples were potted at both ends. Rosette strain gages were placed on the periosteal surface of the bone opposite to the thinnest region of the osteotomy. All samples were loaded to failure at a rate of 0.1 mm/sec or 0.5 degrees/sec, and yield load was determined from the resulting data. Finite element models were then created from the CT scans through a series of softwares, and loading and boundary conditions were added to replicate

the corresponding mechanical testing conditions of each sample (Figure 1).

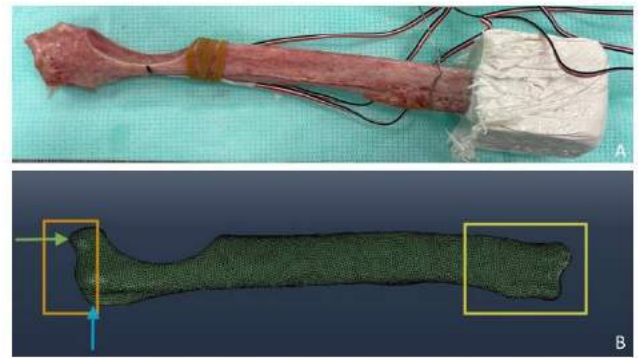


Figure 1: Experimental setup (A) and location of loading and boundary conditions in the FE models (B). All samples had a boundary condition at the proximal end, shown by the yellow box. At the distal end, bending samples were loaded along the blue arrow, compression samples along the green arrow, and torsion samples with a moment applied to the area in the orange box.

Material properties for bone were generated using previously established relationships (Equations 1 and 2) between elastic modulus and density from CT scans for canine bones [3].

$$\rho = 0.9839 + 0.00049332 * HU \quad (1)$$

$$E = 1858 * \rho^{3.09} \quad (2)$$

For the medullary cavity, three different material definitions were tested: one using Equations 1 and 2 for elastic modulus, another with a hollow cavity, and a third with a constant isotropic elastic modulus of 0.02 MPa [4]. It was found that using 0.02 MPa (the effective elastic modulus of bone marrow) produced the highest accuracy and was therefore used in all models.

Simulations were run to the experimental yield load, and stiffness values taken from displacement versus force (or torque) were compared between experimental and finite element results. Finally, the computational models were used to predict yield failure using a maximum principal strain-based criterion [5].

RESULTS

The FE models accurately predicted stiffness, with all samples having less than 8% error and three samples being within 1% (Figure 2). For maximum principal strain, the average difference between finite element and experimental data was 809 $\mu\epsilon$ (11% error), the minimum difference was 235 $\mu\epsilon$ (1.9% error), and the maximum difference was 1858 $\mu\epsilon$ (31.6% error). When comparing loading scenarios, all bending samples yielded below 500 N, compression samples yielded between 800 and 1100 N, and torsion samples yielded between 3.8 and 7.7 Nm. Strain-based yield load predictions (Figure 2) differed from experimental data by an average of 98 N (28.8%) in bending, 207 N (21.9%) in compression, and 2.5 Nm (46%) in torsion. Paired t-test ($\alpha = 0.05$) comparisons (RStudio, Posit, PBC, Boston MA) did not reveal statistical differences between experimental and computational results for stiffness, strain, or yield load.

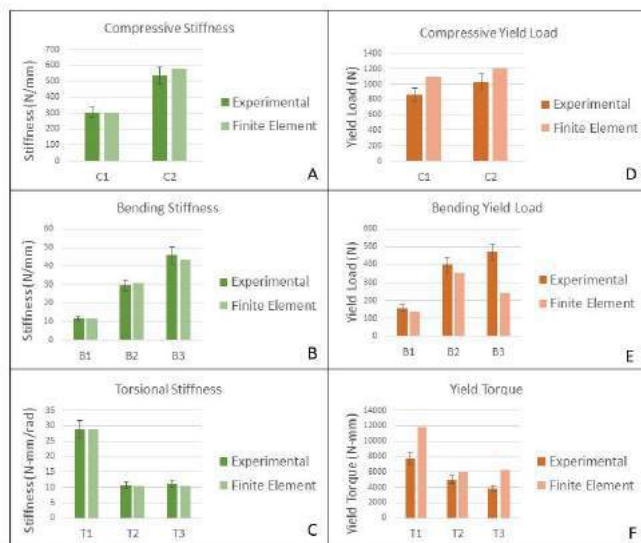


Figure 2: Comparison of experimental and finite element stiffness and yield load. Error bars represent $\pm 10\%$.

DISCUSSION

Overall, the finite element model showed high accuracy in stiffness predictions and moderate accuracy for strain and yield load. Some of the error in the strain-based yield load predictions likely resulted from not taking strain data at the exact location of the fracture, particularly for torsion samples, which exhibited spiral fractures that did not pass through the ROI.

Model validation was supported by statistical analyses, which showed no difference between experimental and FE data for stiffness, strain, and yield load, indicating no overall trends regarding over- or underprediction. Material property definition was an important aspect of the validation; by using an HU to modulus relationship for bone, differences in cortical and trabecular modulus were accounted for, while setting a homogenous modulus for bone marrow greatly reduced error from trying to extrapolate bone relationships to soft tissue.

When loaded under compression, samples generally yielded at a higher load and exhibited greater stiffness than the other loading types, which is consistent with data published by Hart et al. [6] Maximum principal strain, measured at the thinnest point of the osteotomy, was highest in bending, while torsion and compression had similar values. This suggests that samples have the highest fracture risk in bending and are strongest in compression.

Evaluating a clinical example can be useful in the context of this study; in jumping from a height of 0.65 m, peak compression forces on canine forelimbs have been measured to be 30.84 ± 3.66 N/kg [7]. Using the average canine mass in this study of 67.4 kg, this force comes out to be 2078 ± 247 N, suggesting that both compression samples would yield at lower loads than would be observed in this specific scenario. This example shows how an FE model might be used to quantify likelihood of fracture, which could aid doctors in decisions regarding radiotherapy vs stabilization.

This study had some limitations that could affect the overall accuracy and usefulness of the results. The main limitation of this procedure is the amount of manual input required to develop these models, which allows for some slight variation in properties between models, and increases the time required to test a model. These drawbacks limit this method's usefulness in clinical applications, as model creation would require trained personnel and might be expensive for patients. Another limitation is that this study utilizes simple loading conditions, whereas bones *in vivo* are subject to complex combined loading. If this model were to be used in a clinical setting, research would have to be performed regarding the type and magnitude of loading the patient's bone is most likely to endure in order for the fracture prediction to be clinically relevant.

Future studies will further validate this technique using canine radii with clinically diagnosed osteosarcoma; while the tumor was modeled as a completely empty defect in this study, real tumors will have some mechanical properties that may not follow the HU to modulus equations used for healthy bone. Additionally, various types of fixation will be tested to optimize fracture risk reduction, which will ideally be translated to use in human patients. The importance of this study is that it validated a finite element technique to predict yield, which can provide a quantitative measure of fracture risk when compared to common physiologic loads, ultimately helping doctors make treatment decisions for patients with osteosarcoma.

REFERENCES

- [1] Saad, F et al., *Cancer*, 110:1860-1867, 2007.
- [2] Willeumier, J et al., *EFORT Open Rev*, 1:136-145, 2016.
- [3] Laurent, C et al., *J Engineering in Medicine*, 230:639-649, 2016.
- [4] Jansen, L et al., *J Mech Behav Biomed Mater*, 50:299-307, 2015.
- [5] Yosibash, Z et al., *Phil Trans R Soc*, 368:2707-2723, 2010.
- [6] Hart, N et al., *J Musculoskeletal and Neuronal Interactions*, 17:114-139, 2017.
- [7] Pardey, D et al., *Vet Record*, 182:716-716, 2018.

A NEW METHOD FOR GENERATING VIRTUAL BONE SCANS FOR THE PURPOSE OF INVESTIGATING THE EFFECTS OF CORTICAL MICROSTRUCTURE

**Zachary B. Toth (1)
Dr. Joshua Gargac (1)**

(1) Mechanical Engineering, Ohio Northern University, Ada, OH, USA

INTRODUCTION

Globally, bone fractures represent a significant public health issue, affecting 178 million individuals per year, as of 2019 [1]. According to some estimates, the United States alone spends somewhere between \$12.9 and \$16.9 billion per year on non-traumatic fractures [2,3]. Stress fractures, a type of cortical bone fracture most commonly affecting both elderly and physically active people, have a considerable rate of occurrence at approximately 5.7 fractures per 1000 people per year [4,5,6]. The significance of stress fractures lies in the form they take—small cracks in cortical bone caused by repeated mechanical stresses. Because of this, it can be seen that their formation might be influenced by factors such as the geometry and porosity of the cortical bone.

Cortical bone, while somewhat less well understood in regard to bone fragility than trabecular bone, makes up approximately 80% of the human skeleton and serves as a major load-bearing component [7]. According to Augat and Schorlemmer [8], the strength of cortical bone is not only influenced by macro-scale structural properties such as bone cortex thickness and cross-sectional area but is also largely contributed to by microstructural properties such as crystallinity, incidence of microcracks, and cortical porosity. This strength can be measured multiple ways but is primarily either found as a direct measurement through mechanical testing, or derived from Finite Element models of bone scans, such as ultrasounds or micro-Computed Tomography (μ CT) scans [9,10,11].

Evaluating the contribution of microstructure to overall bone strength is tricky since it can be difficult to control changes to pore structure. The ability to easily generate bone samples with their desired microstructural properties would make research into the effects of microstructure more precise. In this vein, designing a program that could do this is a promising solution. Given certain input parameters relating to the desired bone structure, it would generate a 3-dimensional model of micron-scale cortical bone. Ideally, these parameters could be varied to generate images with high similarity to CT scans of cortical

bone thus allowing for the simple generation of additional samples. Additionally, changing the parameters would create opportunities to isolate their specific effect on overall bone strength.

METHODS

In order to mimic cortical bone as closely as possible, previous literature about cortical bone's structure and remodeling mechanics first had to be reviewed. A MATLABTM (MathWorks, Natick, MA) program was then developed that could build an array resembling the network of canals that makes up the haversian systems characteristic of cortical bone. The program generates canals through the array, varying their size, shape, and location based on user-defined input parameters. These parameters include average pore radius, average pore circularity, pore location, and the target porosity. Each of these parameters and their input ranges are based on the current literature [12,13]. Successive canals generate, often in a network with previous canals, until the target porosity is reached. The array is then saved as a TIFF file, which can be opened and processed in other applications.

For comparison, μ CT scans of human cortical bone were acquired. The samples used were obtained from the proximal and mid-diaphysis of an 85-year-old male tissue donor. Samples were machined into cylindrical “dog-bone” specimens with a gauge length of 10 mm and a gauge diameter of 3 mm. Micro-CT scans were acquired (mCT-80, Scanco Medical AG, Brüttisellen, Switzerland) at 10 μ m resolution, 70 kVp voltage and 114 μ A current with 1000 projections at a 600 ms integration time with slices oriented perpendicular to the longitudinal axis of the specimen [14]. The μ CT scans were then processed in ImageJ (U.S. National Institutes of Health, Bethesda, MD) into binary 200 μ m cubic TIFF files.

RESULTS

The 200 μ m cubic bone cores can be opened and visualized in Seg3D (Scientific Computing and Imaging Institute, Salt Lake City,

UT). An example of a generated bone core as compared to one obtained from a CT scan is shown in Figure 1. Images in the first two rows have been inverted to show internal structure by displaying the canals rather than the solid bone. There is a remarkable degree of similarity between an actual CT scans and generated cores, indicating that early builds of the program are able to closely resemble the range of variation within living tissue. This similarity can be most directly seen in the networked nature of the model.

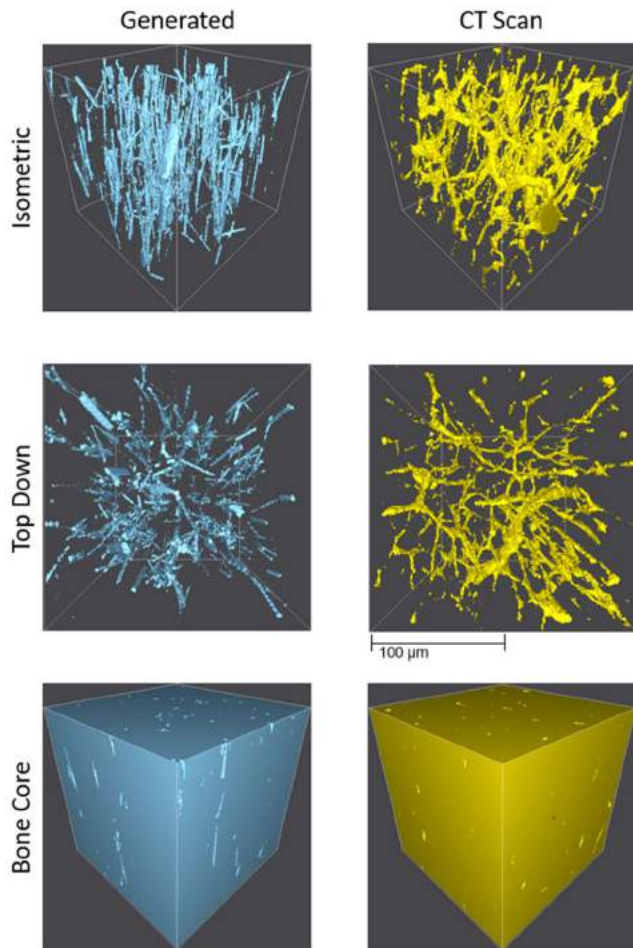


Figure 1: Computer-Generated Sample (Left) and Inverted CT scan of Human Cortical Bone (Right). Three views are shown: An isometric view of the bone core, (Top), a top-down view of the bone core (Center), and a non-inverted isometric view of the bone core (Bottom).

DISCUSSION

In future work, there are two main objectives. First, the program's ability to match geometric features of the μ CT scans must be evaluated and quantified. This would demonstrate the program's efficacy at mimicking real bone and might further inform future parameters for generating bone images. This step will also include identifying which input values are able to most closely approximate bones from different species and age groups. The second objective is to develop a graphical

user interface, which would make the program easier to use once it is published as an open-sourced tool.

This program could be a useful tool for investigating the mechanical effects of different porosities. For example, Schaffler and Burr [15] tested 20 bone core samples, but found that some porosity values were underrepresented due to the relatively small sample size and the variation that comes from nature. With the ability to generate additional samples within this range, less interpolation might have been necessary, potentially leading to more precise data. This program will also enable researchers to isolate the effects of specific variations in pore geometry, such as pore shape. Currently, it is difficult to find samples consisting of mostly tapered pores [16], and therefore researchers are not able to quantify the effects of this microstructural change. Using this program, the presence of these geometric features can be controlled. In practice, this could enable researchers to evaluate the mechanical effects of microstructural changes caused by new medicines [17].

ACKNOWLEDGEMENTS

The authors would like to thank Glen Niebur and Ryan Roeder at the University of Notre Dame for providing the human cortical bone μ CT scans.

REFERENCES

- [1] Wu, A.-M., et al., *The Lancet Healthy Longevity*, 2(9):580-592, 2021. [https://doi.org/10.1016/s2666-7568\(21\)00172-0](https://doi.org/10.1016/s2666-7568(21)00172-0)
- [2] Burge, R., et al., *Journal of Bone and Mineral Research*, 22(3):465–475, 2007. <https://doi.org/10.1359/jbmr.061113>
- [3] Orsini, L. S., et al., *Osteoporosis International*, 16(4):359–371, 2004. <https://doi.org/10.1007/s00198-004-1694-2>
- [4] Waterman, B. R., et al., *Military Medicine*, 181(10):1308–1313, 2016. <https://doi.org/10.7205/milmed-d-15-00571>
- [5] Rizzone, K. H., et al., *Journal of Athletic Training*, 52(10):966–975, 2017. <https://doi.org/10.4085/1062-6050-52.8.01>
- [6] Knowles, S. B., et al., *Journal of athletic training*, 41(2):207–215, 2006. <https://www.ncbi.nlm.nih.gov/pmc/articles/PMC1472638/>
- [7] Ott, S. M., *American Journal of Nephrology*, 47(6):373–375, 2018. <https://doi.org/10.1159/000489672>
- [8] Augat, P., & Schorlemmer, S., *Age and Ageing*, 35(suppl_2):ii27–ii31, 2006. <https://doi.org/10.1093/ageing/afl081>
- [9] Grimal, Q., et al., *Medical Engineering & Physics*, 31(9):1140–1147, 2009. <https://doi.org/10.1016/j.medengphy.2009.07.011>
- [10] Duchemin, L., et al., *Medical Engineering & Physics*, 30(3):321–328, 2008. <https://doi.org/10.1016/j.medengphy.2007.04.008>
- [11] Keyak, J. H., et al., *Medical Engineering & Physics*, 23(9):657–664, 2001. [https://doi.org/10.1016/s1350-4533\(01\)00094-7](https://doi.org/10.1016/s1350-4533(01)00094-7)
- [12] Bakalova, L. P., et al., *Journal of Bone and Mineral Research*, 33(12):2177–2185, 2018. <https://doi.org/10.1002/jbmr.3561>
- [13] Pazzaglia, U. E., et al., *Clinical Orthopaedics & Related Research*, 467(9):2446–2456, 2009. <https://doi.org/10.1007/s11999-009-0806-x>
- [14] Turnbull T. L., et al., *Journal of Biomechanics*, 47(12):3135–3142, 2014. <https://doi.org/10.1016/j.jbiomech.2014.06.022>
- [15] Schaffler, M. B., & Burr, D. B., *Journal of Biomechanics*, 21(1):13–16, 1988. [https://doi.org/10.1016/0021-9290\(88\)90186-8](https://doi.org/10.1016/0021-9290(88)90186-8)
- [16] Pazzaglia, U. E., et al., *Anatomia, Histologia, Embryologia*, 39(1):17–26, 2010. <https://doi.org/10.1111/j.1439-0264.2009.00973.x>
- [17] Tsukamoto, M., et al., *Modern Rheumatology Case Reports*, 6(2):301–304, 2021. <https://doi.org/10.1093/mrcr/rxab048>

DEVELOPING AND TESTING A NOVEL DEVICE FOR DETECTING PERIPHERAL ARTERY DISEASE USING RADIO FREQUENCY ENERGY

J Nelson (1), C Cobb (1), J Keller (2), D Nelson (1), M Francis (3)

(1) William B. Burnsed, Jr. Department of Mechanical, Aerospace, and Biomedical Engineering,
University of South Alabama, Mobile, AL, USA

(2) Department of Health, Kinesiology, and Sport, University of South Alabama, Mobile, AL, USA

(3) Department of Physiology and Cell Biology, University of South Alabama, Mobile, AL, USA

INTRODUCTION

Peripheral Artery Disease (PAD) is a condition characterized by reduced blood flow in the arteries of the arms and legs. People at high risk for PAD include those with diabetes, high cholesterol, and those who smoke. Persons with PAD have an elevated risk of cardiovascular (CV) events such as stroke and heart attack [1,2]. Generally, only people who present symptoms such as claudication and ulcers are tested for PAD. An estimated 20-50% of persons with PAD are asymptomatic, so they are unknowingly at risk for CV events [3].

Early intervention can greatly improve outcomes for persons with PAD by mitigating disease progression from asymptomatic PAD to symptomatic PAD [4,5]. This reduces the risk of claudication, ulcers, amputation, and CV events [5]. PAD disproportionately affects minority populations. In the US, African Americans are roughly twice as likely to have PAD as are non-Hispanic white Americans [6-8]. Racial Minorities also have poorer outcomes [9-12]. Among those with PAD, African Americans experience amputations at twice the rate, and Hispanics at a 50% higher rate than do whites [11]. The importance of early intervention and the racial disparities in patient outcomes presents a need for a widespread screening tool that can be used by anyone in a high-risk group.

Current methods for diagnosing PAD are limited [3,13]. The standard diagnostic tool is the Ankle-Brachial Index (ABI), a ratio of the blood pressure in the arm to the blood pressure in the ankle. ABI is administered to patients presenting with overt symptoms of PAD, meaning asymptomatic people are not tested even if they are at high risk for PAD [3]. Additionally, administering ABI tests requires special training, can be time-consuming, and the results are not always consistent with a patient's PAD status because they can vary with simple exercise such as walking [13,14]. It is not reliable in persons with arterial calcifications, such as those with diabetes, which includes many people in the high-risk categories for PAD [15,16]. This presents the

need for a screening method that can be used on anyone in a high-risk group during routine check-ups.

Infrared (IR) thermography, the process of using infrared light to obtain temperature measurements, is an emerging technology in PAD detection. Static thermal images show that reduced blood flow correlates to lower skin temperature under controlled conditions [17], but factors like skin thickness, ambient temperature, and natural body temperature can affect skin surface temperature [18]. This makes static thermographic images an unreliable method of relating body temperature and blood flow. Using similar principles, thermographic measurements can be taken over a period with a stimulus applied to observe temperature response, which removes limiting factors present in static measurements. This is known as Active Dynamic Thermography (ADT). By applying a known amount of energy to the skin and measuring the rate of skin surface temperature change, a thermal constant can be obtained and used as a normalized metric for identifying PAD.

Our lab is utilizing ADT to develop a tool for noninvasive and portable detection of PAD. This technology (REFLO) uses low-power radio frequency (RF) energy in the Ka band (26.5 – 40 GHz) to heat the skin while simultaneously measuring the surface temperature. The amount of blood flowing through the vasculature affects the temperature of the skin during and after heating, which will allow us to define 'normal' blood flow versus that of PAD [19,20].

We have tested this concept *in vivo* using rabbit pinnae, an accepted model for human skin due to its similar vascular properties [20], and *in silico* with a computer-generated flow model. We have designed an advanced prototype that is more compact and portable than previous versions. It employs a small micropatch antenna and an infrared (IR) temperature sensor, integrated in a compact transducer. A photo of the transducer is shown in Figure 1. The device is battery powered to avoid risk of shock and includes an overheat shutoff feature to avoid burning the skin. During our human subject testing in Spring

2023, measurements will be taken prior to, during, and after tourniquet-induced ischemia, using both the REFLO device and a near-infrared spectroscopy (NIRS) device. We hypothesize that the results as indicated by the REFLO device will correlate with readings from the NIRS device.

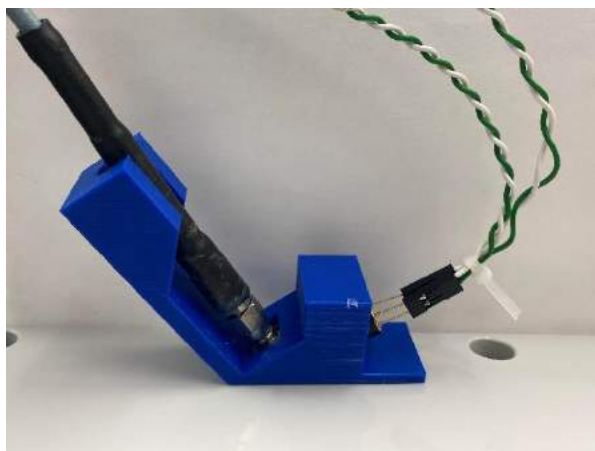


Figure 1. Device transducer.

METHODS

Our human subject experiments are being conducted under a protocol approved by the University of South Alabama Institutional Review Board. Healthy adults of both sexes between the ages of 18 and 31 are eligible to participate. During the study, the REFLO vascular assessment device will be tested and compared to NIRS, an accepted indicator of vascular function. The results will be used to assess the feasibility of using the REFLO device for future screening and diagnosis of PAD and other conditions. Ultimately, this study is designed to collect data in healthy, young adults to develop rationale for future studies within clinical populations.

A vascular occlusion test will be conducted to determine muscle oxygenation via a NIRS device. The participant will undergo 5 minutes of ischemia through a well-accepted protocol routinely used in the associated literature with no known risks other than comparable sensations to a limb “falling asleep”.

During testing of the REFLO device, a small area of skin on the lateral portion of the calf will be heated for a period of up to one minute, or until the surface temperature reaches 40°C, whichever occurs first. Skin surface temperature will be recorded continuously on a computer before, during, and after heating. To ensure safety, a failsafe mechanism in the controller will disconnect the transmitter should the skin temperature exceed 40°C during heating.

Upon the conclusion of our human subject study, thermal constants will be obtained correlating to normal, low, and high flow. We will determine if these constants are statistically significant, indicating whether our device can differentiate between normal and impaired flow.

EXPECTED RESULTS

We predict that the REFLO device will detect the highest rates of heating and cooling during tourniquet-induced ischemia and the lowest rates of heating and cooling during post-occlusive reactive hyperemia. Results will be presented showing the extent to which the rate of temperature change correlates to low, normal, and high flow, indicating the feasibility of our device accurately detecting PAD.

ACKNOWLEDGEMENTS

This work was supported by a Research and Scholarly Development Grant from the University of South Alabama Office of Research and Economic Development.

REFERENCES

- [1] Conte MS et al, Global Vascular Guidelines on the management of chronic limb-threatening ischemia, *J Vasc Surg*, 69(6 Suppl):3S-125S.e40, 2015.
- [2] Neschis D et al, Clinical features and diagnosis of lower extremity peripheral artery disease, *UpToDate*, 2002.
- [3] Alahdab F et al, A systematic review for the screening for peripheral artery disease in asymptomatic patients, *J Vasc Surg*, 61(3, Supplement):42S-53S, 2015.
- [4] Ferket B et al, Systematic Review of Guidelines on Peripheral Artery Disease Screening, *American Journal of Medicine*, 125:198-208, 2012.
- [5] Itoga N et al, Cost-effectiveness analysis of asymptomatic peripheral artery disease screening with the ABI test, *Vasc Med*, 1-10, 2018.
- [6] Selvin, E et al, Prevalence and risk factors for peripheral arterial disease in the United States: results from the National Health and Nutrition Examination Survey, 1999-2000, 110(6):738-743.
- [7] Allison, MA et al, The effect of novel cardiovascular risk factors on the ethnic-specific odds for peripheral arterial disease in the Multi-Ethnic Study of Atherosclerosis (MESA), *J Am Coll Cardiol.*, 48(6) 1190-1197.
- [8] Kullo, IJ et al, Ethnic differences in peripheral arterial disease in the NHLBI Genetic Epidemiology Network of Arteriopathy (GENOA) study, *Vasc Med*, 8(4):237-242, 2003.
- [9] Arya, S et al, Race and socioeconomic status independently affect risk of major amputation in peripheral artery disease, *J Am Heart Assoc*, 7(2):e007425, 2018.
- [10] O'Donnell, TF et al, Regional variation in racial disparities among patients with peripheral artery disease, *J Vasc Surg*, 68(2):519-526, 2018.
- [11] Mustapha, J et al, Explaining racial disparities in amputation rates for the treatment of peripheral artery disease (PAD) using decomposition methods, *J Racial Ethn*, 4(5):784-795, 2017.
- [12] Rizzo, JA et al, Racial disparities in PAD-related amputation rates among Native Americans and non-Hispanic whites: An HCUP analysis, *J Health Care Poor Underserved*, 29(2):782-800, 2018.
- [13] Stein R et al, Limitation of the resting ankle-brachial index in asymptomatic patients with peripheral artery disease, *Vasc Med*, 11(1):29-33, 2006.
- [14] Ankle Brachial Index: Quick Reference Guide for Clinicians, *J Wound Ostomy Continence Nurs.*, 39(2S):S21, 2012.
- [15] Aerden D et al, The Ankle-Brachial Index and the Diabetic Foot: A Troublesome Marriage, *Ann Vasc Surg*, 25(6):770-777, 2011.
- [16] Potier L et al, Use and Utility of Ankle Brachial Index in Patients with Diabetes, *Eur J Vasc Endovasc Surg*, 41(1):110-6, 2011.
- [17] Ilo A et al, Infrared Thermography as a Diagnostic Tool for Peripheral Artery Disease, *Adv Skin Wound Care*, 33(9):482-488, 2020.
- [18] Saiko G, Skin Temperature: The Impact of Perfusion, Epidermis Thickness, and Skin Wetness, *Appl Sci Switz*, 12(14), 2022.
- [19] Latif et al, A novel transducer for measurement of skin blood flow using radio frequency energy, *JESMDT*, 2:041007-1-6, 2019.
- [20] Nelson D et al, Feasibility of using thermal response to Ka band millimeter wave heating to assess skin blood flow, *Physiol. Meas.*, 39(4), 2018.

COMPUTATIONAL MODELING OF FLUID PERFUSION IN A BIPHASIC VOCAL FOLDS TISSUE DURING PHONATION: POTENTIAL ROLE OF PERMEABILITY

Isabella McCollum (1), Alexis Throop (1), Durwash Badr (1), Rana Zakerzadeh (1)

(1) Department of Engineering, Rangos School of Health Sciences
Duquesne University, Pittsburgh, PA, USA

INTRODUCTION

During voice production, pressurized air from the lungs passes through the larynx and the vocal folds (VFs) will start to self-oscillate. This vibration is referred to as phonation and involves complex fluid-structure interactions (FSI) between the tissue of the VFs and the airflow through the larynx. VF modeling provides a prediction of VF dynamics and glottal flow which can lead to an improved understanding of these interactions. When modeling the VF, it is a common assumption to consider the tissue to be an elastic model, however, the folds behave more closely as a poroelastic tissue [1], with an 80% fluid volume fraction, which justifies the use of poroelastic models [2] and making the interactions a fluid-porous structure interaction (FPSI). Previous computational efforts that assumed a biphasic model of the VF tissue ignored the glottal aerodynamics, and the vibration was induced by applying direct load pressures [3, 4]. Combining both the porous model with aerodynamics is a computationally challenging problem but may provide a more realistic model to better help us understand VF behavior and lead to treatment and prevention of voice-related disorders such as vocal fatigue and dehydration that are commonly associated with VF permeability.

The purpose of this study is to investigate the spatiotemporal interstitial fluid dynamics of the porous VF tissue under varying permeability. Compared to previous studies, we develop a Multiphysics computational framework of the airflow through the larynx coupled with the poroelastic tissue dynamics to incorporate both aspects of the interaction. The computational model utilizes FSI methodology to simulate the biphasic behavior of the VFs during phonation as a poroelastic tissue. The effect of permeability on the fluid circulation within the VF tissue and the laryngeal aerodynamics was studied.

METHODS

A three-dimensional model of the VFs within the larynx was constructed using Autodesk Fusion 360 software and computational analysis was implemented in ANSYS Workbench software. To simulate

the dynamic FSI between the airflow and poroelastic tissue, a fully coupled Multiphysics model was created. The airflow dynamics were defined in ANSYS CFX software, while the tissue mechanics were modeled in ANSYS Mechanical.

The airflow was modeled by the unsteady, incompressible Navier-Stokes equations, while the Brinkman equation was used to govern the flow through the porous medium. The VF tissue was assumed to be a one-layer isotropic permeable material. A static inlet pressure of 1 kPa was defined at the subglottal region while the pressure at the outlet of the supraglottal region was fixed at 0 kPa with a zero normal velocity gradient condition applied across the domain. The 3D model and boundary conditions are shown in **Figure 1**. The surfaces of the VF in contact with the fluid domain are free to move with no-penetration conditions. The lateral surfaces of the VFs in contact with the outside are treated with opening conditions for fluid to circulate within the folds. All other exterior surfaces of the domains are treated with no-slip and no-penetration conditions. The FSI occurs on the superior, medial, and inferior surfaces of the VF. The material properties of the VFs and airflow used in numerical simulations were defined in **Table 1**. The permeability constant of the VFs was varied in the range of $k = 10^{-13} \text{ m}^2$ to 10^{-7} m^2 and the coupled system was solved for each case to provide a prediction of the interstitial fluid flow within the VF tissue.

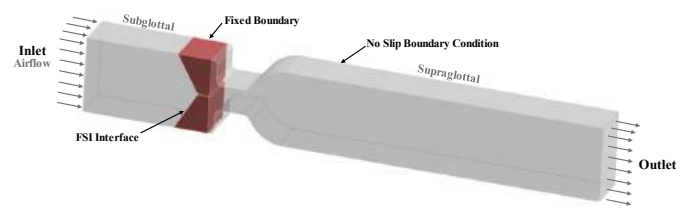


Figure 1: 3D laryngeal model (VFs are shown in red, air domain is depicted in grey) and boundary conditions.

Table 1: Physical parameters and material properties.

Domain	Parameter Description	Parameter Value
Air	Density	1.185 kg/m ³
	Dynamic Viscosity	1.831x10 ⁻⁵ kg/m·s
Vocal Folds	Density	1070 kg/m ³
	Poisson Ratio	0.45
	Young's Modulus	40 kPa

The CFX and Mechanical components were joined along the FSI boundary using the System Coupling component, which solves the fluid and solid domains separately to obtain pressure loads in CFX that are applied to the VFs on the fluid-solid interface, solving for tissue dynamics in Mechanical. This process of the System Coupling algorithm in ANSYS is illustrated in **Figure 2**. The pressure loads obtained from the coupled system were then imported into the second CFX component to capture the fluid circulation within the porous tissue.

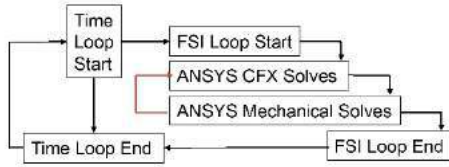


Figure 2: FPSI algorithm in ANSYS Workbench.

RESULTS

The results for the aerodynamics of the glottal flow through the larynx, particularly the pressure and velocity contours, are shown in **Figure 3**. The airflow is driven from the inlet to the outlet by a pressure drop between the subglottal and supraglottal pressures and interacts with the permeable VFs to initiate the flow-induced vibrations.

The uniform velocity streamlines at the inlet reach a maximum value between the folds at the glottis region, then recirculate before exiting the outlet. The subglottal pressure produces a pushing force in the flow direction on the VFs as well as a compressive force in the transverse direction, causing both the inferior and superior surfaces of the fold's tissue to abduct, and thus the glottis opens and closes.

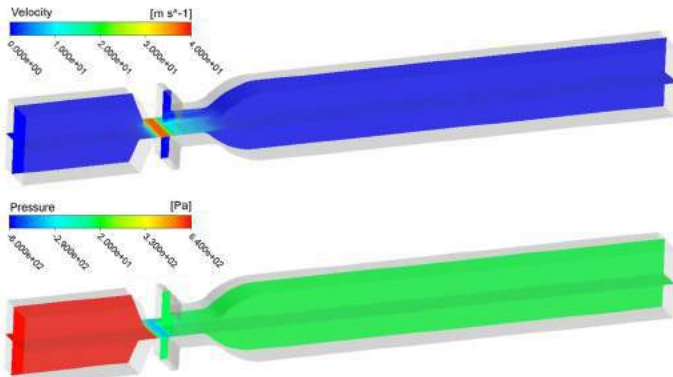


Figure 3: Velocity and pressure contours of airflow in the larynx obtained at the glottal opening time instant.

As the airflow causes the folds to self-oscillate, fluid circulates within the porous tissue of the VFs. The filtration velocity streamlines from four cases with varying permeability are provided in **Figure 4**. The maximum flow velocity during phonation reaches the highest magnitude in the case where the permeability is the highest, as expected.

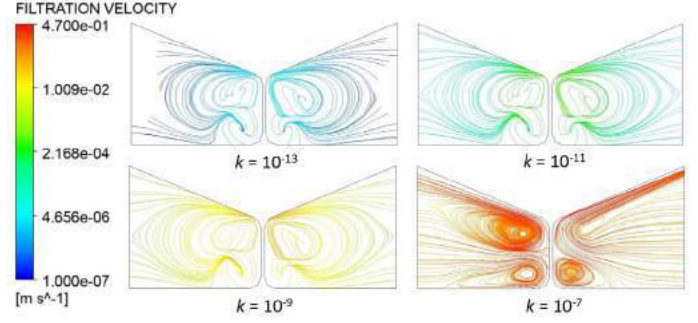


Figure 4: Interstitial fluid streamlines show circulation in porous VF tissue for cases with different VF permeability values.

As an indicator of fluid flow within the VF tissue, we define a measure for the volumetric average of filtration velocity over the VF domain \bar{q}_{VF} calculated by equation (1) below and the corresponding results are reported in **Figure 5** for each permeability value.

$$\bar{q}_{VF} = \frac{\int_{\Omega_{VF}} q_{VF} d\Omega_{VF}}{\int_{\Omega_{VF}} d\Omega_{VF}} \quad (1)$$

It can be observed that both the maximum filtration velocity and the volumetric average of filtration velocity vary with the permeability. The greater the permeability, the faster the flow, and thus a greater circulation of fluid within the porous tissue is observed.

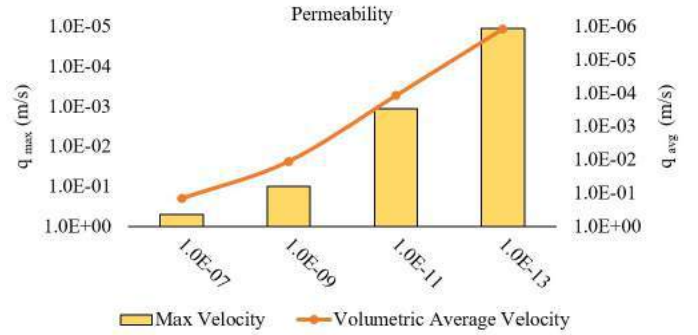


Figure 5: Variation of filtration velocity in the VFs for cases with varying permeability. Bars show the peak value of q_{VF} and the line represents the change in the \bar{q}_{VF} trend.

DISCUSSION

An FPSI framework for the VF was developed to investigate the interstitial fluid dynamics within the VF tissue under varying permeability. Based on our results shown in **Figures 4-5**, we observed that the tissue permeability significantly affects the filtration velocity distribution and its maximum value. Thus, permeability plays a role in tissue perfusion during phonation.

ACKNOWLEDGEMENTS

This project is funded by the Charles Henry Leach II Fund and the National Science Foundation under grant CBET 2138225.

REFERENCES

- [1] Noordzij, J.P., et al. Otolary Clinics of Nor Amer, 39(1): 1-10, 2006.
- [2] Miri, A.K., et al. J Voice, 28(6): 657-667, 2014.
- [3] Kvitt, A.A., et al. J Voice, 29(3): 265-272, 2015.
- [4] Scholp, A., et al. J Acoust Soc of Amer, 148(4): 2161-2172, 2020.

SIGNIFICANCE OF VASA VASORUM OXYGEN SUPPLY IN THE NOURISHMENT OF THE ANEURYSMAL WALL

Manoela Neves (1), Alexis Throop (1), Rana Zakerzadeh (1)

(1) Department of Engineering, Duquesne University
Pittsburgh, PA, USA

INTRODUCTION

An abdominal aortic aneurysm (AAA) represents a progressive localized dilation of the central aorta that asymptotically develops over long periods of time as a result of the remodeling and weakening of the arterial wall extracellular matrix that can suddenly rupture. Most AAAs contain a layer called an intraluminal thrombus (ILT). The presence of an ILT leads to localized oxygen loss (called hypoxia) in the AAA owing to the ILT's limited diffusion, which triggers adventitial angiogenesis and aggravates inflammatory infiltration from the outer vessel layers. Hence, the loss of oxygen supply leads to inflammation, degradation, and finally weakness of the aneurysmal wall, making the aneurysm more likely to grow quickly and rupture.

Although the effects of ILT thickness on oxygen starvation in the AAA wall have been confirmed [1], features such as the adventitial vasa vasorum (VV) blood vessels have been observed to be stenotic in both small and large AAA, with the sac tissue being ischemic and hypoxic. Therefore, given the small number of VV in the abdominal aorta, their stenosis exacerbates tissue hypoxia. A parametric study can be helpful to investigate the importance of this effect, as well as to assess the contribution of VV to AAA nourishment and oxygenation.

The sensitivity of the oxygen distribution to the chosen VV value has previously been studied in idealized AAA geometries [2]; however, the effect and contribution of VV in patient-specific geometries have not been explored. Therefore, the objective of this study is to simulate and examine a patient-specific AAA model and analyze the extent to which different VV oxygen concentrations in ILT presence influence the transport of oxygen to the aortic wall. By implementing a computational model of coupled blood flow and oxygen transport, it is possible to analyze the influence of the model parameters on oxygen delivery to the AAA arterial wall.

METHODS

A patient-specific model of AAA including an ILT is considered (Figure 1). The geometry is reconstructed from computed tomographic

(CT) scans, and SimVascular software is used to segment the lumen and ILT domains. The arterial wall is extruded from the vessel wall in the image with a thickness of 2 mm. Therefore, three domains are constructed: the ILT (shown in red), the lumen, and the arterial wall (shown in grey). All three domains are meshed in the open-source software, Gmsh, using tetrahedral elements.

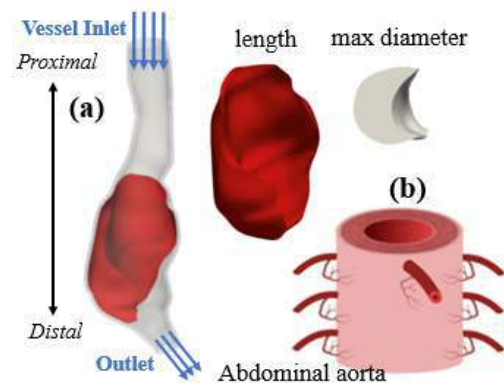


Figure 1: Patient-specific AAA geometry (a) VV vessels in the infrarenal abdominal aorta do not penetrate the medial layer (b).

The blood flow in the lumen is assumed to behave as a Newtonian, incompressible viscous fluid and is represented by the Navier-Stokes equation. The blood flow is coupled with oxygen transport in the lumen, which is governed by the convection-diffusion equation. The oxygen concentration at the inlet of the lumen is prescribed as $5.12 \times 10^{-3} \text{ kg/m}^3$. Moreover, at the lumen inlet, a uniform systolic pressure of $p_f^{in} = 130 \text{ mmHg}$ is applied as a boundary condition. A mass flow rate of 0.075 kg/s is applied at the outlet.

Both the ILT and arterial wall are assumed to be hyperelastic, homogeneous, incompressible, and isotropic materials. Moreover, the second-order Mooney-Rivlin material model is adopted for the arterial wall and ILT. In terms of oxygen transport, the ILT is assumed to be permeable to oxygen molecules through diffusion without any oxygen consumption. Thus, the oxygen transport in the ILT is modeled by the diffusion equation. The oxygen transport in the arterial wall is described by the diffusion-reaction equation, where a reaction term accounts for the metabolic consumption of oxygen. Fixed support boundary conditions are assigned at the inlet and outlet cross sections of the arterial wall. The outer AAA wall is traction-free with no external pressure on the surface.

A fully coupled multiphysics model was created in ANSYS Workbench to account for the dynamic fluid-structure interactions between the blood, ILT, and AAA wall. Hemodynamics and oxygen transport properties are defined in ANSYS CFX while arterial wall and ILT mechanics are modeled in ANSYS Static Structural component. The fluid and solid components directly interact via a single FSI boundary prescribed in the mechanical feature. The simulation is carried out using ANSYS System Coupling. Specific details of the coupled FSI-oxygen transport modeling framework are provided in [3].

In this study, the importance of the VV on oxygen flow is observed by performing numerical simulations with varying levels of oxygen concentration on the adventitia. We considered three cases ranging from neglecting VV to the physiologically normal values for the healthy artery, with oxygen concentration on the exterior wall surface (VV) of VV1 = 0 kg/m³, VV2 = 1.25 × 10⁻³ kg/m³, and VV3 = 2.56 × 10⁻³ kg/m³.

RESULTS

Using the prescribed conditions at the inlet and outlet of the AAA model, the obtained luminal velocity value matches the typical peak systolic blood velocity of 0.23 m/s (see [3] for hemodynamics results). **Figure 2** demonstrates the oxygen concentration along a cross-section on the center of the AAA bulge, which is kept consistent for all three cases. For all three cases, the highest concentration of oxygen is found within the lumen and gradually decreases inside the tissue to reach its minimum value along the arterial wall. The cross-sectional contours show a significant increase in the arterial wall oxygen concentration with increasing VV values.

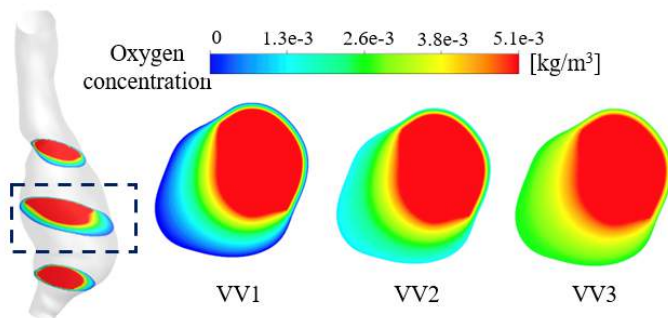


Figure 2: Oxygen concentration contours along a center cross-sectional region of the AAA for three analyzed cases.

The oxygen concentration along the interior interface of the arterial wall in the portion where ILT is located, for cases with varying VV are illustrated and compared in **Figure 3**. In the regions where the ILT is not present within the AAA, the concentration remains consistent among the cases. However, with the presence of the ILT, the change in VV value influences the oxygen concentration within the region.

Similar to **Figure 2**, as the VV value increases from VV1 to VV3, the flow of oxygen to the arterial wall increases.

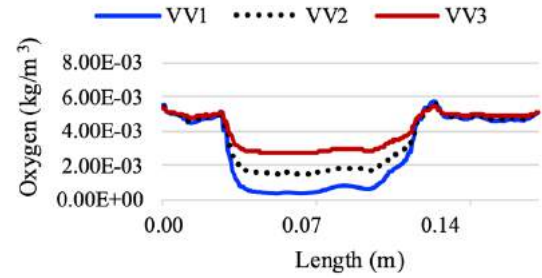


Figure 3: Oxygen concentration along the inner layer of the AAA wall for cases with varying VV oxygen supply.

As an indicator of oxygen transported to the AAA wall, we define a measure for the volumetric average of oxygen concentration over the aortic wall domain \bar{C}_w calculated by equation (1) below, and the corresponding results are reported and visualized in **Figure 4**. The result in **Figure 4** demonstrates an increase in volumetric oxygen concentration within the arterial wall as the adventitial oxygen increases.

$$\bar{C}_w = \frac{\int_{\Omega_w} C_w d\Omega_w}{\int_{\Omega_w} d\Omega_w} \quad (1)$$

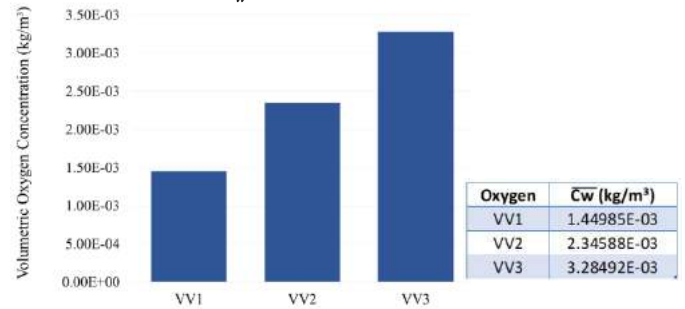


Figure 4: Volumetric average of oxygen concentration in the AAA wall for three cases with varying VV oxygen supply.

DISCUSSION

In this study, using a patient-specific AAA model, the effect of the VV on oxygen transport was explored. The results of **Figures 2-4** indicate that hypoperfusion of adventitial VV (i.e., smaller values for VV) have critical effects on oxygen concentration inside the AAA wall and therefore can cause hypoxia. Particularly, results demonstrate that a lack of the VV blood flow supply would prevent the oxygen from reaching the arterial wall. The oxygen concentration within the AAA wall increased among the cases as the adventitial oxygen concentration increased. These observations indicate that the presence of the VV may play a significant role in AAA wall oxygenation and needs to be taken into consideration in computer simulations.

ACKNOWLEDGEMENTS

Funding for this research is provided by Samuel and Emma Winters Foundation. We would like to thank Shawn Shadden and Miguel Rodriguez for providing us with the AAA computational mesh.

REFERENCES

- [1] Vorop, D., et al. *J. Vasc. Surg.* 2001. **34**: p. 291-299.
- [2] Zakerzadeh R., et al. *Cardiovasc Eng Technol.* 2021. **12**: 166-182.
- [3] Throop, A et al. *Biomech. Model. Mechanobiol* 2022. **21**:1761-1779.

INVESTIGATING SPORT-SPECIFIC PARAMETERS OF IMPACTS IN ICE HOCKEY

**D. Bondi (1), A. Clansey (2), K. Oxland (3), D. Luke (1), A. Rauscher (4), P. van Donkelaar (5),
and L. Wu (1,2)**

- (1) School of Biomedical Engineering, University of British Columbia, Vancouver, BC, Canada
(2) Mechanical Engineering, University of British Columbia, Vancouver, BC, Canada
(3) Department of Science, University of British Columbia, Vancouver, B.C., Canada
(4) Department of Pediatrics, University of British Columbia, Vancouver, BC, Canada
(5) School of Health and Exercise Sciences, University of British Columbia, Okanagan, BC, Canada

INTRODUCTION

Contact is a major part of ice hockey gameplay. Body checking primarily begins at age 13 for male ice hockey players in Canada [1]. Over time, athletes are taught how to control their movements to avoid contact and prevent severe injuries. However, despite how cautious a player may be, contact is still prevalent and fundamental aspect of the game. For example, reports have shown that the median exposure for collegiate male ice hockey players is 287 head impacts per season [2].

Head injury stemming from contact is deeply engrained in the fabric of the sport. In a previous study the concussion rate in male ice hockey players was calculated to be 2.3 per 1,000 impact exposures [3]. However, while several investigations examine the severity and effects of these impacts, there has been limited research regarding the sport-specific factors influencing head impact exposure, specifically ice location, player position, and time (in-game) of when impacts occur. In doing so, “high-risk” areas and situations can be defined, improving player safety in hopes of reducing the high prevalence of head injuries seen in ice hockey. Our objective is to investigate how ice hockey gameplay factors influence head impact exposure in collegiate male ice hockey using instrumented mouthguards [4] during a single competitive season.

METHODS

Twenty-six UBC men’s ice hockey players (H21-00400) were recruited to wear Prevent Biometrics mouthguard sensors [5] for a full season of play (Figure 1). Head impact data were collected in each of the 26 regular-season and playoff games. The mouthguards contained infrared proximity sensors to detect whether the mouthguard is on-teeth during impacts [6]. Impacts that passed an individual on-teeth proximity threshold were included in the dataset. Impact kinematics were transformed to head centre-of-gravity and low-pass filtered using a 4th order Butterworth filter at 200Hz. Peak linear acceleration (PLA), peak angular acceleration (PAA), and peak angular velocity (PAV) were

recorded for each individual impact. Impact data were cross verified with the associated game video to ensure validity of head exposure events. In addition, the location of impact on the rink was estimated through video. We evaluated the effect of ice location, player position, and time in-game on head impact exposure.

RESULTS

419 head impacts were verified and analyzed. Impact kinematics are shown in Table 1. A median head impact was observed to have peak kinematic values of 9.3g for PLA, 567 rad/sec² for PAA, and 8.2 rad/sec for PAV. A 95th percentile impact recorded a PLA value of 23.2g, PAA of 1838 rad/sec², and PAV of 17.7 rad/sec. Segregating impact data by player position produced similar values. Figures 2 and 3 display location-based impact data. Impacts are seen to be clustered on the outer boundaries of the ice surface and in the offensive zone. The majority of head impacts are relatively low severity (93% of impacts below 20g, 79% of impacts below 1000 rad/sec²), and higher severity impacts do not seem to be concentrated in any particular location on ice.

Table 1: Median, 95th percentile, and 95% confidence interval (of median) are displayed for PLA, PAA, and PAV. Shading represents values from entire data set (white), defense only (light grey), and forwards only (dark grey).

	PLA (g)			PAA (rad/sec ²)			PAV (rad/sec)		
Med	9.3	9.8	9.2	567	553	567	8.2	8.3	8.2
95th %	23.2	20.9	24.0	1838	1989	1817	17.7	19.5	17.3
95% CI	0.6	1.4	0.7	67	161	73	0.5	1.1	0.5



Figure 1: Study design

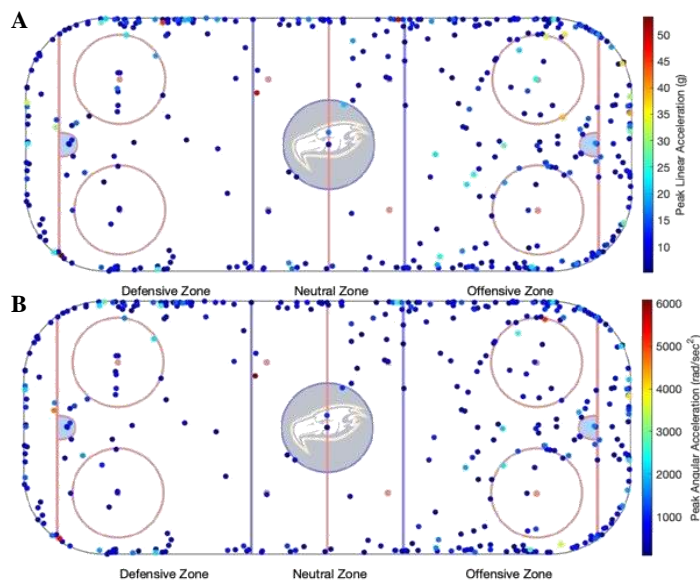


Figure 2: (A) PLA and (B) PAA values from entirety of data set

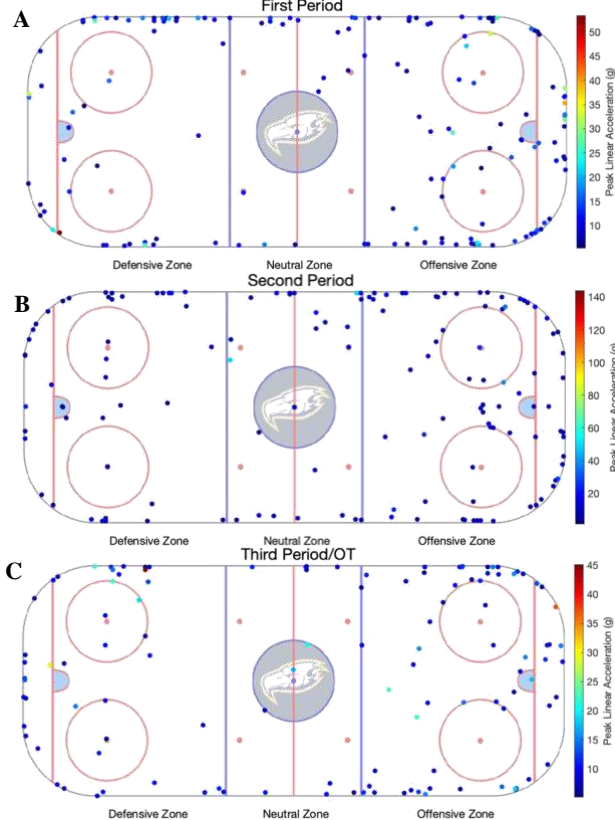


Figure 3: PLA values from 1st (A), 2nd (B), and 3rd/Overtime (C) period impacts. Please note differences in PLA scaling among figures.

DISCUSSION

Previous knowledge is limited in identifying “high-risk” areas of the ice surface during gameplay. While studies have investigated what mechanism of injury is most common [8], impact exposure density based on location has not been adequately explored. Our data suggests that head impact exposure is heavily concentrated around the outer

boundaries of the ice surface, where glass boards protrude and encapsulate the area of play. This may be due to the nature of gameplay. Players with possession of the puck are susceptible to impacts in these areas; a combination of their lack of maneuverability and impaired vision in these positions. Furthermore, our results show that players are more susceptible to impacts in the offensive zone of the ice than defensive. Players can only receive contact when in possession of the hockey puck, which usually occurs in the offensive zone. However, it is worth noting that a higher impact exposure density in the offensive zone is not associated with larger kinematic values for forwards than defense, which is corroborated by previous findings [2, 7].

Our results indicate that head impact severity for median and 95th percentile impacts do not vary based on position, with forward and defense experiencing similar impact kinematics. In support, other researchers found similar magnitude of impacts among collegiate forward and defense hockey players [2]. Similarly, others reported no differences in PLA and PAA among teenage hockey player position [7]. These outcomes may likely be attributed to the lack of specificity in positional gameplay; contact tactics (such as hitting and bodychecking) do not vary by position.

The present findings reveal that head impact exposure varies by period of gameplay. Figure 3 illustrates the variation in magnitude and location of impacts between periods. Our results show that the first period tends to be the most physical of the game, with higher impact exposure density and kinematic values than the second and third periods. Correspondingly, others have found that concussions in the NHL are most common in the first period of play [9]. Hitting requires significant energy from the perpetrator; players may elect to hit less frequently in the latter stages of games, choosing to avoid contact to reduce energy expenditure and manage the onset of fatigue.

The results presented suggest that ice location and timeliness have significant influence on the degree and magnitude of impact exposure, while player position does not. In addition, the offensive area and outer boundaries of the ice can be identified as high-risk areas. Players should be particularly cognizant of potential impacts in these locations and in the early stages of games. Impact exposure data points will continue to be added, which may further reveal trends and important information of situations of “high risk” of head injury.

ACKNOWLEDGEMENTS

We would like to thank the Canadian Institutes of Health Research (CIHR) and Natural Sciences and Engineering Research Council of Canada (NSERC) for their ongoing support and funding of these studies. We would also like to thank the UBC Men’s Hockey Team players, support staff, and coaches for their continued participation in this study. Their cooperation and excitement have propelled this study forward. Finally, we would like to thank Prevent Biometrics and Susan Schmitz of UBC Dentistry for their tireless efforts in supporting our work.

REFERENCES

- [1] Houghton, K et al., *Paediatr Child Health* 17(9):509, 2012.
- [2] Wilcox, B et al., *J Biomech*, 47:109-114, 2014.
- [3] Dick, R, *Br. J. Sports Med*, 43(1):i46-i50
- [4] Wu, L et al., *Ann Biomed Eng*, 44:1234-1245, 2016.
- [5] Bartsch, A et al., *Annu Int Conf IEEE Eng Med Biol Soc*, 2068-2072, 2019.
- [6] Wu, L et al., *IEEE Trans Biomed Eng*, 61(11):2659-2668, 2014.
- [7] Mihalik, J et al., *Ann Biomed Eng*, 40(1):141-149, 2011.
- [8] McKnight C et al., *J Athl Train*, 27(4):338-343, 1992.
- [9] Hutchison M et al., *Br J Sports Med*, 49:547-551, 2015.

NORMAL VARIATION IN FREQUENCY- AND TIME-DOMAIN RESTING STATE EEG METRICS

Eric Liu (1,2), Cidnee Luu (1), Lyndia Wu (1)

- (1) Department of Mechanical Engineering, University of British Columbia, Vancouver, BC, Canada
(2) Department of Engineering Science, University of Toronto, Toronto, ON, Canada

INTRODUCTION

Electroencephalography (EEG) measurements have traditionally reflected brain function changes in epilepsy, neurodegeneration, and brain trauma. Recently, advances in recording hardware and quantitative data analysis methods have expanded the applications of EEG beyond clinical and laboratory settings. Mobile EEG systems and nuanced artifact removal algorithms are now being used to explore brain changes that occur in ambulatory settings. A better understanding of the normal variability of repeated EEG measurements will be important for interpreting these measurements in noisy real-world scenarios.

The literature on the test-retest reliability of common EEG metrics has demonstrated high correlations between repeated trials performed over varying time scales [1,2]. However, external factors such as alertness or physiological stress also influence cognition and may induce underlying EEG changes that can confound the anticipated results. In this study, we characterized the range of normal intra-subject variability in resting state EEG data and examined the effects of potential sources of variability.

METHODS

12 healthy adults (5 females) aged 18 to 26 years (mean age of 22.3 ± 2.6 years) participated in the study. The human participant protocol for our study was approved by the UBC Research Ethics Board (H20-02313) and informed consent was obtained from all the participants. Experiment sessions for each subject were conducted on 2 separate days to examine day-to-day variability. On each day, subjects participated in an “early” session (between 10:00 am and 12:00 pm) and a “late” session (between 3:00 pm and 5:00 pm) to examine time-of-day variability. Each session involved 3 minutes of sitting, treadmill walking (2.5-3.5 mph), and treadmill jogging (4.5-5.5 mph), each followed by 5 minutes of eyes-closed resting state EEG recording.

EEG signals were recorded through 32 Ag/AgCl active electrodes (International 10-20 arrangement) amplified using the BrainVision

LiveAmp amplifier (Brain Products GmbH, Gilching, Germany) at a sampling rate of 500 Hz. We performed all data processing in MATLAB using scripts running EEGLAB functions [3]. The raw EEG signals were first re-referenced to the common average reference, then bandpass filtered at 1-100Hz using a 4th-order forward-backward Butterworth filter. We manually removed large transient artifacts, resulting in an average loss of 5.68s per 300s recording (1.89%). We then used independent component analysis (ICA) to remove components with significant ocular or muscle artifacts.

EEG trials were separated into 2-second epochs, and the power spectrum and sample entropy were calculated for each epoch with a 1-second overlap. For power spectrum band power analysis, we defined EEG frequency bands as delta (1-4 Hz), theta (4-8 Hz), alpha (8-12 Hz), beta (12-22 Hz), and gamma (22-40 Hz). The power spectral density of each epoch was computed using Welch’s modified periodogram. Sample entropy was computed as defined in [4], with $m = 2$ and $r = 0.2$.

We constructed linear mixed-effects models to determine the within-subject effects of experiment day, time of day, activity level, and their interactions on EEG band power and sample entropy. *Post hoc* tests were conducted for all statistically significant fixed effects and interactions, using the Tukey HSD method with adjusted p -values. All statistical testing was performed in R.

RESULTS

Each subject exhibited a wide range of measurements across the 12 recording trials (Figure 1). The most consistent metrics were relative alpha power (average intra-subject mean 0.48 ± 0.03 (6.25%)) and relative beta power (0.11 ± 0.01 (9.09%)). The least consistent metrics were absolute delta power ($5.69 \pm 1.45 \mu V^2$ (25.5%)) and absolute theta power ($3.32 \pm 0.53 \mu V^2$ (16.0%)). Despite these large variations, each subject had an idiosyncratic power spectrum shape (Figure 2). Sample entropy had an average intra-subject mean of 0.58 ± 0.04 (6.90%).

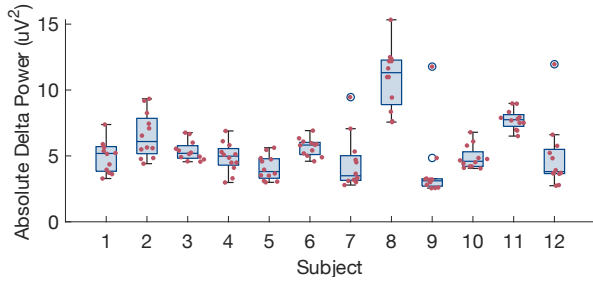


Figure 1: Overall intra-subject variability in absolute delta power.

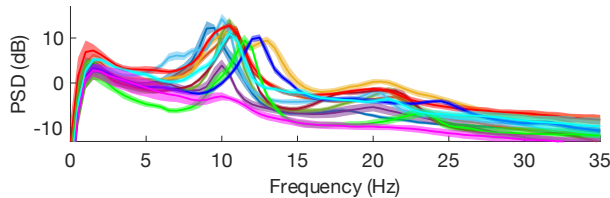


Figure 2: Individual power spectra over all trials. Each color represents the mean power spectrum for a subject and the shading indicates the standard deviation.

Activity level before resting state EEG measurement had a significant effect on relative delta power ($p = 0.027$), relative theta power ($p = 2.92 \times 10^{-6}$), absolute delta power ($p = 7.7 \times 10^{-5}$), and absolute alpha power ($p = 0.025$). *Post hoc* testing using Tukey's HSD found that relative delta power, absolute delta power, and absolute alpha power measured after jogging were higher than those measured after sitting ($p = 0.022$, $p = 0.0002$, and $p = 0.019$, respectively). Relative theta power was significantly decreased with activity in all comparisons (running < sitting, $p < 0.0001$; running < walking, $p = 0.025$; walking < sitting, $p = 0.023$). Time of day had a significant effect on relative beta ($p = 0.002$) and gamma ($p = 0.0009$) power, with the *post hoc* test revealing an increase in these metrics in the PM (Figure 3). There were no significant effects on sample entropy and no significant interactions.

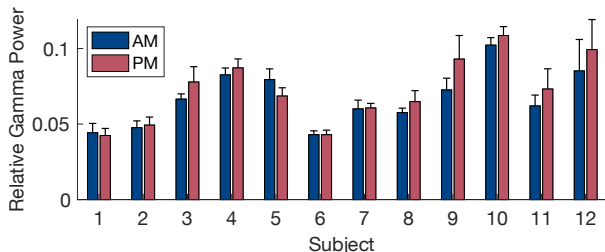


Figure 3: Individual AM vs. PM relative gamma power.

Approximately half (73/144) of the sample entropy time series exhibited a systematic decay pattern over the 5-minute recording trial. These patterns had positive correlations with the high-frequency (beta and gamma) bands and negative correlations with the low-frequency (delta, theta, and alpha) bands (Figure 4). A mixed-effects logistic regression model showed no significant effects of the experimental factors on the presence/absence of decay behavior.

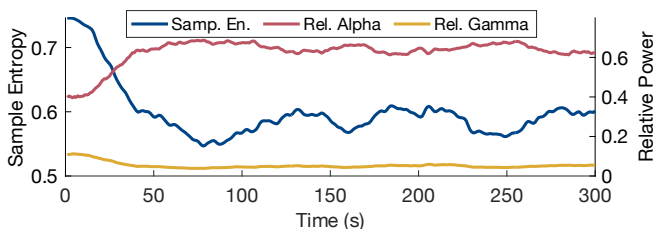


Figure 4: Representative time series of EEG metrics showing a settling pattern with entropy-band power correlations.

DISCUSSION

The large overall intra-subject EEG variabilities observed in this study are important for establishing clinically significant effect sizes for quantitative EEG metrics. For example, studies on Alzheimer's disease (AD) and post-concussive syndrome (PCS) patients have shown a slowing of the EEG rhythm compared to healthy controls (AD: +8.60% in absolute theta power [5]; PCS: +28.6% in absolute theta power [6]). In this case, the effect found in AD falls within our observed normal spread of intra-individual variability—the effect size may be too small to indicate altered brain function in a clinical setting.

Decreases in relative theta power associated with exercise have been reported in the literature [7]. This effect was obtained after subjects performed strenuous exercise, while the decrease in relative theta power observed in our study after a 3-minute walk demonstrates that even small amounts of physical activity can influence EEG measurements. The observed effects of exercise on theta and alpha power indicate an acceleration of the EEG rhythm after physical activity, characteristic of heightened cognitive function or alertness. The large increases in delta power after running may point to residual sweat artifacts—standard artifact removal methods (filtering and ICA) may not be completely effective in EEG applications involving physical activity.

The literature on the circadian rhythm and diurnal cycles of alertness suggests a decrease in alertness and wakefulness in the afternoon [8]. However, the increases in relative beta and gamma power in the afternoon sessions of our study reflect an increase in cognitive activity later in the day. Post-session questionnaire responses explain this unexpected result—while participants indeed reported lower alertness during afternoon sessions, they reported higher thought complexity. This may cause increased high-end spectral power despite the “post-lunch dip” in alertness.

The sample entropy and relative band power time series (Figure 4) reveal that EEG metrics can exhibit transient intra-trial variability. The absence of any significant fixed effects suggests that the observed settling pattern may be an intrinsic attribute of resting-state EEG recordings. The time required for EEG metrics to reach steady-state should be considered in future quantitative analyses of continuous EEG.

This study explored the intra-individual variability of quantitative EEG measurements over repeated trials, which can help to establish a baseline for interpreting results in clinical applications. Our findings can be made more relevant in ambulatory settings by using the same mobile EEG system outside of a controlled environment. Subsequent studies could also use a larger and more varied participant sample to account for within-subject parameters such as differing responses to exercise, diurnal/nocturnal preferences, and sex differences. Finally, the overall power spectrum shape should be further evaluated as a resting state EEG metric for its potential to have excellent test-retest consistency [9].

ACKNOWLEDGEMENTS

This study was funded by the Natural Sciences and Engineering Research Council of Canada (NSERC) and the Canada Foundation for Innovation (CFI).

REFERENCES

- [1] Choi, J et al., *Clin EEG Neurosci*, 51:348-356, 2020.
- [2] Corsi-Cabrera, M et al., *Clin Neurophys*, 118:9-21, 2007.
- [3] Delorme, A et al., *J Neurosci Methods*, 134:9-21, 2004.
- [4] Richman, J et al., *Methods in Enzymology*, 384:172-184, 2004.
- [5] Meghdadi, A et al., *PLoS ONE*, 16:e0244180, 2021.
- [6] Buchanan, D et al., *Brain Sci*, 11:537, 2021.
- [7] Devilbiss, D et al., *J Healthcare Eng*, 2019:4794637, 2019.
- [8] Zhou, Y et al., *Front Public Health*, 9:652849, 2021.
- [9] Levin, A et al., *Front Integr Neurosci*, 14:21, 2020.

MODULATING THE AXIAL DISPLACEMENT OF TWO PHOTON POLYMERIZED HUMAN LAMINA CRIBROSA MODELS

Brock J. Pemberton (1), Remi J. Shittu (1), Jonathan P. Vande Geest (1,2,3)

(1) Department of Bioengineering, University of Pittsburgh, Pittsburgh, PA, USA

(2) Department of Ophthalmology, University of Pittsburgh, Pittsburgh, PA, USA

(3) The McGowan Institute for Regenerative Medicine, University of Pittsburgh, Pittsburgh, Pennsylvania, USA

INTRODUCTION

Primary Open Angle Glaucoma (POAG) is a leading cause of irreversible blindness and is expected to affect 110 million people by 2040 [1]. It is known that in patients with POAG, the lamina cribrosa (LC) becomes remodeled during the progression of the disease [2]. The LC is a porous disc located in the optic nerve head which supports retinal ganglion cell (RGC) axons as they exit the eye [3]. It is suspected remodeling of the LC leads to RGC death and then blindness. Elevated intraocular pressure (IOP) can be another risk factor of POAG. It is suspected that elevated IOP may play a role in LC remodeling, however there are cases of POAG without elevated IOP [4].

It would be very beneficial to model how elevated IOP may remodel the LC. If high fidelity two photon polymerized (TPP) models of the LC can be produced, their mechanics should be quantified. Ideally, the models' mechanics should match the mechanics of a real LC. The purpose of this study was to alter the stiffness of the fabricated LC and to investigate differences in anterior to posterior displacement of the fabricated LC.

METHODS

Model LCs were produced using an Olympus BX51 upright laser-scanning microscope (Insight DS+, Spectra Physics, Santa Clara, CA) controlled with a custom Python script. The laser polymerized NanoscribeTM IP-PDMS at a wavelength of 780nm. Models that were polymerized twice had the script run two times in the same area.

The models were developed for 20 min in 70% ethanol before allowing to air dry. The models measured approximately 2.5mm in diameter. They were then placed over a 2mm diameter

biopsy punched hole in a PDMS sheet. The edges were sealed with liquid PDMS and cured at 60°C for 1 h.

The mounted LCs were placed into a custom Intravital Bioreactor, where pressure was applied to the model using an ElveflowTM OB1 Microfluidic Flow Controller and DI water (Figure 1). Pressure was applied for a range of 0-67.5mmHg in increments of 11.25mmHg.

Two photon imaging was used to measure axial displacement, where the z-depth of the focal plane where the model LC appeared brightest was recorded for each pressure (Figure 2).

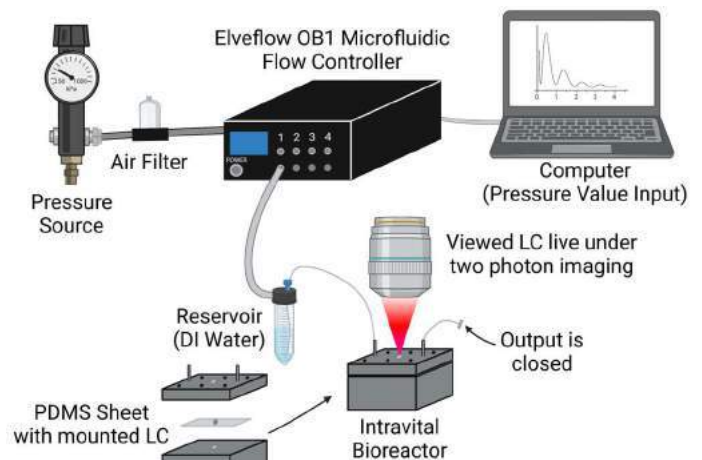


Figure 1: Experimental setup [5]

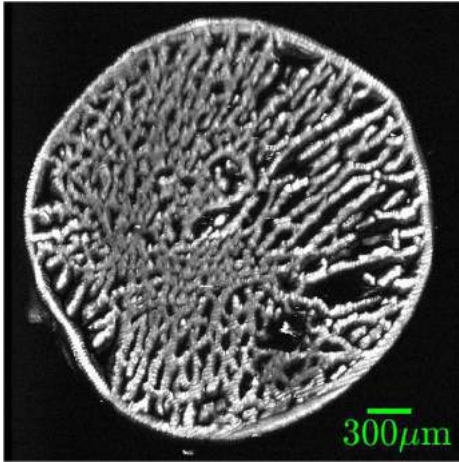


Figure 2: 3D max intensity projection of a twice polymerized LC prior to pressurization (4X, ex: 780nm, em: 620nm)

RESULTS

Preliminary results show that polymerizing a model LC an additional time before development results in a smaller posterior displacement under pressure (Table 1). Furthermore, the rate at which the displacement increases with increasing pressure for a twice polymerized LC appears to be about 0.7 times that of an LC polymerized once (Figure 3).

Table 1: Pressure and Displacement for polymerized LCs

Pressure (mmHg)	1x LC Displacement (μm)	2x LC Displacement (μm)
0.00	0.0	0.0
11.25	189.8	159.4
22.50	373.8	320.6
33.75	596.5	434.1
45.00	737.9	548.8
56.25	900.1	621.9
67.50	1017.6	714.9

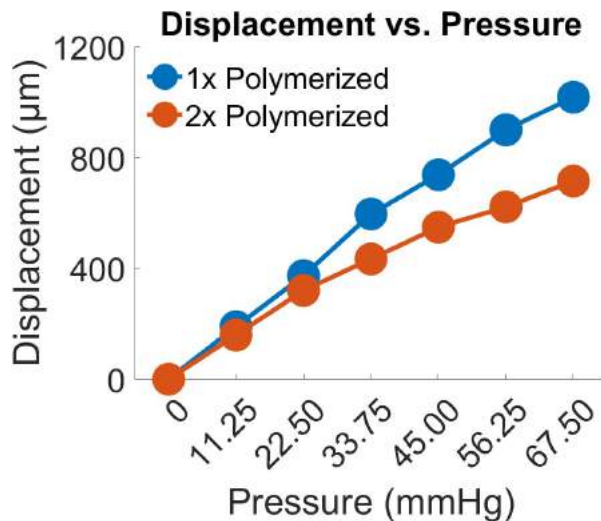


Figure 3: Displacement versus pressure for a once and twice polymerized LC

DISCUSSION

The results show that repeating polymerization of a model LC decreases its axial displacement under pressure. This is consistent with expected results. A second polymerization further cures the photoresin. This increases the stiffness of the model and results in a lower displacement when put under the same pressure as a once polymerized model.

These findings complement previous work that produced models of the LC [6]. It should be noted, however, that these models were produced using subtractive manufacturing, while this study tested models produced using additive manufacturing. Prior to this study, models were similar to an LC in geometry only. These results suggest that it is possible to tune the biomechanical response of patient specific human LCs for future mechanobiological studies.

There are several limitations to this study. In the present study, only one sample for each of the degrees of polymerization were fabricated. Additional models must be created and tested to determine whether there is a statistically significant difference in axial displacement as a function of degree of polymerization. For example, models that have undergone three or more polymerizations would be interesting to compare.

In addition, there is likely some variability in the displacements due to human error. Often, it was difficult to judge at which z-depth the LC was the brightest, since there typically was a z-range where the model was visible, and its morphology changed as it deformed under increasing pressure. However, this may only have offset results by tens of microns. This variability would not have been large enough for the two LCs displacements to be the same overall.

In the future, data similar to that presented here may be used to estimate the biomechanical properties of patient specific LC models. Furthermore, these values may be compared to those derived from *in vivo* studies. Future work will continue to fine tune the biomechanical response of these surrogates for use in studies quantifying LC mechanobiology.

ACKNOWLEDGEMENTS

Research reported in this abstract was supported by the NIH T32EY017271 Interdisciplinary Visual Sciences (IVS) Training Program.

REFERENCES

- [1] Crawford Downs, J et al., *Exp Eye Res*, 93:133-140, 2011.
- [2] Fazio, M A et al., *Invest Ophth Vis Sci*, 55:7189-7198, 2014.
- [3] Quigley, H A et al., *Brit J Ophthalmol*, 90:262-267, 2006.
- [4] Strickland, R G, et al., *Int J Mol Sci*, 23:8068, 2022.
- [5] Figure 1 created with BioRender.com.
- [6] Shittu, R J et al. *Invest Ophth Vis Sci*, 63(7):2718 – A0082, 2022.

NINTENDO LABO FOR SERIOUS GAMING

Amanda M. Wells (1), Logan M. Suiter (1), Jacob G. Colwell (1), Joshua A. Gargac (1),

(1) Department of Mechanical Engineering, Ohio Northern University, Ada, Ohio,
USA

INTRODUCTION

Serious gaming is the practice of using video games, either commercial or specifically designed, for physical rehabilitation. Serious games have emerged in the last decade as a way to increase patient involvement in rehabilitation, increase the likelihood of patients continuing treatment after progress stalls, and generally increasing mental health during treatment [1]. However, the current literature has not kept pace with the evolution of technology and therefore the use of next-generation consoles for serious gaming is underdeveloped. The Nintendo Switch™ (Nintendo, Kyoto, Japan) console could provide new avenues for serious gaming because of the advanced sensing ability of its controllers (Joy-Cons), and the engaging ways in which the Joy-Cons can be used. Joy-Cons are equipped with acceleration sensors, gyroscopes, and infrared depth sensors, and are capable of near field communication and high-precision vibration.

Nintendo has demonstrated the capabilities of these Joy-Con with its LABO™ product. Nintendo LABO is a DIY kit that allows users to build cardboard mechanisms that house the Joy-Cons, called Toy-Cons [2]. Each LABO kit comes equipped with games that can be played by mapping physical motions of the user to the in-game controls. The goal of this research is to 1) identify candidate Toy-Cons for serious gaming, 2) track joint motion with commercially available software, and 3) biomechanically evaluate joint motion while playing the Toy-Con games. Specifically, this study primarily evaluated the fishing rod Toy-Con game from LABO Kit 01 because the game involved repetitive movements utilizing the shoulder, elbow, wrist, and hand, ideal for occupational therapy. Long-term, this data will be compared to current practices employed by occupational therapists for rehabilitation.

METHODS

A total of 5 test participants (2 male and 3 female) between 20 and 22 years of age were analyzed under IRB approval. Motion was tracked using Cortex Software (Motion Analysis Corporation, Santa Rosa, CA) [3]. Reflective markers were attached to the joints involved in the motion while using the Nintendo LABO fishing pole (Fig.1). The markers were placed on the subject's shoulder, elbow, wrist, and hand (Fig. 2). The motion capture system recorded the motion in all three planes of motion by taking position data of each reflective marker at 100 frames per second.

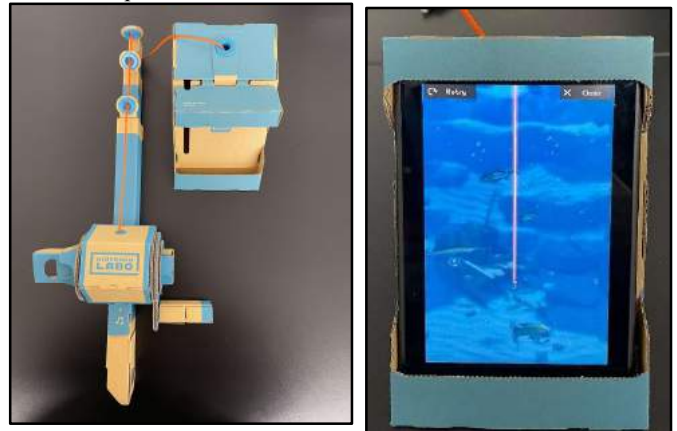


Figure 1: Nintendo LABO fishing pole Toy-Con and fishing interface (game).

Data was collected by utilizing six motion capture cameras located precisely around the subject. The cameras were calibrated before data collection. The subject was positioned so each joint marker was visible by at least 3 cameras. Once the recording started, the subject played the game by flexing and extending their right elbow parallel to the sagittal

plane to precisely move the in-game fishing hook up and down. Rotating the wrist allowed the participants to either reel the virtual fishing hook up (cw. rotation) or down (ccw. rotation). All of the participants were instructed to use their right arms and to hold the fishing rod in their laps relaxed. Each participant was seated in a chair placed one-foot away from the Nintendo Switch screen. The computer software collected and stored position data for each joint marker every frame. To avoid ghost markers, data was collected in dimly lit conditions with undesired reflective material hidden from the cameras. Data was cleaned using Motion Analysis' Cortex Software which allows for active joint motion tracking using the reflective markers referred to as the active marker system. The software utilizes the Ikendo Solver to make precise and accurate calculations [4]. Lost marker data was interpolated by the software utilizing the cubic join and rectify operations filling in any gaps in the recorded data.

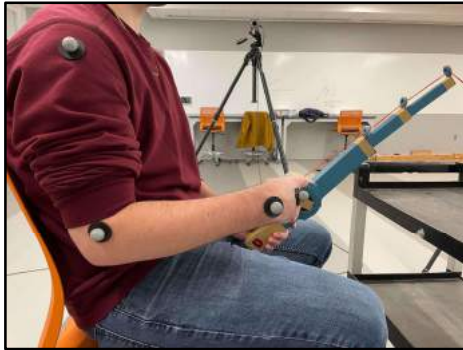


Figure 2: Joint markers were placed at the shoulder, elbow, wrist, and hand.

The data was exported and evaluated using MS Excel (Microsoft, Redmond, WA). The shoulder points were used as the origin for relative position vector analysis. The elbow joint and wrist joint angles were calculated in the appropriate planes (Eqn. 1).

$$A \cdot B = |A||B|\cos\theta \quad (1)$$

RESULTS

The data for the fishing rod show the extremes of wrist and elbow flexion during gameplay (Fig. 3). Both the elbow and wrist angles change in a periodic fashion, and the amplitude of the angle variance changes between subjects. The motion observed can be broken down by joint into both flexion and extension. Flexion involves decreasing the angle formed by the bones of the joint, and extension is increasing the angle that is formed by the bones within the joint.

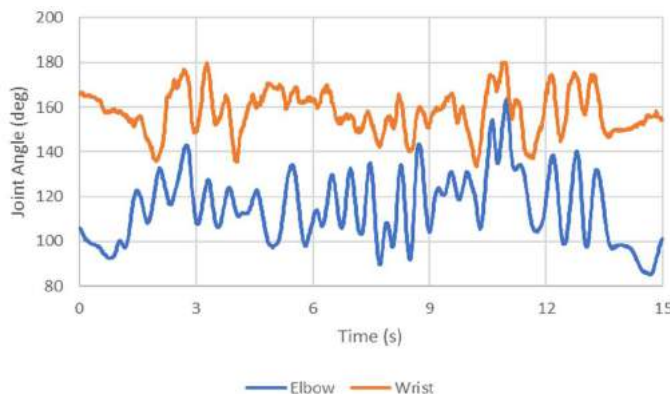


Figure 3: Joint angle variation during 15 seconds of fishing gameplay.

Across five subjects, the average min and max joint angles for both the wrist and the elbow joints were found (Tab. 1). These angles are

achieved when the elbow and wrist go through flexion and extension, and this motion is repeated during game play which is ideal for occupational therapy. On average, the participants completed 20 flexion-extension cycles for both the elbow and wrist joints during the 15 seconds of recorded gameplay.

Table 1: Minimum and maximum angles for elbow joint

	Avg. Maximum Angle (deg)	Avg. Minimum Angle (deg)
Elbow	138.0 ± 21.1	69.2 ± 20.6
Wrist	178.0 ± 32.8	120.0 ± 13.8

DISCUSSION

The primary areas of rehabilitation are the fingers, wrist, elbow, shoulder, and brain [5]. Typical ranges of motion (ROM) for effective rehabilitation of the elbow are from 0° (straight arm) to 121° of flexion for a total angle displacement of 121° [6]. The data suggests that the elbow went through both flexion and extension, between the angles of 54.25° and 163.74° for a total angle displacement of 109.49°. Overall, the motion from the fishing game accounted for 90.4% of the recommended rehabilitation ROM. For wrist flexion and extension recommended ROM is -40° of extension and 38° of flexion for a total displacement of 78° [6]. The data from the fishing game shows that the wrist went through both flexion and extension, between the angles of 89.41° and 179.97° for a total angle displacement of 90.56°. This is 116.1% of the overall recommended rehabilitation range of motion.

The data suggests that the LABO products could be useful in occupational therapy, and further study should be performed to evaluate the remaining Toy-con assemblies. A greater adoption of the Nintendo Switch could have many benefits. Commercially developed games are interactive and fun, which is important for patient retention. Additionally, Nintendo offers four LABO kits each with their own set of Toy-Cons (14 total). This opens the opportunity for different types of motions to be targeted in therapy. Additionally, the Nintendo LABO products are commercially available at a relatively low cost providing ease of access to therapy clinics. Lastly, the Nintendo Switch and LABO products could even be altered to better perform occupational therapy tasks.

ACKNOWLEDGEMENTS

The authors acknowledge Louis DiBerardino for his aid when using the motion capture equipment.

REFERENCES

- [1] Laamarti F. International Journal of Computer Games Technology, Volume 2014, 15 pg, 2014.
- [2] "Nintendo Labo Toy-Con 01 Variety Kit " Nintendo Labo Toy-Con Nintendo. <https://www.nintendo.com/sg/switch/adfu/index.html> (accessed Jan. 28, 2023).
- [3] "Cortex - Our Most Powerful Motion Capture Software Yet," Motion Analysis. <https://motionanalysis.com/software/cortex-software/> (accessed Jan. 28, 2023).
- [4] "BaSix Go - Revolutionary Animation Software for Motion Capture," Motion Analysis. <https://motionanalysis.com/software/basix-go/> (accessed Jan. 31, 2023).
- [5] "Occupational Therapy (OT) at Mellen Center," Cleveland Clinic. <https://my.clevelandclinic.org/health/treatments/4440-occupational-therapy-at-mellen-center>
- [6] Gates D. American Journal of Occupational Therapy, Volume 70, 10 pg, 2016.

OPTIMIZATION OF MOUNTING METHODS FOR TENSION-COMPRESSION TESTING OF MURINE INTERVERTEBRAL DISC JOINTS

J. Veres (1), S. Lim (2), G. D. O'Connell (2,3)

- (1) Bioengineering, University of California Berkeley, Berkeley, CA, U.S.A.
(2) Mechanical Engineering, University of California Berkeley, Berkeley, CA, U.S.A.
(3) Department of Orthopaedic Surgery, UCSF, San Francisco, CA, USA

INTRODUCTION

Intervertebral discs are soft tissues found between vertebrae that give the spine flexibility, distribute mechanical load, and dissipate energy¹. Disc degeneration is a broad diagnosis, characterized by tissue damage through age-related wear-and-tear that often causes pain, limits mobility, and negatively impacts a patient's overall quality of life². Approximately 40% of adults over age 40 and 80% of adults over 80 have some degree of disc degeneration³. Since the primary function of the disc is to withstand large complex loads during daily activities, mechanical properties are a popular metric for assessing changes with degeneration.

Mice are a commonly used animal model for studying the progression or regeneration of disc disease and damage, because they can be genetically manipulated, and their discs are biochemically and mechanically similar to human discs⁵. However, due to their small size and, therefore, high sensitivity to changes in position and environment, assessing material properties of mouse discs can be challenging. In the literature, current methods of testing murine discs require expensive custom jigs or are not described well enough to replicate the methods used, making it difficult and expensive to conduct these tests. The objective of this study was to create an inexpensive, open-source method to mechanically test murine discs that was repeatable across samples and kept the disc as close to physiological alignment and tissue hydration as possible.

METHODS

Sample Preparation Lumbar columns (L1-L5) were acquired from mice through a sample sharing program at UC Berkeley. The spines were stored at -20°C until they were prepared for material testing. Preparation consisted of removing tissue from the lumbar column to expose the discs. Then cuts were made through the transverse plane of the L1/2 and L3/4 discs. Finally, the posterior bony processes were removed, leaving a L2/3 and a L4/5 bone-disc-bone motion segment.

Mechanical Testing Mechanical testing was conducted on an Instron 3400 Series Universal Testing System (Illinois Tool Works Inc., Norwood, MA) and consisted of 20 cycles of tension-compression between -1.0N and +1.0N. All samples were mounted according to one of the variable mounting techniques described below, then loaded into the Instron with the clamp ends fixed. In the final mounting protocol, samples were hydrated for 15 minutes in saline polyethylene glycol (sPEG) before testing⁶. A 17% wt/vol concentration sPEG was used to prevent the tissue from overhydrating before testing. The neutral zone (NZ), compressive, and tensile stiffnesses were measured and normalized to specimen geometry. Compressive and tensile stiffnesses were calculated by curve fitting for data between 80-100% of the maximum applied load (Figure 1A – red lines), and the NZ was determined using the double sigmoid curve-fit method⁷ (Figure 1B – blue line). Data is presented as mean±standard deviation.

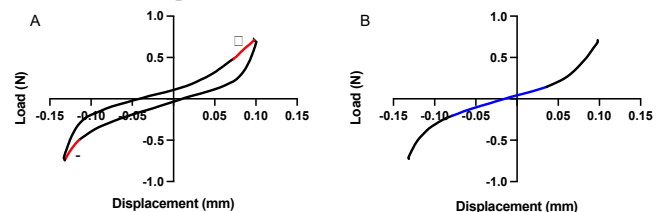


Figure 1. Representative axial-tension compression curves with tensile and compressive stiffnesses and neutral zone highlighted.

Success Criteria The relative success of each mounting method was based on 6 criteria: 1) the transverse plane of the disc remained parallel to the applied load, 2) the disc was kept in a physiologically neutral position, 3) the sample was not damaged, 4) the sample remained fixed in the mount, 5) the disc stayed hydrated during testing, and 6) a tertiary load-displacement curve was observed and repeatable.

Sandpaper Mounting Methods The first sample fixation method consisted of fixing each vertebral body between two sheets of sandpaper with cyanoacrylate (n=6, Figure 2A). The second sample fixation method was identical to the first, but polymethyl methacrylate (PMMA) was used instead of cyanoacrylate (n=7, Figure 2B).

SAM Box Mounting Methods The third method introduced the first iteration of the Sample Aligning Mechanical testing Box (SAM Box). For SAM Box Version 1 (V1), the sample was potted in PMMA in 3D printed pieces that were connected with thin bridges. After the PMMA was cured, the bridges were cut, allowing for each side of the joint segment to articulate separately (Figure 2C). The 3D printed pieces were then loaded into the Instron clamps (n=7).

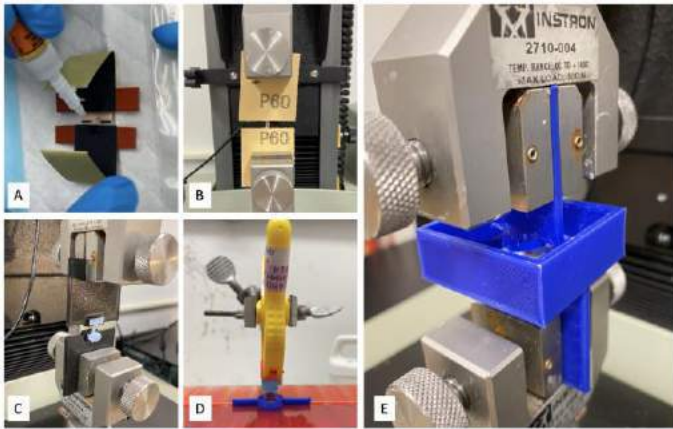


Figure 2. Sample mounting methods. A, B) Cyanoacrylate and PMMA sandpaper methods, C-E) SAM Box Versions 1-3 (V1-V3).

The second iteration of the SAM Box (SAM Box V2; Figure 2D) removed the alignment bridges, instead relying on clamps and the Instron to pot samples directly in their testing configuration (n=6). However, PMMA curing times in the testing configuration led to tissue dehydration prior to testing.

The third iteration of the SAM Box (SAM Box V3) added a bath around the sample, allowing for a 15-minute hydration period after PMMA curing but prior to sample testing (n=7, Figure 2E).

RESULTS

Failed Methods The sandpaper cyanoacrylate method failed 4/6 samples tested. Using this method, the sample did not remain fixed to the sandpaper during testing, parallel alignment was highly variable, and cyanoacrylate often oozed onto the disc. To address this, PMMA was used instead of cyanoacrylate, which limited oozing and created rigid fixation to the sandpaper. However, the sandpaper PMMA method also failed, with 5/7 samples failing. Using the sandpaper and PMMA, parallel alignment was difficult and highly variable.

To improve sample alignment, the SAM Box V1 was used to orient samples during potting. This retained rigid fixation and physiological alignment, but because samples were potted prior to testing, the mounting process often applied unwanted bending or torsional stresses on the joint segment. This led to failure of 7/12 samples. Next, samples were potted in place on the Instron using the SAM Box V2 method. This addressed the alignment difficulties, kept rigid fixation, and protected the disc from extraneous glue, however the added drying time led to sample failure, with 4/6 of the samples failing.

The SAM Box V3 The SAM Box V3 was the most successful prototype with the success criteria being met for all 7 samples. The added bath of the SAM Box V3 allowed for tissue rehydration prior to testing. This method was easy to use, kept samples hydrated and

aligned, and consistently produced load displacement curves that agreed well with data reported in the literature.

Axial compression-tension mechanics were measured with SAM Box V3. The normalized compressive stiffness was 4.177 ± 1.487 MPa, normalized tensile stiffness was 2.830 ± 1.271 MPa, and normalized NZ stiffness was 0.238 ± 0.138 MPa, and (Figure 3).

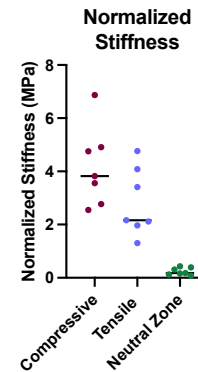


Figure 3. Normalized stiffnesses from SAM Box V3 pilot testing.

DISCUSSION

The SAM Box V3 is a mounting method for murine lumbar disc joints that is easy to use, inexpensive, and mimics physiological conditions. Each SAM Box V3 costs about \$1.00 in polylactic acid filament and takes about an hour to print on an Ultimaker 3.

The results presented here align well with published results. Sarver et al., reported a normalized NZ stiffness of 0.58 ± 0.45 MPa, a normalized compressive stiffness of 3.65 ± 0.98 MPa, and a normalized tensile stiffness of 2.54 ± 0.44 MPa⁸. Additionally, Choi et al. reported a normalized compressive stiffness of 5 ± 0.5 MPa⁹ using a similar test protocol. These results suggest that the SAM Box V3 method is consistent with other methods used in the field, while being cheaper and more adaptable to different fixturing methods.

Despite the consistent results presented here, there are limitations to the SAM Box V3. First, testing was performed at room temperature rather than body temperature (37°C); however, we chose to test at room temperature to better match methods used in the literature for comparison. Additionally, adding 3D printed fixtures to the load chain may result in increased in machine compliance, which needs to be accounted for when analyzing mechanical test data. However, because the applied loads are minimal (approx. 1N), it is unlikely that the 3D printed boxes will experience large deformations.

Overall, the SAM Box V3 allows for easy mounting, gripping, and testing of murine disc joint segments while maintaining hydration and alignment. It is a low-cost method that can be applied in tensile-compression mechanical tests, which is important for studying disc mechanics with degeneration, injury, or regeneration.

ACKNOWLEDGEMENTS

This study was supported by the UC Berkeley SURF Program.

REFERENCES

- [1] Erwin W.M., *J. of Canadian Chiropractic Assoc.*, 1:285-291, 2014.
- [2] Hong C. et al. *Ann. Occup. Environ. Med.*, 16 (33), 2021.
- [3] Medical Advisory Secretariat, *Ontario Health Tech. Assessment*, 6(10):1-98, 2006.
- [4] Adams M. et al., *Spine*, 31:2151-2161, 2006.
- [5] Jin L. et al., *Histol Histopathol*, 33:543-554, 2018.
- [6] Werbner B. et al., *J. Mech. Behav. Biomech. Mater.*, 125(104591), 2021.
- [7] Smit T. et al., *BMC Musculoskelet. Disorders*, 12(38), 2011.
- [8] Sarver J. et al., *J Orthop. Res.*, 23(1):150-5, 2005.
- [9] Choi H et al., *Matrix Biol.*, 70:102-122, 2018.

TESTING THE VALIDITY OF VARIOUS VISCOSITY VALUES FOR A VERSATILE OXYGENATING PERFUSION SYSTEM

A. Fasci (1), S. Salazar (1), J. Oseghale (2), M. Garcia (1), A. Khalil (1), B. Wearden (1), L. Muenchow (3), J. Gonzalez (1), C. Villareal (1), D. Portillo (1)

Faculty Advisor(s)
R.L. Hood (1,2)

- (1) Department of Mechanical Engineering, The University of Texas at San Antonio, San Antonio, TX, USA
(2) Department of Biomedical Engineering, The University of Texas at San Antonio, San Antonio, TX, USA
(3) Department of Biology, The University of Texas at San Antonio, San Antonio, TX, USA

INTRODUCTION

As recently as the last decade, there has been an increased focus on improving efficacy of organ preservation processes for improved transplantation outcomes [1]. The most common approach to organ preservation is static cold storage (SCS), but studies have shown that this method is linked to time-dependent ischemia injury and limited preservation times [2]. More recent methods involve machine perfusion (MP), which prevent ischemia by perfusing the organ with an oxygen-rich blood substitute. Current devices on the market for MP have significant drawbacks to consider. Oftentimes they are bulky and heavy, requiring a cart for mobility purposes. In addition, they can be complicated to operate. In some instances, necessitating an additional person for procedural use. The most limiting aspect of the current devices on the market is their single organ type design, thus creating the difficulty of training personnel on proper use for each device. Our team focused on the drawbacks of the current devices on the market and attempted to solve the bulk of them.

We have designed a versatile oxygenating perfusion system (VOPS) to reduce time-related ischemia injuries and improve the likelihood of organ viability for replantation. The VOPS device was designed to preserve tissues by maintaining a homeostatic environment and allowing oxygen circulation within the tissue, those incorporating MP. It is dimensionally sized to be able to preserve a small limb, heart, kidney, pancreas and liver, and able to be carried by a single person. Some organs require different solutions to maintain organ circulation. We hypothesized that this device is capable of perfusing different levels of viscosities (1-6.5 cP) to the same standard as phosphate-buffered saline (PBS) to improve blood mimicking capabilities [3].

METHODS

Pressurized oxygen was delivered to the tubes in a pulsatile fashion that caused a cyclical effect of inflation and deflation of the tubing. As the pressurized oxygen entered the tubes, the pressure within the pump chamber increased above the hydrostatic pressure in the main organ

chamber. This caused a pressure difference that forced a bolus of oxygenated fluid from the main chamber into the pump chamber through the perfusion port[2]. During the pulsatile process, the silicone tubing experienced deflation, this dropped the pressure in the pump chamber beyond the pressure in the main organ chamber thus a bolus of oxygenated fluid was then forced back into the pump chamber; this process allowed for a pulsatile flow of oxygen throughout the device.



Figure 1: VOPS Device Design Components

VOPS is composed of four main components: the top cap (must be screwed into place onto the pump chamber), helical silicone tubing (Silastic® Laboratory Tubing, DuPont de Nemours, Inc.), pump chamber, organ chamber and base cap. Silicone tubing was placed in the most efficient formation of helical shape and was chosen because it allows oxygen to permeate through its walls[2]. The pump chamber contains the helical silicone tubing that is 6.1 m in length; the organ chamber contains fluid and vascular resistance element. The vascular resistance element is silicone tubing cut to a length that intends to mimic

the resistance a kidney would experience during normal blood flow (0.22 mmHg/mL/min) and was derived from previous research and literature[2]. The device includes six latches that secure the pump chamber to the organ chamber, and O-rings designed to ensure the device has an air-tight seal. The device was manufactured in-house at The University of Texas at San Antonio's machine shop. The top cap, pump chamber and base cap were made of 6061 Aluminum. A silicon tube holder was 3-D printed in-house (Clear Resin, Form 2, Formlabs) to ensure that helical tubing did not kink or compress. The organ chamber was made of acrylic. Use of medical-grade epoxy allowed the organ chamber to be secured in place with the base cap. The pressures that were used for testing are as follows: 27.6, 55.2, 82.7, and 110.3 kPa. Pressure transducers (PX309-030G5V, Omega Engineering, Inc.) were attached to the inlet of the vascular resistance-mimicking PVC tubing and the main organ chamber. The measured difference between the pressures at these tubes indicated the perfusion pressure. The flow rate was measured via a sensor (2PXL-TS410, Transonic Systems Inc.) attached to an exterior flow loop located outside of the device. The pressure transducers and flow sensor provided data that was recorded via a LabVIEW virtual interface (NI 9221 and NI USB-9162, LabVIEW 2019 SP1, National Instruments) and distributed to MATLAB (MATLAB R2020a, The MathWorks, Inc.) for calculation and analysis. Testing was conducted using a pneumatic switching setup with a pulse frequency of 0.25 Hz, 50% duty cycle (2000 ±100 ms open, 2000 ±100 ms closed). This approach allowed the entire system to be mechanical, without the need for batteries or electronic control. The procedure for viscosity testing started with the mixture of anhydrous calcium chloride (Flinn Scientific, Inc, Batavia, IL, USA) and deionized water, the table below describes the viscosity mixture procedure. A Cannon-Fenske Viscometer (CANNON Instrument Company, State College, PA, USA) was used to find the viscosity of the aqueous solutions with the varying mass percentage.

Table 1: Viscosity Mixing Procedure

Viscosity	Mass %	To create a 4 L solution	To create a 1 L solution
1 cP	0%	4000 mL H ₂ O, 0 g CaCl ₂	1000 mL H ₂ O, 0 g CaCl ₂
3 cP	31.53%	3204 mL H ₂ O, 1472.77 g CaCl ₂	801 mL H ₂ O, 368.2 g CaCl ₂
5 cP	37.47%	3023 mL H ₂ O, 1808.2 g CaCl ₂	756 mL H ₂ O, 452.21 g CaCl ₂
6.5 cP	39.99%	2942 mL H ₂ O, 1957.0 g CaCl ₂	736 mL H ₂ O, 489.58 g CaCl ₂

Five tests were performed at each mass percentage and the resulting viscosity data were output in centiStokes[3]. The average of these tests was obtained as the viscosity at the respective mass percentage.

RESULTS

The results of these tests required gathering data both using a baseline parameter set and a tuned set to collect peak perfusion and mean flow rates. Baseline data was accumulated using constant variables of vascular resistance and silicone tube length, however, incorporated varying oxygenation pressures (27.6 to 110.3 kPa). Table 2 shows the peak perfusion pressure (mmHg) and mean flow rate (mL/min) for each of the tested viscosities for both baseline and tuned test results.

Table 2: Viscosity Test Results

Viscosity (cP)	Peak Perfusion Pressure (mmHg)		Mean Flow Rate (mL/min)	
	[Baseline/Tuned]		[Baseline/Tuned]	
1	29.3 - 96.8	15.5 - 70.0	2.5 - 13.2	4.0 -19.4
3	17.2 - 47.5	22.4 - 83.8	5.0 - 16.0	6.4 - 28.2
5	8.6 - 49.2	11.8 - 54.5	1.5 - 12.7	5.2 -26.8
6.5	4.8 - 30.1	5.3 - 24.2	0.6 - 5.7	1.4 - 12.6

The trend that was displayed for this testing showed an inverse relationship with viscosity and peak perfusion pressures. As the viscosity increased, the peak perfusion pressures decreased, regardless of oxygen pressure rate [3]. However, this relationship did not translate to the mean flow rates. The tuned pulse frequency and duty cycle showed a trend of decreasing peak perfusion pressures and increased the mean flow rates. The use of the vascular resistance validates the VOPS device's capacity to deliver the appropriate peak perfusion pressures and mean flow rates within a targeted range gathered by data collected in porcine kidney preservation studies performed by Urbanellis et al. for each viscosity tested[4].

DISCUSSION

The VOPS device has competitive advantages over the current organ preservation devices available on the market due to its portability, versatility, and low cost. Our results indicated ideal viscosity for the current design of the VOPS device in terms of balancing oxygen supply pressures to reach appropriate perfusion parameters for the preservation of a human kidney. While the VOPS device met the perfusion parameters at more oxygen supply pressures with one tested viscosity, all viscosity solutions tested reached the flow parameters essential for kidney preservation. This provides evidence that the VOPS is highly versatile as it can potentially be used with several preservation solutions that are required for various organs.

ACKNOWLEDGEMENTS

This work was funded through a Department of Defense PRMRP; Award Number: W81XWH-18-1-0640. The authors would like to thank Dr. Ender Finol and Dr. Chris Combs for providing data acquisition equipment, and David Kuenstler for assisting with the fabrication of the device.

REFERENCES

[1] Hameed, A. M., Hawthorne, W. J., and Pleass, H. C., 2017, "Advances in organ preservation for transplantation," ANZ journal of surgery, 87(12), pp. 976-980.

[2] Portillo, D. J., Gonzalez, J., Villarreal, C., Salazar, S. J., Fasci, A., Wearden, B., Oseghale, J., Khalil, A., Perillo, T., and Muenchow, L., 2022, "Development and Characterization of a Nonelectronic Versatile Oxygenating Perfusion System for Tissue Preservation," Annals of Biomedical Engineering, pp. 1-13.

[3] Gonzalez, J. M., Villarreal, C., Fasci, A., David Di, R., Salazar, S., Khalil, A., Brandt, W., Oseghale, J., Garcia, M., Portillo, D. J., and Hood, R. L., 2023, "Evaluating the Performance of a Nonelectronic, Versatile Oxygenating Perfusion System across Viscosities Representative of Clinical Perfusion Solutions Used for Organ Preservation," Bioengineering, 10(1), p. 2.

[4] Kathis, J. M., Cen, J. Y., Chun, Y. M., Echeverri, J., Linares, I., Ganesh, S., Yip, P., John, R., Bagli, D., Mucci, I., Ghanekar, A., Grant, D. R., Robinson, L. A., and Selzner, M., 2017, "Continuous Normothermic Ex Vivo Kidney Perfusion Is Superior to Brief Normothermic Perfusion Following Static Cold Storage in Donation After Circulatory Death Pig Kidney Transplantation," American Journal of Transplantation, 17(4), pp. 957-969.

PULSE OXIMETER FOR SIMULATION MANNEQUIN

Marina Walsh (1), Benjamin Aon (1), Hatice S. Emanet (1), Cheyenne M. Miller (1), Chiamaka G. Oduah (1)

Faculty Advisor(s)

Ria Mazumder (1)

(1) Department of Biomedical Engineering, Widener University, Chester, PA, USA

INTRODUCTION

According to the National Council of State Boards of Nursing, 87% of nursing schools are using high-fidelity mannequin-based training in their curriculum.¹ Simulation mannequins provide an immersive learning environment by mimicking real-life clinical scenarios that healthcare workers will potentially encounter in the field. This allows nursing students to train and enhance their skills and competencies in a controlled and risk-free environment. Although today's mannequins are equipped with multiple intricate features that significantly enhances simulation experience, there is still a need for improvement of realism in several basic clinically relevant attributes. For example, the absence of blood flow in mannequins prevent nursing students from using regular pulse oximeters to measure pulse rate and SpO₂ levels.

Both SpO₂ and pulse rate are vital measurements that can indicate different life-threatening conditions (such as acute respiratory distress syndrome, pneumonia, heart failure, etc.). Hence it is important that nurses are trained to read these measurements and determine a plan of action based on the readings.

Currently, there are 2 methods that nursing instructors implement in mannequin-based simulation laboratories which allows nursing students to analyze pulse rate and SpO₂ levels. (1) In high-fidelity mannequins that have the capability to reflect physiological measurements on a monitor, the instructor sets the pulse rate and SpO₂ levels prior to the simulations. During the simulation lab, the nursing students read the measurements from the monitor and makes appropriate interventions based on their observation. (2) In mannequins that aren't equipped with these features the students during simulation use a regular pulse oximeter to mimic the action of clipping it to a finger and when completed correctly the instructor announces the measurements based on the clinical situation being simulated. Neither of these techniques are realistic. Furthermore, these options don't

respond to real-time intervention, that is if the nurses are taking an action such as injecting a drug the numbers don't automatically change in real-time based on this action.

Therefore, the aim of our project is to create a realistic (both visually and operationally) stand-alone pulse oximeter device that can be integrated into any simulation mannequin irrespective of make or model. The device should be able to reflect normal measurements and disease conditions based on the clinical situation being simulated by the instructor. Lastly, the device should be able to update its values in real-time in response to intervention from nursing students during simulation labs.

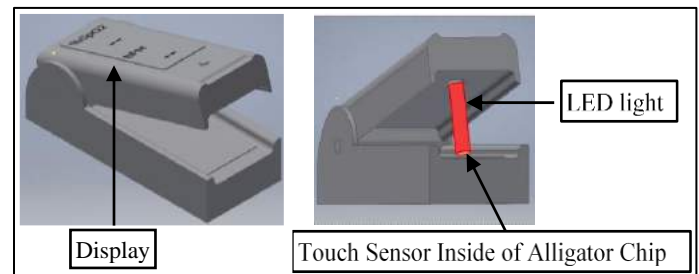


Figure 1: Sketch of the external case (done in Inventor 2020)

PRODUCT DESIGN

Design: Based on our design criteria and constraints the team proposed an app-controlled Bluetooth-based pulse oximeter device as a potential solution.

The design consists of a 3D printed finger-clip casing (Figure 1) that mimics the appearance of an alligator clip pulse oximeter and houses all the electronic components (Figure 2). The device operates via an Arduino mini-UNO microcontroller board that is connected to a wireless Bluetooth receiver, a LED light, a force transducer, and an OLED display. The Bluetooth receiver obtains pulse rate and SpO₂ values transmitted from an app designed using MIT App Inventor (Figure 3). An LED light included underneath the top surface of the case mimics the light

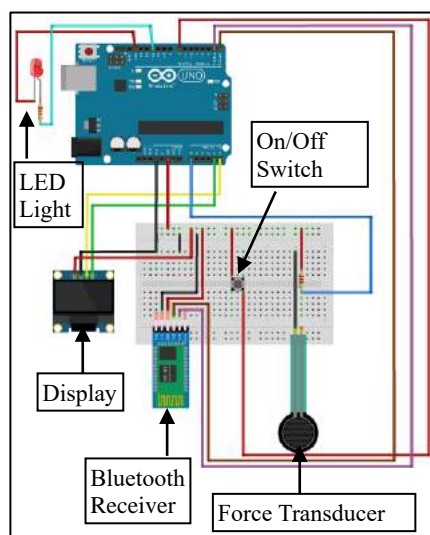


Figure 2: Sketch of the electronic components housed inside the case.

Instructor set-up: The app can be accessed by the instructor either from a cellphone or a computer. Prior to the simulation lab, the instructor sets the appropriate values on the app based on the clinical scenario being simulated and hits submit to transmit the data to the Bluetooth receiver.

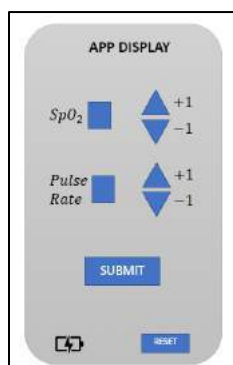


Figure 3: Schematic of the App

Nursing student use: During simulation the nursing students will clip the device onto a simulation mannequin's finger and turn on the device using the push button switch. As the force transducer gets activated by the pressure from the finger, the values submitted by the instructor prior to the simulation is displayed.

Real-time intervention: Based on the observed SpO₂ and pulse rate measurements, if the nursing students plan and execute a course of action, the instructor can update the measurement values to reflect the effect of their action real-time via the app. The updated values will help the nursing students analyze their treatment plan and act accordingly based on improvement or deterioration in the observed measurements.

Design Analysis: There are several benefits of the design. It is easy to use for both the nursing students and instructors, as all that the students need to do is place the device on the mannequin's finger and turn it on and all that the instructor does is adjusts the values through an app. The device is interchangeable on any mannequin's finger (pediatric, adult, low-fidelity, high-fidelity, etc.) as all the device requires is a finger for the force sensor to be activated. The 3D printed casing replicates any over the counter pulse oximeter and the mechanism to operate the device mimics the same both of which

source of an actual pulse oximeter to enhance realism (Figure 1b). The force transducer placed on the inner surface of the case is activated when the device is clipped onto a finger which allows the values transmitted via the Bluetooth to be shown on the OLED display. The case contains a push button switch to turn the device on or off.

enhances realism. The device is designed to encase all electronic circuitry and the battery inside a 3D printed case for safety purposes. The device is equipped with a feedback mechanism that allows nursing students to analyze their intervention during a simulation lab.

BUDGET & MARKET ANALYSIS

According to the 2022 "Mannequin-Based Simulation-Global Market Trajectory & Analytics" report², despite the COVID-19 issue, the global market for mannequin-based simulation, which was earlier predicted to be valued at US\$1.4 billion in 2020, is now estimated to grow to US\$3.7 billion by 2027 at a compound annual growth rate (CAGR) of 14.4%. Patient simulators, one of the market segments the report looked at, is projected to develop at a CAGR of 13.9% and reach US\$2.5 billion by the conclusion of the analysis period. This shows that although the demand for simulation mannequin-based training had increased during the global pandemic (due to the limitations of on-site clinical training), the need has not subsided, and the post-pandemic market continues to grow.

Since our product is vendor independent it can be integrated into already-existing mannequins as well as newly manufactured ones which allows us to address a very large market. The parts cost to build this device is projected to be less than \$150. Given that more than 87% of nursing schools incorporated simulation-based mannequins of some form the team anticipates producing about 50,000 pulse-oximeter units each year to be incorporated both with existing and newly manufactured mannequins with a selling price of \$500 per unit. Since mass production will reduce the cost of parts, the projected income from selling one unit is estimated to be greater than \$350. This income will be used for advertisement, lab space rent, salary for engineers and employees and other related expenses. The team predicts that the device should still provide an overall profit of \$150 per device.

ACKNOWLEDGEMENTS

We would like to extend our thanks to Widener University's School of Nursing for allowing us access to their simulation lab and providing us with feedback.

REFERENCES

- [1] Koukourikos, K., Tsaloglidou, A., Kourkouta, L., Papathanasiou, I. V., Iliadis, C., Fratzana, A., & Panagiotou, A. (2021). Simulation in Clinical Nursing Education. Acta Informatica Medica : AIM : Journal of The Society For Medical Informatics Of Bosnia & Herzegovina : Casopis Društva Za Medicinsku Informatiku BiH, 29(1), 15–20. <https://doi.org/10.5455/aim.2021.29.15-20>
- [2] Mannequin-Based Simulation – Global Market Trajectory & Analytics, (2022) https://www.researchandmarkets.com/reports/338825/mannequinbased_simulation_global_market#product-description

DIRECTIONAL MIGRATION OF OVARIAN CANCER CELLS IN A 3D MICROTISSUE MODEL

Peyton E. Clark (1), Asha Kumari (2), Karthikeyan Mythreye (2),
M.K. Sewell-Loftin (1,3)

- (1) Department of Biomedical Engineering, University of Alabama at Birmingham, Birmingham, AL, USA
(2) Department of Pathology, University of Alabama at Birmingham, Birmingham, AL, USA
(3) O'Neal Comprehensive Cancer Center, University of Alabama at Birmingham, Birmingham, AL, USA

INTRODUCTION

High grade serous ovarian carcinoma (HGSOC) accounts for 90% of deaths as a result of ovarian cancer [1]. Additionally, in the U.S. the median age at diagnosis is 63 and most cases are in post-menopausal women [2]. In contrast with the age of women diagnosed with HGSOC, most *in vivo* models of HGSOC use young animals. This discrepancy may add to the challenges of studying ovarian cancer, as aged animal models are expensive and require extensive care. The process of metastasis of HGSOC begins with an epithelial-to-mesenchymal transition (EMT), which promotes the migration of the cancer cells and decreases intercellular attachment [3]. The hallmarks of EMT include increased expression of alpha smooth muscle actin (α SMA) and Snail1, which promote increased cell migration and matrix remodeling. Recent work has indicated that EMT-like phenotypic shifts may be caused by mechanical forces [4]. To better understand how mechanical forces may drive changes in migration behaviors of ovarian cancer cells, we developed a microfluidic model for biomechanical studies of the tumor microenvironment. The objective of this project was to optimize a 3D microtissue model to study ovarian cancer cell migration. Additionally, we sought to use the microfluidic model to study the contribution of the senescent vasculature from aged tissues on tumor cell behavior.

METHODS

ID8 mouse ovarian surface epithelial cells with *Trp53* Δ deletion (ID8p53) are a previously established HGSOC model that allow for study of the tumor microenvironment [5]. ID8p53 cells were seeded into the center chamber of a three-chamber microfluidic device, where the tissue chambers are adjacent in series to each other [6]. Each chamber of the device is an independent microtissue connected with 20 μ m communication ports to allow cell migration and transfer of nutrients. The cells were suspended in a 9:1 fibrin-collagen matrix to mimic the natural tumor environment, with a total matrix protein concentration of 10mg/ml. The side chambers were loaded with blank, cell-free gels. The

devices were cultured for three days with a flow regime that prevented convective diffusion from occurring between adjacent regions. Before imaging, the left chambers of all devices were treated with TGF- β 1 (10 ng/ml), and an inward (left chamber to center chamber) flow was established. The right-hand chambers received control media with no exogenous TGF- β 1. The devices were imaged over either a 3hr period or an 18hr period with images taken every 5min or 30min, respectively. After treatment, cell migration was quantified using Chemotaxis and Migration Tool V2.0 [7]. After 24hr of treatment, the microtissues were fixed and stained for phalloidin and DAPI for immunofluorescence analysis to further characterize cell migration behaviors.

To measure how age associated vascular senescence differences alter ovarian cancer cell migration, we utilized human SKOV3 cells tagged with a GFP reporter in a conditioned media study. SKOV3-GFP cells were seeded into the center chamber of the device in the same conditions described above with the same 3-day period prior to introduction of conditioned media. On day 3, the left chamber of the device was treated with conditioned media from senescent human ovarian microvascular endothelial cells (HMECs) and the right chamber received conditioned media from non-senescent HMECs. The center chamber was fed with the control media. An inward flow direction was established that caused diffusion of factors in the media from side chambers towards the SKOV3-GFP in the center chamber. Images were taken at the time of initial treatment and every 24 hours for six days. The cells received fresh media every day. Migration into the side chambers was measured as percent area of fluorescence normalized to total area of the side chambers.

RESULTS

The results show that a prolonged exposure to TGF- β 1 is required to trigger a significant change in ID8p53 total migration distance (Figure 1A). For additional characterization, histograms displaying migration angles for individual cells were generated (Figure 1B, C).

Movement towards TGF- β 1 is indicated by 180°. The interquartile ranges (IQR), representing the middle 50% of the data, were determined to compare migration data trends. The immunofluorescence analysis shows that cell migrated into the left chamber with the TGF- β 1, but not into the right chamber (Figure 1D).

In conditioned media studies, our results show that over a period of 5 days, there is increased cell migration in the left chamber, towards the senescent conditioned media (Figure 2A). The differences in migration evened out on day 6. These differences in migration can also be seen in the immunofluorescence images. The left chamber of the microtissue model on day 1 of treatment shows higher levels of cell migration than the right chamber (Figure 2B). This trend is continued on day 5 (Figure 2C).

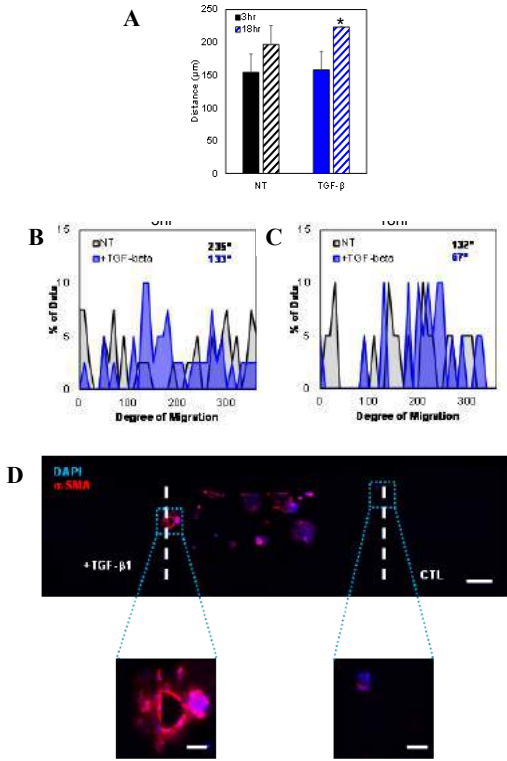


Figure 1: (A) Distance traveled by ID8p53 cells in the microtissue model. Averages \pm SEM shown. N = 2-4 devices, 20-40 cells. * $p < 0.05$ vs. 3hr NT. (B, C) Histograms showing angles of migration for cells in microtissue models. 180° represents migration towards the Left chamber, or source of TGF- β 1. Inset numbers are interquartile ranges (middle 50%) of all measured events, n=20-40 cells. (D) Representative images of microtissue model. Scale bar = 250μm. Tissue chamber borders (white dashed lines) and treatments are shown. (Below) Insets of regions near chamber interfaces. Scale bar = 50μm.

DISCUSSION

Our studies show that we can successfully track and characterize migration events for mouse and human ovarian cancer cell lines in our 3D microtissues models. We were able to control the matrix conditions, flow conditions, and the delivery of growth factors or conditioned media over multiple days while performing real-time imaging. In optimization studies with ID8p53 cells and TGF- β 1, we saw an increase in migratory behavior when exposed to TGF- β 1 over an extended period of time. Treatment with the growth factor resulted in a more directed migration,

indicated by the decreased IQR at both time points. The studies with the mouse cells allowed us to optimize the loading and fluid flow conditions, as well as the method of analysis. Moreover, our pilot studies with conditioned media from senescent endothelial cells demonstrated slight differential migration towards media from senescent cells compared to non-senescent, control cells. Our results suggest that secreted factors from senescent ovarian cancer cells may promote migratory behaviors. This could partially explain differences with ovarian cancer progression in patients of different ages. This proof-of-concept study will be used to develop future experiments to determine which factors may be responsible for the increased migration observed in senescent media-treated samples. Future work will also focus on further optimizing the microtissue model to allow for easier and less expensive study of HGSOc in an environment that closely mimics the natural tumor microenvironment.

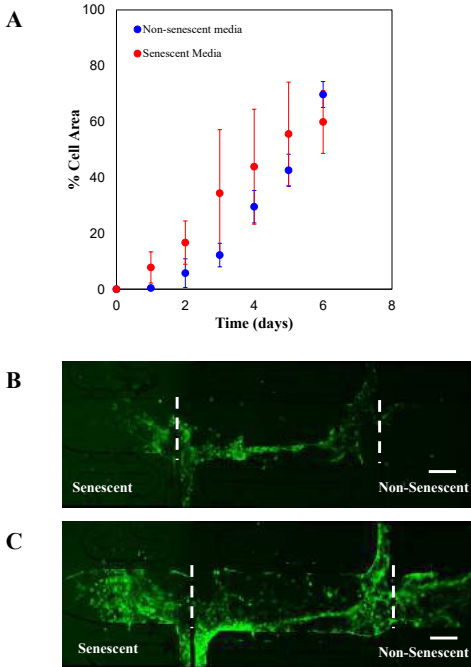


Figure 2: (A) Percent cell area in microtissue model. Quantifications shows total GFP+ area divided by total area of side chambers (ROI area), which was held constant for left/right chambers. Averages \pm SEM shown. N = 2 devices. (B, C) Representative images of cell migration in microtissue model with GFP-tagged SKOV-3 on day 1 (B) or day 5 (C) of treatment. Tissue chamber borders (white dashed lines) and treatments are shown. Scale bar = 250μm

ACKNOWLEDGEMENTS

The authors would like to acknowledge funding for this project: R00-CA230202 (M.K.S.L), IMPACT Award, O'Neal Comprehensive Cancer Center (M.K.S.L), and the Fine Family Philanthropic Grant.

REFERENCES

[1] Kurman, R.J. et al, *Am. J. Pathol.*, 2016, 186(4), 733-747. [2] Lisio, M.-A. et al., *Int. J. Mol. Sci.* 2019, 20, 952. [3] Lengyel, E., *Am. J. Pathol.*, 2010, 177(3), 1053-1064. [4] Sewell-Loftin, M.K. et al., *Sci. Rep.*, 2017(7), 12574. [5] Walton, J., *Cancer Res.* 2016, 76(20), 6118-6129. [6] Sewell-Loftin, M.K. et al., *Lab Chip*, 2020(20), 2776-2787. [7] Trapp, G., *Ibidi GmbH*, 2010

QUANTITATIVE POLARIZED LIGHT IMAGING OF PORCINE PULMONARY VALVE LEAFLETS

Shreya Sreedhar (1), Connor Link (1), Daniel P. Pearce (1), Colleen M. Witzenburg (1)

(1) Department of Biomedical Engineering
University of Wisconsin-Madison
Madison, Wisconsin, USA

INTRODUCTION

Proper alignment of collagen fibers provides strength and support to heart valve leaflets, allowing them to effectively regulate blood flow through the heart. Aberrations in collagen alignment can cause changes in the mechanical properties of the leaflets and increase the risk of valve dysfunction and disease. Following altered loading conditions in the heart, the collagen alignment in the diseased/alterd region is known to rearrange [1]. Studying the full-field collagenous organization of a tissue can be a useful way to quantify its heterogeneous structural properties. A novel imaging technique using division-of-focal-plane polarimetry can be used to measure circularly polarized light transmitted through an unfixed tissue to rapidly quantify its collagen alignment [2]. Quantitative polarized light imaging (QPLI) is a useful tool used to study the full field collagenous organization of thin heterogenous tissues, which provides overall incident light intensity (S0), the angle of linear polarization (AoP), and the degree of linear polarization (DoLP) [3].

This method of quantification has been used previously in studying homogeneous tissues such as tendons and cartilage but has remained underutilized in structurally and mechanically heterogeneous cardiovascular tissues [2,3]. Our objective was to apply QPLI to pulmonary valve leaflets, which are thin heterogeneous cardiovascular tissues. We assessed the hypothesis that pulmonary valve leaflets would exhibit similar spatial patterns in AoP and DoLP to previously tested aortic valve leaflets [5]. We also evaluated the hypothesis that light intensity and tissue thickness are correlated, and we found a negative correlation between the two. These metrics provided by QPLI can help determine trends in the structural properties of pulmonary valve leaflets, and eventually be applied to the changes in properties in diseased states.

METHODS

Sample preparation. Pulmonary heart valves were excised from the hearts of 5–6-month old pigs obtained from a local butcher (Hoesly's Meats, New Glarus, WI). Leaflets were either frozen for later use or stored in phosphate-buffered saline (PBS) and tested within 24 hours. The leaflets were carefully placed on a black platform, ensuring to keep the sample flat. The leaflet was then scanned by the LJ-V7080 laser micrometer (Keyence) at an acquisition rate of 200 Hz to obtain a 3D thickness profile.

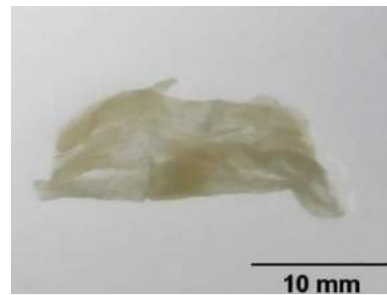


Fig 1: Sample leaflet

Imaging. In order to image the leaflet using QPLI, the sample was transferred to a glass platform using tweezers. The directionality of the leaflet was kept the same as on the black platform for consistency. The glass platform was placed on top of an LED light source with a circularly polarized light filter. The soft tissue was imaged with the highest intensity light setting. The image was obtained using the Polarization GUI (SpinView) at a 20 Hz acquisition frame rate and the "Polarized8" pixel format.

Data Analysis. The raw output data from the polarization GUI provides the intensity of light that passes through the soft tissue at different angles. S0, DoLP, and AoP were computed from the raw data as done previously [3,4]. S0 indicates the overall intensity of incident light. AoP

indicates the angle of linear polarization and is a measure of preferred collagen fiber angle. DoLP indicates the degree of linear polarization and is a measure of that preference, with a value of 0 showing no alignment and 1 showing total alignment. To determine trends between thickness, S0, and DoLP these values were plotted against one another for each leaflet. A Pearson's correlation coefficient (r) was calculated to quantify the correlation and a p-value was calculated to determine the significance of the correlation.

RESULTS

Fig. 2 includes a quiver plot of the AoP overlaid on the DoLP heatmap of a representative leaflet sample. The AoP vector is scaled to the amount of DoLP in that region. The belly region of the tissue exhibited low alignment, while the lower outer region of the sample exhibited high alignment. All samples showed this pattern, and these results are consistent with previously presented data on quantifying heterogeneity in aortic valve leaflets [5].

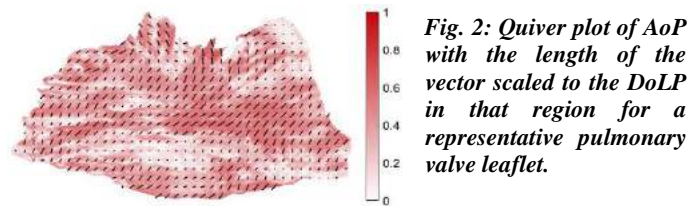


Fig. 3 includes the raw S0 and thickness values from QPLI and laser micrometry, respectively. The leaflets imaged had thicknesses ranging from 0.80 ± 0.01 mm to 1.2 ± 0.02 mm. A visual comparison suggests an inverse relationship between thickness and intensity - in regions of high thickness, there was typically lower intensity and in regions of low thickness there was typically higher intensity.

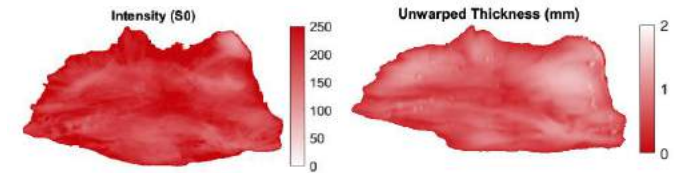


Fig. 3: S0 (left) and Unwarped Thickness (right) for a representative pulmonary valve leaflet.

In order to quantitatively compare each metric, the thickness for each leaflet was warped to fit into the border of the Intensity plot using a rotational matrix. Table 1 displays r values for comparisons between S0 and warped thickness, DoLP and warped thickness, and S0 and DoLP. Each metric was compared using pixel-to-pixel correlation. P-values for every sample were below $1e-10$. The average r value for S0 vs. thickness -0.5 ± 0.09 , indicating a negative correlation between the two metrics. This is consistent with the visual comparison between intensity and thickness. The correlations between DoLP vs. thickness and S0 vs. DoLP, remains inconclusive as there is a large standard error and no strong patterns. Fig. 4 displays the warped thickness, DoLP, and S0 for a representative leaflet.

DISCUSSION

QPLI is a useful tool that can provide full-field information about the collagenous organization of soft tissues, yet few efforts have been made to apply QPLI to structurally heterogeneous cardiovascular soft tissues. Useful metrics such as S0, AoP and DoLP were obtained for pulmonary valve leaflets. All samples showed similar regional patterns to previous studies [5]. We found that light intensity and thickness exhibited a

negative correlation, while thickness and DoLP, and S0 and DoLP were very weakly and weakly correlated, respectively. The strength of this negative correlation between S0 and thickness (-0.58), could indicate that variations in tissue density also impact S0 or that the warping of the thickness negatively affected pixel to pixel correlations. We computed the percent error of the warped thickness, and sample edges exhibited high error. This could be because the outside edges need to be warped most when expanding the tissue into the intensity border. While future work will further investigate the effects of warping there was a consistent negative correlation between thickness and intensity. DoLP of a soft tissue, however, showed weak and very weak correlations to S0 and thickness, indicating it will provide information independent to thickness and intensity on the degree of collagen alignment of a soft tissue. Future work will also include dynamic imaging of leaflets during biaxial loading. Dynamic imaging will provide more information on the collagen fiber alignment and rotation during alternative loading conditions, which can reveal more about the function of the tissue's extracellular matrix.

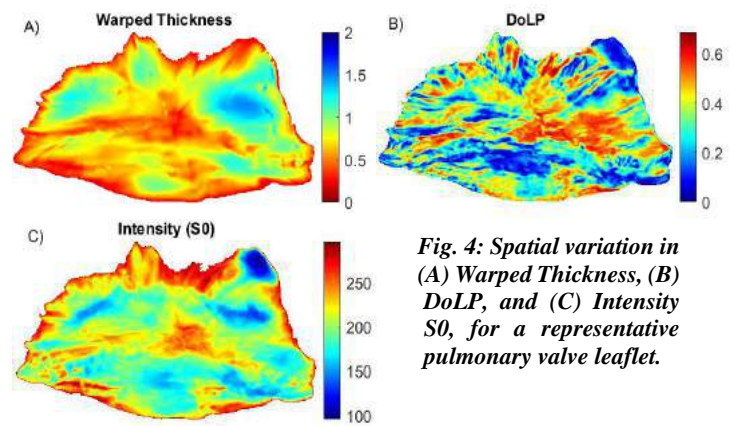


Table 1: Correlation coefficient (r) for S0 vs. warped thickness, DoLP vs. warped thickness and S0 vs. DoLP. *Warped thickness, DoLP and Intensity (S0) for leaflet 3 pictured above in Fig 4.

Leaflet number	S0 vs. warped thickness	DoLP vs. warped thickness	S0 vs. DoLP
1	-0.71	-0.45	0.55
2	-0.52	-0.10	0.21
3*	-0.51	-0.02	0.33
4	-0.48	0.36	0.02
5	-0.58	-0.14	0.35
6	-0.67	-0.24	0.46
Average	-0.58 ± 0.09	-0.10 ± 0.27	0.32 ± 0.19

ACKNOWLEDGEMENTS

This work was funded by a grant from the NSF to C.M.W (2030173).

REFERENCES

- [1] Fomovsky, G et al., J Heart and Circulatory Physiology, 298:H221-H228, 2010
- [2] York, T et al., J Biomedical Optics, 19:066011, 2014
- [3] Perkins, R et al., Optics Express, 18:25815-25824, 2010
- [4] York, T et al., Optics Express, 51:5392-5400, 2012
- [5] Sacks, MS et al., Ann Biomed Eng., 25:678-89, 1997

ANALYSIS OF THE FRICTIONAL FORCES DURING BLOOD CLOT REMOVAL IN EXPERIMENTAL MODELS OF ACUTE ISCHEMIC STROKE

Omar N. Elkhayat (1), Bryan C. Good (1)

(1) Department of Mechanical, Aerospace, and Biomedical Engineering, The University of Tennessee, Knoxville, TN, USA

INTRODUCTION

Every year in the U.S., over 800,000 people suffer from stroke, of which 90% are classified as acute ischemic stroke (AIS) [1]. AIS is defined by the obstruction of blood flow in an artery in the brain due to a lodged embolus. The “MR CLEAN” trial found that treatment of AIS was more effective with the addition of intraarterial treatment, defined as mechanical disruption of the lodged blood clot via mechanical thrombectomy (MT) [2]. Intraarterial treatment can be performed using either a stent retriever (SR) or an aspiration catheter. Although a high rate of recanalization (~85%) was found for patients treated with MT, a large rate of mortality and loss of function still occurred [3]. Currently, *in-vitro* models provide a more practical and cost-effective method of studying AIS and MT. However, Johnson *et al.* discussed the importance of characterizing vessel wall friction for the optimization of *in-vitro* modeling [4], as current experimental models do not accurately mimic the frictional and adhesive forces that occur *in-vivo*. The current gap in knowledge on AIS and MT biomechanics is the motivation for investigating the frictional interactions that occur between blood clots, materials used in *in-vitro* AIS models, nitinol materials found in SRs, and arterial walls. These findings will lead to an increased understanding of the forces involved in MTs, inspiring new surgical techniques and devices to further improve the treatment of AIS.

METHODS

For all experimental testing, custom 3-D printed attachments were made for use on a Single Column Material Testing System (Instron). Static friction testing was conducted similarly to Gunning *et al.* [5], and results were analyzed in ImageJ. Kinetic friction testing was conducted between embolus analogs (EAs) and materials commonly used in *in-vitro* models of AIS (glass, PVC, and silicone), bare nitinol material found in SRs, and carotid artery tissue samples. Additional friction experiments were also performed between a Solitare2 nitinol SR (4x40 mm) (Medtronic) and the same artificial and biomaterial surfaces.

To create EAs for static and kinetic mechanical testing, bovine blood (Lampire Biologic) was collected in CPDA-1 anticoagulated bags, centrifuged to separate red blood cells and plasma, and reconstituted to desired hematocrits (0-40%). Calcium chloride was added to promote coagulation in the blood, which then filled 3-D printed molds (20x20x10 mm) and clotted statically for 2 hours. EAs for static friction testing were formed in bare molds, while EAs for kinetic friction testing were formed in molds with one Velcro-lined wall. Velcro allowed for the fixation of one side of the clot during testing.

For kinetic testing, a modified lap-shear approach was used (**Fig. 1**). Before loading the sample onto the Instron, the initial height of the EA was recorded. The sample was then fixed onto the lower attachment and the testing material brought into contact with the EA. The compressed height of the EA between the slide and testing material was recorded. Having the initial and compressed height (strain) of the EA, the normal stress on the EA can be found using its Young's Modulus. Shearing occurred at 0.1 mm/s to minimize viscoelastic effects.

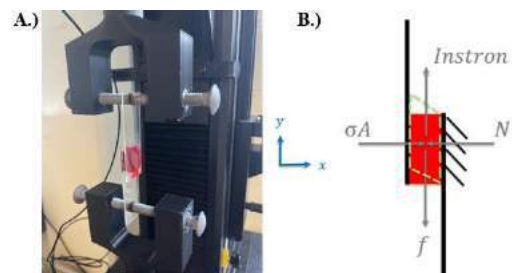


Fig. 1: A.) Instron with custom 3-D printed attachments for kinetic friction testing and B.) FBD of the testing set up.

For kinetic testing between the SR and various material surfaces, a custom 3-D printed attachment helped to translate the testing coordinate system (**Fig. 2**). The SR was unfolded on the testing material and a

weight was placed on the SR, providing a known normal force and to help keep the SR unfolded. To ensure that the coefficient of kinetic friction was accurately measured and did not change, two different loads were used during testing. The SR was pulled at approximately 2 mm/s to mimic rates used in *in-vitro* MT testing.

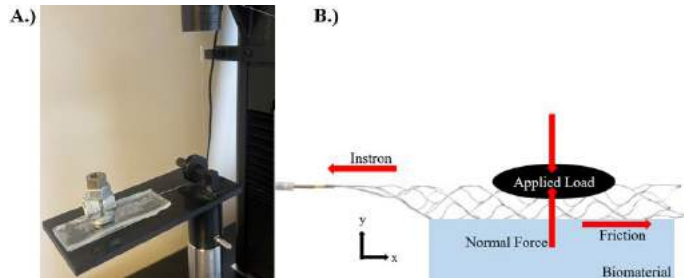


Fig. 2: A.) Instron with custom 3-D printed attachments for testing the Solitaire2 SR and B.) FBD of the testing set up.

RESULTS

The average coefficients of friction of EAs against various material surfaces are shown in **Table 1**. Overall, silicone experienced the highest friction between the EAs while nitinol experienced the lowest. This trend was consistent for all hematocrits in static testing as well as for the 40% EA kinetic tests. The coefficients of kinetic friction were also found to be lower than that of the static friction for all materials and EAs. An observed increase in friction corresponded with decreasing EA hematocrit. Statistical significance was found between the 0% and 40% EAs for all materials for static friction, as well as between the coefficients of static and kinetic friction for the 40% EAs.

Table 1: Average coefficients of static and kinetic friction of EAs against material surfaces, reported with a 95% CI.

EA Hematocrit	Sample Size	Coefficient of Static Friction	Coefficient of Kinetic Friction
Glass			
40%	20	0.096 ± 0.004	0.064 ± 0.010
20%	20	0.121 ± 0.010	-
0%	20	0.139 ± 0.012	-
PVC			
40%	20	0.106 ± 0.005	0.073 ± 0.015
20%	20	0.122 ± 0.006	-
0%	20	0.176 ± 0.032	-
Silicone			
40%	20	0.117 ± 0.005	0.078 ± 0.013
20%	20	0.134 ± 0.009	-
0%	20	0.223 ± 0.048	-
Nitinol			
40%	20	0.097 ± 0.003	0.031 ± 0.004
20%	20	0.115 ± 0.007	-
0%	20	0.128 ± 0.020	-

A summary of the average coefficients of kinetic friction during SR testing is shown in **Table 2**.

Table 2: Average coefficients of kinetic friction of the Solitaire2 SR against material surfaces, reported with a 95% CI.

Load	Sample Size	Coefficient of Kinetic Friction
PVC		
20 g	20	1.66 ± 0.08
30 g	20	1.73 ± 0.06
Silicone		
20g	20	4.40 ± 0.13
30g	20	4.31 ± 0.12

An example of raw SR testing data is shown in **Fig. 3**. The graph depicts a ramp-up region where there is visible stretching of the SR and a constant region in which the SR is sliding against the material. Only the constant region is used for calculations of the kinetic friction. Similar force vs. displacement graphs were observed during kinetic friction testing of EAs, with the addition of a ramp down region to a 0-force reading when EA separated from the testing material.

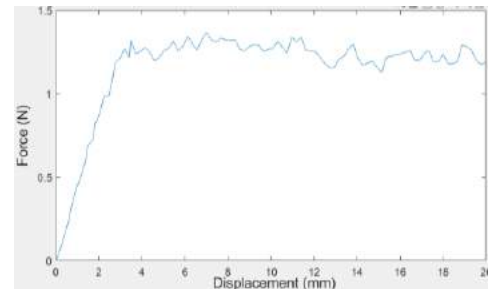


Fig. 3: Raw force vs. displacement data from kinetic testing of the Solitaire2 SR against silicone under a 30 g load.

The results of SR testing (**Table 2**) show no significant change in the coefficients of friction across the differing loads for the same material. Silicone had a significantly higher coefficient of kinetic friction when compared to PVC. The frictional forces obtained between the SR and materials were significantly higher when compared to the interactions between materials and EAs. Preliminary data obtained with bovine carotid arteries show coefficients of static and kinetic friction at around 0.4 and 0.2 for 40% EA hematocrit, respectively, while kinetic friction testing with SRs show significantly higher results at about 2.4.

DISCUSSION

The results of these experiments indicate that, despite EA adhesion increasing with fibrin content (i.e. lower hematocrit), the effect of this is small compared to the adhesion between the SR and the model wall. Previous findings have shown that higher EA removal forces were correlated with vascular tortuosity, which we believe may be a result of increased wall contact with the SR [6]. From this, we expect that the frictional forces between the SR and wall interface have a greater impact on MT removal forces and greater influence on EA removal than that of EA composition. However, to prove these claims, continued testing on the kinetic friction of EAs is required. Preliminary friction results between EAs and bovine carotid arteries suggest that *in-vitro* AIS models are underpredicting the *in-vivo* frictional forces by a factor of 4. Preliminary friction results between SRs and bovine carotid arteries show an underprediction of frictional forces in PVC and overprediction in silicone in *in-vitro* AIS models and needs to be considered in *in-vitro* MT models. Continued testing of vessel walls should also be conducted to confirm this, as well as to determine the efficacy of representing *in-vivo* conditions with current benchtop models. It should be noted that in both *in-vitro* and *in-vivo* environments, the presence of a lubricant (water/blood) is present and could affect the frictional forces. Future testing will be conducted to determine a more accurate representation of the adhesion of the EAs and SRs on wetted material surfaces.

REFERENCES

- [1] Center for Disease Control, 2022.
- [2] Berkhemer, O et al., The New England Journal of Medicine, 2015.
- [3] Grech, R et al., The Neuroradiology Journal, 2015.
- [4] Johnson, S et al., Front. Med. Technol., 2022
- [5] Gunning, G et al., Journal of NeuroInterventional Surgery, 2018
- [6] Poulos, D et al., SB3 Conference, 2022.

PREGNANCY AND AGE DIFFERENTIALLY AFFECT MECHANICALLY-INDUCED COLLAGEN DAMAGE IN MURINE UTEROSACRAL LIGAMENTS

Catalina S. Bastías (1), Lea M. Savard (2), Kathleen Connell (3), Kathryn Jacobson (2), Sarah Calve (1,2,4), Virginia L. Ferguson (1,2,4), Callan M. Luetkemeyer (2,5)

- (1) Biomedical Engineering Program, University of Colorado Boulder, Boulder, CO, USA
(2) Department of Mechanical Engineering, University of Colorado Boulder, Boulder, CO, USA
(3) Department of Obstetrics and Gynecology, University of Colorado Anschutz, Aurora, CO, USA
(4) BioFrontiers Institute, University of Colorado Boulder, Boulder, CO, USA
(5) Department of Mechanical Science and Engineering, University of Illinois Urbana-Champaign, IL, USA

INTRODUCTION

About 50% of women worldwide are affected by pelvic organ prolapse (POP), which is characterized by the descent of any or all the pelvic floor organs (i.e., cervix, uterus, bladder, and rectum) from their natural position. Age, body weight, parity, and delivery type (vaginal or cesarean births), are thought to alter the mechanical properties of the pelvic floor tissues, including the uterosacral ligaments (USLs), resulting in POP [1]. The USLs provide fundamental structural support for the uterus, cervix, and vagina by tethering the cervix to the sacrum. Pregnancy and childbirth are known to impose mechanical strain on the USLs, potentially causing damage, and increasing the possibility of developing POP [1]. Additionally, ageing plays a role in the pathogenesis of POP, but the mechanism is unknown [2].

The mechanical integrity of the USLs is derived from extracellular matrix (ECM) components like collagens, elastin, and proteoglycans. Type I collagen is the major tensile load-bearing ECM component of ligamentous tissues and therefore likely to be involved in USL failure and POP [3].

In this study, we employed a murine model to examine the effects of pregnancy and age on the biochemical composition of the USL and its susceptibility to collagen damage in response to mechanical deformation.

METHODS

Female C57BL/6J mice were obtained and euthanized according to the University of Colorado Boulder's Animal Care and Use Committee. Both mature (>17-weeks, n = 2-3) and young (10-15 weeks, n = 3-5) murine USLs were collected at three different stages of pregnancy: nulliparous (NP), late pregnant gestation day 18.5 (E18.5) and post-partum day 1 (PP1). The USLs were isolated, and a suture was tied at the cervical end. One USL was used for mechanical analysis and was left attached to the pelvis and a piece of the cervix, which were left to act as anchors, and tested while freshly harvested. The contralateral

USL was flash frozen with liquid nitrogen and kept at -80°C until later analyzed with Raman spectroscopy.

Samples used for mechanical testing were placed in a solution of Ghost Dye Red 780 (Tonbo Biosciences), which stains all free amine groups, for 2 hours at 4°C on a rocker. For the last 10 minutes, a dead cell nuclei stain, Sytox Deep Red (ThermoFisher Scientific) was added to the solution. The samples were then placed in a custom loading chamber in a 1×PBS bath connected to a 100 mN FemtoTools load cell under an upright confocal microscope (Leica STELLARIS 5). Each USL was set in a reference configuration of ~500 μN pre-load.

Collagen hybridizing peptide (CHP) was used to determine regions with significant collagen denaturation (damage) [4]. Prior to mechanical testing, the 1×PBS bath was replaced with a 10 μM solution of CHP for 15 minutes. This staining procedure was repeated after each deformation step to record the changes in collagen damage. The samples were imaged at 10× magnification (2.14 μm pixel resolution) before, during, and after deformation. Deformed configurations were prescribed by actuator displacements of 1000, 1500, 2000, and 2500 μm at 50 μm/seconds, and allowed a stress-relaxation period of 5 minutes. For each image stack, max intensity projections were created. 2D displacement fields were estimated using composite Ghost Dye and Sytox images of reference and deformed states with MATLAB's *imregdemon*s function, from which Lagrange strain fields were derived. A moving threshold was used to determine pixels with significant collagen damage,

$$\gamma_i = \mu_i + 2\sigma_1 \quad (1)$$

Where γ_i is the CHP image intensity threshold for the i th reference image, μ_i is the mean CHP intensity of the i th reference image, and σ_1 is the standard deviation in CHP intensity of the original reference image. This thresholding method is robust to increases in image intensity resulting from multiple stain times.

From the strain and damage maps, average axial (E_{11}), transverse (E_{22}), and shear (E_{12}) strains, as well as percent damaged area were

calculated for the intermediate region. A 2-way ANOVA was performed to analyze the effect of stretch state and pregnancy for each age group, with significance indicated at $p < 0.05$.

Raman spectroscopy was used to map the biochemical composition of the contralateral USLs. After thawing at room temperature, the samples were placed on a custom well and evaluated using a confocal Raman microscope system (Renishaw inVia, 785 nm laser, 1.06 μm). A grid of 100 $\mu\text{m} \times 150 \mu\text{m}$ ($\sim 3 \times 12$) spectra along the USL was obtained and heatmaps were developed in MATLAB.

Raman spectra were obtained ($n = 1\text{-}2/\text{group}$) for each sample (Fig. 4). Peaks were correlated with biochemical constituents based on *in vivo* Raman spectroscopy of the human cervix performed by [5]. Our data was normalized using the phosphatidylethanolamine peak (1769 nm). Heat maps of peak area ratios were obtained.

RESULTS

Deformation fields and collagen damage maps were inhomogeneous (Fig 1). Axial strain (E_{11}) along the direction of the collagen fibers and the number of pixels with damage (highlighted in red) increased with the applied global displacement, δ .

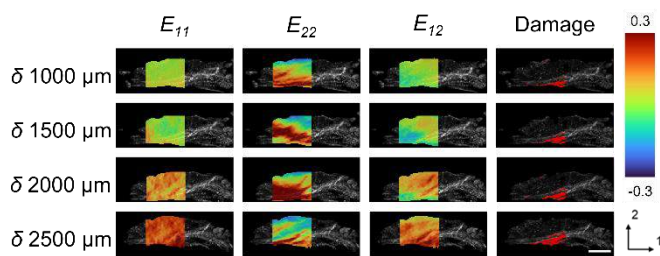


Figure 1: Lagrange strain fields and damage maps at four levels of global displacement, δ , in a young NP (scale bar = 500 μm).

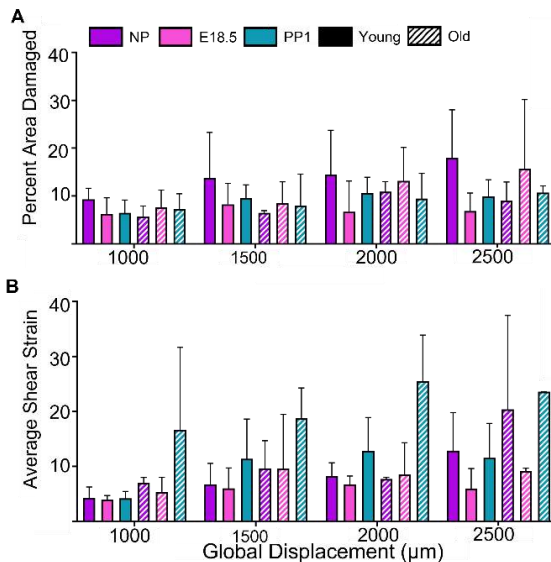


Figure 2: A) Percent damaged area and average shear strain (E_{12}) significantly increased with global displacement and pregnancy.

The least amount of damaged area was induced in USLs from E18.5 mice from the young cohort. B) Average shear strain (E_{12}) differed significantly with pregnancy stage for both old and young cohort ($p < 0.05$).

Percent damaged area differed significantly with pregnancy stage and global displacement for the young cohort ($p < 0.05$), while for the

old age group, only global displacement was a significant factor. Following applied deformation, the damaged area was smallest in USLs from young E18.5 mice (Fig. 2A).

Average shear strain (E_{12}) was significantly different with pregnancy stage in both the young and mature cohorts, with the lowest shear strain observed in the USLs of young, pregnant mice (Fig 2B).

Raman spectra differed along the length of the USLs, with the highest intensities seen in the cervical region and the lowest in the sacral region. This trend was common to all the samples assessed. There were no significant differences in peak ratios with pregnancy stage and age.

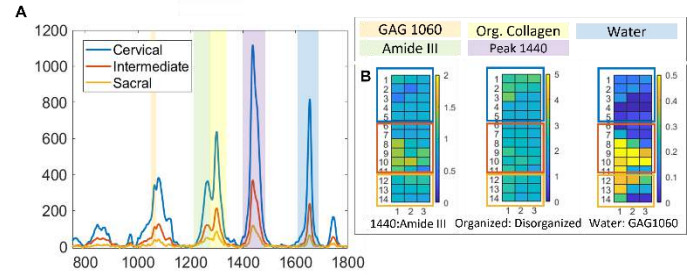


Figure 4: Raman analysis of an old NP USL. A) Representative Raman spectra and B) heat maps of peak ratios show regional (cervical, intermediate, sacral) variations in composition, but these trends were consistent across cohorts).

DISCUSSION

Our work indicates that both pregnancy and age are important factors in USL damage accumulation and mechanics. For young, but not mature mice, mechanically-induced collagen damage was significantly different across pregnancy stages for similar levels of applied strain, with less damage being accrued in USLs from pregnant mice. This suggests that the ECM in the USL remodels during pregnancy to protect it from mechanical injury, but remodeling may be less effective in older individuals. However, Raman spectroscopy did not discern any significant differences in biochemical composition with age or pregnancy stage. Thus, our preliminary results suggest that ECM remodeling during pregnancy may affect organization more than composition. The significant differences observed in average shear strain with pregnancy also point to differences in microstructural organization.

This is the first study to investigate the effects of both age and pregnancy on USL composition, mechanics, and structural damage. Our current limitations include small sample sizes, especially for identifying differences in USL composition. Nevertheless, our data suggest that both pregnancy and age affected collagen damage and mechanics in the USL, possibly due to changes in microstructural organization. Future work will aim to understand the specific microstructural changes that protect the USL from injury.

ACKNOWLEDGEMENTS

This work was supported by CU UROP grant (CB), the NSF GRFP (LS), the University of Colorado Innovative Grant Program, and the Anschutz Boulder Nexus Seed Grant.

REFERENCES

- [1] Donaldson K et al., Ann Biomed Eng, 49(8), 1788-1804 (2021).
- [2] Dietz HP et al., ANZJOG, 48(6), 587-591 (2008).
- [3] Zhu YP et al, Int Urogynecol J, 32(8), 2273-2281 (2021).
- [4] Zitnay, JL et al., Nat Comm, 8(1): 1-12, 2017.
- [5] O'Brien CM et al., AJOG, 218(10), 1362-1372 (2020).

EYE-SPECIFIC 3D MODELS OF LAMINA CRIBROSA HEMODYNAMICS SHOW SHARED TRENDS IN BLOOD FLOW, OXYGENATION AND SENSITIVITY TO VESSEL DIAMETER

Andrew Theophanous (1), Shaharoz Tahir (1), Yuankai Lu (2), Yi Hua (2,3,4), Ian A. Sigal (1,2)

(1) Department of Bioengineering, University of Pittsburgh, Pittsburgh, PA, USA
(2) Department of Ophthalmology, University of Pittsburgh, Pittsburgh, PA, USA
(3) Department of Biomedical Engineering, University of Mississippi, Oxford, MS, USA
(4) Department of Mechanical Engineering, University of Mississippi, Oxford, MS, USA

INTRODUCTION

Millions of people worldwide are blind or have reduced vision due to glaucomatous damage to the retinal ganglion cell axons that carry visual information from the retina to the brain. [1] In glaucoma, axonal damage starts at the lamina cribrosa (LC) within the optic nerve head (Figure 1a). Although the mechanisms of damage remain unclear, low levels of oxygenation within the LC are thought to be a primary contributor. [2] Direct measurement of LC oxygenation remains out of reach. Hence, the characteristics of the LC vasculature that most affect blood perfusion and oxygenation remain unknown. Using an eye-specific 3D vasculature model of the LC we recently found a strong positive relationship between vessel diameter and LC oxygenation. [3] However, eyes vary in anatomy, and it remains unclear how much these differences affect LC hemodynamics. We tested the hypothesis that despite differences between eyes, they will share general aspects of LC blood flow, oxygenation, and sensitivity to vessel diameter.

METHODS

Using methods recently described, we developed four eye-specific vasculature models based on serial histological sections of monkey optic nerve heads (Figure 1b). [3, 4] To account for differences in LC shape and boundary conditions, the region modeled was larger than the LC. LC vessels were identified by the LC collagenous beams. [3] Baseline vessel diameters were uniform. To study the effects of vessel diameter on the LC blood flow and oxygen, we uniformly varied the vessel diameter in each model as follows: 6.4, 7.2, 8.0, 8.8, and 9.6 μm .

Blood was considered as an incompressible Newtonian fluid, and its flow behavior was described by the Hagen-Poiseuille equation. [5] Pressure boundary conditions were applied to each model to estimate blood flow through the vasculature. [3] A Green's function method was then employed to calculate oxygen concentration. [6] We used the minimum (10th percentile) oxygen concentration as potentially indicative of hypoxic conditions.

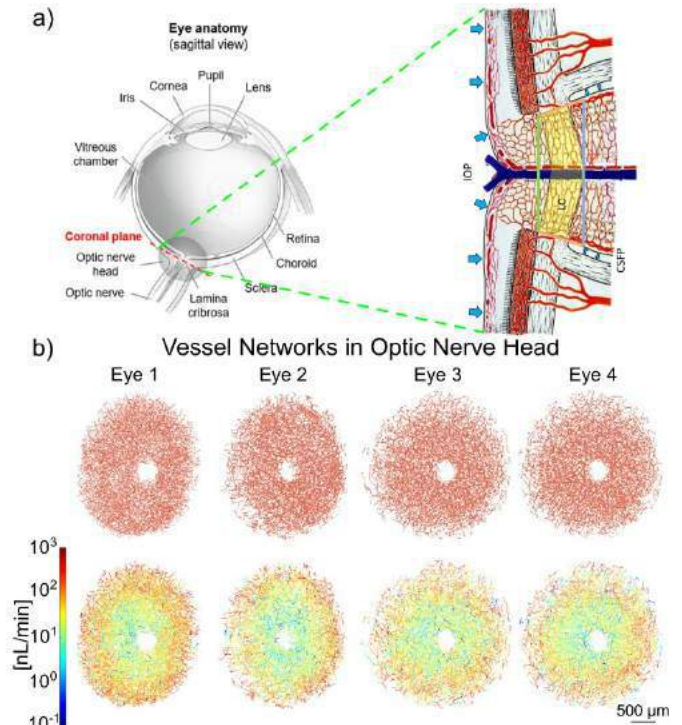


Figure 1: (a) On the left, a schematic longitudinal cross-section of an eye. On the right, optic nerve head close-up with the LC highlighted in yellow [3]. (b) Coronal front views of the four models developed in this study at the baseline vessel diameters of 8 μm . For clarity, we show them with a single color (top row) and colored by blood flow (bottom row). In general, the blood flow was higher at the periphery, decreasing towards the center.

RESULTS

All LCs exhibited variations in blood flow and oxygenation across the region, generally with higher flow and oxygen at the periphery (Figure 1b). Although eyes 1 and 4 had substantially higher minimum oxygen concentrations, all four LCs exhibited similar positive, nonlinear increases in oxygen with diameter (Figure 3).

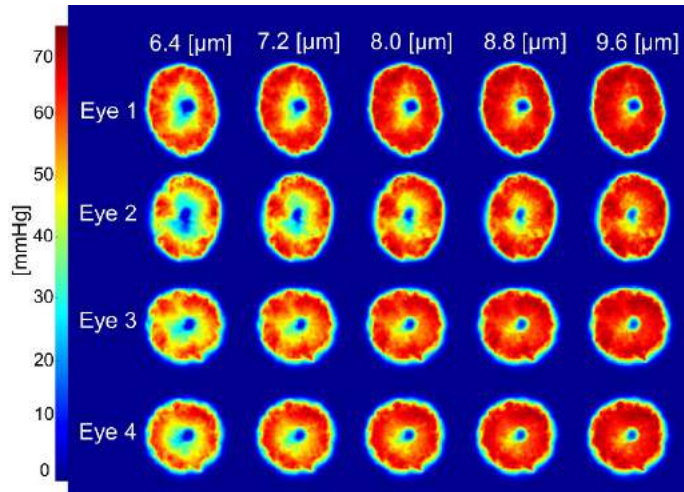


Figure 2: Distribution of oxygen concentration in the optic nerve head neural tissues for various vessel diameters (mid-LC coronal sections). There was higher oxygenation at the periphery than the center, similar to the variations in blood flow observed in Figure 1b. Oxygen concentration increased with the vessel diameter.

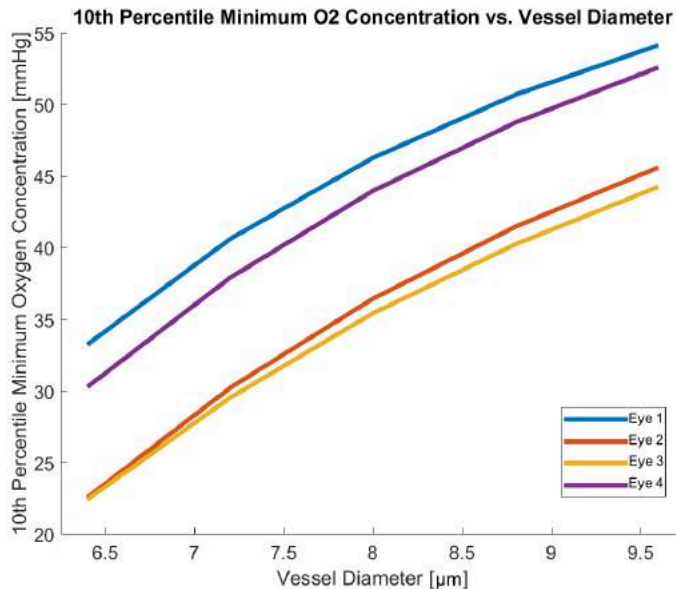


Figure 3: Effects of vessel diameter on the minimum oxygen concentration in the LC. Note that there were no intermediate values between the five diameters we considered (6.4, 7.2, 8.0, 8.8, and 9.6 μm). Results are shown as lines to help discern trends. Although there were differences in minimum oxygen concentration between the eyes, the nonlinear relationships between vessel diameter and the minimum oxygen concentration were fairly consistent across the four eyes.

DISCUSSION

We tested the hypothesis that despite differences between each eye's LC anatomy, they will share general aspects of LC blood flow, oxygenation, and sensitivity to vessel diameter. Our results support the hypothesis: maps of blood flow and oxygenation were similar across the four LCs studied. Furthermore, although there were differences in overall oxygen concentration between eyes, the minimum LC oxygen concentration sensitivity to vessel diameter was fairly consistent.

The effects of vessel diameter on blood flow are reasonable: an increase in vessel diameter decreases the flow resistance, increasing the blood flow rate, and resulting in more efficient oxygen transport and higher oxygen concentration in the LC. In this work, we varied vessel diameter as part of a systematic approach to test its influence on the LC. We therefore assumed that all vessels of all LCs had the same diameters. This is unlikely to be exactly the case. Vessel diameters likely vary between eyes. They can also vary due to tissue deformations induced, for example, by changes in intraocular pressure, or changes in gaze. [7] Tissue distortions may also affect vessel tortuosity. [8] Vessel diameter may also vary due to pericyte action. In the retina, cerebellum, and cerebral cortex, pericytes were found to regulate the capillary diameter, and therefore, the blood flow in response to metabolic demand. [9-11] Although the existence of pericytes in the LC is not established, some human LC cells test positive for PDGFR β , a marker for pericytes. [12] The perfusion-labeling method we used did not allow us to simulate accurately the physiologic perfusion cycles, and therefore, the vessel diameters cannot be guaranteed to be physiologically accurate. We therefore assumed that all the vessels in a particular model had the same diameter. To the best of our knowledge, there are no studies providing detailed maps of LC vessel diameter. Further work could help provide detailed information on vessel diameters. We also assumed the oxygen consumption rate of neural tissues to be uniform throughout the LC based on literature values for other neural tissues. The oxygen consumption rate may vary with regions and/or pressure gradients in the LC. It may be advantageous to incorporate region and pressure-dependent neural tissue oxygen consumption rates in future studies.

In summary, we found that despite anatomical differences, there are important similarities in LC blood flow, oxygenation, and sensitivity to vessel diameter. Considering the strong influence of vessel diameter on LC oxygenation, situations that reduce the diameter, such as high intraocular pressure, may have a high risk of inducing hypoxia.

ACKNOWLEDGEMENTS

Supported by NIH R01-EY023966, R01-EY028662, R01-EY031708, P30-EY008098, R01-HD045590, R01-HD083383, and T32-EY017271; Eye and Ear Foundation (Pittsburgh, Pennsylvania), Research to Prevent Blindness, and BrightFocus Foundation.

REFERENCES

- [1] Quigley, H.A. (2011). *Lancet*, 377: 1367-1377.
- [2] Chuangsuwanich, T. et al. (2016). *IOVS*, 57: 6167-6179.
- [3] Hua, Y. et al. (2022). *Exp Eye Res*, 220: 109105.
- [4] Lee, P.Y. et al. (2022). *J Biomech Eng*, 144: 061006.
- [5] Guidoboni, G. et al. (2013). *JCSMD*, 1: 1-21.
- [6] Secomb, T.W. et al. (2004). *Ann Biomed Eng*, 32: 1519-1529.
- [7] Sigal, I.A. et al. (2014). *IOVS*, 55: 1-15.
- [8] Brazile, B.L. et al. (2020). *IOVS*, 61: 2-2.
- [9] Peppiatt, C.M. et al. (2006). *IOVS*, 58: 3565-3574.
- [10] Wu, D.M. et al. (2003). *Am J Physiol Heart Circ*, 284: H2083-90.
- [11] Hall, C.N. et al. (2014). *Nature*, 508: 55-60.
- [12] Tovar-Vidales, T. et al. (2016). *Exp Eye Res*, 147: 94-97.

FAILURE IN ARTICULAR CARTILAGE: FINITE ELEMENT PREDICTIONS OF STRESS, STRAIN, AND PRESSURE UNDER MICRO-INDENTATION INDUCED FRACTURE

Brandon P. Chelstrom (1), Dipul Chawla (2), Corinne R. Henak (1,2,3)

- (1) Department of Biomedical Engineering, University of Wisconsin-Madison, Madison, WI
(2) Department of Mechanical Engineering, University of Wisconsin-Madison, Madison, WI
(3) Department of Orthopedics and Rehabilitation, University of Wisconsin-Madison, Madison, WI

INTRODUCTION

While articular cartilage exhibits remarkable failure resistance, it can break down under abnormal or repetitive loading¹. Cartilage is a heterogeneous, anisotropic, poroviscoelastic (PVE) material². The solid matrix is made of collagen fibrils and proteoglycans with negatively charged glycosaminoglycans side chains that interact with dissolved solutes to swell the solid matrix². This material complexity has resulted in an incomplete understanding of cartilage failure mechanics³.

To date, there are several postulated failure mechanisms: (§1) cartilage failure is governed by the breaking of collagen fibrils⁴ and (§2) cartilage exhibits two distinct failure^{5,6} regimes based primarily on loading rate. Within rate-dependent regimes, postulated classification includes (§2.1) brittle⁶ failure at fast displacement rates (FDR) due to stress build-up at the articular surface, and shear-based ductile⁶ failure at slow displacement rates (SDR). FDR induces fracture before PVE relaxations have time to occur while SDR induces fracture after the majority of PVE relaxations have occurred⁵. An alternative theory based on crack morphology (§2.2) postulates a pressurization-fragmentation⁵ regime at SDR due to osmotic pressure build up⁷, and a strain-governed⁵ regime at FDR due to lack of fluid flow. However, it has not been resolved which failure theory is accurate.

Therefore, the objective of this study was to develop a PVE finite element (FE) model to predict the stress, strain and fluid pressure during cartilage microindentation, thereby providing insight into the mechanics driving cartilage microfracture.

METHODS

An axisymmetric FE model was analyzed using FEBio⁸. Boundary and loading conditions matched prior experiments that investigated osmolarity (hypo-osmolar, normal osmolarity, and hyper-osmolar) and displacement rate (FDR and SDR) effects⁵ (Fig. 1A). Experiments analyzed the critical displacement, defined as the point of fracture initiation, which occurred at the first drop in load.

Finite Element Model: Cartilage was modeled as a 5° wedge (Fig. 1B) with a neo-Hookean ground matrix⁴, biphasic behavior with strain-dependent permeability⁴, nonlinear fiber behavior with viscoelastic fibrils⁴, and the fluid-solid matrix interactions with Donnan equilibrium swelling. Collagen fibrils were modeled using a continuous spherical fiber distribution with power-law strain energy density⁴. Sample thickness matched the average value for the normal-osmotic condition⁵. Cartilage was discretized into hexahedral and pentahedral elements with mesh density and biasing determined via mesh convergence analysis. The indenter was modeled in SolidWorks 2022 and discretized using Gmsh 4.8.4 with triangular shell elements, and the boundary plane was modeled using a single quadrilateral shell element. Both the indenter and boundary plane were set as rigid body materials. All boundary and loading conditions were prescribed to match the experimental conditions (Fig. 1A) and models were analyzed up to experimental critical displacements.

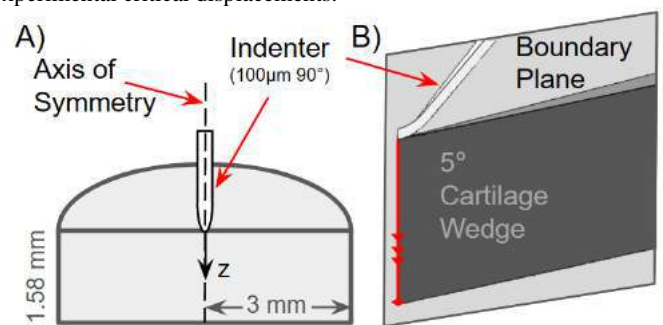


Figure 1: (A) half-symmetry schematic of experimental set-up; (B) FE model where outputs were taken along the axis of symmetry.

Donnan equilibrium constants were fit to match measured changes in sample thickness due to varying osmolarity. Osmotic pressure (π) was

enforced through fixed charge density in the current configuration⁹:

$$\pi = R\theta(\sqrt{(c^F)^2 + (c^*)^2} - c^*) \quad (1)$$

Where R is the universal gas constant, θ is the absolute temperature, c^* is the external bath osmolarity and c^F is the fixed charge density of the solid matrix in the current configuration defined by the fixed charge density in the reference configuration⁹:

$$c^F = \frac{\phi_0^w}{J-1+\phi_0^w} c_0^F \quad (2)$$

Where c_0^F is the initial fixed charged density, ϕ_0^w is the fluid volume fraction in the reference configuration, and J is the relative volume. The initial fixed charge density of $c_0^F = -158 \text{ mM}^{10}$ best fit the relative volume change measured experimentally. Distributions of principal Cauchy stresses, max shear stress, principal solid Cauchy stresses, max solid shear stresses, principal Lagrange strains, max Lagrange shear strains, and fluid pressures at critical displacements were taken along the axis of symmetry as a function of distance from the surface (Fig. 1B). Due to space constraints, not all model outputs are reported here.

Statistical Analysis: The effects of osmolarity, rate, and their interaction were statistically evaluated at the average magnitude of each output. Normality was checked with a Shapiro-Wilk test, QQ-plot, and histogram analysis. A two-way ANOVA evaluated normally distributed outputs. A non-parametric Friedman test was used for outputs that were not normal and could not be transformed to normality. All significance was set with $p \leq 0.05$.

RESULTS

Fluid pressure, stress, and strain directly underneath the indenter tip varied in both magnitude and distribution as a function of rate (Fig. 2, 3). Third principal Lagrange strain (Fig. 2D) had a much steeper gradient at FDR compared to SDR despite reaching much higher critical displacements at SDR. Fluid pressure was also over 20 times higher under FDR compared to SDR (Fig. 3C).

Third principal solid stress showed pair-wise significance between displacement rates at each osmolarity (Fig. 2B, 3A). At FDR, there was no significant difference in the third principal solid stress by osmolarity.

Solid shear stress had pair-wise significant difference between osmolarities at FDR, which was not observed at SDR (Fig. 3B). At the hypo-osmolar case, a pair-wise difference between rate was observed.

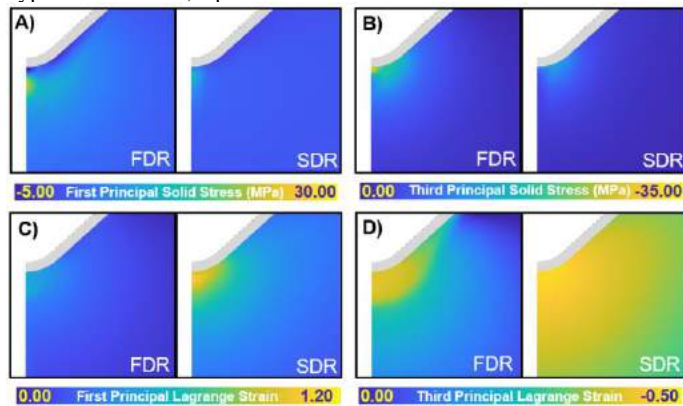


Figure 2: Qualitative distributions of (A) most tensile and (B) most compressive solid stress; (C) most tensile and (D) most compressive strains at mean critical displacement under normal osmolarity.

DISCUSSION

In this study, dramatic differences between FDR and SDR support the existence of two distinct, rate-dependent failure modes (§2) for cartilage⁵⁻⁷ (Fig. 2). Further specifics of the outputs can be interpreted

to provide evidence for failure mechanism (§2.1), ductile-brittle failure⁶; or for (§2.2), pressurization-strain failure⁵.

The predicted mechanics are consistent with (§2.1), the ductile-brittle failure theory. Brittle failure has been shown to cause fractures of the solid matrix at the articular cartilage surface along collagen fiber orientation at FDR⁶. This study predicted no difference in third principal solid stress between osmolarities at FDR, with the maximum value occurring at the articular surface (Fig. 3A); this is consistent with brittle failure. At SDR, the solid shear stress had no significant difference between osmolarity suggesting ductile failure (Fig. 3B).

The predicted mechanics are not consistent with (§2.2), the pressurization-strain failure theory. At FDR, a significant difference between osmolarities of the third principal Lagrange strain was observed (Fig. 2D); this does not suggest a consistent failure metric at FDR. At SDR, fluid pressure had a gentle gradient descending from the cartilage surface, indicating fluid pressure dissipation, while a highly localized maximum directly under the indenter tip at FDR indicates a pressure build-up (Fig. 3C). This is not consistent with a pressurization regime at SDR since pressure is lowest at the cartilage surface where fracture occurred.

In conclusion, this study supports the concept of cartilage failure as rate-dependent with ductile-like failure under SDR and brittle-like failure under FDR.

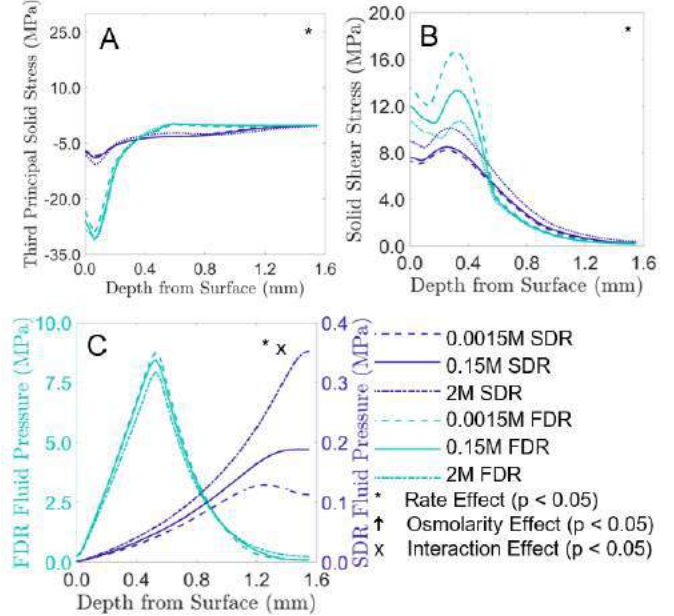


Figure 3: Depth-wise distributions of (A) most compressive solid stress and (B) max shear solid stress, and (C) fluid pressure.

ACKNOWLEDGEMENTS: NSF (CMMI-DCSD-1662456), NSF (CMMI-BMMB-2225174), UW-Madison VCGRE with funding from the Wisconsin Alumni Research Foundation.

REFERENCES

- [1] Maly M et al., *Curr Opin Rheumatol* 547–552, 2008.
- [2] Mow, V et al., *Biomaterials* 13: 67–97, 1991.
- [3] Liu, A et al., *Osteoarthritis Cartilage* 22:178–183, 2014.
- [4] Han, G et al., *J Mech Behav Biomed Mater* 96:186–192, 2019.
- [5] Chawla, D et al., *J Mech Behav Biomed Mater* 136, 2022.
- [6] Silyn-Roberts, H & Broom, N, *Connect Tissue Res* 24:143–156, 1990.
- [7] Stok, K & Oloyede, A, *Connect Tissue Res* 44: 109–120, 2003.
- [8] Maas, S et al., *J Biomech Eng* 134, 2012.
- [9] Ateshian, G et al., *J Biomech Eng* 131, 2009.
- [10] Shapiro, E et al., *Magn Reson Med* 47, 2002

APPLICATION OF 3D PRINTING IN SHAPE MEMORY POLYMER-BASED ENDOVASCULAR EMBOLIZATION FOR PREVENTING INTRACRANIAL ANEURYSM RUPTURE

Tanner Cabaniss (1), Sergio A. Pineda-Castillo (1,2), Bradley N. Bohnstedt (3),
Chung-Hao Lee (1)

- (1) Biomechanics and Biomaterials Design Laboratory (BBDL), School of Aerospace and Mechanical Engineering, University of Oklahoma, Norman, OK, USA
(2) Stephenson School of Biomedical Engineering, University of Oklahoma, Norman, OK, USA
(3) Department of Neurological Surgery, Indiana University School of Medicine, Indianapolis, IN, USA

INTRODUCTION

Intracranial aneurysms (ICAs) are present in approximately 4% of the American population [1], with the risk of aneurysm rupture scaling relative to the size of the aneurysm and the thinning of vessel wall [2]. The most devastating consequence of aneurysm rupture is subarachnoid hemorrhage (SAH) – a significant bleed within the intracranial cavity, with a 30% rate of rupture over the lifetime of the patient [3]. In addition, SAH carries a hospital mortality rate of 18% [4], along with 74% of survivors suffering lifelong complications [5].

The two most prominent treatments for ICA therapy are endovascular coil embolization and neurosurgical clipping. Coiling exhibits operative morbidity rates up to 10 times lower than clipping, which makes it the preferred method for therapy, especially for the elderly [6,7]. However, endovascular technologies suffer from limitations related to low complete and partial ICA occlusion rates, (64% and 34% of cases, respectively) [6]. Therefore, additional research efforts can be made to improve the efficacy of ICA embolization technologies, most prominently in the improvements to the rate of *complete* and *lasting* occlusion.

In this study, we proposed a patient-specific shape memory polymer (SMP)-based device, aiming to enable a higher rate of ICA occlusion for a wider breadth of aneurysm geometries, compared to the traditional coil-based methods. Further, the internal scaffolding of our porous SMP material is expected to promote thrombogenesis within the aneurysm sac that can accelerating occlusion of the aneurysm [8]. Moreover, our preliminary results and ongoing research show the great potential of our proposal method as a viable embolization technique to ameliorate complete occlusion rates of endovascular ICA therapeutics, as demonstrated by successful occlusions through *in vitro* aneurysm phantom models.

METHODS

Template Material Selection: First, we 3D printed porous polyvinyl alcohol (PVA, Form Futura Atlas Support) templates to be

used as leaching/lattice replacement agents. PVA was selected as the template material due to its great water solubility [9], biocompatibility [10], and availability as a 3D-printable filament. A thorough calibration procedure, specific to the PVA filament, was first performed to ensure consistent dimensional accuracy (i.e., line width, layer height, and structural integrity, see the Results section). This calibration procedure included optimization of the extruder temperature, volumetric flow rate, print speed, as well as several other printing parameters.

SMP Foam Fabrication: We next synthesized SMP based on our in-house protocol [11] in a molar ratio of 1:0.32:0.22, of hexamethylene isocyanate (HDI), N,N,N',N'-tetrakis (hydroxypropyl) ethylenediamine (HPED), and triethanolamine (TEA), as described previously [12]. Then, the PVA templates were coated with the liquid SMP solution and placed in a freezer (-20 °C) for 1 h, followed by a 3-step curing procedure in a vacuum oven for 3 h. at 45 °C, 1 hour at 70 °C, and 1 hour at 100 °C. Finally, the total foam construct was dissolved in a sonicator water bath at 50 °C for dissolving the PVA, leaving the porous SMP specimen (Fig. 1).

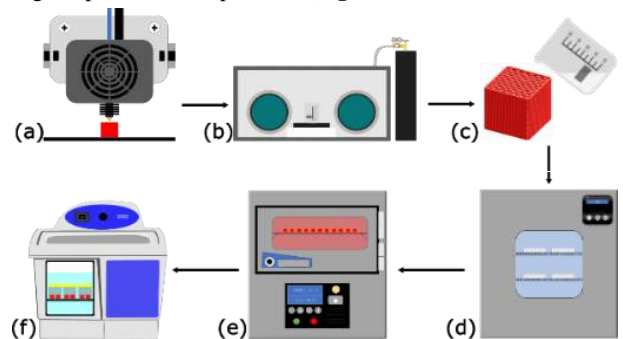


Figure 1: (a) 3D printing of PVA templates, (b) Synthesis of SMP, (c) Coating of templates, (d) Cooling of coated templates, (e) Curing of SMP, (f) Dissolution of PVA templates.

Material Characterization of SMP Porous Foams: Differential scanning calorimetry (DSC), scanning electron microscopy (SEM), Fourier-transform infrared spectroscopy (FTIR), and thermomechanical testing/characterizations were performed to evaluate the material properties of the fabricated porous SMP specimens.

Aneurysm Phantom Fabrication: Polydimethylsiloxane (PDMS) was used in conjunction with a PVA positive mold to fabricate phantoms of the aneurysm sac and surrounding arteries. This enabled testing of the SMP devices under an *in vitro* patient-specific geometry condition (Fig. 2d).

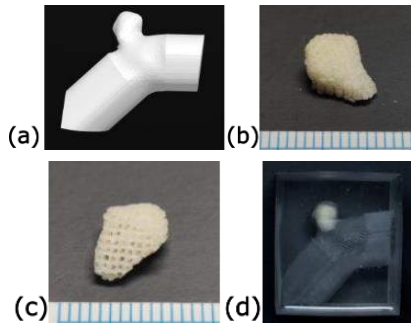


Figure 2: (a) CAD model of aneurysm and adjacent artery, (b) Top view and (c) Bottom view of patient-specific SMP device, (d) Patient-specific SMP device occlusion of *in vitro* phantom aneurysm.

RESULTS

3D Printing Resolution/Accuracy Targeted: Dimensional accuracy was evaluated via electronic calipers with a ± 0.01 mm resolution by measuring each face at the midplane point. The sample of PVA templates ($n = 40$) displayed a mean width of 10.80 ± 0.018 mm and a mean height of 9.99 ± 0.023 mm for a rectangular prism characterization model with a designed base of 10.80×10.80 mm and a height of 10.00 mm. This translated to the SMP specimens ($n = 40$) displaying a mean width of 9.85 ± 0.254 mm and a mean height of 9.99 ± 0.134 mm. The reduction in width is due to the removal of the two external wall layers, 0.4 mm each, during dissolution to expose the internal scaffold structures of the SMP material.

Microstructural Evaluation of Synthesized SMP Foams: SEM enabled the analysis of the internal scaffolds at the micro-scale and the overall geometric characteristic of the SMP specimens, as demonstrated in Figure 3.

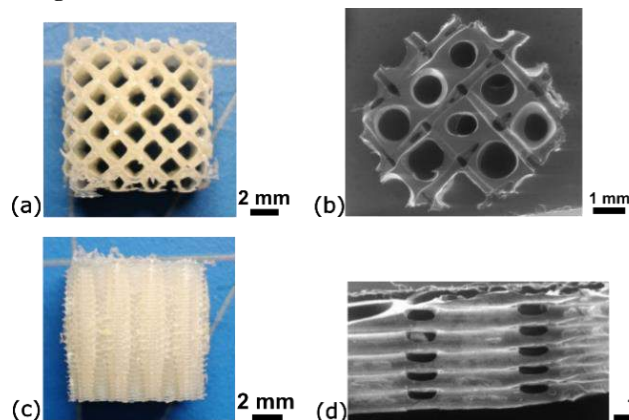


Figure 3: (a,b) Top view and (c,d) Side view of SMP specimen

Evaluation of Glass Transition Temperature: DSC revealed a glass transition temperature (T_g) of 41 °C for the fabricated SMP material which is just above internal body temperature of ~37 °C. This ensures that the

material will not deform from its designed geometries, while the shape recover can be triggered without causing thermal damage to the arterial and aneurysm tissues during the *in vivo* endovascular procedure [13].

Uniaxial Compression – Thermomechanical Characterization: The stress-strain testing revealed cyclical stress behavior with a reduction of elastic modulus over each cycle. Along the Z- and X-axis of compression, the elastic modulus was reduced by ~50% and 15%, respectively, over 10 cycles of 80% uniaxial compression.

DISCUSSION

Current intracranial treatment methods, such as GDCs and hydrogel coils [8], utilize a uniform approach in which there is little to no adaptation for the geometric specificity of each patient's aneurysm. This results in levels of recurrence, up to 13% [6], and often necessitates additional procedures both of which increase the likelihood of debilitating complications. Our patient-specific embolization device attempts to resolve this issue by replicating the geometry of the targeted aneurysm, using additive manufacturing and shape memory technology. This is aimed at enabling more thorough occlusion and more efficient thrombosis. This device aims to reduce the post-operative recurrence rates and greatly reduce the need for follow-up procedures, reducing the risk of complications for the patient.

In addition, the SEM analysis revealed that the dissolution of the PVA templates left tunnels within the SMP internal scaffolds which further increases compressibility of the specimens. This will be vital for adequate compression of small-scale specimens, specifically those to be used in *in vivo* animal testing.

Currently, this device exhibits limitations related to the size of the target aneurysm. Our SMP and PVA template methodology has proven successful with aneurysms ranging from 10-20 mm in major diameter; however, there is still more optimization needed to expand the range of effective use to small aneurysms (<10 mm) and giant aneurysms (>20 mm). Additionally, this device requires several days of preparation to complete the previously described methodology which could limit its use case to non-emergency operations only.

Further work based on this research study will involve evaluating biocompatibility via *in vitro* testing with cell cultures which if successful will aid in the progression towards animal testing and eventual clinical trials.

ACKNOWLEDGEMENTS

This study is supported by the National Heart, Lung, and Blood Institute of the National Institute of Health (NIH R01 HL159475), the Oklahoma Center for the Advancement of Science and Technology (HR18-002), and the Oklahoma Shared Clinical and Translational Resources (OSCTR).

REFERENCES

- [1] Keedy, A. *et al.*, *McGill J Med*, 9(2):141-146, 2006.
- [2] Kashiwazaki, D. *et al.*, *Stroke*, 44:2169-2173, 2013.
- [3] Korja, M. *et al.*, *Stroke*, 45:1958-1963, 2014.
- [4] Lantigua, H. *et al.*, *Crit Care*, 19(1):309, 2015.
- [5] Hijdra, A. *et al.*, *Stroke*, 18:1061-1067, 1987.
- [6] Bradac, G. *et al.*, *Neurosurg Rev*, 30:117-126, 2007.
- [7] Ogilvy, C. *et al.*, *Neurosurgery*, 52:82-87, 2003.
- [8] Pineda-Castillo, S. *et al.*, *Polymers*, 14(13):2526, 2022.
- [9] Harpaz, D. *et al.*, *Materials*, 12(3):343, 2019.
- [10] Alexandre, N. *et al.*, *J. Biomed. Res. A.*, 102(12):4262-4275, 2014.
- [11] Wang, J. *et al.*, *Polymers*, 11(4):631, 2019.
- [12] Pineda-Castillo, S. *et al.*, *Adv. Eng. Mater.*, 23(6):2100322, 2021.
- [13] Wang, H. *et al.*, *Front. Neurosci.*, 8:307, 2014.

3D RECONSTRUCTION OF SYNDACTYLIZED HAND IN AUTODESK RECAP PHOTO WITH ARDUINO

Caleb E. Scheideger (1), Anna S. Dillenbeck (2), Hui Shen (3), Xiangyi Cheng (4)

- (1) Mechanical Engineering, Ohio Northern University, Ada, OH, USA
- (2) Mechanical Engineering, Ohio Northern University, Ada, OH, USA
- (3) Mechanical Engineering, Ohio Northern University, Ada, OH, USA
- (4) Mechanical Engineering, Ohio Northern University, Ada, OH, USA

INTRODUCTION

Syndactyly, one of the most common congenital malformations of the hand, is a result of a failed separation of adjacent digits [1]. These digits are common among congenital limb malformations that affect 1 out of 2,000-3,000 people at birth [2]. For any type of syndactyly, reconstructive surgery would be needed to separate the digital skin, reconstruct the web space between fingers, cover the web space, and separate digits with soft tissues [3]. Soft tissues are usually a certain shape of skin designed by doctors. The simplest design is a dorsal rectangular flap formed by connecting the metacarpal heads and a point on each digit at the midpoint of the proximal phalanx [4]. However, the area of the dorsal rectangular flap may be insufficient to cover the lateral defects at the base of the digit and even the web space [5]. The skin from another site of the body, such as the volar side of the forearm, can be used, which may lead to extended operation time as well as inconsistent skin texture and stress [5]. Other shapes of dorsal flaps were also designed to cover as much area as needed, such as rectangular, hexagonal, pentagonal, and more [5]. The result of using an improper shape and dimension of skin to cover the web commissure can lead to web creep. However, the sufficiency of the dorsal flap is still based purely on intuition and personal experiences.

Conducting a numerical study with known mechanical properties, such as Young's Modulus of the dorsal flap that varies with age, gender, and ethnicity [6], can help understand why web creep occurs and how to prevent it. To the best knowledge of authors, however, no numerical study has been conducted on the effect of the size and shape of the flap on the outcome quantitatively. This leads to analyzing the stress of the dorsal flap using a finite element analysis (FEA) that can be further investigated with 3D hand models of syndactyly digits.

This preliminary research aims to evaluate the feasibility of an autonomous low-cost solution for extracting geometric features in FEA on a dorsal flap, which can be used in optimizing their dimensions and configurations. We utilized Autodesk Recap Photo to reconstruct a 3D hand model using a series of pictures taken by an Arduino camera, the OV2640 ArduCAM model. Geometric features will be extracted from the defective and non-defected hand models to estimate the dimensions and configurations of the dorsal flap. FEA will be performed on the estimated types of dorsal flap to analyze the deformation. This potential solution would help surgeons to select the optimized dimensions and configurations of the individual's hands with precise accuracy and quantitative results and prevent the occurrence of web creep.

PRODUCT DESIGN

To extract geometric features autonomously, we aim to use Autodesk ReCap Photo software to 3D reconstruct an individual's

hand models given a series of images taken from his/her hands. The software produces a 3D model of a still object by using at least 20 in-focus pictures taken from different perspectives of it.

Tests were performed with the iPhone 11 camera and ArduCAM to find proper perspectives and resolution that provides quality pictures for 3D model reconstruction in the software while maintaining a small storage size. Various perspectives have been attempted to qualitatively find the best picture view for 3D model reconstruction. From our tests, we determined that taking pictures from an angled top-down view produced the most completed model. Figure 1(a) displays a skeleton hand model reconstructed using the pictures taken by iPhone 11 and Figure 1(b) displays a tissue box model reconstructed using the pictures taken by an OV2640 ArduCAM. We demonstrated that both an iPhone 11 camera and ArduCAM are qualified to be used. Concluding that the ArduCAM could reduce image uploading time and increase efficiency due to its lower resolution.



Figure 1(a): iPhone 11 camera Figure 1(b): OV2640 ArduCAM

A device was designed to support the functions of the camera to achieve autonomous image capturing in a more effective and efficient way. Figure 2 represents a prototype that is a proof of concept as to how the compatibility between the user and function relates. This design incorporates a movement in one degree of freedom that rotates around an axis (8) where a patient's hand will be. This simple rotation enables the camera to take hand images in the best perspectives we found. This would all be in a potential 4ftx3ft enclosed frame (2) to ensure that the device is sheltered and compact. A single appendage is attached to a stepper motor (4), held by a motor mount (3). The camera (7) would be placed at the end of the angled appendage (6) to capture images facing inwards at a minimum of 1ft away from the center axis of the armrest (1). A slip-ring (5) would be used to allow the wiring to move through the appendage without being tangled during the rotational movement. The wire would lead to a control panel (9) that is placed outside of the control space to house the Arduino UNO breadboard, TFT LCD (thin-film-transistor liquid-crystal-display) touchscreen, and battery.

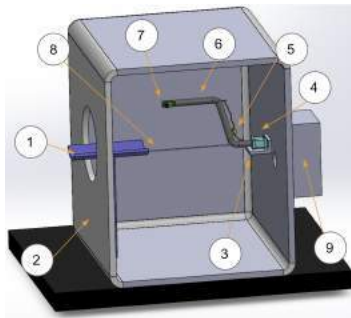


Figure 2: Robotic Appendage Prototype

BUDGET & MARKET ANALYSIS

The budget for the prototype is estimated at \$2,000. To be specific, \$50 budgeting towards the ArduCAM camera and the Arduino UNO Board; \$550 towards the stepper motor that can provide a maximum of 2,124.1oz of torque to the appendage; \$500 towards a frame and mount that provides stability for our device and is aesthetically pleasing for the user; \$200 towards the armrest to provide the user with a comfortable experience during the scanning process; \$120 towards the angled appendage and maintaining wire management; and \$200 towards a control panel that allows the consumer to operate the device.

The predicted market size is around 800 in the United States. This being for hand surgeons can be benefitted from this device, along with the thousands of patients that can also be benefitted. A projected sales price would be \$2,500 per unit with a generated revenue of 2MM. Producing this product in mass with given investments towards moulding the frames, appendages, hand rests, and control panels could equvalate to prices lower than \$1,250. A profit margin of \$1,750 could generate 1.4MM, and an investment of \$500 would have a return on investment of \$2,800.

METHODS

Figure 3 shows the adoption (solid lines) and development testing method (dashed lines) of the proposed autonomous device. The images of the patient's defective hand would be taken by the camera embedded in the device and sent to Autodesk Recap Photo software to create a 3D model. Critical geometric parameters would be extracted from the model using computer vision techniques. These parameters prepare us for performing FEA on dorsal flap. Based on the FEA analysis, a dorsal flap with optimized dimensions and configuration would be recommended to doctors. As for the development testing method in this preliminary study, we plan to manually measure the geometric features, the results of which would serve as ground truth for us to compare the parameters obtained using computer vision. Since this comparison is only for this preliminary test to validate the capability of the device, it will be excluded from the actual use.

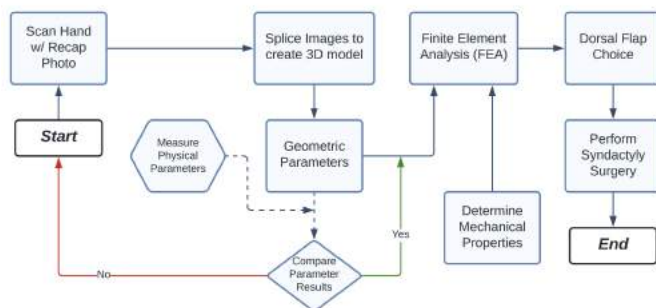


Figure 3: Flowchart of the Adoption and Testing Method

RESULTS

We adopted Autodesk ReCap Photo to create a 3D model using a series of images taken by OV2640 ArduCAM with Arduino Uno, as shown in Figure 1(b). The tissue box was used as our first testing object due to it being easily accessible. Twenty photos were taken with 800x600 quality and from the best perspective we found –

an angled top-down view/ isometric. This demonstrated that this camera module is capable of producing a model that displays significant characteristics of the object. The limitation of the outcome is that the model only rendered three out of four sides, while the fourth side was hollow. Since the current image-taking was done manually, the entire process was time-consuming. We now assume that the missing side is due to the fluctuating lighting that came from time passing. The use of the device will avoid this situation by achieving automatic image capture in a much shorter period.

DISCUSSION

To the best knowledge of authors, this is the first study of conducting FEA to optimize the dimensions and configurations of the dorsal flap to prevent web creep occurrence. The current design is based on proof of concept that can later be improved to design a more aesthetically pleasing and functioning prototype. We have demonstrated the feasibility of using a low-cost OV2640 ArduCAM in 3D model reconstruction. This prepares us for the development of a fully autonomous device, which can take images of patients' hands by enabling coding in Arduino that controls the stepper motor and the capture rate of the ArduCAM, then send the images to Autodesk ReCap Photo for 3D hand model reconstruction. The model would be used for further geometric parameter extraction for FEA analysis in future study.

ACKNOWLEDGMENTS

We want to acknowledge the College of Engineering at Ohio Northern University for contributing towards our budget.

REFERENCES

- [1] Miyamoto, J., Nagasao, T., & Miyamoto, S. (2010). Biomechanical analysis of surgical correction of syndactyly. *Plastic and reconstructive surgery*, 125(3), 963–968. <https://doi.org/10.1097/PRS.0b013e3181cb6743>
- [2] Ahmed H, Akbari H, Emami A, Akbari MR. Genetic Overview of Syndactyly and Polydactyly. *Plast Reconstr Surg Glob Open*. 2017 Nov 2;5(11):e1549. doi: 10.1097/GOX.0000000000001549. PMID: 29263957; PMCID: PMC5732663. <https://www.ncbi.nlm.nih.gov/pmc/articles/PMC5732663/>
- [3] M. C. Manske, C. A. Goldfarb, "Syndactyly", *The Pediatric Upper Extremity*, 2015, p. 277-295. https://doi.org/10.1007/978-1-4614-8515-5_13
- [4] Tara L. Braun, Jeffrey G. Trost, William C. Pederson, "Syndactyly Release", *Seminars in Plastic Surgery*, Vol. 30 No. 4, 2016, p. 162-170. Available: <http://dx.doi.org/10.1055/s-0036-1593478>
- [5] Juan Liu, Huaiyuan Zheng, Zhenbing Chen, Xinyi Dai, Arndt F. Schilling, Hans-Günther Machens, "Dorsal plane-shaped advancement flap for the reconstruction of web space in syndactyly without skin grafting: A preliminary report", *Journal of Plastic, Reconstructive & Aesthetic Surgery*, Volume 68, Issue 11, 2015, p. e167-e173, ISSN 1748-6815. Accessed May 25th 2022, [Online]. Available: <https://www.sciencedirect.com/science/article/pii/S174868151515003071>
- [6] Agache, P.G., Monneur, C., Leveque, J.L. et al. "Mechanical properties and Young's modulus of human skin in vivo". *Archives of Dermatological Research* 269, 221 - 232 (1980). Accessed May 25th 2022. [Online], Available: <https://doi.org/10.1007/BF00406415>

INVESTIGATING THE EFFECT OF TENSILE STRAIN ON THE MECHANICAL MEMORY OF ENDOTHELIAL CELLS

Michael Heim (1), Bronte Miller (1), Mary-Kathryn Sewell-Loftin (1,2)

(1) Department of Biomedical Engineering, University of Alabama at Birmingham, Birmingham, AL, USA

(2) O'Neal Comprehensive Cancer Center, University of Alabama at Birmingham, Birmingham AL, USA,

INTRODUCTION

While much attention has been devoted to the study of the biochemical signaling processes involved in the tumor microenvironment (TME) as targets for anti-cancer therapies, there have been few studies that investigate the mechanical factors involved in supporting tumor progression. As tumors grow and expand, they require additional nutrients and oxygen which can be delivered through angiogenesis, or the process of growing blood vessels from a previously existing vasculature. [1] Recent studies demonstrate that the endothelial cells that make up our blood vessels are mechanically-sensitive, and that mechanoreceptors on these cells may play a role in guiding the growth of nascent blood vessels. Our previous work has shown that mechanical stimulation alone, without the addition of soluble factors such as VEGF, is sufficient to drive vessel growth in 3D *in vitro* models [2,3], although further work is needed to determine the precise mechanism that controls this behavior. A key component in angiogenesis is the membrane receptor vascular endothelial growth factor receptor 2 (VEGFR-2), which binds VEGF as a ligand to promote blood vessel growth. However, anti-cancer therapies that inhibit VEGFR-2 signaling have limited success in patients [4]. We believe this may be partially due to mechanosignaling through the VEGFR-2 pathway. Some studies suggest that VEGFR-2 can be phosphorylated or activated without the ligand [5]. Phosphorylation of specific tyrosine residues in VEGFR-2, Y1054/Y1059, is required to undergo angiogenic activity, while phosphorylation at Y1214 causes the activation of several other pathways, which includes many mechanotransductive transcription factors. [6] In order to identify how prolonged tensile strain alters VEGFR-2 phosphorylation and signaling in endothelial cells and if these changes correspond to differences in blood vessel growth or stability, 3-D models must be refined and utilized. These altered signaling behaviors in the endothelial cells after being strained can be defined as their "strain memory." The existence of a strain memory can be ascertained by observing pro-vasculogenic behaviors of endothelial cells following pro-longed (>24h) cyclic tensile

strain as well as measuring the phosphorylation of Y1214 and Y1054/Y1059 residues. We hypothesize that the Y1054/Y1059 residue will show an increase in phosphorylation after pro-longed cyclic tensile strain.

METHODS

Human microvascular endothelial cells (HMECs) with HMEC media (500 mL MCDDB131 media with 10ng/mL EGF, 1μg/mL hydrocortisone, 50mL HI FBS, 25mL L-Glutamine) every other day. After the cells reached confluence, they were trypsinized and seeded onto FlexCell plates with collagen I coating. In each well, 5x10⁵ cells were loaded and allowed to grow for 48h prior to strain exposure. The FlexCell (FX-6000T) system was used to treat samples with cyclic strain at 9% elongation and 0.3Hz for 24h; control cells were plated on the same FlexCell plates but did not receive mechanical stimulation. After strain treatments, cells were harvested and seeded into 24 well plate as 5x10⁴ cells per well. Once in the 24 well plate, the cells were fed with HMEC media without exogenous VEGF. After 48h, the cells were fixed and stained for pY1054/Y1059 (Invitrogen, 44-1047G, 1:500) followed by secondary (ThermoFisher, Donkey-anti-Mouse Alexa-Fluor 555 A31570, 1:500). The wells were imaged using an Olympus Microscope (IX-83). Images were processed in FIJI to determine area of positive staining to total cell area per each image; samples were run in triplicate. A second study was performed with a set of HMECs treated with strain for 72h. During the incubation prior to staining, some samples received 25ng/mL of exogenous VEGF, and the other half were given standard HMEC media. These samples were counterstained with DAPI at 1:1000. Images were processed in FIJI to determine area of positive staining to total cell area per each image; samples were run in triplicate. Statistical significance was determined using ANOVA followed by post-hoc testing or by student's t-tests assuming unequal variance.

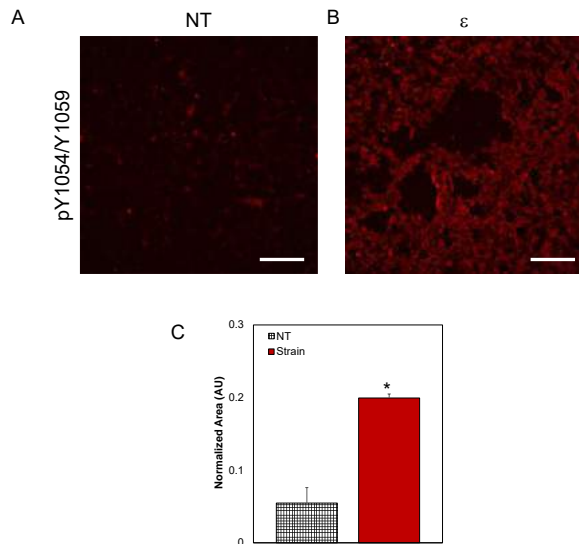


Figure 1: (A,B) Representative immunofluorescence images of pY1054/Y1059 (red) for control no treatment (NT) or strained (ϵ) HMECs. Scale bar = 250 μ m. (C) Quantification of positive area relative to total cell area + SEM. No treatment compared with 24h strained pY1054/Y1059. * $p < 0.05$ vs. NT; $n=3$ samples.

RESULTS

The mechanical memory study performed on the FlexCell, showed a significant increase in area representing phosphorylated Y1054/Y1059 in cells that were strained versus cells that were not strained (Figure 1). Furthermore, HMECs strained for 72h demonstrated a statistical increase in pY1054/Y1059 only when exogenous VEGF was added (Figure 2.)

DISCUSSION

The objective of this project was to investigate how long-term mechanical stimulation (24h or greater) would alter phosphorylation dynamics of VEGFR-2 in HMECs. Our hypothesis was that the cells would demonstrate a strain memory and have altered levels of pY1054/Y1059 with strain treatment compared to non-strained cells. With 24h of strain treatment, the cells demonstrated significantly higher levels of pY1054/Y1059 compared to non-strained controls, suggesting that the HMECs may exhibit this type of strain memory behavior. However, strain alone for 72h did not have a significant difference in pY1054/Y1059 area compared to the non-strained cells. To further explore this, we included exogenous VEGF in the media of HMECs that had been strained for 72h to examine combinatorial effects between ligand and mechanical stimulation. However, the combination of VEGF and strain does increase overall levels of pY1054/Y1059. One possible reason for this could be how the VEGFR-2 receptor internalizes after activation and is degraded to prevent feed-forward signaling. For cells not stimulated with strain, the additional VEGF may not be sufficient to cause prolonged expression of pY1054/Y1059. On the other hand, when 25ng/mL of VEGF was added to the media with strain, there was a greater area of phosphorylation than if there was strain and no VEGF. Overall, the 72h study seems to suggest that longer periods of strain require VEGF to maintain higher levels of pY1054/Y1059. This also suggests these endothelial cells strain memory may be more potent over longer periods of time when VEGF is also involved.

Future studies will focus on taking HMECs that are treated with strain and embedding them in a 3D microtissue model [3] to determine if the strain memory affects vascularization potential of the cells. Additionally, we hope to perform similar experiments to ascertain the amount pY1214 present after different periods of strain.

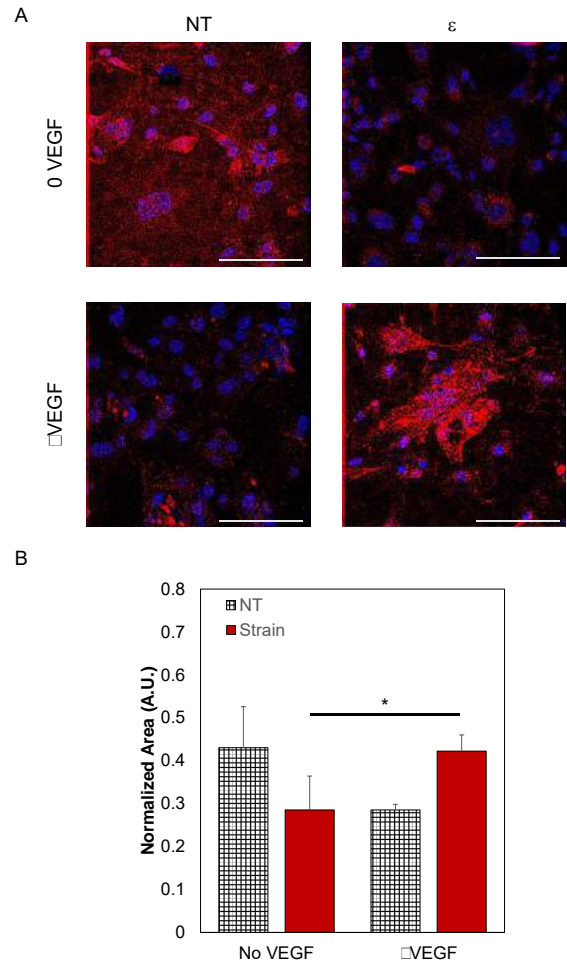


Figure 2: (A) Representative immunofluorescence images of pY1054/Y1059 (red) for control no treatment (NT) or strained (ϵ) HMECs. The scale bar is 500 μ m. (C) Quantification of positive area relative to total cell area + SEM. No treatment compared with 24h strained pY1054/Y1059. * $p < 0.05$; $n=3$ samples.

ACKNOWLEDGEMENTS

The authors would like to acknowledge funding for this project: Blazer Fellowship (B.M); R00-CA230202 (M.K.S.L), IMPACT Award, O'Neal Comprehensive Cancer Center (M.K.S.L).

REFERENCES

- [1] Miller, B. et al. *Front Cardiovasc Med* 8: 804934, 2022.
- [2] Sewell-Loftin, MK et al., *Sci Rep*, 7:12574, 2017.
- [3] Sewell-Loftin, MK et al., *Lab Chip*, 20:2776-2787, 2020.
- [4] Ribatti, D, *Oncotarget*, 7:46668-46677, 2016.
- [5] Warren CM, *Sci Signal* 7:309-ra1, 2014
- [6] Testini C et al. *EMBO* 5:e50309, 2020

THE IMPACT OF LACTATION ON PREGNANCY-INDUCED CARDIAC HYPERTROPHY DURING POSTPARTUM IN MICE

Gracine H. Sime (1), Arden C. Shen (2), Molly S. Kaissar (1), Jennifer L. Anderson (2),
Craig J. Goergen (2), Kyoko Yoshida (1)

(1) Department of Biomedical Engineering, University of Minnesota, Minneapolis, MN, USA
(2) Weldon School of Biomedical Engineering, Purdue University, West Lafayette, IN, USA

INTRODUCTION

Previous research shows that the heart grows in both mass and volume during normal pregnancy and regresses in the months following delivery in humans [1]. These adaptations help the pregnant patient accommodate the increased demand from the growing fetus while maintaining normal cardiovascular function. In some patients, however, maladaptive adaptations trigger cardiovascular dysfunction. Cardiovascular conditions account for half of all pregnancy-related mortalities in the United States. Specifically, pregnancy-associated heart failure is more likely to occur after delivery as it causes 39% of deaths between 43 days to one year postpartum [2].

Heart growth is driven by a combination of hormonal and mechanical cues. Our previous research suggests that increases in circulating progesterone (*P4*) and loading from hemodynamic changes are the primary drivers of heart growth in rat models of pregnancy [3]. However, *P4* and hemodynamic changes in the postpartum period can depend on factors such as lactation status after delivery. For example, lactating rats show elevated *P4* and cardiac output while non-lactating rats return to pre-pregnant values upon weaning [4, 5]. However, direct comparisons of heart growth between lactating and non-lactating models are lacking to date.

Therefore, the objective of this study is to assess the impact of lactation on heart growth in mice. We hypothesize that elevated hormonal levels and mechanical loading continue to drive cardiac hypertrophy after delivery, provoking additional heart growth during lactation. In contrast, we hypothesize that non-lactating mice hearts regress towards pre-pregnant size after delivery. To assess cardiac growth, we tracked changes in left ventricular (LV) size and shape throughout the entire pregnancy and postpartum period using serial cardiac ultrasound measurements. We allowed one group of mice to nurse their pups during the 21-day postpartum period and removed the pups from the other group of mice immediately following delivery. Our findings suggest that the hormonal and mechanical changes associated

with lactation prompt heart growth, while their absence allows the heart to recover to its pre-pregnant state.

METHODS

Changes in left ventricular (LV) mass, dimension, and volume were monitored throughout an average 19-day pregnancy and 21-day postpartum period in nulliparous C57Bl/6J mice using serial cardiac ultrasound measurements. Four nulliparous female mice were paired with male mice and gestational dating was performed through observation of the decidual reaction by high-frequency ultrasound (Fujifilm VisualSonics, Toronto, ON, Canada). Four-dimensional cardiac ultrasound (4DUS) was performed on days 0, 12, and 18 during pregnancy (**D0**, **D12**, **D18**) and on days 1, 7, and 21 postpartum (**PPD1**, **PPD7**, **PPD21**) using a high-frequency Vevo 3100 ultrasound system [6]. Two females were allowed to nurse their pups during the postpartum period (lactating, **L**, *n*=2) and two females had their litters removed immediately after delivery (non-lactating, **NL**, *n*=2).

A custom graphical user interface was used to segment the 4DUS scans [6]. Epicardial and endocardial boundaries were outlined at sequential time points to trace the local wall motion throughout the cardiac cycle. The 4D meshes of the epicardial and endocardial walls were used to calculate cardiac morphometry and function metrics, such as LV mass and stroke volume (SV) (Fig. 1). Researchers were blinded to the lactation status of the mice during analysis.

RESULTS

Throughout the 19-day pregnancy, LV mass increased in all four mice (Fig. 2A, Black). LV mass continued to increase during the postpartum period in the **L** group (Fig. 2A, Maroon). LV mass regressed towards pre-pregnancy values in the **NL** group, plateauing by **PPD7** in both mice (Fig. 2A, Gold).

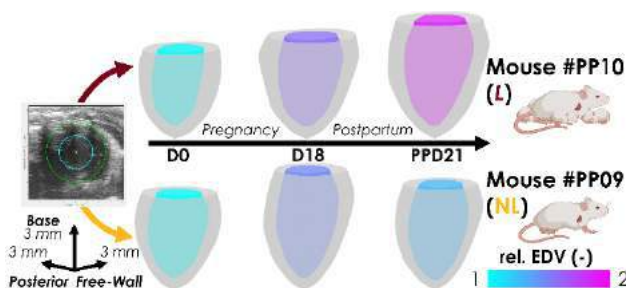


Figure 1: Representative 4D meshes of the LV at the beginning of the study (D0), the end of pregnancy (D18), and the end of the postpartum period (PPD21) from one *L* mouse (#PP10) and one *NL* mouse (#PP09).

Similarly, SV increased in all four mice throughout pregnancy (Fig. 2B, Black). Notably, SV decreased between **D18** and **PPD1** in three out of four mice, independent of lactation status. In the postpartum period, SV remained elevated in the *L* group (Fig. 2B, Maroon), SV returned toward pre-pregnancy volumes in the *NL* group (Fig. 2B, Gold).

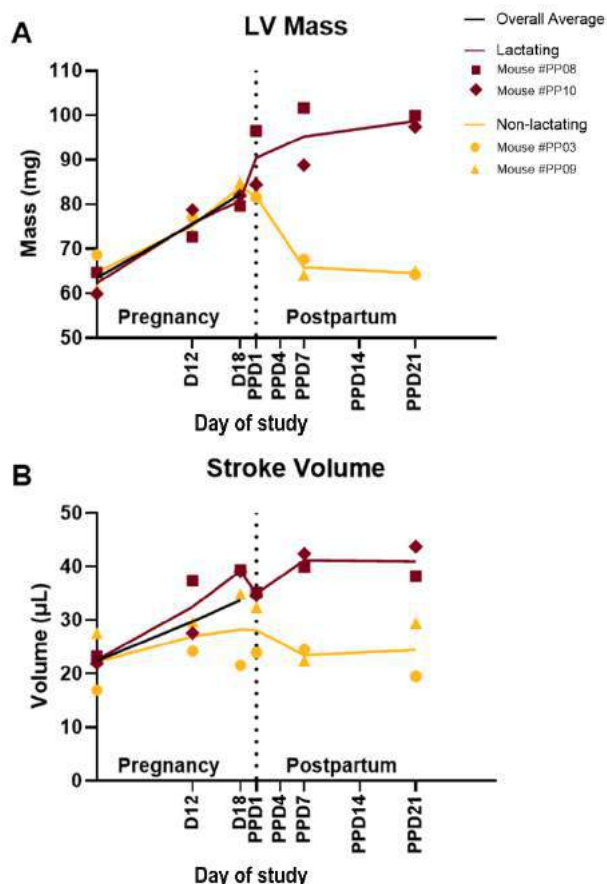


Figure 2: LV mass (A) and SV (B) estimated by ultrasound during pregnancy and the postpartum period in *L* and *NL* mice.

DISCUSSION

This study investigated the impact of lactation on pregnancy-induced cardiac hypertrophy in mice. Our results show that heart growth continued throughout the end of the study in the *L* cohort while growth reversed in their *NL* counterparts by **PPD7**, which is qualitatively

consistent with previously published trends in mice [7, 8]. Our data also demonstrates that hemodynamic metrics like SV remained elevated in the *L* group and decreased in the *NL* group, in agreement with cardiac output changes seen in rats [4]. Coupled with reported increases in serum *P4* concentrations, these findings are consistent with our hypothesis that elevated *P4* levels and cardiac outputs continue driving heart growth following pregnancy in murine models [5, 9].

The postpartum period is at least as long and just as complex as gestation, yet available literature often draws conclusions from a single postpartum measurement taken anywhere from hours to months after delivery [7, 8]. Our study illustrates the necessity of frequent and appropriately timed measurements to further our understanding of cardiac changes during the entire pregnancy and postpartum timeline. For example, SV decreased between **D18** and **PPD1** in three out of four mice, independent of lactation status. This drop in SV is likely an unloading effect from significant blood loss during delivery and subsequent decreased cardiac demand after delivery [10]. Additionally, our results show how significant cardiac changes can occur over a few days during pregnancy and the postpartum period in mice. While the **D18** scans usually occurred ~24 hours before delivery, differences in gestational periods meant that **D18** could fall a day or two before delivery [11]. For example, mouse #PP08 (Fig. 2, Maroon Boxes) gave birth two days after the **D18** scan – creating a three-day gap between **D18** and **PPD1**, during which significant growth occurred.

In conclusion, our findings suggest that *L* mice experience hormonal and mechanical changes that drive additional heart growth, whereas *NL* mice experience hormonal and mechanical changes that drive reverse growth during the postpartum period. One limitation of this work is the low animal numbers, which we are currently addressing with more scans and analysis. In the future, we will investigate how ceasing lactation after 21 days will impact heart size and shape in the *L* mice. We can also repeat this study with additional cohorts that are ovariectomized on **PPD1** to remove the influence of reproductive hormones like *P4* throughout the postpartum period [12]. Ultimately, we aim to characterize cardiac hypertrophy throughout the entire pregnancy and the postpartum timeline so that we can uncover the mechanisms behind pregnancy-induced heart growth.

ACKNOWLEDGEMENTS

We would like to thank Charlotte Cleary, Grace Coomes, and Kyndall Davis for their contributions to the segmentation process. We acknowledge funding from the Gates Foundation, Indiana CTSI, and Purdue University Women's Global Health Institute. MSK was supported by the National Institutes of Health through the Cardiovascular Engineering Training Program at the University of Minnesota (T32-HL139431). JLA was supported by the National Science Foundation under the Graduate Research Fellowship Program (GRFP) (DGE-1842166).

REFERENCES

- [1] Savu O et al. *Circ Cardiovasc Imaging* 5.3 (2012).
- [2] Petersen EE et al. *MMWR Morb Mortal Wkly Rep* 68 (2019).
- [3] Yoshida K et al. *Biomech Model Mechanobiol* 21.3 (2022).
- [4] Hanwell A et al. *J Physiol*, 233.1 (1973).
- [5] McNeilly A et al. *Marshall's Physiology of Reproduction* (1994).
- [6] Damen FW et al. *Am J Physiol Heart Circ*, 321.1 (2021).
- [7] Murata K et al. *Endocrinology*, 154.2, (2013).
- [8] Umar S et al. *J Appl Physiol*, 113.8, (2012).
- [9] Mizoguchi Y et al. *Mol Cell Endocrinol*, 132.1, (1997).
- [10] Pritchard JA et al. *Anesthesiology*, 26.4, (1965).
- [11] Murray SA et al. *PLOS ONE*, 5.8, (2010).
- [12] de Sousa FL et al. *Behav Brain Res*, 212.1, (2010).

3D PRINTED MOUTH GUARD FOR TEMPOROMANDIBULAR JOINT DYSFUNCTION

Christopher N. Barnes (1), Jorge M. Pumachagua (1), Elias P. Saliba (1)

Faculty Advisor(s)

Victor A. Huayamave (1), Alesha Fleming (2)

(1) Mechanical Engineering, Embry-Riddle Aeronautical University, Daytona Beach, Florida, USA

(2) Aerospace Physiology, Embry-Riddle Aeronautical University, Daytona Beach, Florida. USA

INTRODUCTION

Temporomandibular Joint Dysfunction (TMJD) is a disorder where there is an anterior displacement of the articular disk with reference to the condyle. TMJD is a common disorder that affects nearly 10 million Americans [1]. The abnormal jaw mechanics causes major symptoms of discomfortability and pain. These symptoms are clicking, pain of the jaw, difficulty to chew, and severe bruxism. Bruxism is a condition where teeth grind, gnash, or clench involuntarily at any time of the day, especially during sleep time. Bruxism engages the Masseter, Temporalis, Medial Pterygoid and Lateral Pterygoid muscles to continuously be under involuntary movement which leads to the exhaustion of the muscles and jaw joints. Along with, the Temporomandibular Joint (TMJ) is nearly connected with the ear muscles where a misalignment of the articular disk can set excess pressure on the branches of the trigeminal nerve and therefore cause aching pain around the ear; exhibiting how delicate TMJD can be to the human health.

The ideal solution in the current market to treat TMJD remains unknown in the biomedical community. Within the past twenty years, treatment options to help relieve TMJD involved a series of stages and processes, like physical therapy to help alleviate TMJ pain by avoiding extreme jaw movements and using prescribed medications. One such treatment option is dental splints: plastic mouthpieces that fit on the upper and lower teeth. Although this helps with teeth alignment and reduce the effect of bruxism on the excessive wear and damage of the teeth, they do not prevent bruxism, grinding/clenching of the teeth [2]. In addition, dental guards do not alleviate pressure from the TMJ when bruxism occurs, which ultimately results in the patient continuing to experience uncomfortable symptoms. The final option would be surgical methods including arthrocentesis, arthroscopy, discectomy, and joint replacement. Although the surgical methods can help produce a

successful outcome, the process to obtain these surgical methods are lengthy and can be expensive financially. The objective of the design is to produce a dental guard that can relieve the pressure from the TMJ while it is under bruxism, preventing the patient's symptoms to augment. Therefore, the chosen design for this project is to redesign current market dental guards due to it being considerably safer and lower cost than an invasive option. Occurring concern of the lack of protection of the jaw mastication muscles will be taken into consideration.

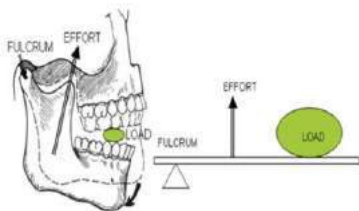
PRODUCT DESIGN

The current prototype has two separate pieces. The upper guard covering the teeth until the premolars and the bottom guard covering the 2nd premolar and 1st molar. The bottom guard will be connected by a strap that it is still being designed. This design is still under research on how to protect the jaw mastication muscles, particularly on the Masseter considering it is the responsible muscle that elevates the mandible for jaw closure.



Figure 1: Prototype CAD model

To conduct research on a possible method to relieve TMJD symptoms, an engineering approach is needed to mechanically understand the phenomenon. The approach taken to understand TMJD is based on the fundamentals of levers. The mandible is classified as a class 3 lever [3]. The fulcrum being at the mandibular condyle. The effort is applied by the four mastication muscles, the medial pterygoid, lateral pterygoid, temporalis, and masseter. Therefore, the load is produced by the action of chewing. Positioning of the fulcrum and effort is crucial since if one of the two are out of alignment, a higher effort is required for the load resulting in a stronger tension on the mastication muscles and mandibular condyle.



A LEVER OF CLASS III

Figure 2: Mandible as a class III lever

Extensive study was concluded on various papers regarding current solutions and cause of TMJ discomfort. An occurring concern among cases is the lack of protection of the jaw mastication muscles. Dental guards can protect the teeth from grinding, excessive wear, and damage, however, there is no proven method to relieve the pressure of the jaw joints. Numerous types of current orthodontic treatments were researched before coming across the Herbst appliance. The Herbst appliance is used to correct an overbite in a patient, although, with modifications to the design, a dental guard can help relieve some of the symptoms of TMJD.

The current market dental guards do not prevent protrusion, protraction, retraction, nor lateral or medial excursion. This is a current issue as the individual is exerting forces on their jaw with the grinding movement causes the articular disk to slip. Subsequently current dental guards do not relieve the jaw muscle average bite force of 700 N on the molars and about 350 N on the incisors [4]. To counter this, the design has an upper guard custom fit with rougher under surface. The front of the upper guard will be thicker than the back portion to prevent the 1st and 2nd molars from touching. This should relieve the 700N at the back of the mouth. In addition to the top guard, there is a bottom guard made of a softer, thicker gel material. The bottom guard will only cover both premolars on both sides. This will help relieve the force on the incisors. This combination will allow for friction to be present between the dental guards under biting force preventing grinding.

BUDGET & MARKET ANALYSIS

The current market of dental guards as of 2021, is valued at 3.7 billion dollars with an average of 40 million dental guards being sold each year [5]. These dental guards come in stock, boil-and-bite, as well as custom made. Our dental guard focuses on the custom section to protect individuals with TMJD. The upper dental guard will be 3D printed with an acrylic 1.75 mm which costs \$50 per roll of 1000g. The bottom guard will be made in an elastic 50A resin with a cost of \$200 per 1020g. The average print weight for a top guard is 28 grams resulting in roughly 35 upper dental guards per acrylic roll. The bottom guard uses about 14g per print resulting in roughly 71 dental guards per elastic

50A resin. Consequently, with a cost of approximately \$300, roughly 70 customers can have a custom dental guard to help protect them from TMJD. The cost of each dental guard will be priced at 200 as current market dental guards price scale is around \$100-\$150 resulting in \$14,000 gross income per batch.

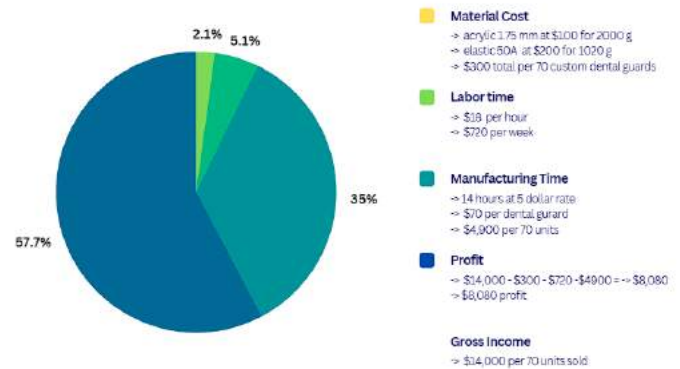


Figure 3: Manufacturing cost estimation of current design

Labor cost will come in about \$18 per hour or \$720 per week. Manufacturing time is set to be 14 hours at a \$5 rate resulting in \$70. The cost breakdown will result in an estimated profit of \$8,080. The previous prices are unofficial as it is an estimation, multiple factors will be considered with a deeper study of the market.

REFERENCES

- [1] Burke, D. (2019, March 13). TMJ (temporomandibular joint) disorders. Healthline. Retrieved from <https://www.healthline.com/health/tmj-disorders#symptoms>
- [2] Guaita, M., & Högl, B. (2016, February 20). Current treatments of bruxism. Current treatment options in neurology. Retrieved from <https://www.ncbi.nlm.nih.gov/pmc/articles/PMC4761372/>
- [3] Walia, M. S., Arora, S., Arora, N., & Rathee, M. (2014, January 1). Temporomandibular Joint (TMJ): A weight bearing joint? Research Gate. Retrieved from https://www.researchgate.net/publication/294428451_Temporomandibular_Joint_TMJ_A_Weight_Bearing_Joint
- [4] Bakke, M. (2016). Jaw Muscle. Jaw Muscle - an overview | ScienceDirect Topics. Retrieved from [https://www.sciencedirect.com/topics/neuroscience/jaw-muscle#:~:text=The%20jaw%20muscles%20move%20the,\(lateral%20pterygoid%20and%20digastric\).](https://www.sciencedirect.com/topics/neuroscience/jaw-muscle#:~:text=The%20jaw%20muscles%20move%20the,(lateral%20pterygoid%20and%20digastric).)
- [5] Sports mouthguard market size & share report, 2022-2030. Sports Mouthguard Market Size & Share Report, 2022-2030. (n.d.). Retrieved from <https://www.grandviewresearch.com/industry-analysis/sports-mouthguard-market#:~:text=The%20global%20sports%20mouthguard%20market,5.9%25%20from%202022%20to%202030.>

ASSISTIVE PADDLE MOUNTING SYSTEM FOR PARA-KAYAKING SPORTS

Betsabe Hernandez (1), Dinh L. Le (1), Weston J. Randall (1), Erin C. Ray (1)

Faculty Advisors

Victor A. Huayamave, PhD (1)
Christine D. Walck, PhD (1)

(1) Mechanical Engineering, Embry-Riddle Aeronautical University, Daytona Beach, Florida, USA

INTRODUCTION

According to the CDC, one in four adults in the U.S. suffer from a disability that affect their major life activities (1). They also report that the most common type of disability is physical, leading to mobility dysfunction (1). A major cause of physical disability is paralysis. Currently, approximately 1 in 50 Americans suffer from some form of paralysis caused by stroke or injury to the nervous system (2) due to a lack of sufficient blood flow to the brain. This poor blood flow kills brain cells in the affected area of the brain, and all neurological problems that occur are reflective of what area of the brain was affected (2). While paralysis is often permanent, the quality of life for these patients can be improved through parasports—sports designed to accommodate the limitations of the disabled— using adaptive and assistive equipment [ref].

The Oceans of Hope Foundation (OOHF) is a non-profit organization in Daytona Beach, FL, which hosts nearly 130 participants each year in adaptive kayaking events. The OOHF provides assistive equipment including the Angle Oar Gamut Hinged Mount shown in Figure 1. The Gamut Hinged Mount is an adaptive kayak mount that assists the user by self-stabilizing, thereby decreasing the stress on the user while kayaking (3). A rotating head, on the support mount, allows the user to have a large range of motion and is advertised by Angle Oar to be ideal for kayakers with rotator cuff injuries, hand, wrist and elbow stiffness, and those suffering from arthritis (3). However, the participants at OOHF have expressed their frustrations with the Gamut Hinged Mount, stating various faults with the system. Some of the most notable faults include the susceptibility to deformation, resulting in failure, when the kayakers exert a large amount of force. Such a failure inherently increases the risk of injuries by the participants in their need to compensate for the force required to paddle. Another notable problem is seen in the paddle path. Currently the path mimics a seesaw movement instead of a 'normal' stroke.



Figure 1: Angle Oar Gamut Hinged Mount

PRODUCT DESIGN

To address the frustrations of the OOHF, a team at Embry-Riddle designed a new assistive device that mimics a more natural paddling path (i.e., paddle stroke) shown in Figure 2. The paddle motion is controlled by a slotted arc allowing the

adjustable attachment to slide within it. This design allows the user a wider range of motion as opposed to the seesaw motion. To further accommodate the users, the ends of the arc are adjustable to allow the distance between the assistive device and their torso to vary.

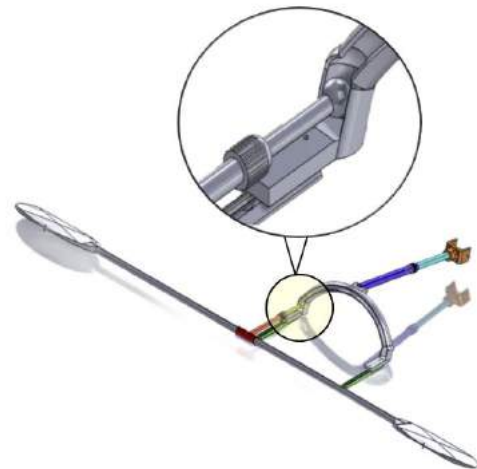


Figure 2: Isometric View of Design's CAD Model

Results:

This design focuses on the viability of the user having the ability to mimic the wide ranges of motion.

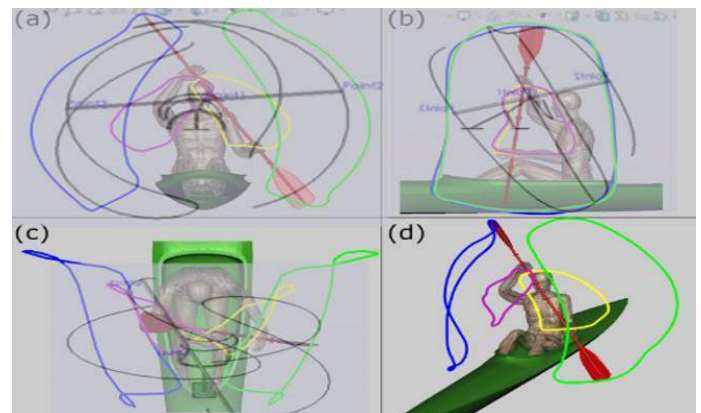


Figure 3: CAD Model Motion Overlay

Figure 3 depicts the allowable ranges of motion the blades of the paddle would have with the assistive device shown in gray. The green and blue shapes depict the average range of motion of the paddle blades, while the pink and yellow show the range for the hands, of a 'normal' kayaker. This device is unique in that the motion of the paddle closely mimics that of a normal kayaker in contrast to similar products.

In collaboration with Embry-Riddle's Biomechanical Analyses Laboratory, the team will validate the prototype using motion capture technologies. The motion capture will aid in forward and inverse kinematics. Allowing the team to post-process the motion path of the kayak paddle when paired with the prototype. The main purpose of testing is to ensure that, not only the device follows the proper path of motion, but that the user can also follow normal and safe ranges in motion while kayaking.

BUDGET & MARKET ANALYSIS

Although a budget of \$1500 was awarded to the team for development and manufacturing, costs were saved through the collaboration with the OOFH. OOFH donated the Gamut Hinged Mount to analyze the pros and cons of the competing market design. In addition, technical papers used for this project were available through University Resources. The program used to design the prototype in a 3D space, SolidWorks, is also provided through the University Resources. Due to the minimal spending on the design process, the majority of the team's budget is going towards 3D printing the mock-up and prototype of the design shown in Figure 2. The mock-up is printed in Polylactic Acid (PLA), which has an average cost between \$15 and \$25 per kilogram, and requires multiple test-prints. With a maximum weight of 6 lbs., and a print time close to 24 hours, the mock-up has an estimated cost of \$300. The prototype is made of polypropylene, which can cost over \$100 per kilogram. To allow for any necessary re-printing the budget for the prototype print is \$600. Within the slotted arc that makes up most of the prototype, there is a ball that slides within the arc. The team needs to print this ball out of a low-friction material, such as Tribo Plus, or purchase a similar part that suits the design parameters. The cost of Tribo Plus is approximately \$200 per kg so, allowing for any necessary re-prints, the estimated cost to print the ball is \$500. The team also needs to purchase basic connectors, such as nuts and bolts which is unlikely to cost more than \$20.

Given the relatively large population of Americans with a physical disability, the potential market size is on a national scale. If just 10% of this population considers purchasing the product, the potential customers may come out to nearly 300,000 over the course of 2 years. Because this market also lacks substantial competition, the product has an even higher potential for success.

Sales predictions can be made using the competitor's sales data, and analyzing more general kayaking market data. Based upon Angle Oar's sales figures, 68% of their customer base are using adaptive kayaking equipment(6). It is likely that sales figures for the new product would be comparable to theirs. Based on the kayaking market predictions from 2020 to 2025, the share is predicted to increase to \$105.37 million, and the growth momentum will accelerate at a CAGR of 2% (7). It can be assumed that the sales of the improved product will follow this trend.

For mass-production, injection molding is the most cost-effective manufacturing option, and Acrylonitrile Butadiene Styrene (ABS) is a viable material choice due to its favorable material properties and reasonable material cost of approximately \$1.30 per pound. The cost for injection molding is dependent on several factors, including weight, complexity, and volume of order. Since the design in mind requires assembly after the injection molding, the manufacturing cost would include those additional charges. Because the part is more easily manufactured in high volumes than the current products on market, the cost of manufacturing should be notably less than the current products (8). Because the market has so little competition, and the new design offers distinct improvements over the original, the projected sales price for potential national roll out of the design is \$300, which is higher than that of the competitors without being unreasonable (3).

In order to build a company for this product, a significant investment is needed to manufacture the molds for injection molding, hire on essential administrative employees, purchase materials, and pay for distribution of the initial production.

ACKNOWLEDGEMENTS

Oceans of Hope Foundation

REFERENCES

- [1] Centers for Disease Control and Prevention. (2020, September 16). Disability impacts all of us. CDC. Disability Impacts All of Us Infographic | CDC
- [2] Centers for Disease Control and Prevention. (2022, April 5). Stroke [Fact sheet]. CDC. (<https://www.cdc.gov/stroke/treatments.htm>)
- [3] Angle Oar. (n.d.). *Gamut paddle holder for sit-on-top kayaks*. Angle Oar. (<https://www.angleoar.com/product-page/gamut-paddle-holder-for-sit-on-top-kayaks>)
- [4] Centers for Disease Control and Prevention. (2018, August 16). *CDC: 1 in 4 US adults live with a disability*. CDC. (<https://www.cdc.gov/media/releases/2018/p0816-disability.html>)
- [5] United States Census Bureau. (2021, May 26). *Anniversary of americans with disabilities act: July 26, 2021*. Census. (<https://www.census.gov/newsroom/facts-for-features/2021/disabilities-act.html>)
- [6] McCall, M. (2020, December 4). *Adaptive Kayaking Snapshot: A 2021 InfoGraphic*. Angle Oar. (<https://www.angleoar.com/post/adaptive-kayaking-infographic-2021>)
- [7] Technavio. (2021, February). *Canoeing and Kayaking Equipment Market Growth, Size, Trends, Analysis Report by Type, Application, Region and Segment Forecast 2021-2025*. Technavio. (<https://www.technavio.com/report/canoeing-and-kayaking-equipment-market-industry-analysis>)
- [8] Neagu, C (2022, March 22). *Understanding Injection Molding Cost for Manufacturers*. Xometry (<https://www.xometry.com/resources/injection-molding/injection-molding-cost/#:~:text=Injection%20molding%20costs%20from%20%2410%2C000,best%20for%20large%20product%20on%20volumes.>)

DESIGN OF A PROPHYLACTIC KNEE BRACE TO PREVENT ACL INJURIES IN FEMALE ATHLETES

J. DiVanna (1), E. LoVerde (2), M. Taibi (3)

Faculty Advisor(s)

P. Saboori (1)

(1) Mechanical Engineering, Manhattan College, Riverdale, NY, United States

INTRODUCTION

Anterior Cruciate Ligament (ACL) tears cause an immense amount of pain in individuals and typically have a lengthy recovery time of between 6-9 months. The susceptibility and long-term consequences of such an injury are further magnified amongst female athletes - who regularly perform the intense, change-of-direction movements which are frequently associated with ACL tears and, as a result, are therefore unable to participate in the entirety of at least one athletic season.^[1-2] Additionally, females are generally 2 to 8 times more likely to tear their ACL in comparison to their male counterparts due to several anatomical and biomechanical differences between the two - most notably cited in a female's wider hips introducing a more compromising valgus force upon their knees during the landing portion of a jump.^[3] During this motion, the hip extensors are unable to control the downward acceleration resulting in the pelvis collapsing forward and causing an increased amount of strain on the knee.^[4]

With the rise in women participating in collegiate sports over the past few decades, the number of ACL injuries sustained amongst female athletes has also grown exponentially. And being that such injuries result in extensive recovery periods in addition to expensive health costs, an ACL tear can prove to be career-ending for some collegiate female athletes - eliminating the potential pathway to becoming a professional athlete and subsequently forfeiting the opportunity to stabilize their financial future with the associated generous salary rates. As such, to try and remedy the compounded effects stemming from this type of ACL issue, it is necessary to develop a knee brace that would effectively "re-train" a female athlete's muscles and landing position to reduce the stress and strain placed on the knee - reducing the risk of sustaining an ACL injury in the process. Since this is such a common injury amongst athletes, a brace would expectedly be in high demand from athletes, coaches, and physical therapists. The brace would be worn during practices to develop muscle memory within the athletes. The brace is designed to counteract the valgus motion and is strong enough to withstand strenuous movement while maintaining knee stability.

PRODUCT DESIGN

The brace was modeled and designed using NX software. The size of the brace was determined by utilizing the measurements of an "average" female adult knee. The brace's diameters are parametrically editable so that when a leg dimension is inputted, the brace automatically adjusts its shape. This allows for a range of braces to be printed depending on the test subjects used. In addition, the brace uses a four-bar mechanism for movement.

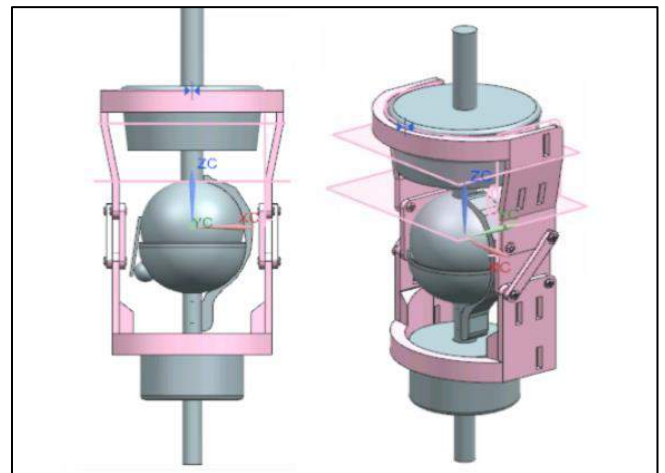


Figure 1: CAD Knee and Knee Brace Model

Once the brace was modeled, it was printed with solid ABS plastic. The ribs of the brace were designed to be in front. They were also modified to be oval-shaped so that the rib would protrude further out and allow for the brace to be positioned deeper onto the leg. The bottom rib has indents near the calf to help taper the transition from the larger-diameter thigh to the smaller-diameter calf. In terms of comfort

for the test subjects, different thicknesses of padding were also used to determine the most agreeable fit during both rest and motion.

Furthermore, the padding was added to provide cushioning for the knee and to give the knee additional support against future stresses and strains. Velcro straps were added to the back of the brace to fit better in the hitches. The Velcro straps also allowed the brace to be adjusted depending on the size of the athlete testing the brace. The thickness of the brace was increased since its original design concept to make sure the brace would be able to withstand any of the forces generated from eventual human testing. Screw countersinks were additionally cut in for a smoother movement of the brace itself and for increased comfort of the test subjects. Two screw countersinks were put into the side plates, positioned at either side of the knee, and another two were placed into the brace’s top and bottom pieces.



Figure 2: Knee Brace CAD and Prototype

This brace will be worn by athletes during their practices, requiring its design to consider the intense, change-of-direction movements commonly associated with many sports and to contain certain features that can withstand the forces generated from such motions. The prophylactic knee brace will look to “retrain” the athletes’ knee muscles to limit the compromising valgus movement that most commonly leads to ACL tears.

To determine an athlete’s pre-existing risk of sustaining an ACL injury, a screening process was also conducted before any further testing takes place. Screening the athletes included observing the degree of valgus already present in their knees during the landing portion of a series of jump squats. Using the tracking system described in Table 1, the degree of pre-existing valgus was scored for each athlete.

Single-leg squat (out of 6)	Knee tracks over inside foot.	1/6
Regular Squat (out of 6)	Knee tracks over first toe.	4/6
Jump Squat (out of 6)	Knee tracks over second and third toes.	6/6

Table 1: Example of Jump Metrics Scale

To test its effectiveness, female athletes were asked to wear the brace for six weeks through a series of leg muscle-building exercises performed twice a week. Every two weeks the athletes were rescreened to observe any changes in the magnitude of their knees’ valgus motion.

At the end of the six-week study, the risk screenings were post-processed for analysis to determine if any significant trends could be identified from the collected data. The expected results include a decreased valgus motion and an increase in knee stability. With repetition of workouts utilizing the brace along with ACL-centered exercises the results will be more apparent.

BUDGET & MARKET ANALYSIS

The prophylactic knee brace will mainly be marketed to female athletes and athletic trainers. Looking at athletes in particular, the brace would be marketed towards younger athletes ranging from 18 to 25 years of age. Since this brace represents a type of preventative care, athletic trainers could also benefit from its purchase in using it to limit their clients’ chance of ACL injury. The budget breakdown to produce the brace comes out to be about \$100/brace. This cost consists of the amount of money required to 3D print the brace, as well as the cost of Velcro, foam, and screws. The customization component adds a unique aspect to the brace which is reflected in the overall cost. The average cost of high-end braces can range between \$200 and \$400, therefore indicating that this brace would be a much more cost-effective option for consumers. However, in the future, this brace could be mass-produced and as a result allow for all its individual pieces (including the padding foam, screws, and Velcro) to become cheaper, and for its overall selling price to decrease too. With this potential for mass production, the brace would ultimately reduce in cost to about \$70/brace and, because a 3D printer will be used for production, each of the braces can be individually customized to comfortably fit each consumer.

ACKNOWLEDGEMENTS

Manhattan College Mechanical Engineering Department

REFERENCES

[1] S. Gupta, L. A. Pierpoint, R. D. Comstock, and M. G. Saper, “Sex-Based Differences in Anterior Cruciate Ligament Injuries Among United States High School Soccer Players: An Epidemiological Study,” *Orthopaedic Journal of Sports Medicine*, vol. 8, no. 5, 2020.

[2] Sanchez, “Anterior Cruciate Ligaments; a literature review on why women have increased susceptibility,” *Cache digital archive*, 2020. [Online]. Available: <https://cache.kzoo.edu/bitstream/handle/10920/38634/Juninho%20Sanchez%20-%20SIP%20PAPER%20Final.pdf?sequence=3&isAllowed=y>.

[3] Giovinazzo, “The Impact of Oral Contraception on Anterior Cruciate Ligament Injury in Young Female Athletes,” *ScholarWorks@Arcadia*, 21-Apr-2020. [Online]. Available: <https://scholarworks.arcadia.edu/showcase/2020/pa/87/>

[4] N. J. Romanchuk, M. J. Del Bel, and D. L. Benoit, “Sex-specific landing biomechanics and energy absorption during unanticipated single-leg drop-jumps in adolescents: implications for knee injury mechanics,” *Journal of Biomechanics*, vol. 113, p. 110064, Dec. 2020.

3D PRINTED PATIENT-SPECIFIC LOWER EXTREMITY MODEL FOR ASSESSING DEVELOPMENTAL DYSPLASIA OF THE HIP

E. Fontz (1), O. Burkowski (1), J. Palmer (1), E. Scott (1), C. Price (2, 3), V. Huayamave (1)

- (1) Mechanical Engineering, Embry-Riddle Aeronautical University, Daytona Beach, Florida, USA
(2) International Hip Dysplasia Institute, Orlando, Florida, USA
(3) Orlando Health, Orlando, Florida, USA

INTRODUCTION

Developmental Dysplasia of the Hip (DDH) is a condition that causes an infant's hip to be easily displaced from the acetabulum. An abnormally formed acetabulum is the most common case and can cause the femoral head to slip from the socket easily. Mechanically, the hip is classified as a ball and socket joint consisting of two bones, the pelvis, and the femur. The ball is defined as the femoral head and the socket is defined as the acetabulum. The joint is formed where the ball and the socket fit together and are held by cartilage and ligaments, allowing the ball to glide easily inside the socket.

Infantile hip dislocation is a common condition affecting 1 in every 1000 children born in the USA [9]. It is unknown what the exact cause of DDH is, but most cases are seen in females, breech presentations, firstborn children, those with genetic risk, and when the fetus is restricted in the womb. The most common case seen is when the acetabulum is formed incorrectly resulting in a shallow socket as shown below in Figure 1, allowing for dislocation of the infant's hip.



Figure 1: Anatomical Differences in Hip Dysplasia Patients [6]

The Barlow and Ortolani maneuvers are used to physically detect DDH by dislocating and relocating the femoral head in the acetabulum. proper training in these two tests can improve the chances of diagnosing DDH, resulting in early treatment by non-surgical methods. During the Barlow maneuver, one hand stabilizes the pelvis while the other grasps and flexes the infant's hip to 90 degrees. The hip is then adducted 10-

20 degrees and a gentle posterior force is applied to see if the femoral head dislocates from the acetabulum. During the Ortolani maneuver, the pelvis is stabilized with one hand and the hip is again flexed to 90 degrees. Then the hip is abducted, and an anterior force is simultaneously applied. The femoral head then returns to the acetabulum, resulting in a palpable clunk [8].

Current simulation trainers, including Laerdal Medical's Hippy Baby, are commonly used to teach the Barlow and Ortolani maneuvers to physicians and medical students. The Hippy Baby model presents only the lower half of the torso and limbs of a newborn and is intended for use with the Barlow and Ortolani maneuvers [7]. One issue with this trainer is the stiffness and rigidity of the model as it does not represent the same range of motion as an infant.

This study was conducted to evaluate the forces applied to the Laerdal Hippy Baby model was used by examiners while performing the Barlow and when various examiners performed measuring the force applied using a force plate. The level of force required to dislocate the femoral head from the acetabulum on the Hippy Baby is 12N, however, the average peak force applied by the examiners was 33N [4]. A medical professional could exert too much force and injure the infant while performing the maneuvers on the infant if they are practicing on the Hippy Baby because of its rigidity. Another issue with the Hippy Baby is that the internal anatomy and mechanics are not visible which hinders the student from visualizing how the femur and acetabulum are behaving while performing the maneuvers on a real infant.

In addition, a new model was developed in an attempt to minimize these limitations of current exam training simulation.

METHODS

The new model was created using the anatomy of an infant with mild hip dysplasia. This anatomy was then scaled down and mirrored, to match a 2-month-old infant with class B DDH on both sides. A transparent section will be added along the pelvic region to allow the students to observe the dislocation and reduction. A water-clear

urethane rubber was used to achieve optimum transparency. Because infant bones are not as rigid as a fully developed adult, it can be difficult to quantify their strength and flexibility. The material properties used in this project, originate from a study that performed tensile testing on cadaver infant femurs. The study consisted of a group of infant femurs ranging from 1 day old to 6 months old. Due to the two- to three-month-old age representation of the Hippy Baby, the 2-month-old subject's results were used. The cadaver bone was found to have a Young's Modulus of 803 MPa and a Poisson's Ratio of 0.30 and all analyses will use these properties [5]. 3D printed materials such as thermoplastic polyurethane (TPU) provide the required flexibility, however, it tends to buckle when put under a sizeable load.

Additionally, to compare the force required to dislocate between the new model and the Hippy Baby, a combination of load cells and force plates will be used. These results will be compared to the study mentioned above [4].

FEA analysis was performed to compare different material combinations with the infant bones. A 33N load was applied axially at a point in between the medial and lateral condyles of the femur. The femoral head was fixed within the acetabulum, to observe only the displacement in the femoral shaft. This FEA model did not allow for any movement, the femoral head was fixed in the acetabulum. Since the deflection/bending in the femur was the most important aspect for this analysis, movement in the acetabulum was negligible. Additionally, muscle activity, ligaments, and cartilage were also assumed to be negligible. All three materials were modeled as linear elastic isotropic, using tetrahedral elements.

The first model used the infant material properties mentioned above, the second uses material properties of TPU with a Young's Modulus of 27.15 MPa and a Poisson's ratio of 0.48 [1]. The final model uses the same properties of TPU along with a 3mm in diameter aluminum rod going through the center, the Young's Modulus for the rod is 68900 MPa and a Poisson's ratio of 0.33 [2].

Tensile testing will be performed on the Ultimaker 95A TPU to verify our extrapolated values for Young's Modulus.

RESULTS

A preliminary study was conducted using a Force Sensitive Resistor (FSR) to determine the force required to dislocate the Hippy Baby's femoral head from the acetabulum. The FSR was attached to the knee of the trainer. Of the 10 trials, the average applied force was 27.4N, similar to the peak force used by examiners. The actual force required to dislocate the trainer is 12N [5].



Figure 2: Hippy Baby Instrumented with a FSR

All three FEA models were tested using an applied axial load of 12N, 27.40N, and 33N. Under a 33N applied axial load, the model with the infant bone had a displacement of 0.74mm across the femur. Under the same loading conditions, the TPU model had a displacement of 22.53mm, a 2,952.85% increase from the infant bone results. With the addition of the aluminum rod, the femur displaced 0.97mm, which is within 0.30mm of the infant model.

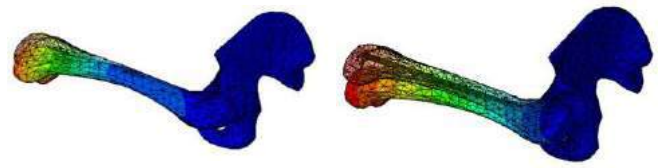


Figure 3: Infant Model (left) with a displacement of 0.74mm and TPU with the Rod (right) with a displacement of 0.97mm under a 33N Axial Load

Amongst all three applied loads, the TPU model had significantly more deflection than the others. The large percent difference between the TPU and infant model confirms the need for an aluminum rod.

DISCUSSION

The model is limited in its anatomical representation of an infant's hip and acetabulum due to the size of the model and the time required to manufacture realistic ligaments and tendons. Even though these structures are not included, the range of motion and movement during the Barlow and Ortolani maneuvers will not be affected due to the lack of strength in the muscles of a real infant to resist these procedures.

The 3D-printed bones have been evaluated using various print orientations and infills. Ultimately, the Ultimaker 95A TPU at 100% infill would be best suited for modeling infant bones. Through FEA analysis it has been determined that an aluminum rod will be inserted into the center of the femur to reduce the flexibility of the TPU in the femoral shaft. Further materials testing will be conducted with tensile testing. A more in-depth study will be performed using load cells and a force plate to compare the applied forces on the current Hippy Baby, to the prototype during the Barlow maneuver.

The next step is to assemble the prototype and ensure the improved model accurately represents the Barlow and Ortolani maneuvers and the material properties of a real infant's bones. The prototype will also be given to the orthopedic surgeon who has been assisting in the project, for extensive feedback.

ACKNOWLEDGEMENTS

Sheridan Perry, B.S. Mechanical Engineering 2022
Office of Undergraduate Research Ignite Grant, ERAU
International Hip Dysplasia Institute

REFERENCES

- [1] 3D Pros. Choosing Infill Percentage for 3D Printed Parts. Pflugerville, Texas. 2021
- [2] Aluminum 6061-T6. ASM material data sheet. (n.d).
- [3] Castro, A. P., et al. Finite element modeling of the developing infant femur using paired CT and MRI scans. PLoS One. 2019
- [4] Chow, Y. W., et al. Measurement of the Forces and Movements Involved In Neonatal Hip Testing. International Society For Low Power Laser Applications In Medicine. 1994.
- [5] Hirsch, C., & Evans, F. G. Studies on some physical properties of infant compact bone. Acta Orthopaedica, 35(1-4), 300-313. 1965.
- [6] International Hip Dysplasia Institute. (n.d.). What is Hip Dysplasia? Retrieved from International Hip Dysplasia Institute.
- [7] Jones D. (1998). Neonatal Detection of Developmental Dysplasia of the Hip. The Journal of Bone and Joint Surgery.
- [8] Stanford Medicine. (n.d.). Barlow and Ortolani Maneuvers. Retrieved from Stanford Medicine.
- [9] Storer, S., & Skaggs, D. L. Developmental Dysplasia of the Hip. American Family Physician, 1310-1316. 2006.

EVALUATING THE UNDERSTANDABILITY OF REAL-TIME SONIFIED BIOFEEDBACK PROTOTYPES FOR BALANCE TRAINING

Vibha R. Iyer (1,2), Mitchell A. Tillman (1), Antonia M. Zaferiou (1)

(1) Biomedical Engineering, Stevens Institute of Technology, Hoboken, NJ, USA

(2) Biomedical Engineering, Georgia Institute of Technology, Atlanta, GA, USA

INTRODUCTION

Sonified biofeedback, which conveys biological signals through sound and musical cues [1], can be harnessed to facilitate balance training. This study's purpose was to evaluate the understandability of two prototype sonified biofeedback designs during dynamic balance tasks, such as walking and turning, with young healthy adults. We asked for quantitative and qualitative feedback to inform future design iterations towards helping improve older adult balance during turns. In prior work, we found that young adults experience unstable conditions during turns by investigating two relevant balance measurements that our prototype system conveys through sound. During turns, young adults experienced larger frontal-plane whole-body angular momentum (Hf) and smaller "lateral distance" (LD), which is the horizontal distance between the body's center of mass and lateral (side-to-side) edge of the base of support (area in contact with the ground) [2].

METHODS

Five participants (two male, three female; age 20.4 ± 1.4 yrs) pursuing engineering-related undergraduate degrees provided informed consent to participate in this pilot study approved by Stevens' IRB. The study was conducted during one two-hour lab visit that began with setting up the participant with optical motion capture reflective markers. The optical motion capture system (Optitrack, Eugene, OR) monitored 3D body positions and streamed data in real-time to a second computer to compute the balance measurements using MATLAB (MathWorks, Natick, MA). The balance measurements were streamed to a third computer that used the interactive media software Max-MSP (Cycling 74, San Francisco, CA) to map biomechanical measurements to sound parameters, and generate the corresponding sound [3] (see [example video](#)). Next, within each of the two sonified biofeedback designs (Hf and LD, in randomized order) there were three sequential phases for the participant to interact with the system: (1) assessment of prior understanding of balance measurements (Hf and LD) and sound

separately, (2) familiarization period with sonification designs, and (3) assessment of understanding of sonification designs. Participant design feedback and user perceptions were quantitatively and qualitatively obtained after each step along with overall user experience at the end of each phase and the end of the entire study. During Phase 1, verbal conversation using scripted descriptions of balance metrics was used to introduce the system and establish initial familiarity with the balance measurements. The scripted descriptions were intended to be in lay terms and included: "*Larger whole body angular momentum, or larger rotation of your body around your center of mass, produce higher pitches*" and "*Smaller lateral distances, or smaller distances between your center of mass and edge of your base of support, produce faster beats*". After, participants familiarized themselves with the sonified biofeedback by performing feet-in-place weight shifting (Hf only), straight line walking, turning while walking, and free movements.

To evaluate their level of understanding, participants were asked to move their bodies to generate specific sound sequences. Sequence 1 was "high-low-high" pitch for Hf or drum beat speed for LD and Sequence 2 was "low-medium-high" pitch for Hf or drum beat speed for LD. Participants completed four trials to evaluate their understanding of each of the two designs by attempting each of the two sequences. The time series of each trial was divided into three sections based on the timing of the verbal cue to move to the next sound level and the median of each section was calculated (using LD and |Hf|). The median values were ranked relative to the previous and subsequent section; if their ranking matched the same pattern as the sound sequence (e.g., high-low-high), they were deemed successful. **Figure 1** depicts a successful Hf trial for Sequence 2 and a successful LD trial for Sequence 1. The horizontal line thresholds on **Figure 1** mark the extrema Hf and LD mapped to sound. Therefore, beyond these thresholds, the sound stayed constant. The Hf threshold was determined from prior research [2] and the LD thresholds were personalized based on the range used during straight-line gait. The rates of successful sequences are reported.

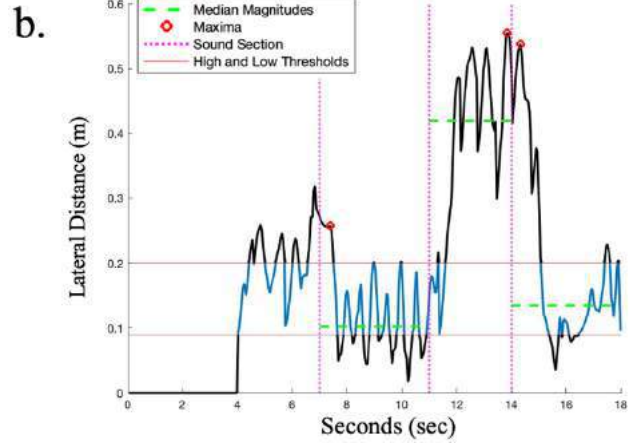
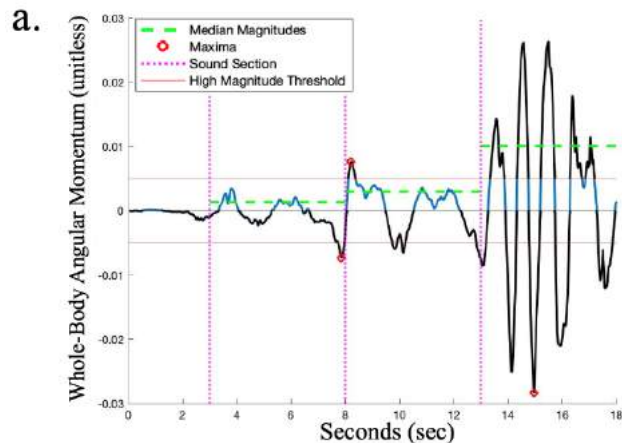


Figure 1: Example timeseries for sound generation task. (a) Hf low-medium-high pitch. (b) LD high-low-high drum speed.

Finally, participants rated their perceptions of “Ease of Use and Usability” of both designs, overall, using a 7-point Likert scale [3].

RESULTS

Overall, 65% of trials generating specific sequences for the designs were successful (Table 1). The average perceived “Ease of Use and Usability” score was 5.4 out of 7 (+/- 0.89 SD) (Table 2).

Table 1: Success of sound generation tasks by sound sequence and sonified biofeedback design.

Participant:	1	2	3	4	5	% Success
Hf Sequence 1	✓		✓	✓		60%
Hf Sequence 2	✓	✓	✓	✓	✓	100%
LD Sequence 1	✓			✓		40%
LD Sequence 2	✓	✓		✓		60%
Successes:	4/4	2/4	2/4	4/4	1/4	

Table 2: Ratings for “Ease of Use & Usability” of biofeedback technology (tech.) 7=“completely agree”, 1=“completely disagree”.

Participant:	1	2	3	4	5	Mean (SD)
“My interaction with the tech. is clear and understandable”	6	5	5	6	6	5.6 (0.5)
“Interacting with the tech. does not require a lot of mental effort”	5	3	6	5	5	4.8 (1.1)
“I find the tech. to be easy to use”	5	4	5	6	6	5.2 (0.8)
“I find it easy to get the tech. to do what I want to do”	4	5	6	6	6	5.4 (0.9)
“I find the tech. to be flexible to interact with”	5	5	6	7	7	6 (1.0)
“Learning how to perform tasks using the tech. was easy”	5	4	6	6	6	5.4 (0.9)
“The tech. has good functionality”	5	5	5	7	7	5.8 (1.1)
“I feel I have an intuitive sense of how to operate the tech.”	4	6	6	6	5	5.4 (0.9)
“I find it easy to remember how to perform tasks using the tech.”	4	5	5	6	5	5 (0.7)
Mean (SD)	4.8 (.7)	4.7 (.9)	5.6 (.5)	6.1 (.6)	5.9 (.8)	

DISCUSSION

Participants performed better with the Hf system, passing 80% of trials, in contrast to only passing 50% of LD trials. All participants

achieved a successful Sequence 2 (low-medium-high) for Hf. In contrast, only two participants achieved a successful sequence 1 (high-low-high) for LD. Some of these results could be because LD was designed to be used during walking and requires the participant walking forward while modulating LD, whereas, the Hf design allows simpler feet-in-place body movements, like tilting the torso side-to-side. Additionally, some participants out-performed others. Participants 1 and 4 successfully completed all four sequences, in comparison to Participant 5, who only succeeded in sequence 2 for Hf.

As for perceived Ease of Use and Usability, the lowest average rating for a question (4.8 / 7) was given in response to “*Interacting with the technology does not require a lot of mental effort*”, which relates to our current research about cognitive load during sonified biofeedback. The best average rating (6 / 7) was given in response to “*I find the technology flexible to interact with*”, which may be a helpful design feature as we seek to use the system for multifaceted balance training.

This was a preliminary evaluation of the level of understanding of complex biomechanical measurements conveyed through musical cues in near real-time. Therefore, the sample size is small and limited to collegiate engineering students and students of related disciplines. The fact that participants may have learned about angular momentum or biomechanics in coursework could bias the results and *re-emphasizes viewing this study as a first step towards a multifaceted user-centered design process* that we are using to develop the system for older adults. Surprisingly, this small cohort still yielded a variety of responses and results in assessments, which may relate to the need to personalize these systems and familiarization protocols in future designs.

Results indicate that there is generally positive perceptions of the ease of use and usability of the systems, but room to improve the understandability of the sonified biofeedback systems. We are currently using the results of this study to improve the overall sonified biofeedback design, descriptions of the balance measurements and the sounds, familiarization tasks. Further, we are also incorporating design feedback from older adults, and physical therapists from focus groups and “think-aloud” user sessions.

ACKNOWLEDGEMENTS

This work is supported by the National Science Foundation, REU/RET Site Grant # 2050921 and NSF CAREER Award #1944207.

REFERENCES

- [1] Hermann, T et al., *The Sonification Handbook*, 1:9-17, 2011
- [2] Tillman, M et al., *J Biomech*, 141:1-10, 2022
- [3] Chen TL et al., *PLoS One*, 12:1-29, 2017

NUMERICAL MODELING FOR INFANTS WITH DUCTAL-DEPENDENT PULMONARY FLOW

S. Mulla (1), M.H. Alzaeim (1), W.S. Basha (1), K.B. Kose (1)

(1) Biomedical Engineering Department, Istanbul Medipol University, Istanbul,Turkiye

INTRODUCTION

The treatment of pulmonary atresia (PA) and Patent Ductus Arteriosus (PDA) requires a comprehensive approach owing to their highly variable morphological features [1]. The decision-making process can be complex, leading to excessive resource and time consumption in both cardiology and cardiac surgery [2]–[4]. It is a very sensitive process to decide whether the treatment will be surgical or catheterization and, in these cases, whether the PDA will remain open or closed.

This study focused on investigating whether utilizing numerical simulations to predict the optimal approach for ductus-dependent congenital circulation has significant consequences. A comparative blood flow simulation study was performed with medical image data and clinical data of selected newborns.

METHODS

Three patients with PA and PDA agreed to participate in this study, and computed tomography image datasets constituted the initial input of the study. The image-based three-dimensional (3D) model was obtained by image processing toolkits [5].

The virtual models were created with open-source computer-aided design tools [6]. The finite element method has been used to simulate patient-specific blood flow[7]. The blood was defined as a Newtonian fluid, with a kinematic viscosity of 0.004 m²/s and a density of 1060 kg/m³ (Eq.1,2).

$$\nabla \cdot \mathbf{u} = 0 \quad (\text{Eq.1})$$

$$\rho \mathbf{u} \cdot \nabla \mathbf{u} = -\nabla p + \nabla \cdot [\mu(\nabla \mathbf{u} + (\nabla \mathbf{u})^T)] \quad (\text{Eq.2})$$

The pulsatile velocity profile of the patient is created on MATLAB and, was defined as the boundary condition (Figure.1) [8].

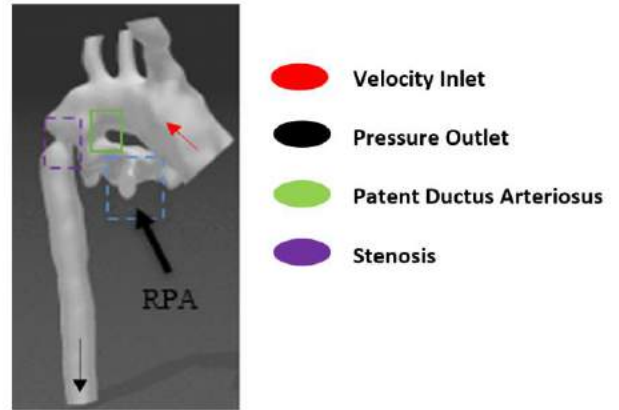


Figure 1: Patient-specific Virtual 3D models anterior (left) and posterior (right) views. RPA: Right pulmonary artery.

RESULTS

For three newborn patients, a hemodynamic visualization was made based on the digital twin model and two virtual 3D models obtained from the pre-operative DICOM image. Virtual repair methods, which did not highlight one of them, gave different results for each patient, as we predicted. Pressure drop

in a congenital artery is typically considered acceptable if it is between 10 mm Hg and 50 mm Hg [9]. In the first patient, the PDA-removed flow visualization results indicated a large pressure drop. It was found to be within the acceptable range in the second patient without aortic coarctation. Velocity streamlines depicted a better result than the pre-operation models in all simulations, it was observed that vortices were found in patients with coarctation, and it was seen that it would affect the decision according to the segment in which it was located. Evaluations for wall shear stress (WSS) provided the most useful findings for clinical decision-making. While the surgical repair was planned for the first patient, the hemodynamic analysis showed that closure of the PDA could provide a more risk-free flow as a result of the numerical simulation (Figure.2).

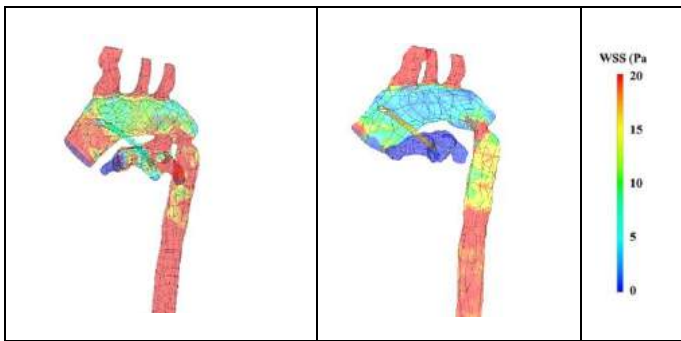


Figure 2: The WSS distribution of the virtual shunt (left) and removed PDA (right) models of the first patient.

DISCUSSION

This hemodynamic methodology has guided our ability to evaluate flow patterns in shunted configurations and the associated unmeasurable but calculable mechanical consequences [10]. The WSS distribution, which was confirmed as the cause of endothelial remodeling, was visualized and compared with actual postoperative findings. It was seen that the evaluation of the dimensions and materials of the shunt configurations on their digital twins for three patients could provide significant contributions to pre-operative planning. In the future steps of this study, it is planned to increase the number of patients and to include anastomosis angles in the evaluation as well as optimal shunt diameter and sizes.

ACKNOWLEDGEMENTS

This study was funded by Istanbul Medipol University BAP (Scientific Research Project) grant on 02.2023.

REFERENCES

- [1] A. C. Glatz *et al.*, “Comparison Between Patent Ductus Arteriosus Stent and Modified Blalock-Taussig Shunt as Palliation for Infants With Ductal-Dependent Pulmonary Blood Flow: Insights From the Congenital Catheterization Research Collaborative,” *Circulation*, vol. 137, no. 6, pp. 589–601, Feb. 2018, doi: 10.1161/CIRCULATIONAHA.117.029987.
- [2] M. Rezaeimoghaddam *et al.*, “Pre-surgical planning of complex congenital heart defects – selected clinical cases and pre-

operative hemodynamic performance Discussion & Conclusion,” 2017.

- [3] Yıldız Okan, Köse K. Banu, Tanıdır İ. Cansaran, Pekkan Kerem, Guzeltas Alper, and Haydin Sertaç, “Single-center experience with routine clinical use of 3D technologies in surgical planning for pediatric patients with complex congenital heart disease,” *Diagnostic and Interventional Radiology*, 2021, doi: DOI 10.5152/dir.2021.20163.
- [4] I. Valverde *et al.*, “Three-dimensional printed models for surgical planning of complex congenital heart defects: an international multicentre study,” *European Journal of Cardio-Thoracic Surgery*, vol. 52, no. 6, pp. 1139–1148, Dec. 2017, doi: 10.1093/ejcts/ezx208.
- [5] I. Technologies, S. A. Gombe, and T. Supervisor, “43D Visualization and Segmentation of Lungs Using Itk / Vtk / Qt Kopsude 3D Visualiseerimine Ja Segmenteerimine Itk / Vtk / Qt,” 2017.
- [6] “FreeCAD: Your own 3D parametric modeler.” <https://www.freecadweb.org/> (accessed Aug. 02, 2019).
- [7] “Simulation Software | Engineering in the Cloud | SimScale.” <https://www.simscale.com/> (accessed Feb. 10, 2023).
- [8] “MATLAB - MathWorks - MATLAB & Simulink.” <https://nl.mathworks.com/products/matlab.html> (accessed Nov. 06, 2022).
- [9] R. Ascutto, N. Ross-Ascutto, J. Wiesman, and S. DeLeon, “Bidirectional glenn shunt as an adjunct to surgical repair of congenital heart disease associated with pulmonary outflow obstruction: Relevance of the fluid pressure drop-flow relationship,” *Pediatr Cardiol*, vol. 29, no. 5, pp. 910–917, 2008, doi: 10.1007/s00246-008-9229-9.
- [10] D. Shav, R. Gotlieb, U. Zaretsky, D. Elad, and S. Einav, “Wall shear stress effects on endothelial-endothelial and endothelial-smooth muscle cell interactions in tissue engineered models of the vascular wall,” *PLoS One*, vol. 9, no. 2, p. e88304, 2014, doi: 10.1371/journal.pone.0088304.

COMPUTATIONAL MODELING OF HEMODYNAMICS IN AORTIC ROOT ENLARGEMENT

Surya Sanjay (1), Mia Bonini (1), Alexander Makkinejad (3), Maximilian Balmus (2), Marc Hirschvogel (2), Nicholas Burris (4), Bo Yang (3), David Nordsletten (1,2,3)

(1) Department of Biomedical Engineering, University of Michigan, Ann Arbor, MI, USA
(2) Department of Biomedical Engineering and Imaging Sciences, King's College London, London, UK
(3) Department of Cardiac Surgery, Michigan Medicine, Ann Arbor, MI, USA
(4) Department of Radiology, University of Michigan, Ann Arbor, MI USA

INTRODUCTION

Aortic stenosis (AS) is the most common valvular condition in the developed world, manifesting in 1.3% to 4% of adults between the ages of 65 and 85.[1] It is characterized by a narrowed orifice area between the leaflets of the aortic valve, often caused by calcification or other factors, such as a congenital bicuspid valve.[2] AS causes obstruction of left ventricular (LV) outflow, increasing the pressure required to drive cardiac output.[3] These changes can lead to heart failure and death.[4] The gold standard for treating AS is (surgical) aortic valve replacement (AVR), comprising of the resection of the diseased leaflets followed by the implantation of a mechanical or bioprosthetic valve.[5]

Patient-prosthesis mismatch (PPM) is a frequent outcome of AVR, wherein the implanted valve is too small to accommodate for the cardiac output required by the patient. PPM is defined as an indexed effective orifice area (i.e. the valvular orifice size standardized to body surface area) of $<0.65 \text{ cm}^2/\text{m}^2$ (severe) or $<0.85 \text{ cm}^2/\text{m}^2$ (moderate).[6] It represents 54% to 65% of cases, and it can cause compensatory remodeling and hypertrophy of the left ventricle.[7, 8] To prevent PPM, aortic root enlargement (ARE) was proposed to be performed in tandem with AVR to increase the aortic annulus size by up to 10 mm.[9, 10] It has been noted that ARE is associated with LV regression and a significant reduction in transvalvular pressure gradient, both of which indicate a trend toward cardiac competency.[9, 11] However, an increase in annular diameter reduces outflow velocity and may cause hemostasis which can increase the risk of thrombosis.[10]

In this study, we utilized computational fluid dynamics (CFD) simulations to model hemodynamics in the aortic root following AVR and AVR+ARE. In doing so, we non-invasively estimate pressure, velocity, and residence time. Using these values, we work to evaluate the risk of thrombosis after aortic root enlargement *in silico*, providing a basis for future longitudinal clinical studies.

METHODS

To evaluate the hemodynamic impact of ARE, CT scans of three AVR patients (Patients 1, 3, & 5) and three patients who underwent AVR+ARE (Patients 2, 4, & 6) were collected, wherein Patients 1 and 2, 3 and 4, and 5 and 6 were paired. These patient pairs were matched on age, sex, ejection

fraction, and native annulus size. As a secondary control, a “virtual” AVR (vAVR) model without an ARE was generated for each AVR+ARE patient using preoperative anatomy and annulus dimensions. Transvalvular pressure, peak velocity, and blood residence time (time to exit the model from a given starting location) over six cardiac cycles were computed at a temporal resolution of 0.02 seconds.

Pre- and post-operative computed tomography (CT) images were acquired for each patient, and 3D models of the ascending aorta and aortic root were segmented using 3DSlicer. Segmented models were imported into SimModeler for smoothing, tetrahedral mesh generation (using boundary layer refinement). Hemodynamic parameters, including heart rate (70 bpm) and stroke volume (73.5 mL/beat), were standardized for all patients to isolate the effects of root anatomy. Meshes were coupled with a closed-loop 0D model that represents the remaining cardiovascular system.[12] CFD simulations were performed on the finite-element multiphysics solver CHeart.[13]

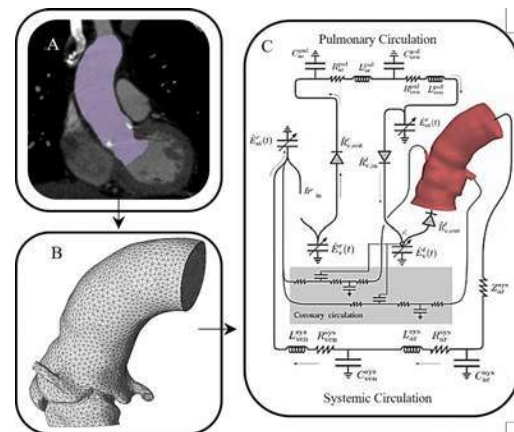


Figure 1: Aortic Root Modeling Pipeline. (A) Pre- and post-operative CT images are segmented to create 3D models of the aortic root blood volume. (B) Tetrahedral volume meshes are generated in SimModeler. (C) Meshes are coupled with a closed-loop 0D model.

Due to poor image resolution, valve leaflets could not be segmented from the CT images. Instead, the aortic valve was modeled in SimModeler as a 2D plane. The location and orientation were based on landmarks in the patient images. The anatomic valvular orifice area (AVOA) was defined on the plane and was based on the patient's implanted valve. This area is used to control flow in the simulations, mimicking the opening and closing of the aortic valve throughout the cardiac cycle.

RESULTS

AVR+ARE increased the annulus diameter by 2 valve sizes in Patient 2 (21 → 29mm), and by 3 sizes in Patients 4 and 6 (23 → 29mm and 21 → 27mm, respectively). CFD simulations demonstrated an expected decrease in mean and peak pressure gradients in AVR+ARE cases compared to AVR (42.9% and 69.8% decrease, respectively) and vAVR (41.3% and 66.4% decrease, respectively). Peak velocity was also reduced after root enlargement by an average of 37.9% and 40.0% relative to AVR and vAVR. Finally, residence time decreased by 0.11% on average ($\sigma = 2.61$) in AVR+ARE models compared to AVR, wherein Patients 2 and 4 had a slight increase and Patient 6 had a slight decrease.

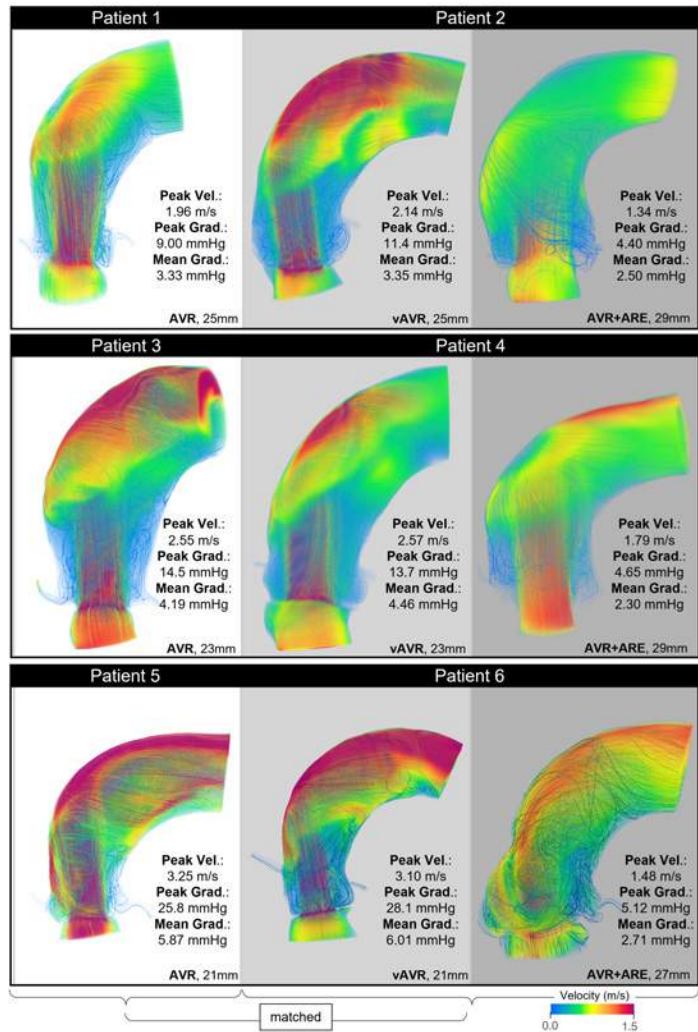


Figure 2: Velocity fields at peak systole are shown for AVR, AVR+ARE, and vAVR. Abbreviations: Vel. = velocity, and Grad. = transvalvular pressure gradient.

DISCUSSION

In this work, we modeled blood flow in AVR and AVR+ARE patients to study how an ARE changes the risk of thrombosis and local hemodynamics. We observed a global decrease in transvalvular peak velocities and pressure gradients following post-ARE in comparison with AVR-only models. This is in line with the results of earlier studies.[11]. We also demonstrate a minimal change in residence time and blood stasis in the si-

nuses following root enlargement. This suggests a limited added risk of thrombosis.

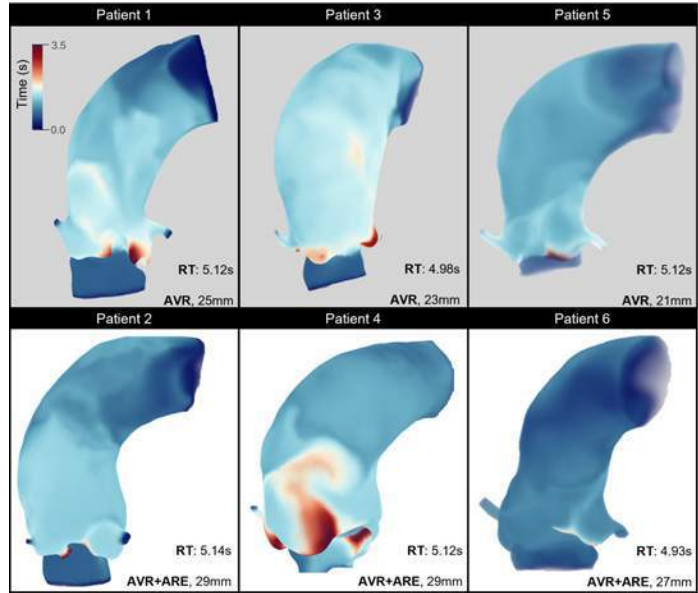


Figure 3: Residence time fields are shown for AVR and AVR+ARE. Abbreviations: RT = residence time.

We observed that patient 6 (AVR+ARE) had a lower residence time than its matched patient, patient 5 (AVR only). This suggests that there are other factors, including possibly the way that a new valve is implanted, that have a competing influence on the occurrence of hemostasis following valve replacement. This might further explain the lack of consensus regarding the longitudinal effects of ARE.[11, 14]

In future work, we plan on examining velocity, pressure, and residence time in models that include dynamic valve leaflets, which more closely matches physiological conditions. In doing so, we hope to further elucidate the longitudinal effects of ARE, as patient-prosthesis mismatch becomes an increasingly debated topic.

ACKNOWLEDGEMENTS

DN acknowledges funding from the Engineering and Physical Sciences Research Council Healthcare Technology Challenge Award (EP/R003866/1).

REFERENCES

[1] Nathaniel S et al. *World J. Cardiol.* 2.6 (2010).
[2] Flachskampf FA et al. *Internist (Berl).* 45.11 (2004).
[3] Carabello BA. *Circ. Res.* 113.2 (2013).
[4] Minamino-Muta E et al. *Sci. Rep.* 1 (2017).
[5] Joseph J et al. *Am. J. Med.* 130.3 (2017).
[6] Pibarot P et al. *Heart* 92.8 (2006).
[7] Fallon JM et al. *Ann. Thorac. Surg.* 106.1 (2017).
[8] Iqbal A et al. *Indian J. Thorac. Cardiovasc. Surg.* 35.1 (2018).
[9] Sujith NS et al. *J. Card. Surg.* 37.10 (2022).
[10] Yang B et al. *Ann. Thorac. Surg.* 114.6 (2022).
[11] Rao V et al. *J. Thorac. Cardiovasc.* (2022).
[12] Hirschvogel M et al. *Int. J. Numer. Method. Biomed. Eng.* 33.8 (2017).
[13] Lee J et al. *SIAM* 38.3 (2016).
[14] Haunschild J et al. *E. J. Cardiothorac. Surg.* 56.2 (2019).

ELERT – A HAPTIC EMERGENCY ALERT SYSTEM FOR THE AUDITORILY IMPAIRED

Emily Bartling (1), Ruth Hammond (1), Deven Cobb (2), Jerritt Gutierrez (1)

Faculty Advisor(s)

J. Miles Canino (1)

- (1) Department of Mechanical Engineering, Rose-Hulman Institute of Technology, Terre Haute, IN, USA
- (2) Department of Biology and Biomedical Engineering, Rose-Hulman Institute of Technology, Terre Haute, IN, USA

INTRODUCTION

According to the U.S. Fire Administration (USFA), there are 11 million deaf or hard of hearing Americans who are unable to rely on the life-saving warning sounds of a smoke alarm [3]. This deficit extends to all life-saving emergency warning devices that utilize auditory alerting. Currently available solutions are expensive and require special installation - limiting such technology to the homes of individuals that can afford them. Examples include bed-vibrating fire alarms and specialized strobe-light systems. Outside of the personal residence, the hearing impaired must rely on cues from their surroundings to interpret nearby emergency alerting. These cues can be difficult to interpret, particularly when the individual is preoccupied with other tasks. Our team designed an affordable, wearable, haptic-rich solution that best addresses this problem.

PRODUCT DESIGN

Emergency Listening, Emergency Responsive, Technology (ELERT) is a wearable device that responds to auditory input via haptic user-interfacing. The current prototype is in the form of a device that can be worn as one would wear a wristwatch. The 3D printed mechanical housing is shown in Figure 1.

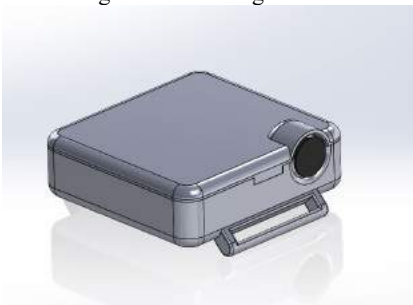


Figure 1: ELERT mechanical housing for the haptic system.

Creating a compact, but feature-rich, device was challenging. The microcontroller, microphone, haptic motors, haptic motor driver, and battery all had to be organized within a compact, ergonomic case. Since the unit would also be vibrating against the user's body, there also had to be careful consideration taken for haptic motor placement, and isolation (mechanical and electrical) of the vibratory motor from other sensitive electronic elements. Figure 2 provides an internal view of the wristwatch case design, with recessed space for components to be seated.

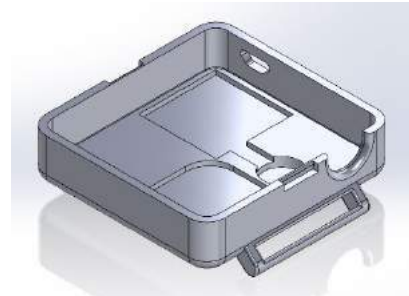


Figure 2: Internal housing depicting integrated electrical cutouts.

The vibrational motor is press-fit into a circular cutout, minimizing the distance between the motor and skin, improving the magnitude of vibratory stimulus transmitted to the user's wrist. When the top and bottom of the case are mated together, there is a circular hole allowing for projection of the microphone sensor, vastly improving auditory signal detection. The case is held together with a snap-fit joint that interfaces with the main mechanical housing, keeping the device together and protected. A hook-and-loop fastener is currently being utilized as the strap, allowing for easy donning, doffing, and adjustability.

The microphone is a KY-037, which is used to sample audio signals at a frequency of 11,000 Hz. The haptic motor is driven by a haptic driver (DRV2605L), vibrating at a frequency of 166 Hz and magnitude of 0.4 G - more than adequate to stimulate the mechanoreceptors located within the skin of the wrist [4]. All of these components are controlled via an Arduino Micro and powered by a coin-cell battery. Figure 3 shows the assembled device.



Figure 3: Assembled device and electronics.

The device was coded using a combination of Arduino and C. The audio signal from the KY-037 microphone was processed using the arduinoFFT data-processing library. This allowed for the extrapolation of the input audio signal’s frequency content, which was then stored and assessed according to a rolling-average of the frequency data. A rolling-average threshold of 2200 Hz was specified for our prototype. When this threshold was met, the device began actuating the haptic motor, alerting the user. The threshold of 2200 Hz was specified in accordance with NFPA 72, the National Fire Alarm and Signaling Code, which requires that emergency alarm systems use a temporal-three sound, produced at a high frequency of about 3,150 Hz [1]. Using a rolling-average accounts for background noises and other frequencies that may be sampled during the pauses of the temporal-three sound.

BUDGET & MARKET ANALYSIS

Our team’s budget for the prototype was \$240.00, provided through a KEEN Engineering Unleashed Fellowship Award. Table 1 depicts the cost-breakdown of the final prototype and anticipated production costs.

Table 1: ELERT prototype and production budget breakdown.

Item Name	Quantity	USD/Unit	Production USD/Unit
KY-037 Microphone	1	\$1.92	\$0.37
Arduino Micro	1	\$24.20	\$0.75
Haptic Motor	1	\$1.95	\$1.56
DRV2605L Haptic Driver	1	\$9.50	\$0.95
Coin Cell Holder	1	\$4.84	\$0.48
Hook & Loop Strap	1	\$5.99	\$0.18
Misc*	-	\$20.00	\$2.00
TOTAL	-	\$68.40	\$6.29

* Cost estimate for plastics, wires, etc.

As seen in Table 1, purchasing components in bulk would reduce the cost of a production model significantly. Costs could also be significantly reduced by choosing a cheaper microcontroller. All of these factors, in combination with mass production methods, brings the cost of a production model to an estimated 6.29 USD. With production overhead, and other costs in mind, we estimate an MSRP of around 15.00 USD. We anticipate that this device would be considered a General Wellness Product and would not be subject to regulation by the FDA [2].

This low cost is highly favorable in the current market. Table 2 provides details on the costs of our product’s market peers, clearly demonstrating that our device has a competitive advantage when it comes to offering an economical alerting device. The ELERT poses as a viable solution to fill a significant gap in the market for the hearing impaired.

Table 2: Cost of ELERT compared to market peers.

Assistive Solution	Description	Cost
First Alert [5]	A fire alarm designed for the hearing impaired with a built-in strobe light	\$100
Safe Awake [6]	Smoke detector with built in bed shaker	\$250
ELERT	Portable, haptic alerting aid	\$~15

DISCUSSION

Currently, the device can alert the wearer to the standard high-frequency temporal-three sound for smoke alarms and the standard high-frequency temporal-three sound for fire alarms. Once these alarms are stopped, the device continues to haptically alert the user for a few seconds. While our device currently targets fire-related emergency alerting, it has the potential to offer users alerts to a wide range of auditory stimulus. This could allow for the user to customize their device to respond to particular auditory signals, such as classroom bells, an infant crying, dog barking, or work-related alert-sounds. We would also like to explore alternative designs for the device, allowing users to wear the device in more intuitive and comfortable ways. This could take the form of a haptic necklace or other wearables. Our device has proven its viability to compete with current market solutions and has the potential to become a customizable wearable solution, supporting the hearing impaired in their everyday life.

REFERENCES

- [1] V. Ziavras, “Low frequency fire and smoke alarms: NFPA,” *National Fire Prevention Association*. January, 2021
- [2] “General Wellness: Policy for Low Risk Devices” U.S. Food and Drug Administration. September, 2019
- [3] “Fire safe and sound - fitchburgtechnologyneighborhood.com.” 2021
- [4] “Vibrotactile threshold measurements at the wrist using parallel vibration actuators,” *ACM Transactions on Applied Perception*. September, 2022
- [5] “First Alert Hardwired led Strobe Light Smoke Alarm with 10-year sealed battery - 7020BSL (1038335),” *First Alert Store*. February, 2023
- [6] “SafeAwake intermittent bed Shaker,” *SafeAwake*. February, 2023

DEVELOPMENT OF A NOVEL ANIMAL MODEL FOR OSTEOCHONDritis DISSECANS: A RADIOFREQUENCY ABLATION APPROACH

Kosisochukwu Ogonna-ukuku (1), Boyuan Liu (2),
Kristine Fischenich (3), Virginia L. Ferguson (1,2)

(1) Biomedical Engineering Program, University of Colorado Boulder, Boulder, CO, USA
(2) Department of Mechanical Engineering, University of Colorado Boulder, Boulder, CO, USA
(3) Department of Orthopaedics, University of Colorado, Anschutz Medical Campus, Aurora, CO, USA

INTRODUCTION

Osteochondritis dissecans (OCD) is an acquired focal knee disorder that occurs in the secondary physis and adjacent subchondral bone in distal femur. The resulting tissue necrosis ultimately can result in partial joint destruction and early degenerative arthritis [1]. Imaging techniques have improved clinical diagnosis of OCD, but a lack of animal models that adequately replicate OCD makes further advances challenging. Existing models frequently involve acute damage to the articular cartilage rather than the underlying bone. These models mimic a focal cartilage defect and do not capture the unique presentation of OCD, which includes cartilage and underlying bone necrosis. Here, we propose to use radiofrequency ablation (RFA) (Fig. 1A) of subchondral trabecular bone, thereby generating a highly controlled tissue necrosis that can precede articular cartilage damage. We propose that this novel approach will enable a translational animal model of OCD to evaluate pathogenesis along with modalities for early detection and treatment.

understand the thermal necrosis during RFA in the knee joint, we seek to develop an ex-vivo RFA experiment, in which by defining power and time inputs we can generate a controlled volume of thermally damaged subchondral bone tissue to guide the development of a novel animal model of OCD. Using these experiments, we aim to demonstrate the efficacy of RFA to generate focal tissue necrosis in subchondral trabecular bone to, later, demonstrate OCD-like outcomes in a live, large animals.

METHODS

For this study, we selected swine models due to the suitable size of the pig's knee joint for conducting RFA and the similarity of the bone, cartilage, and vascular architecture of the distal femur to juvenile human subjects [2]. We designed an ex-vivo ablation experiment in porcine condyle tissue with a commercial RF generator (Medtronic plc) (Fig. 1B). Briefly, fresh cadaveric porcine distal femurs were collected from a local abattoir. An RFA probe (17-gauge, 5 mm active tip) was inserted from the non-loading region of the femoral medial condyle through a hole (slowly drilled by a 1/16-inch drill bit to avoid thermal damage from friction) to a depth that is determined by a computed tomography image of each joint and which is guided by our computational finite element model described below. The probe was connected to the RF generator and applies the RF signal to induce resistive heat thus creating ablation. An in-house fabricated grounding pad (10 mm x 10 mm) was placed on the side of the condyle close to the probe. This custom-designed grounding pad included aluminum foil at the outer layer to connect to the RF generator by wire and a piece of gauze pad at the inner layer that connected the grounding pad contact to the curved condyle surface. An electrode gel (Parker Laboratories, Inc.) applied to gauze pad: 1) adhered the aluminum foil-gauze pad and the gauze pad-condyle connections and 2) enabled electric conduction between the sample and the grounding pad.

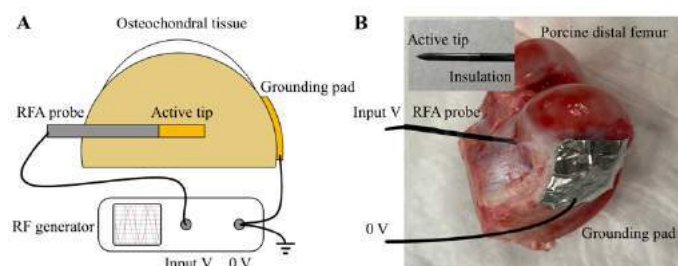


Figure 1: A) Schematic of a radiofrequency ablation system. B) Ex-vivo RFA experimental setup of a porcine condyle tissue.

RFA is commonly used to treat a range of conditions affecting soft tissues. The available protocols and guidelines of clinical RFA apply to human tissue that lacks the structural complexity of bone. Thus, to

RESULTS

To date, we established an experimental setup that will enable us to ablate a controlled region of bone and marrow, with minimal damage to the overlying articular cartilage. We aim to use this experimental setup to optimize experimental parameters and demonstrate proof-of-concept for a novel large animal model of OCD.

In our ongoing studies, we will first conduct experiments that verify our experimental setup and compare results to those in our established computational model. A small RF signal will be sent from the generator to detect the resistance of the whole circuit. We will vary the size and the location of the grounding pad and record the changes in the measured resistance. In our previous simulations, we observed that the grounding configuration have a significant influence on the ablation region. Thus, our experiments will measure the voltage differences between the probe and the different locations of the grounding pad. This process will enable us to determine if the grounding design is sufficient to dissipate the electric current across the whole region and prevent unwanted burning on the condyle surface.

We will next conduct a series of ex-vivo RFA experiments by varying the input voltage to induce different regions of thermal necrosis in the distal femoral condyles from porcine knees. The temperature spread of the tissue will be monitored by thermal probes inserted at different locations of the condyle. Assuming subchondral bone thermal necrosis when temperatures exceed 50 °C [3], we will estimate the necrotic lesion size from the measurements. After the experiments, the tissue will undergo formalin fixation for 14 days. We will employ histology to assess cell death and tissue degradation and compare the size of damaged regions with computational models using the same parameters.

Additional to the experiments, our team has created a computational finite element model based on actual tissue geometry from an X-ray microscope scan of porcine subchondral bone (Fig. 2A). The model simulated heat dissipation during RFA in one-half of the femoral medial condyle (i.e., to reduce computational cost), where articular cartilage, subchondral bone plate, and subchondral cancellous bone were separated and subchondral cancellous bone and marrow were homogenized. A cylindric electrode tip model used in the experiment (17-gauge probe, 5 mm active tip) was included to apply RFA input and a 10 mm x 10 mm pad was placed on the side of the condyle to apply zero voltage grounding boundary condition (Fig. 2B).

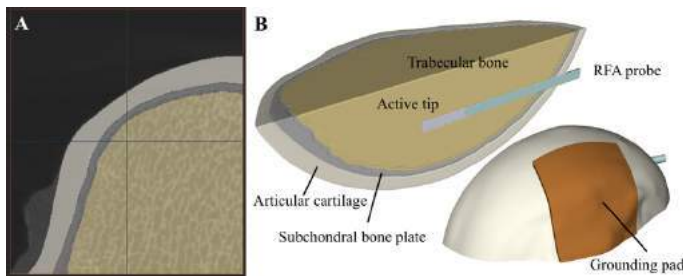


Figure 2: Simulation of RFA in porcine subchondral bone. A) X-ray microscope scan of a porcine femoral medial condyle. B) Reconstructed model of the scanned volume that includes the RFA probe and grounding pad.

Temperature contours of the tissue were plotted to evaluate for thermal necrosis. These initial model inputs will guide selection of optimized inputs (voltage and time) for experiments. Initial simulations were performed with different input voltages were run (10 V, 15 V, and 20 V; 10 mins of heating) to evaluate thermal spread from RF ablation resistive heating using coupled thermal-electrical analysis. An

additional simulation with 15 V input for 20 mins was run to evaluate temperature stability during RFA. Proper material properties and other boundary conditions including body temperature (37°C) were set. Varying the input voltage showed that RF ablation generated maximum internal tissue temperatures of 48.3, 61.8, and 81.1 °C. We observed that the 15 and 20 V inputs generated necrotic lesions with radii of 8 and 15 mm, respectively (Fig. 3A), with the size of thermal necrosis induced by 15 V close to the size of necrosis found in pigs with OCD [4].

With a 15 V input, the peak temperature near the RFA tip was identical (61.8 °C) at 10 min and 20 min time points (Fig. 3B) of the simulation. We believe it is sufficient to run the simulation and future RFA experiments for 10 mins with 15 V input to trigger OCD-like necrosis.

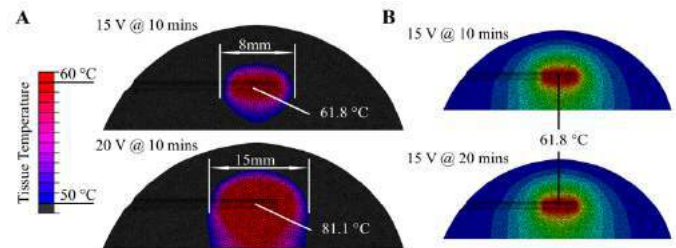


Figure 3: RFA simulation results. A) 15 V and 20 V inputs generated necrotic lesions with radii of 8 mm and 15 mm at the end of the ablation (10 mins). B) Peak temperature near the RFA tip remains the same after 10 mins of ablation.

DISCUSSION

Simulation of a porcine femoral medial condyle model was used to predict thermal spread in subchondral tissue, including trabecular bone and marrow, during RFA. Our results showed that by varying power and time, we can generate a controlled volume of thermally damaged tissue that compares with the volume of necrotic tissue in OCD. Our ex-vivo experiments are ongoing. We are collecting temperature data *in situ* to estimate the thermal necrotic lesion sizes. We will analyze cell death and tissue degradation. These experimental results will help us to 1) validate the simulation model and 2) determine if we can induce the unique presentation of OCD tissue damage using this novel RFA approach.

Using the simulation results, we selected the input voltage and run time for our proposed experiments. Combining these two parameters, our approach will allow us to develop a novel, thermal injury model of OCD to allow for the eventual study of disease progression and evaluation of novel therapeutic approaches. Further, our study can provide guidance to other RF ablation procedures such as removal of tumors in the musculoskeletal system.

ACKNOWLEDGEMENTS

We are grateful for the funding support provided for this research by CCTSI TM-Pilot FY18.220.012, which is supported by NIH/NCATS Colorado CTS Grant Number UL1 TR002535. We thank Robert Behnke and Medtronic Surgical team for loan of the RFA system.

REFERENCES

- [1] Uozumi, H et al., Am J Sports Med, 37(10):2003-2008 (2009).
- [2] Tôth, F et al., J Orthop Res, 37(10):2130-2137 (2019).
- [3] Eriksson, AR et al, J Prosthet Dent, 50(1):101-107 (1983).
- [4] Ytrehus, B et al., Vet Pathol, 44(4):429-448 (2007).

ULTRAPORTABLE EXTRACORPOREAL MEMBRANE OXYGENATION MACHINE

D. Kurtz (1), L. Windover (2), C. Davies (2)

Faculty Advisor(s)

C. Davies (2)

- (1) Department of Chemical Engineering, Queen's University, Kingston, Ontario, Canada
(2) Department of Mechanical and Materials Engineering, Queen's University, Kingston, Ontario, Canada

INTRODUCTION

Extracorporeal membrane oxygenation (ECMO) machines are artificial lung devices used to support patients with significant lung damage, who cannot be kept alive with conventional lung ventilators in an intensive care setting [1]. In the aftermath of COVID-19, the need for such artificial lung mechanisms has been emphasized. ECMO is often a vital treatment for patients suffering from acute respiratory distress, hypothermia, cardiac arrest, and other life-threatening conditions. Recent studies have shown that ECMO improves patient outcomes drastically (36%) for patients that experience a cardiac arrest when it is applied within 15 minutes of the cardiac arrest [2]. Current ECMO machines are expensive and complex to operate, so adoption is mostly limited to larger hospitals, keeping them inaccessible for large portions of the population.

The creation of a portable artificial lung would allow for first responders needing to transport patients to begin blood oxygenation with ECMO immediately. This year, the Queen's Biomedical Innovation Team (QBiT) has undertaken the task to develop the Ultraportable ECMO machine, which will be more affordable, robust, and suited for use in a wide range of conditions. Design aims were assessed for use in hospitals and clinics that do not possess the infrastructure for traditional ECMO, or with pre-hospital critical care teams in the field.

The current ECMO machine market is worth \$740.85 million globally and is expected to grow at a 5.74% compound annual growth rate [3]. QBiT's design is anticipated to sell for approximately \$4,140.50, far lower than market alternatives. Demand for inexpensive, compact ECMO remains high, especially in underserved healthcare settings.

PRODUCT DESIGN

In ECMO, the interconnectedness between the blood and oxygen streams allows for passive diffusion of oxygen (O₂) and carbon dioxide (CO₂). The O₂ gradient will flow from the pure O₂ gaseous stream into the desaturated blood stream, while the CO₂ gradient will flow from the

blood stream into the gaseous stream. The design of the gas transfer system will maximize gas exchange. Sweep gas of 100% O₂ will be supplied through the membrane oxygenator. At a minimum, the sweep gas flow rate should be equal to the blood flow rate. Increasing the sweep gas flow rate will increase CO₂ elimination if necessary. The device will use custom triply periodic minimal (TPM) surfaces, which minimize the spanning area between boundaries and have a continuous shape. They function as a membrane through the laminar mixing and subsequent recombination of the fluid. Compared to a hollow fiber design membrane, TPM surfaces increase the O₂ transfer capabilities by up to 69.8% [1]. This significant increase is possible because TPM surfaces disrupt the laminar boundary layer, the main source of diffusional resistance in hollow fiber membrane oxygenators. The membrane is printed using VeroClear resin and coated in silicone to increase biocompatibility and provide a smooth outer coating. The TPM surface divides the 3D structure into two separated, interconnected channels. These channels possess a high surface area to volume ratio, allowing two flows to pass through simultaneously [1].

The design of the case and internal components of the ECMO device are crucial to the ability of the device to perform as needed, as it must be lightweight, impact and weather resistant and portable. The case and internal components must also not impede the life-saving functions of the device and allow for its operation in any conditions. QBiT has opted to use a wheeled PelicanTM hard case to contain the components such as the dissolved oxygen (DO) and pH sensors, along with semi-rigid foam to cushion any impact, as seen in Figure 1.

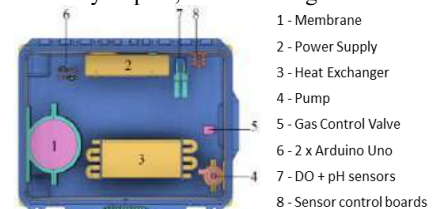


Figure 1: Ultraportable ECMO casing and components.

3D-printed mounting brackets and supports are used to maintain the position of each component in the case, and medical grade tubing is used to ensure proper blood flow through the device.

The electronic components within the Ultraportable ECMO machine perform three main tasks: control blood flow, blood temperature and gas pressure. These tasks facilitate the oxygenator by maintaining O₂ pressure while passing blood through the membrane at the correct temperature and rate for safe human use. The electrical sub team is responsible for designing, implementing, and testing all the included electronics. This includes sourcing appropriate parts, creating a power grid and programming control functionality.

The implementation of the electronics for the Ultraportable ECMO machine is far smaller and less expensive than currently available ECMO machines. Microcontrollers are organized in a two-tiered hub and spoke network, where the lowest level nodes represent sensors and actuators. An Arduino Nano was chosen as the central microcontroller and handles two-way communication between the nodes and the user interface using the I2C protocol. Once the user input has been gathered by the interface and communicated to the nodes, the node controller autonomously uses live sensor data to adjust its actuator output to achieve the target input. Each node runs on its own power rail, generated by a 120 AC-DC converter, and a total of 400 Watts is provided to the system. Shunt regulators are used as they only require three parts, making them small, cost effective, and easy to design in-house.

Blood flow is monitored with an in-line flow sensor. As the fluid flows past a turbine, the speed at which the turbine spins is proportional to the flow rate. The flow is controlled using a Genedey 12V ½ inch brushless centrifugal pump. The pump possesses a 5 m static head and can exceed the optimal blood flow rate for oxygenation, which was determined to be 0.2-5 L/m. Blood temperature is monitored with a non-invasive infrared sensor and temperature can be increased with heating pads, which are fitted to a heat-conducting pipe. The heating element follows an actuator model, through which temperature increases result from increases in the microcontroller duty cycle. The O₂ concentration in the blood is measured with a galvanized steel probe, while the CO₂ concentration is calculated from pH, as measured with a pH probe. The pressure of the gas inside the oxygenator can then be adjusted with a solenoid gas valve. The duty cycle and valve opening size are directly proportional, so as the microcontroller duty cycle increases, the valve will open, with gas influx from the compressed O₂ tank increasing the pressure within the system. Python is used to create a display monitor to organize data collected by an Arduino Nano, as seen in Figure 2.

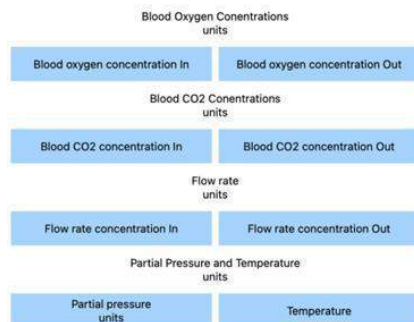


Figure 2: Monitor displaying the collected ECMO data.

The display includes the output temperature [°C], blood flow rate [L/min], blood oxygen saturation [%], and CO₂ concentration [%] displayed to three significant digits. The display allows for real-time monitoring of the sensor data and efficient analysis of a patient's vitals.

BUDGET & MARKET ANALYSIS

The total design budget for the Ultraportable ECMO machine is \$3,185. The cost of materials for the prototype is \$2,475, including all parts necessary for assembly. Additionally, a cost of \$400 is associated with the building of the prototype, and the remaining \$310 is budgeted for testing. The current markup on medical devices is very high, reaching up to 50%. QBiT estimates that the Ultraportable ECMO machine could sell at a 30% markup, or \$4,140.50 [4].

The Covid-19 pandemic has highlighted both the value and scarcity of respiration devices for treating respiratory illnesses in medical emergencies [1]. The target market for the Ultraportable ECMO machine are use in EMS vehicles or remote locations. Studies highlight the benefit of ambulatory respiratory assistance via ECMO machines, with a study from Columbia University Medical Center finding that 80% of patients who received a successful lung transplant were supported by an ECMO machine during ambulatory transport [5]. It is clear that access to ECMO machines is crucial to positive clinical outcomes. The ECMO market is expected to be dominated in North America, with a potential market size projected to grow significantly from 2023 to 2028, reaching multimillion USD by the end of the forecasted period [6].

ACKNOWLEDGEMENTS

We thank the members of the QBiT for their work on this project and review of this abstract. We thank SparQ Queen's for permitting use of their manufacturing equipment, Dr. Ramiro Arellano for his medical expertise, and Dr. Claire Davies for her technical expertise and support as QBiT's faculty advisor. We are grateful for funding from Dean Kevin Deluzio, the Sci'73 foundation, and Makers Making Change to support QBiT's design efforts.

REFERENCES

- [1] F. Hesselmann *et al.*, "Three-dimensional membranes for artificial lungs: Comparison of flow-induced hemolysis," *Artif. Organs*, vol. 46, no. 3, pp. 412–426, 2022, doi: 10.1111/aor.14081.
- [2] "The Role and Impact of Extracorporeal Membrane Oxygenation in Critical Care - PMC," <https://www.ncbi.nlm.nih.gov/pmc/articles/PMC6027718/> (accessed Jan. 08, 2023).
- [3] R. A. Fowler *et al.*, "Critical care capacity in Canada: results of a national cross-sectional study," *Crit. Care*, vol. 19, no. 1, Art. no. 1, Dec. 2015, doi: 10.1186/s13054-015-0852-6.
- [4] G. Nieves, "What Is the Markup on Medical Devices?," *LAC Healthcare Solutions*, Jan. 02, 2021, <https://www.lac.us/blog/what-is-the-markup-on-medical-devices/> (accessed Jan. 06, 2023).
- [5] H. Peng, F. Gao, and W. Hu, "Design, modeling and characterization of triply periodic minimal surface heat exchangers with additive manufacturing," Aug. 2019.
- [6] "Artificial Lung Market Size in 2023 | Overview with the Best Scope to New Players, Trends, Benefits & Opportunities till 2028," *MarketWatch*, <https://www.marketwatch.com/press-release/artificial-lung-market-size-in-2023-overview-with-the-best-scope-to-new-players-trends-benefits-opportunities-till-2028-2022-11-16> (accessed Jan. 07, 2023).

THE EFFECTS OF PROGERIA ON CENTRAL VASCULAR TISSUE, BLOOD FLOW, AND BLOOD PRESSURE

L. Roukoz (1), T. Hopper (1), S. Murtada (2), J. Humphrey (2), C.A. Figueroa (1)

(1) Biomedical Engineering, University of Michigan, Ann Arbor, Michigan, United States
(2) School of Engineering and Applied Science, Yale University, New Haven, Connecticut, United States

INTRODUCTION

Progeria shows an advanced aging phenotype from a young age. It can affect the central vasculature in different ways, inducing changes in thickness, cardiac output, pressure, and stiffnesses compared to healthy controls. These alterations can increase risk of cardiovascular disease, including stroke and heart failure [1]. In this project, we use a mouse model of progeria [2], biomechanical phenotyping to characterize aortic tissue, microCT imaging, flow and pressure data, and computational modeling techniques to study cardiovascular alteration in three progeria mice compared to three wild type controls.

METHODS

Mice were anesthetized to measure flow and characterize aortic anatomy. Doppler ultrasound measurements were taken at the carotid arteries, iliac arteries, and ascending aorta. Mice were placed supine in a microCT scanner to image the aorta and main branches. Pressure was assessed via tail-cuff, while mice were awake. Mice were then sacrificed, and biaxial tissue testing was performed [3] to measure vascular thickness and anisotropic (circumferential and axial) stiffness at the following locations: ascending thoracic aorta (ATA), proximal and distal descending thoracic aorta (pDTA and dDTA), supra-renal abdominal aorta (SAA), and infrarenal abdominal aorta (IAA).

A 3D model was built of the aorta and main branches by generating centerline paths and 2D contours to represent the luminal diameter. Aortic diameter was extracted from these models at the previous 5 locations to linearize in vivo stiffness and thickness values [4]. Values at these 5 locations were then linearly interpolated over the entire aorta and branches.

For the hemodynamic fluid-structure interaction (FSI) analysis, aortic inflow waveforms were prescribed from the ultrasound data. Three-element Windkessel models, consisting of a proximal resistance, a distal resistance, and a compliance, were prescribed at each vessel outlet to represent the distal vasculature. Resistance and compliance

values were iteratively adjusted until computed tail cuff pressure values matched experimental values. Given that flow and anatomy were assessed under anesthetized conditions, but cuff pressure under awake conditions, anesthetized values of pressure were estimated by scaling measured systolic and diastolic pressure by 0.76 and 0.89, respectively. These values were obtained by studying the impact of isoflurane on pressure in wild type mice (ongoing study). Fluid structure interaction (FSI) analyses in progeria and wild type specimens were performed using the open-source software CRIMSON [5].

RESULTS

Vessels in progeria mice are thicker than those in wild type controls, while also having a different pattern of thickness. In wild type mice, the thickness across the entire aorta is relatively constant, while progeria mice have a larger thickness in the ATA, and then relatively constant thickness throughout the rest of the aorta (Fig 1). Circumferential material stiffness is smaller throughout the aorta in the progeria mice, except for the ATA, where it is comparable to the wild type (Fig 2).

Subject-specific flow waveforms were prescribed at the ATA from the available Doppler ultrasound data for progeria and control mice. Values of three-element Windkessel models for each outflow branch were iteratively adjusted until a good match (e.g., discrepancies smaller than 10%) was achieved between simulation and data. Specifically, between pressure computed at the tail and cuff measurements, as well as computed and measured mean iliac flows (Fig 3).

In the distal vasculature, progeria mice have larger resistances and compliances than wild type mice.

Wild type and progeria mice have similar flows in the ATA and DTA. However, due to the smaller caliber of the DTA in the progeria mouse, blood velocities are noticeably larger (Fig 4).

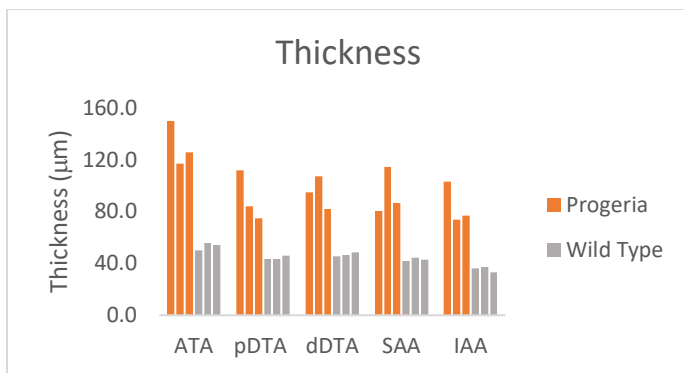


Figure 1: Aortic thickness (μm) for progeria (Orange) and wild type mice (grey).

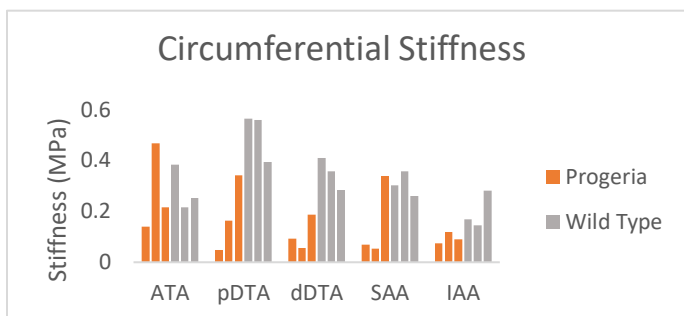


Figure 2: Aortic circumferential stiffness (MPa) for progeria (Orange) and wild type mice (grey).

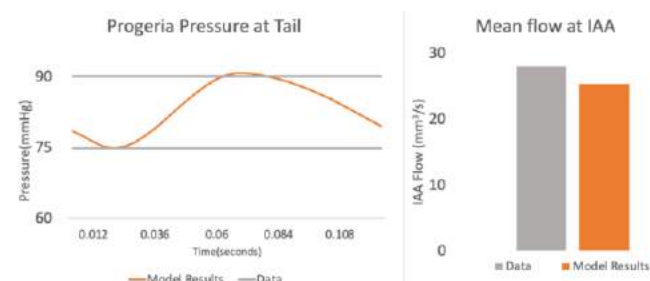


Figure 3: Validation of computational results against available experimental data. Left: pressure cuff data. Right: Mean iliac flow data. Pressure and flow values to indicate validity of the progeria mouse model

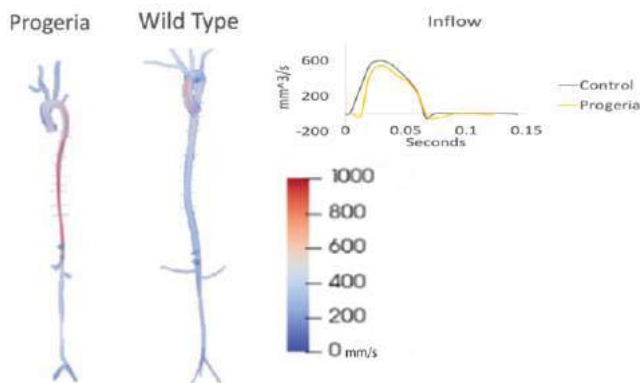


Figure 4: Volume render of blood velocity from a progeria mouse (left) compared to a wild type of mouse(right). Insert shows aortic inflow waveforms for each specimen.

Discussion

Aging is known to affect the stiffness of heart and blood vessels. Over time, elastin fibers degrade and are slowly replaced by collagen, leading to an overall increase in stiffness.[6] Progeria has an extreme ageing phenotype which shows different symptoms than those of simple aging. To quantify some aspects of the exacerbated aging in progeria, we used a rich amount of data on anatomy, flow, pressure, and tissue stiffness, together with the hemodynamics modeling software CRIMSON.

The results show that progeria mice tend to have thicker walls on their central vasculature. This replicates the thickening known to occur with aging in wild type mice [8]. Patterns of stiffness, however, show a different distribution compared to aging mice. Circumferential stiffness, except for the ATA, were all smaller than in wild type mice [2].

Computational modeling, informed by experimental data, can shed light into disease patterns, as well as quantify markers of disease progression that are not attainable through experiments alone. Computational modeling may also facilitate using data acquired under certain physiological conditions, and to combine it with data acquired under different physiological conditions (e.g., anesthetized versus awake).

Some limitations of this study involve accurate delineation of the aortic geometry from the microCT data. Furthermore, parameter estimation is a time-consuming process, requiring many iterations on the Windkessel values to match the available data on flow and pressure.

Progeria shows an advanced ageing phenotype, while also presenting differences compared to normal ageing, especially in central vascular stiffness. While stiffness increases with age in wild type mice, progeria mice show decreased values of material stiffness in most regions of the aorta, except for the ATA. This study is the first step towards understanding alterations in progeria relative to both aged-match wild type as well as normal aging subjects. Future work will extend into studying differences in heart function in these mouse models of progeria.

ACKNOWLEDGEMENTS

This research was supported, in part, by grants from the NIH (RD1 HL105297)

REFERENCES

- [1] Olive, M et al., 2010, doi:10.1161/ATVBAHA.110.209460
- [2] Murtada SI. et al, 2020, doi:10.5061/dryad.mcvdncjw9
- [3] Ferruzzi J et al, 2013, doi:10.1007/s10439-013-0799-1
- [4] Baek, S et al., 2007, doi: 10.1016/j.cma.2006.06.018
- [5] C. J. Arthurs, et al., 2021. doi:10.1371/journal.pcbi.1008881
- [6] Horn, M. Trafford, A. 2016. doi:10.1016/j.yjmcc.2015.11.005
- [7] Hopper S. et al, 2021, doi: 10.3389/fphys.2021.746796
- [8] Cuomo F, et al, 2019, doi:10.1098/rspa.2018.0076

A DIGITAL INCENTIVE SPIROMETER FOR AIDING LUNG RECOVERY POST-SURGERY

Isabella T. Mirro (1), Yi-An Hsieh (1), Jackson C. Dooley (1), Parth K. Mody (1), Josh Freedman (1,2)

Faculty Advisor(s)

David F. Meaney (1), Jeffrey Babin (2)

(1) Bioengineering, University of Pennsylvania, Philadelphia, Pennsylvania, USA
(2) Engineering Entrepreneurship, University of Pennsylvania, Philadelphia, Pennsylvania, USA

INTRODUCTION

Postoperative pulmonary complications (ie. pneumonia, respiratory failure, etc.) occur in ~5% of the 20M inpatient surgeries in the United States and cost the healthcare system over \$3.42 billion annually.^{1,2} The current standard of care (SOC) to prevent postoperative pulmonary complications (PPCs) includes incentive spirometry, which involves patients performing breathing exercises with an incentive spirometer (IS) for 5 minutes every 1-2 hours post-operation under the guidance of a nurse. Incentive spirometry has been shown to reduce the risk of PPCs and healthcare costs, with studies reporting shorter hospital stays, decreased time on ventilators, and lower healthcare costs (by over 500\$ in certain subgroups), in patients that used an IS.^{3,4}

Still, there exist multiple shortcomings of the current ISs used in hospitals. Current devices do not enable providers to accurately and efficiently collect patient-use data. Nurses and physicians are unable to reliably track patient progress and adherence, resulting in ballpark discharge decisions and extra time spent sitting with patients as they complete their IS exercises to ensure adherence and proper use. This creates a significant time burden for nurses keeping them from performing other crucial tasks.⁵ Furthermore, the lack of data collection and low adherence has prevented research on the clinical benefit of incentive spirometry and its impact on patient recovery trajectories.⁶

With more than 19 million ISs prescribed annually in the United States, there exists a need for a device that can 1) accurately collect patient data, 2) improve patient adherence, 3) reduce nurse time burden, and 4) is scalable to personalized treatment applications.⁷

PRODUCT DESIGN

We have designed the inSPIRE digital incentive spirometer with an integrated mobile app to increase adherence to IS exercises, reduce the time burden for nurses, and provide clinicians with more, higher quality patient recovery data (Figure 1). The inSPIRE device utilizes a digital sensor to measure airflow in the device, which enables the collection of patient use data (Figure 1a). A microcontroller with

Bluetooth capability then continuously sends user data to the integrated app accessible to both patients and nurses (Figure 1b). The physical device is made up of 2 components: (1) a detachable and disposable mouth-piece and (2) the connected housing that contains the airflow tube and the electronic components of the device (rechargeable battery, microcontroller, and digital sensor).

To validate our design for measuring airflow, we created a prototype of our airflow chamber with our digital sensor and connected a large syringe to the opening where a patient would be inhaling from. By adding varying weights to pull down on the syringe plunger with constant velocity, we created known and constant airflows in the chamber that our sensor could measure. After using our sensor to measure various airflows, we performed a linear regression on the air flow rates our sensor measured versus the actual airflows. This yielded a slope of 0.999 and an R^2 of 0.989, suggesting that our design accurately measures air flow (Figure 1c).

inSPIRE was designed with incentivizing features and to be easy-to-use for patients. With inSPIRE, patients perform breathing exercises as they would with current ISs while exercise data is automatically stored and displayed on the integrated mobile app. Training modules and real-time visual cues on the app allow patients to easily complete exercises correctly. Patients can track the completion of their daily prescribed exercises with stored data, and a reminder system will notify patients of upcoming and missed exercises for the day. We also gamify the completion of exercises through different games in the app to make completing exercises easier (Figure 1b.). The compact handheld design will also make handling the device easy, with all of these features ultimately improving adherence and thus reducing the risk of PPCs.

Clinicians will benefit from features aimed at streamlining hospital workflows. The app will make patient-use data available to clinicians such that nurses can monitor the adherence of all their patients on one remote system. This will significantly reduce the time nurses spend monitoring patients and ensuring exercise completion. Clinicians will also be able to access quantitative patient lung recovery data based on

exercise performance through the app, enabling informed decisions regarding hospital discharge, ventilation, and other interventions.

Looking forward, inSPIRE’s applications may extend beyond post-surgery settings to include asthma, COPD, Covid, and other chronic respiratory conditions. By leveraging data collection and analysis applied to these indications, inSPIRE will create additional services and value, improving the standard of care in the pulmonary rehabilitation space. In the post-op setting, analyzing the recovery and exercise data collected from our device may enable development of patient-specific training regimens that minimize PPC risk or reveal trends that can be used to detect PPC onset early. This approach could lend itself well to elucidating trends in long-covid recovery and other indications as well.

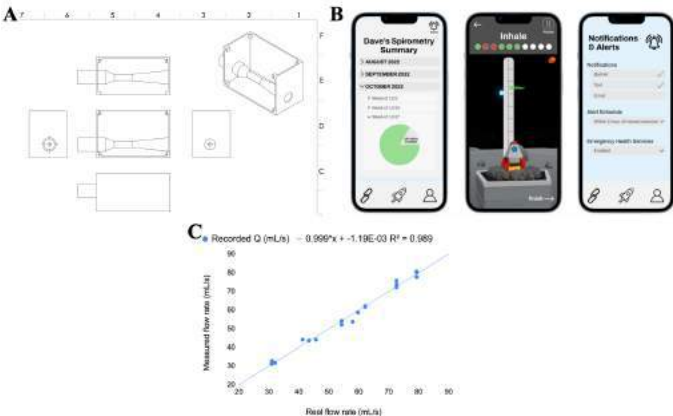


Figure 1: A) Prototype CAD design B) Mockups of mobile app tracking, gamification and reminder features C. Data from validation setup shows a strong correlation between real and measured flow rates.

Digital spirometers currently on the market measure peak expiratory flow as a measure of lung health, and some companies have developed digital breathing trainers, similar to incentive spirometers, for non-clinical use that range from \$100-\$300 (Airofit Pro, MIR Smart One, ViQure Opump). Our device is novel in that its core technology reliably measures airflow and it is catered to in-hospital incentive spirometry applications through our cost-effective, easy-to-use design.

BUDGET & MARKET ANALYSIS

Table 1: Design budget for building prototype

Item	COST PER UNIT (\$)	NUMBER OF UNITS	TOTAL COST PER ITEM (\$)
3D printing elastic material (TPE or TPU)	39	1	39
3D printing non-elastic material (PLA, clear)	24	1	24
Liquid rubber sealant	16	1	16
Screw set	9	1	9
Arduino MKR wifi 1010	39	2	78
Battery	12	2	24
Pressure Sensor	15	2	30
TFT LCD screen	20	2	40
			TOTAL COST: 260

Our revenue model will initially consist of one-time sales of the reusable main body of the inSPIRE device and recurring revenue generated from sales of the disposable mouthpieces. Current single-use incentive spirometers sold to hospitals cost on average \$4.50 per unit. We plan to sell the main body of our device for \$100 and our

mouthpieces for \$1 per patient. As the mouthpiece would be a simple injection-molded part and the main device body would be an injection molded part with a microcontroller and other basic electronics, we believe we can manufacture the components for \$0.20 and \$20 respectively. Assuming an average patient stay of five days post-surgery, there will be a turnover of approximately 73 patients per bed annually. This means that current ISs would cost hospitals \$328.5, whereas implementing our device would cost \$173 per bed annually. With this business model, inSPIRE would undercut the overall cost of current incentive spirometry programs at hospitals and reduce hospital waste.

In addition to saving on implementation costs, inSPIRE may also deliver savings to hospitals through reducing nurse monitoring time and the rate of PPCs. As incentive spirometry instruction is not a billable event for hospitals, our product which will have integrated training, set up, and monitoring of patients will save hospitals costs in nurse hours. As data analysis is used to produce predictive metrics for preventative treatment or other services, our revenue model may adapt to include a subscription to these software elements. This data could also lead to a billable event for hospitals, encouraging them to adopt our device.

The Hospital of the University of Pennsylvania (HUP) and other research hospitals that perform many inpatient surgeries will serve as our beachhead market. With a case study on HUP, which has 988 beds and an average ~70% capacity, we can achieve \$115K ARR if we fully serve the hospital with 660 devices and 48,000 mouthpieces purchased annually. Our beachhead market consists of 55 hospitals of similar size or larger than HUP (>800 beds), totalling to roughly a \$6.5MM annual market. Considering the total postoperative space in the United States and the 19 million patients currently prescribed an IS in the US, we will address a market of ~\$45MM annually, consisting of potentially 260,000 devices and 19 million mouthpieces that could be sold each year. Beyond postoperative use cases, we plan to expand to additional indications needing long term respiratory rehabilitation.

We estimate further physical device development costs to be \$25k and app development costs to be \$100k. Injection molding tooling costs for a simple piece like our mouthpiece should fall around \$15k, while tooling for the main device will be more complex and may cost \$100k. In all, we anticipate development and manufacturing preparation to cost ~\$240k. Despite costs, we hope to generate significant ROI. If by year 2 we capture 10% of our beachhead market, we will be generating \$650k in revenue with gross profits of \$520k. If by year 4 we then capture 15% of the total market, we will be generating \$7MM in revenue with gross profits of \$5.6 MM.

ACKNOWLEDGEMENTS

We are proud to have developed our technology in the Stephenson Foundation Educational Library and Bio-MakerSpace at UPenn. We feel fortunate to have access to the Penn Medicine network, as it was in collaboration with nurses and clinicians at HUP that the unmet needs in respiratory rehabilitation were identified. Our solution was developed and iterated on with feedback from stakeholders and faculty with diverse backgrounds spanning UPenn’s Engineering School, Wharton, Penn Medicine, and the Penn Center for Innovation.

REFERENCES

[1] Fernandez-Bustamante A, et al., *JAMA surgery*, 152.2: 157-166, 2017.
[2] Linde-Zwirble, W. L., et al., *Critical Care*, 14: 1-2, 2010.
[3] Liu, C. J., et al., *BMC Pulmonary Medicine*, 19: 1-8, 2019.
[4] Sweity, E. M., et al., *Journal of Cardiothoracic Surgery*, 16, 2021.
[5] Eltorai A. E., et al., *Respiratory Care*, 63.5: 532-537, 2018.
[6] Eltorai A. E., et al., *Respiratory Care*, 63.3: 347-352, 2018.
[7] Eltorai A. E., et al., *Inquiry*, 55, 2018.

AUTOMATING COLLAGEN GEL IMAGE SEGMENTATION USING DETECTRON2: AN APPLICATION OF MODERN COMPUTER VISION TECHNIQUES

Michael I. Cafiero (1), Spencer P. Lake (2), Michael A. David (3)

- (1) Computer Science, Washington University in St. Louis, St. Louis, MO, USA
 (2) Mechanical Engineering & Materials Science, Washington University in St. Louis, St. Louis, MO, USA
 (3) Orthopedics, University of Colorado Anschutz Medical Campus, Aurora, CO, USA

INTRODUCTION

The collagen gel model system can be used to study cell contraction and the impact of drug treatments [1]. Quantifying gel area change (i.e., degree of contraction) often requires manual segmentation, which is a lengthy process and prone to human-to-human variability. One possible solution to this is machine learning (ML): a predictive modeling approach that uses previous data to perform automated decisions and tasks.

An open-source ML tool that has demonstrated success for object detection and image segmentation resource is Detectron2 (Meta) [2]. Detectron2 is a next-generation computer vision platform that allows for easy training and application of modern models, such as Mask-RCNN, TensorMask, and others. A Mask-RCNN model is designed to generate instance-level segmentation, which allows for more precise identification of individual objects/instances in an image. In this study, we aimed to develop a ML model with the Mask-RCNN framework to automatically segment collagen gels and wells. (Figure 1).

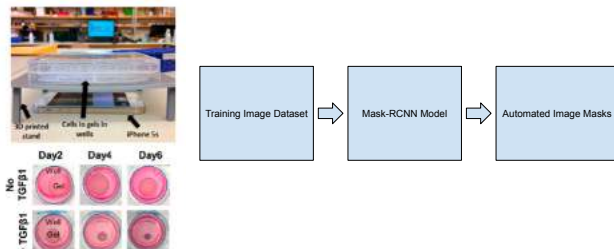


Figure 1: Gel Setup and Images (Adapted from [1]) and Automation Flowchart

METHODS

For this study, a previous database of collagen gel images was used [1]. The Detectron2 underwent training on a set of 50 randomly selected images, which were randomly selected from a total image population of ~8000 images, using an automated API script. This dataset was annotated to facilitate training using COCO (Common Objects In Context) format, a common object identification method for neural network training. Before using the COCO format, the laboratory employed binary image masking, a well-established approach for data analysis. A data pipeline (Figure 2) was constructed to obtain COCO annotations that converted binary image masks into COCO annotations via the identification of the mask perimeter, providing a scalable and efficient solution for image masks of varying shapes.

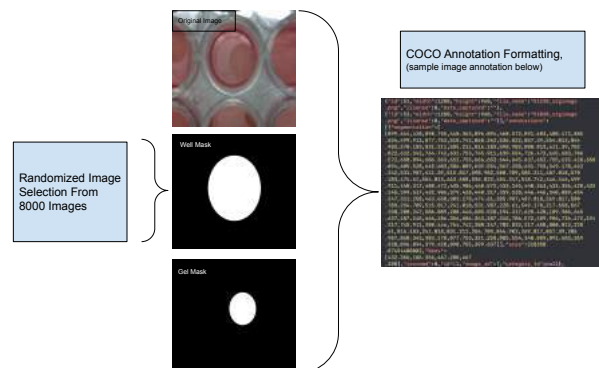


Figure 2: Preprocessing Pipeline Diagram.

For ML applications, a model requires a training dataset, and a testing dataset to validate the model on separate data that the model has not yet been exposed to. The testing dataset was also selected at random from the ~8000 image population and did not contain any images from the training data. The data pipeline facilitated the random selection, annotation, and grouping of images for both training and testing purposes.

To evaluate the model's output, we compared the human-generated mask with the computer-generated mask to calculate the Dice score, which quantifies the similarity between the two masks. We also judged the success of the training process using total loss and accuracy. Total loss is a metric for error that quantifies the performance of the model at each level of optimization. The other key training metric, accuracy, measures the percentage of correctly identified images.

The training procedure was executed for 1000 iterations, with a learning rate of 0.00025 as recommended by the Detectron2 documentation. The standard Detectron2 framework was used for training, with the majority of the initial hyperparameters employed. A Google Colab environment was used for computation with an NVIDIA V100 GPU.

RESULTS

Training of the model took approximately 7 minutes and 30 seconds, without evidence of overfitting. Total loss conformed to a negative logarithmic curve, which is standard for neural networks (Figure 3). Additionally, the accuracy of the Mask RCNN steadily increased during training, until it reached a plateau towards 1000 iterations.

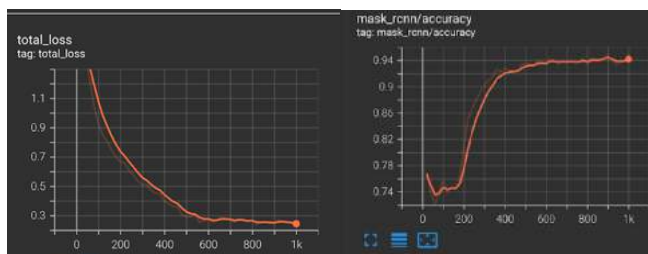


Figure 3: Total loss and accuracy graphs of model training

Results were evaluated on a separate testing dataset containing 100 images randomly selected from the same population as the training dataset (~8000 images). For the well segmentation process, the model yielded a Dice score of 0.989 across the 100 images. Visually, the model produced an accurate trace of the well, which can be seen in purple in the image (Figure 4). Detectron2 provides an easy visualization method, which plots the mask against the original image with a randomized color, as well as the bounding box.

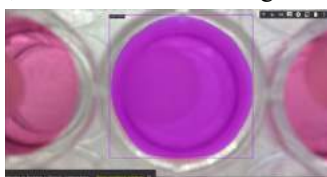


Figure 4: Sample result of well segmentation.

The gel recognition model also performed well, with an average dice score of 0.987 across 100 images. The model precisely identified and segmented the collagen gels within each of the wells, which is a more challenging task to perform visually (Figure 5).

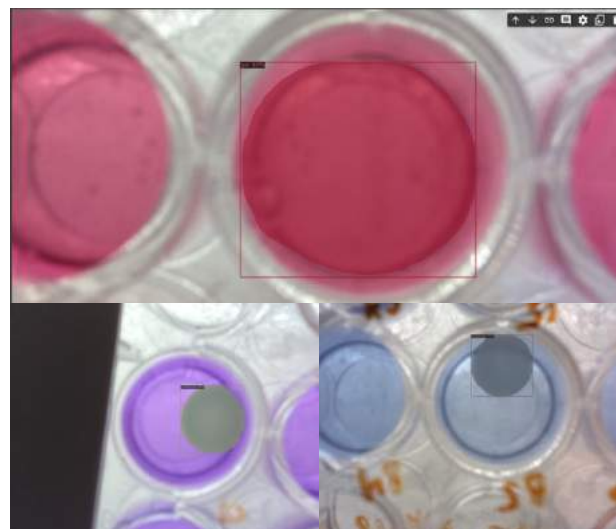


Figure 5: Examples of uncontracted (top) and contracted (bottom) gels and resulting ML gel segmentation.

DISCUSSION

Our results show that Detectron2 can achieve high accuracy and precision in segmenting culture plastic wells and collagen gels, making it a valuable tool for researchers. This technique can be used for future lab automation, and will enable efficient analysis for thousands of gels and their response to different treatments using this *in vitro* model system.

Additionally, the model can be optimized to accurately segment uncontracted collagen gels, which can be difficult to identify by human eye as opposed to contracted gels. Detectron2 also supports multi-object detection, which can be used on images containing several object types, making it a scalable solution for more complex segmentation needs.

To increase practicality, the data preprocessing pipeline can be further developed to support conversion from other annotation types and prevent annotation by hand where possible. Additionally, the model should be further tested to determine its practicality for non-circular object types and robustness. To conclude, this study demonstrates the feasibility of Detectron2 computer vision to automate common lab tracing and segmentation techniques and highlights its ease of use and customizability.

ACKNOWLEDGEMENTS

The authors acknowledge the NIH for funding (R01 AR071444).

REFERENCES

[1] David+, Frontiers, 2022; [2] Wu+, Detectron2, 2019

TRACKING OF PEDICLE SCREWS USING EXTENDERS AND LENTICULAR ARRAYS

**Alicia C. Repka (1), Jacob Sandler (2), Halle Lowe (2), Peter Brunner (3), Robert B. Pless (4), Camilo A. Molina (3)
Eric C. Leuthardt (3), Carl D. Hacker (3), Daniel W. Moran (1), Guy M. Genin (2)**

(1) Biomedical Engineering, Washington University in St. Louis, St. Louis, Missouri, United States
(2) Mechanical Engineering, Washington University in St. Louis, St. Louis, Missouri, United States
(3) Neurosurgery, Washington University School of Medicine in St. Louis, St. Louis, Missouri, United States
(4) Computer Science, George Washington University, Washington, D.C., United States

INTRODUCTION

Spinal correction surgeries require precise placement of pedicle screws in that connect metal bars to vertebrae. Tracking these screws is critical for the efficient and accurate completion of these surgeries, and is essential for inserting patient-specific rods that connect between pedicle screws and determine the patient's final spine disposition. However, this is challenging because the screws lie out of plain sight of the surgeon, and because their orientations are difficult to track. Our goal was therefore to create a simple, user friendly system which obviates tracking issues caused by occlusion of pedicle screws, streamlines the rod-shaping process for surgeons, lowers the total amount of time spent operating, and facilitates better patient outcomes.

We propose to achieve this using removable extenders to pedicle screws that enable the surgeon and the operating room imaging system to identify the positions of the screw ends, and lenticular arrays attached to the ends of these extenders to enable a single camera to identify the three-dimensional (3D) orientation of these extenders.

BACKGROUND

Lenticular Arrays Lenticular arrays reflect different colors when viewed from different directions in a relationship known as the hue response function (HRF). Using the observed color of a given lenticular array, along with its HRF, it is possible to determine its orientation about its major axis[1]. By creating a fiducial marker with two planar lenticular arrays with perpendicular major axes, we propose to determine the orientation and position of the marker in space using complementary information from each of the arrays.

Camera Calibration To identify the camera pose from the lenticular markers, a fully defined system can be solved by calculating the rotation and translation matrix of the lenticular markers according to the five pose constraints outlined in [2]:

$$\mathbf{R}\vec{n}_{hue1} \cdot \vec{r}_1 = 0 \quad (1)$$

$$\mathbf{R}\vec{n}_{hue2} \cdot \vec{r}_2 = 0 \quad (2)$$

$$\mathbf{R}(C_2 - C_1) \cdot (\vec{r}_1 \times \vec{r}_2) = 0 \quad (3)$$

$$(\mathbf{R}C_1 + \mathbf{T}) \times \vec{r}_1 = \vec{0} \quad (4)$$

$$(\mathbf{R}C_2 + \mathbf{T}) \times \vec{r}_2 = \vec{0} \quad (5)$$

where rays \vec{r}_1 and \vec{r}_2 are the rays from the camera to the lenticular marker, \vec{n}_{hue1} and \vec{n}_{hue2} define the unique planes corresponding to the observed hue of the lenticular markers, \mathbf{R} is the rotation matrix, \mathbf{T} is the translation matrix, and C_1 and C_2 are the locations of the markers in world coordinates.

METHODS

Markers and Practical HRF To generate a proof-of-concept HRF, a 1.1 by 1.1 cm lenticular marker was constructed from two lenticular array segments with perpendicular major axes, each measuring 1.1 by 0.55 cm. Photographs of the marker were taken using an iPhone 7 mounted on a 108 cm diameter semicircular track. Photographs were taken at 2.5° intervals ranging from 45° to 135°. Lighting consisted of ambient light from ceiling lights and the camera flash from the iPhone camera. After taking all photographs for the first array of interest, the marker was rotated 90° to obtain photographs for the second array. The average hue of the lenticular marker was mapped to a hue dictionary for each array, and the HRF was found by fitting average hue vs. orientation by a 2-term Fourier series using MATLAB (Natick, The Mathworks). To test the accuracy of the HRF, photographs of the entire marker were taken at 1.25° increments (over 65° – 71.25° along the camera track under the same lighting conditions, and data were used to validate the HRF.

Extenders PLA plastic prototypes of pedicle screw extenders were 3D printed. The initial design focused on driveability of the screw through the extender, integration with existing technology and proprietary threadings, creation of large surface area for markers, and monoaxial constraint of

polyaxial screws. This design (Fig. 1A) consists of a lofted marker attachment and a driving pin coaxially inserted into the loft. The lofted attachment possesses threads matching proprietary threading from the relevant screw tulip brand and size; the screw used in this study was a two-times scale, 3D print modeled after the Stryker EVEREST Screw (Kalamazoo, Stryker). The driving pin integrates with the EVEREST Screw tulip to set into the shank drive, thereby constraining the tulip to monoaxial movement and interlacing any rotation of the driving pin with that of the shank.

To provide rotational freedom, the final design, shown in Figs. 1B, 1C, leverages the pedicle screw tulip's rotational degree of freedom by using a cylinder to interface with the shank drive, thereby retaining the monoaxial configuration of the screw while still allowing independent rotation of the tulip and extender. The second degree of rotational freedom is enabled by the hinge between the marker arm and extender base (Fig. 1C). Locking pegs on the outside of the marker arm interlock with counterpart holes in the extender base on a circular track, allowing the user to rotate the arm in increments of 30°. As a precaution against obstruction by walls of muscle, fat, or tissue, the marker arm can be attached to the extender base before or after it is threaded into the tulip. Two entry slots at 0° and 90° polar angles ensure simple attachment of the marker arm (Fig. 1C).

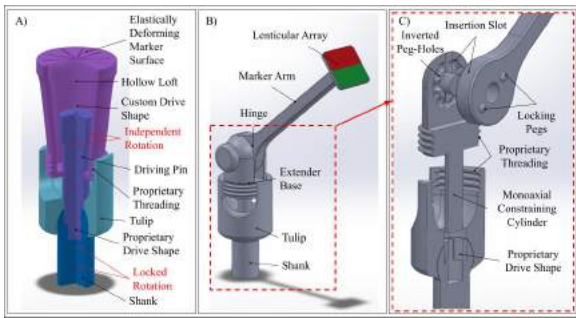


Figure 1: Initial prototype, final design, and section view.

BENCHTOP PROTOTPYE TESTS

The measured HRF for the lenticular arrays was periodic, with some hues were repeated at different angles. This was problematic because the lenticular calibration method requires a unique hue to determine a unique orientation. To address this issue during testing, only angles ranging from 50° to 105° were considered because this range exhibited an approximately affine relationship between hue and orientation. Raw data for angles 45°–135°, raw data for the one-to-one regions ranging for 50°–105°, and the Fourier fits are shown in Figure 2.

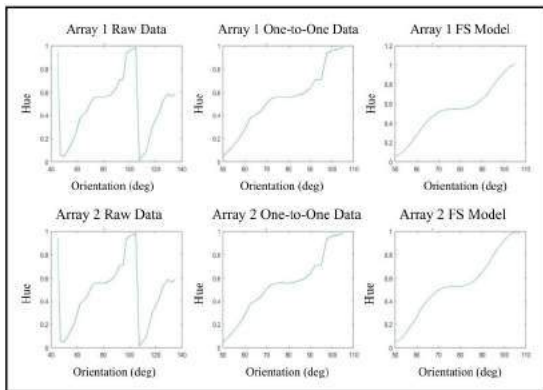


Figure 2: Lenticular calibration model.

Once the HRF fit was generated, photographs were taken every 1.25° from 65° to 71.25° relative to the major axis, beginning from the plane of the marker. The results of the back calculation of camera angle relative to the marker for each photograph are shown in Table 1.

Table 1: Results of lenticular orientation estimation using proof-of-concept HRF.

Measured Angle (deg)	Calculated Angle (deg)	Error (deg)
65	69.35	4.35
66.25	69.90	3.65
67.5	70.99	3.49
68.75	71.50	2.75
70	71.91	1.91
71.25	74.82	3.03

Error Analysis All of the observed errors were within 5°, which is promising considering the technological limitations of the experimental setup. However, it is important to note that much more research is needed. During future research, it will be important to take several hue measurements at each angle in order to establish a variance and to use more precise instruments to measure the camera angle.

DISCUSSION

Camera Calibration In addition to further benchtop testing, goals for future development include investing in a motorized camera track with a fixed speed to take a video of the lenticular array and relate frame to orientation for a more accurate angle measurement. A camera mount to hold the camera perfectly tangential to the arc will also greatly improve accuracy of angle measurements. Finally, designing and printing a perfectly linear hue gradient, to place behind the lenticular array will more practically address the issue of generating a one-to-one HRF. Translational error was not tested in this study, however for a full analysis of the tracking quality of the lenticular arrays, these errors should be collected and compared against those measured in [1].

Extenders As the system stands, the polar angle is chosen within a set of defined values and locked in place by the surgeon in the corresponding peg hole. Although this simplifies communication of the polar angle between the surgical team and computer system, it also limits the closeness with which the plane of the marker can match the image plane. This could be remedied by a more continuous and friction-locking mechanism for choosing polar angle. One solution for this is to make both the extender and its associated screw driveable, which could be accomplished by introducing successive, detachable sheaths. By introducing a sheath which solely interfaces with the tulip threading while remaining coaxial with but rotationally independent from an internal sheath, a stable monoaxial configuration can be achieved for the screw.

Market analysis The spine market of \$13B/year provides ample grounding for a device that can increase the speed of surgery. We anticipate that using these devices can save the surgeon 10-45 minutes per procedure by accelerating the process of bending and inserting a fixation rod. With these surgeries billing at \$10K-\$45K per hour, the price point of \$1K per set is easily justified, with a 1% market share yielding a profit of \$10M per year, including a 50% overhead to the sales and distribution force. The patent space for pedicle screw tracking is dense, but no use of a lenticular array has yet been patented. Our patent application is now under review.

ACKNOWLEDGEMENTS

This work was supported by the Center for Innovation in Neuroscience and Technology at the Washington University School of Medicine.

REFERENCES

- [1] Schillebeeckx I et al. 2015 *International Conference on 3D Vision*. 2015. DOI: 10.1109/3DV.2015.61.
- [2] Schillebeeckx I et al. 2016 *IEEE Conference on Computer Vision and Pattern Recognition (CVPR)*. 2016. DOI: 10.1109/CVPR.2016.358.

MICRO-COMPUTED TOMOGRAPHY FOR THE DETERMINATION OF THE DENTIN-ENAMEL JUNCTION DENSITY GRADIENT WIDTH

Bradley S. Rosenberg (1), Michael Truhlar (2), Sobhan Katebifar (1), Alix C. Deymier (1)

(1) Biomedical Engineering, UConn Health, Farmington, CT, USA
(2) School of Dental Medicine, UConn Health, Farmington, CT, USA

INTRODUCTION

The dentin-enamel junction (DEJ) separates the two mechanically dissimilar tissues in teeth: dentin and enamel, Fig 1. Biological interfaces such as the DEJ are frequently the site of stress concentrations which makes them prone to failure [1]. Despite appearing as an abrupt interface, the DEJ is highly resistant to fracture [2]. This high toughness may be the result of multiscale gradients present at the DEJ. Previous work has shown that gradients in composition and mechanics exist; however, there is no unanimous consensus on the true width of the junction with values being reported from less than 5 microns to as large as 100 microns [1, 3]. Looking at compositional and structural gradients will move the current understanding of the DEJ forward. For this reason, we start by looking at long-range density gradients using high-resolution micro-computed tomography (μ CT). These results will help elucidate the structural features responsible for dissipating stress concentrators at the DEJ.

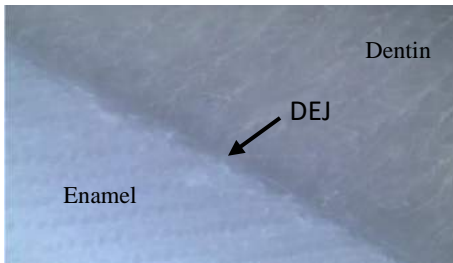


Figure 1: Micrograph of the murine DEJ showing the seemingly abrupt interface between enamel and dentin.

tissue, wrapped in gauze, soaked in a phosphate-buffered saline solution, and placed in a -20° C freezer for storage.

METHODS Tooth

acquisition: 4-5 month old CD-1 mice (Charles River, CT) were sacrificed via CO₂ asphyxiation. Lower right (LR) murine incisors were extracted, cleaned of any remaining soft

Micro-Computed Tomography: Five lower right incisors were thawed and analyzed for structural changes using a Scanco 50 microCT system. Whole teeth were placed in the system and the midsection of each tooth spanning 7.3 mm was imaged at a resolution of 3.4 μ m. μ CT data was reconstructed to obtain cross-sectional data for each region of interest. This data was analyzed to obtain information about the volumetric contribution of each tissue present as well as the density gradient width across the DEJ.

Volumetric analysis: Cross-sectional microCT images were loaded into the CTAnalysis software (CTAn, Bruker), Fig 3. The threshold for pulp, dentin and enamel were separately established by an experienced user to isolate each of the tissues of interest. On a 255 bit density scale the enamel threshold was set between 240-255, dentin between 120-240, and the pulp between 10-120. 3D analyses were then performed to obtain volumes of each tissue for the scanned region. Relative values were calculated as percentages.

Gradient width collection: Three regions of interest were selected in the tooth located several mm from the apical tip, several mm from the coronal tip, and one in the mid-section. For each location 5 sections were analyzed to ensure experimental robustness. For each section, five lines were drawn perpendicular to the DEJ starting from the pulp cavity and extending across the DEJ interface eventually reaching the edge of the enamel boundary, Fig 2. The attenuation coefficients, which are correlated to material density, were collected along each of these lines. This set of 375 lines of density information was then analyzed to determine DEJ gradient widths as well as develop a library of density data.

Gradient width analysis: Gradient widths were calculated using the attenuation coefficient data. The linear outputs were fit using custom MATLAB programs which performed a linear fit on the

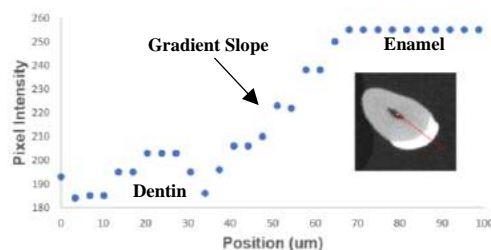


Figure 2: Visualizing pixel intensity changes through the transition from dentin to enamel.

gradient region by minimizing R^2 values across the region of interest. The maximum intensity was divided by the gradient slope to calculate the gradient widths.

Once all gradient widths were determined, a one-way ANOVA test was run for each tooth as well as Tukey's range test to determine if the gradient width changed as a function of location both within a specific tooth and between different teeth.

RESULTS

Volumetric results: On average, dentin makes up the bulk of the tooth composing 81.33% of the total volume. This is followed by enamel at 13.75% and the pulp with 5.02%.

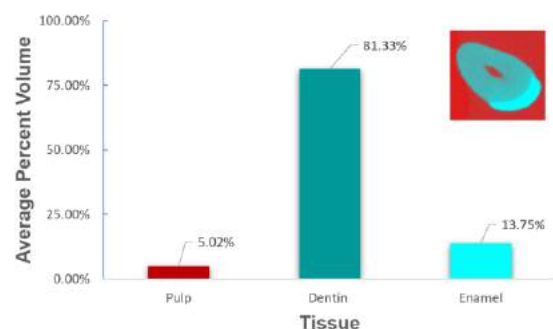


Figure 3: Percent tooth volume of the three main tooth regions.

Gradient results: There is significant variability in gradient width within individual incisor specimens at different locations along the length of a tooth. However, when comparing the average density gradient width of the three locations (C, M, and A) between the five teeth samples, it can be seen that there is no significant difference in the average gradient length. Comparing the different teeth, the mean gradient width of the coronal section was 22.33 μm , which is very similar to that of the middle section (22.89 μm), and the apical section (24.404 μm) as well, Fig 4. Consequently, the total average density gradient width was measured as $23.12 \pm 2.48 \mu\text{m}$.

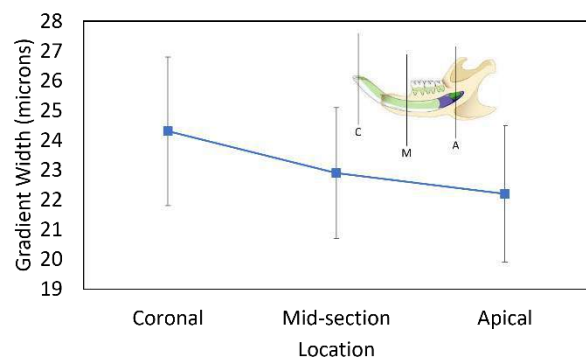


Figure 4: Average density gradient width does not vary with tooth location.

DISCUSSION

Murine incisors grow continuously throughout the animal's life due to the presence of a stem cell niche located at the apical part of the tooth [4]. While variations in density gradient width occurred within individual teeth, ANOVA testing showed that there is no significant difference in gradient width between different tooth samples. In addition to this, no discernable pattern was noted for gradient width discrepancies within individual teeth. For these reasons, it can be seen that the density gradient is ostensibly not a function of tooth location or tooth maturity. While the stages of tooth development are highly conserved across toothed vertebrate species, variations in gradient width were most likely due to the natural inconsistencies associated with the murine DEJ and the formation of surrounding tissues [4].

The literature is very sparse with respect to the DEJ when utilizing μCT to characterize this unique interface. Stock et. al. used synchrotron μCT to differentiate the mineral content present in bulk dentin, enamel, and the region separating the two tissues in one of the only studies involving this technique. Through their investigation utilizing bovine incisors, a region of punctate contrast with diminished mineral deposition was determined to be mantle dentin [5]. Although these tissues can be highly variable when comparing different samples and even more so across species, similarities can be shown as the data presented also depicts a gradient of increasing attenuation coefficient (density) when transitioning from the dentin to the more mineralized enamel, Fig 2.

Using μCT , it has been proposed that the width of the DEJ is approximately 23 μm which is curiously similar to those values suggested by nanoindentation studies [6]. Further studies using Raman spectroscopy to look at compositional gradients, proposed a functional width for the DEJ as small as 4 μm . It is possible that the larger size calculated for the DEJ's width when analyzing the interface with μCT , in addition to the difference in resolution of the technique (3.4 μm for μCT and 0.65 μm for Raman), may be due to the fact that the measurements are taking into account the mantle dentin region which extends beyond the composite interface. Similarly, there may be mechanical and density gradients that exist at a larger scale than any compositional gradients.

It is clear that there are many factors influencing the current understanding of the DEJ's functional width. Higher resolution methods consistently express smaller functional width measurements according to the literature. Moreover, how the junction is defined can also play a large role in how it is measured. Rather than view the structure as a sharp transition between two dissimilar tissues, some investigators propose the DEJ as a relatively broad structural transition zone including the mantle dentin and the inner aprismatic enamel [5]. Our results support this concept and add to the idea that multiple gradients are present at varying length scales.

ACKNOWLEDGEMENTS

Funded by an NIH R03 GRANT13319573. μCT was performed at the UConn Health Imaging Core by Renata Rydzik.

REFERENCES

- [1] Kruize, C et al., *ACS Biomater.Sci.Eng.*, 2021.
- [2] White, S et al., *J.Prosthet.Dent.*, 94(4):330–335, 2005.
- [3] Lin, C et al., *J.Dent.Res.*, 73(5):1072–1078, 1994.
- [4] Catón, J et al., *J.Anat.*, 214(4):502–515, 2009.
- [5] Stock, S et al., *J.Struct.Biol.*, 161(2):162–171, 2008.
- [6] Fong, H et al., *Mater. Sci. Eng. C*, 7(2):119–128, 1999.
- [7] Sharir, A et al., *Nat.Cell.Biol.*, 21:1102–1112, 2019.

MICRO-COMPUTED TOMOGRAPHY FOR THE DETERMINATION OF THE DENTIN-ENAMEL JUNCTION DENSITY GRADIENT WIDTH

Bradley S. Rosenberg (1), Michael Truhlar (2), Sobhan Katebifar (1), Alix C. Deymier (1)

(1) Biomedical Engineering, UConn Health, Farmington, CT, USA
(2) School of Dental Medicine, UConn Health, Farmington, CT, USA

INTRODUCTION

The dentin-enamel junction (DEJ) separates the two mechanically dissimilar tissues in teeth: dentin and enamel, Fig 1. Biological interfaces such as the DEJ are frequently the site of stress concentrations which makes them prone to failure [1]. Despite appearing as an abrupt interface, the DEJ is highly resistant to fracture [2]. This high toughness may be the result of multiscale gradients present at the DEJ. Previous work has shown that gradients in composition and mechanics exist; however, there is no unanimous consensus on the true width of the junction with values being reported from less than 5 microns to as large as 100 microns [1, 3]. Looking at compositional and structural gradients will move the current understanding of the DEJ forward. For this reason, we start by looking at long-range density gradients using high-resolution micro-computed tomography (μ CT). These results will help elucidate the structural features responsible for dissipating stress concentrators at the DEJ.

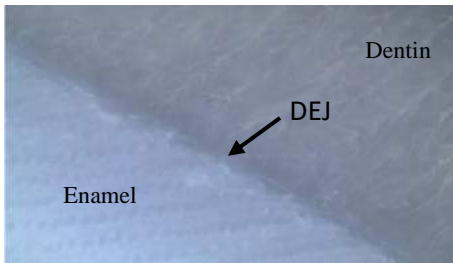


Figure 1: Micrograph of the murine DEJ showing the seemingly abrupt interface between enamel and dentin.

tissue, wrapped in gauze, soaked in a phosphate-buffered saline solution, and placed in a -20° C freezer for storage.

METHODS Tooth

acquisition: 4-5 month old CD-1 mice (Charles River, CT) were sacrificed via CO₂ asphyxiation. Lower right (LR) murine incisors were extracted, cleaned of any remaining soft

Micro-Computed Tomography: Five lower right incisors were thawed and analyzed for structural changes using a Scanco 50 microCT system. Whole teeth were placed in the system and the midsection of each tooth spanning 7.3 mm was imaged at a resolution of 3.4 μ m. μ CT data was reconstructed to obtain cross-sectional data for each region of interest. This data was analyzed to obtain information about the volumetric contribution of each tissue present as well as the density gradient width across the DEJ.

Volumetric analysis: Cross-sectional microCT images were loaded into the CTAnalysis software (CTAn, Bruker), Fig 3. The threshold for pulp, dentin and enamel were separately established by an experienced user to isolate each of the tissues of interest. On a 255 bit density scale the enamel threshold was set between 240-255, dentin between 120-240, and the pulp between 10-120. 3D analyses were then performed to obtain volumes of each tissue for the scanned region. Relative values were calculated as percentages.

Gradient width collection: Three regions of interest were selected in the tooth located several mm from the apical tip, several mm from the coronal tip, and one in the mid-section. For each location 5 sections were analyzed to ensure experimental robustness. For each section, five lines were drawn perpendicular to the DEJ starting from the pulp cavity and extending across the DEJ interface eventually reaching the edge of the enamel boundary, Fig 2. The attenuation coefficients, which are correlated to material density, were collected along each of these lines. This set of 375 lines of density information was then analyzed to determine DEJ gradient widths as well as develop a library of density data.

Gradient width analysis: Gradient widths were calculated using the attenuation coefficient data. The linear outputs were fit using custom MATLAB programs which performed a linear fit on the

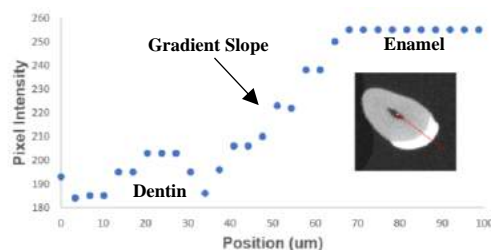


Figure 2: Visualizing pixel intensity changes through the transition from dentin to enamel.

gradient region by minimizing R^2 values across the region of interest. The maximum intensity was divided by the gradient slope to calculate the gradient widths.

Once all gradient widths were determined, a one-way ANOVA test was run for each tooth as well as Tukey's range test to determine if the gradient width changed as a function of location both within a specific tooth and between different teeth.

RESULTS

Volumetric results: On average, dentin makes up the bulk of the tooth composing 81.33% of the total volume. This is followed by enamel at 13.75% and the pulp with 5.02%.

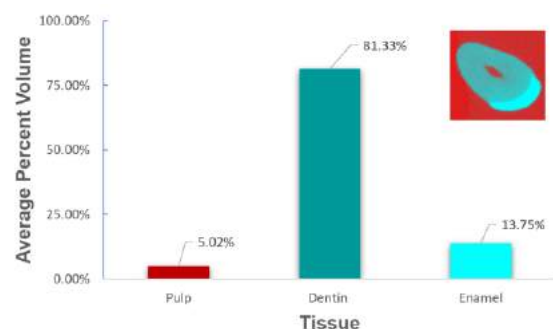


Figure 3: Percent tooth volume of the three main tooth regions.

Gradient results: There is significant variability in gradient width within individual incisor specimens at different locations along the length of a tooth. However, when comparing the average density gradient width of the three locations (C, M, and A) between the five teeth samples, it can be seen that there is no significant difference in the average gradient length. Comparing the different teeth, the mean gradient width of the coronal section was 22.33 μm , which is very similar to that of the middle section (22.89 μm), and the apical section (24.404 μm) as well, Fig 4. Consequently, the total average density gradient width was measured as $23.12 \pm 2.48 \mu\text{m}$.

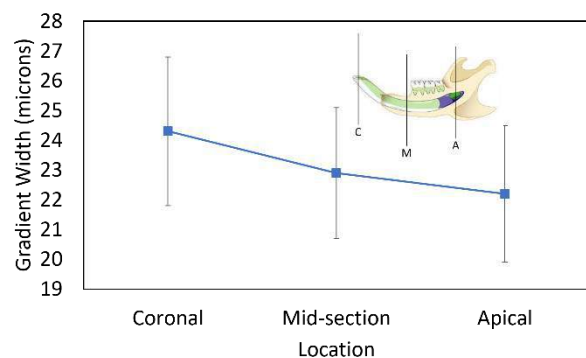


Figure 4: Average density gradient width does not vary with tooth location.

DISCUSSION

Murine incisors grow continuously throughout the animal's life due to the presence of a stem cell niche located at the apical part of the tooth [4]. While variations in density gradient width occurred within individual teeth, ANOVA testing showed that there is no significant difference in gradient width between different tooth samples. In addition to this, no discernable pattern was noted for gradient width discrepancies within individual teeth. For these reasons, it can be seen that the density gradient is ostensibly not a function of tooth location or tooth maturity. While the stages of tooth development are highly conserved across toothed vertebrate species, variations in gradient width were most likely due to the natural inconsistencies associated with the murine DEJ and the formation of surrounding tissues [4].

The literature is very sparse with respect to the DEJ when utilizing μCT to characterize this unique interface. Stock et. al. used synchrotron μCT to differentiate the mineral content present in bulk dentin, enamel, and the region separating the two tissues in one of the only studies involving this technique. Through their investigation utilizing bovine incisors, a region of punctate contrast with diminished mineral deposition was determined to be mantle dentin [5]. Although these tissues can be highly variable when comparing different samples and even more so across species, similarities can be shown as the data presented also depicts a gradient of increasing attenuation coefficient (density) when transitioning from the dentin to the more mineralized enamel, Fig 2.

Using μCT , it has been proposed that the width of the DEJ is approximately 23 μm which is curiously similar to those values suggested by nanoindentation studies [6]. Further studies using Raman spectroscopy to look at compositional gradients, proposed a functional width for the DEJ as small as 4 μm . It is possible that the larger size calculated for the DEJ's width when analyzing the interface with μCT , in addition to the difference in resolution of the technique (3.4 μm for μCT and 0.65 μm for Raman), may be due to the fact that the measurements are taking into account the mantle dentin region which extends beyond the composite interface. Similarly, there may be mechanical and density gradients that exist at a larger scale than any compositional gradients.

It is clear that there are many factors influencing the current understanding of the DEJ's functional width. Higher resolution methods consistently express smaller functional width measurements according to the literature. Moreover, how the junction is defined can also play a large role in how it is measured. Rather than view the structure as a sharp transition between two dissimilar tissues, some investigators propose the DEJ as a relatively broad structural transition zone including the mantle dentin and the inner aprismatic enamel [5]. Our results support this concept and add to the idea that multiple gradients are present at varying length scales.

ACKNOWLEDGEMENTS

Funded by an NIH R03 GRANT13319573. μCT was performed at the UConn Health Imaging Core by Renata Rydzik.

REFERENCES

- [1] Kruize, C et al., *ACS Biomater.Sci.Eng.*, 2021.
- [2] White, S et al., *J.Prosthet.Dent.*, 94(4):330–335, 2005.
- [3] Lin, C et al., *J.Dent.Res.*, 73(5):1072–1078, 1994.
- [4] Catón, J et al., *J.Anat.*, 214(4):502–515, 2009.
- [5] Stock, S et al., *J.Struct.Biol.*, 161(2):162–171, 2008.
- [6] Fong, H et al., *Mater. Sci. Eng. C*, 7(2):119–128, 1999.
- [7] Sharir, A et al., *Nat.Cell.Biol.*, 21:1102–1112, 2019.

DEVELOPMENT AND ASSESSMENT OF A NEW WEB APPLICATION TO MEASURE THE ORIENTATION AND ALIGNMENT OF FIBROUS TISSUE

Katherine J. Fors (1), Kyle Shannon (3), Kate J. Benfield (2), Trevor J. Lujan (1)

- (1) Department of Mechanical & Biomedical Engineering, Boise State University, Boise, ID, USA
(2) Biomedical Engineering Doctoral Program, Boise State University, Boise, ID, USA
(3) Research Computing Support, Boise State University, Boise, ID, USA

INTRODUCTION

Fibrillar networks in soft and hard tissue govern the macro and micro-scale mechanical behavior and are critical to cell function.¹ It is therefore important to accurately quantify structural characteristics of fiber networks to advance a mechanistic understanding of healthy, damaged, healing, and repaired tissue, and to serve as a diagnostic tool for disorders and treatments. To support this need, a number of research groups have developed free software applications to extract descriptive structural parameters from two-dimensional images of fiber networks including mean fiber orientation and fiber alignment (dispersion). Together, these two parameters define material anisotropy and can be directly inserted into material models for computational simulations. Software applications that measure these two parameters include: OrientationJ (ImageJ)², Directionality (Fiji)², CurveAlign³, CytoSpectre,⁴ as well as FiberFit⁵, which was developed by our lab in 2016. These applications have been increasingly used in the biomedical community for a broad range of research projects that include mechanobiology, tissue engineering, and cell biology. However, there are two notable limitations that have hindered their reliable and widespread adoption.

The first notable limitation is the reliability of the values calculated by the software tools. At this time, no study has directly compared the accuracy of different software applications in measuring mean fiber orientation and fiber alignment. Although one recent study did report correlations between the parameters computed by different software, they did not report errors.⁶ Researchers are therefore unable to make informed decisions about what software tool to use, and consequently, reported data may be inaccurate. The second notable limitation is accessibility. Although the previously listed software applications are free to use, they do require the user to download and run an executable that may not be compatible with their operating systems. An attractive alternative is to create web-based applications that allow instant access to anyone with an internet connection.

The first objective of this study was to convert FiberFit software into a web-based application. The second objective was to compare the accuracy of FiberFit with other free software applications that similarly quantify mean fiber orientation and fiber alignment from two-dimensional images.

METHODS

Web Application Development. The portable FiberFit software application⁵ was converted from Python script to a web application (**Fig. 1**). The original Python code (available on GitHub) was installed on a server and a web interface was written in standard HTML, JavaScript, and CSS. The server processes data files in parallel, writing the output

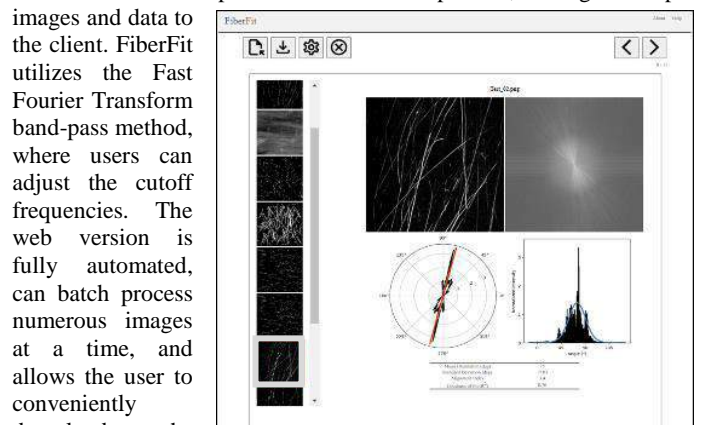


Figure 1: FiberFit web application

images and data to the client. FiberFit utilizes the Fast Fourier Transform band-pass method, where users can adjust the cutoff frequencies. The web version is fully automated, can batch process numerous images at a time, and allows the user to conveniently download the results through generated reports, summary tables, and histogram data. Users can view all uploaded images in a scroll bar to the left, and view the results of any selected image on the right (**Fig. 1**). This web application is now available online at <https://ntm.boisestate.edu/fiber-fit/>.

Accuracy Measurement. A set of 52 unique images of known fiber orientation and alignment were generated using a custom Matlab program (**Fig. 2**). A binary image was populated with straight lines based on a semicircular von Mises probability density function for specified values of alignment k (dispersion) and mean orientation μ . These manufactured images were then input into the five previously mentioned software applications. The programs were run under their default settings according to their manuals with the exception of OrientationJ where a gaussian gradient filter was applied according to our previous work.⁵ The fiber angle distribution histogram generated by each program was then extracted. This data was input into a custom Matlab program that calculates μ and k by curve fitting the data's histograms to a von Mises distribution. The error between the known and measured values of μ and k were calculated (actual – predicted) (**Fig. 2**). Images were broken into two categories: disordered fiber networks ($k \leq 1$) and aligned fiber networks ($k \geq 2$).

Statistics A repeated measures ANOVA was run to determine the effect of each software program (within-subject) on μ and k errors. One-way ANOVAs were run to determine the effect of alignment type (disordered vs aligned) on μ and k error.

RESULTS

FiberFit and CytoSpectre had significantly lower mean orientation and alignment errors than the other three software applications (**Fig. 3A-B**). CurveAlign, Directionality, and OrientationJ had higher errors when calculating mean orientation in disordered fiber networks (**Fig. 3C**). With the exception of FiberFit, all software applications had significantly larger errors when quantifying the fiber alignment (dispersion) in images with highly aligned fiber networks (**Fig. 3D**), with CurveAlign having errors 8-40x greater than other software.

DISCUSSION

This study found that FiberFit and CytoSpectre were the most accurate programs for calculating mean orientation and alignment of fiber networks from manufactured images. While all programs were able to accurately measure the mean fiber orientation in images with highly aligned fiber networks, FiberFit showed the best results in measuring mean orientation in disordered fiber networks (**Fig. 2C**). CurveAlign was unique in having very high errors when measuring fiber alignment in images with highly aligned networks. Based on our findings, we would 1) not recommend CurveAlign for calculating the two tested parameters, and 2) FiberFit or CytoSpectre would be preferred when analyzing images with disordered fiber networks. Differences in error may be related to the underlying algorithms used to generate the fiber angle histogram. FiberFit, CytoSpectre, and

Directionality use Fourier Transforms, while OrientationJ (structure tensor), and CurveAlign (CT-FIRE/CFR) use other algorithms.

To the best of our knowledge, this is the first time the accuracy of these programs has been directly compared. An innovation of this study was to use a standardized process to analyze the fiber distribution histograms generated by each software. By using the same Matlab code to calculate μ and k from downloaded histograms (**Fig. 2**), we were able to quantify differences in accuracy. Importantly, the Matlab code gave mean orientation results very close to the mean orientation calculated by each individual program (average difference of 1.2 degrees), which gives us confidence in the relative errors reported in this study.

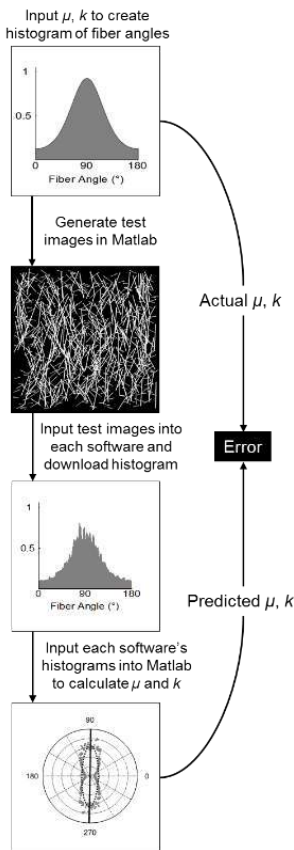


Figure 2: Method to calculate software error.

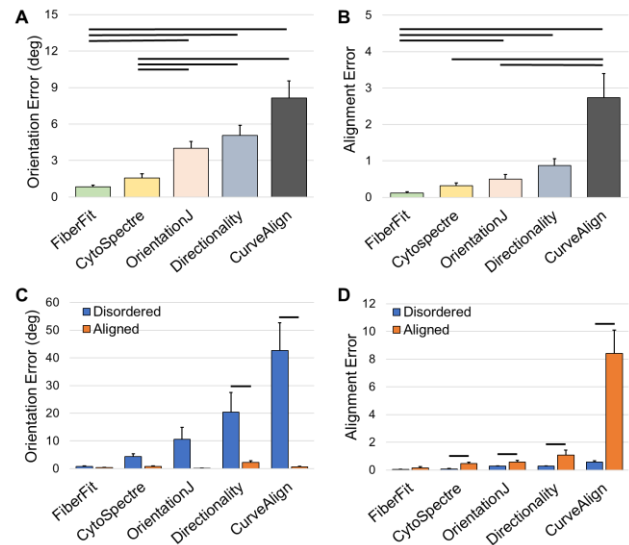


Figure 2: Software comparison. Orientation and alignment error were determined for (A-B) all images and (C-D) aligned or disordered networks. Lines = sig. difference ($p < 0.05$)

There are notable benefits of certain software applications apart from their accuracy in characterizing fiber images. Both FiberFit and CytoSpectre are capable of handling multiple images at a time and are very user-friendly with a short learning curve. Other programs such as CurveAlign, Directionality, and OrientationJ have additional features that may be better suited for specific applications (e.g. collagen interactions with epithelial cells).

In conclusion, this study has developed an accurate web application that can quantify material symmetry in 2-D images. The conversion of FiberFit into a web application will provide on-demand access to a scalable software tool (<https://ntm.boisestate.edu/fiber-fit/>). This will eliminate barriers related to downloading and installation. This study has also provided perspective on differences that exist between available software tools. Future work will expand this assessment by examining software accuracy when using confocal images of soft tissue. The development and adoption of reliable computational tools can help advance a mechanistic understanding of biological materials.

ACKNOWLEDGEMENTS

Support kindly provided by NIH NIAMS 1R15AR075314-01

REFERENCES

- [1] Stender et al. BMBB. 2017. 17(2) [2] Rezakhaniha et al. BMBB. 2012. 11(3-4) [3] Liu et al. Methods Mol Biol. 2017. 1627: 429–451 [4] Kartasalo et al. BMC Bioinformatics. 2015. 16:344 [5] Morrill et al. Biomech Model Mechanobiol. 2016. 15(6) [6] Vries et al. Acta Biomaterialia, 2022. 263-274.

HANDHELD SHEAR WAVE TENSIOMETER MEASUREMENTS ARE SENSITIVE TO REGIONAL LOADING IN PHANTOM COLLATERAL LIGAMENTS

Mary E. Laudon (1), Lesley R. Arant (1), Joshua D. Roth (1,2,3)

- (1) Department of Biomedical Engineering, University of Wisconsin-Madison, Madison, WI, USA
(2) Department of Orthopedics and Rehabilitation, University of Wisconsin-Madison, Madison, WI, USA
(3) Department of Mechanical Engineering, University of Wisconsin-Madison, Madison, WI, USA

INTRODUCTION

Because of their wide attachments, ligaments undergo non-uniform loading that differs with joint angle. Measuring these regional loads is important for characterizing ligament biomechanics and executing surgical procedures such as total knee arthroplasty (TKA). Outcomes after TKA depend, in part, on the proper tensioning of the collateral ligaments [2]. However, existing methods to assess ligament tension are subjective, indirect, and/or invasive [3]; and are unable to capture the non-uniform loads on wide ligaments such as the medial collateral ligament (MCL). Therefore, a method to quantitatively, directly, and non-invasively evaluate non-uniform ligament tension could improve surgical outcomes, streamline the TKA workflow, and enhance our understanding of complex ligament biomechanics.

Our research group has developed a handheld sensor called a shear wave tensiometer to measure ligament tension directly and non-invasively. This technique uses the linear relationship between squared shear wave speed and axial stress to measure tension in load-bearing tissues such as ligaments [4]. This method has been validated in uniformly loaded tissues [5], and a preliminary study in a finite element model recently suggested that shear wave speed varies regionally in non-uniformly loaded tissues [6]. However, it is unknown how tensiometer measurements are affected by non-uniform loading experimentally.

Accordingly, *the aims of this study* were to 1) determine how accurately the tensiometer can measure the total tension in a non-uniformly loaded specimen, and 2) determine the effect of load gradient and tensiometer tip position on measured shear wave speeds. We hypothesized that 1) a tensiometer with a tip width that spans the width of the specimen will measure total tension under varying gradients, and 2) shear wave speeds measured with a smaller tip width will be sensitive to both tip position and the degree of the load gradient.

METHODS

Mechanical Model: We used a mechanical knee model to simulate loading of a phantom collateral ligament during a varus-valgus laxity assessment (**Figure 1**). Our phantom ligament has mechanical properties comparable to those of biological ligaments [7] and dimensions similar to those of the MCL [8]. The phantom wraps around 3D-printed bone contours to mimic MCL wrapping around the femur and tibia. The clamp representing the femoral attachment includes a slotted connection that allows for rotation about its centerline to introduce non-uniform loading (**Figure 1**). The phantom is tensioned by applying a valgus torque to the simulated tibial shaft. We incorporated in-line load cells on the anterior and posterior borders of the phantom ligament (**Figure 1**) to confirm that we created a non-uniform gradient in the phantom.

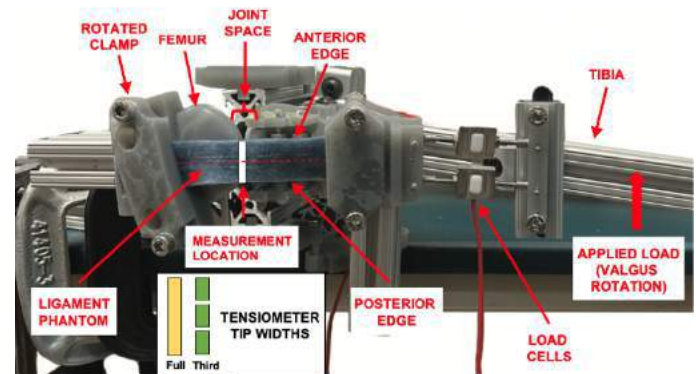


Figure 1: Mechanical knee model with phantom ligament showing positioning of load cell tips to measure regional shear wave speed.

Shear Wave Tensiometer: We measured shear wave speeds using our handheld tensiometer. The tensiometer consists of a voice coil tapper, which excites shear waves, and a downstream piezoelectric load cell, which tracks shear wave propagation along the length of the tissue. We computed the time delay between wave arrivals at the tapper and load cell. Shear wave speed was computed by dividing the distance between the tips by the time delay. For this study, we fabricated two different tensiometer tip widths, including one that spanned the entire width of the phantom and another that spanned a third of the width of the phantom ligament (**Figure 1**).

Experimental Design: We first oriented the femoral clamp such that the load cells displayed equal tensions indicating a uniform load across the phantom. We then positioned the tensiometer on the phantom over the joint space and applied a ramped valgus torque to the model to tension the phantom (**Figure 1**). For the full tip width, we measured shear wave speeds with the tensiometer centered over the phantom. For the third tip width, we measured shear wave speeds with the tensiometer placed over the anterior, central, and posterior portions of the phantom (**Figure 1**). We repeated this measurement process with two different non-uniform tension gradients that were achieved by rotating the clamp counterclockwise by 10 and 15 degrees to increase the tension in the anterior portion of the ligament.

Statistical Analysis: To determine errors between tensiometer-measured tension and total tension in a non-uniformly loaded specimen (Aim 1), we first fit a linear regression between shear wave speed (independent variable) and total tension (dependent variable) for the trials with a uniformly loaded phantom and a centrally positioned tensiometer with a full tip width. We then used this regression to compute tensiometer-measured tension for each non-uniform gradient with a centrally positioned, full-tip-width tensiometer. Errors were computed between the tensiometer-measured tension and the gold-standard total tension, which computed as the sum of the in-line load cell measurements (**Figure 1**).

To determine the effects of tip position and the degree of load gradient on shear wave speeds measured with the third tip width (Aim 2), we performed a two-way ANOVA test with an interaction term. We also performed post hoc pairwise comparisons (Tukey's tests) to identify which tip positions, gradient levels, and tip position-gradient level interactions had significantly different shear wave speeds.

RESULTS

The error analysis revealed that tensiometer-measured tension were greater on average than the gold-standard total tension. The root-mean-square error increased by 22% as the gradient increased from a 10-degree clamp rotation to a 15-degree clamp rotation (**Table 1**).

Table 1: Bias and precision errors between tensiometer-measured tension and gold-standard total tension.

	Bias Error [N]	Precision Error [N]
10-degree gradient	28.4	33.1
15-degree gradient	25.3	49.8

The two-way ANOVA test found a statistically significant difference in measured shear wave speeds with varying tip position and load gradient ($p<0.001$). Pairwise comparisons for tip position revealed that shear wave speeds at the posterior position were significantly different than those at the anterior and center locations ($p<0.001$). Pairwise comparisons for the interaction between tip position and load gradient revealed several interesting differences (**Figure 2**). For example, with the 15-degree gradient, shear wave speeds were significantly higher in the anterior and central regions compared to those in the posterior region ($p<0.001$).

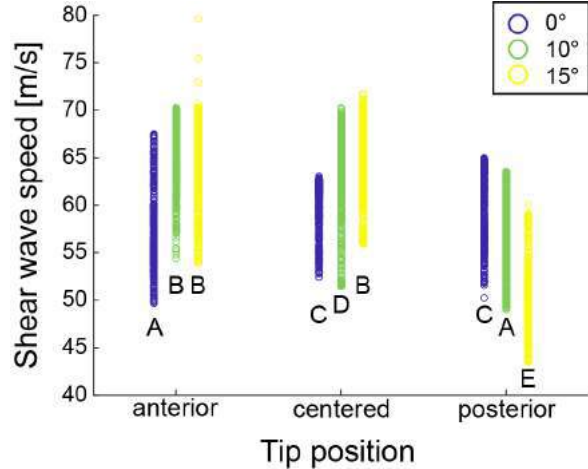


Figure 2: Plot depicts the effect of tip position and gradient on measured shear wave speeds. Data sets labeled with the same letter do not have statistically different shear wave speeds.

DISCUSSION

The errors in total tension (**Table 1**) indicate that a tensiometer with a tip width that spans the entire width of the specimen may over-predict the total tension in the structure when it is calibrated using measurements in a uniformly loaded structure. Thus, measured shear wave speeds may be more sensitive to high-load regions than low-load regions. Tensiometer users should take this over-prediction into account when performing measurements in non-uniformly loaded structures. Despite these errors, our findings indicate that tensiometer measurements still provide information about relative changes in total tension in non-uniformly loaded tissues, which is important for clinical applications such as ligament balancing in TKA.

The ANOVA test indicated that shear wave speed measurements are sensitive to tip position and load gradient. In general, the effect of tip position on shear wave speeds is dependent on the degree of the gradient. There was evidence among non-uniform gradients that measured shear wave speeds increased as tip position moved anteriorly. This is consistent with greater regional tension anteriorly due to our 10- and 15-degree gradients and suggests that the tensiometer captures regional differences in shear wave speed. Our ongoing work includes supplementing these experimental findings with a dynamic finite element model that enables us to perform probabilistic simulations of a wider range of loading gradients, tip widths, and tip positions.

In conclusion, we determined that tensiometers tend to over-predict the total tension in a non-uniformly loaded structure. We also found evidence that tensiometers can capture non-uniform loading across the width of a specimen, as well as the degree of non-uniform loading. Together, our findings demonstrate that our handheld tensiometer is a promising device to quantitatively, directly, and non-invasively measure tension in both uniformly and non-uniformly loaded tissues.

ACKNOWLEDGEMENTS

This work was supported by the Draper Technology Innovation Fund (TIF), administered by Discovery to Product (D2P) at UW–Madison.

REFERENCES

[1] Whiteside, *Clin Orthop Relat Res*, 2000. [2] Gustke, *Bone Joint J*, 2014. [3] Aglietti, *Clin Orthop Relat Res*, 2007. [4] Martin, *Nat Commun*, 2018. [5] Blank, *J Mech Behav Biomed Mate*, 2020. [6] Blank, *SB3C*, 2021. [7] Arant, *J Mech Behav Biomed Mate*, 2022. [8] Liu, F et al., *Journal Orthop Surg Res*, 2010.

COGNIGUARD

J. Funk (1), J. Aikens (2), C. Davies (1)

Faculty Advisor(s)

C. Davies (1)

- (1) Department of Mechanical and Materials Engineering, Queen's University, Kingston, Ontario, Canada
(2) Department of Engineering Physics, Queen's University, Kingston, Ontario, Canada

INTRODUCTION

The recent increase in popularity of running on off-road trails has resulted in numerous serious fall-related injuries [1]. The terrain and environmental factors are subject to unforeseen variation, with fluctuations in altitude, unstable surfaces, and rock falls representing major obstacles to participants [1], [2]. Despite the possibility for severe head injuries on unmaintained trails, many runners do not use helmets. Traditional helmets are often considered too bulky, conspicuous, or expensive, such as the “Vapor Helmet” offered by Track N Trail [3]. A product must be developed that maximizes cranial safety, while being appealing and comfortable for the user.

The Queen's Biomedical Innovation Team (QBiT) is developing the CogniGuard, an inflatable helmet geared toward trail runners and other individuals at risk of fall-based head injuries. The product will detect falls prior to their occurrence using onboard software and sensors and protect the user's head with an embedded inflation system.

This device is being developed to minimize fall-based injuries for trail running, with additional applications including usage by patients with a fall risk, such as individuals recovering from an injury, the elderly or patients with epilepsy and other neurological conditions. The device will detect and protect individuals in case of a fall, and with an aesthetically pleasing design, it will provide an appealing improvement to users over pre-existing helmets.

PRODUCT DESIGN

The user will be able to wear this device like a normal hat. If the sensors incorporated into the helmet detect a fall, the airbag will expand around the user's head, protecting vital areas, including the temples and back of the head. The dark blue patches, as seen in Figure 1, are composed of Nylon 6.6, and will absorb an impact and prevent inflation system rupture in the case of rough or abrasive terrain. The inflation system airbag is composed of two materials, Nylon 6.6 and polyethylene. The dual-material system allows for inconspicuous airbag storage within the helmet and providing a protective external coating.

The primary airbag material chosen, Nylon 6.6, is advantageous due to its high safety factor and lower density than contemporary materials [4]. Polyethylene was used as the secondary material due to its ability to easily fold inside the hat and inflate quickly. Figure 1 below shows a schematic of the helmet with the airbag expanded, connected to the microcontroller armband via wiring.



Figure 1: CogniGuard after airbag inflation.

The casing for the microcontroller and battery will be stored within an armband to reduce helmet weight and potential damage to components. Soft PLA was used as 3D-printer filament for the armband casing due to its durability and vibration-dampening properties [5].

The polyethylene airbag was sewn onto the hat fabric through a multi-directional stitching method, using heat-bonding and silicone as a sealant. This bonding method, also used for car airbags, maximizes airbag integrity [6].

The inflation system integrates a compressed air source and airtight container design to seamlessly transfer gas. Its low weight of approximately 0.45 kg allows for installation within the helmet. A 12-

gram CO₂ cartridge is used for inflation and is installed in a custom 3D-printed holster within the helmet. A ¼" bolt is threaded into the holster and tightened to secure the cartridge. When activated, a microprocessor-controlled, onboard 12-volt push-pull solenoid electromagnet will puncture the seal of the CO₂ canister, inflating the airbag.

Ease of manufacturing was considered for all parts. The main body of the inflation system is 3D-printed so it can easily be produced using the accessible PLA material. PLA was chosen due to its high tensile strength of 50 MPA [7]. The push pull electromagnets can be implemented by hand [8]. The Uxcell electromagnets were chosen because they can be used with only 12 volts of electricity which will be electrically feasible [8]. The 12-gram crosman CO₂ cartridge was chosen because it has a high pressure of 850 psi allowing the size of the canister to be small, only 8.4 cm long [9]. The pressure of an average airbag is 30 psi, so utilizing Equation 1, the volume for the inflated airbag was determined to be 0.674 L.

$$\text{Equation 1: } P_1V_1 = P_2V_2$$

The electrical system of the CogniGuard, contained within the armband casing, consists of sensors for fall detection and a connection from the microcontroller to the inflation system. The electrical system consists of a ESP 32 microcontroller, a GY 521 sensor module, a TIP 120 transistor, 1N4001 diode, and various resistors and batteries. The GY 521 module is comprised of a MPU 6050 tri-axial accelerometer and tri-axial gyroscope, allowing for six degrees of freedom. The GY 521 module connects to the board with I2C protocol for a maximum data transfer rate of 400kHz [10]. The accelerometer and gyroscope values range from ± 2 to $\pm 16^\circ/\text{s}^2$ and ± 250 to $\pm 2000 \text{ dps}$ respectively, allowing for motion capture. The input data is fed into a MATLAB Machine Learning (ML) model that will determine if a fall has occurred. To ensure that the model is universally applicable, over 50 hours of training data will be sourced from different team members. The module includes an on-board voltage regulator to regulate input voltage to 3.3V, allowing it to receive voltages from 2.5-5V and preventing damage from fluctuating output voltages [10]. The solenoid used in the inflation system requires 12V of power, which is not possible to be obtained directly from the ESP 32 microcontroller. As a result, the system uses a TIP 120 transistor to switch to an 18V power source once a fall detection signal is generated to activate the solenoid. The system is also connected to a 1N4001 diode to prevent the reverse voltage spike from solenoid activation from damaging the other electrical components [11]. In addition to the system's accuracy and providing a high data collection rate, the combination of the GY 521 sensor with the ESP 32 controller is a highly accessible and affordable option. The TIP 120 transistor has a low base-emitter voltage of 5V, making it ideal for being controlled by the ESP 32 and it is rated for 60V, which is more than enough to remain operational when connected to the 18V power supply [12].

The software sub-team focused on the embedded system of the inflatable helmet, which would detect a fall and trigger the inflation system. As previously described, accelerometer data would be fed into a ML model to determine if the falling condition is met, so an Arduino-based microcontroller will be utilized to trigger the inflation system, as the embedded system's microcontroller. This is a safety critical system, where reliability is key to maintaining proper function of the device. Therefore, no wireless or internet of things technology was used in the device. These technologies would reduce the reliability of the device as wireless technology is prone to failure, and the conditions in which this device would be used might not have access to the internet.

BUDGET & MARKET ANALYSIS

In the US, in 2017, it was recorded that 9.15 million people trail run, so a large potential market exists for the product [13]. The prototyping budget for one CogniGuard was \$1,609.12 for materials and

\$1,853.20 for manufacturing, and \$1,525.50 for testing, resulting in a total cost of \$4,987.82. The team estimates that production scaling will drop the cost per unit to \$320. Currently, there is a single alternative on the market, the Hövding 3, a Swedish inflatable biking helmet, selling for \$505.07 [14]. Selling the CogniGuard for \$448 will ensure it has a 40% return on investment while being a cheaper and therefore more appealing alternative in the market. The CogniGuard will be a considerable addition to a diverse market of users including trail runners, cyclists, the elderly, and patients with neurological diseases.

ACKNOWLEDGEMENTS

We thank the members of the QBiT for their work on this project and review of this abstract. We thank SparQ Queen's for permitting use of their manufacturing equipment, as well as Dr. Claire Davies for her technical expertise and support as QBiT's faculty advisor. We are grateful for funding from Dean Kevin Deluzio, the Sci'73 foundation, and Makers Making Change for their financial support for QBiT's operations and design efforts.

REFERENCES

- [1] C. T. Viljoen *et al.*, "Epidemiology of Injury and Illness Among Trail Runners: A Systematic Review," *Sports Med.*, vol. 51, no. 5, pp. 917–943, May 2021, doi: 10.1007/s40279-020-01418-1.
- [2] "Helmet Required: Courmayeur, Italy's 2,200 Meter-high Sky Race - Run the Alps," Aug. 12, 2017. <https://runthealps.com/helmet-required-courmayeur-italys-2200-meter-high-sky-race/> (accessed Feb. 09, 2023).
- [3] "Helmets," *Track 'N Trail*. <https://shop.trackntrail.ca/equipment/climb/helmets/?source=facebook> (accessed Jan. 06, 2023).
- [4] "Nylon 6 and Nylon 6/12." <https://www.xometry.com/resources/materials/nylon-6-and-nylon-6-12/> (accessed Feb. 09, 2023).
- [5] "What's Soft PLA Filament & How Does It Compare to TPU? | All3DP." <https://all3dp.com/2/what-s-soft-pla-filament-how-does-it-compare-to-tpu/> (accessed Feb. 01, 2023).
- [6] "Sewing threads for airbags | A&E Gütermann." <https://industry.guetermann.com/en/industry-overview/automotive-airbag/> (accessed Feb. 01, 2023).
- [7] "What is PLA? (Everything You Need To Know)." <https://www.twi-global.com/technical-knowledge/faqs/what-is-pla.aspx> (accessed Jan. 06, 2023).
- [8] "Uxcell.com." https://www.uxcell.com/electromagnets-c-1920_1929.html (accessed Feb. 09, 2023).
- [9] "2311: Powerlet® 12g CO2 Cartridges 25 Count." <https://crosman.ca/cen/2311-powerletr-12g-co2-cartridges-25-count.html> (accessed Jan. 06, 2023).
- [10] "MPU-6000 and MPU-6050 Product Specification Revision 3.4." InvenSense Inc., Aug. 19, 2013. [Online]. Available: <https://invensense.tdk.com/wp-content/uploads/2015/02/MPU-6000-Datasheet1.pdf>
- [11] "Service Bulletin." General Motors, Mar. 2015. [Online]. Available: <https://static.nhtsa.gov/odi/tsbs/2015/MC-10113732-9999.pdf>
- [12] "Plastic Medium-Power Complementary Silicon Transistors." ON Semiconductor, Nov. 2014. [Online]. Available: <https://www.onsemi.com/pdf/datasheet/tip120-d.pdf>
- [13] "Participants in trail running U.S. 2006-2017," *Statista*. <https://www.statista.com/statistics/191333/participants-in-trail-running-in-the-us-since-2006/> (accessed Feb. 09, 2023).
- [14] "Hövding - Airbag for urban cyclists." <https://hovding.com/> (accessed Jan. 09, 2023).

INVESTIGATING ANTHROPOMORPHIC HAND MOVEMENT PATTERNS TO SIGN AMERICAN SIGN LANGUAGE (ASL) ACCURATELY AND REPEATEDLY

Lillie Bukzin (1), Sophi Schneider (1), Julia Zelevinsky (2), Ethan Danahy (2), Samantha Johnson (3)

- (1) Department of Community Health, Tufts University, Boston, MA, USA
(2) Department of Mechanical Engineering, Tufts University, Boston, MA, USA
(3) Tatum Robotics, Hudson, MA, USA

INTRODUCTION

A primary mode of communication for the DeafBlind community is tactile American Sign Language (ASL). Tactile ASL, which follows a similar structure to ASL, involves an individual receiving signs by placing a hand on their signing partner. Research by Johnson *et al.* investigated the potential of an anthropomorphic robot hand that signs tactile ASL in an effort to make an independent communication tool for those with deafblindness [1]. To do this effectively, the focus was placed on accurately and repeatedly recreating ASL handshapes (Fig. 1), the core of all ASL signs. This focus highlighted the need to specifically understand how the hand moves between handshapes to avoid collision and confusion.

Understanding how the human hand moves between handshapes lend itself to faster, more concise, and more fluid signing that eliminates unneeded movements and delays. Fluid hand movements are also essential to forming comprehensible signs and decreasing miscommunication events. Additionally, the community of those who sign is widespread, creating a range of dialects and regional signs. This, as well as individual differences and preferences, leads to specific signs being produced in several different ways [2]. However, since all signs are made up of a finite number of handshapes, by developing transitions for these handshapes, we can ensure fluidity of signing variation.

The complexity of hand anatomy allows for many unique forms of movement and individual degrees of freedom (DoF). The 30 muscles in the hand support movement, allowing for flexion/extension and abduction/adduction around three phalangeal joints [3]. Due to the nuance of human hand motion, as well as ASL signing, a research gap exists surrounding how the hand smoothly transitions between complex handshapes. Our research objectives focus on understanding the movement between handshapes and finding patterns in the varying handshape movements to support efforts of signing phonology and robotics. Specifically, our findings will be tested on an 18-DoF robotic hand to determine accuracy and repeatability.

METHODS

To determine how the human hand moves between handshapes, each motion was analyzed by joint.

Numbering Joint Transitions for Each Handshape. All DoF were assigned a number between one and 18, and documentation was created for every handshape transition (e.g. A \rightarrow Open A, A \rightarrow B, A \rightarrow Open B, etc.). Using previous recordings and background in ASL handshape formation, joints were labeled in an order of movement that enabled a fluid transition from the starting handshape to the ending handshape. Labeling joint transitions in this manner allowed for an easier transfer of knowledge from the document to the robotic hand code. Notably, specific joint angles were not needed at this point; instead, angles were later implemented through joint mapping.

Handshapes Consistency Key (HCK). As the numbering of joint movements between handshapes continued, observations and similarities between various transitions were recorded. To keep transitions consistent between handshapes, a HKC was created. In this key, rules were listed that defined the order that joints should move when multiple are changed within the same transition (e.g. beginning joint movement at the index finger and moving medially). Additionally, this key determined when handshape transitions occurred in two parts to avoid collision during movement in opposing planes. This key provided a resource to produce all future handshape transitions and confirmed the accuracy of existing transitions.

MediaPipe Validation. To validate these handshape transitions, motion capture analysis was completed using MediaPipe, specifically, to confirm two-part handshape transitions and hand timing. For each of the starting handshape transitions, a human hand was recorded completing the specified transition. Using the mapped DoF points, the position of the TIP joints in the X, Y, and Z direction on each finger were mapped across 80 ms frames. Depending on the axis of movement, the change in position (speed) was graphed relative to the frames to display peaks for significant joint movement for each. To only capture relevant information and avoid interference, frames were removed at the

start and end to sanitize the data set. These graphs consequently allowed for the most significant starting frame for each hand to be determined to confirm hand timing.

RESULTS

The proposed HKC was applied to all letter transitions, as seen in Figure 1, to provide reliability and develop patterns. Each joint was assigned a number, name, and place within the movement order. Coloration was assigned to each number in the movement order to aid in pattern identification (coloration remained consistent between all handshake transitions).

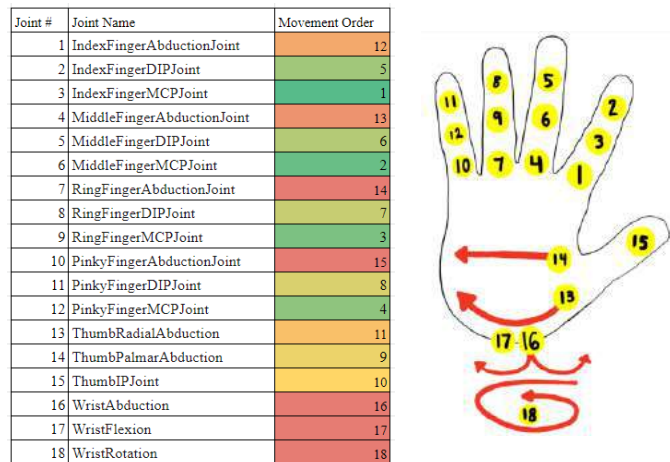


Figure 1: A Sample Transition (A → B) with hand detailing the location of each joint number seen in the first column.

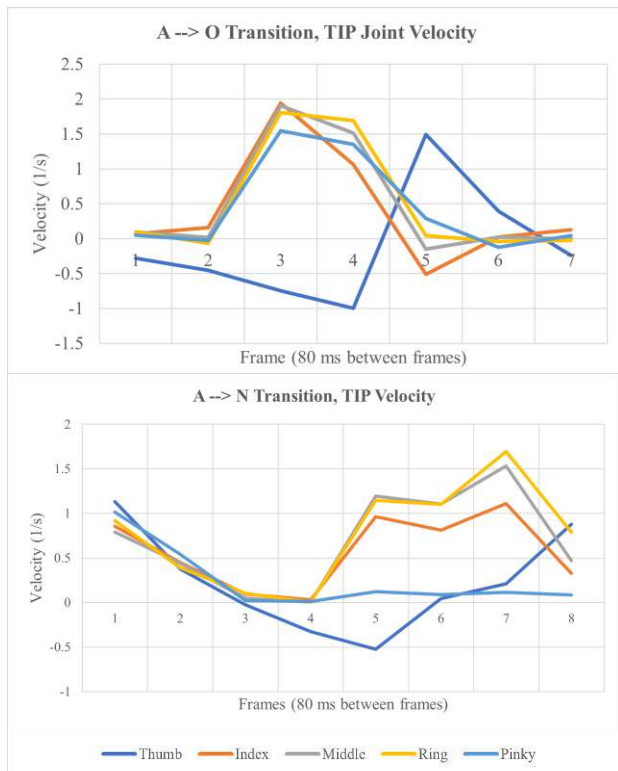


Figure 2: Motion capture validation of A → O and A → N Transitions using velocity of the TIP joints

The HKC contains 25 rules, for example, when the fingers are extending, move all Metacarpal Interphalangeal (MCP) joints before Distal Interphalangeal (DIP) joints. Key HKC rules were analyzed for their use within coded hand transitions. The transition from every

handshape to 'B' (an open handshape) was used to analyze fingers extending and determined that 97.06% of these transitions followed this rule.

Importantly to using the HCK, timing and inherent delays of the transitions were introduced and confirmed using MediaPipe. For example, in Figure 2, the recorded data from the transition from 'A' to 'O' indicate that all non-thumb fingers move first in frame 3, followed by the thumb in frame 5 to complete the transition. The transition from 'A' to 'N' displays the distinct peaks across the frames that denote two parts are needed for the joint sequences to successfully complete the transition without collision. At frame 5, the thumb moves out in the away from the rest of the hand while the non-thumb fingers move upwards. Between the two peaks at frame 5 and 7, the thumb moves into place while the non-thumb fingers stall. This indicates the delay in the movement of the non-thumb fingers to allow the thumb to move to its final position successfully. The lack of movement by the pinky indicates its lack of prevalence in the overall transition. This motion capture result thus portrays how the fingers' movements are timed in ways to prevent collision relative to if the joints were to move immediately to their final positions on the robot.

Testing the proposed transitions with the ASL signing robotic hand, the team was able to determine the functional accuracy of their design. In trials with DeafBlind users (N=5), we saw a recognition rate of 90% of fingerspelled words, confirming the HKC's success. DeafBlind users remarked at the 'fluidity of the signing' and said the transitions made the fingerspelling much 'smoother.'

DISCUSSION

The numbering of the joints with the HKC allowed for a repeatable and concise understanding of overall hand movement. All transition decisions were made to prevent collisions and interference between finger movements. This research takes advantage of what is known anatomically of hand movements to better understand how those movements can be applied in ASL, specifically in relation to natural movements from one handshape to another.

The consistency key enabled the formation of patterns and forced reevaluation of inconsistencies. Validation using the signing robot also provided a secondary measure to confirm the strength of the data. User testimonials demonstrated the practical successes of the transitions to have improved the robot's functionality.

This motion capture validation allowed for the recognition of patterns and confirmed the necessity of two-part transitions. Further, the graphical representation of the hand movement allows for critical analysis of how the hand moves and what role each joint plays in the overall transition and how they interact at the same time frames.

As our next steps, critically, we will compare the motion capture results on the human hand with that of the robot hand and ensure that the proposed transitions are accurately mapping human movements. This extended motion capture analysis will further enhance the ability for pattern recognition and minute differences between various handshape transitions.

Through this research, the team recorded and analyzed realistic anthropomorphic hand movements, highlighting key hand anatomy and the specific application in robotics.

ACKNOWLEDGEMENTS

We would like to thank Tatum Robotics for proposing this project and supporting ongoing research and improvements. Also, we thank Tufts University for its commitment to accessibility projects.

REFERENCES

- [1] Johnson, S. et al., *EMBC*, 10.1109, 2021.
- [2] Lu, J., et al., *Frontiers in Psychology*, 10.3389, 2018.
- [3] Hirt, B. et al., *Thieme Medical Publishers*, 2016.

A MECHANICAL MODEL OF GLENOHUMERAL STABILITY ACROSS SPECIES

S. Li (1), I. Kurtaliaj (2), B. Quinn (3), S. Swartz (3), S. Thomopoulos (2), G. M. Genin (1)

- (1) NSF Science and Technology Center for Engineering MechanoBiology, and Department of Mechanical Engineering and Material Science, Washington University, St. Louis, MO, USA
(2) Orthopedic Surgery, Columbia University, New York, NY, US
(3) Comparative Anatomy, Brown University, Providence, RI, US

INTRODUCTION

Instability of the shoulder leads to a range of debilitating pathologies [1]. At the extremes of athletic performance, human shoulder joints must support loads across a range of angles of up to 140° [2] (Fig. 1). Injuries are frequent in these regimes, and the tendon tears that can result are difficult to repair [3]. Identifying mechanisms that enable shoulder stability at the extremes of motion is important for guiding surgical repairs.

Bats provide an interesting model for this. Although bats have evolved high-force overhead motions (Fig. 1), they do not seem to injure their shoulders as frequently as humans [4]. Our objective was therefore to model the ways that shoulder stability is maintained in bats, and to compare this to mice, similarly sized animals in which overhead motion is not observed.

A range of computational models exists to describe the motion of the shoulder and the resulting strains of tendons that connect to the shoulder [5]. Although these models provide exceptional anatomical accuracy and are predictive of shoulder kinematics, they are not well suited to closed form analysis and parametric study across species. We therefore developed a simplified model of shoulder stability and applied it to enable cross-species study. We hypothesized that the anatomy of bats provides advantages over that of mice to promote shoulder stability.

METHODS

Mathematical model: Based upon CT scans of the bat and mouse glenohumeral joints (not shown), we developed a simplified model of the energy barrier to shoulder instability as a function of the glenoid and insertion angle between tendons and the humeral head. Depicted in **Fig. 2(a)**, The two-dimensional model considered the glenoid as an arc with radius r_{gle} and angle α . The humeral head of radius r_{hum} rests at the bottom of the glenoid with a section of bone with width w . The total length from the bottom of the humeral head to the other end of the bone is H . Distanced a from the edge of the bone, two linear elastic tendons

with gauge (unstretched) length L_0 and initial length L were inserted to both sides of the bone at an angle θ . The other ends of the tendon were fixed. Both tendons were linear elastic with stiffness k .

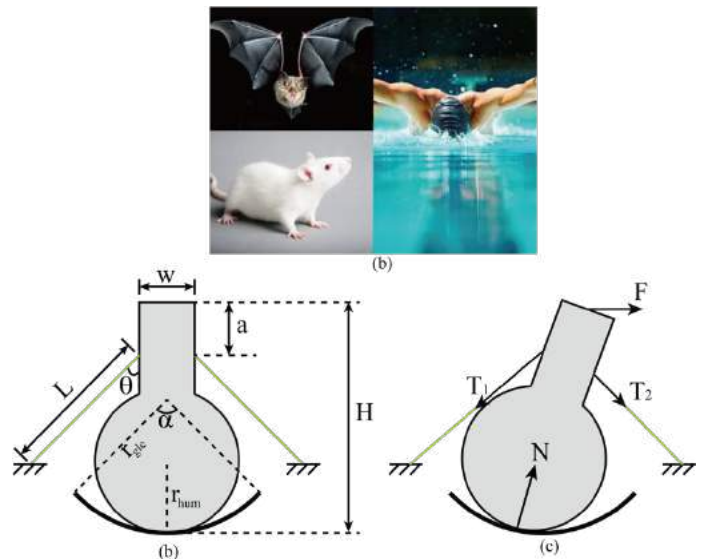


Figure 1: (a) A bat, a mouse, and a butterfly swimmer (photo credits in Acknowledgments). (b) Model of the glenohumeral joint in its initial condition and (c) loaded condition.

To model response to destabilizing forces, a concentrated force F was applied quasistatically as shown in **Fig.1(b)**. Force was ramped linearly until the humeral head became unstable, and the force required to displace it further in the glenoid decreased. To calculate the resistance of the system to instability, the work U done by F up to the point of instability was calculated: $U = \int \vec{F} \cdot d\vec{r}$, where $d\vec{r}$ is the increment of

path length followed by the point of application of the force. Using the Matlab (Natick, The Mathworks) environment, force-displacement curves and U were calculated for different combinations of glenoid arc angles α and tendon insertion angles θ . In all simulations, the following baseline parameters were used: $L_0 = r_{gle} = 7.5$ cm; $r_{hum} = w = 5$ cm; $H = L = 15$ cm; $a = 3$ cm; and $k = 2500$ N/m.

RESULTS

Simulations revealed that the force-displacement relations varied with insertion angle (Fig. 2, for the case of $\alpha = 180^\circ$) and glenoid angle (not shown). Force rose nonlinearly as the humeral head reoriented during its traversal of the glenoid arc. As tendon insertion angle increased, the structural stiffness of the system increased, suggesting that a larger tendon insertion angle leads to stiffer humerus-glenoid assemblies. The peak force needed for instability was highest at intermediate tendon insertion angles, while the maximum displacement of the humerus prior to instability was highest for lower insertion angles.

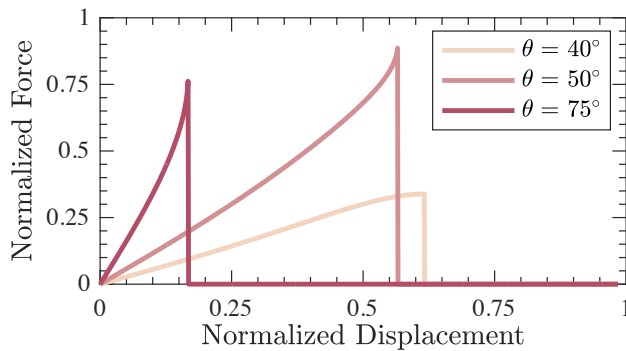


Figure 2: Tendon angles affect the relationship between force and humerus displacement. Here, force was normalized by the kL_0 , and displacement was normalized by the glenoid radius, r_{gle} .

The elastic energy barrier that must be overcome for instability is a function of the stiffness, peak force, and peak displacement, of the tendon-humeral head assembly, as well as of the depth of the glenoid. To evaluate how this energy barrier for instability changes with tendon insertion angles and the depth of the glenoid, a phase diagram was drawn (Fig. 3). In this phase diagram, darker shades of red correspond to higher energy barriers that must be overcome for instability to occur. The plot shows that small tendon insertion angles (ranging from 0° to $\sim 30^\circ$) lead to relatively small energy barriers regardless of glenoid arc angle. On the other hand, for certain tendon insertion angles greater than 30° , the energy barrier increases with glenoid arc angle up to a threshold. The maximum energy barrier occurs for tendon insertion angles in the range of 50° – 60° , although the rise to this is nonmonotonic. The energy barrier is relatively insensitive to the glenoid angle beyond an instability threshold that is associated with full dislocation of the humeral head from the glenoid; thereafter, the instability is associated with a bifurcation in humeral head position within the glenoid, and the energy barrier for this does not vary with the spatial extent of the glenoid.

The range of glenoid angles observed in mice is $42^\circ \pm 10^\circ$, and that of the bat is $73^\circ \pm 10^\circ$ [6]; the insertion angles for both species are more difficult to estimate, but appear to be greater than 45° . In the context of the phase diagram, this places bats in a range that can accommodate a greater range of stable tendon insertion angle than the mouse.

DISCUSSION

The impact of this study lies in understanding the factors that may lead to instability in human shoulders. Comparing mice, which have limited shoulder mobility, to bats, which can perform diverse flying maneuvers

with both mobility and stability [3], is instructive. While the simplified mathematical model certainly does not capture all of the complexity of shoulder motion, it does allow certain comparisons to be made. First, the deep glenoid and larger arc angle of the bat promote stability over a much broader range of tendon insertion angles than does that of the mouse.

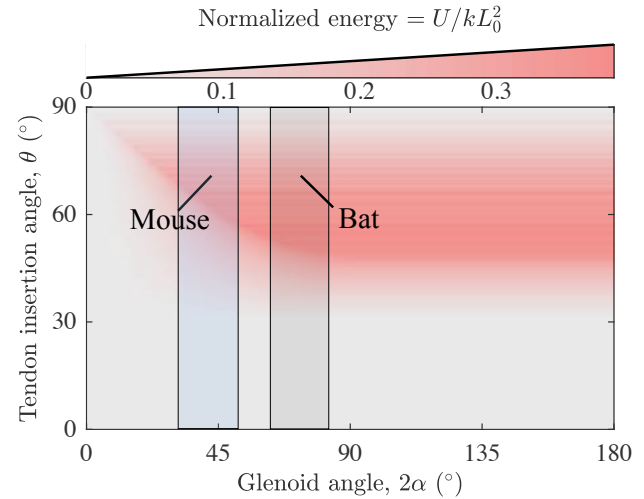


Figure 3: Phase diagram representing the energy barrier that must be overcome for instability of the model shoulder to occur.

Second, in Figure 3 the state of the mouse shoulder lies close to the diagonal line separating regions of low energy barrier to regions of high energy barrier for insertion angles less than 45° . Stability in this region may be enabled by the anatomy of the mouse, which prevents overhead motion [2].

Third, the bat anatomy encompasses the range over which the maximum energy barrier is found (insertion angle of $\sim 60^\circ$ and glenoid arc angle $\sim 60^\circ$), indicating that a larger disturbance is required to dislocate the humeral head from the glenohumeral joint. Beyond about $2\alpha = 75^\circ$, the model predicts that no additional benefit would be found by further increasing the glenoid angle. This suggests that the bat anatomy is well optimized to maximize the energy barrier associated with dislocation, and is significant because it provides a target for human glenoid reconstruction surgeries [7].

We note that the model is idealized. Although the human shoulder can be studied using this model, future studies should add additional detail. Rather than concentrated force, tendons exert distributed force over an enthesis footprint area. Future studies could account for this, as well as the more complex geometries of glenohumeral joints across species. However, even with these limitations, the model provides evidence to support the hypothesis that the anatomy of bats provides advantages over that of mice to promote shoulder stability, and provides insight into targets for surgical reconstruction of the glenoid.

ACKNOWLEDGEMENTS

We gratefully acknowledge funding from the NSF Science and Technology Center for Engineering Mechanobiology (CMMI 1548571), and the NIH (grant R01AR077793).

REFERENCES

- [1] Provencher, et al., 2021. J Am Acad Orth Surg, 29:e51-e61.
- [2] Golman, et al., 2021, Sci. Adv., 7(48), p. eabi5584.
- [3] Arias-Martorell, et al., 2019, Ecol Evol, 9(1), pp. 703–722.
- [4] Bahlman, et al., 2013, Bioinspir. Biomim., 8(1), p. 016009.
- [5] Bolsterlee, et al., 2014. Med Bio Eng Computing 52:283–291.
- [6] Kurtalaj, et al., 2022. Proceedings of the SB3C.
- [7] Zhang, et al., 2022, Shoulder & Elbow, 14(2), pp.123–134.

CHARACTERIZATION OF A POLYMERIC DEVICE FOR LOCALIZED AND CONTROLLED DRUG DELIVERY TO CERVICAL CANCER

P. Phillips (1), M. Elbjorn (2), J. Provencio (2), D. Di Rocco (2), R. L Hood (2,3)

- (1) Department of Biology, University of Texas at San Antonio, San Antonio, Texas, United States of America
(2) Mechanical Engineering, University of Texas at San Antonio, San Antonio, Texas, United States of America
(3) Biomedical Engineering, University of Texas at San Antonio, San Antonio, Texas, United States of America

INTRODUCTION

Despite technological advancements over the past four decades, the mortality rates of cervical cancer, the third most frequent malignancy, have remained about the same [1]. Cervical cancer is often successfully treatable if identified early through routine screening and various stage specific treatment procedures. Currently, treatment options include chemotherapy, radiation therapy, and surgical intervention. Cervical cancer poses a global burden due to the therapeutic challenges low- and middle-income countries face as they are both inaccessible and unaffordable [2].

Biodegradable polymers have enabled many novel approaches to drug delivery. For an effective drug delivery system, it is crucial to deliver medicine to the right place at the right time. Implantable drug delivery systems were developed to overcome problems associated with oral and injectable administration approaches of bioavailability, patient adherence, and first pass metabolism, among others. Polymeric drug delivery systems are versatile and have shown promise to overcome these issues.

The solution proposed is the Multistage Polymer Delivery System (MPDS), which is a biodegradable polymer able to control administration of drugs over 2 to 3 weeks through geometry and composite structures. This study's objective is to demonstrate our MPDS demonstrates a biphasic linear controlled release profile, which we believe would indicate potential as an effective treatment vehicle for cervical malignancies.

METHODS

PCL (Polycaprolactone) was chosen for this study due to its hydrophobicity and slow degradation rate, which were hoped could be leveraged into an effective treatment vehicle to deliver hydrophilic drugs including cisplatin, tetracycline, and carboplatin, which are traditionally used to treat cervical cancer [4]. PLA (Polylactic acid)

was also selected due to its versatility as a biopolymer, ability to exhibit thermoplastic behavior; and previously demonstrated utility in various applications including drug carriers, cancer therapy, and medical tools [5]. Rhodamine B was selected as a model for hydrophilic drugs, due to its similar hydrodynamic radii to those mentioned, water solubility, and ease of detectability [6]. Once submerged in PBS (Phosphate buffered solution), the release of Rhodamine B within the device was tracked through UV-Vis Spectrophotometry.

To batch manufacture polymer devices and ensure minimal error, a two-sided metal injection mold was designed to create twelve 0.100 cm spherical devices. Two g of PCL and 0.002 g of Rhodamine B were weighed out to create twelve devices. A hotplate was used to bring the polymer to 60 °C, the melting point of PCL, so Rhodamine B could be evenly distributed. The polymer mixture was then placed into the metal injection mold and pressed to form equal-sized spheres. These steps were repeated to create the PLA devices.

The purpose of the first experiment was to evaluate the release rate of Rhodamine B over an extended period and determine the replicability of the results. The experiment included 250 mL beakers with 100 mL of PBS. Magnetic rods were placed in each beaker to ensure the solution remained well-mixed. At the start of each experiment (Day 0), the device was submerged into the beaker with PBS and stored at 37°C for 21 days. Each day, 2.5 mL was extracted and replaced with fresh PBS.

The second experiment's purpose was to determine the release rate at different points in the device. PCL and PLA devices were both split into four pieces. The experiment involved submersion of each piece in a separate 50 mL volume of PBS that was maintained by a stir bar. The experiment was conducted at 37°C for 12 days using the same method for daily sampling.

RESULTS

Figure one exhibits the results of the Rhodamine B release experiment: the release rate of PCL and PLA over a 21-day period. The PCL devices exhibited a biphasic linear controlled release profile. However, the PLA devices did not release any Rhodamine B over the 21-day period.

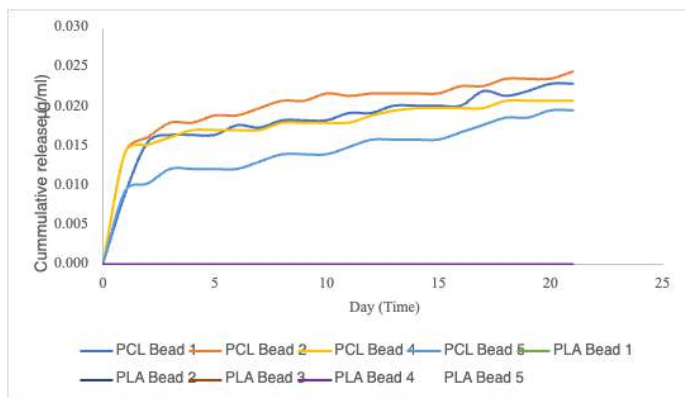


Figure 1. The release rate Rhodamine B in PCL and PLA devices for an extended period

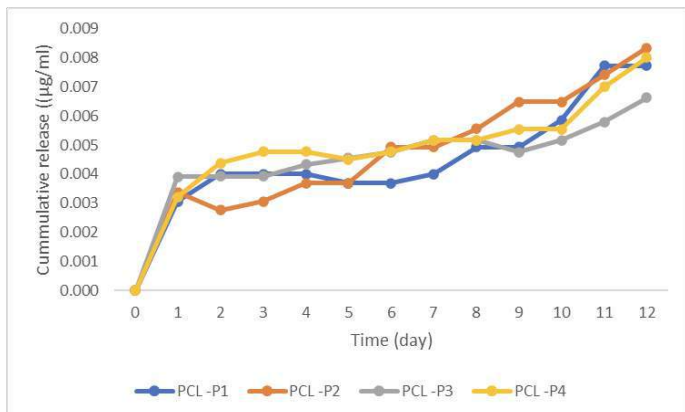


Figure 2. The release rate Rhodamine B in PCL devices when cut in four pieces

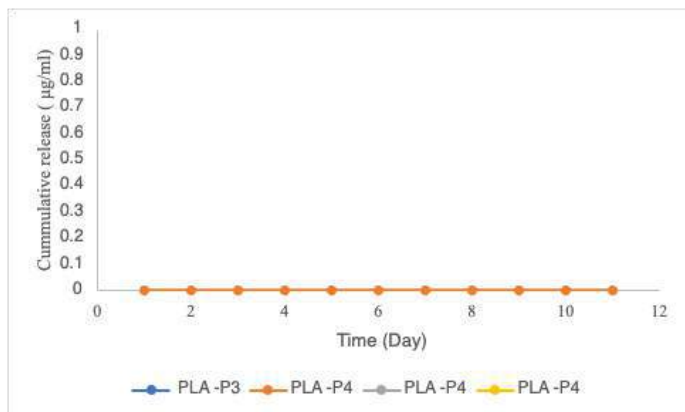


Figure 3. The release rate Rhodamine B in PCL devices when cut in four pieces

Figures two and three exhibit the results for experiment two: the release rate of PCL and PLA devices for a 12-day period when cut into four equal pieces. The variety of mass of each sub-divided piece was normalized for comparison. The PCL devices displayed comparable results to experiment one. Again, figure three exhibits that PLA did not exhibit any release over the 12-day period when cut into four equal pieces.

DISCUSSION

After evaluating the data collected from the two experiments, all the devices display comparable results, which indicate the repeatability of the fabrication process. Experiment one displays a linear biphasic release of Rhodamine B within the PCL device over an extended period. Experiment two displays a comparable release rate which conveys the objective of ensuring each device exhibits similar release. Furthermore, it displays the direct relationship between surface area and release rate.

The biphasic linear behavior of PCL release follows a loading and maintenance dosage administration schedule. The release data from the PCL device fulfilled the biphasic linear profile objective. While PLA did not exhibit release in either of the experiments, it displayed the possibility of creating a polymer composite that could be leveraged to control aqueous access to drug-loaded PCL. The data in this study provides a foundation for future development of this polymeric drug release regulation approach for treating cervical cancer [7].

ACKNOWLEDGEMENTS

The authors acknowledge and appreciate proof-of-concept funding support from the University of Texas at San Antonio.

REFERENCES

- [1] Senapati, S. et al. (2018) Controlled drug delivery vehicles for cancer treatment and their performance. Signal transduction and targeted therapy. [Online] 3 (1), 7–19.
- [2] Burmeister, C. A. et al. (2022) Cervical cancer therapies: Current challenges and future perspectives. Tumour virus research. [Online] 13200238–200238.
- [3] Yang, B. H. et al. (2004) Cervical cancer as a priority for prevention in different world regions: An evaluation using years of life lost. International journal of cancer. [Online] 109 (3), 418–424.
- [4] Tsimberidou, A. M. et al. (2020) Review of precision cancer medicine: Evolution of the treatment paradigm.
- [5] Kamaly, N. et al. (2016) Degradable Controlled-Release Polymers and Polymeric Nanoparticles: Mechanisms of Controlling Drug Release. Chemical reviews. [Online] 116 (4), 2602–2663
- [6] DeStefano, V. et al. (2020) Applications of PLA in modern medicine. Engineered Regeneration. [Online] 176–87.
- [7] Ordikhani, F. et al. (2016) Drug Delivery Approaches for the Treatment of Cervical Cancer. Pharmaceuticals. [Online] 8 (3), 23–.

A BIOREACTOR TOWARDS MECHANICALLY STIMULATING STEM CELL DIFFERENTIATION IN BIOPRINTED ORTHOPEDIC TISSUE CONSTRUCTS

Shreya Garg^{1,2}, Isadora S. dos Passos², Hossein Vahid Alizadeh³, Carolyn Kim^{2,3}, Jiannan Li³, Yunzhi Peter Yang^{1,3,4}

¹Department of Bioengineering, Stanford, Stanford, CA, United States

²Department of Mechanical Engineering, Stanford, Stanford, CA, United States

³Department of Orthopedic Surgery, Stanford, Stanford, CA, United States

⁴Department of Materials Science and Engineering, Stanford, Stanford, CA, United States

INTRODUCTION

Bioprinted scaffolds provide a promising alternative to the current standard of care for orthopedic injuries (ie. autografts, allograft, synthetic implants) in their biomimetics and enhanced functionality [1]. However, the efficacy of these constructs depends on their cellular differentiation and successful integration into the native tissue—a challenge that has yet to be addressed. Previous work has shown that a combination of mechanical and graded biochemical cues can stimulate mesenchymal stem cell (MSC) differentiation into osteoblasts and tenoblasts [2]. This study aims to determine whether such mechanically-stimulated differentiation can be achieved in cell-laden scaffolds by designing a bioreactor that simulates the native tissue environment and generates a stress field of tension-compression forces akin to those endured by musculoskeletal cells around many bony pulleys along the tissue construct. The initial bioreactor was manufactured using acrylic and polyethylene terephthalate glycol (PETG), and a second generation model is being developed with anodic aluminum oxide for increased durability and stability. The stress field due to the cyclic tension induced by the bioreactor was determined via Finite Element Analysis (FEA) and will be correlated to the cell morphologies that arise in tension versus compression regions of the scaffold following sample testing in future studies. If variable differentiation and cell morphology is achieved across the stress gradient, that would inform how bioprinted constructs might react and develop when implanted into musculoskeletal tissue.

METHODS

Ring-shaped scaffold samples consisting of a polycaprolactone (PCL) backbone and gelatin-fibrin hydrogel were synthesized as 7 cm x 1 cm matrices [Fig. 1], and MSC-bearing droplets were deposited within the construct via Acoustic Droplet Ejection (ADE).



Figure 1: Linear scaffold sample consisting of a PCL backbone

and MSC-laden gelatin fibrin bioink. Two 1 cm PCL end strips were sutured together to form a 7 cm-long, ring-shaped scaffold. (1 cm scale bar)

In order to generate a stress field mimicking what the sample would undergo *in vivo*, a bioreactor that subjected the cells to a grade of tension to compression forces was manufactured. The device's loading configuration resulted in a cyclic stress when the bioreactor was in operation [Fig. 2].

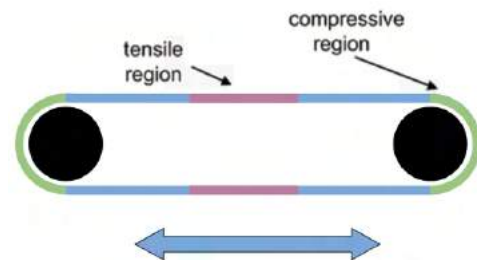


Figure 2: Each ring sample was wrapped around two reciprocating loading rods in a symmetric manner as a representation of a wrap-around tendon on a bony pulley. Linear actuation subjected the rods to cyclic bidirectional movement, resulting in the ring stretching and compressing with a sinusoidally-described displacement and maximum displacement of 3.5 mm.

The bioreactor was fabricated with 3D-printed PETG and laser cut acrylic such that 12 scaffold samples could be loaded for simultaneous tension-compression testing. A rack-and-pinion mechanism in conjunction with linear actuation enabled the bidirectional movement that induced cyclic stress [Fig 3], and movement was calibrated to a frequency of 0.5 Hz and a maximum uniaxial displacement of 3.5 mm (with these values being programmable). This results in 7-10% tensile strain, which is comparable to physiological values [3,4]. Finite element analysis was performed to determine the stress field on the construct and predict resulting cell morphologies.

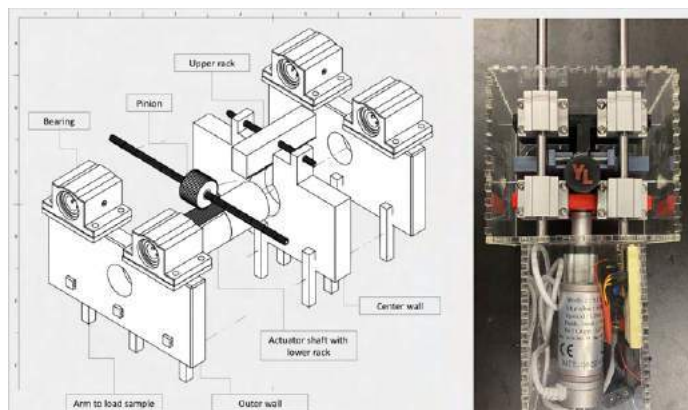


Figure 3: Exploded-view schematic of the bioreactor's internal hardware, consisting of two outer walls that move bidirectionally to the middle wall to induce stretching and compressing of the ring samples loaded around sets of arms. The rack-and-pinion system enables this movement when coupled with a linear actuator that fits into the actuator shaft.

RESULTS

Defined by the mechanical parameters of the scaffold and bioreactor, a computational model of the bioreactor-induced stress field was generated to simulate the viscoelastic deformation of the gelatin fibrin gel using the Finite Element (FE) method in COMSOL Multiphysics (COMSOL Inc., USA) [Fig. 4].

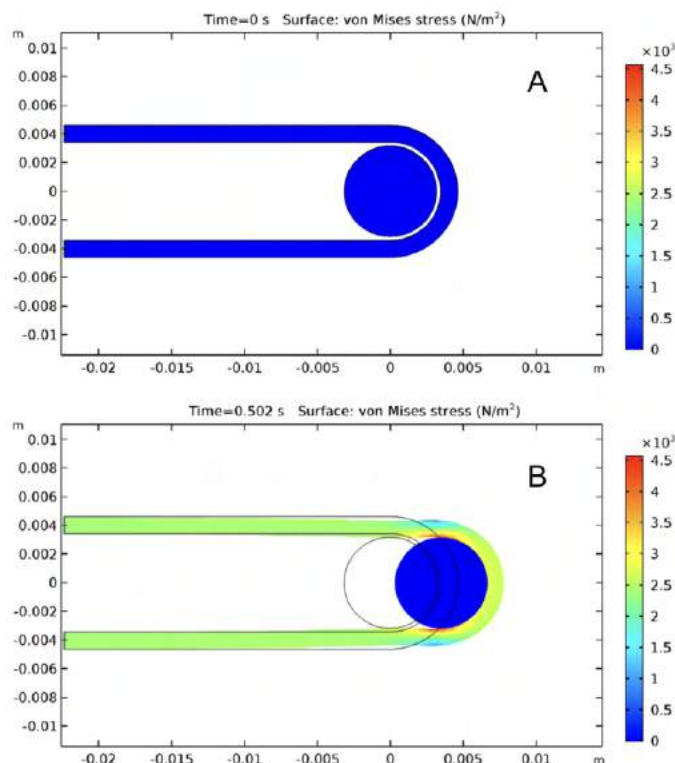


Figure 4: The stresses acting on the scaffold were visualized at

(A) time point $t = 0$ s, when uniaxial displacement across the length of the scaffold $d = 0$ mm and (B) time point $t = 0.5$ s, when displacement was at a maximum of 3.5 mm. The greatest points of stress identified were located at the tensile regions.

The reciprocating rod the samples are loaded onto was modeled as a circular solid with a uniaxial linear motion and a prescribed sinusoidal displacement. The scaffold was modeled as an elastic part that stretches on account of the movement of the rod. The geometry of the model is identical to the experimental setup, and the scaffold material properties were determined experimentally. A triangular mesh was created for the FE model, which was simulated with a time-dependent solver for two motion cycles. The stress and strain distribution inside the hydrogel part was then visualized. The stress distribution is shown in Fig. 4 at two different time points corresponding to 1) the beginning of the scaffold stretch and 2) the maximum stretch at a displacement of 3.5 mm.

DISCUSSION

The FEA model demonstrates that cells along bone/tendon constructs are subjected to a variable stress field under physiological conditions and that consequently, MSC differentiation may differ in accordance to these graded tension and compression forces. To investigate further, the cell morphologies that result from two weeks of mechanical stimulation from cell loading onto this bioreactor will be visualized to study if and how variable stress fields influence MSC differentiation. These morphologies will also be studied when such mechanical cues are delivered in conjunction with biochemical cues (eg. Sox9, Collagen1, Collagen2, Scx, Aggrecan) that are known to incite MSC growth and differentiation. In addition, a second generation bioreactor is being manufactured with anodic aluminum oxide for increased stability and durability, with bidirectional movement induced through a timing belt mechanism that provides more accurate control over displacement length. In tandem with the modelistic results of this study, these future investigations will provide insight into how bioprinted implants will integrate into native tissue, whether targeted cell differentiation can be achieved for regenerative medicine purposes by combining mechanical and biochemical stimuli, and the clinical effectiveness of printed implants in the long run.

ACKNOWLEDGEMENTS

This research was partially funded by DoD grant 81XWH-20-1-0343 and the Stanford Department of Bioengineering.

REFERENCES

- [1] Genova, T et al., *International journal of molecular sciences*, 21: 7012, 2021.
- [2] Li, J et al., *Frontiers in cell and developmental biology*, 9:640388, 2021.
- [3] Wilson, A et al., *Philosophical transactions of the Royal Society of London. Series B, Biological sciences*, 366: 1540–1553, 2011.
- [4] Thomopoulos, S et al., *Tissue Engineering Part A* 17:7-8, 1039-1053, 2011.

PITCH COMPETITION: ON-DEMAND, VOLUMETRIC LIQUID BIOPSY FROM SOLID TUMORS

Y. Kimura (1), MC. Sheehan (2), NR. Raghuraman (2) D. Downing (3) and G. Srimathveeravalli (2)

- (1) Department of Diagnosis and Interventional Radiology, Osaka University Graduate School of Medicine, Suita, Osaka, Japan
(2) Department of Mechanical and Industrial Engineering, University of Massachusetts, Amherst, MA, USA
(3) Department of Biology, University of Massachusetts, Amherst, MA, USA

PROBLEM STATEMENT

Patients suspected to have cancer undergo a medical procedure called biopsy where long, thin needles are used to collect a small tissue sample of the suspicious mass which is then interrogated to determine malignancy. The clinical practice of biopsy typically samples less than 1% of the tumor volume (**Fig. 1a**) whereas tumors are known to exhibit remarkable spatial heterogeneity, with considerable intratumoral variation in protein markers, gene expression, and the presence and status of immune cells [1-2]. Despite major advances in cancer diagnostics and therapy, the practice of biopsy has remained unchanged over several decades, fundamentally limiting our ability to study, understand, and treat cancer.

Several approaches have been tested to bridge this gap, including the

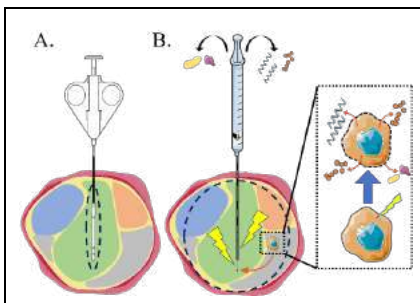


Fig 1. Intratumoral heterogeneity shown with different colors. **A)** Sample volume (dashed line) from conventional biopsy is miniscule. **B)** Our technology can extend the sampling volume to the entire tumor.

use of imaging tools to locally profile the tumor microenvironment or by using physical forces to improve tissue sampling [3-4]. Further translation of imaging approaches to regular clinical usage is hindered by the inability to extract tissue samples that are necessary for pathology and diagnosis. High resource requirements and considerable alteration of clinical workflow are other limiting factors. Our

proposed technology is designed to seamlessly integrate with current

image-guided biopsy procedures while dramatically increasing the data that can be derived from the tumor to guide clinical decision making.

TECHNOLOGY/SOLUTION DESCRIPTION

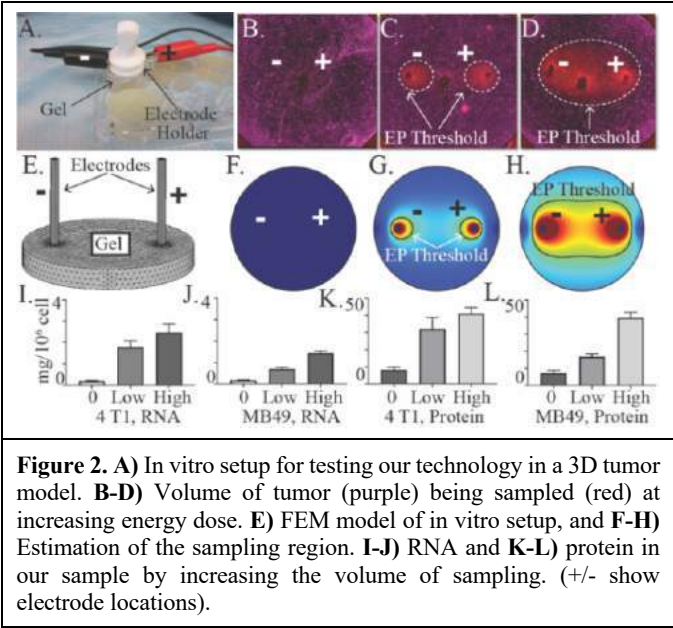
We have established devices, technology and translational techniques to produce on-demand liquid samples from large, defined tissue volumes (e.g., sphere with a 2-3 cm diameter, **Fig. 1b**). This liquid sample is enriched with intracellular material such as DNA, RNA, protein and metabolites that is otherwise inaccessible for diagnostic purposes, or is often heavily degraded due to the degradative conditions in the tumor microenvironment. This high-quality “liquid biopsy” sample can be extracted from the tumor by simple aspiration with needles, then directly fed into existing cancer diagnosis pipelines and genomic sequencing with minimal post-processing.

Our technology functions by placing a long, thin needle into the tissue of interest and delivering an electrical waveform that stimulates release of intracellular materials from cells without harming them. The medical devices we have developed has features that allow simultaneous extraction of the sample by simple aspiration. We have established computational models to guide selection of the electrical waveform based on the desired volume from which sample is to be eluted, and also volumetrically map the sample to the tumor volume from which it was derived (**Fig. 2 b-d, f-h**). For the first time, physicians will be able to extract samples from entire tumor or tissue volumes in a predictable fashion.

We have validated this technology with in vitro models (**Fig. 2 i-l**) and preclinical studies in animals bearing breast and bladder cancer, confirming that the protein and RNA extracted with our technique are representative of what can be obtained by processing the entire tumor (**Fig. 3**). Sequencing results suggest that our liquid biopsy samples have excellent correlation with matched whole tumor lysate, even without optimization. Crucially, this validates the ability for samples acquired with technology to be directly fed into next generation sequencing and

multi-omic platforms that are becoming standard of care for cancer diagnosis. Notably, existing biopsies sample require 2-3 day post-processing for subsequent multi-omic interrogation.

We are currently working on establishing of a prototype device that would be suitable for eventual clinical use and are further optimizing the electrical waveform to allow performing this procedure in an outpatient setting.



BUSINESS CASE

Our promising new technology is expected to broadly impact cancer diagnosis by upgrading clinically used biopsy techniques, specifically, that of fine needle aspirations performed during percutaneous and endoscope guided procedures. We will target prostate cancer as the first clinical indication to develop and validate our technology.

Figure 3. Comparison of protein and RNA levels in conventional (EP-) biopsy versus our technique (EP+) in breast (4T1) and bladder (MB49) tumor models in mice.

Urologists caring for men on active surveillance (AS) for prostate cancer (PCa) are our immediate and ultimate customers respectively. An estimated 50% of all men with PCa in the USA are referred to active surveillance for clinical management of their disease [5-6]. This is performed using blood tests and saturation template biopsies (using 12 – 40 needle placements) every 1-2 years for the duration of the patient’s life. This clinical paradigm for active surveillance presents known risks of under- or over-staging of PCa, and the possibility of false negative results. The current workflow also requires several days before diagnostic results are

available to patients, while being incapable of using technological advances in molecular and genetic techniques to improve precision and prognostic value of diagnosis. We anticipate our product will prove beneficial to men whose cancer is not visible on magnetic resonance imaging, have increasing prostate specific antigen levels on blood tests and are scheduled for conventional template biopsy. This would represent over half the patients on active surveillance, and close to a quarter of all non-metastatic prostate cancer patients. Eventually, we expect our product will improve diagnosis of most solid tumors (e.g., lung, colorectal, breast cancers) and patients with metastatic cancer who are eligible for immuno- or precision therapy.

For our proposed clinical indication, we anticipate our product can generate liquid biopsy samples from an entire prostate sextant with a single needle placement (Fig. 4), allowing reliable multi-omic profiling of a whole prostate gland with fewer than 4 needle placements. The entire process takes a few seconds to complete. Use of liquid biopsy samples for diagnosis would circumvent the current approach of Gleason scoring system that requires heavy involvement of pathologists and has a multi-step processing workflow. Having simultaneous access to genomic, transcriptomic, protein and metabolite sample from the entire prostate would allow creating a definitive picture of the patient’s disease status while also reducing diagnostic inaccuracies from sampling bias.

Regulatory and Commercial Strategy: The choice of preliminary evaluation in the prostate and the need for such technology was driven by input from our clinical advisors. Competing technologies are driven by imaging without acquiring tissue specimens, or are focused on minor improvements in existing biopsy devices. Both approaches lack the ability to retrieve intracellular samples from a predictable volume or seamlessly integrate with existing clinical workflows. Our product will bridge two gaps in cancer care, namely that of acquiring high-quality samples that represents an entire tumor /prostate volume with that of diagnostic capabilities by current generation genomic and molecular diagnostic technologies. Our product is based on FDA cleared predicates (for the electrical waveform) that are already in clinical use for over a decade, providing a clear pathway to regulatory approval. Our technology is positioned as a biological sample acquisition device, thereby our product would not fall under diagnostic or therapeutic categories, qualifying as a Class II device eligible for 510k approval with limited clinical trials documenting safety.

ACKNOWLEDGEMENTS

G.S. acknowledges grant and funding support from the National Cancer Institute and the National Institute of Diabetes, and Digestive and Kidney Diseases of the National Institutes of Health under Award Number R01CA236615 and R01DK129990, and the Dept. of Defense CDMRP PRCRP Award CA170630 and CA190888. Y.K. acknowledges the support of the Uehara Foundation.

REFERENCES

- [1] Pritzker and Nieminen. *Arch. Pathol. Lab. Med.* vol 243, no 11, 2019.
- [2] Iacobuzio-Donahue et al. *Nat. Cancer*, vol 1, no 1, 2019.
- [3] Zhu L et al., *Sci Rep*, 8, 6553, 2018
- [4] Taieb A et al., *SPIE Optic. Metrol.* 2021
- [5] Parker C et al., *Ann of Onc*, 8, 6553, 2018
- [6] Litwin MS and Tan H-J., *JAMA*, Vol 317, no 21, 2017

PITCH COMPETITION: IMPROVING CLINICAL CT IMAGE DATA TO DEVELOP BETTER FRACTURE RISK ALGORITHMS AND PATIENT OUTCOMES

Lance L. Frazer (1), Nathan Louis (1,2), Kal L. Clark (3), Daniel P. Nicolella (1)

- (1) Southwest Research Institute, San Antonio, TX, USA
(2) Electrical Engineering and Computer Science, University of Michigan, Ann Arbor, MI, USA
(3) Department of Radiology, University of Texas Health Science Center at San Antonio, San Antonio, TX, USA

PROBLEM STATEMENT

Osteoporotic fractures commonly occur in the hip and vertebrae and are associated with a \$17 billion burden in healthcare-related costs [1]. Not simply an economic burden, osteoporotic fractures are a significant cause of morbidity and mortality in the aging population [2]. In fact, hip fractures are fatal in 20% of cases and permanently disabling in 50% of cases [3]. It is estimated that 40-46% of women over 50, and 13-22% of men over 50 will suffer an osteoporosis-related fracture [4]. With the number of persons over 60 projected to nearly triple by 2050 [5], a significant increase in at-risk populations for fracture is imminent. Thus, the need is immediate to identify those at greatest risk of bone fracture and provide timely intervention.

Over the past two decades, significant progress has been made in our understanding of bone fragility and fracture [6]. However, over the same period, little progress has been made clinically to reliably identify those at risk of fracture. This has been due in part to the narrow breadth of accessible biomarkers that indicate fracture risk. In fact, the only readily agreed upon clinical measure of fracture risk is bone mineral density (BMD). Unfortunately, since BMD only gives a coarse estimate of the amount of mineralized bone per unit volume, BMD alone has only a 30-50% success rate in predicting fractures [7]. Bone is a complex structure with an intricate microstructural organization and the characterization of this microstructure (an indicator of bone quality) provides a significantly improved estimate of bone's structural integrity [8] compared to BMD. Recently, high-resolution peripheral quantitative computed tomography (HR-pQCT) has emerged as a promising technology to clinically assess bone microstructure. Unfortunately, HR-pQCT is limited both in its low clinical availability and applicability. Only small volumes of bone at specific peripheral locations can be assessed (i.e. distal tibia, distal radius, etc.). A wealth of information describing bone's structural integrity remains inaccessible, and it has been shown that thorough, whole-bone descriptions of structure are

more predictive than single, or few measures of bone structure [9]. A robust solution for assessing bone strength and fracture risk should account for microstructural information like HR-pQCT, but should be applicable to full bone volumes at any region of interest (e.g. hip, spine, etc.) like traditional CT. To this end, we have created a software solution that uses state-of-the-art physics-based deep learning to address the limitation of existing medical image data acquisition technology.

TECHNOLOGY/SOLUTION DESCRIPTION

We have developed and submitted a patent for an algorithm that 1) improves the resolution of medical image data and 2) uses the improved medical image data in a novel fracture risk assessment. In this system, a physics-based generative adversarial neural network is used to predict high-resolution image data from low-resolution image data in a process called super-resolution. CT image data is transformed from a resolution of 250-500 microns to 50-100 microns with sharp, and accurate, delineation in the trabecular microarchitecture consistent with what is visible in a MicroCT scan (Figure 1). From these image data, the novel fracture risk algorithm considers the spatial distribution of microarchitecture. For the first time, microarchitectural parameters are obtainable at sites of frequent fracture and can assist clinicians in diagnosing osteoporotic fracture risk.

The novelty of our algorithm is threefold. 1) A novel, physics-based approach has been implemented to constrain the neural network to physiologically-plausible predictions of microarchitecture. 2) We've curated a unique dataset for training that consists of bones scanned on both a MicroCT machine, as well as traditional lower-resolution clinical CT. In past implementations of super-resolution of medical image data, high-resolution image data is artificially down-sampled to create lower-resolution input data. We've demonstrated that this approach does not faithfully reproduce data that would have originated from a clinical environment (Figure 2). Finally, 3) our fracture risk algorithm is the first

of its kind to consider the spatial distribution of microarchitecture in whole bones. The algorithm considers the same physics that govern fabric tensor-derived material properties of bone shown to accurately reflect its mechanical behavior [13-15]. Detailed bone architecture is now accessible at sites susceptible to fracture (proximal femur, spine, etc.), whereas current high-resolution imaging technology is limited to distal skeletal sites.

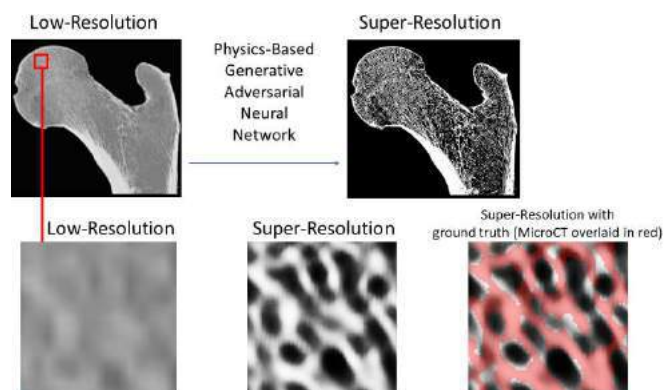


Figure 1. Top: Example of our super-resolution algorithm on the proximal femur of a bone not used in training. Bottom: 5x5 mm section of bone detailing the quality of the super-resolution algorithm compared to MicroCT (right, red overlay).

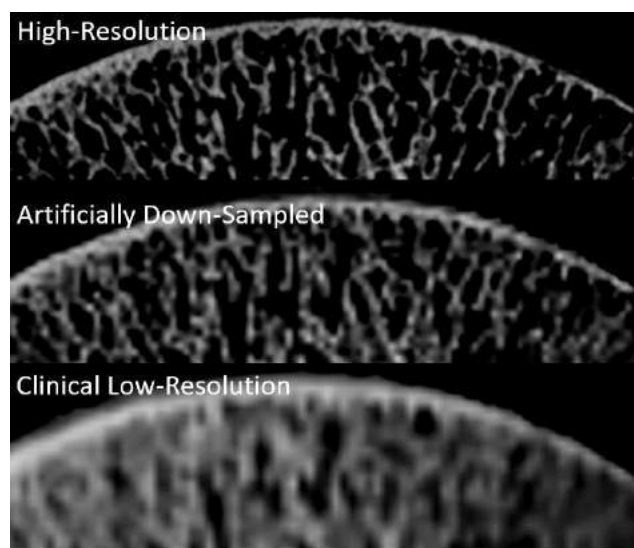


Figure 2. Example of artificial down-sampling providing similar detail to the original high-resolution image. In both the artificial down-sampling image and the clinical low-resolution image, the resolution is theoretically the same.

BUSINESS CASE

The primary use case for this technology is an opportunistic use of available image data at hospitals and imaging centers around the country. Roughly 40% of individuals over the age of 65 will have a CT scan during a typical year. Most of these scans are for reasons other than osteoporotic diagnosis (e.g. abdominal pain) but hip and spine image data are coincidentally present in these scans. The problem is that since these images are not tailored specifically to look for osteoporosis, they often do not provide high enough resolution to make informed decisions about the patient's bone strength, thus limiting any rational treatment

decision-making. We are addressing this issue with our technology that enhances low-resolution image data and can be opportunistically applied to non-osteoporosis-related image data. The value proposition is clear: fix a technological constraint to instantly gain a free, convenient, and large-scale screening tool.

Given the above, a proposed use case is: A hospital pays for our software, such that they can provide large-scale osteoporotic fracture risk screening. In the event an individual has been flagged for high risk of osteoporotic fracture, subsequent screenings and intervention may take place, which provides additional income to the hospital. Since obtaining reimbursement statutes for new medical technology is a long and cumbersome pathway, the opportunistic use case of available image data circumvents the need for reimbursement in the initial adoption of the software. As the software gains adoption through beneficial use and acceptance, the case can be made for a stand-alone practice where image data is gathered for the sole intent of detailed osteoporotic fracture risk assessment.

We are currently working with the University of Texas Health Science Center at San Antonio's department of radiology, as well as clinical partners in the university hospital system to further develop the technology, implement the solution into their medical image data processing workflow, and test the feasibility. Moreover, we are collaborating with a large medical scanner manufacturer to explore additional product opportunities.

As a non-profit research and development organization, the path to market requires a spinoff of a small, startup company. Currently, we are working toward validating our fracture risk assessment in a small, cadaveric study. If successful, a large cohort will be recruited for a clinical study that will accompany the 510(k)-device application to demonstrate the validity in the approach and its clinical utility and accuracy. A 510(k) submission is noted as a precedent has been set for medical image-based fracture risk assessment tools, as well as image enhancement software (e.g. O.N Diagnostics, FRAX, Canon's Advanced Intelligent Clear-IQ Engine, etc.). In the meantime, a Q-submission will be presented to the FDA for their initial feedback and concerns. In addition, an alternative path to market will be explored via simple licensing agreements of our patent to a CT manufacturer. In this way, an established medical device company may implement our software into their existing medical scanners and assume the risk of bringing the product to market. The largest risk of our product is an inability to predict fracture risk better than existing methodologies, such as O.N. Diagnostics, FRAX, and published algorithms in the literature. However, our alternative path to market partially ameliorates this risk, as medical scanner manufacturers are interested in the super-resolution technology alone, which we've demonstrated success with.

ACKNOWLEDGEMENTS

The authors of this submission would like to thank Canon Medical Systems, USA for their funding of the initial research and development.

REFERENCES

- [1] Ferrari, S et al., 2016, Arch Osteoporos, 11(1).
- [2] Melton, L, 2003, J Bone Min Res, 18(6).
- [3] National Clinical Guideline, 2012.
- [4] Kanis, J et al., 2000, Osteoporos.Int., 11(8).
- [5] United Nations, 2009, Population Division of the Department of Economic and Social Affairs of the United Nations Secretariat.
- [6] Hernandez, C et al., 2017, J Bone Min Res, 32(6).
- [7] McCreadie, B et al., 2000, J Bone Min Res, 15(12).
- [8] Gross, T et al., 2013, Biomech Model Mechanobiol, 12(4).
- [9] Bredbenner T et al., 2014, J Bone Min Res, 29(9).

SLIC-VAD: A WIRELESSLY POWERED LVAD WITH MAGNETIC LEVITATION BEARINGS

**Shweta Karnik (1), Huang Chen (1), Simon Kiang (4), Arun Kumar Kota (2), Yaxin Wang (3),
Joseph Cavallaro (4), Oscar H Frazier (3), Lakshmi Prasad Dasi (1)**

- (1) Department of Biomedical Engineering, Georgia Institute of Technology and Emory University,
Atlanta, GA, USA
(2) Mechanical and Aerospace Engineering, North Carolina State University, Raleigh, NC, USA
(3) Innovative Device and Engineering Applications, Texas Heart Institute, Houston, TX, USA
(4) Electrical and Computer Engineering, Rice University, Houston, TX, USA

PROBLEM STATEMENT

Heart failure (HF) is one of the leading causes of death, affecting nearly 6 million people in the United States (US). In 2012, HF contributed to more than 10% of the total health expenditure costs for cardiovascular diseases. These costs are projected to increase by 127% to \$69.8 billion by 2030 [1]. Other than significantly increasing the economic burden, HF greatly reduces patients' mobility and quality of life.

Heart transplantation is the optimal surgical therapy for end stage HF; however, this therapeutic option is progressively limited. Due to the limited availability of donor hearts, left ventricular assist devices (LVADs) have emerged as a primary treatment modality for HF as both bridge-to-transplantation and destination therapy. After the discontinuation of HeartMate II (Abbott labs) and HVAD (Medtronic), Abbott's HeartMate III remains as the only implantable, FDA approved LVAD on the market.

Despite the clinical success, LVAD therapy is known to have adverse effects that negatively impact patient outcomes and may result in fatalities. After LVAD implantation, the stroke rates fall anywhere between 11-47% whereas the incidence of gastrointestinal (GI) bleeding is reported to be around 11-40% [2]. LVADs are driven by percutaneous drivelines, which can cause infection and lead to rehospitalization and surgical intervention. Moreover, the inflow cannula is susceptible to thrombus formation, embolization of thrombus puts the patient at a high risk of ischemic stroke. In case of a thrombosis related LVAD failure, the patient might need undergo a second open heart surgery to replace the implanted device.

There is an urgent unmet need for a long-term, implantable LVAD to cater to the widening gap between the donors and the patients, along with the growing number of patients with end stage HF. To address this need of a reliable LVAD therapy that effectively causes no adverse events post implant, we propose the SLIC-VAD, a centrifugal pump designed using a synergistic amalgamation of material science, fluid

dynamics, wireless energy transfer, magnetic levitation, and hemodynamics.

TECHNOLOGY/SOLUTION DESCRIPTION

The SLIC-VAD is a centrifugal LVAD specifically designed to minimize the post implant complications using our team's expertise. Most of the LVADs aim to utilize one or more of fluid dynamics, magnetic levitation, hemodynamics, material science, wireless energy transfer in their design; SLIC-VAD on the other hand, is designed to be performant on all these fronts (Figure 1Figure 1).

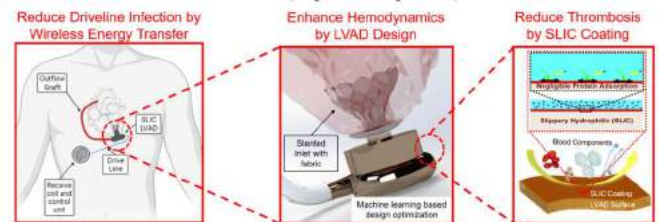


Figure 1 SLIC-VAD with a stented inlet, wireless energy transfer and super hydrophilic (SLIC) coating

The hydrodynamic components of the SLIC-VAD are optimized to offer superior fluid dynamics performance under complex inflow conditions using a state-of-the-art machine learning algorithm. It will include a stented inlet, motivated by the transcatheter aortic valve technology, to improve the inflow hemodynamics and reduce the risk of thrombosis. Furthermore, we plan to incorporate flexible rotors which will open the possibility of low-cost manufacturing.

The blood contacting regions of the SLIC-VAD will be coated with a novel slippery and hydrophilic coating with ice-like hydration layers. This innovative coating would dramatically hinder the subsequent steps of blood coagulation cascade by imparting substantial lateral forces and dislodge adsorbed blood proteins on a molecular scale.

SLIC-VAD will incorporate magnetically levitated bearings to eliminate the contact bearings and avoid blood stasis in the narrow gaps of the device. SLIC-VAD's driveline will be replaced with wireless energy and communication transfer to dramatically reduce the infection caused by the percutaneous drivelines. The wireless communication will enable the clinicians to remotely monitor the device operation and provide real-time management of any complications that may arise.

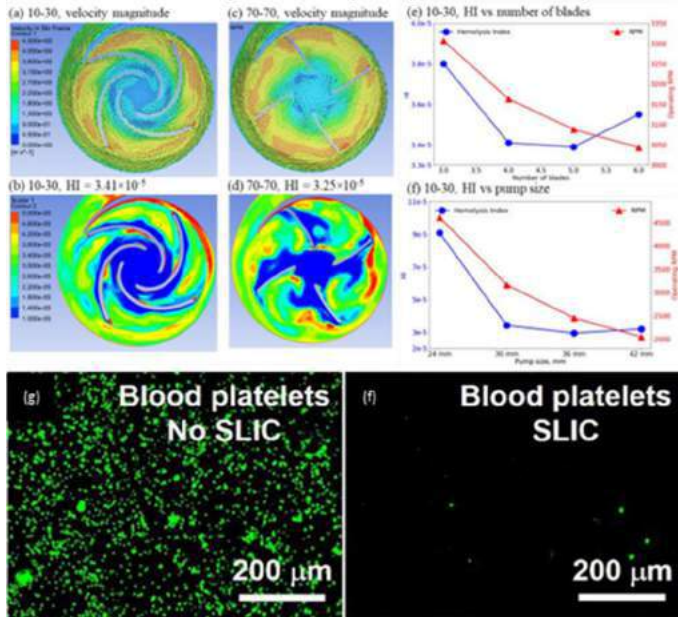


Figure 2 (a & f) Preliminary Results using a validated CFD Model. (g-f) Blood platelets adhesion without and with SLIC coating
SLIC-VAD's initial experimental and CFD analysis have shown its ability to achieve a pressure of 90 mmHg at 5 L/min and 3000 RPM. Figure 2 (a–d) shows the results from our initial design optimization, where in flow field and the hemolysis index (HI) of two rotor designs are compared. We also investigated the effects of the pump size and the number of blades on HI Figure 2 (e–f). It is observed a flow – targeted optimization is insufficient since better flow may not correlate with less blood damage. The fluorescence microscopy images indicate virtually negligible platelet adhesion with our novel SLIC coating (Figure 2(g–f)).

BUSINESS CASE

The global LVAD market is projected to grow significantly at a CAGR of 17.6% from 2021-2028, with a valuation of \$1.8 billion in 2020.

SLIC-VAD is designed to be a destination and bridge-to-transplantation therapy for end-stage HF patients, our primary end users. We also consider family members, caregivers, and healthcare professionals to be our end users. Insurance companies are expected to be the main payer, in addition to government programs covering some or all of the device's cost.

Given the high impact of our work, we plan to incorporate a targeted marketing approach to touch as many patients' lives as we can. We aim to establish a relationship with key stakeholders/decision makers of the LVAD therapy, namely, cardiac surgeons, cardiologists and medical centers specializing in heart transplantation.

SLIC-VAD is a Class III device and will follow the FDA premarket approval (PMA) pathway. The preclinical studies will include 30 day 15 GLP chronic ovine studies post implantation and *ex vivo* hemocompatibility tests. Upon successful completion of the initial

prototype evaluation, we will apply for an Investigational Device Exemption from the FDA to gather early clinical data that will be used for the PMA application.

The clinical trials evaluating the HeartMate III (NCT02224755) utilized 1000 patients in a randomized parallel assignment. We anticipate having a similar study protocol and number of patient volunteers for our SLIC-VAD's randomized trials where HeartMate III would serve as a clinical control. Key performance indicators will include the rate of survival six months after implantation, without stroke or device malfunction. Our work is currently supported by a government funding, we plan on applying for venture capitalist funding and business targeted NIH grants in future.

Bringing a novel LVAD to market successfully is a task that requires us to overcome a multitude of hurdles. Some of the ones we anticipate are related to cost, physician adoption and patient selection. Our key manufacturing concerns include ensuring precise manufacturing and usage of high-quality materials, establishing a robust tracking system for accountability, and implementing a sterilization process to mitigate infection risks.

In 2019, a new high annual volume of 3,198 LVADs implants was recorded in the registry history [3]. We estimate to achieve the design freeze and FDA approval by 2026 and 2032, respectively (Figure 3). With the rapidly increasing HF patient population, we plan to have 20% market penetration by 2035 and generating a cumulative revenue of \$2 billion in the US.



Figure 3 SLIC-VAD's financial projections

Currently the LVAD market is dominated by the companies listed below (Table 1), however, these companies fail to address the comprehensive market needs. SLIC-VAD's unique synergistic approach towards tackling the market needs is what distinguishes it from the rest of its competitors.

Table 1 Competitive Market Analysis

	Optimized Hydrodynamic Components	Stented Inlet	Anti-Thrombotic Coatings	Magnetically Levitated Bearings	Wirelessly Driven	Wireless Communication Enabled
SLIC-VAD	✓	✓	✓	✓	✓	✓
Abbott Laboratories	✓	✗	✗	✓	✗	✗
Abiomed Inc.	✓	✗	✗	✗	✗	✗
Medtronic	✓	✗	✗	✓	✗	✗

ACKNOWLEDGEMENTS

Research supported by the National Institute of Biomedical Imaging & Bioengineering under award number 1R21EB033960-01.

REFERENCES

- [1] Tsao C. W. *et al. Circulation*, vol. 145, no. 8, pp. e153-e639, 2022.
- [2] Sahni A. *et al. Annals of Biomedical Engineering*, 2023
- [3] Guglin M. *The VAD Journal*, vol. 8, no. 1, p. 1, 2022.

I-KINCOR: REVOLUTIONALIZING PEDIATRIC DUCT – DEPENDENT SURGERIES.

Luis René Mata Quiñonez (1), Shweta Karnik (1), Srujana S. Joshi (1), Leon Cheng (1), Holly Bauser-Heaton, MD, PhD(1, 2), Lakshmi Prasad Dasi, PhD(1)

(1) Wallace H Coulter Department of Biomedical Engineering, Georgia Institute of Technology and Emory University, Atlanta, GA, USA
(2) Children's Healthcare of Atlanta, Atlanta, GA, USA

PROBLEM STATEMENT

Congenital heart disease (CHD) is present in 17.9 of every 1000 newborns representing one of the leading causes of neonate mortality [1]. The prevalence of patients with duct-dependent circulation, wherein the ductus arteriosus (DA) is the only pathway for the pulmonary blood supply, is around 8 out of 10,000 births [2][3].

For subsequent surgical repair, the palliative treatment for these patients is maintaining the patency of the DA (PDA). Traditionally, the modified Blalock–Taussig–Thomas shunt (BTTS), which is a surgical connection between the aorta and the pulmonary artery is used. However, it has a high infant mortality rate of about 20% [4]. Previous solutions include formalin infiltration, balloon angioplasty, and thermal balloon dilation, but are associated with complications like variability in the length of duct patency response [5], cardiac and pulmonary artery perforation [6] and aneurysmal dilation and stenosis [7] respectively, making them unsuitable for use.

To overcome these limitations, a minimally invasive procedure of PDA stenting has been used. It involves the percutaneous deployment of coronary stent in the DA, and allows for higher stent patency length, lower operative risks, shorter hospital stay and lower mortality rate than BTTS procedure with a risk ratio of 0.58 [4]. However, there are associated complications to PDA stenting. Meta-analysis shows higher reintervention rates in PDA stent groups when compared to surgical shunt groups with a risk ratio of 1.63 [4]. Furthermore, stenting procedures may also cause pulmonary artery isolation, stent stenosis, thrombosis and fracture [4][8].

One of the most important factors for the successful stenting of the PDA is pre-procedural planning; in which main considerations are: determining the correct stent dimensions, predicting the interaction of the stent with patient anatomy, and ultimately deciding patient candidacy. Hence, there is an unmet need for a surgical planning platform for this procedure.

TECHNOLOGY/SOLUTION DESCRIPTION

We are committed to enhance the pre-procedural planning of ductal stenting, which currently involves visualizing the patent DA and adjacent structures from CT scans to identify the required stent dimensions (length and diameter) and the most optimal surgical access. However, this process does not take into account the complex and tortuous DA anatomy, and unexpected outcomes like partial covering of the duct length, stent malapposition, migration and thrombosis, or even pulmonary isolation might occur [4][8].

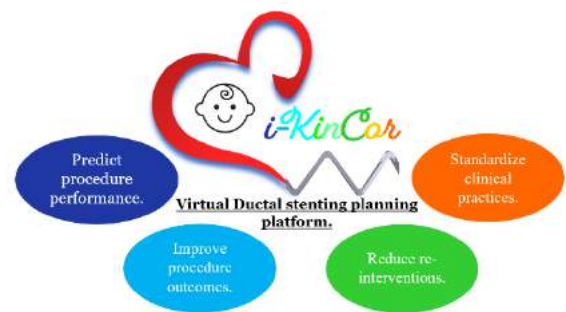


Figure 1. Benefits of i-KinCor.

i-KinCor is a 3D computational modeling framework that will serve as a virtual surgical planning tool for physicians for ductal stenting, and to predict procedural outcomes and complications.

The computational framework will allow simulation of transcatheter stent deployment into patient-specific anatomies and analyze the structural interaction between the stent and native DA. We are pioneers in the application of computational simulations for pre-procedural planning of ductal stenting. Figure 1 lists the benefits of our solution.

Figure 2 presents an outline of the steps of the proposed solution. Pre-procedural chest CT/MRI scans will be analyzed, segmented and discretized for simulations using commercially available software. This process is intended to identify the stent dimensions and the most adequate access to the DA. The selected stent, balloon and guide wires will be collected from our database of CAD models. Finite element analysis (FEA) will be performed on the patient-specific 3D model of DA to simulate transcatheter deployment of the stent. Key anatomic features of the DA and deployment attributes that lead to favorable stenting outcomes will be identified. These data will help the interventional cardiologist to decide if the patient is suited for the procedure and to be aware, in advance, of potential complications that might occur. This innovative approach will revolutionize the pre-procedural planning for ductal stenting resulting into reduced procedure risk and time, selection criteria for patient candidacy, longer duration of palliation and improved communication between the interventional and surgical teams for short and long-term medical decisions. This will also pave the way for a standard solution by homogenizing the best clinical practices regarding the device selection and pre-procedural planning across medical centers.

The pathway towards the commercialization of this technology requires the replication of the computational methods in large populations of patients to contemplate the inherent variability of DA geometries and tissue properties among patients. Applying this iterative process will permit us to refine the solution.

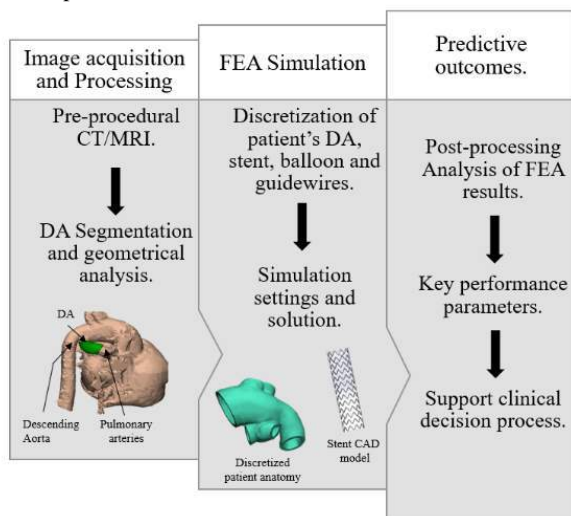


Figure 2. Workflow Schematic of i-KinCor.

BUSINESS CASE

With the increasing prevalence of CHDs in the United States, the pediatric population born with duct-dependent circulation is growing [1]. Due to the complicated patient anatomies and unforeseeable complications, the clinicians have to decide the best course of treatment within limited time frame which may lead to reinterventions and rehospitalizations in future. Currently, there is no available technology for surgical planning of ductal stenting and predicting the post-procedural outcomes. i-KinCor is a niche product which provides a personalized virtual platform to bridge this market gap.

Within the stakeholders of i-KinCor, the primary end users will be the interventional cardiologists, cardiothoracic surgeons to decide the best treatment option. Our technology could be further extended as a surgical training platform for medical residents, thereby increasing the

impact on patient outcomes as well as expanding our market. We expect the pediatric centers specializing in CHDs and the insurance companies to be our main payers.

We aim to establish a relationship with key decision makers as our marketing strategy. We will conduct demonstrations using case studies proving the efficiency of i-KinCor across different hospitals and medical centers. Additionally, we will incorporate digital marketing elements including engagement via website, professional platforms and social media and present at clinical conferences.

To commercialize our technology, we will need a facility with robust IT infrastructure including workstations, servers, access to supercomputers and software licenses. Our team will consist of highly skilled engineers and marketing and sales, finance, and IT departments. We plan on applying for venture capitalist funding and business targeted NIH SBIR and STTR grants for funding our future work.

i-KinCor is a Class II medical device and will follow the FDA 510k pathway. We will use FEops HEARTguide as our predicate device since we use a virtual surgical planning platform. We plan on achieving design freeze and 510k approval by 2025 and 2027, respectively (Figure 3). We estimate to have 20% market penetration by 2033: generating about \$65 million cumulative revenue in the US.

Some of the anticipated risks are the technology adoption, quality of patient scans, and meeting service time. The customers would need to institutionalize the usage of this technology to properly exploit the benefit of an improved planning process.

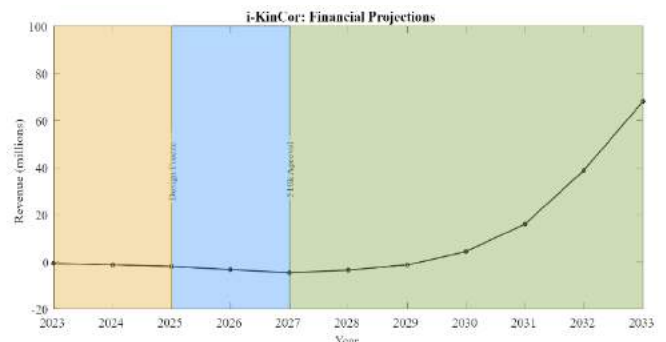


Figure 3. i-KinCor's financial projections.

ACKNOWLEDGEMENTS

We would like to acknowledge the HeRO research funding provided to us by Children's Healthcare of Atlanta.

REFERENCES

- [1] Centers for Disease Control and Prevention. Morbidity and mortality weekly report (MMWR). 2023
- [2] Heaton J, and Heller D. Single Ventricle. In: StatPearls Treasure Island. Publishing; 2022.
- [3] Mai CT, et al. Birth Defects Res. 2019; 111(18): 1420-1435.
- [4] Bauser-Heaton, H et al. Journal of the Society for Cardiovascular Angiography & Interventions, 1(6), 100392. 2022
- [5] Rudolph, A. M et al. The New England journal of medicine, 292(24), 1263–1268.1975
- [6] Walsh, K et al. British heart journal, 69(3), 260–262. 2020
- [7] Annual meeting of the association of european paediatric cardiologists, Oslo, Norway, Pediatric Cardiology, 11(4), 231–256. 1990
- [8] Chamberlain, R. C. et al., Journal of the Society for Cardiac Angiography & Interventions, 95(6), 1141–1148. 2020

PITCH COMPETITION: SOLVING THE PROBLEM OF BICYCLE HELMET FIT

William J. Makowski (1), Thomas L. Martin (2), William A. Schaudt (3)

- (1) Graduate School, Virginia Tech, Blacksburg, VA, USA
(2) Department of Electrical and Computer Engineering, Virginia Tech, Blacksburg, VA, USA
(3) Virginia Tech Transportation Institute, Virginia Tech, Blacksburg, VA, USA

PROBLEM STATEMENT

Evidence shows that the use of bicycle helmets significantly reduces the risk of head injury during a crash [1]. Sadly, the use of improperly fitting helmets and its relationship to greater risk of injury has been continually identified over the last twenty years [2], [3], [4], [5]. Common problems that relate to poor helmet fit are wearing helmets that are too wide, helmet's being too high on the forehead or helmets not being adjusted properly [3], [4], [5].

In an effort to learn about additional problems relating to helmets, I conducted primary qualitative research, through Customer Discovery (CD). For CD, I conducted 166 Problem Interviews, with pro and semipro athletes, masters riders, downhill riders, various demographics of parents and bike industry personnel. Then, I conducted another 118 interviews through the NSF I-Corps program with pediatricians, coordinators at Safe Kids, the primary volunteer for the Bicycle Helmet Safety Institute, bicycle helmet testing lab personnel, as well as researchers at various universities regarding bicycle helmet fit. The CD interviews focused on three types of risk, product risk (problem), market risk (existing alternatives) and customer risk (customer segment) [6].

During the Problem Interviews, I spoke with a group of potential early adopters who I refer to as US Bike Parents, meaning parents who bought a bike from a US kids specific bike company. I conducted thirty one Problem Interviews with US Bike Parents. I am highlighting US Bike Parents as they appear to be a viable group of early adopters, for a solution that will be described in the Technology/Solution Description section of this abstract.

Specific to US Bike Parents, for product risk, I found that eight of the parents experienced a Severe Problem of helmet fit for their child. A Severe Problem of helmet fit means a difficulty so severe, they went to multiple bike shops, returned multiple helmets and/or disregarded a buying option because "it won't work," with severe amounts of frustration expressed. This finding would lead me to believe that helmet

fit was a concern for this demographic of parents and that they are potential early adopters of a solution that would solve that problem.

TECHNOLOGY/SOLUTION DESCRIPTION

Bicycle helmets can reduce peak linear acceleration (PLA), as well as other injurious forces to the brain [7]. Historically, expanded polystyrene (EPS) has been the most commonly used material for bicycle helmets to reduce PLA to the brain in the event of a crash [8]. Due to the material's ability to reduce PLA, it is still commonly used [8], [9].

In 2014, Smith Helmets introduced the Overtake. The Overtake's helmet liner was a combination of EPS and a material called Koroyd, an extruded thermoplastic structure [10], [11]. Bontrager released the next iteration of structure-based helmets with the introduction of Wavecel. Wavecel helmets are a combination of both EPS and Wavecel, a stacked origami thermoplastic structure [12], [13]. Wavecel is a more complex structure than Koroyd and reduces both PLA and rotational acceleration [13]. In 2021, Hexr's additively manufactured hexagonal helmet, is the most recent iteration of helmets with thermoplastic structures [14]. Despite the developments in both design and manufacturing technologies, the safest commercially available bicycle helmets as of February 10th, 2023 are entirely EPS based helmets according to Virginia Tech's Helmet Ratings [15]. However, the one exception is the Bontrager Specter Wavecel helmet, just making the top 30 [15].

The goal of designing additively manufactured structures is not necessarily to produce a "safer" helmet, but rather to use additive manufacturing to create a better fitting helmet, which can be difficult with traditional injection molded foam helmets. To create such a helmet, the development process includes: 1. Designing for fit, which incorporates creating a digital surface; 2. Designing for protection, which incorporates designing a mesostructure; and finally, 3. Developing a feedback loop for evaluating mesostructure performance.

The technologies include scanning, surface generation, mesostructure design, finite element analysis (FEA) and production, resulting in new methods of product development for personal protective equipment.

For initial product development I have focused on step 2. Designing for protection. The basis for the mesostructure design process was split into two groups: Group 1: Recreating structures found in previous research and Group 2: Recreating structures currently on the market. Figure 1 shows three structures I designed in the latticing software nTopology, based on the Group 1 and Group 2 design strategies.

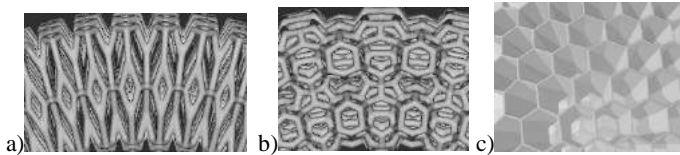


Figure 1: a) Group 1 using a Weaire-Phelan unit type, b) Group 1 using a Kelvin unit type, c) Group 2 using a Hexagonal Honeycomb unit type

For step 2. Designing for protection, I designed and printed several different test coupons, which have gone through four phases of impact testing. The parameters for impact testing were based on the Consumer Product Safety Commission (CPSC) standard for bicycle helmets. The parameters included using the flat anvil, headform A and ambient conditioning [16]. When impact testing, the only difference from the standard was we started with an impact velocity of 3.1m/s, and increased the velocity with each subsequent phase of testing. Recently, we tested the parts at an impact velocity of 6.2m/s, which is the highest velocity impact attenuation test for the CPSC standard [16]. In the standard, during an impact, the parts cannot experience a peak linear acceleration (PLA) above 300g [16]. During testing at 6.2m/s, one of the parts experienced a PLA of 211g, and another part experienced a PLA of 256g. We plan to move to conditioned testing soon.

Additional product development will focus on 1. Designing for fit and 3. Developing a feedback loop for evaluating mesostructure performance. When designing for fit, in order to collect cranial measurements two techniques can be leveraged, 3D scanning and using a photo based software that measures and interprets images, such as photogrammetry. When developing a feedback loop for evaluating mesostructure performance homogenization and impact testing should help determine what geometries are best suited for reducing PLA.

BUSINESS CASE

As previously mentioned in the Problem Statement section, from the Customer Discovery Interviews, US Bike Parents appear to be a viable group of potential early adopters, where the parents are the customers and the children are the end users. Based on the interviews, the value proposition is, parents who want a high quality riding experience for their child will buy a custom fit helmet to eliminate the twenty minutes per week they spend adjusting their child's helmet.

Current revenue models include direct sales through a website, channel sales through product reviewers and US children's specific bicycle companies, as well as retailer sales through bicycle retailers. It is anticipated that orders will be fulfilled through drop shipping, as each helmet is custom made. Based on Customer Discovery, specifically the Solution Interviews, we developed value and cost based pricing models, where we anticipate pricing will be \$150 per helmet.

For bicycle helmets, the primary regulatory body is the CPSC. As directed by their standard, the helmets must pass the peripheral vision test, positional stability test, dynamic strength of retention system test and impact attenuation test [16]. In regards to production, additive

manufacturing has advantages for producing complex lattice structures and customized solutions, when compared to injection molding [17]. However, as we have impact tested parts, the parts have performed inconsistently which is concerning. So we are currently navigating production strategies.

As stated in section Technology/Solution Description, additional product development will include 1. Designing for fit, which involves: developing and improving the user experience when collecting scan data and; optimizing the digital workflow from the collection of scan data to the final print. In addition, product development will include 3. Developing a feedback loop for evaluating mesostructure performance, which involves a combination of static FEA, dynamic FEA and impact testing to achieve lower PLAs and reduce the part weight. Other commercialization activities include offering a pilot program aimed at potential early adopters, as well as establishing a strategy for localized and automated production.

Other commercialization activities include, we have submitted a provisional patent application, through our technology transfer offices. Through CD, another market we identified as a viable group of early adopters are riders who have purchased a high-end or custom built bike. Finally, we have identified cranial helmets and military helmets as additional product categories for custom fit applications.

ACKNOWLEDGEMENTS

First of all we would like to thank Virginia Tech's Institute of Creativity, Arts and Technology for funding initial product development through a SEAD Grant. We thank Dominic LoPinto and Dr. Emily Kieffer for their feedback and expertise in the design process. We are thankful to Dr. Christopher Williams and Bemnet Molla at Virginia Tech's DREAMS Lab for their assistance with printing parts. We also thank Larry Rose for his help during the initial stages of testing. Finally, we would like to thank the Dr. Mark Begonia and Ethan Harris at the Virginia Tech Helmet Lab for their assistance and expertise during impact testing.

REFERENCES

- [1] Lee, R et al., *Injury Prevention*, 15:125-131, 2009.
- [2] Bromell, R & Geddis, D., *J Paediatrics and Child Health*, 53:145-148, 2017.
- [3] Rivara, F et al, *Injury Prevention*, 5:194-197, 1999.
- [4] Rezendes, J, *J Pediatric Nursing*, 21:35-44, 2006.
- [5] Thai, K et al, *Traffic Injury Prevention*, 16:268-275, 2015.
- [6] Maurya, A., *Running Lean*, 2nd Edition, 2012.
- [7] King, A et al, *IRCOBI Conference*, 1-12, 2003.
- [8] Kroeker, S et al., *J of Biomechanical Engineering*, 142:1-11 2020.
- [9] Mills, N., *British J of Sports Medicine*, 24:55-60, 1990.
- [10] Bland, M et al., *Traffic Injury Prevention*, 19:S158-S163, 2018.
- [11] Gokhale, V., *Purdue University*, 2016
- [12] Harris, J., *University of Cambridge*, 2018
- [13] Bliven, E et al., *Accident Analysis & Prevention*, 124:58-65, 2019.
- [14] Jafferson, J et al, *Materials Today*, 46:1247-1260, 2021.
- [15] *Virginia Tech Helmet Ratings*, www.helmet.beam.vt.edu/bicycle-helmet-ratings.html, accessed Feb, 10th 2023.
- [16] CPSC, Consumer Product Safety Commission; 16 CFR Part 1203, 1998.
- [17] Pereira, T et al, *Procedia Manufacturing*, 30:11-18, 2018.

PITCH COMPETITION: FACILIFLOW: AN IMPLANTABLE DEVICE TO PREVENT THE ONSET OF BREAST CANCER-RELATED LYMPHEDEMA

A. Swarup (1), A. Vella (1), K. Rowley (2), J. Frattolin (1), J. Moore Jr. (1)

(1) Department of Bioengineering, Imperial College, London, UK
(2) Lympha Motus Ltd, London, UK

PROBLEM STATEMENT

Approximately one in seven women will develop breast cancer. In 2021, there were some 282,000 new breast cancer diagnoses in the US. The removal of lymph nodes and severing of lymphatic vessels during breast cancer surgery disrupts lymph flow and impairs normal fluid removal from the arm. This leads to debilitating and incurable swelling of the arm (breast cancer-related lymphedema; BCRL) in approximately 21% of breast cancer patients [1]. This translates to 59,220 new cases of BCRL each year, with a prevalence of 760,000.

There is no cure for BCRL, forcing patients to live with a constant reminder of their cancer as well as long term problems with pain, immune dysfunction and recurrent infections. With five-year survival rates for breast cancer now exceeding 90% [2], the incremental costs for BCRL care for the US are estimated at \$6B/year.

Despite the development of at least two surgical procedures, three pharmaceutical approaches and two devices aimed at treating BCRL, it is still considered incurable in the general setting. This is in part because the surgical procedures (which show mixed success rates) require specialized microsurgical skills, but also because once the swollen arm tissue has fibrosed, those adaptations are likely irreversible.

Current surgical BCRL strategies are predominantly aimed at treatment. Lymphovenous Anastomosis (LVA) involves connecting lymphatic vessels to veins, both of which are typically <1mm diameter thus requiring microsurgery. Autologous Lymph Node Transfer (ALNT) requires a lymph node plus surrounding tissue to be harvested from another part of the body and moving it to the axilla. Surgeons must connect the node's blood supply, also requiring microsurgery. LVA and ALNT show mixed success rates, often based on short follow up periods (<3 years). These procedures are generally not covered by insurance or national health programs.

Pharmaceutical approaches to treatment include Lymfactivin, a gene therapy version of vascular endothelial growth factor C (VEGF-C),

widely acknowledged as the most effective compound to promote lymphatic vessel growth [3,4]. Lymfactivin is infused into harvested tissue as an adjuvant to ALNT. Clinical trials showed no benefit, perhaps due to the immature form of VEGF-C produced. CellTaxis is in clinical trials with Acebilustat, targeted at treating BCRL.

The only device in clinical trials is Fibralign's BioBridge (a collagen-based surgical mesh) which aims to treat and prevent BCRL by wicking fluid out of the arm and guiding lymphatic vessel growth. BioBridge is deployed via subcutaneous injections, requiring additional training, surgery and special equipment.

In the absence of widely available, reliable means of prevention or treatment, BCRL patients at best can only manage their disease through complete decongestive therapy (CDT), comprising compression bandaging, specialized massage, skincare, and exercise. CDT requires fastidious patient compliance, and generally will at best only limit further arm swelling. Over 80% of BCRL patients take health-related leave from work, and many suffer social isolation and depression [5,6]. Physical Therapists who help patients manage their BCRL have stated that prevention should be a priority of research and development efforts [7].

We aim to develop an effective, economical means of BCRL prevention that can be easily integrated into the current standard care pathway without additional expertise or equipment.

TECHNOLOGY/SOLUTION DESCRIPTION

Our implantable medical device seeks to prevent, rather than cure, BCRL. FaciliFlow (Figure 1) would be easily implanted by any surgeon at the time of the original cancer surgery to encourage lymphatic vessel regrowth and lymph flow normalization. It is made from materials well-known to the FDA and attached to surrounding tissue with 2-4 sutures in minutes.

Its patented design [8] features multiple parallel channels to minimize resistance to fluid flow, imitating the multiple parallel pathways formed by afferent lymphatic vessels as they approach lymph nodes. It also releases VEGF-C in a controlled manner over 90 days. Fluid flow also increases VEGF-C effectiveness [9]. Preliminary data from a study in rats indicated a success rate of 55% in FaciliFlow's ability to regrow new lymphatic vessels, comparable to the success rate of ALNT + injected VEGF-C protein [10].

FaciliFlow is injection molded from medical-grade silicone, with encapsulated slow-release of fully functional VEGF-C, and a water-soluble excipient that facilitates VEGF-C release. We aim to achieve a therapeutic concentration of 100ng/mL [11] at a distance of 2 cm from the implant for 90 days, providing a consistent, locally-delivered, functional dose following lymphatic injury to elicit healing. Local release should minimize the risk of VEGF-C reaching therapeutic concentrations in tumor locations. We will be monitoring blood VEGF-C levels in preclinical and clinical trials as verification.

FaciliFlow's design is being fully verified under an ISO13485-compliant Quality Management System. Next steps are large animal trials and preparation for clinical trials.

BUSINESS CASE

The total addressable market for BCRL prevention is all breast cancer patients undergoing surgery; approximately 90% of breast cancer patients in the USA, or 253,800 patients. At an anticipated price of \$1000 (based on other medical devices of similar complexity), the USA market is approximately \$250M per year. We estimate the EU market to be of similar size to the USA market.

The device will be attractive to insurance and provider-associated payers who would also be responsible for the care of BCRL patients, costing \$7450 per year for each patient in the first two years (and slightly lesser amounts thereafter, lifelong for each patient).

The primary challenge to this device will be uptake by surgical oncologists. Surgeons may fail to appreciate the extent of the condition because patients must be followed for at least three years to confirm BCRL. The development of node-sparing procedures such as Sentinel Lymph Node Biopsy may lead to the assumption that the condition is declining but we have performed an extensive meta analysis of BCRL incidence (to be published soon) showing that the incidence rate remains at around 20%, the same as Disipio noted in 2013 [1]. We have recruited surgical oncologists and patient advocates to our advisory board and will continue to work with KOLs as we prepare for regulatory approval and reimbursement.

Remaining hurdles to market include preclinical and clinical trials, production of clinical grade VEGF-C, regulatory approval and reimbursement. Our current funding is being used to produce implants under a regulatory-compliant QMS. We are seeking funding for trials. We have received quotes for producing clinical grade VEGF-C (which is already available as research grade).

We are in discussions with regulatory bodies in the UK and US. The FDA will likely consider this a Class III combination product. Other permanent silicone implants that release drugs have been in use since the 1980s. An important determinant of the regulatory pathway will be the primary outcome. We believe that evidence of lymphatic vessel reconnection (which can be done minimally invasively with near-infrared imaging), which should occur within six months, should suffice as a primary outcome. If regulatory bodies insist on BCRL development as a primary outcome, this will greatly increase the costs of the clinical trial.

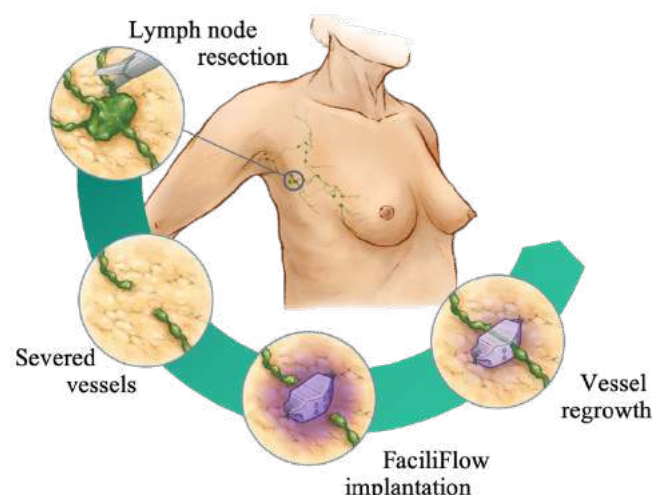


Figure 1: Illustration of lymph node removal during breast cancer surgery, followed by FaciliFlow implantation. Its flow channels are oriented in the original direction of flow and VEGF-C is released locally to promote lymphatic vessel reconnection.

The cost of manufacturing is estimated at <\$4 per device which provides a margin of >95%. The majority of the costs associated with the procedure of implantation will be borne by the underlying procedure rather than needing a separate surgical procedure, given that implantation is performed at the time of lymph node removal.

The breast cancer therapy market is growing at a CAGR of 8.3% [12], thus the US market for FaciliFlow has the potential to grow to \$370M in five years. In addition to the strong market pull for BCRL prevention, there is potential that the device would be of use in other lymphoedema such as cervical, womb, prostate, bladder, and head and neck cancers.

Route to Market and Dissemination: The route to market will likely imitate that for implantable medical devices employing a similar technology or therapeutic mode of action. Commercial exploitation will likely involve acquisition by an established MedTech company with pre-existing distribution networks.

ACKNOWLEDGEMENTS

The authors gratefully acknowledge funding from an NIHR i4i Grant and a Siemens Healthineers EITT Competition Award.

REFERENCES

- [1] DiSipio, T., et al., *Lancet Oncology*, 14(6), 500-515, 2013.
- [2] NCI SEER Database, 2022.
- [3] Szoke et al., *Nature Comms*, 12, 3460, 2021.
- [4] Tervala et al., *J Surg Res*, 196(1), 200-207, 2015.
- [5] Boyages et al., *Psychooncology*, 26(6), 849-855, 2017.
- [6] Moffatt, *QJM*, 96(10), 731-8, 2003.
- [7] Underwood et al., *Lymph Res Biol*, 17(3), 2019.
- [8] US Patent 11,071,618, 2021.
- [9] Goldman et al., *Am J Physiol Heart Circ*, 292(5), H2176-83, 2007.
- [10] Schindewolf et al., *Immun Inflam Dis*, 2(3), 152-161, 2014.
- [11] Sweat et al., *Microcirculation*, 21(6), 532-40, 2014.
- [12] Mordor Intelligence, 2022: <https://www.mordorintelligence.com/industry-reports/breast-cancer-therapeutics-market>

PITCH COMPETITION: PREDICTING FRACTURE HEALING BY MEASURING COMPLIANCE VIA DIRECT ELECTROMAGNETIC COUPLING

**Kevin M. Labus (1), Kirk C. McGilvray (1,2), Branislav Notaros (3), Milan Ilic (4), Julie Dunn (5)
Christian M. Puttlitz (1,2,6)**

- (1) Department of Mechanical Engineering, Colorado State University, Fort Collins, CO, USA
- (2) School of Biomedical Engineering, Colorado State University, CO, USA
- (3) Electrical and Computer Engineering, Colorado State University, Fort Collins, CO, USA
- (4) School of Electrical Engineering, University of Belgrade, Belgrade, Serbia
- (5) University of Colorado Health North, Loveland, CO, USA
- (6) Department of Clinical Sciences, Colorado State University, CO, USA

PROBLEM STATEMENT

Musculoskeletal trauma presents a major medical and financial burden, with long bone fractures accounting for 10% of all nonfatal injuries in the US [1]. Non-union, the failure to heal, occurs in approximately 5-10% of all fractures. Non-unions are gravely concerning, as analyses of direct healthcare costs associated with non-unions have been reported to be in the range of \$20,500-\$53,500 per incident [2]. These estimates do not include the indirect costs associated with non-unions such as lost wages and productivity, which are thought to represent 67-92.3% of total costs [3]. It has been reported that 72% of patients with non-unions continue to experience pain, and 41% have not returned to work 12 months post-fracture [4].

To avoid the tremendous socioeconomical costs likely to be incurred, the ability to recognize potential non-unions early in the post-injury course is of utmost importance. It has been estimated that the deleterious effects and resultant costs can be reduced by approximately 50% if fractures at risk of non-union can be addressed during the acute four-week postoperative time period [5]. Therapies to improve healing, including osteobiologics, rehabilitation, and electromagnetic stimulation, are most effective during this early healing time period. However, the prognosis of improper bony healing remains an obstacle to the early and effective implementation of these treatments. The current gold standard for monitoring healing is via biplanar radiographs. Regrettably, radiographic evidence is unhelpful during the acute healing phase due to the delayed timeframe of visible mineralization in the fracture callus. The current standard of care results in the determination of non-union ranging from 3-9 months. Thus, there remains a profound gap in the market necessitating improved early and quantitative techniques to monitor and predict the course of fracture healing.

Due to formation and remodeling of the soft fracture callus, which occurs prior to radiographically visible mineralization, the quantification of fracture site compliance has shown the ability to accurately predict healing outcomes prior to radiographic diagnosis [6-

7]. However, there are currently no clinically available solutions on the market for monitoring fracture site compliance. Therefore, we have developed a technology that leverages the temporal fracture compliance phenomenon to monitor acute healing and provide an early prediction of non-union.

TECHNOLOGY/SOLUTION DESCRIPTION

We have developed a non-invasive system that utilizes an external radio-frequency antenna to electromagnetically couple to a fractured limb to measure deformations at the fracture site under applied loading ("direct electromagnetic coupling", DEC). The DEC technique works by measuring the resonant frequency shift between the antenna and bone/hardware, which can be calibrated to determine precise deflections of the fracture from which stiffness and/or compliance of the fracture site can be calculated. Our group has (1) established the electromagnetic foundations of the DEC technique via experiments and computational models [8], (2) experimentally demonstrated the efficacy of this technique to monitor changes in stiffness using *in vitro* fracture healing models [9], and (3) validated DEC for distinguishing between normal and non-union healing in a large animal fracture model [10].

Other similar mechanical-monitoring technologies currently in development rely on modifying fracture stabilization implants by adding an implanted sensor and associated circuitry. In contrast, our DEC technology is completely external, which provides two main advantages: (1) It can be applied universally to fractures stabilized with any existing implant(s) including plates and intramedullary nails or to fractures stabilized non-operatively, such as with functional bracing. (2) Since DEC is non-invasive and the radio sensing technology is harmless, it presents no significant risk to the patient, enabling an easier clinical implementation and relatively few regulatory hurdles.

Additionally, we have developed the DEC technology into a telemetric device that can be easily used by the fracture patient in their home, and the data are transmitted for analysis. This telemedicine

approach enables daily data collection, which is crucial for determining the temporal trends in fracture compliance during the acute healing timeframe without requiring additional clinical office visits. We have implemented this telemetric DEC system in a pilot clinical study of tibial fracture patients (Fig. 1). The results of this study have established the feasibility of the self-measurement telemetric approach. One patient out of the eight completed to date experienced a non-union and required a revision surgery 6 months following the original surgery. The temporal compliance data show promise for distinguishing between normal and non-union healing pathways in the early timeframe (Fig. 1).

The DEC technology represents a paradigm shift in the way fracture healing can be evaluated. Therefore, there is a high burden of proof for the clinical community to adopt this method in their practice. In order to advance the technology to the market, we must demonstrate efficacy in predicting non-union by using the device in a much larger patient population and establishing a predictive algorithm based on the collected data. Towards this end, we have begun planning for a large multi-site clinical study of the telemetric tibial DEC system. Additionally, we must show that the collected data are useful for improving patient care by using the predictive algorithm to prescribe treatment interventions, such as the injection of osteobiologics, to improve healing in patients determined to have a high probability of non-union. Finally, to improve the appeal of this technology as a marketable product, we plan to demonstrate efficacy in additional fracture locations. Towards this goal, we are developing humeral and femoral DEC systems and have shown efficacy in cadaveric studies of proximal and diaphyseal humeral fractures.

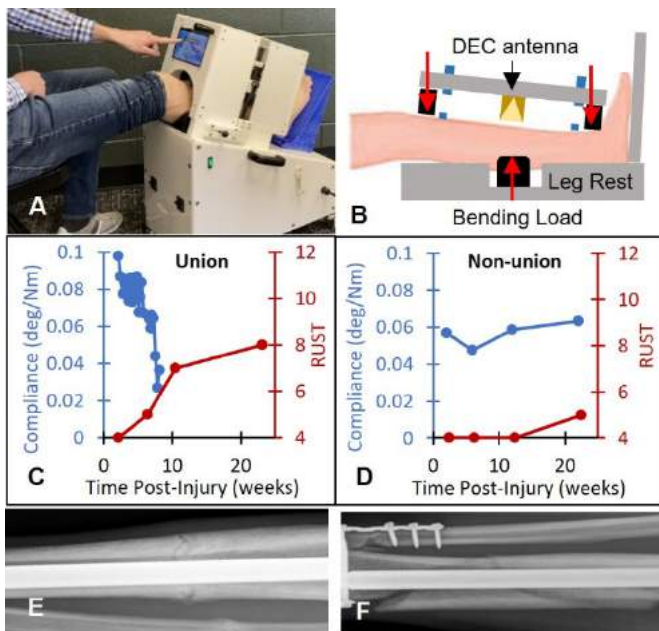


Figure 1: (A) The telemetric tibial DEC device is automated for daily self-use by the patient. (B) The device applies 3-point bending and measures deflection via a calibrated DEC antenna. Example bending compliance data (blue) and corresponding radiographs are shown for patients with (C, E) union and (D, F) non-union healing outcomes. Semiquantitative radiographic union score for tibia (RUST) data are also shown (red), demonstrating for the union patient that large changes in compliance were seen prior to radiographically visible bridging (RUST < 9).

BUSINESS CASE

Our product is an analytic service. Our business would provide the measurement devices to the fracture patients' homes, analyze the data as it is acquired, and provide weekly reports to the attending doctor. The end user is the fracture patient, and human factors studies will ensure device usability and safety. The primary customer and key decision maker for purchasing this product will be orthopaedic trauma surgeons. We plan to collect a robust set of clinical data on the efficacy of our technology in order to use a clinical evidence-based approach to sell to the customers. Since we have a novel product in a niche market, we will utilize a direct sales approach. In the United States, there are approximately 5,000 orthopaedic trauma surgeons in 800 trauma clinics treating approximately 1.5 million long bone fractures annually, 100,000 of which result in non-union. We estimate that there is a \$750 million annual market for identifying and treating problematic fractures, which represents 50% of the direct medical costs of non-union.

The feasibility of this business model will require the primary medical payors (e.g. insurance companies, Medicare, Medicaid, VA) to provide reimbursement. Accomplishing this will necessitate strong clinical evidence supporting the efficacy the technology to predict non-union and show that the overall healthcare savings from treating problematic fractures early outweighs the cost of using our product.

Prior to marketing our product, we will need to obtain regulatory approval. A clinical trial will be conducted under Good Clinical Practice (GCP) regulations, and an investigational device exemption (IDE) will be applied for through the FDA. There will be an administrative burden associated with this. However, since our technology presents no significant risk, the IDE should not be technically challenging to acquire. For FDA marketing approval, our technology would qualify as a Class I device and would be appropriate for a De Novo classification as a novel medical device. The European Union Medical Device Regulation classification is Class Im (a low-risk device with a measuring feature) and will require involvement of a notified body to receive the CE mark. For device fabrication, we will partner with a manufacturer operating under Good Manufacturing Practice (GMP) regulations.

Although we have collected strong evidence supporting the efficacy of the DEC, there remains risk associated with the additional clinical studies needed to advance the technology. There is a risk that the method may not produce a non-union prediction with a high enough confidence to make it valuable. However, we are investigating methods to combine the mechanical evidence the DEC provides with radiographic evidence and healing-related biomarkers to improve predictive analytics. Ultimately, we expect that mechanical measurements using our technology will provide a critical contribution to monitoring healing in the future of fracture care.

ACKNOWLEDGEMENTS

Funding was provided by the National Institutes of Health (R21AR077323) and the Colorado Office of Economic Development and International Trade (CTGGI 2020-2697).

REFERENCES

- [1] Vyrosktek, SB, et al. *MMWR Surveill Summ.* 53(7):1-57, 2004.
- [2] Antonova, E, et al. *BMC Musculoskeletal Disord.* 14: 42, 2013.
- [3] Hak DJ, et al. *Injury.* 45 suppl 2: S3-7, 2014.
- [4] Tay, WH, et al. *Injury.* 45(10): 1653-8.
- [5] Giannoudis, PV, et al. *AAOS.* 2006.
- [6] McGilvray, KC, et al. *J Orthop. Res.* 33(10):1439-46, 2015.
- [7] Richardson, JB, et al. *J Bone Joint Surg Br.* 76(3): 389-94. 1994.
- [8] Labus, KM, et al. *IEEE Access.* 6:68184-68194, 2018.
- [9] Labus, KM, et al. *J Orthop Res.* 37(5):1164-1171.
- [10] Wolynski, JG, et al. *Annals Trans. Med.* 9(5), 2021.

PITCH COMPETITION: TACKLING ANTIMALARIAL DRUG RESISTANCE IN AFRICA USING NOVEL DRUG REPURPOSING AND NANOTECHNOLOGY STRATEGIES.

Samuel W. Uzundu, Petra O. Nnamani, Anthony A. Attama.

Department of Pharmaceutics, University of Nigeria, Nsukka, Enugu State, Nigeria.

PROBLEM STATEMENT

Malaria is a global public health concern that has ravaged particularly Sub-Saharan Africa which accounts for over 90% of the global malaria burden [1]. More worrisome is the fact that Nigeria has consistently topped the chart of Countries with the highest malaria burden in the last five years [1]. Since malaria was first discovered, there has been a lot of therapeutic interventions which led to the introduction and usage of the following classes of antimalarial drugs-4-aminoquinolines eg Chloroquine etc, 8-aminoquinolines eg Primaquine etc, Aminoalcohols eg Mefloquine, Antifolates eg Sulphadoxine etc, Hydroxynaphthoquinones eg atovaquone etc Endoperoxides eg Artemether,

These classes of antimalarial drugs with the exception of the endoperoxides have been taken out by resistance from the malaria parasite; the endoperoxides are currently being threatened by resistance from the malaria parasite [2]. The above drug classes were initially active against the malaria parasite which eventually mustered resistance against them. As a result of this resistance by the malaria parasite, these drugs are no longer in clinical use; a good example is Chloroquine which was very effective against *P.falciparum* until resistance set in. Chloroquine is no longer used in treating malaria.

Resistance is the common denominator in the retirement of these drugs from clinical use. This resistance challenge is what my novel formulation addresses.

TECHNOLOGY/SOLUTION DESCRIPTION

This invention aims at tackling the challenge of antimalarial drug resistance (ADR) through the application of a novel drug combination and Nanotechnology. Chloroquine is not indicated for the treatment of Chloroquine-resistant *P.falciparum* malaria due to resistance by the malaria parasite.

To solve this problem of resistance, Chloroquine was combined with WOG19 (physical combination in a lipid matrix) and formulated into solid lipid nanoparticles and tested for clinical efficacy against the malaria parasite. This novel combination of chloroquine and WOG19 gave the highest reduction in parasitaemia in the Anka strain (resistant strain) of *P.berghei*-infected mice in the curative model (please see Figure 1) and highest average parasitaemia suppression (please see Table 1). THE COMBINATION OF CHLOROQUINE WITH WOG19 EXTENDS THE USE OF CHLOROQUINE TO THE TREATMENT (CURATIVE AND SUPPRESSIVE) OF CHLOROQUINE-RESISTANT MALARIA-WHICH BEFORE NOW WAS NOT POSSIBLE CURATIVELY! DUE TO RESISTANCE BY THE MALARIA PARASITE.

This formulation needs to be optimized in terms of targeted delivery, delivery system, safety and encapsulation efficiency to be market-ready.

BUSINESS CASE

My Antimalarial nanoformulation is novel, cheap, smart, potentially resistance-proof and very effective against resistant malaria parasites, therefore will potentially eliminate Malaria globally particularly in Sub-Saharan Africa which accounts for over 90% of the global malaria burden (World Malaria Report, 2021). Africa will be a huge market for my product (Repurposed Chloroquine for treating Chloroquine-Resistant *P.falciparum* malaria) which should be affordable (a key requirement for therapeutic interventions in Africa) for them. I do not foresee any immediate approval and manufacturing concerns (Licensing by FDA etc); Chloroquine is already an established drug in terms of its safety, efficacy, the only concern would that of WOG19 as to its safety, WOG19 is naturally occurring, results from our toxicity studies show WOG19 is safe for human consumption. I also do not foresee any immediate threat to this product (it is potentially resistance-proof).

Table 1: The Average suppression of parasitaemia in the Anka strain (P<0.05), SLN-Solid Lipid Nanoparticles.

Group	Average Parasitaemia (%)	Average Parasitaemia (%) of Reference	Average Suppression (%)
Placebo	14.000± 1.528	14.000± 1.528	100
Formulation(WOG19-loaded SLNs)	5.400 ± 0.503	14.000± 1.528	61.420 ± 1.029
Combination(Chloroquine plus WOG19-loaded SLNs)	2.200 ± 0.252	14.000± 1.528	84.300 ± 1.015
Positive control(pure Chloroquine solution)	7.600 ± 0.503	14.000 ±0.503	45.700 ± 1.079

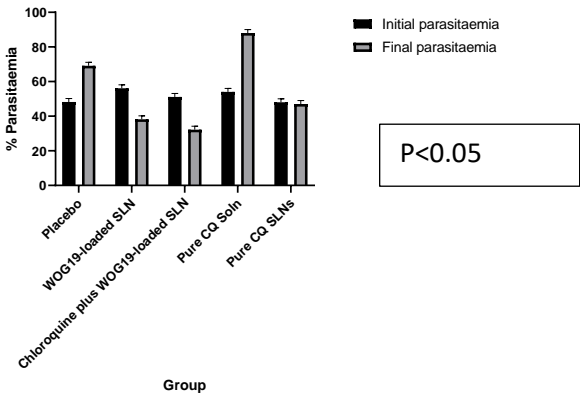


Figure 1: Reduction in parasitaemia in the Anka strain (curative model)

ACKNOWLEDGEMENTS

With every sense of humility, I deeply appreciate Professors Anthony Attama and Petra Nnamani, my Mentors and Supervisors for their priceless support and constant push to bring out the best in me.

REFERENCES

[1]World Malaria Report, 2021.
[2] Van der Pluijm, R et al., Trends in Parasitology, 37:15-24, 2021.

PITCH COMPETITION: TAPPING INTO LIGAMENT TENSION WITH OUR LIGAMENT TENSIO-METER TO ENHANCE OUTCOMES FOLLOWING ORTHOPEDIC PROCEDURES

Lesley R. Arant (1), Kai M. Heineman (1), Josh D. Roth (2, 3)

- (1) Department of Biomedical Engineering, University of Wisconsin-Madison, Madison, WI, USA
(2) Department of Orthopedics and Rehabilitation, University of Wisconsin-Madison, Madison, WI, USA
(3) Department of Mechanical Engineering, University of Wisconsin-Madison, Madison, WI, USA

PROBLEM STATEMENT

Improper ligament tensioning during orthopedic procedures is associated with postoperative joint dysfunction, patient dissatisfaction, and a higher risk of revision procedures. For example, in total knee arthroplasty, under-tensioning the collateral ligaments can lead to instability and pain, while over-tensioning can lead to stiffness and pain [1]. Similarly, in cruciate ligament reconstructions, inadequate graft tension impedes graft healing and fails to reinstate normal anterior laxity [2]. Considering that total knee arthroplasty and ligament reconstructions are among the most frequently performed orthopedic procedures [3], achieving proper ligament tension is necessary to improve patient satisfaction and reduce the economic burden associated with revision procedures.

Despite the well-documented importance of proper ligament tensioning, existing solutions to gauge ligament tension intraoperatively are either subjective or fail to assess tension in an individual ligament. One common technique is a laxity assessment, in which ligament tension is indirectly inferred from joint motion and stiffness [4]. Since this assessment is commonly subjective, its outcomes vary according to a particular surgeon's training and experience [5]. Although distraction devices [6] and contact force sensors [7] provide quantitative measurements, they are unable to assess tension in an individual ligament. Thus, given the lack of adequate devices available, there is no consensus on the proper target or method of assessing ligament tension.

Accordingly, a sensor that provides direct and objective measurements of ligament tension would give orthopedic surgeons the information needed to improve patient function and satisfaction following orthopedic procedures.

TECHNOLOGY/SOLUTION DESCRIPTION

Our technology, termed a ligament tensiometer, shows promise for filling this hole in a surgeon's toolbox because it provides direct and quantitative measurements of ligament tension. The ligament tensiometer is a handheld device placed in contact with the ligament of

interest. It consists of two main components (**Figure 1**): (1) a voice coil actuator that excites low amplitude shear waves in the ligament, and (2) a piezoelectric load cell that tracks the shear wave propagation along the ligament's length. The tensiometer software computes the shear wave speed in the ligament using the time delay between the voice coil actuator and load cell signal (**Figure 1**). The tensiometer software then calibrates measured shear wave speeds to ligament tension using the linear relationship between shear wave speed squared and tension [8,9]. Thus, the output of the tensiometer is a near real-time, quantitative measurement of tension in a specific ligament.

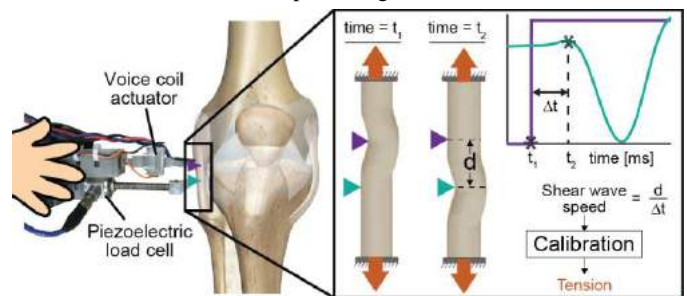


Figure 1: Our ligament tensiometer is a handheld device that uses shear wave speed to measure tension in a particular ligament.

We performed a preliminary error analysis of our tensiometer prototype to assess its accuracy of measuring collateral ligament tension (**Figure 2**). We chose these ligaments to study because of the promising application of the tensiometer in collateral ligament balancing during total knee arthroplasty. We used our ligament tensiometer to measure shear wave speeds in the medial and lateral collateral ligaments of human cadaveric knees ($n=3$) under manually applied loads (**Figure 2a**). We used a calibration algorithm to compute the tensiometer-measured tensions from measured shear wave speeds. We computed the errors between the tensiometer-measured tensions and gold standard

tensions measured using a six degree-of-freedom robot and the principle of superposition [10]. We found that the tensiometer can directly measure ligament tension with low bias errors (**Figure 2b**). Additionally, when the tensiometer was coupled with optical motion capture to track ligament length, the tensiometer could accurately measure ligament engagement length (i.e., length at transition from toe to linear region) (**Figure 2c**). Thus, the tensiometer could be used with existing surgical navigation tools to measure other key metrics of ligament mechanics.

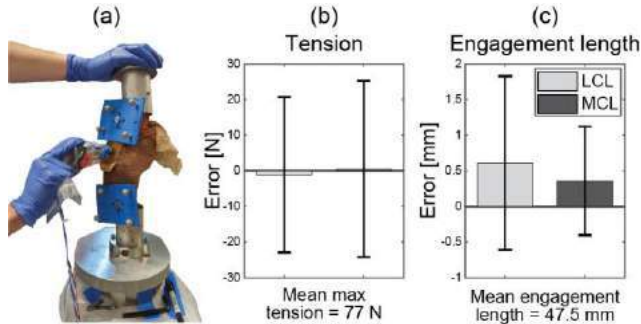


Figure 2: (a) We used the tensiometer to measure lateral and medial collateral ligament (LCL and MCL, respectively) tension during laxity assessments in three cadaveric knees. (b) The tensiometer measured ligament tension with low bias errors. (c) When coupled with optical motion capture, the tensiometer accurately measured ligament engagement length.

The key technical advancement required to take our tensiometer to market is to increase its precision through design optimization. Preliminary data suggests that tensiometer-measured tension is sensitive to tensiometer design factors (e.g., tip spacing, excitation frequency [11]) and use factors (e.g., application force [12], positioning of the tensiometer on the ligament [13]). Thus, we must identify the optimal combinations of these design and use factors that yield repeatable and accurate measures of ligament tension, while maintaining the tensiometer's ease-of-use. Additionally, the size of the tensiometer should be decreased so it can be placed in contact with the intraarticular surface of ligaments, thus avoiding the need for additional surgical incisions. With these key technical advancements, the ligament tensiometer would be a strong candidate for a marketable product.

BUSINESS CASE

Although orthopedic surgeons and other operating room personnel are the end users of the ligament tensiometer, there are additional customers to consider. First, the patients are those who are receiving an orthopedic procedure that involves ligament tensioning, such as total knee arthroplasty or ligament reconstruction. In the United States alone, the number of total knee arthroplasties and cruciate ligament reconstructions are projected to reach 1,272,000 [14] and 700,000 [15], respectively, by 2025. Considering that the tensiometer has potential use in many other procedures, joints, and ligaments, this should be considered a conservative estimate of the patient market size.

The payers are the hospitals, insurance agencies, and the patients who receive the surgery. Once marketed, we envision the cost structure of the tensiometer to be a one-time payment for the device, followed by the purchasing of disposables and software licenses as needed. Thus, we expect this cost to be comparable to existing sensors on the market used to gauge ligament tension. To appeal to each of these customers, we plan to acquire data that shows that tensiometer use improves patient outcomes, decreases surgical time, and/or decreases costs.

Our marketing strategy involves three phases (**Figure 3**). In phase I, we will recruit an interested “champion” surgeon to test the tensiometer on a small subset of patients at the UW Hospital. This phase

requires IRB approval before the tensiometer can be used in live patients. To fund phase I, we plan on seeking Small Business Innovation Research (SBIR) phase I funds totaling \$200,000. In phase II, we will fabricate at least ten tensiometers and send each to a different institution for use by surgeons. In this phase, we will also submit Premarket Notification 510(k) to the FDA because the tensiometer will be considered a Class II medical device. To fund phase II, we will apply for SBIR phase II funds totaling \$1 million. In phase III, we plan to acquire FDA clearance to enable widespread tensiometer use. Several companies with strong footholds in the orthopedic technology industry have already expressed interest in the tensiometer. By selling our small business and any patents to one of these companies, we aim to achieve widespread adoption of the tensiometer in hospitals.

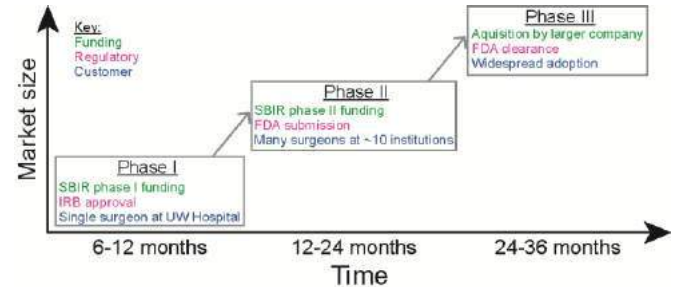


Figure 3: Pathway to market for the ligament tensiometer.

The main hurdle to market is translating our tensiometer from a prototype to a clinically-usable device. In particular, the tensiometer components must be either sterilizable or disposable so that the tensiometer can be reused in different patients. Additionally, to decrease manufacturing cost and time, and increase product robustness, the tensiometer housing must not be made of 3D printed polymers.

The main risk to the developmental pathway of the tensiometer is the reluctance of surgeons to incorporate a new technology into their surgical procedure. If this challenge presents, then we will lean on the support of the existing early adopters to generate more data that supports the benefit of tensiometer measurements to improving patient outcomes. This may lengthen the time to commercialization, but we do not believe this will be a permanent roadblock to translation of our device.

In sum, our three-phase marketing plan aims to recruit surgeons who will fuel the generation of supporting data, which in turn will fuel market expansion. Once commercialized, the ligament tensiometer will enhance the process of ligament tensioning during orthopedic procedures, leading to more consistent, predictable, and positive surgical outcomes for patients suffering from debilitating orthopedic injuries and diseases.

ACKNOWLEDGEMENTS

This work was supported by the Draper Technology Innovation Fund (TIF), administered by Discovery to Product (D2P) at UW–Madison.

REFERENCES

- [1] Babazadeh, S et al., *Orthop Rev (Pavia)*, 1:e26, 2009. [2] Tohyama, H et al., *Knee Surg Sports Traumatol Arthrosc*, 6:S30-S37, 1998.
- [3] Blom, A et al., *BMJ*, 374:n1511, 2021. [4] Casino, D et al., *Knee Surg Sports Traumatol Arthrosc*, 17:369-373, 2009. [5] Järvelin, J et al., *Acta Orthopaedica*, 83:190-196, 2012. [6] Takashima, Y et al., *Knee*, 27:1071-1077, 2020. [7] Park, C et al., *Clin Orthop Surg*, 13:1-9, 2021.
- [8] Martin, J et al., *Nat Commun*, 9:1592, 2018. [9] Blank, J et al., *J Mech Behav Biomed Mater*, 105:103704, 2020. [10] Fujie, H et al., *J Biomech Eng*, 117:1-7, 1995. [11] Arant, L et al., *ORS*, 2022.
- [12] Arant, L et al., *SB3C*, 2022. [13] Blank, J et al., *ORS*, 2020.
- [14] Singh, JA et al., *J Rheumatology*, 46:1134-1140, 2019.
- [15] Grandview Research. *Cruciate Ligament Repair Procedures Market Size, Share & Trends Analysis Report*. 2017.

ORTHOPEDIC CAST SAW

Ryan A. DeJesus (1), Nicholas J. Graham (1), Evan M. Lunney (1), Jaedan D. Morton (1)

(1) Department of Mechanical Engineering, The Pennsylvania State University - Harrisburg,
Middletown PA, United States

PROBLEM STATEMENT

In the medical industry an orthopedic cast saw is used to remove casts. A cast is a supportive device used to stabilize extremities, preventing further injury. The shortcoming with the current cast saw is that it allows the user to plunge the saw too deep causing cuts and burns. This results in an injury to 72 out of every 10,000 casts removed from patients. The Stryker® 940 is designed to minimize cuts using an oscillating blade shown in **Figure 1**. This method cuts through hard material like casting but leaves skin mostly unscathed. Beyond causing harm to the patient, these injuries can cost the company money in lawsuits, and give a bad reputation. The goal of this project, as stated, is to minimize unnecessary injuries during the cast removal process. To reduce injuries to patients, the device needs to include more safety features. The current design lacks the necessary depth control required to stop the user from causing injury. The target customer for this project is primarily orthopedic centers that perform cast removals.



Figure 1

This figure shows the OEM design of the Stryker® 940 Cast saw

TECHNOLOGY/SOLUTION DESCRIPTION

Our proposed prototype implements a modular depth control system. This is achieved by the creation of a new guard shown in **Figure 2**. It is composed of 3 ABS parts along with stainless steel hardware. This guard replaces the OEM guard shown in **Figure 1**. The purpose behind the new guard is to impose limits to the cutting depth which can be set with the knob in the back. Cutting depths are set by moving the guard parallel with the blade in 1-millimeter increments. For each full rotation of the knob, one millimeter of translation will be achieved. A clockwise rotation results in a decrease of cutting depth, while the opposite applies for counterclockwise rotation. Using a Nyloc nut embedded in the base, the knob gets progressed as it goes through the threads of the nut. This resulting motion adjusts the cutting depth.

To increase useability in the medical field, the material must be changed from ABS. Fabrication of a nylon part is critical for sterilization in the medical field. While the current 3-D printed prototypes are functional, injection molding is essential for the future of this product, as it provides a clean and professional finish. The current mechanical design shows a great proof of concept but is lacking features. An electronic design is currently being developed. This design will be controlled with buttons that adjust cutting depth while displaying the current depth of cut on a seven segment LED display. The buttons provide a more accurate method of measuring one rotation since they are paired with a stepper motor.



Figure 2

This figure shows an ABS print of the new guard design

BUSINESS CASE

The adjustable guard is a modular implementation that can be added on the Stryker® 940. By designing this guard to fit on a commonly used cast saw, we are securing a large potential customer base. In the US approximately 6.8 million fractures occur each year. When a fracture occurs, casting is a common practice of immobilization. Breaking bones will always occur, so the use of safe removal processes will always be in demand.

For each of our prototypes, the cost including the hardware was less than \$20 when printed from ABS as shown in **Figure 2**. If nylon was used along with better fabrication processes, the cost of a single product would be around 200\$. This includes electronics, stainless-steel hardware, and injection molded parts. These parts consist of the lid, base, and adjustable guard shown in **Figure 3**. When a larger order is placed, the cost per part along with the cost of electronics will decrease significantly making a more cost-effective solution. This shows the economic viability of the product for orthopedic centers and hospitals. Patients include anyone with a cast, while end users are nurses and techs along with doctors who remove casts.

The CDRH which is a subsection of the FDA controls medical devices produced in the US. Since a cast saw does not have a severe risk of illness or injury, we are not required to submit a premarket approval. The largest risk to this business is that the Striker® 940 is no longer in production. This is not an overwhelming concern since the guard can be easily modified to fit onto other existing saws. Due to the low cost and modular design of our guard, this product can be implemented into hospitals easily. The reward for using this product is high especially when considering its low cost.

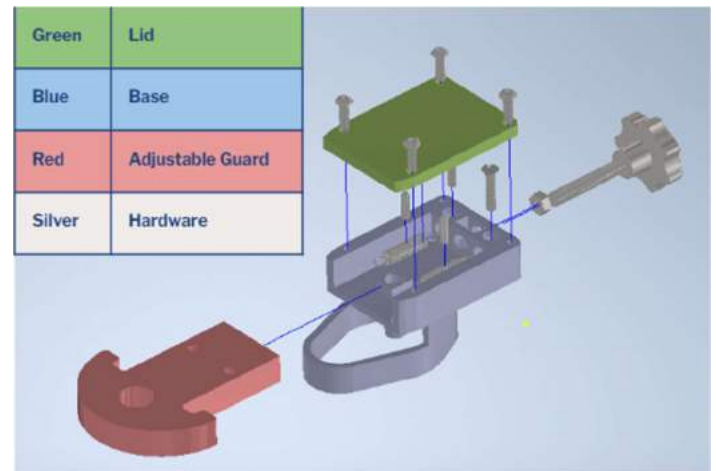


Figure 3

This figure shows the exploded parts diagram of the new guard

ACKNOWLEDGEMENTS

We would like to give a special thanks to Anilchandra Attaluri, PhD, Assistant Professor of Mechanical Engineering, Penn State Harrisburg, and Joseph L. Petfield, MD, Assistant Professor, Pediatric Orthopedic Surgery, Penn State Health. We would also like to give thanks to Penn State Harrisburg for the financial support of the project.

References

- “Fractures.” Fractures | Lehigh Valley Health Network, <https://www.lvhn.org/conditions/fractures#:~:text=A%20bone%20fracture%20is%20a,year%20in%20the%20United%20States.>
- Shore, Benjamin J., et al. “Epidemiology and Prevention of Cast Saw Injuries.” *Journal of Bone and Joint Surgery*, vol. 96, no. 4, 2014, <https://doi.org/10.2106/jbjs.l.01372>.
- “Stryker 940 Cast Cutter Saw.” *Www.atlasprosales.com*, https://www.atlasprosales.com/Stryker_940_Cast_Cutter_Saw_p/t-cc-940.htm.

PITCH COMPETITION: ARTIFICIAL MULTI-ORGAN REPLACEMENT (AMOR) SYSTEM

Nanye Du (1), Suhail Ahmad (2), Shaohang Hao (1), Ziyuan Wang (1), Ye Jin (1), Alexander Novokhodko (1), Dayong Gao (1,3),

- (1) Department of Mechanical Engineering, University of Washington, Seattle, WA, USA
(2) Department of Medicine, University of Washington, Seattle, WA, USA
(3) Department of Bioengineering, University of Washington, Seattle, WA, USA

PROBLEM STATEMENT

Intensive care patients who are acutely ill often have at least one or multi-organ failure (MOF). During the past decades, the prevalence of MOF in critically ill patients has been increasing, and the associated mortality rate remains high. More than 5 million patients are admitted annually to US ICUs for intensive or invasive monitoring [1]. And studies have reported a high prevalence of at least one failure with 70% of the patients at some point during the ICU stay.[2] The MOF even contributes to 50% of the ICU patient deaths and this number has a dramatic increase to 341% during pandemic [3,4]. Critically ill patients are complex and require a systematic approach to ensure excellent care. They are often managed by thinking about each system in turn so that all their maladies are considered and appropriately treated. Unfortunately, MODS is a complex syndrome for which the pathophysiological mechanisms are poorly understood. Despite a physician's best efforts, patients may deteriorate to the point that multiple organs are dysfunctional and heading toward failure. When this occurs, the acuity and complexity of these patients escalates and considerable attention to the details of each system is paramount. Decades of research have ensued to treat and reverse multi-organ dysfunction syndromes (MODS) before it becomes MOF. However, aside from correcting the underlying etiology, there has been no single treatment strategy that can be used to cure all patients. Moreover, salvage therapies are lacking for severe MODS that progress to MOF. [1]

At the most recent development, when MOF happened, the solution was to create extracorporeal support for failing organ-systems by applying multiple single organ support equipment. These organ support systems include kidney dialysis, liver dialysis, fluid removal, gas exchange support, respectively. But applying those individual complex machines together on one patient is quite challenging, risky, and labor intensive. "The timing and degree of any intervention are crucial when saving MOF patients" [5]; With the interviews from nurses

who operate the organ support systems in ICUs, they all have the comments that the manual tubing setup and preparation procedure for organ support machines gave them the most pain as well as frustration. The complex and time-consuming preparation procedure puts patients waiting for treatment at danger, and this is also critical for nurses rushing for an extremely sick patient with MOF. The reliance on current priming technique creates fear for both patients and nurses. Having a solution to demonstrate safety and check for proper priming is essential.

TECHNOLOGY/SOLUTION DESCRIPTION

We are working on a modular AMOR system that can provide easier but more efficient treatment for doctors to apply on single or multi-organ failure patients. AMOR was inspired by the concept that organs do not work indecently in our body. Integrating all these systems into one will also be beneficial to the user experience and save preparation time that is critical to provide treatment. It will minimize the operation procedure, significantly reduce the preparation complexity. Furthermore, an integrated system could monitor patients online and analyze the treatment data from different organ support systems together, which will reduce the nurse workload and minimize potential human error. The modular design makes the treatment set up more flexible. Doctors can easily switch between different organ support modes based on patient situations.

Patients who developed failure of multiple organs such as kidney, central nervous system, lungs and heart with massive anasarca, needing kidney dialysis, various forms of liver support systems such as Molecular Adsorbent Recirculating System™ (MARST™) along with ventilator and vasopressor support. Kidney dialysis is usually effective in treating the biochemical abnormalities of renal failure, such as urea, creatinine, electrolyte abnormalities and metabolic acidosis. But the kidney dialysis is ineffective in treating extra-cellular fluid excess that

usually is massive and adversely affects the pulmonary, cardiac and brain functions and eventual outcome of the patient [6].

Kidney dialysis is also unable to reduce protein bound hepatic toxins such as bilirubin [7]. Several systems based on the concept of using albumin containing dialysate to remove albumin bound toxins, as a consequence of liver failure, were developed. The albumin systems that have been used include the Single-Pass Albumin Dialysis system (SPAD), and the Molecular Adsorbent Recirculating System™ (MARSTM). The MARS is the most commonly used liver support system in the USA. However, this system is expensive and has many limitations such as its ability to treat uremic abnormalities and most importantly, very limited ability to reduce fluid excess. Additional kidney dialysis treatment is required to treat uremic abnormalities. Randomized studies reviewing the results of the MARS use have shown some mortality benefit however there are also reports of hemodynamic instability with its use. For patients with acute on chronic liver failure (AOCLF), the use of MARS has not increased the probability of receiving transplantation compared to the use of standard medical treatment without MARS [8].

A recent device called the Advanced Organ Support (ADVOS) system has been used in acutely ill patients with MOF. The device is reported to provide liver, renal, and respiratory support. It is proposed that the modulation in pH regenerates the albumin in the albumin dialysate and ultrafiltration is proposed to filter out bilirubin and other solutes wastes. The modulation of pH in the dialysate circuit is proposed to help the acid base balance of patient thus supporting renal system [9,10]. Unfortunately, removal of bilirubin from the circuit by ultrafiltration for the albumin regeneration purpose has not been documented by data. Improvement in patient's biomarkers is promising however survival benefit has not been shown [11].

Past work from our group established three key observations: albumin dialysate removes protein-bound toxins across commonly used dialyzer membranes without a need for a specially designed membrane such as reported for MARS (9); charcoal columns can regenerate albumin dialysate by removing clinically relevant toxin(s) (bilirubin) (10). Our theoretical modeling showed that combining albumin dialysis with ultrafiltration produces greater solute clearance than albumin dialysis alone (11). Based on these experiments, we developed a multi-organ support system that uses recirculating regenerating albumin dialysate. Additionally, the combined hemodialysis and albumin dialysate system provides both liver and kidney dialysis simultaneously. Unlike previous systems, our device allows sorbent columns to be regenerated to maintain their functionality for a longer period.

BUSINESS CASE

The AMOR system will initially focus on ICU settings, where most MOF patients are treated while the mortality rate remains high. Follow-on opportunities for the deployment of AMOR system include Emergency Rooms, Emergency Response Unit and Military. There is also portable potential of AMOR system that can achieve home-based use for organ support treatment. The primary customers and early adopters for AMOR system will be physicians and nurses at Intensive Care Unit (ICU) in hospital settings, representing our beachhead market. They are the main potential customers since they are the primary role of treating MOF patients. In the words of the medical director of dialysis services at UW Medical Center, "A device that could maintain patient's multi-organ function would simplify decision making". Additionally, another potential market share that can be added for AMOR system is the consumables which also take up a considerable medical expense through the Medicare systems each year.

We have already filed the PCT patent (US 63/183,482, 2022) with UW CoMotion for our Kidney and Liver combined modular system. We are planning to file the full utility patent once we conduct further regulatory investigation to create a solid patent landscape. For the regulatory aspect of AMOR system to get the clinical approval and payment, we are in the process of figuring out a clear pathway with the regulatory consultants and we are also conducting search for the predicated devices and possible 510(k) pathway that we can follow for accelerating the FDA approval process. The lack of existing solutions or devices for MOF support might require our AMOR system to follow new guidelines and standard codes which would take longer period for the approval process. However, Since AMOR is also a modular platform for each organ support, the existing FDA approved organ support system for kidney, liver, heart and lung can be individually considered for assisting the FDA approval for AMOR system as well.

ACKNOWLEDGEMENTS

This work has been supported, in part, by University of Washington grants and gift funds to Dayong Gao.

REFERENCES

- [1] Mitchell, L et al., "Multiple Organ Dysfunction and Failure", *ClinicalKey*, 259:1432-1439, 2020.
- [2] Pedersen, P et al., "Prevalence and prognosis of acutely ill patients with organ failure at Arrival To Hospital: Protocol for a systematic review," *Systematic Reviews*, vol. 6, no. 1, 2017.
- [3] Zhao, P et al., "Global Research Status of multiple organ dysfunction syndrome during 2001–2021: A 20-year bibliometric analysis," *Frontiers in Medicine*, vol. 9, 2022.
- [4] J. Brogan et al., "Epidemiology of organ failure before and during COVID-19 pandemic surge conditions," *American Journal of Critical Care*, vol. 31, no. 4, pp. 283–292, 2022.
- [5] Piccinni, P et al., "Multiple organ dysfunction syndrome," *Critical Care Nephrology*, pp. 309–312, 2009.
- [6] Hamdi T, *Current Opinion in Nephrology and Hypertension*, Jul;27(4):289–97. 2018.
- [7] Patzer, J, *Principles of Bound Solute Dialysis. Therapher Dial*, Apr;10(2):118–24, 2006.
- [8] Hassanein, T et al., *Randomized controlled study of extracorporeal albumin dialysis for hepatic encephalopathy in advanced cirrhosis. Hepatology*.Dec;46(6):1853–62, 2007.
- [9] Fuhrmann, V et al., *Advanced organ support (ADVOS) in the critically ill: first clinical experience in patients with multiple organ failure. Ann Intensive Care*, Dec;10(1):96. 2020.
- [10] Fuhrmann, V et al., *Registry on extracorporeal multiple organ support with the advanced organ support (ADVOS) system: 2-year interim analysis. Medicine*, Feb 19;100(7):e24653, 2021.
- [11] Kaps, L et al., *Applicability and safety of discontinuous ADVanced Organ Support (ADVOS) in the treatment of patients with acute-on-chronic liver failure (ACLF) outside of intensive care. Kanda T, editor. PLoS ONE*, Apr 1;16(4):e0249342, 2021.
- [12] Pei, Y et al., *ASAIO Journal*, 61(3):324–31, 2015.
- [13] Ding, W et al., *Artificial Organs*, Nov;38(11):954–62, 2014.
- [14] Pei, Y et al., *2013 ICME International Conference on Complex Medical Engineering [Internet], Beijing: IEEE*, p. 528-531, 2013.

A NOVEL HARDWARE AND SOFTWARE DEVICE TO NON-INVASIVELY PREDICT POST THROMBOTIC SYNDROME

Cyrus J. Darvish (1), Pete H. Gueldner (1), Rabih A. Chaer (2),
 David A. Vorp (3-8), and Timothy K. Chung (1)

- (1) Bioengineering, University of Pittsburgh, Pittsburgh, Pennsylvania, USA
 (2) Division of Surgery, University of Pittsburgh Medical Center, Pittsburgh, Pennsylvania, USA
 (3) Mechanical Engineering and Materials Science, University of Pittsburgh, Pittsburgh, Pennsylvania, USA
 (4) McGowan Institute for Regenerative Medicine, University of Pittsburgh, Pittsburgh, Pennsylvania, USA
 (5) Surgery, University of Pittsburgh, Pittsburgh, Pennsylvania, USA
 (6) Chemical and Petroleum Engineering, University of Pittsburgh, Pittsburgh, Pennsylvania, USA
 (7) Cardiothoracic Surgery, University of Pittsburgh, Pittsburgh, Pennsylvania, USA
 (8) Clinical and Translational Sciences Institute, University of Pittsburgh, Pittsburgh, Pennsylvania, USA

PROBLEM STATEMENT

Deep vein thrombosis (DVT) (**Figure 1A**) is a common cardiovascular disorder where a blood clot forms, typically in the lower leg or thigh. DVT affects as high as 3 in 1000 of the general population each year and can lead to a pulmonary embolism (PE), which is the third most common cause of death from a cardiovascular disease [1]. According to the CDC, 900,000 people are diagnosed with DVT in the United States each year, and approximately 300,000 of these patients will die from DVT/PE. Clinical diagnosis of DVT can be accomplished using compression duplex ultrasound and in some rarer cases computed tomography (CT) or magnetic resonance imaging (MRI) [2]. Anticoagulation and compression socks have emerged as a reliable method to treat DVT. However, approximately 50% of symptomatic DVT patients will progress to post thrombotic syndrome (PTS) [3]. PTS is a debilitating disease that is associated with chronic venous insufficiency after an episode of acute DVT. Common symptoms include chronic inflammation, pain, and venous ulcers.

Patients that suffer from PTS will experience a significant reduction in quality of life when compared to DVT patients due to persistent pain and inflammation in the lower legs. PTS is also associated with a higher prevalence in the Black community [4,5]. There are heavy costs to bear when managing PTS (\$10,300 in 1991 US dollars, estimated to be ~22,445 in 2023) and this does not include the downstream complications of the disease [6]. PTS is typically diagnosed 3-6 months after an episode of acute DVT and can only be diagnosed if the symptoms of DVT have previously subsided with treatment [7].

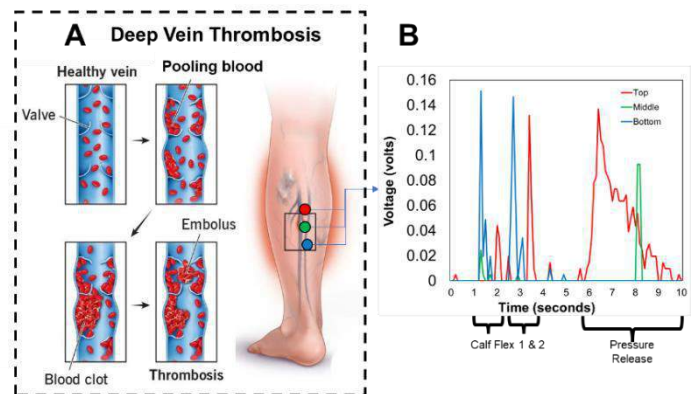


Figure 1: A) Shows the steps that lead towards deep vein thrombosis and post thrombotic syndrome. B) Preliminary data of our device output from sensor array from pressurized calf flexion and pressure release

Diagnosis of PTS is currently limited to a qualitative assessment of clinical signs and symptoms (Villalta scale) [8]. A patient is considered to have PTS if they score greater than five points on the scale, with greater than fifteen points considered severe (10-15% of patients).

An alternative method that has not been widely adopted is air plethysmography. This method tracks the overall volume change with pressure and can measure venous reflux. However, it cannot independently diagnose PTS [9] and ultrasound remains the predominant method to confirm PTS. While diagnosis and treatment of DVT is well established, there is no gold standard for diagnosing PTS or predicting its outcome in patients with acute DVT.

TECHNOLOGY/SOLUTION DESCRIPTION

The penultimate goal of this approach is to design and manufacture a non-invasive low-cost Thrombosis Differentiating Pressure (TDP) cuff that is accompanied by a machine learning (ML) model to pre-emptively identify whether a patient will transition to PTS after DVT (**Figure 2**). Development of the device will include two aims. The first aim will include developing a novel TDP cuff hardware device that will be placed on the lower leg or thigh of a patient with DVT. The cuff will contain a matrix of sensors that will be able to characterize deformations in the deep veins during

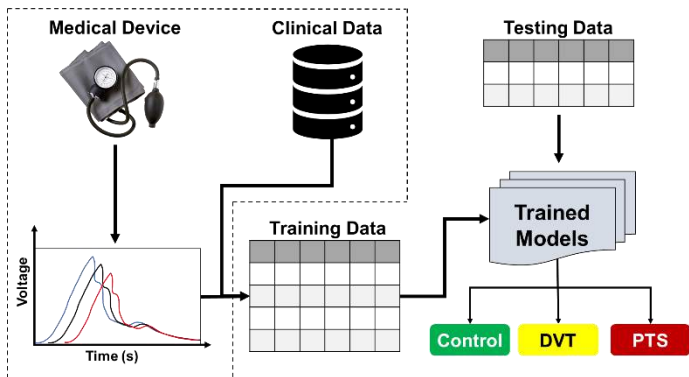


Figure 2: Illustrates the variables and steps of the approach to identify patients at high risk of developing PTS after acute DVT.

pressurization. The inflation of the pressure cuff will compress the vein wall and compliance of the vein can be measured. Gathering compliance data will be used to identify patients who are at high risk of developing PTS after the incidence of acute DVT.

The second aim is to incorporate a ML model to predict patients at risk of transitioning to PTS. The process will include training, testing, and validating a ML model to predict the likelihood of a DVT patient transitioning to PTS using the processed signals from the TDP cuff, patient survey data (Villalta score) and key patient clinical indices (age, sex, race, medications, and other co-morbidities). The device would have a wide range of applications that are not limited to DVT/PTS and could assess venous hypertension for patients during dynamic movements (e.g., walking with the TDP cuff). The approach combines vascular biomechanics and ML to develop a novel non-invasive hardware device paired with an innovative ML software system to predict whether a patient will develop PTS. Accurate predictions would allow clinicians to preemptively treat high risk patients more aggressively, reducing healthcare costs and improving quality of life for the patients.

BUSINESS CASE

As mentioned before, PTS bears a significant socioeconomic impact, increasing cost to the patient when compared to DVT treatment alone (\$10,300 vs. \$6,000 in 1991 dollars, or \$22,445 vs. \$13,074 in 2023). With the 900,000 people affected each year by DVT in the United States that gives an overall market size of nearly \$12 billion.

The purpose of the novel approach is to pre-emptively diagnose PTS before symptoms reappear, allowing clinicians to

treat the initial bout of acute DVT more aggressively. The TDP cuff will be used at the time of treatment to identify at-risk patients. This could significantly reduce costs for follow-up treatments and reduce concern for both patients and clinicians of developing debilitating PTS in the immediate future (3-6 months after a DVT episode). The TDP cuff is a low-cost solution that has the potential to replace ultrasound for patients that suffer from acute DVT.

The primary customers would be primary care offices and specialties that include vascular surgeons and cardiothoracic surgeons that regularly treat DVT patients. The TDP cuff could be used in a primary care facility without the need for a vascular surgeon. The primary advantage is that the hardware device would not add any significant clinical time (i.e., easy to use). The hardware and software approach could potentially replace the need for an ultrasound technician to measure vein functionality during follow-up visits.

The initial TDP cuff will be deployed in a clinic to measure acoustic waveforms from patients diagnosed with DVT and PTS. A pilot study will be conducted to compare the signature waveforms with ultrasound compliance measurements. The pilot study will collect ultrasound and TDP cuff data from normal, DVT, and PTS patients. A validation study will be performed to correlate the signals from the TDP cuff and train a predictive machine learning model.

Clinical adoption is key to overcoming the limitations of the current methods of managing DVT patients. The path towards commercialization includes the protection of intellectual property and regulatory approval. An invention disclosure and provisional patent has been filed by the University of Pittsburgh Innovation Institute. There are current efforts underway to develop the prototype and deploy it in a clinical setting to collect sensor data, clinical data, and ultrasound images from patients (control, DVT, and PTS). After the hardware and ML software model are completed, an FDA pre-submission meeting will be sought after to understand the regulatory path forward. The initial hardware and software approach would be classified as a Class II device with predicates (i.e., not a *de novo* device) for the hardware and Class II for the software as a medical device (SaMD) as it would inform clinical management of DVT/PTS. Lastly, a prospective clinical trial will be performed with an FDA device exemption to demonstrate the efficacy and performance of the TDP cuff in a clinical setting for 510(K) FDA approval as a safe and effective medical device.

ACKNOWLEDGEMENTS

PG was supported by the National Science Foundation Graduate Research Fellowship under Grant #1747452.

REFERENCES

- [1] Cushman, M et al., *Seminars in hematology*, 44(2):62-69, 2007.
- [2] Silickas, J et al., *Methodist Debaque Cardiovasc J.*, 14(3):188-195, 2018.
- [3] Rabniovich, A. And Kahn, S., *JTH*, 15(2):230-240, 2017.
- [4] Haig, Y et al, *JVIR*, 24(1):17-24, 2013.
- [5] White, R and Keenan, C, *Thrombosis Research*, 123(S4):S11-S17, 2009.
- [6] Ashrani, A and Heit, J, *J. Thromb. Thrombolysis*, 28:465-476, 2009.
- [7] Kahn, S.R., *Am Soc Hematol Educ Program*, (1), 2016.
- [8] Kahn, S.R., *JTH*, 884-888, 2009.
- [9] Criado, E et al., *J Vasc. Surg.*, 27(4):660-670, 1998.

PITCH COMPETITION: POLYMERIC TRANSCATHETER AORTIC VALVE REPLACEMENT (TAVR) FOR TREATING AORTIC STENOSIS

B. Kovarovic (1), O.M. Rotman (1), M. Slepian (2), D. Bluestein (1)

- (1) Biomedical Engineering, Stony Brook University, Stony Brook, NY, USA
(2) Sarver Heart Center, University of Arizona, Tucson, AZ, USA

PROBLEM STATEMENT

Aortic stenosis (AS) resulting from progressive calcific aortic valve disease (CAVD) is estimated to be prevalent in 5% of the elderly population above 65 years old and severe AS in 3% of the population about 75 years old [1]. Untreated severe AS is associated with a 50% mortality rate within the two years [2], and thus the highly invasive surgical replacement procedure was considered the gold standard therapy until the minimal transcatheter aortic valve replacement (TAVR) was introduced in 2011 to treat inoperable patients. SAVR held in the market with about 70,000 US patients in 2010 and the introduction of TAVR has expanded the market to about 150,000 combined SAVR/TAVR patients in 2020 [2]. Since the introduction of TAVR, it has been approved in the US to expand from inoperable patients (2011) to high risk (2012), intermediate risk (2016), and low risk/younger patients (2019) as well as for unique aortic valve anatomies such as bicuspid aortic valve. 2019 marked the first year TAVR (72,991) exceeded SAVR (57,626) procedures in the US [3], and this is due to both the experience of interventional heart teams as well as the attraction of patients to the reduced hospital costs and stay. With additional pressure from the COVID-19 pandemic, the global TAVR market reached \$4.4B and is forecasted to reach up to \$13.35B by 2030.

Despite the global acceptance of TAVR because of the minimally invasive nature of the procedure, the current commercial valves are subject to intrinsic and extrinsic structural valve degeneration (SVD) due to the inherent limitations of the chemically fixed bioprosthetic tissues used to create the functional leaflets and sleeve components. The fixed tissues are subject to degradation due to intrinsic inflammatory responses that can lead to thrombosis, endocarditis, and eventually lead to formation of calcific masses within the bioprosthetic tissue. Due to the crimping procedure, in which the metal stent frame is compressed radially onto the delivery catheter for the transcatheter approach to the aortic valve, the bioprosthetic tissue is compressed and is prone to mechanical damage. The damage incurred diminishes the durability and

wear resistance of the prevailing tissue-based valves in the market, leading to increased rates of wear and tear damage. With the recent advancements in TAVR technology, the in vivo durability lifetime of tissue TAVR valves remains uncertain or inconclusive, thereby posing a significant risk to younger patients who opt for TAVR devices instead of surgical alternatives with an established durability record.

The present polymeric valve technology has the potential to rectify the various shortcomings of the prevailing tissue-based TAVR devices, as well as exceed the performance, hemocompatibility, safety, and manufacturability of tissue valves. The idea of using elastic polymer material to cast or mold leaflet structures, known as polymeric valves, has been explored since the 1950s, starting with polyurethane valves. However, the demanding conditions of the aortic valve environment and the limitations of polymer technologies have hindered their success. The polymer properties, in combination with leaflet design that is very limited for tissue valves, has to be able to easily open during systolic forward flow, close and seal during diastole while resisting the largest pressure gradient in the cardiovascular system, and maintain this function at a constant rate of approximately 72 beats per minute throughout the patient's remaining lifespan. In recent years a few materials have been identified to be suitable for polymeric valves and

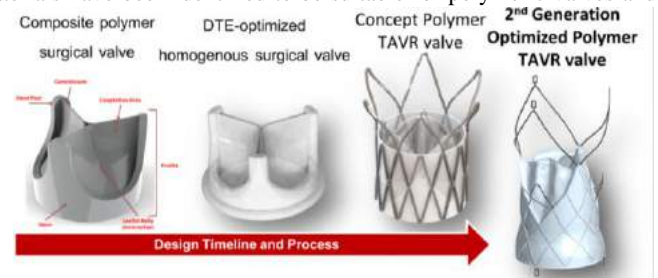


Fig 1: PolyNova Cardiovascular Inc timeline of polymeric TAVR development to the PolyV-2 design.

companies or research groups are beginning the process of study, validation, animal trials, and final approval from the FDA for novel polymeric valve systems. The regulatory approval process will be especially rigorous as the device is a Class III device without 510k pathway due to the novel material. Nevertheless, the prospect of a material that offers an engineered platform with reduced patient risk, along with the rapidly growing TAVR market, is highly appealing to both startup companies and potential investors.

TECHNOLOGY/SOLUTION DESCRIPTION

Our company, PolyNova Cardiovascular Inc (Stony Brook, NY), has been researching and developing polymeric valve technologies since 2014 with the initial focus on surgical valves, and since transitioning to the more attractive TAVR devices (Fig 1). The polymeric material has undergone development into a now cross-linked form of Poly(Styrene-block-IsoButylene-block-Styrene) or xSIBS that we have termed “Flexamer” technology. SIBS based devices have been used in cardiovascular devices for paving coronary stents, Boston Scientific, Marlborough, MA) and for glaucoma shunts. Initial testing involved study of proper material stiffness, degree of cross-linking, and benefits or shortcomings of composite materials. This polymer has been shown to be hemocompatible and thromboresistant, as well as resilient to calcification, crimping damage and wear and tear that has plagued tissue valves [3]. One of the advantages of the “Flexamer” material compared to the competitors, is that the polymer is a thermoset material and utilizes a encased casting/molding platform with either compression, transfer or even injection molding systems. This gives the advantage that our valve can be cast in virtually any shape, configuration, or size with a highly repeatable molding system. Compared to tissue valve, which are hand sutured to the stent frame over numerous days of manual labor and is fraught with human error, we are able to cast the valve on top or around the stent frame, creating the leaflets and attachment simultaneously, in a matter of hours, drastically reducing the error and cost of the final product. The main polymeric valve competitor (Foldax Inc, Salt Lake City, UT), who is currently in first-in-man trials for their surgical valve, utilizes a “dip-coating” system in which a mandrel is coated via controlled dipping and drying process, which requires a robotic arm to reach repeatable products and they lose the ability to finely control the resulting design.

This fine control of the leaflet structure has given us the ability to iterate on the device design, with significant utilization of *in silico* models and optimization from the initial surgical valve design to the current second generation TAVR valve design. The casting technology unlocked the ability to cast variable thickness leaflets in a semi-open configuration via the simulation results informing the design where the largest cycle stresses occur and increases the thickness in this region (Fig 2, Provisional patent UA 22-059 Pro, U.S.S.N. 63/315,286 – March 2022). The variable thickness optimization reduces the peak cycle stress far below the fatigue limit of the polymer, offering a known large factor of safety, as well as increasing the performance of the valve. The first generation TAVR device, PolyV-1, was subjected to a battery of *in vitro* testing in order to confirm the strength of the polymer and functionality as a valve. The polymer offered reduced platelet activation compared to commercial devices, increased performance in both idealized [4] and patient-specific platforms [5], no risk of calcific salts depositions, no risk of crimping damage over long periods [6], and achieving the ultimate benchmark of durability with no performance loss over 1B cycles (25 year *in vivo* equivalent, exceeding the FDA required 200M limit) [7]. The PolyV-1 was designed to evaluate the polymer and the second generation PolyV-2 was redesigned for proper TAVR deployment and on-going animal (ovine) trials. PolyV-2 was scaled up, designed, and optimized [7] To demonstrate the *in vivo* performance and compatibility of the polymeric valve, the valves need

to be properly deployed in an ovine model using an 18F delivery system that minimizes the stent and polymer volume.

BUSINESS MODEL

The current TAVR market is rapidly expanding due to the aging of the “baby boomer” generation, combined with the attractive nature of the risk involved in this minimally invasive procedure, its lower cost and decreased hospital stay. However, the “double-edge” nature of TAVR rapid expansion is demonstrated by the many failing tissue based valves leading to Valve-in-Valve (ViV) rescue operations to correct the failing valves. This creates a situation where there is a requirement to rectify numerous currently deployed devices while

continuing to employ flawed tissue technologies, which puts the patients at risk. Polymer valve technologies have the potential to be disruptive as they offer a viable long-term solution that can overcome the shortcomings of current TAVR tissue valve technology by allowing engineering solution of optimized designs. Consequently, the continued use of tissue valves would offer no clear benefits. With proper design and testing polymer TAVR technologies can replace the need for most surgical valve replacements since only current advantage of surgical valves is their established longer-term durability as compared to tissue TAVR devices. The polymeric valve technology of PolyNova Cardiovascular Inc will effectively address the needs of AS patients as well as the expansion to unique anatomies such as Bicuspid Aortic Valve (BAV) specific devices, and can address the challenges and economic burden of developing nations such as rheumatic heart disease with lower cost polymeric valves. Manufacturing can be completed in a small lab/ clean factory setting without need to massive scale up since the device manufacturing time would be reduced from days to hours. The main hurdle to market is the lengthy and in-depth regulatory process of a complex new Class III device with new material by the FDA. Performing the needed validation testing (ISO 5840) and animal trials is a challenging and costly process. Earlier companies that developed polymeric valves attempted to rush to clinical trials without fully optimizing the design, resulting in resource depletion. We have taken the approach of careful and continued improvement of the device design to mitigate these risks before finally arriving at our current stage of animal trials.

ACKNOWLEDGEMENTS

NIH-NIBIB Phase II-U01EB012487 (DB); NIH-NIBIB 1U01EB026414-01 (DB). Industry Partners: ANSYS, Simulia LHP.

REFERENCES

- [1] Osnabrugge, R et al., *J Am Coll Cardiol*, 62(11):1002-12, 2013.
- [2] Sevilla, J et al., *J of Med Econ*, 25:1, 1051-1060, 2022.
- [3] Carroll, J et al., *J Am Coll Cardiol*, 76:2492-516, 2020.
- [4] Rotman O, et al. *Ann Biomed Eng*, 47, 113–125, 2019.
- [5] Kovarovic B, et al. *Artificial Organs*. 45(4),E41-E52, 2021.
- [6] Rotman O, et al. *ASAIO*, 66(2):190-198, 2020.
- [7] Kovarovic B, et al. *JBME*. 144(6): 061008. 2022

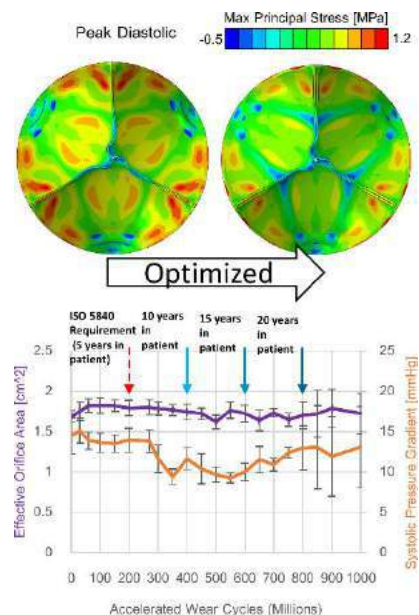


Fig 2: (Top) In silico optimization of the PolyV-2 leaflets with variable thickness. (Bottom) Extended accelerated wear durability testing to 1Billion cycles.

PITCH COMPETITION: AUTOMATICALLY PERFUSABLE HUMAN VESSEL CHIP PLATFORM FOR PRECLINICAL RESEARCH IN HAZARDOUS CONTAINMENT ENVIRONMENTS AND SPACE

J. Eades (1), A. Kumar (1), A. Jain (1,2,3)

- (1) Department of Biomedical Engineering, Texas A&M University, College Station, TX, USA
- (2) Department of Medical Physiology, College of Medicine, Texas A&M University, College Station, TX, USA
- (3) Department of Cardiovascular Sciences, Houston Methodist Hospital, Houston, TX, USA

PROBLEM STATEMENT

In addition to lifestyle factors and coexisting conditions, pathogens and other extrinsic harmful substances have become increasingly recognized as contributors to and direct causes of vasculopathies in humans. Highly common bacterial (e.g., by *Chlamydia pneumoniae*, *Helicobacter pylori*, and *Streptococcus pneumoniae*) and viral infections (e.g., by herpes viruses, hepatitis B and C, influenza, and human immunodeficiency virus) have been linked to cardiovascular diseases including coronary artery disease [1–4], vascular dementia [5,6], endothelial dysfunction [7–9], and thrombosis [10–12]. Most recently, endothelial dysfunction and venous thromboembolism have been identified as major contributors to the risk and severity of coronavirus disease 2019 (COVID-19), cited as having contributed to up to one-third of deaths in some clinical reports [13].

Human vascular pathologies are highly complex diseases that result from a convergence of factors, and many mechanisms of these diseases remain poorly understood [14]. Traditionally, basic biology research and preclinical drug discovery and development testing has been performed using animal (predominantly, murine) research models. However, due to inherent differences between animals and humans ranging from inconsistent genetic profiles to large differences in macroscopic tissue environments and behaviors, these research models do not mimic human physiology sufficiently for understanding the complexities of vascular pathologies [15]. As a result, little is known about many mechanisms of pathogen-induced vascular diseases, and new approaches to treatment have been difficult to identify. Furthermore, drug candidate screening and efficacy and toxicity testing efforts remain limited in their prediction of human drug response. Finally, variabilities in vascular physiology and drug response caused by genetic stochasticity and lifestyle factors result in significant differences in manifestations of disease and responses to therapeutics across populations. In fact, the U.S. Food and Drug Administration

(FDA) recently announced new requirements for greater representation in diverse clinical trials to achieve approval of new therapeutics [16]. Resolving these differences is one of the major challenges in design and execution of clinical trials as many potential adverse effects are not captured during limited clinical trials [17].

In addition to the broad challenges associated with accurately modeling human disease and drug response, studies that must be conducted in hazardous containment environments present unique problems. Recently, the COVID-19 pandemic has highlighted these challenges as biosafety level 3 and 4 (BSL-3 and 4) containment requirements [18] have significantly slowed research into and treatment of severely damaging secondary effects of the disease. These facilities require strict safety measures to be considered for sufficient protection of personnel, and traditional in vitro and animal models are difficult or, in some cases, impossible to implement in accordance with rules and regulations.

Microphysiological systems (MPS) represent a leading candidate technology for addressing the challenges outlined above. These platforms integrate advantages of modern tissue engineering and microfluidics technologies including use of human cells (e.g., primary or iPSC-derived), control of tissue architectures, tunability of tissue microenvironments, perfusion of nutrient-containing solutions and biological fluids, and facile observation of cell and tissue responses sufficient for providing deep mechanistic insights. We have demonstrated novel MPS platforms to model key aspects of vascular physiology and pathology. We have shown inflammation-induced clotting relevant to various systemic human diseases [19, 20]. We have reproduced physiologically relevant hemodynamics and shown their role in formation of deep vein thrombosis [21]. We have also implemented blood-derived endothelial progenitors on these model platforms as a rapid option for developing patient-specific in vitro vascular models [22]. However, despite these and many other advancements in MPS models of human diseases, standard methods and

platform configurations for fluid handling, sample input, and outcome observation do not meet the requirements for use in hazardous containment environments. As a result, there is a significant need for new technologies to translate MPS and similar technologies for applications in studying human pathogens, hazardous materials, and others requiring special research environments.

TECHNOLOGY/SOLUTION DESCRIPTION

To address the challenges associated with studying human physiology and testing drugs in hazardous containment environments, we have developed a platform integrating four key components. First, a pumping system has been constructed with a minimized footprint for easy accommodation in cell culture incubators of various sizes. This instrumentation provides advantages over commercially available platforms in its ability to tightly control fluid flow at the resolutions required to reproduce patterns directly from clinical patient data across the range of flow rates seen in various kinds of cardiovascular regimes while occupying less volume than traditional fluid delivery instruments. Second, an automated three-way valve with a sample injection port is included to alternate between media or biological fluid flow streams and pathogen (or other test case) solutions. This unit provides users the ability to introduce test samples such as pathogens of interest into the vascular tissue model system using only standard operation of a syringe. Third, a MPS vascular tissue model (which can easily be exchanged for other models) is interfaced directly with the fluid handling elements for reliable control of fluid perfusion. This system can include human endothelial cells from a range of sources to model various sections of the human cardiovascular system for research at various scales ranging from pooled experiments for high-level uniformity to single patient resolution for population representation or treatment pre-screening. Finally, a small, inexpensive fluorescent microscope is included within the platform for easy real-time monitoring of cell and tissue responses to test conditions. Additionally, a collection reservoir is provided to allow for cell or lysate extraction with sufficient sample concentration for downstream genomics, transcriptomics, and proteomics assays. Collectively, the components of the platform are packaged in such a way that sterilization and integration into controlled environments is easily achievable even with extensive personnel protection equipment (PPE). Furthermore, operation and sample collection requirements have been optimized so that users need only perform conventionally simple tasks.

The capabilities of this system have been demonstrated both individually and collectively. The fluid handling component has been proven capable of matching human cardiovascular flows in arterial and venous systems with accuracy less than 0.13 mmHg and resolution of 20 ms. The three-way valve is operable using a simple button press. The MPS component has been published previously as an impactful model of human vasculature both as a representation of disease (i.e., deep vein thrombosis) and drug testing (both to test anti-thrombotic therapeutics and to screen for off-target effects). As a prototype platform has been constructed and applied for research at a biosafety level 2 by untrained users (technology readiness level – TRL – 5), future development will be dedicated to addressing user input from alpha and beta testing to maximize ease of use. Additionally, durability testing is currently ongoing to identify the time and number of operations that the platform can withstand reliably.

BUSINESS CASE

The user groups for this technology include researchers studying vascular pathologies induced by harmful pathogens or other substances requiring experimentation in hazardous containment environments.

Such users include academic and medical basic science researchers, drug discovery and early-stage development researchers, pharmaceutical companies, and contract research organizations (CROs) conducting both preclinical and clinical testing. Furthermore, stakeholder interviews have revealed interest by government agencies including the Food and Drug Administration (FDA) for the data offered by a human-representative in vitro model, the Centers for Disease Control (CDC) for the ability to conduct rapid response experimentation in the event of pathogen outbreaks, and the National Aeronautics and Space Administration (NASA) for the ability to deploy these platforms in space to study the effects of anti-gravity environments and aging on the human cardiovascular system.

Because this is an entirely in vitro platform, regulation occurs at the site of deployment based on safety requirements for each use case. Although this system has been developed based on feedback from such safety officers, the lack of a standardized set of requirements between containment facilities and separate use cases will need to be addressed more extensively. Additionally, although manufacturing and distribution companies with proven capabilities in generating individual components for the platform exist and have been identified, the most financially feasible large-scale platform assembly mechanism remains to be determined. Finally, despite the proven capabilities of the individual components of the platform, the initial lack of market awareness and general inertia associated with the use of traditional research strategies will provide initial resistance. This challenge will be addressed using a strategic publication strategy with reputed partners across our prospective user groups both to demonstrate product feasibility and to gain widespread awareness.

ACKNOWLEDGEMENTS

This material is supported by the NHLBI of NIH under Award Number R01HL157790, NSF CAREER Award number 1944322

REFERENCES

- [1] L. Xue et al., *BMC Cardiovasc Disord*, 19:110, 2019.
- [2] H. Liang et al., *Annals of Medicine*, 53:1448–1454, 2021.
- [3] S. Syed et al., *iScience*, 24:102535, 2021.
- [4] E. P. Benditt et al., *Proc. Natl. Acad. Sci.*, 80:6386–6389, 1983.
- [5] K. Shima et al., *Med Microbiol Immunol*, 199: 283–289, 2010.
- [6] Y. Xu et al., *Int'l Journal of Neuroscience*, 126:899–903, 2016.
- [7] S. J. Evani et al., *Front. Microbiol.*, 7, 2016.
- [8] X. Xia et al., *JAHA*, 9:e014120, 2020.
- [9] V. Kondreddy et al., *ATVB*, 41:1987–2005, 2021.
- [10] T. Pessi et al., *Circulation*, 127:1219–1228, 2013.
- [11] G. M. Vail et al., *Infection*, 37:358–364, 2009.
- [12] N. Edington et al., *Archives of Virology*, 90:111–124, 1986.
- [13] D. Wichmann et al., *Annals of Internal Medicine*, Aug. 2020.
- [14] N. R. Sutton et al., *ATVB*, 43:15–29, 2023.
- [15] G. A. Van Norman, *JACC: Basic to Translational Science*, 4:845–854, 2019.
- [16] T. J. Hwang et al., *N Engl J Med*, 387:1347–1349, 2022.
- [17] Improving Representation in Clinical Trials and Research, Washington, D.C.: National Academies Press, 2022.
- [18] NIH Guidelines for Research Involving Recombinant or Synthetic Nucleic Acid Molecules. 2019.
- [19] A. Jain et al., *Nat Commun*, 7:10176, 2016.
- [20] A. Jain et al., *Clin. Pharmacol. Ther.*, 103:332–340, 2018.
- [21] N. K. Rajeeva Pandian et al., *Small*, 16:2003401, 2020.
- [22] T. Mathur et al., *Lab Chip*, 19:2500–2511, 2019.